JANUARY/FEBRUARY 2005
Volume 16, Number 1

© Copyright 2005 by the American Chemical Society

Bioconjugate Chemistry

EDITORIAL: Thanks to Our Reviewers

It is a pleasure to acknowledge the contributions of the reviewers of manuscripts submitted in 2004 for publication in *Bioconjugate Chemistry*. Their unselfish service has been essential in the shaping of the fifteenth volume of the journal. The scientific community is fortunate that its members are willing to share their time and specialized knowledge in this way. The reviewers are listed on the following page.

Claude F. Meares

Editor-in-Chief

10.1021/bc040059l CCC: $30.25 © 2005 American Chemical Society
Published on Web 01/19/2005

List of Reviewers

Samuel Achilefu
Gregory Adams
Sudhir Agrawal
Steve Alley
Carolyn Anderson
Charles Apel
You Bae
Kwamena Baidoo
James Baker
Rolf Barth
Jacqueline Barton
Craig Beeson
Jean-Paul Behr
Alexei A. Bogdanov
Elijah Bolotin
Gian Bonora
Darryl Bornhop
Martin Brechbiel
Stephen Brocchini
Donald Buchsbaum
Jean Cadet
Paolo Caliceti
Chien-Hsing Chang
Mark Davis
Eric Defranq
Sally DeNardo
E. F. M. de Vries
Gene Dubowchik
Richard Ebright
Ramon Eritja
Jose Garcia-Fernandez
Joseph Francisco
Stephen Foulger
Keith Fox
Jean Frechet
Michael Gait
Kieran Geoghegan
Jacquelyn Gervay-Hague
Eli Gilboa
R. Gietz
Malcolm Gilchrist
Barry Gold
Viktor Goldmacher
David Goodwin
Harry Gray
Richard Greenwald
Robert Haener
Kevin Hamblet
Trevor Hambley
Roland Haubner
Fred Hawthorne
Frederic Heitz
Donald Hnatowich
Hideyoshi Harisima
Piet Herdewijn
Greg Hermanson
Ferenc Hudecz
Lee Josephson
Jingyue Ju
Rudi Juliano
Sylvia Jurisson
Shigeo Katoh
John Katzenellenbogen
Risto Kauppinen
Sung Wan Kim
Thomas Kissel
Hiromi Kitano
Toni Kline
Hisataka Kobayashi
Jindrich Kopecek
Felix Kratz
Ulo Langel
Robert Langer
Christopher Leamon
Moses Lee
Jean-Christophe Leroux
Susan Lever
Michael Lewis
Kai Licha
Harri Lonnberg
Hiroshi Maeda
Jean-Pierre Mahy
B. Manjula
Jon Marsh
Niko Meltola
Damon Meyer
Dale Miles
Damon Meyer
Michel Monsigny
Jogeshwa Mukherjee
Yuichi Ohya
Teruo Okano
Daniel Pack
Monica Palcic
William Pardridge
Joon Park
Kinam Park
Tae Gwan Park
Jerry Pickering
Caryn Prudente
David Putnam
Ronald Raines
Tariq Rana
Steven L. Regen
Steven Roffler
Buck Rogers
Steven Rokita
Keith Rose
Vincent Rotello
Ahmad Safavy
Russell Sanderson
Roger Schibli
Nathalie Scholler
Gideon Schreiber
P. August Schubiger
Michael Seidman
Paul Selvin
Wei-Chiang Shen
Dean Sherry
John Shively
Steven Smith
J. Suggs
Francis Szoka, Jr.
David Thompson
Richmond Thompson
Don Tomalia
Eishun Tsuchida
Ching-Hsuan Tung
Ganesan Vaidyanathan
Karen Vasquez
Pierre Vierling
Wynn Volkert
Alan Waggoner
Ernst Wagner
Binghe Wang
Dong Wang
Lai-Xi Wang
Yadong Wang
Michael Welch
Theodore Wensel
C. Werner
D. Scott Wilbur
Eric Wickstrom
Meir Wilchek
Karen L. Wooley
Anna Wu
George Wu
Rickey Yada
John Yates
Samuel Zalipsky
Gang Zheng

BC040059L

REVIEWS

Next Generation, High Relaxivity Gadolinium MRI Agents†

Kenneth N. Raymond* and Valérie C. Pierre

Department of Chemistry, University of California, Berkeley, California 94720-1460 . Received July 27, 2004

Magnetic resonance imaging (MRI) has evolved into one of the most powerful techniques in diagnostic clinical medicine and biomedical research by enabling the acquisition of high resolution, three-dimensional images of the distribution of water in vivo (*1*). The strong expansion of medical MRI has prompted the development of a new class of pharmacological products, called contrast agents. These agents catalytically shorten the relaxation time of nearby water molecules, thereby enhancing the contrast with background tissues. In 1999, approximately 30% of all MRI scans used a contrast agent, most of which were based on gadolinium complexes (*1*). By now, this number has probably increased to between 40 and 50%. This utility has prompted research on improved Gd-based contrast agents, about which several reviews have recently been published (*1*−*15*).

Gd(III) is highly paramagnetic with seven unpaired electrons and a long electronic relaxation time, making it an excellent candidate as a relaxation agent. However, the very high in vivo toxicity of $[Gd(H_2O)_8]^{3+}$ requires that the metal be complexed by strong organic chelators before it is administered to patients. Current MRI agents require injection of gram quantities of Gd in order to obtain satisfactory contrast in the resulting image. With such large doses required for reasonable image enhancement, current contrast agents are limited to targeting sites where they can be expected to accumulate in high concentrations, such as in the blood stream. Ideally, second generation agents will be site-specific; much higher relaxivities will be required to account for the decrease in concentration that accompanies increased tissue specificity.

The image-enhancing capability of a contrast agent is directly proportional to its relaxation of neighboring water molecules by the paramagnetic ion; that is, to the relaxation rate increase, either longitudinal ($1/T_1$) or transverse ($1/T_2$). This effect includes both inner-sphere (from water molecules directly coordinated to the Gd) and outer-sphere contributions (from nearby, H-bonded waters). The latter are usually relatively small and are usually neglected. For Gd(III) complexes, the inner-sphere relaxivity primarily results from a dipolar contribution (through-space interactions due to the random fluctuations of the electronic field) and can be described by the Solomon−Bloembergen−Morgan equation. According to this theory, to increase the relaxivity, r_{1p}, of a Gd contrast agent, one has to design a ligand that will enable the complex to have a greater number of inner-sphere water molecules, q; an optimally short water residence time, τ_m; and a slow tumbling rate, $1/\tau_r$ (Figure 1) while maintaining sufficient thermodynamic stability. This is quite a challenge! The water residence time, τ_m, is probably the least understood and most important parameter that affects relaxivity. Indeed, it has been demonstrated that the relaxivity of a Gd^{III} complex will increase upon slowing down its molecular tumbling (increasing its molecular weight) insofar as its water residence time is close to optimal (*16*−*19*).

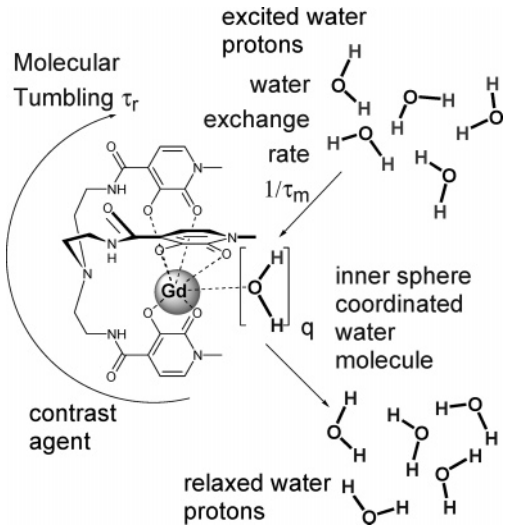

Figure 1. Parameters influencing relaxivity.

Considering the aforementioned properties, current commercial poly(amino-carboxylate) complexes (Figure 2) have several disadvantages (*1*). They have only one coordinated water molecule and fast tumbling rates due to their small size. Attempts to increase their relaxivities by grafting them on macromolecules (slowing τ_r) have led to mixed success due to the accompanying particularly slow water exchange rates, $1/\tau_m$, typically $0.5-5 \times 10^6$ s^{-1} (*1, 20, 21*). These water exchange rates are several orders of magnitude slower than the rate for $Gd(H_2O)_8^{3+}$ and far below levels necessary to achieve high relaxivity ($\tau_m \approx 20$ ns at 20 MHz). Because the fundamental properties of current commercial contrast agents are far from optimal, their resulting relaxivities are very low (~5 mM^{-1} s^{-1}), just a few percentage points of what is theoretically possible. Recent attempts to increase their water exchange rates by destabilizing their nine-coordinate ground state have resulted in less stable complexes (*20, 21*).

* To whom correspondence should be addressed: Tel: +1-510-841-1196; fax: +1-510-486-5283; e-mail: raymond@socrates.berkeley.edu.

† Part of the Special Issue collection on Imaging Chemistry that began in issue 6, 2004. A preliminary description of this work was presented at the Symposium on Chemistry and Biological Applications of Imaging Agents and Molecular Beacons, at the spring 2004 National Meeting of the American Chemical Society.

10.1021/bc049817y CCC: $30.25 © 2005 American Chemical Society
Published on Web 12/21/2004

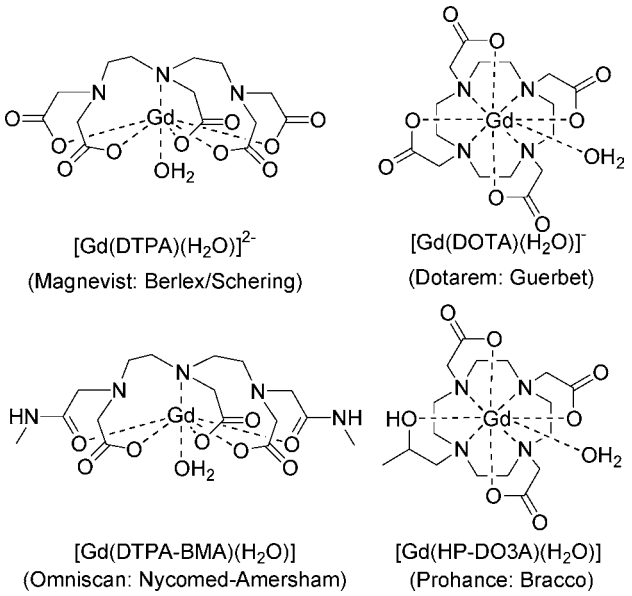

Figure 2. Common commercial Gd(III) contrast agents.

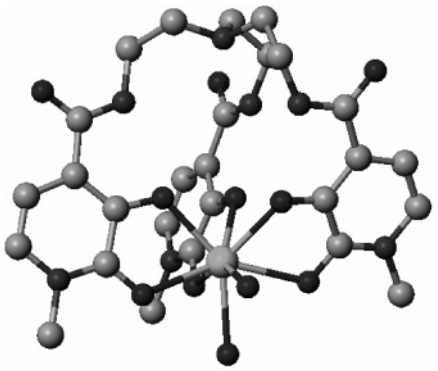

Figure 3. Crystal structure of Gd-TREN-1-Me-3,2-HOPO (**1**).

Gd(III) centers of poly(amino-carboxylate) complexes are coordinated by both oxygen and nitrogen atoms. This is more for synthetic convenience than design, given the high oxophilicity of lanthanide ions (*22*). We have reported a new family of MRI agents composed of all-oxygen donors and based on hydroxypyridinone (HOPO) and related ligands (Figure 4). The first of this family of compounds, Gd-TREN-1-Me-3,2-HOPO (Figure 3), showed particular promise due to its two coordinated water molecules and its fast, near-optimal water exchange rate (*23*). Its relaxivity of 10.5 mM^{-1} s^{-1} is more than double that of commercial contrast agents. Since then, the HOPO family has been extended to include complexes with varying chelating HOPO moieties, including mixed or heteropodal complexes and some complexes with varying caps. Their structures are shown in Figure 4, and their relaxivity and stability properties are given in Table 1. The water exchange rates and relaxivities of HOPO-based complexes are compared to those of commercial agents in Figures 5 and 6, respectively.

The fast, near-optimal water exchange rate is probably the most significant property of this family of complexes. The mechanism of exchange is probably similar to that of the aqua ion. Indeed both are eight-coordinate and both undergo rapid water exchange through an associative mechanism that goes through a nine-coordinate intermediate (Figure 8). This mechanism was recently supported by variable pressure NMR experiments that indicated that the reaction has a small negative activation volume ($\Delta V^{\ddagger} = -5 \pm 1$ cm^3 mol^{-1}) similar to that of the aqua complex ($\Delta V^{\ddagger} = -3.3$ cm^3 mol^{-1}) and indicative of an associative interchange process (*24*). Furthermore, shape analysis of the coordination sphere of the Gd(III) center in the crystal structure of Gd-TREN-1,2-HOPO indicates that the Gd(III) has a bicapped trigonal prism configuration (C.N. 8, Figure 8). Coordination of a new oxygen donor to form a tricapped trigonal prism (C.N. 9 intermediate) does not disturb the original geometry, indicating that this geometry may be predisposed for near optimal water exchange rates (*25*).

The water exchange mechanism of lanthanide aqua complexes are understood because of the classic studies of Merbach et al. (*26*). Earlier lanthanides (La to Nd) are nine-coordinate and exchange water through a dissociative mechanism whereas the heavier lanthanides (Gd to Lu) are eight-coordinate and exchange water through an associative mechanism. The fastest water exchange rates are observed for Sm and Eu for which the 8 and 9 coordination states are energetically identical. Given their fast water exchange rates, the same trend is expected for the HOPO based Gd(III) complexes. This is supported by the structure of La-TREN-1-Me-3,2-HOPO (Figure 9), which is a dimer in which one La is eight-coordinate with square antiprismatic geometry and the other is nine-coordinate with a monocapped square antiprismatic geometry (*27*). This demonstrates that the eight- and nine-coordination states are very close in energy and have similar geometries, which explains the fast water exchange rate observed for the corresponding Gd complex.

A typical NMRD (nuclear magnetic resonance dispersion) profile of a hydroxypyridinone-based complex, Gd-TREN-Me_2-5,4-HOPY (**3**), is shown in Figure 7. The relaxivity increases with decreasing temperature, a typical behavior for small molecular weight compounds for which the rotational correlation time is the limiting parameter. More significantly, at relevant magnetic field strengths the relaxivity peaks at high magnetic fields, typically between 20 and 100 MHz. This peak is a direct consequence of the fast water exchange rates of HOPO-based complexes: these rates are near optimal for high frequency MRI scanners. This behavior is opposite to that observed for commercial contrast agents, which have higher relaxivities at low magnetic fields (below 10 MHz) but significantly lower relaxivities at higher field strengths.

One of the disadvantages of the first hydroxypyridone-based Gd(III) complexes was their poor aqueous solubility. Given the high injection dosage needed to observe sufficient contrast in MR images, a water solubility of ~0.5 M is required. Modifications to improve solubility include the methoxy derivative, Gd-TREN-MOE−3,2-HOPO (**2**), cap in Gd-Ser_3-TREN-Me-3,2-HOPO (**7**), which has OH groups grafted onto the cap, and several

Table 1. Relaxivity, Water Exchange Rate and Stability of Hydroxypyridinone-Based Gd(III) Complexes

compound	**1**	**2**	**3**	**4**	**5**	**6**	**7**	**8**	**9**	**10**	**11**	**12**	**13**	**14**	**15**	**16**	**17**	**18**
$r_{1,p}$ (mM^{-1} s^{-1})[a]	10.5		9.0		9.5	9.1	9.0	6.6		8.8	7.7	7.2		9.1				
τ_m (ns)[b]			2				16			8			19	31	19			
pM[c]	19.2	19.8	18.0	19.5			17.7	16.7	15.6	20.1	16.1	16.2			20.1	20.3	15.2	~13
ref	(23, 31)	(35)	(33)	(31)	(25)	(25)	(36)	(32)	(32)	(27)	(27)	(27)	(28)	(28)	(24)	(34)	(31)	(31)

[a] 20 MHz, 25 °C, pH 7−8. [b] 25 °C. [c] 25 °C, pH 7.4, 0.1 M KCl, $[L]_{total} = 10$ μM, $[Gd]_{total} = 1$ μM.

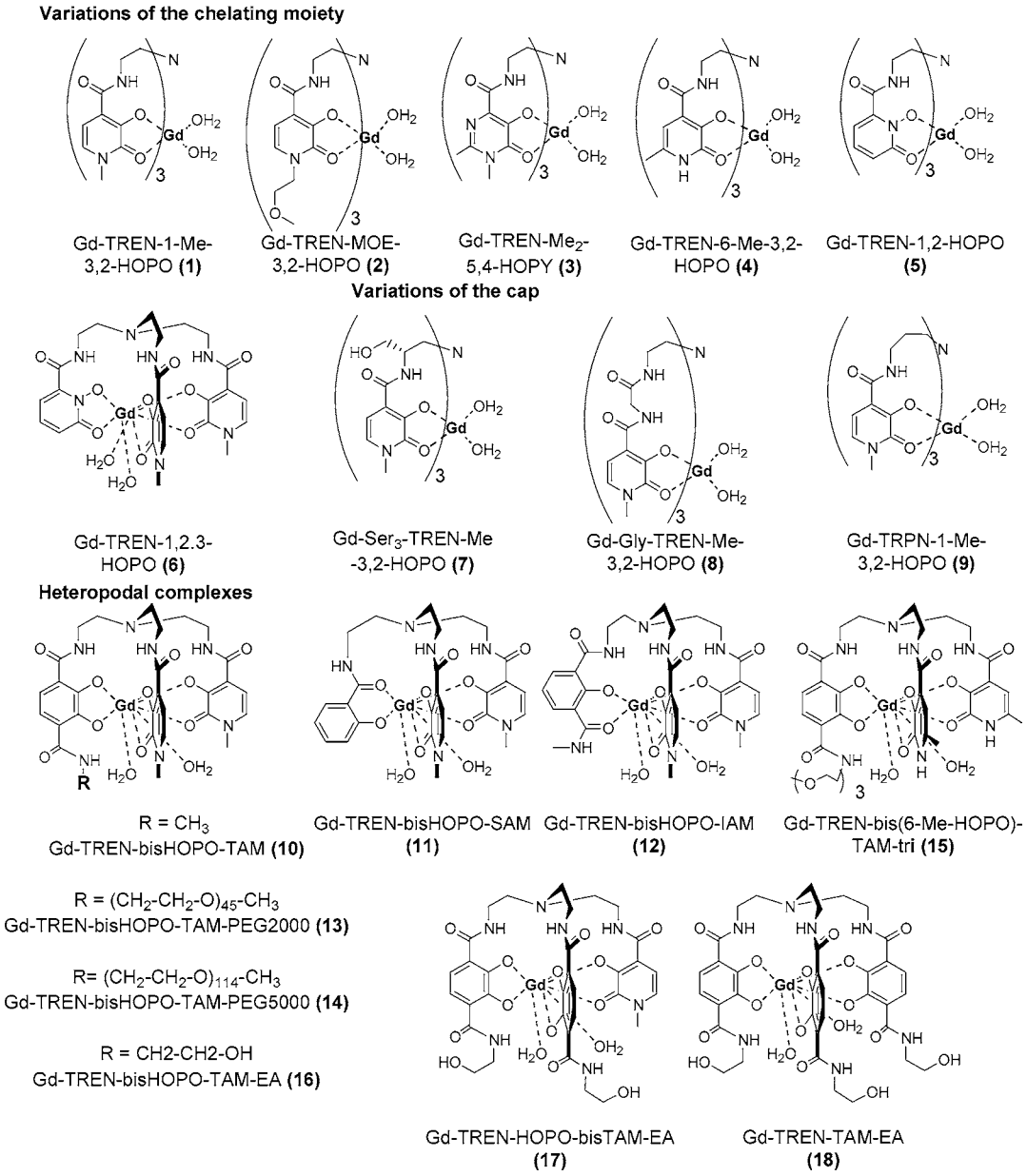

Figure 4. Structure of hydroxypyridinone-based Gd(III) complexes.

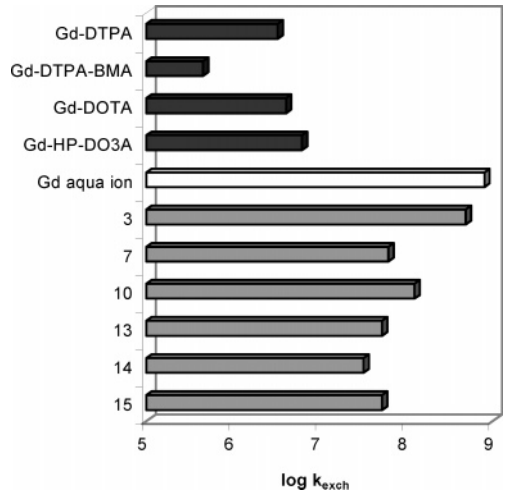

Figure 5. Water exchange rate of HOPO-based Gd complexes (grey) versus commercial agents (black).

isomers of HOPO such as Gd-TREN-6-Me-1,2-HOPO (**4**), Gd-TREN-1,2-HOPO (**5**), and the promising hydroxypyrimidine derivative, Gd-TREN-Me_2-5,4-HOPY (**3**). Mixed or heteropodal complexes containing two 1-Me-3,2-HOPO moieties and either a terephthalamide (**10**), a salicylamide (**11**), an isophthalamide (**12**), or a 1,2-HOPO moiety (**6**) have also been studied (*25, 27, 31, 33, 35, 36*). Fortunately, the addition of these small water-solubilizing moieties and the small variations in the chelating ring do not significantly change the water residence time ($\tau_m \approx 20$ ns), and all complexes demonstrate similar relaxivities ($r_{1p} \approx 9$ mM^{-1} s^{-1}). The exception is Gd-TREN-Me_2-5,4-HOPY (**3**) which not only demonstrates markedly improved solubility (up to 100 mM) but also a noticeably shorter water residence ($\tau_m \approx$ 2 ns), similar to that of the aqua complex (*33*).

The heteropodal HOPO/TAM (terephthalamide) complex offers the further advantage of being easily functionalized via its terminal acid group. Several poly(ethylene glycol) (PEG) derivatives (**13**, **14**, and **15**) bearing PEGs of different length have thus been synthesized. The resulting complexes demonstrate not only markedly improved water solubility but also provide the ability to fine-tune the water residence time (*28*). Addi-

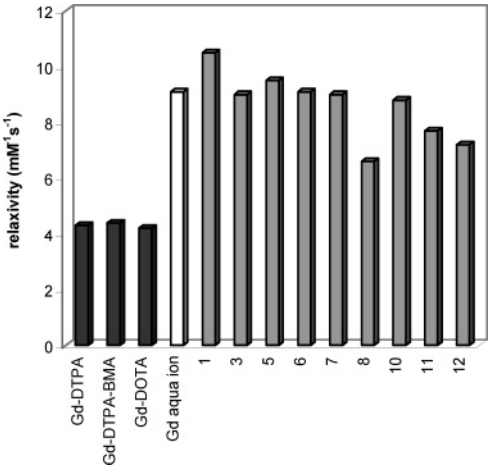

Figure 6. Relaxivity of HOPO-based Gd complexes (q = 2, gray) versus commercial agents (q = 1, black). (20 MHz, 25 °C, pH 7−8).

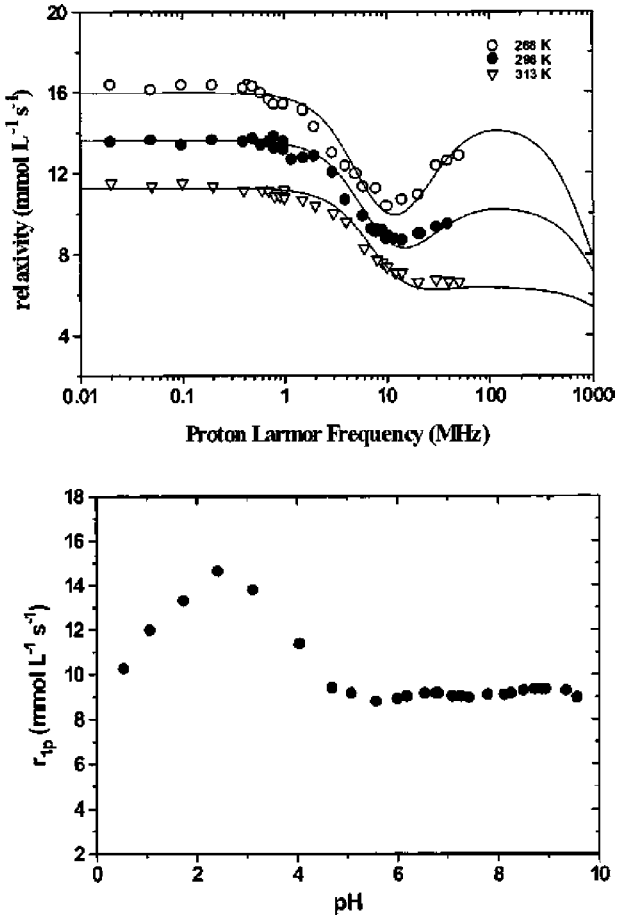

Figure 7. NMRD profile and pH dependence profile of Gd-TREN-Me$_2$-5,4-HOPY (**3**) (*33*).

tion of a PEG chain of MW ≈5000 g/mol increases the water residence time, τ_m, by a factor of 4.

The high toxicity of the Gd^{III} aqua ion (LD_{50} (mice) = 0.1 mmol/kg) requires that it be sequestered, and complexes that are kinetically labile must exhibit high thermodynamic stabilities (*29*). The stabilities of complexes with different number of protonation steps can easily and directly be compared in terms of their pMs (*30*). The stabilities of HOPO-based complexes are given in Table 1. As shown in Figure 11, they have stabilities comparable to commercial agents. Surprisingly, the more basic heteropodal HOPO−TAM complexes do not display

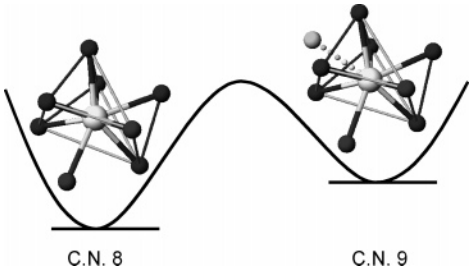

Figure 8. Proposed mechanism of water exchange for q = 2 hydroxypyridinone-based complexes (*25*).

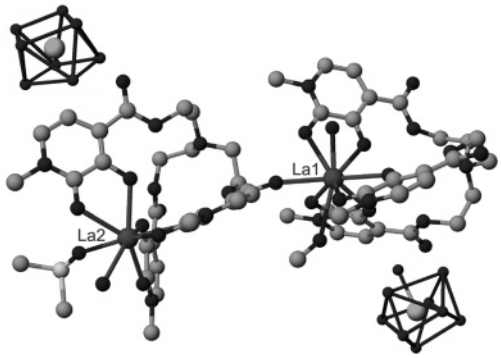

Figure 9. Crystal structure of La-TREN-1-Me-3,2-HOPO. La1 is nine-coordinate with monocapped square antiprismatic geometry while La2 is eight-coordinate with square antiprismatic geometry (*27*).

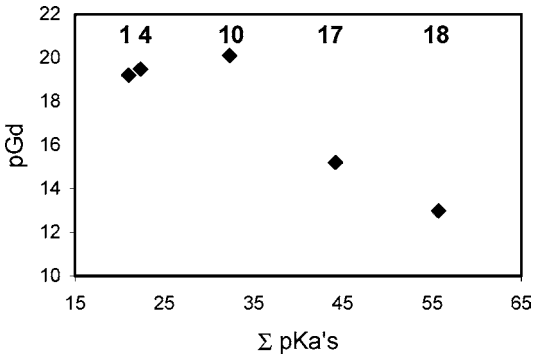

Figure 10. Stability of mixed hydroxypyridinone/terephthalamide Gd(III) complexes as a function of their basicity. 25 °C, pH 7.4, 0.1 M KCl, $[L]_{total}$ = 10 μM, $[Gd]_{total}$ = 1 μM (*31*).

the same linear relationship between stability and basicity that was observed for the more acidic commercial agents. As shown in Figure 10, the substitution of one hydroxypyridinone by one terephthalamide moiety (**16**) slightly increases the stability of the Gd(III) complex, while further substitution (**17** and **18**) significantly decreases the stability (*31*). This indicates that there is an optimal ligand basicity needed to achieve maximum stability, and that it is achieved by the presence of only one TAM moiety.

The TREN capping moiety is another important parameter in achieving high stability. Replacing the TREN cap by an expanded TRPN moiety (**9**) or inserting a glycine spacer (**8**) significantly reduces the stability of the resulting Gd(III) complex. As seen in both these data and the structures, internal H-bonding between the central capping N and the surrounding protons from the three amides noticeably increases the stability of the complexes (*32*).

All hydroxypyridinone Gd(III) complexes are acid sensitive. One HOPO podand protonates around pH 3, and the complex fully dissociates between pH 1 and 2.

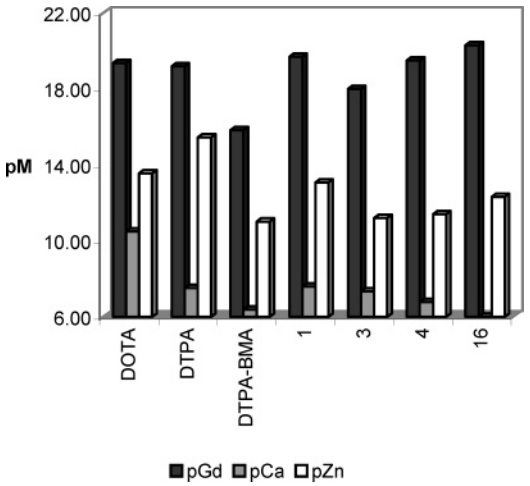

Figure 11. Selectivity of hydroxypyridinone-based ligands for Gd(III) over Ca(II) and Zn(II). 25 °C, pH 7.4, 0.1 M KCl, $[L]_{total} = 10\ \mu M$, $[M]_{total} = 1\ \mu M$ (*33, 34*).

As shown in Figure 7, this thermodynamic behavior, first observed by spectrophotometric titrations, is completely reflected in the pH dependence of the relaxivities (*33*). At pH 3, when one HOPO moiety protonates and dissociates, it is replaced by two water molecules, reflected by the doubling in relaxivity. The relaxivity then decreases toward pH 1 as the complex completely dissociates.

Selectivity is another important parameter to consider for kinetically labile complexes such as the HOPOs, which reach thermodynamic equilibrium with endogeneous cations during their in vivo lifetime. Indeed, it has been demonstrated that for such Gd(III) complexes, their toxicity is not directly related to their stability but rather to the selectivity of the ligand for Gd(III) over physiologically available metals such as Zn(II) (*29*). This selectivity may easily be determined by the difference in pM values between the two metal complexes (i.e. the selectivity for Gd(III) over Zn(II) is pGd-pZn). As shown in Figure 11, hydroxypyridinone ligands have higher selectivity for Gd(III) over Ca(II) and Zn(II) than commercial contrast agents (*34*).

CONCLUSION

Hydroxypyridinone-based Gd(III) complexes demonstrate significantly improved relaxivities due to their higher number of coordinated water molecules and near-optimal water exchange rates-several orders of magnitude faster than those of commercial agents. This optimal τ_m is reflected in the NMRD profiles, which typically show a peak of relaxivity at high magnetic fields where the relaxivities of commercial agents decrease. The fast water exchange is a result of an interchange associative mechanism in which the nine-coordinate intermediate is close in energy to the eight-coordinate ground state. This exchange rate can further be fine-tuned by grafting long poly(ethylene glycol) chains to the pendant acid of a mixed hydroxypyridinone/terephthalamide complex. These complexes also have high thermodynamic stability, and the ligands are more selective for Gd(III) over physiologically available cations such as Ca(II) and Zn(II) than current commercial agents.

ACKNOWLEDGMENT

This work was supported by the National Institutes of Health Grant HL 69832. We also acknowledge a research gift from Schering A.G.

LITERATURE CITED

(1) Caravan, P., Ellison, J. J., McMurry, T. J., and Lauffer, R. B. (1999) Gadolinium(III) chelates as MRI contrast agents: Structure, dynamics, and applications. *Chem. Rev. 99*, 2293−2352.
(2) Parker, D., and Williams, J. A. (1996) Getting excited about lanthanide complexation chemistry. *J. Chem. Soc., Dalton Trans.* 3613−3628.
(3) Aime, S., Botta, M., Fasano, M., and Terreno, E. (1998) Lanthanide(III) chelates for NMR biomedical applications. *Chem. Soc. Rev. 27*, 19−29.
(4) Aime, S., Botta, M., Fasano, M., Crich, S. G., and Terreno, E. (1999) H-1 and O-17-NMR relaxometric investigations of paramagnetic contrast agents for MRI. Clues for higher relaxivities. *Coord. Chem. Rev. 186*, 321−333.
(5) Comblin, V., Gilsoul, D., Hermann, M., Humblet, V., Jacques, V., Mesbahi, M., Sauvage, C., and Desreux, J. F. (1999) Designing new MRI contrast agents: a coordination chemistry challenge. *Coord. Chem. Rev. 186*, 451−470.
(6) Thunus, L., and Lejeune, R. (1999) Overview of transition metal and lanthanide complexes as diagnostic tools. *Coord. Chem. Rev. 184*, 125−155.
(7) Botta, M. (2000) Second coordination sphere water molecules and relaxivity of gadolinium(III) complexes: Implications for MRI contrast agents. *Eur. J. Inorg. Chem.*, 399−407.
(8) Aime, S., Cabella, C., Colombatto, S., Crich, S. G., Gianolio, E., and Maggioni, F. (2002) Insights into the use of paramagnetic Gd(III) complexes in MR-molecular imaging investigations. *J. Magn. Reson. Imaging 16*, 394−406.
(9) Brucher, E. (2002) Kinetic stabilities of gadolinium(III) chelates used as MRI contrast agents. *Top. Curr. Chem. 221*, 103−122.
(10) Frullano, L., Rohovec, J., Peters, J. A., and Geraldes, C. F. G. C. (2002) Structures of MRI contrast agents in solution. *Top. Curr. Chem. 221*, 25−60.
(11) Gries, H. (2002) Extracellular MRI contrast agents based on gadolinium. *Top. Curr. Chem. 221*, 1−24.
(12) Jacques, V., and Desreux, J. F. (2002) New classes of MRI contrast agents. *Top. Curr. Chem. 221*, 123−164.
(13) Toth, E., Helm, L., and Merbach, A. E. (2002) Relaxivity of MRI contrast agents. *Top. Curr. Chem. 221*, 61−101.
(14) Meade, T. J., Taylor, A. K., and Bull, S. R. (2003) New magnetic resonance contrast agents as biochemical reporters. *Curr. Opinion Neurobiol. 13*, 597−602.
(15) Zhang, S. R., Merritt, M., Woessner, D. E., Lenkinski, R. E., and Sherry, A. D. (2003) PARACEST agents: Modulating MRI contrast via water proton exchange. *Acc. Chem. Res. 36*, 783−790.
(16) Nicolle, G. M., Toth, E., Schmitt-Willich, H., Raduchel, B., and Merbach, A. E. (2002) The impact of rigidity and water exchange on the relaxivity of a dendritic MRI contrast agent. *Chem. Eur. J. 8*, 1040−1048.
(17) Tóth, E., Pubanz, D., Vauthey, S., Helm, L., and Merbach, A. E. (1996) the role of water exchange in attaining maximum relaxivities for dendrimeric MRI contrast agents. *Chem. Eur. J. 2*, 1607−1615.
(18) Wiener, E. C., Brechbiel, M. W., Brothers, H., Magin, R. L., Gansow, O. A., Tomalia, D. A., and Lauterbur, P. C. (1994) Dendrimer-Based Metal-Chelates − a New Class of Magnetic-Resonance-Imaging Contrast Agents. *Magn. Reson. Med. 31*, 1−8.
(19) Tóth, E., and Merbach, A. E. (1998) water exchange dynamics: the key for high relaxivity contrast agents in medical magnetic resonance imaging. *ACH Models Chem. 135*, 873−884.
(20) Cheng, T. H., Wang, Y. M., Lin, K. T., and Liu, G. C. (2001) Synthesis of four derivatives of 3,6,10-tri(carboxymethyl)-3,6,-10-triazadodecanedioic acid, the stabilities of their complexes with Ca(II), Cu(II), Zn(II) and lanthanide(III) and water-exchange investigations of Gd(III) chelates. *J. Chem. Soc., Dalton Trans.* 3357−3366.
(21) Laus, S., Ruloff, R., Toth, E., and Merbach, A. E. (2003) Gd−III complexes with fast water exchange and high thermodynamic stability: Potential building blocks for high-relaxivity MRI contrast agents. *Chem. Eur. J. 9*, 3555−3566.

(22) Hancock, R. D., and Martell, A. E. (1989) Ligand Design for Selective Complexation of Metal-Ions in Aqueous-Solution. *Chem. Rev. 89*, 1875−1914.
(23) Xu, J., Franklin, S. J., Whisenhunt, D. W., and Raymond, K. N. (1995) Gadolinium Complex of Tris[(3-Hydroxy-1-Methyl-2-Oxo-1,2-Didehydropyridine-4-Carboxamido)Ethyl]-Amine − a New Class of Gadolinium Magnetic-Resonance Relaxation Agents. *J. Am. Chem. Soc. 117*, 7245−7246.
(24) Thompson, M. K., Botta, M., Nicolle, G., Helm, L., Aime, S., Merbach, A. E., and Raymond, K. N. (2003) A highly stable gadolinium complex with a fast, associative mechanism of water exchange. *J. Am. Chem. Soc. 125*, 14274−14275.
(25) Xu, J., Churchill, D. G., Botta, M., and Raymond, K. N. (2004) Synthesis, Structure, and Shape Analysis of a Novel Gadolinium(III) Hydroxypyridonate-Based Complex: Towards MRI Contrast Agents of High Relaxivity. *Inorg. Chem. 43*, 5492−5494.
(26) Helm, L., and Merbach, A. E. (1999) Water exchange on metal ions: experiments and simulations. *Coord. Chem. Rev. 187*, 151−181.
(27) Cohen, S. M., Xu, J., Radkov, E., Raymond, K. N., Botta, M., Barge, A., and Aime, S. (2000) Syntheses and relaxation properties of mixed gadolinium hydroxypyridinonate MRI contrast agents. *Inorg. Chem. 39*, 5747−5756.
(28) Doble, D. M. J., Botta, M., Wang, J., Aime, S., Barge, A., and Raymond, K. N. (2001) Optimization of the relaxivity of MRI contrast agents: Effect of poly(ethylene glycol) chains on the water-exchange rates of Gd−III complexes. *J. Am. Chem. Soc. 123*, 10758−10759.
(29) Cacheris, W. P., Quay, S. C., and Rocklage, S. M. (1990) The Relationship between Thermodynamics and the Toxicity of Gadolinium Complexes. *Magn. Reson. Imaging 8*, 467−481.
(30) pM is defined as pM = − $\log[M]_{free}$ and is calculated under the standard conditions: $[L]_{total}$ = 10 μM.; $[M]_{total}$ = 1 μM.; pH = 7.4. The more stable the complex, the lower the concentration of free or uncomplexed metal, the higher the pM value.
(31) Doble, D. M. J., Melchior, M., O'Sullivan, B., Siering, C., Xu, J. D., Pierre, V. C., and Raymond, K. N. (2003) Toward optimized high-relaxivity MRI agents: The effect of ligand basicity on the thermodynamic stability of hexadentate hydroxypyridonate/catecholate gadolinium(III) complexes. *Inorg. Chem. 42*, 4930−4937.
(32) O'Sullivan, B., Doble, D. M. J., Thompson, M. K., Siering, C., Xu, J. D., Botta, M., Aime, S., and Raymond, K. N. (2003) The effect of ligand scaffold size on the stability of tripodal hydroxypyridonate gadolinium complexes. *Inorg. Chem. 42*, 2577−2583.
(33) Sunderland, C. J., Botta, M., Aime, S., and Raymond, K. N. (2001) 6-carboxamido-5,4-hydroxypyrimidinones: a new class of heterocyclic ligands and their evaluation as gadolinium chelating agents. *Inorg. Chem. 40*, 6746−6756.
(34) Pierre, V. C., Melchior, M., Doble, D. M. J., and Raymond, K. N. (2004) Toward Optimized High-Relaxivity MRI Agents: Thermodynamic Selectivity of Hydroxypyridonate/Catecholate Ligands. *Inorg. Chem. 43*, 8520−8525.
(35) Johnson, A. R., O'Sullivan, B., and Raymond, K. N. (2000) Synthesis of a ligand based upon a new entry into the 3-hydroxy-*N*-alkyl-2(1*H*)-pyridinone ring system and thermodynamic evaluation of its gadolinium complex. *Inorg. Chem. 39*, 2652−2660.
(36) Hajela, S., Botta, M., Giraudo, S., Xu, J. D., Raymond, K. N., and Aime, S. (2000) A tris-hydroxymethyl-substituted derivative of Gd-TREN-Me-3,2-HOPO: An MRI relaxation agent with improved efficiency. *J. Am. Chem. Soc. 122*, 11228−11229.

BC049817Y

Ligand-Carrying Gas-Filled Microbubbles: Ultrasound Contrast Agents for Targeted Molecular Imaging†

Alexander L. Klibanov*

Cardiovascular Division, University of Virginia, Charlottesville, Virginia 22908. Received April 24, 2004; Revised Manuscript Received December 8, 2004

INTRODUCTION

Molecular imaging is heralded as the solution to many problems of current medicine (*1*). It is supposed to offer convenient, universal, high-resolution, and affordable diagnostic imaging insight into the in vivo biological processes on the molecular and cellular level, aiding with personalized, targeted, and image-guided therapeutic interventions. Contrast agents usually suggested for molecular imaging are radioisotopes, paramagnetic materials, or fluorescent dyes, designed for SPECT/PET, MRI, or infrared optical imaging systems, respectively. Ultrasound as an imaging modality offers a cache of advantages over those techniques; therefore, development of molecular imaging contrast agent for ultrasound will result in many benefits.

Ultrasound imaging is (1) a real-time modality (routinely, 20−30 frames/s or more); (2) consistently used in image-guided biopsy and therapy, such as cryoablation, (3) inexpensive and popular; equipment is widely installed worldwide, and (4) portable: equipment can be taken to the bedside, ambulance, battlefield, or private practice office (including laptop and hand-held ultrasound units).

The concept of ultrasound contrast agent for molecular (targeted) imaging consists of using contrast particles with a specific ligand to the target receptors that are expressed in the area of disease. Targeted contrast is administered intravenously, circulates in the bloodstream, and accumulates in the area of interest via a ligand−receptor interaction. Free circulating agent clears from the bloodstream, and targeted agent signal is then used to demarcate the site and condition of the target diseased tissue (a simplified picture of such imaging is presented on Figure 1). Ultrasound imaging equipment is widely available. Contrast materials for intravenous use are already approved; therefore, targeted agents capable of molecular imaging represent a logical extension of the existing technology.

In this review, we will discuss the chemistry of the preparation of the most efficient targeted ultrasound contrast materials, techniques for ligand attachment, and application of these agents for molecular imaging. In this limited format it is not possible to provide the references to all the existing literature in the field; examples will be provided to demonstrate the general development trends.

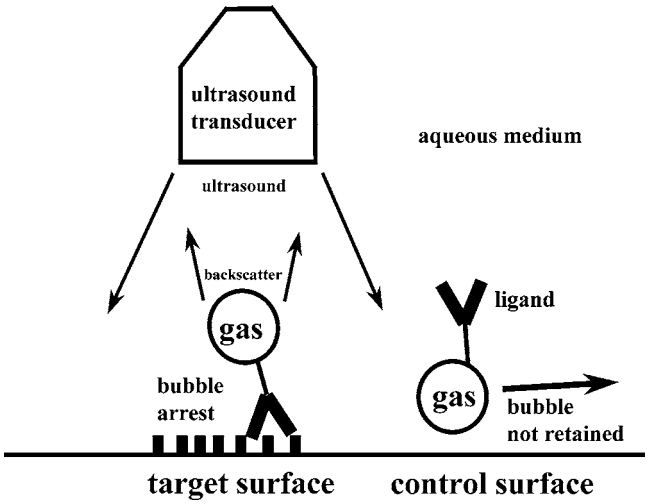

Figure 1. General outline of targeted ultrasound imaging of ligand-carrying microbubble retained on a receptor-coated target surface.

Ultrasound Contrast Particle Design: Physical Considerations and Sensitivity. Ultrasound imaging is performed by signal processing of the reflections of sound waves sent toward the tissues within the body. For general clinical diagnostic imaging 1−10 MHz frequency ultrasound is used, which implies sub-millimeter to millimeter wavelength range and comparable spatial resolution. Higher frequencies, up to 20−50 MHz, provide much higher resolution (down to tens of micrometers) at the expense of penetration depth and are applied for imaging of specific organs, such as in ophthalmology, or in the intravascular probes. Lower frequency ultrasound, ∼1−3 MHz, allows deep penetration within the body. High frequencies provide limited penetration, only several millimeters. Ultrasound scattering by the tissues and borders between tissues is dependent on the mismatch of the acoustic impedance, i.e., difference between the product of the speed of sound in the medium multiplied by the density of that medium (*2*). Therefore, contrast agent particles which present the highest echo response would be the ones that possess the highest acoustic impedance mismatch between the bulk medium (blood has acoustic impedance quite close to water) and the particle microphase.

Several types of contrast particles have been suggested for ultrasound imaging, including liquid-core microemulsions and nanoemulsions (*3*), liposomes (*4*), and gas-filled microbubbles, with the average size of several micrometers (*5*−*7*). Gas-filled microbubbles offer the highest acoustic impedance mismatch and the highest recorded backscatter signals in ultrasound imaging (*2*, *8*). Liquid

* Corresponding author: Alexander L. Klibanov, UVA Cardiovascular Division, Cardiovascular Imaging Center, P.O. Box 800158, Hospital Drive, Cobb Hall, Room 1026, Charlottesville, VA 22908-0158. Telephone: (434)243-9773, telefax (434)982-3183, e-mail alk6n@virginia.edu.

† Part of the Special Issue collection on Imaging Chemistry that began in issue 6, 2004. A preliminary description of this work was presented at the Symposium on Chemistry and Biological Applications of Imaging Agents and Molecular Beacons, at the spring 2004 National Meeting of the American Chemical Society.

10.1021/bc049898y CCC: $30.25 © 2005 American Chemical Society
Published on Web 12/30/2004

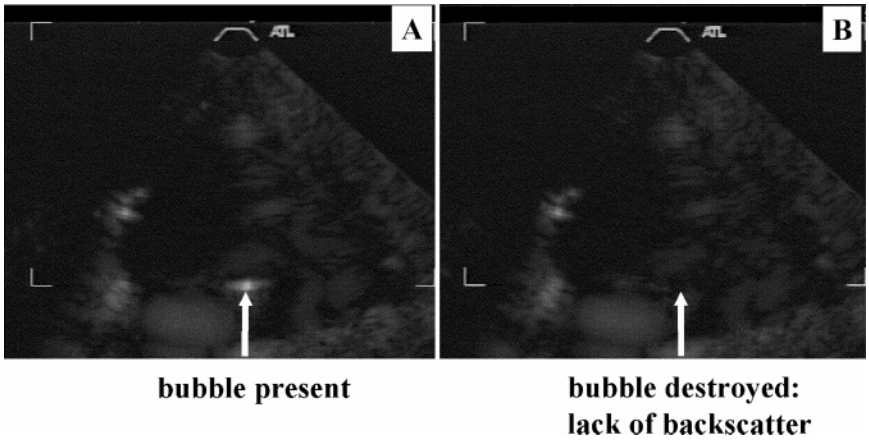

Figure 2. Ultrasound imaging of an individual targeted microbubble immobilized on a Petri dish, using Philips HDI 5000 system, equipped with a P4-2 transducer. (A) Microbubble imaging at MI = 0.2. (B) Dish after microbubble destruction. Reprinted with permission from ref 11. Copyright 2004 Lippincott, Williams and Wilkins.

contrast emulsion particles offer lower acoustic impedance mismatch but enhanced stability and prolonged circulation time (*3*). Multilamellar liposome-based agents were initially hypothesized to provide acoustic response due to their multilamellar lipid structure (*4*); later, it was shown that their acoustic response was caused by incorporated pockets of gas phase (*9*). Such liposomes offer acoustic response that is several orders of magnitude lower than that of microbubble-based agents (*10*). Overall, microbubbles offer the best detection sensitivity and some of these contrast agents are already approved for blood pool indications. Hence, the main focus of this review will be the discussion of the microbubble-based contrast materials, the specific chemistry of their preparation, ligand coupling, and actual molecular imaging applications.

Sensitivity of the detection of gas-filled microbubbles by ultrasound is quite high, even in comparison with other modalities suggested for molecular imaging. Typical approved intravenous human dose of ultrasound contrast microbubble material is at sub-milligram level. Actual detectable amount is considerably less. Experimental detection of *individual* microbubbles with diagnostic imaging clinical ultrasound systems has been reported (*8*, *11*). An estimated mass of the material contained in the shell and gas phase of an average microbubble is about a picogram; it can be clearly observed by ultrasound imaging of targeted microbubble in an in vitro model system (Figures 1 and 2). Within a certain microbubble concentration range, ultrasound backscatter response demonstrated linear dependence on concentration. Therefore, one can expect successful delineation of the areas of microbubble accumulation in the target tissues even if the number of actual targeted tracer particles is low (few thousands of selectively retained microbubbles definitely could be detected at the target area).

Additional imaging and postprocessing schemes can be applied to improve detection of targeted microbubbles on the background of normal tissue (the latter may be actually useful to pinpoint the location of the targeted bubbles in relation to anatomical markers and body structures). One important approach is image subtraction, when an image frame is acquired prior to contrast administration, and next one is obtained when targeted contrast accumulates in the area. Frames are aligned properly, and images are subtracted, so that the targeted contrast signal that constitutes the difference between the frames can be recognized easily. To aid in this procedure, targeted bubble destruction at high ultrasound intensity is often used (*12*). This way, there is no need to wait for many minutes from obtaining the original blank image to acquiring the "targeted" image, with the probe fixed at the same spot. After the "targeted" frame, all the targeted accumulated bubbles can be cleared by ultrasound irradiation, and the control frame is taken just a few seconds later (Figure 3A vs Figure 3C provide an in vitro model comparison). Another advantage of high-intensity destructive ultrasound imaging is a considerably higher acoustic response achieved in these conditions (Figure 3B). When nondestructive imaging of microbubble contrast is performed at a low ultrasound mechanical index (Figure 3A), the signal from targeted microbubbles is relatively low (arrow on the images pointing toward microbubble location), but quite visible and detectable as compared with control image where bubbles were destroyed, Figure 3C. When bubbles are irradiated with a higher-intensity ultrasound pulse, they are destroyed. Actual intensity and frequency of ultrasound pulses applied for bubble destruction and imaging may have to take into account the potential bioeffects of ultrasound (see below). During destruction, bubbles emit a bright acoustic flash at various frequencies. This signal can be detected by the imaging system very efficiently (Figure 3B). The microscopy image of the plate prior to insonation showed that only a small fraction (several percent) of the target surface is covered with targeted bubbles; just a few bubbles as observed optically (Figure 3D) are sufficient to obtain the high signal-to-noise ultrasound images. Overall sensitivity of the ultrasound for the detection of targeted contrast should be sufficient for molecular imaging.

Ultrasound Contrast Particle Design: Microbubble Preparation and Storage Stability. When microbubbles were first proposed as contrast agents, they did not carry a shell; such nonstabilized bubbles could survive only while they were surrounded by the aqueous medium, either normal saline (*13*) or viscous X-ray contrast (*14*). Such bubbles would fuse with each other and with the headspace air above the volume of the aqueous medium in the vial and rapidly disappear even prior to administration in the patient. An inadequate level of storage stability required in situ bubble generation in the immediate proximity to the patient location.

Improvement of microbubble formulation allowed the preparation of microbubbles stabilized with a lipid shell, typically, a lipid monolayer. Most often, lipids applied for microbubble coating possess a high transition tem-

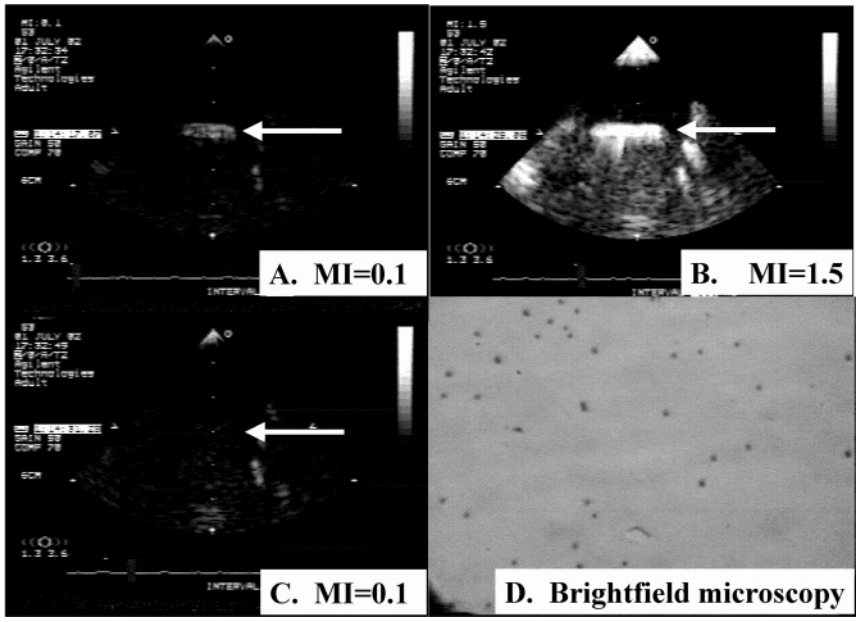

Figure 3. Ultrasound contrast imaging of biotinylated bubbles targeted to a streptavidin-coated Petri dish. A. Imaging at low ultrasound intensity (MI = 0.1). B. Imaging at high ultrasound intensity destructive to microbubbles (MI = 1.5). C. Imaging at low ultrasound intensity (MI = 0.1) after microbubble destruction. Location of microbubbles on the dish marked by arrow. D. Photomicrograph of targeted microbubbles on a dish prior to destruction.

Table 1. Commercially Available Ultrasound Contrast Microbubbles Currently in Clinical Practice[a]

agent name (manufacturer)	gas core	shell composition	design
Levovist (Schering AG)	air	palmitic acid	dry galactose precursor matrix
Albunex (MBI/Mallinckrodt)	air	albumin	albumin shell bubbles stored in albumin aqueous saline
Optison (Mallinckrodt/ Amersham)	octafluoropropane	albumin	albumin shell bubbles stored in albumin aqueous saline
Definity (Bristol Myers Squibb Medical Imaging)	octafluoropropane	phospholipids (DPPC, MPEG-DPPE, DPPA)	precursor: aqueous liposomal solution in a vial with C_3F_8 headspace
Imagent (Alliance/ Photogen)	N_2/perfluorohexane vapor	phospholipid (DMPC)	dry precursor matrix
SonoVue (Bracco)	sulfur hexafluoride	phospholipids (DSPC, DPPG, palmitic acid)	dry precursor matrix

[a] Contrast agent names are trademarks by respective manufacturers.

perature (e.g., DPPC, 42 °C, or DSPC, 56 °C). Monolayers of such lipids are in gel phase and do not fuse as easily as do monolayers of fluid-phase lipids. Lipid-stabilized microbubbles possess somewhat improved stability over shell-free bubbles. To improve microbubble storage stability even further, we need to prevent direct contact between individual microbubbles and thus reduce the rate of shell fusion and bubble coalescence. This is achieved either by adding electrostatically charged molecules as a part of the microbubble shell (typically as 5−15 mol % of a negatively charged lipid within the bulk zwitterionic lipid) (*15*) or by grafting a surface brush of hydrophilic polymer, such as poly(ethylene glycol) (PEG) on the microbubble surface (*16*). PEG brush is similar to the coating of long-circulating liposomes, an established drug delivery system with prolonged circulation time and reduced uptake to Kupffer cells and macrophages. PEG-coated microbubble preparations can be stored for up to several years without a substantial loss of ultrasound contrast response, in our experience.

Actual microbubble preparation is typically accomplished by high-shear (such as probe-type sonication) dispersing of gas in the aqueous medium that contains lipids in a micellar or liposomal form. A most primitive but efficient dispersion apparatus consists of two disposable polypropylene syringes, partly filled with gas and aqueous lipid mixture and connected to each other via a partially closed stopcock (*17*). Liquid and gas are forced from one syringe to another by back and forth movement of the plungers; high shear and resulting microbubbles are generated in the narrow connector orifice. The size of the manufactured bubbles is dependent on the shear flow and also on the composition of the stabilizer lipid. A more sophisticated and widely applied method consists of sonication of the aqueous medium with a probe-type ultrasound disintegrator in the atmosphere of a desirable gas. When the gas is dispersed in the aqueous micellar medium, freshly generated contact surface between the gas and liquid phases is immediately coated and stabilized with the lipid monolayer to reduce surface tension. As individual microbubbles are closed up, they can no longer fuse with their neighbors due to the presence of the newly deposited shell. Typically, instead of air that was used in the early generation bubble preparations, fluorine-containing inert insoluble gases (such as decafluorobutane, octafluoropropane, or sulfur hexafluoride) are predominantly applied in the second generation microbubble materials (see Table 1 for the characteristics of some microbubble contrast agents available).

Commercially developed (nontargeted) microbubbles applied as the markers of circulating blood are stored usually as precursors, mostly dry preparations that

require addition of water for reconstitution prior to injection (*15*) and can only be used within several hours after reconstitution. However, some of the bubble preparations can withstand prolonged (years) storage in the aqueous phase; this requires a thicker shell, such as denatured albumin (*6*) or a shell composed of gel-phase lipid combined with PEG brush coating (*18*) to avoid microbubble fusion. Overall, storage stability of ultrasound contrast microbubble agents is now comparable with that of the agents used in other molecular imaging modalities, and cumbersome preparation or express delivery from the manufacturer to the hospital is not required.

Ultrasound Contrast Particle Design: Ligand Attachment Strategies. There are two general strategies for the attachment of the targeting ligand to the microbubble shell. In the first technique, the ligand is in a separate procedure coupled to the shell-forming molecule or its precursor (such as a lipid residue), to be used as an anchor to retain the ligand attached to the shell monolayer. The bioconjugate is then mixed with the bulk material suited for shell preparation, and bubbles are generated as described above. This approach works well for small organic molecule ligands, such as peptides, peptide mimetics, carbohydrates, hormones, and vitamins (such as biotin). Preparation of ligand−lipid conjugates has been perfected years ago and applied for ligand attachment to microbubbles either directly (*19*) or via a PEG spacer arm (*18*, *20*, *21*). The main advantage of this approach is the ability to perform the synthesis and product purification in the stepwise manner in the fully controlled conditions of an organic chemistry setup, ensuring high product yield and purity.

The second general approach to ligand conjugation with the bubble shell calls for covalent or noncovalent attachment of ligands to preformed microbubbles. This approach is most appropriate for the materials that are unstable in the conditions of continuous sonication, high-speed shear mixing, and resulting high temperatures, that are often associated with the preparation of microbubbles. Large protein molecules, such as antibodies or antibody fragments, are easily denatured in harsh conditions. To avoid denaturation of protein ligands, reactive moieties that are stable enough to withstand bubble preparation conditions can be incorporated in the shell first and then applied for the attachment of the protein ligand to preformed bubbles.

The groupings to achieve protein ligand binding can be suitable for covalent or noncovalent attachment. The noncovalent attachment strategies have been well developed, mostly with biotin−streptavidin-mediated techniques (Figure 4) (*12*). Conveniently, microbubbles can be rapidly purified from excess of free lipid, streptavidin, or biotinylated ligand, by repeated low-speed centrifugal flotation washes (e.g., 400*g* for several minutes). Respectively, after the first round of centrifugal washes during which the microbubbles are purified from excess lipid and biotin−lipid, microbubbles are dispersed in streptavidin solution. Streptavidin is used at an excess over the amount of available biotins on the bubble surface to avoid bubble cross-linking. After a brief incubation, the excess of free streptavidin is removed by flotation. Biotinylated antibody or other ligand is then added to complete the "sandwich" formation on the bubble surface (Figure 4). Coupling yield for the attachment of biotinylated ligands to microbubbles is reasonably high, and large excesses and losses of expensive ligand can be avoided.

Covalent attachment of antibody ligands to preformed microbubbles can be easily accomplished after a carboxylated lipid derivative has been incorporated in the bubble shell; typically, carboxylate is positioned on the outer terminus of a PEG polymer spacer, and the other terminus of PEG is grafted to the lipid anchor embedded in the shell (*22*). Carboxylate can be activated by a water-soluble carbodiimide, such as 1-ethyl-3-(3′-dimethylaminopropyl)carbodiimide in the presence of *N*-hydroxysulfosuccinimide, and resulting active ester can react with an amino group of an antibody or other protein ligand (Figure 5) (*23*, *24*). First, in mildly acidic conditions, the carboxylic acid residue is reacted with the carbodiimide with the formation of an unstable *O*-acylisourea. It is undesirable for this intermediate to be converted to the stable *N*-acylisourea, which would then be permanently attached onto the surface of the microbubble. *N*-Hydroxysulfosuccinimide is therefore added to convert *O*-acylisourea to *N*-hydroxysulfosuccinimide ester, which is reasonably stable in mild acidic environments, but would rapidly hydrolyze with the release of the unaltered carboxyl and *N*-hydroxysulfosuccinimide once the bubble preparation is placed in the mildly alkaline aqueous buffer solution containing the ligand that possesses primary amino groups used for coupling. Irreversible chemical modification of the bubble surface with undesirable *N*-acylisourea will thus be avoided.

The coupling yield of the targeting agent to microbubbles is determined by the rates of two competing

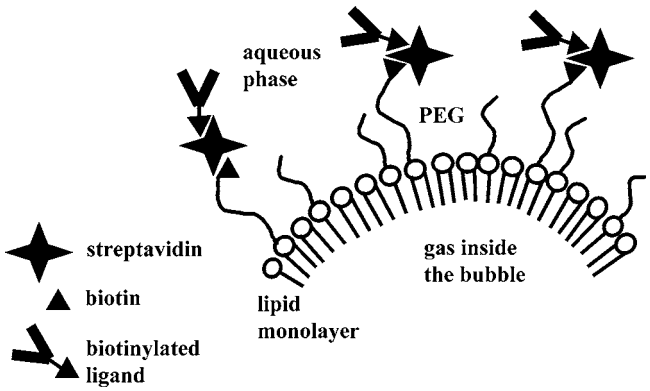

Figure 4. Design of biotinylated microbubble and attachment of biotinylated ligand via a streptavidin linker and PEG spacer arm.

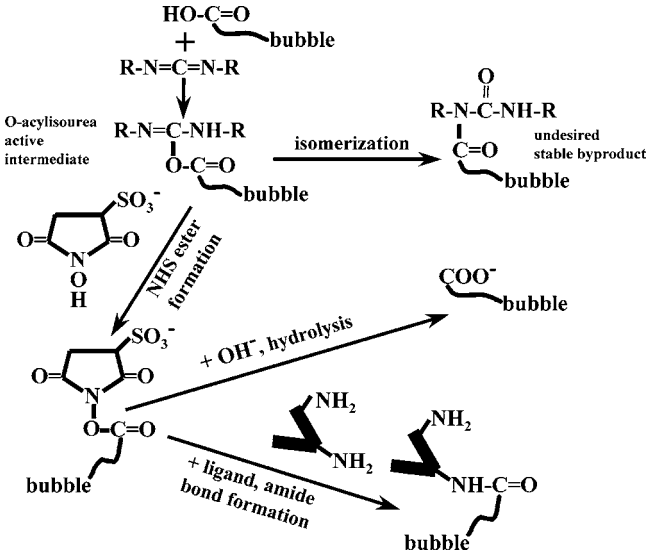

Figure 5. Coupling of amino-containing ligand to carboxyl-carrying microbubbles via water-soluble carbodiimide and *N*-hydroxysulfosuccinimide: the desired and side reactions.

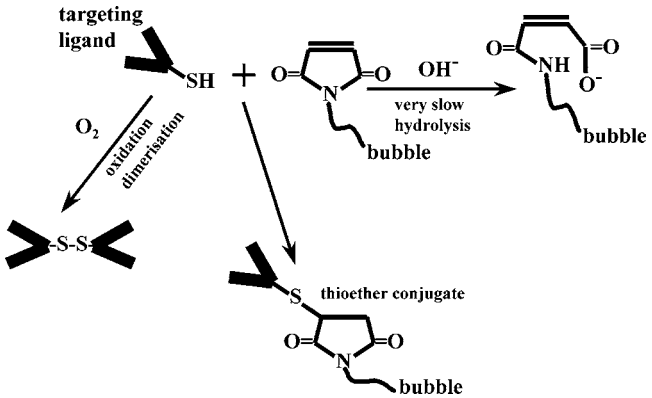

Figure 6. Coupling of thiol-carrying ligand to maleimide-carrying microbubbles: the desired and side reactions.

reactions, hydrolysis of *N*-hydroxysulfosuccinimide ester, and formation of amide bond between the ligand and activated carboxyl. The hydrolysis reaction is pseudo-first-order; the reaction rate constant is dependent on pH (faster at higher pH). The rate of coupling is also dependent on the concentration of primary amine in the deprotonated form (which depends on its p*K* and pH as well). Ligand coupling to active ester is a second-order reaction; the rate and the ligand coupling yield are both dependent on the concentration of reactants. While this coupling chemistry was successfully applied for antibody coupling to liposomal systems, where carboxylated lipid concentration was in the mM range (*24*), it is less than perfect for microbubble-based systems. The overall concentration of lipids that are needed to coat the surface of microbubbles is about 2 orders of magnitude less than a typical liposome lipid concentration, as is the concentration of activated carboxyl in the microbubble preparation. To achieve a decent ($\sim 10^5$ antibody per microbubble) level of coating, a large excess of the expensive antibody ligand has to be added (*22*); most of the antibody is not attached to the bubbles and wasted. To improve coupling yield, one needs to reduce the rate of side reactions of the activated derivative on the bubble surface without reducing the rate of the desired coupling reaction.

A different coupling strategy, attachment of thiol-carrying targeting ligands to the particle surface via maleimide (*25*) or vinyl sulfone, is widely applied in bioconjugate chemistry. Use of maleimide may provide good ligand coupling yield and slow degradation of the reactive group on the bubble surface (Figure 6). Maleimide-PEG-lipid can be easily incorporated in the monolayer shell, and thiol-carrying antibody can be simply added to react with maleimide with a formation of a thioether bond, which is exceptionally stable. The maleimide reactive group possesses much better stability than an NHS ester in the aqueous medium (*26*), and the rate of unproductive side reactions is greatly diminished; therefore, the yield of ligand coupling to the microbubbles can be improved considerably. An alternative side reaction in this case, oxidation of a thiol with atmospheric oxygen with the formation of disulfide bond, should not be a major problem, because microbubble handling should be performed in the perfluorocarbon atmosphere anyway. An additional benefit from the use of the thiol-maleimide approach, the ability to directionally attach the ligand to the bubbles, should also be taken into account. Protein ligands contain dozens of primary amino groups, and carboxylic acid coupling to those with amide bond formation is quite random. Some of the coupling sites may be located close to the binding site of the ligand, which would greatly reduce the affinity to the target receptor. If a single thiol residue is specifically introduced in a desired portion of the ligand, either by site-directed mutagenesis or by synthesis, oriented coupling to the bubbles will be achieved. The chance of ligand inactivation upon coupling via a single thiol will be greatly reduced.

The use of a flexible polymer spacer arm as a linker between the bubble surface and the ligand offers some advantage over a direct attachment of the ligand to the microbubble surface. The microbubble shell, especially one formed from gel-state phospholipids, does not offer rapid ligand mobility along the bubble surface. Therefore, the matching of ligand and receptor pairs along the contact area may require time that is not available during the brief contact between the bubble and the target surface in a flow-through scenario. Use of a flexible polymer tether (such as PEG) allows the ligand to rapidly interrogate the target surface and attach to the target receptors whenever available and in reasonable proximity to the microbubble surface. Additional benefit of placing the ligand on the PEG spacer becomes obvious when microbubbles also carry a grafted PEG polymer brush. If the ligand is attached directly to the lipid anchors, it may be hidden inside the polymer brush layer and become poorly accessible to the target receptor (*27*). When ligand is placed on the extended tether, especially if the length of the tether exceeds the thickness of the PEG brush, a "tiered brush" structure is created on the surface of the bubbles, where the thick brush layer of shorter PEG provides a stabilization coating, and longer polymer chains with tethered ligand are extended into the surrounding medium for efficient target receptor capture.

Ultrasound Contrast Particle Design: Biodistribution and in Vivo Behavior. Initial microbubble contrast preparations were quite unstable in the bloodstream; shell-free microbubbles could not even pass through the lung vasculature, and contrast imaging of myocardium was only possible after intraarterial administration (*13*). Since that time, ultrasound contrast materials' circulation time has improved greatly. Modern microbubble contrasts use appropriate lipid, polymer, or protein shells and can persist in the bloodstream for many minutes (up to 1 h for some preparations). This circulation time scale is quite sufficient to perform the task of targeted mapping of the receptors exposed to vascular lumen. For lipid monolayer-based microbubble design, generally, the coating made from longer-chain fully saturated lipid molecules (such as distearoyl phosphatidylcholine as compared with, for example, dimiristoyl phosphatidylcholine) ensures longer circulation time. In the early generation contrast agents, air was used as the gas phase. Use of low-solubility gases, e.g., decafluorobutane, further improves circulation time, because such gases exit the bubble and dissolve in the surrounding blood slower than oxygen or nitrogen. A lipid monolayer-coated bubble with decafluorobutane gas core can stay in the bloodstream for many minutes. During the circulation, especially while passing through the lung microcirculation, microbubbles gradually deflate and lose ability to scatter ultrasound; majority of the poorly soluble gas incorporated within the bubbles is exhaled within minutes after intravenous injection, which points to the lungs as the major bubble gas elimination site (*28*) (actual circulation and exhalation times depend on the specifics of the gas used).

Some of the microbubble preparations were retained nonspecifically in the vasculature, especially in the areas of inflammation (*29*, *30*); in part this may be caused by the activation of complement by some of the components

of the microbubble shell and triggered by the presence of electrostatically charged lipids on the bubble surface (*31*). Leukocytes, macrophages, and Kupffer cells have a tendency to capture these heavily charged microbubbles, especially the ones carrying phosphatidylserine (*32*). Presence of the PEG brush on the microbubble surface of charged bubbles reduces complement deposition only partially (*31*); therefore, it may be desirable to avoid surface charge in the microbubble formulations, especially if reduction of the nonspecific microbubble tissue uptake is desired.

In all of the imaging modalities used for targeted and molecular imaging, it is critical to achieve not only a high degree of accumulation of contrast material in the target and low accumulation in normal tissues, but also low level of circulating contrast in the bloodstream. For some of the intravenously injected targeted contrasts used in SPECT or MRI, such as antibodies, long-circulating liposomes, or high molecular mass polymers, it may take up to a day to clear from the bloodstream via liver or kidneys. Therefore, diagnostic imaging cannot be performed rapidly and repeated frequently to monitor treatment efficacy. In the case of ultrasound, circulating bubbles may clear from the bloodstream completely within a fraction of an hour, or even faster, depending on the particular shell design and gas core. We can speculate that the microbubbles that had attached to the target tissue should maintain their stability much better than the bubbles still in circulation. Targeted bubbles do not repeatedly pass through the lungs where most of gas exchange and bubble deflation seem to take place. In an in vitro setting, targeted bubbles can be maintained on the antigen-coated surface for at least a day. Even if the majority of the bubbles clears from the bloodstream and other tissues, and only a small fraction of the administered bubbles is retained at the target, high detection sensitivity should allow successful target detection and delineation. Thus, we can expect high target-to-blood ratio within 10−15 min after microbubble contrast administration (*12*), and in this situation further extending contrast circulation time may not bring any benefits for the timely completion of the imaging procedure and successful diagnosis.

Potential Safety Concerns Associated with Targeted Microbubble Systems. Contrast agents need to possess an excellent safety profile to be permitted for clinical use. Therefore, potential safety, toxicity, and side effect concerns affiliated with targeted microbubble agents need to be taken seriously and evaluated in detail. There are generally three groups of safety questions concerning microbubble contrast to be applied in molecular imaging: (1) the general reaction of the organism to contrast agent particles; (2) potential generation of immune response to particle components, such as targeting ligands; (3) ultrasound radiation bioeffects potentiation in the presence of microbubble agents in the living tissues.

Concerns regarding undesired reactions of the organism to the intravascular administration of particle agents had been raised many times over the past years, especially with liposomes (*33*). In some patients an undesired systemic hypersensitivity-type reaction to the particle administration might occur; agent infusion is then to be discontinued and antiinflammatory therapy performed (*34*). One likely explanation for these adverse events is based on the electrostatic surface charge of the particles that results in complement activation leading to the undesired systemic effects (*33*). The administered dose of ultrasound contrast agents is usually lower than the dose of therapeutic liposomes; therefore, the resulting undesirable effects are quite rare. For ultrasound contrast particles, addition of a PEG brush on particle surface might diminish complement-mediated events somewhat, but might not fully solve the problem (*31*) (similarly, liposome therapeutics described above that cause complement activation are PEGylated). The effective solution to this problem would be to formulate the agent without a substantial content of electrostatically charged components, which may be easily achievable for most of the particle systems by careful choice of ligands, coupling chemistries, and coupling anchors.

Concerns regarding immune response to targeted particles, i.e., development of antibodies against targeting ligands (such as full size antibody molecules) and other microbubble shell components, have been evaluated for liposome-based drug carrier systems and should not be very different for the targeted ultrasound contrast particles (*35*). The use of humanized/human antibodies, small antibody fragments, and small molecule ligands is expected to minimize development of secondary antibodies in patients. Monitoring of this issue will ensure safety of repeated clinical application of targeted contrast ultrasound particles.

The presence of gas bubbles may enhance the bioeffects generated by ultrasound (*36*). In clinical practice, the intensity of ultrasound radiation transmitted into the body of the patient by the transducer of the imaging system is strictly controlled and limited; mechanical index (MI) and thermal index quotients are constantly computed and restricted by the equipment according to applicable FDA guidelines (*37*). In vitro and in animal studies it has been shown that in certain conditions, a combination of microbubbles and ultrasound may cause RBC hemolysis (*38*), enhance transfection (a term "Sonoporation" was even coined (*39*)), and in some instances result in the rupture of microvasculature and formation of miniature petechial hemorrhages (*40*) that may actually be applied for enhancement of angiogenesis (*41*) and for drug delivery (*42*). The perceived degree, potential practical importance, and alleged dangers of the ultrasound bioeffects vary. Regarding hemolysis, even if we assume that a billion injected bubbles would in a worst-case scenario damage a billion RBCs (<0.3 mL of blood), the amount of released hemoglobin would be comparable with the background free hemoglobin normally present in blood. Regarding tissue and vascular wall damage, to achieve substantial petechia formation, several parameters of the studies had to be brought to certain levels at the same time. In some animal studies, the skin barrier had to be removed to achieve vascular bioeffects (therefore, we may expect that even a modest degree of attenuation by the tissues in the body would suppress capillary rupture). Microbubble concentration in the blood in those animal studies sometimes was orders of magnitude higher than used in clinic (*40*−*42*). In concurrence to that, bioeffects did not manifest themselves unless lower frequency ultrasound (e.g., ∼1−2 MHz transmit) was applied at high MI (1.0 and above). Intermittent pulsing (1 frame/s) was found to cause petechia formation whereas continuous (30 frames/s) imaging did not (*43*); possibly, intermittent pulsing allowed the microbubbles to reach the capillaries, where size of microbubble is close to the size of vascular lumen and bubble expansion in the sound field may cause maximal effect on the vessel wall. Ultrasound bioeffects at higher frequencies were generally suppressed. Care should be therefore taken to avoid a combination of undesirable conditions (such as

high energy intermittent pulsing at low frequencies) during targeted ultrasound contrast imaging.

Overall, microbubble-based contrast agents are approved for clinical use in many countries; hundreds of thousands of patients have received ultrasound contrast material, and so far, reported side effects from numerous clinical trials have been quite rare (certainly less than manifested in case of X-ray contrast media). When we combine available side effect information with its applicability to targeted bubble imaging paradigm, we may assume that it is unlikely to become a major problem. For targeted imaging, circulating bubbles will be removed to reduce target-to-blood ratio; therefore, we may not expect significant damage to capillaries as observed for circulating bubbles. Low MI and higher frequency imaging will likely be used for detecting targeted bubbles; therefore, bioeffects are not likely to present a significant issue in the ultrasound contrast molecular imaging. It is important to continue in-depth research and monitoring efforts in the area of microbubble-mediated bioeffects, so that patient safety is assured.

Ultrasound Contrast Materials in Molecular Imaging Applications. The general upper limit for the size of an intravascular particulate contrast agent, several micrometers, roughly the same size as red blood cells, is defined by the diameter of capillaries. These micron-size bubble particles would not be able to escape the circulation and enter the extravascular space. Submicron bubbles are mostly not very stable and not very echogenic. Therefore, targeting of micron-size bubbles directed to the receptors on intravascular entities is the most acceptable strategy. Receptors of interest, upregulated on the inner surface of endothelial layer of the vasculature, include proteins from integrin and selectin families. For instance, P-selectin and ICAM-1 are known to be upregulated on the surface of activated endothelium in the tissue that is undergoing inflammatory processes; selectin and integrin upregulation is applied by the body to direct leukocyte accumulation and transmigration into these areas. Leukocyte size and behavior in the blood flow is similar to that of the microbubble contrast agent, so it can be expected that targeting of microbubbles can be as successful as targeting of leukocytes in nature. Indeed, when a monoclonal antibody against P-selectin was attached to the microbubble surface via a PEG spacer and biotin−streptavidin linker technique, selective accumulation of microbubbles in the areas of inflammation and ischemia-reperfusion injury of mouse kidneys was demonstrated by intravital microscopy and ultrasound imaging (*12*), very similar to leukocyte capture and accumulation in those areas. Similarly, anti-ICAM-1 monoclonal antibody attached to the same biotinylated bubbles directed them to the vasculature of rejecting hearts in a heterotopic rat heart transplant model (*44*). Anti-VCAM-1 antibody on the bubble surface directs them to atherosclerotic plaques in animal models (*45*).

This targeting strategy also proved successful for imaging the areas of angiogenesis, which is an important phenomenon defining the process of tumor growth and metastases development (*46*) or could be induced on purpose as a therapeutic procedure for the improvement of the blood flow to ischemic myocardium or other tissues and organs (*47*). Biotinylated antibody against $\alpha_V\beta_3$, or a biotinylated 5.4 KD RGD disintegrin peptide echistatin, coupled to biotinylated microbubbles by the same technique as above, resulted in selective accumulation of targeted bubbles, but not the control bubbles, in the area of elevated surface density of $\alpha_V\beta_3$ on vascular endothelium, such as angiogenesis in a matrigel plug mouse model (*48*) or a tumor growth area in a glioma model in nude rats (*49*). Successful targeting of microbubbles via covalently attached RGD peptides to activated platelets has also been achieved as an approach to blood clot imaging (*20*, *21*).

Overall, a successful clinically suitable targeted microbubble contrast agent is not going to be based on streptavidin−biotin coupling technology due to the need of multiple washes and the use of a foreign, possibly immunogenic protein (streptavidin) in the design; that approach is most appropriate and convenient for early proof-of-principle animal studies, where biotinylated ligands, such as antibodies of a wide variety are easily available commercially. Most of the available monoclonal antibodies are also immunogenic, due to their rat or mouse origin, and the variety of nonimmunogenic human antibodies is still limited. Furthermore, antibodies or other large proteins may be denatured in the harsh conditions of sonication and high shear during microbubble preparation and have to be attached to the preformulated microbubble agents. The preferred strategy would be to obtain small molecule ligands against the desired selectin and integrin targets and attach them to the bubbles via a direct chemical linking, preferably via a PEG spacer arm. Such high-affinity ligands (peptides or peptide mimetics) are becoming available via combinatorial synthesis and library screening methods. High affinity small molecules with nM level K_d have already been identified (*50*). As compared with an antibody with its ~150 kD molecular mass, these molecules are much smaller in size and should easily withstand the conditions of microbubble preparation without loss of binding affinity.

Another advantage of small molecule ligands over antibodies is in the kinetics of the attachment of ligand to receptor. Antibody active site structure is oftentimes designed as a pouch; it binds to the target receptor slowly and holds it firmly, with overall low equilibrium dissociation constant K_d, despite low kinetic k_{on}. Small ligands, on the other hand, can rapidly bind to the target with high k_{on}, which is a great advantage for a situation where a microbubble that flows through the vasculature and bumps into activated endothelium has a very limited time to attach to it. In nature, leukocytes apply PSGL-1, a fast k_{on} ligand with a sialylated sulfated 19-amino acid active site on its N-terminus, to achieve rapid binding to endothelium, resulting in leukocytes slow rolling through the vessels even in high shear flow (*51*). This ligand makes leukocytes as well as model polystyrene beads roll (and even firmly stick) onto endothelial cells that possess high enough surface density of P-selectin. The use of such small ligands (as simple as sialyl Lewis X, or a glycosulfopeptide described above) on the surface of microbubbles, especially in combination with coimmobilized slow k_{on} ligands (such as antibodies) will allow firm adhesion despite rapid blood flow in high wall shear stress conditions (*52*, *53*). A small ligand will provide initial slowdown of the bubbles so that the antibody will obtain a better chance to attach to the target antigen, thus retaining the microbubble on the target surface firmly. We need to note, however, that these elaborate designs might only be necessary for some of the intended targets located in the areas of exceptionally high shear flow (such as vulnerable plaque when accessed from the artery side). For many of the proposed targets, such as tumor vasculature with relatively slow blood flow, existing simple single-ligand designs may be sufficient for successful microbubble targeting and retention.

CONCLUSION

The winning design of a targeted ultrasound contrast agent will most likely be based on a small molecule ligand attached to the shell of a gas-filled microbubble. Preformulated microbubbles will be stable on storage. They will require only a short resuspension procedure prior to the administration to patients. The bubbles will most likely be PEGylated, to improve storage stability, achieve optimal circulation time, and reduce nonspecific background accumulation in normal nondiseased tissues. The injected dose of the material is going to be in submilligram level (of which the ligand will constitute micrograms, quite comparable with PET or SPECT targeted nuclear medicine agents). Due to low dosage and proper shell composition, the possibility of undesirable patient side effects will be eliminated. Current ultrasound imaging technologies and equipment allow excellent sensitivity of microbubble contrast detection in the target tissues, with the capability to count individual bubbles with picogram mass. Targeted ultrasound contrast will find widespread application for imaging, image-guided biopsy, and image-guided therapy of cancer, as well as application for monitoring the status of tissues subjected to ischemia, inflammation, or rejection of transplanted organs.

ACKNOWLEDGMENT

The author is grateful to J.R. Lindner, S. Kaul, K. Ley, and J. Rychak, University of Virginia Cardiovascular Division, Cardiovascular Research Center and Cardiovascular Imaging Center, for support, help, and exchange of ideas. Support (in part) via DOE 43-14702, NIH DK63508, HL64381, and EIF Foundation is acknowledged. Mallinckrodt Inc. (Hazelwood, MO) is acknowledged for the donation of laboratory equipment to University of Virginia so this research could continue at UVA.

LITERATURE CITED

(1) Blasberg, R. Molecular Imaging and Cancer. (2003) *Mol. Cancer Ther. 2*, 335−343.

(2) Leighton, T. G. (1997) *The Acoustic Bubble*, Academic Press, London.

(3) Lanza, G. M., Wallace, K. D., Scott, M. J., Cacheris, W. P., Abendschein, D. R., Christy, D. H., Sharkey, A. M., Miller, J. G., Gaffney, P. J., and Wickline, S. A. (1996) A novel site-targeted ultrasonic contrast agent with broad biomedical application. *Circulation 94*, 3334−3340.

(4) Alkan-Onyuksel, H., Demos, S. M., Lanza, G. M., Vonesh, M. J., Klegerman, M. E., Kane, B. J., Kuszak, J., and McPherson, D. D. (1996) Development of inherently echogenic liposomes as an ultrasonic contrast agent. *J. Pharm. Sci. 85*, 486-490.

(5) Fritz, T. A., Unger, E. C., Sutherland, and G., Sahn, D. (1997) Phase I clinical trials of MRX-115. A new ultrasound contrast agent. *Invest. Radiol. 32*, 735−740.

(6) Meza, M., Greener, Y., Hunt, R., Perry, B., Revall, S., Barbee, W., Murgo, J, P., and Cheirif, J. (1996) Myocardial contrast echocardiography: reliable, safe, and efficacious myocardial perfusion assessment after intravenous injections of a new echocardiographic contrast agent. *Am. Heart J. 132*, 871−881.

(7) Nanda, N. C., Wistran, D. C., Karlsberg, R. P., Hack, T. C., Smith, W. B., Foley, D. A., Picard, M. H., and Cotter, B. (2002) Multicenter evaluation of SonoVue for improved endocardial border delineation. *Echocardiography 19*, 27−36.

(8) Klibanov, A. L., Rasche, P. T., Hughes, M. S., Wojdyla, J. K., Galen, K. P., Wible, J. H. Jr., and Brandenburger, G. H. (2002) Detection of individual microbubbles of an ultrasound contrast agent: fundamental and pulse inversion imaging. *Acad. Radiol. 9*, Suppl 2, S279−S281.

(9) Huang, S. L., Hamilton, A. J., Pozharski, E., Nagaraj, A., Klegerman, M. E., McPherson, D. D., and MacDonald, R. C. (2002) Physical correlates of the ultrasonic reflectivity of lipid dispersions suitable as diagnostic contrast agents. *Ultrasound Med. Biol. 28*, 339−348.

(10) Coussios, C. C., Holland, C. K., Jakubowska, L., Huang, S. L., MacDonald, R. C., Nagaraj, A., and McPherson, D. D. (2004) In vitro characterization of liposomes and Optison by acoustic scattering at 3.5 MHz. *Ultrasound Med. Biol. 30*, 181−190.

(11) Klibanov, A. L., Rasche, P. T., Hughes, M. S., Wojdyla, J. K., Galen, K. P., Wible, J. H., Jr., and Brandenburger, G. H. (2004) Detection of individual microbubbles of ultrasound contrast agents: imaging of free-floating and targeted bubbles. *Invest. Radiol. 39*, 187−95.

(12) Lindner, J. R., Song, J., Christiansen, J., Klibanov, A. L., Xu, F., and Ley, K. (2001) Ultrasound assessment of inflammation and renal tissue injury with microbubbles targeted to P-selectin. *Circulation 104*, 2107−2112.

(13) Gramiak, R., Shah, P. M., and Kramer, D. H. (1969) Ultrasound cardiography: contrast studies in anatomy and function. *Radiology 92*, 939−948.

(14) Feinstein, S. B., Lang, R. M., Dick, C., Neumann, A., Al-Sadir, J., Chua, K. G., Carroll, J., Feldman, T., and Borow, K. M. (1988) Contrast echocardiography during coronary arteriography in humans: perfusion and anatomic studies. *J. Am. Coll. Cardiol. 11*, 59−65.

(15) Bokor, D., Chambers, J. B., Rees, P. J., Mant, T. G., Luzzani, F., and Spinazzi, A. (2001) Clinical safety of SonoVue, a new contrast agent for ultrasound imaging, in healthy volunteers and in patients with chronic obstructive pulmonary disease. *Invest. Radiol. 36*, 104−109.

(16) Klibanov, A. L. (2002) Ultrasound contrast agents: development of the field and current status. In *Topics In Current Chemistry v.222* (*Contrast Agents II)* (Krause, W., Ed.) pp 73−106, Springer-Verlag, Berlin.

(17) Chiang, C. W., Lin, F. C., Fu, M., Fang, B. R., Hsu, T. S., and Lee, Y. S. (1986) Importance of adequate gas-mixing in contrast echocardiography. *Chest 89*, 723−726.

(18) Klibanov, A. L., Gu, H., Wojdyla, J. K., Wible, J. H., Ki, D. H., Needham, D., Villanueva, F. S., and Brandenburger, G. H. (1999) Attachment of ligands to gas-filled microbubbles via PEG spacer and lipid residues anchored at the interface. *Proceedings of 26th International Symposium on Controlled Release of Bioactive Materials*, pp 124−125, Controlled Release Society, Boston.

(19) Tardy, I., Pochon, S., Theraulaz, M., Nanjappan, P., and Schneider, M. (2002) In vivo ultrasound imaging of thrombi using a target-specific contrast agent. *Acad. Radiol. 9*, Suppl 2, S294−S296.

(20) Wu, Y., Unger, E. C., McCreery, T. P., Sweitzer, R. H., Shen, D., Wu, G., and Vielhauer, M. D. (1998) Binding and lysing of blood clots using MRX-408. *Invest. Radiol. 33*, 880−885.

(21) Schumann, P. A., Christiansen, J. P., Quigley, R. M., McCreery, T. P., Sweitzer, R. H., Unger, E. C., Lindner, J. R., and Matsunaga, T. O. (2002) Targeted-microbubble binding selectively to GPIIb IIIa receptors of platelet thrombi. *Invest. Radiol. 37*, 587−593.

(22) Villanueva, F. S., Jankowski, R. J., Klibanov, S., Pina, M. L., Alber, S. M., Watkins, S. C., Brandenburger, G. H., and Wagner, W. R. (1998) Microbubbles targeted to intercellular adhesion molecule-1 bind to activated coronary artery endothelial cells. *Circulation 98*, 1−5.

(23) Hermanson G. (1996) *Bioconjugate Techniques*, Academic Press, San Diego.

(24) Bogdanov, A. A. Jr., Klibanov, A. L., and Torchilin, V. P. (1988) Protein immobilization on the surface of liposomes via carbodiimide activation in the presence of N-hydroxysulfosuccinimide. *FEBS Lett.*, *231*, 381−384.

(25) Kirpotin, D., Park, J. W., Hong, K., Zalipsky, S., Li, W. L., Carter, P., Benz, C. C., and Papahadjopoulos, D. (1997) Sterically stabilized anti-HER2 immunoliposomes: design and targeting to human breast cancer cells in vitro. *Biochemistry 36*, 66−75.

(26) Gregory J. D. (1955) The stability of *N*-ethylmaleimide and its reaction with sulfhydryl groups, *J. Am. Chem. Soc*. *77*, 3922−3923.
(27) Kim, D. H., Klibanov, A. L., and Needham, D., (2000) The Influence of Tiered Layers of Surface-grafted Poly(ethylene glycol) on Receptor−ligand-mediated Adhesion Between Phospholipid Monolayer-stabilized Microbubbles and Coated Glass Beads. *Langmuir 16*, 2808−2817.
(28) Schneider M. (1999) Characteristics of SonoVue. *Echocardiography 16*, 743−746.
(29) Lindner, J. R., Coggins, M. P., Kaul, S., Klibanov, A. L., Brandenburger, G. H., and Ley, K. (2000) Microbubble persistence in the microcirculation during ischemia/reperfusion and inflammation is caused by integrin- and complement-mediated adherence to activated leukocytes. *Circulation*, *101*, 668−675.
(30) Villanueva, F. S., Jankowski, R. J., Manaugh, C., and Wagne, r W. R. (1997) Albumin microbubble adherence to human coronary endothelium: implications for assessment of endothelial function using myocardial contrast echocardiography. *J. Am. Coll. Cardiol. 30*, 689−693.
(31) Fisher, N. G., Christiansen, J. P., Klibanov, A., Taylor, R. P., Kaul, S., and Lindner, J. R. (2002) Influence of microbubble surface charge on capillary transit and myocardial contrast enhancement. *J. Am. Coll. Cardiol. 40*, 811−819.
(32) Lindner, J. R., Song, J., Xu, F., Klibanov, A. L., Singbartl, K., Ley, K., and Kaul, S. (2000) Noninvasive ultrasound imaging of inflammation using microbubbles targeted to activated leukocytes. *Circulation 102*, 2745−2750.
(33) Szebeni, J., Baranyi, L., Savay, S., Milosevits, J., Bunger, R., Laverman, P., Metselaar, J. M., Storm, G., Chanan-Khan, A., Liebes, L., Muggia, F. M., Cohen, R., Barenholz, Y., and Alving, C. R. (2002) Role of complement activation in hypersensitivity reactions to doxil and hynic PEG liposomes: experimental and clinical studies. *J. Liposome Res. 12*, 165−172.
(34) Koukourakis, M. I., Koukouraki, S., Giatromanolaki, A., Archimandritis, S. C., Skarlatos, J., Beroukas, K., Bizakis, J. G., Retalis, G., Karkavitsas, N., and Helidonis, E. S. (1999) Liposomal doxorubicin and conventionally fractionated radiotherapy in the treatment of locally advanced nonsmall-cell lung cancer and head and neck cancer. *J. Clin. Oncol. 17*, 3512−3521.
(35) Harding, J. A., Engbers, C. M., Newman, M. S., Goldstein, N. I., and Zalipsky, S. (1997) Immunogenicity and pharmacokinetic attributes of poly(ethylene glycol)-grafted immunoliposomes. *Biochim. Biophys. Acta 1327*, 181−192.
(36) Miller, M. W., Miller, D. L., and Brayman, AA. (1996) A review of in vitro bioeffects of inertial ultrasonic cavitation from a mechanistic perspective. *Ultrasound Med. Biol. 22*, 1131−1154.
(37) Meltzer, R. S. (1996) Food and Drug Administration ultrasound device regulation: the output display standard, the "mechanical index," and ultrasound safety. *J. Am. Soc. Echocardiogr.* 9, 216−220.
(38) Williams, A. R., Kubowicz, G., Cramer E., and Schlief, R. (1991) The effects of the microbubble suspension SH U 454 (Echovist) on ultrasound-induced cell lysis in a rotating tube exposure system. *Echocardiography 8*, 423−433.
(39) Bao, S., Thrall, B. D., and Miller, D. L. (1997) Transfection of a reporter plasmid into cultured cells by sonoporation in vitro. *Ultrasound Med. Biol. 23*, 953−959.
(40) Miller, D. L, and Quddus, J. (2000) Diagnostic ultrasound activation of contrast agent gas bodies induces capillary rupture in mice. *Proc. Natl. Acad. Sci. U S A 97*, 10179−10184.
(41) Song, J., Qi, M., Kaul, S., and Price, R. J. (2002) Stimulation of arteriogenesis in skeletal muscle by microbubble destruction with ultrasound. *Circulation 106*, 1550−1555.
(42) Price, R. J., Skyba, D. M., Kaul, S., and Skalak, T. C. (1998) Delivery of colloidal particles and red blood cells to tissue through microvessel ruptures created by targeted microbubble destruction with ultrasound. *Circulation 98*, 1264−1267.
(43) Wible, J. H. Jr., Galen, K. P., Wojdyla, J. K., Hughes, M. S., Klibanov, A. L., and Brandenburger, G. H. (2002) Microbubbles induce renal hemorrhage when exposed to diagnostic ultrasound in anesthetized rats. *Ultrasound Med. Biol. 28*, 1535−1546.
(44) Weller, G. E., Lu, E., Csikari, M. M., Klibanov, A. L., Fischer, D., Wagner, W. R., and Villanueva, F. S. (2003) Ultrasound imaging of acute cardiac transplant rejection with microbubbles targeted to intercellular adhesion molecule-1. *Circulation 108*, 218−224.
(45) Davis, C. J., Christiansen, J. P., Klibanov, A. L., Sanders, J., Sarembock, I. J., and Lindner, J. R. (204). Microbubbles targeted to endothelial VCAM-1 adhere to atherosclerotic plaques at physiologic shear rates. *Circulation 108*, Suppl. S, 2837.
(46) Folkman, J. (2002) Role of angiogenesis in tumor growth and metastasis. *Semin. Oncol. 29*, Suppl 16, 15−18.
(47) Villanueva, F. S., Abraham, J. A., Schreiner, G. F., Csikari, M., Fischer, D., Mills, J. D., Schellenberger, U., Koci, B. J., and Lee, J. S. (2002) Myocardial contrast echocardiography can be used to assess the microvascular response to vascular endothelial growth factor-121. *Circulation 105*, 759−765.
(48) Leong-Poi, H., Christiansen, J., Klibanov, A. L., Kaul, S., and Lindner, J. R. (2003) Noninvasive assessment of angiogenesis by ultrasound and microbubbles targeted to alpha v -integrins. *Circulation 107*, 455−460.
(49) Ellegala, D. B., Leong-Poi, H., Carpenter, J. E., Klibanov, A. L., Kaul, S., Shaffrey, M. E., Sklenar, J., and Lindner, J. R. (2003) Imaging tumor angiogenesis with contrast ultrasound and microbubbles targeted to alpha v beta 3. *Circulation 108*, 336−341.
(50) Goodman, S. L., Holzemann, G., Sulyok, G. A., and Kessler, H. (2002) Nanomolar small molecule inhibitors for alpha V beta 6, alpha V beta 5, and alpha V beta 3 integrins. *J. Med. Chem. 45*, 1045−1051.
(51) Goetz, D. J., Greif, D. M., Ding, H., Camphausen, R. T., Howes, S., Comess, K. M., Snapp, K. R., Kansas, G. S., and Luscinskas, F. W. (1997) Isolated P-selectin glycoprotein ligand-1 dynamic adhesion to P- and E-selectin. *J. Cell Biol. 137*, 509−519.
(52) Weller, G. E., Tom, E. M., Felix, M. M., Wagne, W. R., and Villanueva, F. S. (2003) Multi-targeting enhances adhesion of ultrasound contrast microbubbles to inflammatory endothelium. *Circulation 108*, Suppl. S, 2355.
(53) Rychak, J. J., Klibanov, A. L., Leppanen, A., Cummings, R. D., and Ley, K. (2004) Enhanced binding of ultrasound contrast microbubbles targeted to P-selectin using a physiological capture ligand. *FASEB J. 18*, #331.23.

BC049898Y

COMMUNICATIONS

Improving the Integrity of Three-Dimensional Vascular Patterns by Poly(ethylene glycol) Conjugation

Sadhana Sharma,[†,§] Wei Tan,[‡,§] and Tejal A. Desai*[,∥]

Davis Heart & Lung Research Institute, The Ohio State University, Columbus, Ohio 43210, Beckman Institute, University of Illinois at Urbana−Champaign, Urbana, Illinois 61801, and Department of Biomedical Engineering, Boston University, Boston, Massachusetts 02215. Received May 16, 2004; Revised Manuscript Received August 16, 2004

Development of functional tissue-engineering constructs may require that multiple cell types be organized in controlled three-dimensional (3-D) microarchitectures with proper nutrient diffusion and vascularization. In the past few years, a variety of microscale techniques have demonstrated the ability to control protein and cell attachment in defined patterns. Nevertheless, maintenance of these patterns over time has been a significant challenge due to nonspecific protein adsorption and cell migration. To this end, we have investigated the effectiveness of poly(ethylene glycol) (PEG) thin films in maintaining the integrity of 3-D cellular patterns, using human umbilical vein endothelial cells (HUVEC) as a model system. These HUVEC constructs were created using extracellular matrix (ECM)-based microfluidic patterning. Our results indicated that PEG-conjugated substrates improve cell pattern integrity as compared to control silicon. The compliance multifactor (a measure of pattern integrity; higher value means lower pattern integrity) was about 3.66 ± 0.29 on day 5 for PEG-conjugated surfaces, compared with 8.23 ± 0.42 for control surfaces ECM-based microfluidic patterning coupled with stable PEG-conjugated surfaces may serve as a vital tool for vascularized tissue engineering.

INTRODUCTION

Damage or loss of an organ or tissue is one of the most frequent and costly problems in healthcare. Current treatment modalities include transplantation, surgical reconstruction, and mechanical devices such as kidney dialyzers. These therapies have revolutionized medical practice but have limitations. While transplantation is restricted by ever increasing donor shortage, mechanical devices cannot perform all the functions of a single organ, thus providing only temporary benefits (*1, 2*). The emerging and interdisciplinary field of tissue engineering offers to solve the organ transplantation crisis. The creation of functional tissue engineering constructs, however, requires the formation of well-defined biomimetic microenvironments that surround cells and promote controlled cell interactions, maintenance of three-dimensional (3-D) microarchitecture, and proper vascularization.

Vascularization is considered as the main technological barrier for building 3-D human organs, as effective organ perfusion is not possible without an endothelialized vascular tree (*3*). The extracellular matrix (ECM), serving as a natural scaffold and reservoir of signaling molecules in tissues, may provide 3-D biomimetic environments for proper growth of the cells, and hence vascularization. Chemical modifications of matrix components in vitro *may* allow ECM scaffolds to be tailored. Patterning of cells within a 3-D matrix provides an approach that allows for shifting from two-dimensional (2-D) patterned cell cultures to 3-D patterned "tissue"-like culture systems (*4, 5*).

Microfluidic patterning techniques provide ways to spatially control cells and design appropriate configurations of cells and materials for "engineered" products. Chiu et al. (2000) fabricated 3-D microfluidic systems and used them to pattern proteins and mammalian cells on a planar substrate. The channel structure, formed by a microstamp in contact with the surface of the substrate, limited migration and growth of the cells in the channels. Removal of the stamp, however, resulted in the spreading and growth of the different cell types (*6*). It was realized that nonselective adhesion and cell migration were the major reasons for the collapse of these patterns over time.

While the problem of long-term maintenance of 2-D cell patterns created using microcontact printing has been previously addressed, the stability of 3-D cellular patterns remains unexplored (*4*). We previously investigated the pattern integrity of 3-D micropatterns created using microfluidic patterning. Since the ECM naturally stabilizes tissue architecture in vivo (*7*), we used ECM components in microfluidic patterning for better main-

* Correspondence to T. A. Desai, Department of Biomedical Engineering, Boston University, 44 Cummington St., Boston, MA 02215. Tel: 617 358-3054; Fax: 617-353-6766; email: tdesai@bu.edu.

[†] The Ohio State University.

[‡] University of Illinois at Urbana−Champaign.

[∥] Boston University.

[§] Both authors contributed equally to this work.

10.1021/bc049885k CCC: $30.25 © 2005 American Chemical Society
Published on Web 11/06/2004

tenance of pattern integrity. We also demonstrated that the chemical addition of matrix components in vitro would allow the ECM scaffolds to be tailored for superior maintenance of HUVEC patterns (*4*). This method improved the integrity of 3-D HUVEC patterns on Petri dish for a period of two weeks.

PEGs are known for their ability to prevent protein adsorption and cellular adhesion (*8, 9*). Therefore, the use of covalently coupled and stable PEG films may be useful for the modification of surfaces for 3-D ECM microfluidic patterning. This may facilitate improved control over cell proliferation and migration and, in turn, pattern maintenance for longer durations. Previously, Branch et al. (2000) used PEG thin films as a background for 2-D neural patterning. However, these films degraded over time (<4 weeks) resulting in the loss of pattern (*10, 11*). In this study, we investigate the usefulness of PEG conjugation for maintaining the integrity of 3-D HUVEC patterns created using microfluidic patterning. The PEG films used in this study were developed using a one-step covalent coupling procedure (*12*). These PEG films were characterized and investigated for their stability over time (up to 4 weeks) (*13, 14*). Results suggested that these PEG thin films were effective in controlling protein and cell adhesion for the period investigated. In the present research effort, we have examined the effectiveness of PEG thin films in maintaining the integrity of 3-D HUVEC patterns. These HUVEC patterns were created using ECM-based microfluidic patterning with a collagen matrix.

MATERIALS AND METHODS

Preparation and Characterization of PEG-Conjugated Silicon Substrates. PEG-conjugated silicon substrates were created using a one-step covalent coupling procedure. This reaction scheme involves synthesis of PEG-$OSiCl_3$ (called PEG-silane) by reacting PEG with silicon tetrachloride in the presence of triethylamine (catalyst), followed by direct coupling of PEG-silane to a hydrophilized silicon surface. In the present study, PEG (MW: 1000) was coupled to 3-in. silicon wafers (⟨100⟩) using 10 mM of PEG concentration for 1 h. Ellipsometry, contact angle measurement, X-ray photoelectron spectroscopy (XPS), and atomic force microscopy (AFM) were used to analyze the PEG-conjugated surfaces. The details of this procedure have been described elsewhere (*12*).

Cell Culture and Microfluidic ECM-HUVEC Patterning. HUVECs (BioWhittaker, Walkersville, MD) were maintained in endothelial growth medium (BioWhittaker) containing 2% FBS, 2 mL of human fibroblast growth factor (hFGF−B), 0.2 mL of hydrocortisone, 0.5 mL of vascular endothelial growth factor (VEGF), 0.5 mL of human recombinant insulin-like growth factor (R3−IGF-1), 0.5 mL of ascorbic acid, 0.5 mL of human epidermal growth factor (hEGF), 0.5 mL of gentamicin-amphotericin B (GA-1000), and 0.5 mL of heparin in every 500 mL of endothelial basal medium. Cells with passage 3−8 were used in the experiments.

Collagen matrix was used in these experiments to create 3-D HUVEC patterns. This method involves microfluidic patterning of 3-D biopolymer matrices to provide microscale control over cellular microenvironments. The method of preparing prepolymer solution of collagen matrix has been described in detail elsewhere (*15*). The techniques of cell microfluidic patterning have also been demonstrated previously (*6*). Similar procedures were used in this study to pattern HUVECs. For injection, a 1-cm^3 syringe was used, but the needle was replaced with a smaller 26 gauge needle to fit the inner diameter of the tubing. To pattern cell-ECM assemblies, cell-ECM solutions were prepared. The concentration of cells without and within ECM solutions was 1×10^6 cells/mL. First a prepolymer solution, which polymerizes at 37 °C, was prepared on ice and then mixed with the cell suspension just before microfuidic delivery. The control and PEG-conjugated wafers were then immersed in water for 30 min and sterilized by immersion in 70 vol % ethanol for 20 min. Subsequently, they were rinsed in sterile deionized water and dried inside a sterile hood. HUVEC-ECM assemblies were then patterned into a straight microchannel using a PDMS mold (prepared as described in (*4*)). Figure 1 shows a schematic of the microfluidic patterning technique used in this study.

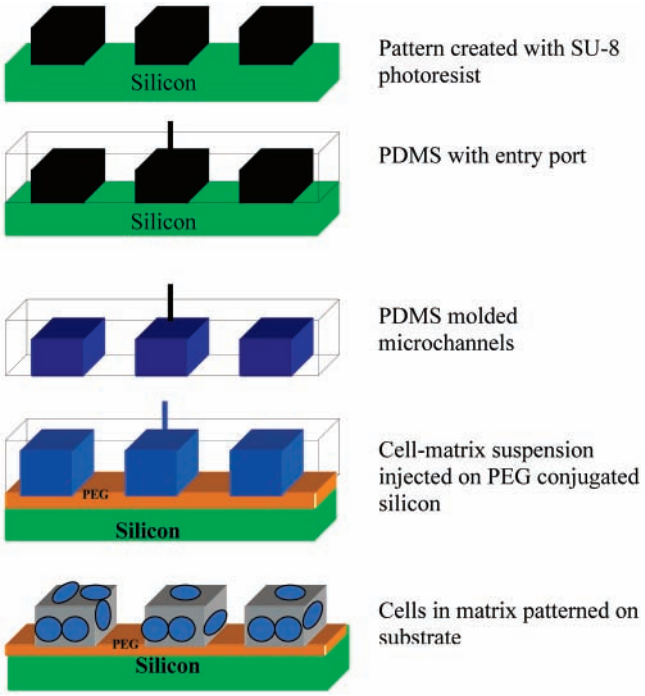

Figure 1. Schematic diagram for microfluidic cellular patterning.

For quantitative assessment of cell spreading, samples were monitored daily for 5 days after removing the PDMS template. Light microscopy was used to acquire images of cells and cell-matrices. Image-Pro Plus software (Media-Cybernetics, Carlsbad, CA) was used for image analysis. Matrix size, spreading area, and cell migration distance were measured by the software tools. In this study, the compliance multifactor was defined as the patterned cell area at time = t over the original patterned cell area at time = 0. Analysis of variance (ANOVA) was used to evaluate the results of compliance multifactor. The significance levels of the experimental data were analyzed with Microsoft (Redmond,WA) Excel.

RESULTS AND DISCUSSION

Surface Characterization of PEG-Conjugated Silicon Substrates. The thickness of PEG films was determined using variable-angle ellipsometry and was found to be 20 ± 0.93 Å. The hydrophilicity/hydrophobicity of the surface was determined by measuring water contact angle in air using the HALF-ANGLE measuring technique by a contact angle goniometer (Tantec Inc., Schaumburg, IL) before and after PEG-conjugation (Table 1). Surfaces with contact angles in the range of 20−60° are generally considered to be hydrophilic and show more

Table 1. Surface Properties of Control Silicon and PEG-Conjugated Silicon Substrates

			surface composition[a] (%)					protein adsorption (ng cm^{-2})	
	film thickness (Å)	contact angle (deg)	C	O	Si	C−O	R_{rms} (nm)	fibrinogen	albumin
silicon	-	<6	13.2	54.2	32.5	0	0.18	751.63 ± 24.94	602.25 ± 16.20
PEG	20.0 ± 0.93	41.7 ± 1.1	21.6	31.8	46.4	66.62	0.68	138.66 ± 32.39	63.79 ± 29.90

[a] For a take-off angle of 65°, defined as the angle spanned by the electron path to the analyzer and the surface of the sample.

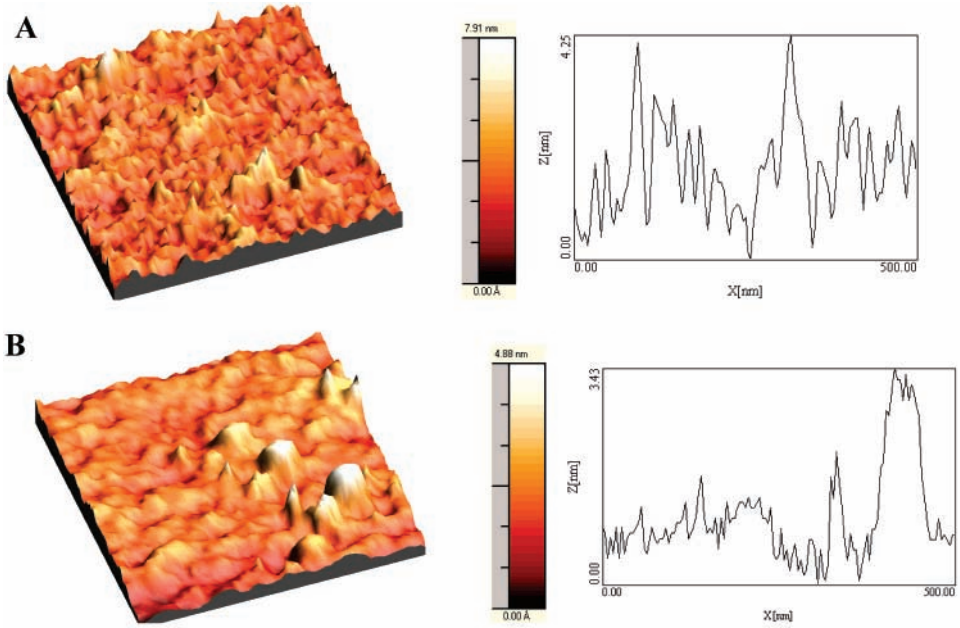

Figure 2. 3-D AFM images and corresponding section plots of 500 nm scans for fibrinogen adsorption on (a) clean silicon, (b) PEG-conjugated silicon.

resistance to protein adsorption and cell adhesion. The water contact angle for these PEG films was ~42°, suggesting their hydrophilic nature. The presence of PEG on silicon surfaces was verified using XPS. Survey spectra, and high-resolution spectra of Si2p and C1s core levels were taken on silicon surfaces before and after conjugation of PEG. The XPS analysis demonstrated an increase in carbon and oxygen content, and a decrease in silicon concentration for the PEG-modified surface (Table 1). An increase in the intensity of the C−O peak in high-resolution C1s spectra further confirmed the presence of PEG on silicon substrate. Surface topography and uniformity of clean and PEG-conjugated surfaces were examined using a tapping mode AFM. The roughness of the surface was assessed by measuring the roughness parameter, R_{rms} (root-mean-square roughness). R_{rms} is defined as the root-mean-square average of the height (h) deviations taken from the mean data plane. It is expressed as: $R_{rms} = \sqrt{(1/N)\sum_{i=1}^{N}(h_i - \bar{h})^2}$. Here, h_i is the current height value, $\bar{h}$ is the height of the mean data plane, and N is the number of points within the box cursor. Table 1 shows RMS roughness parameters for control and PEG-conjugated silicon surfaces. Furthermore, PEG-conjugated silicon substrates were analyzed for their antifouling abilities using albumin and fibrinogen as model proteins. There was an approximately 80% reduction in fibrinogen adsorption and 90% reduction in albumin adsorption on PEG-conjugated surfaces (Table 1). The topography of fibrinogen-adsorbed control and PEG-conjugated surfaces was also examined using AFM. Figure 2 shows 3-D and section plots for 500 nm size scans of protein-adsorbed control and PEG-conjugated silicon. Irregularly defined and nonuniformly distributed peaks were seen in the 3-D image and section plot of protein on PEG-conjugated surfaces compared to control silicon surfaces. A closer examination of the section plots of control and PEG-conjugated surfaces indicated that protein was evenly adsorbed on control silicon surface as compared to random adsorption on PEG-conjugated surfaces. Detailed characterization of these surfaces is described elsewhere (*13*).

HUVEC-ECM Pattern Integrity on Control and PEG-Conjugated Silicon Substrates. Pattern integrity is defined here as the ability of cells to stay in the position where they were originally patterned. It is similar to the notion of pattern compliance which has been used elsewhere (*10, 11*), except that in this study it refers to a 3-D system. To examine the efficacy of PEG in maintaining pattern integrity, first ⟨100⟩ silicon wafers were coated with PEG as described earlier. The change in cellular micropattern width over time was used to evaluate pattern integrity. The width of the cell pattern was determined by drawing two parallel lines as the borders between which most of the cells (>95%) are located, neglecting outliers beyond the borderlines. In our previous paper (*4*), we investigated the influence of the channel size on the compliance and, therefore, defined compliance multifactor as the patterned cell area at time t over the original patterned cell area at $t = 0$, divided by channel size in order to eliminate that factor in the final compliance multifactor value. In this study, the compliance multifactor was defined as the patterned cell area at time = t over the original patterned cell area at time = 0. Smaller values of compliance multifactor mean better maintenance of the pattern i.e., greater pattern integrity. Cell number was estimated from micrograph image areas of 1 mm^2.

Figure 3 shows the results for the HUVEC-ECM patterns created on unmodified and PEG-modified silicon. The cells patterned on PEG-conjugated substrates

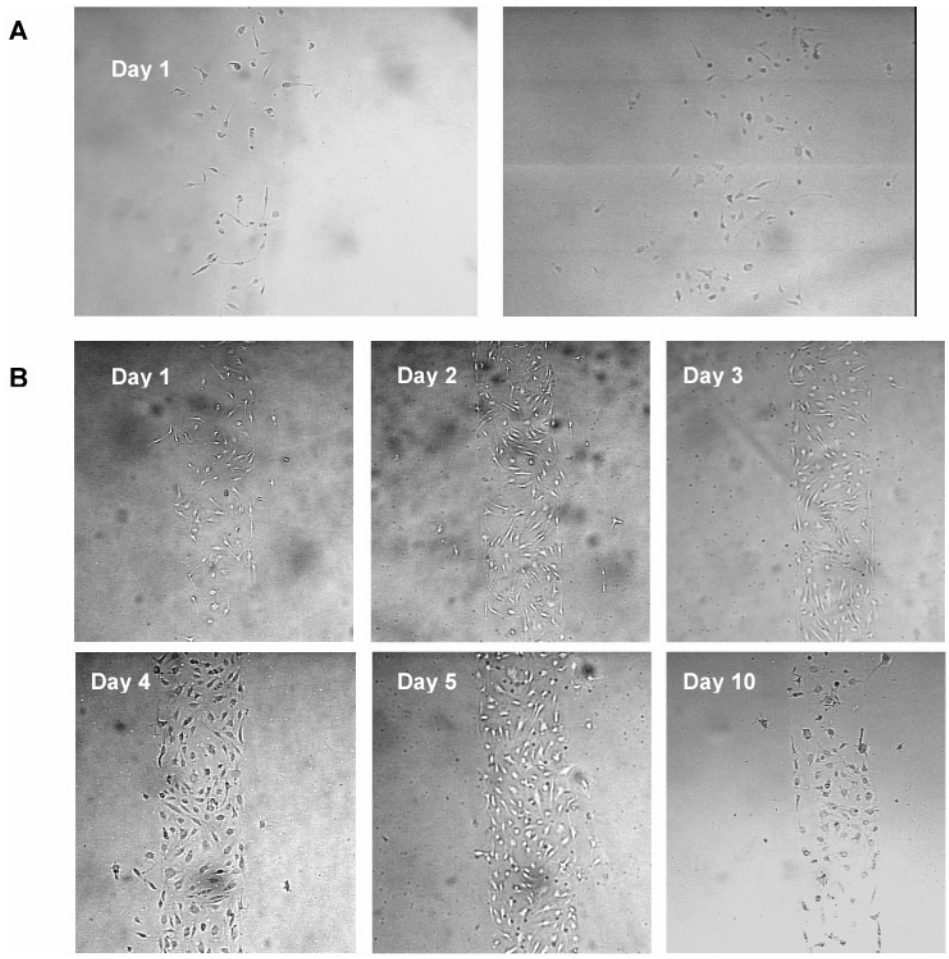

Figure 3. (A) Control silicon: pictures of cells cultured for 1−2 days. After 3 days, we had to take two frames to add images up to get the compliance multifactor; (B) PEG conjugated silicon: pictures of cells cultured for 1−5 days and day 10. After 10-day culture, cells apoptosized due to the overconfluency in the channel area.

displayed greater compliance with the original pattern, with a slower rate of pattern loss in the first 5 days of culture as compared to control silicon. For control silicon substrates, images from two frames were taken to obtain the compliance multifactor after 3 days. Cell migration and proliferation contribute to the loss of a cellular pattern over time. As compared to our previous study, here we used a different type of substrate, i.e., silicon instead of Petri dish. Because of the limited size of the silicon piece we used and higher compliance multifactor on the silicon piece than that on the dish surface, we could only follow the changes in control silicon sample till day 6 as compared to two weeks on Petri dish. While the compliance multifactor continued to increase for cells patterned on bare silicon, its value begins to plateau for PEG-conjugated silicon. On day 5, the compliance multifactor was about 3.66 ± 0.29 for PEG-conjugated surfaces, compared with 8.23 ± 0.42 for control silicon surfaces (Figure 4). Lower values of compliance multifactor for PEG-conjugated surfaces indicate the superior ability of PEG to maintain cell patterns for the period investigated.

In this study, we combined three different approaches: microfluidic patterning for spatial control, collagen matrix materials for chemical/ material control, and PEG in order to improve the pattern integrity. This model may also be useful for providing quantitative measurements of cell−matrix interactions, and eventually generating tissue-like structures in vitro. Our previous studies indicated that the modified collagen

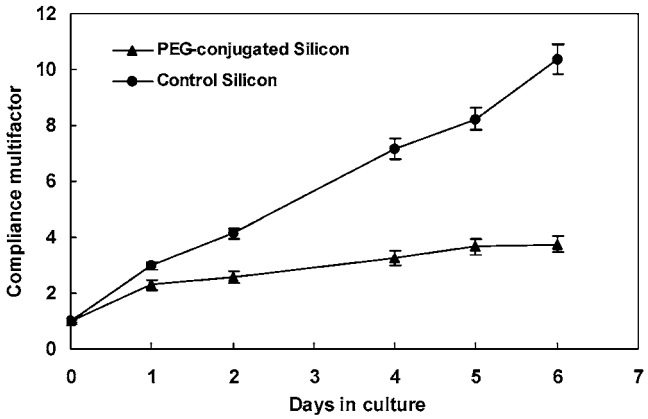

Figure 4. Compliance multifactor of HUVEC on control silicon and PEG-conjugated silicon wafers.

(collagen−chitosan or collagen−chitosan−fibronectin) matrices maintain cell pattern integrity better than the collagen-only matrix (*4*). Our future studies would, therefore, be directed toward combining modified collagen matrices with PEG-conjugated substrates to achieve compliance multifactor values (∼1) suitable for long-term culture.

ACKNOWLEDGMENT

This work was funded by the Whitaker Foundation and the National Science Foundation (ECS-9820829).

LITERATURE CITED

(1) Langer, R., and Vacanti, J. P. (1993) Tissue engineering. *Science 260*, 920.
(2) Niklason, L. E., and Langer, R. (2001) Prospects for organ and tissue replacement. *JAMA 285* (5), 573−576.
(3) Borenstein, J. T., Terai, H., King, K. R., Weinberg, E. J., Kaazempur-Mofrad, M. R., and Vacanti, J. P. (2002) *Biomed. Microdev. 4* (3), 167−175.
(4) Tan, W., and Desai, T. A. (2003) Microfluidic Patterning of cells in extracellular matrix biopolymers: Effects Of Channel Size, Cell Type, and Matrix Composition on Pattern Integrity. *Tissue Eng. 9* (2), 255−267.
(5) Tan, W., and Desai, T. A. (2003) Microfluidic Patterning of cellular biopolymer matrices for biomimetic 3-D structures. *Biomed. Microdev. 5* (3), 235−244.
(6) Chiu, D. T., Jeon, N. L., Huang, S., Kane, R. S., Wargo, C. J., Choi, I. S., Ingber, D. E., and Whitesides, G. M. (2000) Patterned deposition of cells and proteins onto surfaces by using three-dimensional microfluidic systems. *Proc. Natl. Acad. Sci. U.S.A. 97*, 2408−2413.
(7) Alberts, B., Bray, D., Lewis, J., Raff, M., Roberts, K., and Watson, J. (1994) *Molecular Biology of Cells*, Garland Publishing, New York.
(8) Harris, J. M. (Ed.) (1992) *Poly(ethylene glycol) Chemistry: Biotechnical and Biomedical Applications*. Plenum. New York.
(9) Sharma, S., Popat, K. C., and Desai, T. A. (2003). Nanostructured non-fouling films for BioMEMS applications, in *Handbook of nanostructured biomaterials and their applications* (Nalwa, H. S., Ed.) Academic Press, San Diego (invited chapter, in press).
(10) Branch, D. W., Wheeler, B. C., Brewer, G. J., and Leckband, D. E. (2000) Long-term maintenance of patterns of hippocampal pyramidal cells on substrates of poly(ethylene glycol) and microstamped polylysine. *IEEE Trans Biomed Eng. 47* (3), 290−300.
(11) Branch, D. W., Wheeler, B. C., Brewer, G. W., and Leckband, D. E. (2001) Long-term stability of grafted polyethyleneglycol surfaces for use with microstamped substrates in neuronal cell culture. *Biomaterials 22*, 1035−1047.
(12) Sharma, S., Johnson, R. W., and Desai, T. A. (2003) Ultrathin poly(ethylene glycol) films for silicon-based microdevices. *Appl. Sur. Sci. 206* (1−4), 218−229.
(13) Sharma, S., Popat, K. C., and Desai, T. A. (2002) Controlling non-specific protein interactions in silicon bio-microsystems with poly(ethylene glycol) films. *Langmuir 18* (23), 8728−8731.
(14) Sharma, S., Johnson, R. W., and Desai, T. A. (2004) Evaluation of the stability of nonfouling ultrathin poly(ethylene glycol) films for silicon-based microdevices. *Langmuir 20* (2), 348−356.
(15) Tan, W., Krishnaraj, R., and Desai, T. A. (2001) Effects of chitosan on cell viability and proliferation in three-dimensional collagen gels. *Tissue Eng. 7*, 203−210.

BC049885K

Human Serum Albumin Bearing Covalently Attached Iron(II) Porphyrins as O_2-Coordination Sites

Rong-Min Wang,[†,‡] Teruyuki Komatsu,[†] Akito Nakagawa,[†] and Eishun Tsuchida*[,†]

Advanced Research Institute for Science and Engineering, Waseda University, 3-4-1 Okubo, Shinjuku-ku, Tokyo 169-8555, Japan, and Institute of Polymer, Northwest Normal University, Lanzhou 730070, China . Received June 17, 2004; Revised Manuscript Received September 25, 2004

Tetrakis{(α,α,α,α-*o*-pivalamido)phenyl}porphinatoiron(II) with a bifunctional tail possessing an axially coordinated imidazolyl group and a protein attachable succinimidyl(glutamyl) group (FeP-GluSu) has been synthesized. It can efficiently react with the lysine residues of recombinant human serum albumin (rHSA), giving a new albumin−heme conjugate [rHSA(FeP-Glu)]. MALDI-TOFMS showed a distinct molecular ion peak at *m/z* 70 643, which indicates that three FeP-Glu molecules were covalently linked to the rHSA scaffold. The binding number of FeP-Glu is approximately three (mol/mol) and independent of the mixing ratio. The CD spectrum and Native PAGE revealed that the albumin structure remained unaltered after the covalent bonding of the hemes. This rHSA(FeP-Glu) conjugate can bind and release O_2 reversibly under physiological conditions (pH 7.3, 37 °C) in the same manner as hemoglobin and myoglobin. The O_2-adduct complex had a remarkably long lifetime ($\tau_{1/2}$: 5 h). The O_2-binding affinity [$P_{1/2}^{O_2}$: 27 Torr] was identical to that of human red cells. Laser flash photolysis experiments gave the O_2- and CO-association rate constants and suggested that there are two different geometries of the imidazole binding to the central ion.

Human serum albumin (HSA), which is the major plasma protein component in our bloodstream, has no prosthetic group; however it nonspecifically captures many endogenous and exogenous compounds by weak interactions, *e.g.,* H-bond, ionic attraction, and hydrophobic interaction, namely noncovalent bonds (*1*−*3*). Synthetic heme, 2-[{8-*N*-(2-methylimidazolyl)octanoyl}-oxy]methyl-5,10,15,20-tetrakis{(α,α,α,α-*o*-pivalamido)-phenyl}porphinatoiron(II) (FeP, Chart 1 a) is also incorporated into recombinant HSA (rHSA), and the obtained albumin−heme (rHSA-FeP) hybrid can reversibly coordinate O_2 under physiological conditions (pH 7.3, 37 °C) (*4*). This O_2-carrying plasma hemoprotein could be of medical importance as a blood replacement composition (*4e*−*g*). Nevertheless, the major driving force of the heme-binding to albumin is a hydrophobic interaction; therefore, its binding constants (10^4−10^6 M^{-1}) are not high enough to maintain the heme concentration in the circulatory system for a long period (*4a*). The administration of the albumin−heme hybrid solution into rats demonstrated that the lifetimes of the heme was less than 6 h (*4e, 5*). To immobilize the heme group to the albumin scaffold more tightly and retain its O_2-transport efficacy, we have combined the O_2-coordination site FeP to the rHSA structure through a covalent bond. In this communication, we report, for the first time, the synthesis of a novel FeP analogue with a bifunctional branched-tail including an axially coordinated imidazolyl group and a protein-attachable succinimidyl(glutamyl) group (FeP-GluSu, Chart 1 a), and the properties of the rHSA conjugate bearing covalently linked FeP-Glu as a new O_2-carrying hemoprotein.

Chart 1. (a) 5,10,15,20-Tetrakis{(α,α,α,α-*o*-pivalamido)-phenyl}porphinatoiron Derivatives with a Bifunctional Tail Group. (b) Space-Filling Representation of the Oxygenated FeP-GluSu by Insight II (see ref 11)

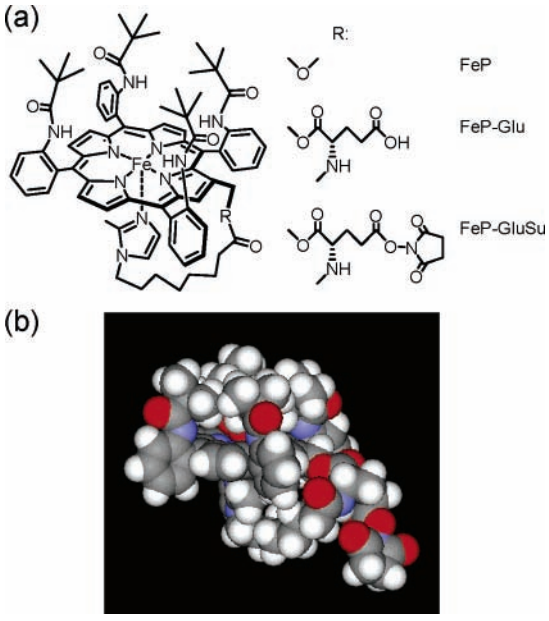

As a functional side-chain of FeP, which directly makes a covalent bond to rHSA, we selected the succinimidyl group, because it selectively reacts with the NH_2 group of lysine in the range of pH 6.3−8.6 with high yield. The branched tail that includes the imidazolyl and succnimidyl groups via a glutamate junction was introduced into the parent porphyrin **1** (*6*) as shown in Scheme 1 (*7*).

* Corresponding author. Phone: +81 3-5286-3120. Fax: +81-3-3205-4740. E-mail: eishun@waseda.jp.
† Waseda University.
‡ Northwest Normal University.

10.1021/bc049859m CCC: $30.25 © 2005 American Chemical Society
Published on Web 11/12/2004

Scheme 1. Synthetic Scheme of FeP-GluSu

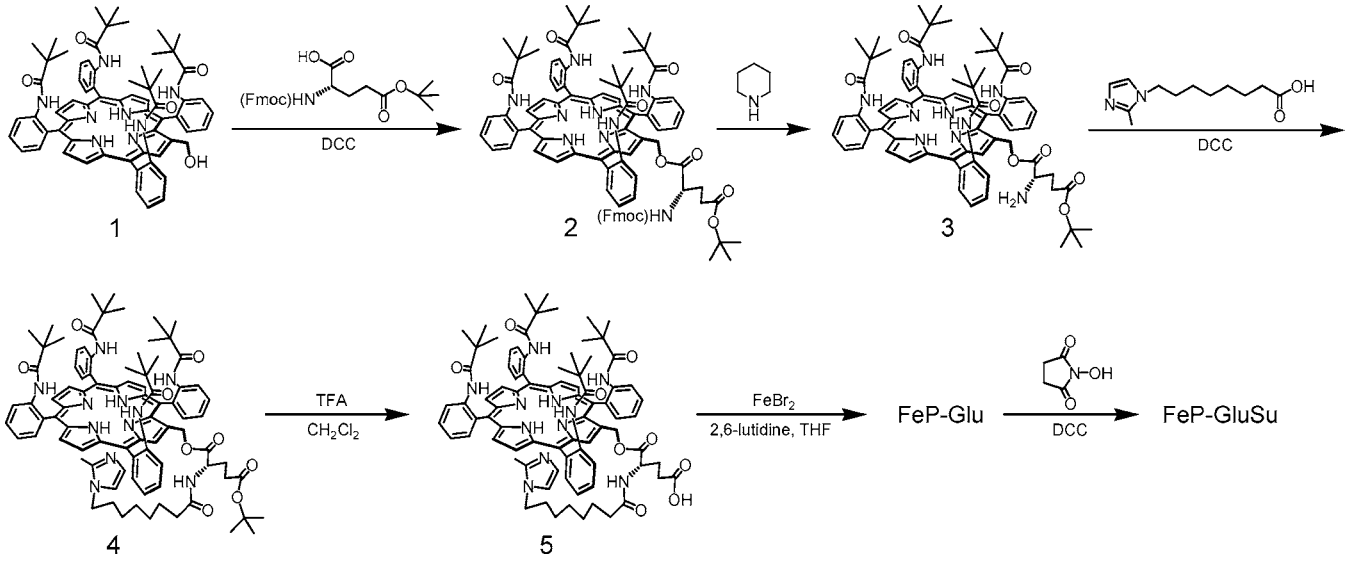

Table 1. CO-and O_2-Binding Parameters of rHSA(FeP-Glu) Conjugate in Phosphate−Buffered Solution (pH 7.3) at 25 °C

	$10^{-6}\ k_{on}^{CO}(M^{-1}\,s^{-1})$		$10^{-7}\ k_{on}^{O_2}(M^{-1}\,s^{-1})$		$10^{-2}\ k_{off}^{O_2}(s^{-1})$		$P_{1/2}^{O_2}$(Torr)[a]
system	fast	slow	fast	slow	fast	slow	
rHSA(FeP-Glu) conjugate	6.2	1.1	2.8	–	3.3	–	9 (27)
rHSA-FeP hybrid[b]	4.7	0.66	3.2	1.0	7.2	2.2	13 (35)
Hb(T-state)α[c]	0.22	–	0.29	–	1.8	–	40

[a] At 37 °C in parenthesis. [b] From ref 4c. [c] From refs 13−15.

First, Fmoc-L-Glu(g-*tert*-butyl ester) was bound to the OH group at the β-pyrrolic position of the porphyrin **1** by DCC. After removal of the Fmoc protecting group with piperidine, 8-*N*-(2-methylimidazolyl)octanoic acid was reacted with the obtained compound **3** in CH_2Cl_2, giving the imidazolyl-tailed porphyrin (**4**). The *tert*-butyl group was then removed by TFA, and the central iron insertion was carried out by the general $FeBr_2$ method to afford the iron-porphryin FeP-Glu. Finally, the reaction of *N*-hydroxysuccinimide with DCC gave the FeP-GluSu. All reactions can be performed at room temperature with high yields. The analytical data of all compounds described above were satisfactory obtained (*7*).

The FeP-Glu was converted to the ferrous complex by reduction in a heterogeneous two-phase system (toluene/aqueous $Na_2S_2O_4$) under an N_2 atmosphere (*6, 8*). The UV−vis absorption spectrum of the orange solution showed five-*N*-coordinated Fe(II) species (λ_{max}: 440, 531, 563 nm) via intramolecular imidazole binding (*6, 8, 9*). Upon exposure to CO, its UV−vis absorption immediately moved to that of the CO adduct complex. On the other hand, the dioxygenation was unstable at 25 °C, which is likely due to the presence of the neighboring glutamic acid proton.

The EtOH solution of the carbonyl FeP-GluSu (2 mL) was then injected into the phosphate-buffered solution of rHSA (8 mL, pH 7.3) (molar ratio 4/1), and the mixture was gently stirred for 1 h at room temperature. The solution was dialyzed against phosphate buffer (pH 7.3) to remove EtOH. The MALDI-TOFMS demonstrated a single molecular ion peak at *m/z* 70 643 (Figure 1). Attempts to measure the molecular weight of the rHSA-FeP hybrid, in which the FePs are noncovalently accommodated, failed using MALDI- and ESI-TOFMS; the molecular ion peak of rHSA (65 500) was only observable because the FePs are dissociated from the albumin during the ionization process (*10*). Therefore, we can conclude that the FeP-Glu is conjugated with rHSA

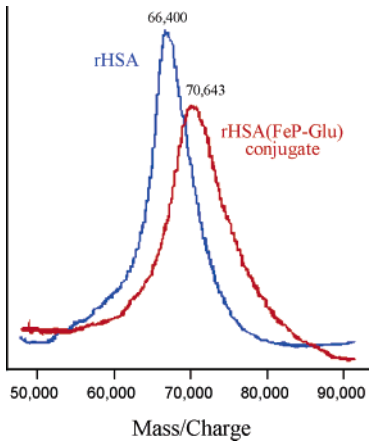

Figure 1. MALDI-TOFMS of the rHSA(FeP-Glu) conjugate. Matrix: 2,5-dihydroxybenzoic acid.

through amide bond formation. The average number of FeP-Glu in an rHSA was estimated to be 2.9−3.5, and this number is not dependent on the mixing molar ratio of FeP-GluSu/rHSA that ranged from 4 to 10. There are a total of 59 NH_2 groups in the rHSA structure, but only three of them are presumably active for the FeP-GluSu binding.

The conjugation of FeP-GluSu did not induce any change in the circular dichroism spectrum of rHSA in the 200−250 nm region. The Native PAGE of rHSA(FeP-Glu) also showed a single band with same migration distance of rHSA. Both results suggested that the secondary structure, molecular shape, and surface charge of albumin remained unaltered after the covalent binding of the hemes.

The UV−vis absorption spectrum of the rHSA(FeP-Glu) conjugate under an N_2 atmosphere showed a typical five-*N*-coordinated complex as seen in the toluene solution of FeP-Glu (Figure 2) (*4a,b, 6, 8, 9*). Upon exposure

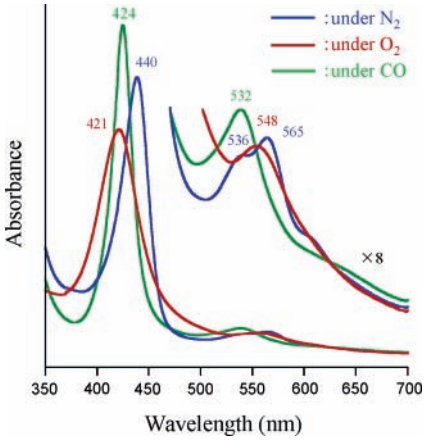

Figure 2. UV−vis absorption spectral changes of the rHSA-(FeP-Glu) conjugate in phosphate-buffered solution (pH 7.3) at 25 °C.

of this solution to O_2, the spectrum changed to that of the O_2-adduct complex under physiological conditions (pH 7.3, 37 °C) (*4a*−*c*). This dioxygenation was reversibly observed to be dependent on the O_2 partial pressure in the same manner as hemoglobin (Hb) and myoglobin. The half-lifetime of the O_2 adduct (ca. 5 h at 37 °C) was significantly longer than that of the noncovalent rHSA-FeP hybrid ($\tau_{1/2}$: 2 h) (*4d*). The covalent linkages of FeP-Glu to the protein scaffold obviously retarded the oxidation process of the central ferrous ion. Molecular simulation of the structure of FeP-GluSu revealed that the geometry of the imidazole ring against the porphyrin platform was perpendicular, which suggests that the spacer moiety between the imidazole and the porphyrin periphery does not produce an unfavorable distortion of the axial coordination and will not influence the O_2-binding behavior (see Chart 1b) (*11*).

The O_2-binding affinity [$P_{1/2}{}^{O_2}$] of the rHSA(FeP-Glu) conjugate was determined to be 27 Torr at 37 °C (*3b,c, 6, 7, 9, 10*), which is almost the same as that of the rHSA-FeP hybrid [$P_{1/2}{}^{O_2}$: 33 Torr] (*3b*−*d*) and identical to that of human red cells (*12*). The laser flash photolysis experiments provided the association rate constants of the O_2- and CO-bindings ($k_{on}{}^{O_2}$, $k_{on}{}^{CO}$) (*6, 8, 9a*). The absorption decays accompanying the O_2- and CO-recombination to the noncovalent rHSA-FeP hybrid were composed of two phases of the first-order kinetics, and the curves were fit by a double-exponential equation to determine k_{on} (fast) and k_{on} (slow) (Table 1) (*4c*). We supposed that the O_2- and CO-association to the FeP in the hydrophobic domains of the albumin was influenced by the molecular microenvironments around each O_2-coordination site, e.g., steric hindrance of the amino acid residue and difference in polarity (*4b*−*d*). The time dependence of the absorption change in the CO recombination to the rHSA(FeP-Glu) conjugate also showed double-exponential profile, but the rebinding process of O_2 obeyed monophasic decay. On the basis of studies on synthetic model hemes, it has been known that the proximal-side effect is the only primary factor which influences the association rate for CO but not for O_2 (*8, 9a*). We assume that there are two different geometries of the imidazole coordination and that each one shows the individual kinetics of the CO association. The covalent linkages between the axially coordinated imidazolyl side-chain and the albumin structure may provide an additional strain of the Fe−N(imidazole) bond and gives two conformations of the proximal-base binding. Since the $k_{on}{}^{O_2}$ value of rHSA(FeP-Glu) was nearly the same as the $k_{on}{}^{O_2}$ (fast) of the rHSA-FeP hybrid (Table 1), the FeP-Glu molecules are likely to locate on the surface of rHSA.

In conclusion, reaction of the newly synthesized tetrakis{(α,α,α,α-*o*-pivalamido)phenyl}porphinatoiron(II) with a proximal base and succinimidyl(glutamyl) group to rHSA produced a novel albumin conjugate bearing covalently attached heme groups as O_2-coordination sites. The molecular weight of rHSA(FeP-Glu) was directly measured by MALDI-TOF MS. In nature, one can find unique heme-linked proteins, e.g., cyctochrome *c*. The rHSA(FeP-Glu) conjugate presumably becomes a valuable model of these hemoproteins. The obtained rHSA-(FeP-Glu) can reversibly absorb O_2 under physiological conditions, and its O_2-binding affinity showed an identical value to that for human erythrocytes. These results suggest that this novel plasma protein may efficiently transport O_2 in the bloodstream as an O_2-carrier with a long circulation time.

ACKNOWLEDGMENT

This work was partially supported by Grant-in-Aid for Scientific Research (No. 16350093) from JSPS, Grant-in-Aid for Exploratory Research (No. 16655049) from MEXT Japan, and Health Science Research Grants (Regulatory Science) from MHLW Japan. R.M.W. acknowledges NNSFC (No. 20274034). The authors are grateful to NIPRO Corp. for their supporting the oxygen-infusion project.

Supporting Information Available: Experimental details of the compounds **2**, **3**, **4**, **5**, FeP-Glu, and FeP-GluSu and their spectroscopic data. This material is available free of charge via the Internet at http://pubs.acs.org.

LITERATURE CITED

(1) Peters, T., Jr. (1996) All about albumin. *Biochemistry, Genetics, and Medical Applications*, Academic Press, San Diego; and reference therein.

(2) Kragh-Hansen, U. (1981) Molecular aspects of ligand binding to serum albumin. *Pharmacol. Rev. 33,* 17−53.

(3) Curry, S., Brick, P., and Franks, N. P. (1999) Fatty acid binding to human serum albumin: new insights from crystallographic studies. *Biochim. Biphys. Acta 1441*, 131−140.

(4) (a) Komatsu, T., Hamamatsu, K., Wu, J., and Tsuchida, E. (1999) Physicochemical properties and O_2-coordination structure of human serum albumin incorporating tetrakis(*o*-pivamido)phenylporphyrinatoiron(II) Derivatives. *Bioconjugate Chem. 10*, 82−86. (b) Tsuchida, E., Komatsu, T., Matsukawa, Y., Hamamatsu, K., and Wu, J. (1999) Human serum albumin incorporating tetrakis(*o*-pivalamido)phenylporphinatoiron(II) derivative as a totally synthetic O_2-carrying hemoprotein. *Bioconjugate Chem. 10*, 797−802. (c) Komatsu, T., Matsukawa, Y., and Tsuchida, E. (2000) Kinetics of CO- and O_2-binding to human serum albumin-heme hybrid. *Bioconjugate Chem. 11*, 772−776. (d) Komatsu, T., Matsukawa, Y., and Tsuchida, E. (2002) Effect of heme structure on O_2-binding properties of human serum albumin-heme hybrids: intramolecular histidine coordination provides a stable O_2-adduct complex. *Bioconjugate Chem. 13*, 397−402. (e) Tsuchida, E., Komatsu, T., Hamamatsu, K., Matsukawa, Y., Tajima, A., Yoshizu, A., Izumi, Y., and Kobayashi, K. (2000) Exchange transfusion of albumin-heme as an artificial O_2-infusion into anesthetized rats: physiological responses, O_2-delivery and reduction of the oxidized hemin sites by red blood cells. *Bioconjugate Chem. 11*, 46−50. (f) Kobayashi, K., Komatsu, T., Iwamaru, A., Matsukawa, Y., Watanabe, M., Horinouchi, H., and Tsuchida, E. (2003) Oxygenation of hypoxia region in solid tumor by administration of human serum albumin incorporating synthetic hemes. *J. Biomed. Mater. Res. 64A*, 48−51. (g) Tsuchida, E., Komatsu, T., Matsukawa, Y., Nakagawa, A., Sakai, H., Kobayashi, K., and Suematsu, M. (2003) Human serum albumin incorporating synthetic heme: red blood cell substitute

without hypertension by nitric oxide scavenging. *J. Biomed. Mater. Res. 64A*, 257−261.

(5) Russo, S. M., Pepe, J. Y., Donohue, S., Cable E. E., Lambrecht, R. W., and Bonkovsky, H. L. (1995) Tissue distribution of zinc-mesoporphyrin in rats: relationship to inhibition of heme oxygenase. *J. Pharmacol. Exp. Ther. 272*, 766−774.

(6) Tsuchida, E., Komatsu, T., Ando, K., Kumamoto, S., and Nishide, H (1995) Synthesis and O_2-binding properties of tetraphenylporphyrinatoiron(II) derivatives bearing a proximal imidazole covalently bound at the β-pyrrolic position. *J. Chem. Soc., Perkin Trans. 2* 1995, 747−753.

(7) The synthetic details and spectroscopic data of the porphyrins can be obtained from the Supporting Information.

(8) Tsuchida, E., Komatsu, T., Arai, K., and Nishide, H. (1993) Synthesis and dioxygen-binding properties of double-sided porphyrinatoiron(II) complexes bearing covalently bound axial imidazole. *J. Chem. Soc., Dalton Trans.* 2465−2469.

(9) (a) Collman, J. P., Brauman, J. I., Collins, T. J., Iverson, B. L., Lang, G., Pettman, R. B., Sessler, J. L., and Walters, M. A. (1983) Synthesis and characterization of the "Pocket" porphyrins. *J. Am. Chem. Soc. 105*, 3038−3052. (b) Collman, J. P., Brauman, J. I., Iverson, B. L., Sessler, J. L., Morris, R. M., and Gibson, Q. H. (1983) O_2 and CO binding to iron(II) porphyrins: a comparison of the "Picket Fence" and "Pocket" porphyrins. *J. Am. Chem. Soc. 105*, 3052−3064.

(10) Tsuchida, E., Komatsu, T., and Yanagimoto, T. (2000) Molecular environment effect on O_2-binding to lipidporphyrinatoiron(II) complexes in aqueous media, *J. Porphyr. 4*, 81−87.

(11) The esff force field simulation was performed using an Insight II system (Molecular Simulations Inc.). The structure was generated by alternative minimizations and annealing dynamic calculations from 1,000 K to 100 K.

(12) Severinghaus, J. W. (1966) Blood gas calculator. *J. Appl. Physiol. 21*, 1108−1116.

(13) Sawicki, C. A., and Gibson G. H. (1977) Properties of the T State of Human Oxyhemoglobin Studied by Laser Photolysis. *J. Biol. Chem. 252*, 7538−7547.

(14) Sharma, V. S., Schmidt, M. R., and Ranney, H. M. (1976) Dissociation of CO from Carboxyhemoglobin. *J. Biol. Chem. 251*, 4267−4272.

(15) Steinmeier, R. C., and Parkhurst, L. J. (1975) Kinetic Studies on the Five Principle Components of Normal Adult Human Hemoglobin. *Biochemistry 14*, 1564−1573.

BC049859M

ARTICLES

Positron-Labeled Dopamine Agonists for Probing the High Affinity States of Dopamine Subtype 2 Receptors

Dah-Ren Hwang,* Raj Narendran, and Marc Laruelle

Department of Psychiatry, Columbia University, 1051 Riverside Drive, Unit 31, New York, New York 10032.
Received July 12, 2004; Revised Manuscript Received October 14, 2004

It is well documented that guanidine nucleotide-coupled dopamine subtype 2 receptors (D_2) are configured in high and low affinity states for the dopamine agonist in vitro. However, it is still unclear whether these functional states exist in vivo. We hypothesized that positron-labeled D_2 agonist and Positron Emission Tomography can be used to probe these functional states noninvasively. Recently, we demonstrated in nonhuman primates that *N*-[^{11}C]propyl-norapomorphine (NPA), a full D_2 agonist, is a suitable tracer for imaging the high affinity states of D_2 receptors in vivo. We also developed kinetic modeling method to derive receptor parameters, such as binding potential (BP) and specific uptake ratios (V_3''). When coupled with a dopamine releasing drug, amphetamine, NPA was found to be more sensitive than antagonist tracers, such as [^{11}C]raclopride (RAC), to endogenous dopamine concentration changes (by about 42%). This finding suggests that NPA is a superior tracer for reporting endogenous DA concentration. In addition, the difference of the BP or V_3'' of NPA and RAC under control and amphetamine challenge conditions could be used to estimate the functional states of D_2 receptors in vivo. On the basis of our findings and the assumptions that NPA binds only to the high affinity states and RAC binds equally to both affinity states, we proposed that about 70% of the D_2 receptors are configured in the high affinity states in vivo.

INTRODUCTION

The hyperdopaminergic hypothesis of schizophrenia is well supported by compelling evidence such as that all antipsychotics are potent dopamine D_2 receptor antagonists and that hyperdopaminergic activities of schizophrenic patients are detectable by neuroimaging techniques. However, the functional states of the D_2 receptors in this disease are still unknown.

Like other guanine nucleotide protein (G-protein)-coupled receptors, D_2 receptors are configured into G-protein-coupled (GR) and -uncoupled (R) states, as proposed in the ternary complex model (*1*, *2*). In this model, dopamine (DA) or other D_2 agonists bind with high affinity to GR ($D_{2\ high}$) and low affinity to the low affinity states ($D_{2\ low}$). However, a D_2 antagonist will bind with equal potency to the high and the low affinity states. Therefore, an agonist tracer is needed to probe the $D_{2\ high}$ receptors in vivo. In addition, since DA binds with high affinity to the $D_{2\ high}$, an agonist tracer will be more sensitive to endogenous DA concentration changes, and hence it will be a superior tracer for reporting endogenous DA concentrations.

Single photon emission computed tomography (SPECT) and positron emission tomography (PET) have been used successfully to study the competition between endogenous DA and radiotracers (*3*). These neuroimaging techniques involved a baseline scan followed by a drug challenge scan. The baseline uptake of the tracer (such as [^{123}I]IBZM or RAC) is first determined. Then, a DA enhancing drug, such as amphetamie (AMPH), is given. The drug leads to massive increases of DA in the synapse that compete with tracer binding and result in the decrease of tracer uptake. The difference of tracer bindings between these two scans becomes an index of synaptic dopamine concentrations.

The endogenous concentrations of DA at baseline and after AMPH challenge can be measured using microdialysis technique. A linear relationship exists between the changes of tracer binding (detected by IBZM SPECT or RAC PET scans) and the DA concentration (measured by microdialysis) (Figure 1) (*4*, *5*). With increasing doses of AMPH (0.3, 0.5, and 1 mg/kg), a 7-, 10-, and 15-fold increase in endogenous DA concentration and 20%, 30%, and 40% decrease of tracer bindings, respectively, were observed. The linear relationship of the AMPH dose response curve demonstrated that the decrease of tracer uptake is an index of endogenous DA concentration. It also revealed that a 40% increase in DA concentration only resulted in 1% decrease of [^{123}I]IBZM, and a 44% increase in DA concentration resulted in 1% decrease of RAC binding. The low sensitivity of antagonist to dopamine competition is observed. Examining the RAC PET images in Figure 1, one can easily appreciate the small 10% difference between the control (top image) and the AMPH (0.3 mg/kg, bottom).

Importantly, the AMPH challenge image paradigm has revealed that the decrease in tracer binding under the AMPH condition is more in the schizophrenic patients (−15%) than in the normal controls (−9%). This observation offered a direct evidence of hyperdopaminergic activity in schizophrenia. The role of noninvasive brain imaging technique in understanding the pathophysiology of schizophrenia has recently been reviewed (*6*).

* To whom correspondence should be addressed. Tel: (212) 543 5901; Fax: (212) 568 6171; e-mail: hd72@columbia.edu.

10.1021/bc049834n CCC: $30.25 © 2005 American Chemical Society
Published on Web 12/29/2004

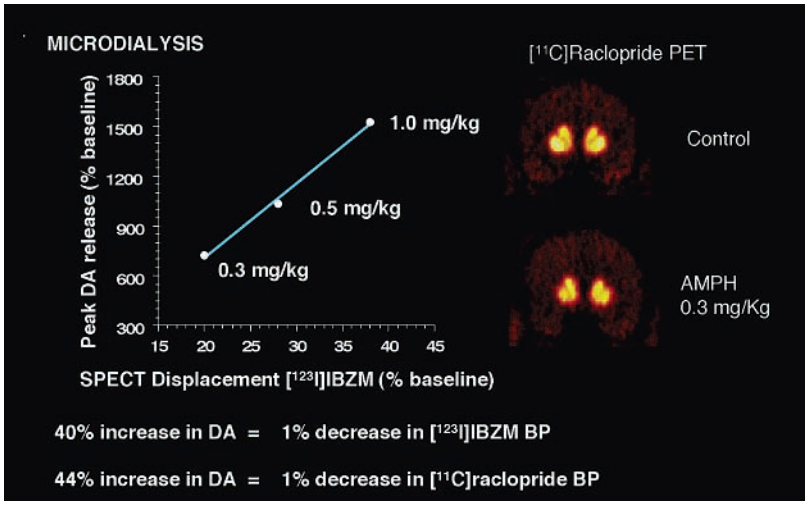

Figure 1. Microdialysis and neuroimaging measurements of amphtamine-induced DA release. The graph on the left showed the linear relationship between the percent of displacement of [^{123}I]IBZM binding (*X*-axis) and the peak dopamine concentration measured by microdialysis. The PET images on the right were obtained in healthy controls using [^{11}C]raclopride. The top panel is the images under control conditions and the bottom panel is the image after a dose of amphetamine (0.3 mg/kg).

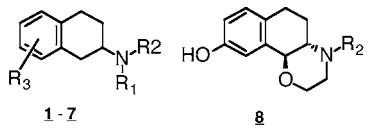

1 - 7 8

	R_1	R_2	R_3	STR/CER	Species	Ref
1	4-Me-Ph-Et-	^{18}F-Pr-	5-OH	1	rat	7
2	4-F-Ph-Et-	^{18}F-Pr-	5-OH	1	rat	7
3	Pr	$CH_3CH_2{}^{11}CH_2$-	5-OH	2	monkey	12
4	Ph-Et-	$CH_3CH_2{}^{11}CH_2$-	5-OH	1.5	monkey	13
5	C_6H_{11}-Et-	$CH_3CH_2{}^{11}CH_2$-	5-OH	1.5	monkey	13
6	Pr	^{18}F-$(CH_2)_5$-	5-OH	2	monkey	11
7	Pr	$CH_3CH_2{}^{11}CH_2$-	7-OH	1	monkey	8
8	-	$CH_3CH_2{}^{11}CH_2$-	-	-		9

Figure 2. Positron-labeled aminotetralin derivatives.

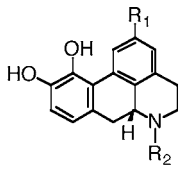

	R_1	R_2	K_i(nM)	STR/CER	Species	Ref
9	H	$^{11}CH_3$-	11	1.5	rat	15
10	H	^{18}F-Pr-	-	1	rat	14
11	OH	$C_2H_5{}^{11}CH_2$-	0.17	2	monkey	16
12	O-^{11}Me	Pr	0.05	low uptake	monkey	16
NPA	H	$C_2H_5{}^{11}CH_2$-	0.8	2.8	baboon	19

Figure 3. Positron-labeled apomorphine derivatives.

Unfortunately, this image paradigm revealed a ceiling effect of 40% decrease of tracer binding by DA enhancing drugs (*3*). This is based on the results from eight nonhuman primates (five with RAC and three with IBZM) and 11 human studies (six RAC and five IBZM). In these studies, the decrease of tracer binding potential (which is the ratio of striatal uptake to tracers activity in the blood) ranged from 10% to 40% with doses of AMPH ranged from 0.2 to 1 mg for nonhuman primates and 0.2−0.5 mg for humans. One possible explanation of the ceiling effect is that antagonist tracers (such as IBZM and RAC) bind with equal affinity to both high and low affinity states. However, only the bindings to the high affinity states are vulnerable to endogenous DA challenge. The 40% ceiling effect suggested that 40% of the D_2 receptors are configured in the high affinity state. However, the best way to confirm the high and low affinity function states of D_2 receptors is to use agonist tracer.

Because DA agonist binds with high affinity to the high affinity states, it is expected that an agonist tracer will be more sensitive to endogenous DA concentration changes than that of an antagonist tracer. Therefore, an agonist tracer will be a superior probe for reporting endogenous DA concentration.

Since the early 1990s, two classes of D_2 agonists, apomorphine and aminotralin derivatives, have been evaluated as potential agonist PET tracers (Figures 2 and 3). In the aminotralin series, both 5- and 7-hydroxy-aminotetralin derivatives have been prepared and evaluated. In 1993, Zijlstra et al. reported two fluoropropyl derivatives of 5-hydroxy-2-aminotetralin, compounds **1** and **2** in Figure 2 (*7*). However, both tracers showed no selective bindings in vivo. In 1994, Halldin et al. evaluated [^{11}C]-7-hydroxy-2-*N*,*N*-dipropylaminotetralin (7-OH-DPAT, **7**, prepared by N-alkylation with [^{11}C]propyl iodide) as a potential ligand for D_3 receptor, and a striatum (target tissue) to cerebellum (reference tissue) ratio of 2.2 in monkey brain was reported (*8*). However, since the initial report, no detailed studies of 7-OH-DPAT were reported. Similarly, Brown et al. reported the preparation of [^{11}C]PHNO, **8**, via the formation of [^{11}C]-propionic amide followed by reduction, but in vivo evaluation of the tracer was never reported (*9*). More recently, Shi et al. reported that several 5-hydroxy-2-aminotetralin derivatives (both C-11 and F-18 labeled tracers, compounds **3** to **6** in Figure 2) have high affinity for the D_2 receptors (*10*−*13*). The agonist properties of these tracers were demonstrated by in vitro autoradiography using rat brain slices. When tissues were incubated in the presence of nonhydrolyzable guanine nucleotide, GppNHp, which converts the high to the low affinity states, tracer uptakes are completely blocked. Monkey PET studies of tracers **3** to **6** revealed a striatum/cerebellum ratios of about 2. Detailed evaluation of these tracers (particularly the optically active tracers) has not been reported.

For the apomorphine series (Figure 3), Zijlstra et al. evaluated both [^{11}C]apomorphine, **9**, and [^{18}F]fluoropropylnorapomorphine, **10**, in rodents (*14*, *15*). [^{11}C]Apo-

morphine had a striatum/cerebellum ratio of about 1.5, but the fluoro derivative did not show any specific uptake. Because of the low selective uptake, these tracers were not further evaluated. Halldin et al. reported two [^{11}C]-labeled *N*-propyl-nor-apomorphine (NPA) derivatives, 2-hydoxy-[^{11}C-propyl]NPA, **11**, and 2-O-[^{11}C]methoxy-NPA, **12**. Initial primate studies showed that comppound **11** (prepared by reacting the norpropyl precursor with [^{11}C]propyl iodide) had low brain uptake (*16*). On the other hand, 2-[^{11}C]methoxy-NPA, prepared by reacting 2-hydroxy-NPA with [^{11}C]methyl iodide, showed a moderate striatum/cerebellum ratio of 2 in monkey. Unfortunately, this tracer was not further characterized.

Interestingly, one of the best characterized D_2 agonist, *N*-propyl-norapomorphine (NPA), has not been the focus of PET tracer development. NPA is a full D_2 agonist with K_i values of 0.4 nM and 23 nM for the $D_{2\ high}$ and $D_{2\ low}$, respectively (*17*, *18*). It also has high affinity for another D_2 family receptors, the D_3 subtype ($K_i = 0.3$ nM). It has good D_2 selectivity over other receptors (K_i for D_1, 340 nM; α_2, 480 nM; all other receptors, >1 μM). More importantly it has been used in humans for treating Parkinson's disease. In addition, norapomorphine, the starting material for the radiolabeling of NPA, is commercially available. This greatly facilitated our preparation and evaluation of [^{11}C]-labeled NPA.

This article will focus on the use of [^{11}C]-labeled NPA for in vivo imaging of the high affinity states of D2 receptors. The sensitivities of an agonist verse an antagonist PET tracer to endogenous dopamine concentration changes will be presented.

EXPERIMENTAL PROCEDURES

Radiochemistry. [^{11}C]NPA was prepared according to our published procedure (*19*). Briefly, a two-step labeling procedure, N-propionylation of norapomorphine followed by LAH reduction, was used for the preparation of [^{11}C]NPA (*19*). This procedure yielded high specific activity (>1.5 mCi/nmol) and radiochemical purity (>95%) of NPA. [^{11}C]Raclopride was prepared from desmethyl raclopride and [^{11}C]methyl triflate with similar specific activity and radiochemical purity.

Baboon PET Imaging. Detailed procedures can be found in two published articles (*20*, *21*). Briefly, the baboon was anesthetized with isoflurane and body temperature maintained by a water blanket. After tracer injection, 120-min dynamic PET scans were started. For amphetamine challenge studies, amphetamine was given 5 min prior to tracer injection. Arterial blood samples were taken at different interval to get input function and to do metabolite analysis. Plasma free fraction was measured using ultrafiltration technique.

PET Image Analysis. Detailed description can be found in our published article (*21*). Briefly, the outcome measures are the tissue distribution volume (V_T), binding potentials (BP), and selective uptake ratios (V_3''). These terms are defined as follows:

$$V_T = C_{tissue}/C_{blood} \quad (1)$$

$$BP_{tissue} = V_{T\ tissue} - V_{T\ reference\ region} = \text{bound/free} = f_1 B_{max}/K_D \quad (2)$$

$$V_3'' = BP_{tissue}/V_{T\ reference\ region} \quad (3)$$

where C_{tissue} is the radioactivity in the tissue detected by PET scan, C_{blood} is the amount of the parent tracer in the plasma (determined by measuring the radioactivity in the plasma at different time point and corrected for the metabolites), B_{max} is the total receptor density, K_D is the tracer's affinity for D_2 receptors, and f_1 is the plasma free fraction of the tracer.

The effect of AMPH on tissue's selective uptake is calculated as the difference of the BP or V_3'' of the pre- and post-AMPH scans divided by the BP or V_3'' of the pre-AMPH scan as defined in eqs 4 and 5:

$$\Delta BP = (BP_{pre} - BP_{post})/BP_{pre} \quad (4)$$

$$\Delta V_3'' = (V_3''_{pre} - V_3''_{post})/V_3''_{pre} \quad (5)$$

Table 1. Reproducibility of $\Delta V_3''$ and ΔBP Following Amphetamine (0.5 mg/kg) in the Same Baboon

tracer	condition	$\Delta V_3''$, %	ΔBP, %
[^{11}C]raclopride	test	−26	−26
	retest	−25	−21
[^{11}C]NPA	test	−48	−41
	retest	−46	−52

RESULTS AND DISCUSSION

For the radiosynthesis of NPA, a two-step labeling procedure, N-propionylation of norapomorphine followed by LAH reduction, was developed (*19*). This procedure yielded high SA (>1.5 mCi/nmol) and radiochemical purity (>95%) of NPA. Biodistribution in rats showed a striatum/cerebellum ratio of 4.4 at 60 min post tracer injection.

Baboon PET scans showed moderate striatal uptakes and the striatum/cerebellum ratio reached 2.8 at 45 min post tracer injection, which is higher than any D_2 agonist PET tracer reported to date. More importantly, the uptake was blocked by haldol at an iv dose of 0.2 mg/kg. These results strongly suggest that NPA is a selective D_2 receptor PET ligand.

Recently, we demonstrated that a one-tissue-compartment kinetic modeling method with metabolite corrected arterial input function is suitable for deriving receptor parameters, such as the tissue distribution volume (V_T), binding potentials (BP) and selective uptake ratios (V_3'') (*20*).

Table 1 shows the $\Delta V_3''$ of RAC and NPA in the same baboon using a dose of 0.5 mg/kg AMPH. A decrease of 26% and 48% was observed for RAC and NPA, respectively (*21*). The reliability of this outcome measure under test and retest conditions is excellent. The $\Delta V_3''$ value is more consistent than the ΔBP value. The voxelwise V_3'' maps of RAC and NPA under control and AMPH conditions in the same baboon are shown in Figure 4. The large effect of amphetamine on NPA V_3'' is evident.

More detailed studies were then conducted in three additional baboons (*21*). Each baboon received both RAC and NPA and studied under control and AMPH treated conditions (3 doses: 0.3, 0.5, and 1 mg/kg). A total of 36 scans were performed. For these scans, there were no significant difference in injected dose, mass (both control and AMPH conditions), free fractions, clearance rate, and the reference tissue distribution volume ($V_{T\ CER}$). However, the $V_{T\ CER}$ did drop under AMPH conditions, which only results in underestimates of the true effect.

The AMPH dose effects on the $\Delta V_3''$ of RAC and NPA are shown in Figure 5. Under all doses examined, NPA consistently shows higher decreases of selective uptakes and the difference are significant in all doses examined. If we compare the AMPH effect on NPA (triangle) and antagonist tracers (RAC circle and IBZM square), one can clearly see that a ceiling effect (60%) is observed with NPA (Figure 6). Assuming that NPA binds only to the

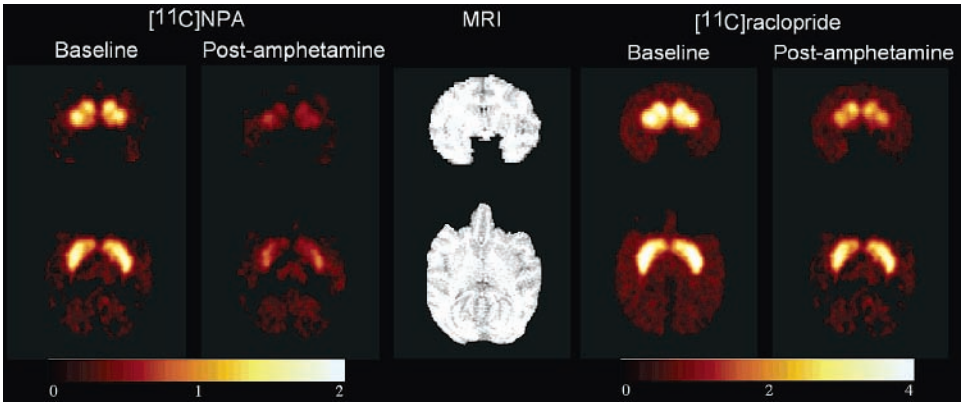

Figure 4. Voxelwise V_3'' maps of [^{11}C]NPA and [^{11}C]raclopride in the same baboon under control and post amphetamine (0.5 mg/kg) challenge conditions. The left panel is the [^{11}C]NPA V_3'' maps under baseline (left) and post amphetamine challenge (right). The middle panel is the MRI images of the baboon brain correspond to those of the PET images. The right panel is the [^{11}C]raclopride V_3'' maps under baseline (left) and post amphetamine challenge (right). In this paired study the displacement ($\Delta V_3''$) for [^{11}C] NPA and [^{11}C]raclopride are − 48% and − 26%, respectively.

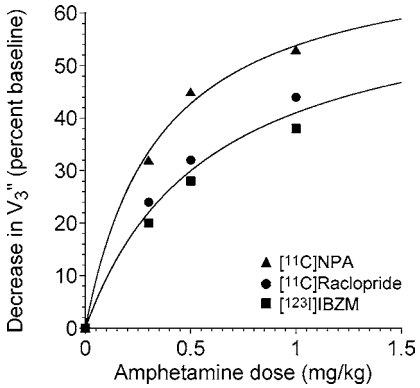

Figure 5. Effect of amphetamine on V_3'' of [^{11}C]NPA (solid triangle), [^{11}C]raclopride (solid circle), and [^{123}I]IBZM (solid square). The *X*-axis is the dose of amphetamine (mg/kg), and the *Y*-axis is the percent change of V_3'' ($\Delta V_3''$). The figure illustrates that the effect of amphetamine on agonist tracer ([^{11}C]NPA, K_{high} = 0.2 nM) is larger than antagonist tracers ([^{11}C]raclopride, K_D = 1.2 nM; and [^{123}I]IBZM, K_D = 0.4 nM). Its effect on antagonists is similar. These results imply that the agonist tracer is more sensitive to endogenous dopamine concentration changes than antagonist tracer.

$D_{2\ high}$, the percent of high affinity states (ratio of R_{high} to B_{max}) can be calculated from the ratios of ΔBP_{RAC} and ΔBP_{NPA} according to the following equation:

$$R_{high}/B_{max} = [\Delta BP_{RAC}/\Delta BP_{NPA}]\,(1 - \alpha) + \alpha \quad (6)$$

where α is the percent of receptor occupied by DA. Detailed derivation of the equations can be found in our recent paper (*21*).

Since only 60% of the NPA binding ($D_{2\ high}$) was displaceable by endogenous DA, this portion of $D_{2\ high}$ is defined as R_{HS} (synaptic high affinity states) and the rest of $D_{2\ high}$ as R_{HNS} (nonsynaptic high affinity states). This means that R_{HS} equals 60% of $D_{2\ high}$ that are not occupied by DA.

Our results showed a $\Delta BP_{RAC}/\Delta BP_{NPA}$ ratio of 0.7 (*21*). If we assume α equals 10% (i.e. 10% of the $D_{2\ high}$ is already occupied by DA), a R_{high}/B_{max} ratio of 0.73 was obtained from eq 6. It suggested that 73% of the D_2 receptors are configured in the high affinity state (i.e. $D_{2\ high}/B_{max}$ = 73%). Since we assume that 10% of the $D_{2\ high}$ are occupied by DA and we observed a maximum of 60% of NPA binding that can be displaced by endogenous DA, the percent of R_{HS} and R_{HNS} are calculated to be 38% (i.e. 0.6 × (0.73 − 0.1)) and 25%, respectively.

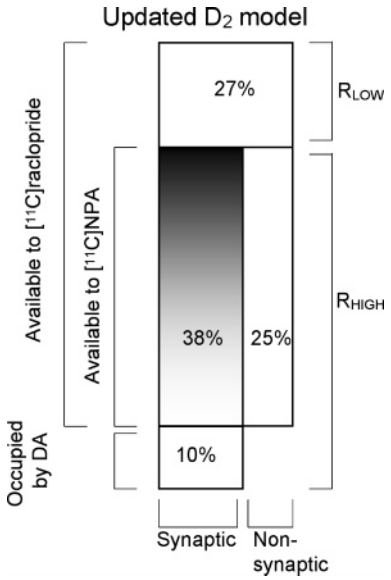

Figure 6. Revised model of D_2 receptors. The extended model (panel B) is derived from our present result. The new model divides the receptors into $D_{2\ high}$ and $D_{2\ low}$. An 10% of the $D_{2\ high}$ are assumed to be occupied by dopamine at baseline. Our result suggests that 40% of $D_{2\ high}$ are protected from dopamine challenge. Therefore, the $D_{2\ high}$ was further divided into synaptic and nonsynaptic compartments. Since we observed a 70% difference between the effect of amphetamine on [^{11}C]NPA and [^{11}C]raclopride, this suggests that 73% of the receptors are the $D_{2\ high}$. Thus we calculated the following proportion of receptors for the extended model: 10% occupied by dopamine at baseline, 38% of the R_{high} are vulnerable to dopamine challenge (synaptic $D_{2\ high}$), 25% of the R_{high} are protected from dopamine occupancy (nonsynaptic $D_{2\ high}$), and 27% are R_{low}.

On the basis of these results, we modified the original D_2 model, which suggests that only 50% of the D_2 receptors are configured in high affinity states, to the new model that 73% of the D_2 receptors are configured in the high affinity states ($D_{2\ high}$). We also proposed that, among the 73% of $D_{2\ high}$, 10% is already occupied by DA at baseline, 38% is the synaptic high affinity state that is vulnerable to AMPH challenge, and 25% is the nonsynaptic high affinity state that is not vulnerable to challenge.

Recently, we performed in vivo saturation binding studies in baboon with both NPA and RAC (unpublished results). From these experiments we obtained the in vivo K_D of 1.44 nM for RAC and 0.15 nM for NPA. The B_{max} obtained with RAC and NPA are 26 and 20 nM, respec-

tively. From these numbers, the percent of $D_{2\ high}$ is calculated to be 79%, which is remarkably close to the number we derived from the combined RAC and NPA studies.

In conclusion, we found that in vivo binding of NPA is more vulnerable to competition by endogenous DA than that of RAC (by 42%). NPA appears to be a superior probe to report on endogenous DA fluctuations. We also found that about 60% of the NPA bindings are vulnerable to endogenous competition (versus 44% for RAC), which agrees with previous findings in mice using [^{3}H]NPA (*22*). Assuming that, at tracer dose, NPA binds only to $D_{2\ high}$, our results implied that about 70% of D_2 receptors are $D_{2\ high}$. Recent saturation studies confirmed that NPA B_{max} (= R_{high}) is 70% of RAC B_{max}.

There is no doubt that neuroimaging techniques such as PET and SPECT are powerful tools to explore biochemistry in vivo. This technique depends on the successful development of appropriate tracers. It is obvious that chemists play a vital role in this field. Equally important is to establish collaborations among different disciplines that widen the scope of the application.

ACKNOWLEDGMENT

This research was supported by a grant from NIMH (RO1 62089-01) and a Young Investor Award form NARSAD. We thank the technical supports of the members of the Division of Functional Brain Mapping.

LITERATURE CITED

(1) De Lean, A., Stadel, J., and Lefkowitz, R. (1980) A ternary complex model explains the agonist-specific binding properties of the adenylate cyclase-coupled beta-adrenergic receptors. *J. Biol. Chem*. *255*, 7108−7117.

(2) Samama, P., Cotecchia, S., Costa, T., and Lefkowitz, R. (1993) A mutation-induced activated state of the beta 2-adrenergic receptor. Extending the ernary complex model. *J. Biol. Chem*. *268*, 4625−4636.

(3) Laruelle, M. (2000) Imaging synaptic neurotransmission with in vivo binding competition techniques: a critical review. *J. Cereb. Blood Flow Metab*. *20*, 423−451.

(4) Laruelle, M., Iyer, R., Al-Tikriti, M., Zea-Ponce, Y., Malison, R., Zoghbi, S., Baldwin, R., Kung, H., Charney, D., Hoffer, P., Innis, R., and Bradberry, C. (1997) Microdialysis and SPECT measurements of amphetamine-induced dopamine release in nonhuman primates. *Synapse 25*, 1−14.

(5) Endres, C., Kolachana, B., Saunders, R., Su, T., Weinberger, D., Breier, A., Eckelman, W., and Carson, R. (1997) Kinetic modeling of [^{11}C]raclopride: combined PET-microdialysis studies. *J. Cereb. Blood Flow Metab*. *17*, 932−942.

(6) Laruelle, M. (2000) The role of endogenous sensitization in the pathophysiology of schizophrenia: Implications from recent brain imaging studies. *Brain Res. Rev*. *31*, 371−384.

(7) Zijlstra, S., Elsinga, P., Oosteruis, E., Visser, G., Korf, J., and Vaalburg, W. (1993) Synthesis and in vivo distribution in the rat of several fluorine-18 labeled 5-hydroxy-2-aminoetraline derivatives. *Appl. Radiat. Isot*. *44*, 473−480.

(8) Halldin, C., Swahn, C., Suhara, L., Farde, L., Karlsson, P., Sokoloff, P., and Sedvall, G. (1994) Preparation of (+)-[propyl-^{11}C]7-OH-DPAT, a selecive dopamine D3 receptor agonist for PET. *J. Labelled Compd. Radiopharm*. *35*, 471−472.

(9) Brown, D., Luthra, S., Brad, F., Prenant, C., Dijkstra, D., Wikstrom, H., and Brooks, D. (1997) Labeling of the D2 agonist using [^{11}C]-propionyl chloride. *J. Labelled Compd. Radiopharm*. *40*, S565.

(10) Shi, B., Narayanan, T., Yang, Z., Christian, B., and Mukherjee, J. (1999) Radiosynthesis and in vitro evaluation of 2-(N-alkyl-N-1′-^{11}C-propyl)amino-5-hydroxytetralin analogues as high affinity agonists for dopamine D2 receptors. *Nucl. Med. Biol*. *26*, 725−735.

(11) Shi, B., Narayanan, T., Christian, B., Chattopadhyay, S., and Mukherjee, J. (2004) Synthesis and biological evaluation of the binding of dopamine D2/D3 receptor agonist, (R, S)-5-hydroxy-2-(N-propyl-N−(5′-^{18}F-fluoropentyl)aminotetralin (^{18}F-5-OH−FPPAT) in rodents and nonhuman primates. *Nucl. Med. Biol*. *31*, 303−311.

(12) Mukherjee, J., Narayanan, T., Christian, B., Shi, B., Dunigan, K., and Mantil, J. (2000) In vitro and in vivo evaluation of the binding of the dopamine D2 receptor agonist [^{11}C]-(R,S)-5-hydroxy-2-(di-*n*-propylamino)tetralin in rodents and nonhuman primate. *Synapse 37*, 64−70.

(13) Mukherjee, J., Narayanan, T. K., Christian, B. T., Shi, B., and Yang, Z. Y. (2004) Binding characteristics of high-affinity dopamine D2/D3 receptor agonists, [^{11}C]-PPHT and [11C]-ZYY-339 in rodents and imaging in non-human primates by PET. *Synapse 54*, 83−91.

(14) Zijlstra, S., Visser, G., Korf, J., and Vaalburg, W. (1993) Synthesis and in vivo distribution in the rat of several fluorine-18 labeled N-fluoroalkyl-aporphine. *Appl. Radiat. Isot*. *44*, 651−658.

(15) Zijlstra, S., Van Der Worp, H., Wiegman, T., Visser, G., Korf, J., and Vaalburg, W. (1993) Synthesis and in vivo disribution in the rat of a dopamine agonist: N-[^{11}C]methyl-norapomorphine. *Nucl. Med. Biol*. *20*, 7−12.

(16) Halldin, C., Swahn, C., Neumeyer, J., Hall, H., Gao, Y., Karlsson, P., and Farde, L. (1992) Preparation of two potent and selective dopamine D2 receptor agonist: (R)-[^{11}Cpropyl]-2-OH−NPA and (R)-[^{11}Cmethyl]-2-OCH3−NPA. *J. Labelled Compd. Radiopharm*. *35*, S265−266.

(17) Gardner, B., and Strange, P. (1998) Agonist action at D2(long) dopamine receptors: ligand binding and functional assays. *Br J Pharmacol*. *124*, 978−984.

(18) Neumeyer, J., Neustadt, B., Oh, K., Weinhardt, K., Boyce, C., Rosenberg, F., and Teiger, D. (1973) Aporphines. 8. Total synthesis and pharmacological evaluation of (±)-N−*n*-propylnorapomorphine, and (±)-N−*n*-propylnorapocodeine. *J Med Chem*. *16*, 1223−1228.

(19) Hwang, D., Kegeles, L., and Laruelle, M. (2000) (−)-N-[^{11}C]Propyl-norapomorphine: a positron-labeled dapamine agonist for PET imaging of D2 receptors. *Nucl. Med. Biol*. *27*, 533−539.

(20) Hwang, D., Narendran, R., Huang, Y., Slifstein, M., Talbot, P., Sudo, Y., Van Berckel, B., Kegeles, L., Martinez, D., and Laruelle, M. (2004) Quantitative analysis of (−)-N-[^{11}C]-propyl-norapomorphine in vivo binding in nonhuman primates. *J Nucl. Med.. 45*, 338−346.

(21) Narendran, R., Hwang, D., Slifstein, M., Talbot, P., Erritzoe, D., Huang, Y., Cooper, T., Martinez, D., Kegekes, L., Abi-Dargham, A., and Laruelle, M. (2004) In vivo vulnerability to competition by endogenous dopamine: comparison of the D2 receptor agonist radiotracer (−)-[^{11}C]propyl-norapomorphine ([^{11}C]NPA) with the D2 receptor antagonist radiotracer [^{11}C]raclopride. *Synapse 52*, 188−208.

(22) Cumming, P., Wong, D., Gillings, N., Hilton, J., Scheffel, U., and Gjedde, A. (2002) Specific binding of [^{11}C]raclopride and N-[^{3}H]propyl-norapomorphine to dopamine recepotrs in living mouse striatum: occupancy by dendogenous dopamine and guanosine triphosphae free G protein. *J. Cereb. Blood Flow Metab*. *22*, 596−604.

BC049834N

Chlorophyll-a Analogues Conjugated with Aminobenzyl-DTPA as Potential Bifunctional Agents for Magnetic Resonance Imaging and Photodynamic Therapy†

Guolin Li,[▽,‡] Adam Slansky,[▽,‡] Mahabeer P. Dobhal,[▽] Lalit N. Goswami,[▽] Andrew Graham,[▽,§] Yihui Chen,[▽] Peter Kanter,[∥] Ronald A. Alberico,[‡] Joseph Spernyak,[⊥] Janet Morgan,[§] Richard Mazurchuk,[⊥] Allan Oseroff,[§] Zachary Grossman,[‡,*] and Ravindra K. Pandey[▽,‡,*]

Photodynamic Therapy Center, Department of Nuclear Medicine and Radiology, Department of Dermatology, Department of Toxicology/Medicine, and Preclinical MR Imaging Resource, Roswell Park Cancer Institute, Buffalo, New York 14263. Received August 12, 2004; Revised Manuscript Received October 21, 2004

A clinically relevant photosensitizer, 3-devinyl-3-(1-hexyloxyethyl)pyropheophorbide-a (HPPH, a chlorophyll-a derivative), was conjugated with Gd(III)-aminobenzyl-diethylenetriaminepentaacetic acid (DTPA), an experimental magnetic resonance (MR) imaging agent. In vivo reflectance spectroscopy confirmed tumor uptake of HPPH−aminobenzyl-Gd(III)-DTPA conjugate was higher than free HPPH administered intraveneously (iv) to C_3H mice with subcutaneously (sc) implanted radiation-induced fibrosarcoma (RIF) tumor cells. In other experiments, Sprague−Dawley (SD) rats with sc implanted Ward Colon Carcinoma cells yielded markedly increased MR signal intensities from tumor regions-of-interest (ROIs) 24 h post-iv injection of HPPH−aminobenzyl-Gd(III)-DTPA conjugate as compared to unconjugated HPPH. In both in vitro (RIF tumor cells) and in vivo (mice bearing RIF tumors and rats bearing Ward Colon tumors) the conjugate produced significant increases in tumor conspicuity at 1.5 T and retained therapeutic efficacy following PDT. Also synthesized were a series of novel bifunctional agents containing two Gd(III) atoms per HPPH molecule that remained tumor-avid and PDT-active and yielded improved MR tumor conspicuity compared to their corresponding mono-Gd-(III) analogues. Administered iv at a MR imaging dose of 10 μmol/kg, these conjugates produced severe skin phototoxicity. However, by replacing the hexyl group of the pyropheophorbide-a with a tri(ethylene glycol) monomethyl ether (PEG-methyl ether), these conjugates produced remarkable MR tumor enhancement at 8 h post-iv injection, significant tumoricidal activity (80% of mice were tumor-free on day 90), and reduced skin phototoxicity compared to their corresponding hexyl ether analogues. The poor water-solubility characteristic of these conjugates was resolved by incorporation into a liposomal formulation. This paper presents the synthesis of tumor-avid contrast enhancing agents for MR imaging and thus represents an important milestone toward improving cancer diagnosis and tumor characterization. More importantly, this paper describes a new family of bifunctional agents that combine two modalities into a single cost-effective "see and treat" approach, namely, a single agent that can be used for contrast agent-enhanced MR imaging followed by targeted photodynamic therapy.

INTRODUCTION

For many years, in vivo imaging of human organs was largely dependent upon intravenous administration of radioactive molecules for nuclear scanning or nonradioactive iodinated chemicals for radiography (*1*−*4*). However, over the past decade, magnetic resonance (MR) imaging has become the method-of-choice for many procedures (*4*). Unlike nuclear scanning, conventional radiography or computed tomography, MR often relies on "contrast-enhancing agents" to improve inherent contrast between normal and diseased tissue. MR signal intensity or signal intensity differences (contrast) is dependent upon longitudinal (1/*T*1) and transverse relaxation rates (1/*T*2) of tissue protons. Agents containing paramagnetic ions have been shown to effectively alter 1/*T*1 and/or 1/*T*2 by changing the local magnetic field when they come in close proximity to water protons. The paramagnetic ion most widely used in this regard is gadolinium [Gd(III)] because of its seven unpaired electrons and large paramagnetic moment. At present, three similar Gd(III)-derived MR contrast enhancing agents have been approved by the Food and Drug Administration (FDA) for clinical use in the United States, the bis-*N*-methylglucamine salt of Gd(III)-diethylenetriamine pentaacetic acid (DTPA) (Magnavist, Berlex Laboratories, Wayne, NJ), the bis-*N*-methylamide of Gd(III)-DTPA (Omniscan, Amersham Health, Princeton, NJ), and the Gd(III) chelate of the 20-(2-hydroxypropyl) derivative of 1,4,7,10-tetraazacyclododecane-*N*,*N*′,*N*″,*N*‴-1,4,7-tetraacetic acid (Prohance, Bracco Diagnostics, Princeton, NJ). All three of these agents are carboxylate-containing,

* To whom correspondence should be addressed. R.K.P.: Phone: 716-845-3203. Fax: 716-845-8920. E-mail: ravindra.pandey@roswellpark.org. Z.G.: Phone: 716-845-8015. E-mail: zachary.grossman@roswellpark.org.

† Part of the Special Issue collection for Imaging Chemistry that began in Issue 6, 2004. A preliminary description of this work was presented at the Symposium on Chemistry and Biological Applications of Imaging Agents and Molecular Beacons, at the spring 2004 National Meeting of the American Chemical Society.

▽ Photodynamic Therapy Center.
‡ Department of Nuclear Medicine and Radiology.
§ Department of Dermatology.
∥ Department of Toxicology/Medicine.
⊥ Preclinical MR Imaging Resource.

10.1021/bc049807x CCC: $30.25 © 2005 American Chemical Society
Published on Web 01/04/2005

water-soluble complexes. While several agents look promising, no macromolecular MR contrast-enhancing agent has been approved for human use. Conventional MR contrast media rely on tumor enhancement secondary to altered tumor capillary permeability. The time course of tumor enhancement with these agents, therefore, is to a great extent dependent upon intravascular contrast agent concentration. As an administered MR contrast-enhancing agent clears from the circulation, tumor conspicuity may appear to increase due to rising tumor-to-background ratio. Thereafter, tumor MR signal intensity declines as nonbound contrast media clears from a given lesion. Typical plasma clearance rates for FDA approved agents are on the order of 15 min or less, thereby limiting the usable time frame for MR data acquisition, which can take between 5 and 15 min per acquisition. Moreover, several additional disadvantages exist for current FDA-approved MR contrast media. Because current FDA approved MR agents do not preferentially bind specific molecular targets, they cannot reliably differentiate neoplasm from inflammation. Finally, because the tumor selectivity of current MR contrast-enhancing agents is singularly dependent upon perturbations in normal vascular permeability, small foci of metastatic tumor cells, particularly those in minimally enlarged or normal-sized lymph nodes, may not be detectable by current methods. However, by selective or nonselective binding of a MR contrast-enhancing agent to a tumor target or by simply slowing in vivo tumor clearance rates, several improvements might be realized. For example, additional data sets or repeat MR acquisitions might be obtained, thereby enabling screening of additional body regions or more detailed MR characterization of specific locations.

Previously, gadolinium-based porphyrin contrast media, particularly gadoporphyrin-2, have been extensively studied and found to be necrosis-avid (*5*, *6*). Although such compounds may be useful for tumor imaging (5−30% tumor mass is commonly necrotic), a MR agent that targets living tumor cells, particularly those that are actively undergoing metabolic processes, would be superior. For the last several years, our laboratory has focused our research efforts on developing various long wavelength-absorbing photosensitizers (660−800 nm) derived from chlorophyll-a and bacteriochlorophyll-a for photodynamic therapy (PDT) (*7*−*14*). Among these compounds, HPPH is currently at Phase II human clinical trials and others are at various stages of preclinical studies (*15*, *16*). Because HPPH demonstrated both tumor avidity and limited skin phototoxicity (a major drawback with most of the porphyrin-based compounds), we were interested in studying HPPH as a "vehicle" for delivering gadolinium complexes to tumors. Our goal was to develop a single bifunctional agent that could be clinically utilized both as a MR contrast-enhancing agent and a photosensitizer for PDT.

EXPERIMENTAL PROCEDURES

^{1}H and ^{13}C NMR spectra were recorded on Bruker AMX-400 Spectrometer at 400.1 and 100.6 MHz, respectively. Unless otherwise stated, chemical shifts are reported in ppm and referenced to residual solvent resonance peaks ($CDCl_3$: for ^{1}H, 7.26 ppm and ^{13}C, 77.2 ppm; methanol-d_4: for ^{1}H, 3.31 ppm). UV−vis spectra were recorded on a Varian (Cary-50 Bio) spectrophotometer. Column chromatographic separations were performed over silica gel 60 (70−230 mesh) or neutral alumina (Brockmann grade III, ∼150 mesh).

HPPH−DTPA-*tert*-butyl Ester (3). A mixture of HPPH **2** (91 mg, 0.143 mmol), **7** (167 mg, 0.215 mmol), *N*,*N*′-dicyclohexylcarbodiimide (DCC, 35 mg, 0.170 mmol), and (dimethylamino)-pyridine (DMAP, 21 mg, 0.172 mmol) in dry dichloromethane (5 mL) was stirred at room temperature under nitrogen for 16 h. Water (1 mL) was then added, and the mixture was stirred for 15 min. The organic layer was separated, dried with Na_2SO_4, filtered, and concentrated. The residue was dissolved in minimum amount of dichloromethane (∼2 mL) and refrigerated for 1 h. It was then filtered, and the solid (1, 3-dicyclohexylurea) was washed with dichloromethane. The filtrate was concentrated and purified with column chromatography over neutral alumina (Brockmann grade III, ∼150 mesh) eluting with hexanes−EtOAc (v/v 3/1) and then hexanes−EtOAc (v/v 5/2). The fractions containing the product **3** were combined and concentrated. The residue was purified by another column chromatography over neutral alumina (Brockmann grade III) eluting with CH_2Cl_2-EtOAc (v/v 8/1) and then $CH_3OH-CH_2Cl_2$ (3%) to provide the title compound **3** (167 mg, 0.120 mmol) as a dark blue oil in 84% yield. UV−vis in CH_2Cl_2 [λ_{max} (ϵ)]: 410 (117540), 505 (10650), 536 (10740), 604 (8950), 660 (54460). ^{1}H NMR ($CDCl_3$) δ 9.81 (1H, splitting s, H-5), 9.00 (1H, splitting s, H-10), 8.53 (1H, s, H-20), 7.24 (1H, br, CONH), 7.17 (2H, m, H-2′ and 6′), 7.05 (2H, m, H-3′ and 5′), 5.93 [1H, m, CH_3(O-hexyl)*CH*-3], 5.22 (2H, dd, AB system, J = 20.0 Hz, $COCH_2$-15), 4.60 (1H, m, H-18), 4.42 (1H, m, H-17), 3.78−3.17 (20H, m, H-1″, CH_3-2, CH_3-7, CH_3CH_2-8 and 5 × NCH_2CO_2C), 3.09−2.90, 2.90−2.52, 2.50−2.28, 2.24−2.03 [total 19H, m, CH_3-12, HNCO-CH_2CH_2-17, H-7′, 8′, 9′, 10′, 11′, CH_3(O-hexyl)CH-3], 1.82 (3H, d, J = 7.4 Hz, CH_3-18), 1.78 (2H, m, H-2"), 1.59 (3H, m, CH_3-CH_2-8), 1.40, 1.39, 1.37 [45H, each s, 5×-$OCOC(CH_3)_3$], 1.40 (2H, m, overlapped with *tert*-butyls, H-3"), 1.25 (4H, m, H-4″ and H-5″), 0.80 (3H, m, H-6″), 0.46 (1H, br, NH), −1.59 (1H, s, NH). ^{13}C NMR ($CDCl_3$): δ 196.5, 172.2, 171.5, 170.9, 170.7, 160.4, 155.6, 151.0, 149.2, 145.3, 141.7, 141.6, 140.0, 137.7, 136.3, 136.0, 135.9, 132.6, 132.5, 130.2, 129.8, 128.0, 119.7, 106.2, 104.1, 98.3, 98.2, 92.8, 80.9, 80.7, 73.1, 69.9, 63.2, 56.3, 56.2, 53.8, 53.1, 52.7, 51.9, 50.3, 48.4, 36.8, 34.0, 32.0, 30.4, 28.4, 28.3, 26.3, 25.0, 24.9, 23.3, 22.8, 19.6, 17.5, 14.2, 14.1, 11.7, 11.5, 11.2. MS (FAB) *m*/*z* 1397.9 (MH^+, 100). HRMS (FAB): Calcd for $C_{80}H_{117}N_8O_{13}$ (MH^+) 1397.8739; Found 1397.8750.

HPPH−DTPA (4). **3** (130 mg) was dissolved in trifluoroacetic acid (TFA, 3 mL). The solution was stirred at room temperature for 3 h. TFA was removed with under high vacuum at room temperature. The residue was dissolved in toluene (10 mL), and then the solvent was removed with rotavapor. The process was repeated three times to give **4** as dark blue powder. ^{1}H NMR (50% $CDCl_3$, 50% CD_3OD and one drop of C_5D_5N) δ 9.77 (1H, splitting s, H-5), 9.46 (1H, s, H-10), 8.60 (1H, s, H-20), 7.31 (2H, m, H-2′ and 6′), 7.01 (2H, m, H-3′ and 5′), 5.92 [1H, m, CH_3(O-hexyl)*CH*-3], 5.20 (2H, dd, AB system, J = 19.6 Hz, $COCH_2$-15), 4.62 (1H, m, H-18), 4.34 (1H, m, H-17), 3.81−2.23 (36H, m, H-1", CH_3-2, CH_3-7, CH_3-12, CH_3CH_2-8, HNCOCH_2CH_2-17, H-7′, 8′, 9′, 10′, 11′ and 5×-NCH_2CO_2C. Note: CH_3-2, CH_3-7, and CH_3-12 appeared at 3.37, 3.26, and 3.58, respectively), 2.12 [3H, d, J = 6.6 Hz, CH_3(O-hexyl)CH-3], 1.84 (3H, d, J = 7.2 Hz, CH_3-18), 1.72 (2H, m, H-2″), 1.69 (3H, t, J = 7.4 Hz, CH_3CH_2-8), 1.38 (2H, m, H-3″), 1.21 (4H, m, H-4″ and H-5″), 0.75 (3H, t, J = 7.2 Hz, H-6″). MS (ESI) *m*/*z* 1117.7 (MH^+, 100).

HPPH−DTPA-Gd Complex (5). To a solution of **4** (135 mg, 0.121 mmol) in pyridine (15 mL) was added a solution of $GdCl_3 \cdot 6H_2O$ (45 mg, 0.121 mmol) in deionized water (2 mL). The solution was stirred at room temperature for 3 h. Solvent was removed, and deionized water (10 mL) was added to the residue. A dark blue solid formed. The mixture was filtered and washed with water. The dark blue solid was collected and dried with high vacuum in a desiccator to provide **5** (141 mg) in 90% yield. Anal. Calcd for $C_{60}H_{75}N_8O_{14}Gd$: C, 55.84; H, 5.86; N, 8.69. Found: C, 56.71; H, 5.88; N, 8.37.

Compound 8. A mixture of **2** (228 mg, 0.358 mmol), di-*tert*-butyl iminodiacetate (132 mg, 0.538 mmol), DCC (89 mg, 0.431 mmol), and DMAP (53 mg, 0.434 mmol) in dry dichloromethane (6 mL) was stirred at room temperature under nitrogen for 15 h. Water (1 mL) was then added, and the mixture was stirred for 15 min. The organic layer was separated, dried with Na_2SO_4, filtered, and concentrated. 1,3-Dicyclohexylurea was removed as described in the preparation of **3**. The crude product was purified with column chromatography over neutral alumina (Brockmann grade III, ∼150 mesh) eluting with hexanes−EtOAc (v/v 1/1) to provide the title compound **8** (306 mg) as a

dark blue oil in 99% yield. UV−vis in CH_2Cl_2 [λ_{max} (ϵ)]: 318 (25650), 410 (128140), 505 (11750), 536 (11750), 605 (9720), 661 (60760). ^{1}H NMR ($CDCl_3$) δ 9.79 (1H, s, H-5), 9.53 (1H, s, H-10), 8.53 (1H, s, H-20), 5.92 [1H, q, J = 6.6 Hz, CH_3(O-hexyl)*CH*-3], 5.22 (2H, dd, AB system, J = 20.7 Hz, $COCH_2$-15), 4.51 (1H, q, J = 6.9 Hz, H-18), 4.39 (1H, m, H-17), 4.03 (2H, splitting s, H-1′ or H-2′), 3.79−3.53 (9H, m, CH_3CH_2-8, 1× ring CH_3, H-1′ or 2′, H-1″), 3.39, 3.28 (each 3H, s, 2 × ring CH_3), 2.75, 2.47 (each 1H, m, $HNCOCH_2CH_2$-17), 2.42, 2.14 (each 1H, m, $HNCOCH_2$-CH_2-17), 2.12 [3H, two set of doublets, J = 6.6, 7.3 Hz, CH_3(O-hexyl)CH-3], 1.81 (3H, d, J = 7.6 Hz, CH_3-18), 1.75 (2H, m, H-2″), 1.72 (3H, t, J = 7.6 Hz, CH_3CH_2-8), 1.50−1.40 [11H, m, H-3″, 1 × $OCOC(CH_3)_3$], 1.23 (4H, m, H-4″ and H-5″), 1.04, 1.03 [9H, two singlets, 1 × $OCOC(CH_3)_3$], 0.79 (3H, m, H-6″), 0.43 (1H, br, NH), −1.72 (1H, s, NH). MS (FAB) *m/z* 864.4 (MH^+, 100). HRMS (FAB): Calcd. for $C_{51}H_{70}N_5O_7$ (MH^+) 864.5275; Found 864.5280.

HPPH−di-DTPA-*tert*-butyl Ester (10). Compound **8** (626 mg, 0.725 mmol) was dissolved in TFA (10 mL). The solution was stirred at room temperature for 2 h. TFA was removed, and the residue was dried with high vacuum. DCC (907 mg, 4.39 mmol), DMAP (268 mg, 2.19 mmol), **7** (2.21 g, 2.84 mmol), and dry CH_2Cl_2 (20 mL) were then added. The resultant mixture was stirred at room temperature under nitrogen for 20 h. Water (10 mL) was then added, and the mixture was stirred for 15 min. The organic layer was separated, dried with Na_2SO_4, filtered, and concentrated. 1,3-Dicyclohexylurea was removed as described in the preparation of **3**. The product was purified with column chromatography over neutral alumina (Brockmann grade III, ∼150 mesh) eluting with hexanes−EtOAc (v/v 1/2) to remove excess **7** and some other impurity and then eluting with CH_3OH−CH_2Cl_2 (3%) to give **10** (1.13 g) in 68.6% yield. UV−vis in CH_2Cl_2 [λ_{max} (ϵ)]: 319 (21870), 411 (109150), 506 (9960), 537 (10010), 604 (8280), 660 (50080). ^{1}H NMR ($CDCl_3$) δ 10.59 (1H, br, 1 × CO*NH*-phenyl), 9.76 (1H, splitting s, H-5), 9.49 (1H, s, H-10), 8.46 (1H, s, H-20), 8.14 (1H, br, 1 × CO*NH*-phenyl), 7.65 (2H, m, 2 × phenyl H), 7.48 (2H, m, 2 × phenyl H), 7.23 (4H, m, 4 × phenyl H), 5.87 [1H, m, CH_3(O-hexyl)*CH*-3], 5.16 (2H, dd, AB system, J = 20.0 Hz, $COCH_2$-15), 4.40 (1H, m, H-18), 4.28 (1H, m, H-17), 4.07, 3.84 (4H, m, H-1′ and H-1″), 3.76−3.53 (7H, m, H-1‴, CH_3-12, CH_3CH_2-8), 3.53−3.28 (23H, CH_3-2 and 10 × NCH_2CO_2C), 3.25 (3H, s, CH_3-7), 3.10 (2H, m, H-3′ and H-3″), 2.98−2.15 (20H, m, $HNCOCH_2CH_2$-17, H-2′, 2″, 4′, 4″, 5′, 5″, 6′, 6″), 2.07 [3H, m, CH_3(O-hexyl)CH-3], 1.69 (8H, m, H-2‴, CH_3CH_2-8, CH_3-18), 1.61−1.28 [92H, m, H-3‴, 10 × $OCOC(CH_3)_3$], 1.20 (4H, m, H-4‴ and H-5‴), 0.76 (3H, t, J = 6.8 Hz, H-6″), 0.43 (1H, br, NH), −1.75 (1H, s, NH). MS (FAB) *m/z* 2274.0 (MH^+, 100). HRMS (FAB): Calcd for $C_{125}H_{189}N_{13}O_{25}$-Na ($MNa^+$) 2295.3814; Found 2295.3820.

HPPH-di-DTPA (11). 10 (30 mg) was treated with TFA (2 mL) as described in the preparation of **4** to provide **11** in quantitative yield. ^{1}H NMR (60% $CDCl_3$, 40% CD_3OD and one drop of C_5D_5N, TMS as internal standard) δ 9.83 (1H, splitting s, H-5), 9.57 (1H, s, H-10), 8.58 (1H, s, H-20), 7.68−7.37 (4H, m, 4 × phenyl H), 7.22−6.94 (4H, m, 4 × phenyl H), 5.92 [1H, m, CH_3(O-hexyl)*CH*-3], 5.13 (2H, dd, AB system, J = 19.8 Hz, $COCH_2$-15), 4.58−3.99 (6H, m, overlapped with water signal, H-18, H-17, H-1′ and H-1″), 3.84−2.20 (55H, m, H-1‴, CH_3-2, CH_3-7, CH_3-12, CH_3CH_2-8, 10 × NCH_2CO_2C, $HNCOCH_2CH_2$-17, H-2′, 2″, 3′, 3″, 4′, 4″, 5′, 5″, 6′, 6″), 2.12 [3H, m, CH_3(O-hexyl)CH-3], 1.85−1.63 (8H, m, H-2‴, CH_3CH_2-8, CH_3-18), 1.35 (2H, m, H-3‴), 1.22 (4H, m, H-4‴ and H-5‴), 0.76 (3H, m, H-6″). MS (ESI) *m/z* 1713.9 (MH^+, 100).

HPPH−di-DTPA-di-Gd Complex (12). A solution of **10** (700 mg, 0.308 mmol) in TFA (10 mL) was stirred at room temperature for 3 h. TFA was then removed with a ratovapor. The resultant residue was dissolved in pyridine (10 mL). A solution of $GdCl_3$·$6H_2O$ (230 mg, 0.619 mmol) in deionized water (2 mL) was added to above solution. The mixture was stirred at room temperature for 3 h. Solvent was removed, and deionized water (20 mL) was added to the residue. Dark blue solid formed. The mixture was filtered and washed with water. The dark blue solid was collected and dried with high vacuum in a desiccator to provide **12** (630 mg) in 99.5% yield. Anal. $C_{85}H_{107}N_{13}O_{27}Gd_2$. Calcd: C, 49.57; H, 5.24; N, 8.85. Found: C, 50.63; H, 5.10; N, 8.21.

Compound 14. Methylpyropheophorbide-a **13** (2.13 g, 3.88 mmol) was dissolved in HBr−AcOH (30%, 40 mL). The solution was stirred at room temperature for 2 h. HBr and acetic acid were removed under high vacuum. To the residue was added tri(ethylene glycol) monomethyl ether (5 mL) and potassium carbonate (2.0 g) and dry CH_2Cl_2 (20 mL). The mixture was stirred at room temperature for 1 h. It was then diluted with CH_2Cl_2 and washed with water and 5% $NaHCO_3$. The organic layer was dried with Na_2SO_4, filtered, and concentrated. The resultant residue was purified with column chromatography over alumina (Grade III) using CH_2Cl_2−acetone (v/v 9/1) as eluant to give D-20, which was crystallized from CH_2Cl_2−hexanes to provide pure **14** (1.50 g) in 54.2% yield. ^{1}H NMR ($CDCl_3$) δ 9.75 (1H, s, H-5), 9.50 (1H, s, H-10), 8.54 (1H, s, H-20), 6.02 [1H, q, J = 6.7 Hz, CH_3(O-PEG)*CH*-3], 5.18 (2H, dd, AB system, J = 19.8 Hz, $COCH_2$-15), 4.49 (1H, m, H-18), 4.30 (1H, m, H-17), 3.66, 3.62, 3,40, 3.28 (15H, each s, 3 × ring CH_3, $COOCH_3$, H-7″), 3.95−3.48, 3.40 (14H, m, CH_3CH_2-8, H-1″, 2″, 3″, 4″, 5″, 6″), 2.69, 2.55, 2.28 (1H, 1H, 2H, m, $CH_3OOCCH_2CH_2$-17), 2.15 [3H, two set of doublets, J = 6.8, 6.6 Hz, CH_3(O-hexyl)-CH-3], 1.82 (3H, d, J = 7.8 Hz, CH_3-18), 1.72 (3H, t, J = 7.6 Hz, CH_3CH_2-8), 0.43 (1H, br, NH), −1.72 (1H, s, NH). MS (ESI) *m/z* 735.9 (MNa^+, 100).

Compound 15. To a solution of **14** (1.5 g) in THF (80 mL) were added methanol (40 mL) and a solution of LiOH·H_2O (1.0 g) in water (20 mL). The mixture was stirred at room temperature for 4 h. It was then neutralized with 2% acetic acid (200 mL). The mixture was extracted CH_2Cl_2 (4 × 200 mL). The organic layers were combined and washed with water (5 × 400 mL), dried over Na_2SO_4, filtered, and concentrated. The resultant residue was crystallized with CH_2Cl_2−hexanes to provide **15** (1.46 g) in 99.3% yield. UV−vis in CH_2Cl_2 [λ_{max} (ϵ)]: 320 (21230), 410 (106603), 505 (9822), 536 (9671), 604 (8160), 661 (49864). ^{1}H NMR ($CDCl_3$) δ 9.72 (1H, splitting s, H-5), 9.49 (1H, s, H-10), 8.51 (1H, s, H-20), 5.99 [1H, q, J = 6.4 Hz, CH_3(O-PEG)*CH*-3], 5.18 (2H, dd, AB system, J = 20.2 Hz, $COCH_2$-15), 4.47 (1H, q, J = 7.0 Hz, H-18), 4.31 (1H, m, H-17), 3.65, 3.37, 3,26, 3.25 (12H, each s, 3 × ring CH_3, H-7″), 3.89−3.45, 3.39 (14H, m, CH_3CH_2-8, H-1″, 2″, 3″, 4″, 5″, 6″), 2.69, 2.59, 2.29 (1H, 1H, 2H, m, $CH_3OOCCH_2CH_2$-17), 2.12 [3H, two set of doublets, J = 6.6, 6.7 Hz, CH_3(O-hexyl)CH-3], 1.80 (3H, d, J = 6.9 Hz, CH_3-18), 1.69 (3H, t, J = 7.7 Hz, CH_3CH_2-8), −1.72 (1H, s, NH). MS (FAB) *m/z* 699.2 (MH^+, 100). HRMS (FAB): Calcd for $C_{40}H_{51}N_4O_7$ (MH^+) 699.3757; Found 699.3730.

Compound 16. By following the procedure for the preparation of **8**, reaction of **15** (1.45 g, 2.07 mmol) with di-*tert*-butyl iminodiacetate (770 mg, 3.14 mmol) in the presence of DCC (650 mg, 3.15 mmol) and DMAP (382 mg, 3.13 mmol) provided **16** (1.60 g) in 83.3% yield. UV−vis in CH_2Cl_2 [λ_{max} (ϵ)]: 318 (18008), 411 (92100), 505 (8335), 537 (8438), 605 (6895), 661 (43426). ^{1}H NMR ($CDCl_3$) δ 9.74 (1H, splitting s, H-5), 9.53 (1H, s, H-10), 8.53 (1H, s, H-20), 6.01 [1H, m, CH_3(O-hexyl)*CH*-3], 5.21 (2H, dd, AB system, J = 19.8 Hz, $COCH_2$-15), 4.50 (1H, m, H-18), 4.38 (1H, m, H-17), 4.02 (2H, splitting s, H-1′ or 2′), 3.68, 3.34, 3,29, 3.27 (12H, each s, 3 × ring CH_3, H-7″), 3.91−3.50, 3.42 (14H, m, CH_3CH_2-8, H-1″, 2″, 3″, 4″, 5″, 6″), 3.39 (2H, s, H-1′ or 2′), 2.74, 2.43, 1.94 (1H, 2H, 1H, m, $CH_3OOCCH_2CH_2$-17), 2.13 [3H, d, J = 6.7 Hz, CH_3(O-hexyl)CH-3], 1.80 (3H, d, J = 7.5 Hz, CH_3-18), 1.72 (3H, t, J = 7.5 Hz, CH_3CH_2-8), 1.47, 1.43 1.07, 1.03 [6H, 6H, 3H, 3H, each s, 2 × $OCOC(CH_3)_3$], 0.79 (3H, m, H-6″), 0.39 (1H, br, NH), −1.75 (1H, s, NH). MS (FAB) *m/z* 926.3 (MH^+, 100). HRMS (FAB) Calcd for $C_{52}H_{72}N_5O_{10}$ (MH^+) 926.5279; Found 926.5316.

Compound 18. By following the procedure for the preparation of **10**, compound **16** (3.70 g, 3.99 mmol) was treated with TFA (40 mL) to afford compound **17**. Without purification, reacting **17** with **7** (7.50 g, 9.63 mmol) in the presence of DCC (2.04 g, 9.89 mmol) and DMAP (1.22 g, 9.99 mmol) provided **18** (5.91 g) in 63.3% yield. UV−vis in CH_2Cl_2 [λ_{max} (ϵ)]: 318 (22525), 412 (112301), 505 (10336), 537 (10243), 605 (8528), 661 (51863). ^{1}H NMR ($CDCl_3$): δ 10.79 (1H, br, 1 × CO*NH*-phenyl), 9.72 (1H, splitting s, H-5), 9.45 (1H, splitting s, H-10), 8.76 (1H, br, 1 × CO*NH*-phenyl), 8.47 (1H, s, H-20), 7.71 (2H, m, 2 × phenyl H), 7.54 (2H, d, J = 7.9 Hz, 2 × phenyl H), 7.25 (2H, m, 2 × phenyl H), 7.20 (2H, d, J = 8.2 Hz, 2 × phenyl H), 5.96 [1H, m, CH_3-(O-hexyl)*CH*-3], 5.15 (2H, dd, AB system, J = 20.4 Hz, $COCH_2$-

Scheme 1

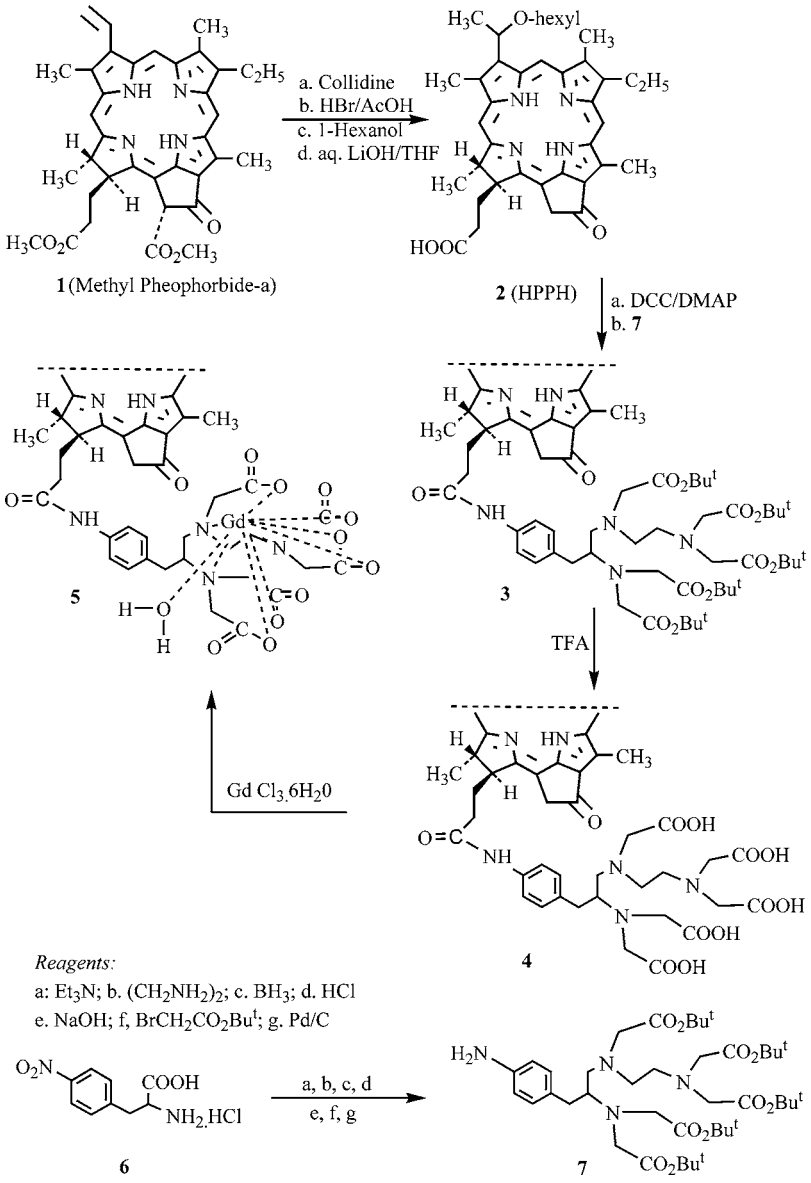

15), 4.41 (1H, m, H-18), 4.26 (1H, m, H-17), 3.94 (2H, m, H-1′ or H-1"), 3.87−3.20 (48H, m, H-1′ or H-1″, H-1‴, 2‴, 3‴, 4‴, 5‴, 6‴, 7‴, 10 × N*CH*$_2$CO$_2$C, CH$_3$-2, CH$_3$-7, CH$_3$-12, CH$_3$*CH*$_2$-8), 3.11 (2H, m, H-3′ and H-3″), 2.98−2.30 (20H, m, HNCO-*CH*$_2$*CH*$_2$-17, H-2′, 2″, 4′, 4″, 5′, 5″, 6′, 6″), 2.10 [3H, m, *CH*$_3$-(PEG)CH-3], 1.68 (6H, m, *CH*$_3$CH$_2$-8, CH$_3$-18), 1.55−1.30 [90H, m, 10 × OCOC(CH$_3$)$_3$], 0.38 (1H, s, NH), −1.77 (1H, s, NH). MS (FAB) *m/z* 2336.1 (MH$^+$, 68), 2358.1 (MNa$^+$, 100). HRMS (FAB): Calcd for $C_{126}H_{191}N_{13}O_{28}Na$ (MNa$^+$) 2357.3818; Found 2357.3820.

Gd(III) Complex 20. A solution of **18** (5.90 g, 2.52 mmol) in TFA (50 mL) was stirred at room temperature for 3 h. TFA was then removed under vacuum. The resultant residue was washed with water, dried under vacuum, and dissolved in pyridine (70 mL). To this solution was added a solution of $GdCl_3 \cdot 6H_2O$ (1.91 g, 5.14 mmol) in deionized water (5 mL). The mixture was stirred at room temperature for 2.5 h. Solvent was removed to dryness, and deionized water (100 mL) was added to the residue. The dark blue solid was washed several times with water (5 × 100 mL) and dried under high vacuum in a desiccator to provide **20** (5.20 g) in 97.1% yield. Analysis for $C_{86}H_{109}N_{13}O_{30}Gd_2$. Calculated: C, 48.69; H, 5.18; N, 8.59. Found: C, 48.91; H, 4.99; N, 8.85.

Formulation Procedure. To formulate the compound into the liposome mixture, a ratio of 2:1 60% lecithin to cholesterol (Sigma) by mass is dissolved into a minimal amount of dichloromethane in a large-mouthed test tube. The dichloromethane was then evaporated by purging nitrogen slowly while the test tube was kept warm by inserting the test tube in a warm water bath. The test tube was then placed into desiccator under high vacuum for 1 h in order to ensure total removal of the dichloromethane. The compound was weighed out in a ratio of 2:1 60% lecithin to compound by mass and placed into another large test tube. PBS (6 mL) (pH 7.2) was added to the compound and sonicated for 5−10 min. This mixture was then pipetted into the test tube with the liposome film and sonicated for 2 h. The solution must be surrounded by cold water since sonication produces heat. After 2 h the solution was filtered through a 0.45 μm filter into a plastic culture tube and wrapped in aluminum foil.

Whole Body MRI Imaging. Rats (female SD rats, three rats/group) with subcutaneously implanted Ward colon carcinomas (1 cm^3) were imaged in a 1.5 T magnetic resonance imaging system using a standard wrist coil (GE Horizon 5.8, GE Medical Systems, Milwaukee, WI). Preinjection imaging was T_1 weighted (TR = 500 ms, TE = 14 ms) in axial and coronal planes. Image thickness was 3 mm with a 1 mm interscan gap. Matrix size was 256 × 192 with 1.5 excitations and an 8 × 8 cm field-of-view.

***T*1/*T*2 Relaxivity Experiments:** The R1 and R2 relaxivity measurements were acquired on a General Electric 4.7T/33 cm horizontal bore magnet (GE NMR instruments, Fremont, CA)

Scheme 2

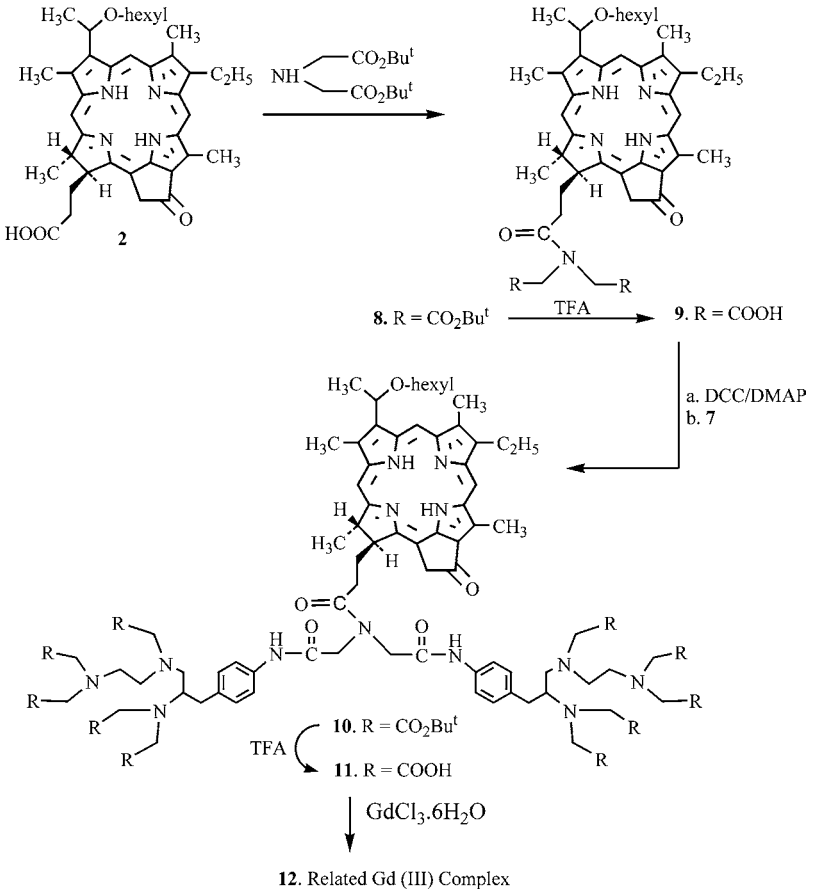

incorporating AVANCE digital electronics (Bruker BioSpec platform with Paravision version 2.1 acquisition software, Bruker Medical, Billerica, MA).

T1 relaxation rates (R1) were acquired for a range of contrast agent concentrations with a saturation recovery spin−echo (SE) sequence with a fixed TE = 10 ms and TR times ranging from 125 to 8000 ms (FOV = 32 × 32 mm, slice thickness = 1 mm, slices = 3, interslice gap = 2 mm, matrix = 128 × 128, NEX = 2). Signal intensities at each repetition time was obtained by taking the mean intensity within ROIs using Analyze 5.0 (Biomedical Imaging Resource, Mayo Foundation, Rochester, MN), and R1 and S_{MAX} were determined by nonlinear fitting of the equation:

$$S_{(TR)} = S_{MAX}(1 - e^{-(R1 \cdot TR)}) + \text{background noise}$$

using Matlab's Curve Fitting Toolbox (Matlab 6.5, MathWorks Inc., Natick, MA). Similarly, T2 relaxation rates (R2) were acquired with multi-echo, CPMG SE sequence with a fixed TR of 4500 ms and TE times ranging from 100 to 2000 ms. R2 and S_{MAX} were determined as described above using the equation:

$$S_{(TE)} = S_{MAX}(e^{-(R2 \cdot TE)}) + \text{background noise}$$

Animal and Tumor Systems. RIF-1 tumors were propagated in 6−9 week old female C3H/He mice. Tumors were obtained by subcutaneous injection of 2×10^5 RIF cells, prepared from established tumors by enzymatic digestion, into the right flanks of the animals. Prior to tumor-cell injection all hair was removed from the inoculation site by shaving and use of a commercially available depilatory, e.g. Nair. Tumors were used for experimentation when they reach a diameter of 5−6 mm and a width and thickness of ~4 mm.

Light Sources. An 18-W argon laser pumping a dye laser (model 171/375; Spectra-Physics) using DCM dye (Exciton, Inc.) tuned to 665 nm wavelength filter was employed. The output beam was split using a custom-made eight-way beam splitter device coupled to 400 μm diameter optical fibers. Each fiber was terminated with a microlens of a focal length of 3.5 mm in order to supply an even light distribution over the treatment field. The power density (75 mW cm^{-2}) was measured by a thermopile power meter (Coherent), and treatment field size was typically 1 cm in diameter.

Assessment of Tumor Response and Cure. The tumor's length (the longest dimension) and width (perpendicular to the long axis) was measured with electronic calipers. The volume was calculated as $V = {}^1/_2(L \times W^2)$. The hours-to-endpoint (HTE; time to 400 mm^3) was calculated by linearly interpolating between the times just before and after this volume is reached, using log(tumor volume) for the calculations; this was done using Microsoft Excel-based software developed by the RPCIC Biomathematics Resource. Mice were routinely sacrificed just after their tumors reached the endpoint. For nonrecurrent tumors, animals were followed for at least 30 days from the time of treatment. Individual experiment included at least five mice. Toxic death was defined as deaths taking place within 48 h of treatment. Toxic deaths only occur after intense PDT treatments.

Mice were used to elucidate important questions regarding the PDT efficacy. The primary therapeutic endpoint was based on the time for tumor regrowth to 400 mm^3. These procedures fall into Class 1 (little or no pain and distress) or Class 2 (mild stress) categories. The designed toxicity endpoint, normal (foot) tissue damage, is a Class 3 procedure; early toxic death is a nondesigned toxicity endpoint. PDT experiments using these endpoints are covered in an approved Institute Animal Care and Use (IACUC) protocol.

Determination of Intracellular Localization by Fluorescence Light Microscopy. In our attempt to investigate the site(s) of localization of the conjugates, these compounds were coincubated in the RIF cells with Mitotracker Green (Molecular Probes, Eugene, OR) which target mitochondria. Briefly, 1×10^5 cells were plated on poly-L-lysine-coated coverslips and grown for 2 days. Cells were incubated with photosensitizer(s) for 4 or 24 h at 37 °C, 5% CO_2, in the dark, and then washed

Scheme 3

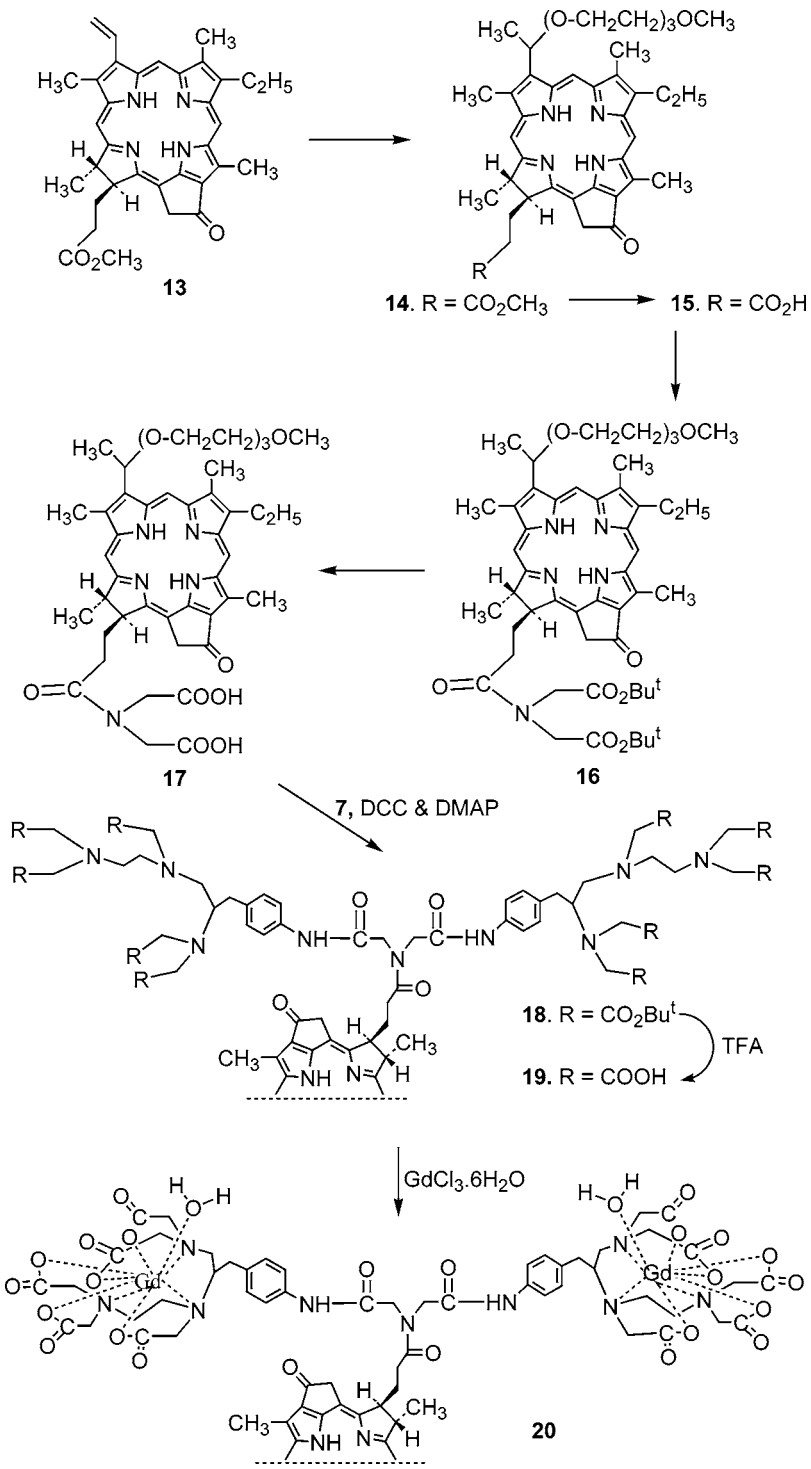

with fresh growth medium for 1 h to remove loosely bound drug, and gently rinsed with PBS immediately prior to microscopy (Zeiss Axiovert 200, Inverted Fluorescence Microscope, Carl Zeiss Inc., Germany). Localization was similar at both time-points. For the coincubation studies, Mitotracker Green (200 nM) was added 24 h before washing with PBS and examining by microscopy. Fluorescence was imaged with an AxioCam MRM monochrome digital camera. The images were captured and processed by MRGrab Software (Carl Zeiss, Inc., Germany). The cells were illuminated by a Fluoarc HBO 103 mercury vapor arc lamp filtered through a filter cube containing a 390−430 nm excitation filter, a 505 nm dichroic filter, and a 650−700 nm emission filter for detection of photosensitizers. Mitotracker Green was detected using a 450−490 nm excitation filter, a 495 nm dichroic, and a 500−550 nm emission filter. Images of photosensitizers and Mitotracker Green were taken in rapid succession.

RESULTS AND DISCUSSION

Chemistry. *HPPH Conjugated with One Gd(III)-Aminobenzyl-DTPA Complex.* For the preparation of the conjugate, methyl pheophorbide *a*, **1**, was isolated from *Spirulina pacifica* (*17*, *18*) and was converted into the corresponding 3-devinyl-3-(1-hexyloxy)ethyl-pyropheophorbide *a* (HPPH), **2**, by following the improved methodology developed in our laboratory. For the preparation of the MR agent, HPPH **2** was reacted with 4-aminobenzyl-

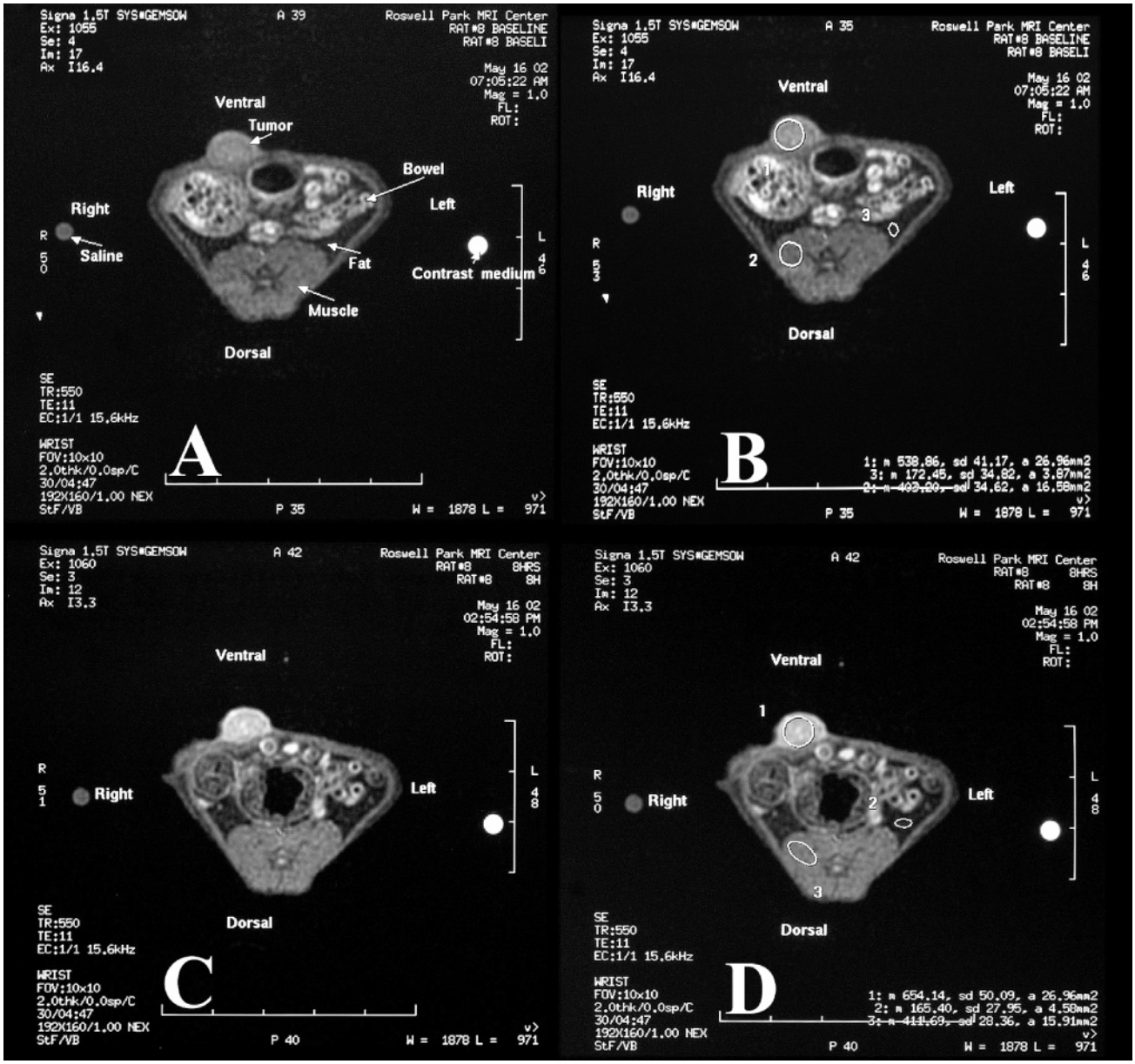

Figure 1. MRI images of tumors (Word Colon) implanted in rats (SD) from conjugate **20** (10 μmol/kg) before and at 8 h postinjection (for details see the text).

DTPA penta-*tert*-butyl ester **7** [which in turn was obtained in several steps from **6** by slightly modifying the methodology reported by Cummins et al. (*19*)] via the carbodiimide approach as illustrated in Scheme 1. For the preparation of the Gd(III) complex, the *tert*-butyl ester functionalities in **3** were converted into the corresponding carboxylic acid **4**, by reacting with trifluoroacetic acid (yield 100%). It was then dissolved in pyridine and reacted with gadolinium chloride hexahydrate dissolved in deionized water at room temperature for 2 h. The solvents were removed, and the residue was washed with deionized water several times and dried under high vacuum. The desired compound **5** was isolated (92% yield).

HPPH Conjugated with Two Gd(III)-Aminobenzyl-DTPA Complexes. The tumor avidity of any scanning agent, whether receptor-based (monoclonal antibodies, peptides) or porphyrin-based, generally improves only slightly by molecular redesign. An alternate approach for improving MR relaxivity would be to increase the number of Gd(III) atoms per molecule. Our approach was based on the hypothesis that HPPH conjugated with two or more Gd(III) chelates per molecule would further enhance tumor conspicuity and/or lower the dose required for MR imaging. For the synthesis of the desired conjugate, HPPH **2** was first reacted with di-*tert*-butyl iminodiacetate by following the carbodiimide approach as described for the preparation **3** (Scheme 1), and the intermediate amide analogue **8** was obtained (quantitative yield). The two *tert*-butyl functionalities present in the intermediate were cleaved on reacting with TFA, and the corresponding carboxylic acid **9** was isolated in quantitative yield. In a sequence of reactions, amide analogue **9** on reacting first with 4-aminobenzyl-DTPA **7** (Scheme 1) and then with TFA and $GdCl_3$ produced the desired compound **12** (90% overall yield). The structures of the intermediates and the final products were confirmed by ^1H NMR and/or mass spectrometry.

Di-Gd(III)-DTPA Conjugate of Pyropheophorbide-PEG. Previous SAR and QSAR efficacy studies on a series of alkyl ether analogues of pyropheophorbide-a (*8*) has shown that lipophilicity is one of the determinants for PDT. Therefore, to investigate the effect of hydrophilic substituent in tumor imaging, PDT efficacy, and skin

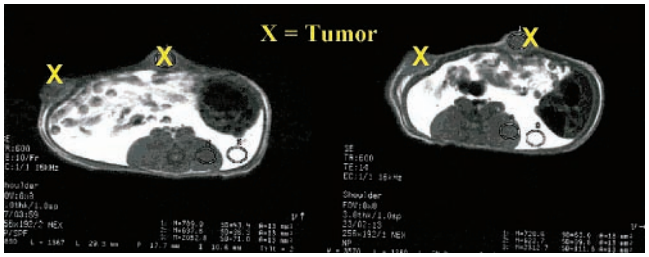

Figure 2. Tumor images rats implanted with Word Colon tumors) before (A) and 8 h postinjection (B) of Magnavist (1 mmol/kg).

phototoxicity, the hexyl ether group present at position-3 in compound **12** was replaced by a poly(ethylene glycol) methyl ether group by following the methodology depicted in Scheme 3, and conjugate **20** was isolated in good yield (see Experimental Procedures).

Body Tumor MR Imaging. *HPPH−Mono-Gd(III)-aminobenzyl-DTPA Conjugate **5**, HPPH−Di-Gd(III)-aminobenzyl-DTPA Conjugate **12**, and the Related PEG Derivative **20**.* Imaging was repeated at 1 and 24 h postinjection of Gd−HPPH **5** (11.25 μmol/kg) with identical imaging parameters (see Experimental Procedures). Region of interest measurements were obtained over the tumor paraspinal muscles and intraabdominal fat, using a workstation (GE Advantage Windows 3.1, GE Medical Systems, Milwaukee, WI). The tumor area of interest increased markedly, from 623 to 881 intensity units. The effect was striking both visually and quantitatively. Signal enhancement was largely restricted to tumor. The signal obtained from fat was essentially unchanged (1998 to 1939 intensity units), and muscle enhancement was minimal. The Gd−HPPH **5** was insoluble in water and required solubilization in 1% Tween-80/water solution, which represents a major barrier to human use because of its known toxicity at higher doses. Therefore, the formulation was revised to Gd−HPPH liposomal formulation (see Experimental Procedures), which has achieved a 25-fold increase in solubility.

To prove that the liposome preparation remains tumor-avid, we successfully produced images virtually identical to the Tween 80 formulation using 10 μmol/kg of conjugate **5**. We also observed that the "higher payload" tumor-avid double-Gd−HPPH compound **12** was equally soluble with liposomal capsulation and enhanced tumor signal. However, the effect was not linear (the signal enhancement was largely restricted to tumor, whose intensity rises markedly from 370 (pre-injection) to 582 (24 h) to 715 at 48 h postinjection.

No tumor enhancement with conjugate **20** over baseline was detected, either visually or quantitatively, at doses of 2.5 μmol/kg and 5.0 μmol/kg in rats. At a dose of 10 μmol/kg, the best enhancement of tumor signal relative to baseline developed 8 h after drug injection. A baseline supine transaxial image viewed from the caudal end (Figure 1, A) demonstrates transplanted tumor (1 cm^3) growing out of the ventral abdominal wall. Muscle, fat, and bowel were clearly defined. Baseline signal measurements (Figure 1B) of tumor, muscle, fat, and control tubes of saline and contrast medium were 538, 403, 172, 385, and 1684. Eight hours after intravenous injection of 10.0 μmol/kg of the Gd(III) complex of Pyro-PEG **20** (Figure 1C) the tumor was visually enhanced and the tumor signal measurement (Figure 1D) increased 22% to 654. Fat and muscle signal changed minimally, from 172 and 403 (baseline measurement) to 165 and 411 (after the conjugate injection), respectively. On the 8-h images, saline and contrast medium control tubes measured 359 and 1746, representing a variation of 15% and 5% respectively from baseline measurements, due to normal system "drift".

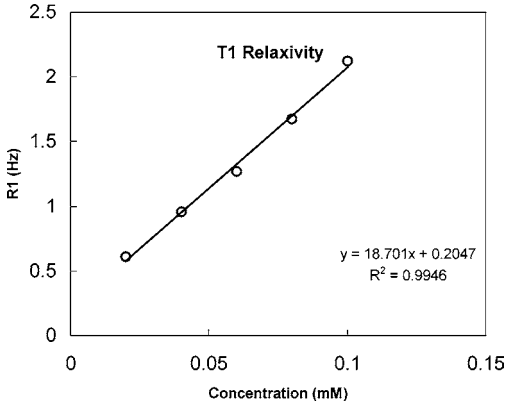

Figure 3. T1 relaxivity of conjugate **20**.

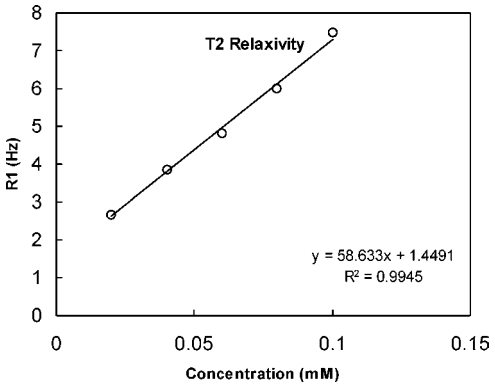

Figure 4. T2 relaxivity of conjugate **20**.

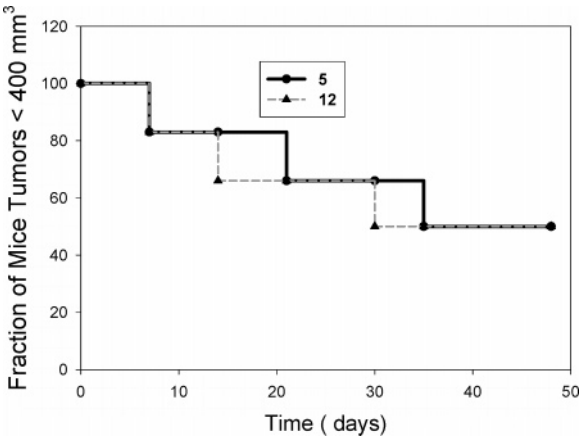

Figure 5. In vivo photosensitizing efficacy of DTPA conjugates **5** and **12** (liposomal formulation) at a dose of 0.47 μmol/kg in C_3H mice (six mice/group) implanted with RIF tumors. The 4−6 mm diameter tumors were exposed to light [130 J/cm^2 (75 mW/cm^2)] for 30 min from a tunable dye laser tuned to the maximum red absorption peak (λ_{max}665 nm)] 24 h postinjection. At day 50, 3/6 mice were tumor-free.

Comparative Study with Magnavist. At present, Magnavist [Gd(III) complex of DTPA] is a standard MRI agent that clinicians use on an almost daily basis. It, however, works by penetrating damaged tumor vascular beds and does not bind to tumor cells, so that when it rapidly clears from the circulation, the tumor concentration also falls rapidly. It has a very brief temporal "window" for MR imaging (5 to 10 min), and therefore to use Magnavist as a tumor-enhancing agent one must know where to image with MRI in advance as it clears

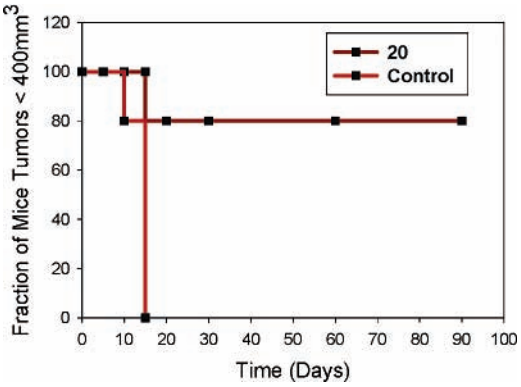

Figure 6. Mice (C3H/HeJ, six mice/group) bearing RIF tumors were treated with **20** (10 μmol/kg) with light (75mW, 135 J/cm^2) for 30 min at 8 h postinjection. Control: No light treatment. At day 90, 5/6 mice were tumor-free.

from tumors within minutes. In the present study, Magnavist was used to image tumors implanted in Fisher rats. The best images were obtained at 5, 10 min postinjection (data not shown). However, at 1, 4, 8, and 24 h postinjection, no tumor enhancement was observed (Figure 2, images at 8 h postinjection), whereas the lead compound (e.g. **20**) remains in tumors for a reasonable time, so that MRI could scan several large body areas and later treat transcutaneously by PDT.

T1 and T2 relaxivity of each compound was determined by taking the slope of linear least-squares fit of contrast agent concentration vs relaxation rate (for compound **20** see Figures 3 and 4). For comparison, relaxivity of Gd-DTPA (Magnevist, Berlex, Wayne, NJ) at 4.7 T was acquired under identical conditions. Compound **20** formulated in liposome demonstrated a relatively high T1 relaxivity of 18.70 $mM^{-1}\cdot s^{-1}$ at 4.7 T as compared to Gd-DTPA (3.25 $mM^{-1}\cdot s^{-1}$), as well as a high T2 relaxivity of 58.63 $mM^{-1}\cdot s^{-1}$.

*In Vivo Photosensitizing Efficacy of Liposome-Encapsulated Mono-Gd−HPPH Conjugate **5** and Di-Gd(III) Conjugate **12**:* The photosensitizing efficacies of the mono- **5** and di-Gd(III)-DTPA **12** were evaluated in C3H mice (six mice/group) bearing RIF tumors (*7*, *8*) at a dose of 0.47 μmol/kg. The compounds in liposomal formulation produced the same PDT efficacy (Figure 3). As can be seen, the presence of an additional Gd(III)-DTPA molecule did not inhibit PDT activity. By day 35 the effect of each compound was equal to 50% tumor cure (3/6 mice were tumor free and both formulations produced the same PDT efficacy (Figure 3). However, compound **12** at the tumor-imaging dose (10 μmol/kg), after light exposure (135 J/cm^2, 24 h postinjection), was found to be toxic and produced 100% mortality (without light exposure, no toxicity was observed).

*In Vivo Photosensitizing Activity of the PEG Analogue **20** at MR Imaging Dose.* Compound **20** at the tumor imaging dose (10.0 μmol/kg) was evaluated for PDT efficacy in C3H mice (10 mice/group) bearing RIF tumors under the light treatment conditions described for compounds **5** and **12** [130 J/cm^2 (75 mW/cm^2) for 30 min] at 8 h postinjection (tumor-imaging time). As can be seen from Figure 6, in preliminary screening, the PEG analogue **20** was found to be quite effective (80% of mice were tumor-free on day 90) and did not produce any mortality or adverse effects at the imaging dose before and after the light treatment. All treated mice showed normal behavior.

Skin Phototoxicity of the Conjugates and Advantages of the Related PEG Analogue. Conjugates **5**, **12**, and **20** (10 μmol/kg, the imaging dose) were injected (iv) individually to rats (three rats/group), and the foot was exposed to light (*18*). The feet of each rat (one exposed to light and another used as a control) response was observed daily. Skin response was significantly different for conjugates **5**, **12**, and **20**. Both **5** and **12** were found

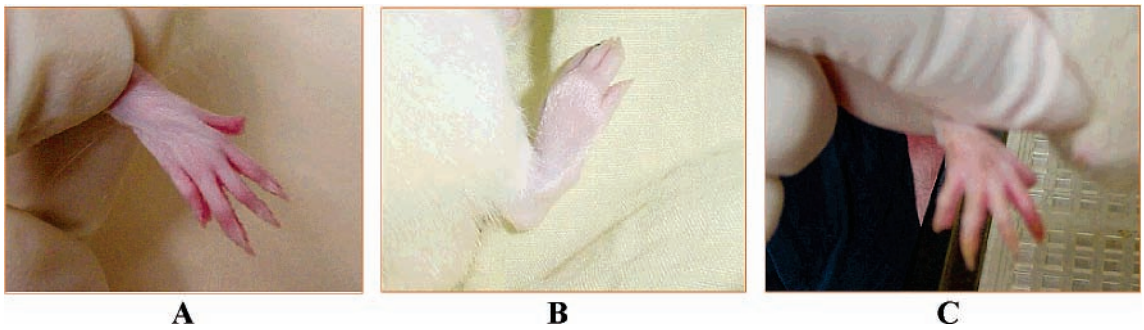

Figure 7. Foot response in female SD rats injected with 10 μmol/kg of compound **20** [A: before light exposure, B: light exposure at 24 h and C: at 96 h postinjection]. At 24 h, swelling of toes and at 96 h, light edema (almost normal) was observed (for details see the text).

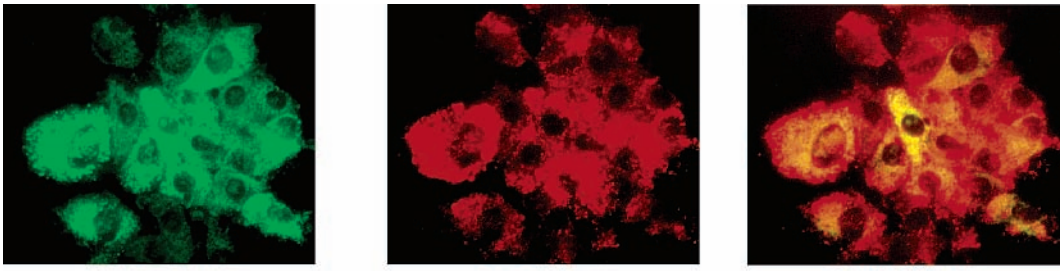

Figure 8. Comparative localization of Mitotracker Green (Mitochondrial marker) and conjugate **20** (1.0 μM) in RIF cells, determined by fluorescence light microscopy (false colors). Similar patterns were obtained from the mono- and di-Gd(III)-aminophenyl-DTPA conjugates **5** and **12** respectively (for details, see the text).

to be extremely phototoxic whereas compound **20** showed significantly reduced skin phototoxicity. The foot response was scored by following the literature procedure and was recorded as follows: At 24 h: 1.8 (moderate dry desquamation and swelling of toes); 72 h: 1.0 (erythema with edema and slight depilation); 96 h: 0.1 (light edema); 120 h: 0 (normal, no reaction) (Figure 7). Thus, initial mild-to-moderate phototoxicity resolved to some extent on day 4 and 5. Therefore, the introduction of a more hydrophilic group certainly helped in clearance of the drug from the skin, resulting in reduced phototoxicity.

Intracellular Localization. It has been shown by us and others that photosensitizers that localize in mitochondria are generally more effective than those that localize in lysosomes (*20*−*24*). Therefore, the localization characteristics of HPPH (localize in mitochondria) was compared with the related DTPA-Gd(III) conjugates including the PEG analogue (for details, see Experimental Procedures). The HPPH and the related DTPA-Gd(III) conjugates **5** and **12** and the PEG analogue **20** were found to localize in mitochondria. A representative example of the DTPA conjugate **20** is shown in Figure 8. Localization images by fluorescence light microscopy (see Experimental Procedures) were taken in rapid sessions. The results (Figure 8) indicate that Mitotracker Green and conjugate **20** localize to the same subcellular region, the mitochondria.

CONCLUSION

The preliminary data suggest that di-DTPA-Gd(III) conjugate **12** is a more effective MRI imaging agent than the related mono-DTPA analogue **5**. Therefore, for designing an improved imaging agent, it is advantageous to have two Gd(DTPA) moieties in the conjugates. However, for both HPPH conjugates (mono-DTPA-Gd(III) **5** and di-DTPA-Gd(III)) **12**, the imaging dose (10.0μmol/kg) produced severe skin phototoxicity. Interestingly, conjugate **20** in which the hexyl substituent (conjugate **12**) was replaced with PEG-monomethyl ether was found to be an effective MRI agent (at 8 h postinjection) at a dose of 10 μmol/kg, with enhanced in vivo photosensitizing efficacy and reduced skin phototoxicity. Measured T1 and T2 relaxivities for liposome-formulated Pyro-PEG-di-DTPA-Gd(III) contrast media **20** were significantly increased as compared to a commercially available mono-DTPA-Gd(III) MR contrast-enhancing agent and were consistent with theoretical values expected for a di-DTPA-Gd(III) conjugate (*25*).

Though the PEG conjugate is not entirely free from phototoxicity, the imaging and photosensitizing results obtained from our systematic synthetic design provides an excellent approach for developing improved bifunctional agents. These characteristics raise the concept of a single "see and treat" agent that could be injected intravenously to image the tumors by MRI and then treat them by exposing to light (PDT) introduced either endoscopically or by a thin fiber optic cable, following guided needle puncture. On the basis of these results, we extrapolate that an improved dual agent can be developed by (a) selecting those photosensitizers as substrates that possess higher tumor selectivity than HPPH, (b) the desired overall lipophilicity can be tuned by introducing mono- or di-PEG substituents at the peripheral position of the chromophore, (c) the depth of tissue penetration could further be increased by conjugating Gd(III)-DTPA with those photosensitizers that exhibit long-wavelength absorption near 750−800 nm. Such dual conjugates may have advantages in treating large and deeply seated tumors. These studies are currently in progress.

ACKNOWLEDGMENT

The authors are thankful to the NIH (CA 55791, 1 R21 CA109914-01), Oncologic Foundation of Buffalo, Roswell Park Alliance, and the shared resources of the Roswell Park Cancer Center Support Grant (P30CA16056) for financial support. We are thankful to Adam Sumlin, PDT Center, for his help in evaluating the foot-response assay (skin phototoxicity). The technical assistance provided by Schlossin and Carol Kaminskiin in tumor imaging is highly appreciated.

LITERATURE CITED

(1) Caravan, P., Ellison, J. J., McMurry, T. J., and Lauffer, R. B. (1999) Gadolinium(III) chelates as MRI contrast agents: Structure, dynamics, and applications. *Chem. Rev. 99*, 2293−352.

(2) Wagner, H. N., Szabo, Z., and Buchanan, J. W. (1995) Nuclear Medicine: What it is and what it does? In *Principles of Nuclear Medicine*, 2nd ed., Chapter 1, W. B. Saunders Co., Philadelphia.

(3) McAfee J. G., and Subramanian, G. (1984) Clinical Radionuclide Imaging. In *Radioactive Agents for Imaging* (Freeman, L. M., Ed.) Chapter 3, Grune & Stratton, Inc., Philadelphia.

(4) Grossman, Z. D., and Rosebrough, S. F. (1990) *Clinical Radioimmunoimaging*, Grune & Stratton, Inc., Philadelphia.

(5) Ni, Y., Adzamli, K., Miao, Y., Cresens, E., Yu, J., Periasamy, M. P., Adama, M. D., and Marchal, G. (2001) MRI contrast enhancement of necrosis by MP-2269 and gadoporphyrin-2 in a rat model of liver infarction. *Invest. Radiol. 36* (2), 97−103.

(6) Hoffmann, B., Bogdanov A., Jr., Marecos E., Ebert, W., Semmler, W., and Weissleder, R. (1999) Mechanism of gadoporphyrin-2 accumulation in tumor necrosis. *J. Magn. Reson. Imaging 9*, 336−41.

(7) Pandey, R. K., Sumlin, A. B., Potter, W. R., Bellnier, D. A., Henderson, B. W., Constantine, S.; Aoudia, M.; Rodgers, M. A. J., Smith, K. M., and Dougherty, T. J. (1996) Synthesis, photophysical properties and photodynamic efficacy of the alkyl ether analogues of chlorophyll-a derivatives. *Photochem. Photobiol. 63*, 194−205.

(8) Henderson, B. W., Bellnier, D. A., Greco, W. R., Sharma, A., Pandey, R. K., Vaughan, L., Weishaupt, K. R., and Dougherty, T. J. (1997) A quantitative structure−activity relationship for a congeneric series of pyropheophorbide derivatives as photosensitizers for photodynamic therapy. *Cancer Res. 57*, 4000−4007.

(9) Zheng, G., Potter, W. R., Sumlin, A., Dougherty, T. J., and Pandey, R. K. (2000) Photosensitizers related to purpurin-18-N-alkylamides. A comparative in vivo tumoricidal ability of ester vs amide functionalities. *Bioorg. Med. Chem. Lett. 10*, 123−127.

(10) Rungta, A., Zheng, G., Missert, J. R., Potter, W., Dougherty, T. J., and Pandey, R. K. (2000) Purpurinimides as photosensitizers: Effect of the presence and position of the substituents in in vivo photodynamic efficacy. *Bioorg. Med. Chem. Lett. 10*, 1463−1466.

(11) Zheng, G., Camacho, S., Potter, W., Bellnier, D. A., Henderson, B. W., Dougherty, T. J., and Pandey, R. K. (2001) Synthesis, tumor uptake and in vivo photosensitizing efficacy of a homologous series of 3-devinyl-3-(1-hexyloxyethyl)-purpurin-18-*N*-alkylimides. *J. Med. Chem. 44*, 1540−1559.

(12) Chen, Y., Graham. A., Potter, W., Morgan, J., Vaughan, L., Bellnier, D. A., Henderson, B. W., Oseroff, A., Dougherty, T. J., and Pandey, R. K. (2002) Bacteriopurpurinimides: Highly stable and potent photosensitizers for photodynamic therapy. *J. Med. Chem. 45*, 255−258.

(13) Li, G., Graham. A., Dobhal, M. P., Morgan, J., Oseroff, J., Dougherty, T. J., and Pandey, R. K. (2003) Synthesis, in vitro/in vivo photosensitizing efficacy, intracellular localization,

HAS (site II) binding ability of various bacteriochlorins derived from chlorophyll-a. *J. Med. Chem. 46*, 5349−5359.
(14) Chen, Y., Sumlin, A., Morgan, J., Gryshuk, A., Oseroff, A., Henderson, B. W., Dougherty, T. J., and Pandey, R. K. (2004) Synthesis and photosensitizing efficacy of isomerically pure bacteriopurpurinimides. *J. Med. Chem. 47*, 4814−4817.
(15) Dougherty, T. J., Pandey, R. K., Nava, H. R., Smith, J. A., Douglass H. O., Edge, S. B., Bellnier, D. A., O.Malley, L., and Cooper, M. (2000) Preliminary clinical data on a new photodynamic therapy photosensitizer HPPH for treatment of obstructive esophageal cancer. *Proc. SPIE*, *3909*, 25−27.
(16) Bellnier, D. A., Greco, W. R., Loewen, G. M., Nava V., Oseroff, A. R., Pandey, R. K., Tsuchida, T., and Dougherty, T. J. (2003) Population pharmacokinetics of the photodynamic therapy agent HPPH in cancer patients. *Cancer Res. 63*, 1806−1813.
(17) Smith, K. M., Goff, D. A., and Simpson, D. J. (1985) Meso substitution of chlorophyll derivatives: direct route for transformation of bacteriopheophorbide-*d* into bacteriopheophorbide-c. *J. Am. Chem. Soc*. *107*, 4941−4954.
(18) Pandey, R. K., Bellnier, D. A., Smith, K. M., and Dougherty, T. J. (1991) Chlorin and porphyrin derivatives as potential photosensitizers in photodynamic therapy. *Photochem. Photobiol*. *53*, 65−72.
(19) Cummins, C. H., Rutter, E. W., and Fordyce, W. A. (1991) A convenient synthesis of bifunctional chelating agents based on diethylenetriaminepentaacetic acid, their coordination chemistry with Yttrium(III). *Bioconjugate Chem*. *2*, 180−186.
(20) Kessel, D., and Luo, Y. (1999) Mitochondrial photodamage and PDT induced apoptosis. *Cell Differ. 6*, 28−35.
(21) MacDonald, I., Morgan, J., Bellnier, D. A., Paszkiewicz, G. M., Whitaker, J. E., Litchifeld, D. J., and Dougherty, T. J. (1999) Subcellular localization patterns and their relationship to photodynamic activity of pyropheophorbide-a derivatives. *Photochem. Photobiol. 70*, 789−97.
(22) Kessel, D., and Woodburn K. (1993) Biodistribution of photosensitizing agents. *Int. J. Biochem. 10*, 1377−1383.
(23) Malik, Z., and Amit, I. (1997) Subcellular localization of sulfonated tetraphenyl porphines in colon carcinoma cells by spectrally resolved imaging. *Photochem. Photobiol*. *65*, 389−396.
(24) Kessel, D. Chemical and biochemical determinants of porphyrin localization. In porphyrin localization and treatment tumors (Doiron, D. R., and Gomer, C. J., Eds.) pp 405−418, Alan R. Liss, New York.
(25) Viglianti, B. L., Abraham, S. A., Michelich, C. R., Yarmolenko, P. S., MacFall, J. R., Bally, M. B., and Dewhirst, M. W. (2004) In Vivo Monitoring of Tissue Pharmacokinetics of Liposome/Drug Using MRI: Illustration of Targeted Delivery. *Magn. Reson. Med. 51*, 1153−1162.

BC049807X

A New High Affinity Technetium-99m-Bombesin Analogue with Low Abdominal Accumulation

Kuo-Shyan Lin,[†] Andrew Luu,[†] Kwamena E. Baidoo,*[,†] Hossein Hashemzadeh-Gargari,[†] Ming-Kai Chen,[†] Kenneth Brenneman,[†] Roberto Pili,[‡] Martin Pomper,[§] Michael A. Carducci,[‡] and Henry N. Wagner, Jr.[†]

Department of Environmental Health Sciences, The Johns Hopkins Medical Institutions, 615 North Wolfe Street, Baltimore, Maryland 21205, and Department of Oncology, The Sidney Kimmel Comprehensive Oncology Center, The Johns Hopkins Medical Institutions, Cancer Research Building, 1650 Orleans Street, Baltimore, Maryland 21231, and Department of Radiology, The Johns Hopkins Medical Institutions, 600 N. Wolfe Street, Baltimore, Maryland 21287. Received July 23, 2004; Revised Manuscript Received October 6, 2004

^{99m}Tc-labeled bombesin analogues have shown promise for noninvasive detection of many tumors that express bombesin (BN)/gastrin-releasing peptide (GRP) receptors. ^{99m}Tc-labeled peptides, however, have a tendency to accumulate in the liver and intestines due to hepatobiliary clearance as a result of the lipophilicity of the ^{99m}Tc chelates. This makes the imaging of lesions in the abdominal area difficult. In this study, we have synthesized a new high affinity ^{99m}Tc-labeled BN analogue, [DTPA^1, Lys^3(^{99m}Tc-Pm-DADT), Tyr^4]BN, having a built-in pharmacokinetic modifier, DTPA, and labeled with ^{99m}Tc using a hydrophilic diaminedithiol chelator (Pm-DADT) to effect low hepatobiliary clearance. In vitro binding studies using human prostate cancer PC-3 cell membranes showed that the inhibition constant (K_i) for [DTPA^1, Lys^3(^{99}Tc-Pm-DADT), Tyr^4]BN was 4.1 ± 1.4 nM. Biodistribution studies of [DTPA^1, Lys^3(^{99m}Tc-Pm-DADT), Tyr^4]BN in normal mice showed very low accumulation of radioactivity in the liver and intestines (1.32 ± 0.13 and 4.58 ± 0.50% ID, 4 h postinjection, respectively). There was significant uptake (7.71 ± 1.37% ID/g, 1 h postinjection) in the pancreas which expresses BN/GRP receptors. The uptake in the pancreas could be blocked by BN, partially blocked by neuromedin B, but not affected by somatostatin, indicating that the in vivo binding was BN/GRP receptor specific. Scintigraphic images showed specific, high contrast delineation of prostate cancer PC-3 xenografts in SCID mice. Thus, the new peptide has a great potential for imaging BN/GRP receptor-positive cancers located even in the abdomen.

INTRODUCTION

Bombesin (BN), the first cancer cell autocrine peptide growth factor to be discovered (*1*), is a 14 amino acid peptide initially isolated from frog skin (*2*). The main mammalian members of the bombesin family of peptides are gastrin releasing peptide (GRP), a 27 amino acid peptide first isolated from porcine stomach (*3*), and neuromedin B (NMB), a 10 amino acid peptide first isolated from porcine spinal cord (*4*). Bombesin-like peptides produce many physiological activities that include stimulation of the release of numerous gastrointestinal hormones and peptides (*5, 6*), stimulation of pancreatic enzyme secretion (*7*), effects on the central nervous system (CNS) such as thermoregulation (*8*), and inhibition of thyroid-stimulating hormone (TSH) (*9*). Many tumors such as glioblastoma, small cell lung cancer, prostate, breast, gastric, colon, and pancreatic cancer (*10*−*18*) are also known to express cell surface receptors to bombesin-like peptides. The receptor system is accessible as a marker for the development of tracers for noninvasive detection and therapy of the cancers.

Radionuclides, such as ^{111}In, ^{125}I, ^{105}Rh, and ^{99m}Tc (*19*−*28*), have been used to label BN/GRP analogues for noninvasive in vivo imaging of BN/GRP receptor-positive cancers. Of these radionuclides, ^{99m}Tc is more advantageous because of its ready availability, low cost, excellent imaging properties (141 keV photon energy and 89% photon flux), favorable dosimetry, and high specific activity. Many ^{99m}Tc-labeled peptides, however, have a tendency to accumulate in the liver and intestines as a result of hepatobiliary clearance. Hepatobiliary clearance is the preferred excretion route because of the lipophilicity conferred on the labeled peptide by many Tc chelates. The high accumulation of radioactivity in the liver and intestines will jeopardize the imaging of BN/GRP receptor-positive cancers and their metastases in the abdominal area. Radiotracers with higher hydrophilicity tend to be excreted trough the urinary system (*29*−*31*), Strategies for decreasing abdominal accumulation have included the use of hydrophilic bifunctional chelating agents (BFCA) (*28*) or coligands (*32*). Recently, we reported the use of a built-in pharmacokinetic modifier in the form of diethylenetriaminepentaacetic acid (DTPA) to reduce hepatobiliary clearance (*33*).

In this study, we present a new high affinity, hydrophilic ^{99m}Tc-labeled BN/GRP analogue, [DTPA^1, Lys^3(^{99m}Tc-Pm-DADT), Tyr^4]BN, having the build-in pharmacokinetic modifier, DTPA, at the N-terminus and labeled with ^{99m}Tc using a hydrophilic diaminedithiol (DADT) chelate, Pm-DADT (Figure 1), to direct its clearance through the urinary system. The design and synthesis of [DTPA^1, Lys^3(^{99m}Tc-Pm-DADT), Tyr^4]BN as well as its initial biological evaluation are discussed here.

* To whom correspondence should be addressed. Telephone: (410)-955-7706. Fax: (410) 955-6222. E-mail: kbaidoo@jhsph.edu.
[†] Department of Environmental Health Sciences.
[‡] Department of Oncology.
[§] Department of Radiology.

10.1021/bc049820h CCC: $30.25 © 2005 American Chemical Society
Published on Web 12/31/2004

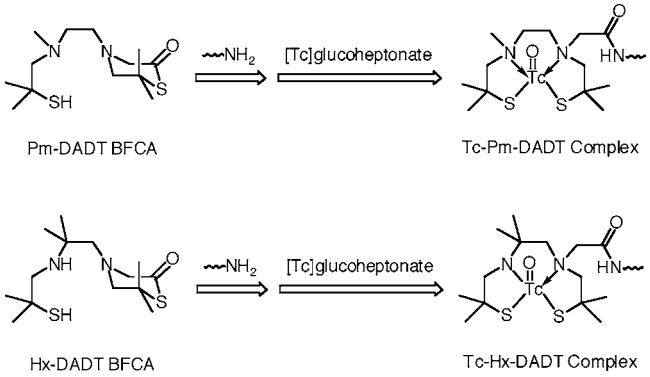

Figure 1. The structures of the diaminedithiol (DADT) bifunctional chelating agents (BFCA) and their Tc complexes. Reaction of the bifunctional chelating agents Hx-DADT and Pm-DADT with amine nucleophiles results in the release of a thiol group to complete the chelating core of the diaminedithiol chelating system for subsequent chelation of Tc from labile Tc complexes such as Tc-glucoheptonate.

MATERIALS AND METHODS

BN, neuromedin B, and somatostatin were purchased from Advanced ChemTech (Louisville, KY). [^{99}Tc]NH_4TcO_4 and [^{125}I-Tyr^4]BN were purchased from NEN Life Science Products (Boston, MA). [^{99m}Tc]$NaTcO_4$ was purchased as a solution in physiologic saline from Syncor (Timonium, MD). The Glucoscan kit was purchased from the Du Pont Radiopharmaceutical Division (Billerica, MA). All other chemicals were obtained from either Aldrich Chemical Co. (Milwaukee, WI) or Sigma Chemical Company (St. Louis, MO). Solvents and chemicals were reagent grade and used as received without further purification. Pm-DADT was synthesized according to our previously published procedure (*34*).

Male CD-1 mice were purchased from the Charles River Laboratories (Charles River, MA). The PC-3 cell line was obtained from the American Type Culture Collection (Rockville, MD) and grown in the Cell Culture Laboratory, School of Medicine, The Johns Hopkins University (Baltimore, MD). Amino acid analyses and MALDI mass spectral analyses were performed by AnaSpec, Inc. (San Jose, CA).

HPLC was performed with a Waters Chromatography Division (Milford, MA) HPLC System equipped with two model 510EF pumps, a model 680 automated gradient controller, a model 490 UV absorbance detector, and a Bioscan NaI scintillation detector connected to a Bioscan Flow-count System. The output from two channels of the UV detector and the output from the Flow-count system were fed into a Gateway 2000 P5−133 computer fitted with an IN/US System, Inc. (Tampa, FL) computer card. HPLC acquisition and analysis were performed with the Winflow software from IN/US. The semipreparative column (C18 Novapak cartridge, 25 mm × 10 cm, 6 μm), the analytical column (C18 Novapak cartridge, 8 mm × 10 cm, 4 μm), and the C18 Light Sep-Pak cartridge were purchased from Waters Chromatography Division. The G3000SW size exclusion column (silica, 7.5 mm × 30 cm, particle size 10 μm, pore size 25 nm) was purchased from TosoHaas (Montogomeryville, PA). HPLC solvents consisted of acetontrile containing 0.1% trifluoroacetic acid (solvent A) and water containing 0.1% trifluoroacetic acid (solvent B). Liquid scintillation counting for quantification of ^{99}Tc activity was performed on an LKB Wallac instrument model 1219 Rackbeta using Ecolume (ICN pharmaceuticals, Inc., Costa Mesa, CA) as cocktail. Filtration of in vitro assay mixtures was performed on a BRANDEL, 48M Harvester. ^{125}I activity on filters from in vitro assays and ^{99m}Tc activity of tissues from biodistribution and blocking studies were counted on an automated gamma counter (Pharmacia-Wallac model 1282). Analyses of in vitro binding assay results were performed using the EBDA/LIGAND programs from Biosoft (Milltown, NJ). ^{99m}Tc activity for synthetic reactions was measured in a Capintec CRC-7 Dose Calibrator.

Synthesis of [DTPA^1, Lys^3(Pm-DADT), Tyr^4]BN. The basic peptide sequence, [DTPA^1, Lys^3, Tyr^4]BN was assembled in an Advanced ChemTech 90 Tabletop Peptide Synthesizer using the *tert*-butyloxycarbonyl (Boc) protocol starting with Boc-L-methionine-*p*-methylbenzhydrylamine resin (3 g, 1 mmol/g). Coupling was performed for 30 min with DIC (9 mmol) and HOBt (9 mmol) using the appropriate Boc-protected amino acid (9 mmol) which included N^{im}-tosyl-His, N^{in}-formyl-Trp, *N*-γ-xanthyl-Gln, *N*-β-xanthyl-Asn, *O*-2,6-dichlorobenzyl-Tyr, and N^{ϵ}-2-chlorobenzyloxycarbonyl-Lys in methylene chloride/dimethylformamide (1:1). The coupling reactions were monitored with the nynhydrin test and was repeated if the test was positive. The Boc group was deprotected during each cycle with trifluoroacetic acid (25%) in methylene chloride. DTPA was conjugated at the last step of peptide assembly using the method of Mokotoff et al. (*35*). At the end of peptide assembly, cleavage and side chain deprotection were performed using anhydrous hydrogen fluoride (14 g) at 0 °C for 1.5 h in the presence of anisole (19.7 mmol). After removal of hydrogen fluoride using a slow stream of nitrogen, the residue was washed with ether, dried, and then extracted with 5% aqueous acetic acid (50 mL) and lyophilized. The lyophilized powder was dissolved in water (50 mL), and the solution was adjusted to pH 11 with 2.5 M NaOH. After 5 min, the solution was readjusted to pH 7 with 6 N HCl. The crude product was purified by HPLC using a linear gradient from solvent A (15%)/solvent B (85%) to solvent A (40%)/solvent B (60%) over the course of 50 min at a flow rate of 6 mL/min using the semipreparative column monitored on-line for UV absorption at 220 nm. Eluates containing the product with a retention time of 26.0 min were collected, pooled, and lyophilized. The purity of [DTPA^1, Lys^3, Tyr^4]BN was >95% as assessed by analytical HPLC. The yield of [DTPA^1, Lys^3, Tyr^4]BN was 968 mg (17%).

Pm-DADT was coupled to [DTPA^1, Lys^3, Tyr^4]BN according to Scheme 1. Pm-DADT·2HCl (9.9 mg, 27.2 μmol) and [DTPA^1, Lys^3, Tyr^4]BN (9.0 mg, 4.7 μmol) were dissolved in borate buffer (500 μL, 0.1 M, pH 9) and acetonitrile (500 μL), and the pH was readjusted to 9 with triethylamine. The mixture was incubated at room temperature for 3 h and then extracted with ether (3 × 2 mL). The aqueous fraction was chromatographed by HPLC with a linear gradient from solvent B (100%) to solvent A (80%)/solvent B (20%) over the course of 60 min at a flow rate of 6 mL/min using the semipreparative column monitored on-line for UV absorption at 220 nm. The product with a retention time of 30.8 min was collected, followed by lyophilization. The synthetic yield of [DTPA^1, Lys^3(Pm-DADT), Tyr^4]BN was 5.2 mg (50%). Amino acid analysis gave the expected amino acid ratios; calc/found Asn (1/0.88), His (1/1.14), Val (1/0.98), Leu (1/0.95), Lys (1/0.81), Gln(2/1.79), Gly (2/2.19), Ala (1/0.98), Tyr (1/1.09), Met (1/0.97). MALDI MS: calc MW for [DTPA^1, Lys^3(Pm-DADT), Tyr^4]BN, 2195.0; found $[M + H]^+$ 2195.1.

^{99m}Tc Labeling of [DTPA^1, Lys^3(Pm-DADT), Tyr^4]BN. ^{99m}Tc labeling of [DTPA^1, Lys^3(Pm-DADT), Tyr^4]BN was performed as depicted in Scheme 1. A glucoheptonate kit (Glucoscan) was reconstituted with water (1.0 mL). From this solution, [^{99m}Tc]glucoheptonate

Scheme 1. Synthesis of [DTPA^1, Lys^3(Tc−Pm-DADT), Tyr^4]BN

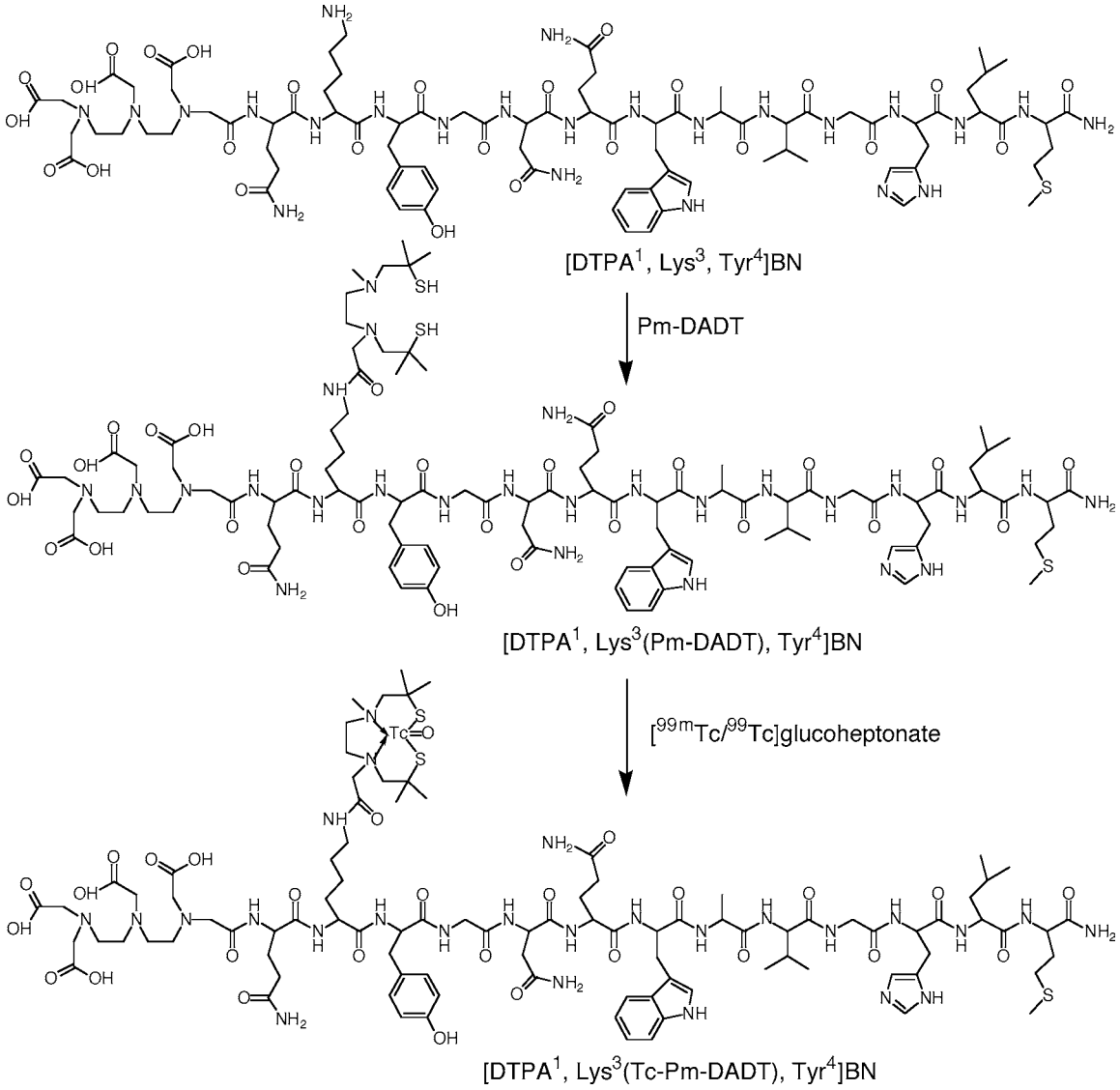

was prepared by addition of an aliquot (200 μL) to a [^{99m}Tc]pertechnetate solution (500 μL, 10−20 mCi), and the mixture was vortexed for 1 min. Then, the [^{99m}Tc]glucoheptonate solution (300 μL) was added to a solution of the [DTPA^1, Lys^3(Pm-DADT), Tyr^4]BN (0.5 μmol) in water (500 μL), and the mixture was vortexed for 1 min and incubated at room temperature for 10 min. The reaction was followed by HPLC using a linear gradient from solvent A (25%)/solvent B (75%) to solvent A (55%)/solvent B (45%) over the course of 60 min at a flow rate of 2 mL/min using the analytical column monitored on-line for UV absorption at 220 nm and scintillation for radioactivity. [DTPA^1, Lys^3(^{99m}Tc-Pm-DADT), Tyr^4]BN was obtained as a single product peak with a retention time of 35.1 min compared with a retention time of 27 min for [DTPA^1, Lys^3(Pm-DADT), Tyr^4]BN, the unlabeled precursor. The yield was > 90%.

Preparation of the ^{99}Tc Analogue of [DTPA^1, Lys^3-(Pm-DADT)Tyr^4]BN. A solution of [^{99}Tc]glucoheptonate in water (20 μL, 20 mM) was added to a solution of [DTPA^1, Lys^3(Pm-DADT), Tyr^4]BN (0.8 mg, 0.36 μmol) in methanol (400 μL) and water (400 μL), and the mixture was incubated at room temperature for 10 min. A similar product was obtained as described above for the ^{99m}Tc analogue. The product was isolated by HPLC using the same conditions above for the purification of the ^{99m}Tc analogue. The yield of the product was 17%. MALDI MS: calc MW for [DTPA^1, Lys^3(^{99}Tc-Pm-DADT), Tyr^4]BN 2308.0, found $[M + H]^+$ 2307.8.

In Vitro Binding Assay of BN Analogues. In vitro binding studies were performed using a modified method of Reile et al. (*36*). Briefly, membrane protein (10 μg) was incubated at 25 °C for 35 min with [^{125}I-Tyr^4]BN (100 pM) in the presence or absence of various concentrations of BN, somatostatin, [DTPA^1, Lys^3, Tyr^4]BN, [DTPA^1, Lys^3-(Pm-DADT), Tyr^4]BN or [DTPA^1, Lys^3(^{99}Tc-Pm-DADT), Tyr^4]BN ranging from 10 pM to 10 μM in the assay buffer (50 mM Tris-HCl buffer, pH 7.4, containing 1 mg/mL bovine serum albumin (BSA) and 2 μg/mL bacitracin) (125 μL total volume). Nonspecific binding was determined in the presence of 1 μM bombesin. The reaction was terminated by rapid filtration through Whatman GF/B glass fibers presoaked for 30 min in the wash buffer (50 mM Tris-HCl buffer, pH 7.4, containing 1 mg/mL BSA). The filter was washed 3 × 5 mL with ice cold wash buffer. Radioactivity on the filters was counted using the automated gamma counter. The results of the assay were analyzed by the EBDA/LIGAND computer programs (*37*). The assays were performed in duplicate and the whole experiment was repeated three times.

Biodistribution of [DTPA^1, Lys^3(^{99m}Tc-Pm-DADT), Tyr^4]BN in Normal Mice. The HPLC-purified [DTPA^1,

Lys^3(^{99m}Tc-Pm-DADT), Tyr^4]BN was isolated from the HPLC eluate by solid-phase extraction using the C18 Light Sep-Pak cartridge. The Sep-Pak cartridge was first washed with ethanol (5 mL) followed by a solution of ammonium acetate (0.05 M, 5 mL). The HPLC eluate containing [DTPA^1, Lys^3(^{99m}Tc-Pm-DADT), Tyr^4]BN was diluted five times with ammonium acetate (0.05 M) and then passed through the Sep-Pak cartridge. The Sep-Pak cartridge was washed with an ammonium acetate solution (0.05 M, 5 mL) and then [DTPA^1, Lys^3(^{99m}Tc-Pm-DADT), Tyr^4]BN was eluated with ethanol (300 μL). The ethanolic solution was diluted with physiologic saline to make the final injectate (10 μCi/mL) containing <0.5% ethanol.

Normal male CD-1 mice (average weight 31.6 ± 1.0 g) were used for the biodistribution studies. [DTPA^1, Lys^3(^{99m}Tc-Pm-DADT), Tyr^4]BN (2 μCi, 200 μL) was injected into mice via the tail vein. At 15 min, 1, 2, and 4 h postinjection, four mice for each time point were euthanized by cervical dislocation. Major organs were dissected, weighed, and counted in the automated gamma counter with aliquots of the injectate as standards counted at the same time. The percent injected dose per organ (% ID/organ) and the percent injected dose per gram (% ID/g) were calculated. The % ID in blood was estimated with the assumption that the total blood volume is 6.5% of the body weight.

In blocking studies, each mouse received a subcutaneous injection of 700 μg BN, neuromedin B, or somatostatin in saline (100 μL) or saline vehicle (100 μL) 30 min before the intravenous injection of [DTPA^1, Lys^3(^{99m}Tc-Pm-DADT), Tyr^4]BN. One hour after the injection of the tracer, the mice were sacrificed and major organs were dissected, weighed, and counted as described above.

Stability Test of [DTPA^1, Lys^3(^{99m}Tc-Pm-DADT), Tyr^4]BN in Human Serum. The purified ethanolic solution (300 μL) of [DTPA^1, Lys^3(^{99m}Tc-Pm-DADT), Tyr^4]BN was diluted with saline (3 mL), and then 100 μL of this diluted solution was mixed with 900 μL of human serum. The mixture was incubated in a 37 °C water bath. After 2, 4, and 6 h, an aliquot (100 μL) was removed and analyzed by HPLC.

The HPLC conditions were isocratic at a flow rate of 1 mL/min using the size exclusion column monitored online for UV absorption at 280 nm and scintillation for radioactivity. The eluent consisted of phosphate buffer (0.2 M, pH 7.15) containing 10% acetonitrile and 0.05% sodium azide. The serum proteins eluted at the retention time ranging from 5 to 10 min, and [DTPA^1, Lys^3(^{99m}Tc-Pm-DADT), Tyr^4]BN eluted at the retention time of 13.2 min.

Scintigraphic Imaging of Prostate Cancer PC-3 Xenografts Using [DTPA^1, Lys^3(^{99m}Tc-Pm-DADT), Tyr^4]BN. Male SCID mice (24.0−32.6 g) were injected subcutaneously with 10^6 PC-3 human prostate cancer cells in matrigel (0.3 mL) in one flank. The mice having palpable tumors after 8 weeks were used for imaging studies. HPLC purified [DTPA^1, Lys^3(^{99m}Tc-Hx-DADT), Tyr^4]BN (200 μCi) was injected through the tail vein. Each mouse was injected with HPLC purified [DTPA^1, Lys^3(^{99m}Tc-Pm-DADT), Tyr^4]BN (200 μCi) through the tail vein. For comparison, another group of mice were preinjected subcutaneously with 0.7 mg BN to block BN/GRP receptors in vivo 30 min before receiving radiotracer. At 12 h postinjection of tracer, the mice were anaesthesized with urethane and placed directly on the face of one crystal head of a Phillips IRIX VT camera fitted with a low energy high resolution parallel hole collimator and imaged. Image analysis was performed using the Odyssey FX 8.9C software. The target to nontarget ratio on the image was calculated from regions of interest drawn over the tumor area (target) and the contralateral region (nontarget) of each mouse image.

RESULTS AND DISCUSSION

The development of biomarkers for early detection of cancer is important in patient management. Because they are rapidly metabolized in blood, autocrine growth peptides such as bombesin/GRP, are not suitable as biomarkers for detection. The receptors, on the other hand, can be used as biomarkers for detection if suitable tracers could be developed for identifying them in vivo. In many instances, such as in small cell lung cancer (*38, 39*) and gastric cancer (*18*), there are practically no receptors present in surrounding normal tissue making this system amenable to good target to non target differentiation that can be taken advantage of in both imaging and therapy.

Currently, there is significant evidence of the presence of BN receptors in human biopsy samples of prostate, breast, stomach, colon, and small cell lung cancer (*17, 18, 40*−*44*). The incidence of high-density binding sites appears to be near 100% for prostate cancer (*17*) and small cell lung cancer (*42, 45, 46*). In breast cancer 63% of invasive ductal carcinoma and ductal carcinoma in situ as well as all lymph node metastases from the primary tumors express the receptor (*40*). The incidence is 57% for stomach cancer (*18*) and about 40% for colon cancer (*44*). Thus far, in a limited number of patients, the feasibility of imaging bombesin receptors in humans has been demonstrated (*24, 27*).

It is becoming increasingly evident that the BN/GRP receptor becomes expressed early in the process of carcinogenesis in a number of cancers that have been investigated. For example, pulmonary BN/GRP receptor levels in adult lung are extremely low or nonexistent under normal conditions. However, prolonged tobacco exposure, transformed cells, and lung cancer result in marked increases in pulmonary BN/GRP levels and the expression of their receptors (*45, 47*). In human prostate cancer tissue, a massive bombesin/GRP receptor overexpression has been demonstrated in prostatic intraepithelial proliferative lesions, a premalignant condition, and in prostatic carcinoma but not in normal tissues or other prostate hyperplasias (*17*). Similar results have also been reported for gastric cancer where a high density of receptors is present in gastric cancer and Menetrier's disease, a mucosal disorder known to be premalignant, but absent in the surrounding normal tissues (*18*). Such data are not only of biological significance but also provide a molecular basis for potential applications such as bombesin/GRP-receptor scintigraphy for biochemical characterization of the cancers with respect to the extent of bombesin/GRP receptor expression on the cells. The benefits of such characterization would include early diagnosis including the monitoring of high risk individuals such as heavy smokers, imaging of the extent of disease, and the selection of patients to benefit from therapies based on bombesin/GRP receptors.

For these reasons efforts continue to be made to develop ^{99m}Tc-labeled bombesin analogues for imaging neoplasia that express the receptor (*22*−*28*). Because the binding of Tc, an inorganic metal, to the peptide is weak, it is necessary to provide a Tc chelating site on the peptide that can bind Tc in a stable fashion. A number of chelating systems have been investigated for this purpose. We have been investigating the use of diaminedithiol ligands, in the form of the bifunctional

chelating agents depicted in Figure 1, as the carrier of the Tc label. DADT ligands have been shown to be one of the most promising chelators for labeling substrates with Tc and Re. The advantages of the ligand system include stable and well characterized complexes. DADT ligands have been used to label both proteins and peptides with Tc for applications such as cancer and inflammation imaging (*22, 34, 48, 49*).

Previously, we showed in model studies that the labeling of Lys^3-BN with ^{99m}Tc, using Pm-DADT as the bifunctional chelating agent resulted in reduced hepatobiliary activity compared to that of Hx-DADT (intestines and liver, 29% vs 96% ID, 3 h postinjection) (*22*). On chelation of the $[Tc(V)\text{-}oxo]^{3+}$ core using Hx-DADT derived ligands, the resulting TcO-Hx-DADT complex core (Figure 1) is neutral as a consequence of the deprotonation of two sulfhydryl and one secondary amine groups (*50*). In contrast, TcO-Pm-DADT (Figure 1) exhibits one positive charge due to the deprotonation of only the two sulfhydryl groups (*34*). Thus, in applying the two bifunctional chelating agents to label Lys^3-BN, a more hydrophilic product, $Lys^3(^{99m}Tc\text{-}Pm\text{-}DADT)BN$, is obtained from Pm-DADT, compared with $Lys^3(^{99m}Tc\text{-}Hx\text{-}DADT)BN$ which is derived from Hx-DADT. The hydrophilicity of $Lys^3(^{99m}Tc\text{-}Pm\text{-}DADT)BN$ accounts for its lower accumulation in the hepatobiliary system. Recently (*33*), we also explored the use of DTPA as a built-in pharmacokinetic modifier to reduce the excretion of a ^{99m}Tc-labeled BN analogue, [$DTPA^1$, $Lys^3(^{99m}Tc\text{-}Hx\text{-}DADT)$, Tyr^4]BN, through the hepatobiliary system. For this compound, Hx-DADT was used to chelate ^{99m}Tc. Compared to $Lys^3(^{99m}Tc\text{-}Hx\text{-}DADT)BN$ (also labeled using Hx-DADT), the excretion of [$DTPA^1$, $Lys^3(^{99m}Tc\text{-}Hx\text{-}DADT)$, Tyr^4]BN through the hepatobiliary pathway was greatly reduced (from 96% for $Lys^3(^{99m}Tc\text{-}Hx\text{-}DADT)BN$ to 21% for [$DTPA^1$, $Lys^3(^{99m}Tc\text{-}Hx\text{-}DADT)$, Tyr^4]BN), indicating the success of the pharmacokinetic modifier in modulating the biodistribution of [$DTPA^1$, $Lys^3(^{99m}Tc\text{-}Hx\text{-}DADT)$, Tyr^4]BN. These results showed that both the more hydrophilic TcO-Pm-DADT and the use of the pharmacokinetic modifier could independently lower the hepatobiliary clearance of the resulting ^{99m}Tc-labeled BN analogues. However, further reduction of the hepatobiliary clearance is necessary to lower the background radioactivity for better imaging of BN/GRP receptor-positive cancers and their metastases located in the abdominal area. In this study, therefore, we combined the two strategies of pharmacokinetic modifier and hydrophilic chelate in the same peptide in an effort to further lower the hepatobiliary accretion of the labeled peptide.

In the design of the target molecule, [$DTPA^1$, Lys^3-$(^{99m}Tc\text{-}Pm\text{-}DADT)$, Tyr^4]BN, we sought modifications only at the N-terminus of BN. The C-terminal octapeptide, which is required for receptor binding (*51*), was left intact in order to preserve high affinity binding to the receptor. Pyr at the N-terminus of BN was replaced by DTPA, which serves as the pharmacokinetic modifier. Arg at the third position of BN was replaced by Lys to provide the essential ϵ-amino group for coupling to the bifunctional chelating agent, Pm-DADT. Coupling of Pm-DADT at the Lys side chain which is placed at a distance from the receptor binding region was designed to minimize the interference of the Tc-chelate with the receptor binding site. Leu at the fourth position was also replaced by Tyr to facilitate the potential direct iodination of the resulting analogue.

The peptide backbone [$DTPA^1$, Lys^3, Tyr^4]BN was assembled using the Boc technology. Coupling of the bifunctional chelating agent, Pm-DADT, to [$DTPA^1$, Lys^3, Tyr^4]BN was performed at pH 9 using a Pm-DADT: [$DTPA^1$, Lys^3, Tyr^4]BN ratio of 6:1 (Scheme 1). After 3 h incubation at room temperature, the excess Pm-DADT was removed by extraction with ether and the [$DTPA^1$, Lys^3(Pm-DADT), Tyr^4]BN adduct purified by semipreparative reversed phase HPLC. Side chain protection was unnecessary since the indole and imidazole groups of Trp and His, respectively, are weak neucleophiles under the coupling conditions. The purified adduct was characterized by both mass spectrometry and amino acid analysis.

Table 1. Results of in Vitro Binding Studies of Bombesin Analogues to PC-3 Cell Membranes

compound	K_i[a] (nM)
bombesin	1.7 ± 0.6
[$DTPA^1$, Lys^3, Tyr^4]BN	3.1 ± 1.3
[$DTPA^1$, Lys^3(Pm-DADT), Tyr^4]BN	15.5 ± 1.2
[$DTPA^1$, $Lys^3(^{99}Tc\text{-}Pm\text{-}DADT)$, Tyr^4]BN	4.1 ± 1.4
somatostatin	>10000

[a] Values represent the mean ± SD ($n = 3$).

We prepared both no-carrier-added (^{99m}Tc) and milligram quantities (^{99}Tc) of the Tc-labeled BN analogue, [$DTPA^1$, Lys^3(Tc-Pm-DADT), Tyr^4]BN. These Tc derivatives were prepared in ligand exchange reactions by incubation of a mixture of [$DTPA^1$, Lys^3(Pm-DADT), Tyr^4]BN with [^{99m}Tc]- or [^{99}Tc]glucoheptonate at room temperature (Scheme 1). Only one product was obtained in both cases. The yield of ^{99m}Tc product was >90% after incubation for 10 min at room temperature as determined by HPLC. The ^{99}Tc product with 17% isolated yield was characterized by chromatographic comparison to the ^{99m}Tc analogue and mass spectrometry.

Both DTPA and the DADT chelating ligands can coordinate Tc. Therefore, a major issue in the design of [$DTPA^1$, $Lys^3(^{99m}Tc\text{-}Pm\text{-}DADT)$, Tyr^4]BN was the site of Tc chelation. The mass spectrometry results of [$DTPA^1$, $Lys^3(^{99}Tc\text{-}Pm\text{-}DADT)$, Tyr^4]BN indicated that only one [Tc-oxo] center was chelated to [$DTPA^1$, Lys^3(Pm-DADT), Tyr^4]BN. This could either be at the DADT or DTPA site. In the stability studies, only 6.8% of radioactivity was transferred to serum proteins even after 6 h incubation at 37 °C. This is an indication of the strong binding of Tc to the peptide, suggesting binding at the DADT site. The labeling of proteins with ^{99m}Tc via DTPA results in poor stability both in vitro and in vivo (*52*). Furthermore, we have shown in previous studies that in the presence of the benzylamine derivative of Pm-DADT, more than 100 fold excess DTPA cannot compete for the chelation of ^{99m}Tc (*34*). Taken together, the likelihood is strong that the ^{99m}Tc is chelated via the DADT ligand site rather than DTPA.

As a first step in the evaluation of the biological activity of [$DTPA^1$, Lys^3(Tc-Pm-DADT), Tyr^4]BN, we have investigated the ability of [$DTPA^1$, Lys^3(Tc-Pm-DADT), Tyr^4]-BN to bind to the BN/GRP receptor in human prostate cancer PC-3 cell membrane preparations according to a modified method of Reile et al. (*36*). These studies involved competitive binding experiments using the authentic BN receptor ligand [^{125}I-Tyr^4]BN. Results of analysis with the EBDA/LIGAND computer programs are shown in Table 1. The apparent affinities (K_i) of [$DTPA^1$, Lys^3, Tyr^4]BN (3.1 ± 1.3 nM) and [$DTPA^1$, $Lys^3(^{99}Tc\text{-}Pm\text{-}DADT)$, Tyr^4]BN (4.1 ± 1.4 nM) for the BN receptor were comparable to that of BN (1.7 ± 0.6 nM) itself. The unlabeled Pm-DADT adduct, [$DTPA^1$, Lys^3-(Pm-DADT), Tyr^4]BN, had slightly lower affinity (15.5 ± 1.2 nM). Somatostatin which does not bind to the receptor system had a $K_i > 10000$ nM.

Table 2. Biodistribution Results (% ID/organ)[a] of [DTPA[1], Lys[3](99mTc-Pm-DADT), Tyr[4]]BN in normal Mice at Different Time Points

	15 min	1 h	2 h	4 h
blood[b]	5.07 ± 0.50	2.78 ± 0.50	1.52 ± 0.13	1.22 ± 0.07
brain	0.05 ± 0.02	0.03 ± 0.01	0.02 ± 0.01	0.017 ± 0.004
heart	0.15 ± 0.02	0.07 ± 0.02	0.06 ± 0.03	0.03 ± 0.01
lung	0.37 ± 0.02	0.19 ± 0.04	0.21 ± 0.08	0.16 ± 0.05
kidneys	9.14 ± 1.47	7.67 ± 1.47	6.11 ± 0.90	3.40 ± 0.76
spleen	0.14 ± 0.08	0.07 ± 0.03	0.06 ± 0.02	0.05 ± 0.01
pancreas	1.85 ± 0.24	1.49 ± 0.40	1.29 ± 0.38	1.33 ± 0.24
intestines	5.51 ± 0.56	7.25 ± 0.90	6.15 ± 0.50	4.58 ± 0.50
stomach	0.88 ± 0.07	0.74 ± 0.13	0.61 ± 0.08	0.43 ± 0.23
liver	4.26 ± 0.81	1.70 ± 0.31	1.66 ± 0.41	1.32 ± 0.13

[a] Values represent the mean ± SD ($n = 4$). [b] The blood volume is estimated to be 6.5% of the body weight.

Table 3. Radioactivity Concentration (% ID/g)[a] of [DTPA[1], Lys[3](99mTc-Pm-DADT), Tyr[4]]BN in Normal Mice Organs at Different Time Points

	15 min	1 h	2 h	4 h
blood	2.44 ± 0.24	1.39 ± 0.24	0.74 ± 0.07	0.58 ± 0.05
brain	0.12 ± 0.04	0.07 ± 0.03	0.05 ± 0.03	0.04 ± 0.01
heart	0.96 ± 0.15	0.46 ± 0.13	0.38 ± 0.15	0.23 ± 0.02
lung	1.72 ± 0.15	0.78 ± 0.13	0.73 ± 0.21	0.69 ± 0.08
kidneys	16.4 ± 2.80	15.3 ± 3.11	11.9 ± 2.58	6.66 ± 0.94
spleen	1.09 ± 0.37	0.68 ± 0.22	0.57 ± 0.22	0.55 ± 0.15
pancreas	8.95 ± 0.98	7.71 ± 1.37	5.99 ± 1.56	5.45 ± 0.36
intestines	1.62 ± 0.11	2.61 ± 0.29	2.00 ± 0.17	1.47 ± 0.25
stomach	1.69 ± 0.74	1.61 ± 0.48	1.08 ± 0.49	0.87 ± 0.42
liver	1.95 ± 0.24	0.93 ± 0.16	0.84 ± 0.27	0.77 ± 0.11
muscle	0.67 ± 0.08	0.39 ± 0.12	0.30 ± 0.09	0.11 ± 0.02

[a] Values represent the mean ± SD ($n = 4$).

Results of the biodistribution studies of [DTPA[1], Lys[3]-(99mTc-Pm-DADT), Tyr[4]]BN in normal mice are summarized in Tables 2 and 3. [DTPA[1], Lys[3](99mTc-Pm-DADT), Tyr[4]]BN showed fast clearance from the blood pool (0.58 ± 0.05% ID/g, 4 h postinjection) in good agreement with our previous findings (*22*). However, the radioactivity excreted through the hepatobiliary system (liver and intestines, ~6% ID, 4 h postinjection) was much lower compared to the results of Lys[3](99mTc-Hx-DADT)BN (96% ID, 3 h postinjection), Lys[3](99mTc-Pm-DADT)BN (29% ID, 3 h postinjection) and [DTPA[1], Lys[3](99mTc-Hx-DADT), Tyr[4]]BN (21% ID, 4 h postinjection) from our previous studies (*22, 33*). These results indicated the success of the pharmacokinetic modifier, DTPA, and the combination with the hydrophilic Tc-Pm-DADT chelate, in reducing the radioactivity in the hepatobiliary system. Only small amounts of activity remained in the stomach and liver 4 h postinjection (0.43 ± 0.23 and 1.32 ± 0.13% ID, respectively). The pancreas, which expresses the BN/GRP receptor, showed significant uptake (7.71 ± 1.37% ID/g, 1 h postinjection) of radioactivity. This demonstrated the ability of [DTPA[1], Lys[3]-(99mTc-Pm-DADT), Tyr[4]] to target BN/GRP receptor expressing cells in vivo. The pancreas/blood, pancreas/muscle, and pancreas/liver ratios were highest at 4 h postinjection at 9.1, 50, and 7.1, respectively.

To determine if the distribution of [DTPA[1], Lys[3](99m-Tc-Pm-DADT), Tyr[4]]BN in vivo was specific, we conducted experiments in which bombesin, neuromedin-B, somatostatin, or saline vehicle was preinjected in normal mice prior to the administration of [DTPA[1], Lys[3]-(99mTc-Pm-DADT), Tyr[4]]BN. Results of these receptor blocking studies in vivo are shown in Table 4. The difference in the uptake of [DTPA[1], Lys[3](99mTc-Pm-DADT), Tyr[4]]BN with and without subcutaneous injection of 700 μg of BN is significant in the pancreas (0.48 ± 0.07 vs 8.71 ± 0.99% ID/g) and intestines (0.68 ± 0.11 vs 2.20 ± 0.01% ID/g). Acini cells of the pancreas, submucosal layer of the small intestine, longitudal and circular muscle, and submucosal layer of the colon all have been shown to express BN/GRP receptors (*53, 54*). Neuromedin B (*55*), another mammalian analogue of BN, which shows moderate affinity (K_i, 150−350 nM against [^{125}I-Tyr[4]]BN) toward BN/GRP receptors in acini cells of rat pancreas partially blocked the uptake of radioactivity in pancreas (4.87 ± 0.06 vs 8.71 ± 0.99% ID/g). In contrast, biodistribution of the group with the preinjection of somatostatin, which does not bind to the BN/GRP receptor, was similar to that of the unblocked group. Thus, blocking in vivo followed the expected rank order with respect to the affinity of the blocking agents to the BN/GRP receptor in the pancreas. These results show the specificity of the uptake of [DTPA[1], Lys[3](99mTc-Pm-DADT), Tyr[4]]BN in receptor rich tissue in vivo. Furthermore, [DTPA[1], Lys[3](99mTc-Pm-DADT), Tyr[4]]BN appears to have subtype selectivity on account of the limited ability of neuromedin-B to block its binding in vivo.

Table 4. Results (% ID/g[a]) of Blocking Studies in Normal Mice

	unblocked	bombesin[b]	neuromedin b[b]	somatostatin[b]
blood	1.34 ± 0.17	1.54 ± 0.19	1.59 ± 0.14	1.42 ± 0.16
heart	0.54 ± 0.11	0.55 ± 0.06	0.59 ± 0.05	0.51 ± 0.03
lung	1.40 ± 0.21	1.10 ± 0.14	1.20 ± 0.14	1.36 ± 0.11
kidneys	13.65 ± 0.61	14.32 ± 2.40	15.20 ± 1.18	12.26 ± 2.05
spleen	0.56 ± 0.16	0.57 ± 0.16	0.74 ± 0.12	0.80 ± 0.06
pancreas	8.71 ± 0.99	0.48 ± 0.07	4.87 ± 0.51	8.90 ± 1.51
intestines	2.20 ± 0.01	0.68 ± 0.11	1.88 ± 0.05	1.96 ± 0.30
stomach	3.09 ± 0.71	2.42 ± 0.47	3.28 ± 0.38	4.83 ± 0.59
liver	1.31 ± 0.16	1.39 ± 0.18	1.74 ± 0.08	1.55 ± 0.12
muscle	0.29 ± 0.03	0.34 ± 0.35	0.31 ± 0.01	0.30 ± 0.03

[a] Values represent the mean ± SD ($n = 4$). [b] 700 μg (in 100 μL saline) BN, neuromedin B, or somatostatin was injected subcutaneously 30 min before the injection of [DTPA[1], Lys[3](99mTc-Pm-DADT), Tyr[4]]BN.

The incidence of the specific subtype of receptors present in human tumors has begun to be investigated. Preston et al. found the predominant subtype in stomach cancer was the BB_2. Recently, Reubi et al. (*46*) also studied the incidence of bombesin receptor subtypes in human tumors. They reported in their series of 161 human tumors that 12/12 prostate cancers, 41/51 breast cancers, and 5/5 gastrinomas expressed the BB_2 receptor subtype predominantly. The study confirmed previous studies that indicate that for prostate and breast cancers, the predominant subtype expressed in high density is the BB_2 subtype (*17, 40, 41*). Other tumors in this series such as small cell lung cancer (3/9) and renal cell carcinomas (6/16) also showed BB_2 receptor subtype expression. Lower incidence of expression of the BB_1 and BB_3 receptor subtypes were reported in bronchial carcinoids, renal cancer, Ewing sarcomas except intestinal carcinoids that showed 11/24 BB_1 receptors, and small cell lung cancer that showed 4/9 BB_3 receptors in this series. The results of our blocking studies suggest that [DTPA[1], Lys[3](99mTc-Pm-DADT) may be more specific for the BB_2 subtype, the predominant subtype expressed in many tumors. This is because neuromedin-B has higher affinity for the BB_1 receptor than the BB_2 receptor. Further work is ongoing in our laboratory to investigate the subtype specificity of [DTPA[1], Lys[3](99mTc-Pm-DADT) Tyr[4]].

In preliminary studies, we investigated the feasibility of imaging human prostate cancer PC-3 xenografts in SCID mice. In these studies, one group of mice were injected with unlabeled bombesin prior to the injection of the tracer to block the receptors while the other group

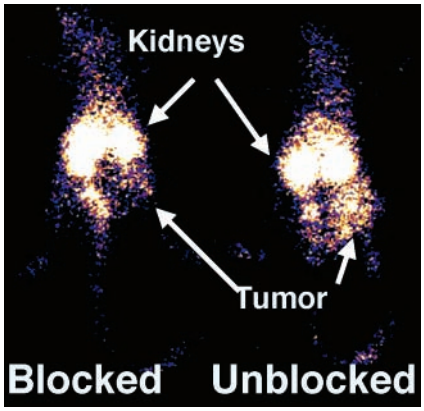

Figure 2. Representative images of human prostate cancer PC-3 tumors in SCID mice injected with [DTPA[1], Lys[3](99mTc-Pm-DADT), Tyr[4]]BN. Each mouse received a 200 μCi injection of [DTPA[1], Lys[3](99mTc-Pm-DADT), Tyr[4]]BN. One group of mice received 700 μg of BN subcutaneously (blocked) and another group received saline vehicle (unblocked) 30 min before the intravenous injection of tracer. The mice were imaged at 12 h postinjection. The target/nontarget ratios were 2 and 10 for the blocked versus unblocked mice, respectively.

only received the tracer. Representative images obtained after 12 h postinjection are shown in Figure 2. The tumor could more clearly be seen in the mice that received no blocking dose of bombesin, whereas the tumors could barely be seen in the mice whose receptors were blocked. Analysis of regions of interest drawn over tumor areas compared to contralateral regions in the same mice showed that the target (tumor) to nontarget (contralateral region) ratios were 2 and 10 for the blocked versus unblocked mice, respectively. The results show that the binding of [DTPA[1], Lys[3](99mTc-Pm-DADT), Tyr[4]]BN in vivo in the tumor is specific and indicates the potential of the tracer for imaging prostate cancer.

In conclusion, the use of the built-in pharmacokinetic modifier, DTPA, combined with the hydrophilic Tc-Pm-DADT chelate, showed minimum abdominal accumulation and the ability to target BN/GRP receptor-positive tissues. This will enable [DTPA[1], Lys[3](99mTc-Pm-DADT), Tyr[4]]BN to be used for imaging BN/GRP receptor-positive cancers and their metastases located even in the abdominal area. DADT ligands are also capable of forming highly stable complexes with Re, the congener of Tc. Thus, the 186Re and 188Re analogues of [DTPA[1], Lys[3](Pm-DADT), Tyr[4]]BN would be directly applicable for the radiotherapy of many cancers. When used together, the Tc and Re analogues would represent a diagnostic and therapeutic pair of radiopharmaceuticals. The Tc analogues could then be used to select the patients that could benefit from therapy using the Re analogues.

ACKNOWLEDGMENT

This work was supported by PHS Research Grant numbers CA32845, CA096817, SAIRP grant CA92871, and Training Grant CA09199 support for A.L., H.H.G., and K.B. from the National Cancer Institute.

LITERATURE CITED

(1) Cuttita, F., Carney, D. N., Mulshine, J., Moody, T. W., Fedorko, J., Fischler, A., and Minna, J. D. (1986) Bombesin-like peptides can function as autocrine growth factors in human small cell lung cancer. *Nature 316*, 823−825.

(2) Anastasi, A., Erspamer, V., and Bucci, M. (1971) Isolation and structure of bombesin and alytesin, two analogous active peptides from the skin of the European amphibian *Bombina Alytes*. *Experientia 27*, 166−167.

(3) McDonald, T. J., Jornvall, H., Nilsson, G., Vagne, M., Ghatei, M., Bloom, S. R., and Mutt, V. (1979) Characterization of a gastrin releasing peptide from porcine nonantral gastric tissue. *Biochem. Biophys. Res. Commun. 90*, 227−233.

(4) Minamino, N., Kangawa, K., and Matsuo, H. (1983) Neuromedin B: A novel bombesin-like peptide identified in porcine spinal cord. *Biochem. Biophys. Res. Commun. 114*, 541−548.

(5) Ghatei, M. A., Jung, R. T., Stevenson, J. C., Hillyard, C. J., Adrian, T. E., Lee, Y. C., Christtofides, N. D., Sarson, D. L., Mashiter, K., MacIntyre, I., and Bloom, S. R. (1982) Bombesin: action on gut hormones and calcium in man. *J. Clin. Endocrinol. Metab. 54*, 980−985.

(6) Kaneto, A., Kaneko, T., Nakaya, S., Kajinuma, H., and Kosaka, K. (1978) Effect of bombesin infused intrapancreatically on glucagon and insulin secretion. *Metabolism 27*, 549−553.

(7) Jensen, R. T., Coy, D. H., Saeed, Z. A., Heinz-Erian, P., Mantey, S., and Gardner, J. D. (1988) Interaction of bombesin and related peptides with receptors on pancreatic acinar cells. *Ann. N.Y. Acad. Sci. 547*, 138−149.

(8) Brown, M. R., Carver, K., and Fisher, L. A. (1988) Bombesin: central nervous system actions to affect the autonomic nervous system. *Ann N.Y. Acad Sci 547*, 174−182.

(9) Rettori, V., Pazos-Moura, C. C., Moura, E. G., Polak, J., and McCann, S. M. (1992) Role of neuromedin B in control of the release of thyrotropin in hypothyroid and hyperthyroid rats. *Proc. Natl. Acd. Sci U.S.A. 89*, 3035−3039.

(10) Moody, T. W., Carney, D. N., Cuttitta, F., Quattrocchi, K., and Minna, J. D. (1985) High affinity receptors for bombesin/GRP-like peptides on human small cell lung cancer. *Life Sci. 37*, 105−113.

(11) Moody, T. W., Mahmoud, S., Staley, J. S., Naldini, L., Cirillo, D., South, V., Felder, S., and Kris, R. (1989) Human glioblastoma cell lines have neuropeptide receptors for bombesin/gastrin releasing peptide. *J. Mol. Neurosci. 1*, 235−242.

(12) Farre, A., Ishizuka, J., Gomez, G., Parekh, D., Koo, J. Y., Townsend, C. M., Jr., and Thompson, J. C. (1993) Bombesin stimulates growth of colon cancer in mice and decreases their survival. *Surg. Oncol. 2*, 169−173.

(13) Qin, Y., Ertl, T., Cai, R. Z., Halmos, G., and Schally, A. V. (1994) Inhibitory effect of bombesin receptor antagonist RC-3095 on the growth of human pancreatic cancer cells in vivo and in vitro. *Cancer Res. 54*, 1035−1041.

(14) Qin, Y., Halmos, G., Cai, R. Z., Szoke, B., Ertl, T., and Schally A. V., Bombesin antagonist inhibit in vitro and in vivo growth of human gastric cancer and binding of bombesin to its receptors. *J. Cancer Res. Clin. Oncol. 120*, 519−528.

(15) Yano, T., Pinski, J., Groot, K., and Schally, A. V. (1992) Stimulation by bombesin and inhibition by bombesin/gastrin releasing peptide antagonist RC-3095 of growth of human breast cancer cell lines. *Cancer Res. 52*, 4545−4547.

(16) Giacchetti, S., Gauville, C., de Cremoux, P., Bertin, L., Berthon, P., Abita, J−P., Cuttitta, F., and Calvo, F. (1990) Characterization, in some human breast cancer cell lines, of gastrin-releasing peptide-like receptors which are absent in normal breast epithelial cells. *Int. J. Cancer 46*, 293−298.

(17) Markwalder, R., and Reubi, J. C. (1999) Gastrin-releasing peptide receptors in the human prostate: relation to neoplastic transformation. *Cancer Res. 59*, 1152−1159.

(18) Preston, S. R., Woodhouse, L. F., Jones-Blackett, S., Wyatt, J. I., and Primrose J. N. (1993) High affinity binding sites for gastrin releasing peptide on human gastric cancer and Ménétrier's mucosa. *Cancer Res. 53,* 5090−5092.

(19) Breeman, W. A., De Jong, M., Bernard, B. F., Kwekkeboom, D. J., Srinivasan, A., van der Pluijm, M. E., Hofland, L. J., Visser, T. J., and Krenning, E. P. (1999) Pre-clinical evaluation of [(111)In-DTPA-Pro(1), Tyr(4)]bombesin, a new radioligand for bombesin-receptor scintigraphy. *Int. J. Cancer 83*, 657−663.

(20) Li, N., Struttman, M., Higginbotham, C., Grall, A. J., Skerlj, J. F., Vollano, J. F., Bridger, S. A., Ochrymowycz, L. A., Ketring, A. R., Abrams, M. J., and Volkert, W. A. (1997) Biodistribution of model 105Rh-labeled tetradentate thiamacrocycles in rats. *Nucl. Med. Biol. 24*, 85−92.

(21) Mantey, S., Frucht, H., Coy, D. H., and Jensen, R. T. (1993) Characterization of bombesin receptors using a novel, potent,

radiolabeled antagonist that distinguishes bombesin receptor subtypes. *Mol. Pharmacol. 43*, 762−774.
(22) Baidoo, K. E., Lin, K−S., Zhan, Y., Finley, P., Scheffel, U., and Wagner, H. N., Jr. (1998) Design, synthesis, and initial evaluation of high-affinity technetium bombesin analogues. *Bioconjugate Chem. 9*, 218−225.
(23) Nock, B., Nikolopoulou, A., Chiotellis, E., Loudos, G., Maintas, D., Reubi, J. C., and Maina, T. (2003) (99m)Tc]-Demobesin 1, a novel potent bombesin analogue for GRP receptor-targeted tumour imaging. *Eur. J. Nucl. Med. Mol. Imaging 30*, 247−58.
(24) Scopinaro, F., Varvarigou, A., Ussof, W., De Vincentis, G., Sourlingas, T. G., Evangelatos, G. P., Datsteris, J., and Archimandritis, S. C. (2002) Technetium labeled bombesin-like peptide: preliminary report on breast cancer uptake in patients. *Cancer Biother. Radiopharm. 17*, 327−335.
(25) La Bella, R., Garcia-Garayoa, E., Langer, M., Blauenstein, P., Beck-Sickinger, A. G., and Schubiger, P. A. (2002) In vitro and in vivo evaluation of a 99mTc(I)-labeled bombesin analogue for imaging of gastrin releasing peptide receptor-positive tumors. *Nucl. Med. Biol. 29*, 553−560.
(26) Gali, H., Hoffman, T. J., Sieckman, G. L., Owen, N. K., Katti, K. V., and Volkert, W. A. (2001) Synthesis, characterization, and labeling with 99mTc/188Re of peptide conjugates containing a dithia-bisphosphine chelating agent. *Bioconjugate Chem. 12*, 354−363.
(27) Van de Wiele, C., Dumont, F., Vanden Broecke, R., Oosterlinck, W., Cocquyt, V., Serreyn, R., Peers, S., Thornback, J., Slegers, G., and Dierckx, R. A. (2000) Technetium-99m RP527, a GRP analogue for visualisation of GRP receptor-expressing malignancies: a feasibility study. *Eur. J. Nucl.Med. 27*, 1694−1699.
(28) Karra, S. R., Schibli, R., Gali, H., Katti, K. V., Hoffman, T. J., Higginbotham, C., Sieckman, G. L., and Volkert, W. A. (1999) 99mTc-labeling and in vivo studies of a bombesin analogue with a novel water-soluble dithiadiphosphine-based bifunctional chelating agent. *Bioconjugate Chem. 10*, 254−260.
(29) Decristoforo, C., and Mather, S. J. (1999) 99m-Technetium -labeled peptide-HYNIC conjugates: effects of lipophilicity and stability on biodistribution. *Nucl. Med. Biol. 26*, 389−396.
(30) Trejtnar, F., Laznicek, M., Laznickova, A., and Mather, S. J. (2000) Pharmacokinetics and renal handling of 99mTc-labeled peptides. *J. Nucl. Med. 41*, 177−182.
(31) Marmion, M. E., Woulfe, S. R., Neumann, W. L., Nosco, D. L., and Deutsch, E. (1999) Preparation and characterization of technetium complexes with Schiff base and phosphine coordination. 1. Complexes of technetium-99 g and −99m with substituted $acac_2en$ and trialkyl phosphines (where $acac_2en$ = N, N′- ethylenebis[acetylacetone iminato]). *Nucl. Med. Biol. 26*, 755−770.
(32) Edwards, D. S., Liu, S., Barrett, J. A., Harris, A. R., Looby, R. J., Ziegler, M. C., Heminway, S. J., and Carroll, T. R. (1997) New and versatile ternary ligand system for technetium radiopharmaceuticals: water soluble phosphines and tricine as coligands in labeling a hydrazinonicotinamide-modified cyclic glycoprotein IIb/IIIa receptor antagonist with ^{99m}Tc. *Bioconjugate Chem. 8*, 146−154.
(33) Lin, K−S., Baidoo, K. E., Hashemzadeh-Gargari, H., Scheffel, U., and Wagner, H. N., Jr. (1999) Design of a new hydrophilic Tc-99m labeled bombesin receptor binding analogue. *J. Nucl. Med. 40*(*Suppl.*), 79 p.
(34) Baidoo, K. E., and Lever, S. Z. (1990) Synthesis of a diaminedithiol bifunctional cheating agent for incorporation of technetium-99m into biomolecules. *Bioconjugate Chem. 1*, 132−137.
(35) Mokotoff, M., Swanson, D. P., Jonnalagadda, S. S., Epperly, M. W., and Brown, M. L. (1997) Evaluation of laminin peptide fragments labeled with indium-111 for the potential imaging of malignant tumors. *J. Pept. Res. 49*, 510−516.
(36) Reile, H., Armatis, P. E., and Schally, A. V. (1994) Characterization of high-affinity receptors for bombesin/gastrin releasing peptide on the human prostate cancer cell lines PC-3 and DU-145: Internalization of receptor bound [^{125}I-Tyr^4]bombesin by tumor cells. *Prostate 25*, 29−38.
(37) McPherson, G. A. (1985) Analysis of radioligand binding experiments. A collection of computer programs of the IBM PC. *J. Pharmacol. Methods 14*, 213−228.
(38) Sunday, M. E., Kaplan, L. M., Motoyama, E., Chin, W. W., and Spindel, E. R. (1988) Gastrin-releasing peptide (mammalian bombesin) gene expression in health and disease. *Lab. Invest. 59*, 5−24.
(39) Moody, T. W., and Cuttitta, F. (1993) Growth factor and peptide receptors in small cell lung cancer. *Life Sci. 52*, 1161−1173.
(40) Gugger, M., and Reubi, J. C. (1999) GRP receptors in non-neoplastic and neoplastic human breast. *Am J Pathol. 155*, 2067−2076.
(41) Halmos, G., Wittliff, J. L., and Schally, A. V. (1995) Characterization of bombesin /gastrin releasing peptide receptors in human breast cancer and their relationship to steroid receptor expression. *Cancer Res. 55*, 280−287.
(42) ToiScott, M., Jones, C. L., and Kane, M. A. (1996) Clinical correlates of bombesin-like peptide receptor subtype expression in human lung cancer cells. *Lung Cancer 15*, 341−354.
(43) Carroll, R., Matnowskyj, K. A., Chakrabarti, S., McDonald, T. J., and Benya, R. V. (1999) Aberrant expression of gastrin-releasing peptide and its receptor by well differentiated colon cancers in humans. *Am. J. Physiol. 276*, G655−665.
(44) Radulovic, S., Milovanovic, S., Cai, R−Z., and Schally, A. V. (1992) The binding of bombesin and somatostatin and their analogues to human colon cancers. *Proc. Soc. Exp. Biol. Med. 200*, 394−401.
(45) Shriver, S. P., Bourdeau, H. A., Gubish, C. T., Tirpak, D. L., Davis, A. L. G., Luketich, J. D., and Siegfried, J. M. (2000) Sex-specific expression of gastrin-releasing peptide receptor: relationship to smoking history and risk of lung cancer. *J. Natl. Cancer Inst. 92*, 24−33.
(46) Reubi, J. C., Wenger, S., Schmuckli-Maurer, J., and Schaer, J−C., Gugger, M. (2002) Bombesin receptor subtypes in human cancers: detection with the universal radioligand ^{125}I-[D-Tyr^6, b-Ala^{11}, Phe^{13}, Nle^{14}]BN(6−14). *Clin. Cancer Res. 8*, 1139−1146.
(47) Siegfried, J. M., DeMichele, M. A. A., Hunt, J. D., Davis, A. G., Vohra, K. P., and Pilewski, J. M. (1997) Expression of mRNA for gastrin-releasing peptide receptor by human bronchial epithelial cells: Association with prolonged tobacco exposure and responsiveness to bombesin-like peptides. *Am. J. Respir. Crit. Care Med. 156*, 358−366.
(48) Baidoo, K. E., Scheffel, U., and Lever, S. Z. (1990) Technetium-99m labeling of proteins: Initial evaluation of a novel diaminedithiol bifunctional chelating agent. *Cancer Res. 50*(*Suppl.*), 799s−803s.
(49) Baidoo, K. E., Scheffel, U., Stathis, M., Finley, P., Lever, S. Z., Zhan, Y., and Wagner,H. N., Jr. (1998) High Affinity No Carrier Added Technetium-99m Labeled Chemotactic Peptides for Studies of Inflammation In Vivo. *Bioconjugate Chem. 9*, 208−217.
(50) Baidoo, K. E., Lever, S. Z., and Scheffel, U. (1994) A bifunctional chelator for facile preparation of neutral technetium complexes. *Bioconjugate Chem. 5*, 114−118.
(51) Heimbrook, D. C., Boyer, M. E., Garsky, V. M., Balishin, N. L., Kiefer, D. M., Oliff, A., and Riemen, M. W. (1988) Minimal ligand analysis of gastrin releasing peptide: receptor binding and mitogenesis. *J. Biol. Chem. 263*, 7016−7019.
(52) Childs, R. L., and Hnatowich, D. J. (1985) Optimum conditions for labeling of DTPA-coupled antibodies with technetium-99m. *J Nucl Med 26*, 293−299.
(53) Zhu, W−Y., Göke, B., and Williams, J. A. (1991) Binding, internalization, and processing of bombesin by rat pancreatic acini. *Am. J. Physiol. 261*, G57−64.
(54) Moran, T. H., Moody, T. W., Hostetler, A. M., Robinson, P. H., Godrich, M., and McHugh, P. R. (1988) Distribution of bombesin binding sites in the gastrointestinal tract. *Peptide 9*, 643−649.
(55) Von Schrenck, T., Heinz-Erian, P., Moran, T., Mantey, S. A., Gardner, J. D., and Jensen, R. T. (1989) Neuromedin B receptor in esophagus: evidence for subtypes of bombesin receptors. *Am. J. Physiol. 256*, G747−758.

BC049820H

Multivalent Carbocyanine Molecular Probes: Synthesis and Applications[§]

Yunpeng Ye,[†] Sharon Bloch,[†] Jeffery Kao,[‡] and Samuel Achilefu*,[†]

Department of Radiology and Department of Chemistry, Washington University, St. Louis, Missouri 63110.
Received August 31, 2004; Revised Manuscript Received October 18, 2004

Synergistic multivalent interactions can amplify desired chemical or biological molecular recognitions. We report a new class of multicarboxylate-containing carbocyanine dye constructs for use as optical scaffolds that not only serve as fluorescent antennas but also participate in structural assembly of the multivalent molecular construct. Three generations of carboxylate-terminating multivalent near-infrared carbocyanine probes from a dicarboxylic acid precursor dye (cypate) were prepared via its imino diacetic acid derivatives. Conjugation of the probes with D-(+)-glucosamine afforded dendritic arrays of the carbohydrates on an inner NIR chromophore core. All the multicarboxylate probes and their glucosamine conjugates have similar NIR spectral properties because conjugation occurred at distal positions to the inner chromophore core, thereby providing consistent and predictable spectral properties for their biological applications. Although light-induced photodamage equally affected the precursor dye, multicarboxylate probes, and their glucosamine derivatives, we observed that octacarboxylcypate (multivalent probe) was remarkably stable in different mediums at physiologically relevant temperatures relative to cypate, especially in basic mediums. Biodistribution studies in tumor-bearing nude mice show that all the glucosamine conjugates localized in the tumor but cypate was almost exclusively retained in the liver at 24 h postinjection. The tumor uptake does not correlate with the number of glucosamine tether on the multicarboxylate probe. Overall, the triglucosamine derivative appears to offer the best balance between high tumor uptake and low retention in nontarget tissues. These results suggest that multivalent molecular beacons are useful for assessing the beneficial effects of multivalency and for optimizing the biological and chemical properties of tissue-specific molecular probes.

INTRODUCTION

Optical imaging is attractive for studying molecular recognitions of chemical and biological importance because minute fluorescent tracers can be detected in homogeneous and heterogeneous media with existing laboratory instruments. For in vivo biological applications, near-infrared (NIR) fluorescent carbocyanine molecular probes are valuable for optical imaging because light in the 700−900 nm wavelengths propagates several centimeters in tissue (*1*, *2*). As a result, diseases in deep tissues can be monitored noninvasively by NIR optical methods. Additionally, NIR excitation also minimizes tissue autofluorescence that confounds spectral analysis in the visible wavelengths. Thus, development of NIR molecular probes with high specificity, selectivity, sensitivity, and stability are highly desirable.

Several reports have successfully demonstrated the potential of NIR dye bioconjugates for imaging diseases in small animals (*3*−*5*). Recent studies have focused on developing dye conjugates of small bioactive molecules to improve rapid diffusion to target tissue, identify, and optimize new molecular beacons by combinatorial library and high throughput strategies and enhance in vivo stability of the compounds (*4*, *6*−*10*). Most of these studies were performed with carbocyanine-based molecular probes because of the exceptionally high biocompatibility and desirable spectral properties of indocyanine green (ICG), which is a member of this class of compounds (*7*, *11*). Because ICG itself does not readily react with biomolecules, we recently developed a reactive carbocyanine dye called cypate (**1**), which has similar spectral, blood clearance, and excretion profiles as ICG (*12*). Bioconjugates of cypate are not toxic to animals up $>10\ \mu$mol/kg body weight. Despite these successes, direct labeling of bioactive molecules to optimize the probes for clinical applications remains a challenge.

Synthetic dendrimers, nanoparticles, quantum dots, and other polyvalent compounds use synergistic multivalent interactions to amplify desired chemical or biological molecular recognitions (*13*−*15*). Labeling the multivalent materials at their reactive peripheral sites with fluorescent antennas provides a highly sensitive approach to track, visualize, and quantify different molecular interactions by optical methods. Although this strategy allows for conjugating multiple chromophores, the resulting molecular constructs may quench fluorescence, induce aggregation, disrupt bioactive conformations of adjacent small molecules, and destabilize the chromophore systems because of their exposure to harsh and metabolically active mediums.

Recently, we reported a new class of multicarboxylate-containing carbocyanine probes for use as optical scaffolds that not only serve as fluorescent antennas but also

* Corresponding author. Samuel Achilefu, Department of Radiology, Washington University School of Medicine, 4525 Scott Ave., CB 8225, St. Louis, MO 63110. Phone: 314-362-8599. Fax: 314-747-5191. E-mail: achilefus@mir.wustl.edu.

[†] Department of Radiology.

[‡] Department of Chemistry.

[§] Part of the Special Issue on Imaging Chemistry that began in issue 6, 2004. A preliminary description of this work was presented at the Symposium on Chemistry and Biological Applications of Imaging Agents and Molecular Beacons, at the spring 2004 National Meeting of the Americal Chemical Society.

10.1021/bc049790i CCC: $30.25 © 2005 American Chemical Society
Published on Web 12/23/2004

participate in structural assembly of the multivalent molecular probes (*16*). The peripheral carboxylic acids that are distal to the chromophore core allow facile conjugation with biomolecules and retain the desirable NIR spectral properties of the dendritic molecule. Herein, we report the synthesis, spectral properties, stability, and biodistribution of multivalent NIR carbocyanine-based molecular probes. The results show that multivalent constructs have increased solution stability over the precursor dye in different mediums and physiologically relevant temperatures. Biodistribution of the glucosamine derivatives shows that the distribution of the compounds in target tumor does not correlate directly with the number of glucosamine moieties but reveals the potential of using multivalency to optimize molecular probes for different biomedical applications.

EXPERIMENTAL PROCEDURES

General. All solvents and chemicals were reagent grade and used without further purification. Benzotriazol-1-yloxy-tris(pyrrolidino)phosphonium hexafluorophosphate (PyBOP) and *N*-hydroxybenzotriazole (HOBt) were purchased from AnaSpec (San Jose, CA). Trifluoroacetic acid (TFA) and DIEA were purchased from Advanced ChemTech (Louisville, KY). Diisopropylcarbodiimide (DIC) and glutaconaldehyde dianilide monohydrochloride were purchased from Lancaster Synthesis (Windham, NH). Dichloromethane (DCM), *N*,*N*-dimethyformamide (DMF), methanol, and acetonitrile were from purchased from Fisher Scientific (Pittsburgh, PA). Other commercial chemicals were purchased from Aldrich (Milwaukee, WI). Mass spectra were obtained in dilute methanol solutions using Waters ZQ 4000 positive electrospray at cone voltage 67 V. All the compounds including the intermediates and final products were fully identified by ES-MS. The identity of final glucosamine conjugates were also confirmed by MALDI-TOF high-resolution mass spectrometry.

HPLC Purification and Analysis. HPLC analysis was performed on a Vydac C-18 column (250 × 4.6 mm) at a flow rate of 1.0 mL/min. Semipreparative HPLC was performed on a Vydac C-18 column (25 × 2.2 cm) at 9.5 mL/min. HPLC solvents consist of water containing 0.05% TFA (solvent A) and acetonitrile containing 0.05% TFA (solvent B). The elution protocol for analytical HPLC starts with 90% A for 1 min, followed by a linear gradient to 30% A over 20 min, held at 30% A for 5 min, continued to 10% A over 5 min, and finally returned to 90% A over 2 min. The elution profile was monitored by UV absorbance at 254 and 214 nm.

NMR Analysis. NMR spectra were recorded on a Varian Inova-600 (Varian Assoc., Palo Alto, CA) spectrometer, and the data were processed off-line with VNMR software. Proton and carbon chemical shifts were measured in ppm downfield from an external 3-(trimethylsilyl) propionic acid (TSP) standard. Proton spectra were obtained in DMSO-d_6 with a 5200-Hz spectral width collected into 32k data points using a 5.0 s preacquisition delay. Carbon spectra were obtained with a 27 000-Hz spectral width collected into 64k data points. The proton-detected heteronuclear multiple quantum coherence (HMQC) spectrum was recorded using a 0.5 s $^1H-^{13}C$ nulling period. The 90° ^1H pulse width was 9.5 μs, and the 90° ^{13}C pulse width was 14 μs. The proton spectral width was set to 5200 Hz and the carbon spectral width was set to 27 000 Hz. Phase sensitive 2D spectra were obtained by employing the Hypercomplex method. A 2 × 256 × 2048 data matrix with 64 scans per t1 value was collected. Gaussian line broadening was used in weighting both the t2 and the t1 dimensions. After 2D Fourier transform, the spectra resulted in 512 × 2048 data points, which were phase- and baseline-corrected in both dimensions.

UV−Vis and Emission Analysis. Absorbance spectra were measured on a Beckman Coulter DU 640 UV−visible spectrophotometer. Fluorescence spectra were recorded on a Fluorolog-3 fluorophotometer (JOBIN YVON/HORIBA, Edison, NJ). Stock solutions (1.0 mM) of the dye and its conjugates were prepared by dissolving each sample in anhydrous DMSO (99.99%). UV−vis and fluorescence measurements were carried out by sequentially adding 0.5−2.0 μL aliquots of the stock solutions via a micropipet into 3 mL of 20% aqueous DMSO solution or other solvents in a quartz cuvette. The mixtures were stirred briefly for equilibration prior to data acquisition.

1,1,2-Trimethyl[1H]-benz[*e*]indole-3-propanoic Acid. A mixture of 1,1,2-trimethyl-[1H]-benz[*e*]indole (40.0 g, 19.11 mmol) and 3-bromopropanoic acid (40.0 g, 26.15 mmol) in 1,2-dichlorobenzene (200 mL) was heated with stirring at 110 °C for 18 h. After the resulting mixture was cooled to room temperature, the precipitate was collected by filtration, followed by trituration in DCM to remove the unreacted material, and dried under vacuum to afford 1,1,2-trimethyl[1H]-benz[*e*]indole-3-propanoic acid (57 g, 82.4%). ESI-MS: 281.31 ($[MH]^+$).

Cypate (1). A solution of Ac_2O (1.20 g, 11.75 mmol) in DCM (5 mL) was added dropwise to a cooled, stirring suspension of glutaconaldehyde dianil monohydrochloride (2.84 g, 9.97 mmol) and DIEA (2.60 g, 20.11 mmol) in DCM (20 mL). The resulting clear solution was stirred for 1 h and added dropwise to a refluxing solution of 1,1,2-trimethyl[1H]-benz[*e*]indole-3-propanoic acid (8.2 g, 22.64 mmol) and sodium acetate (3.2 g, 39.01 mmol) in acetonitrile/water (95/5 mL). The mixture was refluxed for 16 h, cooled, filtered, and washed with acetonitrile, 5% HCl solution, and ethyl ether. About 6 g (85%) of **1** was obtained. ESI-MS: 625.34 ($[MH]^+$).

Tricarboxylic Acid-Containing Cypate Derivative (2). To a cooled solution of **1** (352.5 mg, 0.5 mmol) in DMF (15 mL) was added EDCI (114.6 mg, 0.6 mmol). After 20 min, HOBt (81.2 mg, 0.60 mmol) and di-*tert*-butyl iminodiacetate (147.0 mg, 0.60 mmol) were added. The mixture was stirred at room temperature for 2 h and concentrated. The residue was dissolved in DCM (35 mL), washed with HCl solution (1 M, 3 × 15 mL) and brine, and dried over $MgSO_4$. The filtrate was concentrated and purified by flash column chromatography using dichloromethane/methanol (100:6 v/v) to afford 154 mg (33%). ES-MS: 852.41 ($[MH]^+$).

The above compound (70 mg, 0.075 mmol) was dissolved in TFA (10 mL) and stirred for 1 h, concentrated, and dried to afford 59 mg of **2**, which was further purified by HPLC for both UV−vis and fluorescence assays. ES-MS: 740.28 ($[MH]^+$); HR-MS: 740.2987($[MH]^+$).

Tetracarboxylic Acid-Containing Cypate Derivative (3). The *tert*-butyl ester of **3** (348 mg, 60%) was prepared from **1** (352.5 mg, 0.5 mmol), EDCI (382.0 mg, 2.0 mmol), HOBt (270 mg, 2.0 mmol), and di-*tert*-butyl iminodiacetate (490.0 mg, 2.0 mmol), as described for **2** above. ES-MS: 1079.49 ($[MH]^+$).

The ester (200 mg, 0.17 mmol) was dissolved in TFA (30 mL) and stirred for 1 h, concentrated, and dried to afford 154 mg (97%) of **3**, which was further purified by HPLC for both UV−vis and fluorescence assays. ES-MS: 855.20 ($[MH]^+$).

Hexacarboxylic Acid-Containing Cypate Derivative (4). The *tert*-butyl ester of **4** (72.0 mg, 30%) was prepared from **2** (130 mg, 0.16 mmol), EDCI (275.1 mg, 1.44 mmol), HOBt (194.4 mg, 1.44 mmol), and a solution of di-*tert*-butyl iminodiacetate (352.8 mg, 1.44 mmol), as described for **2** above. ES-MS: 1422.60 ($[MH]^+$).

The ester (15 mg, 0.01 mmol) was dissolved in TFA (10 mL) and stirred for 1 h, concentrated, and dried to afford **4** (11 mg, 95%) which was further purified by HPLC for both UV−vis and fluorescence assays. ES-MS: 1085.23 ($[MH]^+$).

Octacarboxylic Acid-Containing Cypate Derivative (5). The *tert*-butyl ester of **5** (55.0 mg, 30%) was prepared from **3** (94 mg, 0.10 mmol), EDCI (229.2 mg, 1.20 mmol), HOBt (162 mg, 1.20 mmol), and a solution of di-*tert*-butyl iminodiacetate (196.0 mg, 0.80 mmol) in DMF (3 mL), as described for **2** above. (ES-MS: 1764.61 ($[MH]^+$).

The ester (25 mg, 0.0136 mmol) was dissolved in TFA (10 mL) and stirred for 2 h, concentrated, and dried to afford **5** (18 mg, 95%), which was further purified by HPLC for both UV−vis and fluorescence assays. ES-MS: 1315.21 ($[MH]^+$); HR-MS: 1315.5061($[MH]^+$).

Mono-D-(+)-glucosamine-Containing Cypate (6). To a cooled (−5 °C) solution of **1** (15 mg, 0.0213 mmol), HBTU (10.26 mg, 0.027 mmol), and HOBt (3.7 mg, 0.027 mmol) in DMF (5 mL) was added a solution of D-(+) glucosamine·HCl (12.0 mg, 0.054 mmol) and DIEA (14 mg, 0.108 mmol) in DMSO (1 mL). The mixture was stirred at room temperature for 2 h and added into ether (25 mL) with stirring. The precipitate was collected and purified by HPLC (10%-80% of A over 30 min) to afford 2.4 mg (13%) of **6**. ES-MS: 786.30 ($[MH]^+$); HR-MS: 786.4157 ($[MH]^+$).

Di-D-(+)-glucosamine-Containing Derivative of Cypate (7). We used a similar procedure described for **6** above to prepare **7** from **1** (15 mg, 0.0213 mmol), HBTU (25.8 mg, 0.068 mmol), HOBt (9.2 mg, 0.068 mmol), and a solution of D-(+) glucosamine·HCl (32.4 mg, 0.15 mmol) and DIEA (36.5 mg, 0.28 mmol) in DMSO (1 mL). The crude product was purified by HPLC to afford 6.6 mg (30%) of 7. ES-MS: 947.39 ($[MH]^+$); HR-MS: 947.5096 ($[MH]^+$).

Tri-D-(+)-glucosamine-Containing Derivative of Cypate (8). We used a similar procedure described for **6** above to prepare **8** from **2** (15 mg, 0.0183 mmol), HBTU (38.0 mg, 0.10 mmol) and HOBt (13.5 mg, 0.10 mmol), and a solution of D-(+) glucosamine·HCl (43.2 mg, 0.20 mmol) and DIEA (52.0 mg, 0.40 mmol) in DMSO (1.5 mL). Purification by HPLC afforded 6.0 mg (25%) of **8.** ES-MS: 1223.46 ($[MH]^+$); HR-MS: 1223.4759 ($[MH]^+$).

Tetra-D-(+)-glucosamine-Containing Derivative of Cypate (9). We used a similar procedure described for **6** above to prepare **9** from **3** (16 mg, 0.0171 mmol), HBTU (129.2 mg, 0.34 mmol), HOBt (46.0 mg, 0.34 mmol), and a solution of D-(+) glucosamine·HCl (73.5 mg, 0.34 mmol) and DIEA (129.0 mg, 1.0 mmol) in DMSO (1.5 mL). The mixture was purified by HPLC to afford 7.0 mg (26%) of **9**. ES-MS: 1499.41 ($[MH]^+$).

Hexa-D-(+)-glucosamine-Containing Derivative of Cypate (10). We used a similar procedure described for **6** above to prepare **10** from **4** (20 mg, 0.0172 mmol), HBTU (380.0 mg, 1.0 mmol), HOBt (135 mg, 1.0 mmol), and a mixture of D-(+) glucosamine·HCl (216.0 mg, 1.0 mmol) and DIEA (322.5 mg, 2.5 mmol) in DMSO (8 mL). The crude product was purified by HPLC to afford 7.3 mg (20%) of **10**. ES-MS: 2052.39 ($[MH]^+$), 1026.83 $[MH_2]^{2+}$; HR-MS: 2052.5934 ($[MH]^+$).

Octa-D-(+)-glucosamine-Containing Derivative of Cypate (11). We used a similar procedure described for **6** above to prepare **11** from **5** (20 mg, 0.0143 mmol), HBTU (380 mg, 1.0 mmol), HOBt (135 mg, 1.0 mmol), and a mixture of D-(+) glucosamine·HCl (432.0 mg, 2.0 mmol) and DIEA (516 mg, 4.0 mmol) in DMSO (12.0 mL). HPLC purification afforded 8.0 mg (21%) of **11**. ES-MS: 2606.49 ($[MH]^+$), 1302.47 ($[MH_2]^{2+}$); HR-MS: 2604.5407 ($[MH]^+$).

Solution Stability Studies. The stability of representative probes in four different media was monitored by UV−vis. The test solutions (10 μM) were prepared by adding stock solutions (1 mM, 30 μL) into 2970 μL of five different mediums: aqueous NaOH (0.01 M), aqueous HCl (0.01 M), PBS buffer (pH 7.2), 50% aqueous acetonitrile, and 50% aqueous acetonitrile containing 0.01 M DIEA. The solutions were kept at room temperature or incubated at 37 °C for analysis by UV−vis. The difference between the initial and subsequent absorbances of the solution at λ_{max} for each compound was used to determine their stability under different conditions.

Photostability Studies. Photostability studies were monitored by UV−vis at a probe concentration of 5.56 μM in 20% aqueous DMSO under three different conditions: in the dark (cuvette containing the solution was wrapped in aluminum foil), normal room fluorescent light (monitored at 24 h intervals for one week), and direct exposure to 60 W light bulb (sample was placed 30 cm from the light source and monitored at 0.5 h intervals for 8 h). Changes in the initial and subsequent absorbances of **1**, **5**, and **11** were recorded at the λ_{max} for each compound.

Biodistribution Assays. All animal studies were performed in compliance with the Guidelines for the Care and Use of Research Animals established by Washington University's Animal Studies Committee. To establish tumors, 1×10^7 CA20948 cells, grown in DMEM medium containing 10% fetal calf serum, were injected subcutaneously into the left flank of male nude mice. The CA20948 tumor typically grows to 3−5 mm between 14 and 21 days postinjection. The tumor bearing mice were anesthetized with ketamine/xylazine via intraperitoneal injection and each probe in 20% aqueous DMSO (0.3 μmol/kg body weight) was administered retroorbitally into the mice. At 24 h postinjection, the animals were euthanized and selected organs were removed, washed, and placed on a dark background for fluorescence imaging.

A noninvasive in vivo continuous wave fluorescence imaging apparatus was used to assess the localization and distribution of the probes, as described previously (*12*). Briefly, two 780 nm laser diodes were launched into fiber optic bundles to excite the probes and the emitted fluorescence was captured with a Photometrics CoolSnap HQ charge-coupled device (CCD) camera equipped with an 830 nm interference filter. We used two laser diodes to produce as much uniform illumination of the organs as possible. Images were acquired and processed using WinView software from Princeton Instruments. Tissue parts, instead of whole organs, were used to determine the relative fluorescence intensity in each organ to minimize problems associated with depth-dependent nonlinear fluorescence emission. A statistical program in the WinView package was used to estimate the mean fluorescence intensity per organ part.

RESULTS AND DISCUSSION

Synthesis. *Improved Synthesis of Cypate, the First Generation Dye.* The improved procedure is summarized

Scheme 1. Improved Synthesis of Cypate via Preacylation Approach[a]

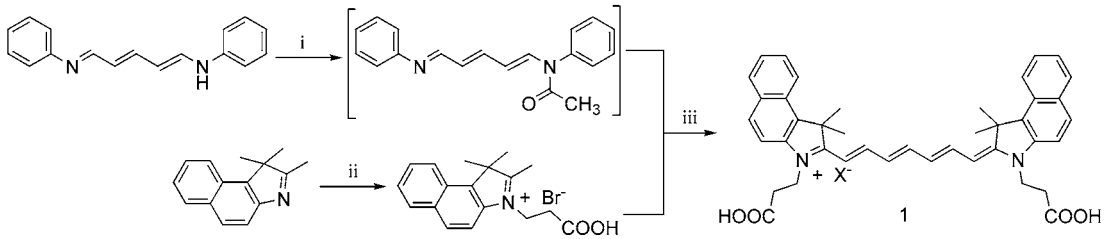

[a] Reagents and conditions: (i) acetic anhydride/DIEA/DCM; (ii) 3-bromopropanoic acid/1,2-dichlorobenzene/110 °C; (iii) CH_3COONa/CH_3CN/H_2O/refluxed.

in Scheme 1. Cypate (**1**) was originally designed to mimic the absorption, fluorescence emission, excretion pathway, and blood clearance profiles of indocyanine green (ICG) because of the in vivo biocompatibility in humans and desirable spectral properties of ICG (*1*, *9*, *11*, *12*). Unlike ICG, **1** can serve as an optical scaffold for multivalent molecular designs because it contains two carboxylic acid functional sites for further derivatization. Initially, we synthesized **1** by a conventional method where a mixture of carboxypropyl benzoindole, glutaconaldehyde dianil monohydrochloride, and sodium acetate were refluxed in ethanol (*12*). Unfortunately, the isolated yield was low (<10%). Consequently, we explored alternative approaches to improve cypate synthesis by optimizing the reaction conditions (*6*, *12*, *16*).

Previous studies indicate that N-acetylation of the intermediate glutaconaldehyde may play an important role in the reaction of aldehydes with benzoindole to form tricarbocyanine dyes (*17*, *18*). This reaction is routinely performed in situ by using a mixture of acetic anhydride/acetic acid. However, the synthesis we conducted in acetic anhydride/acetic acid solution did not improve the yield of **1**. Therefore, we explored preacetylation of glutaconaldehyde with acetic anhydride prior to condensation with benzoindole intermediate at 110 °C to minimize the formation of byproducts generated at higher temperatures. As summarized in Scheme 1, the reaction of 1,1,2-trimethyl-[1H]-benz[*e*]indole and 3-bromopropanoic acid at 110 °C in dichlorobenzene afforded 1,1,2-trimethyl-[1H]-benz[*e*]indole-3-propanoic acid, which was conveniently purified by trituration in DCM and filtration to afford the compound in >80% yield. Reaction of glutaconaldehyde dianil monohydrochloride with acetic anhydride in the presence of triethylamine in DCM afforded acetyl glutaconaldehyde dianil. The solution was added to a refluxing mixture of 1,1,2-trimethyl[1H]-benz[*e*]-indole-3-propanoic acid and sodium acetate in ethanol at 70 °C. The resulting mixture was refluxed for about 16 h, concentrated, and washed with a solution of dilute HCl to afford the desired compound. Although this procedure improved the isolated yield of **1** over previous methods, the purification was still difficult because of the formation of solvent-mediated mono- and diethyl ester byproducts.

After conducting the reactions in different solvent systems, we found that a mixture of acetonitrile/water (7:3) eliminates the ester byproduct formation and significantly increased the isolated yield of **1**. The condensation reaction progressed smoothly at 70 °C in the aqueous acetonitrile solution, suggesting that the dye formation is favored by entropy and higher reaction temperatures are avoidable. The desired compound **1** was obtained in >80% yield by recrystallization. ES-MS, NMR, and HPLC analyses confirmed its identity and purity. The facile workup, non-HPLC-based purification, and gram-scale preparation attest to the importance of preacetylating glutaconaldehyde in reducing the formation of byproducts, making this protocol attractive for efficient large-scale synthesis of **1** and related compounds.

Synthesis of Multivalent Cypate Analogues. The synthetic procedure is summarized in Scheme 2 (*16*). Amide bonds are commonly used as a linker because of its facile formation, derivation to anchor different functionalities, high solution stability, and biocompatibility. For these reasons, we introduced multivalency on carbocyanine dye inner cores via multicarboxamide functionalities. Although the amide formation appears straightforward, we found the use of highly reactive coupling reagents such as HBTU, PyBOP, and HATU in the presence of organic bases such as DIEA lead to the decomposition of **1**, as identified by HPLC, UV−vis, and ES-MS. After evaluating the most commonly used coupling methods, we found that the relatively mild carbodiimide-mediated coupling of **1** and its derivatives with amine-containing compounds gives amide products in good yields. As identified by MS in some reaction mixtures, inactive *N*-acylurea byproducts were formed through O−N migration of the active *O*-acylurea intermediate (*19*). This migration can be minimized by adding HOBt to the reaction mixture, which also catalyzes the reaction. Therefore, we finally used a combination of EDIC/HOBt to prepare the multivalent compounds. Reaction of **1** with di-*tert*-butyl imino diacetate in the presence of EDCI/HOBt, followed by TFA-mediated deprotection, gave two of the second-generation multivalent probes (tri- (**2**) and tetra (**3**) carboxylate-containing derivatives). Further reactions of **2** and **3** with di-*tert*-butyl imino diacetate in the presence of EDIC/HOBt and subsequent TFA-mediated deprotection afforded two of the third-generation multivalent probes (hexa- (**4**) and octa- (**5**) carboxylate-containing derivatives (Scheme 2)). The compounds were purified and obtained in moderate to good yields as follows: **2** (33%), **3** (60%), **4** (30%), and **5** (30%). The NIR multivalent molecular probes were used to prepare dendritic arrays of diverse bioactive moieties on a carbocyanine inner core for molecular recognitions.

Dendritic Arrays of Glucosamine on Carbocyanine Core. Carbohydrates play important roles in molecular recognitions. These polyhydroxylated molecules typically enhance the intended biological event via multivalent interactions in glycoside clusters (*20*). To explore the potentials of the multivalent carbocyanines in molecular recognition studies, we constructed a library of multivalent glucosamine-containing carbocyanine conjugates as molecular beacons. Accordingly, a series of compounds including **6**, **7**, **8**, **9**, **10**, and **11** (Figure 1) were prepared by conjugating D-(+)-glucosamine with **1**, **2**, **3**, **4**, and **5** in the presence of HBTU/HOBT/DIEA in moderate yields (*16*).

HPLC Analysis. The purity and homogeneity of all the glucosamine conjugates were analyzed by HPLC. Figure 2 shows two RP-HPLC chromatograms of compound **5** and its conjugate **11**. Expectedly, conjugation of

Scheme 2. Synthesis of Multi-carboxylic Acid-containing Carbocyanine Dyes[a]

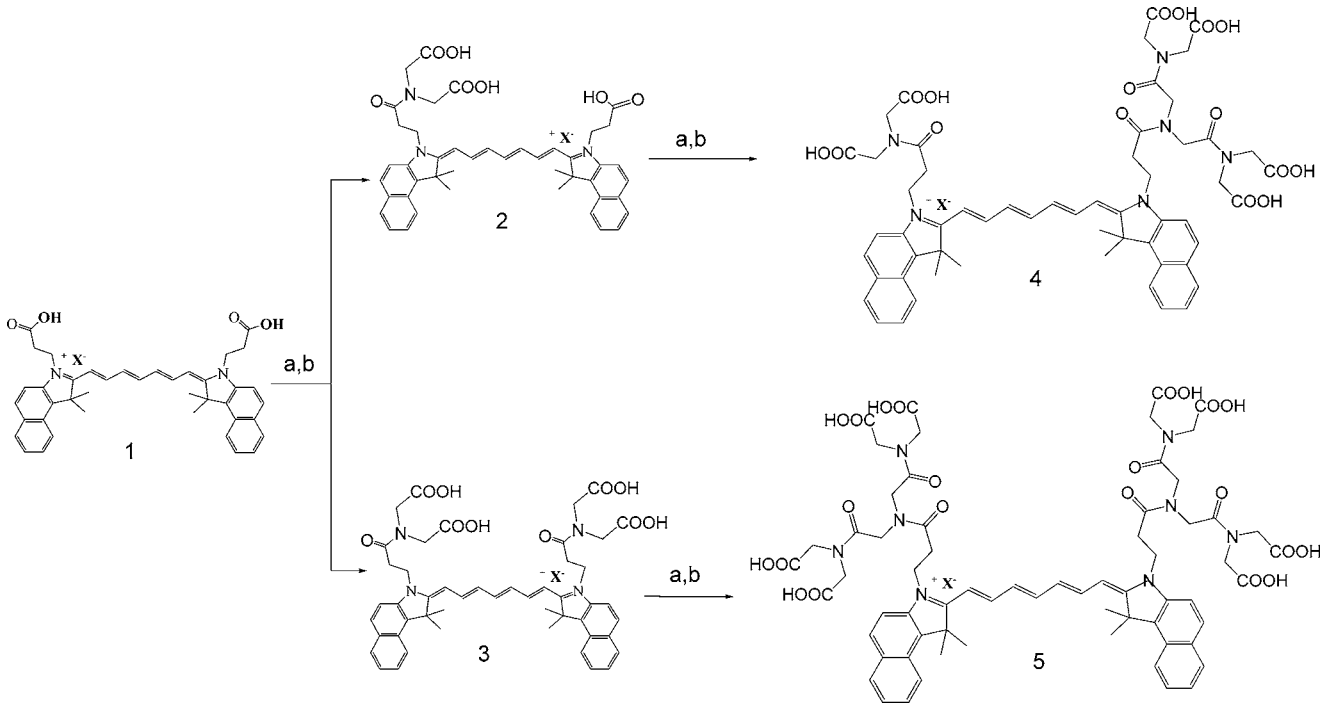

[a]Reagents and conditions: (a) EDCI/HOBT/di-*tert*-butyl iminodiacetate/rt/8 h; (b) TFA.

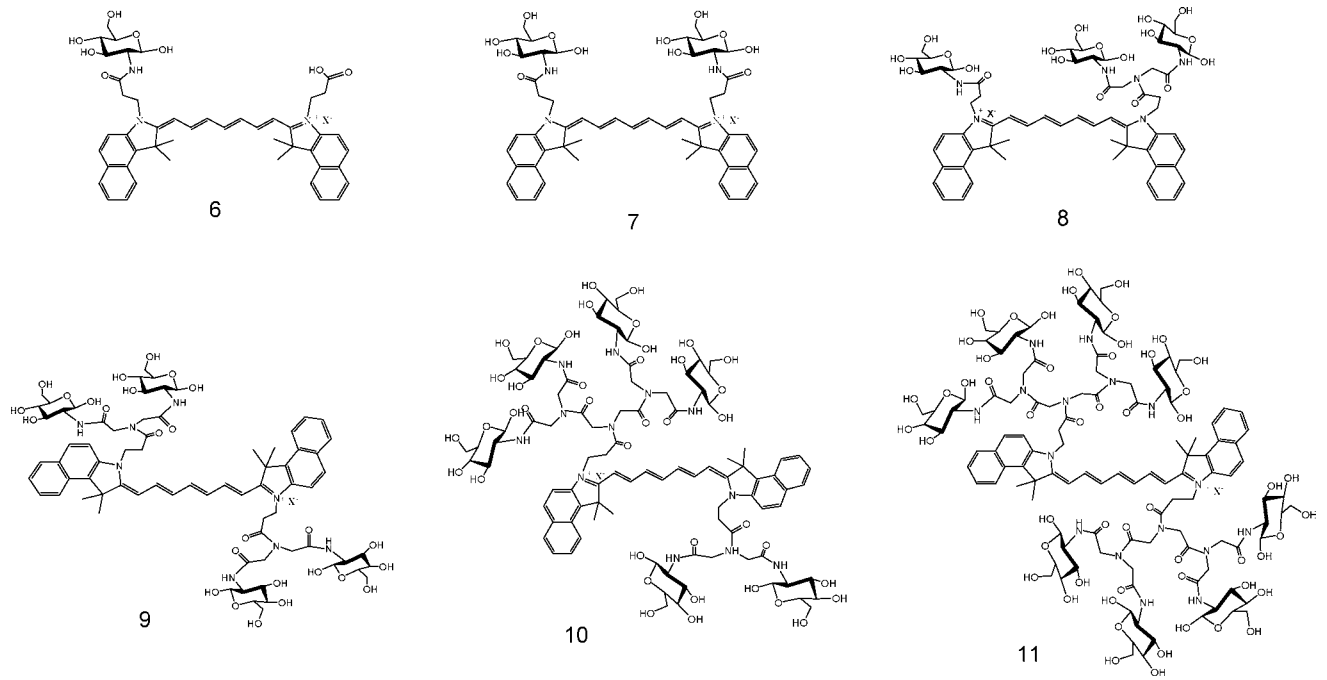

Figure 1. Structures of representative dendritic arrays of glucosamine on an inner NIR carbocyanine core.

the multivalent probes with glucosamine increases the hydrophilicity of the conjugate, as reflected in the shorter HPLC retention time compared with the precursor dye. The enhanced water solubility facilitates formulation of the probes in aqueous buffers for in vivo application.

NMR Analysis. ^{1}H and ^{13}C NMR analysis was performed on representative molecular probes **1**, **5**, and **11**. Structure of **1** was confirmed by proton 1D spectrum and 2D COSY and HMQC experiments. In Figure 3(A), the doublet at 6.45 ppm is assigned to the terminal protons at the conjugated double bond that are next to the indole ring. Spin propagation from the center proton (a in Figure 4(A)) toward the terminal proton (d in Figure 4A) further confirms the symmetrically conjugated seven-carbon double-bonded fragment. Assigned carbon resonances range from 104 to 156 ppm in HMQC (Figure 4B, a, b, c, d), indicating the conjugated double bonds are indeed present in **1**. Compounds **5** and **11** were identified by comparing their ^{13}C spectra with **1**. Additional resonances at 168−171 ppm and 47−50 ppm (Figure 5B) confirm the presence of octacarboxylic acid and 12 methylene groups, respectively, in **5**. Furthermore, the spectrum in Figure 5C indicates that the sugar carbons in **11** spans from 54 to 95 ppm. Comparison of the 2D HMQC spectra between **5** and **11** confirms the presence of glucosamine's anomeric H1′ protons at 4.92 and 4.43 ppm while those of H2′ to H6′ range from 3.02 to 3.59 ppm (Figure 6). Proton integration suggests that there is a 6:2 ratio between the

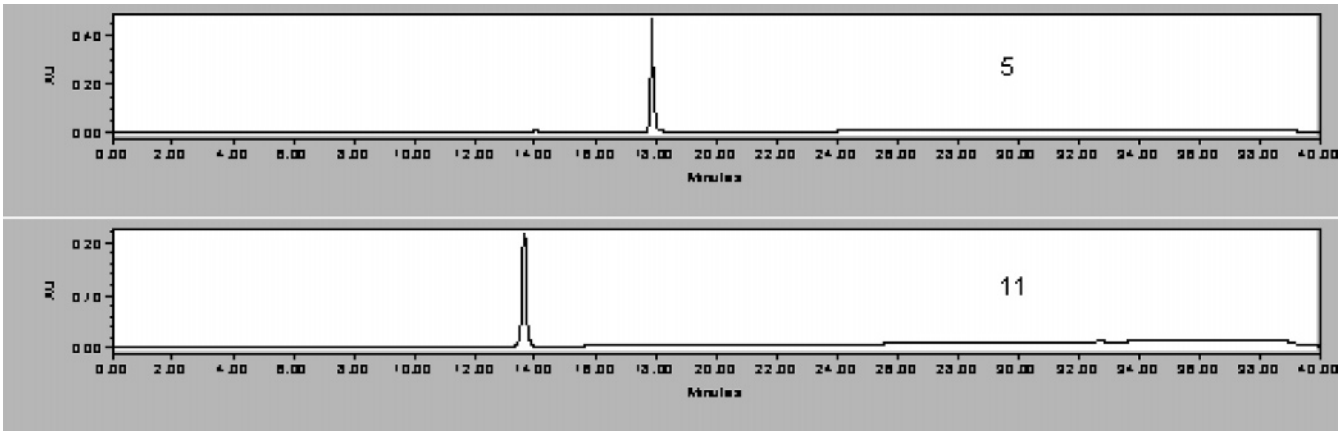

Figure 2. HPLC profiles of compound **5** (top) and **8** (bottom) detected at 254 nm.

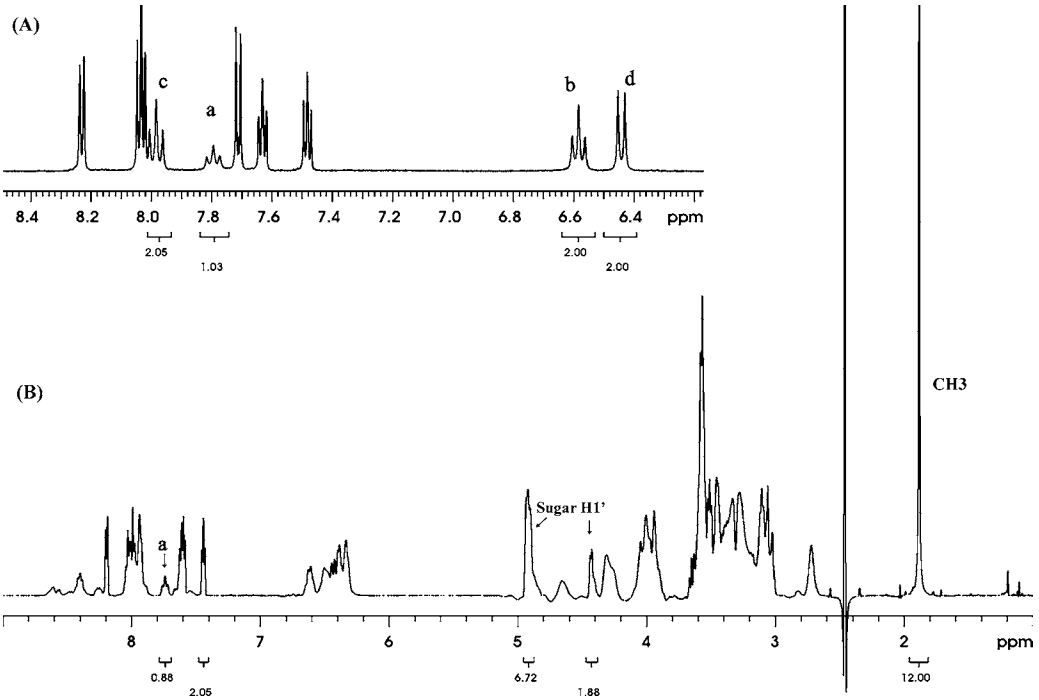

Figure 3. 600 MHz proton spectra of (A) compound **1**, and (B) compound **11** in DMSO-d_6 at 25 °C. Resonance a: center proton, d: terminal vinyl protons next to indole ring, b: protons adjacent to a, and c: protons adjacent to d.

two H1′ resonances (Figure 3B) and further confirms **11** possesses eight sugar moieties in the structure.

Absorption and Emission Properties. The absorption and emission spectra of all the compounds evaluated are similar, with their maxima centered around 780 and 810 nm, respectively. Figure 7 shows the normalized absorption and emission spectra of **1**, **5**, and **11**. Expectedly, the spectral properties of the dendritic arrays are also similar to the precursor multivalent beacons in the same solvent because conjugation occurred at distal positions to the inner chromophore core. This feature demonstrates another advantage of this series of multivalent molecular probes in providing consistent and predictable spectral properties for biological applications. All the compounds have exceptionally high molar absorptivity in a variety of solvents (Table 1).

Solution Stability Studies. Understanding the stability of molecular probes in different solvent systems will guide researchers in selecting the appropriate medium to formulate the compounds, perform reactions, and optimize storage conditions for each probe. To this effect, we assessed the stabilities of **1** (precursor dye), **5** (carboxylic acid tethered multivalent dye), and **11** (dendritic array of glucosamine on the multivalent dye **5**) in different mediums and temperatures. Dilute NaOH and HCl were chosen to represent the mild basic or acidic conditions frequently encountered in diverse applications. Because we typically lyophilize the compounds in aqueous acetonitrile (ACN) and conduct reactions in DIEA-containing organic solutions, we also evaluated the stabilities of the probes in 50% aqueous ACN and 0.01 M DIEA solution in 50% aqueous ACN. Phosphate-buffered saline (PBS, pH 7.2) is conventionally used to formulate products for biological applications, and hence prolonged stability of the probes in PBS is highly desirable. The stabilities of the probes (10 μM) in different mediums were monitored by UV−vis at λ_{max} of each probe.

As with most carbocyanine dyes, all the compounds tested are relatively stable in acidic condition at room temperature (Figure 8) and 37 °C (Figure 9). Possibly, protonation of the "donor" tertiary amine of the benzoindole carbocyanine stabilizes the probes. Similarly, solutions of the probes in 50% aqueous ACN are exceptionally stable for up to 18 h at 37 °C. These results suggest that workup and storage conditions in acidic and aqueous

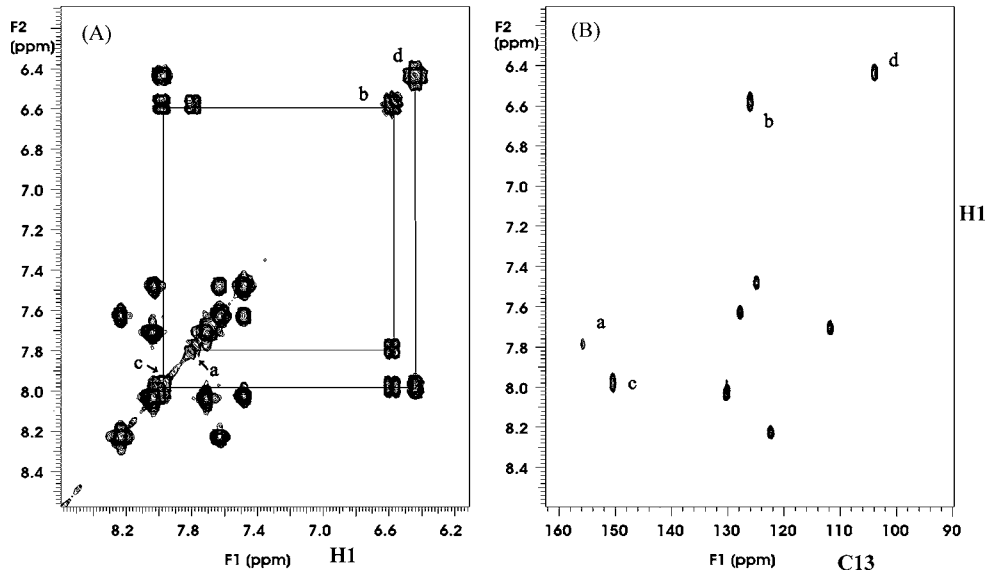

Figure 4. Expansions of the 600 MHz (A) COSY and (B) HMQC spectra of compound **1** in DMSO-d_6 at 25 °C. Same figure labels as in Figure 1.

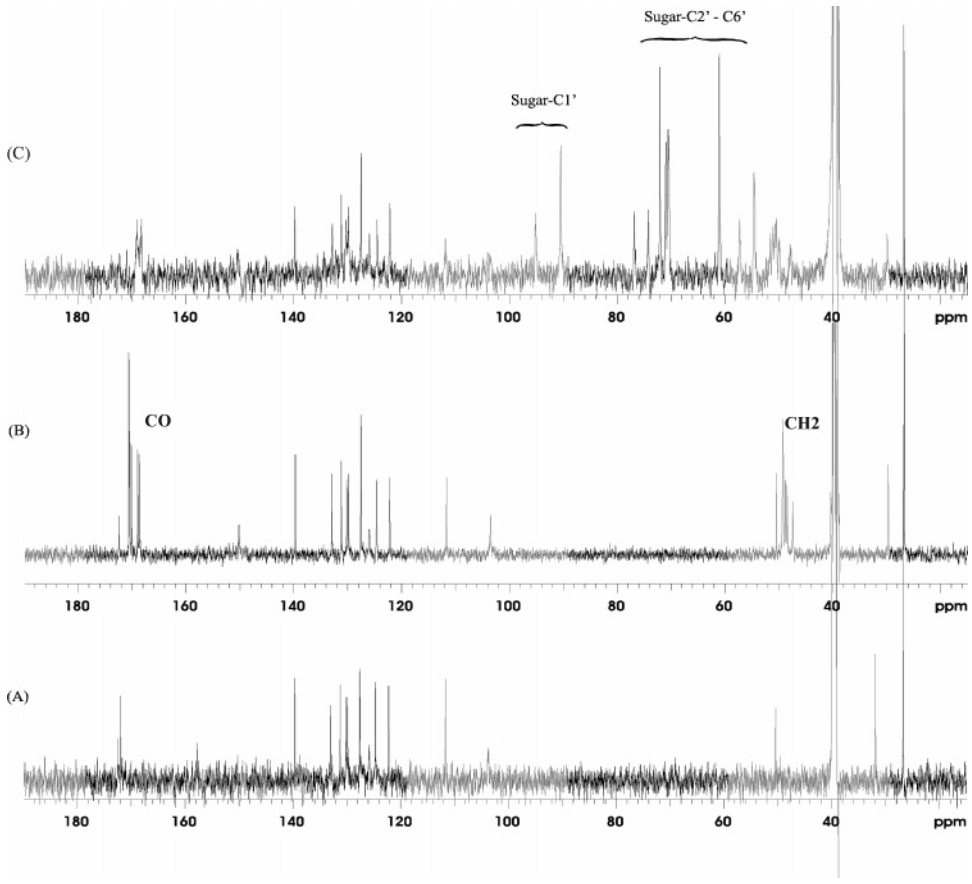

Figure 5. Carbon-13 spectra of (A) compound **1**, (B) compound **5**, and (C) compound **11** in DMSO-d_6 at 25 °C.

ACN mediums do not destabilize the chromophore system. In contrast, stabilities of the compounds in NaOH were different. While **5** was relatively stable in this medium up to 96 h, **1** and **11** were adversely affected. At 16 h, the percent absorbance of **1** in NaOH decreased to <80% and further dropped to <30% at room temperature after 96 h (Figure 8). A similar trend was obtained at 37 °C (Figure 9). This mild but progressive destabilization of **1** in NaOH may be due to the initial formation of the sodium carboxylate salt, followed by the generation of hydroxide zwitterions with the quartenary amine group of benzoindole. The strong basic hydroxide counterion can destabilize the conjugated π-system by abstracting acidic protons or reversing the aldehyde−trimethylbenzoindole condensation (Scheme 1). This inner salt effect by a strong basic counterion is supported by the minimal destabilization of **1** in the mild basic DIEA solution in aqueous ACN (Figure 9). Stability of **11** in basic mediums is abysmal and appears to correlate with the basicity of the medium, with stability in NaOH < DIEA solutions. This can be attributed to the hydrolysis of the glucosamine moieties under basic conditions, which gener-

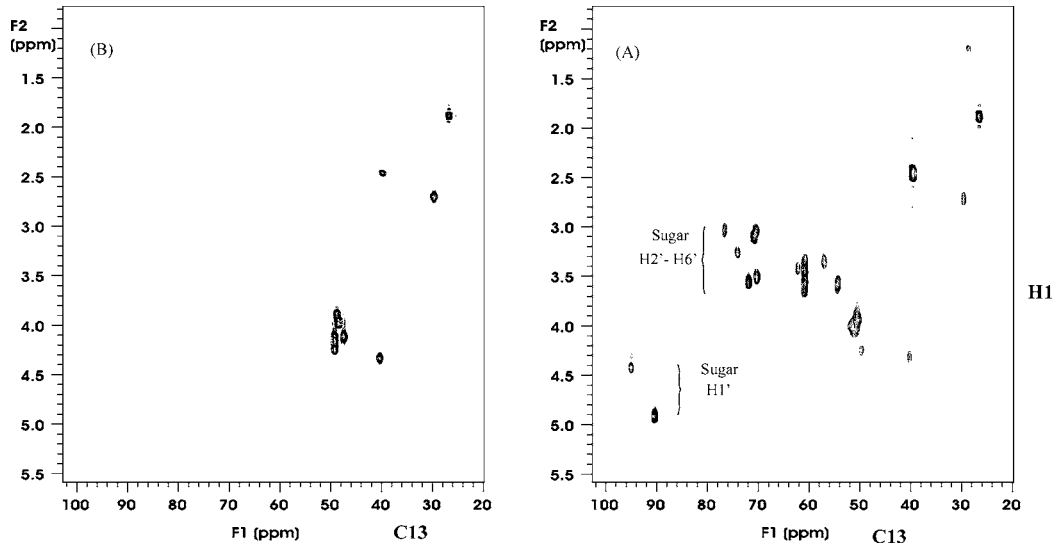

Figure 6. Expansions of the 600 MHz HMQC spectra of (a) compound **11** and (b) compound **5** in DMSO-d_6 at 25 °C.

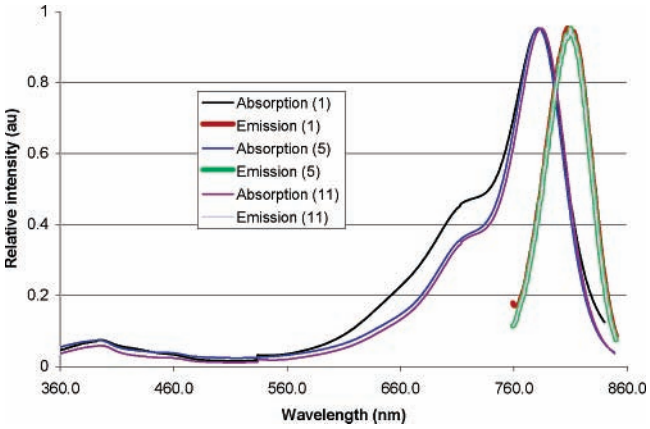

Figure 7. Normalized absorption and emission spectra of **1**, **5**, and **11** in 20% aqueous DMSO.

ates a mixture of byproducts that interfere with the spectral properties of the probe. Based on HPLC profile (not shown), the retention time of the byproducts (10.9 min), which increased in intensity as a function of time, is close to that of **5** (11.7 min) under the same HPLC condition, suggesting an incomplete hydrolysis of **11** toward the precursor probe **5**. However, **11** is most stable in PBS relative to **1** and **5** at room temperature after 96 h (Figure 8). This interesting observation indicates that the dendritic glucosamine probes can be formulated and stored in PBS for biological assays.

The results of the solution stability studies show that constructing multivalency on an inner chromophore core produced a robust NIR multivalent molecular probe (**5**) with exceptionally high stability in different mediums and at physiologically relevant temperatures, compared with the precursor dye (**1**). Stability of the dendritic array of biomolecules on the multivalent probes depends on the inherent stability of the biomolecule itself. In this study, the glucosamine cluster (**11**) is remarkably stable in acidic (dilute aqueous HCl) and buffered (PBS, pH 7.2) solutions but unstable under basic conditions.

Photostability Studies. Photostability studies were performed at a concentration of 5.56 μM in 20% aqueous

Table 1. Photophysical Properties of NIR Multivalent Probes in Different Solvents

compd	solvent	λ_{max}^{ab} (nm)	λ_{max}^{em} (nm)	$\Delta\lambda$ (nm)	ϵ (10^5) mol^{-1} cm^{-1}	compd	solvent	λ_{max}^{ab} (nm)	λ_{max}^{em} (nm)	Δ_λ (nm)	ϵ (10^5) mol^{-1} cm^{-1}
1	20% DMSO	782	808	26	2.24	**7**	20% DMSO	783	810	27	2.24
	PBS (pH 7.2)	778	805	27			PBS (pH 7.2)	779	805	26	
	water	778	803	25			water	779	806	27	
	95% ethanol	787	816	29			95% ethanol	786	813	27	
2	20% DMSO	782	812	30	1.90	**8**	20% DMSO	784	811	27	1.97
	PBS (pH 7.2)	778	806	28			PBS (pH 7.2)	780	806	26	
	water	778	805	27			water	779	806	27	
	95% ethanol	785	814	29			95% ethanol	789	814	25	
3	20% DMSO	782	808	26	2.15	**9**	20% DMSO	783	808	25	1.87
	PBS (pH 7.2)	777	807	30			PBS (pH 7.2)	779	809	30	
	water	777	805	28			water	779	809	30	
	95% ethanol	785	813	28			95% ethanol	783	812	29	
4	20% DMSO	782	808	26	2.01	**10**	20% DMSO	784	809	25	2.19
	PBS (pH 7.2)	778	805	27			PBS (pH 7.2)	780	808	28	
	water	778	811	33			water	780	808	28	
	95% ethanol	785	814	29			95% ethanol	792	819	27	
5	20% DMSO	782	810	28	1.85	**11**	20% DMSO	784	810	26	1.99
	PBS (pH 7.2)	778	804	26			PBS (pH 7.2)	780	807	27	
	water	778	810	32			water	780	807	27	
	95% ethanol	787	814	27			95% ethanol	791	816	25	
6	20% DMSO	783	809	26	2.24						
	PBS (pH 7.2)	778	805	27							
	water	778	806	28							
	95% ethanol	786	815	29							

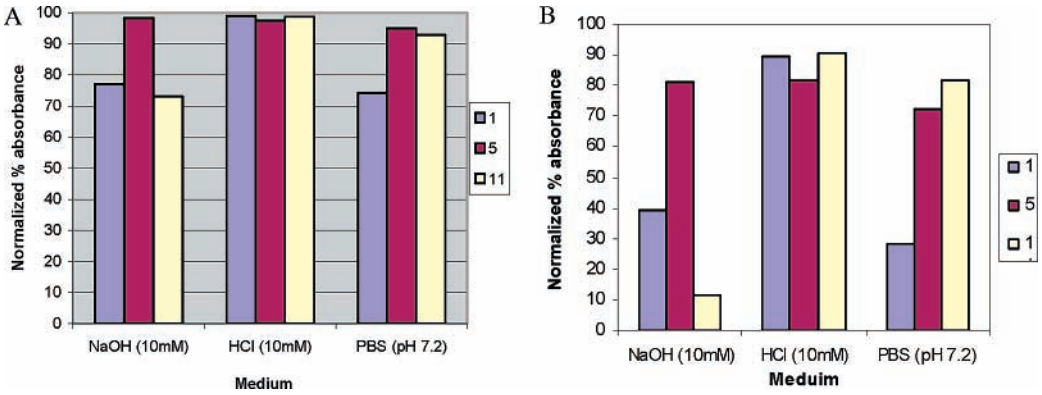

Figure 8. Absorbance of **1**, **5**, and **11** in different mediums at room temperature: (A) 16 h and (B) 96 h. The initial absorbance at $t = 0$ for each medium is normalized as 100%.

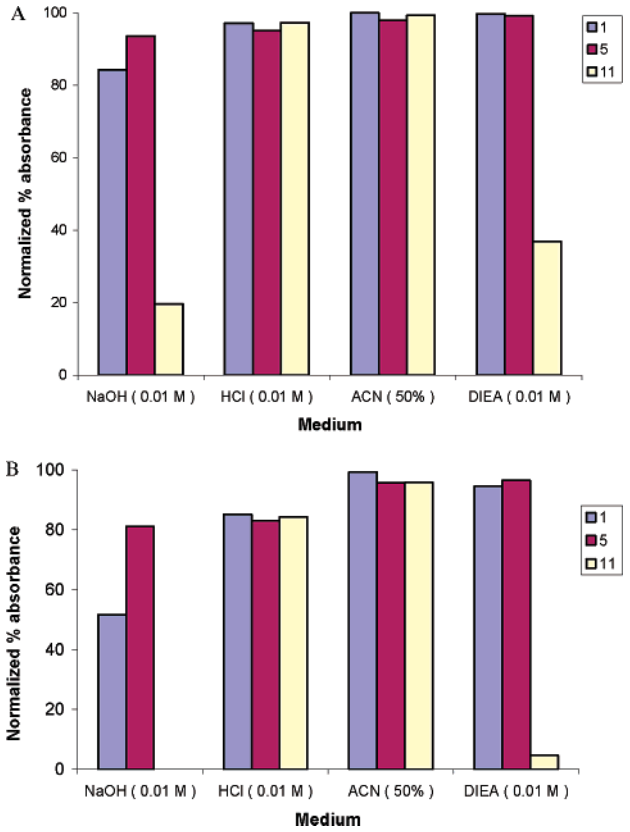

Figure 9. Absorbance of **1**, **5**, and **11** in different mediums at room temperature: (A) 16 h and (B) 96 h. The initial absorbance at $t = 0$ for each medium is normalized as 100%.

DMSO under three different conditions. A solution of the probe in a cuvette was (1) wrapped in aluminum foil and stored in a dark room, (2) placed on a laboratory shelf and exposed to normal fluorescent room light (condition A), and (3) exposed to a bright 60 W light bulb placed within 30 cm from the sample (condition B). UV−vis spectra were recorded at 0.5 h intervals for over 8 h under condition B and at 24 h intervals over one week for condition A. We found that the photophysical stability of all the molecular probes were identical. In the dark, the absorbance remained nearly constant for >1 week. Under fluorescent room light, no appreciable change in absorbance was observed for up to 24 h. However, the absorbance gradually decreased to 20% after 5 days. In contrast, all of the solutions were very unstable on exposure to bright light (Figure 10). The decrease in absorbance appears to follow a two-phase exponential model with a linear decay constant of about $-7.2\ s^{-1}$. The photostability data demonstrates that the multivalency does not protect the chromophore system from photodegradation and that the conventional storage in the dark is still recommended for the multivalent compounds. The observed decrease is probably due to photobleaching.

In Vivo Biodistribution. Glucose is the primary monosaccharide from carbohydrate digestion that is transported to cells to generate energy for normal physiological functions. Internalization of glucose in cells is typically mediated by glucose transporters (GLUTs) where it is phosphorylated by mitochondrial hexokinase (*21*). The metabolic fate of glucose hinges on the intricate interplay between extracellular glucose level, GLUTs and mitochondrial hexokinase. Abnormal, hypermetabolizing cells such as cancers, overexpress GLUTs to enhance this equilibrium-dependent glucose transport relative to normal surrounding cells. Therefore, molecules that are recognized by GLUTs but not further metabolized once internalized in cells accumulate in diseased tissues, thereby providing a method to image and treat pathologic tissues. This strategy is widely used to image hypermetabolizing cells by positron emission tomography after administering a radioactive glucose analogue, ^{18}fluorodeoxyglucose (^{18}FDG) to patients (*22*). Previous studies have shown that a fluorescent probe-labeled glucosamine derivative, 2-(*N*-(7-nitrobenz-2-oxa-1,3- diazol-4-yl)amino)-2-deoxyglucose (2-NBDG), is a viable nonradioactive method to monitor glucose transport and uptake in cells (*23*). More recent studies have shown that conjugation of glucosamine to NIR fluorescent dyes (*24*) or photosensitizers (*25*) results in high tumor uptake of the compounds. Although carbohydrates are known to interact strongly with their target via glycosidic clusters (*20*), these studies did not explore the potential beneficial effects of multivalency. Therefore, we evaluated the in vivo distribution of the NIR fluorescent dendritic arrays of glucosamine in highly proliferating pancreatic tumor (CA20948) bearing mice.

Each mouse received 0.3 μmol of the beacons per kg body weight of mouse via tail vein injection. The in vivo and ex vivo distribution of the molecular beacons were monitored by NIR fluorescence imaging using two collimated solid 780 nm laser sources for excitation and a CCD camera equipped with 830 nm interference filter to capture the fluorescence emission (*12*). At 24 h postinjection, the nude mice were sacrificed. Aliquots of blood and some major organs were harvested and washed with distilled water. The mean fluorescence count in each tissue was determined for each compound and normalized relative to 100% of the organ with highest fluorescence intensity (Figure 11). Negative control studies show that the precursor dye **1** was not retained in the tumor

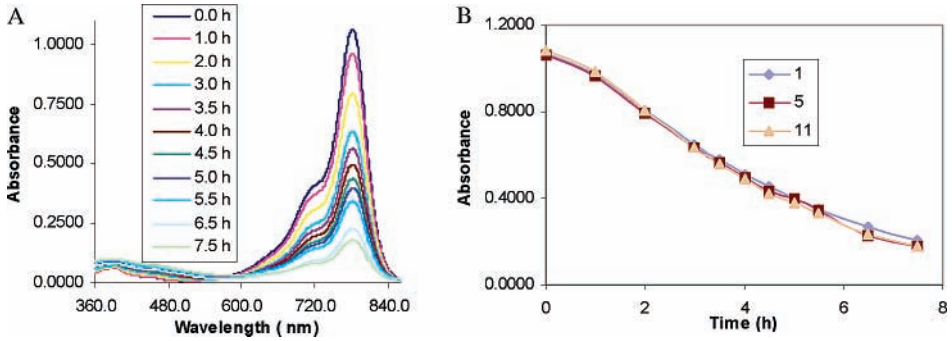

Figure 10. Spectra of the changes in the absorbance of **5** with time and (B) photostability of **1**, **5**, and **11** in 20% aqueous DMSO exposed to 60 W light bulb.

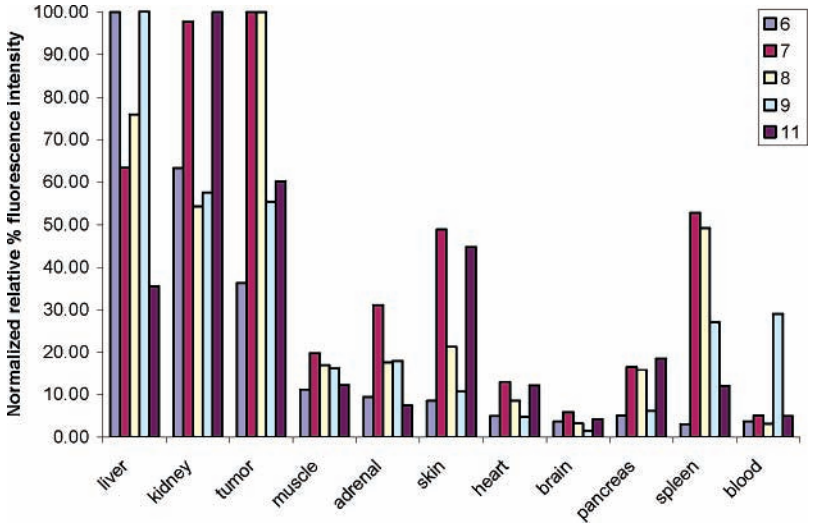

Figure 11. Biodistribution of dendritic arrays of glucosamine in CA20948 pancreatic tumor-bearing mice at 24 h postinjection of the probes.

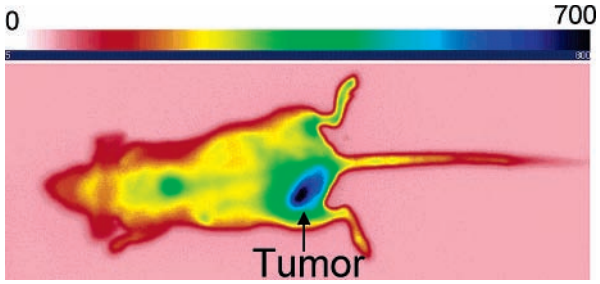

Figure 12. False color fluorescence image of compound **8** in CA20948 tumor-bearing nude mouse at 24 h postinjection of the probe.

but accumulated in the liver at about 1 h postinjection. This observation was also noted in previous studies with the same tumor model in male Lewis rats (*9*, *12*).

In contrast, all of the dendritic arrays of glucosamine were retained in the tumor up to 24 h postinjection (Figure 11). Compounds **7** and **8** have the highest tumor uptake at 24 h postinjection. However, the high retention of **7** in the skin increases background fluorescence, which is not desirable for noninvasive optical imaging. A significant amount of compound **9** is retained in blood at 24 h postinjection, making it the best agent for applications that require long-circulating probes with low skin uptake. The octaglucosamine probe (**11**) rapidly accumulates in the target tumor tissue within 6 h postinjection but at 24 h, the tumor uptake reduced to about 50% of the fluorescence intensity relative to the kidneys, which became the predominant retention organ. Surprisingly, the skin uptake of **11** was also high. Of all the glucosamine derivatives examined, the triglucosamine derivative (**8**) appears to have a good balance between high tumor uptake and decreased retention in nontarget tissues (Figure 12). Overall, there is an intricate relationship between the probe distribution and the multivalent compounds but the molecular basis for the selective uptake in some tissues is not clear at this time. Nonetheless, these results demonstrate that each compound can be used for different biomedical applications. For example, compound **9**, which is retained in blood for >24 h, could serve as a blood pool agent for monitoring blood flow and imaging blood vessels.

CONCLUSION

NIR carbocyanine dyes can effectively serve as optical scaffold for anchoring multiple functionalities and providing multivalency for molecular recognition studies. On the basis of the synthetic strategy developed, higher generations of the multivalent compounds are also accessible. Because the reactive functional groups are distal to the chromophore core, both multicarboxylate probes and their dendritic glucosamine derivatives have similar spectral properties, thereby improving data reproducibility and enabling the use of the same excitation source and filter for sample analysis. Photophysical stability studies show that neither the multivalent probes nor their corresponding dendritic array of biomolecules confer greater photostability to the chromophore core relative to the precursor dye. However, the multivalency appears to remarkably enhance the solution stability of the multicarboxylate probes in different mediums at physi-

ologically relevant temperatures. Overall, the stability studies provide guidance for reaction mediums and storage conditions. Biodistribution studies in tumor-bearing nude mice showed that all the glucosamine conjugates localized in the tumor but the precursor dye, cypate was almost exclusively retained in the liver. The pattern of probe distribution in various tissues suggests that each of the NIR fluorescent glucosamine derivatives could be useful for different but complimentary biological applications.

ACKNOWLEDGMENT

Funding for this project was provided by the NSF Bioengineering grant (BES 0119489).

LITERATURE CITED

(1) Hawrysz, D. J., and Sevick-Muraca, E. M. (2000) Developments toward diagnostic breast cancer imaging using near-infrared optical measurements and fluorescent contrast agents. *Neoplasia 2*, 388−417.

(2) Mahmood, U., and Weissleder, R. (2003) Near-infrared optical imaging of proteases in cancer. *Mol. Cancer Ther. 2*, 489−496.

(3) Tung, C. H., Mahmood, U., Bredow, S., and Weissleder, R. (2000) In vivo imaging of proteolytic enzyme activity using a novel molecular reporter. *Cancer Res. 60*, 4953−4958.

(4) Achilefu, S. (2004) Lighting up tumors with receptor-specific optical molecular probes. *Technol. Cancer Res. Treat. 3*, 393−409.

(5) Sevick-Muraca, E. M., Houston, J. P., and Gurfinkel, M. (2002) Fluorescence-enhanced, near-infrared diagnostic imaging with contrast agents. *Curr. Opin. Chem. Biol. 6*, 642−650.

(6) Ye, Y., Li, W. P., Anderson, C. J., Kao, J., Nikiforovich, G. V., et al. (2003) Synthesis and characterization of a macrocyclic near-infrared optical scaffold. *J. Am. Chem. Soc. 125*, 7766−7767.

(7) Frangioni, J. V. (2003) In vivo near-infrared fluorescence imaging. *Curr. Opin. Chem. Biol. 7*, 626−634.

(8) Becker, A., Hessenius, C., Licha, K., Ebert, B., Sukowski, U., et al. (2001) Receptor-targeted optical imaging of tumors with near-infrared fluorescent ligands. *Nat. Biotechnol. 19*, 327−331.

(9) Bugaj, J. E., Achilefu, S., Dorshow, R. B., and Rajagopalan, R. (2001) Novel fluorescent contrast agents for optical imaging of in vivo tumors based on a receptor-targeted dye-peptide conjugate platform. *J. Biomed. Opt. 6*, 122−133.

(10) Achilefu, S., Jimenez, H. N., Dorshow, R. B., Bugaj, J. E., Webb, E. G., et al. (2002) Synthesis, in vitro receptor binding, and in vivo evaluation of fluorescein and carbocyanine peptide-based optical contrast agents. *J. Med. Chem. 45*, 2003−2015.

(11) Ntziachristos, V., Yodh, A. G., Schnall, M., and Chance, B. (2000) Concurrent mri and diffuse optical tomography of breast after indocyanine green enhancement. *Proc. Natl. Acad. Sci. U.S.A. 97*, 2767−2772.

(12) Achilefu, S., Dorshow, R. B., Bugaj, J. E., and Rajagopalan, R. (2000) Novel receptor-targeted fluorescent contrast agents for in vivo tumor imaging. *Invest. Radiol. 35*, 479−485.

(13) Mammen, M., Choi, S. K., and Whitesides, G. M. (1998) Polyvalent interactions in biological systems: Implications for design and use of multivalent ligands and inhibitors. *Angew. Chem.-Int. Edit. 37*, 2755−2794.

(14) Yordanov, A. T., Kobayashi, H., English, S. J., Reijnders, K., Milenic, D., et al. (2003) Gadolinium-labeled dendrimers as biometric nanoprobes to detect vascular permeability. *J. Mater. Chem. 13*, 1523−1525.

(15) Gopidas, K. R., Whitesell, J. K., and Fox, M. A. (2003) Nanoparticle-cored dendrimers: Synthesis and characterization. *J. Am. Chem. Soc. 125*, 6491−6502.

(16) Ye, Y. P., Bloch, S., and Achilefu, S. (2004) Polyvalent carbocyanine molecular beacons for molecular recognitions. *J. Am. Chem. Soc. 126*, 7740−7741.

(17) Becker, A., Riefke, B., Ebert, B., Sukowski, U., Rinneberg, H., et al. (2000) Macromolecular contrast agents for optical imaging of tumors: Comparison of indotricarbocyanine-labeled human serum albumin and transferrin. *Photochem. Photobiol. 72*, 234−241.

(18) Lin, Y. H., Weissleder, R., and Tung, C. H. (2002) Novel near-infrared cyanine fluorochromes: Synthesis, properties, and bioconjugation. *Bioconjugate Chem. 13*, 605−610.

(19) Volonterio, A., and Zanda, M. (2003) Domino condensation/aza-michael/o→n acyl migration of carbodiimides with activated [alpha],[beta]-unsaturated carboxylic acids to form hydantoins. *Tetrahedron Lett. 44*, 8549−8551.

(20) Bolam, D. N., Xie, H. F., White, P., Simpson, P. J., Hancock, S. M., et al. (2001) Evidence for synergy between family 2b carbohydrate binding modules in cellulomonas fimi xylanase 11a. *Biochemistry 40*, 2468−2477.

(21) Pauwels, E. K. J., Ribeiro, M. J., Stoot, J., McCready, V. R., Bourguignon, M., et al. (1998) Fdg accumulation and tumor biology. *Nucl. Med. Biol. 25*, 317−322.

(22) Gambhir, S. S. (2002) Molecular imaging of cancer with positron emission tomography. *Nat. Rev. Cancer 2*, 683−693.

(23) Yamada, K., Nakata, M., Horimoto, N., Saito, M., Matsuoka, H., et al. (2000) Measurement of glucose uptake and intracellular calcium concentration in single, living pancreatic beta-cells. *J. Biol. Chem. 275*, 22278−22283.

(24) Chen, Y., Zheng, G., Zhang, Z. H., Blessington, D., Zhang, M., et al. (2003) Metabolism-enhanced tumor localization by fluorescence imaging: In vivo animal studies. *Opt. Lett. 28*, 2070−2072.

(25) Zhang, M., Zhang, Z. H., Blessington, D., Li, H., Busch, T. M., et al. (2003) Pyropheophorbide 2-deoxyglucosamide: A new photosensitizer targeting glucose transporters. *Bioconjugate Chem. 14*, 709−714.

BC049790I

Rapid Binding of Concanavalin A and Maltose−Polyrotaxane Conjugates Due to Mobile Motion of α-Cyclodextrins Threaded onto a Poly(ethylene glycol)

Tooru Ooya,[†,‡] Hideto Utsunomiya,[†] Masaru Eguchi,[†] and Nobuhiko Yui[†,‡,*]

School of Materials Science and The 21st Century COE Program, Japan Advanced Institute of Science and Technology, 1-1 Asahidai, Tatunokuchi, Ishikawa 923-1292, Japan. Received August 4, 2004; Revised Manuscript Received October 31, 2004

Maltose−polyrotaxane conjugates (Mal-PRXs), in which maltose-conjugated α-cyclodextrins (α-CDs) are threaded onto a poly(ethylene glycol) (PEG) chain capped with benzyloxycarbonyl-L-tyrosine, were characterized in terms of their molecular motion and the relation to multivalent interactions between the maltose moiety and concanavalin A from *Canavalia ensiformis* (Con A). Spin−lattice relaxation time (T_1) and spin−spin relaxation time (T_2) of α-CD C(1), maltosyl C(1), and PEG methylene protons in the Mal-PRXs revealed that the mobile motion of α-CDs in the polyrotaxane governed the molecular motion of maltosyl groups in α-CDs and threading PEG chain. The association constant (K_a) of the Mal-PRXs with 22, 38 and 53% of α-CD threading was 5.7×10^4, 1.1×10^6, and 5.3×10^5 (M^{-1}-maltose), respectively. The largest K_a value of the Mal-PRX with 38% of α-CD threading was well correlated with the T_1 and T_2 values of maltosyl groups and α-CD, suggesting that the mobile motion of maltose-conjugated α-CDs in the Mal-PRX contributes to the highest affinity with Con A. Initial rate of binding with Con A was also governed by the mobile motion of maltose-conjugated α-CDs. Therefore, we concluded that both highly molecular motion due to the mobile motion of maltose-conjugated α-CDs and multivalency of the Mal-PRXs contributes to inducing rapid Con A binding.

INTRODUCTION

Multivalent interactions between ligands and binding proteins have been extensively studied to obtain high association constants for targeting ligand−polymer conjugates to specific cells (*1*) and mimicking saccharide−protein interactions (*2*−*4*). Especially, saccharide−polymer conjugates enhance the interaction with concanavalin A (Con A), one of plant lectins from *Canavalia ensiformis*, resulting in the increased association constant (*5*−*7*). These effects are due to the multivalent interactions that are dependent on molecular weight (*8*), the number of ligands per one polymeric backbone (*9*), and flexibility of the polymeric backbone and linkers (*10*, *11*). In these factors, flexibility of the backbone and linkers is thought to be important because the flexible motion is considered to reduce steric hindrance of ligands toward the binding sites of lectins. Increasing the number of ligands per one polymeric backbone increases local density of the ligands, resulting in the enhanced opportunity of the multivalent interaction. Recently, architectural effects of the saccharide scaffolds on the multivalent interaction have been investigated (*12*) using linear neoglycopolymers (*9*), dendrimers (*13*, *14*), dendrigraft (*15*), nanoparticles (*16*), cyclic peptides (*17*), and cyclodextrins (CDs) (*18*, *19*). However, the increased local density and the number of saccharides often cause lectin recognition mismatching, so that reduction of the mismatching by the design of biomaterials is required to improve the multivalent feature.

To enhance the multivalent interaction, we have focused on mechanically locked structures of polyrotaxanes, in which many α-cyclodextrins (α-CDs) are threaded onto a poly(ethylene glycol) (PEG) chain capped with bulky end-groups (*20*). In our previous study, the mechanically locking structure of polyrotaxane is utilized for the conjugation of biotin (*21*, *22*) and a valyl-lysine dipeptide (*23*), and each conjugate is multivalently recognized by a streptavidin and peptide transporter, respectively. Moreover, maltosyl groups are successfully introduced to the polyrotaxane with a different number of α-CDs for multivalent interaction with Con A. When the threading percentage of α-CDs against the stoichiometric number was 38%, the highest mobility of maltosyl groups is observed, which demonstrates the highest relative potency of Con A-induced hemagglutination (*24*). Also, the maltose−polyrotaxane conjugate (Mal-PRX) with a highly mobile nature maintains water cluster structure that is clarified by Raman spectroscopy (*25*). Those findings suggest that the Mal-PRXs seem to be inert in aqueous solution, and the high mobility of maltosyl groups allows multivalent interaction. However, it has been unclear how the molecular motions of both α-CDs and PEG in the Mal-PRXs are related to the highly molecular motion of the maltosyl group. Moreover, the data of Con A-induced hemagglutination did not give us the direct binding aspects with Con A.

In this study, we examined Mal-PRXs in detail to understand the close relationship between whole molecular motions of the polyrotaxane backbone and multivalent binding with Con A. Molecular motion of maltosyl groups, α-CDs, and PEG in the Mal-PRXs was analyzed by spin−lattice relaxation time (T_1) and spin−spin relaxation times (T_2), and we discuss how the α-CD threading percentage in the Mal-PRXs affects the whole

* To whom correspondence should be addressed. Phone and Fax: +81-761-51-1640. E-mail: yui@jaist.ac.jp.
† School of Materials Science.
‡ The 21st Century COE Program.

10.1021/bc049809h CCC: $30.25 © 2005 American Chemical Society
Published on Web 12/24/2004

molecular motion. Association constants (K_a) and initial binding rate of the multivalent interaction between the Mal-PRXs and Con A are estimated, and we also discuss in detail how the molecular motions of maltosyl groups, α-CDs, and PEG in the Mal-PRXs take part in the multivalent interaction.

MATERIALS AND METHODS

Materials. α-Cyclodextrin (α-CD) was purchased from Bio-Research Corporation of Yokohama (Yokohama, Japan). Poly(ethylene glycol) (PEG, M_n = 20 000), poly(acrylic acid) (PAA, M_n = 25 000) and *N,N*-diisopropylethylamine (DIEA) were purchased from Wako Pure Chemical Co. Ltd (Osaka, Japan). α,ω-Diamino PEG was synthesized according to previously reported method via tosylation, phthalimidation, and its hydorazine substitution (*26*). Benzotriazol-1-yloxytris(dimethylamino)phosohonium hexafluorophosphate (BOP reagent) and 1-hydroxybenzotriazole (HOBt) were purchased from Nacalai Tesque, Inc. (Kyoto, Japan). Benzyloxycarbonyl-L-tyrosine (Z-L-Tyr) was purchased from Kokusan Chemical Co., Ltd (Tokyo, Japan). Concanavalin A (Con A) from *Canavalia ensiformis* was purchased from Sigma Co. (MI). Fluorescein-labeled Con A was purchased from Vector Laboratories, Inc. (CA). Other chemicals used were of highest purity available.

Measurements. Gel permeation chromatography (GPC) was carried out using GPC columns TSK_{gel} G-5000H_{HR} + TSK_{gel} G-3000H_{HR} (Tosoh Co. Ltd., Tokyo, Japan) using DMSO (HPLC grade, Kishida Chemical Co. Ltd., Osaka, Japan) as the eluent. The eluent was detected with a chiral detector (OR-990, Japan Spectroscopic Co., Ltd., Tokyo, Japan). ^{1}H NMR spectra were recorded on a 750 MHz FT-NMR spectrometer (Varian, Unity plus, CA). Turbidity change at 420 nm was recorded on a UV−vis spectrometer (V-550, Japan Spectroscopic Co., Ltd., Tokyo, Japan). Fluorescent spectra were recorded on a spactrofluorometer (FP-777, Japan Spectroscopic Co., Ltd., Tokyo, Japan).

Synthesis of Maltose−Polyrotaxane Conjugates (Mal-PRXs, 1−3) (24). Polypseudorotaxanes (inclusion complex of α-CDs and α,ω-diamino PEG, M_n: 20 000) were prepared according to the previously reported procedure by Harada et al. (*20*). The number of threading α-CD was calculated to be ca. 120 from ^{1}H NMR spectra, comparing the integrations of the signals at 4.8 ppm (C(1)H of α-CD) with those at 3.5 ppm (CH_2 of PEG).

The synthetic method of Z-Tyr-terminated PRXs was followed by our previous report with some modifications (*24*). To introduce Z-L-Tyr as the terminal groups of polyrotaxanes, a condensation reaction was carried out. Z-L-Tyr (3.9 g, 12.4 mmol), BOP (5.5 g, 12.4 mmol), HOBt (1.9 g, 14.0 mmol), and DIEA (2.2 mL, 12.4 mmol) were dissolved in dry DMF (10 mL). The solution was added to a suspension of the polypseudorotaxane (85 g, 0.62 mmol) in a mixture of DMF and DMSO (40 mL), and the reaction mixture was stirred at room temperature for 6 h. Here, volume ratio of DMF and DMSO (DMF/DMSO) was varied so as to be 85/15, 90/10, and 100/0. After that, the mixture was poured into excess acetone to precipitate crude products and to remove BOP, HOBt, DIEA, and unreacted α,ω-diamino PEG. The precipitate was collected by centrifugation and washed with ethanol and pure water to remove impurities including free α-CDs. The resulting precipitate was dried in vacuo at room temperature to obtain Z-Tyr-terminated PRXs as white powders. By changing the DMF/DMSO from 85/15 to 100/0, the number of α-CDs was varied to be ca. 50, 85, and 120, respectively, which was calculated by ^{1}H NMR spectra. The obtained Z-Tyr-terminated PRXs were soluble only in DMSO.

To introduce carboxyl groups to hydroxyl group of α-CDs in Z-Tyr-terminated PRXs, carboxyethyl ester PRXs (CEE-PRXs) were prepared using the Z-Tyr-terminated PRXs according to our method (*24*). The Z-Tyr-terminated PRXs and succucinic anhydride (same mol. of hydroxyl groups in the Z-Tyr-terminated PRXs) were dissolved in dry pyridine and stirred at room temperature. The reaction mixture was poured into excess ether and washed with ether three times. The precipitate was collected by centrifuging and dried in vacuo to give the CEE-PRXs. The degree of substitution of CEE groups in the polyrotaxane was estimated from the ratio of the methylene peak of CEE (2.3 ppm) and C(1)H of α-CD (4.9 ppm) on ^{1}H NMR spectra. In this synthetic condition, all the primary hydroxyl groups were converted to the CEE, i.e., the number of CEE per one α-CD molecule was ca. 6.

Finally, maltosyl groups were introduced to CEE groups in the CEE-PRXs (Scheme 1). β-Maltosylamine (Mal-amine) was prepared by the method of Kobayashi et al. (*27*) (yield: 85%). The CEE-PRXs (concentrated of CEE: 3.0 mM) were dissolved in dry DMSO. A solution of BOP, HOBt, and DIEA in DMSO (6.0 mM each) was added to the solution. The reaction mixture was stirred at 25 °C for several minutes. Then, Mal-amine in DMSO was added (final concentration of Mal-amine: 8.8 mM) and stirred at 25 °C for 10 h. The solution was poured into an excess acetone, and then the crude products were purified by dialysis against water using Spectra/Por CE 6 (MWCO: 8000) to obtain the maltose-polyrotaxane conjugates (Mal-PRX, **1**−**3**) as white powders (yields: 70−80%).

In a similar manner, a maltose−α-CD conjugate (Mal-CD, **4**) and maltose−poly(acrylic acid) conjugates (Mal-PAA, **5**) were synthesized. α-CD (2.5 g, 2.6 mmol) and succinic anhydride (8.2 g, 54.6 mmol) were dissolved in dry pyridine (100 mL) and stirred for 24 h at room temperature. The reaction mixture was poured into excess ether. The precipitate was collected by centrifuging and dried in vacuo to give a crude product. The crude product was dissolved in distilled water. The solution was dialyzed in distilled water for 3 days using Spectra/Por CE (MWCO = 500) and then lyophilized to obtain CEE-α-CD (the number of CEE per one α-CD molecule was ca. 6). Finally, Mal-amine (2.0 mM) was introduced to the CEE-α-CD (concentrated of CEE: 3.8mM) in the presence of BOP, HOBt, and DIEA in DMSO (4.6 mM each) as well as the Mal-PRXs. As for the Mal-PAA **5**, Mal-amine (8.8 mM) was introduced to the PAA (concentrated of carboxyl groups: 7.0 mM) in the presence of BOP, HOBt, and DIEA in DMSO (17.5 mM each).

The degree of substitution of maltose in the polyrotaxane was calculated from the ratio of the C(1)H and C(1′) of maltose (2H, 5.3 ppm) and C(1)H of α-CD (1H, 4.9 ppm) on the ^{1}H NMR spectra. Average molecular weights of the Mal-PRXs **1**−**3** and the Mal-PAA **5** were calculated by ^{1}H NMR and GPC. As for the GPC, both the number average molecular weight (M_n) and the weight average molecular weight (M_w) were calculated from a calibration curve of pullulan standard. The M_w of the Mal-CD **4** was determined by MALDI-TOF mass spectrum using Voyager-DE2RP (PE Biosystems, Foster city, CA) in linear mode. Samples for mass spectrum were prepared by casting the matrix compound (2,5-dihydroxyacetophenone) with the Mal-CD **4** (0.2 mg/mL in water) onto the

Scheme 1. Synthesis of Maltose−Polyrotaxane Conjugates Using a Carboxyethyl Ester (CEE)−Polyrotaxane and *β*-Maltosylamine

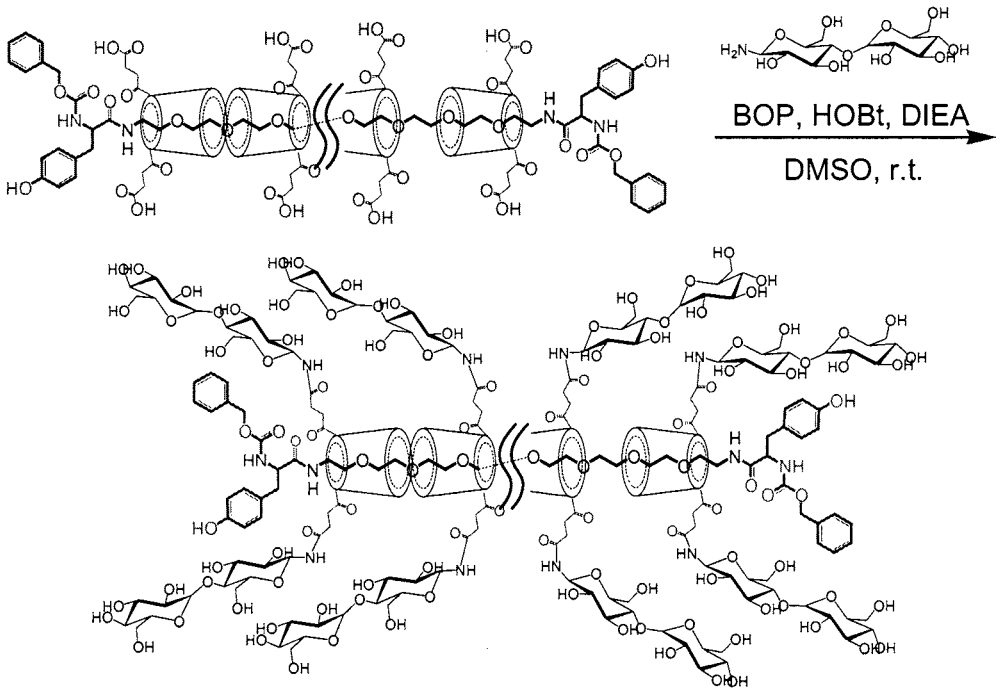

slide, and the solvent was evaporated. Ionization was accelerated with 20 kV.

1: ^{1}H NMR [750 MHz, D_2O containing 0.05v/v % *t*-BtOH ppm]: *δ* 7.9−7.3 (d, NH's), 5.3−5.0 (C(1)H and C(1′)H of maltose, d, 460 H), 5.1−4.6 (C(1)H of α-CD, d, 300 H), 3.9−3.3 (C(3)H, C(5)H, C(6)H, C(4)H and C(2)H of α-CD and C(3)H, C(3′)H, C(5)H, C(5′)H, C(6)H, C(6′)H, C(4)H, C(4′)H, C(2)H and C(2′)H of maltose, m, 4560 H), 3.55 (CH_2 of PEG, s, 455 H), 2.9−2.3 (CH_2 of carboxyethyl ester, m, 1200 H).

2: ^{1}H NMR [750 MHz, D_2O containing 0.05v/v % *t*-BtOH ppm]: *δ* 7.9−7.3 (d, NH's), 5.3 (C(1)H and C(1′)H of maltose, d, 488 H), 5.1−4.6 (C(1)H of α-CD, d, 480H), 3.9−3.3 (C(3)H, C(5)H, C(6)H, C(4)H and C(2)H of α-CD and C(3)H, C(3′)H, C(5)H, C(5′)H, C(6)H, C(6′)H, C(4)H, C(4′)H, C(2)H and C(2′)H of maltose, m, 5990 H), 3.55 (CH_2 of PEG, s, 455 H), 2.9−2.3 (CH_2 of carboxyethyl ester, m, 2040 H).

3: ^{1}H NMR [750 MHz, D_2O containing 0.05v/v % *t*-BtOH ppm]: *δ* 7.9−7.3 (d, NH's), 5.3 (C(1)H and C(1′)H of maltose, d, 480 H), 5.2−4.6 (C(1)H of α-CD, d, 720H), 3.9−3.3 (C(3)H, C(5)H, C(6)H, C(4)H and C(2)H of α-CD and C(3)H, C(3′)H, C(5)H, C(5′)H, C(6)H, C(6′)H, C(4)H, C(4′)H, C(2)H and C(2′)H of maltose, m, 7200 H), 3.55 (CH_2 of PEG, s, 455 H), 2.9−2.3 (CH_2 of carboxyethyl ester, m, 2880 H).

4: ^{1}H NMR [750 MHz, D_2O containing 0.05v/v % *t*-BtOH ppm]: *δ* 7.9−7.3 (d, NH's), 5.3 (C(1)H and C(1′)H of maltose, d, 6 H), 5.2−4.6 (C(1)H of α-CD, bs, 6 H), 4.2−3.2 (C(3)H, C(5)H, C(6)H, C(4)H and C(2)H of α-CD and C(3)H, C(3′)H, C(5)H, C(5′)H, C(6)H, C(6′)H, C(4)H, C(4′)H, C(2)H and C(2′)H of maltose, m, 48 H), 2.9−2.3 (CH_2 of carboxyethyl ester, m, 24 H).

5: ^{1}H NMR [750 MHz, D_2O containing 0.05v/v % *t*-BtOH ppm]: *δ* 8.1−7.3 (d, NH's), 5.3 (C(1)H and C(1′)H of maltose, d, 470 H), 4.2−3.2 (C(3)H, C(3′)H, C(5)H, C(5′)H, C(6)H, C(6′)H, C(4)H, C(4′)H, C(2)H and C(2′)H of maltose, m, 2820 H), 3.7 (CH of PAA, s, 87 H), 1.9 (CH of PAA, s, 174 H).

^{1}H NMR Spin−Lattice Relaxation Time (T_1) and Spin−Spin Relaxation Time (T_2). The Mal-PRXs were dissolved in 0.1 M phosphate buffer (pH 7.4, D_2O + 0.02 M NaH_2PO_4 + 0.08 M Na_2HPO_4 + 0.1 mM $CaCl_2$ + 0.1 mM $MgCl_2$). ^{1}H NMR spin−lattice relaxation times (T_1) C(1)H of maltosyl groups, C(1)H of α-CDs, and methylene of PEG were determined by inversion−recovery method, using the pulse sequence 180°− t−90°−acquire, where t is a variable delay. ^{1}H NMR spin−spin relaxation times (T_2) of C(1)H of maltosyl groups, C(1)H of α-CDs, and methylene of PEG were determined by the Carr−Purecell−Meiboom−Gill (CPMG) method. The ^{1}H CPMG spectra measurements were performed using the standard $\pi/2\text{-}[\tau-\pi-\tau]_n$ CPMG sequence at room temperature.

Fluorescent Assay for Multivalent Interaction between Mal-PRXs and Con A. Aliquots (1 μL) of a stock solution of the conjugates (0.75 mM as maltose units) were added every 15 min to a solution of fluorescein-labeled Con A (5.9×10^{-7} mmol/1.5 mL, 393 nM) in the PBS (pH 7.4) containing 0.1 mM $CaCl_2$ + 0.1 mM $MgCl_2$. Fluorescence intensity at 520 nm was measured with excitation at 490 nm at 25 °C.

Turbidity Assay. One mL of Con A dissolved in the PBS (0.8 mg/mL, 7.97 μM) was added to a cuvette. A solution of the 20 mM per maltose residue dissolved in the PBS was added. Absorbance at 420 nm was recorded for 20 min.

Inhibition of Con-A-Induced Hemaggulutination (24). To evaluate how the number of maltosyl groups per α-CD molecule in the series of Mal-PRXs, Mal-PRXs **1**−**3** with different number of maltosyl groups were prepared by changing the feed ratio of Mal-amine and CEE-PRXs (*24*). The concentration of Con A was fixed to be 4-fold minimum concentration required for hemagglutination of erythrocyte (*28*), Twenty microliters of a 3% erythrocyte (rat blood) suspension in a 0.1 M phosphate buffer (PBS, pH7.4) containing 0.1 mM $CaCl_2$ and 0.1 mM $MgCl_2$ was pipetted into each well of the 2-fold dilution series of Con A (20 μL) in 96-holes microtiter plate and incubated at 37 °C for 1 h. The minimum concentration of Con A was determined, and its 4-fold concentration was used for the following Con A-induced hemaggultination assay.

Table 1. Characterization of Mal-PRXs 1−3, Mal-α-CD 4, and Mal-PAA 5

sample code[a]	no. of α-CDs[b]	total no. of Mal	M_n NMR[c]	M_n GPC[d]	M_w	M_w/M_n
Mal-PRX, **1**	50 (22)	230	181 300	199 400	334 000[d]	1.7
Mal-PRX, **2**	85 (38)	244	237 500	257 700	412 300[d]	1.6
Mal-PRX, **3**	120 (53)	240	291 100	293 700	469 900[d]	1.6
Mal-CD, **4**	−	3	−	−	2542 [− H], 2418 [− Na], 2318 [− Na], 2218 [− Na][e]	−
Mal-PAA, **5**	−	240	109 600	102 300	358 000[d]	3.5

[a] M_n of PEG for **1**−**3**: 20 000, Mn of poly(acrylic acid) for **5**: 25 000. [b] Parentheses were α-CD threading %. [c] Calculated from ^{1}H NMR spectra. [d] Calculated from a calibration curve using pullulan standard. [e] Calculated from MALDI-TOF mass spectroscopy: 2542 [− H]: Mal-α-CD with three maltosyl groups and three CEE groups, 2418 [− Na]: Mal-α-CD with three maltosyl groups and two CEE groups, 2318 [− Na]: Mal-α-CD with three maltosyl groups and one CEE group and 2218 [− Na]: Mal-α-CD with three maltosyl groups without CEE groups.

Table 2. T_1 and T_2 Values of Mal-PRXs 1−3, Mal-α-CD 4, and Mal-PAA 5

	T_1 (sec)			T_2 (sec)		
sample code	C(1)H of Mal	C(1)H of α-CD	CH_2 of PEG	C(1)H of Mal	C(1)H of α-CD	C(1)H of PEG
Mal-PRX, **1**	2.31	3.85	0.91	0.12	0.17	0.09
Mal-PRX, **2**	1.46	3.09	0.92	0.23	0.25	0.06
Mal-PRX, **3**	2.42	3.63	0.98	0.08	0.06	0.13
Mal-CD, **4**	1.42	1.37	−	0.24	0.08	−
Mal-PAA, **5**	1.26	−	−	0.04	−	−

An aliquot (20 μL) of Con A (7.83 μg/mL) in the buffer was added to each hole of 96-holes microtiter plates. The malotose conjugates dissolved in the buffer with various concentrations were added to the each hole (20 μL) and incubated at 37 °C for 1 h. Then, 3% erythrocyte suspension (40 μL) was added to the holes and incubated at 37 °C for 1 h. Agglutination of erythrocytes was observed, and the minimum concentration (MIC) of maltose was determined. All the experiments were carried out triplicate.

RESULTS AND DISCUSSION

Synthesis, Characterization and Molecular Motion of Mal-PRXs. A variation of the Mal-PRXs **1**−**3** with different number of threading α-CDs (no. of CDs: 50, 85, and 120) and the same number of maltose (ca. 230−240) was prepared using PEG with M_n of 20 000 (Table 1). If α-CDs are stoichiometrially threaded onto a PEG chain, two ethylene glycol units should be included in each α-CD cavity (*20*). Since the stoichiometric number is ca. 227 for PEG with M_n of 20 000, the threading % of α-CDs in Mal-PRX **1**, **2**, and **3** were 22, 38, and 53%, respectively. The obtained data of M_n from the GPC were well consistent with those from ^{1}H NMR, suggesting that the M_n calibrated by pullulan did not include any artifacts of the instruments such as pressure variations.

Our previous studies of the Mal-PRXs regarding the molecular motion of maltosyl groups suggest that highly flexible motion of maltosyl groups in the Mal-PRX **2** dominates the multivalent recognition of Con A (*24*). However, it has been unclear that the relation between the molecular motion of maltosyl groups and mechanically locking structure between α-CDs and PEG. ^{1}H NMR relaxation studies of each component (maltose, α-CDs, and PEG in the Mal-PRXs **1**−**3**) can provide information of the mobility in solution, because the relaxation parameters have long been used to provide a dynamic description of biomacromolecules such as protein structures (*29*). Table 2 summarizes the results of T_1 and T_2 values of C(1)H of maltosyl groups, C(1)H of α-CD, and methylene groups of PEG in the Mal-PRXs **1**−**3**. T_1 has been used for analyzing molecular motion of CDs before and after including guest molecules (*30*), and longer T_1 values of CDs in the presence of guest molecules suggest the decreased molecular motion of CDs due to locating the guest molecules in the cavity. The Mal-PRX **1** (α-CD threading: 22%) and **3** (α-CD threading: 53%) were longer in the T_1 values of both C(1)Hs of maltosyl groups (2.31 and 2.42 s) and α-CD (3.85 and 3.63 s) than those of Mal-PRX **2** (α-CD threading: 38%) (1.46 and 3.09 s). Since the Mal-CD **4** showed smaller T_1 values (1.42 and 1.37 s) than the Mal-PRXs, the larger T_1 values of the Mal-PRXs **1** and **3** seem to indicate slower motion of both maltosyl groups and α-CDs. On the other hand, T_1 values of PEG showed similar motion (Table 2). Thus, the T_1 values were one of good parameters to discuss the molecular motion of Mal-PRXs. However, it is still difficult to image how the molecular motions of maltosyl groups, α-CDs, and PEG are related to each other. Since T_2 values are strongly influenced by heterogeneous conditions of magnetic fields, which is related to solubility, association, molecular motion, and so on, T_2 can also give us important information of molecular motion. The Mal-PRX **2** was much longer in the T_2 value of C(1)H of α-CD than the others. Similar tendency was observed for the T_2 value of C(1)H of maltosyl groups (Table 2). In addition, the Mal-PRX **2** exhibited almost the same T_2 as the Mal-CD **4** (*24*). Generally, slow molecular motions in magnetic fields show longer and shorter T_1 and T_2 values, respectively, while fast motions show both longer values. Therefore, the difference between T_1 and T_2 values ($T_1 - T_2$) should provide the real information of molecular motions: big difference between T_1 and T_2 values indicates slow molecular motions. As shown in Figure 1, $T_1 - T_2$ of both C(1)Hs of maltosyl groups and α-CDs in the Mal-PRX **2** was smaller than the Mal-PRXs **1** and **3**. On the other hand, $T_1 - T_2$ of C(1)H maltosyl groups in the Mal-PAA **5** showed the largest value of all the sample series. These results indicate that the mobile motion of α-CDs in the polyrotaxane governed the molecular motion of maltosyl groups in α-CDs, and the mechanically locking structure between maltose-conjugated α-CDs and PEG contributes to increasing the mobility of maltosyl groups. Contribution of α-CD-mobile motion was discussed from the relation between C(1)Hs of α-CDs and maltosyl groups or methylene groups of PEG (Figure 2). As mentioned above, T_2 values of C(1)H maltose was increased with C(1)H α-CDs, suggesting

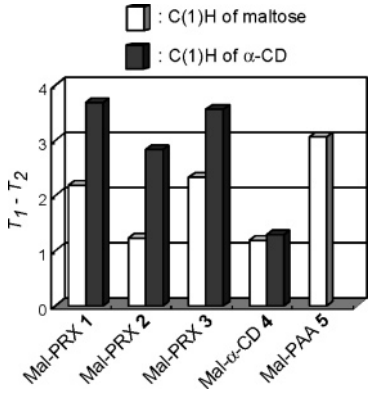

Figure 1. The difference between T_1 and T_2 values ($T_1 - T_2$) of C(1)H of maltosyl groups and α-CDs in the Mal-PRXs **1**−**3**, the Mal-α-CD **4**, and the Mal-PAA **5**.

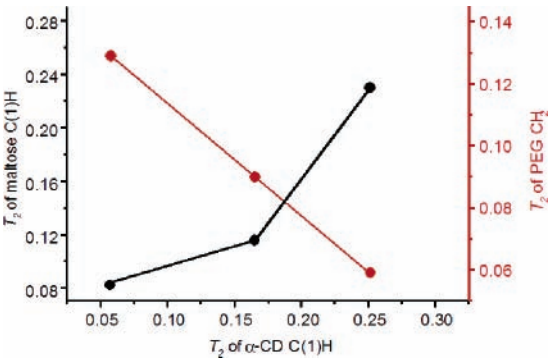

Figure 2. The relation of T_2 values of C(1)Hs of α-CDs with those of maltosyl groups and methylene groups of PEG.

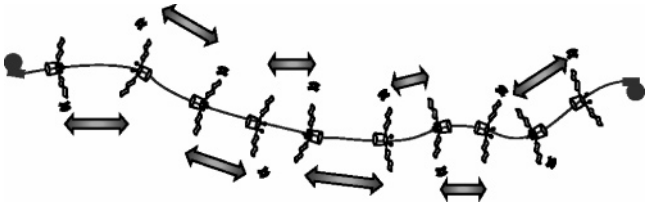

Figure 3. Image of molecular motion of the Mal-PRX **2** based on the results of ^{1}H NMR relaxation studies.

both the mobile motions are not independent. On the other hand, T_2 values of PEG methylene groups was inversely proportional to the values of C(1)H α-CDs, This means that PEG molecule existed in magnetically heterogeneous conditions with increasing the molecular motion of maltose governed by the mobile motion of α-CDs. Therefore, it can be speculated that the highest mobile motion of maltose-conjugated α-CDs in the Mal-PRX **2** is sliding along the PEG chain with diffusion of the Mal-PRX **2** itself (Figure 3). With increasing the α-CD threading % (the Mal-PRX **3**), some intra- and/or intermolecular hydrogen bonds between the maltose-conjugated α-CDs are likely to occur, resulting in the decreased motion of maltose-conjugated α-CDs and the increased motion of the exposed PEG. With a decrease of the α-CD threading % (the Mal-PRX **1**), it is supposed that the terminal Z-L-Tyr moieties intermolecularly associate, because an increase in hydrophilically modified α-CD threading in polyrotaxanes contributes to decreasing association number in water (*31*). Such an association may become slower the molecular motions of the Mal-PRX **1** in comparison with the Mal-PRX **2**.

Affinity of Mal-PRXs to Con A. Our previous results of Con A-induced hemagglutination of the Mal-PRXs (*24*) made us hypothesize that Con A bound effectively with

Table 3. K_a for the Binding of Con A with Mal-PRXs 1−3, Mal-α-CD 4, and Mal-PAA 5 at 25 °C

sample code	K_a ($\times 10^3$ M^{-1})
Mal-PRX,**1**	57
Mal-PRX,**2**	1100
Mal-PRX,**3**	530
Mal-CD, **4**	3.0
Mal-PAA,**5**	140
maltose	1.1[a]

[a] Determined by isothermal titration calorimetry (ITC). In ref 34, 1.2×10^3 M^{-1}.

maltosyl groups of the Mal-PRX **2** via highly molecular motion of maltosyl group. As mentioned in the previous section, highly mobile motion of α-CDs dominated the highly molecular motion of the maltosyl group in the Mal-PRX **2**. Therefore, determination of association constant (K_a) will provide us the direct evidence of the mobile effect on Con A binding. The K_a of the multivalent interaction between the Mal-PRXs and Con A was quantitatively determined by fluorescent assay using fluorescein-labeled Con A. The addition of an increasing amount of the Mal-PRXs decreased the fluorescent intensity of fluorescein at 520 nm. The decrement of fluorescence intensity ($\Delta F/F_0$) was plotted against the concentration per maltose unit of the conjugate. Apparent K_a was calculated by the following equation (*10*, *32*):

$$\frac{F_0}{\Delta F}[\text{maltose}] = \frac{F_0}{\Delta F_{max}}[\text{maltose}] + \frac{F_0}{\Delta F_{max} K_a}$$

where [maltose] was the concentration of maltose (M). The obtained K_a values of the multivalent saccharides (the Mal-PRXs **1**−**3** and the Mal-PAA **5**) were summarized in Table 3. The K_a values of the Mal-PRXs **1**−**3** and the Mal-PAA **5** (the number of maltose: 230−240) were 1−3 powers higher than those of monomeric compound (maltose), indicating the multivalent effect. The Mal-CD **4** displayed three maltosyl groups in one conjugate. The magnitude of the power in the Mal-CD **4** was the same with maltose, indicating that the oligomeric number of maltose conjugation is not effective for the affinity to Con A. The K_a values of the Mal-PRX **1**, **2**, and **3** were 5.7×10^4, 1.1×10^6, and 5.3×10^5 (M^{-1}-maltose), respectively. This result indicates that the K_a values of the Mal-PRX **1**, **2**, and **3** were 52, 1000, and 480 times higher than maltose. Since the number of maltosyl groups per one Mal-PRX molecule is similar level (230−240), the number of maltosyl groups in the Mal-PRXs should not be the main factor of the difference. The most considerable factors are local density of maltose and mobile motion of maltose-conjugated α-CDs in the Mal-PRXs. The K_a value of the Mal-PRX **1** seems to be too small compared with the Mal-PRX **3**, because the Mal-PRX **1** showed similar degree of the molecular motions with the Mal-PRX **3** (Figure 1). The number of maltose per one α-CD molecule in the Mal-PRX **1**, **2**, and **3** was 4.6, 2.9, and 2.0, respectively, so that the local density of maltosyl groups attached to α-CD molecule in the Mal-PRXs is the considerable factor. To evaluate the influence of the local density, the Mal-PRXs **1**−**3** with different number of maltosyl groups were prepared and examined the inhibition of Con A-induced hemagglutination. The hemagglutination assay is useful for the evaluation of the difference in the number of ligands (*11*). As shown in Figure 4, the relative potency, calculated from the minimum inhibition concentration, of the Mal-PRX **2** was increased with the number of maltosyl groups per one α-CD molecule and reached to the highest value

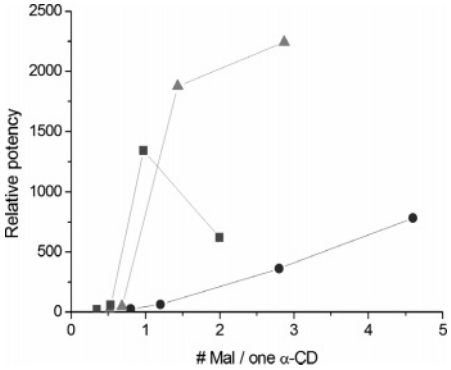

Figure 4. Dependence of hemagglutination inhibition on the number of maltosyl groups per α-CD. (closed circle): the Mal-PRX **1**. (closed triangle): the Mal-PRX **2**, (closed square): the Mal-PRX **3**.

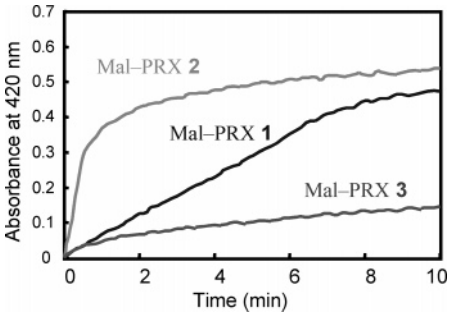

Figure 5. Time course of turbidity measurements in a 0.1 M phosphate buffer containing 0.1 mM $CaCl_2$ and 0.1 mM $MgCl_2$ (pH 7.4) at 25 °C. Concentration of Con A and the Mal-PRX was 7.97 μM and 20 mM maltose units, respectively.

at the 2.9 maltosyl groups per one α-CD molecule. The relative potency of the Mal-PRX **3** was increased with the number up to 1.0 and then was decreased with a further increase in the number. These results suggest that the decrease in the relative potency of the Mal-PRX **3** is due to steric hindrance: all the maltosyl groups cannot necessarily bind to the binding sites of Con A. However, such the steric hindrance in the Mal-PRX **2** was eliminated, presumably due to the highly mobile motion of maltose-conjugated α-CDs (Figures 1 and 2). On the other hand, the relative potency of the Mal-PRX **1** was smaller than the Mal-PRXs **2** and **3** and proportionally increased with the number of maltosyl groups per one α-CD molecule. This result suggests that the molecular motion of the Mal-PRX **1** do not reflect the inhibition of Con A-induced hemagglutination, and the steric hindrance from the number of maltose per one α-CD molecule was small. Presumably, intra- and/or intermolecular association of Mal-PRX **1** due to smaller number of threading α-CD as mentioned before exists, and therefore the Mal-PRX **1** showed the smallest K_a value.

Initial Rate of Binding with Con A. Turbidimetric assay is one of good methods to monitor the rate of lectin clustering with saccharide derivatives (*9*, *33*, *34*). After mixing the solution of the Mal-PRXs and Con A, the absorbance was increased with a certain rate and then slowly increased (Figure 5). The increased absorbance means the cross-linking of the Mal-PRXs with Con A under high concentrations of both the Mal-PRXs and Con A. It is known that a change in the initial rate of turbidity is directly related to Con A clustering mediated by saccharide-based multivalent polymers (*9*). From the initial binding curve in Figure 5, the absorbance of the Mal-PRX **2** was increased and reached to 0.3 within 0.6 min while the time to finish the initial binding of the Mal-PRX **1** and **3** was 7.5 and 0.7 min, respectively. Since the large value of the absorbance (turbidity) shows the formation of higher order and cross-linked structure (*9*), the Mal-PRX **2** is considered to be rapidly cross-linked with Con A with high order. The cross-linking between the Mal-PRX **2** and Con A was faster than the Mal-PRX **1**, but the extent of cross-linking seems to be the same level with the Mal-PRX **2**. This result indicates that the Mal-PRX **2** is superior to the Mal-PRX **1** in terms of rapid formation of the high order-cross-linking structure. On the other hand, the extent of cross-linking between the Mal-PRX **3** and Con A was very small (Figure 5). This result suggests that the Mal-PRX **3** is intramolecularly cross-linked with Con A compared with the Mal-PRXs **1** and **2**.

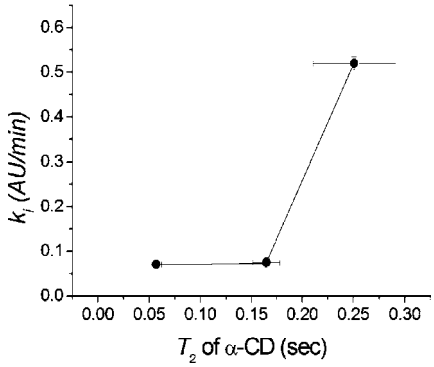

Figure 6. Initial rate of precipitation (k_i) as a function of T_2 values of α-CD C(1)H in the Mal-PRXs.

Table 4. Initial Rate of Con A Precipitation (k_i) Using Mal-PRXs

sample code	k_i (AU/min)
Mal-PRX, **1**	0.075 ± 0.011
Mal-PRX, **2**	0.52 ± 0.015
Mal-PRX, **3**	0.071 ± 0.004

To qualify the initial rate for binding, initial rate of the precipitation (k_i) was calculated using following equation:

$$k_i = \mathrm{abs}_{420}/\mathrm{min}$$

Table 4 shows the k_i of the Mal-PRXs **1**–**3**. The k_i of the Mal-PRX **2** showed the highest value, even in the same number of maltosyl groups per one conjugate with the Mal-PRXs **1** and **3**. Figure 6 shows the relationship between T_2 values of C(1)H of α-CD in each conjugate and k_i. Similar relationship between the T_2 values of C(1)H of maltosyl groups and Con A was observed (data not shown). Thus, the mobile motion of maltose-conjugated α-CDs in the Mal-PRX **2** contributes to the highest binding rate with Con A.

CONCLUSIONS

Maltose–polyrotaxane conjugates (Mal-PRXs) with the same number of maltose (230–240) and different α-CD threading percentage (22, 38, and 53%) were examined to clarify the molecular motion of the Mal-PRXs and those relations to Con A binding. ^{1}H NMR relaxation time analysis revealed that the mobile motion of α-CDs in the polyrotaxane governed molecular motion of the maltosyl group in α-CDs and threading PEG chain. The largest K_a value of the Mal-PRX **2** was well correlated with large T_1 and T_2 values of maltosyl groups and α-CD, suggesting that mobile motion of maltose-conjugated α-CDs in the Mal-PRX contributes to the highest affinity with Con A.

Highly mobile motion of maltose-conjugated α-CDs in the Mal-PRX **2** is likely to enhance initial rate of binding with Con A. Therefore, it is concluded that the mobile motion due to the mechanically locking structure plays a key role for inducing rapid multivalent interaction.

ACKNOWLEDGMENT

The authors acknowledged Mr. Koichi Higashimine (JAIST) for measuring the 750 MHz ^{1}H-NMR spectra. T_1 and T_2. This work was financially supported by a Grant-in-Aid for Scientific Research (B) (No. 14380397), a program for the "Supporting young researchers with fixed-term appointments" in Special Coordination Funds for Promoting Science and Technology, from the Ministry of Education, Science, Sports and Culture, Japan, and the 21st century COE program "Scientific Knowledge Creation Based on Knowledge Science", JAIST.

LITERATURE CITED

(1) (a) Kopecek, J., Kopecková, P., Minko, T., Lu, Z.-R., and Peterson, C. M. (2001) Water soluble polymers in tumor targeted delivery. *J. Controlled Release 74*, 147−158. (b) Lu, Z.-R.; Kopecková, P.; J. Kopecek, J. (1999) Polymerizable Fab' antibody fragments for targeting of anticancer drugs. *Nat. Biotechnol. 17*, 1101−1104.

(2) Mammen, M., Choi, S.-K., and Whitesides, G. N. (1998) Polyvalent interactions in biological systems: implications for design and use of multivalent ligands and inhibitors. *Angew. Chem., Int. Ed. 37*, 2754−2794.

(3) Kiessling, L. L., Gestwicki, J. E., and Strong, L. E. (2000) Synthetic multivalent ligands in the exploration of cell-surface interactions. *Curr. Opin. Chem. Biol. 4*, 696−703.

(4) Dwek, R. A. (1996) Glycobiology: Toward understanding the function of sugars. *Chem. Rev. 96*, 683−720.

(5) Kiessling, L. L., and Pohl, N. L. (1996) Strength in numbers: nonnatural polyvalent carbohydrate derivatives. *Chem. Biol. 3*, 71−77.

(6) Dimick, S. M., Powell, S. C., McMahon, S. A., Moothoo, D. N., Naismith, J. H., and Toone, E. J. (1999) On the meaning of affinity: Cluster glycoside effects and concanavalin A. *J. Am. Chem. Soc. 121*, 10286−10296.

(7) Lundquist, J. J., and Toone, E. J. (2002) The cluster glycoside effect. *Chem. Rev. 102*, 555−578.

(8) Kanai, M., Mortell, K. H., and Kiessling, L. L. (1997) Varying the size of multivalent ligands: The dependence of concanavalin A binding on neoglycopolymer length. *J. Am. Chem. Soc. 119*, 9931−9932.

(9) Cairo, C. W., Gestwicki, J. E., Kanai, M., and Kissling L. L. (2002) Control of multivalent interactions by binding epitope density. *J. Am. Chem. Soc. 124*, 1615−1619.

(10) Hasegawa, T., Kondoh, S., Matsuura, K., and Kobayashi, K. (1999) Rigid helical poly(glycosyl phenyl isocyanide)s: Synthesis, conformational analysis, and recognition by lectins. *Macromolecules 32*, 6595−6603.

(11) Corbell, J. B., Lundquist, J. J., and Toone, E. J. (2000) A comparison of biological and calorimetric analyses of multivalent glycodendrimer ligands for concanavalin A. *Tetrahedron: Asymmetry 11*, 95−111.

(12) Gestwicki, J. E., Cairo, C. W., Strong, L. E., Oetjen, K. A., and Kiessling, L. L. (2002) Influencing receptor−Ligand binding mechanisms with multivalent ligand archtechture. *J. Am. Chem. Soc. 124*, 14922−14933.

(13) Pagé, D., and Roy, R. (1997) Synthesis and biological properties of mannosylated starburst poly(amidoamine) dendrimers. *Bioconjugate Chem. 8*, 714−723.

(14) Aoi, K., Itoh, I., and Okada, M. (1995) Globular carbohydrate macromolecules "Sugar Balls". 1. Synthesis of novel sugar-persubstituted poly(amido amine) dendrimers. *Macromolecules 8*, 5391−5393.

(15) Reuter, J. D., Myc, A., Hayes, M. M., Gan, Z., Roy, R., Qin, D., Yin, R., Piehler, L. T., Esfand, R., Tomalia, D. A., and Baker, J. R., Jr. (1999) Inhibition of viral adhesion and infection by sialic-acid-conjugated dendritic polymers. *Bioconjugate Chem. 10*, 271−278.

(16) Joralemon, M. J., Murthy, K. S., Remsen, E. E., Becker, M. L., and Wooley, K. L. (2004) Synthesis, characterization, and bioavailability of mannosylated shell cross-linked nanoparticles. *Biomacromolecules 5*, 903−913.

(17) Renaudet, O., and Dumy, P. (2003) Chemoselectively template-assembled glycoconjugates as mimics for multivalent presentation of carbohydrates. *Org. Lett. 5*, 243−246.

(18) Ortega-Caballero, F., Gimenez-Martinez, J. J., Garcia-Fuentes, L., Ortiz-Salmeron, E., Santoyo-Gonzalez, F., and Vargas-Berenguel, A. (2001) Binding affinity properties of dendritic glycosides Based on a β-cyclodextrin core toward guest molecules and concanavalin A. *J. Org. Chem. 66*, 7786−7795.

(19) Nelson, A., and Stoddart, J. F. (2003) Dynamic multivalent lactosides displayed on cyclodextrin beads dangling from polymer strings. *Org. Lett. 5*, 3783−3786.

(20) (a) Harada, A., and Kamachi, M. (1990) Complex formation between poly(ethylene glycol) and α-cyclodextrin. *Macromolecules 23*, 2821−2823. (b) Harada, A., Okada, M., Li, J., and Kamachi, M. (1995) Preparation and characterization of inclusion complexes of poly(propylene glycol) with cyclodextrins. *Macromolecules 28*, 8406−8411.

(21) Ooya, T., Kawashima, T., and Yui, N. (2001) Synthesis of polyrotaxane-biotin conjugates and surface plasmon resonance analysis of streptavidin recognition. *Biotechnol. Bioprocess Eng. 6*, 1−6.

(22) Ooya, T., and Yui, N. (2002) Multivalent interactions between biotin-polyrotaxane conjugates and streptavidin as a model of new targeting for transporters. *J. Controlled Release 80*, 219−228.

(23) Yui, N., Ooya, T., Kawashima, T., Saito, Y., Tamai, I., Sai, Y., and Tsuji, A. (2002) Inhibitory effect of supramolecular polyrotaxane-dipeptide conjugates on digested peptide uptake via intestinal human peptide transporter. *Bioconjugate Chem. 13*, 582−587.

(24) Ooya, T., Eguchi, M., and Yui, N. (2003) Supramolecular design for multivalent interaction: maltose mobility along polyrotaxane enhanced binding with concanavalin A. *J. Am. Chem. Soc. 125*, 13016−13017.

(25) Hirose, H., Sano, H., Mizutani, G., Eguchi, M., Ooya, T., and Yui, N. (2004) The effect of the mobility of ligands in polyrotaxanes on order structure of water clusters. *Langmuir 20*, 2852−2854.

(26) Harada, A., Li, J., and Kamachi, M. (1994) Preparation and characterization of a polyrotaxane consisting of monodisperse poly(ethylene glycol) and α-cyclodextrins. *J. Am. Chem. Soc. 116*, 3192−21096.

(27) Kobayashi, K., Tawada, E., Akaike, T., and Usui, T. (1997) Artifical glycopolypeptide conjugates: simple synthesis of lactose- and *N,N'*-diacatylchitobiose-substituted poly(L-glutamic acid)s through *N*-β-glycoside linkages and their interaction with lectins. *Biochim. Biophys. Acta 1336*, 117−122.

(28) Kawagishi, H., Yamawaki, M., Isobe, S., Usui, T., Kimura, A., and Chiba, S. (1994) Two lectins from the marine sponge Halichondria okadai. An *N*-acetyl- sugar-specific lectin (HOL-I) and an *N*-acetyllactosamine-specific lectin (HOL-II). *J. Biol. Chem. 269*, 1375−1379.

(29) Lian, L.-Y. (1993) Dynamic and exchange processes in macromolecules studied by NMR spectroscopy, in *Methods in Molecular Biology vol. 17: Spectroscopic Methods and Analyses: NMR, Mass Spectrometry, and Metalloprotein Techniques* (Jones, C., Mulloy, B., and Thomas, A. H., Eds.) pp 169−189, Humana Press, Totowa, NJ.

(30) (a)Eliseev, E. V., and Schneider, H.-J. (1994) Molecular recognition of nucleotides, nucleosides, and sugars by aminocyclodextrins. *J. Am. Chem. Soc. 116*, 6081−6088. (b) Okada, M., Kamachi, M., and Harada, A. Preparation and characterization of inclusion complexes of poly(propylene glycol) with methylated cyclodextrins. *J. Phys. Chem. B. 103*, 2067−2613.

(31) Ooya, T., and Yui, N. (1998) Supramolecular dissociation of biodegradable polyrotaxanes by terminal hydrolysis. *Macromol. Chem. Phys. 199*, 2311−2320.

(32) Akasaka, T., Matsuura, K., and Kobayashi, K. (2001) Transformation from block-type to graft-type oligonucleotide-

glycopolymer conjugates by self-organization with half-sliding complementary oligonucleotides and their lectin recognition. *Bioconjugate Chem. 12*, 776−785.
(33) Kitano, H., Sumi, Y., and Tagawa, K. (2001) Recognition of novel lipopolypeptides with many pendent sugar residues by lectin. *Bioconjugate Chem*. *12*, 56−61.
(34) Roy, R., Page, D., Perez, S. F., and Bencomo, V. V.(1998) Effect of shape, size, and valency of multivalent mannosides on their binding properties to phytohemagglutinins. *Glycoconjugate J. 15*, 251−263.

BC049809H

Noninvasive Molecular Imaging of *MYC* mRNA Expression in Human Breast Cancer Xenografts with a [^{99m}Tc]Peptide–Peptide Nucleic Acid–Peptide Chimera

Xiaobing Tian,[†] Mohan R. Aruva,[‡] Wenyi Qin,[∥] Weizhu Zhu,[∥] Edward R. Sauter,[∥] Mathew L. Thakur,[‡,§] and Eric Wickstrom[†,§,*]

Departments of Biochemistry and Molecular Pharmacology, Radiology, and Kimmel Cancer Center, Thomas Jefferson University, Philadelphia, Pennsylvania 19107, and Department of Surgery, University of Missouri, Columbia, Missouri 65212. Received August 28, 2004; Revised Manuscript Received October 28, 2004

Human estrogen receptor-positive breast cancer cells typically display elevated levels of Myc protein due to overexpression of *MYC* mRNA, and elevated insulin-like growth factor 1 receptor (IGF1R) due to overexpression of *IGF1R* mRNA. We hypothesized that scintigraphic detection of *MYC* peptide nucleic acid (PNA) probes with an IGF1 peptide loop on the C-terminus, and a [^{99m}Tc]chelator peptide on the N-terminus, could measure levels of *MYC* mRNA noninvasively in human *IGF1R*-overexpressing MCF7 breast cancer xenografts in nude mice. We prepared the chelator-*MYC* PNA-IGF1 peptide, as well as a 4-nt mismatch PNA control, by solid-phase synthesis. We imaged MCF7 xenografts scintigraphically and measured the distribution of [^{99m}Tc]probes by scintillation counting of dissected tissues. MCF7 xenografts in nude mice were visualized at 4 and 24 h after tail vein administration of the [^{99m}Tc]PNA probe specific for *MYC* mRNA, but not with the mismatch control. The [^{99m}Tc]-probes distributed normally to the kidneys, livers, tumors, and other tissues. Molecular imaging of oncogene mRNAs in solid tumors with radiolabel-PNA–peptide chimeras might provide additional genetic characterization of preinvasive and invasive breast cancers.

INTRODUCTION

MYC was one of the first proto-oncogenes to be identified (*1*), and *MYC* was the first oncogene to be inhibited by antisense oligonucleotides, blocking the transition from G1 to S phase in normal peripheral blood mononuclear cells (*2*) and in promyelocytic leukemia cells (*3*). *MYC* mRNA and Myc protein are overexpressed in a variety of cancers, including breast (*4*), bladder (*5*), kidney (*6*), lung cancer (*7*), and lymphoma (*8*). *MYC* antisense oligonucleotides were able to ablate Myc protein levels in peripheral blood mononuclear cells of Eμ-*myc* transgenic mice (*9*), delay the onset of congenital lymphoma in Eμ-*myc* transgenic mice (*10*), and delay the proliferation of Eμ-*myc* lymphoma cells transplanted into congenic parental mice (*11*). Similarly, in patients with advanced solid tumors, a phase I trial of our *MYC* antisense oligonucleotide sequence, combined with cisplatin, revealed no significant toxicity at therapeutic doses, and displayed clinical responses in ovarian and colorectal cancer (*12*).

Myc is a nuclear phosphoprotein in the basic/helix-loop-helix/leucine zipper family of transcription factors that associates with Max to activate proliferative genes (*13*). Myc protein accelerates cells into S phase by induction of cyclin D1 (*14*), which increases shortly after estrogen induction of *MYC* mRNA expression in mammary cells (*15*) via an atypical estrogen response element (*16*).

As a corollary of *MYC* overexpression in breast cancers (*4*), *MYC* antisense oligonucleotides inhibited estrogen-stimulated MCF7 breast cancer cell proliferation, as well as the estrogen-independent MDA-MB-231 breast cancer line (*17*). Correspondingly, induction of *MYC* expression in antiestrogen-arrested cells mimicked the effects of estrogen by reinitiating cell cycle progression (*18*), while constitutive overexpression of Myc protein conferred resistance to antiestrogen treatment in human MCF7 breast cancer cells (*19*). In the cell signaling pathway, antisense inhibition of *MYC* mRNA in MCF7 breast cancer cells inhibited cyclin D1 expression and cell proliferation (*15*, *20*), even though *MYC* gene induction did not increase cyclin D1 expression. Thus, while cyclin D1 expression is dependent on Myc protein, *MYC* gene expression is not limited by cyclin D1.

Clinical examination and mammography, the currently accepted breast cancer screening methods, miss almost half of breast cancers in women younger than 40 years, approximately one-quarter of cancers in women aged 40–49 years, and one-fifth of cancers in women over 50 years old (*21*). The breast is the most common site of noncutaneous cancer in US women (*22*). Moreover, if an abnormality is found, an invasive diagnostic procedure must still be performed to determine if the breast contains atypia or cancer. Despite recent improvements in BI-RADS standardization of mammography (including the use of two views of the breast rather than one, spot compression, and digital images) that have improved sensi-

* Corresponding author: Dr. Eric Wickstrom, Department of Biochemistry and Molecular Pharmacology, Thomas Jefferson University, 219 Bluemle Life Sciences Building, 233 S. 10th St., Philadelphia PA 19107-5541, voice: 215-955-4578, fax: 215-955-4580 or 215-923-9214, eric@tesla.jci.tju.edu, website: http://tesla.jci.tju.edu.

[†] Department of Biochemistry and Molecular Pharmacology, Thomas Jefferson University.

[‡] Department of Radiology, Thomas Jefferson University.

[§] Kimmel Cancer Center, Thomas Jefferson University.

[∥] University of Missouri.

10.1021/bc0497923 CCC: $30.25 © 2005 American Chemical Society
Published on Web 12/31/2004

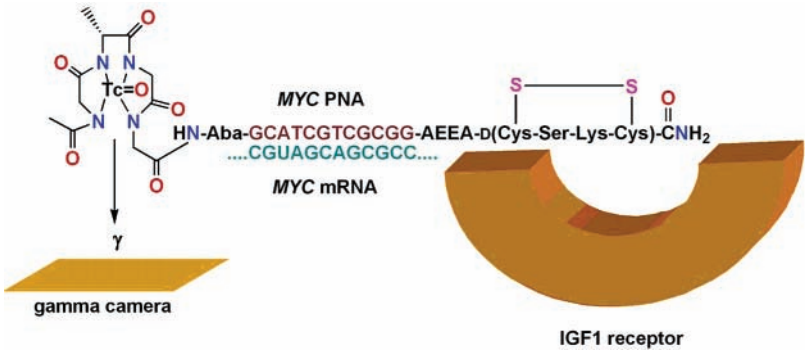

Figure 1. [^{99m}Tc]AcGlyD(Ala)GlyGlyAba-*MYC* PNA-AEEA-D(CysSerLysCys), WT4219, designed to bind to the receptor for IGF1, internalize, and hybridize with *MYC* mRNA. Scintigraphic imaging of γ-particles emitted upon decay of ^{99m}Tc might identify sites of high *MYC* mRNA expression.

tivity and specificity (*23*), 66−85% of women with suspicious mammograms who undergo surgery are found to have a benign abnormality (*24*). In many other patients recently determined to have a benign mammogram, clinical examination reveals a mass found to be malignant.

A noninvasive method to evaluate women for the presence of atypia and/or cancer of the breast would be very beneficial. SestaMIBI has demonstrated utility in imaging lesions in a dense breast, but is limited by the fact that other cell types with high mitochondrial activity avidly take up the tracer, leading to false positive results in breasts with inflammation/infection (*25*), false negatives due to sensitivity limits of the technology, in which tumors <8 mm in diameter are difficult to visualize (*26*), and the potential for false negatives with well differentiated, slowly growing tumors due to their lower mitochondrial content.

Recent evidence from gene expression profiling suggests that alterations in mRNA conferring the potential for invasive breast cancer are already present in preinvasive disease, supporting the rationale for this approach (*27*). However, transcription profiles of breast cancer tissue by microarray analysis have not yet identified detectable overexpression of those markers (*28*), and that approach requires an invasive biopsy. As a step in characterizing preinvasive disease, such as ductal carcinoma in situ, it might be helpful to identify sites of *MYC* overexpression externally, without a biopsy.

Therefore, we hypothesized that noninvasive imaging of a radiolabeled oligonucleotide hybridized to *MYC* mRNA inside breast cancer cells might identify sites of neoplastic transformation. Previously, a [^{99m}Tc]6-hydrazinonicotinate-conjugated *MYC* antisense oligonucleotide phosphorothioate failed to show differences in uptake among cell lines with high, normal, or low levels of *MYC* mRNA (*29*). Those negative results might have been due to nonspecific affinity of phosphorothioate oligonucleotides for proteins, limiting efflux of unbound label, and to destruction of the oncogene message being measured by RNase H attack on the RNA target due to hybridization of the labeled antisense DNA, or to lack of a receptor targeting ligand. While specific tumor uptake of [^{111}In]-*MYC* phosphorothioate (*30*) and [^{68}Ga]*KRAS* phosphorothioate (*31*) have been asserted, those reports have not been replicated as yet.

Morpholino phosphorodiamidates provide a useful alternative to phosphorothioates as hybridization agents, but suffer from poor uptake (*32*). However, radiolabeled morpholino oligonucleotides have exhibited good pharmacokinetic and tissue distribution properties (*33*). Avoidance of cytosines in morpholino sequences reduces renal accumulation (*34*), while conjugation of basic peptides elevates cellular uptake of morpholino oligomers (*35*).

To address those drawbacks, we turned to peptide nucleic acids (PNAs), which hybridize more tightly and more specifically to RNA than morpholino oligonucleotides (*36*, *37*), resist nuclease attack, and demonstrate antisense activity upon microinjection of PNAs into cellular nuclei (*38*). RNA hybridized to uncharged oligonucleotide derivatives, such as PNA, is not recognized by RNase H. Therefore, PNA does not catalyze degradation of its analyte, the bound RNA (*39*), but inhibits mRNA translation solely by hybridization arrest, and thus provides an opportunity for diagnostic application (*38*). The requirement for intracellular PNA microinjection, however, stems from their poor cellular uptake, which was reported to be 10 times less efficient than uptake of phosphorothioates in a variety of mammalian cells (*40*).

Cellular uptake of PNAs can be improved by the addition of ligands (*41*). Previously we observed that synthesis of an *IGF1R* PNA dodecamer with an N-terminal D-peptide analogue of IGF1, D(CysSerLysCys), provided cell-type specificity, and increased cellular uptake 5−10-fold in BALB/c3T3 cells transformed with human *IGF1R* (*42*) and in human *IGF1R*-overexpressing MCF7 breast cancer cells (*43*). Only background levels of uptake were seen with control cell lines or control peptides. In prostate cancer cells, for comparison, addition of dihydrotestosterone or a nuclear localization peptide to a *MYC* antisense PNA permitted some nuclear localization and Myc reduction in LNCaP cells expressing androgen receptor after 24 h exposure to 10 μM PNA (*44*). It appears that the use of a peptide analogue specific for a cell surface receptor is more effective than a steroid capable of binding to a cytoplasmic protein after unassisted uptake.

We have pursued this cell-specific approach to enable application of PNAs as gene expression diagnostics in vivo, developing methods for the synthesis of peptide−PNA−peptide chimeras, which exhibit the same melting temperatures with complementary RNA targets as do PNAs alone without peptides (*45*). For noninvasive scintigraphic imaging of oncogene mRNA in malignant lesions, we developed a method to label PNA−peptide hybridization probes with ^{99m}Tc by including a chelating peptide GlyD(Ala)GlyGlyAba (Aba = γ-aminobutanoate) (TP3654) (*46*) coupled by continuous solid-phase synthesis to the N-terminus of PNA-AEEA-D(CysSerLysCys) (AEEA = aminoethoxyethoxyaceate) (*45*). Fluoresceinyl-GlyD(Ala)GlyGlyAba−*CCND1* PNA-AEEA-D(CysSerLysCys) lowered cyclin D1 protein in *IGF1R*-overexpressing MCF7 xenografts in immunocompromised mice upon

Scheme 1. Assembly of Chelator Peptide−*MYC* PNA−Peptides

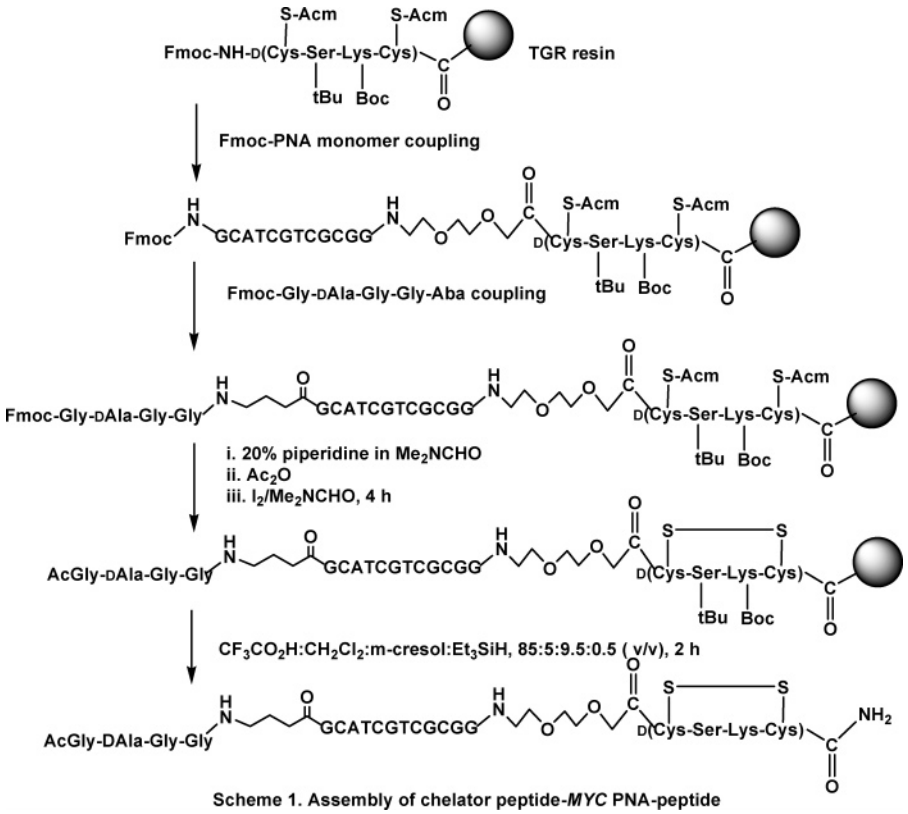

Scheme 1. Assembly of chelator peptide-*MYC* PNA-peptide

intratumoral injection (*43*). The γ-emitting [^{99m}Tc]AcGlyD(Ala)GlyGlyAba−*CCND1* PNA-AEEA-D(CysSerLysCys) visualized *IGF1R*-overexpressing, *CCND1*-overexpressing MCF7 xenografts in immunocompromised mice at 12 and 24 h after intravenous administration. In all of those experiments, control PNA and peptide sequences were unable to produce similar images (*43*).

Because *MYC* mRNA is overexpressed in a broad spectrum of cancers, it might be a valuable target for diagnostic imaging in many cases. We report here imaging of *MYC* mRNA levels in human estrogen receptor-positive MCF7:IGF1R breast cancer xenografts in immunocompromised mice following intravenous administration of [^{99m}Tc]AcGlyD(Ala)GlyGlyAba-*MYC* PNA-AEEA-D(CysSerLysCys) chimera, designed to bind to the receptor for IGF1, internalize, and hybridize with *MYC* mRNA (Figure 1).

MATERIALS AND METHODS

Peptide−PNA−Peptide Synthesis. The peptide−PNA−peptide chimeras were assembled (Scheme 1), purified, and characterized as described previously (*45*). Briefly, the IGF1 analogue D(CysSerLysCys), or the mismatch control D(CysAlaAlaCys), was assembled by Fmoc coupling on NovaSyn TGR resin (0.2−0.3 mmol/g) (Novabiochem, San Diego CA) on an Applied Biosystems 430A peptide synthesizer. Then the linker Fmoc-AEEA and PNA monomers (Applied Biosystems, Foster City CA) were sequentially coupled to the N-terminus of the peptide-resin on an Applied Biosystems 8909 DNA synthesizer, running the manufacturer's PNA 2 μmol protocol. Finally, the chelator peptide Fmoc-GlyD(Ala)-GlyGlyAba (Novabiochem) was coupled to the N-terminus of the PNA−peptide using a long coupling cycle protocol (*45*), then acetylated. The cysteine residues were cyclized on solid phase with 10 equivalents of I_2 in Me_2NCHO for 4 h at room temperature (*45*).

The chimeras were cleaved and deprotected with 85% CF_3CO_2H, 5% CH_2Cl_2, 9.5% *m*-cresol, and 0.5% Et_3SiH for 2 h at room temperature (*45*), then purified by reversed phase liquid chromatography on a 10 × 250 mm Alltima C_{18} column eluted with a gradient linear 25 min. from 5% to 45% CH_3CN in aqueous 0.1% CF_3CO_2H, at 1 mL/min, at 50 °C, monitored at 260 nm. Matrix-assisted laser desorption ionization time-of-flight mass spectrometry (MALDI-TOF MS, Ciphergen Corp., Fremont, CA) was carried out from an α-cyano-hydroxycinnamic acid matrix excited at 338 nm, and calibrated with porcine neuropeptide Y.

Cell Lines and Xenografts. Human MCF7:IGF1R estrogen receptor-positive breast cancer cells, clone 17, transformed to express 1×10^6 IGF1R/cell constitutively from a cytomegalovirus promoter (*47*) were maintained in DMEM plus 5% calf serum, 50 U/mL penicillin, 5 μg/mL streptomycin, 2 mM glutamine, and 7.5 nM 17-β-estradiol (Sigma) at 37 °C under 5% CO_2. For tumor induction, $5-6 \times 10^6$ cells in 0.2 mL of culture medium were implanted intramuscularly through a sterile 27 gauge needle into the thighs of female Balb/c nude mice obtained from NIH. Tumors were allowed to grow to no more than 0.5 cm in diameter. Each injection included 10 mg of Matrigel. A 60-day release pellet containing 4.5 mg of 17-β-estradiol (Innovative Research of America, Sarasota, FL) was implanted subdermally in each mouse. All animal studies were conducted in accordance with federal and state guidelines governing the laboratory use of animals, and under approved protocols reviewed by the Animal Care and Use Committee at Thomas Jefferson University. All animals were anesthetized by approved methods, and when required, the animals were restrained using methods and devices specifically designed to provide a minimum of discomfort to the animal. Animals were euthanized in a halothane chamber, con-

Scheme 2 ^{99m}Tc Labeling of Peptide−PNA−peptides

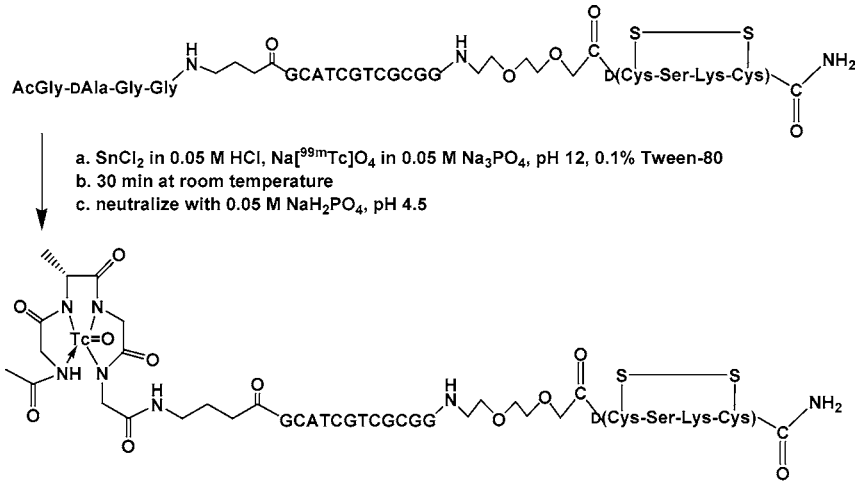

Scheme 2. ^{99m}Tc labeling of peptide-*MYC* PNA-peptides

sistent with USDA regulations and American Veterinary Medical Association recommendations.

Radiolabeling. Purified peptide−PNA−peptide chimeras were labeled with ^{99m}Tc (Scheme 2) essentially as described previously (*48*). Briefly, 20 μg of peptide−PNA−peptide chimera and 45−60 μg of $SnCl_2 \cdot 2H_2O$ were vortexed in 20 μL of 0.05 M HCl. Next, 12 mCi of $Na^{99m}TcO_4$ freshly eluted from the ^{99m}Tc generator with 200 μL of 0.15 M NaCl were vortexed with 600 μL of 0.05 M Na_3PO_4, pH 12, 0.1% Tween 80. The radionuclide mixture was then added to the peptide−PNA−peptide/$SnCl_2$ solution and incubated for 30 min at room temperature. Finally, the solution was neutralized by the addition of 1 mL of 0.05 M NaH_2PO_4, pH 4.5.

Reaction mixtures were analyzed to determine free ^{99m}Tc and chelated ^{99m}Tc by reversed phase liquid chromatography on a 4.5 × 250 mm reversed phase C_{18} microbond HPLC column (Rainin, Emeryville, CA) coupled to a UV detector, NaI (Tl) radioactivity monitor, and a rate meter. The column was eluted with a 28 min. gradient from 10% to 100% CH_3CN in aqueous 0.1% CF_3CO_2H, at 1 mL/min, at 25 °C. Unchelated free ^{99m}Tc (R_f 1.0) was also determined by instant thin-layer chromatography on silica gel (ITLC−SG, Gelman Sciences, Ann Arbor, MI) developed with methylethyl ketone. Colloid formation (R_f 0.0) was determined on ITLC−SG developed with pyridine/HOAc/H_2O (3:5:1.5). These preparations were stable at 22 °C for more than 4 h, as determined by HPLC, and were stable to challenges with 100-fold molar excesses of diethylenetriaminepentaacetic acid, human serum albumin, or cysteine.

Systemic Administration and Tissue Distribution of Labeled Probes. To assess chimera distribution and imaging, 7.4−11.1 MBq (0.2−0.3 mCi) of the [^{99m}Tc]-peptide−PNA−peptides in 0.2 mL of sterile 0.1 M Na_2HPO_4, pH 7, was administered to groups of five mice each through a lateral tail vein using a sterile 27 gauge needle. For the 24 h distribution, 29.6−34.2 MBq (0.8−0.9 mCi) of probe was administered. At 4 and 24 h postinjection, mice were lightly anesthetized, then imaged using a Starcam (GE Medical, Milwaukee, WI) gamma camera equipped with a parallel hole collimator. For each image, 300 000 counts were collected. Digital scanning of region-of-interest intensities with the interfaced Entegra computer (GE Medical) across each scintigraphic image from the tumor-free left flank to the tumor-bearing right flank provided quantitation of tumor images.

Mice were then euthanized, and tissues were dissected. These were washed free of blood, blotted dry, and weighed, and radioactivity associated with each tissue was counted in an automatic gamma counter (Packard Series 5000, Meridien, CT), together with a standard radioactive solution of a known quantity prepared at the time of injection. Results were expressed as percent of injected dose per gram of tissue (% I.D/g).

In Vivo Stability. Urine was collected up to 2−3 h postinjection from groups of 5 mice injected with [^{99m}Tc]-peptide−PNA−peptide probes for assessment of probe stability. The urine samples were combined, sedimented at 2000*g* for 10 min, filtered through Millipore HAWP 025 membranes with 0.22 μm pores, and analyzed by RP-HPLC as described in Radiolabeling above.

Statistical Methods. Statistical analysis of differences among groups was determined by applying the standard error of the mean, Student's *t* test, Kruskal and Wallis's one-way analysis of variance on ranks, or the Holm−Sidak pairwise multiple comparison procedure, using SigmaStat 3.0 (SPSS, Chicago, IL).

RESULTS

Peptide−PNA−Peptides. We prepared a cyclized peptide−PNA−peptide chimera AcGlyD(Ala)GlyGlyAba-GCATCGTCGCGG-AEEA-D(CysSerLysCys), WT4219, specific for *MYC* mRNA and the IGF1 receptor (Figure 1). Preparative RP-HPLC of the crude product yielded a main peak containing 98.05% of the absorbance at 260 nm (Figure 2A). The overall yield following preparative RP-HPLC was 27.2%. MALDI-TOF MS confirmed the identity of the main product peak at 4221.6 Da (Figure 2B). Similarly, we prepared a *MYC* PNA 4-mismatch control, AcGlyD(Ala)GlyGlyAba-GCATGTCTGCGG-AEEA-D(CysSerLysCys), WT4235, with 30.6% overall yield following preparative RP-HPLC (Figure 3A), and MALDI-TOF mass of 4234.7 Da (Figure 3B).

[^{99m}Tc]Peptide−PNA−Peptides. Twenty microgram aliquots of the *MYC* peptide−PNA−peptide antisense probe, WT4219, labeled well at 22 °C (Figure 4A). Free ^{99m}Tc was only 0.36%, and colloids were only 4.84%. The PNA mismatch, WT4235, labeled well also (Figure 4B). Free ^{99m}Tc was 0.99%, and colloids were 4.84%.

Systemic Administration. To test our hypothesis that a complementary [^{99m}Tc]peptide−PNA−peptide probe specific for *MYC* mRNA and the IGF1 receptor could visualize a *MYC*-expressing tumor, we administered approximately 0.5 mCi [^{99m}Tc]peptide PNA−peptide *MYC* probes to cohorts of five nude mice bearing approximately 0.5 cm MCF7:IGF1R xenografts to determine the specificity and sensitivity of scintigraphic imaging 4 h and 24

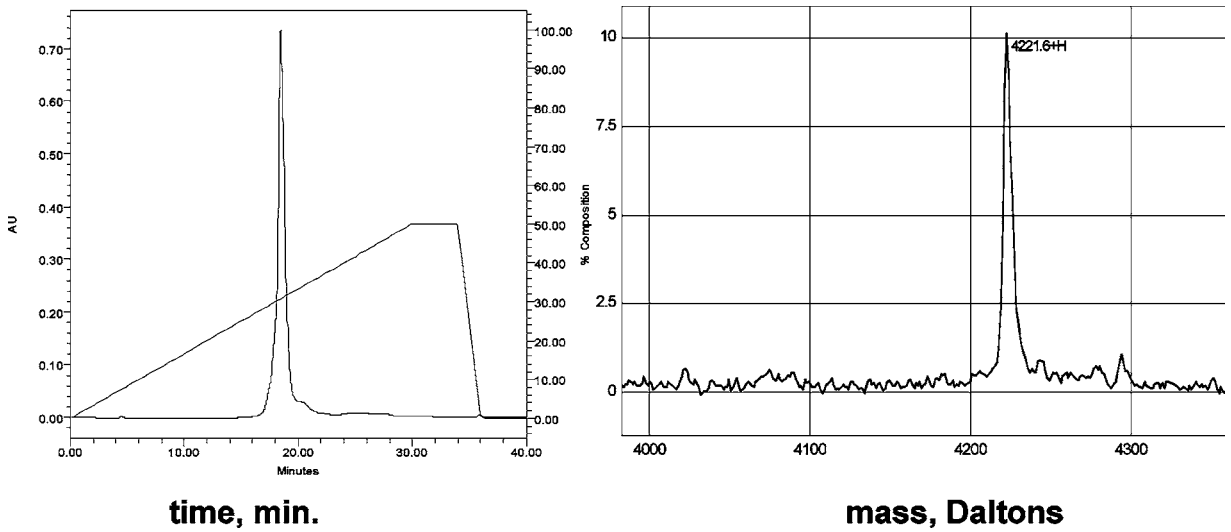

Figure 2. Characterization of cyclized *MYC* antisense chimera AcGlyD(Ala)GlyGlyAba-GCATCGTCGCGG-AEEA-D(CysSerLysCys), WT4219. A. Preparative reversed phase liquid chromatography of cyclized chimera on a 10 × 250 mm Alltima C_{18} column eluted with a linear 30 min. gradient from 5% to 45% CH_3CN in aqueous 0.1% CF_3CO_2H, at 1 mL/min, at 50 °C, monitored at 260 nm. B. MALDI-TOF mass spectrum of chimera in a matrix of α-cyano-hydroxycinnamic acid. Experimental mass: 4221.6 Da; calculated mass: 4219.0 Da.

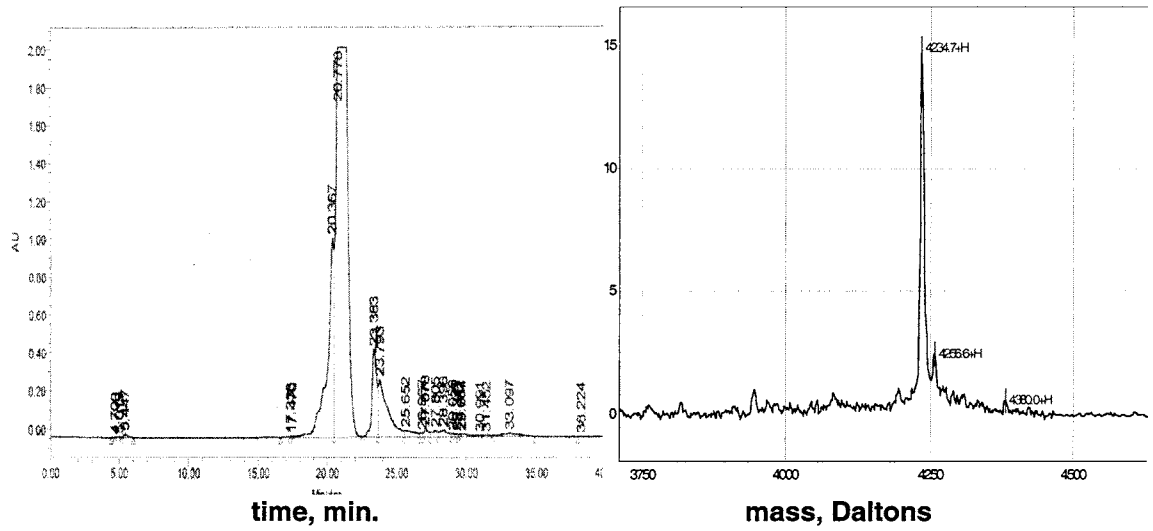

Figure 3. Characterization of cyclized *MYC* mismatch chimera AcGlyD(Ala)GlyGlyAba-GCATGTCTGCGG-AEEA-D(CysSerLysCys), WT4235. A. Preparative C_{18} HPLC of cyclized chimera as in Figure 2. B. MALDI-TOF mass spectrum of chimera as in Figure 2. Experimental mass: 4234.7 Da; calculated mass: 4235.0 Da.

h after administration (Figure 5). We previously tested whether the PNA-free chelator plus IGF1 analogue control probe would bind to tumor cells expressing high levels of IGF1 receptor, which it did not (*43*).

To test whether a probe containing four central PNA mismatches would bind to tumor cells expressing high levels of IGF1 receptor and *MYC* mRNA, we administered the PNA mismatch control, WT4235. We did not observe tumor signals at 4 h or 24 h postinjection. Finally, to test whether the complementary probe with correct IGF1 analogue would bind to tumor cells expressing high levels of IGF1 receptor and *MYC* mRNA, we administered the PNA antisense chimera, WT4219. In this case, we observed faint tumor signals at 4 h and intermediate tumor signals at 24 h postinjection.

Digital scanning of the tumor site region-of-interest on the right flank vs the mirror image tumor-free region-of-interest on the left flank enabled quantitation of tumor images. The ratios of tumor site:control site intensities are plotted in Figure 6 as a function of time. One presumes that any ratio greater than 1 implies some preferential probe concentration. No tumor image was obvious in Figure 5 following administration of the PNA mismatch control, WT4235, which includes the IGF1 peptide analogue, but the digitized tumor site:control site ratio was 3.33 ± 0.30 at 4 h, and 2.72 ± 0.44 at 24 h. A faint tumor image was apparent in Figure 5 four h after administration of the antisense probe, WT4219, which correlated with the tumor site:control site ratio of 4.35 ± 0.58. At 24 h postinjection, the ratio increased to 7.01 ± 0.90.

Kruskal−Wallis one-way analysis of variance on ranks determined that the four groups were significantly different from each other ($p < 0.001$). When all four groups were compared by the Holm−Sidak method, the antisense group was not significantly different from the mismatch group at 4 h postinjection ($p = 0.244$). However, at 24 h postinjection, Holm−Sidak comparison revealed a statistically significant difference ($p < 0.001$) between the antisense group and the mismatch group. The test performed had a power of 0.985 with $\alpha = 0.050$.

In Vivo Stability. RP-HPLC of radioactivity in the combined 3-h urine sample from mice injected with [^{99m}-

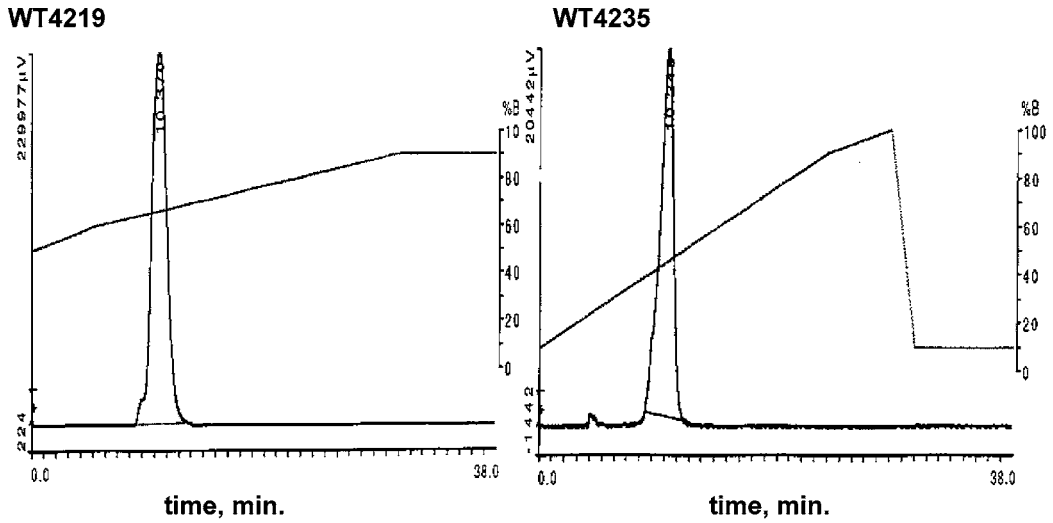

Figure 4. Analysis of [^{99m}Tc]peptide−PNA−peptides. An aliquot of each labeling reaction was analyzed by RP-HPLC on a 10 × 250 mm Rainin Microbond C_{18} column eluted with a 28 min gradient from 10% to 100% CH_3CN in aqueous 0.1% CF_3CO_2H, at 1 mL/min, at 25 °C. %B (CH_3CN) is shown on the right *y*-axis, and NaI (Tl) radiometric gamma emission is shown on the left *y*-axis. Left: antisense probe, WT4219. The single labeled peak eluted at 10.37 min. Right: mismatch probe, WT4235. The single labeled peak eluted at 10.25 min.

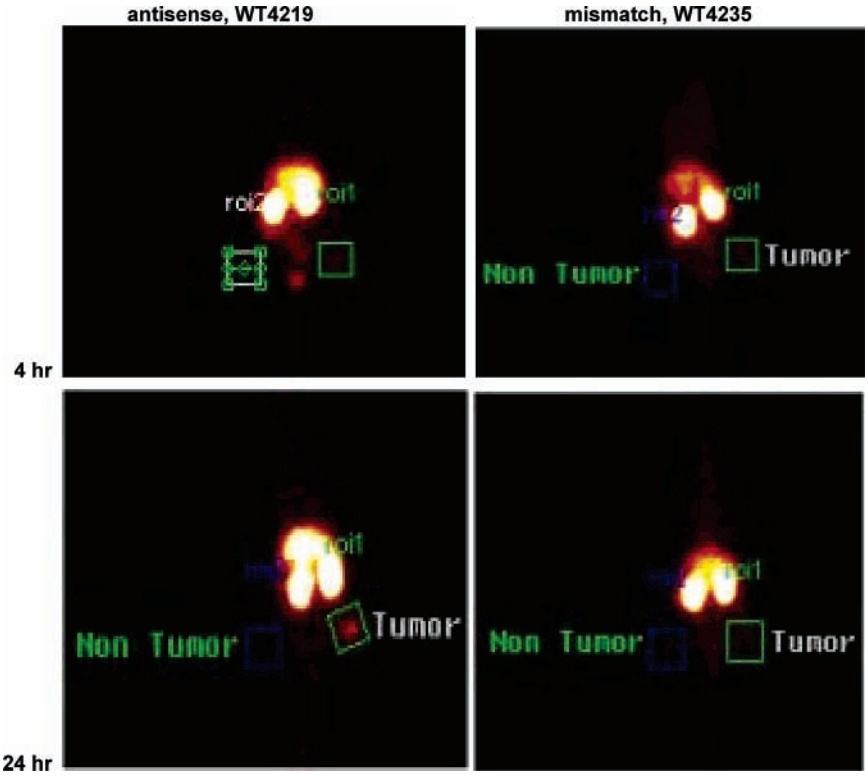

Figure 5. Scintigraphic images of γ−particles emitted by decaying ^{99m}Tc in immunocompromised mice carrying human MCF7: IGF1R ER+ breast tumor cell xenografts at 4 h and 24 h after injection of [^{99m}Tc]peptide−PNA−peptides. Left: [^{99m}Tc]*MYC* PNA antisense probe, WT4219; right: [^{99m}Tc]*MYC* PNA mismatch control, WT4235.

Tc]*MYC* antisense probe, WT4219, showed no void volume peak of free ^{99m}Tc, but only an intact probe peak at 10.7 min (Figure 7, left). RP-HPLC of radioactivity in the combined 2-h urine sample from mice injected with [^{99m}Tc]*MYC* mismatch probe revealed a void volume peak of free ^{99m}Tc, 44% of radioactivity, and a probe peak at 10.3 min with 56% of the radioactivity (Figure 7, right). Breakdown fragments of the peptide−PNA−peptide probe were not detected from either probe.

Tissue Distribution. Tissue distribution of each probe was measured in all subjects at 4 and 24 h after administration. Table 1 presents the data for the antisense group and the mismatch group at 4 h, while Table 2 shows the 24 h results. As the time after injection elapsed, the radioactivity in all tissues decreased, including that in the tumors. However, the tumor to blood and tumor-to-muscle ratios increased for WT4219 as time went on. This is consistent with the scintigraphic images in Figure 5 and the tumor (right)-to-muscle (left) image intensity ratios provided in Figure 6, which were higher than the tumor/muscle distribution ratios from scintillation counting for WT4219. While the tumors were readily detectable by scintigraphy with WT4219, but not with WT4235, the tumor distribution counts of % injected dose/g for the antisense group and the mismatch group were not remarkably different, except for the heart. The

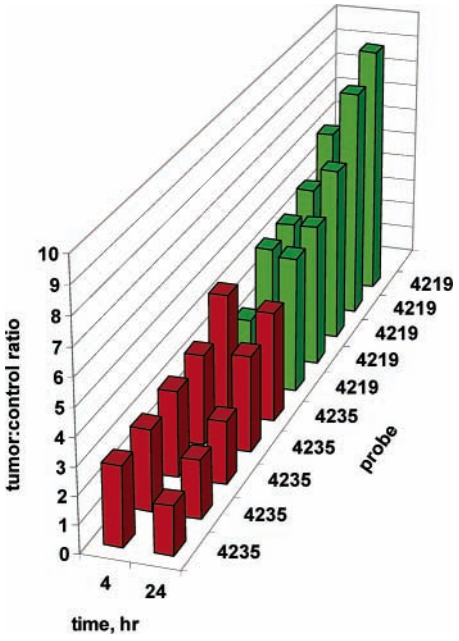

Figure 6. Tumor site:control site gamma intensity ratios after systemic administration of [^{99m}Tc]peptide−PNA−peptide chimeras for all subjects in Figure 5. red, [^{99m}Tc]*MYC* PNA mismatch control, WT4235; green, [^{99m}Tc]*MYC* PNA antisense probe, WT4219.

increased accumulation of the mismatch probe WT4235 in heart tissue invited a BLAST search with the WT4235 sequence for heart-specific or mitochondrial-specific murine mRNAs. Unfortunately, no complementary homologies were identified, so the concentration of mismatch probe in the heart remains unexplained.

The tissue distribution data indicated that renal excretion was the primary route of elimination and renal uptake was highest among all tissues, but the extent differed from agent to agent.

DISCUSSION

In this report we tested the feasibility of using a [^{99m}Tc]chelator peptide-*MYC* PNA receptor-targeting hybridization probe to image *MYC* mRNA at modest copy number in ER+ breast cancer cells that overexpress IGF1R, a receptor that is overexpressed is a high percentage of breast cancer cells.

Quantitative reverse transcription-polymerase chain reaction measurements of *MYC* mRNA in total MCF7:IGF1R cell RNA revealed 4-fold inhibition after preannealing with 0.1 μM N-Gly$_D$(Ala)GlyGlyAba-*MYC* PNA-Gly$_4$D(CysSerLysCys) probe before adding PCR primers, and 8-fold inhibition after preannealing with 1.0 μM probe (*39*). The *MYC* mismatch control had no effect, consistent with the hypothesis that the complementary PNA probe would bind strongly to the mRNA target. That probe was essentially the same as WT4219, except for substitution of Gly$_4$ for the AEEA linker (*39*). The specificity of RT inhibition implies that the peptide−PNA−peptides hybridize to their intended *MYC* mRNA target.

Previously, denaturing NaDodSO$_4$ gel electrophoresis (*43*) of a comparable [^{99m}Tc]peptide−*CCND1* PNA−peptide probe showed a radioactive band that co-electrophoresed with the main radioactive band from the [^{99m}Tc]*CCND1* probe labeling mixture. Similarly, fluorescence microscopy illustrated that the peptide−*CCND1* PNA−peptide probes were taken up inside MCF7:IGF1R breast cancer cells, if and only if the IGF1 peptide analogue sequence was correct (*43*), as was reported previously for p6 cells (*42*).

We carried out a variety of tests of the hypothesis that overexpression of *MYC* mRNA in MCF7:IGF1R breast cancer xenografts could be detected specifically and noninvasively by scintigraphic imaging of ^{99m}Tc-peptide−PNA−peptide probes. We previously measured *MYC* oncogene mRNA copy number in MCF7:IGF1R human breast cancer cells by quantitative reverse transcription-polymerase chain reaction (*43*). Comparison of threshold cycle numbers for *MYC* mRNA with those for TATA-box binding protein mRNA yielded an average ratio of 8 for MCF7:IGF1R cells over two logs of RNA template. On the basis of the previously reported TATA-box binding protein mRNA copies per breast cancer cell of 1000−2000 (*49*), we estimated approximately 8000 *MYC* mRNAs per MCF7:IGF1R cell. Assuming 8000 mRNAs per cell and 10^9 cells per gram of tumor, there would be an estimated 8×10^{12} mRNA copies available for binding in a 1 g tumor. Our data suggest that 0.1% of the injected [^{99m}Tc]-WT4219 antisense probe (specific activity 2 Ci/μmol) was associated with the tumors at 24 h. This suggests that approximately 3×10^{11} molecules of [^{99m}Tc]WT4219 were bound to the mRNA in a 1 g tumor, or about 4% of the *MYC* mRNAs, despite nonuniform distribution of radioactivity in the tumor. In a high specific activity or carrier-free preparation, this would be equivalent to 500 μCi of ^{99m}Tc, suggesting the possibility of up to 500 times greater sensitivity than we observed in this initial study.

To estimate the fraction of internalized PNA probes that could be hybridized to available *MYC* mRNAs in live tumor cells, one must begin with the observed T_m of approximately 80 °C for 2.5 μM peptide−PNA−peptide 12-mers with 2.5 μM RNA (*45*). A copy number of approximately 8000 *MYC* mRNAs per 1 pL cell translates to 13 nM, while the [^{99m}Tc]WT4219 appeared to be less than 1/10 of that, 1 nM. The T_m, the probe concentration, and the 13-fold excess mRNA concentration enable prediction (*36*) of virtually complete hybridization of available intracellular probe.

Interestingly, concentration of label in tumors was very faint at 4 h after injection of the antisense PNA *MYC* sequence with IGF1 analogue, WT4219, although the digital scan revealed detectable concentrations of label. We interpret that observation to mean that uptake, intracellular trafficking, hybridization of label, and efflux of unbound label are all slow processes that do not reveal a strong tumor signal at 4 h. Because labeled antisense PNA in the tumors could be visualized at 24 h, we hypothesize that 24 h was sufficient for unbound probe to efflux from cells and to be excreted. With respect to the hybridized label, bound PNA probe dissociates negligibly from complementary RNA by 12−24 h (*25*, *36*). In the end, we found that the MCF7:IGF1R xenografts that overexpress *MYC* mRNA could be imaged reliably and specifically at 24 h postinjection.

The [^{99m}Tc]*MYC* mismatch probe was also administered to immunocompromised mice to assess metabolism in vivo. Urinalysis by RP-HPLC (Figure 7), showing intact [^{99m}Tc]*MYC* antisense and mismatch probes, implied reasonable stability of the peptide−PNA agent in vivo, consistent with the hypothesis that a [^{99m}Tc]D-peptide−PNA would be resistant to proteases and nucleases in blood and tissues. In the case of the mismatch probe, free ^{99m}Tc void volume peak probably resulted from reoxidation of probe-bound Tc(III) to free Tc(VII) in the liver. The lack of a free ^{99m}Tc void volume peak in the case of the antisense probe is remarkable. One may speculate that the antisense probe was only excreted

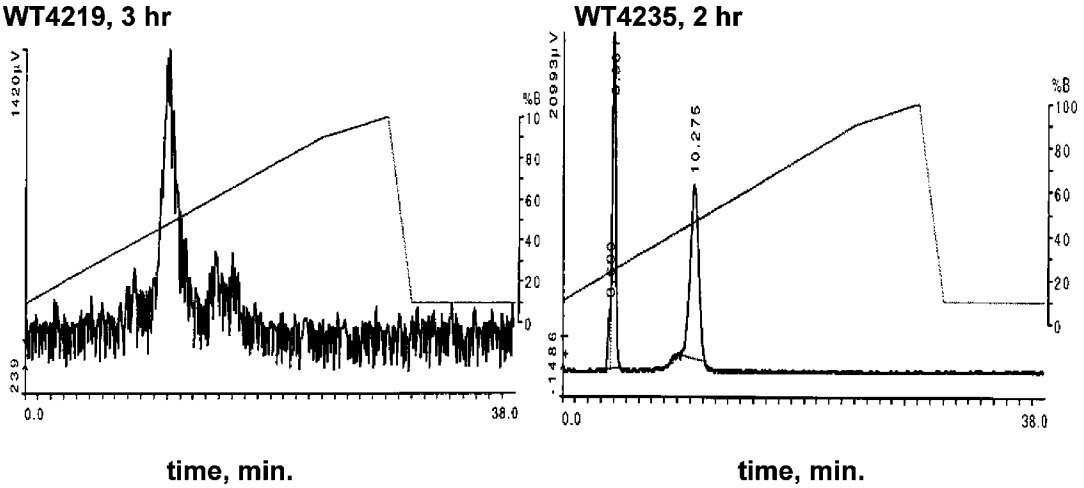

Figure 7. Analytical HPLC of [^{99m}Tc]peptide−PNA−peptide probes that were recovered from mouse urine 2−3 h after administration, chromatographed as in Figure 4 above. Left, [^{99m}Tc]*MYC* antisense probe, WT4219, 3 h after administration; right, [^{99m}Tc]*MYC* mismatch probe, WT4235, 2 h after administration.

Table 1. Tissue Distribution (% injected dose/g) of the [^{99m}Tc]*MYC* Antisense Chimera, WT4219, and the [^{99m}Tc]*MYC* Mismatch Chimera, WT4235, at 4 h after Systemic Administration (n = 5)

tissues	antisense	mismatch	null prob.
muscle	0.08 ± 0.02	0.11 ± 0.03	0.11
intestine	0.10 ± 0.03	0.11 ± 0.01	0.18
heart	0.09 ± 0.02	0.68 ± 0.15	0.00003
lungs	0.52 ± 0.19	0.70 ± 0.27	0.25
blood	0.18 ± 0.03	0.24 ± 0.03	0.01
spleen	3.64 ± 1.71	4.44 ± 0.98	0.39
kidneys	31.54 ± 3.14	37.47 ± 3.42	0.02
liver	5.55 ± 0.77	3.43 ± 0.51	0.00091
tumor	0.20 ± 0.05	0.23 ± 0.05	0.47
T/M ratio	2.57 ± 0.96	2.26 ± 0.78	0.59
T/B ratio	1.14 ± 0.17	0.97 ± 0.29	0.30

Table 2. Tissue Distribution (% injected dose/g) of the [^{99m}Tc]*MYC* Antisense chimera, WT4219, and the [^{99m}Tc]*MYC* Mismatch Chimera, WT4235, at 24 h after Systemic Administration (n = 5)

tissues	antisense	mismatch	null prob.
muscle	0.04 ± 0.01	0.05 ± 0.01	0.45
intestine	0.04 ± 0.00	0.05 ± 0.00	0.008
heart	0.03 ± 0.00	0.24 ± 0.03	0.0000004
lungs	0.15 ± 0.04	0.25 ± 0.03	0.002
blood	0.04 ± 0.01	0.05 ± 0.01	0.06
spleen	3.47 ± 0.88	3.32 ± 1.41	0.84
kidneys	21.65 ± 6.50	20.06 ± 4.64	0.67
liver	4.95 ± 0.58	2.93 ± 0.75	0.001
tumor	0.10 ± 0.03	0.11 ± 0.03	0.63
T/M ratio	2.59 ± 0.88	2.19 ± 0.30	0.37
T/B ratio	2.48 ± 0.56	2.09 ± 0.55	0.30

upon the first pass through the kidney, and that antisense probes that distributed to tissues did not re-enter the bloodstream to be metabolized by the liver, at least up to 3 h.

The tissue distribution and urinalysis results were comparable to our previous observations with [^{99m}Tc]-GlyD(Ala)GlyGlyAba-GCATCGTCGCGG, WT4219 lacking the IGF1 analogue (*39*). The tissue distribution results were also comparable with those for [^{99m}Tc]-AcGlyD(Ala)GlyGlyAba−*CCND1* PNA-IGF1 analogues and controls (*43*). As noted above, a BLAST search with the mismatch sequence did not uncover any complementary cardiac or mitochondrial mRNAs.

Although there was no significant difference in tumor: muscle ratios between the *MYC* probe and its mismatch control, the MCF7:IGF1R xenografts were imaged clearly with WT4219, but not with WT4235. That is because the tissue distribution data report radioactivity in the entire excised masses, which include some surrounding normal tissue, the actively proliferating cells on the periphery of the tumors, and the necrotic cores. The radioactive *MYC* probes were predicted to concentrate in the actively proliferating cells. However, the surrounding normal tissues, which do not express human *MYC* mRNA, and the nectrotic cores, which exhibit poor uptake of macromolecules (*50*) and are not proliferating, were not dissected away before measuring tissue radioactivity. As a result, the apparent % uptake of ^{99m}Tc/g tumor was diluted by inclusion of extra nonproliferating tissue. Hence, the tumor/muscle ratios of *MYC* probe radioactivity were reduced to the range of the mismatch probe. This same difference between clear scintigraphic images and modest % uptake of ^{99m}Tc/g tumor was also observed earlier for [^{99m}Tc]GlyD(Ala)GlyGlyAba-vasoactive intestinal peptide, which revealed occult tumors in patients despite apparent tumor uptake of only 0.3% injected dose/g in xenografts in immunocompromised mice (*46*, *48*, *51*), and for [^{99m}Tc]AcGlyD(Ala)GlyGlyAba−*CCND1* PNA-IGF1 analogues and controls in MCF7:IGF1R xenografts (*43*). Digital scanning, however, of scintigraphic intensities determined the radioactivity per pixel in the tumor region-of-interest, revealing *MYC* mRNA expression in the actively proliferating cells on the periphery of the tumors. In this case, the necrotic centers presumably did not contribute to the measurement, eliminating the possibility of label dilution. Thus, the tumor/contralateral scintifigraphic intensity ratios in Figure 6 probably provided more accurate results than the scintillation counting tissue distribution ratios in Tables 1 and 2.

High grade renal cell carcinomas exhibit elevated cytoplasmic Myc protein, but not in the nuclei, and not in normal renal cells (*40*, *52*). Therefore, concentration of the PNA antisense probe WT4219 in the kidneys was probably not due to labeling of *MYC* mRNA in kidney cells, but to nonspecific binding to negative charges on renal parenchyma. Simultaneous L-lysine administration has been shown to reduce renal accumulation of [^{111}In]-DTPA-octreotide in rats (*53*). Preliminary results from a study underway in our laboratory with our [^{99m}Tc]*CCND1* probe administered to tumor-bearing mice are consistent with that report.

Our observation of scintigraphic imaging of *MYC* mRNA expression in xenografts could be applicable to

patients at risk for new or recurrent breast cancer, including those with a strong family history of breast cancer, or when standard detection techniques provide ambiguous results. Imaging of mRNA expression with chelator−PNA−peptide chimeras labeled with ^{99m}T, ^{64}Cu, or other radionuclides might also be applicable to other oncogenes or to other cell surface receptors.

Targeting altered expression of oncogenes provides the promise of specificity, ultimately leading to the elimination of diagnostic surgical biopsy. *MYC* overexpression is a common event in and highly associated with the presence of breast cancer. While not sufficiently sensitive to be used alone, noninvasive measurement of mRNA expression by one or more oncogenes to confirm the presence or absence of cancer by γ-particle emission or by positron emission tomography when an imaging study is abnormal provides a mechanism for more accurate diagnosis of breast cancer.

ACKNOWLEDGMENT

We thank Dr. Eva Surmacz for her advice and the gift of MCF7 cells that constitutively overexpress IGF1R, Zuping Qu for maintaining the MCF7 cells under a variety of conditions, Dr. Zhi-xian Lu for assembly of linear peptide-resin supports, and Dr. Richard Wassell for assistance in measuring mass spectra of peptide−PNA−peptides. This work was supported by DOE ER63055 to E.W. and NIH HL59769 to M.L.T.

LITERATURE CITED

(1) Duesberg, P. H., Bister, K., and Vogt, P. K. (1977) The RNA of avian acute leukemia virus MC29. *Proc. Natl. Acad. Sci. U. S. A. 74*, 4320−4324.

(2) Heikkila, R., Schwab, G., Wickstrom, E., Loke, S. L., Pluznik, D. H., Watt, R., and Neckers, L. M. (1987) A c-myc antisense oligodeoxynucleotide inhibits entry into S phase but not progress from G0 to G1. *Nature 328*, 445−449.

(3) Wickstrom, E. L., Bacon, T. A., Gonzalez, A., Freeman, D. L., Lyman, G. H., and Wickstrom, E. (1988) Human promyelocytic leukemia HL-60 cell proliferation and c-myc protein expression are inhibited by an antisense pentadecadeoxynucleotide targeted against c-myc mRNA. *Proc. Natl. Acad. Sci. U. S. A. 85*, 1028−1032.

(4) Orr, M. S., Fornari, F. A., Randolph, J. K., and Gewirtz, D. A. (1995) Transcriptional down-regulation of c-myc expression in the MCF-7 breast tumor cell line by the topoisomerase II inhibitor, VM-26. *Biochim. Biophys Acta 1262*, 139−145.

(5) Schmitz-Drager, B. J., Schulz, W. A., Jurgens, B., Gerharz, C. D., van Roeyen, C. R., Bultel, H., Ebert, T., and Ackermann, R. (1997) c-myc in bladder cancer. Clinical findings and analysis of mechanism. *Urol. Res. 25 Suppl 1*, S45−S49.

(6) Mizutani, Y., Bonavida, B., Fukumoto, M., and Yoshida, O. (1995) Enhanced susceptibility of c-myc antisense oligonucleotide-treated human renal cell carcinoma cells to lysis by peripheral blood lymphocytes. *J. Immunother. Emphasis Tumor Immunol. 17*, 78−87.

(7) Rygaard, K., Vindelov, L. L., and Spang-Thomsen, M. (1993) Expression of myc family oncoproteins in small-cell lung-cancer cell lines and xenografts. *Int. J. Cancer 54*, 144−152.

(8) Hernandez, L., Hernandez, S., Bea, S., Pinyol, M., Ferrer, A., Bosch, F., Nadal, A., Fernandez, P. L., Palacin, A., Montserrat, E., and Campo, E. (1999) c-myc mRNA expression and genomic alterations in mantle cell lymphomas and other nodal non-Hodgkin's lymphomas. *Leukemia 13*, 2087−2093.

(9) Wickstrom, E., Bacon, T. A., and Wickstrom, E. L. (1992) Down-regulation of c-*MYC* antigen expression in lymphocytes of Eμ-c-myc transgenic mice treated with anti-c-myc DNA methylphosphonates. *Cancer Res. 52*, 6741−6745.

(10) Huang, Y., Snyder, R., Kligshteyn, M., and Wickstrom, E. (1995) Prevention of tumor formation in a mouse model of Burkitt's lymphoma by 6 weeks of treatment with anti-c-myc DNA phosphorothioate. *Molecular Medicine 1*, 647−658.

(11) Smith, J. B., and Wickstrom, E. (1998) Antisense c-myc and immunostimulatory oligonucleotide inhibition of tumorigenesis in a murine B-cell lymphoma transplant model. *J. Natl. Cancer Inst. 90*, 1146−1154.

(12) Gelmon, K. A., Batist, G., Chi, K., Sandor, K., Webb, M., D'Aloisio, S., Burge, C., Saltman, D., Goldie, J., and Miller, W. A dose escalation phase I study of c-MYC antisense in combination with cisplatin in the treatment of solid tumours and lymphomas. Presented at the AACR-NCI-EORTC International Conference on Molecular Targets and Cancer Therapeutics, Miami Beach, FL, Oct 29−Nov 2, 2001.

(13) Nair, S. K., and Burley, S. K. (2003) X-ray structures of Myc-Max and Mad-Max recognizing DNA. Molecular bases of regulation by proto-oncogenic transcription factors. *Cell 112*, 193−205.

(14) Perez-Roger, I., Kim, S. H., Griffiths, B., Sewing, A., and Land, H. (1999) Cyclins D1 and D2 mediate myc-induced proliferation via sequestration of p27(Kip1) and p21(Cip1). *Embo J. 18*, 5310−5320.

(15) Doisneau-Sixou, S. F., Sergio, C. M., Carroll, J. S., Hui, R., Musgrove, E. A., and Sutherland, R. L. (2003) Estrogen and antiestrogen regulation of cell cycle progression in breast cancer cells. *Endocr. Relat. Cancer 10*, 179−186.

(16) Dubik, D., and Shiu, R. P. (1992) Mechanism of estrogen activation of c-myc oncogene expression. *Oncogene 7*, 1587−1594.

(17) Watson, P. H., Pon, R. T., and Shiu, R. P. (1991) Inhibition of c-myc expression by phosphorothioate antisense oligonucleotide identifies a critical role for c-myc in the growth of human breast cancer. *Cancer Res. 51*, 3996−4000.

(18) Prall, O. W., Rogan, E. M., Musgrove, E. A., Watts, C. K., and Sutherland, R. L. (1998) c-Myc or cyclin D1 mimics estrogen effects on cyclin E-Cdk2 activation and cell cycle reentry. *Mol. Cell Biol. 18*, 4499−4508.

(19) Venditti, M., Iwasiow, B., Orr, F. W., and Shiu, R. P. (2002) C-myc gene expression alone is sufficient to confer resistance to antiestrogen in human breast cancer cells. *Int. J. Cancer 99*, 35−42.

(20) Carroll, J. S., Swarbrick, A., Musgrove, E. A., and Sutherland, R. L. (2002) Mechanisms of growth arrest by c-myc antisense oligonucleotides in MCF-7 breast cancer cells: implications for the antiproliferative effects of antiestrogens. *Cancer Res. 62*, 3126−3131.

(21) Rosenberg, R. D., Hunt, W. C., Williamson, M. R., Gilliland, F. D., Wiest, P. W., Kelsey, C. A., Key, C. R., and Linver, M. N. (1998) Effects of age, breast density, ethnicity, and estrogen replacement therapy on screening mammographic sensitivity and cancer stage at diagnosis: review of 183, 134 screening mammograms in Albuquerque, New Mexico. *Radiology 209*, 511−518.

(22) American Cancer Society (2004) *Cancer Facts and Figures*, American Cancer Society, Atlanta GA, http://www.cancer.org/downloads/STT/CAFF_finalPWSecured.pdf.

(23) Diekmann, F., Diekmann, S., Bollow, M., Hermann, K. G., Richter, K., Heinlein, P., Schneider, W., and Hamm, B. (2004) Evaluation of a wavelet-based computer-assisted detection system for identifying microcalcifications in digital full-field mammography. *Acta Radiol. 45*, 136−141.

(24) Fahy, B. N., Bold, R. J., Schneider, P. D., Khatri, V., and Goodnight, J. E., Jr. (2001) Cost-benefit analysis of biopsy methods for suspicious mammographic lesions; discussion 994−5. *Arch. Surg. 136*, 990−994.

(25) Pappo, I., Horne, T., Weissberg, D., Wasserman, I., and Orda, R. (2000) The Usefulness of MIBI Scanning to Detect Underlying Carcinoma in Women with Acute Mastitis. *Breast J. 6*, 126−129.

(26) Lumachi, F., Zucchetta, P., Marzola, M. C., Ferretti, G., Povolato, M., Paris, M. K., Brandes, A. A., and Bui, F. (2002) Positive predictive value of 99mTc sestamibi scintimammography in patients with nonpalpable, mammographically detected, suspicious, breast lesions. *Nucl. Med. Commun. 23*, 1073−1078.

(27) Ma, X. J., Salunga, R., Tuggle, J. T., Gaudet, J., Enright, E., McQuary, P., Payette, T., Pistone, M., Stecker, K., Zhang,

B. M., Zhou, Y. X., Varnholt, H., Smith, B., Gadd, M., Chatfield, E., Kessler, J., Baer, T. M., Erlander, M. G., and Sgroi, D. C. (2003) Gene expression profiles of human breast cancer progression. *Proc. Natl. Acad. Sci. U. S. A. 100*, 5974−5979.

(28) Martin, K. J., Kritzman, B. M., Price, L. M., Koh, B., Kwan, C. P., Zhang, X., Mackay, A., O'Hare, M. J., Kaelin, C. M., Mutter, G. L., Pardee, A. B., and Sager, R. (2000) Linking gene expression patterns to therapeutic groups in breast cancer. *Cancer Res. 60*, 2232−2238.

(29) Stalteri, M. A., and Mather, S. J. (2000) In-vitro studies on 99m-Tc-labeled HYNIC-conjugated oligonucleotides. *Nucl. Med. Commun. 21*, 374.

(30) Dewanjee, M. K., Ghafouripour, A. K., Kapadvanjwala, M., Dewanjee, S., Serafini, A. N., Lopez, D. M., and Sfakianakis, G. N. (1994) Noninvasive imaging of c-myc oncogene messenger RNA with indium-111-antisense probes in a mammary tumor-bearing mouse model. *J. Nucl. Med. 35*, 1054−1063.

(31) Roivainen, A., Tolvanen, T., Salomaki, S., Lendvai, G., Velikyan, I., Numminen, P., Valila, M., Sipila, H., Bergstrom, M., Harkonen, P., Lonnberg, H., and Langstrom, B. (2004) 68Ga-Labeled Oligonucleotides for In Vivo Imaging with PET. *J. Nucl. Med. 45*, 347−355.

(32) Summerton, J., and Weller, D. (1997) Morpholino antisense oligomers: design, preparation, and properties. *Antisense Nucleic Acid Drug Dev. 7*, 187−195.

(33) Liu, G., Zhang, S., He, J., Liu, N., Gupta, S., Rusckowski, M., and Hnatowich, D. J. (2002) The influence of chain length and base sequence on the pharmacokinetic behavior of 99mTc-morpholinos in mice. *Q. J. Nucl. Med. 46*, 233−243.

(34) Liu, G., He, J., Dou, S., Gupta, S., Vanderheyden, J. L., Rusckowski, M., and Hnatowich, D. J. (2004) Pretargeting in tumored mice with radiolabeled morpholino oligomer showing low kidney uptake. *Eur. J. Nucl. Med. Mol. Imaging 31*, 417−424.

(35) Zhang, Y. M., Liu, C. B., Liu, N., Ferro Flores, G., He, J., Rusckowski, M., and Hnatowich, D. J. (2003) Electrostatic binding with tat and other cationic peptides increases cell accumulation of 99mTc-antisense DNAs without entrapment. *Mol. Imaging Biol. 5*, 240−247.

(36) Egholm, M., Buchardt, O., Christensen, L., Behrens, C., Freier, S. M., Driver, D. A., Berg, R. H., Kim, S. K., Norden, B., and Nielsen, P. E. (1993) PNA hybridizes to complementary oligonucleotides obeying the Watson-Crick hydrogen-bonding rules. *Nature 365*, 566−568.

(37) Urtishak, K. A., Choob, M., Tian, X., Sternheim, N., Talbot, W. S., Wickstrom, E., and Farber, S. A. (2003) Targeted gene knockdown in zebrafish using negatively charged peptide nucleic acid mimics. *Dev. Dynam. 228*, 405−413.

(38) Good, L., and Nielsen, P. E. (1997) Progress in developing PNA as a gene-targeted drug. *Antisense Nucleic Acid Drug Dev. 7*, 431−437.

(39) Rao, P. S., Tian, X., Qin, W., Aruva, M. R., Sauter, E. R., Thakur, M. L., and Wickstrom, E. (2003) 99mTc-peptide-peptide nucleic acid probes for imaging oncogene mRNAs in tumours. *Nucl. Med. Commun. 24*, 857−863.

(40) Gray, G. D., Basu, S., and Wickstrom, E. (1997) Transformed and immortalized cellular uptake of oligodeoxynucleoside phosphorothioates, 3′-alkylamino oligodeoxynucleotides, 2′−O-methyl oligoribonucleotides, oligodeoxynucleoside methylphosphonates, and peptide nucleic acids. *Biochem. Pharmacol. 53*, 1465−1476.

(41) Soomets, U., Hallbrink, M., and Langel, U. (1999) Antisense properties of peptide nucleic acids. *Front Biosci. 4*, D782−D786.

(42) Basu, S., and Wickstrom, E. (1997) Synthesis and characterization of a peptide nucleic acid conjugated to a D-peptide analogue of insulin-like growth factor 1 for increased cellular uptake. *Bioconjugate Chem. 8*, 481−488.

(43) Tian, X., Aruva, M. R., Qin, W., Zhu, W., Duffy, K. T., Sauter, E. R., Thakur, M. L., and Wickstrom, E. (2004) External imaging of CCND1 cancer gene activity in experimental human breast cancer xenografts with Tc-99m-peptide-PNA-peptide chimeras. *J. Nucl. Med. 45*, 2070−2082.

(44) Boffa, L. C., Scarfi, S., Mariani, M. R., Damonte, G., Allfrey, V. G., Benatti, U., and Morris, P. L. (2000) Dihydrotestosterone as a selective cellular/nuclear localization vector for antigene peptide nucleic acid in prostatic carcinoma cells. *Cancer Res. 60*, 2258−2262.

(45) Tian, X., and Wickstrom, E. (2002) Continuous solid-phase synthesis and disulfide cyclization of peptide−PNA−peptide chimeras. *Organic Lett. 4*, 4013−4016.

(46) Pallela, V. R., Thakur, M. L., Chakder, S., and Rattan, S. (1999) 99mTc-labeled vasoactive intestinal peptide receptor agonist: functional studies. *J. Nucl. Med. 40*, 352−360.

(47) Bartucci, M., Morelli, C., Mauro, L., Ando, S., and Surmacz, E. (2001) Differential insulin-like growth factor I receptor signaling and function in estrogen receptor (ER)-positive MCF-7 and ER-negative MDA-MB-231 breast cancer cells. *Cancer Res. 61*, 6747−6754.

(48) Thakur, M. L., Marcus, C. S., Saeed, S., Pallela, V., Minami, C., Diggles, L., Le Pham, H., Ahdoot, R., and Kalinowski, E. A. (2000) 99mTc-labeled vasoactive intestinal peptide analogue for rapid localization of tumors in humans. *J. Nucl. Med. 41*, 107−110.

(49) Bièche, I., Laurendeau, I., Tozlu, S., Olivi, M., Vidaud, D., Lidereau, R., and Vidaud, M. (1999) Quantitation of MYC gene expression in sporadic breast tumors with a real-time reverse transcription-PCR assay. *Cancer Res. 59*, 2759−2765.

(50) Jain, R. K. (1998) The next frontier of molecular medicine: delivery of therapeutics. *Nat. Med. 4*, 655−657.

(51) Thakur, M. L., Pallela, V. R., Consigny, P. M., Rao, P. S., Vessileva-Belnikolovska, D., and Shi, R. (2000) Imaging vascular thrombosis with 99mTc-labeled fibrin alpha-chain peptide. *J. Nucl. Med. 41*, 161−168.

(52) Lipponen, P., Eskelinen, M., and Syrjanen, K. (1995) Expression of tumour-suppressor gene Rb, apoptosis-suppressing protein Bcl-2 and c-Myc have no independent prognostic value in renal adenocarcinoma. *Br. J. Cancer 71*, 863−867.

(53) de Jong, M., Rolleman, E. J., Bernard, B. F., Visser, T. J., Bakker, W. H., Breeman, W. A., and Krenning, E. P. (1996) Inhibition of renal uptake of indium-111-DTPA-octreotide in vivo. *J. Nucl. Med. 37*, 1388−1392.

BC0497923

Structure−Photodynamic Activity Relationships of Substituted Zinc Trisulfophthalocyanines

Nicole Cauchon, Hongjian Tian, Réjean Langlois, Carole La Madeleine, Stephane Martin, Hasrat Ali, Darel Hunting, and Johan E. van Lier*

Department of Nuclear Medicine and Radiobiology, Faculty of Medicine, Université de Sherbrooke, Sherbrooke, Québec, Canada J1H 5N4. Received June 30, 2004; Revised Manuscript Received October 20, 2004

To identify optimal features of metalated sulfophthalocyanine dyes for their use as photosensitizers in the photodynamic therapy of cancer, we synthesized a series of alkynyl-substituted trisulfonated phthalocyanines and compared their amphiphilic properties to a number of parameters related to their photodynamic potency. Varying the length of the substituted alkynyl side-chain modulates the hydrophobic/hydrophilic properties of the dyes providing a linear relationship between their *n*-octanol/water partition coefficients and retention times on reversed-phase HPLC. Aggregate formation of the dyes in aqueous solution increased with increasing hydrophobicity while monomer formation was favored by the addition of serum proteins or organic solvent. Trisulfonated zinc phthalocyanines bearing hexynyl and nonynyl substituents exhibited high cellular uptake with strong localization at the mitochondrial membranes, which coincided with effective photocytotoxicity toward EMT-6 murine mammary tumor cells. Further increase in the length of the alkynyl chains (dodecynyl, hexadecynyl) did not improve their phototoxicity, likely resulting from extensive aggregation of the dyes in aqueous medium and reduced cell uptake. Aggregation was evident from shifts in the electronic spectra and reduced capacity to generate singlet oxygen. When monomerized through the addition of Cremophor EL all sulfonated zinc phthalocyanines gave similar singlet oxygen yields. Accordingly, differences in the tendency of the dyes to aggregate do not appear to be a determining factor in their photodynamic potency. Our results confirm that the latter in particular relates to their amphiphilic properties, which facilitate cell uptake and intracellular localization at photosensitive sites such as the mitochondria. Combined, these factors play a significant role in the overall photodynamic potency of the dyes.

INTRODUCTION

Photodynamic therapy (PDT)[1] is an alternative treatment for cancer and several other medical conditions requiring a concerted action of a photosensitizer, oxygen, and light (*1*−*3*). Upon illumination with light of the appropriate wavelength (630−800 nm), the photosensitizer is excited to its triplet state and the excited photosensitizer interacts with its environment to produce highly reactive intermediates (for example, singlet oxygen, superoxide anion, and hydroxyl radical) that are cytotoxic and cause tumor regression either directly by cell inactivation (*4*, *5*) and/or indirectly by destruction of the tumor vascular microcirculation (*6*−*8*). PDT using Photofrin as a sensitizer has been approved for clinical treatment of many cancers worldwide, including cancer of the skin, mouth, esophagus, bladder, lung, breast, and some reproductive organs (*9*, *10*). Advantages of PDT over other conventional cancer therapies are that neither the photosensitizer nor the light used for its activation are toxic, allowing the treatment to target diseased tissue selectively while sparing surrounding healthy tissue.

The well-known limitations and drawbacks of Photofrin, i.e., chemical heterogeneity, relatively low absorption coefficient at the activation wavelength of 630 nm, and prolonged cutaneous photosensitivity, has led to an extensive search for new, well-defined sensitizers with highly effective photoactivity and less side effects (*11*). Many different classes of new sensitizers have been advanced for PDT and are under development at various stages of preclinical or clinical trials (*12*). Among the second-generation photosensitizers for PDT, phthalocyanines (Pc) have received particular attention due to the selective retention by tumor cells, lack of toxicity, and chemical and photochemical stability combined with a high molar absorption coefficient ($\epsilon > 10^5\ M^{-1}\ cm^{-1}$, 640−710 nm) in the clinically useful red part of the spectrum (*13*). Nonsubstituted Pc are extremely hydrophobic and insoluble in water. Sulfonation is a well documented method to render them suitable for use in biological systems. Sulfonated Pc are water soluble and have been shown to be effective photosensitizers to kill tumor cells in vitro and tumor regression in vivo. We have previously synthesized zinc, gallium, and aluminum Pc with various degrees of sulfonation by either condensation or sulfonation methods (*14*). Depending on the degree of sulfonation, Pc exhibit varying hydrophobic and hydrophilic

* To whom correspondence should be addressed. Tel: (819) 564-5409; Fax: (819) 564-5442. E-mail: johan.e.vanlier@usherbrooke.ca.

[1] Abbreviations: AlOHPcS4, aluminum tetrasulfophthalocyanine; CRM, Cremophor EL; DMF, dimethylformamide; FBS, fetal bovine serum; HBSS/HEPES, Hanks's Balanced Salt Solution/*N*-2-hydroxyethylpiperazine-*N*′-2-ethanesulfonic acid; HPPI, 3α-hydroperoxy-1,2,3,3α,8,8α-hexahydropyrrolo[2,3*β*]-indole-2-carboxylic acid; LD_{90} and LD_{50}, light dose required to inactivate 90% or 50% cells at a given drug dose; MTT, 3-(4,5-dimethylthiazol-2-yl)-2,5-diphenyltetrazolium bromide; PBS, phosphate-buffered saline; Pc, phthalocyanine; PDT, photodynamic therapy; t_R, retention time on C-18 reverse-phase HPLC.; $ZnPcS_2$, disulfonated ZnPc; $ZnPcS_3$, trisulfonated ZnPc; $ZnPcS_3C_2$, ethynyl-$ZnPcS_3$; $ZnPcS_3C_6$, hexynyl-$ZnPcS_3$; $ZnPcS_3C_9$, nonynyl-$ZnPcS_3$; $ZnPcS_3C_{12}$, dodecynyl-$ZnPcS_3$; $ZnPcS_3C_{16}$, hexadecynyl-$ZnPcS_3$.

10.1021/bc049848t CCC: $30.25 © 2005 American Chemical Society
Published on Web 12/24/2004

properties, affecting the tendency to aggregate, changing their ability to generate $^1O_2$ and resulting in very different photodynamic effects (*15*). Hydrophobic photosensitizers tend to aggregate in aqueous solution (*16*), decreasing their photodynamic activity while hydrophilic photosensitizers display decreased cell uptake (*17*), target less photosensitive sub cellular sites (*18*), and are rapidly cleared in vivo (*19*).

Many investigators have reported that photodynamic treatment induce lesions in mitochondria, lysosomes, golgi, membranes, and/or other organelles as well as essential biomolecules including DNA (*20*−*22*). Photosensitizers rarely reach the cell nucleus and accordingly this target is less important for photodynamic cytotoxicity. The cytoplasmic organelles constitute the more accessible targets for photosensitizers mainly owing to the permeability of cytoplasmic membrane. Mitochondria are the principal target for most photosensitizers and damage to this organelle quickly induces cell death by apoptosis (*9*). Deregulation or dysfunction of the mitochondria induces fast cell death due to respiratory failure. The Golgi apparatus is a specialized type of endoplasmic reticulum involved in the transport of macromolecules and degradation products. Damage to the Golgi disrupts protein synthesis/routing and excretion of breakdown products. The lysosomes are the excretory vesicles produced by the Golgi to eliminate undesirable compounds (exocytosis) and their rupture releases such materials together with harmful acidic hydrolases into the cytosol.

Cellular response to PDT-induced oxidative stress involves complex signal transduction pathways and alterations in gene expression leading either to repair of induced lesions, altered cell functions, or cell death (*23*). Even though specific damage to sub-cellular structures or functions has been demonstrated, it is difficult to show a clear causal relationship between intracellular damage and cell death (*24*). Furthermore, sensitivity to PDT differs a great deal among various cell types (*25*). Thus photodynamic activity depends largely on intracellular distribution patterns that in turn depend on both cell type and the nature of the photosensitizer. The relative contribution of these various factors to the overall photodynamic response remains to be elucidated.

Under in vitro conditions, amphiphilic photosensitizers are in general more photodynamically active than hydrophobic or hydrophilic molecules of the same class of compounds (*17*, *26*). It has also been suggested that favorable pharmacokinetics to ensure tumor selectivity and rapid systemic clearance is likewise related to the amphiphilic properties of the photosensitizer (*10*). Among the sulfophthalocyanine dyes, adjacently substituted, disulfonated compounds have the appropriate amphiphilic properties for optimal cell membrane penetration, resulting in high photodynamic activity both against tumor cells in culture and experimental animal tumors (*27*−*30*). However such derivatives are difficult to purify as single isomeric products. We have also demonstrated that addition of some hydrophobic groups onto the fourth benzyl ring of trisulfonated Pc can improve their amphiphilic properties resulting in an increase in cell uptake and in vitro photocytotoxicity (*31*, *32*). Woehrle and collaborators showed that introducing different lengths of alkyl chains to a series of positive-charged Pc tips the balance of the hydrophilic/lipophilic character of a Pc-based sensitizer (*33*). Pandey's studies on a series of purpurinimides containing alkyl substituents established that the overall lipophilicity did not affect singlet oxygen yields of the monomerized compound; however, the position of the alkyl groups was shown to play an important role in the in vivo efficacy of the photosensitizer (*34*).

Since the core of the Pc macro ring system is hydrophobic and peripherally attached sulfonate groups are hydrophilic, substituting different lipophilic alkyl chains onto a sulfonated Pc permits modulation of the amphiphilic properties of the dye. Using indole or pyrrole as a protecting group of the sulfonate substituent (*35*) in combination with the palladium-catalyzed cross-coupling reaction (*36*) allowed us to prepare a series of novel trisulfonated Pc substituted with different lengths of alkynyl carbon chains on the fourth, nonsulfonated benzyl ring (*37*). In this paper we compare their amphiphilic properties to tendencies to aggregate, cell uptake, intracellular distribution, and photocytotoxicity to arrive at structure−activity relationships.

EXPERIMENTAL PROCEDURES

Photosensitizers. The di- and trisulfonated zinc(II) Pc ($ZnPcS_{2a}$ and $ZnPcS_3$) were prepared via condensation of sulfonated precursors and purified by extensive C-18 reversed-phase HPLC fractionation (Waters Corp., Milford, MA; Column: RCM 8 × 10, Millipore, Milford, MA), using a linear gradient from 100% aqueous 5.0 mM phosphate buffer (pH 5) to 100% methanol over 30 min (1.5 mL/min) (*14*). A preliminary note on the syntheses of the substituted trisulfonated Pc ($ZnPcS_3C_{2-16}$) has previously been reported (*37*). Briefly, their preparation involves the synthesis of the indole-protected monoiodo $ZnPcS_3I$ (**3**) via the mixed condensation of 1-(3,4-dicyanophenylsulfonyl)indole (**1**) with 4-iodophthalonitrile (**2**) followed by facile purification over a silica gel column (Scheme 1). The protected monoiodo **3** was reacted with the different terminal alkynes under palladium/Cu(I)-catalyzed conditions to yield the series of protected $ZnPcS_3C_{2-16}$ (**4**−**8**) with different functionalized alkynyl substituents. After further purification over a silica gel column, the protected $ZnPcS_3C_{2-16}$ were hydrolyzed with lithium methoxide in methanol/THF to yield the pure alkynyl derivatives **9**−**13** in >85% yield.

2-Iodo-9,16,23-tris(1′-indolylsulfonyl)phthalocyanine Zinc(II) (3). 4-Iodophthalonitrile (**1**) (1 mmol), 1-(3,4-dicyanophenylsulfonyl)indole (**2**) (3 mmol), and zinc acetate (5 mmol) were ground together and heated at 200 °C for 2 h. The crude mixture was dissolved in $CHCl_3$ and purified by silica gel column chromatography eluted with 5% ethyl acetate in toluene to yield **3** as a dark blue solid in 20%. UV−vis ($CHCl_3$) λ_{max}/nm (log ϵ) 687.5 (5.26), 673.5 (5.26). ^1H NMR (DMSO-d_6) 9.2 (m), 8.8 (m), 8.4 (m), 8.22 (m), 8.18 (m), 7.9 (m), 7.4 (m), 7.2 (m), 6.7 (m).

General Procedure for the Coupling of 3 with Alkynes. Compound **3** (0.1 mmol) and alkyne (0.13 mmol) were dissolved under N_2 in anhyd THF (5 mL). To this were added $Pd(ph_3P)_2Cl_2$ (18 mg), CuI (18 mg), and triethylamine (9 mL), and the mixture was heated at reflux for 15−24 h. The products were purified by silica gel column chromatography and isolated in 85−90% yield.

2-Ethynyl-9,16,23-tris(1′-indolylsulfonyl) PcZn(II) (4): UV−vis ($CHCl_3$) λ_{max}/nm (log ϵ) 690 (5.26), 676 (5.26), 615 (4.65), 359 (4.90), MS (FAB) *m/z* calculated for $C_{61}H_{39}N_{11}O_6S_3Zn$ 1211.70, found, 1211.0.

2-(1′-Hexyne)-9,16,23-tris(1′-indolylsulfonyl) PcZn(II) (5): UV−vis ($CHCl_3$) λ_{max}/nm (log ϵ) 691 (5.28), 676 (5.26), 613 (4.59), 361 (4.89), MS (FAB) *m/z* calculated for $C_{62}H_{39}N_{11}O_6S_3Zn$ 1195.62, found, 1195.1.

2-(1′-Nonyne)-9,16,23-tris(1′-indolylsulfonyl) PcZn(II) (6): UV−vis ($CHCl_3$) λ_{max}/nm (log ϵ) 691 (5.28), 677

Scheme 1[a]

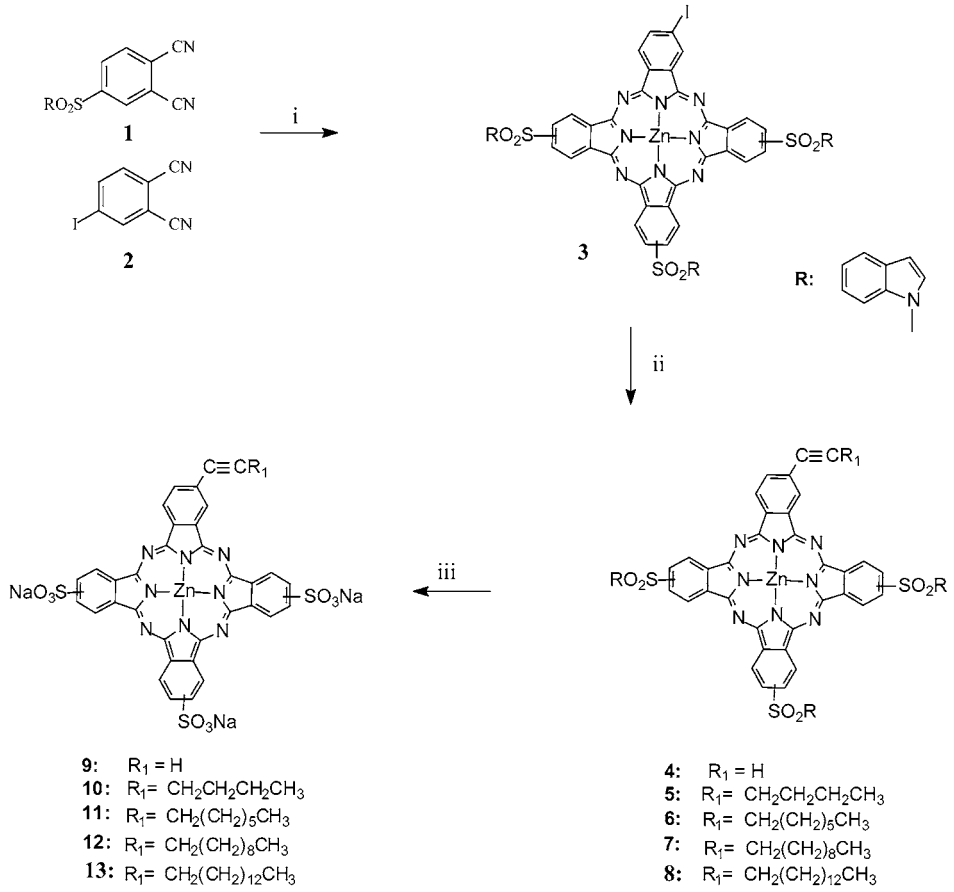

[a] Reagents and conditions: *i*: ZnAc·2H_2O, 200-220 °C, 30 min, 19%; *ii*: alkyne, $PdCl_2(Ph_3P)_2$, CuI, THF, Et_3N, rt, 15−24 H, 85∼95%; *iii*: LiOMe, MeOH, THF, reflux, 24 h, 80∼85%.

(5.26), 614 (4.60), 362 (4.88), MS (FAB) *m/z* calculated for $C_{65}H_{45}N_{11}O_6S_3Zn$ 1237.70, found, 1237.0.

2-(1′-Dodecyne)-9,16,23-tris(1′-indolylsulfonyl) PcZn(II) (7): UV−vis ($CHCl_3$) λ_{max}/nm (log ϵ) 692 (5.27), 675 (5.25), 613 (4.59), 362 (4.90), MS (FAB) *m/z* calculated for $C_{68}H_{51}N_{11}O_6S_3Zn$ 1279.78, found, 1278.9.

2-(1′-Hexadecyne)-9,16,23-tris(1′-indolylsulfonyl) PcZn(II) (8): UV−vis ($CHCl_3$) λ_{max}/nm (log ϵ) 692 (5.23), 676 (5.22), 614 (4.58), 362 (4.87), MS (FAB) *m/z* calculated for $C_{72}H_{59}N_{11}O_6S_3Zn$ 1335.89, found, 1234.9.

General Procedure for the Deprotection of Indolysulfonyl PcZn(II) 4−8. To a solution of lithium (80 mg) in MeOH (5 mL) was added **4**−**8** (50 mg) in THF (10 mL). The solution was refluxed for 24 h, the solvent was evaporated, and the crude mixture was purified by medium-pressure reversed-phase C-18 column chromatography using MeOH and phosphate buffer (5 mmol; pH 5).

2-Ethynyl-9,16,23-trisulfosodium PcZn(II) (9): UV−vis (MeOH) λ_{max}/nm (log ϵ) 671 (5.27), 607 (4.58), 344 (4.81), MS (Electron-spray) *m/z* calculated for $C_{34}H_{16}N_8O_9S_3Zn$ 842.11, found, 840.8 (M-1). ^{1}H NMR (DMSO-d_6) δ: 9.75 (m, 3H), 9.48 (m, 5H), 8.52 (m, 4H).

2-(1′-Hexyne)-9,16,23-trisulfosodium PcZn(II) (10): UV−vis (MeOH) λ_{max}/nm (log ϵ) 671 (5.20), 607 (4.48), 344 (4.79), MS Electron-spray) *m/z* calculated for $C_{38}H_{24}N_8O_9S_3Zn$ 898.22, found, 896.9 (M-1). ^{1}H NMR (DMSO-d_6) δ: 9.72 (m, 3H), 9.38 (m, 5H), 8.50 (m, 3H), 8.18 (m, 1H), 2.72 (t, 2H), 1.85 (m, 2H), 1.28 (m, 2H), 1.15 (t, 3H, CH_3).

2-(1′-Nonyne)-9,16,23-trisulfosodium PcZn(II) (11): UV−vis (MeOH) λ_{max}/nm (log ϵ) 671 (5.31), 607 (4.52), 345 (4.82), MS (Electron-spray) *m/z* calculated for $C_{41}H_{30}N_8O_9S_3Zn$ 940.30, found, 939.0 (M-1).

2-(1′-Dodecyne)-9,16,23-trisulfosodium PcZn(II) (12): UV−vis (MeOH) λ_{max}/nm (log ϵ) 671 (5.30), 607 (4.51), 345 (4.81), MS Electron-spray) *m/z* calculated for $C_{44}H_{36}N_8O_9S_3Zn$ 982.38, found, 981.0 (M-1). ^{1}H NMR (DMSO-d_6) δ: 9.75 (m, 3H), 9.45 (m, 5H), 8.55 (m, 3H), 8.20 (m, 1H), 2.78 (t, 2H), 1.2−1.8 (m, 12H), 1.08 (t, 3H, CH_3).

2-(1′-Hexadecyne)-9,16,23-trisulfosodium PcZn(II) (13): UV−vis (MeOH) λ_{max}/nm (log ϵ) 678 (5.14), 607 (4.36), 356 (4.68), MS Electron-spray) *m/z* calculated for $C_{48}H_{44}N_8O_9S_3Zn$ 1038.49, found, 1037.8 (M-1). ^{1}H NMR (DMSO-d_6) δ: 9.68 (m, 3H), 9.42 (m, 5H), 8.55 (m, 3H), 8.18 (m, 1H), 2.72 (t, 2H), 0.9−1.81 (m, 26H), 0.82 (t, 3H, CH_3).

Formulation of Photosensitizers. To prepare the phosphate-buffered saline (PBS) dye solutions, a few mg of Pc were dissolved in 1% PBS (pH 7.4) and sonicated for a few minutes. The solution was filtered on Millex-GV 0.22 μm (Millipore, Ont.) under sterile condition. The final concentration of the dyes was determined by UV−vis spectroscopy after 50-fold dilution in methanol or dimethylformamide (DMF).

Lipophilic Properties of the Dyes. The hydrophilic and hydrophobic properties of the various Pc were determined by their retention time (t_R) on C-18 reversed-phase HPLC and by their partition coefficient (P) between *n*-octanol and water.

(a) Retention Time. Analytical HPLC was conducted on a Waters system composed of a model 600 pump, 2487 UV−visible detector, helium degasser, model 600 control-

ler, and a Rheodyne injector. The HPLC column consisted of a Radial-Pak cartridge (10 × 0.8 cm) filled with 4 μm Nova Pak C18 reversed-phase packing (Waters) and operated with a 1−30% linear gradient of methanol in aqueous 10.0 mM sodium phosphate buffer (pH 5.0) over a period of 30 min followed by isocratic elution with 100% methanol for 5 min, at 1.0 mL min^{-1}. Eluted Pc were detected by the absorbency of the monomeric dyes at 670−700 nm and t_R were calculated as the weighted average of the t_R of the regional isomers.

(b) Partition Coefficient. To 2 mL of the various sulfonated ZnPc solutions (50 μM) in PBS (pH 7.4) was added 2 mL of *n*-octanol. The mixture was vortexed for 2 min and then centrifuged 10 min (900 g) at room temperature to separate the phases. The concentrations of Pc in both phases was determined spectrophotometrically (U-2000, Hitachi) after diluting a sample 50-fold in DMF and measuring the absorbency at 340−360 nm (ϵ = 80 000 M^{-1} cm^{-1}). The Pc concentration found in *n*-octanol was then divided by that found in PBS to give the partition coefficient (*P*).

Spectral Properties. The stock $ZnPcS_3C_{2-16}$ and $ZnPcS_{3/2a}$ solutions in PBS were diluted to 5 μM in different media (methanol, DMF, PBS, 1% and 55% FBS in Waymouth, 1% CRM in PBS) and incubated for different time intervals (0, 1, and 24 h). The electronic spectra were recorded (U-2000, Hitachi, Japan) and evaluated for the degree of aggregation by calculating the absorbency of the monomer at about 675 nm and the aggregate about 635 nm from the deconvoluted spectra. The dye concentrations can be measured independently from their aggregation state by their absorbency at 340−360 nm (ϵ = 80 000 $M^{-1}cm^{-1}$).

L-Tryptophan Photooxidation (*38*). A solution of 1 mL containing ZnPcS (50 μM) and l-tryptophan (5 mM) in PBS with and without 1% CRM was irradiated in a glass test tube (16 × 100 mm). The light source consisted of a high-intensity xenon short arc 300 W lamp model LX300F (ILC Technology, Sunnyvale, CA). Light was fed through a liquid guide fiber optic (model 77556, Oriel Corp. Stratford, CT) and two filters LS-700 and LL-600 (Corion, Holliston, MA), thus transmitting light between 600 and 700 nm at a fluence rate of 150 mW cm^{-2} (measured with a Power-Energy meter model 365 with a sensor model 38-0101, Scientech, Boulder, CO). The solution was kept at 4 °C and bubbled with air to ensure O_2 saturation. After 2 and 4 min of illumination, 80 μL samples were collected and analyzed by HPLC to quantify the characteristic hydroperoxide products 3α-hydroperoxy-1,2,3,3α,8,8α-hexahydropyrrolo[2,3β]indole-2-carboxylic acid (HPPI isomers) (t_R HPPI = 13.5 and 18.0 min, t_R tryptophan = 30.0 min) derived from $^1O_2$ oxidation of tryptophan. The relative HPPI yield for each photosensitizer was measured from the HPPI chromatogram peak areas, taking the area produced by $AlOHPcS_4$ as 100%. HPLC analysis was done on a Radial Pak cartridge (10 × 0.8 cm) filled with 4 μm Nova Pak C_{18} reversed-phase packing eluted at 1.0 mL/min with a linear gradient of 0.1% trifluoroacetic acid (TFA) in water and methanol (0.1% TFA) over 30 min from (1 to 30% methanol). The UV−vis detector was set at 215 nm.

Cell Cultures. The cell line used was the EMT-6 murine mammary tumor line, maintained in Waymouth medium culture (Gibco, Burlington, Canada) supplemented with 15% fetal bovine serum (FBS), 1% glutamine, and 1% pen−strep (Gibco). This corresponds to a complete medium.

Cell Uptake of Dyes. The EMT-6 cells (1.5 × 10^5 cells per well) in 1 mL Waymouth's growth medium were incubated in 24 multiwell plates (Falcon) overnight at 37 °C under 5% CO_2. The medium was removed and the monolayer rinsed twice with 1% PBS and then overlaid with 500 μL of the dye solution (10 μM) in medium culture supplemented with 1% FBS. For the longer incubation times of 24 and 48 h, the medium was supplemented with 4% of FBS to reduce cell death. After the incubation, the dye solution was removed and the cells were washed twice with 1% PBS. The cells were lysed with 500 μL of 0.1 N NaOH. An aliquot (50 μL) was removed to determine cellular protein according to the Bradford method (Bio-Rad Protein Assay) (*39*). DMF (450 μL) and 1% PBS (100 μL) were added to the remaining cell lysate, the mixture was centrifuged for 30 min at 4 °C, 3500 rpm, and dye concentration in the clear supernatant was assayed by fluorescence spectroscopy (F-2000, Hitachi) (λ_{ex} = 608 nm, 5 nm band-pass, λ_{em} = 687 nm, 5 nm band-pass). Standard curves were made using cell lysates treated as above with known amounts of the appropriate Pc solution added. The results were expressed as nmole of Pc per mg of cellular protein.

Intracellular Distribution. The cell suspension (1 × 10^5 cells/mL) was plated onto glass cover slips and incubated for 18−24 h at 37 °C, 5% CO_2, to allow for cell adhesion. The medium was removed, and the cells were rinsed twice with PBS and then overlaid with 1 mL of the dye solution (10 μM) in medium culture supplemented with 1% FBS. After 3 h at 37 °C, the dye solution was removed and the cells were washed twice with PBS and twice more with low phosphate buffer (HBSS/HEPES). The cells were incubated at 37 °C under 5% CO_2 with different tracker dyes (Invitrogen Inc., Ontario, Canada) including SYTO 13 (10 nM, 1 h), Myto-Tracker green (150 nM, 45 min), Lyso-Tracker Green (200 nM, 1 h), TMA-DPH (5 μM, 1 h), and NBDC6 Ceramide (5 μM, 1 h). Only the latter dye needs to be rinsed three times with the same buffer where after new medium is added, and the cells are incubated for another 30 min. After the last incubation, all samples were washed twice with PBS and mounted for microscopic observations. Cells were examined with a scanning confocal microscope (NORAN Instruments Inc, Middleton, WI) coupled to an inverted microscope with a 100× oil immersion objective (Nikon). Specimens were excited by krypton/argon laser at 488 or 568 nm and emitted fluorescence was measured using barrier filters (525/25 nm band-pass or 590 nm long-pass, respectively). Optical sections were collected at 0.25-μm intervals with 10 μm pinhole aperture (minimal opening in order to yield a maximal confocal component). Digitized images of 512 × 480 pixels were obtained with 256 times line averaging and enhanced with Intervision software (NORAN Instruments Inc) on a Silicon Graphics O2-workstation (Mountain View, CA).

Cell Photoinactivation. Cell cultures were trypsinated to give a 1.5 × 10^5 cells/mL suspension of which 100 μL per well were plated in 96 multiwell plates and incubated overnight at 37 °C under 5% CO_2. One column did not receive cells to serve as a blank. Attached cells were rinsed twice with PBS and incubated with 50 μL of dye solution (1 μM) in Waymouth 1% FBS for 1 or 24 h. One control column was filled with dye-free Waymouth 1% FBS. The cells were then rinsed twice with PBS, refed with 100 μL of Waymouth 15% FBS, and exposed for varying time intervals to red light (10 mW cm^{-2} at 660−700 nm). Plates were incubated overnight at 37 °C under 5% CO_2. Cell survival was measured by a colorimetric method, using the tetrazolium salt MTT (3-(4,5-dimethylthiazol-2-yl)-2,5-diphenyltetrazolium bromide) (Sigma).

Table 1. *n*-Octanol/Water Partition Coefficients (*P*), Reversed-phase HPLC Retention Times (t_R), Tryptophan Photooxidation Yields (HPPI), and Monomer Concentration of PcS in Various Solvents

			HPPI yield (%)[c]		monomer formation (%)[d]				
sensitizer	P ($P \times 10^{-3}$)[a]	t_R (min)[b]	PBS	CRM	PBS	CRM	methanol	1% FBS	55% FBS
$AlOHPcS_4$	n.a.[e]	8.6	0.97	1.00	40.4	66.8	n.a	n.a	n.a
$ZnPcS_{2a}$	5.6 ± 0.9	25.5	0.18	1.16	9.6	62.4	58.8	16.0	51.4
$ZnPcS_3$	1.33 ± 0.5	22.4	0.29	1.14	10.4	83.4	95.4	12.6	23.4
$ZnPcS_3C_2$ (**9**)	3.5 ± 0.5	23.4	0.09	1.15	7.2	59.8	57.0	9.0	16.8
$ZnPcS_3C_6$ (**10**)	26.9 ± 6.0	27.2	0.05	1.15	4.2	81.0	68.0	6.6	18.8
$ZnPcS_3C_9$ (**11**)	34.2 ± 4.0	28.8	0.03	1.25	2.4	99.6	46.2	5.0	15.2
$ZnPcS_3C_{12}$ (**12**)	38.7 ± 5.0	29.9	n.d.[e]	1.26	1.0	75.8	60.2	8.8	15.2
$ZnPcS_3C_{16}$ (**13**)	43.0 ± 7.0	31.3	n.d.	1.11	3.0	88.0	52.8	4.6	6.0

[a] *P*: *n*-Octanol/water partition coefficient. [b] t_R: HPLC retention times of PcS (in minutes, weighted average of regional isomers) on a C-18 reversed-phase column. [c] The relative amount of hydroperoxide (HPPI) formed from the photooxidation of l-tryptophan using different PcS in PBS (with and without 1% CRM) is expressed relative to that obtained with a standard ($AlOHPcS_4$). The quantum yield for singlet oxygen production of $AlOHPcS_4$ is 0.4. [d] The monomer concentration was estimated from its molar absorbance at 675 nm after deconvolution analysis and expressed as % of total PcS (5 μM). [e] n.d.: No detectable HPPI formation. n.a.: not applicable.

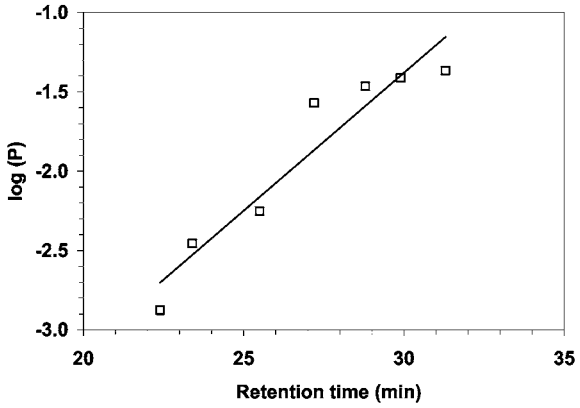

Figure 1. *n*-Octanol/water partition coefficient (log *P*) vs reversed-phase HPLC retention time (t_R).

Eight-fold replicates were run and experiments were repeated at least three times.

MTT Assay. This assay was adapted from the method described by Tada et al. (*40*). A stock solution of MTT at 0.5% in PBS was prepared and kept at 4 °C in the dark. The solution was diluted 5-fold in Waymouth 15% FBS, and 50 μL was added in each well. After 4 h incubation (37 °C, 5% CO_2), 100 μL sodium dodecyl sulfate (10% in 0.01 N HCl) was added to the wells to stop MTT reduction and to dissolve the blue formazan crystals produced by mitochondrial hydrogenases in living cells. After 24 h incubation, the plates were read on a microplate reader (Molecular Devices, Thermomax) for their optical densities at 570 nm. The survival curves were plotted as a function of light dose and LD_{90} values were calculated.

RESULTS

Lipophilic Properties of the Dyes. The retention times (t_R) of the substituted $ZnPcS_3C_n$ on reversed-phase HPLC and their partition coefficients (*P*) between *n*-octanol and water are summarized in Table 1. A plot of log *P* versus the retention time on HPLC shows a linear correlation (Figure 1). t_R values of the $ZnPcS_3C_n$ increase with increasing "*n*", i.e., the length of the alkynyl side chain, reflecting their increased lipophilicity. Addition of a six-carbon chain to the $ZnPcS_3$ to give $ZnPcS_3C_6$ (**10**) increases the t_R from 22.4 to 27.2 min, which is similar to the t_R of the adjacent substituted disulfonated $ZnPcS_{2a}$ (25.5 min), suggesting that their amphiphilic characters are comparable. The partition coefficients indicate however that the $ZnPcS_3C_6$ (**10**) is more lipophilic than the $ZnPcS_{2a}$.

Spectral Properties. The spectra of all dyes in PBS show a strong absorption peak at 460 nm, a characteristic peak of the monomer at 675 nm, and a characteristic peak for the aggregated dye at 630 nm (Figure 2). Aggregation of the monomers results in a blue shift of the Q-band, from 675 to 630 nm while the intensity of the absorption band at 460 nm remains constant (*15*, *41*−*43*). In Waymouth 1% FBS the intensity of the aggregate peak at 630 nm is decreased while the intensity of monomeric Q-band at 675 nm is increased. Augmenting the FBS concentration to 55% further increases the absorption peak at 675 nm. This suggests that binding of the Pc to FBS proteins facilitates the formation of monomers. In methanol and DMF the monomeric peak at 675 nm is prominent for most of the $ZnPcS_3$ derivatives. Addition of an emulsifier such as Cremophor EL (1%) to an aqueous solution of the dye likewise results in monomerization of the aggregates. Examples of the spectral shifts in different media are presented in Figure 2a−d.

To estimate the concentration of monomeric or aggregated Pc in different media, deconvolution spectra of the overlapping absorption peaks were generated. To this end, the spectra were analyzed by a Lorentzian non linear curve fit (*44*). Table 1 summarizes the monomer concentration (μM) of the various sulfonated ZnPc (5 μM) measured in five different media after an equilibrium period of 24 h. In all media a linear relationship between retention time (t_R) and the monomer concentration is evident with the highest percentage of monomers occurring for the hydrophilic $ZnPcS_3$ lacking the hydrocarbon side chain. Monomerization is minimal in PBS. The addition of 1% FBS has little effect, while 55% FBS results in a balance between the concentration of monomer and aggregate except for $ZnPcS_3C_{16}$ (**13**), which is not affected. In contrast the monomer concentration of $ZnPcS_{2a}$ increases by 5-fold upon addition of 55% FBS, approaching the monomerization level obtained in methanol. In methanol, the monomer concentration of all sulfonated ZnPc derivatives is higher than 2.3 μM, with the nonsubstituted $ZnPcS_3$ approaching near 100% monomerization.

L-Tryptophan Photooxidation. Upon excitation, phthalocyanine monomers generate $^1O_2$, which in turn can photooxidize lipids and amino acids such as L-tryptophan. L-Tryptophan photooxidation yields characteristic hydroperoxide isomers (HPPI) that can be quantified using HPLC. Singlet oxygen quantum yields ($\Phi\ ^1O_2$) can be established by comparison of the HPPI yields of the ZnPc with $AlOHPcS_4$ ($\Phi\ ^1O_2 = 0.43$) (*45*). Table 1 shows the HPPI hydroperoxide yields for the various

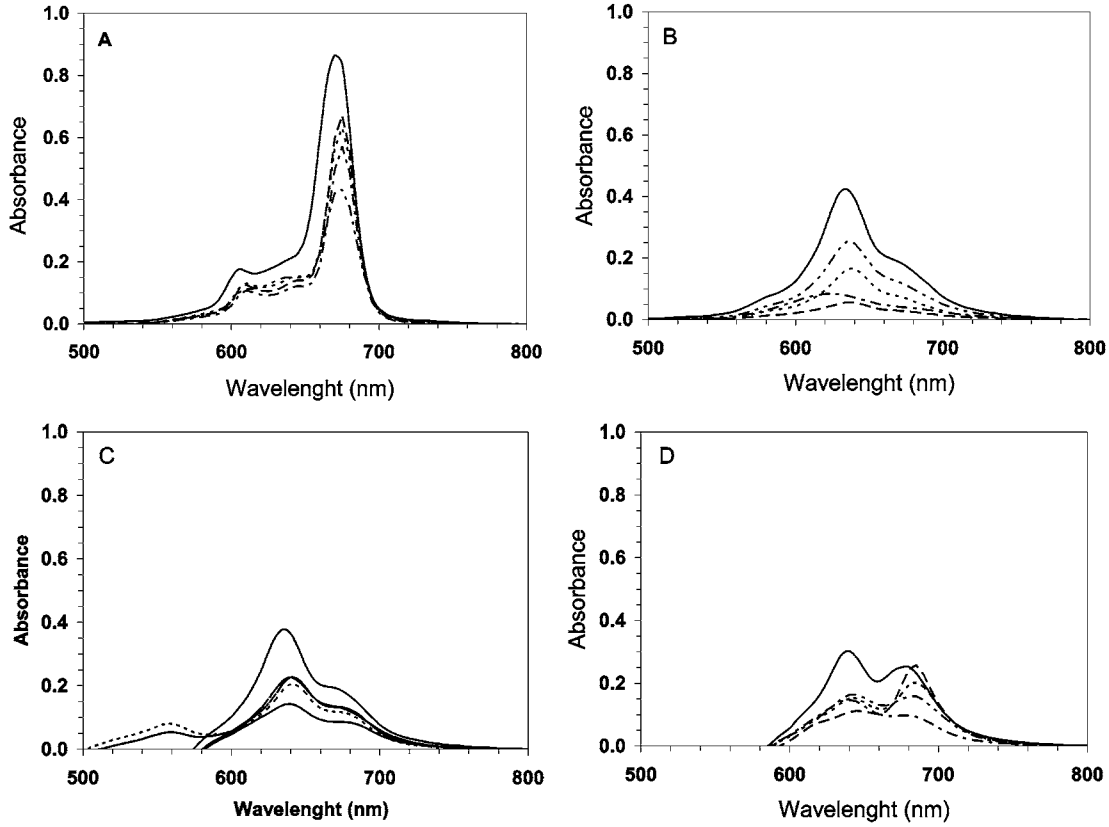

Figure 2. Absorption spectra of $ZnPcS_3$ (−), $ZnPcS_3C_2$ (− · · −), $ZnPcS_3C_6$ (· · · ·), $ZnPcS_3C_9$ (− − −) and $ZnPcS_3C_{16}$ (− · − ·) in different media. A: methanol, B: PBS, C: Waymouth's +1% FBS, D: Waymouth's +55% FBS.

ZnPcS derivatives together with their monomer concentrations. In PBS the photooxidation of l-tryptophan is greatly decreased when $ZnPcS_3$ is substituted with lipophilic chains to give $ZnPcS_3C_n$. This is in agreement with their absorption spectra that indicate that the $ZnPcS_3C_n$ are highly aggregated in this medium. However, addition of 1% CRM results in >60% monomerization revealing that all $ZnPcS_3C_n$ have similar capacities to generate $^1O_2$, which are higher than that of the reference dye AlO-$HPcS_4$.

Cell Uptake. Dye uptake by the EMT-6 cells as a function of incubation time is presented in Figure 3. The concentrations in nmole Pc per mg cell protein after 1 and 24 h incubation with 10 μM ZnPcS are shown together with cell survival after PDT with 1 μM ZnPcS as a function of the light dose required for 50% and 90% cell kill (LD_{50} and LD_{90}). After 1 h of incubation, $ZnPcS_3C_9$ (**11**) shows the highest uptake among the various $ZnPcS_3C_n$. Prolonged incubation of 24 h results in further increase of the dye concentration by about an order of magnitude. $ZnPcS_3$ substituted with longer aliphatic side chains ($n > 9$) are taken up by the EMT-6 cells to a lesser extent.

Intracellular Distribution. Figure 4a−e shows the intracellular localization of the ZnPcS derivatives (10 μM) in EMT-6 cells after 3 h incubation, together with the localization of different tracker dyes. The presence of the ZnPcS is evident from their red fluorescence (Figure 4, center images). The different tracker dyes are detected by their intense green fluorescence (left images), while colocalization with the ZnPcS results in a yellow fluorescence (right images). The ZnPcS are mainly localized in the cytoplasm: Mitochondria (Figure 4a), Golgi (Figure 4b), and lysosomes (Figure 4c), while almost excluded from the cell nucleus (Figure 4d). The sensitizers mostly cross the cytoplasmic membrane by passive diffusion; however, colocalization with the tracker dyes in Golgi and lysosomes indicates that part of the transport involves endocytosis. The latter is confirmed by the detection of ZnPcS as a punctuate pattern colocalized with membrane tracker dye (Figure 4e). The parent $ZnPcS_3$ and its analogue substituted with a short C2 chain exhibit a similar distribution pattern while substitution with the longer C12 and C16 chains reduces uptake in the cytoplasmic organelles. The most amphiphilic $ZnPcS_{2a}$, $ZnPcS_3C_6$ (**10**) and $ZnPcS_3C_9$ (**11**), show the highest accumulation in the mitochondria (Figure 4).

Photocytotoxicity. No dark toxicity toward EMT-6 cells was observed with any of the dyes under study up to 100 μM over a 24 h incubation period in Waymouth 1% FBS. LD_{50} and LD_{90} after 1 h and 24 h incubation with the dyes as a function of light dose (J cm^{-2}) are summarized in Table 2 and were derived from the corresponding survival curves (not shown). To directly compare cell uptake with photocytotoxicity of the $ZnPcS_3C_n$ series, the LD_{50}, LD_{90}, and cell uptake values vs retention time are shown on the same plots (Figure 3). The most photoactive dye is the $ZnPcS_{2a}$ followed by $ZnPcS_3C_6$ (**10**) and $ZnPcS_3C_9$ (**11**). The latter exhibit substantial higher photocytotoxicity than the parent $ZnPcS_3$ or the $ZnPcS_3C_n$ bearing the shorter ($n = 2$) or longer ($n = 16$) alkynyl side chain.

DISCUSSION

In this study we compare the hydrophilic/lipophilic properties of a series of structurally related sulfonated Pc dyes with a number of parameters that impact on their photodynamic potential. The lipophilic properties of the various $ZnPcS_3C_n$ were determined by two methods, *n*-octanol/water partition coefficient (*P*) and reversed-phase HPLC retention time (t_R). The first shows the

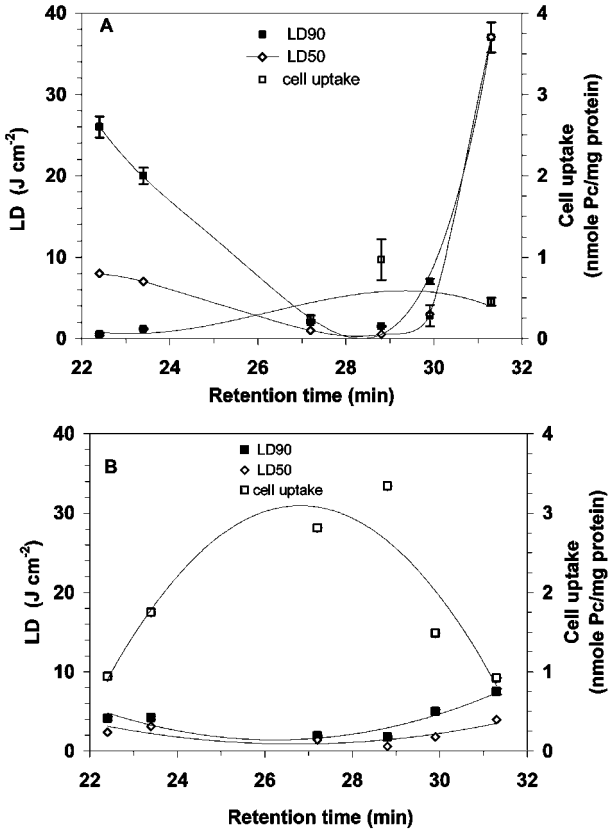

Figure 3. Comparison of EMT-6 cell phototoxicity (LD_{90} and LD_{50} in J cm^{-2}) and cell uptake (in nmol Pc/mg protein) of a series of ZnPcS derivatives as a function of their HPLC retention times, after (A): 1 h and (B): 24 h incubation periods.

preference of the dyes for organic solvent (*n*-octanol) and the second determines the strength of hydrophobic interactions. Both methods give a measure of the lipophilic properties of the dyes and the relationship between these two parameters was shown to be linear (Figure 1). Longer t_R correlate with a higher partition coefficient (log *P*) reflecting stronger lipophilic properties of a given dye.

Singlet oxygen ($^1O_2$) yields have shown to be inversely proportional to the extent of aggregation of a sensitizer (*15*, *43*). Tendency to aggregate is largely modulated by the ring substituents and the nature of axial ligands on the central metal ion. Monomeric Pc molecules with the identical central metal ion and varying degrees of sulfonation retain the same photochemical activity. Pc aggregation is easily detected by a 30−50 nm blue-shift of the Q-band around 675 nm to yield a broad and less absorption peak around 630 nm in the UV−vis absorption spectrum (*15*). Upon excitation with light, aggregated photosensitizers dissipate their energy through internal conversion to the ground-state rather than triplet formation with subsequent singlet oxygen production (*16*). Hydroperoxide (HPPI) formation from L-tryptophan by our ZnPcS in PBS increased proportionally with the monomer concentration (Table 1). The more lipophilic compounds with longer HPLC retention times aggregated more readily in aqueous solution, thus reducing their photochemical activities. When the Pc derivatives were solubilized in 1% Cremophor EL, HPPI formation of all $ZnPcS_3C_n$ derivatives surpassed that of the reference $AlOHPcS_4$ (Table 1). Margaron et al. reported similar findings using a series of ZnPc, where the most lipophilic compound, a tetraiodinated ZnPc entered the cells to a lesser extent due to low affinity for the plasma membrane (*26*).

It is generally believed that amphiphilic properties of photosensitizers play a significant role in their efficiency in photodynamic therapy (*46*). We previously reported that increasing the number of sulfonated groups on a metallo Pc led to a decrease in the photocytotoxicity under both in vitro and in vivo conditions, which coincided with decreased cellular uptake (*47*, *48*). The disulfonated dye bearing two sulfonated groups on adjacent benzyl rings was found to be the most photoactive derivative. On the other hand, it was reported that amphiphilic dyes interact with the lipid portion of plasma membranes (*49*), thereby facilitating their transport into the cell (*27*). It has also been reported that the same amphiphilic properties allows for more efficient binding to low density lipoprotein (LDL), which has been implicated in the transport of porphyrin-based sensitizers to tumor tissue (17). Amphiphilic properties of sulfonated Pc strongly correlate with their cell uptake and photocytotoxic potency (*26*). Our current data confirm that adding a lipophilic hydrocarbon side chain to $ZnPcS_3$ improves cell uptake (Table 2). However, adding longer chain lengths, e.g., $n > 9$ for $ZnPcS_3C_n$, results in a decrease in cell uptake providing a parabolic relationship between cell uptake vs retention time, inverse to that observed for phototoxicity vs retention time (Figure 3). This is particularly evident after a 24 h incubation period (Figure 3B). Comparing the LD_{90} of the $ZnPcS_3C_n$ with their relative cell uptake values, both after a 1-h and 24-h incubation periods, reveals a linear regression with higher cell uptake capacity correlating to lower photocytotoxicity (Figure 5). This phenomenon is particularly evident after the shorter 1-h incubation period. This confirms that variations in cellular phototoxicity between the dyes cannot simply be explained by differences in cell uptake. Instead, our data strongly suggest that variations in cell uptake rates and intracellular distribution pattern are responsible for differences in photoactivity.

On such account we examined possible correlations between amphiphilicity and tendencies to aggregate, which in turn could impact both on cell uptake kinetics and capacity to produce singlet oxygen as well as intra-

Table 2. Phototoxicity and EMT-6 Cell Uptake of a Series of ZnPcS Derivatives

	1 h			24 h		
sensitizer	cell uptake[a]	LD_{50}[b]	LD_{90}[b]	cell uptake[a]	LD_{50}[b]	LD_{90}[b]
$ZnPcS_{2a}$	0.16± 0.04	0.5	1.0	1.75 ± 0.06	0.2	0.6
$ZnPcS_3$	0.05 ± 0.01	8.0	26.0	0.94± 0.02	2.4	4.1
$ZnPcS_3C_2$ (**9**)	0.12 ± 0.01	7.0	20.0	1.75 ± 0.15	3.1	4.2
$ZnPcS_3C_6$ (**10**)	0.24 ± 0.03	1.0	2.0	2.81 ± 0.07	1.4	1.9
$ZnPcS_3C_9$ (**11**)	0.97 ± 0.25	0.5	1.5	3.34 ± 0.10	0.6	1.8
$ZnPcS_3C_{12}$ (**12**)	0.28 ± 0.13	3.0	7.0	1.49 ± 0.10	1.8	5.0
$ZnPcS_3C_{16}$ (**13**)	0.45 ± 0.05	>37.0	>37.0	0.92 ± 0.05	4.0	7.5

[a] EMT-6 cells were incubated with ZnPcS (10 μM) for 1 h or 24 h and analyzed for dye content as described under materials and methods. Values are in nmole Pc per mg of cell protein (±SEM). [b] The LD_{50} or LD_{90} is the light dose (J cm^{-1}) required to induce cell survival by 50% or 90% after incubating EMT-6 cells with 1 μM dye for 1 h or 24 h.

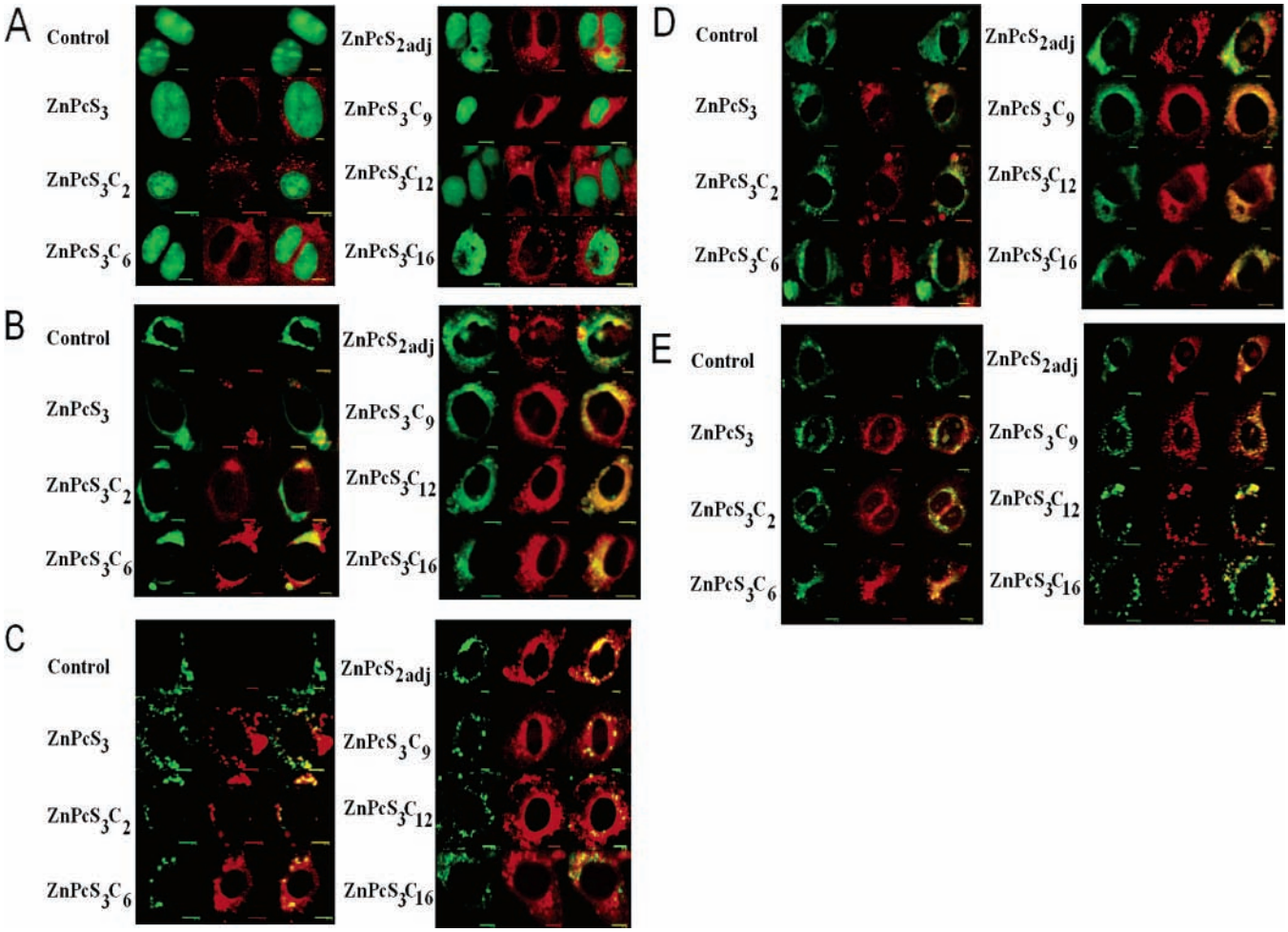

Figure 4. Comparative intracellular localization of ZnPcS derivatives (10 μM) in EMT-6 cells after incubation for 3 h (center images) with various tracker dyes (left images) and superimposed images (right images). A: nucleus (syto 13), B: mitochondria (mytotracker green), C: lysosomes (lyso-tracker green), D: golgi (NBD-6 Ceramide), and E: endocytose (TMA-DPH).

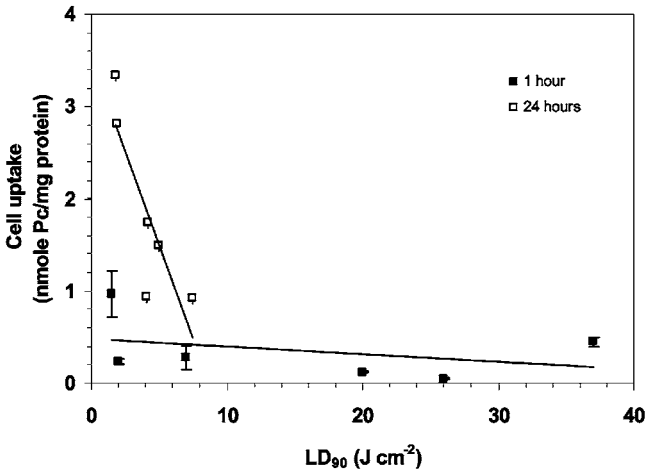

Figure 5. Comparison of EMT-6 cell uptake and phototoxicity (LD_{90} and LD_{50}) of a series of ZnPcS derivatives after 1 h (■) and 24 h (□) incubation times.

cellular localization pattern. Increasing hydrophobicity of $ZnPcS_3$ by the addition of lipophilic side chains affects the tendencies to aggregate in a milieu-dependent manner. In PBS or culture medium, with the addition of 1% FBS protein, aggregation remains high and similar for all derivatives tested (Table 1). These data show that the most hydrophilic parent $ZnPcS_3$ is in fact the least aggregated. Adding 55% protein to the medium breaks up the stacked ZnPcS aggregates resulting in doubling of the monomer concentration to ~20%. Only the $ZnPcS_3C_{16}$ is less affected by the added protein and its monomer concentration remains low (6%). In contrast $ZnPcS_{2a}$ interacts strongly with protein resulting in a 5-fold increase of the monomer concentration (>50%). In methanol monomerization is high, i.e., above 50% for most dyes tested. Of the five media the aqueous buffer fortified with 55% FBS most closely mimics the intracellular environment where the dyes localize, suggesting that a similar monomerization process occurs at the cellular level. This implies that amphiphilicity of the dye plays an important role in reaching optimal monomer/aggregated ratios at the target site, contributing to the desired phototoxic effects.

Longer side chains facilitate aggregation of the dyes resulting in loss of their capacity to generate singlet oxygen, a phenomena that is confirmed by their diminished capacity to photooxidize L-tryptophan to its characteristic HPPI hydroperoxide products (Table 1). Steric hindrance may also contribute to diminished cell uptake and loss of phototoxicity. Rosenthal et al. attributed the absence of significant uptake of the lipophilic tetraneopentoxy ZnPc to steric hindrance of the bulky neopentoxy groups (*50*). We previously demonstrated that adding long axial hydrocarbon chains to silicon naphthalocyanine increased their hydrophobicity, but that increased steric hindrance reduced cellular uptake resulting in reduced cellular phototoxicity (*51*).

However, differences between the intracellular localization patterns of the dyes may yet play the most important role in exerting their photodynamic action. The high reactivity of the cytotoxic singlet oxygen produced upon photoexcitation of the dyes limits their action range such that most of the photodamage occurs at the site where the dyes localize (*24*). The importance of intracellular localization relates to the many cytoplasmic targets, the extent of the damage generated, and the capacity of the cell to repair these injuries. The nucleus's DNA is prone to damage and as such is the first target to consider in cell death. However, access to the nucleus is limited due to the selectivity of the nuclear membrane. Our phthalocyanines, as well as other photosensitizers, tend to accumulate on the surface of the nuclear membrane without traversing this barrier (Figure 4A). Even though the nucleus is not directly affected by our phthalocyanines, its role in cell death after PDT is evident since damage at other intracellular sites initiates a cascade of biochemical reactions that affect the nucleus (*20*).

Our $ZnPcS_3C_n$ localize mainly at the mitochondria and Golgi apparatus (Figure 4B,C). There are, however, significant differences between the dye preparations with the most amphiphilic $ZnPcS_3C_6$ and -C_9 giving the highest colocalization with mitotracker green. Shorter or longer lipophilic side chains show reduced uptake. Furthermore, uptake by the lysosomes provides an active pathway to attack vital organelles as part of the overall photodynamic response. The relationship between the intracellular localization pattern of our ZnPcS and their photodynamic potency obviously does not constitute the only parameter to consider. Other factors that may play a role include the quantity of singlet oxygen produced, interaction between different organelles within the cell, the extent of damage, changes in permeability of the various membrane structures, cell uptake kinetics, etc. Evaluation of all such parameters is essential to establish a reliable structure−photodynamic activity relationship and experiments to this end are currently in progress.

In summary, the amphiphilic properties of trisulfonated ZnPc can be improved by introducing a lipophilic alkynyl chain to the Pc macro cycle. The amphiphilic properties of the $ZnPcS_3C_n$ play a key role in cell uptake and photocytotoxicity, and also affect the aggregation of sulfonated Pc in biological systems. Adding a C6−C9 linear carbon chain to $ZnPcS_3$ ($ZnPcS_3C_6$ and $ZnPcS_3C_9$) gave Pc that readily localized in the mitochondria and the Golgi apparatus resulting in comparable photodynamic activities as those reported for the amphiphilic, adjacent disulfonated $ZnPcS_{2a}$, which is considered as one of the most active sulfonated Pc-based photosensitizers for PDT. The advantage of these new derivatives over $ZnPcS_{2a}$ as potential photosensitizers for PDT lies in their chemistry: They are more easily prepared and purified to give well identified products.

ACKNOWLEDGMENT

This work was supported by the Canadian Institutes for Health Research (CIHR grant MOP-37768). The authors are grateful to Dr. Leonid Volkov for his expertise help with the confocal fluorescence microscopy. JEvL is the holder of the Jeanne and J.-Louis Lévesque Chair in radiobiology.

LITERATURE CITED

(1) Dougherty, T. J., Gomer, C. J., Henderson, B. W., Jori, G., Kessel, D. Korbelik, M., Moan J., and Peng, Q. (1988) Photodynamic therapy. *J. Natl. Cancer Inst. 90*, 889−905.

(2) MacDonald, I. J., and Dougherty, T. J. (2001) Basic principles of photodynamic therapy. *J. Porphyrins Phthalocyanines 5*, 105−129.

(3) Fisher, A. M. R., Murphree, A. L., and Gomer, C. J. (1995) Clinical and preclinical photodynamic therapy. *Lasers Surg. Med. 17*, 2−31.

(4) Henderson, B. W., and Dougherty, T. J. (1992) How does photodynamic therapy work? *Photochem. Photobiol. 55*, 145−157.

(5) Hilf, R. (1992) Cellular targets of photodynamic therapy. In *Photodynamic therapy. Basic Principles and Clinic Applications* (Henderson, B. W., and Dougherty, T. J., Eds.) pp 47−54, Marcel Dekker, New York.

(6) Star, W. M., Marijnissen, P. A., van den Berg-Blok, A. E., Versteeg, J. A. C., Franken, K. A., and Reinhold, H. S. (1986) Destruction of rat mammary tumor and normal tissue microcirculation by hematoporphyrin derivative photoradiation observed in vivo in sandwich observation chambers. *Cancer Res. 46* 2532−2540.

(7) Nelson, J. S., Liaw, L. H., Orenstein, A., Roberts, W. G., and Berns, M. W. (1988) Mechanism of tumor destruction following photodynamic therapy with hematoporphyrin derivative, chlorin, phthalocyanine. *J. Natl. Cancer Inst. 80*, 1599−1605.

(8) Hamblin, M. R., and Newman, E. L. (1994) On the mechanism of tumor-localising effect in photodynamic therapy. *J. Photochem. Photobiol. B. Biol. 23*, 3−8.

(9) Moan, J., and Peng, Q. (2003) An Outline of the Hundred-Year History of PDT. *Anticancer Res. 23*, 3591−3600.

(10) Bonnett, R. (1999) Photodynamic therapy in historical perspective. *Rev. Contemp. Pharmacother. 10*, 1−17.

(11) Ali, H, and van Lier, J. E. (1999) Metal complexes as photo- and radiosensitizers. *Chem. Rev. 99*, 2379−2450.

(12) Sharman, W. M., Allen, C. M, and van Lier, J. E. (1999) Photodynamic therapeutics: Basic principles and clinical applications. *Drug Discovery Today 4*, 507−517.

(13) Allen, C. M., Sharman, W. M., and van Lier, J. E. (2001) Current status of phthalocyanines in the photodynamic therapy of cancer. *J. Porphyrins Phthalocyanines 5*, 161−169.

(14) Ali, H., Langlois, R., Wagner, J. R., Brasseur, N., Paquette, B., and van Lier, J. E. (1988) Biological activities of phthalocyanines-X. Syntheses and analyses of sulfonated phthalocyanines. *Photochem. Photobiol. 47*, 713−717.

(15) Wagner, J. R., Ali, H., Langlois, R., Brasseur N., and van Lier, J. E. (1987) Biological activities of phthalocyanines VI. Photooxidation of L-tryptophan by selectively sulfonated gallium phthalocyanines: Singlet oxygen yields and effect of aggregation. *Photochem. Photobiol. 45*, 587−594.

(16) Philips, D. (1997) Chemical mechanisms in photodynamic therapy with phthalocyanines. *Prog. Reaction Kinet. 22*, 175−300.

(17) Kessel, D., Thompson, P., Saatio K., and Nantwi, K. D. (1987) Tumor localization and photosentization by sulfonated derivatives of tetraphenylporphine. *Photochem. Photobiol. 45*, 787−790.

(18) Kongshaug, M., Moan, J., and Brown S. B. (1989) The distribution of porphyrins with different tumor localizing ability among human plasma proteins. *Br. J. Cancer 59*, 184−188.

(19) Woodburn, K., Stylli, S., Hill, J. S., Kaye, A. H., Reiss J. A., and Phillips, D. R. (1992) Evaluation of tumour and tissue distribution of porphyrins for use in photodynamic therapy. *Br. J. Cancer 65*, 321−328.

(20) Oleinick, N. L., Morris, R. L., and Belichenko, I. (2002) The role of apoptosis in response to photodynamic therapy: what, where, why and how. *Photochem. Photobiol. Sci. 1*, 1−21.

(21) Ali, S. M., and Olivo, M. (2002) Bio-distribution and subcellular localization of Hypericin and its role in PDT induced apoptosis in cancer cells. *Int. J. Oncol. 21*, 531−540.

(22) Kessel, D., and Luo, Y. (2001) Intracelluar sites of photodamage as a factor in apoptotic cell death. *J. Porphyrins Phthalocyanines 5*, 181−184.

(23) Ferri, K. F., and Kroemer, G. (2001) Organelle-specific initiation of cell death pathways. *Nat. Cell Biol. 3*, 255−263.

(24) Korbelick, M. and Cecic, I. (2003) Mechanism of Tumor Destruction by photodynamic therapy. In *Handbook of Pho-*

tochemistry and Photobiology (Nalwa, H. S., Ed.) vol. 4, Chapter 2, pp 39−77, American Scientific Publishers, Stevenson Ranch, CA.

(25) Nonaka, M., Ikeda, H., and Inokuchi, T. (2004) Inhibitory effect of heat shock protein 70 on apoptosis induced by photodynamic therapy in vitro. *Photochem. Photobiol. 79*, 94−98.

(26) Margaron, P., Grégoire, M.-J., Scasnar, V., and van Lier, J. E. (1996) Structure−photodynamic activity relationships of a series of 4-substituted zinc phthalocyanines. *Photochem. Photobiol. 63*, 217−223.

(27) Paquette, B., Ali, H., Langlois, R., Brasseur, N., and van Lier, J. E. (1988) Biological activities of phthalocyanines-VIII. Cellular distribution in V-79 Chinese hamster cells and phototoxicity of selectively sulfonated aluminum phthalocyanines. *Photochem. Photobiol. 47*, 215−220.

(28) Brasseur, N., Ali, H., Langlois, R., and van Lier, J. E. (1988) Biological activities of phthalocyanine-IX. Photosensitization of V-79 Chinese hamster cells and EMT-6 mouse mammary tumor by selectively sulfonated zinc phthalocyanines. *Photochem. Photobiol. 47*, 705−711.

(29) Margaron, P., Madarnas, P., Ouellet, R., and van Lier, J. E. (1996) Biological activities of phthalocyanines-XVII. Histopathological evidence for different mechanisms of EMT-6 tumor necrosis induced by photodynamic thereapy with disulfonated aluminum phthalocyanine or photofrin. *Anticancer Res. 16*, 613−620.

(30) Chan, W.-S., Ali, H., and van Lier, J. E (1996) Evidence for different mechanisms of EMT-6 tumor necrosis by photodynamic therapy with disulfonated aluminum phthalocyanine or photofrin: Tumor cell survival and blood flow. *Anticancer Res. 16*, 1887−1892.

(31) Paquette, B., Boyle, R. W., Ali, H., MacLennan, A. H., Truscott, T. G., and van Lier, J. E. (1991) Sulfonated phthalimidomethyl aluminum phthalocyanine: The effect of hydrophobic substituents on the in vitro phototoxicity of phthalocyanines. *Photochem. Photobiol. 53*, 323−327.

(32) Kudrevich, S., Brasseur, N., La Madeleine, C., Gilbert, S., and van Lier, J. E. (1997) Syntheses and photodynamic activities of novel trisulfonated zinc phthalocyanine derivatives. *J. Med. Chem. 40*, 389−3904.

(33) Whoerle, D., Iskander, N., Graschew, G., Sinn, H., Friedrich, E. A., Maier-Borst, W., Stern, J., and Schlag, P. (1990) Synthesis of positive charge phthalocyanines and their activity in the photodynamic therapy of cancer cells. *Photochem. Photobiol. 51*, 351−356.

(34) Zheng, G., Potter, W. R., Camacho, S. H., Missert, J. R., Wang, G., Bellnier, D. A., Henderson, B. W., Rodgers, M. A. J., Dougherty, T. J., and Pandey, R. K. (2001) Synthesis, photophysical properties, tumor uptake, and preliminary in vivo Photosensitizing efficacy of a homologous series of 3-(1′-Alkykloxy)ethyl-3-devinylpurpurin-18-*N*-alkylimides with variable lipophilicity. *J. Med. Chem. 44*, 1540−1559.

(35) Li, Z., van Lier, J. E., and Leznoff, C. C (1999) Heterocyclic aromatic amide protected groups for aryl and phthalocyaninesulfonic acids. *Can. J. Chem. 77*, 138−145.

(36) Sharman, W. M., and van Lier, J. E. (2000) The use of palladium catalysis in the synthesis of novel porphyrins and phthalocyanines. *J. Porphyrins Phthalocyanines 4*, 441−453.

(37) Tian, H., Ali, H., and van Lier, J. E. (2000) Synthesis of water soluble trisulfonated phthalocyanines via palladium-catalysed cross coupling reactions. *Tetrahedron Lett. 41*, 8435−8438.

(38) Langlois, R., Ali, H., Brasseur, N., Wagner, J. R., and van Lier, J. E. (1986) Biological activities of phthalocyanines-IV. Type II sensitized photooxidation of L-tryptophan and cholesterol by sulfonated metallophthalocyanines. *Photochem. Photobiol. 44*, 117−123.

(39) Bradford, M. M. (1976) A rapid and sensitive method for the quantitation of microgram quantities of protein utilizing the principle of protein-dye binding. *Anal. Biochem. 72*, 248−254.

(40) Tada, H., Shiho, O., Kuroshima, K., Koyama, M., and Tsukamoto, K. (1986) An improved colorimetric assay for interleukin 2. *J. Immunol. Methods 93*, 157−165.

(41) Bernauer, K., and Fallad, S. (1961) Phthalocyanine in wasseriger Losung I. *Helv. Chim. Acta 44*, 1287−1292.

(42) Harriman, A., and Richoux, M.-C. (1980) Attempted photoproduction of hydrogen using sulfophthalocyanines as chromophores for three-component systems. *J. Chem. Soc., Faraday Trans. 2 76*, 1618−1626.

(43) Spike, J. D., and Bommer, J. C. (1986) Zinc phthalocyanine as a photodynamic sensitizer for biomolecules. *Int. J. Radiat. Biol. 50*, 41−45.

(44) Papoulis, A. (1984) *Probability, Random Variables, and Stochastic Processes*, 2nd ed., p 104, McGraw-Hill, New York.

(45) Redmond, R. W., and Gamlin, J. N. (1999) A compilation of singlet oxygen yields from biologically relevant molecules. *Photochem. Photobiol. 70*, 391−475.

(46) van Lier, J. E. and Spikes, J. D. (1989) The chemistry, photophysics and photosensitizing properties of phthalocyanines. In *Photosensitizing Compounds*: *their chemistry*, *Biology and Clinical Use* (Dougherty, T. J., Bock, G. H., and Harnett, S., Eds.) pp 17−32, Ciba Foundation Symposium 146, Wiley, Chichester.

(47) Brasseur, N., Ali, H., Langlois, R., and van Lier, J. E. (1987) Biological activities of phthalocyanine −VII. Photoinactivation of V-79 Chinese hamster cells by selectively sulfonated gallium phthalocyanines. *Photochem. Photobiol. 46*, 739−744.

(48) Brasseur, N., Ali, H., Langlois, R., Wagner, J. R., Rousseau, J., and van Lier, J. E. (1987) Biological activities of phthalocyanine-V. Photodynamic therapy of EMT-6 mammary tumors in mice with sulfonated phthalocyanines. *Photochem. Photobiol. 45*, 581−586.

(49) Chatelier, R. C, Sawyer, W. H., Swincer, A. G., and Ward, A. D. (1985) *Methods in porphyrin photosensitization* (Kessel, D., Ed.) p 169. Plenum Press, New York.

(50) Rosenthal, I., Ben-Hur, E., Greenberg, S., Concepcion-Lam, A., Drew, D. M., and Leznoff, C. C. (1988) Substituted phthalocyanines as photodynamic sensitizers. In *Oxygen Radicals in Biology and Medicine* (Simic, M. G., Taylor, K. A., Ward J. F., and von Sonntag, C., Eds.) Basic Life Science vol. 49, pp 467−472, Plenum Press, New York.

(51) Brasseur, N., Nguyen, T.-L., Langlois, R., Ouellet, R., Marengo, S., Houde, D., and van Lier, J. E. (1994) Synthesis and photodynamic activities of silicon 2,3-naphthalocyanine derivatives. *J. Med. Chem. 37*, 415−420.

BC049848T

Synthesis of a Lipid Conjugate of SO_3Le^a and Its Enhancement on Liposomal Binding to Activated Platelets

Feng Yan,[§] Jie Xue,[§] Junmin Zhu,[†] Roger E. Marchant,[†,*] and Zhongwu Guo[§,*]

Departments of Chemistry and Biomedical Engineering, Case Western Reserve University, 10900 Euclid Avenue, Cleveland, Ohio 44106. Received August 13, 2004; Revised Manuscript Received October 20, 2004

3′-O-Sulfated Le^a (SO_3Le^a) is one of the most potent natural oligosaccharide ligands of selectins. The specific interactions between SO_3Le^a and E-/P-selectins are critical in the inflammation process. This paper described an efficient synthesis of a lipid conjugate of SO_3Le^a and its combination with phospholipid and cholesterol to form SO_3Le^a-coated liposomes by the freeze-thaw and extrusion method. The size ($D = 78$ nm) and stability of the resultant glycoliposomes were comparable to that of liposomes without the glycoconjugate. It was further observed that the incorporation of SO_3Le^a into liposomes could significantly enhance their adhesion to activated platelets as a result of the specific binding between SO_3Le^a on the glycoliposome and the P-selectin on activated platelets. The glycoliposome constructs may be useful for antiinflammation or for targeted delivery of drugs to endothelial cells that express E- and P-selectins.

INTRODUCTION

Liposomes are colloidal structures consisting of a lipid bilayer and an encapsulated aqueous volume to locate useful components. Since the encapsulated volume and components are isolated from the outside environment, they are not easily disturbed until the liposome is disrupted. Consequently, liposomes have been studied extensively as drug delivery systems (*1*−*7*), in the hope of improving the stability, therapeutic efficiency, and pharmacokinetic properties of drugs while reducing their side effects. As drug delivery systems, liposomes have the advantage of being biodegradable and nontoxic, as well as the beneficial properties that their surface chemistry and lipid composition can be easily modified to address targeting requirements. Moreover, the high lateral mobility of liposome-associated molecules facilitates their formation of subdomains on liposome surface and enables the multivalent interactions between liposomes and cells.

In recent years, the cell surface glycocalyx has emerged as a useful model to create carbohydrate-modified liposomes, namely glycoliposomes, for the targeting of specific organs or tissues (*8*−*10*). An important discovery in this respect is that liposomes coated with different carbohydrates have distinct properties. For instance, by primarily inhibiting the uptake of liposomes into the reticuloendothelial system (RES) in liver and spleen, GM1 ganglioside enhances liposomal circulation lifetimes in vivo (*11*−*13*) in a manner comparable to that observed with the sterically stabilized poly(ethylene glycol) (PEG) liposomes (*14*, *15*). In contrast, trisialoganglioside GT1 liposomes were quickly cleared into the RES, due to the specific binding between GT1 and its receptors in RES (*16*). These results suggest that the recognition of special oligosaccharide epitopes by cells may play an important role in determining the in vivo fate of glycoliposomes (*10*, *14*). Consequently, glycoliposomes are extensively investigated for targeted drug delivery, taking advantage of their interactions with specific carbohydrate receptors on cells (*10*). This approach can give rise to highly selective and efficient delivery devices and further reduce the adverse systemic side effects of drugs.

Numerous carbohydrate recognition proteins are known to exist on mammalian cell surfaces (*17*−*22*). For the purpose of tissue targeting, the galactose- and mannose-binding receptors on hepatic cells have been broadly studied (*8*, *10*, *22*−*25*). Another important target is the selectins present on activated endothelial cells and platelets (*26*−*29*).

Selectins are a family of lectins that bind Lewis type carbohydrate antigens specifically (*30*, *31*). Three selectins have been identified, including E-, P-, and L-selectins. P- and E-selectins are expressed on activated vascular endothelial cells and platelets; L-selectin is expressed on activated leukocytes. The specific interactions between selectins and their ligands regulate the adhesion of leukocytes to endothelium, the first step of inflammation (*30*−*32*). Therefore, much effort is currently focused on the development of new therapeutic strategies for inflammatory diseases based on Lewis type antigens (*33*−*35*).

The natural selectin ligands, such as sialyl Lewis x (sLe^x **1**), sialyl Lewis a (sLe^a **2**), and 3′-O-sulfated Lewis a (SO_3Le^a **3**) (Figure 1), share a common recognition motif, namely the Lewis type antigen which is a fucosylated trisaccharide with a negatively charged species, e.g. a sialic acid or a sulfate unit, attached to the galactose 3-O-position.

It has been well established that Lewis type carbohydrates can interrupt the adhesion of leukocytes to the endothelium and thus inhibit the inflammatory process (*33*). Alternatively, the specific binding of Lewis type carbohydrates to endothelial cells can also be used for the selective targeting of the endothelium (*26*). To explore the promise of these applications, we synthesized the lipid conjugate of SO_3Le^a, one of the most potent natural ligands of selectin (*36*), incorporated the conjugate into

* Corresponding authors: Z.G., tel. 1-216-368-3736, fax 1-216 368-3006, e-mail zxg5@case.edu; R.E.M., tel. 1−216-368-3005, fax 1−216-368-4969, e-mail: rxm4@case.edu.

[§] Department of Chemistry.

[†] Department of Biomedical Engineering.

10.1021/bc049805c CCC: $30.25 © 2005 American Chemical Society
Published on Web 12/30/2004

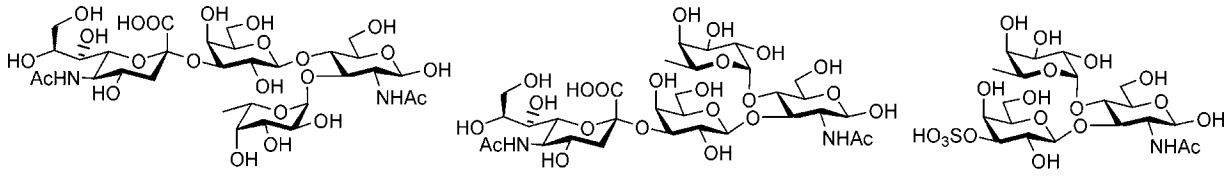

Figure 1. The natural carbohydrate ligands of selectins.

liposomes, and studied the properties of the resultant glycoliposomes. One objective of this work was to establish a practicable method to synthesize the lipid conjugates of Lewis type antigens with the lipid moiety linked to the carbohydrate reducing end. Another objective was to investigate the physical and biological properties of the glycoliposomes coated with a Lewis type antigen.

EXPERIMENTAL PROCEDURES

General Methods. NMR spectra were recorded on a 300 or 600 MHz NMR spectrometer with chemical shifts reported in ppm (δ) relative to Me_4Si (^1H), $CDCl_3$ (^{13}C), and $CFCl_3$ (^{19}F), respectively. Coupling constants (J) are reported in hertz (Hz). Thin-layer chromatography (TLC) was performed on silica gel 60 GF_{256} with detection by charring with phosphomolibdic acid in EtOH or 5% H_2SO_4 in EtOH. Commercial solvents and reagents were directly used without further purification.

***O*-(2,4,6-Tri-O-acetyl-3-*O*-chloroacetyl-*β*-D-galactopyranosyl)-(1→3)-2-deoxy-4,6-*O*-phenylmethylene-2-phthalimido-*β*-D-glucopyranosyl Azide (9).** A solution of TfOH (200 μL) in CH_2Cl_2 (2 mL) was added dropwise to a mixture of **7** (1.80 g, 2.86 mmol), **8** (0.80 g, 0.93 mmol), and NIS (0.62 g, 1.45 mmol) in CH_2Cl_2 (50 mL) at −10 °C. After the reaction was completed (monitored by TLC), saturated $NaHCO_3$ solution was added (30 mL). The organic phase was separated, and the aqueous phase was extracted with CH_2Cl_2 (50 mL). The organic solutions were combined and washed with $Na_2S_2O_3$ solution (2 × 25 mL) and dried over anhydrous Na_2SO_4. The solvent was removed under reduced pressure, and the residue was subjected to column chromatography to afford **9** (0.82 g, 55%) as a white solid. TLC: R_f = 0.25 (hexane and acetone, 3:2); ^1H NMR (300 MHz, $CDCl_3$): δ 7.94−7.77 (m, 4 H, aromatic), 7.49−7.23 (m, 5 H, aromatic), 5.60 (s, 1 H, C*H*Ph), 5.35 (bd, *J* 9.5 Hz, 1 H, H-1), 5.20 (d, *J* 3.4 Hz, 1 H, H-4′), 5.02 (dd, *J* 8.0, 10.4 Hz, 1 H, H-2′), 4.81 (dd, *J* 3.4, 10.4 Hz, 1 H, H-3′), 4.79 (dd, *J* 8.9, 9.7 Hz, 1 H, H-3), 4.56 (d, *J* 8.0 Hz, 1 H, H-1′), 4.40 (dd, 1 H, H-6a), 4.23 (dd, *J* 3.4, 10.4 Hz, 1 H, H-2), 4.03 (dd, *J* 8.3, 11.1 Hz, 1 H, H-6b), 3.88−3.72 (m, 6 H, H-4, 5, 6′a, 6′b, CH_2Cl), 3.50 (m, 1 H, H-5), 2.09, 1.93, 1.59 (s, 3 H each, 3 Ac); FAB-MS: Calcd for $C_{35}H_{35}ClN_4O_{15}$ (M^+) 787.1, Found 787.1.

***O*-(2,4,6-Tri-O-acetyl-3-*O*-chloroacetyl-*β*-D-galactopyranosyl)-(1→3)-6-*O*-benzyl-2-deoxy-2-phthalimido-*β*-D-glucopyranosyl Azide (10).** A freshly prepared saturated solution of HCl in diethyl ether (8 mL) was added dropwise to a suspension of **9** (1.0 g, 1.1 mmol) and $NaBH_3CN$ (0.78 g, 11.0 mmol) in THF (60 mL) at 0 °C. After **9** was completely consumed, solid $NaHCO_3$ (1.5 g) was added to quench the reaction. The mixture was stirred at room temperature for 5 min and then diluted with ethyl acetate (300 mL). After the organic solution was washed with saturated $NaHCO_3$ solution (2 × 150 mL) and brine (2 × 150 mL), it was dried over anhydrous Na_2SO_4. The solvent was removed under reduced pressure and the residue was separated by column chromatography to afford **10** (0.90 g, 90%) as a colorless foamy solid. TLC: R_f = 0.23 (hexane and acetone, 3:2); $[\alpha]_D$ −3.6 (*c* 1.0, $CHCl_3$); ^1H NMR (600 MHz, $CDCl_3$): δ 7.94−7.77 (m, 4 H, aromatic), 7.49−7.23 (m, 5 H, aromatic), 5.29 (d, *J* 3.6 Hz, 1 H, H-4′), 5.20 (d, *J* 9.6 Hz, 1 H, H-1), 5.12 (dd, *J* 9.8, 11.2 Hz, 1 H, H-2′), 4.84 (dd, *J* 3.6, 11.2 Hz, 1 H, H-3′), 4.65 (s, 2 H, CH_2Ph), 4.50 (dd, *J* 7.8, 10.8 Hz, 1 H, H-3), 4.40 (d, *J* 7.8 Hz, 1 H, H-1′), 4.50 (dd, *J* 9.6, 10.8 Hz, 1 H, H-2), 4.13−4.09 (m, 2 H), 4.00 (s, 1 H, OH), 3.95 (m, 1 H), 3.86−3.70 (m, 5 H), 3.67 (t, *J* 9.6 Hz, 1 H). 2.14, 2.09, 2.01 (s, 3 H each, 3 Ac); ^{13}C NMR (25 MHz, $CDCl_3$): δ 170.6, 170.3, 168.9, 166.6, 138.0, 134.8, 131.30, 128.56, 128.53, 128.47, 127.96, 127.92, 127.84, 127.76, 127.72, 123.9, 100.9, 85.6, 81.8, 77.75, 77.59, 77.2, 76.7, 73.72, 73.67, 73.63, 72.5, 71.2, 69.6, 69.1, 68.3, 66.8, 61.55, 61.52, 54.2, 40.21, 40.18, 20.63, 20.60, 20.57, 20.54, 19.79; FAB-MS: Calcd for $C_{35}H_{36}ClN_4NaO_{15}$ ($M - H + Na)^+$ 811.1, Found 811.2.

***O*-(2,4,6-Tri-O-acetyl-3-*O*-chloroacetyl-*β*-D-galactopyranosyl)-(1→3)-[*O*-(2,3,4-tri-*O*-benzyl-α-L-fucopyranosyl)-(1→4)]-6-*O*-benzyl-2-deoxy-2-phthalimido-*β*-D-glucopyranosyl Azide (11).** A mixture of **10** (0.070 g, 0.089 mmol), **6** (0.105 g, 0.23 mmol), and freshly activated MS 4 Å in CH_2Cl_2 (10 mL) and DMF (10 mL) was stirred at 20 °C for 2 h, whereupon $CuBr_2$ (0.070 g, 0.30 mmol) and Bu_4NBr (0.10 g, 0.32 mmol) were added. After the mixture was stirred at room temperature for 36 h, the solid material was filtered off and washed with CH_2Cl_2 (2 × 20 mL). The combined filtrates were washed with diluted aq HCl solution, saturated aq $NaHCO_3$ solution, and brine, dried over Na_2SO_4, and concentrated under reduced pressure. The residue was purified by flash chromatography to afford **11** (0.80 g, 78%) as a colorless foamy solid. TLC: R_f = 0.30 (hexane and acetone, 2:1); $[\alpha]_D$ −22.8 (*c* 1.0, $CHCl_3$); ^1H NMR (600 MHz, $CDCl_3$): δ 7.94−7.77 (m, 4 H, aromatic), 7.49−7.23 (m, 20 H, aromatic), 5.20 (dd, *J* 1.2, 3.6 Hz, 1 H, H-4′), 5.19 (d, *J* 12.0 Hz, 1 H, CH_2Ph), 5.10 (d, *J* 9.6 Hz, 1 H, H-1), 5.02 (dd, *J* 8.4, 10.4 Hz, 1 H, H-2′), 4.98 (d, *J* 12.0 Hz, 1 H, CH_2Ph), 4.88 (d, *J* 12.0 Hz, 1 H, CH_2Ph), 4.84 (dd, *J* 3.6, 11.2 Hz, 1 H, H-3), 4.83 (m, 3 H, H-2″, H-4″, H-3″), 4.78 (d, *J* 12.0 Hz, 1 H, CH_2Ph), 4.70 (d, *J* 12.0 Hz, 1 H, CH_2Ph), 4.70 (m, 1 H, H-5″), 4.48 (dd, *J* 3.6, 10.6 Hz, 1 H, H-3′), 4.44 (s, 2 H, CH_2Ph), 4.20 (m, 4 H, H-5′, H-1′, H-2, H-1″), 4.08−3.93 (m, 3 H, H-4, H-6), 3.80 (m, 2 H, CH_2Cl), 3.74−3.64 (m, 3 H, H-5, H-6), 3.65 (m, 1 H), 1.99, 1.98, 1.71 (s, 3 H each, 3 Ac), 1.12 (d, *J* 6.2 Hz, 3 H, Fuc-6); ^{13}C NMR (25 MHz, $CDCl_3$): δ 170.3, 169.92, 169.19, 166.63, 138.71, 138.63, 138.23, 135.02, 128.78, 128.49, 128.47, 128.41, 128.33, 127.92, 127.71, 127.60, 127.56, 127.44, 127.01, 123.89, 100.4, 97.8, 85.3, 80.9, 77.9, 77.48, 77.06, 76.64, 76.27, 75.5, 75.05, 74.51, 73.94, 73.18, 72.73, 72.35, 72.3, 70.23, 67.5, 66.4, 66.1, 55.8, 40.3 20.63, 20.49, 20.38, 16.97; FAB-MS: Calcd for $C_{62}H_{65}ClN_4O_{19}$ (M^+) 1204, Found 1204.

***O*-(2,4,6-Tri-*O*-acetyl-*β*-D-galactopyranosyl)-(1→3)-[*O*-(2,3,4-tri-*O*-benzyl-α-L-fucopyranosyl)-(1→4)]-6-*O*-benzyl-2-deoxy-2-phthalimido-*β*-D-glucopyranosyl Azide (12).** After 16 h of refluxing, the mixture of thiourea (25 mg, 0.033 mmol), 2,6-lutidine (16 μL, 14 mg)

and **11** (80 mg, 0.066 mmol) in EtOH and CH_2Cl_2 (1:4, 50 mL) was concentrated in a vacuum. The residue was purified on a silica gel column to give **12** (64 mg, 86%) as a foamy solid. TLC: R_f = 0.27 (toluene and ethyl acetate, 2:1); $[\alpha]_D$ −9.7 (*c* 0.8, $CHCl_3$); ^{1}H NMR (600 MHz, $CDCl_3$): δ 7.94−7.77 (m, 4 H, aromatic), 7.49−7.23 (m, 20 H, aromatic), 5.07 (d, *J* 19.2 Hz, 2 H, CH_2Ph), 5.05 (d, *J* 9.6 Hz, 1 H, H-1), 4.91 (d, *J* 12.0 Hz, 1 H, CH_2Ph), 4.83 (d, *J* 12.0 Hz, 1 H, CH_2Ph), 4.83−4.62 (m, 6 H, H-2″, H-4″, H-3″, H-3, H-2′, H-4′), 4.20 (t, *J* 9.6 Hz, 1 H, H-2), 4.14−3.87 (m, 7 H, H-5′, H-1′, H-4, H-1″, H-6′), 3.65−3.54 (m, 4 H), 3.16 (dd, *J* 3.6, 9.6 Hz, 1 H, H-3′), 2.00, 1.96, 1.68 (s, 3 H each, 3 Ac), 1.13 (d, *J* 6.2 Hz, 3 H, Fuc-6); ^{13}C NMR (25 MHz, $CDCl_3$): δ 171.7, 170.2, 170.1, 138.76, 138.60, 138.25, 138.06, 134.84, 128.79, 128.59, 128.49, 128.43, 128.34, 127.92, 127.75, 127.69, 127.6, 127.55, 127.50, 127.44, 127.05, 123.778, 100.2, 97.9, 85.4, 80.9, 78.0, 77.5, 77.07, 76.66, 76.27, 75.50, 75.05, 74.34, 73.97, 73.19, 72.52, 72.33, 71.78, 71.63, 70.56, 68.90, 66.88, 66.35, 60.18, 55.75, 29.8, 20.72, 20.64, 20.60, 17.02; FAB-MS: Calcd for $C_{60}H_{64}N_4O_{18}$ (M^+) 1128, Found 1128.

***O*-(2,4,6-Tri-*O*-acetyl-3-*O*-sulfo-*β*-D-galactopyranosyl)-(1→3)-[*O*-(2,3,4-tri-*O*-benzyl-α-L-fucopyranosyl)-(1→4)]-6-*O*-benzyl-2-deoxy-2-phthalimido-*β*-D-glucopyranosyl Azide (13).** While the mixture of **12** (70 mg, 0.062 mmol) and SO_3·NMe_3 (0.173 g, 1.24 mmol) in pyridine (15 mL) was stirred at room temperature, the reaction progress was monitored by TLC. When the reaction completed about 24 h later, the mixture was concentrated in a vacuum. The residue was dissolved in $CHCl_3$ (30 mL), and the solution was washed with brine, dried over Na_2SO_4, and concentrated under reduced pressure. Purification was performed on a silica gel column to produce **13** (54 mg, 72%) as a white foamy solid. TLC: R_f =0.28 (DCM and MeOH, 8:1); ^{1}H NMR (600 MHz, $CDCl_3$): δ 7.94−7.77 (m, 4 H, aromatic), 7.49−7.23 (m, 20 H, aromatic), 5.33 (dd, 1 H, H-4′), 5.07 (d, *J* 9.6 Hz, 1 H, H-1), 4.89 (d, *J* 11.4 Hz, 1 H, CH_2Ph), 4.80−4.59 (m, 6 H), 4.38 (m, 2 H, CH_2Ph), 4.17−4.07 (m, 3 H), 3.96−3.87 (m, 4 H), 3.65−3.60 (m, 4 H), 2.00, 1.94, 1.76 (s, 3 H each, 3 Ac), 1.13 (d, *J* 6.2 Hz, 3 H, Fuc-6); ^{13}C NMR (25 MHz, $CDCl_3$): δ 171.7, 170.2, 170.1, 138.76, 138.60, 138.25, 138.06, 134.84, 128.79, 128.59, 128.49, 128.43, 128.34, 127.92, 127.75, 127.69, 127.6, 127.55, 127.50, 127.44, 127.05, 123.778, 100.2, 97.9, 85.4, 80.9, 78.0, 77.5, 77.07, 76.66, 76.27, 75.50, 75.05, 74.34, 73.97, 73.19, 72.52, 72.33, 71.78, 71.63, 70.56, 68.90, 66.88, 66.35, 60.18, 55.75, 29.8, 20.72, 20.64, 20.60, 17.02; FAB-MS: Calcd for $C_{60}H_{63}N_4Na_2O_{21}S$ ($M - H + 2\ Na)^+$ 1253, Found 1253.

***O*-(3-*O*-Sulfo-*β*-D-galactopyranosyl)-(1→3)-[*O*-(2,3,4-tri-*O*-benzyl-α-L-fucopyranosyl)-(1→4)]-2-acetamido-6-*O*-benzyl-2-deoxy-*β*-D-glucopyranosyl Azide (5).** After the mixture of **13** (0.25 g, 0.21 mmol) and ethylenediamine (1 mL, 15 mmol) in BuOH (10 mL) was stirred at 90 °C overnight, the solution was concentrated in a vacuum, and the residue was dissolved in MeOH (20 mL). To this solution were added triethylamine (2.0 mL) and Ac_2O (1.5 mL) at room temperature. The mixture was stirred for 10 min and then condensed. Purification of the residue with silica gel column twice gave **5** (0.11 g, 52%) as a white foamy solid. TLC: R_f = 0.49 (DCM and MeOH, 8:1); $[\alpha]_D$ −27.5 (*c* 1.0, $CHCl_3$); ^{1}H NMR (600 MHz, $CDCl_3$−CD_3OD): δ 7.18−7.39 (m, 20 H, aromatic), 5.04 (d, *J* 3.0 Hz, 1 H, H-1″), 4.88 (d, *J* 11.4 Hz, 1 H), 4.78 (d, *J* 11.4 Hz, 1 H), 4.75 (d, *J* 10.8 Hz, 1 H), 4.72 (m, 1 H, 5-H″), 4.69 (d, *J* 11.4 Hz, 1 H), 4.58 (d, *J* 10.8 Hz, 1 H), 4.55 (d, *J* 9.6 Hz, 1 H, H-1), 4.50 (d, *J* 12.0 Hz, 1 H), 4.48 (d, *J* 11.4 Hz, 1 H), 4.39 (d, *J* 10.2 Hz, 1 H, H-1′), 4.38 (d, *J* 12.0 Hz, 1 H), 4.14 (d, *J* 2.4 Hz, 1 H), 4.10 (dd, *J* 9.6, 3.0 Hz, 1 H), 3.80−3.97 (m, 8 H), 3.65 (d, *J* 10.8 Hz, 1 H), 3.61 (m, 2 H), 3.43 (m, 2 H), 1.95 (s, 3 H), 1.12 (d, *J* 6.0 Hz, 3 H); MALDI-TOF-MS: Calcd for $C_{48}H_{58}N_4NaO_{17}S$ ($M - H + Na)^+$ 1016, Found 1015.

5-{*O*-(3-*O*-Sulfo-*β*-D-galactopyranosyl)-(1→3)-[*O*-(2,3,4-tri-*O*-benzyl-α-L-fucopyranosyl)-(1→4)]-2-acetamido-6-*O*-benzyl-2-deoxy-*β*-D-glucopyranosylamino}-5-oxopentanoic Acid 2(*R*,*S*),3-Dioctadecanoyloxypropanyl Ester (16). Lindlar's catalyst (20 mg) was added to a solution of **5** (50 mg, 0.05 mmol) in dry DCM and MeOH (1:1, 10 mL), and the mixture was stirred vigorously under a H_2 atmosphere at room temperature for 2 h. TLC showed a clean and complete reaction. The catalyst was filtered off, and the filtrate was directly applied to the next step without further treatment. Thus, to this solution were added **15** (74 mg, 0.1 mmol), HOBt (34 mg, 0.25 mmol), and EDC (96 mg, 0.5 mmol) at 0 °C, and the mixture was stirred at room temperature for 48 h, before it was concentrated in a vacuum. The residue was dissolved in diethyl ether, and the solution was washed with water, dried over Na_2SO_4, and finally condensed. Purification of the residue with a silica gel column gave the coupling product **16** (60 mg, 70%). TLC: R_f = 0.65 (DCM and MeOH, 8:1); ^{1}H NMR (600 MHz, $CDCl_3$−CD_3OD): δ 7.16−7.39 (m, 20 H, aromatic), 5.21 (m, 1 H, H-2^{gly}), 5.03 (br, 1 H, H-1″), 4.94 (d, *J* 8.4 Hz, 1 H, H-1), 4.88 (d, *J* 11.4 Hz, 1 H), 4.78 (d, *J* 11.4 Hz, 1 H), 4.72 (t, 1 H), 4.71 (d, *J* 10.8 Hz, 1 H), 4.69 (d, *J* 11.4 Hz, 1 H), 4.58 (d, *J* 10.8 Hz, 1 H), 4.43 (d, *J* 10.8 Hz, 1H, H-1′), 4.25−4.31 (m, 3 H), 4.09−4.14 (m, 5 H), 3.80−3.97 (m, 7 H), 3.61 (m, 3 H), 3.41 (t, *J* 9.0 Hz, 2 H), 2.33 (t, *J* 7.2 Hz, 2 H), 2.28 (t, *J* 7.2 Hz, 4 H), 2.20 (t, *J* 7.2 Hz, 2 H), 1.90 (s, 3 H), 1.86 (m, 2 H), 1.57 (m, 4 H), 1.23 (br, 56 H), 1.12 (d, *J* 6.6 Hz, 3 H), 0.83 (t, *J* 7.2 Hz, 6 H); ^{13}C/^{1}H NMR (150/600 MHz, HMQC): 103.0/4.43 (Gal-1), 97.5/5.03 (Fuc-1), 78.8/4.94 (Glu-1), 69.2/5.21 (Glycerol-2); MALDI-TOF-MS: Calcd for $C_{92}H_{139}N_2Na_2O_{24}S$ ($M - H + 2\ Na)^+$ 1734, Found 1733.

5-{*O*-(3-*O*-Sulfo-*β*-D-galactopyranosyl)-(1→3)-[*O*-α-L-fucopyranosyl)-(1→4)]-2-acetamido-2-deoxy-*β*-D-glucopyranosylamino}-5-oxopentanoic Acid 2(*R*,*S*),3-Dioctadecanoyloxypropanyl Ester (4). A mixture of **16** (25 mg, 14.8 μmol) and 10% Pd/C (25 mg) in DCM and MeOH (2:1, 3 mL) was stirred at room temperature in an H_2 atmosphere for 2 days. The solid material was filtered off through a syringe filter and washed with a mixture of MeOH and CH_2Cl_2 (1:1). The filtrates were combined and concentrated in a vacuum to afford **4** (22 mg, 95%) as a white solid. ^{1}H NMR (600 MHz, $CDCl_3$−CD_3OD): δ 5.21 (m, 1 H, Gly-H-2), 4.91 (d, *J* 9.0 Hz, 1 H, H-1); MALDI-TOF-MS: Calcd for $C_{64}H_{116}N_2Na_2O_{24}S$ ($M + 2\ Na)^+$ 1375, Found 1375.

Preparation of Liposomes. Liposomes were prepared by the extrusion method.[31] Briefly, desired volume of lipid stock solutions (20 mg/mL) in chloroform and methanol (3:1, v/v) (6.0 μmol of DSPC for DSPC liposomes, 0.55 μmol of DSPC with 0.05 μmol of PEG-DSPC for PEG liposomes, and 0.55 μmol of DSPC with 0.05 μmol of glycolipid **4** for glycoliposomes) was mixed with a cholesterol stock solution (10 mg/mL) in chloroform (0.154 mL, 4.0 μmol) in a 10-mL round-bottom flask. The total volume was made up to 1 mL by chloroform. The mixtures were deposited in a thin film on the interior of the flask by rotary evaporation under reduced pressure for 30 min, followed by drying in a vacuum oven at room-temperature overnight. Following addition of phosphate-buffered saline (PBS) (1 mL), lipid thin films were

Scheme 1

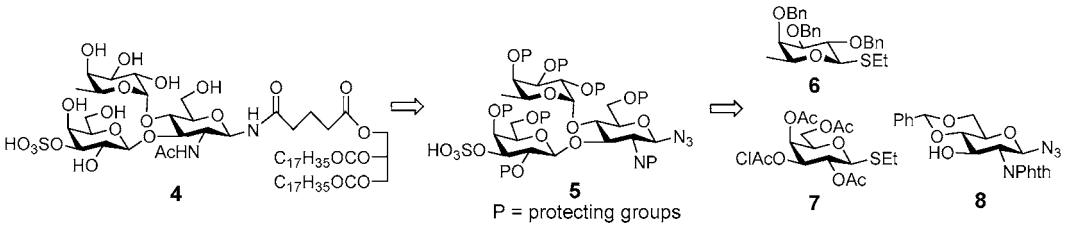

hydrated in 70 °C water bath for 30 min to obtain multilamellar vesicles (MLVs). MLV suspension was subjected to 3−5 freeze−thaw cycles, involving quenching in liquid nitrogen, followed by an immersion at 70 °C in a water bath. Unilamellar vesicles (ULVs) were produced by extrusion through Nucleopore track-etch polycarbonate membranes (Avanti Polar Lipids Inc.) with pore size of 100 nm for 10 times on an Avanti Mini-Extruder (Avanti Polar Lipids Inc.) operated at 75 °C. Then half of the liposomes thus obtained were extruded through 50-nm membranes for 10 more times by the same method. The extruded liposomes were stored at room temperature and followed by measuring the particle size and distribution.

Platelet Preparation. Whole blood (20 mL) was drawn from healthy, medication-free human donors into two 10-mL tubes each containing 1 mL of 3.8% sodium citrate anticoagulant, which was centrifuged at 800 rpm for 15 min to collect platelet-rich plasma (PRP). Platelets were obtained by centrifuging PRP at 1500 rpm for 15 min at 25 °C and resuspended in an equal volume of phosphate-buffered saline (PBS) containing 1% bovine serum albumin (BSA).

Fluorescence Microscopy. Fluorescence microscopy was used to characterize SO_3Le^a liposomes binding to platelets. Liposomes for use in fluorescence experiments were prepared by incorporating 1 mol % of nitrobenzodiazole (NBD)-modified phosphatidylcholine (NBD-PC, Avanti) with other lipids. PRP was incubated on collagen III coated glass coverslips in a multiwell cell culture plate at room temperature for 1 h. Then the coverslips were gently washed with PBS and incubated with NBD-labeled liposomes for 1 h, followed by washing with PBS and fixing in 4% paraformaldehyde. The coverslips were mounted onto glass microscope slides. The uniform distribution of platelets on coverslips was confirmed on a Nikon Diaphot phase-contrast microscope. Fluorescence micrographs were imaged on a Nikon Diaphot epifluorescence inverted microscope fitted with a Spot RT chilled CCD camera. All coverslips were run in triplicate, and multiple fields were examined for each coverslip.

RESULTS AND DISCUSSION

Synthesis of the Lipid Conjugate of SO_3Le^a. In the natural form, Lewis antigens are attached through their reducing ends to lipids and/or proteins. However, the semisynthetic lipid conjugates of Lewis antigens employed in previous studies (*26*, *27*, *37*) had the lipids attached to the 2-amino group of the glucosamine residue, as this position is easily distinguishable from the free hydroxyl groups of the oligosaccharides to enable a regioselective reaction affording well-defined products. Even though the resultant glycoliposomes showed promising properties (*26*, *27*, *37*), a problem with these glycolipids is that the artificial linkage may affect the conformations of the antigens and thereby their binding to selectins. Moreover, although several Lewis antigens including SO_3Le^a were synthesized previously (*35*, *38*−*43*), the reported syntheses did not focus on the conjugation of the antigens to other structures, and the reducing end of the synthetic antigens was usually capped by an unreactive group. Therefore, it would be generally useful to have a practicable method to prepare glycolipids of Lewis antigens with the lipid moiety on the carbohydrate reducing end.

Herein, we design to attach a lipid, 1,2-distearoyl-*sn*-glycerol, to the reducing end of SO_3Le^a via an amide bond using the glutaric group as a bifunctional linker (as shown in the structure of synthetic target **4**, Scheme 1). An important advantage of this design is that it may lead to a highly convergent synthetic procedure. Since an amino group is more reactive than a hydroxyl group, and a carboxylic compound can be conveniently and selectively attached to the amino group of a glycosylamine even in the presence of free hydroxyl groups (*44*), the introduction of the lipid chain can be achieved at the final stage of the glycolipid synthesis. In this case, an azido group that can be selectively reduced to a primary amine under mild condition can be used as a latent amino group. Moreover, since an azido group can withstand most transformations involved in carbohydrate synthesis, it may also serve as a protecting group of the oligosaccharide reducing end to further simplify the synthetic plan, especially in regard to protection tactics. Another useful property of the designed glycolipid **4** is that, compared to natural O-glycosides, a glycosyl amide is less susceptible to glycosidases, and consequently, **4** should be more stable under physiological conditions.

The retrosynthetic analysis of **4** (Scheme 1) results in an azido derivative **5** of SO_3Le^a as the logical key intermediate, whereas **5** can be further disconnected into three monosaccharide blocks **6**, **7**, and **8**. To facilitate the regioselective sulfation of the galactose 3-O-position at a later step, this position was protected by a chloroacetyl (ClAc) group that can be selectively removed in the presence of other acyl groups. Monosaccharide **8** is designed to have the azido group linked to its anomeric carbon.

Scheme 2 outlines the synthesis of the key intermediate **5**. First, the glycosylation of **8** by **7** was accomplished with *N*-iodosuccinimide (NIS) and trifluoromethanesulfonic acid (TfOH) as promoters to form the β-linked disaccharide **9** (H-1: δ 5.35, J = 9.5 Hz; H-1′: δ 4.56, J = 8.0 Hz). Next, the benzylidene ring was regioselectively opened by reaction with sodium cyanoborohydride ($NaBH_3CN$) under a strong acidic condition to afford **10**. The fucosylation of **10** by **6** with tetrabutylammonium bromide and CuBr as promoters (*45*, *46*) gave the α-glycosylation product **11** in an excellent yield (78%) and stereoselectivity, while the same reaction with NIS and TfOH as promoters showed little stereoselectivity. After the chloroacetyl group of **11** was removed by thiourea, a sulfate group was introduced to the same position by reaction with sulfur trioxide trimethylamine complex ($SO_3{\cdot}NMe_3$) in pyridine. This reaction was very clean, and the product **13** could be readily purified by column

Scheme 2 [a]

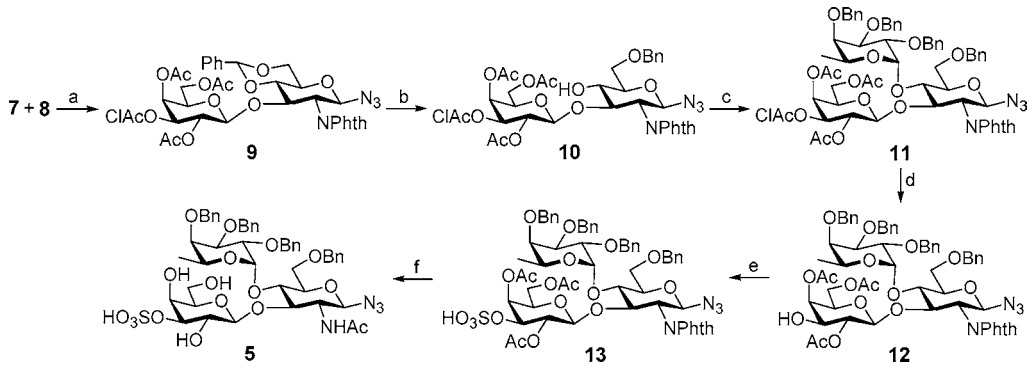

[a] Reagents and conditions: (a) NIS, TfOH, MS 4 Å, CH_2Cl_2, −10 °C to room temperature, overnight, 55%; (b) $NaCNBH_3$, HCl, MS 4 Å, THF, 0 °C, 2 h, 90%; (c) **6**, CuBr, $(n\text{-}Bu)_4NBr$, DMF−CH_2Cl_2 (1:1), rt, 6 h, 78%); (d) thiourea, 2,6-lutidine, EtOH−CH_2Cl_2 (1:4), reflux, 16 h, 86%; (e) $SO_3{\cdot}NMe_3$, pyridine, rt, 24 h, 72%; (f) $H_2NCH_2CH_2NH_2$, butanol, 90 °C, overnight; then Ac_2O, MeOH, rt, 1 h, 50%.

Scheme 3 [a]

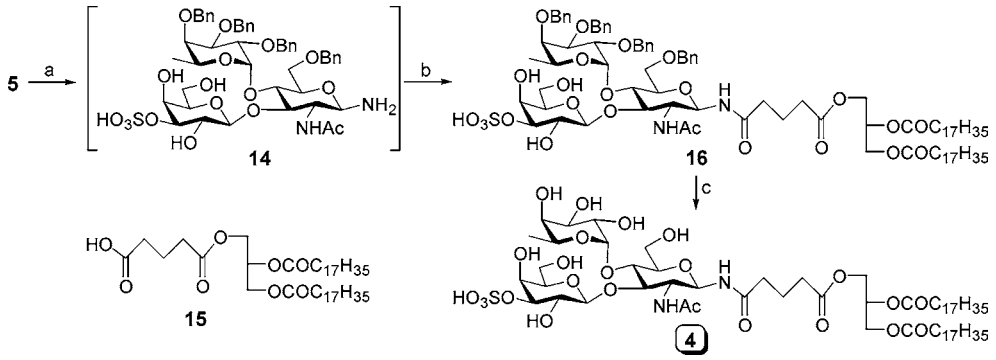

[a] Reagents and conditions: (a) H_2, Lindlar catalyst, MeOH−CH_2Cl_2 (1:1), rt, 2 h; (b) **15**, HOBt, EDC, MeOH−CH_2Cl_2 (1:1), rt, 48 h, 70% (two steps); (c) H_2, 10% Pd/C, MeOH−CH_2Cl_2 (1:2), rt, 48 h, 95%.

chromatography. The removal of the phthalyl and acetyl groups of **13** proved to be problematic. We first examined the reaction using hydrazine, but it afforded a very low yield of the expected product, presumably due to the involvement of the azido group. The deprotection was eventually achieved by heating **13** with ethylenediamine at 90 °C overnight, under which condition the sulfate group was unaffected. Subsequent acetylation of the resultant free amino group was performed in a one-pot manner to give the trisaccharide **5**. The two combined steps afforded a moderate yield (50%). It is worthy noting that the *O*-acetyl groups must be removed at this stage, or it would be impossible to remove the acetyl groups selectively after introducing the lipid moiety that also possesses ester bonds.

To facilitate the coupling of the sulfated trisaccharide **5** and the glycerol lipid via a glutaric group (Scheme 3), **5** was converted into a glycosylamine by selective hydrogenation under the influence of Lindlar catalyst. The resultant amine **14** was immediately treated with 1-[3-(dimethylamino)propyl]-3-ethylcarbodiimide hydrochloride (EDC) and a glutarate of the lipid moiety **15**. The reaction proceeded smoothly to afford the expected glycolipid **16** in a good yield (70%) after column chromatography. Finally, global debenzylation of **16** was realized with 10% Pd/C in a hydrogen atmosphere, leading to the desired free glycolipid **4** that did not require further purification. The structures of the synthetic intermediates and the final product were verified by their NMR and MS spectra.

Properties of SO_3Le^a Modified Liposomes. The resultant glycolipid **4** was incorporated into liposomes in a 5% molar concentration, using 1,2-distearoyl-sn-glycero-3-phosphocholine (DSPC) and cholesterol in a molar ratio of 3:2, by a freeze-thaw and extrusion method (*47*, *48*). The liposomes were sequentially extruded through two membranes of 100 and 50 nm pore size, respectively. The resultant glycoliposome gave a mean vesicle size of 78 nm (Table 1), which is comparable to that of DSPC liposome (63 nm) and 5% mol PEG-modified

Table 1. Particle Size of Various Liposomes

	vesicle size (extrusion by 50 nm membrane)	
liposome[a]	D_v[b] ± SD[c] (nm)	PDI[d]
DSPC	63.3 ± 1.4	0.13
PEG	66.4 ± 1.4	0.12
SO_3Le^a	78.5 ± 1.5	0.20

[a] All liposomes were made with 60 mol % of total lipid and 40 mol % of cholesterol. [b] Average diameter. [c] Standard deviation. [d] Polydispersity index.

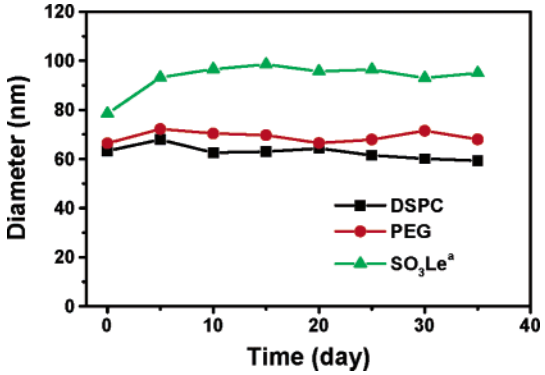

Figure 2. The size of different liposomes at room temperature.

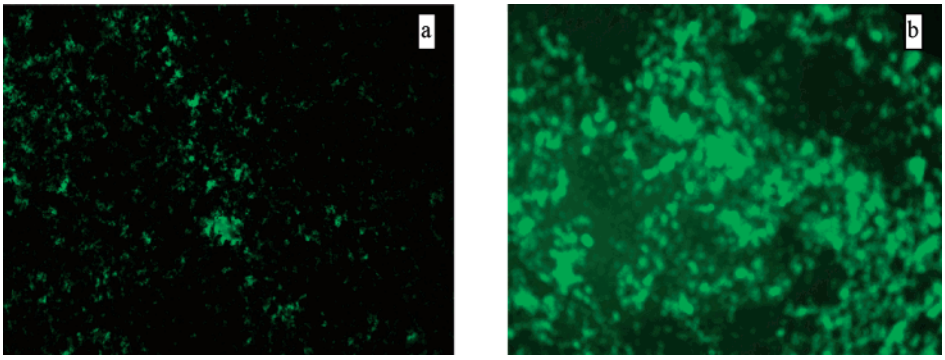

Figure 3. Fluorescence micrographs of platelets labeled with DSPC liposome (a) and SO_3Le^a liposome (b).

liposome (66 nm). The slightly larger size (by ca. 15−20%) of the former may result from the relatively large polar head of the glycolipid.

To investigate whether the increased size of SO_3Le^a-coated liposome would affect its stability, the three kinds of liposome were kept at room temperature for an extended period while the vesicle sizes were analyzed. We found that the size of the glycoliposome increased to about 98 nm at the initial stage but remained unchanged later on for at least one month (Figure 2). The results indicate that the stability of the glycoliposome was comparable to that of DSPC- and PEG-modified liposomes. It may suggest that the glycoliposome is stable enough for practical uses.

The binding of DSPC- and SO_3Le^a-coated liposomes to activated platelets was studied by the fluorescence microscopy method (*49*). The liposomes used in these experiments were prepared by incorporating 1 mol % of nitrobenzodiazole (NBD)-modified phosphatidylcholine which shows green fluorescence. On the other hand, since P-selectin is a component of the α-granule membrane of resting platelets and is only expressed on the activated platelet surface after α-granule secretion, we employed collagen coating on the coverslips to activate and adhere platelets (*50*) in order to observe the platelets more easily by the fluorescence microscope. Thus, the platelet-rich plasma was incubated on collagen III-coated glass coverslips in a multiwell cell culture plate at room temperature. The coverslips were then gently washed with PBS and incubated with NBD-labeled liposomes, followed by washing with PBS and fixing in 4% paraformaldehyde. Fluorescence micrographs of the coverslips were imaged, and the intensity of their green fluorescence from NBD label was calculated by Adobe Photoshop (Version 6.0). It was observed that the color intensity of SO_3Le^a-containing liposome-treated coverslips (Figure 3b) was at least 6.5 times higher than that of DSPC liposome-treated ones (Figure 3a). These results suggested that the SO_3Le^a-coated liposome had much higher binding to activated platelets than the DSPC liposome without SO_3Le^a. The significant increase in binding of the former to activated platelets is attributed to the specific interactions between SO_3Le^a on the glycoliposome and the P-selectin on activated platelets.

In summary, this paper has described an efficient method to prepare the lipid conjugate of SO_3Le^a with the lipid moiety attached to the reducing end of the carbohydrate chain through a bifunctional glutaric group. In the synthesis, the glycosidic azido derivative **5** of SO_3Le^a was employed as a key intermediate. This design facilitated a convergent synthetic procedure with the selective coupling of the lipid moiety to SO_3Le^a achieved at the final stage, which also significantly simplified the design of protection tactics. The strategies developed in this research may be applicable to the synthesis of other glycolipids. Our preliminary studies of the target glycolipid **4** indicate that it can form stable liposomes with DSPC and cholesterol, and the resultant glycoliposomes can bind to activated platelets effectively. These results suggest that SO_3Le^a-coated liposomes may be used to target endothelium for the selective delivery of drugs or be used as antiinflammatory agents via inhibition of the binding of lymphocytes to endothelial cells. These potential applications as well as the multivalent effects necessary for the selectin−carbohydrate ligand interactions are currently under further investigations.

ACKNOWLEDGMENT

This work was supported by a grant from National Institute of Health (R01 HL70263).

LITERATURE CITED

(1) Sapra, P., and Allen, T. M. (2003) Ligand-targeted liposomal anticancer drugs. *Prog. Lipid Res. 42*, 439−462.
(2) Chrai, S. S., Murari, R., and Ahmad, I. (2003) Liposomes, Part II: drug delivery systems. *Pharm. Technol. Eur. 15*, 53−56.
(3) Budai, M., and Szogyi, M. (2001) Liposomes as drug carrier systems. Preparation, classification and therapeutical advantages of liposomes. *Acta Pharm. Hung. 71*, 114−118.
(4) Sharma, A., and Sharma, U. S. (1997) Liposomes in drug delivery: Progress and limitations. *Int. J. Pharm. 154*, 123−140.
(5) Allen, T. M., and Moase, E. H. (1996) Therapeutic opportunities for targeted liposomal drug delivery. *Adv. Drug Delivery Rev. 21*, 117−133.
(6) Lasic, D. D., and Barenholz, Y. (1996) Liposomes: Past, Present, and Future. *Handbook of Nonmedical Applications of Liposomes* (Lasic, D. D. and Barenholz, Y., Eds.) pp 299−315, Volume 4, CRC, Boca Raton, FL.
(7) Weiner, N., Martin, F., and Riaz, M. (1989) Liposomes as a drug delivery system. *Drug Dev. Indust. Pharm. 15*, 1523−1554.
(8) Kawakami, S., Yamashita, F., Nishida, K., Nakamura, J., and Hashida, M. (2002) Glycosylated cationic liposomes for cell-selective gene delivery. *Crit. Rev. Ther. Drug Carrier Syst. 19*, 171−190.
(9) Sihorkar, V., and Vyas, S. P. (2001) Potential of polysaccharide anchored liposomes in drug delivery, targeting and immunization. *J. Pharm. Pharm. Sci. 4*, 138−158.
(10) Jones, M. N. (1994) Carbohydrate-mediated liposomal targeting and drug delivery. *Adv. Drug Delivery Rev. 13*, 215−249.
(11) Allen, T. M., Hansen, C., and Rutledge, J. (1989) Liposomes with prolonged circulation times: Factors affecting uptake by reticuloendothelial and other tissues. *Biochim. Biophys. Acta 981*, 27−35.
(12) Mori, A., Klibanov, A. L., Torchilin, V. P., and Huang, L. (1991) Influence of the steric barrier activity of amphipathic poly(ethyleneglycol) and ganglioside GM1 on the circulation

time of liposomes and on the target binding of immunoliposomes in vivo. *FEBS Lett. 284*, 263−266.
(13) Liu, D., A., M., and Huang, L. (1992) Role of liposome size and RES blockade in controlling biodistribution and tumor uptake of GM1-containing liposomes. *Biochim. Biophys. Acta 1104*, 95−101.
(14) Oku, N., and Namba, Y. (1994) Long-circulating liposomes. *Crit. Rev. Ther. Drug Carrier Syst. 11*, 231−270.
(15) Allen, T. M., Hansen, C., Martin, F., Redemann, C., and Yau-Young, A. (1991) Liposomes containing synthetic lipid derivatives of poly(ethyleneglycol) show prolonged circulation half-lives in vivo. *Biochim. Biophy. Acta 1088*, 29−36.
(16) Gabizon, A., and Papahadjopoulos, D. (1992) The role of surface charge and hydrophilic groups on liposome clearance in vivo. *Biochim. Biophy. Acta 1103*, 94−100.
(17) Ashwell, G., and Harford, J. (1982) Carbohydrate-specific receptors of the liver. *Annu. Rev. Biochem. 51*, 531−554.
(18) Vasta, G. R., M., Q., Ahmed, H., and O'Leary, N. (1999) C-type lectins and galectins mediate innate and adaptive immune functions: Their roles in the complement activation pathway. *Dev. Comp. Immunol.* 401−420.
(19) Yamazaki, N., Kojima, S., Bovin, N., Andre, S., Gabius, S., and J., G. H. (2000) Endogenous lectins as targets for drug delivery. *Adv. Drug Delivery Rev. 43*, 225−244.
(20) Sharon, N. (1984) Carbohydrates as recognition determinants in phagocytosis and in lectin-mediated killing of target cells. *Biol. Cell. 51*, 239−246.
(21) Gordon, S., Perry, V. H., Rabinowitz, S., P., C. L., and Rosen, H. (1988) Plasma membrane receptors of the mononuclear phagocyte system. *J. Cell. Sci. 9 (Suppl.)*, 1−26.
(22) Opanasopit, P., Higuchi, Y., Kawakami, S., Yamashita, F., Nishikawa, M., and Hashida, M. (2001) Involvement of serum mannan binding proteins and mannose receptors in uptake of mannosylated liposomes by macrophage. *Biochim. Biophys. Acta 1511*, 134−145.
(23) Vyas, S. P., Katare, Y. K., Mishra, V., and Sihorkar, V. (2000) Ligand directed macrophage targeting of amphotericin B loaded liposomes. *Int. J. Pharm. 210*, 1−14.
(24) Nag, A., and Ghosh, P. (1999) Assessment of targeting potential of galactosylated and mannosylated sterically stabilized liposomes to different cell types of mouse liver. *J. Drug Target. 6*, 427−438.
(25) Kawakami, S., Munakata, C., Fumoto, S., Yamashita, F., and Hashida, M. (2001) Novel galactosylated liposomes for hepatocyte-selective targeting of lipophilic drugs. *J. Pharm. Sci. 90*, 105−113.
(26) DeFrees, S. A., Phillips, L., Zalipsky, S., and Guo, L. (1996) Sialyl Lewis x liposomes as a multivalent ligand and inhibitor of E-selectin-mediated cellular adhesion. *J. Am. Chem. Soc. 118*, 6101−6104.
(27) Murohara, T., Margiotta, J., Phillips, L. M., Paulson, J. C., DeFrees, S., Zalipsky, S., Guo, L. S., and Lefer, A. M. (1995) Cardioprotection by liposome-conjugated sialyl Lewis x-oligosaccharide in Myocardial Ischaemia and reperfusion Injury. *Cardiovasc. Res. 30*, 965−974.
(28) Zeisig, R., Stahn, R., Wenzel, K., Behrens, D., and Fichtner, I. (2004) Effect of sialyl Lewis X-glycoliposomes on the inhibition of E-selectin-mediated tumour cell adhesion in vitro. *Biochim. Biophys. Acta 1660*, 31−40.
(29) Vodovozova, E. L., Moiseeva, E. V., Grechko, G. K., Gayenko, G. P., Nifant′ev, N. E., Bovin, N. V., and Molotkovsky, J. G. (2000) Antitumor activity of dytotoxic liposomes equipped with selectin ligand siaLeX, in a mouse mammary adenocarcinoma model. *Eur. J. Cancer 36*, 942−949.
(30) McEver, R. P. (1991) Selectins: Novel receptors that mediate leukocyte adhesion during inflammation. *Thromb. Haemost. 65*, 223−228.
(31) Bertozzi, C. R. (1995) Cracking the carbohydrate code for selectin recognition. *Chem. Biol. 2*, 703−708 and references therein.
(32) Somers, W. S., Tang, J., Shaw, G. D., and Camphausen, R. T. (2000) Insights into the molecular basis of leukocyte tethering and rolling revealed by structures of P- and E-selectin bound to sLe (X) and PSGL-1. *Cell 103*, 467−479.
(33) Mulligan, M. S., Paulson, J. C., Frees, S. D., Zhang, Z.-L., Lowe, J. B., and Ward, P. A. (1993) Protective effects of oligosaccharides in P-selectin-dependent lung injuries. *Nature 364*, 149−151.
(34) Xie, X., Rivier, A.-S., Zakrzewicz, A., Bernimoulin, M., Zeng, X.-L., Wessel, H. P., Schapira, M., and Spertini, O. (2000) Inhibition of selectin-mediated cell adhesion and prevention of acute inflammation by nonanticoagulant sulfated saccharides. *J. Biol. Chem. 275*, 34818−34825.
(35) DeFrees, S. A., Kosch, W., Way, W., Paulson, J. C., Sabesan, S., Halcomb, R. L., Huang, D.-H., Ichikawa, Y., and Wong, C.-H. (1995) Ligand recognition by E-selectin: Synthesis, inhibitory activity and conformational analysis of bivalent sialyl Lewis x analogues. *J. Am. Chem. Soc. 117*, 66−79.
(36) Yuen, C.-T., Bezouska, K., B′Brien, J., Stoll, M., Lemoine, R., Lubineu, A., Kiso, M., hasegawa, A., Bockovich, N. J., Nicolaou, K. C., and Feizi, T. (1994) Sulfated blood group Lewis a: A superior oligosaccharide ligand for human E-selectin. *J. Biol. Chem. 269*, 1595−1598.
(37) Zalipsky, S., Mullah, N., Harding, J. A., Gittelman, J., Guo, L., and DeFrees, S. A. (1997) Poly(ethylene glycol)-grafted liposomes with oligopeptide or oligosaccharide ligands appended to the termini of the polymer chains. *Bioconjugate Chem. 8*, 111−118.
(38) Kameyama, A., Ishida, H., Kiso, M., and Hasegawa, A. (1991) Total synthesis of sialyl Lewis x. *Carbohydr. Res. 209*, c1-c4.
(39) Blixt, O., and Norberg, T. (1998) Solid-phase enzymatic synthesis of a sialyl Lewis X tetrasaccharide on a sepharose matrix. *J. Org. Chem. 63*, 2705−2710.
(40) Kiyoi, T., Nakai, Y., Kondo, H., Ishida, H., Kiso, M., and Hasegawa, A. (1996) A highly practical synthesis of the sialyl Lewis X pentasaccharide and an investigation of binding to E-, P-, and L-selectins. *Bioorg. Med. Chem. 4*, 1167−1176 (and references therein).
(41) Rosch, M., Herzner, H., Dippold, W., Wild, M., Vestweber, D., and Kunz, H. (2001) Synthetic Inhibitors of Cell Adhesion: A Glycopeptide from E-Selectin Ligand 1 (ESL-1) with the Arabino Sialyl Lewisx Structure. *Angew. Chem., Int. Ed. 40*, 3836−3839.
(42) Nicolaou, K. C., Bockovich, N. J., and Carcanague, D. R. (1993) Total synthesis of sulfated Le^x and Le^a-type oligosaccharide selectin ligands. *J. Am. Chem. Soc. 115*, 8843−8844.
(43) Kretzschmar, G., and Stahl, W. (1998) Large scale synthesis of linker-modified sialyl Lewis X, Lewis X and N-acetyllactosamine. *Tetrahedron 54*, 6341−6358.
(44) Wen, S., and Guo, Z. (2001) Unprotected oligosaccharides as phase-tags: Solution-phase synthesis of glycopeptides with solid-phase workups. *Org. Lett. 3*, 3773−3776.
(45) Lemieux, R. U., Hendriks, K. B., Stick, R. V., and James, K. (1975) Halide ion catalyzed glycosidation reactions. Syntheses of α-linked disaccharides. *J. Am. Chem. Soc. 97*, 4056−4062.
(46) Dan, A., Lergenmüller, M., Amano, M., Nakahara, Y., Ogawa, T., and Ito, Y. (1998) p-Methoxybenzylidene-tethered β-mannosylation for stereoselective synthesis of asparagine-linked glycan chains. *Chem. Eur. J. 4*, 2182−2190.
(47) Olson, F., Hunt, C. A., Szoka, F. C., Vail, W. J., and Papahadjopoulos, D. (1979) Preparation of liposomes of defined size distribution by extrusion through polycarbonate membranes. *Biochim. Biophys. Acta 557*, 9−23.
(48) Hope, M. J., Bally, M. B., Webb, G., and Cullis, P. R. (1985) Production of large unilamellar vesicles by a rapid extrusion procedure. Characterization of size distribution, trapped volume and ability to maintain a membrane potential. *Biochim. Biophys. Acta 812*, 55−65.
(49) Lestini, B., Sagnella, S. M., Xu, Z., Shive, M. S., Richter, N. J., Jayaseharan, J., Case, A. J., Kottke-Marchant, K., Anderson, J. M., and Marchant, R. E. (2002) Surface modification of liposomes for selective cell targeting in cardiovascular drug delivery. *J. Controlled Release 78*, 235−247.
(50) Michelson, A. D., Barnard, M. R., Krueger, L. A., Frelinger, A. L., and Furman, M. I. (2000) Evaluation of platelet function by flow cytometry. *Methods 21*, 259−270.

BC049805C

Affinity Capture of a Mammalian DNA Polymerase β by Inhibitors Immobilized to Resins Used in Solid-Phase Organic Synthesis

Kouji Kuramochi,[†] Tetsuya Haruyama,[‡] Ryo Takeuchi,[‡] Takashi Sunoki,[#] Madoka Watanabe,[‡] Masahiko Oshige,[†] Susumu Kobayashi,[†,#] Kengo Sakaguchi,[†,‡] and Fumio Sugawara*[,†,‡]

Genome and Drug Research Center, Department of Applied Biological Science, and Faculty of Pharmaceutical Sciences, Tokyo University of Science, Noda, Chiba 278-8510, Japan. Received August 24, 2004; Revised Manuscript Received November 28, 2004

The application of resins normally used in solid-phase organic synthesis to the affinity capture of a mammalian DNA polymerase β (pol β) is reported. Lithocholic acid (LCA), an inhibitor of pol β, was immobilized on various solid supports, and the batch affinity purification of pol β from a mixture of proteins using these LCA-immobilized resins was examined. Of the resins tested, TentaGel was the most effective at purifying pol β and at resisting nonspecific absorption of proteins. The immobilized LCA recognized pol β specifically, which resulted in pol β binding to the resin. Using the LCA-immobilized resin, it was possible to purify pol β from a mixture of proteins. Furthermore, it was possible to concentrate pol β from a crude nuclear extract of human T lymphoma Molt4 cells. To facilitate the immobilization of compounds on TentaGel resins, we also designed and prepared photoaffinity beads containing a photoreactive group at the free termini of the TentaGel resin. The pol β inhibitors LCA, C_{18}-β-SQDG, and epolactaene were immobilized on the photoaffinity beads by photoreaction. The batch affinity purification of pol β from a protein mixture could be also achieved with these beads.

INTRODUCTION

DNA replication, repair, and recombination are important processes for all organisms. Many classes of DNA polymerases (pols) have been identified in multicellular eukaryotes, and recent investigations have revealed that eukaryotic cells contain at least 14 types of DNA pol (*1*). The purification of DNA pols is still a laborious and time-consuming endeavor. For example, a combination of many types of column chromatography (for example, phosphocellulose, human serum conjugated sepharose, rabbit IgG conjugated sepharose, and monoclonal antibody conjugated sepharose column chromatography) has been often used for the purification of DNA polymerase β.

One approach to studying the various roles of each of the DNA pols is to use inhibitors as tools and molecular probes to distinguish among the various DNA pols and to clarify their biological and in vivo functions. We previously identified a number of such inhibitors against DNA pols by screening both natural and synthetic products (*2*–*5*). Use of these inhibitors against DNA pols as molecular probes is also important for purifying DNA pols and for understanding their biological functions in detail.

Lithocolic acid (LCA), one of the bile acids, has been reported to promote tumorigenesis induced by *N*-methyl-*N*′-nitro-*N*-nitrosoguanidine in rats (*6*–*8*) and to possess inhibitory activities against eukaryotic DNA pol α and β (*9*–*11*). We previously found that both the hydrophilic end (carboxyl group) and the hydrophobic region (steroidal skeleton) greatly influence the inhibitory activity of LCA, and that LCA binds to the 8-kDa DNA binding domain of DNA pol β (*11*). $^{1}H-^{15}N$ HMQC NMR analysis of the 8-kDa domain of pol β bound to LCA showed that LCA binds to the N-terminal 8-kDa domain of pol β as a 1:1 complex and interacts mainly with three amino acids (Lys 60, Leu 77, and Thr 79) in this domain (*10*, *11*). In addition, we previously prepared biotinylated LCA derivatives and developed affinity chromatography for the separation of DNA pol α and β from a mixture of the two proteins (*12*).

Recently, small molecules have been immobilized on solid surfaces to facilitate the purification, and to profile the cellular activities, of their binding proteins (*13*–*18*). Several matrixes for affinity purification have been reported, including a glycidyl methacrylate (GMA)-covered GMA-styrene copolymer core (*15*), a poly(methacrylate) polymer (*16*, *17*), and a poly(ethylene glycol) dimethylacrylamide (PEGA) copolymer (*18*), among others.

Affinity purification of proteins is usually performed in aqueous solutions; however, the immobilization of bioactive compounds is usually performed in organic solvents. For this reason, we are interested in applying resins used for solid-phase organic synthesis to the development of methods for the affinity capture of proteins (*16*–*18*). Resins for solid-phase organic synthesis represent an ideal matrix for affinity purification because they are stable in both aqueous and organic media as well as under synthetic conditions (*16*, *17*, *19*). In addition to these attractive features, significant advances in solid-phase synthesis, coupled with improvements in solid polymer supports and linkers, have made it possible to attach structurally complex and diverse compounds onto

* Corresponding author. Tel: +81-(0)4-7124-1501. Fax: +81-(0)4-7123-9767. E-mail: sugawara@rs.noda.tus.ac.jp.
[†] Genome and Drug Research Center.
[‡] Department of Applied Biological Science.
[#] Faculty of Pharmaceutical Sciences.

10.1021/bc0497970 CCC: $30.25 © 2005 American Chemical Society
Published on Web 12/31/2004

the resins. Herein we report the application of resins used for organic synthesis to the detection and purification of DNA pol β.

EXPERIMENTAL PROCEDURES

Compounds **2** and **5** were prepared according to the reported procedures (*12*, *20*−*22*). The determination of compound **2**, **5**, and LCA was performed by measuring ^{1}H NMR, ^{13}C NMR, IR, and MS data. ^{1}H and ^{13}C NMR spectra were recorded on a JEOL JNM-400 (Japan) or on a BRUKER DXR400 or DRX600 instrument (Germany). Chemical shifts were reported in δ, parts per million (ppm), relative to TMS as an internal standard or were calibrated by using residual undeuterated solvent as an internal reference. IR spectra were recorded on a JASCO FT/IR-410 spectrometer (Japan). Mass spectra were obtained on an ABI QSTAR Pulsar spectrometer equipped with an ESI ion source. UV irradiation was performed by an UM-453-A instrument (Ushio Inc., Japan). Column chromatography was carried out with Fuji Silisia PSQ100B silica gel (Japan). The immobilization of **2** and **5** on resins and cleavage of LCA from **3a** were checked by analytical thin-layer chromatography (TLC). TLC was performed on precoated Merck silica gel 60 F_{254} plates (Germany), and compounds were visualized by UV illumination (254 nm) or by heating the plates to 150 °C after spraying them with phosphomolybdic acid in ethanol. THF was distilled from sodium/benzophenone; CH_2Cl_2 was distilled from P_2O_5; and DMSO was distilled from CaH_2. All other solvent and reagents were obtained from commercial sources and used without further purification. Organic extracts were dried over $MgSO_4$, filtered, and concentrated by using a rotary evaporator. Involatile oils and solids were vacuum-dried.

Succinimidyl carbonate TentaGel resins (0.5 mmol/g) were purchased from Advanced ChemTech (USA); *p*-Nitrophenyl carbonate Merrifield resins (1.0 mmol/g) were obtained from Novabiochem (USA); and succimidyl carbonate Wang resins (1.0 mmol/g) were purchased from Aldrich (USA).

The fluorescein amine isomer II-immobilized resins were scanned for fluorescence by Xioskop2 plus, ebg 100 ISOLATED-2 and AxioCam HRm instrumentation (Carl Zeiss Co., Germany).

We used the following buffers: His-buffer A, containing 0.5 M NaCl, and 20 mM Tris-HCl (pH 7.9) buffer and 5 mM immidazole; His-buffer B, containing 0.5 M NaCl, and 20 mM Tris-HCl (pH 7.9) buffer and 60 mM immidazole; His-buffer C, containing 0.5 M NaCl, and 20 mM Tris-HCl (pH 7.9) buffer and 1 M immidazole; TEG buffer A, containing 50 mM Tris-HCl (pH 7.5), 1 mM EDTA, 10% (v/v) glycerol and 50 mM NaCl; TEG buffer B, containing 50 mM Tris-HCl (pH 7.5), 1 mM EDTA, 10% (v/v) glycerol and 1 M NaCl; TEG buffer C, containing 50 mM Tris-HCl (pH 7.5), 1 mM EDTA, 10% (v/v) glycerol and 100 mM NaCl; TEG buffer D, containing 50 mM Tris-HCl (pH 7.5), 1 mM EDTA, 10% (v/v) glycerol and 500 mM NaCl; sucrose buffer A, containing 50 mM Tris-HCl (pH 7.5), 50 mM NaCl, 1 mM EDTA, 5 mM 2-mercaptoethanol, 0.01% Nonidet-40, protease inhibitors (1 μg/mL leupeptin, 1 μg/mL pepstatin A, and 1 mM phenylmethylsulfonyl fluoride) and 0.25 M sucrose; and sucrose buffer B, containing 50 mM Tris-HCl (pH 7.5), 50 mM NaCl, 1 mM EDTA, 5 mM 2-mercaptoethanol, 0.01% Nonidet-40, protease inhibitors, and 1 M sucrose.

General Method for the Preparation of LCA-immobilized Resins. A suspension of each resin **1a**−**c** (1.0 equiv), 3-(3′-aminopropionyl)lithocholic acid (**2**) (1.2 equiv) and diidopropylethylamine (3 equiv) in DMSO-acetone-$CHCl_3$ (3:1:1, v/v) was stirred at 50 °C for 3 days. The processes of the reactions were checked by TLC. Each mixture was quenched by the addition of MeOH (1 mL) and then stirred at 50 °C for a further 1 h. Each mixture was filtered and washed with MeOH three times and dried in vacuo.

General Method for the Preparation of Methyl Carbonate Resins. A suspension of each resin **1a**−**c** (1 equiv) and K_2CO_3 (3 equiv) in MeOH was stirred at room temperature (rt) for 1 day. Each mixture was filtered and washed with MeOH three times. The resulting resins were dried in vacuo.

General Determination of the Amount of LCA on the Resins. A suspension of each LCA-immobilized resin (50 mg) and 1 N NaOH aq (0.5 mL) in THF−MeOH−H_2O (3:1:1 v/v, 2.5 mL) was stirred at room temperature for 1 day. The processes of the reactions were checked by TLC. Each mixture was filtered and washed with EtOAc three times. The filtrate was acidified to pH 1 and extracted with EtOAc three times. The organic layer was dried ($MgSO_4$) and evaporated. The residue was purified by silica gel chromatography to yield lithocholic acid (LCA). The determination of LCA was performed by measuring ^{1}H NMR, ^{13}C NMR, IR, and MS data.

Preparation of the Photoaffinity Beads. To a solution of TentaGel-CO_2Su (0.5 mmol/g, 56.0 mg) and **5** (20.0 mg, 0.056 mmol) in DMF (0.6 mL) was added *i*-Pr_2NEt (0.02 mL, 0.11 mmol) at room temperature. The mixture was then stirred for 34 h at room temperature. The processes of the reactions were checked by TLC. After filtration, the beads obtained were washed with MeOH three times to yield photoaffinity beads.

General Method for the Immobilization of Compounds on Photoaffinity Beads. A solution of photoaffinity beads (0.165 mmol/g, 30.0 mg) and substrate (5.0 μmol) in MeOH was stirred for 30 min. The solvent was removed under reduced pressure and the beads were dried in vacuo. After irradiation of the photoaffinity beads and substrate by a high-pressure mercury arc lamp for 1 h, the beads were washed with MeOH (3 times) and dried in vacuo.

Expression and Purification of Six Histidine Tagged-DNA Polymerase β (pol β) (*23*). The cDNA encoding pol β from *Rattus norvegicus* was cloned into the expression vector pET28b(+), and the *Escherichia coli* BL21 (DE3) was transformed with the vector. A single colony was used to incubate 600 mL of LB medium containing 1% glucose and 50 μg/mL of kanamycin at 30 °C. The cells were grown overnight and used to incubate 6 L of the same medium at 30 °C. After 3 h of growth, 1 mM IPTG was added. After 4 h of growth at 30 °C, the cells were harvested by centrifugation at 4000 rpm for 10 min at 4 °C in a HITACHI 10A rotor. The cells were resuspended in His-buffer A, sonicated 20 times for 20 s, and centrifuged for 30 min at 15 000 rpm in a HITACHI 20−2 rotor (Japan) at 4 °C. The supernatant was loaded onto His-Bind Resin preequilibrated with His-buffer A. The column was washed with His-buffer B, and the bound proteins were eluted with His-buffer C. The fraction containing the six-histidine-tagged pol β protein was dialyzed against TEG buffer (containing 50% (v/v) glycerol and 100 mM NaCl) and stored at −20 °C until use.

SDS−PAGE Analysis. Analyses by SDS−PAGE were generally done with 15% SDS−polyacrylamide gels and CBB staining. The eluted fractions of the resins from the nuclear extract were analyzed by SDS−PAGE (10−20% gel) and the gel was stained with silver.

Western Blotting Analysis (*24*). For Western blotting analysis, purified proteins were first resolved on SDS−PAGE gel (10−20%) and then transferred to nitrocellulose membranes and probed with a primary antibody, DNA polymerase β Ab-3 rabbit polyclonal antibody (Lab vision corporation, USA). Anti-rabbit IgG conjugated with horseradish peroxidase (VECTOR Laboratories, Inc., USA) was used as a secondary antibody. The antigen−antibody complex was visualized using Super-Signal West Dura (PIERCE). The chemiluminescence of the bands corresponding to human DNA polymerase β was quantified using Luminescent image analyzer, according to the manufacturer's instructions (LAS-1000 plus, Fuji Film, Japan).

Affinity Purification Using the LCA-Immobilized TentaGel, Merrifield, and Wang Resins. All procedures were performed at 4 °C. Each resin (20 mg), preequilibrated with TEG buffer A, was added to a solution (1.0 mL) of proteins (pol β, 8 nmol; hemoglobin, 15 nmol; trypsin inhibitor, 15 nmol; lysozyme, 15 nmol) in TEG buffer A, and the batch adsorption of proteins to the proteins was carried out overnight. Hemoglobin, trypsin inhibitor, and lysozyme were purchased from Wako Pure Chemical Industry (Japan). The resin was collected by centrifugation, and 800-μL aliquots of each supernatant (flow through) were kept for analysis. The resins were then washed 4 times with 800 μL TEG buffer A, and 800-μL aliquots of each supernatant (wash) were kept for analysis. Elution was performed 3 times with 100 μL of TEG buffer A containing 1% Tween20 and 80-μL aliquots of each supernatant (eluate) were kept for analysis. The resins were then boiled at 100 °C in 20 μL of SDS−PAGE loading buffer containing 1.25 mM DTT, 2.5% SDS, 100 mM Tris-HCl pH 6.8, 12.5% (v/v) glycerol and 0.01% BPB and 20-μL aliquots of each sample were kept for analysis.

Determination of the Amount of pol β bound To the Photoaffinity Beads Immobilized pol β Inhibitors (*25*). Each resin (10 mg) was suspended in 800 μL of TEG buffer and then 200 μL of pol β predialyzed against TEG buffer C was added. The batch adsorptions of proteins were carried out overnight. The amount of the His- tagged pol β protein bound to the beads was determined by Bradford assay, with absorbance measured at 595 nm.

Detection of pol β from Human T lymphoma Molt4 Cells by Using LCA-Immobilized TentaGel Resin. All procedures were performed at 4 °C. Frozen Molt4 cells (1 g) were crushed and suspended in 10 mL of sucrose buffer A. The Molt4 suspension was homogenized, and then centrifuged for 10 min at 9000 rpm in a HITACHI 20-2 rotor. The precipitate was then resuspended in 10 mL of sucrose buffer A. The suspension was layered in a thin band on top of 30 mL of sucrose buffer B, and then centrifuged for 30 min at 9000 rpm in a HITACHI 20-2 rotor. The precipitate was suspended in 5 mL of TEG buffer C containing 5 mM 2-mercaptoethanol, 0.01% Nonidet-40, and protease inhibitors, sonicated, and incubated on ice for 20 min, before being centrifuged for 20 min at 15 000 rpm in a HITACHI 20-2 rotor. The supernatant was further centrifuged for 30 min at 40 000 rpm in a HITACHI 70 Ti rotor (Japan).

The LCA-immobilized TentaGel resin (10 mg) and nonimmobilized one (10 mg), which were preequilibrated with TEG buffer C, were added to the supernatant (5 mg; 1.2 mL) to adsorb proteins. After incubation of the sample for 3.5 h, aliquots of the supernatant were removed and kept for the analysis. These resins were first batch washed five times with 1 mL of TEG buffer C for 10 min and 1-mL aliquots of each supernatant were kept. Next TEG buffer D (200 μL) was added to each resin, batch elution was carried out for 10 min, and 200-μL aliquots of each supernatant were kept. Then TEG buffer B (200 μL) was then added to each resin, batch elution was carried out for 10 min, and then 200-μL aliquots of each supernatant were kept for analysis. Finally, TEG buffer B (200 μL) containing 1% Tween20 was added to each resin, batch elution was carried out for 10 min, and 200-μL aliquots of each supernatant were kept.

Scheme 1. Preparation of LCA-immobilized Resins[a]

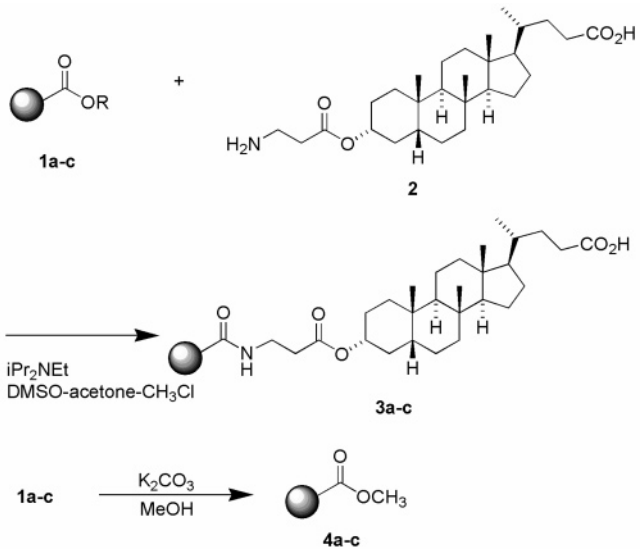

[a] (a) TentaGel resins. (b) Merrifield resins. (c) Wang resins. R = *N*-succinimidyl (**1a** and **1c**) and R = *p*-nitrophenyl (**1b**).

RESULTS AND DISCUSSION

Initially, lithocholic acid (LCA) was immobilized on TentaGel resins (**1a**), Merrifield resins (**1b**), and Wang resins (**1c**). We previously found that the carboxyl group of LCA plays an important role in the inhibitory activity of LCA toward DNA pols (*11*, *12*). Therefore, LCA was immobilized on the resins with the 3-hydroxyl group rather than the carboxyl group (*12*). Treatment of carbonate resins **1a**−**c** and 3-(3′-aminopropionyl)lithocholic acid (**2**) with *i*Pr_2NEt in DMSO−acetone−$CHCl_3$ gave LCA-immobilized resins **3a**−**c** (Scheme 1). The amount of LCA immobilized was determined from the amount of LCA cleaved by hydrolysis from the resins. As a result, the amount of LCA immobilized on **3a**−**c** was 0.14, 0.48, and 0.10 μmol/mg of resin, respectively. Methyl carbonate resins **4a**−**c** were also prepared to examine the nonspecific binding of proteins.

To test the ability of these affinity resins, the maximum amount of pol β (*23*) binding to each resin (10 mg) was determined by monitoring absorbance at 595 nm (Figure 1). After **3a**−**c** (10 mg each) were equilibrated with a buffered solution of pol β (0.21 mg, 5.4 nmol), the amount of pol β that bound to the resins was determined by the colorimetric method reported by Bradford (*25*). From the amount of pol β that bound to **4b** and **4c** (0.014 and 0.012 mg, respectively), about 30% of the amount of pol β that bound to **3b** and **3c** was due to nonspecific binding. By contrast, only a small amount (0.003 mg) of pol β bound to **4a**; thus, the nonspecific binding of pol β to resin **3a** was far less (∼10%). We consider that the poly(ethylene glycol) (PEG) grafted on the TentaGel resin used in **3a** and **4a** prevented the nonspecific binding of pol β (*26*, *27*).

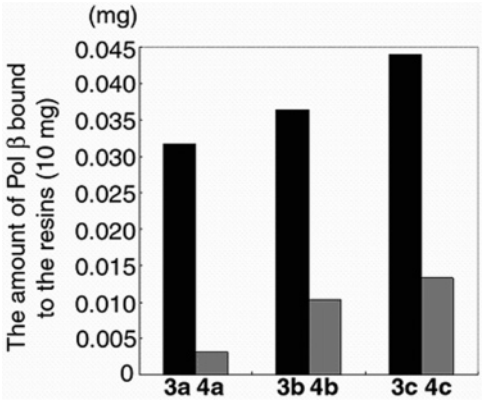

Figure 1. Pol β binding to resins **3a**−**c** and **4a**−**c**. Methyl carbonate resins (**4a**−**c**) were used as a negative control. The amount of pol β bound to each resin was determined by Bradford assay (*25*) by monitoring absorption at 595 nm.

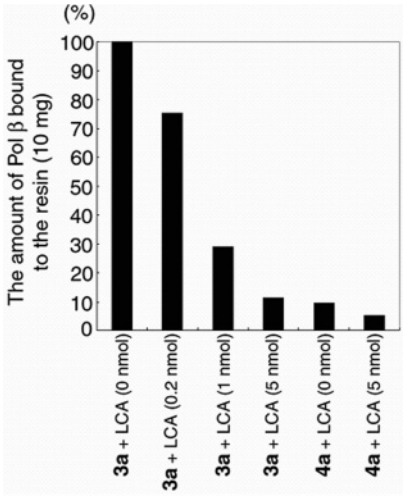

Figure 2. Inhibition of pol β adsorption to the resins by the addition of free LCA. The relative amount of pol β bound to **3a** in the absence and presence of increasing concentrations of free LCA was determined. The amount of pol β bound to **3a** in the absence of free LCA was arbitrarily taken to be 100%. Resin **4a** was used as a negative control.

The total amount of LCA that was immobilized on 10 mg of **3a** was 1.4 μmol, whereas the amount of pol β binding to 10 mg of **3a** was only 0.81 nmol (0.032 mg). The low absorption capacity of **3a** for pol β will be the low affinity between LCA and pol β. Our previous NMR experiments suggested that the 8-kDa domain of pol β binds to free LCA in a 1:1 ratio with a dissociation constant (K_D) of 1.56 mM (*10*). Use of resins bearing the higher affinity inhibitor against pol β will improve the absorption capacity, and the greater the amount of **3a** that is used, the greater the amount of pol β that will bind to **3a**. Indeed, 1.8 nmol (0.070 mg) of pol β was absorbed onto 20 mg of **3a** (data not shown).

To confirm that the LCA immobilized on the surface of **3a** specifically recognized pol β, we carried out competition assays of pol β adsorption to the resins in the presence of free LCA (Figure 2). The amount of pol β bound to **3a** in the absence and presence of increasing amounts of LCA was determined. The results showed that the greater the amount of free LCA that was added, the greater the amount of pol β that was unbound. This competitive inhibition of binding between **3a** and pol β by the addition of free LCA indicated that pol β bound to the LCA immobilized on **3a** in a specific manner.

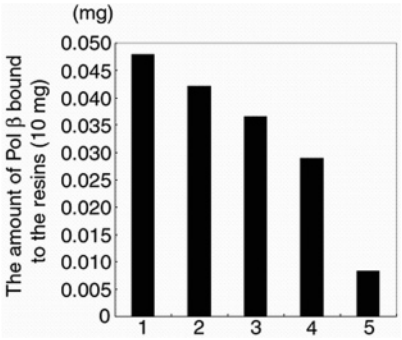

Figure 3. Relationship between the amount of LCA immobilized on **3a** and the amount of pol β bound to the resin. The amount of LCA immobilized on TentaGel resins was as follows: lane 1, 0.16 μmol/mg of resin; lane 2, 0.14 μmol/mg of resin; lane 3, 0.09 μmol/mg of resin; lane 4, 0.07 μmol/mg of resin; lane 5, 0.04 μmol/mg of resin.

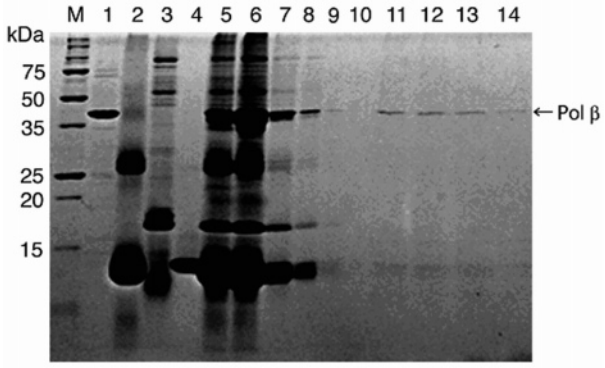

Figure 4. SDS−PAGE of input materials (pol β, hemoglobin, lysozyme, and trypsin inhibitor), flow-through, wash, elute, and resin during affinity purification with **3a**. Lane 1, pol β; lane 2, hemoglobin; lane 3, trypsin inhibitor; lane 4, lysozyme; lane 5, mixture of these proteins; lane 6, flow-through; lane 7−10, wash; lane 11−13, elute; lane 14, resin; M, molecular weight marker.

We next examined the relationship between the amount of LCA immobilized and the amount of pol β bound to the resin (Figure 3). Resins, **3a** with various concentrations of immobilized LCA (0.04 $\sim$ 0.16 μmol/mg resin), were prepared, and the amount of pol β bound to each resin was determined by Bradford assay. The amount of the LCA immobilized was determined by the amount of LCA cleaved by hydrolysis from the resins. The immobilization of **2** on **1a** under various conditions was also examined; however, the maximum concentration of immobilized LCA was found to be only 0.16 μmol/mg of resin. This low reactivity is probably due to the insolubility of **2** in organic solvents. In Figure 3, the amount of pol β bound to the resin is plotted against the decreasing amounts of immobilized LCA. It can be seen that the more LCA that was immobilized on TentaGel resins, the more pol β that bound to the LCA-immobilized TentaGel resins; however, pol β binding seemed to reach a maximum when the LCA immobilized reached a concentration of 0.16 μmol/mg of resin.

An example of the affinity purification of pol β from a mixture of proteins by **3a** is shown in Figure 4. After **3a** was equilibrated with a mixture of pol β, hemoglobin, trypsin inhibitor, and lysozyme, the resins were washed with TEG buffer A. Bound pol β was then eluted by the addition of 1% Tween20. Although the flow-through contained all of the charged proteins, which had various isoelectric points, pol β was certainly retained and purified by the LCA-immobilized resin. This result

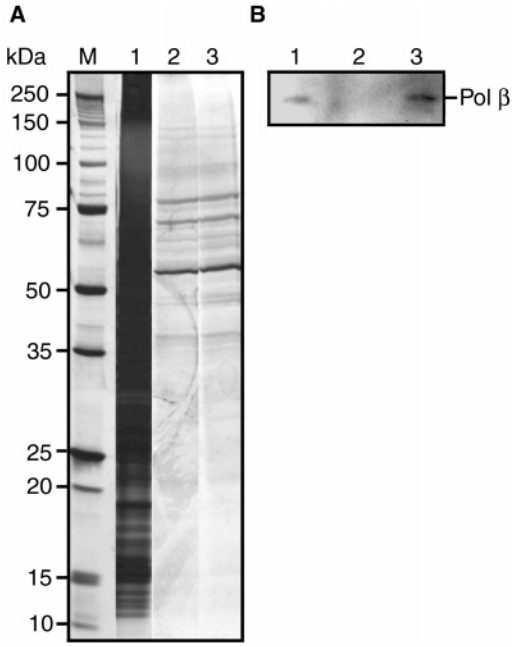

Figure 5. Partial purification of pol β from Molt4 nuclear extracts by the resin **3a**. (A) SDS−PAGE analysis of the eluted samples from the resin **3a** and **4a**. The gel was stained with silver: lane 1, nuclear extract; lane 2, elute from **4a** with TEG buffer B containing 1% Tween20; lane 3, elute from **3a** with TEG buffer B containing 1% Tween20; M, molecular weight marker. (B) Western blotting analysis for pol β. Proteins were transferred to a nitrocellulose membrane, and pol β was detected with anti-pol β polyclonal antibody. Lanes were the same as those for panel A.

indicates that only pol β specifically bound to the LCA-immobilized resins.

To test whether the LCA-immobilized resins can retain pol β from many kinds of proteins, the capture of pol β from a crude nuclear extract of human T lymphoma Molt4 cells by using **3a** was examined (Figure 5). Resins **3a** and **4a** were respectively incubated with the nuclear extract (5 mg). After the resins were washed with TEG buffer C, TEG buffer D, and TEG buffer B, the bound fraction was eluted with 1% Tween20. Figure 5A shows SDS−PAGE analysis of the nuclear extract (lane 1) and the fractions eluted from **4a** and **3a** (lanes 2 and 3, respectively). Although the total proteins in the fraction eluted from **3a** was obviously less than those in the nuclear extract (lane 1 versus lane 3), it was difficult to identify the band corresponding to pol β. However, pol β was successfully detected by Western blotting using an anti-pol β polyclonal antibody (Figure 5B) (*24*). Thus, pol β was certainly retained from the crude nuclear extract by **3a** and eluted with 1% Tween20 (lane 3, Figure 5B). On the other hand, pol β was not detected by Western blotting in the eluted fraction from **4a** (lane 2, Figure 5B). These observations suggest that pol β specifically recognized LCA on the surface of **3a**. Furthermore, the signal intensity of the band in lane 1 was approximately equal to that in lane 3 in Figure 5B (lane 1/lane 3 = 100: 99). Unfortunately, it was unable to identify how pure the eluted fraction from the resin **3a** was because the amount of the proteins in the eluted fractions was too little to determine the protein concentration by Bradford assay. Indeed, several nonspecific binding proteins were observed in the eluted fraction, but it is possible to concentrate pol β from the crude nuclear extract by **3a**. These results suggest that a combination of the inhibitor-

Scheme 2. Preparation of Photoaffinity Beads (6)

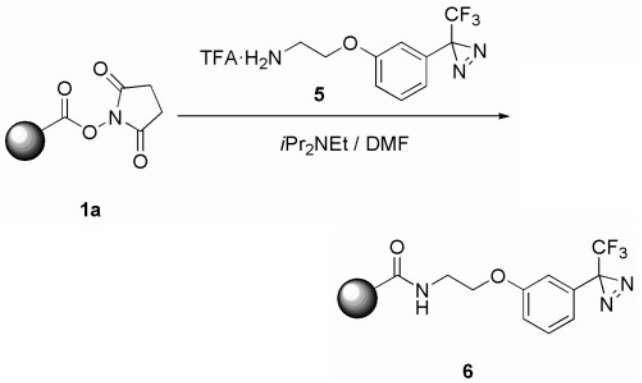

Scheme 3. Photoaffinity Reaction of Photoaffinity Beads (7) and Fluorescein Amine Isomer II (8)

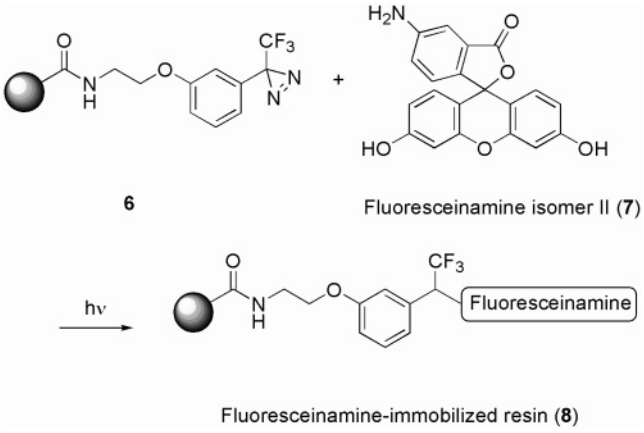

immobilized resins and classical column chromatography may facilitate the purification of pol β from a crude extract.

Nonspecific binding of proteins to **3a** would be due to hydrophobic interactions between proteins and the matrix of **3a** (*16*). As shown in Figure 1, LCA-immobilized Merrifield resins (**3b**) and Wang resins (**3c**) exhibited much more nonspecific protein binding. The matrixes of **3b** and **3c** are more hydrophobic than that of TentaGel (**3a**). Introduction of hydrophilic spacers on **3a** could reduce the nonspecific binding proteins (*15*, *17*).

To facilitate the immobilization of compounds on the resins, we prepared photoaffinity beads (**6**), that is, TentaGel resin beads with a photoreactive group at the free termini (*20*−*22*, *28*). Small molecules can be immobilized to such groups on a glass slide by a photolabeling reaction, as described in the small-molecules microarrays reported by Kanoh et al. (*28*) We therefore considered that, by using this methodology, small molecules, proteins, oligosaccharides, and DNA could be immobilized on the resin by UV irradiation. Photoaffinity beads (**6**) were prepared according to Scheme 2, in which a highly reactive carbene would be generated following the UV irradiation of **6** and would react with compounds in a nonspecific manner.

To check immobilization on the photoaffinity beads (**6**) following a photoreaction, the fluorescein amine isomer II (**7**) was immobilized on TentaGel resin by UV irradiation (Scheme 3). A solution of **6** and **7** in MeOH was stirred for 30 min at room temperature (rt). The solvent was removed under reduced pressure, and the beads were dried in vacuo. After irradiation of the solution of **6** and **7** by a high-pressure mercury arc lamp for 1 h, the beads were washed with MeOH (3 times) and dried in vacuo.

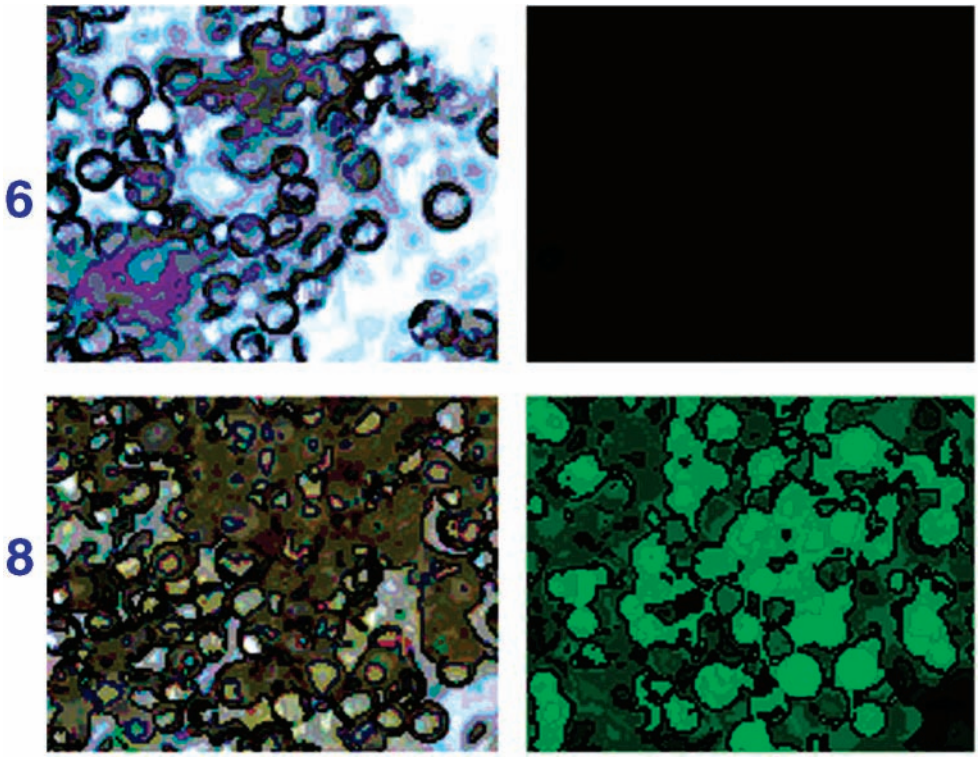

Figure 6. Microscopy (left) and the fluorescence (right) images of resins **6** and **8**.

Scheme 4. Photoaffinity Reaction of Photoaffinity Beads (6) and pol β Inhibitors 9a−c

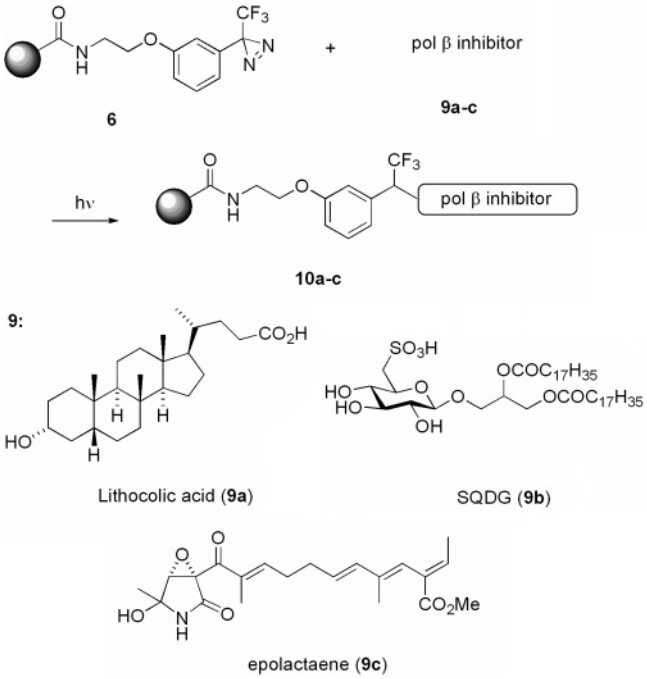

The resulting beads (**8**) were scanned for fluorescence by using a fluorescence microscope (Figure 6). The strong yellowish green fluorescence signals produced by **8** indicated that the fluorescein amine II (**7**) had been immobilized on the surface of resin **6** by the photoaffinity reaction.

Because LCA (**9a**), SQDG (**9b**) (*29*−*31*), and epolactaene (**9c**) (*32*−*34*) inhibit the activities of pol β in a dose-dependent manner, each of these molecules was immobilized on the photoaffinity beads (**6**) in the same way to obtain the inhibitor-immobilized TentaGel resins

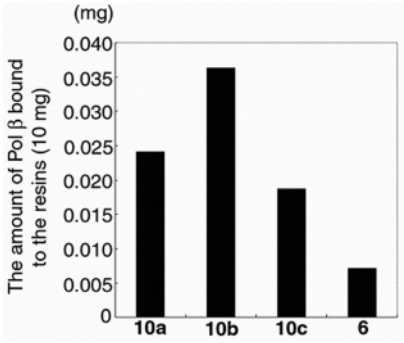

Figure 7. Amount of pol β bound to resins **10a**−**c**. Resin **6** was used as a negative control.

10a−**c** (Scheme 4). The maximum amount of pol β binding to **10a**−**c** (10 mg) was determined by monitoring absorbance at 595 nm (Figure 7). Whereas only 0.0075 mg of pol β bound to **6**, pol β was absorbed onto all of the inhibitor-immobilized resins. The amount of pol β bound to **10a**−**c** (10 mg) was 0.024, 0.037, and 0.019 mg, respectively. The immobilization of **9a**−**c** on **6** proceeded in a nonspecific manner; however, some of the immobilized **9a**−**c** did not lose the ability to bind pol β.

As mentioned above, the carboxylic group plays an important role in the interaction of LCA andpol β. Therefore, LCA was immobilized on **3a** through its 3-hydroxyl group. By contrast, LCA was immobilized in a nonspecific manner on **10a**−**c**. However, there was not much difference between the amount of pol β binding to **3a** and that binding to **10a** (0.032 mg for **3a**; 0.024 mg for **10a**). These findings show that the immobilization of protein inhibitors by a photoaffinity reaction will be effective not only for detecting the interactions between small molecules and proteins, but also for purifying proteins via these interactions.

Finally, the affinity purification of pol β from a mixture of proteins containing pol β, hemoglobin, trypsin inhibi-

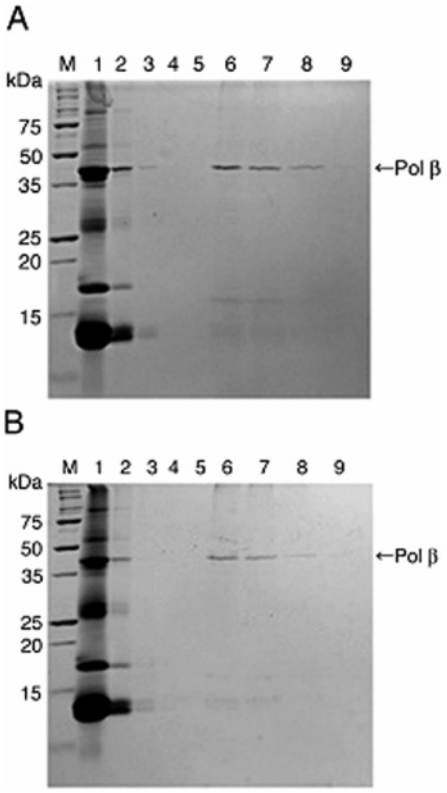

Figure 8. (A) SDS−PAGE of starting materials (pol β, hemoglobin, lysozyme, and trypsin inhibitor), flow-through, wash, elute, and resin during affinity purification with resin **10a**. (B) SDS−PAGE of starting materials (pol β, hemoglobin, lysozyme, and trypsin inhibitor), flow-through, wash, elute, and resin during affinity purification with resin **10b**. Lane 1, flow-through; lane 2−5, wash; lane 6−8, elute; lane 9, resin; M, molecular weight marker.

tor, and lysozyme was also successfully achieved with photoaffinity beads **10a** and **10b** (Figure 8).

CONCLUSION

We report here the application of resins normally used in solid-phase organic synthesis to the affinity capture of DNA pol β. LCA, an inhibitor of a mammalian DNA polymerase β, was immobilized on Merrifield resins, Wang resins, and TentaGel resins, and the batch affinity purification of pol β from a mixture of proteins using these LCA-immobilized resins was examined. Among the resins, TentaGel resins were found to be the most effective for both purifying pol β and reducing nonspecific protein absorption. Furthermore, with the LCA-immobilized TentaGel resin, it was possible to concentrate pol β from a crude cell extract.

To facilitate the immobilization of compounds on TentaGel resins, we also designed and prepared photoaffinity beads containing a photoreactive group at the free termini of the TentaGel resin. The immobilization of compounds on the resins was easily achieved by UV irradiation. LCA, C_{18}-β-SQDG, and epolactaene, which all inhibit pol β, were immobilized on the photoaffinity beads by photoreaction. Pol β was successfully bound by all three of the immobilized pol β inhibitors. The batch affinity purification of pol β from a protein mixture was also achieved by the use of these resins.

We believe that these inhibitor-immobilized resins will facilitate the purification of pol β from a crude extract. As this methodology for the affinity capture of proteins is based on ligand−receptor interactions, it will be applicable to the affinity capture of other proteins based not only on small molecule−protein interactions but also protein−protein interactions, DNA−protein interactions, and so on. Studies of the use of resins in further proteomics applications are currently under way.

ACKNOWLEDGMENT

This work was supported in part by a Grant-in-aid of the JSPS.

LITERATURE CITED

(1) Sakaguchi, K., Sugawara, F., and Mizushina, Y. (2002) DNA polymerase inhibitors. *Seikagaku 74*, 244−251.
(2) Sakaguchi, K., Hotta, Y., and Stern, H. (1980) Chromatin-associated DNA polymerase activity in meiotic cells of lily and mouse. *Cell Struct. Funct. 5*, 323−334.
(3) Mizushina, Y., Tanaka, N., Yagi, H., Kurosawa, T., Onoue, M., Seto, H., Horie, T., Aoyagi, N., Yamaoka, M., Matsukage, A., Yoshida, S., and Sakaguchi, K. (1996) Fatty acids selectively inhibit eukaryotic DNA polymerase activities in vitro. *Biochim. Biophys. Acta 1308*, 256−262.
(4) Mizushina, Y., Kamisuki, S., Mizuno, T., Takemura, M., Asahara, H., Linn, S., Yamaguchi, T., Matsukage, A., Hanaoka, F., Yohida, S., Saneyoshi, M., Sugawara, F., and Sakaguchi, K. (2000) Dehydroaltenusin, a mammalian DNA polymerase α inhibitor. *J. Biol. Chem. 275*, 33957−33961.
(5) Mizushina, Y., Kamisuki, S., Kasai, N., Shimazaki, N., Takemura, M., Asahara, H., Linn, S., Yohida, S., Matsukage, A., Koiwai, O., Sugawara, F., Yoshida, H., and Sakaguchi, K. (2002) A plant phytotoxin, solanapyrone A, is an inhibitor of DNA polymerase β and λ. *J. Biol. Chem. 277*, 630−638.
(6) Narisawa, T., Magadia, N. E., Weisburger, J. H., and Wynder, E. L. (1974) Promoting effect of bite acids on colon carcinogenesis after intrarectal instillation of *N*-methyl-*N*′-nitro-*N*-nitrosoguanidine. *J. Natl. Cancer Inst. 53*, 1093−1097.
(7) Reddy, B. S., Narisawa, T., Weisburger, J. H., and Wynder, E. L. (1976) Promoting effect of sodium deoxycholate on colon adenocarcinomas in germfree rats. *J. Natl. Cancer Inst. 56*, 441−442.
(8) Reddy, B. S., and Watanabe, K. (1979) Effect of cholesterol metabolites and promoting effect of lithocolic acid in colon carcinogenesis in germ-free and conventional F344 rats. *Cancer Res. 39*, 1521−1524.
(9) Ogawa, A., Murate, T., Suzuki, M., Nimura, Y., and Yoshida, S. (1998) Lithocholic acid, a putative tumor promoter, inhibits mammalian DNA polymerase beta. *Jpn. J. Cancer Res. 89*, 1154−1159.
(10) Mizushina, Y., Ohkubo, T., Sugawara, F., and Sakaguchi, K. (2000) Structure of lithocolic acid binding to the *N*-terminal 8-kDa domain of DNA polymerase β. *Biochemistry 39*, 12606−12613.
(11) Mizushina, Y., Kasai, N., Miura, K., Hanashima, S., Takemura, M., Sugawara, F., and Sakaguchi, K. (2004) Structural relationship of lithocholic acid derivatives binding to the *N*-terminal 8-kDa domain of DNA polymerase β. *Biochemistry 43*, 10669−10677.
(12) Watanabe, M., Hanashima, S., Mizushina, Y., Yoshida, H., Oshige, M., Sakaguchi, K., and Sugawara, F. (2002) Biotinylated lithocholic acids for affinity chromatography of mammalian DNA polymerases α and β. *Bioorg. Med. Chem. Lett. 12*, 287−290.
(13) Harding, M. W., Galat, A., Uehling, D. E., and Schreiber, S. L. (1989) A receptor for the immunosuppressant FK506 is a cis−trans peptidyl-prolyl isomerase. *Nature 341*, 758−760.
(14) Taunton, J., Hassig, C. A., and Schreiber, S. L. (1996). A mammalian histone deacetylase related to the yeast transcriptional regulator Rpd3p. *Science 272*, 408−411.
(15) Shimizu, N., Sugimoto, K., Tang, J., Nishi, T., Sato, I., Hiramoto, M., Aizawa, S., Hatakeyama, M., Ohba, R., Hatori, H., Yoshikawa, T., Suzuki, F., Oomori, A., Tanaka, H., Kawaguchi, H., Watanabe, H., and Handa, H. (2000) High-performance affinity beads for identifying drug receptors. *Nat. Biotechnol. 18*, 877−881.

(16) Tamura, T., Terada, T., and Tanaka, A. (2003) A quantitative analysis and chemical approach for the reduction of nonspecific binding proteins on affinity resins. *Bioconjugate Chem. 14*, 1222−1230.

(17) Shiyama, T., Furuya, M., Yamazaki, A., Terada, T., and Tanaka, A. (2004) Design and synthesis of nobel hydrophilic spacers for the reduction of nonspecific binding proteins on affinity resins. *Bioorg. Med. Chem. 12*, 2831−2841.

(18) Sucholeiki, I., Toledo-Sherman, L. M., Hosfield, C. M, Boutilier K., DeSouza, L. V., and Stover, D. R. (2004) Novel magnetic supports for small molecule affinity capture of proteins for use in proteomics. *Molec. Diversity 8*, 9−19.

(19) Poschalko, P., Rohr, T., Gruber, H., Bianco, A., Guichard, G., Briand, J.-P., Weber, V., and Falkenhagen, D. (2003) SUBPOL: A novel sucrose-based polymer support for solid-phase peptide synthesis and affinity chromatography applications. *J. Am. Chem. Soc. 125*, 13415−13426.

(20) Hatanaka, Y., Hashimoto, H., Kurihara, H., Nakayama, H., and Kanaoka, Y. (1994) A novel family of aromatic diazirines for photoaffinity labeling. *J. Org. Chem. 59*, 383−387.

(21) Hatanaka, Y., Hashimoto, M., Nakayama, H., and Kanaoka, Y. (1994) Syntheses of nitro-substituted aryl diazirines. An entry to chromogenic carbene precursors for photoaffinity labeling. *Chem. Pharm. Bull. 42*, 826−831.

(22) Hashimoto, M., Kanaoka, Y., and Hatanaka, Y. (1997) A versatile approach for functionalization of 3-aryl-3-trifluoromethyldiazirine photophor. *Heterocycles 46*, 119−122.

(23) Date, T., Yamaguchi, M., Hirose, F., Nishimoto, Y., Tanihara, K., and Matsukage, A. (1988) Expression of active rat DNA polymerase beta in *Escherichia coli*. *Biochemistry* 27, 2983−2990.

(24) Towbin, H., Staehelin, J., and Godon, J. (1979) Electrophoretic transfer of proteins from polyacrylamide gels to nitrocellulose sheets: procedure and some applications. *Proc. Natl. Acad. Sci. U.S.A. 76*, 4350−4354.

(25) Bradford, M. M. (1976) A rapid and sensitive method for the quantitation of microgram quantities of protein utilizing the principle of protein dye binding. *Anal. Biochem. 2*, 248−254.

(26) Ostuni, E., Chapman, R. G., Holmlin R. E., Takayama, S., and Whitesides, G. M. (2001). A survey of structure−property relationships of surfaces that resist the adsorption of protein. *Langmuir 17*, 5605−5620.

(27) Matsuya, T., Tashiro, S., Hoshino, N., Shibata N., Nagasaki, Y., and Kataoka, K. (2003) A core−shell-type fluorescent nanosphere possessing reactive poly(ethylene glycol) tethered chains on the surface for zeptomole detection of protein in time-resolved fluorometric immunoassay. *Anal. Chem. 75*, 6124−6132.

(28) Kanoh, N., Kumashiro, S., Simizu S., Kondoh, Y., Hatakeyama, S., Tashiro, H., and Osada, H. (2003) Immobilization of natural products on glass slides by using a photoaffinity reaction and the detection of protein-small-molecule in reactions. *Angew. Chem. Int. Ed. 42*, 5584−5587.

(29) Ohta, K., Mizushina, Y., Hirata, N., Takemura, M., Sugawara, F., Matsukage, A., Yoshida, S., and Sakaguchi, K. (1998). Action of a new mammalian DNA polymerase inhibitor, sulfoquinovosyldiacylglycerol. *Biol. Pharm. Bull. 22*, 111−116.

(30) Ohta, K., Mizushina, Y., Hirata, N., Takemura, M., Sugawara, F., Matsukage, A., Yoshida, S., and Sakaguchi, K. (1998) Sulfoquinovosyldiacylglycerol, KM043, a new potent inhibitor of eukaryotic DNA polymerases and HIV-reverse transcriptase type 1 from a marine red alga, *Gigartina tenella*. *Chem. Pharm. Bull. 46*, 684−686.

(31) Hanashima, S., Mizushina, Y., Ohta, K., Yamazaki, T., Sugawara, F., and Sakaguchi, K. (2000) Structure−activity relationship of a novel group of mammalian DNA polymerase inhibitors, synthetic sulfoquinovosylacylglycerol. *Jpn. J. Cancer Res. 91*, 1073−1083.

(32) Kakeya, H., Takahashi, I., Okada, G., Isono, K., and Osada, H. (1995) Epolactaene, a novel neuritogenic compound in human neuroblastoma cells, produced by a marine fungus. *J. Antibiot. 48*, 733−735.

(33) Mizushina, Y., Kobayashi, S., Kuramochi, K., Nagata, S., Sugawara, F., and Sakaguchi, K. (2000) Epolactaene, a novel neuritogenic compound in human neuroblastoma cells, selectively inhibits the activities of mammalian DNA polymerases and human DNA topoisomerase II. *Biochem. Biophys. Res. Commun. 273*, 784−788.

(34) Kuramochi, K., Mizushina, Y., Nagata, S., Sugawara, F., Sakaguchi, K., and Kobayashi, S. (2004) Structure−activity relationships of epolactaene analogs as DNA polymerases inhibitors. *Bioorg. Med. Chem. 12*, 1983−1989.

BC0497970

Synthesis and in Vitro Characterization of Organometallic Rhenium and Technetium Glucose Complexes against Glut 1 and Hexokinase

Roger Schibli,*[,†,‡] Cécile Dumas,[†] Jeannine Petrig,[†] Loredana Spadola,[‡] Leonardo Scapozza,[‡] Elisa Garcia-Garayoa,[†] and P. August Schubiger[†,‡]

Center for Radiopharmaceutical Science, ETH-PSI-USZ, Paul Scherrer Institute, 5232 Villigen PSI, Switzerland, and Department of Chemistry and Applied Biosciences ETHZ, 8093 Zurich, Switzerland. Received September 20, 2004; Revised Manuscript Received December 7, 2004

A series of nine organometallic technetium-99m and rhenium complexes of glucose are presented and characterized in vitro regarding their potential as surrogates of [^{18}F]-2-fluoro-desoxy glucose ([^{18}F]-FDG). The glucose derivatives are functionalized at positions C-1, C-2, C-3, and C-6. Different spacer lengths and chelating systems have been introduced at these sites. For the (radio)labeling, the organometallic precursors $[^{99m}Tc(H_2O)_3(CO)_3]^+$ and $[ReBr_3(CO)_3]^{2-}$ respectively have been used. The resulting complexes have been characterized chemically and radiochemically. The formation of uniform products has been observed on the macroscopic (Re) and no-carrier-added level (^{99m}Tc). The Tc-99m complexes revealed good inertness against ligand exchange (Cys and His) and excellent stability in physiological buffered saline as well as in human plasma over a period of 24 h at 37 °C. The rhenium complexes have been tested for competitive inhibition of the (yeast) hexokinase. Only for C-2 derivatized glucose complexes with extended spacer functionalities K_i values in the millimolar and sub-millimolar range have been observed. In silico molecular docking experiments supported these experimental findings. However, the competitive inhibitors are not recognized as a pseudosubstrate of hexokinase. The cellular uptake of all ^{99m}Tc-complexes into HT-29 colon carcinoma cells via Glut1 was generally low and unspecific independent of the position at the hexose ring, the chelating systems, or the overall charge of the corresponding metal complexes. The current results seem to preclude the use of these compounds as [^{18}F]-FDG surrogates primarily due to the low cellular uptake via Glut1.

INTRODUCTION

The radioactive labeled glucose analogue [^{18}F]-2-fluoro-desoxy glucose ([^{18}F]-FDG)[1] (^{18}F: β^+, $T_{1/2} = 109$ min) has gained tremendous relevance in clinical tumor diagnosis in recent years. [^{18}F]-FDG is taken up by tumor cells mainly by facile diffusion through the glucose transport protein Glut1. Phosphorylation of [^{18}F]-FDG to [^{18}F]-2-fluoro-desoxy glucose-6-phosphate ([^{18}F]-FDG-6-P) is accomplished by hexokinase (HK), and consequently [^{18}F]-FDG-6-P is metabolically trapped inside the cell. There is evidence that the phosphorylation via HK appears as the rate determining step in [^{18}F]-FDG accumulation in cancer cells, although this issue is controversially discussed in the literature (*1*−*3*). The clinical relevance of [^{18}F]-FDG prompted already some years ago the development of inexpensive and readily available ^{99m}Tc (γ; 150 keV, $T_{1/2} = 6.0$ h) labeled glucose analogues (*4*−*6*). Apart from the low costs of Tc-99m, a Re-186 (β^-; 1.1 MeV, $T_{1/2} = 90.6$ h) or Re-188 (β^-; 2.1 MeV, $T_{1/2} = 16.9$ h) labeled "FDG" analogue would open the opportunity for radiotherapy of various tumors with a simple and unspecific tracer. However, the ^{99m}Tc(V)-glucose complexes reported so far do not match the criteria and characteristics of FDG, such as active transport via Glut1 and phosphorylation via hexokinase. It can be speculated that this is due to steric reasons or the fact the transition metal coordination occurs via functional groups of the carbohydrate moiety important, for example, for substrate recognition.

Our group reasoned to employ the pendent approach for the radiolabeling of glucose to maintain its biological activity. For the radiolabeling, the organometallic precursor $[^{99m}Tc(H_2O)_3(CO)_3]^+$ was chosen. Other than technetium and rhenium in high oxidation states such as +V/+III, the low-valent, organometallic M(+I)-tricarbonyl (M = Tc, Re) moiety reveals a low affinity toward hard donor groups such as hydroxyl functionalities (ubiquitous in carbohydrates) but a high affinity toward medium soft and soft donor functionalities.

Recently, several groups including our group have reported the preparation of organometallic glucose and glucosamine analogues of technetium and rhenium, respectively (*7*−*11*). However, until now there are no in vitro or in vivo results of such compounds reported, with respect to Glut1 and/or HK.

In this work, we present the biological characterization of a series of organometallic technetium- and rhenium-tricarbonyl complexes of glucose, derivatized at positions C-1, C-2, C-3, and C-6 with various chelating systems

* Author of correspondence. E-mail: roger.schibli@psi.ch. Phone: +41-(0)56-310 2837. Fax: +41-(0)56-310 2849.

† Center for Radiopharmaceutical Science.

‡ Department of Chemistry and Applied Biosciences ETHZ.

[1] Abbreviations: HK, hexokinase; [^{18}F]-FDG, [^{18}F]-2-fluoro-desoxy glucose; [^{18}F]-FDG-6-P, [^{18}F]-2-fluoro-desoxy glucose-6-phosphate; PBS, phosphate buffered saline; ATP, adenosin triphosphate; ADP, adenosin diphosphate; NADH, nicotinamide adenine dinucleotide hydrate; $NADP^+$, nicotinamide adenine dinucleotide phosphate; NADPH, nicotinamide adenine dinucleotide phosphate, reduced form; G6PDH, phosphenol-pyruvate, PEP, glucose-6-phosphate-dehydrogenase; PyK, pyruvate-kinase; LDH, lactate-dehydrogenase; TEOA, triethanolamine hydrochloride buffer; IDA, iminodiacetic acid; TEAP, triethylammonium phosphate.

10.1021/bc049774l CCC: $30.25 © 2005 American Chemical Society
Published on Web 12/24/2004

Scheme 1

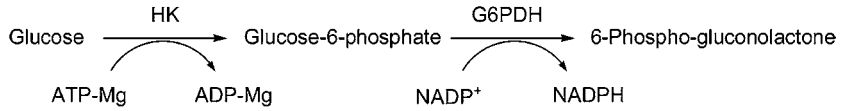

(Scheme 3). The Tc-99m complexes have been tested for cell internalization and transport via Glut1 in HT29 colon carcinoma cells. The corresponding rhenium complexes were assessed for competitive inhibition of HK or pseudosubstrate activity. Results of molecular docking studies between the metal complexes and human HK-I are also reported.

EXPERIMENTAL PROCEDURES

Materials and Methods. All chemicals and enzymes were purchased from Fluka (Buchs, Switzerland) and used without further purification. The syntheses of the glucose derivatives **1**−**9** and the rhenium complexes **10**, **14**−**16** have been described elsewhere (*9*, *11*, *12*). $(NEt_4)_2$-$[ReBr_3(CO)_3]$ was synthesized according to previously published procedures (*13*). The IsoLink kit was used to prepare the radioactive precursor $[^{99m}Tc(H_2O)_3(CO)_3]^+$ for the radiolabeling (*14*). All ^{99m}Tc glucose complexes have been prepared similar to the procedure published earlier (*9*). Na[$^{99m}TcO_4$] was eluted from a ^{99}Mo/^{99m}Tc generator (Mallinckrodt, Petten, The Netherlands) using 0.9% saline. UV/vis spectra were recorded on Beckman DU640 spectrometer. HPLC analyses were performed on a Merck-Hitachi L-7000-system equipped with an L-7400 tunable absorption detector, and a Berthold LB 506 B radiometric detector. HPLC solvents consisted of aqueous 0.05 M TEAP buffer, pH = 2.25 (solvent A) and methanol (solvent B). For the radiochemical analyses, a Macherey-Nagel C-18 reversed phase column (10 μm, 150 × 4.1 mm) was used. The HPLC system started with 100% of A from 0 to 3 min. The eluent switched at 3 min to 75% A and 25% B and at 9 min to 66% A and 34% B followed by a linear gradient 66% A/34% B to 100% B from 9 to 20 min. The gradient remained at 100% B for 2 min before switching back to 100% A. The flow rate was 1 mL/min. Human plasma samples were measured on a Superdex 10 size exclusion column. PBS was used as the mobile phase. The flow was set to 0.8 mL/min. Gamma samples were measured in a Packard COBRA II gamma counter. Scintillation analyses were performed on a Canberra Packard 1900TR beta counter.

Preparation of the Tc-99m Complexes 10a−**18a.** To 250 μL of a 10^{-4} M solution of compounds **1**−**9** in physiological phosphate buffer (pH = 7.4), 250 μL of the neutralized IsoLink solution were added. The mixtures were heated at 75° C for 45 min. The reactions and products were analyzed by means of HPLC. Yields varied between 70 and 95%. The compounds were purified via HPLC for the in vitro tests.

Synthesis of Complexes 11b−**13b and Complexes 17b and 18b.** The complexes have been prepared similar to the method described for complex **10** in ref *9*. The disodium salt of ligands **2**−**4** was dissolved in water (5 mL) and 1 equiv of $(NEt_4)_2[ReBr_3(CO)_3]$ was added. After 2 h at 50 °C, the solvent was evaporated and the residue was dried overnight in a desiccator. The crude reaction product was redissolved in a minimum amount of methanol and applied on a SepPak C18 cartridge, preconditioned according to the manufacturer's protocol. Unreacted starting material and byproducts were eluted with H_2O. The final product was eluted with MeOH/H_2O (1:1). Analytical data for complex **11b**: ^{1}H NMR (CD_3OD, 25 °C): 5.49 (d, 0.5H), 4.65 (d, 0.5H), 4.10−3.54 (m, 10H), 3.54−3.00 (m, 4H), 2.40−2.01 (m, 2H); IR (KBr): 3444 br, 2024 vs, 1892 vs, 1650 vs, 1400 m, 1064 m cm^{-1}; MS (ES): *m/z* (%) 624 (100%) [M$^-$]. Analytical data for complex **12b**: ^{1}H NMR (DMSO-d_6, 50 °C) 5.24−5.17 (m, 0.3H), 5.04−4.99 (m, 0.5H), 4.86−4.81 (m, 0.2H), 4.51−4.45 (m, 0.4H), 4.29−4.15 (m, 0.6H), 4.02−3.50 (m, 8H), 3.50−3.31 (m, 2H), 3.31−3.14 (m, 3H), 1.84−1.70 (m, 2H), 1.70−1.54 (m, 2H), 1.51−1.26 (m, 8H); IR (KBr): 3432 br, 2020 vs, 1884 vs, 1656 m, 1640 w, 1630 m, 1390 m, 1034 m cm^{-1}; MS (ES): *m/z* (%) 692 [M$^-$] (100). Analytical data for complex **13b**: IR (KBr): 3445 br, 2022 vs, 1883 vs, 1646 m, 1653 w, 1637 w, 1617 s, 1458 w, 1092 w cm^{-1}; MS (ES): *m/z* (%) 633 [M − $C_2H_5O_2$] (100). Analytical data of complex **17b**: ^{1}H NMR (CD_3OD): δ 7.26 (d, 2 H), 7.12 (d, 2 H), 6.49 (s, 1 H), 3.87 (s, 6 H), 3.58−3.72 (m, 4 H), 3.75 (d, 2 H), 3.69−3.63 (m, 1 H), 3.34 (t, 1 H), 2.25−2.20 (m, 1 H), 1.78−1.72 (m, 1 H); IR (KBr): 3750 br, 2026 vs, 1896 vs, 1654 w, 1458 w, 1080 m cm^{-1}; MS (ES): *m/z* (%) 668 [M$^+$] (100). Analytical data of complex **18b**: ^{1}H NMR (CD_3OD) 5.94 (d, 0.5H), 5.09 (d, 0.5H), 5.07−5.02 (m, 1H), 5.01−4.96 (m, 1H), 4.70 (d, 0.5H), 4.54−4.39 (m, 0.5H), 4.39−4.28 (m, 0.5H), 4.17−3.92 (m,1.5H), 3.86−3.65 (m, 1H), 3.96 (d, 2H), 3.72 (d, 2H), 3.56−3.47 (m, 2H), 3.43−2.30 (m, 2H), 1.89−1.76 (m, 2H); IR (KBr): 3426 br, 2008 vs, 1892 vs, 1638 s, 1458 m, 1260 w, 1032 m cm^{-1}; MS (ES): *m/z* (%) 638 [M$^-$] (100).

Hexokinase Assay. A slightly modified procedure described by Roche-Applied-Science has been used to assess the inhibition effect of the rhenium complexes (*15*). Commercial yeast hexokinase has been used instead of human HK1. The phosphotransferase activity was followed spectrophotometrically (340 nm) in the presence of an excess of G6PDH at 37 °C (as depicted in Scheme 1). The assay was validated with 2-*N*-acetyl glucosamine, a known HK inhibitor. Stock solution of 10^{-2} M of the complexes **10b**−**18b** in TEOA (pH = 7.6) buffer have been prepared. Inhibition with respect to glucose was studied at three different concentrations. The reaction mixture contained 50−250 μL of the stock solution of the complexes in 0.1 M TEOA, 100 μL of 10 mM NADP, 50 μL of 0.66 mM ATP, 200 μL of 10 mM $MgCl_2$, 75−250 μL of 1 mM glucose, 5 μL of a stock solution of glucose-6-phosphate dehydrogenase (G6PDH; 140 U/mL), and 10 μL of a stock solution of HK (150 U/mL). The sample volume was matched to a final volume of 1 mL with 0.1 M TEAO buffer. Disturbance of the absorption of NADP$^+$ and NADPH were not detected at the applied concentrations of complexes.

Pseudosubstrate Assay. The PyK assay method has been described by Tietz and Ochoa (Scheme 2) (*16*). The

Scheme 2

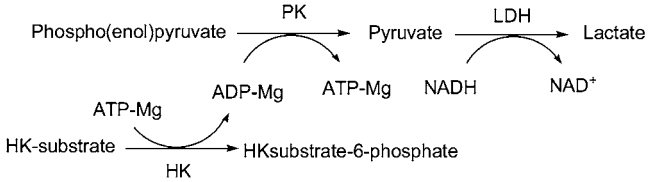

assay was validated with D-glucose and 2-deoxy-D-glucose. Stock solutions of 10^{-2} M glucose and complexes **11b**−**13b** have been prepared in 30 mM phosphate

buffer. The substrate activity was tested at a concentration of 10^{-3} M of glucose and 10^{-3} M of complexes, respectively. Reactions were carried out at 37 °C and followed at 340 nm. A mixture of 590 μL of phosphate buffer 100 μL of glucose or complex solution, 10 μL of HK (150 U/mL), 150 μL of 10 mM $MgCl_2$, 50 μL of 1 mM ATP, 50 μL of phosphor(enol)pyruvate (8 mM), 65 μL of NADH (1.6 mM) and 35 μL of LDH (500 U/mL; freshly prepared) was incubated for 3 min at 37 °C. The reaction was launched by addition of 5 μL of freshly prepared PyK (170 U/mL) in phosphate buffer.

Measurement of Cell Uptake. Cellular uptake was assayed as previously described with few modifications (*17*). HT29 cells were grown in McCoy's 5A with 10% fetal calf serum (FCS). Confluent cells were placed in 12-well plates (106 cells/well) and allowed to attach overnight. Before the assay, cells were incubated for 5 h at 37 °C with McCoy's + 0.5% bovine serum albumin (BSA). Prior to the uptake studies, cells were preincubated with PBS + 1% BSA for 30 min at 37 °C. The assay was validated with [^{3}H]-2-deoxyglucose (2 μCi/mL, 160 nmol/mL). The effect of insulin, cytochalasin B, and D-glucose on [^{3}H]-2-deoxyglucose uptake was also tested. Cells were incubated for 30 min at 37 °C with insulin (0−100 nM), cytochalasin B (0−50 μM), and D-glucose (0−10 mM) before the 30 min incubation with [^{3}H]-2-deoxyglucose or the complexes **10a**, **15a**, and **17a** (Figure 4). For the Tc-99m complexes, the cells (106 cells/well) were incubated for 20 min at 37 °C with increasing concentrations of the different derivatives (0−1 MBq/mL, approximately 0−52 pM). The uptake was terminated by aspiration of the medium. Cells were washed three times with cold PBS and lysed with 1 N NaOH.

In Vitro Stability Tests. HPLC purified samples (100 μL) of the Tc-99m complexes were mixed with 900 μL of physiological phosphate buffer, human plasma, and 10^{-2} M solutions of cystein and histidine and incubated at 37 °C for 24 h. Aliquots were taken at 1, 4, and 24 h and analyzed via HPLC.

Computational Details. The analysis of the glucose binding site was carried out based on the crystal structure (resolution 2.8 Å) of HKI (*18*) using the program GRID (version 19) (*19*). The energy surface was calculated using H_2O as a probe, which contoured the space available in the active site for a ligand at 0 kcal/mol. The structure of the IDA complex moiety was taken from a reported crystal structure (*20*).

RESULTS AND DISCUSSION

Synthesis and Characterization of ^{99m}Tc and Re Complexes 10−18. The structure and composition of all tested rhenium complexes have been unambiguously characterized by means of ^{1}H NMR, IR spectroscopy, and/or mass spectrometry. The chemical analyses revealed that the metal-tricarbonyl center was in all cases tridentately coordinated via IDA- (**1**−**5** and **9**), picolylamine mono acetic acid (**6**), and histidyl (**7**), or via bisimidazolyl amino methane (**8**) chelates (Scheme 3). The resulting rhenium complexes showed high stability over a period of several weeks in aqueous media as evident from HPLC and NMR analyses. They were all soluble in aqueous media, which was essential to perform the in vitro experiments. However, complexes with chelating systems containing aromatic functionalities (**15b**−**17b**) and the complex **12b** with an octyl chain were less soluble in buffered systems than the complexes **10b**, **11b**, **13b**, **14b**, and **18b**.

The glucose analogues **1**−**9** were reacted with the radioactive precursor $[^{99m}Tc(H_2O)_3(CO)_3]^+$ under physiological conditions. The formation of single products was observed in all cases. The yields of the labeling reactions were generally good (70−95%) but slightly depended on the nature of the chelating system. As previously reported by our group, chelating systems containing one or more aromatic amine functionalities (derivatives **6**−**8**) gave rise to higher yields than those with the IDA chelate at a ligand concentration of 10^{-4} M (*21*). However, we did not observe a significant dependence of the labeling efficiency either on the position where glucose was functionalized or on the spacer length. The HPLC analysis of the Tc-99m complexes **10a**−**18a** revealed similar retention times as for the corresponding rhenium complexes **10b**−**18b**. Thus, it can be concluded that Tc-99m complexes have the identical structure and composition as the analogous rhenium complexes.

Molecular Docking Studies. From high-resolution crystal structures of the enzyme dimer and monomer, it is evident that, for example, in yeast HK and human HK-I, the C-terminal and N-terminal domains are separated by a deep cleft (*18*, *22*). Glucose binds at the very bottom of the cleft and causes the small lobe of the molecule to rotate by 12° relative to the large lobe (*23*). Competitive HK inhibitors bind at the same site of the domain. The glucopyranose has to adopt a C-1 (chair equatorial) conformation. The C-3 and C-4 hydroxyl group of the sugar make specific interactions with the side chains of the protein. However, no direct interaction with side chains of the protein is observed for the OH group at position C-2. Thus, it is obvious that most of the known inhibitors of HK are C-2 functionalized, e.g., *o*-toluoyl glucosamine. Therefore, we performed molecular docking experiments with C-2 functionalized complexes. Simple alkyl spacers of different length were introduced between the sugar moiety and the Tc/Re-tricarbonyl entity. The molecules were manually docked into the active site. It was calculated that the introduction of a heptyl spacer would be sufficient to accommodate the metal entity in a large cavity at the outer surface of the protein without rearranging the glucose moiety in the active site. Figure 1 depicts the grid surface of the active site of HK in the "open" and the "closed" conformation with the corresponding glucose complex with a heptyl spacer.

Kinetic Studies of Rhenium Complexes 11b−18b against Hexokinase. The number of inhibitors for different types and subtypes of HKs (yeast, bovine brain, rabbit and human muscle) reported in the literature is rather limited. (i) Deoxy derivatives of hexoses which are competitive inhibitors with K_i values in the range of the K_m value of glucose (approximately 1 mM) (*24*, *25*). (ii) Hexose-6-phosphate analogues which inhibit human HK by interacting at regulatory sites (*26*). (iii) Glucosamine derivatives (*22*, *27*, *28*). However, to the best of our knowledge the inhibition of hexokinase by transition metal complexes and particularly organometallic glucose complexes has never been reported until now.

The complexes **10b**−**18b** have been tested for competitive inhibition of yeast hexokinase. Table 1 gives the inhibition constants of the different complexes. The kinetic data were calculated from Lineweaver−Burk plots ($1/v$ versus 1/[glucose]) and replots (slope versus concentration of inhibitor) with respect to glucose. Complexes **12b**, **13b**, **15b**, and **17b** competed with the substrate glucose for the active site of the enzyme however with variable efficiency. Two trends could be observed: (i) C-2 functionalized derivatives with a long alkyl and poly(ethylene glycol) spacer (**12b** and **13b**) exhibited low K_i values in the micromolar range (Table 1). For a comparison, the known HK inhibitor *N*-acetyl-

Scheme 3 [a]

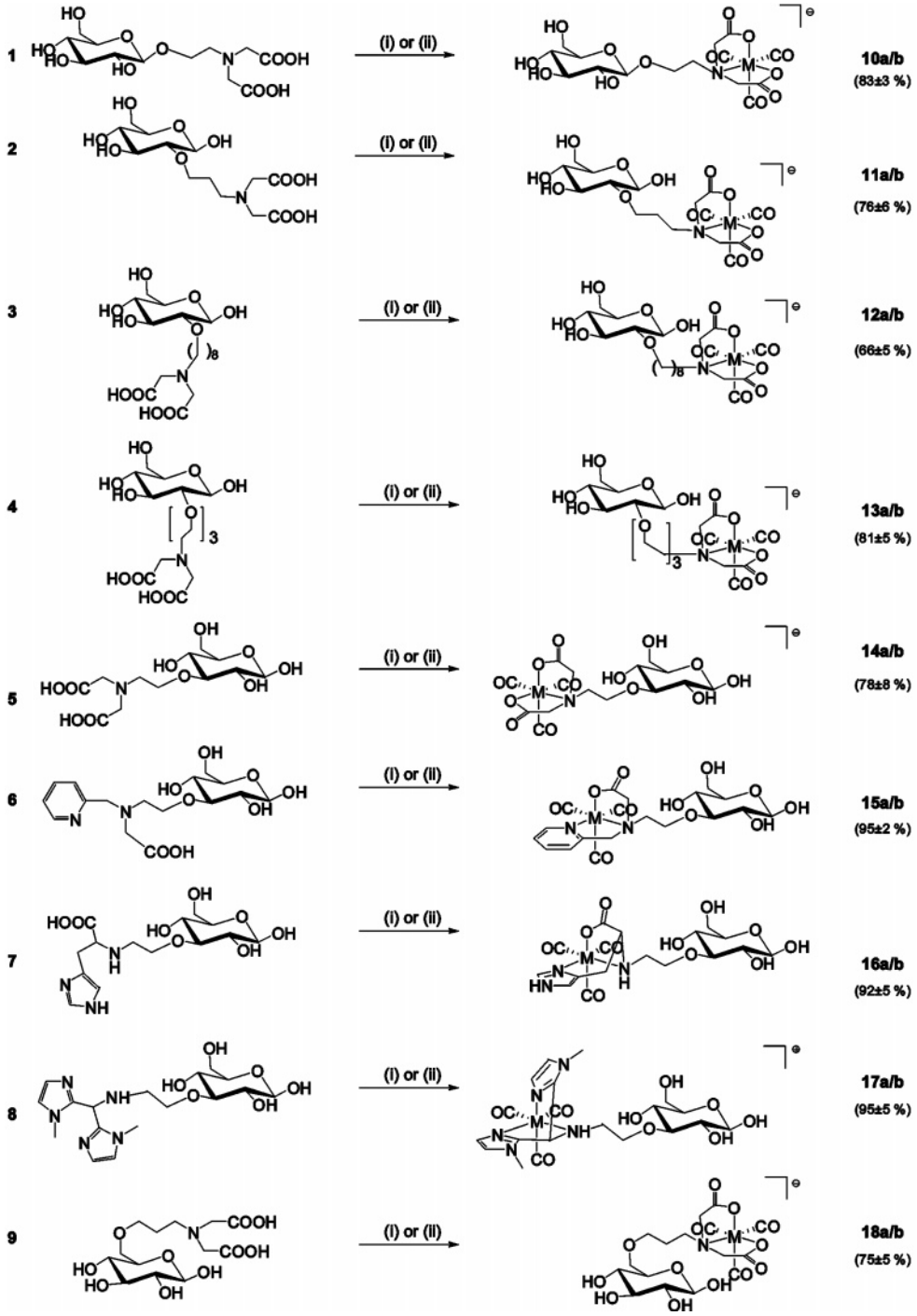

[a] (i) M = ^{99m}Tc: $[^{99m}Tc(H_2O)_3(CO)_3]^+$, PBS, pH = 7.5, 45 min, 75 °C; (ii) M = Re: $(NEt_4)_2[ReBr_3(CO)_3]$, methanol or water, 2 h, 50 °C. (Yields given for ^{99m}Tc complexes only).

glucosamine revealed in our test system a K_i value of 3.26 ± 0.01 mM (literature value 2.72 ± 0.05 mM (*27*)). (ii) For the anionic complex **11b** functionalized at position C-2 with a short spacer and for the glucose complexes functionalized at C-1 and C-3 no or only moderate inhibition of the enzyme was detected independent of the overall charge of the complexes. These experimental data are in accordance with the results obtained during the above-mentioned molecular docking experiments.

It is worth mentioning that none of the metal-free glucose derivatives **1**−**9** showed inhibition of HK. Similar observations have been made with organometallic functionalized thymidine analogues toward human cytosolic thymidine kinase. Also in those cases only the corresponding rhenium-tricarbonyl complexes revealed inhibition of the targeted enzyme (*29*). It can be speculated that the neutralization of a negative charge at the chelating entity and/or the reorganization of the functional groups after complexation is the reason for this effect.

Evaluation of Pseudosubstrate Activity of Rhenium Complexes 12b and 13b. Theoretically complexes **10**−**17**, which have a free OH group at position C-6, may also act as pseudosubstrates and could potentially be phosphorylated by ATP. Thus, formation of ADP can be used as an indication for substrate and pseudosubstrate activity of glucose analogues. The C-2 functionalized rhenium glucose analogues **12b** and **13b** which exhibited reasonable K_i were qualitatively tested for pseudosub-

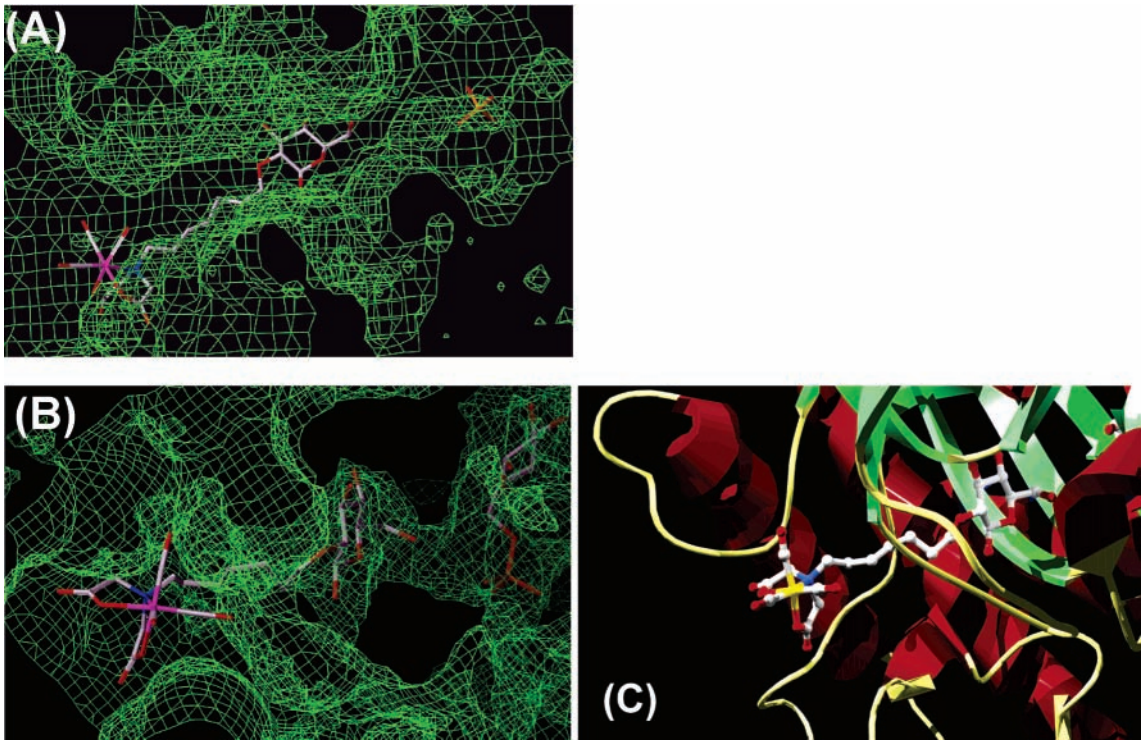

Figure 1. Catalytic site of HK: The green grids represent surface of the protein. (A) Active site of HK in the "open" conformation and (B) active site of HK in the "closed" conformation comprising a C-2 functionalized glucose "M(IDA)$(CO)_3$ complex" (M = Tc, Re) with a heptyl spacer; (C) ribbon representation of closed conformation.

Table 1. Inhibition Constants of Complexes 10b−18b with Respect to Yeast Hexokinase

complex	K_i [mM]	tested conc of inhibitor (mM)
10b	not detectable	1−2.5
11b	not detectable	1−2.5
12b	5.8 ± 0.9	1−2.5
13b	0.25 ± 0.01	1−2.5
14b	not detectable	1−7.6
15b	>100	1−2
16b	not detectable	0.1−2
17b	>100	1−3.8
18b	not detectable	0.1−2

strate activity. The formation of the ADP was measured via the ATPase assay ($\Delta Abs_{340nm}/\Delta t$ resulting from the oxidation of NADH is indirectly proportional to ADP formation). However, we observed only negligible activities for both Re complexes (Figure 2). By contrast, experiments with D-glucose and 2-deoxy-D-glucose revealed a significant rate of reaction as expected.

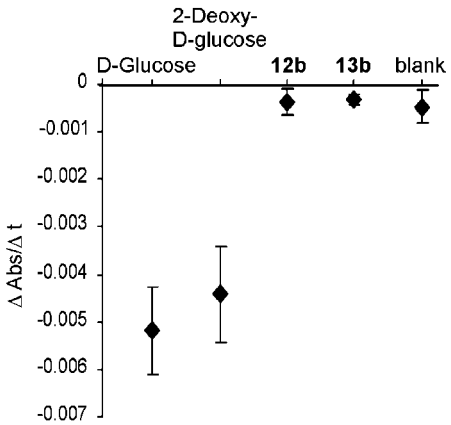

Figure 2. Rate of oxidation of NADH by LDH in the presence of HK, PyK, and complexes **12b**, **13b**, D-glucose, and 2-deoxy-D-glucose.

In Vitro Stability of Complexes 10a−18a. Previous to the cell experiments, all radioactive complexes **10a−18a** were tested in vitro in physiological phosphate buffer (pH = 7.4) and human serum at 37 °C for 24 h. Only minor decomposition of the complexes or back oxidation of the metal center to $^{99m}TcO_4^-$ (5−10%) could be observed during this time. The Tc-99m complexes were also challenged against the amino acids Cys and His. The complexes showed only insignificant transchelation or decomposition in the presence of Cys (<5%). Complexes with the IDA chelating moiety (**10a−14a** and **18a**) revealed minor ligand exchange in the presence of excess His (5−10%), whereas the complexes **15a−17a** were completely inert.

Cell Internalization Experiments via Glut1. It is well documented that Glut1 exists in two conformations and offers an extracellular as well as an intracellular binding site for D-glucose. Earlier it was reported that the OH groups at positions C-1, C-2, and C-3 of glucose interact with the transport protein at the extracellular binding site (*30*). The OH groups at positions C-4 and C-6 are described to be important for interaction with the intracellular binding sites. It was also reported that Glut1 tolerates some modification of the transported substrate. Speizer et al. reported that 6-deoxy-*N*-(7-nitrobenzyl-2-oxa-1,3-diazol-4-yl)amino glucose is transported via Glut1 (*31*) and recently, Zhang et al. published that pyropheophorbide 2-deoxyglucosamide functionalized at C-1 targets and transports via Glut1 (*32*).

We tested all our Tc-99m complexes for transport through the cell membrane via Glut1 and indirectly also for Glut1 interaction/inhibition. For these experiments, the colon carcinoma cell line HT29 has been used. The cells have been validated for exclusive overexpression of the sodium-independent Glut1 transport systems. For our tests, the cells have been incubated for 30 min at 37 °C with the freshly prepared and HPLC-purified technetium-99m complexes **10a−18a** and different amounts of

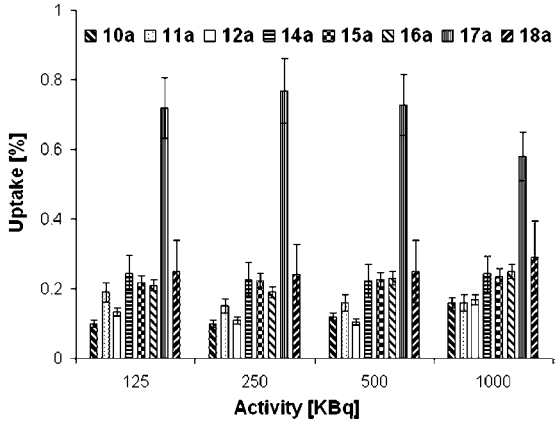

Figure 3. Dose-dependent cellular uptake of the complexes **10a**−**18a** in HT-29 colon carcinoma cells (after 30 min at 37 °C).

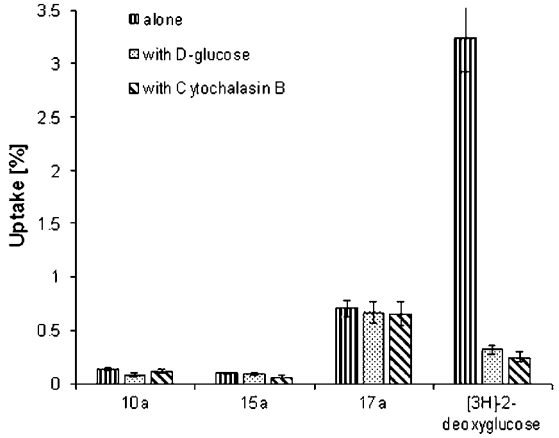

Figure 4. Cellular uptake of complex **10a**, **15a**, **17a**, and [3H]-2-deoxyglucose in the presence of 10 mM D-glucose or 50 μM cytochalasin B.

activity (125−1000 KBq). The results are depicted in Figure 3. Cellular uptake of the complexes **10a**−**16a** and **18a** ranged between 0.1 and 0.3% of total activity. Only complex **17a** revealed a significantly higher uptake (0.7 ± 0.08%). Compared to [^{3}H]-2-deoxyglucose (approximately 3 ± 0.38% after 30 min), the uptake was relatively low (Figure 4). In addition, the cellular uptake was not dose dependent.

The internalization of complexes **13a** (C-2), **17a** (C-3), and **18a** (C-6) was challenged in the presence of 10 mM D-glucose and cytochalasin B (50 μM), a potent Glut1 inhibitor, to verify specific transport via Glut1 or binding to Glut1. It was observed that within the standard deviation the internalization of the selected complexes was not affected by cytochalasin B (Figure 4). Therefore, it can be concluded that our complexes are not transported via Glut1. Since cytochalasin B is binding intracellularly, it still could be speculated that the complexes are interacting at the extracellular binding site of glucose (*33*, *34*). However, the fact that a large excess of D-glucose did not affect or reduce internalization of the complexes gives evidence that they do not compete for a common binding site. Unspecific uptake via passive diffusion rather than active transport via the sodium-independent Glut1 transporter can be postulated for all complexes based on these observations. Facilitated passive diffusion of the very lipophilic complex **17a** is presumably the reason for its increased (unspecific) internalization.

Almost simultaneously to our findings, Fischbarg and co-workers have recently published an improved three-dimensional structure of Glut1 by an evolutionary homology strategy based on the structure of glycerol-3-phosphate transporter from *Escherichia coli* (PDB 1PW4 (*35*)) (*34*). This model is still under investigation and validation, and the results should presumbaly be handled and interpreted with the necessary caution. A putative docking site of D-glucose was found near the extracellular opening of the transport channel as expected. According this model, D-glucose forms initially H-bonds with the pyranose oxygen (and lysine 38) as well as with the OH group at position C-6 (and glutamic acid 41), which is contrary to what was published earlier. The conserved QLS motif, which has been recognized earlier to be important for the selectivity of sugars transported (*36*), was also found near the entrance forming a tight bottleneck nearly impassable for compounds larger than glucose. Thus, it is very likely that our (and presumably any other) technetium glucose complexes are sterically too demanding for recognition at the extracellular binding site and/or transportation via Glut1. In addition, Fischbarg proposed that only one or two H-bonds are formed between the transporter and the substrate at any time, giving evidence for a rolling mechanism during substrate migration along the transport channel. It can be speculated that any modification preventing glucose from this rolling mechanism (as our modification of glucose with technetium complexes most likely do) will not be transported. Glut1 inhibitors such as forskolin and phloretin where found to form simultaneously three and five H-bonds, respectively, immobilizing these compounds and therefore blocking Glut1. Thus, it would eventually be interesting to target Glut1-overexpressing cancer cells with technetium complexes based on scaffold of a potent Glut1 inhibitor.

CONCLUSION

We have synthesized, radiolabeled, and characterized in vitro a series of organometallic technetium and rhenium complexes of glucose functionalized with different chelating systems at positions C-1, C-2, C-3, and C-6 of the hexose. The formation of well-defined and stable complexes has been observed in all cases. Competitive inhibitors were only found among glucose complexes functionalized at position C-2. Molecular docking experiments support this tendency. Other than [^{18}F]-FDG, the inhibitors are not phosphorylated by the enzyme in the presence of excess ATP. Furthermore, all tested complexes seem not to be recognized and transported via the Glut1 transporter. A critical evaluation of the data of our compounds preclude at the moment their use as [^{18}F]-FDG surrogates. The poor in vitro results do not currently justify further in vivo experiments with the presented technetium glucose complexes. However, it cannot be excluded that these compounds have the potential for other diagnostic (and therapeutic) indications or targets. Therefore, we are currently screening and evaluating other cellular transport systems such as Glut3 and SDGLT1-3, which show lower substrate specificity and are overexpressed on various cancer types.

ACKNOWLEDGMENT

We thank Judith Stahel for preparing the technetium-99m complexes and performing enzyme kinetic experiments. This work has been financially supported by Mallinckrodt-Tyco Inc.

LITERATURE CITED

(1) Aloj, L., Caraco, C., Jagoda, E., Eckelman, W. C., and Neumann, R. D. (1999) Glut-1 and hexokinase expression: Relationship with 2-fluoro-2- deoxy-D-glucose uptake in A431 and T47D cells in culture. *Cancer Res. 59*, 4709−4714.

(2) Mathupala, S. P., Rempel, A., and Pedersen, P. L. (1997) Aberrant glycolytic metabolism of cancer cells: A remarkable coordination of genetic, transcriptional, post-translational, and mutational events that lead to a critical role for Type II hexokinase. *J. Bioenerg. Biomembr. 29*, 339−343.

(3) Torizuka, T., Tamaki, N., Inokuma, T., Magata, Y., Sasayama, S., Yonekura, Y., Tanaka, A., Yamaoka, Y., Yamamoto, K., and Konishi, J. (1995) In-Vivo Assessment of Glucose-Metabolism in Hepatocellular- Carcinoma with Fdg-Pet. *J. Nucl. Med. 36*, 1811−1817.

(4) Ozker, K., Collier, B. D., Lindner, D. J., Kabasakal, L., Liu, Y., Krasnow, A. Z., Hellman, R. S., Edwards, S. D., Bourque, C. R., and Crane, P. D. (1999) Biodistribution of Tc-99(m)-labelled 5-thio-D-glucose. *Nucl. Med. Commun. 20*, 1055−1058.

(5) Caner, B. E., Ercan, M. T., Bekdik, C. F., Varoglu, E., Muezzinoglu, S., Duman, Y., and Erbengi, G. F. (1991) Visualization of Bone Pathologies and Lung-Cancer with Tc-99 Glucose Phosphate—a Comparative-Study. *Nuklearmedizin 30*, 132−136.

(6) Risch, V. R., Honda, T., Heindel, N. D., Emrich, J. L., and Brady, L. W. (1977) Distribution of Tc-99m 1-Thioglucose in Rats—Effect of Administration Route on Pancreatic Specificity. *Radiology 124*, 837−838.

(7) Dumas, C., Petrig, J., Schibli, R., Stahel, J., Schubiger, A. P., Spadola, L., Scapozza, L., and Mertens, J. (2001) Functionalization of glucose for the labeling with 99mTc-tricarbonyl. *J. Labelled Compd. Radiopharm. 44 Suppl. 1*, S57−S59.

(8) Banerjee, S. R., Zubieta, J. A., and Babich, J. W. (2004) A new bifunctional amio acid chelator targeting glucose transporter. *J. Nucl. Med. 45*, 465P.

(9) Petrig, J., Schibli, R., Dumas, C., Alberto, R., and Schubiger, P. A. (2001) Derivatization of glucose and 2-deoxyglucose for transition metal complexation: Substitution reactions with organometallic Tc-99m and Re precursors and fundamental NMR investigations. *Chem.--Eur. J. 7*, 1868−1873.

(10) Bayly, S. R., Fisher, C. L., Storr, T., Adam, M. J., and Orvig, C. (2004) Carbohydrate conjugates for molecular imaging and radiotherapy: Tc-99m(I) and Re-186(I) tricarbonyl complexes of *N*-(2′-hydroxybenzyl)-2-amino-2-deoxy-D-glucose. *Bioconjugate Chem. 15*, 923−926.

(11) Dumas, C., Schibli, R., and Schubiger, A. P. (2003) Versatile Routes to Synthesize C-(2) and C-(6) Iminodiacetic Acid Functionalized Glucose Derivatives. *J. Org. Chem. 68*, 512−518.

(12) Dumas, C., Petrig, J., Spingler, B., Schubiger, A. P., and Schibli, R. (2004) Syntheses and Characterization of organorhenium complexes of C-3 functionalized glucose. *Bioconjugate Chem.*, manusript submitted.

(13) Alberto, R., Schibli, R., Egli, A., Schubiger, P. A., Herrmann, W. A., Artus, G., Abram, U., and Kaden, T. A. (1995) Metal Carbonyl Syntheses XXII. Low-Pressure Carbonylation of $[MOCl_4]^-$ and $[MO_4]^-$: The Technetium(I) And Rhenium-(I) Complexes $[NEt_4]_2[MCl_3(CO)_3]$. *J. Organomet. Chem. 493*, 119−127.

(14) Alberto, R., Ortner, K., Wheatley, N., Schibli, R., and Schubiger, A. P. (2001) Synthesis and Properties of Boranocarbonate: A convenient in situ CO source for the aqueous preparation of $[^{99m}Tc(H2O)_3(CO)_3]^+$. *J. Am. Chem. Soc. 123*, 3135−3136.

(15) http://www.roche-applied-science.com, 2004.

(16) Tietz, A., and Ochoa, S. (1958) Fluorokinase and Pyruvic Kinase. *Arch. Biochem. Biophys. 78*, 477−493.

(17) Cooper, D. R., Watson, J. E., Patel, N., Illingworth, P., Acevedo-Duncan, M., Goodnight, J., Chalfant, C. E., and Mischak, H. (1999) Ectopic Expression of Protein Kinase C beta II, -delta, and -epsilon, but not -beta I or -zeta, Provide for Insulin Stimulation of Glucose Uptake in NIH-3T3 Cells. *Arch. Biochem. Biophys. 372*, 69−79.

(18) Aleshin, A. E., Zeng, C. B., Bourenkov, G. P., Bartunik, H. D., Fromm, H. J., and Honzatko, R. B. (1998) The mechanism of regulation of hexokinase: new insights from the crystal structure of recombinant human brain hexokinase complexed with glucose and glucose-6-phosphate. *Structure 6*, 39−50.

(19) Goodford, P. J. (1985) A Computational-Procedure for Determining Energetically Favorable Binding-Sites on Biologically Important Macromolecules. *J. Med. Chem. 28*, 849−857.

(20) Schibli, R., Schwarzbach, R., Alberto, R., Ortner, K., Schmalle, H., Dumas, C., Egli, A., and Schubiger, A. P. (2002) Steps Toward High Specific Activity Labeling of Biomolecules for Therapeutic Application: Preparation of Precursor $[^{188}Re(H_2O)_3(CO)_3]^+$ and Synthesis of Tailor-Made Bifunctional Ligand Systems. *Bioconjugate Chem. 13*, 750−756.

(21) Schibli, R., La Bella, R., Alberto, R., Garcia-Garayoa, E., Ortner, K., Abram, U., and Schubiger, P. A. (2000) Influence of the denticity of ligand systems on the in vitro and in vivo behavior of Tc-99m(I)-tricarbonyl complexes: A hint for the future functionalization of biomolecules. *Bioconjugate Chem. 11*, 345−351.

(22) Steitz, T. A., Anderson, W. F., Fletterick, R. J., and Anderson, C. M. (1977) High-resolution crystal strucutre of yeast hexokinase complexes with substrate, activators, and inhibitors. *J. Biol. Chem. 252*, 4497−4500.

(23) McDonald, R. C., Steitz, T. A., and Engelman, D. M. (1979) Yeast hexokinase in solution exhibits a large conformational change upon binding glucose or glucose 6-phosphate. *Biochemistry 18*, 338−342.

(24) Swarup, G., and Kenkare, U. W. (1980) Reaction of brain hexokinase with a substrate-like reagent. Alkylation of a single thiol at the active site. *Biochemistry 19*, 4058−4064.

(25) Schirch, D. M., and Wilson, J. E. (1987) Rat brain hexokinase: Location of the substrate hexose binding site in a structural domain at the C-terminus of the enzyme. *Arch. Biochem. Biophys. 254*, 385−396.

(26) Mehta, A., Jarori, G. K., and Kenkare, U. W. (1988) Brain hexokinase has no preexisting allosteric site for glucose 6-phosphate. *J. Biol. Chem. 263*, 15492−15497.

(27) Willson, M., and Perie, J. (1999) Inhibition of yeast hexokinase: a kinetic and phosphorus nuclear magnetic resonance study. *Spectrochim. Acta Part A 55*, 911−917.

(28) Willson, M., Sanejouand, Y.-H. P., Jacques, Hannaert, V., and Opperdoes, F. (2002) Sequencing, Modeling, and Selective Inhibition of *Trypanosoma brucei* Hexokinase. *Chem. Biol. 9*, 839−847.

(29) Schibli, R., Netter, M., Scapozza, L., Birringer, M., Schelling, P., Dumas, C., Schoch, J., and Schubiger, P. A. (2003) First organometallic inhibitors for human thymidine kinase: synthesis and in vitro evaluation of rhenium(I)- and technetium(I)-tricarbonyl complexes of thymidine. *J. Organomet. Chem. 668*, 67−74.

(30) Kahlenbe, A, and Dolansky, D. (1972) Structural Requirements of D-Glucose for Its Binding to Isolated Human Erythrocyte-Membranes. *Can. J. Biochem. 50*, 638−643.

(31) Speizer, L., Haugland, R., and Kutchai, H. (1985) Asymmetric Transport of a Fluorescent Glucose Analog by Human-Erythrocytes. *Biochim. Biophys. Acta 815*, 75−84.

(32) Zhang, M., Zhang, Z. H., Blessington, D., Li, H., Busch, T. M., Madrak, V., Miles, J., Chance, B., Glickson, J. D., and Zheng, G. (2003) Pyropheophorbide 2-deoxyglucosamide: A new photosensitizer targeting glucose transporters. *Bioconjugate Chem. 14*, 709−714.

(33) Basketter, D., and Widdas, W. (1978) Asymmetry of the hexose transfer system in human erythrocytes. Comparison of the effects of cytochalasin B, phloretin and maltose as competitive inhibitors. *J. Physiol. 278*, 389−401.

(34) Salas-Burgos, A., Iserovich, P., Zuniga, F., Vera, J. C., and Fischbarg, J. (2004) Predicting the Three-Dimensional Structure of the Human Facilitative Glucose Transporter Glut1 by a Novel Evolutionary Homology Strategy: Insights on the Molecular Mechanism of Substrate Migration, and Binding

Sites for Glucose and Inhibitory Molecules. *Biophys. J. 87*, 2990−2999.
(35) Huang, Y., Lemieux, M. J., Song, J., Auer, M., and Wang, D.-N. (2003) Structure and Mechanism of the Glycerol-3-Phosphate Transporter from *Escherichia coli*. *Science 301*, 616−620.
(36) Olsowski, A., Monden, I., Krause, G., and Keller, K. (2000) Cysteine Scanning Mutagenesis of Helices 2 and 7 in GLUT1 Identifies an Exofacial Cleft in Both Transmembrane Segments. *Biochemistry 39*, 2469−2474.

BC049774L

Characterization of Site-Specific ScFv PEGylation for Tumor-Targeting Pharmaceuticals

Arutselvan Natarajan, Cheng-Yi Xiong, Huguette Albrecht, Gerald L. DeNardo, and Sally J. DeNardo*

University of California Davis Medical Center, Sacramento, California 95816. Received August 2, 2004; Revised Manuscript Received November 24, 2004

New radiopharmaceuticals are possible using site-specific conjugation of small tumor binding proteins and poly(ethylene glycol) (PEG) scaffolds to provide modular multivalent, homo- or heterofunctional cancer-targeting molecules having preferred molecular size, valence, and functionality. Residence time in plasma can be optimized by modification of the size, number, and charge of the protein units. However, random PEG conjugation (PEGylation) of these small molecules via amine groups has led to variations of structural conformation and binding affinity. To optimize PEGylation, scFvs have been recombinantly produced in a vector that adds an unpaired cysteine (c) near the scFv carboxy terminus (scFv-c), thus providing a specific site for thiol conjugation. To evaluate the general applicability of this unpaired cysteine for PEGylation of scFv-c, conjugation efficiency was determined for four different scFvs and several PEG molecules having thiol reactive groups. The effect of the PEG molecular format on scFv-c PEG malignant cell binding was also addressed. ScFvs produced as scFv-c and purified by anti E-TAG affinity chromatography were conjugated using PEG molecules with maleimide (Mal) or *o*-pyridyl disulfide (OPSS). Conjugations were performed at pH 7.0, with 2 molar excess TCEP/scFv and PEG-(Mal) or PEG-OPSS, using 5:1 (PEG/scFv). PEG-Mal conjugation efficiency was also evaluated with 1:5 (PEG/scFv). PEGylation efficiency was determined for each reaction by quantitation of the products on SDS−PAGE. ScFv-c conjugation with unifunctional maleimide PEGs resulted in PEG conjugates incorporating 30−80% of the scFv-c, but usually above 50%. Efficiency of scFv-c conjugation to both functional groups of the bifunctional PEG-$(Mal)_2$ varied between the PEG and scFv-c molecules studied. A maximum of 45% of scFv-c protein was conjugated as PEG-$(scFv\text{-}c)_2$ using the smallest PEG-$(Mal)_2$ (2 kDa). No significant increase in scFv-c conjugation was observed by the use of greater than a 5 molar excess of PEG/scFv-c. Under the same conjugation conditions, PEG as OPSS yielded less than 10% PEG-scFv-c. PEG-$(scFv)_2$ conjugates had increased binding in ELISA using malignant cell membranes, when compared with unmodified scFv-c. PEGylated-scFv binding was comparable with unmodified scFv-c. In summary, scFv-c can be PEGylated in a site-specific manner using uni- or bivalent PEG-Mal, either linear or branched. ScFv-c was most efficiently conjugated to smaller PEG-Mal molecules, with the smallest, 2 kDa PEG-Mal, usually PEGylating 60−90% of the scFv-c. ScFv-c conjugation to form PEG-$(scFv\text{-}c)_2$ reached greatest efficiency at 45%, and its purified form demonstrated greater binding than the corresponding scFv-c.

INTRODUCTION

Radiolabeled monoclonal antibodies (MAb) have proven to be effective therapy for some radiosensitive cancers (*1, 2*). Because of their large size, blood clearance and tumor uptake occur slowly, decreasing the tumor to marrow therapeutic index. Unless bone marrow support is provided, hematological toxicity precludes administration of sufficient radiopharmaceutical to deliver effective radiation to most solid tumors (*3, 4*). Recombinant production of selected single chain Fv antibody fragments (scFv) provides small molecules for new paradigms designed to enhance the therapeutic index of tumor-targeted or pretargeted radionuclide therapy (*5*−*7*). With advances in antibody engineering and phage-display, antibody fragments can be generated that have a high degree of target specificity and a range of binding affinities (*8, 9*).

* Corresponding author: Sally J. DeNardo, M.D., Radiodiagnosis and Therapy, Molecular Cancer Institute, University of California, Davis Medical Center, 1508 Alhambra Blvd., Rm. 3100, Sacramento, CA 95816. Telephone: 916-734-3787, Fax: 916-451-2857, E-mail: sjdenardo@ucdavis.edu.

Pharmacokinetic studies with radiolabeled scFvs have shown that their small size leads to rapid blood and renal clearance and insufficient opportunity for tumor uptake (*10, 11*). These small antigen-binding proteins can also serve as modules in multivalent tumor-targeting constructs designed to enhance radioimaging and therapy (*12, 13*). Poly(ethylene glycol) (PEG) polymers have the characteristics necessary to serve as scaffolds for these modules. PEGylation, the covalent attachment of PEG to other molecules, has become a validated drug delivery method, and several PEGylated drugs have been approved by the FDA. Better stability, decreased proteolysis, enhanced solubility, and longer circulation and body retention of PEGylated pharmaceuticals have led to their enhanced efficacy (*14, 15*).

PEGylation of biologically active drugs has historically been accomplished by covalent conjugation to available primary amines of lysine residues. Significant loss of target binding or biologic activity frequently resulted as a consequence of conformational change or steric hindrance (*16, 17*). Since small molecules such as scFv allow little room for error, an expression vector has been

10.1021/bc0498121 CCC: $30.25 © 2005 American Chemical Society
Published on Web 12/31/2004

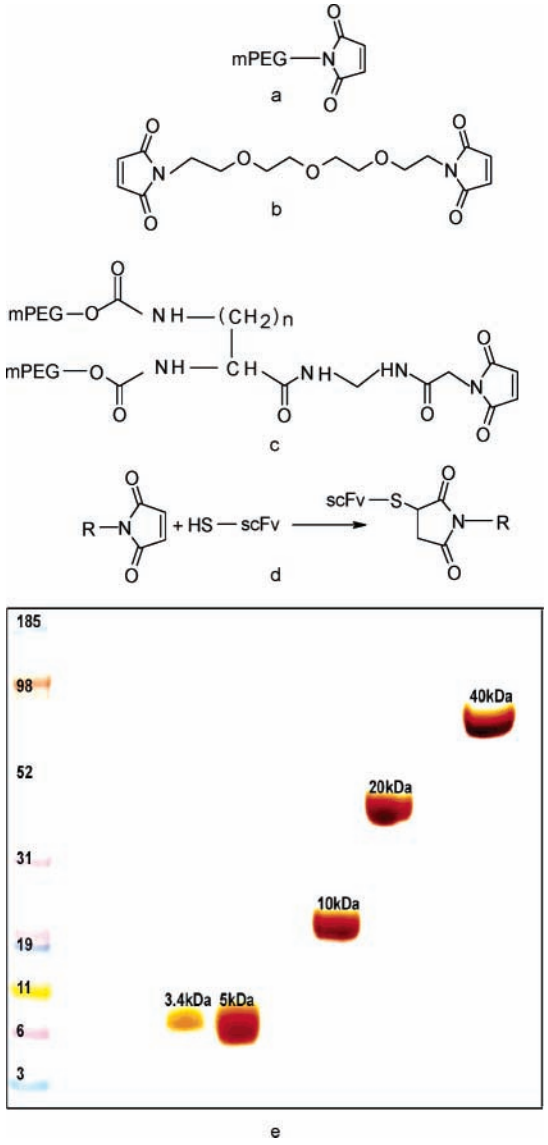

Figure 1. PEG maleimide (PEG-Mal) structures and the maleimide (Mal) thiol conjugation reaction with scFv-c (scFv-SH): (a) Methoxy-PEG-Mal. (b) PEG-$(Mal)_2$. (c) Branched methoxy-PEG-Mal. (d) Formation of thioether bond between maleimide and cysteine of scFv-c. (e) PEG-Mal structures electrophoresed on SDS−PAGE gel (4−12%) under reducing conditions and stained by barium iodide, demonstrating relative mobility prior to protein conjugation.

engineered for the addition of a free cysteine (c) near the carboxyl end of the scFv (scFv-c), thereby providing a specific site for thiol conjugation of scFv-c produced in the vector (*18*). To determine the general applicability of scFv-c PEGylation, we evaluated the relative conjugation efficiency of several scFv-c with PEG molecules varying in size, structure, and thiol reactive groups, including mono- and bifunctional PEG molecules in linear and branched formats (Figure 1, Table 1). Evidence of a relationship between PEG structure, size, and the efficiency of scFv-c PEGylation was observed.

MATERIALS AND METHODS

Materials. Methoxy-PEG-maleimide (PEG-Mal) of 3.4, 5, 20, and 40 kDa and a bifunctional maleimide-PEG-Mal (PEG-$(Mal)_2$) of 3.4 kDa were purchased from Nektar Therapeutics (San Carlos, CA). PEG-Mal of 10 and 20 kDa, methoxy-PEG-*o*-pyridyl disulfide (OPSS) of 5, 10, and 20 kDa, and PEG-$(Mal)_2$ of 2 kDa were obtained from

Table 1. List of Various PEG Molecules Used for Site-Specific PEGylation

no.	functionalized PEGs	molecular weight (kDa)
1	PEG-$(Mal)_2$	2, 3.4
2	NHS-PEG-Mal	3.4
3	PEG-Mal	5
4	PEG-Mal	10
5	PEG-Mal	20
6	$(PEG)_2$-Mal	40
7	PEG-$(OPSS)_2$	2
8	PEG-OPSS	3.4
9	PEG-OPSS	10
10	PEG-OPSS	20

[a] Methoxy-PEG: PEG, Mal: maleimide, OPSS: *o*-pyridyl disulfide, NHS: hydroxysuccinimide, PEG-$(Mal)_2$/$(OPSS)_2$: PEG have been functionalized at both ends.

Sunbio PEG-Shop (Anyang City, S. Korea). These were stored under N_2 atmosphere. Titrisol Iodine solution was obtained from EM Science (Gibbstown, NJ) and tris(2-carboxyethyl)phosphine hydrochloride (TCEP) from Molecular Probes (Eugene, OR). The Micro BCA Protein Assay Reagent kit was obtained from Pierce Biotechnology (Rockford, IL) and the RPAS purification module from Amersham Biosciences Corp (Piscataway, NJ). All other chemicals were obtained from Sigma-Aldrich (St. Louis, MO).

Production and Purification of scFv-c. Four MUC-1 positive scFv-c were selected from previously developed MUC-1 immune phage display scFv libraries (*19, 20*). MUC-1 is a high molecular weight glycoprotein molecule, composed of an extracellular domain with tandem repeats of 20 amino acids, a transmembrane region, and a cytoplasmic tail. In many epithelial cancers, the extracellular domain presents novel epitopes of shortened carbohydrate chains and exposed portions of the 20 amino acid tandem repeats, hence providing unique relatively tumor specific targets for antibodies (*20*). Anti MUC-1 scFv gene inserts were isolated by SfiI/NotI double digestion and ligated into the pCANTAB 5E Cys vector (*18*). Clones isolated from transformants after electroporation into *E. coli* HB2151 were sequenced to confirm the presence of the extra cysteine-specifying codon at the 3′ end of the scFv (scFv-c). In the scFv-c protein, cysteine (C) is transcribed from this vector codon, at the end of the linked Vh-Vl sequence, immediately after the amino acid sequence of the NotI insertion site (underlined) and before the E-TAG amino acid sequence (bold): (Vh-Vl...TKLELKRAAAC**GAPVPYPDPLEPRAA**) (*20*).

All the scFvs-c were produced in shaker flasks and purified as previously described (*18, 20*). Briefly, periplasmic extracts were prepared and affinity purified by anti E-Tag chromatography of the scFv-c proteins using the RPAS purification module and buffer-exchanged into phosphate-buffered saline (PBS) pH 7.4 (*18, 20*). The protein concentration (mg/mL) of each E-Tag purified scFv-c product was determined by using the micro BCA protein reagent kit. To ensure the scFv-c was in the monomeric form for conjugation, the scFv-S−S-scFv linkage from the unpaired thiol groups was prevented by addition of the reducing agent, TCEP, in 2-fold molar excess. As shown previously (*18*), nearly 100% reduction of that thiol group could be maintained in this manner with no evidence of effect on the two intramolecular disulfide bridges of the scFv-c. The advantage of TCEP as the reducing agent was stability over time in a broad pH range (5.0−8.0); however, increased signal in ELISA studies has been noted at these concentrations, so that samples with and without TCEP are evaluated.

Estimation of Maleimide Reactivity as PEG-Mal. To estimate the degree of functional maleimide groups available for conjugation in the PEG reagents, functional group analysis of the various PEG-Mal was carried out by adding up to a 5 M excess of cysteine to each PEG-Mal in 0.1 M sodium phosphate, pH 7, with 1 mM EDTA (Table 1, nos. 1−6). Free cysteine was then measure by reaction with DNTB as previously published (*21*). The results indicated that maleimide functional groups in all the PEG-Mal reagents were greater than 90% reactive toward cysteine and thus thiol groups.

PEGylation of scFv-c. The PEG to scFv molar ratio for conjugation reactions was initially studied with scFv-c as D5-c PEG-$(Mal)_2$ (2 kDa) at 2, 5,10, 20, and 50-fold molar excess of PEG. Since no increase in scFv conjugation was demonstrated in ratios over 5:1, PEGylation studies of all 4 scFv-c with the PEG-Mal and PEG-OPSS reagents was performed at a molar ratio of 5:1 (PEG: scFv). The reaction was carried out in 0.1M sodium phosphate buffer, pH 7.0, 2 mM EDTA, at 1−2 mg/mL scFv-c and 2-fold molar excess TCEP, and incubated under N_2 atm at 37 °C overnight (*22, 23*).

PEGylation efficiency was analyzed using separation of scFv-c and PEG-scFv species with SDS−PAGE (Novex XCell II) in 4−12% Bis-Tris NuPAGE gel and MES running buffer, according to the manufacturer's methods (*17, 22, 24*). Coomassie blue and barium iodide staining detected scFvs (free and conjugated) and PEG molecules, respectively, and comparisons were made to the molecular weight standards. Coomassie blue-stained proteins in the PAGE gels were digitally scanned for permanent images and quantitation of the bands. The gels were then rinsed with distilled water, and 5% barium chloride solution was added for 10 min and again rinsed and placed in 0.1 M Titrisol iodine solution for color development (*17, 25*) (Figure 2).

PEGylation yields were calculated from quantitation of the initial scFv-c compared to the resulting scFv-c as PEG-scFv conjugates vs unconjugated scFv-c. The relative amounts of each species in each reaction were obtained by calculations of digital information from densitometry performed on the scanned gel images and protein standards (Personal Densitometer S1, model PDS1, Molecular Dynamics Inc., Sunnyvale, CA), as previously described (*26*).

Western Blot Analysis of scFv-c E-Tag-Purified Products. The 4 scFv-c and separately BA1-c and the purified BA1-c PEG-$(scFv)_2$ products were evaluated with anti-E Tag by Western blotting. Two hundred and fifty nanograms of purified scFv-c and PEG-$(scFv)_2$ were subjected to SDS−PAGE, transferred onto a PVDF (polyvinylidine difluoride) membrane to which HRP-conjugated anti-E Tag (Amersham Biosciences) was added. After washings, reactivity was detected with the Super Signal (Pierce, Rockford, IL) substrate and exposed to chemiluminescent-sensitive film. Specific attention was given to the 17 and 19 kDa products seen on PAGE but not on Western with anti-E-Tag (Figure 3).

Protein N-Terminal Sequencing of the 17 and 19 kDa Fragments. After separation of the BA1-c protein forms by nonreducing SDS−PAGE, ~9.5 and 19 μg of BA1-c nonreduced scFv fragments, respectively, were loaded into two lanes of a 4−12% NuPAge gel (Invitrogen), and the proteins were electroblotted onto a PVDF membrane (Biorad, Hercules, CA) for direct N-terminal sequencing by Edman's degradation. This protein microsequencing was performed on an ABI Procise HT Edman Sequencer System (Perkin-Elmer/Applied Biosystems, Foster City, CA) at the Molecular Structure Facility at University of California−Davis.

Cell Lines and Cell Lysate Preparation. MUC-1 positive human breast adenocarcinoma MCF-7 cells (American Type Culture Collection (ATCC) Manassas, VA) were grown to 75% confluence in DMEM (Gibco, Invitrogen Corp., Carlsbad, CA) medium supplemented with 5% fetal calf serum (FCS) (Gibco, Invitrogen Corp.). MUC-1-positive DU145 human prostate cancer cells (ATTC) were grown to 100% confluence in RPMI-1640 medium (Gibco, Invitrogen Corp.) supplemented with 10% FCS.

Purification of PEG Conjugates. PEG-$(BA1)_2$ reaction mixture, as shown in the (Figure 3a, lane B) containing 250 μg of PEGylated protein, was purified by molecular sieving column chromatography on a 30 × 1.5 cm glass column (Bio-Rad, Hercules, CA) packed with sephadex G-75 (Sigma Chemicals, St. Louis, MO). The column was preconditioned in 100 mM sodium phosphate buffer pH 7.0 and operated at a flow rate of 0.3 mL/min. Fractions were collected (200 μL), and the PEG-$(scFv\text{-}c)_2$ (65 kDa) was eluted immediately after the void volume. ScFv-c (31kDa) and PEG-scFv-c (34kDa) eluted together at midcolumn volume.

Immunoreactivity. ELISA was used to determine immunoreactivity of PEGylated scFv against breast (MCF-7) and prostate cancer (DU145) cell membranes. Pro-Bind ELISA assay plates (Becton Dickinson Lab Ware, Franklin Lakes, NJ) were coated with 100 μL of cell lysate at 1 mg/mL. The wells were dried by warming the plates at 37 °C. Nonspecific binding was blocked with 200 μl/well of PBS/0.1% Tween 20 (Sigma-Aldrich) containing 3.0% nonfat dry milk (Bio-Rad, Hercules, CA) for 1 h at 37 °C. E-Tag-purified scFv-c, the reaction mixture of scFv-c and PEGylated scFv, and the purified PEG-$(scFv\text{-}c)_2$ were each studied in triplicate on three occasions, using 1 μg of scFv-c/well, a total volume of 100 μL/well (PBS/0.01% Tween 20/0.3% nonfat dry milk), and 1 h incubation at 37 °C. Following each incubation, the plates were washed six times with PBS containing 0.01% Tween 20. Anti-E-Tag-HRP MAb (100 μL) diluted to 1:4000 in PBS/0.1% Tween/0.3% nonfat milk solution was added and incubated in the same manner. Following the last wash step, the 2,2′-amino-bis-3-ethylbenzthiazoline-6-sulfonic acid (ABTS) substrate (Sigma-Aldrich), containing 0.3% H_2O_2, was added. As soon as color had developed, the content of each well was transferred to a new plate. Plates were read at $A_{405\ nm}$ (Dynex microplate reader, Chantilly, VA).

RESULTS

Evaluation of scFv-c Preparations. PAGE gels of the ETAG-purified products of each scFv-c in TCEP are illustrated in Figures 2. The major band, approximately 30 kDa, corresponds to the monomeric form of the scFv-c for CC6-c (Figure 2a), AD3-c (Figure 2b), D5-c (Figure 2c), and BA1-c (Figure 2d). Lower molecular weight recombinant products of AD-3-c, D5-c, and BA1-c can be seen approximating 17 and 19 kDa. These were demonstrated to have no E-Tag by Western Blot analysis, as exemplified by BA1-c (Figure 3). Minor bands at approximately 52 kDa were detected only in the initial BA1-c (Figure 2d) and were not studied.

PEGylation of scFv-c. PEGylation was studied using PEG with either of two thiol reacting groups, Mal or OPSS (*16, 27, 28*). Effective conjugations were only obtained with Mal as either PEG-Mal or PEG-$(Mal)_2$. The

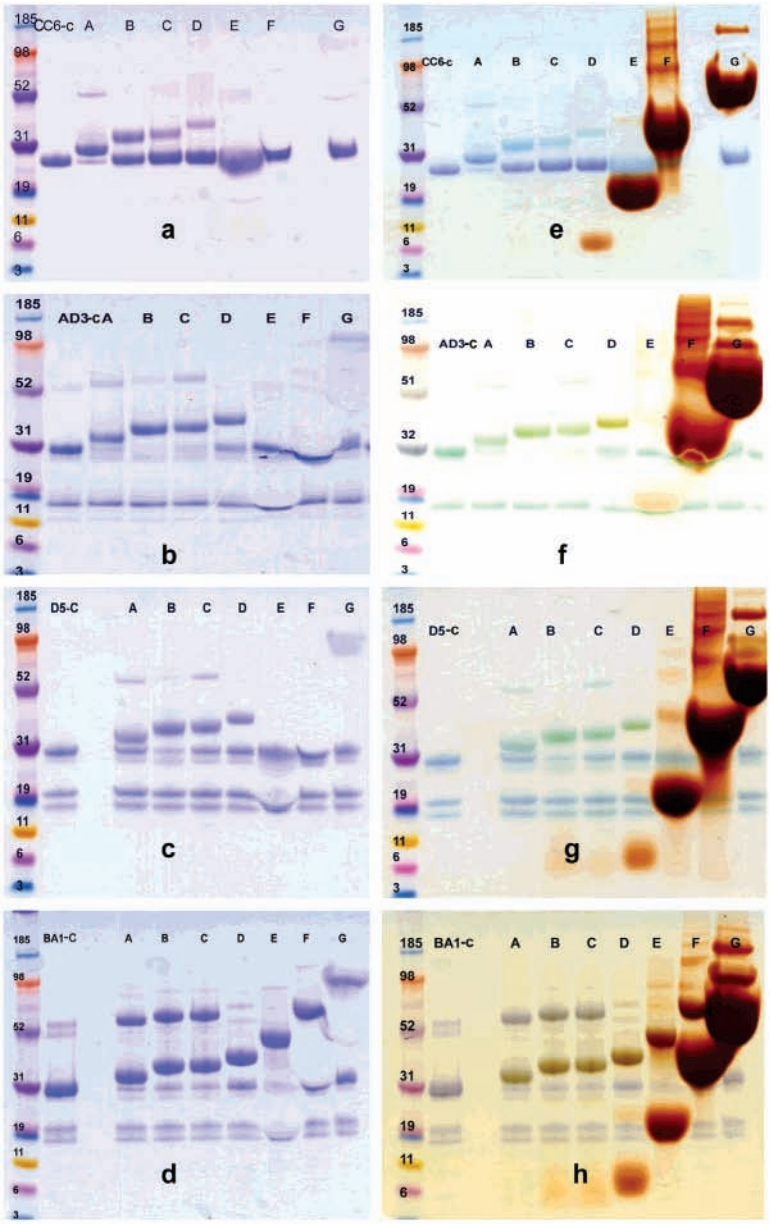

Figure 2. PEG-scFv conjugates on SDS−PAGE gel (4−12%) under reducing conditions. (Left) (a−d) Stained with Coomassie blue for protein identification. ScFv-c in each series of conjugation reactions, a: CC6-c, b: Ad3-c, c: D5-c, and d: BA1-c. (Right) (e−h) Stained with Coomassie blue for protein followed by barium iodide for PEG, allowing both scFv-PEG and PEG identification, e: CC6-c, f: Ad3-c, g: D5-c, and h: BA1-c. Lanes A and C are the results from PEGylation with PEG-$(Mal)_2$, 2 and 3.4 kDa; Lane B, NHS-PEG-Mal 3.4 kDa; and Lanes D−G PEG-Mal of 5, 10, 20, and (branched) 40 kDa. Note should be made that lanes D−G showed PEGylation with increasing PEG molecule size. The identification of PEG and scFv-PEG by barium iodide and Coomassie blue is shown in Figure 2e−h with three different colors: blue (scFv), green/gray (PEG-scFv), and brown (PEG), providing identification of various molecules to confirm the PEG-scFv conjugation. Lanes A to F (Figures a−d), with Coomassie blue staining, show gradual increase in molecular weight in accordance with the molecular weight of the PEG used in the conjugation.

PEG with OPSS was evaluated (5:1), PEG-OPSS/scFv, and resulted in less than 10% scFv conjugation. PEGylation with identical molar ratios of PEG-Mal to scFv-c (5:1) was much more effective with all scFvs (Figures2 and 4). The PEG-Mal conjugated 30−85% of the scFvs (Figure 4), and the percent of scFv that conjugated as bi-scFv on PEG-$(Mal)_2$ ranged from 15 to 35% for both 2 and 3.4 kDa PEG-$(Mal)_2$ polymers. ScFv BA1-c had the highest efficiency of bi-scFv-c conjugation to produce PEG- $(scFv)_2$ (Figure 4). Using the hetero-bifunctional PEG (3.4 kDa) (Table 1; no. 2) containing one Mal and *N*-hydroxysuccinimide (NHS), the latter for amine reactions, correlated with no effective production of bifunctional PEG-$(scFv)_2$ with CC6-c, AD3-c, or D5-c (Figure 2a,b,c; lane B), but BA1-c conjugated with the NHS group resulting in 40% of that scFv-c as PEG$(scFv)_2$, although the reactivity of NHS should be minimized at this pH (Figure 2d, lane B).

With different sizes of PEG, the PEGylation of scFv-c as one scFv-c per PEG resulted with scFv-c conjugation efficiency ranging from 45% to 75% (2 kDa), 30 to75% (3.4 kDa), 25 to 85% (5 kDa), and 10 to 70% (40 kDa) of the original scFv-c protein (Figure 4, blue bar). With PEG-$(Mal)_2$, 15 to 45% (2 kDa), and 15 to 40% (3.4 kDa), the initial scFv-c protein PEGylated as two scFv per PEG (PEG-$(scFv)_2$) (Figure 4, green bar). Conjugation efficiency with PEG varied moderately among the four scFv with BA1-c > AD3-c ≅ D5-c > CC6-c. The 10 and 20 kDa PEG-Mal PEGylated less than 5% of three out of the four scFv-c.

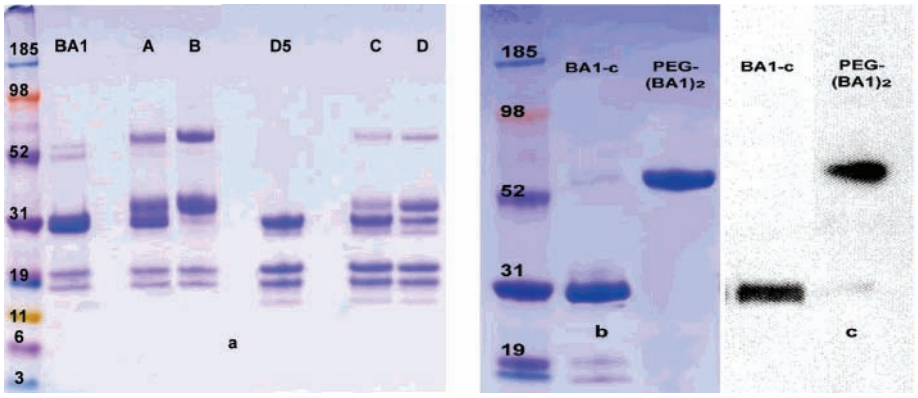

Figure 3. (a) SDS−PAGE reducing gel (4−12%) of 2 kDa PEG-$(Mal)_2$ conjugation reactions with two different scFvs, BA1-c and D5-c, using two different molar ratios of scFv/PEG: 5:1 (lanes A and C), and 1:5 (lanes B and D). It should be noted that bivalent PEG-$(scFv)_2$ product yield was not enhanced by multifold increase in scFv-c to PEG. (b) SDS−PAGE gel and (c) Western blot analysis of BA1-c compared to the purified PEG-$(BA1)_2$ product from the conjugation reaction mixtures seen in part b. The Western blot was performed using HRP-conjugated anti-E-TAG antibody. Bands at 17 and 19 kDa in parts a and b demonstrate no E-TAG binding on Western blot. Prior sequencing indicates that these represent an scFv fragment, with the protein sequence from the amino terminus of VH through the linker region.

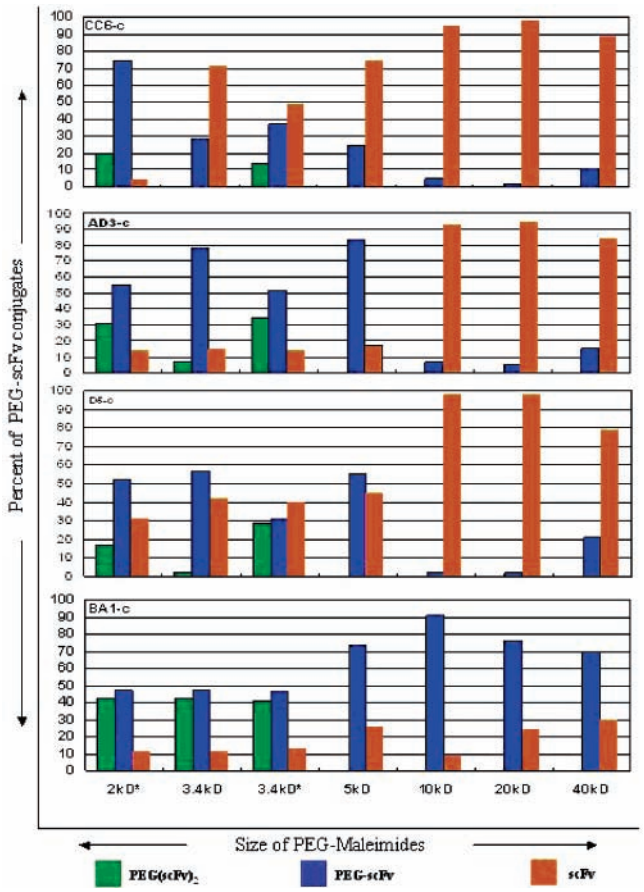

Figure 4. Yields of scFv-c and with PEG-Mal conjugation. The percent scFv-c protein conjugated by PEG-Mal (conjugation yield) calculated from densitometry of the Coomassie blue-stained PAGE gel images. Conjugation yield of scFv-c with PEG-$(Mal)_2$ and PEG-Mal are separately color-coded: green, PEG-$(scFv\text{-}c)_2$; blue, PEG-scFv-c; and orange, unconjugated scFv-c. The scFv-c protein percent yield as PEG-scFv conjugates are on the *x*-axis and PEG-Mal sizes are on the *y*-axis. * PEG-$(Mal)_2$. Panel of scFvs used in these studies were CC6-c, AD3-c, D5-c, and BA1-c, respectively.

The comparison of conjugation reactions of PEG-Mal molecules consisting of various molecular weights ranging from 2 kDa to 40 kDa (Figure 1) demonstrated higher efficiency scFv PEGylation with smaller PEG molecules and lower with larger PEG molecules (Figure 4). The percent yield of PEG-scFvs was 45 to 75, 30 to 75, 25 to 80, and 10 to 70% for 2, 3.4, 5, and 40 kDa PEGs, respectively. BA1 (scFv) had above 40% conjugation with all size of PEG-Mal. AD3 had an exceptionally high percent conjugation of 85% with 5 kDa PEG-Mal. However, unexpectedly 10 and 20 kDa linear PEG-Mal compounds did not react with CC6, D5, and AD3, but BA1 had greater than 75% conjugation. The 40 kDa PEG-Mal branched PEG (Figure 1) conjugated with all four scFv-c (Figures 2 and 4) (*29*). We speculate that this may be due to the influence of the location of the Mal in the branched polymer, as the 10 and 20 kDa were terminal on the linear molecule (*29, 30*).

SDS−PAGE Analysis of PEG-scFv and PEG-$(scFv)_2$ Products. The SDS−PAGE of protein by Coomassie blue is shown in Figure 2a−d. The identification of PEG and scFv-PEG by barium iodide and Coomassie blue is shown in Figure 2e−h with three different colors: blue (scFv), gray (PEG-scFv), and brown (PEG), providing identification of various molecules to confirm the PEG-scFv conjugation.

The SDS−PAGE gel (Figure 1e) of the PEG reagents stained with barium iodide showed decreased mobility of the PEG molecules of 2, 3.4, 5,10, 20, and 40 kDa with increased molecular size (*25*). Lanes A to E and F (Figures 2a−d), of Coomassie blue staining, demonstrated gradual increase in protein conjugate molecular weight (bands) in accordance with the molecular weight of the PEG (Figure 1) used in the conjugation.

The typical conjugation yield of PEG-scFvs varied between 20 and 80%. In Figure 2a−d, lanes A and C, we have used PEG-$(Mal)_2$ for the conjugation, which showed 15−45% PEG-$(scFv)_2$. Figure 2e−h, lanes A and C, supported this, as the light green/gray color of these bands confirmed bifunctional PEGylation. Figure 2d, lane G, demonstrated substantial PEGylation product of BA1-c and the branched PEG-Mal 40 kDa (98 kDa), while Figure 2a (lane G) of the scFv (CC6) showed less than 10% branched PEG-Mal 40 kDa conjugation product.

Lanes E and F for the 10 and 20 kDa linear PEG with the three scFvs (CC6, AD3, and D5) showed very faint bands for the PEGylation yield. Lane G of the Figure 2e−h did not demonstrate visible green color for PEGylation due to masking by the dark brown color by high concentrations of PEG. Data from these conjugations is presented in Figure 4.

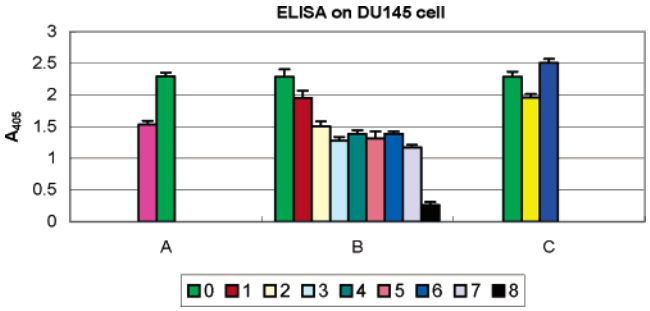

Figure 5. Comparison of MUC-1 binding by ELISA of BA1-c and its PEGylated products on DU145 cell lysate. Two micrograms of protein from each product were used. (A) BA1-c, no TCEP (pink) and BA1-c, with 2-fold molar excess of TCEP (green). (B) PEG-BA1 products (unpurified), code corresponds to conjugation reaction mixture tested i.e., 0 = BA1-c, 1 = 2kDa PEG-$(BA1)_2$, 2 = 3.4 kDa PEG-$(BA1)_2$, 3 = 3.4 kDa PEG-BA1, 4 = 5 kDa PEG-BA1, 5 = 10 kDa PEG-BA1, 6 = 20 kDa PEG-BA1 7 = 40 kDa PEG-BA1, and 8 = negative scFv-PEG control. (C) BA1-c with TCEP (green); 2 kDa PEG-$(BA1)_2$, unpurified (yellow); 2 kDa PEG-$(BA1)_2$, purified (blue). These data demonstrate that binding was generally retained after PEGylation. Further, binding of purified bifunctional 2kDa PEG-$(BA1)_2$ was increased over the original scFv-c with or without the TCEP addition. Since TCEP has demonstrated enhanced ELISA signal at the concentrations used; scFv-c with and without TCEP were controls in these binding studies. Reaction mixture samples had negligible TCEP because of buffer exchange/concentration and therefore no enhanced signal. The control BA1-c (pink), without TCEP, seen in A, represents a more appropriate comparison for PEG-scFv reaction mixture than the BA1-c with TCEP (green). PEGylated monofunctional scFv-c products demonstrated binding very similar to the initial BA1-c, and the binding of the bifunctional 2 kDa PEG-$(BA1)_2$ seen in C (blue) was enhanced. Graphs were derived from mean absorbance values normalized to background (no scFv). Corresponding standard errors (SE) from three experiments with triplicates in each of the three experiments are shown. Mean background values and SE was 0.11 (±0.009) for DU145 cell lysate.

PAGE and Western Blot Analysis. Figure 3a–c show the conjugation reaction mixture and purified product of BA1-c conjugated as PEG-$(scFv)_2$ analyzed by SDS–PAGE and anti E-Tag probing of the Western blot. SDS–PAGE of BA1-c show the two bands frequently seen, corresponding to 17 and 19 kDa, which did not appear with anti E-Tag probing of the Western blot, indicating that these two proteins have no E-Tag (Figure 3c).

Immunoreactivity. ELISA studies of in vitro binding to tumor cell membrane lysate were performed on the various PEGylation products, with varied results, particularly noted in samples with low PEGylation yield. Since the most efficient PEGylation with the various PEG structures was demonstrated with BA1-c (Figures 2 and 4), providing comparable samples for study, all of the BA1-c unpurified PEGylation products and the purified bivalent PEG-$(BA1\text{-}c)_2$ from conjugation with 2 kDa PEG-$(Mal)_2$ were selected for further study. ELISA results of these BA1-c PEGylation products seen on SDS–PAGE in Figure 2d demonstrated good binding with all univalent products and better binding with the bivalent PEG-$(BA1\text{-}c)_2$ (Figure 5). The purified PEG-$(BA1\text{-}c)_2$, in PBS with no TCEP, demonstrated the best results compared to the BA1-c with or without TCEP (Figure 5). Results on MCF-7 were remarkably similar and therefore are not shown.

DISCUSSION

Intact antibodies represent epitope specific, bivalent molecules that are used to specifically target a selected antigen for radiodiagnosis or therapy (*31*). If there is abundant antigen present, simultaneous or serial binding to two adjacent antigen molecules leads to increased "functional affinity" (avidity) and enhanced retention time on the target. Abundant antigen target on the malignant cell membrane is frequently found in cancer because of up-regulation of gene products. Univalent antibody fragments, such as Fab fragments or scFv, exhibit faster blood clearance and better tissue penetration and provide similar epitope-binding specificity and single valance affinity, but substantially lower avidity (*32*). The selection and production of target-specific scFv proteins is well established (*23*, *33*). The characteristics of the molecular format in which they can be used most effectively for tumor targeting depends on the diagnostic or therapeutic purpose so that the required molecular formats and pharmacokinetics vary. Small molecules, with rapid tissue penetration and clearance, provide high target to nontarget (T/NT) imaging agents for PET; larger heterofunctional formats, having longer blood and malignant cell residence, provide pretargeting molecules for multistep radioisotope therapy.

To increase avidity and to generate both homo- and heterofunctional molecules, Fab and scFv have been engineered previously into dimeric, trimeric, or tetrameric conjugates through the use of either chemical or recombinant technology (*33–35*). The work reported here addresses another more generally applicable approach to create multimeric scFv molecules for cancer targeting, by site-specific conjugation to functionalize PEG (*18*).

PEGylation has demonstrated the ability to increase in vivo bioactivity of a number of peptides, including asparaginase, interferon alpha, recombinant interleukin-2, tumor necrosis factor-alpha, cytokine conjugated toxin, and photodynamic agents such as chlorine polymers (*29*, *36–38*). The ability to control blood clearance based upon the selection of molecular size for PEGyated peptides has been demonstrated (*39, 40*). Increasing the "effective" molecular size of PEGylated recombinant interlecukin-2 from 40 kDa to 208 kDa increased the slow phase of plasma clearance, by more than 8-fold (*39*).

The FDA has approved a number of PEGylated proteins for imaging (*41*) and therapy (*38*, *42*). Other PEGylated compounds, to prolong circulation time and reduce immunogenicity, are in clinical trials (*43*). In general, PEGylation of proteins, including radiolabeled proteins, results in increased molecular size, increased blood retention, and decreased renal glomerular filtration (*44*). However, uptake of PEGylated proteins into renal tubular cells and hepatocytes, compared to non-PEGylated proteins, has been variable: increased (*45–47*), decreased (*48*), or unchanged (*49*). Conceptually, tumor to normal tissue concentration ratios can be enhanced for targeted radionuclide therapy with PEGylation of small tumor binding modules, but this has yet to be realized (*23*).

PEGylation also affords the opportunity to form multidentate versions of peptides and scFv through the use of branched or star PEG polymers, with the likelihood of increasing avidity and residence time on target sites (*50*). Studies of the effects of PEGylation on biodistribution of antibody fragments with linear PEG structures have shown that linear PEGylated fragments have prolonged circulation times and increased tumor uptake (*36, 39, 45, 50–53*).

In most cases, PEGylation has been performed by random conjugation with any of the many lysine residues of the protein. In small molecules, such as scFv, an

increased fraction of available lysine is located in or near the binding site (*17*). The resultant PEGylated proteins tend to be heterogeneous, composed of molecules having PEG conjugated at different positions, thus creating variable binding affinities (*17*). To overcome this major problem, an approach wherein the recombinant scFv production vectors encode an unpaired cysteine near the C terminus of any inserted scFv for site-specific PEGylation was devised; scFv-c from the pCANTAB 5E Cys vector was used to study thiol PEGylation in this report (*18*). The advantage of employing sulfhydryl-directed moieties in scFv engineering is that the four disulfide-bonded cysteines of the scFv framework needed for the structural configuration are completely buried by the molecular conformation, thus relatively protected (*19*). Unpaired cysteines are relatively unprotected and not naturally present, thus providing a unique site-specific target for conjugation of any scFv-c made in this manner (*54*).

In the PEGylation of scFv for developing tumor-targeting radiopharmaceuticals, efficient conjugation of thiol-reacting PEG to scFv-c is needed. Although the proof of principle of site-specific PEGylation has been previously published (*18, 23*), the general applicability and efficiencies of conjugation of various scFv-c with a panel of PEG molecules have not been demonstrated. Using four MUC-1 scFvs, having different target epitopes and sequences (*20*), the relative scFv-c thiol conjugation was evaluated with an array of functionalized PEG molecules. Focus was particularly made on linear uni- and bifunctional maleimide PEG molecules of varying molecular weights. In light of these studies, at least 60% (60−90%) of all four scFv could be conjugated with maleimide, demonstrating that the added cysteine provided an available SH for site-specific conjugation, as shown in Figures 2 and 4,

ScFv-PEG molecular size increased consistent with the size of PEG attached, as expected (Figure 2a−d). However, when the molecular weight of PEG-Mal increased above 5 kDa, PEGylation efficiency substantially decreased despite evidence of appropriate Mal reactivity on these larger PEG molecules. Steric hindrance of the Mal group by coiling of the linear PEG polymers may provide an explanation. With the 40 kDa branched polymer, better conjugation yield over the linear 10 and 20 kDa PEG may also be due to less steric hindrance of PEG on Mal interaction with the cysteine, since Mal is at the "v" branching point in this PEG configuration (Figure 1) (*29*).

Bifunctional conjugation was demonstrated with 2 and 3.4 kDa PEG bimaleimide. Using the same 1:5 scFv/PEG ratio with the (2 kDa and 3.4 kDa) PEG-$(Mal)_2$, 20, 30, 15, and 42% of the 4 scFv-c was conjugated as $(scFv)_2$-PEG, with 2−40% scFv-c left unconjugated. The efficiency of scFv-c reacting with Mal-PEG in all formats did seem to relate to the specific scFv-c, although three of four scFv-c demonstrated more complete conjugation with smaller and linear PEG-Mal molecules. Little or no divalent PEG-$(scFv)_2$, however, with the NHS-PEG-Mal was expected since NHS should not be conjugating at the pH used. This was the case with three of four scFvs. However, BA1-c did conjugate 40% of the BA1-c as scFv-PEG-scFv with NHS-PEG-Mal. This mixed bifunctional PEG formed a resultant PEG-$(BA1)_2$ that did bind tumor membranes well on ELISA (Figure 5). An available reactive group near the C-terminus of this scFv-c may be responsible.

The PEG-$(scFv)_2$ demonstrated improved binding to the cell membrane antigen when compared to the monomeric scFv-c. The improved binding of S−S linked homodimers (di-scFv) and PEG-$(scFv)_2$ over the univalent scFv-c or scFv would also be expected because of the increase in avidity with bivalent binding (*18, 55−57*). However, selected PEG-linked scFv bioconjugates are expected to be superior in vivo tumor targeting agents compared to di-scFv or diabody forms since (i) PEGylated proteins have shown enhanced stability in the circulation in vivo; (ii) increased molecular size should result in decreased rapid kidney clearance, as the threshold for first pass elimination is approximately 65 kDa (*58*); (iii) the addition of PEG is likely to decrease proteolysis at the tumor site (*42*).

In summary, 30-40% of the scFv-c protein from E-TAG-purified recombinant products was converted to malignant cell membrane binding PEG-$(scFv)_2$ in three of the four scFv-c studied. In these three studied, 50−90% could be conjugated as univalent PEG-scFv, with comparable malignant cell binding before and after PEGylation. These results provide further evidence that novel constructs for imaging and therapy can be developed from scFv-c modules through site-specific PEGylation.

ACKNOWLEDGMENT

U.S. Department of Energy Grant DE-FG01-00NE22944, National Cancer Institute Grant PO1 CA47829, and Department of Defense Grant DAMD17-01-0177 supported this work. We thank Trevor Peterson for excellent technical assistance to producing scFv for this work under a Society of Nuclear Medicine Extension and Research fellowship.

LITERATURE CITED

(1) DeNardo, S. J., DeNardo, G. L., O'Grady, L. F., Macey, D. J., Mills, S. L., Epstein, A. L., Peng, J.-S., and McGahan, J. P. (1987) Treatment of a patient with B cell lymphoma by I-131 Lym-1 monoclonal antibodies. *Int. J. Biol. Markers 2*, 49−53.

(2) Juweid, M. E., Stadtmauer, E., Hajjar, G., Sharkey, R. M., Suleiman, S., Luger, S., Swayne, L. C., Alavi, A., and Goldenberg, D. M. (1999) Pharmacokinetics, dosimetry and initial therapeutic results with ^{131}I- and ^{111}In-/^{90}Y-labeled humanized LL2 anti-CD22 monoclonal antibody (MAb) in patients with relapsed/refractory non-Hodgkin's lymphoma (NHL). *Clin. Cancer Res. 5*, 3292s−3303s.

(3) DeNardo, S. J., DeNardo, G. L., Yuan, A., Richman, C. M., O'Donnell, R. T., Lara, P. N., Kukis, D. L., Natarajan, A., Lamborn, K. R., Jacobs, F., and Siantar, C. L. (2003) Enhanced therapeutic index of radioimmunotherapy (RIT) in prostate cancer patients: comparison of radiation dosimetry for 1,4,7,10-tetraazacyclododecane-N,N′,N″,N‴-tetraacetic acid (DOTA)-peptide versus 2IT-DOTA monoclonal antibody linkage for RIT. *Clin. Cancer Res. 9*, 3938s−3944s.

(4) Jain, R. K. (1990) Physiological barriers to delivery of monoclonal antibodies and other macromolecules in tumors. *Cancer Res. 50*, 814s−819s.

(5) Winthrop, M. D., DeNardo, S. J., and DeNardo, G. L. (1999) Development of a hyper immune anti-MUC-1 single chain antibody fragments phage display library for targeting breast cancer. *Clin. Cancer Res. 5*, 3088s−3094s.

(6) DeNardo, S. J., DeNardo, G. L., DeNardo, D. G., Xiong, C. Y., Shi, X. B., Winthrop, M. D., Kroger, L. A., and Carter, P. (1999) Antibody phage libraries for the next generation of tumor targeting radioimmunotherapeutics. *Clin. Cancer Res. 10*, 3213−3218.

(7) Winter, G., Griffiths, A. D., Hawkins, R. E., and Hoogenboom, H. R. (1994) Making antibodies by phage display technology. *Annu. Rev. Immunol. 12*, 433−455.

(8) Carter, P. (2001) Improving the efficacy of antibody-based cancer therapies. *Nat. Rev. Cancer 1*, 118−129.

(9) Maynard, J., and Georgiou, G. (2000) Antibody engineering. *Annual Review of Biomed. Eng. 2*, 339−376.

(10) Adams, G. P. (1998) Improving the tumor specificity and retention of antibody-based molecules. *In Vivo 12*, 11−22.
(11) Adams, G. P., McCartney, J. E., Tai, M. S., Oppermann, H., Huston, J. S., Stafford, W. F., Bookman, M. A., Fand, I., Houston, L. L., and Weiner, L. M. (1993) Highly specific in vivo tumour targeting by monovalent and divalent forms of 741F8 anti-c-erbB-2 single-chain Fv. *Cancer Res. 53*, 4026−4034.
(12) Larson, S. M., El-Shirbiny, A. M., Divgi, C. R., Sgouros, G., Finn, R. D., Tschmelitsch, J., Picon, A., Whitlow, M., Schlom, J., Zhang, J., and Cohen, A. M. (1997) Single chain antigen binding protein (scFv CC49). *Cancer 80*, 2458−2468.
(13) Fitch, J. C., Rollins, S., Matis, L., Alford, B., Aranki, S., Collard, C. D., Dewar, M., Elefteriades, J., Hines, R., Kopf, G., Kraker, P., Li, L., O'Hara, R., Rinder, C., Rinder, H., Shaw, R., Smith, B., Stahl, G., and Shernan, S. K. (1999) Pharmacology and biological efficacy of a recombinant, humanized, single-chain antibody C5 complement inhibitor in patients undergoing coronary artery bypass graft surgery with cardiopulmonary bypass. *Circulation 100*, 2499−2506.
(14) Katre, N. V. (2004) The conjugation of proteins with poly(ethyleneglycol) and other polymers. Altering properties of proteins to enhance their therapeutic potential. *Adv. Drug Delivery Rev. 10*, 91−114.
(15) Bailon, P., and Berthold, W. (1998) Poly(ethyleneglycol)-conjugated pharmaceutical proteins. *Pharm. Sci. Technol. Today 1*, 352−356.
(16) Veronese, F. M. (2001) Peptide and protein PEGylation: a review of problems and solutions. *Biomaterials 22*, 405−417.
(17) Yamamoto, Y., Tsutsumi, Y., Yoshioka, Y., Nishibata, T., Koybayashi, K., Okamoto, T., Muka Shimizu, T., Nakagawa, S., and Mayumi, T. (2003) Site-specific PEGylation of a lysine-deficient TNF-alhpa with full bioactivity. *Nat. Biotechnol. 21*, 546−552.
(18) Albrecht, H., Burke, P. A., Natarajan, A., Xiong, C. Y., Kalicinsky, M., DeNardo, G. L., and DeNardo, S. J. (2004) Production of soluble ScFvs with C-terminal-free thiol for site-specific conjugation or stable dimeric ScFvs on demand. *Bioconjugate Chem. 15*, 16−26.
(19) Padlan, E. A. (1994) Molecular biology intelligence unit: Antibody−antigen complexes. *The structure of antibodies*, pp 17−30, R.G. Landes Company, Austin, TX.
(20) Winthrop, M. D., DeNardo, S. J., Albrecht, H., Mirick, G. R., Kroger, L. A., Lamborn, K. R., Venclovas, C., Colvin, M. E., Burke, P. A., and DeNardo, G. L. (2003) Selection and characterization of Anti-MUC-1 scFvs intended for targeted therapy. *Clin. Cancer Res. 9,* 3845s−3853s.
(21) Creighton, T. E. (1989) *Protein Structure: A practical Approach* (Creighton, T. E., Ed.) pp 155−167, Oxford University Press, Oxford.
(22) Bailon, P., Palleroni, A., Schaffer, C. A., Spence, C. L., Fung, W. J., Porter, J. E., Ehrlich, G. K., Pan, W., Xu, Z. X., Modi, M. W., Faird, A., Berthold, W., and Graves, M. (2001) Rational design of a potent, long-lasting form of interferon: a 40 kDa branched poly(ethylene glycol)-conjugated interferon alpha-2a for the treatment of heptitis C. *Bioconjugate Chem. 12*, 195−202.
(23) Yang, K., Basu, A., Wang, M., Chintala, R., Hsieh, M. C., Liu, S., Hua, J., Zhou, J., Li Phyu, H., Mendez, M., Janjua, H., Peng, P., Longley, C., Borowski, V., Mehlig, and M., Fil, D. (2003) Tailoring structure−function and pharmacokinetic properties of single-chain Fv proteins by site-specific PEGylation. *Protein Eng. 16*, 761−770.
(24) Laemmli, U. K. (1970) Cleavage of structural proteins during the assembly of the head of bacteriophage T4. *Nature 227*, 680−685.
(25) Kurfurst, M. M. (1992) Detection and molecular weight determination of poly(ethyleneglycol) modified hirudin by staining after sodium dodecyl sulfate-polyacrylamide gel electrophoresis. *Anal. Biochem. 200*, 244−248.
(26) Makmura, L., Hamann, M., Areopagita, A., Furuta, S., Munoz, A., and Momand, J. (2001) Development of a Sensitive Assay to Detect Reversibly Oxidised Protein Cysteine Sulfhydryl Groups. *Antiox. Redox Signaling 3,* 1105−1118.
(27) Roberts, M. J., Bentley, M. D., and Harris, J. M. (2002) Chemistry for peptide and protein PEGylation. *Adv. Drug Delivery Rev. 54*, 459−476.
(28) Olafsen, T., Cheung, C., Yazaki., P. J., Li, L., Sundaresan, G., Gambhir, S. S., Sherman, A. M., Williams, E. M., Shively, E. J., Raubitschek, A. A., and Wu, A. M. (2004) Covalent disulfide-linked anti-CEA diabody allows sie-specific conjugation and radiolabeling for tumor targeting applications. *Protein Eng., Des. Select. 17*, 21−27.
(29) Monfardini, C., Schiavon, O., Caliceti, P., Morpurgo, M., Harris, J. M., and Veronese, F. M. (1995) A Branched Monomethoxypoly(ethylene glycol) for Protein Modification. *Bioconjugate Chem. 6,* 62−69.
(30) Veronese, F. M., Caliceti, P., and Schibler, M. J. (1997) Branched and Linear poly(ethylene glycol): Influence of the polymer structure on enzymological, pharmacokinetic, and immunological properties of protein conjugates. *J. Bioact. Compat. Polym. 12,* 196−207.
(31) Brekke, H. O., and Sandlie, I. (2003) Therapeutic Antibodies For Human Diseases at the Dawn of the Twenty-First Century. *Nat. Rev. Drug Discovery 2,* 52−62.
(32) Hudson, P. J., and Souriau, C. (2004) Engineered Antibodies. *Nat. Med. 9,* 129−134.
(33) Carter, P. (2001) Improving the Efficacy of Antibody-based Cancer Therapies. *Nat. Rev./Cancer 1,* 118−129.
(34) Tomlinson, I., and Holliger, P. (2000) Methods for generating multivalent and bispecific antibody fragments. *Methods Enzymol. 326,* 461−479.
(35) Todorovska, A. (2001) Design and application of diabodies, triabodies and tetrabodies for cancer targeting. *J. Immunol. Methods 248*, 47−66.
(36) Delgado, C., Francis, G. E., and Fischer, D. (1992) Uses and properties of PEG-linked proteins. *Crit. Rev. Ther. Drug Carrier Syst. 9,* 249−304.
(37) Katre, N., Knauf, M. J., and Laird, W. J. (1987) Chemical modification of recombinant interleukin 2 by polyetheylene glycol increases its potency in the murine Meth A sarcoma model. *Proc. Natl. Acad. Sci. U.S.A. 84,* 1487−1491.
(38) Reddy, K. R., Wright, T. L., Pockros, P. J., Shiffman, M., Everson, G., Reindollar, R., Fried, M. W., Purdum, P. P., Jensen, D., Smith, C., Lee, W. M., Boyer, T. D., Lin, A., Pedder, S., and DePamphilis, J. (2001) Efficacy and safety of pegylated (40-kd) interferon alpha-2a compared with interferon alpha-2a in noncirrhotic patients with chronic hepatitis C. *Hepatology 33,* 433−438.
(39) Knauf, M. J., Bell, D. P., Hirtzer, P., Luo, Z. P., Young, J. D., and Katre, N. V. (1988) Relationship of effective molecular size to systemic clearance in rats of recombinant interleukin-2 chemically modified with water-soluble polymers. *J. Biol. Chem. 263,* 15064−15070.
(40) DeNardo, S. J., Yao, Z., Lam, K. S., Song, A., Burke, P. A., Mirick, G. R., Lamborn, K. R., O'Donnell, R. T., and DeNardo, G. L. (2003) Effect of molecular size of PEGylated peptide on the pharmacokinetics and tumor targeting in lymphoma bearing mice. *Clin. Cancer Res. 9,* 3854s−3864s.
(41) Chen, X., Park, R., Shahinian, A., Bading, J., and Conti, P. (2004) Pharmacokinetics and tumor retention of 125I-labeled RGD peptide are improved by PEGylation. *Nucl. Med. Biol. 1,* 11−19.
(42) Crawford, J. (2002) Clinical uses of pegylated pharmaceuticals in oncology. *Cancer Treatment Rev. 28,* 7−11.
(43) Harris, J. M., and Chess, R. B. (2003) Effect of pegylation on pharmaceuticals. *Nat. Rev. Drug Discovery 2,* 214−221.
(44) Behr, T. M., Goldenberg, D. M., and Becker, W. (1998) Reducing the renal uptake of radiolabeled antibody fragments and peptides for diagnosis and therapy: present status, future prospects and limitations. *Eur. J. Nucl. Med. 25,* 201−212.
(45) Delgado, C., Pedley, R. B., Herraez, A., Boden, R., Boden, J. A., Keep, P. A., Chester, K. A., Fisher, D., Begent, R. H. J., and Francis, G. E. (1996) Enhanced tumour specificity of anti-carcinoembryonic antigen Fab′ fragment by poly(ethylene glycol) (PEG) modification. *Br. J. Cancer 73,* 175−182.
(46) Eno-Amooquaye, E. A., Searle, F., Boden, J. A., Sharma, S. K., and Burke, P. J. (1996) Altered biodistribution of an antibody-enzyme conjugate modified with poly(ethyleneglycol). *Br. J. Cancer 73,* 1323−1327.

(47) Pepinsky, R. B., Shapiro, R. I., Wang, S., Chakraborty, A., Gill, A., Lepage, D. J., Wen, D., Rayhorn, P., Horan, G. S. B., Taylor, F. R., Garber, E. A., Galdes, A., and Engber, T. M. (2002) Long-acting forms of sonic hedgehog with improved pharmacokinetic and pharmacodynamic properties are efficacious in a nerve injury model. *J. Pharm. Sci. 91,* 371−387.

(48) Wen, X., Wu, Q., Ke, S., Ellis, L., Charnsangavej, C., Delpassand, A. S., Wallace, S., and Li, C. (2001) Conjugation with ^{111}In-DTPA-poly(ethylene glycol) improves imaging of anti-EGF receptor antibody C225. *J. Nucl. Med. 42,* 1530−1537.

(49) Fang, J., Sawa, T., Akaike, T., and Maeda, H. (2002) Tumor-targeted delivery of poly(ethyleneglycol)-conjugated D-amino acid oxidase for antitumor therapy via enzymatic generation of hydrogen peroxide. *Cancer Res. 62,* 3138−3143.

(50) Lee, L. S., Conover, C., Shi, C., Whitlow, M., and Filpula, D. (1999) Prolonged circulating lives of single-chain Fv proteins conjugated with poly(ethylene glycol): A comparison of conjugation chemistries and compounds. *Bioconjugate Chem. 10,* 973−981.

(51) Kozlowski, A., Charles, S. A., and Harris, J. M. (2001) Development of pegylated interferons for the treatment of chronic hepatitis C. *Biodrugs 15,* 419−429.

(52) Ensor, C. M., Holtzberg, F. W., Bomalaski, J. S., and Clark, M. A. (2002) Pegylated arginine deiminase (ADI−SS $PEG_{20,000mw}$) inhibits human melanomas and hepatocellular carcinomas in vitro and in vivo. *Cancer Res. 62,* 5443−5450.

(53) Wang, M., Lee L. S., Nepomich A., Yang J.-D., Conover C., Whitlow M., and Fipula, D. (1998) Single-chain Fv with manifold *N*-glycans as bifunctional scaffolds for immunomolecules. *Protein Eng. 11,* 1277−1283.

(54) Kabat, E. A., Wu, T. T., Perry, H. M., Gottesman, K. S., and Foeller, C. (1991) *Sequences of Proteins of Immunological Interest*, US Department of Health and Human Services, Bethesda, MD.

(55) Karacay, H., Sharkey, R. M., Govindan, S. V., McBride, W. J., Goldenberg, D. M., Hansen, H. J., and Griffiths, G. L. (1997) Development of a streptavidin-anti-carcinoembryonic antigen antibody, radiolabeled biotin pretargeting method for radioimmunotherapy of colorectal cancer. Reagent development. *Bioconjugate Chem. 8,* 585−594.

(56) Wu, A. M., Chen, W., Raubitschek, A., Williams, L. E., Neumaier, M., Fischer, R., Hu, S. Z., Odom-Maryon, T., Wong, J. Y., and Shively, J. E. (1996) Tumor localization of anti-CEA single-chain Fvs: improved targeting by non-covalent dimers. *Immunotechnology 2,* 21−36.

(57) Le Gall, F., Kipriyanov, S. M., Moldenhauer, G., and Little, M. (1999) Di-, tri-, and tetrameric single chain Fv antibody fragments against human CD19: effect of valency on cell binding. *FEBS Lett. 453,* 164−168.

(58) Maack, T., Johnson, V., Kan, S. T., Figueiredo, J., and Sigulem, D. (1979) Renal filtration, transport and metabolism of low molecular weight proteins: a review. *Kidney Int. 16,* 251−270.

BC0498121

Preparation and Biological Characterization of Polymeric Micelle Drug Carriers with Intracellular pH-Triggered Drug Release Property: Tumor Permeability, Controlled Subcellular Drug Distribution, and Enhanced in Vivo Antitumor Efficacy

Younsoo Bae,[†] Nobuhiro Nishiyama,[‡] Shigeto Fukushima,[†] Hiroyuki Koyama,[‡] Matsumura Yasuhiro,[§] and Kazunori Kataoka*,[†]

Department of Materials Science and Engineering, Graduate School of Engineering, The University of Tokyo, 7-3-1 Hongo, Bunkyo-ku, Tokyo 113-8656, Japan, Department of Clinical Vascular Regeneration, Graduate School of Medicine, The University of Tokyo, 7-3-1 Hongo, Bunkyo-ku, Tokyo 113-8655, Japan, and Investigative Treatment Division, National Cancer Center Research Institute East, 6-5-1 Kashiwanoha, Kashiwa, Chiba 277-8577, Japan. Received July 28, 2004; Revised Manuscript Received October 31, 2004

A novel intracellular pH-sensitive polymeric micelle drug carrier that controls the systemic, local, and subcellular distributions of pharmacologically active drugs has been developed in this study. The micelles were prepared from self-assembling amphiphilic block copolymers, poly(ethylene glycol)-poly(aspartate hydrazone adriamycin), in which the anticancer drug, adriamycin, was conjugated to the hydrophobic segments through acid-sensitive hydrazone linkers. By this polymer design, the micelles can stably preserve drugs under physiological conditions (pH 7.4) and selectively release them by sensing the intracellular pH decrease in endosomes and lysosomes (pH 5−6). In vitro and in vivo studies show that the micelles have the characteristic properties, such as an intracellular pH-triggered drug release capability, tumor-infiltrating permeability, and effective antitumor activity with extremely low toxicity. The acquired experimental data clearly elucidate that the optimization of both the functional and structural features of polymeric micelles provides a promising formulation not only for the development of intracellular environment-sensitive supramolecular devices for cancer therapeutic applications but also for the future treatment of intractable cancers with limited vasculature.

INTRODUCTION

The selective augmentation of drug concentrations in avascular tumor tissues is the most challenging issue of current cancer chemotherapy using macromolecular bioconjugates (*1*−*3*). Most anticancer drugs are pharmacologically effective but limited in their clinical applications due to serious toxicity and low water solubility; thereby, the altered biodistribution of these drugs has an important meaning not only to reduce the toxicity but also to improve therapeutic effects (*4*−*6*). For these reasons, interest has centered on the creation of drug carriers that safely and precisely deliver the appropriate amounts of active drugs to solid tumors (*7*−*10*). Indeed, several macromolecular drug carriers are under clinical trials or used practically, which include water-soluble polymer−drug conjugates (*11*), liposomal carriers (*12*), and polymeric micelles (*13*). However, even though these carriers have made significant advancements in cancer therapy, recent studies point out their antitumor activities are subject to change according to the cancer species with pathological, pharmacological, and biochemical differences (*14*).

There are three major reasons why the present macromolecular drug carriers have difficulties in clinical use. First, the carriers injected into the body encounter in vivo barriers such as nonspecific systemic accumulation and phagocytotic clearance by the host defense system (*15*). Second, even after the carriers accumulated in solid tumors avoiding these in vivo barriers, they still have to overcome the heterogeneous tumor microenvironments that are characterized by insufficient blood supply, disordered vasculatures, and diffusion-limited interstitum (*16*). Third, the carriers that successfully accessed the inside of tumor tissues should release the loaded drugs back into active forms in order to exert the antitumor effect (*17*). Among these reasons, poor permeability of the carriers inside the tumor tissues and low concentrations of active drugs throughout solid tumors become particularly serious problems (*18, 19*). For these reasons, understanding the correlation between the physicochemical properties of drug carriers and their behaviors in the body is very important, and the combination of these two features is required for the design of ultimate carriers (*20*).

In this article, we will report that such tantalizing problems may be overcome by a novel tumor-infiltrating drug carrier, the pH-sensitive polymeric micelle, whose structural and functional features were optimized for the intracellular drug delivery (Figure 1A). The micelle is a nanosized supramolecular assembly from the self-assembling amphiphilic block copolymers, poly(ethylene glycol)-poly(aspartate hydrazone adriamycin) [PEG-p(Asp-Hyd-ADR)]. The anticancer drug, adriamycin (ADR), is

* To whom correspondence should be addressed. Phone: +81-3-5841-7138, Fax: +81-3-5841-7139, E-mail: kataoka@bmw.t.u-tokyo.ac.jp.

[†] Department of Materials Science and Engineering, The University of Tokyo.

[‡] Department of Clinical Vascular Regeneration, The University of Tokyo.

[§] National Cancer Center Research Institute East.

10.1021/bc0498166 CCC: $30.25 © 2005 American Chemical Society
Published on Web 12/22/2004

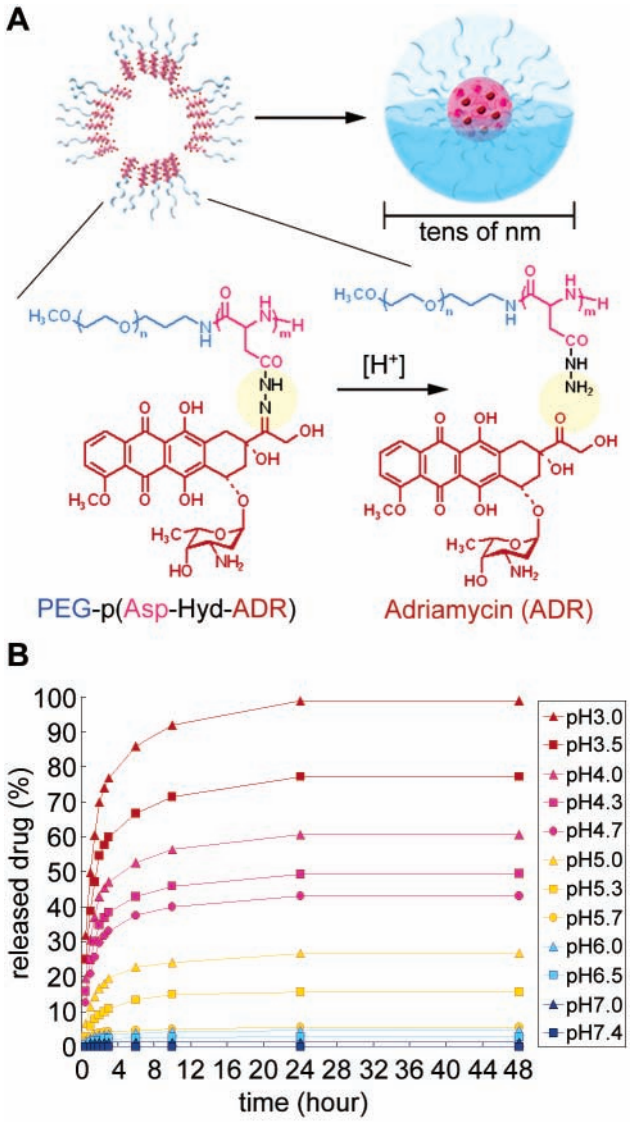

Figure 1. Preparation of tumor-infiltrating polymeric micelles with intracellular pH-sensitivity. (A) Micelles with tens of nm size diameter were prepared from self-assembling amphiphilic block copolymers, PEG-p(Asp-Hyd-ADR), in which the anticancer drug, adriamycin (ADR), was conjugated through acid-sensitive hydrazone linkers. (B) The micelles released the loaded drugs under acidic conditions below pH 6.0 corresponding to intracellular space, but remained stable under the conditions of vascular and extracellular space (pH 7.4−7.0).

conjugated to the core-forming segments through the hydrazone linkers that are stable under physiological conditions (pH 7.4) but cleavable under acidic intracellular environments in endosomes and lysosomes (pH 5−6). This carrier design allows the micelle to safely protect hydrophobic drugs from the host defense system in the body and to selectively exert cytotoxicity due to intracellular pH-triggered drug release, improving both the delivery effect and therapeutic efficacy of the drugs (*21*). Therefore, the characteristic in vitro and in vivo behaviors of the micelles would offer intriguing information taking into account the future design and development of bioresponsive supramolecular carrier systems for the intracellular trafficking of biologically active molecules.

EXPERIMENTAL PROCEDURES

Materials. β-Benzyl-L-aspartate was from Sigma and α-methoxy-ω-amino poly(ethylene glycol) (PEG; MW = 12 000) was from Nippon Oil & Fats, Japan. PEG was purified using an ion-exchange gel column (CM-Sephadex C-50, Amersham Pharmacia Biotech) prior to the synthesis of the block copolymers. Adriamycin hydrochloride-(ADR−HCl) was from Nippon Kayaku, Japan, and its purity was checked by reversed phase liquid chromatograpy (RPLC). Sephadex LH-20 gel was from Amersham Pharmacia Biotech, Sweden.

Cell Lines and Animals. A human small cell lung cancer cell line SBC-3 and murine colon adenocarcinoma 26 (C26) cells were from the National Cancer Center Research Institute, Japan, and cultured in a medium (DMEM, Sigma, St. Louis, MO) containing 10% fetal bovine serum in a humidified atmosphere with 5% CO_2 at 37 °C. CDF-1 mice (female, 6 weeks old) were from Charles River, Japan. The animals were cared for and all experiments were performed in compliance with the Guide for the Care and Use of Laboratory Animals as adopted and promulgated by the National Institutes of Health.

Preparation of the pH-Sensitive Polymeric Micelles. The self-assembling amphiphilic block copolymer, PEG-p(Asp-Hyd-ADR), was synthesized as reported elsewhere (*22*). Briefly, poly(ethylene glycol)-poly(β-benzyl-L-aspartate) (PEG-PBLA) was synthesized from the ring-opening polymerization of β-benzyl-L-aspartate *N*-carboxy-anhydride using PEG as a macro initiator, followed by substitution of the benzyl groups of PEG-PBLA with hydrazide groups for drug binding (see also Supporting Information). Unbound ADR was completely removed using Sephadex LH-20 gel, and the obtained polymers were redissolved in dimethylacetamide to prepare the micelle by a dialysis method.

Evaluation of Acid-Sensitive Drug Release from the Micelles. Reversed phase liquid chromatograpy (RPLC) analysis, using a μ-Bondasphere 5 μm C4-300A column (Nihon Waters, Japan), was used to assess the pH sensitivity of the micelle. The micelle with a 10 mg/mL concentration was incubated under various buffered conditions from pH 7.4 to 3.0 [20 mM phosphate buffer (pH 7.4−6.0), 20 mM acetate buffer (pH 5.8−3.0)], and time- and pH-dependently released drugs were measured from the peak intensity by a UV detector (485 nm).

Observations on Intracellular Drug Release and Localization of the Micelles. Multicellular tumor spheroid (MCTS) was prepared from a C26 cell line using a spheroid culture plate, Sumiloncelltight (Sumitomo Bakelite, Japan); 200 μm size MCTS were sorted and used for the experiments. Fluorescence images were observed using a confocal laser scanning microscope (LSM 510, Carl Zeiss, Germany) with a 20× objective (Plan-Apochromat, Carl Zeiss, Germany) and a 63× objective (C-Apochromat, Carl Zeiss, Germany) at excitation wavelengths of 488 nm (Ar laser) and 364 nm (UV laser) for ADR and Hoechst 33258, respectively. The concentrations of the micelles in the medium were adjusted to 10 μg/mL (ADR equivalent). All images were acquired and processed with the accompanying software.

In Vitro Growth Inhibition Assay. A tetrazolium dye method, called the MTT assay, was used to evaluate the growth-inhibitory effect of the micelle. Using 96-well culture plates, exponentially growing SBC-3 cells were seeded (2000 cell/well) and preincubated for 24 h, followed by coincubation with ADR and the micelle samples. After exposure for 3, 10, and 24 h, the medium was discarded and each cell was reincubated in fresh medium for another 24 h. The cells were then counted using a Bio-RAD Microplate Reader 550 (Bio-Rad Laboratories Inc.).

In Vivo Antitumor Activity and Body Weight Change of Mice. The antitumor activity of the micelles was evaluated with tumor bearing, 7-week-old, female SPF CDF1 mice (n = 6, Charles River, Japan). After implanting C26 cells 10 days earlier, injection of the samples took place using a volume of 0.1 mL/10 g body weight. The regimens of the micelles were scheduled by changing the administration dose (20, 40, and 60 mg/kg) three times with a 4-day interval, based on the optimized regimens of ADR as a control. However, in the case of ADR, only limited doses (5, 10, and 15 mg/kg) were applied to the mice due to the drugs toxicity. The mice were monitored daily, and tumor growth and body weights were measured at 2-day intervals. Tumor volume is calculated as follows: volume = $1/2 \times LW^2$ (L is the long diameter and W is the short diameter of a tumor).

Biodistribution and Pharmacokinetics. The CDF1 mice (n = 6), when the tumor volume reached ca. 100 mm^3, were injected with ADR and the micelles in a volume of 0.1 mL/10 g body weight for the experiments. The dose was either 10 mg/kg for ADR or the micelles (ADR equivalent). After the injection, blood, tumor, and major organs (heart, kidney, liver and spleen) were collected at 0.5, 1, 3, 6, 9, 24, and 48 h, followed by HPLC anaylsis (see Supporting Information for the detailed protocol).

Fluorescence Microscopic Observations of Solid Tumors and Their Peripheral Blood Vessels. The tumor-bearing mice were sacrificed at 24 h after the injection of the micelles with a 10 mg/kg dose. The intact tumor tissues with their peripheral blood vessels were harvested for macroscopic observations using a fluorescence microscope (Axiovert 200, Carl Zeiss, Germany) equipped with a 2.5× objective (Plan-Neofluar, Carl Zeiss, Germany) and a filter set15 (BP546/12, FT580, LP590, mercury lamp excitation, Carl Zeiss, Germany).

RESULTS

Preparation of the Intracellular pH-Sensitive Polymeric Micelles. The polymer backbone of PEG-p(Asp-Hyd-ADR) consisted of poly(ethylene glycol) (PEG) with a molecular weight of 12 000 g/mol for the hydrophilic shell-forming segment and 37 repeating units of polyaspartate (PAsp) for the core-forming segment (MW = 28 679), which were determined by gel permeation chromatography and ^{1}H NMR measurements. The 28 side chains in the PAsp block were replaced by hydrazide groups for the binding of the drugs. Adriamycin (ADR) was then conjugated to the polymer backbone through hydrazone bonds between the carbonyls at the C13 of ADR and the hydrazide groups of the PEG-p(Asp-Hyd) block copolymer. Even though the biological and chemical background of binding ADR to polymer backbone through hydrazone linkages has been delineated in our previous work (*22*) as well as many studies (*23*−*26*), it must be noticed that the hydrazone linkage is the most popularly used as pH-sensitive linkers due to the fact that this bond is quite stable at pH 7.4 but hydrolyzes under mild acidic conditions with pH 5−6. Therefore, to ensure that drug release from the micelles occurs only when acid-labile hydrazone linkers are cleaved, any unbound free ADR were completely removed in this study. These were confirmed by a reversed phase liquid chromatograpy (RPLC) analysis that is generally used for separating and purifying materials due to the differences in their hydrophobic properties (further details are described below). RPLC analysis showed the drug loading content of PEG-p(Asp-Hyd-ADR) was 42.5 wt % with respect to a single block copolymer chain. The obtained PEG-p(Asp-Hyd-ADR) block copolymers self-assembled into micelles in aqueous solutions; the prepared micelles had a 65 nm diameter, which was confirmed by dynamic light scattering measurements.

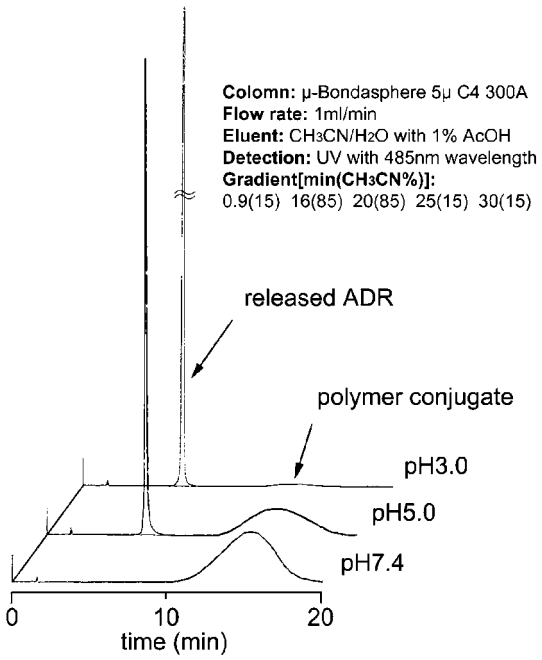

Figure 2. Acid-sensitive cleavage of drug-binding hydrazone bonds evaluated by reversed phase liquid chromatography (RPLC) analysis. RPLC separates free drugs and polymer conjugates due to the differences in their hydrophobic properties, demonstrating absence of free drugs at pH 7.4 possibly binding to polymer conjugates in a physical way. On the other hand, it clearly shows that the amount of released drugs increases under acidic conditions in which the drug-binding hydrazone linkers can be cleaved.

The Micelles Selectively Release the Loaded Drugs by Sensing a pH Decrease. To confirm the acid-sensitive drug release profile, the micelles were incubated under various pH conditions from 7.4 to 3.0, and the released drugs were measured using RPLC analysis. Figure 1B shows that the micelles released the loaded drugs time- and pH-dependently as the external pH decreased, while they were stable under physiological conditions at pH 7.4 for over 48 h. The results indicate the micelles should release the loaded drugs in the intracellular acidic regions (pH 5−6) such as endosomes and lysosomes in which the drug-binding hydrazone linkers can be cleaved most effectively. Chemical evidence for absence of free drugs and acid-sensitive cleavage of hydrazone linkers to induce drug release was also presented by RPLC analysis (Figure 2). As described above, ADR is conjugated to amphiphilic block copolymers through pH-sensitive hydrazone linkers. If the drugs were simply entrapped in the micelles by physical interaction instead binding to polymers via chemical linkers, a sharp peak corresponding to the free drug should be separated from drug−polymer conjugates by RPLC and appeared in the physiological condition (pH 7.4) where the acid-labile hydrazone bond remains stable. However, the peak from the free drug was not shown at pH 7.4 but gradually increased in acidic conditions while the broad peak from polymer conjugates decreased. Eventually, almost 100% of the drugs were released at pH 3.0, and on the basis of this, we calculated the drug loading content of polymer conjugate described above. These results demonstrate that acid-sensitive cleavage

Table 1. Growth Inhibitory Effects of the Micelles against Cancer Cells[a]

sample	exposure time (hour)	IC_{50}[b] (μg/mL±SD)	relative index[c]
ADR	3	0.041 ± 0.035	1.05
	10	0.048 ± 0.026	1.23
	24	0.039 ± 0.025	1
micelle	3	1.08 ± 0.12	27.69
	10	0.45 ± 0.061	11.54
	24	0.27 ± 0.038	6.92

[a] Eight independent experiments were carried out using a human small cell lung cancer cell line SBC-3 ($n = 8$). [b] IC_{50} denotes the inhibitory concentration of the drugs required for 50% reduction in cell population. Concentrations of the micelles are calculated with free ADR equivalents. [c] Relative index denotes the ratio between a control and the object for comparison. Here, we evaluated the growth inhibitory effect of the micelles by converting their concentrations with respect to ADR after a 24 h incubation as the control.

of hydrazone linkers between drugs and polymer chains obviously induced drug release.

Regenerated Drugs Were Pharmaceutically Active Inhibiting Cell Growth in Vitro. To verify whether the released drugs are pharmacologically active, an in vitro growth-inhibition test was carried out. The test revealed that the cytotoxic activity of the micelles was as high as 1/7-fold with respect to that of the free drugs after a 24 h exposure time (Table 1). Interestingly, the micelles showed delayed cytotoxicity that was drastically changed depending on the incubation time, which reflects that the drug release from the micelles took place and correlated with the cell metabolism.

The Micelle Infiltrates into the Avascular Tumor Model Multicellular Tumor Spheroids. Recently, it has been reported that the fluorescence quenching effect of the micelles provides a useful tool to observe the intracellular behaviors of the micelles (*22*). The fluorescence intensity of ADR, playing a role not only as an anticancer drug, but also as a fluorescence probe in this study, is quenched due to the locally increased high concentration in the micelle core; however, the fluorescence becomes detectable again as the micelles start to release ADR under acidic conditions. Consequently, the micelles emit intense fluorescence signals with the release of the entrapped ADR; a series of processes such as intracellular trafficking, drug release, and localization were able to be directly monitored in live cells accompanying the structural change. In the meantime, the multicellular tumor spheroid (MCTS) was used as an in vitro tumor model for the experiments because it is the most similar to avascular tumor regions of practical solid tumors in vivo that are characterized by limited accessibility of cell subpopulations (Figure 3). For example, MCTS reproduces adverse microenvironmental conditions of solid tumors in vivo such as hypoxia and nutritional depletion, and the extracellular matrix between tumor cells instead of intratumoral normal cell populations (*27*−*28*).

For these reasons, the intracellular behaviors of the micelles were observed within solid tumors using fluorescence quenching effect and the MCTS. The micelles were coincubated with the MCTS, and the change in the fluorescence intensity was monitored using a confocal laser scanning microscope (CLSM). The three-dimensional CLSM images demonstrated the time-dependent change in the fluorescence intensity of the micelle systems and their distributions throughout the MCTS with a 200 μm diameter depending on the incubation time (Figure 4A). The 200 μm diameter of MCTS was

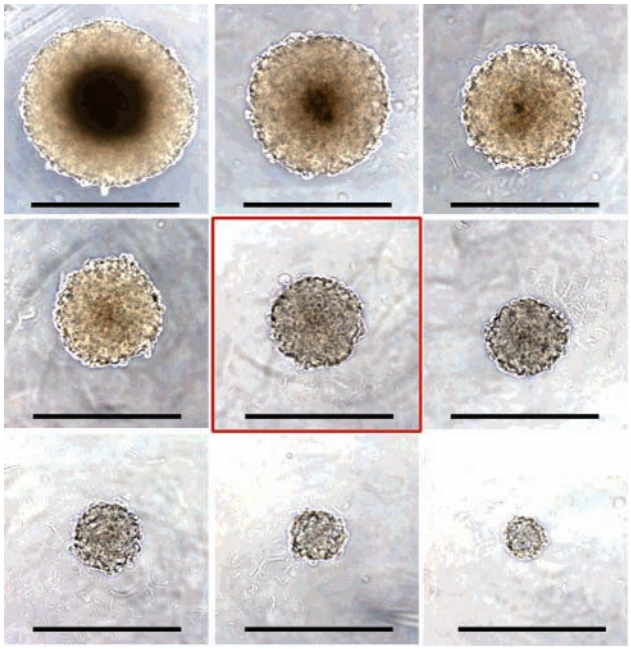

Figure 3. Preparation of multicellular tumor spheroid (MCTS). MCTS with diameter ranging from 100 to 500 μm was prepared from a C26 cell line. Among them, MCTS with a 200 μm diameter (red-edged) was used as an in vitro tumor model because it has the most suitable size for reproducing in vivo avascular tumor regions that are characterized by limited accessibility of cell subpopulations (bar = 500 μm).

determined as the most suitable size for the experiments, considering the fact that the maximum distance between the capillary blood vessels within avascular solid tumor is 200 μm or less (*29*). The fluorescence of the micelle system remained quenched at 1 h after incubation, but it was detected at 3 and 24 h. It is notable that most cell nuclei remained blue at 3 h. The images, therefore, suggest that the micelles began to intracellularly release the drugs but the released drugs were still localized in the cytoplasm. However, the intense fluorescence of ADR was eventually detected in most of the cell nuclei after 24 h. These results reflect that the micelles would access every cell in the avascular region of tumor tissues in vivo to release the drugs.

The Micelles Enter the Cell Interior and Release the Drugs. To get a better understanding of the intracellular distributions of the micelles and their released drugs, further observations of the MCTS coincubated with the micelles under high magnification were carried out using a 63× objective (Figure 4B). These images show clear evidence of the intracellular drug release from the micelles and accumulation of the released drugs in the cell nuclei. The localization of the ADR fluorescence in the cytoplasm after 3 h incubation is supporting our speculation that the micelles internalized the cells releasing the drugs. After additional incubation up to 24 h, the presence of the drugs both in the cytoplasm and cell nuclei was confirmed. When the same experiments were carried out with free ADR, all the cell nuclei in the MCTS became red within 1 h because the ADR with a low molecular weight rapidly penetrated into each cell, and we were not able to observe this unique time-dependent fluorescence change in intensity and its distribution. Therefore, it is obvious that the micelles are precisely functioning in the intracellular regions as we designed, and the possible drug release from the micelles in the extracellular regions is negligible.

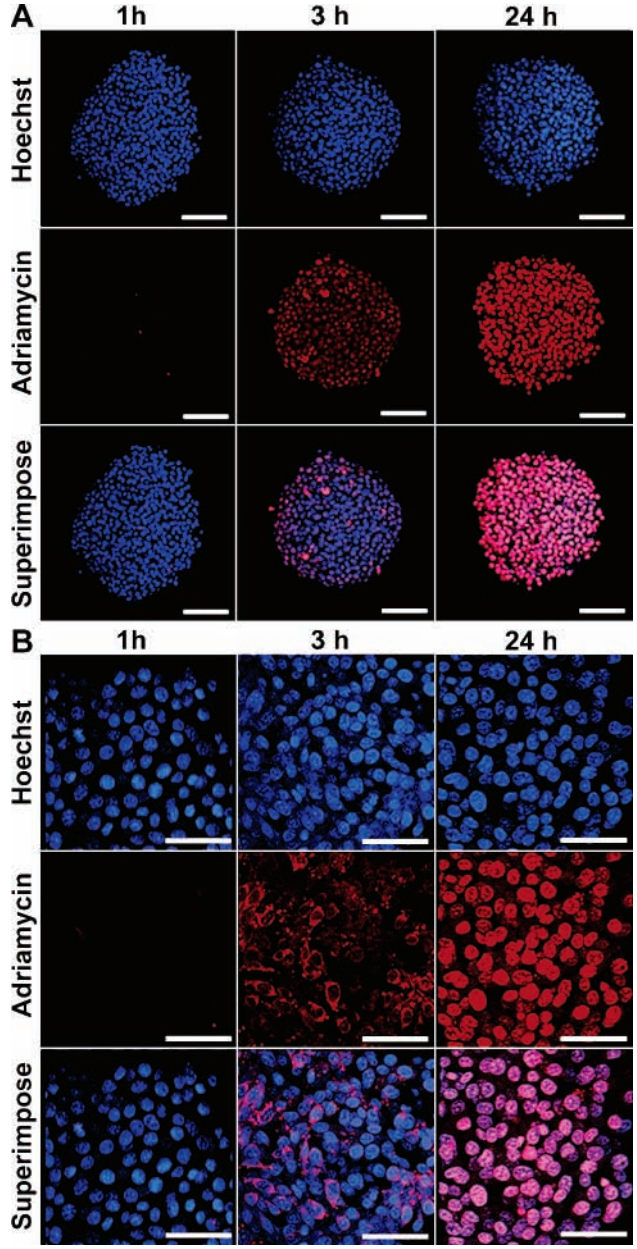

Figure 4. Observation of tumor permeability and intracellular drug release behaviors of the micelles. (A) CLSM observations showed the time-dependent change in the fluorescence intensities of ADR in the micelle system in MCTS. The images showed that the micelles can access the inside of the MCTS and release the loaded drugs (bar = 100 μm). (B) The intracellular drug release and localization of the micelles in each cell of MCTS were observed in detail using a high-magnification 63× objective. The images clearly demonstrated that the micelles internalized into the cells and released drugs, and that the released drugs eventually accumulated in the cell nuclei (bar = 50 μm).

The Micelles Suppress Tumor Growth in Mice with Enhanced Therapeutic Efficacy and Lowered Toxicity. The animal tests revealed that the micelles exerted an effective antitumor activity over a broad range of injection doses to suppress tumor growth in mice, showing some of the clear comparisons with ADR (Figure 5). In the case of ADR, tumor growth was suppressed with a 10 mg/kg dose, but the mice treated with a 15 mg/kg dose were dead due to the drug's toxicity. This corresponds well to the fact that the lethal dose of ADR killing 50% of the test animals within a designated period, called LD_{50}, is generally 12.7−13.2 mg/kg. On the contrary, the micelles were safely injectable up to a 40 mg/kg dose, while three of six mice were completely cured and there was no death among the treated mice. Notably, the body weights of the mice that slightly decreased during the micelle administration recovered, or even increased, on day 30 with respect to the controls (Table 2). Such behavior was not observed in the case of ADR, and the mice were emaciated with a 10 mg/kg dose that was the optimum dose for ADR to suppress tumor growth. Namely, the therapeutic efficacy of the micelles was significantly improved over that of ADR within this animal experiment setting, which distinguishes the micelles from ADR that has a narrow therapeutic window between 10 and 15 mg/kg. In the meantime, the tumor-suppressing antitumor activity of the micelles is shown from a 20 mg/kg dose. The micelles also extended the duration of tumor growth reaching a 5-fold initial tumor volume up to 22 and 28 days for the 20 and 40 mg/kg doses, respectively. These results indicate that the micelles achieved both enhanced therapeutic efficacy and a reduced toxicity of the loaded drugs, which are of great advantage to create effective and safe drug carrier systems.

Table 2. In Vivo Antitumor Activity of the Micelles against C26 Tumor-Bearing Mice

sample	dose (mg/kg)[a]	body weight change on day 30 (%)[b]	toxic death	duration days of tumor growth[c]	complete cure
control	0	−2.18 ± 1.74	0/6	3.7	0/6
ADR	5	−13.35 ± 0.59	0/6	4.2	0/6
	10	−16.84 ± 1.26	0/6	14.6	1/6
	15	−	6/6	−	−
micelle	5	−0.89 ± 1.68	0/6	3.9	0/6
	10	−4.51 ± 1.44	0/6	4.0	0/6
	20	3.13 ± 1.60	0/6	22.1	2/6
	40	−4.07 ± 0.92	0/6	27.9	3/6
	60	−	6/6	−	−

[a] Administrations were carried out three times with a 4-day interval, and doses were determined in free ADR equivalents. [b] Body weights were measured on day 30 after the first injection to compare the long-term toxicity between ADR and the micelles. Values are expressed as mean ± SEM. [c] Duration time to reach 5-fold initial tumor volume.

The Micelles Circulate for a Long Time in the Blood and Selectively Accumulate in Solid Tumors. Effective antitumor activity and low toxicity imply that the micelles are stable in the blood without drug release (or leakage); therefore, their systemic and local distribution may dominate the tumor-suppressing antitumor activity. To demonstrate this, we investigated the in vivo dispositions of the micelles in detail using a biodistribution study. The levels of the micelles in the blood, tumor, and major organs, such as the heart, kidney, liver, and spleen, are expressed as percentage of each dose at specific times after the intravenous injection (Figure 6A). As summarized in Table 3, the micelles circulated in the blood for a prolonged time, and the area under the concentration curve (AUC) of the blood was 15-fold greater than that of ADR. In particular, it is noteworthy that the AUC values of the micelles in the heart and kidney decreased as compared to ADR, indicating that their tumor selectivity (AUC_{tumor}/AUC_{organ}) increased 6- and 5-fold higher with respect to the heart and the kidney, respectively. Such tumor-selective accumulation of the micelles may reduce the side effects of ADR such as cardiotoxicity and nephrotoxicity. In the meantime, the micelles showed a relatively low uptake in the liver and spleen despite the long residence time in the blood in comparison with tumors. These results suggest that the micelles may rapidly evacuate from these reticular

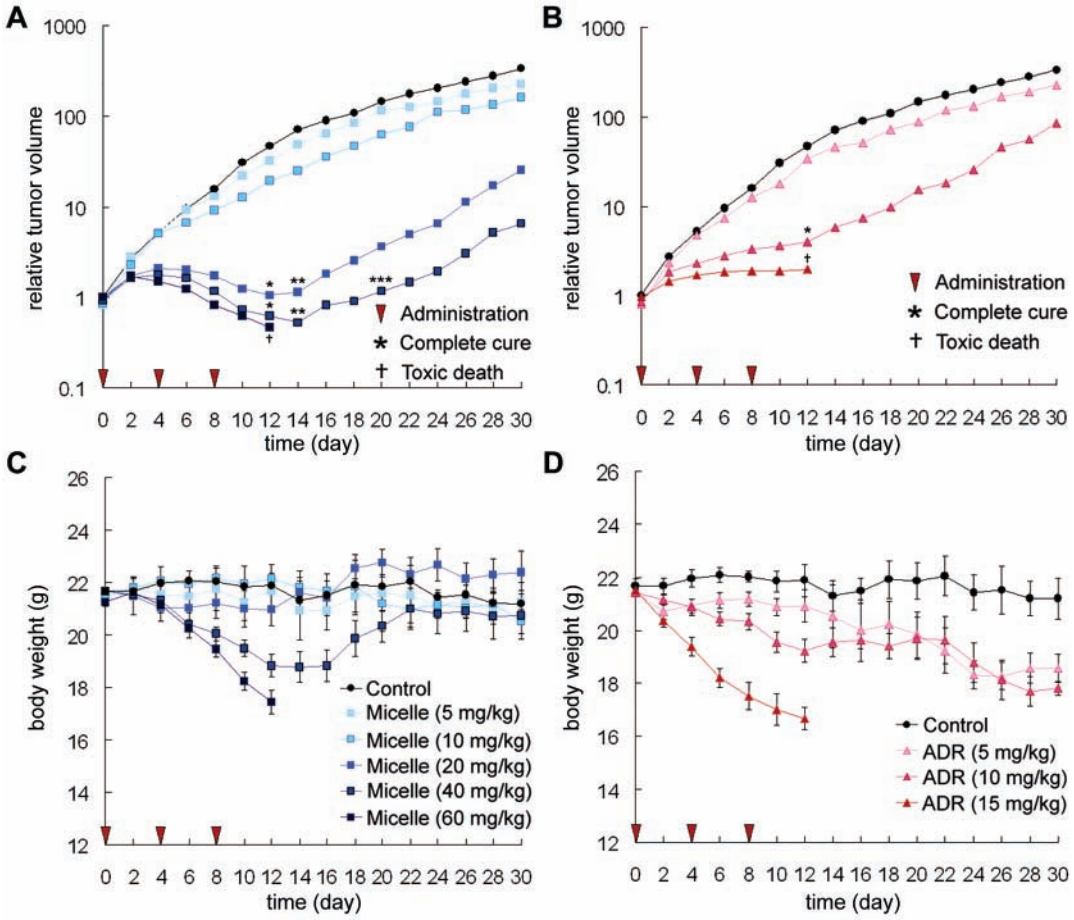

Figure 5. Tumor size and body weight changes of the treated mice. The figures show effective tumor-suppressing activity and low change in body weights over a broad range of injection doses of the micelles (A and C). To the contrary, ADR showed a narrow therapeutic window between 10 and 15 mg/kg does avoiding toxic death (B and D). Administrations were carried out three times with a 4-day interval into tumor bearing CDF1 mice (female, 6-week-old, $n = 6$). The micelle doses are shown as ADR equivalents. Values are expressed as mean and mean ± SEM for the tumor volume and body weight, respectively.

connective tissues without interacting with monocytes and macrophages that are responsible for engulfing and removing cellular debris, old cells, and unwelcome external invaders from the bloodstream. On the contrary, tumor tissues are characterized by a large vascular permeability and high interstitial diffusivity while a lack of lymphatic drainage is observed. This phenomenon is explained by the enhanced permeability and retention (EPR) effect, which significantly affects distributions of the macromolecules facilitating their access and accumulation in tumors (*30, 31*). Consequently, the micelles that accumulated in the solid tumors through the EPR effect can stay for a prolonged time. The biodistribution study, therefore, showed that the cytotoxicity of the micelles seems to depend on their retention time as well as in the accumulated amounts in each organ, which may be crucial in attaining both an effective antitumor activity and reduced toxicity in a single drug carrier system.

In vivo antitumor activity test showed that the micelles effectively suppressed tumor growth in mice over a broad range of injection doses while toxicity remained extremely low. On the other hand, the biodistribution study revealed that the micelles circulated in the blood for a long period of time and accumulated in normal organs as well as the tumors. These results are very interesting because the micelles showed organ-dependent differences in cytotoxicity. To elucidate this, we investigated the localization of the micelles in each organ by calculating the tissue-to-blood concentration ratio K_b (Table 4). The K_b value is defined as $[K_b = C_{tissue}/C_{blood}]$ where C_{tissue} and C_{blood} denote the tissue concentration and the blood concentration of the micelles, respectively. Each K_b value indicates distribution of the micelles in vascular space ($K_b < 0.1$), extracellular space ($0.1 < K_b < 0.5$), and intracellular space ($0.5 < K_b$) (*32, 33*). The data revealed that the micelles localized in the cell interior of tumor tissues but mainly distributed in the extracellular space of other organs after accumulation. It is in good accordance with our previous results published elsewhere (*34, 35*). We speculate that such drastic alterations might be due to the pathological differences in vasculatures and lymphatic drainages between organs. Consequently, even though the micelles accumulate in normal organs, they can be excreted from the body before releasing drugs. The organ-dependent cytotoxicity of the micelles, therefore, probably would depend on their retention time as well as the accumulated amounts in each organ.

The Micelles Regulate the Local Drug Distribution within Solid Tumors. In view of their tumor-specific accumulation and intracellular distribution, the micelles should release the drugs in solid tumors along with emitting fluorescence as we observed in the intracellular drug release experiment using MCTS. In contrast, if the micelles released the drugs slowly or not at all, the fluorescence of ADR would remain quenched. On the basis of this hypothesis, we observed the solid tumors and their peripheral blood vessels in mice after intravenous injection of the micelles using a fluorescence microscope (Figure 6B). The observations were carried out at 24 h after injection because the micelles needed to

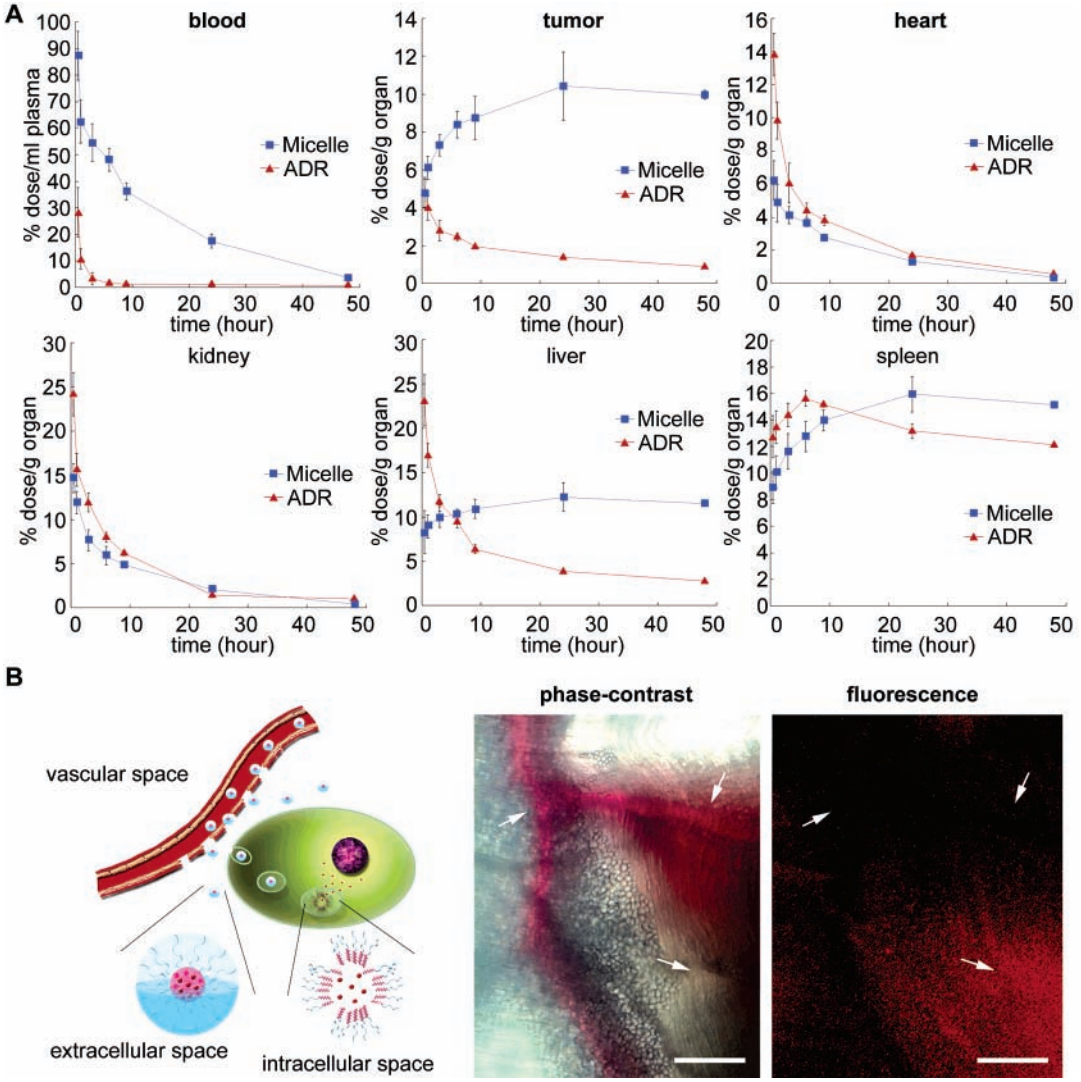

Figure 6. Tumor-specific accumulation of the micelles and locally increased drug concentrations. (A) Biodistribution study revealed the prolonged circulation in the blood and tumor-specific accumulation of the micelles. (B) Fluorescence microscopic observations of the solid tumor and its peripheral regions at 24 h after micelle injection demonstrate that the drug concentrations in the tumor tissues selectively increased due to the tumor-specific accumulation and controlled drug release from the micelles (bar = 500 μm).

Table 3. Tumor-Specific Accumulation of the Micelles

	AUC[a]		AUC ratio	tumor selectivity[b] (AUC_{tumor}/AUC_{organ})		tumor selectivity ratio $[(AUC_{tumor}/AUC_{organ})_{micelle}/(AUC_{tumor}/AUC_{organ})_{ADR}]$
	ADR	micelle	($AUC_{micelle}/AUC_{ADR}$)	ADR	micelle	
blood	58.86	858.54	14.59	–	–	–
tumor	49.59	210.21	4.24	–	–	–
heart	94.70	65.24	0.69	0.52	3.22	6.19
kidney	151.56	117.80	0.78	0.33	1.78	5.39
liver	176.15	261.17	1.48	0.28	0.80	2.86
spleen	341.38	329.66	0.97	0.15	0.64	4.27

[a] AUC denotes the area under a concentration curve that is obtained from the biodistribution study. Values are calculated based on the trapezoidal rule up to 24 h after intravenous injection. [b] Tumor selectivity of ADR and the micelles was determined by calculating the relative accumulated concentrations between the tumor tissues and each organ (AUC_{tumor}/AUC_{organ}). Their ratios indicate the change in the tumor selectivity of the micelles with respect to ADR.

accumulate in the tumor tissues enter the cells and release the drugs intracellularly as long as they were present in the blood. A phase-contrast image showed that the tumor blood vessels containing the micelles begin to leak into the extravascular compartment of the solid tumors (note the red color of the micelles). However, no fluorescence was detected at the corresponding part but in the limited regions of the solid tumor. Therefore, even though colloidal drug carriers are generally considered to localize in the limited peripheral regions of the solid tumors due to poor accessibility, we have confirmed that the micelles can infiltrate into tumor tissues after accumulation, thus increasing the local drug concentration. This conclusion is in good accordance with the results from the permeability testing of the micelles into MCTS.

DISCUSSION

This paper has revealed a new potency of the polymeric micelle drug carrier systems that they can directly deliver drugs to the interior of targeted cells in vivo by infiltrat-

Table 4. Tissue-to-blood Concentration Ratio (K_b) in Each Organ[a]

	organ				
time (h)	tumor	heart	kidney	liver	spleen
0.5	0.0545	0.0714	0.168	0.0946	0.1023
1	0.0976	0.0772	0.1903	0.1429	0.1617
3	0.134	0.0755	0.1402	0.1834	0.2136
6	0.1747	0.0764	0.1226	0.2141	0.2651
9	0.2412	0.0762	0.134	0.3014	0.3859
24	0.5992	0.0761	0.1162	0.7037	0.9158

[a] K_b value is defined as [$K_b = C_{tissue}/C_{blood}$] where C_{tissue} and C_{blood} were the tissue concentration and the blood concentration of the micelles, respectively. Each K_b value indicates the distribution of the drugs in vascular space ($K_b < 0.1$), extracellular space ($0.1 < K_b < 0.5$), and intracellular space ($0.5 < K_b$).

ing into solid tumors. These findings provided a clear answer to the questions whether the nanosized supramolecular drug carriers can access the cells in the avascular region of the solid tumors without structural and functional breakdown, which is also crucial to other intracellular environment-sensitive macromolecular bioconjugates that are injected through the vein for tumor targeting.

For the past several decades, natural and artificial macromolecules have evolved into a very useful class of drug delivery media (*36*−*39*). However, their in vivo applications are not always successful because limited accessibility inside solid tumors causes stagnation of drug carriers at the periphery of the tumor vasculatures, inducing low concentrations of active drugs in the targeted tumor tissues (*40*). Such a poor delivery efficiency of active drugs to the solid tumors is considered a serious problem facing recent cancer therapy using drug carriers. In this regard, we considered that the intrinsic characteristics of drug carriers may play a critical role in determining their in vivo behaviors, such as tumor permeability, drug release property, and antitumor activity. To confirm this, a suitable carrier model is required that controls the release of drugs while its structural features are optimized for a tumor-targeting drug delivery, and we prepared a new type of drug carrier in this study by adding an intracellular pH-triggered drug release property to the polymeric micelle drug carrier system whose chemical and biological properties are clearly identified (*41*).

As shown in the experimental results, the prepared micelle behaves not only as a biocompatible nanosized drug carrier with a high drug-loading content but also as a bioresponsive device with intracellular pH-sensitivity to control the drug release. These characteristic behaviors suggest that the nanosized core−shell structure of the micelles seems important to take the best advantage of the PEG shielding, imparting both stability and fragility into a single carrier system. The micelles safely protect the loaded drugs and functional linkers by providing a nanocompartment in the core that is completely segregated from the external environments; they maintain a high water-solubility with the hydrophilic shell that prevents the adsorption of proteins and the adhesion of cells so as to circumvent the uptake by reticuloendothelial systems during blood circulation (*42, 43*). In the meantime, intracellular trafficking of the micelles in the solid tumors is evident, which indicates that PEG shielding of the micelle may behave as a kinetic barrier that regulates the condition of the molecular affinity interaction between the micelles and cell membrane according to the exposure or retention time. As explained by the EPR effect, solid tumors feature a large vascular permeability, high interstitial diffusivity, and poor lymphatic drainage; this is a fact that results in tumor-specific retention over a long period of time required for interacting with tumor cells. The retention time in each organ influences the intracellular trafficking of the micelles; thereby, any undesirable cytotoxicity to the normal organs is avoided. Consequently, the intracellular pH-triggered drug release property of the micelles should be the major reason for in vivo antitumor activity with low toxicity.

In conclusion, the intracellular pH-sensitive polymeric micelles exemplify the supramolecular drug carriers that control the systemic, local, and subcellular distribution of the active drugs. They show a higher bioavailability than free drugs, and therefore, the intracellular delivery of drugs would be the most effective and promising formulation for cancer chemotherapy with enhanced therapeutic efficacy and low toxicity. Moreover, the study reveals that the biocompatible structure and environment-sensitive functionality should be considered as a single event in order to realize the carrier systems that are related to these intracellular environments and material transports for the future treatment of cancers with avascular tumor tissue.

ACKNOWLEDGMENT

This research was supported by a Grant-in-Aid for Scientific Research from the Ministry of Education, Culture, Sports, Science and Technology (MEXT), Japan, and by Core Research for Evolutional Science and Technology (CREST), Japan Science and Technology Corporation (JST).

Supporting Information Available: Synthetic scheme for PEG-p(Asp-Hyd-ADR) block copolymer. HPLC analysis protocol for biodistribution. This material is available free of charge via the Internet at http://pubs.acs.org.

LITERATURE CITED

(1) Duncan, R. (2003) The dawning era of polymer therapeutics. *Nat. Rev. Drug Discovery 2*, 347−360.
(2) Maeda, H. (2001) SMANCS and polymer-conjugated macromolecular drugs advantages in cancer chemotherapy. *Adv. Drug Delivery Rev. 46*, 169−185.
(3) Jain, R. K. (2001) Delivery of molecular and cellular medicine to solid tumors. *Adv. Drug Delivery Rev. 46*, 149−168.
(4) Kopecek, J. (2003) Smart and genetically engineered biomaterials and drug delivery systems. *Eur. J. Pharm. Sci. 20*, 1−16.
(5) Nishiyama, N., Okazaki, S., Cabral, H., Miyamoto, M., Kato, Y., Sugiyama, Y., Nishio, K. Matsumura, Y., and Kataoka, K. (2003) Novel cisplatin-incorporated polymeric micelles can eradicate solid tumors in mice. *Cancer Res. 63*, 8977−8983.
(6) Lewanski, C. R. I., and Stewart, S. (1999) PEGylated liposomal adriamycin: a review of current and future applications. *Pharm. Sci. Technol. Today 2*, 473−477.
(7) Jensen, K. D., Nori, A., Tijerina, M., Kopeckova, P., and Kopecek, J. (2003) Cytoplasmic delivery and nuclear targeting of synthetic macromolecules. *J. Controlled Release 87*, 89−105.
(8) Lian, T., and Ho, R. J. Y. (2001) Trends and developments in liposome drug delivery systems. *J. Pharm. Sci. 90*, 667−680.
(9) Kataoka, K., Kwon, G., Yokoyama, M., Okano, T., and Sakurai, Y. (1993) Block-copolymer micelles as vehicles for drug delivery. *J. Controlled Release 24*, 119−132.
(10) Ringsdorf, H. (1975) Structure and properties of pharmacologically active polymers. *J. Polym. Sci. Polym. Symp. 51*, 135−153.

(11) Vasey, P. A., Kaye, S. B., Morrison, R., Twelves, C., Wilson, P., Duncan, R., Thomson, A. H., Murray, L. S., Hilditch, T. E., Murray, T., Burtles, S., Fraier, D., Frigerio, E., and Cassidy, J. (1999) Phase I clinical and pharmacokinetic study of PK1 [N-(2-hydroxypropyl)methacrylamide copolymer doxorubicin]: first member of a new class of chemotherapeutic agents − drug-polymer conjugates. *Clin. Cancer Res. 5*, 83−94.
(12) Gordon, A. N., Fleagle, J. T., Guthrie, D., Parkin, D. E., Gore, M. E., and Lacave, A. J. (2001) Recurrent epithelial ovarian carcinoma: a randomized phase III study of pegylated liposomal doxorubicin versus topotecan. *J. Clin. Oncol. 19*, 3312−3322.
(13) Nakanishi, T., Fukushima, S., Okamoto, K., Suzuki, M., Matsumura, Y., Yokoyama, M., Okano, T., Sakurai, Y., and Kataoka, K. (2001) Development of the polymer micelle carrier system for doxorubicin. *J. Controlled Release 74*, 295−302.
(14) Jain, R. K. (1994) Barriers to drug delivery in solid tumors. *Sci. Am. 271*, 58−65.
(15) Takakura, Y., and Hashida, M. (1996) Macromolecular carrier systems for targeted drug delivery: Pharmacokinetic considerations on biodistribution. *Pharm. Res. 13*, 820−831.
(16) Dvorak, H. F., Nagy, J. A., Dvorak, J. T., and Dvorak, A. M. (1998) Identification and characterization of the blood vessels of solid tumors that are leaky to circulating macromolecules. *Am. J. Pathol. 133*, 95−109.
(17) Ishida, T., Kirchmeier, M. J., Moase, E. H., Zalipsky, S., and Allen, T. M. (2001) Targeted delivery and triggered release of liposomal doxorubicin enhances cytotoxicity against human B lymphoma cells. *Biochim. Biophys. Acta Biomembranes 1515*, 144−158.
(18) Tsukioka, Y., Matsumura, Y., Hamaguchi, T., Koike, H., Moriyasu, F., and Kakizoe, T. (2002) Pharmaceutical and biomedical differences between micellar doxorubicin (NK911) and liposomal doxorubicin (Doxil). *Jpn. J. Cancer Res. 93*, 1145−1153.
(19) Unezaki. S., Maruyama, K., Hosoda, J., Nagae, I., Koyanagi, Y., Nakata, M., Ishida, O., Iwatsuru, M., and Tsuchiya, S. (1996) Direct measurement of the extravasation of poly(ethyleneglycol)-coated liposomes into solid tumor tissue by in vivo fluorescence microscopy. *Int. J. Pharm. 144*, 11−17.
(20) Suzuki, H., Nakai, D., Seita, T., and Sugiyama, Y. (1996) Design of a drug delivery system for targeting based on pharmacokinetic consideration. *Adv. Drug Delivery Rev. 19*, 335−357.
(21) Jones, A. T., Gumbleton, M., and Duncan, R. (2003) Understanding endocytic pathways and intracellular trafficking: a prerequisite for effective design of advanced drug delivery systems. *Adv. Drug Delivery Rev. 55*, 1353−1357.
(22) Bae, Y., Fukushima, S., Harada, A., and Kataoka, K. (2003) Design of environment-sensitive supramolecular assemblies for intracellular drug delivery: polymeric micelles that are responsive to intracellular pH change. *Angew. Chem., Int. Ed. 42*, 4640−4643.
(23) D'souza, A. J. M., and Topp, E. M. (2004) Release from polymeric prodrugs: linkages and their degradation. *J. Pharm. Sci. 93*, 1962−1979.
(24) Ulbrich, K., and Subr, V. (2004) Polymeric anticancer drugs with pH-controlled activation. *Adv. Drug Delivery Rev. 56*, 1023−1050.
(25) Willner, D., Trail, P. A., Hofstead, S. J., King, H. D., Lasch, S. J., Braslawsky, G. R., Greenfield, R. S., Kaneko, T., Firestone, R. A. (1993) (6-Maleimidocaproyl)hydrazone of doxorubicin. A new derivative for the preparation of immunoconjugates of doxorubicin. *Bioconjugate Chem. 4*, 521−527.
(26) Kaneko, T., Willner, D., Monkovic, I., Knipe, J. O., Braslawsky, G. R., Greenfield, R. S., and Vyas D. M. (1991) New hydrazone derivatives of adriamycin and their immunoconjugates − a correlation between acid stability and cytotoxicity. *Bioconjugate Chem. 2*, 133−141.
(27) Hamilton, G. (1998) Multicellular spheroids as an in vitro tumor model. *Cancer Lett. 131*, 29−34.
(28) Sutherland, R. M. (1988) Cell and environment interactions in tumor microregions: the multicell spheroid model. *Science 240*, 177−184.
(29) Konerding, M. A., Fait E., and Gaumann, A. (2001) 3D microvascular architecture of pre-cancerous lesions and invasive carcinomas of the colon. *Br. J. Cancer 84*, 1354−1362.
(30) Maeda, H., Wu, J., Sawa, T., Matsumura, Y., and Hori, K. (2000) Tumor vascular permeability and the EPR effect in macromolecular therapeutics: a review. *J. Controlled Release 65*, 271−284.
(31) Matsumura, Y., and Maeda, H. (1986) A new concept of macromolecular therapeutics in cancer chemotherapy: mechanism of tumoritropic accumulation of proteins and the antitumor agent SMANCS. *Cancer Res. 46*, 6387−6392.
(32) Jain, R. K. (1988) Determinants of tumor blood flow: a review. *Cancer Res. 48*, 2641−2658.
(33) Baxter, L. T., Daniel, H. Z., Mackensen, G., and Jain, R. K. (1994) Physiologically based pharmacokinetic model for specific and nonspecific monoclonal antibodies and fragments in normal tissues and human tumor xenografts in nude mice. *Cancer Res. 54*, 1517−1528.
(34) Yamamoto, Y., Nagasaki, Y., Kato, Y., Sugiyama, Y., and Kataoka, K. (2001) Long-circulating poly(ethylene glycol)-poly(D, L-lactide) block copolymer micelles with modulated surface charge. *J. Control. Release 77*, 27−38.
(35) Nishiyama, N., Kato, Y., Sugiyama, Y., and Kataoka, K. (2001) Cisplatin-loaded polymer−metal complex micelle with time-modulated decaying property as a novel drug delivery system. *Pharmaceut. Res. 18*, 1035−1041.
(36) Torchilin, V. P., Lukyanov, A. N., Gao, Z. G., and Papahadjopoulos-Sternberg, B. (2003) Immunomicelles: Targeted pharmaceutical carriers for poorly soluble drugs. *P. Natl. Acad. Sci. USA. 100*, 6039−6044.
(37) Adams, M. L., Lavasanifar, A., and Kwon, G. (2003) Amphiphilic block copolymers for drug delivery. *J. Pharm. Sci. 92*, 1343−1355.
(38) Shiah, J. G., Dvorak, M., Kopeckova, P., Sun, Y., Peterson, C. M., and Kopecek, J. (2001) Biodistribution and antitumour efficacy of long-circulating N-(2-hydroxypropyl)methacrylamide copolymer-doxorubicin conjugates in nude mice. *Eur. J. Cancer 37*, 131−139.
(39) Kopecek, J., Kopeckova, P., Minko, T., Lu, Z. R., and Peterson, C. M. (2001) Water soluble polymers in tumor targeted delivery. *J. Controlled Release 74*, 147−158.
(40) Emanuel, N., Kedar, E., Bolotin, E. M., Smorodinsky, N. I., and Barenholz, Y. (1996) Targeted delivery of doxorubicin via sterically stabilized immunoliposomes: Pharmacokinetics and biodistribution in tumor-bearing mice. *Pharm. Res. 13*, 861−868.
(41) Kataoka, K., Harada, A., and Nagasaki, Y. (2001) Block copolymer micelles for drug delivery: design, characterization and biological significance. *Adv. Drug. Delivery Rev. 47*, 113−131.
(42) Yokoyama, M., Okano, T., Sakurai, Y., Fukushima, S., Okamoto, K., and Kataoka, K. (1999) Selective delivery of adriamycin to a solid tumor using a polymeric micelle carrier system. *J. Drug Target. 7*, 171−186.
(43) Kwon, G., Suwa, S., Yokoyama, M., Okano, T., Sakurai, Y., and Kataoka, K. (1994) Enhanced tumor accumulation and prolonged circulation times of micelle-forming poly(ethylene oxide-aspartate) block copolymer-adriamycin conjugates. *J. Controlled Release 29*, 17−23.

BC0498166

Role of Biotin-Binding Affinity in Streptavidin-Based Pretargeted Radioimmunotherapy of Lymphoma⊗

Kevin J. Hamblett,[†,⊥] Oliver W. Press,[§,||] Damon L. Meyer,[§,⊥] Don K. Hamlin,[‡] Don Axworthy,[§] D. Scott Wilbur,[‡] and Patrick S. Stayton*[,†]

Departments of Bioengineering, Medicine, and Radiation Oncology, University of Washington, Seattle, Washington 98195, and The Fred Hutchinson Cancer Research Center, Seattle, Washington 98109-1024 Received March 30, 2003; Revised Manuscript Received June 23, 2004

One pretargeting approach to cancer radioimmunotherapy utilizes an antibody−streptavidin conjugate that is first localized to the tumor. A "clearing agent" is then administered to remove the excess bioconjugate from blood, followed by injection of the radiolabeled biotin therapeutic. In this study, the role of streptavidin−biotin affinity in this pretargeting system was investigated for the first time in vivo, with a reduced affinity, site-directed streptavidin mutant and with radiolabeled bis-biotin reagents. The S45A streptavidin mutant (SA-S45A), which displays a faster off-rate for biotin, was utilized with a bivalent biotin carrier that retains high avidity for the streptavidin mutant. Mice were fed either a normal or biotin-deficient diet, yielding serum endogenous biotin concentrations of 31 nM and 5 nM, respectively. Lymphoma-bearing nude mice pretargeted with 1F5 Antibody-SA-Wild Type (WT) bioconjugates produced ^{125}I-bis-biotin tumor concentrations of 2.2%ID/g and 7.0%ID/g in mice fed normal diets vs biotin-deficient diets. ^{125}I-bis-biotin tumor concentrations of mice pretargeted with 1F5-SA-S45A were 12%ID/g and 10%ID/g for mice fed normal and biotin-deficient diets, respectively. However, poor clearance of the 1F5-SA-S45A with the biotinylated clearing agent led to high normal organ concentrations of ^{125}I-bis-biotin. A galactosylated human serum albumin (HSA) modified with bis-biotin was then tested, and normal organ ^{125}I-bis-biotin concentrations were significantly reduced. Tumor-to-organ ratios achieved for 1F5-SA-S45A with the HSA-bis-biotin clearing agent in mice with high serum biotin were similar to those achieved with 1F5-SA-WT in mice with low serum biotin. These results demonstrate that exchange of bound endogenous biotin with lower affinity streptavidin mutants is possible, and that corresponding use of bis-biotin carriers can nearly eliminate the differences in therapeutic radioactivity at the tumor site in animals on normal vs biotin-deficient diets. The results also interestingly demonstrate, however, that improved clearance agents capable of removing the lower affinity streptavidin-antibody conjugate are needed to achieve comparable specificity in tumor to blood or normal organ ratios.

INTRODUCTION

Anti-CD20 antibody therapies have yielded high response rates in patients with B cell lymphomas (*1*). However, only 6% to 20% of patients achieve complete remissions, and few are cured using the antibody as a single agent. The therapeutic effectiveness of anti-CD20 antibodies can be enhanced by conjugating to radionuclides. This has been demonstrated in a recent randomized clinical trial that compared ^{90}yttrium-labeled ibritumomab tiuxetan (Zevalin), an anti-CD20 antibody, to rituximab (*2*). The radiolabeled anti-CD20 antibody achieved an overall response rate of 80% and complete remissions in 30% of lymphoma patients, compared with an overall response rate of 56% ($p = 0.002$) and a complete response rate of 16% ($p = 0.04$) with the nonradioactive anti-CD20 antibody (*2*). To further improve the response rates, myeloablative doses of radioactivity can be administered to further improve the response rates; however, this strategy subsequently requires stem cell transplantation (*3*).

A potential strategy for delivering higher levels of radioactivity to tumors without requiring myeloablative doses is multistep radioimmunotherapy (RIT) with pretargeting. One pretargeting approach consists of an antibody−streptavidin (Ab-SA) conjugate, a "clearing agent" to remove Ab-SA conjugate from the blood, and the radiolabeled biotin therapeutic. Clearing the excess Ab-SA conjugate from the blood has two significant advantages. First, the Ab-SA conjugate in the blood is quickly eliminated through the liver, limiting the nonspecific radiation exposure due to the presence of excess Ab-SA in the blood. Second, higher concentrations of Ab-SA can be injected because this nonspecific exposure is

⊗ Part of the Special Issue collection for Imaging Chemistry that began in issue 6, 2004. A preliminary description of this work was presented at the Symposium on Chemistry and Biological Applications of Imaging Agents and Molecular Beacons, at the spring 2004 National Meeting of the American Chemical Society.

* To whom correspondence should be addressed. Phone: 206-685-8148. Fax: 206-685-8256. E-mail: stayton@u.washington.edu.
† Department of Bioengineering.
|| Department of Medicine.
‡ Department of Radiation Oncology.
§ The Fred Hutchinson Cancer Research Center.
⊥ Present address: Seattle Genetics, Inc., Bothell, WA 98026.

[1] Abbreviations: Ab-SA, monoclonal antibody−streptavidin conjugate: BSA, bovine serum albumin; CA, clearing agent; HSA, human serum albumin; NAGB, *N*-acetylgalactosamine-biotin; RIT, radioimmunotherapy; rt, room temperature; SA, streptavidin; SA-S45A, streptavidin mutant having the serine at residue 45 replaced with an alanine, SA-WT, wild type streptavidin; 1F5-SA-WT, monoclonal antibody 1F5 conjugated to wild-type streptavidin; 1F5-S45A, monoclonal antibody 1F5 conjugated to the streptavidin mutant S45A; cpm, counts per minute; %ID/g, percent of injected dose per gram.

10.1021/bc034049g CCC: $30.25 © 2005 American Chemical Society
Published on Web 12/16/2004

Chart 1. Structures for Bis-biotin-NCS and ^{125}I-Bis-biotin

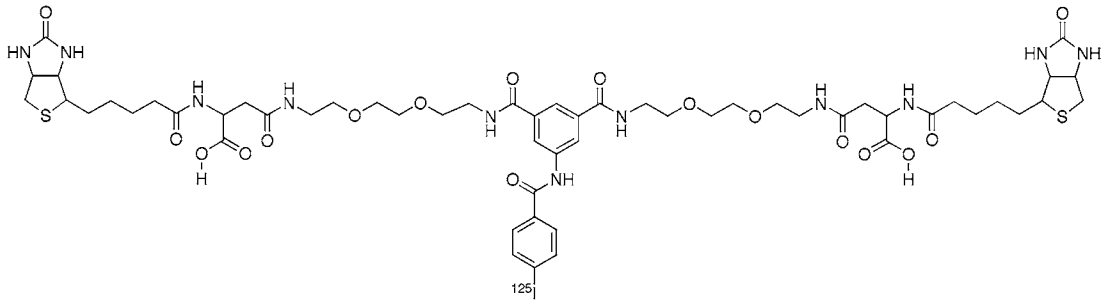

^{125}I-bis-biotin

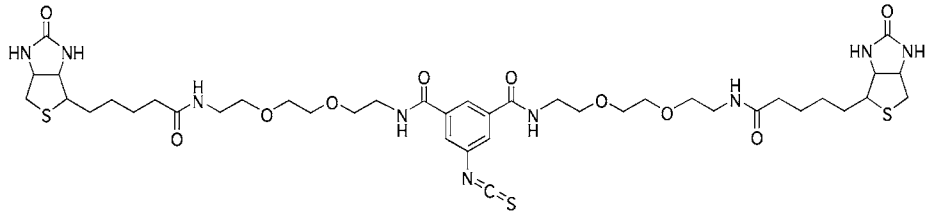

bis-biotin-NCS

reduced, leading to higher concentration gradients and better tumor penetration of the antibody−streptavidin complex. Pretargeting has been shown to be an effective strategy for directing radioactivity to tumor xenografts in mice (*4*−*6*). Although SA-biotin pretargeting has demonstrated promise, the immunogenicity of SA and the presence of competing endogenous biotin represent potential limitations (*7*, *8*). Endogenous biotin binds and effectively blocks biotin-binding sites of SA due to its slow dissociation rate ($T_{1/2}$ = 6.5 h) (*9*). Mice are generally fed a biotin-deficient diet for several days prior to pretargeted radioimmunotherapy to reduce endogenous biotin concentration in serum (*7*, *10*). The extent of the endogenous biotin problem in humans is less clear, but patient dietary restrictions are difficult at best and even low levels of endogenous biotin can block available biotin-binding sites of streptavidin (*4*, *8*). Serum biotin levels also do not reveal the entire extent of endogenous biotin, as the liver has been suggested as a storage/release depot for biotin (*11*), and biotin levels in colon adenocarcinoma were found to be 3-fold higher than the surrounding tissue (*12*).

In this study we have investigated the role of the high affinity streptavidin binding in the pretargeting system. The high affinity of streptavidin for biotin provided the initial rationale for using this binding pair in pretargeting, but it conversely leads to the limitations associated with blocking by endogenous biotin. We have recently shown that SA-mutants can be used in combination with a bivalent biotin derivative to allow exchange of biotin, while retaining the high affinity with the bivalent biotin ligand in an in vitro binding system (*13*). Here we have characterized a site-directed mutant of SA in an anti-CD20 pretargeting system that exhibits lower affinity and a faster biotin off-rate than wild-type SA (SA-WT) (*9*, *14*−*16*). We report here an in vivo investigation using a mouse lymphoma xenograft system to determine whether this modified streptavidin−biotin system could circumvent blocking of biotin-binding sites by endogenous biotin while maintaining blood clearance capabilities and tumor targeting specificity. The study provided interesting insight into the tradeoff of high affinity in relation to endogenous ligand competition versus clearing agent effectiveness.

EXPERIMENTAL PROCEDURES

Reagent Preparation. SA-WT and SA-S45A were expressed, refolded, and purified as previously described (*9*, *15*, *16*). Conjugation of intact 1F5, an anti-CD20 antibody, to SA was performed as previously described (*5*, *17*). Briefly, Ab was reduced using DTT and SA was conjugated with SMCC in two separate reaction vials. Reduced Ab and maleimide-modified SA were reacted and then purified in two steps using iminobiotin and cation exchange columns. The Ab-SA conjugates were analyzed by HPLC and found to be >90% of the preparations had antibody:SA ratios of 1:1. ^{125}I-bis-biotin (Chart 1) was prepared and radioiodinated as previously described (Chart 1) (*13*).

To prepare the HSA-bis-biotin clearing agent, 0.3 mL of a 20 mg/mL in 50 mM sodium bicarbonate, pH 8.5, solution of HSA (6 mg, 0.09 μmol) was added to 0.15 mL of a 9.5 mg/mL solution of bis-biotin-NCS (1.4 mg, 1.5 μmol), shown in Chart 1, in the same buffer. The reaction mixture was slowly tumbled at room-temperature overnight. The entire mixture was then passed over a Sephadex G-25 column (PD-10, Phamacia, Piscataway, NJ) and collected in 0.9% saline. The protein containing fractions were combined, concentrated in a Centricon-30 (Millipore, Bedford, MA), and washed three times with 0.9% saline, concentrating between each wash. To the final volume of 0.25 mL was added 0.75 mL of 0.5 M sodium borate, pH 8.0, followed by 3 mg (9.6 0.09 μmol) of solid β-galactopyranosylphenyl isothiocyanate (Sigma, St. Louis, MO). The mixture was then allowed to tumble at room-temperature overnight before passing over a Sephadex G-25 column. The protein containing fractions were combined, concentrated, and washed three times with 0.9% saline, concentrating between washes.

Effect of Diet on Serum Biotin Levels. To measure the levels of biotin in serum, a competition assay was performed as previously described (*18*). Bovine serum albumin (BSA) mixed with biotinylated-BSA (100:1) at

a total protein concentration of 10 mg/mL was added to a 96-well plate at a total protein concentration of 10 mg/mL and allowed to incubate at room temperature for 1 h. The wells were washed three times with 10 mM Tris, 150 mM NaCl, 0.05% Tween 20 at pH = 7.5, referred to as TNTw buffer. Biotin standards or samples were added to the wells, followed by the addition of SA-HRP (1.25 mg/mL) (Zymed Laboratories, San Francisco, CA) at a 1:5000 dilution mixed with BSA at 1 mg/mL, and the mixtures were incubated at room temperature for 30 min. Wells were washed three times with TNTw buffer, followed by the addition of 0.1 M citric acid, 0.012% H_2O_2, and *o*-phenylenediamine dihydrochloride at a concentration of 1 mg/mL, pH = 4.5, which was incubated for 30 min at room temperature. The absorbance at 450 nm was measured for each well using a plate reader. The absorbance of biotin standards were plotted versus the logarithm of concentration. A standard curve was fit to a one-site competition model using Graphpad Prism version 3.02 for Windows, GraphPad Software, San Diego, CA (www.graphpad.com).

BALB/c nu/nu mice were separated into two groups of four mice each. Both groups were initially fed a normal diet (Irradiated Lab Diet #5053: Rodent Diet #20, [Purina, St. Louis, MO]). Mice were starved for 2 h at the same time every day, followed by retro-orbital phlebotomy. After the first blood draw, defined as time = 0, one group of mice was placed on a biotin-deficient diet (TD 81079 [Harlan Teklad, Madison, WI]), and the other group remained on the normal diet. Blood was removed for the next 4 days at the same time each day after a 2 h starvation. Blood was immediately collected into 1.5 mL tubes and allowed to clot. Blood samples were centrifuged at 4000 rpm for 3 min, the supernatant was removed, and the process was repeated. Supernatant was removed, and biotin concentrations were determined at various serum dilutions using the biotin assay described above. Serum samples for the mice at each time point were tested at three dilutions in order to obtain the most accurate reading range. Absorbance readings were used to calculate the corresponding biotin concentration in nmoles from the standard curve.

Effect of Streptavidin−Biotin System on Bis-Biotin Tumor Concentration on Normal or Biotin-Deficient Diets. BALB/c nu/nu mice (B & K Universal, Fremont, CA) were separated into two groups and fed either a normal or biotin-deficient diet. 10×10^6 Ramos lymphoma cells were injected subcutaneously into the flank of each mouse. One group of mice fed a biotin-deficient diet was injected with ^{125}I-bis-biotin ip, mice were sacrificed 24 h later, and tissues were harvested as described below. Upon the emergence of palpable tumors, the remaining mice were injected ip with 300 μg (6 nmol biotin binding sites) of either ^{131}I-1F5-SA-WT conjugate or ^{131}I-1F5-SA-S45A conjugate, labeled by the chloramine-T method. The mice were separated into four groups (n = 5), a normal diet and biotin-deficient diet for each 1F5-SA conjugate. Twenty-four hours after conjugate injection, 50 μg (6 nmol biotin) of a *N*-acetylgalactosamine-biotin (NAGB) clearing agent, graciously supplied by the NeoRx Corporation (*19*), was administered ip. ^{125}I-Bis-biotin (2.8 nmol biotin) was injected ip into the mice 3 h later, and the mice were sacrificed 24 h later. Organs were harvested and weighed, and the radioactivity was measured by a Cobra II gamma counter (Packard Bioscience). Tissue concentrations were calculated as the percent of injected dose per gram of tissue (%ID/g) and reported ± standard deviation. Statistical analysis was performed using the nonparametric Mann−Whitney test to compare groups.

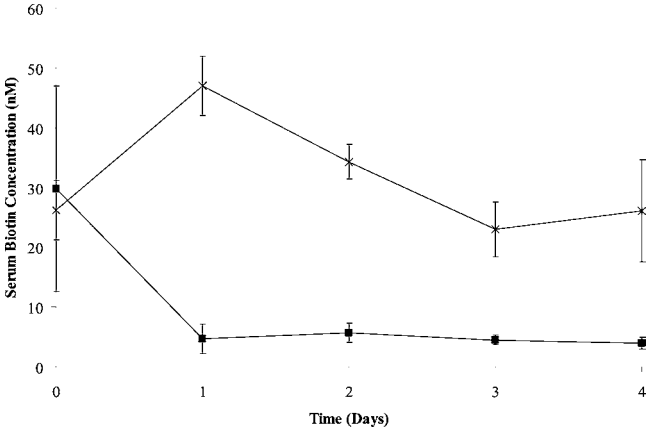

Figure 1. The effect of diet on serum biotin concentration. Mice were fed either a normal diet (×) or a biotin-deficient diet (■), with four mice per group. Blood samples were removed by a retro-orbital blood draw, and serum biotin concentration was measured using a biotin assay.

Pharmacokinetics of 1F5-SA Using Different Clearing Agents. Alternative clearing agents were investigated to improve the clearance of the mutant conjugate, 1F5-SA-S45A. Human serum albumin (HSA) was modified by conjugation of galactose residues and 2−2.5 equiv of bis-biotin molecules, to produce HSA-bis-biotin. Mice were fed a normal diet and separated into cohorts of four mice. Mice were injected ip with 75 μg (5.6 nmol biotin binding sites) ^{125}I-SA-S45A. At 4 h after the initial reagent, mice were injected ip with either 200 μg (11 nmol biotin) of HSA-bis-biotin, 100 μg of NAGB (12 nmol biotin), or 200 μg of HSA (control group). Blood samples were obtained at various time points throughout the experiment. The percent of injected dose per gram of blood (%ID/g) was calculated and plotted as a function of time.

Biodistributions in Mice Pretargeted with 1F5-SA, Cleared with a HSA-Bis-Biotin Clearing Agent. BALB/c nu/nu mice were injected with 10×10^6 Ramos cells subcutaneously in the right flank. Mice were fed either a normal or biotin-deficient diet. With the formation of palpable tumors, mice were injected with 300 μg (6 nmol biotin binding sites) of either ^{131}I-1F5-SA-WT or ^{131}I-1F5-SA-S45A. HSA-bis-biotin at a dose of 200 μg (11 nmol biotin) was administered 24 h later. Three hours later ^{125}I-bis-biotin (2.8 nmol biotin) was injected into the mice, and mice were sacrificed 24 h later. Tissue samples were collected, organs were weighed, and radioactivity was measured.

RESULTS

Assessment of Serum Biotin Concentrations for Normal vs Biotin-Deficient Diets. The serum levels of biotin were characterized for comparison between the normal mouse diets and the biotin-deficient diets. Prior to the determination of serum biotin levels, a standard curve was established using 11 different biotin concentrations ranging from 0.1 nM to 400 nM. The standards yielded a curve that was well fit to a one-site competition model after logarithmic transformation of the concentration. Mice that remained on the normal diet had serum biotin concentrations of 31 ± 5 nM. After beginning a biotin-deficient diet, serum biotin concentrations dropped to 4.7 ± 1.5 nM in 1 day as shown in Figure 1.

Effect of Streptavidin Affinity on Bis-Biotin Tumor Concentration with Normal vs Biotin-Defi-

cient Diets. A biodistribution study was conducted to test whether a bis-biotin therapeutic could be used in combination with a 1F5-SA-mutant conjugate to reduce the blocking of biotin-binding sites by endogenous biotin. SA-S45A has an affinity for biotin (2.1×10^{-10} M) (*14*) that is approximately 3 orders of magnitude lower than SA-WT (2.3×10^{-13} M) (*20*). Decreasing the affinity for biotin was expected to promote exchange of endogenous biotin, diminishing the blocking of biotin-binding sites by endogenous biotin on mice fed normal diets. The biodistribution of ^{125}I-bis-biotin was first measured in mice fed a biotin-deficient diet 24 h postinjection (Supporting Information). The concentration in all tissues was below 0.1%ID/g, indicating that the molecule does not localize nonspecifically to any of the tissues tested. Following this initial evaluation, a dual-label biodistribution experiment was conducted in mice on normal vs biotin-deficient diets. An outline of the injection times and groups used in both biodistribution experiments is shown in Scheme 1.

Tumor-bearing mice were split into two groups and fed either a biotin-deficient diet or a normal diet. These groups were further sub-divided and administered with either 1F5-SA-WT or 1F5-SA-S45A, with all groups injected with the NAGB clearing agent. The concentrations of the ^{131}I-1F5-SA conjugates in different tissues are shown in Figure 2A, 24 h after ^{125}I-bis-biotin administration. The blood concentration of ^{131}I-1F5-SA-WT was 17.7 ± 8.6%ID/g with the normal diet and 7.9 ± 6.0%ID/g for the biotin-deficient diet, indicating that endogenous biotin blocked the action of the biotin-based clearing agent. The blood concentration of the ^{131}I-1F5-SA-S45A conjugate was 21.4 ± 4.9%ID/g with the normal diet and remained relatively high at 14.2 ± 6.8%ID/g with the biotin-deficient diet. The high blood concentrations of ^{131}I-1F5-SA-S45A indicated suboptimal clearance of the low affinity mutant conjugate by the NAGB clearing agent. The concentration of ^{125}I-bis-biotin in different tissues at 24 h after injection is displayed in Figure 2B for the four groups of mice. The ^{125}I-bis-biotin concentrations at the tumors with 1F5-SA-S45A were 12 ± 4.6%ID/g and 10 ± 4.4%ID/g for normal vs biotin-deficient diets, respectively, whereas the concentrations with 1F5-SA-WT were 2.2 ± 1.1%ID/g and 7.0 ± 1.6%ID/g for normal vs biotin-deficient diets, respectively. These results demonstrate that the blocking of radiolabeled biotin by endogenous biotin observed in the 1F5-SA-WT system can be overcome with the lower affinity SA-S45A mutant. However, the concentrations of ^{125}I-bis-biotin in all normal organs was also significantly higher ($p < 0.05$) compared to mice receiving 1F5-SA-WT, due to the high blood concentrations of the 1F5-SA-S45A conjugate. The lower affinity of SA-S45A for biotin thus reduced the effectiveness of the NAGB clearing agent, necessitating the use of a new clearing agent with higher affinity to the mutant conjugate.

Effect of Different Clearing Agents on the Pharmacokinetics of SA-S45A and 1F5-SA-S45A. In initial pilot experiments, we assessed the efficiencies of modified clearing agents at removing unconjugated ^{125}I-SA-S45A from the circulation of mice fed a normal diet. The use of a divalent biotin-based agent was investigated based on the "avidity" effect previously demonstrated with the lower affinity streptavidin mutants (*13*). The NAGB clearing agent was tested at twice its usual dose (100 μg). Additionally, a galactosylated HSA-based clearing agent was constructed by conjugation with bis-biotin-NCS (see methods). Unmodified HSA was used as a control. Blood concentrations of ^{125}I-SA-S45A as a function of time are shown in Figure 3 for groups of mice injected with each clearing agent. HSA-bis-biotin reduced the blood concentration of ^{125}I-SA-S45A from 15.9 ± 2.8%ID/g to 1.0 ± 0.01%ID/g at 30 min after injection. The clearing results with the NAGB clearing agent showed a bimodal distribution where two mice showed no reduction in blood %ID/g, while two mice showed a reduction equivalent to that with the HSA-bis-biotin (leading to the average reduction from 16.8 ± 2.4%ID/g to 7.5 ($\pm$ 4.5−7.1) %ID/g, with the large standard deviation bars in Figure 3). Separate experiments showed that the NAGB clearing agent efficiency with the SA-S45A mutant streptavidin was sensitive to mouse diet, and the bimodal results most likely reflected that two of the mice had recently con-

Scheme 1. Schematic Depicting Time Course of Reagent Injections and Tissue Distribution in the Aminal Experiments[a]

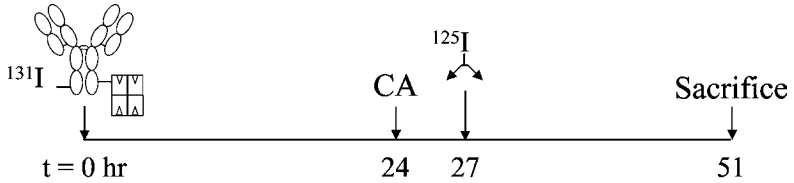

	Group	Conjugate	CA	Diet
Experiment 1	1	1F5-SA-WT	NAGB	Normal
	2	1F5-SA-WT	NAGB	Biotin-Deficient
	3	1F5-SA-S45A	NAGB	Normal
	4	1F5-SA-S45A	NAGB	Biotin-Deficient
Experiment 2	5	1F5-SA-WT	HSA-bis-biotin	Normal
	6	1F5-SA-WT	HSA-bis-biotin	Biotin-Deficient
	7	1F5-SA-S45A	HSA-bis-biotin	Normal
	8	1F5-SA-S45A	HSA-bis-biotin	Biotin-Deficient

[a] ^{131}I-1F5−SA was injected at time 0, followed 24 h later by clearing agent. Three hours later ^{125}I-bis-biotin was administered, and mice were sacrificed after an additional 24 h. Two biodistribution experiments were performed, and the reagents used in each group are listed in the table.

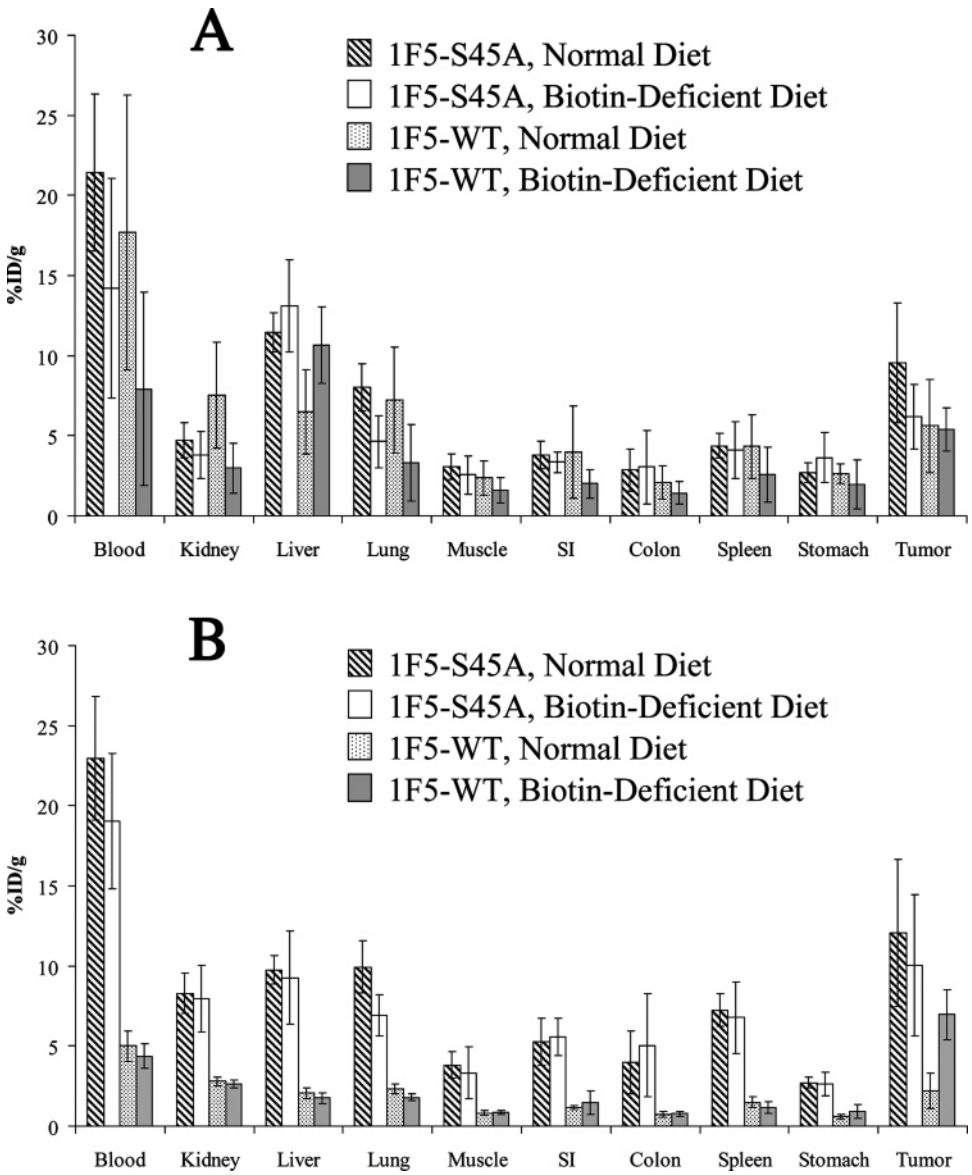

Figure 2. Tissue distributions of (A) ^{131}I-1F5-SA and (B) ^{125}I-bis-biotin in a pretargeting protocol using the NAGB clearing agent. ^{131}I-1F5-SA-WT and ^{131}I-1F5-SA-S45A were injected into mice on either normal or biotin-deficient diets. Twenty-four hours after the initial injection, the NAGB clearing agent was injected, followed 3 h later by administration of ^{125}I-bis-biotin. Mice were sacrificed 24 h after ^{125}I-bis-biotin injection, the tissues were harvested and weighed, and radioactivity was measured. The %ID/g of each tissue is shown for each group. From left to right in each column: 1F5-SA-S45A, normal diet; 1F5-SA-S45A, biotin-deficient diet; 1F5-SA-WT, normal diet; and 1F5-SA-WT, biotin-deficient diet. Average values are shown ± standard deviation.

sumed normal diet pellets. The HSA-bis-biotin was chosen for further studies to match best to the reduced affinity of the SA-S45A reagents under the broadest set of diet conditions.

Biodistributions in Mice Pretargeted with 1F5-SA and Cleared with HSA-Bis-Biotin. In a second biodistribution experiment, Ramos-bearing nude mice were split into two groups and fed either a biotin-deficient diet or a normal diet. These groups were further subdivided and administered with either 1F5-SA-WT or 1F5-SA-S45A. The HSA-bis-biotin clearing agent was used to determine if 1F5-SA-S45A in mice fed a normal diet could yield high ^{125}I-bis-biotin tumor concentrations and low ^{125}I-bis-biotin concentrations in the blood and normal organs. Figure 4A depicts the Ab-SA localization in each organ. The blood concentration of ^{131}I-1F5-SA-S45A 24 h after the ^{125}I-bis-biotin injection was 5.4 ± 3.0%ID/g with the normal diet and 4.4 ± 0.8%ID/g in the biotin-deficient group. 1F5-SA-WT exhibited a blood concentration of 9.7 ± 3.7%ID/g in mice fed a normal diet and 4.2 ± 2.7%ID/g in mice fed a biotin-deficient diet. ^{125}I-bis-biotin biodistributions are displayed in Figure 4B. Tumor concentrations of ^{125}I-bis-biotin 24 h after injection were 0.2 ± 0.03%ID/g for 1F5-SA-WT with the normal diet, and 0.1 ± 0.05%ID/g on the biotin-deficient diet. The tumor concentrations of ^{125}I-bis-biotin were 4.9 ± 3.2%ID/g and 3.4 ± 0.6%ID/g for 1F5-SA-S45A on normal vs biotin-deficient diets, respectively. Blood concentrations of ^{125}I-bis-biotin for 1F5-SA-S45A with the normal vs biotin-deficient diets were 2.5 ± 0.6%ID/g and 3.9 ± 0.7%ID/g, respectively. A comparison of tumor/normal organ ratios of the nonoptimized vs optimized 1F5-SA-S45A conjugate with the normal diet is compared to the optimized 1F5-SA-WT conjugate on the biotin-deficient diet in Figure 5. It can be observed that the bis-biotin clearing agent improves the overall performance of the 1F5-SA-S45A conjugate similar to the best 1F5-SA-WT conjugate system, with the advantage of attaining this performance on a normal biotin diet.

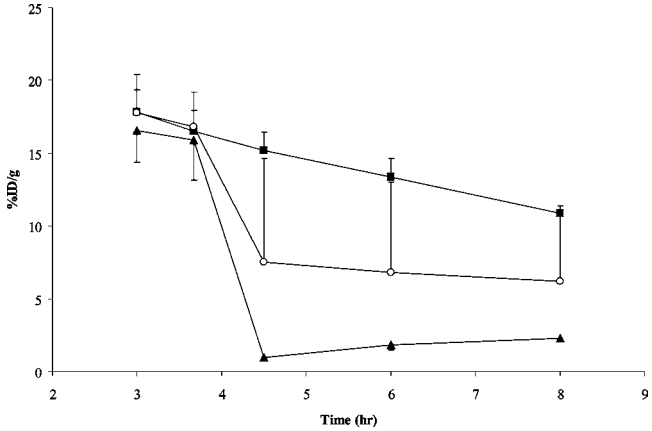

Figure 3. The effect of clearing agents on blood pharmacokinetics of SA-S45A. Three groups of mice ($n = 4$) were fed a normal diet and injected with ^{125}I-SA-S45A, and 4 h later the clearing agent was injected. Blood samples were removed at various time points, the radioactivity was measured, and %ID/g was calculated for each group: HSA control (■) NAGB (○), and HSA-bis-biotin (▲). Average values are shown ± standard deviation.

DISCUSSION

In this study, we have investigated the role of streptavidin affinity, modified therapeutic ligands, and clearing agents in a pretargeting system designed for treating B-cell lymphoma. In particular, the tradeoffs between the advantage of faster biotin off-rates for the rapid exchange of bound endogenous biotin with the biotinylated therapeutic, and the disadvantages of poorer therapeutic retention and blood clearance, have been clarified and initially optimized. The major conclusion is that the low affinity streptavidin mutant can be used with bis-biotin therapeutics of higher effective affinity (avidity) to achieve exchange of blocking endogenous biotin and excellent retention at the tumor. To achieve high tumor/normal organ ratios, it was also found that the clearing agent must be modified to the bis-biotin derivative in order to effectively clear the radiolabeled biotin therapeutic from the blood. When the optimized therapeutic and clearing agents were utilized with the lower affinity mutant, the performance of the pretargeting system with mice on normal diets reached that of the WT streptavidin system on biotin-deficient diets. In addition to providing useful insight into the role of biotin off-rates in pretargeting systems, this finding suggests that the engineered pretargeting system could reduce the impact of endogenous biotin and reduce the quantities of antibody−streptavidin conjugates needed to achieve effective radiation doses at the tumor site.

The bis-biotin strategy was based on previous in vitro work using SA affinity mutants and bivalent biotin ligands (*13*). The bivalent binding of optimized bis-biotin ligands raised their affinity with a site-directed SA-Y43A mutant to that comparable to biotin and wild-type SA. This property allows displacement of monovalent endogenous biotin due to the faster off-rate of the SA mutant, while maintaining the high affinity retention of the bis-biotin once it is exchanged. Initial evaluation of the Y43A streptavidin mutant used in the in vitro studies suggested that a faster off-rate was necessary in the in vivo pretargeting system, and thus the SA- S45A mutant was utilized in this study. The half-life of biotin dissociation from SA-WT is over 6.5 h at 37 °C, while for SA-S45A it is only 14 s. To test the impact of high and low biotin serum concentrations on wild-type and mutant SA biotin and bis-biotin systems, we conducted a series of experiments with mice possessing variable serum concentrations of endogenous biotin as a result of dietary manipulations. The biotin-deficient diets rapidly lowered the serum biotin concentration by 6-fold, from 31 nM to 4.7 nM. While a biotin-deficient diet was sufficient to reduce endogenous biotin serum concentrations 6-fold in mice within 1 day, in rats a 6-fold reduction of plasma biotin concentration took six weeks (*7*). Endogenous biotin levels in human plasma were reported between 1.3 and 2.2 nM (*10*, *21*), which is lower than reported above in nude mice (31 nM) and in rats (5.3 nM) (*7*). Tumor biopsies of patients in the clinic treated with NR-LU-10-SA (WT) revealed a reduction in the biotin-binding capacity over time, which was hypothesized to be due to blockage by endogenous biotin (*22*). As highlighted by Sharkey et al. (*23*), the presence of biotin storage sites may play a role in blocking biotin-binding sites. Development of cutaneous and neurological disorders in the aforementioned rats by 3−5 weeks suggests that reducing endogenous biotin levels in humans with such a diet would require close monitoring.

The tumor concentration of ^{125}I-bis-biotin in mice pretargeted with 1F5-SA-WT and low concentrations of endogenous biotin (biotin-deficient diet) was 7.0%ID/g compared to 2.2%ID/g in mice with high concentrations of serum endogenous biotin (normal diet). Tumor concentration of ^{125}I-bis-biotin was 12%ID/g in mice with high serum biotin concentrations treated with 1F5-SA-S45A, indicating endogenous biotin was unable to block the biotin-binding sites of 1F5-SA-S45A as it did 1F5-SA-WT. There was a concomitant increase in the concentrations of ^{125}I-bis-biotin in normal tissues, especially the blood. This finding highlighted an important tradeoff with the SA mutant: the normal biotin-based clearing agent also had an increased off-rate that prevented effective blood clearance. Biotinylated HSA modified with galactose residues was one of the first clearing agents used to remove Ab-SA conjugates from the blood (*4*). The same strategy was used to construct the multivalent clearing agent that was designed to exhibit the same increase in effective affinity through the avidity effect observed with the bis-biotin therapeutic. The HSA-bis-biotin clearing agent, used with the 1F5-SA-S45A conjugate and ^{125}I-bis-biotin, reduced normal organ concentrations in mice fed a normal diet to similar levels as those observed with the combination of the NAGB clearing agent, the 1F5-SA-WT conjugate, and ^{125}I-biotin in mice fed biotin-deficient diets (Figure 2). We have thus shown that the blocking of biotin-binding sites by endogenous biotin can be mitigated by using a SA-mutant with a lower affinity for biotin coupled with a bivalent bis-biotin therapeutic and clearing agent. Further optimization of the clearing agent and the streptavidin affinity will be necessary to fine-tune the composite activity and specificity (tumor-tissue ratios) further, but these results demonstrate the potential for engineering protein and ligands to optimize the overall pretargeting system.

ACKNOWLEDGMENT

We thank Dr. John Pagel and Dr. David Hyre for insightful discussions. This work was supported by the NIH (NCI Grant CA76287 and DK49655), the Whitaker Foundation (Graduate Fellowship for K.J.H.), and the Department of Energy, Medical Applications and Biophysical Research Division, Office of Biological and Environmental Research under grant number DE-FG03-98ER62572.

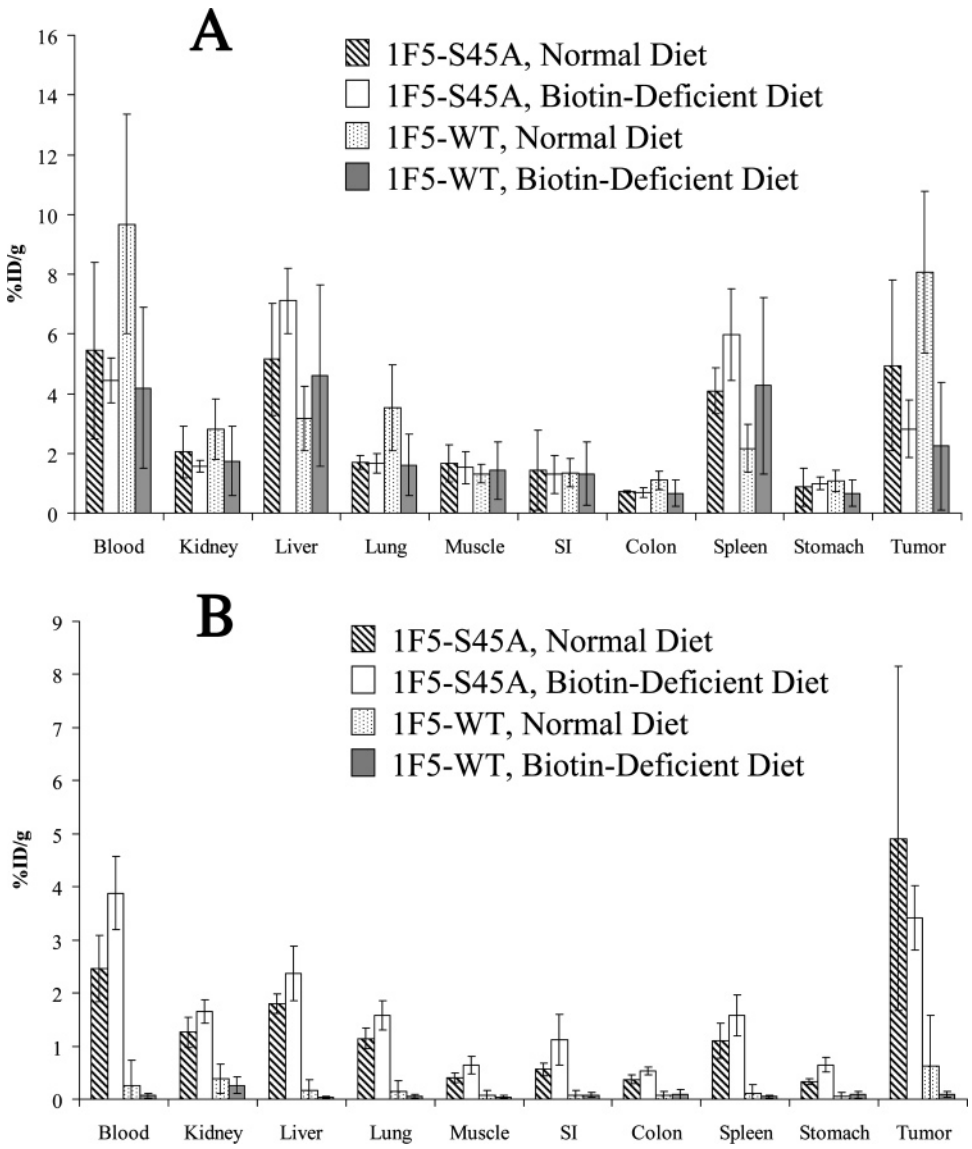

Figure 4. Tissue distributions of (A) ^{131}I-1F5-SA and (B) ^{125}I-bis-biotin in a pretargeting protocol using the HSA-bis-biotin clearing agent. ^{131}I-1F5-SA-WT and ^{131}I-1F5-SA-S45A were injected into mice on either normal or biotin-deficient diets. Twenty-four hours after injection HSA-bis-biotin clearing agent was injected, followed 3 h later by administration of ^{125}I-bis-biotin. Mice were sacrificed 24 h after ^{125}I-bis-biotin injection, the tissues were harvested and weighed, and radioactivity was measured. The %ID/g of each tissue is shown for each group. From left to right in each column: 1F5-SA-S45A, normal diet; 1F5-SA-S45A, biotin-deficient diet; 1F5-SA-WT, normal diet; and 1F5-SA-WT, biotin-deficient diet. Average values are shown ± standard deviation.

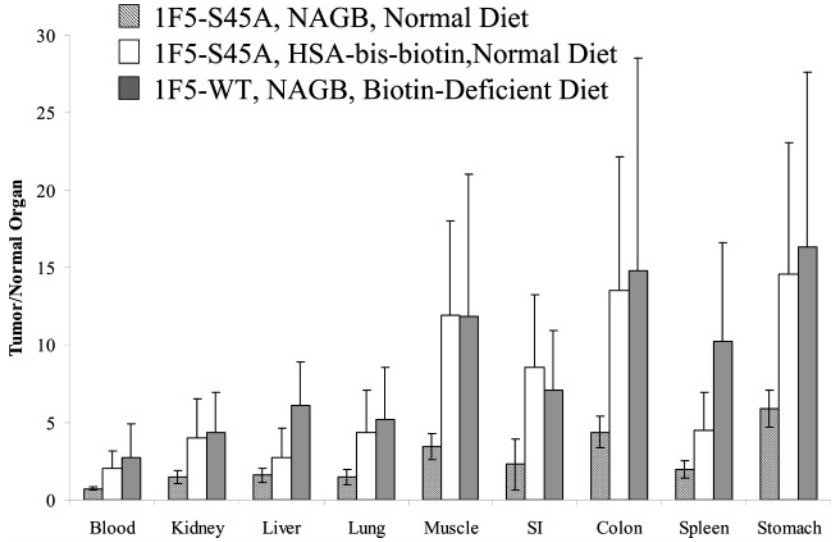

Figure 5. Graph displaying tumor/normal tissue ratios. Tumor/normal tissue ratios of ^{125}I-bis-biotin were calculated from the biodistribution experiments. The following groups are displayed from left to right: 1F5-SA-S45A, NAGB clearing agent, normal diet; 1F5-SA-S45A, HSA-bis-biotin clearing agent, normal diet; and 1F5-SA-WT, NAGB clearing agent, biotin-deficient diet.

LITERATURE CITED

(1) Mclaughlin, P. (2002) Progress and Promise in the Treatment of Indolent Lymphomas. *Oncologist 7*, 217−225.
(2) Witzig, T. E., Gordon, L. I., Cabanillas, F., Czuczman, M. S., Emmanouilides, C., Joyce, R., Pohlman, B. L., Bartlett, N. L., Wiseman, G. A., Padre, N., Grillo-Lopez, A. J., Multani, P., and White, C. (2002) Randomized Controlled Trial of Yttrium-90-Labeled Ibritumomab Tiuxetan Radioimmmunotherapy Versus Rituximab Immunotherapy for Patients With Relapsed or Refractory Low-Grade, Follicular, or Transformed B−Cell Non-Hodgkin's Lymphoma. *J. Clin. Oncol. 20*, 2453−2463.
(3) Press, O. W., Eary, J. F., Appelbaum, F. R., Martin, P. J., Nelp, W. B., Glenn, S., Fisher, D. R., Porter, B., Matthews, D. C., Gooley, T., and Bernstein, I. D. (1995) Phase II Trial of I^{131}-B1 (Anti-CD20) Antibody Therapy with Autologous Stem Cell Transplantation for Relapsed B Cell Lymphomas. *Lancet 346*, 336−340.
(4) Axworthy, D. B., Reno, J. M., Hylarides, M. D., Mallett, R. W., Theodore, L. J., Gustavson, L. M., Su, F. M., Hobson, L. J., Beaumier, P. L., and Fritzberg, A. R. (2000) Cure of Human Carcinoma Xenografts by a Single Dose of Pretargeted Yttrium-90 with Negligible Toxicity. *Proc. Natl. Acad. Sci. 97*, 1802−1807.
(5) Press, O. W., Corcoran, M., Subbiah, K., Hamlin, D. K., Wilbur, D. S., Johnson, T., Theodore, L., Yau, E., Mallett, R., Meyer, D. L., and Axworthy, D. (2001) A Comparative Evaluation of Conventional and Pretargeted Radioimmunotherapy of CD20-Expressing Lymphoma Xenografts. *Blood 98*, 2535−2543.
(6) Schultz, J., Lin, Y., Sanderson, J., Zuo, Y., Stone, D., Mallet, R., Wilbert, S., and Axworthy, D. (2000) A tetravalent single-chain antibody-streptavidin fusion protein for pretargeted lymphoma therapy. *Cancer Res. 60*, 6663−6669.
(7) Mock, D. M., and DuBois, D. B. (1986) A sequential, solid-phase assay for biotin in physiologic fluids that correlates with expected biotin status. *Anal. Biochem. 153*, 272−278.
(8) Rusckowski, M., Fogarasi, M., Fritz, B., and Hnatowich, D. J. (1997) Effect of endogenous biotin on the applications of streptavidin and biotin in mice. *Nucl. Med. Biol. 24*, 263−268.
(9) Klumb, L., Chu, V., and Stayton, P. S. (1998) Energetic Roles of Hydrogen Bonds at the Uriedo Oxygen Binding Pocket Streptavidin−Biotin Complex. *Biochemistry 37*, 7657−7663.
(10) Baker, H. (1985), Assessment of Biotin Status: Clinical Implications. *Ann. N. Y. Acad. Sci. 447*, 129−132.
(11) Shriver, B., Roman-Shriver, C., and Allred, J. B. (1993), Depletion and Repletion of Biotinyl Enzymes in Liver of Biotin-Deficiet Rats: Evidence of a Biotin Storage System. *J. Nutr. 123*, 1140−1149.
(12) Baker, H., Frank, O., Chen, T., Feingold, S., DeAngelis, B., Baker, E. R. (1981) Elevated vitamin levels in colon adenocarcinoma as compared with metastatic liver adenocarcinoma from colon primary and normal adjacent tissue. *Cancer 47*, 2883−2886.
(13) Hamblett, K. J., Kegley, B. B., Hamlin, D. K., Chyan, M., Hyre, D. E., Press, O. W., Wilbur, D. S., and Stayton, P. S. (2002), A Streptavidin−Biotin Binding System That Minimizes Blocking By Endogenous Biotin. *Bioconjugate Chem. 13*, 588−598.
(14) Hyre, D. E., Le Trong, I., Freitag, S., Stenkamp, R. E., and Stayton, P. S. (2000) Ser45 plays an important role in managing both the equilibrium and transition state energetics of the streptavidin−biotin system. *Protein Sci. 9*, 878−885.
(15) Chu, V., Freitag, S., Le Trong, I., Stenkamp, R. E., and Stayton P. S. (1998) Thermodynamic and structural consequences of flexible loop deletion by circular permutation in the streptavidin−biotin system. *Protein Sci. 7*, 848−859.
(16) Chilkoti, A., Tan, P. H., and Stayton, P. S. (1995) Site-directed mutagenesis studies of the high-affinity streptavidin−biotin complex: contributions of tryptophan residues 79, 108, and 120. *Proc. Natl. Acad. Sci. 92*, 1219−1224.
(17) Hylardies, M., Mallett, R. W., and Meyer, D. L. (2001) A Robust Method for the Preparation and Purification of Antibody/Streptavidin Conjugates. *Bioconjugate Chem. 12*, 421−427.
(18) Huang, E. Z., and Rogers, Y. (1997) Competitive enzymatic assay of biotin. *Methods Enzymol. 279*, 304−308.
(19) Weiden, P. L., Breitz, H. B., Press, O., Appelbaum, J. W., Bryan, J. K., Gaffigan, S., Stone, D., Axworthy, D., Fisher, D., and Reno, J. (2000) Pretargeted radioimmunotherapy (PRIT) for treatment of non-Hodgkin's lymphoma (NHL): initial phase I/II study results. *Cancer Biother. Radiopharm. 15*, 15−29.
(20) Green, N. (1975) Avidin. *Adv. Protein Chem. 29*, 85−133.
(21) Wood, H. G. (1998) *Biotin*, in *Vitamins: Fundamental Aspects in Nutrition & Health* (Combs, G. F., Ed.) pp 349−363, Academic Press, San Diego,
(22) Breitz, H. B., Weiden, P. L., Beaumier, P. L., Axworthy, D. B., Seiler, C., Su, F., Graves, S., Bryan, K., and Reno, J. M. (2000) Clinical optimization of pretargeted radioimmunotherapy with antibody-streptavidin conjugate and ^{90}Y-DOTA-biotin. *J. Nucl. Med. 41*, 131−140.
(23) Sharkey, R. M., Karacay, H., Griffiths, G. L., Behr, T. M., Blumenthal, R. D., Mattes, M. J., Hansen, H. J., and Goldenberg, D. M. (1997) Development of a Streptavidin-Anti-Carcinoembryonic Antigen Antibody, Radiolabeled Biotin Pretargeting Method for Radioimmunotherapy of Colorectal Cancer. Studies in a Human Colon Cancer Xenograft Model. *Bioconjugate Chem. 8*, 595−604.

BC034049G

Amphiphilic Core–Shell Nanoparticles with Poly(ethylenimine) Shells as Potential Gene Delivery Carriers

Junmin Zhu,[†] Angie Tang,[†] Lai Pang Law,[†] Min Feng,[†] Kin Man Ho,[†] Daniel K. L. Lee,[†] Frank W. Harris,[‡] and Pei Li*[,†]

Department of Applied Biology and Chemical Technology, and Open Laboratory of Chirotechnology of the Institute of Molecular Technology for Drug Discovery and Synthesis, The Hong Kong Polytechnic University, Hung Hom, Kowloon, P. R. China, and Maurice Morton Institute of Polymer Science, University of Akron, Akron, Ohio 44325-3909. Received April 29, 2004

Spherical, well-defined core–shell nanoparticles that consist of poly(methyl methacrylate) (PMMA) cores and branched poly(ethylenimine) shells (PEI) were synthesized via a graft copolymerization of methyl methacrylate from branched PEI induced by a small amount of *tert*-butyl hydroperoxide. The PMMA-PEI core–shell nanoparticles were between 130 to170 nm in diameter and displayed zeta-potentials near +40 mV at pH 7 in 1 mM aqueous NaCl. Plasmid DNA (pDNA) was mixed with nanoparticles and formed complexes of approximately 120 nm in diameter and was highly monodispersed. The complexes were characterized with respect to their particle size, zeta-potential, surface morphology, and DNA integrity. The complexing ability of the nanoparticles was strongly dependent on the molecular weight of the PEI and the thickness of the PEI shells. The stability of the complexes was influenced by the loading ratio of the pDNA and the nanoparticles. The condensed pDNA in the complexes was significantly protected from enzymatic degradation by DNase I. Cytotoxity studies using MTT colorimetric assays suggested that the PMMA-PEI (25 kDa) core–shell nanoparticles were three times less toxic than the branched PEI (25 kDa). Their transfection efficiencies were also significantly higher. Thus, the PEI-based core–shell nanoparticles show considerable potential as carriers for gene delivery.

INTRODUCTION

The search for a DNA carrier system that can provide safe and efficient gene delivery continues to be one of the most challenging tasks of gene therapy. A desirable vector must be able to protect DNA from enzymatic degradation, bind to target cells, cross the cell membrane, escape from the endosome, and release the therapeutic DNA or RNA resulting in gene expression. The vector should not be toxic or induce an immune response. For good systemic circulation in vivo, the size of the vector should be less than 200 nm in diameter and monodisperse (*1*, *2*).

In the past decade, viral and nonviral vectors have been extensively developed for DNA and oligonucleotide delivery. Viral vectors, although more efficient, are plagued by safety concerns, including virus replication and inflammatory reactions (*3*). With nonviral vectors, the efficiency of gene transfer to cells is very low due to the lack of receptor recognition, endosome escape, and poor nuclear targeting, but nonviral vectors are easy to manufacture on a large scale at an acceptable cost and have superior safety profiles and low immunogenicity. Targeting ligands can also be readily attached. Furthermore, the nonviral vectors can protect DNA from degradation by nucleases in the lysosome and bloodstream. Thus, nonviral systems are more amenable for use in commercial products (*4*).

Nonviral vectors that have been investigated include naked DNA, cationic lipids, liposomes, peptides, surfactants, polymers, dendrimers, polymeric particles, and other systems (*2*). Although many of these delivery systems have been evaluated in vivo, there is still no system that provides the efficacy, safety, and formulation stability required for clinical use. Thus, new nonviral gene delivery systems are continuously being developed in the hope that they will meet these stringent requirements.

Cationic polymers have received particular attention because they can condense with DNA via electrostatic interaction to form small particles, which protect the DNA from degradation and enhance uptake via endocytosis. Furthermore, they can be easily manufactured and conjugated to targeting ligands or intracellular trafficking enhancers (*5*). Of the various types of cationic polymers, linear and branched poly(ethylenimine)s are considered to be the most promising because they combine excellent transfection efficiency with high complex stability (*6*, *7*). The high transfection efficiency of PEI has been attributed to the so-called proton sponge effect (*8*). Since the amine groups on branched and linear PEI are not fully protonated at physiological pH after the PEI/DNA complexes enter the endo/lysosomal compartment, the PEI is able to buffer the acidic pH of the lysosome, protecting the DNA from degradation. Protonation of the PEI also results in an expansion of the polymeric network due to intramolecular charge repulsion. This causes an osmotic swelling/rupture of the vesicles, releasing the DNA into the cytoplasm. The positively charged PEIs are also endocytosed by the cells, thus facilitating endosomal escape. However, a major problem associated with PEI and many other cationic polymer–DNA complexes is their tendency for particle aggregation, resulting in the

* Corresponding author. E-mail: bcpeili@polyu.edu.hk.
[†] The Hong Kong Polytechnic University.
[‡] University of Akron.

10.1021/bc049895l CCC: $30.25 © 2005 American Chemical Society
Published on Web 11/24/2004

formation of large particles (even μm-sized) with broad size distributions. The large particles have poor diffusion in vascular periphery and low internalization capacity to the cells *(9*, *10)*. Thus, the desirable in vivo vectors should be approximately 100 nm in diameter for good systemic circulation and effective endosytosis. Monodisperse vectors having homogeneous compositions are preferred, as they enable pharmacokinetic analysis of a single active species.

The objective of this work was to address the abovementioned problems through the use of monodisperse, amphiphilic core−shell nanoparticles with PEI shells as the gene carriers. The nanoparticles were prepared by our recently developed procedure (*11*, *12*) and treated with plasmid DNA. The resulting pDNA−nanoparticles complexes of approximately 100 to 120 nm in diameter were evaluated with regards to their morphology, physical and chemical properties, ability to protect and release the pDNA, cytotoxicity, and transfection efficiency.

EXPERIMENTAL PROCEDURES

Materials. Branched polyethylenimine with weight average molecular weight of 25 kDa (PEI25K) (waterfree) and 750 kDa (PEI750K) (50 wt % solution in water) were obtained from Aldrich. The phenolic inhibitor in methyl methacrylate (Aldrich) was removed by washing three times with 10% sodium hydroxide solution and then with deionized water until the pH of the water layer dropped to 7. It was further purified by vacuum distillation. *tert*-Butyl hydroperoxide (70% solution in water) was obtained from Acros. GIBCO Dulbecco's modified Eagle medium (DMEM) and Lipofectamine were purchased from Invitrogen Corporation. Poly(aspartic acid) (pASP, molecular weight based on viscosity of 8300 to 11 000 with a DP= 80) and in vitro MTT-based toxicology assay kit were obtained from Sigma. DNase I was purchased from Amersham (7500 units/μL). The human HeLa cell line was purchased from the American Type Culture Collection (ATCC, Maryland). LAR II Luciferase Substrate was from Promega. Freshly deionized and distilled water (ddH_2O) was used as the dispersion medium.

Synthesis of PMMA-PEI Core−Shell Nanoparticles. The PMMA-PEI core−shell nanoparticles were prepared according to our previously described method with minor modifications (*12*). PEI25K (0.84 g) was dissolved in water, and the pH of the solution was adjusted to 7 with 2 M HCl. Purified MMA (0.42 g) was added to the PEI solution in a water-jacketed flask equipped with a thermometer, a condenser, a magnetic stirrer, and a nitrogen inlet. After the solution was stirred under nitrogen for 30 min at 50 °C, *tert*-butyl hydroperoxide (0.25 mL of 1.0×10^{-2} M solution) was added dropwise. The mixture (total 30 mL) was heated at 80 °C for 2 h under nitrogen. The MMA conversion was then determined gravimetrically. The nanoparticles were carefully purified by repeated centrifugation of the dispersion at 13 000 rpm, followed by decantation. This procedure was repeated until conductivity of the supernatant was close to that of the water used. The nanoparticles were further purified by placing their final dispersion in a dialysis tube with a 50 K molecular weight cutoff (Spectra/PorCE) and dialyzed against 5 L of water, which was changed daily for one week at room temperature.

Characterization of Nanoparticles. Infrared spectra were recorded on a Nicolet 750 FT-IR spectrophotometer using KBr disks. Particle size and distribution were measured on a Coulter LS 230 Particle Size Analyzer. The diameters of the nanoparticle/pDNA (NP/pDNA) complexes and their zeta-potentials were determined with a Malvern Zetasizer 3000HS (Malvern, UK) in a 1 mM NaCl aqueous solution. The morphologies of nanoparticles were determined with a JEM 100 CX transmission electron microscope (TEM) with an accelerating voltage of 100 kV. Each sample was prepared by wetting a carbon-coated grid with a small drop of the dilute particle dispersion. The dry nanoparticles were treated with a small drop of 2% phosphotungstic acid (PTA) for 30 min and dried at room temperature. The morphologies of the PMMA-PEI nanoparticles and NP/pDNA complexes were examined with scanning electron microscope (SEM, Stereoscan 440, Leica). To prepare the samples, a drop of dilute latex dispersion was spread on to a glass surface and dried in a dust-free environment at room temperature. The dried specimen was then coated under vacuum with a thin layer of gold to a depth of ca. 5 Å.

Purification of Plasmid DNA. Commercially available plasmid DNA of pGL3-control (Promega) encoding the luciferase reporter gene was used in this study. This plasmid carries the SV40 promoter and enhancer that drive the firefly luciferase gene. The pGL3 plasmid was amplified in transformed JM109 *E.coli* cells in 5 mL of Luria Bertani agar broth supplemented with 50 μg/mL ampicillin (Sigma) at 37 °C. The mixture was gently shaken overnight at 225 rpm. The amplified plasmid DNA was purified using the Concert Rapid Plasmid Miliprep Kit (Life Biotechnologies). The concentration of pDNA was then measured by ultraviolet absorbance with a GeneQuant DNA/RNA Calculator at 260 nm (Pharmacia). The purity of the pDNA was confirmed using double restriction enzyme digestion with BamH1 and HindIII, followed by 0.8% agarose gel electrophoresis.

Nanoparticle/pDNA Complex Formation. The PMMA-PEI nanoparticle dispersions were diluted with ddH_2O to 1 mg/mL. Different amounts of the nanoparticle dispersion were mixed with 0.3 μg of pDNA in TE buffer, and the mixtures were incubated at room temperature for 20 min.

Gel Retardation Assay. pDNA binding to nanoparticles (i.e. complex formation) was studied by means of an agarose gel retardation assay. The agarose gel was prepared by dissolving 0.8% (w/v) agarose in 0.5× Tris−boric acid−EDTA (TBE) buffer containing 0.5 μg/mL ethidium bromide. The samples were mixed with appropriate amounts of 6× gel-loading buffer (Promega) and then loaded into the slots of the gel and subjected to electrophoresis at a voltage of 80 V for 40 min. The pDNA in the gel were visualized by ultraviolet transillumination and photographed by a Lumi-Imager. A 1 kb stepladder marker (Promega) was used as a DNA size marker.

Release of pDNA from Nanoparticles Complexes. The reversible nature of the nanoparticle/pDNA complexes was investigated through the addition of a polyanion, poly(aspartic acid) (pAsp). The complexes were incubated at room temperature with pAsp at a pAsp/pDNA molar ratio ranging from 10 to 100. Various incubation times were used (5, 10, 15, 30, 60, and 120 min), and the released pDNA was analyzed with 0.8% agarose gel electrophoresis.

DNase I Proection Assay. Nanoparticle/pDNA complexes [5:1 (w/w)] were incubated for 10 min at 37 °C with 1, 2, 3, 4, 6, 8, 10 unit/μL of DNase I (1 unit/μL), respectively. The DNase I was then inactivated by adding ethylenediaminetetraacetic acid (EDTA) (0.5 M, pH 8.0), followed by heating it at 80 °C for 2 min. The pDNA was then released from the nanoparticle complexes by pAsp

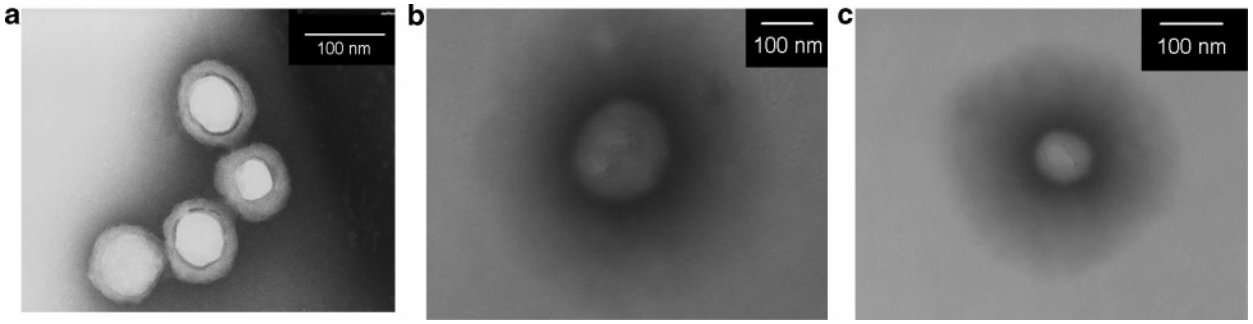

Figure 1. TEM micrographs of PMMA-PEI core−shell nanoparticles: (a) NP1, (b) NP1 at a high magnification, and (c) NP5 at a high magnification.

(molar ratio of pAsp to pDNA = 67:1), and its integrity was assessed by agarose gel electrophoresis.

Cell Culture. The human HeLa cells were cultured in DMEM medium with low glucose, supplemented with 10% (v/v) heat-inactivated fetal bovine serum (FBS) at 37 °C under 5% CO_2. The cells were subcultured before reaching confluence, about every 7 to 8 days.

Cytotoxicity Assay. HeLa cells were seeded at 1.0 × 10^5 cells per well in 96-well plates using DMEM medium containing 10% FBS, 2 mM glutamine, 1 μg/mL insulin, 100 units/mL penicillin, and 100 μg/mL streptomycin and then incubated at 37 °C for 24 h under a 5% CO_2. After incubation, the medium was removed from the wells, and the cells were washed three times with 1× phosphate buffered saline (PBS) solution. Various concentrations of nanoparticles and PEI25K, ranging from 10 to 400 μg/mL, were prepared in the DMEM medium. 200 μL of the nanoparticle dispersion or PEI25K solution was added to each well and subsequently incubated with the cells for 16 h at 37 °C under 5% CO_2. The medium was then removed and replaced with 20 μL of 3-(4,5-dimethylthiazol-2-yl)-2,5-diphenyltetrazolium bromide (MTT) solution (5 mg/mL in PBS). The mixtures were further incubated at 37 °C for 4 h. The MTT solution was then carefully removed from each well, and 200 μL of MTT solubilization solution (containing 10% Triton X-100 plus, 0.1 N HCl in anhydrous 2-propanol) was added to dissolve the MTT formazan crystals. Plates were incubated for an additional 5 min before absorbances at 570 nm were determined spectrophotometrically using an ELISA microplate reader (Bio-Rad). The cell viability (%) was calculated according to the following equation:

$$\text{cell viability (\%)} = (A_{\text{sample}}/A_{\text{control}}) \times 100$$

where A_{sample} is the absorbance of the nanoparticles or PEI treated cells and A_{control} is the absorbance of the untreated cells. Each experiment was done in triplicate and repeated a minimum of three times.

Transfection Study. Cells were seeded at a concentration of 1.0 × 10^5 cells/well in six-well plates and incubated at 37 °C under 5% CO_2 for 24 h. Nanoparticle/pNDA and PEI25K/pDNA complexes of various nitrogen-to-phosphate (N/P) ratios were prepared. 200 μL of each complex suspension prepared, containing 1 μg plasmid, was added to each well. After incubation for 4 h at 37 °C under 5% CO_2, the medium was replaced by DMEM supplemented with 10% FBS and incubated for additional 20 h. The cells in each well were then washed with PBS (1 mL) and lysed with 500 μL of 1× Passive Lysis Buffer (PLB) with gentle shaking at room temperature for 15 min. 20 μL of the cell lysate was transferred into a luminometer tube containing 40 μL of LAR II Luciferase substrate. The relative luminescence unit (RLU) was measured with a Turner Designes TD-20/20 Luminometer (Promega).

Table 1. Preparation of PMMA-PEI Core−Shell Nanoparticles[a]

sample code	PEI (M_w, kDa)	MMA/PEI[b] (w/w)	D_v (nm)	D_n (nm)	D_v/D_n[c]	ξ-potential[d] (mV)
NP1	750	4:1	155	137	1.12	40
NP2	25	4:1	172	152	1.13	42
NP3	25	2:1	133	122	1.09	41
NP4	25	1:1	137	124	1.10	39
NP5	25	1:2	148	135	1.10	41

[a] The PEI and MMA were heated at 80 °C for 2 h in the presence of 0.08 mM TBHP. The pH of the reaction mixtures was 7, and solid content was approximately 4%. [b] Weight ratio of MMA to PEI charged. [c] D_n and D_v are the number and volume average particle diameters, respectively. D_v/D_n is the polydispersity index of the particle size distribution. [d] Zeta-potential was measured in 1 mM NaCl solution.

RESULTS AND DISCUSSION

Preparation of Core−Shell Nanoparticles with PEI Shells. A series of core−shell nanoparticles consisting of poly(methyl methacrylate) cores with branched poly(ethyleneimine) shells was prepared (Table 1). The procedure involved the *tert*-butyl hydroperoxide-initiated graft copolymerization of MMA from branched PEI in water at 80 °C. These particles include high and low molecular weight PEI shells and different shell thicknesses. Conversions of MMA monomer in all systems were around 90%. Small amounts of unreacted PEI, water-soluble copolymer and MMA monomer were removed from the particle dispersions through repeated centrifugation and decantation, followed by dialysis. The properties of the nanoparticles are summarized in Table 1. When the ratio of MMA to PEI was held constant (4:1 w/w), the use of lower molecular weight PEI resulted in slightly larger particle sizes. When the MMA to PEI ratio was decreased from 4:1 to 1:2, particle diameters decreased initially and then increased. This probably reflected the decrease in the diameter of the PMMA core followed by the increase in the thickness of the PEI shell. The nanostructures of the particles were examined with TEM (Figure 1). The micrographs clearly reveal that the nanoparticles are spherical and have well-defined core−shell nanostructures with very hairy PEI shells. The different core diameters and shell thicknesses were easily differentiated at high levels of magnification (Figures 1b and 1c). Furthermore, the nanoparticles all displayed positive surface charges of around +40 mV, regardless of the molecular weight of PEI or shell thickness. Such high positive zeta-potential of the PMMA-PEI core−shell nanoparticles indicated that these nanoparticles were

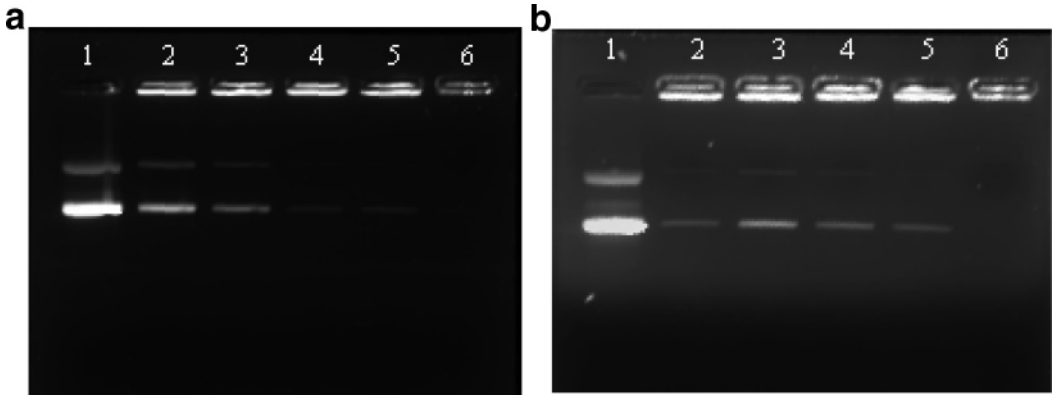

Figure 2. Ratio of nanoparticles to pDNA (w/w) required for complete complexation: (a) NP1/pDNA, Lane 1: pDNA; Lanes 2−6 are NP1/pDNA at weight ratios of 6:1, 8:1, 10:1, 12:1, and 14:1. (b) NP2/pDNA, Lane 1: pDNA; Lane 2−6 are NP2/pDNA at weight ratio of 30:1, 35:1, 40:1, 45:1, and 50:1.

very stable in aqueous and capable of condensing negatively charged pDNA.

Effect of the Molecular Weight of the PEI in the Shell on the Complexation of pDNA. DNA condensation onto a carrier is the first step in gene delivery. Thus, the effects of several parameters on the ability of the nanoparticles to complex with pDNA were examined. The effect of the molecular weight of the PEI shell was determined by incubating pDNA with various amounts of NP1 and NP2 nanoparticles. The amount of pDNA complexed with the nanoparticles was observed with agarose gel electrophoresis (Figure 2). When using the NP1 nanoparticles prepared from a high molecular weight of PEI (750 kDa), the pDNA was completely bound at nanoparticles to pDNA ratio of 14:1 (w/w) (Figure 2a). However, a ratio of 50:1 (w/w) was needed to bind all the pDNA with the NP2 nanoparticles, which were prepared with a low molecular weight PEI (25 kDa) (Figure 2b). Thus higher molecular weight PEI had much greater DNA binding capacity. Complicating this result is the fact that the molecular weight of PEI affects the transfection efficiency and the cytotoxicity *(13−15).* Although PEI with a molecular weight greater than 25 kDa provides high transfection efficiency, it is usually highly toxic, nonbiodegradable, and cannot be excreted. On the other hand, PEI carriers with molecular weights below 18K are not toxic, but have much lower transfection efficiency. Thus, even though the nanoparticles with high molecular weight of PEI shells bind DNA more effectively, the nanoparticles prepared from a low molecular weight of PEI (25 kDa) will probably have more potential for use in gene delivery.

Effect of the Thickness of the PEI Shell on Complexation with pDNA. To determine the effect of the thickness of the shell on the binding ability of the nanoparticles, a series of nanoparticles with an increase of shell thicknesses [MMA to PEI weight ratio of 4:1 (NP2), 2:1 (NP3), 1:1 (NP4) and 1:2 (NP5)] was prepared using PEI with a molecular weight of 25 kDa. The amount of nanoparticles necessary to completely complex a given amount of pDNA (0.3 μg) was then determined using agarose gel electrophoresis. Results in Table 2 show that the nanoparticles containing larger amounts of PEI were much more effective in complexing the pDNA. In fact, as the amount of PEI in the nanoparticle, i.e., the thickness of the shell, increased, the amount of nanoparticles required to complex the given amount of pDNA significantly decreased from 50:1 to 2:1. Thus, the NP5 nanoparticles were used for all subsequent studies.

Surface Properties and Stability of Complexed Nanoparticles. Surface charges of nanoparticles play a major role in controlling particle aggregation, which strongly affect the biodistribution and intracellular uptake in tissue (*16*, *17*). Since positive charges of nanoparticle surfaces decrease upon complexation of the negatively charged pDNA, the nanoparticles are expected to become less stable and more susceptible to aggregation as the amount of pDNA in the complex is increased. Thus, a study was carried out to determine the effect of pDNA loading on nanoparticle stability. Loading of pDNA was varied by complexing different amounts of the NP5 nanoparticles with a standard amount of pDNA at weight ratios of 2:1, 5:1, and 10:1. The stability of the complexes was determined with particle size measurement (Figure 3). Although the gel electrophoresis has indicated that NP5 nanoparticles could completely complex all the pDNA at the ratio of 2:1 (Table 2), the complexed particles were unstable and aggregated to form large particles with a mean size of 1612 nm (Figure 3b). However, the stability of the complexes could be greatly improved when increasing the nanoparticles to pDNA ratios to 5:1 or 10:1 (Figure 3 c and 3d). These complexed particles had mean sizes of 124 and 123 nm in diameter, which were smaller than the original NP5 particles (146 nm in diameter). The reduction of particle sizes was due to the negatively charged pDNA partially neutralizing the positively charged PEI shell. Thus the PEI shell became less water-soluble and shrunk. Measurement of surface charges of the complexes indicated that the zeta potential of the NP5 nanoparticles was reduced from +39.3 mM to +17.1 mV upon complexation with pDNA at a ratio of 5:1, confirming the electrostatic adsorption of pDNA on the PEI shell. Thus NP5 and pDNA complexation at weight ratio of 5:1 [estimated nitrogen to phosphorus (N/P) ratio = 5.5:1] was used for all the subsequent studies. The fact that the particle size of the complexes are around 100 nm with positive surface charges is very important for successful gene delivery because they provide good systemic circulation in vivo and facilitate cell uptake.

Table 2. Weight Ratios of Nanoparticles to pDNA Required for Complete Complexation

sample	MMA/PEI (w/w)	nanoparticle/pDNA (w/w) required to completely complex 0.3 μg of pDNA
NP2	4:1	50:1
NP3	2:1	20:1
NP4	1:1	12:1
NP5	1:2	2:1

The particle diameters and size distributions of the NP5 nanoparticles and their pDNA complexes were

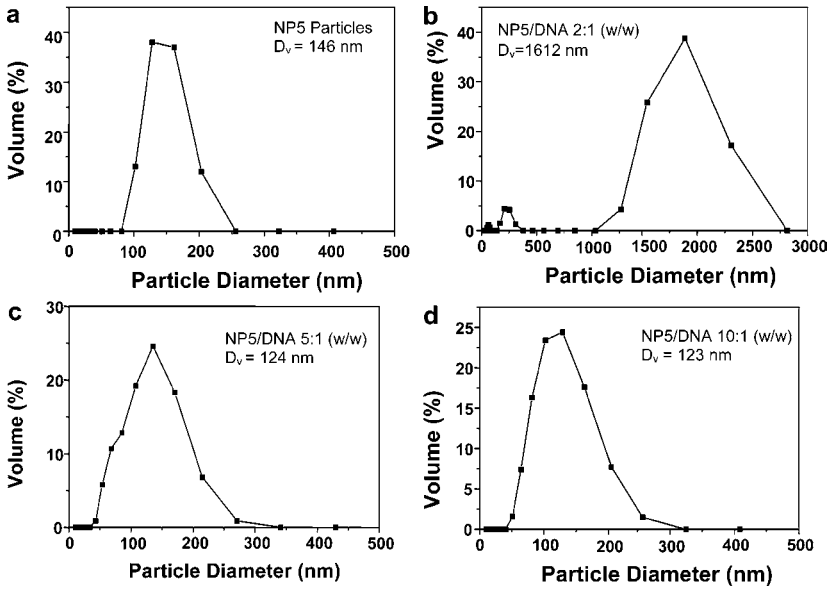

Figure 3. Particle diameters (Dv) of NP5 nanoparticles and NP5/pDNA complexes: (a) NP5 nanoparticles; (b) NP5:pDNA = 2:1 (w/w); (c) NP5:pDNA = 5:1 (w/w); (c) NP5:pDNA = 10:1 (w/w).

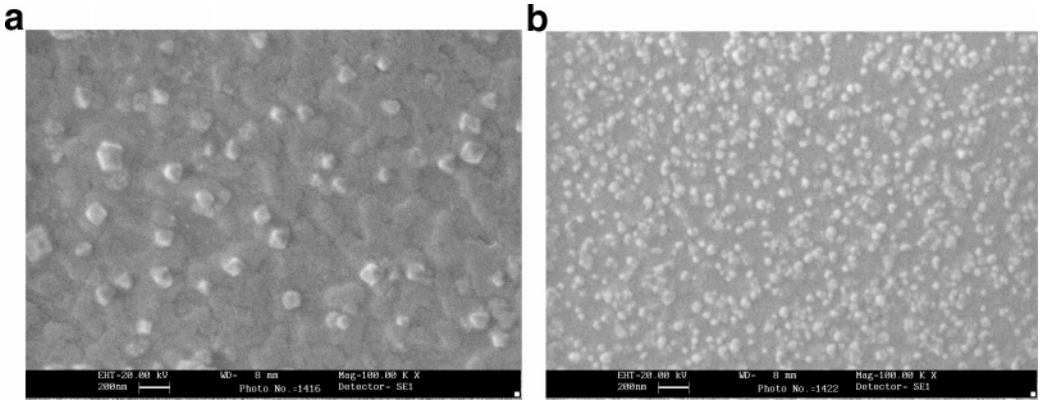

Figure 4. SEM micrographs of (a) NP5 nanoparticles, and (b) NP5/pDNA complexes at 5:1 ratio (w/w).

further studied with a scanning electron microscope (SEM) (Figure 4). The results confirmed that the average size of the NP5 nanoparticles was reduced to approximately 100 nm in diameter after complexing the pDNA. The monodispersity of the nanoparticles was also quite evident.

When the branched PEI25K was complexed with pDNA using N/P ratios of 4.4:1, 5.5:1, and 11:1, bimodal particle size distributions were obtained in all cases. The diameters of the complexed particles ranged from 70 to100 nm, while those of the larger particles were between 400 and 650 nm. Thus, use of the core−shell nanoparticles as the carrier has obvious an advantage over the branched PEI with regards to the nanosize and monodispersity.

DNA Integrity and Release of pDNA from the Complexes. Physical integrity of the DNA after complexation is a prerequisite for biological activity of the DNA to mediate successful transfection. Disassembly of DNA from the carrier is another critical step in the final stage of gene expression. The disassembly reaction is believed to occur between the ionic complex of DNA with other anionically charged macromolecules or cellular components such as mRNA, sulfated sugars, and nuclear chromatin in the cell (*18*). Therefore, it is important to examine whether the pDNA remain intact after complexation and can be released through an exchange reaction with a polyanion. Figure 5 shows the results of releasing pDNA after incubating the complexed nanoparticles with poly(aspartic acid) (pAsp) for 2 h at room temperature. There was no pDNA band in Lane 2, indicating that the pDNA had formed a stable complex with NP5 nanoparticles. When 10 and 23 times excess

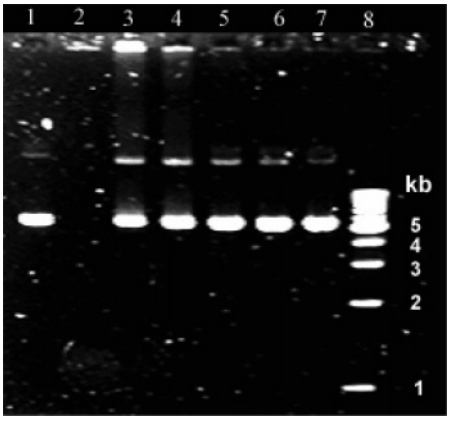

Figure 5. Release of pDNA from NP5/pDNA complexes by the addition of pAsp at various molar ratios. Lane: (1) plasmid DNA; (2) NP5/pDNA complexes at 5:1 weight ratio; (3−7) NP5/pDNA complexes with increasing proportions of pAsp (10, 23, 34, 45, and 55-fold excess of pAsp); (8) 1 kb DNA stepladder size marker. The band comigrating with the 5 kb size marker is the supercoiled form of pDNA, while the slower running and fainter band is the relaxed circular form.

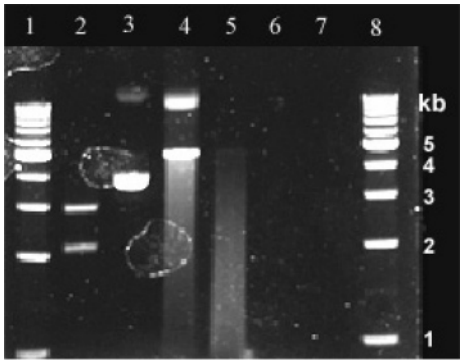

Figure 6. Determination of an optimal amount of DNase I to completely digest 0.3 μg of pDNA. Lane: (1 and 8) 1 kb DNA step ladder size marker; (2) double digestion of pDNA with BamH1 and Hind III for 90 min at 37 °C; (3) untreated plasmid DNA; (4−7) pDNA incubated with increasing amounts of DNase I [0.1, 0.5, 1, and 5 units].

of pAsp to pDNA (molar ratio) were used to release pDNA from the complexed particles (Land 3 and 4), both pDNA bands and smear appeared. Further increasing the molar ratios to 34, 45, and 55 could release all the pDNA from the complexes (Lane 5, 6, and 7). The nature of pDNA released was the same as the uncomplexed pDNA (Lane 1). These results clearly indicate that pDNA molecules remain intact after complexation and can be easily disassembled by polyanions. We also studied the minimum time required to completely release the pDNA from the complexed nanoparticles using 46-fold excess of pAsp and found that the pDNA could be all released within 5 min of incubation time.

Protection of pDNA against DNase I Digestion. For a useful gene delivery system, the carriers must be able to protect DNA from degradation by cellular nucleases abundant in serum and extracellular matrix. In this study, the extent of protection offered by the nanoparticles was investigated. Figure 6 showed that when naked pDNA (0.3 μg) was treated with 0.1 unit/μL of DNase I (Lane 4), a smear migrated ahead of the main band of the supercoiled pDNA, indicating some of the pDNA molecules were degraded. Increasing the DNase I concentration to 0.5 unit/μL could degrade most of the pDNA (Lane 5). Further increasing DNase I concentration to 1 or 5 unit/μL could completely degrade the pDNA (Line 6 and 7). When the same amount of pDNA (0.3 μg) was complexed with the NP5 nanoparticles and treated with 1 or 2 unit/μL of DNase I, no significant degradation of the pDNA was observed (Lanes 6 and 7, Figure 7). An increase of the intensity of the slower running band indicated the presence of more pDNA molecules in relaxed circular form. This change may be attributed to the fact that the DNase generates a single nick at one strand of the DNA, which can be repaired when they are inside the cell. The extent of the protection was further demonstrated using 3 to 10 unit/μL of DNase I to treat the NP5/pDNA complexes (Lanes 8−12, Figure 7). The majority of pDNA remained intact even though degradation became more and more apparent. The lack of complete protection against DNase I may be due to the degradation through surface erosion of DNA that is dynamically mobile on the particle shell. The porous nature of the nanoparticles shell layer also allowed the access of DNase, which could degrade the bounded pDNA (*19*). On the other hand, the level of nucleases in human serum at physiological conditions is approximately 0.1 unit/μL. At this level, the DNA complexed onto the nanoparticles should be totally protected against enzymatic degradation.

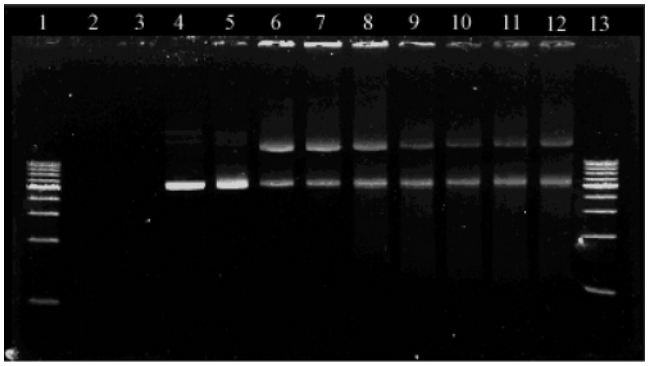

Figure 7. Protection of pDNA against DNase I after complexation with NP5 nanoparticles (NP5 to pDNA at a weight ratio of 5:1). Lane: (1 and 13) 1 kb step ladder size marker; (2) NP5 nanoparticles; (3) NP5/pDNA complexes; (4) plasmid DNA control; (5) pDNA released from the complexes without DNase treatment; (6−12) pDNA released from complexes treated with increasing amounts of DNase I [1, 2, 3, 4, 6, 8, and 10 units/μL].

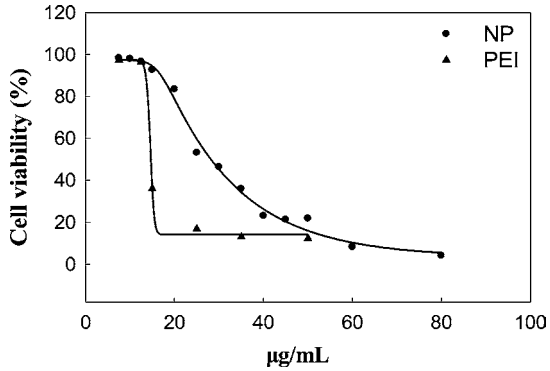

Figure 8. The percentage of viable cells at various concentrations for the NP5 nanoparticles (NP) and the free PEI (25kDa) polymer.

Cytotoxicity Study. The cytotoxicities of the PMMA-PEI core−shell nanoparticles (e.g. NP5) and the PEI25K polymer were compared using a cell viability assay (Figure 8). Various amounts of NP5 nanoparticles and PEI25K polymer were separately incubated with 1.0×10^5 HeLa cells (per well) in culture for 16 h at 37 °C. The cell viability was determined using MTT assay by measuring conversion of the MTT tetrazolium compound to formazan. The PMMA-PEI nanoparticles showed a significant reduction of cytotoxicity compared with the PEI (Figure 8). IC_{50} concentrations of the NP5 nanoparticles and PEI were 30 μg/mL and 10 μg/mL, respectively, indicating that the NP5 nanoparticles were three times less toxic than the PEI. In addition, a very sharp drop in the number of viable cells was observed with PEI, but much more gradual with NP5. This indicates that a much wider window between the beginning of metabolic down-regulation and the complete loss of viability is available with the nanoparticles. It should be noted that these cytotoxicity results were based on the use of nanoparticles and free PEI polymer. In general, the cytotoxicity of cationic carriers is reduced after complexation of the DNA (*8*). The cause of PEI cytotoxicity may be due to the multiple attachment of PEI to the cell surface, resulting in lysis of the cell (*20*, *21*). In our case, the PEI macromolecules are covalently linked to the PMMA particle surface. Thus, the number of possible PEI attachments to cell surfaces may be reduced, resulting in a lower cytotoxicity to the cell.

Transfection Activity. The effectiveness of PMMA-PEI core−shell nanoparticle (NP5) as carriers in gene

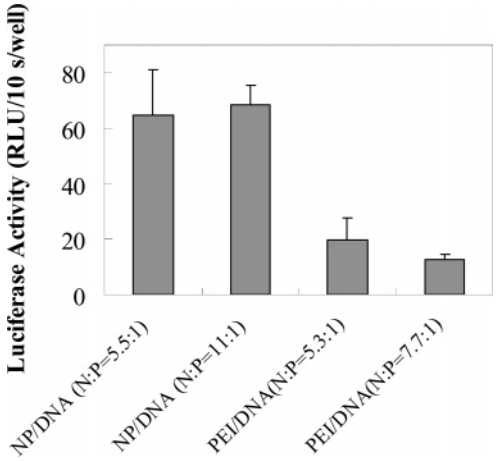

Figure 9. Transfection efficiency of NP5 and PEI25K at various N/P ratios in HeLa cells.

delivery was compared with PEI25K by assessing the level of expression of the reporter gene, firefly luciferase, carried into the HeLa cell in culture. The transfection efficiency was determined by the activity of firefly luciferase in relative luminescence units (RLU). Our results showed that the use of NP5 nanoparticles as carriers gave much higher transfection efficiency than that of PEI (Figure 9). For example, NP5/DNA complexes with N:P ratio of 5.5:1 were three times more efficient than PEI/DNA complexes with N/P ratio of 5.3:1. Increasing the N/P ratio of NP/DNA to 11:1 slightly enhanced the transfection efficiency. However, an opposite effect was observed with PEI/DNA complexes.

CONCLUSION

Various core−shell nanoparticles consisting of poly(methyl methacrylate) cores with branched poly(ethylenimine) shells were synthesized via a TBHP-induced graft copolymerization of methyl methacrylate from branched poly(ethylenimine). These core−shell nanoparticles were able to condense pDNA to form nanoparticle/pDNA complexes. Compared with the use of the branched PEI (25kDa) alone, PMMA-PEI core−shell nanoparticles formed much more stable complexed nanoparticles around 120 nm in diameter with a narrow size distribution. They were also three times less toxic than the branched PEI polymer and at least three times more efficient as gene carriers in transfecting cells. Although high molecular weight PEI (750 kDa) showed greater pDNA binding ability than the low molecular weight PEI (25 kDa), the cytotoxicity issue limited its potential application in gene delivery. Increasing PEI shell thickness using low molecular weight PEI (25 kDa) significantly increased the pDNA binding ability. The complexed pDNA remained intact and could be disassembled from the nanoparticle by the poly(aspartic acid). The PMMA-PEI core−shell nanoparticles also showed strong pDNA protection against enzymatic degradation. Thus, our PEI-based core−shell nanoparticles clearly demonstrate great potential as carriers for gene delivery. Studies of transfection efficiency with different cells and under different conditions, distribution of the nanoparticles inside the cell, and attachment of targeting ligands onto the nanoparticle surface will be the subjects of future investigation.

ACKNOWLEDGMENT

We gratefully acknowledge the Hong Kong Polytechnic University, Research Grants Council of the Hong Kong Special Administrative Region (Project No. PolyU 5283/02P), and The University Grants Committee Area of Excellence Scheme (Hong Kong) for their financial support of this research.

Supporting Information Available: A figure of the weight ratios of various nanoparticles to pDNA required for complete complexation of 0.3 μg of pDNA. A figure of particle sizes and size distributions of PEI25K/pDNA complexes at various N/P ratios. This material is available free of charge via the Internet at http://pubs.acs.org.

LITERATURE CITED

(1) Norton, P. A., and Steel, L. F. (2000) *Gene transfer methods: introducing DNA into living cells and organisms*, BioTechniques Books Publication, Eaton Publishing, Westborough, MA.
(2) McAllister, K., Sazani, P., Adam, M., Cho, M. J., Rubinstein, M., Samulski, R. J, and DeSimone, J. M. (2002) Polymeric nanogels produced via inverse microemulsion polymerization as potential gene and antisense delivery agents. *J. Am. Chem. Soc. 124*, 15198−15207.
(3) Cavazzana-Calvo, M., Thrasher, A., and Mavilio, F. (2004) The future of gene therapy. *Nature 427*, 779−781.
(4) Mountain, A. (2000) Gene therapy: the first decade. *Trends in Biotech. 18*, 119−128.
(5) De Smedt, S. C., Demeester, J., and Hennink, W. E. (2000) Cationic polymer based gene delivery systems. *Pharm. Res. 17*, 113−126.
(6) Kircheis, R., Wightman, L., and Wagner, E. (2001) Design and gene delivery activity of modified polyethylenimines. *Adv. Drug Delivery Rev. 53*, 341−358.
(7) Brissault, B., Kichler, A., Guis, C., Leborgue, C., Danos, D., and Cheradame, H. (2003) Synthesis of linear polyethylenimine derivatives for DNA transfection. *Bioconjugate Chem. 14*, 581−587.
(8) Godbey, W. T., Wu, K. K., and Mikos, A. G. (1999) Poly(ethylenimine) and its role in gene delivery. *J. Controlled Release 60*, 149−160.
(9) Vinogradov, S. V., Bronick, T. K., and Kabanov, A. X. (1998) Self-Assembly of polyamine-poly(ethylene glycol) copolymers with phosphorothioate oligonucleotides. *Bioconjugate Chem. 9*, 805−812.
(10) Nakai, T., Kanamori, T., Sando, S., and Aoyama, Y. (2003) Remarkably size-regulated cell invasion by artificial viruses. Saccharide-dependent self-aggregation of glycoviruses and its consequences in glycoviral gene delivery. *J. Am. Chem. Soc. 125*, 8465−8475.
(11) Li, P., Zhu, J. M., and Harris, F. W. (2003) Amphiphilic core−shell latexes. US Patent 6,573,313.
(12) Li, P., Zhu, J., Sunintaboon, P., and Harris, F. W. (2002) New route to amphiphilic core−shell polymer nanospheres: graft copolymerization of methyl methacrylate from water-soluble polymer chains containing amino groups. *Langmuir 18*, 8641−8646.
(13) Godbey, W. T., Wu, K. K., and Mikos, A. G. (1999) Size matters: Molecular weight affects the efficiency of poly(ethylenimine) as a gene delivery vehicle. *J. Biomed. Mater. Res. 45*, 268−275.
(14) Fischer, D., Bieber, T., Li, Y., Elsässer, H., and Kissel, T. (1999) A novel nonviral vector for gene delivery based on low molecular weight, branched polyethylenimine: effect of molecular weight on transfection efficiency and cytotoxicity. *Pharm. Res. 16*, 1273−1279.
(15) Kunath, K., Harpe, A. V., Fischer, D., Petersen, H., Bickel, U., Voigt, K., and Kissel, T. (2003) Low-molecular-weight polyethylenimine as a nonviral vector for DNA delivery: comparison of physicochemical properties, transfection efficiency and in vivo distribution with high-molecular weight polyethylenimine. *J. Controlled Rel*ease *89*, 113−125.
(16) Pouton, C. W., and Seymour, L. W. (2000) Key issues in nonviral gene delivery. *Adv. Drug Delivery Rev. 46*, 187−203.
(17) Mislick, K. A., and Baldeschwieler, J. D. (1996) Evidence for the role of proteoglycans in cation-mediate gene transfer. *Proc. Natl. Acad. Sci. U.S.A. 93*, 12349−12354.

(18) Eracher, P., Roche, A. C., Monsigny, M., and Midoux, P. (1995) Glycosylated polylysine/DNA complexes: Gene transfer efficiency in relation with the size and substitution level of glycosylated polylysines and with the plasmid size. *Bioconjugate Chem. 6*, 401−410.
(19) Truong-Le Vu L., Walsh S. M., Schweibert E., Mao H. Q., Guggino W. B., August J. T., and Leong K. W. (1999) Gene Transfer by DNA Gelatin Nanospheres. *Arch. Biochem. Biophys. 361*, 47−56.
(20) Choksakulnimitr, S., Masuda, S., Tokuda, H., Takakura, Y., and Hashida, M. (1995) In vitro cytotoxicity of macromolecules in different cell culture systems. *J. Controlled Release 34*, 233−241.
(21) Ryser, H. J. (1967) A membrane effect of basic polymers dependent on molecular size. *Nature 215*, 934−936.

BC049895L

PEG-Modified Protamine with Improved Pharmacological/ Pharmaceutical Properties as a Potential Protamine Substitute: Synthesis and in Vitro Evaluation

Li-Chien Chang,[†,*] Hsiao-Feng Lee,[‡] Meng-Ju Chung,[†] and Victor C. Yang[§]

School of Pharmacy, National Defense Medical Center, Taipei, Taiwan, ROC, Industrial Science & Technology Network Inc., York, Pennsylvania 17404, and College of Pharmacy, The University of Michigan, Ann Arbor, Michigan 48109. Received January 15, 2004; Revised Manuscript Received September 4, 2004

Cardiopulmonary bypass (CPB) procedures are frequently associated with massive inflammatory responses, resulting in a high rate of morbidity and mortality in routine cardiac operations. One recognized attribute of these deleterious responses is the synergic effect of heparin and protamine, which elicit the activation of the complement system in vivo. To circumvent such toxic effects following protamine reversal of heparin anticoagulation in the CPB procedures, we proposed that poly(ethylene glycol) (PEG)-modified protamine could retain the heparin-neutralization ability and yet diminish the induced complement activation by the formed heparin−protamine complexes (HPC), thereby providing highly improved pharmacological properties. PEGylation of protamine was carried out by utilizing *N*-hydroxysuccinimidyl (NHS) conjugation chemistry. Size exclusion chromatography (SEC), reverse-phase high performance liquid chromatography (RP-HPLC), and matrix-assisted laser desorption mass spectrometry (MALDI-MS) were used to assess the conjugation stiochiometry, the purity of the conjugates, and the site of PEG modification, respectively. The heparin-neutralizing activity was determined by using heparin affinity chromatography and various biological assays including the plasma-activated partial thromboplastin time (aPTT), anti-Xa, and anti-IIa methods. The potency in inducing complement activation was examined in vitro using the CH_{50} hemolytic assay. The PEG-modified protamine was successfully synthesized with a PEG/protamine stiochiometry of 1:1. Only one conjugation site for PEG that was located at the N-terminal end of protamine was obtained. In the biological evaluations, the PEG-modified protamine displayed a full retention of the heparin-neutralizing ability of protamine and a significantly reduced activity in complement activation following its complexation with heparin. Results from studies of the particle size and zeta potential indicated that the PEG-modified protamine formed substantially smaller aggregates with heparin, rendering them less effective in triggering the size-dependent complement responses. As with protamine, PEG-modified protamine exhibited an enhanced aqueous solubility, therefore attaining significantly improved pharmaceutical properties. These preliminary results suggested that the PEG-modified protamine conjugate might serve as a potential protamine substitute with improved therapeutic and pharmaceutical properties in heparin reversal.

1. INTRODUCTION

Protamine is a low molecular weight protein (average MW: 4500 Da) rich in basic arginine residues. It is employed universally in the reversal of heparin anticoagulant activity following various surgical procedures including cardiopulmonary bypass (CPB), peripheral vascular surgery, and invasive cardiac angiography (*1*). It is estimated that more than 600 000 procedures are encountered in the mandatory use of these two drugs each year in the United States (*2*).

Despite decades of clinical use, safety concerns, however, have been remunerated on these two drugs. It has been widely reported that the synergic effects of heparin and protamine on the complement system would result in a variety of postoperative complications, such as increased pulmonary capillary permeability, anaphylactic reactions, organ failures (*3*, *4*), and ultimately many unpredictable deaths (*5*, *6*). Although intravenous administration of protamine alone could produce systemic hypotension, myocardial depression, and an increase in vascular permeability (*7*, *8*), it has been demonstrated clinically that the combined use of protamine and heparin actually triggers the activation of complement system that subsequently elicits more toxic responses (*9*, *10*). The quest for a better protamine alternative is therefore in profound scrutiny in recent years (*11*−*14*).

It has been recognized that inflammatory responses in CPB is, in large part, attributed to complement activation (*15*, *16*). Alleviation in complement activation has been shown to significantly diminish the CPB-associated inflammatory responses (*17*, *18*). On the basis of this reason, it has been hypothesized by us (*19*−*21*) and other investigators (*22*) that reduction of protamine-related complement activation is an effective method to improve the safety of CPB operations. Previously, we demonstrated that a chain-shortened low molecular weight protamine (LMWP) peptide with diminished

* Correspondence and reprint requests should be addressed to Li-Chien Chang, Ph.D.; School of Pharmacy, National Defense Medical Center; 161 MinChuan E. Road, Sec. 6, Taipei, Taiwan; Tel: 886-2-87923100 ext 18890; Fax: 886-2-87919890; e-mail: lichien@ndmctsgh.edu.tw.

† National Defense Medical Center.

‡ Industrial Science & Technology Network Inc.

§ The University of Michigan.

10.1021/bc0499735 CCC: $30.25 © 2005 American Chemical Society
Published on Web 12/09/2004

complement-activating ability elicited no toxic responses in a clinical dog model. This LMWP peptide, which was derived from thermolysin digestion of protamine, however, suffers with the shortcoming of yield (15%) that renders its prospect in comprehensive protamine substitution and as a universal heparin antidote. In this regard, the main objective of this study is to design an alternative approach in achieving a less toxic protamine substitute via the modification of protamine with the poly(ethylene glycol) (PEG) polymer.

It has been well documented that modification of a protein with PEG would help it elude the recognition by the immune system and retard the plasma clearance in vivo (*23*). Since the primary attribute of protamine toxicity lies in its cross-linking with the complement proteins (*11*), the major components of the immune system, it is of great interest to investigate if modification of protamine with PEG would attenuate the risk of protamine-mediated complement activation and enhance the safety of heparin/protamine therapies. Herein, we present a detailed investigation on this protamine PEGylation hypothesis, including synthesis, purification, characterization, and in vitro efficacy and toxicity evaluation of two PEG (PEG^{2000} and PEG^{5000}) modified protamine conjugates. The objective of this study is to demonstrate that the PEG-modified protamine would retain the original heparin-neutralizing ability of protamine, yet devoid of its complement-activating activity.

2. MATERIALS AND METHODS

2.1. Materials. Methoxypoly(ethylene glycol)-succinimidyl propionate (mPEG-SPA, 2000 and 5000 Da) was purchased from Shearwater Polymers (Huntsville, AL). Protamine sulfate (salmine, Grade X), human antithrombin III (A7388), and trifluoroacetic acid (TFA) were obtained from Sigma Chemical Co. (St. Louis, MO). Porcine intestine heparin (167 IU/mg) and S-2238 substrate were purchased from Pharmacia Hepar Inc. (Franklin, OH). HiTrap heparin affinity column was obtained from Amarshan Pharmacia Biotech Inc. (Piscataway, NJ). Freshly frozen human plasma in citrate was obtained from the American Red Cross (Detroit, MI). Acetonitrile was HPLC grade, and all solutions were prepared using distilled and deionized water (ddH_2O).

2.2. Preparation of PEG−Protamine Conjugates. Synthesis of the PEG (2000 or 5000 Da)−protamine conjugates was carried out by using the succinimidyl derivative of PEG propionic acid (PEG-SPA). In brief, a 10-fold molar excess of PEG-SPA (75 mmol) was allowed to react with protamine (7.5 mmol) in 5 mL of PBS (pH 7.5) buffer at room temperature for 2 h. The reaction mixture was then loaded on an Econo-Pac CM (Biorad) column preequilibrated with PBS. The column was washed with 10 volumes of PBS and then eluted with a linear NaCl gradient (0−2 M) in PBS. The appropriate fraction of PEG−protamine conjugate was collected, desalted, lyophilized, and then stored at −20 °C prior to use.

2.3. Characterization of PEG−Protamine Conjugates. Purified PEG−protamine conjugates were analyzed by size exclusion HPLC chromatography (SEC−HPLC, Shimadzu) equipped with a UV detector on a Tricorn Superdex Peptide (Amersham) column. For each measurement, the chromatography was performed with detection at 215 nm using an isocratic mobile phase of PBS with a flow rate of 0.7 mL/min.

Purity of the PEG−protamine conjugates was assessed by reverse-phase HPLC using an Alltech HPLC system equipped with a UV/VIS detector for continuously monitoring the absorbance of the eluent at 215 nm. A 4.6 × 250-mm, 5 μm Macrosphere (Alltech) C-4 column was equilibrated with 0.1% aqueous trifluoroacetic acid (solvent A) at a flow rate of 1.0 mL/min. Following sample injection (50 μL), a linear gradient of 2.0%/min solvent B (0.09% trifluoroacetic acid in acetonitrile) was applied to the column for a period of 50 min.

MALDI-TOF MS analyses were performed by the Protein and Carbohydrate Research Center at the University of Michigan using a Vestec-2000 Laser Tec Research laser desorption linear time-of-flight mass spectrometer. The matrix employed for all samples was α-cyano-4-hydroxycinnamic acid.

2.4. Bioactivity Measurements. Affinity of the PEG−protamine conjugates toward heparin was evaluated by using a heparin affinity chromatography. In brief, the purified conjugates were applied to a HiTrap heparin column (Pharmacia), and the affinity toward the immobilized heparin was determined from the elution time using a linear NaCl gradient (0−2 M) for 30 min. The flow rate was set at 1 mL/min, and the elution was monitored at 215 nm.

To comprehensively evaluate the heparin-neutralizing activity of PEG−protamine conjugates, three heparin assays routinely used in clinical laboratories including the activated partial thromboplastin time (aPTT), anti-Xa, and anti-IIa assays were employed. In brief, for the aPTT assay, 15 μL of heparin solution (5 U/mL) was mixed with 15 μL of sample solution containing various concentrations of protamine (0−30 μg/mL) or PEG−protamine conjugates (0−200 μg/mL), followed by the addition of 100 μL of actin cephaloplastin and 100 μL of plasma. After 3 min of incubation, 100 μL of 20 mM calcium chloride (preheated to 37 °C) were added and the clotting time was immediately measured using a fibrometer. For the anti-Xa assay, the procedure of Chang et al. (*19*) was followed. Briefly, 20 μL of heparinized human plasma (0.6 U/mL) was mixed with 75 μL of human antithrombin III (0.1 U/mL). After 2 min of incubation at 37 °C, 75 μL of factor Xa (4 nkat/mL), 75 μL of S-2222 substrate (1.9 mmol/mL), and 5 μL of protamine (or PEG−protamine conjugates) were added. Following 10 min of incubation, the absorbance of the solution was measured at 405 nm. The heparin-neutralizing ability of protamine (or PEG−protamine conjugates) was proportional to the absorbance increase at 405 nm. The protocol for measuring the anti-IIa activity was similar to that of anti-Xa except that factor IIa (thrombin) and S-2238 were used in replacement of factor Xa and S-2222, respectively. Details of this anti-IIa assay were described in a previous publication (*20*).

2.5. Complement Activation. Complement activation by protamine (or PEG−protamine) or heparin−protamine (or PEG−protamine) complexes was assessed by a modified hemolytic complement assay (*20*) using sensitized sheep erythrocytes (SRBC). In brief, 150 μL of diluted (1:60) serum containing an increasing concentration of protamine (or PEG−protamine) or heparin−protamine (or PEG−protamine) complexes, 75 μL of sensitized SRBC, and 150 μL of 0.02 M triethanolamine buffer saline (TBS) buffer containing 0.15 M NaCl were mixed together. The mixture was incubated at 37 °C for 60 min with occasional agitation. The reaction was then quenched by the addition of ice-cold TBS. After centrifugation, 200 μL of the supernatant were pipetted into the wells of a microplate, and the amount of released hemoglobin was determined at 541 nm using a microplate reader. The absorbance in the reaction mixture by adding TBS buffer

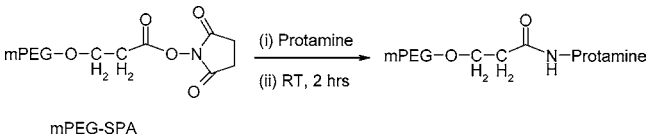

Figure 1. Scheme for chemical coupling of poly(ethylene glycol) (PEG) polymers to the N-terminal amino residues of protamine using methoxy(ethylene glycol)-succinimidyl propionate (mPEG-SPA).

and H_2O as the test samples was used as the control to represent 0% and 100% lysis, respectively. The degree of complement consumption (Y) was obtained from the equation:

$$Y = \left(1 - \frac{\text{test OD} - \text{TBS lysis OD}}{\text{H}_2\text{O lysis OD} - \text{TBS lysis OD}}\right) \times 100$$

2.6. Size and Charge of the Heparin−Protamine Complex (HPC). The heparin−protamine (or PEG−protamine conjugates) complexes (HPC) were prepared by mixing protamine (or PEG−protamine conjugates) with heparin (1U/mL). The dose of protamine used to form HPC was estimated based on the stiochiometric neutralization ratio of 1 mg protamine per 100 U of heparin (*24*), whereas the dose of PEG−protamine conjugates was determined by the ratio of achieving complete neutralization according to the aPTT assay. The solution was allowed to stand for 30 min at 20 °C to allow for a complete complex formation. The formed HPC were then examined for their size and zeta potential by using the HORIBA LB-500 (particle size) and ZetaPlus (zeta potential) analyzers, respectively. The particle size was presented as the effective mean diameter.

3. RESULTS AND DISCUSSION

3.1. Synthesis, Purification, and Characterization. Numerous methods for attaching PEG to a protein have been reported in the literature (*25*). Coupling reactions involving the amino groups of a protein and the monomethyl ester group of a modified PEG are the most widely used method. Among them, conjugation of a protein with the succinimidyl ester-modified PEG was shown to yield a linkage stable in most biological buffers and physiological conditions. For this reason, activated PEG-SPA (succinimidyl propionic acid) was selected to synthesize the PEG−protamine conjugates.

Conjugation was carried out under a slightly basic condition (pH 7.5). Normally, PEGylation of a protein occurs at the α-amino group of the N-terminal residue or the ϵ-amino groups of surface lysine residues when utilizing the *N*-hydroxysuccinimidyl (NHS) conjugation chemistry. Due to lack of lysine residues in the protamine sequence (*19*), the PEGylation reaction in our case is expected to occur only at the α-amino group, indeed, the imino moiety of the N-terminal proline residue of protamine (see Figure 1). Providentially, this conjugation process was actually preferred because it would allow for a site-specific 1:1 PEGylation of protamine at the N-end while preserving its intact structure for heparin neutralization.

To identify the PEGylation chemistry, the synthesized PEG−protamine conjugates were first examined by size exclusion chromatography (SEC). It can be seen in the chromatograms in Figure 2 that for either conjugation reaction (PEG^{2000}−protamine and PEG^{5000}−protamine) the desired mono-PEGylated protamine conjugates were predominantly produced and nearly homogeneous conjugates were obtained, suggesting that using the PEG-succinimidyl propionate reacted at a slightly basic pH could selectively produce N-terminally PEGylated protamines without branch reactions. The purity of the formed PEG−protamine conjugates was then assessed by using reverse-phase HPLC. As seen in Figure 3, only a single peak was eluted from the RP-column, indicating the production of highly pure (>95%) PEG−protamine conjugates. Although the PEG polymer did not absorb light at 215 nm, the separated PEG−protamine conjugate was not likely to contain un-reacted PEG simply because PEG possessed a very weak affinity to the ion exchange column.

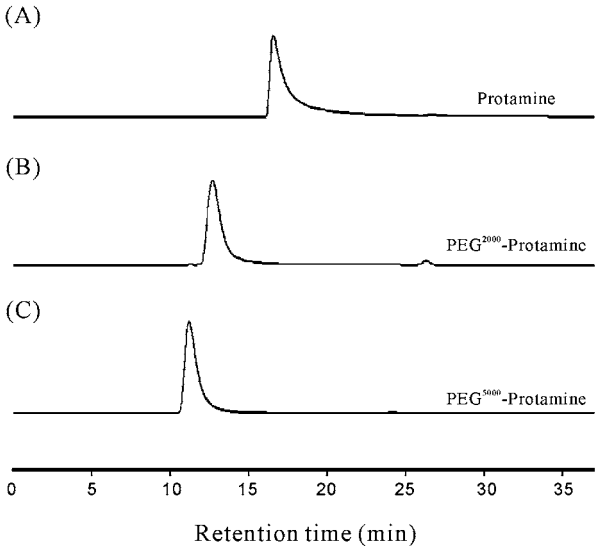

Figure 2. Size exclusion HPLC chromatograms of (A) protamine, (B) PEG^{2000}−protamine conjugate, and (C) PEG^{5000}−protamine conjugate. The PEG−protamine samples were prepurified by cationic ion-exchange chromatography as described in Materials and Methods.

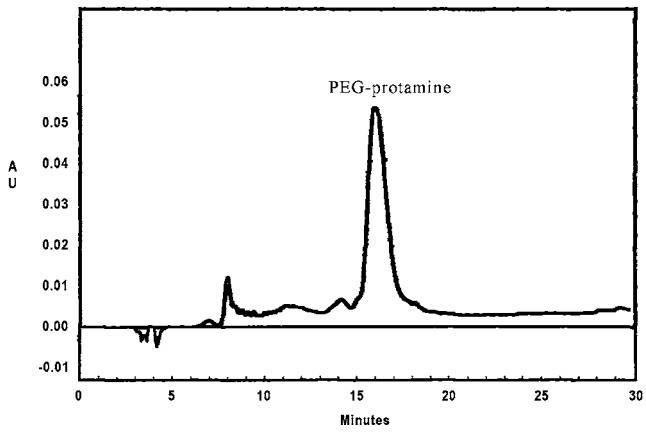

Figure 3. Reverse-phase HPLC chromatogram of PEG^{2000}−protamine conjugate. HPLC traces for PEG^{5000}−protamine conjugate were nearly identical to that of PEG^{2000}−protamine conjugate.

MALDI-TOF analysis was performed to further confirm the SEC results and to determine the molecular weight polydispersity of the formed PEG−protamine conjugates. As seen in Figure 4, the most probable mass peak was 6305.6 *m/z* for PEG^{2000}−protamine conjugate and 9970.5 *m/z* for PEG^{5000}−protamine conjugate, respectively, and in either spectrum a small double-charged mass (M^{2+}) peak was also present. Considering the molecular weight of protamine (4000−4300 Da (*19*)) and two PEGs (2000 and 5000), the obtained mass of the conjugates was very consistent with the calculated mass

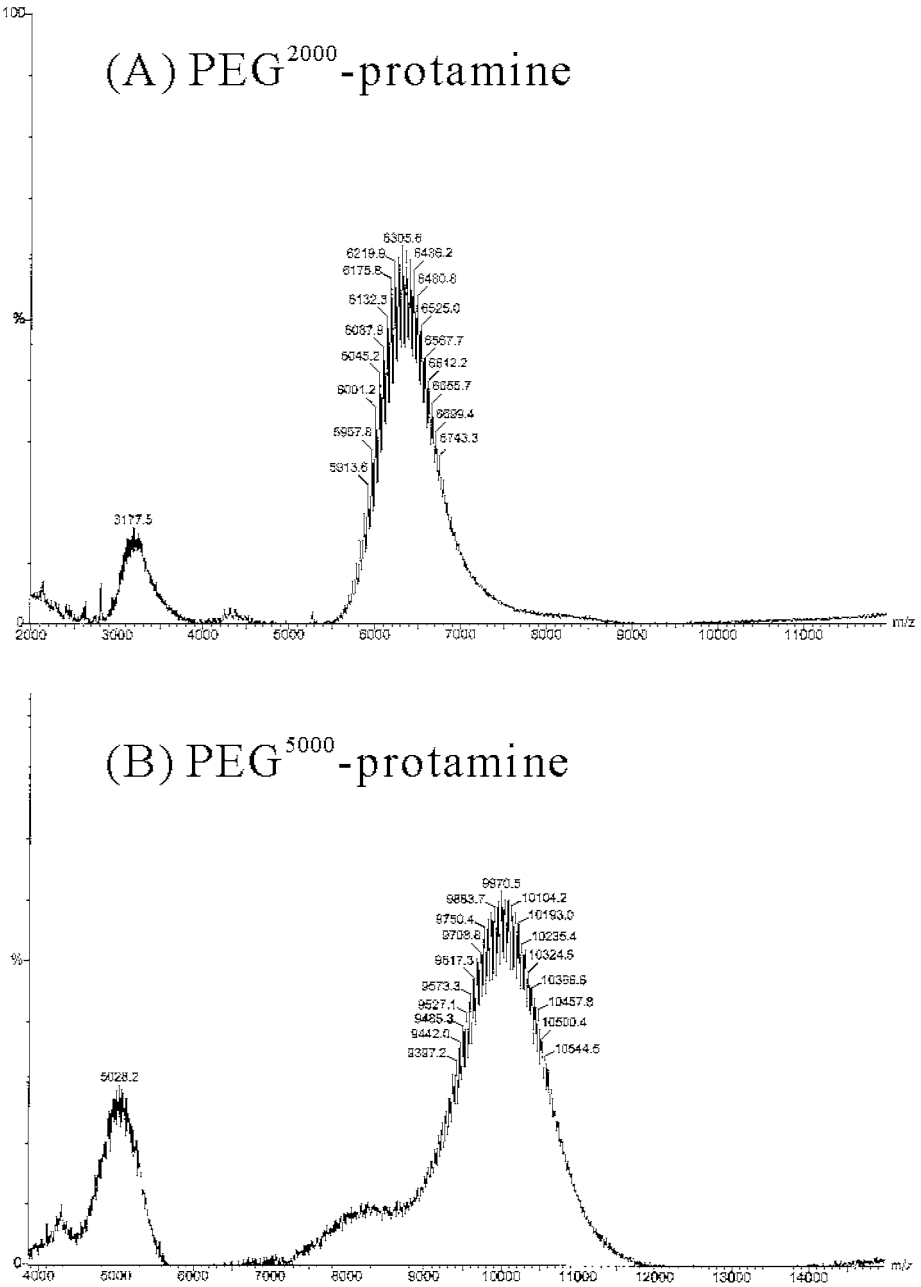

Figure 4. MALDI-TOF spectra of (A) PEG^{2000}−protamine and (B) PEG^{5000}−protamine conjugates. The molecular weight of protamine is about 4000−4300 Da (*19*). The most probable mass of PEG^{2000}−protamine and PEG^{5000}−protamine conjugates are 6305.6 and 9970.5 Da, respectively.

sum of individual molecules. Therefore, both the SEC and MALDI-TOF results clearly indicated that each protamine molecule was attached with only one PEG polymer chain with no intra- or intermolecular cross-linking being detected. Although the broad width of the peaks seen in both figures in Figure 4 suggested the polydispersity in molecular weight of the PEG−protamine conjugates, such a behavior was likely attributed to the polydispersity of the used PEG polymer rather than that of protamine, because the molecular weight distribution of protamine was relatively narrow (ca. 300 Da). Taken together, these data provided conclusive evidence that a homogeneous conjugation with a stiochiometry of 1:1 between PEG and protamine was achieved.

3.2. Binding Affinity and Neutralization Efficacy. It is well documented that the binding between protamine and heparin is primarily an electrostatic interaction. Both the structural integrity and charge density of protamine appear to be essential for its binding and neutralization activity toward heparin. In this regard, one could speculate that protamine modified by PEG at the N-terminal should preserve most of the heparin binding and neutralizing abilities. To validate this hypothesis, a previously established heparin affinity chromatographic method (*19*) was applied. Table 1 shows the elution ionic strength of the conjugates from a heparin column. As seen, while the original protamine was eluted

Table 1. Properties of PEG−Protamine Conjugates

compound	MW[a] (Da)	conjugation stoichiometry	heparin affinity[b] (NaCl concentration, M)
Protamine	4200	- -	~1.4
PEG^{2000}−Protamine	6400	1:1	~1.3
PEG^{5000}−Protamine	9800	1:1	~1.2

[a] Approximate value as determined by using MALDI-TOF mass analysis. [b] Elution concentration from a heparin affinity column.

with an ionic strength of 1.4 M NaCl, the PEG−protamine conjugates (PEG^{2000}−protamine and PEG^{5000}−protamine) were eluted at lower NaCl concentrations (i.e. 1.3 and 1.2 M, respectively), suggesting that the conjugation process might more or less impair the heparin-binding affinity of protamine. Nevertheless, it is well-known that protamine neutralizes heparin by its stronger affinity to heparin than antithrombin III (AT III). Therefore, the PEG−protamine conjugates should still possess a sufficient heparin-neutralizing ability, since the previous study revealed that AT III was eluted at a lower ionic strength (i.e. 0.75−1.3 M NaCl (*19*)) than those of the PEG−protamine conjugates.

It has been suggested that protamine may possess two active sites, one of which is utilized for heparin neutralization (*26*). Our previous investigation supported this speculation and further suggested that this site was near the C-terminal of the protamine molecule (*19*). In this regard, though most modification methods would result in loss of the biological functions of the parent protein, the N-terminal modification approach employed here might be able to achieve a maximum retention of the heparin-neutralizing ability of protamine. This is because the PEG polymer was conjugated to the N-terminal of protamine, and it was therefore not likely to exert any influence to the binding events that occurred at the C-terminal of protamine. To examine this postulation, a full spectrum of heparin biological assays, including the anti-IIa and anti-Xa chromogenic assays as well as the activated partial thromboplastin time (aPTT) method, was employed. As seen in Figure 5A, the dose required to achieve a complete neutralization of the anti-Xa activity was not significantly affected by PEG conjugation. For instance, each unit of heparin required 3 nmol of protamine to completely neutralize the anti-Xa activity, whereas it would require about 3.2 and 4.3 nmol of PEG^{2000}−protamine and PEG^{5000}−protamine conjugates, respectively, to achieve a full reversal. Interestingly, the sigmoid dose response curve of PEG^{2000}−protamine conjugate almost superimposed with that of native protamine, suggesting a complete retention by the conjugate of protamine's function in neutralizing heparin-induced anti-Xa activity. Figure 5B showed that the anti-IIa activity of heparin was also completely neutralized by protamine, PEG^{2000}−protamine, and PEG^{5000}−protamine conjugates at the protamine/heparin dose ratios of 2, 6.5, and 7 nmol/U, respectively. When comparing with the anti-Xa results seen in Figure 5A, however, PEG modification seemed to result in a larger reduction of the conjugates in protamine's function in neutralizing the anti-IIa activity of heparin. Altogether, the results implicated that conjugation of PEG at the N-terminal of protamine might offset the heparin-neutralizing functions of protamine more on the anti-IIa activity as opposed to the anti-Xa activity.

Heparin neutralization by protamine is often assessed by the activated partial thromboplastin time (aPTT) assay, a method that is used clinically to examine the effects on the intrinsic pathway of the hemostatic system. Figure 5C displays the dose-dependent profiles in the neutralization of heparin's aPTT activity by protamine, PEG^{2000}−protamine, and PEG^{5000}−protamine. As seen, the aPTT activity was completely neutralized by protamine at a protamine/heparin dose ratio of 1.8 nmol/U. On the other hand, this aPTT activity was also completely neutralized by PEG^{2000}−protamine and PEG^{5000}−protamine but at a higher protamine/heparin ratio of 2.3 and 3.9 nmol/U, respectively. Interestingly, the aPTT heparin-neutralizing ability seemed to be inversely proportional to the chain length of PEG, as the protamine conjugate of PEG^{2000} is more potent than that of PEG^{5000} with regard to the heparin neutralizing activity. This phenomenon could be accounted for the fact that the heparin neutralizing ability of PEG−protamine conjugates may be dependent on the size of PEG polymer chain which is presumably in relation to its yielded steric hindrance.

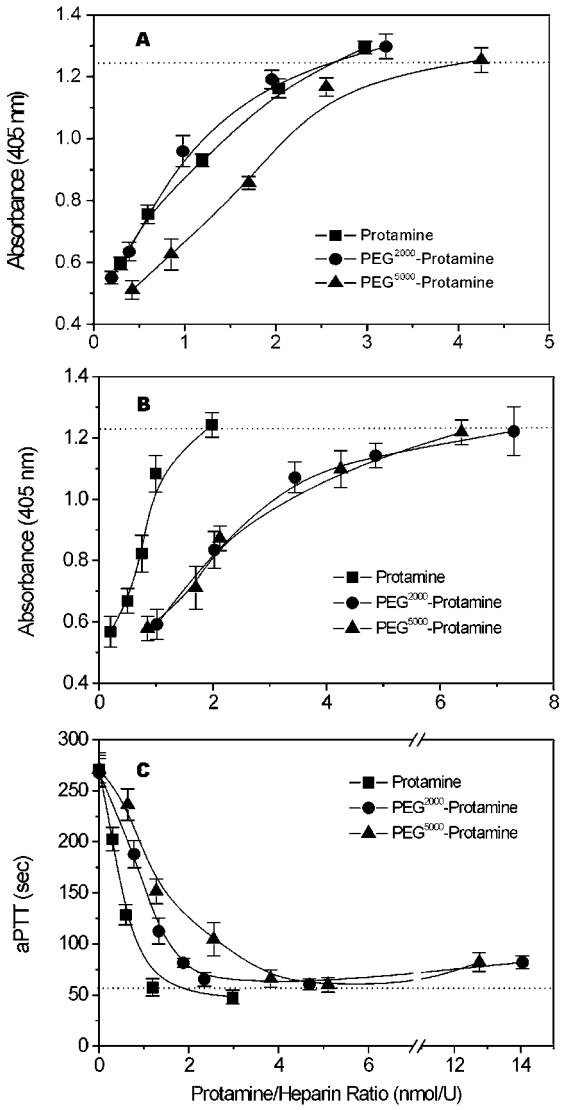

Figure 5. Neutralization of heparin by protamine, PEG^{2000}−protamine, and PEG^{5000}−protamine as measured by (A) anti-Xa, (B) anti-IIa chromogenic assays, and (C) aPTT clotting assay. Dotted line represents the control (i.e. 100% neutralization) for chromogenic assays and the baseline clotting time for clotting assay, respectively.

To further explain the impairment on the anti-heparin ability of the protamine conjugates by PEG modification, it is necessary to consider other factors such as the conjugation site of PEG and the specific binding affinity of protamine toward heparin. It is well documented that thrombin (factor IIa) binds heparin via an electrostatic interaction (*27*), whereas the anti-Xa activity of heparin is mediated by the specific binding of antithrombin III (ATIII) to the pentasaccharide sequence in heparin (*28*). For this reason, neutralization of the anti-Xa activity of heparin would probably require a specific sequence in protamine that possesses a unique heparin binding affinity in order to compete with AT III. If this assumption is true, our previous investigation indicated that this

specific heparin-binding domain evidently would be near the C-terminal of the protamine sequence. To this end, the N-terminal conjugation strategy employed in this study would be very keen in preserving the functions of the PEG−protamine conjugates in neutralizing the anti-Xa activity of heparin. For instance, while the doses required to neutralize the anti-Xa activity of heparin by protamine and the PEG^{2000}−protamine conjugate was about the same, the dose by the PEG^{5000}−protamine conjugate was increased by merely 1.5-fold. On the other hand, since the anti-IIa activity of heparin relies on a nonspecific binding by thrombin, any added PEG polymer chain on protamine would interfere with this nonspecific thrombin binding, resulting in a reduction of the conjugate in neutralizing the anti-IIa activity of heparin. As a consequence, both PEG^{2000}- and PEG^{5000}−protamine conjugates were significantly impaired in their abilities in neutralizing heparin-induced anti-IIa activity, and the doses required to neutralize such a heparin activity was increased by nearly identical 3.5-fold. Because the aPTT activity is mediated by the overall reactions of the coagulation proteins in the intrinsic pathway, it is of no surprise that the impairment on the aPTT neutralization by the conjugates was affected by both PEG conjugation and the chain length of the PEG polymers.

3.3. Complement Function. In general, protamine-induced toxicity is mediated by either a nonimmunological or an immunological pathway (*3*). For the former, the primary event is that the complement proteins bind either to Ig or directly to a particle surface and initiate deleterious complement responses. Therefore, measurements of complement consumption induced by this mechanism can be used as a key index to assess the toxicity of protamine and its PEG-derived analogues. Figure 6A showed the dose-dependent consumption of complement components by protamine and PEG^{5000}−protamine conjugate. As seen, protamine alone did not elicit any detectable complement consumption until its concentration was raised beyond 1 mg/mL, whereas about 30% of complement consumption was seen for the PEG^{5000}−protamine conjugate at a dose of 0.5 mg/mL. Nevertheless, these results did not seem to pose any clinical concern because the concentration was far beyond dose range (i.e. 0.01−0.05 mg/mL) employed clinically following a CPB procedure.

It has been reported that protamine by itself causes the depletion of the complement components in vitro only at a relatively high concentration (*9*). Coadministration of heparin and protamine, however, triggered a significant degree of complement responses at the much lower clinical dose range both in vitro and in vivo (*9*, *10*). Although the exact mechanism of complement activation by heparin and protamine remained unclear, related studies nevertheless suggested that activation of the complement system was mediated by formation of the heparin−protamine complexes, namely HPC. Indeed, this activation requires the HPC aggregates to reach a critical size in order to bind to C1q, the prelude of the activation event, as the binding of C1q moiety with other molecules is known to require the presence of repeating binding sites to bind the multiple heads of C1q molecule (*29*). Therefore, previously we demonstrated that the use of a chain-shortened low molecular weight protamine (LMWP) in HPC formation would significantly attenuate the HPC-induced complement activation in vitro (*20*), primarily due to the presence of an insufficient size or inappropriate structure of the formed HPC.

Following the same theory, protamine (or PEG^{5000}−protamine) was added to serum samples containing an increasing amount of heparin at the dose equivalent to the neutralization ratio (i.e. for each unit of heparin, 10 μg and 50 μg of protamine and PEG^{5000}−protamine were used, respectively, see results in Figure 5) to examine the effects of HPC on the complement system. Figure 6B showed that at a serum heparin concentration between 2.5 and 10 U/mL, which was the dose normally encountered during a cardiovascular surgical procedure, HPC produced by protamine and PEG^{5000}−protamine yielded 60−70% and 40% complement consumption, respectively. Although the CH50 method was a qualitative rather than a quantitative assay for measuring complement activation, the observed difference between these two HPC aggregates clearly suggested that the HPC by PEG^{5000}−protamine yielded significantly reduced complement activation. This phenomenon might be rationalized by the charge neutralization, and shielding effects of PEG on protamine abrogated the unwanted interactions of the formed HPC with complement proteins, alleviating the induced toxic side effects.

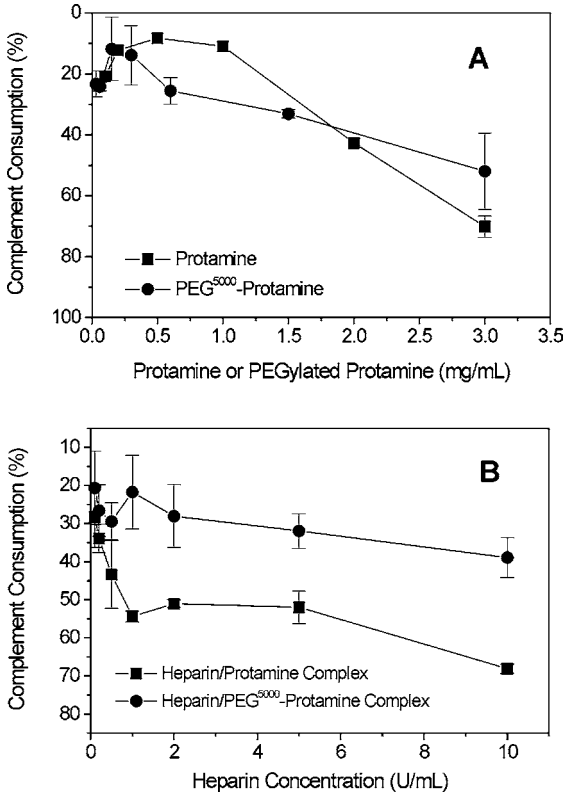

Figure 6. (A) Effects of protamine and PEG^{5000}−protamine alone on complement consumption. (B) Effects of heparin−protamine complexes and heparin-PEG^{5000}−protamine complexes on complement consumption. Complexes were prepared by the addition of protamine (or PEG^{5000}−protamine) to serum samples containing an increasing concentration of heparin at the respective neutralization ratio. That is, for each unit of heparin, 10 μg or 50 μg of protamine and PEG^{5000}−protamine conjugate, respectively, were added for the formation of heparin-(PEG^{5000}−protamine) complexes (HPC).

It has been shown that the CPB-induced inflammatory response can be significantly diminished via the reduction of complement activation. Clinical strategies aimed at reducing complement activation thus far include the use of corticosteroids (*30*), specific complement inhibitors (e.g. compstatin that inhibits the C3-mediated activation (*31*), and anti-properdin monoclonal antibody that would block the interaction of properdin and C3 convertase (*32*)). Although such strategies have been shown to be relatively useful, there still exist concerns of utilizing

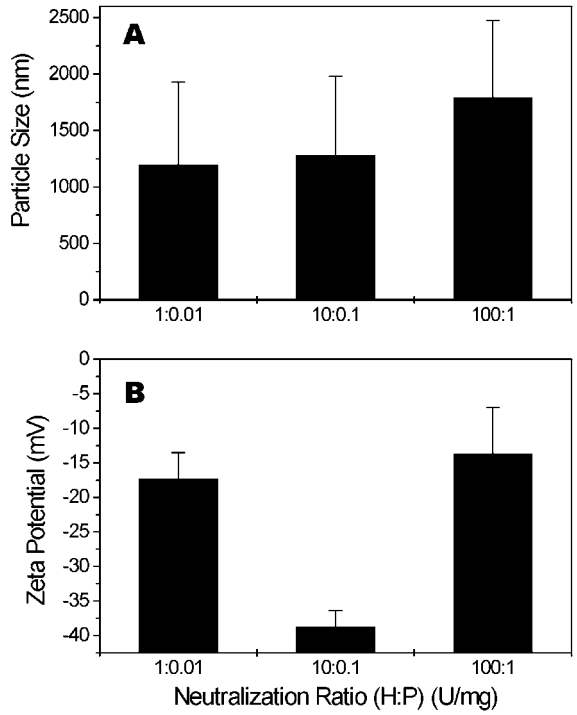

Figure 7. (A) Particle size and (B) zeta potential of the HPC aggregates formed by various amounts of heparin neutralized by their equivalent protamine. Data are presented as mean ± standard deviation.

these approaches, such as that compounds blocking the complement pathways may cause an increased susceptibility to pathogenic infection. Indeed, these drawbacks have already been reported in the literature with the use of soluble complement receptor 1 (sCR1) (*33*). In this regard, our approach by preventing the interaction with complement proteins instead of blocking the complement system should be more beneficial for use in clinical practice.

3.4. Particle Size and Zeta Potential. As discussed previously, complement activation by HPC was governed by their binding with C1q. Therefore, it deems necessary to further examine the particle size and zeta potential of the formed HPC aggregates. To determine the particle size and zeta potential of HPC, three concentrations (i.e. 1, 10, 100 U/mL) of heparin solution were mixed with appropriate amounts of protamine (or PEG−protamine conjugates) by using the previously determined neutralization ratios to yield the HPC aggregates. Figure 7 displayed the size distribution and zeta potential of the formed HPCs. As seen, while HPC aggregates with a mean size greater than 1000 nm occurred at all three test concentrations, the zeta potentials of these aggregates were −17.3, −38.7, and −13.7 for HPC formed with the heparin concentration of 1, 10, and 100 U/mL, respectively. Although the size of the HPC aggregates was sometimes influenced by the mixing speed (i.e. the size might be increased to 5000 nm if mixing of heparin and protamine was conducted more rapidly), the data nevertheless suggested that surface of the HPC aggregates was polyanionic; which was in good agreement with findings reported elsewhere (*34*). On the other hand, the aggregates produced by mixing heparin with PEG−protamine displayed a significantly reduced size, as in the range of ∼60 nm for heparin-PEG^{5000}−protamine complexes (data not shown). In fact, five out of the six measurements did not provide meaningful readings when using the light-scattering detection method, suggesting that the hydrophilic PEG polymer might help solubilize the HPC resulting in virtually no detectable aggregates when mixing heparin with the PEG−protamine conjugates. In concurrence, these PEG−protamine-derived HPC aggregates neither disclosed any meaningful value in the zeta potential measurement because soluble aggregates could not reflect light.

Introduction of PEG to a cationic carrier peptide as a block or graft copolymer is a well-known approach for stabilization of the cationic peptide and DNA complexes in gene delivery systems (*35*, *36*). While the cationic PEG−peptide conjugate hybrids with anionic DNA in an aqueous medium, the electrostatic interaction between anionic DNA segments and cationic counterparts is known to drive the formation of a polyelectrolyte complex inner core, whereas PEG segments constitute a PEG surrounding corona (*37*). In this regard, our result seemed to be in good agreement with this phenomenon that the cationic PEG−protamine conjugate interacted with anionic heparin to form such soluble micelle. As a consequence, the surrounding hydrophilic PEG segments of the core HPC aggregate could not only improve the aqueous solubility of the formed aggregate, but also protect the aggregate from serum protein binding, owing to the steric hindrance effect of the flexible PEG chains.

Rossmann et al. studied the composition of the heparin protamine aggregates in vitro and in vivo using different staining procedures and light or electron microscopy (*34*). The heparin−protamine complexes were described as particles of up to 500 nm in diameter, slightly oval, and sharply contoured. The surface of these aggregates was polyanionic, thus allowing them to bind strongly to scavenger receptor-bearing cells (e.g. macrophage) and trigger varying responses via the release of mediators such as thromboxane A2. Stehle et al. suggested that the amount, size, and charge density of the complexes were the determinants that evoke the deleterious complement responses (*38*). In this study, owing to the possible existence of the polyelectrolyte complex micelles structure between the cationic PEG−protamine conjugate and anionic heparin, a different mechanism by which the PEG−protamine conjugate could function might thus be as follow: First, PEG is a adhesion-resistant polymer that forms a flexible shield on the surface of HPC, avoiding the recognition by the immune system and binding with complement proteins. Second, the grafted hydrophilic PEG polymer enhances the solubility and reduces the size of HPC, therefore decreasing the magnitude of complement responses. (Note: the larger the HPC, the more significant the complement responses). In addition, the increased solubility of PEG−protamine conjugate would improve its stability, compatibility, and bioavailability, favorable pharmaceutical properties for dosage formulation. Overall, modification of protamine with PEG appears to be an attractive strategy to improve the pharmacological/pharmaceutical function of protamine for its important clinical application.

4. CONCLUSION

A simple approach via PEG modification of protamine was successfully used to create a potentially less toxic protamine alternative. On the basis of the selectivity of NHS conjugation chemistry and the unique composition of the protamine sequence, a mono-PEG molecule was covalently linked to the protamine N-terminal residue, producing a linear PEG−protamine conjugate. The conjugates maintain the high reactivity of protamine to heparin and graft the steric effect of PEG to the surface

of the HPC, therefore enabling an improved pharmacological activity. In addition, the grafted PEG polymer increases the solubility of HPC aggregates, a favorable pharmaceutical property for dosage formulation. Thus, it is rational to suggest that the PEG−protamine conjugate could be an effective, but less toxic, protamine alternative. While there is no real alternative for reducing heparin-inducing bleeding risks without inflicting patients with protamine-associated toxic effects presently, the PEG−protamine conjugate discloses many attractive pharmacological and pharmaceutical properties to be a safer heparin antidote. Additional studies focused on investigation of the complement inactivation mechanism, immunogenicity, and in vivo efficacy of the PEG−protamine conjugates are currently in progress in our laboratories.

LITERATURE CITED

(1) Conrad, S. A., and Rycus, P. T. (1998) Extracorporeal life support 1997. *ASAIO J. 44*, 848−852.

(2) Association, A. H. (1999) *2000 heart and stroke statistical update*, Amercian Heart Association, Dallas, TX.

(3) Horrow, J. C. (1985) Protamine: a review of its toxicity. *Anesth. Analg. 64*, 348−361.

(4) Kimmel, S. E., Sekeres, M. A., Berlin, J. A., Goldberg, L. R., and Strom, B. L. (1998) Adverse events after protamine administration in patients undergoing cardiopulmonary bypass: risks and predictors of under-reporting. *J. Clin. Epidemiol. 51*, 1−10.

(5) Gupta, S. K., Veith, F. J., Ascer, E., Wengerter, K. R., Franco, C., Amar, D., el-Gaweet, E. S., and Gupta, A. (1989) Anaphylactoid reactions to protamine: an often lethal complication in insulin-dependent diabetic patients undergoing vascular surgery. *J. Vasc. Surg. 9*, 342−350.

(6) Neidhart, P. P., Meier, B., Polla, B. S., Schifferli, J. A., and Morel, D. R. (1992) Fatal anaphylactoid response to protamine after percutaneous transluminal coronary angioplasty. *Eur. Heart J. 13*, 856−858.

(7) Kien, N. D., Quam, D. D., Reitan, J. A., and White, D. A. (1992) Mechanism of hypotension following rapid infusion of protamine sulfate in anesthetized dogs. *J. Cardiothorac. Vasc. Anesth. 6*, 143−147.

(8) Conahan, T. J., Andrews, R. W., and MacVaugh, H., (1981) Cardiovascular effects of protamine sulfate in man. *Anesth. Analg. 60*, 33−36.

(9) Rent, R., Ertel, N., Eisenstein, R., and Gewurz, H. (1975) Complement activation by interaction of polyanions and polycations. I. Heparin-protamine induced consumption of complement. *J. Immunol. 114*, 120−124.

(10) Cavarocchi, N. C., Schaff, H. V., Orszulak, T. A., Homburger, H. A., Schnell, W. A., Jr., and Pluth, J. R. (1985) Evidence for complement activation by protamine-heparin interaction after cardiopulmonary bypass. *Surgery 98*, 525−531.

(11) Yang, V. C., Port, F. K., Kim, J. S., Teng, C. L., Till, G. O., and Wakefield, T. W. (1991) The use of immobilized protamine in removing heparin and preventing protamine-induced complications during extracorporeal blood circulation. *Anesthesiology 75*, 288−297.

(12) Levy, J. H., Cormack, J. G., and Morales, A. (1995) Heparin neutralization by recombinant platelet factor 4 and protamine. *Anesth. Analg. 81*, 35−37.

(13) Michelsen, L. G., Kikura, M., Levy, J. H., Lee, M. K., Lee, K. C., Zimmermann, J. J., and Szlam, F. (1996) Heparinase I (neutralase) reversal of systemic anticoagulation. *Anesthesiology 85*, 339−346.

(14) Hendrikx, M., Leunens, V., Vandezande, E., Wallyn, A., and Flameng, W. (1997) The use of a heparin removal device: a valid alternative to protamine. *Int. J. Artif. Organs 20*, 166−174.

(15) Asimakopoulos, G. (1999) Mechanisms of the systemic inflammatory response. *Perfusion 14*, 269−277.

(16) Wan, S., LeClerc, J. L., and Vincent, J. L. (1997) Inflammatory response to cardiopulmonary bypass: mechanisms involved and possible therapeutic strategies. *Chest 112*, 676−692.

(17) Rinder, C. S., Rinder, H. M., Smith, B. R., Fitch, J. C., Smith, M. J., Tracey, J. B., Matis, L. A., Squinto, S. P., and Rollins, S. A. (1995) Blockade of C5a and C5b-9 generation inhibits leukocyte and platelet activation during extracorporeal circulation. *J. Clin. Invest. 96*, 1564−1572.

(18) Soulika, A. M., Khan, M. M., Hattori, T., Bowen, F. W., Richardson, B. A., Hack, C. E., Sahu, A., Edmunds, L. H., Jr., and Lambris, J. D. (2000) Inhibition of heparin/protamine complex-induced complement activation by Compstatin in baboons. *Clin. Immunol. 96*, 212−221.

(19) Chang, L. C., Lee, H. F., Yang, Z., and Yang, V. C. (2001) Low molecular weight protamine (LMWP) as nontoxic heparin/low molecular weight heparin antidote (I): preparation and characterization. *AAPS PharmSci 3*, E17.

(20) Chang, L. C., Liang, J. F., Lee, H. F., Lee, L. M., and Yang, V. C. (2001) Low molecular weight protamine (LMWP) as nontoxic heparin/low molecular weight heparin antidote (II): in vitro evaluation of efficacy and toxicity. *AAPS PharmSci 3*, E18.

(21) Lee, L. M., Chang, L. C., Wrobleski, S., Wakefield, T. W., Yang, V. C., Liang, J. F., Lee, H. F., and Yang, Z. (2001) Low molecular weight protamine as nontoxic heparin/low molecular weight heparin antidote (III): preliminary in vivo evaluation of efficacy and toxicity using a canine model. *AAPS PharmSci 3*, E19.

(22) Metz, S., and Horrow, J. C. (1994) Protamine and Newer Heparin Antagonists. *Pharmacology & Physiology in Anesthetic Practice* (Stoelting, R. K., Ed.) pp 1−15, J. B. Lippincott Company, Philadelphia.

(23) Francis, G. E., Fisher, D., Delgado, C., Malik, F., Gardiner, A., and Neale, D. (1998) PEGylation of cytokines and other therapeutic proteins and peptides: the importance of biological optimisation of coupling techniques. *Int. J. Hematol. 68*, 1−18.

(24) Jaques, L. B. (1979) Heparins−anionic polyelectrolyte drugs. *Pharmacol. Rev. 31*, 99−166.

(25) Roberts, M. J., Bentley, M. D., and Harris, J. M. (2002) Chemistry for peptide and protein PEGylation. *Adv. Drug Delivery Rev. 54*, 459−476.

(26) Wolzt, M., Weltermann, A., Nieszpaur-Los, M., Schneider, B., Fassolt, A., Lechner, K., Eichler, H. G., and Kyrle, P. A. (1995) Studies on the neutralizing effects of protamine on unfractionated and low molecular weight heparin (Fragmin) at the site of activation of the coagulation system in man. *Thromb. Haemost. 73*, 439−443.

(27) Casu, B. (1985) Structure and biological activity of heparin. *Adv. Carbohydr. Chem. Biochem. 43*, 51−134.

(28) Rosenberg, R. (1987) Basic Principles and Clinical Practice. *Hemostasis and Thrombosis* (Colman, R. W., Marder V. J., Hirsh J., Eds.) pp 1373−1392, J. B. Lippincott Company, Philadelphia.

(29) Cooper, N. R. (1983) Activation and regulation of the first complement component. *Fed. Proc. 42*, 134−138.

(30) Asimakopoulos, G., and Gourlay, T. (2003) A review of antiinflammatory strategies in cardiac surgery. *Perfusion 18*, 7−12.

(31) Morikis, D., Assa-Munt, N., Sahu, A., and Lambris, J. D. (1998) Solution structure of Compstatin, a potent complement inhibitor. *Protein Sci. 7*, 619−627.

(32) Gupta-Bansal, R., Parent, J. B., and Brunden, K. R. (2000) Inhibition of complement alternative pathway function with anti-properdin monoclonal antibodies. *Mol. Immunol. 37*, 191−201.

(33) Swift, A. J., Collins, T. S., Bugelski, P., and Winkelstein, J. A. (1994) Soluble human complement receptor type 1 inhibits complement-mediated host defense. *Clin. Diagn. Lab. Immunol. 1*, 585−589.

(34) Rossmann, P., Matousovic, K., and Horacek, V. (1982) Protamine-heparin aggregates. Their fine structure, histochemistry, and renal deposition. *Virchows Arch. B Cell Pathol. Incl. Mol. Pathol. 40*, 81−98.

(35) Choi, Y. H., Liu, F., Kim, J. S., Choi, Y. K., Park, J. S., and Kim, S. W. (1998) Poly(ethylene glycol)-grafted poly-L-lysine as polymeric gene carrier. *J. Controlled Release 54*, 39−48.
(36) Toncheva, V., Wolfert, M. A., Dash, P. R., Oupicky, D., Ulbrich, K., Seymour, L. W., and Schacht, E. H. (1998) Novel vectors for gene delivery formed by self-assembly of DNA with poly(L-lysine) grafted with hydrophilic polymers. *Biochim. Biophys. Acta 1380*, 354−368.
(37) Kataoka, K., Harada, A., and Nagasaki, Y. (2001) Block copolymer micelles for drug delivery: design, characterization and biological significance. *Adv. Drug Delivery Rev. 47*, 113−131.
(38) Stehle, G., Wunder, A., Sinn, H., Schrenk, H. H., Friedrich, E. A., Dempfle, C. E., Maier-Borst, W., and Heene, D. L. (1995) Complexes of a modified low-molecular-weight heparin with protamine are predominantly cleared by a macrophage scavenger receptor-mediated process in rats. *J. Surg. Res. 58*, 197−204.

BC0499735

Cationic Lipids with Increased DNA Binding Affinity for Nonviral Gene Transfer in Dividing and Nondividing Cells

Ajit S. Narang,[†] Laura Thoma,[†] Duane D. Miller,[†] and Ram I. Mahato[†,‡,*]

Departments of Pharmaceutical Sciences and Biomedical Engineering, University of Tennessee Health Science Center, Memphis, Tennessee 38163. Received July 27, 2004; Revised Manuscript Received September 30, 2004

Effect of headgroup structure on catonic lipid-mediated transfection was investigated with either a (i) tertiary amine, (ii) quaternary amine with a hydroxyl, or (iii) quaternary amine with mesylate as headgroups. Liposomes were formulated using cholesterol or dioleoyl phosphatidyl ethanolamine (DOPE) as colipids, and transfection efficiencies were determined in rapidly dividing colon carcinoma (CT 26) and rat aortic smooth muscle (RASM) cells as well as in nondividing human pancreatic islets using luciferase and green fluorescent protein expression plasmids, pcDNA3-Luc and pCMS-EGFP, respectively. Liposome/pDNA complexes were evaluated for DNA conformational state by circular dichroism (CD), DNA condensation by electrophoretic mobility shift assay (EMSA), particle size and zeta potential by laser diffraction technique, and surface morphology by transmission electron microscopy (TEM). Encouraging transfection results were obtained with the mesylate headgroup based lipid in liposome formulations with DOPE as a colipid, which were higher than the commercially available Lipofectamine formulation. We hypothesize that the additional hydrogen bonding or covalent interactions of the headgroup with the plasmid DNA, leading to higher binding affinity of the cationic lipids to pDNA, results in higher transfection. This hypothesis is supported by TEM observations where elongated complexes were observed and more lipid was seen associated with the DNA.

INTRODUCTION

Cationic lipid-based nonviral gene delivery system is an attractive approach for therapeutic gene transfer. Most cationic lipids have three parts: (i) a hydrophobic lipid anchor group, (ii) linker group, such as an ester, amide, or carbamate, and (iii) a positively charged headgroup, which interacts with pDNA, leading to its condensation (*1*, *2*). Among all the basic components of the cationic lipid, the type of headgroup has been shown to have a dominant role in transfection efficiency and toxicity. Three functional properties characterize the activity of any cationic liposome formulation: (i) efficient DNA condensation, (ii) increased cellular uptake due to interaction of positively charged complexes with negatively charged biological surfaces, and (iii) membrane fusion or transient membrane destabilization with the plasma membrane or the endosome to achieve delivery into the cytoplasm while avoiding degradation in the lysosomal compartment (*3*).

Since the introduction in 1987 of the transfection reagent Lipofectin, a 1:1 w/w mixture of the cationic lipid *N*-[1-(2,3-dioleoyloxy)propyl]-*N*,*N*,*N*-trimethylammonium (DOTMA) and dioleoyl phosphatidyl ethanolamine (DOPE) (*4*), many cationic lipids bearing either a single tertiary or quaternary ammonium headgroup or which contain protonatable polyamines linked to dialkyl or cholesterol anchors have been designed for transfection of a variety of cell types in culture (*5*, *6*). Commercially available cationic lipids used as liposome formulations or alone for gene delivery include DOTMA; 2,3-dioleyloxy-*N*-[2-spermine carboxamide] ethyl-*N*,*N*-dimethyl-1-propanammonium trifluoroacetate (DOSPA), 1,2-bis(oleoyloxy)-3-(trimethylammonio)propane (DOTAP), *N*-[1-(2,3-dimyristyloxy)propyl]-*N*,*N*-dimethyl-*N*-(2-hydroxyethyl)ammonium bromide (DMRIE), *3β*-[*N*-(*N*′,*N*′-dimethylaminoethane)carbamoyl]cholesterol (DC-Chol), and dioctadecyl amidoglyceryl spermine (DOGS, Transfectam). A few such compounds have also been used in initial clinical studies (*7*). However, many of the cationic lipids used in early clinical trials such as DC-Chol (*8*), DMRIE (*9*), and GL-67 (*10*), although effective in vitro, have proven inefficient in vivo, especially when compared with viral vectors.

Based on the structures of their cationic headgroups, cationic lipids can be classified into quaternary ammonium lipids, lipopolyamines, cationic lipids bearing both quaternary ammonium and polyamine moieties, amidinium and guanidinium salt lipids, and heterocyclic cationic lipids. A quaternary ammonium headgroup is widely used in many of the established cationic lipids such as DOTAP, DOTMA, and DMRIE, with the exception of Lipofectamine, which is a combination of both a polyamine and a quaternary cation. There are fewer lipids containing a primary, secondary, or tertiary amine headgroup. An example is DC-Chol, with a tertiary amino headgroup linked to cholesterol (*5*).

We have earlier studied the effect of cationic lipid structures, cationic lipid to colipid molar ratios, liposome size, charge ratio, and DNA dose on in vivo gene expression (*11*). Since liposome/plasmid complexes did not disperse well inside the solid tumor after local intratumoral injection (*12*) but showed beneficial effect in tumor regression (*13*), we later developed water soluble lipopolymers for gene delivery (*14*, *15*). Although water

* Corresponding author. Ram I. Mahato, Ph.D., Department of Pharmaceutical Sciences, University of Tennessee Health Science Center, 26 S. Dunlap Street, Feurt Building, Room 413, Memphis, TN 38163. Tel: (901) 449 6929. Fax: (901) 448 6092. E-mail: rmahato@utmem.edu.

[†] Department of Pharmaceutical Sciences.

[‡] Department of Biomedical Engineering.

10.1021/bc049818q CCC: $30.25 © 2005 American Chemical Society
Published on Web 12/31/2004

soluble lipopolymers were effective in transfecting various cells, they were not effective in transfecting nondividing human pancreatic islets. Therefore, we decided to use Lipofectamine for gene delivery to human islets. We observed low transfection efficiency, possibly due to poor nuclear translocation, as the nuclear membrane remains intact in these cells at all times (*16*, *17*). This is also because islets are a compact cluster of ~1000 nondividing cells (*18*). To further enhance the transfection efficiency in both dividing and nondividing cells, we have designed novel cationic lipids based on C_{18} monounsaturated oleoyl esters of glycerol backbone to be used as liposomes. C_{18} chain length was selected based on the previous studies by various groups who have shown that carbon chain length significantly influences transfection efficiency, and C_{18} is the most commonly used and efficient in transfection (*3*, *11*, *19*). Moreover, smaller chain length lipids tend to provide more fluidity and weaker binding (*19*, *20*). Furthermore, introduction of unsaturation into carbon chain is known to give higher transfection (*21*).

MATERIALS AND METHODS

RPMI medium 1640 and trypsin−ethylenediaminetetraacetic acid (EDTA) were procured from Gibco, Invitrogen Corporation (Grand Island, NY). Dulbecco's phosphate-buffered saline (DPBS), heat-inactivated fetal bovine serum (FBS), and penicillin (10000 units/mL penicillin G sodium)−streptomycin solution (10000 μg/mL streptomycin sulfate) in 0.85% saline were purchased from Cellgro, Mediatech, Inc. (Herndon, VA). Luciferase Assay System, Luciferase Cell Culture Lysis Reagent 5X (CCLR), and Sca I restriction enzyme were procured from Promega Corporation (Madison, WI). QIAfilter plasmid maxi kit was purchased from Qiagen, Inc. (Valencia, CA); 96-well flat-bottom white LIA plate from Greiner Bio-One, Inc. (Longwood, FL); BCA protein assay kit from Pierce (Rockland, IL); Terrific Broth (Modified), Luria Agar (Miller's LB agar), glycerol, agarose, ethidium bromide aqueous solution (10 mg/mL), 2-propanol, absolute ethyl alcohol, sodium hydroxide pellets, oleoyl chloride, 2-bromoethanol, and various organic solvents including chloroform, acetone, ethanol, methylene chloride, phosphomolybdic acid spray reagent, and *N*,*N*-dimethylformamide (DMF) were purchased from Sigma-Aldrich Co. (St. Louis, MO). SURE-2 supercompetent cells were purchased from Stratagene, Inc. (La Jolla, CA), SOC medium from Invitrogen (Carlsbad, CA), 3-(dimethylamino)-1,2-propanediol, silica gel, and methanesulfonyl chloride from Aldrich Chemical Co., Inc. (Milwakee, WI), deuterated chloroform from Cambridge Isotope Labs, Inc. (Andover, MA), and cholesterol and 1,2-dioleoyl-*sn*-glycero-3-phosphoethanolamine (DOPE) from Avanti Polar Lipids, Inc. (Alabaster, AL). Carbon-coated 300-mesh copper grids were purchased from Electron Microscopy Sciences, Inc. (Fort Washington, PA). pCMS-EGFP plasmid was procured from BD Biosciences Clontech (Palo Alto, CA) and pcDNA3-Luc plasmid was a kind gift from Expression Genetics, Inc. (Huntsville, AL).

Synthesis and Purification. The synthesis scheme of tertiary, quaternary, and mesylate cationic lipids is shown in Figure 1. 3-(Dimethylamino)-1,2-propanediol (I) was reacted with oleoyl chloride (II) in anhydrous chloroform overnight at room temperature. The reaction mixture was extracted sequentially with 0.1 N sodium hydroxide, water and brine followed by dehydration in sodium sulfate and evaporation of chloroform in a rotary evaporator. Complete removal of starting materials was ascertained by ^{1}H nuclear magnetic resonance (NMR) spectroscopy using Bruker ARX-300 (Bruker Biospin

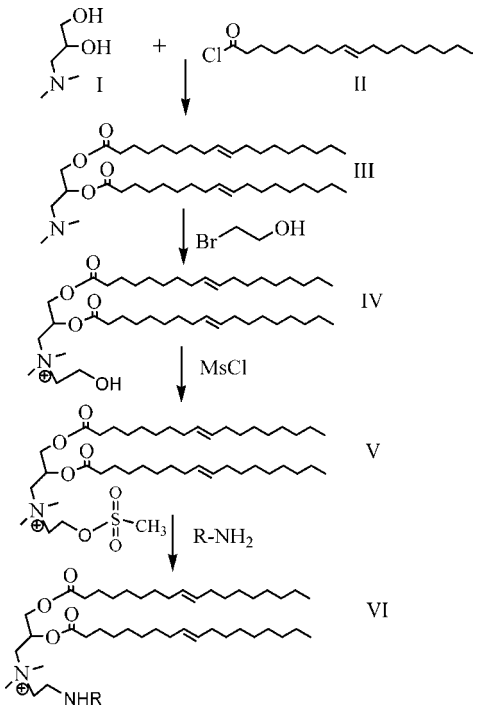

Figure 1. Synthesis scheme for 3-(dimethylamino)-1,2-dioleoylpropanediol (DADP, III), 3-(*N*-2-hydroxyethyl dimethylamino)-1,2-dioleoylpropanediol (HE-DADP, IV), and 3-(*N*-ethyl-2-methanesulfonyldimethylamino)-1,2-dioleoylpropanediol (EMS-DADP, V) cationic lipids starting with 3-(dimethylamino)-1,2-propanediol (I) esterification using oleoyl chloride (II), followed by quaternization using 2-bromoethanol and mesylation of the free hydroxyl group. EMS-DADP can be attached to various amine headgroups to yield transfection reagents with the structure (VI).

Corporation, Billerica, MA). The product, 3-(dimethylamino)-1,2-dioleoylpropanediol (DADP, III), was dehydrated in a desiccator and stored at −20 °C (yield >90%). The quaternary amine compound, 3-(*N*-2-hydroxyethyldimethylamino)-1,2-dioleoylpropanediol (HE-DADP, IV), was synthesized by reacting (III) in 1:1 molar quatity in *N*,*N*-dimethylformamide at 105 °C for 24 h followed by solvent evaporation under high vacuum. Reaction conditions were optimized through ^{1}H NMR monitoring to minimize the formation of side products and maximize the reaction yield, which was 80%. The product was identified by both NMR and electrospray ionization-mass spectrometry (ESI-MS) using Bruker Esquire-LC Ion Trap LC/MS (Bruker Biospin Corporation, Billerica, MA). The mesylate derivative, 3-(*N*-ethyl-2-methanesulfonyldimethylamino)-1,2-dioleoylpropanediol (EMS-DADP, V), was synthesized by reacting HE-DADP with methanesulfonyl chloride in the presence of triethylamine as the base, in methylene chloride on ice, followed by room temperature, for 3 h. Following characterization using thin-layer chromatography (TLC) using acetone/NaOH medium with spot visualization using phosphomolybdic acid/heat gun treatment, the reaction mixture was extracted using silica gel chromatography using acetone: 0.1 N aqueous NaOH (97/3) as the mobile phase. The Product eluted in the second fraction at an $R_f \sim 0.6$. purified product was identified by both NMR and ESI-MS.

Plasmid Preparation and Purification. Luciferase expression plasmid, pcDNA3-Luc, driven by cytomegalovirus (CMV) promoter, and enhanced green fluorescent protein (EGFP) expression plasmid, pCMS-EGFP, were transformed in SURE-2 supercompetent cells. Colonies were grown in 50 μg/mL ampicillin containing LB Agar

plates, followed by growth of single colonies in ampicillin containing terrific broth media. After sufficient bacterial growth, the cells were pelleted by centrifugation at 5000*g* and 4 °C for 20 min followed by plasmid extraction using QIAfilter plasmid maxiprep kit as per vendor's protocol. Plasmid purity was assessed by UV spectrophotometry ($A_{260/280} > 1.75$), agarose gel electrophoresis, and restriction digestion using *Sca I* enzyme.

Preparation of Liposomes and Lipid/Plasmid Complexes. Liposomes were prepared from a cationic lipid and a colipid (cholesterol or DOPE) at various molar ratios. Briefly, lipids were mixed in chloroform at desired molar ratios and evaporated to dryness in a 50-mL round-bottom flask using a rotary vacuum evaporator. Ethanol was used in the case of EMS-DADP due to the limited solubility of the mesylate compound in chloroform. The lipid film was hydrated in purified water to produce multilamellar vesicles, which were passed through an extruder (Lipex Biomembranes, Vancouver, Canada) using 100, 400, and 800 nm pore size polycarbonate membrane 10 times. The liposomes were stored at 4 °C as colloidal dispersions until used.

Plasmid and cationic liposomes were diluted separately to a volume of 250 μL with a final glucose concentration of 5% w/v, and then the DNA was added to the liposomes with mild mixing by pipeting. Complex formation was allowed to proceed for 45 min at room temperature. Lipid/plasmid complexes of different charge ratios were prepared by adjusting the stoichiometry of plasmid and cationic liposomes. The complexes were characterized for condensation efficiency, particle size, and ξ-potential as described previously (*11*, *22*, *23*). Briefly, complex formation and DNA condensation were determined using 1% agarose gel electrophoresis at 60V. The mean particle size of lipid/plasmid complexes was determined at 90° by dynamic light scattering using 90Plus Particle Sizer (Brookhaven Instruments Corp., Holtsville, NY). Particle size data is reported as a mean ± SD of three samples. ξ-Potential was measured by measuring electrophoretic mobility in aqueous solution at 25 °C and pH 7 utilizing a 30 mW laser and 0 to 3.2 kV/m field strength. The ξ-potential is reported as an average of 10 separate readings for a single sample.

Cell Culture and Transfection. Colon carcinoma (CT-26) and rat aortic smooth muscle (RASM) cells were cultured in 162 cm^2 flasks in RPMI 1640 media supplemented with 10% FBS and 1% penicillin/streptomycin antibiotic−antimycotic mixture. About 50 000 cells were plated in each well of 12-well cell culture plates. When the cells reached ~80% confluency (about 48 h after plating), cells were washed with cold Dulbecco's phosphate buffered saline (DPBS) and were incubated with cationic liposome/pDNA complexes in 500 μL serum free medium. At 6 h posttransfection, the culture media was replaced with serum containing media. In the case of EGFP expression plasmid, cells were incubated for additional 46−48 h and analyzed for transfection efficiency by fluorescence microscopy and flow cytometry. For luciferase expression plasmid, 48 h posttransfection the cells were washed with cold PBS and lysed in 500 μL of luciferase cell culture lysis reagent. Total protein was measured using BCA protein assay kit. Luciferase activity was measured in terms of relative light units (RLU) using a 96-well plate Labsystems Luminoskan RS luminometer (Albertville, MN). Human pancreatic islets were isolated, purified, counted, and cultured as described earlier (*16*, *17*). For transfection experiments, 1000 I.E. were suspended in 48-well plates and incubated for 12 h with pDNA/liposome complexes at the dose of 1 μg/well, followed by addition of more media and incubation at 37 °C in 5% CO_2 incubator for 48 h until cell lysis. $N = 6$ replicas were used for each sample.

Circular Dichroism. Circular dicrhroism (CD) spectra of plasmid DNA and pDNA/liposome complexes were obtaind using the Aviv 62A spectrometer (Lakewood, NJ). Samples were scanned through a wavelength range of 220−360 nm at 25 °C using a 0.5 mL quartz cuvette, with a path length of 1 cm. Each sample was scanned four times with an integration time of 5 s, and the values were averaged. Scanning was done at 1 nm steps, and the slit width was 1 nm. Liposome/pDNA complexes were prepared at 3/1 +/− charge ratio at 50 μg/mL pDNA concentration. Sample values were subtracted from those obtained for dextrose solution (for pDNA) or corresponding liposome solution in dextrose (for liposome/pDNA complexes) as blank.

Transmission Electron Microscopy. Liposome/pDNA complexes prepared at 3/1 (+/−) charge ratio were visualized by transmission electron microscopy (TEM) using 300-mesh carbon coated copper (Cu) grids, at 60 kV and magnifications ranging from 40 000× to 300 000×. Complexes were prepared at 3/1 charge ratio and 0.01 μg/μL pDNA concentration. Ten microliter complexes were loaded on the Cu grid for 2 min followed by blotting of the excess liquid and incubation for another 2 min with 1% uranyl acetate followed by blotting. The grid was air-dried for another 2 min and visualized under the electron microscope. Digital images were captured using the instrument software.

Statistical Analysis. Statistical significane of differences between samples was evaluated using one-way and two-way ANOVA using SPSS software (SPSS Inc., Chicago, IL) with Tukey's posthoc analysis. Significance level used for all studies was $p = 0.05$.

RESULTS

Syntheses and Purification. Tertiary amine (DADP, III), quaternary amine (HE-DADP, IV), and mesylate (EMS-DADP, V) derivatives of a two-chain fatty acid containing cationic lipid with only one positively charged headgroup were synthesized using dimethylaminoglycerol (I) as a template (Figure 1). Oleoyl chloride (II) was conjugated to the free hydroxyls of the glycerol backbone by esterification in chloroform followed by extraction in a series of aqueous solutions to give DADP. DADP was converted to HE-DADP by reaction with 2-bromoethanol in *N*,*N*-dimethylformamide, followed by mesylation in methylene chloride to yield EMS-DADP. Purity of the isolated compounds was assessed by both NMR and electrospray ionization-mass spectroscopy (ESI-MS). The mesylate compound was further converted to polyamine derivative (VI) using polyethyleneimine of low molecular weight (PEI 423) by simple heating.

NMR results of DADP are as follows (Figure 2a). ^{1}H NMR (300 MHz, chloroform-d_1): δ ~0.8−1.0 ppm (H of terminal (CH_3) of lipid chains (a)); δ ~1.2−1.7 (H of (CH_2) methylenes of lipid chains except the ones neighboring the double bond and the carbonyl (b)); δ ~2.0−2.1 (H of (CH_2) methylenes of lipid chains neighboring the double bond (c)); δ ~5.3−5.5 (H of (CH=) groups of lipid chains participating in double bond (d)); δ ~2.1−2.3 (H of (CH_3) methyl groups attached to the tertiary nitrogen (e)); δ ~4.3−4.4 (H of (CH_2) methylene of glycerol backbone (f)); δ ~2.2−2.4 (H of (CH_2) methylenes next to carbonyl on the lipid chains (g)); δ ~4.1 (H of (CH) from the glycerol backbone (h)); δ ~2.3−2.5 (H of (CH_2) methylene of the glycerol backbone connecting the amine (i)).

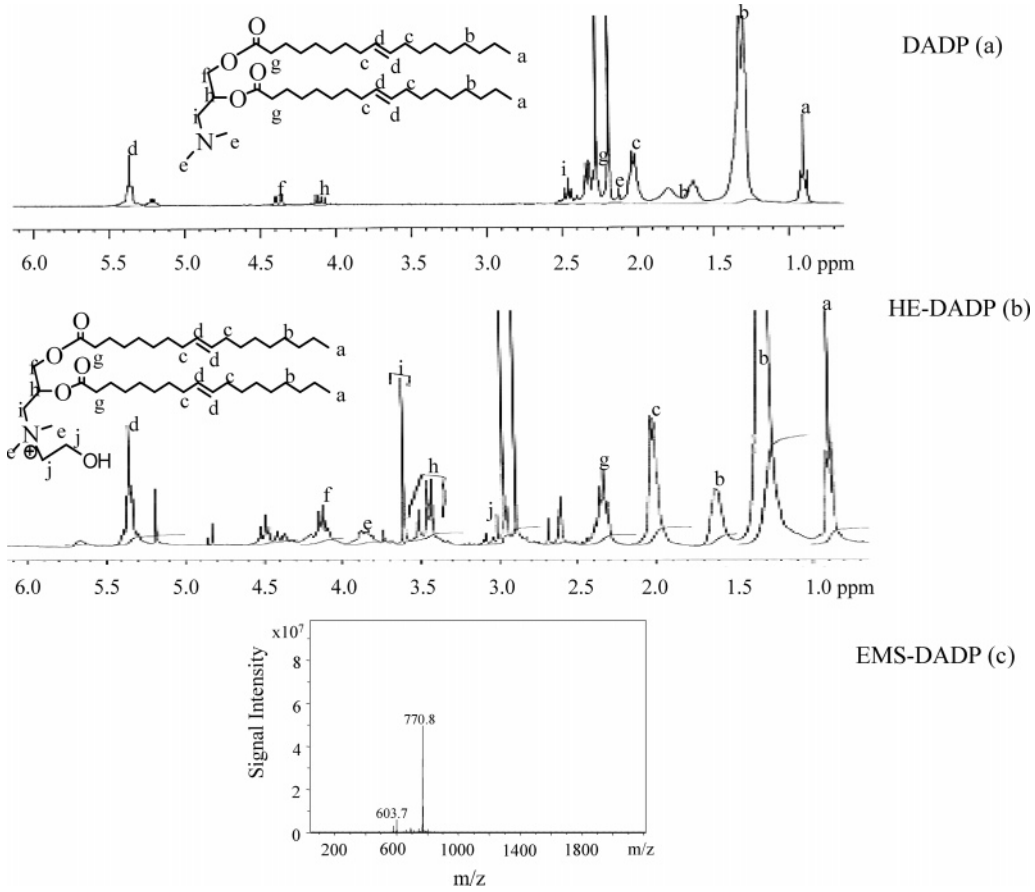

Figure 2. Proton nuclear magnetic resonance (NMR) spectra for 3-(dimethylamino)-1,2-dioleoylpropanediol (DADP, III) and 3-(*N*-2-hydroxyethyl dimethylamino)-1,2-dioleoyl propanediol (HE-DADP, IV) and electrospray ionization (ESI) mass spectrum (MS) for 3-(*N*-ethyl-2-methanesulfonyldimethylamino)-1,2-dioleoylpropanediol (EMS-DADP, V).

NMR results of HE-DADP are as follows (Figure 2b). ^{1}H NMR (300 MHz, chloroform-d_1): δ ~0.9 ppm (H of terminal (CH_3) of lipid chains (a)); δ ~1.2−1.7 (H of (CH_2) methylenes of lipid chains except the ones neighboring the double bond and the carbonyl (b)); δ ~2.1 (H of (CH_2) methylenes of lipid chains neighboring the double bond (c)); δ ~5.4 (H of (CH═) groups of lipid chains participating in double bond (d)); δ ~3.8−3.9 (H of (CH_3) methyl groups attached to the tertiary nitrogen (e)); δ ~4.1−4.2 (H of (CH_2) methylene of glycerol backbone (f)); δ ~2.2−2.4 (H of (CH_2) methylenes next to carbonyl on the lipid chains (g)); δ ~3.3−3.5 (H of (CH) from the glycerol backbone (h)); δ ~3.6 (H of (CH_2) methylene of the glycerol backbone connecting the amine (i)); δ ~2.9−3.1 (H of (CH_2) methylenes of hydroxy ethanol attached to the quaternary nitrogen (j).

EMS-DADP was also analyzed by NMR; however, the spectrum was too complicated to clearly distinguish product formation (data not shown). Hence, product formation and purity of EMS-DADP were assessed by the ESI-MS appearance of the molecular ion peak (770.8 corresponding to M. W. of 770, Figure 2c).

DNA Condensation. To determine the effect of cationic lipid headgroup structures, cationic lipid-to-colipid ratio, cationic lipid to pDNA charge ratio, and pH on DNA condensation, pDNA complexes were prepared by adjusting the stoichiometry of plasmid and cationic liposomes, using liposomes prepared from a cationic lipid (DADP, HE-DADP, or EMS-DADP) and a colipid (cholesterol or DOPE) at various molar ratios. Effective DNA condensation was achieved with cationic liposomes prepared using HE-DADP or EMS-DADP at charge ratios 3/1 and above, as no mobility of pDNA was observed at these charge ratios (data not shown). In contrast, DADP was relatively inefficient at DNA condensation, as some free DNA was seen even at 5/1 (+/−) charge ratio (data not shown). At a given charge ratio, cationic lipid to colipid molar ratios had little influence on DNA condensation (data not shown).

Formulation Factors Influencing Transfection Efficiency. The effect of various physicochemical parameters on in vitro transfection into CT-26 colon carcinoma cells was examined as a function of cationic lipid headgroup structure, colipid type, cationic lipid/colipid molar ratio, cationic lipid/DNA charge ratio, and liposome size.

The headgroup of most effective cationic lipids is either a polyamine or a quaternary amine, with the exception of Lipofectamine, which is a combination of both the motifs. Lipofectamine is composed of the cationic lipid DOSPA with colipid DOPE at 3/1 weight ratio. Since Lipofectamine gives one of the best transfection efficiencies and was used in our previous studies on gene delivery to human pancreatic islets (*16*, *17*), we compared the transfection efficiency of this commercially available reagent with our newly synthesized DADP, HE-DADP, and EMS-DADP lipid-based formulations. Transfection efficiency is reported as % relative light units (RLU) per mg of total protein content, expressed as a percentage of the transfection activity observed with Lipofectamine. Each bar in Figure 3 represents an average of six samples, with standard deviation being ≤10%.

The molar ratio of cationic lipid to colipid influences the surface chemistry of lipid/plasmid complexes and phase transition temperature of the liposomes. This may affect the plasmid uptake, opsonization, and endosomal

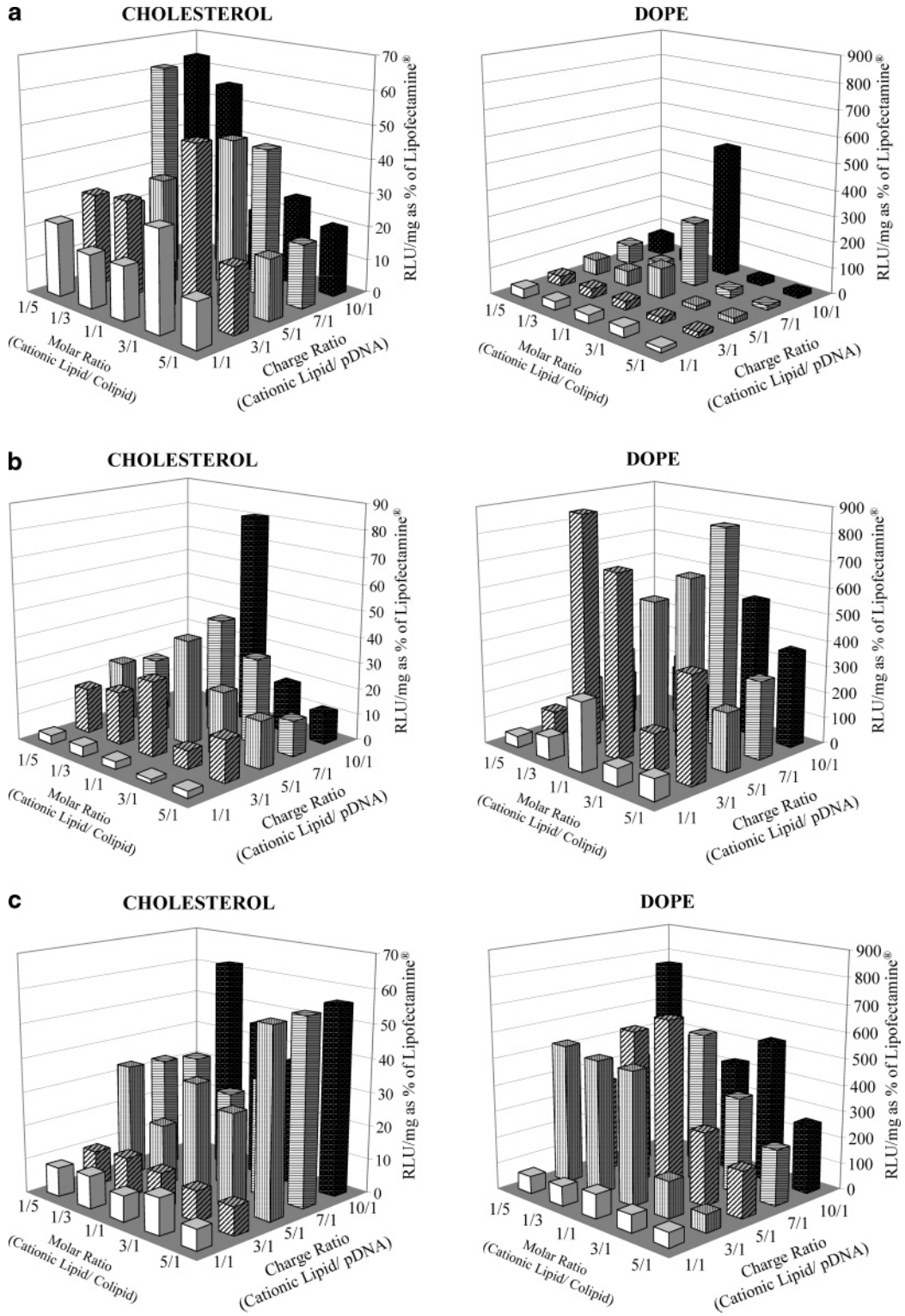

Figure 3. Transfection efficiency of liposomes prepared with 3-(dimethylamino)-1,2-dioleoylpropanediol (DADP) (a), 3-(*N*-2-hydroxyethyldimethylamino)-1,2-dioleoylpropanediol (HE-DADP) (b), or 3-(*N*-ethyl-2-methanesulfonyldimethylamino)-1,2-dioleoylpropanediol (EMS-DADP) (c) lipid derivatives prepared with cholesterol or DOPE as a colipid, as % relative light units (RLU) measured by luciferase assay, per mg of protein for $n = 6$. Transfection efficiency of Lipofectamine was considered 100% for comparison purpose.

release thus affecting the efficiency of gene expression. Most of the cationic liposome formulations incorporate colipids, but the colipid amount does not normally exceed 50% because of the need for high cationic lipid content to complex with and neutralize the large number of negative charges of DNA.

As shown in Figure 3, transfection efficiency was strongly influenced by the relative proportions of cationic lipid, colipid, and plasmid DNA. In general, at a fixed DNA concentration, the cationic lipid dose−response curves were bell-shaped due to the toxicity of cationic lipid at higher dose or charge ratios. The transfection efficiency of these cationic lipids was in the following order: DADP < HE-DADP < EMS-DADP. The use of cholesterol as a colipid showed poor transfection, while DOPE as a colipid gave higher transfection.

Transfection efficiency of DADP was higher for the 3/1 molar ratio of cationic lipid/colipid while decreasing on

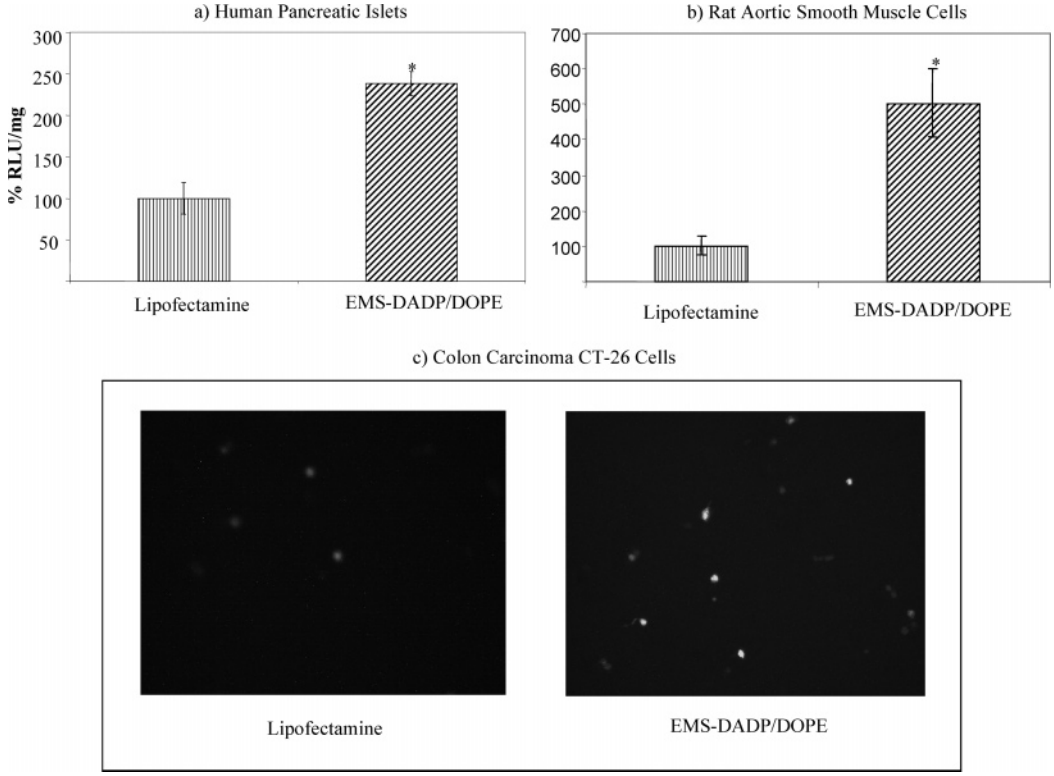

Figure 4. Transfection efficiency of pcDNA3-Luc/EMS-DADP (3/1, +/−) complexes in human pancreatic islets (a) and in rat aortic smooth muscle cells (b), by luciferase assay, and of pCMS-EGFP//EMS-DADP (3/1, +/−) complexes in colon carcinoma CT-26 cells (c), by fluorescence microscopy. (*) indicates statistically significantly ($p < 0.05$) differences in transfection efficiency by two-way ANOVA analysis.

either side, except for the 10/1 (+/−) cationic lipid/pDNA charge ratio for transfection. With respect to the influence of charge ratio, in liposomes with higher cholesterol content (1/5 and 1/3 molar ratios) transfection efficiency was higher with increasing charge ratios while liposomes with equal or less colipid content (1/1, 3/1, or 5/1 molar ratios) showed higher transfection efficiencies at intermediate charge ratios of 3/1 and 5/1.

HE-DADP showed a distinct trend of higher transfection activity at 1/1 molar ratio and decreasing trend with an increase in either the cationic or the colipid component of liposomes. However, the transfection efficiency of DADP, HE-DADP, and EMS-DADP was less when cholesterol was used as a colipid compared to Lipofectamine, with none of them exceeding 80% of the efficiency observed with Lipofectamine (Figure 3a). In contrast, transfection efficiency was signficantly higher for HE-DADP and EMS-DADP when DOPE was used as a colipid for liposome preparation. There was, furthermore, a clear trend of the transfection being dependent on the molar ratio of cationic lipid/colipid with 1/1 ratio giving higher activity than increasing the content of either component. HE-DADP and EMS-DADP/DOPE liposome/pDNA complexes, however, presented much higher transfection efficiency than DADP (∼2−5 times), as well as the commercially available reagent Lipofectamine (∼5 times) (Figure 3b). In the case of EMS-DADP/DOPE liposomes, the transfection activity was higher at higher molar ratios of DOPE.

We have previously reported that transfection efficiency of Lipofectamine/pCAGGS-hVEGF complexes into human islets is low and dependent on the incubation period of islets with the complexes (*16*, *17*). There are also reports of low transfection of Lipofectin/pDNA, Lipofectamine/pDNA, DOSPA:DOPE liposome/pDNA, and polyethylenimine (PEI)/pDNA complexes into intact mouse, rat, and porcine islets (*26*). Unlike the 3:1 w/w ratio Lipofectamine/pDNA used in the present study, Benhamou et al. (*24*) used relatively large amount of cationic lipid (DOTAP, complexes were formulated at 12/1 DOTAP/pDNA weight ratio). These authors also suggested that islet transfection is predominantly in the peripheral cells due to the relative inaccessibility of the central core cells to the vector. Low transfection efficiency in islets was also reported by Saldeen et al. (*25*) To compensate for low transfection efficiency, some workers transfect the dispersed islet cells, as opposed to intact islets, which gives higher transfection due to greater number of cells becoming exposed to the transfection agent after dispersion (*24*, *26*). This, however, often compromises the glucose response function of β-cells and will not be suitable for transplantation (*25*). In the present study, transfection efficiency was observed to be ∼2.5 times higher than Lipofectamine in the human pancreatic islets, and ∼5 times in RASM cells (Figure 4 a,b). In an attempt to further enhance transfection efficiency in human islets, we are in process of testing our lead formulations in conjunction with fusogenic peptides.

We also analyzed GFP positive CT-26 cells by flow cytometry after transfection with Lipofectamine and the lead formulation EMS-DADP/DOPE (1/1) complexed with pDNA at 3/1 (+/−) charge ratio. The results indicated that the transfection efficiency for EMS-DADP/DOPE liposomes was ∼1.5 times higher than Lipofectamine. Concurrent fluorescence microscopic observations of the same samples indicated higher levels of and difference in GFP expression. This could be because flow cytometric analysis would only capture cells that are relatively brightly fluorescent.

We and others (*3*, *11*, *27*) have shown that the transfection efficiency of larger size liposomes is higher than small size liposomes. To test the validity of this observa-

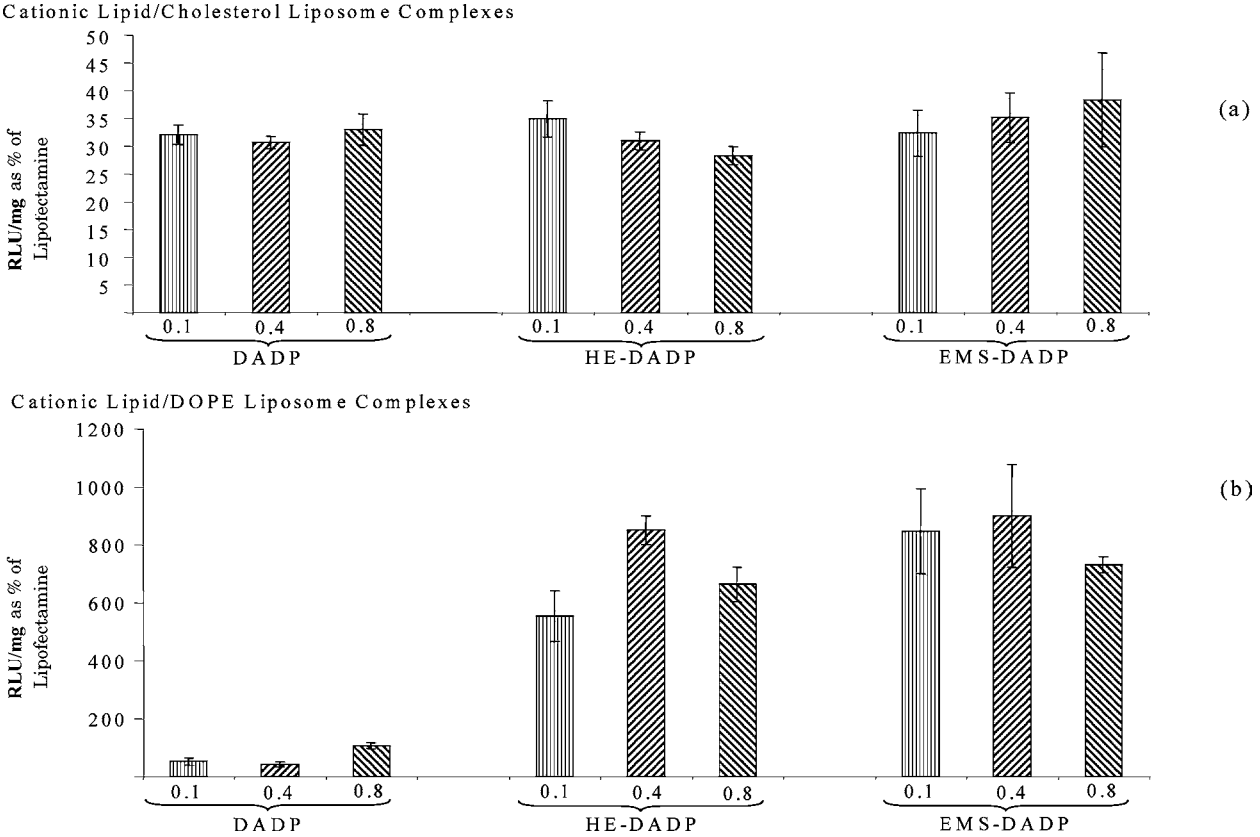

Figure 5. Effect of liposome size on transfection efficiency of pDNA/liposome complexes using DADP, HE-DADP, and EMS-DADP liposomes, extruded through 0.1, 0.4, and 0.8 μm polycarbonate membranes, using (a) cholesterol or (b) DOPE as a colipid. Transfection activity is expressed as % relative light units (RLU) measured by luciferase assay per mg of protein for $n = 6$. Transfection efficiency of Lipofectamine was considered 100% for comparison. There was no significant difference ($p = 0.05$) in transfection efficiency between different liposome size samples of the same lipid-based formulations.

tion with our novel lipids, we examined the effect of liposome size on transfection efficiency by extrusion of liposomes through 100, 400, and 800 nm pore size polycarbonate membranes and complex formation with pcDNA3-Luc at 3/1 (+/−) charge ratio (Figure 5). In the present study, liposome size did not show any significant effect on transfection efficiency for DOPE and cholesterol-based liposome/pDNA complex formulations, since 100, 400, and 800 nm extruded liposomes showed similar %RLU/mg total protein (Figure 5).

Particle Size and Zeta Potential. Particle diameter of liposome/pDNA complexes (Figure 6a) was ~500 nm for DADP and HE-DADP with both colipids, while EMS-DADP had a larger particle size (~1.0 μm with cholesterol as a colipid and ~1.8 μm with DOPE as a colipid). The particle size of complexes of all liposomes was larger than that of Lipofectamine and was closer to the membrane size used for extrusion of liposomes i.e., 400 nm (Figure 6a).

Zeta potential of liposome/pDNA complexes was ~ +40mV for both HE-DADP and EMS-DADP liposomes with either cholesterol or DOPE as colipids (Figure 6b). These were comparable to the zeta potential observed for Lipofectamine, ~ +45mV. The ξ-potential for complexes with DADP liposomes was, however, on the negative side (~−15mV). This was indicative of insufficient positive charge on the tertiary nitrogen to cause effective DNA condensation.

Circular Dichroism. Circular dichroism spectra were recorded for naked plasmid and lipid/plasmid complexes in 5% dextrose solution. Since dextrose is a chiral molecule, CD spectra of dextrose alone was subtracted from that of pDNA in dextrose solution to obtain the profile for pDNA. Similarly, the spectra of complexes were recorded with background normalization to the profiles of corresponding liposomes alone in dextrose solution. The spectra were recorded from 220 nm to 360 nm to observe changes in the conformation of pDNA arising from its interactions with the cationic lipids. The charge ratio of cationic lipids to pDNA as well as the molar ratio of cationic lipids to colipids was kept constant in order to delineate the differences arising from different structures of cationic lipids. The CD spectra of naked DNA and lipid/plasmid complexes are shown in Figure 7. The spectrum of naked DNA presented B-type DNA curve. The CD spectra of liposome/pDNA complexes indicated a significant change in DNA conformation being brought about by the interaction with cationic lipids. CD spectra of Lipofectamine/plasmid complexes were also recorded as a positive control. These data indicated that the difference in transfection efficiency obtained with these different liposome formulations could not be directly correlated to the change in DNA conforamation/winding of the duplex brought about by the cationic lipids.

Transmission Electron Microscopy. Morphology of lipid/plasmid complexes was visualized at magnifications of 40000 to 300000 under the transmission electron microscope after negative staining of DNA using uranyl acetate. The complexes formed with cationic lipids were compared with those formed with Lipofectamine (Figure 8a). The complexes with EMS-DADP had the tendency to be elongated and have more surface area than those formed with Lipofectamine, which were relatively compact. Furthermore, some incompletely condensed pDNA molecules could be visualized in these samples (Figure 8b), which indicated that a significantly higher amount

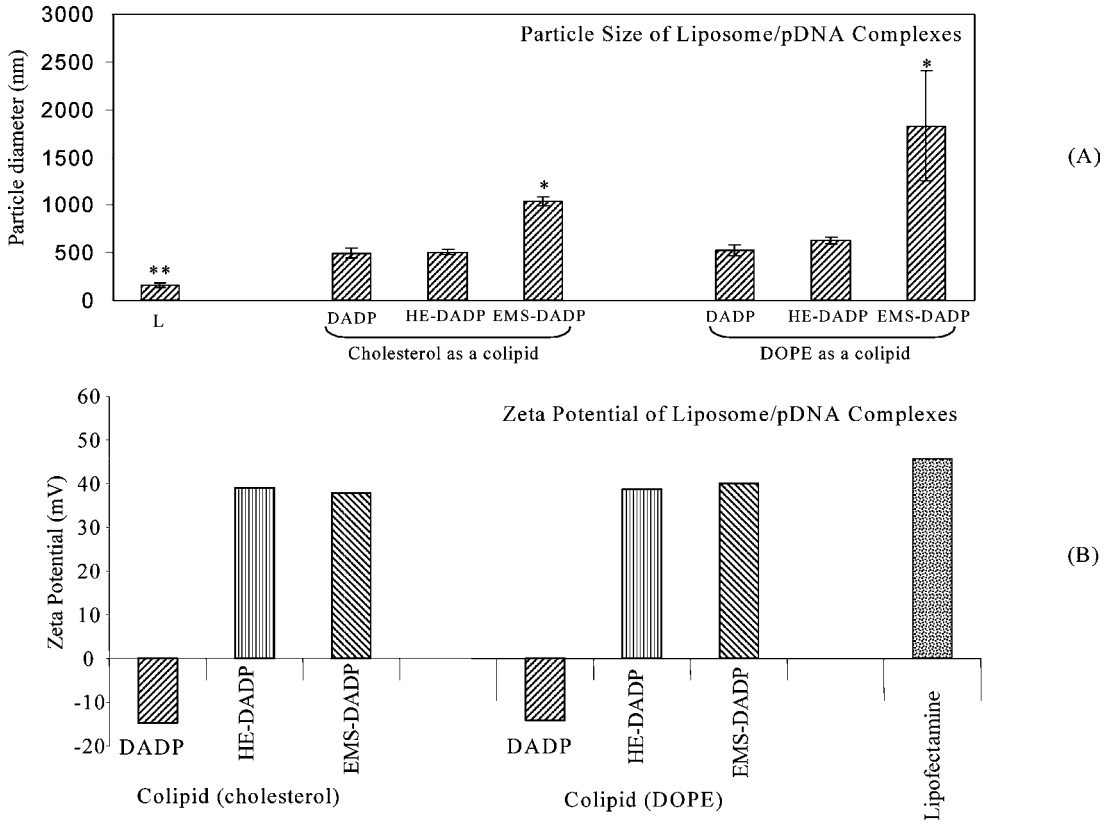

Figure 6. Particle size (a) and zeta potential (b) of liposome/pDNA complexes prepared at 3/1 (+/−) charge ratio using either 3-(dimethylamino)-1,2-dioleoylpropanediol (DADP), 3-(*N*-2-hydroxyethyldimethylamino)-1,2-dioleoylpropanediol (HE-DADP), or 3-(*N*-ethyl-2-methanesulfonyldimethylamino)-1,2-dioleoylpropanediol (EMS-DADP) as a cationic lipid and cholesterol or DOPE as a colipid at 1/1 molar ratio. Lipofectamine/pDNA complexes (3/1 molar ratio) were used as a control. (*) indicates statistically significant difference of these EMS-DADP samples from DADP, HE-DADP, and Lipofectamine. Lipofectamine (**) sample was significantly different from all other samples. Two-way ANOVA was used to assess statistical signficance of differences at $p < 0.05$ level. Significance tests could not be applied to the zeta potential data since it was based on only one sample readings.

of the lipids were attached to the DNA molecules in the case of EMS-DADP than Lipofectamine.

DISCUSSION

Cationic lipid structure, colipid type, lipid/DNA ratio, cationic lipid/colipid ratio, and liposome size have been shown to influence gene transfer efficiency both in vitro and in vivo (*2*, *3*, *11*). Here we report the effect of these parameters on the transfection efficiency of our newly synthesized cationic lipids in vitro. These lipid derivatives have two C_{18} oleoyl lipid chains attached to the glycerol backbone through an ester linkage. To the C-3 carbon of the glycerol backbone is attached either a tertiary or a quaternary amine as a hydrophilic headgroup. A review of research (*2*−*4*, *28*−*35*) and review (*36*−*42*) papers, and patents (US 5550289, 4897355, 5736392, 5527928, 5744625, 5892071, 5869715, 5171678, 5824812, 6251433, 6376248, 6051429, 6087325, 6143716, 6339069, 5736392, 5334761, and 6346516), revealed various design features and structure−activity relationships of cationic lipids. On the basis of this information, it was concluded that a two chain symmetrical C_{18} mono-unsaturated oleoyl ester chain based lipid conjugate would be the most suitable with a glycerol backbone connecting it to the cationic headgroup.

Significant differences were observed in the transfection efficiency of the three lipid derivatives prepared viz. DADP, HE-DADP, and EMS-DADP (Figure 3). The charge ratio of cationic lipid to pDNA, type of colipid, and molar ratio of cationic lipid to colipid affected the transfection efficiency of liposome/plasmid complexes. One possible reason for different transfection efficiency is the difference in their DNA condensing ability. Unlike most quaternary lipids currently being used for transfection, HE-DADP has an additional hydroxyl functionality separated from the quaternary amine by a two-carbon chain alkyl moiety that confers to it a distance of ∼ 5 Å. The hydroxyl group can participate in hydrogen bond formation as both a hydrogen bond donor and/or acceptor. The distance of the hydroxyl group from the quaternary amine correlates with the molecular distances within the DNA bases, indicating a possibility of concurrent hydrogen bond interactions along with electrostatic interactions, thus leading to better DNA condensation.

On the basis of the high transfection obtained with lipid/plasmid complexes prepared at 3/1 (+/−) charge ratio and 1/1 molar ratio of cationic lipid/colipid, we selected formulations of DADP, HE-DADP, and EMS-DADP with both cholesterol and DOPE as colipids for further studies. Plasmid DNA solution in water was used as a control. We hypothesize that the higher transfection efficiency of HE-DADP and EMS-DADP is due to stronger interactions between cationic lipid and plasmid DNA that originate in the presence of the hydroxyl functionality in HE-DADP and the methylsulfonate group in the case of EMS-DADP. The hydroxyl group has the potential for hydrogen bonding interactions both as a hydrogen bond donor as well as an acceptor. The position of the hydroxyl group on HE-DADP is such that it is only two carbons away from the positively charged nitrogen. Given the interaction of the positive nitrogen with the negative phosphate on the DNA backbone, which would bring the

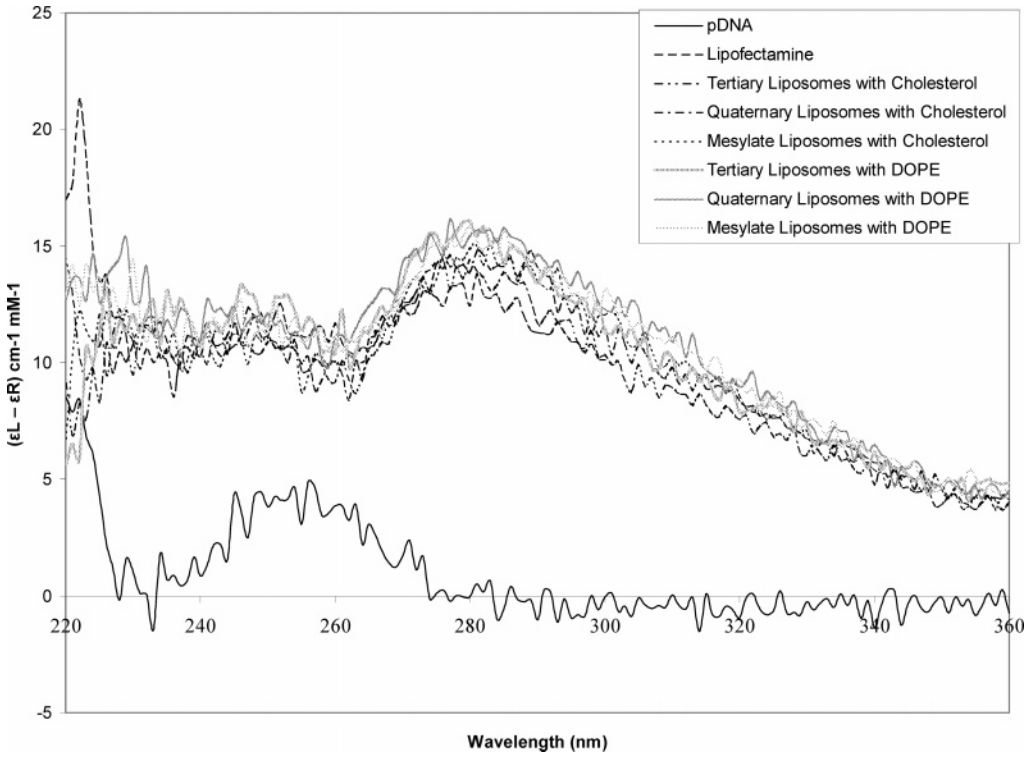

Figure 7. Circular dichroism (CD) spectra of lipid/plasmid complexes. Liposomes were prepared at 1/1 molar ratio of either 3-(dimethylamino)-1,2-dioleoylpropanediol (DADP), 3-(*N*-2-hydroxyethyldimethylamino)-1,2-dioleoylpropanediol (HE-DADP), or 3-(*N*-ethyl-2-methanesulfonyldimethylamino)-1,2-dioleoylpropanediol (EMS-DADP) as a cationic lipid and cholesterol or DOPE as a colipid. Complexes were prepared at 3/1 charge ratio of cationic lipid/colipid, and CD was recorded at a pDNA concentration of 50 μg/mL. The CD spectra has been compared to the profile for pDNA alone. Spectral profiles of liposomes with dextrose or of dextrose alone were subtracted as blank.

headgroup of the cationic lipid in close proximity to the DNA, the hydroxyl group possibly engages in hydrogen bonding interactions, either directly or through water bridge(s), with the neighboring polar or charged groups on the surface of DNA duplex. Multiple hydrogen bonding interaction of the cationic lipids with surface charged groups on the DNA double helix would be sufficient to significantly increase the overall strength of interaction between the lipid and the plasmid DNA.

In the case of EMS-DADP, the presence of the uncharged, bulky methanesulfonyl group above the quaternary amine headgroup is expected to hinder the electrostatic interactions between the positively charged nitrogen with the negatively charged phosphates on the DNA backbone. However, the transfection efficiency of EMS-DADP was not reduced compared to the quaternary compound, HE-DADP. Mesylates have been shown to alkylate DNA (*43*−*47*) and can react with amine functionalities in aqueous conditions at room temperature (*48*). Furthermore, the steric positioning of the mesylate group is expected to be close to the neighboring phosphates on the surface of double stranded DNA molecule, when the quaternary nitrogen forms electrostatic bonds with the anionic phosphates. The mesylate group, therefore, possibly forms a covalent bond or engages in hydrogen bonding interactions through the water bridges.

We have earlier evaluated in vivo transfection efficiency of cationic liposomes in mice after tail vein injection of lipid/plasmid complexes. Human growth hormone (hGH) gene expression level in the serum was about 6-fold higher when 400 nm extruded liposomes were used compared to 100 nm extruded liposomes (*11*). Ross et al. (1999) also observed a linear increase in lipoplex association, cellular uptake, and gene expression with increase in liposome size, composed of DOTAP as the cationic lipid and DOPE as the colipid (*49*). Also, Zelphati et al. (1998) have shown the transfection activity to be almost double for an increase in particle size from 100 nm to 400 nm (*50*). Felgner et al. (1994) have evaluated different particle size formulations of the cationic lipid DORIE, which is very similar to our lipid HE-DADP, and observed a 2-fold difference in the transfection efficiency of larger multilamellar vesicles and smaller unilamellar vesicles of these liposomes (*3*). In contrast, we did not observe a signficant (p 0.05, ANOVA) difference in transfection efficiency with increase in liposome size for all cationic lipids (Figure 5).

Zeta potential of the complexes has an important role in transfection efficiency by promoting adhesion of the complexes to the negatively charged cell membrane. The ξ-potential of lipid/plasmid complexes prepared using HE-DADP and EMS-DADP was ∼(+)40 mV, which was comparable to that for Lipofectamine/plasmid complexes (∼ +45 mV) indicating that higher ξ-potential was not the reason for higher transfection. The ξ-potential for complexes prepared with the liposomes of DADP was ∼ −15 mV. The low transfection efficiency of DADP could be correlated to negative zeta potential.

We have earlier shown that interaction with cationic lipopolymers significantly affects the conformation of pDNA, as inferred by CD, and that this is a function of +/− charge ratio used for the preparation of complexes (*14*). Therefore, in the present study, we have scanned pDNA and liposome/pDNA complexes over a range of 220−360 nm at a fixed charge ratio of 3/1 (+/−), to assess the comparative degree of change in conformational state of plasmid DNA with liposomes of different cationic lipids. The CD profile obtained for a given pDNA molecule depends on its sequence of base pairs, %AT content of bases, and the interactions among bases (*51*, *52*).

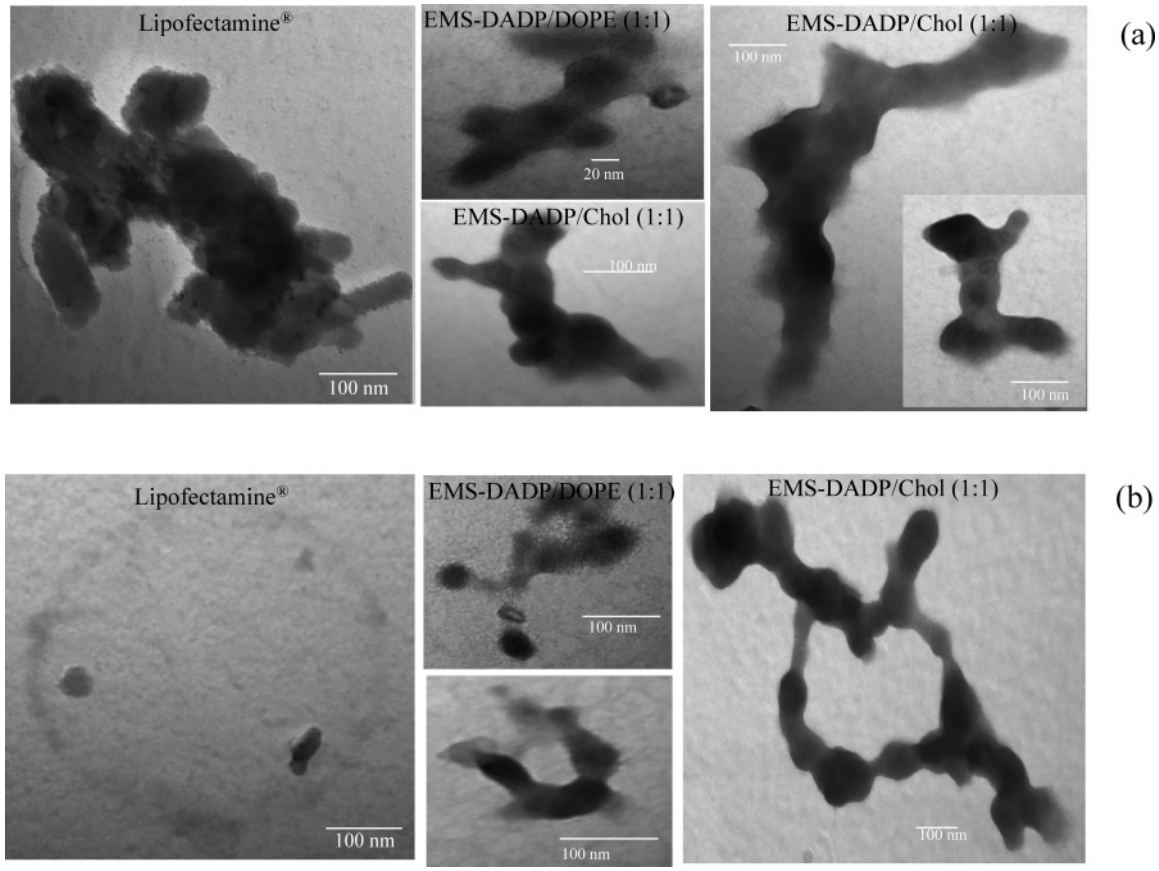

Figure 8. Transmission electron microscopy (TEM) images of cationic liposome/pDNA complexes and occasional uncondensed plasmid DNA when complexes were prepared at 3/1 (+/−) charge ratio using cationic liposomes prepared with 1/1 molar ratio of the cationic lipid with the colipid. Samples were prepared at the pDNA concentration of 0.01 μg/μL and negatively stained on carbon-coated copper grids using uranyl acetate aqueous solution. Complexes of the mesylate lipid with either DOPE or cholesterol as a colipid in liposome formulations have been compared with Lipofectamine.

Hence, the CD spectra of pDNA obtained in our current study was somewhat different than that obtained earlier (*14*) and seems closer to the poly [d(A-C-C). d(G-G-T)] two repeating trinucleotide polymer at 67% GC content shown by Gray et al. (*51*). The goal of our study here was to examine the relative difference in changes in conformation induced by different cationic lipids. The results (Figure 7) indicated a significant change in the conformation of pDNA upon complexation with the cationic lipids in the appearance of a significant positive peak ~ 280 nm, where there was a positive peak at ~ 255 nm in the naked pDNA and the disappearance of the slight negative peak at ~235 nm. However, the relative difference in the pDNA profile with different cationic lipids, including Lipofectamine, was insignificant. This indicated that the degree of conformational change/winding-up of the helix caused by the cationic lipids was similar in all cases examined.

The particle size data (Figure 6) as well as the results of transfection studies (Figure 3) implied the possibility that the higher in vitro transfection could be due to the aggregation/agglomeration of complexes. Therefore, we sought to visualize the complexes using transmission electron microscopy (TEM) to confirm the observations of particle size data and any possible aggregation of the complexes. The size, agglomeration, and structural geometry of the complexes has been shown to depend greatly upon the +/− charge ratio of the cationic polymer/liposomes to pDNA. Lower charge ratios of 1/1.2 to 1/1.3 were shown to form large-sized complexes and aggregates (*53*). Pitaard et al. (1997) had shown the progressive decrease in diameter and increase in compactness of complexes formed at (+/−) charge ratios of 0.3/1, through 1.65/1 to 6/1 (*54*). Rackstraw et al. (2002) had shown the increase in density and size of complexes formed at 1/1 to 5/1 charge ratio (*55*). The complexes were seen to be compact and spheroidal in all cases. Aggregate formation was also visible in some cases, especially at lower charge ratios. An interesting observation was reported by Thomas et al. (2003), with the deposition of a lot of lipid on the circular pDNA at an extremely high charge ratio of 150/1 (*56*). We have seen similar phenomena in the case of pDNA/EMS-DADP:DOPE liposome complexes but at a lower charge ratio of 3/1 (+/−).

The TEM of the pDNA complexes of Lipofectamine liposomes was also visualized as a control. Both complexes (Figure 8a) as well as occasional uncondensed pDNA (Figure 8b) could be seen. The observation of uncondensed DNA could be due to the relatively lower amount of liposomes used for pDNA condensation. The results indicated the size of most of the complexes to be in the range of the particle size data obtained using light scattering technique (Figure 6a). Furthermore, two significant differences were observed between Lipofectamine/plasmid and EMS-DADP:DOPE liposome/plasmid complexes. While the former appeared more compact in nature, the latter were more 'spread-out' and elongated, with higher surface area (Figure 8). The observation of elongated complexes indicated that the higher particle size obtained with the light scattering technique for EMS-DADP complexes could be due to the varying orientation of the elongated structures. This would also explain the significantly higher variability seen with the EMS-DADP/DOPE complexes in Figure 6a. The amount of lipid

attached to the plasmid DNA was seen to be significantly higher for EMS-DADP than for Lipofectamine complexes. This observation is in line with our hypothesis that the conformational placement of the hydroxyl or the mesylate group allows them to form additional bonding interactions with the DNA double helix, leading to a greater degree of attraction between the lipid molecules and the plasmid DNA. This results in more amount of lipid 'sticking' to the pDNA. This also explains the relatively elongated or spread-out nature of the complexes formed with EMS-DADP as being due to the packing of an excessive amount of material on the DNA duplex with a limited surface area.

The observation of uncondensed DNA could be due to the relatively lower amount of liposomes used for pDNA condensation. Although electrophoretic mobility of plasmid DNA was seen to be prevented at charge ratios of 3/1 and higher, effective charge neutralization might not result in formation of compact lipid/DNA complexes for all 100% molecules at 3/1 (+/−) charge ratio. Hence, some incompletely compacted pDNA molecules, which did have the lipid attached, were observed under the electron microscope at this charge ratio, although they were very few.

Bennett et al. (1997) have evaluated in vivo transfection efficiency and lipid hydration of a series of cationic lipids with variations in headgroup structures (*57*). Among other lipids, their lipid structure RI, which is the same as HE-DADP, was compared with its methoxy derivative (MEP) to evalute the difference in hydration and the role of hydrogen bonding interactions. They observed an increase in lipid hydration with increasing bulk of the polar headgroup with methoxy modification, which was attributed to reduced interactions with the colipid, DOPE. Thus, greater exclusion of interstitial water in the case of hydroxyl containing lipids due to intermolecular hydrogen bonding, would lead to reduced lipid hydration with increased tendency of liposomes to form nonbilayer structures. Such lipids were observed to be more active than the non-hydroxyl-containing lipids. The same lipid, HE-DADP, was also studied by Felgner et al. (1994) as DORI in their evaluation of a series of cationic lipid structures differing in headgroup as well as lipid domain structures (*3*). Addition of a hydroxyalkyl moiety on the quaternary amine in DORI was seen to give ~2-fold higher transfection than the non-hydroxyl group-containing lipid, DOTMA. Presence of polar hydroxyl functionality was postulated to affect hydrogen bonding associations with DOPE to form a heterodimer with different net charge dependent on the medium pH. The authors proposed that ion pair heterodimer formation with DOPE would help maintain the integrity of bilayer structure with changing pH, resulting in different aggregation and fusion properties of vesicles that impact intracellular trafficking. Hence, the hydrogen bonding potential of the hydroxyl functionality in the headgroup has been postulated to improve transfection efficiency either by destabilization of liposomes due to reduced hydration or maintaining the integrity of bilayer structure with changing pH.

Irrespective of the hypothesis regarding vesicle properties that influence transfection activity, cationic lipid interactions with the colipid DOPE were deemed important to the higher transfection efficiency of hydroxyl-containing cationic lipids by both Bennet et al. (*57*) and Felgner et al. (*3*). Felgner et al. also showed that an alternate colipid, dioleoyl phosphatidylcholine (DOPC), which had a permanently positively charged quaternary amine in the headgroup, which would display pH independent charge of the cationic lipid/colipid heterodimer. Lower transfection efficiency was seen with DOPC as a colipid in liposome formulations as compared to DOPE. Hence, the role of colipid remains very important to transfection efficiency because of its potential interactions with the cationic lipid. We expect that this should be true also for cholesterol versus DOPE as a colipid in our formulations.

Indeed, the transfection efficiency of EMS-DADP with DOPE-based liposomes is much higher than that with cholesterol based liposomes (Figure 3). The observation of higher amount of lipid attachment to plasmid DNA with mesylate lipid-based liposomes, however, is consistent with both types of colipids (Figure 8). This indicates that more lipid attachment is not the only mechanism involved. Literature also suggests that membrane fusion, promoted by lipid attachment to DNA, may not be the predominant mechanism for cell penetration (*58*). The predominant mechanism for membrane penetration is endocytosis rather than fusion. Membrane fusion and disruption, however, is a critical requirement for the next stage of endosomal escape. Higher affinity of the mesylate headgroup for DNA would also promote higher colipid attachment to pDNA because of the proximity of both lipids in the liposome formulation. Also, the attachment of DOPE as a colipid may be more than cholesterol because of zwitterionic nature of DOPE and its possible interactions with EMS-DADP as well as plasmid DNA. The fusogenic colipid DOPE is known to have significantly higher impact on endosomal disruption than cholesterol. Hence, we hypothesize that while higher lipid attachment may be protective for plasmid DNA and slightly enhancing cell penetration in the case of either colipid, higher transfection efficiencies are seen only with DOPE as a colipid because of its role in membrane fusion and disruption at the stage of endosomal escape. This is indicated by the significantly higher transfection efficiency of EMS-DADP liposomes having a higher molar content of DOPE in the liposomes (1/5, 1/3, and 1/1 EMS-DADP/DOPE molar ratios consistently give higher transfection than 3/1 and 5/1 molar ratios irrespective of the charge ratio used, Figure 3b). No such significant effect of colipid content was seen with cholesterol-based liposomes (Figure 3a). Hence, these cationic lipid formulations may be acting predominantly at a stage of endosomal disruption and prevention of lysosomal degradation instead of cellular internalization. These hypotheses will be the subject of our further investigations in this area.

The incomplete condensation observed at 3/1 (+/−) charge ratio may adversely impact in vivo gene expression of lipid/plasmid complexes. However, there is a need to maintain a delicate balance between transfection efficiency and toxicity. High charge ratios are known to efficiently condense DNA and increase transfection efficiency, but also increase cytotoxicity. Moreover, high charge ratios of cationic lipid to pDNA in complexes is known to cause complement activation after systemic administration (*59*). To minimize cytotoxicity, we will use 3/1 (+/−) charge ratio complexes for further evaluation of our novel lipids.

While our compounds with both polyamine and the quaternary amine were water-soluble and had lower transfection efficiencies than the commercially available Lipofectamine (data not shown), the HE-DADP and EMS-DADP showed unexpectedly higher transfection efficiencies. The cytotoxicity observed with these compounds, however, was not significantly higher than Lipofectamine, which was used as a positive control. We conclude that the possible reason for the higher transfection efficiency

observed with EMS-DADP lipsomes is due to increased lipid affinity for and attachment to the plasmid DNA.

ACKNOWLEDGMENT

This work was supported by the University of Tennessee New Faculty Start-up Fund and the UT Vascular Biology Center of Excellence.

LITERATURE CITED

(1) Mahato, R. I., Rolland, A., and Tomlinson, E. (1997) Cationic lipid-based gene delivery systems: pharmaceutical perspectives. *Pharm. Res. 14*, 853−859.

(2) Lee, E. R., Marshall, J., Siegel, C. S., Jiang, C., Yew, N. S., Nichols, M. R., Nietupski, J. B., Ziegler, R. J., Lane, M. B., Wang, K. X., Wan, N. C., Scheule, R. K., Harris, D. J., Smith, A. E., and Cheng, S. H. (1996) Detailed analysis of structures and formulations of cationic lipids for efficient gene transfer to the lung. *Hum. Gene Ther. 7*, 1701−1717.

(3) Felgner, J. H., Kumar, R., Sridhar, C. N., Wheeler, C. J., Tsai, Y. J., Border, R., Ramsey, P., Martin, M., and Felgner, P. L. (1994) Enhanced gene delivery and mechanism studies with a novel series of cationic lipid formulations. *J. Biol. Chem. 269*, 2550−2561.

(4) Felgner, P. L., Gadek, T. R., Holm, M., Roman, R., Chan, H. W., Wenz, M., Northrop, J. P., Ringold, G. M., and Danielsen, M. (1987) Lipofection: a highly efficient, lipid-mediated DNA-transfection procedure. *Proc. Natl. Acad. Sci. U.S.A. 84*, 7413−7417.

(5) Gao, X., and Huang, L. (1991) A novel cationic liposome reagent for efficient transfection of mammalian cells. *Biochem. Biophys. Res. Commun. 179*, 280−285.

(6) Behr, J. P., Demeneix, B., Loeffler, J. P., and Perez-Mutul, J. (1989) Efficient gene transfer into mammalian primary endocrine cells with lipopolyamine-coated DNA. *Proc. Natl. Acad. Sci. U.S.A. 86*, 6982−6986.

(7) Edelstein, M. L., Abedi, M. R., Wixon, J., and Edelstein, R. M. (2004) Gene therapy clinical trials worldwide 1989−2004-an overview. *J. Gene. Med. 6*, 597−602.

(8) Hui, K. M., Ang, P. T., Huang, L., and Tay, S. K. (1997) Phase I study of immunotherapy of cutaneous metastases of human carcinoma using allogeneic and xenogeneic MHC DNA-liposome complexes. *Gene Ther. 4*, 783−790.

(9) Galanis, E., Hersh, E. M., Stopeck, A. T., Gonzalez, R., Burch, P., Spier, C., Akporiaye, E. T., Rinehart, J. J., Edmonson, J., Sobol, R. E., Forscher, C., Sondak, V. K., Lewis, B. D., Unger, E. C., O'driscoll, M., Selk, L., and Rubin, J. (1999) Immunotherapy of advanced malignancy by direct gene transfer of an interleukin-2 DNA/DMRIE/DOPE lipid complex: phase I/II experience. *J. Clin. Oncol. 17*, 3313−3323.

(10) Ruiz, F. E., Clancy, J. P., Perricone, M. A., Bebok, Z., Hong, J. S., Cheng, S. H., Meeker, D. P., Young, K. R., Schoumacher, R. A., Weatherly, M. R., Wing, L., Morris, J. E., Sindel, L., Rosenberg, M., Van Ginkel, F. W., Mcghee, J. R., Kelly, D., Lyrene, R. K., and Sorscher, E. J. (2001) A clinical inflammatory syndrome attributable to aerosolized lipid-DNA administration in cystic fibrosis. *Hum. Gene Ther. 12*, 751−761.

(11) Mahato, R. I., Anwer, K., Tagliaferri, F., Meaney, C., Leonard, P., Wadhwa, M. S., Logan, M., French, M., and Rolland, A. (1998) Biodistribution and gene expression of lipid/plasmid complexes after systemic administration. *Hum. Gene Ther. 9*, 2083−2099.

(12) Nomura, T., Nakajima, S., Kawabata, K., Yamashita, F., Takakura, Y., and Hashida, M. (1997) Intratumoral pharmacokinetics and in vivo gene expression of naked plasmid DNA and its cationic liposome complexes after direct gene transfer. *Cancer Res. 57*, 2681−2686.

(13) Nomura, T., Yasuda, K., Yamada, T., Okamoto, S., Mahato, R. I., Watanabe, Y., Takakura, Y., and Hashida, M. (1999) Gene expression and antitumor effects following direct interferon (IFN)-gamma gene transfer with naked plasmid DNA and DC-chol liposome complexes in mice. *Gene Ther. 6*, 121−129.

(14) Wang, D. A., Narang, A. S., Kotb, M., Gaber, A. O., Miller, D. D., Kim, S. W., and Mahato, R. I. (2002) Novel branched poly(ethylenimine)-cholesterol water-soluble lipopolymers for gene delivery. *Biomacromolecules 3*, 1197−1207.

(15) Han, S., Mahato, R. I., Sung, Y. K., and Kim, S. W. (2000) Development of biomaterials for gene therapy. *Mol. Ther. 2*, 302−317.

(16) Mahato, R. I., Henry, J., Narang, A. S., Sabek, O., Fraga, D., Kotb, M., and Gaber, A. O. (2003) Cationic lipid and polymer-based gene delivery to human pancreatic islets. *Mol. Ther. 7*, 89−100.

(17) Narang, A. S., Cheng, K., Henry, J., Zhang, C., Sabek, O., Fraga, D., Kotb, M., Gaber, A. O., and Mahato, R. I. (2004) Vascular endothelial growth factor gene delivery for revascularization in transplanted human islets. *Pharm. Res. 21*, 15−25.

(18) Gaber, A. O., Fraga, D. W., Callicutt, C. S., Gerling, I. C., Sabek, O. M., and Kotb, M. Y. (2001) Improved in vivo pancreatic islet function after prolonged in vitro islet culture. *Transplantation 72*, 1730−1736.

(19) Ferrari, M. E., Rusalov, D., Enas, J., and Wheeler, C. J. (2002) Synergy between cationic lipid and co-lipid determines the macroscopic structure and transfection activity of lipoplexes. *Nucleic Acids Res. 30*, 1808−1816.

(20) Matulis, D., Rouzina, I., and Bloomfield, V. A. (2002) Thermodynamics of cationic lipid binding to DNA and DNA condensation: roles of electrostatics and hydrophobicity. *J. Am. Chem. Soc. 124*, 7331−7342.

(21) Floch, V., Le Bolc'h, G., Audrezet, M. P., Yaouanc, J. J., Clement, J. C., Des Abbayes, H., Mercier, B., Abgrall, J. F., and Ferec, C. (1997) Cationic phosphonolipids as non viral vectors for DNA transfection in hematopoietic cell lines and CD34+ cells. *Blood Cells Mol. Dis. 23*, 69−87.

(22) Mahato, R. I., Kawabata, K., Nomura, T., Takakura, Y., and Hashida, M. (1995) Physicochemical and pharmacokinetic characteristics of plasmid DNA/cationic liposome complexes. *J. Pharm. Sci. 84*, 1267−1271.

(23) Mahato, R. I., Lee, M., Han, S., Maheshwari, A., and Kim, S. W. (2001) Intratumoral delivery of p2CMVmIL-12 using water-soluble lipopolymers. *Mol. Ther. 4*, 130−138.

(24) Benhamou, P. Y., Moriscot, C., Prevost, P., Rolland, E., Halimi, S., and Chroboczek, J. (1997) Standardization of procedure for efficient ex vivo gene transfer into porcine pancreatic islets with cationic liposomes. *Transplantation 63*, 1798−1803.

(25) Saldeen, J., Sandler, S., Bendtzen, K., and Welsh, N. (2000) Liposome-mediated transfer of IL-1 receptor antagonist gene to dispersed islet cells does not prevent recurrence of disease in syngeneically transplanted NOD mice. *Cytokine 12*, 405−408.

(26) Saldeen, J., Curiel, D. T., Eizirik, D. L., Andersson, A., Strandell, E., Buschard, K., and Welsh, N. (1996) Efficient gene transfer to dispersed human pancreatic islet cells in vitro using adenovirus-polylysine/DNA complexes or polycationic liposomes. *Diabetes 45*, 1197−1203.

(27) Liu, Y., Mounkes, L. C., Liggitt, H. D., Brown, C. S., Solodin, I., Heath, T. D., and Debs, R. J. (1997) Factors influencing the efficiency of cationic liposome-mediated intravenous gene delivery. *Nat. Biotechnol. 15*, 167−173.

(28) Byk, G., Dubertret, C., Escriou, V., Frederic, M., Jaslin, G., Rangara, R., Pitard, B., Crouzet, J., Wils, P., Schwartz, B., and Scherman, D. (1998) Synthesis, activity, and structure−activity relationship studies of novel cationic lipids for DNA transfer. *J. Med. Chem. 41*, 229−235.

(29) Banerjee, R., Mahidhar, Y. V., Chaudhuri, A., Gopal, V., and Rao, N. M. (2001) Design, synthesis, and transfection biology of novel cationic glycolipids for use in liposomal gene delivery. *J. Med. Chem. 44*, 4176−4185.

(30) Regelin, A. E., Fankhaenel, S., Gurtesch, L., Prinz, C., Von Kiedrowski, G., and Massing, U. (2000) Biophysical and lipofection studies of DOTAP analogues. *Biochim. Biophys. Acta 1464*, 151−164.

(31) Venkata Srilakshmi, G., Sen, J., Chaudhuri, A., Ramadas, Y., and Madhusudhana Rao, N. (2002) Anchor-dependent lipofection with nonglycerol based cytofectins containing

single 2-hydroxyethyl headgroups. *Biochim. Biophys. Acta 1559*, 87−95.
(32) Heyes, J. A., Niculescu-Duvaz, D., Cooper, R. G., and Springer, C. J. (2002) Synthesis of novel cationic lipids: effect of structural modification on the efficiency of gene transfer. *J. Med. Chem. 45*, 99−114.
(33) Vigneron, J. P., Oudrhiri, N., Fauquet, M., Vergely, L., Bradley, J. C., Basseville, M., Lehn, P., and Lehn, J. M. (1996) Guanidinium-cholesterol cationic lipids: efficient vectors for the transfection of eukaryotic cells. *Proc. Natl. Acad. Sci. U.S.A. 93*, 9682−9686.
(34) Ren, T., Song, Y. K., Zhang, G., and Liu, D. (2000) Structural basis of DOTMA for its high intravenous transfection activity in mouse. *Gene Ther. 7*, 764−768.
(35) Gaucheron, J., Wong, T., Wong, K. F., Maurer, N., and Cullis, P. R. (2002) Synthesis and properties of novel tetraalkyl cationic lipids. *Bioconjugate Chem. 13*, 671−675.
(36) Miller, A. D. (1998) Cationic Liposomes for Gene Therapy. *Angew Chem., Int. Ed. 37*, 1768−1765.
(37) Niculescu-Duvaz, D., Heyes, J., and Springer, C. J. (2003) Structure−activity relationship in cationic lipid mediated gene transfection. *Curr. Med. Chem. 10*, 1233−1261.
(38) Liu, D., Ren, T., and Gao, X. (2003) Cationic Transfection Lipids. *Curr. Med. Chem. 10*, 1005−1013.
(39) Nicolazzi, C., Garinot, M., Mignet, N., Scherman, D., and Bessodes, M. (2003) Cationic lipids for transfection. *Curr. Med. Chem. 10*, 1263−1277.
(40) Kumar, V. V., Singh, R. S., and Chaudhuri, A. (2003) Cationic transfection lipids in gene therapy: successes, setbacks, challenges and promises. *Curr. Med. Chem. 10*, 1297−1306.
(41) Miller, A. D. (2003) The problem with cationic liposome/micelle-based nonviral vector systems for gene therapy. *Curr. Med. Chem. 10*, 1195−1211.
(42) Behr, J. P. (1994) Gene transfer with synthetic cationic amphiphiles: prospects for gene therapy. *Bioconjugate Chem. 5*, 382−389.
(43) Bartsch, H., Terracini, B., Malaveille, C., Tomatis, L., Wahrendorf, J., Brun, G., and Dodet, B. (1983) Quantitative comparison of carcinogenicity, mutagenicity and electrophilicity of 10 direct-acting alkylating agents and of the initial O6: 7-alkylguanine ratio in DNA with carcinogenic potency in rodents. *Mutat. Res. 110*, 181−219.
(44) Eder, E., Kutt, W., and Deininger, C. (2001) On the role of alkylating mechanisms, O-alkylation and DNA-repair in genotoxicity and mutagenicity of alkylating methanesulfonates of widely varying structures in bacterial systems. *Chem. Biol. Interact. 137*, 89−99.
(45) Peterson, A. R. (1980) DNA synthesis, mutagenesis, DNA damage, and cytotoxicity in cultured mammalian cells treated with alkylating agents. *Cancer Res. 40*, 682−688.
(46) Platzek, T., and Bochert, G. (2000) DNA alkylation studies of combined treatment with methylnitrosourea and ethylmethanesulfonate in mice. *Teratog., Carcinog., Mutagen 20*, 27−34.
(47) Snyder, R. D., and Bhatt, S. (1993) Alterations in repair of alkylating agent-induced DNA damage in polyamine-depleted human cells. *Cancer Lett 72*, 83−90.
(48) Hudson, R. F., and Withey, R. J. (1964) Nucleophilic reactivity. V. The reaction between amines and ethyl methanesulfonate. *J. Chem. Soc.* 3513−3517.
(49) Ross, P. C., and Hui, S. W. (1999) Lipoplex size is a major determinant of in vitro lipofection efficiency. *Gene Ther. 6*, 651−659.
(50) Zelphati, O., Nguyen, C., Ferrari, M., Felgner, J., Tsai, Y., and Felgner, P. L. (1998) Stable and monodisperse lipoplex formulations for gene delivery. *Gene Ther. 5*, 1272−1282.
(51) Gray, D. M., Johnson, K. H., Vaughan, M. R., Morris, P. A., Sutherland, J. C., and Ratliff, R. L. (1990) The vacuum UV CD bands of repeating DNA sequences are dependent on sequence and conformation. *Biopolymers 29*, 317−323.
(52) Allen, F. S., Gray, D. M., and Ratliff, R. L. (1984) On the first-neighbor analysis of nucleic acid CD spectra: the definitive T matrix and considerations of various methods. *Biopolymers 23*, 2639−2659.
(53) Gustafsson, J., Arvidson, G., Karlsson, G., and Almgren, M. (1995) Complexes between cationic liposomes and DNA visualized by cryo-TEM. *Biochim. Biophys. Acta 1235*, 305−312.
(54) Pitard, B., Aguerre, O., Airiau, M., Lachages, A. M., Boukhnikachvili, T., Byk, G., Dubertret, C., Herviou, C., Scherman, D., Mayaux, J. F., and Crouzet, J. (1997) Virus-sized self-assembling lamellar complexes between plasmid DNA and cationic micelles promote gene transfer. *Proc. Natl. Acad. Sci. U.S.A. 94*, 14412−14417.
(55) Rackstraw, B. J., Stolnik, S., Davis, S. S., Bignotti, F., and Garnett, M. C. (2002) Development of multicomponent DNA delivery systems based upon poly(amidoamine)-PEG copolymers. *Biochim. Biophys. Acta 1576*, 269−286.
(56) Thomas, M., and Klibanov, A. M. (2003) Conjugation to gold nanoparticles enhances polyethylenimine's transfer of plasmid DNA into mammalian cells. *Proc. Natl. Acad. Sci. U.S.A. 100*, 9138−9143.
(57) Bennett, M. J., Aberle, A. M., Balasubramaniam, R. P., Malone, J. G., Malone, R. W., and Nantz, M. H. (1997) Cationic lipid-mediated gene delivery to murine lung: correlation of lipid hydration with in vivo transfection activity. *J. Med. Chem. 40*, 4069−4078.
(58) Bloomfield, V. A. (1996) DNA condensation. *Curr. Opin. Struct. Biol. 6*, 334−341.
(59) Plank, C., Mechtler, K., Szoka, F. C., Jr., and Wagner, E. (1996) Activation of the complement system by synthetic DNA complexes: a potential barrier for intravenous gene delivery. *Hum. Gene Ther. 7*, 1437−1446.

BC049818Q

Template-Directed Assembly and Characterization of Metallosalen–DNA Conjugates

Jennifer L. Czlapinski† and Terry L. Sheppard*

Department of Chemistry and The Robert H. Lurie Comprehensive Cancer Center, Northwestern University, 2145 Sheridan Road, Evanston, Illinois 60208-3113. Received October 17, 2004

Nucleic acid template-directed synthesis represents a powerful method for the encoded synthesis of new bioconjugates. Our laboratory previously reported a strategy for the synthesis of a new metal–DNA hybrid, metallosalen–DNA, by the DNA or RNA template-directed cross-linking of two salicylaldehyde-modified DNA oligonucleotides. The current manuscript describes the optimal assembly requirements and biophysical characterization of metallosalen–DNA conjugates containing nickel and manganese ions. Competitive assembly reactions demonstrated the template-directed nature of metallosalen–DNA formation. A single metallosalen–DNA conjugate was assembled selectively in the presence of two pairs of salicylaldehyde precursor strands and a single DNA template. Assembly reactions were sensitive to base pair mismatches in the pairing arms. Single base mismatches resulted in a loss of metallosalen–DNA conjugate yield. Metallosalen–DNA assembly yields depended on the identity and length of the template spacer, the reaction pH, and the type of metal and diamine utilized in the assembly reaction. Metallosalen–DNA conjugates were stable to a variety of conditions, including extended incubation at 50 °C. Nickel metallosalen–DNA remained unchanged after incubation at 80 °C for 24 h, while decomposition of manganese metallosalen–DNA was observed under the same conditions. Circular dichroism (CD) spectroscopy indicated that DNA duplexes containing internal metallosalen moieties adopted B-form double helices. UV thermal denaturation analysis demonstrated that 32-nucleotide duplexes containing internal metallosalen modifications displayed melting temperatures ~5 °C less than unmodified DNA duplexes.

INTRODUCTION

Metal ions are essential to nucleic acid structure and biochemistry. Nucleic acid duplexes and RNA tertiary structures are stabilized by metal ion binding (*1*, *2*), and numerous catalytic nucleic acids require divalent metal ions for their function (*3*, *4*). Despite a growing understanding of nucleic acid–metal interactions, the rational design or combinatorial discovery of metal-binding sites is still in its infancy. However, chemists have united the properties of metal ions with the coding abilities of nucleic acids by developing methods for the covalent conjugation of metal complexes to oligonucleotides. Early metal–DNA complexes involved the covalent attachment of EDTA to an oligonucleotide (*5*), for use in iron-mediated DNA cleavage. Since this discovery, numerous metal–DNA hybrids have been developed for applications ranging from nucleic acid cleavage (*6–12*) to DNA electron transfer studies (*13–19*). Other metal–DNA conjugates have been utilized as DNA hybridization probes and sensors (*20–23*) and for mechanistic studies of the anticancer drug, cisplatin (*24*). Recently, metal complexes have been utilized as scaffolds for metal-mediated DNA base pairs (*25–31*).

Metal–DNA hybrids have been synthesized by several methods. One common approach involved the conjugation of the metal complex to a functional group "handle" on a DNA oligonucleotide (*17–21*). A second procedure was based on the synthesis of oligonucleotides modified with metal ligands, followed by metal complexation (*5–8*, *22*). Metal complexes also have been inserted into oligonucleotides directly by DNA automated synthesis (*12–15*, *23*, *24*). In a recent advance, a DNA polymerase was used to incorporate a metal-containing nucleoside triphosphate into an oligonucleotide (*32*). Our laboratory became interested in template-directed synthesis as a new method for the assembly of metal–DNA hybrids.

In template-directed synthesis, substrate oligonucleotides bearing complementary reactive groups are brought into proximity by Watson–Crick base pairing with a nucleic acid template, which accelerates the selective formation of chemical bonds between the functionalized oligonucleotides. Initially, template-directed synthesis employed oligonucleotide strands containing chemically modified phosphate backbones (*33–35*). More recently, template-directed ligation reactions were expanded for the detection of DNA and RNA point mutations (*36*, *37*). Reversible chemical ligation strategies also have been developed (*33*, *38*) and adapted for the ligation of thymidine oligomers (*39*). Remarkably, DNA and RNA templates have directed the synthesis of a range of chemical structures across diverse reaction classes (*40–46*). In addition, nucleic acid mimics, including hexitol nucleic acids (*47*) and peptide nucleic acids (*48*, *49*), have demonstrated potential as templates in directed assembly reactions. More recently, template-directed synthesis has supported the construction of complex organic molecule–DNA conjugates (*50–52*), in some cases, with stereoselectivity (*53*) and in multistep transformations (*54*).

We recently reported a new metal–DNA hybrid, metallosalen–DNA, which was assembled by DNA or RNA

* To whom correspondence should be addressed. Tel: 847-467-7636; Fax: 847-491-7713; E-mail: t-sheppard@northwestern.edu.

† Current address: Department of Chemistry, University of California, Berkeley, CA 94720.

10.1021/bc049753r CCC: $30.25 © 2005 American Chemical Society
Published on Web 12/23/2004

Scheme 1. Template-directed Metallosalen−DNA Conjugate Assembly.

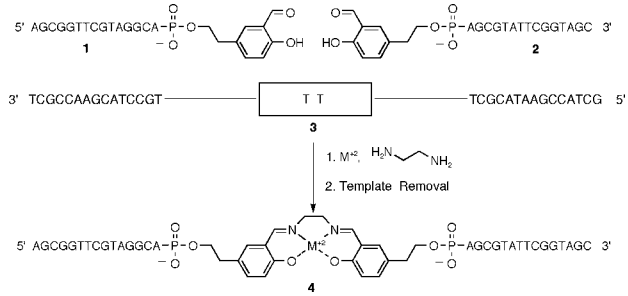

template-directed synthesis (*55*, *56*). In our method, the metal complex was site-specifically incorporated into DNA by the diamine cross-linking of salicylaldehyde-modified DNA on an external template (Scheme 1). Two complementary DNA oligonucleotides were modified with a salicylaldehyde moiety at either the 3′- or 5′-end (**1** and **2**, respectively). The substrates were aligned on the template strand, and the addition of a diamine and a divalent metal ion led to the formation of a metallosalen−DNA hybrid. Herein we describe the variables that control optimal template-directed assembly of metallosalen−DNA conjugates containing nickel and manganese ions. Metallosalen−DNA assembly is controlled by the composition and length of template spacers that bridge the assembly site, reaction pH, the identities of the metal ion and diamine, and the presence of a complementary DNA template in the assembly reaction. Metallosalen−DNA conjugates form B-form DNA duplexes, as judged by circular dichroism (CD) studies, and their presence destabilizes a 32-oligonucleotide duplex by ∼5 °C in melting temperature.

EXPERIMENTAL PROCEDURES

General. All molecular biology reagents were purchased from Sigma. Metals for metallosalen−DNA conjugate formation were purchased from Aldrich as metal acetates, unless otherwise stated. T4 Polynucleotide kinase was obtained from US Biochemical, and [γ-^{32}P]-ATP (7000 Ci/mmol) was purchased from ICN. Radioactive bands in polyacrylamide gels were visualized using a Molecular Dynamics Storm Phosphorimager and quantitated using Molecular Dynamics ImageQuant software. 4-(2-Hydroxyethyl)-1-piperazineethanesulfonic acid (HEPES), 2-(4-morpholino)ethanesulfonic acid (MES), and 2-(cyclohexylamino)ethanesulfonic acid (CHES) were purchased as molecular biology grade reagents from Sigma. Matrix-assisted laser desorption ionization time-of-flight (MALDI-TOF) mass spectrometry was performed on a PerSeptive Biosystems, Inc. (Foster City, CA), Voyager-DE PRO Biospectrometry Workstation MALDI-TOF mass spectrometer as described (*55*).

DNA Synthesis, Deprotection, and Purification. Standard unmodified DNA oligonucleotides were synthesized by Integrated DNA Technologies (Coralville, IA). Modified oligonucleotides were synthesized on a Pharmacia Gene Assembler Plus at the 1.3 μmol scale using phosphoramidites with labile base protecting groups for the natural nucleotides, as described (*55*). All oligonucleotides were purified by reverse-phase HPLC (RP-HPLC), lyophilized, and resuspended in 0.5× Tris-EDTA buffer (5 mM Tris and 0.5 mM EDTA, pH = 7.5). Purified oligonucleotides were quantified by UV spectroscopy, as previously described (*55*).

5′-GCCGATACCACGCTCTTCACCGACGATTG-CCT-3′ (7). Oligonucleotide **7** was synthesized by Integrated DNA Technologies and purified by RP-HPLC.

Salicylaldehyde-Modified DNA Synthesis. Salicylaldehyde-modified DNA strands were synthesized by solid-phase DNA synthesis using standard methods for the natural nucleoside phosphoramidites and 2-(1,3-dioxan-2-yl)-3-benzoyloxyphenyl-4-ethyl-*O*-(2-cyanoethyl)-*N*,*N*′-diisopropylphosphoramidite (*55*) (**27**, 0.11 M solution in anhydrous CH_3CN). After synthesis, oligonucleotides were deprotected as described (*55*) and purified by RP-HPLC.

5′-AGGCAATCGTCGGTG-SAL-3′ (5). Oligonucleotide **5** was synthesized in the 5′-to-3′ direction using a dA-5′-CPG 500 solid support (Glen Research, 33.4 mg, 31 μmol/g loading, 1.03 μmol scale), using standard 5′-β-cyanoethyl nucleoside phosphoramidites and **27**. MALDI-TOF (*m/z*): $[M]^-$ calcd for **5**, 4860; found, 4860.

5′-SAL-GAGCGTGGTATCGGC-3′ (6). Oligonucleotide **6** was synthesized in the traditional 3′-to-5′ direction using standard 3′-nucleoside phosphoramidites (Glen Research, Ultramild) and **27** on a 1.3 μmol scale. MALDI-TOF (*m/z*): $[M]^-$ calcd for **6**, 4877; found, 4877.

5′-Radiolabeling. Oligonucleotide **1** or **5** (24 pmol) was radiolabeled as described (*55*). The reaction was purified by 20% PAGE, eluted from the gel slice (10 mM Tris-HCl, 200 mM NaCl, 1 mM EDTA, pH 7.5), and recovered by precipitation with two volumes of 2-propanol, which had been supplemented to 0.3 M NaOAc, pH 5.2. The oligonucleotide was redissolved in ddH_2O.

Mn Metallosalen−DNA Conjugate Formation Reactions (Mn-4 or Mn-8). A mixture of **1**−**3** (or **5**−**7**), each at 4 μM in 10 mM HEPES, pH 8.0 and 150 mM NaCl, were annealed by heating to 95 °C and slow cooling to RT over 2 h. Solutions of manganese acetate (2 mM) and ethylenediamine (EN, 500 μM) were added to give final concentrations of 400 μM $Mn(OAc)_2$ and 100 μM EN. Each strand was present in a final concentration of 2 μM. The solution was incubated at 37 °C for 1 h. Preparative scale reactions were performed on a 4 nmol scale in 50 mM HEPES, pH 8.0 and 150 mM NaCl. Conjugates were analyzed and purified by 20% polyacrylamide gel electrophoresis (PAGE) using TB buffer (89 mM Tris, 89 mM borate, no EDTA). The metallosalen−DNA complex was visualized using a handheld UV lamp and recovered by electroelution with TB buffer in a Schleicher & Schuell Elutrap (30 min, 200 V at RT). **Mn-4** or **Mn-8** were concentrated in a Millipore Microcon YM-3 filter, washed twice with 200 μL of ddH_2O, and eluted into 50 μL of ddH_2O for storage.

Ni Metallosalen−DNA Conjugate Formation Reactions (Ni-4 or Ni-8). Ni metallosalen−DNA formation reactions followed the same general procedure as for **Mn**; however, the $Ni(OAc)_2$ and EN had final concentrations of 300 μM and 150 μM, respectively, in a pH 6.5 buffer solution (10 mM MES and 150 mM NaCl). Preparative scale reactions required no changes in the reaction buffer.

Competitive Metallosalen−DNA Assembly. Two sets of reactions were prepared, one for formation of **Ni-4** and the other for **Mn-4**, using the buffer conditions listed above. For each metal, three reactions were performed: (1) a mixture of strands **1**−**3** (2 μM) with 20 fmol of radiolabeled **1**; (2) 2 μM each of **1**−**3** and **5**−**6** with 20 fmol of radiolabeled **1**; and (3) 2 μM each of **1**−**3** and **5**−**6** with 20 fmol of radiolabeled **5**. The appropriate amount of metal and diamine was added, and the reactions were incubated at 37 °C and analyzed by 20% PAGE using 1× TB as the running buffer.

Nonspecific Metallosalen–DNA Assembly. To assay for nonspecific metallosalen–DNA formation, a series of assembly reactions was performed for each metal ion. Two reactions were assembled for each time point: one that contained **1**–**3** (each at 2 μM) with 20 fmol radiolabeled **1**, and the other with 2 μM of **1** and **2** with 20 fmol radiolabeled **1**. Since assembly could not be quenched, the reactions were initiated in order of decreasing time. At the end of the time course, products were analyzed by 20% PAGE with TB as the running buffer.

Mismatch Metallosalen–DNA Formation. Reactions containing 2 μM each of **1**, **2**, template **3** or one of the mismatched templates **9**–**13**, and 20 fmol of radiolabeled **1**, were initiated under standard conditions. Reactions were performed with both $Mn(OAc)_2$ and $Ni(OAc)_2$ for each template and were assayed by 20% PAGE electrophoresis with TB buffer.

Metallosalen–DNA Formation with Diverse Metal Ions. Metal ion assays were performed using 2 μM each of **1**–**3** with 20 fmol of radiolabeled **1**. Each reaction was incubated for 1 h at 37 °C with 500 μM of metal salt and 250 μM of EN in 10 mM buffer at the required pH with 150 mM NaCl, as indicated by metal speciation data (*57*). $Cu(OAc)_2$ at pH 9.0 (CHES), $VOSO_4$ at pH 7.0 (HEPES), and $RhCl_3$ and $ZnSO_4$ at pH 7.5 (HEPES). Reaction products were analyzed by PAGE using 1× TB as the running buffer.

Metallosalen–DNA Thermal Stability and EDTA Decomposition. Radiolabeled **Mn-4** and **Ni-4** conjugates were prepared as described above. For thermal stability, solutions containing radiolabeled conjugate **4** were incubated at various temperatures (RT, 37 °C, 50 °C, and 80 °C), and reaction aliquots were taken over 48 h. The time points were analyzed by 20% PAGE with TB running buffer. For EDTA decomposition analysis, the radiolabeled conjugates were prepared in smaller quantities (2 μM strand concentrations) with 20 fmol of radiolabeled **1**. **Mn-4** and **Ni-4** formation reactions were treated with EDTA, pH 8.0 (final concentration: 0–40 mM) for 15 min at RT. Product decomposition was followed by 20% PAGE with TB as the running buffer.

Circular Dichroism Spectroscopy. CD spectra were recorded using a Jasco J-715 CD spectropolarimeter. Oligonucleotide duplex samples were prepared by mixing solutions of 1 μM of each strand in 10 mM sodium phosphate, 150 mM NaCl, pH 7.0. Spectra were recorded from 200 to 350 nm at 25 °C in a quartz cuvette (1 cm path length). The sample compartment was purged with inert atmosphere (N_2) during data acquisition. Each spectrum represents a baseline corrected average of four accumulations per scan, and all data were corrected by subtracting the buffer reference signal.

UV Thermal Denaturation Analysis. UV thermal denaturation data were acquired on a Cary 500 spectrophotometer equipped with a multicuvette thermoelectric controller in 1 cm quartz cuvettes. Solutions of 1 μM duplex oligonucleotides in 10 mM sodium phosphate, 150 mM NaCl, pH = 7.0 were annealed by heating to 95 °C for 5 min, then cooled to 25 °C over 2 h. The samples were degassed under vacuum for 3 min prior to melting analysis. The absorbance was measured at 260 nm as the samples were heated from 30 °C to 90 °C at 0.5 °C/min. Data sets for the downward transition from 90 °C to 30 °C also were collected at 0.5 °C/min; all melting profiles were fully reversible to within 1.0 °C. Melting temperatures (T_m) were determined from plots of dA_{260}/dT vs T as described (*58*) and are derived from replicate melting experiments using at least two independently prepared samples.

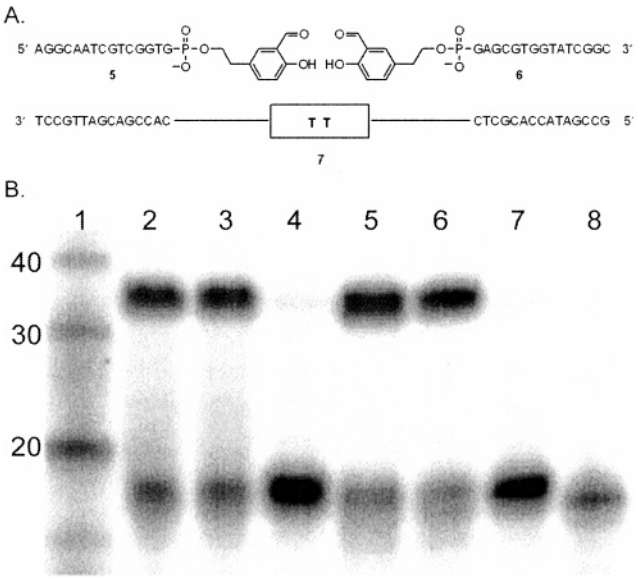

Figure 1. Metallosalen–DNA formation reactions for **Mn-4** and **Ni-4**. (A) SAL–DNA sequences **5** and **6** align on complementary template **7** to support assembly of **Mn-8** and **Ni-8**. (B) Gel electrophoresis assay of metallosalen–DNA competitive assembly. Lane 1: 10 bp marker. Lanes 2–4: Mn assembly reactions at pH 8.0 for 1 h. Lane 2: All components: 400 μM $Mn(OAc)_2$, **1**, **2**, and template **3**, 100 μM EN, radiolabeled **1**. Lane 3: +SAL strands **5** and **6**. Lane 4: +**5** and **6**, -radiolabeled **1** and + radiolabeled **5**. Lanes 5–7: Analogous reactions to Lanes 2–4, but with 300 μM $Ni(OAc)_2$ and 150 μM EN at pH 6.5 for 24 h. Lane 8: Radiolabeled **1**.

RESULTS AND DISCUSSION

Generality of Template-Directed Metallosalen–DNA Synthesis. Our approach to metallosalen–DNA by template-directed synthesis was reported previously for the formation of **Mn-4** and **Ni-4**, as shown in Scheme 1 (*55*). We provided evidence that complementary template **3**, a diamine, and either manganese or nickel ions were required for the assembly of metallosalen–DNA **4** from **1** and **2**. To demonstrate the generality of template-directed synthesis of metallosalen–DNA, a second set of SAL–DNA precursors were prepared that varied the DNA sequences flanking the metallosalen–DNA. SAL–DNA sequences (**5** and **6**, Figure 1A) were synthesized, purified, and characterized by MALDI-TOF MS as described previously for **1** and **2** (*55*). Template-directed assembly reactions of metallosalen–DNA conjugates **Mn-8** and **Ni-8** from **5** and **6** and the complementary template **7** were analyzed by denaturing polyacrylamide gel electrophoresis (PAGE). When DNA **5** and **6** were hybridized to template **7** and incubated at 37 °C in the presence of 100 μM ethylenediamine (EN) and 400 μM $Mn(OAc)_2$, a new DNA product, corresponding to **Mn-8**, was produced in 50% yield. Similarly, **Ni-8** was prepared in 70% yield after 24 h, when 150 μM EN and 300 μM $Ni(OAc)_2$ were incubated with **5** and **6** in the presence of **7**. Metallosalen–DNA assembly required EN, divalent metal ion, and template **7** for optimal assembly, and **Mn-8** and **Ni-8** were produced in yields comparable to those of conjugates **4** (*55*). To confirm the identities of these new metallosalen–DNA hybrids, preparative syntheses (4 nmol) of **Mn-8** and **Ni-8** were performed with an RNA template. Purification of the conjugates was attempted by selective RNase H digestion of the RNA template as previously described (*55*). Although this strategy was effective for the purification of **Mn-4** and **Ni-4**, it was not reliable when applied to metallosalen–

DNA conjugates **Mn-8** and **Ni-8**. Thus, a more general method for the purification of metallosalen−DNA conjugates was developed, which utilized complementary DNA templates that were four nucleotides shorter than **7** (two nucleotides were removed from both the 5′- and 3′-ends). The shorter templates facilitated the separation of the desired metallosalen−DNA from the template strand by gel electrophoresis. Using this approach, **Mn-8** and **Ni-8** were purified by 20% PAGE, and their identities were confirmed by MALDI-TOF MS and base composition analysis (*55*) (see Supporting Information).

Template Specificity of Metallosalen−DNA Assembly. Given the sequence generality of metallosalen−DNA formation, further studies were performed to evaluate the effects of template specificity on the assembly reactions. To assay the template dependence of metallosalen−DNA conjugate assembly, a series of competitive assembly reactions were performed. Four noncomplementary salicylaldehyde-modified (SAL) oligonucleotides were combined with a template that was complementary to only one pair of SAL strands. Upon addition of a diamine and a divalent metal ion, only one metallosalen−DNA should be produced, dependent on the identity of the template strand present in the reaction. A series of reactions using the four SAL strands (**1**−**2** and **5**−**6**) and complementary DNA templates, **3** and **7**, respectively, were undertaken to assay metallosalen−DNA formation under competitive conditions. Three independent metallosalen−DNA reactions were performed and assayed by PAGE using radiolabeled SAL strands as tracers for the assembly of two different metallosalens, **4** and **8**. The first reaction was a typical assembly of **4** (Scheme 1) from SAL strands **1** and **2**, and template **3**, where radiolabeled **1** was used as a tracer. The second and third reactions contained four SAL strands, **1/2** and **5/6**, and the complementary template to **1** and **2** (oligonucleotide **3**). The second reaction, which included the radioactive tracer strand **1** (to track assembly of **4**), was designed to demonstrate that the correct templated conjugate, **4**, was formed even in the presence of other SAL oligonucleotides. The presence of labeled strand **5** in the third reaction was used to follow the assembly of **8** and show that strands **5** and **6** do not form metallosalen−DNA conjugate **8** in the presences of the "wrong" template (**3**).

Gel electrophoretic analysis of the competition reactions is shown in Figure 1B for metallosalen−DNA assembly with manganese and nickel ions. When **1** and **2** were hybridized to their complementary template **3** and incubated for 1 h at 37 °C in the presence of 100 μM EN and 400 μM $Mn(OAc)_2$, **Mn-4** was produced in 57% yield (lane 2). The addition of SAL strands **5** and **6**, which were noncomplementary to **3**, did not disrupt **Mn-4** formation (58%, lane 3). In the absence of labeled **1** (lane 4) and the presence of labeled **5**, no formation of **Mn-8** was observed. The assembly reactions performed with nickel provided similar results. When **1** and **2** were hybridized to complementary **3** and incubated for 24 h at 37 °C in the presence of 150 μM EN and 300 μM $Ni(OAc)_2$, **Ni-4** was produced in 73% yield (lane 5). The addition of unlabeled noncomplementary SAL oligonucleotides (**5** and **6**) did not alter the yield of **Ni-4** (72%, lane 6). However, when noncomplementary **1** was present as the labeled strand, no assembly of metallosalen−DNA **Ni-4** was observed (lane 7). Taken together, the results shown in Figure 1B demonstrated that metallosalen−DNA formation was template-directed, and that a single DNA template was capable of directing the synthesis of a unique metallosalen−DNA conjugate from a mixture of SAL−DNA strands.

Table 1. Mismatched Template Sequences and Yields for Mn-4 Formation Fidelity[a]

sequence		% yield **Mn-4**
5′-GCTACCGAATACGCTTTTGCCTACGAACCGCT-3′	(**3**)	64
5′-GCTACCGAATACGCTTT**G**GCCTACGAACCGCT-3′	(**9**)	58
5′-GCTACCGAATACGCTTT$\underline{\mathbf{C}}$GCCTACGAACCGCT-3′	(**10**)	60
5′-GCTACCGA**C**TACGCTTT$\underline{\mathbf{C}}$TGCCTACGAACCGCT-3′	(**11**)	55
5′-GCTACCGAATACGCTTTTGCCTACG***C***AACCGCT-3′	(**12**)	51
5′-GCTACC_AATACGCTTTTGCCTACGAACCGCT-3′	(**13**)	40

[a] The bolded/underlined letter indicates the mismatched nucleotide; the nucleotide in bold italics is an additional base; and the underscore shows a missing nucleotide.

Nonspecific Metallosalen−DNA Assembly and Effects of Mismatched Base Pairs. To better assess how DNA templates enhance the rates of metallosalen−DNA assembly reactions, a measurement of the background rate of nonspecific metallosalen assembly was required. Nonspecific metallosalen−DNA assembly results from the cross-linking of two SAL−DNA strands in the absence of the corresponding DNA template. To monitor the nonspecific formation of metallosalen−DNA in reactions that lacked a template strand, the background rate of nonspecific metallosalen−DNA assembly was measured by following the formation of metallosalen−DNA product in a reaction containing only the two noncomplementary SAL−DNA strands in the presence of a diamine and a divalent metal ion, but in the absence of a template DNA. SAL strands **1** and **2** (including radiolabeled **1** as a tracer) were incubated under standard assembly conditions. For reactions with Mn(II), the nonspecific yield of material that comigrated with **Mn-4** was found to be 1% at 1 h. Nonspecific product formation increased gradually to 34% at 48 h of reaction. Although the yields of nonspecific conjugate formation increased at longer incubation times, template-directed **Mn-4** reactions typically were completed in 1 h (70% yield), which guaranteed that the major product of template-directed synthesis was the desired **Mn-4** under these conditions. As seen earlier (*56*), nonspecific assembly reactions with Ni(II) were considerably slower than those with manganese ions. No detectable nonspecific products were formed within 48 h, which was 24 h after templated **Ni-4** and **Ni-8** formations were generally complete. Thus, both manganese and nickel ion template-directed metallosalen−DNA assembly reactions were completed before significant amounts of nonspecific products were formed.

Numerous template-directed chemical ligation reactions have been shown to be sensitive to single base pair mismatches at or near the ligation site (*36*, *43*, *45*, *48*). As a result, the effect of base pair mismatches on metallosalen−DNA conjugate formation was assayed. A series of DNA templates (Table 1) for synthesis of metallosalen−DNA **4** (template a) or **8** (template b) were prepared that contained a range of mismatch types and sites: adjacent to the metallosalen assembly site (**9** and **10**), at the center of one metallosalen−DNA arm (**11**), an insertion of a dC nucleotide (**12**) or deletion of a single dG nucleotide (**13**) in the template strands.

Utilizing the conditions for **Mn-4** formation, the four mismatched templates **9**-**13** were hybridized with SAL strands **1** and **2** and incubated in the presence of 100 μM EN and 400 μM $Mn(OAc)_2$ at 45 °C for 1 h. Under these conditions, the mismatched templates led to lower yields of **Mn-4** (Table 1). The **Mn-4** yields with mismatched templates **9**−**13** were between 4 and 24% lower than with complementary template **3** (64%). When the mismatches were near the metallosalen formation site, the yields did not decrease significantly: **9** (58%, G·A

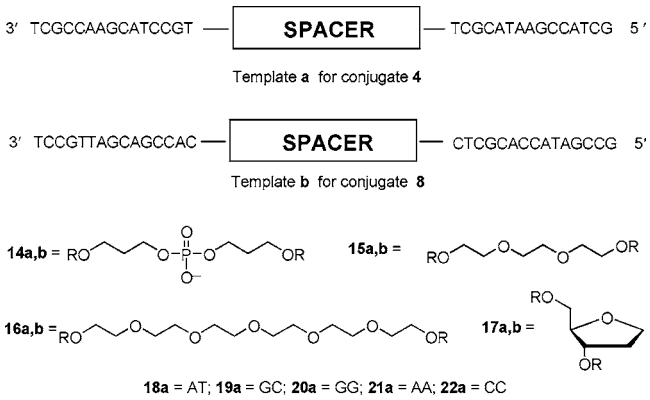

Figure 2. Template sequences and spacers used to evaluate the effects of spacer length and composition on metallosalen–DNA conjugate (**4** and **8**) formation. The spacer identities include a three-carbon linker (**14**), a nine-atom glycol linker (**15**), an eighteen-atom glycol linker (**16**), two D-spacers (**17**), and various dinucleotides: AT (**18**), GC (**19**), GG (**20**), AA (**21**), and CC (**22**).

mismatch) and **10** (60%, C·A mismatch). A more substantial decrease in yield occurred when the mismatch was centrally located within a DNA arm of the metallosalen (**11**, C·T mismatch, 55%) or with a single base insertion (**12**, 51%). The best discrimination was observed with a single base deletion (**13**, 40%).

The results in Table 1 indicate that metallosalen–DNA formation may not be sensitive to mismatches near central assembly site. Due to the lack of standard base pairing of the salicylaldehyde groups with bases in the templates and the likely requirement for flexibility at the assembly site, the loss of an additional base pair interaction by mismatch pairing may not perturb the assembly process. Nonetheless, there is a measurable decrease in yield for the other mismatched templates.

Effects of Template Spacers, Reaction pH, and Metal Ion Identity on Metallosalen–DNA Assembly Reactions. We previously established that efficient template-directed metallosalen–DNA assembly was dependent on several variables, including the identity of the template spacer nucleotides, the metal ion selected for the assembly reaction, and pH that was optimal for the selected metal ion (*55*). We now elaborate on the variables that affect the efficiency of template-directed metallosalen–DNA synthesis.

Other studies have revealed that the rate of bond formation in a template-directed reaction is relatively independent of the distance between the reactive partners (*51*). Thus, we evaluated the effect of the chemical identity and length of the central template spacer (See Scheme 1, Figure 1A) on the efficiency of metallosalen–DNA assembly reactions. Our initial report of metallosalen–DNA assembly (*55*) employed a DNA template with a central spacer consisting of two thymidine residues (TT, Scheme 1). We prepared a panel of template spacers to determine the effect of the chemical nature and the distance of the spacer groups on template-directed synthesis yields (Figure 2). Specifically, we examined spacers with flexible backbones (**14**–**16**), D-spacer abasic site analogues (**17**), and dinucleotides (**18**–**22**), which are shown in Figure 2. The optimal template for each metallosalen–DNA conjugate depended on the metal ion used in the assembly reaction and, in some cases, the oligonucleotide sequence. For example, significant template spacer effects were observed for assembly of manganese-containing metallosalen–DNA. For **Mn-4** assembly, optimal yields were achieved with template **3** (66%, TT spacer), followed by **14a** (51%, two three carbon spacers). The two glycol spacer templates, **15a** and **16a**, gave the next highest yields, at 49% each. The best template for **Mn-8** formation was the nine-atom glycol spacer in **15b** (61%), followed by **16b** (55%, eighteen atom glycol spacer), and **7** (50%, TT spacer). The rest of the templates gave similar yields of **Mn-8**: **17b** (two D-spacers, 25%) and **14b** (21%).

Table 2. Assembly Yields for Mn-4 and Ni-4 Metallosalen–DNA Conjugates with Different Nucleotide Spacer Templates

		% yield	
template	spacer	**Mn-4**	**Ni-4**
3	TT	77	86
18	AT	54	78
19	GC	66	72
20	GG	68	73
21	AA	71	76
22	CC	71	74

In contrast, more consistent results were observed for the assembly of the two different nickel-containing metallosalens. **Ni-4** and **Ni-8** formation was optimal with template spacers of similar type. For **Ni-8**, the original template **7** (TT spacer) exhibited the highest yield (70%). The next highest yielding template was **16b** (67%), while the rest of the templates yielded 30–40% less **Ni-8** than the standard thymidine dinucleotide template (**7**). The results for **Ni-4** were similar: the original template **3**, containing two thymidines, gave the optimal yield (69%). Other templates yielded between 12 and 62% less of the desired **Ni-4**, with **15a** yielding the least **Ni-4** (6%). In general, the formation of conjugates **4** and **8** was optimal when the templates contained natural nucleotides (T spacers, **3** or **7**) compared with the flexible organic spacers (**14**–**16**) and the abasic "D-spacers" (**17**). The organic spacers were chosen to provide flexibility and low steric demand at the assembly site. Likewise, templates with D-spacers were designed to maintain the natural helical pitch of the DNA backbone while eliminating steric hindrance at the assembly site by nucleotide bases. The results shown here were unexpected, given that templates that contained non-nucleotidyl spacers yielded 12 to 62% less metallosalen–DNA conjugate than the templates containing two natural thymidine residues.

With the successful formation of metallosalen–DNA conjugates using templates containing two thymidine spacers, other dinucleotide template spacers were evaluated: AT (**18a**), GC (**19a**), GG (**20a**), AA (**21a**), and CC (**22a**, Figure 2). Using **3** and the new templates **18a**–**22a**, the assembly reactions for **Mn-4** and **Ni-4** were examined, and the results are shown in Table 2. The yields for the metallosalen–DNA conjugates (**4**) with nickel and manganese ions showed comparable trends. Overall, template **3**, with its TT spacer, provided the maximal yield for the metallosalen–DNA conjugate **4** (77% for **Mn-4** and 86% for **Ni-4**). For templates **19a**–**22a**, which varied the identity of the internal dinucleotide spacer, results for **Mn-4** and **Ni-4** assembly reactions followed a similar trend: TT (**3**) ≫ AA (**21a**) ≥ CC (**22a**) > GG (**20a**) > GC (**19a**). Template **18a** (AT spacer) was unusual in that conjugate yields were dependent on the metal used. Template **18a** yielded 54% of **Mn-4**, which was lower than with the GC spacer (**19a**, 66%). However, yields of **Ni-4** with **18a** (78%) were similar to AA (76%, **21a**) and CC (74%, **22a**). We suggest that the differences may be accounted for by differential metal ion binding abilities of the spacer sites or by unique hydrogen bonding interactions with the salicylaldehyde moiety of

the SAL−DNA precursors. Evaluation of these hypotheses will require further structural studies of duplexes containing metallosalen−DNA. Nevertheless, Table 2 clearly shows that, of the templates screened, templates with two thymidine nucleotide spacers (**3** or **7**) are the optimal complementary strands for formation of the corresponding metallosalen−DNA derivatives.

A major reason for the initial selection of metallosalens as a target for template-directed synthesis was their ability to accommodate a variety of metal ions and diamines (*59*). To determine the range of metal ions and diamines that were able to support metallosalen−DNA assembly, a series of assays was performed using SAL strands **1** and **2** with template **3**. Metal ion assays were performed using concentrations of 500 μM of each metal and 250 μM of EN. The reactions were evaluated after 1 and 24 h of incubation at 37 °C and assayed by PAGE. Several water-soluble transition metals were assayed for their metallosalen−DNA formation ability, and the metal ions that supported metallosalen−DNA assembly were Mn(III), Ni(II), VO(II), Zn(II), Cu(II), and Rh(III) (see Supporting Information). As demonstrated previously, $Mn(OAc)_2$ and $Ni(OAc)_2$ provided the highest yields of metallosalen−DNA conjugates. Iron (II) also displayed early promise, but DNA aggregation has been observed above concentrations of 40 μM (*60*), which limited further studies. Copper(II) produced metallosalen−DNA conjugate in 36% yield, and the yields of **VO-4** and **Zn-4** were 15 and 21%, respectively. Formation of **Rh-4** proceeded poorly, in a maximal yield of 5%. Other studies have shown that metallosalen−DNA conjugate assembly reactions also accept Al(III) (*61*), opening the possibility for template directed synthesis of more diverse metallosalen−DNA conjugates.

All of the work described to date utilized ethylenediamine (EN) (*55*, *56*) as the cross-linker for the two precursor SAL−DNA strands. To explore the tolerance of the metallosalen−DNA assembly reaction to other diamines, two diamines were examined for metallosalen−DNA conjugation reactions: racemic *trans*-1, 2-diaminocyclohexane (CA) and 1,2-phenylenediamine (PA). CA was chosen because its molecular structure is more constrained than EN, while PA was selected to investigate formation with a rigid, achiral diamine. Utilizing the standard assembly conditions for **Mn-4** and **Ni-4**, the comparative ability of EN, CA, and PA to support metallosalen−DNA formation was assessed by gel electrophoretic studies. The yield of metallosalen−DNA, composed of different diamines, was dependent on the combination of metal and diamine used in the assembly reaction. For assembly with Mn(II), metallosalen−DNA yields for CA were similar to EN (54% and 55%, respectively), whereas the metallosalen derived from PA was formed in significantly lower yield (16%). The opposite trend occurred with nickel-metallosalen assembly: PA and EN yielded 44% and 40% of the metal−DNA respectively, while CA yielded 3% of the Ni metallosalen−DNA conjugate. These investigations suggested that use of diverse diamines should support the construction of a broad range of metallosalen−DNA backbones, including chiral diamine cross-linkers.

Physical Properties of the Metallosalen−DNA Conjugates. A second motivation for selection of metallosalen−DNA as a target for DNA template-directed synthesis was our interest in using metallosalen−DNA for applications in targeted DNA cleavage (*62*), catalysis, and materials design. As a result, we became interested in the inherent chemical and thermal stability of metallosalen−DNA and the stability of DNA duplexes containing metallosalen−DNA. To evaluate the metallosalen−DNA conjugates for thermal and chemical stability, radioactive samples of **Mn-4** and **Ni-4** were prepared using 0.4 nmol of **1**, **2**, template **3**, and a trace amount of radiolabeled **1** with the appropriate concentrations of metal and EN. The assembly reactions were incubated at 37 °C for 1 h (**Mn-4**) or 24 h (**Ni-4**) and purified by PAGE. The purified metallosalens, **Mn-4** or **Ni-4**, were subjected to various conditions, and the rates of decomposition were assayed by PAGE.

The effect of temperature on metallosalen−DNA stability was explored. At room temperature, there was no detected decomposition of **Mn-4** or **Ni-4** over several days. Incubation at higher temperatures also demonstrated little effect on the conjugates: no **Mn-4** or **Ni-4** decomposition was seen over 2 days at 50 °C. The degradation of **Mn-4** was slow (1−2% per h) at 80 °C and produced a product that comigrated with the SAL−DNA starting material. Thus, we hypothesized that the major decomposition mechanism was hydrolysis of the metallosalen. Conjugate **Ni-4** displayed no degradation at 80 °C over 24 h. Repeated thaws from −20 °C of nonradiolabeled **Mn-4** and **Ni-4** samples over several months to a year proceeded with no detectable loss of the conjugates.

Given the demonstrated thermal stability of conjugates **Mn-4** and **Ni-4**, we examined the stability of the metallosalen groups to the metal chelator, EDTA. Early in our investigations of template-directed metallosalen−DNA syntheses, EDTA was removed from all buffers to prevent removal of the metal from the salen ligand. The extent of metallosalen−DNA EDTA decomposition was assayed by incubation of **Mn-4** and **Ni-4** radiolabeled samples with increasing concentrations of EDTA (0−40 mM) for 15 min. The only visible products were the starting strand **1** and the metallosalen−DNA conjugate, **4**, suggesting that the major mechanism for decomposition was salen hydrolysis following metal removal. The **Mn-4** conjugate was stable in buffers containing up to 5 mM EDTA, above which the fraction of **Mn-4** remaining steadily decreased. At and above 40 mM EDTA, the amount of **Mn-4** remained at 6% of the starting amount. In contrast to the instability of **Mn-4**, **Ni-4** was stable to all EDTA concentrations examined, with no decomposition to component SAL−DNA strands being detected. Thus, the thermal and EDTA stability assessments of **Mn-4** and **Ni-4** indicated that nickel metallosalen−DNA conjugates were the more robust complexes, and the manganese metallosalen−DNA were more labile.

With the stabilities of the metallosalen−DNA conjugates established, the helical properties of the metallosalen−DNA conjugates **4** and **8** within duplex DNA were examined by circular dichroism (CD) spectroscopy. Metallosalen−DNA strands were hybridized to their complementary templates (**4•3** and **8•7**, TT spacers) in 10 mM sodium phosphate, 150 mM NaCl, pH 7.0. For comparison, all−DNA duplexes of templates **3** and **7** with complementary oligonucleotides (**23** and **24**, respectively) also were evaluated. Representative CD spectra for **Mn-4•3** and **Ni-4•3** and **3•23** are compared in Figure 3A. The spectrum of each duplex displays a positive band at 280 nm and a negative band at 250 nm, indicative of a B-form helix (*63*). All metallosalen−DNA conjugate duplexes provided similar CD spectra (see Supporting Information), indicating that the metallosalen does not disrupt B-form helicity.

The thermal stabilities of the metallosalen−DNA/template duplexes were evaluated by UV-thermal denaturation studies. Utilizing the same annealing conditions as the CD studies, the UV melting profiles were obtained

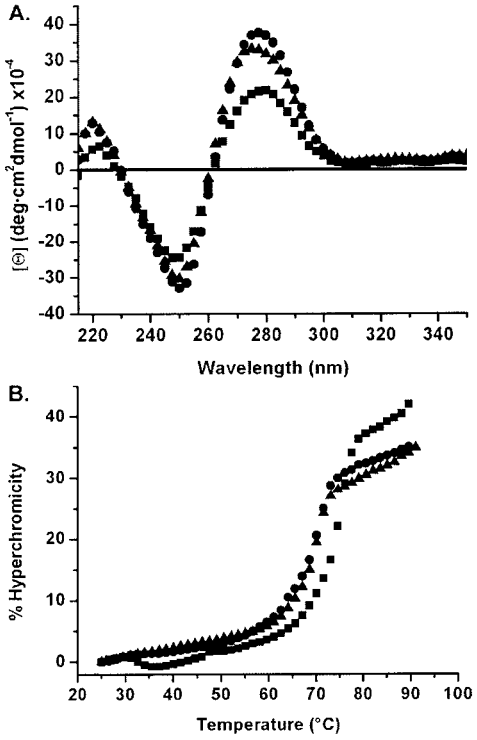

Figure 3. Biophysical properties of metallosalen–DNA **Mn-4•3** (circles) and **Ni-4•3** (triangles) duplexes compared to the control duplex of **3•23** (squares). (A) CD spectra of duplexes (1 μM each strand) in 10 mM sodium phosphate, 150 mM NaCl, pH 7.0. CD spectra were recorded at 25 °C. (B) UV thermal denaturation data were acquired under conditions identical to part A at 260 nm with a temperature ramp rate of 0.5 °C/min.

by heating the samples from 30 °C to 90 °C at 0.5 °C/min. The melting profiles of **Mn-4•3** and **Ni-4•3** and **3•23** are shown in Figure 3B. Metallosalen DNA conjugate duplexes of **Mn-4•3** and **Ni-4•3** demonstrated sharp melting transitions at 70.6 ± 0.1 °C and 70.5 ± 0.1 °C, respectively. The control duplex comprised of **3•23** displayed a slightly higher melting temperature (T_m) of 75.6 ± 0.3 °C. Thus, the replacement of two base pair interactions with the metallosalen led to a thermal stability loss of 5 °C in these duplexes. A similar decrease was observed in the **Ni-8** duplex T_m ($\Delta T_m = -6$ °C) compared with the unmodified duplex of **7•24**. Duplex **Ni-8•7** displayed a melting transition of 72.1 ± 0.5 °C compared to the T_m of 78.0 ± 0.1 °C for the control duplex **7•24.** The **Mn-8•7** duplex melted with a T_m of 69.1 ± 0.1 °C, but with a broad curvature, indicating a less cooperative denaturation profile. The UV-thermal denaturation studies indicated that the metallosalen of a metallosalen–DNA conjugate creates a minor destabilization of duplex DNA ($\Delta T_m = -5$ to -6 °C). The melting profiles of the conjugate duplexes were similar to unmodified duplexes **3•23** and **7•24** indicating that insertion of a metallosalen did not alter the mode of duplex denaturation. Although a duplex destabilization was expected with the replacement of two base pair interactions with a metallosalen, the disruption of duplex stability was relatively minor for these 32-nucleotide duplexes.

In conclusion, we have demonstrated the generality of template-directed metallosalen–DNA synthesis through the preparation and characterization of a new metallosalen–DNA conjugate (**8**). A second-generation purification methodology was developed that involved the use of shorter DNA templates, which permitted the isolation and characterization of four metallosalen–DNA conjugates. Our assembly approach for metallosalen–DNA conjugates was shown to be specific and template-directed, even in the presence of noncomplementary SAL–DNA strands. The optimal templates for efficient metallosalen–DNA conjugate synthesis contained dinucleotide spacers, usually TT, compared to flexible organic spacers or abasic site analogues. CD spectroscopy demonstrated that duplexes containing metallosalens adopted B-form helices, and UV-thermal denaturation studies indicated that the metallosalen destabilizes 32-mer duplexes by 5–6 °C. These studies establish the key features necessary for the template-directed syntheses and applications of metallosalen–DNA.

ACKNOWLEDGMENT

We acknowledge funding from the ACS Petroleum Research Fund (34740-G4). J.L.C. was supported by an Institutional NRSA Training Grant in Molecular Biophysics (GM08382). T.L.S. is a recipient of a Burroughs Wellcome Fund New Investigator Award in the Toxicological Sciences. The MALDI-TOF MS instrument was purchased with funds provided by NIH Scientific Instrumentation grant 1-S10-RR13810. We acknowledge the use of instruments in the Keck Biophysics Facility at Northwestern University.

Supporting Information Available: Synthesis of oligonucleotides **23**–**26**, characterization, CD, and UV thermal denaturation data for **Mn-8** and **Ni-8**, assays of metal ions and templates **3**, **7**, and **14**–**17** for the assembly of metallosalen–DNA conjugate **4**. This material is available free of charge via the Internet at http://pubs.acs.org/bc.

LITERATURE CITED

(1) Saenger, W. (1984) *Principles of Nucleic Acid Structure*, Springer-Verlag, New York.
(2) Zarrinkar, P. P., and Williamson, J. R. (1994) Kinetic Intermediates in RNA Folding. *Science 265*, 918–924.
(3) Feig, A. L., and Uhlenbeck, O. C. (1999) in *The RNA World* (Gesteland, R. F., Cech, T. R., and Atkins, J. F., Eds.) pp 287–319, CSHL Press, Cold Spring Harbor, NY.
(4) Pyle, A. M. (1993) Ribozymes: A Distinct Class of Metalloenzymes. *Science 261*, 709–714.
(5) Dreyer, G. B., and Dervan, P. B. (1985) Sequence-specific cleavage of single-stranded DNA: oligodeoxynucleotide-EDTA-Fe(II). *Proc. Natl. Acad. Sci. U.S.A. 82*, 968–972.
(6) Bashkin, J. K., Frolova, E. I., and Sampath, U. (1994) Sequence-Specific Cleavage of HIV mRNA by a Ribozyme Mimic. *J. Am. Chem. Soc. 116*, 5981–5982.
(7) Bergstrom, D. E., and Gerry, N. P. (1994) Precision Sequence-Specific Cleavage of a Nucleic Acid by a Minor-Groove-Directed Metal-Binding Ligand Linked through N-2 of Deoxyguanosine. *J. Am. Chem. Soc. 116*, 12067–12068.
(8) Chen, C. B., and Sigman, D. S. (1988) Sequence-specific scission of RNA by 1,10-phenanthroline-copper linked to deoxyoligonucleotides. *J. Am. Chem. Soc. 110*, 6570–6572.
(9) Sakamoto, S., Tamura, T., Furukawa, T., Komatsu, T., Ohtsuka, E., Kitamura, M., and Inoue, H. (2003) Highly efficient catalytic RNA cleavage by the cooperative action of two Cu(II) complexes embodied within an antisense oligonucleotide. *Nucleic Acids Res. 31*, 1416–1425.
(10) Hall, J., Husken, D., and Haner, R. (1997) Sequence-specific cleavage of RNA using macrocyclic lanthanide complexes conjugated to oligonucleotides: a structure activity study. *Nucleosides Nucleotides 16*, 1357–1368.
(11) Dubey, I., Pratviel, G., and Meunier, B. (2000) Synthesis and DNA cleavage of 2′-O-amino-linked metalloporphyrin-oligonucleotide conjugates. *J. Chem. Soc., Perkin Trans. 1* 3088–3095.
(12) Magda, D., Crofts, S., Lin, A., Miles, D., Wright, M., and Sessler, J. L. (1997) Synthesis and Kinetic Properties of Ribozyme Analogs Prepared Using Phosphoramidite De-

rivatives of Dysprosium(III) Texaphyrin. *J. Am. Chem. Soc. 119*, 2293−2294.

(13) Lewis, F. D., Helvoigt, S. A., and Letsinger, R. L. (1999) Synthesis and spectroscopy of Ru(II)-bridged DNA hairpins. *Chem. Commun*. 327−328.

(14) Khan, S. I., Beilstein, A. E., Tierney, M. T., Sykora, M., and Grinstaff, M. W. (1999) Solid-Phase Synthesis and Photophysical Properties of DNA Labeled at the Nucleobase with Ru(bpy)2(4-m-4′-pa-bpy)$^{2+}$. *Inorg. Chem. 38*, 5999−6002.

(15) Bannwarth, W., Pfleiderer, W., and Mueller, F. (1991) Energy transfer within oligonucleotides from a lumazine (pteridine-2,4(1H,3H)-dione) chromophore to bathophenanthroline-ruthenium(II) complexes. *Helv. Chim. Acta 74*, 1991−1999.

(16) Yoo, J., Delaney, S., Stemp, E. D. A., and Barton, J. K. (2003) Rapid radical formation by DNA charge transport through sequences lacking intervening guanines. *J. Am. Chem. Soc. 125*, 6640−6641.

(17) Ortmans, I., Content, S., Boutonnet, N., Kirsch-De Mesmaeker, A., Bannwarth, W., Constant, J. F., Defrancq, E., and Lhomme, J. (1999) Ru-labeled oligonucleotides for photoinduced reactions on targeted DNA guanines. *Chem. Eur. J. 5*, 2712−2721.

(18) Meade, T. J., and Kayyem, J. F. (1995) Electron transfer through DNA: site-specific modification of duplex DNA with ruthenium donors and acceptors. *Angew. Chem., Int. Ed. 34*, 352−354.

(19) Meggers, E., Kusch, D., and Giese, B. (1997) An efficient synthesis of enantiomerically pure D- and L-ruthenium(II)-labeled oligonucleotides. *Helv. Chim. Acta 80*, 640−652.

(20) Telser, J., Cruickshank, K. A., Schanze, K. S., and Netzel, T. L. (1989) DNA oligomers and duplexes containing a covalently attached derivative of tris(2,2′-bipyridine)ruthenium(II): synthesis and characterization by thermodynamic and optical spectroscopic measurements. *J. Am. Chem. Soc. 111*, 7221−7226.

(21) Schubert, F., Kluetsch, T., and Cech, D. (1997) Anionic manganese meso-tetraphenyl porphine/oligonucleotide conjugates − synthesis and utilization in chemiluminescent DNA-probe detection. *Nucleosides Nucleotides 16*, 277−289.

(22) Bannwarth, W., Schmidt, D., Stallard, R. L., Hornung, C., Knorr, R., and Mueller, F. (1988) Bathophenanthroline-ruthenium(II) complexes as non-radioactive labels for oligonucleotides which can be measured by time-resolved fluorescence techniques. *Helv. Chim. Acta 71*, 2085−2099.

(23) Hurley, D. J., and Tor, Y. (1998) Metal-Containing Oligonucleotides: Solid-Phase Synthesis and Luminescence Properties. *J. Am. Chem. Soc. 120*, 2194−2195.

(24) Manchanda, R., Dunham, S. U., and Lippard, S. (1996) Automated Solid-Phase Synthesis of Site-Specifically Platinated Oligodeoxyribonucleotides. *J. Am. Chem. Soc. 118*, 5144−5145.

(25) Zimmermann, N., Meggers, E., and Schultz, P. G. (2002) A Novel Silver(I)-Mediated DNA Base Pair. *J. Am. Chem. Soc. 124*, 13684−13685.

(26) Weizman, H., and Tor, Y. (2001) 2,2′-Bipyridine Ligandoside: A Novel Building Block for Modifying DNA with Intra-Duplex Metal Complexes. *J. Am. Chem. Soc. 123*, 3375−3376.

(27) Meggers, E., Holland, P. L., Tolman, W. B., Romesberg, F. E., and Schultz, P. G. (2000) A Novel Copper-Mediated DNA Base Pair. *J. Am. Chem. Soc. 122*, 10714−10715.

(28) Tanaka, K., Yamada, Y., and Shionoya, M. (2002) Formation of Silver(I)-Mediated DNA Duplex and Triplex through an Alternative Base Pair of Pyridine Nucleobases. *J. Am. Chem. Soc. 124*, 8802−8803.

(29) Tanaka, K., Tengeiji, A., Kato, T., Toyama, N., and Shionoya, M. (2003) A Discrete Self-Assembled Metal Array in Artificial DNA. *Science 299*, 1212−1213.

(30) Weizman, H., and Tor, Y. (2001) Oligo-ligandosides: a DNA mimetic approach to helicate formation. *Chem. Commun*. 453−454.

(31) Wagenknecht, H.-A. (2003) Metal-mediated DNA base pairing and metal arrays in artificial DNA: Towards new nanodevices. *Angew. Chem., Int. Ed. 42*, 3204−3206.

(32) Weizman, H., and Tor, Y. (2002) Redox-active metal-containing nucleotides: Synthesis, tunability, and enzymatic incorporation into DNA. *J. Am. Chem. Soc. 124*, 1568−1569.

(33) Goodwin, J. T., and Lynn, D. G. (1992) Template-directed synthesis: use of a reversible reaction. *J. Am. Chem. Soc. 114*, 9197−9198.

(34) Gryaznov, S. M., and Letsinger, R. L. (1993) Chemical ligation of oligonucleotides in the presence and absence of a template. *J. Am. Chem. Soc. 115*, 3808−3809.

(35) Fedorova, O. A., Gottikh, M. B., Oretskaya, T. S., and Shabarova, Z. A. (1996) Cyanogen bromide-induced chemical ligation: mechanism and optimization of the reaction conditions. *Nucleosides Nucleotides 15*, 1137−1147.

(36) Xu, Y., Karalkar, N. B., and Kool, E. T. (2001) Nonenzymatic autoligation in direct three-color detection of RNA and DNA point mutations. *Nat. Biotechnol. 19*, 148−152.

(37) Sando, S., Abe, H., and Kool, E. T. (2004) Quenched Auto-Ligatind DNAs: Multicolor Identification of Nucleic Acids at Single Nucleotide Resolution. *J. Am. Chem. Soc. 126*, 1081−1087.

(38) Zhan, Z.-Y. J., and Lynn, D. G. (1997) Chemical Amplification through Template-Directed Synthesis. *J. Am. Chem. Soc. 119*, 12420−12421.

(39) Li, X., Zhan, Z.-Y. J., Knipe, R., and Lynn, D. G. (2002) DNA-Catalyzed Polymerization. *J. Am. Chem. Soc. 124*, 746−747.

(40) Summerer, D., and Marx, A. (2002) Highlight: DNA-templated synthesis: More versatile than expected. *Angew. Chem., Int. Ed. 41*, 89−90.

(41) Wu, T., and Orgel, L. E. (1992) Nonenzymatic template-directed synthesis on oligodeoxycytidylate sequences in hairpin oligonucleotides. *J. Am. Chem. Soc. 114*, 317−322.

(42) Bruick, R. K., Dawson, P. E., Kent, S. B. H., Usman, N., and Joyce, G. F. (1996) Template-directed ligation of peptides to oligonucleotides. *Chem. Biol. 3*, 49−56.

(43) Letsinger, R. L., Wu, T., and Elghanian, R. (1997) Chemical and photochemical ligation of oligonucleotide blocks. *Nucleosides Nucleotides 16*, 643−652.

(44) Gryaznov, S. M., Schultz, R., Chaturvedi, S. K., and Letsinger, R. L. (1994) Enhancement of selectivity in recognition of nucleic acids via chemical autoligation. *Nucleic Acids Res. 22*, 2366−2369.

(45) Liu, J., and Taylor, J. S. (1998) Template-directed photoligation of oligodeoxyribonucleotides via 4-thiothymidine. *Nucleic Acids Res. 26*, 3300−3304.

(46) Luther, A., Brandsch, R., and von Kiedrowski, G. (1998) Surface-promoted replication and exponential amplification of DNA analogs. *Nature 396*, 245−248.

(47) Kozlov, I. A., De Bouvere, B., Van Aerschot, A., Herdewijn, P., and Orgel, L. E. (1999) Efficient Transfer of Information from Hexitol Nucleic Acids to RNA during Nonenzymatic Oligomerization. *J. Am. Chem. Soc. 121*, 5856−5859.

(48) Mattes, A., and Seitz, O. (2001) Mass-spectrometric monitoring of a PNA-based ligation reaction for the multiplex detection of DNA single-nucleotide polymorphisms. *Angew. Chem., Int. Ed. 40*, 3178−3181.

(49) Mattes, A., and Seitz, O. (2001) Sequence fidelity of a template-directed PNA-ligation reaction. *Chem. Commun*. 2050−2051.

(50) Gartner, Z. J., Grubina, R., Calderone, C. T., and Liu, D. R. (2003) Two enabling architectures for DNA-templated organic synthesis. *Angew. Chem., Int. Ed. 42*, 1370−1375.

(51) Gartner, Z. J., and Liu, D. R. (2001) The Generality of DNA-Templated Synthesis as a Basis for Evolving Non-Natural Small Molecules. *J. Am. Chem. Soc. 123*, 6961−6963.

(52) Calderone, C. T., Puckett, J. W., Gartner, Z. J., and Liu, D. R. (2002) Directing otherwise incompatible reactions in a single solution by using DNA-templated organic synthesis. *Angew. Chem., Int. Ed. 41*, 4104−4108.

(53) Li, X., and Liu, D. R. (2003) Stereoselectivity in DNA-Templated Organic Synthesis and Its Origins. *J. Am. Chem. Soc. 125*, 10188−10189.

(54) Gartner, Z. J., Kanan, M. W., and Liu, D. R. (2002) Multistep small-molecule synthesis programmed by DNA templates. *J. Am. Chem. Soc. 124*, 10304−10306.
(55) Czlapinski, J. L., and Sheppard, T. L. (2001) Nucleic Acid Template-Directed Assembly of Metallosalen−DNA Conjugates. *J. Am. Chem. Soc. 123*, 8618−8619.
(56) Czlapinski, J. L., and Sheppard, T. L. (2004) Template-Directed Assembly of Metallosalen-DNA Hairpin Conjugates. *ChemBioChem 5*, 127−129.
(57) Pourbaix, M. (1966) *Atlas of Electrochemical Equilibria in Aqueous Solutions*, Pergamon Press, Oxford.
(58) Marky, L. A., Kallenbach, N. R., McDonough, K. A., Seeman, N. C., and Breslauer, K. J. (1987) The melting behavior of a DNA junction structure: a colorimetric and spectroscopic study. *Biopolymers 26*, 1621−1634.
(59) Katsuki, T. (2003) Some recent advances in metallosalen chemistry *Synlett* 281−297.
(60) Mandelkern, M., Dattagupta, N., and Crothers, D. M. (1981) Conversion of B DNA between solution and fiber conformations. *Proc. Natl. Acad. Sci. U.S.A. 78*, 4294−4298.
(61) Brown, R. S., Nielsen, M., and Gothelf, K. V. (2004) Self-assembly of aluminium-salen coupled nanostructures from encoded modules with cleavable disulfide DNA-linkers. *Chem. Commun.* 1464−1465.
(62) Czlapinski, J. L., and Sheppard, T. L. (2004) Site-Specific Oxidative Cleavage of DNA by Metallosalen-DNA Conjugates. *Chem. Commun.* 2468−2469.
(63) Gray, D. M., Ratliff, R. L., and Vaughan, M. R. (1992) Circular dichroism spectroscopy of DNA. *Methods Enzymol. 211*, 389−406.

BC049753R

Synthesis of a Metallopeptide–PNA Conjugate and Its Oxidative Cross-Linking to a DNA Target

Olga Kornyushyna, Ann J. Stemmler, Daina M. Graybosch, Ikuko Bergenthal, and Cynthia J. Burrows*

Department of Chemistry, University of Utah, 315 S. 1400 East, Salt Lake City, Utah 84112-0850.
Received October 8, 2004; Revised Manuscript Received November 18, 2004

A nickel(II)–PNA bioconjugate was prepared by formation of a salicylaldimine complex with the amino terminus of a peptide–PNA hybrid with the sequence Arg-His-Gly-$[TACCTAGCAT]_{PNA}$-Arg-$CONH_2$. Hybridization to complementary oligodeoxynucleotides was demonstrated, and covalent adduct formation was observed upon addition of $KHSO_5$ as oxidant. In the absence of PNA, the reactivity of the phenolic radical generated as an intermediate was found to be G ≫ T ≫ C, A; by inclusion of the PNA delivery agent, cross-links between the two oligomers could be observed with T and C bases in the vicinity of the nickel complex, although G was still the most reactive site. The metal complex could be removed by treatment with EDTA following which the Schiff base linkage was readily hydrolyzed. The final result in this case is a salicylaldehyde moiety appended at the target site in DNA.

INTRODUCTION

Both nucleic acids and proteins are rich in nucleophilic sites as well as containing heterocyclic components susceptible to oxidation. Oxidation of either of the two biopolymers generates an electron-deficient site that can lead to covalent bond formation with a nucleophilic partner. For example, oxidative adducts to DNA bases include the well characterized addition of tyrosine's phenol group to both cytosine and thymine heterocycles as part of the molecular basis of DNA–protein cross-linking (*1*, *2*). Additionally, our laboratory has shown that a phenolic radical generated as part of a metallosalicylaldehyde complex undergoes facile addition to guanine forming a covalent adduct to RNA or DNA (*3*–*5*). Such a radical can be effectively produced with a nickel(II) salen complex (Scheme 1, M = Ni) whose one-electron oxidation is predominantly centered on the ligand rather than the metal (*6*). The N-terminal peptide sequence XXH (X = any amino acid) is also a good binding site for nickel(II) producing a redox-active complex and allowing conjugation of the complex to any peptide or protein sequence via elaboration of the C-terminus of XXH to include a DNA-binding sequence. Indeed, both metallosalens and metallopeptides have served as reactive components of bioconjugates for site-selective modification of DNA (*7*–*10*). By combining these two motifs, the ability of nickel(II) salen to form oxidative adducts (*11*) and the peptide features of the NiXXH complex (*12*), we designed the Ni(sal-XH) complex. In this complex, the minimal peptide unit is a dipeptide in which the second amino acid is histidine to provide a strong coordination site for the metal, and the first amino acid is any primary amine-containing α-amino acid (i.e. X ≠ proline) such that the amino terminus can form a Schiff base with salicylaldehyde (Scheme 1).

We previously reported the structure and properties of a prototype complex, Ni(sal-RH), the first tetradentate metal complex of a peptide-salicylaldimine (*13*). Crystallographic analysis showed the formation of a highly planar nickel(II) complex with coordination to the phenolate oxygen, the imine nitrogen, one deprotonated amide nitrogen, and an imidazole nitrogen with no additional axial ligands. An arginine residue at the N-terminal position enhanced both water solubility of the complex and its electrostratic interaction with DNA. Oxidation of the nickel(II) complex could be triggered in either of two ways, using the strong oxidant $KHSO_5$, or by adding a reducing agent, HSO_3^- to an aerobic aqueous solution of Ni(sal-RH). In the latter case, the nickel complex serves initially as a catalyst for in situ autoxidation of sulfite to HSO_5^- (*14*–*16*) and subsequently as a substrate for ligand-centered oxidation.

In the initial study, we found guanine bases in oligodeoxynucleotides exhibited the highest intrinsic reactivity with the Ni(sal-RH) complex under oxidative conditions (*13*), as was the case for other nickel salen-type complexes (*3*, *5*, *17*, *18*). Our subsequent goal was to explore the utility of Ni(sal-XH) as a DNA modifying agent under conditions where the salicylaldimine radical could be delivered site specifically to bases other than guanine. Targeted delivery of DNA alkylating agents has

Scheme 1. Design of the M(sal-XH) Motif

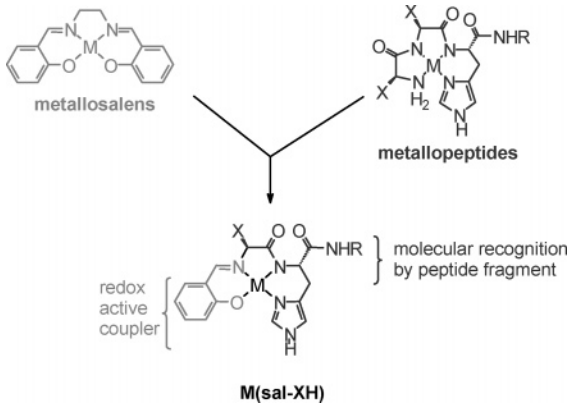

* To whom correspondence should be addressed. E-mail: burrows@chem.utah.edu.

10.1021/bc0497564 CCC: $30.25 © 2005 American Chemical Society
Published on Web 12/21/2004

Scheme 2. Structure of 1, Ni(sal-RH)G-[TACCTAGCAT]$_{PNA}$-RCONH$_2$

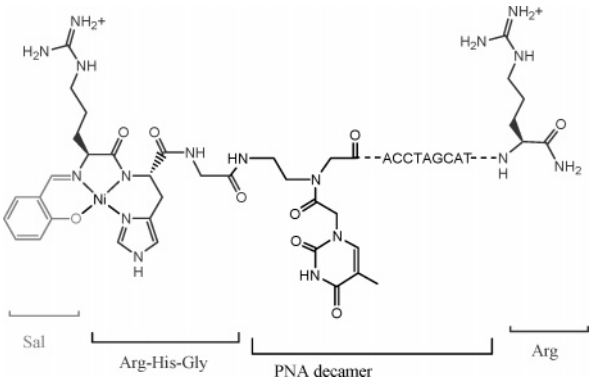

been demonstrated for a variety of conjugates to distamycin analogues (*19*, *20*), and metallopeptides have been used for site-specific cleavage of nucleic acids via conjugation to proteins (*9*), distamycin-like polyamides (*21*), and PNA (*7*). In the present work, we examine the ability of PNA conjugates of the Ni(sal-XH) motif to covalently attach the salicylaldehyde unit to various bases of an oligodeoxynucleotide in order to demonstrate the utility of the Ni(sal-XH) to ultimately modify DNA with a unique aldehyde moiety.

Peptide nucleic acid (PNA) can serve as an ideal delivery agent to target specific sites in nucleic acids due to its exceptional properties for nucleic acid binding and ease of synthesis (*22*). PNAs have high binding affinity for DNA because of their neutral charge, and because PNA-DNA duplexes show higher melting temperatures than DNA–DNA duplexes, shorter sequences can be used to impart high stability to a duplex. PNA is less tolerant of base pair mismatches than is DNA; a single mismatch typically leads to an 8–20 °C lowering of the T_m in a PNA–DNA duplex ensuring higher sequence selectivity than for DNA–DNA duplexes (*23*–*25*). We therefore designed the Ni(sal-XH)–PNA conjugate, **1** (Scheme 2), that includes a PNA decamer conjugated to an N-terminal RHG peptide for formation of the appropriate redox-active nickel complex. Its reactivity toward complementary targets presenting any of the four natural bases in proximity to the metal complex was then examined.

EXPERIMENTAL PROCEDURES

Synthesis of NH$_2$-RHG-[TACCTAGCAT]-R-CONH$_2$. The PNA–peptide conjugate was prepared at a 0.1 mmol scale using Rink Amide AM resin (0.145 g) to build the conjugate. Fmoc- and Bhoc-protected monomers for PNA synthesis were purchased from Perseptive Biosystems; other protected amino acids were purchased from Nova-Biochem. The initial arginine at the C-terminus was coupled to the resin using standard peptide synthesis protocols. The solvent system was DMF, the activating agent was *N*-methylmorpholine in DMF, and the deprotecting agent was 20% piperidine in DMF. The peptide synthesizer was then switched to an NMP (*N*-methylpyrrolidine)-based solvent system (20% DMSO in NMP) (*26*) for addition of the Bhoc-protected PNA monomers. The activating agent was 10% DIPEA (*N*,*N*-diisopropylethylamine) and 10% lutidine in 20% DMSO/NMP, and the deprotecting agent was 30% piperidine in 20% DMSO/NMP. Each PNA monomer (0.1 mmol) was weighed into vials along with HBTU (0.3 mmol). An endcapping reagent (3 mL) was used that consisted of 5% acetic anhydride and 6% lutidine in 20% DMSO/NMP. The mixing times and activating/deprotecting steps reflected published protocols (*22*). Next, the solvent system of the synthesizer was switched back to DMF, as described above, to add the three N-terminal amino acids. Fmoc-Gly-OH, Fmoc-His(trt)-OH, and Fmoc-Arg(pbf)-OH were added sequentially using standard protocols. Endcapping was achieved using acetic anhydride. The final step was deprotection of the last amino acid without endcapping.

The PNA–peptide was cleaved from the resin using a cleavage cocktail of 95% trifluoroacetic acid, 4% *m*-cresol (necessary to cleave Bhoc protecting group) and 1% triisopropylsilane (a radical scavenger). The cocktail was shaken with the beads at room temperature for 1 h. The PNA–peptide conjugate was dried and washed three times with diethyl ether and then dried by evaporation. The sample was HPLC purified using an analytical C18 column (Viadac, 4.6 × 250 mm). The dried sample was dissolved in 35 mL of 0.1% TFA and filtered. A gradient from 100% solvent A (0.1% aqueous TFA) to 18% solvent B (acetonitrile) was used. The peak at 26 min. was analyzed by ESI-LC-MS (see Supporting Information) and showed a molecular mass at 3193.4 (calcd = 3193.7).

Synthesis and Purification of DNA Oligomers. Oligodeoxynucleotides were synthesized using standard automated solid-support chemistry protocols on an Applied Biosystems Model 392B synthesizer using the manufacturer's protocols. Gel electrophoresis on 20% polyacrylamide gels with 7M urea at 40 W provided the purified oligodeoxynucleotides. The purity of synthesized oligodeoxynucleotides was confirmed by mass spectral analysis on a Micromass Quattro II instrument.

Electrophoretic Mobility Shift Assays. The 14nt oligodeoxynucleotides were 5′-end labeled using T4 polynucleotide kinase and [(γ-^{32}P] ATP. Unreacted [(γ-^{32}P] ATP was separated from labeled oligonucleotides with MicroSpin G-25 columns (Amersham Pharmacia Biotech). DNA oligonucleotides were annealed to the PNA–peptide strand in 10 μL solutions of 10 mM NaH_2PO_4. The DNA concentration was kept constant (2.2 μM) while the PNA–peptide concentration varied from 0 to 2.2 μM. The resultant duplexes were applied to a 15% nondenaturing polyacrylamide gel and subjected to electophoresis at 2 W for 4.5 h in the cold box (4 °C). Radiolabeled duplex formation was quantified by storage phosphor autoradiography (Molecular Dynamics Storm 860).

Formation of the 1:DNA Duplexes. 5′-[^{32}P]-End-labeled oligodeoxynucleotides (3N14, N = A, C, G, T) were annealed to the PNA–peptide strand in 200 μL solutions containing 100 mM NaCl plus10 mM NaH_2PO_4 (pH = 8) to yield 1 μM solutions of DNA/PNA–peptide duplexes. Ni(sal)$_2$ was prepared by mixing stoichiometric amounts of Ni(OAc)$_2$ in 4:1 ethanol:water and salicylaldehyde in ethanol and collection of the precipitate. Approximately 1.5 mg of Ni(sal)$_2$ was added to each duplex solution and shaken overnight in the cold box at 4 °C. Excess amounts of Ni(sal)$_2$ were removed by filtration through SPIN-X columns, followed by washes with 100 μL of distilled H_2O (final volume = 300 μL). The solution volume was then reduced to 100 μL to yield 2 μM **1**:DNA duplex.

Cross-Link Formation. A 20-μL aliquot of 2 μM radiolabeled **1**:DNA duplex was added to 4 μL of 1 mM $KHSO_5$ in a 40-μL solution of 100 mM NaCl/10 mM NaH_2PO_4 (pH = 7) and incubated for 15 min at room temperature. Reactions were quenched by adding 2 μL of 20 mM EDTA and 2 μL of 50 mM HEPES followed by dialysis

Peptide-[PNA]/DNA duplexes:

NH_2 -RHG- [TAC CTA GCA T]-R-$CONH_2$
3′-AAA-A-ATG GAT CGT A-5′ (3A14)
3′-CCC-A-ATG GAT CGT A-5′ (3C14)
3′-GGG-A-ATG GAT CGT A-5′ (3G14)
3′-TTT-A-ATG GAT CGT A-5′ (3T14)

Figure 1. Sequences of the peptide−PNA conjugate and oligodeoxynucleotides used in these studies.

overnight. Oxidized and unmodified **1**:DNA duplex was then treated with 0.2 M piperidine for 30 min at 90 °C. Both unmodified and oxidized **1**:DNA duplex not treated with piperidine were used as controls in these experiments. All reactions were lyophilized to dryness, resuspended in 4 μL of loading buffer, applied to a 15% polyacrylamide gel in the presence of 7M urea, and subjected to electrophoresis for 3 h at 40 W. Formation of the high molecular weight products was then monitored by storage phosphor autoradiography (Molecular Dynamics Storm 860).

Adduct Formation of Ni(sal-RH) with Plasmid DNA. Ni(sal-RH) was prepared as previously described (*13*). Reactions with the single-stranded plasmid from M13mp18 phage were conducted using 100 μM Ni(sal-RH) and 50 μM Na_2SO_3 using the same reaction and buffer conditions as for oligonucleotide work. Primer extension and PCR were performed using 5′-[^{32}P]-end labeled d(GTTTTCCCAGTCACGAC), the −40 primer relative to the Hind III restriction site, according to the procedure for the Thermo Sequenase cycle sequencing kit (Amersham). Analysis and imaging was conducted as described above.

RESULTS AND DISCUSSION

The peptide bioconjugate **1** was designed to comprise a 10-mer PNA sequence for hybridization to its complementary sequence in DNA along with the N-terminal XH motif for formation of the redox-active Ni(sal-XH) complex. A glycine spacer was added between the metal ligating peptide and the PNA sequence, and arginines were included at both the N terminus and the C terminus for additional water solubility and electrostratic interactions with DNA. Although lysine residues could also have served this purpose, they may have interfered with Schiff base formation at the amino-terminal site. Finally, the C terminus of the oligomer was left as a neutral amide rather than a carboxylate group by synthesis on Rink Amide resin, again for facilitating binding to DNA. The synthesis of the peptide−PNA portion of **1** was achieved through a combination of standard protocols for peptide and for PNA synthesis on solid support. The nickel salicylaldimine complex of the peptide could be prepared either before or after hybridization to the DNA complement. The completed synthesis of **1** was analyzed by ESI-MS (see Supporting Information) after HPLC purification of the peptide−PNA ligand.

The PNA conjugate **1** was tested for hybridization to DNA complements by both thermal melting studies and gel mobility shift analysis using the four oligodeoxynucleotides shown in Figure 1. Each of the 14-mers contained the 10-mer complementary sequence to the PNA segment at its 5′ end, a one-nucleotide spacer of deoxyadenosine, thought to be the least reactive of the four bases, and a trinucleotide NNN sequence at the 3′ end that would be oriented in proximity to the Ni(sal-RH) group and would serve as the target sites for oxidative adduct formation. T_m values were above 55 °C, and a gel shift experiment indicated tight binding between the PNA−peptide conjugate and each of the 3N14 complements. A representative assay is shown in Figure 2 for 3T14.

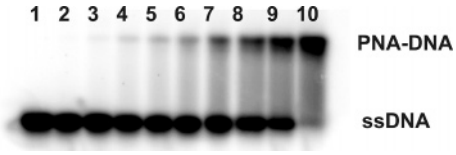

Figure 2. PNA−peptide binding examined by the gel mobility shift assay. In a total volume of 10 μL, a radiolabled DNA (3T14) was incubated with various amounts of a complementary PNA−peptide as described in the Experimental Procedures. The samples were analyzed on the 15% nondenaturing polyacrylamide gel. PNA concentrations in lanes 1−10 were 0, 0.011, 0.022, 0.034, 0.069, 0.14, 0.28, 0.55, 1.1, and 2.2 μM.

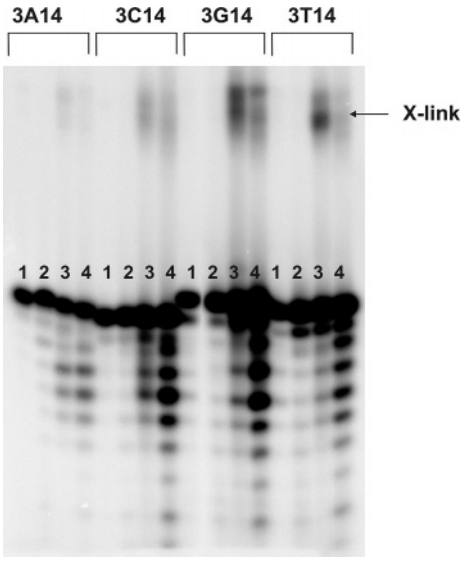

Figure 3. DNA−PNA cross-link formation after incubation DNA + bioconjugate **1** with $KHSO_5$ as described in the Experimental Procedures. For each series, lane 1 contains unoxidized DNA·**1** in buffer; lane 2 contains unoxidized DNA·**1** treated with 0.2 M piperidine; lane 3 − DNA·**1** incubated with 100 μM $KHSO_5$; lane 4 − DNA·**1** incubated with 100 μM $KHSO_5$ and treated with 0.2 M piperidine. All reactions were subjected to electrophoresis on a denaturing 15% polyacrylamide gel. The positions of the high molecular weight products are indicated by the arrow.

To assess the ability of the PNA−Ni(sal-RH) bioconjugate to form covalent cross-links to target oligodeoxynucleotides, we analyzed both oxidation and adduct formation by denaturing gel electrophoresis (Figure 3). For each of the DNA 14-mers containing the complement to the PNA sequence plus a 3′-NNNA overhang near the Ni(sal-RH) complex, the **1**:DNA duplex was treated with $KHSO_5$ to trigger oxidation of the nickel(II) complex. Because nickel−salicylaldimine complexes typically undergo ligand-centered oxidation, the resulting phenolic radical is expected to couple to one of the 3′ overhanging nucleotides. For each set of experiments, the first two lanes represent control studies without oxidant and −/+ piperidine treatment. Piperidine treatment would be expected to result in strand scission at sites of base oxidation and/or adduct formation (*27*). Lanes 3 and 4 show adduct formation and strand scission −/+ piperidine treatment, respectively.

It is clear from the results in Figure 3 that guanosine nucleotides retain the highest level of reactivity toward oxidative cross-link formation with thymidine also showing substantial adduct formation. The ability of dC to undergo adduct formation was apparent but small, while that of dA was almost nonexistent. Treatment of the

Scheme 3. Proposed Mechanism of Cross-Link Formation and Hydrolysis

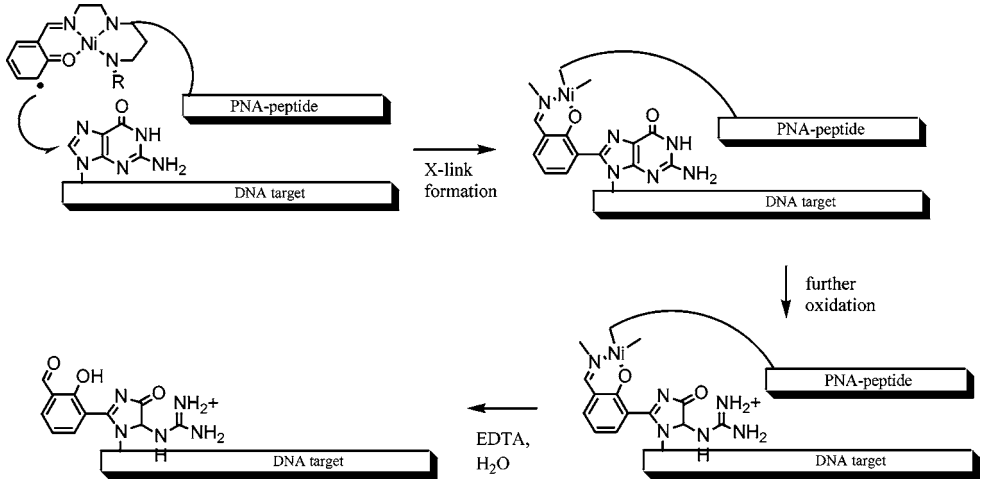

cross-linked duplexes with piperidine led to some loss of intensity presumably due to strand scission as was previously shown for the parent complex, Ni(sal-RH) (*13*). In all cases, the overhanging nucleotides appear also to be subject to oxidative damage leading to strand scission as evidenced by the bands observed below starting material on the gel. This is likely due to the rather high concentration of $KHSO_5$ employed in the reaction (100 μM). Previously, we found that Na_2SO_3 could be used in place of $KHSO_5$ wherein the nickel complex served to catalyze in situ oxidation of sulfite to monoperoxysulfate, avoiding the use of excess oxidant (*13*); however, trials with Na_2SO_3 in the present system led to lower yields of cross-link formation as well.

On the basis of prior work in our laboratory and others, we propose the following mechanism of covalent adduct formation. First, the PNA strand hybridizes with DNA delivering the redox-active nickel complex to the vicinity of the 3′-overhang of the DNA target strand. Reaction with $KHSO_5$ as oxidant (or nickel-catalyzed autoxidation of Na_2SO_3) leads to ligand-centered oxidation generating a phenol radical on the salicylaldimine moiety. Radical attack at C8 of guanine (Scheme 3) or the 5,6 double bond of T or C leads to covalent adduct formation. The adducts appear to be sensitive to piperidine treatment, giving rise to strand scission at the site of cross-linking under Maxam–Gilbert conditions (Figure 3, lanes 4). In the case of guanine C8 phenolic adducts, we previously showed that the adducts were highly sensitive to further oxidation by a pathway analogous to that of 8-oxoguanosine, leading to a guanidinohydantoin derivative. This further oxidation product likely accounts for the additional high-molecular weight band observed by PAGE (Figure 3) under conditions where relatively high concentrations of oxidant were used. This was well characterized for the parent compound Ni(sal-RH) by ESI-MS analysis of the various adducts isolated from the gel (*13*). Furthermore, it was demonstrated that the peptide delivery vehicle could be released from its target by treatment with EDTA. Removal of the coordinating nickel ion presumably sensitizes the salicylaldimine to hydrolysis. The final product after EDTA treatment is therefore the original strand with a salicylaldehyde moiety tagging the site of adduct formation.

The extent of reaction at the various positions of the NNN overhang were analyzed after piperidine treatment. While all three positions were reactive, there was in each case a slight preference for reaction at the internal positions, N_{12} and N_{13}, as opposed to the final nucleotide,

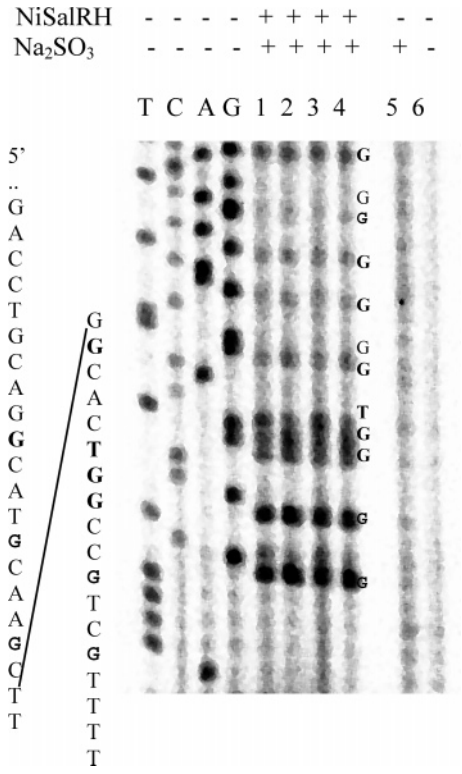

Figure 4. Primer extension analysis of single-stranded phage DNA (M13mp18) cross-linked to Ni(sal-RH). A portion of the sequence analyzed is shown at left with reactive sites in boldface. Lanes T, C, A, G are Sanger sequencing lanes of the single-stranded phage using ddATP, ddGTP, ddTTP, and ddCTP, respectively. Lanes 1–4 are reaction lanes. Cross-linking of Ni(sal-RH) with ss phage M13mp18 sterically inhibits Thermo Sequenase and hence primer extension stops before bases cross-linked to Ni(sal-RH). Control lane 5 demonstrates the effect of Na_2SO_3 in the absence of Ni(sal-RH). Control lane 6 is primer extension in the absence of Na_2SO_3 and Ni(sal-RH).

N_{14} (see Supporting Information), and the trend was the same for all bases except T, for which all three positions were equally reactive. An explanation consistent with these data is that bioconjugate **1** positions the reactive phenol radical nearest the bases that are 2–3 nucleotides beyond the complementary duplex region.

To examine whether the observed reactivity of the nickel salicylaldimine group with T or C, in addition to G, could be found in a larger sample of DNA, we analyzed the single-stranded plasmid M13mp18 with the parent complex, Ni(sal-RH), lacking the PNA delivery unit.

Scheme 4. Utility of the Ni(sal-XH) Motif in Bioconjugates for Delivery of an Aldehyde Functional Group to Specific Sites in DNA

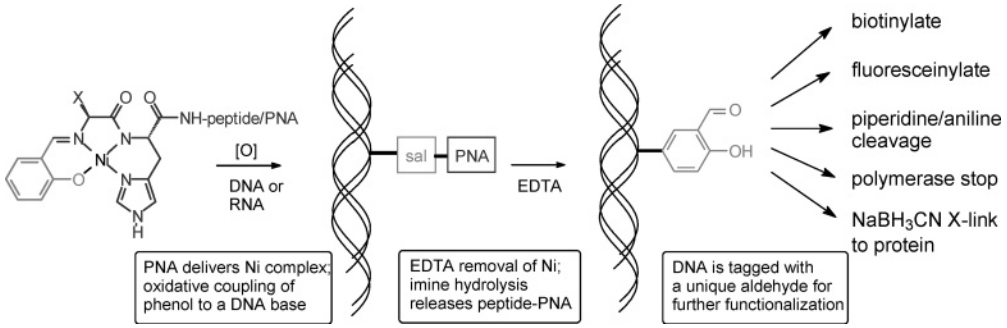

Conditions were chosen under which we previously observed a high degree of adduct formation as opposed to simple oxidative damage. These conditions involved the use of relatively low concentrations of sulfite such that the strong oxidant HSO_5^- was only formed via nickel-mediated autoxidation, and the concentration of HSO_5^- remained negligible. Oxidative adduct formation was analyzed using Thermo Sequenase, an exonuclease-free thermostable DNA polymerase. Primer extension was inhibited by the presence of an adduct, and thus the bands analyzed in lanes 1−4 of Figure 4 represent adduct sites that are one nucleotide shorter than the dideoxy sequencing lanes for which insertion opposite the template base has occurred. The data shown represent a small segment of a larger analysis. In general, reactivity still was seen only at guanines; however, a small number of thymines were also observed to form adducts. These data is therefore in keeping with the assessment that the overall reactivity preference of the phenolic radical generated from the Ni(sal-RH) complex is G > T > C ≫ A.

CONCLUSIONS

We have demonstrated that a Schiff base complex of nickel(II) can be readily appended to a synthetic peptide−PNA conjugate for oxidative cross-linking to a complementary strand of DNA. Minimal requirements for the formation of the nickel complex are an N-terminal XH dipeptide motif in which X represents any α-amino acid with a primary amine available for imine formation with salicylaldehyde. The nickel(II) complex can then be prepared before or after conjugation of PNA to its DNA target. Oxidation with $KHSO_5$, or in situ formation of this oxidant by nickel-catalyzed sulfite autoxidation, leads to oxidative coupling between the phenol ring of salicylaldehyde and a DNA base. Although the intrinsic reactivity of the phenol radical is greatest toward guanosine (G > T > C > A), the reactivity of T and C is enhanced by delivery of the redox-active metal complex in proximity to these bases by the PNA conjugate. Even with delivery, however, adenine remains low in reactivity.

The ability to remove the metal complex and its PNA targeting agent by simple addition of EDTA is a further benefit of this design. The final result is a DNA strand whose targeted site bears a salicylaldehyde tag (Scheme 4). Such a unique aldehyde may be further functionalized with aldehyde reactive reagents leading to site-specific biotinylation, fluorescent labeling, or cross-linking to DNA binding proteins via reductive amination. Such features greatly expand the arsenal of metallo−PNA conjugates that has recently seen development in other laboratories as well (*28*−*33*).

ACKNOWLEDGMENT

We thank Dr. James G. Muller for assistance with mass spectrometry. This work was supported by a grant from the National Science Foundation (0137716).

Supporting Information Available: ESI-MS characterization of **1** and quantitative analysis of PAGE results for site reactivity of **1** in oligo targets. This material is available free of charge via the Internet at http://pubs.acs.org.

LITERATURE CITED

(1) Margolis, S. A., Coxon, B., Gajewski, E., and Dizdaroglu, M. (1988) Structure of a hydroxyl radical induced cross-link of thymine and tryosine. *Biochemistry 27*, 6353−6359.

(2) Gajewski, E., and Dizdaroglu, M. (1990) Hydroxyl radical induced cross-linking of cytosine and tyrosine in nucleohistone. *Biochemistry 29*, 977−980.

(3) Woodson, S. A., Muller, J. G., Burrows, C. J., and Rokita, S. E. (1993) A primer extension assay for modification of guanine N7 by Ni(II) complexes. *Nucleic Acids Res. 21*, 5524−5525.

(4) Muller, J. G., Paikoff, S. J., Rokita, S. E., and Burrows, C. J. (1994) DNA modification promoted by water-soluble nickel(II) salen complexes: A switch to DNA alkylation. *J. Inorg. Biochem. 54*, 199−206.

(5) Muller, J. G., Kayser, L. A., Paikoff, S. J., Duarte, V., Tang, N., Perez, R. J., Rokita, S. E., and Burrows, C. J. (1999) Formation of DNA adducts using nickel(II) complexes of redox-active ligands: A comparison of salen and peptide complexes. *Coord. Chem. Rev. 185*−*186*, 761−774.

(6) Goldsby, K. A. (1988) Symmetric and unsymmetric nickel(II) Schiff base complexes: Metal-localized versus ligand-localized oxidation. *J. Coord. Chem. 19*, 83−90.

(7) Footer, M., Egholm, M., Kron, S., Coull, J. M., and Matsudaira, P. (1996) Biochemical evidence that a D-loop is part of a four-stranded PNA-DNA bundle. Nickel-mediated cleavage of duplex DNA by a Gly-Gly-His Bis-PNA. *Biochemistry 35*, 10673−10679.

(8) Routier, S., Bernier, J.-L., Catteau, J.-P., and Bailly, C. (1997) Recognition and cleavage of DNA by a distamycin-salen-copper conjugate. *Bioorg. Med. Chem. Lett. 7*, 1729−1732.

(9) Harford, C., Narindrasorasak, S., and Sarkar, B. (1996) The designed protein M(II)-Gly-Lys-His-Fos(138−211) specifically cleaves the AP-1 binding site containing DNA. *Biochemistry 35*, 4271−4278.

(10) Long, E. C. (1999) Ni(II)-Xaa-Xaa-His metallopeptide- -DNA/RNA interactions. *Acc. Chem. Res. 32*, 827−836.

(11) Rokita, S. E., and Burrows, C. J. (2003) in *Small Molecule DNA and RNA Binders* (Demeunynck, M., Bailly, C., and Wilson, W. D., Eds.) pp 126−145, Wiley-VCH, Weinheim.

(12) Harford, C., and Sarkar, B. (1997) Amino terminal Cu(II)- and Ni(II)-binding (ATCUN) motif of proteins and peptides: Metal binding, DNA cleavage, and other properties. *Acc. Chem. Res. 30*, 123−130.

(13) Stemmler, A. J., and Burrows, C. J. (1999) The Sal-XH mofif for metal-mediated oxidative DNA−peptide cross-linking. *J. Am. Chem. Soc. 121*, 6956−6957.
(14) Muller, J. G., Hickerson, R. P., Perez, R. J., and Burrows, C. J. (1997) DNA damage from sulfite autoxidation catalyzed by a nickel(II) peptide. *J. Am. Chem. Soc. 119*, 1501−1506.
(15) Lepentsiotis, V., Domagala, J., Grgic, I., van Eldik, R., Muller, J. G., and Burrows, C. J. (1999) Mechanistic information on the redox cycling of Ni(II/III) complexes in the presence of sulfur oxides and oxygen. Correlation with DNA damage experiments. *Inorg. Chem. 38*, 3500−3505.
(16) Wietzerbin, K., Pratviel, G., Bernadou, J., Meunier, B., Muller, J. G., Jameton, R. A., and Burrows, C. J. (1999) Hydroxylation, epoxidation and DNA cleavage reactions mediated by the biomimetic MnTMPyP/O2/sulfite oxidation system. *Inorg. Chem. 38*, 4123−4127.
(17) Zhou, X., Shearer, J. M., and Rokita, S. E. (2000) A Ni-(salen)-biotin conjugate for rapid isolation of accessible DNA. *J. Am. Chem. Soc. 122*, 9046−9047.
(18) Mandal, S. S., Varshney, U., and Bhattacharya, S. (1997) Role of the central metal ion and ligand charge in the DNA binding and modification by metallosalen complexes. *Bioconjugate Chem. 8*, 798−812.
(19) Bailly, C., and Chaires, J. B. (1998) Sequence-specific DNA minor groove binders. Design and synthesis of netropsin and distamycin analogues. *Bioconjugate Chem. 9*, 513−538.
(20) Kumar, D., Veldhuyzen, W. F., Zhou, Q., and Rokita, S. E. (2004) Conjugation of a hairpin pyrrole-imidazole polyamide to a quinone-methide for control of DNA cross-linking. *Bioconjugate Chem. 15*, 915−922.
(21) Bailly, C., Sun, J.-S., Colson, P., Houssier, C., Hélène, C., Waring, M. J., and Henichart, J.-P. (1992) Design of a sequence-specific DNA-cleaving molecule which conjugates a copper-chelating peptide, a netropsin residue, and an acridine chromophore. *Bioconjugate Chem. 3*, 100−103.
(22) Nielsen, P. E., and Egholm, M. (1999) *Peptide Nucleic Acids: Protocols and Applications,* Horizon Scientific Press, Wymondham, UK.
(23) Ratilainen, T., Holmen, A., Tuite, E., Nielsen, P. E., and Norden, B. (2000) Thermodynamics of sequence-specific binding of PNA to DNA. *Biochemistry 39*, 7781−7791.
(24) Ratilainen, T., Holmen, A., Tuite, E., Haaima, G., Christensen, L., Nielsen, P. E., and Norden, B. (1998) Hybridization of peptide nucleic acid. *Biochemistry 37*, 12331−12342.
(25) Jensen, K., Orum, H., Nielsen, P. E., and Norden, B. (1997) Kinetics for hybridization of peptide nucleic acids (PNA) with DNA and RNA studied with the BIAcore technique. *Biochemistry 36*, 5072−5077.
(26) Thomson, S. A., Josey, J. A., Cadilla, r., Gaul, M. D., Hassman, C. F., Luzzio, M. J., Pipe, A. J., Reed, K. L., Ricca, D. J., Wiethe, R. W., and Noble, S. A. (1995) Fmoc mediated synthesis of peptide nucleic acids. *Tetrahedron 51*, 6179−6194.
(27) Burrows, C. J., and Muller, J. G. (1998) Oxidative nucleobase modifications leading to strand scission. *Chem. Rev. 98*, 1109−1151.
(28) Petersen, L., de Koning, M. C., van Kuik-Romeijn, P., Weterings, J., Pol, C. J., Platenburg, G., Overhand, M., van der Marel, G. A., and van Boom, J. H. (2004) Synthesis and in vitro evaluation of PNA−peptide-DETA conjugates as potential cell penetrating artificial ribonucleases. *Bioconjugate Chem. 15*, 576−582.
(29) Mokhir, A., Kraemer, R., and Wolf, H. (2004) Zn^{2+}-Dependent peptide nucleic acids probes. *J. Am. Chem. Soc. 126*, 6208−6209.
(30) Mokhir, A., Kraemer, R., Voloshin, Y. Z., and Varzatskii, O. A. (2004) Synthesis and DNA binding properties of dioxime-peptide nucleic acids. *Bioorg. Med. Chem. Lett. 14*, 2927−2930.
(31) Mokhir, A. A., and Kraemer, R. (2003) Conjugates of PNA with naphthalenediimide derivatives having a broad range of DNA affinities. *Bioconjugate Chem. 14*, 877−883.
(32) Verheijen, J. C., van der Marel, G. A., van Boom, J. H., and Metzler-Notle, N. (2000) Transition metal derivatives of peptide nucleic acid (PNA) oligomers—synthesis, characterization, and DNA binding. *Bioconjugate Chem. 11*, 741−743.
(33) Bigey, P., Soennichsen, S. H., Meunier, B., and Nielsen, P. E. (1997) DNA Binding and cleavage by a cationic manganese porphyrin−peptide nucleic acid conjugate. *Bioconjugate Chem. 8*, 267−270.

BC0497564

Synthesis of New Bivalent Peptides for Applications in the Affinity Enhancement System

L. Morandeau,[†] E. Benoist,[‡] A. Loussouarn,[§] A. Ouadi,[∥] P. Lesaec,[†] M. Mougin,[†] A. Faivre-Chauvet,[†] J. Le Boterff,[†] J. F. Chatal,[†] J. Barbet,[†] and J. F. Gestin*,[†]

Inserm U.601, Institut de Biologie, 9 Quai Moncousu, 44093 NANTES Cedex 01, France, Laboratoire de Chimie Inorganique, Université Paul Sabatier, Bat. IIR1, Route de Narbonne, 31062 TOULOUSE, France, Chelatec SAS, Institut de Biologie, 9 Quai Moncousu, 44093 Nantes Cedex 01, France, and IRES, CNRS/IN2P3 and Université L. Pasteur, B.P.28, 67037 Strasbourg Cedex 2, France. Received September 21, 2004; Revised Manuscript Received November 22, 2004

The feasibility of two-step radioimmunotherapy (RIT) of cancer by the Affinity Enhancement System (AES) has been demonstrated in experimental and clinical studies. This technique, associating a bispecific antibody and a bivalent peptide radiolabeled with iodine-131, has been developed to reduce toxicity and to improve therapeutic efficacy compared to one-step targeting methods. The use of AES with different beta-emitters such as rhenium-188, samarium-153, or lutetium-177 or alpha-emitters such as actinium-225 or bismuth-213 is now considered. Thus three new peptides, designed to allow for the coupling of a variety of bifunctional chelating agents BCA, were synthesized by associating two glycyl-succinyl-histamine (GSH) arms, which are recognized by the 679 monoclonal antibody (mAb-679), with different binding agents, such as *p*-nitrophenylalanine or *N,N*-bis(carboxymethyl)-4-*N*′-(9-fluorenylmethyloxycarbonyl)aminobenzylamine. Immunoreactivity and serum stability evaluation were performed for each synthesized peptide. One of the three peptides (**LM218**) proved to be more stable than the others, and three different BCAs were coupled to **LM218** (CITC-DTPA, CITC-TTHA, and CITC−CHXA″DTPA). One of these products, **LM218-BzTTHA** was radiolabeled with indium-111 without loss of immunoreactivity toward the mAb-679. These new peptides will allow pretargeted RIT with a large variety of radionuclides, to adapt the choice of the radionuclide (LET, half-life, penetrating emission) to the nature and size of targeted tumors.

INTRODUCTION

The targeting of cancer cells depends on the capacity of monoclonal antibodies to recognize antigens expressed at the surface of malignant tumors. These antibodies are used as vectors for radionuclides acting within the tumor mass. They were originally radiolabeled with a gamma emitter and used for diagnostic purposes in immunoscintigraphy (IS) of solid tumors (*1*). This concept was then extended to radioimmunotherapy (RIT[1]), using β- or α-emitters (*2*). However, this system often involves high irradiation of normal tissues, an undesirable effect due in part to the low uptake of monoclonal antibodies in tumor sites (0.01% ID/g tumor), which requires the infusion of large radioactivity doses (*3*), and the relatively slow clearance of excess activity (several hours). Pretargeting techniques allow substantial reduction of nonspecific irradiation of normal tissues. The Affinity Enhancement System (AES) is based on the use of a bispecific antibody (antitumor antigen x anti-hapten) and a radiolabeled peptide carrying two haptens (*4*, *5*). The principle consists of administering the bispecific antibody intravenously and to allow it to bind tumor cells. After a few days to allow elimination of excess free antibody, the radiolabeled bivalent peptide is injected, which is recognized by the bispecific antibody prelocalized in the tumor. Because of its small size, the peptide diffuses rapidly toward the target, and its clearance is much faster than that of a radiolabeled monoclonal antibody. The di-DTPA-TL peptide (Figure 1), which is bivalent with respect to the DTPA-indium hapten, has been used for immunoscintigraphy of colon cancer (*6*) and medullary thyroid carcinoma (*7*), and RIT of medullary thyroid carcinoma (*8*) and small-cell lung cancer (*9*) in association with the F6-734 (anti-CEA x anti-DTPA-indium) bispecific antibody. This peptide is currently tested in clinical trials for the therapy of CEA-expressing tumors (*10*) in association with the hMN14-734 (anti-CEA x anti-DTPA-indium) bispecific antibody. The di-DTPA-TL peptide allows radiolabeling with indium-111 on the DTPA groups and radiolabeling with iodine-131 on the aromatic ring of the tyrosine present in the linker peptide. A similar bivalent hapten based on DTPA-indium has been tested with the AES to target indium-111 to renal cell carcinoma in animals (*11*) and a derivative of this

* To whom correspondence should be addressed. L.M.M.: E-mail: laurence.morandeau@health.wa.gov.au. J.F.G.: Phone: 33 (0) 2 40 08 47 19. Fax: 33 (0) 2 40 35 66 97. E-mail: jfgestin@nantes.inserm.fr.

[†] Inserm U.601, Institut de Biologie.

[‡] Université Paul Sabatier.

[§] Chelatec SAS, Institut de Biologie.

[∥] IRES, CNRS/IN2P3 and Université L. Pasteur.

[1] Abbreviations: RIT, radioimmunotherapy; AES, Affinity Enhancement System; mAb, monoclonal antibody; GSH, glycyl-succinyl-histamine; BCA, bifunctional chelating agent; AcOEt, ethyl acetate; CDI, carbonyldiimidazole; DCC, dicyclohexylcarbodiimide; DHU, dicyclohexylurea; DMF, dimethylformamide; THF, tetrahydrofuran; TFA, trifluoroacetic acid; CITC-DTPA, *p*-isothiocyanatobenzyldiethylentriaminepentaacetic acid; CITC-TTHA, *p*-isothiocyanatobenzyltriethylentetraaminehexaacetic acid; CITC−CHXA″DTPA, *N*-[(*R*)-2-Amino-3-(*p*-isothiocyanatophenyl)propyl]-*trans*-(*S,S*)-cyclohexane-1,2-diamine-*N,N,N′,N″,N″*-pentaacetic acid.

10.1021/bc0497721 CCC: $30.25 © 2005 American Chemical Society
Published on Web 12/24/2004

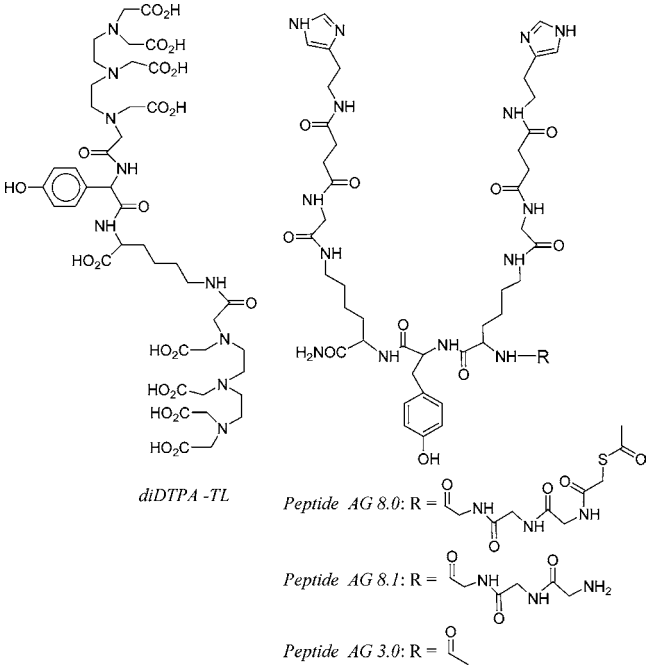

Figure 1. di-DTPA-TL, AG8.0, AG8.1 and AG3.0 Peptides.

peptide, designed to be labeled with technetium-99m and rhenium-188, has also been tested in animals in a colon cancer model (*12*). Peptides AG3.0 and AG8.1 (*13*) (Figure 1) in association with bispecific antibody F6-679 (anti-CEA x anti-GSH) allow direct radiolabeling with iodine-131 on the aromatic ring of tyrosine. Peptide AG8.0 was designed to allow radiolabeling with rhenium-188 and technetium-99m (*14*). However, in vivo targeting with rhenium-188 was not entirely satisfactory (*15*).

Iodine-131, the main radionuclide currently used in RIT, possesses satisfactory specific activity and is fairly easy to radiolabel. However, its radiophysical properties (low-energy β^- radiation, strong gamma emission, and long half-life) do not make it the best radionuclide for RIT applications (*16*). Radionuclides such as actinium-225, samarium-153, yttrium-90, lutetium-177, holmium-166, rhenium-186/188, and astate-211 possess very interesting properties. The possibility of labeling a peptide with each of these radionuclides would provide a therapeutic tool adaptable to different tumor targets. The intrinsic properties of each β- or α-emitter (physical half-life, linear energy transfer, range, energy) could be exploited as a function of the nature and size of the tumor targets to be destroyed. However, the use of these radionuclides within the AES requires their complexation by a bifunctional chelating agent (BCA) (*17*−*20*) coupled to the peptide. In this line of work Sharkey et al. (*21*) have tested in animals, in a colon cancer model, GSH containing peptides bearing a 1,4,7,10-tetraazacyclododecane-*N*,*N*′,*N*″,*N*‴-tetraacetic acid (DOTA) that forms stable complexes with radionuclides such as lutetium-177, yttrium-90, and other radiometals.

The purpose of the present study was to design and synthesize new versatile peptides capable of being coupled to a variety of BCAs. This would allow iodine-131, which is currently used in RIT, to be replaced by other potentially more efficient radionuclides. An analogue of peptide AG8.1 was synthesized, which conserves the recognition properties of AG8.1 for mAb-679 (*22*) and bears a BCA coupling site. To this effect, an aromatic amine ($pK_a = 3$ to 5) was used, as a coupling site, allowing the coupling reaction to be carried out at pH 6, when the amine functions of imidazole ($pK_a = 7.1$) are not reactive. The introduction of a BCA on this new position is less susceptible to interfere in the recognition of the GSH site by mAb-679. On the other hand, the choice of an aromatic amine allows its transformation in isothiocyanate, so the coupling reaction to the BCA can occur either after activation of the peptide or activation of the BCA.

Three analogues of peptide AG8.1 have been synthesized: peptides **LM085**, **LM054**, and **LM218**. Their binding to mAb-679 was checked first, in comparison with that of peptide AG8.1, and their stability in serum was then evaluated. These tests showed that peptide **LM218** was the best candidate. **LM218** was coupled to several BCAs (CITC-DTPA (*17*), CITC-TTHA (synthesis nondescribed), and CITC−CHXA″DTPA (*18*, *19*)). One of the obtained bivalent peptides, **LM218-BzTTHA**, was radiolabeled with indium-111. The resulting radiolabeled product was fully immunoreactive toward mAb-679.

MATERIAL AND METHODS

General. All chemicals were of the highest purity commercially available (Sigma-Aldrich Company). Indium-111 was purchased from CIS bio international as a solution of indium-111 in HCl 0.05 M (specific activity: 370 MBq/μg; volumetric activity 370 MBq/mL). AG8.1 was kindly provided by Dr A. Gruaz-Guyon (Inserm, Paris, France) and mAb-679 by Dr. D. M. Goldenberg (IBC Pharmaceuticals, Inc. Morris Plains, NJ). The HPLC solvents were purchased from Carlo-Erba. TLC was performed using precoated Kieselgel 60 plates F_{254} (TLC plates, Carlo-Erba) and was visualized by UV or iodine. Silica gel (230−400 mesh, Carlo-Erba) was purchased from Merck. High-Performance Liquid Chromatography was carried out at 211 nm on a Waters 600 HPLC System using analytical reverse phase HPLC (SymmetryShield 5 μm RP-18 4.5 × 150 mm, Waters) and semipreparative reverse phase HPLC columns (SymmetryShield 7 μm RP-18, 19 × 300 mm, Waters). The elution solvents are as follows: solvent A: TFA/H_2O 0.1%; solvent B: acetonitrile. HPLC conditions will be given in details for each case. NMR spectra were recorded on a BRUKER AC 250 apparatus (250.133 MHz for ^1H). Chemical shifts are indicated in δ values (ppm) downfield from internal TMS and coupling constants (*J*) are given in Hertz (Hz). Multiplicities were recorded as s (singlet), d (doublet), t (triplet), and m (multiplet). Mass spectra were recorded using a Bruker Esquire LC electrospray mass spectrometer with methanol or water as carrier solvent. Competition curves and serum stability were performed in polypropylene tubes coated with mAb-679. The radiochemical purity was measured by thin layer silica gel chromatography, and the chromatograms were analyzed after exposure on a phosphorus screen (Molecular Dynamics, Sunnyvale, CA) using IPLab-Gel software (Analytics Corp., Atlanta, GA).

Synthesis: N_α-(Benzyloxycarbonyl)lysine Ethyl Ester (1). A suspension of N_α-(benzyloxycarbonyl)lysine (4.02 g, 14.3 mmol) in 600 mL of EtOH was saturated with HCl_g until total dissolution. The solution was stirred at room temperature for 4 h. After concentration to dryness, the residue was taken up in AcOEt and washed with 1 M NaOH. The organic layer was dried with Na_2SO_4, filtered, concentrated, and dried under reduced pressure. 3.74 g of yellow oil were obtained (85%).^1H NMR ($CDCl_3$): δ (ppm) 1.27 (t, 3H, $J = 7.1$ Hz); 1.31−1.92 (m, 8H); 2.65 (t, 2H, $J = 6.8$ Hz); 4.18 (q, 2H, $J = 7.1$ Hz); 4.35 (q, 1H, $J = 6.1$ Hz); 5.10 (s, 2H); 5.40 (d, 1H, $J = 6.1$ Hz); 7.33 (s, 5H). ^{13}C NMR ($CDCl_3$): δ (ppm) 14.5; 22.9; 32.8; 33.4; 41.1; 54.2; 61.7; 67.2; 127.0−128.4 (5C); 136.7; 156.3; 172.9. MS (ES^+) *m/z* 309 [MH^+].

Glycyl-N_α-(benzyloxycarbonyl)lysine Ethyl Ester (2). *N*-(*tert*-Butyloxycarbonyl)glycine *p*-nitrophenyl ester (3.59 g, 12 mmol) and **1** (3.74 g, 12 mmol) were dissolved in 20 mL of anhydrous THF under nitrogen atmosphere. After addition of triethylamine (0.72 g, 7.2 mmol), the solution was stirred at room temperature for 2 h and then concentrated to complete dryness. The residue was taken up in AcOEt and washed with 0.2 M HCl. The organic layer was dried with Na_2SO_4, filtered, and concentrated under vacuum. The residue was purified by column chromatography on silica gel eluting with dichloromethane−ethyl acetate (1:1) (R_f = 0.3) to give 4.25 g of *N*-(*tert*-butyloxycarbonyl)glycyl-N_α-(benzyloxycarbonyl)-lysine ethyl ester as a colorless oil (86%). ^{1}H NMR ($CDCl_3$): δ (ppm) 1.24 (t, 3H, J = 7.1 Hz); 1.30−1.81 (m, 15H); 3.24 (m, 2H,); 3.73 (d, 2H, J = 5.8 Hz); 4.15 (q, 2H, J = 7.1 Hz); 4.35 (m, 1H); 5.30 (bs, 3H); 5.43 (d, 1H, J = 8.1 Hz); 6.21 (m, 1H); 7.35 (s, 5H). ^{13}C NMR ($CDCl_3$): δ (ppm) 14.5; 22.8; 28.6 (3C); 29.3; 32.5; 39.3; 44.7; 54.1; 61.8; 67.3; 80.5; 128.4−128.9 (5C); 137.0; 156.5 (2C); 170.0; 172.8. MS (ES^+) *m/z* 466 [MH^+]. Trifluoroacetic acid (4 mL, 52 mmol) was slowly added to *N*-(*tert*-butyloxycarbonyl)glycyl-N_α-(benzyloxycarbonyl)lysine ethyl ester (4 g, 8.6 mmol) at 0 °C. The mixture was stirred for 2 h at 30 °C before the excess of TFA was evaporated in vacuo. The residue was taken up in CH_2Cl_2 and washed with 1 M NaOH. The organic layer was dried with Na_2SO_4, filtered, and concentrated to dryness. 2.75 g of compound **2** was obtained as a yellow oil (88%). ^{1}H NMR ($CDCl_3$): δ (ppm) 1.23 (t, 3H, J = 7.1 Hz); 1.31−1.81 (m, 8H); 3.19−3.27 (m+s, 4H); 4.15 (q, 2H, J = 7.1 Hz); 4.30 (m, 1H); 5.10 (s, 1H); 5.60 (d, 1H, J = 8.3 Hz); 7.33 (s; 6H). ^{13}C NMR ($CDCl_3$): δ (ppm) 14.5; 22.9; 28.7; 32.4; 38.8; 45.1; 54.1; 61.8; 67.2; 128.4−128.9 (5C); 136.7; 156.4; 172.8; 173.2. MS (ES^+) *m/z* 366 [MH^+].

Succinylhistamine (2bis). Succinic anhydride (1.76 g, 17.6 mmol) was dissolved in 15 mL of anhydrous DMF, under nitrogen atmosphere. A solution of histamine (1.77 g, 15.9 mmol) in 25 mL of anhydrous DMF was added dropwise. The reaction mixture was stirred 1 h at room temperature. The DMF was removed under vacuum. Then 20 mL of ethanol was added, and the reaction mixture was chilled at 4 °C for a night. The white precipitate was filtered, washed with cold ethanol, and dried in vacuo. 2.83 g of a white solid was obtained (84%). ^{1}H NMR (CD_3OD): δ (ppm) 2.39 (m, 2H); 2.53 (m, 2H); 2.80 (t, 2H, J = 6.8 Hz); 3.42 (t, 2H, J = 6.8 Hz); 7.07 (d, 1H, J = 1.2 Hz); 8.12 (d, 1H, J = 1.2 Hz). ^{13}C NMR (CD_3OD): δ (ppm) 27.0; 32.7 (2C); 40.4; 118.4 (2C); 136.2; 175.6; 179.1. MS (ES^+) *m/z* 212 [MH^+].

Histaminosuccinylglycyl-N_α-(benzyloxycarbonyl)-lysine Ethyl Ester (3). To 1.055 g (5 mmol) of **2bis** dissolved in 20 mL of hot anhydrous DMF, was added, at 0 °C, 0.830 g (6 mmol) of *p*-nitrophenol, under nitrogen atmosphere. The reaction mixture was stirred 30 min at 0 °C before DCC (1.03 g, 5 mmol) was added. After 4 h at 0 °C a solution of **2** (1.83 g, 5 mmol) dissolved in 20 mL of anhydrous DMF was added slowly. The reaction mixture was stirred overnight at room temperature and then DMF was removed under vacuum. 15 mL of MeOH was added, and the reaction mixture was chilled at 4 °C for a night. After filtration of DHU, the filtrate was evaporated to dryness and purified by column chromatography on silica gel eluting with ethyl acetate and then methanol (R_f (MeOH) = 0.5). After crystallization in acetone, 1.09 g of white powder was obtained (39%). ^{1}H NMR (CD_3OD): δ (ppm) 1.20 (t, 3H, J = 7.1 Hz); 1.41−1.77 (m, 6H); 2.48 (m, 4H); 2.74 (t, 2H, J = 7.0 Hz); 3.18 (t, 2H, J = 6.9 Hz); 3.36 (t, 2H, J = 7.0 Hz); 3.79 (s, 2H); 4.11 (m, 3H); 5.07 (s, 2H); 6.82 (d, 1H, J = 1.1 Hz); 7.33 (s, 5H); 7.60 (d, 1H, J = 1.1 Hz). ^{13}C NMR (CD_3OD): δ (ppm) 14.8; 24.4; 28.1; 30.0; 32.1; 32.4; 32.5; 40.3; 40.8; 44.3; 55.9; 62.6; 67.9; 119.0 (2C); 129.1−129.8 (5C); 136.4; 138.5; 159.0; 172.1; 174.6; 174.9; 175.9. MS (ES^+) *m/z* 559 [MH^+].

Histaminosuccinylglycyllysine Ethyl Ester (4). Catalytic hydrogenation of **3** (558 mg, 1 mmol) in methanol (20 mL) over 10% Pd/C (0.3 equiv; w/w) was carried out at atmospheric pressure. After 4 h, the catalyst was filtered off (Celite) and the filtrate was removed under reduced pressure. 420 mg of a white solid was obtained (99%). ^{1}H NMR (CD_3OD): δ (ppm) 1.21 (t, 3H, J = 7.1 Hz); 1.43−1.80 (m, 6H); 2.50 (m, 4H); 2.64 (t, 2H, J = 7.0 Hz); 3.18 (t, 2H, J = 6.9 Hz); 3.37 (t, 2H, J = 7.0 Hz); 3.65 (m, 1H); 3.80 (s, 2H); 4.11 (q, 2H, J = 7.1 Hz); 6.72 (d, 1H, J = 1.1 Hz); 7.56 (d, 1H, J = 1.1 Hz). ^{13}C NMR (CD_3OD): δ (ppm) 14.8; 24.4; 26.1; 26.6; 28.0; 32.2; 32.3; 39.6; 40.7; 44.0; 55.7; 62.6; 119.2 (2C); 136.7; 172.2; 174.3; 174.7; 175.8. MS (ES^+) *m/z* 425 [MH^+].

Histaminosuccinylglycyl-N_α-(benzyloxycarbonyl)-lysine (4bis). Compound **3** (200 mg, 0.36 mmol) was dissolved in 1 mL of 1 M NaOH. After 2 h at room temperature, the mixture was evaporated in vacuo. The residue was taken up in 1 mL of water, and 1 M HCl was added until pH of the solution was 3. The solution was evaporated to dryness, and the white solid resulting was taken up in 1 mL of anhydrous MeOH. After 12 h at 4 °C, sodium chloride was filtered off and the filtrate evaporated. 189 mg of a white solid were obtained (99%). ^{1}H NMR (CD_3OD): δ (ppm) 1.39−1.78 (m, 6H); 2.37 (s, 4H); 2.99 (t, 2H, J = 6.1 Hz); 3.29 (m, 2H); 3.64 (m, 2H); 3.89 (m, 3H); 5.06 (s, 2H); 7.10 (s, 1H); 7.21 (s, 1H); 7.38 (s, 5H). ^{13}C NMR (CD_3OD): δ (ppm) 23.9; 26.1; 29.8; 30.1; 31.4; 32.3; 39.1; 40.0; 43.7; 55.5; 67.6; 118.2 (2C); 128.7 (2C); 129.0; 129.4 (2C); 135.8; 138.2; 159.0; 171.8; 175.4; 176.3; 176.7. MS (ES^+) *m/z* 531 [MH^+].

***N*-(*tert*-Butoxycarbonyl)-*p*-nitrophenylalanine *p*-Nitrophenyl Ester (5)**. To a solution of *N*-(*tert*-butoxycarbonyl)-*p*-nitrophenylalanine (200 mg, 0.64 mmol) and *p*-nitrophenol (98 mg, 0.70 mmol) in 5 mL of anhydrous THF was added dropwise, at 0 °C and under nitrogen atmosphere, a solution of DCC (133 mg, 0.64 mmol) in 10 mL of anhydrous THF. The reaction mixture was taken 4 h at 0 °C and 16 h at room temperature. DHU was filtered and washed with 5 mL of anhydrous DMF. The filtrate was evaporated to dryness, and the residue was taken up in 10 mL of anhydrous MeOH. After 4 h, the precipitated formed was filtered, washed with 10 mL of cold anhydrous MeOH, and dried in vacuo. 175 mg of a white solid was obtained (63%). ^{1}H NMR ($CDCl_3$): δ (ppm) 1.44 (s, 9H); 3.35 (m, 2H); 4.86 (m, 1H); 5.08 (d, 1H, J = 8.6 Hz); 7.23 (d, 2H, J = 9.2 Hz); 7.44 (d, 2H, J = 8.9 Hz); 8.23 (d, 2H, J = 8.9 Hz); 8.29 (d, 2H, J = 9.2 Hz). ^{13}C NMR ($CDCl_3$): δ (ppm) 28.2 (3C); 38.0; 54.4; 80.7; 122.1 (2C); 123.9 (2C); 125.4 (2C); 130.2 (2C); 143.3; 143.7; 174.3; 154.7; 158.6; 170.3. MS (ES^+) *m/z* 432 [MH^+].

Histaminosuccinylglycyl(*O*-ethyl)lysyl-*p*-nitrophenylalanine Hydrochloride (6). To a solution of compound **5** (158 mg, 0.37 mmol) in 1 mL of anhydrous DMF were added, under nitrogen atmosphere, **4** (204 mg, 0.48 mmol) and triethylamine (67 μL, 0.48 mmol). The reaction was stirred overnight at room temperature. After evaporation, the residue was taken up in 5 mL of $CHCl_3$ and washed three times with 5 mL of 0.5 M NaOH. The organic layer was dried over Na_2SO_4, filtered, and evaporated to dryness. The crude material was purified

by column chromatography on silica gel, eluting with ethyl acetate and then methanol (R_f (MeOH) = 0.5) to give 249 mg of a white solid (95%). To a solution of this compound (72 mg, 0.1 mmol) in 2 mL of acetone was added 700 μL of 3 M HCl. The reaction mixture was kept 4 h at room temperature. The solvents were removed, and the residue was dried under vacuum. 63 mg of a white solid was obtained (96%). ^{1}H NMR (CD_3OD): δ (ppm) 1.21 (t, 3H, J = 7.1 Hz); 1.32−1.78 (m, 6H); 2.40 (m, 4H); 2.68 (m, 2H); 3.01 (d, 2H, J = 7.4 Hz); 3.18 (t, 2H, J = 7.0 Hz); 3.37 (t, 2H, J = 7.2 Hz); 3.70 (s, 2H); 3.98 (t, 1H, J = 7.2 Hz); 4.02 (q, 2H, J = 7.1 Hz); 4.31 (m, 1H); 6.85 (s, 1H); 7.38 (d, 2H, J = 8.6 Hz); 7.67 (s, 1H); 8.07 (d, 2H, J = 8.6 Hz). ^{13}C NMR (CD_3OD): δ (ppm) 14.5; 23.9; 27.7; 28.6; 29.7; 31.9; 32.1; 39.3; 39.9; 40.5; 43.7; 53.8; 56.7; 62.3; 118.1 (2C); 124.4 (2C); 131.7 (2C); 136.1; 146.8; 148.3; 171.8; 173.3; 173.6; 174.5; 175.6. MS (ES^+) m/z 617 [MH^+].

LM054. To a solution of **4bis** (198 mg, 0.36 mmol) and *p*-nitrophenol (50 mg, 0.36 mmol) in 2 mL of anhydrous DMF was added, at 0 °C and under nitrogen atmosphere, a solution of DCC (74 mg, 0.36 mmol) in 6 mL of anhydrous DMF. After 4 h at 0 °C and a night at room temperature, **6** (234 mg, 0.36 mmol) and triethylamine (57 μL, 0.40 mmol) were added to the solution. The reaction mixture was stirred 8 h and then evaporated to dryness. The residue was taken up in 5 mL of anhydrous MeOH and chilled at 4 °C overnight. DHU was filtered and washed with cold MeOH, and the filtrate was concentrated to dryness. The crude product was purified by semipreparative HPLC at 211 nm. Semipreparative HPLC conditions: gradient: 0−15 min, 80%-50% A; 15−16 min, 50%-0% A; 16−24 min, 0% A; 24−25 min, 0%-80% A. Flow rate: 17 mL/min. Retention time: 9.43 min. 50 mg of pure product were collected (12%). ^{1}H NMR (CD_3OD): δ (ppm) 1.13 (t, 3H, J = 6.8 Hz); 1.22−1.75 (m, 12H); 2.38 (s, 8H); 2.77 (t, 4H, J = 6.6 Hz); 3.05 (m, 4H); 3.22 (m, 2H); 3.33 (t, 4H, J = 6.4 Hz); 3.53 (m, 1H); 3.72 (m, 1H); 3.86 (t, 1H, J = 7.0 Hz); 4.02 (q, 2H, J = 6.8 Hz); 4.25 (m, 1H); 5.10 (s, 2H); 7.21 (s, 5H); 7.22 (s, 2H); 7.38 (d, 2H, J = 8.6 Hz); 8.01 (d, 2H, J = 8.6 Hz); 8.67 (s, 2H). ^{13}C NMR (CD_3OD): δ (ppm) 14.5; 23.9; 24.0; 25.6 (4C); 29.6; 29.7; 31.7 (3C); 32.0; 32.5; 38.5; 39.3; 39.9; 40.0; 43.7 (2C); 53.8; 55.0; 56.6; 62.4; 67.8; 117.6 (2C); 124.4 (2C); 128.8; 129.1 (2C); 129.5 (2C); 131.7 (2C); 133.0 (2C); 134.8 (2C); 138.0; 146.4; 148.3; 158.5; 171.8; 171.9; 172.8; 173.3; 174.8; 174.9 (2C); 175.5 (2C). Analytical HPLC: gradient: 0−15 min, 80−50% A; 15−16 min, 50%-0% A; 16−24 min, 0% A; 24−25 min, 0%-80% A; flow rate 1 mL/min; retention time: 9.40 min. MS (ES^+) m/z 1130 [MH^+].

***p*-Aminobenzylamine Hydrochloride (7).** Catalytic hydrogenation of *p*-nitrobenzylamine hydrochloride (1.10 g, 5.8 mmol) in methanol (15 mL) over 10% Pd/C (10% w/w) was carried out at atmospheric pressure. After 3 h, the catalyst was filtered off (Celite) and the solvent was removed under reduced pressure. 900 mg of a yellow solid was obtained (98%). ^{1}H NMR (DMSO-d_6): δ (ppm) 3.82 (s, 2H); 5.27 (s, 2H); 6.58 (d, 2H, J = 8.3 Hz); 7.15 (d, 2H, J = 8.3 Hz); 8.19 (s, 2H). ^{13}C NMR (DMSO-d_6): δ (ppm) 43.3; 113.8 (2C); 120.7 (2C); 130.3; 149.2. MS (ES^+) m/z 123 [MH^+].

***N,N*-Bis(ethoxycarbonylmethyl)-4-aminobenzylamine (8).** A mixture of **7** (420 mg, 2.65 mmol), sodium carbonate (1.13 g, 10.6 mmol), potassium iodide (441 mg, 2.65 mmol), and ethyl bromoacetate (665 mg, 3.97 mmol) in acetonitrile (20 mL), under nitrogen atmosphere, was refluxed for 2 h. The insoluble materials were filtered off, and the solvent was removed under reduced pressure. The residue was purified on silica gel column using ethyl acetate-chloroform (1:1) as eluent to yield a yellow oil (469 mg, 60%). ^{1}H NMR ($CDCl_3$): δ (ppm) 1.25 (t, 6H, J = 7.1 Hz); 3.51 (s, 4H); 3.77 (s, 2H); 4.15 (q, 4H, J = 7.1 Hz); 6.61 (d, 2H, J = 8.5 Hz); 7.14 (d, 2H, J = 8.5 Hz). ^{13}C NMR ($CDCl_3$): δ (ppm) 14.8 (2C); 54.7 (2C); 58.1; 60.7 (2C); 115.3 (2C); 128.3; 131.0 (2C); 146.1; 171.9. MS (ES^+) m/z 295 [MH^+].

Disodium Salt of *N,N*-Bis(carboxymethyl)-4-aminobenzylamine (9). To 476 mg (1.6 mmol) of compound **8** in 500 μL of ethanol was added 3.20 mL of 2 M NaOH. The reaction mixture was stirred at 35 °C for 2 h and then concentrated to dryness. 452 mg of desired product was obtained as a pale orange solid (100%). ^{1}H NMR (D_2O): δ (ppm) 3.12 (s, 4H); 3.65 (s, 2H); 6.80 (d, 2H, J = 8.3 Hz); 7.16 (d, 2H, J = 8.3 Hz). MS (ES^+) m/z 239 [MH^+].

***N,N*-Bis(carboxymethyl)-4-*N′*-(9-fluorenylmethyloxycarbonyl)aminobenzylamine (10).** To 1.57 g (5.6 mmol) of compound **9** in a mixture of 10% Na_2CO_3 (15 mL) and dioxane (10 mL) was slowly added, at 0 °C, 1.5 g (5.6 mmol) of 9-fluorenylmethyl chloroformate. After 4 h at 0 °C and overnight at room temperature, the solvents were removed. 1 mL of H_2O was added to the residue followed by 3 M HCl until the pH rose to Congo. The obtained precipitate was filtered, washed with cold water, and dried under reduced pressure. 1.55 g of a white solid was obtained (60%). ^{1}H NMR (DMSO-d_6): δ (ppm) 3.71 (s, 4H); 4.17 (t, 1H, J = 6.7 Hz); 4.21 (s, 2H); 4.40 (d, 2H, J = 6.7 Hz); 7.25 (m, 8H); 7.59 (d, 2H, J = 6.9 Hz); 7.70 (d, 2H, J = 6.9 Hz). ^{13}C NMR (DMSO-d_6): δ (ppm) 46.9; 53.7 (2C); 56.9; 65.8; 118.4 (2C); 120.4 (2C); 125.3 (2C); 127.3 (2C); 127.9 (2C); 129.4 (2C); 132.5; 138.3; 141.0 (2C); 144.0 (2C); 153.6; 172.4 (2C). MS (ES^+) m/z 461 [MH^+].

***N′*-Fmoc-*N,N*-(histaminosuccinylglycyl-(*O*-ethyl)-lysyl-carboxymethyl)-*p*-aminobenzylamine (11).** To a solution of **10** (1.04 g, 2.26 mmol) in 5 mL of anhydrous DMF, was added, under nitrogen, CDI (878 mg, 5.42 mmol). When the effervescence stopped, a solution of **4** (2.3 g, 5.42 mmol) in 5 mL of anhydrous DMF was added. The reaction mixture was stirred at room-temperature overnight and then concentrated to dryness. The residue solubilized in 3 mL of MeOH was added dropwise at 0 °C in 100 mL of water. The precipitate was filtered, washed twice with cold water, and dried under vacuum. 2 g of a white solid was obtained (71%). ^{1}H NMR (CD_3OD): δ (ppm) 1.13 (t, 6H, J = 7.0 Hz); 1.18−1.79 (m, 12H); 2.40 (m, 8H); 2.66 (t, 4H, J = 7.0 Hz); 3.06 (t, 4H, J = 6.8 Hz); 3.27 (t, 4H, J = 7.0 Hz); 3.56 (s, 2H); 3.60 (s, 4H); 3.67 (s, 4H); 4.02 (q, 4H, J = 7.0 Hz); 4.15 (t, 1H, J = 6.5 Hz); 4.24 (m, 2H); 4.35 (d, 2H, J = 6.5 Hz); 6.72 (s, 2H); 7.13−7.33 (m, 8H); 7.49 (s, 2H); 7.57 (d, 2H, J = 7.2 Hz); 7.70 (d, 2H, J = 7.2 Hz). ^{13}C NMR (CD_3OD): δ (ppm) 14.5 (2C); 24.2 (2C); 26.0 (2C); 26.7 (2C); 27.2 (2C); 31.8 (2C); 32.1 (2C); 34.7; 40.1 (2C); 40.4 (2C); 43.7 (2C); 53.7 (2C); 58.2 (2C); 59.3; 62.4 (2C); 67.7; 118.1 (4C); 119.9 (2C); 121.0 (2C); 126.2 (2C); 128.2 (2C); 128.8 (2C); 131.2 (2C); 133.1; 136.0 (2C); 139.7; 142.6 (2C); 145.3 (2C); 155.8; 171.8 (2C); 173.5 (4C); 174.5 (2C); 175.5 (2C). MS (ES^+) m/z 1273.5 [MH^+].

LM085. Compound **11** (300 mg, 0.24 mmol) and 240 μL (2.3 mmol) of diethylamine were dissolved in 2 mL of anhydrous DMF. The reaction mixture was stirred under nitrogen atmosphere for 2 h and then concentrated. 10 mL of water was added to the residue. The aqueous layer was extracted four times with ethyl acetate (10 mL). The aqueous layer was then evaporated and dried under reduced pressure to yield desired compound as a white

solid (225 mg, 91%). ^{1}H NMR (CD_3OD): δ (ppm) 1.09 (d.t, 6H, J = 7.0 Hz); 1.36-1.75 (m, 12H); 2.38 (m, 8H); 2.63 (t, 4H, J = 7.0 Hz); 3,07 (t, 4H, J = 6.9 Hz); 3.25 (t, 4H, J = 7.0 Hz); 3.50 (s, 2H); 3.57 (s, 4H); 3.67 (s, 4H); 4.02 (q, 4H, J = 7.0 Hz); 4.24 (m, 2H); 6.57 (d, 2H, J = 8.4 Hz); 6.72 (s, 2H); 6.97 (d, 2H, J = 8.4 Hz); 7.48 (s, 2H). ^{13}C NMR (CD_3OD): δ (ppm) 14.5 (2C); 24.2 (2C); 27.6 (2C); 29.8 (2C); 31.8 (2C); 32.0 (2C); 32.1 (2C); 40.1 (2C); 40.4 (2C); 43.73 (2C); 52.8 (2C); 58.1; 59.4 (2C); 62.4 (2C); 116.4 (2C); 118.1 (4C); 129.5; 131.6 (2C); 135.7 (2C); 148.4; 171.8 (2C); 173.5 (2C); 173.6 (2C); 174.5 (2C); 175.5 (2C). Analytical HPLC: gradient: 0−5 min, 100% A; 5−35 min, 100%-0% A; 35−36 min, 0%-100% A; flow rate 1 mL/min; retention time: 15.0 min. MS (ES^+) *m/z* 1052 [MH^+].

LM218. Anhydrous $NH_{3(g)}$ was bubbled into a stirring solution of **11** (70 mg, 55 μmol) in 5 mL of MeOH. An ice bath was used to keep the solution at 5 °C. The formation of the product was monitored by electrospray mass spectra. Anhydrous $NH_{3(g)}$ was bubbled punctually until total reaction. The reaction mixture was reduced to dryness, the residue was taken up in 2 mL of water, and the aqueous layer was washed with $CHCl_3$ (5 × 5 mL). The aqueous layer was concentrated and dried under vacuum to give 40 mg of a yellow solid (74%). ^{1}H NMR (CD_3OD): δ (ppm) 1.17−1.82 (m, 12H); 2.50 (s, 8H); 2.74 (t, 4H, J = 6.6 Hz); 3.15 (t, 4H, J = 6.6 Hz); 3.34 (s, 4H); 3.39 (t, 4H, J = 7.1 Hz); 3.58 (s, 2H); 3.79 (s, 4H); 4.13 (m, 2H); 6.74 (d, 2H, J = 8.3 Hz); 6.89 (s, 2H); 7.13 (d, 2H, J = 8.3 Hz); 7.69 (s, 2H). ^{13}C NMR (CD_3OD): δ (ppm) 25.3 (2C); 28.8 (2C); 30.8 (2C); 33.7 (6C); 41.9 (2C); 45.5 (2C); 51.8 (2C); 56.1 (2C); 60.6; 62.0 (2C); 119.0 (2C); 119.9 (4C); 130.4; 133.7 (2C); 137.5 (2C); 148.8; 174.2 (2C); 176.5 (2C); 177.3 (2C); 178.3 (2C); 179.3 (2C). Analytical HPLC: gradient: 0−5 min, 100% A; 5−35 min, 100%-0% A; 35−36 min, 0%-100% A; flow rate 1 mL/min; retention time: 14.3 min. MS (ES^+) *m/z* 993 [MH^+].

General Procedure for LM218-BCA Coupling. A solution of **LM218**, BCA, and Et_3N in 500 μL of anhydrous DMF was stirred under nitrogen atmosphere for 16 h. The solvent was then evaporated, and the residue was purified by semipreparative reverse phase HPLC at 211 nm. Semipreparative HPLC conditions: isocratic, solvent A: 83%, solvent B: 17%. Flow rate: 17 mL/min.

LM218-BzDTPA. Using 6 mg (6.0 μmol) of **LM218,** 8 mg (12 μmol) of CITC-DTPA (17), and 5 μL (37.2 μmol) of triethylamine, 3 mg of pure **LM218-BzDTPA** was collected (Retention time: 6.4 min, yield = 30%). MS (ES^+) *m/z* 1533 [MH^+]. Analytical HPLC: gradient: 0−5 min, 100% A; 5−30 min, 100%-0% A; 30−40 min, 0%A; flow rate 1 mL/min; retention time: 16.5 min.

LM218-BzTTHA. Using 6 mg (6.0 μmol) of **LM218,** 9.4 mg (12 μmol) of CITC-TTHA (synthesis not described), and 8.3 μL (48.9 μmol) of triethylamine, 3.3 mg of pure **LM218-BzTTHA** was collected (Retention time: 6.7 min, yield 33%). MS (ES^+) *m/z* 1635 [MH^+]. Analytical HPLC: gradient: 0−5 min, 100% A; 5−30 min, 100%-0% A; 30−40 min, 0% A; flow rate 1 mL/min; retention time: 17.4 min.

LM218-CHXA″DTPA. Using 6 mg (6.0 μmol) of **LM218,** 8.5 mg (12.1 μmol) of CITC−CHXA"DTPA (*18*, *19*), and 7.6 μL (54.4 μmol) of triethylamine, 3 mg of **LM218-CHXA″DTPA** was collected (Retention time: 5.7 min, yield = 32%). MS (ES^+) *m/z* 1635 [MH^+]. Analytical HPLC: gradient: 0−5 min, 100% A; 5−30 min, 100%-0% A; 30−40 min, 0% A; flow rate 1 mL/min; retention time: 16.7 min.

Preparation of mAb-679-Coated Tubes. A series of 50 polypropylene tubes was coated by adding 0.5 mL of a solution of mAb-679 at 20 μg mL^{-1}. After 12 h incubation at 37 °C, the supernatant was removed and 0.5 mL of phosphate-buffered saline (PBS) supplemented with 0.5% bovine serum albumin (BSA) was added. Tubes were kept at 4 °C until used.

Preparation of AG8.1-^{125}I. AG8.1 was labeled with ^{125}I using chloramine-T (*23*). After labeling, the hapten was purified using a SepPak C_{18} cartridge (Millipore, Saint Quentin Yvelines, France) by successive injections of the labeling solution. The SepPak C_{18} cartridge was first eluted with 5 mL of 0.05% trifluoroacetic acid in water and then with 5 mL of a 3:2 mixture of 0.1 M phosphate buffer solution pH 7 and ethanol. Under these conditions, free ^{125}I was eluted in the acid aqueous phase and the radiolabeled hapten was eluted in the first 2 mL of the ethanol phase. The radiochemical purity of the purified solution was measured by thin layer silica gel chromatography using methanol as eluent. The immunoreactive fraction was determined by the percentage of activity of the mAb-679-coated tubes.

Competition Tests. For each competition test, peptide AG8.1 was used as a reference. The immunoreactivity tests of the synthesized peptides and AG8.1 peptide toward mAb-679 were performed in mAb-679-coated tubes. Two series of seven tubes were prepared for each peptide. In the first series, the tubes were charged with (1) a constant amount of AG8.1 peptide (0.2 pmol) radiolabeled with Iodine-125, (2) an increasing amount of cold AG8.1 peptide (C = 0, 0.25, 0.5, 1, 5, 10, and 100 pmol), (3) 200 μL of PBS/0.5% BSA for the **LM054** and **LM085** series or 250 μL for the **LM218** series. In the second series, the tubes were charged with (1) a constant amount of AG8.1 peptide (0.2 pmol) radiolabeled with Iodine-125. (2) an increasing amount of cold synthesized peptides **LM054**, **LM085**, or **LM218** (n = 0, 0.25, 0.5, 1, 5, 10, and 100 pmol), (3) 200 μL of PBS/0.5% BSA for the **LM054** and **LM085** series or 250 μL for the **LM218** series. After a night at 37 °C, the radioactivity of each tube was measured before (T) and after (B) three washes with 500 μL of PBS/1% Tween 20.

Serum Stability. Two solutions of AG8.1 peptide at 250 pmol/mL and 50 pmol/mL in serum and two solutions of **LM054**, **LM085**, or **LM218** peptide at the same concentrations were incubated at 37 °C. The immunoreactivity of each solution was determined at different times (0, 4 h, 24 h, 48 h, 144 h); for each point, 0.2 pmol of AG8.1 peptide radiolabeled with ^{125}I and 200 μL of the solutions of AG8.1 peptide in serum were incubated in a first series of mAb-679-coated tubes and 0.2 pmol of AG8.1 peptide radiolabeled with ^{125}I and 200 μL of the solutions of synthesized peptide (**LM054**, **LM085**, or **LM218**) in serum (50 pmol and 10 pmol) in another series of mAb-679-coated tubes. After 1.5 h of incubation at 37 °C, the radioactivity of each tube was measured before (T) and after (B) three washes with 500 μL of PBS supplemented with 1% Tween 20.

Radiolabeling of LM218-BzTTHA. 20 μL of a solution of $^{111}InCl_3$, 3.2 μL of sodium citrate/sodium acetate buffer 0.25 M/1.5 M pH 5.5, and 9 μL of a solution of **LM218-BzTTHA** at 20 pmol μL^{-1} were mixed and incubated 16 h at room temperature. A reference solution containing 20 μL of $InCl_3$ solution, 9 μL of H_2O, and 3.2 μL of sodium citrate/sodium acetate 0.25 M/1.5 M pH 5.5 buffer was also incubated 16 h at room temperature. The reference and the radiolabeled peptide were purified through a Sep-Pack C_{18} cartridge (Millipore, Saint-Quentin Yvelines, France) conditioned with sodium citrate buffer 0.1 M pH 5.5. The columns were first eluted with 5 mL of sodium citrate 0.1 M pH 5.5 buffer followed

Scheme 1. Synthesis of GSH Arms 4 and 4Bis[a]

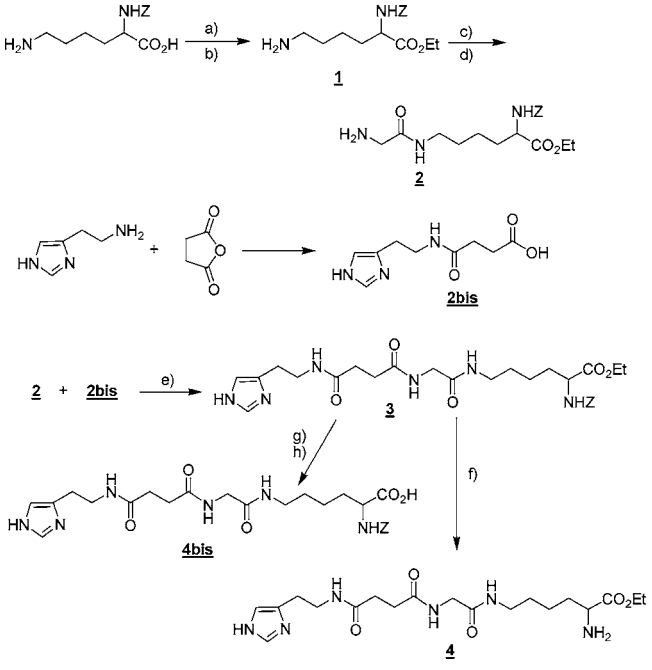

[a] Reagents: (a) HCl gas, EtOH; (b) NaOH; (c) *N*(Boc)glycine *p*-nitrophenyl ester; (d) CF_3CO_2H; (e) *p*-nitrophenol, DCC; (f) H_2, Pd/C; (g) NaOH 1 M; (h) HCl 1 M.

by 5 mL of EtOH/sodium citrate buffer 0.1 M pH 5.5 10% and 5 mL of EtOH. Reference $InCl_3$ eluted in the first 5 mL of citrate buffer. **LM218-BzTTHA-^{111}In** eluted in the 5 mL of EtOH/sodium citrate buffer 0.1 M pH 5.5 and in the first 1 mL of EtOH.

Immunoreactivity of LM218-BzTTHA-^{111}In. A series of mAb-679-coated tubes was loaded with increasing volumes (0, 2, 4, 6, 8, 10, 12, 15, and 20 μL) of the purified fraction of **LM218-BzTTHA-^{111}In**. Each tube was adjusted to a 250 μL volume with PBS/0.5% BSA. After 2 h at 37 °C, the radioactivity of each tube was measured before (T) and after (B) three washes with 500 μL of PBS/1% Tween 20.

RESULTS

Synthesis. Three peptides containing two GSH arms were synthesized. The GSH arms **4** and **4bis** were prepared by conventional peptide synthesis (*24*) (Scheme 1). Briefly, *N*(CbZ)-lysine ethyl ester **1** was obtained by esterification of commercial *N*(CbZ)-lysine by treatment with HCl gas in ethanol. Compound **1** was condensed with *N*(Boc)-glycine *p*-nitrophenyl ester with a 86% yield, followed by removal of the Boc group by TFA treatment (88%). **2bis** was obtained by coupling succinic anhydride to histamine. The condensation reaction between **2** and **2bis** was performed after activation of **2bis** with DCC/*p*-nitrophenol. Catalytic hydrogenation or basic hydrolysis of the resulting **3** yielded respectively intermediates **4** (99%) or **4bis** (99%). The synthesis of **LM054** was performed with an overall yield of 7% (Scheme 2). Compound **6** was obtained by coupling the activated ester **5** on compound **4**, followed by cleavage of the protective Boc group with TFA. Condensation between **4bis**, activated by *p*-nitrophenol in the presence of DCC, and **6** led to peptide **LM054** with a 12% yield after purification by semipreparative high-performance liquid chromatography (HPLC).

LM085 was synthesized with an overall yield of 22% (Scheme 3). The two acid functions of compound **10** were activated simultaneously by CDI and coupled with two

Scheme 2. Synthesis of LM054[a]

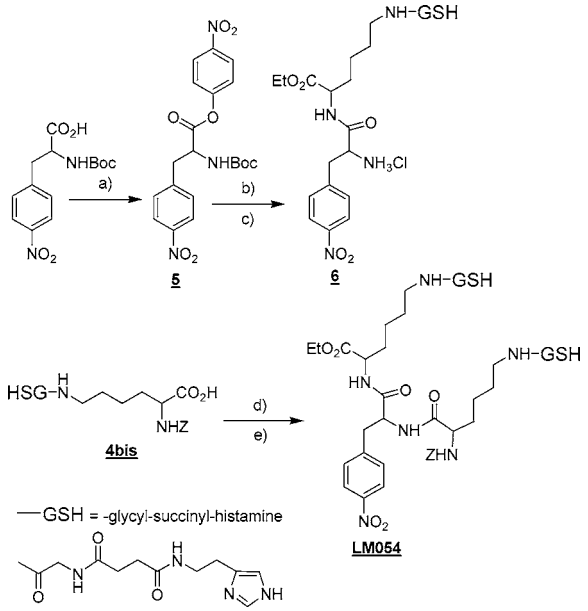

[a] Reagents: (a) *p*-nitrophenol, DCC; (b) compound **4**; (c) HCl 3 M; (d) *p*-nitrophenol, DCC; (e) compound **6**, Et_3N.

Scheme 3. Synthesis of LM085 and LM218[a]

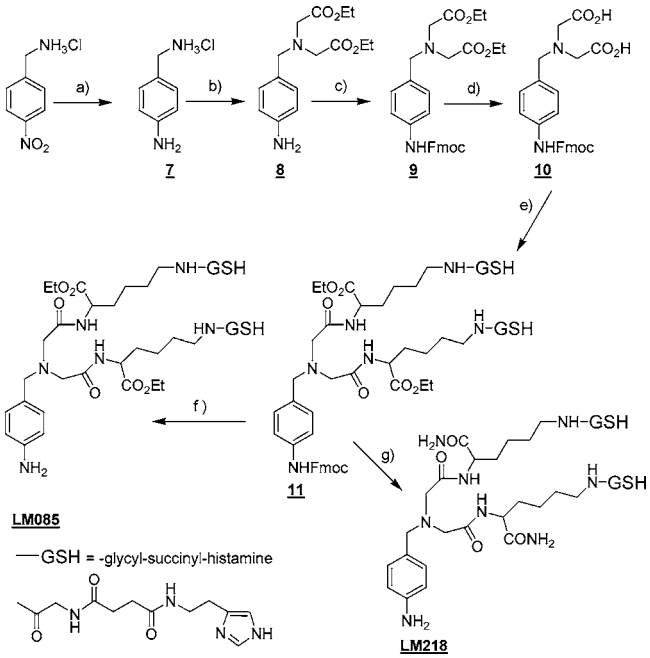

[a] Reagents: (a) H_2, Pd/C; (b) Na_2CO_3, KI, $BrCH_2CO_2Et$; (c) NaOH 2 M; (d) FmocCl; (e) CDI (2.4 equiv); compound **4** (2.4 equiv); (f) Et_2NH; (g) NH_3 gas.

GSH arms (compound **4**). Compound **11**, obtained with a 70% yield, did not require HPLC purification. The cleavage of the Fmoc group performed in the presence of diethylamine gave **LM085**. **LM218** was synthesized with an overall yield of 16% (Scheme 3). $NH_{3(g)}$ treatment of previously described compound **11** allowed the substitution of the two ethyl ester functions into amide functions and the cleavage of the protective Fmoc group.

LM218-BzDTPA, LM218-BzTTHA, and **LM218-CHXA′DTPA.** The coupling reaction of peptide **LM218** with CITC-DTPA, CITC-TTHA, and CITC−CHXA′DTPA was achieved in anhydrous organic medium in the presence of triethylamine. Purification by semiprepara-

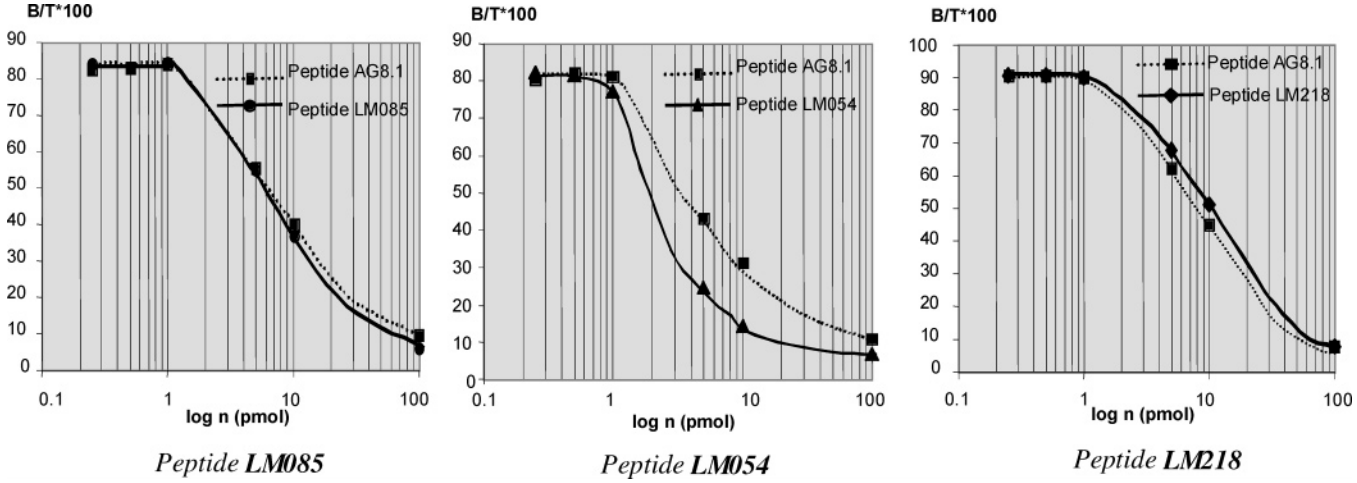

Figure 2. Competition tests. The synthesized peptides (**LM054**, **LM085**, and **LM218**) and peptide AG8.1 (reference) are compared in their ability to displace the fixation of a constant amount of tracer AG8.1-^{125}I on mAb-679-coated tubes. % of tracer AG8.1-^{125}I fixed on total amount introduced was plotted as a function of quantity of cold peptide (0.25 to 100 pmol).

tive HPLC allowed the expected conjugate to be obtained with an average yield of 30%.

AG8.1-^{125}I Radiolabeling. AG8.1-^{125}I was obtained with a 40% yield after addition of 253 MBq of iodine-125 to 11 nmol of AG8.1. The specific activity of AG8.1-^{125}I after purification was 11.1 MBq/nmol, with a radiochemical purity of 100% by chromatography. The immunoreactive fraction was measured between 85 and 90%.

Competition Studies (Figure 2). To evaluate the affinity of the synthesized peptides toward mAb-679, binding a trace amount of AG8.1-^{125}I to mAb-679-coated tubes was measured in the presence of increasing concentration of **LM054**, **LM085**, and **LM218**. The three synthesized peptides and AG8.1 itself showed similar competition curves with tracer AG8.1-^{125}I. Thus, it was considered that peptides AG8.1, **LM054**, **LM085**, and **LM218** had the same affinity for antibody mAb-679.

Serum Stability Tests (Figure 3). The serum stability of **LM054**, **LM085**, and **LM218** was studied by incubating each peptide at two different concentrations (250 and 50 pmol/mL) in human serum at 37 °C. Solutions of peptide AG8.1 at the same concentrations were used as references. The binding of a trace amount of AG8.1-^{125}I to mAb-679-coated tubes in the presence of 200 μL of the peptide solutions in serum was measured at selected time intervals, by incubation in mAb-679-coated tubes. Loss of immunoreactivity of the tested peptide results in a decreased competition toward the tracer AG8.1-^{125}I and in an increasing bound to total (B/T) ratio. AG8.1 remained stable for 48 h in the two series of tests. At 144 h, a loss of about 10% of immunoreactivity was observed for the 50-pmol/mL concentration. **LM054** at 50 pmol/mL lost 8% of its immunoreactivity in 4 h and 30% in 24 h. At 144 h, immunoreactivity was almost totally absent for both concentrations (250 and 50 pmol/mL). **LM085** retained its immunoreactivity at 4 h and lost 9% and 4% respectively for concentrations 50 and 250 pmol/mL at 24 h and 15% for both concentrations at 144 h. Until 24 h, peptide **LM218** showed practically the same immunoreactivity for mAb-679, as did peptide AG8.1. At 144 h, there were slight losses of immunoreactivity (6% and 3% respectively) compared to peptide AG8.1 for concentrations of 250 and 50 pmol/mL.

LM218-BzTTHA-^{111}In. Radiolabeling of **LM218-BzTTHA** was performed in sodium citrate/sodium acetate 0.25 M/1.5 M pH 5.5 buffer for 16 h at room temperature. A reference solution containing $InCl_3$ in the same buffer was also prepared. Purification of both solution on a Sep-Pack C_{18} cartridge (Millipore, Saint Quentin Yvelines, France) was performed, showing that free indium eluted in the first 5 mL of sodium citrate buffer 0.1 M pH 5.5, and **LM218-BzTTHA-^{111}In** in the 5 mL of EtOH/sodium citrate buffer 0.1 M pH 5.5 and in the first 1 mL of the EtOH fraction. The concentration of this last 1 mL fraction was evaluated to be 18 pmol mL^{-1}.

Immunoreactivity of LM218-BzTTHA-^{111}In. Conservation of the immunoreactivity of **LM218-BzTTHA** after radiolabeling was checked by introducing increasing amounts of **LM218-BzTTHA-^{111}In** in mAb-679-coated tubes. The EtOH fraction, estimated at 18 pmol mL^{-1}, was used. A series of nine mAb-679-coated tubes was loaded with 0, 2, 4, 6, 8, 10, 12, 15, and 20 μL of the EtOH fraction and adjusted to 250 μL with PBS/0.5% BSA. After 2 h at 37 °C, the radioactivity of each tube was measured before (T) and after (B) three washes with 500 μL of PBS/1% Tween 20. The B/T ratio was calculated. For each tube a constant immunoreactive fraction of 85% was found.

DISCUSSION

The original development of the AES pretargeting technology by Immunotech S.A. (Marseille, France) was performed in a large part as a collaboration with our laboratory (*25*, *26*). Later on, the advantage of bivalent haptens for pretargeting has been confirmed independently by Boerman and co-workers (*11*), and the AES was considered for RIT by IBC Pharmaceuticals (*10*). While the current clinical trials are still being performed using DTPA-indium bivalent haptens (Figure 1), the need for other haptens allowing a broader range of radionuclides to be used has been recognized. Thus, bivalent haptens of varying structures and lengths of the linker peptide chain using glycyl-succinyl-histamine (GSH) as the hapten have been synthesized (*13*, *14*, *27*). Peptide AG3.0 (Figure 1) proved to be the best candidate, both for its affinity for mAb-679 and its stability in vivo (*27*). In this peptide, the two GSH arms are linked together by a Lys-Tyr-Lys link, in which tyrosine allows direct radiolabeling with iodine-131. However, the physical characteristics of iodine-131 (low-energy β^- radiation, strong gamma emission, and long half-life) set limits to its use in RIT even using AES (*26*).

To circumvent this problem, the synthesis of heteropeptides recognized by mAb-679 (anti-GSH) and bearing

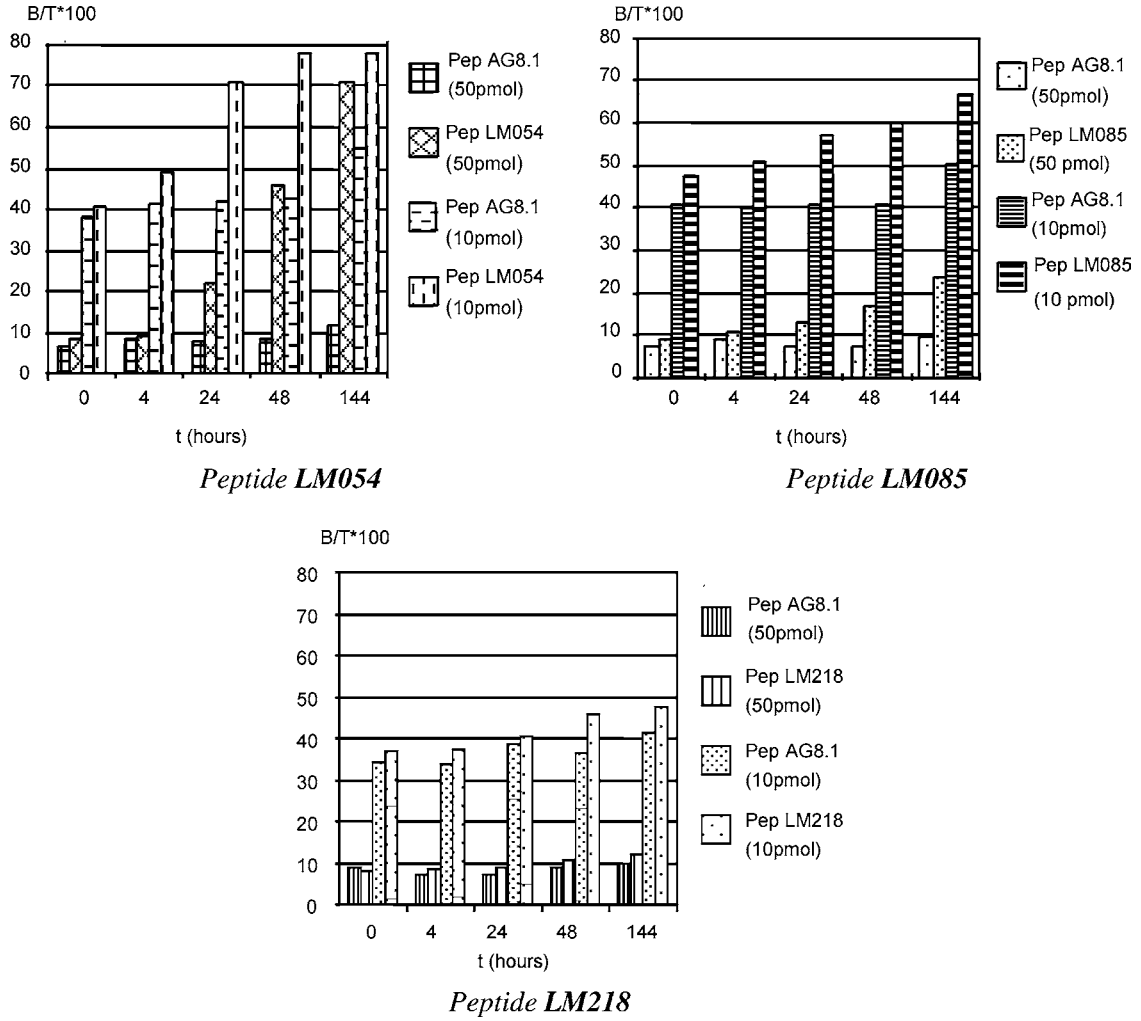

Figure 3. Serum stability. 50 pmol and 10 pmol of synthesized peptides (**LM054**, **LM085**, and **LM218**) and peptide AG8.1 (reference) were incubated in human serum at 37 °C. Aliquots of the serum solutions were put in competition with a constant amount of AG8.1-^{125}I in mAb-679-coated tubes. The percentage of bound AG8.1-^{125}I was plotted as a function of time of incubation for the two concentrations (50 and 10 pmol). Increased B/T corresponds to a loss of immunoreactivity of the tested peptide.

a site for coupling BCA's capable of forming a stable complex with a variety of radionuclides was undertaken. All three synthesized peptides showed good affinity toward mAb-679 (Figure 2). However, stability tests (Figure 3) showed that **LM054** was very rapidly degraded in serum at 37 °C, making it unsuitable for RIT. Thus, the synthetic process involving reduction of the nitro-aromatic function and/or cleavage of the benzyloxycarbonyl group was not carried on. The synthesis of a second peptide involved the coupling of the amine functions of compound **4** with the diacid [carboxymethyl-(4-nitrobenzyl)amino]acetic acid. Simultaneous activation of the two acid functions and subsequent coupling with two GSH arms (compound **4**) were performed with a good yield. Unfortunately, the final step involving catalytic hydrogenation of the nitro-aromatic function failed, producing side-products associated with benzylic rupture. To overcome this difficulty, another strategy was adopted by beginning the synthesis with an aromatic amino group protected by Fmoc. Reduction of the nitro group of the *p*-nitrobenzylamine followed by Fmoc-protection of the aryl amino group and N,N-dialkylation of the aliphatic amino group gave the diacid **10** in 70% yield. This intermediate reacted with two GSH arms to give, after removal of the Fmoc group, peptide **LM085** (Scheme 3). This compound precipitated in water and required no HPLC purification. Deprotection of the Fmoc group caused essentially no side reactions. Competition tests (Figure 2) showed that **LM085** and AG8.1 have the same affinity toward mAb-679. However, serum tests (Figure 3) were not satisfactory as **LM085** had poorer serum stability than AG8.1. To improve the serum stability and to mimic peptide AG8.1, the ethyl ester functions of **LM085** were replaced by amide functions. The treatment with NH_3 gas of compound **11** allowed both deprotection of the Fmoc function and afforded the amide functions (Scheme 3). The resulting compound **LM218**, like **LM054** and **LM085**, has the same affinity for mAb-679 as AG8.1, but also showed good serum stability for up to 144 h. As **LM218** met our criteria (satisfactory immunoreactivity and good serum stability), it was selected to validate the model. Thus **LM218** was coupled to three well-known BCAs, CITC-DTPA, CITC-TTHA, and CITC−CHXA″DTPA (Figure 4) in anhydrous organic medium. Unlike aqueous medium, in which a large excess of BCA is necessary, the anhydrous organic solvent allowed us to work with 2 equiv of BCA relative to the peptide. Finally, one of the conjugates, **LM218-BzTTHA**, was radiolabeled successfully with indium-111, and the immunoreactive fraction of the resulting radiolabeled product was measured as 85% or better.

There was a triple advantage in replacing the aliphatic amine function on the side chain of peptide AG8.1 by an aromatic amine function as the coupling site on the new

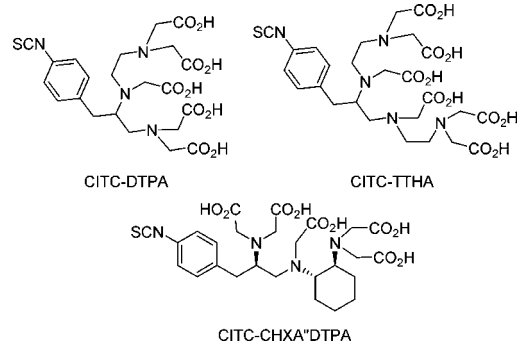

Figure 4. Chemical structures of CITC-DTPA, CITC-TTHA, and CITC−CHXA″DTPA.

peptides. First, the coupling of the BCA on this coupling site is less susceptible to interfere in the recognition of the GSH arms by mAb-679. Second, the low pK_a (3−5) of the aromatic amine allowed coupling to the BCA at a lower pH than with an aliphatic amine (pK_a = 9) and avoided undesirable interaction with the amine functions of imidazole (pK_a = 7.1). Third, the aromatic amine function can be easily activated after transformation to isothiocyanate (results not shown). This possible introduction of an isothiocyanate makes possible the coupling of BCA presenting aliphatic and aromatic amine functions.

In summary, a new bivalent peptide capable of binding mAb-679 was synthesized for applications in the Affinity Enhancement System. This peptide has been coupled to different BCAs and radiolabeled by indium-111, affording a radiolabeled product with excellent immunoreactivity toward mAb-679. These encouraging results indicate that this peptide could be used to couple a large variety of BCAs and thus to use a great variety of radionuclides for in vivo tumor pretargeting. Further studies are now in progress in this direction and will be reported in a future publication. AES-pretargeted RIT using radionuclides with better radiophysical properties than iodine-131 should prove even more efficient for tumor ablation and less toxic.

ACKNOWLEDGMENT

This work was supported by a grant from "La Ligue départementale Contre le Cancer de Vendée". The authors are indebted to Dr Anne Gruaz-Guyon for providing peptide AG8.1 and to IBC Pharmaceuticals, Inc., for the gift of mAb-679.

LITERATURE CITED

(1) Kairemo, K. J., and Liewendahl, K. (1994) Radioimmunodetection of malignant solid tumors. *Scand. J. Clin. Lab. Invest. 54* (8), 569−583 (Review).

(2) Hoefnagel, C. A. (1991) Radionuclide therapy revisited. *Eur. J. Nucl. Med. 18* (6), 408−431 (Review).

(3) Chatal, J. F., Peltier, P., Bardies, M., Chetanneau, A., Thedrez, P., Faivre-Chauvet, A., and Gestin, J. F. (1992) Does immunoscintigraphy serve clinical needs effectively? Is there a future for radioimmunotherapy? *Eur. J. Nucl. Med. 19* (3), 205−213.

(4) Le Doussal, J. M., Martin, M., Gautherot, E., Delaage, M., and Barbet, J. (1989) In vitro and in vivo targeting of radiolabeled monovalent and divalent haptens with dual specificity monoclonal antibody conjugates: enhanced divalent hapten affinity for cell-bound antibody conjugate. *J. Nucl. Med. 30* (8), 1358−1366.

(5) Le Doussal, J. M., Gautherot, E., Martin, M., Barbet, J., and Delaage, M. (1991) Enhanced in vivo targeting of an asymmetric bivalent hapten to double-antigen-positive mouse B cells with monoclonal antibody conjugate cocktails. *J. Immunol. 146* (1), 169−175.

(6) Le Doussal, J. M., Chetanneau, A., Gruaz-Guyon, A., Martin, M., Gautherot, E., Lehur, P. A., Chatal, J. F., Delaage, M., and Barbet, J. (1993) Bispecific monoclonal antibody-mediated targeting of an indium-111-labeled DTPA dimer to primary colorectal tumors: pharmacokinetics, biodistribution, scintigraphy and immune response. *J. Nucl. Med. 34* (10), 1662−1671.

(7) Peltier, P., Curtet, C., Chatal, J. F., Le Doussal, J. M., Daniel, G., Aillet, G., Gruaz-Guyon, A., Barbet, J., and Delaage, M. (1993) Radioimmunodetection of medullary thyroid cancer using a bispecific anti-CEA/anti-indium-DTPA antibody and an indium-111-labeled DTPA dimer. *J. Nucl. Med. 34* (8), 1267−1273.

(8) Kraeber-Bodere, F., Bardet, S., Hoefnagel, C. A., Vieira, M. R., Vuillez, J. P., Murat, A., Ferreira, T. C., Bardies, M., Ferrer, L., Resche, I., Gautherot, E., Rouvier, E., Barbet, J., and Chatal, J. F. (1999) Radioimmunotherapy in medullary thyroid cancer using bispecific antibody and iodine131-labeled bivalent hapten: preliminary results of a phase I/II clinical trial. *Clin. Cancer. Res. 5* (10 Suppl), 3190s−3198s.

(9) Vuillez, J. P., Kraeber-Bodere, F., Moro, D., Bardies, M., Douillard, J. Y., Gautherot, E., Rouvier, E., Barbet, J., Garban, F., Moreau, P., and Chatal, J. F. (1999) Radioimmunotherapy of small cell lung carcinoma with the two-step method using a bispecific anti-carcinoembryonic antigen/anti-diethylenetriaminepentaacetic acid (DTPA) antibody and iodine-131Di-DTPA hapten: results of a phase I/II trial. *Clin. Cancer. Res. 5* (10 Suppl), 3259s−3267s.

(10) Kraeber-Bodere, F., Faivre-Chauvet, A., Ferrer, L., Vuillez, J. P., Brard, P. Y., Rousseau, C., Resche, I., Devillers, A., Laffont, S., Bardies, M., Chang, K., Sharkey, R. M., Goldenberg, D. M., Chatal, J. F., and Barbet, J. (2003) Pharmacokinetics and dosimetry studies for optimization of anti-carcinoembryonic antigen x anti-hapten bispecific antibody-mediated pretargeting of Iodine-131-labeled hapten in a phase I radioimmunotherapy trial. *Clin. Cancer. Res. 9* (10 Pt. 2), 3973s−3181s.

(11) Boerman, O. C., Kranenborg, M. H., Oosterwijk, E., Griffiths, G. L., McBride, W. J., Oyen, W. J., de Weijert, M., Oosterwijk-Wakka, J., Hansen, H. J., and Corstens, F. H. (1999) Pretargeting of renal cell carcinoma: improved tumor targeting with a bivalent chelate. *Cancer Res. 59* (17), 4400−4405.

(12) Karacay, H., McBride, W. J., Griffiths, G. L., Sharkey, R. M., Barbet, J., Hansen, H. J., and Goldenberg, D. M. (2000) Experimental pretargeting studies of cancer with a humanized anti-CEA x murine anti-[In-DTPA] bispecific antibody construct and a (99m)Tc-/(188)Re-labeled peptide. *Bioconjugate Chem. 11* (6), 842−854.

(13) Gruaz-Guyon, A., Janevik-Ivanovska, E., Raguin, O., De Labriolle-Vaylet, C., and Barbet, J. (2001) Radiolabeled bivalent haptens for tumor immunodetection and radioimmunotherapy. *Q. J. Nucl. Med. 45* (2), 201−206.

(14) Gruaz-Guyon, A., Le Doussal, J. M., Delaage, M., and Barbet, J. (1994) Bihaptenic derivates for binding of technetium or rhenium, process for their preparation, application to diagnosis and therapy, kits and immunological reagents comprising them. French Patent 2,697,255.

(15) Gestin, J. F., Loussouarn, A., Bardies, M., Gautherot, E., Gruaz-Guyon, A., Sai-Maurel, C., Barbet, J., Curtet, C., Chatal, J. F., and Faivre-Chauvet, A. (2001) Two-step targeting of xenografted colon carcinoma using a bispecific antibody and 188Re-labeled bivalent hapten: biodistribution and dosimetry studies. *J. Nucl. Med. 42* (1), 146−153.

(16) Bardies, M., and Chatal, J. F. (1994) Absorbed doses for internal radiotherapy from 22 beta-emitting radionuclides-beta-dosimetry of small spheres. *Phys. Med. Biol. 39* (6), 961−981.

(17) Corson, D., and Meares, C. F. (2000) Efficient Multigram Synthesis of the Bifunctional Chelating Agent (*S*)-1-*p*-Isothiocyanatobenzyl-diethylenetetraminepentaacetic Acid. *Bioconjugate Chem. 11* (2), 292−299.

(18) Wu, C., Kobayashi, H., Sun, B., Yoo, T. M., Paik, C. H., Gansow, O. A., Carrasquillo, J. A., Pastan, I., and Brechbiel,

M. W. (1997) Stereochemical influence on the stability of radio-metal complexes in vivo. Synthesis and evaluation of the four stereoisomers of 2-(*p*-nitrobenzyl)-*trans*-CyDTPA. *Bioorg. Med. Chem. 5* (10), 1925−1934.

(19) Brechbiel, M. W., and Gansow, O. A. (1992) Synthesis of C-functionalized trans-cyclohexyldiethylenetriaminepentaacetic acid for labeling of monoclonal antibodies with the Bismuth-212 α- particle emitter. *J. Chem. Soc., Perkin Trans. 1* 1173−1178.

(20) Liu, S., and Edwards, D. S. (2001) Bifunctional chelators for therapeutic lanthanide radiopharmaceuticals. *Bioconjugate Chem. 12* (1), 7−34.

(21) Sharkey, R. M., McBride, W. J., Karacay, H., Chang, K., Griffiths G. L., Hansen, H. J., and Goldenberg, D. M. (2003) A universal pretargeting system for cancer detection and therapy using bispecific antibody. *Cancer Res. 63*, 354−363.

(22) Morel, A., Darmon, M., and Delaage, M. (1990) Recognition of imidazole and histamine derivatives by monoclonal antibodies. *Mol. Immunol. 27* (10), 995−1000.

(23) Greenwood, F., and Hunter, W. (1963) The preparation of I-131-labeled human growth hormone of high specific radioactivity. *Biochem. J. 89*, 114−123.

(24) Benoist, E. (1997) Synthèse de ligands tétradentés N_2S_2 en vue du radiomarquage de vecteurs immunospécifiques pour des applications diagnostiques et thérapeutiques en cancérologie. Ph.D.*,* University of Nantes.

(25) Hosono, M., Hosono, M. N., Kraeber-Bodere, F., Devys, A., Thedrez, P., Faivre-Chauvet, A., Gautherot, E., Barbet, J., and Chatal, J. F. (1999 Jul) Two-step targeting and dosimetry for small cell lung cancer xenograft with anti-NCAM/antihistamine bispecific antibody and radioiodinated bivalent hapten. *J. Nucl. Med. 40* (7), 1216−1221.

(26) Kraeber-Bodere, F., Faivre-Chauvet, A., Sai-Maurel, C., Campion, L., Fiche, M., Gautherot, E., Le Boterff, J., Barbet, J., Chatal, J. F., and Thedrez, P. (1999) Toxicity and efficacy of radioimmunotherapy in carcinoembryonic antigen-producing medullary thyroid cancer xenograft: comparison of iodine 131-labeled $F(ab')_2$ and pretargeted bivalent hapten and evaluation of repeated injections. *Clin. Cancer. Res. 5* (10 Suppl), 3183s−3189s.

(27) Janevik-Ivanovska, E., Gautherot, E., Hillairet de Boisferon, M., Cohen, M., Milhaud, G., Tartar, A., Rostene, W., Barbet, J., and Gruaz-Guyon, A. (1997) Bivalent hapten-bearing peptides designed for iodine-131 pretargeted radioimmunotherapy. *Bioconjugate Chem. 8* (4), 526−533.

BC0497721

Fluorescent Nanometer Microspheres as a Reporter for Sensitive Detection of Simulants of Biological Threats Using Multiplexed Suspension Arrays

L. Wang,*,† K. D. Cole,† A. K. Gaigalas,† and Yu-Zhong Zhang‡

Biotechnology Division, National Institute of Standards and Technology, Gaithersburg, Maryland 20899-8312, and Molecular Probes, Inc., 4849 Pitchford Avenue, Eugene, Oregon 97402-9165. Received August 18, 2004; Revised Manuscript Received November 18, 2004

We succeeded in using 40 nm FRET (fluorescence resonance energy transfer) microspheres conjugated to antibodies as the fluorescent reporters to perform the multiplexing suspension array measurements on two simulants of biological threats, ricin (A chain) and a crude spore preparation of *Bacillus globigii* (Bg). The microspheres were impregnated with two types of fluorophores in equal number (~140 fluorophores in total per microsphere) and displayed bright PE-like fluorescence via a fluorescence resonance energy transfer mechanism. Activated microspheres (aldehyde groups) were directly coupled to antibodies and used to form sandwich-type immunoassays in a suspension array. For the crude preparations of Bg, the assay sensitivity using antibody-conjugated microspheres is an order of magnitude higher than that using the conventional fluorescent reporter, *R*-phycoerythrin (PE). Using the microspheres, Bg at the concentration of 5 ng/mL can be easily detected. For ricin, the assay sensitivity was similar to that obtained using PE as the reporter, but washing the reaction mixtures resulted in the fluorescence signals that were 2−3 times higher compared to those using PE. Ricin at a concentration of 1 ng/mL can be readily identified. Importantly, the two simulants do not interfere with each other in the multiplexing experiments. The 40 nm FRET microspheres are a new sensitive alternative as fluorescent reporters for detection in suspension arrays.

INTRODUCTION

Over the past 20 years, flow cytometry has become an indispensable measurement tool for clinical diagnostics and basic research. It is exquisitely suited to multiplexing analysis because the technology is capable of analyzing multiple wavelengths of emitted fluorescence from thousands of particles per second with excellent sensitivity (*1, 2*). When compared to conventional flow cytometers with multiple lasers for the respective fluorophores, the latest design of the suspension array flow cytometer (Luminex 100 from Luminex Corp.) provides high sensitivity, high throughput, and multiplex detection at a lower cost. The instrument is designed to take advantage *R*-phycoerythrin (PE) as the reporter. The suspension arrays utilize polystyrene microbeads (5.5 μm in diameter) that are impregnated with precise ratios of red and infrared fluorescent dyes yielding an array of 100 bead sets, each with a unique intensity address in the instrument. A 635 nm, 10 mW red diode laser excites the two classification fluorophores embedded in the microbeads, and a 532 nm, 13 mW yttrium aluminum garnet (YAG) laser provides the excitation of the fluorescent reporter PE. The immunoassays adopt a typical sandwich immunoassay format where antigen-specific capture antibodies are immobilized on the microbeads, antigen is then added and allowed to bind to capture beads, and the bound antigen is subsequently recognized by the biotinylated secondary antibodies that are identified by streptavidin-PE (*3*). Because the reporter fluorescence does not overlap with the classification signal, no fluorescent compensation is required.

High-throughput suspension arrays have been used for disease diagnostics (*4*) and for detections of biological threats because of the sensitivity, specificity, and multiplex capabilities (5, *6*). McBride and co-workers (*6*) have developed and tested a fully autonomous pathogen detection system for monitoring airborne biological threat agents. This system is designed to automate the sample collection, preparation, and multiplex detection of biological threat agents (bacteria, viruses, and toxins) using suspension arrays. The technological characteristics exhibit advantages over other immunoassay formats, such as enzyme-linked immunosorbent assay (ELISA) and time-resolved fluorescence (TRF) assays (*7*). To fulfill the need of the public health against the biological threats, it's important to develop simulants of biothreat agents for the purposes of rapid and accurate detection, remediation, and personnel training.

In the present study, two simulants of biological threats, ricin (A chain) and a spore preparation of *Bacillus globigii* (Bg), have been chosen as the model systems for detection using suspension arrays. Ricin, a glycoprotein toxin derived from castor plant beans, is one of the most poisonous naturally occurring substances known and has great potential for harm due to its wide availability and superior stability. The A chain portion of the ricin heterodimer has the enzymatic activity that binds and depurinates a specific adenine in the 28S subunit of ribosomes. The B chain portion of ricin is required for it to efficiently enter cells (*8, 9*). Bg is a nonpathogenic relative of *Bacillus anthracis* and the spore size and properties are similar to *Bacillus anthracis*

* Corresponding author: Lili Wang, National Institute of Standards and Technology, 100 Bureau Dr., Stop 8312, Gaithersburg, MD 20899-8312, (301) 975-2447, lili.wang@nist.gov.
† National Institute of Standards and Technology.
‡ Molecular Probes, Inc.

10.1021/bc0498020 CCC: $30.25 © 2005 American Chemical Society
Published on Web 12/23/2004

spores. The dormant spores can endure a wide range of extreme environmental stresses while retaining the capacity to rapidly return to vegetative growth (germination process) when environmental conditions are favorable (*10*). These two simulants (Bg and ricin A-chain) can safely be used as internal controls to increase the confidence of the results obtained from suspension arrays.

PE has an extremely high extinction coefficient and high fluorescence quantum yield and is widely used in conventional sandwich immunoassays. The Luminex 100 instrument was specifically designed to use PE as the fluorescent reporter. Since new types of brightly fluorescent reporter molecules are being developed continuously, the choice of the fluorescent reporter is likely to play an important role in increasing the sensitivity and reliability of immunoassays using liquid suspension arrays (manuscript in preparation). Although fluorescent microspheres (μm size) are widely used as standards for flow cytometry and fluorescence microscopy (*11*), nanometer-sized microspheres imbedded with fluorophores have been developed and conjugated to antibodies or streptavidin for immunology studies using flow cytometry, fluorescence microscopy, and ELISAs (*12*−*15*). These brightly fluorescent microspheres possess many advantages, such as high photostability and signal-to-noise ratio, environmental insensitivity, and incorporation of multiple dyes to make a set of probes that fluoresce at different wavelengths with a single excitation wavelength. In the present study, 40 nm FRET microspheres impregnated with two types of fluorophores were used as the fluorescent reporter for the sandwich assays detecting both ricin A chain and Bg simultaneously. We have focused on the application of these new FRET microspheres for multiplex assays and compared the results to PE, that is the reporter with the best sensitivity and greatest number of previous applications.

MATERIALS AND METHODS

An aqueous suspension of 40 nm FRET microspheres ($\sim 3.0 \times 10^{14}$/mL) with aldehyde functional groups on the surface was from Molecular Probes (Eugene, OR).[1] These microspheres are impregnated with two types of orange BODIPY dyes in equal number ($\sim$140 fluorophores in total per microsphere) and display bright PE-like fluorescence via a fluorescence resonance energy transfer mechanism. The dried preparation of *Bacillus globigii* (Bg, *Bacillus atropheus*) spores (lot Sept. 17, 2002) was obtained from U. S. Army Edgewood Chemical Biological Center (Edgewood, MD). The spore preparation gave an average of 1×10^5 colonies per μg of powder when suspended in water or buffer. Stock spore suspensions in PBS were stored at 4 °C. Ricin A chain (1 mg/mL, #L-1190, Vector Laboratories, Burlingame, CA) was diluted in PBS containing 5 mM dithiothreitol and 1% (w/w) BSA. Diluted solutions of the Bg spore and ricin A chain were prepared in PBS and used as the multiplex antigen samples. The polyclonal antibody against *Ricinus communis* agglutinin I & II was also purchased from Vector Laboratories. The antibody stock solution was prepared by adding 0.5 mL of water to obtain a final concentration of 2 mg/mL in phosphate buffer, pH 7.8 (10 mM phosphate, 0.15 M NaCl, 0.08% sodium azide, and sucrose). The polyclonal antibody against Bg was provided by Tetracore Inc. (Gaithersburg, MD) and was dissolved in phosphate-buffered saline, pH 7.4, (0.01 M phosphate, 0.138 M NaCl, 0.0027 M KCl, 0.05% (w/w) NaN_3) at a concentration of 3.6 mg/mL.

The immobilization of the polyclonal antibodies to Luminex carboxylated microspheres was accomplished through formation of a carbodiimide bond and carried out according to the manufacturer-recommended procedures. A FluoReporter Mini-Biotin-XX-Protein Labeling Kit from Molecular Probes was used for biotinylation of the antibodies, and the coupling reaction of biotins to the antibody was carried out according to the manufacturer-recommended procedures. The conjugation of the antibodies to 40 nm FRET microspheres was through the formation of an amide bond between amine groups of the antibodies and aldehyde groups on the surface of microspheres (*16*) and was carried out as follows. A 20 μL of antibody stock solution was diluted into 400 μL water, and then a proper volume of 40 nm FRET microsphere suspension was slowly added to the antibody solution. The labeling reaction carried out overnight with gentle vortexing. To prepare antibody-conjugated microspheres with different molar ratios between antibody and microsphere, the volume of microsphere suspension added was adjusted while the amount of antibody was kept constant. The agarose gel electrophoresis was used to detect the fluorescent products of the labeling reactions and help out finding of the optimal molar ratio of antibody and microsphere.

A commercial Luminex 100 instrument (Luminex Corp., Austin, TX) was used to perform the multiplexing sandwich assays detecting surrogates of biological threat agents, ricin A chain and Bg. Polyclonal antibodies coupled to specific Luminex beads (1500−3000 beads, 14 μL) were used for the primary analyte-capture step. After incubation with analytes (20 μL) for 20 min with gentle vortexing, the biotin-labeled antibodies (30 μL, 0.8 μg) were added and incubated for 20 min to form the sandwich-type complexes. PE-labeled streptavidin (10 μL, 1.5 μg) was then added as the conventional fluorescent reporter for the detection of ricin toxin and Bg. The final volume of the reaction mixture was 74 μL. On the other hand, microsphere-conjugated antibodies were utilized as an alternative, bright fluorescent reporter to detect the two analytes. The addition of the prior labeled antibodies combines the last two steps in conventional Luminex sandwich assays (Figure 1). When washing steps were employed, the assays were performed in 1.5 μL centrifuge tubes. The sandwich reaction mixtures were centrifuged at a g-force of 9000 for 2 min. The supernatant was discarded and 500 μL of blocking buffer, pH 7.4, (0.01 M phosphate, 0.138 M NaCl, 0.0027 M KCl, 1% (w/w) bovine serum albumin, 0.05% (w/w) NaN_3) was added. The centrifugation step described above was repeated, and the supernatant was again discarded. After the addition of 74 μL of blocking buffer, the reaction mixtures were vortexed and transferred to a 96-well plate (Model P, Corning Incorporated, Corning, NY) and prepared for detection. For the multiplexing sandwich assays, the blank signals were obtained in the absence of the antigens and were subtracted from the fluorescence signals of the sandwich complexes in the presence of the two analytes.

RESULTS AND DISCUSSION

The various steps of sandwich assays are illustrated in Figure 1. The analyte is recognized by the polyclonal

[1] Certain commercial equipment, instruments, and materials are identified in this paper to specify adequately the experimental procedure. In no case does such identification imply recommendation or endorsement by the National Institute of Standards and Technology, nor does it imply that the materials or equipment are necessarily the best available for the purpose.)

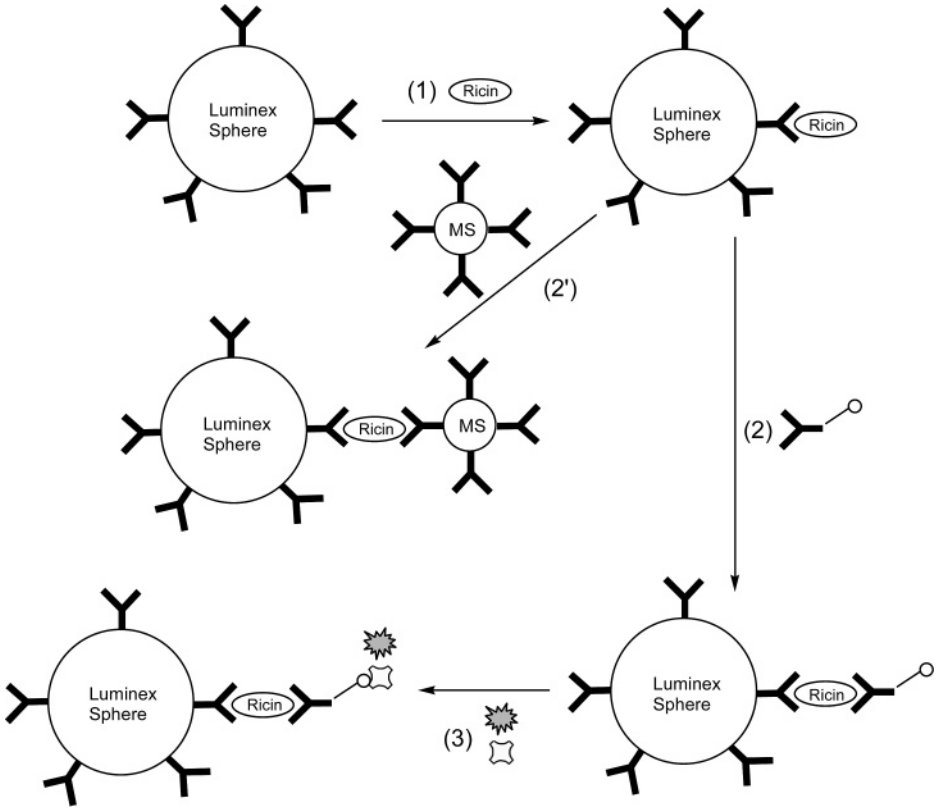

Figure 1. The schematic of immunological assays implemented in the study. As a first step, an analyte such as ricin A chain, for example, is bound to beads coated with a layer of polyclonal antibodies raised against ricin. Subsequently, biotinylated antibodies are added to the suspension in conventional immunoassays (2). Finally *R*-phycoerythrin (PE)-labeled streptavidin as the fluorescent reporter is added to the suspension to conclude the conventional sandwich assay (3). Alternatively, we have employed antibody-conjugated 40 nm FRET microspheres (MS) as the fluorescent reporter for the sandwich assay (2′). The 40 nm FRET microsphere is impregnated with as many as 140 fluorophores and is highly fluorescent compared to PE. The sizes of beads (5.5 μm) and 40 nm microspheres are not proportional in the illustration.

antibody immobilized on the surface of the beads (Step 1). Used in conventional immunoassays, biotin-labeled antibodies are subsequently bound to the analytes to form sandwich-type complexes (Step 2). Last, *R*-phycoerythrin (PE)-labeled streptavidin is added as the fluorescent reporter for intensity measurements by the instrument (Step 3). Alternatively, the antibody conjugated microspheres (40 nm in diameter) replaces the biotin-labeled antibodies and the strepavidin−PE steps in a single step (Step 2′). Since each 40 nm FRET microsphere, on the average, contains about 140 fluorophores, and a resonance energy transfer method (equal numbers of donor and acceptor) is used, about 70 fluorophores are sufficient for the final emission. It is known that a single PE is equivalent to ~20 fluorophores. Therefore, when the microspheres are used as the fluorescent label, in theory, the fluorescence signal should be about 3.5 times higher than that using *R*-PE as the fluorescent reporter. Since the 40 nm FRET microspheres are largely made of hydrophobic polystyrene, however, effort may be needed for preventing nonspecific adsorption.

Because of light scattering by the 40 nm polystyrene spheres, the absorbance of the dye molecules cannot be accurately measured through simple subtraction of the absorbance from the blank microspheres. The absorbance below 500 nm is affected by the light scattering. Wittmershaus and co-workers have measured the absorbance of different BODIPY dyes embedded in microspheres via the method of index matching (*17*). Given that the absorption of dye molecules impregnated in microspheres should be proportional to the fluorescence signal obtained at the same excitation wavelength when the emission wavelength is held constant (*18*), we measured the excitation spectrum of the dye-embedded microspheres. The excitation and emission spectra of the microspheres are shown in Figure 2. The maximal absorbance and fluorescence are at 538 nm and at 570 nm, respectively. These properties are ideal for applications using Luminex 100 instruments that are equipped with a 532 nm laser beam and a 575 ± 12 nm band-pass filter for the excitation and detection of fluorescent reporters, respectively. As shown in the inset of Figure 2, two types of BODIPY dyes are needed to maximize fluorescence signal for detections using Luminex 100 instrument**.** Upon excitation, the first BODIPY fluorophores whose emission spectrum shown as dash dot line in the inset will transfer its energy to the second BODIPY dye molecules (shown as dash line) via dipole−dipole interactions with ~95% transfer efficiency (*19*). Because these fluorophores are imbedded in the microspheres, their photostabilities are superior to the commonly used *R*-PE (*17*, *20*).

To minimize nonspecific adsorption of the microspheres to various hydrophobic assay components, the reactive aldehyde groups on the outer surfaces of the microspheres were saturated with antibodies. We have used agarose gel electrophoresis to detect the fluorescent products of the labeling reactions between antibodies and aldehyde microspheres. Figure 3 shows the gel electrophoresis of the conjugation reactions with various molar ratios of antibody and microsphere as well as pure reactive microspheres as a control (lane 1 in Figure 3A). Since the polystyrene microspheres are neutral on the outer surface, they hardly move into the gel. At relative low molar ratios of ricin antibody and microsphere from

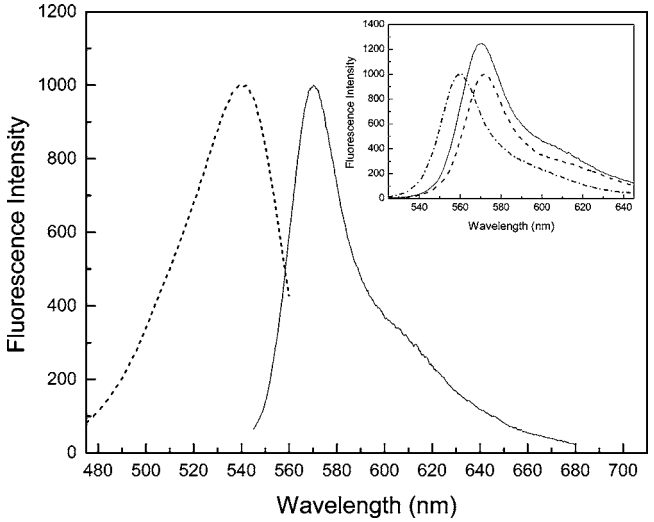

Figure 2. Normalized excitation (short dash line) and emission (solid line) spectra of the 40 nm FRET microspheres suspended in water. The fluorescence was monitored at 570 nm for the excitation spectrum and the excitation wavelength was set at 532 nm for the emission spectrum, respectively. The inset displays emission spectra (arbitrary units) of 40 nm microspheres with one type of BODIPY dye (dash and dash dot lines) and FRET microspheres imbedded with two types of BODIPY dye (solid line). The excitation wavelength was set at 490 nm for the spectral comparison. The Stokes shifts for both types of BODIPY dye are about 20 nm. The slits for excitation and emission monochromators were set at 4 nm for these measurements.

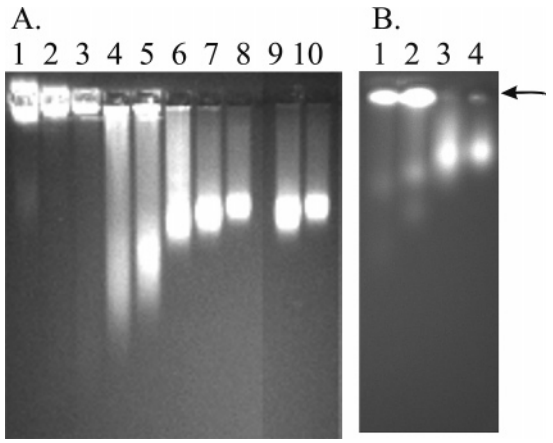

Figure 3. Agarose gel electrophoresis of microsphere preparations. The samples were electrophoresed for 3 h at 6 V/cm in 0.75% agarose using 0.5 × TBE buffer (45 mM TRIS, 45 mM boric acid, 1 mM EDTA, pH 8.3). Samples with diluted with 4% Ficoll 400 and a trace of bromphenol blue before loading. The arrow indicts the sample loading position. (A) The samples are microspheres (lane 1) and antibody-conjugated microspheres with various molar ratios of antibody against ricin and microsphere: 4:1 (lane 2), 8:1 (lane 3), 16:1 (lane 4), 24:1 (lane 5), 32:1 (lane 6), 48:1 (lane 7), 64:1 (lane 8), 48:1 from earlier preparation (lane 9), and 64:1 from earlier preparation (lane 10). (B) The conjugation reactions with four different molar ratios of antibody against Bg and microsphere: 32:1 (lane 1), 48:1 (lane 2), 64:1 (lane 3), 96:1 (lane 4). The gel was placed on a Dark Reader illuminator (output 400 nm to 500 nm, Clare Chemical Research, Denver, CO) and photographed using the supplied filter.

4:1 to 32:1 (Figure 3A: lane 2 to lane 6), not all microspheres are labeled with antibodies given that bare microspheres are seen near the loading well. At the ratios of 48:1 (Figure 3A: lane 7 and 9) and 64:1 (Figure 3A: lane 8 and 10), almost all the microspheres are conjugated with antibodies that are shown by the distinct

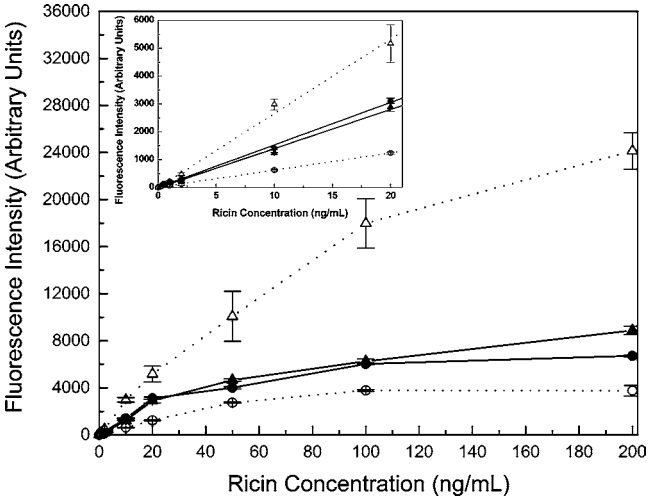

Figure 4. Standard curves of the immunoassays for ricin A chain generated by using two different fluorescent reporters, PE (circle and solid line) and antibody-conjugated microspheres with the molar ratio of antibody and microsphere of 48:1 (triangle and solid line), and implementing the two-step washing after completion of the sandwich complexes with the use of antibody-conjugated microspheres (open triangle and dot line) or PE (open circle and dot line). The error bars in the figure show the standard deviations obtained from multiple experimental repeats ($N = 4$). The inset shows the standard curves in the low concentration region of ricin A chain where the fluorescence signal corresponds linearly to ricin concentration. Various lines in the inset are the linear fitting curves.

fluorescent band that moved into the gel. The conjugation reactions (Figure 3A: lane 9 and 10) were made two weeks earlier than those (Figure 3A: lane 7 and 8), and the antibody-conjugated microspheres were stable as shown in the figure. Both ratios (48:1 and 64:1) were used to perform the sandwich assays and gave similar results.

Microspheres conjugated with the antibodies against Bg run more slowly in agarose gel than those labeled with anti-ricin antibodies (Figure 3B). At two ratios of Bg antibody and microspheres, 32:1 (Figure 3B, lane 1) and 48:1 (Figure 3B, lane 2), there were excess microspheres present near the loading wells and the coupling reactions were inefficient. With the increase of this ratio to 64:1 (Figure 3B, lane 3) and 96:1 (Figure 3B, lane 4), however, most microspheres were conjugated with antibodies, which could be visualized as a fluorescent band in the gel. The conjugated microspheres with the ratio of 64:1 were used for Bg to carry out the multiplexing experiments. The excitation and emission spectral shapes of these conjugated microspheres are the same as those shown in Figure 2.

Figure 4 displays the standard curves of the multiplexing immunoassays for ricin A chain in the presence of Bg using two different fluorescent reporters, PE (circle and solid line) and antibody-conjugated microspheres at the molar ratio of ricin antibody and microsphere of 48:1 (triangle and solid line). The two standard curves agree with each other. At low ricin concentrations ($\leq$20 ng/mL) the fluorescence signal reacts with ricin in a linear fashion, and at high concentrations of ricin ($\geq$20 ng/mL) the signal slowly approaches a plateau. Because of the possibility of the nonspecific adsorption by the microspheres, we further explored the effect of implementing a two-step washing step prior to the fluorescence detection. With the addition of the washing step, the standard curve with the use of antibody-conjugated microspheres (open triangle and dot line) was obtained with a highly improved sensitivity. In contrast, with the use of PE, the

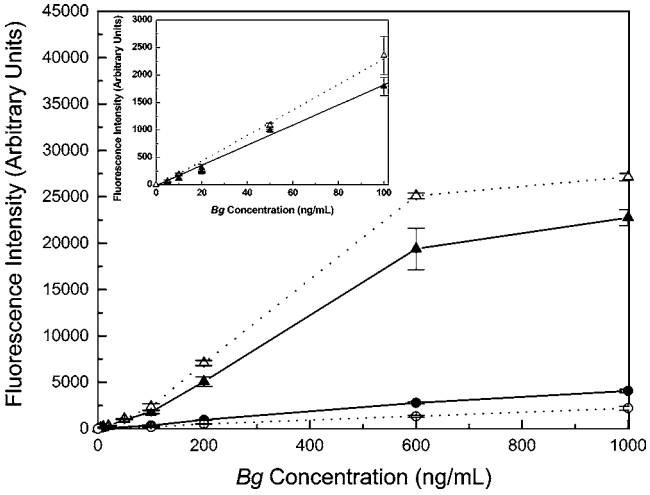

Figure 5. Standard curves of the immunological assays for *Bacillus globigii* (Bg) generated by using two fluorescent reporters, PE (circle and solid line) and antibody-conjugated microspheres with the molar ratio of antibody and microsphere of 64:1 (triangle and solid line), and employing the washing step after formation of the sandwich complexes in the presence of the antibody-conjugated microspheres (open triangle and dot line) or PE (open circle and dot line). The error bars show the standard deviations obtained from multiple experimental repeats ($N = 4$). The inset shows the standard curves in the low concentration region of Bg where the fluorescence signal responds to antigen concentration in a linear fashion. The two lines in the inset are the linear fitting curves.

assay sensitivity has dropped (open circle and dot line). The inset of the figure shows the standard curves in the low concentration region of the analyte where the fluorescence signal from the reporter responds linearly to analyte concentration. The larger slope of the linear fitting curve demonstrates the high sensitivity of ricin A chain detection by using the antibody-conjugated microspheres. The fluorescence enhancement achieved by the washing step is likely due to the minimization of the self-quenching between 40 nm dye-imbedded microspheres. As we anticipated, the fluorescence signals from the sandwich complexes with conjugated microspheres are 2 to 3 times larger than those using PE as the fluorescent reporter. Additionally, the presence of Bg did not interfere with the detection of ricin A chain since the fluorescence signals of the ricin sandwich complexes are about the same in the presence and absence of Bg (data not shown). The error bars in the figure show the standard deviations obtained from multiple experimental repeats.

The samples of Bg spores used in this study are crude preparations that would be representative of an environmental sample. The Bg samples must be constantly mixed to prevent settling during sampling and during the antigen capture step. The biological activity of these samples can be expressed in colony forming units ($\sim 1 \times 10^5$ colonies per μg), but comparison to other results done with different preparations of spores is not very meaningful because the total antigen content is not well defined in these samples. There is a real need for developing well-defined spore samples in both highly pure and crude forms. In the absence of standardized spore preparations, it makes the most sense to look at the relative differences in the detection limits when comparing the different reporters using the same samples.

The standard curves of the sandwich assays for Bg in the presence of ricin A chain are shown in Figure 5 with the use of two fluorescent reporters, PE (circle and solid line) and antibody-conjugated microspheres at the molar ratio of Bg antibody and microsphere of 64:1 (triangle and solid line). The assay sensitivity by using antibody-conjugated microspheres is much higher than that using the conventional PE. For instance, the fluorescence signals of the sandwich complexes at the Bg concentration of 5 ng/mL are distinctively above the signal of the negative control. However, with the use of PE as the reporter, the fluorescence signals of the formed complexes and of the negative control are about the same at the Bg concentration of 50 ng/mL. McBride and co-workers (*5*) showed that the sensitivity of Bg detection (using PE as the reporter) in suspension arrays was more than an order of magnitude higher compared to that using ELISAs.

We further explored the detection of Bg spores using the microspheres by adding a washing step. The fluorescence signals were only slightly improved by the washing step (open triangle and dot line) compared to the signals without the washing step (triangle and solid line). Similar to ricin assays shown in Figure 4, applying the washing steps with the use of PE as the reporter results in decrease of signals (open circle and dot line) when compared to the signals without the washing step (circle and solid line).

The high fluorescence signals obtained with the microspheres are likely attributed to several factors. As described earlier, each microsphere could emit, in principle, a ~3.5 times higher fluorescence signal than that of a single PE molecule. Additionally, because of the large size of Bg spore (~ 1 μm long and 0.7 μm wide) (*21*), it could be recognized by multiple polyclonal antibodies raised against Bg. With the use of microsphere-labeled antibodies, the signals of formed Bg complexes at high Bg concentrations are about 6 times higher than that using PE-conjugated antibodies (Figure 5). This implies that self-quenching between PE molecules is likely at high analyte concentration. The FRET microspheres coated with a layer of Bg antibodies may be less susceptible to self-quenching and therefore more versatile in recognizing the analyte (a crude spore preparation of Bg). The inset of the figure shows the standard curves in the low concentration region of the analyte where the fluorescence signal from antibody-conjugated microspheres responds to Bg concentration in a linear fashion. Using PE as the fluorescent reporter, the signals were hardly distinguishable from the background at the Bg concentration of 50 ng/mL.

CONCLUSIONS

To detect small amount of biological threats, it is critical to search for better fluorescent reporters that give brightest possible fluorescence for detection using high-throughput suspension arrays. In the present study, we have used 40 nm FRET microsphere-conjugated antibodies as the fluorescent reporters that emit about 3 times higher fluorescence than that of the conventional PE reporter used in suspension arrays to perform the multiplexing array experiments. In the case of Bg, the assay sensitivity using antibody-conjugated microspheres is an order of magnitude higher than that using the conventional PE without the implementation of the washing step. With the use of antibody-coupled microspheres, Bg at the concentration of 5 ng/mL can be easily detected. In the case of ricin A chain, the assay sensitivity is as good as that using PE as the fluorescent reporter without the washing step. While employing the washing step, however, the fluorescence signals of the sandwich complexes are 2−3 times higher than those using PE. Ricin A chain at concentration of 1 ng/mL can be readily

identified. Importantly, the two simulants do not interfere with each other in the multiplexing experiments. Thus, the present 40 nm FRET microspheres can be visualized as a unique class of fluorescence reporters for sensitive detections using suspension arrays.

ACKNOWLEDGMENT

The authors are indebted to D. Hancock for making antibody-coated Luminex beads and biotinylated antibodies.

LITERATURE CITED

(1) Martinez, A., Pittaluga, S., Villamor, N., Colomer, D., Rozman, M., Raffeld, M., Montserrat, E., Campo, E., and Jaffe, E. S. (2004) Clonal T-cell Populations and Increased Risk for Cytotoxic T-cell Lymphomas in B−CLL Patients: Clinicopathologic Observations and Molecular Analysis. *Am. J. Surg. Pathol. 28*, 849−858.

(2) Xu, H., Sha, M. Y., Wong, E. Y., Uphoff, J., Xu, Y., Treadway, J. A., Truong, A., O′Brien, E., Asquith, S., Stubbins, M., Spurr, N. K., Lai, E. H., and Mahoney, W. (2003) Multiplexed SNP Genotyping Using the Qbeads System: a Quantum Dot-encoded Microsphere-based Assay. *Nucleic Acids Res*. *31*, e43.

(3) Kellar, K. L.; Iannone M. A. (2002) Multiplexed Microsphere-based Flow Cytometric Assays. *Exp. Hematol*. *30*, 1227−1237.

(4) Pickering, J. W., Martins, T. B., Carl Schroder, M., and Hill, H. R. (2002) Comparison of a Multiplex Flow Cytometric Assay with Enzyme-Linked Immunosorbent Assay for Quantitation of Antibodies to Tetanus, Diphtheria, and *Haemophilus influenzae* Type b. *Clin. Diagn. Lab. Immunol*. *9*, 872−876.

(5) McBride, M. T., Gammon, S., Pitesky, M., O′Brien, T. W., Smith, T., Aldrich, J., Langlois, R. G., Colston, B., and Venkateswaran, K. S. (2003) Multiplexed Liquid Arrays for Simultaneous Detection of Simulants of Biological Warfare Agents. *Anal. Chem*. *75*, 1924−1930.

(6) McBride, M. T., Masquelier, D., Hindson, B. J., Makarewicz, A. J., Brown, S., Burris, K., Metz, T., Langlois, R. G., Tsang, K. W., Bryan, R., Anderson, D. A., Venkateswaran, K. S., Milanovich, F. P., and Colston, B. W., Jr. (2003) Autonomous Detection of Aerosolized *Bacillus anthracis* and *Yersinia pestis*. *Anal. Chem*. *75*, 5293−5299.

(7) Peruski, A. H., Johnson, L. H., III., and Peruski, L. F., Jr. (2002) Rapid and Sensitive detection of Biological Warfare Agents Using Time-Resolved Fluorescence Assays. *J. Immunol*. *Methods 263*, 35−41.

(8) Robertus, J. D. (1991) The Structure and Action of Ricin, a Cytotoxic N-glycosidase. *Semin. Cell Biol*. *2*, 23−30.

(9) Vitetta, E. S. and Thorpe, P. E. (1991) Immunotoxins Containing Ricin or Its A Chain. *Semin. Cell Biol*. *2*, 47−58.

(10) Moir, A., Corfe, B. M., and Behravan, J. (2002) Spore Germination. *Cell. Mol*. *Life Sci*. *59*, 403−409.

(11) Vogt, R. F., Cross, G. D., Phillips, D. L., Henderson, L. O., and Hannon, W. H. (1991) Interlaboratory Study of Cellular fluorescence Intensity Measurements with Fluorescein-Labeled Microbead Standards. *Cytometry 12*, 525−536.

(12) Bhalgat, M. K., Haugland, R. P., Pollack, J. S., Swan, S., and Haugland, R. P. (1998) Green- and Red-fluorescent Nanospheres for the Detection of Cell Surface Receptors by Flow Cytometry. *J. Immunol*. *Methods 219*, 57−68.

(13) Zhao, X., Hilliard, L. R., Mechery, S. J., Wang, Y., Bagwe, R. P., Jin, S., and Tan, W. (2004) A Rapid Bioassay for Single Bacterial Cell Quantitation Using Bioconjugated Nanoparticles. *Proc. Natl. Acad. Sci. U.S.A. 101*, 15027−15032.

(14) Väisänen, V., Härmä, H., Lilja, H., and Bjartell, A. (2000) Time-resolved Fluorescence Imaging for Quantitative Histochemistry Using Lanthanide Chelates in Nanoparticles and Conjugated to Monoclonal Antibodies. *Luminescence 15*, 389−397.

(15) Schaertl, S., Meyer-Almes, F., Lopez-Calle, E., Siemers, A., and Krämer, J. (2000) A Novel and Robust Homogeneous Fluorescence-based Assay Using Nanoparticles for Pharmaceutical Screening and Diagnostics. *J. Biomol. Screen*. *5*, 227−237.

(16) Hermanson, G. T. (1996) *Bioconjugate Techniques*, Chapter 7, Academic Press, San Diego, CA.

(17) Wittmershaus, B. P., Skibicki, J. J., McLafferty, J. B., Zhang, Yu-Zhong, and Swan, S. (2001) Spectral Properties of Single BODIPY Dyes in Polystyrene Microspheres and in Solutions. *J. Fluoresc. 11*, 119−127.

(18) Schwartz, A., Wang, L., Early, E., Gaigalas, A., Zhang, Yu-zhong, Marti, G. E., and Vogt, R. F. (2002) Quantitating Fluorescence Intensity from Fluorophore: The Definition of MESF Assignment. *J. Res. Natl. Inst. Stand. Technol*. *107*, 83−91.

(19) Roberts, D. V., Wittmershaus, B. P., Zhang, Yu-Zhong, Swan, S., and Klinosky, M. P. (1998) Efficient Excitation Energy Transfer among Multiple Dyes in Polystyrene Microspheres. *J. Luminesc. 79*, 225−231.

(20) White, J. C. and Stryer, L. (1987) Photostability Studies of Phycobiliprotein Fluorescent Labels. *Anal. Biochem. 161*, 442−452.

(21) Chada, V. G. R., Sanstad, E. A., Wang, R., and Driks, A. (2003) Morphogenesis of *Bacillus* Spore Surfaces. *J. Bacteriol*. 185, 6255−6261.

BC0498020

A Long-Acting, Highly Potent Interferon α-2 Conjugate Created Using Site-Specific PEGylation

Mary S. Rosendahl,*,† Daniel H. Doherty,† Darin J. Smith,† Sharon J. Carlson,† Elizabeth A. Chlipala,‡ and George N. Cox†

Bolder BioTechnology, Inc., 4056 Youngfield Street, Wheat Ridge, Colorado 80033, BolderPATH, Inc., Campus Box 347, University of Colorado, Boulder, Colorado 80309. Received November 30, 2004

Recombinant interferon α-2 (IFN-α2) is used clinically to treat a variety of viral diseases and cancers. IFN-α2 has a short circulating half-life, which necessitates frequent administration to patients. Previous studies showed that it is possible to extend the circulating half-life of IFN-α2 by modifying lysine residues of the protein with amine-reactive poly(ethylene glycol) (PEG) reagents. However, amine-PEGylated IFN-α2 comprises a heterogeneous product mixture with low specific activity due to the large number and critical locations of lysine residues in IFN-α2. In an effort to overcome these problems we determined the feasibility of creating site-specific, mono-PEGylated IFN-α2 analogues by introducing a free (unpaired) cysteine residue into the protein, followed by modification of the added cysteine residue with a maleimide-PEG reagent. IFN-α2 cysteine analogues were expressed in *Escherichia coli* and purified, and their in vitro bioactivities were measured in the human Daudi cell line growth inhibition assay. Several cysteine analogues were identified that do not significantly affect in vitro biological activity of IFN-α2. Certain of the cysteine analogues, but not wild-type IFN-α2, reacted with maleimide-PEG to produce mono-PEGylated proteins. The PEG−Q5C analogue retained high in vitro bioactivity (within 3- to 4-fold of wild-type IFN-α2) even when modified with 20- and 40-kDa PEGs. Pharmacokinetic experiments indicated that the 20-kDa PEG−Q5C and 40-kDa PEG−Q5C proteins have 20-fold and 40-fold longer half-lives, respectively, than IFN-α2 following subcutaneous administration to rats. These studies demonstrate the feasibility of using site-specific PEGylation technology to create a long-acting, mono-PEGylated IFN-α2 protein with high specific activity.

INTRODUCTION

α-Interferons (IFN-α) comprise a family of at least 25 nonallelic genes and pseudogenes that encode proteins with 70% or greater amino acid identity (Henco et al., 1985; Blatt et al., 1996). IFN-α2 is the best-studied member of this family. IFN-α2 is a 19 kDa protein that exhibits antiviral, antiproliferative, and immunomodulatory effects on many cell types (Pestka and Langer, 1987; Gutterman, 1994). Recombinant IFN-α2 has proven useful for the treatment of a variety of human viral diseases and cancers (Gutterman, 1994). Recombinant IFN-α2 has a short circulating half-life and generally is administered to patients by daily or thrice weekly injections. Previous studies showed that it is possible to increase the circulating half-life of IFN-α2 by covalent modification of the protein with amine-reactive poly(ethylene glycol) (PEG) reagents, which typically attach to lysine residues or the N-terminal amino acid (Monkarsh et al., 1997; Wang et al., 2000; Bailon et al., 2001). A limitation of the use of amine-reactive PEGs for modifying IFN-α2 is the fact that IFN-α2 contains 10 (or 11, depending upon the subtype) lysine residues in addition to the N-terminal amino acid. Monkarsh et al. (1997) found that all 11 lysine residues in IFN-α2a are modified to varying extents using amine-reactive PEG reagents. In addition to these 11 positional isomers, amine-PEGylated IFN-α comprises a mixture of mono-, di-, and multiply-PEGylated species. The various positional isomers and mono- and multiply-PEGylated IFN-α2 species have different specific activities (Monkarsh et al., 1997). Amine-PEGylated IFN-α2 also has significantly reduced in vitro bioactivity (4- to 14-fold) compared to IFN-α2 (Monkarsh et al., 1997; Wang et al., 2000; Bailon et al., 2001), which increases the amount of protein required to treat patients. Loss of bioactivity is greatest when IFN-α2 is modified with large PEGs (e.g., 20- and 40-kDa PEGs), which are the most useful PEGs for extending the half-life of the protein, and when the protein is modified with more than one PEG (Monkarsh et al., 1997; Bailon et al., 2001). IFN-α2 contains several lysine residues that are located in regions of the protein believed to be important for receptor binding (Radhakrishnan et al., 1996). It is likely that modification of one or more of the critical lysine residues contributes to the loss of activity upon PEGylation of IFN-α2 with amine-reactive PEG reagents.

In an effort to overcome the heterogeneity and loss of activity problems associated with amine-PEGylation of IFN-α2, we tested the feasibility of using site-specific PEGylation (Goodson and Katre, 1990) to modify IFN-α2. Site-specific PEGylation involves introducing a "free" cysteine residue, that is, a cysteine residue not involved in a disulfide bond, into a target protein using site-directed mutagenesis, followed by covalent modification of the added cysteine residue with a cysteine-specific PEG reagent. A key technical challenge with this technology is the identification of a site(s) in the target protein where

* Corresponding author. Tel: (303) 420-4420. Fax: (303) 420-4426. E-mail: mrosendahl@bolderbio.com.
† Bolder BioTechnology, Inc.
‡ BolderPATH, Inc.

10.1021/bc049713n CCC: $30.25 © 2005 American Chemical Society
Published on Web 01/04/2005

a cysteine residue can be introduced and PEGylated without significantly affecting in vitro biological activity of the protein. In this report, we demonstrate the utility of this approach for creating a long-acting, highly potent PEGylated cysteine analogue of IFN-α2.

EXPERIMENTAL PROCEDURES

Cloning DNA Sequences Encoding IFN-α2 and IFN-α2 Cysteine Analogues. DNA encoding IFN-α2b (Henco et al., 1985) was amplified using the polymerase chain reaction (PCR) method from human genomic DNA (CLONTECH, Inc., Palo Alto, CA) using primers BB93 (5′-CGCGAATTCGGATATGTAAATAGATACACAGTG-3′) and BB94 (5′-CGCAAGCTTAAAAGATTTAAATCGT-GTCATGGT-3′). The PCR product was digested with *Eco*RI and *Hin*dIII and cloned into similarly digested plasmid pCDNA3.1(+) (Invitrogen Corporation, Carlsbad, CA), creating plasmid pBBT160. The IFN-α2 gene in pBBT160 was modified initially for cytoplasmic expression in *Escherichia coli* by using PCR mutagenesis to add a methionine codon immediately prior to the first residue (C1) of the mature IFN-α2 protein and to add a TAA stop codon following the carboxy-terminal residue, E165. In addition, *Xba*I and *Sal*I sites were added and a *Bgl*II site was eliminated to provide convenient restriction sites for subsequent mutagenesis. None of these alterations changed the amino acid sequence of IFN-α2. Primers used in this PCR reaction were BB99 (5′-CGCAAGCT-TCATATGTGTGATCTGCCTCAAACCCACAGCCTGG-GTTCTAGAAGGACCTTGATGCTC-3′) and BB100 (5′-CGCGAATTCTTATTCCTTACTTCTTAAACTTTCTTG-CAAGTTTGTCGACAAAGAAAAGGATCTCATGAT-3′). The PCR product was digested with *Hin*dIII and *Eco*RI and cloned into plasmid pCDNA3.1(+), creating pBBT164. The *Nde*I−*Eco*RI fragment of pBBT164 containing the met-IFN-α2 sequence was subcloned into pUC18 (Sigma-Aldrich, Inc., St. Louis, MO) to generate plasmid pBBT168.

A secreted form of IFN-α2 was created by fusing DNA encoding the *E. coli* heat-stable enterotoxin gene (STII) signal sequence (Picken et al., 1983) to the coding sequence of mature IFN-α2 via two sequential PCR reactions. The first reaction used forward primer BB101 (5′-GCATCTATGTTCGTTTTCTCTATCGCTACCAAC-GCTTACGCATGTGATCTGCCTCAAACCCACAGC-3′) and reverse primer BB100 with pBBT164 DNA. The PCR product was used as DNA template in a second PCR reaction, which used reverse primer BB100 and forward primer BB11 (5′-CCCCCTCTAGACATATGAAGAAGAA-CATCGCATTCCTGCTGGCATCTATGTTCGTTTTCTC-TATCG-3′). The PCR product was digested with *Nde*I and *Xba*I, and the ∼100 bp *Nde*I−*Xba*I fragment containing the STII leader sequence and amino-terminal 30 bp of IFN-α2 was purified and cloned into similarly digested pBBT168 DNA, creating pBBT177. The STII-IFN-α2 gene was subcloned as an *Nde*I−*Eco*RI fragment into expression vector pCYB1 (New England Biolabs, Beverly, MA), creating pBBT178.

Mutant IFN-α2 genes were constructed by site-directed PCR-based mutagenesis (Higuchi, 1990; Horton et al., 1993), using plasmid pBBT177 as the DNA template. PCR products were digested with appropriate restriction endonucleases and cloned into similarly digested pBBT177 DNA. Correct DNA sequences of all cysteine analogues were confirmed. The STII-IFN-α2 genes encoding the cysteine analogues were excised from the pUC18-based pBBT177 derivatives as *Nde*I−*Eco*RI fragments and subcloned into pCYB1 for expression in *E. coli*.

Expression and Purification of IFN-α2 and IFN-α2 Cysteine Analogues. pCYB1 plasmids encoding STII-IFN-α2 and STII-IFN-α2 cysteine analogues were transformed into *E. coli* strain W3110. Overnight cultures were diluted to an optical density at 600 nm of ∼0.02 in Luria Broth (LB) media, 100 mM MES (pH 5.5), containing 100 μg/mL ampicillin. Typically, cells were grown at 37 °C until the optical densities of the cultures reached 0.3−0.4. Isopropyl-β-D-thiogalactopyranoside (IPTG) was then added to a final concentration of 0.5 mM, and the induced cultures were shifted to 28 °C and incubated for about 16 h. Cultures were subjected to osmotic shock as described by Koshland and Botstein (1980). This procedure was modified for the IFN-α2 cysteine analogues to include 5 mM cystine in the osmotic shock buffers. The osmotic shock supernatant and pellet fractions were processed immediately or stored frozen at −80 °C.

IFN-α2 and certain IFN-α2 cysteine analogues were purified from the osmotic shock supernatants by S-Sepharose and Cu^{2+} immobilized metal affinity chromatography (IMAC) column chromatography (Voss et al., 1994; Khan and Rai, 1990). The osmotic shock supernatants were adjusted to pH 3 and centrifuged, and the supernatants were loaded onto a 5 mL HiTrap S-Sepharose column (Amersham Biosciences Corporation, Piscataway, NJ) equilibrated in 20 mM MES, pH 5.0. The bound proteins were eluted with a linear salt gradient from 0% to 100% 500 mM NaCl, 20 mM MES, 10% ethylene glycol, pH 5.0. Column fractions enriched for the IFN-α2 proteins were identified by nonreducing SDS−PAGE. These fractions were pooled and loaded onto a 1 mL Cu^{2+} IMAC HiTrap column (Amersham Biosciences Corporation) equilibrated in 40 mM sodium phosphate, pH 6.0, 1 M NaCl, 0.1% Tween 20. The IFN-α2 proteins were eluted with a reverse pH gradient from 5.5 to 4.1 in 40 mM sodium phosphate, 1 M NaCl, 0.1% Tween 20. Column fractions were analyzed by nonreducing SDS−PAGE, and fractions containing properly folded IFN-α2 protein and no visible contaminants were pooled and stored at −80 °C.

The osmotic shock pellets containing insoluble IFN-α2 cysteine analogues were treated with B-PER bacterial protein extraction reagent (Pierce Chemical Company, Rockford, IL) according to the manufacturer's directions. Insoluble material was recovered by centrifugation, washed with water, and solubilized in 5 mL of 6 M guanidine, 50 mM cysteine in 20 mM Tris base. The mixture was stirred for 30 min and then dialyzed overnight at 4 °C against 400 mL of 40 mM sodium phosphate, 150 mM NaCl, pH 8.0. The refold mixture was then adjusted to pH 3.0 and centrifuged, and refolded IFN-α2 proteins were purified from the supernatants by S-Sepharose and Cu^{2+} IMAC column chromatography as described above.

For larger scale production of the Q5C analogue, the osmotic shock step was omitted, and the protein was refolded from whole cells as follows. Frozen cells from 400 mL cultures were thawed and resuspended in 10 mL of 8M guanidine, 20 mM cysteine, 2% Tween 20, 20 mM MES, pH 3. After mixing for 3 h, the solution was diluted 20-fold, the guanidine concentration was adjusted to 0.6 M, urea and copper sulfate were added to final concentrations of 1 M and 40 μM, respectively, and the solution was adjusted to pH 6. The refold mixture was incubated for 1−2 days, adjusted to pH 3, and clarified by centrifugation. The refold mixture was diluted 4-fold with H_2O, and refolded Q5C protein was purified by S-Sepharose and Cu^{2+} IMAC column chromatography as described above.

PEGylation of IFN-α2 Cysteine Analogues. IFN-α2 proteins were incubated at room temperature with a 10- to 15-fold molar excess of Tris[2-carboxyethylphosphine] hydrochloride (TCEP, Pierce Chemical Company) and a 15- to 20-fold molar excess of 5 kDA maleimide PEG, 10 kDa maleimide PEG, 20 kDa maleimide PEG or 40 kDa branched maleimide PEGs (Nektar, Inc., Huntsville, AL) at pH 8.5 for 60 min. The PEGylation reactions were then diluted 10-fold with 20 mM MES, pH 5.0, adjusted to pH 3.0, and subjected to S-Sepharose column chromatography using the conditions described above.

In Vitro Bioactivity Measurements. The human Daudi B cell line (Horoszewicz et al., 1979; Evinger and Pestka, 1981) was obtained from the American Type Culture Collection (Rockville, MD) and maintained in RPMI 1640 media supplemented with 10% fetal bovine serum (FBS), 2 mM glutamine, 50 units/mL penicillin, and 50 μg/mL streptomycin (assay media). For bioassays, washed cells were resuspended at a concentration of 4×10^5 cells/mL in assay media, and 50 μL (2×10^4 cells) of the cell suspension was aliquotted per well of a flat bottom 96 well tissue culture plate. Serial 3-fold dilutions of the protein samples were prepared in assay media, and 50 μL of the diluted protein samples were added to the test wells. Protein samples were assayed in triplicate wells. Control wells contained media but no cells. A commercial wild-type IFN-α2 (Endogen, Inc.), and wild-type IFN-α2 prepared by us were analyzed in parallel to control for interday variability in the assay. Plates were incubated for 4 days at 37 °C in a humidified 5% CO_2 tissue culture incubator. Following the incubation period, 20 μL of CellTiter 96 AQueous One Solution Reagent (Promega Corporation, Madison, WI) was added to each well, and the plates were incubated at 37 °C in the tissue culture incubator for 1−4 h. Absorbance was read at 490 nm using a microplate reader.

Pharmacokinetic Experiments in Rats. Animal experiments were performed with the approval of BolderPATH's Institutional Animal Care and Use Committee. Groups of three male Sprague Dawley rats, weighing approximately 350 g each, received a single intravenous injection (lateral tail vein) of Roferon (recombinant *E. coli*-derived IFN-α2a, Roche), 10-kDa PEG−IFN-α2 Q5C, 20-kDa PEG−IFN-α2 Q5C, or 40-kDa PEG−IFN-α2 Q5C, each at a dose of 100 μg of protein/kg of body weight. At selected time points, blood samples (0.4 mL) were drawn from the rats into EDTA anticoagulant tubes. The blood samples were centrifuged, and the plasma samples were stored at −80 °C. A predose sample (0 h) was drawn 1 day prior to injection of the test compounds. Plasma levels of the test proteins were quantitated using human IFN-α2 ELISA kits (Pierce Chemical Company.). Serial dilutions of plasma samples from one animal in each test group were analyzed in the in vitro bioassay to identify dilutions that fell within the linear range of the ELISA (25.6−1000 pg/mL). Duplicate samples of appropriate dilutions of plasma samples from all rats were then analyzed in the ELISA. A subcutaneous pharmacokinetic experiment was performed in the same manner except that the protein samples were injected subcutaneously into the lateral sides of the rats. Pharmacokinetic parameters were analyzed using the WinNonlin software package (Pharsight, Inc., Mountain View, CA) using noncompartmental methods.

Biochemical Methods. Protein samples were analyzed by SDS−polyacrylamide gel electrophoresis (SDS−PAGE) on precast Tris−glycine polyacrylamide gels (Invitrogen Corporation, Carlsbad, CA) and stained with Coomassie Blue. 2-Mercaptoethanol was added to a final concentration of 1−5% (v/v) to reduce the proteins. Protein concentrations were determined using a Bradford protein assay kit (Bio-Rad Laboratories, Richmond, CA), using bovine serum albumin as the protein standard.

RESULTS

***E. coli* Expression, Purification, and Bioactivity of IFN-α2 and IFN-α2 Cysteine Analogues.** Human IFN-α2 has a compact globular structure, comprising five α helices joined by loops (Radhakrishnan et al., 1996; Klaus et al., 1997). The five α helices are termed A−E beginning from the N-terminus of the protein. The loop regions are referred to by the helices they join, for example, the A−B loop joins helices A and B. We constructed seven cysteine analogues in various nonhelical regions of IFN-α2. We constructed one cysteine substitution analogue in the amino-terminal region preceding helix A (Q5C), three cysteine substitution analogues in the CD loop (Q101C, T106C, E107C), and one cysteine substitution analogue in the carboxy-terminal region following helix E (S163C). We also constructed one cysteine addition analogue, *166C, that adds a cysteine residue following the carboxy-terminal residue, E165. In addition, we constructed the C98S analogue, which eliminates the nonessential C1−C98 disulfide (Morehead et al., 1984) and creates an unpaired cysteine (C1) in the region preceding helix A.

Wild-type IFN-α2 and IFN-α2 cysteine analogues were expressed as periplasmic secreted proteins in *E. coli* strain W3110 using the *E. coli* STII leader sequence, as described in Experimental Procedures. Voss et al. (1994) reported that correct processing of the STII secretion signal from IFNα2 was pH-dependent, being enhanced when culture pH was maintained at or below 6.7. Similarly, we found that Luria Broth medium buffered with 100 mM MES to a pH of 5.5 gave optimum yields of correctly processed IFN-α2 and IFN-α2 cysteine analogues (data not shown), and it was used routinely for expression of the proteins. Induced cell cultures were subjected to osmotic shock (Koshland and Botstein, 1980) to release the soluble contents of the periplasm. Approximately 25−50% of the correctly processed wild-type IFN-α2 protein was recovered in the supernatant fraction following centrifugation of the osmotic shock-treated cells. Wild-type IFN-α2 was purified from the osmotic shock supernatant by S-Sepharose column chromatography followed by affinity chromatography using a Cu^{2+} IMAC column (Figure 1). Purified wild-type IFN-α2 had a similar mean IC_{50} to a commercial IFN-α2 standard in the human Daudi B cell line growth inhibition assay (Figure 2 and Table 1). Relative IC_{50}'s for these proteins were consistent between experiments, although their absolute IC_{50} values varied by up to 2- to 3-fold in assays performed on different days; therefore comparisons between proteins were made on samples analyzed on the same days.

In contrast to wild-type IFN-α2, most IFN-α2 cysteine analogues were present in the osmotic shock supernatants at significantly reduced levels relative to wild-type IFN-α2 (data not shown). The cysteine analogues partitioned primarily into the osmotic shock pellets. Only the Q5C and S163C proteins were present at appreciable levels in the osmotic shock supernatants. These analogues were purified from the osmotic shock supernatants by S-Sepharose and Cu^{2+} IMAC chromatography as described for wild-type IFN-α2, with the exception that 5 mM cystine was added to the osmotic shock buffers. In

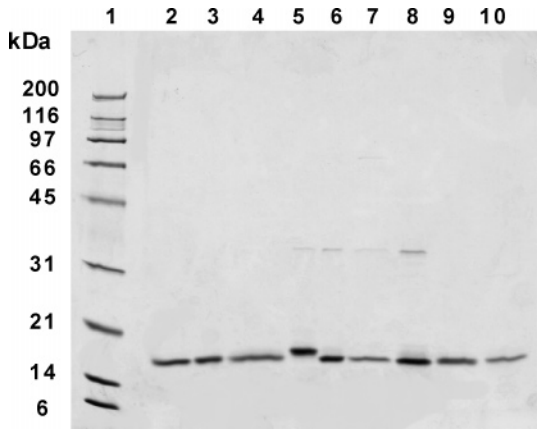

Figure 1. Nonreduced SDS−PAGE analysis of column pools of purified recombinant wild-type IFN-α2 and IFN-α2 cysteine analogues: lane 1, molecular weight markers; lane 2, wild-type IFN-α2 prepared by us; lane 3, Q5C soluble, periplasmically expressed; lane 4, Q5C, refolded; lane 5, C98S; lane 6, Q101C; lane 7, T106C; lane 8, E107C; lane 9, S163C; lane 10, *166C.

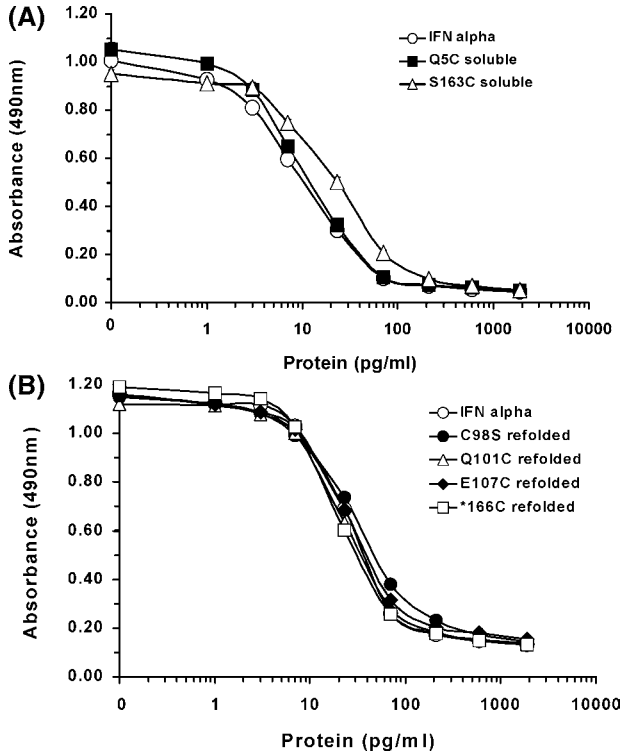

Figure 2. Dose response curves of IFN-α2 cysteine analogues and wild-type IFN-α2 for inhibiting proliferation of Daudi cells. Data are means of triplicate wells ± SD from representative experiments. SDs were less than 10% of the means. Proteins shown in the same panel were analyzed on the same days. Wild-type IFN-α2 used in the bioassay shown in panel A was prepared by us. Wild-type IFN-α2 used in the bioassay shown in panel B was purchased from Endogen, Inc. The Q5C and S163C proteins analyzed in panel A were purified from the soluble (supernatant) fraction of osmotic shock lysates; the C98S, Q101C, E107C, and *166C proteins analyzed in panel B were refolded from the insoluble (pellet) fraction of the osmotic shock lysates (see Experimental Procedures).

the absence of cystine, the cysteine analogues eluted in multiple fractions throughout the column gradients rather than as single peaks (data not shown).

SDS−PAGE analyses revealed that the C98S, Q101C, T106C, E107C, and *166C cysteine analogues expressed well but accumulated primarily in the osmotic shock pellets, suggesting that they were insoluble. When denatured and reduced these analogues comigrated with wild-type IFN-α2, indicating that the STII leader had been removed. Insoluble IFN-α2 cysteine analogues were refolded from the osmotic shock pellets and purified by S-Sepharose and Cu^{2+} IMAC column chromatography. The Q5C protein was recovered in both the pellet and the supernatant of the osmotic shock lysate and was purified from both sources. Nonreducing SDS−PAGE analysis of the purified Q5C, C98S, Q101C, T106C, E107C, S163C, and *166C proteins is shown in Figure 1. The cysteine analogues were recovered predominantly as monomers that comigrated with wild-type IFN-α2 under reducing and nonreducing SDS−PAGE conditions. The C98S analogue migrated with a slightly greater apparent molecular mass than the other INF-α2 analogues under nonreducing conditions, presumably due to the absence of the native C1−C98 disulfide bond (Morehead et al., 1984). Certain of the purified IFN-α2 analogues (C98S, Q101C, T106C, E107C) contained small amounts of disulfide-linked IFN-α2 dimers, which were apparent when the proteins were analyzed by nonreducing SDS−PAGE (Figure 1).

Table 1. In Vitro Bioactivities of IFN-α2 Cysteine Analogs

IFN-α2 protein	free cysteine location[a]	form assayed[b]	IC_{50} (pg/mL)[c]
IFN-α2[d]			13 ± 5
IFN-α2[e]		soluble	12 ± 4
Q5C	preceding helix A	soluble	13 ± 4
Q5C	preceding helix A	refolded	17 ± 3
C98S	preceding helix A[f]	refolded	28 ± 5
Q101C	C−D loop	refolded	18 ± 7
T106C	C−D loop	refolded	18 ± 0
E107C	C−D loop	refolded	18 ± 9
S163C	following helix E	soluble	27 ± 8
*166C	C-terminus	refolded	15 ± 6

[a] Based upon the IFN-α2 structure described by Radhakrishnan et al. (1996). [b] Soluble and refolded forms purified from the osmotic shock supernatant and pellet fractions, respectively. [c] Means ± SD for at least three assays for each protein except for the T106C analogue, which was assayed twice. [d] Wild-type IFN-α2 standard (Endogen, Inc.). [e] Wild-type IFN-α2 prepared by us. [f] Mutation creates a free cysteine (C1) in the region preceding helix A.

The Q5C, Q101C, T106C, E107C, and *166C proteins had in vitro bioactivities (IC_{50}'s) that were indistinguishable from that of wild-type IFN-α in the Daudi cell assay. In contrast, IC_{50}'s for the C98S and S163C proteins were consistently reduced about 2-fold relative to the IC_{50} of wild-type IFN-α2. Q5C recovered from the soluble periplasmic fraction and Q5C recovered from the insoluble fraction and refolded had IC_{50}'s equivalent to each other and to wild-type IFN-α2. These data are summarized in Table 1. Dose response curves for representative cysteine analogues are shown in Figure 2.

Preparation and in Vitro Bioactivity of PEG−Q5C. For PEGylation, the purified IFN-α2 cysteine analogues were reacted for 1 h at room temperature with TCEP and 5 kDa maleimide PEG at pH 8.5, as described in Experimental Procedures. Under these conditions, the Q5C analogue showed the greatest reactivity with the PEG reagent, yielding about 60% mono-PEGylated Q5C protein without detectable di- or tri-PEGylated protein (Figure 3). Control experiments (not shown) demonstrated that inclusion of a reducing agent such as TCEP in the PEGylation reaction was required for efficient PEGylation of Q5C and other IFN-α2 cysteine analogues. Wild-type IFN-α2 showed no detectable PEGylation under identical conditions, indicating that the native disulfide bonds of the protein are not disrupted by the

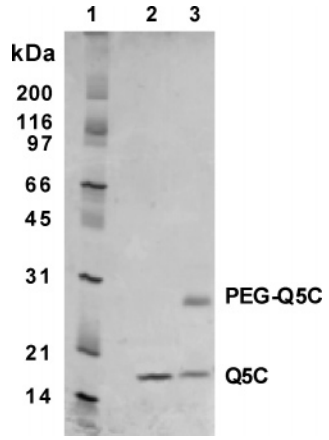

Figure 3. Nonreducing SDS−PAGE of Q5C and wild-type IFN-α2 PEGylation reaction products: lane 1, molecular weight markers; lane 2, wild-type IFN-α2 PEGylation reaction products; lane 3, Q5C PEGylation reaction products. Reaction conditions were as described in Experimental Procedures.

reaction conditions (Figure 3). The T106C, E107C, and S163C analogues also generated mono-PEGylated proteins using these PEGylation conditions, but the extent of PEGylation was less than that observed for the Q5C analogue (data not shown). The C98S, Q101C, and *166C proteins reacted only weakly with the PEG reagent under these conditions (data not shown).

The Q5C protein was modified at a larger scale with 5-, 10-, 20-, and 40-kDa maleimide-PEGs. PEG−Q5C was separated from unreacted Q5C protein by S-Sepharose column chromatography. A representative column elution profile for the 5-kDa PEG−Q5C PEGylation reaction mixture is shown in Figure 4A. The S−Sepharose column elution profile showed two major peaks. The early-eluting peak was determined to be mono-PEGylated Q5C by nonreducing SDS−PAGE (Figure 4B). The late-eluting peak was determined to be unreacted Q5C protein. Fractions containing PEG−Q5C and no visible unmodified protein were pooled and used for bioactivity measurements. Similar procedures were used to prepare Q5C modified with 10-, 20- and 40-kDa PEGs. Nonreducing SDS−PAGE of the purified PEG−Q5C proteins is shown in Figure 5.

When tested in the in vitro Daudi cell growth inhibition assay, bioactivity of the 5-kDa PEG−Q5C protein was reduced approximately 2-fold (IC_{50} of 22 ± 7 pg/mL; N = 3) compared to bioactivities of wild-type IFN-α2 (IC_{50} of 13 ± 6 pg/mL) and unmodified Q5C protein (IC_{50} of 13 ± 5 pg/mL) analyzed in the same assays (Figure 6A). Bioactitvities of the 10-, 20- and 40-kDa PEG−Q5C proteins were reduced approximately 3- to 4-fold relative to bioactivities of wild-type IFN-α and unmodified Q5C proteins analyzed in the same assays (Figure 6B and Table 2).

Pharmacokinetic Studies of PEG−Q5C Proteins. Circulating half-lives of the PEG−Q5C proteins were compared to that of wild-type IFN-α2 (Roferon, Roche) following intravenous and subcutaneous injection in rats. Circulating levels of the proteins were measured by ELISA. Following intravenous injection (Figure 7A), wild-type IFN-α2 cleared rapidly from the rats with a terminal half-life of 0.5 h, similar to what is reported in the literature (Bailon et al., 2001). In contrast, terminal half-lives for the 10-, 20-, and 40-kDa PEG−Q5C proteins were 22, 24, and 32 h, respectively. The initial distribution phase also appeared to be lengthened in the PEG−Q5C proteins relative to wild-type IFN-α2; however, not

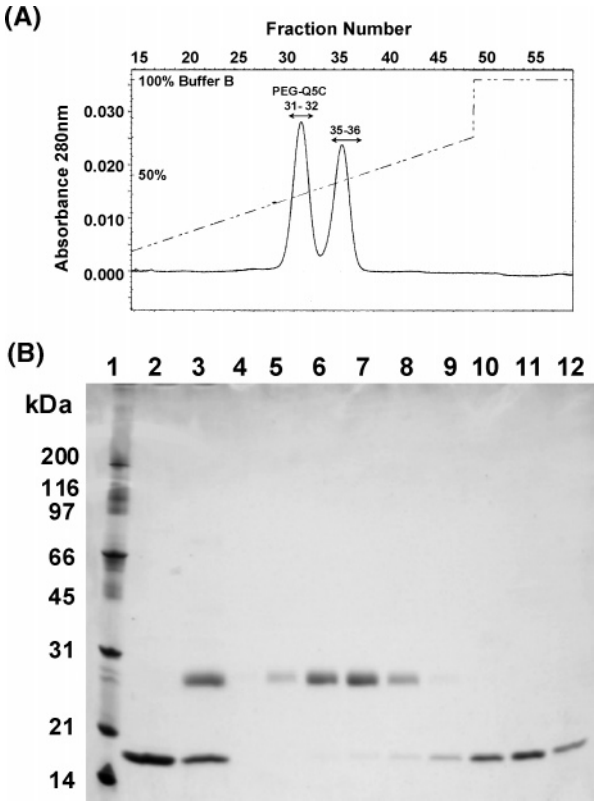

Figure 4. Purification of 5-kDa PEG−Q5C by S-Sepharose column chromatography: (A) the elution profile for the PEG reaction mixture applied to an S-Sepharose column; (B) nonreducing SDS−PAGE analysis of Q5C (lane 2), the Q5C PEGylation reaction products (lane 3), and fractions 29−37 recovered from the column (lanes 4−12). Fractions 31 and 32 (lanes 6−7) were pooled. Fractions 34−37 (lanes 9−12) contain predominantly unreacted Q5C. Molecular weight markers are shown in lane 1.

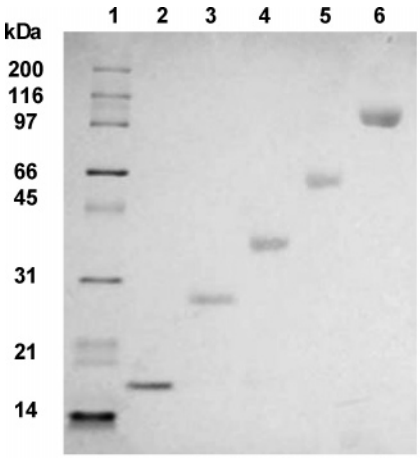

Figure 5. Nonreducing SDS−PAGE analysis of Q5C modified with different molecular weight PEGs: lane 1, molecular weight markers; lane 2, wild-type IFN-α2 prepared by us; lane 3, 5-kDa PEG−Q5C; lane 4, 10-kDa PEG−Q5C; lane 5, 20-kDa PEG−Q5C; lane 6, 40-kDa PEG−Q5C.

enough early time points were sampled to obtain accurate values for the distribution phase.

Following subcutaneous administration (Figure 7B), plasma concentrations of wild-type IFN-α2 peaked 1 h after administration (10.2 ng/mL) and decreased to undetectable levels by 24 h postinjection. The terminal half-life was 1.2 h. In contrast, maximum plasma levels of the PEG−Q5C proteins were not attained until 10 h

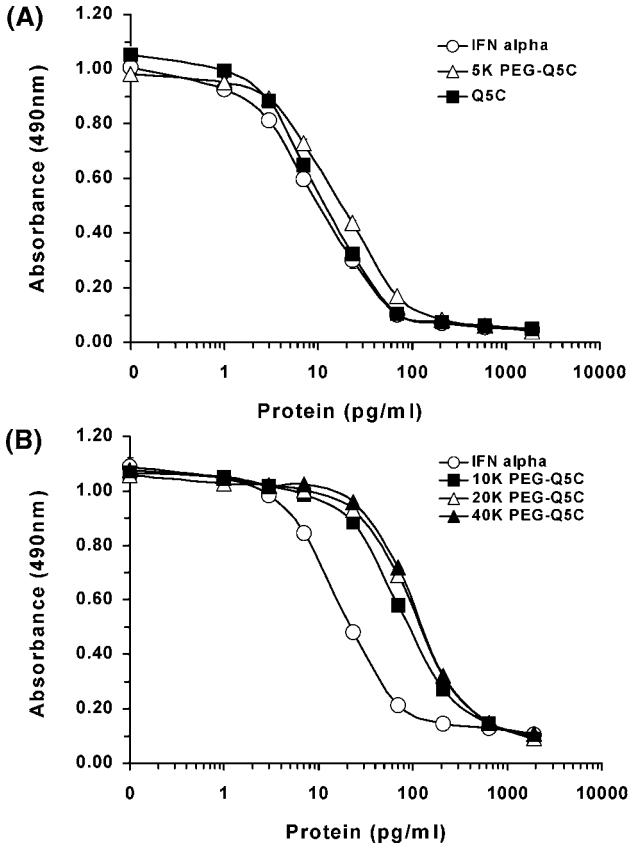

Figure 6. Dose response curves for PEG−Q5C proteins, unmodified Q5C, and wild-type IFN-α2 for inhibiting proliferation of Daudi cells: (A) comparison of the activities of commercial wild-type IFN-α2, Q5C, and 5-kDa PEG−Q5C; (B) comparison of the activities of commercial wild-type IFN-α2, 10-kDa PEG−Q5C, 20-kDa PEG−Q5C, and 40-kDa PEG−Q5C. Data are means of triplicate wells ± SD from representative experiments. SD were less than 10% of the means.

Table 2. In Vitro Bioactivities of PEG−Q5C Proteins

protein	IC_{50} (pg/mL)[a]
IFN-α2[b]	24 ± 5
IFN-α2[c]	29 ± 1
Q5C[d]	31 ± 2
10-kDa PEG-Q5C[d]	70 ± 0
20-kDa PEG-Q5C[d]	100 ± 7
40-kDa PEG-Q5C[d]	108 ± 11

[a] Means ± SD for at least three assays for each protein, except for the 10-kDa PEG−Q5C protein and our wild-type IFN-a2 protein, which were assayed twice. [b] Wild-type IFN-α2 standard (Endogen, Inc.). [c] Wild-type IFN-α2 prepared by us. [d] Q5C protein refolded from whole cells.

(10-kDa PEG−Q5C, 15.9 ng/mL), 24 h (20-kDa PEG−Q5C, 20.7 ng/mL), and 48 h (40-kDa PEG−Q5C, 33.3 ng/mL) postinjection (Figure 7B), and the PEG−Q5C proteins were cleared much more slowly than IFN-α. Terminal half-lives for the 10-, 20-, and 40-kDa PEG−Q5C proteins were 17, 27, and 48 h, respectively.

DISCUSSION

Our goal was to identify a site(s) in IFN-α2 where a cysteine residue can be introduced and PEGylated without significant loss of in vitro bioactivity. We focused mutagenesis efforts away from the presumptive receptor binding sites in IFN-α2, which have been localized to the N-terminal end of the A−B loop, helices C and D and the D−E loop (Uze et al., 1995; Rhadhakrishnan et al., 1996; Klaus et al., 1997; Roisman et al., 2001). The three

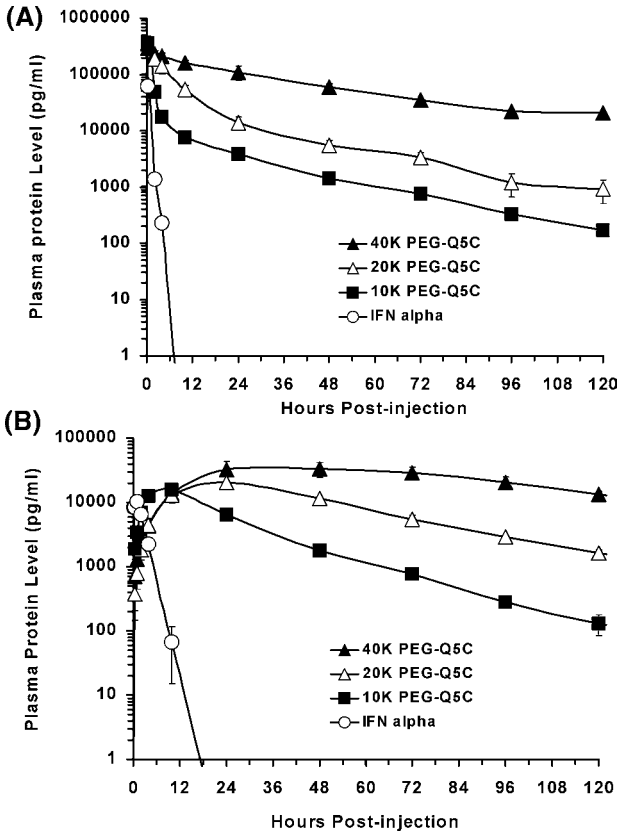

Figure 7. Changes in plasma protein levels following (A) intravenous and (B) subcutaneous administration of IFN-α2 (Roferon) and Q5C modified with 10-, 20-, and 40-kDa maleimide PEGs to rats. Protein levels were measured using human IFN-α2 ELISA kits. Data are means ± SD for three rats per group. SDs were generally less than 25% of the means.

regions chosen for mutational analysis, the region preceding helix A, the C−D loop, and the region following helix E, exhibit significant flexibility and high solvent exposure (Klaus et al., 1997). We found that the cysteine analogues analyzed in these regions retained complete (Q5C, Q101C, T106C, E107C, and *166C) or near complete (C98S, S163C) in vitro biological activity. Our data for the C98S analogue confirm previous studies indicating that the C1−C98 disulfide is not absolutely required for IFN-α2 bioactivity (Morehead et al., 1984; DeChiara et al., 1986). This is in contrast to the C29−C138 disulfide bond, which is required for IFN-α2 bioactivity (Morehead et al., 1984). We found that addition of cystine to the osmotic shock buffers and use of cysteine in the refold buffers was beneficial in improving recoveries of the IFN-α2 cysteine analogues from *E. coli*. We postulate that cystine/cysteine react with the free cysteine residues in the analogues to form a stable mixed disulfide that prevents or minimizes disulfide shuffling and aggregation of the proteins during subsequent column purification steps. This hypothesis is consistent with the finding that the purified cysteine analogues must be exposed to a reducing agent such as TCEP (presumably to reduce the mixed disulfide) for optimal reactivity with maleimide PEGs.

The Q5C protein was chosen for further study because it expressed well, displayed wild-type in vitro biological activity, and PEGylated efficiently. The mono-PEGylated Q5C protein could be purified readily from non-PEGylated protein by ion-exchange chromatography. The PEG−Q5C protein eluted as a single symmetrical peak, consistent with the PEG−protein having a homogeneous

structure. In contrast, amine-PEGylated IFN-α2 elutes as multiple peaks from ion-exchange columns due to heterogeneity resulting from the large number of positional isomers and multiply-PEGylated species (Monkarsh et al., 1997). In vitro bioactivity of the purified 5-kDa PEG−Q5C protein was within 2-fold of wild-type IFN-α2, whereas in vitro bioactivities of the Q5C protein modified with 10-, 20-, and 40-kDa PEGs were within 3- to 4-fold of wild-type IFN-α2. By contrast, in vitro bioactivity of IFN-α2 is reduced 4- to 5-fold when modified with 5-kDa amine-reactive PEGs and at least 14-fold when modified with 40-kDa amine-reactive PEGs (Monkarsh et al., 1997; Wang et al., 2000; Bailon et al., 2001). Thus, targeted attachment of PEG to IFN-α2 using site-specific PEGylation not only provides a structurally homogeneous product but also appears to yield a PEGylated IFN-α2 protein with higher specific activity than comparable amine-PEGylated IFN-α2 proteins. Pharmacokinetic studies showed that the circulating half-life of the Q5C protein varied depending upon the size of the attached PEG moiety, larger PEGs extending the half-life more than smaller PEGs. Attachment of a single 40-kDa PEG to the Q5C protein increased its half-life up to 40-fold relative to wild-type IFN-α2 following subcutaneous administration to rats. Modification of the Q5C protein with PEG also significantly slowed absorption of the protein from the injection site following subcutaneous administration, larger PEGs slowing absorption more than smaller PEGs. The half-life of the 40-kDa PEG−Q5C protein following subcutaneous administration to rats (48 h) is similar to that reported for IFN-α2a modified with a 40-kDa amine-reactive PEG following subcutaneous administration to rats (51 h; Bailon et al., 2001).

Two amine-PEGylated IFN-α2 products, PEG-Intron (Schering-Plough) and PEGASYS (Roche), are approved for use in humans. Both products have longer half-lives than IFN-α2, can be administered less frequently than IFN-α2 (once per week), and are more efficacious than IFN-α2 at treating hepatitis C (Craxi and Licata, 2003; Foster, 2003; Pedder, 2003). Clinical trials of these PEGylated IFN-α2 products in cancer patients are in progress (Choueiri et al., 2003). Although both products are prepared using amine-PEGylation technologies, the PEGylated proteins have quite different physical properties due to the PEGs used to prepare the proteins. PEG-Intron is modified with a 12 kDa linear PEG, whereas PEGASYS is modified with a 40 kDa branched PEG (Pedder, 2003). PEGASYS has lower activity than PEG-Intron in in vitro bioassays but a longer half-life than PEG-Intron in vivo (Gilbert and Park-Cho, 1999; Bailon et al., 2001; Pedder, 2003). The site-specific PEGylated Q5C protein described here is distinguished from PEG-Intron and PEGASYS by possessing both high in vitro bioactivity and a long half-life. Whether these unique features of PEG−Q5C will lead to a more potent or efficacious PEG-IFN-α2 product in vivo remains to be determined.

In conclusion, these studies demonstrate the feasibility of using site-specific PEGylation to create a long-acting IFN-α2 conjugate with high specific activity. Because of the shared structural features of members of the IFN gene family (IFN-α, IFN-β, IFN-γ, IL-10) information gained from these studies may prove useful for creating long-acting, site-specific PEGylated forms of other interferon species.

ACKNOWLEDGMENT

This work was supported by Grants 1R43 CA79361 and 2R44 CA79361 to G.C. from the National Cancer Institute. The contents of the publication are solely the responsibility of the authors and do not necessarily represent the official views of the National Cancer Institute.

LITERATURE CITED

(1) Bailon, P., Palleroni, A., Schaffer, C. A., Spence, C. L., Fung, W.-J., Porter, J. E., Ehrlich, G. K., Pan, W., Xu, Z.-X., Modi, M. W., Farid, A., and Berthold, W. (2001) Rational design of a potent, long-acting form of interferon: a 40 kDa branched polyethylene glycol-conjugated interferon α2a for the treatment of hepatitis C. *Bioconjugate Chem. 12*, 195−202.

(2) Blatt, L. M., Davis, J. M., Klein, S. B., and Taylor, M. W. (1996) The biological activity and molecular characterization of a novel synthetic interferon-alpha species, consensus interferon. *J. Interferon Cytokine Res. 16*, 489−499.

(3) Choueiri, T. K., Hutson, T. E., and Bukowski, R. M. (2003) Evolving role of pegylated interferons in metastatic renal cell carcinoma. *Expert Rev. Anticancer Ther. 3*, 823−829.

(4) Craxi A., and Licata, A. (2003) Clinical trial results of peginterferons in combination with ribavirin. *Semin. Liver Dis. 23* (Suppl. 1), 35−46.

(5) DeChiara, T. M., Erlitz, F., and Tarnowski, S. J. (1986) Procedures for in vitro DNA mutagenesis of human leukocyte interferon sequences. *Methods Enzymol. 119*, 403−415.

(6) Evinger, M., and Pestka, S. (1981) Assay of growth inhibition in lymphoblastoid cell cultures. *Methods Enzymol. 79*, 362−368.

(7) Foster, G. R. (2003) Pegylated interferon with ribavirin therapy for chronic infection with hepatitis C virus. *Expert Opin. Pharmacother. 4*, 685−691.

(8) Gilbert, C. W., and Park-Cho, M. (1999) Interferon polymer conjugates. U.S. Patent 5,951,974.

(9) Goodson, R. J., and Katre, N. V. (1990) Site-directed pegylation of recombinant interleukin-2 at its glycosylation site. *Biotechnology 8*, 343−346.

(10) Gutterman, J. U. (1994) Cytokine therapeutics: Lessons from interferon α. *Proc Natl. Acad. Sci. U.S.A. 91*, 1198−1205.

(11) Henco, K., Brosius, J., Fujisawa, J. I., Haynes, J. R., Hochstadt, J., Kovacic, T., Pasek, M., Schambock, A., Schmid, J., Todokoro, K., Walchli, M., Nagata, S., and Weissmann, C. (1985) Structural relationship of human interferon alpha genes and pseudogenes. *J. Mol. Biol. 185*, 227−260.

(12) Higuchi, R. (1990) Recombinant PCR. *PCR Protocols: A Guide to Methods and Applications*. (Innis, M. A., Gelfand, D. H., Sninsky, J. J., and White, T. J., Eds.) pp 177−183, Chapter 22, Academic Press, San Diego, CA.

(13) Horoszewicz, J. S., Leong, S. S., and Carter, W. A. (1979) Noncycling tumor cells are sensitive targets for the antiproliferative activitiy of human interferon. *Science 206*, 1091−1093.

(14) Horton, R. M. (1993) In Vitro Recombination and mutagnesis of DNA. SOIng together tailor-made genes. *Methods in Molecular Biology*, *Vol. 15: PCR Protocols: Current Methods and Applications* (White, B. A., Ed.) pp 251−2266, Chapter 25, Humana Press, Totawa, NJ.

(15) Khan, F. R., and Rai, V. R. (1990) Large-scale production of recombinant proteins: human leukocyte interferon. *Bioprocess Technol. 7*, 161−169.

(16) Klaus, W., Gsell, B., Labhardt, A. M., Wipf, B., and Senn, H. (1997) The three-dimensional high-resolution structure of human interferon α-2a determined by heteronuclear NMR spectroscopy in solution. *J. Mol. Biol. 274*, 661−675.

(17) Koshland, D., and Botstein, D. (1980) Secretion of beta-lactamase requires the carboxy end of the protein. *Cell 20*, 749−760.

(18) Monkarsh, S. P., Ma, Y., Aglione, A., Bailon, P., Ciolek, D., DeBarbieri, B., Graves, M. C., Hollfelder, K., Michel, H., Palleroni, A., Porter, J. E., Russoman, E., Roy, S., Pan, Y.-C., et al. (1997) Positional isomers of monopegylated inter-

feron α-2a: isolation, characterization and biological activity. *Anal. Biochem. 247*, 434−440.
(19) Morehead, H., Johnson, P. D., and Wetzel, R. (1984) Roles of the 29−138 disulfide bond of subtype A of human α interferon in its antiviral activity and conformational stability. *Biochemistry 23*, 2500−2507.
(20) Pedder, S. C. J. (2003) Pegylation of interferon alpha: structural and pharmacokinetic properties. *Semin. Liver Dis. 23* (Suppl. 1), 19−22.
(21) Pestka, S., and Langer J. A. (1987) Interferons and their actions. *Annu. Rev. Biochem. 56*, 727−777.
(22) Picken, R. N., Mazaitis, A. J., Maas, W. K., Rey, M., and Heyneker, H. (1983) Nucleotide sequence of the gene for heat-stable enterotoxin II of *Escherichia coli*. *Infect. Immun. 42*, 269−275.
(23) Radhakrishnan, R., Walter, L. J., Hruka, A., Reichert, P., Trotta, P. P., Nagabhushan, T. L., and Walter, M. R. (1996) Zinc mediated dimer of human interferon-alpha 2b revealed by X-ray crystallography. *Structure 4*, 1453−1463.
(24) Roisman, L. C., Piehler, J., Trosset, J.-Y., Scheraga, H. A., and Schreiber, G. (2001) Structure of the interferon-receptor complex determined by distance constraints from double mutant cycles and flexible docking. *Proc. Natl. Acad. Sci. U.S.A. 98*, 13231−13236.
(25) Uze, G., Lutfalla, G., and Mogensen, K. E. (1995) Alpha and beta interferons and their receptor and their friends and relations. *J. Interferon Cytokine Res. 15*, 3−26.
(26) Voss, T., Falkner, E., Ahorn, H., Krystek, E., Maurer-Fogy, I., Bodo, G., and Hauptmann, R. (1994) Periplasmic expression of human interferon alpha 2c in *Escherichia coli* results in a correctly folded molecule. *Biochem. J. 298*, 719−725.
(27) Wang, Y.-S., Youngster, S., Bausch, J., Zhang, R., McNemar, C., and Wyss, D. F. (2000) Identification of the major positional isomer of PEGylated interferon alpha-2b. *Biochemistry 39*, 10634−10640.

BC049713N

Transfection Activity of Polyamidoamine Dendrimers Having Hydrophobic Amino Acid Residues in the Periphery

Kenji Kono,* Hitoshi Akiyama, Toshinari Takahashi, Toru Takagishi, and Atsushi Harada

Department of Applied Materials Science, Graduate School of Engineering, Osaka Prefecture University, 1-1 Gakuen-cho, Sakai, Osaka 599-8531, Japan. Received September 10, 2004; Revised Manuscript Received December 1, 2004

We designed poly(amidoamine) dendrimers with phenylalanine or leucine residues at their chain ends. Thereby, we achieved efficient gene transfection of cells through synergy of the proton sponge effect, which is induced by the internal tertiary amines of the dendrimer, and hydrophobic interaction by the hydrophobic amino acid residues in the dendrimer periphery. Dendrimers having 16, 29, 46, and 64 terminal phenylalanine residues were prepared by the reaction of the amine-terminated poly(amidoamine) G4 dendrimer and L-phenylalanine using condensing reagent 1,3-dicyclohexylcarbodiimide. Transfection activity of these phenylalanine-modified dendrimers for CV1 cells, an African green monkey kidney cell line, increased concomitant with the increasing number of the terminal phenylalanine residues, except for the dendrimer with 64 phenylalanine residues, which showed poor water solubility and hardly formed a complex with DNA at neutral pH. However, under weakly acidic conditions, the dendrimer with 64 phenylalanine residues formed a complex with DNA, thereby achieving highly efficient transfection. In contrast, the attachment of L-leucine residues was unable to improve the transfection activity of the parent dendrimer, probably because of the relatively lower hydrophobicity of this amino acid. The phenylalanine-modified dendrimer exhibited a higher transfection activity and a lower cytotoxicity than some widely used transfection reagents. For that reason, the phenylalanine-modified dendrimers are considered to be promising gene carriers.

INTRODUCTION

Development of safe and efficient nonviral vectors is an important task in the field of gene therapy. Despite many efforts to develop nonviral vectors, their ability to transfect cells has yet to be improved (*1*, *2*). A variety of nonviral systems have been studied for this purpose. Cationic polymers offer some advantages such as a large diversity of molecular structures and freedom of molecular design (*3*, *4*). Cationic polymers can form stable complexes, so-called polyplexes, with DNA through electrostatic interactions. Positively charged polyplexes interact strongly with negatively charged cell membranes and are taken up by the cells through an endocytic pathway. However, many cationic polymers cannot achieve efficient transfection. A major cause is that, when internalized into the cell and taken up in the endosome, a large fraction of their complexes with DNA is delivered to the lysosome and is ultimately degraded there.

Nevertheless, several kinds of cationic polymers can mediate relatively efficient transfection of various animal cells. Poly(ethylenimine) (PEI) and poly(amidoamine) (PAMAM) dendrimers are among these polymers (*5*−*8*). These polymers possess many secondary and tertiary amino groups, which become protonated under weakly acidic conditions. These amino groups suppress the lowering of pH in endosomes and lysosomes by adsorbing protons and prohibiting their degradation in the lysosome. In addition, endosome buffering by these polymers is thought to induce osmotic swelling of the endosome interior, engendering rupture of the endosome and subsequent release of DNA into cytoplasm (*9*, *10*). Such a function of these secondary and tertiary amino groups of polymers is called the proton sponge effect (*6*).

PAMAM dendrimers are unique synthetic macromolecules with highly branched structure and globular shape (*11*, *12*). Molecular size of the dendrimers is increased stepwise via the repetition of a reaction sequence. Consequently, their size and structure are highly controllable and their molecular weight distribution is generally very narrow (*12*). Taking into account the high controllability of structure of the PAMAM dendrimers and their relatively high transfection activity, PAMAM dendrimers are highly attractive materials for the design of gene carriers. For that reason, many studies have been carried out to produce efficient gene carriers using PAMAM dendrimers as base materials (*13*). For example, Haensler and Szoka attempted to improve their transfection activity by conjugation of a pH-sensitive membrane-active peptide that destabilizes the endosomal membrane and promotes the escape of DNA into the cytosol (*5*). Arima and colleagues also prepared conjugates of PAMAM dendrimers with cyclodextrins, concluding that this conjugation greatly enhanced the transfection activity of PAMAM dendrimers (*14*, *15*). In addition, modification of PAMAM dendrimers with various molecules, such as a hydrophobic fluorescent dye (*16*) and poly(ethylene glycol) (*17*), demonstrably improves their efficiency for gene and oligonucleotide delivery.

Many studies have established that hydrophobic moieties affect transfection activity of cationic polymers (*18*−*22*). The hydrophobic nature of gene carriers will influence formation and stability of complexes between the

* Corresponding author. Kenji Kono. Department of Applied Materials Science, Graduate School of Engineering, Osaka Prefecture University, 1-1 Gakuen-cho, Sakai, Osaka 599-8531, Japan. Tel: +81-722549330. Fax: +81-722549913. E-mail: kono@ams.osakafu-u.ac.jp.

10.1021/bc049785e CCC: $30.25 © 2005 American Chemical Society
Published on Web 12/30/2004

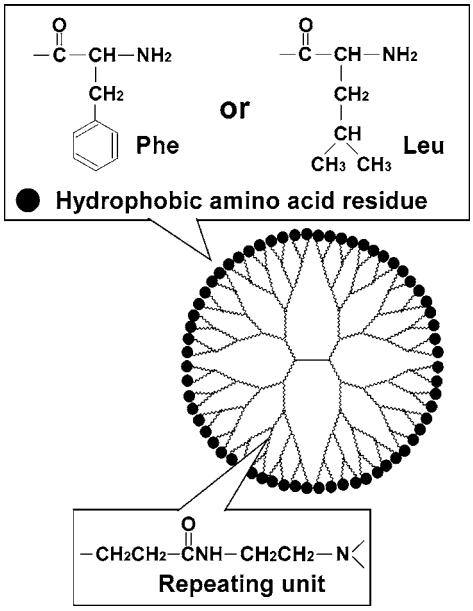

Figure 1. Structure of phenylalanine- or leucine-modified PAMAM G4 dendrimer.

carriers and DNA as it enhances interactions between the carriers and cells. In a previous study (*23*), we prepared PAMAM dendrons having two dodecyl groups. That study found that dendrons with hydrophobic moieties showed much higher transfection activity than PAMAM dendrimers of the same generation. That result suggests that introduction of an appropriate amount of hydrophobic moieties to the dendrimers can elevate their transfection efficiency.

In this study, we designed PAMAM G4 dendrimers having hydrophobic amino acid residues to produce efficient nonviral vectors that achieve cell transfection by synergistic actions of hydrophobic interactions and the proton sponge effect. We prepared PAMAM G4 dendrimers having phenylalanine or leucine residues at the dendrimer chain ends (Figure 1). Subsequently, we investigated their abilities to form a polyplex with plasmid DNA and to transfect CV1 cells, an African green monkey kidney cell line. The remarkable improvement of transfection activity of the PAMAM G4 dendrimer achieved by incorporation of phenylalanine is described.

EXPERIMENTAL PROCEDURES

General Methods. PAMAM (starbust) G4 dendrimer with an ethylenediamine core was purchased from Aldrich Chemical (Milwaukee, WI). *N*-(*tert*-Butoxycarbonyl)-L-phenylalanine (Boc-Phe) and *N*-(*tert*-butoxycarbonyl)-L-leucine (Boc-Leu) were obtained from Peptide Institute, Inc. (Osaka, Japan). 1, 3-Dicyclohexylcarbodiimide (DCC) and *N*-hydroxysuccinimide were supplied from Tokyo Kasei Kogyo (Tokyo, Japan). Trifluoroacetic acid, triethylamine, 2-amino-2-hydroxymethyl-1,3-propanediol (Tris), and *N*,*N*-dimethylformamide (DMF) were from Kishida Chemical (Osaka, Japan). Dimethyl sulfoxide (DMSO) and ethidium bromide were from Wako Pure Chemical Industries (Osaka, Japan). Fetal calf serum (FCS) was from JRH Biosciences (Tokyo, Japan). Agarose was from Sigma (St. Louis, MO). Dulbecco's modified Eagle's medium (DMEM) was from Nissui Pharmaceutical (Tokyo, Japan). 3-(4,5-Dimethyl-2-thiazolyl)-2,5-diphenyl-2*H*-tetrazolium bromide (MTT) was obtained from Dojin Laboratories (Kumamoto, Japan). Lipofectamine and SuperFect were purchased from Invitrogen (Carlsbad, CA) and Qiagen (Hilden, Germany), respectively. Plasmid DNA pCMV-Luc, which contains the cDNA of firefly luciferase driven by a human cytomegalovirus immediate-early promoter, was a gift from Dr. Kazuo Maruyama, Teikyo University.

Synthesis of Phenylalanine-Modified PAMAM G4 Dendrimers. The PAMAM dendrimers having varying numbers of phenylalanine residues at the chain terminals were prepared by the reaction of the amine-terminated PAMAM G4 dendrimers with varying amounts of Boc-Phe using *N*-hydroxysuccinimide and DCC and subsequent deprotection of Boc-Phe residues attached to the dendrimers using trifluoroacetic acid and thioanisole. A typical procedure was as follows: *N*-hydroxysuccinimide (44 mg, 0.380 mmol) and DCC (85 mg, 0.412 mmol) were added to Boc-Phe (84 mg, 0.317 mmol) dissolved in DMF (2 mL) and stirred for 7 h. Then, the PAMAM G4 dendrimer (46.9 mg, 3.30 nmol) and triethylamine (0.066 mL, 0.475 mmol) dissolved in DMSO (2 mL) were added to the solution and stirred for 7 days at room temperature. The obtained Boc-Phe-attached G4 dendrimer was purified with a Sephadex LH-20 column using methanol as the eluent. Boc groups of the dendrimer were removed by the treatment with trifluoroacetic acid (4 mL) and thioanisole (1 mL) at room temperature for 8 h. The dendrimer was purified by dialysis against distilled water and recovered by freeze-drying. Yield, 45.6 mg. Other Phe-modified dendrimers were prepared by the same procedure.

Synthesis of Leucine-Attached PAMAM G4 Dendrimer. *N*-Hydroxysuccinimide (102 mg, 0.883 mmol) and DCC (197 mg, 0.956 mmol) were added to Boc-Leu (170 mg, 0.735 mmol) dissolved in DMF (2 mL) and stirred for 3.5 h. Then, the PAMAM G4 dendrimer (108.9 mg, 7.66 nmol) and triethylamine (0.153 mL, 1.10 mmol) dissolved in DMSO (4 mL) were added to the solution and stirred for 8 days at room temperature. The obtained Boc-Leu-attached dendrimer was purified with a Sephadex LH-20 column using methanol as eluent. The deprotection of Boc-Leu-attached dendrimer and purification of the resultant dendrimer were carried out by the same procedure. Yield, 87.7 mg.

Agarose Gel Electrophoresis. The dendrimer−DNA polyplexes with varying N/P ratios were prepared by mixing plasmid DNA (1 μg) dissolved in 20 mM Tris-HCl buffer (5 μL) and the dendrimer dissolved in PBS (5 μL). After 10-min incubation at room temperature, the samples (10 μL) were electrophoresed on 0.6 wt % agarose gel in 40 mM Tris, 20 mM sodium acetate, and 2 mM EDTA buffer containing 1 μg/mL ethidium bromide at 100 V for 30 min. The ethidium bromide-stained bands were visualized and photographed using an Eagle Eye II Still Video System (Stratagene).

Transfection. For the preparation of dendrimer−plasmid DNA polyplexes, plasmid DNA (1 μg) dissolved in 20 mM Tris-HCl buffer (pH4.0−7.4, 50 μL) was mixed with the dendrimer dissolved in PBS of the same pH (0.2−5 g/l, 50 μL). The mixed solution was incubated for 10 min at room temperature to afford a polyplex with a given ratio of primary amino group of Phe-G4 to DNA phosphate (N/P ratio). The CV1 cells were seeded in 0.5 mL of DMEM supplemented with 10% FCS in 24-well culture plates at 5.0×10^4 cells per well the day before transfection. The cells were washed with PBS containing 0.36 mM $CaCl_2$ and 0.42 mM $MgCl_2$ [PBS(+)] and then covered with DMEM (1 mL). The polyplex containing plasmid DNA (1 μg) was added gently to the cells and incubated at 37 °C for 4 h. Then, the cells were rinsed with PBS(+), covered with DMEM containing 10% FCS,

and incubated at 37 °C. After 40 h, the cells were lysed by adding 50 μL of Luc-PGC-50 detergent (Toyo Ink, Tokyo, Japan). A 20 μL aliquot from each dish was used for one luciferase assay using a kit (Toyo Ink) and a Lumat LB9507 luminometer (Berthold, Bad Wildbad, Germany). The protein content of the lysate was measured by Coomassie Protein Assay Reagent (Pierce, IL) using bovine serum albumin as the standard. Transfection by Lipofectamine and Superfect was performed according to protocols recommended by the manufacturers.

Cytotoxicity. The cytotoxycity of complexes of the dendrimer, Lipofectamine, and Superfect with plasmid DNA was assessed by MTT assay (*24*). The cells were seeded in 1 mL of DMEM supplemented with 10% FCS in 12-well culture plates at 1.5×10^5 cells per well the day before transfection. The cells were washed with PBS (+) and then covered with DMEM (1 mL). The dendrimer−, Lipofectamine−, or SuperFect−DNA complex containing plasmid DNA (3μg) was added gently to the cells and incubated at 37 °C for 4 h. Then, the culture medium was carefully replaced with 0.5 mL of fresh DMEM containing 10% FCS, and 70 μL of MTT dissolved in PBS (5 mg/mL) was added to each well. After 4-h incubation at 37 °C, the medium was removed and the cells were solubilized in 500 μL of 2-propanol containing 0.1 M HCl. The number of viable cells was determined by absorbance at 570 nm. The cytotoxicity of the dendrimer, Lipofectamine, and Superfect without plasmid DNA was also measured by the same procedure.

RESULTS AND DISCUSSION

Design and Synthesis of Phenylalanine-Modified Dendrimers. The PAMAM dendrimers are currently considered to be extremely potent and promising nonviral vectors. These polymers can achieve efficient transfection of cells by the proton sponge effect, which induces suppression of gene degradation by lysosomal enzymes and promotes the transfer of DNA into the cytosol, resulting in transfection of the cells. This study prepared PAMAM dendrimers having hydrophobic amino acid residues because such dendrimers are expected to achieve an efficient transfection by a synergy of the proton sponge effect and hydrophobic interactions with cellular membranes.

We used phenylalanine for modification of PAMAM G4 dendrimers because this amino acid has a highly hydrophobic side group. We have already shown that amino acid molecules can be attached to terminal amino groups of the PAMAM dendrimers using condensing agent, DCC (*25*). Therefore, in this study, we combined phenylalanine with the dendrimer chain ends by the same method. Figure 2 depicts ^{1}H NMR spectra for the PAMAM G4 dendrimer (A), phenylalanine (B), and the dendrimer after reaction with 96 equiv of phenylalanine (C). Figure 2C shows that the spectrum of the dendrimer after the reaction exhibits signals corresponding to the PAMAM dendrimer and signals corresponding to phenylalanine, indicating that the amino acid residues are combined with the dendrimer. The number of phenylalanine residues attached to the dendrimer can be evaluated using the integral ratio of the signal at 2.2 ppm to 7−7.2 ppm. Table 1 lists the numbers of amino acid molecules added per dendrimer molecule for the reaction and the numbers of the amino acid residues combined to the dendrimer after the reaction. The number of phenylalanine residues combined to the dendrimer was controllable by adjusting the quantities of amino acids added for the condensation

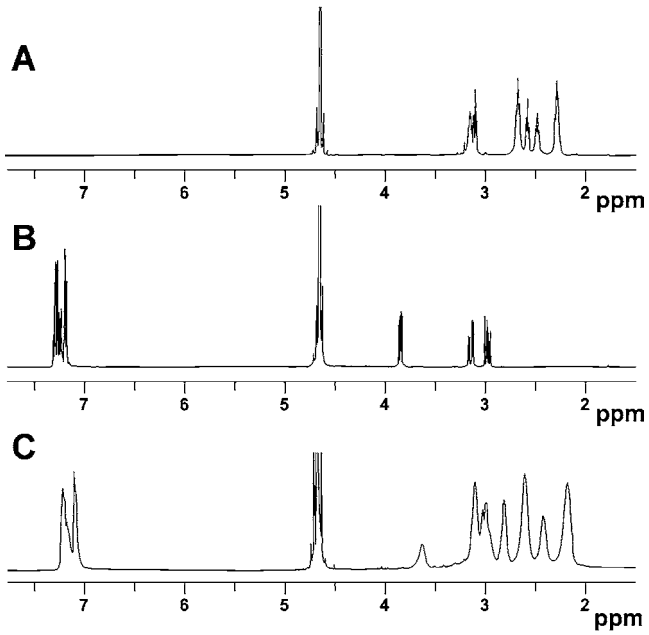

Figure 2. ^{1}H NMR spectra for PAMAM G4 dendrimer (A), L-phenylalanine (B), and (Phe)64-G4 dendrimer (C) in D_2O.

Table 1. Preparation of Phe- and Leu-Modified PAMAM G4 Dendrimers[a]

	number of amino acids per dendrimer	
dendrimer	in feed (mol/mol)	product (mol/mol)
$(Phe)_{16}$-G4	19.2	16.4
$(Phe)_{29}$-G4	32.0	29.2
$(Phe)_{46}$-G4	48.0	46.3
$(Phe)_{64}$-G4	96.0	64.5
$(Leu)_{63}$-G4	96.0	63.2

[a] Evaluated by ^{1}H NMR spectra.

reaction. When 96 equiv quantities of phenylalanine were reacted with the dendrimer, 64 phenylalanine residues were combined to the dendrimer, indicating that this Phe-modified dendrimer has a phenylalanine residue at every chain end. Consequently, we prepared four kinds of phenylalanine-modified dendrimers, (Phe)16-G4, (Phe)-29-G4, (Phe)46-G4, and (Phe)64-G4, which possessed 16, 29, 46, and 64 phenylalanine residues, respectively (Table 1).

Evaluation of Complex Formation with Plasmid DNA. The PAMAM dendrimers can form complexes efficiently with plasmid DNA through electrostatic interaction between the protonated primary amine of the dendrimer and negatively charged phosphodiester groups of DNA (*8*, *26*). Nevertheless, attachment of phenylalanine to the primary amine may affect the dendrimers' ability to form the complex with DNA. For that reason, we examined the influence of attachment of phenylalanine residues to the dendrimer on its ability of complex formation using agarose gel electrophoresis (Figure 3). In this experiment, the plasmid DNA was incubated with the dendrimer having varying numbers of phenylalanine residues for 10 min at pH 7.4, and electrophoresed on an agarose gel. Figure 3 shows that the free DNA band was not seen at the N/P ratio of 1 for the unmodified PAMAM dendrimer, indicating that all plasmid DNA molecules were associated with the dendrimer. However, for dendrimers having phenylalanine residues, the free DNA band can be observed at N/P ratios higher than 1. In addition, dendrimers having more phenylalanine residues needed a higher N/P ratio to complete their complex formation with DNA. For the fully phenylala-

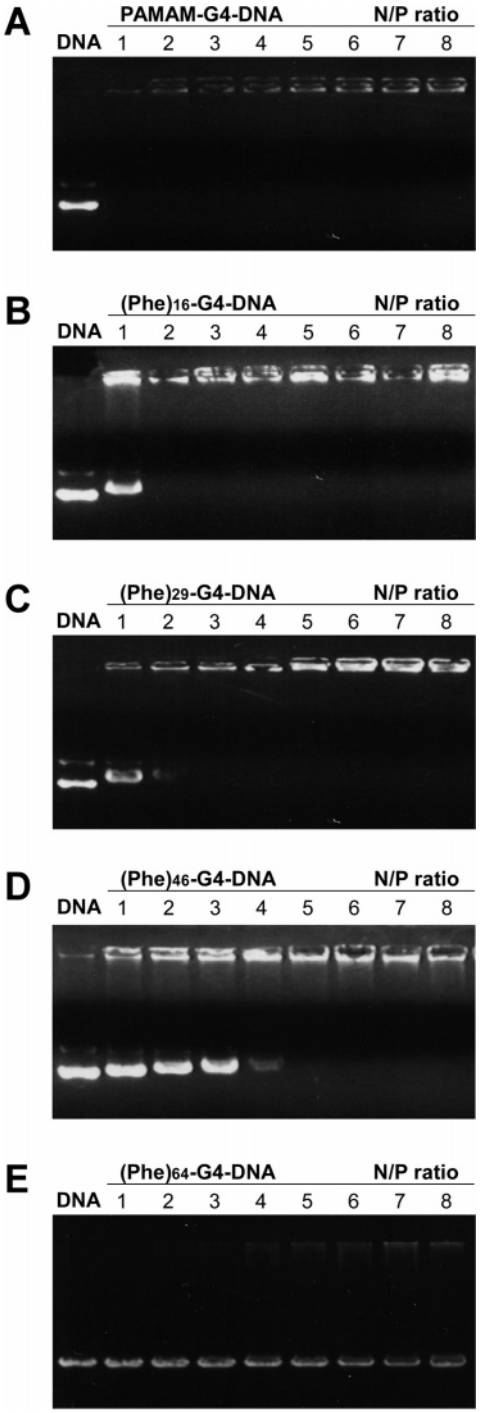

Figure 3. Agarose gel electrophoretic analysis for polyplex formation of PAMAM G4 dendrimers with varying numbers of phenylalanine residues: A, unmodified G4; B, (Phe)16-G4; C, (Phe)29-G4; D, (Phe)46-G4; E, (Phe)64-G4. Dendrimers and plasmid DNA were mixed at varying charge ratios and incubated for 10 min at room temperature. Then, the mixed solution was applied to the agarose gel and electrophoresed at 100 V for 30 min.

nine-substituted dendrimer, the free DNA band did not disappear, even at the N/P ratio of 8. These results emphasize that attachment of phenylalanine residues showed less ability to form a complex with DNA. Considering that protonation of the primary amino groups of the dendrimer occurs between pHs 7 and 10 (*27*) and the pK_a of α-amino group of phenylalanine is 9.1, these amino groups possess similar basicity. However, when combined to the dendrimer chain terminal, phenylalanine

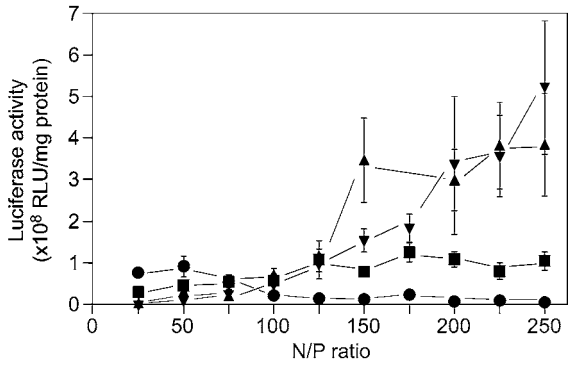

Figure 4. Luciferase activities of CV1 cells treated with polyplexes consisting of plasmid DNA and PAMAM G4 dendrimers with varying amounts of phenylalanine residues with varying N/P ratios: ■, unmodified G4; ●, (Phe)16-G4; ▲, (Phe)-29-G4; ▼, (Phe)46-G4 dendrimers. The cells (5×10^4) were treated with the polyplexes containing 1 μg DNA. Each point represents the mean ± SD ($n = 3$).

residues were able to form a hydrophobic environment in the periphery of the dendrimer, reducing protonation of their α-amino groups. Consequently, the phenylalanine-modified dendrimer showed smaller ability to form a complex with DNA.

Transfection Activity of Phenylalanine-Modified Dendrimers. Transfection activity of cationic polymer−DNA complexes varies depending on their composition. Therefore, we prepared dendrimer−DNA complexes at various N/P ratios and examined their transfection activity for CV1 cells. Figure 4 depicts luciferase activity of the cells treated with complexes consisting of plasmid DNA containing firefly luciferase gene and the dendrimers having varying numbers of phenylalanine residues. The (Phe)16-G4 dendrimer showed a similar or smaller transfection activity compared to the unmodified dendrimer. However, the dendrimer having 29 or 46 phenylalanine residues exhibited higher transfection activity. This result suggests that increased hydrophobicity enhances the transfection activity of the dendrimer. For that reason, it is expected that a fully phenylalanine-substituted dendrimer may exhibit the highest transfection activity among phenylalanine-modified dendrimers. Nevertheless, this dendrimer exhibited poor ability to form a complex with plasmid DNA, as mentioned above.

Transfection Activity of Phenylalanine-Modified Dendrimers at Acidic pH. Although the (Phe)64-G4 dendrimer hardly formed a complex with DNA at pH 7.4, it is possible that this dendrimer exhibits a higher ability to form the complex under acidic conditions because such conditions would enhance protonation of the amino groups contained in the (Phe)64-G4 dendrimer. Agarose gel electrophoresis was performed for mixtures of the dendrimer and DNA at various N/P ratios at pH 4−6 to examine the influence of pH on the ability of the dendrimer to form the complex. As shown in Figure 5, the N/P ratio at which the free DNA band disappears decreases with decreasing pH. This indicates that the ability of the dendrimer to perform complex formation increases with decreasing pH.

We next examined transfection activity of complexes prepared by mixing the (Phe)64-G4 dendrimer and plasmid DNA at varying N/P ratios at mildly acidic pHs. Figure 6A depicts luciferase expression of CV1 cells treated with these complexes. Transfection activity of these complexes was affected markedly by their composition. However, complexes with N/P ratios of 50−60 exhibited remarkably high transfection activity. We

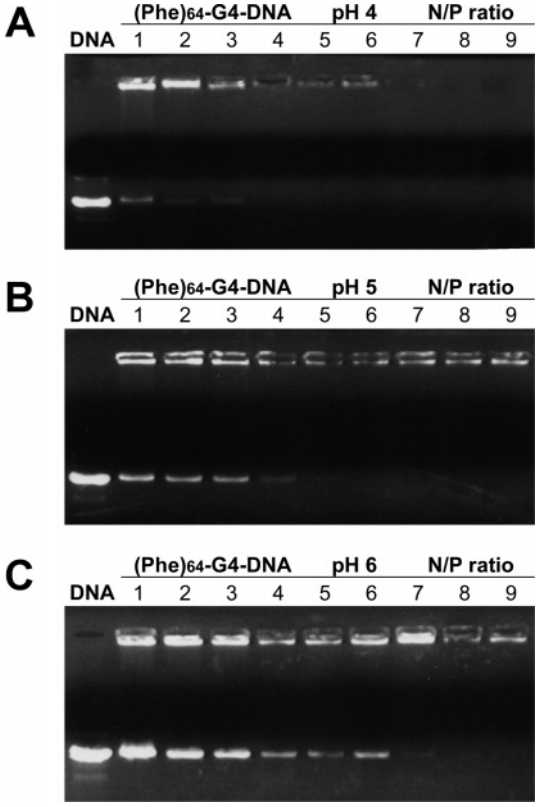

Figure 5. Agarose gel electrophoretic analysis for polyplex formation of (Phe)64-G4 dendrimer at pHs 4.0 (A), 5.0 (B), and 6.0 (C). The dendrimer and plasmid DNA were mixed at varying charge ratios and incubated for 10 min at room temperature. Then, the mixed solution was applied to the agarose gel and electrophoresed at 100 V for 30 min.

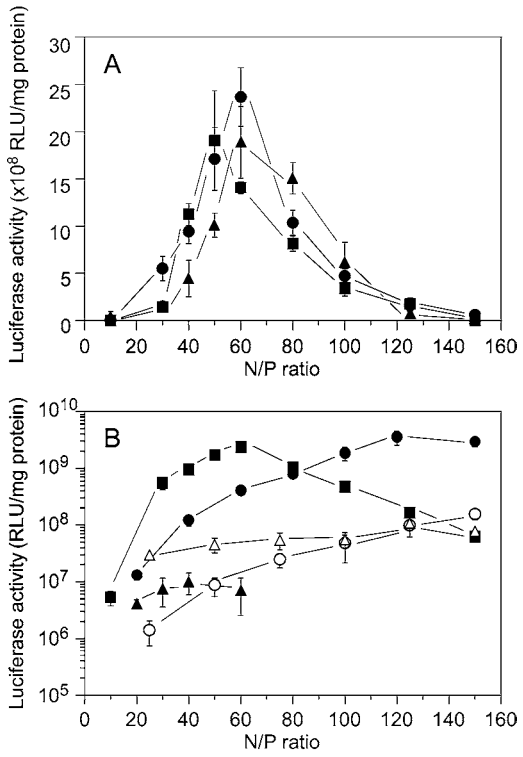

Figure 6. Influence of preparation pH on transfection activity of polyplex. (A) Luciferase activities of CV1 cells treated with (Phe)64-G4 polyplex with varying N/P ratios prepared at pHs 4.0 (■), 5.0 (●), and 6.0 (▲). (B) Luciferase activities of CV1 cells treated with (Phe)64-G4 (squares), (Phe)46-G4 (circles), and unmodified G4 (triangles) dendrimer polyplexes prepared at pHs 7.4 (open symbols) and 5.0 (closed symbols). The cells (5×10^4) were treated with the polyplex containing 1 μg DNA. Each point represents the mean ± SD ($n = 3$).

compared the (Phe)46-G4 dendrimer−DNA complex with the N/P ratio of 250 prepared at pH 7.4, which shows the highest activity among the polyplexes prepared at pH 7.4 (Figure 4), and the (Phe)64-G4 dendrimer−DNA polyplexes with the N/P ratio of 60 prepared at pH 5.0. The latter exhibited five times higher expression of luciferase gene, although the amount of the dendrimer contained in the latter polyplex was about one-fourth of that contained in the former polyplex. In addition, compared with the polyplex of the unmodified dendrimer, the (Phe)64-G4 dendrimer−polyplex exhibited about 30 times higher activity.

We further examined cell transfection by the polyplexes of (Phe)46-G4 or unmodified G4 dendrimer prepared at pH 5.0 and compared the result with that of the (Phe)64-G4 dendrimer-containing polyplex (Figure 6B). Thereby, we determined the influence of the pH of polyplex formation on transfection activity. The polyplex of the unmodified dendrimer showed decreased activity when prepared at pH 5.0. Because the charge density of the dendrimer is very high, DNA molecules might be bound very tightly to the dendrimer, resulting in the reduced transfection activity. However, regarding the (Phe)46-G4 dendrimer-containing polyplex, when prepared at pH 5.0, its activity increased 1 order of magnitude over that of the polyplex prepared at pH 7.4. A mildly acidic condition appears to moderately increase protonation of amino groups with reduced basicity in the dendrimer periphery; the resultant polyplex might show high transfection activity because of its hydrophobic nature and proton sponge effect. In comparison with the (Phe)64-G4−dendrimer polyplex, the (Phe)46-G4−dendrimer polyplex required a much higher N/P ratio. Consequently, that polyplex required a much higher amount of the dendrimer to achieve maximum activity, even though these polyplexes with the optimized compositions show approximately the same transfection activity.

Comparison between Phe-Modified and Leu-Modified Dendrimers. We first examined the effect of the attachment of L-phenylalanine on transfection activity of the PAMAM dendrimer. Next, L-leucine was used to modify the dendrimer as another hydrophobic amino acid. An excess of leucine was reacted with the PAMAM G4 dendrimer using DCC. The resultant dendrimer contained 63 leucine residues per dendrimer, as evaluated by ^{1}H NMR (Table 1). The ability of the (Leu)63-G4 dendrimer to form polyplexes was examined using agarose gel electrophoresis. The plasmid DNA was incubated with the leucine-modified dendrimer for 10 min at pH 7.4; then it was electrophoresed on an agarose gel. In contrast to the case of the (Phe)64-G4 dendrimer, no free DNA band was observed even at the N/P ratio of 1, indicating that the (Leu)63-G4 dendrimer has a much higher ability to form a polyplex with DNA (results not shown).

We examined the effect of attachment of leucine residues on transfection activity of the PAMAM dendrimer. CV1 cells were treated with the (Leu)63-G4 dendrimer polyplexes prepared at pH 7.4 and pH 5.0. Expression of luciferase in the treated cells was estimated, and the results were compared with the case of (Phe)64-G4 dendrimer polyplexes. We expected that incorporation of leucine residues to the chain ends of the dendrimer would elevate its transfection activity. How-

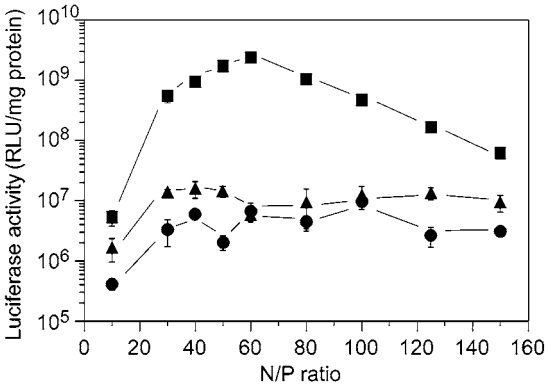

Figure 7. Comparison of transfection activity of luecine- and phenylalanine-modified dendrimers. Luciferase activities of CV1 cells treated with (Phe)64-G4 polyplex prepared at pH 5.0 (■) and (Leu)63-G4 polyplexes prepared at pHs 7.4 (▲) and 5.0 (●) containing 1 μg DNA with varying N/P ratios were shown in the figure. Each bar represents the mean ± SD (n = 3).

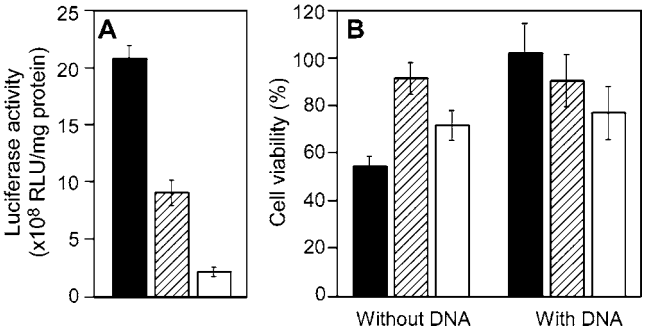

Figure 8. Comparison of transfection activity and cytotoxicity of (Phe)64-G4 dendrimer with widely used vectors. (A) Luciferase activities of CV1 cells treated with complexes of (Phe)-64-G4 dendrimers (closed bars), Lipofectamine (hatched bars), and SuperFect (open bars) containing 1 μg of DNA. Each bar represents the mean ± SD (n = 4). (B) Viability of CV1 cells treated with (Phe)64-G4 dendrimers (closed bars), Lipofectamine (hatched bars), and SuperFect (open bars) with or without plasmid DNA. Viability was expressed as the percentage of the untreated control cells. Each bar represents the mean ± SD (n = 3). The (Phe)64-G4 dendrimer polyplex with N/P ratio of 60 prepared at pH 5.0 was used.

ever, as shown in Figure 7, leucine residues did not increase its transfection activity at either pH compared with the unmodified dendrimer. Consequently, the (Leu)-63-G4 dendrimer−polyplexes exhibited a significantly lower activity than the (Phe)64-G4 dendrimer polyplexes.

As mentioned previously, we designed phenylalanine-modified and leucine-modified PAMAM dendrimers because we expected that these dendrimers express high transfection activity by synergistic actions of the proton sponge effect and hydrophobic interactions with cells. In fact, the attachment of phenylalanine increased the transfection activity of the parent dendrimer by about 2 orders of magnitude over that of the parent dendrimer (Figure 6). In contrast, the attachment of leucine showed no remarkable enhancement of dendrimer activity even though this amino acid is also hydrophobic. As a measure of hydrophobicity of the amino acid, Nozaki and Tanford used differences in free energy between a hydrophobic moiety of an amino acid in ethanol (or dioxane) and in water and showed that the free energies of transfer for phenylalanine and for leucine are 2500 and 1800 cal/mol, respectively (*28*), indicating that phenylalanine is more hydrophobic. We observed that (Phe)64-G4 dendrimer showed poor water solubility at pH 7.4, whereas (Leu)-63-G4 dendrimer was soluble in water at the same pH, although both dendrimers have essentially the same number of amino acid residues. This fact implies that the attachment of phenylalanine to the dendrimer lent a highly hydrophobic character to the dendrimer periphery. In fact, Meijer and co-workers reported that phenylalanine residues, when combined to the chain ends of poly(propylenimine) dendrimers, form a densely packed shell on the dendrimer surface (*29*, *30*). Therefore, the highly hydrophobic surface of densely packed phenylalanine residues of the dendrimer might enhance interaction of the dendrimer−DNA polyplexes and cellular membranes, engendering efficient transfection.

Recently, Shibata et al. reported that a random copolymer of L-lysine and L-phenylalanine translocates phospholipid membranes much faster than a poly(L-lysine) (*31*). This rapidity is probably attributable to the random incorporation of hydrophobic phenylalanine residues into the positively charged poly(lysine) chain. Those residues lowered the potential barrier in the hydrophobic region of the lipid membrane for the polypeptide translocation (*31*). Considering that observation, it is possible that the hydrophobic shell of phenylalanine on the dendrimer surface interacts strongly with the hydrophobic region of the cellular membranes and causes their destabilization, thereby enhancing translocation of the gene through the membrane.

Transfection Activity of Phe-modified Dendrimers and Some Vectors. We compared the respective activities of Lipofectamine and SuperFect, both of which are widely used and commercially available vectors, to evaluate the potential of phenylalanine-modified dendrimers as a gene carrier. We treated CV1 cells with (Phe)64-G4 dendrimer−DNA polyplex, Lipofectamine−DNA complex, and SuperFect−DNA complex; then we evaluated the cells' expression of luciferase. Figure 8A shows that the (Phe)64-G4 dendrimer polyplex induced about 2.3-fold higher and about 10-fold higher expression of luciferase, respectively, than Lipofectamine and SuperFect complexes that contained identical amounts of plasmid DNA.

The potential use of the phenylalanine-modified dendrimer as a gene carrier was also estimated from the viewpoint of cytotoxicity. Figure 8B depicts the viability of the cells treated with the (Phe)64-G4 dendrimer, Lipofectamine, and SuperFect, and their complexes with the plasmid DNA. The (Phe)64-G4 dendrimer itself was shown to be relatively toxic compared to these commercially available reagents. It is likely that the phenylalanine-modified dendrimer interacts strongly with the cell membranes and damages the cells because of the hydrophobic nature of the phenylalanine. However, in the form of the complex with DNA, the toxicity of the phenylalanine-modified dendrimer decreased remarkably. This decrease is attributable to the weakening of their strong interaction with cellular membranes by complexation with the hydrated DNA molecule. These results indicate that the phenylalanine-modified dendrimer can be considered as an efficient vector.

CONCLUSION

In this study, we prepared PAMAM G4 dendrimers having hydrophobic amino acid residues, which achieve an efficient transfection of cells through synergy of the proton sponge effect induced by the dendrimer tertiary amines and hydrophobic interaction by the amino acid residues. Transfection activity was not improved when leucine was attached to the dendrimer. However, the attachment of phenylalanine greatly increased the trans-

fection activity of the parent dendrimer. Activity of the fully phenylalanine-substituted dendrimer was shown to be higher than for some widely used vectors. Transfection activity of the PAMAM dendrimers is known to increase with generation (*5*, *8*). Therefore, the phenylalanine-modified dendrimers with higher generations may exhibit still higher activity than the present dendrimers. For this reason, the findings obtained in this study will engender the development of efficient gene carriers. We are currently studying the effect of dendrimer generation on transfection activity of phenylalanine-modified dendrimers.

ACKNOWLEDGMENT

This work was partly supported by the Grant-in-Aid from Japanese Ministry of Education, Culture, Sports, Science, and Technology (16300159) and the Mitsubishi foundation.

LITERATURE CITED

(1) Mountain, A. (2000) Gene therapy: the first decade. *Trends Biotechnol. 18*, 119−128.
(2) Crystal, R. G. (1995) Transfer of genes to humans: early lessons and obstacles to success. *Science 270*, 404−410.
(3) Brown, M. D., Schätzlein, A. G., and Uchegbu, I. F. (2001) Gene delivery with synthetic (non viral) carriers. *Int. J. Pharm. 229*, 1−21.
(4) Behr, J. P. (1993) Synthetic gene-transfer vectors. *Acc. Chem. Res. 26*, 274−278.
(5) Haensler, J., and Szoka, F. C., Jr. (1993) Polyamidoamine cascade polymers mediate efficient transfection of cells in culture. *Bioconjugate Chem. 4*, 372−379.
(6) Boussif, O., Lezoualc'h, F., Zanta, M. A., Mergny, M. D., Scherman, D., Demeneix, B., and Behr, J. P. (1995) A versatile vector for gene and oligonucleotide transfer into cells in culture and in vivo: Polyethylenimine. *Proc. Natl. Acad. Sci. U.S.A. 92*, 7297−7301.
(7) Tang, M., Redemann, C. T., and Szoka, F. C., Jr. (1996) In vitro gene delivery by degraded polyamidoamine dendrimers. *Bioconjugate Chem. 7*, 703−714.
(8) Kukowska-Latallo, J. F., Bielinska, A. U., Johnson, J., Spindler, R., Tomalia, D. A., and Baker, J. R., Jr. (1996) Efficient transfer of genetic material into mamalian cells using Starburst polyamidoamine dendrimers. *Proc. Natl. Acad. Sci. U.S.A. 93*, 4897−4902.
(9) Zou, S. M., Behr, J. P., Goula, D., and Demeneix, B. (2000) Gene delivery with polyethylenimine. In *Gene Therapy: Therapeutic mechanisms and strategies* (Templeton, N. S., Lasic, D. D., Eds.) pp 131−139, Marcel Dekker, New York.
(10) Sonawane, N. D., Szoka, F. C., Jr., and Verkman, A. S. (2003) Chloride accumulation and swelling in endosomes enhances DNA transfer by polyamine-DNA polyplexes. *J. Biol. Chem. 278*, 44826−44831.
(11) Tomalia, D. A., Baker, H., Dewald, J., Hall, M., Kallos, G., Martin, S., Roeck, J., Ryder, J., and Smith, P. (1985) A new class of polymers: starburst-dendritic macromolecules. *Polym. J. 17*, 117−132.
(12) Tomalia, D. A., Naylor, A. M., and Goddard, W. A. (1990) Starburst dendrimers: molecular-level control of size, shape, surface chemistry, topology, and flexibility from atoms to macroscopic matter. *Angew. Chem., Int. Ed. 29*, 138−175.
(13) Kubasiak, L. A., and Tomalia, D. A. (2004) Cationic dendrimers as gene transfection vectors: dendri- poly(amidoamines) and dendri- poly(propyleneimines). In *Polymeric Gene Delivery: Principles and Applications* (Amiji, M. M., Eds.) Chapter 9, pp 133−157, CRC Press, Boca Raton, FL.
(14) Arima, H., Kihara, F., Hirayama, F., and Uekama, K. (2001) Enhancement of gene expression by polyamidoamine dendrimer conjugates with α-, *β*-, and *γ*-cyclodextrins. *Bioconjugate Chem. 12*, 476−484.
(15) Kihara, F., Arima, H., Tsutsumi, T., Hirayama, F., and Uekama, K. (2002) Effects of structure of polyamidoamine dendrimer on gene transfer efficiency of the dendrimer conjugate with α-cyclodextrin. *Bioconjugate Chem. 13*, 1211−1219.
(16) Yoo, H., and Juliano, R. L. (2000) Enhanced delivery of antisense oligonucleotides with fluorofore-conjugated PAMAM dendrimers. *Nucleic Acids Res. 28*, 4225−4231.
(17) Luo, D., Haverstick, K., Belcheva, N., Han, E., and Saltzman, W. M. (2002) Poly(ethylene glycol)-conjugated PAMAM dendrimer for biocompatible, high-efficiency DNA delivery. *Macromolecules 35*, 3456−3462.
(18) Zhou, X., Klibanov, A. L., and Huang, L. (1991) Lipophilic polylysines mediate efficient DNA transfection in mammalian cells. *Biochim. Biophys. Acta 1065*, 8−14.
(19) Remy, J. S., Sirlin, C., Vierling, P., and Behr, J. P. (1994) Gene transfer with a series of lipophilic DNA-binding molecules. *Bioconjugate Chem. 5*, 647−654.
(20) Kurisawa, M., Yokoyama, M., and Okano, T. (2000) Transfection efficiency increases by incorporating hydrophobic monomer units into polymeric gene carriers. *J. Controlled Release 68*, 1−8.
(21) Han, S., Mahato, R. I., and Kim, S. W. (2001) Water-soluble lipopolymer for gene delivery. *Bioconjugate Chem. 12*, 337−345.
(22) Wang, D., Narang, A. S., Kotb, M., Gaber, A. O., Miller, D. D., Kim, S. W., and Mahato, R. I. (2002) Novel branched poly(ethylenimine)-cholesterol water-soluble lipopolymers for gene delivery. *Biomacromolecules 3*, 1197−1207.
(23) Takahashi, T., Kono, K., Itoh, T., Emi, N., and Takagishi, T. (2003) Synthesis of novel cationic lipids having polyamidoamine dendrons and their transfection activity. *Bioconjugate Chem. 14*, 764−773.
(24) Mosmann, T. (1983) Rapid colorimetric assay for cellular grouth and survival: application to proliferation and cytotoxicity assays. *J. Immunol. Methods 65*, 55−63.
(25) Kojima, C., Haba, Y., Fukui, T., Kono, K., and Takagishi, T. (2003) Design of biocompatible dendrimers with environment-sensitivity. *Macromolecules 36*, 2183−2186.
(26) Tang, M. X., and Szoka, F. C., Jr. (1997) The influence of polymer structure on the interactions of cationic polymers with DNA and morphology of the resulting complexes. *Gene Ther. 4*, 823−832.
(27) Niu, Y., Sun, L., and Crooks, R. M. (2003) Determination of the intrinsic proton binding constants for poly(amidoamine) dendrimers via potentiomentric pH titration. *Macromolecules 36*, 5725−5731.
(28) Nozaki, Y., and Tanford, C. (1971) The solubility of amino acids and two glycine peptides in aqueous ethanol and diaxane solutions. *J. Biol. Chem. 246*, 2211−2217.
(29) Jansen, J. F. G. A., de Brabander-van den Berg, E. M. M., and Meijer, E. W. (1994) Encapsulation of guest molecules into a dendritic box. *Science 266*, 1226−1229.
(30) Jansen, J. F. G. A., and Meijer, E. W. (1995) The dendritic box: Shape-selective liberation of encapsulated guests. *J. Am. Chem. Soc. 117*, 4417−4418.
(31) Shibata, A., Murata, S., Ueno, S., Liu, S., Futaki, S., and Baba, Y. (2003) Synthetic copoly(Lys/Phe) and poly(Lys) translocate through lipid bilayer membranes. *Biochim. Biophys. Acta 1616*, 147−155.

BC049785E

A New Highly Efficient Photoreactive Analogue of dCTP. Synthesis, Characterization, and Application in Photoaffinity Modification of DNA Binding Proteins

Sergey V. Dezhurov,† Svetlana N. Khodyreva,† Ekaterina S. Plekhanova, and Olga I. Lavrik*

Institute of Chemical Biology and Fundamental Medicine, Siberian Division, Russian Academy of Sciences, Prospect Lavrentieva 8, Novosibirsk, 630090 Russia. Received September 7, 2004; Revised Manuscript Received November 30, 2004

A new base-substituted analogue of dCTP, *exo-N*-{2-[*N*-(4-azido-2,5-difluoro-3-chloropyridine-6-yl)-3-aminopropionyl]aminoethyl}-2′-deoxycytidine-5′-triphosphate (FAP-dCTP) has been synthesized and characterized. FAP-dCTP is an efficient substrate of mammalian DNA polymerase β in the reaction of primer elongation displaying substrate properties as an analogue of dCTP and dTTP. FAP-dCTP was used for the photoaffinity modification of mammalian DNA polymerase β. Two approaches to photoaffinity labeling were utilized. In one approach, photoreactive FAP-dCTP was first incorporated into radiolabeled primer−template, and photoreactive DNA was UV-irradiated in the presence of DNA polymerase β, which resulted in the polymerase labeling by photoreactive primer. In an alternate approach, FAP-dCTP was first UV-cross-linked to the enzyme; subsequently, radiolabeled primer−template was added, and the enzyme-linked FAP-dCTP was incorporated into the 3′-end of radioactive primer. This "catalytic" modification pathway was shown to be less specific in recognition of FAP-dCTP as an analogue of dCTP than dTTP. FAP-dCTP was used as substrate of endogenous DNA polymerases of HeLa cell extract to synthesize photoreactive DNAs for photoaffinity modification of cell proteins. UV irradiation results in modification of DNA binding proteins of cell extract. The level of photoaffinity labeling of protein targets in the cell extract was strongly dependent on the efficiency of synthesis of photoreactive DNA.

INTRODUCTION

The photoaffinity labeling technique in the study of DNA replication/repair machineries is based on UV-light-induced cross-linking of photoreactive DNA to proteins. The most easy-to-use way to synthesize photoreactive probes is the in situ introduction of photoreactive dNMP moieties into the 3′ end of a DNA primer via the activity of DNA polymerases with photoreactive dNTP analogues used as substrates. A wide range of base-substituted dNTP analogues containing photoreactive groups of different photoreactivity and spacers of various lengths have been synthesized and characterized (*1*−*3*). Photoreactive dNTP analogues have been shown to be effective substrates of viral, bacterial, and eukaryotic DNA polymerases. These analogues were widely applied in study of proteins belonging to DNA replication/repair machineries in the systems reconstituted from purified proteins (*4*−*6*) and in cell extracts (*7*, *8*). Photoreactive dNMP moieties varied substantially in their ability to form covalent cross-links with target protein depending on the type of photoreactive group used. The efficiency of covalent adduct formation may become a parameter restricting applicability of the method when applied in cell extracts for identification of unknown proteins because their concentrations are limited. Another factor that should be considered when photoreactive probes are synthesized in cell extracts via activity of the endogenous DNA polymerases is catalytic efficiency of dNTP derivatives since the concentrations of DNA polymerases are limited, which may restrict the yield of photoreactive DNA. It should be noticed that photoreactive dNTP analogues displayed different kinetic parameters in the primer elongation catalyzed by Pol β[1] (*9*). In our previous studies, we clearly recognized the factors that influence the efficiency of protein cross-linking. The most significant factors are the nature of photoreactive group and its position at the heterocyclic base. For example, among dUTP derivatives bearing substituents at the 5th position of the uridine ring, the most efficient in protein cross-linking was shown to be DNA containing FAP-dUMP moieties (*10*). As far as dCTP derivatives, the most efficient in protein cross-linking were FABO- and FABC-containing photoreactive DNA when these analogues were introduced opposite to an adenine of the template (*11*). As has been previously shown, dCTP derivatives

* To whom correspondence should be addressed. Tel: 7(3832) 344296. Fax: 7(3832) 333677. E-mail: lavrik@niboch.nsc.ru.

† The authors wish it to be known that in their opinion, the first two authors should be regarded as joint first authors.

[1] Abbreviations: FAP-dCTP, *exo-N*-{2-[*N*-(4-azido-2,5-difluoro-3-chloropyridine-6-yl)-3-aminopropionyl]aminoethyl}-2′-deoxycitidine-5′-triphosphate (lithium salt); FABO-dCTP, *exo-N*-[(4-azido-2,3,5,6-tetrafluorobenzylideneaminooxy)-butyloxy]-2′-deoxycytidine-5′-triphosphate (lithium salt); FABC-dCTP, *exo-N*-[2-(4-azido-2,3,5,6-tetrafluorobenzylideneaminooxymethylcarbonyl)-aminoethyl]-2′- deoxycytidine-5′-triphosphate (lithium salt); FAB-dCTP, *exo-N*-[2-(4-azidotetrafluorobenzoyl)-aminoethyl]-2′-deoxycytidine-5′-triphosphate (lithium salt); FAP-dUTP, 5-{*N*-[*N*-(4-azido-2,5-difluoro-3-chloropyridine-6-yl)-3-aminopropionyl]-*trans*-3-aminopropenyl-1}-2′-deoxyuridine-5′-triphosphate (lithium salt); FABC-dUTP, 5-[*N*-(4-azido-2,3,5,6-tetrafluorobenzylideneaminooxymethylcarbonyl)-methylcarbamoyl]-*trans*-3-aminopropenyl-1]-2′-deoxyuridine-5′-triphosphate (lithium salt); Pol β, DNA polymerase β; N_3dATP, 2-azidoadenosine triphosphate.

10.1021/bc0497867 CCC: $30.25 © 2005 American Chemical Society
Published on Web 12/23/2004

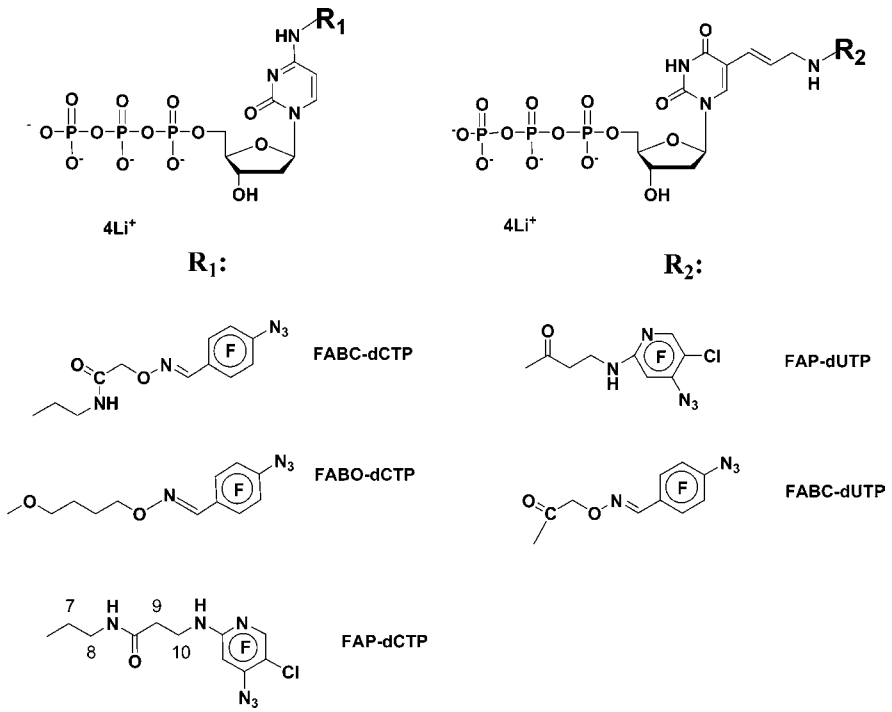

Figure 1. Structures of photoreactive analogues of dNTP.

were recognized by DNA polymerases as dTTP due to the shift of tautomeric equilibrium from the amino to the imino form cased by introduction of the photoreactive group (*9*). A characteristic feature of FABO- and FABC-dCTP derivatives is an electron-deficient atom of nitrogen, which is involved in π-system of the arylazido group (Figure 1).

Comparison of the efficiencies of photoreagent cross-linking to Pol β when DNA probes contain the same FABC group attached to either the 4th or 5th positions of the pyrimidine ring (moieties of FABC-dCMP and FABC-dUMP, respectively) clearly demonstrated that the former was more effective (*11*).

FAB-dCTP used to study the interactions of base excision repair proteins in mouse embryonic fibroblast extract with DNA intermediates synthesized in situ by endogenous DNA polymerases was efficiently incorporated in the primer (*12*). This analogue displayed rather good parameters in primer elongation catalyzed by Pol β but provided a low level of enzyme modification being incorporated in the primer chain. The main target for cross-linking of the photoreactive dCMP-containing primer was shown to be the complementary template chain (*9*). The corresponding efficiencies of the photoreactive primer cross-linking to Pol β and the template were 2% and 84%, respectively.

Thus, taking together all these data prompted us to synthesize a dCTP analogue substituted at the 4th position with a FAP group, which provided rather effective modification of Pol β as a part of a FAP-dUMP containing primer. We expected the new analogue to combine good substrate properties in DNA synthesis with effective cross-linking to proteins when introduced into DNA that would make it suitable for photoaffinity modification both in reconstituted systems and in cellular extracts. We tested FAP-dCTP as a substrate in the primer elongation catalyzed by Pol β and endogenous DNA polymerases of HeLa cell extract. Photoreactive DNA with FAP-dCMP moieties synthesized in situ was used for photoaffinity modification of Pol β and DNA binding proteins in the cell extract.

EXPERIMENTAL PROCEDURES

Materials. Ethylenediaminetetraacetic acid (EDTA), dCTP, glycine, Tris, *N*,*N*,*N*′,*N*′-tetramethylethylenediamine (TEMED), and Coomassie G-250 were from Sigma (St. Louis, MO); $MgCl_2$ and formamide were from Fluka (Buchs, Switzerland); β-mercaptoethanol was from Serva (Heidelberg, Germany); acrylamide, *N*,*N*′-methylenebisacrylamide, and urea were from ICN (Aurora, OH); γ-[^{32}P]ATP (>110 TBq/mmol) and T4 polynucleotide kinase were from Biosan (Novosibirsk, Russia). The ^{1}H, ^{19}F, and ^{31}P NMR spectra were recorded with a Bruker AM-400 spectrometer. UV spectra were recorded with UV 2100 Shimadzu (Kyoto, Japan).

Oligonucleotides 5′-GGAAGACCCTGACGTT**G**CCCA-ACTTAATCGCC-3′ (36-mer template I), 5′-GGAAGAC-CCTGACGTT**A**CCCAACTTAATCGCC-3′ (36-mer template II), and 5′-GGCGATTAAGTTGGG-3′ (15-mer primer) Sibenzyme (Novosibirsk, Russia) were used for synthesis of photoreactive DNA. The primers were the 5′-end-labeled with [^{32}P] using T4 polynucleotide kinase and γ-[^{32}P]ATP (*13*) and then purified by denaturing PAGE in 7 M urea (*14*). The radioactive primer was mixed with the template at 1:1.5 molar ratio, and the DNA duplexes were formed by heating to 90 °C and slowly cooling to room temperature.

Recombinant rat DNA polymerase β (EC 2.7.7.7) was purified as described (*15*). Plasmid pRSET containing the cDNA of rat DNA polymerase β was the kind gift of Dr. S. H. Wilson (National Institute of Environmental Health Sciences, USA). HeLa cells were kindly provided by Dr. M. A. Zenkova (Institute of Chemical Biology and Fundamental Medicine, Novosibirsk). The whole cell extract was prepared as described (*16*).

FABO-dCTP and FABC-dCTP synthesized as described (*1*) were a generous gift of Dr. I. V. Safronov (Institute of Chemical Biology and Fundamental Medicine, Novosibirsk).

Synthesis and Characterization of FAP-dCTP. Synthesis of *exo*-*N*-{2-[*N*-(4-azido-2,5-difluoro-3-chloropyridine-6-yl)-3-aminopropionyl]aminoethyl}-2′-deoxyciti-

Scheme 1. Synthesis of FAP-dCTP

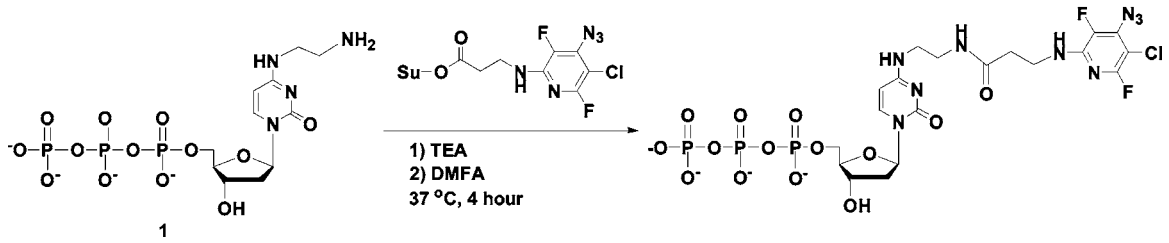

1

dine-5′-triphosphate (lithium salt) was carried out according to the standard method of the introduction of photoreactive groups (*1*). *N*-(4-Azido-2,5-difluoro-3-chloropyridine-6-yl)-3-aminopropionic acid *N*-hydroxysuccinimidyl ester (0.5 mmol) dissolved in DMFA (1 M, 500 μL) was mixed with 114 μmol (16 μL) of triethylamine and 0.4 mmol of triphosphate **1** (Scheme 1) dissolved in 2 mL of DMFA. When the reaction was completed (2 h, 37 °C), 50 mL of a 2% solution of $LiClO_4$ in acetone was added to the reaction mixture. The resulting precipitate was separated by centrifugation and washed with acetone and Et_2O. FAP-dCTP was purified by large scale HPLC using chromatographic complex Waters and column Lichroprep RP-18 (5−20 μm). Solvent was removed under reduced pressure; the residue was precipitated with a 2% solution of $LiClO_4$ in acetone and washed with Et_2O (61 mg, 20%). The purity of the analogue was 95% as estimated by analytical HPLC. The product was homogeneous according to TLC with $R_f = 0.21$ (dioxane−ammonia−water, 6:4:0.3); UV (H_2O) $\lambda_{max} = 237$ ($\epsilon = 26\,000$), $\lambda_{max} = 322$ ($\epsilon = 4000$), $\lambda_{min} = 280$ ($\epsilon = 1450$); NMR spectra (D_2O), ^{31}P (δ, ppm) −5.95 (d, $J = 20$ Hz, P_γ, 1P,), −10.21 (d, $J = 20$ Hz, P_α, 1P), −20.31 (t, $J = 20$ Hz, P_β, 1P), ^1H (δ, ppm) 2.2−2.4 (d, bs, H2′, 2H), 2.4−2.6 (t, bs, H9, 2H), 3.3−3.7 (m, H7, H8, H10, 6H), 4.1−4.3 (m, bs, H4′, H5′, 3H), 4.5 (s, H3′, 1H), 6.1 (d, H5, 1H), 6.4 (d, H1′, 1H), 7.9 (d, H6, 1H), ^{19}F (δ, ppm) 7.9 (d, $J = 23$ Hz, F5, 1F), 86.7 (d, $J = 23$ Hz, F2, 1F).

Mass Spectrometry. The mass spectra were recorded by MALDI-TOF mass spectrometer REFLEX III (Bruker Daltonics, Bremen, Germany), equipped with a single stage reflector giving an effective 3.0 m flight path and using the instrument's standard 337 nm nitrogen laser and microchannel plate detector. Range of operational parameters was 20 kV acceleration voltage, 0 ns extraction delay, and 90% grid voltage. Generally the extraction delay and grid voltage were set to optimize resolving power. Spectra were obtained as averages of 60 laser shots, and the laser energy was generally set 25% above the ionization threshold. The matrix was 3-hydroxypicolinic acid. Saturated solution of matrix (50 mg/mL) was prepared in 1:1 acetonitrile/water containing 1% diammonium hydrogen citrate.

Substrate Properties of FAP-dCTP. DNA synthesis catalyzed by Pol β was carried out in buffer containing 50 mM Tris-HCl (pH 8.8), 50 mM KCl, and 10 mM $MgCl_2$. In addition, the reaction mixture contained 1.5 μM template, 1 μM 5′-[^{32}P]-primer, and FAP-dCTP in variable concentrations (10−300 μM). The reaction was started by the enzyme addition to the final concentration of 20 or 2000 nM depending on the primer−template system and performed at 37 °C. Aliquots of 10 μL were taken out of the 200 μL reaction mixture at different time intervals (0.167−15 min) and quenched by the addition of loading buffer containing 80% formamide and 50 mM EDTA. After being heated (5 min, 90 °C), the samples were analyzed by electrophoresis in 20% PAG under denaturing conditions (*14*). Distribution of radioactivity in the gel was quantified using Molecular Imager (Bio-Rad, USA) and software "Quantity One". For each of the reaction mixtures, the efficiency of the primer elongation was determined. The data obtained were used for calculation of the K_m and k_{cat} values using the software Origin 6.0 (Microcal Software Inc., USA).

Determination of the Modification Rate Constant (k) and the Time of Half-Modification ($\tau_{1/2}$) of Pol β by Photoreactive Primers. The reaction mixtures for DNA synthesis (200 μL) contained standard components described above, but the concentration of Pol β and FAP-dCTP were 3 and 10 μM, respectively. The reaction mixtures were incubated for 30 min at 37 °C to introduce a photoreactive FAP-dCMP moiety into the 3′-end of the primer by the activity of Pol β. After primer elongation, the reaction mixtures were placed in water bath (25 °C). Photolysis was induced by UV light using a DRK-120 VIO-1 UV lamp ('LOMO', Saint Petersburg, Russia) supplemented with glass filter UFS-6 ($\lambda = 313-365$ nm) at a distance of 110 mm. During the irradiation, 15 μL aliquots were taken at definite time intervals (1−30 min). The reactions were stopped by adding the Laemmli loading buffer and heating at 90 °C for 5 min. The covalent adducts of Pol β with the [5′-^{32}P] DNA primer were separated from the free DNA primer and the products of template modification by 12% PAGE as described (*17*). Distribution of radioactivity in the gel was quantified as described above. The rate constants of modification (k) were calculated from the time dependence of the amount of modification products, assuming that the modification reaction is of the first order. The half-time of modification was calculated by the formula $\tau_{1/2} = (\ln 2)/k$, which corresponds to the formation of the half of the maximum amount of adducts under these conditions.

Determination of the Efficiency of Modification of Pol β (W_R). Pol β was cross-linked to photoreactive DNA as described in the previous sections by irradiation for the time $t \gg \tau_{1/2}$ (15 min). The covalent adducts of the [5′-^{32}P] DNA primer with DNA polymerase were separated from the other components of the reaction mixture by 12% PAGE (*17*). Distribution of radioactivity in the gel was quantified as describe above. The efficiency of modification was calculated from the equations $W_R = W_r/x$, $W_r = 100\%[A_1/(A_1 + A_2)]$ where A_1 is the amount of the primer covalently linked to Pol β, A_2 is the amount of the unbound radioactive DNA primer, and x is the part of extended primer. The A_1 and A_2 values were determined by counting the corresponding areas of the gel.

Determination of the Efficiency of DNA Template Modification. The modification of DNA template, which occurred along with the modification of Pol β, was determined quantitatively after the separation of the products by 20% PAGE under denaturing conditions (*14*). Distribution of radioactivity in the gel was quantified as describe above. The modification efficiency was calculated as the ratio of the template modification products to the total amount of the reactive [5′-^{32}P] DNA primer.

Catalytic Modification of Pol *β*. Modification of Pol β by the catalytic pathway was realized via initial UV irradiation of the enzyme in the presence of FAP-dCTP for the time $t \gg \tau_{1/2}$ followed by addition of primer−template and further incubation for 30 min at 37 °C. Concentrations of components were the same as for direct modification described in previous section.

Photoaffinity Modification of DNA Binding Proteins in Cellular Extract. Photoreactive dCMP moieties were incorporated in the primer by endogenous DNA polymerases of cell extract. The reaction mixtures (15 μL) contained standard components described above, but DNA duplex was 0.1 μM. One of the photoreactive dCTP analogues was added to the final concentration of 30 μM. The reaction mixtures contained 33 μg of total HeLa cell proteins. The reaction of incorporation of photoreactive dCMP residue was started by addition of cellular extract and allowed to proceed for 15 min at 37 °C. Two microliter aliquots were taken after completing DNA synthesis to analyze the efficiency of primer elongation. The rest of the reaction mixtures were placed on ice and irradiated for 15 min as described above. The efficiencies of primer elongation and cross-linking to proteins were quantified as described above.

RESULTS AND DISCUSSION

Characterization of FAP-dCTP. FAP-dCTP (Figure 1) was synthesized according to the standard method of the introduction of photoreactive groups (*1*) as shown in Scheme 1. FAP-dCTP was purified by large scale HPLC. The purity of the analogue was 95% as estimated by analytical HPLC. Data of NMR and UV spectroscopy confirmed the structure of the obtained compound.

Characterization of photoreactive derivatives of nucleoside triphosphates by MALDI-MS is poorly represented in the literature. We have found a single example, where the authors have determined MALDI-TOF spectra to characterize N_3dATP and a few nonnucleoside aryl azide derivatives (*18*). In the negative ion MALDI spectra of these ATP analogues, "fingerprint" peaks corresponding to [M − 10 − 1], [M − 12 − 1], [M − 16 − 1], [M −26 − 1], [M −28 − 1], [M − 41 − 1], and [M − 42 − 1] were observed. The model of a fragmentation of cited photoreactive compounds induced by ultraviolet laser has been suggested. It seems clear that [M − 28 − 1] corresponds to the nitrene and its isomers and [M − 42 − 1] indicates that it is possible for the azide to lose N_2 and N to form a free radical, for example. The MALDI-MS analysis for FAP-dCTP revealed analogous products [M − 1], [M − 41 − 1], and [M − 42 − 1], but the main peaks [M − 1], [M − 26 − 1], and [M − 28 − 1] were shifted (+7) in *m/z* values; these products represent the adducts containing Li^+ ions (Figure 2).

Substrate Properties. Substrate properties of FAP-dCTP in reaction of DNA primer elongation catalyzed by Pol β was characterized for two DNA duplexes, in which FAP-dCTP is incorporated either as a dCTP (PT1) or a dTTP analogue (PT2). Under conditions used, a single FAP-dCMP moiety was incorporated on both PT1 and PT2.

Data on kinetic parameters of primer elongation are listed in Table 1. It should be emphasized that on PT2 when FAP-dCTP was used as a dTTP analogue the efficiency of incorporation was substantially lower in comparison with PT1. In the former case, the concentration of Pol β in the reaction mixture was enhanced about 1000 times to register incorporation of the analogue. Since the concentrations of Pol β and template−primer

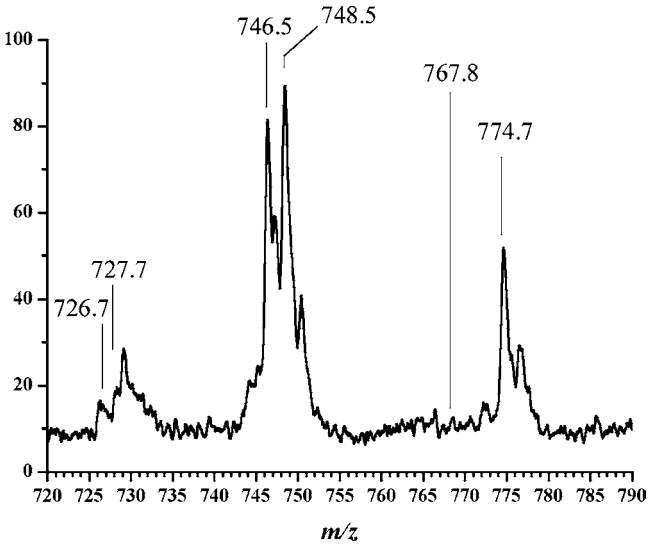

Figure 2. MALDI-TOF analysis of FAP-dCTP: peaks [M − 1], [M − 1 − 41], and [M − 1 − 42] (corresponding *m/z* values are 767.8, 727.7, and 726.7) and peaks of Li^+-containing adducts [M − 1 + Li], [M − 1 − 26 + Li], and [M − 1 − 28 + Li] (corresponding *m/z* values are 774.7, 748.5, and 746.5).

Table 1. Kinetic Parameters of Primer Elongation Catalyzed by DNA Polymerase *β*

case	k_{cat}, s^{-1}	$K_m \times 10^5$, M
as analogue of dCTP (PT1)	0.33 ± 0.04	1 ± 0.5
as analogue of dTTP (PT2)	0.005 ± 0.0005	3 ± 1.5

in this case were comparable, that is, the Michaelis−Menten approximation does not hold, the kinetic parameters of FAP-dCTP incorporation as an analogue of dTTP should be regarded only as a crude estimate.

K_m values for FAP-dCTP are rather close on both template−primer duplexes and differ insignificantly from K_m values for dCTP and dTTP, which were determined in refs *9* and *11*, respectively. K_m values for FABO-dCTP and FABC-dCTP were 10-fold higher than that of dCTP (*9*). When these analogues were used as dTTP, a 10-fold increase in K_m values in comparison with that for dTTP was also detected (*11*). Unlike dCTP derivatives bearing FABO or FABC groups, FAP-dCTP appears not to face steric hindrance in the interactions with the enzyme binding site. k_{cat} values for FAP-dCTP differ 65-fold depending on the template−primer duplex. When FAP-dCTP replaced dCTP, the k_{cat} value was in close agreement with that of dCTP (*9*). Thus, FAP-dCTP displays the best substrate properties among all photoreactive dCTP derivatives synthesized by us until now. When FAP-dCTP was used as dTTP the k_{cat} value was substantially lowered. DNA polymerase β appears to recognize FAP-dCTP in this case as an incorrect dNTP. Such a behavior conforms to the mechanism that is responsible for Pol β fidelity. DNA polymerase β provides dNTP selection mainly at the step of phosphodiester bond formation, but this enzyme can also discriminate between the correct and incorrect dNTP during stage of nucleotide binding (*19*).

Photoaffinity Modification of Pol *β*. We characterized all previously synthesized photoreactive dNTP analogues in their ability to cross-link Pol β when they were incorporated at the 3′ end of primers (*9, 10, 11*). To study the efficiency of FAP-dCMP-containing DNA as a photoreagent for protein modification, we used the same approach. We studied kinetics of the covalent attachment of photoreactive primer to Pol β. FAP-dCMP moieties were introduced in situ by Pol β using both template−

Scheme 2. Catalytic and Direct Pathways of Photoaffinity Modification of Pol β

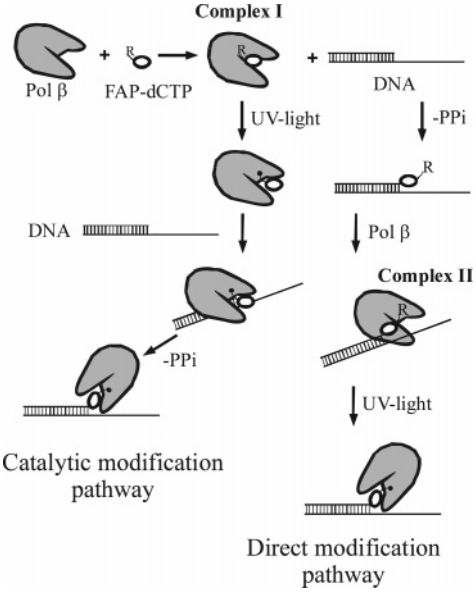

primer duplexes PT1 and PT2. Molar ratio of template−primer duplex to Pol β and their concentrations provided practically complete binding of DNA duplex by Pol β. Under these conditions, the unproductive photolysis of photoreactive DNA in solution, which does not lead to formation of covalent adducts with Pol β, is minimized.

When FAP-dCTP was used as dCTP analogue, that is, on PT1, the efficiency of primer elongation prior to UV-irradiation was more than 90%. The kinetics of formation of covalent adducts of photoreactive primer with Pol β and the template strand fitted the exponential equation of the first order as was the case with other photoreactive dNTP derivatives (*10, 11*). We have estimated the rate constant of formation of covalent adducts and half-time of Pol β modification. The obtained values were shown to be similar to those for photoreactive primers with FAP-dUMP moiety bearing the same photoreactive group (*10*).

When FAP-dCTP was used as dTTP, that is, on PT2, the yield of cross-linking of photoreactive primer to Pol β was abnormal. The level of cross-linking (W_r) was 43% and exceeded the extent of conversion of the initial primer to the photoreactive form, which was less than 25%. This fact prompted us to propose that the additional amount of the covalent adducts of Pol β with the photoreactive primer was formed by an unusual pathway. The conventional pathway proceeds via prior incorporation of photoreactive dNMP moiety into the 3′ end of the primer followed by UV-light-induced cross-linking of photoreactive DNA to the protein. But, in the last unusual case, the process appears to proceed via the following steps (Scheme 2): first, cross-linking of photoreactive dCTP analogue to dNTP binding site of Pol β and, second, rather fast transfer of dNMP moiety onto the 3′ end of the primer from the dCTP analogue, which is covalently attached to the enzyme surface.

Such a way of Pol β labeling by using a similar photoreactive analogue of dCTP was suggested by us earlier (*20*). This pathway appears to provide the surplus in the level of covalent adduct formation.

To prove this proposal, we compared the rates of the primer elongation by Pol β and the cross-linking of the photoreactive primer to the enzyme. When FAP-dCTP was used as dTTP analogue, the rate of the primer elongation was approximately 10 times lower than the rate of cross-linking (data not shown). The rate of the primer elongation when FAP-dCTP was used as dCTP analogue was too high at the used concentration of Pol β to register the contribution of the second pathway. Thus, the more efficient covalent adducts Pol β−DNA primer formation appears to occur via saturation of dNTP binding site with the covalently attached dCTP analogue, from which a dCMP residue is transferred to the 3′ end of the primer.

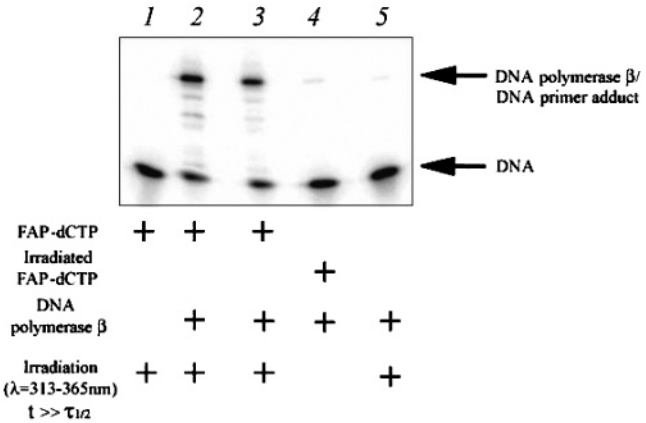

Figure 3. SDS−PAGE analysis of products of Pol β photoaffinity labeling: lane 1, no Pol β; lanes 2 and 3, direct and catalytic adduct formation, respectively; lane 4, FAP-dCTP irradiated (15 min) prior to addition to the reaction mixture; lane 5, no FAP-dCTP.

Table 2. Parameters of FAP-dCTP as Photoreagent

case	k, min^{-1}	x, %	W_R, %	W_r, %	W_{DNA},%
as analogue of dCTP (PT1)	0.23 ± 0.05	70 ± 2	57 ± 5	40 ± 5	*a*
as analogue of dTTP (PT2)	0.55 ± 0.2	20 ± 2	*b*	43 ± 2	10 ± 2

[a] Not determined. [b] Not applicable.

The additional argument for the proposed mechanism comes from the experiments where Pol β was UV-irradiated in the presence of FAP-dCTP with the reaction mixtures being devoid of DNA duplex during UV-irradiation. After completion of irradiation, the reaction mixtures were supplemented with DNA duplex and further incubated. The following analysis revealed the efficient formation of the covalent adducts. The data are presented in Figure 3. The amounts of DNA−protein adducts formed in each of the pathways are comparable, which speaks in favor of the essential contribution of catalytic labeling of Pol β in the total level of its modification.

Covalent fixation of a dNTP analogue in the active site of Pol β probably allows the enzyme to skip the stage of selection of the complementary dNTP. The transfer of the NAB-dUMP moiety from the dUTP analogue covalently fixed in the active site of Pol β onto the 3′ end of the oligonucleotide in a DNA duplex with a blunt end, that is, without a templating base, was shown by us earlier (*21*).

The data on the efficiency of Pol β modification are listed in Table 2. The relative efficiency (W_R) of cross-linking, that is, the part of photoreactive DNA primer cross-linked to Pol β, was the highest achieved so far with any photoreactive analogue used by us, although when FAP-dCTP was used as dTTP, the value of the relative efficiency is ill-defined due to the considerable contribution of catalytic modification of Pol β in the total level of the modification. Therefore, the W_R value (the amount of photoreactive primer cross-linked to Pol β normalized

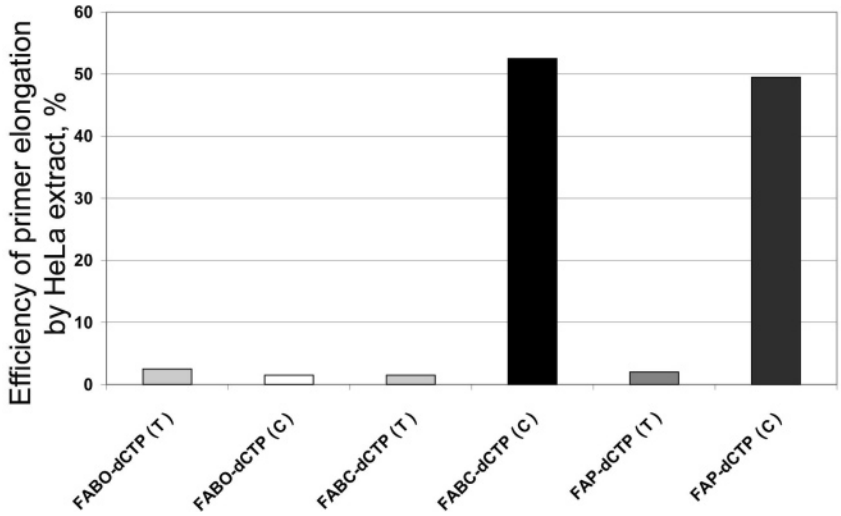

Figure 4. Efficiencies of incorporation of different dCTP analogues by endogenous DNA polymerases of HeLa cell extract. Letters in parentheses designate as what deoxynucleoside triphosphate dCTP or dTTP the analogue was used.

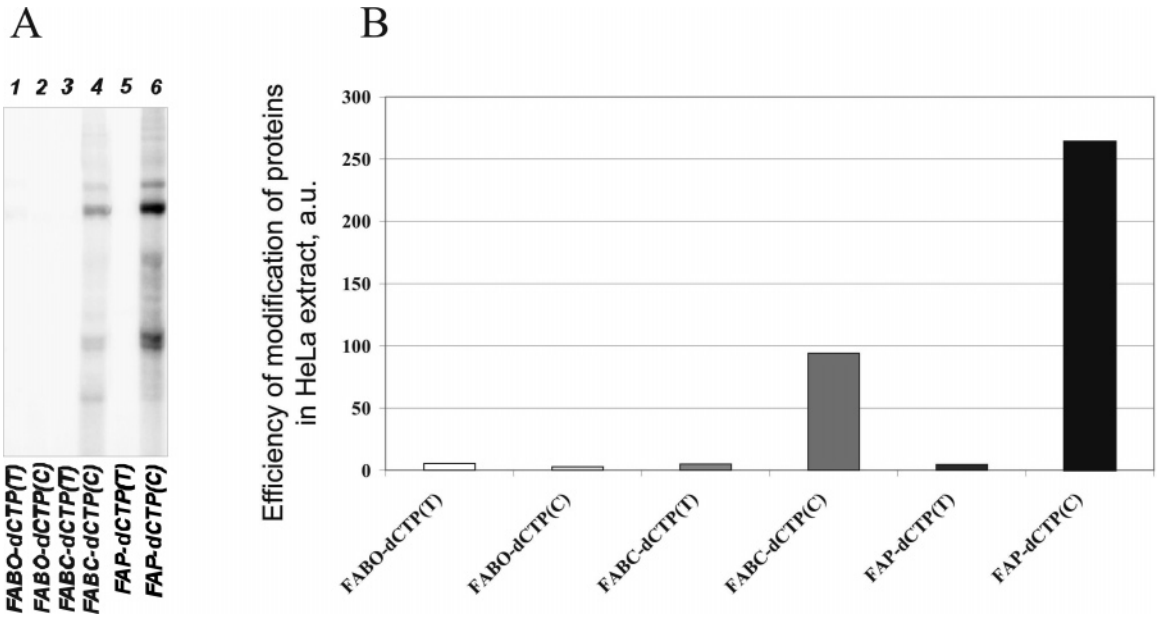

Figure 5. SDS−PAGE analysis (A) of products of photo-cross-linking of DNA binding proteins in HeLa cell extract by photoreactive DNAs synthesized in situ by endogenous DNA polymerases with different dCTP analogues as substrates and efficiencies of protein labeling (B) in HeLa cell extract by photoreactive DNAs (a.u. = arbitrary units). Letters in parentheses designate as what deoxynucleoside triphosphate dCTP or dTTP the analogue was used.

on the amount of the photoreactive primer synthesized prior to irradiation) is not shown in the Table 2. However, the W_r value directly determined from the experiment is rather high in comparison with the primers bearing other photoreactive dCMP moieties.

When FAP-dCMP was placed opposite an adenosine of the template chain, the modification of the template did not practically occurred. Location of FAP-dCMP moiety opposite the template guanosine residue resulted in less than 10% cross-linking of the photoreactive primer to the complementary template chain. The levels of the template modification containing A or G opposite FAP-dCMP correlates with the nucleophilicity of these bases. Rather low levels of the template modification were also observed in the case of FABC-dCMP and FABO-dCMP primers (*11*). Thus, these analogues can be considered as protein-directed reagents.

Thus, newly synthesized FAP-dCTP displays the best substrate characteristics among dCTP analogues in primer elongation catalyzed by Pol β and provides the highest level of Pol β modification achieved for any photoreactive dNTP derivatives synthesized and used by us until now.

Application of FAP-dCTP in Cell Extract. The most easy-to-use and adequate way to synthesize photoreactive probes is the in situ introduction of photoreactive dNMP moieties into DNA via activity of endogenous DNA polymerases using photoreactive dNTP analogues as substrates. In cell extracts, where the concentrations of DNA polymerases are rather low, the poor substrate properties of dNTP analogues may become the limiting factor in DNA synthesis, which, in turn, restricts the applicability of the analogue in these systems. We demonstrated good substrate properties of FAP-dCTP in the primer elongation catalyzed by Pol β, but in cell extracts the efficiency of incorporation of photoreactive moieties into DNA can be modulated by the presence of other DNA polymerases and proteins, which can influence the activity of Pol β. Therefore, the most adequate way to estimate the potential of the analogue as a reagent

for the in situ synthesis of photoreactive DNA probes in cell extracts is the direct measurement of the efficiency of its incorporation. We compared the efficiencies of incorporation of photoreactive dCMP moieties into DNA in HeLa cell extract using FAP-dCTP, FABO-dCTP, and FABC-dCTP as substrates. DNA containing FABO-dCMP and FABC-dCMP residues provide efficient cross-linking to Pol β, but corresponding dCTP analogues vary substantially in their substrate properties as dCTP or dTTP analogues in DNA synthesis catalyzed by Pol β (*9, 11*). Both FABC-dCTP and FABO-dCTP were used as dTTP to synthesize DNA probes for photoaffinity modification of proteins in HeLa cell extract (*11*). FABC-dCTP was shown to be less efficient in protein labeling than FABO-dCTP, but the data were not quantified. Here we quantitatively compare the levels of incorporation of these three analogues and efficiencies of photoaffinity modification of DNA binding proteins in HeLa cell extract by DNA synthesized in situ. The data on the efficiencies of analogue incorporation both as dCTP and dTTP by endogenous DNA polymerases in HeLa cell extract are presented in Figure 4.

FAP-dCTP and FABC-dCTP were rather efficiently incorporated as dCTP analogues, but considerably worse when used as dTTP. FABO-dCTP was rather inefficient in the extract both as dCTP and dTTP.

Photoreactive DNAs synthesized in situ were used for photoaffinity modification of DNA binding proteins in HeLa extract. A pattern of protein modification in HeLa cell extract is shown in Figure 5A. Quantitative estimation of the efficiencies of protein cross-linking to photoreactive DNA synthesized on the basis of different photoreactive dCTP analogues clearly demonstrates that the efficiencies are determined by the levels of analogue incorporation (Figure 5B). The yield of cross-linking products also depends on the type of photoreactive group. For example, FAP-dCTP and FABC-dCTP were incorporated as dCTP with comparable efficiencies, but DNA primer containing FAP-dCMP provided at least 2.5-fold higher level of protein labeling. Analogous dependencies of the efficiencies of protein labeling in HeLa cell extract on substrate properties of the analogues and the types of photoreactive groups were demonstrated for the set of photoreactive dUTP analogues (*11*).

The patterns of protein labeling were rather similar for all three analogues except the efficiency of cross-linking. Thus, the performance requirements for photoreactive dNTP analogues depend on the system, in which the analogues are planned to be used; and in the systems with limited DNA polymerase activities, the substrate characteristics of the analogues in DNA synthesis become very important. Taking together, the data clearly shows that newly synthesized FAP-dCTP possessing the best substrate and photochemical characteristics among the photoreactive dNTP analogues synthesized by us until now meets the requirements to be applied to the systems reconstituted from purified proteins and crude cellular extracts.

ACKNOWLEDGMENT

The work was supported by grants from the Russian Foundation for Basic Research, Project Nos. 04-04-48525, 03-04-48562, and 04-03-32490, and by a grant from HFSP, No. RG0007/2004-C104. We thank Dr. Vladimir Koval for recording the MALDI-MS.

LITERATURE CITED

(1) Safronov, I. V., Shcherbik, N. V., Khodyreva, S. N., Vlasov, V. A., Dobrikov, M. I, Shishkin, G. V., and Lavrik, O. I. (1997)- New photoreactive N^4-substituted dCTP analogues: Preparation, photochemical characteristics, and substrate properties in HIV-1 reverse transcriptase-catalyzed DNA synthesis. *Russ. J. Bioorgan. Chem. 23*, 531−539.

(2) Wlassoff, W. A., Dobrikov, M. I., Safronov, I. V., Dudko, R. Y., Bogachev, V. S., Kandaurova, V. V., Shishkin, G. V., Dymshits, G. M., and Lavrik, O. I. (1995) Synthesis and characterization of (d)NTP derivatives substituted with residues of different photoreagents. *Bioconjugate Chem. 6*, 352−360.

(3) Kolpashchikov, D. M., Ivanova, T. M., Bogachev, V. S., Nasheuer, H. P., Weisshart, K., Favre, A., Pestryakov, P. E., and Lavrik, O. I. (2000) Synthesis of base-substituted dUTP analogues carrying a photoreactive group and their application to study human replication protein A. *Bioconjugate Chem. 11*, 445−451.

(4) Lavrik, O. I., Kolpashchikov, D. M., Weisshart, K., Nasheuer, H.-P., Khodyreva, S. N., and Favre, A. (1999) RPA subunit arrangement near the 3'-end of the primer is modulated by the length of the template-strand and cooperative protein interactions. *Nucleic Acids Res. 27*, 4235−4240.

(5) Kolpashchikov, D. M., Hughes, P., Favre, A., Baldacci, G., and Lavrik, O. I. (2001) Localization of the large subunit of replication factor C near the 5′ end of DNA primers. *J. Mol. Recognit. 14*, 239−244.

(6) DellaVecchia, M. J., Croteau, D. L., Skorvaga, M., Dezhurov, S. V., Lavrik, O. I., and Van Houten, B. (2004) Analyzing the handoff of DNA from UvrA to UvrB utilizing DNA-protein photoaffinity labeling. *J. Biol. Chem.*, in press.

(7) Doerhoefer, S., Khodyreva, S., Safronov, I. V., Wlassoff, W. A., Anarbaev, R., Lavrik, O. I., and Holler, E. (1998) Molecular constituents of the replication apparatus in the plasmodium of *Physarum polycephalum*: identification by photoaffinity labeling. *Microbiology 144*, 3181−3193.

(8) Lebedeva, N. A., Rechkunova, N. A., Khodyreva, S. N., Favre, A., and Lavrik, O. I. (2002) Photoaffinity labeling of proteins in bovine testis nuclear extract. *Biochem. Biophys. Res. Commun. 297*, 714−721.

(9) Drachkova, I. A., Petruseva, I. O., Safronov, I. V, Zakharenko, A. L., Shishkin, G. V., Lavrik, O. I., and Khodyreva, S. N. (2001) Reagents for modification of protein-nucleic acid complexes: Site-specific photomodification of mammalian DNA polymerase β complexes with primers extended by dCTP *exo-N*-substituted arylazido derivatives. *Russ. J. Bioorgan. Chem. 27*, 173−179.

(10) Dezhurov, S. V., Khodyreva, S. N., Rechkunova, N. I., Kolpaschikov, D. M., and Lavrik, O. I. (2003) A comparative study of the modification efficiency of DNA polymerases and DNA template by the DNA Primers with various photoreactive groups at their 3′- termini. *Russ. J. Bioorgan. Chem. 29*, 75−82.

(11) Dezhurov, S. V., Grin, I. R., Safronov, I. V., Shishkin, G. V., Lavrik, O. I., and Khodyreva, S. N. (2004) High-efficiency modification of DNA-polymerase β under conditions of direct and sensitized activation of photoreactive DNA. Modification of proteins of cellular extract. *Russ. Chem. Bull.*, in press.

(12) Lavrik, O. I., Prasad, R., Sobol, R. W., Horton, J. K., Ackerman, E. J., and Wilson, S. H. (2001) Photoaffinity labeling of mouse fibroblast enzymes by a base excision repair intermediate. Evidence for the role of poly(ADP-ribose) polymerase-1 in DNA repair. *J. Biol. Chem. 276*, 25541−25548.

(13) *Protocols and Applications Guide* (1991) pp 150−152, Promega, Madison, WI.

(14) Maniatis, T. (1989) *Molecular cloning: a laboratory manual*, Cold Spring Harbor University Press, Cold Spring Harbor, NY.

(15) Beard, W. A., and Wilson, S. H. (1995) Purification and domain-mapping of mammalian DNA polymerase beta. *Methods Enzymol. 262*, 98−107.

(16) Biade, S., Sobol, R. W., Wilson, S. H., and Matsumoto, Y. (1998) Impairment of proliferating cell nuclear antigen-dependent apurinic/apyrimidinic site repair on linear DNA. *J. Biol. Chem. 273*, 898−902.

(17) Laemmli, U.K. (1970) Cleavage of structural proteins during the assembly of the head of bacteriophage T4. *Nature 277*, 680−685.

(18) Chen, X., Siems, W. F., Asbury, G. R., and Yount, R. G. (1999) Fingerprint patterns from laser-induced azido photochemistry of spin-labeled photoaffinity ATP analogues in matrix-assisted laser desorbtion/ionization mass spectrometry. *J. Am. Soc. Mass Spectrom. 10*, 1337−1340.
(19) Sweasy, J. B. (2003) Fidelity mechanisms of DNA polymerase beta. *Prog. Nucleic Acid Res. Mol. Biol*. *73*, 137−169.
(20) Lavrik, O. I., Prasad, R., Beard, W. A., Safronov, I. V., Dobrikov, M. I., Srivastava, D. K., Shishkin, G. V., Wood, T. G., and Wilson, S. H. (1996) dNTP binding to HIV-1 reverse transcriptase and mammalian DNA polymerase beta as revealed by affinity labeling with a photoreactive dNTP analogue. *J. Biol. Chem. 271*, 21891−21897.
(21) Lavrik, O. I., Zakharenko, A. L., Prasad, R., Vlasov, V. A., Bogachev, V. S., and Favre, A. (1998) dNTP, covalently bound to DNA polymerases through a base, active in nucleotidyl transfer reactions. *Mol. Biol. (Mosk.) 32*, 621−628.

BC0497867

Synthesis and Characterization of Poly(ethylene oxide)-*block*-poly(methylidene malonate 2.1.2) Block Copolymers Bearing a Mannose Group at the PEO Chain End

Peggy Studer,[†,‡] David Limal,[†,‡] Pascal Breton,[†] and Gérard Riess*[,‡]

VIRSOL, 46 Rue Boissière, 75116 Paris, France, and Laboratoire de Chimie Macromoléculaire, Ecole Nationale Supérieure de Chimie de Mulhouse/Institut de Chimie des Surfaces et Interfaces, 3 Rue Alfred Werner, 68200 Mulhouse, France. Received August 13, 2004; Revised Manuscript Received December 3, 2004

A poly(ethylene oxide)-*block*-poly(methylidene malonate 2.1.2) block copolymer (PEO-*b*-PMM 2.1.2) bearing a mannose moiety at the poly(ethylene oxide) chain end was synthesized by sequential anionic polymerization of ethylene oxide (EO) and methylidene malonate 2.1.2 (MM 2.1.2), followed by a coupling reaction between its poly(ethylene oxide) amino- or aldehyde-end group and a sugar derivative. Different coupling procedures, either in organic media or in aqueous micellar solutions, were examined in order to optimize the poly(ethylene oxide) end-glycosylation yield. The micellar size of the functionalized block copolymers was determined by dynamic light scattering.

INTRODUCTION

There is a growing interest in the development of novel drug delivery systems to reach an increased bioavailability of drugs with controlled release profiles to the targeted cells and to reduce their side effects, especially in the field of cancer chemotherapy (*1, 2*). To this aim, biocompatible amphiphilic block copolymers, which have the tendency to self-assemble into micelles in a selective solvent, can be utilized as potential carriers for hydrophobic drugs or other bioactive molecules (*3*−*7*). The good water solubility properties, the biocompatibility, and the lack of immunogenicity of poly(ethylene oxide) (PEO) provide these nanostructures with a suitable outer corona of PEO that prevents protein adsorption and cell adhesion, which are the first steps before their uptake by the mononuclear phagocyte system and their rapid blood clearance (*8*). The drug release kinetics being affected by the drug/polymer interactions as well as by the polymer microstructure and erosion/degradation properties, the chemical composition, and architecture of the polymers have to be tailored to accommodate drugs with varying hydrophobicity, molecular weight, etc. The polymer matrixes and particularly the hydrophobic block have to be chosen in order to achieve the desired biocompatibility, polymer degradation and/or erosion, and drug release kinetics. The synthetic degradable polymers used for biomedical applications are typically poly(amino acids), poly(esters), and poly(anhydrides) with hydrolyzable bonds along the backbone (*9*). Another category of biocompatible polymers bears enzymatically cleavable side chains leading to water-soluble polymers through a bioerosion mechanism. These bioerodible polymers can be poly(cyanoacrylates) (PACA) (*10*) or poly(methylidene malonate 2.1.2) (PMM 2.1.2). The latter is prepared by polymerization of 1-ethoxycarbonyl-1-ethoxycarbonylmethylenoxycarbonyl ethene (MM 2.1.2, Scheme 1) and has been shown to be less toxic than PACA (*11, 12*).

Scheme 1. Structure of Methylidene Malonate 2.1.2 (MM 2.1.2) and of the Mannose Derivatives a and b

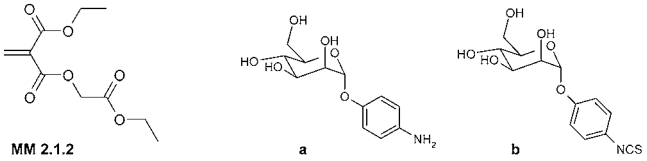

More recently, it has been proposed to introduce reactive groups on the surface of this kind of polymeric micelles and to use them as a basic system for active targeting (*4, 13*). Thus, PEGylation chemistry is retaining more and more attention in the field of biomedical materials (*14*−*16*). To improve the potential utility of polymeric micelles for drug targeting, Nagasaki et al. (*17*) reported the functionalization of the outer surface of the micelle by an easy and quantitative method allowing the synthesis of heterobifunctional poly(ethylene oxide) and block copolymers such as poly(ethylene oxide)-*b*-poly(D,L-lactide) (PEO-*b*-PDLLA), poly(ethylene oxide)-*b*-poly(dimethylaminoethyl methacrylate) (PEO-*b*-PDMAEMA) and many others. By using a sugar derivative as an initiator, the authors also developed a novel one-pot synthesis of PEO-*b*-PDLLA block copolymers bearing one sugar end-group, like glucosyl or galactosyl, at the PEO chain end (*18, 19*). Indeed, by an adequate protection of four out of five hydroxyl groups, a retained hydroxyl group can be used as an initiator for the monosaccharide-induced EO polymerization.

As the synthesis of nonfunctionalized PEO-*b*-PMM 2.1.2 is already known using diphenylmethylpotassium as an initiator (*20, 21*), the aim of this study was to develop a novel route to prepare functionalized PEO-*b*-PMM 2.1.2 block copolymers allowing the coupling of various ligands such as sugars (*22*), peptides (*23*), folic acid (*24*), fluorescent markers (*25*), etc. Our main purpose was to develop α-functionalized PEO-*b*-PMM 2.1.2 block copolymers and to demonstrate the reactivity of these

* To whom correspondence should be addressed. Tel +33-3-89-33-68-54; fax +33-3-89-33-68-54; e-mail: gerard.riess@uha.fr.
† VIRSOL.
‡ Ecole Nationale Supérieure de Chimie de Mulhouse/Institut de Chimie des Surfaces et Interfaces.

10.1021/bc0498065 CCC: $30.25 © 2005 American Chemical Society
Published on Web 12/24/2004

Scheme 2. Synthetic Route to α-Amino and α-Aldehyde-Functionalized PEO-*b*-PMM 2.1.2 Copolymers 1 and 3

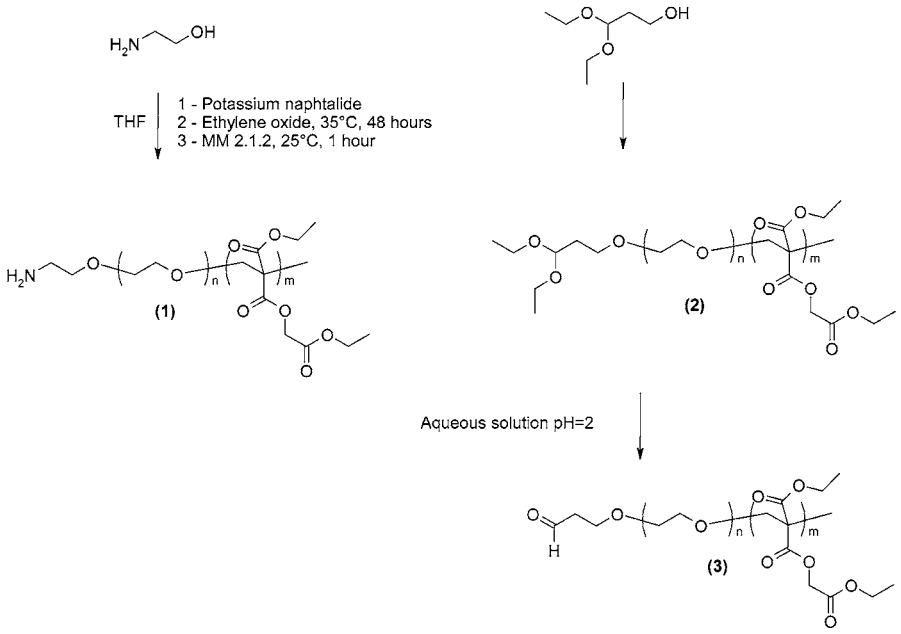

PEO end functions, so that the latter are enabled to carry out the ligand-anchoring with targeting agents such as a mannosyl residue. In the present study, a mannose moiety was conjugated through two different coupling procedures, either in aqueous micellar solutions or in organic solvents, to the α-amino and α-aldehyde reactive PEO end groups of the PEO-*b*-PMM 2.1.2 block copolymers, which were introduced during the initiation step.

EXPERIMENTAL PROCEDURES

Materials. All the reagents and chemicals used in this study were of the highest purity available. THF was purified using conventional methods (*20*). 2-Aminoethanol (Aldrich) was purified by distillation under CaH_2. The sodium phosphate buffer solution pH 7.0 was prepared as described by Yamamoto et al. (*13*). A 100 mL sodium carbonate buffer solution pH 9.5 was prepared as follows: 4.8 mL of a 0.2 M sodium carbonate solution and 20.3 mL of a 0.2 M sodium bicarbonate solution were diluted to 100 mL with distilled water. Methylidene malonate 2.1.2, prepared according to the Bru-Magniez et al. procedure (*26*), was kept under sulfur dioxide at −20 °C. Potassium naphthalide was prepared by the method of Scherf et al. (*27*), and its concentration (0.3 M) was determined by titration.

Preparation of the Sugar Derivatives. Sugar derivatives were prepared by combining different reaction steps described in the literature (*28*−*31*). (4-Aminophenyl)-α-D-mannopyranose **a** (Scheme 1) was obtained through a four-step synthesis (*29*). Briefly, mannose acylation according to Lerner et al. (*28*) consisted of the protection of the hydroxyl groups in positions 2, 3, 4, and 6 of α-D-mannopyranose, thus allowing the introduction on position 1 of the *p*-nitrophenyl group as described by Smits et al. (*30*). Deprotection of the hydroxyl groups was achieved on an Amberlyte resin, followed by a catalytic hydrogenolysis on Pd/C (*31*) that gave **a** with a global yield of 20%. As described by Monsigny et al. (*31*), (4-isothiocyanatophenyl)-α-D-mannopyranose **b** (Scheme 1) was obtained with a 94% yield by the reaction of **a** with thiophosgene.

Polymer Characterization. ^1H and ^{13}C NMR spectra were recorded in $CDCl_3$ using a Bruker AC 250F spectrometer, respectively, at 250 and 62.9 MHz. Gel permeation chromatography measurements were performed by using a Waters 2690 Alliance system equipped with a sequence of Waters Styragel HR4, HR1 and HR0.5 columns and an internal RI Waters 410 detector (flow rate = 1 mL/min). THF was used as an eluant, and standards were poly(ethylene oxide) and poly(styrene).

Preparation and Characterization of the Polymeric Micelles. The procedure for micelle formation has been described previously (*20*). Briefly, 25 mg of copolymer was dissolved in 5 mL of a mixture THF/water 1/1 (v/v), and the polymer solution was transferred into a preswollen membrane SpectraPor 7 (molecular weight cut-off: 1000) and dialyzed against water for 24 h. The mean diameter of the polymeric micelles was determined by dynamic light scattering using a Coulter N4 Plus particle size analyzer (Coultronics).

Synthesis of α-Amino PEO-*b*-PMM 2.1.2 Block Copolymers (1) (Scheme 2). Polymerizations were carried out under nitrogen atmosphere in reactors equipped with a magnetic stirring device. As described by Mosquet et al. (*32*) for PEO, a typical procedure for the synthesis of the amino-bearing PEO-*b*-PMM 2.1.2 block copolymers **1** was as follows: 3.3 mL of potassium naphthalide solution (1 mmol) was added to 150 mL of dry THF containing 1 mmol (60 μL) of 2-aminoethanol to prepare the insoluble metalated alcoholate initiator. Afterward, this heterogeneous system was stirred for 5 min, and then 114 mmol (5 g) of EO was added via a sealed ampule to the THF solution containing the initiator. The polymerization of EO was carried out at 35 °C for 2 days. The PEO solution was then divided into two equivalent parts. The first one was deactivated by a small amount of methanol and kept for the determination of the molecular weight, the polydispersity, and the end functionality of the PEO thus prepared. A degassed MM 2.1.2 in THF solution (1 g/15 mL) was quickly introduced under efficient stirring into the second reaction vessel, resulting in the discoloration of the solution, and the reaction was carried out for an additional 1 h at room temperature. After the polymerization was stopped by the addition of a few drops of methanol, the mixture was then concentrated under reduced vacuum and finally precipitated

into a large amount of diethyl ether. The precipitated polymer was collected by filtration and dried under vacuum at room temperature (yield = 95%). *HO-PEO-NH_2 Homopolymer.* GPC (THF, PEO standards): number-average molecular weight (M_n) = 4470; weight-average molecular weight (M_w) = 5810; polydispersity index (I_p) = 1.30. ^{1}H NMR (250 MHz, $CDCl_3$, δ in ppm): 2.85 (t, CH_2NH_2, 2H), 3.60 (m, CH_2 of PEO, 4H). ^{13}C NMR (62.9 MHz, $CDCl_3$, δ in ppm): 41.6 (CH_2NH_2), 60.1 (CH_2OH), 70.0 (CH_2 of PEO), 72,3 (CH_2 in β position of OH), 73.3 (CH_2 in β position of NH_2). End functionality = 98%. *PMM 2.1.2-b-PEO-NH_2 Copolymer.* GPC (THF, PS standards): polydispersity index (I_p) = 1.32. ^{1}H NMR (250 MHz, $CDCl_3$, δ in ppm): 1.30 (m, CH_3 of PMM 2.1.2, 6H), 2.80 (m, CH_2 of the main chain of PMM 2.1.2, 2H), 3.60 (m, CH_2 of PEO, 4H), 4.10 (m, CH_2 of CH_2CH_3 of PMM 2.1.2, 4H), 4.50 (m, CH_2 of PMM 2.1.2, 2H). End functionality = 98%.

Synthesis of α-Acetal PEO-*b*-PMM 2.1.2 Block Copolymers (2) (Scheme 2). As reported by Yamamoto et al. (*13*) for PEO-*b*-PDLLA block copolymers, the synthesis of α-acetal-PEO-*b*-PMM 2.1.2 block copolymers **2** was as follows: 4.1 mL of potassium naphthalide (1.25 mmol) was added to 150 mL of dry THF containing 1.25 mmol (197 μL) of 3,3-diethoxypropan-1-ol to prepare the soluble metalated alcoholate initiator. After this mixture was stirred for 5 min, 114 mmol (5 g) of EO was then added via a sealed ampule to the THF solution containing the initiator. The polymerization of EO was carried out as described above. After dividing the solution into two equivalent parts, a degassed MM 2.1.2 in THF solution (4 g/15 mL) was quickly introduced under vigorous stirring into the second reaction vessel, and the reaction was carried out for an additional 1 h at room temperature. The polymerization was then stopped and the purification of the polymer was carried out as described before (yield = 95%). *HO-PEO-acetal Homopolymer.* GPC (THF, PEO standards): number-average molecular weight (M_n) = 4200; weight-average molecular weight (M_w) = 4960; polydispersity index (I_p) = 1.18. ^{1}H NMR (250 MHz, $CDCl_3$, δ in ppm): 1.18 (t, CH_3, 6H), 1.88 (q, CH_2, 2H), 3.60 (m, CH_2 of PEO, 4H), 4.62 (t, CH, 1H). ^{13}C NMR (62.9 MHz, $CDCl_3$, δ in ppm): 15.3 (CH_3), 34.0 (CH_2), 60.1 (CH_2OH), 61.4 (CH_2 of CH_2CH_3), 61.5 (CH_2O), 70 (CH_2 of PEO), 72.3 (CH_2 in β position of OH), 100.5 (CH). End functionality = 98%. *PMM 2.1.2-b-PEO-acetal Copolymer.* GPC (THF, PS standards): polydispersity index (I_p) = 1.32. ^{1}H NMR (250 MHz, $CDCl_3$, δ in ppm): 1.18 (t, CH_3, 6H), 1.30 (m, CH_3 of PMM 2.1.2, 6H), 1.88 (q, CH_2, 2H), 2.80 (m, CH_2 of the main chain of PMM 2.1.2, 2H), 3.60 (m, CH_2 of PEO, 4H), 4.10 (m, CH_2 of CH_2CH_3 of PMM 2.1.2, 4H), 4.50 (m, CH_2 of PMM 2.1.2, 2H), 4.62 (t, CH, 1H). End functionality = 95%.

Synthesis of α-Aldehyde PEO-*b*-PMM 2.1.2 Block Copolymers (3) (Scheme 2). An aqueous micellar solution of the acetal-PEO-*b*-PMM 2.1.2 copolymer **2** was prepared as described above, and the acetal group was transformed into an aldehyde group by acid treatment as follows: the aqueous solution of α-acetal-PEO-*b*-PMM 2.1.2 micelles was acidified to pH 2.0 by 1 N HCl added dropwise. After being stirred for 2 h at room temperature, the solution was neutralized by 0.1 N NaOH. The micellar solution was then desalted by dialysis against water. After 24 h, the micelles were then freeze-dried. *HO-PEO-CHO Homopolymer.* GPC (THF, PEO standards): number-average molecular weight (M_n) = 4290; weight-average molecular weight (M_w) = 5060; polydispersity index (I_p) = 1.18. ^{1}H NMR (250 MHz, $CDCl_3$, δ in ppm): 2.67 (td, CH_2CHO, 2H), 3.60 (m, CH_2 of PEO, 4H), 9.77 (t, CHO, 1H). ^{13}C NMR (62.9 MHz, $CDCl_3$, δ in ppm): 43.6 (CH_2), 60.1 (CH_2OH), 64.6 (CH_2O), 70.0 (CH_2 of PEO), 72.3 (CH_2 in β position of OH), 201.0 (CHO). End functionality = 87%. *PMM 2.1.2-b-PEO-CHO Copolymer*. GPC (THF, PS standards): polydispersity index (I_p) = 1.30. ^{1}H NMR (250 MHz, $CDCl_3$, δ in ppm): 1.30 (m, CH_3 of PMM 2.1.2, 6H), 2.67 (td, CH_2-CHO, 2H), 2.80 (m, CH_2 of the main chain of PMM 2.1.2, H), 3.60 (m, CH_2 of PEO, 4H), 4.10 (m, CH_2 of CH_2-CH_3 of PMM 2.1.2, 4H), 4.50 (m, CH_2 of PMM 2.1.2, 2H), 9.77 (t, CHO, 1H). End functionality = 95%.

Table 1. Coupling Reactions Yields between Copolymer 1 and (4-Isothiocyanatophenyl)-α-D-mannopyranose b According to Experimental Conditions (Procedure A)

run	reaction medium	[**b**]/[(1)] (mol/mol)	α-end functionalization yield (%)[a]
1	micellar solution[b]	5	18
2		10	18
3		25	21
4	THF	10	40
5		25	59
6	DMF	10	23
7		25	40

[a] Coupling reaction with MM 2.1.2$_{(7)}$-EO$_{(102)}$-NH_2 block copolymer end functionalization yield = 98%. [b] Carbonate buffer pH 9.5.

Coupling of Mannosyl Derivatives to α-Amino PEO-*b*-PMM 2.1.2 or α-Aldehyde PEO-*b*-PMM 2.1.2 Copolymers 1 and 3. *Procedure A: Synthesis of Mannosylated PEO-b-PMM 2.1.2 Block Copolymers **4** by Conjugation between the Copolymer 1 and (4-Isothiocyanatophenyl)-α-D-mannopyranose **b** (Table 1).* In a buffer solution pH 9.5*:* A typical procedure for coupling H_2N-PEO-*b*-PMM 2.1.2 copolymer **1** to an isothiocyanate-bearing mannosyl derivative was as follows: a solution of 150 mg of copolymer **1** in 12 mL of *N*,*N*-dimethylacetamide was dialyzed against a carbonate buffer solution pH 9.5. Subsequently, 5, 10, and 25 mol equiv per polymer of **b** were added to the micellar solution, which was stirred for 24 h at room temperature. The micelle solutions were then dialyzed against water for 24 h and finally lyophilized. In organic solvent*:* **1** (150 mg) was dissolved in 20 mL of DMF or THF. Subsequently, 10 and 25 mol equiv per polymer of **b** and 50 mol equiv per polymer of *N*-methylmorpholine were added to the mixture. After a one-day reaction, unreacted mannosyl derivatives were removed from the solution by dialysis for 24 h. The micelle solutions were collected and lyophilized. ^{1}H NMR (250 MHz, $CDCl_3$, δ in ppm): 1.30 (m, CH_3 of PMM 2.1.2, 6H), 2.80 (m, CH_2 of the main chain of PMM 2.1.2, 2H), 3.60 (m, CH_2 of PEO, 4H), 4.10 (m, CH_2 of CH_2CH_3 of PMM 2.1.2, 4H), 4.50 (m, CH_2 of PMM 2.1.2, 2H), 5.40 (d, H_{ano}, 1H), 7.10 (d, aromatics, 2H), 7.22 (d, aromatics, 2H).

*Procedure B: Synthesis of Mannosylated PEO-b-PMM 2.1.2 Block Copolymers **5** by Reductive Amination between Copolymer 3 and (4-Aminophenyl)-α-D-mannopyranose **a*** (Table 2). In buffer solution pH 7.0*:* A typical procedure for the coupling of OHC-PEO-*b*-PMM 2.1.2 block copolymers with an amino-bearing mannose was as follows: a solution of 150 mg of polymer **3** in 30 mL of *N*,*N*-dimethylacetamide was dialyzed against carbonate buffer solution pH 7.0. Subsequently, 5 and 10 mol equiv per polymer of **a** were added to the micelle solution. After 1 h stirring, 5 and 10 mol equiv per polymer of $NaBH_3CN$ were introduced into the reactor to reduce the Schiff's base formed between the aldehyde groups of **3** and the primary amino groups of **a**. After a four-day reaction, the micelle solutions were then dialyzed against water for

Table 2. Coupling Reactions Yields between Copolymer 3 and (4-Aminophenyl)-α-D-mannopyranose a According to Experimental Conditions (Procedure B)

run	solvent	ratio [**a**]/[(**3**)] (mol/mol)	reducing agent	α-end functionalization yield (%)[a]
8	micellar solution[b]	5	$NaBH_3CN$	44
9		10		37
10	anhydrous DMF	5	$NaBH(OAc)_3$	74
11		10		85

[a] Coupling reaction with MM $2.1.2_{(30)}$-$EO_{(96)}$-CHO block copolymer end functionalization yield = 95%. [b] Phosphate buffer pH 7.

24 h in order to remove the unreacted mannosyl derivatives and the salts and finally lyophilized. In organic solvent: Anhydrous DMF (25 mL) was added to 100 mg of **3**. Amounts of 5 and 10 mol equiv per polymer of **a** were then added to the mixture which was stirred for 1 h. Subsequently, 5 and 10 mol equiv per polymer $NaBH(OAc)_3$ were introduced into the reactor, and the mixtures were stirred for 24 h. The purification procedure was the same as described before. ^{1}H NMR (250 MHz, $CDCl_3$, δ in ppm): 1.30 (m, CH_3 of PMM 2.1.2, 6H), 1.85 (quin, CH_2, 2H), 2.80 (m, CH_2 of the main chain of PMM 2.1.2, 2H), 3.60 (m, CH_2 of PEO, 4H), 4.10 (m, CH_2 of CH_2CH_3 of PMM 2.1.2, 4H), 4.50 (m, CH_2 of PMM 2.1.2, 2H), 5.38 (d, H_{ano}, 1H), 6.53 (d, aromatics, 2H), 6.87 (d, aromatics, 2H) (Figure 1).

As described by Monsigny et al. (*33*), the sugar contents in the polymer samples were determined by a microscale colorimetric assay, in which the mannose residue reacts with resorcinol in the presence of 75% sulfuric acid solution. This easy-to-handle microplate assay has been found to be suitable to quantitatively determine the sugar content of samples. Note that we checked by GPC that the dialysis-purified polymer samples do not contain free mannosyl derivative.

RESULTS AND DISCUSSION

The synthesis of mannosylated PEO-*b*-PMM 2.1.2 block copolymers was carried out through the two following steps: (i) synthesis of α-amino or α-aldehyde PEO-*b*-PMM 2.1.2; (ii) coupling of the mannosyl derivatives to these α-functionalized copolymers.

The PEO precursor was analyzed by GPC using PEO standards for the determination of its molecular weight and polydispersity index. From the chemical composition of the purified copolymers determined by ^{1}H NMR, molecular weights of copolymers were calculated on the assumption that the block copolymer samples contained neither unreacted PEO nor PMM 2.1.2 homopolymer. In fact, it was clearly established from GPC profiles that copolymer samples did not contain a detectable amount of PEO homopolymer. The elimination of eventual traces of PMM 2.1.2 homopolymer from block copolymers was achieved by precipitation of the copolymerization reaction products into a large amount of diethyl ether, a well-known and good solvent of PMM 2.1.2.

The α-end functionalization yield was determined as following. The number-average molecular weight of the α-functionalized PEO homopolymer, which is the precursor for the preparation of the functionalized PEO-*b*-PMM 2.1.2 copolymers, was determined by GPC and allowed the calculation of the number *n* of ethylene oxide units per chain and thus per end group, whatever its functionality. The relative intensity of the signals corresponding to the α-end group protons as compared to that of the methylene protons of the PEO segment were obtained from the ^{1}H NMR spectra and allowed the determination of the number of functionalized end groups per *n* units and thus the calculation of the α-end functionalization yield. Calculations of α-functionalized PEO-*b*-PMM 2.1.2 copolymers **2**−**5** made use of ^{1}H NMR signals corresponding to the PMM 2.1.2 protons. Peaks corresponding to protons adjacent to or characteristic from amino, acetal, aldehyde, or mannosyl moieties were clearly observed in the spectra of the α-functionalized PEO homopolymers and/or of the PEO-*b*-PMM 2.1.2 block copolymers and enabled the easy determination of end functionalization yields. Furthermore, the chemical nature of the end group was confirmed by ^{13}C NMR (*29*), and the values obtained were in good agreement with those given by Zalipsky (*34*).

Synthesis and Characterization of α-Amino PEO-*b*-PMM 2.1.2 Block Copolymers 1. Most of them involving amino-protected initiators, different methods have been previously reported in the literature for the synthesis of α-amino PEO (*32, 35*−*38*). We selected the easiest one that consists of initiating the polymerization of EO by aminoethanolate as described by Mosquet et al. (*32*). These authors showed that due to the high reactivity of the potassium alcoholate with respect to those of the amino group, the ring opening reaction of ethylene oxide by the amino group is avoided in a dry aprotic medium like THF. In our study, the number-average molecular weight and polydispersity index were 4470 g/mol and 1.30, respectively, for the α-amino PEO, i.e., a degree of polymerization of 102. The weight-average molecular weight of the PMM 2.1.2 segment was estimated to be 1500 g/mol based on the molecular weight of the PEO segment and on the MM 2.1.2/EO ratio as determined by ^{1}H NMR. Probably due to the low solubility of the potassium 2-aminoethanolate in THF, the polydispersity index of the α-amino PEO is slightly higher than those obtained with soluble initiators (*32*). This MM $2.1.2_{(7)}$-$EO_{(102)}$-NH_2 copolymer thus prepared has an excellent α-amino end-functionality of 98% which was confirmed by acido-basic titration with NaOH. Moreover, the elemental analysis of the nitrogen content was in good agreement with the NMR/GPC data (*29*).

Synthesis and Characterization of α-Acetal PEO-*b*-PMM 2.1.2 Block Copolymers 2. The synthesis of α-acetal and α-aldehyde PEO homopolymers or corresponding copolymers has already been extensively described by Kataoka et al. (*39*−*42*). For the α-acetal PEO synthesized in the present study, the number-average molecular weight and polydispersity index were 4200 g/mol and 1.18, respectively. As expected, when soluble initiators are used, the polydispersity index value is lowered. The weight-average molecular weight of the PMM 2.1.2 segment was estimated at 6760 g/mol based on the molecular weight of the PEO segment and on the MM 2.1.2/EO molar ratio obtained from ^{1}H NMR data. This MM $2.1.2_{(30)}$-$EO_{(96)}$-acetal copolymer showed a good α-acetal end-functionalization yield of 95%, which was in agreement with those given by Scholz et al. (*41*).

Synthesis and Characterization of α-Aldehyde PEO-*b*-PMM 2.1.2 Block Copolymers 3. In water, core−shell-structured micelles were formed by the segregation of the hydrophobic PMM 2.1.2 blocks into the core, which is surrounded by a hydrophilic shell composed of PEO blocks. Thus, as confirmed by ^{1}H NMR, this structure prevents possible acidic hydrolysis of the PMM 2.1.2 esters, the MM 2.1.2/EO ratio being the same before and after the 2-h hydrolysis. The MM $2.1.2_{(30)}$-$EO_{(96)}$-CHO copolymer thus prepared showed an α-aldehyde end-

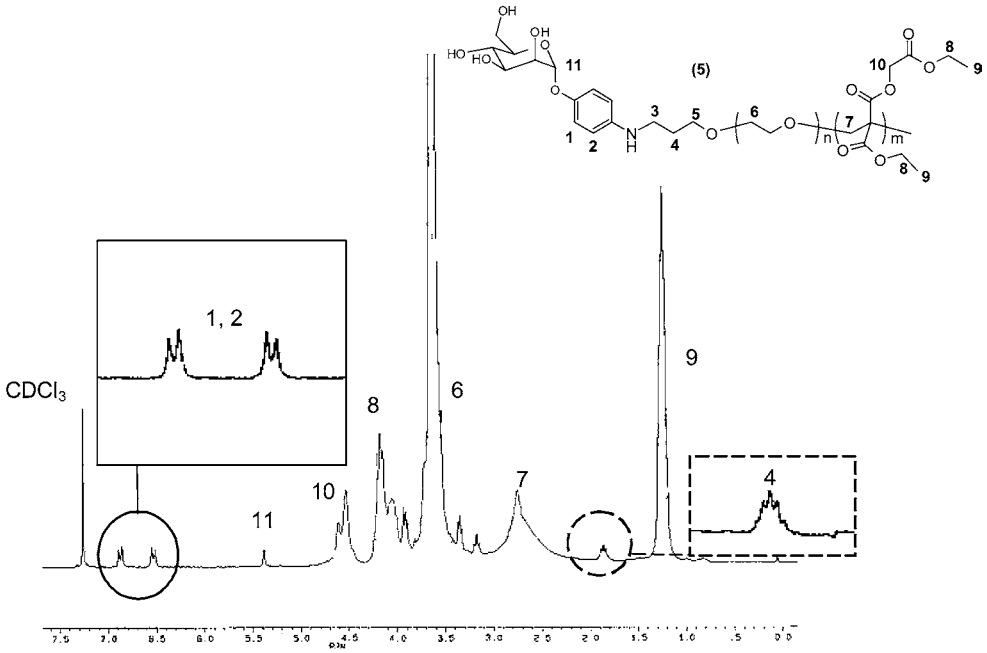

Figure 1. ^{1}H NMR spectrum of α-mannosyl-functionalized POE-*b*-PMM 2.1.2 **5** prepared by reductive amination.

Scheme 3. Coupling Reaction between (4-Isothiocyanatophenyl)-α-D-mannopyranose b and the α-amino Ended Copolymer (1)

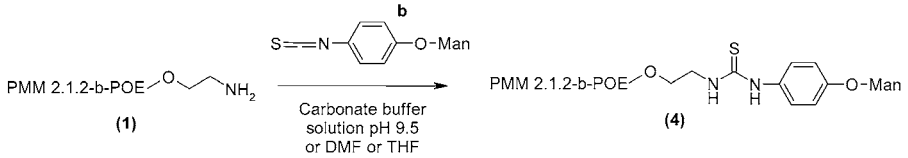

functionalization yield of 95%, similar to the previous one given above.

Coupling of Mannosyl Derivatives to α-Amino PEO-*b*-PMM 2.1.2 and to α-Aldehyde PEO-*b*-PMM 2.1.2 Copolymers 1 and 3. Mannosyl derivatives were conjugated to the α-functionalized PEO end, either by reaction of the amine function of **1** with the phenylisothiocyanate group of **b**, or by the reaction of the aldehyde function of **3** with the amino group of **a**. The bound mannosyl derivative content was determined by the resorcinol colorimetric method after free unreacted mannosyl derivatives were completely removed by dialysis. As mentioned by Yamamoto et al. (*13*), there might be about 5% mol equiv ligand per polymer being noncovalently linked to the block copolymer; hence, the measured mannosyl derivative content could include a small amount of physically adsorbed sugar. In fact, a GPC calibration test showed that less than 0.08% (w/w) of free mannose derivatives (either **a** or **b**) per purified copolymer sample could be detected, that corresponded to a maximum of 3% mol equiv per polymer of unbound mannosyl derivative, in considering a polymer sample with a weight-average molecular weight of 10000 g/mol (*29*). Furthermore, the accuracy of the coupling yields were confirmed by ^{1}H NMR analysis. The reaction conditions and the α-glycosylation yields are summarized in Table 1. No change in the GPC peak profile was observed by mannosylation of the precursor polymers.

Our goal was to implement a strategy to compare the efficiency of two different coupling reactions: (i) one using α-amino copolymers **1**; (ii) the other using α-aldehyde copolymers **3**.

H_2N-PEO-b-PMM 2.1.2 Block Copolymer. The coupling reaction (Scheme 3) was performed either in a heterogeneous buffer solution at pH 9.5 (micellar solution) or in a homogeneous medium such as THF or DMF. The results given in Table 1 show that, probably because of the better solubility of copolymer **1** in these solvents, the highest coupling efficiency were achieved in organic solvents and especially in THF.

OHC-PEO-b-PMM 2.1.2 Block Copolymer. The two most commonly used reductive amination methods differ in the nature of the reducing agent. In the first one, the catalytic hydrogenation involving platinum or palladium catalysts gives a mixture of products and has limited use especially in the presence of reducible functional groups. The second one utilizes hybride reducing agents such as borohydrides. The reductive amination between the α-aldehyde ended copolymer **3** and the amine-bearing mannosyl derivative **a** were carried out with two different reducing agents. The choice of the reducing agent was critical for the success of the reaction, since the latter must reduce imines selectively over aldehydes under the reaction conditions. In our procedure, the reductive amination was indirect, as the reaction involved the preformation of the imine intermediate followed by reduction in a subsequent separate step. Depending on the nature of the reducing agent, the coupling reaction (Scheme 4) was performed either in aqueous buffer solution pH = 7.0 as described by Yamamoto et al. (*13*) or in anhydrous DMF as suggested by Abdel-Magid et al. (*43*). The results given in Table 2 show that the reductive amination was an efficient procedure. In the presence of $NaBH_3CN$, which is a specific reducing agent in buffer solution, the coupling yields were similar to those of Yamamoto et al. (*13*) obtained for the coupling of amino acids with PDLLA-*b*-PEO-CHO. Note that excellent coupling yields could be reached with sodium

Scheme 4. Coupling Reaction between the (4-aminophenyl)-α-D-mannopyranose a and the α-Aldehyde Ended Copolymer (3)

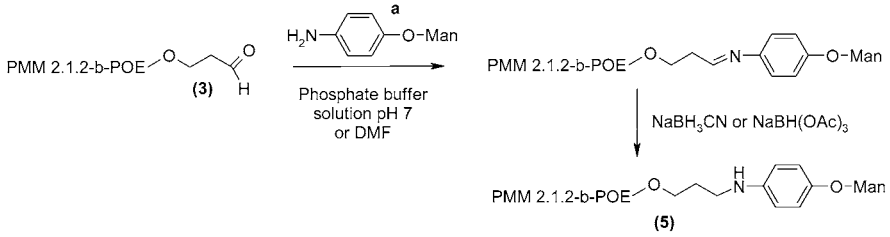

Table 3. Size of Micelles Obtained with Various α-Substituted Copolymers

copolymer	functionalization	average diameter in weight (nm)[a]
2	acetal	56.2 ± 2.3
3	CHO	56.2 ± 2.0
5	O-Man	56.0 ± 1.9

[a] Acetal-$EO_{(96)}$-MM $2.1.2_{(30)}$ block copolymer (end functionalization yield = 95%) was used as a starting material.

triacetoxyborohydride $NaBH(OAc)_3$ in DMF, this mild and selective reducing agent being suitable for reductive reactions to be carried out in organic solvents such as DMF as mentioned by Abdel-Magid et al. (*43*). Figure 1 shows the ^1H NMR spectrum of α-mannosyl-functionalized PEO-*b*-PMM 2.1.2 as a typical example.

From these results, it turned out that the synthesis of α-mannosyl-functionalized PEO-*b*-PMM 2.1.2 has preferably to be carried out in an organic medium such as THF or DMF which are common solvents of both sequences of the block copolymers. Furthermore, it appeared that the highest coupling yield (74−85%) is obtained in organic medium by reductive amination between α-aldehyde-ended copolymers **3** and amine-bearing mannosyl derivative **a**, this yield being quite comparable to those of 65% and 90% given by Nakamura et al. (*18*) and Yasugi et al. (*19*), respectively, which were obtained by initiating the polymerization with a protected monosaccharide residue. In addition, this procedure has a double-advantage: (i) compared to α-amino-functionalized copolymers **1**, α-aldehyde-functionalized copolymers **3** have been obtained with a lower polydispersity index; (ii) the amine-bearing mannosyl derivative **a** was produced in a four-step synthesis, whereas the phenylisothiocyanate-bearing mannosyl derivative **b** needed five steps.

Micellization of the α-Acetal, α-Aldehyde and α-Mannosyl-Functionalized PEO-*b*-PMM 2.1.2 Block Copolymers 2, 3, and 5. As the primary application of these α-substituted PEO-*b*-PMM 2.1.2 block copolymers consists of preparing polymeric colloidal vectors for drug delivery, it was of interest to determine their micellar characteristics. In aqueous media, these block copolymers self-associate, leading to spherical micelles with a PMM 2.1.2-made hydrophobic core surrounded by a corona of hydrated PEO segments. A typical example of micellar characteristics of α-substituted block copolymers with various end groups is given in Table 3, the composition and molecular weight of the copolymer being kept constant.

Dynamic light scattering studies indicated that, in our micellization procedure, the block copolymer leads to a monodisperse micelle population with an average diameter of 56 ± 2 nm, which is in agreement with the predicted value of 49 nm given by Larras et al. (*20*) for PEO-*b*-PMM 2.1.2 block copolymers. It was confirmed that the micelle diameter did not change, neither after the hydrolysis of the acetal group as pointed out by Kataoka et al. (*13*) nor after the coupling reaction with the mannosyl derivatives **a** or **b**.

CONCLUSION

Well-controlled molecular weight α-amino and α-aldehyde-functionalized PEO-*b*-PMM 2.1.2 block copolymers were synthesized with high mean yields. These block copolymers were then successfully conjugated to a mannosyl derivative for the preparation of bioerodible nanocarriers with the aim of developing active tissue targeting strategies. Reductive amination of the α-aldehyde end-functionalized copolymer with amine-bearing mannosyl derivative in the presence of sodium triacetoxyborohydride in DMF appeared to be the most suitable functionalization procedure. A maximum of 85% of the PEO chain end was α-conjugated to mannosyl derivative without any change in the micellar size. Our studies result in a panel of novel macromolecular entities that can be used as starting materials on which to anchor various targeting ligands bearing various chemical functionalities. The latter can be adapted to the nature of the α-ending reactive function of the PEO-*b*-PMM 2.1.2 block copolymer, whereas the initiation process by a monosaccharide residue is limited to the sugar moiety only.

ACKNOWLEDGMENT

The authors gratefully acknowledge the financial support by Dr. Bru. We thank Drs. Nathalie Colin and Sophie Ruiz for their assistance in the determination of the copolymer-bound mannosyl derivative. We are grateful to Drs. Virginie Larras and Serge Sagodira for their helpful discussions.

LITERATURE CITED

(1) Yang, L., and Alexandris, P. (2000) Physicochemical aspects of drug delivery and release from polymer-based colloids *Curr. Opin. Colloid Interface Sci. 5*, 132−143.

(2) Nishiyama, N., Okazaki, S., Cabral, H., Miyamoto, M., Kato, Y., Sugiyama, Y., Nishio, K., Matsumura, Y., and Kataoka, K. (2003) Novel cisplatin-incorporated polymeric micelles can eradicate solid tumors in mice. *Cancer Res. 63*, 8977−8983.

(3) Kwon, G. S. (1998) Diblock copolymer nanoparticles for drug delivery *Crit. Rev. Ther. Drug Carrier Syst. 15*, 481−512.

(4) Kataoka, K., Harada, A., and Nagasaki, Y. (2001) Block copolymer micelles for drug delivery: design, characterization and biological significance. *Adv. Drug Delivery Rev. 47*, 113−131.

(5) Torchilin, V. P. (2001) Structure and design of polymeric surfactant-based drug delivery systems. *J. Controlled Release 73*, 137−172.

(6) Harris, J. M., and Zalipsky, S. (1997) *Poly(ethylene glycol) chemistry: biotechnical and biomedical applications* (Harris, J. M., and Zalipsky, S. Eds.) pp 99−116, Plenum Publishing Corporation, New York.

(7) Allen, C., Maysinger, D., and Eisenberg, A. (1999) Nano-engineering block copolymer aggregates for drug delivery. *Colloids Surf. B: Biointerfaces 16*, 3−27.

(8) Davis, S. S. (1997) Biomedical applications of nanotechnology − implications for drug targeting and gene therapy. *Trends Biotechnol. 15*, 217−224.
(9) Riess, G. (2003) Micellization of block copolymers. *Prog. Polym. Sci. 28*, 1107−1170.
(10) Couvreur, P. (1988) Polyalkylcyanocrylates as colloidal drug carriers. *Crit. Rev. Ther. Drug Carrier Syst. 5*, 1−20.
(11) Lherm, C., Müller, R. H., Puisieux, F., and Couvreur, P. (1992) Alkylcyanoacrylate drug carriers: II. Cytotoxicity of cyanoacrylate nanoparticles with different alkyl chain length. *Int. J. Pharm. 84*, 13−22.
(12) Lescure, F., Seguin, C., Breton, P., Bourrinet, P., Roy, D., and Couvreur, P. (1994) Preparation and characterization of novel poly(methylidene malonate 2.1.2)-made nanoparticles. *Pharm. Res. 11*, 1270−1277.
(13) Yamamoto, Y., Nagasaki, Y., Kato, M., and Kataoka, K. (1999) Surface charge modulation of poly(ethyleneglycol)-poly-(D,L-lactide) block copolymer micelles: conjugation of charged peptides. *Colloids Surf. B: Biointerfaces 16*, 135−146.
(14) Harris, J. M. (1985) Laboratory synthesis of poly(ethyleneglycol) derivatives. *Macromol. Chem. Phys. C25*, 325−373.
(15) Harris, J. M., Struck, A. C., Case, M. G., Paley, M. S., Van Alstine, and J. M., Brooks, D. E. (1984) Synthesis and characterization of poly(ethylene glycol) derivatives. *J. Polym. Sci., Polym. Chem. 22*, 341−352.
(16) Zalipsky, S., Gilon, C., and Zilkha, A. (1983) Attachment of drugs to poly(ethyleneglycol)s. *Eur. Polym. J. 19*, 1177−1183.
(17) Nagasaki, Y., and Kataoka, K. (1998) Heterotelechelic poly-(ethylene glycol)s and their derivatives for active targeting drug delivery systems. *ACS Polym. Prepr. 39*, 190−191.
(18) Nakamura, T., Nagasaki, Y., and Kataoka, K. (1998) Synthesis of heterobifunctional poly(ethylene glycol) with a reducing monosaccharide residue at one end. *Bioconjugate Chem. 9*, 300−303.
(19) Yasugi, K., Nakamura, T., Nagasaki, Y., Kato, M., and Kataoka, K. (1999) Sugar-installed polymer micelles: synthesis and micellization of poly(ethylene glycol)-poly(D,L-lactide) block copolymers having sugar groups at the PEG chain end. *Macromolecules 32*, 8024−8032.
(20) Larras, V., Bru, N., Breton, P., and Riess, G. (2000) Synthesis and micellization of amphiphilic poly(ethylene oxide)-*block*-poly(methylidene malonate 2.1.2) diblock copolymers. *Macromol. Rapid Commun. 21*, 1089−1092.
(21) Bru-Magniez, N., Larras, V., Riess G., Breton, P, Couvreur, P., and Roques Carmes, C. Novel surfactant copolymers based on methylidene malonate. WO 99/38898 (1999)/FR19980001001 (1998)
(22) Seymour, L. W. (1994) Soluble polymers for lectin-mediated drug targeting. *Adv. Drug Delivery Rev. 14*, 89−111.
(23) Gariepy, J. G., and Kawamura, K. (2001) Vectorial delivery of macromolecules into cells using peptide-based vehicles. *Trends Biotechnol. 19*, 19−26.
(24) Sudimack, J., and Lee, R. J. (2000) Drug targeting via the folate receptor. *Adv. Drug Delivery Rev. 41*, 147−162.
(25) Rihova, B., Ulbrich, K., Kopecek, J., and Mancal, P. (1983) Immunogenicity of N−(2-hydroxypropyl)-methacrylamide copolymers-potential hapten or drug carriers. *Folia Microbiol. 28*, 217−227.
(26) Bru-Magniez, N., De Cock, C., Poupaert, J., De Keyser, J. L., and Dumont, P. (1988) Monoesters or diesters of endo-ethano-9,10-dihydro-9,10-anthracene dicarboxylic-11,11 acid, process for their preparation, and their use in the preparation of symmetric or asymmetric methylidene malonates. EP 0283364.
(27) Scherf, G. W. H., and Brown, R. K. (1960) Potassium derivatives of fluorene as intermediates in the preparation of C-9-substituted fluorenes. II. Comparative reactivities of the alkali metals, lithium, sodium, and potassium, with fluorene in glycol dimethyl ether, glycol diethyl ether, tetrahydrofuran, and dioxane. *Can. J. Chem. 38*, 2450−2456.
(28) Lerner, L. M., and Mennitt, G. (1994) A new synthesis of L-talose and preparation of its adenine nucleosides. *Carbohydr. Res. 259*, 191−200.
(29) Studer, P. (2001) Ph.D. Thesis, University of Haute-Alsace (France), Synthèse et caractérisation de polymères fonctionnalisés et de copolymères à base de méthylidène malonate 2.1.2. Application à la vectorisation de principes actifs.
(30) Smits, E., Engberts, J. B. F. N., Kellogg, R. M., and Van Doren, H. A. (1996) Reliable method for the synthesis of aryl β-D-glucopyranosides, using boron trifluoride-diethyl ether as catalyst. *J. Chem. Soc., Perkin Trans. 1* 2873−2877.
(31) Monsigny, M., Roche, A. C., and Midoux, P. (1984) Uptake of neoglycoproteins via membrane lectin(s) of L1210 cells evidenced by quantitative flow cytometry and drug targeting. *Biol. Cell. 51*, 187−196.
(32) Mosquet, M., Chevalier, Y., Le Perchec, P., and Guicquero, J. P. (1997) Synthesis of poly(ethylene oxide) with a terminal amino group by anionic polymerization of ethylene oxide initiated by amino alcoholates. *Macromol. Chem. Phys. 198*, 2457−2474.
(33) Monsigny, M., Petit, C., and Roche, A. C. (1988) Colorimetric determination of neutral sugars by a resorcinol sulfuric acid micromethod. *Anal. Biochem. 175*, 525−530.
(34) Zalipsky, S. (1995) Functionalized poly(ethylene glycol) for preparation of biologicaly relevant conjugates. *Bioconjugate Chem. 6*, 150−165.
(35) Kim, Y. J., Nagasaki, Y., Kataoka, K., Kato, M., Yokoyama, M., Okano, T., and Sakurai, Y. (1994) Heterobifunctional poly-(ethylene oxide) − One pot synthesis of poly(ethylene oxide) with a primary amino group at one end and a hydroxyl group at the other end. *Polym. Bull. 33*, 1−6.
(36) Yokoyama, M., Okano, T., Sakurai, Y., Kikuchi, A, Ohsako, N, Nagasaki, Y, and Kataoka, K. (1992) Synthesis of poly-(ethylene oxide) with heterobifunctional reactive groups at its terminals by an anionic initiator. *Bioconjugate Chem. 3*, 275−276
(37) Nagasaki, Y., Iijima, M., Kato, and M., Kataoka, K. (1995) Primary amino-terminal heterobifunctional poly(ethylene oxide). Facile synthesis of poly(ethylene oxide) with a primary amino group at one end and a hydroxyl group at the other end. *Bioconjugate Chem. 6*, 702−704.
(38) Cammas, S., Nagasaki, Y., and Kataoka, K. (1995) Heterobifunctional poly(ethylene oxide): synthesis of α-hydroxy-ω-amino PEOs with the same molecular weights. *Bioconjugate Chem. 6*, 226−230.
(39) Otsuka, H., Nagasaki, Y., and Kataoka, K. (2000) Surface characterization of functionalized polylactide (PLA) through the coating with heterobifunctional poly(ethylene glycol)(PEG)/PLA block copolymers. *Biomacromolecules 1*, 39−48.
(40) Scholz, C., Iijima, M., Nagasaki, Y., and Kataoka, K. (1998) Polymeric micelles as drug delivery systems: a reactive polymeric micelle carrying aldehyde groups. *Polym. Adv. Technol. 9*, 1−9.
(41) Scholz, C., Iijima, M., Nagasaki, and Y., Kataoka, K. (1995) A novel reactive polymeric micelle − Polymeric micelle with aldehyde groups on its surface. *Macromolecules 28*, 7295−7297.
(42) Nagasaki, Y., Kutsuna, T., Iijima, M., Kato, M., Kataoka, K., Kitano, S., and Kadoma, Y. (1995) Formyl-ended heterobifunctional poly(ethylene oxide): synthesis of poly(ethylene oxide) with a formyl group at one end and a hydroxyl group at the other end. *Bioconjugate Chem. 6*, 231−233.
(43) Abdel-Magid, A. F., Carson, K. G., Harris, B. D., Maryanoff, C. A., and Shah, R. D. (1996) Reductive amination of aldehydes and ketones with sodium triacetoxyborohydride. Studies on direct and indirect reductive amination procedures. *J. Org. Chem. 61*, 3849−3862.

BC0498065

TECHNICAL NOTES

Copoly(styrene-maleic acid)−Pirarubicin Micelles: High Tumor-Targeting Efficiency with Little Toxicity[1]

Khaled Greish,[†,§] Akinori Nagamitsu,[‡] Jun Fang,[†,⊥] and Hiroshi Maeda*[,†,§,∥]

Division of Advanced Biomedical Sciences, Department of Microbiology, Graduate School of Medical Sciences, Kumamoto University, Honjo 1-1-1, Kumamoto 860-8556, Japan, Hakuaikai Hospital, 4-3 Konnya-ima machi, Kumamoto 860-0012, Japan, and Biodynamics Research Laboratory, Cooperative Research Center, Kumamoto University, Techno Research Park, 2081-7 Tabaru, Mashiki-machi, Kumamoto, 861-2202, Japan.
Received March 23, 2004; Revised Manuscript Received July 20, 2004

The copolymer of styrene-maleic acid (SMA) was used to construct micelles containing pirarubicin (4′-*O*-tetrahydropyranyladriamycin, or THP) as a new anticancer drug formulation. The procedure for the preparation of the micelles was simple, the component consisting of only SMA and pirarubicin in a noncovalent association, possibly by hydrophobic interaction between the styrene portion of SMA and pirarubicin chromophore. This method ensures more than 80% recovery of pirarubicin by weight, and 60% of drug loading (by weight) was achieved. The micelles obtained (SMA−THP) showed high solubility in water and a constant pirarubicin release rate of about 3−4%/day in vitro. SMA−THP micelles had an average molecular size of about 34 kDa according to gel chromatography; this size is a marked increase from the 627.6 Da of free THP, which suggests the formation of a micellar structure. When albumin was added, the molecular size of the micelles increased to about 94 kDa, which indicates binding to albumin, a unique characteristic of SMA. SMA−THP micelle preparation had a cytotoxic effect (93−101%) on MCF-7 breast cancer cells and SW480 human colon cancer cells in vitro that was comparable to that of free THP. An in vivo assay of SMA−THP at doses of 20 mg/kg in ddY mice bearing S-180 tumor revealed complete tumor eradication in 100% of tested animals. Mice survived for more than 1 year after treatment with micellar drug doses as high as 100 mg/kg pirarubicin equivalent. This marked antitumor activity can be attributed to the enhanced permeability and retention (EPR) effect of macromolecular drugs seen in solid tumors, which enables selective delivery of drugs to tumor and thus much fewer side effects. Complete blood counts, liver function test, and cardiac histology showed no sign of adverse effects for intravenous doses of the micellar preparation. These data thus suggest that intravenous administration of the SMA−THP micellar formulation can enhance the therapeutic effect of pirarubicin more than 50-fold.

INTRODUCTION

Pirarubicin, (4′-*O*-tetrahydropyranyladriamycin, or THP[2]) is an anthracycline antibiotic that was developed during a search for less cardiotoxic agents among the 4′-O-substituted anthracyclines (*1*). Pirarubicin proved effective against hematological malignancies and was used for treatment of acute leukemias and malignant lymphomas, as well as breast cancer (*2*, *3*). The drug has both lipophilic and hydrophilic properties, which allows either intravenous (iv) or intraarterial injection with Lipiodol used as a carrier for treatment of liver metastasis and hepatocellular carcinoma (*4*). Unfortunately, THP lacks specificity for cancer cells, and its potent cytotoxicity, like that of many other low-molecular-weight cytotoxic anticancer agents, leads to severe side effects. As in most conventional chemotherapeutic drug regimens, this nonselective cytotoxicity is the primary reason for dose limitation.

We previously found that drugs of large molecular size, i.e., those of more than 40 kDa, preferentially accumulate in tumor tissue because of the unique characteristics of the tumor vasculature (*5*−*11*). Solid tumor tissue usually

* To whom correspondence should be addressed. Tel.: +81-96-373-5098; Fax: +81-96-214-5356. E-mail address: msmaedah@gpo.kumamoto-u.ac.jp.

† Division of Advanced Biomedical Sciences, Kumamoto University.

‡ Hakuaikai Hospital.

§ Biodynamics Research Laboratory, Kumamoto University.

∥ Present address: Sojo University, Ikeda 4-22-1, Kumamoto 860-0082, Japan.

⊥ Department of Pathology, Duke University, Durham, NC.

[1]The definition of "micelles" may not be precisely as defined in polymer science; however, we deliberately use micelles as naïve definition. These SMA-micelles have a discrete size distribution in gel chromatography and by ultracentrifugation, and it is a complex of SMA and THP.

[2]Abbreviations: EPR, enhanced permeability and retention effect in solid tumor; THP, 4′-*O*-tetrahydropyranyladriamycin, which is also known as pirarubicin; SMA, copoly(styrene-maleic acid/anhydride); SDS, sodium dodecyl sulfate; EDAC, ethyldimethylaminopropylcarbodiimide; MTT, 3-(4,5-dimethylthiazol-2-yl)-2,5-diphenyltetrazolium bromide; MALDI-TOF, matrix-assisted laser desorption−ionization/time-of-flight; H&E, haematoxylin and eosin.

10.1021/bc040297g CCC: $30.25 © 2005 American Chemical Society
Published on Web 11/25/2004

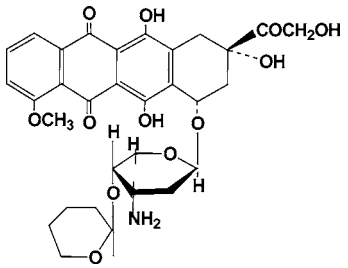

Figure 1. Chemical structure of pirarubicin (THP).

shows increased vascular density caused by angiogenesis, impaired lymphatic recovery system, and lack of a smooth muscle layer in the blood vessels. More important, functional augmentation of enhanced vascular permeability in tumor tissues has been identified and involves extensive production of vascular mediators such as bradykinin, nitric oxide, prostaglandins, matrix metalloproteinases, and vascular endothelial growth factor/vascular permeability factor, among others (*12*−*17*). We named this phenomenon the "enhanced permeability and retention (EPR) effect of macromolecular drugs in solid tumors" (*5*, *6*). In the present study, we developed micelles containing copoly(styrene-maleic acid) (SMA) and pirarubicin (THP) (Figure 1) with a large molecular size, to take advantage of the EPR effect and achieve tumor-selective drug delivery as well as an excellent therapeutic effect.

One advantage of using SMA for polymeric drug development relates to its noncovalent binding to albumin, which thus permits plasma albumin, one of the most biocompatible macromolecules, to serve as a secondary carrier of the drug (*18*). This SMA-micelle preparation takes advantage of the EPR effect. The amphiphilic nature of SMA enables a wide range of formulation possibilities, including an aqueous formulation for iv injection and an oily formulation for intraarterial or oral administration (*18*, *19*−*23*). With higher lipophilic nature, we demonstrated facilitated uptake into cells (*24*). In addition, we previously showed that when animals were treated with SMA conjugates, the SMA moieties conferred immunopotentiating activity (*25*−*28*); this result is in clear contrast to the immunosuppression caused by conventional small-molecular-size anticancer drugs.

We recently reported preparation and characterization of SMA−doxorubicin micelles, which showed marked tumor accumulation in tumor after iv administration compared with that obtained with free doxorubicin, i.e., a 13-fold increase in tumor uptake of drug and a 25-fold increase in the plasma level of drug (AUC) in a 24-h period (*29*). The SMA−doxorubicin micelle preparation produced a potent antitumor effect with fewer side effects at doses as high as 100 mg/kg of doxorubicin equivalent; in contrast, the parent drug had an LD_{100} of 10 mg/kg (*29*).

In this paper, we describe the preparation and characterization of SMA−THP micelles and the anticancer properties of this formulation.

EXPERIMENTAL PROCEDURES

Materials. Pirarubicin (also referred to as THP) was a generous gift from Meiji Seika Kaisha, Ltd, Tokyo, Japan. SMA as the anhydride form of a maleyl group with a mean molecular size of 1435 Da (M_w/M_n: 1.1), the range being between 901 and 1781 Da, was generously supplied by Kuraray Ltd, Kurashiki, Japan. Other reagents were of commercial reagent grade and were used without further purification.

Chemical Analysis. Visible/UV absorption was determined by use of a spectrophotometer (U-200, Hitachi Ltd., Tokyo, Japan). THP content was quantified via analysis of UV absorption at 487 nm. Fluorescence spectra were obtained by use of a fluorescence spectrophotometer (F-4500, Hitachi), excitation at 480 nm and emission at 450−750 nm. Infrared (IR) spectra were recorded with a JIR-6500w spectrometer (JEOL, Tokyo, Japan) using a KBr disk. Mass spectra were obtained by means of matrix-assisted laser desorption−ionization/time-of-flight (MALDI-TOF) mass spectrometry (Voyager System 6192, ABI, Foster City, CA).

Preparation of SMA−THP Micelles. Micelles were prepared as previously described in SMA−doxorubicin micelles preparation (*29*). Briefly, SMA (anhydrous) copolymer was hydrolyzed in 0.05 M NaOH. Hydrolysis produced an increase of 18 Da. Consequently, the mean molecular size of each repeating unit becomes 220 Da (Figure 2A). IR spectra showed the appearance of an OH signal at about 3400 cm^{-1} (Figure 2B, a, b).

To form the micelles, SMA powder was dissolved in water at pH 5.0 at 10 mg/mL, and then THP solution at a concentration of 10 mg/mL was added to this solution, followed by addition of the water soluble carbodiimide, ethyldimethylaminopropylcarbodiimide (EDAC), to 10 mg/mL. Resulting precipitates were washed and collected by centrifugation at 8000 rpm, solubilized, and then reconstituted in pH 7.0. The micelle solution (about 10 mg of THP/mL) was washed and concentrated to one tenth of the original volume by means of the ultrafiltration method with the Amicon ultrafiltration system (YM-10 membrane; cutoff molecular size of 10 kDa), which was repeated three times.

Sephadex G-50 and G-150 Gel Filtration. Size-exclusion chromatography with Sephadex G-50 Fine column (Pharmacia LKB, Uppsala, Sweden) was performed to separate the large-molecular-size SMA−THP micelles (with 0.2 M $NaHCO_3$, pH 8.2, as eluant, and a column size of Ø 3 × 52 cm), and the peak fraction was lyophilized. The powder thus obtained was subjected to IR and UV/visible spectroscopy.

To define the apparent molecular size of the micelles more accurately, various known globular proteins were used as standards. For this analysis, a Sephadex G-150 chromatography column of Ø 2.5 × 64 cm, with 0.25 M $NaHCO_3$, pH 8.2, as eluant, was used.

Release of Free Drug from the SMA−THP Micelles. To verify the release of free drug from SMA−THP micelles in vitro, 20 mg of the micellar preparation was dissolved in 5 mL of distilled water and placed in sealed dialysis tubes (M_r cutoff of 1000 Da; Spectrapor, Spectrum Laboratories Inc., San Diego, CA). The dialysis tubes were submerged in one of three different solutions: (a) 100% ethanol; (b) aqueous solution, pH 7.4; or (c) aqueous solution, pH 5.5. The dialysis tubes, with 25 mL of each solution above, were reciprocally shaken at 1 Hz for several days at 37 °C in the dark. Aliquots of dialysate solution were taken at predetermined time points, and the amount of THP in the dialysate was quantified by absorption at 487 nm.

In Vitro Cytotoxicity. In vitro cytotoxicity of SMA−THP micelles was determined by means of the 3-(4,5-dimethylthiazol-2-yl)-2,5-diphenyltetrazolium bromide (MTT) assay (*30*) with human breast cancer MCF-7 cells and colon cancer SW480 cells, which were plated in 96-well culture plates (3000 cells/well). Cells were cultured overnight in Dulbecco's modified Eagle's medium with

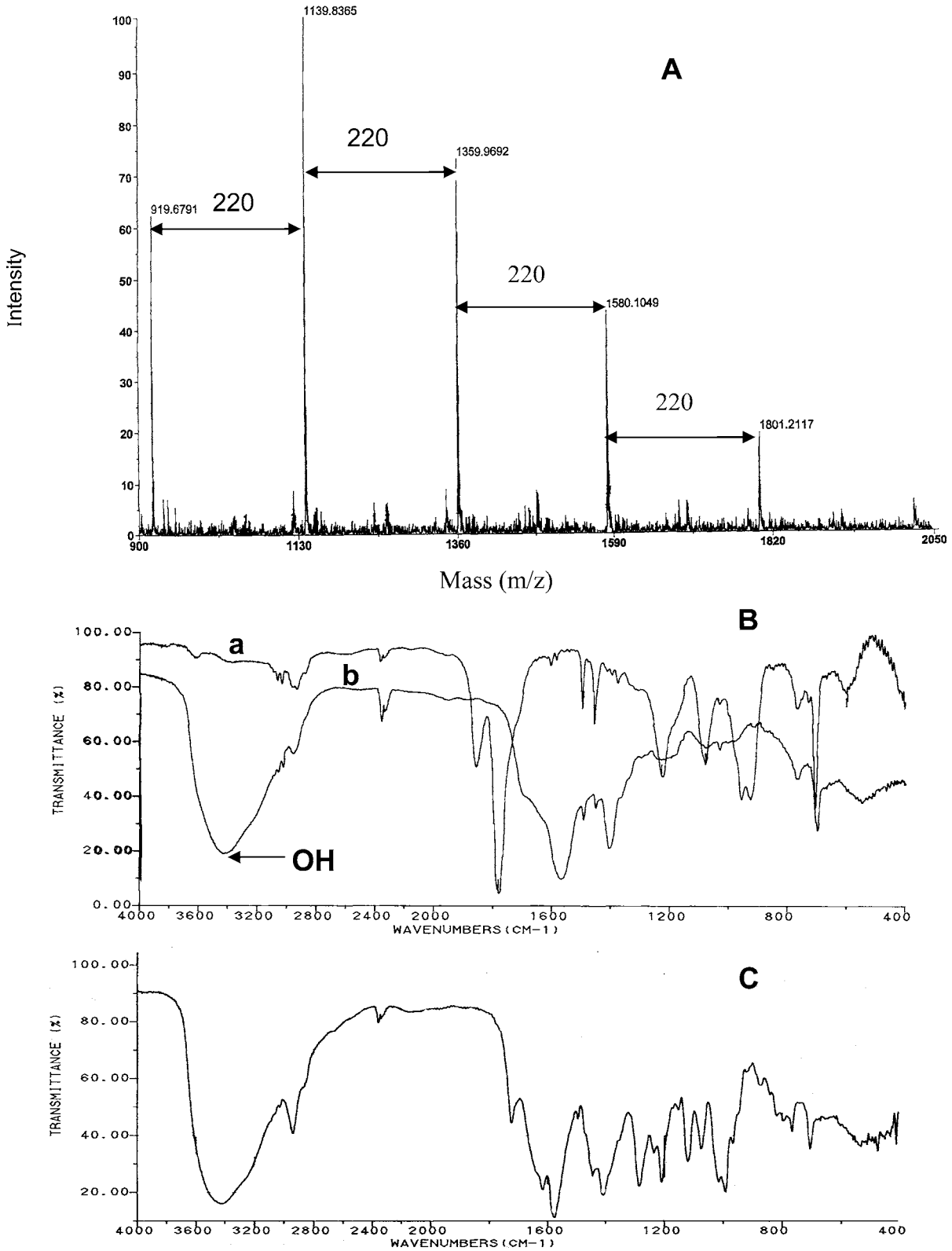

Figure 2. (A) MALDI-TOF mass spectra of styrene maleic acid. The increment of the molecular size of each unit from 202 to 220 Da clearly indicates integration of the H_2O molecule. (B) IR spectra of anhydrous SMA before (a) and after (b) hydrolysis. The appearance of a strong OH signal at 3434 cm^{-1} indicates hydrolysis of anhydrous SMA (a) to the water-soluble styrene-maleic acid (b). (C) IR spectrum of SMA−THP micelles.

10% fetal calf serum. The cells were then incubated in the presence of free THP or SMA−THP micelles for 3 days. Toxicity was quantified as the fraction of cells surviving relative to untreated controls.

Evaluation of the Antitumor Effect of SMA−THP Micelles in an Animal Tumor Model. Mouse sarcoma S-180 cells (2×10^6 cells), maintained as an ascitic tumor in ddY mice, were implanted subcutaneously in the dorsal skin of 6-week-old ddY mice each weighing 30−35 g. On day 7 after tumor cell inoculation, when tumor size was 5−7 mm in diameter but contained no necrotic areas, iv injections of free THP or SMA−THP micelles, in distilled

water at the desired concentration, were administrated into the tail vein in four equal doses every other day. Concentrations of the solutions were standardized via visible absorbance at 487 nm. All experiments were carried out according to the guidelines of the Laboratory Protocol of Animal Handling, Kumamoto University. Tumor growth was measured every 2 days by size of the tumors with a digital caliper, the tumor volume (V) being estimated by using the measured longitudinal cross section (L) and transverse section (W) according to the formula,

$$V = (L \times W^2)/2$$

The day of tumor implantation was set as day 0; the tumor volume was expressed in cm^3.

Side Effects of Treatment with SMA−THP Micelles. Mice with S-180 tumors of about 5−7 mm in diameter were used for this study. Either free THP or SMA−THP micelles were administered as described above. One, two, and three weeks after drug administration, 20 μL samples of blood were collected from the medial canthus for complete blood counts by means of an automated blood counter (F-800 Microcell Counter, Toa Medical Electronics, Kobe, Japan). For measurements of alanine aminotransferase, aspartate aminotransferase, lactate dehydrogenase, and total creatine kinase, mice were killed 36 h after administration of either free drug or micellar THP, and 1 mL samples of blood were obtained from the inferior vena cava. Blood was kept at 0 °C until centrifugation at 4 °C, 3000 rpm for 15 min, and plasma was separated and stored at −80 °C until analyses by use of the Auto Analyzer system (Hitachi Ltd., Tokyo, Japan). At the time of blood collection, tissue specimens (heart, spleen, liver, and kidney) were also obtained; reperfusion with 20 mL of physiological saline containing heparin (5 units/mL) had been performed to remove blood components in blood vessels of the tissues. These tissue specimens were fixed in formalin and then embedded in paraffin and stained with hematoxylin−eosin (H&E).

Statistical Analyses. All data were expressed as means ± SD. Student's t-test was used to compare differences between experimental groups.

RESULTS AND DISCUSSION

Synthesis of SMA−THP Micelles. In the present study, we found that SMA, the styrene moiety of the amphiphilic polymer, formed a complex with pirarubicin (THP) to yield SMA−THP micelles. We also found that hydrolysis of SMA was essential for this complex formation: the hydrolyzed SMA was highly water-soluble and could form micelles rapidly. Treatment of anhydride acid of SMA with alkali resulted in the opening of the maleic anhydride ring in SMA via hydrolysis and the addition of an OH group, as evidencd by a 3400 cm^{-1} signal in the IR spectrum (Figure 2B,C) and an increase in the unit molecular size of SMA from 202 Da (styrene-maleic anhydride) to 220 Da (styrene maleate) because of the addition of 18 Da of H_2O (Figure 2A).

The loading efficiency of THP in the micelles was rather high: the micelles contained 60% (w/w) THP, as determined by spectroscopy and elemental analysis (i.e., N, C, and H content). The yield of drug from the micelles was more than 80% (by weight). It is most likely that the surface of the micellar outer shell has the polar, ionized carboxyl group of the maleic acid and the inner core consists mainly of the hydrophobic styrene group and pirarubicin chromophore.

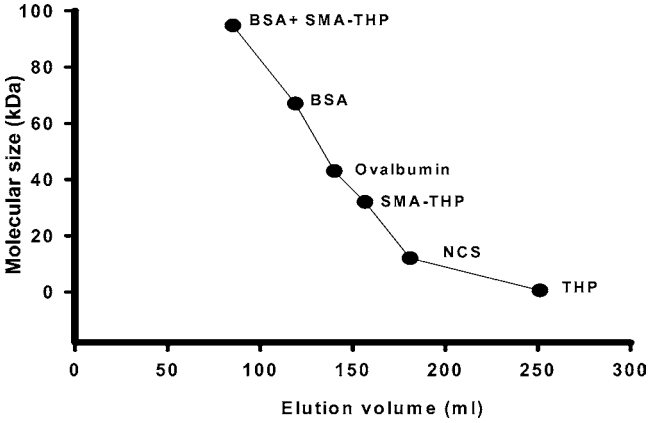

Figure 3. Average molecular size of SMA−THP micelles compared with standard molecular size markers. Sephadex G-150 Fine gel was used with a 2.5 × 64 cm column; each fraction was eluted with 0.2 M $NaHCO_3$, pH 8.2. BSA, bovine serum albumin; NCS, neocarzinostatin.

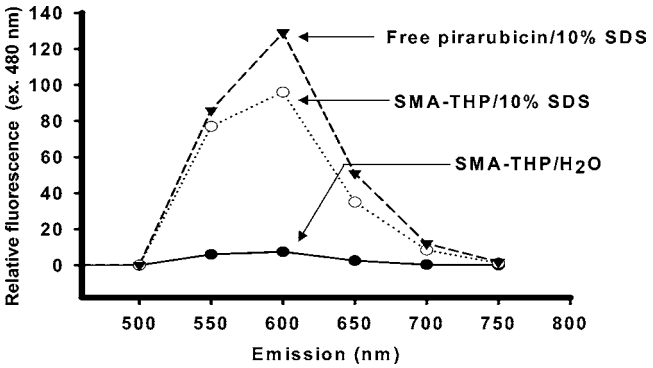

Figure 4. Change in fluorescence intensity of SMA−THP compared with that of free THP. SMA−THP micelles or free THP, each at 10 μM, was prepared in distilled water or in 10% SDS. Each solution was excited at 480 nm, and the resulting fluorescence emissions at 450−750 nm were recorded.

As shown in Figure 3, the SMA−THP micelles had a clearly increased molecular size compared with free pirarubicin. The average molecular size of the micelles was approximately 34 kDa (Figure 3), as determined by Sephadex G-150 column chromatography. The molecular size of the micelles increased to about 94 kDa when bovine serum albumin (40 mg/mL) was added, which indicates binding of SMA−THP to albumin (Figure 3).

Studies on Micellar Formation. Our initial intent regarding the SMA−THP complex was to induce covalent cross-links between the amino group of pirarubicin and the carboxyl group of maleic acid in SMA by treatment with EDAC, facilitated by a dehydration reaction to produce a carboamide linkage (*5*). However, this reaction did not proceed. In contrast, as described above, SMA and THP formed micelles, as evidenced, in part, by the ease with which free THP was liberated from the SMA−THP micelles without the use of harsh hydrolytic conditions, that is, by either ethanol or 10% sodium dodecyl sulfate (SDS) (Figure 4). IR spectroscopy of SMA−THP micelles showed the absence of signals corresponding to amide I and amide II, in contrast to other cases in our study (*31*). Furthermore, we found that other polyamines used instead of EDAC could serve a similar catalytic function for molecular orientation during formation of SMA micelles (not shown).

When excited at 480 nm, free THP showed intense fluorescence emission with a maximum peak between 550 and 600 nm (maximum at about 590 nm) (Figure 4). This

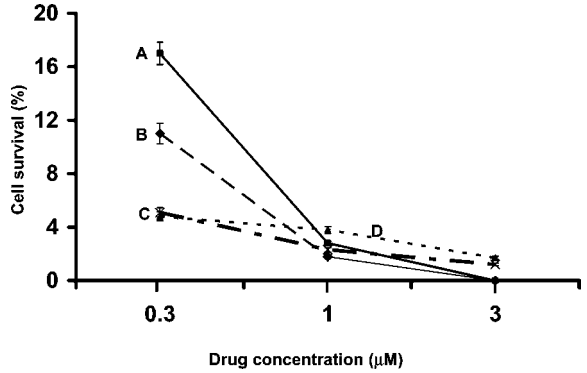

Figure 5. In vitro cytotoxicity of SMA−THP compared with that of free THP in MCF-7 and SW480 cells. (A) SMA−THP in MCF-7 cells. (B) Free THP in MCF-7 cells. (C) SMA−THP in SW480 cells. (D) Free THP in SW480 cells. Cells were exposed to free drug or to SMA−THP for 3 days. Cell viability was determined by the MTT assay. Values are means ± SD; n = 12.

fluorescence was almost completely quenched when the THP molecules were closely attached to or interacting with other aromatic molecules, the styrene moiety of SMA, in the binding pocket of albumin (or other proteins), or other high-affinity species (*32*). We thus anticipated that the energy transfer from the THP chromophore to aromatic residues of styrene in the micelles would result in efficient quenching and suppression of fluorescence. Figure 4 shows that, in fact, the fluorescence spectrum of the SMA−THP complex was markedly quenched when compared with that of the free drug, perhaps because the THP molecules form part of the core of the SMA−THP micelles, or are in very close contact with SMA (or styrene). The fluorescence intensity was restored when the micelles were disrupted by exposure to 10% SDS, which destroyed the micellar association between the anthracycline ring and the hydrophobic styrene residue of SMA.

Consequantly, Sephadex G-50 chromatography showed that SMA−THP exposed to 10% SDS had a distinctly smaller molecular weight equivalent to free THP, compared to the untreated micelles (data not shown).

Free Drug Release from SMA−THP Micelles. Free pirarubicin was released very slowly from the SMA−THP complex in aqueous media, about 3% per day at pH 7.4 and 4% per day at pH 5.5, which indicated higher stability of the micelles at neutral pH. When the solution outside the dialysis tubes was replaced by ethanol, the release rate increased markedly, which indicates that disruption of the micelles occurred, as described above. This stability of the micelles at physiological pH would thus prevent rapid release of free THP from micelles during circulation. The free drug would not be able to gain access to critical organs and tissues, which would be protected from the toxic effects of THP. Such stable micelles or macromolecular drugs will also benefit the functioning of the EPR effect for SMA−THP: the slower drug release rate during circulation than the rate of drug uptake into tumor ensured a greater antitumor effect without systemic toxicity.

In Vitro Biological Activity of SMA−THP Micelles. As shown in Figure 5, the cytotoxic effect of SMA−THP micelles on MCF-7 and SW480 cells was quite similar to that of free drug (93−101%) after 72 h of incubation. However, lower in vitro cytotoxicity is known for other polymeric anthracycline conjugates or complexes such as hydroxypropyl methacrylate copolymer-conjugated doxorubicin, (*33*, *34*). To explain the cause of

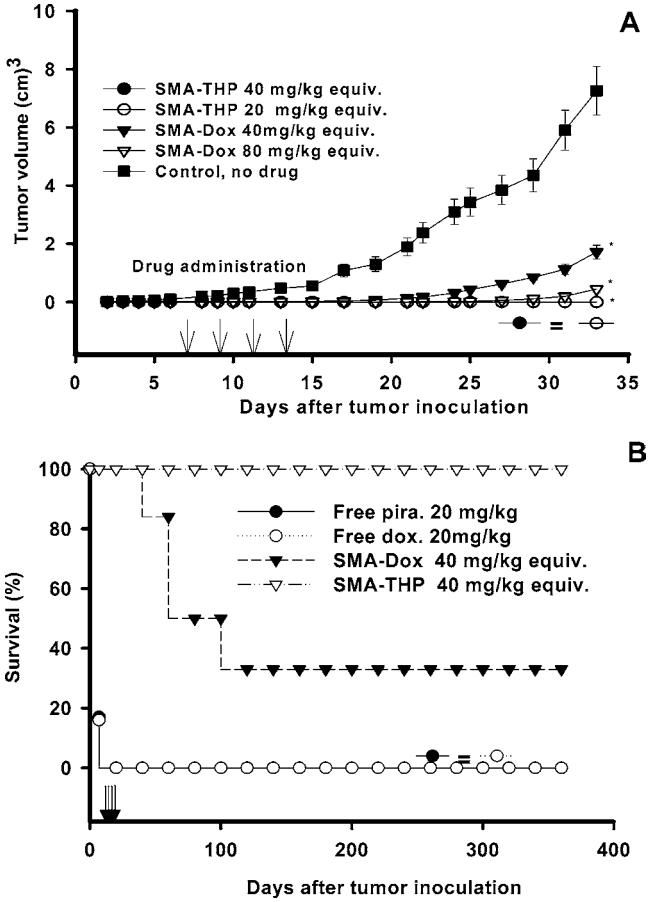

Figure 6. (A) Antitumor effect of SMA−THP micelles on implanted S-180 solid tumor in mice compared with that of control and SMA−doxorubicin micelles. Animals receiving similar dosage of free pirarubicin died within 1 week. Data are means ± SD for 12 tumors; *p < 0.001. (B) Survival of ddY mice after administration of both SMA−THP and SMA−Dox micelles compared with that after treatment with free drugs. Drugs were administered in four equal iv injections into the tail vein during a 1-week period. Observations continued for >1 year.

the similar in vitro cytotoxicity of the free drug and the micellar drug, we are currently investigating the possibility of receptor-mediated uptake, which may account for the high activity of the SMA−THP micelles. In addition to the endocytic mechanism by which most polymeric drugs operate, receptor-mediated uptake may occur: the one extra pyranyl residue in pirarubicin, compared with doxorubicin, may be involved in a receptor-mediated transport (*35*).

Antitumor Activity of SMA−THP Micelles in Vivo. For evaluation of antitumor activity tumor volume was measured in ddY mice bearing S-180 tumors for more than 30 days (Figure 6A), and survival of these mice was followed for more than 300 days as (Figure 6B). Treatment with SMA−THP micelles at two dosages, 20 and 40 mg/kg of free THP equivalent (given in four equal injections), completely suppressed tumor growth. All mice treated with SMA−THP micelles were tumor free. This finding is in great contrast to treatment with free THP, at 10 mg/kg total dose, which caused all mice to die within 1 week because of toxicity. In addition, mice given the 40 mg/kg of free THP equivalent dosage of the SMA−THP micelles demonstrated 100% survival for more than 300 days without any delectable tumor.

Potential Toxicity of SMA−THP Micelles. Tables 1 and 2 show results of blood assays and cardiac and liver function tests for mice receiving 33 mg/kg SMA−THP

Table 1. Blood Analysis for ddY Mice Receiving a Single Dose of 10 mg/kg Free Pirarubicin or 20 mg/kg Pirarubicin Equivalent as SMA−THP[a]

drug treatment	time when measured	hemoglobin (g/dL)	white blood cell count (cells/μL)	platelet count (/mm^3)
control		14.9 ± 1.3	8012 ± 1559	132.8 ± 15.3
free pirarubicin	1 week[b]	11.1 ± 2.6[c]	2533 ± 305[c]	67.6 ± 2.5[c]
SMA−THP	1 week	15.0 ± 2.5	6016 ± 1622	141.3 ± 16.1
	2 weeks	14.1 ± 1.6	5900 ± 2128	130.3 ± 10.9
	3 weeks	15.9 ± 0.4	6366 ± 1903	120.0 ± 32.5

[a] Values are means ± SD; n= 4. [b] Only one animal survived after the first week. [c] The difference from the control was statistically significant ($p < 0.05$).

Table 2. Liver Function and Cardiac Enzyme Assays for ddY Mice Receiving a Single Dose of 10 mg/kg Free Pirarubicin or 20 mg/kg Pirarubicin Equivalent Dose as SMA−THP[a]

drug treatment	CK (U/L)	LDH (IU/L)	ALT (IU/L)	AST (IU/L)
control	309 ± 42	260 ± 62.4	37 ± 12	81 ± 7.3
free pirarubicin	1704 ± 102[b]	634 ± 58[b]	53 ± 8.2	239 ± 18[b]
SMA−THP	381 ± 35	318 ± 42	58 ± 11	73.5 ± 6

[a] Values are means ± SE. CK, creatine kinase; LDH, lactate dehydrogenase; ALT, alanine aminotransferase; AST, aspartate aminotransferase. [b] The difference from the control was statistically significant ($p < 0.05$).

micelles (20 mg/kg free pirarubicin equivalent) and for mice receiving 10 mg/kg free pirarubicin. The values obtained for mice receiving the micellar drug (33 mg/kg) were not statistically different from those of normal healthy mice. In contrast, animals receiving free pirarubicin showed serious side effects, with significant differences from the control group without drug on all measurements.

All S-180 tumor-bearing mice receiving a total dose of 166 mg/kg of the micellar preparation (100 mg/kg free pirarubicin equivalent), by four iv injections (41.5 mg/kg × 4) in 1 week, or 133 mg/kg as a single iv bolus, survived for more than 12 months. In contrast, mice receiving a total dose of 20 mg/kg free THP by four iv injections (5 mg/kg × 4) had a much reduced survival: 83% died within 1 week and the remaining 17% died within 3 weeks (Figure 6B).

The reduced toxicity of the micelles can be attributed to the EPR effect and tumor-selective drug targeting. This EPR effect is a molecular size-dependent phenomenon, which is seen for molecular sizes above M_r 40 000 (*8*, *9*). For example, molecular size of THP with biocompatible SMA, which binds with albumin, becomes larger (Figure 3). Such large macromolecules leak out of tumor vessels into tumor tissues (interstitium) and remain sequestered in the vicinity of the tumor as a result of anatomical and pathophysiological abnormalities of tumor tissues, i.e., by EPR effect (*5*, *8*, *11*, *36*−*41*). The dependence on molecular size of drug uptake into tumor is inversely correlated with the renal clearance of small molecular compounds (*5*, *8*−*11*). Therefore, the SMA−THP micelles, with an apparent molecular size in plasma of 94 kDa, will remain in circulation and, as a result of the EPR effect, lead to more selective targeting of drug to tumor.

Pathological examination of cardiac tissue by H&E staining showed extensive inflammation in animals receiving injections of free THP (5 mg/kg × 4), whereas tumor-bearing mice receiving SMA−THP (41.5 mg/kg × 4) showed no abnormalities. This high safety profile of these SMA−THP micelles can be attributed to the nature of the distribution of polymeric drugs (i.e., the EPR effect). In our previous work, we showed that SMA−doxorubicin micelles accumulated in tumors 13-fold more than that did free doxorubicin. Further more, doxorubicin delivered to cardiac tissue after administration of these micelles was only 8%. However, as is evident from results presented in Figure 6A and B, the new SMA−THP micelles had a far better antitumor effect, with even lower doses of the micellar drug, and produced longer survival; these effects may be attributed to better targeting of drug to tumor and improved accumulation of drug in tumor (*29*). This EPR effect-dependent distribution profile (high drug concentration in tumor but low drug level in normal tissues) ensures a higher margin of safety for normal organs and tissues, the end result being safer dose escalation of the SMA−THP micelle preparation, up to 15 times higher than the maximum tolerable dose of free pirarubicin.

In addition to its pharmacokinetic and pharmacodynamic advantages, SMA is known to confer immunopotentiating effects, such as activation of macrophages, T-cells, and natural killer cells, and induction of interferon (*25*−*28*). These immune system modifications can be considered another benefit of SMA-based micelles.

In summary, the present study described the preparation and characterization of SMA−THP micelles, the antitumor effect of this formulation, and preliminary safety data in mice. Further study of this micellar preparation is warranted.

ACKNOWLEDGMENT

The authors thank both Judith Gandy and Yukiko Koga for their valuable editorial help in the manuscript. This work was supported in part by Grants-in-Aid for Cancer Research to H.M. from the Ministry of Education, Culture, Sports, Science and Technology of Japan.

LITERATURE CITED

(1) Tsuruo, T., Iida, H., Tsukagoshi, S., and Sakurai, Y. (1982) 4′-O-Tetrahydropyranyladriamycin as a potential new antitumor agent. *Cancer Res*. *42*, 1462−1467.

(2) Kimura, K. (1986) A phase II study of (2″R)-4′-O-tetrahydropyranyladriamycin (THP) in patients with hematological malignancies. THP Study Group. *Jpn. J. Cancer Chemother. 13*, 368−375.

(3) Enomoto, K., Abe, O., Tominaga, T., Abe, R., Iino, Y., Koyama, H., Fujimoto, M., and Nomura, Y. (1990) Clinical study of pirarubicin for breast cancer in Japan. Clinical Study Group of THP for Breast Cancer in Japan. Am. *J. Clin. Oncol. 13*, Suppl 1, S48−53.

(4) Izumi, N., and Goto, Y. (1990) A clinical trial of transarterial chemoembolization for hepatocellular carcinoma using 4-O-tetrahydropyranyladriamycin. *Jpn. J. Cancer Chemother. 17*, 1303−1307.

(5) Matsumura, Y., and Maeda, H. (1986) A new concept for macromolecular therapeutics in cancer chemotherapy: Mechanism of tumor tropic accumulation of proteins and antitumor agent SMANCS. *Cancer Res. 46*, 6387−6392.

(6) Maeda, H. (1991) SMANCS and polymer-conjugated macromolecular drugs: Advantages in cancer chemotherapy. *Adv. Drug Delivery Rev*. *6*, 181−202.

(7) Maeda, H., Seymour, L. W., and Miyamoto, Y. (1992) Conjugates of anticancer agents and polymers: Advantages of macromolecular therapeutics in vivo. *Bioconjugate Chem. 3*, 351−362.
(8) Noguchi, Y., Wu, J., Duncan, R., Strohalm, J., Ulbrich, K., Akaike, T., and Maeda, H. (1998) Early phase tumor accumulation of macromolecules: A great difference in clearance rate between tumor and normal tissues. *Jpn. J. Cancer Res. 89*, 307−314.
(9) Maeda, H., Wu, J., Sawa, T., Matsumura, Y., and Hori, K. (2000) Tumor vascular permeability and the EPR effect in macromolecular therapeutics: A review. *J. Controlled Release 65*, 271−284.
(10) Maeda, H., Sawa, T., and Konno, T. (2001) Mechanism of tumor-targeted delivery of macromolecular drugs, including the EPR effect in solid tumor and clinical overview of the prototype polymeric drug SMANCS. *J. Controlled Release 74*, 47−61.
(11) Maeda, H. (2001) The enhanced permeability and retention (EPR) effect in tumor vasculature: The key role of tumor-selective macromolecular drug targeting. *Adv. Enzyme Regul. 41*, 189−207.
(12) Folkman, J. (1971) Tumor angiogenesis in cancer: Therapeutic implications. *N. Engl. J. Med. 285*, 1182−1186.
(13) Maeda, H., Matsumura, Y., and Kato, H. (1988) Purification and identification of [hydroxyprolyl3]bradykinin in ascitic fluid from a patient with gastric cancer. *J. Biol. Chem. 263*, 16051−16054.
(14) Maeda, H., Noguchi, Y., Sato, K., and Akaike, T. (1994) Enhanced vascular permeability in solid tumor is mediated by nitric oxide and inhibited by both new nitric oxide scavenger and nitric oxide synthase inhibitor. *Jpn. J. Cancer Res. 85*, 331−334.
(15) Wu, J., Akaike, T., and Maeda, H. (1998) Modulation of enhanced vascular permeability in tumors by a bradykinin antagonist, a cyclooxygenase inhibitor, and a nitric oxide scavenger. *Cancer Res. 58*, 159−165.
(16) Wu, J., Akaike, T., Hayashida, K., Okamoto, T., Okuyama, A., and Maeda, H. (2001) Enhanced vascular permeability in solid tumor involving peroxynitrite and matrix metalloproteinases. *Jpn. J. Cancer Res. 92*, 439−451.
(17) Senger, D., Galli, S., Dvorak, A., Perruzzi, C., Harvey, V., and Dvorak, F. (1983) Tumor cells secrete a vascular permeability factor that promotes accumulation of ascites fluid. *Science 219*, 983−985.
(18) Kobayashi, M., Oda, T., and Maeda, H. (1988) Protein binding of macromolecular anticancer agent SMANCS: Characterization of poly(styrene-*co*-maleic acid) derivatives as an albumin binding ligand. *J. Bioact. Compat. Polym. 3*, 319−333.
(19) Oka, K., Miyamoto, Y., Matsumura, Y., Tanaka, S., Oda, T., Suzuki, F., and Maeda,H. (1990) Enhanced intestinal absorption of a hydrophobic polymer-conjugated protein drug, SMANCS, in an oily formulation. *Pharm. Res. 7*, 852−855.
(20) Iwai, K., Maeda, H., and Konno, T. (1984) Use of oily contrast medium for selective drug targeting to tumor: Enhanced therapeutic effect and X-ray image. *Cancer Res. 44*, 2114−2121.
(21) Iwai, K., Maeda, H., Konno, T., Matsumura, Y., Yamashita, R., Yamasaki, K., Hirayama, S., and Miyauchi, Y. (1987) Tumor targeting by arterial administration of lipids: Rabbit model with VX2 carcinoma in the liver. *Anticancer Res. 7*, 321−327.
(22) Konno, T., Maeda, H., Iwai, K., Maki, S., Tashiro, S., Uchida, M., and Miyauchi, Y. (1984) Selective targeting of anti-cancer drug and simultaneous image enhancement in solid tumors by arterially administered lipid contrast medium. *Cancer 54*, 2367−2374.
(23) Maki, S., Konno, T., and Maeda, H. (1985) Image enhancement in computerized tomography for sensitive diagnosis of liver cancer and semiquantitation of tumor selective drug targeting with oily contrast medium. *Cancer 56*, 751−757.
(24) Oda, T., Sato, F., and Maeda, H. (1987) Facilitated internalization of neocarzinostatin and its lipophilic polymer conjugate, SMANCS, into cytosol in acidic pH. *J. Natl. Cancer Inst. 79*, 1205−1211.
(25) Oda, T., Morinaga, T., and Maeda, H. (1986) Stimulation of macrophage by polyanions and its conjugated proteins and effect on cell membrane. *Proc. Soc. Exp. Biol. Med. 181*, 9−17.
(26) Suzuki, F., Munakata, T., and Maeda, H. (1988) Interferon induction by SMANCS: A polymer-conjugated derivative of neocarzinostatin. *Anticancer Res. 8*, 97−103.
(27) Suzuki, F., Pollard, R. B., Uchimura, S., Munakata, T., and Maeda, H. (1990) Role of natural killer cells and macrophages in the nonspecific resistance to tumors in mice stimulated with SMANCS, a polymer-conjugated derivative of neocarzinostatin. *Cancer Res. 50*, 3897−3904.
(28) Masuda, E., and Maeda, H. (1996) Changes in cellular components of spleen and lymph node cells and the effector cells responsible for Meth A tumor eradication induced by zinostatin stimalamer. *Cancer Res. 56*, 1868−1873.
(29) Greish, K., Sawa, T., Fang, J., Akaike, T., and Maeda, H. (2003) SMA-doxorubicin, a new polymeric micellar drug for effective targeting to solid tumours. *J. Controlled Release 97*, 219−230.
(30) Mosmann, T. (1983) Rapid colorimetric assay for cellular growth and survival: Application to proliferation and cytotoxicity assay. *J. Immunol. Methods 65*, 55−63.
(31) Sahoo, S. K., Sawa, T., Fang, J., Tanaka, S., Miyamoto, Y., Akaike, T., and Maeda, H. (2002) Pegylated zinc protoporphyrin: A water-soluble heme oxygenase inhibitor with tumor-targeting capacity. *Bioconjugate Chem. 13*, 1031−1038.
(32) Sidney, U. (1969) Proteins and peptides. *Fluorescence Assay in Biology and Medicine* (Sidney, U., Ed.) pp 272−274, Academic Press, London.
(33) Duncan, R. (1999) Polymer conjugates for tumour targeting and intracytoplasmic delivery. The EPR effect as a common gateway? *Pharm. Sci. Technol. Today 2*, 441−449.
(34) Kopecek, J., Kopeckova, P., Minko, T., and Lu, Z. R. (2000) HPMA copolymer-anticancer drug conjugates: Design, activity, and mechanism of action. *Eur. J. Pharm. Biopharm. 50*, 61−81.
(35) Kato, Y., and Sugiyama, Y. (1997) Targeted delivery of peptides, proteins, and genes by receptor-mediated endocytosis. *Crit. Rev. Ther. Drug Carrier Syst. 3*, 287−331.
(36) Konno, T. (1992) Targeting chemotherapy for hepatoma: Arterial administration of anticancer drugs dissolved in Lipiodol. *Eur. J. Cancer 28*, 403−409.
(37) Seymour, L., Miyamoto, Y., Maeda, H., Brereton, M., Strohalm, J., Ulbrich, K., and Duncan, R. (1995) Influence of molecular weight on passive tumour accumulation of a soluble macromolecular drug carrier. *Eur. J. Cancer 31*, 766−770.
(38) Muggia, F. (1999) Doxorubicin-polymer conjugates: Further demonstration of the concept of enhanced permeability and retention. *Clin. Cancer Res. 5*, 7−8.
(39) Maeda, H., Takeshita, J., and Kanamaru, R. (1979) A lipophilic derivative of neocarzinostatin. A polymer conjugation of an antitumor protein antibiotic. *Int. J. Pept. Protein Res. 14*, 81−87.
(40) Maeda, H., and Kojima Y. (1997) Polymer-drug conjugates. *Desk Reference of Functional Polymers: Synthesis and Application* (Arshady, R., Ed.) pp 753−767, American Chemical Society, Washington, DC.
(41) Greish, K., Fang, J., Inutsuka, T., Nagamitsu, A., and Maeda, H. (2003) Macromolecular therapeutics: Advantages and prospects with special emphasis on solid tumourtargeting. *Clin. Pharmacokinet. 42*, 1089−1105.

BC040297G

Conjugation of DOTA Using Isolated Phenolic Active Esters: The Labeling and Biodistribution of Albumin as Blood Pool Marker

Walter Mier,*,† Johannes Hoffend,† Susanne Krämer,† Jochen Schuhmacher,‡ William E. Hull,‡ Michael Eisenhut,‡ and Uwe Haberkorn†

Department of Nuclear Medicine, Universitätsklinikum Heidelberg, INF 400, 69120 Heidelberg, Germany, and German Cancer Research Center, 69120 Heidelberg, Germany. Received November 28, 2003; Revised Manuscript Received September 28, 2004

A convenient method for the functionalization of proteins with DOTA (1,4,7,10-tetraazacyclododecane-1,4,7,10-tetraacetic acid) has been developed. For this purpose DOTA was converted into a series of different monoreactive activated phenolic esters. The esters were prepared in a single step from commercially available DOTA, using 1-ethyl-3-[3-(dimethylamino)propyl]carbodiimide or 1,3-dicyclohexylcarbodiimide as coupling agent. The resulting activated esters were isolated by HPLC, lyophilized, and stored for future applications. In solid form the compounds exhibit high hydrolytic stability. The reactions with proteins proceeded in good yields. The conjugation and subsequent radiolabeling of the 4-nitrophenol ester of DOTA with ^{67}Ga was investigated with rat serum albumin. A time-dependent biodistribution study in tumor bearing rats was conducted to demonstrate the integrity of the albumin conjugate. These results suggest that phenolic esters of DOTA represent versatile reagents to conjugate DOTA with proteins and other biomolecules in high yields.

Bifunctional chelating agents have been shown to be potent ligands for the labeling of molecules such as peptides and antibodies with radioactive isotopes or paramagnetic metals. As there is strong interest in the development of these agents, for example for the application of radioactive metals toward "targeted" diagnosis and therapy of cancer, a variety of bifunctional chelating agents have been synthesized and summarized in a review (*1*).

DOTA (1,4,7,10-tetraazacyclododecane-1,4,7,10-tetraacetic acid) is known to complex a large number of main group and transition metal ions with extremely high stability constants, coordinating, for example, Y^{3+} with the four cyclic nitrogens and the three carboxylates. Because of their high stability constant, metal complexes of DOTA conjugates exhibit better in vivo stability than other chelates such as DTPA (diethylenetriaminepentaacetate).

Potential classes of molecules, which can be conjugated to the chelating agents, are peptides, saccharides, nucleic acids, and proteins. However, the convenient high yield protocols for the conjugation of chelating agents to biomolecules still need to be improved. These conjugation protocols are needed for diagnostic and therapeutic applications as well as for screening peptides in radiopharmaceutical research.

At present, the preferred derivatives of DOTA for the conjugation to proteins are the isothiocyanate *p*-isothiocyanatobenzyl-1,4,7,10-tetraazacyclododecane-1,4,7,10-tetraacetic acid and esters of NHS (*N*-hydroxysuccinimide) that can be obtained by in situ activation (*2*). The in situ activation of the chelating agents leads to a mixture of mono- and multiply activated chelating agents which may react to more than one target molecule. As a consequence, the conjugation reaction is prone to the formation of intra- or intermolecular cross-links. To secure the formation of defined products, extensive efforts have been made to optimize the reaction conditions. Under these conditions, reactions with less than 1% of intermolecular cross-linked species are achievable (*3*). The reaction of more than one carboxylic acid of the chelating agent might lead to a decrease of complex stability. To optimize the in situ activation, the reaction mixture must contain a large excess of chelating agent (typically a 100-fold excess). This excess of chelating agent can nonspecifically aggregate to the target molecules. These aggregates may prolong the purification step and dissociate in vivo, leading to an undefined biodistribution of the label.

Another possibility is to generate spacer-modified chelating agents carrying active groups such as isothiocyanate for the conjugation with target molecules (*4, 5*). This approach necessitates a sophisticated, laborious synthesis of the precursor molecules. Advances have been made to develop spacer-modified linkers that allow the modulation of the pharmacokinetics of the chelator conjugates (*6, 7*). Several other methods for the specific conjugation of DOTA have been developed (*8*−*12*). Defined products of chelating agents with target molecules can be obtained by using selectively protected chelating agents (*13*). The remaining unblocked functional group can then be used for conjugation with the target molecule. However, the synthesis of the partially protected precursor is laborious, and after conjugation, a deprotection step is needed which leads to the denaturation of sensitive biomolecules, in particular in the case of proteins.

The application of activated monoesters represents an efficient method for the preparation of DOTA−protein conjugates. Because of the lability of these compounds, only limited information is available for the preparation, purification, and analysis of the active esters of DOTA.

* To whom correspondence should be addressed. Tel.: 0049-6221-567720, e-mail: walter_mier@med.uni-heidelberg.de.
† Universitätsklinikum Heidelberg.
‡ German Cancer Research Center.

10.1021/bc034216c CCC: $30.25 © 2005 American Chemical Society
Published on Web 12/07/2004

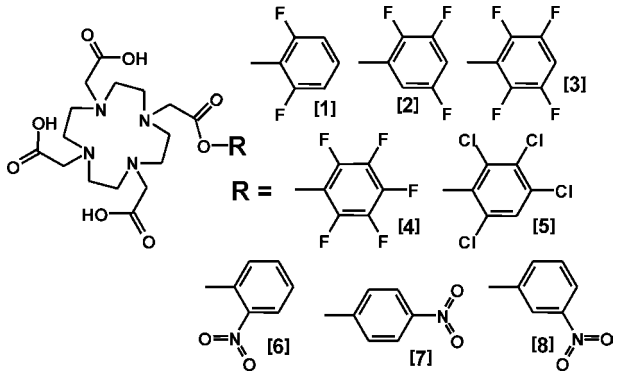

Figure 1. Chemical structures of the active esters of DOTA investigated.

Hitherto the NHS-ester and its water soluble derivative, the sulfo-NHS-ester, were the only active esters of DOTA described in the literature. During our investigations, an elaborate synthesis of the tetrafluorophenyl ester of DOTA was described (*14*). Other activated esters have not yet been reported. As compared to NHS-esters, phenolic esters (*15*, *16*) offer the advantage of an aromatic chromophore favoring UV detection during HPLC separation. These reasons prompted us to develop a straightforward synthesis of a DOTA monoester applicable for conjugation in solution or for solid-phase syntheses (*17*).

Because of the low solubility of unprotected DOTA under nonaqueous conditions, the reaction was conducted in aqueous solution containing acetonitrile using the water-soluble carbodiimide 1-ethyl-3-[3-(diamino)propyl]-carbodiimide × hydrochloride (EDAC) or diisopropylcarbodiimide as condensing agent. Another possibility is the synthesis using higher concentrations of the cosolvents such as acetonitrile or DMF. In this case, the carbodiimide *N*,*N*′-dicyclohexylcarbodiimide (DCC) can be used as a condensing agent. The highest yields of the phenolic esters could be obtained using stoichiometric amounts of DOTA, the substituted phenol and EDAC, or DCC.

The activated esters were obtained by dissolving 500 mg (1.24 mmol) of DOTA (Fluka, Taufkirchen, Germany) in 10 mL of water. A solution of 1.24 mmol of the particular phenol in 8 mL of acetonitrile was added. A solution of 255 mg (1.24 mmol) of *N*,*N*′-dicyclohexylcarbodiimide in 8 mL of pyridine was added dropwise with vigorous stirring. The reaction mixture was stirred for 90 min and concentrated to dryness under reduced pressure. The residue was taken up in 20% acetonitrile in water. The suspension was filtered to remove *N*,*N*′-dicyclohexylurea, and the filtrate was lyophilized. RP-HPLC (RP-select B column 10 μm, 250 × 10 mm Merck, Darmstadt, Germany) with a linear gradient from 0 to 60% acetonitrile (flow = 4 mL/min over 15 min) afforded the pure activated esters (34−65% yield) after lyophilization. Under these conditions, the monoactivated phenolic esters could be formed with surprisingly high selectivity. Compounds **1**−**8** (Figure 1) were characterized by analytical HPLC-chromatography and mass spectrometry. MALDI-MS or ESI-MS (*m*/*z*) for $[M + H]^+$: observed (calculated): **1** = 518 (517.49), **2** = 535 (535.48), **3** = 552 (553.47), **4** = 572 (571.47), **5** = 619 (619.29), **6** = 527 (526.51), **7** = 527 (526.51), **8** = 527 (526.51). The DOTA-bis-phenol-esters were the major byproducts formed under these conditions. The purification proved to be uncomplicated because the product eluted as a single peak. The HPLC profiles of a typical reaction mixture are shown in Figure 2A. The reaction mixture obtained with PNP and DCC is shown as a second example in Figure 2B. Using 2 equiv of DCC, the proportion of multiply activated species is strongly increased. The identity of the lyophilized compounds was further proven by NMR spectroscopy of **7**. This NMR analysis turned out to be complicated because several stable conformers result in broad signals at ambient temperature. At high temperature (373.5 K), a good resolution was achieved (Figure 3).

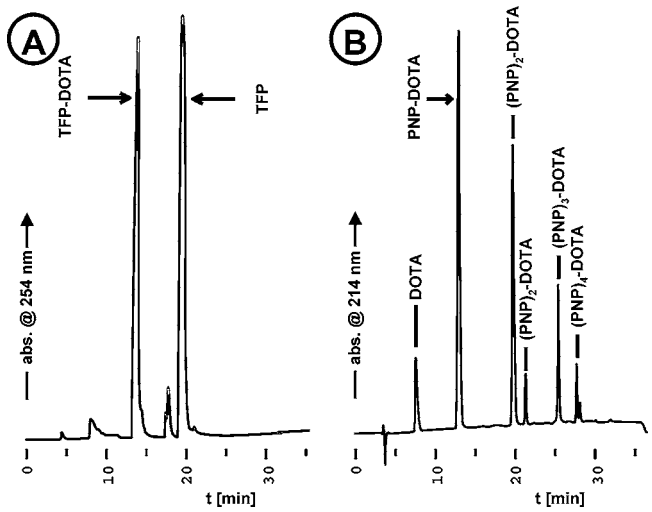

Figure 2. Reverse phase HPLC profiles of two representative reaction mixtures [A] TFP + EDAC and DOTA (1:1:1) and [B] PNP + DCC and DOTA (1:2:1) on a LiChrospher RP-select B 5 μm, 250 × 4 mm column (Merck, Darmstadt, Germany) using a linear gradient from 100% H_2O to 100% acetonitrile (both containing 0.1% TFA) in 30 min, flow rate: 0.7 mL/min).

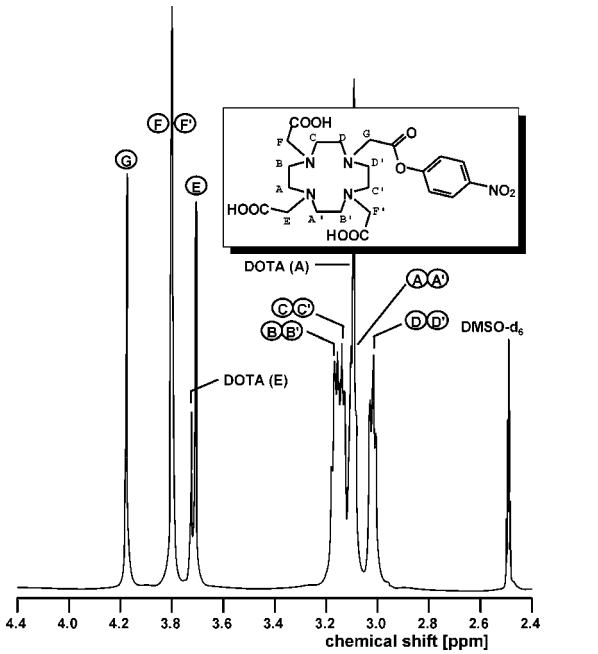

Figure 3. ^{1}H NMR spectrum (aliphatic hydrogens) of **7** in DMSO-d_6 at 80 °C. At high-temperature hydrolysis is observed to yield DOTA (signals A and E).

To characterize the feasibility of these esters, the rate of hydrolysis under different pH conditions was examined at room temperature. As the hydrolysis competes with the aminolysis (which leads to the amide-bonded product), this pH-dependent stability investigation allows the choice of appropriate reaction conditions for an active ester chosen. The comparison of the stability of **1**, **3**, and **7** and the NHS-ester of DOTA obtained from Macrocyclics (Dallas, TX) is shown in Figure 4. As expected, there is

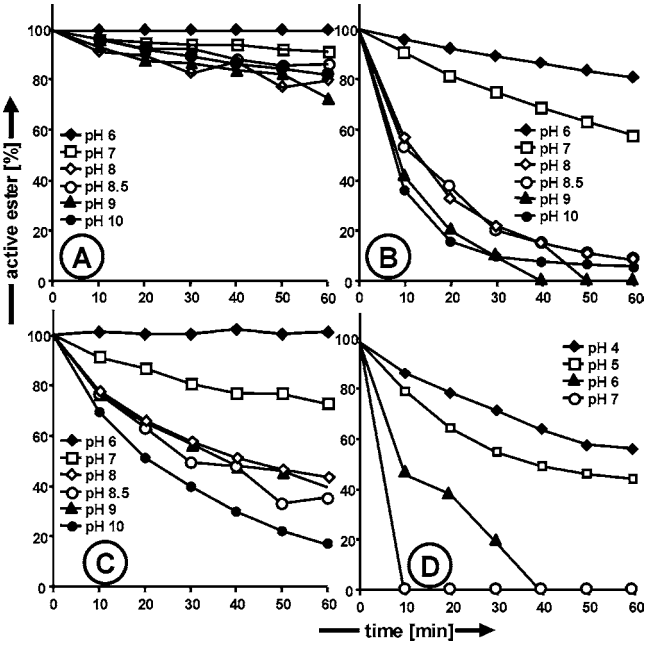

Figure 4. Stability of the phenolic esters **1** [A], **3** [B] and **7** [C] as compared to the NHS-ester of DOTA [D] in aqueous solution under a range of pH conditions. The active esters **1**, **3** and **7** were dissolved at a concentration of 1 mg/mL in borate buffer, the NHS-ester of DOTA was dissolved in citrate buffer. At various time points samples were taken and the concentration determined by RP-HPLC.

a substantial difference between the esters **1** and **3**. Whereas for **1** a relative high stability was found for pH values from 6 to 10, for **3** a slow cleavage was found even at neutral pH-values. The ester **7** revealed a stability profile which appears to be suitable for conjugation reactions at pH values from 7 to 9. The NHS-ester was rapidly hydrolyzed at neutral pH values.

The DOTA conjugation using active phenolic esters was utilized for the modification of rat serum albumin. Albumin was chosen because of the potential utility of albumin-derived radiotracers for making blood pool corrections for myocardial perfusion imaging as well as for the characterization of angiogenetic tumors.

The conjugation reaction was carried out by adding a solution of 10 mg of rat serum albumin (Sigma, Taufkirchen, Germany) in 0.1 M phosphate buffer pH 8.0 to 10 equiv of the lyophilized DOTA-phenolic ester (e.g. 875 μg of **7**). The components were mixed and incubated at room-temperature overnight. The conjugate was purified by gel filtration on a Superdex 75 column (Amersham Pharmacia, Freiburg, Germany) eluted with 0.05 M sodium phosphate 0.15 M NaCl buffer at pH 7. The eluted product was concentrated by 10 kDa molecular weight cutoff ultrafiltration membrane centrifugal filter devices (Amicon Ultra, Millipore). Protein concentrations were quantitated by the Bradford method (*18*).

The labeling was achieved by incubating the DOTA−albumin conjugate (obtained from **7**) with $^{67}Ga^{3+}$ chloride (Bristol-Myers Squibb) in 0.1 M ammonium acetate buffer pH 5 for 6 h at 42 °C. The labeling efficiency of the preparations was >90% as assessed by size exclusion HPLC under the conditions described above. Purification of the labeled compound by size exclusion HPLC led to a product typically with >98% of the radioactivity corresponding to ^{67}Ga-DOTA−albumin.

The number of functional chelates per albumin molecule was determined by isotopic dilution titration using trace amounts of $^{67}Ga^{3+}$ in the presence of a range of concentrations of 'cold' Ga^{3+} in 0.1 M ammonium acetate buffer pH 5.0. After 12 h at 42 °C, excess of DTPA was added and the amount of albumin-bound ^{67}Ga determined by TLC (ITLC−SG, Pall, Dreieich Germany) using 0.9% NaCl in water as the mobile phase. This analysis revealed that the conjugation of DOTA using **7** was effective with an approximate reaction-to-hydrolysis ratio of 1:4. A standard batch obtained from the reaction of 10 mg rat serum albumin with 760 μg of **7** (10 equiv of activated ester) resulted in approximately two functional DOTA chelates per albumin molecule.

The biodistribution of ^{67}Ga-DOTA−albumin was evaluated in male ACI rats bearing subcutaneous MH3924A Morris hepatoma (*19*). The experiments were performed in compliance with German laws relating to the conduct of animal experimentation. Tumor cells (4×10^6) were transplanted subcutaneously into the right thigh of male young adult ACI rats weighing 200−250 g and grown for approximately three weeks to a volume of 1.5 cm in diameter. A solution of ^{67}Ga-DOTA−albumin (2 MBq in 0.2 mL) was intravenously injected via the lateral tail vein. At selected times, rats were sacrificed and the radioactivity contained in the blood, heart, spleen, liver, kidney, muscle, brain, and tumor was measured in a γ-counter (Canberra Packard, Rüsselsheim, Germany) and expressed as a percentage of injected dose per gram of tissue (%ID/g) (Figure 5). Three rats were used for each

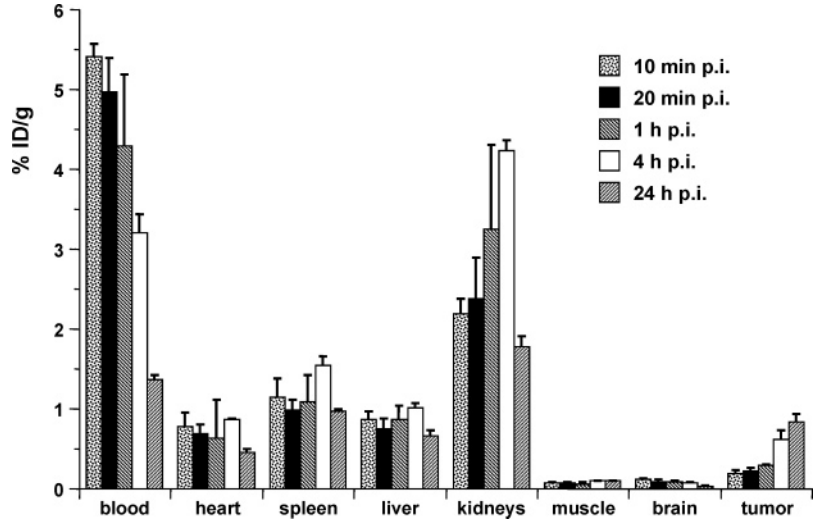

Figure 5. Time dependent organ distribution of ^{67}Ga labeled rat serum albumin in hepatoma-bearing rats.

time point. The data were in accordance with literature data obtained for both ^{125}I-labeled and ^{67}Cu-labeled benzyl-TETA albumin (*20*). As compared to ^{67}Cu-labeled benzyl-TETA-HSA a significantly lower liver uptake was observed (0.86%ID/g vs 2.37%ID/g) because of the intense hepatic metabolism and retention of copper radioisotopes.

Owing to the long circulation time, albumin can also be used as a high molecular weight carrier for drug delivery purposes. However, the biological half-life of albumin is known to be sensitive to high loading ratios (*21*). The best results were obtained with an approximate 1:1 cargo-to-albumin ratio (*22*). A higher number of molecules conjugated to albumin causes alterations of the secondary and tertiary structure, consecutively triggering the rapid sequestration by the monocyte−phagocyte system. The long circulation times allow albumin to passively accumulate in the tumor through the Enhanced Permeability and Retention (EPR) effect (*23*). This phenomenon is due to the increased permeability of tumor vasculature that permits large macromolecules to extravasate into the tumor tissue where they are retained due to an impaired reticuloendothelial/lymphatic clearance of macromolecules.

In summary, the method described here transforms the commercially available DOTA to useful active esters (**1** to **8**) which after purification can be stored and used for DOTA conjugation reactions. The stability of these active esters is suitable to optimize protocols for an efficient, controlled conjugation to proteins, peptides, and other molecules of biological interest, without the necessity of subsequent removal of protecting groups.

ACKNOWLEDGMENT

This study was supported by grants from the Wilhelm Sander-Stiftung (grant number 1999.085.1) and the 'Tumorzentrum Heidelberg/Mannheim'.

LITERATURE CITED

(1) Liu, S., and Edwards, D. S. (2001) Bifunctional chelators for therapeutic lanthanide radiopharmaceuticals. *Bioconjugate Chem. 12*, 7−34.

(2) Lewis, M. R., Raubitschek, A., and Shively, J. E. (1994) A facile, water-soluble method for modification of proteins with DOTA. Use of elevated temperature and optimized pH to achieve high specific activity and high chelate stability in radiolabeled immunoconjugates. *Bioconjugate Chem. 5*, 565−576.

(3) Lewis, M. R., Kao, J. Y., Anderson, A. L., Shively, J. E., and Raubitschek, A. (2001) An improved method for conjugating monoclonal antibodies with *N*-hydroxysulfosuccinimidyl DOTA. *Bioconjugate Chem. 12*, 320−324.

(4) Li, M., and Meares, C. F. (1993) Synthesis, metal chelate stability studies, and enzyme digestion of a peptide-linked DOTA derivative and its corresponding radiolabeled immunoconjugates. *Bioconjugate Chem. 4*, 275−283.

(5) Li, M., Meares, C. F., Zhong, G. R., Miers, L., Xiong, C. Y., and DeNardo, S. J. (1994) Labeling monoclonal antibodies with 90yttrium- and 111indium-DOTA chelates: a simple and efficient method. *Bioconjugate Chem. 5*, 101−104.

(6) Peterson, J. J., and Meares, C. F. (1998) Cathepsin substrates as cleavable peptide linkers in bioconjugates, selected from a fluorescence quench combinatorial library. *Bioconjugate Chem. 9*, 618−626.

(7) Hoffman, T. J., Gali, H., Smith, C. J., Sieckman, G. L., Hayes, D. L., Owen, N. K., and Volkert, W. A. (2003) Novel series of 111In-labeled bombesin analogues as potential radiopharmaceuticals for specific targeting of gastrin-releasing peptide receptors expressed on human prostate cancer cells. *J. Nucl. Med. 44*, 823−831.

(8) Anelli, P. L., Lattuada, L., Gabellini, M., and Recanati, P. (2001) DOTA tris(phenylmethyl) ester: a new useful synthon for the synthesis of DOTA monoamides containing acid-labile bonds. *Bioconjugate Chem. 12*, 1081−1084.

(9) Corsi, D. M., Elst, L. V., Muller, R. N., van Bekkum, H., and Peters, J. A. (2001) Inulin as a carrier for contrast agents in magnetic resonance imaging. *Chemistry 7*, 64−71.

(10) Lewis, M. R., and Shively, J. E. (1998) Maleimidocysteineamido-DOTA derivatives: new reagents for radiometal chelate conjugation to antibody sulfhydryl groups undergo pH-dependent cleavage reactions. *Bioconjugate Chem. 9*, 72−86.

(11) Peterson, J. J., Pak, R. H., and Meares, C. F. (1999) Total solid-phase synthesis of 1, 4, 7, 10-tetraazacyclododecane-N, N′, N″, N‴-tetraacetic acid-functionalized peptides for radioimmunotherapy. *Bioconjugate Chem. 10*, 316−320.

(12) Li, L., Tsai, S. W., Anderson, A. L., Keire, D. A., Raubitschek, A. A., and Shively, J. E. (2002) Vinyl sulfone bifunctional derivatives of DOTA allow sulfhydryl- or amino-directed coupling to antibodies. Conjugates retain immunoreactivity and have similar biodistributions. *Bioconjugate Chem. 13*, 110−115.

(13) Heppeler, A., Froidevaux, S., Maecke, H. R., Jermann, E., Behe, M., Powell, P., and Hennig, M. (1999) Radiometal-labeled macrocyclic chelator-derivatised somatostatin analogue with superb tumour-targeting properties and potential for receptor-mediated internal radiotherapy. *Chem. Eur. J. 5*, 1974−1981.

(14) Mukai, T., Namba, S., Arano, Y., Ono, M., Fujioka, Y., Uehara, T., Ogawa, K., Konishi, J., and Saji, H. (2002) Synthesis and evaluation of a monoreactive DOTA derivative for indium-111-based residualizing label to estimate protein pharmacokinetics. *J. Pharm. Pharmacol. 54*, 1073−1081.

(15) Becker, J. M., Wilchek, M., and Katchalski, E. (1971) Irreversible inhibition of biotin transport in yeast by biotinyl-*p*-nitrophenyl ester. *Proc. Natl. Acad. Sci. U.S.A. 68*, 2604−2607.

(16) Kasina, S., Rao, T. N., Srinivasan, A., Sanderson, J. A., Fitzner, J. N., Reno, J. M., Beaumier, P. L., and Fritzberg, A. R. (1991) Development and biologic evaluation of a kit for preformed chelate technetium-99m radiolabeling of an antibody Fab fragment using a diamide dimercaptide chelating agent. *J. Nucl. Med. 32*, 1445−1451.

(17) Mier, W., Haberkorn, U., and Eisenhut, M. (2001) Synthesis and isolation of active esters of DOTA. *J. Labelled Comp. Radiopharm. 44*, S814−S816.

(18) Bradford, M. M. (1976) A rapid and sensitive method for the quantitation of microgram quantities of protein utilizing the principle of protein-dye binding. *Anal. Biochem. 72*, 248−254.

(19) Haberkorn, U., Altmann, A., Morr, I., Knopf, K. W., Germann, C., Haeckel, R., Oberdorfer, F., and vanKaick, G. (1997) Monitoring gene therapy with herpes simplex virus thymidine kinase in hepatoma cells: Uptake of specific substrates. *J. Nucl. Med. 38*, 287−294.

(20) Mathias, C. J., Welch, M. J., Green, M. A., Diril, H., Meares, C. F., Gropler, R. J., and Bergmann, S. R. (1991) In vivo comparison of copper blood-pool agents: potential radiopharmaceuticals for use with copper-62. *J. Nucl. Med. 32*, 475−480.

(21) Staud, F., Nishikawa, M., Morimoto, K., Takakura, Y., and Hashida, M. (1999) Disposition of radioactivity after injection of liver-targeted proteins labeled with In-111 or I-125. Effect of labeling on distribution and excretion of radioactivity in rats. *J. Pharm. Sci. 88*, 577−585.

(22) Stehle, G., Sinn, H., Wunder, A., Schrenk, H. H., Schutt, S., MaierBorst, W., and Heene, D. L. (1997) The loading rate determines tumor targeting properties of methotrexate-albumin conjugates in rats. *Anticancer Drugs 8*, 677−685.

(23) Kissel, M., Peschke, P., Subr, V., Ulbrich, K., Strunz, A. M., Kuhnlein, R., Debus, J., and Friedrich, E. (2002) Detection and cellular localisation of the synthetic soluble macromolecular drug carrier pHPMA. *Eur. J. Nucl. Med. Mol. Imaging 29*, 1055−1062.

BC034216C

MARCH/APRIL 2005
Volume 16, Number 2

© Copyright 2005 by the American Chemical Society

Bioconjugate Chemistry

COMMUNICATIONS

Coupling Biomolecules to Fullerenes through a Molecular Adapter

Marcello Capaccio, Vasilis G. Gavalas, Mark S. Meier, John E. Anthony,* and Leonidas G. Bachas*

Department of Chemistry and Advanced Carbon Materials Center, University of Kentucky, Lexington, Kentucky 40506-0055. Received June 15, 2004; Revised Manuscript Received December 12, 2004

A novel biotinylated fullerene has been synthesized to facilitate the attachment of biotin-conjugated proteins to C_{60} through the use of streptavidin as a molecular adapter. The strong biotin-streptavidin interaction enables the attachment of fullerenes to streptavidin and, because of the availability of four biotin-binding sites on streptavidin, to biotinylated biomolecules. The feasibility of this approach is demonstrated by using biotinylated alkaline phosphatase. Due to the insolubility of fullerenes in aqueous media, the immobilized enzyme can be eventually recovered by simple centrifugation with no significant loss in activity.

In recent years, fullerene derivatives have found applications in many fields of science and technology due to their special photophysical (strong absorption in the UV region and significant absorptions in the visible region) and electrochemical (electron accepting) properties (*1*−*3*). A variety of C_{60} derivatives have been successfully applied to biological/medical related studies (*4*−*8*). Moreover, C_{60} derivatives have some unique characteristics, related to the spherical shape and dimensions of the fullerene unit, which make them an attractive class of compounds from a biochemical point of view (*9*). For instance, the possibility of treating HIV with fullerenes has been explored by taking advantage of the complimentarily of C_{60} derivatives to structural features on HIV-1 protease, thus causing the inhibition of the enzyme (*10, 11*). An interesting example of coupling proteins and fullerenes was given in a recent report, in which the redox protein azurin was bound to a thiol-selective C_{60} derivative (*12*). Additionally, a biotinylated lipophilic fullerene was synthesized and used as a novel type of transmembrane anchor (*13*). Finally, C_{60} derivatized with a polyanionic dendrimer (*14*) or a histone-derived peptide (*15*) has been employed to form fullerene−protein conjugates through noncovalent interactions.

We are interested in using fullerene derivatives as building blocks to create hybrid biomolecule/fullerene nanoparticles as shown in Scheme 1. Moreover fullerenes, because of their insolubility in water and their nanosize dimensions, present advantages as immobilization supports for enzyme catalysts. Their nanometer size reduces substrate diffusion limitations that are commonly encountered with macroscopic support media. We recently described a method in which a mutant subtilisin was produced (by using molecular biology methods) and subsequently bound to a maleimidopropionyl C_{60} derivative (*16*). We now report a different strategy to attach fullerenes to biomolecules that involves the use of molecular adapters. This can be achieved through a two-step coupling procedure utilizing the strong affinity of streptavidin for biotin. Unlike prior approaches of pre-

* Corresponding authors. bachas@uky.edu. Fax: +1(859)-3231069; Tel: +1(859)2576350. anthony@uky.edu Fax: +1(859)3231069; Tel: +1(859)2578844.

10.1021/bc049861d CCC: $30.25 © 2005 American Chemical Society
Published on Web 03/01/2005

Scheme 1. Schematic Representation of the Hybrid Nanoparticle Formation through the Molecular Adapter, Streptavidin

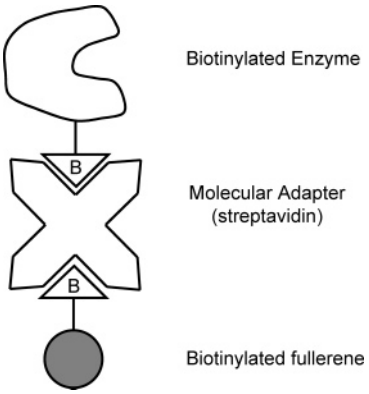

Scheme 2. Preparation of *N*-6-[(Biotinamido)-hexanoyl]-3,4-fulleropyrrolidine

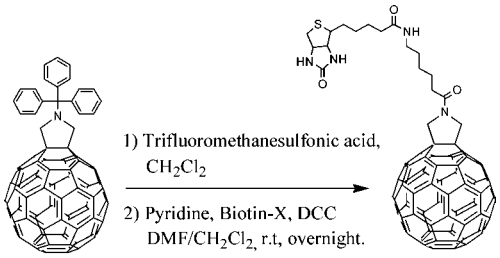

paring fullerene−protein conjugates, where a fullerene derivative is reacted with functional groups on the protein of interest, this manuscript describes a versatile method to prepare these conjugates using a molecular adapter strategy.

A new biotinylated fullerene derivative, *N*-6-[(biotinamido)hexanoyl]-3,4-fulleropyrrolidine, **2**, was synthesized as in Scheme 2. *N*-(Triphenylmethyl)-3,4-fulleropyrrolidine, **1**, was synthesized and deprotected with trifluoromethanesulfonic acid as described previously (*12*, *17*). The biotin unit was added to a fulleropyrrolidine by dicyclohexylcarbodiimide (DCC) coupling of 6-((biotinoyl)-amino)hexanoic acid (biotin-X) with **1**. In particular, anhydrous pyridine (0.6 mL) was added to a sonicated suspension of **1** (40 mg in 10 mL of dry CH_2Cl_2). In a different flask, 37.2 mg (2 equiv) of biotin-X was dissolved in 8 mL of hot dry DMF and added to the suspension with stirring. A dicyclohexylcarbodiimide solution (21.4 mg in 2 mL of dry DMF, 2 equiv) was combined with the rest of the reactants at 0 °C. The reaction mixture was stirred for 30 min in an ice bath and then at room-temperature overnight. The solution was diluted with CH_2Cl_2 (30 mL) and filtered, and the filtrate was evaporated under reduced pressure. The solid residue was washed in a Soxhlet extractor first with water and then with benzene and finally with HPLC-grade pentane; after each washing step, the solid was oven-dried at 50 °C before washing it with the subsequent solvent. A brown powder was recovered from the dried thimble, and any residual solvent adhering to the solid particles was evaporated under reduced pressure. The residue was finally dried over P_2O_5 to yield *N*-6-[(biotinamido)hexanoyl]-3,4-fulleropyrrolidine (**2**, 37.3 mg, 65%). Brown solid; ^{1}H NMR (400 MHz, Me_2SO-d_6/CS_2/C_6D_6/1:1:0.5), δ 1.26 (m, 2H), 1.30 (m, 2H), 1.32 (m, 2H), 1.44 (m, 2H), 1.5 (m, 2H), 1.6 (m, 2H), 2.06 (t, 2H), 2.56 (d, 2H), 2.65 (t, 2H), 2.8 (m, 2H), 3.08 (m, 2H), 4.13, 4.3 (m, NH*CHCH*NH of bridge of biotin ring, 2H), 5.44, 5.54 (singlets, CH_2NCH_2 of pyrrolidine ring, 4H), 6.3, 6.41 (singlets, *NH*CO*NH* of biotin ring, 2H), 7.75 (t, CO*NH* of biotin side chain, 1H); *m/z* (MS-FAB) 1102 (M^-, 10%), 720 (C_{60}, 100%).

The mass spectrometric analysis shows the presence of a single biotin moiety (1102 (M^-)) in the biotinylated C_{60} (*N*-6-[(biotinamido)hexanoyl]-3,4-fulleropyrrolidine) product. This result is consistent with data obtained using a 2-anilinonaphthalene-6-sulfonic acid (ANS) displacement assay (*18*). ANS has distinct fluorescence emission and excitation spectra depending on whether it resides in the binding pocket of streptavidin. Thus, ANS could be used as a probe to evaluate the binding of biotinylated compounds to streptavidin since the wavelength of maximum emission shifts from 422 nm (ANS bound to streptavidin) to 468 nm (free ANS) upon displacement from the binding pocket of the protein. The change in fluorescence intensity at 468 nm was the same when a solution of preformed ANS/streptavidin complex was exposed to either a biotinylated fullerene solution or to an equimolar biotin solution. These data also indicate that, despite the modification of biotin at the carboxyl group, which has been shown to reduce its affinity for streptavidin (*19*, *20*), the interaction between the biotinylated fullerene and streptavidin is strong enough to displace ANS from the binding pocket of the protein.

The aminohexanoate spacer was incorporated between biotin and C_{60} to reduce the possibility of the fullerene affecting the streptavidin−biotin interaction. Indeed, it has been demonstrated previously that when bound to streptavidin, biotin lies well below the protein surface (*21*) and at a depth that is equivalent to the length of the aminohexanoate spacer (*22*, *23*).

Initially, the specificity of the binding between the biotinylated fullerene and streptavidin was determined using a fluorescein-conjugated streptavidin (SAV−FITC). A solution of SAV−FITC (2 mg/mL) was stirred with the biotinylated fullerene (0.7 mg) for 4 h at 4 °C, and then the solution was centrifuged to remove the fullerene with the attached SAV−FITC. The fluorescence signal of the supernatant was determined, which corresponded to unbound SAV−FITC. In parallel, two control experiments were performed. In one experiment, a solution of SAV−FITC (2 mg/mL) was stirred for 4 h with C_{60} (0.5 mg) at 4 °C; in a second experiment, a solution of SAV−FITC (2 mg/mL) was first stirred with an excess of biotin (10 min) to block the binding sites, and then with the biotinylated fullerene (4 h at 4 °C). In all cases, after the incubation step the solution was centrifuged to remove the bound SAV−FITC, and the fluorescence of the supernatant was recorded (proportional to the unbound protein). A fourth solution containing only SAV−FITC was stirred under the same conditions and used as a control as well. As shown in Figure 1, when SAV−FITC was incubated with the biotinylated fullerene, the amount of unbound protein was small compared to the control (Figure 1A,C). SAV−FITC did not bind to unmodified fullerene as verified by the insignificant change in the fluorescence signal in this case (Figure 1B,C). These results demonstrate that the attachment of the biotinylated fullerene to streptavidin takes place only through the biotin moiety and is not due to nonspecific interactions of the protein with the fullerene.

When the binding sites of SAV−FITC were blocked with regular biotin, the protein did not bind to the biotinylated fullerene, as confirmed by the emission spectrum (Figure 1D). This proves that the interaction of the biotinylated fullerene with the SAV−FITC occurs

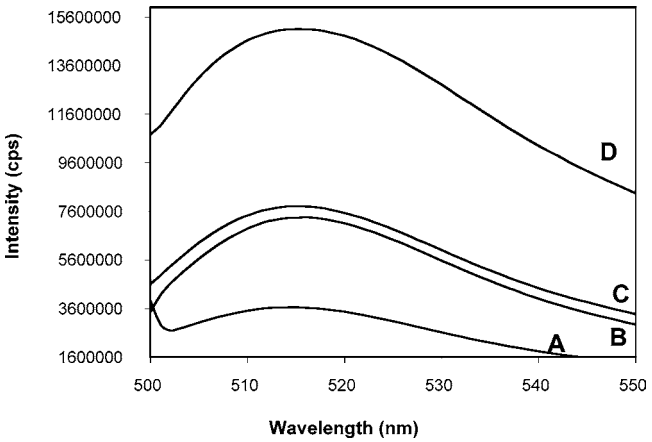

Figure 1. Fluorescence signal of supernatant solutions (λ_{ex} 490 nm) after the removal of the bound streptavidin−FITC by centrifugation. Supernatant derived from a stirred streptavidin−FITC solution: (A) with biotinylated fullerene, (B) with unmodified C_{60}, (C) untreated solution, and (D) with biotin to saturate the four binding sites first and then with biotinylated fullerene.

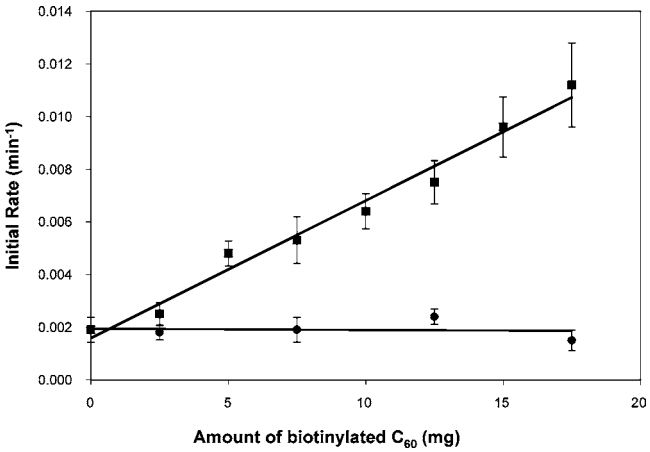

Figure 2. (■) Enzymatic activity (hydrolysis of *p*-NPP) of the hybrid fullerene−streptavidin−alkaline phosphatase nanoparticles. (●) Hydrolysis of *p*-NPP in the presence of the same amount of uncoupled biotinylated fullerene. Data are averages ± standard deviation ($n = 3$).

through the binding sites of the protein. Interestingly, in this case (Figure 1D) the signal increases upon biotin binding compared to the emission spectrum of unbound SAV−FITC (Figure 1C). This phenomenon has been observed previously with biotin binding to SAV−FITC (*24*) and has been attributed to the structural changes of SAV−FITC upon biotin binding (*21*).

The streptavidin−biotin interaction represents a very powerful means of attaching proteins to biotinylated fullerene. This approach becomes more universal if one considers the variety of biotinylated enzymes and streptavidin-conjugated enzymes that are commercially available or easily accessible through synthesis. We investigated the binding of biotinylated alkaline phosphatase to a streptavidin−biotinylated fullerene complex. Alkaline phosphatase catalyzes the hydrolysis of *p*-nitrophenyl phosphate (*p*-NPP) to give *p*-nitrophenol, which absorbs at 400 nm. The coupling reaction was performed by initially forming a complex between streptavidin and biotinylated alkaline phosphatase. In particular, a molar amount of biotinylated alkaline phosphatase, equivalent to saturating one of the four binding sites of streptavidin, was added to a solution of streptavidin in glycine buffer, pH 9.6. The 1:1 molar ratio was selected to limit any inhibitory effect of streptavidin on biotinylated alkaline phosphatase (excess of streptavidin commonly causes inhibition of biotinylated enzymes) (*23*) as well as avoid the formation of aggregates that could precipitate out of solution. After stirring for 10 min, an excess of biotinylated fullerene was added, and the suspension was sonicated at 4 °C. The suspension was then stirred overnight at 4 °C. At this point, the solid was recovered by centrifugation and washed three times with buffer to eliminate any unbound streptavidin. The solid was resuspended, and different amounts of the obtained suspension were added to a cuvette containing a solution of the *p*-NPP substrate. As a control experiment, the same amounts of unreacted biotinylated fullerene were added to a cuvette containing the same concentration of *p*-NPP. The results (Figure 2) verify that the biotinylated alkaline phosphatase was coupled to the fullerene through the streptavidin molecular adapter. Interestingly, we found that unlike suspensions of C_{60} that settle within minutes in water, the fullerene-immobilized enzyme remains in suspension for extended periods of time (several hours). This is an additional advantage of enzymes conjugated to fullerenes over those immobilized on more conventional (macroscopic) supports. It was also demonstrated that the fullerene-immobilized enzyme could be reused without any significant loss of activity. This was accomplished by combining previously used suspensions containing fullerene-immobilized enzyme. After centrifugation, the recovered solid was washed with buffer and its enzymatic activity was subsequently measured. No significant loss of activity was observed.

In conclusion, the biotin−streptavidin interaction enables the attachment of a fullerene to streptavidin and correspondingly to any available biotinylated biomolecules. This was demonstrated by using biotinylated alkaline phosphatase as a model enzyme. Overall, these studies show that streptavidin can be effectively utilized to connect biotinylated nanosized building blocks by taking advantage of its highly selective molecular recognition and affinity properties for biotin.

ACKNOWLEDGMENT

We thank NSF-MRSEC and ARL for financial support; we also acknowledge Prof. M. Maggini (Universita' degli Studi di Padova, Padova, Italy) and Dr. B. Lynn (University of Kentucky Mass Spectrometry Center, Lexington, KY) for their collaboration.

LITERATURE CITED

(1) Martin, N., Sanchez, L., Illescas, B., and Perez, I. (1998) C_{60}-based electroactive organofullerenes. *Chem. Rev. 98*, 2527−2547.

(2) Dai, L., and Mau, A. W. H. (2001) Controlled synthesis and modification of carbon nanotubes and C_{60}: carbon nanostructures for advanced polymeric composite materials. *Adv. Mater. 13*, 899−913.

(3) Innocenzi, P., and Brusatin, G. (2001) Fullerene-based organic−inorganic nanocomposites and their applications. *Chem. Mater. 13*, 3126−3139.

(4) Pantarotto, D., Tagmatarchis, N., Blanco, A., and Prato, M. (2004) Synthesis and biological properties of fullerene-containing amino acids and peptides. *Mini Rev. Med. Chem. 4*, 805−814.

(5) Gavalas, V. G., and Chaniotakis, N. A. (2000) [60]Fullerene-mediated amperometric biosensors. *Anal. Chim. Acta 409*, 131−135.

(6) Chuang, C.-W., and Shih, J.-S. (2001) Preparation and application of immobilized C_{60}-glucose oxidase enzyme in fullerene C_{60}-coated piezoelectric quartz crystal glucose sensor. *Sens. Actuators B 81*, 1−8.

(7) Chen, B. X., Wilson, S. R., Das, M., Coughlin, D. J., and Erlanger, B. F. (1998) Antigenicity of fullerenes: Antibodies specific for fullerenes and their characteristics. *Proc. Natl. Acad. Sci.*, *USA 95*, 10809−10813.

(8) Eiichi, N., and Hiroyuki I. (2003) Functionalized fullerenes in water. The first 10 years of their chemistry, biology, and nanoscience. *Acc. Chem. Res. 36*, 807−815.

(9) Wilson, S. R. (2000) Biological aspects of fullerenes. *Fullerenes* (Kadish, K. M., and Ruof, R. S., Eds.) pp 437−465, Wiley, New York.

(10) Friedman, S. H., De Camp, D. L., Sijbesma, R. P., Srdanov, G., Wudl, F., and Kenyon, G. L. (1998) Inhibition of the HIV-1 protease by fullerene derivatives: model building studies and experimental verification. *J. Am. Chem. Soc. 115*, 6506−6509.

(11) Zhu, Z., and Schuster, D. I. (2002) Molecular dynamics study of the connection between flap closing and binding of fullerene-based inhibitors of the HIV-1 protease. *Biochemistry 42*, 1326−1333.

(12) Kurz, A., Halliwell, C. M., Davis, J. J., Hill, H. A., and Canters, G. W. (1998) A fullerene-modified protein. *Chem. Commun.*, 433−434.

(13) Braun, M., Camps, X., Vostrowsky, O., Hirsch, A., Endreb, E., Bayerl, T., Birkert, O., and Gauglitz, G. (2000) Synthesis of a biotinated lipofullerene as a new type of transmembrane anchor. *Eur. J. Org. Chem.*, 1173−1181.

(14) Braun, M., Atalick, S., Guldi, D. M., Lanig, H., Brettreich, M., Burghardt, S., Hatzimarinaki, M., Ravanelli, E., Prato, M., van Eldik, R., and Hirsh, A. (2003) Electrostatic complexation and photoinduced electron transfer between Zn−Cytochromic c and polyanionic fullerene dendrimers. *Chem. Eur. J. 9*, 3867−3875.

(15) Bianco, A., Pantarotto, D., Briand, J.-P., and Prato M. (2003) Solid-phase synthesis and characterization of a novel fullerene-peptide from histone H3. *Org. Biomol. Chem. 1*, 4141−4143.

(16) Nednoor, P., Capaccio, M., Gavalas, V. G., Meier, M. S., Anthony, J. E., and Bachas L. G. (2004) Hybrid nanoparticles based on organized protein immobilization on fullerenes. *Bioconjugate Chem. 15*, 12−15.

(17) Prato, M., Maggini, M., Giacometti, C., Scorrano, G., Sandoná, G., and Farmia, G. (1996) Synthesis and electrochemical properties of substituted fulleropyrrolidines. *Tetrahedron 52*, 5221−5234.

(18) Wilchek, M., and Bayer, E. A. (1990) Fluorometric assay for avidin−biotin interaction. *Methods Enzymol. 184*, 234−240.

(19) Torreggiani, A., and Fini, J. (1998) The binding of biotin analogues by streptavidin: a Raman Spectroscopic study. *Biospectroscopy 4*, 197−208.

(20) Chan, B. P., Chilkoti, A., Reichert, W. M., and Truskey, G. A. (2003) Effect of streptavidin affinity mutants on the integrin-independent adhesion of biotinylated endothelial cells. *Biomaterials 24*, 559−570.

(21) Weber, P. C., Ohlendorf, D. H., Wendoloski, J. J., and Salemme, F. R. (1989) Structural origins of high-affinity biotin binding to streptavidin. *Science 243*, 85−88.

(22) Pazy, Y., Kulik, T., Bayer, E. A., Wilchek, M., and Livnahi, O. (2002) Ligand exchange between proteins. *J. Biol. Chem. 277*, 30892−30900.

(23) Barbarakis, M. S., Daunert S., and Bachas, L. G. (1992) Effect of different binding proteins on the detection limits and sensitivity of assays based on biotinylated adenosine deaminase. *Bioconjugate Chem. 3*, 225−229.

(24) Smith-Palmer, T., Barbarakis, M. S., Cynkowski, T., and Bachas, L. G. (1993) Fluorescence-based flow-injection determination of biotin and biotinylated compounds. *Anal. Chim. Acta 279*, 287−292.

BC049861D

Preparation of a Gradient Biotinylated Polyethylene Surface To Bind Streptavidin–FITC

Moon Suk Kim,[†,§] Kwang Su Seo,[‡,§] Gilson Khang,[‡] and Hai Bang Lee*[,†]

Nanobiomaterials Laboratory, Korea Research Institute of Chemical Technology, P.O. Box 107, Yuseong, Daejeon 305-600, Korea, and Department of Polymer/Nano Science and Technology, Chonbuk National University, 664-14, Duckjin, Jeonju 561-756, Korea. Received June 16, 2004; Revised Manuscript Received February 1, 2005

A novel biotinylated gradient surface was designed to bind a streptavidin–FITC. The gradient polyethylene (PE) surface was prepared by a corona treatment with a power increase along the PE length, and successively, biotinylated gradient PE surface was prepared by the reaction of polyethylenimine (PEI) and biotin. Surface properties of the gradient PE surface changed according to PE length and chemical modification. The biotinylated gradient PE surface provided a continuous gradient of streptavidin–FITC through binding of avidin–biotin. The luminosity of fluorescence that corresponds to a streptavidin-bound FITC on the biotinylated gradient PE surface increased gradually on the surface along the PE length.

INTRODUCTION

When polymer materials are introduced in in vivo, they can act as a substrate for attaching extracellular matrix (ECM) proteins or cells but they simultaneously induce immunogenic responses (*1*–*4*). To prevent or decrease immunogenic responses, recent development of polymer materials has focused on the design of biomimetic materials that are able to recognize ECM or specific cell (*5*–*8*). The surface modification of materials was expected to be particularly useful in the design of biomimetic materials modified by bioactive molecules with biomolecular recognizable properties (*9*, *10*). The introduction of the bioactive molecules was usually performed by either physical or chemical reaction (*11*–*16*). The bioactive molecule-modified biomaterials can recognize the targetable receptor molecules that are present under biological conditions. The interactions between bioactive molecules and targetable receptors are also important for the design of biomimetic materials, because the evaluation of biomimetic materials can be affected by binding efficiency. The interactions are dependent on several factors such as the affinity between bioactive molecules and targetable receptors, the density of bioactive molecules, and the spatial distribution of bioactive molecules (*17*–*19*). Thus, the design of biomimetic materials that can selectively detect or identify targetable biomolecules as well as minimize nonspecific binding of biomolecules was a challenging subject; in addition, the designed biomimetic materials may offer the potential of biomedical applications such as biomolecular interactions (*20*–*22*), cell motility (*23*–*25*), and diagnostic studies (*26*, *27*).

However, the surface modification has some limitations. Since the surface modification has been performed on a uniform surface, the evaluation of the behavior of bioactive molecules on the biomaterial has been tediously conducted through several experiments.

Scheme 1

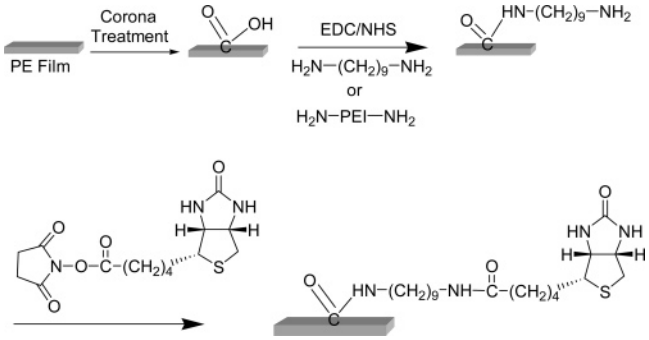

A gradient surface is the surface on which a gradually varying chemical composition exists along its length. If

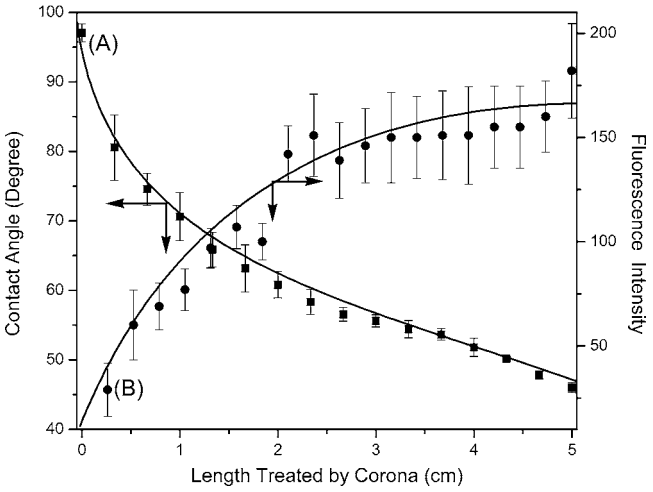

Figure 1. Plot of (A) water contact angle versus length treated by corona and (B) fluorescence intensity versus length treated by corona.

* Corresponding author. E-mail: hblee@krict.re.kr, tel: 82-42-860-7220, fax: 82-42-861-4151).

† Korea Research Institute of Chemical Technology.

‡ Chonbuk National University.

§ M. S. Kim and K. S. Seo contributed equally to this paper.

10.1021/bc049860l CCC: $30.25 © 2005 American Chemical Society
Published on Web 02/23/2005

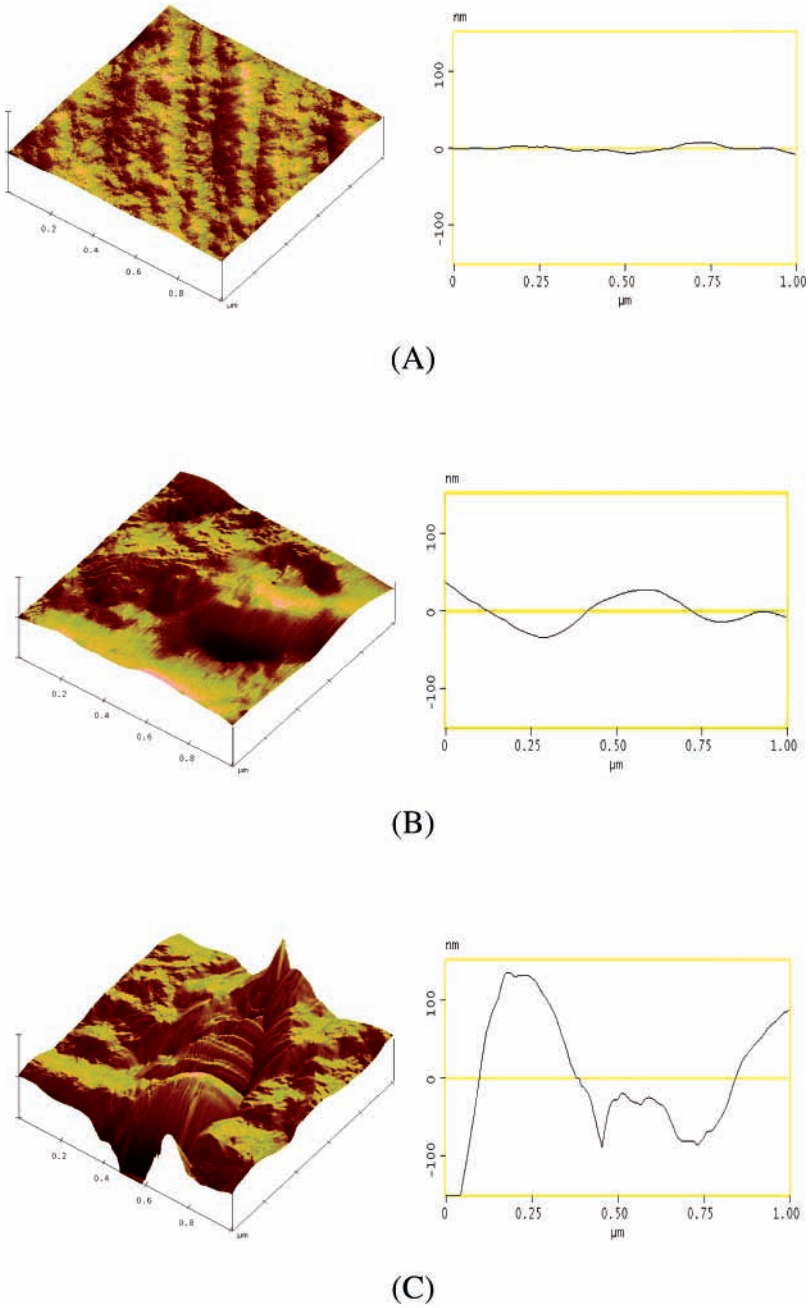

Figure 2. AFM images at the position (A) 0.5 cm, (B) 2.5 cm, and (C) 4.5 cm after corona treatment.

a bioactive molecule is introduced on a gradient surface, the gradient bioactive molecule on the gradient surface can illustrate various results through a single experiment. This can be a powerful tool to evaluate the ability of bioactive molecules (*28*−*30*). However, there were few studies on the interaction between a gradient surface with a bioactive molecule and a targetable biomolecule.

The aim of our research was to develop a simple applicable method using gradient surfaces for biomedical applications. We present here the first approach for design of a novel gradient polyethylene (PE) surface by an incorporation of biotin and the binding of streptavidin−FITC on the biotinylated gradient surface.

RESULTS AND DISCUSSION

Corona discharge treatment is one of the useful methods for introducing functional groups and/or roughness onto a polymer surface. We recently reported the preparation of a gradient surface by radiofrequency corona discharge with knife-type electrodes and the applications as biomaterials (*31*, *32*). In this work, the chemical modification after corona discharge treatment was carried out as shown in Scheme 1. In the first step, the hydrocarbon backbone on the PE surface was activated to the carbon radicals form by the corona discharge treatment. The activated carbon radicals in the presence of oxygen provided a number of functional groups such as the hydroxyl group, ether, ketone, aldehyde, carboxylic acid, and carboxylic ester on the PE surface. Since the corona power gradually increased along the PE length, the density of functional groups gradually increased. To examine the surface property after corona treatment, the gradient PE surface was examined by water contact angle, Fourier transform infrared attenuated total reflectance (FTIR-ATR) spectroscopy, atomic force microscopy (AFM), and electron spectroscopy for chemical analysis (ESCA). The water contact angle of untreated PE surface was 99°, indicating a complete hydrophobic

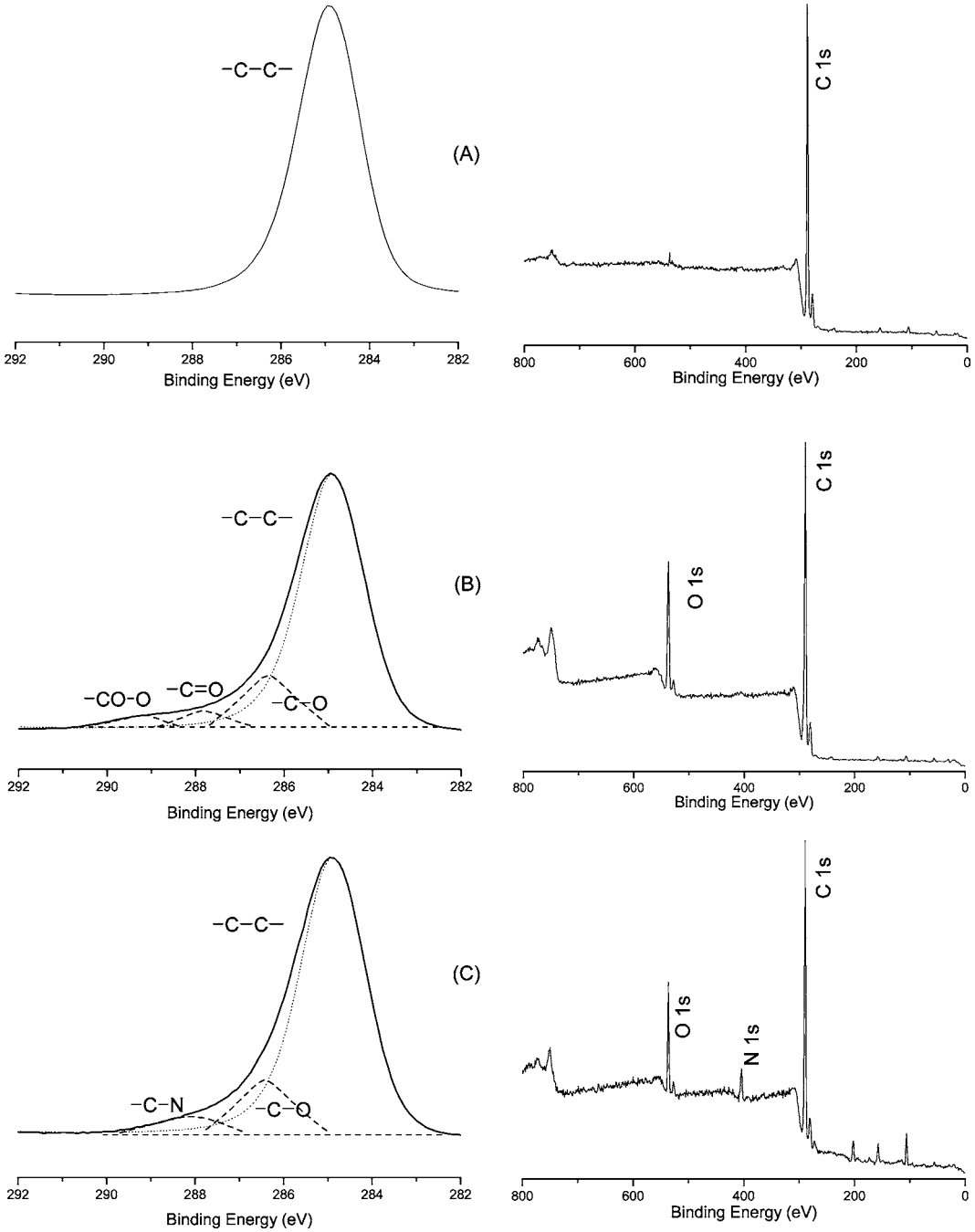

Figure 3. ESCA spectra of (A) untreated PE, (B) corona-treated PE, and (C) PEI-modified PE at the position 4.5 cm. (Left: carbon 1s core level spectra, Right: survey scan spectra).

surface property. As shown in Figure 1A, the water contact angle of PE surface decreased gradually from 99° to 45−50° along the PE length with increasing corona power, indicating the gradual wettability change from completely hydrophobic to extremely hydrophilic. FTIR-ATR spectra showed a peak assignable to the C═O functional group at 1735 cm^{-1} and gradual peak intensity increase as the corona power increased (*33*). Figure 2 shows AFM images along the PE length after corona treatment. The PE surface exhibited a gradient roughness increase from 10 to 100 nm as corona power increases.

The chemical structure changes of the corona-treated PE surface were also investigated by ESCA (Figure 3). The untreated PE surface exhibited only a broad C1*s* peak at a binding energy of 285 eV (Figure 3A). After corona discharge treatment, new peaks assignable to ketone or aldehyde groups, hydroxyl or ether groups, and carboxylic acid or ester groups were observed at 287.9, 286.3 and 289.1 eV, respectively (Figure 3B). We confirmed the formation of various functional groups, especially the carboxylic acid group that can serve as reaction site on the PE surface. The carboxylic acid on the surface may chemically react with a functional group such as NH_2.

Polyamine compounds that have long spacers can be used for immobilization of the surface and consequently allow flexible and multifunctional sites on the surface in a biological environment. Thus chemical modification of the surface using polyamine was performed. First, the carboxylic group on the corona-treated PE surface was activated by *N*-hydroxysuccinimide (NHS) and EDC (*N*-ethyl-*N*′-(3-dimethylaminopropyl)carbodiimide). The activated carboxylic group reacted with the amine com-

Scheme 2

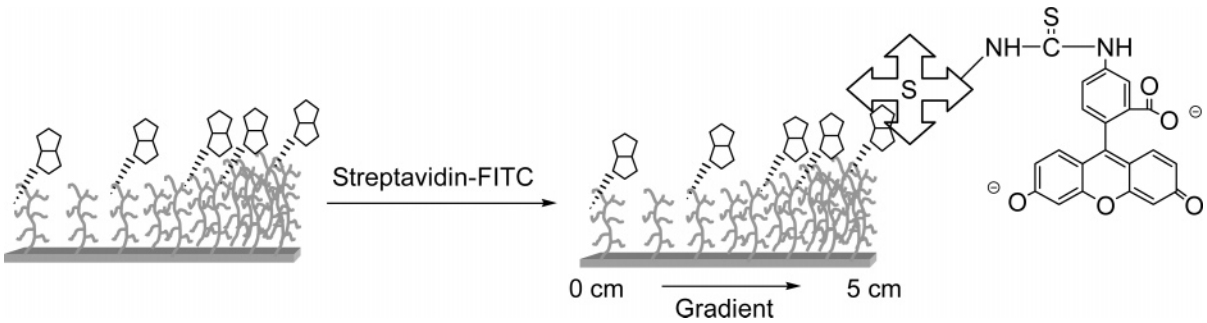

pounds such as 1,9-nonanediamine (ND) or polyethylenimine (PEI). In FTIR-ATR, the peak assignable to the C=O functional group almost disappeared at 1735 cm^{-1}, while a new peak was observed at around 1586 cm^{-1} after reaction with ND or PEI.

The ESCA spectrum of PEI modified on the gradient PE surface is shown in Figure 3C. A gradual increase in height of the C1*s* shoulder at 288.2 eV due to the C−N species within the PEI was observed along the PE length. In addition, 1s of nitrogen was observed at 399 eV in the survey scan spectrum (Figure 3C), and the intensity also gradually increased along the PE length, implying a nitrogen content increase on the PE surface (Table S1) (*34*). The results of FTIR-ATR and ESCA indicated that amine compounds were gradually modified on the gradient PE surface.

Among several binding systems, the binding affinity of the avidin−biotin interaction ($K_D \sim 10^{-15}$ M) is one of the highest to occur in nature as noncovalent bonding (*35*, *36*). Thus, we choose the binding system of avidin−biotin to design a gradient PE surface with a bioactive molecule. The amine-modified gradient PE surface was reacted with biotin that was preactivated by NHS and EDC. The new signal appeared at 1725 cm^{-1} after the reaction of biotin in FTIR-ATR spectrum (*33*). In the subsequent step, the gradient biotinylated PE surface was incubated in a solution of streptavidin−FITC (Scheme 2). The binding of the streptavidin−FITC to the gradient biotinylated PE surfaces was characterized by fluoresence microscopy. The fluorescence microscope image, which corresponds to a streptavidin-bound FITC bonded on the gradient biotinylated PE surfaces, is shown in Figure 4

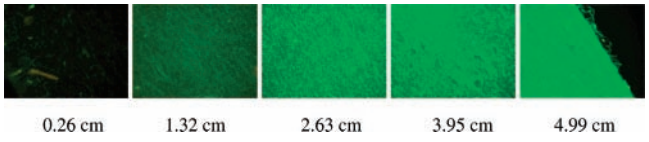

Figure 4. Change of fluorescence images on the gradient PE surface from 0 to 5 cm after the binding of streptavidin−FITC.

(*37*). The luminosity of fluorescence increased gradually on the surface when corona power for the surface increased along the length (*38*). Plotting of the length treated by corona versus the fluorescence intensity of the streptavidin−FITC reveals a gradient as shown in Figure 1B (*39*). The longer the length treated by corona, the smaller the water contact angle value and the stronger the fluorescence intensity , which could well explain the gradient PE surface.

In conclusion, we prepared a gradient PE surface using a corona treatment with power increase along the PE length and biotinylated gradient PE surface through the reaction of PEI and biotin. The biotinylated gradient PE surface provided a continuous gradient of streptavidin−FITC through recognizing their binding partners from solution. We believe that this method will be useful in the study of the analysis of functional bioactive molecules on the gradient surface through one experiment because the designed gradient PE surface is experimentally simpler than using a uniform surface.

ACKNOWLEDGMENT

We would like to thank KMOICE (N11-A08-1402-05-1-3) for funding.

Supporting Information Available: Experimental procedures, Table S1, and Figures S1−S6. This material is available free of charge via the Internet at http://pubs.acs.org.

LITERATURE CITED

(1) Metzger, D. W. (2002) Immune responses to tissue-engineered extracellular matrix used as a bioscaffold. *Ann. N. Y. Acad. Sci. 961*, 335−336.

(2) Vogel, V., and Baneyx, G. (2003) The tissue engineeting puzzle: a molecular perspective. *Annu. Rev. Biomed. Eng. 5*, 441−463.

(3) Sarraf, C. E., Harris, A. B., McCulloch, A. D., and Eastwood, M. (2003) Heart valve and arterial tissue engineering. *Cell Prolif. 36*, 241−254.

(4) Rihova, B. (2000) Immunocompatibility and biocompatibility of cell delivery systems. *Adv. Drug Delivery Rev. 42*, 65−80.

(5) Prokop, A. (2001) Bioartificial pancreas: materials, devices, function, and limitations. *Diabetes Technol. Ther. 3*, 431−449.

(6) Shin, H., Jo, S., and Mikos, A. G. (2003) Biomimetic materials for tissue engineering. *Biomaterials 24*, 4353−4364.

(7) Courtney, J. M., Zhao, X. B., Qian, H., and Sharma, A. (2003) Modification of polymer surfaces: optimization of approaches. *Perfusion 18*, 33−39.

(8) Reyes, C. D., and Garcia, A. J. (2003) Engineering integrin-specific surfaces with a triple-helical collagen-mimetic peptide. *J. Biomed. Mater. Res. 65*, 511−523.

(9) Zhi, Z. L., Morita, Y., Hasan, Q., and Tamiya, E. (2003) Micromachining microcarrier-based biomolecular encoding for miniaturized and multiplexed immunoassay. *Anal. Chem. 75*, 4125−4131.

(10) Quirk, R. A., Chan, W. C., Davies, M. C., Tendler, S. J., and Shakesheff, K. M. (2001) Poly(L-lysine)-GRGDS as a biomimetic surface modifier for poly(lactic acid). *Biomaterials 22*, 865−872.

(11) Bures, P., Huang, Y., Oral, E., and Peppas, N. A. (2001) Surface modifications and molecular imprinting of polymers in medical and pharmaceutical applications. *J. Controlled Release 72*, 25−33.

(12) Brash, J. L. (2000) Exploiting the current paradigm of blood-material interactions for the rational design of blood-compatible materials. *J. Biomater. Sci. Polym. Ed. 11*, 1135−1146.

(13) Ryu, D. D., and Nam, D. H. (2000) Recent progress in biomolecular engineering. *Biotechnol. Prog. 16*, 2−16.

(14) Neff, J. A., Caldwell, K. D., and Tresco, P. A. (1998) A novel method for surface modification to promote cell attachment to hydrophobic substrates. *J. Biomed. Mater. Res. 40*, 511−519.
(15) Latkany, R., Tsuk, A., Sheu, M. S., and Loh, I. H., Trinkaus-Randall, V. (1997) Plasma surface modification of artificial corneas for optimal epithelialization. *J. Biomed. Mater. Res. 36*, 29−37.
(16) Sharma, C. P., Chandy, T., and Sunny, M. C. (1987) Inhibition of platelet adhesion to glow discharge modified surfaces. *J. Biomater. Appl. 1*, 533−552.
(17) Spadaccini, R., and Temussi, P. A. (2001) Natural peptide analgesics: the role of solution conformation. *Cell Mol. Life Sci. 58*, 1572−1582.
(18) Kao, W. J. (1999) Evaluation of protein-modulated macrophage behavior on biomaterials: designing biomimetic materials for cellular engineering. *Biomaterials 20*, 2213−2221.
(19) Thibault, R. J., Jr., Galow, T. H., Turnberg, E. J., Gray, M., Hotchkiss, P. J., and Rotello, V. M. (2002) Specific interactions of complementary mono- and multivalent guests with recognition-induced polymersomes. *J. Am. Chem. Soc. 124*, 15249−15254.
(20) D'Souza, S. F. (2001) Immobilization and stabilization of biomaterials for biosensor applications. *Appl. Biochem. Biotechnol. 96*, 225−238.
(21) Quirk, R. A., Chan, W. C., Davies, M. C., Tendler, S. J., and Shakesheff, K. M. (2001) Poly(L-lysine)-GRGDS as a biomimetic surface modifier for poly(lactic acid). *Biomaterials 22*, 865−872.
(22) Cox, J. D., Curry, M. S., Skirboll, S. K., Gourley, P. L., and Sasaki, D. Y. (2002) Surface passivation of a microfluidic device to glial cell adhesion: a comparison of hydrophobic and hydrophilic SAM coatings. *Biomaterials 23*, 929−935.
(23) Upadhyaya, A., and van Oudenaarden, A. (2003) Biomimetic systems for studying actin-based motility. *Curr. Biol. 13*, R734−744.
(24) Cuvelier, D., Rossier, O., Bassereau, P., and Nassoy, P. (2003) Micropatterned "adherent/repellent" glass surfaces for studying the spreading kinetics of individual red blood cells onto protein-decorated substrates. *Eur. Biophys. J. 32*, 342−354.
(25) Carlier, M. F., Le Clainche, C., Wiesner, S., and Pantaloni, D. (2003) Actin-based motility: from molecules to movement. *Bioessays 25*, 336−345.
(26) Gorbunov, V., Fuchigami, N., Stone, M., Grace, M., and Tsukruk, V. V. (2002) Biological thermal detection: micromechanical and microthermal properties of biological infrared receptors. *Biomacromolecules 3*, 106−115.
(27) Fields, G. B., Lauer, J. L., Dori, Y., Forns, P., Yu, Y. C., and Tirrell, M. (1998) Protein-like molecular architecture: biomaterial applications for inducing cellular receptor binding and signal transduction. *Biopolymers 47*, 143−151.
(28) Elwing, H. (1998) Protein absorption and ellipsometry in biomaterial research. *Biomaterials 19*, 397−406.
(29) Garcia, A. J., and Ducheyne, P. (1994) Numerical analysis of extracellular fluid flow and chemical species transport around and within porous bioactive glass. *J. Biomed. Mater. Res. 28*, 947−960.
(30) Maruno, S., Itoh, H., Ban, S., Iwata, H., and Ishikawa, T. (1991) Micro-observation and characterization of bonding between bone and HA-glass-titanium functionally gradient composite. *Biomaterials 12*, 225−230.
(31) Lee, J. H., Lee, S. J., Khang, G., and Lee, H. B. (2000) The Effect of Fluid Shear Stress on Endothelial Cell Adhesiveness to Polymer Surfaces with Wettability Gradient. *J. Colloid Interface Sci. 230*, 84−90.
(32) Lee, J. H., Lee, J. W., Khang, G., and Lee, H. B. (1997) Interaction of cells on chargeable functional group gradient surfaces. *Biomaterials 18*, 351−358.
(33) FTIR-ATR spectra of gradient PE surface are illustrated in the Supporting Information (Figure S2).
(34) Nitrogen content of the gradient PE surface is summarized in the Supporting Information (Table S1).
(35) Green, N. (1963) Avidin. 1. The use of (14-C) biotin for kinetic studies and for assay. *Biochem. J. 89*, 585−591.
(36) Brandts, J. F., and Lin, L. N. (1990) Study of strong to ultratight protein interactions using differential scanning calorimetry. *Biochemistry 29*, 6927−6940.
(37) All fluorescence microscope images of the gradient PE surface are presented in the Supporting Information (Figures S3 and S4).
(38) Histograms for fluorescence intensity are illustrated in the Supporting Information (Figures S5).
(39) Plots of length treated by corona versus green intensity of streptavidin−FITC from 1,9-nonanediamine-modified PE and PEI-modified PE are illustrated in the Supporting Information (Figures S6).

BC049860L

ARTICLES

Yeast Transformation Process Studied by Fluorescence Labeling Technique

Hu-Zhi Zheng,[†] Hui-Hui Liu,[‡] Shao-Xing Chen,[‡] Zhe-Xue Lu,[†] Zhi-Ling Zhang,[†] Dai-Wen Pang,*[,†] Zhi-Xiong Xie,*[,‡] and Ping Shen[‡]

College of Chemistry & Molecular Sciences and College of Life Sciences, Wuhan University, Wuhan 430072, P. R. China. Received July 14, 2004; Revised Manuscript Received February 1, 2005

A new method based on fluorescence imaging and flow cytometry was developed to investigate the transformation process of *Saccharomyces cerevisiae* AY. Yeast and fluorescent-labeled plasmid pUC18 were used as models of cells and DNA molecules, respectively. Binding of DNA molecules to yeast cell surfaces was observed. Factors influencing DNA binding to cell surfaces were investigated. It has been found that poly(ethylene glycol) (PEG) could induce DNA binding to yeast surfaces, while Li^+ showed a weak effect on the binding. When both Li^+ and PEG were used, synergetic effect occurred, resulting in the binding of pUC18 to the surface of more yeast cells compared with that in the presence of PEG or Li^+ only. It was also confirmed that heat shock, Li^+, and PEG all can increase the permeability of yeast cells. This simple method is helpful for understanding the process of yeast transformation and can be used to investigate the interaction of DNA with cell surfaces.

1. INTRODUCTION

The term "transformation" is used to describe DNA uptake in both prokaryotes and eukaryotes, as detected by consequent changes in phenotype (*1*). Genetic transformation of *Saccharomyces cerevisiae* was first reported in 1960 (*2*). Several methods for yeast transformation, such as spheroplast (*3*), Li^+ intact yeast cell, electroporation (*4*), glass beads (*5*), and biolistic (*6*), were developed.

Li^+ intact yeast cell transformation, which is a simple method with no special equipment required and with relatively high transformation efficiency, was first established by Ito in 1983 (*7*) and subsequently improved (*8*−*11*) and standardized (*12*). So, this method has been widely used.

The natural transformation process of bacteria usually includes three steps: first, DNA is bound to cell surfaces; second, the uptake of DNA by cells occurs; last, DNA molecules are integrated into chromosomal DNA or replicated as extrachromosomal genetic elements (*13*).

Although the details in the yeast transformation process are unknown, it can be supposed that the process involves the contact of DNA to yeast cells, the uptake of DNA by yeast cells, and the integration of DNA. Factors influencing these three steps will affect transformation efficiency. Some reports suggested that DNA could bind to yeast cell surfaces (*11*). It can be believed that factors facilitating DNA binding to cell surfaces will increase transformation efficiency. However, strong binding of DNA to the cell surfaces will result in reduced transformation efficiency (*11*). Increasing cell wall permeability to DNA enhanced transformation efficiency also (*14*).

Herein, DNA binding sites on yeast cell surfaces were observed, and factors that affect DNA binding to cell surfaces and cell permeability were explored in detail. Nevertheless, the integration of DNA molecules into chromosomal DNA cannot be studied by the current method. It is evident that this new method is helpful to understand the transformation process and can be promising in studying the transformation of other cells and the interaction of DNA with cells.

2. MATERIALS AND METHODS

Lithium acetate (LiAc), PEG4000, yeast extract, polypepton, Tris buffer, glucose, glass slides, and cover glass were all purchased from Sigma. YOYO-1 was a product of Molecular Probes. Plasmid pUC18 was obtained from Sino-American Biotechnology Co. Ultrapure water (18.2 MΩ) was prepared with a Labconco system and used throughout. *Saccharomyces cerevisiae* AY was obtained from Prof. Ping Shen's lab and used as a cell model. Before use, it was dispersed on a YPD plate (1.0% yeast extract, 2.0% polypepton, 2.0% glucose, 1.5% agar) and cultured for 2−3 days at 30 °C. Subsequently, a single colony was selected and dispersed on another YPD plate and cultured and then kept at 4 °C.

Plasmid pUC18 was labeled with YOYO-1 at a ratio of 50:1 (base pairs to YOYO-1) in the dark for 90 min at 4 °C immediately before use (*15*). At such a ratio of base pairs to YOYO-1, there is almost no free YOYO-1 because of its complete binding to DNA. A titration experiment demonstrated that addition of excess unlabeled DNA did not result in increase in fluorescence (*16*).

* Corresponding authors. Dai-Wen Pang: phone, 86-27-68756759; fax, 86-27-68754067; e-mail address, dwpang@whu.edu.cn. Zhi-Xiong Xie: e-mail address, hsiech@263.net.

[†] College of Chemistry and Molecular Sciences, Wuhan University.

[‡] College of Life Sciences, Wuhan University.

10.1021/bc049833v CCC: $30.25 © 2005 American Chemical Society
Published on Web 02/19/2005

The Li^+ intact yeast cell transformation protocol was as previously reported (*1*). Yeast was precultured overnight in 5 mL of YPD (1.0% yeast extract, 2.0% polypepton, 2.0% glucose). A suitable volume of precultured cell suspension was added in 50 mL of YPD and incubated at 30 °C with shaking until cell growth reached the late logarithm phase. The cells were then harvested by centrifugation at 5000 rpm for 5 min, washed twice with ultrapure water, and resuspended in ultrapure water at 10^9 cells/mL. One hundred microliters of sample was centrifuged for 5 min at 5000 rpm, and the supernatant was discarded. The pellets were resuspended in 360 μL of transformation mixture (240 μL of 50% PEG4000 (w/v), 36 μL of 1.0 M LiAc, 50 μL of 2.0 mg/mL single-stranded carrier DNA, YOYO-1-labeled pUC18 DNA diluted to 34 μL with water). The cells in transformation mixture were incubated at 30 °C in the dark with shaking for 30 min, and then heat shocked at 42 °C in dark for 15 min.

Cells for experiments were dropped on glass slides and covered with a cover glass and then observed with a fluorescence microscope (FM) (Axiovert 200M, Zeiss) equipped with an oil-immersion objective (100× objective, Zeiss, N.A. = 1.25) or a confocal laser scanning microscope (CLSM) (TCS SP, Leica) equipped with an oil immersion objective (Leica, N.A. = 1.40). Cell samples were filtered with a 300 mesh filter and then diluted by several hundred times with 0.1 M Li^+-containing solution for cells in solution containing Li^+ or with ultrapure water for cells in Li^+-free solution before being analyzed with a flow cytometer (Beckman Coulter Epics Altra) coupled with a 488 nm Ar^+ laser and a 525 nm bandpass filter. The ultrapure-water-washed yeast cells were used as the negative control sample.

To examine yeast cell permeability, 10 μL of 10 μM YOYO-1 was added into 100 μL of water-washed cells, and then, Li^+, PEG, or both were added. The mixture was incubated at 30 °C with shaking in the dark for 30 min and then heat shocked at 42 °C in the dark for 15 min. At last, it was diluted and analyzed with a flow cytometer.

Atomic force microscopic (AFM) images of cell surfaces were obtained using an atomic force microscope (Picoscan, Molecular Imaging) in contact mode with a commercial MAClever type II probe (Molecular Imaging).

3. RESULTS AND DISCUSSION

3.1. Binding of DNA to Yeast Cell Surfaces. A widely used cell-impermeable fluorescent probe, YOYO-1, was used to label pUC18 plasmid DNA. After intercalation into double-stranded DNA, fluorescence intensity of YOYO-1 is enhanced by more than 1000 times (*17*). So, a very high ratio of signal-to-noise can be obtained using YOYO-1 to label DNA.

A commercial plasmid DNA, pUC18, was used to investigate the interaction of DNA with yeast cell surfaces, although it cannot be translated in yeast. Because pUC18 is short in strand length (2686 base pairs), each pUC18 molecule can only combine with a small number of YOYO-1 molecules (no more than 60 molecules) under our experimental conditions, the fluorescence of which is too weak to observe. When pUC18 molecules labeled with YOYO-1 are bound to cell surfaces, the fluorescence intensity is strong enough to observe since more labeled pUC18 molecules are concentrated on the surfaces.

The yeast cell wall acts as a barrier to DNA (*1*), and most DNA molecules are bound to the cell wall (*11*). So, all the fluorescence signals arose from DNA binding to cell surfaces, and the fluorescence of cells will indicate DNA binding to their surfaces. It was confirmed that the binding of YOYO-1 to DNA was of high affinity, thereby preventing the migration of YOYO-1 label from one DNA molecule to another (*17*, *18*). The addition of excessive single-stranded DNA does not affect the fluorescence of YOYO-1-labeled plasmid DNA.

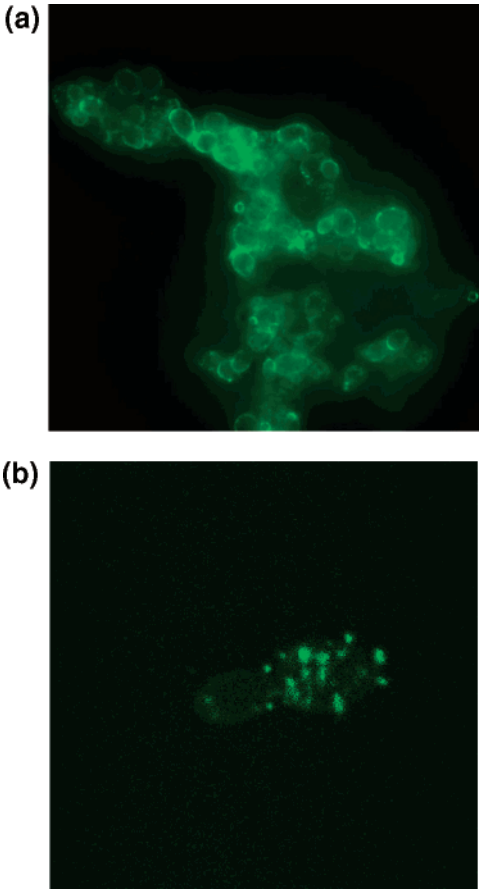

Figure 1. Fluorescence images of DNA binding to yeast cell surfaces: (a) a big field of view obtained by using a FM; (b) a small field of view containing two cells obtained by using a CLSM. Conditions were as follows: ca. 10^8 yeast cells treated with 20 ng of pUC18 stained with YOYO-1; image size ca. 80 × 80 μm^2 (a) and 25 × 25 μm^2 (b).

Because the cell wall of dead cells is not intact, YOYO-1-labeled DNA might diffuse into dead cells and make them fluoresce. So, the presence of dead cells will make difficult the judgment of DNA binding to cell surfaces. To ensure the reliability of experimental results, cells pretreated with the transformation mixture were labeled with methylene blue to determine whether the cells were dead (*19*). It was found that no more than 5% of cells were stained blue; that is, no more than 5% cells were dead.

Binding sites of DNA molecules on yeast cell surfaces were found (Figure 1). As the concentration of pUC18 increased, more pUC18 molecules would be bound to the cell surface. When 80 ng of pUC18 DNA was added into the mixture containing ca. 10^8 cells (the ratio of DNA molecules to cells was about 200:1), the DNA would be bound to the whole cell surface (Figure 2a). These results indicated that DNA binding sites on the surface of one yeast cell could be saturated in the presence of excessive DNA. Excessive pUC18 on the cell surfaces can be washed off (Figure 2b).

3.2. Factors Influencing DNA Binding to Yeast Cell Surfaces. Li^+ and PEG can facilitate DNA binding

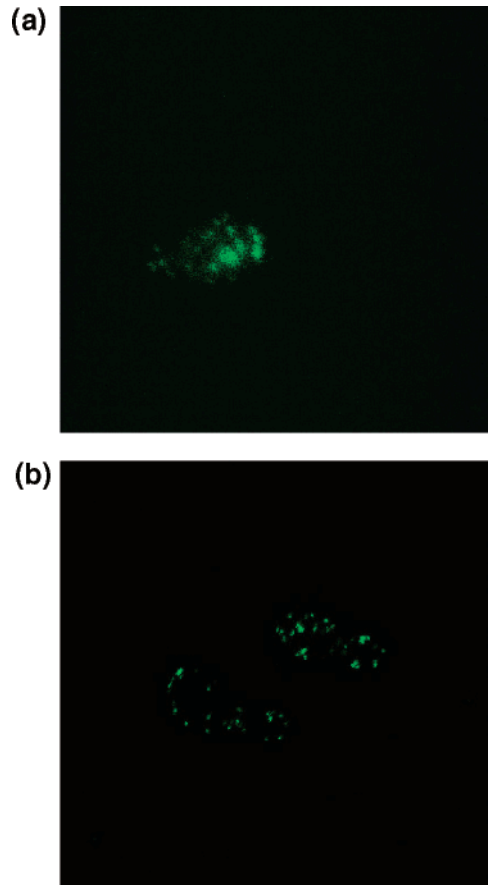

Figure 2. Fluorescence images of saturation of DNA binding to yeast cells. Conditions were as follows: ca. 10^8 yeast cells treated with 80 ng of pUC18 stained with YOYO-1 without washing (a) and with washing (b); 100× oil-immersion objective (N.A. = 1.40) (a) and 40× objective (N.A. = 0.70) (b); image size 25 × 25 μm^2 (a) and 40 × 40 μm^2 (b).

Table 1. Factors Influencing DNA Binding to Cell Surfaces

	percentage of cells with bound DNA (%)				
condition[a]	YOYO-1 labeled DNA	Li^+	PEG	PEG and Li^+	PEG, Li^+, and ss-DNA
a	1.2	6.1	9.8	44.8	
b	3.9	8.3	44.9	95.5	27.9
c	10.6	23.1	61.7	98.2	69.9

[a] Yeast cells (ca. 10^8) were treated with 4 (a), 20 (b), and 80 (c) ng of pUC18 stained with YOYO-1. Negative control sample was water-washed yeast cells.

to the yeast cell surface. Table 1 shows the percentage of fluorescent yeast cells treated with Li^+, PEG, or both in the presence of pUC18 of different concentrations. As mentioned above, the fluorescence of yeast cells was from labeled pUC18 on their surfaces; hence the percentage of fluorescent cells suggests the percentage of the cells with pUC18 bound on their surfaces. Li^+ can induce DNA binding to yeast cell surfaces, but its inducing effect was weak. PEG can induce DNA binding to yeast cell surfaces more strongly than Li^+. In our experiments, it was found that the use of both PEG and Li^+ in the transformation mixture could most strongly induce the binding.

The percentage of cells with bound pUC18 was 1.2%, 3.9%, and 10.6% in the presence of three different concentrations of YOYO-1-labeled pUC18 as listed in Table 1. But in the presence of Li^+, the percentage increased to 6.1%, 8.3%, and 23.1%, showing that Li^+ can induce DNA binding to yeast cell surfaces. As known,

Table 2. Transformation Frequency[a]

transformation frequency			
control	Li^+	PEG	Li^+ and PEG
0	0	5.12×10^{-5}	3.57×10^{-4}

[a] For details, see Supporting Information.

both DNA and the yeast cell surface are partly negatively charged (*20*); they will electrostatically repel. Li^+ can weaken such repulsion, inducing DNA molecules to be bound to yeast cell surfaces. Other cations, such as Na^+ and Cs^+, have been also used for yeast cell transformation (*7*, *8*), most probably due to their reduction of the repulsion between DNA and cell surfaces.

PEG has a strong effect on inducing DNA binding to yeast cell surfaces. In the presence of PEG, the percentages of cells with bound pUC18 on their surfaces increased to 9.8%, 44.9%, and 61.7% at three different labeled pUC18 concentrations (Table 1). It has been reported that PEG facilitates DNA deposition onto yeast cells (*11*). The effect of PEG may be attributed to its changing charges of cell surfaces (*7*). Such changes may induce both conformational changes and aggregation of cells (*7*). And it was also found that PEG could induce a drastic change in the conformation of plasmid DNA molecules (*8*). Perhaps both the conformational changes of DNA molecules and cell surfaces were propitious to the binding of DNA molecules to cell surfaces.

The use of both PEG and Li^+ induced DNA binding to yeast cell surfaces more effectively than PEG or Li^+ only. At three different concentrations of labeled pUC18, the percentage of fluorescent cells was 44.8%, 95.5%, and 98.2%, which might be attributed to a synergetic effect.

These results are exactly consistent with the transformation results (Table 2 and Supporting Information): in the presence of Li^+, PEG, or PEG plus Li^+, the transformation frequency was 0, 5.12×10^{-5}, and 3.57×10^{-4}, respectively.

Single-stranded carrier DNA can be bound more effectively to the yeast cell surfaces and occupy the DNA binding sites. It was reported that 500-fold excess single-stranded DNA decreased the strong binding of DNA to cell surfaces so that most of the plasmid was available for uptake, resulting in high transformation efficiency (*11*). Our results are in agreement with this. Single-stranded DNA decreased the percentage of cells with pUC18 bound to their surfaces from ca. 95% down to 28% in the case of ca. 20 ng of pUC18 in the transform mixture containing ca. 10^8 cells (Table 1).

3.3. Factors Influencing Cell Permeability. As mentioned above, the permeability of cells will affect the transformation for it can influence the cell uptake of DNA. Increasing cell permeability will result in high transformation efficiency. The factors influencing cell permeability were investigated with YOYO-1 by flow cytometry.

As a cell-impermeable reagent, YOYO-1 cannot pass through intact cell membranes, so it has been used to distinguish dead from living cells (*21*). Intact living yeast cells treated with YOYO-1 will not be fluorescent, but dead cells will be fluorescent. For our experiments, it was found that 19.1% (incubated at 30 °C), 73.1% (treated with Li^+), 83.1% (with PEG), and 99.4% (with Li^+ and PEG) of yeast cells were fluorescent (Table 3). However, methylene blue staining experiments showed that almost all of the fluorescent cells were alive. With increasing permeability of living cells, YOYO-1 can get into cells and be bound to the in-cell DNA, making living cells fluorescent. The cells that fluoresce should be permeable.

Table 3. Factors Increasing Cell Permeability[a]

percentage of permeable cells				
incubation at 30 °C	heat shock	Li^+	PEG	PEG and Li^+
19.1	36.1	73.1	83.1	99.4

[a] Negative control sample was water-washed yeast cells.

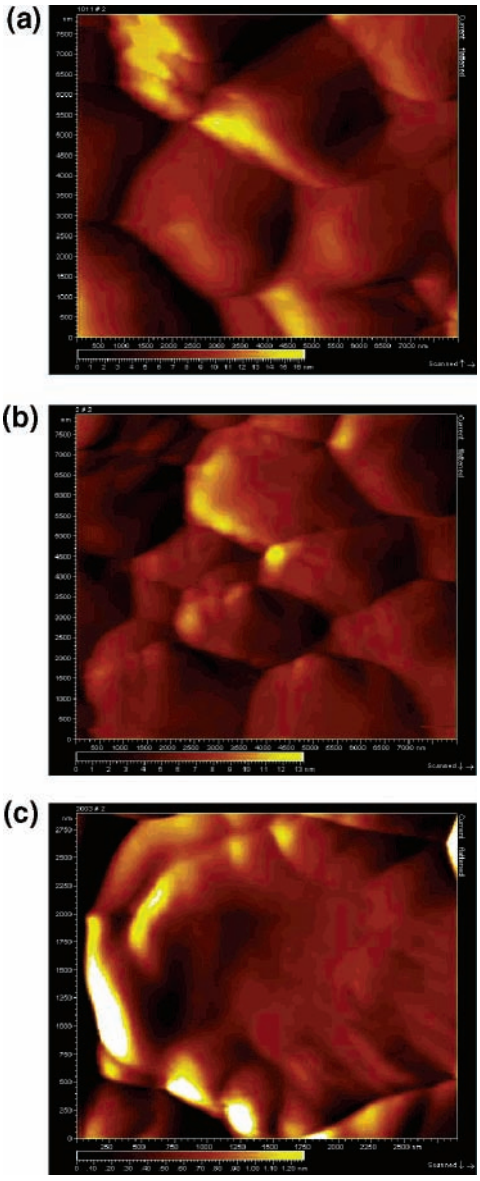

Figure 3. AFM images of some yeast cells (a), Li^+-treated yeast cells (b), and the cell wall of a Li^+-treated single yeast cell (c). Cell sample preparation was as follows: after being cultured and harvested, yeast cells were suspended at ca. 10^9 cells/mL in ultrapure water (a) or 0.1 M Li^+ solution (b, c) and subsequently incubated at 30 °C with shaking for 30 min, and then ca. 50 μL of cell sample was cast onto freshly cleaned slides (1.5 $\times$ 1.5 cm^2).

Treating with Li^+ can increase yeast cell permeability (*14*). Our results from AFM imaging (Figure 3) showed that cells treated with Li^+ had rougher surfaces than cells not treated with Li^+, indicating that the increase in cell permeability was perhaps attributed to the change of the cell surface structure. PEG is essential in yeast transformation (*7*, *8*). Many authors suggested that PEG was responsible for the adsorption of the DNA on the yeast cell surfaces. But our results revealed that PEG could also increase the cell permeability. Because PEG contaminates AFM probe tips seriously, cells treated with PEG cannot be studied by AFM. The use of both PEG and Li^+ can largely increase cell permeability probably due to synergetic effect. This result partly coincides with the transformation results. Although Li^+ can strongly increasing cell permeability, the transformation frequency was zero when only Li^+ was used to treat cells, which may be due to its weak effect on inducing DNA binding to cell surfaces.

Heat shock plays a significant role in transformation. It was reported that heat-shock proteins acted as molecular chaperones, protecting important structural proteins and enzymes from stress-induced degradation (*22*). Heat-shock-induced changes in the level of activities of specific proteins might affect either the transport of plasmid DNA from the cell membrane to the nucleus or elimination of cellular components that can degrade plasmid DNA (*11*). It was found, in our research, that heat shock caused 36.1% of cells to be permeable (19.1% for samples not treated with heat shock) (Table 3), suggesting that heat shock can also increase cell permeability.

4. CONCLUSIONS

A new way to study of yeast transformation process has been explored based on various techniques: fluorescence imaging to examine the DNA binding sites on yeast cell surfaces, flow cytometry to investigate the factors influencing DNA binding to cell surfaces and cell permeability, and AFM to observe cell surfaces to provide complementary information on the cell permeability.

Our research confirmed that there are DNA binding sites on yeast cell surfaces. At a high concentration of DNA, DNA binding sites will be saturated, and DNA molecules will adhere to the whole yeast cell surface.

Heat shock can apparently increase cell permeability. Li^+ is able to weakly promote DNA binding to yeast cell surfaces and strongly increase cell permeability. PEG can strongly induce DNA binding to cell surfaces and increase cell permeability, which are perhaps responsible for the increase of transformation efficiency. PEG can more effectively promote DNA binding to cell surfaces than Li^+. Use of both Li^+ and PEG will result in synergetic effect, which extremely strongly induces DNA binding to cell surfaces and increases cell permeability. Single-stranded carrier DNA is able to decrease strong binding of plasmid DNA to cell surfaces.

ACKNOWLEDGMENT

This work was supported by the National Science Fund for Distinguished Young Scholars (Grant No. 20025311), National Natural Science Foundation of China (Grant Nos. 20305011, 20299034, 20207005, and 30170268), and the Ministry of Education of China (Grant No. 200065). The authors wish to thank Ms. Jing Zhang (Institute of Hydrobiology, Chinese Academy of Sciences, Wuhan, China), Prof. Ming-Sheng Zu, and Prof. Yi-Peng Qi (College of Life Sciences, Wuhan University).

Supporting Information Available: Description of the transformation experiment with a table of the transformation frequencies. This material is available free of charge via the Internet at http://pubs.acs.org.

LITERATURE CITED

(1) Gietz, R. D., and Woods, R. A. (2001) Genetic transformation of yeast. *BioTechniques 30*, 816−831.

(2) Oppenoorth, W. F. F. (1960) Modification of the Hereditary Character of Yeast by Ingestion of Cell-Free Extracts. *J. Microbiol. Serol. 26*, 129−147.

(3) Burgers, P. M. J., and Percival, K. J. (1987) Transformation of Yeast Spheroplasts without Cell Fusion. *Anal. Biochem. 163*, 391−397.
(4) Becker, D. M., and Guarente, L. (1991) Highly efficiency transformation of yeast by electroporation. *Methods Enzymol. 194*, 182−187.
(5) Costanza, M. C., and Fox, T. D. (1988) Transformation of yeast by agitation with glass beads. *Genetics 120*, 667−670.
(6) Johnston, S. A., Anziano, P. Q., Shark, K., Sanford, J. C., and Butow, R. A. (1988) Mitochondrial transformation in yeast by bombardment with microprojectiles. *Science 240*, 1538−1541.
(7) Ito, H., Fukuda, Y., Murata, K., and Kimura, A. (1983) Transformation of Intact Yeast Cells Treated with Alkali Cations. *J. Bacteriol. 153*, 163−168.
(8) Ito, H., Murata, K., and Kimura, A. (1984) Transformation of Intact Cells Treated with Alkali Cations or Thiol Compounds. *Agric. Biol. Chem. 48*, 341−347.
(9) Yanakawa, M., Hishinuma, F., and Gunge, N. (1985) Intact Cell Transformation of *Saccharomyces cervisiae* by Polyethylene Glycol. *Agric. Biol. Chem. 49*, 869−871.
(10) Gietz, R. D., and Schiestl, R. H. (1991) Applications of High Efficiency Lithium Acetate Transformation of Intact Yeast Cells using Single-Stranded Nucleic Acids as Carrier. *Yeast 7*, 253−263.
(11) Gietz, R. D., Schiestl, R. H., Willems, A. R., and Woods, R. A. (1995) Studies on the Transformation of Intact Yeast Cells by the LiAc/SS-DNA/PEG Procedure. *Yeast 11*, 355−360.
(12) Gietz, R. D., and Schiestl, R. H. (1995) Transforming yeast with DNA. *Methods Mol. Cell. Biol. 5*, 255−269.
(13) Palmen, R., and Hellingwerf, K. J. (1997) Uptake and processing of DNA by *Acinetobacter calcoaceticus*-a review. *Gene 192*, 179−190.
(14) Brzobohaty, B., and Kovac, L. (1986) Factors enhancing genetic transformation of intact yeast cells modify cell wall porosity. *J. Gen. Microbiol. 132*, 3089−3093.
(15) Gurrieri, S., Wells, K. S., Johnson, I. D., and Bustamante, C. (1997) Direct Visualization of Individual Microscopy: Characterization of the Factors Affecting Signal/Background and Optimization of Imaging Condition Using YOYO. *Anal. Biochem. 249*, 44−53.
(16) McCoy, S. L., Hausman, F. A., Deffebach, M. E., Bakke, A., Merkens, L. S., Bennett, R. M., and Hefeneider, S. H. (2000) Quantification of DNA binding to cell-surfaces by flow cytometry. *J. Immunol. Methods 241*, 141−146.
(17) Rye, H. S., Yue, S., Wemmer, D. E., Quesada, M. A., Haugland, R. P., Mathies, R. A., and Glazer, A. N. (1992) Stable fluorescent complexes of double-stranded DNA with bis-intercalating asymmetric cyanine dyes: properties and applications. *Nucleic Acids Res. 20*, 2803−2812.
(18) Glazer, A. N., and Rye, H. S. (1992) Stable dye-DNA intercalation complexes as reagents for high-sensitivity fluorescence detection. *Nature* 359, 859−861.
(19) Fang, C. X., An, Z. D., Shen, P., Li G. W., He, F., Chen, X. D., Fan, X. R., Zheng, C. Y., Yang, T. Q., Lin, Q. H., Tang, B., Cao, Q. W., and Peng, Z. R. (1999) *Microbiological Experiments*, 3rd ed. (Shen, P., Fan, X. R., and Li, G. W., Eds.) pp 42−43, Higher Education Press, Beijing, China.
(20) Fang, C. X., An, Z. D., Shen, P., Li, G. W., He, F., Chen, X. D., Fan, X. R., Zheng, C. Y., Yang, T. Q., Lin, Q. H., Tang, B., Cao, Q. W., and Peng, Z. R. (1999) *Microbiological Experiments*, 3rd ed. (Shen, P., Fan, X. R., and Li, G. W., Eds.) p 27, Higher Education Press, Beijing, China.
(21) Haugland, R. P. (1996) *Handbook of Fluorescent Probes and Research Chemicals*, 6th ed. (Spence, M. T. Z., Ed.), pp 380−381, Chapter 16, Molecular Probes, Inc., Eugene, OR.
(22) Ellis, R. J., and van der Vies, S. M. (1991) Molecular chaperones. *Annu. Rev. Biochem. 60*, 321−347.

BC049833V

Design and Synthesis of Functionalized Cyclopentadienyl Tricarbonylmetal Complexes for Technetium-94m PET Imaging of Estrogen Receptors

Heather M. Bigott,[†] Ephraim Parent,[‡] Leonard G. Luyt,[‡] John A. Katzenellenbogen,[‡] and Michael J. Welch*,[†]

Division of Radiological Sciences, Washington University School of Medicine, 510 S. Kingshighway, Campus Box 8225, St. Louis, Missouri 63110, and Department of Chemistry, University of Illinois, 600 South Mathews Avenue, Urbana, Illinois 61801. Received September 21, 2004; Revised Manuscript Received December 30, 2004

Cyclopentadienyl tricarbonylmetal (CpTM, M = Re, ^{94m}Tc) complexes, some based on a typical nonsteroidal estrogen, were prepared with the aim of developing technetium- and rhenium-labeled imaging agents for estrogen receptor (ER) positive breast tumors. CpT[^{94m}Tc] compounds with simple cyclopentadienyl substituents were first synthesized using a modified double ligand transfer reaction. The in vivo biodistribution of one of these CpT[^{94m}Tc] complexes was determined by tissue dissection and microPET imaging. Novel C-ring substituted analogues of cyclofenil, a nonsteroidal compound known to bind the ER, were also prepared, and their ER binding was measured. Because of their low ER affinity, however, labeling and imaging studies of these compounds were not pursued. It is notable that the highest ER binding analogue, a CpTRe cyclofenil derivative, could be synthesized from the corresponding ferrocenyl cyclofenil analogue by the double ligand transfer reaction. This further demonstrates the versatility of the double ligand transfer reaction and indicates that the synthesis of technetium and rhenium radiolabeled agents for breast tumor imaging and therapy is also likely to be successful.

INTRODUCTION

Breast cancer continues to be the most common form of cancer and the third leading cause of cancer death among women in the United States (*1*). Early detection and accurate staging of cancer play key roles in the treatment planning and ultimate outcome of the patient. For breast cancer, proper staging includes the determination of the estrogen receptor (ER)[1] status, because this receptor is upregulated in many breast cancers. Breast tumors that have high ER levels, termed estrogen receptor positive (ER+) tumors, can often be successfully treated through hormone therapy with anti-estrogens. Some breast cancers express only low ER levels (ER−); these cancers generally have a poorer response to anti-estrogen therapy and usually require a more invasive treatment course (*2*). The high level of estrogen receptor expression in ER+ tumors can be exploited in imaging and therapy studies by the administration of ER-targeting compounds labeled with an appropriate radionuclide. Compounds that selectively bind to the receptor with high affinity yield higher activity accumulation in the ER+ tumor tissue than in surrounding nontarget and ER− tissues. Such imaging methods for in vivo assessment of the ER status of breast tumors are attractive because they simultaneously and noninvasively provide information on all tumor sites.

Previously, ER ligands have been labeled with fluorine-18 and other cyclotron-produced, short-lived radionuclides to develop in vivo imaging agents (*3*−*12*). For example, 16α-[^{18}F]fluoro-estradiol (FES) was used to image primary and metastatic breast tumors, and the FES images were shown to have value in predicting the clinical effectiveness of hormone therapy with tamoxifen, the most commonly used anti-estrogen drug (*13*, *14*). Short-lived, cyclotron-produced radionuclides, however, are expensive and are not widely available, which limits the utility of ER imaging agents such as FES for routine clinical studies.

The development of technetium- and rhenium ER-targeting compounds is attractive for several reasons. Compounds labeled with the inexpensive and widely available, single photon emission computed tomography (SPECT) technetium radionuclide, ^{99m}Tc ($t_{1/2}$ = 6.0 h, $E_{\beta+}$ = 140.5 keV, Iγ = 87.2%), could be used as ER imaging agents for routine clinical imaging studies. Rhenium, a nonradioactive congener of technetium, has very similar chemical and physical properties to technetium; in fact, rhenium complexes are commonly used to facilitate the development and characterization of technetium compounds. Rhenium also has two radionuclides that have been proven useful for therapy studies, ^{186}Re ($t_{1/2}$ = 3.71 d, $E_{\beta(\mathrm{avg})}$ = 0.36 MeV, $E\gamma$ = 137 keV) and ^{188}Re ($t_{1/2}$ = 16.8 h, $E_{\beta(\mathrm{avg})}$ = 0.77 MeV, $E\gamma$ = 155 keV) (*15*−*19*). Technetium and rhenium analogues of an ER-targeting compound could therefore be used in dual imaging/therapy studies. Furthermore, the replacement of the SPECT radionuclide, ^{99m}Tc, with the positron emission tomography (PET) radionuclide, ^{94m}Tc ($t_{1/2}$ = 52.0 min, β^+ = 70%, $E_{\beta+\max}$ = 2.44 MeV), could generate ER imaging agents for efficient screening and dosimetry calculations

* To whom correspondence should be addressed. Tel: (314) 362-8436, Fax: (314) 362-8399, e-mail: welchm@wustl.edu.

[†] Washington University School of Medicine.

[‡] University of Illinois.

[1] Abbreviations: Estrogen receptor (ER), single photon emission computed tomography (SPECT), positron emission tomography (PET), cyclopentadienyl tricarbonylmetal (CpTM, M = Tc, Re), relative binding affinity (RBA), postinjection (pi).

10.1021/bc049770g CCC: $30.25 © 2005 American Chemical Society
Published on Web 02/24/2005

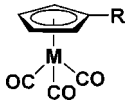

Figure 1. The basic structure of the cyclopentadienyl tricarbonylmetal unit (CpTM, M = Tc, Re).

Scheme 1

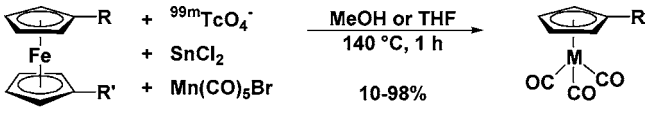

R = acid, ester, amide or ketone
R' = acid, ester, amide, ketone or H

M = ^{99m}Tc, Mn

of new Tc and Re compounds through the quantitation of PET images.

A number of attempts have been made to conjugate technetium and rhenium to estradiol, the natural ER ligand, to create agents suitable for imaging the ER in vivo (*20*−*31*). These steroid-based methods included both pendant and integrated approaches incorporate of the metal. In the pendant design, an inorganic or organometallic metal-containing moiety is covalently attached to the steroid; by contrast, the integrated approach involves replacement of part of the steroid backbone by a metal chelate. Many of these large, lipophilic complexes suffered from low receptor binding affinity, high nonspecific binding, and/or low complex stability, and were therefore not useful in imaging. For reasons that are not yet well understood, even those estradiol complexes with good in vitro binding to the ER did not give favorable tissue distribution in vivo.

The use of nonsteroidal ligands for the development of ER radiopharmaceuticals with organometallic radiometal tethers has also been investigated (*32*−*34*). An organometallic complex potentially useful in the development of ER imaging agents is cyclopentadienyl tricarbonylmetal (CpTM, M = Tc, Re). The CpTM unit (Figure 1) is small, has a lipophilic core of high chemical stability, and can be derivatized by altering the substituent (R) attached to the Cp ring. Wenzel et al. described the preparation of CpTM (M = ^{99m}Tc, Mn) via a quick and relatively mild transformation in which the reduction, carbonylation, and cyclopentadienylation of ^{99m}Tc was carried out in a one-pot reaction (Scheme 1) (*35*). We later studied the scope of this reaction and improved it by both increasing the yield through the use of a different reducing agent ($CrCl_3$ for $SnCl_2$) and by eliminating the Mn side-products of the original method by replacing the carbonyl donor ($Mn(CO)_5Br$ with $Cr(CO)_6$) (*36*). This method is termed a double ligand transfer reaction (DLT) because two different ligands (CO and Cp) on two different metal atoms (Mn/Cr and Fe) become transferred to a third metal atom (Tc/Re). Other methods have also been explored to synthesize the CpTM unit (*37*−*39*).

Jaouen et al. showed the potential of ER-targeting complexes containing the CpTM organometallic moiety by reporting the synthesis of a CpTRe β-ring substituted tamoxifen analogue that not only bound the ER, but also behaved as an anti-estrogen, with nearly identical efficacy as the active metabolite of tamoxifen (*33*). Cyclofenil is another nonsteroidal compound that has been shown to have good binding affinity for the ER (Figure 2a) (*40*). Muthyala et al. have reported several bridged bicyclic C-ring analogues of cyclofenil that have high ER binding affinity (*40*, *41*), as much as five times that of estradiol. This suggests that C-ring substitutions of cyclofenil with CpTM might also be possible without loss of ER binding affinity.

The overall goal of the work described herein was to investigate the synthesis of CpTRe and CpTTc compounds, including CpTM cyclofenil analogues, and to explore their potential use as ER imaging agents. As we are also developing methods for quantitative biodistribution studies derived from animal imaging sessions on microPET scanners, the PET radionuclide ^{94m}Tc was selected for labeling studies. We began our synthetic efforts by establishing labeling conditions for the production of CpT[^{94m}Tc] compounds with simple cyclopentadienyl substituents. To demonstrate that these model compounds could be obtained in sufficient yield, purity, and compatibility for use in animal studies, one of the compounds was used in microPET imaging and tissue dissection studies. To add an ER targeting component to the CpTM system, cyclofenil analogues with C-ring substitutions were synthesized and evaluated for their ability to bind the ER.

EXPERIMENTAL PROCEDURES

Materials and Chemical Methods. Reagents, solvents and deuterated solvents were purchased from Acros Organics of Fisher Scientific (Pittsburgh, PA), Aldrich (Milwaukee, WI), Fisher (Pittsburgh, PA), and Strem (Newburyport, NH). Methylene chloride and tetrahydrofuran were dried by a Solvent Delivery System (SDS) (neutral alumina columns) fabricated by J. C. Meyer (Irvine, CA), based on a design published by Pangborn et al. (*42*). All solutions were prepared using distilled, deionized water (Milli-Q; >18 MΩ resistivity). All air-sensitive reactions were carried out under nitrogen or argon atmosphere, using flame- or oven-dried glassware. Reaction progress was monitored by analytical thin-layer chromatography (TLC) on silica gel medium. Visualization was achieved either by UV light (254 nm) or phosphomolybdic acid indicator. Flash chromatography was performed using Woelm silica gel (0.040−0.063 mm) packing.

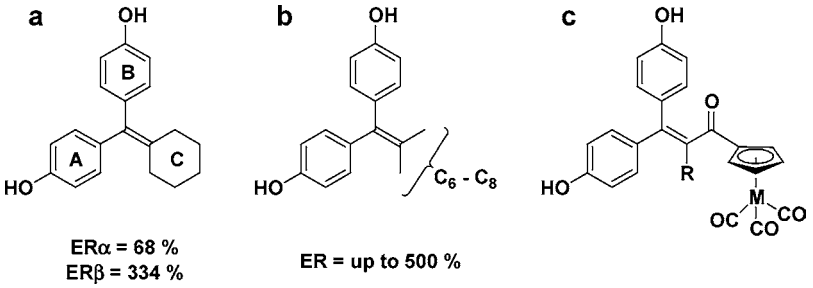

Figure 2. The structures of cyclofenil (**a**) (*39*), literature C-ring substituted analogues (**b**) (*39*−*40*), and proposed C-ring substituted CpTM analogues (**c**). The binding affinities listed are for the ER subtypes α and β and are relative to estradiol which is set as 100%.

^{1}H and ^{13}C NMR spectra were recorded on a Unity 500 Varian FT-NMR spectrometer. Chemical shifts (δ) are reported in parts per million downfield from internal tetramethylsilane and/or referenced from solvent resonances. NMR coupling constants are reported as absolute values in Hertz (Hz). Low resolution electron impact (EI) mass spectra and high-resolution EI mass spectra (HRMS) were obtained on Micromass 70-VSE. Melting points were determined on a Thomas-Hoover melting point apparatus and are uncorrected.

A CS-15 cyclotron (Cyclotron Corporation, Berkeley, CA) with proton beam energy of 14.5 MeV was used for the in-house production of ^{94m}Tc. Methods for the production and purification of $^{94m}TcO_4^-$ have been described (*43*−*45*).[2] Briefly, ^{94m}Tc was produced by proton irradiation of an enriched molybdenum target, according to the ^{94}Mo(p,n)^{94m}Tc nuclear reaction. After irradiation, the ^{94m}Tc was separated from the molybdenum starting material by sublimation. The $^{94m}TcO_4^-$ was removed from the quartz sublimation apparatus either in dilute NaOH solution and was isolated using a Sep-Pak Light alumina N cartridge, or it was removed directly into MeOH and used without purification. Radioactive samples were counted in a radionuclide calibrator (Capintec, Inc., Ramsey, NJ) for determination of activity in millicuries and in a Beckman 8000 (Beckman Fullerton, CA) or a Cobra II (Packard, Meridian, CT) γ-counter for activity in counts per minute. Radionuclidic purity was determined by analysis on a Canberra multichannel analyzing gamma spectrometer (Canberra Industries, Inc., Meriden, CT). MicroPET imaging was performed on a microPET-R4 instrument (Concorde MicroSystems Inc., Knoxville, TN).

Acetylcyclopentadienyltechnetium-94m(I) Tricarbonyl (2a). Alumina purified $^{94m}TcO_4^-$ (5.50 mCi) in 0.5 mL saline was added to a pressure tube and evaporated to dryness with heat under a flow of argon. 1,1′-Diacetylferrocene (0.5 mg, 0.002 mmol), chromium(III) chloride (0.5 mg, 0.003 mmol), chromium hexacarbonyl (1 mg, 0.004 mmol), and 0.5 mL of dry methanol were added, and the tube was then sealed and heated in an aluminum bomb for a total of 45 min (30 min at 180 °C). After cooling to −78 °C, the tube was opened and the solvent evaporated with heat under argon, being careful not to distill off the product. The crude mixture was dissolved in ether and passed through a silica plug, then evaporated under an argon flow, leaving 1.07 mCi (65% decay-corrected). Purification was carried out by HPLC (C_{18} reverse-phase, 50% acetonitrile/50% water), and eluent fractions from 12 to 13.5 min were collected, as determined by the radioactive trace and by comparison to the mass peak of the nonradioactive rhenium analogue (*36*). The product was extracted into ether (x 3), and the combined organic layers were evaporated to give 439 μCi (45% decay-corrected, this was slightly lower than the usual yield of ∼55% and was likely due to loss of the pressure tube seal during heating). This material was dissolved in 10% DMSO/90% saline solution for injection. Note: the above procedure was also carried out using unpurified ^{94m}Tc, as a mixture of pertechnetate and technetium oxides (36% oxide content) in methanol. The isolated yield was 58% (decay-corrected) with greater than 95% purity based on HPLC analysis.

Methoxycarbonylcyclopentadienyltechnetium-94m(I) Tricarbonyl (2b). Alumina purified $^{94m}TcO_4^-$ (1.44 mCi) in 0.75 mL saline was added to a pressure tube and evaporated to dryness with heat under a flow of argon. 1,1′-Ferrocenedicarboxylate methyl ester (10.0 mg, 0.033 mmol), chromium(III) chloride (6 mg, 0.038 mmol), chromium hexacarbonyl (16 mg, 0.073 mmol), and 0.5 mL of dry methanol were added, and the tube was then sealed and heated in an aluminum bomb for a total of 45 min (30 min at 180 °C). After cooling to −78 °C, the tube was opened and the solvent evaporated with heat under argon, being careful not to distill off the product. The crude mixture was dissolved in acetonitrile and passed through a silica plug, then partially evaporated under an argon flow leaving 210 μCi (84% decay-corrected). An aliquot was purified by HPLC (C_{18} reverse-phase, 50% acetonitrile/50% water), and eluent fractions from 10.5 to 12 min were collected, as determined by the radioactive trace and by comparison to the mass peak of the nonradioactive rhenium analogue (*36*). The decay-corrected yield was 56%.

1,1-Bis-(4-methoxy-phenyl)-propan-1-ol (4). A 2 M THF solution of EtMgCl (1.34 mL, 2.68 mmol) was added to a solution of 4,4′-dimethoxybenzophenone (260 mg, 1.07 mmol) in dry THF (5 mL) at 0 °C. The solution was allowed to warm to room temperature over the course of 4−5 h, and a saturated solution of NH_4Cl (25 mL) was then slowly added. To this was added CH_2Cl_2 (25 mL), the phases were separated, and the aqueous phase was extracted with CH_2Cl_2 (2 × 25 mL). The combined organic phases were dried with $MgSO_4$, filtered, and concentrated under vacuum. The residual oil was purified by flash column chromatography (20:80 ethyl acetate:hexanes) to afford **4** as a pale yellow oil (136 mg, 47%). ^{1}H NMR (500 MHz, $CDCl_3$): δ = 0.87 (t, 3H, J = 7.3 Hz), 1.99 (s, 1H), 2.25 (q, 2H, J = 7.3 Hz), 3.79 (s, 6H), 6.82−6.85 (m, 4H), 7.29−7.32 (m, 4H). ^{13}C NMR (125 MHz, $CDCl_3$): δ = 8.21, 34.63, 55.17, 77.93, 113.32, 127.33, 139.43, 158.25.

1,1-Bis-(4-methoxy-phenyl)-1-propene (5). *p*-Toluenesulfonic acid (5.5 mg, 0.029 mmol) was added to a solution of **4** (120 mg, 0.441 mmol) in benzene (30 mL), and the mixture was heated under reflux for 30 min. The solution was cooled, washed successively with saturated solutions of $NaHCO_3$ (2 × 30 mL) and NaCl (2 × 30 mL), then dried over $MgSO_4$, filtered, and concentrated under vacuum. The crude product was purified by flash column chromatography (20:80 ethyl acetate:hexanes) to give **5** as a white solid (104 mg, 93%), mp 100−101 °C (lit. mp (*46*) 97−100 °C). ^{1}H NMR (500 MHz, $CDCl_3$): δ = 1.76 (d, 3H, J = 7.1), 3.80 (s, 3H), 3.85 (s, 3H), 6.03 (q, 1H, J = 7.1 Hz), 6.79−6.82 (m, 2H), 6.90−6.94 (m, 2H), 7.09−7.17 (m, 4H). ^{13}C NMR (125 MHz, $CDCl_3$): δ = 15.66, 55.18, 55.22, 113.37, 113.44, 122.13, 128.32, 131.15, 132.51, 136.11, 141.36, 158.37, 158.54. MS (EI): *m/z* 254 (M^+, 100%); HRMS calcd for $C_{17}H_{18}O_2$ 254.1307, found 254.1313.

3,3-Bis-(4-methoxy-phenyl)-2-methyl-1-phenyl-propenone (6). A solution of benzoyl chloride (37 mL, 0.32 mmol) in CH_2Cl_2 (1 mL) was slowly added to a small flask containing a mixture of **5** (54 mg, 0.21 mmol), aluminum-(III) chloride (85 mg, 0.64 mmol), and CH_2Cl_2 (5 mL) at 0 °C. The solution was allowed to warm to room-temperature overnight. A saturated solution of $NaHCO_3$ (10 mL) was added to quench the reaction and the resulting thick solution was passed through a Celite plug. The aqueous phase was separated and extracted with CH_2Cl_2 (3 × 10 mL). The combined organic phases were dried with $MgSO_4$, filtered, and concentrated under vacuum. The residual oil was purified by flash column chromatography (20:80 ethyl acetate:hexanes) to afford **6** as a pale yellow oil (41 mg, 54%). ^{1}H NMR (500 MHz, $CDCl_3$): δ = 2.16 (s, 3H), 3.62 (s, 3H), 3.83 (s, 3H), 6.51−

[2] Bigott, H. M., Laforest, R., Ruangma, A. and Welch, M. J., unpublished results.

6.55 (m, 2H), 6.89−6.94 (m, 4H), 7.20−7.25 (m, 4H), 7.30−7.35 (m, 1H), 7.76−7.79 (m, 2H). ^{13}C NMR (125 MHz, $CDCl_3$): δ = 19.99, 54.96, 55.18, 113.04, 113.43, 127.99, 129.06, 131.27, 131.36, 132.27, 133.06, 133.47, 134.25, 137.08, 143.62, 158.88, 158.99, 201.59. MS (EI): *m/z* 358 (M^+, 100%); HRMS calcd for $C_{14}H_{22}O_3$ 358.1569, found 358.1564.

3,3-Bis-(4-methoxy-phenyl)-2-methyl-1-ferrocenyl-propenone (9). Pyridine (one drop) and oxalyl chloride (375 mL, 4.30 mmol) were slowly added to a suspension of ferrocenecarboxylic acid (200 mg, 0.869 mmol) in CH_2Cl_2 (6 mL) at 0 °C. The mixture was stirred for 30 min at 0 °C and another 30 min while warming to room temperature, during which time it became a clear rust color. The solvent was removed directly into a trap via cannulation, and the residue was dried for 2 h under vacuum. The ferrocene acid chloride residue (**8**) was dissolved in CH_2Cl_2 (7.5 mL), and the solution was slowly added to a flask containing a mixture of **5** (149 mg, 0.586 mmol), aluminum(III) chloride (272 mg, 2.04 mmol), zinc dust (1.77 g, 27.1 mmol), and CH_2Cl_2 (7.5 mL) at −78 °C. After 2 h, the mixture was stirred for 5 min with a saturated solution of $NaHCO_3$ (15 mL) and was then passed through a Celite plug to remove the zinc solids. The aqueous phase was separated and extracted with CH_2Cl_2 (3 × 10 mL). The combined organic phases were washed once with a saturated solution of NaCl, dried with $MgSO_4$, filtered, and concentrated under vacuum. The crude product was purified by flash column chromatography (3:97 ethyl acetate:methylene chloride) to afford **9** as a rust-colored solid (156 mg, 57%), mp 176−177 °C. ^{1}H NMR (500 MHz, $CDCl_3$): δ = 2.23 (s, 3H), 3.66 (s, 3H), 3.85 (s, 3H), 4.18 (s, 5H), 4.28 (t, 2H, J = 1.9 Hz), 4.57 (t, 2H, J = 1.9 Hz), 6.56−6.60 (m, 2H), 6.91−6.94 (m, 4H), 7.14−7.17 (m, 2H). ^{13}C NMR (125 MHz, $CDCl_3$): δ = 20.68, 55.18, 55.40, 69.90, 70.36, 71.97, 78.84, 113.23, 113.63, 131.50, 131.63, 134.18, 134.37, 134.60, 142.06, 159.06 (x2), 205.93. MS (EI): *m/z* 466 (M^+, 55%); HRMS calcd for $C_{28}H_{26}O_3Fe$ 466.1231, found 466.1235.

3,3-Bis-(4-methoxy-phenyl)-2-methyl-1-(cyclopentadienylrhenium(I) Tricarbonyl)-propenone (10). A pressure vessel was charged with **9** (89 mg, 0.19 mmol), potassium perrhenate (56.6 mg, 0.196 mmol), chromium(III) chloride (60.0 mg, 0.379 mmol), and chromium hexacarbonyl (256 mg, 1.16 mmol). Dry methanol (0.5 mL) was added, and the tube was then sealed and heated in an aluminum bomb for a total of 75 min (60 min at 165 °C). After cooling to −78 °C, the tube was opened and the solution was transferred with CH_2Cl_2 (9 mL) to a separatory funnel and washed once with a saturated solution of NaCl (10 mL). The aqueous phase was separated and extracted with CH_2Cl_2 (2 × 10 mL). The combined organic phases were dried with $MgSO_4$, filtered, and concentrated under vacuum. The crude product was purified by flash column chromatography (3:97 ethyl acetate:methylene chloride) to give **10** as an off-white solid (34 mg, 29%). ^{1}H NMR (500 MHz, $CDCl_3$): δ = 2.12 (s, 3H), 3.76 (s, 3H), 3.84 (s, 3H), 5.10 (t, 2H, J = 2.1 Hz), 5.71 (t, 2H, J = 2.1 Hz), 6.71−6.75 (m, 2H), 6.89−6.93 (m, 2H), 7.00−7.04 (m, 2H), 7.10−7.14 (m, 2H). ^{13}C NMR (125 MHz, $CDCl_3$): δ = 21.28, 55.20, 55.26, 84.35, 88.89, 94.49, 113.61, 113.65, 131.44, 131.68, 132.89, 133.04, 134.27, 143.15, 159.32, 159.67, 195.62, 211.53. MS (EI): *m/z* 616 (M^+, 33%); HRMS calcd for $C_{26}H_{21}O_6{}^{187}Re$ 616.0896, found 616.0893.

4,4′-(1-Propenylidene)bis-phenol (5a). To a solution of **5** (30 mg, 0.12 mmol) in CH_2Cl_2 (2 mL) was added $BF_3{\cdot}S(CH_3)_2$ (745 μL, 7.08 mmol) at room temperature. The solution was stirred for 4 h until the complete conversion to the diphenol, at which time the reaction was quenched with methanol (1 mL), and the solvent was removed under a stream of N_2. The rust orange-colored residue was partitioned between ethyl acetate (4 mL) and water (4 mL), and the mixture was stirred for 20 min. The aqueous phase was separated and extracted once with ethyl acetate (5 mL). The combined organic phases were quickly washed with saturated solutions of $NaHCO_3$ (10 mL) and NaCl (2 × 10 mL), dried over $MgSO_4$, filtered, and concentrated under vacuum. The crude product was dissolved in 40:60 ethyl acetate:hexanes (0.5 mL), passed through a plug of silica gel in a Pasteur pipet, eluted with 40:60 ethyl acetate:hexanes, and concentrated under vacuum to yield a nearly pure **5a** as a pale peach solid (18 mg, 69%). ^{1}H NMR (500 MHz, $(CD_3)_2CO$): δ = 1.68 (d, 3H, J = 6.9 Hz), 5.95 (q, 1H, J = 6.9 Hz), 6.70−6.75 (m, 2H), 6.83−6.87 (m, 2H), 6.95−6.99 (m, 2H), 7.01−7.05 (m, 2H), 8.25 (s, 1H), 8.34 (s, 1H). MS (EI): *m/z* 226 (M^+, 68%).

3,3-Bis-(4-hydroxy-phenyl)-2-methyl-1-ferrocenyl-propenone (9a). To a solution of **9** (19 mg, 0.041 mmol) in CH_2Cl_2 (0.68 mL) was added $BF_3{\cdot}S(CH_3)_2$ (257 μL, 2.44 mmol) at room temperature. The solution was stirred for 5 h until the complete conversion to the diphenol, at which time the reaction was quenched with methanol (1 mL), and the solvent was removed under a stream of N_2. The black residue was partitioned between ethyl acetate (4 mL) and water (4 mL), and the mixture was stirred for 15 min. The aqueous phase was separated and extracted once with ethyl acetate (5 mL). The combined organic phases were quickly washed with saturated solutions of $NaHCO_3$ (10 mL) and NaCl (2 × 10 mL), dried over $MgSO_4$, filtered, and concentrated under vacuum. Flash column chromatography (40:60 ethyl acetate:hexanes) gave nearly pure **9a** as a red rust-colored solid (15 mg, 54%). ^{1}H NMR (500 MHz, $(CD_3)_2CO$): δ = 2.18 (s, 3H), 4.17 (s, 5H), 4.27 (t, 2H, J = 1.9 Hz), 4.53 (t, 2H, J = 1.9 Hz), 6.50−6.53 (m, 2H), 6.78−6.81 (m, 2H), 6.85−6.89 (m, 2H), 7.09−7.13 (m, 2H), 8.27 (s, 1H), 8.49 (s, 1H). MS (EI): *m/z* 438 (M^+, 100%).

3,3-Bis-(4-hydroxy-phenyl)-2-methyl-1-(cyclopentadienylrhenium(I) Tricarbonyl)-propenone (10a). To a solution of **10** (19 mg, 0.031 mmol) in CH_2Cl_2 (1.0 mL) was added $BF_3{\cdot}S(CH_3)_2$ (162 μL, 1.54 mmol) at room temperature. The solution was stirred for 18 h, until the complete conversion to the diphenol, at which time the reaction was quenched with methanol (8 mL), and the solvent was removed under a stream of N_2. The deep red-colored residue was partitioned between ethyl acetate (5 mL) and water (5 mL), and the mixture was stirred for 30 min. The aqueous phase was separated and extracted once with ethyl acetate (5 mL). The combined organic phases were quickly washed with saturated solutions of $NaHCO_3$ (10 mL) and NaCl (10 mL), dried over $MgSO_4$, filtered, and concentrated under vacuum. The crude product was dissolved in 40:60 ethyl acetate:hexanes (0.5 mL), passed through a plug of silica gel in a Pasteur pipet, eluted with 40:60 ethyl acetate:hexanes, and concentrated under vacuum to yield a nearly pure **10a** as a yellow solid (4 mg, 22%). ^{1}H NMR (500 MHz, $(CD_3)_2CO$): δ = 2.05 (overlapped by solvent peak, should be s, 3H), 5.42 (t, 2H, J = 2.2 Hz), 5.92 (t, 2H, J = 2.2 Hz), 6.69−6.73 (m, 2H), 6.86−6.95 (m, 4H), 7.06−7.10 (m, 2H), 8.55 (s, 1H), 8.57 (s, 1H). MS (EI): *m/z* 588 (M^+, 9%).

Synthetic Notes of Diphenolic Compounds. The diphenolic compounds proved difficult to purify because they tended to decompose in solution and upon exposure

to light and heat. 2-D TLC verified that decomposition was not due to incompatibility with the silica gel. Therefore, when decomposition prevented typical column chromatography, short plugs of silica gel were instead used. This resulted in the isolation of nearly pure compounds that were then quickly used without further purification. The mechanism of decomposition (oxidative vs inherent structural instability) is uncertain since the formation of multiple new compounds with similar polarities is suggested by TLC, and the NMR spectra do not provide clear enough signals to identify these impurities. Methods attempted to stabilize the diphenolic compounds and to prevent oxidative decomposition failed. These included using either the radical scavenger, 3,5-di-*tert*-butyl-4-hydroxy-anisole (BHA), or the weak acid, acetic acid, during chromatography. As seen in the absence of these radical scavengers, decomposition was observed with mostly higher polarity compounds being formed. Decomposition was slowed by shielding the product from light, limiting its time in solution, and by storing it in vessels covered in aluminum foil, either on a high vacuum line or at −20 °C under N_2.

Estrogen Receptor Binding Affinity. Relative binding affinities (RBAs) were determined by competitive radiometric binding assays using [^{3}H]estradiol, following previously published procedures (*47*, *48*). The RBAs are expressed as a percentage, relative to estradiol binding being 100%. The receptor sources were lamb uterine cytosol, purified full-length human ERα, or purified full-length human ERβ (Pan Vera Inc., Madison, WI). The RBA values are reported as the average of two or more determinations ± the range ($n = 2$) or standard deviation ($n > 2$).

Biodistribution Study. All animal experiments were conducted in compliance with guidelines established by the Washington University Animal Studies Committee. Tissue distribution studies were performed on C57/Bl6 male mice. The mice were anesthetized with 1−2% isofluorane/oxygen, and a bolus injection of ∼10 μCi of **2a** (100 μL, 10% DMSO in saline) was administered via the tail vein. The animals were sacrificed by cervical dislocation at 2 h postinjection (pi). The tissues and organs were promptly removed and weighed, and the radioactivity of each sample was determined by a gamma counter.

PET Imaging. Positron emission tomography imaging was performed on a microPET-R4 system (Concorde Microsystems Inc, Knoxville, TN) which is based on the design of Cherry and colleagues (*49*). The microPET-R4 has a field of view of 8 cm axially by 11 cm transaxially and is capable of a spatial resolution of 2 mm and an absolute sensitivity of 920 cps/μCi in the middle of the field of view. Data were acquired in list mode and histogrammed into frames. Images were then reconstructed by Fourier Rebinning (FORE) followed by 2D-Filtered Back Projection (2D-FBP) with ramp filter cutoff at the Nyquist frequency, using data from all tilt angles (*50*). The microPET imaging study was carried out on a female C57/Bl6 mouse, anesthetized with 1−2% isofluorane/oxygen and placed in an immobilizing scanner support. Compound **2a** was administered as a bolus injection via the tail vein (175 μCi). Single position imaging was performed at five timepoints (5, 15, 30, 60 and 100 min pi), each consisting of 10 min static data collections.

RESULTS AND DISCUSSION

Design and Synthesis of Representative CpT-[^{94m}Tc] Systems (*51, 52*). Technetium-94m is a positron-emitting radionuclide that can be used in small animal PET imaging as well as standard tissue dissection biodistribution analysis. The relatively short half-life (52 min) of ^{94m}Tc must be considered when designing synthetic schemes utilizing this radionuclide. Ideally, the incorporation of ^{94m}Tc should be in the final synthetic step, and isolation and purification of the final compound should be rapid. To achieve conditions for the time-efficient and reproducible synthesis of CpT[^{94m}Tc] compounds, two model systems with simple cyclopentadienyl substituents were generated, CpT[^{94m}Tc]-$COCH_3$ (**2a**) and CpT[^{94m}Tc]-CO_2CH_3 (**2b**). Compounds **2a** and **2b** were made using a DLT reaction adapted from the reported synthesis of the analogous nonradioactive rhenium compounds, CpTRe-$COCH_3$ and CpTRe-CO_2CH_3 (*36*) (Scheme 2). The modifications made included increasing the reaction temperature from 160 to 180 °C, reducing the reaction time from 60 to 30 min, and purifying the reaction products by HPLC versus column chromatography. Each of these changes was aimed at minimizing synthesis and purification times to better suit the use of the short-lived ^{94m}Tc radiometal.

Scheme 2

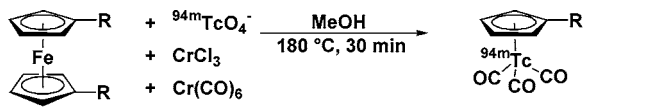

1a R = $COCH_3$ **2a** R = $COCH_3$ (55%)
1b R = $COOCH_3$ **2b** R = CO_2CH_3 (56%)

In general, a pressure vessel was charged with a saline solution of $^{94m}TcO_4^-$, and the solvent was evaporated with heating under a flow of argon. At room temperature, the appropriate ferrocenyl compound, other nonradioactive reagents, and dry MeOH were added. The tube was sealed and heated at 180 °C for 30 min. Compounds **2a** and **2b** were shown to be radiochemically homogeneous and free from chemical impurities after purification by normal phase HPLC. As is typically the case, the characterization of the compounds was facilitated by comparison to the nonradioactive rhenium analogues. The yields reported in Scheme 2 (55% for CpT[^{94m}Tc]-$COCH_3$ and 56% for CpT[^{94m}Tc]-CO_2CH_3) were reasonably high. Additionally, considering that the reaction time was cut in half, these yields compared well to those reported for the rhenium compounds (60% for CpTRe-$COCH_3$ and 88% for CpTRe-CO_2CH_3) (*36*).

From these experiments, the observation was made that the volume of the $^{94m}TcO_4^-$ saline solution should be minimized. First, as the DLT reaction is most efficient with MeOH as the solvent (*36*), the use of a $^{94m}TcO_4^-$ saline solution required a time-consuming evaporation of the aqueous solvent and reconstitution of the residue in MeOH. Therefore, larger solution volumes required longer evaporation times, resulting in greater decay loss of ^{94m}Tc. Second, initial reaction attempts following the concentration of relatively large volumes of $^{94m}TcO_4^-$ in saline (1−3 mL) yielded salty reaction mixtures that, when filtered, caused appreciable amounts of the activity to become trapped in the filters. Optimization experiments for the isolation of $^{94m}TcO_4^-$ following the cyclotron production of ^{94m}Tc led to the development of a combination concentration and purification step.[2] Of the multiple columns and cartridges tested, the shortest processing times and smallest solution volumes were obtained using a Sep-Pak Light alumina N cartridge. In this way, highly concentrated and pure solutions of $^{94m}TcO_4^-$ in just 400 μL of normal saline were made and used in

the reactions. Consequently, the yields were improved from both shortened preparation times and reduced activity loss during filtration due to minimized salt content. The values reported in Scheme 2 are isolated yields and were achieved in reactions that followed the use of this method.

Methanolic solutions of $^{94m}TcO_4^-$ were also used in the DLT reactions of the CpT[^{94m}Tc] compounds. Here, the ^{94m}Tc activity was removed from the quartz distillation apparatus with hot methanol and the unpurified solution was quickly concentrated to the desired volume with heating under a flow of argon.[2] Similar decay-corrected isolated yields were obtained (i.e., 58% and 55% for **2a** from methanol and saline solutions, respectively), and the processing time from end of bombardment to end of synthesis was shortened. Although a direct comparison was not carried out, this suggests that the methanol recovery method would generate higher overall yields (i.e., in mCi), due to reduced ^{94m}Tc decay loss.

It should be pointed out that since no purification of the $^{94m}TcO_4^-$ was performed following the MeOH recovery, a technetium oxide radiochemical impurity (probably $^{94m}TcO_3$, see (*53*)) was present. Interestingly, this species did not appear to interfere with the DLT reaction. In fact, in one case, a methanolic solution of $^{94m}TcO_4^-$ that had an unusually high amount of $^{94m}TcO_3$ (36%) resulted in a 58% isolated yield of compound **2a**. It is unlikely that the $^{94m}TcO_4^-$ species alone reacted to give this yield as it was only 64% of the starting activity (a loss of only 6% would be remarkable). Rather, the technetium oxide impurity was likely also reduced and reacted with the ferrocene starting material.

To confirm the ability of technetium oxide to react in the DLT reaction, the analogous reaction was performed using rhenium(VI) oxide as the metal source. After heating for 1 h at 180 °C, followed by chromatographic purification, acetylcyclopentadienylrhenium(I) tricarbonyl was isolated in a yield of 87% while the methoxycarbonylcyclopentadienyl rhenium(I) tricarbonyl was isolated in 72% yield (experimental details not included). From this, one can conclude that both pertechnetate/perrhenate and technetium/rhenium oxide are suitable metal sources for the DLT reaction.

MicroPET Imaging and Biodistribution Studies of CpT[^{94m}Tc]-COCH$_3$ in Mice (*51, 52*). The simple cyclopentadienyl substituents and overall structure of the model CpT[^{94m}Tc] compounds prepared by the DLT reaction were not expected to target the ER. Nevertheless, to demonstrate the ability to synthesize adequate activity for animal imaging studies and in a chemical formulation compatible for safe iv administration into animals, compound **2a** was synthesized as discussed and used in both tissue distribution and microPET imaging studies of mice. Figure 3 shows a representative coronal microPET image slice of a C57/Bl6 mouse at 5 min pi of 175 μCi of **2a**. No significant differences in activity distributions were observed at later timepoints (out to 2 h pi) and are therefore not shown. This small, lipophilic compound shows high uptake in the liver and kidney area, as well as activity in the bladder, as would be expected in the hepatobiliary and renal clearance of such a compound. Tissue distribution studies of C57/Bl6 mice were also performed following low activity injections of compound **2a** (~10 μCi). These data, presented in Table 1, also show high activity in the clearance organs at 2 h pi.

Design and Synthesis of C-Ring Substituted Cyclofenil Analogues. The ligand binding pocket of the estrogen receptor has been shown to have a substantial amount of unoccupied space (~200 Å^3) when bound to estradiol, particularly in the middle of the ligand binding pocket, near the B and C rings (*54*) (Figure 4a). Several bridged bicyclic C-ring derivatives of cyclofenil have recently been reported to have high RBA for the ER (*40*, *41*), suggesting the potential of other C-ring modifications. Figure 4 shows the structural similarity of the cyclofenil analogues reported here compared to both estradiol and to an example of the reported bicyclic cyclofenil analogues.

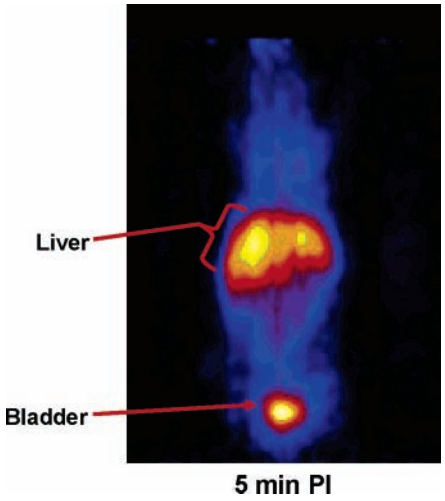

Figure 3. Representative coronal microPET image slice of a C57/Bl6 female mouse at 5 min post tail vain injection of CpT[^{94m}Tc]-COCH$_3$ (**2a**, 175 μCi). Liver and bladder are highlighted with arrows.

Table 1. Biodistribution of CpT[^{94m}Tc]-COCH$_3$ (2a) in Male C57/Bl6 Mice[a]

tissue	**2a**	tissue	**2a**
blood	0.22 ± 0.05	muscle	0.36 ± 0.29
lung	15.25 ± 1.55	fat	1.13 ± 0.80
liver	30.35 ± 2.22	brain	0.04 ± 0.02
spleen	0.17 ± 0.08	bone	0.77 ± 0.74
kidney	13.49 ± 2.64	prostate	1.76 ± 1.88
gallbladder	13.35 ± 2.54	testes	0.26 ± 0.22

[a] % Injected dose per gram at 2 h pi; values are reported as the mean ± SD; $n = 4$ for each time point.

The conditions for the incorporation of ^{94m}Tc into Cp-substituted CpT[^{94m}Tc] systems from the corresponding Cp-substituted ferrocene via the DLT reaction had been established (Scheme 2). We, therefore, sought to synthesize the DLT ferrocene precursor (**9**) necessary for the generation of the CpT[^{94m}Tc] cyclofenil analogue. A model synthesis, to produce a benzoyl cyclofenil analogue (**6**), was performed to assist in the development of effective synthetic conditions. The CpTRe cyclofenil compound (**10**), for characterization and RBA determination, was also synthesized. These syntheses, described briefly here, are detailed in the Experimental Procedures section.

Synthesis of the benzoyl model compound **6** began with the preparation of the known precursor **5**, as shown in Scheme 3 (*55*). Stirring the commercially available 4,4′-dimethoxybenzophenone **3** with the Grignard reagent ethylmagnesium chloride gave the alcohol **4** as the major product. Some formation of the alkene **5** was also observed. Dehydration was effected by refluxing the collected mixture of **4** and **5** in benzene with *p*-toluenesulfonic acid. Friedel−Crafts acylation of **5** with benzoyl chloride to yield the benzoyl cyclofenil analogue **6** was carried out by slow addition of benzoyl chloride to a cooled solution of **5** and aluminum chloride, followed by stirring

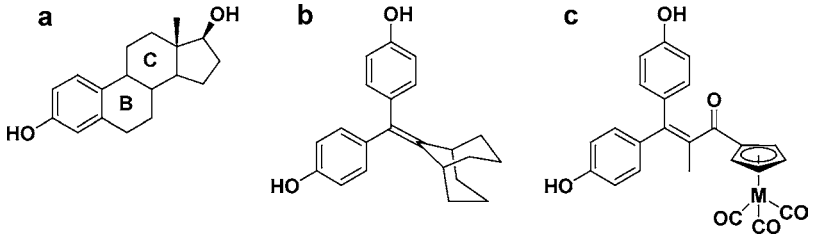

Figure 4. The structures of estradiol (**a**), a literature C-ring substituted analogue (**b**) (*40*), and a C-ring substituted CpTM analogue (**c**).

Scheme 3

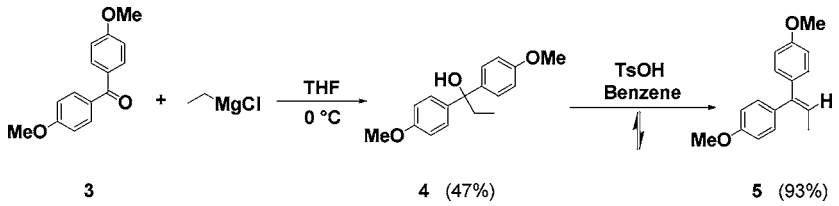

Scheme 4

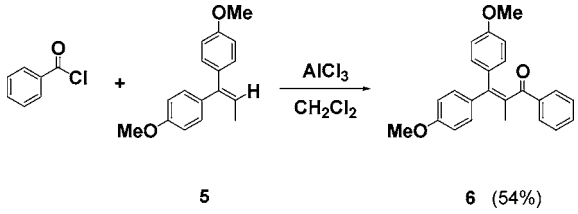

at room-temperature overnight. This gave **6** in 54% yield whereas other orders of addition and changing the Lewis acid resulted in poor yields (10−20%).

The ferrocene cyclofenil **9** analogue was prepared as outlined in Scheme 5. Conversion of the commercially available ferrocene carboxylic acid **7** to the ferrocene acid chloride **8** was quickly accomplished with oxalyl chloride (the use of thionyl chloride resulted in a thick black material) (*56*). Yields of this reaction were very high, provided that anhydrous conditions were strictly maintained. Initial efforts to synthesize **9** with Friedel−Crafts conditions based on the model reaction in Scheme 4 gave low and variable yields (<5−20%). The use of a large excess of Zn dust prevented the oxidation of the ferrocene and resulted in significantly increased and reproducible yields (*57*). The reaction time was also cut from 12 to 2 h, as the formation of the multiple side products worsened with time. The reduction in yield from this considerably shorter reaction time was found to be less than 5%. One of the side products was isolated and shown to be ferrocene anhydride, presumably from the reaction of the **8** with unreacted or hydrolyzed **7**.

Scheme 6 illustrates the synthesis of the CpTRe cyclofenil compound **10** via a DLT reaction on **9**. The ferrocene precursor used here was monosubstituted, as opposed to the 1,1′-disubstituted precursors used in Scheme 2. We and others have reported that a carbonyl group must be directly attached to the Cp ring to effect the ring transfer (*36, 58*); therefore, the DLT reaction in Scheme 6 was predicted to react preferentially on the substituted Cp ring of **9**. As expected, we found no evidence of a ring transfer reaction occurring on the bare Cp ring. Other monosubstituted ferrocene precursors have been successfully labeled, though typically with yields much lower than with the 1,1′-disubstituted counterparts (*36*, *59*). Hence, the lower yield of the reaction in Scheme 6 relative to those in Scheme 2 was not surprising (the lower temperatures may also have accounted, in part, for the lower yields). Though modest, the yield of this reaction produced adequate material for characterization, deprotection and RBA studies; optimization of temperature and reaction time was not performed.

Structural studies of ER binding have indicated the need of a pharmacophore with two free phenols, similar to those of estradiol (spaced approximately 11 Å apart, (*54*)); therefore, good binding of the methyl ether protected compounds **5**, **6**, **9**, and **10** would not be expected, and deprotection conditions were investigated. This proved to be somewhat of a challenge. Deprotection of the phenolic methyl ethers using various reagents (BBr_3, BBr_3 with Zn, $AlCl_3$, $AlCl_3$ with EtSH) and reaction temperatures resulted in either no reaction or product decomposition. Under the conditions in Scheme 7, the deprotection of both phenols appeared, by TLC, to go to completion (*32*). However, the diphenolic compounds were difficult to isolate and purify, as they were found to be sensitive to heat, air and light to varying degrees. Nevertheless, the desired bisphenols **5a**, **9a**, and **10a** could be obtained in reasonable yields. The deprotected benzene compound was the most unstable and could not be prepared. Details and attempts to stabilize the compounds are given above in the Synthetic Notes of Diphenolic Compounds section.

Estrogen Receptor Binding Affinity Determination. Table 2 presents the binding affinity data of the cyclofenil analogues developed in this study. Binding affinities were determined by competitive radiometric binding assays with [^{3}H]estradiol, using cytosol preparations of lamb uterus (considered to be almost all ERα) or full-length human ERα and ERβ, as previously described (*47, 48*). Binding affinities are expressed relative to that of the standard, estradiol, as relative binding affinity (RBA) values, where the affinity of estradiol is 100%.

Binding affinities are presented for both the protected and deprotected compounds. As expected, the deprotected compounds (**5a**, **9a**, and **10a**) all gave significantly higher binding affinities than their protected counterparts (**5**, **9**, and **10**), ranging from 19- to 213-fold increases, which is a typical differential between phenols and their corresponding methyl ethers. The diphenolic alkene compound **5a** showed a small preference for the ERβ subtype, while the CpTRe cyclofenil analogue **10a** had a small preference for the ERα subtype, and the ferrocene cyclofenil analogue **9a** showed no subtype preference. The CpTRe cyclofenil analogue **10a** gave the highest RBA of

Scheme 5

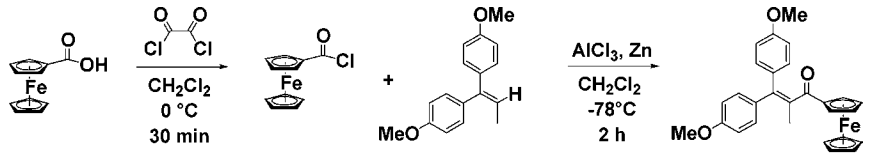

7 **8** (90+%) **5** **9** (57%)

Scheme 6

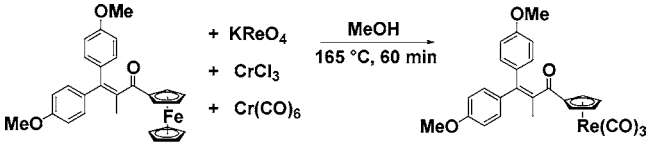

9 **10** (29%)

Scheme 7

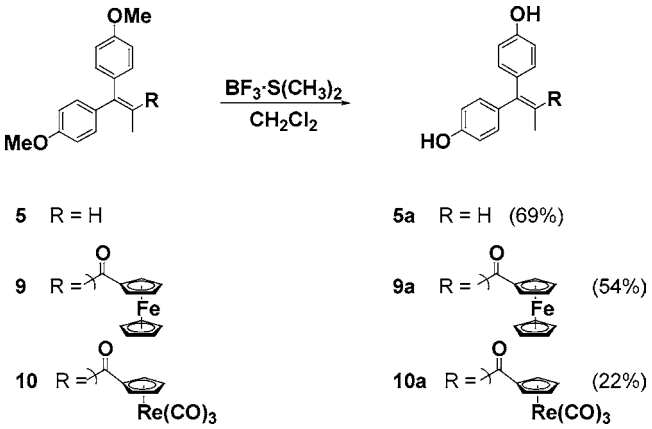

Table 2. Relative Binding Affinities (RBA) of Cyclofenil Analogues[a]

	RBA (%)		
ligand	cytosol	ERα	ERβ
estradiol	100	100	100
5	0.005 ± 0.001	0.006 ± 0.002	0.016 ± 0.004
6	0.004 ± 0.001	0.008 ± 0.002	<0.003
9	0.010 ± 0.003	0.014 ± 0.008	0.031 ± 0.004
10	0.014 ± 0.013	0.009 ± 0.006	0.034 ± 0.037
5a	0.274 ± 0.064	0.408 ± 0.109	1.399 ± 0.534
9a	0.648 ± 0.395	0.773 ± 0.205	0.868 ± 0.019
10a	0.357 ± 0.010	1.920 ± 0.467	0.634 ± 0.028

[a] Values are reported as the mean ± range ($n = 2$) or SD ($n > 2$) of 2−4 independent determinations. Under these conditions, the K_d for estradiol is 0.2 nM for ERα and 0.5 nM for ERβ.

nearly 2% that of estradiol for the ERα subtype. This value, although the highest in this study, is quite low compared with many of the reported ER-targeting compounds in recent literature (*25*, *32*, *41*). As the chemical and physical behavior of rhenium and technetium are very much alike, a CpT[^{94m}Tc] cyclofenil analogue, if synthesized, would also be expected to have a low affinity for the ER. Considering the low RBAs coupled with the handling difficulties of the free phenolic compounds, ^{94m}Tc labeling and imaging studies of these compounds were not pursued.

In conclusion, methods were developed for the rapid incorporation of the short-lived radionuclide ^{94m}Tc into two representative CpT[^{94m}Tc] systems (**2a** and **2b**) with sufficient yield, purity, and iv formulation compatability for animal studies. Qualitative analysis of the microPET images of compound **2a** match the tissue distribution studies of **2a**, suggesting that screening of new radiopharmaceuticals is possible with ^{94m}Tc and microPET. The synthesis of three C-ring substituted cyclofenil analogues was accomplished. Additionally, the conversion of the ferrocene analogue (**9**) into the CpTRe analogue (**10**) by the DLT reaction further demonstrated its utility for the synthesis of CpTM systems with both large and small cyclopentadienyl substituents. This predicts the use of this reaction for the successful incorporation of rhenium and technetium radionuclides into this and other cyclofenil analogues. While literature precedent suggested CpTM cyclofenil compounds as logical targets, the analogues synthesized in the present study had low relative binding affinities for the ER. A new direction may be to vary the C-ring bulk of the CpTM cyclofenil compounds, potentially leading to greater affinity for the ER. This may be accomplished, for example, by the use of a series of alkene precursors and/or extending the linker between the alkene and the ferrocene moieties. However, this approach may not resolve the handling difficulties of this class of diphenolic compounds.

ACKNOWLEDGMENT

We are grateful for support of this research through grants from the National Institute of Health (PHS 5R37 CA25836 [J.A.K.]) and the Department of Energy (DE FG02 84ER60218 [M.J.W.] and DE FG02 86ER60401 [J.A.K.]). Technetium-94m was produced at Washington University Medical School and partially funded through a National Cancer Institute grant (R24 CA86307). MicroPET imaging was partially supported by an NIH/NCI SAIRP grant (1 R24 CA83060). We thank the Small Animal Imaging Core of the Alvin J. Siteman Cancer Center at Washington University and Barnes-Jewish Hospital in St. Louis, MO, for additional support of the microPET imaging. The Core is supported by an NCI Cancer Center Support Grant (1 P30 CA91842). NMR spectra were obtained in the Varian Oxford Instrument Center for Excellence in NMR Laboratory at the University of Illinois. Funding for this instrumentation was provided in part from the W. M. Keck Foundation, the National Institutes of Health (PHS 1 S10 RR104444-01), and the National Science Foundation (NSF CHE 96-10502). Mass spectra were obtained on instruments supported by grants from the National Institute of General Medical Sciences (GM 27029), the National Institutes of Health (RR 01575), and the National Science Foundation (PCM 8121494). We also thank Kathryn Carlson at the University of Illinois for the binding affinity measurements and Eric Mull currently at Boehringer-Ingelheim for his assistance in the preliminary CpTM synthesis efforts.

LITERATURE CITED

(1) The American Cancer Society webpage: Cancer facts and figures 2004 (Accessed Feb. 2004) http://www.cancer.org/docroot/GI/content/GI_3_11x_Cancer_Facts_And_Figures_2004.asp.

(2) McGuire, W. L. (1995) *Estrogen receptors in human breast cancer*, Raven Press, New York.
(3) Jonson, S. D., d'Avignon, D. A., Katzenellenbogen, J. A., and Welch, M. J. (1998) Methyl hypofluorite in the synthesis of 16-methoxyestradiol stereoisomers. *Steroids 63*, 470−478.
(4) VanBrocklin, H. F., Rocque, P. A., Lee, H. V., Carlson, K. E., Katzenellenbogen, J. A., and Welch, M. J. (1993) 16β-[^{18}F]-Fluoromoxestrol: a potent, metabolically stable positron emission tomography imaging agent for estrogen receptor positive human breast tumors. *Life Sci. 53*, 811−819.
(5) Hostetler, E. D., Jonson, S. D., Welch, M. J., and Katzenellenbogen, J. A. (1999) Synthesis of 2-[^{18}F]fluoroestradiol, a potential diagnostic imaging agent for breast cancer: strategies to achieve nucleophilic substitution of an electron-rich aromatic ring with [^{18}F]F. *J. Org. Chem. 64*, 178−185.
(6) Seimbille, Y., Ali, H., and Van Lier, J. E. (2002) Synthesis of 2, 16α- and 4, 16α-difluoroestradiols and their 11β-methoxy derivatives as potential estrogen receptor-binding radiopharmaceuticals. *J. Am. Chem. Soc., Perkin Trans. 1* 657−663.
(7) Seimbille, Y., Rousseau, J., Benard, F., Morin, C., Ali, H., Avvakumov, G., Hammond, G. L., and Van Lier, J. E. (2002) ^{18}F-labeled difluoroestradiols: preparation and preclinical evaluation as estrogen receptor-binding radiopharmaceuticals. *Steroids 67*, 765−775.
(8) Dence, C. S., Napolitano, E., Katzenellenbogen, J. A., and Welch, M. J. (1996) Carbon-11-labeled estrogens as potential imaging agents for breast tumors. *Nucl. Med. Biol. 23*, 491−496.
(9) French, A. N., Napolitano, E., Vanbrocklin, H. F., Hanson, R. N., Welch, M. J., and Katzenellenbogen, J. A. (1993) Synthesis, radiolabeling and tissue distribution of 11β-fluoroalkyl- and 11β-fluoroalkoxy-substituted estrogens: target tissue uptake selectivity and defluorination of a homologous series of fluorine-18-labeled estrogens. *Nucl. Med. Biol. 20*, 31−47.
(10) Pomper, M. G., VanBrocklin, H., Thieme, A. M., Thomas, R. D., Kiesewetter, D. O., Carlson, K. E., Mathias, C. J., Welch, M. J., and Katzenellenbogen, J. A. (1990) 11β-Methoxy-, 11β-ethyl, and 17α-ethynyl-substituted 16α-fluoroestradiols: receptor-based imaging agents with enhanced uptake efficiency and selectivity. *J. Med. Chem. 33*, 3143−3155.
(11) Kiesewetter, D. O., Kilbourn, M. R., Landvatter, S. W., Heiman, D. F., Katzenellenbogen, J. A., and Welch, M. J. (1984) Preparation of four fluorine-18-labeled estrogens and their selective uptakes in target tissues of immature rats. *J. Nucl. Med. 25*, 1212−1221.
(12) Vanbrocklin, H. F., Pomper, M. G., Carlson, K. E., Welch, M. J., and Katzenellenbogen, J. A. (1992) Preparation and evaluation of 17-ethynyl-substituted 16α-[18F]fluoroestradiols: selective receptor-based PET imaging agents. *Nucl. Med. Biol. 19*, 363−374.
(13) Mortimer, J. E., Dehdashti, F., Siegel, B. A., Trinkaus, K., Katzenellenbogen, J. A., and Welch, M. J. (2001) Metabolic flare: indicator of hormone responsiveness in advanced breast cancer. *J. Clin. Oncol. 19*, 2797−2803.
(14) Dehdashti, F., Flanagan, F. L., Mortimer, J. E., Katzenellenbogen, J. A., Welch, M. J., and Siegel, B. A. (1999) Positron emission tomographic assessment of "metabolic flare" to predict response of metastatic breast cancer to antiestrogen therapy. *Eur. J. Nucl. Med. 26*, 51−56.
(15) Dilworth, J. R., and Parrott, S. J. (1998) The biomedical chemistry of technetium and rhenium. *Chem. Soc. Rev. 27*, 43−55.
(16) Alberto, R. (1996) High- and low-valency organometallic compounds of technetium and rhenium. *Top. Curr. Chem. 176*, 149−187.
(17) Schwochau, K. (1994) Technetium radiopharmaceuticals − fundamentals, synthesis, structure, and development. *Angew. Chem., Int. Ed. Engl. 33*, 2258−2267.
(18) John, E., Thakur, M. L., DeFulvio, J., McDevitt, M. R., and Damjanov, I. (1993) Rhenium-186-labeled monoclonal antibodies for radioimmunotherapy: preparation and evaluation. *J. Nucl. Med. 34*, 260−267.
(19) Lisic, E. C., Mirzadeh, S., and Knapp, F. F., Jr. (1993) Synthesis of carrier-free rhenium-188(V)DMSA using triphenylphosphine as a facile reducing agent. *J. Labelled Compd. Radiopharm. 33*, 65−75.
(20) Luyt, L. G., Bigott, H. M., Welch, M. J., and Katzenellenbogen, J. A. (2003) 7α- and 17α-Substituted estrogens containing tridentate tricarbonyl rhenium/technetium complexes: synthesis of estrogen receptor imaging agents and evaluation using microPET with technetium-94m. *Bioorg. Med. Chem. 11*, 4977−4989.
(21) Skaddan, M. B., and Katzenellenbogen, J. A. (1999) Integrated "3+1" oxorhenium(V) complexes as estrogen mimics. *Bioconjugate Chem. 10*, 119−129.
(22) Top, S., Vessieres, A., and Jaouen, G. (1994) Synthetic strategy for organometallic complexes of rhenium with exceptionally high affinity for the estradiol receptor; their potential use as imaging and therapeutic agents. *Chem. Commun.* 453−454.
(23) Spradau, T. W., and Katzenellenbogen, J. A. (1998) Ligands for the estrogen receptor containing cyclopentadienyltricarbonylrhenium units. *Bioorg. Med. Chem. Lett. 8*, 3235−3240.
(24) Skaddan, M. B., Wust, F. R., Jonson, S., Syhre, R., Welch, M. J., Spies, H., and Katzenellenbogen, J. A. (2000) Radiochemical synthesis and tissue distribution of Tc-99m-labeled 7α-substituted estradiol complexes. *Nucl. Med. Biol. 27*, 269−278.
(25) Skaddan, M. B., Wuest, F. R., and Katzenellenbogen, J. A. (1999) Synthesis and binding affinities of novel Re-containing 7α-substituted estradiol complexes: models for breast cancer imaging agents. *J. Org. Chem. 64*, 8108−8121.
(26) Arterburn, J. B., Rao, K. V., and Perry, M. C. (2000) Solid-supported hydrazine substrate for labeling estradiol ligands with rhenium. *Angew. Chem., Int. Ed. 39*, 771−772.
(27) Wust, F., Carlson, K. E., Katzenellenbogen, J. A., Spies, H., and Johannsen, B. (1998) Synthesis and binding affinities of new 17α-substituted estradiol-rhenium "n+1" mixed-ligand and thioethercarbonyl complexes. *Steroids 63*, 665−671.
(28) Wuest, F., Spies, H., and Johannsen, B. (1996) Synthesis of "3+1" mixed-ligand oxorhenium(V) complexes containing modified 3, 17β-estradiol. *Bioorg. Med. Chem. Lett. 6*, 2729−2734.
(29) Hom, R. K., and Katzenellenbogen, J. A. (1997) Synthesis of a tetradentate oxorhenium(V) complex mimic of a steroidal estrogen. *J. Org. Chem. 62*, 6290−6297.
(30) Top, S., El Hafa, H., Vessieres, A., Quivy, J., Vaissermann, J., Hughes, D. W., McGlinchey, M. J., Mornon, J.-P., Thoreau, E., and Jaouen, G. (1995) Rhenium carbonyl complexes of β-estradiol derivatives with high affinity for the estradiol receptor: an approach to selective organometallic radiopharmaceuticals. *J. Am. Chem. Soc. 117*, 8372−8380.
(31) Wenzel, M., and Klinger, C. (1994) Estradiol-derivatives. Synthesis, organ distribution and tumor affinity. *J. Labelled Compd. Radiopharm. 34*, 981−987.
(32) Mull, E. S., Sattigeri, V. J., Rodriguez, A. L., and Katzenellenbogen, J. A. (2002) Aryl cyclopentadienyl tricarbonyl rhenium complexes: novel ligands for the estrogen receptor with potential use as estrogen radiopharmaceuticals. *Bioorg. Med. Chem. 10*, 1381−1398.
(33) Jaouen, G., Top, S., Vessieres, A., Pigeon, P., Leclercq, G., and Laios, I. (2001) First anti-estrogen in the cyclopentadienyl rhenium tricarbonyl series. Synthesis and study of antiproliferative effects. *Chem. Commun.* 383−384.
(34) Top, S., Kaloun, E. B., and Jaouen, G. (2000) A novel and mild metal-exchange reaction in the organometallic cyclopentadienyl series: 1, 1′-diaryl 2-cymantrenyl 1-butene as an example. *J. Am. Chem. Soc. 122*, 736−737.
(35) Wenzel, M. (1992) Technetium-99m labeling of cymantrene analogs with various substituents. A new preparation of technetium-99m radiodiagnostics. *J. Labelled Compd. Radiopharm. 31*, 641−650.
(36) Spradau, T. W., and Katzenellenbogen, J. A. (1998) Preparation of cyclopentadienyltricarbonylrhenium complexes using a double ligand-transfer reaction. *Organometallics 17*, 2009−2017.
(37) Minutolo, F., and Katzenellenbogen, J. A. (1998) A convenient three-component synthesis of substituted cyclopentadienyl tricarbonyl rhenium complexes. *J. Am. Chem. Soc. 120*, 4514−4515.

(38) Minutolo, F., and Katzenellenbogen, J. A. (1998) Boronic acids in the three-component synthesis of carbon-substituted cyclopentadienyl tricarbonyl rhenium complexes. *J. Am. Chem. Soc. 120*, 13264−13265.
(39) Top, S., Lehn, J.-S., Morel, P., and Jaouen, G. (1999) Synthesis of cyclopentadienyltricarbonylrhenium(I) carboxylic acid from perrhenate. *J. Organomet. Chem. 583*, 63−68.
(40) Muthyala, R. S., Carlson, K. E., and Katzenellenbogen, J. A. (2003) Exploration of the bicyclo[3.3.1]nonane system as a template for the development of new ligands for the estrogen receptor. *Bioorg. Med. Chem. Lett. 13*, 4485−4488.
(41) Muthyala, R. S., Sheng, S., Carlson, K. E., Katzenellenbogen, B. S., and Katzenellenbogen, J. A. (2003) Bridged bicyclic cores containing a 1,1-diarylethylene motif are high-affinity subtype-selective ligands for the estrogen receptor. *J. Med. Chem. 46*, 1589−1602.
(42) Pangborn, A. B., Giardello, M. A., Grubbs, R. H., Rosen, R. K., and Timmers, F. J. (1996) Safe and convenient procedure for solvent purification. *Organometallics 15*, 1518−1520.
(43) Roesch, F., Novgorodov, A. F., and Qaim, S. M. (1994) Thermochromatographic separation of ^{94m}Tc from enriched molybdenum targets and its large-scale production for nuclear medical application. *Radiochim. Acta 64*, 113−120.
(44) Roesch, F., and Qaim, S. M. (1996) Nuclear data relevant to the production of the positron emitting technetium isotope ^{94m}Tc via the ^{94}Mo(p,n)-reaction. [Erratum to document cited in *Chem. Abstr. 120*, 88184]. *Radiochim. Acta 75*, 227.
(45) Qaim, S. M. (2000) Production of high purity ^{94m}Tc for positron emission tomography studies. *Nucl. Med. Biol. 27*, 323−328.
(46) Kitamura, T., Kobayashi, S., and Taniguchi, H. (1982) Photochemistry of vinyl halides. Vinyl cation from photolysis of 1,1-diaryl-2-halopropenes. *J. Org. Chem. 47*, 2323−2328.
(47) Katzenellenbogen, J. A., Johnson, H. J., Jr., and Myers, H. N. (1973) Photoaffinity labels for estrogen binding proteins of rat uterus. *Biochemistry 12*, 4085−4092.
(48) Carlson, K. E., Choi, I., Gee, A., Katzenellenbogen, B. S., and Katzenellenbogen, J. A. (1997) Altered ligand binding properties and enhanced stability of a constitutively active estrogen receptor: evidence that an open pocket conformation is required for ligand interaction. *Biochemistry 36*, 14897−14905.
(49) Cherry, S. R., Shao, Y., Silverman, R. W., Meadors, K., Siegel, S., Chatziioannou, A., Young, J. W., Jones, W. F., Moyers, J. C., Newport, D., Boutefnouchet, A., Farquhar, T. H., Andreaco, M., Paulus, M. J., Binkley, D. M., Nutt, R., and Phelps, M. E. (1997) MicroPET: a high-resolution PET scanner for imaging small animals. *IEEE Trans. Med. Imag. 44*, 1161−1166.
(50) Defrise, M., Kinahan, P. E., Townsend, D. W., Michel, C., Sibomana, M., and Newport, D. F. (1997) Exact and approximate rebinning algorithms for 3-D PET data. *IEEE Trans. Med. Imag. 16*, 145−158.
(51) Portions of this work were presented at the 14th International Symposium on Radiopharmaceutical Chemistry: Bigott, H. M., McCarthy, D. W., Wust, F. R., Dahlheimer, J. L., Piwnica-Worms, D. R., and Welch, M. J. (2001) Production, processing and uses of ^{94m}Tc. *J. Labelled Compd. Radiopharm. 44*, S119−S121.
(52) Portions of this work were presented at the 14th International Symposium on Radiopharmaceutical Chemistry: Luyt, L. G., Mull, E. S., Katzenellenbogen, J. A., Bigott, H. M., and Welch, M. J. (2001) Preparation of cyclopentadienyltricarbonyl technetium-94m complexes. *J. Labeled Compd. Radiopharm. 44*, S489−S490.
(53) Gibson, J. K. (1993) High-temperature oxide and hydroxide vapor species of technetium. *Radiochim. Acta 60*, 121−126.
(54) Brzozowski, A. M., Pike, A. C. W., Dauter, Z., Hubbard, R. E., Bonn, T., Engstrom, O., Ohman, L., Greene, G. L., Gustafsson, J., and Carlquist, M. (1997) Molecular basis of agonism and antagonism in the estrogen receptor. *Nature 389*, 753−758.
(55) Suzuki, K., Kobayashi, T., Nishikawa, T., Hori, Y., and Hagiwara, T. (2002) Preparation of 2,2-(diaryl)vinylphosphine compounds, palladium catalyst thereof, and a process for producing arylamine, diaryl, or arylalkyne with the catalyst. EP 1167372, 42 pp.
(56) Abell, A. D., Morris, K. B. and Litten, J. C. (1990) Synthesis and deprotection of [1-(ethoxycarbonyl)-4-[(diphenylmethoxy)-carbonyl]-1-methyl-2-oxobutyl]triphenylphosphonium chloride: a key intermediate in the Wittig reaction between a cyclic anhydride and a stabilized ylide. *J. Org. Chem. 55*, 5217−5221.
(57) Bhatt, J., Fung, B. M., and Nicholas, K. M. (1992) Synthesis and thermal properties of mesomorphic 1, 1′-bis[w-(4′-cyano-4-biphenyloxy)alkyl]ferrocenes. *Liq. Cryst. 12*, 263−272.
(58) Kuntschke, D. (1994) Ph.D. Dissertation, Freien Universitat Berlin, Berlin, Germany.
(59) Cesati, R. R., III, Tamagnan, G., Baldwin, R. M., Zoghbi, S. S., Innis, R. B., and Katzenellenbogen, J. A. (1999) Synthesis of cyclopentadienyl tricarbonyl technetium phenyltropane derivatives by direct double ligand transfer with ferrocene precursors. *J. Labelled Compd. Radiopharm. 42*, S150−S152.

BC049770G

Polymer–Oligonucleotide Conjugate Synthesis from an Amphiphilic Block Copolymer. Applications to DNA Detection on Microarray

Bertrand de Lambert, Carole Chaix,* Marie-Thérèse Charreyre, Alain Laurent, Arnaud Aigoui, Agnès Perrin-Rubens, and Christian Pichot

Unité Mixte CNRS/bioMérieux, Ecole Normale Supérieure de Lyon, 46 allée d'Italie, 69364 Lyon Cedex 07, France. Received August 30, 2004; Revised Manuscript Received January 3, 2005

An amphiphilic block copolymer poly(*tert*-butylacrylamide-*b*-(*N*-acryloylmorpholine-*N*-acryloxysuccinimide)) (poly(TBAm-*b*-(NAM/NAS)) and a random copolymer poly(NAM/NAS), synthesized by the reversible addition–fragmentation chain transfer (RAFT) polymerization process, have been used as support for oligonucleotide (ODN) synthesis, to elaborate polymer–oligonucleotide conjugates. In a first step, starters of ODN solid-phase synthesis were coupled to activated ester functions of polymers, and second, resulting functionalized polymers were covalently grafted onto hydroxylated controlled pore glass (CPG) support to further accomplish ODN synthesis. An efficient capping of residual hydroxyl functions of CPG was performed before synthesis, with both acetic anhydride and diethoxy-*N*,*N*-diisopropyl-phosphoramidite reagents, to suppress parasite-free ODN population present in conjugate crude material and resulting from syntheses directly initiated on silica beads. After purification, conjugates were evaluated in a DNA hybridization assay on a microarray, as macromolecules being able to favor capture of the target. Conjugate coating conditions were studied on the dT25/dA25 model. The role of the hydrophobic part (poly(TBAm)) of the conjugate synthesized with the block copolymer in the orientation of the conjugate after coating was revealed by spotting experiments achieved in a mixed solvent (DMF/H_2O). The use of block copolymer–dT25 conjugate afforded a significant sensitivity improvement of the hybridization assay.

INTRODUCTION

DNA biochip technology on microsystems has been intensively developed this past decade to answer the increasing need of DNA sequence multianalyses in reduced time and in small volumes. In a general manner, DNA microarrays are elaborated by two main methods: (i) in situ synthesis of oligonucleotides (ODNs) either by means of photolithographic techniques (*1*) or spotting robot device (*2*), (ii) mechanical deposition of presynthesized oligonucleotides via ink-jet printing technology (*3*). To develop low-density DNA probe microarrays, the latter strategy of ODN spotting appeared to be more suitable. By this technique and using a nanodroplet ink-jetting piezoelectric device, spot sizes can be varied between 150 and 250 μm and spot densities can reach 2500 spots/cm^2 (*4*).

DNA microarrays are elaborated with different sets of known oligonucleotide sequences (ODN probes) immobilized on precisely defined locations of a solid support. An important feature of a successful DNA microarray is a sensitive and discriminating detection of each event, for instance, hybridization of a complementary target sequence with ODN probes. Concerning the detection, fluorescence is the optical technique which offers the highest sensitivity because of a low background noise (*4*). After DNA target hybridization with the ODN probes, a positive signal arises from the labeled target (either by a fluorophore or by a specific enzyme which can convert a substrate into a fluorescent product).

To amplify the sensitivity of DNA detection, the use of polymers at the surface of the solid support has been reported in the literature. Acrylamide gels (*5*–7), dendritic structures (*8, 9*), and poly(pyrrole) films (*10*) favored the covalent immobilization of a high density of ODN probes (150–250 fmol/mm^2) which improved the capture of the DNA target.

Different strategies have been described to introduce these polymers in association with ODN probes onto the solid surface, to elaborate a DNA microarray by droplet spotting: (i) polymers can be deposited on the whole surface of the chip prior to spot the ODN probes (*5, 9*); (ii) ODN probes bearing polymerizable groups can be addressed individually on the chip surface, and the anchoring can proceed by copolymerization with comonomer mixtures (*6, 10*); (iii) polymer–ODN conjugates can be prepared in a first step prior to be spotted on the chip (*7*).

Our laboratory early focused on the elaboration of polymer–ODN conjugates which could improve DNA target capture efficiency and consequently enhance DNA detection sensitivity of these diagnostic assays. Reactive polymers such as poly(maleic anhydride-methyl vinyl ether) (*11*) and poly(*N*-vinyl pyrrolidone-*N*-acryloxysuccinimide) (*12*) were used to bind ODN probes, and the resulting conjugates were adsorbed onto the conical polymer support of a VIDAS instrument (bioMérieux Co.). To avoid the aggregation observed during the coupling reaction of the ODN to the polymer, as well as to control ODN amount and orientation onto the polymer chain, a new method of conjugate synthesis has been developed. Direct syntheses of oligonucleotides were performed from starters bound along the polymer chain further grafted on a solid support (controlled pore glass), either on poly(maleic anhydride-ethylene) (*13*) or on poly(*N*-acryloylmorpholine-*N*-acryloxysuccinimide) (*14*). This latter

* To whom correspondence should be addressed. Tel: 00 33 (0)4 72 72 83 60. Fax: 00 33 (0)4 72 72 85 33. E-mail: carole.chaix@ens-lyon.fr.

10.1021/bc049791a CCC: $30.25 © 2005 American Chemical Society
Published on Web 02/16/2005

method allowed us to synthesize conjugates with a high density of ODN per chain (up to 135 ODN per chain).

The adsorption of these conjugates produced from linear random copolymers results from nucleic base hydrophobic interactions with the polymeric support. In an attempt to control conjugate anchoring orientation on the solid support to favor ODN probe accessibility for DNA capture, we focused on the use of an amphiphilic block copolymer. The hydrophobic part of the resulting conjugate should adsorb preferentially onto the hydrophobic support, inducing an orientation of the hydrophilic part bearing the ODN probes toward the aqueous phase. The designed amphiphilic copolymer was the poly(*tert*-butylacrylamide-*b*-(*N*-acryloylmorpholine-*N*-acryloxysuccinimide)), poly(TBAm-*b*-(NAM/NAS)), containing both hydrophilic and reactive poly(NAM/NAS) block known to efficiently bind starters and an hydrophobic block poly-(TBAm). This latter block was chosen since TBAm is an hydrophobic monomer which polymerizes efficiently by the controlled radical polymerization technique used to synthesize the block copolymer, namely the reversible addition−fragmentation chain transfer (RAFT) polymerization process (*15*). Moreover, as TBAm is also an acrylamide derivative, it facilitates the synthesis of the second block (acrylamide and acrylate comonomers) from the poly(TBAm) block.

We aim at describing herein the direct synthesis of oligonucleotides from a block copolymer poly(TBAm-*b*-(NAM/NAS)) and a random copolymer poly(NAM/NAS), synthesized by RAFT process (*16, 17*). The use of these conjugates to elaborate DNA microarrays by ink-jet spotting techniques is studied, and the influence of the hydrophobic part of the conjugate on the performance of the diagnostic test is assessed.

MATERIALS AND METHODS

Reagents and Analyses. Controlled pore glass (CPG, 2000 Å mean pore diameter; 40−85 μm particle size; 9.2 m^2/g surface area) was ordered from Fluka. Anhydrous DMF (99.9%) was purchased from Aldrich. 6-(Trifluoroacetylamino)-1-hexanol (>98% from Fluka), (3-*O*-dimethoxytrityl-1,3-diol)-[(β-cyanoethyl)-*N*,*N*-(diisopropyl)]-phophoramidite (Spacer C3, Glen Research), DMAP (99% from Aldrich), hexa(ethylene glycol) (97% from Aldrich), triethylamine (99.5% from Aldrich), glycidyloxypropyltrimethoxysilane (97% from Fluka), and fluorescamine (Acros) were used as received.

Poly(TBAm-*b*-(NAM/NAS)) and poly(NAM/NAS) were synthesized as described in previous papers (*16, 18*). ODNs were synthesized on an Applied Biosystems DNA synthesizer (Model 394) by β-cyanoethyl phosphoramidite chemistry. Purity of the polymer−ODN conjugates was determined by aqueous SEC, using a Waters UltraHydrogel column 500 Å, a Kontron HPLC pump 422, a Kontron HPLC autosampler 465, and a Kontron diode array detector 440. The eluent was a phosphate buffer (0.1 M, pH = 6.8), at a flow rate of 0.5 mL/min. UV detection was achieved at 260 nm.

HPLC analyses of ODNs was performed on an Alliance Instrument from Waters, using XTerra RP 18 column with elution in acetonitrile/triethylammonium acetate buffer 0.05 M gradient (from 4.5% to 8.5% V/V) at 37°C. The flow rate was of 1 mL/min and UV detection was achieved at 260 nm.

Fluorescence measurements were carried out on a Perkin-Elmer LS50. ESI Mass Spectrometry analyses of starter **1** were performed on a Api 165 PE SCIEX instrument (Applied Biosystems). ^{1}H NMR spectra were recorded on an Avance 200 MHz Bruker spectrometer.

(3-*O*-Dimethoxytritylpropane-1,3-diol)−(6-aminohexyl) Phosphate (Starter 1) Synthesis. 84 mg (0.4 mmol) of 6-(trifluoroacetylamino)-1-hexanol were coevaporated with dry acetonitrile and dissolved afterward in 1 mL of this solvent. Then, 1.1 equiv (250 mg, 0.44 mmol) of (3-*O*-dimethoxytritylpropan-1,3-diol)-[(β-cyanoethyl)-*N*,*N*-(diisopropyl)] phosphoramidite (Spacer C3, Glen Research) and 1.3 equiv of ^{1}H-tetrazole (0.52 mmol of a 0.45 M solution/acetonitrile, Glen Research) were successively added to the solution and the mixture was stirred at room temperature during 3 h, under argon atmosphere. Then, 20 mL (5 equiv) of iodine solution (0.1 M in H_2O/pyridine/THF from Glen Research) was added, and the mixture was stirred during 30 min prior to concentrate the solution under reduced pressure. The residue was dissolved in CH_2Cl_2, and the organic phase was washed once with $NaHCO_3$, and twice with H_2O before evaporation to dryness in vacuo. Then, the residue was resuspended in KOH solution (0.2M in ethanol), and the deprotection reaction was achieved in 16 h at room temperature. After concentration in vacuo, the residue was chromatographed on a column of silica gel with (CH_2Cl_2/triethylamine 95/5) and methanol gradient to give starter **1** (70% yield). ^{1}H NMR ($CDCl_3$): 1.15−1.70 (m, 8H, $CH_2CH_2CH_2CH_2CH_2CH_2$); 1.33 (t, CH_3 TEA) 1.82 (m, 2H, $OCH_2CH_2CH_2O$); 2.71 (m, 2H, CH_2NH_2); 3 (q, CH_2 TEA); 3.05 (m, 2H, CH_2-ODMT); 3.70 (s, 6H, OCH_3); 3.84−3.90 (m, 4H, CH_2OPOCH_2); 6.70−7.35 (m, 13H, H Ar); 7.90−8.60 (large peak, NH_3^+). ESI mass analysis in negative mode: $[M - H]^- = 556.3$.

CPG Bead Functionalization. The functionalization step was adapted from a previous procedure published by Maskos and Southern (*19*). First, 1.38 g of underivatized CPG 2000 Å (Fluka) was suspended in chromic−sulfuric acid solution (saturated solution of chromium(VI) oxide in sulfuric acid (purity >95%)). After 3 h activation at 120°C, a large proportion of silane groups on the surface was in silanol form. Activated beads were filtered, carefully washed with water and acetone, and rapidly dried in vacuo prior to use for silanization.

To the beads suspended in 22.3 mL of dry toluene were added 6.8 mL of (glycidyloxypropyl)trimethoxysilane (Fluka) and 1.9 mL of triethylamine (Aldrich). The suspension was gently stirred overnight at 80 °C, then filtered, washed with anhydrous acetone, and dried during 2 h at 120 °C. In a second step, these beads were suspended in 5.52 mL of hexa(ethylene glycol) (Aldrich) with 3.1 μL of sulfuric acid (purity >95%), and the mixture was gently stirred at 80 °C overnight. Finally, the functionalized beads were carefully washed with anhydrous acetone and dried in desiccator.

Coupling of Starter 1 Kinetics onto Random and Block Copolymers. The same protocol was carried out for the two copolymers, poly(TBAm-*b*-(NAM/NAS)) and poly(NAM/NAS). First, 4 mg of block copolymer (or 3.65 mg of random copolymer) was dissolved in 500 μL of anhydrous DMF. In parallel, 3.1 mg of starter **1** (0.6 equiv in comparison with NAS units) was dissolved in 500 μL of the same solvent and added to the polymer solution containing 0.375 mg of DMAP (0.3 equiv). The mixture was stirred at room temperature during 10 days. At defined times, aliquots (10 μL) were withdrawn from the mixture and added to 240 μL of a fluorescamine solution (0.3 mg/mL in DMF) to follow the kinetics via primary amine titration. After 4 h storage in darkness, samples were analyzed by fluorimetry (λ_{em} = 392 nm, λ_{ex} = 463 nm). The fluorescence intensity was related to the concentration of starter **1** in the solution, using a calibration curve $I_{fluo} = f$([starter **1**]) previously obtained under

Table 1. Characteristics of the Block Copolymer, Poly(TBAm-*b*-(NAM/NAS)), and of the Random Copolymer, Poly(NAM/NAS)

sample	copolymer composition (mol %) (^{1}H NMR)	Mn (g/mol) (SEC/LS)	PDI
block: poly(TBAm-*b*-(NAM/NAS))	9/57/34	14000/103000[a]	1.4
random: poly(NAM/NAS)	60/40	71000	1.1

[a] Theoretical mass for the second block.

the same conditions. With this titration method of residual starter **1** in solution, the kinetics of the coupling reaction on the polymer have been obtained.

Grafting of Polymer–Starter 1 Conjugate onto Functionalized CPG Beads. After 10 days of the coupling reaction between copolymer and starter **1**, 150 mg of functionalized CPG beads was added to the mixture, and the grafting reaction was continued under gentle stirring during 5 additional days. Supports were then filtered and carefully washed with anhydrous DMF and anhydrous acetone prior to drying in vacuo for several hours.

ODN Synthesis on Polymer-Functionalized CPG Beads. Columns were loaded with 25 mg of polymer-functionalized beads and a standard 1 μmol β-cyanoethyl phosphoramidite coupling cycle was used for ODN syntheses on an Applied Biosystems 394 instrument. Before syntheses, different capping steps were studied. Ac_2O capping was either achieved directly on the instrument, i.e., three runs of 15 s of Ac_2O capping reagents (acetic anhydride/pyridine/THF; *N*-methylimidazole/THF) alternated with waits of 5 min, or in a flask, i.e., reaction with 1 mL of acetic anhydride in 1 mL of acetonitrile stirred during 120 min. An additional capping was achieved by 10 min reaction with diethoxy-*N*,*N*-diisopropyl-phophoramidite (DPP) 0.1 M or 0.5 M in acetonitrile directly on the instrument. Then, after washing the CPG with acetonitrile, an oxidation step was achieved with iodine (I_2/pyridine/H_2O). During syntheses, the stepwise yield of coupling reaction was automatically determined by dimethoxytrityl cations measurement. For the cleavage and deprotection step, ammonia (30% aqueous) was used for 16 h at 60°C. After concentration in vacuo, conjugates were resuspended in water and purified by filtration on Centricon (Millipore, cutoff of 100000 g/mol) and analyzed by SEC.

Microarray Setup. DNA microarray was elaborated from standard 96-well microplates. Capture probes (polymer–ODN conjugates or ODN) were diluted at 10 μM (ODN concentration) in a coating buffer (150 mM Na_2HPO_4/NaH_2PO_4, from 50 to 400mM NaCl, 1 mM EDTA, pH 7.4). The standard coating buffer used in the study contained 400 mM NaCl. Spotting of this solution in the microplate wells was carried out with a Biochip Arrayer (Perkin-Elmer), which is based on a submicroliter noncontact, drop-on-demand piezoelectric dispensing technology providing a typical spot diameter of 250 μm. Each probe was deposited in duplicate spots, following the circular format of the 96-wells microplate (Apibio microarray). After spotting of the capture probe solution and drying under controlled pressure and temperature, microplates were rinsed with PBS-Tween 20, 0.05%. Then, microarrays were dried in vacuo before storage.

OLISA Test: Capture and Detection Procedures. The fluorescent ODN target 5′CY3-dA25 was diluted in 30 μL of reaction buffer (0.1 M Na_2HPO_4/NaH_2PO_4, 0.5 M NaCl, 0.6% Tween 20, 2% PEG 4000, pH 7). The solution was incubated in the spotted well for 1 h at 37 °C. The well was rinsed twice with PBS-Tween 20, 0.05%.

Then, the array was imaged with the automated Apimager system (Apibio, Grenoble, France). Spot densities were analyzed by calculation of the mean gray level of each spot minus that of the corona surrounding the spot. Pixel densities were scaled from 0 (no signal) to 65 536 (saturating signal) and expressed in arbitrary units (a.u.).

RESULTS AND DISCUSSION

Polymer Synthesis and Characterization. The polymers used in this study were synthesized by a controlled radical polymerization technique, namely the reversible addition–fragmentation chain transfer (RAFT) polymerization, as described in recent papers from our laboratory (*17*, *20*). The RAFT polymerization of the *N*-acryloylmorpholine/*N*-acryloxysuccinimide comonomer pair was performed in the presence of either a dithioester to give a random (statistical distribution of each monomer) copolymer poly(NAM/NAS) (*18*) or a macrodithioester (chains of poly(*tert*-butylacrylamide) also synthesized by RAFT (poly(TBAm)) to produce a block copolymer poly(TBAm-*b*-(NAM/NAS)) (*16*). The two copolymers used in this study (Figure 1) were characterized by ^{1}H NMR and size exclusion chromatography with an on-line light scattering detector (SEC/LS) (*16*, *17*) (Table 1). Both copolymers are homogeneous in size (polydispersity index, PDI < 1.5) and present a long hydrophilic chain (M_n > 70 000 g mol^{-1}). In the block copolymer, the presence of the hydrophobic block of poly(TBAm) induces an amphiphilic behavior. For instance, a similar block copolymer poly(TBAm-*b*-NAM) of 14 000/90 000 g/mol has a critical micellar concentration (CMC) of 1 g/L.

Conjugate Elaboration Strategy. Polymer–ODN conjugates were obtained via a strategy of ODN direct synthesis from polymer chains previously grafted onto hydroxylated silica support, as displayed in Figure 2.

In a first step (A), the polymer was functionalized with a starter of ODN synthesis (starter **1**). The amine

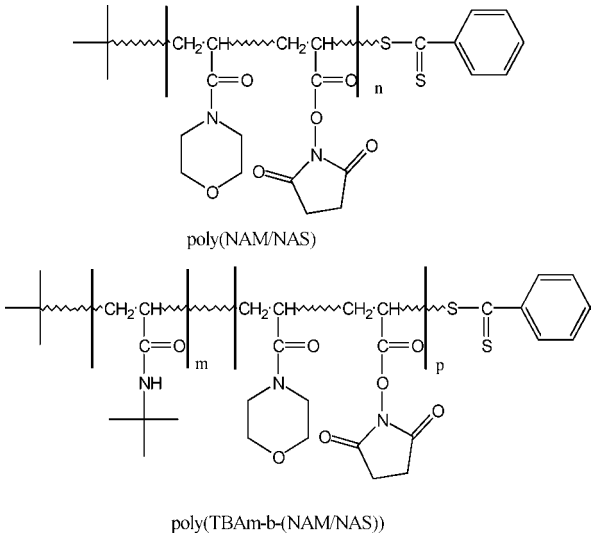

Figure 1. Random copolymer poly(NAM/NAS) and block copolymer poly(TBAm-*b*-(NAM/NAS)) structures.

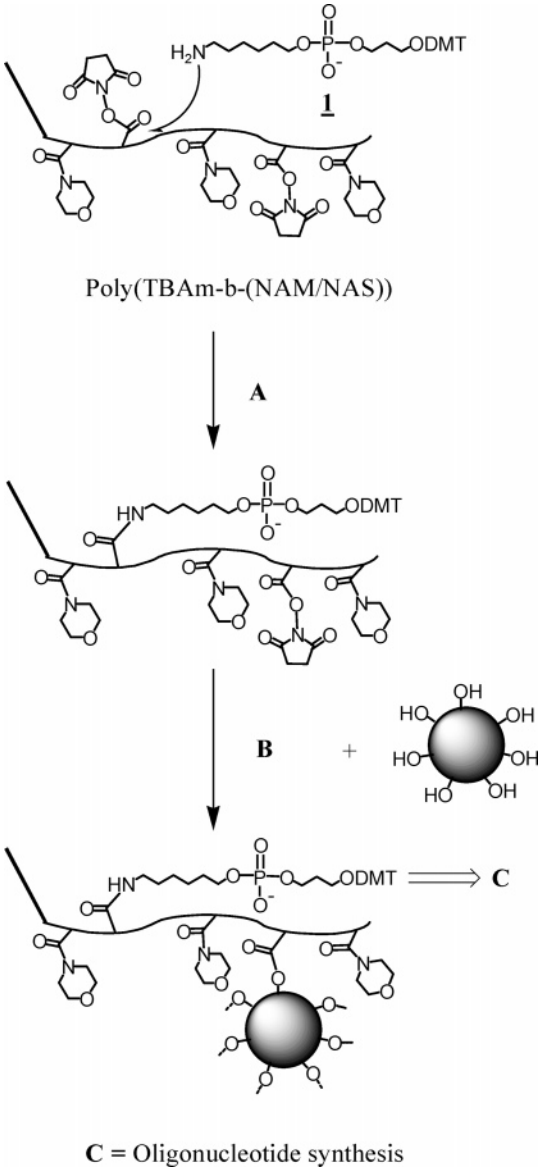

Figure 2. Strategy of conjugate synthesis; step A: Starter **1** functionalization of polymer; step B: grafting of (starter **1**−Polymer) onto HEG-CPG; step C: oligonucleotide synthesis.

function of **1** reacted with the activated ester of polymer. Then, in a second step, the starter-containing polymer was immobilized on CPG through reaction between hydroxyl groups from solid surface and some residual activated ester functions of the polymer (step B). As starter, **1** bears, on one extremity of its alkyl chain, a hydroxyl protected by a dimethoxytrityl (DMT) group. After DMT cleavage under acid treatment, the recovered OH group will be used to initiate oligonucleotide synthesis (step C).

*Starter **1** Synthesis.* Starter **1** structure was designed in order to avoid different hurdles encountered in this laboratory with other molecules elaborated for the same purpose: (i) a nucleotide analogue (5′-dimethoxytrityl-2′-deoxythymidine-3′-(6-aminohexyl phosphate)) which was described to react with maleic anhydride copolymers (*13*) or poly(NAM/NAS) copolymers (*14*) not only via the terminal amino group but also via the intracyclic amine function of the nucleic base, forming an unstable link (in ammonia) between polymer and starter, (ii) a neutral starter, DMT-O$(CH_2)_6NH_2$, efficiently coupled to poly(NAM/NAS) but appearing to inhibit further grafting reaction onto CPG (step B) (unpublished results). According to this latter observation, we aimed at introducing one phosphate group (bringing a charge) in the alkyl chain of the molecule, to restore the grafting ability of the resulting starter **1**−polymer conjugate onto hydroxylated silica support.

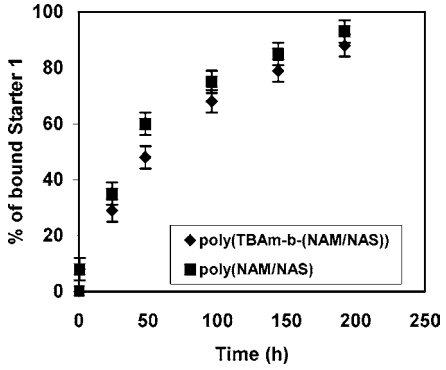

Figure 3. Kinetics of starter **1** coupling reaction to poly(TBAm-*b*-(NAM/NAS)) and to poly(NAM/NAS) (0.6 equiv of **1** per NAS units).

In this work, a new starter of DNA synthesis was designed (starter **1**, Figure 2) presenting at one extremity of its alkyl chain a primary amino function, at the other extremity a hydroxyl function protected by a dimethoxytrityl group, and a phosphate group included inside the chain.

Starter **1** synthesis was achieved via phosphoramidite coupling reaction with good yield (70%), as described in the experimental part.

*Coupling of Starter **1** to Block and Random Copolymers (Step A).* The coupling kinetics of starter **1** to polymer were investigated on both poly(TBAm-*b*-(NAM/NAS)) and poly(NAM/NAS). Conversions were determined by fluorimetry, as described in the experimental part. At different times, the amount of residual starter **1** was quantified using a specific titration of primary amine functions with fluorescamine. An excess of fluorescamine was used (> 5 equiv); preliminary studies showed that neither DMF nor polymers led to a reaction with fluorescamine.

The kinetics were followed with three different initial concentrations of starter **1** in solution, i.e., 0.6, 0.3, and 0.1 equiv of **1** per NAS units in the polymer (Figure 3, case of 0.6 equiv).

As a result, functionalization rates were similar for the two polymers. A reaction time around 8 days led to coupling yields higher than 95%. At this edge, residual starter quantification became difficult because of the too low concentration remaining in solution (sensitivity limit of the spectrofluorimeter). Then, 10 days were preferred to reach an optimized coupling yield (> 95%). Kinetics obtained with 0.3 and 0.1 equiv of **1** per NAS units were similar to the ones of Figure 3.

Grafting of Polymer−Starter Conjugate onto HEG-Functionalized CPG Beads (Step B). In the second step (B, Figure 2), the resulting polymer−starter **1** conjugate was grafted onto controlled pore glass (CPG) support (pore diameter of 2000 Å) which had been previously derivatized with hexa(ethylene glycol) (HEG), following protocols described by Maskos and co-workers (*19*).

As previously described (*14*), polymer grafting onto functionalized CPG was optimum after 5 days reaction. Grafting efficiency of the polymer−starter **1** conjugate was controlled through quantification of dimethoxytrityl groups released from starters **1** bound to polymer chain. The obtained amount of DMT cations released per gram

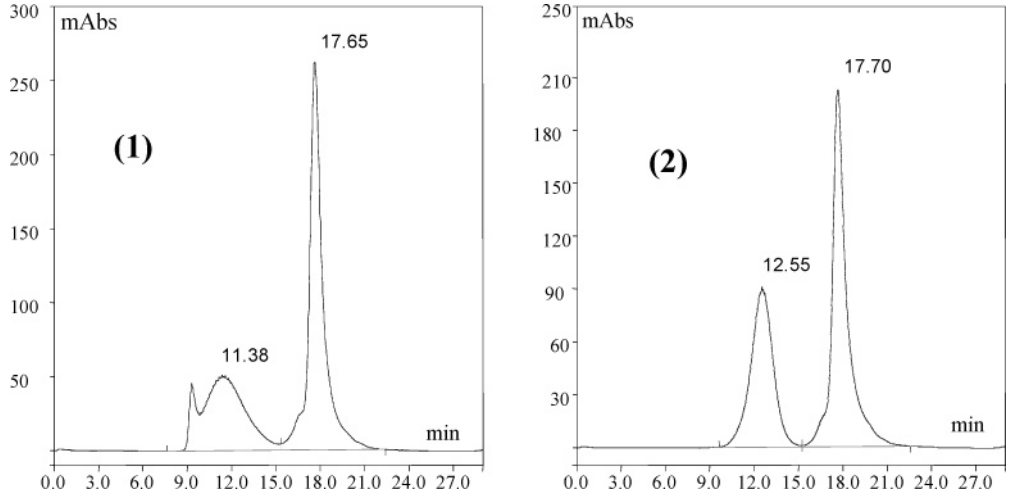

Figure 4. SEC analyses of polymer–ODN conjugates (0.6 equiv of starter **1** per NAS units). (**1**) poly(TBAm-*b*-(NAM/NAS))–dT25; (**2**) poly((NAM/NAS))–dT25.

Table 2. DMT Cation Quantification of Starter 1 Anchored onto CPG through the Polymer Chain

	block	random	block	random	block	random
Initial equivalent of **1**/NAS[a]	0.1	0.1	0.3	0.3	0.6	0.6
Amount of **1** on CPG (μmol/g)[b]	1.4	1.3	3.4	3.4	5.7	5.1

[a] Coupling reaction of **1** onto polymer (step A on Figure 2). [b] Starter **1** DMT cation quantification, after (copolymer–starter **1**) grafting onto CPG (step B on Figure 2).

of support are reported in Table 2 (with different ratios of starter **1** introduced at the first step of the reaction).

Regarding results in Table 2, the higher the amount of starter **1** bound to the polymer chain, the higher the loading of conjugate onto CPG. In addition, functionalization yields were very similar for the two polymers indicating that the hydrophobic part of the block copolymer did not affect grafting reaction.

Oligonucleotide Synthesis on Polymer-Functionalized CPG Beads (Step C). Poly(TBAm-*b*-(NAM/NAS))- and poly-(NAM/NAS)-functionalized CPG beads were introduced in a DNA synthesizer (Applied Biosystems). Then, 25mer polythymidylates (dT25) were synthesized from the bound starters using standard 1 μM phosphoramidite cycle, as described in the experimental part.

Average coupling yield of thymidine synthon was estimated around 98% per cycle. After syntheses, standard ammonia treatment released the polymer–ODN conjugates which were analyzed by SEC. In both cases, chromatograms (at 260 nm) revealed the presence of two populations of nucleic acids (Figure 4).

The first population, eluted at 11.4 min for poly(TBAm-*b*-(NAM/NAS)) and at 12.55 min for poly(NAM/NAS), corresponded to the expected polymer–ODN conjugates. The same amount of conjugate was obtained in both cases (similar peak area on both chromatograms). An additional peak, eluted at 9 min, was observed for block copolymer conjugate which could result from a micellar aggregation of a part of the conjugate due to the hydrophobic block of the polymer. This observation confirmed the potential influence of the hydrophobic block on the conjugate structure in an aqueous medium.

The second population, eluted at 17.7 min, corresponded to free ODN. This parasite population directly initiated from HEG-CPG was systematically observed during conjugate syntheses, even with polymers of different nature, as for instance maleic anhydride copolymers (*13*, *21*).

The two populations were separated by filtration on Centricon membranes (cutoff of 100 000 g/mol). Conjugates were efficiently purified to almost 100% as confirmed by SEC analysis of the resulting material (Figure 5).

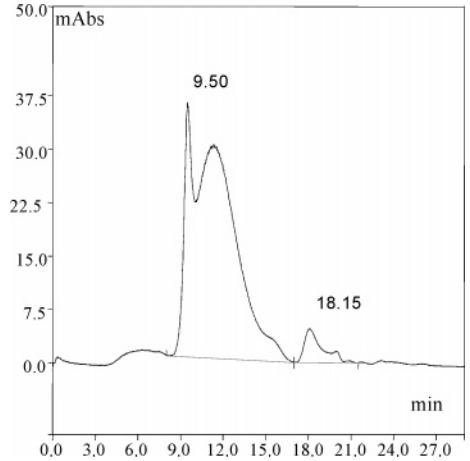

Figure 5. Poly(TBAm-*b*-(NAM/NAS))–dT25 conjugate SEC analysis after purification.

Parasite ODN Population Analysis. Aiming at investigating on the origin of parasite ODN population, a GACTGACT sequence model (including the four nucleotides) was synthesized from poly(TBAm-*b*-(NAM/NAS))-functionalized CPG. Prior to oligonucleotide synthesis, a capping step with acetic anhydride was achieved directly on the DNA synthesizer, as described in the experimental part, to mask residual hydroxyl functions on CPG surface. Under these conditions, coupling yields of the nucleotide phosphoramidites were satisfactory (DMT^+ quantification > 97% per cycle).

After ODN synthesis and release of the polymer–ODN conjugate in solution with ammonia, the parasite-free ODN population was recovered from membrane filtration and analyzed on reverse phase HPLC (Figure 6).

Amazingly, chromatographic analysis revealed a main population of ODN (eluted at 25.8 min) different from the expected GACTGACT oligonucleotide of which reten-

Table 3. Capping Study on Poly(TBAm-*b*-(NAM/NAS))-Functionalized CPG

entry	capping reaction	free ODN, %	conjugate synthesized from poly(TBAm-*b*-(NAM/NAS)) CPG,[a] %
1	no capping	85.7	14.3
2	Ac_2O	69	31
3	Ac_2O + DPP (0.1 M)	65	35
4	Ac_2O + DPP (0.5 M)	49	51

[a] Conjugate peak area/(conjugate + free ODN) peak areas on SEC chromatograms (in percentage).

tion time was measured at 13.8 min (data not shown). This fraction was then collected and analyzed by MALDI-TOF MS. The main peak (m/z = 2753.28) corresponds to GACTGACT-3′-HEG product (calculated M − H = 2753.7 g/mol). This unexpected result suggested that a strong adsorption of HEG may occurred on CPG surface during its derivatization. Further experiments are in progress to better understand this HEG adsorption mechanism.

Capping Study on Polymer-Functionalized CPG. As unexpected ODN synthesis could be initiated from residual hydroxyl groups present on the surface of polymer-functionalized CPG, the acetic anhydride capping step performed in the synthesizer before ODN elongation appeared to be only partially efficient. Then, an additional capping step was evaluated with a more reactive reagent (diethoxy-*N*,*N*-diisopropylphosphoramidite, DPP) described to efficiently react with hydroxyl groups on silica surface (*22*). Best results were obtained when achieving successively Ac_2O capping and DPP (0.5 M in acetonitrile) capping directly inside the synthesizer. A total reduction of 93% of parasite ODN population was reached in these conditions on HEG-CPG.

This capping strategy was assessed on poly(TBAm-*b*-(NAM/NAS))-functionalized CPG, aiming at suppressing free ODN population during conjugate synthesis. Table 3 indicates resulting conjugate amount in solution (in percentage calculated from SEC peak areas) after different cappings of the support before dT25 ODN synthesis.

Compared to experiment 1 performed without capping, Ac_2O and further DPP capping reactions clearly reduced parasite-free ODN population. The best result was reached in experiment 4 (Ac_2O + DPP (0.5 M)). Nevertheless, free ODN peak disappearance was not as important as the one preliminary observed on HEG-CPG (reduction of 93% of parasite ODN synthesis). Two hypotheses can be suggested to explain such a difference: (i) the polymer−starter conjugate immobilized on the bead surface could reduce access of capping reagents to the hydroxyl groups, (ii) a part of the free ODN would not result from a parasite ODN synthesis on the bead, but from a partial degradation of the polymer−ODN conjugate in ammonia after ODN synthesis. It was then important to check the stability of the conjugate during its release from the CPG beads.

Stability Study of Polymer−ODN Conjugate in Ammonia. After ODN synthesis, ammonia treatment (NH_4OH 30%, 16 h, 60°C) was achieved on CPG directly to release the polymer−ODN conjugate in solution and to remove the base protecting groups. Conjugate stability in these conditions was studied by SEC. After 16 h of reaction in ammonia, around 25% of initial conjugate peak area has disappeared on the benefit of free ODN peak (data not shown). This study confirmed that a part of bound ODN were cleaved from polymer under basic treatment.

To avoid this degradation, we attempted to reduce the time of basic treatment from 16 h to 8 h. However, SEC analysis of crude material revealed an incomplete release of the conjugate from the CPG beads (only 80% of conjugate were recovered in solution compared to the amount released after 16 h reaction). According to degradation kinetics showing low difference between 8 h and 16 h of ammonia treatment, the standard treatment of 16 h at 60°C was preferred.

Purity Analysis of the Conjugate's Oligonucleotides. The above study revealed a conjugate degradation under basic conditions (aqueous NH_4OH 30%, at 60 °C) leading to a free ODN population in solution. Thus, to control the quality of the oligonucleotides obtained from direct synthesis on polymer chain, we applied these conditions to a prepurified poly(TBAm-*b*-(NAM/NAS))−dT25 conjugate (purity > 95%). After 48 h treatment, the cleaved ODNs were recovered and purified from residual conjugate by filtration on Centricon membrane (cutoff of 100 000 g/mol). Reverse phase HPLC analysis of the ODNs resulting from conjugate degradation is shown on Figure 7. A main peak is observed on chromatogram, eluted at 22.5 min, that corresponds to the full length oligonucleotide plus an additional fragment at its 3′ extremity resulting from the cleavage process. This chromatographic profile showing a main peak of full length dT25, and on the other hand, a low amount of truncated sequences (peaks between 8 and 22 min) attested to the good quality of oligonucleotides directly

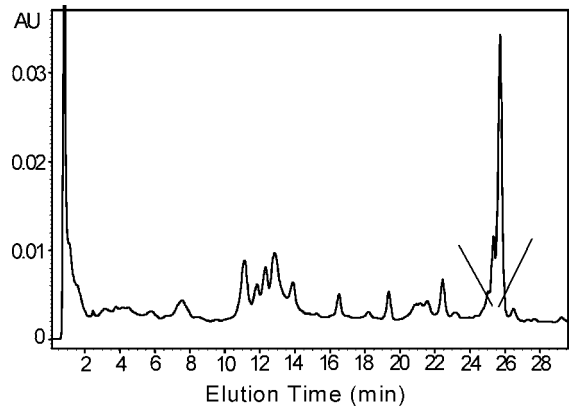

Figure 6. HPLC analysis of ODN population present in conjugate synthesis solutions.

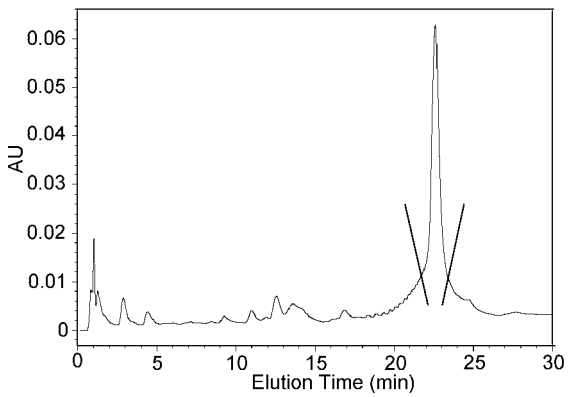

Figure 7. HPLC of ODNs bound to poly(TBAm-*b*-(NAM/NAS)); analysis achieved after conjugate degradation in ammonia.

synthesized onto polymer. To understand the conjugate degradation mechanism occurring in ammonia, the population eluted at 22.5 min during HPLC (Figure 7) was collected and analyzed by MALDI-TOF MS. The obtained mass (7681.56 g/mol) corresponded to a dT25−3′-O−PO_2−O-propanol (calculated M − H = 7680.7 g/mol). This surprising result suggested that the cleavage between ODNs and polymer chain in ammonia preferentially proceeded on the phosphate group of starter **1** instead of on the amide function binding the starter **1** to the polymer chain (Figure 2). In the literature, hydrolysis of phosphate diester groups of various molecules in basic medium was indeed described (*23, 24*). Two different cleavage mechanisms were reported, i.e., via a reaction on either C−O or P−O bound, which depended on the nature of the radicals borne by the phosphate. Results revealed that less sterically hindered phosphodiester groups were cleaved more rapidly, by an efficient nucleophilic attack on the carbon of C−O−P bound. When regarding the polymer−dT25 conjugate chemical structure in our case, the starter **1** phosphodiester group was less sterically hindered than the other phosphate groups of the oligonucleotide. This point could explain the specific cleavage observed on starter **1** phosphate diester linkage in aqueous ammonia, leading to conjugate degradation.

To conclude from the present results on conjugate elaboration, the strategy of direct synthesis of oligonucleotides from polymer can be applied to a block copolymer. In relation with the number of starter **1** bound to the polymeric chain, we can target conjugates with a broad range of ODN per chain (from 17 to 100). Prior to ODN synthesis, two capping steps must be performed on the functionalized CPG, with acetic anhydride and DPP reagents successively. This more efficient capping of residual hydroxyl groups from CPG beads allowed us to increase the amount of conjugate obtained in solution from 14.3% to 51% (percentages calculated in comparison with free ODN population). A slight degradation of conjugates was observed during the ammonia treatment. After investigation on the nature of the ODNs released from degradation, it seems that the cleavage preferentially proceeded on starter **1** phosphate diester group that linked ODN to polymer chain. HPLC analysis of ODN population recovered from conjugate degradation confirmed the good quality of oligonucleotides synthesized from the polymer. Conjugates were purified up to 95% prior to be used in hybridization assays in order to evaluate their performances in the capture phase.

Assessment of Polymer−ODN Conjugates in DNA Diagnostic Microarrays. Poly(TBAm-*b*-(NAM/NAS))−dT25 conjugates were evaluated in a microarray system based on a standard 96-well microtiterplate format functionalized in each well by 16 different spots. The Figure 8a shows the circular format of spots in the well. Biological species solutions are automatically deposited by droplet spotting technology (see experimental part). In a perspective of multidetection, the 16 spots could be addressed independently by ODN probes or proteins in order to develop in parallel oligosorbent and immunosorbent assays (*25*). In this work, we have evaluated conjugate ability to enhance signal of oligosorbent assay schemed in Figure 9.

Microarrays were functionalized by spotting either dT25 or copolymer−dT25 conjugates in phosphate buffer as described in Materials and Methods. It is worth noting that the concentration of free ODN or ODN bound to polymer in the case of conjugate were similar in spotting solutions. An assay performed with the poly(TBAm-*b*-(NAM/NAS))−dT25) conjugate is shown on Figure 8b. The picture corresponds to the resulting fluorescent signal obtained in the well after target hybridization. This experiment carried out at 10 nM of dA25-CY3 revealed that the assay run with conjugate was much more efficient (signal amplification × 5).

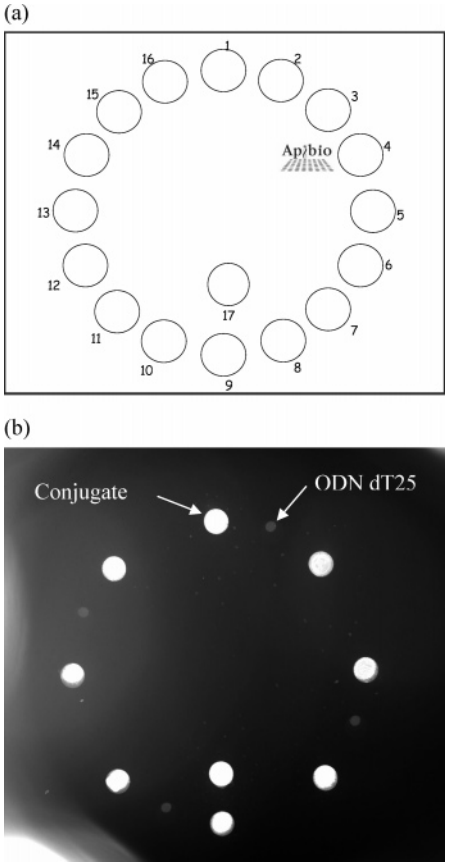

Figure 8. (a) Circular format of spots in wells of a microtiterplate from Apibio. (b) Circular microarray fluorescence resulting from 5′CY3-dA25 hybridization at 10 nM, after the spotting on surface of either ODN dT25 or poly(TBAm-*b*-(NAM/NAS))−dT25 conjugate at 10 μM (dT25 concentration) in standard buffer.

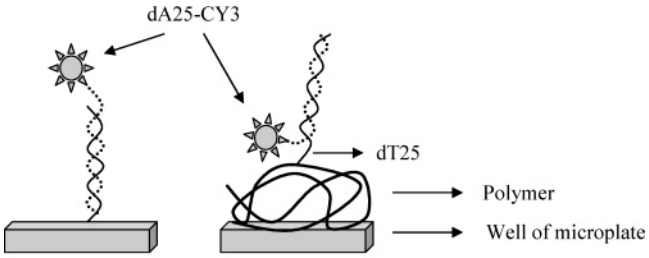

CY3 : carbonyl-indocyanine

Figure 9. Direct hybridization of 5′CY3-dA25 target on dT25 or on poly(TBAm-*b*-(NAM/NAS))−dT25 spotted on a microarray (detection by fluorescence).

Influence of Salt Concentration in Spotting Buffer. Experiments were achieved in order to study the influence of salt concentration in coating buffer on the fluorescent signal obtained after target hybridization. Similar ODN concentration (10 μM) was used for both spottings of dT25 and poly(TBAm-*b*-(NAM/NAS))−dT25 conjugate solutions.

As shown on graph of Figure 10, variation of salt concentration in coating buffer clearly influenced the fluorescent signal resulting from hybridization with the target. Best results were obtained by spotting conjugates

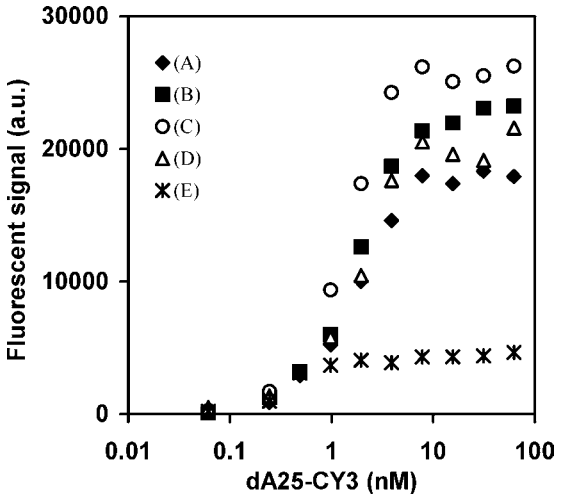

Figure 10. Influence of salt concentration in coating buffer (150 mM phosphate buffer, pH 7.4) on resulting fluorescent signal obtained in the assay. (A): [NaCl] = 400 mM, block copolymer−dT25 conjugate coating; (B): [NaCl] = 200 mM, block copolymer−dT25 conjugate coating; (C): [NaCl] = 100 mM, block copolymer−dT25 conjugate coating; (D): [NaCl] = 50 mM, block copolymer−dT25 conjugate coating; (E): [NaCl] = 400 mM, ODN dT25 coating.

in phosphate buffer (150 mM, pH 7.4) containing 100 mM NaCl. It is worth noting that the use of conjugate instead of oligonucleotide efficiently enhanced the fluorescent signal when dA25-CY3 concentration was higher than 1 nM. The use of conjugate increased dynamic range of dA25-CY3 detection (dynamic range from 0.2 nM to 1 nM using dT25 and from 0.2 nM to 10 nM using block copolymer−dT25 conjugate). To conclude from this study, phosphate coating buffer with 100 mM NaCl appeared to be good conditions for both conjugate anchoring on solid surface (salts suppress intermolecular electrostatic repulsions and so favor conjugate adsorption) and ODN probes expansion in solution. This latter parameter probably improves resulting accessibility of immobilized ODN probes for DNA capture.

Influence of ODN Number per Polymer Chain. According to the amount of starter **1** coupled to polymer chain, conjugates with different ODN numbers could be obtained. As described in Table 2, polymers were functionalized with three different amounts of **1** per NAS, i.e., 0.1, 0.3, and 0.6 equiv. Considering the coupling reaction yield of 95%, the number of ODN bound to the polymer could be estimated from the following equation:

$$f_{\mathrm{ODN}} = n_{(1)} \times Y \times N_{(\mathrm{NAS})}$$

with f_{ODN} the number of ODN per polymer chain, $n_{(1)}$ the equivalent number of starter **1**, Y the coupling yield of **1** to polymer, and $N_{(\mathrm{NAS})}$ the number of NAS units in the polymer chain ($N_{(\mathrm{NAS})}$ = 235 and 168 for block and random copolymers, respectively).

Taking into account the conjugate degradation in ammonia, we can estimate that 25% of ODN bound to polymer were cleaved during basic deprotection as described in the following equation:

$$F_{\mathrm{ODN}} = f_{\mathrm{ODN}} \times 0.75$$

with F_{ODN} the estimation of the final number of ODN per polymer chain. Calculated ODN number per chain (F_{ODN}) for the different polymer−ODN conjugates used in this study are mentioned on the graph of Figure 11. To evaluate the influence of ODN number per polymer chain

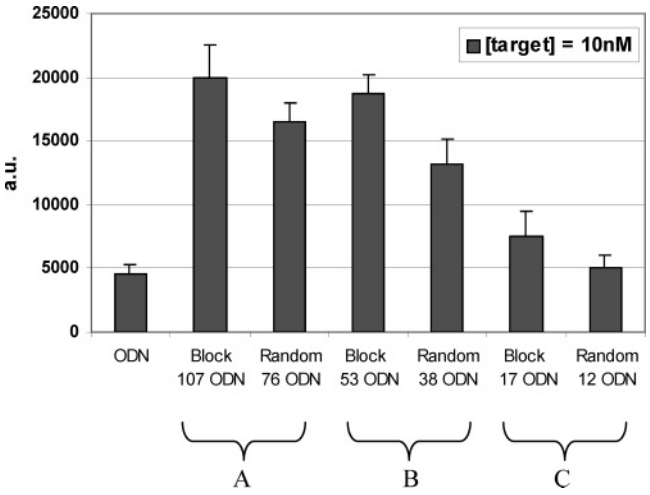

Figure 11. Influence of the number of ODNs per polymer chain on resulting fluorescent signal for block and random conjugates. Polymer functionnalization in conditions A: 0.6 equiv of **1** per NAS; B: 0.3 equiv of **1** per NAS; C: 0.1 equiv of **1** per NAS.

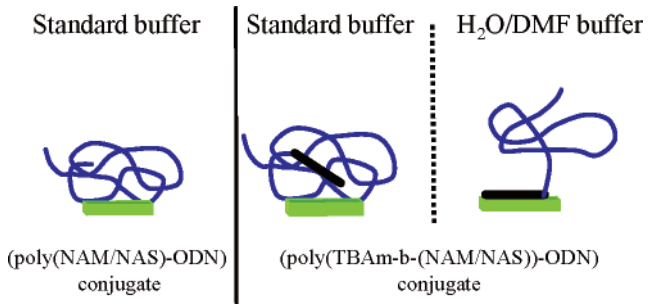

Figure 12. Schematic illustration of the hypothesis of conjugate conformation onto the solid support according to the nature of coating buffer.

on the fluorescent signal, the various conjugates were spotted on a microarray (Figure 11).

Efficient signal amplification was observed using conjugates from columns A and B, in comparison with free dT25. On the other hand, conjugates of column C, bearing a low amount of ODN, did not significantly amplify the signal. In conclusion from this study, a minimal amount of ODN per chain was necessary to impact the signal of the test on the microarray. Although experiments with conjugates of A and B columns led to quasi similar results, we can observe a slight enhancement of signal by using a block copolymer instead of a random copolymer.

Conjugate Spotting in Organic Solvent. We have demonstrated that the use of polymer−oligonucleotide conjugates instead of ODN for coating of microarrays improved DNA target capture from biological samples and thus enhanced fluorescent signal of the assays. But no significant difference was observed in the performances of the test, whether or not a block or a random copolymer was used. At this time, it was anticipated that aqueous buffer used for conjugate coating was not the best medium for favoring the solvation and the expansion of the hydrophobic block of poly(TBAm-*b*-(NAM/NAS)). In this medium, the poly(TBAm) may be hidden inside the hydrophilic part of conjugate and thus may have difficulties to access to solid surface (Figure 12). To validate our hypothesis and overcome the problem, coating of the conjugate was evaluated in a medium containing some organic solvent. The graph in Figure 13 shows signals obtained with poly(TBAm-*b*-(NAM/NAS))−ODN and poly-((NAM/NAS))−ODN coated in mixed media (20% DMF/

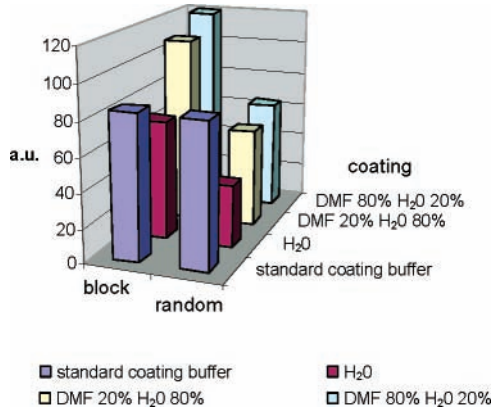

Figure 13. The influence of coating buffer on the sensitivity of the assay ([target] = 0.5 nM) for poly(TBAm-*b*-(NAM/NAS))–ODN (block) and poly(NAM/NAS)–ODN (random) conjugates (0.6 equiv of **1** per NAS).

80%H_2O and 80% DMF/20% H_2O), in comparison with data obtained in phosphate buffer and in Milli-Q water. The best results were observed for spots coated with poly(TBAm-*b*-(NAM/NAS))–ODN in organic mixtures. This would corroborate the above-mentioned hypothesis. The poly(TBAm) chain should indeed be well solvated so as to have the chance to interact with the solid surface during the coating step. It may be suggested that in DMF-rich solvent, the conjugate probably adopts a conformation favoring the anchoring on the surface via the hydrophobic arm, with a subsequent improvement of the capture probes accessibility. Finally, this would enhance the fluorescent signal of the DNA target detection.

CONCLUSION

An amphiphilic block copolymer poly(*tert*-butylacrylamide-*b*–*N*-acryloylmorpholine-*N*-acryloxysuccinimide) and a random copolymer poly(*N*-acryloylmorpholine-*N*-acryloxysuccinimide), synthesized by controlled radical polymerization (RAFT process) were used (number average molecular weights (Mn) of 14 000/103 000 g/mol and 71 000 g/mol, respectively) to elaborate polymer–ODN conjugates. A strategy of direct synthesis of ODN from the polymeric chain previously grafted onto solid support (controlled pore glass, CPG) was achieved. A preliminary step was performed to bind starters of oligonucleotide synthesis along the chain. For that purpose, (3-*O*-dimethoxytritylpropan-1,3-diol)-(6-aminohexyl) phosphate (starter **1**) was synthesized and characterized. The activated ester functions of the NAS units along the polymer chain efficiently reacted with the amino spacer arm of **1**, reaching coupling yield close to 100% after 10 days of reaction. Resulting polymer–starter **1** conjugates were grafted onto hydroxylated CPG beads and 25mer polythymidylates were synthesized from the functionalized polymer. Then, polymer–ODN conjugates were released in solution by ammonia treatment and analyzed by SEC. Two populations were observed on the chromatograms: one population eluted between 9 and 15 min, ascribed to polymer–ODN conjugate, and the other population eluted between 15 and 22 min, attributed to free ODN material. In an attempt to suppress this parasite ODN population resulting from syntheses directly initiated from hydroxylated CPG, the capping reaction of silica beads with diethoxy-*N*,*N*-diisopropylphosphoramidite (DPP) was studied. Performing DPP capping in addition to standard acetic anhydride capping reduced efficiently but not completely parasite ODN syntheses. Then, conjugates were purified by filtration on controlled pore size membrane up to 95% purity and evaluated in DNA hybridization assay as macromolecules being able to favor capture of the target. The microarray system used for the study was based on a standard 96-well microtiterplate format, presenting 16 different spots in each well. Conjugates were spotted by nanodroplet inkjetting technique. Both conjugates, elaborated from either block or random copolymers, enhanced signal of the DNA hybridization assay in standard spotting buffer (phosphate buffer with 400 mM NaCl). The role of the hydrophobic part (poly(TBAm)) of conjugate synthesized from the block copolymer was revealed by coating both types of conjugates in a mixed solvent (DMF/H_2O). In these conditions, poly(TBAm) block was more accessible for adsorption onto the surface of the well, inducing an orientation of the hydrophilic part of the conjugate (bearing ODN) toward the aqueous media. In conclusion, poly(TBAm-*b*-(NAM/NAS))–ODN conjugates spotting in a mixed solvent afforded a significant sensitivity improvement of hybridization assay performed with model dT25–dA25 on a microarray. Using this strategy, further experiments are in course with various biological models and will be reported in due time.

ACKNOWLEDGMENT

We wish to thank David Duracher and Thibault Martin from Apibio for the provision of oligosorbent microarrays spotted with conjugates.

Supporting Information Available: (a) MALDI-TOF MS analysis (in negative mode) of ODN population present in conjugate synthesis solutions (after collect of the peak eluted on HPLC at 25.8 min (Figure 6)). (b) Capping studies with Ac_2O and DPP on HEG-CPG. (c) Stability study of (block copolymer–ODN) conjugate in ammonia. This material is available free of charge via the Internet at http://pubs.acs.org.

LITERATURE CITED

(1) Pease, A., C., Solas, D., Sullivan, E. J., Cronin, M. T., Holmes, C., P., and Fodor, S. P. A. (1994) Light-generated oligonucleotides arrays for rapid DNA sequence analysis. *Proc. Natl. Acad. Sci. U.S.A. 91*, 5022–5026.

(2) Hughes, T., R., Mao, M., Jones, A. R., Burchard, J., Marton, M., J., Shannon, K., W., and Lefkowitz, S., M. et al. (2001) Expression profiling using microarrays fabricated by an ink-jet oligoucleotide synthesizer. *Nat. Biotechnol. 19*, 342–347.

(3) Cheung, V., G., Morley, M., Aguilar, F., Massimi, A., Kucherlapati, R., and Childs, G. (1999) Making and reading microarrays. *Nat. Genet. 21* (suppl.), 15–19.

(4) Campas, M., and Katakis, I. (2004) DNA biochip arraying, detection and amplification strategies. *Trends Anal. Chem. 23* (1), 49–62.

(5) Timofeev, E., and Mirzabelov, A. (2001) Binding specificity and stability of duplexes formed by modified oligonucleotides with a 4096-hexanucleotide microarray. *Nucleic Acids Res. 29* (12), 2626–2634.

(6) Rehman, F., N., Audeh, M., Abrams, E., S., Hammond, P., W., Kenney, M., and Boles, T. C. (1999) Immobilization of acrylamide-modified oligonucleotides by co-polymerization. *Nucleic Acids Res. 27* (2), 649–655.

(7) Efimov, V., A., Buryakova, A. A., and Chakhmakhcheva, O., G. (1999) Synthesis of polyacrylamides N-substituted with PNA-like oligonucleotide mimics for molecular diagnostic applications. *Nucleic Acids Res. 27* (22), 4416–4426.

(8) Beier, M., and Hoheisel, J., D. (1999) Versatile derivatisation of solid support media for covalent bonding on DNA-microchips. *Nucleic Acids Res. 27* (9), 1970–1977.

(9) Le Berre, V., Trévisiol, E., Dagkessamanskaia, A., Sokol, S., Caminade, A.-M., Majoral, J.-P., Meunier, B., and Fran-

çois, J. (2003) Dendrimeric coating of glass slides for sensitive DNA microarrays analysis. *Nucleic Acids Res. 31* (16), e88.
(10) Lassalle, N., Roget, A., Livache, T., Mailley, P., and Vieil, E. (2001) Electropolymerisable pyrrole-oligonucleotide: synthesis and analysis of ODN hybridation by fluorescence and QCM. *Talanta 55*, 993−1004.
(11) Delair, T., Charles, M.-H., Cros, P., Laayoun, A., Mandrand, B., and Pichot, C. (1998) Synthesis and characterization of nucleic acid-(co)polymer conjugates: application to diagnostics. *Polym. Adv. Technol. 9*, 349−361.
(12) Erout, M.-N., Troesch, A., Pichot, C., and Cros, P. (1996) Preparation of conjugates between oligonucleotides and *N*-vinylpyrrolidone/*N*-acryloxysuccinimide copolymers and applications in nucleic acid assays to improve sensitivity. *Bioconjugate Chem. 7*, 568−575.
(13) Minard-Basquin, C., Chaix, C., Pichot, C., and Mandrand, B. (2000) Oligonucleotide-polymer conjugates: effect of the method of synthesis on their structure and performance in diagnostic assays. *Bioconjugate Chem. 11*, 795−804.
(14) Minard-Basquin, C., Chaix, C., D′Agosto, F., Charreyre, M.-T., and Pichot, C. (2004) Oligonucleotide synthesis onto poly(N-acryloylmorpholine-*co*-N-acryloxysuccinimide); assessment of the resulting conjugates in a DNA sandwich hybridization test. *J. Appl. Polym. Sci. 92*, 3784−3795.
(15) De Lambert, B., Charreyre, M.-T., Chaix, C., and Pichot, P. (2005) RAFT polymerization of hydrophobic acrylamide derivatives. *Polymer 46*, 623−637.
(16) De Lambert, B., Charreyre, M.-T., Chaix, C., and Pichot, C. (2004) Synthesis of amphiphilic block copolymers of acrylamide derivatives via the RAFT polymerization. *Polymer*, submitted.
(17) Favier, A., Charreyre, M.-T., and Pichot, C. (2004) Study of the RAFT polymerization of a water soluble bi-substituted acrylamide derivative; influence of experimental parameters. *Polymer 45*, 8661−8674.
(18) Favier, A., D′Agosto, F., Charreyre, M.-T., and Pichot, C. (2004) Synthesis of N-acryloxysuccinimide copolymers by the RAFT process as reactive building blocks with full control of composition and molecular weights. *Polymer 45*, 7821−7830.
(19) Maskos, U., and Southern, E. M. (1992) Oligonucleotide hybridisations on glass supports: a novel linker for oligonucleotide synthesis and hybridisation properties of oligonucleotides synthesised *in situ*. *Nucleic Acids Res. 20* (7), 1679−1684.
(20) Favier, A., Charreyre, M.-T., Chaumont, P., and Pichot, C. (2002) Study of the RAFT Polymerization of a Water-Soluble Bisubstituted Acrylamide Derivative. 1. Influence of the Dithioester Structure. *Macromolecules 35* (22), 8271−8280.
(21) Chaix, C., Minard-Basquin, C., Delair, T., Pichot, C., and Mandrand, B. (1998) Oligonucleotide synthesis on maleic anhdride copolymers covalently bound to silica spherical support and characterization of the obtained conjugates. *J. Appl. Polym. Sci. 70*, 2487−2497.
(22) Yu, D., Tang, J.-Y., Iyer, R., P., and Agrawal, S. (1994) Diethoxy N, N− diisopropyl phosphoramidite as an improved capping reagent in the synthesis of oligonucleotides using phosphoramidite chemistry. *Tetrahedron Lett. 35* (46), 8565−8568.
(23) Wolfenden, R., Ridgway, C., and Young, G. (1998) Spontaneous hydrolysis of ionized phosphate monoesters and diesters and the proficiencies of phosphatases and phosphodiesterases as catalysts. *J. Am. Chem. Soc. 120*, 833−834.
(24) Williams, N. H., and Wyman, P. (2001) Base-catalyzed phosphate diester hydrolysis. *Chem. Commun.* 1268−1269.
(25) Perrin, A., Duracher, D., Perret, M., Cleuziat, P., and Mandrand, B. (2003) A combined oligonucleotide and protein microarray for the codetection of nucleic acids and antibodies associated with human immunodeficiency virus, hepatitis B virus, and hepatitis C virus infections. *Anal. Biochem. 322*, 148−155.

BC049791A

Intrinsically Fluorescent Cytotoxic Cisplatin Analogues as DNA Marker Molecules

Julio J. Criado,*,† Emilio R. Fernández,† Juan L. Manzano,† Angel Alonso,‖ Susana Barrena,‡ Manuel Medarde,§ Rafael Pelaez,§ M. Dolores Tabernero,⊥ and Alberto Orfao‡

Departamentos de Química Inorgánica and Química Farmacéutica, Facultad de Farmacia, and Centro de Investigación del Cáncer (CIC), Campus "Miguel de Unamuno", Universidad de Salamanca, 37007-Salamanca (Spain), Departamento de Química Analítica, Facultad de C. Químicas, Plz. de la Merced s/n, Universidad de Salamanca, 37008-Salamanca, (Spain), and Unidad de Investigación, Hospital Universitario de Salamanca, 37007-Salamanca (Spain). Received September 3, 2004;
Revised Manuscript Received December 22, 2004

Two square planar derivatives of $Pt(en)Cl_2$ with intrinsic fluorescence in aqueous solution at room temperature, with quantum yields (Φ) 0.11 and 0.10, respectively, have been synthesized and characterized as [Pt(en)(CG)Cl] (Complex **1**) and [$Pt(en)(CG)_2$] (Complex **2**) (en = ethylenediamine, CG = cholylglycinate). Complexes **1** and **2** exchange just one ligand (chloride or cholylglycinate, respectively) when reacted with water or 5′-GMP to give the same chemical species. After reaction with DNA oligonucleotides or DNA plasmids, they show enhanced emission in the visible region, which lasts for long periods of time and makes them potentially useful DNA marker molecules. Incubation with nucleated blood cells followed by microscopic analyses revealed that they enter the cells within minutes of exposure, selectively stain the DNA, and persist after more than 48 h of exposure. Complexes **1** and **2** display cell cycle phase-independent cytotoxic activity against cisplatin-resistant CHO (Chinese hamster ovarian) tumor cells, with an early onset of their effects. Their slightly different biological effects, as compared to cisplatin, are considered to be linked to the bile acids and their vector properties and to the preferential formation of monoadducts.

INTRODUCTION

Cisplatin has become one of the most widely used anticancer agents, being especially effective in the treatment of patients with testicular and ovarian cancers as well as of hematologic malignancies, such as Hodgkins disease and childhood leukemias (*1*). Its severe toxicity and the development of resistance to the drug has led to the synthesis and evaluation of thousands of cisplatin analogues (*2*). In such complexes, leaving groups appear to influence solubility, toxicity, and both the tissue and intracellular distribution of the drug, while stable (carrier) am(m)ine ligands determine the structure of DNA adducts and cellular responses (*1*). The only analogues approved worldwide for patient treatment, the dicarboxylates carboplatin and oxaliplatin, appear to follow these rules (*2*, *3*).

Many and diverse biochemical and biophysical methods have been applied to elucidate critical aspects of the mechanisms of action of cytotoxic platinum complexes, in particular those of cisplatin (*4*). Platinum(II) complexes are considered to be nonfluorescent in solution at room temperature (except those carrying additional fluorophores), and, to the best of our knowledge, no intrinsically fluorescent cisplatin analogue with cytotoxic activity has been described so far. Recently reported approaches using platinum complexes with appended fluorophores have been only partially successful since, once inside the cell, fluorescence was not long-lasting (*5*). To achieve dynamic pictures of the biological effects of cisplatin analogues, it would be very interesting to have intrinsically fluorescent compounds with cytotoxic activity, especially against drug-resistant cell lines (*6*, *7*).

In recent years, we and others have explored the potential usefulness of bile acids as exchangeable platinum(II) ligands (*8*), which might reduce both toxicity and resistance owing to their lower lability (carboxylate vs chloride ligands), their amphipathic character, and their vectoriality (drug targeting) (*9*−*11*). In the present paper we describe for the first time two new intrinsically fluorescent square-planar platinum(II) complexes carrying one or two cholylglycinate ligands (**1** and **2**, Figure 1) that emit at room-temperature both once free in solution and after reaction with DNA. They were synthesized from $Pt(en)Cl_2$ using previously described protocols, and their reactions with different potential cellular ligands, such as water, GMP and DNAs of different sizes and sources, together with their fluorescence and cytotoxic properties have been studied. The implications on the cellular and biological effects of these compounds are also discussed.

EXPERIMENTAL SECTION

Chemicals. Dichloro(ethylenediamine)platinum(II), $Pt(en)Cl_2$, was purchased from Aldrich (St Louis, MO). Sodium cholylglycinate (NaCG), guanosine 5′-monophos-

* To whom correspondence should be addressed. Fax: +34-923 29 45 15. E-mail: jjct@usal.es.
† Departamento de Química Inorgánica, Universidad de Salamanca.
§ Departamento de Química Farmacéutica, Universidad de Salamanca.
‡ Centro de Investigación del Cancer (CIC), Universidad de Salamanca.
‖ Departamento de Química Analítica, Universidad de Salamanca.
⊥ Hospital Universitario de Salamanca.

10.1021/bc049788r CCC: $30.25 © 2005 American Chemical Society
Published on Web 02/24/2005

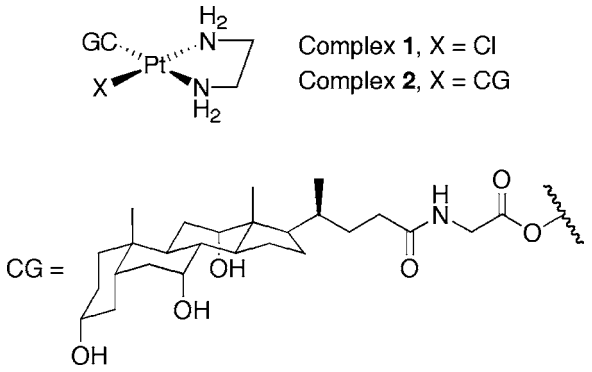

Figure 1. Structures of the platinum complexes **1** and **2**.

phate (sodium salt; 5′-GMP), penicillin/streptomycin, sucrose, spermine tetrahydrochloride, trypsin, trypsin inhibitor, RNAse, Nonidet Np40, and propidium iodide were obtained from Sigma (St Louis, MO). HBSS (Hank's balanced salt solution), DMEM cell culture medium, L-glutamine, fetal calf serum, and sodium citrate were all purchased from Gibco BRL (Carlsbad, CA). Trisodium citrate and dimethyl sulfoxide were obtained from Merck (Darmstadt, Germany). All other reagents were of high purity and were used as purchased without any further purification. Oligonucleotides **I** (self-complementary) 5′-3′d(TATGATCATA), **II** (self-complementary) 5′-3′d(TGATCATGATCA), and **III** (single strand, non self-complementary) 5′-3′d(TTAGGGTTA) were purchased from Sigma Genosys (Cambridge, UK), with purification in reverse phase. Purified *Trichoderma harzianum* HH3-DNA (linear, 563 bp) was kindly provided by the Department of Microbiology (University of Salamanca, Salamanca, Spain), and the CH1cisR ovarian cancer cell line was kindly provided by Dr. J. M. Pérez (Madrid, Spain).

Analytical Methods. Chemical analyses for C, H, and N were performed on a Perkin-Elmer 2400 elemental analyzer (Applied Biosystems, Foster City, CA). Platinum was determined by atomic absorption on a Hitachi Z-8100 flameless graphite furnace spectrophotometer (Hitachi, Tokio, Japan) set at a wavelength of 265.9 nm, using the following temperature program: 90 °C (20 s), 100 °C (20 s), 800 °C (20 s), 1600 °C (30 s), 2800 °C (5 s), and 3000 °C (4 s). Infrared (IR) spectra were recorded in the 4000−200 cm^{-1} range on a Perkin-Elmer FT-IR 1730 instrument coupled to a Perkin-Elmer Data Station (Applied Biosystems). KBr pellets and spectrophotometric grade Nujol (Fluka, St. Louis, MO) or polyethylene disks (Aldrich) were used to record the spectra above and below 400 cm^{-1}, respectively. Electrospray ionization mass spectra (ESI-MS) were recorded on a Waters ZQ 4000 (Waters S.A., Milford, MA); positive and negative ion mass spectra were obtained by signal averaging of 25 consecutive shots; MALDI-TOF spectra were recorded on a Bruker, Reflex III (delayed extraction) instrument (Bruker, Karlsruhe, Germany) equipped with a nitrogen laser (λ = 337 nm, 3 ns pulse width). Electrical conductivity in solution was measured using a CDM2e conductimetry radiometer with a CDC-104 immersion cell (Radiometer, Copenhagen, Denmark). Temperature was controlled in a Unitherm water bath (Selecta, Barcelona, Spain) with a precision of ±0.01 °C. ^{1}H (400 MHz), ^{13}C (102.6 MHz), and ^{195}Pt (64.5 MHz) NMR spectra were obtained in D_2O, methanol-d_4 or DMSO-d_6 solutions on a Bruker DX400 instrument (Bruker, Germany). Carbon resonances were distinguished by DEPT-90 and DEPT-135 experiments. TMS was used as internal standard for ^{1}H and ^{13}C spectra. Using K_2PtCl_6 (δ = 0 ppm) as external standard, 300.000 scans, 2 s relaxation delay, and a 48 h acquisition time were used to obtain the ^{195}Pt spectra. Fluorescence measurements were performed in water at room temperature in a Shimadzu RF 5000 spectrofluorometer system (Shimadzu, Tokyo, Japan) equipped with a 150 W xenon lamp and a sensitivity unit. The optimal excitation wavelength was obtained from a fluorescence excitation spectra acquired at the optimal emission wavelength. Excitation and emission peaks were as follows: (1) free [Pt(en)(CG)Cl] and free [Pt(en)$(CG)_2$] in solution (301 nm, 384 nm) and (330 nm, 436 nm), respectively, (2) platinum complexes bound to oligonucleotides **I**, **II**, and **III** (352 nm, 437 nm), and (3) platinum complexes bound to HH3-DNA (350 nm, 437 nm).

Synthesis and Characterization of the Platinum Compounds. *Ethylenediaminechlorocholylglycinateplatinum(II), Pt(en)(CG)Cl*. Complex **1** was obtained by slowly adding a 1 mM NaCG solution to a 1 mM Pt(en)Cl_2 solution at 50 °C, with subsequent stirring for 24 h in the darkness (final pH = 5.6−5.7) (*10*, *12*). Liquid−liquid extraction on C18 cartridges yielded (after final methanol extraction) the newly formed platinum complexes (60% from the starting NaCG) free of excess unreacted Pt(en)Cl_2. Preparative TLC chromatography using butyl acetate/methanol 65/35 (v/v) gave complex **1** (R_f = 0.30, final yield 29%) as a yellow solid after evaporation to dryness in P_4O_{10}.

*Complex **1**, Pt(en)(CG)Cl*. Yellowish solid. Soluble in H_2O, MeOH, DMSO. Mp (with dec) = 173 ± 2 °C. EA Calcd. for $C_{28}H_{50}ClN_3O_6Pt$: % C 44.53; % H 6.67; % N 5.56; % Pt 25.83. Found: % C 45.16; % H 6.81; % N 5.52; % Pt 26.11. IR (ν, cm^{-1}): 3392, 1601, 1409, 542, 349. ESI-MS (*m/z*): 754.7 $[M]^+$, 741.4 $[M - Cl - H + Na]^+$, 718.6 $[M - Cl - H]^+$, 510.4 $[CG + 2Na]^+$, 488.4 $[CG + H + Na]^+$. ^{1}H NMR (CD_3OD) δ = 0.71 (3H, s; Me-18); 0.90 (3H, s; Me-19); 1.03 (3H, d, J = 6.5 Hz; Me-21); 2.53 (4H, bs; en); 3.37 (1H, m; H-3); 3.80 (1H, bs; H-7); 3.96 (1H, bs; H-12); 4.02 (2H, s; H-25). ^{13}C NMR (CD_3OD) δ = 188.6 (C- 26); 179.6 (C-24); 72.7 (C-12); 71.4 (C-3); 67.8 (C-7); 53.5 (C-25); 48.2 (en); 46.5 (C-17); 46.0 (C-13); 45.4 (en); 41.6 (C-5); 41.6 (C-14); 39.4 (C-8); 38.8 (C-4); 35.8 (C-20); 35.0 (C-1); 34.4 (C-6); 34.3 (C-10); 31.9 (C-22); 30.5 (C-23); 29.4 (C-2); 29.2 (C-11); 27.9 (C-16); 26.3 (C-9); 22.7 (C-15); 21.6 (C-19); 16.5 (C-21); 11.5 (C-18). ^{195}Pt NMR (D_2O) δ = −1970 ppm.

Ethylenediaminebischolylglycinateplatinum(II), Pt(en)$(CG)_2$. Complex **2** was obtained using two different approaches: The first was identical to that described above, except that 2 equiv of NaCG was used, giving complex **2** (R_f = 0.24, 12% final yield). The second method was used in order to remove traces of complex **1**: a 1 mM solution of Pt(en)Cl_2 was reacted with an excess of $AgNO_3$ for 24 h; the precipitate formed was filtered out, and 2 equiv of NaCG was slowly added as a 1 mM solution. The subsequent procedures were identical to those described above for complex **1**. At the end, complex **2** gave a single TLC band (R_f = 0.24, 35% final yield).

*Complex **2**, Pt(en)$(CG)_2$*. Yellow solid. Soluble in H_2O, MeOH, DMSO. Mp (with dec) = 184 ± 2 °C. EA Calcd. for $C_{54}H_{92}N_4O_{12}Pt$: % C 54.76; % H 7.83; % N 4.73; % Pt 16.47. Found: % C 54.93; % H 7.78; % N 4.52; % Pt 17.01. IR (ν, cm^{-1}): 3429, 1617, 1384, 536. MALDI-TOF-MS (*m/z*): 1228.8 $[M + 2Na - 1]^+$, 1207.9 $[M + Na + 1]^+$, 1184.6 $[M + 1]^+$, 997.8 $[(NaCG)_2 + Na]^+$, 719.5 $[M - CG]^+$, 510.4 $[CG + 2Na]^+$, 488.4 $[CG + Na]^+$. ^{1}H NMR (CD_3OD) δ = 0.70 (3H, s; Me-18); 0.90 (3H, s; Me-19); 1.02 (3H, d, J = 6.5 Hz; Me-21); 2.48 (2H, bs; en); 3.35 (1H, m; H-3); 3.73 (2H, bs; H-25); 3.78 (1H, bs; H-7); 3.95 (1H, bs; H-12). ^{13}C NMR (CD_3OD) δ = 176.5 (C-26); 176.3 (C-24); 74.0 (C-12); 72.9 (C-3); 69.0 (C-7); 48.1 (C-17); 47.5

(en); 47.5 (C-13); 44.6 (C-25); 43.2 (C-14); 42.9 (C-5); 41.0 (C-8); 40.4 (C-4); 37.0 (C-20); 36.5 (C-1); 35.9 (C-6); 35.8 (C-10); 34.3 (C-22); 33.3 (C-23); 31.3 (C-2); 29.5 (C-11); 28.7 (C-16); 27.8 (C-9); 24.3 (C-15); 23.2 (C-19); 17.7 (C-21); 13.0 (C-18). ^{195}Pt NMR (D_2O) $\delta = -1420$ ppm.

NMR Reaction of Complexes 1 and 2 with 5′-GMP. One milligram of complex **1** (or complex **2**) was added as a solid to 0.5 mg (or 0.3 mg) of 5′-GMP sodium salt dissolved in 400 μL of 10 mM phosphate buffer in D_2O (pH = 7.2). Complex **2** immediately gave a clear solution, but complex **1** only dissolved after 24 h at 50 °C. ^{1}H NMR spectra at different time-points were recorded at 25 °C using a presaturation pulse to remove the residual solvent peak (spectral width = 8000 Hz). ROESY and DQF−COSY spectra of the final 1:1 complexes were also acquired at 25 °C.

Microscopic Analyses. Peripheral blood (PB) samples were collected from three healthy volunteers. Three 100 μL aliquots from each PB sample were incubated with 2 mL of an hypotonic solution (Quicklysis, Cytognos, Salamanca, Spain) for 10 min at room temperature to lyse nonnucleated red cells. After this incubation period, nucleated cells were centrifuged (5 min at 540*g*) and washed once in a phosphate-buffered saline (PBS) solution (pH = 7.6). Then, the cell pellet was resuspended in 50 μL of PBS and placed on a slide to which 50 μL of a solution of either complex **1** (5 μM) or complex **2** (5 μM) in water or just 50 μL of water was added. Fluorescence measurements were performed using an Olympus BX40 fluorescence microscope (Olympus, Hamburg, Germany) equipped with a mercury arc lamp using a 350 ± 25 nm band-pass excitation filter and a 400 ± 10 nm long pass emission filter. Fluorescence emission was captured through a CCD camera and printed in a 512 × 512 pixel picture.

Cytotoxicity Assays. The cytotoxic activity of the two newly synthesized platinum compounds **1** and **2** was evaluated in comparison with that of the most widely used platinum compound, cisplatin. To this end, CH1cisR ovarian cancer cells were cultured in parallel in the presence of different concentrations (0, 1, 2.5, 5, and 10 μM) of complex **1**, complex **2**, or cisplatin in DMEM medium supplemented with 10% fetal calf serum, 1% L-glutamine, and 1% penicillin/streptomycin. For the analysis of the cytotoxic activity, cells were harvested either prior to adding the platinum compounds or at 24 and 48 h after they were placed in culture. To harvest the cells they were incubated (5 min at 37 °C) with a solution containing 0.25% (w/v) of trypsin in Hank's balanced salt solution.

Evaluation of the cytotoxic activity was performed using conventional flow cytometry (FACScalibur, Becton/Dickinson Biosciences, San Jose, CA) techniques that allow the simultaneous measurement of cell death and cell proliferation. Briefly, harvested cells were centrifuged (5 min at 540*g*) and resuspended at a concentration of 10^4 cells/μL of 70% ethanol. After an incubation period of at least 30 min at 4 °C, cells were washed once in sodium citrate buffer−sucrose 250 mM, trisodium citrate 40 mM, 5% (v/v) dimethyl sulfoxide, 0.1% (v/v) Nonidet P40, 0.5 mM trishydroxymethylaminomethane, and 1.5 mM spermine tetrahydrochloride and resuspended in the same citrate buffer at a concentration of 10^4 cells/μL. To 10^6 cells in 100 μL, 1.5 mL of a solution containing 0.5 g/L of RNAse and 0.1 g/L of trypsin inhibitor in citrate buffer was added; after gently mixing, cells were incubated for another 10 min at room temperature. Once this incubation period had ended, 1.5 mL of a solution containing 0.42 g/L of propidium iodide in sodium citrate buffer was added, and another incubation for 15 min (room temperature) was performed in the darkness. Measurements of cell DNA contents were performed for at least 10^4 cells for each experimental condition.

Statistical Analysis. The equations for kinetic studies were adjusted to the experimental data by means of a nonlinear regression program available in the SIMFIT in the statistics package (Bardsley 1992 SIMFIT package 3.2. Department of Obstetrics and Gynecology, Manchester, UK).

For the calculation of the ratio of dead/apoptotic cells and the distribution of surviving cells in the different cell cycle phases, the ModFIT software program was used (Verity Software, Topsham, MA). The Mann−Whitney *U* test was used to estimate the statistical significance of the differences observed between groups. *P* values <0.05 were considered to be associated with statistical significance.

RESULTS

Structure of the Platinum Complexes 1 and 2. Both platinum complexes were characterized by a combination of spectroscopic techniques, since no crystals suitable for X-ray diffraction studies were available. In the MS, the peaks corresponding to platinated species were easily recognized due to six different isotopic masses for the metal (190, 192, 194, 195, 196, and 198). The observed molecular ions (754.7 for complex **1** and 1184.6 for complex **2**) are consistent with the molecular formulas $C_{28}H_{50}ClN_3O_6Pt$ (calcd. mass: 754.3) and $C_{54}H_{92}N_4O_{12}Pt$ (calcd. mass: 1183.64). Remarkable fragmentation peaks corresponded to the loss of a chloride from complex **1** or a cholylglycinate from complex **2** ($[M\mathbf{1} - Cl - H]^+ = 718.6$ and $[M\mathbf{2} - CG]^+ = 719.5$).

The ^{195}Pt NMR resonance for complex **1** is centered at −1970 ppm indicating a square planar complex with a PtN_2OCl environment, while the ^{195}Pt NMR signal for complex **2** is centered at −1470 ppm indicating a PtN_2O_2 square planar complex (*13*). The carboxylate ν_{as} and ν_s absorption bands in the IR spectra of complex **1** (1601 and 1409 cm^{-1}) and complex **2** (1637 and 1384 cm^{-1}) also point to monodentate binding of the cholylglycinate ligands (*10*). For complex **1**, a typical stretching vibrational mode of Pt−Cl at 349 cm^{-1} was observed (*10*, *14*).

The ^{1}H NMR and ^{13}C NMR spectra for complex **1** showed peaks corresponding to one cholylglycinate and to the ethylenediamine. The ^{1}H NMR and ^{13}C NMR spectra for complex **2** displayed peaks corresponding to two cholylglycinates and to the ethylenediamine. There is a single set of resonances for the two cholylglycinate ligands in complex **2** and the two ethylenediamine carbons of complex **2** are isochronous.

Both complexes are soluble in methanol and DMSO and dissolve over time in water, complex **2** being more water soluble than complex **1** (*14*). Aqueous solutions of both compounds showed a concentration-dependent, broad, and unstructured (*15*−*17*) fluorescence emission band (Figure 3), which persisted for weeks. The absorption spectra of these platinum compounds were typically formed by very intense charge-transference bands in the UV zone (Figure 2). These bands hide weaker d−d transitions located to greater wavelengths which did not show up at the concentrations used (10^{-4} M) in the registered absorption spectra.

The quantum yields (Φ) in water were calculated as being of 0.11 for complex **1** and of 0.10 for complex **2** (relative to quinine sulfate) (*18*).

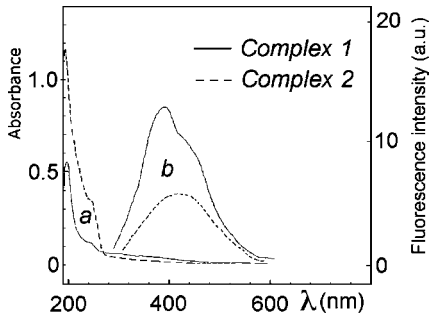

Figure 2

Figure 2. Electronic absorption (a) and emission (b) spectra at room temperature of platinum complexes in water solution ($c = 1 \times 10^{-4}$ M). Excitation wavelength: $\lambda_{ex} = 301$ nm (Complex **1**); $\lambda_{ex} = 330$ nm, (Complex **2**); fluorescence intensity in arbitrary units.

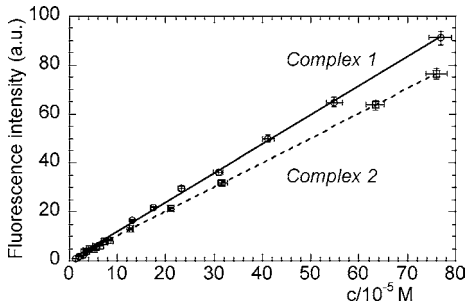

Figure 3. Concentration dependency of the fluorescence intensity of the platinum complexes. Concentrations are expressed in 10^{-5} M and the fluorescence intensity in arbitrary units (a.u.). Emission wavelengths for each complex were selected from the emission spectra (Figure 2) to achieve the maximal emission intensity: Complex **1**, $\lambda_{ex} = 301$ nm, $\lambda_{em} = 384$ nm; Complex **2**: $\lambda_{ex} = 330$ nm, $\lambda_{em} = 436$ nm. For each concentration series, small aliquots of a recently prepared aqueous solution of the corresponding complex were sequentially added to the cuvette, equilibrated for 10 min and measured at room temperature.

Kinetic Studies. Molar conductivities at 37 °C of complexes **1** or **2** (10^{-3} M solutions) were of 144 and 150 S cm^2 mol^{-1}, respectively, in agreement with a 1:1 electrolyte ratio. The hydrolysis kinetics at 37 °C in water and in solutions of increasing NaCl concentrations (4, 150, and 500 mM) were followed by the overtime variation in absorbance at 245 nm. The decay curve was adjusted to a pseudo first-order rate equation, $A = A_0e^{-kt} + C$, where A is absorbance at time t; A_0 is absorbance at time zero; k_{obs} is the rate constant (h^{-1}), and C is a constant term introduced to take into account the baseline variation and the absorption of other nonreacting species (Figure 4). The calculated values for the rate constants (k_{obs}) and the half-lives are summarized in Table 1.

Reactivity of Complexes 1 and 2 with 5-GMP. The reaction between complex **1** or complex **2** and 5′-GMP at 37 °C in a 1:1 molar ratio (10^{-4} M each) was followed by mass spectrometry (Figure 5). Briefly, unreacted 5′-GMP was quantified by peak integration (35 spectra) relative to an internal standard and comparison with a calibration curve (obtained by fitting different 5′-GMP standards to a straight line). Total 5′-GMP was estimated as the sums of the $m/z = 362$ [(5′-GMP) − H]$^+$ and $m/z = 384$ [5′-GMP) − H + Na]$^+$ ions (calibration curve: $0.999 > r^2 < 0.999$, $n = 4$, RSD = 0.3% − 0.03%). Both complexes reacted slowly since 5′-GMP consumptions greater than 95% took 187 and 124 h, respectively.

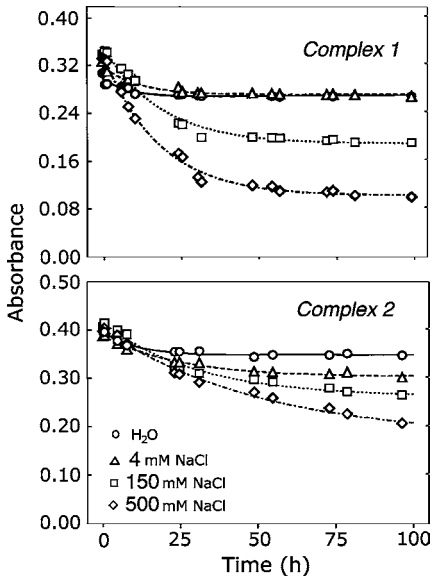

Figure 4. Absorbance vs time curves for complexes **1** and **2**. The hydrolysis reactions for complexes **1** and **2** were followed by monitoring the decay of the 245 nm absorption band at 37 °C. Increasing concentrations of sodium chloride (4, 150, and 500 mM) were selected to mimic the effect of different environments on the hydrolysis kinetics. The traces connecting the experimental data-points were drawn by SIMFIT and correspond to first order decays.

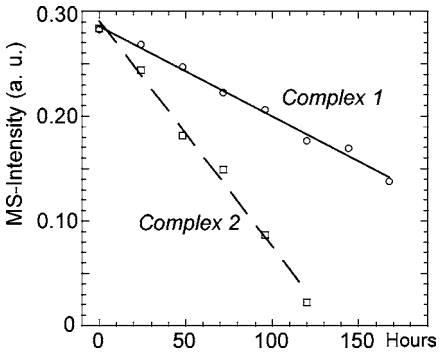

Figure 5. Effect of complex **1** and complex **2** on free 5′-GMP concentration according to time curves in the presence of complexes **1** and complex **2**. Free 5-GMP concentration was monitored by the MS-intensity measured at different time points (see text for details).

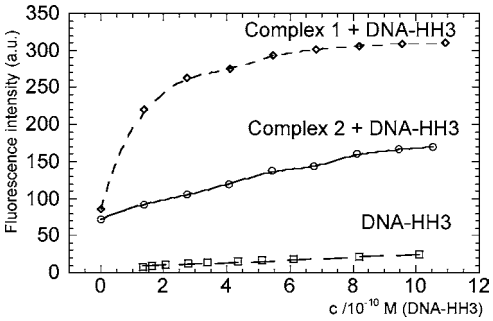

Figure 6. Fluorescence of the platinum complex **1** and complex **2** after incubation with HH3-DNA. Fluorescence intensity of increasing concentrations of HH3-DNA incubated for 24 h. with a 7.2×10^{-4} M solution of complex **1** in water and a 1.3×10^{-4} M solution of complex **2**. ($\lambda_{ex} = 350$ nm, $\lambda_{em} = 437$ nm.) The solutions remained fluorescent for periods of time longer than two months.

NMR monitoring of the reaction of complexes **1** and **2** with 5′-GMP revealed an over time decrease in the signal corresponding to the guanosine H8 proton (8.1 ppm),

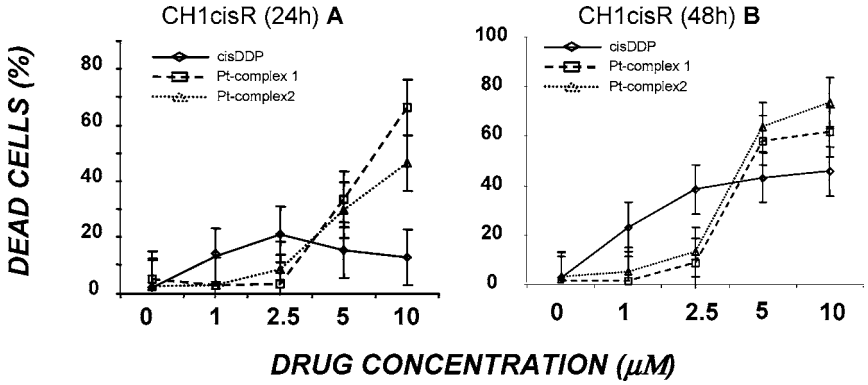

Figure 7. Cytotoxic activity of different doses of Pt complex **1** and complex **2** as compared to cisplatin against CH1cisR ovarian cancer cells after 24 h (panel A) and 48h (panel B) of culture. Results expressed as percentage of dead CH1cisR cells. Statistically significant differences ($p < 0.04$) were observed for the percentage of dead cells at 24 h for cisplatin as compared to both complex **1** and complex **2** at doses of 10 μM.

Table 1. Kinetic Parameters for Hydrolysis Reactions [$C = 10^{-4}$ M, 37 °C, final pH = 4.5 for Complex 1 and pH 6.0 for Complex 2]

	H_2O	4 mM NaCl	150 mM NaCl	500 mM NaCl
		Complex **1**		
k_{obs} (h^{-1})	$1.22 \pm 0.02 \times 10^{-1}$	$8.4 \pm 0.02 \times 10^{-2}$	$5.38 \pm 0.01 \times 10^{-2}$	$5.24 \pm 0.01 \times 10^{-2}$
$t_{1/2}$ (h)	5.68	8.23	12.88	13.22
		Complex **2**		
k_{obs} (h^{-1})	$0.93 \pm 0.01 \times 10^{-1}$	$0.39 \pm 0.02 \times 10^{-1}$	$0.32 \pm 0.02 \times 10^{-1}$	$0.19 \pm 0.01 \times 10^{-1}$
$t_{1/2}$ (h)	7.45	17.77	21.66	36.48

together with the appearance of a new resonance at 8.7 ppm (identical for both platinum compounds). The chemical shift changes for the sugar and the steroid moieties were less pronounced.

Fluorescence Properties of the Platinum Complexes 1 and 2 after Reaction with DNAs. All measurements were performed under the conditions employed for the microscopic experiments ($\lambda_{ex} = 350$ nm and $\lambda_{em} = 437$ nm) described below, to render the comparisons meaningful. The complexes were reacted separately with 5′-GMP, oligonucleotides **I**, **II**, and **III** (see Experimental Section) and HH3-DNA.

Incubation of 10^{-4} M [Pt(en)(CG)Cl] (**1**) and [Pt(en)-(CG)$_2$] (**2**) solutions with a 1:1 molar ratio of 5′-GMP led to fluorescence "quenching" . On the other hand, addition of increasing amounts of either oligonucleotides **I**, **II**, or **III** or HH3-DNA led, after 5 min, to an increase in fluorescence intensity higher than the sum of the fluorescence intensities of the individual components (*19*). The solutions remained fluorescent for periods longer than 2 months. No major differences in fluorescence emission were observed with increasing salt concentration (4, 150, and 500 mM of sodium chloride) when compared with aqueous solution (Figure 6).

Cytotoxic Activity of Platinum Complexes 1 and 2 and Microscopic Analyses. As shown in Figure 7, platinum complexes **1** and **2** displayed an important cytotoxic activity against the CH1cisR ovarian cancer cell line. This cytotoxic activity was already evident after 24 h of culture, and its maximum was reached for the highest doses assayed: 5 and 10 μM. Interestingly, after 24 h no significant differences were observed between the proportion of dead cells obtained with both complexes ($p > 0.05$). In contrast, the cytotoxic activity of these two complexes after 24 h of culture was significantly ($p < 0.04$) higher than that of cisplatin, this latter compound requiring longer periods of time (48 h) to reach identical cytotoxic effects, see Figure 7.

Analysis of the relative distribution of surviving cells in culture along the G_0/G_1, S and G_2/mitosis cell cycle

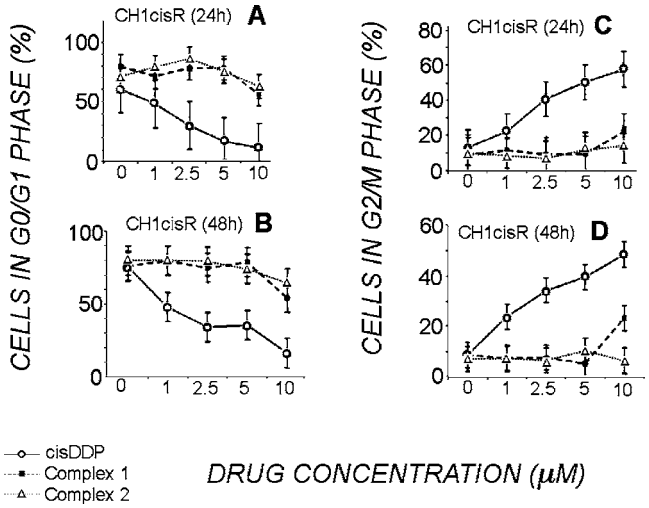

Figure 8. Cell cycle distribution of live CH1cisR (panels A to D) cells, after being cultured for 24 h (panels A, C), and 48 h (panels B, D), in the presence of Pt complex **1**, complex **2**, and cisplatin. Percentage value of G_0/G_1 cells is shown in panels A and B, and the proportion to G_2/M cells is displayed in the other panels (C and D). Statistically significant differences ($p < 0.03$) were found in the percentage of both G_2/M- and G_0/G_1-cell cycle phase cells cultured in the absence versus the presence of cisplatin at doses >2.5 μM for 24 and 48 h, except for the comparisons of the percentage of G_2/M cells treated with 2.5 μM cisplatin for 24 h.

phases showed that neither of the two platinum complexes synthesized induced a significant accumulation of cells in any specific cell cycle phase ($p > 0.05$). By contrast, cisplatin induced a dose-dependent accumulation of CH1cisR cells in the G_2/M cell cycle phases ($p < 0.03$), in line with previous findings (*20*). At identical doses, cisplatin requires that cells must have reached G_2, to enter apoptosis and finally die (*20*, *21*), see Figure 8.

PB nucleated cells incubated with either platinum complexes **1** or **2** became fluorescent after 10 min, mainly within the cells' nuclei, under microscopic analysis

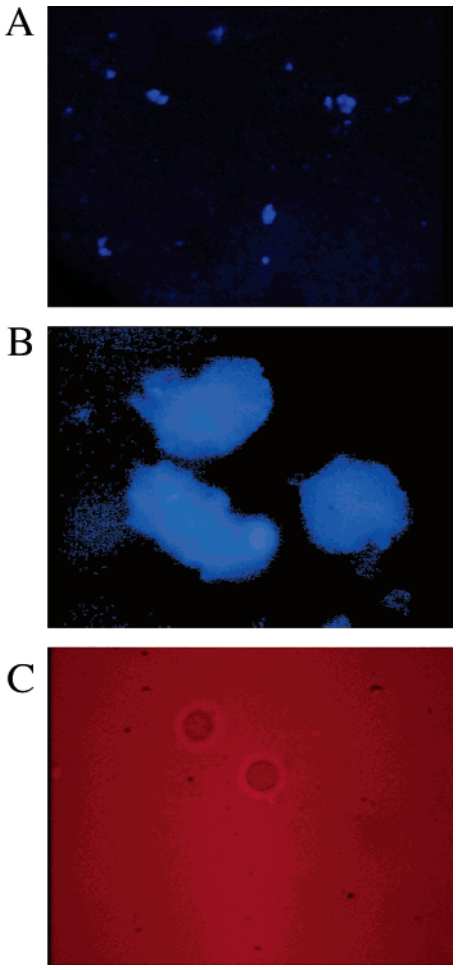

Figure 9. Illustrative photographs of the fluorescence emission observed after incubating peripheral blood nucleated cells with complex **1** (complex **2** leads to very similar photographs). Panel A shows a 20× magnification and panel B a 500× magnification. Panel C shows that these cells remained alive and did not incorporate propidium iodide.

(Figure 9). Cells treated with both platinum complexes remained fluorescent for more than five weeks.

DISCUSSION

The spectroscopic data for complex **1** and complex **2** agree with the expected [Pt(en)(CG)Cl] and [Pt(en)$(CG)_2$] square planar complexes, very similar to the closely related [$Pt(NH_3)_2$(CG)Cl] and [$Pt(NH_3)_2(CG)_2$] compounds we have recently described (*10*). Both complexes carry two putative leaving ligands, one chloride and one cholylglycinate for complex **1** and two cholylglycinates for complex **2**. The cholylglycinate ligands in both complexes are spectroscopically very similar, suggesting identical binding modes. Minor differences are seen for the atoms next to the Pt atom, the C-26 carboxylates and the ethylenediamine carbons and protons, which are isochronous in the NMR spectra of complex **2** but not in the asymmetric complex **1** (with different trans ligands: chloride and cholylglycinate). In complex **2**, the two cholylglycinates give rise to only one set of resonances, indicating a rapid rotation on the NMR time scale of the bile acids ring system, as would be expected for a freely rotating linear chain linking the Pt atom and the steroid skeleton.

Aqueous solutions of either complex show a persistent, concentration-dependent, broad, and unstructured fluorescence emission band. To the best of our knowledge, there are no previous reports of fluorescent platinum complexes in water at room temperature (other than those with attached fluorescent ligands) (*5*). The half-lives for the complexes measured in the kinetic studies (see Table 1) imply that both complexes are almost completely hydrolyzed after 48 h in pure water, but their solutions remain fluorescent.

Substitution of the chloride ion by water in cisplatin is the first kinetic step in its mechanism of action (*22*−*25*), prior to reaction with its final targets. Complexes **1** and **2** show higher aqueous solubility but slower kinetic profiles than cisplatin. The higher stability in water of complex **2** as compared to complex **1** relates to the substitution of the chloride ligand by the second carboxylate group (a worse leaving group). Such a substitution in cisplatin analogues (e.g. carboplatin and oxaliplatin) is considered to be responsible for their increased water solubility, as well as their reduced kinetic reactivity and toxicity (*1*). For complexes **1** and **2**, the higher the NaCl concentration, the longer their half-lives, as observed upon increasing NaCl concentrations from those observed in the cytoplasmic compartment (4 mM) to the plasma ones (150 mM). This behavior parallels that of cisplatin and accounts for its higher intracellular than extracellular reactivity (*1*).

The hydrolysis reactions of the two complexes follow single decay kinetics of increasing rates with decreasing NaCl concentrations (see Table 1). The two complexes initially hydrolyze to the same putative aquo-complex (*26*), $[Pt(en)(CG)H_2O]^+$, in agreement with the equivalent fragmentation peaks of the MS ($[M\mathbf{1} - Cl - H]^+ = 718.6$ and $[M\mathbf{2} - CG]^+ = 719.5$):

$$[Pt(en)(CG)Cl] + H_2O \rightarrow [Pt(en)(CG)H_2O]^+ + Cl^-$$

$$[Pt(en)(CG)_2] + H_2O \rightarrow [Pt(en)(CG)H_2O]^+ + CG^-$$

A second decay curve is not observed for either complex, even for very long reaction times. This observation suggests that there is only one replaceable ligand in these complexes, as opposed to cisplatin and its analogues, where two substitutions are seen from the kinetics of hydrolysis reactions. These double substitutions allow the formation of DNA bis-adducts, which are deemed important for the cytotoxic activity of cisplatin analogues (probably due to intra- and interstrand DNA cross-links) (*2*−*4*).

As a model system, the reaction of the complexes with 5′-GMP (cisplatin reacts with 5′-GMP to give mixtures of the mono- and the bisadducts) were studied by MS and NMR. The final time-points showed the [Pt(en)(CG)(5′-GMP)]$^+$ monoadduct with $m/z = 1082.5$, together with the residual unreacted complex. No platinated peak which could be ascribed to the generation of a [Pt(en)-$(5′\text{-GMP})_2]^+$ bis-adduct was detected, in agreement with the previously described kinetic studies. The ^{1}H NMR chemical shift changes are in agreement with the N7 platination of guanine. Guanine N7 is readily accessible in the DNA major groove and, owing to its high basicity among the four nucleotide bases, it is the major binding target on DNA for antitumor platinum complexes (*27*−*29*). Summarizing, complex **1** and **2** seem to have a single reactive ligand, the second one being inert or reacting much slower under the experimental conditions used, and they both lead to the same chemical species. The reaction of the complexes with 5′-GMP led to a substantial decrease in their fluorescence intensities. The endpoint

solutions gave, after correcting for the concentration differences, fluorescent intensities very similar to each other, as expected if they contain the same final products.

To determine the nature of the fluorescent species observed in the microscopic images described below, we further studied the reactivity of the complexes against different oligonucleotides and DNA structures by following changes in the emission spectra. A substantial increase in fluorescence intensity is observed, ascribed to the formation of monoadducts of the complexes with the guanine bases of the DNA. There was no fluorescence decay observed even for periods longer than 2 months, suggesting that the monoadducts are stable in vitro and do not evolve toward bis-adducts, even for oligonucleotide **III**, which bears three Gs in a row. The decreased fluorescence intensity of the 5′-GMP adducts and the increased emission attained with oligonucleotides and other DNAs is very fortunate, since it reduces the background fluorescence in microscopic images.

The microscopic studies confirmed that complexes **1** and **2** in individual cells mainly target the cells' nuclei, supporting their preferential binding to DNA. Interestingly, the increase in cell fluorescence was rapidly observed after 10 min, in keeping with the results described using oligonucleotides **I**, **II**, and **III**, and HH3-DNA. In addition, cells treated with both platinum complexes remained fluorescent for more than five weeks. Accordingly, both complexes emit enough fluorescence to allow unequivocal identification of cells containing the platinum complexes bound to their DNA and they remain stable. Such features, in a heterogeneous sample composed of a mixture of different cell subsets, would facilitate the visualization of individual cells containing platinum complexes inside by conventional microscopic techniques. This also indicates that even if cells containing platinum remained alive for relatively long periods of time they would not be able to rapidly eliminate such platinum complexes from the nuclei into the cytoplasmic compartment or the extracellular media. This would further facilitate a close analysis of the activity of these compounds through the possibility of identifying the cells targeted, provided that both platinum complexes do in fact retain cytotoxic activity.

The two synthesized platinum complexes showed a dose-dependent cytotoxic activity. Interestingly, once compared to cisplatin, both complex **1** and complex **2** showed significantly a higher cytotoxic activity at early time periods after they have been added to the cell culture, even in the absence of a high number of DNA bis-adducts. Since the formation of bis-adducts appears to be directly linked to the cytotoxic activity of cisplatin, our results suggest that the two platinum complex assayed might have formed other different type of adducts (*19*, *30*−*33*) which would also be capable of inducing cytotoxicity. The linkage of platinum compounds to bile acids would also help to explain the different pharmacokinetics observed for the two new complexes as compared to cisplatin. In addition, they exert their cytotoxic effects in the absence of significant accumulation of cells at a specific cell cycle phase.

Analysis of the relative distribution of surviving cells in culture along the G_0/G_1, S, and G_2/mitosis cell cycle phases showed that neither of the two platinum complexes synthesized induced a significant accumulation of cells in any specific cell cycle phase ($p > 0.05$). By contrast, cisplatin induced a dose-dependent accumulation of CH1cisR cells in the G_2/M cell cycle phases ($p < 0.03$), in line with previous findings (*20*). At identical doses, cisplatin requires that cells must have reached G_2, to enter apoptosis and finally die (*20*, *21*).

Such cell-cycle associated differences could be explained, at least to a certain extent, in terms of the formation of different adducts with the platinum complexes **1** and **2** as compared to cisplatin, which could lead to the occurrence of different interactions of the platinum compound once inside the cell. A potential advantage of the newly synthesized platinum complexes would rely on their potential cytotoxic effects on proliferating and resting tumor cells, provided the fact that this is not associated with an increase in normal tissue toxicity. Further studies are necessary to explore these potential advantages.

ACKNOWLEDGMENT

This work has been supported by grants from the Junta de Castilla y León (Grants SA 050/03 and SA073/02) and the D.G.I.-M.C.T. (PPQ2001-1977). We wish to thank the C.I.D.T.A. for allowing us to use their equipment, Dr. Anna Lithgow for acquiring the NMR spectra, Dr. César Raposo for the MS, N. Skinner for revising the manuscript, and Dr. José M. Perez for providing the ovarian cancer cell lines.

LITERATURE CITED

(1) Rosenberg, B. (1999) *Platinum complexes for the treatment of cancer: why the search goes on* (Lippert, B., Ed.) 1st ed., pp 3−30, Wiley−VCH, Zurich.

(2) Wong, E., and Giandomenico, C. M. (1999) Current Status of Platinum-Based Antitumor Drugs. *Chem. Rev. 99*, 2451−2466.

(3) Lebwohl, D., and Canetta, R. (1998) Clinical development of platinum complexes in cancer therapy: an historical perspective and an update. *Eur. J. Cancer 34*, 1522−1534.

(4) Jamieson, E. R., and Lippard, S. J. (1999) Structure, Recognition, and Processing of Cisplatin-DNA Adducts. *Chem. Rev. 99*, 2467−2498.

(5) Molenaar, C., Teuben, J.-M., Heerebrij, R. B., Tanke, H. J., and Reedijk, J. (2000) New insights in the cellular processing of platinum antitumor compounds, using fluorophore-labeled platinum complexes and digital fluorescence microscopy. *J. Biol. Inorg. Chem. 5*, 655−665.

(6) Brooks, J. (2002) Synthesis and Characterization of Phosphorescent Cyclometalated Platinum Complexes. *Inorg. Chem. 41*, 3055−3066.

(7) Yang, Q. Z., Wu, L. Z., Wu, Z. X., Zhang, L. P., and Tung, C. H. (2002) Long-Lived Emission from Platinum(II) Terpyridyl Acetylide Complexes. *Inorg. Chem. 41*, 5653−5655.

(8) Konno, T. (1992) Targeting chemotherapy for hepatocarcinoma. Administration of anticancer drugs dissolved in lipiodol. *Eur. J. Cancer 28*, 403−409.

(9) Criado, J. J., Macías, R. I. R., Medarde, M., Monte, M. J., Serrano, M. A., and Marín, J. J. G. (1997) Synthesis and characterization of the new cytostatic complex *cis*-diammineplatinum(II) chlorocholylglycinate. *Bioconjugate Chem. 8*, 453−458.

(10) Criado, J. J., Domínguez, M. F., Medarde, M., Rodriguez, E., Macías, R. I. R., and Marín, J. J. G. (2000) Structural characterization, kinetic studies and in vitro biological activity of new cis-diamminebis-cholylglycinate(O,O′)Pt(II) and cis diamminebisursodeoxycholate(O,O′)Pt(II) complexes. *Bioconjugate Chem. 11*, 167−174.

(11) Paschke, R., Kalbitz, J., and Paetz, C. (2000) Novel spacer linked bile acid-cisplatin compounds as a model for specific drug delivery, synthesis and characterization. *Inorg. Chim. Acta 304,* 241−249.

(12) Altman, J., Castrillo, T., Beck, W., Bernhardt, G., and Schönemberg, H. (1991) Metal complexes with biologically important ligands. 62. Platinum(II) complexes of 3-(2-aminoethoxy)estrone and estradiol. *Inorg. Chem. 30*, 4085−4088.

(13) Watabe, M., Takayama, T., Kuwahara, A., Kawahashi, T., Koike, Y., Horiuchi, A., Suzuki, M., Watanabe, T., Mikami, K., Matsumoto, T., and Narusawa, Y. (1995) Preparation and ^{13}C and ^{195}Pt NMR spectra of platinum(II) peptide complexes and their growth-inhibitory activity against mouse meth a solid tumor in vivo. *Bull. Chem. Soc. Jpn. 68*, 2559−2565.
(14) Appleton, T. G. (1997) Donor atom preferences in complexes of platinum and palladium with amino acids and related molecules. *Coord. Chem. Rev. 166*, 313−359.
(15) Lever, A. B. P. (1984) *Inorganic Electronic Spectroscopy*, 2nd ed., Elsevier, Amsterdam.
(16) Lin, Y., Weissleder, R., and Tung, C.-H. (2002) Novel Near-Infrared Cyanine Fluorochromes: Synthesis, Properties, and Bioconjugation. *Bioconjugate Chem. 13*, 605−610.
(17) Corte, M., Carney, J. T., Oppenheimer, J. D., Downey, K. E., and Cummings, S. D. (2002) Photoinduced electron transfer and energy transfer reactions of hydroxo-(2,2′:6′,2″-terpyridine) platinum(II). *Inorg. Chim. Acta 333*, 148−151.
(18) Lakowicz, J. R. (1999) *Principles of Fluorescence Spectroscopy*, 2nd ed., Kluwer Academic/Plenum, New York.
(19) Bauer, C., Peleg-Shulman, T. J., Gibson, D., and Wang, A. H. J. (1998) Monofunctional platinum amine complexes destabilize DNA significantly. *Eur. J. Biochem 256*, 253−260.
(20) Sorenson, C. M., and Eastman, A. (1988) Influence of cis-diamminedichloroplatinum(II) on DNA synthesis and cell cycle progression in excision repair proficient and deficient Chinese hamster ovary cells. *Cancer Res. 48*, 6703−6707.
(21) Bose, R. N. (2002) Biomolecular targets for platinum antitumor drugs. *Mini Rev. Med. Chem. 2*, 103−111.
(22) Bancoft D. P., Lepre, C. A., and Lippard, S. J. (1990) Platinum-195 NMR kinetic and mechanistic studies of cis- and trans-diamminedichloroplatinum(II) binding to DNA *J. Am. Chem. Soc. 112*, 6860−6871.
(23) Peleg-Shulman, T., Katzhendler, J., and Gibson, D. (2000) Effects of monofunctional platinum binding on the thermal stability and conformation of a self-complementary 22-mer. *J. Inorg. Biochem. 81*, 313−323.
(24) Hambley, T. V. (2001) Platinum binding to DNA: structural controls and consequences. *J. Chem. Soc., Dalton Trans.* 2711−2718.
(25) Robillard, M. S., Galanski, M., Zimmermann, W., Keppler, B. K., and Reedijk, J. (2002) Aminoethanol-dichloroplatinum-(II) complexes: influence of the hydroxyethyl moiety on 5′-GMP and DNA binding, intramolecular stability, the partition coefficient and anticancer activity. *J. Inorg. Biochem. 88*, 254−259.
(26) Costa, L. A. S., Rocha, W. R., de Almeida, W. B., and Dos Santos, H. F. (2004) The solvent effect on the aquation processes of the cis-dichloro(ethylenediamine)platinum(II) using continuum solvation models. *Chem. Phys. Lett. 387*, 182−187.
(27) Zhao, G., Lin, H., Zhu, S., Sun, H., and Chen, Y. (1998) Dinuclear palladium(II) complexes containing two monofunctional $[Pd(en)(pyridine)Cl]^+$ units bridged by Se or S. Synthesis, characterization, cytotoxicity and kinetic studies of DNA-binding. *J. Inorg. Biochem. 70*, 219−226.
(28) Qu, Y., Fitzgerald, J. A., Rauter, H., and Farrell, N. (2001) Approaches to Selective DNA Binding in Polyfunctional Dinuclear Platinum Chemistry. The Synthesis of a Trifunctional Compound and Its Interaction with the Mononucleotide 5′-Guanosine Monophosphate. *Inorg. Chem. 40*, 6324−6327.
(29) Djuran, M. I., Milinkovic, S. U., Habtemariam, A., Parsons, S., and Sadler, P. J. (2002) Crystal packing and hydrogen bonding in platinum(II) nucleotide complexes: X-ray crystal structure of $[Pt(MeSCH_2CH_2SMe)(5'\text{-GMP-}N7)_2]\cdot 6H_2O$. *J. Inorg. Biochem. 88*, 268−273.
(30) Bierbach, U., Sabat, M., and Farrell, N. (2000) Inversion of the Cis Geometry Requirement for Cytotoxicity in Structurally Novel Platinum(II) Complexes Containing the Bidentate N,O-Donor Pyridin-2-yl-acetate. *Inorg. Chem. 39*, 1882−1890.
(31) Schmidt, K., Filippov, D. V., Meeuwenoord, N. J., van der Marel, G. A., van Boom, J. H., Sorenson, C. M., Barry, M. A., and Eastman, A. (1990) Analysis of events associated with cell cycle arrest at G2 phase and cell death induced by cisplatin. *J. Natl. Cancer Inst. 82*, 749−755.
(32) El-Mehasseb, I, M., Kodaka, M., Okada, T., Tomohiro, T., Okamoto, K., and Okuno, H. (2001) Platinum (II) complex with cyclometalating 2-phenylpyridine ligand showing high cytotoxicity against cisplatin-resistant cell. *J. Inorg. Biochem. 84*, 157−158.
(33) Kasparkova, J., Novakova, O., Farrell, N., and Brabec, V. (2003) DNA Binding by Antitumor *trans*-$[PtCl_2(NH_3)(thiazole)]$. Protein Recognition and Nucleotide Excision Repair of Monofunctional Adducts. *Biochemistry 42*, 792−800.

BC049788R

Polyphenylene Dendrimers as Scaffolds for Shape-Persistent Multiple Peptide Conjugates

Gueorgui Mihov,[†] Dörthe Grebel-Koehler,[†] Anke Lübbert,[†] Guido W. M. Vandermeulen,[†] Andreas Herrmann,[†] Harm-Anton Klok,[‡] and Klaus Müllen*,[†]

Max Planck Institute for Polymer Research Ackermannweg 10D-55128 Mainz, Germany, and Ecole Polytechnique Fédérale de Lausanne (EPFL) Institut des Matériaux, Laboratoire des Polymères Bâtiment MX-D, CH 1015 Lausanne, Switzerland. Received July 8, 2004; Revised Manuscript Received February 2, 2005

The present work describes synthetic concepts for the coupling of peptides to polyphenylene dendrimers (PPDs). Novel functionalized cyclopentadienones have been synthesized whose Diels−Alder cycloaddition with various core molecules leads to polyphenylene dendrimers possessing (protected) amino or carboxyl groups. In addition, the resulting functionalized molecules exhibit the characteristic shape-persistence and monodispersity of PPDs. Their functions have been used for the attachment of polylysine to the dendritic scaffold. Three different methods for the decoration of dendrimers with polypeptides are presented. First, polylysine segments are grafted from the surface of the dendrimers employing α-amino acid *N*-carboxyanhydride (NCA) polymerization. Second, the *C*-terminal carboxyl groups of protected polypeptides are activated and then coupled to the amino groups on the surface of the PPD. Finally, cysteine terminated, unprotected peptide sequences are attached to polyphenylene dendrimers utilizing the addition of the sulfhydryl group of a cysteine to the maleimide functions on the dendrimer surface. Moreover, Diels−Alder cycloaddition of suitably functionalized cyclopentadienons to a desymmetized core molecule allows the design of a dendritic scaffold with a specific number of different anchor groups on its periphery. These approaches are important for the tailoring of new, shape-persistent, polyfunctional multiple antigen conjugates.

1. INTRODUCTION

Dendrimers are monodisperse, highly branched macromolecules (*1*−*3*). Their synthesis involves either a convergent or divergent protocol, both implicating the creation of a core molecule and an iterative procedure for the construction of the dendrimer. The high number of functional groups and the well-defined structure make dendrimers attractive carriers for the design of nanoparticles with potential uses in clinical and diagnostic applications. Recent advances in the biomedical applications of various dendritic structures are reviewed by Stiriba et al. (*4*). The polyphenylene dendrimers (PPDs)[1] described here are unique shape-persistent and polyfunctional molecules bearing topologically isolated, noninterfering functional groups (*5*). This is essential for the active function of PPDs decorated with short peptide sequences because the bioactivity of the latter is strongly influenced by inter- and intramolecular chain interactions. The attachment of a defined number of oligopeptides onto PPDs has been inspired by the recent achievement of multiple antigen peptides (MAPs) (*6*).

MAPs are nanoparticles, which, when introduced to an organism, are able to trigger an immune response. In nature, the recognition of foreign bodies (antigens) by antibodies proceeds via the so-called key and lock principle, in which the shape of the antibodies' receptors is complementary to a given pattern on the surface of the antigen that is to be recognized. Complex antigens have a variety of epitopes on different parts of their surface, each of which can be recognized separately by a different antibody. Antigens of special interest are so-called immunogens that trigger an immune response, i.e., the production of antibodies.

Very often, the identifiable part for the antibody is a polypeptide segment. The attachment of several recognizable polypeptides to a nanoparticle is referred to as a MAP. These structures have proven to exhibit amplified immunogenicity and pave the way toward fully synthetic vaccines (*7*). Currently, MAPs are constructed by attaching the desired polypeptides to a dendritic matrix composed, most frequently, of branched polylysine. It has been shown that a stronger immunogenic effect may be achieved when the MAP system contains two different antigen peptides (*8*).

However, the oligolysine carriers do not possess a defined spatial structure, which is believed to have an unfavorable effect on their function (*6*). In fact, inter- and intramolecular interactions of the antigens may modify their secondary structure as well as limit their acces-

* To whom correspondence should be addressed. Prof. Dr. Klaus Müllen, Max Planck Institute for Polymer Research, Ackermannweg 10, D-55128 Mainz, Germany. Phone: +49 (0) 6131 379150/151. Fax: +49 (0) 6131 379350. E-mail: muellen@mpip-mainz.mpg.de.

[†] Max Planck Institute for Polymer Research.

[‡] Ecole Polytechnique Fédérale de Lausanne (EPFL) Institut des Matériaux.

[1] Abbreviations: PPD, polyphenylene dendrimers; NCA, *N*-carboxyanhydride; MAP, multiple antigen peptides; PDI, perylenediimide; GPC, gel permeation chromatography; HBTU, *O*-benzotriazole-*N*,*N*,*N*′,*N*′-tertramethyluronium hexafluorophosphate; HOBt, *N*-hydroxybenzotriazole; DCM, dichloromethane; EDC, *N*-(3-dimethylaminopropyl)-*N*′-ethylcarbodiimide hydrochloride; DIPEA, diisopropylethylamine; NMWLs, nominal molecular weight limits; PTFE, polytetrafluorethylene; M_w, weight-average molecular weight; M_n, number- average molecular weight; TFE, 2,2,2-trifluoroethanol; $[\Theta]_{222}$, mean residue elipticity at 222 nm; GnTd, n-generation dendrimer with tetrahedral core; GnPDI, n-generation dendrimer with PDI core.

10.1021/bc049839k CCC: $30.25 © 2005 American Chemical Society
Published on Web 03/01/2005

sibility. Therefore, the synthesis of nanosized peptide carriers comprising a well-defined structure and shape-persistence may provide improved MAPs. In this respect, the polyphenylene dendrimers are very promising templates due to their structural perfection and precise spatial definition of functional units in the center, in the dendritic scaffold, or at the periphery. Furthermore, they are chemically inert under the conditions of living organisms, which is another important prerequisite for biologically oriented applications.

In addition, the polyphenylene dendrimers can be synthesized not only as all-carbon structures but also using a strongly fluorescent perylenediimide core (PDI). Recently, we have described several synthetic approaches toward water-soluble and fluorescent PDI chromophores (*9*). The chromophore adds a further important property, namely, the possibility of facile optical detection of the dendritic conjugate, and such molecules may find diagnostic application. Thus, the aim of the present work is the development of reliable and expandable synthetic routes affording peptide-functionalized polyphenylene dendrimers with prospective application for attachment of antigen peptides onto a shape-persistent, polyphenylene scaffold. A further development is the synthesis of polyphenylene dendrimers bearing two different polypeptides. While we have recently described routes toward the synthesis of novel polyphenylene dendrimers with lysine and glutamic acid moieties anchored on the surface (*10*), we herein extend this idea by employing different synthetic approaches for the preparation of peptide−PPD conjugates. Polyphenylene dendrimers were functionalized with polylysine following three parallel routes. First, oligolysines were grafted directly from the surface of polyphenylene dendrimers employing α-amino acid *N*-carboxyanhydride (NCA) polymerization. Second, protected pentalysine moieties were coupled to PPDs via carbodiimide activation. Third, unprotected hexapeptides, composed of five lysine residues and a *C*-terminal cysteine, were specifically attached to the polyphenylene scaffold. This was achieved employing a Michael addition of the thiol containing peptides to maleimide functions on the dendrimer periphery. An important prerequisite for the synthesis of polyphenylene dendrimers decorated with two different peptide units is the creation of a core comprising two types of anchor groups, allowing the independent coupling of different peptide sequences.

2. EXPERIMENTAL SECTION

General Information. Unless stated otherwise, all solvents and reagents are commercially available and were used as received. ^{1}H NMR spectra were recorded on Bruker AMX 250, Bruker AMX 300, Bruker Advance DRX 500 or 700 spectrometers. Spectra were referenced to the residual proton signal of the deuterated solvent. Molecular weights were determined with matrix-assisted laser desorption/ionization time-of-flight (MALDI-TOF) or field desorption (FD) mass spectrometry; MALDI-TOF mass spectra were recorded on a Bruker MALDI-TOF mass spectrometer, and FD mass spectra were recorded on VG Instruments ZAB 2 Se-FPD. Peptide syntheses were carried out on an Applied Biosystems peptide synthesizer model 433A. Ultraviolet-visible (UV−vis) spectra and fluorescence spectra were recorded using a Perkin-Elmer Lambda 9 and SPEX Fluorolog 2 spectrophotometer, respectively. Circular dichroism (CD) spectra were measured on a Jasco J-715 spectropolarimeter. Gel permeation chromatography (GPC) was performed at 60 °C with a setup consisting of a Waters 510 pump and a series of three styrene-divinylbenzene columns (300 × 8 mm) with pore sizes of 500, 10^5, and 10^6 Å (Polymer Standard Services, Mainz, Germany). The elemental analyses were carried out by the Microanalytical Laboratory of the University of Mainz (Germany).

The amino acids were free acids, and coupling was facilitated by the use of *O*-benzotriazole-*N*,*N*,*N*′,*N*′-tertramethyluronium hexafluorophosphate (HBTU) and *N*-hydroxybenzotriazole (HOBt). Purity was checked using analytical reverse-phase high performance liquid chromatography (RP-HPLC, AKTA-Purifier, Amersham-Pharmacia Biotech). The column used was a reverse-phase C8 column (Sephasil peptide C8, volume 4.155 mL, 5 μm particle size). The synthesis of first- and second-generation dendrimers with maleimide functionalities **13a**−**d** and conjugates **38a**−**d** have been described previously (*10*). Compounds **1** (*11*), **2** (*12*), **3** (*13*), **4** (*14*), and **16** (*15*) were synthesized according published procedures.

Procedures. Compound 7a. 3-(4-Aminophenyl)-2,4,5-triphenylcyclopenta-2,4-dienone (**6a**) (1.4 g, 3.55 mmol), *N*-BOC-γ-aminobutyric acid (2.4 g, 17.71 mmol), *N*-(3-dimethylaminopropyl)-*N*′-ethylcarbodiimide hydrochloride (EDC) (2.4 g, 17.71 mmol), and DMAP (1.3 g, 10.6 mmol) were dissolved in 50 mL of DMF and stirred for 48 h under an argon atmosphere. Thereafter, DCM (50 mL) was added, and the reaction mixture was washed twice with water. The organic phase was isolated, dried over magnesium sulfate, and filtrated, and the solvent was evaporated. The dried residue was purified by column chromatography with DCM/acetone (10:1) eluent to give **7a** as brown powder. Yield: 2.07 g (82.1%). FD (M^+): m/z = 585.5; ^{1}H NMR (250 MHz, CD_2Cl_2) δ_H 7.43 (d, 2H, J = 8.48 Hz), 7.32−7.18 (m, 13H, arom.), 6.98 (d, 2H, J = 7.85 Hz), 6.87 (d, 2H, J = 7.89 Hz), 3.21 (q, 2H, J = 6.28 Hz), 2.23 (t, 2H, J = 6.28 Hz), 1.81 (t, 2H, J = 6.28 Hz), 1.44 (s, 9H); ^{13}C NMR (75 MHz, DMSO-d_6) δ_C 199.6, 171.1, 171.0, 155.5, 154.5, 139.6, 139.5, 132.7, 130.7, 130.5, 129.7, 129.6, 128.8, 128.5, 128.0, 127.9, 127.5, 127.4, 126.8, 124.9, 124.1, 118.1, 117.9, 77.4, 33.7, 28.2, 25.3, 11.0; mp 106 °C.

Compound 7b. 3,4-Bis-(4-aminophenyl)-2,5-diphenylcyclopenta-2,4-dienone (**6b**) (1.1 g, 2.69 mmol), *N*-BOC-γ-aminobutyric acid (5.46 g, 26.9 mmol), EDC (5.16 g, 26.9 mmol), and DMAP (1.97 g, 16.1 mmol) were dissolved in 50 mL of DMF and stirred for 48 h under an argon atmosphere. DCM (50 mL) was added, the reaction mixture was washed twice with water, and the organic phase isolated, dried over magnesium sulfate, and filtrated, and the solvent was evaporated. The dried residue was purified by column chromatography with DCM/acetone (2:1) as eluent to give **7b** as brown powder. Yield: 1.54 g (73%). FD (M^+): m/z = 782.6; ^{1}H NMR (250 MHz, DMSO-d_6) δ_H 7.43 (d, 2H, J = 8.85 Hz), 7.30−7.13 (m, 10H, arom.), 6.83 (d, 2H, J = 8.53 Hz), 2.92 (q, 4H, J = 6.63 Hz), 2.26 (t, 4H, J = 7.27 Hz), 1.65 (p, 4H, J = 7.27 Hz), 1.35 (s, 18H); ^{13}C NMR (75 MHz, DMSO-d_6) δ_C 199.8, 171.2, 155.8, 154.5, 139.8, 139.7,139.0, 130.0, 129.9, 128.2, 127.6, 127.1, 124.5, 118.2, 77.6, 34.0, 28.5, 25.5, 11.2.

Compound 8a. This compound was prepared analogously to **7a** using **6a** (1.4 g, 3.55 mmol), *N*-*Z*-γ-aminobutyric acid (3.37 g, 14.2 mmol), EDC (2.72 g, 14.2 mmol), and DMAP (1.04 g, 8.5 mmol) in 50 mL of DMF. The crude product was purified by column chromatography with DCM/acetone (10:1) as eluent to give **8a** as brown powder. Yield: 1.8 g (82%). FD (M^+): m/z = 619.4; ^{1}H NMR (250 MHz, DMSO-d_6) δ_H 7.44−7.12 (m, 20H, arom.), 6.96 (d, 2H, J = 7.9 Hz), 6.83 (d, 2H, J = 8.85 Hz), 4.99 (s, 2H), 3.01 (q, 2H, J = 6.64 Hz), 2.89 (t, 2H, J = 7.26 Hz), 1.75 (p, 2H, J = 6.63 Hz); ^{13}C NMR (75

MHz, DMSO-d_6) δ_C 199.7, 171.1, 156.1, 154.6, 154.5, 139.6, 139.5, 137.2, 135.8, 132.8, 130.7, 130.5, 129.8, 129.7, 128.9, 128.6, 128.4, 128.3, 128.0, 127.9, 127.7, 127.5, 127.4, 126.8, 125.0, 124.1, 118.0, 106.1, 65.1, 46.1, 33.6, 25.3; mp 80 °C.

Compound 8b. This compound was prepared analogously to **7b** using **6b** (1.1 g, 2.69 mmol), *N*-*Z*-γ-aminobutyric acid (6.39 g, 26.9 mmol), EDC (7.92 g, 26.9 mmol), and DMAP (1.97 g, 16.1 mmol) in 50 mL of DMF. The crude product was purified by column chromatography with DCM/acetone (2:1) as eluent to give **8b** as brown powder. Yield: 1.75 g (76.2%). FD (M^+): m/z = 853; ^{1}H NMR (250 MHz, DMSO-d_6) δ_H 7.44 (d, 4H, J = 8.53 Hz), 7.33−7.13 (m, 24H, arom.), 6.84 (d, 4H, J = 8.53 Hz), 4.99 (s, 4H), 3.02 (q, 4H, J = 6.32 Hz), 2.29 (t, 4H, J = 7.27 Hz), 1.65 (p, 4H, J = 5.95 Hz); ^{13}C NMR (75 MHz, DMSO-d_6) δ_C 199.8, 171.3, 171.2, 156.3, 154.5, 139.8, 139.7, 137.4, 131.0, 130.0, 128.5, 128.5, 127.9, 127.6, 127.1, 124.6, 118.3, 65.4, 46.4, 33.8, 25.3; mp 248 °C.

Compound 9. This compound was prepared analogously to **7a** using **6a** (0.7 g, 1.8 mmol), hexanedioic acid monomethyl ester (1.44 g, 9 mmol), EDC (1.72 g, 9 mmol), and DMAP (0.66 mg, 5.4 mmol) in 50 mL of DMF. The crude product was purified by column chromatography with DCM/acetone (50:1) as eluent to give **9** as brown powder. Yield: 0.830 g (85%). FD (M^+): m/z = 542; ^{1}H NMR (250 MHz, CD_2Cl_2) δ_H 7.51−7.16 (m, 15H, arom.), 6.96 (d, 2H, J = 6.91 Hz), 6.85 (d, 2H, J = 8.5 Hz), 3.63 (s, 3H), 2.49−2.25 (m, 4H), 1.80−1.58 (m, 4H); ^{13}C NMR (75 MHz, CD_2Cl_2) δ_C 199.9, 179.0, 130.8, 130.7, 129.8, 129.0, 128.6, 128.5, 128.4, 127.9, 119.1, 51.9, 34.1, 24.8, 24.7.

Compound 14a. Compounds **3** (0.1 g, 0.085 mmol) and **7a** (0.597 g, 1.02 mmol) were dissolved in 31.5 mL of a *o*-xylene/toluene/DMSO mixture (5/5/2). The resulting solution was heated at 150 °C for 36 h under an argon atmosphere. The reaction mixture was precipitated in petroleum ether, and the crude product was purified by chromatography (silica gel, CH_2Cl_2/acetone 2:1) to give **14a.** Yield: 202 mg (70%). MALDI-TOF MS ((M + Na)$^+$): m/z = 3426; ^{1}H NMR (250 MHz, d^6-DMSO) δ_H 9.65, 9.59 (2H, NH), 7.91 (s, 4H, arom.), 7.42 (s, 4H, arom.), 7.33−6.66 (m, 98H, arom.), 2.89 (q, 8H, ^3J = 6.63 Hz), 2.69 (sept, 4H, ^3J = 6.32 Hz), 2.17 (q, 8H, ^3J = 7.27 Hz), 1.59 (p, 8H, ^3J = 7.27 Hz), 1.34 (s, 36H), 1.02 (d, 24H, ^3J = 5.68 Hz), ^{13}C NMR (125 MHz, DMSO-d_6) δ_C 170.4, 170.3, 170.3, 162.4, 155.3, 154.9, 153.2, 145.5, 141.3, 141.2, 141.1, 141.0, 140.4, 140.2, 139.8, 139.5, 139.4, 139.3, 139.2, 139.1, 139.0, 138.9, 138.8, 138.7, 137.5, 136.7, 136.6, 136.4, 136.3, 134.3, 134.0, 132.3, 131.0, 131.0, 131.0, 130.9, 130.8, 130.5, 130.2, 130.1, 129.3, 129.0, 127.3, 127.3, 126.6, 126.5, 126.3, 126.0, 125.4, 125.3, 125.2, 123.4, 122.5, 119.9, 119.7, 119.3, 118.5, 117.3, 117.0, 77.3, 33.6, 28.1, 25.2, 23.3.

Compound 14b. Compounds **3** (0.1 g, 0.085 mmol) and **7b** (1.07 g, 2.04 mmol) were dissolved in 42 mL of a *o*-xylene/toluene/DMSO mixture (5/5/2). The resulting solution was heated for 36 h at 150 °C under an argon atmosphere. The reaction mixture was precipitated in petroleum ether, and the crude product was purified by chromatography (silica gel, CH_2Cl_2/acetone 1:1) to give **14b.** Yield: 315 mg (88%). MALDI-TOF MS ((M + Na)$^+$): m/z = 4225; ^{1}H NMR (250 MHz, DMSO-d_6) δ_H 9.66, 9.61 (2s, NH), 7.90 (s, 4H, arom.), 7.43−6.68 (m, 94H, arom.), 2.88 (q, 16H, ^3J = 6.32 Hz), 2.69 (sept, 4H, ^3J = 6.31 Hz), 2.17 (q, 16H, ^3J = 7.27 Hz), 1.60 (p, 16H, ^3J = 7.27 Hz), 1.34 (s, 72H), 1.02 (d, 24H, ^3J = 5.68 Hz), ^{13}C NMR (125 MHz, DMSO-d_6) δ_C 170.4, 170.3, 170.2, 162.4, 155.3, 154.9, 153.2, 145.5, 141.2, 140.4, 139.4, 139.1, 139.0, 137.6, 136.7, 136.6, 136.4, 136.3, 134.4, 134.1, 132.3, 131.0, 131.0, 130.9, 130.5, 130.1, 129.3, 129.0, 127.3, 126.6, 126.0, 125.9, 125.4, 123.4, 122.5, 119.9, 119.7, 119.3, 118.5, 117.4, 117.1, 117.0, 77.3, 33.6, 28.2, 25.2, 23.4.

Compound 15a. Compound **14a** (0.2 g, 0.06 mmol) was dissolved in 4 mL of 50% trifluoroacetic acid in dichloromethane and stirred at room temperature for 2 h. The reaction mixture was added to saturated $NaHCO_3$ solution, and the precipitated product **15a** was filtrated and dried under reduced pressure. Yield: 172 mg (98%). MALDI-TOF MS ((M + Na)$^+$): m/z = 3023; ^{1}H NMR (500 MHz, DMSO-d_6) δ_H 7.93 (s, 4H, arom.), 7.45−7.42 (m, 6H, arom.), 7.31 (d, 4H, ^3J = 7.62 Hz, arom.), 7.17−6.68 (m, 92H, arom.), 2.70 (sept, 4H, ^3J = 6.41 Hz), 2.23 (q, 8H, ^3J = 7.63 Hz), 1.60 (p, 8H, ^3J = 6.72 Hz), 1.24 (s, NH), 1.04 (d, 24H, ^3J = 6.41 Hz); ^{13}C NMR (75 MHz, DMSO-d_6) δ_C 177.2, 171.0, 162.7, 155.0, 153.3, 145.5, 141.8, 141.2, 141.1, 140.5, 140.4, 139.9, 139.7, 139.6, 139.5, 139.4, 139.1, 138.9, 138.8, 137.6, 136.9, 134.3, 134.0, 133.5, 132.5, 131.2, 131.0, 130.6, 129.5, 127.7, 127.0, 126.7, 126.4, 125.8, 123.8, 122.6, 120.1, 119.5, 119.4, 118.9, 117.3, 116.9, 53.0, 44.3, 33.9, 28.4, 23.7.

Compound 15b. Compound **14b** (0.2 g, 0.05 mmol) was dissolved in 4 mL of 50% trifluoroacetic acid in dichloromethane and stirred at room temperature for 2 h. The reaction mixture was added to a saturated $NaHCO_3$ solution, and the precipitated product **15b** was filtrated and dried under reduced pressure. Yield: 158 mg (98%). MALDI-TOF MS ((M + Na)$^+$): m/z = 3423; ^{1}H NMR (250 MHz, DMSO-d_6) δ_H 7.92 (s, 4H, arom.), 7.44 (t, ^3J = 7.62 Hz, 2H, arom.), 7.39 (s, 4H, arom.), 7.31 (d, ^3J = 7.62 Hz, 4H, arom.), 7.19−6.69 (m, 88H, arom.), 2.70 (sept, ^3J = 6.72 Hz, 16H), 2.23 (q, ^3J = 7.63 Hz, 8H), 1.60 (p, ^3J = 6.72 Hz, 8H), 1.24 (s, NH), 1.04 (d, 24H, ^3J = 6.41 Hz); ^{13}C NMR (75 MHz, DMSO-d_6) δ_C 170.8, 166.8, 162.7, 155.0, 153.3, 145.5, 141.4, 141.2, 140.5, 140.0, 139.6, 139.1, 137.6, 136.9, 136.8, 136.6, 134.5, 134.2, 132.4, 131.3, 130.8, 130.6, 129.5, 129.3, 127.7, 126.9, 126.4, 125.7, 125.6, 123.8, 122.6, 120.1, 119.9, 119.3, 118.9, 117.3, 117.0, 114.0, 66.9, 33.6, 31.3, 28.4, 23.8.

Compound 17a. Compounds **16** (0.1 g, 0.036 mmol) and **8a** (0.797 g, 1.29 mmol) were dissolved in 9 mL of a tetraethyleneglycol/diphenyl ether mixture (1:1). The resulting solution was heated for 24 h at 170 °C under an argon atmosphere. The reaction mixture was precipitated in methanol, and the crude product was purified by chromatography (silica gel, CH_2Cl_2/acetone 1:4) to give **17a**. Yield: 197 mg (73%). MALDI-TOF MS ((M + Na)$^+$): m/z = 7640; ^{1}H NMR (300 MHz, DMSO-d_6) δ_H 9.64, 9.58 (2s, NH), 7.92 (s, 4H, arom.), 7.37−6.69 (m, 298H, arom.), 4.98 (s, 16H), 2.97 (br, 16H), 2.72 (sept, 4H, ^3J = 6.31 Hz), 2.20 (br, 16H), 1.63 (br, 16H), 1.02 (br, 24H); ^{13}C NMR (75 MHz, DMSO-d_6) δ_C 170.5, 156.3, 156.1, 141.4, 141.2, 141.0, 140.4, 139.8, 139.3, 139.0, 138.4, 137.6, 137.1, 136.7, 136.6, 134.6, 134.2, 131.5, 131.1, 131.0, 129.5, 128.3, 127.8, 126.8, 126.4, 117.3, 116.8, 60.2, 60.1, 33.7, 28.8, 25.3, 23.9.

Compound 17b. Compounds **16** (0.12 g, 0.043 mmol) and **8b** (0.879 g, 1.03 mmol) were dissolved in 18 mL of a tetraethyleneglycol/diphenyl ether mixture (1:1). The resulting solution was heated at 170 °C for 24 h under an argon atmosphere. The reaction mixture was precipitated in methanol and the crude product purified by chromatography (silica gel, CH_2Cl_2/acetone 1:4) to give **17b**. Yield: 286 mg (71%). MALDI-TOF MS ((M + Na)$^+$): m/z = 9434; ^{1}H NMR (300 MHz, DMSO-d_6) δ_H 9.65, 9.59 (2s, NH), 7.90 (s, 4H, arom.), 7.31−6.43 (m, 298H, arom.), 4.98 (s, 32H), 2.98 (br, 32H), 2.71 (sept,

4H, ^3J = 6.31 Hz), 2.20 (br, 32H), 1.64 (br, 32H), 1.02 (br, 24H); ^{13}C NMR (75 MHz, DMSO-d_6) δ_C 170.6, 156.1, 156.0, 141.5, 141.3, 140.9, 140.3, 139.7, 139.4, 139.0, 138.4, 137.5, 137.2, 136.8, 136.5, 134.6, 134.2, 131.6, 131.2, 130.9, 129.5, 128.3, 127.7, 126.7, 126.3, 117.3, 116.9, 60.2, 60.1, 33.6, 28.9, 25.2, 23.8.

Compound 18a. Compound **17a** (0.26 g, 0.035 mmol) was dissolved in 6 mL of trifluoroacetic acid and 210 μL of 5.7 M HBr in acetic acid was added. The reaction mixture was stirred at room temperature for 2 h and added to a saturated $NaHCO_3$ solution. The precipitate **18a** was filtrated and dried under reduced pressure. Yield: 215 mg (97%). ^{1}H NMR (300 MHz, DMSO-d_6) δ_H 7.95 (s, 4H, arom.), 7.03−7.80 (m, 246H, arom.), 2.04 (br, 16H), 1.82 (br, 16H), 1.43 (br, NH), 1.01 (br, 24H); ^{13}C NMR (75 MHz, DMSO-d_6) δ_C 170.0, 162.7, 158.3, 157.8, 155.0, 153. 3, 145.5, 141.8, 141.3, 140.9, 140.3, 140.1, 139.9, 139.6, 139.3, 138.9, 138.6, 138.4, 137.9, 137.6, 137.1, 136.7, 136.2, 134.6, 134.3, 132.5, 131.9, 131.3, 130.9, 130.7, 130.6, 129.9, 129.5, 129.2, 129.0, 128.7, 128.3, 128.0, 127.7, 126.8, 126.6, 126.4, 125.5, 123.8, 122.6, 120.1, 119.3, 118.9, 117.3, 116.9, 115.3, 49.9, 32.8, 28.3, 23.7, 22.

Compound 18b. Compound **17b** (0.23 g, 0.025 mmol) was dissolved in 6 mL of trifluoroacetic acid and 280 μL of 5.7 M HBr in acetic acid were added. The reaction mixture was stirred at room temperature for 2 h and added to a saturated $NaHCO_3$ solution. The precipitate **18b** was filtrated and dried under reduced pressure. Yield: 170 mg (96%). ^{1}H NMR (300 MHz, DMSO-d_6) δ_H 7.90 (s, 4H, arom.), 7.69−6.44 (m, 238H, arom.), 2.29 (br, 32H), 1.76 (br, 32H), 1.40 (br, NH), 1.18 (br, 24H); ^{13}C NMR (75 MHz, DMSO-d_6) δ_C 170.7, 170.1, 162.7, 161.0, 158.8, 158.4, 157.9, 157.5, 153.3, 145.5, 141.3, 140.9, 140.3, 139.7, 139.4, 139.0, 138.4, 138.0, 137.6, 136.6, 136.1, 134.8, 134.4, 134.2, 132.5, 131.3, 130.6, 129.5, 128.6, 12.5, 128.2, 128.1, 128.0, 127.9, 127.7, 126.8, 126.4, 124.2, 123.2, 122.6, 120.2, 119.7, 119.3, 118.9, 118.7, 117.4, 117.0, 115.3, 47.6, 33.9, 32.9, 28.9, 23.8, 22.9.

Compound 19. Compounds **2** (0.100 g, 0.137 mmol) and **5b** (0.408 g, 0.55 mmol) in *o*-xylene (15 mL) were heated at 160 °C for 24 h under an argon atmosphere. The reaction mixture was concentrated to one-fourth of the initial volume, and the product was purified by precipitation from a mixture of methanol and water (7:1) to give a yellow powder. Yield: 0.250 g (84%). MALDI-TOF MS (M^+): m/z = 2159; ^{1}H NMR (250 MHz, CD_2Cl_2) δ_H 7.72−6.70 (m, 78H, arom.), 6.61−6.49 (m, 8H, arom.), 6.34−6.21 (m, 8H, arom.), 1.18−1.05 (m, 42H); ^{13}C NMR (75 MHz, CD_2Cl_2) δ_C 166.3, 153.2, 132.2, 131.7, 131.4, 130.8, 130.4, 128.5, 128.1, 126.3, 123.3, 108.1, 90.3, 64.1, 19.0, 11.6.

Compound 20. To a solution of **19** (0.220 g, 0.102 mmol) in THF (20 mL) was added (*tert*-Bu)$_4$NF·3H$_2$O (0.130 g, 0.41 mmol). The reaction mixture was stirred for 5 h at room temperature. Water (20 mL) was added, and the product was extracted with DCM (3 × 15 mL). The organic phase was isolated, dried over magnesium sulfate, filtrated, and concentrated to 5 mL. The product was purified by precipitation from a mixture of methanol and water (7:1) to give a yellow powder. Yield: 0.160 g (85%). MALDI-TOF MS (M^+): m/z = 1848; ^{1}H NMR (250 MHz, CD_2Cl_2) δ_H 7.74−6.70 (m, 78H, arom.), 6.62−6.50 (m, 8H, arom.), 6.35−6.22 (m, 8H, arom.), 3.12 (s, 2H); $_{13}$C NMR (75 MHz, CD_2Cl_2) δ_C 166.3, 153.2, 132.2, 131.8, 131.4, 130.8, 130.4, 128.5, 128.1, 126.3, 123.3, 85.7, 79.4, 64.1.

Compound 21. Compounds **20** (0.100 g, 0.054 mmol) and **9** (0.105 g, 0.204 mmol) were dissolved in *o*-xylene (15 mL) and heated at 160 °C for 24 h under an argon atmosphere. The reaction mixture was concentrated to one-fourth of the initial volume, and the product was purified by precipitation from methanol to give a yellow powder. Yield: 0.130 g (84%). MALDI-TOF MS (M^+): m/z = 2875; ^{1}H NMR (250 MHz, CD_2Cl_2) δ_H 7.74−6.21 (m, 134H, arom.), 3.62 (s, 6H), 2.32−2.18 (m, 8H), 1.69−1.55 (m, 8H); ^{13}C NMR (75 MHz, CD_2Cl_2) δ_C 171.0, 168.1, 149.4, 149.0, 144.9, 144.6, 142.9, 142.5, 141.5, 141.3, 141.1, 140.7, 140.4, 140.2, 140.0, 139.7, 139.3, 136.5, 136.3, 135.9, 132.9, 132.3, 132.2, 130.8, 130.4, 130.1, 129.7, 129.2, 128.6, 128.5, 128.4, 128.2, 127.3, 126.7, 126.0, 120.2, 120.0, 118.3, 118.0, 114.2, 113.9, 63.9, 51.9, 37.6, 34.1, 25.3, 24.9.

Compound 22. To a solution of **20** (0.100 g, 0.035 mmol) in tetrahydrofuran (2 mL) was added an aqueous solution of LiOH (0.300 mL, 2.3 M), and the mixture was heated at 80 °C for 12 h under an argon atmosphere. The reaction mixture was added to distilled water, and the product was extracted with DCM (3 × 20 mL). The organic phases were collected, washed twice with water, and dried with $MgSO_4$, and the solvent was evaporated to give **22** as yellow powder. Yield: 0.093 g (94%). MALDI-TOF MS: m/z = 2847 g/mol (M^+), 2869 g/mol ((M + Na)$^+$); ^{1}H NMR (250 MHz, CD_2Cl_2) δ_H 7.75−6.15 (m, 134H, arom.), 2.16−1.55 (m, 16H); ^{13}C NMR (75 MHz, CD_2Cl_2) δ_C 169.0, 167.9, 149.2, 148.8, 144.8, 144.4, 142.7, 142.3, 141.8, 141.1, 140.9, 140.5, 140.3, 140.0, 139.9, 139.5, 138.5, 136.3, 135.7, 135.4, 132.7, 132.1, 131.6, 131.3, 130.9, 130.5, 130.3, 129.9, 129.7, 129.5, 129.1, 128.9, 128.6, 128.4, 128.3, 128.2,127.9, 127.5, 127.2, 126.5, 125.8, 120.6, 120.0, 119.8, 115.5, 114.2, 113.7, 63.8, 37.3, 30.1, 25.2.

Compound 23. Compound **22** (0.080 g, 0.032 mmol) was dissolved in THF (0.5 mL), and 2 N HCl (1 mL) added. After 10 min, the mixture was cooled with ice and concentrated HCl (0.5 mL) added. The mixture was stirred for 20 min, and the solvents were evaporated under high vacuum. The final product was isolated as a bright brown powder, which was used in the next step without additional purification. Yield: 0.055 g (89%).

Compound 24. Compound **23** (0.065 g, 0.034 mmol) and 4-(2,5-dioxopyrrol-1-yl)butanoyl chloride (0.085 g, 0.41 mmol) were dissolved in a mixture of DMF (5 mL) and triethylamine (0.5 mL). The solution was stirred for 6 h at RT under an argon atmosphere. The product was purified by precipitation in methanol to give a dark yellow powder. Yield: 0.080 g (92%). MALDI-TOF MS ((M + Na)$^+$) m/z = 2873 g/mol; ^{1}H NMR (250 MHz, CD_2Cl_2) δ_H 7.56−6.53 (m, 102H, arom.), 3.59−3.48 (m, 8), 2.45−2.12 (m, 16H), 1.95−1.65 (m, 16H); ^{13}C NMR (175 MHz, DMSO-d_6) δ_C 174.1, 170.9, 169.9, 162.2, 143.7, 141.2, 140.2, 140.0, 139.5, 139.0, 136.7, 136.4, 134.3, 132.9, 131.2, 130.0, 129.5, 128.5, 128.4, 127.6, 126.8, 126.6, 126.2, 125.4, 117.3, 116.9, 36.8, 35.7, 33.4, 30.7, 24.4, 24.1, 23.6.

Compounds 36a−d. The PDI dendrimers **15a**,**b** and **18a**,**b** together with 5 equiv of peptide and 20 equiv of HOBT and HBTU were dissolved in a minimum quantity DMF and treated with 50 equiv of diisopropylethylamine (DIPEA). The reaction was stirred for 5 days at room temperature, and the product afterward was precipitated from diethyl ether. The resulting powder contained dendrimer−peptide−conjugate and peptide. Purification by dialysis proved impossible, and thus the mixture was dissolved in TFA and deprotected with HBr in acetic acid by the method described above. The crude product was precipitated from diethyl ether and subsequent ultrafil-

Table 1. Synthesis and Properties of Peptide-Decorated PDI-Dendrimers[a]

sample	generation	$Q_{Initiator}$ [mg]	Q_{NCA} [mg]	NMWL [kDa]	yield [mg]	yield [%]	theoretical m	UV/ VIS $m_{Lys,\ UV}$	GPC^{UV}_{DMF} $m_{Lys,GPC}$	GPC^{UV}_{DMF} M_w/M_n
30a	$n = 1$ $x = 4$	100	408	10	210	69.5	10	9	14	1.11
30b		22.5	459	30	195	72.5	50	50	54	1.16
30c		14.3	587	50	286	84.3	100	85	84	1.15
31a	$n = 1$ $x = 8$	66.4	479	10	265	88.3	10	9	12	1.09
31b		15.8	567	50	273	83.8	50	68	60	1.08
31c		7.64	552	50	238	76.1	100	76	74	1.10
32a	$n = 2$ $x = 8$	110.5	420	10	195	64.1	10	6	9	1.17
32b		27.7	526	30	175	55.7	50	28	22	1.42
32c		15.1	572	50	120	34.8	100	41	37	1.27
33a	$n = 2$ $x = 16$	77.5	524	30	298	87.4	10	14	16	1.26
33b		17.8	603	50	253	73.0	50	41	58	1.50
33c		8.6	578	50	245	75.4	100	89	68	1.42

[a] Notation: x, number of polypeptide chains per molecule; m, number of lysine residues per chain. The polydispersity (M_w/M_n) of the peptide−dendrimer conjugates is calculated from the gel permeation chromatography data, obtained in DMF against polystyrene standards.

tration in water [nominal molecular weight limits (NMWLs) 10 000] and freeze-drying yielded the products **36a**−**d**.

36a. Yield: 159 mg (61%). ^{1}H NMR (700 MHz, DMSO-d_6) δ_H 7.91−6.70 (m, 130H, arom. + NH), 4.26−4.23(br, 20H), 3.96−3.10 (m, NH), 2.69 (br, 40H), 2.22 (br, 8H), 1.67−1.23 (m, 120H), 1.05 (br, 24H), GPC (UV, $\lambda = 280$ nm; PS): $M_n = 15700$ g/mol, $M_w/M_n = 1.1$.

36b. Yield: 169 mg (48%). ^{1}H NMR (700 MHz, DMSO-d_6) δ_H 7.90−6.71 (m, 150H, arom. + NH), 4.26−4.19 (br, 40H, H_c), 3.51−3.0 (m, NH), 2.71 (br, 80H, H_e), 2.24 (br, 16H, Hb), 1.67−1.24 (m, 240H, H_d), 1.05 (br, 24H, H_a); GPC (UV, $\lambda = 280$ nm; PS): $M_n = 20100$ g/mol, $M_w/M_n = 1.1$.

36c. Yield: 129 mg (52%). ^{1}H NMR (700 MHz, DMSO-d_6) δ_H 7.95−6.49 (m, 300H, arom. + NH), 4.26−4.20 (br, 40H, H_c), 3−64−3.08 (m, NH), 2.75 (br, 80H, H_e), 2.24 (br, 16H, Hb), 1.68−1.24 (m, 240H, H_d), 1.04 (br, 24H, H_a); GPC (UV, $\lambda = 280$ nm; PS): $M_n = 28600$ g/mol, $M_w/M_n = 1.16$.

36d. Yield: 131 mg (39%). ^{1}H NMR (700 MHz, DMSO-d_6) δ_H 7.95−6.45 (m, 340H, arom. + NH), 4.30−4.15 (br, 80H, H_c), 3.35 (br, NH), 2.74 (br, 160H, H_e), 2.26 (br, 32H, Hb), 1.68−1.04 (m, 504H, H_{d+a}); GPC (UV, $\lambda = 280$ nm; PS): $M_n = 35800$ g/mol, $M_w/M_n = 1.12$.

Polymerization. An argon-filled and thoroughly dried Schlenk-tube fitted with a drying tube was charged with a filtered (0.45 μm, PTFE) solution of the initiator (**15ab** and **18ab**) in dry dimethylformamide. A solution NCA in dry dimethylformamide was added via a syringe driven filter, so that the final NCA concentration in the mixture reaches approximately $c = 0.15-0.2$ g/L. The mixture was stirred under the exclusion of light for 5 days at room temperature, and the product was precipitated by dropwise addition of a 15-fold (v/v) excess of water. The precipitate was filtered through a glass frit, washed extensively with Et_2O to remove unreacted monomer, and dried under vacuum.

Deprotection of the Polymers. The polymer was dissolved in TFA, and a 4-fold excess (per lysine unit) of HBr in an AcOH solution (5.7 mol/L) was added. After 1 h reaction time, the product was precipitated by the addition of Et_2O. The precipitate was then filtered through a glass frit, purified via ultrafiltration against Milli-Q-water until a constant conductivity was reached, and finally lyophilized. The membranes used had NMWLs of 10 000 and 30 000 (regenerated cellulose), and 50 000 (polyethersulfone). All yields and molecular masses are listed in Table 1.

Scheme 1

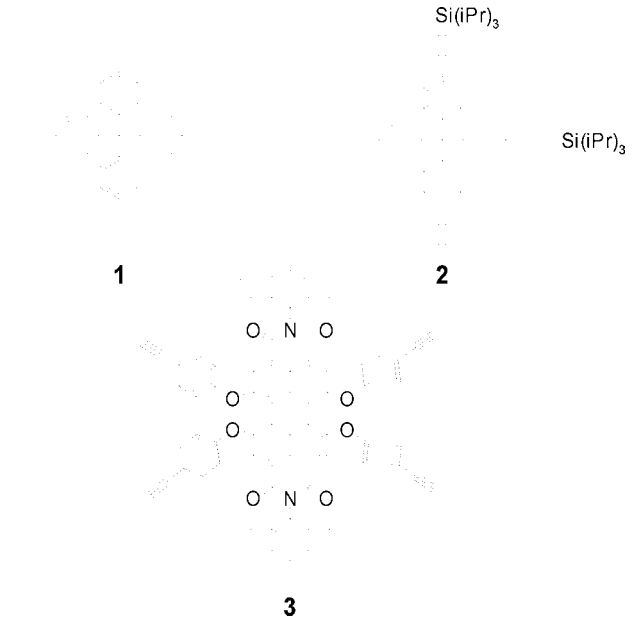

3. RESULTS AND DISCUSSION

The synthesis of polyphenylene dendrimers commences with a multi-ethynyl-substituted core molecule, namely, tetrakis-(4-ethynylphen-1-yl)-methane (**1**), its desymmetrized derivative **2**, as well as the PDI core **3** (Scheme 1).

We emphasize that the geometry of the core determines the overall shape of the resulting cascade molecules (*16*). The growth of each dendritic layer is based upon an iterative process including a Diels−Alder reaction and subsequent deprotection of ethynyl functions (*5*). Scheme 2a introduces a functionalized cyclopentadienone **4** used as A_2B-type branching agent (*16*). This molecule can act both as diene and after removal of the silyl protective groups from the ethynyl groups, as dienophile. In the [4+2]-cycloaddition between the cyclopentadienone and a free ethynyl group of the core molecule or the preceding dendrimer generation, a pentaphenylbenzene unit is formed under the extrusion of carbon monoxide (*17*−*19*).

3.1. Synthesis of Functionalized Cyclopentadienones. By using prefunctionalized cyclopentadienones **5ab**, **7ab**, **8ab**, **9** in the Diels−Alder reaction, polyphenylene dendrimers with chemical functions are obtained. These functions are either protected amino (**5ab**, **7ab**, **8ab**) or carboxyl (**9**) groups that can be readily converted into versatile anchor groups. The synthesis of the func-

Scheme 2[a]

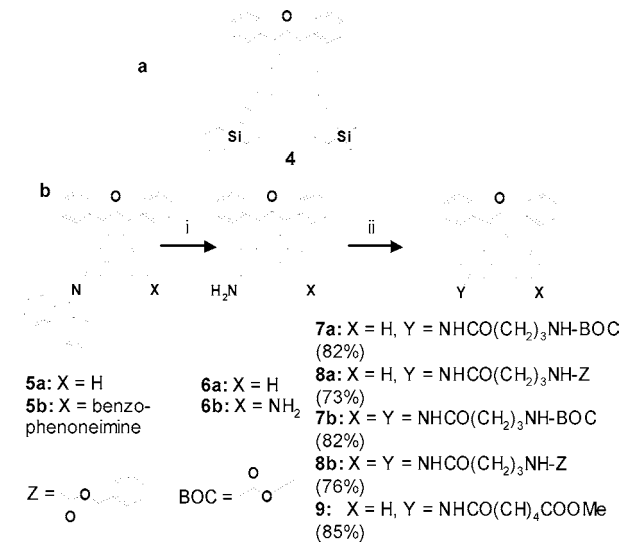

[a] (a) A_2B-branching unit 3,4-bis-(4-triisopropylsilylethynylphenyl)-2,5-diphenyl-cyclopenta-2,4-dien-1-one **4**; (b) synthesis of functionalized cyclopentadienones; i: HCl, RT, THF; ii: corresponding *N*-protected amino acid or hexanedioic acid monomethyl ester, EDC, DMAP, DMF, RT.

tionalized cyclopentadienones is depicted in Scheme 2b. The preparation of the imino- (**5a**,**b**) and amino- (**6a**,**b**) functionalized cyclopentadienones has been described previously (*10*).

γ-Aminobutyric acid-functionalized building blocks **7ab**, **8ab** were obtained by EDC-catalyzed coupling of **6a**,**b** and the corresponding *N*-protected amino acid derivatives in DMF at room temperature. The products were purified by flash chromatography, and the structures were confirmed by ^{1}H NMR spectroscopy and FD mass spectrometry. Monocarboxy-functionalized cyclopentadienone **9** was synthesized analogously via a carbodiimide induced reaction of **6a** with hexanedioic acid monomethyl ester.

3.2. Synthesis of Polyphenylene Dendrimers. For the sake of brevity, the terminology introduced in Figure 1 will be used for the central dendritic polyphenylene units.

Scheme 3 summarizes the synthesis of amino- and maleimide-functionalized dendrimers. We have previously described the preparation of maleimide-decorated polyphenylene dendrimers **13a**−**d** (*10*). The Diels−Alder reaction of the functionalized cyclopentadienones **5ab** with either the core **1** or the octaethynyl-functionalized dendrimer **10** yielded the benzophenoneimino dendrimers **11a**−**d**. Subsequently, the complete cleavage of the protective groups was achieved with HCl in THF at room temperature, and the resulting amino dendrimers **12a**−**d** were reacted without additional purification with 4-(2,5-dioxo-pyrrol-1-yl)-butanoyl chloride to afford polyphenylene dendrimers with different numbers of maleimide anchor groups **13a**−**d**.

The synthesis of first-generation BOC-protected amino-functionalized PDI-dendrimers **14ab** proceeded via the Diels−Alder cycloaddition of **7ab** with the perylenediimide core **3.** The subsequent removal of the BOC groups with trifluoroacetic acid in dichloromethane (*20*) afforded

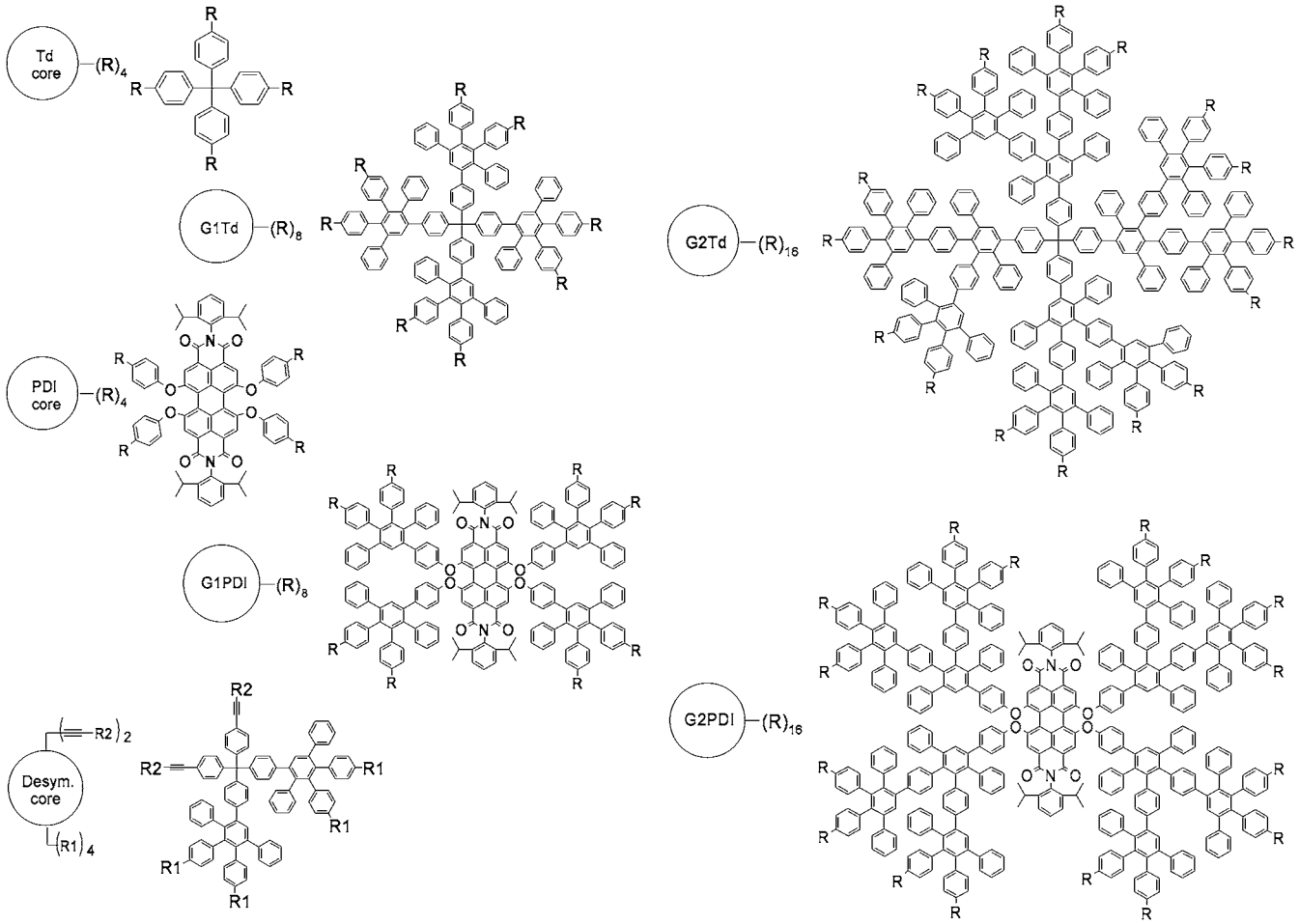

Figure 1. Symbols used to represent the polyphenylene scaffold of dendrimers in the schemes hereafter. The abbreviation in the circles shows the dendrimer generation and the central core unit.

Scheme 3. Synthesis of Functionalized Dendrimers[a]

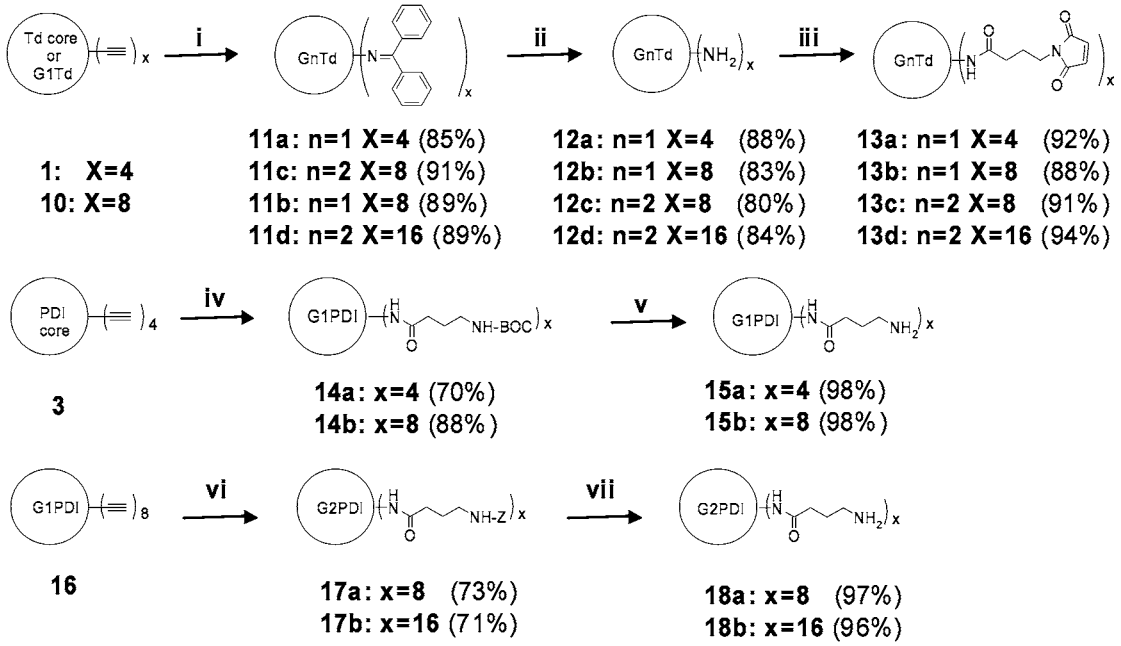

[a] (i) **5a/5b**, *O*-xylene, 150 °C; (ii) HCl, THF; (iii) 4-(2,5-dioxo-2,5-dihydropyrrol-1-yl)butanoyl chloride, DMF, triethylamine; (iv) **7a/7b**, *O*-xylene, toluene, DMSO, 150 °C; (v) TFA, DCM, RT; (vi) **8a/8b**, diphenyl ether, tetraethylene oxide, 170 °C; (vii) HBr, acetic acid. Notation: n, generation of the dendrimer.

the amino compounds **15ab**. Employing the reagents **8ab** in a Diels–Alder reaction with **16** yielded the PDI dendrimers of the second generation **17ab**, which were readily converted to **18ab** by treatment with HBr in glacial acetic acid (*21*). The amino groups of compounds **15ab** and **18ab** are more stable against oxidation and more accessible for the coupling of polypeptides than amino groups of the aniline derivatives **12a–d**.

The synthesis of polyphenylene dendrimers possessing two different chemical functions is depicted in Scheme 4. First, cyclopentadienone **5b** was reacted with the diethynyl core **2** to afford compound **19**. After deprotection of the ethynyl groups, the subsequent Diels–Alder cycloaddition of **9** produced compound **20**. Note that **20** has both (protected) amino and carboxyl anchor groups. The ester groups were converted to free carboxyl groups by LiOH in THF at 80 °C (*22*), while the deprotection of the amino groups was achieved by HCl in THF. Finally, the maleimide groups were introduced via reaction with 4-(2,5-dioxo-pyrrol-1-yl)-butanoyl chloride in DMF at room temperature to obtain the bifunctional compound **24**.

3.3. Coupling of Polylysines to Polyphenylene Dendrimers. Scheme 5 gives an overview of the three synthetic routes toward peptide-decorated PPDs. Here we demonstrate the synthetic versatility of polyphenylene dendrimers as 3D carriers for the preparation of spatially defined bioactive conjugates. Three different strategies for peptide coupling were employed. We emphasize that the developed strategies are versatile and may be used for coupling of various oligopeptide fragments, according to the desired application.

3.3.1. Grafting of Protected Polypeptide from the PPD. The grafting of the polylysine from the surface of the polyphenylene dendrimers **15ab** and **18ab** was achieved by ring opening polymerization (Scheme 5a) of α-amino acid *N*-carboxyanhydrides (NCA). The ϵ-benzyloxycarbonyl-L-lysine *N*-carboxyanhydride (Lys(Cbz)-NCA) **25** was prepared following a literature procedure (*23–25*). **15a**,**b** and **18a**,**b** can be regarded as macroinitiators to which the corresponding amount of Lys(Cbz)-

Scheme 4. Synthesis of PPD Decorated with Different Anchor Groups[a]

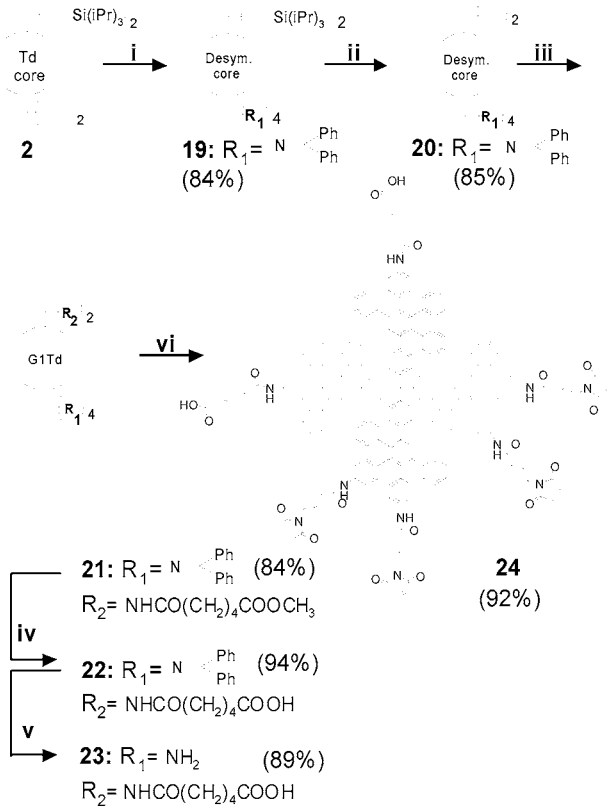

[a] (i) **5b**, *O*-xylene, 145 °C; (ii) $(t\text{-}Bu)_4NF{\cdot}3H_2O$, THF; (iii) **9**, *O*-xylene, 145 °C; (iv) LiOH, THF, 80 °C; (v) 2 N HCl, THF; (vi) 4-(2,5-dioxo-2,5-pyrrol-1-yl)-butanoyl chloride, DMF, triethylamine.

NCA was added, depending on the desired length of the peptide. The reaction proceeded in DMF at room temperature for 5 days.

The products **26a–c**, **27a–c**, **28a–c**, **29a–c** were precipitated in water. Unreacted monomer was removed

Scheme 5. Different Strategies for the Preparation of Peptide-dendrimer Conjugates[a]

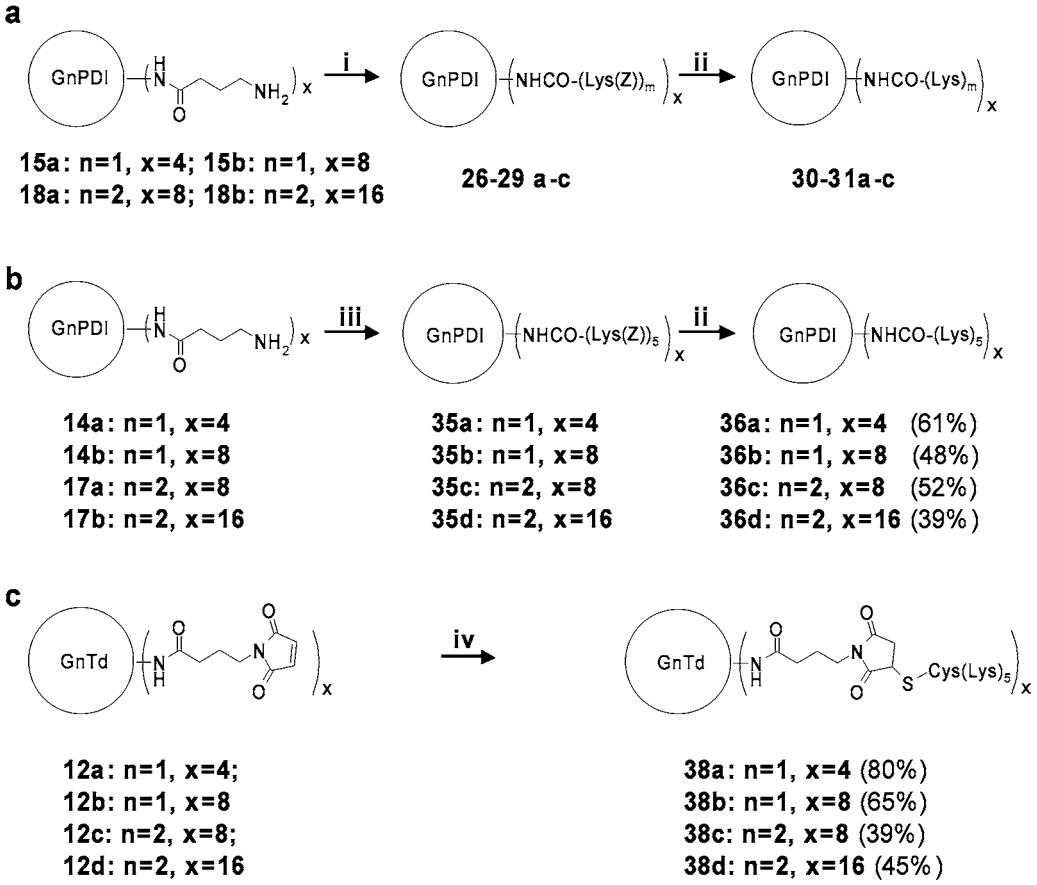

[a] (i) ϵ-benzyloxycarbonyl-L-lysine *N*-carboxyanhydride (**25**), DMF; (ii) HBr, acetic acid; (iii) HOOC-(Lys(Z))$_5$-NHZ (**34**), HBTU, HOBT, DIPEA, DMF; (iv) HOOC-Cys-(Lys)$_5$-NH$_2$ (**37**), DMF. Notation: n, generation of the dendrimer; m, number of lysine residues per chain.

by extensive washing with Et_2O. Finally, the deprotection of the side chains of the lysine residues yielded **30a**−**c**, **31a**−**c**, **32a**−**c**, **33a**−**c** (Table 1). This reaction scheme permits control of the polypeptide length via the amount of the Lys(Cbz)-NCA added to the reaction. The dendrimers bear different numbers of polylysine chains of variable length (Table 1). These variable polypeptide lengths were used in the investigation of the secondary structure of the polylysine shell attached to a polyphenylene core (see section 2.4.). The Cbz-groups of the lysine residues were removed by HBr in glacial acetic acid, followed by precipitation in diethyl ether. To investigate the conjugates in salt-free solutions **30**−**33a**−**c** were purified via ultrafiltration in milli-Q water.

3.3.2. Attachment of Protected Pentalysine. In this case, the *C*-terminus of a Cbz-protected pentalysine **34** is coupled to the amino groups on the surface of the PDI dendrimers (Scheme 5b). The peptide was obtained by solid-phase peptide synthesis using standard Fmoc protecting group chemistry (*26*). The activation of the *C*-terminal carboxyl group of the peptides was achieved using HOBT, HBTU, and DIPEA as activating agents (*27*).

The dendrimers **15a**,**b** or **18 a**,**b**, peptide **34**, HOBT, HBTU, and DIPEA were allowed to react for 5 days in dry DMF under an inert atmosphere at room temperature. After precipitation of the sample in diethyl ether, the crude product was found to contain the target compounds **35a**−**d** and the unreacted polypeptide. Since purification at this stage was not possible, the Z-groups were removed by the same protocol as mentioned in 3.3.1. Subsequent utrafiltration in water (NMWLs 10 000) and freeze-drying yielded the water soluble conjugates **36a**−**d**. The structure and purity of these compounds were verified by means of ^{1}H NMR spectroscopy and gel permeation chromatography. The decoration of PDI dendrimers with preformed polypeptide sequences has the important advantage that no byproducts such as imperfect polypeptide chains occur. Note that the removal of such byproducts in the subsequent purification steps would be rather laborious (*28*).

3.3.3. Coupling of Unprotected Pentalysine. We also demonstrate a functionalization of the dendrimers with unprotected peptidesequences employing the Michael addition of the sulfhydryl group of terminal cysteine to the maleimide units on the dendrimer surface (Scheme 5c). Hexapeptide **37** is composed of a *C*-terminal cysteine and five lysine residues. The peptide was prepared via solid-phase peptide synthesis. The reaction of **13a**−**d** with **37** was performed in DMF at room temperature and the products **38a**−**d** were purified by dialysis and high performance liquid chromatography (HPLC). As for the method described in section 3.3.2, the absence of byproducts with wrong peptide sequences is a considerable advantage. Furthermore, in this case one circumvents the deprotection step(s), making this method especially convenient for coupling of polypeptide sequences sensitive to the deprotection procedures. It should be mentioned that the coupling via the SH group of the cysteine residue is not restricted to polypeptides.

3.4. Properties. 3.4.1. Circular Dichroism (CD). The intrinsic properties of proteins are achieved via secondary, tertiary, and quaternary structures. Therefore, a self-organization of the polypeptide shell attached

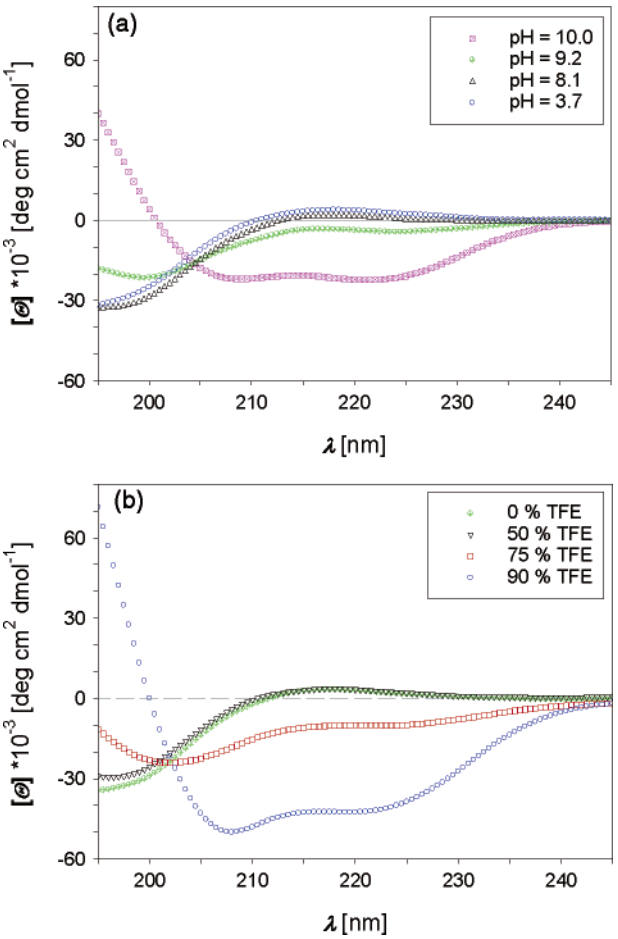

Figure 2. CD spectra of **30c** as a function of pH (a) and concentration of 2,2,2-trifluoro ethanol (b).

to a dendrimer core is essential for targeting bioproperties as for example antigen−antibody recognition. This motivated us to study the effect of either solvent or length of the peptides on the secondary structure of attached polylysine moieties.

PPDs bearing polylysine chains longer than six amino acid residues were investigated by CD spectroscopy. It is known that 2,2,2-trifluoroethanol (TFE) (*29*) as well as high pH (*23*) induce coil-to-helix transition in polylisine moieties. We employed these protocols to study how the polyphenylene scaffold affects the capability of the attached polypeptides of forming secondary structure. Figure 2 shows the CD spectra of **30c** (c = 1.1 μmol/L) as a function of pH (Figure 2a) and concentration of TFE (Figure 2b), respectively. The data are representative of all studied compounds **30a**−**c**, **31a**−**c**, **32a**−**c**, and **33a**−**c**, and the following conclusions can be drawn.

Below pH 9, the polypeptide chains form random coils. Above this pH value, the coils turn into helices. Above pH 10, however, the polypeptides begin to precipitate.

Coil-to-helix transformation can be induced by the exchange of the solvent, namely, when the concentration of TFE is above 75% vol.

The coil-to-helix transition with TFE as a solvent is induced because the intramolecular repulsion is suppressed (*29*−*31*). The same effect can be obtained by the basicity of the aqueous solution being increased (*23*). The helix content at pH 9.9 and in 90% TFE was calculated for all polylysine-decorated PPDs according to the method of Chen et al. (*32*−*34*). The mean residue ellipticity of a polylysine with 100% helix content at 222 nm was taken to be −37 600 deg cm^2 dmol^{-1} (*29*). The results are summarized in Table 2. For all studied compounds, the helix content at pH 9.9 is about 40% or above. Furthermore, the helix content determined in 90% TFE is higher than that determined at pH 9.9.

Table 2. Helix Content in Percent from the CD Spectra (80 μg/mL) in Water at pH = 9.9 and the Percentage in Comparison with the Measurements in a 90% TFE Solution

sample	generation	$m_{\mathrm{Lys,\,UV}}$	pH	α-helix [%]	$[\Theta]_{222}^{\mathrm{water}}/[\Theta]_{222}^{90\%\mathrm{TFE}}$ [%]
30a	$n = 1$ $x = 4$	9	9.9	43.6	78.2
30b		50	9.9	46.4	47.5
30c		85	10	60.6	53
31a	$n = 1$ $x = 8$	9	9.9	35.2	66.8
31b		68	10.1	27.6	26.2
31c		76	9.8	47	45
32a	$n = 2$ $x = 8$	6	9.9	46.4	1133
32b		28	10	44.4	40.2
32c		41	9.9	43.2	42.5
33a	$n = 2$ $x = 16$	14	10	24.8	22.8
33b		41	9.9	80.6	71.2
33c		89	10.1	43.3	38

[a] Notation: $m_{\mathrm{Lys,UV}}$, number of lysine residues per chain, calculated by UV absorption of dendrimers.

The dissociation of polypeptide coiled coils and their organization into single-stranded helices are also evidenced by the ratio of the mean residue ellipticities at 222 and 208 nm (*33*, *35*). Figure 3a shows the ratio $[\Theta]_{222}/[\Theta]_{208}$ measured at pH 9.9 and in 90% TFE for all studied compounds. As evident from the plot, for polypeptide chains longer than 10 lysine residues, the ratio $[\Theta]_{222}/[\Theta]_{208}$ remains constant whatever the generation and number of polypeptide chains.

In water the ratio of the mean residue ellipticities at 222 and 208 nm is nearly one and indicates aggregation between the helices, whereas the value of the measurements in 90% TFE is around 0.8 points at dissociation. Shorter chains, comprising less than 10 residues, are less spatially organized and exhibit higher coil content, the latter being evidenced by the minimum in the ellipticity located in the region below 206 nm. An example is presented in Figure 3b where the CD spectra of **30a** and **30c** are compared.

The main conclusion from the CD data is that polypeptides attached on the dendrimers periphery are capable of forming secondary structures. This finding is essential for the design of synthetic multi-immunogens since the secondary structure of epitopes is responsible for the unique antigen−antibody recognition.

3.4.2. UV−Vis Absorption and Fluorescence. The compounds **30a**, **31a**, **32a**, and **33a**, each containing a PDI core, were characterized by UV−Vis and fluorescence spectroscopy. As an example, the absorption and emission spectra of **33c**, recorded in water and 90% TFE, are shown in Figure 4. Absorption and emission maxima in aqueous solution are at 580 and 614 nm, respectively, while a small bathochromic shift occurs when changing the solvent from water to 90% TFE with maxima at 597 (absorption) and 624 nm (emission).

For all compounds studied, the maxima of absorption are observed at 580−600 nm, being essentially independent of the dendrimer generation and number of peptide residues. Interestingly, the extinction in the less polar solvent water (58 000−88 000 cm^2 mol^{-1}) is lower than the extinction in TFE solutions (81 000−103 000 cm^2 mol^{-1}). All of the compounds **31**−**33** exhibit fluorescence. The emission maxima were detected at wavelengths between 615 and 630 nm upon excitation at 560 nm. The quantum yields in aqueous solutions of all compounds

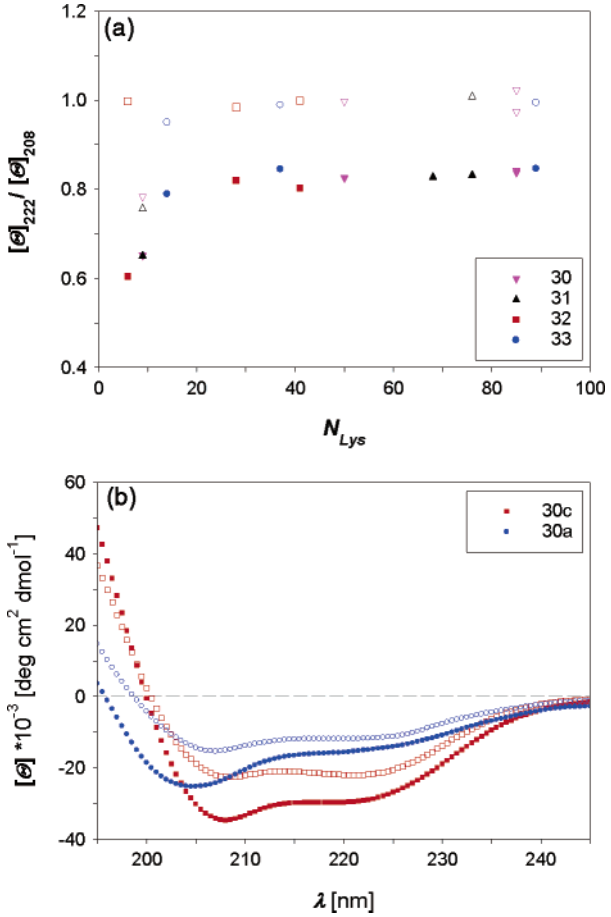

Figure 3. (a) Ratio of the mean residue ellipticities at 222 and 208 nm. $[\Theta]_{222}$/ $[\Theta]_{208}$ of different generations: **30** (red down triangles), **31** (black up triangles) **32** (red squares), **33** (blue circles) in 90% TFE (filled symbols) and at pH 9.9 ± 0.1 (empty symbols). (b) CD spectra of **30a** and **30c**. CD spectra of **30a** (circles) and **30c** (squares) in 90% TFE (filled symbols) and at pH 9.9 (empty symbols).

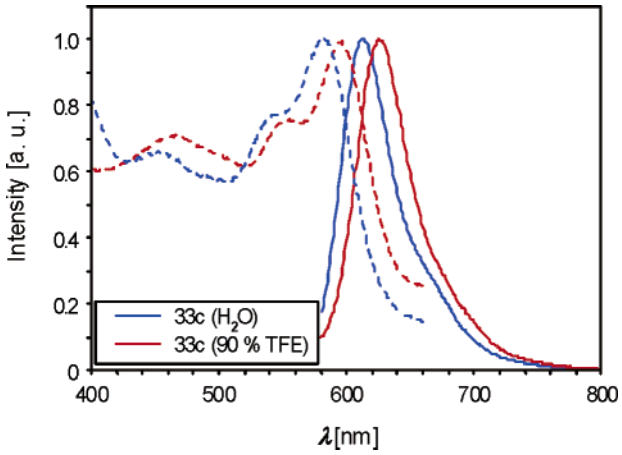

Figure 4. UV−vis absorbance and fluorescence emission spectra of **33c** in 90% TFE and in aqueous solution pH 9.9.

were low (about 1%). Nevertheless, the optical properties (strong absorption at 580−600 nm and fluorescence in water) of the peptide-decorated PDI dendrimers allow their identification in complex mixtures of biological samples. These features are very important for in vitro/ in vivo studies and pharmaceutically oriented applications since at wavelengths greater than 550 nm cells and tissue usually do not show any chromophoric properties.

4. CONCLUSIONS

We have demonstrated the synthesis of new amino acid functionalized cyclopentadienones. Their Diels−Alder reactions with different core molecules lead to polyphenylene dendrimers functionalized with amino or carboxyl groups. Polylysine fragments were then coupled to these dendrimers employing three different methods.

(i) Grafting of the peptides from the surface of the dendrimer by applying the NCA polymerization strategy. This route affords a decoration of PPDs with polypeptides, connected via their *C*-terminus. Furthermore, the attached polypeptide chains are able to fold into defined secondary structures, an important prerequisite for the preparation of functional bioconjugates.

(ii) Carbodiimide coupling of a protected peptide. The C-terminal carboxyl groups of the peptides are activated employing HBTU/ HOBT and are attached to the surface amino groups of the dendrimers.

(iii) Specific attachment of unprotected peptide fragments under mild conditions via Michael addition of a thiol group of the terminal cysteine of the polypeptide to the maleimide of the PPD. This method allows both *C*- and *N*-terminal attachment of the polypeptide.

The resulting dendrimers have good solubility in water and combine shape-persistence with a controlled number of surface functions. Additionally, when perylenediimide PPDs are used as cores, absorption and fluorescence techniques can be employed for their identification.

By using an asymmetric core molecule and appropriately functionalized cyclopentadienones in a Diels−Alder reaction, we have obtained PPDs bearing two different functional groups. For example, compound **33**, a PPD bearing carboxyl and maleimide functions in isolated surface domains, is a scaffold for the creation of a conjugate possessing two different polypetide sequences.

We have recorded circular dichroism (CD) spectra of PPDs bearing different numbers of polypeptide chains of various degrees of polymerization. On the basis of these data, we have concluded that at pH 9.9, as well as in the presence of more than 75% TFE, the attached polypeptide is capable of forming an α-helical secondary structure. This fact is of particular importance for the design of MAP since the secondary structure is essential for the intrinsic properties of its distinct sites. In addition, conjugates synthesized with the perylenediimide core strongly absorb at 580−600 nm and are fluorescent in water.

Our synthetic methods are not restricted to oligolysines but may be easily adapted to the substitution of PPD with various polypeptide sequences. This opens the way to biofunctonalized compounds with perspectives as spatially defined MAPs with a hydrophilic shell formed of certain epitopes and chromophor-labeled shape-persistent scaffolds.

ACKNOWLEDGMENT

This work was supported by the Deutsche Forschungsgemeinschaft (SFB 625).

LITERATURE CITED

(1) Newcome, G. R., Moorefield, C. N., and Vögtle, F. (1996) *Dendritic Molecules*, VCH Verlagsgesellschaft GmbH, Weinheim.

(2) Bosman, A. W., Janssen, H. M., and Meijer, E. W. (1999) About Dendrimers: Structure, Physical Properties, and Applications. *Chem. Rev. 99*, 1665−1688.

(3) Fréchet, J. M. J., and Hawker, C. J. (1996) Synthesis and Properties of Dendrimers and Hyperbranched Polymers in

Comprehensive Polymer Science (S. L. Aggarwal, S. Russo, S, Eds.) 2nd Suppl., Pergamon Press, Oxford.
(4) Stiriba, S.-E., Frey, H., and Haag, R. (2002) Dendritic Polymers in Biological Applications: From Potential to Clinical Use in Diagnostics and Therapy. *Angew. Chem., Int. Ed. 41*, 1329−1334.
(5) Wiesler, U.-M., Weil, T., and Müllen, K. (2001) Nanosized Polyphenylene Dendrimers. *Top. Curr. Chem. 212*, 1−40.
(6) Veprek, P., and Jezek, J. (1999) Peptide and glycopeptide dendrimers. Part II. *J. Peptide Sci. 5*, 203−220.
(7) Tam, J. P. (1996) Recent advances in multiple antigen peptides. *J. Immun. Methods 196*, 17−32.
(8) Tam, J. P., and Lu, Y.-A. (1989) Vaccine engineering: Enhancement of immunogenicity of synthetic peptide vaccines related to hepatitis in chemically defined models consisting of T- and B-cell epitopes. *Biochemistry 86*, 9084−9088.
(9) Kohl C., Weil, T., Qu, J., and Müllen K. (2004) Towards Highly Fluorescent and Water-Soluble Perylene Dyes *Chem.-Eur. J. 10*, 5297−5310.
(10) Herrmann, A., Mihov, G., Vandermeulen, G.W. M., Klok, H.-A., and Müllen, K. (2003) Peptide-functionalized polyphenylene dendrimers. *Tetrahedron 59*, 3925−3935.
(11) Kohn, F., Hofkens, J., Wiesler, U.-M., Cotlet, M., Van der Auweraer, M., Müllen, K., and De Schryver, F. C. (2001) Single-molecule spectroscopy of a dendrimer-based host−guest system. *Chem. Eur. J. 7*, 4126−4133.
(12) Grimsdale, A. C., Bauer, R., Weil, T., Tchebotareva, N., Wu, J., Watson, M., and Müllen, K. (2002) The Chemical Desymmetrisation of Two- and Three-Dimensional Polyphenylenes as a Key Step to Functional Nanoparticles. *Synthesis (Stuttgart) 9*, 1229−1239.
(13) Qu, J., Pschirer, N. G., Liu, D., Stefan, A., De Schryver, F. C., and Müllen, K. (2004) Dendronized perylenetetracarboxdiimides with peripheral triphenylamines for intramolecular energy and electron transfer. *Chem.-Eur. J. 10*, 528−537.
(14) Morgenroth, F., Reuther, E., and Müllen, K. (1997) Polyphenylene dendrimers: From three-dimensional to two- dimensional structures. *Angew. Chem., Int. Ed. Engl. 36*, 631−634.
(15) Qu, J., Zhang, J., Grimsdale, A. C., and Müllen, K. (2004) Dendronized Perylene Diimide Emitters: Synthesis, Luminescence, and Electron and Energy Transfer Studies. *Macromolecules 37*, 8297−8306.
(16) Wiesler, U.-M., Berresheim, A. J., Morgenroth, F., Lieser, G., and Müllen, K. (2001) Divergent Synthesis of Polyphenylene Dendrimers: The Role of Core and Branching Reagents upon Size and Shape. *Macromolecules 34*, 187−199.
(17) Morgenroth, F., Kübel, C., and Müllen, K. (1997) Nanosized polyphenylene dendrimers based upon pentaphenylbenzene units. *J. Mater. Chem. 7*, 1207−1211.
(18) Morgenroth, F., and Müllen, K. (1997) Dendritic and hyperbranched polyphenylenes via a simple Diels−Alder route. *Tetrahedron 53*, 15349−15366.
(19) Morgenroth, F., Reuther, E., and Mullen, K. (1997) Polyphenylene Dendrimers: From Three-Dimensional to Two-Dimensional Structures. *Angew. Chem., Int. Ed. 36*, 631−634.
(20) Sakai, N., and Ohfune, Y. (1992) Total Synthesis of Galantin I. Acid-Catalyzed Cyclization of Galantinic Acid. *J. Am. Chem. Soc. 114*, 998−1010.
(21) Ben-Ishai, D., and Berger, A. (1952) Cleavage of N-Carbobenzoxy Groups by dry Hydrogen Bromide and Hydrogen Chloride. *J. Org. Chem. 17*, 1564−1570.
(22) Ram, R. N., and Charles, I. (1997) Selective esterification of aliphatic nonconjugated carboxylic acids in the presence of aromatic or conjugated carboxylic acids catalysed by $NiCl_2 \cdot 6H_2O$. *Tetrahedron 53*, 7335−7340.
(23) Klok, H.-A., Hernandez, J. R., Becker, S., and Mullen, K. (2001) Star-Shaped Fluorescent Polypeptides. *J. Polym. Sci. Pol. Chem. 39*, 1572−1583.
(24) Poché, D. S., Moore, M. J., and Bowles, J. L. (1999) An Unconventional Method for Purifying the N-Carboxyanhydride Derivates of gamma-Aklyl-L-glutamates. *Synth. Commun. 29*, 843−854.
(25) Kricheldorf, H. R. (1987) α-*Amino Acid-N-Carboxyanhydrides and Related Heterocycles*, Springer-Verlag, Berlin-Heidelberg-New York.
(26) Fields, G. B., and Noble, R. L. (1990) Solid-phase peptide synthesis utilizing 9-fluorenylmethoxycarbonyl amino acids. *Int. J. Peptide Res. 35*, 161−214.
(27) Choi, J. S., Lee, E. J., Choi, Y. H., Jeong, Y. J., and Park J. S. (1999) Poly(ethylene glycol)-*block*-poly(L-lysine) Dendrimer: Novel Linear Polymer/Dendrimer Block Copolymer Forming a Spherical Water-Soluble Polyionic Complex with DNA. *Bioconjugate Chem. 10*, 62−65.
(28) Chaves, F., Calvo, J. C., Carvajal, C., Rivera, Z., Ramirez, L., Pinto, M., Trujillo, M., Guzman, F., and Patarroyo, M. E. (2001) Synthesis, isolation and characterization of Plasmodium falciparum antigenic tetrabranched peptide dendrimers obtained by thiazolidine linkages. *J. Peptide Res. 58*, 307−316.
(29) Maeda, Y., Nakagawa, T., and Kuroda, Y. (2003) Oligopeptide-mediated helix stabilization of model peptides in aqueous solution. *J. Peptide Sci. 9*, 106−113.
(30) Cammers-Goodwin, A., Allen, T. J., Oslick, S. L., McClure, K. F., Lee, J. H., and Kemp, D. S. (1996) *J. Am. Chem. Soc. 118*, 3082−3090.
(31) Huang, K., Park, Y. D., Cao, Z. F., and Zhou, H. M. (2001) Reactivation and refolding of rabbit muscle creatine kinase denatured in 2,2,2-trifluoroethanol solutions. *Biochim. Biophys. Acta 1545*, 305−313.
(32) Chen, Y.-H., Yang, J. T., and Chau, K. H. (1974) Determination of the helix and β form of proteins in aqueous solution by circular dichroism. *Biochemistry 13*, 3350−3359.
(33) Lau, S. Y. M., Taneja, A. K., and Hodges, R. S. (1984) Synthesis of a model protein of defined secondary and quaternary structure. Effect of chain length on the stabilization and formation of two-stranded alpha-helical coiled-coils. *J. Biol. Chem. 259*, 13253−13261.
(34) Yang J. T., Wu, C.-S., and Martinez, C. H. M. (1986) *Calculation of Protein Conformation from Circular Dichroism*, Academic Press, New York.
(35) Chitra, R., and Smith, P. E. (2001) Properties of 2,2,2-trifluoroethanol and water mixtures. *J. Chem. Phys. 114*, 426−435.

BC049839K

MicroPET Imaging of MCF-7 Tumors in Mice via unr mRNA-Targeted Peptide Nucleic Acids

Xiankai Sun,[†,‡] Huafeng Fang,[§] Xiaoxu Li,[§] Raffaella Rossin,[†] Michael J. Welch,[†] and John-Stephen Taylor*[,§]

Division of Radiological Sciences, Mallinckrodt Institute of Radiology, Washington University School of Medicine, St. Louis, Missouri 63110, and Department of Chemistry, Washington University, St. Louis Missouri 63130.
Received September 14, 2004; Revised Manuscript Received February 3, 2005

As more becomes known about the expression profiles of normal and cancerous cells, it should become possible to design antisense-based imaging agents for the early detection of cancer noninvasively. In this report, we rationally designed and synthesized three antisense and one sense hybrid PNA (peptide nucleic acid) to the unr mRNA that is highly overexpressed in a breast cancer cell line (MCF-7). The conjugates had a four-lysine tail at the carboxy terminus for cell permeation and a DOTA (1,4,7,10-tetraazacyclododecane-N,N′,N″,N‴-tetraacetic acid) chelating moiety at the amino terminal end for chelating ^{64}Cu for biodistribution and microPET imaging studies. Biodistribution of two ^{64}Cu-labeled conjugates with antisense and sense sequences (PNA50 and PNA50S) showed high uptake and long retention in kidney and low uptake and efficient clearance in blood and muscle in normal balb/c mice when administered intravenously or intraperitoneally. Intraperitoneal administration, however, gave a much slower release rate. MCF-7 tumors (100−320 mg) in CB-17 SCID mice were imaged with all four ^{64}Cu-labeled PNA conjugates by microPET, but the image contrast varied with different time points and different conjugates. Of the conjugates studied, ^{64}Cu-DOTA-Y-PNA50-K4 showed the best tumor image quality at all time points with a tumor/muscle ratio of 6.6 ± 1.1 at 24 h postinjection, which is among the highest reported for radiolabeled oligonucleotides. Our work further strengthens the potential of antigene and antisense PNAs to be utilized as specific molecular probes for early detection of cancer and ultimately for patient specific radiotherapy.

INTRODUCTION

Noninvasive imaging techniques are revolutionizing the way of understanding diseases at the cellular and molecular levels. Among the current available imaging modalities, positron emission tomography (PET) has demonstrated its great potential in the field of molecular imaging. The success of PET is due to its superior sensitivity and specificity in diverse applications and the ability to quantitatively analyze the regions of interest (*1*, *2*). Since the completion of human genome sequence, there has been considerable research interest in assessing gene expression through noninvasive molecular imaging approaches. Currently, the number of genes is estimated to be between 24 000 and 30 000 and that alternative polyadenylation and splicing could result in the formation of between 46 000 and 85 000 messenger RNAs (mRNA) (*3*). Of the various PET probes that have been developed to image gene expression in small animal models, oligodeoxynucleotides (ODNs) appear to be an inexhaustible gold mine for the development of new tracers with high specificity considering that an ODN with more than 12 bases could target a unique sequence in the whole human genome (*4*).

Naturally occurring ODNs cannot be directly used for nuclear imaging because they are rapidly degraded in vivo by endo- and exonucleases (*5*). Furthermore, ODNs can cause degradation of the target mRNA by RNAse H. To increase the in vivo stability of ODNs without significant alteration of their pharmacokinetics and targeting properties, many chemical modifications have been made to the sugar−phosphate backbone. Modifications include morpholino, phosphorothioate, phosphoroamidate, methylphosphonate, 2′- or 3′-modifications, 2′−4′ bridges (locked nucleic acid), and complete replacement of the backbone with an amide backbone (peptide nucleic acid or PNA) (*6*−*8*). PNAs are unique types of oligonucleotides, which were initially introduced by Nielsen et al. in 1991 as ligands for the double-stranded DNA recognition (*9*). They are synthetic DNA mimics featuring a chain with repeating N-(2-aminoethyl) glycine units instead of the sugar−phosphate backbone. Because of the structural characteristics (e.g., neutral and flexible), PNAs are resistant to in vivo enzymatic degradation and bind complementary DNAs or RNAs with high affinity and specificity even under low ionic strength (*10*). They also do not activate RNAse H degradation of mRNA. Recent work has shown that PNAs can be used as molecular hybridization probes (*11*), nuclear imaging tracers (*8*, *12*−*16*), and to control gene expression and splicing (*6*, *17*−*19*).

Using antisense PNAs as molecular imaging probes has a major obstacle in that they are not able to penetrate biologic membranes. To overcome this obstacle, researchers have resorted to drug delivery techniques such as

* To whom correspondence should be addressed. Tel: 314-935-6721. Fax: 314-935-4481. E-mail: taylor@wustl.edu.
† Washington University School of Medicine.
‡ Current address: Department of Radiology, the University of Texas Southwestern Medical Center at Dallas, Dallas, TX 75390.
§ Washington University.

10.1021/bc049783u CCC: $30.25 © 2005 American Chemical Society
Published on Web 02/26/2005

using cationic lipids (or polyamines) and liposomes (*20*−*23*), nanoparticles (*24*), and direct conjugation with monoclonal antibodies (*12*, *13*) or peptides (*6*, *25*−*32*), etc. Recently, it was reported that PNAs with four lysines at the C terminus (PNA-K4 oligomers) were able to penetrate cells in cell culture (*33*) and enter the cells of most organs of a mouse by their ability to restore correct splicing to an otherwise defective reporter gene (*6*).

To be useful as a probe, an antisense PNA must target a unique or a uniquely overexpressed mRNA in the disease cell. Analysis of mRNA expression levels within cancer cells by DNA chip or array analysis (*34*−*37*) and by serial analysis of gene expression (SAGE) (*38*, *39*) have revealed that there are many overexpressed mRNAs, some of which may be present in more than 50-fold greater abundance than in normal cells. To ensure good detection sensitivity and selectivity, a unique or uniquely overexpressed mRNA target should also be highly abundant, and initially we imagined that there would be a number of such candidate mRNA triggers already validated for antisense cancer therapy (*40*). Most of all the validated antisense targets for cancer have been picked, however, on the basis of biological function and not on abundance, and many of the target mRNAs turn out not to be uniquely overexpressed in the cancer cells as judged from an examination of SAGE databases. A search of the NCBI SAGE database for mRNAs that are uniquely overexpressed (>10-fold) and in high copy number in cancer cells identified the unr (upstream of N-ras) (*41*−*44*) mRNA as a potential target. The unr mRNA is more than 10-fold more highly expressed in the MCF-7 breast cancer cell line than it is in any normal tissue cell line, and that it is present in about 5000 copies per cell, making it an ideal initial target for imaging studies.

An additional criterion for the preparation of any PET probe is the ability to rapidly introduce the radionuclide at the last step in the synthesis and under conditions that do not damage the ligand. The important role of copper radiotracers in these regards has been well-recognized in the applications of PET imaging and radiotherapeutic agents in recent years. ^{64}Cu can be rapidly attached to a ligand by chelation to an appended high affinity chelator. Of the four copper radionuclides that can be used as PET imaging agents, ^{64}Cu has shown its versatility in diverse applications for PET imaging (*45*−*51*) and radiotherapy of cancer (*52*−*56*) due to its decay characteristics ($t_{1/2}$ = 12.7 h; β^+: 0.653 MeV, 17.4%; β^-: 0.578 MeV, 39%) and the ability to produce it in high yield and specific activity on a small biomedical cyclotron (*57*, *58*). In this study, we introduced a DOTA moiety to the N terminus of our designed PNAs so that they can be radiolabeled with ^{64}Cu, which enabled the in vivo visualization of our PNAs targeting MCF-7 tumor in mice via microPET and biodistribution studies.

EXPERIMENTAL PROCEDURES

Materials. DOTA-tris(*tert*-Butyl ester) was from Macrocyclics Inc. (Dallas, TX), and diisopropylethylamine (DIEA), trifluoroacetic acid (TFA), *m*-cresol, and diethyl ether (anhydride) were purchased from Aldrich (St. Louis, MO). α-N-9-Fluorenylmethoxycarbonyl (Fmoc)-protected amino acids [D-Lys(Boc)-OH and Tyr(tBu)-OH] were purchased from NovaBiochem (La Jolla, CA). O-(7-Azabenzo-triazol-1-yl)-1,1,3,3-tetramethyluronium hexafluorophosphate (HATU), Fmoc-XAL PEG-PS resin, PNA building blocks [Fmoc-A-(Bhoc)-OH, Fmoc-C-(Bhoc)-OH, Fmoc-G-(Bhoc)-OH, and Fmoc-T-OH], and other reagents and solvents for PNA and peptide synthesis were purchased from Applied Biosystems (Foster City, CA). UV spectral data were acquired on a Bausch and Lomb Spectronic 1001 spectrophotometer or Varian Cary 100 Bio UV−visible Spectrophotometer. Matrix-assisted laser desorption ionization (MALDI) mass spectra of PNA−peptide conjugates were measured on PerSeptive Voyager RP MALDI-time-of-flight (TOF) mass spectrometer using sinapinic acid as a matrix and calibrated vs insulin (average $[M + H^+] = 5734.5$) that was present as an internal standard. High-pressure liquid chromatography was carried out on a Beckman Coulter System Gold 126 with an array detector. Copper-64 was prepared on the Washington University Medical School CS-15 cyclotron by the ^{64}Ni(p,n)^{64}Cu nuclear reaction at a specific activity of 50−200 mCi/μg at the end of bombardment as previously described (*58*). Water was distilled and then deionized (18 MΩ/cm^2) by passing through a Milli-Q water filtration system (Millipore Corp., Bedford, MA). Diethylenetriaminepentaacetic acid (DTPA), ammonium acetate, and sodium chloride were purchased from Fluka Chemie AG (Buchs, Switzerland). Dry powder in foil pouches for the preparation of 10 mM phosphate buffer saline (PBS), pH 7.4, and 4-(2-hydroxyethyl)piperazine-1-ethanesulfonic acid (HEPES) were purchased from Sigma-Aldrich. Solvents (e.g., acetone, methanol, etc.) were purchased from Fisher Scientific (Pittsburgh, PA) and used as received. Saline (0.9% NaCl solution) was purchased from American Pharmaceutical Partners, Inc. (Schaumburg, IL). Centricons (YM-3: MWCO 3000 Da) were purchased from Millipore Corporation. Fast protein liquid chromatography (FPLC) and radio-FPLC were performed using an Amersham Pharmacia Biotech ÄKTA FPLC (Amersham Biosciences Corp., Piscataway, NJ) equipped with a Beckman 170 Radioisotope Detector (Beckman Instruments, Inc., Fullerton, CA). The Superdex 75 was bought from Amersham Biosciences Corp. PBS, trypsin/EDTA, and cell culture media and additives were purchased from the tissue culture support center of Washington University School of Medicine (St. Louis, MO). Fetal bovine serum (FBS), Earle's balanced salt solution (BSS), and insulin were bought from Sigma. Balb/c and CB-17 SCID mice were purchased from the Charles River Laboratories (Wilmington, MA).

Tissue Culture and Animal Model. The MCF-7 cell line was obtained from the American Type Culture Collection (ATCC, Manassas, VA). MCF-7 cells were grown in Eagle's minimum essential medium (MEM) with Earle's BSS and 2 mM L-glutamine modified to contain 1 mM sodium pyruvate, 0.1 mM nonessential amino acids, 1.5 mg/mL sodium bicarbonate supplemented with 10% FBS and 0.01 mg/mL bovine insulin. To establish MCF-7 human breast xenografts, each CB-17 SCID mice was implanted with a 60-day subcutaneous (s.c.) slow release estrogen pellet (1.7 mg 17β-estradiol/pellet; Innovative Research of America, Sarasota, FL) 48 h prior to the s.c. injection of MCF-7 cells into the nape of neck. Cultured MCF-7 cells were harvested from monolayer using PBS and trypsin/EDTA, and suspended in media with FBS. The cell suspension was centrifuged and resuspended in PBS at the concentration of 1×10^8 cells per milliliter. It was then mixed 1:1 with Matrigel and injected s.c. (1×10^7 cells per mouse, injection volume 200 μL) into the nape of the neck of CB-17 SCID mice (5−6 weeks of age). After the cell injection, the animals were monitored twice a week by general observations. The tumor was noticed to grow in the first week and allowed to grow five weeks to reach a palpable size for microPET imaging studies. The tumor weight was 100−320 mg as determined by post imaging biodistribution.

Synthesis of the DOTA-(D)-Y-PNA-K4 Conjugates. NH_2-Y-PNA-K4 conjugates were synthesized continuously on universal support XAL-PEG-PS resin on a 2 μmol scale with standard solid phase Fmoc off chemistry on an Expedite 8909 Synthesizer (Applied Biosystems) by loading the fifth and sixth building block channels with Fmoc-D-Lys and Fmoc-Tyr(tBu), respectively, and programming the sequence accordingly under standard automated PNA synthesis protocol. DOTA-tris(*tert*-butyl ester) (11.5 mg, 20 μmol) was dissolved in 100 μL of *N*-methylpyrrolidone, and then, 100 μL of HATU in dimethylformamide (DMF) solution (0.2 M) and 100 μL of base solution (0.2 M DIEA, 0.3 M 2,6-lutidine in DMF) were added, the mixture was introduced into the cartridge containing PNA-K4 resin manually with a syringe and pushed back and forth with a second syringe to agitate the resin suspension every 10 min for 1 h. Then, the resin was washed with DMF and dichloromethane and dried by passing nitrogen. Treatment of the resin with TFA/*m*-cresol (4:1) for 2 h at RT was used to cleave the conjugates and remove the side chain protective groups. Ethyl ether (8−10 volumes) was added to the TFA solution to precipitate the product as a yellow solid. The crude product was purified by reversed phase HPLC on a Microsorb C18 column (300 Å pore, 5 μm particle size, 4.6 × 250 mm) using a 5−70% linear gradient of solvent B (0.1% TFA in acetonitrile) in A (0.1% TFA in water) over 65 min at the flow rate of 1 mL/min. The effluent was monitored by absorbance at 260 nm and the major peaks were collected, concentrated to dryness in vacuum, and characterized by MALDI-TOF mass spectrometry.

Radiolabeling of DOTA-Y-PNA-K4 Conjugates with ^{64}Cu. Copper-64 chloride (typically in 0.1 M HCl) was converted to ^{64}Cu-citrate by adding an appropriate volume of 0.1 M ammonium citrate buffer (pH 7.0) to the $^{64}CuCl_2$ solution. Prior to labeling, the stock solutions of DOTA-Y-PNA-K4 conjugates were heated at 80 °C for 10 min to minimize aggregation and plastic wall sticky property of the PNA conjugates. To 200 μL of a DOTA-Y-PNA-K4 conjugate solution (40 μM), 20 μL of ^{64}Cu-citrate was added (2−4 mCi). The resulting solution was incubated at 60 °C for 1−2 h in a thermomixer (1000 rpm). After incubation, 5 μL of 10 mM DTPA solution was added to the ^{64}Cu-DOTA-Y-PNA-K4 solution. The solution was vortexed for a few seconds and left at RT for 10 min. It was then centrifuged at least two times through a Centricon YM-3 (MWCO 3000 Da) with 10 mM PBS buffer (pH 7.4) to remove the ^{64}Cu−DTPA complex and/or free ^{64}Cu-activity. The radiochemical purity (RCP) of the ^{64}Cu-labeled DOTA-Y-PNA-K4 conjugate was monitored by FPLC. The product was then diluted with 10 mM PBS buffer (pH 7.4) to prepare appropriate doses for biodistribution and microPET imaging studies.

FPLC Analysis. A 100 μL of analyte was injected into a Superdex 75 gel filtration column, which was then eluted with 20 mM HEPES and 150 mM NaCl (pH 7.3) buffer at an isocratic flow rate of 0.5 mL/min. The UV wavelength was preset to 280 nm, the radioactivity was monitored by an online Beckman radio-detector. Under these conditions, the retention times of the ^{64}Cu-DOTA-Y-PNA-K4 and DOTA-Y-PNA-K4 were ca. 31−35 min.

Biodistribution Studies. All animal studies were performed in compliance with guidelines set by the Washington University Animal Studies Committee. Copper-64 labeled DOTA-Y-PNA-K4 solutions were diluted with saline. Normal balb/c mice weighing 20−30 g (n = 3 per time point) were anesthetized with isoflurane and injected with 10−12 μCi of activity via the tail vein (i.v.) or ca. 55 μCi of radioactivity via intraperitoneal (i.p.) injection. The injected volume of activity per mouse was 100 μL. The mice were anesthetized prior to sacrifice (by decapitation) at each time point. Organs of interest were removed, weighed, and counted. Standards were prepared and counted along with the samples to calculate the percent injected dose per gram (%ID/g) and percent injected dose per organ (%ID/organ).

MicroPET Imaging Studies. The microPET imaging studies were carried out using the microPET R4 (rodent) scanner (Concorde Microsystems Inc., Knoxville, TN) (*59*). MCF-7 tumor-bearing CB-17 SCID mice were anesthetized with 1−2% vaporized isoflurane and injected with ca. 200−400 μCi of activity in 120 μL saline via the tail vein (^{64}Cu-DOTA-Y-PNA50, 210 μCi; ^{64}Cu-DOTA-Y-PNA50S, 347 μCi; ^{64}Cu-DOTA-Y-PNA5, 253 μCi; ^{64}Cu-DOTA-Y-PNA7, 361 μCi). At specific time points (1, 4, and 24 h) postinjection, the mice were reanesthetized and then immobilized in a supine position on custom-built support beds with attached anesthetic gas nose cones for data collection. Within 4 h p.i., the imaging collection time was 10 min; at 24 h p.i., the imaging collection time was 20 min.

Radioactive tracer accumulation (^{64}Cu-labeled PNAs) in a targeted organ was measured using the standardized uptake value (SUV). The SUVs were obtained by the quantification of the regions of interest (ROIs) by viewing these areas in the selected tissues and averaging the activity concentration corrected for decay over the contained voxels (multiple image slices) at the time points p.i. (*60*).

$$\mathrm{SUV} = \frac{\text{radioactivity concentration in ROI } (\mu\text{Ci/cc})}{\text{injection dose } (\mu\text{Ci})/\text{animal weight (g)}}$$

After the microPET imaging at 24 h p.i., the animals were sacrificed and biodistribution studies were performed. The ratios of tumor to blood (T/B) and tumor to muscle (T/M) were calculated. The unpaired t-test on the biodistribution and microPET quantitation data was performed using Prism, v. 4.00 (Graphpad, San Diego, CA).

Assaying Unr mRNA Expression. Total RNA was extracted from MCF-7 cells and grafted mouse tissues with TRIzol (Invitrogen Corp., Carlsbad, CA). For the adult mouse tissues, samples were harvested and immediately submerged in RNAlater Tissue collection RNA stabilization solution (Ambion, Inc., Austin, TX) and then homogenized prior to mRNA extraction. Relative RT-PCR was carried out according to the manufacturer's procedures (Ambion). The cDNA was prepared with SuperScriptII reverse transcriptase (Invitrogen Life Technologies, Carlsbad, CA) and PCR was carried out with human-specific and nonspecific unr mRNA primers that were designed based on the available human and mouse unr sequences (gi:56117851, gi:16877279) along with QuantumRNA Classic I 18S Internal Standard competimer primer mix (1:1) as an internal control (Ambion). For human unr mRNA 5′-TGGGGGACATGGTCGAGTAT-3′ and 5′-ACATTCCACTGTGGCCCTG-3′ were used, and for both human and mouse unr mRNA 5′-AGCTTGTCCAAAGGCAAAG-3′ and 5′-AAGCCAAACTGATCTTTCACAC-3′ were used. PCR was performed with Pfx polymerase (Invitrogen) using a 3 min 94 °C preincubation followed by 24 cycles of 45 s 94 °C, 45 s at 56 °C for human-specific primers and 52 °C for the nonspecific primers, and 45 s at 68 °C. The samples were then kept at 68 °C for 2 min and then loaded into a 1% agarose gel and ethidium bromide stained.

Table 1. PNAs Used in PET Imaging Studies and Their Characterization by MALDI-TOF

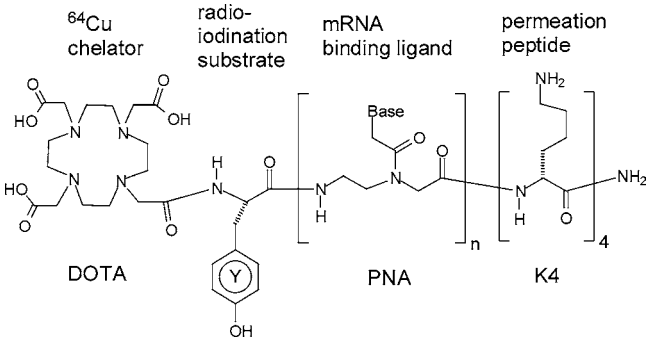

PNA	site[a]	PNA sequence	calcd avg MW (M + 1)	observed (M + 1)
50	2848	TGGTGTGCTTTGTGGATG	6066.67	6068.95
7	673	TTTCCCAGTCCGTCGGTC	5876.54	5879.07
5	476	CATTATGTCCATTGTTGT	5930.29	5930.3
50S	sense	CATCCACAAAGCACACCA	5849.53	5852.87

[a] Start codon at 448.

RESULTS

Selection of the Antisense PNAs. The sequences of the antisense PNAs were selected by a procedure that will be described in greater detail elsewhere but in brief consisted of using a modification of a recently described RT-ROL (reverse transcriptase−random ODN library) method for mapping antisense binding sites on native mRNA (*61*). ODNs complementary to these sites were synthesized and their binding affinity for the unr mRNA determined. Hybrid PNAs corresponding to ODNs with the highest binding affinities and containing a C-terminal K4 (Lys_4) sequence and an amino terminal Cys-Tyr sequence were then synthesized, radioiodinated with ^{131}I on tyrosine, and their binding affinities determined. Three of these antisense PNAs and one sense PNA were selected for imaging studies: PNA50 with a K_d of 21 pM, PNA5 with a K_d of 22 pM, PNA7 with a K_d of 15 pM, and PNA50S (sense form of PNA50) with a K_d of >10 nM in 0.1 M NaCl, 50 mM EDTA, 2 mM cacodylic acid (Table 1). The sites on the mouse unr mRNA corresponding to the antisense PNA binding sites on the human mRNA are shown in (Table 2), two of which differ in sequence by two nucleotides (PNA50 and PNA7 sites), and one by only one nucleotide (PNA5 site). All the mouse sites have stretches of less than 14 nucleotides of complete complementarity to the PNAs, as compared to 18 for the human mRNA.

Synthesis of DOTA-Y-PNA-K4 Conjugates. The PNA conjugates (Table 1) were synthesized using standard automated solid phase Fmoc synthesis on an ABI 8909 DNA synthesizer with a PNA option (unfortunately, this synthesizer is no longer commercially available). The unnatural D-isomer of lysine was used to inhibit enzymatic degradation of the K4 permeation peptide unit. The DOTA group was added manually in the last step of the synthesis to the amino terminal ("5′-end") of the PNA via the commercially available tri-*tert*-butylester, and the HPLC purified products characterized by MALDI-TOF (Table 1).

Radiolabeling of DOTA-Y-PNA-K4 Conjugates. Four DOTA-Y-PNA-K4 conjugates were all successfully radiolabeled with ^{64}Cu in 0.1 M ammonium citrate buffer (pH 7.0) under mild conditions (at 60 °C for 1−2 h) in yields of 32−61% (decay corrected). After DTPA challenge of nonspecifically bound ^{64}Cu activity and Centricon YM-3 (MWCO: 3000 Da) separation, the radiochemical purity of the ^{64}Cu-labeled PNA conjugates was nearly 100% as determined by radio-FPLC: both the radioactivity and UV (280 nm) curves only showed a single strong peak with the same retention time in the range of 30−35 min. The ^{64}Cu-labeled PNA conjugates remained 100% intact after being kept in saline overnight.

Biodistribution of ^{64}Cu-DOTA-Y-PNA-K4 Conjugates in Normal Balb/c Mice. To better evaluate the in vivo kinetics of the ^{64}Cu-labeled PNA conjugates, the biodistribution studies were carried out with two different injection modes in normal balb/c mice: intravenous (tail vein) injection (i.v.) and intraperitoneal injection (i.p.).

Tail Vein Injection. The biodistribution data of ^{64}Cu-DOTA-Y-PNA50-K4 and ^{64}Cu-DOTA-Y-PNA50S-K4 in blood, liver, kidneys, and muscle are presented as percent of injected dose per organ (%ID/organ) at 20 min, 1 h, and 4 h postinjection (p.i.) in Figure 1. Both conjugates exhibited high kidney uptake and long retention. Within 1 h p.i., ^{64}Cu-DOTA-Y-PNA50-K4 showed slightly higher kidney accumulation (37.4 ± 1.8%ID/kidney at 20 min p.i. and 45.8 ± 0.7%ID/kidney at 1 h p.i.) than ^{64}Cu-DOTA-Y-PNA50S−K4 (35.6 ± 0.6%ID/kidney at 20 min p.i. and 42.3 ± 0.2%ID/kidney at 1 h p.i.). Out to 4 h p.i., ^{64}Cu-DOTA-Y-PNA50-K4 exhibited significant kidney clearance (36.1 ± 3.6%ID/kidney at 4 h p.i. $P < 0.02$ as compared to the value at 1 h p.i.), while a drastic accumulation was observed for ^{64}Cu-DOTA-Y-PNA50S-K4 (60.5 ± 3.6%ID/kidney at 4 h p.i. $P < 0.005$ as compared to the value at 1 h p.i.). In blood, liver, and muscle, the uptake of ^{64}Cu-DOTA-Y-PNA50-K4 was slightly lower than that of ^{64}Cu-DOTA-Y-PNA50S-K4 out to 4 h p.i. Both conjugates showed around 4%ID/organ of uptake in bone at 20 min p.i., but they were cleared to < 1%ID/organ at 4 h p.i. Negligible uptake was observed in lung, spleen, heart, and brain for both compounds (<1%ID/organ).

Intraperitoneal Injection. The biodistribution of ^{64}Cu-DOTA-Y-PNA50-K4 and ^{64}Cu-DOTA-Y-PNA50S-K4 via the intraperitoneal injection mode was performed in normal balb/c mice ($n = 3$) at 24 and 48 h p.i. The biodistribution data in selected organs are shown in

Table 2. Complementarity of PNAs Used in This Study to Human and Mouse mRNAs

PNA	mRNA	mRNA sequence with mismatches underlined	longest stretch of homology
PNA50	human unr	CATCCACAAAGCACACCAT	18
	mouse unr	CGTCCACAAAGCACATCAT	13
PNA5	human unr	AC̲AACAATGGACATAA̲TG	18
	mouse unr	ACAACAATGGACACAATG	13
PNA7	human unr	GACCGACGGACTG̲G̲GAAA	18
	mouse unr	GACCGG̲AGGACTGGGAAA	11
	mouse Slc37a3	A̲GAGG̲AC̲GGACTGGGAA̲G	14
	mouse pleckstrin	G̲C̲C̲TCACGGACTGGGAA̲A̲	13
PNA50S	human GALNT5	TC̲A̲TG̲TGCTTTGTGGATG	15

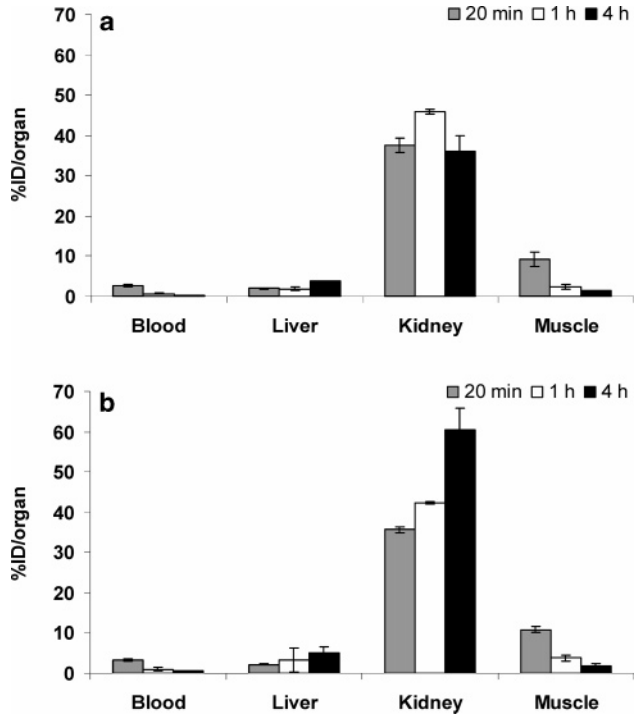

Figure 1. Biodistribution data of ^{64}Cu-DOTA-Y-PNA-K4 conjugates in selected organs of normal balb/c mice via the tail vein injection (n = 3). Injection dose: 10−12 μCi/100 μL. Upper: ^{64}Cu-DOTA-Y-PNA50-K4; lower: ^{64}Cu-DOTA-Y-PNA50S-K4. Data are present as %ID/organ ± SD.

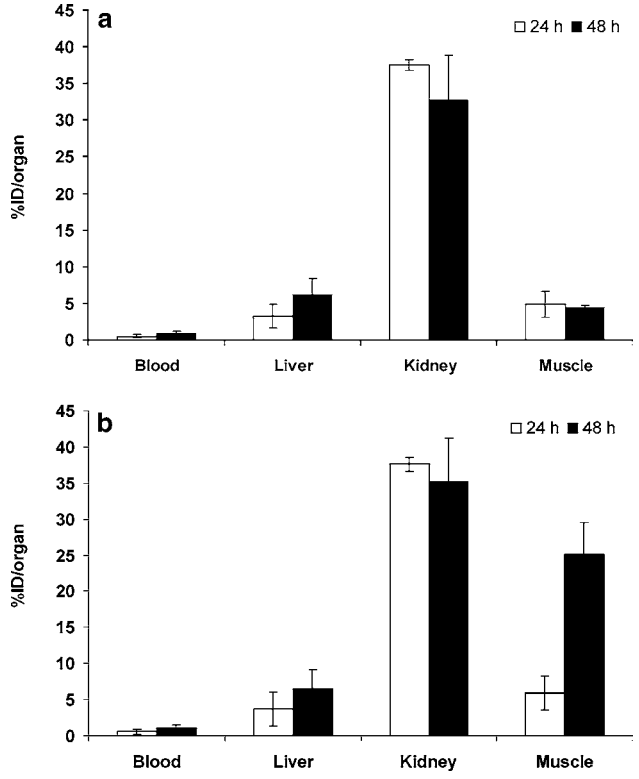

Figure 2. Biodistribution data of ^{64}Cu-DOTA-Y-PNA-K4 conjugates in selected organs of normal balb/c mice via intraperitoneal injection (n = 3). Injection dose: 55 μCi/100 μL. Upper: ^{64}Cu-DOTA-Y-PNA50-K4; lower: ^{64}Cu-DOTA−PNA50S-K4. Data are present as %ID/organ ± SD.

Figure 2. Both compounds exhibited similar uptake in kidney and liver at 24 h p.i. (^{64}Cu-DOTA-Y-PNA50-K4: 37.5 ± 0.7%ID/kidney and 3.2 ± 1.6%ID/liver; ^{64}Cu-DOTA-Y-PNA50S-K4: 37.6 ± 1.0%ID/kidney and 3.7 ± 2.4%ID/liver), which is comparable to the data of the i.v. mode at 20 min p.i. While no significant clearance was observed from kidney at 48 h p.i. for either compound (^{64}Cu-DOTA-Y-PNA50-K4: 33 ± 6%ID/kidney; ^{64}Cu-DOTA-Y-PNA50S-K4: 35 ± 6%ID/kidney), it is apparent that both conjugates were accumulating in liver out to 48 p.i. (^{64}Cu-DOTA-Y-PNA50-K4: 6.1 ± 2.1%ID/liver; ^{64}Cu-DOTA-Y-PNA50S-K4: 6.5 ± 2.6%ID/liver). Surprisingly, the muscle uptake of ^{64}Cu-DOTA-Y-PNA50S-K4 drastically increased from 5.9 ± 2.4%ID/muscle at 24 h p.i. to 25.0 ± 4.4%ID/muscle at 48 h p.i., while ^{64}Cu-DOTA-Y-PNA50-K4 maintained the same uptake level from 24 h (4.9 ± 1.8%ID/muscle) to 48 h p.i. (4.5 ± 0.2%ID/muscle). Both compounds exhibited low accumulation in other tissues (<1%ID/organ in lung, spleen, heart, and brain; < 2%ID/organ in blood and bone; and < 3%ID/organ in fat at 48 h p.i.).

MicroPET Imaging of ^{64}Cu-DOTA-Y-PNA-K4 Conjugates in MCF-7 Tumor Bearing Mice. The microPET imaging was performed in MCF-7 tumor-bearing CB-17 SCID mice with ^{64}Cu-DOTA-Y-PNA-K4 conjugates at 1, 4, and 24 h p.i. Of the four compounds, ^{64}Cu-DOTA-Y-PNA50-K4 exhibited visually the highest image contrast of the tumor, which was implanted in the nape of the neck, from 1 h out to 24 h p.i. (Figure 3a). Consistent with the biodistribution results, the microPET images (Figure 4) showed that the kidneys were the primary organ of accumulation of the PNA conjugates. As shown in Figure 3b, the solid tumor was also discernible from the surrounding tissues with ^{64}Cu-DOTA-Y-PNA50S-K4. The tumor was clearly imaged with ^{64}Cu-DOTA-Y-PNA5-K4 at 1 h p.i. (Figure 3c), but was not visible at either 4 or 24 h p.i. In contrast, ^{64}Cu-DOTA-Y-PNA7-K4 was able to give a fairly good image of the tumor at 24 h p.i. (Figure 3d) but not at the earlier time points.

The microPET images were analyzed by the quantification of radiotracer accumulation in the regions of interest (ROIs). The time−activity curves of the four PNA conjugates in the kidneys (represented by the left kidney), liver, and tumor are shown in Figure 5. It is apparent that the quantitative data are in agreement with the microPET images (Figures 3 and 4). The kidneys had the highest concentrations of all four compounds as shown by the standard uptake values (SUVs). The ^{64}Cu-labeled conjugates of PNA50, PNA50S, and PNA5 showed slow clearance from the kidneys and significant accumulation in the liver from 1 to 24 h p.i. While these three compounds exhibited similar uptake and retention in the kidneys and liver, ^{64}Cu-DOTA-Y-PNA7-K4 demonstrated significantly different behavior. In the kidneys, it showed the lowest uptake and the most efficient clearance out to 24 h p.i., whereas its liver concentration was the highest, at around five times those of other compounds at 1 h p.i., and remained at about the same level out to 24 h p.i. Copper-64-DOTA-Y-PNA50-K4 showed the highest SUV (0.076 ± 0.009) in tumor, followed by ^{64}Cu-DOTA-Y-PNA5-K4 (SUV: 0.034 ± 0.003) and ^{64}Cu-DOTA-Y-PNA50S-K4 (SUV: 0.018 ± 0.004) at 1 h p.i. While ^{64}Cu-DOTA-Y-PNA50-K4 exhibited rapid washout from tumor out to 4 h p.i., the accumulation level of ^{64}Cu-DOTA-Y-PNA50S-K4 remained steady within 24 h p.i. Consistent with the microPET images (Figure 3d), an appreciable amount of ^{64}Cu-DOTA-Y-PNA7-K4 accumulated in the tumor at 24 h p.i. (SUV: 0.031 ± 0.003).

Postimaging Biodistribution Data. The post imaging biodistribution experiments were carried out right after the microPET imaging at 24 p.i. The concentrations

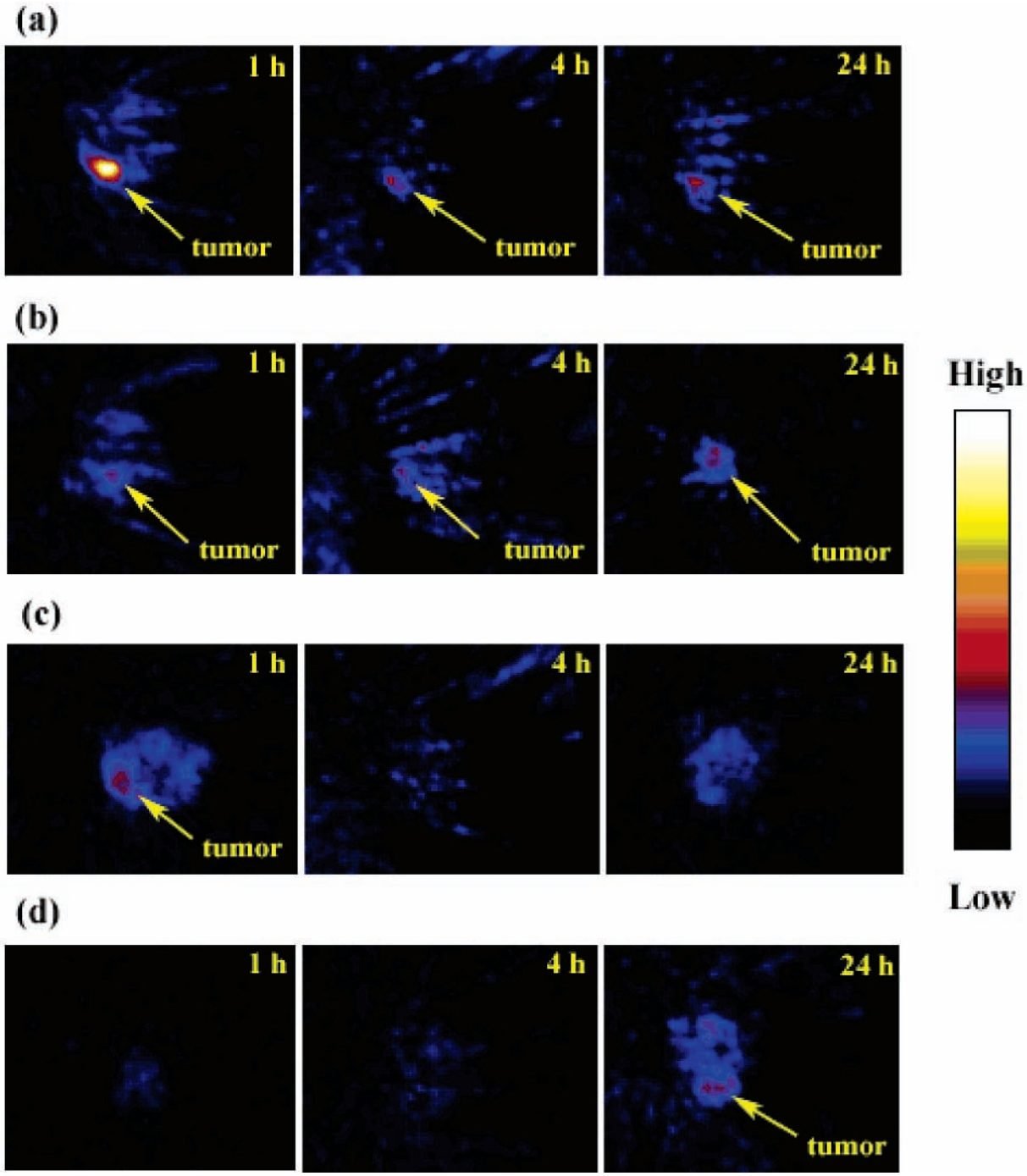

Figure 3. MicroPET transaxial images of ^{64}Cu-labeled PNA conjugates in MCF-7 tumor bearing CB-17 SCID mice. (a) ^{64}Cu-DOTA-Y-PNA50-K4 (injection dose: 210 μCi). (b) ^{64}Cu-DOTA-Y-PNA50S-K4 (injection dose: 347 μCi). (c) ^{64}Cu-DOTA-Y-PNA5-K4 (injection dose: 253 μCi). (d) ^{64}Cu-DOTA-Y-PNA7-K4 (injection dose: 361 μCi). The intensity of the images was decay-corrected and normalized to the injection dose.

of the four PNA conjugates in blood, liver, kidneys, muscle, and tumor were represented by percent of injected dose per gram of tissue (%ID/g) as shown in Figure 6. Copper-64-DOTA-Y-PNA50-K4 exhibited the highest concentration in the kidneys (280 ± 35%ID/g), followed by ^{64}Cu-DOTA-Y-PNA5-K4 (251 ± 50%ID/g), ^{64}Cu-DOTA-Y-PNA50S-K4 (174 ± 54%ID/g), and ^{64}Cu-DOTA-Y-PNA7-K4 (143%ID/g). While ^{64}Cu-DOTA-Y-PNA50-K4, ^{64}Cu-DOTA-Y-PNA50S-K4 and ^{64}Cu-DOTA-Y-PNA5-K4 showed similar low concentrations in the liver (5.6 ± 0.3%ID/g, 5.2 ± 2.2%ID/g, and 7.7 ± 1.1%ID/g, respectively), the concentration of ^{64}Cu-DOTA-Y-PNA7-K4 was much higher (28%ID/g). This observation is consistent with quantification of the microPET images. Although ^{64}Cu-DOTA-Y-PNA50-K4 and ^{64}Cu-DOTA-Y-PNA5-K4 showed similar tumor uptake (1.50 ± 0.11%ID/g and 1.35 ± 0.11%ID/g, respectively), the tumor/muscle (T/M) ratio of the former (T/M: 6.6 ± 1.1; $n = 2$) is about five times that of the latter due to the high concentration of ^{64}Cu-DOTA-Y-PNA5-K4 in muscle as shown in Figure 7. The T/M ratios of ^{64}Cu-DOTA-Y-PNA50S-K4 (3.0 ± 0.2; $n = 2$) and ^{64}Cu-DOTA-Y-PNA7-K4 (2.75; $n = 1$) are in between. Copper-64-DOTA-Y-PNA50-K4 also demonstrated the highest tumor/blood (T/B) ratio (T/B: 3.4 ± 0.0; $n = 2$) among the ^{64}Cu-labeled PNA conjugates at 24 h p.i.

Assay for Human and Mouse Unr mRNA Expression. To verify that the MCF-7 tumors were indeed

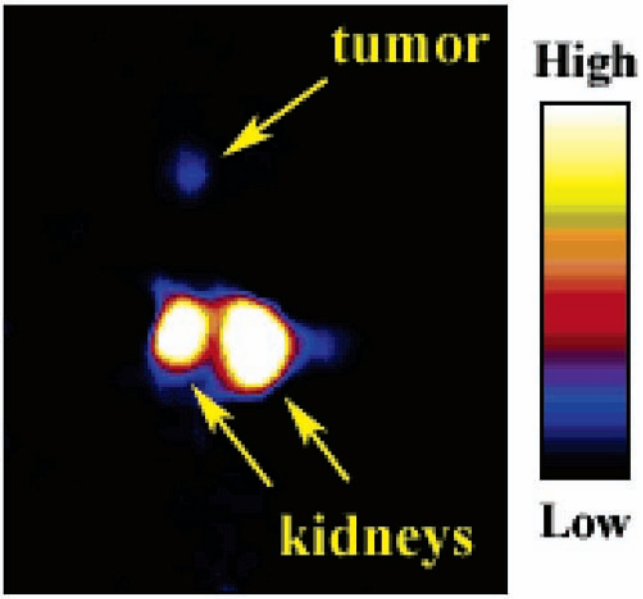

Figure 4. MicroPET coronal image of ^{64}Cu-DOTA-Y-PNA50-K4 in an MCF-7 tumor bearing CB-17 SCID mouse at 1 h p.i. The intensity of the images was scaled by max/min of frame.

producing human unr mRNA, unr mRNA expression was assayed by relative RT PCR using 18S rRNA as an internal control. Human unr mRNA-specific and nonspecific primers were designed based on the available sequences of human and mouse unr mRNA, and used to assay unr mRNA production in MCF-7 cells from tissue culture and from the tumor and other tissue specimens in a tumor-bearing mouse. The primers for the 18S RNA were nonspecies specific. As can be seen from Figure 8A, human unr mRNA was detected in the MCF-7 tumor in the mouse and was not detected in any other tissue samples. Use of the nonspecific PCR primers with the same tissue samples shows that mouse unr mRNA is produced in a number of tissues at variable levels (Figure 8B). The amount of unr mRNA detected with the human specific primers relative to the 18S rRNA is slightly greater in the tumor sample than it is in the MCF-7 cells from tissue culture, indicating that the expression level in the tumor is at least the same, if not more than it is in tissue culture. The amount of the unr mRNA detected with the nonspecific primers relative to the 18S rRNA is also slightly greater for the tumor than for the cultured cells indicating that the majority of the unr mRNA is being expressed by the MCF-7 cells.

DISCUSSION

Antisense oligonucleotides have been reported as nuclear imaging probes (PET and SPECT) in forms of unmodified oligomers or viral/nonviral carrier-oligomer conjugates (*8*, *14*, *15*, *62*). While the carrier systems could significantly enhance the tumor accumulation of oligonucleotides due to the increased payload of the carriers (*63*), a major concern is how to address the extent to which the biodistribution is determined by the carrier or the oligomer. Carrier-oligomer conjugates may also encounter the common difficulties of drug delivery systems, such as sequestration by reticulo-endothelial system (RES) and immunogenicity of the carriers (*8*). It is

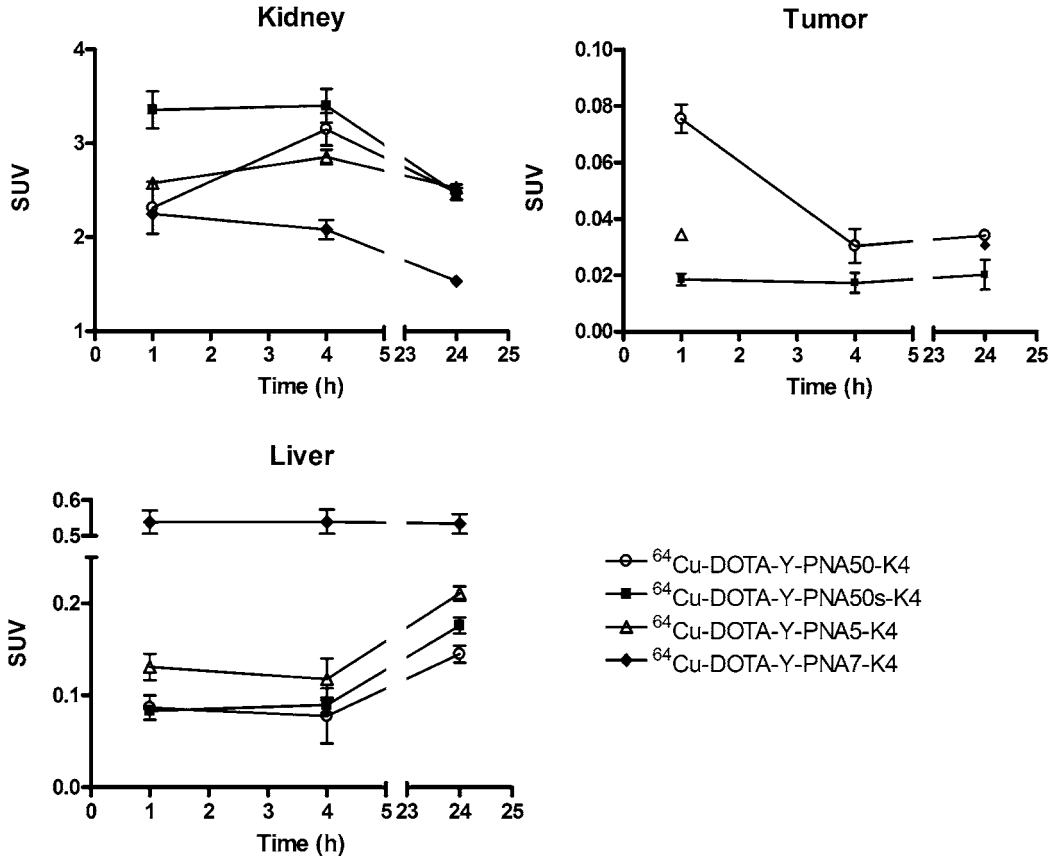

Figure 5. Time−activity curves of ^{64}Cu-DOTA-Y-PNA-K4 conjugates in MCF-7 tumor bearing CB-17 SCID mice. Data are obtained from averaging multiple microPET image slices in the selected organs and tumor and presented as mean SUV ± SD. Because of the low tumor to background contrast of ^{64}Cu-DOTA-Y-PNA5-K4 and ^{64}Cu-DOTA-Y-PNA7-K4, their SUV data in tumor are only obtainable at 1 and 24 h p.i., respectively.

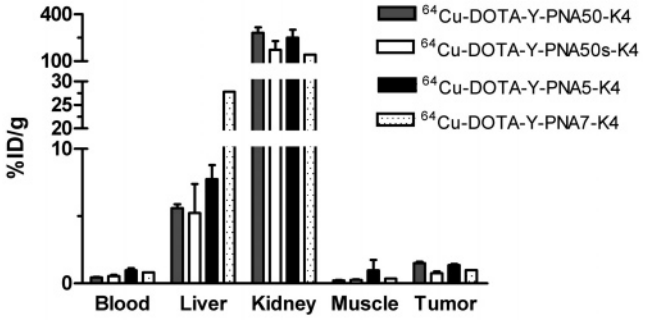

Figure 6. Biodistribution data of ^{64}Cu-DOTA-Y-PNA-K4 conjugates in MCF-7 tumor bearing CB-17 SCID mice post-microPET imaging at 24 h p.i. (n = 2). Data are present as %ID/g ± SD.

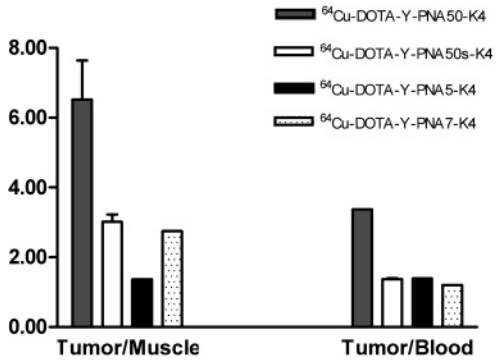

Figure 7. Ratios of tumor to muscle and tumor to blood of ^{64}Cu-DOTA-Y-PNA-K4 conjugates in MCF-7 tumor bearing CB-17 SCID mice at 24 h p.i. Data were calculated from biodistribution results of post-microPET imaging.

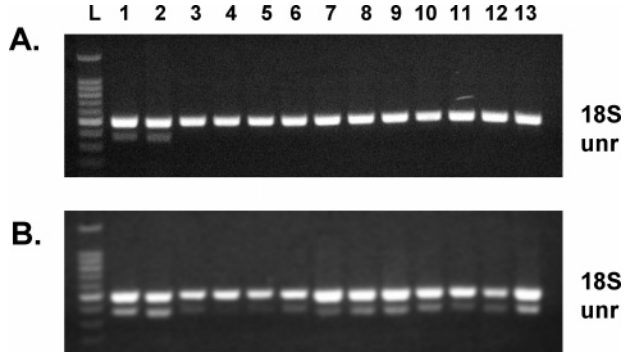

Figure 8. Relative RT-PCR assay for (A) human unr mRNA and (B) both human and mouse unr mRNA using 18S rRNA as an internal control. Lanes: 1, MCF-7 cells; 2, tumor; 3, muscle; 4, brain; 5, fat; 6, heart; 7, intestine; 8, kidney; 9, liver; 10, lung; 11, ovary; 12, spleen; and 13, uterus. The 18S PCR band is 488 nt, and the unr PCR band is 368 nt.

self-evident that unmodified or minimally modified oligonucleotides should be studied in-depth before they could be applied to the gene transfection or drug delivery systems for various proposes.

As a special class of oligonucleotide analogues, the biological behavior of PNAs has been extensively studied in vitro and in vivo since they were first proposed (*14*, *28*, *32*, *64*−*72*). In contrast, the utilization of PNAs as imaging probes of cancer for PET and SPECT is very limited, probably because the accumulation of the PNA imaging probes in the tumors could barely reach a detectable level. Recently, Sazani et al. reported that a PNA with four lysine at its N-terminus exhibited superior in vitro and vivo properties and sequence-specific activity compared to its analogue with one lysine (*6*, *33*).

Design of Cell Specific Imaging Probes. Our approach to the design of cell-specific PNA-based imaging agents is to: (1) identify an abundant, unique or uniquely overexpressed mRNA in the target cell, (2) identify high affinity antisense PNAs binding sites on the target mRNA, (3) covalently attach a permeation peptide to the PNAs that allows for reversible cell entry, and (4) attach a positron-emitting radionuclide with high specific activity to the PNA-permeation peptide conjugate. In our approach, the biological function of the mRNA is irrelevant, all that matters is that it is uniquely overexpressed and abundant in the target cell. As such this approach differs from other antisense approaches that often target oncogenes, which are only present in low copy number (<100). For this initial study we used SAGE analysis to identify the uniquely overexpressed (approximately 10-fold) and abundant unr mRNA in the MCF-7 cancer cell line (approximately 5000 copies/cell), and an RT-ROL assay to identify high affinity antisense binding sites on the mRNA. PNAs complementary to these sites were conjoined to the recently described permeation peptide Lys_4 (K4) (*6*, *33*) and the highest affinity PNA-K4 conjugates were linked to the ^{64}Cu binding ligand DOTA to create the MCF-7 cell-specific PET imaging agents.

As can be seen from Table 2, the antisense unr PNA sequences used also have partial complementarity to the mouse unr mRNA sequences and to some other mouse and human sequences. Though not determined in this study, the affinity of the PNAs to the mouse unr mRNA is expected to be diminished by the single and double mismatches, as well as by any changes in mRNA folding that would affect the accessibility of the antisense binding sites. Likewise, binding of PNA7 to two other mouse sequences is likely to be even more diminished by the presence of triple mismatches, even if these sites were accessible. While PNA50S was designed not to bind to the human unr mRNA, a search of the human genome revealed that it is complementary to the human GALNT5 mRNA. This mRNA is not likely to contribute to targeting of PNA50S to the tumor because it was not detected in the MCF-7 SAGE libraries, and has only been detected at very low levels in normal pooled brain and central retina SAGE libraries.

The labeling of DOTA-Y-PNA-K4 conjugates with ^{64}Cu was straightforward. The radiochemical yields were reasonably high, and a nearly perfect radiochemical purity was achieved after DTPA challenge of nonspecifically bound ^{64}Cu and centricon separation. The specific activity of the ^{64}Cu-labeled PNA conjugates was ca. 200 mCi/μmol (7400 MBq/μmol) at the injection time, which is the highest specific activity ever achieved for radiolabeled oligonucleotides (*62*, *73*, *74*) to the best of our knowledge. The radiolabeling conditions were optimized from the trials varying reaction temperature, time, pH, and media (data not shown).

Biodistribution of PNA Conjugates in Normal Mice. Concerned that our PNA conjugates might have rapid in vivo kinetics, we carried out biodistribution experiments in normal mice via i.v. and i.p. modes. The biodistribution via i.v. was performed within a short time period (4 h) postinjection, while the i.p. experiment was conducted at 24 and 48 h p.i. All four PNA conjugates showed high kidney uptake and long retention throughout time (Figures 1 and 2), no matter the injection mode. This observation is in agreement with McMahon's report on the in vivo behavior of PNAs (*75*). It differs, however, from what was observed for PNA50 and PNA50S lacking the DOTA group that were labeled at tyrosine with ^{131}I.

These PNAs showed predominant uptake in the liver (data not shown), indicating that the DOTA group influences the biodistribution properties of the PNA-K4 moiety.

While both PNA conjugates with unr mRNA antisense (PNA50) and sense (PNA50S) sequences exhibited a very similar pattern of tissue distribution within 1 h p.i., the conjugate with sense sequence showed a remarkably higher accumulation in kidney than its antisense counterpart ($P < 0.005$) at 4 h p.i. (Figure 1) which must be related to the differences in their base composition or sequence. As a result of the rapid pharmacokinetics of PNAs (*75*), our PNA conjugates showed a very low level of uptake in blood (<4%ID/blood) at the first time point of the i.v. biodistribution (20 min p.i.), and efficient clearance after then (Figure 1). The liver uptake was only around 5%ID/organ, which is similar to the levels previously reported for PNAs (*13*, *14*, *75*). The i.p. biodistribution showed the same profile as the i.v. experiment (Figures 1 and 2), which indicates that the tissue distribution of the PNA conjugates cannot be significantly altered by the administration modes.

Interestingly, the PNA conjugates with the sense sequence exhibited a significantly higher muscle accumulation at 48 h p.i. as compared to its antisense analogue ($P < 0.002$). It is possible that the sense PNA is complementary to the same or similar sequence found in mouse muscle, or that it shows some preferential affinity to some other biomolecule in muscle. A search of the mouse genome database, however, did not reveal any such homologous sequence (Table 2). As can also be seen from the table, all the antisense unr PNA sequences also show partial complementary to the mouse unr mRNA sequences, and to some other mouse and human sequences. The extent of binding to these sequences would depend on the folding of the mRNA and the effect of the mismatches, both of which are unknown at this time. The human GALNT5 has only been detected in a normal pooled brain and in a human central retina SAGE libraries at a level of 15 and 9 ppm, respectively, and is not present in the MCF-7 SAGE library, suggesting that any localization of PNA50S to the MCF-7 tumor is not due to the presence of another complementary mRNA.

Tumor Imaging with the PNA Conjugates. As shown in the microPET images (Figure 3), a tumor with a size of 100−320 mg in CB-17 SCID mice can be imaged with all four ^{64}Cu-labeled PNA conjugates. This is probably due in part to their high specific activity, which is about 5 times higher than that of the most recently reported ^{68}Ga-labeled oligonucleotide (*62*). The image contrast of the tumor at different time points varies greatly, however, with different compounds. At 1 and 4 h p.i., the tumor was not detectable with ^{64}Cu-DOTA-Y-PNA7-K4, whereas it gave a good tumor contrast at 24 h p.i. (Figure 3d). This behavior is what would be expected for an antisense PNA that slowly accumulates inside the tumor by binding to the target mRNA, which anchors the PNA within the cell, while PNA washes out from cells lacking the target mRNA. Interestingly, ^{64}Cu-DOTA-Y-PNA5-K4 behaved in the opposite way: it could only image the tumor at 1 h p.i. and not at either 4 or 24 h p.i. (Figure 3c). Both ^{64}Cu-DOTA-Y-PNA50-K4 and ^{64}Cu-DOTA-Y-PNA50S-K4 showed a tumor image at all the three time points, but the former conjugate exhibited a much higher tumor to background contrast, especially at 1 h p.i. (Figure 3a,b).

Quantitative analysis of the microPET images are in good agreement with the post imaging biodistribution data (Figures 5 and 6). This further confirmed the quantitation capability of microPET techniques in the field of molecular imaging. Copper-64-DOTA-Y-PNA5-K4 exhibited a similar tumor uptake to ^{64}Cu-DOTA-Y-PNA50-K4, however, the tumor was not discernible from the surrounding tissue at 24 h p.i. due to its relatively high accumulation in muscle and blood (Figure 6). This observation clearly demonstrates that the rapid and efficient clearance from blood and muscle is one of the essential criteria for a good imaging agent besides the high uptake in target organs. The comparatively high accumulation in muscle and blood may be due in part to targeting of the mouse unr mRNA, which differs by only a single nucleotide (Table 2) and appears to be present in muscle (Figure 8).

To the best of our knowledge, ^{64}Cu-DOTA-Y-PNA50-K4 has shown the highest and reproducible tumor/muscle ratio at 4 h (7.9 ± 3.3, data not presented) and at 24 h p.i. (6.6 ± 1.1) among the reported noncarrier bound oligonucleotides in the detection of cancer in vivo via nuclear imaging modalities (*14*, *62*). The tumor/muscle ratios for ^{64}Cu-DOTA-Y-PNA50-K4 are also 3.7 and 2.2 times greater than for ^{64}Cu-DOTA-Y-PNA50S-K4 at 4 and 24 h, respectively. The enhanced selectivity of ^{64}Cu-DOTA-Y-PNA50-K4 is consistent with selective binding of the PNA portion of the imaging agent to the unr mRNA inside the cell, though further studies will be needed to verify this. Further modification of the DOTA−PNA50 conjugate and others is under investigation to increase the selectivity of tumor targeting and to minimize accumulation in kidneys.

CONCLUSION

In conclusion, we have designed and synthesized four PNAs with a four-lysine tail at the C terminus, one with a sense sequence and three with antisense sequences for the unr mRNA, which is overexpressed in MCF-7 cell line. To evaluate their in vivo behavior and tumor-targeting property, we incorporated a DOTA moiety into the PNAs so that the conjugates can be radiolabeled with ^{64}Cu for biodistribution and microPET imaging studies in normal and MCF-7 tumor bearing mice. Of the PNA conjugates studied, ^{64}Cu-DOTA-Y-PNA50-K4 showed the best image contrast of MCF-7 tumor in CB-17 SCID mice, and its tumor/muscle ratio is reproducible and the highest among the radiolabeled oligonucleotides that have been reported for in vivo detection of tumor. On the other hand, the tumor/muscle ratio of ^{64}Cu-DOTA-Y-PNA50-K4 is only about 4-fold better at best than the corresponding sense sequence, indicating that factors other than sequence complementarity to the unr mRNA play a significant role in tumor localization. Likewise, the two other antisense PNA conjugates did not behave like ^{64}Cu-DOTA-Y-PNA50-K4, showing either higher uptake in muscle (^{64}Cu-DOTA-Y-PNA5-K4) or increasing contrast with time (^{64}Cu-DOTA-Y-PNA7-K4). While our studies further indicate that antisense PNAs have great potential to be developed as oncogene or mRNA specific probes for early diagnosis and treatment of specific cancers when ^{64}Cu is delivered in higher amounts (*52*−*56*), there is much to be learned about what governs distribution and localization kinetics of PNA conjugates in vivo.

ACKNOWLEDGMENT

We thank Nicole Fettig, John Engelbach, Lynne Jones, Susan Adams, and Terry Sharp for technical assistance in the biodistribution and microPET imaging studies and Jerrel Rutlin for quantitative analysis of the microPET

images. We also thank Xuan Yue for obtaining the MALDI-TOF of the PNAs. This research was supported by an NCI/NASA Biomolecular Sensors contract (N01-CO-27103). The copper-64 was provided by Washington University School of Medicine and partially funded through NCI Grant R24 CA86307 (M.J.W.).

LITERATURE CITED

(1) Rowland, D. J., Lewis, J. S., and Welch, M. J. (2002) Molecular imaging: The application of small animal positron emission tomography. *J. Cell. Biochem. Suppl. 39*, 110−115.

(2) Rohren, E. M., Turkington, T. G., and Coleman, R. E. (2004) Clinical applications of PET in oncology. *Radiology 231*, 305−332.

(3) Claverie, J. M. (2001) Gene number. What if there are only 30,000 human genes? *Science 291*, 1255−1257.

(4) Woolf, T. M., Melton, D. A., and Jennings, C. G. (1992) Specificity of antisense oligonucleotides in vivo. *Proc. Natl. Acad. Sci. U.S.A. 89*, 7305−7309.

(5) Tavitian, B., Terrazzino, S., Kuhnast, B., Marzabal, S., Stettler, O., Dolle, F., Deverre, J. R., Jobert, A., Hinnen, F., Bendriem, B., Crouzel, C., and Di Giamberardino, L. (1998) In vivo imaging of oligonucleotides with positron emission tomography. *Nat. Med. 4*, 467−471.

(6) Sazani, P., Gemignani, F., Kang, S. H., Maier, M. A., Manoharan, M., Persmark, M., Bortner, D., and Kole, R. (2002) Systemically delivered antisense oligomers upregulate gene expression in mouse tissues. *Nat. Biotechnol. 20*, 1228−1233.

(7) Sazani, P., Astriab-Fischer, A., and Kole, R. (2003) Effects of base modifications on antisense properties of 2′-O-methoxyethyl and PNA oligonucleotides. *Antisense Nucleic Acid Drug Dev. 13*, 119−128.

(8) Younes, C. K., Boisgard, R., and Tavitian, B. (2002) Labeled oligonucleotides as radiopharmaceuticals: Pitfalls, problems and perspectives. *Curr. Pharm. Des. 8*, 1451−1466.

(9) Nielsen, P. E., Egholm, M., Berg, R. H., and Buchardt, O. (1991) Sequence-selective recognition of DNA by strand displacement with a thymine-substituted polyamide. *Science 254*, 1497−1500.

(10) Larsen, H. J., Bentin, T., and Nielsen, P. E. (1999) Antisense properties of peptide nucleic acid. *Biochim. Biophys. Acta 1489*, 159−166.

(11) Paulasova, P., Andreo, B., Diblik, J., Macek, M., and Pellestor, F. (2004) The peptide nucleic acids as probes for chromosomal analysis: Application to human oocytes, polar bodies and preimplantation embryos. *Mol. Hum. Reprod. 10*, 467−472.

(12) Shi, N., Boado, R. J., and Pardridge, W. M. (2000) Antisense imaging of gene expression in the brain in vivo. *Proc. Natl. Acad. Sci. U.S.A. 97*, 14709−14714.

(13) Lee, H. J., Boado, R. J., Braasch, D. A., Corey, D. R., and Pardridge, W. M. (2002) Imaging gene expression in the brain in vivo in a transgenic mouse model of Huntington's disease with an antisense radiopharmaceutical and drug-targeting technology. *J. Nucl. Med. 43*, 948−956.

(14) Rao, P. S., Tian, X., Qin, W., Aruva, M. R., Sauter, E. R., Thakur, M. L., and Wickstrom, E. (2003) ^{99m}Tc-peptide-peptide nucleic acid probes for imaging oncogene mRNAs in tumours. *Nucl. Med. Commun. 24*, 857−863.

(15) Tian, X., Aruva, M. R., Rao, P. S., Qin, W., Read, P., Sauter, E. R., Thakur, M. L., and Wickstrom, E. (2003) Imaging oncogene expression. *Ann. N. Y. Acad. Sci. 1002*, 165−188.

(16) Tian, X., Aruva, M. R., Qin, W., Zhu, W., Sauter, E. R., Thakur, M. L., and Wickstrom, E. (2005) Noninvasive molecular imaging of MYC mRNA expression in human breast cancer xenografts with a [(99m)Tc]peptide-peptide nucleic acid-peptide chimera. *Bioconjugate Chem. 16*, 70−79.

(17) McMahon, B. M., Stewart, J. A., Jackson, J., Fauq, A., McCormick, D. J., and Richelson, E. (2001) Intraperitoneal injection of antisense peptide nucleic acids targeted to the mu receptor decreases response to morphine and receptor protein levels in rat brain. *Brain Res. 904*, 345−349.

(18) McMahon, B. M., Stewart, J. A., Bitner, M. D., Fauq, A., McCormick, D. J., and Richelson, E. (2002) Peptide nucleic acids specifically cause antigene effects in vivo by systemic injection. *Life Sci. 71*, 325−337.

(19) McMahon, B. M., Stewart, J., Fauq, A., Younkin, S., Younkin, L., and Richelson, E. (2002) Using peptide nucleic acids as gene-expression modifiers to reduce beta-amyloid levels. *J. Mol. Neurosci. 19*, 71−76.

(20) Filipovska, A., Eccles, M. R., Smith, R. A., and Murphy, M. P. (2004) Delivery of antisense peptide nucleic acids (PNAs) to the cytosol by disulphide conjugation to a lipophilic cation. *FEBS Lett. 556*, 180−186.

(21) Herbert, B., Pitts, A. E., Baker, S. I., Hamilton, S. E., Wright, W. E., Shay, J. W., and Corey, D. R. (1999) Inhibition of human telomerase in immortal human cells leads to progressive telomere shortening and cell death. *Proc. Natl. Acad. Sci. U.S.A. 96*, 14276−14281.

(22) Hamilton, S. E., Simmons, C. G., Kathiriya, I. S., and Corey, D. R. (1999) Cellular delivery of peptide nucleic acids and inhibition of human telomerase. *Chem. Biol. 6*, 343−351.

(23) Mologni, L., Marchesi, E., Nielsen, P. E., and Gambacorti-Passerini, C. (2001) Inhibition of promyelocytic leukemia (PML)/retinoic acid receptor-alpha and PML expression in acute promyelocytic leukemia cells by anti-PML peptide nucleic acid. *Cancer Res. 61*, 5468−5473.

(24) Coester, C., Kreuter, J., von Briesen, H., and Langer, K. (2000) Preparation of avidin-labeled gelatin nanoparticles as carriers for biotinylated peptide nucleic acid (PNA). *Int. J. Pharm. 196*, 147−149.

(25) Sun, L., Fuselier, J. A., Murphy, W. A., and Coy, D. H. (2002) Antisense peptide nucleic acids conjugated to somatostatin analogues and targeted at the n-myc oncogene display enhanced cytotoxity to human neuroblastoma IMR32 cells expressing somatostatin receptors. *Peptides 23*, 1557−1565.

(26) Bertrand, J. R., Sumbatyan, N., and Malvy, C. (2003) Covalent coupling of a PIM-1 oncogene targeted PNA with an antennapedia derived peptide. *Nucleosides Nucleotides Nucleic Acids 22*, 1611−1613.

(27) de Koning, M. C., van der Marel, G. A., and Overhand, M. (2003) Synthetic developments towards PNA-peptide conjugates. *Curr. Opin. Chem. Biol. 7*, 734−740.

(28) Eriksson, M., Nielsen, P. E., and Good, L. (2002) Cell permeabilization and uptake of antisense peptide-peptide nucleic acid (PNA) into *Escherichia coli*. *J. Biol. Chem. 277*, 7144−7147.

(29) Gait, M. J. (2003) Peptide-mediated cellular delivery of antisense oligonucleotides and their analogues. *Cell. Mol. Life Sci. 60*, 844−853.

(30) Gallazzi, F., Wang, Y., Jia, F., Shenoy, N., Landon, L. A., Hannink, M., Lever, S. Z., and Lewis, M. R. (2003) Synthesis of radiometal-labeled and fluorescent cell-permeating peptide-PNA conjugates for targeting the bcl-2 proto-oncogene. *Bioconjugate Chem. 14*, 1083−1095.

(31) Lewis, M. R., Jia, F., Gallazzi, F., Wang, Y., Zhang, J., Shenoy, N., Lever, S. Z., and Hannink, M. (2002) Radiometal-labeled peptide-PNA conjugates for targeting bcl-2 expression: Preparation, characterization, and in vitro mRNA binding. *Bioconjugate Chem. 13*, 1176−1180.

(32) Koppelhus, U., and Nielsen, P. E. (2003) Cellular delivery of peptide nucleic acid (PNA). *Adv. Drug Delivery Rev. 55*, 267−280.

(33) Sazani, P., Kang, S. H., Maier, M. A., Wei, C., Dillman, J., Summerton, J., Manoharan, M., and Kole, R. (2001) Nuclear antisense effects of neutral, anionic and cationic oligonucleotide analogues. *Nucleic Acids Res. 29*, 3965−3974.

(34) DeRisi, J., Penland, L., Brown, P. O., Bittner, M. L., Meltzer, P. S., Ray, M., Chen, Y., Su, Y. A., and Trent, J. M. (1996) Use of a cDNA microarray to analyse gene expression patterns in human cancer. *Nat. Genet. 14*, 457−460.

(35) Duggan, D. J., Bittner, M., Chen, Y., Meltzer, P., and Trent, J. M. (1999) Expression profiling using cDNA microarrays. *Nat. Genet. 21*, 10−14.

(36) De Vos, J., Thykjaer, T., Tarte, K., Ensslen, M., Raynaud, P., Requirand, G., Pellet, F., Pantesco, V., Reme, T., Jourdan, M., Rossi, J. F., Orntoft, T., and Klein, B. (2002) Comparison of gene expression profiling between malignant and normal plasma cells with oligonucleotide arrays. *Oncogene 21*, 6848−6857.

(37) Tan, Z. J., Hu, X. G., Cao, G. S., and Tang, Y. (2003) Analysis of gene expression profile of pancreatic carcinoma using cDNA microarray. *World J. Gastroenterol. 9*, 818−823.

(38) Velculescu, V. E., Zhang, L., Vogelstein, B., and Kinzler, K. W. (1995) Serial analysis of gene expression. *Science 270*, 484−487.

(39) Zhang, L., Zhou, W., Velculescu, V. E., Kern, S. E., Hruban, R. H., Hamilton, S. R., Vogelstein, B., and Kinzler, K. W. (1997) Gene expression profiles in normal and cancer cells. *Science 276*, 1268−1272.

(40) Stahel, R. A., and Zangemeister-Wittke, U. (2003) Antisense oligonucleotides for cancer therapy-an overview. *Lung Cancer*, *41* (Suppl. 1), S81−S88.

(41) Jeffers, M., Paciucci, R., and Pellicer, A. (1990) Characterization of unr; a gene closely linked to N-ras. *Nucleic Acids Res. 18*, 4891−4899.

(42) Boussadia, O., Amiot, F., Cases, S., Triqueneaux, G., Jacquemin-Sablon, H., and Dautry, F. (1997) Transcription of unr (upstream of N-ras) down-modulates N-ras expression in vivo. *FEBS Lett. 420*, 20−24.

(43) Triqueneaux, G., Velten, M., Franzon, P., Dautry, F., and Jacquemin-Sablon, H. (1999) RNA binding specificity of Unr, a protein with five cold shock domains. *Nucleic Acids Res. 27*, 1926−1934.

(44) Ferrer, N., Garcia-Espana, A., Jeffers, M., and Pellicer, A. (1999) The unr gene: Evolutionary considerations and nucleic acid-binding properties of its long isoform product. *DNA Cell. Biol. 18*, 209−218.

(45) Anderson, C. J., Connett, J. M., Schwarz, S. W., Rocque, P. A., Guo, L. W., Philpott, G. W., Zinn, K. R., Meares, C. F., and Welch, M. J. (1992) Copper-64-labeled antibodies for PET imaging. *J. Nucl. Med. 33*, 1685−1691.

(46) Anderson, C. J., Rocque, P. A., Weinheimer, C. J., and Welch, M. J. (1993) Evaluation of copper-labeled bifunctional chelate-albumin conjugates for blood pool imaging. *Nucl. Med. Biol. 20*, 461−467.

(47) Anderson, C. J., and Welch, M. J. (1999) Radiometal-labeled agents (non-technetium) for diagnostic imaging. *Chem. Rev. 99*, 2219−2234.

(48) Anderson, C. J., Dehdashti, F., Cutler, P. D., Schwarz, S. W., Laforest, R., Bass, L. A., Lewis, J. S., and McCarthy, D. W. (2001) ^{64}Cu-TETA-Octreotide as a PET imaging agent for patients with neuroendocrine tumors. *J. Nucl. Med. 42*, 213−221.

(49) Li, W. P., Lewis, J. S., Kim, J., Bugaj, J. E., Johnson, M. A., Erion, J. L., and Anderson, C. J. (2002) DOTA-D-Tyr(1)-octreotate: A somatostatin analogue for labeling with metal and halogen radionuclides for cancer imaging and therapy. *Bioconjugate Chem. 13*, 721−728.

(50) Philpott, G. W., Schwarz, S. W., Anderson, C. J., Dehdashti, F., Connett, J. M., Zinn, K. R., Meares, C. F., Cutler, P. D., Welch, M. J., and Siegel, B. A. (1995) RadioimmunoPET: Detection of colorectal carcinoma with positron-emitting copper-64-labeled monoclonal antibody. *J. Nucl. Med. 36*, 1818−1824.

(51) Rogers, B. E., Bigott, H. M., McCarthy, D. W., Della Manna, D., Kim, J., Sharp, T. L., and Welch, M. J. (2003) MicroPET imaging of a gastrin-releasing peptide receptor-positive tumor in a mouse model of human prostate cancer using a ^{64}Cu-labeled bombesin analogue. *Bioconjugate Chem. 14*, 756−763.

(52) Anderson, C. J., Jones, L. A., Bass, L. A., Sherman, E. L. C., McCarthy, D. W., Cutler, P. D., Lanahan, M. V., Cristel, M. E., Lewis, J. S., and Schwarz, S. W. (1998) Radiotheraphy, toxicity and dosimetry of copper-64-TETA-octreotide in tumor-bearing rats. *J. Nucl. Med. 39*, 1944−1951.

(53) Lewis, J. S., R., L. M., Cutler, P. D., Srinivasan, A., Schmidt, M. A., Schwarz, S. W., Morris, M. M., Miller, J. P., and Anderson, C. J. (1999) Radiotherapy and dosimetry of ^{64}Cu-TETA-Tyr3-octreotate in a somatostatin receptor-positive, tumor-bearing rat model. *Clin. Cancer Res. 5*, 3608−3616.

(54) Lewis, J. S., Laforest, R., Lewis, M. R., and Anderson, C. J. (2000) Comparative dosimetry of copper-64 and yttrium-90-labeled somatostatin analogues in a tumor-bearing rat model. *Cancer Biother. Radiopharm. 15*, 593−604.

(55) Connett, J. M., Anderson, C. J., Guo, L. W., Schwarz, S. W., Zinn, K. R., Rogers, B. E., Siegel, B. A., Philpott, G. W., and Welch, M. J. (1996) Radioimmunotherapy with a ^{64}Cu-labeled monoclonal antibody: A comparison with ^{67}Cu. *Proc. Natl. Acad. Sci. U.S.A. 93*, 6814−6818.

(56) Zimmermann, K., Grunberg, J., Honer, M., Ametamey, S., Schubiger, P. A., and Novak-Hofer, I. (2003) Targeting of renal carcinoma with $^{67/64}$Cu-labeled anti-Li-CAM antibody chCE7: Selection of copper ligands and PET imaging. *Nucl. Med. Biol. 30*, 417−427.

(57) McCarthy, D. W., Bass, L. A., Cutler, P. D., Shefer, R. E., Klinkowstein, R. E., Herrero, P., Lewis, J. S., Cutler, C. S., Anderson, C. J., and Welch, M. J. (1999) High purity production and potential applications of copper-60 and copper-61. *Nucl. Med. Biol. 26*, 351−358.

(58) McCarthy, D. W., Shefer, R. E., Klinkowstein, R. E., Bass, L. A., Margeneau, W. H., Cutler, C. S., Anderson, C. J., and Welch, M. J. (1997) Efficient production of high specific activity ^{64}Cu using a biomedical cyclotron. *Nucl. Med. Biol. 24*, 35−43.

(59) Knoess, C., Siegel, S., Smith, A., Newport, D., Richerzhagen, N., Winkeler, A., Jacobs, A., Goble, R., Graf, R., Wienhard, K., and Heiss, W. (2003) Performance evaluation of the microPET R4 PET scanner for rodents. *Eur. J. Nucl. Med. Mol. Imaging 30*, 737−747.

(60) Patlak, C. S., Blasberg, R. G., and Fenstermacher, J. D. (1983) Graphical evaluation of blood-to-brain transfer constants from multiple-time uptake data. *J. Cereb. Blood Flow Metab. 3*, 1−7.

(61) Allawi, H. T., Dong, F., Ip, H. S., Neri, B. P., and Lyamichev, V. I. (2001) Mapping of RNA accessible sites by extension of random oligonucleotide libraries with reverse transcriptase. *RNA 7*, 314−327.

(62) Roivainen, A., Tolvanen, T., Salomäki, S., Lendvai, G., Velikyan, I., Numminen, P., Välilä, M., Sipilä, H., Bergström, M., Härkönen, P., Lönnberg, H., and Långström, B. (2004) ^{68}Ga-labeled oligonucleotides for in vivo imaging with PET. *J. Nucl. Med. 45*, 347−355.

(63) Sato, N., Kobayashi, H., Saga, T., Nakamoto, Y., Ishimori, T., Togashi, K., Fujibayashi, Y., Konishi, J., and Brechbiel, M. W. (2001) Tumor targeting and imaging of intraperitoneal tumors by use of antisense oligo-DNA complexed with dendrimers and/or avidin in mice. *Clin. Cancer Res. 7*, 3606−3612.

(64) Boffa, L. C., Scarfi, S., Mariani, M. R., Damonte, G., Allfrey, V. G., Benatti, U., and Morris, P. L. (2000) Dihydrotestosterone as a selective cellular/nuclear localization vector for antigene peptide nucleic acid in prostatic carcinoma cells. *Cancer Res. 60*, 2258−2262.

(65) Good, L., Sandberg, R., Larsson, O., Nielsen, P. E., and Wahlestedt, C. (2000) Antisense PNA effects in *Escherichia coli* are limited by the outer-membrane LPS layer. *Microbiology 146* (Part 10), 2665−2670.

(66) Fraser, G. L., Holmgren, J., Clarke, P. B., and Wahlestedt, C. (2000) Antisense inhibition of delta-opioid receptor gene function in vivo by peptide nucleic acids. *Mol. Pharmacol. 57*, 725−731.

(67) Pooga, M., Land, T., Bartfai, T., and Langel, U. (2001) PNA oligomers as tools for specific modulation of gene expression. *Biomol. Eng. 17*, 183−192.

(68) Pooga, M., and Langel, U. (2001) Targeting of cancer-related proteins with PNA oligomers. *Curr. Cancer Drug Targets 1*, 231−239.

(69) Siwkowski, A. M., Malik, L., Esau, C. C., Maier, M. A., Wancewicz, E. V., Albertshofer, K., Monia, B. P., Bennett, C. F., and Eldrup, A. B. (2004) Identification and functional validation of PNAs that inhibit murine CD40 expression by redirection of splicing. *Nucleic Acids Res. 32*, 2695−2706.

(70) Pellestor, F., and Paulasova, P. (2004) The peptide nucleic acids, efficient tools for molecular diagnosis (review). *Int. J. Mol. Med. 13*, 521−525.
(71) Kristensen, E. (2002) In vitro and in vivo studies on the pharmacokinetics and metabolism of PNA constructs in rodents. *Methods Mol. Biol. 208*, 259−269.
(72) Crooke, S. T. (2004) Progress in antisense technology. *Annu. Rev. Med. 55*, 61−95.
(73) Watanabe, N., Sawai, H., Endo, K., Shinozuka, K., Ozaki, H., Tanada, S., Murata, H., and Sasaki, Y. (1999) Labeling of phosphorothioate antisense oligonucleotides with yttrium-90. *Nucl. Med. Biol. 26*, 239−243.
(74) Kuhnast, B., Dolle, F., Terrazzino, S., Rousseau, B., Loc'h, C., Vaufrey, F., Hinnen, F., Doignon, I., Pillon, F., David, C., Crouzel, C., and Tavitian, B. (2000) General method to label antisense oligonucleotides with radioactive halogens for pharmacological and imaging studies. *Bioconjugate Chem. 11*, 627−636.
(75) McMahon, B. M., Mays, D., Lipsky, J., Stewart, J. A., Fauq, A., and Richelson, E. (2002) Pharmacokinetics and tissue distribution of a peptide nucleic acid after intravenous administration. *Antisense Nucleic Acid Drug Dev. 12*, 65−70.

BC049783U

Design of Phosphoramidite Monomer for Optimal Incorporation of Functional Intercalator to Main Chain of Oligonucleotide

Yun Shi, Kenzo Machida, Akinori Kuzuya, and Makoto Komiyama*

Research Center for Advanced Science and Technology, The University of Tokyo, 4-6-1 Komaba, Meguro-ku, Tokyo 153-8904, Japan. Received December 22, 2004

Chirally pure phosphoramidite monomers bearing 9-amino-6-chloro-2-methoxyacridine were synthesized from D- or L-threoninol and ω-aminocarboxylic acid, and incorporated into oligonucleotides. These acridine−DNA conjugates formed stable duplexes with complementary RNA because of intercalation of the acridine to DNA/RNA heteroduplexes. The stability of duplexes was not very dependent on either the chirality of the central carbon bearing the acridine or the length of the side chain. However, the ability for site-selective activation of the phosphodiester linkage in front of the acridine, which induced Lu(III)-promoted RNA scission, was strongly dependent on these two factors. The largest activation was achieved when the monomer unit was prepared from L-threoninol and 4-aminobutyric acid and the acridine was bound to the amino group. By attaching the more acidic 9-amino-2-methoxy-6-nitroacridine to this optimized scaffold, a quite effective acridine−DNA conjugate for site-selective RNA scission was obtained.

INTRODUCTION

To date, various conjugates of oligonucleotides with functional molecules (e.g., intercalating agents, fluorescent dyes, metal complexes, and others) have been prepared because of their attractive potentials for biological and biochemical applications (*1*−*4*). In many cases, functional molecules were tethered to either appropriate position in the nucleotide or the terminus of the main chain of the oligonucleotide. The introduction of functional molecules to the middle of main chain is also attractive, since these molecules can be placed at predetermined positions in helically structured duplexes and thus show various specific functions (*5*−*13*). One of the most important factors in this main chain modification is the design of a monomer unit that bears the functional molecules. Its structure must be optimized in order for the functional molecules to exert their designated roles satisfactorily.

Recently, we incorporated an acridine to the main chain of oligonucleotides and used these conjugates for site-selective scission of RNA (*14*, *15*). When these conjugates form heteroduplexes with complementary RNA, the acridine intercalates into the duplex and activates the confronting phosphodiester linkages of the RNA. As a result, these linkages are selectively hydrolyzed by metal ions such as lanthanide(III), Zn(II), and Mn(II). The RNA activation was ascribed to both acid catalysis by the ring nitrogen of acridine and the conformational change of the RNA backbone (*15*, *16*).

In those studies, the monomer unit for the introduction of acridine was prepared from 1,3-propanediol, which involves a prochiral carbon. The oligonucleotide additives were used as a mixture of two diastereomers derived from the chirality of this central carbon in the main chain. Accordingly, a detailed study on the relationship between the structure of the acridine−oligonucleotide conjugate and its RNA-activating ability was difficult. In this paper, a series of DNA conjugates bearing 9-amino-6-chloro-2-methoxyacridine are synthesized in chirally pure forms by using D- or L-threoninol as starting material (*17*). Thermodynamic stabilities of duplexes between these conjugates and their complementary RNA, as well as the mode of interactions of the acridine with these duplexes, are systematically studied, and their dependencies on the chirality of central carbon and the length of the side chain are quantitatively clarified. Furthermore, the RNA-activating abilities of these acridine−DNA conjugates (and thus the rates of the resultant site-selective RNA scission) are also investigated, since they should strongly reflect even subtle change in the interactions of the acridine with the confronting phosphodiester linkages.

EXPERIMENTAL PROCEDURES

Materials. The phosphoramidite monomers for the preparation of chiral acridine−DNA conjugates were synthesized from D- or L-threoninol, ω-aminocarboxylic acid, and acridine, as described in the Supporting Information. Details of the spectroscopic characterization of the products and the intermediates are presented there. The solvents used for their synthesis (pyridine, DMF, and dichloromethane) were sufficiently dried by molecular sieves. Unless noted otherwise, conventional 9-amino-6-chloro-2-methoxyacridine was used. Introduction of 9-amino-2-methoxy-6-nitroacridine to the phosphoramidite monomer (and thus to oligonucleotides) was achieved according to a preliminary communication (*16*). Other reagents and solvents were obtained from Glen Research Co., Tokyo Kasei Organic Chemicals, Aldrich Chemical Co., or Wako Pure Chemical Industries, Ltd.

Measurement of Melting Temperatures (T_m) of the Heteroduplexes between Acridine−DNA Conjugate and Its Complementary RNA. Melting profiles were measured on a JASCO V-530 UV/vis spectrophotometer. The absorbance at 260 nm was measured from 20 °C to 60 °C (only for DNA_2-S/RNA_2, from 5 °C to 60 °C) in a quartz cell of 1 cm path length with a heating

* Author to whom correspondence should be addressed. Tel: +81-3-5452-5200. Fax: +81-3-5452-5209. E-mail: komiyama@mkomi.rcast.u-tokyo.ac.jp.

10.1021/bc049698m CCC: $30.25 © 2005 American Chemical Society
Published on Web 03/01/2005

rate of 1.0 °C/min. The specimens contained DNA_2-**X** (1 μM), RNA_2 (1 μM), and NaCl (200 mM) in pH 8.0 Tris-HCl buffer (10 mM).

Spectroscopy. Fluorescence spectra were measured at 10 °C on a JASCO FP-750 spectrofluorometer with the excitation of the acridine at 346 nm. The specimens containing DNA_2-**X** conjugate (5 μM), Tris-HCl buffer (10 mM), and NaCl (200 mM) were titrated with 0.0, 0.5, 1.0, 1.5, and 2.0 equiv of RNA_2 (0−10 μM). The CD spectra were obtained on a JASCO J-820 spectropolarimeter at 10 °C in pH 8.0 phosphate buffer (10 mM); [DNA_2-**X**] = 0.5 mM, [RNA_2] = 0.5 mM, and [NaCl] = 200 mM in a quartz cell of 0.1 cm path length. For UV/vis absorption spectroscopy, a JASCO V-530 spectrometer was used.

Molecular Modeling. The Insight II/Discover 98.0 program package was used for conformational energy minimization. The acridine residue attached to the 36-mer DNA strand was built using the graphical program. In the energy minimization, neither water nor counterions were explicitly included, and their effects were simulated by a sigmoidal and distance-dependent dielectric function. The AMBER95 force field was used for the calculation. Computations were carried out on a Silicon Graphics Octane workstation with the operating system IRIX64 Release 6.5.

Assay of the Abilities of Acridine−DNA Conjugates for Lu(III)-Promoted Site-Selective RNA Hydrolysis. The site-selective RNA hydrolysis was carried out as described previously (*15*). The substrate RNA (RNA_1, 5 μM), labeled with 6-carboxyfluorescein (FAM) at the 5′-end, and the acridine−DNA conjugate (DNA_1-**X**, 10 μM) were dissolved in 10 mM Tris-HCl buffer (pH 8.0) containing NaCl (200 mM). The mixture was heated to 90 °C for 1 min, and slowly cooled to room temperature. Then, $^1/_{10}$ volume of an aqueous solution of $LuCl_3$ was added to the mixture (its final concentration was 100 μM). The mixtures were shielded from ambient light in order to avoid the possibility of any concurrent photoreactions (it later turned out that this procedure is not necessarily required). After a predetermined period of time at 37 °C, the reaction was quenched by 100 mM EDTA−2Na solution and analyzed on 20% denaturing PAGE. Quantitative analysis of the gel-electrophoresis patterns was carried out on a FUJIFILM FLA-3000G fluorescent imaging analyzer. The pseudo-first-order rate constants k_{obs} for the RNA scission were determined by conventional first-order plots.

RESULTS AND DISCUSSION

Acridine−DNA Conjugates for Site-Selective RNA Scission by Lu(III). The phosphoramidite monomers bearing 9-amino-6-chloro-2-methoxyacridine (**X** = **1D**, **1L**, **2D**, **2L**, **3D**, **3L**, **4D**, and **4L** in Figure 1) were synthesized from D- or L-threoninol and ω-aminocarboxylic acid. Thus, all of the eight 36-mer acridine−DNA conjugates (DNA_1-**X**), as well as 9-mer acridine−DNA conjugates (DNA_2-**X**) used for the spectroscopic studies, are chirally pure with respect to the configuration of the central carbon in the main chain. In **5D** and **5L**, the 6-chlorine atom of the acridine residue in **3D** and **3L** was replaced with a nitro group. In all the acridine−DNA conjugates, the **X** residue bearing the acridine is placed in front of U-19 in the substrate RNA_1.

Figure 2b shows typical gel-electrophoresis patterns for the RNA hydrolysis at pH 8.0 and 37 °C. In the absence of acridine−DNA conjugates, RNA_1 was almost randomly hydrolyzed by Lu(III) (lane 1). In their presence, however, RNA_1 was site-selectively hydrolyzed at U-19 as the target site (lanes 2−9). The phosphodiester linkage in the 5′-side of U-19 is the primary scission site (the lower bands designated by the arrow). This linkage is not cleaved at all when a modified DNA involving a 1,3-propanediol linker (in place of **X** in DNA_1-**X**) is used, and is efficiently hydrolyzed only with the use of the acridine−DNA conjugates (*15*). The following part of this paper deals with this scission.

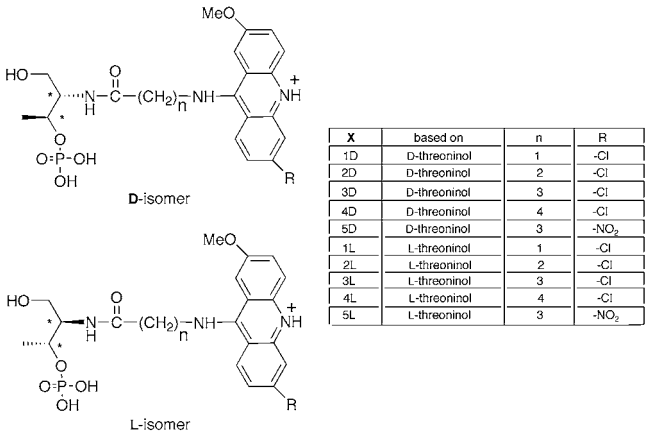

X	based on	n	R
1D	D-threoninol	1	-Cl
2D	D-threoninol	2	-Cl
3D	D-threoninol	3	-Cl
4D	D-threoninol	4	-Cl
5D	D-threoninol	3	-NO_2
1L	L-threoninol	1	-Cl
2L	L-threoninol	2	-Cl
3L	L-threoninol	3	-Cl
4L	L-threoninol	4	-Cl
5L	L-threoninol	3	-NO_2

Figure 1. The structures of acridine-bearing monomer units synthesized in the present study.

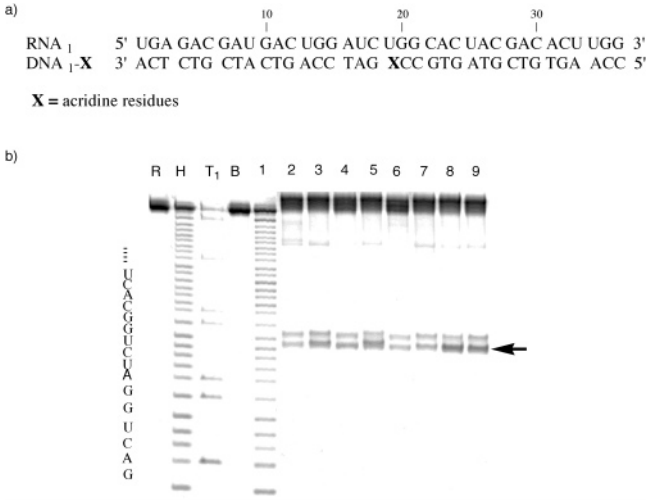

Figure 2. (a) Sequences of substrate RNA_1 and DNA conjugates used for the scission reaction. (b) PAGE for RNA_1 scission by Lu(III) in the presence of DNA conjugate bearing 9-amino-6-chloro-2-methoxyacridine. Lane 1, Lu(III) only; lane 2, with DNA_1-**1D**; lane 3, DNA_1-**2D**; lane 4, DNA_1-**3D**; lane 5, DNA_1-**4D**; lane 6, DNA_1-**1L**; lane 7, DNA_1-**2L**; lane 8, DNA_1-**3L**; lane 9, DNA_1-**4L**. At pH 8.0 and 37 °C for 4 h; [RNA_1] = 5 μM; [DNA] = 10 μM; [Lu(III)] = 100 μM; [Tris-HCl] = 10 mM; [NaCl] = 200 mM. All the scission fragments have 2′-(or 3′-)-phosphate termini, although their mobilities are slightly smaller than the corresponding fragment in lane 1 because of duplex formation with the acridine−DNA conjugates (see ref *18* for more details). R, RNA_1 only; H, alkaline hydrolysis; T_1, RNase T_1 digestion; B, control reaction in buffer solution.

Dependence of RNA-Activating Ability on Either the Chirality of the Central Carbon in the Main Chain or the Length of the Side Chain. First, the effect of side-chain length on the RNA-activating ability was examined for the L-series of conjugates, prepared using the phosphoramidite monomers derived from L-threoninol (**1L**, **2L**, **3L**, and **4L**). The numbers of methylene chains (n) in the side chain are 1, 2, 3, and 4, respectively. As presented in Figure 3a, the RNA-activating ability is notably dependent on the side-chain length. Of these four conjugates, DNA_1-**3L** is the most active (the

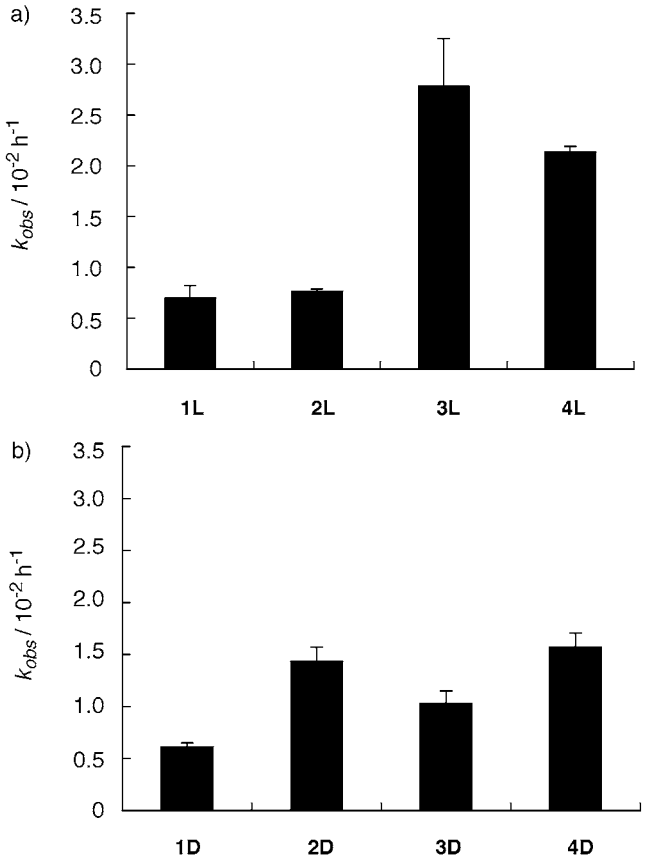

Figure 3. The pseudo-first-order rate constant k_{obs} for the site-selective scission of RNA_1 at the 5′-side of U-19 with (a) L-acridine−DNA conjugates and (b) D-acridine−DNA conjugates. The reaction conditions are the same as shown in Figure 2.

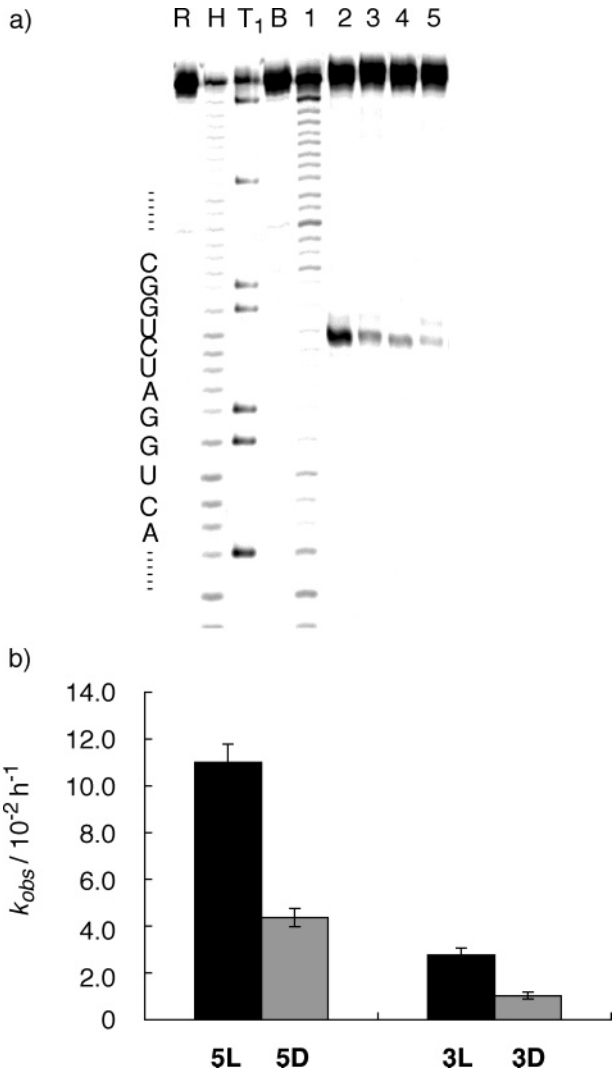

Figure 4. (a) Site-selective RNA_1 scission by Lu(III) in the presence of DNA conjugates bearing 9-amino-2-methoxy-6-nitroacridine (**5D** and **5L**). Lane 1, Lu (III) only; lane 2, with DNA_1-**5L**; lane 3, DNA_1-**5D**; lane 4, DNA_1-**3L**; lane 5, DNA_1-**3D**; R, RNA_1 only; H, alkaline hydrolysis; T_1, RNase T_1 digestion; B, control reaction in the buffer solution. The reaction conditions are the same as in Figure 2. The pseudo-first-order rate constants k_{obs} for the site-selective RNA_1 scission are presented in panel b.

pseudo-first-order rate constant k_{obs} for the RNA scission is 0.027 h^{-1}). This conjugate is about 4 times as active as DNA_1-**1L** and DNA_1-**2L**, and slightly exceeds DNA_1-**4L**. On the other hand, the RNA-activating ability of the D-series of acridine−DNA conjugates (**1D**, **2D**, **3D**, and **4D**) is less affected by the side-chain length (Figure 3b). In most cases (except for **2L** vs **2D**), the L-isomer is more active than the corresponding D-isomer. The difference is the largest when $n = 3$ (DNA_1-**3L** is 2.7 times as active as DNA_1-**3D**). Thus, the best monomer unit to bind 9-amino-6-chloro-2-methoxyacridine for the site-selective scission involves a trimethylene side chain on the central carbon of L-configuration and is prepared from L-threoninol and 4-aminobutyric acid.

Further Promotion of RNA-Activating Ability Using More Acidic Acridine. 9-Amino-2-methoxy-6-nitroacridine is more acidic than 9-amino-6-chloro-2-methoxyacridine (the pK_a values for the protonation at the ring nitrogen are 8.8 and 10.5, respectively). Since the present RNA activation is at least partially associated with acid catalysis by the protonated acridine, still greater RNA-activating ability is expected when 9-amino-2-methoxy-6-nitroacridine is employed (*16*). Accordingly, this acridine was introduced to the oligonucleotide having the scaffold which has been optimized above (the monomer unit prepared from L-threoninol and 4-aminobutyric acid). Exactly as designed, DNA_1-**5L** ($k_{obs} = 0.11$ h^{-1}) is 4.1 times as active as DNA_1-**3L** bearing 9-amino-6-chloro-2-methoxyacridine (Figure 4). By attaching a highly acidic acridine to the optimized backbone of oligonucleotides, an efficient RNA activator has been obtained.

Consistently with these results on the L-isomer, replacement of 9-amino-6-chloro-2-methoxyacridine in DNA_1-**3D** with 9-amino-2-methoxy-6-nitroacridine promoted the RNA-activating ability by 4.4-fold. The increase in the acidity of acridine induces almost the same magnitude of promotion for both D- and L-isomers, and thus DNA_1-**5L** is about 3 times active as DNA_1-**5D**.

Formation of Heteroduplexes between Acridine−DNA Conjugates and Complementary RNA. The T_m values of heteroduplexes between 9-mer acridine-modified DNA_2-**X** (5′-TGCCXGATC-3′) and its complementary 9-mer RNA_2 (5′-GAUCUGGCA-3′) are shown in Table 1. This RNA has the same sequence as the middle part (G15−A23) of RNA_1 used above for the site-selective scission by Lu(III), and the central U corresponds to the target scission site (U-19) in RNA_1. All the DNA conjugates form sufficiently stable duplexes with RNA_2. The T_m values are not very dependent on either the chirality of central carbon in the main chain or the length of the side chain (they take an A-type helix, as evidenced by the CD spectra in the 200−350 nm region: see the Supporting Information). Significantly, DNA_2-**X**/RNA_2 duplexes have considerably higher T_m values than the

Table 1. The Melting Points of the Duplexes between Acridine−DNA Conjugate and RNA_2 as Well as the Quenching of Fluorescence from the Acridine on the Duplex Formation

acridine−DNA conjugate	T_m[a] (°C)	ΔT_m[b] (°C)	fluorescence intensity of the acridine[c] ss	ds	quenching efficiency, %
DNA_2-**1D**	33.1	−4.3	39.5	4.7	88.1
DNA_2-**2D**	37.6	0.2	14.1	1.5	89.4
DNA_2-**3D**	37.5	0.1	12.4	1.2	90.3
DNA_2-**4D**	37.4	0.0	12.5	1.6	87.2
DNA_2-**5D**	37.5	0.1	*d*	*d*	
DNA_2-**1L**	36.5	−0.9	35.3	2.7	92.4
DNA_2-**2L**	40.0	2.6	23.4	5.6	76.1
DNA_2-**3L**	38.0	0.6	24.3	2.2	90.9
DNA_2-**4L**	37.5	0.1	13.2	1.5	88.6
DNA_2-**5L**	38.9	1.5	*d*	*d*	
DNA_2-A	37.4				
DNA_2-S[e]	10.3	−27.1			

[a] Conditions: $[RNA_2] = 1\ \mu M$, $[DNA_2\text{-}\mathbf{X}] = 1\ \mu M$, [Tris-HCl] = 10 mM, and [NaCl] = 200 mM; heating rate, 1 °C/min. [b] The difference between the T_m of the heteroduplex and the value of completely complementary DNA_2-A/RNA_2 duplex. [c] $[RNA_2] = 0.0$ (for ss) or $7.5\ \mu M$ (for ds), $[DNA_2\text{-X}] = 5\ \mu M$, [Tris-HCl] = 10 mM, and [NaCl] = 200 mM at 10 °C; emission wavelength = 494 nm (excitation at 346 nm). [d] Both DNA_2-**5D** and DNA_2-**5L** are fluorescence-silent. [e] DNA_2-S involves a simple 1,3-propanediol linker in place of **X**, and thus has no acridine.

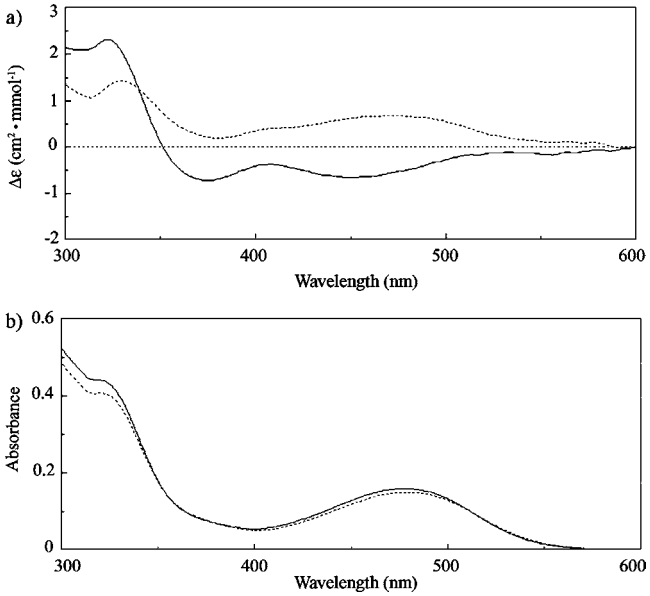

Figure 5. The CD spectra (a) and UV spectra (b) of the DNA_2-**5L**/RNA_2 duplex (solid line) and the DNA_2-**5D**/RNA_2 duplex (dotted line). Measurements were carried out at 10 °C in 10 mM phosphate buffer/200 mM sodium chloride (the T_m values of DNA_2-**5L**/RNA_2 and DNA_2-**5D**/RNA_2 duplexes under these conditions are 38.9 and 37.5 °C, respectively).

RNA_2 duplex of DNA_2-S in which the **X** residue in DNA_2-**X** is replaced by a simple 1,3-propanediol group. Compared with the completely complementary DNA_2-A/RNA_2 duplex, the DNA_2-S/RNA_2 duplex is less stable because of the removal of one A-U Watson−Crick base pair (T_m values are 37.4 and 10.3 °C, respectively). However, DNA_2-**X**/RNA_2 duplexes are mostly more stable than DNA_2-A/RNA_2 (ΔT_m is positive). Even the duplexes of DNA_2-**1L** ($\Delta T_m = -0.9$ °C) and DNA_2-**1D** ($\Delta T_m = -4.3$ °C) are far more stable than the DNA_2-S/RNA_2 duplex. It is strongly indicated that the acridine intercalates into the duplex and the corresponding energy gain sufficiently compensates the removal of one A-U pair. This argument is consistent with the finding by Kool (*1*) that stable duplexes are formed even when nucleobases are replaced by non-hydrogen-bonding aromatic residues.

Intercalation of the acridine into the heteroduplexes is further substantiated by the fact that the fluorescence from the acridine of DNA_2-**X** was notably quenched when it hybridized with RNA_2 (Table 1). For example, more than 90% of the fluorescence was quenched upon the formation of either the DNA_2-**3D**/RNA_2 or DNA_2-**3L**/RNA_2 duplex. Apparently, the acridine in the DNA_2-**X** deeply intercalates into the DNA_2-**X**/RNA_2 duplexes, and its fluorescence is quenched mainly by the adjacent guanine residues. The efficiency of fluorescence quenching is not very dependent on the chirality of the central carbon atom.

Effect of the Chirality of the Central Carbon in the Main Chain on the Position of Acridine. The CD spectra of DNA_2-**5L**/RNA_2 and DNA_2-**5D**/RNA_2 in the 420−520 nm region (due to the absorption of 9-amino-2-methoxy-6-nitroacridine) are entirely different from each other (Figure 5a), although their UV spectra are superimposed almost completely (Figure 5b). The sign of the induced CD is negative for DNA_2-**5L**/RNA_2 (solid line), whereas a positive CD is induced for DNA_2-**5D**/RNA_2 (dotted line). Apparently, the intercalating acridines take considerably different orientations depending on the chirality of the central carbon in the main chain. The molecular modeling in Figure 6 has substantiated this interpretation. Here, the intercalation mode of acridine is viewed from the 3′-side of RNA_1. In the DNA_1-**5L**/RNA_1 duplex (a), the side-chain portion first protrudes from the central carbon toward the major groove side, and then winds to the intercalating position. Thus the longitudinal axis of the acridine is rotated by about 80° counterclockwise with respect to the longitudinal axis of the Watson−Crick base pair in the 3′-side (the pair depicted in white). In DNA_1-**5D**/RNA_1 (b), however, the side chain runs more directly toward the intercalating position, and the corresponding angle between the two axes is only 30° counterclockwise. The difference of CD spectra between the D-isomer and the L-isomer (in Figure 5) is ascribed to this orientational difference (*19*). Almost the same structures were obtained for the DNA_1-**3L**/RNA_1 and DNA_1-**3D**/RNA_1 heteroduplexes involving 9-amino-6-chloro-2-methoxyacridine (data not presented).

On the basis of these analyses, the effect of chirality of the central carbon on the RNA-activating ability is tentatively ascribed to different orientation of intercalating acridine, which in turn induces a difference in local perturbation of the RNA backbone. In the heteroduplex between RNA_1 and DNA_1-**5L**, the conformation at the target scission site is probably more favorable for intramolecular nucleophilic attack of 2′O toward the P atom. It is noteworthy that the binding activity of the L-isomer to RNA_1 is comparable with that of the D-isomer (the T_m values of the DNA_2-**5L**/RNA_2 and DNA_2-**5D**/RNA_2 duplexes are almost the same: see Table 1). The fluorescence quenching efficiency for DNA_2-**3L**/RNA_2 is also almost the same as that for DNA_2-**3D**/RNA_2 (direct analysis on DNA_2-**5L**/RNA_2 and DNA_2-**5D** cannot be made since DNA_2-**5L** and DNA_2-**5D** are fluorescence-silent). There is no drastic difference in the overall structures of these two intercalation products. These facts further support the crucial role of orientation of the intercalating acridine for the present site-selective scission. The possibility that the L-isomer provides more efficient acid catalysis than the D-isomer is unlikely, since the increase in the acidity of acridine (exchange of 9-amino-6-chloro-2-methoxyacridine for 9-amino-2-meth-

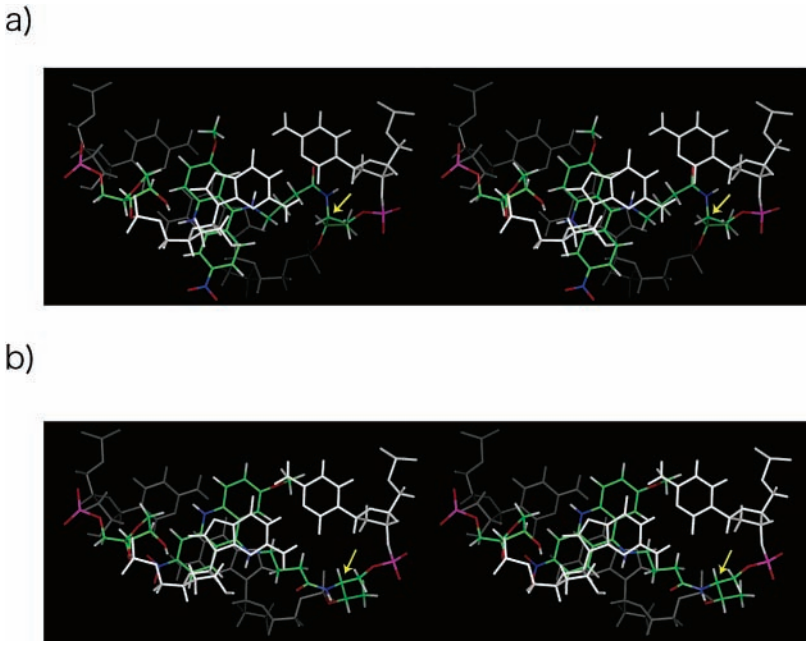

Figure 6. Molecular modeling of the duplex between RNA_1 and either (a) DNA_1-**5L** or (b) DNA_1-**5D**. The Watson−Crick base pair in white is located in the 3′-side of the central U (opposite the acridine (in green)) in RNA_1, whereas the gray one is in its 5′-side. The chiral carbons in the main chains of DNA_1-**5L** and DNA_1-**5D** are indicated by arrows. For the modeling, the nucleobase in front of the acridine was removed to simplify the calculation.

oxy-6-nitoroacridine) induces almost the same promotion effect for both isomers (Figure 4).

CONCLUSION

Using various phosphoramidite monomers, 9-amino-6-chloro-2-methoxyacridine has been incorporated into oligonucleotides in chirally pure forms (with respect to the configuration of central carbon in the main chain). All of these acridine−DNA conjugates form stable heteroduplexes with complementary RNA, and induce selective scission of the RNA by Lu(III) ion at the phosphodiester linkages in front of the acridine. The ability for the activation of confronting phosphodiester linkages strongly depends on both the chirality of the central carbon bearing the acridine and the length of the side chain. In most cases, the L-series of acridine−DNA conjugates are more active than the corresponding D-isomers. On the basis of CD spectroscopy, these results have been interpreted in terms of a subtle difference of orientation of the acridine in the RNA/DNA duplexes and the resulting different perturbation of the RNA backbone. Interestingly and importantly, these differences are not explicitly detected by either the T_m measurements or the fluorescence quenching experiments.

The optimized monomer unit for the RNA activation involves a trimethylene side chain on an L-configuration central carbon, and is prepared from L-threoninol and 4-aminobutyric acid. By combining this optimized monomer unit with the highly acidic 9-amino-2-methoxy-6-nitroacridine, a quite efficient acridine−DNA conjugate has been obtained.

The present systematic study has shown that the position and orientation of the intercalator in helical structures of DNA/RNA heteroduplexes can be regulated by the appropriate design of the monomer unit (chirality of the central carbon and the side-chain length). Thermodynamic stability of a "non-natural" heteroduplex involving this intercalator is not very dependent on the chirality of the central carbon. However, the functional properties (e.g., catalyses) are notably affected by the structure of monomer unit. These findings should be useful for rational design of various functionalized oligonucleotides in which intercalators take significant roles in a direct or indirect way.

ACKNOWLEDGMENT

This work was supported by PROBRAIN. A Grant-in-Aid for Scientific Research from the Ministry of Education, Science, Sports, Culture and Technology, Japan, and the support by JSPS Research Fellowships for Young Scientists (for A.K.) are also acknowledged.

Supporting Information Available: The synthesis and analyses of chirally pure acridine phosphoramidite monomers and acridine−DNA conjugates. The CD spectra of DNA_2-**5L**/RNA_2 and DNA_2-**5D**/RNA_2 duplexes at 200−350 nm. This material is available free of charge via the Internet at http://pubs.acs.org.

LITERATURE CITED

(1) Kool, E. T. (2002) Replacing the nucleobases in DNA with designer molecules. *Acc. Chem. Res. 35*, 936−943.

(2) Komiyama, M., Sumaoka, J., Kuzuya, A., and Yamamoto, Y. (2001) Sequence-selective artificial ribonucleases. *Methods Enzymol. 341*, 455−468.

(3) Asseline, U., Thuong, N. T., and Hélène, C. (1997) Synthesis and properties of oligonucleotide covalently linked to intercalating agents. *New J. Chem. 21*, 5−17.

(4) Goodchild, J. (1990) Conjugates of oligonucleotides and modified oligonucleotides: a review of their synthesis and properties. *Bioconjugate Chem. 1*, 165−187.

(5) Nelson, P. S., Kent, M., and Muthini, S. (1992) Oligonucleotide labeling methods. 3. Direct labeling of oligonucleotides employing a novel, nonnucleosidic, 2-aminobutyl-1,3-propanediol backbone. *Nucleic Acids Res. 20*, 6253−6259.

(6) Putnam, W. C., Daniher, A. T., Trawick, B. N., and Bashkin, J. K. (2001) Efficient new ribozyme mimics: direct mapping of molecular design principles from small molecules to macromolecular, biomimetic catalysts. *Nucleic Acids Res. 29*, 2199−2204.

(7) Neuner, P. (1996) New non nucleosidic phosphoramidite reagent for solid phase synthesis of biotinylated oligonucleotides. *Bioorg. Med. Chem. Lett. 6*, 147−152.
(8) Schneider, K. C., and Benner, S. A. (1990) Oligonucleotides containing flexible nucleoside analogs. *J. Am. Chem. Soc. 112*, 453−455.
(9) Yamana, K., Takei, M., and Nakano, H. (1997) Synthesis of oligonucleotide derivatives containing pyrene labeled glycerol linkers: Enhanced excimer fluorescence on binding to a complementary DNA sequence. *Tetrahedron Lett. 38*, 6051−6054.
(10) Endo, M., Azuma, Y., Saga, Y., Kuzuya, A., Kawai, G., and Komiyama, M. (1997) Molecular design for a pinpoint RNA scission. Interposition of oligoamines between two DNA oligomers. *J. Org. Chem. 62*, 846−852.
(11) Francois, J. C., and Hélène, C. (1999) Recognition of hairpin-containing single-stranded DNA by oligonucleotides containing internal acridine derivatives. *Bioconjugate Chem. 10*, 439−446.
(12) Fukui, K., Tanaka, K., Fujitsuka, M., Watanabe, A., and Ito, O. (1999) Distance dependence of electron transfer in acridine-intercalated DNA. *J. Photochem. Photobiol., B 50*, 18−27.
(13) Davis, W. B., Hess, S., Naydenova, I., Haselsberger, R., Ogrodnik, A., Newton, M. D., and Michel-Beyerle, M. E. (2002) Distance-dependent activation energies for hole injection from protonated 9-amino-6-chloro-2-methoxyacridine into duplex DNA. *J. Am. Chem. Soc. 124*, 2422−2423.
(14) Kuzuya, A., and Komiyama, M. (2000) Sequence-selective RNA scission by non-covalent combination of acridine-tethered DNA and lanthanide(III) ion. *Chem. Lett.* 1378−1379.
(15) Kuzuya, A., Mizoguchi, R., Morisawa, F., Machida, K., and Komiyama, M. (2002) Metal ion-induced site-selective RNA hydrolysis by use of acridine-bearing oligonucleotide as cofactor. *J. Am. Chem. Soc. 124*, 6887−6894.
(16) Kuzuya, A., Machida, K., and Komiyama, M. (2002) A highly acidic acridine for efficient site-selective activation of RNA leading to an eminent ribozyme mimic. *Tetrahedron Lett. 43*, 8249−8252.
(17) Shi, Y., Kuzuya, A., and Komiyama, M. (2003) Stereochemically pure acridine-modified DNA for site-selective activation and scission of RNA. *Chem. Lett. 32*, 464−465.
(18) Kuzuya, A., Mizoguchi, R., Sasayama, T., Zhou, J. M., and Komiyama, M. (2004) Selective activation of two sites in RNA by acridine-bearing oligonucleotides for clipping of designated RNA fragments. *J. Am. Chem. Soc. 126*, 1430−1436.
(19) Eriksson, M., and Norden, B. (2001) Linear and circular dichroism of drug-nucleic acid complexes. *Methods Enzymol. 340*, 68−98.

BC049698M

Electrochemical Detection of Lesions in DNA

Amie K. Boal and Jacqueline K. Barton*

Division of Chemistry and Chemical Engineering, California Institute of Technology, Pasadena, California 91125. Received November 4, 2004; Revised Manuscript Received January 19, 2005

Electrochemical DNA-based sensors that exploit the inherent sensitivity of DNA-mediated charge transport (CT) to base pair stacking perturbations are capable of detecting base pair mismatches and some common base damage products. Here, using DNA-modified gold electrodes, monitoring the electrocatalytic reduction of DNA-bound methylene blue, we examine a wide range of base analogues and DNA damage products. Among those detected are base damage products O4-methyl-thymine, O6-methyl-guanine, 8-oxo-guanine, and 5-hydroxy-cytosine, as well as a therapeutic base, nebularine. The efficiency of DNA-mediated CT is found not to depend on the thermodynamic stability of the helix. However, general trends in how base modifications affect CT efficiency are apparent. Modifications to the hydrogen bonding interface in Watson−Crick base pairs yields a substantial loss in CT efficiency, as does added steric bulk. Base structure modifications that may induce base conformational changes also appear to attenuate CT in DNA as do those that bury hydrophilic groups within the DNA helix. Addition and subtraction of methyl groups that do not disrupt hydrogen bonding interactions do not have a large effect on CT efficiency. This sensitive detection methodology based upon DNA-mediated CT may have utility in diagnostic applications and implicates DNA-mediated CT as a possible damage detection mechanism for DNA repair enzymes.

INTRODUCTION

DNA is remarkably susceptible to chemical modification (*1*−*3*). Hydrolytic damage is the most common form of DNA base modification and often leads to deamination of cytosine and depurination. Oxidative damage results in a variety of base modifications, but 8-oxo-G is thought to be the most prevalent of these lesions. Nonenzymatic alkylation by endogenous and exogenous alkylating agents is also an important type of base damage (*2*). Modification of DNA bases can disrupt DNA replication and transcription by altering the base pairing properties of the DNA base and stalling the protein machinery associated with these processes. Base damage may also be an important indicator in the diagnosis and treatment of cancer, as high levels of damaged bases are often the result of exposure to carcinogens (*4*).

The base pair π-stack, formed when duplex DNA assumes a helical conformation, is capable of mediating charge transport (CT) (*5*−*9*). This chemistry is exquisitely sensitive to changes in base pair structure and dynamics; intervening mismatches in base pairing lead to a loss in the ability to transfer charge from an electron donor to an electron acceptor (*10*), as do bulges (*11*) or structural perturbations in base pair stacking induced by proteins (*12, 13*). While an in vivo role for DNA-mediated CT has yet to be established, it is interesting to consider that DNA-mediated CT may be involved in DNA damage and repair (*14*). Long-range DNA-mediated CT provides a potential route for funneling oxidative damage to specific regions of the genome and insulating alternate regions (*14, 15*). We have proposed that DNA repair proteins may take advantage of the sensitivity of DNA-mediated CT to DNA structural modifications in order to scan the genome for damage as an efficient long-range detection scheme (*14*, *16*).

* To whom correspondence should be addressed at jkbarton@caltech.edu.

The remarkable sensitivity of DNA-mediated CT to perturbations in base pair stacking and dynamics suggested that this chemistry could be applied in the design of sensors that detect base pair mismatches and damage products. Our laboratory has developed one such sensor for the detection of single base mutations in duplex DNA (*17, 18*). In this device, a monolayer of thiol-terminated DNA oligonucleotide duplexes is assembled on a gold surface; a redox-active intercalator bound near the top of the film acts as the probe of DNA CT chemistry. The DNA-mediated reduction of the intercalator is easily monitored electrochemically if the DNA is fully Watson−Crick base paired. However, the presence of a single base pair mismatch or other structural perturbation within the base pair stack attenuates intercalator reduction. This sensor is unique in that it does not exploit differences in hybridization thermodynamics to detect mutations, but instead differences in electronic coupling within the π-stack. Greater sensitivity to perturbations in the π-stack is attained by coupling the DNA-mediated reduction of the intercalative probe into an electrocatalytic cycle with an oxidant in solution capable of reoxidizing the intercalator. Figure 1 illustrates this cycle utilizing the intercalator methylene blue as the electrocatalyst for ferricyanide reduction. The integrity of the DNA π-stack is repeatedly probed via electron transfer in this catalytic cycle, and thus any perturbations in base pair stacking are amplified. Using this methodology, all single base mismatches in DNA, irrespective of sequence context or thermal stability, can be readily detected (*18*). Indeed recently, a full range of DNA-based biosensors have been developed (*19*, *20*).

Here we examine the scope of this methodology. We are interested in determining the primary factors governing the detection of DNA lesions by DNA charge transfer chemistry and the range of lesions that may be detected. How effective, for example, is this chemistry in detecting DNA methylation? Are base analogues

10.1021/bc0497362 CCC: $30.25 © 2005 American Chemical Society
Published on Web 02/17/2005

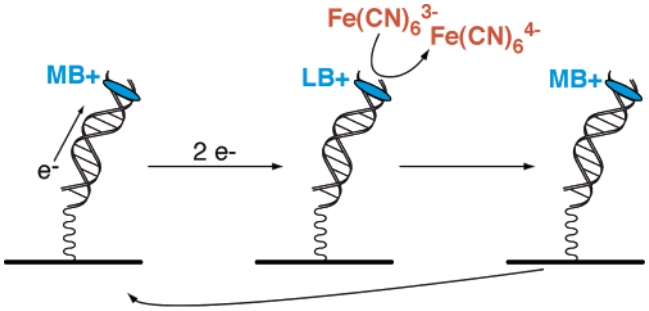

Figure 1. Scheme for electrocatalysis at a DNA-modified electrode. MB^+ denotes methylene blue as the redox-active intercalative probe. MB^+ is reduced to leucomethylene blue (LB^+) in a DNA-mediated electron-transfer process. Ferricyanide ($Fe(CN)_6^{3-}$) is oxidized by LB^+ to regenerate the redox-active intercalative probe.

utilized as probes of nucleic acid processes or as therapeutics readily detected? We have already observed that the conformational distortions in synthetic oligonucleotides containing constrained sugar−phosphate backbones can be detected electrochemically (*21*), and this may be an important consideration in their application in antisense therapeutics. Perhaps most importantly, our understanding of the sensitivity and scope of DNA CT chemistry in the detection of lesions provides a foundation for the consideration of possible roles for DNA CT in mechanisms of DNA repair.

EXPERIMENTAL SECTION

Materials. All reagents for DNA synthesis were purchased from Glen Research (including all unnatural DNA base phosphoramidites). Methylene blue, ferricyanide, and reagents used in the synthesis of thiol-modified DNA were purchased from Aldrich in the highest available purity and used as received. All buffers were prepared with Milli-Q water and filtered with a sterile, 0.2 μm filter.

Preparation of DNA-Modified Electrodes. Oligonucleotides were prepared using standard phosphoramidite synthesis on an ABI 392 model DNA synthesizer. Oligonucleotide composition was verified by mass spectrometry. Thiol-modified duplexes were prepared using a solid-phase coupling procedure (*17*). The modified DNA was HPLC-purified on a semipreparative C18 column after either the amino modification or attachment of the disulfide moiety and again after the thiol deprotection. Thiol-modified DNA and the appropriate complementary strand were prepared in a 100 μM solution and annealed on a thermocycler. The resulting duplexes were self-assembled overnight (12−24 h) on polished (0.3 μm, 0.05 μm alumina) and etched (CV from +1575 mV to −250 mV, 20 cycles in 1 M H_2SO_4) bulk gold electrodes. $MgCl_2$ (100 mM) was added to the DNA solution prior to incubation to ensure a well-packed film. All DNA films were confirmed to be densely packed using a standard ferricyanide assay (*22*). At least three trials were performed for each base modification.

Electrochemical Analysis of DNA Films. Cyclic voltammetry and chronocoulometry experiments were carried out on a BAS CV50W model electrochemical analyzer. Experiments were executed in 50 mM NaCl, 5 mM sodium phosphate, pH 7, at ambient temperatures under an inert atmosphere. A three-compartment electrochemical cell was used with a Pt wire auxiliary electrode, 0.02 cm^2 gold working electrode, and saturated calomel reference electrode separated from the working electrode by a modified Luggin capillary.

Thermal Denaturation Studies. DNA duplexes (1.6 μM) were tested in 50 mM NaCl, 5 mM sodium phosphate, 100 mM $MgCl_2$, pH 7.0, in a quartz cell (with the exception of the lesions in group 4 which were analyzed in the absence of $MgCl_2$ and without the thiol tether). Absorbance at 260 nm was measured on a Beckman DU7400 spectrophotometer as the temperature decreased from 90 °C to 20 °C in a 0.5 °C/min linear gradient. Melting curves were fit to a sigmoidal function using ORIGIN software. The T_m is defined as the midpoint of these sigmoidal curves.

RESULTS

Methodology. Base lesions are incorporated into 15mer thiol-terminated duplexes using standard phosphoramidite chemistry, and the DNAs containing the base lesions are self-assembled into monolayers on gold electrodes. These DNA-modified electrodes are then investigated electrochemically using noncovalent methylene blue (MB) as a redox-active probe either directly or, in conjunction with ferricyanide, electrocatalytically. When MB is used as a direct probe, the DNA-modified electrodes are immersed in a buffered solution containing 2 μM MB. Note that it is the reduction of MB that is monitored using cyclic voltammetry from 0 to −650 mV; some of the lesions examined are easily oxidized but the conditions monitored here do not promote redox chemistry on the bases themselves. MB is also used as a catalytic reductive probe, when the DNA modified electrode is placed in a solution containing 2 mM ferricyanide and 0.5 μM MB. The redox activity of MB is then monitored primarily using chronocoulometry. In the experiments described here, charge is monitored for a period of 5 s while the potential steps from 0 to −350 mV.

The lesions investigated here encompass a wide variety of modifications to DNA bases. Some of these lesions occur physiologically as a result of enzymatic modification to DNA or as a result of oxidative and/or hydrolytic damage. Other lesions represent synthetic modifications to DNA bases, damage to bases that is the result of exposure to alkylating agents, bases used as therapeutics, and fluorescent bases commonly used as synthetic probes of DNA.

Group 1 Lesions. The group 1 lesions are all associated with DNA damage processes. O4-methyl-thymine (OMT) and O6-methyl-guanine (OMG) are methylation damage products occurring at sites involved in hydrogen bonding, and 5-hydroxy-cytosine (OHC) and 8-oxo-guanine (OG) are common oxidative damage products (*23*). The structures of these lesions are shown in Figure 2. DNA films containing OMG base paired with cytosine can be distinguished electrochemically, either with or without electrocatalysis, from those containing well-matched unmodified base pairs (Figure 2). OMT base paired with adenine can also be detected with and without electrocatalysis, but detection is greatly enhanced using electrocatalysis. As illustrated in Table 1, incorporation of these lesions into DNA duplexes also leads to dramatically reduced T_m values. It is noteworthy, however, that duplexes containing OMG have a lower T_m than those containing OMT, yet show less attenuation in MB reduction.

The oxidative damage products OG and OHC can also be detected electrochemically both with and without electrocatalysis (Figure 2). OG is examined here base paired with both A and C (OG:A and OG:C, respectively). In both base pairing contexts, OG is detectable when MB

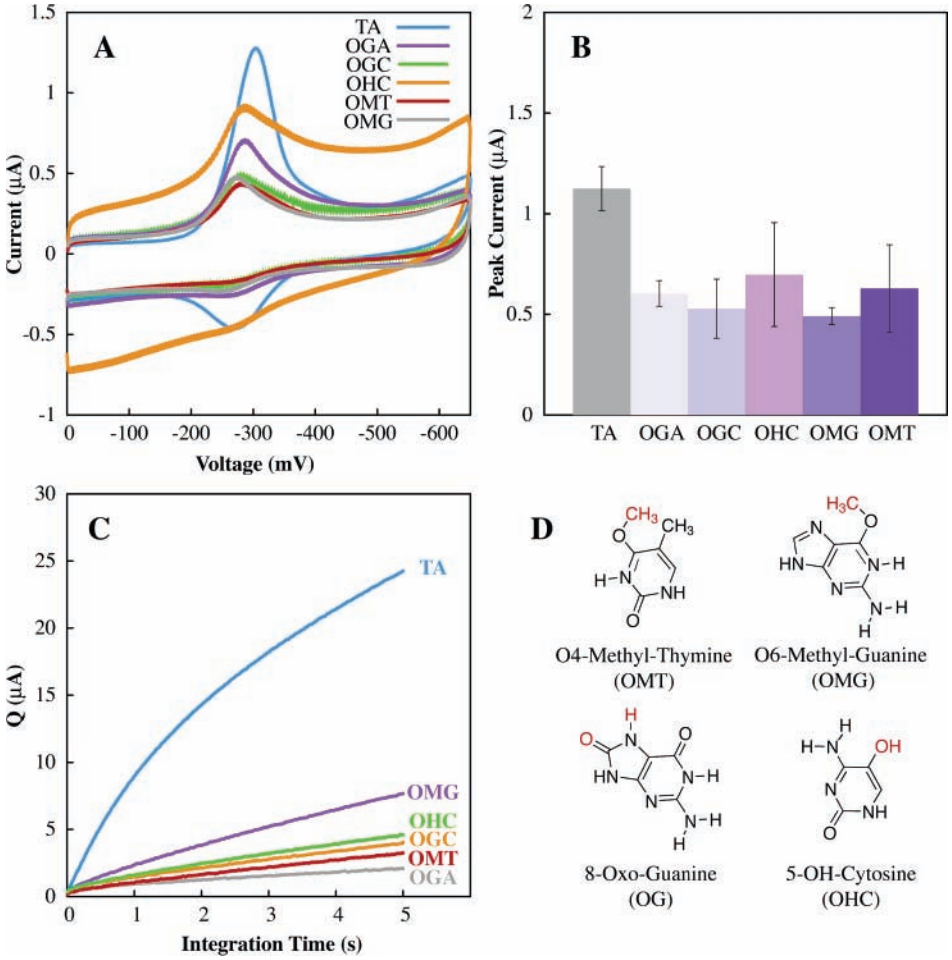

Figure 2. Electrochemical Detection of Group 1 Lesions. (A) Cyclic voltammetry. without electrocatalysis. (B) Bar graph representing peak current attained in cyclic voltammetry experiments without electrocatalysis. (C) Chronocoulometry with electrocatalysis. (D) Structures of group 1 lesions. Deviations from standard base pairs are shown in red.

Table 1. Electrochemical Detection of Group 1 Lesions

Lesion	Sequence[a]	T_m (°C)	Q (μA) w/out electrocatalysis[b]	Q (μA) with electrocatalysis[c]
no lesion (TA)	SH – 5′ – AGT ACA GTC ATC GCG 3′ – TCA TGT CAG TAG CGC	60.0	1.27 ± 0.12	23.9 ± 1.7
O4-Methyl-Thymine (OMT)	SH – 5′ – AGT ACA GTC ATC GCG 3′ – TCA TG**T** CAG TAG CGC	49.4	0.63 ± 0.22	3.1 ± 1.0
O6-Methyl-Guanine (OMG)	SH – 5′ – AGT ACA GTC ATC GCG 3′ – TCA TGU CA**G** TAG CGC	47.8	0.492 ± 0.041	8.1 ± 2.4
5-Hydroxy-Cytosine (OHC)	SH – 5′ – AGT ACA GTC ATC GCG 3′ – TCA TGT **C**AG TAG CGC	54.9	0.70 ± 0.25	5.1 ± 1.1
8-Oxo-Guanine:C (OGC)	SH – 5′ – AGT ACA GTC ATC GCG 3′ – TCA TGT CA**G** TAG CGC	53.6	0.53 ± 0.15	4.1 ± 0.6
8-Oxo-Guanine:A (OGA)	SH – 5′ – AGT ACA GTC ATC GCG 3′ – TCA TG**G** CAG TAG CGC	52.3	0.604 ± 0.064	2.9 ± 0.5

[a] SH-5′ represents $SH(CH_2)_2CONH(CH_2)_6NHCO$ at 5′-OH. [b] Electrochemical detection using 2 μM methylene blue (MB) as redox probe. Q = current at CV peak. [c] Electrochemical detection with electrocatalysis: 0.5 μM MB, 2 mM $Fe(CN)_6^{3-}$. Q = integrated current at 5 s.

is used as a direct probe. In the electrocatalysis experiments, OG is detectable when paired with C or A, but detection of OG:A is especially pronounced. OHC is also easily detectable with electrocatalysis. It is noteworthy that a higher background current is consistently observed in DNA films containing OHC; possibly this reflects a

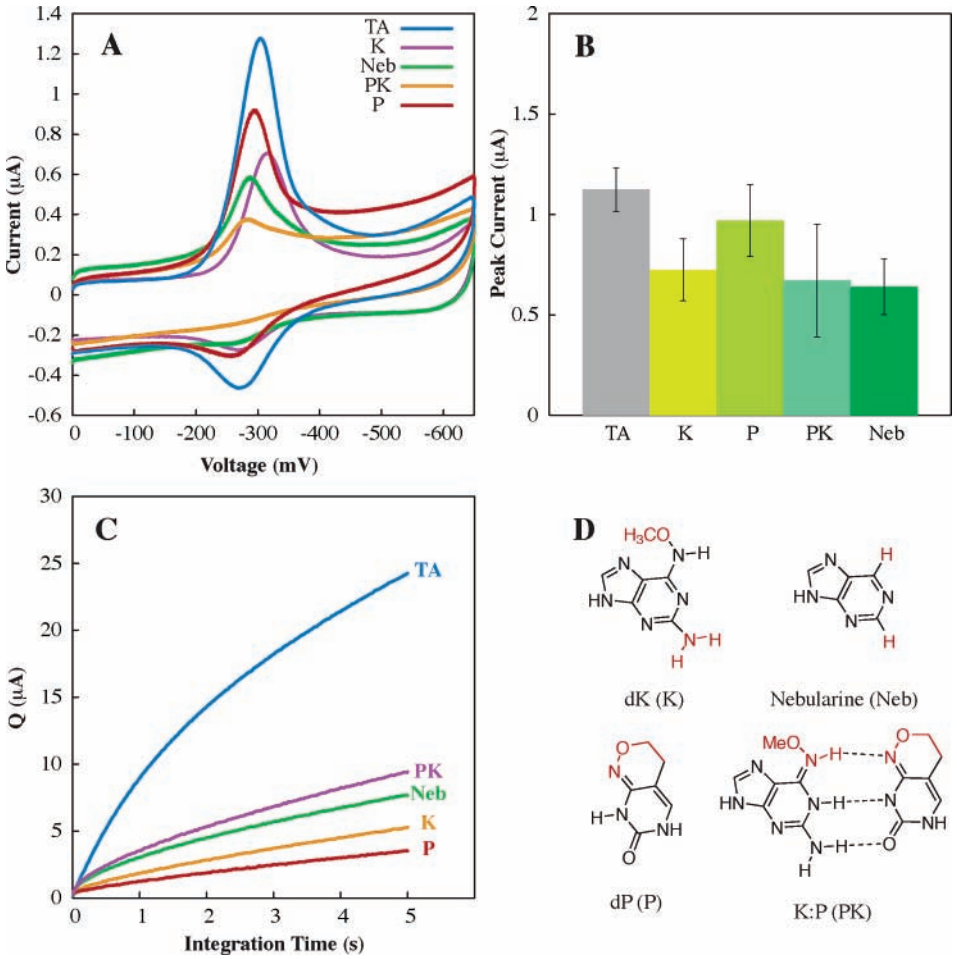

Figure 3. Electrochemical Detection of Group 2 Lesions. (A) Cyclic voltammetry without electrocatalysis. (B) Bar graph representing peak current attained in cyclic voltammetry experiments without electrocatalysis. (C) Chronocoulometry with electrocatalysis. (D) Structures of group 2 lesions. Deviations from standard base pairs are shown in red.

difference in film morphology. Note that all data, irrespective of film capacitance, were first background corrected.

As evident in Table 1, these lesions are somewhat thermodynamically destabilizing; duplexes containing these modifications have lower melting temperatures than unmodified duplexes (TA). Nonetheless, incorporation of these lesions in DNA films leads to a dramatic attenuation in CT efficiency.

Group 2 Lesions. Group 2 includes the synthetic base analogues, P and K, that function as degenerate bases; they can pair with either purine (P) or pyrimidine (K) (*24*). Nebularine (Neb) is a natural product that also has greater base pairing degeneracy than the natural purines (*25*). As illustrated in Figure 3, each of these lesions causes a profound decrease in DNA-mediated CT monitored with electrocatalysis. Significantly, P and K base paired to each other results in a higher charge accumulation when compared to P or K base paired to a natural base. As evident in Table 2, it is also interesting that the duplex with the highest charge accumulation (Q) with electrocatalysis has the lowest T_m. This result provides another indication that CT attenuation does not correlate with duplex melting temperature.

Group 3 Lesions. This group includes the therapeutic base 5-fluoro-uracil (FlU) (*26*), fluorescent bases, 2-aminopurine (2Ap) (*27*), and etheno-adenine (EA) (*28*), and synthetic base analogues 7-deaza-guanine (ZG) (*29*) and 7-deaza-adenine (ZA) (*30*). Group 3 represents structural modifications to DNA bases that are either completely synthetic (ZA, ZG, FlU, 2Ap) or the result of exposure to exogenous mutagens (EA).

Figure 4 illustrates, in DNA films containing these lesions, the reduction of MB without electrocatalysis as measured by cyclic voltammetry. None of these lesions are appreciably distinguished without electrocatalysis. Figure 4 also shows these data in bar graph form, further demonstrating that these lesions, within error, all have the same ability to facilitate CT as a fully matched duplex (TA). When MB is used electrocatalytically, ZA, ZG, and 2Ap are still not distinguishable. Interestingly, FlU or EA incorporation, examined through electrocatalysis, does lead to some attenuation in CT. Table 3 summarizes these data and shows melting temperatures for each duplex. All group 3 lesions, with the exception of EA, also show little deviation in melting temperature from a fully matched duplex.

Group 4 Lesions. Group 4 lesions, 5-methyl-cytosine (MC), N6-methyl-adenine (NA), and uracil (UA) are biologically relevant lesions that are the product of enzymatic methylation (MC and NA) or polymerase misincorporation (U base paired with A) (*31*−*33*). Each of these lesions is the result of the addition or subtraction of a methyl group in a location that does not appreciably hinder Watson−Crick hydrogen bonding ability.

Figure 5 shows the direct DNA-mediated reduction of MB (without electrocatalysis) measured by cyclic voltammetry. Without electrocatalysis, MB reduction is equivalent for DNAs containing these lesions when compared to a duplex that does not contain any lesions (TA). Figure

Table 2. Electrochemical Detection of Group 2 Lesions

Lesion	Sequence[a]	T_m (°C)	Q (μA) w/out electrocatalysis[b]	Q (μA) with electrocatalysis[c]
no lesion (TA)	SH – 5′ – AGT ACA GTC ATC GCG 3′ – TCA TGT CAG TAG CGC	60.0	1.27 ± 0.12	23.9 ± 1.7
dP (P)	SH – 5′ – AGT ACA GTC ATC GCG 3′ – TCA TGP CAG UAG CGC	56.8	0.97 ± 0.18	5.9 ± 2.2
dK (K)	SH – 5′ – AGT ACA GTC ATC GCG 3′ – TCA TGT CKG TAG CGC	53.4	0.73 ± 0.15	6.6 ± 2.5
P:K (PK)	SH – 5′ – AGT ACA GPC ATC GCG 3′ – TCA TGT CKG TAG CGC	50.2	0.67 ± 0.28	10.1 ± 2.1
Nebularine (Neb)	SH – 5′ – AGT ACA GTC ATC GCG 3′ – TCA TGT CNG TAG CGC	53.7	0.64 ± 0.14	9.7 ± 2.3

[a] SH-5′ represents $SH(CH_2)_2CONH(CH_2)_6NHCO$ at 5′-OH. [b] Electrochemical detection using 2 μM methylene blue (MB) as redox probe. Q = current at CV peak. [c] Electrochemical detection with electrocatalysis: 0.5 μM MB, 2 mM $Fe(CN)_6^{3-}$. Q = integrated current at 5 s.

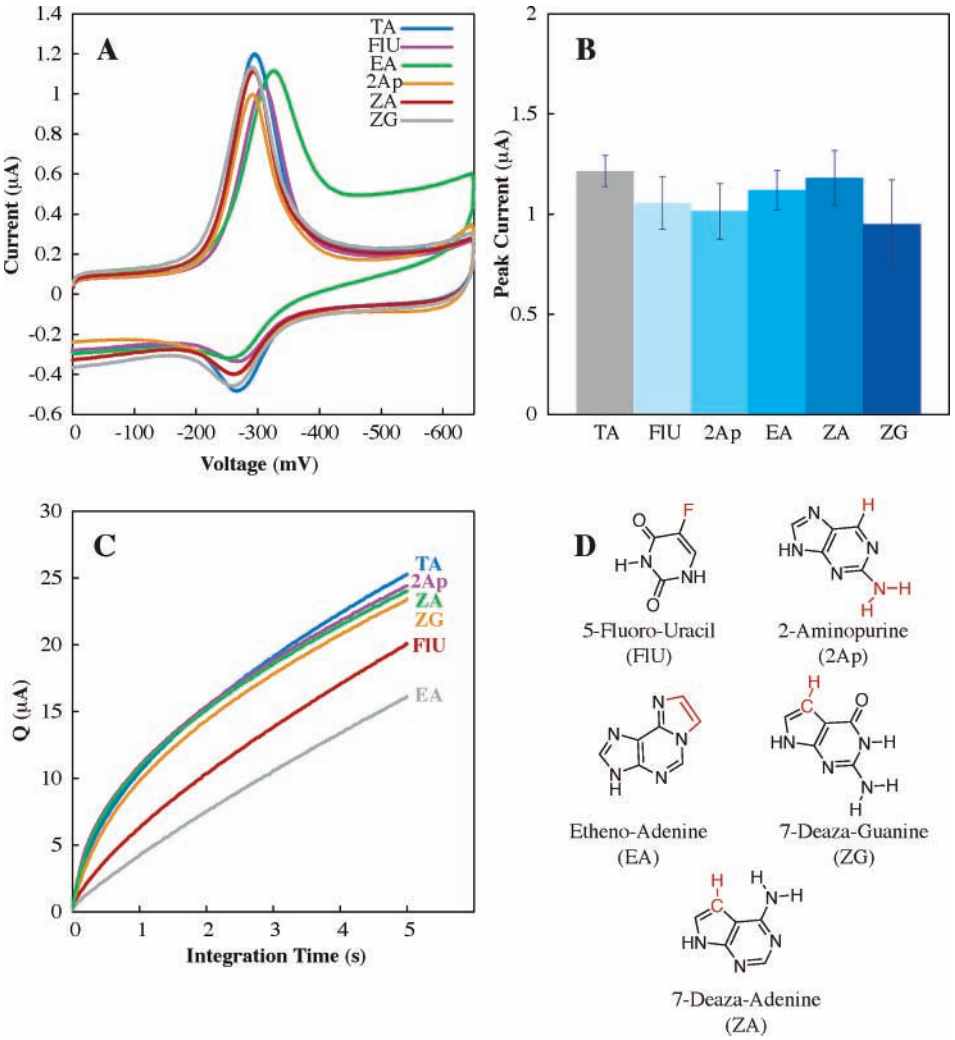

Figure 4. Electrochemical Detection of Group 3 Lesions. (A) Cyclic voltammetry without electrocatalysis. (B) Bar graph representing peak current attained in cyclic voltammetry experiments without electrocatalysis. (C) Chronocoulometry with electrocatalysis. (D) Structures of group 3 lesions. Deviations from standard base pairs are shown in red.

5 also shows these data as a bar graph, illustrating quantitatively that these lesions are not electrochemically detectable by this method. In addition, data from chronocoulometry experiments using electrocatalysis, our most sensitive assay, show that these lesions are not well detected even when MB is used as catalytic probe. These data are summarized in Table 4. Also shown in Table 4 are melting temperatures for these duplexes. It is note-

Table 3. Electrochemical Detection of Group 3 Lesions

Lesion	Sequence[a]	T_m (°C)	Q (μA) w/out electrocatalysis[b]	Q (μA) with electrocatalysis[c]
no lesion (TA)	SH – 5′ – AGT ACA GTC ATC GCG 3′ – TCA TGT CAG TAG CGC	60.0	1.27 ± 0.12	23.9 ± 1.7
5-Fluoro-Uracil (FlU)	SH – 5′ – AGT ACA GTC ATC GCG 3′ – TCA TGT CAG UAG CGC	59.9	1.06 ± 0.13	20.8 ± 0.93
2-Aminopurine (2Ap)	SH – 5′ – AGT ACA GTC ATC GCG 3′ – TCA TGU CPG TAG CGC	57.3	1.01 ± 0.14	20.6 ± 3.3
Etheno-Adenine (EA)	SH – 5′ – AGT ACA GTC ATC GCG 3′ – TCA TGT CEG TAG CGC	50.9	1.12 ± 0.10	18.8 ± 5.1
7-Deaza-Adenine (ZA)	SH – 5′ – AGT ACA GTC ATC GCG 3′ – TCA TGT CZG TAG CGC	60.0	1.12 ± 0.14	24.5 ± 3.5
7-Deaza-Guanine (ZG)	SH – 5′ – AGT ACA GTC ATC GCG 3′ – TCA TGT CAZ TAG CGC	59.5	0.95 ± 0.22	24.0 ± 1.4

[a] SH-5′ represents $SH(CH_2)_2CONH(CH_2)_6NHCO$ at 5′-OH. [b] Electrochemical detection using 2 μM methylene blue (MB) as redox probe. Q = current at CV peak. [c] Electrochemical detection with electrocatalysis: 0.5 μM MB, 2 mM $Fe(CN)_6^{3-}$. Q = integrated current at 5 s.

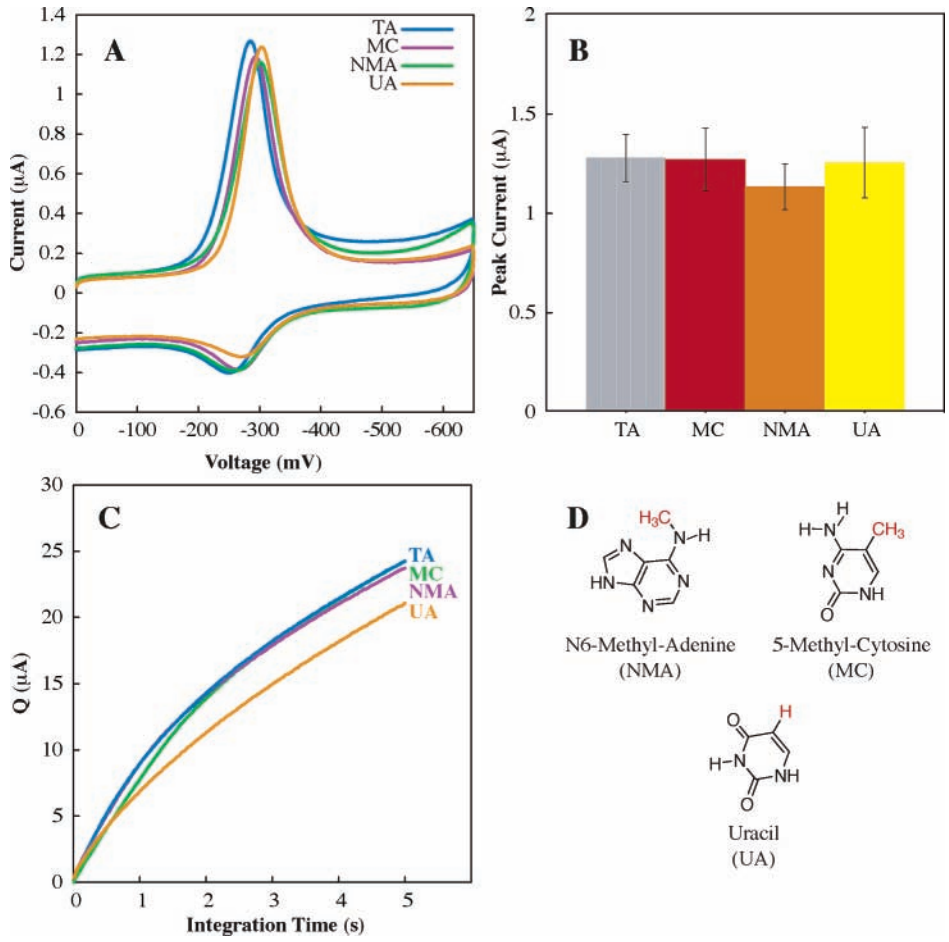

Figure 5. Electrochemical Detection of Group 4 Lesions. (A) Cyclic voltammetry without electrocatalysis. (B) Bar graph representing peak current attained in cyclic voltammetry experiments without electrocatalysis. (C) Chronocoulometry with electrocatalysis. (D) Structures of group 4 lesions. Deviations from standard base pairs are shown in red.

worthy that these lesions do not promote a decrease in melting temperature.

Charge-Transfer Efficiency versus Duplex Stability. Figure 6 shows the quantitative comparison of melting temperatures for the DNA duplexes, and charge accumulation in the DNA films, our measure of CT efficiency. Integrated charge accumulated after 5 s (Q), as measured by our electrochemical assay, is plotted

Table 4. Electrochemical Detection of Group 4 Lesions

Lesion	Sequence[a]	T_m (°C)	Q (μA) w/out electrocatalysis[b]	Q (μA) with electrocatalysis[c]
no lesion (TA)	SH – 5′ – AGT ACA GTC ATC GCG 3′ – TCA TGT CAG TAG CGC	54.3	1.27 ± 0.12	23.9 ± 1.7
5-Methyl-Cytosine (MC)	SH – 5′ – AGT ACA GTC ATC GCG 3′ – TCA TGT CAG TAG CGC	54.3	1.26 ± 0.16	22.8 ± 1.5
Uracil:A (UA)	SH – 5′ – AGT ACA GTC ATC GCG 3′ – TCA TGU CAG TAG CGC	53.2	1.25 ± 0.02	22.4 ± 1.0
N6-Methyl-Adenine (NA)	SH – 5′ – AGT ACA GTC ATC GCG 3′ – TCA TGT CAG TAG CGC	53.1	1.13 ± 0.12	23.47 ± 0.72

[a] SH-5′ represents $SH(CH_2)_2CONH(CH_2)_6NHCO$ at 5′-OH. [b] Electrochemical detection using 2 μM methylene blue (MB) as redox probe. Q = current at CV peak. [c] Electrochemical detection with electrocatalysis: 0.5 μM MB, 2 mM $Fe(CN)_6^{3-}$. Q = integrated current at 5 s.

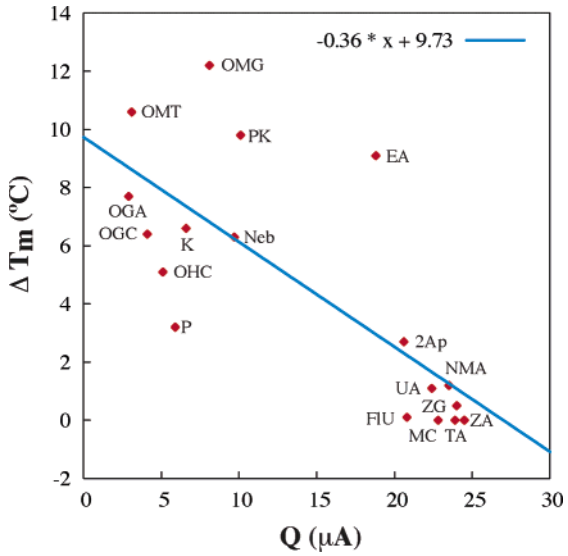

Figure 6. Plot of Q versus ΔT_m based upon data in Tables 1−4. The best linear fit is shown, although $R^2 = 0.57$.

versus the absolute change in T_m from well-matched DNA (TA) for each duplex. The parameter ΔT_m, rather than absolute T_m, is used to account for any differences in experimental conditions among measurements on the lesion-containing DNAs (see Table 4). As evident in the plot, little statistical correlation is observed between the CT efficiency and the thermodynamic stability of the duplex; the squared correlation coefficient for these data (R^2) equals 0.57. The electrochemical assay used here depends on different characteristics of the π-stacked DNA duplex rather than thermodynamic stability.

DISCUSSION

Electrochemical DNA-based biosensors offer a sensitive method for detecting a range of modified bases in DNA. Many of the lesions examined here are implicated in a variety of cancers (*34*−*36*), so that new assays for low levels of lesions that employ electrocatalysis may provide a novel, early diagnostic tool.

The results presented here also establish the general trends in how base modifications affect CT efficiency. Alteration of the Watson−Crick hydrogen bonding interface yields a profound loss in CT efficiency (OMT, OMG, Neb, P, and K), as does added steric bulk (P, K, OMT, and OMG). Base structure modifications that may induce base conformation changes (OG:A) also appear to diminish CT in DNA, as do those that place hydrophilic groups within the DNA helix (OHC). The presence or absence of methyl groups (MC, NMA, and UA) that do not disrupt hydrogen bonding interactions have little effect on CT efficiency. Little correlation between CT efficiency and thermal stability of duplex DNA containing a particular lesion is evident.

How are these lesions detected within the cell? The lesions examined here fall into three categories: oxidatively damaged bases, alkylated bases, and synthetic base analogues. The bases arising from oxidative or alkylation damage (OHC, OG, OMG, OMT) are all recognized by the cellular repair machinery. Enzymatic recognition by DNA repair systems is considered to involve similar factors that affect CT efficiency: hydrogen bonding patterns between the lesion and the opposite base, steric fit, the strength of the glycosidic bond, and base pair dynamics (*37*). OG is thought to be distinguished in part owing to protonation of the N7 nitrogen atom; N7 is not protonated in unmodified guanine (*38*). Repair of OG is also highly dependent on its base pairing environment. For instance, MutY, an enzyme that excises A from OG:A mispairs, can discriminate OG through stacking interactions involving an intercalated tyrosine coupled with hydrogen bonding of the OG to a serine (*39*). OHC is repaired by Endo III, a repair enzyme with a wide substrate specificity that targets oxidized pyrimidines (*40*). With this somewhat nondiscriminate enzyme, recognition is thought to involve both the lability of the lesion glycosidic bond and hydrogen bonding of the enzyme with the base opposite the lesion (*41, 42*). Direct damage reversal, where aberrant alkylation is transferred from DNA to a reactive cysteine in the repair protein, is the process that repairs O-methylation in DNA (*43*). OMT and OMG are recognized by methyltransferases and these enzymes likely recognize their substrates by sensing the instability of the lesion base pair (*44*). A consensus has not yet been reached regarding the exact protein/DNA interactions that determine specificity, but structural studies indicate that hydrophobic residues near the reactive cysteine may be involved in recognizing the site of alkylation (*45, 46*).

Many of these lesions associated with DNA damage have been previously reported as thermally destabilizing lesions (*47*−*49*), consistent with our findings here. Base modifications are also associated with dynamical changes in structure. OG is known to switch from the anti to the syn conformation while pairing with A (*50*). This conformational change is usually invoked as the basis for the mutagenic potential of OG (*51*), but it could also explain

the drastic CT efficiency attenuation observed with the OG:A base pair. O-methylation (OMG, OMT) is also known to alter Watson−Crick hydrogen bonding patterns (*48, 49*); OMG base paired with C does not form any hydrogen bonds unless C is protonated at the N3 position (*52*). OMT is similarly associated with increased flexibility at the lesion base pair (*49*), a property that, while linked to thermal instability and enzymatic recognition, may also be a factor in attenuation of CT efficiency. Synthetic lesions P, K, and Neb are not targeted by repair systems but can be thermally destabilizing (*24*, *53*).

Among the lesions not well-detected in this assay are ZA and ZG, purines where the nitrogen atom at the 7 position is replaced by a carbon atom. This modification is known to lower the redox potential of the base, but the 7-deaza modification is not thought to cause destabilization or altered base pairing and stacking interactions (*54*). 2-Aminopurine base paired with thymine is similarly found to be thermodynamically stable and well stacked in the helix; thus, it is not surprising that these three lesions are not easily detected using DNA CT (*5*, *55*). FlU, when base paired with adenine, is also thermodynamically stable and not a source of structural distortion (*56*). EA, a sterically bulky lesion, is only marginally detected here. Structural studies indicate that EA forms no hydrogen bonds with thymine and assumes a nonplanar conformation to accommodate the excess steric bulk of the lesion. Yet the lesion remains intrahelical, does not disrupt the structure of any flanking base pairs, and is purported to have stabilizing stacking interactions both with the bases above and below it and with the thymine opposite (*57*); perhaps these properties are sufficient to allow for some DNA-mediated reduction of MB in the presence of EA. Notably the poor coupling of EA in the base pair stack has been considered to account for the slow rate of base-base CT seen (*5*).

While O-methylation can be detected through CT, simple base alkylation, MC and NMA, cannot. Enzymatic methylation is generally thought to have a stabilizing effect on duplex DNA (*58, 59*). MC can lead to a higher melting temperature for DNA duplexes (*59*) and methylation at the 5 position on the pyrimidine ring, in general, is purported to reduce base pair opening rates (*60*). NMA, also not significantly thermally destabilizing, exhibits more favorable stacking interactions with bases above and below (*58*). Since methylation, if anything, further stabilizes a well-stacked conformation, then, our inability to detect methylation through DNA CT should not be surprising.

Given that DNA CT offers a sensitive strategy to detect a variety of DNA base lesions, might DNA CT chemistry play some role in DNA repair? While recent crystal structures provide some insight into how lesions may be structurally discriminated, in most cases, it is not well understood how DNA damage is first located within the genome; this is especially true in the case of base excision repair, the process that is responsible for removing single instances of base damage (*37*). The results described here certainly support the idea that DNA-mediated CT could potentially provide the foundation for a method of long range detection of DNA damage by repair enzymes. In this context, the detection of 5-hydroxy-cytosine and 8-oxo-guanine is especially significant as these are substrates for DNA repair glycosylases containing iron−sulfur cofactors that recently have demonstrated redox activity when bound to DNA (*16*).

Conclusions. Electrocatalysis at well-packed DNA films as measured by chronocoulometry is an effective detection technique for biologically relevant lesions and base analogues. This work points out the general trends in base modification that impact charge-transfer efficiency in DNA. These include modifications that lead to decreased or altered base pairing at the lesion site, modifications that add excess steric bulk, alterations that result in burial of polar groups, and modifications with the potential to induce conformational changes. Successful detection of common base damage products with this DNA CT based technique has important implications for the use of DNA-mediated CT as a damage detection mechanism for DNA repair enzymes.

ACKNOWLEDGMENT

We are grateful to the NIH (GM61077) for their financial support of this research.

LITERATURE CITED

(1) Friedberg, E. C., Walker, G. C., and Siede, W. (1995) *DNA Repair and Mutagenesis*, ASM Press, Washington, DC.

(2) Lindahl, T. (1993) Instability and decay of the primary structure of DNA. *Nature 362*, 709−715.

(3) Cadet, J., Delatour, T., Douki, T., Gasparutto, D., Pouget, J. P., Ravanat, J. L., and Sauvaigo, S. (1999) Hydroxyl radicals and DNA base damage. *Mutat. Res. 424*, 9−21.

(4) Hemminki, K., Koskinen, M., Rajeniemi, H., and Koskinen, M. (2000) DNA adducts, mutations, and cancer 2000. *Regul. Toxicol. Pharmacol. 32*, 264−275.

(5) Kelley, S. O., and Barton, J. K. (1995) Electron transfer between bases in double helical DNA. *Science 283*, 375−81.

(6) Kelley, S. O., Holmlin, R. E., Stemp, E. D. A., and Barton, J. K. (1997) Photoinduced electron transfer in ethidium-modified DNA duplexes: dependence on distance and base stacking. *J. Am. Chem. Soc. 119*, 9861−70.

(7) Holmlin, R. E., Dandliker, P. J., and Barton, J. K. (1997) Charge transfer through the DNA base stack. *Angew. Chem., Int. Ed. Engl. 36*, 2715−30.

(8) Schuster, G. B. (2000) Long-range charge transfer in DNA: transient structural distortions control the distance dependence. *Acc. Chem. Res. 33*, 253−60.

(9) Giese, B. (2002) Long-distance electron transfer through DNA. *Annu. Rev. Biochem. 71*, 51−70.

(10) Bhattacharya, P. K. and Barton, J. K. (2001) Influence of intervening mismatches on long-range guanine oxidation in DNA duplexes. *J. Am. Chem. Soc. 123*, 8649−56.

(11) Hall, D. B., and Barton, J. K. (1997) Sensitivity of DNA-mediated electron transfer to the intervening -stack: a probe for the integrity of the DNA base stack. *J. Am. Chem. Soc. 119*, 5045−5046.

(12) Rajski, S. R., and Barton, J. K. (2001) How different DNA-binding proteins affect long-range oxidative damage to DNA. *Biochemistry 40*, 5556−5564.

(13) Boon, E. M., Salas, J. E., and Barton, J. K. (2002) An electrical probe of protein-DNA interactions on DNA-modified surfaces. *Nat. Biotechnol. 20*, 282−286.

(14) Rajski, S. R., Jackson, B. A., and Barton, J. K. (2000) DNA repair: models for damage and mismatch recognition. *Mutat. Res. 447*, 49−72.

(15) Friedman, K. A. and Heller, A. (2001) On the nonuniform distribution of guanine in introns of human genes: possible protection of exons against oxidation by proximal intron poly-G sequences. *J. Phys. Chem. B 105*, 11859−11865.

(16) Boon, E. M., Livingston, A. L., Chmiel, N. H., David, S. S., and Barton, J. K. (2003) DNA-mediated charge transfer for DNA repair. *Proc. Natl. Acad. Sci. U.S.A. 100*, 12543−12547; *ibid. 101,* 4718.

(17) Kelley, S. O., Boon, E. M., Barton, J. K., Jackson, N. M., and Hill, M. G. (1999) Single-base mismatch detection based on charge transduction through DNA. *Nucleic Acids Res. 27*, 4830−4837.

(18) Boon, E. M., Ceres, D. M., Drummond, T. G., Hill, M. G., and Barton, J. K. (2000) Mutation detection by electrocatalysis at DNA-modified electrodes. *Nat. Biotechnol. 18*, 1096−1100.
(19) Drummond, T. G., Hill, M. G., and Barton, J. K. (2003) Electrochemical DNA Sensors. *Nat. Biotechnol. 21*, 1192−1199.
(20) Thorp, H. H. (2004) Electrocatalytic DNA oxidation. *Topics Curr. Chem. 237*, 159−181.
(21) Boon, E. M., Barton, J. K., Pradeepkumar, P. I., Isaksson, J., Petit, C., and Chattopadhyaya, J. (2003) An electrochemical probe of DNA stacking in an antisense oligonucleotide containing a C3′-endo-locked sugar. *Angew. Chem., Int. Ed. 41*, 3402−3405.
(22) Kelley, S. O., Barton, J. K., Jackson, N. M., and Hill, M. G. (1997) Electrochemistry of methylene blue bound to a DNA-modified electrode. *Bioconjugate Chem. 8*, 31−37.
(23) Bjelland, S., and Seeberg, E. (2003) Mutagenicity, toxicity and repair of DNA base damage induced by oxidation. *Mutat. Res. 531*, 37−80.
(24) Hill, F., Loakes, D., and Brown, D. M. (1998) Polymerase recognition of synthetic oligodeoxyribonucleotides incorporating degenerate pyrimidine and purine bases. *Proc. Natl. Acad. Sci. U.S.A. 95*, 4258−4263.
(25) Brown, G. B., and Weliky, V. S. (1953) The synthesis of 9-beta-D-ribofuranosylpurine and the identity of nebularine. *J. Biol. Chem. 204*, 1019−1024.
(26) Pratt, W. B., Ruddon, R. W., Ensminger, W. D., and Maybaum, J. (1994) *The Anticancer Drugs*, 2nd ed., Oxford University Press, New York.
(27) Ward, D. C., Reich, E., and Stryer, L. (1969) Fluorescence studies of nucleotides and polynucleotides I. Formycin, 2-aminopurine riboside, 2,6-diaminopurine riboside, and their derivatives. *J. Biol. Chem. 244*, 1228−1237.
(28) Barrio, J. R., Secrist, J. A., and Leonard, N. J. (1972) Fluorescent adenosine and cytidine derivatives. *Biochem. Biophys. Res. Commun. 46*, 597−604.
(29) Latimer, L. J., and Lee, J. S. (1991) Ethidium bromide does not fluoresce when intercalated adjacent to 7-deazaguanine in duplex DNA. *J. Biol. Chem. 266*, 13849−13851.
(30) Porello, S. L., Williams, S. D., Kuhn H., Michaels M. L., and David, S. S., (1996) Specific recognition of substrate analogues by the DNA mismatch repair enzyme MutY. *J. Am. Chem. Soc. 118*, 10684−10692.
(31) Bird, A. (1992) The essentials of DNA methylation. *Cell 70*, 5−8.
(32) Desrosiers, R., Friderici, K., and Rottman, F. (1974) Identification of methylated nucleosides in messenger RNA from Novikoff hepatoma cells. *Proc. Natl. Acad. Sci. U.S.A. 71*, 3971−3975.
(33) Blount, B. C., Mack, M. M., Wehr, C. M., MacGregor, J. T., Hiatt, R. A., Wang, G., Wickramasinghe, S. N., Everson, R. B., and Ames, B. N. (1997) Folate deficiency causes uracil misincorporation into human DNA and chromosome breakage: implications for cancer and neuronal damage. *Proc. Natl. Acad. Sci. U.S.A. 94*, 3290−3295.
(34) Goth, R., and Rajewsky, M. F. (1974) Persistence of O6-ethylguanine in rat-brain DNA: correlation with nervous system-specific carcinogenesis by ethylnitrosourea. *Proc. Natl. Acad. Sci. U.S.A. 71*, 639−643.
(35) Georgiadis, P., Xu, Y. Z., and Swann, P. F. (1991) Nitrosamine-induced cancer: O4-alkylthymine produces sites of DNA hyperflexibility. *Biochemistry 30*, 11725−11732.
(36) Olinski, R., Gackowski, D., Rozalski, R., Fokinski, M., and Bialowski, K. (2003) Oxidative DNA damage in cancer patients: a cause or a consequence of the disease? *Mutat. Res. 531*, 177−190.
(37) David, S. S., and Williams, S. D. (1998) Chemistry of glycosylases and endonucleases involved in base-excision repair. *Chem. Rev. 98*, 1221−1262.
(38) Bruner, S. D., Norman, D. P. G., and Verdine, G. L. (2000)-Structural basis for recognition and repair of the endogenous mutagen 8-oxoguanine in DNA. *Nature 403*, 859−866.
(39) Fromme, C. J., Banarjee, A. A., Huang, S. L., and Verdine, G. L. (2004) Structural basis for removal of adenine mispaired with 8-oxoguanine by MutY adenine DNA glycosylase. *Nature 427*, 652−656.
(40) Hatahett, Z., Kow, Y. W., Purmal, A. A., Cunningham, R. P., and Wallace, S. S. (1994) New substrates for old enzymes. *J. Biol. Chem. 269*, 18814−18820.
(41) Fromme, J. C., and Verdine, G. L. (2003) Structure of a trapped endonuclease III-DNA covalent intermediate. *EMBO J. 22*, 3461−3471.
(42) Berdal, K. G., Johansen, R. F., and Seeberg, E. (1998) Release of normal bases from intact DNA by a native DNA repair enzyme. *EMBO J. 17*, 363−367.
(43) Sassanfar, M., Posanjh, M. K., Essigman, J. M., and Samson, L. (1991) Relative efficiencies of the bacterial, yeast, and human DNA methyltransferases for the repair of O6-methylguanine and O4-methylthymine. Suggestive evidence for O4-methylthymine repair by eukaryotic methyltransferases. *J. Biol. Chem. 266*, 2767−2771.
(44) Duguid, E. M., Mishina, Y., and He, C. (2003) How do DNA repair proteins located potential base lesions? A chemical cross-linking method to investigate O6-alkylguanine-DNA methyltransferases. *Chem. Biol. 10*, 827−835.
(45) Daniels, D. S., Mol, C. D., Arvai, A. S., Kanugula, S., Pegg, A. E., and Tainer, J. A. (2000) Active and alkylated human AGT structures: a novel zinc site, inhibitor and extrahelical base binding. *EMBO J. 19* 1719−1730.
(46) Moore, M. H., Gulbis, J. M., Dodson, E. J., Demple, B., and Moody, P. C. (1994) Crystal structure of a suicidal DNA repair protein: the Ada O6-methylguanine-DNA methyltransferase from E. coli. *EMBO J. 13*, 1495−501.
(47) Oda, Y., Uesugi, S., Ikehara, M., Nishimura, S., Kawase, Y., Ishikawa, H., Inoue, H., and Ohtsuka, E. (1991) NMR studies of a DNA containing 8-hydroxydeoxyguanosine. *Nucleic Acids Res. 19*, 1407−1412.
(48) Gaffney, B. L., and Jones, R. A. (1989) Thermodynamic comparison of the base pairs formed by the carcinogenic lesion O6-methylguanine with reference both to Watson−Crick pairs and to mismatched pairs. *Biochemistry 28*, 5881−5889.
(49) Cruzeiro-Hansson, L., and Goodfellow, J. M. (1994) Flexibility and curvature of DNA duplexes containing O4-methylthymine: implications for DNA repair. *Carcinogenesis 15*, 1525−1533.
(50) Kouchakdjian, M., Bodepudi, V., Shibutani, S., Eisenberg, M., Johnson, F., Grollman, A. P., and Patel, D. J. (1991) NMR structural studies of the ionizing radiation adduct 7-hydro-8-oxodeoxyguanosine (8-oxo-7H-dG) opposite deoxyadenosine in a DNA duplex. 8−0xo-7H-dG(syn): dA(anti) alignment at lesion site. *Biochemistry 30*, 1403−1412.
(51) Cheng, K. C., Cahill, D. S., Kasai, H., Nishimura, S., and Loeb, L. A. (1992) 8-Hydroxyguanine, an abundant form of oxidative DNA damage, causes G−T and A−C substitutions. *J. Biol. Chem. 267*, 166−172.
(52) Williams, L. D., and Shaw, B. R. (1987) Protonated base pairs explain the ambiguous pairing properties of O6-methylguanine. *Proc. Natl. Acad. Sci. U.S.A. 84*, 1779−1783.
(53) Jiricny, J., Wood, S. G., Martin, D., and Ubasawa, A. (1986) Oligonucleotide duplexes containing inosine, 7-deazainosine, tubercidin, nebularine and 7-deazanebularine as substrates for restriction endonucleases HindII, SalI and TaqI. *Nucleic Acids Res. 14*, 6579−6590.
(54) Baik, M., Silverman, J. S., Yang, I. V., Ropp, P. A., Szalai, V. A., Yang, W., and Thorp, H. H. (2001) Using density functional theory to design base analogues with low oxidation potentials. *J. Phys. Chem. B 105*, 6437−6444.
(55) Law, S. M., Eritja, R., Goodman, M. F., and Breslauer, K. J. (1996) Spectroscopic and calorimetric characterizations of DNA duplexes containing 2-aminopurine. *Biochemistry 35*, 12329−12337.
(56) Kramer, A. B., Mikita, T., and Beardsley, G. P. (1987) Chemical consequences of the incorporation of 5-fluorouracil as studied by NMR. *Biochemistry 26*, 391−397.
(57) Kouchakdjian, M., Eisenberg, M., Yarema, K., Basu, A., Essigmann, J., and Patel, D. J. (1991) NMR studies of the exocyclic 1, N6-ethenodeoxyadenosine adduct (dA) opposite thymidine in a DNA duplex. Nonplanar alignment of dA(anti) and dT(anti) at the lesion site? *Biochemistry 30*, 1820−1828.

(58) Engel, J. D., and von Hippel, P. H. (1977) Effects of methylation on the stability of nucleic acid conformations. *J. Biol. Chem. 253*, 927−934.
(59) Marcourt, L., Cordier, C., Couesnon, T., and Dodin, G. (1999) Impact of C5-cytosine methylation on the solution structure of d(GAAAACGTTTTC)$_2$. An NMR and molecular modeling investigation. *Eur. J. Biochem. 265*, 1032−1042.
(60) Warmlander, S., Sponer, J. E., Sponer, J., and Leijon, M. (2002) The influence of the thymine C5 methyl group on spontaneous base pair breathing in DNA. *J. Biol. Chem. 277*, 28491−28497.

BC0497362

Supramolecular Gene Delivery Vectors Showing Enhanced Transgene Expression and Good Biocompatibility

Xintao Shuai,† Thomas Merdan,† Florian Unger, and Thomas Kissel*

Department of Pharmaceutics and Biopharmacy, Philipps-University of Marburg, Ketzerbach 63, D-35032 Marburg, Germany. Received June 30, 2004; Revised Manuscript Received January 23, 2005

Soluble supramolecular inclusion complexes were formed by threading α-cyclodextrin (α-CD) molecules over poly(ethylene glycol) (PEG) and poly(ϵ-caprolactone) (PCL) chains of ternary block copolymers of PEG, PCL and polyethylenimine (PEI). Characteristic shifts of PCL absorptions in FTIR, ^{1}H NMR and UV spectra strongly suggest that α-CD is threaded over PEG and PCL blocks. Due to the reduced hydrophobic interaction between PCL blocks, the resulting supramolecular complexes displayed a dramatically increased solubility, in comparison with the ternary block copolymers. Their ability to complex DNA was almost as efficient as that of branched PEI 25 kDa, as shown in the ethidium bromide fluorescence quenching experiments. Resulting DNA polyplexes displayed a size of around 200 nm and a neutral surface charge. Microscopy studies in 3T3 fibroblasts revealed an efficient cellular uptake. Transfection efficiencies of inclusion complexes were in the same order of magnitude as PEI. In contrast to PEI a 100× lower toxicity was observed by MTT-assay, allowing the administration of nitrogen-to-phosphate ratios of up to 20. These new gene delivery systems merit further characterization under in vivo conditions.

INTRODUCTION

Various nonviral gene delivery systems consisting of DNA and polycations, dubbed as "polyplexes", have been investigated (*1*−*3*). Poly(ethylenimine), PEI, has attracted considerable interest due to its high positive charge density and consequently strong DNA binding. Another beneficial feature of PEI is the "proton-sponge effect", which is thought to facilitate endosomal/lysosomal escape of DNA into the cytoplasm (*4*). PEI with molecular weights >2000 Da seems to be necessary for effective gene delivery (*5*−*7*). PEI and PEI/DNA complexes were found to be cytotoxic in molecular weight and composition dependent manner due to their electrostatic interactions with negatively charged cell membranes (*5*, *7*).

Copolymers of PEI with hydrophilic macromolecules forming DNA polyplexes with neutral surface charge have extensively been investigated recently (*8*−*12*). Most studies utilize nonionic hydrophilic polyethers, e.g. poly(ethylene glycol) (PEG), as a building block to generate block or graft copolymers with linear or branched PEIs. When these copolymers were mixed with pDNA in aqueous solution, the cationic PEI segment of the copolymer first binds DNA via electrostatic interactions and then the neutralized polyions aggregate to form an insoluble core. The nonionic water-soluble PEG chains act as a hydrophilic shell stabilizing the resulting nanoscale polyelectrolyte complexes (*8*). Polyplexes thus prepared show a lower positive surface charge compared to PEI, and consequently less cytotoxicity was observed. Unfortunately, the transfection efficiency was also decreased.

We recently synthesized a new type of ternary block-copolymers by grafting diblock copolymers of PEG and PCL onto branched PEI. Intensive hydrogen bonding between PCL and PEI blocks was noted in the bulk materials, and solubility was strongly affected by composition, i.e., block length and graft density. DNA polyplexes formed with soluble copolymers or copolymers possessing a high critical micelle concentration (cmc) showed significant transfection efficiency under in vitro conditions. By contrast, those copolymers with a high graft density and long PCL blocks showed very poor gene expression. In the latter case, access and binding of DNA to PEI was seriously hindered by hydrophobic PCL chains surrounding the hydrophilic PEI head. Hydrogen bonding between PCL and PEI blocks is also believed to be an impediment for the DNA complexation with PEI (*13*). Therefore, breaking of hydrogen bonds between PCL and PEI as well as the dissolution of PCL block in aqueous media seem to be key factors for improving gene transfection efficiency of these copolymers.

In this publication, we present an unusual way to dissolve the PCL blocks of the ternary copolymers in aqueous solution by including them inside the α-cyclodextrin (α-CD) cavities. α-CD is a cyclic oligosaccharide consisting of six glucose units (*15*). One of its distinctive characters is its amphipathy, i.e., it possesses a hydrophobic cavity of 4.5 Å in diameter with a hydrophilic outer layer supporting many hydroxyl groups (*15, 16*). Supramolecular inclusion complexes (ICs), organized by noncovalent interactions, can be formed by threading α-CD molecules onto various polymer chains (*17*−*23*). The driving force for the threading process is probably due to intermolecular hydrogen bonding between neighboring CDs, as well as steric compatibility and hydrophobic interactions between host and guest molecules. It has been demonstrated that α-CD forms inclusion complexes with both poly(ethylene glycol) (PEG) (*17, 18*) and PCL (*24*−*28*) chains. In most cases, a full coverage of individual polymer chains with α-CD bracelets leads to crystalline water-insoluble inclusion complexes. In

* To whom correspondence should be addressed. Tel +49-6421-282-5881. Fax +49-6421-282-7016. E-mail: kissel@staff.uni-marburg.de.

† These authors have equally contributed to this work.

10.1021/bc0498471 CCC: $30.25 © 2005 American Chemical Society
Published on Web 02/23/2005

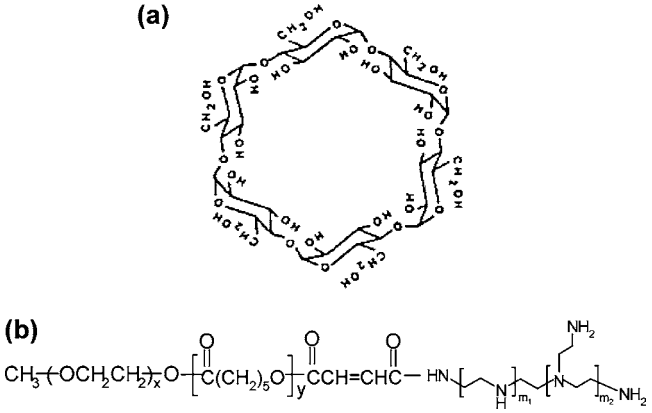

Figure 1. The chemical structures of α-cyclodextrin (a) and copolymer of PEI, PCL and PEG (b).

dilute solutions a partial coverage of PEG or PCL chains with α-CD can be achieved. In the latter case, inclusion complexes with PCL may be completely soluble in water.

Here we investigate supramolecular physicochemical and biological properties of supramolecular inclusion complexes as carriers for gene delivery.

EXPERIMENTAL SECTION

Materials. ϵ-Caprolactone (from Aldrich) was purified by vacuum distillation over CaH_2. Monomethoxyl-poly(ethylene glycol) (MPEG) (Aldrich) was dried by azeotropic distillation with dry toluene. The PEI with a molecular weight of 25 kDa (abbreviation: PEI25k) was a gift from BASF (Germany). This PEI is a highly branched molecule. Its contents of primary, secondary, and tertiary amine units are 42%, 33%, and 25% respectively. α-CD was purchased from Aldrich and vacuum-dried at 40 °C prior to use.

Diblock copolymers of PCL and PEG were synthesized by ring-opening polymerization of ϵ-caprolactone and then grafted to PEI, as described in our recent publication (*13*). The chemical structures of these copolymers and threading of α-CD are shown in Figure 1. Molecular characteristics of polymers used in this study are shown in Table 1. To prepare inclusion complexes, the predetermined amount of α-CD aqueous solution (e.g. 5 mg/mL, 20 mL) was added stepwise to the copolymer micelle solution (e.g. 4.2 mg/mL, 15 mL) in a glass vial immersed in an ultrasonic water bath at room temperature. Sonication was applied for 30 min during and after the addition of the α-CD solution. The mixed solution was then stirred magnetically overnight at room temperature, frozen at ∼−40 °C, and then freeze-dried to yield a powdered sample (*30*).

pCMV−Luc encoding for luciferase as a reporter gene was purchased from Plasmid Factory, Bielefeld, Germany. NIH/3T3 (Swiss mouse embryo) cell line was purchased from the German Collection of Microorganisms and Cell Cultures (DSMZ, Braunschweig, Germany). Cells were cultured according to the protocols suggested by the supplier.

Cell Culture. NIH/3T3 cells (DSMZ#: ACC 59) were cultured under conditions recommended by the supplier in Dulbecco's modified Eagle medium containing 10% fetal bovine serum.

Spectroscopic Measurements of Copolymers and Inclusion Complexes. FTIR spectral studies were carried out using a Nicolet 510P FTIR spectrometer with a resolution of 2 cm^{-1}. Powder samples were compressed into KBr pellets for FTIR measurements. ^1H NMR spectra were recorded on a JEOL GX 400 D spectrometer in deuterated water (D_2O) at room temperature. UV spectra of solution samples were recorded on a Shimadzu UV-160 UV−visible recording spectrophotometer.

Ethidium Bromide Exclusion Assay. DNA condensation was measured by the decrease in ethidium bromide fluorescence, as described earlier (*31, 32*). The assay was performed in 96-well plates in triplicate using 8 μg of salmon testes DNA was dissolved in 79 μL of water and 50 μL of 60 mM Tris buffer pH 7.4 were added to each well. Volumes were adjusted to 300 μL using water. Subsequently, appropriate volumes of 0.05 mg/mL polymer solutions were added to yield N/P ratios between 0.2 and 4. After 10 min 20 μL of a 0.1 mg/mL ethidium bromide solution were added. Wells were mixed thoroughly, and the fluorescence was measured using a fluorescence plate reader with an excitation wavelength at 518 nm and an emission wavelength of 605 nm.

Polyplex Formation. Luciferase plasmid (pCMV-luc) and the appropriate amount of polymer or inclusion complex were dissolved separately in 0.9% sodium chloride solution of pH = 7. The two solutions were mixed by vigorous pipetting, and complexes were allowed to interact for 10 min before use. Polyplexes were prepared for transfection experiments with 4 μg of plasmid in 300 μL of NaCl 0.9% and the appropriate amount of polymer or conjugate in 300 μL of sodium chloride solution (0.9%, pH = 7).

Photon Correlation Spectroscopy. Hydrodynamic diameters of the DNA/polymer complexes were determined by photon correlation spectroscopy. Measurements of micelle solutions were performed on a Zetasizer 3000 HS from Malvern Instruments, Herrenberg, Germany (10 mW HeNe laser, 633 nm). Scattering light was detected at 90° angle through a 400 μm pinhole at a temperature of 25 °C. For data analysis, the viscosity (0.88 mPa·s) and the refractive index (1.33) of distilled water at 25 °C were used. The instrument was routinely calibrated using Standard Reference latex particles (AZ 55 Electrophoresis Standard Kit, Malvern Instruments). Measurements were analyzed by the CONTIN algorithm. Values given are the means of 5 runs of 60 s ± standard deviation.

Zeta Potential Measurements. pCMV−Luc plasmid (16 μg) was complexed with the appropriate amount of polymer in 800 μL of NaCl 150 mM as described above. Zeta-potential measurements of polyplexes formed at N/P 7 were carried out in the standard capillary electrophoresis cell of the Zetasizer 3000 HS from Malvern Instruments at position 17.0 at 25 °C. Sampling time was set to automatic. Average values were calculated with the data of 5 runs.

Fluorescent Labeling of PEI and DNA for Confocal Laser Scanning Microscopy Experiments. Polymer or inclusion complexes (20 mg) were dissolved in 2 mL 0.1 M sodium bicarbonate solution at pH 9. Oregon Green 488 carboxylic acid succinimidyl ester (1 mg, Molecular Probes) was dissolved in 200 μL of dimethyl sulfoxide and added dropwise under stirring to the polymer solution. The mixture was stirred in the dark for 3 h at room temperature before the labeled polymer was purified by ultrafiltration in an Amicon cell (regenerated cellulose membrane, molecular weight cut off 10 000) and washed with 0.1 M borate/1.0 M sodium chloride solution pH 7.5. The washing procedure was performed until no absorption was detectable at 488 nm in the cell outflow. As a final step, the buffer was exchanged with distilled water. Plasmid (pCMV−Luc) was labeled with Cy3 using a commercial kit (Mirrus Label It, Mobitec, Göttingen, Germany). Procedure was performed according to the manufacturer's manual.

Table 1. Molecular Characteristics of Polymers Used in This Study

polymers[a]	molecular weights of blocks (Da) PEI	PCL	PEG	grafting density[b]	solubility[c] (mmol/L)
PEI25k	25000				S[d]
PEI25k-*g*-(PCL580-*b*-PEG5k)$_{2.9}$	25000	580	5000	2.9	S
PEI25k-*g*-(PCL2k-*b*-PEG2k)$_{2.8}$	25000	2000	2000	2.8	0.031
PEI25k-*g*-(PCL1.2k-*b*-PEG2k)$_{5.1}$	25000	1200	2000	5.1	<0.012

[a] In these polymer abbreviations, "*g*" and "*b*" indicates "graft" and "block", respectively. [b] Average number of side chain grafting to each PEI molecule. [c] Solubility which is also the cmc in water at 25 °C. [d] Water soluble polymers without detected cmc.

Table 2. DNA Complexes Formed Respectively with Copolymers and Copolymer/α-CD Inclusion Complexes at N/P 7[a]

copolymer	copolymer size (nm) (± SD)	copolymer ξ-potential (mV)	inclusion complex α-CD[b] (%)	inclusion complex PEI[b] (%)	inclusion complex size (nm) (± SD)	inclusion complex ξ-potential (mV)
PEI25k	164.6 ± 5.4	20.9 ± 2.7	nc[c]	nc	nc	nc
PEI25k-*g*-(PCL580-*b*-PEG5k)$_{2.9}$	207.8 ± 6.2	−0.4 ± 1.9	34	40	208.5 ± 7.2	0.3 ± 1.8
PEI25k-*g*-(PCL2k-*b*-PEG2k)$_{2.8}$	234.4 ± 9.8	−3.5 ± 0.3	62	26	217.5 ± 9.6	−1.5 ± 1.9
PEI25k-*g*-(PCL1.2k-*b*-PEG2k)$_{5.1}$	208.4 ± 8.6	−3.0 ± 0.9	44	34	222.5 ± 12.7	1.4 ± 1.4

[a] Detected with dynamic light scattering. [b] Weight contents in the inclusion complexes. [c] No detected inclusion with α-CD.

Confocal Laser Scanning Microscopy Experiments. A Zeiss Axiovert 100M microscope coupled to a Zeiss LSM 510 scan module was used. NIH/3T3 cells were seeded at a density of 50 000 cells per well in 8-well chamber slides (Lab Tek, Nunc, Wiesbaden, Germany). After 24 h the medium was removed and complexes of 0.5 μg of Oregon Green-labeled polymer or the appropriate amount of inclusion complex and 0.5 μg Cy3 labeled plasmid were added in new medium. After an additional 4 h, medium was removed again and cells were washed four times with phosphorus buffered saline (PBS). Fixation of cells was done by incubation with 400 μL of paraformaldehyde solution 3% in PBS for 20 min. Cells were washed again for four times and incubated for an additional 20 min with a 0.1 mg/mL DAPI (4′,6-diamidino-2-phenylindole, dihydrochloride) (Molecular Probes, Leiden, The Netherlands) solution in PBS. For excitation of DAPI fluorescence, an Enterprise UV laser with an excitation wavelength 364 nm was used. Excitation of Oregon Green was performed using an argon laser with an excitation wavelength of 488 nm and for excitation of Cy3 a helium−neon laser with an excitation wavelength of 543 nm was used.

In Vitro Cytotoxicity Using MTT Assay. L929 mouse fibroblasts were grown in Dulbecco's modified Eagle's medium (DMEM) (Gibco, Germany) supplemented with 10% fetal calf serum (Cytogen, Germany), 2 mM glutamine, penicillin (100 U/ml) and streptomycin (100 μg/mL; both Invitrogen, Germany).

In vitro cytotoxicity of the polymers was evaluated using the MTT assay as described previously (*5*). L929 cells were seeded into 96-well microtiter plates (Nunclon, Nunc, Germany) at a density of 8000 cells/well. After 24 h the culture medium was replaced with 100 μL/ well of serial dilutions of polymer stock solutions in antibiotic-free DMEM ($n = 4$). After an incubation period of 24 h, MTT (3-(4,5-dimethylthiazol-2-yl)-2,5-diphenyltetrazolium bromide) (Sigma-Aldrich, Germany) was dissolved in phosphate buffered saline at 5 mg/mL and 20 μL were added to each well reaching a final concentration of 0.5 mg MTT/ml. After an incubation time of 4 h, unreacted dye was removed by aspiration and the purple formazan product was dissolved in 200 μL/well dimethyl sulfoxide and quantified by a plate reader (Titertek plus MS 212, ICN, Germany) at wavelengths of 570 and 690 nm. The relative cell viability [%] related to control wells containing cell culture medium without polymer was calculated by [A] test/[A] control × 100. Poly(ethylene imine) 25 kDa (BASF, Germany) was used as a positive control.

Transfection Experiments. Transfection experiments were performed with 4 μg of pCMV−Luc. NIH/3T3 cells were seeded in 12-well plates at a density of 50 000 cells per well. After 24 h, medium was removed and complexes were added in 1.5 mL of fresh media. Media was exchanged again after 4 h, and cells were incubated for a further 44 h. Luciferase gene expression was quantified using a commercial kit (Promega) and photon counting with a luminometer (Sirius, Berthold). Results in relative light units per second (RLU/s) were converted into ng luciferase by creating a calibration curve with recombinant luciferase (Promega). Protein concentration in each sample indicating cell viability was determined using a BCA assay. All experiments were performed in triplicate and data were expressed in ng luciferase per mg protein.

RESULTS AND DISCUSSION

Formation of Soluble Inclusion Complexes. Among the three copolymers listed in Table 2, only the copolymer containing the shortest PCL blocks (PCL of molecular weight 580) shows a high solubility in water. The other two copolymers showed a distinct critical micellization concentration (cmc) (*13*). To form an inclusion complex, the α-CD solution of predetermined concentration was added stepwise to the dilute micellar solution of the ternary block copolymer under sonication. During this process, dynamic light scattering (DLS) measurements were employed to monitor the micelle dissolution upon dilution and addition of α-CD. When the turbid solution became transparent upon addition of an aqueous α-CD solution, nanoparticles were no longer detectable by DLS measurement, suggesting the dissolution of micelles.

The effect of added α-CD on the solubility of the copolymers depends largely on the copolymer compositions, as illustrated in Figure 2. A soluble inclusion complex was obtained when the weight ratio of α-CD and PEI25k-*g*-(PCL2k-*b*-PEG2k)$_{2.8}$ reached a critical value of 1.66. In contrast, a soluble inclusion complex was obtained as well when the weight ratio of α-CD and PEI25k-*g*-(PCL1.2k-*b*-PEG2k)$_{5.1}$ reached 0.78. It is known that the cavity depth of α-CD molecules is 7 Å, which is equal to the length of approximately 0.86 repeat units of PCL or approximately 2 repeat units of PEG (*36*). Therefore, even if only the PCL blocks of the copolymer were fully covered by α-CD molecules, the PEI contents in PEI25k-*g*-(PCL580-*b*-PEG5k)$_{2.9}$, PEI25k-*g*-(PCL1.2k-*b*-PEG2k)$_{5.1}$ and PEI25k-*g*-(PCL2k-*b*-PEG2k)$_{2.8}$ should be

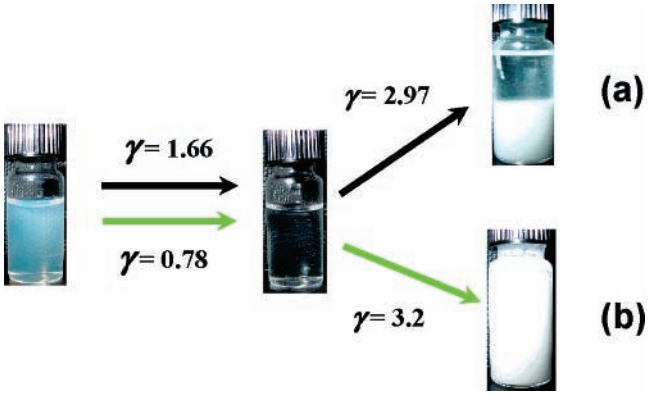

Figure 2. Phase transition phenomena of PEI25k-*g*-(PCL2k-*b*-PEG2k)$_{2.8}$ (a) and PEI25k-*g*-(PCL1.2k-*b*-PEG2k)$_{5.1}$ (b) upon adding α-CD solution. γ is the weight ratio of added α-CD and copolymer.

approximately 43%, 24% and 27%, respectively. The actual PEI content of complexes shown in Table 2 is close to (40% vs 43%, and 26% vs 27%) or much higher (34% vs 24%) than these values. Since PEG may also form an inclusion complex with α-CD, apparently the copolymer side chains (PCL-*b*-PEGs) were only partially covered by α-CD molecules in these soluble inclusion complexes. Interestingly, a white precipitate was formed when the weight ratio of α-CD and PEI25k-*g*-(PCL2k-*b*-PEG2k)$_{2.8}$ reached 2.97 at which the α-CD amount is sufficient to cover ~92% of total side chains (i.e. total length) of both PCL and PEG blocks. However, a gel was formed when the weight ratio of α-CD and PEI25k-*g*-(PCL1.2k-*b*-PEG2k)$_{5.1}$ reached 3.2 at which α-CD can cover ~76% of total side chains. These results are reasonable because the inclusion complex of cyclodextrins and polymer may form insoluble crystals and these insoluble crystals may cross-link the highly branched polymer in solution, as reported by Yui et al. (*35*).

The threading of α-CD molecules onto the copolymer PCL blocks was illustrated in Figure 3 and demonstrated spectroscopically. Figure 4 shows an expansion of the FTIR spectra covering the carbonyl bands of a diblock copolymer of PCL and PEG (MPEG-*b*-PCL), its corresponding ternary copolymer and inclusion complex with α-CD. The inclusion complex powder sample was obtained by freeze-drying of the aqueous sample solution and was allowed to crystallize at room temperature for one month before the FTIR measurements. It is known that the expanded $\nu_{C=O}$ absorption band of the semicrystalline PCL is very indicative of the PCL phase structure in the FTIR measurements (*27*, *28*). In agreement with these reports, the PCL carbonyl absorption band (s, $\nu_{C=O}$) of PCL-*b*-MPEG can be well resolved into a peak at 1726 cm^{-1} and a prominent shoulder at 1736 cm^{-1}, corresponding to the carbonyl absorption of the crystalline and the amorphous PCL phases, respectively. The carbonyl absorption of the crystalline phase (1726 cm^{-1}) is much stronger than that of the amorphous one, suggesting high PCL crystallinity in the diblock copolymer. Upon grafting onto PEI, the absorption of crystalline PCL at 1725 cm^{-1} becomes weak, while the absorption of the amorphous PCL at 1736 cm^{-1} appears as the main peak, as shown in spectrum b. These results indicate that the crystallization of PCL blocks has been suppressed but not completely eliminated in the copolymers. By contrast, as shown in spectrum c, the C=O absorption of crystalline PCL regions completely disappears, and only the C=O absorption of noncrystalline PCL blocks is detected in the spectrum of the ICs. These results suggest that PCL

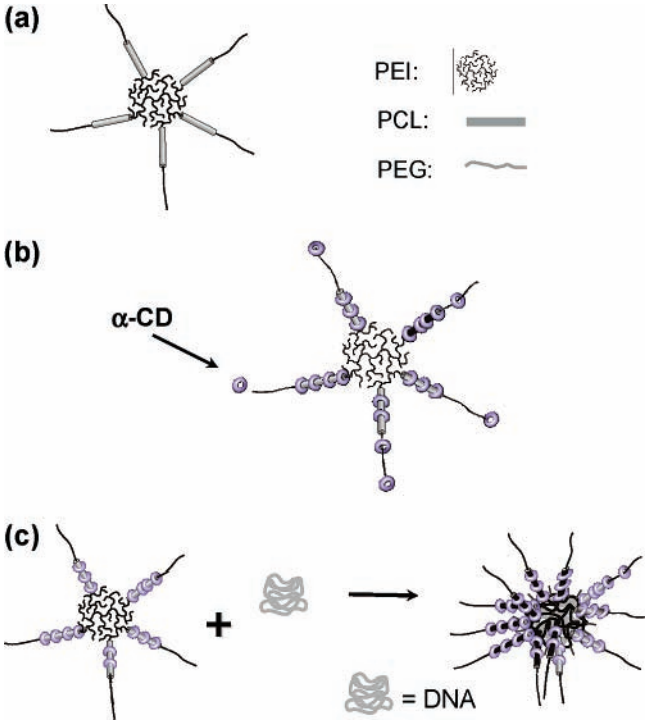

Figure 3. Schematic copolymer structure (a), formation of inclusion complex (b) and formation of polyplex (c).

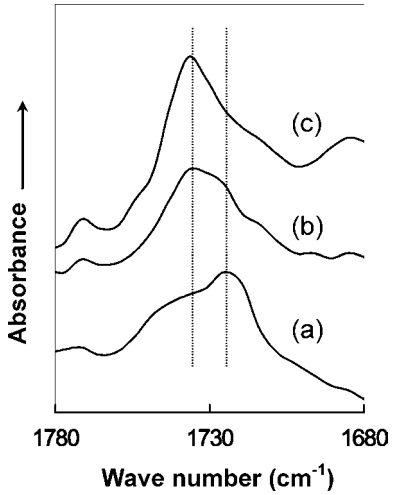

Figure 4. FTIR spectra of hydroxyl-terminated diblock copolymer PCL2k-*b*-MPEG2k (a), PEI25k-*g*-(PCL2k-*b*-PEG2k)$_{2.8}$ (b) and inclusion complex of α-CD and PEI25k-*g*-(PCL2k-*b*-PEG2k)$_{2.8}$ (c).

chains, individually inserted into α-CD channels, were not able to fold and aggregate in order to form any PCL crystals.

^{1}H NMR spectroscopy further corroborates the preferential complexation of PCL block with α-CD. In Figure 5 the ^{1}H NMR spectra of PEI25k-*g*-(PCL580-*b*-PEG5k)$_{2.9}$ and inclusion complex of α-CD and PEI25k-*g*-(PCL2k-*b*-PEG2k)$_{2.8}$ are shown. Unfortunately, PEI25k-*g*-(PCL2k-*b*-PEG2k)$_{2.8}$ has too low solubility (i.e. cmc) and does not show good resonance signals in the ^{1}H NMR measurement. Therefore, we have to turn to the highly soluble PEI25k-*g*-(PCL580-*b*-PEG5k)$_{2.9}$ for ^{1}H NMR measurement and compare its ^{1}H NMR signals with those of the soluble inclusion complex. The soluble copolymer PEI25k-*g*-(PCL580-*b*-PEG5k)$_{2.9}$ in deuterated water showed clear PCL resonance signals at 1.44, 1.66 and 2.4 ppm, Figure 2a. ^{1}H NMR spectra of copolymer micelles did not show

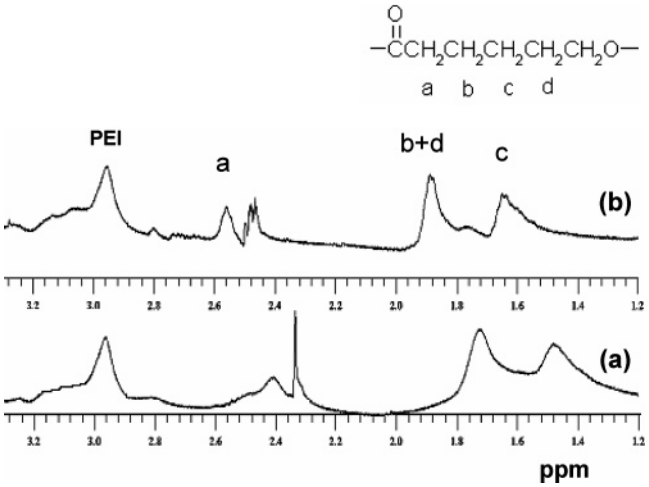

Figure 5. ^{1}H NMR spectra of PEI25k-*g*-(PCL580-*b*-PEG5k)$_{2.9}$ (a) and soluble inclusion complex of α-CD and PEI25k-*g*-(PCL2k-*b*-PEG2k)$_{2.8}$ in D_2O (b).

detectable resonance signals of PCL blocks due to the suppressed chain mobility (data not shown). When the micelles were dissociated upon addition of α-CD, clear PCL resonance signals were observed in the ^{1}H NMR measurements. However, these resonance signals of PCL blocks showed significant downfield shift upon forming the inclusion complex with α-CD, as shown in Figure 5b. These results are consistent with previous reports in which similar downfield shifts were observed when polymer chains were included inside CD cavities (*29*, *37*).

It was reported that protonated poly(iminooligomethylene)s may form soluble inclusion complexes with α-CD and result in the similar downfield chemical shift of oligomethylene signals. However the threading process was very slow at room temperature. In our work, PEI block signal did not show downfield shifts upon mixing with α-CD even after several days at room temperature. A model study with PEI25k showed the same results. Thus apparently, PEI does not form an inclusion complex with α-CD at room temperature. The different behavior of PEI and poly(iminooligomethylene)s may be due to the fact that the reported poly(iminooligomethylene)s contain long oligomethylene chains which are known to form an inclusion complex with α-CD. Indeed, polyethylene is known to form an inclusion complex with α-CD (*38*). In addition, the branched structure of the used PEI might be another reason that it cannot form inclusion complex with α-CD. It is well-known that PEG can also form inclusion complexes with α-CD. However, ^{1}H NMR signals of the PEG blocks of the copolymer complexes listed in Table 2 did not show any significant downfield shifts. These results suggest that the α-CD molecules have preferably formed an inclusion complex with the PCL block in these complexes, in case that the α-CD molar amount was stoichiometrically insufficient for the whole side chain (MPEG-*b*-PCL-) inclusion, as discussed in Figure 2.

Formation of an inclusion complex between α-CD and PCL block was confirmed by UV measurements as well. As shown in Figure 6, upon adding α-CD, the UV absorption peak of the PCL carbonyl of the soluble PEI25k-g-(PCL580-*b*-PEG5k)$_{2.9}$ showed a clear red-shift from 216 to 226 nm due to the interaction between α-CD and the included PCL chain. The other two copolymers are not soluble and form micelles in aqueous solution. Therefore, they are not suitable for the UV study.

The stability of these inclusion complexes still remains unclear. One concern is that α-CD molecules may unthread the copolymer chains and form inclusion complexes with competing ligands present in the cell culture media and blood plasma. So far there is no experimental evidence to substantiate this concern.

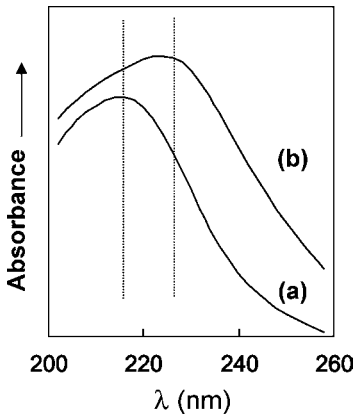

Figure 6. UV spectra of PEI25k-*g*-(PCL580-*b*-PEG5k)$_{2.9}$ (a) and its inclusion complex (b) in water.

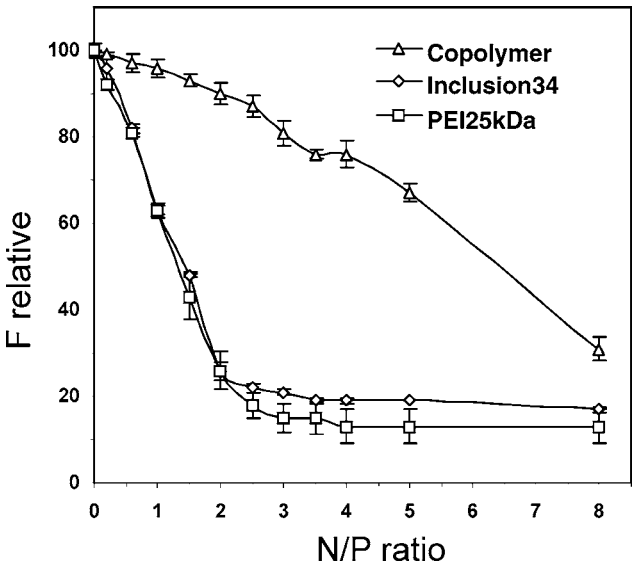

Figure 7. Condensation potential of PEI25k, PEI25k-*g*-(PCL1.2k-*b*-PEG2k)$_{5.1}$ and its inclusion complex with α-CD, as determined by EtBr assay.

Ethidium bromide (EtBr) exclusion assay for DNA condensation. Fluorescence of ethidium bromide added to polyplex solutions was determined to monitor DNA condensation. While free ethidium bromide in solution only shows weak fluorescence, fluorescence intensity strongly increases when it intercalates with DNA. If the DNA is condensed by a polycation, EtBr cannot intercalate with DNA any more. Therefore, condensation of DNA by polycations can be monitored by the decrease of EtBr fluorescence. As shown in Figure 7, increasing amount of PEI25k and inclusion complex both led to a significant decrease in relative fluorescence intensity from 100% to 26% until N/P ratio reached 2. By contrast, the relative fluorescence intensity was only slightly decreased to 90% at this N/P scale when DNA was condensed with PEI25k-*g*-(PCL1.2k-*b*-PEG2k)$_{5.1}$. Similar data were obtained for other inclusion compounds and their CD-free counterparts. Apparently, PEI and the inclusion complexes are much more efficient for DNA condensation, in comparison to the non-α-CD-complexed copolymers.

Size, Zeta-Potential and Biocompatibility of Polyplex Polyplexes. The particle size and ξ-potential of various pDNA/copolymer complexes formed at an N/P

Table 3. 3T3 Cell Viability in the Transfection with DNA Complexes Based on Polymers and Inclusion Complexes

	cell viability[a] (%)					
	N/P = 3		N/P = 7		N/P = 20	
polymer	polymer	IC[b]	polymer	IC	polymer	IC
PEI25k	80 ± 18		69 ± 19		0 ± 0	
PEI25k-*g*-(PCL580-*b*-PEG5k)$_{2.9}$	99 ± 4	101 ± 8	94 ± 4	91 ± 9	46 ± 23	83 ± 9
PEI25k-*g*-(PCL1.2-*b*-PEG2k)$_{5.1}$	100 ± 7	103 ± 2	95 ± 9	100 ± 5	45 ± 18	97 ± 10
PEI25k-*g*-(PCL2*k*-*b*-PEG2*k*)$_{2.8}$	91 ± 4	100 ± 4	90 ± 8	88 ± 5	41 ± 25	84 ± 8

[a] Calculated based on the protein level detected. [b] DNA complexes prepared with inclusion complexes.

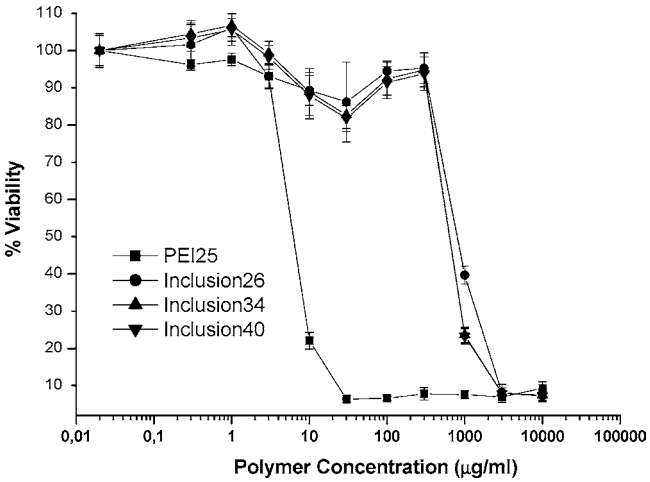

Figure 8. Estimation of cytotoxicity employing an MTT-assay. An about 100-fold less cytotoxicity of inclusion complexes can be observed compared to PEI 25 kDa.

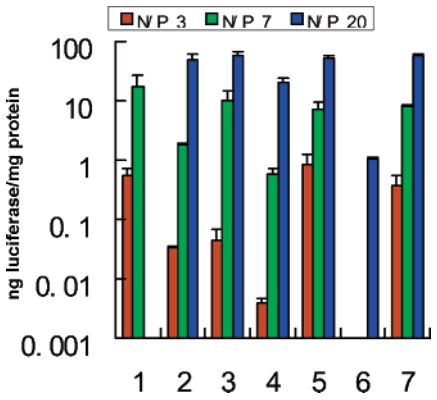

Figure 9. Transfection efficiency of polyplexes to 3T3 cells based on (1) PEI25k, (2) PEI25k-*g*-(PCL580-*b*-PEG5k)$_{2.9}$, (3) inclusion complex of PEI25k-*g*-(PCL580-*b*-PEG5k)$_{2.9}$, (4) PEI25k-*g*-(PCL2k-*b*-PEG2k)$_{2.8}$, (5) inclusion complex of PEI25k-*g*-(PCL2k-*b*-PEG2k)$_{2.8}$, (6) PEI25k-*g*-(PCL1.2k-*b*-PEG2k)$_{5.1}$ and (7) inclusion complex of PEI25k-*g*-(PCL1.2k-*b*-PEG2k)$_{5.1}$.

ratio of 7 are summarized in Table 2. PEI25k formed the smallest polyplexes of approximately 160 nm in diameter. It is noteworthy that threading of α-CD does not increase the particle size of polyplexes, i.e., polyplex sizes detected are all around 200 nm no matter whether α-CD was incorporated or not. As expected, the $\xi-$potential of the polyplexes with PEI 25k are very high (21mV), suggesting highly positive charge on the particle surface. In contrast, polyplexes based on both copolymer and inclusion complexes possess approximately neutral surfaces (−3.5 to 1.4 mV $\xi-$potential).

In Vitro Cytotoxicity Using MTT Assay. Estimations of cytotoxicity by determining protein content after transfection could be confirmed using an MTT cytotoxicity assay. Figure 8 shows data obtained by a MTT assay comparing cytotoxicity of inclusion complexes to PEI 25k. A dramatically reduced toxicity could be observed which is about 100 times lower compared to PEI25k. This notion was also supported by the viability of 3T3 cells observed during the transfection experiments, as shown in Table 3. At N/P ratios of 3 and 7, cells remained viable when transfected with complexes based on the copolymers and their inclusion complexes. By contrast, cell viability dropped to 80% and 69%, respectively, when transfected with the PEI25k-based polyplex. As the N/P ratio reached 20, all cells were killed. However, cells retained about 50% of their viability when transfected with copolymer-based polyplexes. Furthermore, cell viability is even higher (>80%) when cells were transfected with inclusion complex-based polyplexes at N/P 20. A part of this reduced toxicity is probably due to the neutral surface charge of complexes; however, our data suggest also that cyclodextrin further improves biocompatibility.

Gene Transfection Efficiency of Polyplexes. The transfection efficiency to 3T3 cells with polyplexes based on three copolymers and their inclusion complexes is shown in Figure 9. Although PEI25k-*g*-(PCL580-*b*-PEG5k)$_{2.9}$ was soluble in a wide concentration range and showed quite good performance in DNA condensation and transgene expression (*13*), threading of α-CD onto the PCL blocks may further enhance the gene transfection of this copolymer-based polyplex by further reducing the hydrophobic hindrance of DNA binding to PEI blocks. Effect of incorporating α-CD on the transgene transfection of polyplexes of other two copolymers appears to be more significant. Surprisingly, at N/P 3 and 7, although PEI25k-*g*-(PCL1.2k-*b*-PEG2k)$_{5.1}$ did not transfect the cells at all, the polyplex based on the inclusion complex of this copolymer exhibited excellent transfection efficiency.

Intracellular Uptake of Polyplexes. After incubating the NIH 3T3 fibroblasts for 3 h, a typical confocal laser scanning microscope image of an inclusion complex containing polyplex is shown in Figure 10. The micrograph demonstrates the efficient internalization of polyplexes, despite their neutral surface charge. Both DNA and copolymer colocalize in punctuate vesicles, probably in the lysosomal compartment. The mechanism by which the polyplexes escape from the endo/lysosome is presently under investigation. Most likely, the PEI component of the copolymer acts as proton sponge, while inclusion complex formation modulates complex solubility and cytotoxicity. No significant differences could be observed between the subcellular distribution of IC-containing polyplexes compared to PEI25k (data not shown).

CONCLUSION

Upon formation of inclusion complexes between α-CD and preferably the PCL blocks of the ternary copolymers, the copolymers lost their amphipathy and became more hydrophilic. This effect not only led to an increase in water solubility of copolymers but also favored the access and binding of DNA. Consequently, enhanced gene transfection efficiency was detected in transfection ex-

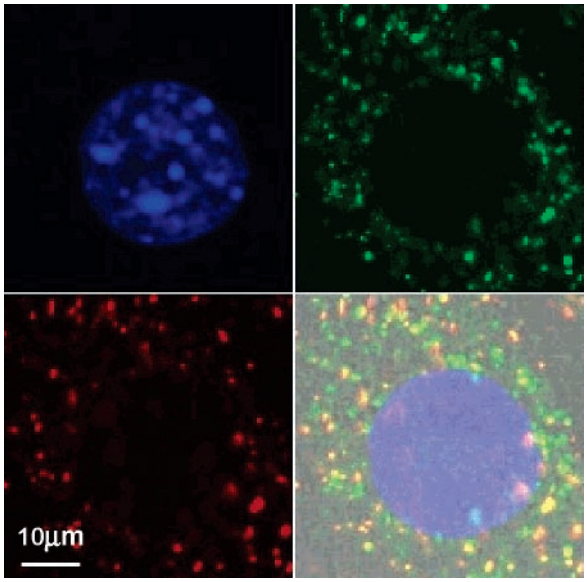

Figure 10. LSCM micrographs of internalization of fluorescent-labeled polyplex based on inclusion complex of PEI25k-*g*-(PCL2k-*b*-PEG5k)$_{2.8}$ into 3T3 fibroblasts after 3 h of incubation. Images assignment: Red: DNA, green: inclusion complex, and blue: nucleus. The image on the right at the bottom is an overlay of the three fluorescent colors and the light microscopic image.

periments, especially for the two copolymers showing distinct CMC. Furthermore these delivery systems showed an excellent biocompatibility, a property that makes them interesting candidates for further in vivo investigations.

ACKNOWLEDGMENT

We thank the Deutsche Forschungsgemeinschaft (DFG) for financial support. X.S. is grateful to the Alexander von Humboldt Foundation (Germany) for a research fellowship.

LITERATURE CITED

(1) Boussif, O., Lezoualc'h, F., Zanta, M. A., Mergny, M. D., Scherman, D., Demeneix, B., and Behr, J. P. (1995) A versatile vector for gene and oligonucleotide transfer into cells in culture and in vivo: polyethylenimine. *Proc. Nat. Acad. Sci. U.S.A. 92*, 7297−7301.

(2) Choi, Y. H., Lui, F., Kim, J. S., Choi, Y. K., Park. J. S., and Kim, S. W. (1998) Polyethylene glycol-grafted poly-L-lysine as polymeric gene carrier. *J. Controlled Release 54*, 39−48.

(3) Lim, Y. B., Kim, S. M., Lee, Y., Lee, W. K., Yang, T. G., Lee, M. J., Suh, H., and Park, J. S. (2001) Cationic hyperbranched poly(amino ester): a novel class of DNA condensing molecule with cationic surface, biodegradable three-dimensional structure, and tertiary amine groups in the interior. *J. Am. Chem. Soc. 123*, 2460−2461.

(4) Behr, J. P. (1997) The proton sponge: a trick to enter cells the viruses did not exploit. *Chimia 51*, 34−36.

(5) Fischer, D., Bieber, T., Li, Y., Elsässer, H. P., and Kissel, T. (1999) A novel nonviral vector for DNA delivery based on low molecular weight, branched polyethylenimine: effect of molecular weight on transfection efficiency and cytotoxicity. *Pharm. Res. 16*, 1273−1279.

(6) Erbacher, P., Remy, J. S., and Behr, J. P. (1999) Gene transfer with synthetic virus-like particles via the integrin-mediated endocytosis pathway. *Gene Ther. 6*, 138−145.

(7) Fischer, D., Harpe, A. V., Kunath, K., Peterson, H., Li, Y., and Kissel, T. (2002) Copolymers of ethylene imine and N−(2-hydroxyethyl)-ethylene imine as tools to study effects of polymer structure on physiochemical and biological properties of DNA complexes. *Bioconjugate Chem. 13*, 1124−1133.

(8) Vinogradov, S. V., Bronich, T. K., and Kabanov, A. V. (1998) Self-assembly of polyamine-poly(ethylene glycol) copolymers with phosphorothioate oligonucleotides. *Bioconjugate Chem. 9*, 805−812.

(9) Bronich, T., Kabanov, A. V., and Marky, L. A. (2001) A thermodynamic characterization of the interaction of a cationic copolymer with DNA. *J. Phys. Chem. B 105*, 6042−6050.

(10) Petersen, H., Martin, A. L., Stolnik, S., Roberts, C. J., Davies, M. C., and Kissel, T. (2002) The macrostopper route: a new synthesis concept leading exclusively to diblock copolymers with enhanced DNA condensation potential. *Macromolecules 35*, 9854−9856.

(11) Petersen, H., Fechner, P. M., Fischer, D,. and Kissel, T. (2002) Synthesis, characterization, and biocompatibility of polyethylenimine-graft-poly(ethylene glycol) block copolymers. *Macromolecules 35*, 6867−6874.

(12) Petersen, H., Fechner, P. M., Martin, A. L., Kunath, K., Stolnik, S., Roberts, C. J., Fischer, D., Davies, M. C., and Kissel, T. (2002) Polyethylenimine-graft-poly(ethylene glycol) block copolymers: influence of copolymer block structure on DNA complexation and biological activities as gene delivery system. *Bioconjugate Chem. 13*, 845−854.

(13) Shuai, X., Merdan, T., Unger, F., Wittmar, M., and Kissel, T. (2003) Novel biodegradable ternary copolymers *hy*-PEI-*g*-PCL-*b*-PEG: synthesis, characterization, and potential as efficient nonviral gene delivery vectors. *Macromolecules 36*, 5751−5759.

(14) Wenz, G. (1994) Cyclodextrins as building-blocks for supramolecular structures and functional units. *Angew. Chem., Int. Eng. Ed. 33*, 803−822.

(15) Harada, A., Li J., and Kamachi, M. (1994) Double-stranded inclusion complexes of cyclodextrin threaded on poly(ethylene glycol). *Nature 370*, 126−128.

(16) Harada, A., Li, J., and Kamachi, M. (1992) The molecular necklace: a rotaxane containing many threaded α-cyclodextrins. *Nature 356*, 325−327.

(17) Harada., A., and Kamachi, M. (1990) Complex formation between poly(ethylene glycol) and α-cyclodextrin. *Macromolecules 23*, 2821−2823.

(18) Harada, A., and Kamachi, M. (1994) Preparation and characterization of a polyrotaxane consisting of monodisperse poly(ethylene glycol) and a-cyclodextrins. *J. Am. Chem. Soc. 116*, 3192−3196.

(19) Huh, K. M., Ooya, T., Sasaki, S., and Yui, N. (2001) Polymer inclusion complex consisting of poly(ϵ-lysine) and α-cyclodextrin. *Macromolecules 34*, 2402−2404.

(20) Shigekawa, H., Miyake, K., Sumaoka, J., Harada, A., and Komiyama, M. (2000) The molecular abacus: STM manipulation of cyclodextrin necklace. *J. Am. Chem. Soc. 122*, 5411−5412.

(21) Harada, A. (2001) Cyclodextrin-based molecular machines.*Acc. Chem. Res. 34*, 456−464.

(22) Li, J., Ni, X., and Leong, K. (2003) Block-selected molecular recognition and formation of polypseudorotaxanes between poly(propylene oxide)-poly(ethylene oxide)-poly(propylene oxide) triblock copolymers and α-cyclodextrin. *Angew. Chem., Int. Ed. 42*, 69−72.

(23) Li, J, Ni, X., Zhou, Z., and Leong, K. W. (2003) Preparation and characterization of polypseudorotaxanes based on block-Selected inclusion complexation between poly(propylene oxide)-poly(ethylene oxide)-poly(propylene oxide) triblock copolymers and α-cyclodextrin. *J. Am. Chem. Soc. 125*, 1788−1795.

(24) Rusa, C., and Tonelli, A. E. (2000) Polymer/polymer inclusion compounds as a novel approach to obtaining a PLLA/PCL intimately compatible blend. *Macromolecules 33*, 5321−5324.

(25) Rusa, C., Luca, C., and Tonelli, A. E. (2001) Polymer-cyclodextrin inclusion compounds: Towards new aspects of their inclusion mechanism. *Macromolecules 34*, 1318−1322.

(26) Lu, J., Mirau, P. A., and Tonelli, A. E. (2001) Dynamics of isolated polycaprolactone chains in their inclusion complexes with cyclodextrin. *Macromolecules 34*, 3276−3284.

(27) Shuai, X., Porbeni, F. E., Wei, M., Bullions, T., and Tonelli, A. E. (2002)Inclusion complex formation between α,γ-cyclodextrins and a triblock copolymer and the cyclodextrin-type-dependent microphase structures of their coalesced samples. *Macromolecules 35*, 2401−2405.

(28) Shuai, X., Porbeni, F. E., Wei, M., Shin, I. D., and Tonelli, A. E. (2001) Formation of and coalescence from the inclusion complex of a biodegradable block copolymer and α-Cyclodextrin: a novel means to modify the phase structure of biodegradable block copolymers. *Macromolecules 34*, 7355−7361.

(29) Weickenmeir, M., and Wenz, G. (1997) Threading of cyclodextrins onto a polyester of octanedicarboxylic acid and polyethylene glycol. *Macromol. Rapid. Commun. 18*, 1109−1115.

(30) There is another way to prepare the soluble IC at room temperature. Copolymer was dissolved in a 1:2 mixture of acetone and water, and then an aqueous solution of predetermined amount of α-CD was added stepwise. The mixed solution was stirred vigorously while allowing acetone to evaporate completely. Powder IC sample was obtained via lyophilization.

(31) Kunath, K., Merdan, T., Hegener, O., Häberlein, H., and Kissel, T. (2003) Integrin targeting using RGD-PEI conjugates for in vitro gene transfer. *J. Gene Med. 5*, 588−599.

(32) Petersen, H., Kunath, K., Martin, A. L., Stolnik, S., Roberts, C. J., Davies, M. C., and Kissel, T. (2002) Star-shaped poly(ethylene glycol)-*block*-polyethylenimine copolymers enhance DNA condensation of low molecular weight polyethylenimines. *Biomacromolecules 3*, 926−936.

(33) Ogris, M., Steinlein, P., Carotta, S., Brunner, S., and Wagner, E. (2001) DNA/polyethylenimine transfection particles: influence of ligands, polymer size, and PEGylation on internalization and gene expression. *AAPS Pharm. Sci. 3*, E21.

(34) Ruponen, M., Ronkko, S., Honkakoski, P., Pelkonen, J., Tammi, M., and Urtti, A. (2001) Extracellular glycosaminoglycans modify cellular trafficking of lipoplexes and polyplexes. *J. Biol. Chem. 276*, 33875−33880.

(35) Huh, K. M., Ooya, T., Lee, W. K., Sasaki, S., Kwon, I. C., Jeong, S. Y., and Yui, N. (2001) Supramolecular-structured hydrogels showing a reversible phase transition by inclusion complexation between poly(ethylene glycol) and grafted dextran and α-cyclodextrin. *Macromolecules 34*, 8657−8662.

(36) Shuai, X., Porbeni. F. E., Wei, M., Bullions, T., and Tonelli, A. E. (2002) Stereoselectivity in the Formation of Crystalline Inclusion Complexes of Poly(3-hydroxybutyrate)s with Cyclodextrins. *Macromolecules 35*, 3778−3780.

(37) Harada, A., Adachi, H., Kawaguchi, Y., and Kamachi, M. (1997) Recognition of alkyl groups on a polymer chain by cyclodextrins. *Macromolecules 30*, 5181−5182.

(38) Harada, A., Suzuki, S., Okada, M., and Kamachi., M. (1996) Preparation and characterization of inclusion complexes of polyisobutylene with cyclodextrins. *Macromolecules 29*, 5611−5614.

BC0498471

Synthesis, Cellular Transport, and Activity of Polyamidoamine Dendrimer–Methylprednisolone Conjugates

Jayant Khandare,[†,‡] Parag Kolhe,[†,§] Omathanu Pillai,[‡] Sujatha Kannan,[‡] Mary Lieh-Lai,[‡] and Rangaramanujam M. Kannan*[,†]

Department of Chemical Engineering and Material Science, and Biomedical Engineering, Wayne State University, Detroit, Michigan 48202, and Department of Pediatrics (Critical Care Division), Children's Hospital of Michigan, Wayne State University, Detroit, Michigan 48201. Received August 19, 2004; Revised Manuscript Received January 26, 2005

Dendrimers have emerged as promising multifunctional nanomaterials for drug delivery due to their well-defined size and tailorability. We compare two schemes to obtain methylprednisolone (MP)–polyamidoamine dendrimer (PAMAM-G4-OH) conjugate. Glutaric acid (GA) was used as a spacer to facilitate the conjugation. In scheme A, PAMAM-G4-OH was first coupled to GA and then further conjugated with MP to obtain PAMAM-G4–GA–MP conjugates. This scheme yields a lower conjugation ratio of MP, presumably because of lower reactivity and steric hindrance for the steroid at the crowded dendrimer periphery. In scheme B, this steric hindrance was overcome by first preparing the MP–GA conjugate, which was then coupled to the PAMAM-G4-OH dendrimer. The ^{1}H NMR spectrum of the conjugate from scheme B indicates a conjugation of 12 molecules of MP with the dendrimer, corresponding to a payload of 32 wt %. In addition, conjugates were further fluorescent-labeled with fluoroisothiocynate (FITC) to evaluate the dynamics of cellular entry. Flow cytometry and UV/visible spectroscopic analysis showed that the conjugate is rapidly taken up inside the cell. Fluorescence and confocal microscopy images on A549 human lung epithelial carcinoma cells treated with conjugates show that the conjugate is mostly localized in cytosol. MP–GA–dendrimer conjugate showed comparable pharmacological activity to free MP, as measured by inhibition of prostaglandin secretion. These conjugates can potentially be further conjugated with a targeting moiety to deliver the drugs to specific cells in vivo.

INTRODUCTION

Dendrimers represent a relatively new class of well-defined monodisperse macromolecules with striking features such as controlled structure, globular shape, and a high density of "tunable" surface functional groups in their periphery (*1–5*). A variety of dendrimers have been synthesized and tailored for diverse applications (*6*). Encapsulation of drugs in PEGylated dendrimers led to increased circulation time (*7, 8*). Various strategies have been devised to load dendrimers with drug molecules, genetic materials, targeting agents, dyes, and imaging agents either by encapsulation, complexation, or conjugation (*9–15*). Although investigation of cellular delivery of drugs using dendrimers is at an early stage, these nanomaterials offer several advantages when compared to liposomes and microparticles. Their multiple, surface functional groups can be easily modified to potentially attach a large number of drug molecules, ligands, and antibodies, making them ideal vehicles for targeted drug delivery. They have been shown to be rapidly internalized into cells. Thus, they are promising nanovehicles in several therapeutic areas, where the target is intracellular (*16–21*). The present investigation demonstrates the potential of dendrimers as promising vehicles for delivering steroids to lung epithelial cells.

A critical issue in dendritic drug delivery systems is achieving a high drug payload. However, the payload that each polymer can carry typically depends on the total number of reactive groups. For example, a linear PEG molecule with two reactive end groups can be conjugated to two drug molecules, whereas, for the same molecular weight, hyperbranched polymers (HBPs) such as dendrimers with multiple reactive end groups can be conjugated to several drug molecules (*17*). Genes, targeting agents, and imaging agents have been linked with dendrimers to increase therapeutic efficacy. In most cases, achieving adequate drug loading has been a challenge. It may be possible that some of the dendrimer–drug conjugates show less therapeutic activity compared to free drug, due to relatively low drug payload and the lack of drug release from conjugate. This is especially true for the anticancer agents such as doxorubicin and methotrexate (*18*).

Despite the fact that dendrimers possess a high density of surface functional groups for chemical modification, the nanoscale architecture of a dendrimer (~10 nm) causes steric hindrance for covalent conjugation of drugs in general, and large steroid molecules in particular. This results in typical drug payloads of less than 10% for high molecular weight drugs (*1*). Achieving high drug payload for steroidal drugs ($M_w \sim 374.5$ Da) is challenging, since both the dendrimer and the steroid exhibit steric hindrance for covalent conjugation. Therefore, the main focus of this study was to (i) synthesize dendrimer–drug

* To whom correspondence should be addressed. Phone: 313-577-3879, Fax: 313-577-3810; E-mail: rkannan@chem1.eng.wayne.edu.

† Department of Chemical Engineering and Material Science, and Biomedical Engineering.

‡ Department of Pediatrics (Critical Care Division).

§ Currently at Schering-Plough.

10.1021/bc0498018 CCC: $30.25 © 2005 American Chemical Society
Published on Web 02/26/2005

conjugates with relatively high steroidal drug payload, (ii) demonstrate the potential of such conjugates to deliver high drug concentrations inside the cells, and (iii) evaluate their pharmacological activity.

We have previously investigated PAMAM-G4-NH_2 dendrimer−ibuprofen complexes involving ionic interaction between surface amine groups of the dendrimer and carboxyl groups of ibuprofen. The complexes demonstrated rapid cell entry into A549 human lung epithelial carcinoma cell lines and showed antiinflammatory activity by suppressing the COX-2 gene in the in vitro studies (*19*). But, since complexation or encapsulation of drug is a weak ionic interaction, the concern arises that the drug may decouple in vivo before it reaches the target site. Unlike these complexes, covalently conjugated drugs will be more stable at physiological pH, making them more suitable for in vivo applications. We have earlier reported dendrimer−ibuprofen conjugates with high payload using PAMAM G4-OH-terminated dendrimer (*20*).

The suitability of a dendrimer for delivering drug will depend on its molecular weight, generation number, end functionality, and charge. The polycationic systems show toxicity and higher elimination rate from the circulation. Anionic systems exhibit reduced uptake of molecules in cultured cells and are rapidly removed via the scavenger receptor in animal models (*21*). Conjugation of drug, targeting moiety, or imaging agent to the dendrimer also depends on the physicochemical properties of the agent to be coupled. This is especially true for a steroidal drug such as methylprednisolone. Covalent and noncovalent conjugations of drugs, genetic materials, and lipids to dendrimers have previously been reported (*22*). The conjugation of bulkier molecules such as steroids to dendrimers aims to address the issues of drug reactivity, stability, and most importantly the steric hindrance. To synthesize high payload drug−dendrimer conjugates using steroids, it is essential to overcome the steric hindrance and low reactivity of the drug molecule. The methodology reported here is an attempt to increase the payload of MP with dendrimer by increasing reactivity and at the same time minimizing steric hindrance.

Methylprednisolone (MP) is a corticosteroid, 6α-methyl-11β,17α,21-trihydroxy-1,4-pregnadiene-3,20-dione. It decreases inflammation by stabilizing leukocyte lysosomal membrane and has a greater antiinflammatory potency than prednisolone. The corticosteroid has three OH groups at 11β, 17α, and 21. The hydroxyl group at C21 is a primary OH and therefore is most favorable for the covalent conjugation with terminal COOH groups of the dendrimer. Previously, MP has been conjugated with dextran by using succinate as a linker (*23*). The ester bond so formed was enzymatically hydrolyzed in rat blood. However, the rate of hydrolysis was very slow, corresponding to a half-life of ~25 h of MP in dextran−MP conjugates.

In this paper, we evaluate synthetic approaches for obtaining MP−dendrimer (PAMAM G4-OH) conjugate with a high drug payload. We report conjugation of MP to PAMAM G2.5-COOH terminal dendrimer and PAMAM G4-OH terminal dendrimer using glutaric acid as a spacer. In addition, fluoroisothiocynate (FITC) was covalently linked with free MP and MP−dendrimer conjugate to investigate the cellular transport of free and dendrimer-conjugated MP. The dynamics of cell entry of the conjugate was studied using A549 human lung epithelial carcinoma cell line. Flow cytometry and UV/visible spectroscopy were used to follow the time-dependent transport of FITC-labeled MP and dendrimer−MP into lung epithelial cells. Fluorescence and confocal microscopy were used to visualize the cellular localization of the conjugate. In vitro pharmacological activity of the conjugate was demonstrated by measuring the prostaglandin (PGE_2) levels in cell supernatant.

EXPERIMENTAL SECTION

Materials and Methods. PAMAM-G-2.5-COOH (M_w ~ 6,267 Da, 32 end groups), PAMAM-G4-OH (M_w ~ 14,279 Da, 64 end groups) dendrimers, methylprednisolone USP (M_w ~ 374.5 Da), and dicyclohexylcarbodiimide (DCC) were purchased from Aldrich. Glutaric acid (M_w ~ 132 Da) (Matheson Coleman and Bell Co.), fluorescent probe fluoroisothiocynate (FITC) (Fluka), Interleukin (IL-2β) and lipopolysaccharide (LPS) (Sigma), ELISA kit for prostaglandin estimation (Cayman Chemical), and dialysis membrane of molecular weight cutoff of 3500 Da (Spectra Pore) were purchased. Dimethyl sulfoxide (DMSO), dimethyl formamide (DMF), methanol, and diethyl ether were purchased from Fischer Scientific. All other chemicals used were analytical grade.

Synthesis of PAMAM-G2.5-COOH−MP Conjugates. PAMAM-G2.5-COOH (0.088 g, 0.014 mmol) and MP (0.168 g, 0.449 mmol) were dissolved in anhydrous dimethyl sulfoxide (DMSO). (On the basis of the molecular weights, this corresponds to a molar ratio of dendrimer to MP of 1:32, one drug molecule for each dendrimer end group). To this solution was added DCC (0.093 g, 0.45 mmol) as a coupling agent. The reaction was carried out at room temperature for 3 days and filtered to remove dicyclohexylurea (DCU). The solution was further dialyzed (dialysis membrane of molecular weight cutoff = 3500 Da) against DMSO for 24 h to remove unreacted methylprednisolone. The contents from dialysis bag were dried under vacuum and characterized by ^{1}H NMR (*24*).

Conjugates Were Prepared Using Two Different Synthetic Strategies. (1) GA was first conjugated to PAMAM-G4-OH dendrimer, and then this conjugate was coupled with MP (scheme A).

(2) GA was first conjugated to MP, and then the conjugate was coupled with PAMAM-G4-OH (scheme B).

Scheme A. *A.1: Synthesis of PAMAM-G4-OH−Glutaric Acid Conjugates.* PAMAM-G4-OH (0.300 g, 0.021 mmol) and glutaric acid (0.180 g, 1.34 mmol) were dissolved in anhydrous dimethyl sulfoxide (DMSO). This corresponds to a mole ratio of dendrimer to GA of 1:64, with one GA molecule for every OH end group on the dendrimer. DCC (0.276 g, 1.33 mmol) was added as a coupling agent and stirred continuously for 2 days at room temperature. The resulting solution was filtered to remove DCU obtained as a byproduct during the reaction. The filtrate was dialyzed extensively with anhydrous DMSO (dialysis membrane of molecular weight cutoff = 3500 Da) for 24 h to remove unreacted glutaric acid. The contents from the dialysis bag were dried under vacuum. Repurification was carried out using diethyl ether, and the conjugate was dried under vacuum. ^{1}H NMR revealed that 50 molecules of GA are conjugated per dendrimer.

A.2: Synthesis of PAMAM-G4-OH−Glutaric Acid−Methylprednisolone Conjugates. PAMAM-G4−glutaric acid conjugate (0.12 g, 0.00574 mmol) and MP (0.1 g, 0.287 mmol) were dissolved in anhydrous dimethyl sulfoxide (DMSO). (The ratio of dendrimer−GA conjugates (50 molecules of GA per dendrimer) to MP was 1:50). To this solution was added DCC as a coupling agent, and the mixture was stirred continuously for 3 days. The DCU obtained was removed by filtration and was then dialyzed extensively with anhydrous DMSO

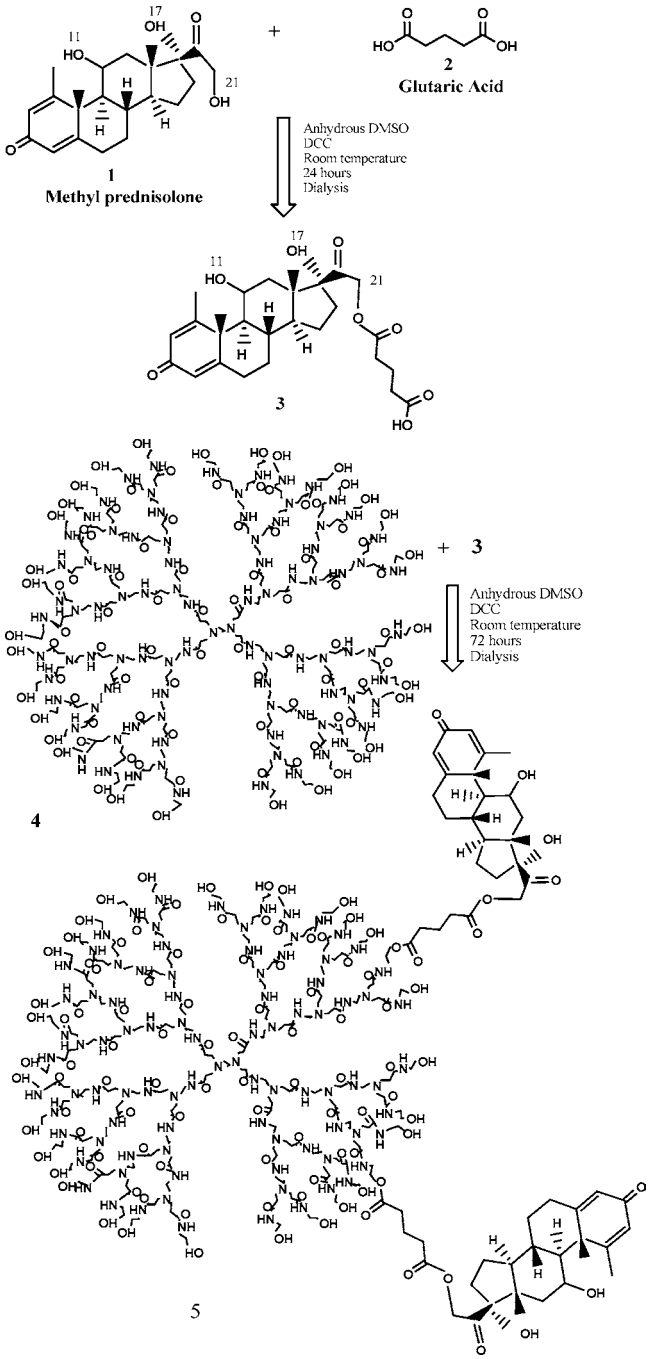

Figure 1. Schematic for dendrimer−glutaric acid−methylprednisolone conjugate synthesis multiplets corresponding to ring structure of methylprednisolone.

(dialysis membrane of molecular weight cutoff = 3500 Da) for 24 h to remove unreacted MP−glutaric acid and DCC. The contents from the dialysis bag were dried under vacuum to obtain the conjugate. ^{1}H NMR was used to characterize the conjugate. The conjugation ratio was extremely low (one molecule of MP per dendrimer). Therefore, the synthetic approach was changed as described below.

Scheme B. *B.1: Synthesis of Glutaric Acid−MP Conjugates (Figure 1*). MP (0.1 g, 0.265 mmol) and GA (0.036 g, 0.26 mmol) were dissolved in anhydrous DMSO. Dicyclohexylcarbodiimide (DCC) (0.056 g, 0.26 mmol) was added as a coupling agent to the above solution. The reaction was carried out for 24 h at room temperature and filtered to remove DCU obtained as a byproduct during this reaction. The filtrate was evaporated under vacuum to obtain MP−glutarate conjugate.

B.2: Conjugation of PAMAM-G4-OH Dendrimer to MP−Glutarate (Figure 1). PAMAM-G4-OH (0.032 g, 0.0024 mmol) and MP−glutaric acid conjugate (M_w ∼506) (0.077 g, 0.152 mM) were dissolved in anhydrous dimethyl sulfoxide (DMSO). (This corresponds to a mole ratio of dendrimer to MP−GA of 1:50). DCC (0.056 g, 0.26 mmol) was added as coupling agent, and the reaction was stirred for 3 days and filtered to remove DCU. The filtrate was dialyzed against anhydrous DMSO for 24 h (dialysis membrane of M_w cutoff = 3500 Da) to remove unreacted MP−glutaric acid conjugate, free MP, free GA, and DCC. The solvent was removed from the contents of dialysis bag, and the conjugate was evaporated under vacuum. The conjugate was characterized using ^{1}H NMR (Figure 2).

Conjugation of FITC to MP and PAMAM-G4-Dendrimer−GA−MP. MP (0.1 g, 0.265 mmol) and FITC (0.011 g, 0.28 mmol) or dendrimer−GA−MP (M_w ∼ 20 351 Da) (0.020 g, 0.00078 mmol) and FITC (0.01 g, 0.26 mmol) were dissolved in anhydrous DMSO (This corresponds-to-mole ratio of dendrimer to FITC 1:10). Dicyclohexylcarbodiimide (0.0054 g, 0.265 mmol) was added as a coupling agent for conjugation of FITC to MP and (0.00284 g, 0.014 mmol) for conjugation with dendrimer−GA−MP. The reaction was carried out for 24 h at room temperature and filtered to remove DCU. The FITC−dendrimer−GA−MP conjugate filtrate was dialyzed against anhydrous DMSO for 24 h (dialysis membrane of molecular weight cutoff = 3500 Da) to remove unreacted FITC and DCC. In addition, free FITC was removed by using excess acetone. The absence of free FITC in the conjugates was verified by thin-layer chromatography (TLC), using chloroform and methanol (1:1) as solvents (*25*). The conjugates were dried under vacuum to obtain FITC-labeled conjugates.

Cell Culture. Human lung carcinoma epithelial cell line A549 was obtained from Children's Hospital of Michigan Cell Culture facility and used for the cell entry and activity studies. Cells were incubated in RPMI 1640 (Gibco-BRL) cell culture medium supplemented with 10% fetal calf serum (FCS) and 1% penicillin−streptomycin at 37 °C with 5% CO_2 in a cell culture incubator. The cells were subcultured every 48 h and harvested from subconfluent cultures (60 to 70%) using 0.05% trypsin (Sigma-Aldrich).

Cell Entry of Fluorescent-Tagged Conjugate. A549 cells were seeded at 2×10^5 cells/mL and cultured on 60 × 15 mm culture plates using RPMI 1640 cell culture medium supplemented with 10% fetal calf serum (FCS) and 1% penicillin. When the cells were 60% confluent, they were treated with FITC-labeled MP or FITC-labeled dendrimer−GA−MP conjugate. The supernatant was removed at times 0, 5, 10, 15, 20, 240, and 360 min, and the amount of FITC present in the supernatant was estimated by measuring the UV/visible absorbance at 490 nm for FITC−MP and 498 for FITC−MP−dendrimer conjugate and quantified with a calibration curve (of known concentrations of FITC−MP and FITC-labeled MP−dendrimer conjugates) using appropriate supernatant as blank solution. The pH of the cell supernatant remained unchanged throughout the experiment.

After removing the cell supernatant at each time point, the cells were washed with phosphate-buffered saline (PBS), trypsinized, and centrifuged at 1500 rpm for 5 min to obtain a cell pellet. The cells were then rinsed with PBS buffer, spun down twice, resuspended in PBS, and subsequently analyzed using a flow cytometer (FACS

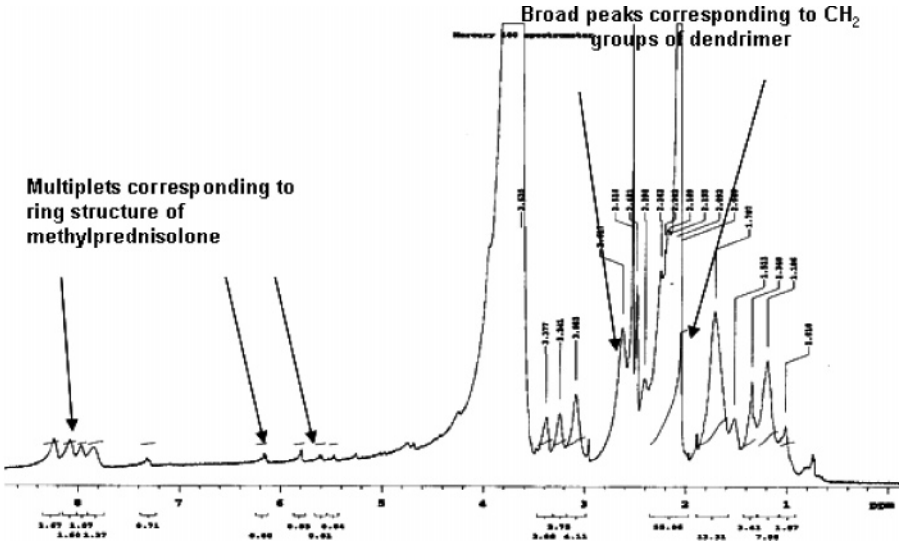

Figure 2. ^{1}H NMR spectrum of dendrimer–glutaric acid–methylprednisolone conjugates.

caliber, Becton Dickinson) by counting 10 000 events. (The mean fluorescence intensity of the cells was calculated using the histogram plot).

Fluorescence Microscopy. The procedure for cell culture and drug treatment was the same as described in previous section. After treatment with the conjugates for 2 h, the cells were washed with phosphate-buffered saline (pH 7.4). A few drops of the buffer was added before observing under the fluorescence microscope (Leica DM1L inverted microscope) using a magnification of 400×. Images were captured and stored using SensiCam-QE 12 bit monochrome camera and Camware 3.1 software, respectively.

Confocal Laser Scanning Microscopy. The procedure for cell culture and drug treatment was the same as described in previous section. After treating A549 cells for 2 h with FITC-labeled free dendrimer or MP conjugated dendrimer, the cells were washed with phosphate-buffered saline (pH 7.4). A few drops of the buffer and antifade reagent (Molecular Probes) was added before observing under the confocal microscope (Zeiss LSM 310) using a magnification of 63 × 1.2. The emission and excitation wavelengths were 488 and 518 nm for FITC.

Pharmacological Activity of Dendrimer–MP Conjugates. A 549 lung epithelial cells (2×10^5 cells/mL/well) was seeded in 24-well plates and allowed to grow overnight in RPMI medium supplemented with 10% FCS and 1% penicillin and streptomycin. When the cells were 60% confluent, the medium was removed and washed with serum-free medium (SFM). Each well was treated with 500 μL of SFM, and prostaglandin (PGE_2) secretion was induced by addition of lipopolysaccharide (LPS) and interleukin (IL- β2) to each well. After 30 min, either 5 μg of free MP or dendrimer–GA–MP conjugate (5 μg equivalent of MP) in ethanol was added. Control treatments with solvent, polymer, and positive control with no treatment, and negative controls without PGE_2 induction, were also studied. The supernatant was removed after 4 h and analyzed for PGE_2 concentration using a commercial ELISA kit. Results were represented as percent inhibition of PGE_2 compared to positive control.

RESULTS AND DISCUSSION

1. Design and Synthesis of Dendrimer–Drug Conjugates. To obtain dendrimer–drug conjugates with high drug payload, it is important to (1) decrease the steric hindrance of the surface functional groups, which are very close to each other. (This could be complicated by the potential back folding of end groups as explained below), and (2) increase the reactivity of the steroidal drug molecule and the dendrimer surface functional groups. Recently we have reported a high payload (on an average 53 molecules of drug per hyperbranched polymer) for the highly reactive and conformationally stable ibuprofen (*20*).

The hydrodynamic radius (R_h) of generation 4-poly-(glycerol succinic acid) (PGLSA-OH) dendrimers was estimated by quasielastic light scattering (QELS) method to be 7 nm (*6*). The authors reported the encapsulation of one Reichardt's dye per dendrimer molecule. As a consequence, R_h of the dendrimer reduced from 7 to 4 nm, suggesting the collapse of aliphatic dendrimer around the dye. Therefore, the factors that affect drug loading in dendrimers include (1) potential collapse of aliphatic groups and lowering of R_h in organic solvents, and (2) reduced *distance* between the two peripheral reactive groups. In addition, the reactivity of dendrimers may not be significantly high for direct covalent conjugation with drugs, especially with conformationally unstable and bulkier steroidal drugs such as MP. Such drugs have low reactivity, higher molecular weight, and steric hindrance.

The objective of present work was to obtain high payloads of MP with PAMAM dendrimers using DCC as a coupling agent. Therefore, we designed two synthetic approaches for conjugating MP with the dendrimer (schemes A and B). For comparison, the drug (MP) was conjugated directly to PAMAM G2.5-COOH dendrimer. The resulting conjugate had one drug molecule per dendrimer. In the first approach (scheme A), glutaric acid was incorporated as a flexible spacer, first by coupling it to OH end groups of PAMAM G4 dendrimer. This would present the highly reactive COOH group of the flexible GA spacer at the dendrimer surface, potentially relieving part of the crowding effect at the surface. The resulting dendrimer–glutarate conjugate was then linked to 21-OH group of MP. The drug loading to dendrimer molecule was estimated using ^{1}H proton integration method (*24*, *25*). However, ^{1}H NMR revealed the incorporation of only one MP molecule per mole of dendrimer. This suggests the presence of steric hindrance and low reactivity of the GA-modified dendrimer conjugate with MP. Therefore, the synthetic approach was slightly modified. In the second approach, the spacer molecule (GA) was first attached to MP, in an attempt to enhance the reactivity

of MP (scheme B). The reaction of glutaric acid to MP (Figure 1) is more favorable to primary hydroxyl group at 21, compared to C_9 (secondary) and C_{11} (tertiary) positions (*23*). MP was first linked to GA and further conjugated with OH groups of G4 dendrimer. ^{1}H NMR spectrum (Figure 2) shows the multiplets between δ 2.0 to 4.0 ppm, which correspond to the presence of 985 protons of CH_2 of PAMAM-G4-OH. Multiplets between δ 5.0 to 8.2 ppm correspond to four protons of the aromatic ring of methylprednisolone. The integration ratio of PAMAM-G4-OH to multiplets of methylprednisolone is 0.047, suggesting that 46.78 protons ($0.047 \times 985 = 46.295$) of methylprednisolone are present. Since four protons correspond to one molecule, on an average, 12 molecules of MP were incorporated per dendrimer molecule. The high payload of MP (32%) per dendrimer indicates that conjugation of a small spacer molecule such as glutaric acid increases the reactivity of MP molecule. In addition the MP−spacer conjugate overcomes the steric hindrance at the dendrimer surface for the large steroid. The resulting ester bond in the conjugate can potentially be hydrolyzed in the cell by lysosomal enzymes.

To study the cellular transport of the conjugates, FITC was conjugated to free MP and MP−GA−dendrimer conjugate using DCC as a coupling agent. Unreacted FITC was removed by membrane dialysis using DMSO for 24 h. Any remaining trace amount of free FITC was removed by an additional repurification step using excess acetone. The absence of free FITC in the conjugate was verified by thin-layer chromatography (TLC), using chloroform and methanol (1:1) as solvents (*25*). The proton integration ratio of MP−GA−dendrimer conjugate was compared to the additional protons arising from FITC molecules in MP−GA−dendrimer-FITC conjugate. ^{1}H NMR reveals that on an average of six FITC molecules are conjugated to MP−GA−dendrimer conjugate (^{1}H NMR not shown).

2. In Vitro Evaluation of Dendrimer−GA−MP Conjugates. When the conjugates were dissolved in DMSO and kept in a dialysis bag, no drug release was evident even after several hours, as verified by HPLC and UV/visible spectroscopy. To demonstrate the therapeutic potential of dendrimer−GA−MP conjugates, we evaluated these conjugates in A549 human lung epithelial carcinoma cell lines. The cells were treated with FITC-labeled-MP or dendrimer−GA−MP−FITC conjugate. Cell supernatant was analyzed for a period of 4 h by UV/visible spectroscopy, to estimate FITC concentration and the cellular uptake. As seen in Figure 3a,b, based on UV/visible analysis of the cell supernatant, ~85% of MP−FITC and 35% of dendrimer−GA−MP−FITC conjugate entered the cell within 1 h. The cellular entry of free and dendrimer-conjugated MP was further confirmed by flow cytometry by measuring the intracellular fluorescence intensity. By flow cytometry (Figure 3a,b), it was found that ~50% of free MP and 65% of dendrimer−GA−MP was inside the cell. The discrepancy between the UV/visible spectroscopy measurements (for extracellular concentration) and flow cytometry (for intracellular concentration) can be attributed to the adsorption of drug molecules on the cell surface. When the extracellular concentration is measured by UV/visible spectroscopy, it does not take into account the molecules that are adsorbed onto the cell and those that are internalized. Since the cells were repeatedly washed with PBS (to remove any adsorbed molecules on the cell surface) after removing the cell supernatant, flow cytometry would be more indicative of measuring fluorescence

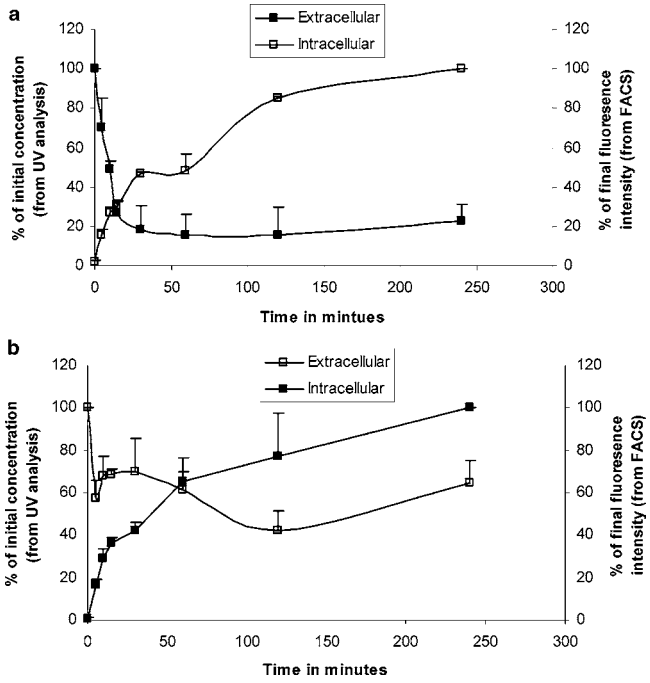

Figure 3. Decrease in FITC concentration in the cell supernatant (from UV/visible spectroscopy shown with open squares on the left-hand *y*-axis) and increase in the FITC intensity inside the cell (calculated from mean fluorescence intensity using flow cytometry and is shown with closed squares on the right-hand *y*-axis) for (a) MP−FITC and (b) dendrimer−GA−MP−FITC conjugate.

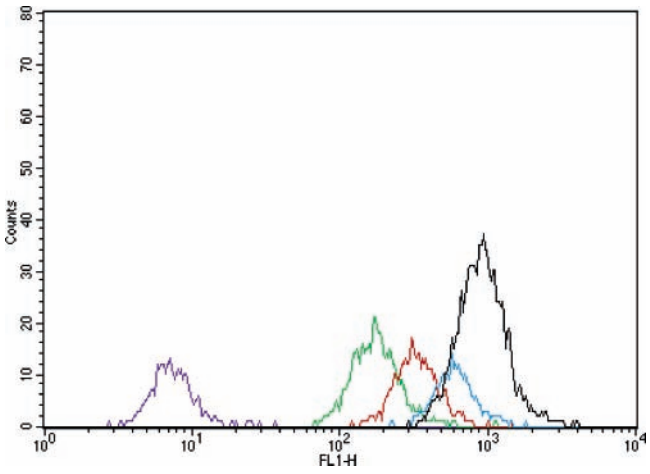

Figure 4. Fluorescence activated cell sorter analysis of the cell entry dynamics of methylprednisolone−glutaric acid−dendrimer−FITC conjugate in A549 lung epithelial cell line shows rapid internalization of the conjugates within 5 min. The log of FITC absorption intensity (FL1-H on *x*-axis) is plotted against the number of cells (counts on *y*-axis). Key: violet, 0 min; green, 5 min; red, 15 min; light blue, 60 min; black, 240 min.

intensity of only those molecules that are internalized into the cell. This is further demonstrated in Figure 4, where rapid internalization of the MP−GA−dendrimer conjugate is noted within 5 min and the fluorescence intensity gradually increases over a period of 4 h. From the present findings, it appears that the measurement of intracellular fluorescence intensity using flow cytometry might be a better method to follow the transport of free drug or drug−polymer conjugates.

At the end of 2 h, the cells were observed under fluorescence microscopy to identify the cellular localization of the free and drug conjugated dendrimer (Figure 5a−c). The cells without FITC showed no fluorescence

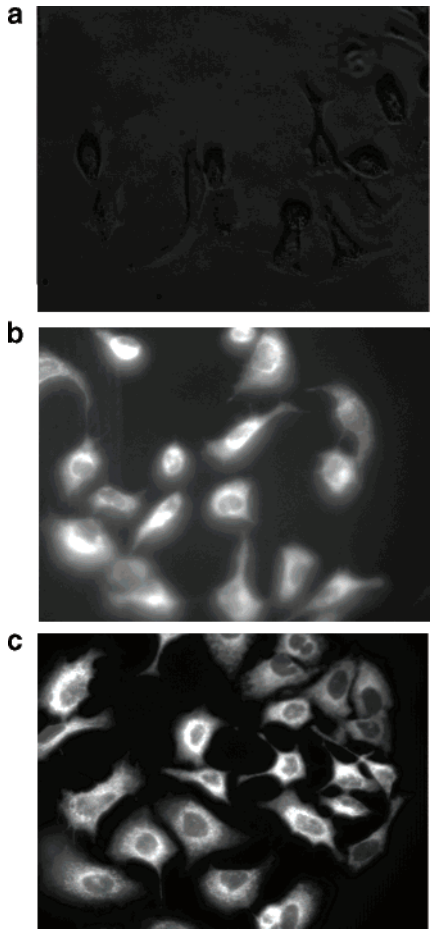

Figure 5. Fluorescence microscopic images (magnification 400×) of A549 cells 4 h of treatment with (a) control (no treatment), (b) FITC-labeled methylprednisolone, and (c) FITC-labeled dendrimer−GA−methylprednisolone conjugate.

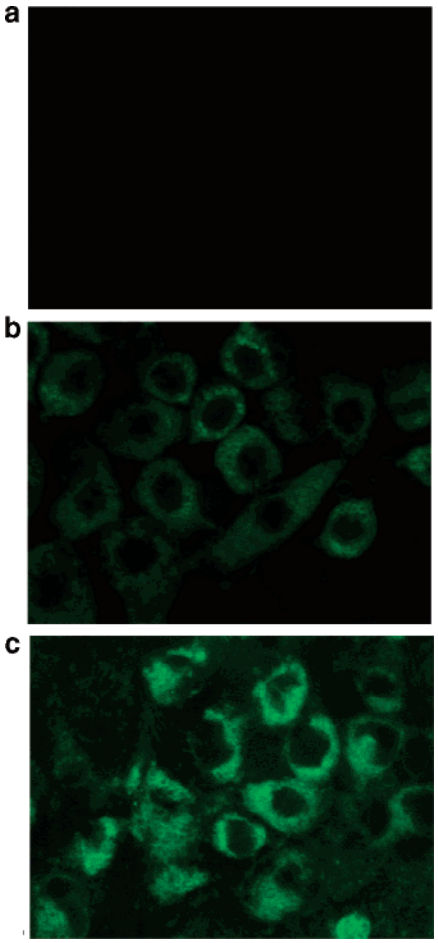

Figure 6. Confocal microscopic images (magnification 63 × 1.2) of A549 cells after 2 h of treatment with (a) control (no treatment), (b) FITC-labeled dendrimer, and (c) FITC-labeled dendrimer−methylprednisolone conjugate. The conjugates appear to be mainly localized in the cytoplasm.

as expected (Figure 5a). Both free and drug conjugated dendrimer were mainly found to be localized in the cell cytoplasm (Figure 5b,c). Further, this was substantiated from confocal microscopic images in Figure 6b,c, where the fluorescence is seen mostly in the cytoplasm. This suggests that the free dendrimer and MP−dendrimer conjugate are mainly localized in the cytosol in the cell.

Epithelial cells are known to possess anionic charge, and charged dendrimers such as PAMAM-NH_2-terminated dendrimers can be transported across the cell by electrostatic interactions (*14*, *26*). However, PAMAM-G4-OH terminal dendrimers are not charged and hence may be transported by selective absorptive endocytosis mechanism. It appears that the free MP enters the cells faster than the MP−dendrimer conjugate. From the results, it appears that the efficiency of the endocytosis mechanism is influenced by the molecular size and further studies are required to understand the cellular uptake mechanism. Simple passive diffusion of drug molecules (which is the case with free MP) across the cell membrane is a less efficient means to deliver drugs into the cells, as the drug molecules can diffuse in and out of the cell depending on the concentration gradient. Unlike passive diffusion, the endocytotic uptake of cells (in case of MP−dendrimer conjugate) is unidirectional; hence, the drug is not only more efficiently transported but is also retained at the site of action inside the cell. For MP, cytoplasmic delivery is required, since it exerts the pharmacological action by binding to the glucocorticoid receptors in the cytoplasmic compartment (*27*).

Antiinflammatory activity of free and dendrimer-conjugated MP was evaluated in vitro using A549 cells, which were pretreated with lipopolysaccharide and interleukin (IL-2β) to induce prostaglandin synthesis. Neither the free dendrimer nor the solvent showed any PGE_2 suppression. Dendrimer−GA−MP conjugate inhibited prostaglandin synthesis to the same extent ($p > 0.05$) as free MP (Figure 7) after 4 h of treatment. The results indicate that the conjugate was able to enter the cell and produce the desired pharmacological action. From these results, it appears that high drug payload in the dendrimer conjugate produces a high local drug concentration inside the cell to elicit a significant therapeutic response. At this point, it is unclear whether the MP is released from the dendrimer conjugate inside the cell or if the drug is effective even in the conjugated form. However, once the conjugate enters the cell, it is conceivable that the acidic pH and the enzymes in the endosomes would eventually hydrolyze the ester bond in the conjugate to release the free drug in the cytosol (*28*). Based on the previous report on dextran−MP conjugate, the hydrolysis process is likely to take much longer than the time frame used in current studies (*23*). Therefore, we may tentatively conclude that the conjugate may not have released the drug appreciably in 4 h. Nevertheless, the high payload drug conjugate show significant therapeutic activity. It may be possible that the conjugate may slowly release the drug over a sustained period providing therapeutic effect over longer times. Further studies are underway to investigate the stability of dendrimer−drug

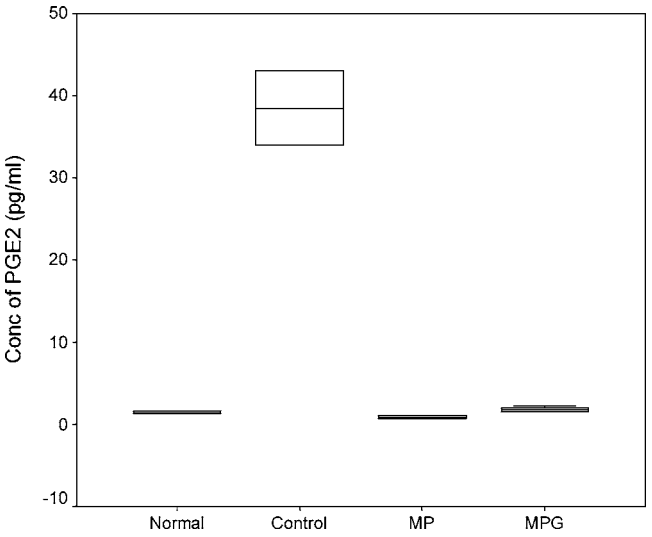

Figure 7. Box plot showing prostaglandin (PGE_2) concentration in the cell supernatant for different treatments ($n = 4$). Normal indicates the cells with no induction of prostaglandin synthesis. Control represents cells with prostaglandin induction with LPS+IL1β but with no drug treatment. MP and MPG indicate the cells, which were induced with LPS+IL1β to secrete prostaglandin and were treated for 4 h with free methylprednisolone and dendrimer−GA−MP conjugate, respectively. The cells treated with MP/MPG-suppressed prostaglandin secretion, and the PGE_2 levels were comparable to normal cells. Induced cells treated with dendrimer and solvent alone were similar to that of control (not shown). This indicates that the pharmacological activity of the conjugated MP has remained similar to that of the free drug.

conjugate at various pHs and in the presence of enzymes to understand the intracellular hydrolysis of the conjugate.

MP is used in the treatment of asthma, but systemic therapy is associated with severe side effects such as gastrointestinal hemorrhage, hypertension, endocrine, metabolic disturbances, immune suppression, and neuropsychiatric disturbances. (*29*). However, when both MP and a targeting ligand are conjugated to dendrimer, it may not only deliver the drug efficiently to the target site inside the cell, but also reduce the systemic side effects. By achieving a high local drug concentration at the target site, one could overcome the systemic adverse effects of free MP and improve the therapeutic efficacy significantly with a reduced dose. Current studies are ongoing to deliver the dendritic conjugate 'directly' to the lung through intranasal administration, in an in vivo lung inflammation model in mice (*30*). Furthermore, as the conjugates are expected to be stable in blood, it would achieve more sustained drug levels leading to reduce dosing frequency. Hence, the advantages of using dendrimers for delivery of MP would include (i) a high local concentration of MP in the lung through high drug payload (example, 12 MP molecules in a ~6 nm diameter spherical dendrimer), (ii) superior residence time in the lung enabled by the dendrimer (unpublished data), and (iii) slow hydrolysis of the ester bond enabling sustained delivery inside the cell.

CONCLUSIONS

A dendrimer−MP conjugate with a relatively high payload (12 steroid molecules per dendrimer) was prepared by first attaching glutaric acid to MP, then conjugating GA-MP to PAMAM-G4-OH dendrimers. This allowed us to (1) overcome the steric hindrance at the dendrimer surface for the large steroid molecule, and (2) improve the stability and reactivity of MP. The conjugate entered the cell rapidly and achieved a high local drug concentration to elicit the desired pharmacological action. It appears that, at least over the time period of this study, the conjugates are localized primarily in the cytosol, as imaged through fluorescence and confocal microscopy. The conjugate showed comparable therapeutic activity to the free drug, even at short times, where the drug may not have released from the dendrimer.

LITERATURE CITED

(1) Kono, K., Liu, M., Frechet, J. M. J. (1999) Design of Dendritic Macromolecules Containing Folate or Methotrexate Residues. *Bioconjugate Chem. 10*, 1115−1121.

(2) Ihre, H. R., Padilla De Jesús, O. L., Szoka, F. C., Jr., Fréchet, J. M. J. (2002) Polyester Dendritic Systems for Drug Delivery Applications: Design, Synthesis, and Characterization. *Bioconjugate Chem. 13*, 443−452.

(3) Grainger, D. W., Okano, T. (2003) Biomedical Micro- and Nano-Technology. *Adv. Drug Delivery. Rev. 55*, 311−313.

(4) Liu, M. J., Frechet, J.M. J. (1999) Designing Dendrimers for Drug Delivery. *Pharm. Sci. Technol. Today 2*, 393−401.

(5) Newcome, G. R., Moorfileld, C. N., Keith, J. N., Baker, G. R., Escamilla, G. H. (1994) Chemistry Within a Unimolecular Micelle Precursor: Boron Superclusters by Site- and Depth-Specific Transformations of Dendrimers. *Angew. Chem. Int. Ed. Engl. 33*, 2413−2420.

(6) Morgan, M. T., Carnahan, M. A., Immoos, C. E., Ribeiro, A. A., Finkelstein, S., Lee, S. J., Grinstaff, M. W. (2003) Dendritic Molecular Capsules for Hydrophobic Compounds. *J. Am. Chem. Soc. 125*, 15485−15489.

(7) Liu, M. J., Kono, K., and Frechet, J. M. J. (2002) Water Soluble Dendrimer-Poly (ethylene glycol) Star Like Conjugates as Potential Drug Carriers. *J. Controlled Release 65*, 121−131.

(8) Yang, H., Morris, J. J., and Lopina, S. T. (2004) Polyethylene Glycol-Polyamidoamine Dendritic Micelle as a Solubility Enhancer and the Effect of the Length of Polyethylene Glycol Arms on the Solubility of Pyrene in Water. *J. Controlled Release 273*, 148−154.

(9) Patri, A. K, Majoros, I. J., and Baker, J. R., Jr. (2002) Dendritic Polymer Macromolecular Carriers for Drug Delivery. *Curr. Opin. Chem. Biol. 6*, 466−471.

(10) Kojima, C., Kono, K., Maryama, K., and Takagishi, T. (2000) Synthesis of Polyamidoamine Dendrimers having Poly(ethylene glycol) Grafts and Their Ability to Encapsulate Anticancer Drugs. *Bioconjugate. Chem. 11*, 910−917.

(11) Rmaileh, R. A., Attwood, D., and D'Emanuele, A. (2003) Dendrimers in Cancer Therapy. *dds & s.* 3, 65−70.

(12) Twyman, L. J., Beezer, A. E., Esfand, R., Hardy, M. J., and Mitchell, J. C. (1999). The Synthesis of Water Soluble Dendrimers and Their Application as Possible Drug Delivery Systems. *Tetrahedron Lett. 40*, 1743−1746.

(13) Tomalia, D. A., Baker, H., Dewald, J. R., Hall, M., Kallos, G., Martin, S., Roeck, J., and Ryder, J. P. Smith. (1985) A New Class of Polymers-Starburst-Dendritic Macromolecules. *Polym. J. 17*, 117−132.

(14) Tajarobi, F., El-Sayed, M., Rege, B. D., Polli, J. E., and Ghandehari, H. (2001) Transport of Polyamidoamine Dendrimers across Madin-Darby Canine Kidney Cells. *Int. J. Pharm. 215*, 263−267.

(15) Malik, N., Wiwattanapatapee, R., Klopsch, R., Lorenz, K., Frey, H., Weener, J. W., Meijer, E. W., Paulus, W., and Duncan, R. (2000) Dendrimers: Relationship Between Structure and Biocompatibility in vitro, and Preliminary Studies on the Biodistribution of I-Labeled Polyamidoamine Dendrimers in vivo *J. Controlled Release 65*, 133−148.

(16) Nigavekar, S. S., Sung, L. Y., Llanes, M., El-Jawahri, A., Lawrence T. S., Becker, C. W., Balogh, L., and Khan, M. K. (2004) ^{3}H Dendrimer Nanoparticle Organ/Tumor Distribution. *Pharm. Res. 21*, 476−483.

(17) Henry, C. M. (2002) Drug Delivery. *Chem. Eng. N*ews *80* (34), 39−47.

(18) Quintana, E., Raczka, L., Piehler, I., Lee, A., Myc, I., Majoros, A. K., Patri, T., Thomas, J., Mulé, J., and Baker (2002) Design and function of a dendrimer-based therapeutic nanodevice targeted to tumor cells through the folate receptor. *Pharm. Res*. *19*, 1310−1316.

(19) Kolhe, P., Misra, E., Kannan, R. M., Kannan, S., and Lieh-Lai, M. (2003) Drug complexation, in vitro release and cellular entry of dendrimers and hyperbranched polymers. *Int. J. Pharm. 259*, 143−148.

(20) Kolhe, P., Khandare, J., Pillai, O, Kannan, R. M., Kannan, S., and Lieh-Lai, M. (2004). Hyperbranched Polymer Drug Conjugates With High Drug Payload for Enhanced Drug Delivery. *Pharm Res. 21* (12), 2185−2195.

(21) Meijer, D. K., and Molema, G. (1995) Targeting of Drugs to The Liver. *Semin. Liver Dis. 15*, 202−256.

(22) Hong, S., Bielinska, A. U., Mecke, A., Keszler, B., Beals, J. L., Shi, X., Balogh, L., Orr, B. G., Baker, J. R., Jr., and Banaszak H., M. M. (2004) Interaction of Poly (amidoamine) Dendrimers with Supported Lipid Bilayers and Cells: Hole Formation and the Relation to Transport., *Bioconjugate Chem. 15* (4), 774−782.

(23) Mehvar, R., Dann R. O., and Hoganson D. A. (2000) Kinetics of Hydrolysis of Dextran-Methylprednisolone Succinate, a Macromolecular Prodrug of Methylprednisolone, In Rat Blood and Liver Lysosomes. *J. Controlled Release 68*, 53−61.

(24) Wiwattanapatapee, R., Lomlim, L., and Saramunee, K. (2003) Dendrimers Conjugates for Colonic Delivery of 5-Aminosalicylic Acid. *J. Controlled Release 88*, 1−9.

(25) Jevprasesphant, R., Penny, J., Attwood, D., McKeown, N. B., and Emanuele, A. D. (2003) Engineering of Dendrimer Surfaces to Enhance Transepithelial Transport and Reduce Cytotoxicity. *Pharm. Res*. *20*, 1543−1550.

(26) Kannan, S., Kolhe, P., Raykova, V., Gilbatec, M., Kannan, R. M., Leih-Lai, M., Basset, D. (2004) Dynamics of Cellular Entry and Drug Delivery by Dendritic Polymers into Human Lung Epithelial Carcinoma Cells *J. Biomaterial Sci.: Polym. Ed. 15*, 311−330.

(27) Adcock, I. M., (2000) Molecular Mechanisms of Glucocorticosteroid Actions. *Pulm. Pharmacol. Ther. 13*, 115−126.

(28) Mcgraw, T. E., Maxifield, F. R., Juliano, R. L., (1991) Targeted Drug Delivery, pp 11−41, Springer-Verlag , New York.

(29) *Physician's Desk Reference* (2002) pp 2486−2488, Medical Economics Company, Inc., Montvale, NJ.

(30) DeLorme, M. P., Gao, X., Doyon R. N., Barraclough- M. B., and Bassett, D. (2002) Inflammatory Effects of Inhaled Endotoxin-Contaminated Metal Working Fluid Aerosols in Rats. *J. Toxicol. Environ. Health. Part A*, *65*, 101−118.

BC0498018

Affinity Enhancement Bivalent Morpholino for Pretargeting: Initial Evidence by Surface Plasmon Resonance

Jiang He,* Guozheng Liu, Jean-luc Vanderheyden, Shuping Dou, Rusckoswki Mary, and Donald J. Hnatowich*

Division of Nuclear Medicine, Department of Radiology, University of Massachusetts Medical School, 55 Lake Avenue North, Worcester, Massachusetts 01655. Received November 22, 2004; Revised Manuscript Received January 31, 2005

Pretargeting with bivalent effectors capable of bridging antitumor antibodies has been reported to provide superior results by affinity enhancement. Morpholinos (MORFs) and other DNA analogues used for pretargeting are ideally suited as bivalent effectors since they are easily synthesized and the distance between binding regions, likely to be a determinant of binding, may be adjusted simply by lengthening the chain. The goal of this investigation was to synthesize a bivalent MORF and to determine by surface plasmon resonance (SPR) whether the bivalent MORF exhibited bimolecular binding and whether the MORFs showed improved in vitro hybridization affinity in its bivalent form compared to its monovalent form. An 18 mer amino-derivitized MORF was made bivalent by dimerizing with disuccinimidyl suberate (DSS) in 1-methyl-2-pyrrolidinone (NMP) with *N*,*N*-diisopropylethylamine (DIEA) followed by purification by ion exchange chromatography. The in vitro hybridization affinity of bivalent compared to monovalent MORF was then measured by SPR. For these measurements, the complementary biotinylated cDNA was immobilized at coating densities that provided an average spacing of 20−100 Å and used to investigate the influence of this spacing on binding of the bivalent MORF with its binding regions separated by 25 Å. The yield of bivalent MORF was as high as 45%, and the structure was confirmed by MALDI-TOF mass spectroscopy. When the sensograms obtained by SPR were analyzed using different binding models, the evidence was consistent with bimolecular binding of the bivalent MORF. The dissociation rate constant of the bivalent compared to monovalent MORF was more than 10-fold lower at 2.14 compared to 0.27×10^{-5} (1/s) ($p < 0.05$), and since the association rate constants were similar at 8.53 and 5.64×10^5 (1/M·s) ($p = 0.08$), the equilibrium constant for hybridization to the immobilized cDNA of the bivalent compared to the monovalent MORF was almost 20-fold higher at 3.99 compared to 0.21×10^{10} (1/M) ($p < 0.05$). In addition, qualitative evidence for bivalent binding of the bivalent MORF was apparent in the lower concentrations necessary to saturate the cDNA. Finally, the stoichiometry interpretation of the binding data provided estimates of the fraction of bivalent MORF binding bimolecularly. Under one set of conditions, this value was 20%. In conclusion, a bivalent MORF was easily synthesized by dimerization of a monovalent MORF. A lower dissociation rate constant and higher equilibrium constant was measured by SPR for the bivalent compared to monovalent MORF in their binding to an immobilized cDNA. These results show that bimolecular binding was occurring in the case of the bivalent MORF and suggest that bivalency may be superior to monovalency in MORF pretargeting applications.

INTRODUCTION

While conventional immunoscintigraphy using monoclonal antibody promises to provide reliable noninvasive detection and localization of tumor, it still often provides marginal results in that image interpretation is often obscured by nonspecific accumulations of radioactivity in bone marrow, liver, in the vascular system, and other organs. As such, alternative methods with superior target/nontarget ratio are needed. Arguably one of the more attractive alternative approaches involves pretargeting (*1*). Preclinical studies of pretargeting have clearly demonstrated efficacy, and early clinical trials in several laboratories are providing encouraging results. These studies usually involve procedures based on the interaction of biotin with (strept)avidin, bispecific antibodies with a radiolabeled hapten, and oligonucleotides with their complement (*1*−*3*).

Even though (strept)avidin can be immunogenic, especially when conjugated to antibodies, and endogenous biotin can interfere, recent developments in avidin derivatives and biotin dimers or trimers are providing encouraging results (*4, 5*). However, the alternative approach using bifunctional antibodies as the first injectate and bivalent haptens (i.e. effector) as the second injectate has occasionally provided excellent results in animals with high tumor/normal tissue ratios and absolute tumor accumulations (*6*−*8*). These successes have been attributed in large part to affinity enhancement resulting from the bridging of two antibodies on the tumor surface by the radiolabeled bivalent hapten effector (i.e. "affinity enhancement system" or AES). The bivalent haptens used successfully include Ac-Lys(In-DTPA)-Tyr-Lys(In-DTPA)-Lys(TscG-Cys-)-NH_2 (*6, 9*), Janus bivalent hapten (*10*), pGlu-Leu-Tyr-Glu-Asn-Lys(DTPA)-Pro-Arg-Arg-Pro-Tyr-Ile-Leu and DTPA-Gly-

* To whom correspondence should be addressed. Phone: 508-856-2187 (J.H.); 508-856-4256 (D.J.H.); Fax: 508-856-4572 (J.H. and D.J.H.). E-mail: jiang.he@umassmed.edu; Donald.hnatowich@umassmed.edu.

10.1021/bc049719c CCC: $30.25 © 2005 American Chemical Society
Published on Web 03/01/2005

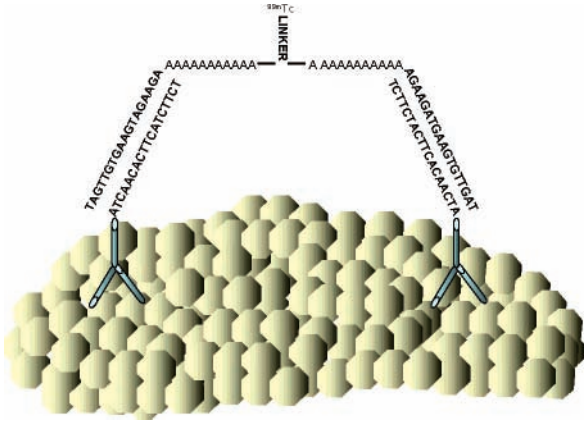

Figure 1. Artist's conception of a bivalent MORF bridging two complementary MORFs immobilizaed on a tumor cell.

Glu-Leu-Tyr-Glu-Asn-Lys(Ac)-Pro-Arg-Arg-Pro-Tyr-Ile-Leu (DTPA-Gly-NT) (*11*), and Ac-Phe-Lys(-DTPA)-Tyr-Lys(DTPA)-NH_2 (*12*) and have been variously radiolabled with ^{99m}Tc, ^{188}Re, ^{125}I, ^{131}I, ^{111}In, and most recently ^{68}Ga for radioimmunodetection and radiotherapy of tumor models (*13*−*21*). From these studies, it may be estimated that about 25 Å between the binding sites has been successfully used previously. Furthermore, a recent publication has shown that a bivalent receptor binding agent showed a 200-fold increase in affinity as the spacer between binding sites varied from 4 to 20 carbon atoms (i.e. 5−25 Å) (*22*).

This laboratory has previously reported encouraging results in tumored mice with pretargeting but using DNA and its analogues (collectively: oligomers). Instead of bifunctional antibodies, an antitumor antibody conjugated with a phosphodiamidate morpholine (MORF) serves as the first injection while the radiolabel is administered later on the complementary MORF (i.e. cMORF) as effector (*23*−*26*).

One advantage of using oligomers for pretargeting is the ease with which bivalent effectors for AES targeting may be constructed and the ease with which the molecular dimension separating the binding sites may be shortened or elongated. To accomplish the first goal of preparing the bivalent effector, MORFs with a primary amine were purchased and dimerized as described below. In future studies, the dimensions between binding sites will be investigated by purchasing the MORFs with additional bases in the chain.

The concept is shown schematically in Figure 1. In this investigation, we describe an initial test in which one bivalent MORF was synthesized and investigated for its properties of hybidization compared to its monovalent form. To measure these properties, a biotinylated cDNA was immobilized on a sensor chip at two concentrations, and, by surface plasmon resonance (SPR), the hybridization properties of MORF were measured in its bivalent form and compared to its monovalent form.

MATERIALS AND METHODS

All 18 mer MORFs and cMORFs [collectively: (c)MORFs] whether biotinylated or amine modified on the 3′ equivalent end were purchased prepurified (Gene-Tools, Corvallis, OR) and were used as received. The MORF base sequence was 5′-equivalent-TCT-TCT-ACT-TCA-CAA-CTA-linker-primary amine. The linker for amine modification was $-C(O)OCH_2C_6H_4CH_2NH_2$. The base sequences of the cMORFs were complementary with the linker and primary amine also on the 3′ equivalent end. The molecular weights were 6164 and 6422 Da. Biotinylated (c)DNA having the same sequences as the (c)MORF were purchased from Qiagen Inc. (Valencia, CA) and were also used as received. Disuccinimidyl suberate (DSS) was purchased from Pierce (Rockford, IL). Anhydrous dimethylformamide (DMF), *N*-methyl-2-pyrrodinone (NMP), and diisopropylethylamine (DIEA) were purchased from Sigma-Aldrich (St. Louis, MO). All other chemicals were reagent grade and were used without purification.

Preparation of Bivalent MORF. About 1.5 mg (0.25 μmol) of amino-derivitized MORF was dissolved in 1.0 mL of 1-methyl-2-pyrrolidinone (NMP). A 0.125 μmol of disuccinimidyl suberate (DSS) in NMP solution at 2 mg/mL was added and followed by 0.66 μmol of *N*,*N*-diisopropylethylamine (DIEA). This mixture was incubated at room temperature for 2 days. The bivalent MORF was purified by Q Sepharose ion exchange chromatography. The collected fractions of bivalent MORFs were passed through a PD-10 column in 50 mM phosphate buffer. The molecular weight of the product was confirmed by MALDI-TOF before storage at freezer temperatures for future use.

Chromatography. Ion Exchange (IE) HPLC was performed on a HiTrap Q HP column (Amersham Biosciences, Uppsala Sweden) using 0.01 N NaOH (solvent A) and 0.01 N NaOH in 2 N NaCl (solvent B) at a flow rate of 1.0 mL/min going from 100% A to 70% A over the 30 min. Before each analysis, the column was stabilized with 0.01 N NaOH, and after each analysis the column was cleaned with solvent B. For small scale of preparative purification, samples were loaded on the column by several injections in running solvent A but without exceeding the column's maximum binding capability. The bivalent MORF was collected in fractions during the gradient elution.

Surface Plasmon Resonance Measurements. The surface plasmon resonance analysis (SPR) was performed on a BIAcore 2000 (BIAcore, Piscataway, NJ) instrument operating at room temperature. In these measurements DNAs rather than MORFs were immobilized because of earlier difficulties in immobilizing biotinylated (c)MORFs. Several 5−10 μL amounts of biotinylated(c)DNAs at 20 nM were each added to a separate new streptavidin−dextran-coated sensor chip (SA) at a flow rate of 20 μL/min until a response of about 100 (±10) or 500 (±30) response units (RU) was reached. The absence of mass transfer effects was confirmed by running separately one concentration of free MORFs at three different flow rates (10, 30, and 75 μL/min) and demonstrating identical response and curve shape for both concentrations. When the identical measurement was performed on a sensor chip to which DNA was added to a response of 750 RU, evidence of mass transfer effects was observed, and accordingly this chip was not used in subsequent studies. Solutions of free monovalent and bivalent MORF were prepared at eight concentrations from 0.0 to 500 nM in the same running buffer (10 mM HEPES, 150 mM NaCl, 3.4 mM Na_2EDTA, 0.005% P20, pH 7.4) and injected separately onto the active (cDNA) or control (DNA) surface. Dissociation was followed for 25 min or 4 h. The chip surface was regenerated by injection of 100 mM HCl. To correct for nonspecific binding and refractive index changes, the control responses were subtracted from those obtained from the active surface. A minor baseline drift resulting from a slow dissociation of the complex on the active and control surfaces was eliminated by also subtracting sensograms obtained following the injection of running buffer (*27*).

In the first series of experiments, samples of monovalent and bivalent MORFs were run at seven concentrations on both the 100 and 500 RU chips and with a dissociation time of only 25 min. In the second series of experiments, all seven concentrations were again run but with a dissociation time of 4 h to obtain more accurate values for the dissociation rate constants. To conserve instrument time, the longer analysis was performed only on the 100 RU chip. Each measurement was repeated four times, and, as mentioned above, each sample was run on both the cDNA and DNA chips at the same surface density so that results with the latter could be use to correct for bulk refractive index changes (*27*).

Sensorgram Kinetic Analysis. Sensorgram curves were evaluated using numerical intergration algorithms (BIAevaluation 3.0, BIAcore, Piscataway, NJ). The algorithm may be programmed for simple monomolecular 1:1 Langmuir interactions of a monvalent analyte or for a bivalent analyte binding monomolecularly (i.e. A+L→AL where A is the analyte, in this case MORF, and L is immobilized ligand, in this case cDNA) or binding bimolecularly (i.e. AA+L→AAL and AAL+ L→LAAL). In addition the algorithm may be programmed to analyze globally (i.e. all analyte concentrations considered together to provide one value for each of the two rate constants, association and dissociation) or locally (i.e. each analyte concentration considered separately to provide one value for each of the two rate constants for each analyte concentration). In addition, in the case of bimolecular binding, the bimolecular binding algorithm can provide one value for each of the two rate constants for the first and second binding. An added complication in the case of bivalent analyte binding is the possibility that the binding may be either monomolecular or bimolecular and thus cannot be accurately modeled. To emphasis this fact, the rate constants in this report for bivalent MORFs are referred to as "apparent". Finally, the program provides for each analysis a Chi2 (χ^2) value which is a statistical measure of how closely the model fits the experimental data. In general, χ^2 values lower than about 10 signify a good fit. In each of these investigations comparing monovalent to bivalent MORFs, the concentrations were adjusted to the same molarity of analyte and therefore the MORF molarity of the bivalent analyte was twice that of the monovalent analyte.

Stoichiometry of Bivalent MORF Binding. The BIAcore instrument measures the mass of molecules bound to the sensor surface. Thus, the stoichiometry of the surface molecular complex (i.e. the number of analyte molecules per ligand molecule) can be determined using eq 1:

$$\text{stoichiometry} = (R_{A(max)} \times MW_L)/(MW_A \times R_L) \quad (1)$$

where MW refers to molecular weight of the analyte (MW_A) and immobilized ligand (MW_L) while R refers to the response in RU of the analyte (R_A) and the ligand (R_L). $R_{A(max)}$ refers to the maximum response (i.e. binding capacity) of R_A for any ligand concentration R_L (i.e. either 100 or 500 RU) and can be obtained by analyzing locally the sensograms obtained at different analyte concentrations (*4, 28, 29*). If the stoichiometry value provided by eq 1 for monovalent MORF is fixed at 1.00, pure bimolecular binding of the bivalent MORF must provide a stoichiometry value of 0.50. To eliminate uncertainties related to ligand concentration in this investigation, the monovalent and bivalent MORFs were compared on the same sensor chips (and thus at the same MW_L and R_L) and the stoichimetry of the bivalent MORF is expressed as a ratio of that of the bivalent over the monovalent MORF.

RESULTS

Preparation of Bivalent MORF. To prepare the bivalent MORF, the amine derivatized MORF was dimerizing with disuccinimidyl suberate (DSS) for 2 days in the presence of 1-methyl-2-pyrrolidinone (NMP) and *N*,*N*-diisopropylethylamine (DIEA). The IE HPLC UV profile for the reaction mixture is shown in Figure 2C with peaks at 10.8, 11.8, and 13.9 min that are thought to represent the excess native MORF (shown in Figure 2A), DSS modified but monovalent MORF and the desired bivalent MORF, respectively. To help confirm these identifies, MORF was also reacted with succinic anhydride to give a compound similar to the DSS modified but monovalent MORF especially in the negative charge (Figure 2B). In this way, the remaining peak at 13.9 min was identified as the bivalent MORF (Figure 2D). Changing from alkaline solution to phosphate buffer or water was performed on a PD-10 column. Correct structure of the bivalent MORF was confirmed by MALDI-TOF MS (calculated MW: 12466; found: 12474 ± 8).

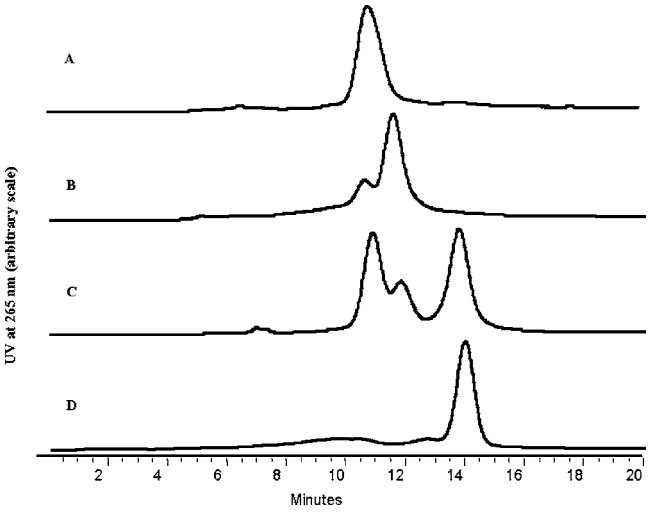

Figure 2. Chromatograms of native MORF (panel A), derivatized but monovalent MORF (panel B), the reaction mixture (panel C), and purified bivalent MORF (panel D) obtained by IE HPLC with UV detection.

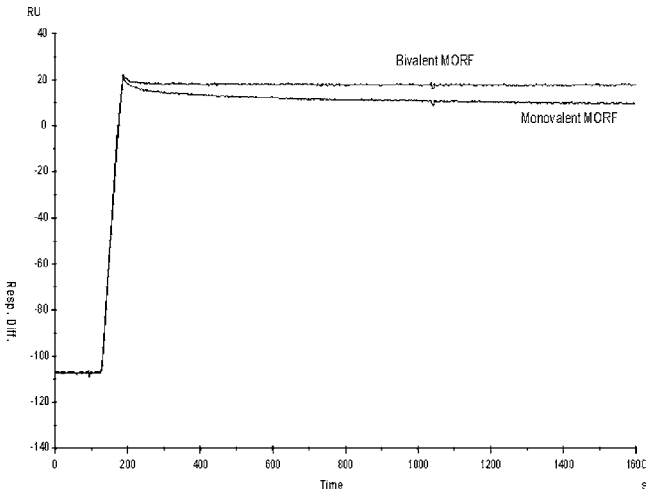

Figure 3. Typical sensograms (normalized) of monovalent and bivalent MORF and obtained at one concentration (40 nM) and at one cDNA density (100 RU).

Table 1. Comparison of Apparent Kinetics Rate Constants and Equilibrium Constants for the Interaction of Monovalent and Bivalent MORF with Immobilized cDNA by Global Fitting Using the 1:1 Langmuir Interaction Model[a]

			k_d (1/s) × 10^{-5}				
cDNA density	analyte	k_a (1/M·s) × 10^5	k_d	k_d fast	k_d slow	K_{equ} (1/M·s) × 10^{10}	$\chi 2$
100 RU	bivalent MORF	8.52(1.32)	2.14(0.39)	26.3(4.7)	0.22(0.04)	3.99(0.83)	17(8)
	monovalent MORF	5.64(0.65)	26.7(1.92)	37.5(6.2)	0.72(0.06)	0.21(0.07)	8(4)
500 RU	bivalent MORF	6.31(0.75)	5.63(0.93)	20.6(5.3)	0.14(0.03)	1.12(0.21)	42(20)
	monovalent MORF	5.12(0.71)	29.3(1.24)	33.1(9.4)	0.68(0.05)	0.18(0.48)	12(7)

[a] k_a: association rate constant; k_d: dissociation rate constant; K_{equ}: equilibrium constant; χ^2: index for goodness of fit. Standard deviations in parentheses.

Table 2. Comparison of Equilibrium Constants for the Binding of Monovalent MORF and Bivalent MORF to Immobilized cDNA by Local Fitting Using the 1:1 Langmuir Interaction Model[a]

concentration (nM)		400	250	160	80	40	20	10
500 RU, bivalent MORF	K_{equ}((1/M·s) × 10^9)	17.4	6.76	4.94	4.23	3.23	1.75	2.31
	χ^2	6.23	7.77	3.56	5.21	1.32	0.23	4.02
500 RU, monovalent MORF	K_{equ}((1/M·s) × 10^9)	2.74	2.13	1.34	3.65	4.23	2.39	2.45
	χ^2	1.35	6.53	5.66	4.32	2.65	2.79	4.36
100 RU, bivalent MORF	K_{equ}((1/M·s) × 10^9)	1.00	2.23	19.9	18.7	2.22	1.42	9.69
	χ^2	1.85	2.64	0.76	1.93	0.55	0.72	16
100 RU, monovalent MORF	K_{equ}((1/M·s) × 10^9)	3.69	3.42	2.16	1.97	2.75	3.20	1.26
	χ^2	0.63	1.12	0.98	3.12	0.71	2.65	1.63

[a] K_{equ}: equilibrium constant; χ^2: index for goodness of fit.

Table 3. Comparison of Apparent Kinetic Rate Constants for the Binding of Bivalent MORF with cDNA Immobilized at 100 RU by Using the Bivalent Binding Model and Local Fitting

concentration of bivalent MORF (nM)	400	250	160	80	40	20	10
$k_a(1 \times 10^5)$ (1/M·s)	4.74	1.03	7.25	6.89	3.99	2.18	9.92
$k_d(1 \times 10^{-4})$ (1/s)	20.3	9.07	31.4	35.1	30.3	3.39	2.59
$k_a(2 \times 10^{-3})$ (1/M·s)	9.40	1.30	4.30	2.30	0.20	0.80	4.36
$k_d(2 \times 10^{-5})$ (1/s)	21.7	6.68	5.02	2.41	1.39	3.52	1.72
χ^2	0.677	4.99	0.545	1.01	1.89	15.3	0.65

Sensorgram Kinetic Analysis. Figure 3 is a composite presenting typical sensorgrams for the monovalent and the bivalent MORFs obtained at 40 nM concentration with cDNA immobilized at 100 RU. The figure shows that the dissociation of bivalent MORF is slower compared to monovalent MORF and almost imperceptible over the 23 min dissociation period, a result of its high binding affinity. To measure more accurately the dissociation rate constant, the binding studies were repeated with a 4 h dissociation period. The measurement was performed for both surface densities of 100 and 500 RU and at seven concentrations of the monovalent and bivalent MORF from 0.5 to 500 nM. The results for different models and fitting method (globally or locally) are reported in Tables 1−3. Table 1 presents a comparison of the results obtained in the analysis of sensograms obtained with the monovalent and bivalent by the simpler 1:1 Langmuir interaction algorithm with global fitting. Table 2 presents analysis of the same data by the 1:1 Langmuir interaction algorithm but with local fitting. Finally Table 3 presents an analysis of only those sensograms obtained with the bivalent MORF using local fitting but with the bivalent algorithm rather than 1:1 Langmuir interaction algorithm. In each case, the χ^2 value is included as a statistical measure of how closely the model fits the experimental data.

As shown in the table, by globally fitting using a 1:1 Langmuir interaction algorithm, the association rate constants are similar for both monovalent and bivalent MORF. However, there is a significant difference in dissociation rate constants providing an equilibrium constants 15−20 times higher for the bivalent MORF at both cDNA densities.

A key step in interpreting the BIAcore results may be the separation of the dissociation rate constants into fast and slow phases since that may provide a method of distinguishing bimolecular binding of the bivalent MORF from monomolecular binding (*30, 31*). In the case of bivalent MORF, monomolecular binding should provide the same dissociation behavior as monovalent MORF while bimolecular binding should show different and slower dissociation kinetics. As described below, by inspection of the dissociation curves, the fast phase was defined as completed by 2 min following the end of the injection while the slow phase continued thereafter. The results are presented in Table 1 as k_d of fast and slow phases.

As shown in Table 2, a more complicated analysis again using the 1:1 Langmuir interaction algorithm but with local fitting has provided a better fit with more reasonable χ^2 usually less than 8. As shown, for the bivalent MORF the highest affinity at the 100 RU density was found in the concentration range of 80−160 nM while at density of 500 RU the highest affinity started at 250 nM.

Table 3 presents the apparent kinetics rate constants of bivalent MORF at different concentrations under condition of 100 RU DNA density and using the bivalent binding model instead of the 1:1 Langmuir interaction algorithm. The bivalent model considers the association and dissociation of the first and second bindings separately. Using a bivalent model to locally fit the sensorgrams of bivalent MORF has generally produced even lower χ^2 values and therefore a superior fit.

Figure 4 A and B presents sensograms of the monovalent and bivalent MORFs at different concentrations and at one cDNA density. Interpretation of the senso-

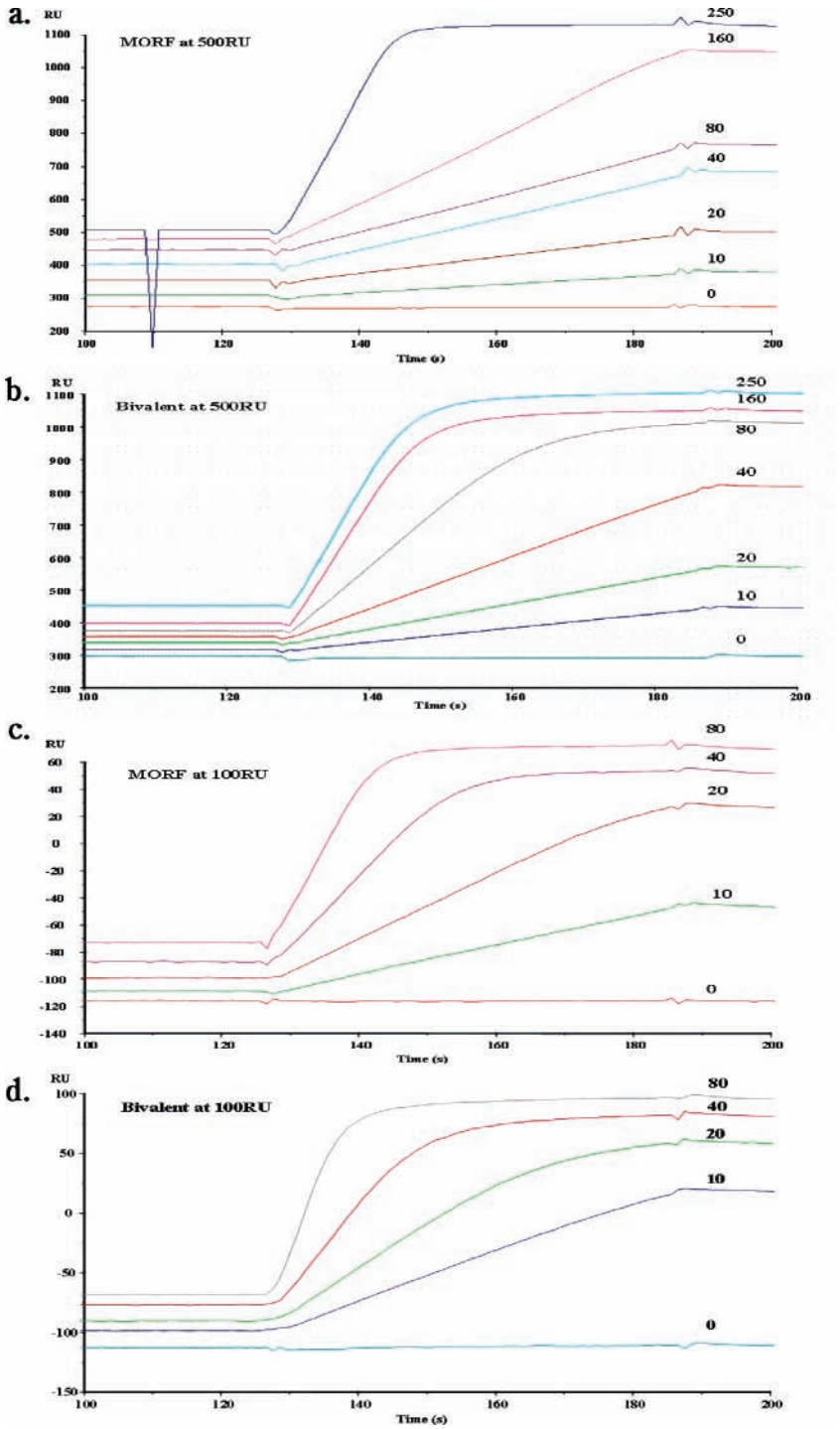

Figure 4. Sensograms at 500 RU cDNA density of the monovalent (panel A) and bivalent MORF (panel B) and at 100 RU cDNA density of the monovalent (panel C) and bivalent MORF (panel D) at the concentrations shown. The MORF concentrations of the bivalent MORF are twice the analyte concentrations. Concentraions are all in nM.

grams involves inspection of the behavior during injection (125 to 185 s). In the absence of saturation, the response will increase linearly throughout the entire period of the injection. In the presence of saturation, the response will level off before the end of the injection. Examples of both may be found in the sensograms of the bivalent MORF (Figure 4B). When injected at concentrations of 40 nM or less, the response increases linearly throughout while at higher concentration, the response becomes horizontal before the end of the injection and does so earlier with increasing concentration. The monovalent MORF clearly reaches a steady response more rapidly than bivalent MORF at this cDNA density and also does so at the lower cDNA density (Figure 4C and 4D). The sensograms may also be inspected for the shape of the curves as saturation approaches. In the case of the monovalent MORF, incapable of bimolecular binding, the sensograms shows a relatively abrupt change from increasing to horizontal response (Figure 4A and 4C). By contrast, the bivalent MORF shows a slower transition as evidence that more complex binding is occurring probably involving both monomolecular and bimolecular binding.

Stoichiometry of Bivalent MORF with Immobilized cDNA. The results of applying eq 1 to the sensograms showed that at both cDNA densities, the ratio of stoichiometry values for the bivalent over the monovalent

MORF is approximately 0.85 at all concentrations. Since this value is between the 1.0 for pure monomolecular binding and 0.5 for pure bimolecular binding, these results imply that the bivalent MORF under all conditions exhibits a mixture of monomolecular and bimolecular binding.

DISCUSSION

In this investigation, SPR was used to study the behavior of a bivalent MORF compared to its monovalent form during hybridization to immobilized cDNA. The bivalent MORF, AA, may bind to one cDNA ligand, L, to form the complex AAL, or it may bridge two ligands to form the complex LAAL. The probability of monomolecular binding (AAL) compared to bimolecular binding (LAAL) will depend on the molecular dimensions of the bivalent analyte and the concentration (spacing) and flexibility of the ligand molecules on the immobilized surface (*32*). Since bimolecular binding may be expected to provide higher hybridization affinities (equilibrium constants) than monomolecular binding, bimolecular binding of bivalent analytes may be expected to be favored under favorable conditions.

By inspection of the sensograms, it is possible to conclude that bimolecular binding of the bivalent MORF was observed in this investigation. The slower dissociation kinetics of the bivalent compared to the monovalent MORF (Figure 3) may be best explained by bimolecular binding of the bivalent MORF leading to slower dissociation. Additional evidence is provided by examination of the dissociation rate in Table 1. As is evident from the Table, the dissociation rate is largely independent of cDNA density in the case of the monovalent MORF but shows a strong dependence on the cDNA density in the case of the bivalent MORF. At the lower cDNA density, monomolecular binding of the bivalent MORF is favored as a result of the larger spacing between cDNAs. The fraction of the bivalent MORF binding bimolecularly may be expected to increase with increasing cDNA density (and therefore decreasing spacing), and therefore the dissociation rate will decrease as shown.

Finally, the sensograms may be inspected for the shape of the association/dissociation phase during injection. At the higher 500 RU cDNA density, saturation (evident by a horizontal response before the end of the injection) required concentrations greater than 40 nM for the bivalent MORF while saturation was not achieved for the monovalent MORF at less than 160 nM. Even considering that the MORF concentration of the bivalent MORF is half that of the monovalent MORF at the same analyte concentration, it is apparent that higher concentrations are required to achieve saturation in the case of the monovalent MORF presumably because the bivalent MORF is capable of bridging cMORFs by bimolecular binding.

Evidence of bimolecular binding is also apparent in the results of applying eq 1 to estimate the stoichometry of binding. Since the response by SPR increases linearly with the molecular weight of the analyte, it should be possible to distinguish between monomolecular and bimolecular binding in the case of the bivalent MORF. Monomolecular binding of the bivalent MORF will provide a response related to its molecular weight that is double that of bimolecular binding for the same number of cDNAs bound. But in the case of bimolecular binding, the response between monovalent and bivalent MORF for the same number of cDNAs will be lower as bivalent MORF bridges two binding sites. This analysis is based on the assumption that the larger bivalent MORF shows no steric hindrance to cDNA binding monomolecularlly compared to the smaller monovalent MORF. There is therefore a different response at the same number of cDNA binding sites for pure bimolecular binding and pure monomolecular binding in the case of bivalent MORF that can be used to estimate the fraction of bivalent MORF that is binding bivalently. To correct for variations in cDNA density and MORF concentrations, the results of stoichiometry analysis have been presented as a ratio. Thus, pure monomolecular binding would results in a stoichiometry value of 1.00 while pure bimolecular binding would results in a value of 0.50. That the results are fairly constant at about 0.79−0.93 regardless of cDNA density or MORF concentration indicates that a substantial and fairly constant fraction of the bivalent binding is bimolecular under all conditions. A value of 0.8 corresponding to the binding of about four bivalent MORF to five cDNAs or only one of four bivalent MORF binding bimolecularily or 25%. In this manner it may be estimated that less than 20% of bivalent MORF was binding bimolecular under the conditions in this study.

Evidence for bimolecular binding may also be apparent from sensorgram analysis using numerical intergration algorithms (BIAevaluation 3.0, BIAcore, Piscataway, NJ). In this investigation, the dissociation curves were analyzed by separately considering a fast and a slow dissociation phase. Dissociation of the bivalent MORF will involve both the dissociation of monomolecular bound bivalent MORF similar to that of the monovalent MORF and the dissociation of biomolecularily bound MORF unique to the bivalent MORF (*30, 31*). In case of the bivalent MORF, monomolecular binding should therefore provide the same dissociation behavior as monovalent MORF while bimolecular binding should show different and slower dissociation kinetics. In this study, the fast phase was defined as completed by 2 min following the end of injection while the slow phase continued thereafter. The k_d values for both phases are reported separately in Table 1 for both monovalent and bivalent MORF. In general, low cDNA density and higher MORF concentrations will not favor bimolecular binding, in the first instance because of the greater spacing between cDNAs and in the latter instance because the cDNAs are more likely to be saturated with MORF bound monomolecularly (see below). As evident in the table, at both cDNA densities, the k_d fast values are similar for monovalent and bivalent MORF (indicating monomolecular binding) while the k_d slow values for the bivalent MORF are significantly smaller ($p = 0.03$) at both densities (indicative of bimolecular binding). Thus, these results suggest that the bivalent MORF is binding bimolecularally at least in part.

The evidence presented above confirms that bimolecular binding was observed. It is then possible to examine the influence of bimolecular binding on the rate and equilibrium constants of hybridization. Bimolecular binding would be expected to result in lower dissociation rate constants and higher equilibrium constants. The results of analyzing the sensograms obtained in this investigation confirm that this is the case. As shown in Table 1, by globally fitting using a 1:1 Langmuir interaction algorithm, an important differences in dissociation rate constants is apparent between monovalent and bivalent MORF providing an equilibrium constant about 15−20 times higher for the bivalent MORF. Reanalysis using local fitting provided separate equilibrium constants for each MORF concentration. As shown in Table 2, in the

case of 500 RU cDNA density, the equilibrium constants for monovalent and bivalent MORFs are similar at concentrations below about 160 nM while at higher concentrations, the equilibrium constant for the bivalent MORF is approximately 2−8 times higher. The results of reanalyzing the data obtained at 100 RU cDNA density also shows similar equilibrium values at concentrations of 80 nM or less and about 9 times higher values for the bivalent MORF at concentrations of 80 and 160 nM. For reasons not understood, the trend reverses at higher concentrations with the monovalent MORF exhibiting higher equilibrium constants than the bivalent. Thus higher equilibrium constants and therefore affinity enhancement only occurred over a particular range of analyte concentrations in our bivalent MORF system instead of at all low concentrations as in other multivalent systems (*30*−*34*). This observation may be due to conformation changes during association of both the long, linear, and flexible cDNA linear ligands and MORF analytes and the complexity of oligomer hybridization itself involving many base pairs.

Table 3 presents the results of reanalyzing the results obtained for the bivalent MORF at each concentration but only at the 100 RU cDNA density. This analysis was capable of calculating separately an apparent first and second association and dissociation rate constants. As shown in the table, the apparent first association rate constant for all concentrations are similar ($(1-7) \times 10^5$ 1/M·s), indicating similar behavior in the first binding step regardless of concentration as is reasonable for consistent monomolecular binding. Furthermore, the first association rate constant is much larger (i.e. more rapid first association) compared to second association rate constant as is reasonable since bimolecular binding requires reorientation. Therefore, high concentrations of bivalent MORF will tend to saturate cDNA sites with monomolecular binding first, reducing the chances for bimolecular binding and therefore reducing the equilibrium constant. This phenomenon may be expected to be more pronounced at lower cDNA concentrations.

It is important to point out that in the sensogram analysis, quantitative evaluation was made difficult by the high cDNA densities required in this investigation to achieve bimolecular binding. These high densities can result in mass transport effects and, furthermore, can complicate the analysis by permitting rebinding during dissociation. In this investigation it was possible to prevent mass transport complications by adjusting the flow rate to be in a range where the response was shown to be flow-rate-independent. However, it was not possible to eliminate rebinding effects, and thus rebinding contributed partially to the resulting kinetic analysis. However, as rebinding would be hindered under conditions of ligand saturation, the fact that bivalent MORF saturated the cDNA at much lower concentrations than monvalent MORF would imply more favorable affinity of bivalent MORF than estimated in this study.

In this investigation, affinity enhancement was observed for the bivalent MORF on chips with cDNA densities as low as 100 RU. The RU unit can be approximately converted to mass of protein in the dextran layer by the relation 1 RU = 1 pg/mm^2 (*35*). With a new SA chip at 10000 RU in strepavidin, there are 10000 pg SA/mm^2 or 1.66×10^{-13} mol SA/mm^2. Using an 18 mer biotin-cDNA (MW ∼ 6K) as the ligand and assuming binding to all four sites of strepavidin, the maximun binding capacity of biotinylated cDNA may be estimated as 4.11 ng cDNA/mm^2 or 6.64×10^{-13} mol cDNA/mm^2 which corresponds to 4000 RU of cDNA. Initially in this study, 100 RU, 500 RU, and 750 RU of cDNA were immobilized which correspond to a 82, 25, and 17 Å distance between two neighboring cDNA. However, at a practical coating density of 750 RU, the effects of mass transport limitation were evident (data not shown), and for this reason only the 100 RU and 500 RU coating densities were used for further studies. It may be surprising that the 82 Å average spacing between cDNAs at 100 RU density did allow bimolecular binding for the bivalent MORF with about 25 Å between two MORF. This could be explained both by the relatively long 17-atom linker by which the cDNA is tethered to the chip via the biotin group and that the MORF itself is about 61 Å long. The bivalent MORF may be expected to have a large access range.

CONCLUSION

A synthesis of bivalent MORF has been described. The bivalent MORF exhibited significant enhanced affinity compared to monovalent MORF as demonstrated by BIAcore measurements. These results suggest that bivalency may be superior to monovalency in MORF pretargeting applications. Studies using less flexible ligand immobilization, lower coating density, and bivalent MORF with different length of linker will be necessary to optimize the influence of affinity enhancement of bivalent MORFs in pretargeting applications.

ACKNOWLEDGMENT

Financial support for this investigation was provided, in part, by the National Institutes of Health (CA79507 and CA 94994). The authors are grateful to Dr. Yongfu Li of Gene-Tools, Inc. (Corvallis, OR) for advice on the MORF purification.

LITERATURE CITED

(1) Goodwin, D. A., Meares, C. F., McTigue, M., Mccall, M. J., and David, G. S. (1986). Rapid localization of haptens in sites containing previously administered antibody for immunoscintigraphy with short half-life tracers [abstract]. *J. Nucl. Med. 27*, 959−959.

(2) Hnatowich, D. J., Virzi, F., and Rusckowski, M. (1987) Investigations of avidin and biotin for imaging applications. *J. Nucl. Med. 28*, 1294−302.

(3) Kuijpers, W. H., Bos, E. S., Kaspersen, F. M., Veeneman, G. H. and van Boeckel, C. A. (1993) Specific recognition of antibody-oligonucleotide conjugates by radiolabeled antisense nucleotides: a novel approach for two-step radioimmunotherapy of cancer. *Bioconjugate Chem. 4*, 94−102.

(4) Hamblett, K. J., Kegley, B. B., Hamlin, D. K., Chyan, M. K., Hyre, D. E., Press, O. W., Wilbur, D. S., and Stayton, P. S. (2002) A streptavidin−biotin binding system that minimizes blocking by endogenous biotin. *Bioconjugate Chem. 13*, 588−598.

(5) Wilbur, D., Pathare, P. M., Hamlin, D. K., and Weerawarna, S. A. (1997) Biotin Reagents for Antibody Pretargeting. 2. Synthesis and in Vitro Evaluation of Biotin Dimers and Trimers for Cross-Linking of Streptavidin. *Bioconjugate Chem. 8*, 819−832.

(6) Karacay H., McBride W. J., Griffiths G. L., Sharkey R. M., Barbet J., Hansen, H. J., and Goldenberg, D. M. (2000) Experimental pretargeting studies of cancer with a humanized anti-CEA x murine anti-[In-DTPA] bispecific antibody construct and a 99mTc-/188Re-labeled peptide. *Bioconjugate Chem. 11*, 842−854

(7) Gruaz-Guyon, A., Janevik-Ivanovska, E., Raguin, O., De Labriolle-Vaylet, C., and Barbet, J. (2001) Radiolabeled bivalent haptens for tumor immunodetection and radioimmunotherapy. *Q. J. Nucl. Med. 45*, 201−6.

(8) Chang, C., Sharkey, R. M., Rossi, E. A., Karacay, H., McBride, W., Hansen, H. J., Chatal, J., Barbet, J., and

Goldenberg, D. M. (2002) Molecular advances in pretargeting radioimmunotherapy with bispecific antibodies. *Mol. Cancer Ther. 1*, 553−563.

(9) Cardillo, T. M., Karacay, H., Goldenberg, D. M., Yeldell, D., Chang, C. H., Modrak, D. E., Sharkey, R. M., and Gold, D. V. (2004) Improved targeting of pancreatic cancer: experimental studies of a new bispecific antibody, pretargeting enhancement system for immunoscintigraphy. *Clin. Cancer Res. 10*, 3552−3561.

(10) Goodwin, D. A., Meares, C. F., McTigue, M., Chaovapong, W., Diamanti, C. I., Ransone, C. H., and McCall, M. J. (1992) Pretargeted immunoscintigraphy: Effect of hapten valency on murine tumor uptake. *J. Nucl. Med. 33*, 2006−2013.

(11) Hillairet De Boisferon, M., Raguin, O., Thiercelin, C., Dussaillant, M., Rostene, W., Barbet, J., Pelegrin, A., and Gruaz-Guyon, A. (2002) Improved tumor selectivity of radiolabeled peptides by receptor and antigen dual targeting in the neurotensin receptor model. *Bioconjugate Chem. 13*, 654−662.

(12) Boerman, O. C., van Eerd, J., Oyen, W. J. G., and Corstens, F. H. M. (2002) A 3-Step Pretargeting Strategy to Image Infection. *J. Nucl. Med. 42*, 1405−1411.

(13) Barbet, J., Peltier, P., Bardet, S., Vuillez, J. P., Bachelot, I., Denet, S., Olivier, P., Leccia, F., Corcuff, B., Huglo, D., Proye, C., Rouvier, E., Meyer, P., and Chatal, J. F. (1998) Radioimmunodetection of medullary thyroid carcinoma using indium-111 bivalent hapten and anti-CEA x anti-DTPA-indium bispecific antibody. *J. Nucl. Med. 39*, 1172−1178.

(14) Bardies, M., Bardet, S., Faivre-Chauvet, A., Peltier, P., Douillard, J. Y., Mahe, M., Fiche, M., Lisbona, A., Giacalone, F., Meyer, P., Gautherot, E., Rouvier, E.; Barbet, J., and Chatal, J. F. (1996) Bispecific antibody and iodine-131-labeled bivalent hapten dosimetry in patients with medullary thyroid or small-cell lung cancer. *J. Nucl. Med. 37*, 1853−1859.

(15) Gautherot, E., Rouvier, E., Daniel, L., Loucif, E., Bouhou, J., Manetti, C., Martin, M., Le Doussal, J. M., and Barbet, J. (2000) Pretargeted radioimmunotherapy of human colorectal xenografts with bispecific antibody and 131I-labeled bivalent hapten. *J. Nucl. Med. 41*, 480−487.

(16) Gestin, J. F., Loussouarn, A., Bardies, M., Gautherot, E., Gruaz-Guyon, A., Sai-Maurel, C., Barbet, J., Curtet, C., Chatal, J. F., and Faivre-Chauvet, A. (2001) Two-step targeting of xenografted colon carcinoma using a bispecific antibody and 188Re-labeled bivalent hapten: biodistribution and dosimetry studies. *J. Nucl. Med. 42*, 146−153.

(17) Griffiths, G. L., Chang, C. H., McBride, W. J., Rossi, E. A., Sheerin, A., Tejada, G. R., Karacay, H., Sharkey, R. M., Horak, I. D., Hansen, H. J., and Goldenberg, D. M. (2004) Reagents and methods for PET using bispecific antibody pretargeting and 68Ga-radiolabeled bivalent hapten-peptide-chelate conjugates. *J. Nucl. Med. 45*, 30−39.

(18) Hosono, M., Hosono, M. N., Kraeber-Bodere, F., Devys, A., Thedrez, P., Fiche, M., Gautherot, E., Barbet, J., and Chatal, J. F. (1998) Biodistribution and dosimolecular study in medullary thyroid cancer xenograft using bispecific antibody and iodine-125-labeled bivalent hapten. *J. Nucl. Med. 39*, 1608−1613.

(19) Hosono, M., Hosono, M. N., Kraeber-Bodere, F., Devys, A., Thedrez, P., Faivre-Chauvet, A., Gautherot, E., Barbet, J., and Chatal, J. F. (1999) Two-step targeting and dosimetry for small cell lung cancer xenograft with anti-NCAM/antihistamine bispecific antibody and radioiodinated bivalent hapten. *J. Nucl. Med. 40*, 1216−1221.

(20) Kraeber-Bodere, F., Bardet, S., Hoefnagel, C. A., Vieira, M. R., Vuillez, J. P., Murat, A., Ferreira, T. C., Bardies, M., Ferrer, L., Resche, I., Gautherot, E., Rouvier, E., Barbet, J., and Chatal, J. F. (1999) Radioimmunotherapy in medullary thyroid cancer using bispecific antibody and iodine 131-labeled bivalent hapten: preliminary results of a phase I/II clinical trial. *Clin. Cancer Res. 5(Suppl.)*, 3190s−3198s.

(21) Kraeber-Bodere, F., Faivre-Chauvet, A., Sai-Maurel, C., Campion, L., Fiche, M., Gautherot, E., Le Boterff, J., Barbet, J., Chatal, J. F., and Thedrez, P. (1999) Toxicity and efficacy of radioimmunotherapy in carcinoembryonic antigen-producing medullary thyroid cancer xenograft: comparison of iodine 131-labeled F(ab′)2 and pretargeted bivalent hapten and evaluation of repeated injections. *Clin Cancer Res. 5(10 Suppl)*, 3183s−3189s.

(22) Sridhar, J., Wei, Z., Nowak, I., Lewin, N. E., Ayers, J. A., Pearce, L. V., Blumberg, P. M., and Kozilowski, A. P. (2003) New bivalent PKC ligands linked by a carbon spacer: Enhancement in binding affinity. *J. Med. Chem. 46*, 4196−4204.

(23) Mang'era, K. O., Liu, G., Wang, Y., Zhang, Y., Liu, N., Gupta, S., Rusckowski, M., and Hnatowitch, D. J. (2001) Initial investigations of 99mTc-labeled morpholinos for radiopharmaceutical applications. *Eur. J. Nucl. Med. 28*, 1682−1689.

(24) Liu, G., Mang'era, K., Liu, N., Gupta, S., Rusckowski, M., and Hnatowich, D. J. (2002) Tumor pretargeting in mice using 99mTc-labeled morpholino, a DNA analog. *J. Nucl. Med. 43*, 384−391.

(25) Liu, G., Liu, C., Zhang, S., He, J., Liu, N., Gupta, S., Rusckowski, M., and Hnatowich, D. J. (2003) Investigations of technetium-99m morpholino pretargeting in mice. *Nucl. Med. Commun. 24*, 697−705.

(26) He, J., Liu, G., Gupta, S., Zhang, Y., Rusckowski, M., and Hnatowich, D. J. (2004) Amplification targeting: a modified pretargeting approach with potential for signal amplification-proof of a concept. *J. Nucl. Med. 45*, 1087−1095.

(27) He, J., Liu, G., Zhang, S., Vanderheyden, J.-L., Liu, N., Liu, C., Zhang, Y., Gupta, S., Rusckowski, M., and Hnatowich, D. J. (2003) A comparison of in vitro and in vivo stability in mice of two morpholino duplexes differing in chain length. *Bioconjugate Chem. 14*, 1018−1023.

(28) Mistrik, P., Moreau, F., and Allen, J. M. (2004) BiaCore analysis of leptin-leptin receptor interaction: evidence for 1:1 stoichiometry. *Anal. Biochem. 327*, 271−277.

(29) Rossi, E. A., Sharkey, R. M., McBride, W., Karacay, H., Zeng, L., Hansen, H. J., Goldenberg, D. M., and Chang, C. H. (2003) Development of new multivalent-bispecific agents for pretargeting tumor localization and therapy. *Clin. Cancer Res. 9(10 Pt 2)*, 3886s−3896s.

(30) Pack, P., Muller, K., Zahn, R., and Pluckthun, A. (1995) Tetravalent miniantibodies with high avidity assembling in Escherichia coli. *J. Mol. Biol. 246*, 28−34.

(31) Svensson, H. G., Wedemeyer, W. J., Ekstrom, J. L., Callender, D. R., Kortemme, T., Kim, D. E., Sjobring, U., and Baker, D. (2004) Contributions of amino acid side chains to the kinetics and thermodynamics of the bivalent binding of protein L to Ig kappa light chain. *Biochemistry. 43*, 2445−2457.

(32) Muller, K. M., Arndt, K. M., and Pluckthun, A. (1998) Model and simulation of multivalent binding to fixed ligands. *Anal. Biochem. 261*, 149−158.

(33) Kortt, A. A., Lah, M., Oddie, G. W., Gruen, C. L., Burns, J. E., Pearce, L. A., Atwell, J. L., McCoy, A. J., Howlett, G. J., Metzger, D. W., Webster, R. G., and Hudson, P. J. (1997) Single-chain Fv fragments of anti-neuraminidase antibody NC10 containing five- and ten-residue linkers form dimers and with zero-residue linker a trimer. *Protein Eng. 10*, 423−433.

(34) Jenkins, J. L., Lee, M. K., Valaitis, A. P., Curtiss, A., and Dean, D. H. (2000) Bivalent sequential binding model of a Bacillus thuringiensis toxin to gypsy moth aminopeptidase N receptor. *J. Biol. Chem. 275*, 14423−31.

(35) Stenberg, E., Persson, B., Roos, H., and Urbaniczky, C. (1991) Quantitative determination of surface concentration of protein with surface plasmon resonance using radiolabeled proteins *J. Colloid Interface Sci. 143*, 513−526.

BC049719C

An Anti-MUC1 Antibody–Calicheamicin Conjugate for Treatment of Solid Tumors. Choice of Linker and Overcoming Drug Resistance

Philip R. Hamann,* Lois M. Hinman, Carl F. Beyer, Lee M. Greenberger, Clara Lin, Delores Lindh, Ana T. Menendez, Rosalyn Wallace, Frederick E. Durr, and Janis Upeslacis

Wyeth Research, 401 N. Middletown Road, Pearl River, New York 10965. Received August 26, 2004; Revised Manuscript Received December 3, 2004

The anti-MUC1 antibody, CTM01, has been chosen to target the potently cytotoxic calicheamicin antitumor antibiotics to solid tumors of epithelial origin that express this antigen. Earlier calicheamicin conjugates relied on the attachment of a hydrazide derivative to the oxidized carbohydrates that occur naturally on antibodies. This produced a "carbohydrate conjugate" capable of releasing active drug by hydrolysis in the lysosomes where the pH is low. Conjugates have now been made that are formed by reacting a calicheamicin derivative containing an activated ester with the lysines of antibodies. This gives an "amide conjugate" that is stable to hydrolysis, leaving the disulfide that is present in all calicheamicin conjugates as the only likely site of drug release from the conjugate. As previously shown for the carbohydrate conjugate, this amide conjugate of CTM01 produces complete regressions of xenograft tumors at doses of 300 μg/kg (calicheamicin equivalents) given three times. This indicates that hydrolytic drug release is not necessary for potent, selective cytotoxicity for calicheamicin conjugates of CTM01. Although the unconjugated calicheamicins are in general less active in cells expressing the multidrug resistance phenotype, both in vitro and in vivo results of studies reported here suggest that the efficacy of the calicheamicins toward such tumors is unexpectedly enhanced by antibody conjugation, especially for the "amide conjugate". These hydrolytically stable conjugates are also active toward cisplatin-resistant ovarian carcinoma cells as well. Such studies indicate that the calicheamicin amide conjugate of CTM01 may have potential for the treatment of MUC1-positive solid tumors, including some types of resistant tumors.

INTRODUCTION

The calicheamicins are highly potent antitumor antibiotics of the enediyne family. Originally isolated from a broth extract of the soil microorganism *M. echinospora* ssp. *calichensis*, they were detected in a screen for potent DNA damaging agents (*1*). The parent of this family of xenobiotics, calicheamicin γ_1^I (**1**, Figure 1), associates with the minor groove of DNA and, following reduction with glutathione (*2*), causes sequence-specific, double-stranded DNA cleavage (*3*, *4*). Due to their mode of action and potency, several analogues of the calicheamicins have been tested in preclinical models as potential antitumor agents. Their development as single agent therapies has not been pursued because of delayed toxicity that limits the therapeutic dose range for treatment. However, their potency makes them appealing candidates for antibody-targeted chemotherapy, where limits in antigen expression make the potency of the cytotoxic agent crucial (*5*–*9*). Even when antigen expression appears to be high enough to allow for the use of less potent agents in animal models (*10*), clinical success has not yet been achieved.

The murine monoclonal antibody CTM01, also known as CT-M-01 or 7F11C7 (*11*), is an internalizing IgG_1 that recognizes the MUC1 antigen present on a broad spectrum of solid tumors of epithelial origin. The MUC1 antigen is a glycoprotein that is expressed on the nonvascular surface of normal epithelial cells, where it is normally inaccessible from circulation. It is present in under-glycosylated form on the nonvascular as well as the vascular surface of a number of epithelial cancer cells, such as breast, lung, ovarian, and colon carcinomas, thereby making it accessible for targeting. This antigen undergoes cycling between the surface and the interior of the cell and carries any bound antibody with it into the cell (*11*). Our results with CTM01 as well as numerous other antibodies suggest that they must be internalized to make effective targeting agents for the calicheamicins (*12*, *13*). CTM01 was selected after comparison of this antibody with a panel of anti-MUC1 monoclonal antibodies (*14*). Successful targeting to tumors in human subjects has been demonstrated (*15*).

The activity of a series of calicheamicin analogues conjugated to CTM01 has previously been described (*16*, *17*). From these studies, the feasibility of conjugating calicheamicin to oxidized carbohydrates on antibodies was established. Using these carbohydrate conjugates, the correlation between the potency of structural analogues of the calicheamicins and their therapeutic potential as conjugates was investigated. Linker variations were also examined in an effort to optimize the therapeutic window for such conjugates. From these studies, NAc-gamma calicheamicin DMH[1] (***3***, Figure 1), which contains a modified aminosugar residue and a disulfide

* To whom correspondence should be addressed. Phone: (845) 602-3423. Fax: (845) 602-5561. E-mail: hamannp@wyeth.com.

[1] Abbreviations: cal equiv, calicheamicin equivalents; DM, dimethyl; DMA, dimethyl acid; DMF, dimethylformamide; DMH, dimethylhydrazide; gamma calicheamicin, calicheamicin γ_1^I; MDR, multidrug resistance; MED, minimum effective dose; MTD, maximum tolerated dose; NAc, *N*-acetyl; OSu ester, *N*-hydroxysuccinimide ester; Pgp, P-glycoprotein; TR, therapeutic ratio (= MTD/MED).

10.1021/bc049795f CCC: $30.25 © 2005 American Chemical Society
Published on Web 02/24/2005

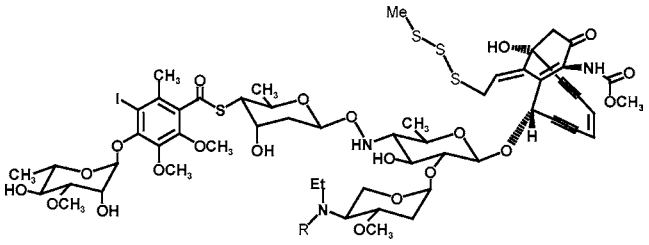

1 Calicheamicin γ_1^I (gamma), R = H
2 NAc-gamma calicheamicin, R = acetyl

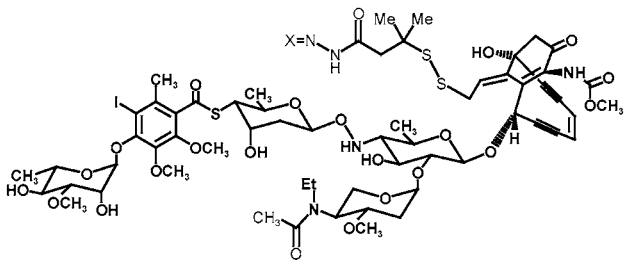

3 NAc-gamma calicheamicin DMH, X = H_2
4 Carbohydrate conjugate, X = Antibody-CH=
(hydrazone with oxidized antibody)

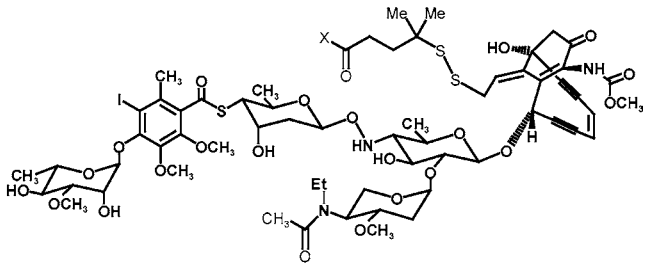

5 NAc-gamma calicheamicin DMA, X = OH
6 NAc-gamma calicheamicin DMA, OSu ester,
X = N-succinimidyloxy
7 Amide conjugate, X = Antibody-NH
(amide bond to lysine groups)

Figure 1. Structures of calicheamicin derivatives and conjugates.

that is sterically hindered by two methyl groups, was chosen as the optimal drug for conjugation.

The carbohydrate conjugate of the anti-CD33 antibody, P67.6, was previously shown to be more efficacious than the corresponding amide conjugate (*18*), presumable due to the need for hydrolytic release of the calicheamicin from the antibody in the acidic lysosomes. In this report, the carbohydrate and amide conjugates of the CTM01 antibody are compared against a variety of tumors of epithelial origin. In contrast to the results with P67.6, both of these classes of conjugates exhibit potent, selective cytotoxicity. However, the amide conjugates show enhanced activity against tumors expressing multidrug resistance (MDR). These studies suggest the hypothesis that attaching a cytotoxic agent, such as calicheamicin, by way of a serum stable linker to an internalizing carrier protein may help to bypass normal membrane-based mechanisms of drug resistance. There is precedence for this with other types of conjugates (*19*), although further research with various drugs and antibodies would be required to adequately define this possibility. Good activity versus a cisplatin-resistant ovarian carcinoma line is also demonstrated.

The amide conjugate selected has been in clinical trials for ovarian cancer (*20*−*22*) as well as lung cancer (unpublished) with only limited evidence of activity. This is in contrast to gemtuzumab ozogamicin (Mylotarg) (*23*), which is an anti-CD33 calicheamicin conjugate approved for AML. The differences that may be responsible for the lesser activity include the presence of circulating antigen (*24*), possible detrimental effects of the predose of native antibody given in an attempt to clear the circulating antigen (*25*), differences in the linkers used (*18*), possible differences in resistance mechanisms (*26*), possible insufficient targeting of the conjugate to large solid tumors, etc. It is also possible that choosing a different tumor type, dosing patient after surgical removal of the primary tumor, or use in combination would show activity. Ongoing efforts may help to clarify these issues. Preclinical data on two more calicheamicin−antibody conjugates have recently been reported (*12*, *13*). Clinical experience with these two conjugates will also expand our understanding of the important issues that need to be addressed in order to make successful chemoimmunoconjugates.

EXPERIMENTAL PROCEDURES

Monoclonal Antibodies. CTM01 is a murine IgG_1 that recognizes the MUC1 (PEM) antigen (*11*). CTM01 was produced and purified from tissue culture supernatants by Celltech. MOPC-21 is a secreted murine myeloma IgG_1 that does not bind to any known antigen (*27*) and was also produced and purified from tissue culture supernatants by Celltech. Lym-1 is a murine IgG_1 reactive with human B-lymphocytes (*28*) and was produced and purified from tissue culture supernatants by Techniclone. These last two antibodies were used as controls.

The radioimmunoassay used for the determination of the immunoreactivity of the conjugates has been described previously (*16*), and involves competition with ^{125}I-labeled CTM01.

Antibody Conjugates. The synthesis of the carbohydrate conjugates (**4**) of NAc-gamma calicheamicin DMH have been reported previously (*16*). Drug loadings of 2 to 3 mol of calicheamicin per mole of antibody were seen and free calicheamicin (predominantly structure **3**) was normally 1−3%.

The procedures for the synthesis of amide conjugates (**7**) have also been published (*18*). Drug loadings of 2 to 3 mol of calicheamicin per mole of antibody were seen and free calicheamicin (predominantly structure **5**) was normally 0.5−1%.

All conjugates were characterized as monomeric by analytical gel-exclusion chromatography (aggregate < 3%) and loading was determined by the ratio of UV absorption at 280 nm (protein) and 333 nm (calicheamicin) as reported (*16*, *18*). Neither conjugation procedure significantly affected the immunoaffinity of the conjugates reported in this paper versus the starting native antibodies, as determined by competitive binding with antibody that had been radiolabeled with ^{125}I-Bolton−Hunter reagent, as detailed below.

Cells and Culture Methods. A549 is a NSC lung carcinoma, ATCC# CCL 185. Raji is a Burkitt's lymphoma cell line, ATCC# CCL 86. OVCAR-3 is an ovarian carcinoma line, ATCC# HTB161. A2780 is an ovarian carcinoma. A2780DDP was derived from A2780 by exposure to cisplatin (*29*) and was a gift from K. L. Scanlon. Lu-78 is a lung carcinoma (*30*). MX-1 is a breast carcinoma line obtained from the NCI. MX-1E was derived from the MX-1 breast carcinoma by exposure to

Table 1. In Vitro Cytotoxicity of CTM01 Carbohydrate and Amide Conjugates[a]

	1 h exposure			continuous exposure		
	IC_{50}, ng/mL[b]			IC_{50}, ng/mL[b]		
sample	MX-1	Raji	select.[c]	MX-1	Raji	select.[c]
CTM01 carbohydrate conjugate (**4**)	12.4	313	1180	0.13	0.11	3.6
CTM01 amide conjugate (**7**)	29.8	>500	>860	0.72	84.4	3800
NAc-gamma calicheamicin (**2**)	154.5	3.03	–	11.77	0.36	–

[a] Results of a single experiment. All IC_{50} values are from well behaved plots of concentration versus inhibition. All IC_{50} values for individual species on each cell line were confirmed in previous and/or subsequent experiments. [b] [^{3}H]Thymidine uptake assay. Doses are given in calicheamicin equivalents. The corresponding concentration of antibody is on average 40-fold greater. [c] Selectivity = IC_{50}(Raji−conjugate)/IC_{50}(MX1−conjugate)/IC_{50}(Raji−NAc-gamma)/IC_{50}(MX1−NAc-gamma).

progressively higher concentrations of gamma calicheamicin and has elevated levels of Pgp. KB8.5 is an MDR cell line derived from the KB oral epidermoid carcinoma (ATCC# CCL17) and was a gift from Drs. Pastan and Gottesman at the NCI. SW620 is a colon carcinoma. SW620R was derived from SW620 by incubation with 20 ng/mL of adriamycin. S1 B1-20 cells were derived from a subclone of LS174T, designated S1, by selection in the presence of bisantrene. The methods used for cell culture have been described previously (*16*).

Photoaffinity assays were performed to determine the tendency of calicheamicin to bind to p-glycoprotein (Table 3.) One hundred micrograms of enriched plasma membranes from S1 of S1-B1-20 cells was incubated in 4 nM IAAP (^{125}I-iodoarylazidoprazosin, 2200 Ci/mmol; DuPont-NEN) with or without test agent as previously described (*31*). S1-B1-20 cells overexpress Pgp and have the MDR phenotype. After 1 h incubation at 25 °C and UV irradiation (5 min, 4 °C), material was solubilized in Laemmli sample buffer and resolved on SDS−PAGE. Gels were dried and subjected to autoradiography. Radioactive bands that contained IAAP bound to Pgp were identified, cut from the gel, and counted in a gamma counter. Binding of calicheamicin to Pgp caused an inhibition of this binding and, hence, lowered the amount of radioactivity associated with the Pgp.

In Vitro Cytotoxicity Assays. Two different assays were used to evaluate cytotoxicity in cell culture: a 1-h limited exposure to treatment and continuous exposure. For both assays, concentrations of the test substances were all normalized to equivalents of calicheamicin (NAc-gamma DMH or NAc-gamma DMA, both 1478 Da) and a medium control was included. All samples were run in triplicate. For the 1-h assay, viable cells (10^5/0.2 mL) were aliquoted into 15 mL test tubes which contained 0.2 mL of the sample to be tested at the appropriate concentration. Tubes were vortexed and incubated at 37 °C. The pellets were washed twice after 1 h with 8 mL of medium and 1 mL of medium was added to each pellet. The cells were then vortexed and 0.2 mL of suspended cells was removed and placed in a well of a 96-well plate (2×10^4 cells). For the continuous assay, triplicate 0.1 mL aliquots of cell suspension were added to microtiter wells already containing 0.1 mL aliquots of sample. For both assays, the cells were incubated for 3 days, at which time 0.1 mL of supernatant was removed and replaced with 0.2 μCi of [^{3}H]thymidine in 0.1 mL of fresh medium. Incubation was resumed for an additional 24 h at which point the cells were harvested and counted. Growth inhibition curves of each drug or conjugate were plotted and the IC_{50} value (concentration of drug equivalents needed for 50% [^{3}H]thymidine uptake inhibition) of each sample was determined.

In Vivo Tests for Antitumor Activity. The cell lines were passaged as ascites tumors in athymic mice or in tissue culture, and, for each experiment, 8×10^6 cells were routinely implanted subcutaneously. Tumors were allowed to become established for 4 days or longer to achieve a size of 50−300 mg prior to dosing ip at the indicated doses on days 1, 5, and 9 after staging. There were five or six mice per test group and 10 in the buffer-treated control group. Tumor mass was determined by measuring the tumor length and width once weekly for at least 28 days post tumor staging. Antitumor activity was defined by the ratio of tumor size of the treated animals and those of the controls (T/C). An agent was considered active if it had a sustained T/C of at least 58% with greater than 65% survivors. A therapeutic ratio (TR) was defined as the maximum tolerated dose/minimum effective dose (MTD/MED) and used as a measure of the therapeutic window for the conjugates or drugs tested.

RESULTS

Carbohydrate and Amide Conjugates of CTM01. Calicheamicin was conjugated to CTM01 by two methods. One method involved oxidizing the naturally occurring carbohydrates of the antibody and reacting the resultant aldehydes with a calicheamicin derivative referred to as NAc-gamma calicheamicin DMH (**3**). (See Figure 1 for structures.) This method gave a "carbohydrate conjugate" containing a hydrazone bond that is hydrolytically labile, especially at the low pH found in lysosomes (*32*, *33*). The second method involved reacting the ϵ-amino groups of lysines on the antibody with a calicheamicin derivative referred to as NAc-gamma calicheamicin DMA, OSu ester (**6**). This method gave an "amide conjugate" which does not have a bond that is hydrolytically labile under physiological conditions. Both of these conjugates contain a disulfide bond that can react with glutathione (or other cellular thiol) to release the calicheamicin from the antibody.

Comparative in Vitro Activity. Previous work showed that carbohydrate conjugates of calicheamicin and CTM01 (**4**) are potently and selectively cytotoxic toward MUC1-expressing cell lines in tissue culture (*16*). Table 1 shows representative data for a comparison of that conjugate with the amide conjugate. Both these conjugates, as well as unconjugated NAc-gamma calicheamicin (**2**), were incubated with either the antigen-positive MX-1 line or the antigen negative Raji cell line for either 1 h or continuously as indicated. Cytotoxicity of the two conjugates and an unconjugated calicheamicin derivative is compared using IC_{50}s expressed in equivalents of calicheamicin (NAc-gamma calicheamicin DMH, ***3***).

With a 1-h drug exposure period, the conjugates are 5 to 12-fold more cytotoxic toward the antigen expressing MX-1 cells than NAc-gamma calicheamicin (**2**) and at least 100-fold less cytotoxic than compound **2** toward the antigen negative Raji cells. Each of the conjugates, therefore, shows about 1000-fold selectivity for the target

Table 2. In Vitro Selectivity of the CTM01 Amide Conjugate versus a Conjugate of a Nonbinding Control Antibody

	IC_{50}, ng/mL cal equiv, 1 h exposure		
cell line	CTM01 conjugate (**7**)	MOPC-21 conjugate (**7**)	select.[a]
A2780DDP	2.4	189	79
ZR-75−1	6.6	>500	>76

[a] Selectivity = IC_{50}(MOPC-21 conjugate) ÷ IC_{50}(CTM01 conjugate).

versus nontarget lines when corrected for the difference in drug sensitivity. With continuous exposure (four-day), the amide conjugate retains this selectivity, although all the IC_{50}s are shifted to far lower values. However, the carbohydrate conjugate loses much of its selectivity due to increased activity on the antigen negative line, presumably due to extracellular hydrolytic release of the calicheamicin derivative in the medium. Some selectivity is still retained if the difference in sensitivity of the two cell lines with respect to NAc-gamma calicheamicin (**2**) is considered.

Comparative in Vitro Activity. In vitro specificity of the CTM01 carbohydrate conjugate with respect to a nonbinding control conjugate has previously been demonstrated (16). The selectivity of the CTM01 amide conjugate was likewise confirmed in a series of experiments in which it was compared with an isotype-matched amide conjugate, prepared with the nontargeting antibody MOPC-21. In vitro cytotoxicity comparisons of the CTMO1 and MOPC-21 amide conjugates and NAc-gamma calicheamicin (**2**) were made in a number of different MUC1-expressing cell lines. MUC1 expression was determined by the ability of the cells to selectively bind radiolabeled CTM01. As shown in Table 2, both the A2780DDP line as well as the ZR-75-1 line show selectivity comparable to that seen previously with CTM01 carbohydrate conjugates.

Comparative in Vivo Activity. Previous work has shown that carbohydrate conjugates of CTM01 were active in multiple xenograft tumor models with long-term, tumor-free survivors being common (*16*). Significant growth inhibition of many MUC1 expressing tumors was also seen with the CTM01 amide conjugate, also with long-term, tumor-free survivors. In the experiment shown in Figure 2, treatment of athymic mice bearing 50 mg subcutaneous tumors with the CTM01 amide conjugate produced dose-dependent growth inhibition of a non small cell lung tumor, Lu-78. The CTM01 amide conjugate was active over a 6-fold dose range and produced complete regressions of the tumor in 10 of 12 animals treated at the two highest doses of 200 and 300 μg/kg given three times. In contrast, a comparable conjugate prepared with the nonbinding MOPC-21 antibody failed to produce sustained inhibition of the tumor growth at the maximum tolerated dose of 300 μg/kg. NAc-gamma calicheamicin (**2**) was included in this test as a control and was lethal at doses greater than 25 μg/kg and produced no sustained responses at nonlethal doses. Similar results were obtained for all treatments in a repeat experiment with tumors that were approximately 300 mg in size at dosing (data not shown).

Pronounced antitumor effects have been observed with both the CTM01 carbohydrate and amide conjugates in additional MUC1-expressing xenograft tumors, including two ovarian carcinomas, OVCAR-3 and A2780 (data not shown). These conjugates were active against these

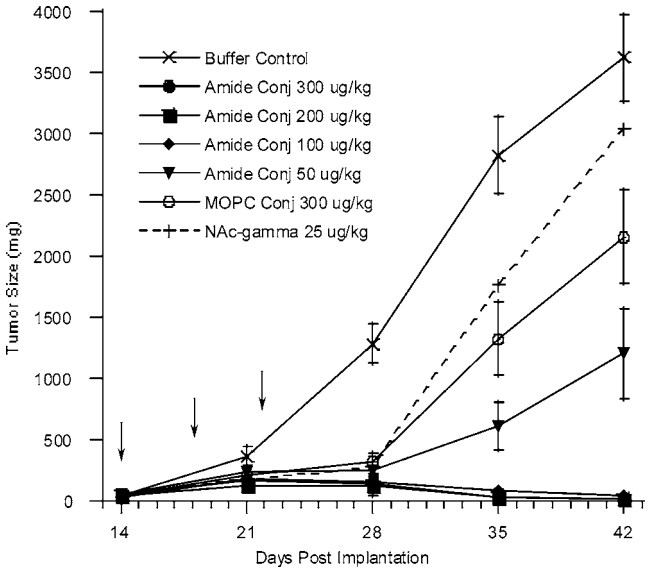

Figure 2. Time-course of the response of Lu-78 xenograft tumors to the CTM01 amide conjugate (**7**), to a similar control conjugate (**7**) made with the nonbinding MOPC-21 antibody, and to treatment with a representative calicheamicin derivative alone. Athymic mice were implanted sc with Lu-78 cells and then dosed when tumors were approximately 50 mg in size. The doses indicated were given on days 14, 18, and 22, as indicated by the arrows, and are given in calicheamicin equivalents. The corresponding concentration of antibody is 40-fold greater. There were no deaths in any group, except for one with NAc-gamma calicheamicin. Error bars are SEMs and were omitted for NAc-gamma calicheamicin (dosed at the MTD) for clarity.

subcutaneous tumors in nude mice over a 4- to 6-fold dose range, expressed in terms of drug equivalents, with an MED of 50 μg/kg/dose × 3 doses and an MTD of >300 μg/kg × 3. As with the Lu-78 study shown in Figure 2, the top nonlethal dose of NAc-gamma calicheamicin (**2**) was lower than the MED for the conjugate and at that dose no sustained antitumor effects were seen with this or other unconjugated calicheamicin derivatives.

Figure 3 shows a comparison between an amide and carbohydrate conjugate of CTM01 on the more difficult to treat nonsmall cell lung carcinoma A549 where the carbohydrate conjugate showed somewhat reduced antitumor effects at lower doses and thus was effective over only a two to 3-fold dose range, instead of the four to 6-fold range seen with the amide conjugates.

In Vitro MDR Results. Screening of the calicheamicin family in vitro indicated that these compounds can serve as substrates for Pgp and thus might be less active against tumors expressing the MDR phenotype. Table 3 shows the results of photoaffinity labeling experiments with Pgp comparing calicheamicin with the known substrate vincristine. A 50-, 500-, and 5000-fold excess of gamma calicheamicin effectively inhibited the photoaffinity labeling of Pgp with 4 nM [^{125}I]-iodophenylazidoprazosin. These data indicate that calicheamicin binds to Pgp nearly as well as vinblastine.

Because of the assumed detrimental consequences of MDR on the clinical use of calicheamicin conjugates, the CTM01 amide conjugate has been compared in tissue culture against a parental cell line and a subclone expressing Pgp. In Table 4, the cytotoxicity of NAc-gamma calicheamicin (**2**) toward the antigen-expressing tumor line, SW620, and its adriamycin-resistant subclone, SW620R, are compared. The MDR ratio as defined in the table is a measure of the reversal of resistance quinidine exhibits on the SW620R cell line corrected for the effects of quinidine on the SW602 parental line. A

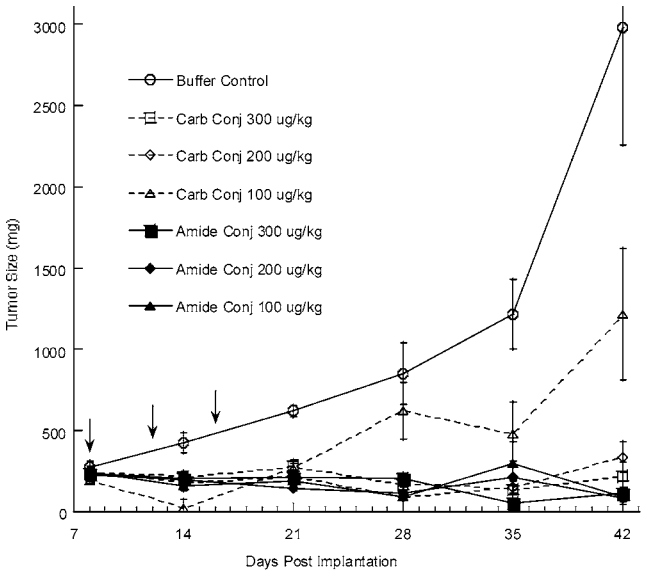

Figure 3. Response of A549 xenograft tumors to the CTM01 amide (**7**) and carbohydrate (**4**) conjugates. Athymic mice were implanted sc with A549 cells and then dosed when tumors were approximately 250 mg in size. The doses indicated were given on days 8, 12, and 16, as indicated by the arrows, and are given in calicheamicin equivalents. The corresponding concentration of antibody is 40-fold greater. Error bars are SEMs.

Table 3. Photoaffinity Labeling of Pgp in the Presence of Gamma Calicheamicin

drug	concn (μM)	vs control, %	±SE[a]	no. exp.
vinblastine	0.2	27	±16	2
	2.0	3.8	±1.7	6
	20	1.8	±1.6	8
gamma calicheamicin (**1**)	0.2	43		1
	2.0	12.3	±5.2	4
	20	1.9	±1.6	2

[a] Standard error of the mean.

Table 4. In Vitro Cytotoxicity of the CTM01 Amide Conjugate and a Nonbinding Control Conjugate versus Adriamycin-Resistant Cells

	IC_{50}, ng/mL cal equiv				
	SW620		SW620R		
sample	−Q[a]	+Q[a]	−Q[a]	+Q[a]	ratio[b]
NAc-gamma calicheamicin (**2**)	0.7	0.18	64.5	2.9	5.7
CTM01 amide conjugate (**7**)	1.0	0.25	3.6	0.6	1.5
Lym-1 amide conjugate (**7**)[c]	294	91.0	>500	401	>0.4

[a] −Q, +Q = without or with 1.2 μg/mL quinidine added. [b] Ratio = IC50(−Q, SW620R)/IC_{50}(+Q, SW620R)/IC_{50}(−Q, SW620)/IC_{50}(+Q, SW620). [c] Nonbinding control conjugate.

high ratio results from a large shift in the IC_{50} relative to that seen in the parental line and implies a high degree of MDR resistance, while a ratio of one would imply no resistance, as far as quinidine at this concentration is able to reverse it. The higher ratio for NAc-gamma calicheamicin confirms the role of Pgp in the SW620R cell lines. The much lower ratio for the CTM01 amide conjugate indicates that MDR is significantly less important for this conjugate.

In Vivo MDR Results. The human epidermoid xenograft tumor, KB8.5, has the MDR phenotype (*34*) and also expresses the MUC1 antigen. In the study described in Figure 4, a comparison was made of the carbohydrate and amide conjugates of CTM01 over a 6-fold dose range. In this study, NAc-gamma calicheamicin DMH (**3**) and

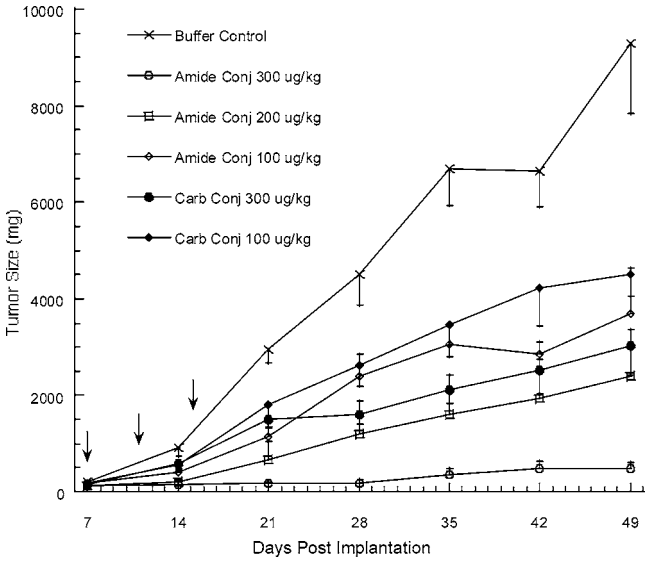

Figure 4. Response of MDR-resistant KB8.5 xenograft tumors to the CTM01 amide (**7**) and carbohydrate (**4**) conjugates. Athymic mice were implanted sc with KB8.5 cells and then dosed when tumors were approximately 200 mg in size. The doses indicated were given on days 7, 11, and 15, as indicated by the arrows, and are given in calicheamicin equivalents. The corresponding concentration of antibody is 40-fold greater. Error bars are SEMs and are given in the negative direction for buffer and the carbohydrate conjugate and in the positive direction for the amide conjugate. (The 200 μg/kg dosing group for the carbohydrate conjugate was omitted due to unusually large variability in that group.)

NAc-gamma calicheamicin DMA (**5**) were included as controls (data not shown). At the maximum tolerated doses of 200 μg/kg given three times, NAc-gamma calicheamicin DMA was completely ineffective while NAc-gamma calicheamicin DMH showed only marginally significant activity. The CTM01 amide conjugate showed pronounced activity over a 4-fold dose range of 100 to 400 μg/kg with two deaths seen in the 400 μg/kg treatment group (not plotted) and with no deaths at lower doses. In contrast, the carbohydrate conjugate was uniformly toxic at the 400 μg/kg dose (not plotted) and showed more modest activity at the 100 and 300 μg/kg doses.

In Vivo Platinum Resistance. The choice between the CTM01 amide and carbohydrate conjugates has also been examined with respect to the potential cross resistance to cisplatin-resistant tumors using the ovarian carcinoma line A2780 and its cisplatin-resistant subclone A2780DDP. Selective in vitro activity against the cisplatin-resistant line was shown in Table 2. Both the CTM01 amide and carbohydrate conjugates gave long-term tumor-free survivors in xenograft experiments with the parental A2780 ovarian line at the maximum tolerated dose and also at 50% of the usual maximum tolerated dose (data not shown). Although these conjugates are less effective against the cisplatin-resistant A2780DDP line, the amide conjugate was still significantly active over a 6-fold dose range of 50 to 300 μg/kg and produced dose-dependent inhibition of the tumor growth (Figure 5). In comparison with the CTM01 amide conjugate, the CTM01 carbohydrate conjugate caused more deaths at the 300 μg/kg dose (three deaths out of six animals versus none), was equally effective at the 150 μg/kg dose, and was somewhat less effective at the 50 μg/kg dose.

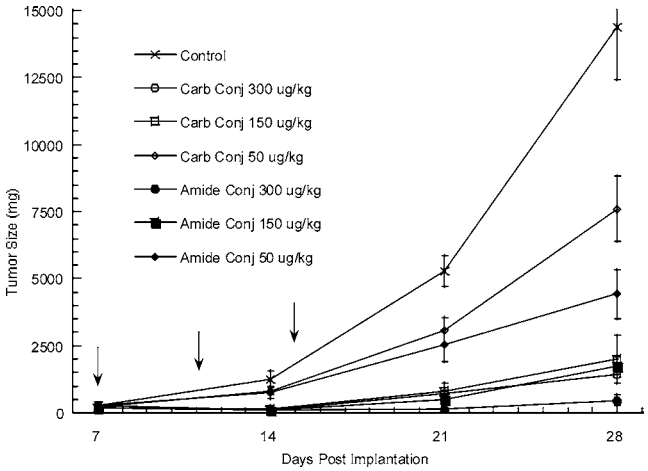

Figure 5. Response of cisplatin-resistant A2780DDP xenograft tumors to the CTM01 amide (**7**) and carbohydrate (**4**) conjugates. Athymic mice were implanted sc with A2780DDP cells and then dosed when tumors were approximately 250 mg in size. The doses indicated were given on days 7, 11, and 15, as indicated by the arrows, and are given in calicheamicin equivalents. The corresponding concentration of antibody is 40-fold greater. Error bars are SEMs.

DISCUSSION

The MUC1 antigen is a glycoprotein that is expressed on the nonvascular surface of normal epithelial cells, where it is normally inaccessible from circulation. It is also present in under-glycosylated form on the nonvascular as well as the vascular surface of a number of epithelial cancer cells, such as breast, non small cell lung, ovarian, and colon carcinomas. Successful targeting of the CTM01 antibody to tumor sites in human subjects has been demonstrated (*15*). MUC1 undergoes cycling between the surface and the interior of the cell (*11*) and carries the bound CTM01 with it into the cell. Our results with CTM01 as well as with a number of other antibodies suggest that drug conjugates must be internalized to be effective targeting agents.

Our previous reports on conjugates prepared with CTM01 concerned carbohydrate conjugates which were designed to release the drug in the acidic lysosomes by acid-catalyzed hydrolysis. The amide conjugates described herein have equivalent activity to that of the carbohydrate conjugates in many in vitro and in vivo test systems (e.g., Figures 2 and 3). These data show that the hydrolytic release inherent in the carbohydrate conjugates offers no known advantage for calicheamicin conjugates of CTM01. This stands in marked contrast to calicheamicin conjugates of another antibody, the anti-CD33 P67.6, which require hydrolytic release of the drug for optimum activity (*35*).

The mode of release for the amide conjugates is presumed to be disulfide exchange with reduced glutathione (*2*), which is at 100-fold higher concentrations inside most cells than in circulation (*36, 37*). This disulfide exchange is closely tied to the triggering of the calicheamicins that is required for the double-stranded DNA cleavage (*2*). Unfortunately, the potency of the calicheamicins and the consequential low concentrations of drug in cells required to produce cytotoxicity has precluded attempts to determine the site or rate of release of any calicheamicin derivatives from the CTM01 conjugates in cellular systems.

Although the CTM01 amide conjugate is in many cases equivalent to the carbohydrate conjugate, there are circumstances where the amide conjugate is superior. The in vitro data from Table 1 clearly shows that when cells are exposed to the carbohydrate conjugate for extended periods of time, there is an erosion of the selectivity, presumably due to the slow, extracellular, hydrolytic release of the cytotoxic calicheamicin derivative. This is consistent with the somewhat increased toxicity of the CTM01 carbohydrate conjugate over that of the CTM01 amide conjugate in numerous xenograft experiments as well as in preclinical toxicology assessments (data not included). Similar observations were made in earlier work that showed that increasing the stability of the disulfide decreased the toxicity of the conjugates (*17*). The toxicity seen with the less stable disulfides is presumed to be due to premature reductive release of a cytotoxic calicheamicin derivative in circulation.

The CTM01 amide conjugate also retains its selectivity in vitro when compared with a nonbinding control conjugate. This is shown in Table 2 for the nonbinding MOPC-21 antibody versus two different cell lines.

An important issue in the development of a potential therapy for solid tumors is the effect of resistance that might inherently exist or may have developed to previous chemotherapies. It is clear from the binding data in Table 3 that the calicheamicins are recognized by Pgp. The data in Table 4 further shows that cells which display the MDR phenotype are cross-resistant to calicheamicin, and that this resistance is reversed by standard reversal agents, such as quinidine. It has also been shown that incubating the MX-1 cell line with sublethal concentrations of gamma calicheamicin created a resistant subclone, MX-1E, that overexpressed Pgp. These MX-1E cells were cross-resistant to vincristine and adriamycin.

As shown in Figure 4, Pgp-mediated resistance is another circumstance where the amide conjugate is superior to the carbohydrate conjugate. The KB8.5 tumor line has an 8.5-fold increase in Pgp expression (*38*). These data, together with the in vitro studies described above, support the conclusion that a significant increase in sensitivity to the calicheamicins is achieved in resistant cells by conjugation of the drug to an internalizing antibody, especially through a stable amide linker.

Due to the presumed importance of glutathione in the chemistry of calicheamicin and its conjugates, it was of interest to examine cisplatin-resistant cell lines, where glutathione levels tend to be increased (*39*). Preliminary data suggest that the higher intracellular levels of glutathione may actually promote cleavage of the disulfide bond in calicheamicin conjugates and activate the drug. This may partly explain why the CTM01 amide conjugate is quite active against the A2780DDP cell line in vivo as shown in Figure 5. This is in spite of the fact that the calicheamicins are DNA active agents and that the A2780DDP cell line tends to be resistant to most DNA-damaging agents, in part due to a 2-fold increase in intracellular glutathione levels (*40*, *41*).

For the antibody P67.6, a site of hydrolytic release was necessary and the corresponding amide conjugate had much lower selectivity and potency (*18*). This is in stark contrast to the results in this report. An explanation of these somewhat contradictory results will require detailed studies on the mechanism of antibody processing for both antibodies in their respective target cell lines. One possibility that might be speculated is that the carbohydrate conjugates release the calicheamicin closer to the surface, allowing for easier access to the Pgp pump, while the amide conjugates may undergo the release of the calicheamicin at an unknown site closer to the DNA than the cell surface, thereby avoiding the Pgp pump to some extent. Another possibility is that the derivatives

released from the carbohydrate conjugates, NAc-gamma calicheamicin DMH, may simply be pumped better than the unknown derivative or derivatives released from the amide conjugate. However, the most important conclusion from the P67.6 and CTM01 calicheamicin conjugates is that one optimal design of conjugate does not exist for all antibodies. Each antibody must be examined separately, and a variety of different types of conjugates must be tried in order to individually optimize a specific delivery system.

In the case of P67.6, the incorporation of a site of hydrolytic release was crucial for the success of the conjugate. This site helped make the conjugate a potent and selective agent targeted toward CD33 positive cells in cell culture, xenograft experiments, and ex vivo models of AML. Subsequent optimization of the design of a hydrolytically labile linker resulted in the "hybrid" linker found in the approved antibody targeted chemotherapeutic agent gemtuzumab ozogamicin (Mylotarg) for use in AML (*42*, *43*). In contrast, the amide conjugate of CTM01 is every bit as potent and selective as the CTM01 carbohydrate conjugate against many tumor lines both in vitro and in vivo. However, the amide conjugate more successfully overcomes MDR resistance in a xenograft model of a cell line that overexpresses Pgp. There is precedence for overcoming MDR resistance by intracellular delivery of cytotoxic agents with the delivery of doxorubicin via folate-targeted liposomes (*44*). In addition, the amide conjugate of CTM01 is effective against a cisplatin-resistant cell line.

In conclusion, the calicheamicin conjugates, especially the "amide conjugate", show significant promise for targeted delivery. Through the process of antibody conjugation, a potent cytotoxic agent can be converted into an effective antitumor agent, with a significant therapeutic window for treating solid tumors in preclinical models. A conjugate made with a genetically engineered human version of CTM01 has been in clinical trials (*20*, *21*) (see the Introduction for discussion) and is the subject of another report (*45*).

ACKNOWLEDGMENT

We thank George Ellestad and May Lee for helpful discussions about calicheamicin chemistry. We are also grateful to Lucy Colina for her help with the biological testing of the conjugates and to Martha Godwin and J. Philip James for their assistance in conjugate preparation and purification.

LITERATURE CITED

(1) Lee, M. D., Dunne, T. M., Siegel, M. M., Chang, C. C., Morton, G. O., and Borders, D. B. (1987) Calicheamicins, a novel family of antitumor antibiotics, 1. Chemistry and partial structure of calicheamicin γ_1^I. *J. Am. Chem. Soc. 109*, 3464−3466.

(2) Myers, A. G., Cohen, S. B., and Kwon, B. M. (1994) A study of the reaction of Calicheamicin γ_1^I with glutathione in the presence of double-stranded DNA. *J. Am. Chem. Soc. 116*, 1255−1271.

(3) Ellestad, G. A., Ding, W.-D., Zein, N., and Townsend, C. A. (1995) DNA-cleaving properties of calicheamicin γ_1. *Enediyne Antibiotics as Antitumor Agents* (Borders, D. B., and Doyle, T. W., Eds.) pp 137−160, Marcel Dekker, New York.

(4) Lee, M. D., Ellestad, G. A., and Borders, D. B. (1991) Calicheamicins: Discovery, structure, chemistry, and interaction with DNA. *Acc. Chem. Res. 24*, 235−243.

(5) Liu, C., and Chari, R. V. J. (1997) The development of antibody delivery systems to target cancer with highly potent maytansinoids. *Expert Opin. Invest. Drugs 6*, 169−172.

(6) Chari, R. V. J., Jackel, K. A., Bourret, L. A., Derr, S. M., Tadayoni, B. M., Mattocks, K. M., Shah, S. A., Liu, C., Blättler, W. A., and Goldmacher, V. S. (1995) Enhancement of the selectivity and antitumor activity of a CC-1065 analog through immunoconjugate formation. *Cancer Res. 55*, 4079−4084.

(7) King, H. D., Staab, A. J., Pham-Kaplita, K., Yurgaitis, D., Firestone, R. A., Lasch, S. J., and Trail, P. A. (2003) BR96 conjugates of highly potent anthracyclines. *Bioorg. Med. Chem. Lett. 13*, 2119−2122.

(8) Doronina, S. O., Toki, B. E., Torgov, M. Y., Mendelsohn, B. A., Cerveny, C. G., Chace, D. F., DeBlanc, R. L., Gearing, R. P., Bovee, T. D., Siegall, C. B., Francisco, J. A., Wahl, A. F., Meyer, D. L., and Senter, P. D. (2003) Development of potent monoclonal antibody auristatin conjugates for cancer therapy. *Nat. Biotechnol. 21*, 778−784 and 941a.

(9) Baloglu, E., Miller, M. L., Roller, E. E., Leece, B. A., Goldmacher, V. S., and Chari, R. V. J. (2003) Studies toward novel taxoid-monoclonal antibody conjugates. *Abstracts of Papers*, 226th American Chemical Society National Meeting, New York, NY September 7−11, 2003, American Chemical Society: Washington, DC, 2003; MEDI-261.

(10) Trail, P. A., Willner, D., Lasch, S. J. Henderson, A. J., Hofstead, S., Casazza, A. M., Firestone, R. A., Hellström, I., and Hellström, K. E. (1993) Cure of xenografted human carcinomas by Br96-doxorubicin immunoconjugates. *Science 261*, 212−215.

(11) Aboud-Pirak, E., Sergent, T., Otte-Slachmuylder, C., Abarca, J., Trouet, A., and Schneider, Y. J. (1988) Binding and endocytosis of a monoclonal antibody to a high molecular weight human fat globule membrane-associated antigen by cultured MCF-7 breast carcinoma cells. *Cancer Res. 48*, 3188−96.

(12) DiJoseph, J. F., Armellino, D. C., Boghaert, E. R., Khandke, K., Dougher, M., Sridharan, L., Kunz, K., Hamann, P. R., Gorovits, B., Udata, C., Moran, J. K., Popplewell, A. G., Stephens, S., Frost, P., and Damle, N. K. (2004) Antibody-targeted chemotherapy with CMC-544: A CD22-targeted immunoconjugate of calicheamicin for the treatment of B lymphoid malignancies. *Blood 103*, 1807−1814.

(13) Boghaert, E. R., Sridharan, L., Armellino, D. C., Khandke, K. M., DiJoseph, J. F., Kunz, A., Dougher, M. M., Jiang, F., Kalyandrug, L. B., Hamann, P. R., Frost, P., and Damle, N. K. (2004) Antibody-targeted chemotherapy with the calicheamicin conjugate hu3S193-*N*-acetyl γ calicheamicin dimethyl hydrazide targets Lewis^Y and eliminates Lewis^Y-positive human carcinoma cells and xenografts. *Clin. Cancer Res. 10*, 4538−4549.

(14) Baker, T. S., Bose, C. C., Caskey-Finney, H. M., King, D. J., Lawson, A. D,. Lyons, A., Mountain, A., Owens, R. J., Rolfe, M. R., Sehdev, M., Yarranton, G. T., and Adair, J. R. (1994) Humanization of an anti-mucin antibody for breast and ovarian cancer therapy. *Adv. Exp. Med. Biol. 1994*, 35361−35382.

(15) Prinssen, H. M., Molthoff, C. F., Verheijen, R. H., Broadhead, T. J., Kenemans, P., Roos, J. C., Davies, Q., van Hof, A. C., Frier, M., den Hollander, W., Wilhelm, A. J., Baker, T. S., Sopwith, M., Symonds, E. M., and Perkins, A. C. (1998) Biodistribution of ^{111}In-labeled engineered human antibody CTM01 (hCTM01) in ovarian cancer patients: Influence of prior administration of unlabeled hCTM01. *Cancer Immunol. Immunother. 47*, 39−46.

(16) Hinman, L. M., Hamann, P. R., Wallace, R., Menendez, A. T., Durr, F. E., and Upeslacis, J. (1993) Preparation and characterization of monoclonal antibody conjugates of the calicheamicins: A novel and potent family of antitumor antibiotics. *Cancer Res. 53*, 3336−3342.

(17) Hinman, L. M., Hamann, P. R., and Upeslacis, J. (1995) Preparation of conjugates to monoclonal antibodies. *Enediyne Antibiotics as Antitumor Agents* (Borders, D. B., and Doyle, T. W., Eds.) pp 87−105, Marcel Dekker, New York.

(18) Hamann, P. R., Hinman, L. M., Beyer, C. F., Lindh, D., Upeslacis, J., Flowers, D. A., and Bernstein, I. (2002) An anti-CD33 antibody-calicheamicin conjugate for treatment of acute myeloid leukemia, choice of linker. *Bioconjugate Chem. 13*, 40−46.

(19) Goren, D., Horowitz, A. T., Tzemach, D., Tarshish, M., Zalipsky, S., and Gabizon, A. (2000) Nuclear delivery of doxorubicin via folate-targeted liposomes with bypass of multidrug-resistance efflux pump. *Clin. Cancer Res. 6*, 1949−1957.

(20) Gillespie, A. M., Broadhead, T. J., Chan, S. Y., Owen, J., Farnsworth, A., Sopwith, M., and Coleman, R. E. (2000) Phase I open study of the effects of ascending doses of the cytotoxic immunoconjugate CMB-401 (hCTM01-calicheamicin) in patients with epithelial ovarian cancer. *Ann. Oncol. 11*, 735−41.

(21) Chan, S. Y., Gordon, A. Y., Coleman, R. Y., Hall, J. Y., Berger, M. S., Sherman, M. Y., Eten, C. Y., and Finkler, N. Y. (2003) A phase 2 study of the cytotoxic immunoconjugate CMB-401 (hCTM01-calicheamicin) in patients with platinum-sensitive recurrent epithelial ovarian carcinoma. *Cancer Immunol. Immunother. 52*, 243−248.

(22) Broadhead, T. J., Gillespie, A. M., Coleman, R. E., Owen, J., Skelton, L., Stephens, S., Farnsworth, A., Sopwith, M., and Chan, S. Y. (1998) Phase I study of the cytotoxic immunoconjugate CMB-401 (hCTM01-calicheamicin) in patients with epithelial ovarian cancer: Immune response and pharmacokinetics following repeated intravenous administration. *Proceedings of the American Society of Clinical Oncology*, ASCO Annual Meeting, May 16−19, 1998, Los Angeles, CA, American Society of Clinical Oncology: Alexandria, VA, 1998, abstract 1693.

(23) Bross, P. F., Beitz, J., Chen, G., Chen, X. H., Duffy, E., Kieffer, L., Roy, S., Sridhara, R., Rahman, A. R., Williams, G., and Pazdur, R. (2001) Approval summary: Gemtuzumab ozogamicin in relapsed acute myeloid leukemia, *Clin. Cancer Res. 7*, 1490−1496.

(24) Davies, Q., Perkins, A. C., Fries, M., Watson, S., Lalani, E.-N., and Symonds, E. M. (1997) The effect of circulating antigen on the biodistribution of the engineered human antibody hCTM01 in a nude mice model. *Eur. J. Nuclear Med. 24*, 206−209.

(25) Broadhead, T. J., Davies, Q., Van Hof, A. C., Molthoff, C. F. M., Perkins, A. C., Roos, J. C., Prinssen, W. M., Verheijen, R. H. M., den Hollander, W., Sopwith, M., Frier, M., Kenemans, P., and Symonds, E. M. (1998) Clinical study to investigate the potential of an engineered human monoclonal antibody, hCTM01, for targeted chemotherapy of ovarian cancer. *Tumor Target. 3*, 55−57.

(26) Walter, R. B., Raden, B. W., Cronk, M. R., Bernstein, I. D., Appelbaum, F. R., and Banker, D. E. (2004) The peripheral benzodiazepine receptor ligand PK11195 overcomes different resistance mechanisms to sensitize AML cells to gemtuzumab ozogamicin. *Blood 103*, 4276−4284.

(27) Melchers, F. (1970) Biosynthesis of the carbohydrate portion of immunoglobulins. *Biochem. J. 119*, 765−772.

(28) Epstein, A., Marder, R. J., Winter, J., Stathopoulos, E., Chen, F.-M., Parker, J. W., and Taylor, C. R. (1987) Two new monoclonal antibodies, Lym-1 and Lym-2, reactive with human B-lymphocytes and derived tumors, with immunodiagnostic and immunotherapeutic potential. *Cancer Res. 47*, 830−840.

(29) Newman, E. M., Lu, Y., Kashani-Sabet, M., Kesavan, V., and Scanlon, K. J. (1988) Mechanisms of cross-resistance to methotrexate and 5-fluorouracil in an A2780 human ovarian carcinoma cell subline resistant to cisplatin. *Biochem. Pharmacol. 37*, 443−447.

(30) Wallace, R. E., Lindh, D., and Durr, F. E. (1989) Arabinofuranosyl-5-azacytosine: Activity against human tumors in athymic mice. *Cancer Chemother. Pharm. 25*, 117−123.

(31) Zhang, X. P., Ritke, M. K., Yalowich, J. C., Slovak, M. L., Ho, J. P., Collins, K. I., Annable, T., Arceci, R. J., Durr, F. E., and Greenberger, L. M. (1994) P-glycoprotein mediates profound resistance to bisantrene. *Oncol. Res. 6*, 291−301.

(32) Van Dyke, R. W., Root, K. V., Schreiber, J. H., and Wilson, J. M. (1992) Role of CFTR in lysosomal acidification. *Biochem. Biophys. Res. Commun. 184*, 300−305.

(33) Ohkuma, S., and Poole, B. (1978) Fluorescence probe measurement of the intralysosomal pH in living cells and the perturbation of pH by various agents. *Proc. Natl. Acad. Sci. U.S.A. 75*, 3327−3331.

(34) Shen, D.-W., Fojo, A., Chin, J. E., Roninson, I. B., Richet, N., Pastan, I., and Gottesman, M. M. (1986) Human multidrug-resistant cell lines: Increased MDR1 expression can precede gene amplification. *Science 232*, 643−645.

(35) Hamann, P. R., Hinman, L. M., Hollander, I., Beyer, C. F., Lindh, D., Holcomb, R., Hallett, W., Upeslacis, J., Shochat, D., Mountain, A., Flowers, D. A., and Bernstein, I. (2002) A potent and selective anti-CD33 antibody-calicheamicin conjugate for treatment of acute myeloid leukemia. *Bioconjugate Chem. 13*, 47−58.

(36) Mamsoor, M. A., Svardal, A. M., and Ueland, P. M. (1992) Determination of the in vivo redox status of cysteine, cysteinylglycine, homocysteine, and glutathione in human plasma. *Anal. Biochem. 200*, 218−229.

(37) Mistry, P., and Harrap, K. R. (1991) Historical aspects of glutathione and cancer chemotherapy. *Pharm. Ther. 49*, 125−132.

(38) Shen, D.-W., Cardarelli, C., Hwang, J., Cornwell, M., Richet, N., Ishii, S., Pastan, I., and Gottesman, M. M. (1986) Multiple drug-resistant human KB carcinoma cells independently selected for high-level resistance to colchicine, adriamycin, or vinblastine show changes in expression of specific proteins. *J. Biol. Chem. 261*, 7762−7770.

(39) El-Akawi, Z. Zdanowicz, J., Creaven, P. J., Abu-Hadid, M., Perez, R., and Pendyala, L. (1996) Induction of γ-glutamyl transpeptidase mRNA by platinum complexes in a human ovarian carcinoma cell line. *Oncol. Res. 8*, 415−423.

(40) Goto, S., Yoshida, K., Morikawa, T. Urata, Y., Suzuki, K., and Kondo, T. (1995) Augmentation of transport for cis-platin-glutathione adduct in cisplatin-resistant cancer cells. *Cancer Res. 55*, 4297−4301.

(41) Okuno, S., Sato, H., Kuriyama-Matsumura, K., Tambe, M., Wang, H., Sodha, S., Hamada, H., Yoshikawa, H., Kondo, T., and Bannai, S. (2003) Role of cystine transport in intracellular glutathione level and cisplatin resistance in human ovarian cancer cell lines. *Br. J. Cancer 88*, 951−956.

(42) Berger, M. S., Leopold, L. H., Dowell, J. A., Korth-Bradley, J. M., and Sherman, M. L.. (2002) Licensure of gemtuzumab ozogamicin for the treatment of selected patients 60 years of age or older with acute myeloid leukemia in first relapse. *Invest. New Drugs 20*, 395−406.

(43) Linenberger, M. L., Hong, T., Flowers, D., Sievers, E. L., Gooley, T. A., Bennett, J. M., Berger, M. S., Leopold, L. H., Appelbaum, F. R., and Bernstein, I. D. (2001) Multidrug-resistance phenotype and clinical responses to gemtuzumab ozogamicin. *Blood 98*, 988−994.

(44) Goren, D., Horowitz, A. T., Tzemach, D., Tarshish, M., Zalipsky, S., and Gabizon, A. (2000) Nuclear delivery of doxorubicin via folate-targeted liposomes with bypass of multidrug-resistance efflux pump. *Clin. Cancer Res. 6*, 1949−1957.

(45) Hamann, P. R., Hinman, L. M., Beyer, C. F., Lindh, D., Upeslacis, J., Shochat, D., and Mountain, A. (2002) A calicheamicin conjugate with a fully humanized anti-MUC1 antibody shows potent antitumor effects in breast and ovarian tumor xenografts. *Bioconjugate Chem. 16*, 354−360.

BC049795F

A Calicheamicin Conjugate with a Fully Humanized Anti-MUC1 Antibody Shows Potent Antitumor Effects in Breast and Ovarian Tumor Xenografts

Philip R. Hamann,*,† Lois M. Hinman,† Carl F. Beyer,† Delores Lindh,† Janis Upeslacis,† Dan Shochat,† and Andrew Mountain‡

Wyeth Research, 401 N. Middletown Road, Pearl River, New York 10965 and Celltech R & D, 216 Bath Road, Slough, England, SL1-4EN. Received August 26, 2004; Revised Manuscript Received December 6, 2004

Murine CTM01 is an internalizing murine IgG_1 monoclonal antibody that recognizes the MUC1 antigen expressed on many solid tumors of epithelial origin. Calicheamicin conjugates of this antibody have previously been shown to be potent, selective antitumor agents in preclinical models. A conjugate has now been made with a genetically engineered human version of this antibody, hCTM01. The hCTM01 is an IgG_4 isotype, has an immunoaffinity approximately 30% higher than mCTM01 by competitive RIA, and is efficiently internalized into target cells. The hCTM01−NAc-gamma calicheamicin DM amide conjugate, referred to as CMB-401, shows targeted killing of MUC1-expressing cells in vitro and produces pronounced dose-related antitumor effects over an 8-fold dose range against a MUC1-expressing, ovarian xenograft tumor, OvCar-3. The specificity of CMB-401 was confirmed by comparing its antitumor effects with those of an isotype-matched nonspecific conjugate against the MX-1 breast carcinoma. CMB-401, given either ip or iv, was highly active in these models in single and multiple dose regimens and gave complete regressions at the highest doses examined with good overall therapeutic ratios. CMB-401 also gave good antitumor effects at similar doses with a cisplatin-resistant MUC1-expressing cell line.

INTRODUCTION

The calicheamicins are highly potent antitumor antibiotics of the enediyne family. Originally isolated from a broth extract of the soil microorganism *M. echinospora* ssp. *calichensis*, the calicheamicins were detected in a screen for potent DNA damaging agents (*1*). The parent of this family of xenobiotics, calicheamicin γ_1^I (**1**, Figure 1), associates with the minor groove of DNA and, following reduction with glutathione (*2*), causes sequence-specific, double-stranded DNA cleavage (*3*, *4*). Due to their mode of action and potency, several analogues of the calicheamicins have been tested in preclinical models for their usefulness as antitumor agents. Their development as single agent therapies has not been pursued because of delayed toxicities that limit the therapeutic dose range for treatment. However, their potency makes them appealing candidates for antibody-targeted chemotherapy, where limits in antigen expression make the potency of the cytotoxic agent crucial.

The murine monoclonal antibody CTM01, also known as CT-M-01 or 7F11C7 (*5*), is an internalizing IgG_1 that recognizes the MUC1 antigen present on a broad spectrum of solid tumors of epithelial origin. The MUC1 antigen is a glycoprotein that is expressed on the nonvascular surface of normal epithelial cells, where it is normally inaccessible from circulation. It is present in underglycosylated form on the nonvascular as well as the vascular surface of a number of epithelial cancer cells, such as breast, lung, ovarian, and colon carcinomas, thereby making it accessible for targeting. This antigen undergoes cycling between the surface and the interior of the cell (*5*) and carries any bound antibody with it into the cell. Our results with CTM01 as well as numerous other antibodies suggest that they must be internalized to make effective targeting agents for potent drugs such as the calicheamicins (*6*, *7*). CTM01 was selected for development after comparison of this antibody with a panel of anti-MUC1 monoclonal antibodies (*8*). Successful targeting of this antibody to tumors in humans has been demonstrated (*9*).

A series of conjugates of the calicheamicins and mCTM01 have previously been described (*10*, *11*). Initial examination of the structural requirement for the calicheamicin portion of the molecule led to the selection of the carbohydrate conjugate **4** which contains NAc-gamma[1] calicheamicin as the calicheamicin core, a disulfide stabilized by two adjacent methyl groups, and a hydrazone linkage to the oxidized carbohydrates of the antibody as a site of hydrolytic release (*10*). Further work showed that the inclusion of the hydrazone was necessary for the anti-CD33 antibody, P67.6, for potent, selective cytotoxicity (*12*). However, for CTM01, including this hydrolyzable bond was not necessary for activity, and the lysine-linked conjugate **7**, referred to as the mCTM01 amide conjugate, was equivalent or even superior in all preclinical models that were examined, especially against resistant cell lines (*13*).

CTM01 has now been fully humanized by genetic engineering as an IgG_4 isotype (*8*) in order to decrease immunogenicity and permit repeated administration in

* To whom correspondence should be addressed. Phone: (845) 602-3423. Fax: (845) 602-5561. E-mail: hamannp@wyeth.com.
† Wyeth Research.
‡ Celltech R & D.

[1] Abbreviations: cal equiv, calicheamicin equivalents; MTD, maximum tolerated dose; MED, minimum effective dose; ip, intraperitoneal; iv, intravenous, sc, subcutaneous; NAc, *N*-acetyl; DMA, dimethyl acid; gamma calicheamicin, calicheamicin γ_1.

10.1021/bc049794n CCC: $30.25 © 2005 American Chemical Society
Published on Web 02/24/2005

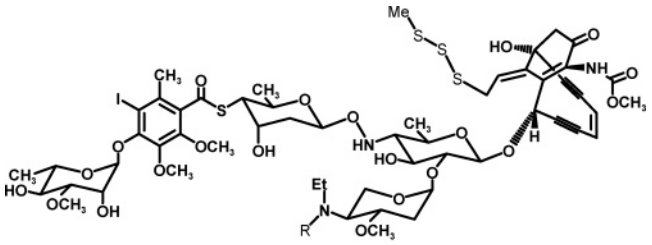

1 Calicheamicin γ_1^I (gamma), R = H
2 NAc-gamma calicheamicin, R = acetyl

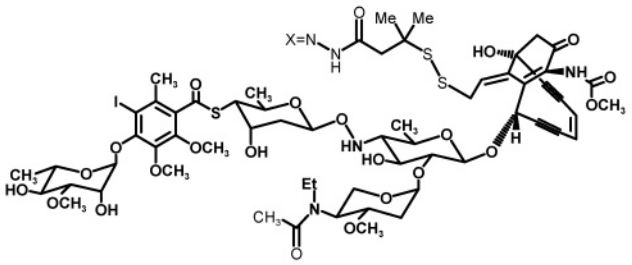

3 NAc-gamma calicheamicin DMH, X = H_2
4 Carbohydrate conjugate, X = Antibody-CH=
(hydrazone with oxidized antibody)

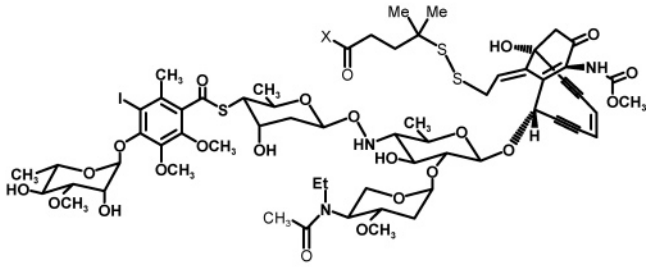

5 NAc-gamma calicheamicin DMA, X = OH
6 NAc-gamma calicheamicin DMA, OSu ester,
X = N-succinimidyloxy
7 Amide conjugate, X = Antibody-NH
(amide bond to lysine groups)

Figure 1. Structures of calicheamicin derivatives and conjugates.

humans. This fully humanized antibody, hCTM01, has been evaluated for its potential for targeted therapy by examining its ability to bind to and internalize into target cells. The potency and selectivity of the amide conjugate of hCTM01, referred to as CMB-401, in in vitro and in vivo tumor models is also described.

CMB-401 (**7**) has been in clinical trials for ovarian cancer (*14*−*16*) as well as lung cancer (unpublished) with only limited evidence of activity. This is in contrast to gemtuzumab ozogamicin (Mylotarg) (*17*), which is an anti-CD33 calicheamicin conjugate approved for AML. The differences that may be responsible for the lesser activity include the presence of circulating antigen (*18*), possible detrimental effects of the predose of native antibody given in an attempt to clear the circulating antigen (*19*), differences in the linkers used (*12*), possible differences in resistance mechanisms (*20*), possible insufficient targeting of the conjugate to large solid tumors, etc. It is also possible that choosing a different tumor type, dosing patients after surgical removal of the primary tumor, or use in combination would show activity. Ongoing efforts may help to clarify these issues. Preclinical data on two more calicheamicin−antibody conjugates have recently been reported (*6*, *7*). Clinical experience with these two conjugates will also expand our understanding of the important issues that need to be addressed in order to make successful chemoimmunoconjugates.

EXPERIMENTAL PROCEDURES

Antibodies. The mCTM01 used in these studies was produced and purified from tissue culture supernatants by Celltech (Lot 122 88JC00-01). The fully humanized version of CTM01 was prepared by Celltech (*8*). hP67.6, an IgG_4, anti-CD33 antibody that served as a nonbinding antibody control (*21*), and MOPC-21, also a nonbinding control (*22*), were also prepared by Celltech.

Antibody Conjugates. The synthesis of the carbohydrate conjugates (**4**) of NAc-gamma calicheamicin DMH have been reported previously (*10*). Drug loadings averaged between 2 and 3 mol of calicheamicin per mole of antibody and free calicheamicin (predominantly structure **3**) was normally 1−3%.

The procedures for the synthesis of amide conjugates (**7**) have also been published (*12*). Drug loadings of 2 to 3 mol of calicheamicin per mole of antibody were seen and free calicheamicin (predominantly structure **5**) was normally 0.5−1%.

All conjugates were characterized as monomeric by analytical gel-exclusion chromatography (aggregate < 3%) and loading was determined by the ratio of UV absorption at 280 nm (protein) and 333 nm (calicheamicin) as reported (*10*, *12*). Neither conjugation procedure significantly affected the immunoaffinity of the conjugates reported in this paper versus the starting native antibodies, as determined by competitive binding with antibody that had been radiolabeled with ^{125}I-Bolton−Hunter reagent, as detailed below.

Cell Lines. MX-1 is a human ductal breast carcinoma cell line obtained from the National Cancer Institute. MCF-7 is a human breast adenocarcinoma, pleural effusion. ZR-75-1 is a human breast carcinoma. Raji is a Burkitt's Lymphoma cell line, ATCC # CCL 86. A2780 (*23*) is an ovarian carcinoma, and A2780DDP (*24*) was derived from A2780 by exposure to cisplatin and has enhanced DNA repair. The ovarian adenocarcinoma tumor OvCar-3 was obtained from the ATCC line HTB 161 and was passaged as an ascites tumor in nude mice.

Culture Methods. The basic methods used are as published previously (*10*). Cells were propagated in RPMI 1640 medium containing 5% fetal calf serum, 5 μg/mL insulin and transferrin, 5 ng/mL selenium, and 50 μg/mL gentamicin. Cultures were maintained in a humidified, 5% CO_2 incubator at 37 °C and were subcultured once or twice a week as needed. For in vitro cytotoxicity tests, streptomycin (50 μg/mL) and penicillin (50 U/mL) were incorporated into the medium.

Relative immunoaffinity of the antibodies and conjugates was measured by a competitive radioimmunoassay (RIA) in which several dilutions of the test sample were competed with iodinated CTM01 for binding to live cells. For each assay, 10^6 A2780DDP cells in 0.1 mL were incubated with 0.05 mL of 4 μg/mL ^{125}I-CTM01 (specific activity about 0.3−0.5 μCi/μg) and serial 4-fold dilutions of the test samples, the highest concentration being 200 μg/mL. After a 1 h incubation at 0−4 °C, the cells were washed three times with cold Dulbecco's phosphate-buffered saline (PBS) and transferred to fresh tubes and counted. Binding inhibition curves were plotted and calculated IC_{50} values for each conjugate were compared with that of the unmodified control antibody as a relative measure of retention of immunoaffinity.

Determination of Antibody Internalization by Target Cells. The acid-dissociation method (*25*) has been

adapted to quantitatively assess internalization of mCTM01 and hCTM01 by the human breast carcinoma cell line, MCF-7, and the cisplatin-resistant human ovarian carcinoma cell line, A2780DDP. Cells were collected by trypsinization and washed; viable cells were enumerated by Trypan Blue exclusion, and the suspension was adjusted to 5×10^6 viable cells/mL in medium (RPMI-1640 containing 5% heat-inactivated fetal calf serum and 0.02 M HEPES, pH 7.4). This suspension was chilled on ice, and ^{125}I-labeled antibody (labeled with Bolton-Hunter reagent; specific activity about 0.5 mCi/mg) was added to give a final concentration of 1−2 mg/10^6 cells. This suspension was distributed to two sets of duplicate tubes at 0.5 mL/tube. One set of tubes (control) was kept on ice throughout the incubation period; the other set was immediately transferred to a 37 °C water bath. At various times, the cell suspensions in duplicate tubes from each set were diluted with 2.5 mL of cold medium and centrifuged. The supernatants were decanted, and the cell pellets were washed with 3 mL of cold medium. The supernatants were decanted again, and the pellets were resuspended in 0.5 mL of 0.05 M glycine and 0.10 M NaCl, pH 2.8. These suspensions were incubated for 20 min at room temperature and then centrifuged. The acid supernatants were carefully removed and transferred to clean tubes; the pellets were resuspended in 0.5 mL of medium and also transferred to clean tubes. The radioactivity associated with cell pellets and acid supernatants was determined by gamma counting. This method is based on the finding that molecules of CTM01 that are bound to the outer plasma membrane of cells are released by exposure to isotonic pH 2.8 buffer, whereas internalized antibody molecules are not released. Thus, it is possible to distinguish between surface-bound and internalized CTM01 by this technique. Over time, there is a shift of radioactivity from the acid supernatants to the cell pellets for samples incubated at 37 °C but not for the controls incubated on ice. From the acid-stable, cell-associated cpm in the experimental samples (corrected for the small, constant, acid-stable cpm in the control samples) and the specific radioactivity of the antibody, the number of molecules of antibody internalized per cell (net uptake) is plotted vs time of incubation.

In Vitro Cytotoxicity Assays. To evaluate the cytotoxicity of drug or conjugate samples, viable cells (10^5/0.2 mL) were aliquoted into 15 mL test tubes which contained 0.2 mL of the sample to be tested at the appropriate concentration. Concentrations were all normalized to ng/mL calicheamicin equivalents (cal equiv). Tubes were vortexed and incubated at 37 °C for 1 h, and the pellets were washed 3 times with 8 mL of medium. One milliliter of medium was added to each pellet, the cells were vortexed, and 0.2 mL was removed and placed in a well of a 96-well plate (2×10^4 cells). Alternately for continuous exposure, cells were plated without removing unbound test article by washing. These cells were incubated for 3 days, at which time 0.1 mL of supernatant was removed and replaced with 0.2 mCi of [^{3}H] thymidine in 0.1 mL of fresh medium. Incubation was resumed for an additional 24 h at which point the cells were harvested and counted. Growth inhibition curves of each drug or conjugate were plotted, and the IC_{50} value (concentration of drug equivalents needed for 50% [^{3}H]thymidine uptake inhibition) of each sample was determined.

In Vivo Tests for Antitumor Activity. The cell lines were passaged in tissue culture or as ascites tumors in nude mice (OvCar-3). For each experiment, 8×10^6 cells were implanted subcutaneously into athymic mice. Tumors were staged for 4 to 10 days to achieve a size of

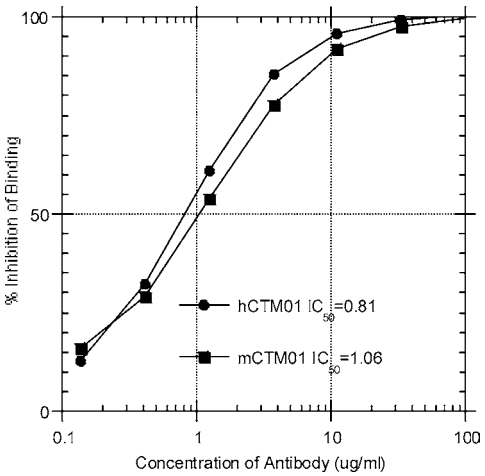

Figure 2. Competitive radioimmunoassay for mCTM01 and hCTM01. Affinity of the humanized antibody relative to the murine antibody is 1.3.

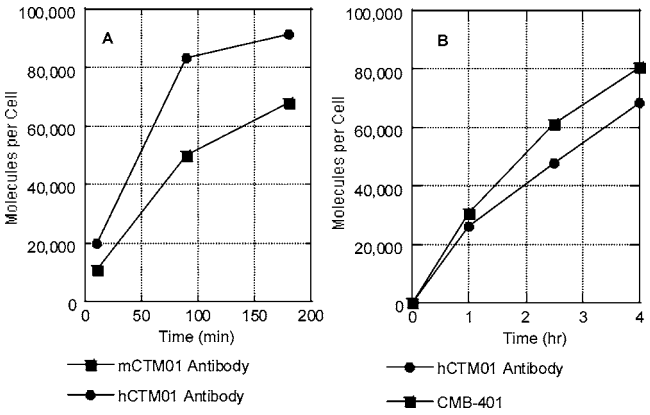

Figure 3. Internalization by MCF-7 (A) and A2780DDP (B) human cell lines. Frame A shows the effect of humanization on uptake, while frame B shows the effect of conjugation to make CMB-401 (**7**) on uptake of humanized antibody.

100−150 mg prior to treating ip at the indicated dose levels on days 1, 5, and 9 after staging. There were five or six mice per test group and 10 in the buffer control group. Tumor mass was determined by measuring two tumor dimensions once weekly for at least 28 days post-tumor staging. Antitumor activity was defined as a sustained 58% minimum inhibition of mean tumor mass (NCI standard criteria) compared with untreated controls in groups with greater than 65% survivors. A therapeutic ratio was defined as the maximum tolerated dose/minimum effective dose (MTD/MED) and used as a measure of the therapeutic window for the conjugates or drugs tested.

RESULTS

Relative Affinities of mCTM01 and hCTM01. The affinities of the murine and humanized versions of CTM01 were compared using ^{125}I-labeled mCTM01 in a competition assay. As shown in Figure 2, the binding data follow a normal curve and show that hCTM01 has ∼30% increased affinity with respect to the murine antibody.

Internalization of mCTM01, hCTM01, and CMB-401. Internalization of the two CTM01 antibodies and CMB-401 was examined on two cell lines using a modification of the acid-dissociation method. The increased affinity of the genetically engineered antibody resulted in increased internalization into the MCF-7 cell line, as shown in Figure 3A, and these results confirmed the observation (*5*) that MUC1 is efficiently internalized. In

Table 1. In Vitro Cytotoxicity of CMB-401 and the mCTM01 Amide Conjugate

	IC_{50}, 1 h[a]			IC_{50}, 4 days[a]		
sample	MX-1	Raji	index[b] specificity	MX-1	Raji	index[b] specificity
CMB-401	14.9	>500	>1000	0.05	>100	>70000
mCTM01 conjugate[c]	54.2	>500	>300	0.61	>100	>6000
NAc-gamma cal.	>20	0.53	**1**	1.08	0.03	**1**

[a] IC_{50}s are given in ng/mL cal equiv, doses of antibody are approximately 40-fold higher. [b] The specificity index is defined as (IC_{50} of conjugate of Raji/IC_{50} of conjugate on MX-1) ÷ (IC_{50} of NAc-gamma on Raji/IC_{50} of NAc-gamma on MX-1). [c] Same conjugate as CMB-401, but with murine antibody.

Table 2. In Vitro Activity of the CMB-401 and the MCTM01 Amide Conjugate

	IC_{50} (ng/mL)		
sample	A2780DDP	ZR-75-1	MCF-7
CMB-401	1.8	9.8	17
mCTM01 conjugate[d]	2.4	ND[b]	20
MOPC-21 conjugate[e]	189	ND[b]	305
hP67.6 conjugate[e]	ND[b]	331	ND[b]
NAc-gamma calicheamicin	0.056	0.038	1.8
selectivity index[c]	105	34	18

[a] IC_{50}s are given in ng/mL cal equiv, doses of antibody are approximately 40-fold higher. [b] ND = not determined. [c] Selectivity index = IC_{50}(MOPC-21 or hP67.6 conjugate) ÷ IC_{50}(CMB-401). [d] Same conjugate as CMB-401, but with murine antibody. [e] Same conjugate as CMB-401, but with indicated antibody.

this example at least 50 000 molecules per cell were internalized within the first hour of incubation at 37 °C. Figure 3B shows that the A2780DDP cell line had a slightly lower rate of internalization for hCTM01, but that CMB-401 was internalized at least as well, indicating that conjugating calicheamicin to the antibody does not interfere with internalization.

Comparative Activity of CMB-401 and the Corresponding Murine Conjugate in Vitro. The mCTM01 amide conjugate and CMB-401 routinely had drug loadings of 2 to 3 mol of calicheamicin per mole of antibody and retained >80% of their immunoaffinity (data not shown). The in vitro activity of CMB-401 was compared with that of the mCTM01 amide conjugate. The MX-1 breast line was used as the antigen-positive cell line and Raji as an antigen-negative control cell line with either 1-h exposure or continuous (4-day) exposure to conjugate. Additionally, the activities of all the conjugates were compared with that of unconjugated NAc-gamma calicheamicin (**2**). As summarized in Table 1, CMB-401 had lower IC_{50}s and higher specificities in both the 1-h incubation and continuous exposure protocols than seen with the mCTM01 amide conjugate.

To evaluate the selectivity of these amide conjugates for other MUC1-expressing tumor cell lines, an in vitro comparison of CMB-401 with a nonspecific antibody conjugate, prepared with identical calicheamicin chemistries, was made. In this study, the mCTM01 amide conjugate and CMB-401 along with both NAc-gamma calicheamicin (**2**) and the nonbinding control conjugate of the murine IgG_1 monoclonal antibody, MOPC-21, or the isotype-matched conjugate of hP67.6 were all tested against two human breast and one ovarian tumor cell lines. As the data in Table 2 indicate, both the mCTM01 amide conjugate and CMB-401 were equivalently active against the MUC1-expressing cell lines, with IC_{50}s in the 10 ng/mL of cal equiv dose range. The specificity of CMB-401 ranged from 20 to 100 with respect to a nonbinding conjugate. Table 2 also shows that both CTM01 amide conjugates were at least as potent on the cisplatin resistant cell line A2780DDP as on the other two cisplatin sensitive cell lines.

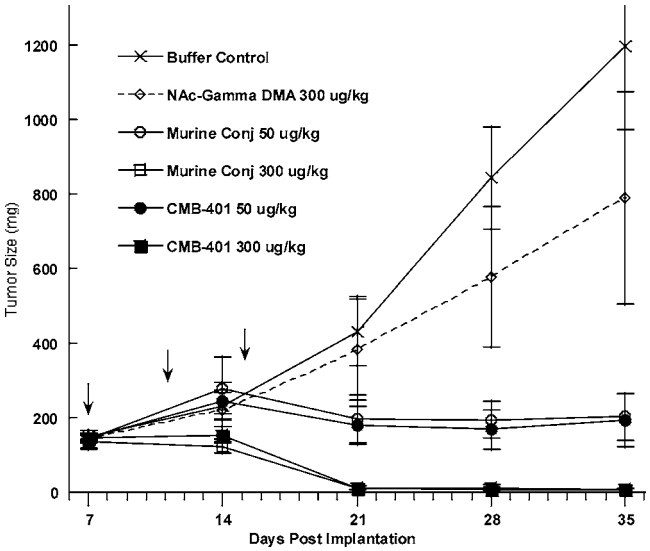

Figure 4. Response of OvCar-3. Xenograft tumors were treated with CMB-401 (**7**), the murine conjugate (**7**), or a representative calicheamicin derivative (**6**) alone. Athymic mice were implanted sc with OvCar-3 cells and then dosed when tumors were approximately 150 mg in size. The doses indicated were given on days 7, 11, and 15, as indicated by the arrows, and are given in calicheamicin equivalents. The corresponding concentration of antibody is 40-fold greater. Error bars are SEMs.

In Vivo Efficacy of CMB-401 versus OvCar-3. As shown in Figure 4, the mCTM01 amide conjugate and CMB-401 were both highly effective against the OvCar-3 ovarian carcinoma xenograft at doses ranging from 50 to 300 μg/kg cal equiv given three times each, with four out of five animals tumor-free in each of the 300 μg/kg treatment groups. This experiment was done with tumors staged to 150 mg prior to treatment. The conjugates were still effective at doses as low as 50 μg/kg, indicating a therapeutic ratio (MTD/MED) ≥ 6. In contrast, neither the NAc-gamma calicheamicin (**2**, not shown) nor the NAc-gamma calicheamicin DMA (**5**, shown) used as controls, gave substantial antitumor effects at the MTD. The dose−response behavior of the conjugates in this experiment is described in Figure 5. With both conjugates, 13 of the 25 treated animals were tumor-free at day 28 of the test as indicated in the figure. Native antibody itself has no effect in this or any other xenograft experiment that has been performed.

Evaluation of Specificity and Efficacy in Vivo versus MX-1. As shown in Figure 6, CMB-401 was compared with a conjugate prepared with the isotype-matched, genetically engineered IgG_4 antibody, hP67.6, that does not target to MX-1, conjugated to the same calicheamicin derivative. In this study, the two conjugates were administered ip on days 11, 15 and 19 post tumor implantation. At doses ranging from 150 to 450 μg/kg cal equiv per injection the specific hCTM01 amide conjugate was active while the nontargeting hP67.6 conjugate had comparatively modest activity (T/C = 43%) at the top dose tested.

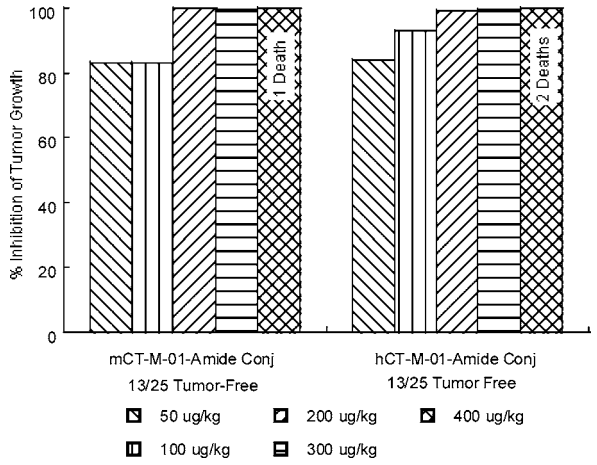

Figure 5. Dose−response of the OvCar-3 ovarian xenograft tumors. Athymic mice were implanted sc with OvCar-3 cells and then dosed with the conjugates (**7**) when tumors were approximately 150 mg in size. The doses indicated were given on days 7, 11, and 15 and are given in calicheamicin equivalents. The corresponding concentration of antibody is 40-fold greater. Data shown is for day 28.

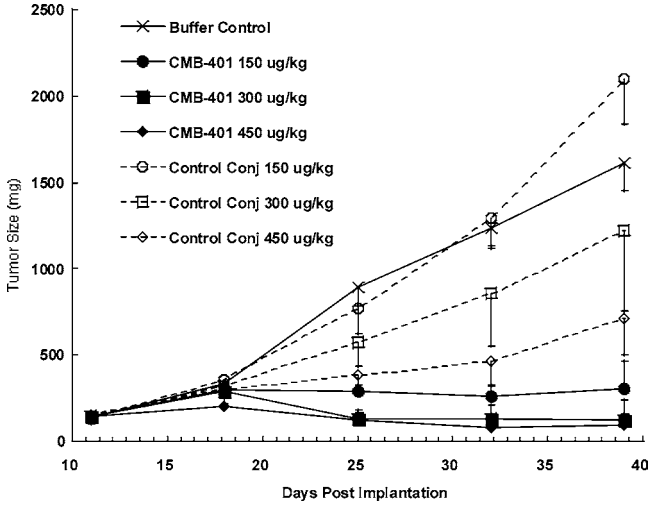

Figure 6. Response of the MX-1 breast xenograft tumors. Athymic mice were implanted sc with MX-1 cells and then dosed with the conjugates (**7**) when tumors were approximately 150 mg in size. The control conjugate is an identical conjugate made with the nonbinding, isotype-matched antibody, P67.6. The doses indicated were given on days 11, 15, and 19 and are given in calicheamicin equivalents. The corresponding concentration of antibody is 40-fold greater. Error bars are SEMs and are given in the negative direction for the control conjugate and in the positive direction for CMB-401.

Evaluation of Dose Schedule and Route of Administration. The MX-1 breast carcinoma was used to examine both route of administration and dose schedule for CMB-401. Figure 7 shows no difference in the activity of CMB-401 administered ip as a larger bolus injection versus the standard three doses separated by 4 days. There was also no significant difference in activity between the conjugates as a function of route of administration, ip versus iv, regardless of whether the conjugate was given as a bolus or as split doses (bolus iv not shown in graph for clarity).

DISCUSSION

The feasibility of conjugating calicheamicin to oxidized carbohydrates on antibodies has previously been demonstrated (*10*). Using these carbohydrate conjugates, the

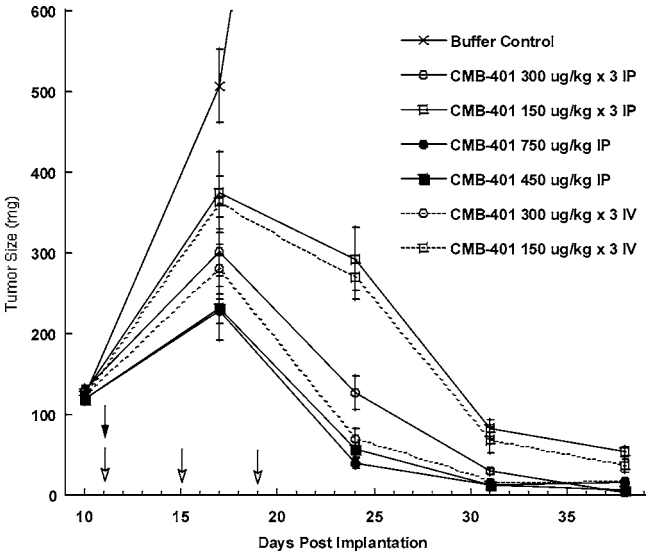

Figure 7. Effect of changing the fractionated dose IP to either a fractionated dose iv or to a bolus dose IP. Athymic mice were implanted sc with MX-1 cells and then dosed with CMB-401 (**7**) when tumors were approximately 150 mg in size. The doses indicated were given either on day 11, as indicated by the solid arrow (single dose), or on days 11, 15, and 19, as indicated by the open arrows, and are given in calicheamicin equivalents. The corresponding concentration of antibody is 40-fold greater. Error bars are SEMs.

correlation between the potency of calicheamicin analogues and their therapeutic potential as conjugates was investigated, and linker variations were also examined in an effort to optimize the therapeutic window for the conjugates. From these studies, the mCTM01 carbohydrate conjugate (**4**), which contains an NAc group, a disulfide that is sterically hindered by two methyl groups, and a hydrazone that allows for hydrolytic drug release, was chosen as the optimal drug for conjugation. Although incorporation of the NAc group lowered the potency of the conjugate somewhat, it significantly improved the therapeutic index. Increasing the stability of the disulfide is thought to decrease premature release and triggering of the calicheamicin in circulation. The hydrazone linkage was originally thought to be required for efficient drug release, as is the case for conjugates of other antibodies (*12*).

The site of hydrolytic release was subsequently removed by attaching an appropriate calicheamicin derivative to the epsilon-amino groups of lysines (*11*). The mCTM01 amide conjugate (**7**) is not only as efficacious as the hydrazone conjugate in many in vitro and in vivo tumor models, but also shows enhanced activity over the hydrazone conjugate against tumors overexpressing P-glycoprotein-mediated multidrug resistance (MDR) (*13*). These studies suggest the hypothesis that attaching a cytotoxic agent, such as calicheamicin, by way of a serum stable linker to an internalizing carrier protein may help to bypass normal membrane-based mechanisms of drug resistance. There is precedence for this with other types of conjugates (*26*), although further research with various drugs and antibodies would be required to adequately define this possibility. The amide conjugate also shows good activity versus a cisplatin-resistant ovarian carcinoma line. That this conjugate has activity equal to or greater than that of the CTM01 carbohydrate conjugate indicates that the hindered disulfide offers ample means for release of the drug intracellularly, presumably through interaction with glutathione and other reduced thiols (*2*). Preliminary experiments indicate that the reaction rate

of a model calicheamicin disulfide with glutathione is consistent with reasonable stability in circulation where glutathione concentrations are lower, but sufficient reactivity to allow for release of an active calicheamicin derivative intracellularly where glutathione concentrations are 100-fold higher (*27*, *28*). Specifically, about 2% reaction of the calicheamicin was seen at 0.02 mM glutathione in pH 7.4 phosphate buffer, which approximates the conditions in circulation, and 55% reaction was seen at 2 mM, which approximates the concentrations seen in cells.

The next step in the development of the CTM01 calicheamicin conjugates has been the replacement of the murine antibody with a genetically engineered human antibody that should be much less immunogenic in patients. The data presented in this report demonstrate that the resultant hCTM01 amide conjugate is well-behaved and is equivalent or superior to the corresponding murine version in all preclinical models. Good binding and internalization of this and all other calicheamicin conjugates is felt to be crucial for good activity. Binding and internalization has been shown to be unaffected by the change from mCTM01 to hCTM01 and by conjugation to calicheamicin. In fact, both the native hCTM01 antibody as well as its conjugate bind and internalize better than the murine counterparts.

In vitro*,* CMB-401 is potently cytotoxic with IC_{50}s in the 0.05 to 17 ng/mL cal equiv range and is highly selective with specificity indices of 20 to over 70 000, depending on the cell line and assay conditions. Specificity has been demonstrated both versus a nontargeted cell line and a nontargeting conjugate on various cell lines. The reason for modest selectivity in some cases is unknown; however, the activity in xenograft models reaffirms the potential of these conjugates. CMB-401 exhibits good stability in vitro as demonstrated by the retention of specificity seen after 4 days of the continuous exposure to conjugate at pH 7.4 and 37 °C.

In vivo, CMB-401 is virtually indistinguishable from the murine counterpart. The MED for multiple experiments falls in the range of 25 to 50 μg/kg cal equiv while the MTD ranges from 300 to 400 μg/kg, in each case being given three times spaced by 4 days. The therapeutic window in multiple experiments is always > 6. CMB-401 produced regressions of well established (150 mg) OvCar-3 ovarian xenograft tumors with long-term, tumor-free survivors being common not only at the MTD, but often at lower doses as well. Good activity is maintained over a 10-fold dose range in some experiments. The targeting of CMB-401 is demonstrated by its superior activity with respect to a conjugate made from the hP67.6 antibody which does not target the MX-1 breast xenograft. The nontargeting conjugate shows only modest in vivo activity at a dose that is almost 10 times the MED for CMB-401. Such modest activity is likely due to the tendency of xenograft tumors to accumulate macromolecules, but is significantly less than seen with the targeting antibody, where internalization takes the calicheamicin into the cell.

Experiments which examine the dosing schedule show that similar activity is seen with a higher bolus dose instead of three fractionated doses spaced 4 days apart. This is somewhat surprising, because chemotherapeutics are often fractionated to maximize effect while minimizing toxicity. Administration iv was seen to give the same results as the more normally used ip administration. Data from previous experiments also show that the CTM01 conjugates are as potent, both in vitro as well as in vivo, on the MUC1-expressing, cisplatin-resistant cell line A2780DDP as against the cisplatin-sensitive target cell lines (*11*). These observations were important since clinical evaluation of CMB-401 activity was initially made in ovarian carcinoma patients who had relapsed following cisplatin-based chemotherapy (*14*, *15*).

CMB-401 is a very potent antitumor agent, being routinely effective and nontoxic in the dose range of 50−300 μg/kg cal equiv. This potency is crucial considering that uptake of antibody conjugates by solid tumors in humans is low, typically in the range of 0.001−0.01% injected dose/g. The potential of the calicheamicins for targeted delivery with a fully humanized anti-MUC1 antibody has been demonstrated in preclinical models. The lack of sufficient activity in clinical trials (see the Introduction for discussion) was disappointing, but it gives us additional incentive to explore the many other properties a chemoimmunoconjugate and the tumors it targets must possess for ultimate success.

LITERATURE CITED

(1) Lee, M. D., Dunne, T. M., Siegel, M. M., Chang, C. C., Morton, G. O., and Borders, D. B. (1987) Calicheamicins, a novel family of antitumor antibiotics, 1. Chemistry and partial structure of calicheamicin γ_1^I. *J. Am. Chem. Soc. 109*, 3464−3466.

(2) Myers, A. G., Cohen, S. B., and Kwon, B. M. (1994) A study of the reaction of calicheamicin γ_1^I with glutathione in the presence of double-stranded DNA. *J. Am. Chem. Soc. 116*, 1255−1271.

(3) Ellestad, G. A., Ding, W.-D., Zein, N., and Townsend, C. A. (1995) DNA-cleaving properties of calicheamicin γ_1. *Enediyne Antibiotics as Antitumor Agents* (Borders, D. B., and Doyle, T. W., Eds.) pp 137−160, Marcel Dekker, New York.

(4) Lee, M. D., Ellestad, G. A., and Borders, D. B. (1991) Calicheamicins: Discovery, structure, chemistry, and interaction with DNA. *Acc. Chem. Res. 24*, 235−243.

(5) Aboud-Pirak, E., Sergent, T., Otte-Slachmuylder, C., Abarca, J., Trouet, A., and Schneider, Y.-J. (1988) Binding and endocytosis of a monoclonal antibody to a high molecular weight human milk fat globule membrane-associated antigen by cultured MCF-7 breast cancer cells. *Cancer Res. 48*, 3188−3196.

(6) DiJoseph, J. F., Armellino, D. C., Boghaert, E. R., Khandke, K., Dougher, M., Sridharan, L., Kunz, K., Hamann, P. R., Gorovits, B., Udata, C., Moran, J. K., Popplewell, A. G., Stephens, S., Frost, P., and Damle, N. K. (2004) Antibody-targeted chemotherapy with CMC-544: A CD22-targeted immunoconjugate of calicheamicin for the treatment of B lymphoid malignancies. *Blood 103*, 1807−1814.

(7) Boghaert, E. R., Sridharan, L., Armellino, D. C., Khandke, K. M., DiJoseph, J. F., Kunz, A., Dougher, M. M., Jiang, F., Kalyandrug, Lyka B., Hamann, P. R., Frost, P., Damle, N. K. (2004) Antibody-targeted chemotherapy with the calicheamicin conjugate hu3S193−*N*-acetyl γ calicheamicin dimethyl hydrazide targets $Lewis^Y$ and eliminates $Lewis^Y$-positive human carcinoma cells and xenografts. *Clin. Cancer Res. 10*, 4538−4549.

(8) Baker, T. S., Bose, C. C., Caskey-Finney, H. M., King, D. J., Lawson, A. D., Lyons, A., Mountain, A., Owens, R. J., Rolfe, M. R., Sehdev, M., Yarranton, G. T., and Adair, J. R. (1994) Humanization of an anti-mucin antibody for breast and ovarian cancer therapy. *Adv. Exp. Med. Biol. 1994*, 35361−35382.

(9) Prinssen, H. M., Molthoff, C. F., Verheijen, R. H., Broadhead, T. J., Kenemans, P., Roos, J. C., Davies, Q., van Hof, A. C., Frier, M., den Hollander, W., Wilhelm, A. J., Baker, T. S., Sopwith, M., Symonds, E. M., and Perkins, A. C. (1998) Biodistribution of ^{111}In-labeled engineered human antibody CTM01 (hCTM01) in ovarian cancer patients: Influence of prior administration of unlabeled hCTM01. *Cancer Immunol. Immunother. 47*, 39−46.

(10) Hinman, L. M., Hamann, P. R., Wallace, R., Menendez, A. T., Durr, F. E., and Upeslacis, J. (1993) Preparation and characterization of monoclonal antibody conjugates of the

calicheamicins: A novel and potent family of antitumor antibiotics. *Cancer Res. 53*, 3336−3342.
(11) Hinman, L. M., Hamann, P. R., and Upeslacis, J. (1995) Preparation of conjugates to monoclonal antibodies. *Enediyne Antibiotics as Antitumor Agents* (Borders, D. B., and Doyle, T. W., Eds.) pp 87−105, Marcel Dekker, New York.
(12) Hamann, P. R., Hinman, L. M, Beyer, C. F., Lindh, D., Upeslacis, J., Flowers, D. A., and Bernstein, I. (2002) An anti-CD33 antibody-calicheamicin conjugate for treatment of acute myeloid leukemia. Choice of linker. *Bioconjugate Chem. 13*, 40−46.
(13) Hamann, P. R., Hinman, L. M., Beyer, C. F., Greenberger, L., Lin, C., Lindh, D., Menendez, A. T., Wallace, R., Durr, F. E., and Upeslacis, J. (2004) An anti-MUC1 antibody-calicheamicin conjugate for treatment of solid tumors, choice of linker and overcoming drug resistance. *Bioconjugate Chem. 16*, 346−353.
(14) Gillespie, A. M., Broadhead, T. J., Chan, S. Y., Owen, J., Farnsworth, A., Sopwith, M., and Coleman, R. E. (1998) Phase I study of ascending doses of the cytotoxic immunoconjugate CMB-401 (hCTM01-calicheamicin) in patients with epithelial ovarian cancer. *Br. J. Cancer 78*, 20.
(15) Chan, S. Y., Gordon, A. Y., Coleman, R. Y., Hall, J. Y., Berger, M. S., Sherman, M. Y., Eten, C. Y., and Finkler, N. Y. (2003) A phase 2 study of the cytotoxic immunoconjugate CMB-401 (hCTM01-calicheamicin) in patients with platinum-sensitive recurrent epithelial ovarian carcinoma. *Cancer Immunol. Immunother. 52*, 243−248.
(16) Broadhead, T. J., Gillespie, A. M., Coleman, R. E., Owen, J., Skelton, L., Stephens, S., Farnsworth, A., Sopwith, M., and Chan, S. Y. (1998) Phase I study of the cytotoxic immunoconjugate CMB-401 (hCTM01-calicheamicin) in patients with epithelial ovarian cancer: Immune response and pharmacokinetics following repeated intravenous administration. *Proceedings of the American Society of Clinical Oncology*, May 16−19, 1998, Los Angeles, CA, American Society of Clinical Oncology: Alexandria, VA, 1998, abstract 1693.
(17) Bross, P. F., Beitz, J., Chen, G., Chen, X. H., Duffy, E., Kieffer, L., Roy, S., Sridhara, R., Rahman, A. R., Williams, G., and Pazdur, R. (2001) Approval summary: Gemtuzumab ozogamicin in relapsed acute myeloid leukemia, *Clin. Cancer Res. 7*, 1490−1496.
(18) Davies, Q., Perkins, A. C., Fries, M., Watson, S., Lalani, E.-N., and Symonds, E. M. (1997) The effect of circulating antigen on the biodistribution of the engineered human antibody hCTM01 in a nude mice model. *Eur. J. Nuclear Med. 24*, 206−209.
(19) Broadhead, T. J., Davies, Q., Van Hof, A. C., Molthoff, C. F. M., Perkins, A. C., Roos, J. C., Prinssen, W. M., Verheijen, R. H. M., den Hollander, W., Sopwith, M., Frier, M., Kenemans, P., and Symonds, E. M. (1998) Clinical study to investigate the potential of an engineered human monoclonal antibody, hCTM01, for targeted chemotherapy of ovarian cancer. *Tumor Target. 3*, 55−57.
(20) Walter, R. B., Raden, B. W., Cronk, M. R., Bernstein, I. D., Appelbaum, F. R., and Banker, D. E. (2004) The peripheral benzodiazepine receptor ligand PK11195 overcomes different resistance mechanisms to sensitize AML cells to gemtuzumab ozogamicin. *Blood 103*, 4276−4284.
(21) Hamann, P. R., Hinman, L. M., Hollander, I., Beyer, C. F., Lindh, D., Holcomb, R., Hallett, W., Tsou. H.-R., Upeslacis, J., Shochat, D., Mountain, A., Flowers, D. A., and Bernstein, I. (2002) Gemtuzumab ozogamicin, a potent and selective anti-CD33 antibody-calicheamicin conjugate for treatment of acute myeloid leukemia. *Bioconjugate Chem. 13*, 47−58.
(22) Melchers, F. (1970) Biosynthesis of the carbohydrate portion of immunoglobulins. *Biochem. J. 119*, 765−772.
(23) Ozols, R. F. and Young, R. C. (1984) Chemotherapy of ovarian cancer. *Semin. Oncol. 11*, 251−263.
(24) Newman, E. M., Lu, Y., Kashani-Sabet, M., Kesavan, V., and Scanlon, K. J. (1988) Mechanisms of cross-resistance to methotrexate and 5-fluorouracil in an A2780 human ovarian carcinoma cell subline resistant to cisplatin. *Biochem. Pharmacol. 37*, 443−7.
(25) Matzku, S., Bröcker, E.-B., Brüggen, J., Dippold, W. G., and Tilgen, W. (1986) Modes of binding and internalization of monoclonal antibodies to human melanoma cell lines. *Cancer Res. 46*, 3848−3854.
(26) Goren, D., Horowitz, A. T., Tzemach, D., Tarshish, M., Zalipsky, S., and Gabizon, A. (2000) Nuclear delivery of doxorubicin via folate-targeted liposomes with bypass of multidrug-resistance efflux pump. *Clin. Cancer Res. 6*, 1949−1957.
(27) Mamsoor, M. A., Svardal, A. M., and Ueland, P. M. (1992) Determination of the in vivo redox status of cysteine, cysteinylglycine, homocysteine, and glutathione in human plasma. *Anal. Biochem*. *200*, 218−229.
(28) Mistry, P. and Harrap, K. R. (1991) Historical aspects of glutathione and cancer chemotherapy. *Pharm. Ther. 49*, 125−132.

BC049794N

pH-Responsive Copolymer Assemblies for Controlled Release of Doxorubicin

Elizabeth R. Gillies and Jean M. J. Fréchet*

Center for New Directions in Organic Synthesis, Department of Chemistry, University of California, Berkeley, California 94720-1460. Received June 26, 2004; Revised Manuscript Received December 13, 2004

pH-Responsive drug carriers have the potential to provide selective drug release at therapeutic targets including tumors and in acidic intracellular vesicles such as endosomes and lysosomes. We have developed a new approach to the design of acid-sensitive micelles by incorporating hydrophobic acetal groups on the core block of a micelle-forming block copolymer. Hydrolysis of the acetals at mildly acidic pH is designed to reveal polar groups on the core-forming block, thus changing its solubility and disrupting the micelle, triggering drug release. The anticancer drug doxorubicin (DOX) was encapsulated in these pH-sensitive micelles, and the acetal hydrolysis rates and DOX release rates were determined in the pH range of 4.0 to 7.4 and were compared to those of control systems. The micelle disruption was investigated by dynamic light scattering. The in vitro toxicities of the empty and DOX-loaded micelles were determined, and the intracellular fate of the encapsulated DOX was compared to free DOX using fluorescence confocal microscopy.

INTRODUCTION

In recent years there has been increased interest in the development of drug delivery systems to improve the properties, increase the effectiveness, and reduce the harmful side effects of therapeutic molecules. Micelles formed by the assembly of amphiphilic block copolymers in aqueous solution have been investigated as potential drug carriers and offer many attractive characteristics (*1*−*3*). For example, these nanocontainers are capable of encapsulating hydrophobic drugs in their core, thus improving the drug's water solubility. In addition, the size of copolymer micelles, typically between 20 and 100 nm, is effective in avoiding rapid renal exclusion, but is also small enough to avoid undesirable uptake by the reticuloendothelial system (*4*). Therefore, the circulation of the micellar carrier and encapsulated drug is prolonged, but since the micelles are composed of polymer chains that are small enough to be eliminated by renal filtration, the eventual disintegration of the micelle will allow the polymer to be excreted. This is important since the long-term build-up of polymer in the body could lead to toxicity. The size and prolonged circulation of copolymer micelles also facilitates their passive accumulation at pathological sites such as tumors where the vasculature has increased permeability (*5*). This selective targeting of the drug carrier is ideal in terms of increasing the effectiveness and lowering the systemic toxicity of the drug payload.

An important issue determining the effectiveness of a micellar drug carrier is the ability to control the location and time over which drug release occurs. This challenge has motivated the development of micelle systems that are designed to release their drug load in a controlled manner, upon arrival at the target site. For example, temperature has been used to modulate drug release from thermoresponsive micelles (*6*, *7*), while ultrasound has been reported to trigger drug release from Pluronic micelles (*8*, *9*). Both these approaches require the presence of external stimuli, but it is also possible to exploit naturally occurring changes in the physiological environment. Change in acidity is a particularly useful stimulus to consider in the development of drug carriers because of the numerous pH gradients that exist in both normal and pathophysiological states. For example, it is well documented that the extracellular pH of tumors is slightly more acidic than the blood and normal tissue (*10*−*12*). In addition, it is proposed that micelles are taken up by cells via an endocytosis process (*13*, *14*). Although the endocytic pathway begins near the physiological pH of 7.4, it drops to a lower pH of 5.5−6.0 in endosomes and approaches pH 4.5−5.0 in lysosomes (*15*). Therefore, polymeric micelles that are responsive to pH can be designed to selectively release their payload in tumor tissue or within tumor cells.

Several different approaches have been taken to the development of pH-sensitive micelles (*16*). One approach is to incorporate "titratable" groups such as amines or carboxylic acids into the block copolymers such that the micelle formation is altered by the protonation of these groups. However, only a few of these systems have been demonstrated to undergo transitions in the physiologically relevant pH range of 5.0−7.4 and have the proven capacity to encapsulate drugs (*17*−*21*). Another approach that remains less explored is to incorporate acid degradable linkages into the copolymer for the direct attachment of drugs to the copolymer backbone or such that degradation of the linkage provides sufficient structural change in the polymer to trigger drug release. The groups of Park (*22*) and Kataoka (*23*) have demonstrated the first approach by attaching the anticancer drug doxorubicin (DOX) to the micelle-forming copolymer by an acid-sensitive hydrazone linkage. Heller and co-workers have developed micelles based on poly(ethylene oxide)(PEO)-polyortho ester block copolymers where the core-forming polyortho ester block degrades under acidic conditions (*24*, *25*).

* To whom correspondence should be addressed. E-mail: frechet@cchem.berkeley.edu.

10.1021/bc049851c CCC: $30.25 © 2005 American Chemical Society
Published on Web 02/11/2005

We have recently introduced a new approach to acid-sensitive micelles using PEO−dendrimer hybrids as backbones (*26*, *27*). The approach involves the attachment of hydrophobic groups to the periphery of the core-forming dendrimer block by an acid-sensitive acetal linkage. The system is designed such that upon hydrolysis of the linkage and loss of the hydrophobic groups, the core-forming block becomes hydrophilic, thus destabilizing the micelle and enabling escape of the drug from its encapsulating micellar compartment. The stepwise synthesis and controlled multivalency of the PEO-dendrimer backbone afford a high degree of control over the polymer structures. This has allowed us to tune properties such as the rate of micelle disruption, the critical micelle concentration (CMC), and the size of the micelles by adjusting the length of the PEO block, the generation and chemical structure of the dendrimer block, and the method for attaching the hydrophobic acetals to the polymer (*27*). Here we describe the application of this new approach for the development of a pH-responsive delivery system for DOX. DOX is an ideal candidate for incorporation into this micelle system because it has previously been shown to benefit from the increased circulation time, tumor targeting, and decreased systemic toxicity provided by drug delivery systems such as liposomes (*28*−*30*), polymeric micelles (*31*, *32*), and polymer−drug conjugates (*33*, *34*). The loading and pH-dependent release of DOX from micelles based on a PEO−dendritic polyester hybrid are described here. Investigations of the micelle degradation by dynamic light scattering (DLS) and UV−visible spectroscopy are also described, and preliminary in vitro studies of the DOX-loaded micelles are reported.

MATERIALS AND METHODS

Preparation of DOX-Loaded Micelles. Copolymers **1** and **4** were synthesized as previously reported (*26*, *35*). DOX was loaded into the copolymer micelles using a modification of the previously reported oil/water emulsion method (*31*, *36*). With sonication, DOX (0.75 mg) was dissolved in 0.15 mL of chloroform with 3.0 equiv of NEt_3. This solution was added dropwise to a stirred solution containing 2.5 mg of copolymer in 5 mL of water. The resulting emulsion was stirred overnight in the dark at room temperature, open to the atmosphere allowing the chloroform to evaporate. Insoluble, free DOX was removed by centrifugation at 2000*g* for 5 min. Soluble, free DOX was removed from the micelles by ultrafiltration (triplicate) using a membrane with a molecular weight cutoff of 30 000 g/mol (Amicon YM30). DOX loading was quantified by absorbance using a UV−visible spectrometer (CARY 50 Conc) (*37*). Fluorescence spectra of DOX and DOX-loaded micelles were obtained at a concentration of 10 μg/mL DOX equiv using an ISA/SPEX Fluorolog 3.22 equipped with a 450 W Xe lamp, double excitation and double emission monochromators, and a digital photon-counting photomultiplier. An excitation wavelength of 490 nm was used, and the emission spectra were recorded from 510 to 700 nm.

Determination of Acetal Hydrolysis Rates. A solution of DOX-loaded micelles was adjusted to a buffer concentration of 0.1 M at the desired pH (pH 4.0, 5.0: acetate; pH 6.0: citrate; pH 7.4: phosphate). A micelle concentration of approximately 0.5 mg/mL was used. The samples were stored at 37 °C, and formation of the 2,4,6-trimethoxybenzaldehyde hydrolysis product was detected over time by measuring the absorbance of the sample at 290 nm in a quartz cuvette having a path length of 1 mm. To determine the absorbance at 100% hydrolysis, a drop of concentrated HCl was added to the sample to effect complete hydrolysis.

Determination of DOX Release Rates. A solution of DOX or DOX-loaded micelles (approximately 20 μg/mL DOX equiv) was added to a Slid-A-Lyzer dialysis cassette (Pierce) with a molecular weight cutoff of 10 000. The solution was dialyzed at 37 °C against 0.1 M buffer of the required pH (pH 4.0, 5.0: acetate; pH 6.0: citrate; pH 7.4: phosphate). The solution was removed periodically from the dialysis cassette and the absorbance at 490 nm was measured, then the solution was returned to the dialysis cassette. The amount of released DOX was determined by the decrease in absorbance of the solution in the dialysis cassette.

Dynamic Light Scattering. Micelle sizes were determined by dynamic light scattering using a Zetasizer Nano ZS (Malvern Instruments) equipped with a 4 mW He−Ne laser at 633 nm. Copolymer concentrations were 1 mg/mL in the appropriate 0.1 M buffer (pH 5.0: acetate; pH 7.4: phosphate). The samples were incubated at 37 °C in the temperature-controlled instrument and size measurements were taken automatically every 20−30 min. over a period of 72 h.

Cell Cytotoxicity Assay. MDA-MB-231 breast cancer cells were cultured by the UC Berkeley Cell Culture Facility in a medium consisting of Dulbecco's Modified Eagle medium (DMEM), containing 10% FBS. The cytotoxicity of the empty micelles, DOX-loaded micelles, and free DOX were determined using the MTT assay (*38*). Cells were seeded onto a 96-well plate at a density of 1.6×10^4 cells per well in 100 μL of medium and incubated overnight (37 °C, 5% CO_2). The medium of each well was then replaced by 100 μL of new medium (DMEM, 10% FBS, 1% penicillin−streptomycin) containing various concentrations of micelles, DOX-loaded micelles, or free DOX. The tests were conducted in replicates of four for each concentration. The cells were incubated for 72 h, the medium was aspirated, and 100 μL of fresh medium was added, followed by 20 μL of MTT solution (5 mg/mL). The cells were incubated for 4 h, and then the medium was carefully aspirated. To the resulting purple crystals was added 200 μL of DMSO, followed by 25 μL of pH 10.5 glycine buffer (0.1 M glycine, 0.1 M NaCl). The optical densities at 570 nm were obtained using a SpectraMAX 190 microplate reader (Molecular Devices). Optical densities measured for wells containing cells that received no polymer or drug were considered to represent 100% growth.

Laser Scanning Confocal Microscopy. MDA-MB-231 cells (4.8×10^5 cells per well) were seeded onto a six-well plate containing collagen I-coated coverslips (round, 2.2 cm diameter, BD Biosciences). After incubation overnight (37 °C, 5% CO_2), the medium was carefully aspirated and replaced with 2.0 mL of medium (DMEM, 10% FBS, 1% penicillin−streptomycin) containing 1.0 μg/mL DOX equiv of DOX-loaded micelles or free DOX. The cells were incubated for 24 h, and then the medium was carefully removed. The wells were each rinsed twice with 3 mL of PBS. Two milliliters of 1% paraformaldehyde was added, and the cells were fixed for 10 min. The solution was aspirated, the wells were rinsed three times with PBS, and then the coverslips were transferred to glass slides. Images were obtained using a confocal laser scanning microscope (LSM 510, Carl Ziess Inc.) using a 40× objective and an excitation wavelength of 543 nm (He−Ne laser).

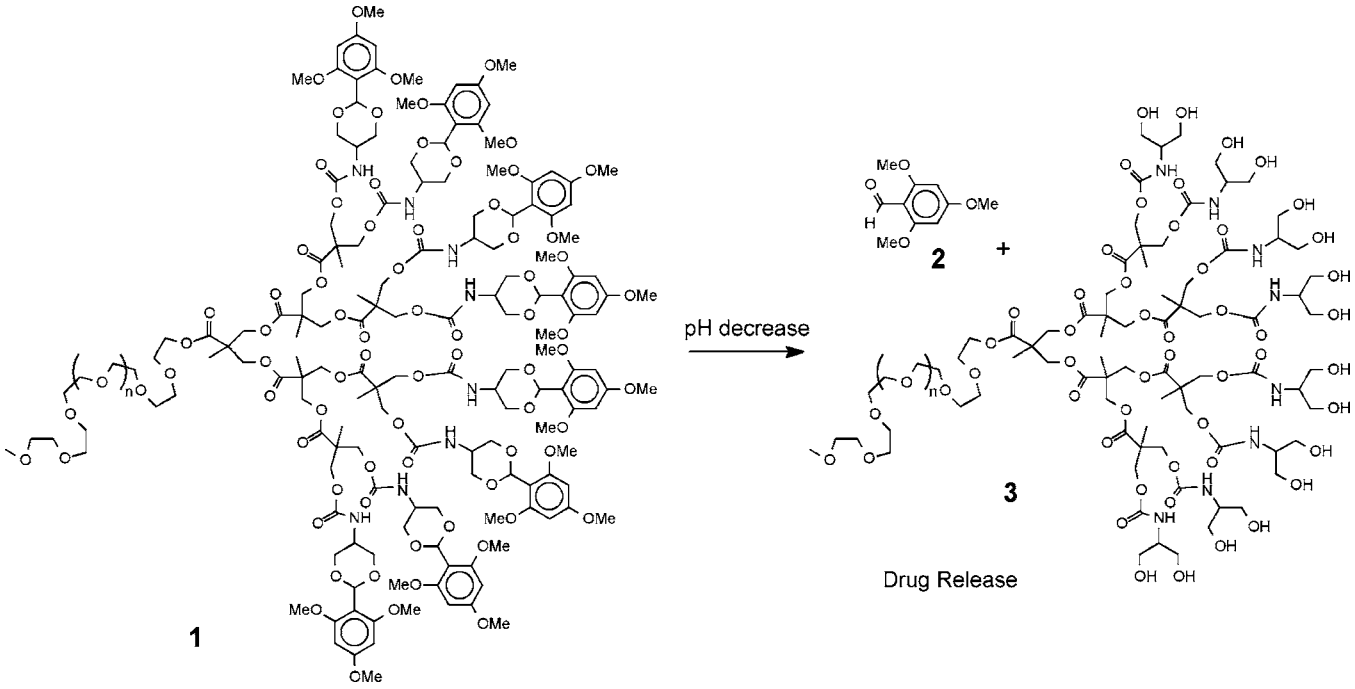

Figure 1. Hydrolysis of acetals on the dendrimer periphery of the micelle-forming copolymer **1** leads to a solubility change designed to disrupt micelle formation and trigger the release of drug.

RESULTS AND DISCUSSION

Preparation of DOX-Loaded Micelles. Copolymer **1** (Figure 1), composed of a 10 000 MW PEO block and a third generation polyester dendrimer with cyclic acetals of 2,4,6-trimethoxybenzaldehyde attached to the periphery was prepared as previously reported (*27*). As illustrated in Figure 1, hydrolysis of the cyclic acetals on the dendrimer periphery releases 2,4,6-trimethoxybenzaldehyde (**2**) and reveals polar 1,3-diol moieties on the dendrimer periphery to provide **3** after complete hydrolysis. This change in solubility of the dendrimer block is designed to trigger the disruption of the micelle and release of drug. Of the various polymers prepared in previous studies, **1** was selected for development of a DOX delivery system because of the ideal micelle size of 27 nm, a CMC of 40 mg/L, and the relatively rapid rate of micelle degradation (*27*).

DOX was loaded into micelles of **1** by an oil/water emulsion method similar to that described previously by Kataoka and co-workers (*31*, *36*). Chloroform was used as the organic phase, and 3 equiv of NEt_3 was used relative to DOX, as the drug is known to partition most effectively into the chloroform phase and into the micelle upon deprotonation of the glycosidic amine (*31*). Using 30 wt % of DOX relative to copolymer, a drug loading of approximately 12 wt % was typically obtained after centrifugation to remove insoluble free DOX particles and ultrafiltration to remove soluble unencapsulated DOX. DOX loadings were determined according to absorbance using UV−visible spectroscopy (*37*). As shown in Figure 2, that DOX is encapsulated in the micelles is supported by the significant attenuation in fluorescence (>20 times) observed for DOX-loaded micelles relative to a solution of free DOX of the same absorbance. This fluorescence attenuation has been observed previously for micellar DOX solutions and is attributed to fluorescence self-quenching of the drug molecules, which are within close proximity at the micelle core (*36*, *37*).

Hydrolysis of Acetals at the Micelle Core. A cyclic acetal composed of 2,4,6-trimethoxybenzaldehyde and the 1,3-diol moiety of serinol was selected as the pH-sensitive

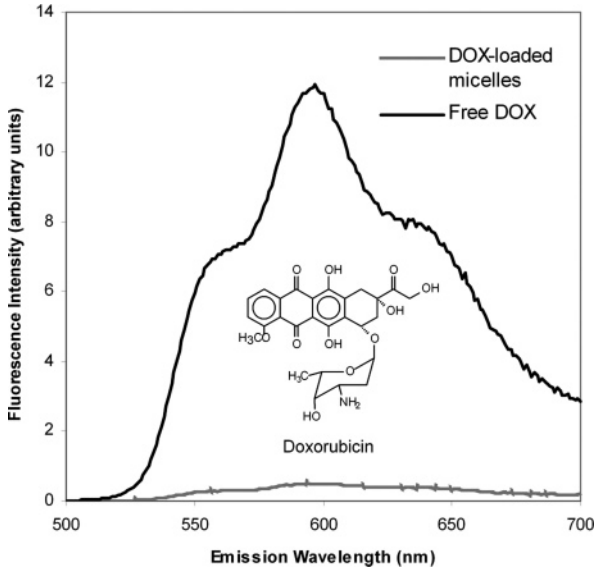

Figure 2. Fluorescence quenching of DOX-loaded micelles compared to free DOX (normalized for absorbance).

linkage for this system. While cyclic acetals are known to hydrolyze quite slowly in comparison to noncyclic acetals (*39*), the introduction of electron-donating methoxy groups at the ortho and para positions on the aromatic ring accelerates the hydrolysis rate significantly. We have also found that when these acetals are incorporated into the core block of a micelle-forming copolymer, the hydrolysis half-life is strongly dependent on the chemical environment at the micelle core. For example, while the half-life for a water-soluble low molecular weight model compound containing the same acetal is 1 h at pH 5, and several days at pH 7.4 (*27*), the rate is slowed to 50% hydrolysis after 4 h at pH 5.0 for micelles of copolymer **1** (*27*). This rate can be accelerated by the incorporation of hydrophilic spacers between the acetal and the dendrimer periphery that make the micelle core more hydrophilic, or slowed further by use

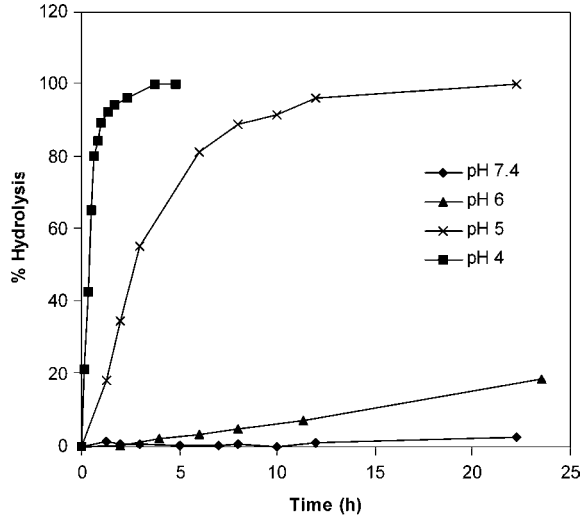

Figure 3. Hydrolysis rates of the acetals in DOX-loaded micelles of copolymer **1** at pH's ranging from 4 to 7.4.

of an even more hydrophobic linkage between the acetal and dendrimer or increasing the generation of the hydrophobic dendrimer block, making the dendrimer core more hydrophobic (*27*). Therefore, we were interested in the effect on the hydrolysis rate of incorporating DOX into the micelle core. The acetal hydrolysis rates at pH's ranging from 4 to 7.4 were investigated for the DOX-loaded micelles of copolymer **1**. Production of 2,4,6-trimethoxybenzaldehyde upon hydrolysis was detected by its absorbance at 290 nm. As shown in Figure 3, the amount of hydrolysis at pH 7.4 is quite negligible over a period of 24 h, while approximately 20% hydrolysis occurs at pH 6 over the same time period. At pH 4.0, the rate is rapid, with 50% hydrolysis after less than 30 min and at pH 5.0 the rate is very similar to that of the empty micelles with 50% hydrolysis after approximately 3 h. Therefore, the incorporation of DOX into the micelle core has only a small effect on the acetal hydrolysis rate. This may be because the hydrophobic aromatic portion of the DOX molecule is balanced by the hydrophilic glycosidic fragment, thus giving only a small change in the overall polarity of the micelle core.

pH-Dependent Release of DOX from the Micelles. The release of DOX from the micelles at different pH's was investigated using a dialysis procedure. A solution of the DOX-loaded micelles in a dialysis cassette was dialyzed against 100 mM buffer of the desired pH and the solution in the cassette was sampled at various times over a 72 h period to determine the amount of DOX remaining in the micelles. As shown in Figure 4a, a significant amount of DOX is released in a pH-dependent manner in the pH range of 4.0−6.0, while at pH 7.4 the system is very stable with less than 10% of the DOX released over 72 h.

As a control, the release of free DOX from a dialysis cassette was investigated at pH 5.0 and pH 7.4. As illustrated in Figure 4b, the release rates are very similar at both pH's, with essentially complete release after less than 10 h. This is consistent with the expected rate of diffusion for low molecular weight molecules across the dialysis membrane. Additionally, the release of DOX from micelles formed from copolymer **4** (Figure 5a) was also investigated as a control. In contrast to the highly sensitive cyclic acetals on the dendrimer periphery of **1**, the simple benzylidene acetals of **4** do not undergo hydrolysis at mildly acidic pH (*40*). Copolymer **4** was prepared as previously reported (*35*), and the micelles were prepared and loaded with DOX as described above for micelles of copolymer **1**. As shown in Figure 5b, the release rates of DOX from these micelles at both pH 5.0 and pH 7.4 are significant, with somewhat faster release at pH 5.0 as observed previously by Kataoka and co-workers using a pH-insensitive micelle system based on a PEO-poly(benzylasparate) block copolymer (*31*). These results indicate that the release of DOX from micelles is generally pH-dependent to some degree due to the increased aqueous solubility of DOX at mildly acid pH; However, the pH-sensitive micelle system based on copolymer **1** shows a stronger dependence of the release rate on pH (i.e. a greater difference between the rates at pH 7.4 and pH 5.0), suggesting that the hydrolysis of the pH-sensitive acetals likely plays a role. In addition, the increased stability of the pH-sensitive system at pH 7.4 is advantageous so that DOX will not be released during blood circulation, thus avoiding the undesirable organ accumulation and toxicity associated with the free drug. The slower release rate at pH 7.4 for micelles of **1** versus **4** highlights the fact that subtle changes in the polymer structure have a significant effect on the compatibility

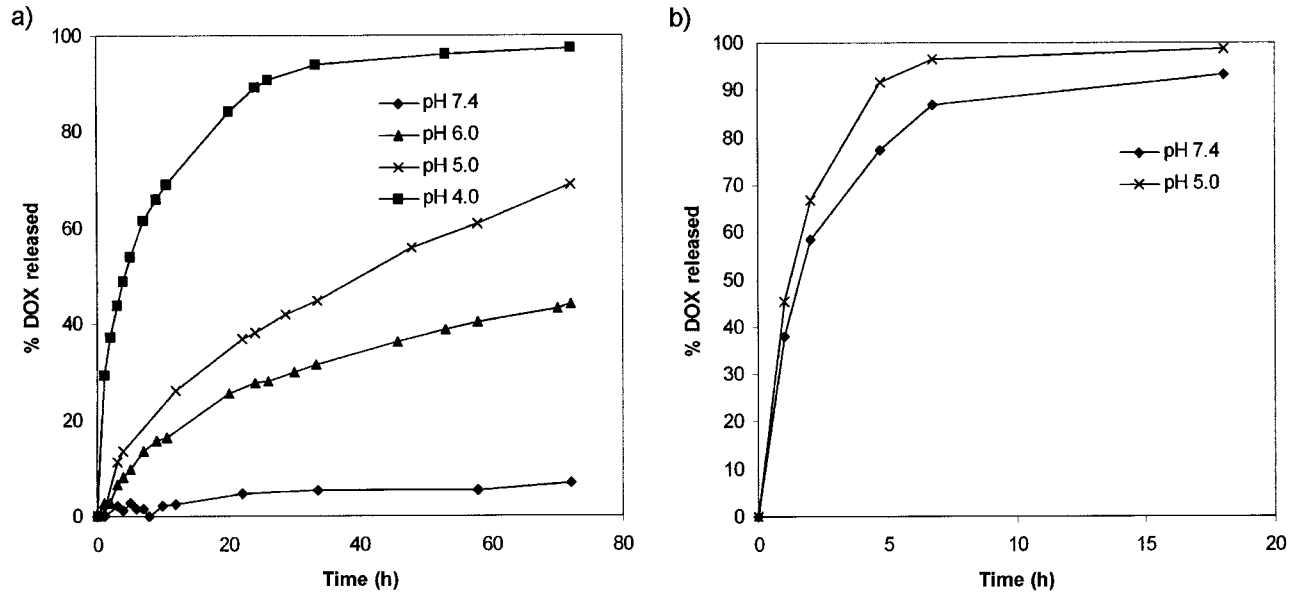

Figure 4. (a) pH-Dependent release of DOX from micelles of copolymer **1**. (b) Release of free DOX from a dialysis cassette.

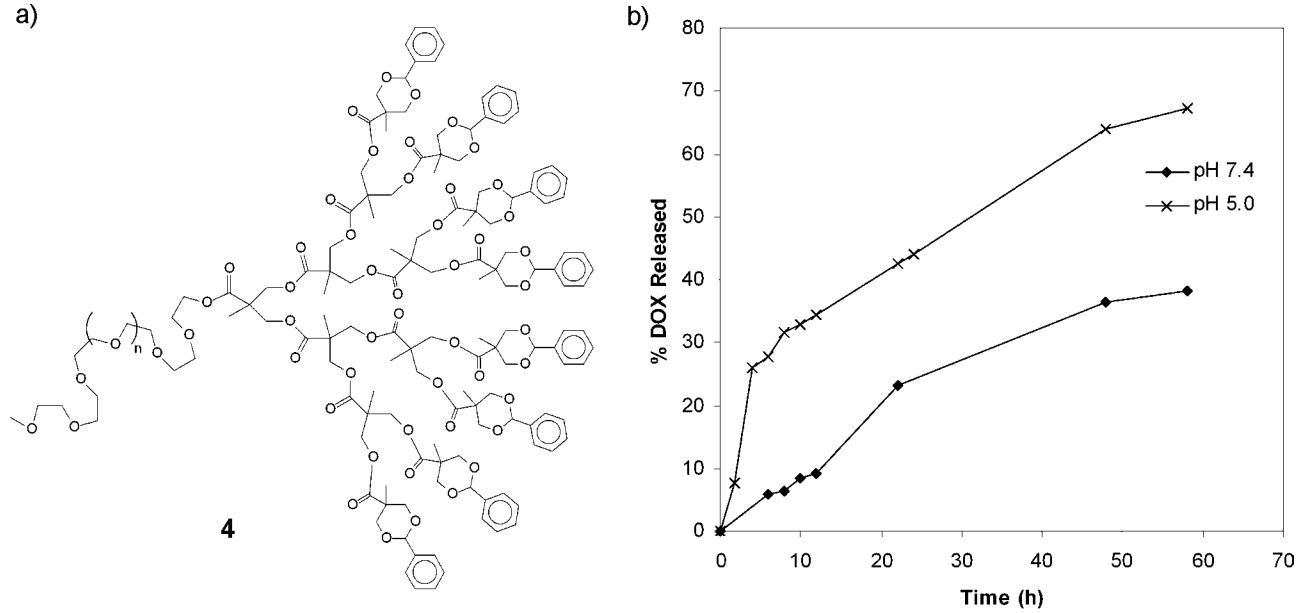

Figure 5. (a) Chemical structure of copolymer **4** forming micelles that are not pH-sensitive at mildly acidic pH. (b) Release of DOX from the pH-insensitive micelles.

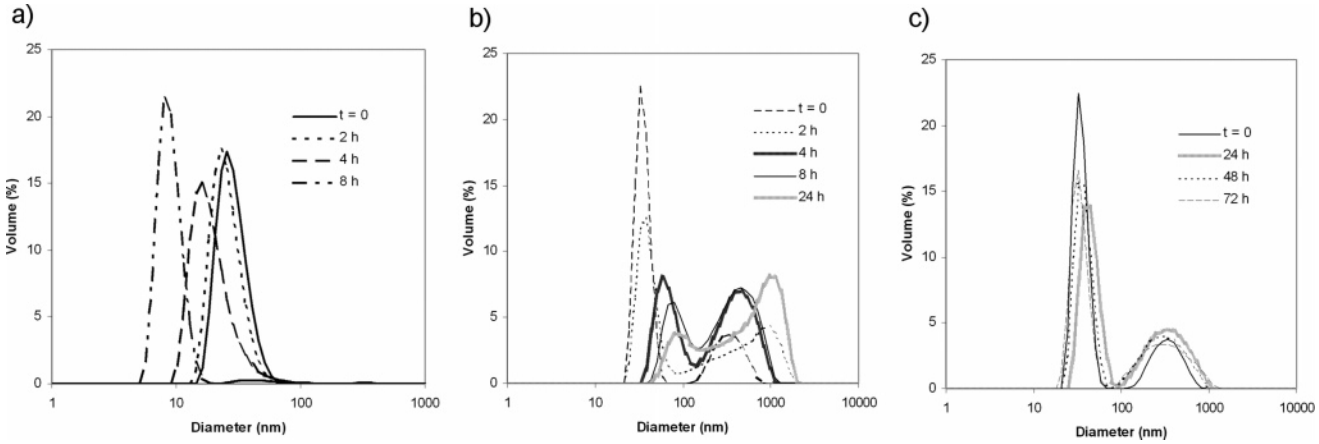

Figure 6. Dynamic light scattering measurements on micelles of copolymer **1**: (a) Degradation of empty micelles at pH 5.0. (b) Disruption of DOX-loaded micelles at pH 5.0. (c) Stability of DOX-loaded micelles at pH 7.4.

of the micelle core with the drug, thus altering the drug's overall release rate, and making the design of ideal model systems challenging. While exhibiting high stability under neutral conditions, the release of DOX from micelles of copolymer **1** at pH 5.0 is somewhat faster than that reported for other micelle systems where DOX is covalently bound to the polymer by a pH-sensitive linkage (*22*, *23*). Therefore, overall these results indicate that the pH-sensitive DOX-loaded micelles of **1** have characteristics ideal for the selective release of DOX in mildly acidic physiological environments.

Investigation of Micelle Degradation by Dynamic Light Scattering. Although DOX is steadily released from the micelles of copolymer **1** at mildly acidic pH, the release rates are generally slower than the acetal hydrolysis rates. Furthermore, even after 100% acetal hydrolysis, not all of the DOX is immediately released. Therefore, we were interested in probing the degradation of the DOX-loaded micelles by dynamic light scattering (DLS) to determine the time dependence of the micelle size. While the empty micelles have an initial volume average diameter of 27 nm, the DOX-loaded micelles are somewhat larger with a diameter of 35 nm and a small fraction of aggregates in the size range of 200−400 nm is observed. As shown in Figure 6a, the size of the empty micelles decreases over several h at pH 5.0, consistent with the disintegration of the micelles into soluble copolymer molecules. In contrast, over several h at pH 5.0, the size of the DOX-loaded micelles increases and the fraction of aggregates in the population becomes greater as shown in Figure 6b. This aggregation probably occurs upon disruption of the micelles due to acetal hydrolysis and is facilitated by the tendency of DOX to form aggregates by π-stacking. The lack of appearance of a population with a size less than 10 nm indicates that after acetal hydrolysis, the copolymers are probably associated with the aggregates rather than being dissociated in solution. It is likely that some DOX release occurs during rearrangement of the micelles to aggregates, while the remainder of the release over a longer time period occurs from the aggregates and is assisted by the increased water solubility of DOX at acidic pH upon protonation of the glycosidic amine. At pH 7.4, the micelles are stable over several days, with no significant changes in the size distribution over this time period (Figure 6c).

In Vitro Investigation of DOX-Loaded Micelles. Preliminary in vitro studies were conducted to compare the toxicities of the empty micelles, DOX-loaded micelles, and free DOX in MDA-MB-231 breast cancer cells using

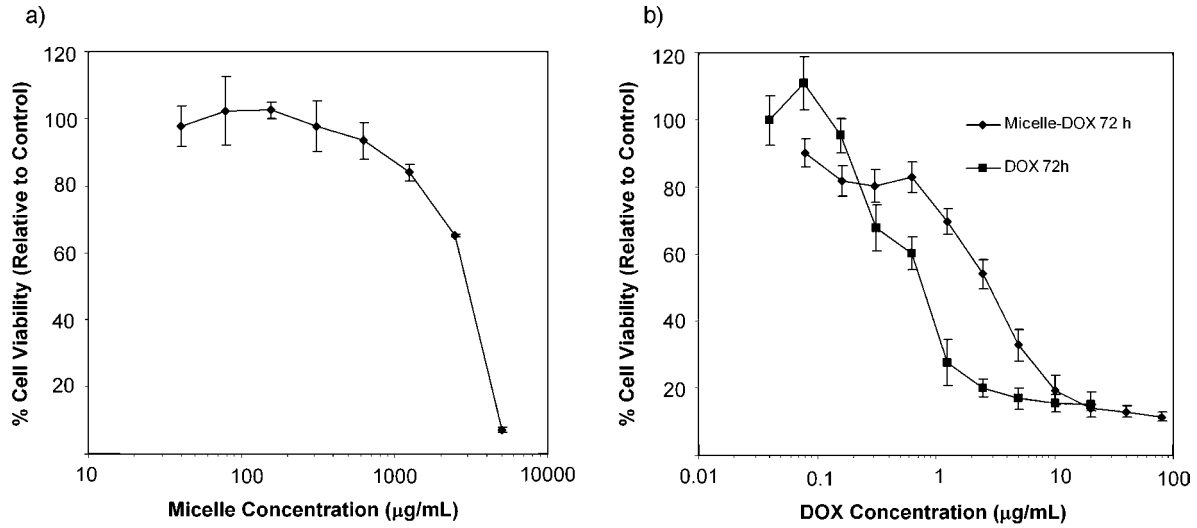

Figure 7. In vitro toxicity of (a) empty micelles and (b) free DOX and DOX-loaded micelles of copolymer **1** with MDA-MB-231 cells after a 72 h incubation (MTT assay).

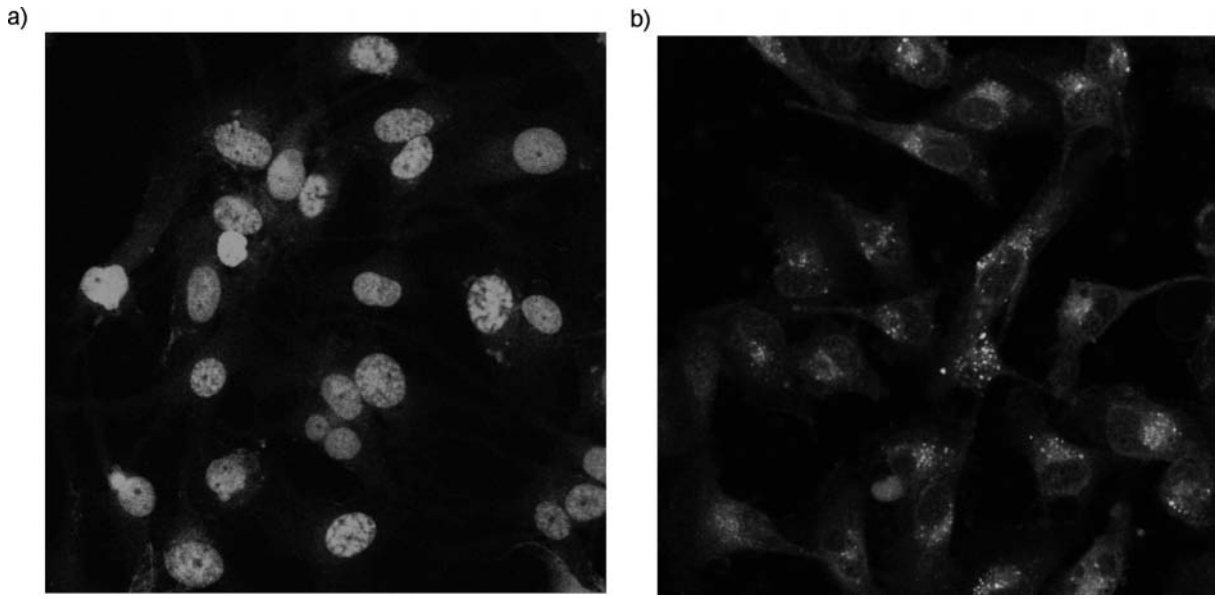

Figure 8. Laser scanning confocal microscopy images of (a) DOX and (b) DOX-loaded pH-sensitive micelles incubated with MDA-MB-231 cells for 24 h.

the MTT assay (*38*). As shown in Figure 7a, the empty micelles of copolymer **1** are nontoxic at concentrations up to 1 mg/mL, with an IC_{50} of approximately 2 mg/mL. The toxicity of the DOX-loaded micelles was investigated at a constant, nontoxic copolymer concentration of 0.2 mg/mL, and the concentration of DOX was varied. As shown in Figure 7b, above 1 μg/mL DOX equiv, the DOX-loaded micelles were toxic and an IC_{50} of approximately 3 μg/mL was determined. For comparison, the toxicity of free DOX was also investigated and the IC_{50} was found to be about 0.8 μg/mL. The fact that the micelle formulation is toxic, with an IC_{50} on the same order of magnitude as free DOX is consistent with the release of free and active DOX in the cells and is encouraging for the therapeutic potential of the system. The somewhat lower toxicity of the micelle system may result from the gradual release of DOX within the cell and from differences in the released drug's cellular localization relative to the free drug. However, the potential for the selective accumulation of the micelle system in tumor tissue by the enhanced permeation and retention effect may enhance its overall therapeutic efficacy in vivo relative to free DOX (*5*).

The intracellular localization of both free DOX and DOX-loaded micelles was investigated using confocal microscopy. As shown in Figure 8a, cells exposed to free DOX show significant accumulation of DOX in the nucleus after 24 h, consistent with the results of previous studies (*41*). In contrast, cells exposed to DOX-loaded pH-sensitive micelles have a punctate fluorescence that is concentrated in the cytoplasm after 24 h as shown in Figure 8b. These observations are important for several reasons. First, the absence of DOX fluorescence in the nucleus suggests that the micelles are stable in the presence of cells and serum-containing cell medium, as the rapid destabilization of the micelles in the extracellular environment and subsequent release of DOX outside the cell would be expected to result in an image similar to that observed for free DOX. In addition, the fluorescence in the cytoplasm suggests that the DOX-loaded micelles are indeed taken up by cells, and its punctate nature is consistent with the localization of the drug in subcellular organelles. While it is not possible with these data to determine the precise mechanism of cellular uptake or localization of the DOX-loaded micelles or the released drug, comparisons with similar images

previously reported for both pH-sensitive DOX-loaded micelles (*23*) and polymer-DOX conjugates (*42*) suggest that the fluorescence may be associated with organelles such as lysosomes, mitochondria, and the golgi apparatus. While one important mechanism of action of DOX involves DNA intercalation (*43*), other mechanisms have also been proposed, including the inhibition of mitochondrial function (*44*), thus explaining the toxicity of this and other delivery systems that do not lead to the accumulation of DOX in the nucleus. More in vitro studies with these DOX-loaded pH-sensitive micelles will be necessary in order to further explore their mechanism of cell uptake and intracellular trafficking.

CONCLUSIONS

In summary, the anticancer drug doxorubicin was encapsulated in pH-sensitive micelles formed from a PEO−dendritic polyester copolymer with acid-labile acetal groups on the core-forming dendrimer periphery. It was found that the acetal groups undergo hydrolysis and that DOX is selectively released at acidic pH's such as those encountered in tumor tissue and in endocytic vesicles including endosomes and lysosomes. In comparison with a non-pH-sensitive micelle control, the release of DOX from the pH-sensitive system was much more dependent on pH, although the release of DOX at acidic pH is clearly to some degree due to its increased aqueous solubility. Dynamic light scattering studies revealed that while the pH-sensitive micelles are stable at pH 7.4, acetal hydrolysis at acidic pH results in disruption of the micelles and rearrangment to form larger aggregates. In vitro toxicity studies revealed that the empty micelles are relatively nontoxic, while DOX encapsulated in the micelles has a toxicity quite similar to that of the free drug. Laser scanning confocal microscopy images support the localization of DOX in intracellular organelles in contrast to free DOX, which is localized in the cell nucleus after 24 h. This suggests that the DOX-loaded micelles are indeed taken up by cells and that the mechanism of action of the released drug may differ from that of the free drug. Future in vitro and in vivo studies will further explore the biological properties of these micelles. Thus far, these new pH-responsive drug carriers show promise for the controlled release of therapeutics in mildly acidic physiological environments.

ACKNOWLEDGMENT

We thank the National Institute of Health (GM 65361 and EB 002047) and the U.S. Department of Energy (DE-AC03-765F00098) for support of this research. We thank Ann Fisher and Young Kwon for help with in vitro studies. The Center for New Directions in Organic Synthesis is supported by Bristol-Myers Squibb as a Sponsoring Member and Novartis Pharma as Supporting Member.

LITERATURE CITED

(1) Kataoka, K., Harada, A., and Nagasaki, Y. (2001) Block copolymer micelles for drug delivery: design, characterization and biological significance. *Adv. Drug Delivery Rev. 47*, 113−131.

(2) Lavasanifar, A., Samuel, J., and Kwon, G. S. (2002) Poly(ethylene oxide)-*block*-poly(L-amino acid) micelles for drug delivery. *Adv. Drug Delivery Rev. 54*, 169−190.

(3) Kabanov, A. V., Batrakova, E. V., and Alakhov, V. Y. (2002) Pluronic block copolymers as novel polymer therapeutics for drug and gene delivery. *J. Controlled Release 82*, 189−212.

(4) Kwon, G. S., and Okano, T. (1996) Polymeric micelles as new drug carriers. *Adv. Drug Delivery Rev. 21*, 107−116.

(5) Maeda, H., and Matsumura, Y. (1986) A new concept in macromolecular therapeutics in cancer chemotherapy: mechanism of tumoritropic accumulation of proteins and the antitumor agent SMANCS. *Cancer Res. 46*, 6387−9392.

(6) Cammas, S., Suzuki, K., Sone, C., Sakurai, Y., Kataoka, K., and Okano, T. (1997) Thermo-responsive polymer nanoparticles with a core−shell micelle structure as site-specific drug carriers. *J. Controlled Release 48*, 157−164.

(7) Chung, J. E., Yokoyama, M., and Okano, T. (2000) Inner core segment design for drug delivery control of thermo-responsive polymeric micelles. *J. Controlled Release 65*, 93−103.

(8) Husseini, G. A., Myrup, G. D., Pitt, W. G., Christensen, D. A., and Rapoport, N. Y. (2000) Factors affecting acoustically triggered release of drugs from polymeric micelles. *J. Controlled Release 69*, 43−52.

(9) Rapoport, N., Pitt, W. G., Sun, H., and Nelson, J. L. (2003) Drug delivery in polymeric micelles: from in vitro to in vivo. *J. Controlled Release 91*, 85−95.

(10) Engin, K., Leeper, D. B., Cater, J. R., Thistlethwaite, A. J., Tupchong, L., and McFarlane, J. D. (1995) Extracellular pH distribution in human tumors. *Int. J. Hypertherm. 11*, 211−216.

(11) Ojugo, A. S. E., Mesheehy, P. M. J., McIntyre, D. J. O., McCoy, C., Stubbs, M., Leach, M. O., Judson, I. R., and Griffiths, J. R. (1999) Measurement of the extracellular pH of solid tumors in mice by magnetic resonance spectroscopy: a comparison of exogenous 19F and 31P probes. *NMR Biomed. 12*, 495−504.

(12) van Sluis, R., Bhujwalla, Z. M., Ballerteros, P., Alverez, J., Cerdan, S., Galons, J. P., and Gillies, R. J. (1999) In vivo imaging of extracellular pH using 1H MSRI. *Magn. Reson. Med. 41*, 743−750.

(13) Kabanov, A. V., Slepnev, V. I., Kuznetsova, L. E., Batrakova, E. V., Alakhov, V. Y., Melik-Nubarov, N. S., and Sveshnikov, P. G. (1992) Pluronic micelles as a tool for low-molecular weight compound vector delivery into a cell: Effect of *Staphylococcus aureus* enterotoxin B on cell loading with micelle incorporated fluorescent dye. *Biochem. Int. 26*, 1035−1042.

(14) Luo, L., Tam, J., Maysinger, D., and Eisenberg, A. (2002) Cellular internalization of poly(ethylene oxide)-*b*-poly(caprolactone) diblock copolymer micelles. *Bioconjugate Chem. 13*, 1259−1265.

(15) Mellman, I., Fuchs, R., and Helenius, A. (1986) Acidification of the endocytic and exocytic pathways. *Annu. Rev. Biochem. 55*, 773−700.

(16) Gillies, E. R., and Fréchet, J. M. J. Development of acid sensitive copolymer micelles for drug delivery. *Pure Appl. Chem. 76*, 1295−1308.

(17) Lee, E. S., Na, K., and Bae, Y. H. (2003) Polymeric micelle for tumor pH and folate-mediated targeting. *J. Controlled Release 91*, 103−113.

(18) Leroux, J., Roux, E., Garrec, D., Hong, K., and Drummond, D. C. (2001) N-isopropylacrylamide copolymers for the preparation of pH-sensitive liposomes and polymeric micelles. *J. Controlled Release 72*, 71−84.

(19) Kabanov, A. V., Vinogradov, S. V., Suzdaltseva, Y. G., and Alakhov, V. Y. (1995) Water-soluble block polycations as carriers for oligonucleotide delivery. *Bioconjugate Chem. 6*, 639−643.

(20) Katayose, S., and Kataoka, K. (1997) Water-soluble polyion complex associates of DNA and poly(ethylene glycol)-poly(L-lysine) block copolymer. *Bioconjugate Chem. 8*, 702−707.

(21) Zhang, G.-D., Harada, A., Nishiyama, N., Jiang, D.-L., Koyama, H., Aida, T., and Kataoka, K. (2003) Polyion complex micelles entrapping cationic dendrimer porphyrin: effective photosensitizer for photodynamic therapy of cancer. *J. Controlled Release 93*, 141−150.

(22) Yoo, H. S., Lee, E. A., and Park, T. G. (2002) Doxorubicin-conjugated biodegradable polymeric micelles having aicd-cleavable linkages. *J. Controlled Release 82*, 17−27.

(23) Bae, Y., Fukushima, S., Harada, A., and Kataoka, K. (2003) Design of environment-sensitive supramolecular assemblies for intracellular drug delivery: polymeric micelles that are

responsive to intracellular pH change. *Angew. Chem., Int. Ed. 42*, 4640−4643.
(24) Heller, J., Barr, J., Ng, S. Y., Abdellauoi, K. S., and Gurny, R. (2002) Poly(ortho esters): synthesis, characterization, properties and uses. *Adv. Drug Delivery Rev. 54*, 1015−1039.
(25) Ng, S. Y., Heller, J. (2003) US 2003152630.
(26) Gillies, E. R., and Fréchet, J. M. J. (2003) A new approach towards acid sensitive copolymer micelles for drug delivery. *Chem. Commun.* 1640−1641.
(27) Gillies, E. R., Jonsson, T. B., and Fréchet, J. M. J. (2004) Stimuli-responsive supramolecular assemblies of linear-dendritic copolymers. *J. Am. Chem. Soc. 126*, 11936−11943.
(28) Ceh, B., Winterhalter, M., Frederik, P. M., Vallner, J. J., and Lasic, D. D. (1997) Stealth liposomes: from theory to product. *Adv. Drug Delivery Rev. 24*, 165−177.
(29) Gabizon, A. A. (1992) Selective tumor localization and improved therapeutic index of anthracyclins encapsulated in long-circulating liposomes. *Cancer Res. 52*, 891−896.
(30) Huang, S. K., Mayhew, E., Gilani, S., Lasic, D. D., Martin, F. J., and Papahadjopoulos, D. (1992) Pharmacokinetics and Therapeutics of Sterically Stabilized Liposomes in Mice Bearing C-26 Colon Carcinoma. *Cancer Res. 52*, 6774−6781.
(31) Kataoka, K., Matsumoto, T., Yokoyama, M., Okano, T., Sakurai, Y., Fukushima, S., Okamoto, K., and Kwon, G. S. (2000) Doxorubicin-loaded poly(ethylene glycol)-poly(b-benzyl-L-aspartate) copolymer micelles: Their pharmaceutical characteristics and biological significance. *J. Controlled Release 64*, 143−153.
(32) Danson, S., Ferry, D., Alakhov, V., Margison, J., Kerr, D., Jowle, D., Brampton, M., Halbert, G., and Ranson, M. (2004) Phase I dose escalation and pharmacokinetic study of pluronic polymer-bound doxorubicin (SP1049C) in patients with advanced cancer. *Br. J. Cancer 90*, 2085−2091.
(33) Vasey, P. A., Kaye, S. B., Morrison, R., Twelves, C., Wilson, P., Duncan, R., Thomson, A. H., Murray, L. S., Hilditch, T. E., Murray, T., Burtles, S., Fraier, D., Frigerio, E., and Cassidy, J. (1999) Phase I clinical and pharmacokinetic study of PK1 [N−(2-hydroxypropyl)methacrylamide copolymer doxorubicin]: First member of a new class of chemotherapeutic agents − drug-polymer conjugates. *Clin. Cancer Res. 5*, 83−94.
(34) Duncan, R., Dimitrijevic, S., and Evagorou, E. G. (1996) The role of polymer conjugates in the diagnosis and treatment of cancer. *S. T. P. Pharma. Sci. 6*, 237−263.
(35) Ihre, H., Padilla De Jesús, O. L., and Fréchet, J. M. J. (2001) Fast and convenient divergent synthesis of aliphatic ester dendrimers by anhydride coupling. *J. Am. Chem. Soc. 123*, 5908−5917.
(36) Kwon, G., Naito, M., Yokoyama, M., Okano, T., Sakurai, Y., and Kataoka, K. (1997) Block copolymer micelles for drug delivery: Loading and release of doxorubicin. *J. Controlled Release 48*, 195−201.
(37) Kwon, G. S., Naito, M., Yokoyama, M., Okano, T., Sakurai, Y., and Kataoka, K. (1995) Physical Entrapment of Adriamycin in AB Block Copolymer Micelles. *Pharm. Res. 12*, 192−195.
(38) Freshney, I. R. (2000) *Culture of Animal Cells: A Manual of Basic Technique,* 4th ed., pp 336−338, Wiley-Liss, New York.
(39) Fife, T., Jao, L. (1965) Substituent effects in acetal hydrolysis. *J. Org. Chem. 30*, 1492−1495.
(40) Greene, T. W., and Wuts, P. G. M., (1999) *Protective groups in organic synthesis,* 3rd ed., pp 57−58, Wiley and Sons Inc., New York.
(41) Coley, H. M., Amoa, W. B., Twentyman, P. R., and Workman, P. (1993) Examination by laser scanning confocal fluorescence imaging microscopy of the subcellular localization of anthracyclines in parent and multidrug resistant cells lines. *Br. J. Cancer 67*, 1316−1323.
(42) Rodrigues, P. C. A., Beyer, U., Schumacher, P., Roth, T., Fiebig, H. H., Unger, C., Messori, L., Orioli, P., Paper, D. H., Mulhaupt, R., and Kratz, F. (1999) Acid-sensitive poly(ethylene glycol) conjugates of doxorubicin: preparation, in vitro efficacy and intracellular distribution. *Bioorg. Med. Chem. 7*, 2517−2524.
(43) Gabbay, E. J., Grier, D., Fingerie, R. E., Reimer, R., Levy, R., Pearce, S. W., and Wilson, W. D. (1976) Interaction specificity of the anthracyclines with DNA. *Biochemistry 15*, 2062−2070.
(44) Nicolay, K., and De Kruijff, B. (1987) Effects of adriamycin on respiratory chain activities in mitochondria from rat liver, rat heart and bovine heart. Evidence for preferential inhibition of complex III and IV. *Biochim. Biophys. Acta 892*, 320−330.

BC049851C

Cytotoxic Activity of a Tumor Protease-Activated Pore-Forming Toxin

C. Potrich,*[,†] R. Tomazzolli,[†] M. Dalla Serra,[†] G. Anderluh,[‡] P. Malovrh,[‡] P. Maček,[‡] G. Menestrina,[†] and M.Tejuca[†,§]

CNR-ITC Istituto di Biofisica Sezione di Trento, Via Sommarive 18, 38050 Povo (TN) Italy, Department of Biology, Biotechnical Faculty, University of Ljubljana, Večna pot 111, 1000 Ljubljana, Slovenia, and Departamento de Bioquimica, Facultad de Biologia, Universidad de la Habana, Calle 23 e/I y J, La Habana, Cuba. Received May 31, 2004; Revised Manuscript Received December 21, 2004

Equinatoxin II is a pore forming toxin produced by the sea anemone *Actinia equina*. It is able to kill very unspecifically most cell types by the membrane-perturbing action of an amphiphilic α-helix located at its N-terminal. A normally active N-terminal mutant, containing one single cys in the amphiphilic α-helix, becomes totally inactive when it is bound to avidin via a biotinylated linker. By choosing, as a linker, a peptide containing a tumor protease cleavage site, we were able to construct an enzymatically activable conjugate which should be selective for tumor cells. The introduced cleavage site was designed in order to be digested by both cathepsin B and matrix metalloproteases (MMPs). We confirmed that this conjugate could be activated in vitro by cathepsin B and MMPs. After having measured the enzymatic activity of fibrosarcoma and breast carcinoma cells, we analyzed the cytotoxic effect of the conjugate on the same lines and on human red blood cells (HRBC) as controls. We found that the conjugate was activated, at least in part, by the tumor cell lines used, whereas it was inactive on HRBC. That the activation process was dependent on the enzymatic action of cathepsin B and MMPs, was indicated by three lines of evidence: (1) binding occurred normally on all type of cells including HRBC which however were insensitive being devoid of enzymes; (2) the cytotoxic effect correlated with the amount of cathepsin B activity expressed by the cells; (3) conjugate activation was reduced by specific inhibitors of cathepsin B and MMPs. These results demonstrate the possibility of tumor cell killing by a pore-forming toxin conjugate specifically activated by tumor proteases.

INTRODUCTION

Immunotoxins and mitotoxins are chimeric molecules in which specific ligands are coupled to toxins. If the ligand moiety is specific for a tumoral cell line, the chimeric toxin can kill those cells selectively. Several reviews describe the construction and the activity of chimeric toxin produced by genic fusion or chemical linking to either antibodies (immunotoxins) or growth factors (mitotoxins) (*1*, *2*).

The toxins usually used for conjugation are derived either from bacteria (e.g. *Pseudomonas* exotoxin A or diphtheria toxin (*3*, *4*)), or from plants (e.g. ricin or abrin (*5*)). Both types of toxins kill cells by inhibiting protein synthesis (*6*). To exert their effect these complexes must enter the cell, where only a portion of the internalized immunotoxin escapes degradation and reaches the cytoplasmic target. In some cases internalization can be a rate-limiting step, which reduces the immunotoxin efficacy. One way to overcome this problem is to use membrane-active toxins (*7*), such as hemolysins and cytolysins (*8*, *9*). These pore forming toxins attack the lipid phase of cell membranes disintegrating vital membrane functions. They could provide very powerful antitumoral drugs, when conjugated with an appropriate targeting molecule. Some examples of the construction of such molecules have been reported, using membrane damaging toxins of different origin e.g. from animals (cytolysins from sea anemones (*10*−*13*)), plants (*Pyrularia* thionin (*14*)) or from bacteria (*Bacillus thuringiensis* δ-endotoxin (*15*), *Staphylococcus aureus* α-toxin (*16*), *Bacillus anthracis* anthrax toxin (*17*)). However, the main problem of most of the immunotoxins constructed with membrane active proteins is the poor cellular specificity associated to the capacity of the toxin to bind to almost any cell membrane. The purpose of this study was to overcome much unspecificity. To this aim we present the construction of a modular inactive conjugate between a sea anemone cytolysin (the EqTII-I18C mutant) and avidin and its activation mediated by tumor cells proteases. To construct this tumor protease-activated pore-forming toxin we chose two classes of proteases, cathepsins and metalloproteinases (MMPs),[1] which are known to be associated to several tumors. Numerous reports in

* Corresponding author. Tel: ++39 0461 314257. Fax: ++39 0461 810628. E-mail: cpotrich@itc.it.

† CNR-ITC Istituto di Biofisica Sezione di Trento.

‡ University of Ljubljana.

§ Universidad de la Habana.

[1] Abbreviations: BMH: bismaleimidohexane; biotin-HPDP: *N*-[6-(biotinamido)hexyl]-3′-(2′-pyridyldithio)propionamide; DTT: dithiothreitol; E64: *trans*-epoxysuccinyl-L-leucylamido-(4-guanidino)butane; EDTA: ethylenediaminetetraacetic acid; EqTII: *Actinia equina* equinatoxin II.; FBS: fetal bovine serum; GM 6001: *N*-[(2*R*)-(hydroxamidocarbonylmethyl)-4-methylpentanoyl]-L-tryptophan methylamide; HC_{50}: concentration which causes 50% of hemolysis; HIC: hydrophobic interaction chromatography; HRBC: human red blood cells; HT 1080: human fibrosarcoma; IC_{50}: concentration which reduces by 50% viability in a citotoxicity assay; MCF 7: human breast adenocarcinoma; MMPs: matrix metalloproteinases; MTT: 3-(4,5-dimethylthiazol-2-yl)-2,5-diphenyltetrazolium bromide; SDS: sodium dodecyl sulfate; ZR 751: human breast carcinoma.

10.1021/bc049873z CCC: $30.25 © 2005 American Chemical Society
Published on Web 02/16/2005

the literature describe circumstantial evidence that cathepsin B and L contribute to tumor progression and metastasis (*18*, *19*). Cathepsin B is found at higher levels in a number of human cancers (i.e. colorectal, lung and bladder), suggesting that it may be useful as a diagnostic and prognostic marker. The MMPs are involved in a wide range of proteolytic events, in normal and pathological circumstances (*20*). Pathological processes involving MMPs include tumor growth and migration (*21*).

This approach is intended as a conceptual proof to demonstrate that a relatively simple chemistry could be used to conjugate a cytolysin to a ligand moiety via a peptide containing cleavage sites of tumor-associated proteolytic enzymes. We further demonstrated that the conjugate could be specifically cleaved by these enzymes, leading to its possible application as antitumoral drug. The advantage of the activable pore-forming system, for the construction of immunotoxins, is the reduction of the unspecific activity. In this way two mechanisms of target would be present in a single hybrid molecule, the recognizing of tumor cell through the ligand moiety and the specific activation of the toxin by the tumor-associated proteases.

EXPERIMENTAL PROCEDURES

Materials. *Actinia equina* equinatoxin II-I18C mutant was produced in an *E. coli* expression system as described previously (*22*). *N*-[6-(Biotinamido) hexyl]-3′-(2′-pyridyldithio)propionamide (biotin-HPDP) and bismaleimidohexane (BMH) were purchased from Pierce, the peptide NH_2-C-N-K-S-R-L-G-L-G-K-biotin-COOH was from Primm (Milan), cathepsin B, matrix metalloproteinase 7 (MMP-7), avidin, *N*-[(2*R*)-(hydroxamidocarbonylmethyl)-4-methylpentanoyl]-L-tryptophan methylamide (GM 6001) and cathepsin B substrate III (Z-R-R-AMC) from Calbiochem; 5,5′-dithio-bis-(2-nitrobenzoic acid) (DTNB or Ellman's reagent) from Acros; *trans*-epoxysuccinyl-L-leucylamido-(4-guanidino)butane (E64), dithiothreitol (DTT) and 3-(4,5-dimethylthiazol-2-yl)-2,5-diphenyltetrazolium bromide (MTT) were obtained from Sigma. The metalloproteinase specific substrate Mca-P-L-G-L-Dap(Dpn)-A-R-NH_2 was purchased from Bachem (catalog number M-1895), while Prionex (porcine hydrolyzed collagen of average mass 20 kDa) was purchased from Pentapharm Ltd.

Cell Lines. Cells used in these assays were ZR 751 (human breast carcinoma), MCF 7 (human breast adenocarcinoma) and HT 1080 (human fibrosarcoma) obtained from the Istituto Zooprofilattico Sperimentale (Brescia, Italy). After every week new cells were thawed and cultured in RPMI 1640 (ZR 751) or Eagle's minimum essential medium (MCF 7 and HT 1080) with 10% fetal bovine serum (FBS, EuroClone), 2 mM L-glutamine and 0.15 mg/mL gentamicin. The MCF 7 cell line was also supplemented with 1 mM sodium pyruvate. All reagents and media were obtained from Sigma.

Conjugation via HPDP. EqTII-I18C was incubated with biotin-HPDP in a 1:8 molar ratio in 20 mM Na_2HPO_4, 150 mM NaCl, 1 mM EDTA pH 7.4 for 90 min at room temperature. EqTII-I18C, that was S−S linked to biotin via a long spacer arm, was separated from unreacted HPDP using a HIC column (Metachem) equilibrated with 25 mM Na_2HPO_4, 0.5 M $(NH_4)_2SO_4$, pH 7. Elution was with a linear gradient of $(NH_4)_2SO_4$ decreasing from 100% to 0% in 15 min. When avidin was added, we obtained the following conjugated molecule: EqTII-I18C_S−S-$(CH_2)_2$CONH $(CH_2)_6$NH-biotin_avidin (or EqTII-I18C_biotin_avidin).

Conjugation Mediated by Ellman's Reagent or BMH. The cysteine of EqTII-I18C mutant was either activated by using the Ellman's reagent or covalently modified with the homobifunctional cross-linking reagent BMH. EqTII-I18C was incubated for 30 min at room temperature in 0.1 M Na_2HPO_4 pH 8 with Ellman's reagent in a probe to toxin molar ratio of 60:1. Alternatively, it was incubated in 20 mM Na_2HPO_4, 150 mM NaCl pH 7.0 with BMH for 30 min at room temperature in a probe:toxin molar ratio of 30:1. Excess of reagent was removed by desalting (Sephadex G-25, NAP-5 column, Pharmacia Biotech Amersham Bioscences). The resulting activated or modified EqTII-I18C was incubated with the biotinylated peptide in a peptide to toxin molar ratio of 40:1, at room temperature for 2 days, and again the excess of peptide was removed by gel filtration. An excess of avidin (avidin:biotinylated toxin in a 4:1 or 2:1 molar ratio) was added at room temperature, and after 1 h the resulting conjugate was purified from unbound components via HIC. The column was equilibrated with 25 mM Na_2HPO_4, 2 M $(NH_4)_2SO_4$ pH 7; the bilinear gradient of $(NH_4)_2SO_4$ was decreasing from 100% to 15% in 12 min and from 15% to 0% in 8 min. The concentration of the conjugate among the collected aliquots was estimated by measuring the absorbance at 280 nm and by titrating the hemolytic activity of the fractions before and after reduction with 2.5 mM DTT. The concentration of the conjugate was approximately calculated using a molar extinction coefficient of 132 840 M^{-1} cm^{-1} at 280 nm on the basis of a molar composition of one toxin per avidin molecule (confirmed by electrophoretic experiments, see Figure 3E). The conjugate produced with BMH was EqTII-I18C_S-maleimide-$(CH_2)_6$-maleimide-S-peptide-biotin_avidin, while by using Ellman's reagent, or no reagents at all, we obtained the following molecule: EqTII-I18C_S−S-peptide-biotin_avidin.

Enzymatic Digestion. Cathepsin B was first activated with 10 mM DTT at 37 °C for 15 min. For peptide digestion, a 1.2 mM peptide solution was incubated with activated cathepsin B (at final concentration of 3.5 μM) in 30 mM sodium acetate pH 5, or 0.35 mM peptide was incubated with 3.8 μM MMP-7 in 0.2 M NaCl, 50 mM Tris/HCl, 5 mM $CaCl_2$, 20 μM $ZnCl_2$ pH 7.6, both at 37 °C for 2 h. The specificity of the cleavage was checked by adding 50 μM E64 for cathepsin B or 8 μM GM6001 for MMP-7.

For conjugate digestion a 6.3 μM conjugate solution was incubated with activated cathepsin B (at final concentration of 0.9 μM) in 80 mM Na H_2PO_4 pH 5 or 2.8 μM conjugate was digested by 2.3 μM MMP-7 in 0.2 M NaCl, 50 mM Tris/HCl, 5 mM $CaCl_2$, 20 μM $ZnCl_2$ pH 7.6, at 37°C for 2 h. To check the specificity of the cleavage, parallel experiments were performed by adding 11.4 μM E64 or 4.7 μM GM6001, respectively.

In both cases the products were separated by hydrophobic interaction chromatography under the same conditions used for conjugate separation. The products of the conjugate digestion were also tested by hemolytic assays.

Mass Spectrometry Analysis. Digested peptides (same conditions as described above) were passed on a Jupiter C4 column by Phenomenex with a 15 min linear gradient from 5 to 95% acetonitrile in water. LC-MS analysis was performed on a Hewlett-Packard Series 1100 liquid chromatograph coupled to a Bruker Esquire-LC ion trap mass spectrometer equipped with an atmospheric pressure ESI interface. A Rheodyne 7725 (Cotati, CA) injection valve equipped with a 200 μL internal loop was used for the injections. The PDA (photodiode-array) detector (HP Series 1100) was set at a wavelength of 215 nm, and a 7:3 split of the column effluent was used to achieve a flow rate of 300 μL/min into the ESI source.

Hemolytic Assays. Hemolytic activity of EqTII-I18C and different conjugates was determined turbidimetrically at 650 nm with a microplate reader (UVmax from Molecular Devices, Sunnyvale, CA) supported by the computer program SOFTmax. Briefly, human RBC were prepared from fresh heparinized blood by washing thrice (700 g for 10 min) and resuspending in the saline buffer: 140 mM NaCl, 10 mM Tris/HCl, pH 7.4. Finally, the concentration of HRBC was adjusted to an apparent absorbance of 0.1 at 650 nm with the buffer. Toxin and conjugates were 2-fold serially diluted in saline buffer using flat-bottom 96-well microplates, previously treated for 30 min with 0.1 mg/mL Prionex to saturate the unspecific protein binding sites of plastic which can reduce toxin concentration. One volume of HRBC was added to each well, and the time course of hemolysis was followed for 30 min at room temperature. Percentage of hemolysis was determined as follows:

$$\text{hemolysis (\%)} = (A_{max} - A_{t10})/(A_{max} - A_{min}) \times 100$$

where A_{max} and A_{min} represent the absorbance values for intact and completely hemolysed RBC respectively and A_{t10} is the absorbance value in each well after 10 min from the beginning of the kinetic.

Electrophoretic Analysis. SDS−PAGE was performed according to Laemmli using precast minigels with density gradients ranging 8−25% (Amersham Pharmacia, Uppsala, Sweden). A semiautomatic horizontal unit (PhastSystem by Pharmacia) was used. Gels were stained with Coomassie brilliant blue followed by silver stain.

Fluorescence Measurements. Cathepsin B and MMP activities associated to the tumor cells were evaluated using specific fluorogenic peptides and choosing conditions as similar as possible to the citotoxicity test. In fact cells were prepared as in the cytotoxicity assay using the appropriated media without serum. In the cathepsin test 1×10^5 cells were incubated with cathepsin B substrate III (final substrate concentration 40 μM; $\lambda_{exc} = 320$ nm, $\lambda_{em} = 460$ nm) at room temperature and fluorescence was measured for 15 h every 5 min with a fluorescence microplate reader (Fluostar, SLT, Austria). In the MMP test, the quantity of cells used was between 0.6 and 0.9 $\times 10^5$ and the specific MMP substrate was at 10 μM. The fluorescence was monitored at $\lambda_{exc} = 320$ nm, $\lambda_{em} = 395$ nm for 30 min at 25 ± 3°C with a photon-counting fluorimeter (SPEX Fluoromax, JY Horiba, Edison, NJ). Ultramicro quartz cuvettes of 100 μL volume and 1 cm path length were used. In both tests the pH was about 7.

Tetrazolium-Based Assay of Cytotoxicity. In vitro toxicity against three tumor cell lines (MCF 7, ZR 751 and HT 1080) was measured by the MTT reduction assay. Cells were grown as monolayers in a humidified air atmosphere with 5% CO_2, at 37°C, and when reaching 80% confluence, they were trypsinized (2.5 g/L porcine trypsin in Hanks's balanced salt solution), washed three times, resuspended in the appropriate media (without FBS) and added to 96-microwell plates at similar cellular densities. The conjugate, treated with or without 1 mM DTT, was serially diluted (2-fold at each step) with appropriate medium without FBS on 96-well microtiter plates treated with Prionex. In some cases 0.1 mM MMP inhibitor GM6001 was added. All solutions used were filtered for sterility. A range 1.6 to 2.8×10^4 cells was added to each well in a final volume of 100 μL. Plates were then incubated at 37°C, 5% CO_2 for 2 h and then supplemented with 10% serum and incubated again for 16 to 38 h. MTT was finally added to each well (0.2 mg/mL), and the cells were cultured for two more hours before adding 100 μL of 10% SDS in 0.01 N HCl to dissolve the dark blue crystals. After overnight incubation under the same conditions, the optical density at 575 nm of each well was measured with a microplate reader (UVmax from Molecular Devices).

Percentage of cell viability was determined as follows:

$$\text{viability (\%)} = (A_s - A_0)/(A_c - A_0) \times 100$$

where A_s represents the absorbance value of the sample, A_c is the absorbance of nontreated cells (control) and A_0 is the blank value.

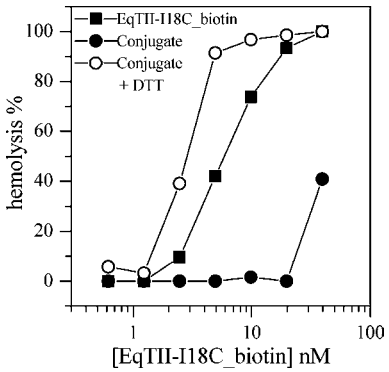

Figure 1. Hemolytic activity of the conjugate. The hemolytic activity of EqTII-I18C_biotin (squares) and the conjugate (EqTII-I18C_biotin_avidin) with or without 2.5 mM DTT (open or closed circles, respectively) was estimated using HRBC. The percentage of hemolysis was determined with a microplate reader after 10 min of interaction. The concentrations (nM) indicated are equivalent to the toxin content, and, in the case of the conjugate, they are the same because only one toxin molecule is present in the conjugate, as determined by SDS−PAGE (see Figure 3E).

Binding of the Conjugate to HRBC and Cells. To determine the binding of the conjugate to human red blood cells, the hemolytic activity of 0.19 μg/mL conjugate with or without 10 mM DTT was measured. Erythrocytes incubated with nonactivated conjugate (in the absence of DTT) were sedimented by centrifugation (3 min at 700 g), resuspended in 10 mM Tris/HCl 140 mM NaCl pH 7.4 and treated with or without 10 mM DTT. Binding to ZR 751 and HT 1080 cells was studied performing a citoxicity assay as described previously. The conjugate was serially diluted (2-fold at each step) beginning from the nontoxic concentration of 1.5 μg/mL, and cells were added. To activate the conjugate 10 mM DTT was added at different times (after 1, 2 and 3 h). Cell viability was then determined by MTT test.

RESULTS AND DISCUSSION

Inhibition of EqTII Activity by Conjugation with Avidin. As a preliminary step biotin was directly linked to EqTII-I18C by using biotin-HPDP. In this case, the addition of an excess of avidin to the biotinylated mixture removed the hemolytic activity (Figure 1, solid circles). Only at the highest concentration (about 40 nM), the fraction of biotinylated mutant treated with avidin showed a modest activity (6% of the DTT treated sample) due probably to the presence of a small amount of nonbiotinylated EqTII-I18C. The inactivation due to avidin was reversible. In fact, it was possible to restore the hemolytic activity by removing it with DTT (Figure 1, open circles). DTT reduced the disulfide bond between the EqTII cysteine and the biotin, thus releasing the active free toxin. The biotinylated EqTII-I18C appeared

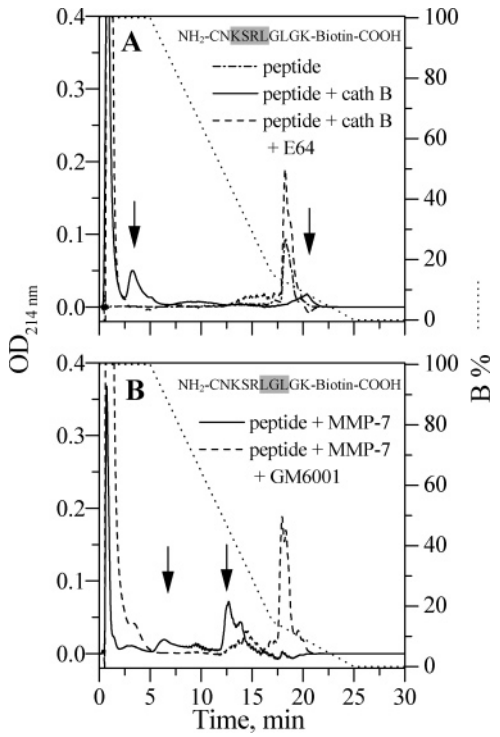

Figure 2. Separation of the peptide cathepsin/MMP digestion products. The peptide sequence is shown on top, and the cleavage sites for cathepsin B (KSRL) or MMP (LGL) are highlighted, respectively in A and B. A: Cathepsin B digestion. After 2 h of incubation of the peptide solution with activated cathepsin, the products were separated by HIC on a 50 × 4.6 mm C3 Metachem column at a flow rate of 1 mL/min. Samples were eluted with a gradient of Buffer B (2 M $(NH_4)_2SO_4$, 25 mM Na H_2PO_4, pH 7) in Buffer A (25 mM Na H_2PO_4, pH 7). The percentage of Buffer B present at any time is indicated by the dotted line. The solid line indicates the profile of the digested peptide (50 μg), while the dashed line corresponds to the same quantity of peptide combined with cathepsin and the specific inhibitor E64. The arrows indicate the main digestion products. The dashed−dotted line is referred to the peptide (25 μg) without any treatment. B: MMP-7 digestion. The conditions are the same as in A. 50 μg of the peptide was digested by MMP-7 in the presence (dashed line) or absence (solid line) of the specific MMP inhibitor GM6001. The arrows indicate the principal products derived from the cleavage.

to be slightly less hemolytic ($HC_{50} \cong 5.7$ nM) than EqTII-I18C released from the conjugate by DTT ($HC_{50} \cong 2.9$ nM). This could be due to a steric effect introduced by the presence of biotin which is removed by DTT. These experiments demonstrated that avidin, bound to the N-term of EqTII, was able to block the hemolysis by introducing a sterical hindrance into the mutant (the molecular weight of avidin, 66 kDa, is roughly thrice that of the toxin).

Construction of an Enzymically Activable Conjugate. *Choice of the Peptide.* To conjugate EqTII-I18C to avidin we next decided to use a biotinylated peptide containing a general cleavage sites for matrix metalloproteinases (MMPs) and cathepsin B, two classes of enzymes that are associated to tumor cells. The peptide sequence is given in Figure 2. The presence of one cysteine at the N-terminus allowed its coupling to the EqTII mutant; it was followed by an asparagine, that increased solubility and served to link the cysteine to the cathepsin B cleavage site: KSRL (*16*, *23*, *24*). The general MMP cleavage site, LGL (*21*), was inserted next. We have chosen this site because it could be cleaved by a large number of soluble MMPs (for example MMP-2, MMP-7, MMP-9) and by membrane MMPs such as MMP-14 (*25*, *26*). Moreover, the LGL sequence is present in the fluorescent metalloproteinase specific substrate we used to evaluate the MMPs activity of our cell lines. The remaining amino acids, GK, made the linking to biotin more flexible and introduced one additional charge to further increase solubility. Biotin was used for avidin binding.

That the enzymes could cut this peptide was confirmed by exposing it to human cathepsin B or MMP-7 and separating the digested products by hydrophobic interaction chromatography (Figure 2A and 2B, respectively). We chose MMP-7 as a representative member of the MMP family. The peak corresponding to the peptide disappeared almost completely from the chromatogram when incubated with cathepsin B or with MMP-7. Meanwhile, two main peaks appeared, marked by arrows in Figure 2, indicating digestion. On the contrary, when the peptide was incubated with the enzyme and the appropriated inhibitor, no cleavage was observed (comparison between the dashed and the dashed−dotted line, Figure 2A). We further demonstrated that the enzymatic cleavage was specific through LC-ESI-MS measurements. From the digestion with MMP-7 we found two major peaks which UV absorption well correlated with the MS signal. In fact, the fragments for LGK-biotin and LGLGK-biotin were detected as $[M + Na]^+$ ions at the nominal mass of 678 Da and at 848 Da respectively, as expected from the complete digestion. Similarly, when we treated the peptide with cathepsin B, three major peaks have been detected both by UV detector and by ESI ionization. In particular, by the latter technique $[M + Na]^+$ ions corresponding to the fragments (i) K-biotin at *m/z* 508, (ii) GK-biotin at *m/z* 565 and (iii) LGK-biotin at *m/z* 565 have been found in order of increasing elution time. These fragments derive from the carboxypeptidase action of the cathepsin B, which is preferred in the presence of a free C-term. It was possible to detect also LGLGK-biotin (*m/z* 848 as $[M + Na]^+$) and CNKSR (*m/z* 607 as M^+), the fragments expected from the classical endopeptidase activity of cathepsin B (*16*).

Preparation and Characterization of the Conjugate. EqTII-I18C was S−S linked to the biotinylated peptide. The disulfide bond between the cysteine of the mutant and the cysteine of the peptide, which formed spontaneously at low rate, was favored by activating the mutant with Ellman's reagent. As an alternative to the disulfide bond, we used BMH to form a thioether bond. This reagent increased the toxin−avidin distance, allowing the construction of a conjugate potentially more sensitive to the protease action. Furthermore, BMH was chosen to have a control conjugate free of the reducible disulfide bond. Unfortunately, this goal was only partially obtained since, from hemolytic assays, we noticed the permanence of some DTT-inducted activity, which could be attributed to the presence of spontaneously formed conjugate (not shown).

The toxin was first separated from the excess of reagent and then from the excess of peptide by filtration on Sephadex G25. The resulting fraction was incubated with an excess of avidin to give a conjugate which was separated from unreacted components by HIC (Figure 3A). As indicated by comparison with the chromatograms of free proteins, the conjugation mixture contained free toxin (nonbiotinylated and, possibly, some biotinylated, but not avidin bound), avidin and conjugate (marked by an arrow). In some cases avidin eluted as a double peak, the minor one corresponding to avidin bound to the peptide without toxin. All peaks, collected after HPLC, were tested for the hemolytic activity before and after

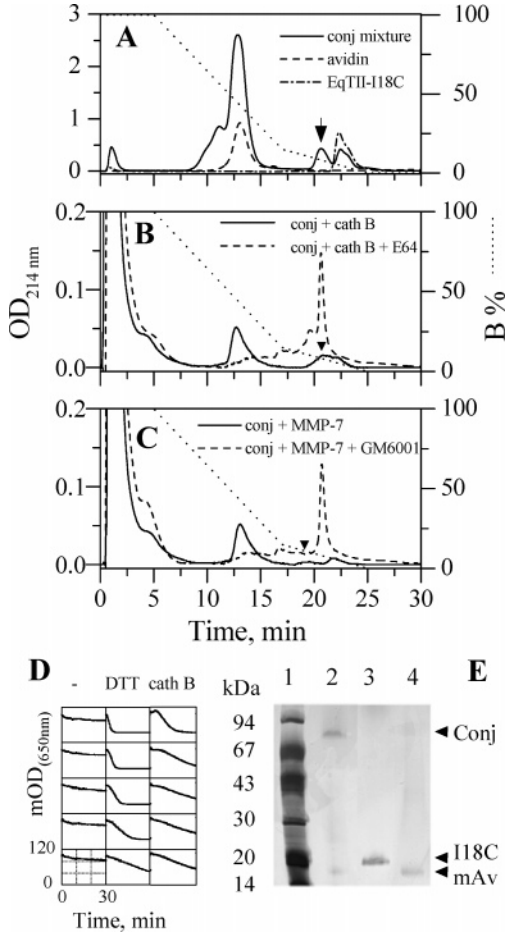

Figure 3. A: Purification and characterization of EqTII-I18C_S−S-peptide-biotin_avidin. EqTII-I18C and avidin, linked via the biotinylated peptide, were purified by HIC as in Figure 2. The solid line indicates the profile of conjugate reaction mixture (composted by 95 μg of toxin previously biotinylated and 1.1 mg of avidin), while the dashed−dotted line corresponds to free EqTII-I18C (180 μg) and the dashed one to free avidin (300 μg). The conjugate was in the peak indicated by the arrow as demonstrated by measuring its hemolytic activity and by SDS−PAGE 8−25% (Figure 3D and 3E, respectively). B, C: Separation of the cathepsin B/MMP-7 digestion products. The products of the conjugate digestion were separated by HIC (solid line), as in part A. Dashed line: conjugate (24 μg) incubated with cathepsin B or MMP-7 and the specific inhibitor, E64 or GM6001, respectively. The positions of the enzymes are marked by an arrowhead. D: Hemolytic activity of the conjugate alone (−), treated with DTT (DTT) or cathepsin B (cath B). It is reported the time course of the turbidity decrease of a HRBC suspension exposed to various doses of the conjugate, 2-fold diluted at each step from top to bottom. The conjugate concentration in the first well was 2.5 μg/mL for columns marked with "−" and DTT and 1.4 μg/mL for the column marked with cath B. The axis scales are the same for all the wells and are reported only on the bottom left one. Conditions of incubation with cathepsin B: 0.11 μM conjugate, 0.36 μM cathepsin; 2 hs at 37°C. E: SDS−PAGE analysis. The SDS−PAGE shows the conjugate (100 ng, lane 2), EqTII-I18C (100 ng, lane 3) and avidin (50 ng, lane 4). The bands indicated by arrows heads correspond approximately to MW of 86 kDa, 20 kDa and 16 kDa, as determined by comparison with standards (lane 1; the molecular weights corresponding to the different bands are reported on the left), and were identified as conjugate, EqTII-I18C and monomeric avidin.

reduction with DTT. This analysis confirmed the presence of the conjugate in the peak indicated by the arrow. In fact the protein in that fraction was able to permeabilize the erythrocyte membrane only after DTT reduction of the S−S bridge (Figure 3D). An HC_{50} of 1.1 nM of toxin was determined, for the reduced conjugate, after 30 min. As a control we observed that, under the same conditions, avidin was not hemolytic at all whereas the hemolytic activity of the mutant itself was always expressed independently of DTT. SDS−PAGE analysis of the purified conjugate under nonreducing conditions (Figure 3E, lane 2) confirmed the presence of high molecular weight compounds (around 90 kDa), as expected from the binding of one molecule of toxin (lane 3) to one molecule of avidin (lane 4, monomeric form). A minor band corresponding to monomeric avidin was also present. From the HPLC profiles (Figure 3A) we estimated that about 25% of the EqTII-I18C used was present in the conjugate. The yield varied from one preparation to another and sometimes was higher. The HPLC-purified conjugate was rechromatographed and it appeared to be free of other components (not shown).

Activation of the Conjugate by Human Cathepsin B and Matrix Metalloproteinase **7***.* That either human cathepsin B or MMP-7 were able to cleave the conjugate had been shown by HIC of the digestion products (Figure 3B and 3C). The HPLC profile demonstrated that cathepsin B and MMP-7 could cleave the conjugate releasing free avidin and toxin. In both cases, the first peak obtained (centered at about 13 min) corresponded to avidin (compare Figure 3A) while the peak corresponding to the free toxin was centered at about 22 min. The positions of the enzymes are marked by an arrowhead in Figure 3B and 3C, indicating that the cathepsin B peak (Figure 3B) was observed at the same position as the conjugate peak. The latest peak was still present when we treated it with the inhibitors (dashed line, Figure 3B and 3C), showing that the cleavage was specific.

In agreement, the hemolytic assay (Figure 3D, line marked by cathB) clearly demonstrated that cathepsin B can cut the linker peptide and restore the hemolytic activity of EqTII-I18C. The HC_{50} after 30 min, due to the mutant released by cathepsin B, was 1.0 nM (concentration of toxin), almost the same as that obtained by treating the conjugate with DTT (Figure 3D, line DTT). In a similar way we found that also trypsin could cleave the conjugate producing a hemolytic fragment ($HC_{50} \cong$ 0.8 nM; data not shown), thus confirming that the peptide inside the conjugate was accessible by enzymes.

Enzymatic Activity of ZR 751, HT 1080 and MCF 7 Tumor Cell Lines. All cell lines used were characterized for the presence of MMPs and cathepsin B activity in our experimental conditions using specific fluorogenic peptides (Figure 4). Cells were trypsinized, washed and resuspended in the appropriate culture media (without FBS) to reproduce similar conditions as the cytotoxicity assay. After addition of cells, the fluorescence of the substrate was monitored (Figure 4). The MMP activities, calculated as the relationship between the initial slopes and the total number of cells in the assay, of the three cell lines were quantitatively similar. The ratio between the enzymatic activities of ZR 751 and MCF 7, with respect of that of HT 1080 cells, was approximately one in both cases, with values ranging from 0.8 ± 0.2 for ZR 751 to 1.1 ± 0.6 for MCF 7 (mean of three experiments). Cathepsin B activities, instead, were different in the three lines. In particular, the higher activity was found for MCF 7 (10.0 ± 3.6 higher than HT 1080) and an intermediate value for ZR 751 (3.4 ± 0.8 higher than HT 1080). In our experimental conditions, MMP activity was always better than cathepsin activity (Figure 4).

To check if the resulting activity was due to the specific enzymes or if there was any unspecific cleavage, we

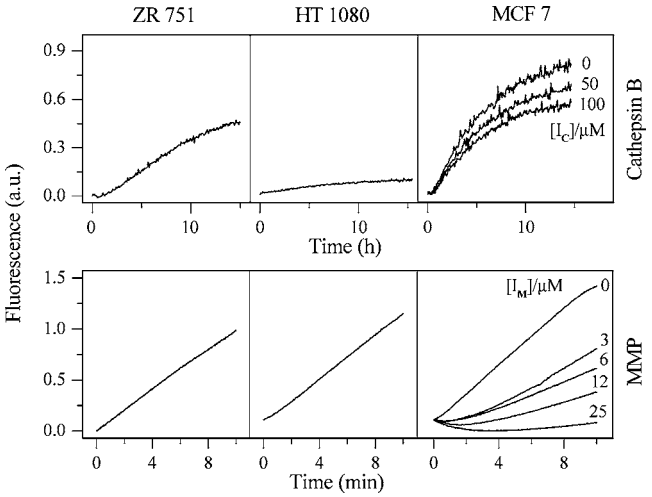

Figure 4. Cathepsin B and MMP enzymic activity associated to the tumor cell lines ZR 751, HT 1080 and MCF 7 evaluated with specific fluorogenic peptides. Upper panel: cathepsin B test. The fluorescence was measured every 5 min with a microplate reader, 1×10^5 cells were used and the substrate concentration was 40 μM. Lower panel: MMP test. A fluorimeter was used, the quantity of cells was between 0.6 and 0.9×10^5 and the substrate concentration was 10 μM. On the y axis fluorescence is represented as 10^6 cps. For MCF 7 cell line the activities in the presence of specific inhibitors was reported. I_C: cathepsin inhibitor (E64); I_M: MMP inhibitor (GM6001).

added appropriate inhibitors. The enzymatic activities were significantly reduced by the MMP inhibitor. As an example, MCF 7 MMP enzymatic activity was inhibited from 47 to 98% when the GM6001 inhibitor ranged from 3 to 25 μM. Some inhibition was also verified when the cathepsin inhibitor E64 was added. In this case MCF 7 enzymatic activity was inhibited by 16 or 30% using the inhibitor at a concentration of 50 and 100 μM, respectively. This suggested that the measured enzymatic activity was due, at least in part, to the specific enzymes studied.

Cytotoxic Effects of the Conjugate on the Tumor Cells. Contrary to the case of erythrocytes (Figure 5A, insert), even in the absence of DTT the conjugate displayed cytotoxic activity on the tumor cell lines studied (Figure 5). The MCF 7 cell line was the most sensitive, with an IC_{50} of 0.3 μg/mL of the conjugate in the absence and 0.2 μg/mL in the presence of DTT (Figure 5A). Both the other cell lines were less affected by the conjugate; in particular, the IC_{50} was 5.8 μg/mL for ZR 751 and 14.2 μg/mL for HT 1080 cells (Figure 5B and C).

This correlates nicely with the cathepsin B activity (see Figure 4), but not with MMP activity, that was similar in all three cell lines. However, by studying the effect of the specific MMP inhibitor GM6001 on the conjugate activity toward MCF 7 tumor cells, we observed that some MMP enzymatic activity was also involved in cytotoxicity. In fact, in the presence of 100 μM inhibitor and 0.2 μg/mL of conjugate (Figure 6) we observed that the cell fraction killed by the conjugate treated with the inhibitor was one-fifth in comparison with the one without inhibitor.

Binding of the Conjugate to the Cell Membrane. Finally, we wanted to evaluate if the conjugate was able to bind to the cells even when not permeabilizing them (Figure 7). The EqTII-I18C_S−S-peptide-biotin_avidin conjugate was added to HRBC at the concentration of 0.19 μg/mL (Figure 7A). The cells were then washed, resuspended in physiological buffer and treated or not with DTT. Only under reducing conditions we observed

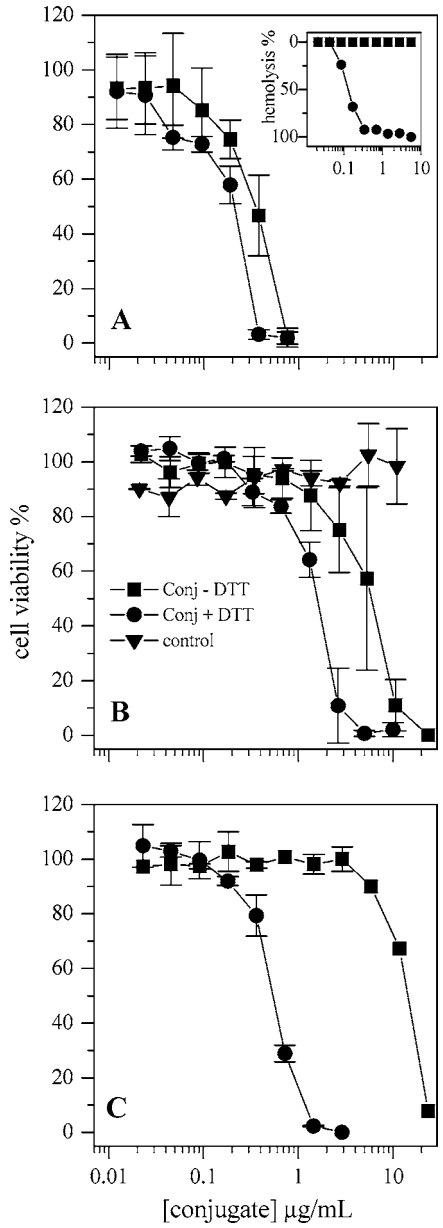

Figure 5. Cytotoxic effects of the conjugate toward cancer cells. The cytotoxic effect was evaluated on three tumor cell lines. Cells in a concentration ranging from 1.6 to 2.8×10^5 cells/mL were incubated at 37°C, 5% CO_2 for 2 h with different conjugate doses with (circles) or without (squares) 1 mM DTT and then supplemented with 10% serum. Triangles represent cells not incubated with conjugate (control experiment). Cells viability was measured after a minimum of 18 h and a maximum of 40 h from the addition of conjugate, by the MTT assay. Results represent the mean ± SEM of at least three experiments. In B and C the conjugate was produced by using BMH. HRBC are shown in the insert of panel A as an example of cells without any MMP or cathepsin enzymic activity. Hemolytic test was performed as in Figure 1. A: MCF 7; B: ZR 751; C: HT 1080.

hemolytic activity, indicating that the conjugate was indeed bound to the erythrocyte membrane but could not permeabilize them until activated by DTT. In this way, we could demonstrate that membrane-bound conjugate is stable and active for a long time; in fact even when DTT was added after 80 min, the permeabilization was complete. Similarly we found that, at sub-cytotoxic concentrations, the same conjugate could bind to tumor cells and that it could be activated by DTT even after 1 h from the washout (Figure 7B). We tested the time-course of this availability, finding that after 2 h the

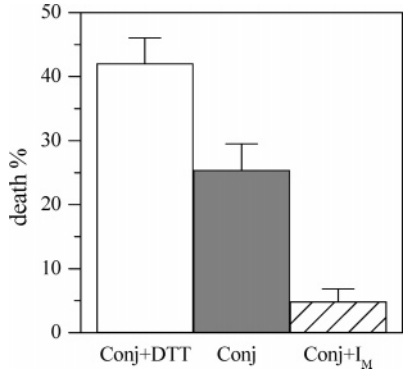

Figure 6. Inhibition of the conjugate activity toward MCF 7 cells. It is represented as the percentage of death of MCF 7 cells in the presence of the conjugate treated or not with 1 mM DTT (white and gray bars, respectively), or in the presence of MMP inhibitor (striped bar). Cells viability was measured by MTT test as in Figure 5. The concentration of the MMP specific inhibitor used in the experiment was 100 μM, while the cell suspension was 1.9×10^5 cells/mL. Results represent the mean $\pm$ SEM of three experiments.

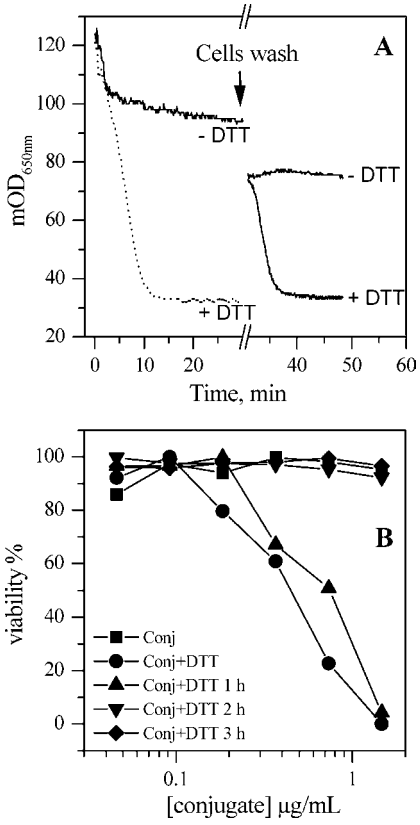

Figure 7. Binding of the EqTII-I18C_S−S-peptide-biotin_avidin conjugate to the cell membrane. Panel A. Binding to human red blood cells. Dotted line: hemolytic activity of 0.19 μg/mL conjugate with 10 mM DTT (the conditions are as in Figure 1). Solid lines: erythrocytes incubated with nonactivated conjugate (− DTT), sedimented by centrifugation (interruption of 10 min), resuspended and treated or not with 10 mM DTT. The hemolytic activity was followed for another 20 min. Panel B. Binding to human breast carcinoma cells (ZR 751). The conjugate was added at sub-cytotoxic concentration and was activated with 10 mM DTT at different times (1, 2, 3 h; up triangles, down triangles and diamonds, respectively). Viability assay was determined by the MTT test. Squares represent the conjugate without DTT and circles a conjugate immediately activated with DTT.

conjugate was no longer available for cleavage. This was true for ZR 751 (Figure 7) as well as for HT 1080 cells (data not shown).

CONCLUSIONS

The biotin−avidin conjugation method, pioneered for anticancer immunotoxins (*27*) and already exploited also for the construction of an antiparasite (*11*) and an anticancer immunotoxin (*12*), is presented here in a version with a linker-peptide. This has the advantage of being very versatile. Simply by changing the sequence of the biotinylated peptide it is possible, at least in principle, to activate a pore-forming toxin like EqTII onto different cell types. In fact, by introducing in the peptide the cleavage sequence for an enzyme expressed by a certain tumor cell, or even by tumor surrounding stromal cells, only in the proximity of that cell will the peptide be cleaved. The killer toxic moiety will be released, directly killing the tumor cell itself or the cells which support the tumor.

The use of peptides to construct immunotoxins was already described (*28*, *29*) but only to help the transport of the toxic moiety, or to improve the extent of covalent conjugation between an antibody and a toxin. Here we propose a new system, which is useful to specifically target the conjugate. In fact we could show that a peptide, containing the cleavage sites for cathepsin and MMP, renders the conjugate active against several tumoral cell lines expressing those enzymes, but not against erythrocytes, which are devoid of them. For the conjugation we selected EqTII-I18C mutant, because this links the avidin molecule to the N-terminal α-helix of EqTII (*30*), which is a crucial element for the toxin−membrane interaction and should be free to move for activity (*31*−*33*).

The most sensitive tumor cells were found to be MCF 7 which also express the highest enzymic activity. The extent of cytotoxicity on the different cell lines correlated with the amount of cathepsin B activity expressed; however, at least on MCF 7 cells, the conjugate activity was also significantly inhibited by the specific MMP inhibitor GM6001, suggesting a contribution of both cathepsin B and MMP to the conjugate activation. This conclusion is supported by the fact that erythrocytes, which do not possess such enzymes, are not damaged by the conjugate. At subtoxic concentrations, the conjugate is still capable of binding to the cells in a form that can be activated, e.g. by DTT, for at least 1 h. Such binding is not cell specific and may be mediated by the toxin moiety. To avoid such unspecific binding we are planning to select for the conjugation a different EqTII mutant, which could not bind to the cell surface. Attaching a biotinylated antitumor antibody to the avidin of such conjugate, we could produce a promising immunotoxin with two levels of specific activation: antibody targeting and enzymic activation.

ACKNOWLEDGMENT

This work was financially supported by the Italian Consiglio Nazionale delle Ricerche (CNR), by the Istituto Trentino di Cultura (ITC), by the Fondazione Trentina per la Ricerca sui Tumori (FTRT) and by the grant F/2886-1 from International Foundation for Science (IFS) to M.T. It was also partially supported by Fondazione Cariverona, Bando 2001 "Ambiente e sviluppo sostenibile". We wish to thank Dr. Mercedes Ferreras for giving us MMP substrate and Prof. Graziano Guella for the support in ESI-MS experiments. We also thank the referee for the useful suggestions of additional experiments and references on the topic.

LITERATURE CITED

(1) Kreitman, R. J. and Pastan, I. (1998) Immunotoxins for targeted cancer therapy. *Adv. Drug Delivery Rev. 31*, 53−88.
(2) Forero, A. and Lobuglio, A. F. (2003) History of antibody therapy for non-Hodgkin's lymphoma. *Semin. Oncol. 30*, 1−5.
(3) Pastan, I. (2003) Immunotoxin containing Pseudomonas exotoxin A: a short history. *Cancer Immunol. Immunother. 52*, 338−341.
(4) Frankel, A. E., Powell, B. L., and Lilly, M. B. (2002) Diphtheria toxin conjugate therapy of cancer. *Cancer Chemother Biol Response Modif. 20*, 301−313.
(5) Baluna, R., Coleman, E., Jones, C., Ghetie, V., and Vitetta, E. S. (2000) The effect of a monoclonal antibody coupled to ricin A chain-derived peptides on endothelial cells in vitro: Insights into toxin-mediated vascular damage. *Exp. Cell Res. 258*, 417−424.
(6) Thrush, G. R., Lark, L. R., Clinchy, B. C., and Vitetta, E. S. (1996) Immunotoxins: an update. *Annu. Rev. Immunol. 14*, 49−71.
(7) Tritton, T. R. and Hickman, J. A. (1990) How to kill cancer cells: membranes and calcium signaling as targets in cancer chemotherapy. *Cancer Cells 2*, 95−105.
(8) Harvey, A. L. (1990) Cytolytic toxins. In *Handbook of toxinology* (Shier, W. T., Ed.), pp 1−66. Marcel Dekker, New York.
(9) Anderluh, G.; G. Menestrina (2001) Pore-forming proteins from sea anemones and the construction of immunotoxins for selective killing of harmful cells. In *Bio-organic compounds: chemistry and biomedical applications* (Fingerman, M., Ed.), pp 131−148, Science Publishers, Inc., Enfield, NH.
(10) Pederzolli, C., Belmonte, G., Dalla Serra, M., Maček, P., and Menestrina, G. (1995) Biochemical and cytotoxic properties of conjugates of transferrin with equinatoxin II, a cytolysin from a sea anemone. *Bioconjugate Chem. 6*, 166−173.
(11) Tejuca, M., Anderluh, G., Maček, P., Alvarez, C., Lanio, M. E., Marcet, R., Torres, D., Sarracent, J., Dalla Serra, M., and Menestrina, G. (1999) Antiparasite activity of sea anemone cytolysins on Giardia duodenalis and specific targeting with anti-Giardia antibodies. *Int. J. Parasitol. 29*, 489−498.
(12) Potrich, C., Viero, G., Tejuca, M., Anderluh, G., Maček, P., and Menestrina, G. (2000) Construction of new immunotoxins by linking equinatoxin II to monoclonal antibodies via the biotin−avidin interaction. Cytotoxic effects on human tumor cells. *Acta Biol. Sloven. 43*, 47−51.
(13) Avila, A. D., de Acosta, M. C., and Lage, A. (1988) A new immunotoxin built by linking a hemolytic toxin to a monoclonal antibody specific for immature T lymphocytes. *Int. J. Cancer 42*, 568−571.
(14) Gasanov, S. E., Rael, E. D., Gasanov, N. E., and Vernon, L. P. (1995) In vitro evaluation of Pyrularia thionin-anti-CD5 immunotoxin. *Cancer Immunol. Immunother. 41*, 122−128.
(15) Al Yahyaee, S. A. S. and Ellar, D. J. (1996) Cell targeting of a pore-forming toxin, CytA delta-endotoxin from *Bacillus thuringiensis* subspecies *israelensis*, by conjugating CytA with anti-thy 1 monoclonal antibodies and insulin. *Bioconjugate Chem. 7*, 451−460.
(16) Panchal, R. G., Cusak, E., Cheley, S., and Bayley, H. (1996) Tumor protease-activated, pore-forming toxins from a combinatorial library. *Nat. Biotechnol. 14*, 852−856.
(17) Liu, S. H., Bugge, T. H., and Leppla, S. H. (2001) Targeting of tumor cells by cell surface urokinase plasminogen activator-dependent anthrax toxin. *J. Biol. Chem. 276*, 17976−17984.
(18) Rozhin, J., Sameni, M., Ziegler, G., and Sloane, B. F. (1994) Pericellular pH affects distribution and secretion of cathepsin B in malignant cells. *Cancer Res. 54*, 6517−6525.
(19) Mai, J., Waisman, D. M., and Sloane, B. F. (2000) Cell surface complex of cathepsin B/annexin II tetramer in malignant progression. *Biochim. Biophys. Acta 1477*, 215−230.
(20) Koblinski, J. E., Ahram, M., and Sloane, B. F. (2000) Unraveling the role of proteases in cancer. *Clin. Chim. Acta 291*, 113−135.
(21) Barrett, A. J., Rawlings, N. D., and Woessner, F. J. (2003) *Handbook of Proteolyic Enzymes, two-Volume Set with CD ROM*, 1−2, Academic Press, Cambridge.
(22) Anderluh, G., Barlič, A., Podlesek, Z., Maček, P., Pungerčar, J., Gubensek, F., Zecchini, M., Dalla Serra, M., and Menestrina, G. (1999) Cysteine scanning mutagenesis of an eucaryotic pore-forming toxin from sea anemone: topology in lipid membranes. *Eur. J. Biochem 263*, 128−136.
(23) Takahashi, T., Dehdarani, A. H., Yonezawa, S., and Tang, J. (1986) Porcine spleen cathepsin B is an exopeptidase. *J. Biol. Chem. 261*, 9375−9381.
(24) Chapman, H. A., Riese, R. J., and Shi, G. P. (1997) Emerging roles for cysteine proteases in human biology. *Annu. Rev. Physiol. 59*, 63−88.
(25) Nagase, H. and Fields, G. B. (1996) Human matrix metalloproteinase specificity studies using collagen sequence-based synthetic peptides. *Biopolymers 40*, 399−416.
(26) Turk, B. E., Huang, L. L., Piro, E. T., and Cantley, L. C. (2001) Determination of protease cleavage site motifs using mixture-based oriented peptide libraries. *Nat. Biotechnol. 19*, 661−667.
(27) Meyer, B. F., Stoner, M. L., Raphael, C. L., Davis, R. E., and Herrmann, R. P. (1991) Streptavidin−biotin immunotoxins: a new approach to purging bone marrow. *Exp. Hematol. 19*, 710−713.
(28) Keller, J., Heisler, I., Tauber, R., and Fuchs, H. (2001) Development of a novel molecular adapter for the optimization of immunotoxins. *J. Controlled Release 74*, 259−261.
(29) Kleinschmidt, M., Rudolph, R., and Lilie, H. (2003) Design of a modular immunotoxins connected by polyionic adapter peptides. *J. Mol. Biol. 327*, 445−452.
(30) Athanasiadis, A., Anderluh, G., Maček, P., and Turk, D. (2001) Crystal structure of the soluble form of equinatoxin II, a pore-forming toxin from the sea anemone Actinia equina. *Structure 9*, 341−346.
(31) Malovrh, P., Viero, G., Dalla Serra, M., Podlesek, Z., Lakey, J. H., Maček, P., Menestrina, G., and Anderluh, G. (2003) A novel mechanism of pore-formation: equinatoxin penetration of membrane by a N-terminal amphipatic region. *J. Biol. Chem. 278*, 22678−22685.
(32) Anderluh, G., Dalla Serra, M., Viero, G., Guella, G., Maček, P., and Menestrina, G. (2003) Pore formation by equinatoxin II, an eukaryotic protein toxin, occurs by induction of nonlamellar lipid structures. *J. Biol. Chem. 278*, 45216−45223.
(33) Hong, Q., Gutierrez-Aguirre, I., Barlič, A., Malovrh, P., Kristan, K., Podlesek, Z., Maček, P., Turk, D., Gonzalez-Manas, J. M., Lakey, J. H., and Anderluh, G. (2002) Two-step membrane binding by Equinatoxin II, a pore-forming toxin from the sea anemone, involves an exposed aromatic cluster and a flexible helix. *J. Biol. Chem. 277*, 41916−41924.

BC049873Z

Synthesis, Characterization, and Pharmacokinetic Studies of PEGylated Glucagon-like Peptide-1

Sang-Heon Lee,[†] Seulki Lee,[‡] Yu Seok Youn,[†] Dong Hee Na,[†] Su Young Chae,[‡] Youngro Byun,[‡] and Kang Choon Lee*,[†]

Drug Targeting Laboratory, College of Pharmacy, SungKyunKwan University, 300 Chonchon-dong, Jangan-ku, Suwon City 440-746, Korea, and Center for Cell and Macromolecular Therapy, Gwangju Institute of Science and Technology, 1 Oryung-dong, Buk-gu, Gwangju 500-712, Korea. Received November 5, 2004; Revised Manuscript Received December 28, 2004

Glucagon-like peptide-1-(7−36) (GLP-1) is a hormone derived from the proglucagon molecule, which is considered a highly desirable antidiabetic agent mainly due to its unique glucose-dependent stimulation of insulin secretion profiles. However, the development of a GLP-1-based pharmaceutical agent has a severe limitation due to its very short half-life in plasma, being primarily degraded by dipeptidyl peptidase IV (DPP-IV) enzyme. To overcome this limitation, in this article we propose a novel and potent DPP-IV-resistant form of a poly(ethylene glycol)-conjugated GLP-1 preparation and its pharmacokinetic evaluation in rats. Two series of mono-PEGylated GLP-1, (i) N-terminally modified PEG_{2k}-N^{ter}-GLP-1 and (ii) isomers of Lys^{26}, Lys^{34} modified PEG_{2k}-Lys-GLP-1, were prepared by using mPEG-aldehyde and mPEG-succinimidyl propionate, respectively. To determine the optimized condition for PEGylation, the reactions were monitored at different pH buffer and time intervals by RP-HPLC and MALDI-TOF-MS. The in vitro insulinotropic effect of PEG_{2k}-Lys-GLP-1 showed comparable biological activity with native GLP-1 ($P = 0.11$) in stimulating insulin secretion in isolated rat pancreatic islet and was significantly more potent than the PEG_{2k}-N^{ter}-GLP-1 ($P < 0.05$) that showed a marked reduced potency. Furthermore, PEG_{2k}-Lys-GLP-1 was clearly resistant to purified DPP-IV in buffer with 50-fold increased half-life compared to unmodified GLP-1. When PEG_{2k}-Lys-GLP-1 was administered intravenously and subcutaneously into rats, PEGylation improved the half-life, which resulted in substantial improvement of the mean plasma residence time as a 16-fold increase for iv and a 3.2-fold increase for sc. These preliminary results suggest a site specifically mono-PEGylated GLP-1 greatly improved the pharmacological profiles; thus, we anticipated that it could serve as potential candidate as an antidiabetic agent for the treatment of non-insulin-dependent diabetes patients.

INTRODUCTION

Glucagon-like peptide-1-(7−36) (GLP-1) is a proglucagon-derived peptide secreted from the L-cells in the gastrointestinal tract in response to orally ingested nutrients (*1*). Initial clinical interest in GLP-1 was based on its glucose-dependent insulinotropic effect, which was thought to be a potential advantage over conventional antidiabetic agents that secrete insulin via glucose-independent mechanism (*2*, *3*). GLP-1 also exerts actions suit for non-insulin-dependent diabetes mellitus (NIDDM) patients such as inhibition of glucagons secretion, inhibition of gastric emptying, and a decrease in appetite (*4*). Moreover, numerous recent studies indicated direct effects of GLP-1 on pancreatic β-cells. For example, GLP-1 is involved in β-cell growth and survival by stimulating cell proliferation and differentiation into new β-cells which could lead to increased β-cell mass (*5*, *6*). On the basis of the advantages as described above, GLP-1 has a great therapeutic potential to treat NIDDM diabetes. However, GLP-1 is quite unstable in vivo (half-life; < 2 min for iv injection) and clinical application requires frequent administration at high dosages. These limitations pose great challenges in the development of GLP-1 as an antidiabetic pharmaceutical agent.

The rapid clearance and degradation of GLP-1 in plasma is mainly due to N-terminal cleavage of the first two amino acids, His^8-Ala^9, by the enzyme dipeptidyl peptidase IV (DPP-IV) (*7*). Until now, the main approach that has been used to improve the therapeutic level of GLP-1 is development of enzyme-resistant GLP-1 analogues by substituting one or two amino acids of the peptide (*8*). Design of GLP-1 analogues showed a number of promising results; however, it still remains difficult to optimize conditions such as control of enzyme resistance and biological potency in vivo. Chemical conjugation of several substances to GLP-1 has been also proposed to improve clinical efficiency. For instance, fatty acid acylation, NN2211 (*9*), was found to extend action via binding to an existing serum protein derivative while albumin conjugation, CJC-1131 (*10*), showed prolonged half-life compared to the circulating half-life of albumin itself. Protein modification is one of the convenient alternative ways to improve therapeutic profiles of native proteins; however, little work was done with GLP-1.

We previously reported site specifically poly(ethylene glycol) (PEG)-modified salmon calcitonin (sCT) exhibited improved pharmacokinetic and pharmacodynamic profiles with pronounced stability compared to intact sCT in vitro and in vivo (*11*−*15*). PEG-modified proteins often have extended plasma half-lives, decreased proteolytic

* To whom correspondence should be addressed. Phone: 82-31-290-7704, Fax: 82-31-290-7724, E-mail: kclee@skku.edu.
[†] SungKyunKwan University
[‡] Gwangju Institute of Science and Technology

10.1021/bc049735+ CCC: $30.25 © 2005 American Chemical Society
Published on Web 02/23/2005

degradation, and reduced immunogenecity (*16*, *17*). However, the nonspecific PEGylation process frequently results in substantial loss of biological activity when PEG binds around the protein's active sites (*18*). This may show inconsistent pharmacodynamic profiles. Therefore, it is important to strike a balance between biological stability and therapeutic activity of PEGylated proteins under physiological conditions. In this respect, we hypothesized that covalent coupling of PEG to a specific site of GLP-1 may improve the overall therapeutic profile of GLP-1 while maintaining biological activity. In this work, we have prepared and characterized novel PEGylated GLP-1 conjugates in vitro and investigated pharmacokinetic profiles in vivo.

MATERIALS AND METHODS

Materials. GLP-1 was purchased from Bachem (Torrance, CA). Succinimidyl propionate monomethoxypoly(ethylene glycol) (mPEG-SPA) and aldehyde monomethoxypoly(ethylene glycol) (mPEG-ALD) were purchased from Shearwater Polymers (Huntsville, AL). Trifluoroacetic acid (TFA) and acetonitrile (ACN) was purchased from Sigma (St. Louis, MO). All reagents and organic solvents used were at least ACS grade.

Preparation of Mono-PEGylated GLP-1 Conjugates. The positional isomers of mono-PEGylated GLP-1 conjugates were prepared and purified according to the procedures described previously (*11*). In brief, GLP-1 (100 μL, 1 mg/mL) in various 50 mmol/L buffer solutions was reacted with 2 mole excess of $mPEG_{2k}$-SPA (pH adjusted from 7.5 to 9.0 with 50 mmol/L Tris-HCl buffer) at room temperature for 1 h and $mPEG_{2k}$-ALD (pH adjusted from 4.5 to 5.5 with 50 mmol/L sodium acetate buffer) at 4 °C for 2 h, respectively. The mono-PEGylated GLP-1 conjugates were monitored and purified by reversed-phase high-pressure liquid chromatography (RP-HPLC) on X-tera C_{18} (4.6 × 250 mm, 5 μm, Waters, Milford, MA) at room temperature. The mobile phase consisted of 0.1% TFA in distilled water (eluent A) and ACN containing 0.1% TFA (eluent B). The mobile phase was run with a linear gradient from 30 to 60% eluent B for 20 min at a flow rate of 1 mL/min and the UV absorbance of the eluent was monitored at 215 nm. The HPLC fractions corresponding to respective peaks were collected separately, purged with nitrogen, and lyophilized.

Lys-C Digestion of Mono-PEGylated GLP-1. To determine the positions where the PEG molecules were attached, a lysyl endoproteinase, Lys-C, digestion was employed as described previously (*19*). Each purified mono-PEGylated conjugate was dissolved in 50 μL of triethylamine-HCl buffer (10 mmol/L; pH 7.4) to a concentration of 1 mg/mL. Following the addition of 50 μL of enzyme (1 mg/mL), the reaction was allowed to incubate for 1 h at 37 °C. To quench the digestion, 5 μL of 10% (v/v) TFA was added and reaction mixture was analyzed by MALDI-TOF MS.

MALDI-TOF MS. Molecular weight was obtained from MALDI-TOF mass spectrometry using a Voyager Biospectrometry Workstation (PerSeptive Biosystem, Framingham, MA). Samples were prepared by mixing 1 μL of aliquot with 2 μL of the matrix solution, a saturated solution of α-cyanohydroxycinnamic acid in 50% of water/ACN with 0.3% TFA. One microliter of the sample mixture was spotted into a well of the sample plate and dried by vacuum prior to mass spectrometry. Data for 2 ns pulses of the 337 nm nitrogen laser were averaged for each spectrum in a linear mode, and positive ion TOF detection was performed using an accelerating voltage of 25 kV.

Insulinotropic Actions from Isolated Rat Pancreatic Islets. Pancreatic islets were isolated from male Sprague−Dawley rats weighting 250−270 g by the modified method of Lacy and Kostianovsky (*20*). Briefly, anesthesia was induced by intraperitoneal injection of pentobarbital sodium (50 mg/kg). The donor pancreas was inflated by injection of cold Hank's balanced buffered salt solution (HBSS, pH 7.4, Sigma) containing 1.5 mg/mL type V collagenase (Sigma). Isolated islets were purified by centrifugation with a discontinuous Ficoll (Amersham Biosciences AB, Uppsala, Sweden) gradient at 2400 rpm for 25 min. Purified islets were cultured with RPMI-1640 culture medium (Sigma) supplemented with 10% fetal bovine serum (FBS, Gibco, Carlsbad, CA) and 1% penicillin−streptomycin (Gibco) at 37 °C with an atmosphere of 95% air and 5% CO_2. After the 2 day maintenance period, the islets were washed and incubated in a Krebs−Ringer bicarbonate buffer. Twenty islets were incubated for 2 h in 2 mL of KRB−HEPES at 37 °C with an atmosphere of 95% air and 5% CO_2, containing the respective stimulus. The insulin release was measured by a radioimmunoassay kit (Insulin Kit, ICN Pharmaceuticals, Orangeburg, NY).

Stability to DPP−IV in Vitro. GLP-1 (100 μL, 5 nmol/L) and an equivalent amount of purified mono-PEGylated GLP-1 were prepared in triethylamine·HCl buffer (10 mmol/L; pH 7.4). DPP-IV (5 mU, 900 μL) was added, and the solutions were incubated at 37 °C. At the indicated time points, 100 μL was removed from the reaction mixture, and reactions were terminated by the addition of 5 μL of 10% (v/v) TFA. Each sample was analyzed by MALDI-TOF MS and RP-HPLC as described.

Pharmacokinetics in Vivo. Male Sprague−Dawley (SD) rats were cannulated in jugular vein day before the experiment. The animals were randomly divided into four groups, and the GLP-1 and molar equivalent amount of mono-PEGylated GLP-1 dissolved in saline was intravenously (1 μg/kg) and subcutaneously (10 μg/kg) administered. Blood samples were drawn at predetermined time points in an ice-chilled polyethylene tube containing DPP-IV inhibitor (10 μL per mL of blood; Linco Research Inc., St. Charles, MO). The plasma samples were obtained by centrifugation and stored at −70 °C until assay. The concentration of GLP-1 in rat plasma was analyzed by a commercial sandwich enzyme-linked immunosorbent assay (ELISA) kit (Linco Research Inc.) with GLP-1 and PEGylated conjugates as standards. The peptide concentration beyond the calibration range was diluted by addition of blank rat plasma.

Data Analysis. Data are expressed as mean ± SD. The pharmacokinetic parameters were calculated from the plasma concentrations after administration. The area under the time curves was calculated using the linear trapezoidal method. Differences between treatments were evaluated using paired Student's t tests. $P < 0.05$ was considered statistically significant.

RESULTS AND DISCUSSION

Monitoring of PEGylation. The GLP-1 molecule has three possible sites for the PEGylation; they are the primary amino group of N-terminus (His^7) and two lysine residues (Lys^{26} and Lys^{34}) (Figure 1). Two different chemical approaches were used to PEGylate free amino functional group of the peptide. In the first approach, mPEG-SPA was used to form an amide bond with Lys^{26} and Lys^{34}. In the second approach, reductive alkylation was carried out by reaction mPEG-ALD with His^7, followed by $NaCNBH_3$ reduction. To determine the

His^{7}-Ala-Glu-Gly-Thr-Phe-Thr -Ser-Asp-Val-

Ser-Ser-Tyr-Leu-Glu-Gly-Gln-Ala-Ala-Lys^{26}-

Glu-Phe-Ile-Ala-Trp-Leu-Val-Lys^{34}-Gly-Arg-NH_2

Figure 1. Primary structure of GLP-1. Possible PEGylated sites are His^7, Lys^{26}, and Lys^{34}.

optimized condition for PEGylation that would selectively label the target site, the feed molar ratio between GLP-1 and PEG was fixed as 1 to 2 and reactions were carried out at different pH and were monitored at different time intervals by HPLC over an 8 h period. For the lysine, pH was varied from 7.5 to 9.0 and for the histidine, pH was varied from 4.5 to 5.5. Figure 2 illustrates the RP-HPLC analysis of the reaction mixture obtained after the termination of the each reaction. Increasing the pH from 7.5 to 9.0 decreased the yield of PEG_{2k}-Lys-GLP-1, while decreasing the pH from 5.5 to 4.5 led to an increased yield of PEG_{2k}-N^{ter}-GLP-1. Selective pH affected the final yield of PEGylated product; however, the reaction time did not influence the production yield much. Each of the purified mono-PEGylated GLP-1 derivatives was then subjected to the lysyl endoproteinase, Lys-C, proteolysis to determine the positional substitution of PEG molecules. After incubation with Lys-C, reaction mixtures were directly characterized by MALDI-TOF MS (Figure 3). By peptide mapping (Table 1), it was confirmed that (i) purified PEGylated GLP-1 conjugates were purely monosubstituted and (ii) PEG_{2k}-Lys-GLP-1 consisted of two different isomers, PEG_{2k}-Lys^{26}-GLP-1 and PEG_{2k}-Lys^{34}-GLP-1. In addition, the amount of proteolytic fragment of Glu^{27}-Arg^{36} is more predominant than His^7-Lys^{34} (Figure 3C). MALDI-TOF MS is one of the direct determination techniques for the peptide content (*21*), and the result indicates that most of the PEG_{2k}-Lys-GLP-1 consisted of PEG_{2k}-Lys^{34}-GLP-1. This result well matches what we expected based on the natural characteristics of PEG molecule. Once PEG binds to Lys^{34}-GLP-1, the Lys^{26} position has a reduced chance to form a chemical bond with PEG due to the steric hindrances induced by the closely attached PEG molecule at the Lys^{34} position. However, we could not completely purify two different PEG_{2k}-Lys-GLP-1 isomers by using HPLC, mainly due to the small physicochemical differences between PEG_{2k}-Lys^{26}-GLP-1 and PEG_{2k}-Lys^{34}-GLP-1. Similarly, the chemical structure of N-terminally PEGylated PEG_{2k}-N^{ter}-GLP-1 was also confirmed, with good yield (Figure 3D,E, Table 1). After characterization of mono-PEGylated GLP-1 conjugates, the fractions were collected, pooled, and lyophilized. The BCA protein analysis was then carried out to determine the concentration of peptide.

Biological Activities. The influence of GLP-1 and mono-PEGylated GLP-1 conjugates on insulin secretion was investigated in isolated rat islets to determine biological activities indirectly in vitro. The primary physiological response to GLP-1 observed is glucose-dependent insulin secretion. Since the effect of GLP-1 under low glucose concentration (2.8 mmol/L) is not that significant compared to high glucose concentration (16.8 mmol/L), the biological activity of GLP-1 conjugates was evaluated under high glucose conditions. Culturing only islets in 16.8 mmol/L glucose resulted in increases in the rate of insulin secretion of 7.8 ± 1.2-fold per islet over those observed in the presence of 2.8 mmol/L glucose (Figure 4). Insulin release was clearly stimulated by the addition of 100 nmol/L GLP-1, a significant enhancement to 3.4 ± 0.7-fold ($p < 0.001$) per islet compared to without stimulant in 16.8 mmol/L glucose. The high concentration of peptide was chosen for in vitro study because the reported receptor binding (EC_{50}) value of GLP-1 is around 1 nmol/L and was also shows no further increase of insulin release in islets at concentrations above 100 nmol/L of GLP-1 (*22*). At equivalent molar concentrations of mono-PEGylated conjugates, PEG_{2k}-Lys-GLP-1 was at least as potent as native peptide in stimulating insulin secretion (306.6 ± 72.8 vs 368.9 ± 82.9 pmol/L, $P = 0.117$) and was significantly more potent than PEG_{2k}-N^{ter}-GLP-1 which showed 1.5 ± 0.5-fold increase of insulin secretion per islet compared to that without stimulant. It is well-known that certain residues or regions of residues are important for biological activity of therapeutic proteins, and for GLP-1, the N-terminus plays an important role in receptor binding which could directly affect the therapeutic action in vivo. It is postulated that conjugation of PEG moieties to the N-terminus of GLP-1 pro-

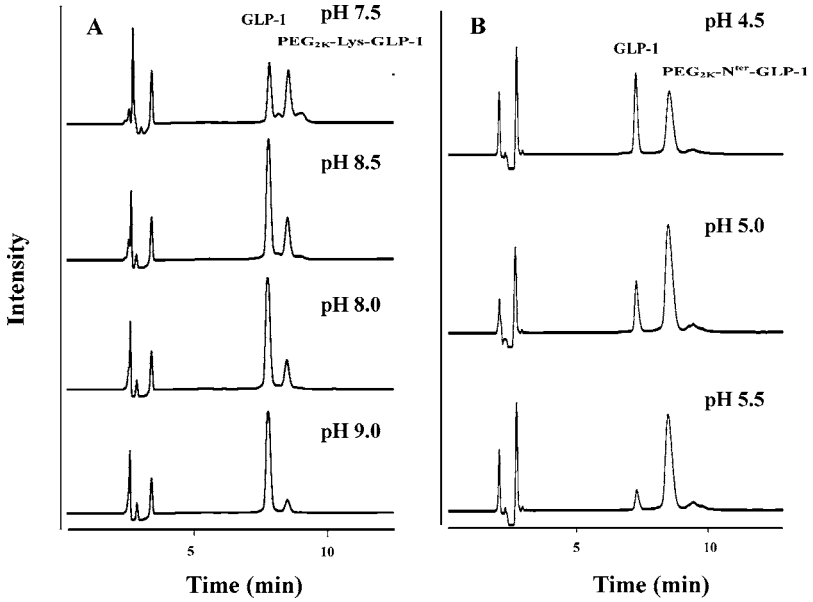

Figure 2. RP−HPLC analysis of the reaction mixture obtained by reaction of (A) mPEG-SPA and (B) mPEG-ALD with GLP-1 at different pHs as indicated. Analysis was performed on a X-tera C18 column with water/acetonitrile/TFA as eluent and a flow rate of 1 mL/min, and peaks were monitored at 215 nm.

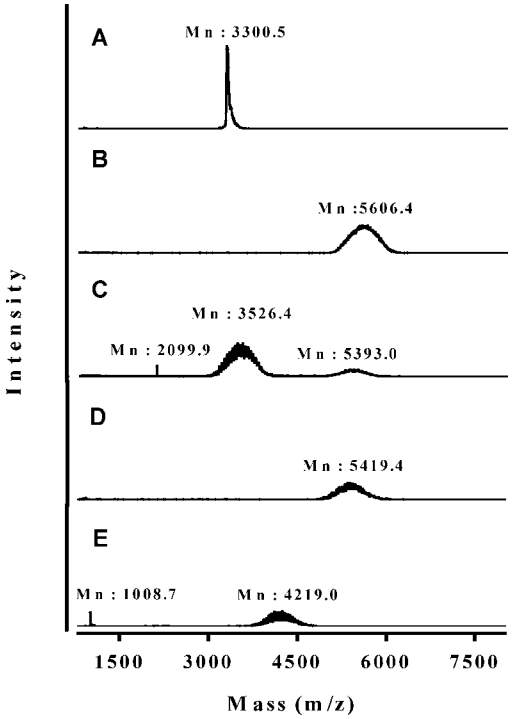

Figure 3. Mass analysis of (A) intact GLP-1, (B) purified PEG_{2k}-Lys-GLP-1, (C) proteolytic fragments of PEG_{2k}-Lys-GLP-1, (D) purified PEG_{2k}-N^{ter}-GLP-1, and (E) proteolytic fragments of PEG_{2k}-N^{ter}-GLP-1. Proteolysis was performed by incubating each purified peptide with lysyl endoproteinase, Lys-C, and the mass of each proteolytic fragment was directly evaluated by MALDI-TOF MS.

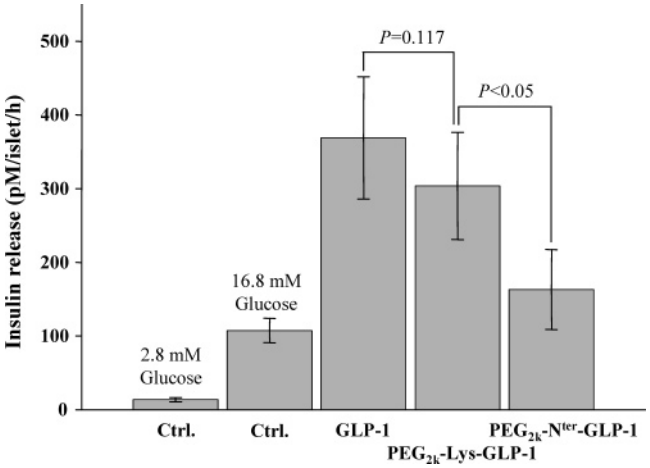

Figure 4. Stimulation of insulin secretion from rat pancreatic islets by 100 nM of GLP-1 and an equivalent amount of PEGylated GLP-1 conjugates. Rat islets were isolated by collagenase digestion, and static incubation of 20 islets per sample was performed for 2 h at 37 °C in the presence of 16.8 mM glucose (2.8 mM indicates basal). Insulin release was measured by RIA as described in Materials and Methods. Values are mean ± SD (n = 6−8).

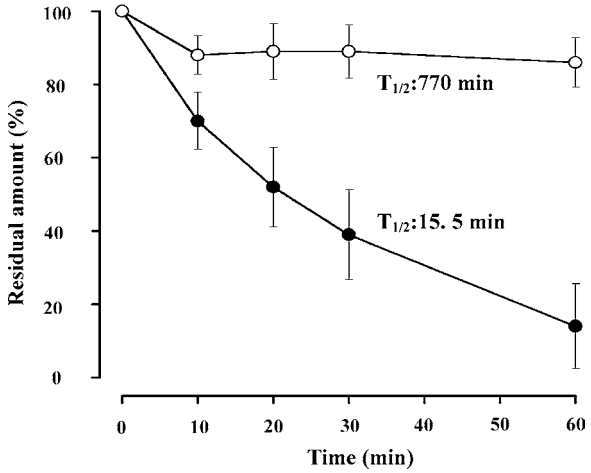

Figure 5. Stability of PEG_{2k}-Lys-GLP-1 toward enzymatic degradation by DPP-IV in comparison with intact GLP-1. Unmodified GLP-1 (●) and PEGylated GLP-1 (○) were incubated with purified DPP-IV at 37 °C. At the indicated time points, aliquots were subjected to analytical HPLC. The quantity of the peptide (peak area) at t = 0 was assigned to 100%. Values are mean ± SD (n = 3).

duces conformational disturbances mainly by steric hindrance, which may perturb the receptor−ligand interaction and lead to lower biological activity. Because N-terminally modified GLP-1 conjugates showed a markedly reduced potency in stimulating insulin secretion, PEG_{2k}-Lys-GLP-1 was selected for further experiments.

Stability of Mono-PEGylated GLP-1. Enzymatic resistance to DPP-IV of intact GLP-1 and PEG_{2k}-Lys-GLP-1 was evaluated. GLP-1 was degraded by the purified DPP-IV in vitro at 37 °C, with a half-life value of 15.5 min. In contrast, PEGylated GLP-1 revealed a significantly prolonged half-life compared to intact GLP-1 itself with a value of 770 min (Figure 5). Degradation profiles was also monitored and indirectly quantified by MALDI-TOF MS as GLP-1 (3297.1 Da) and N-terminally truncated GLP-1 metabolite, GLP-1 (9−36) amide (3087.1 Da) (Figure 6). The mass difference between two peaks (210.0 Da) corresponds to mass of cleaved two amino acids (His^7, Ala^8) at the N-terminals. The relative height of the metabolite peak was increased as time passes. At 10 min postincubation with DPP-IV, nearly one-third was recovered as GLP-1 (9−36), and at 60 min, most of the intact GLP-1 was degraded. In contrast, mono-PEGylated GLP-1 was significantly resistant to proteolytic enzyme. Most of the PEG_{2k}-Lys-GLP-1 remained in original form after 60 min incubation and could still be detected even at 2 h postincubation. From the literature, some of the N-terminally substituted GLP-1 analogues by addition of various different kinds of amino acids showed potent biological activity with decreased degradation profiles (*23*). However, this process generally needs a large screening process to search for analogues with balanced stability and activity. In the case of our system, PEG_{2k}-Lys-GLP-1, even simple selective attachments of PEG not far from the site of cleavage showed significantly improved proteolytic stability in vitro while maintaining

Table 1. Molecular Mass of PEGylated GLP-1 after Lys-C Protease Digestion As Determined by MALDI-TOF (calcd/found)

proteolytic fragment	calcd mass (GLP-1 std)	PEG_{2k}-N^{ter}-GLP-1	PEG_{2k}-Lys^{26}-GLP-1	PEG_{2k}-Lys^{34}-GLP-1
His^7-Lys^{26}	2098.2	4217.3/4219.0[a]	-	2098.2/2099.9
Glu^{27}-Lys^{34}	1005.2	1005.2/1008.7	-	-
Gly^{35}-Arg^{36}	231.2	N.D.[b]	N.D.[b]	-
His^7-Lys^{34}	3085.4	-	5391.3/5393.0[a]	-
Gly^{27}-Arg^{36}	1218.5	-	-	3524.4/3526.4[a]

[a] PEGylated fragments. [b] Not determined.

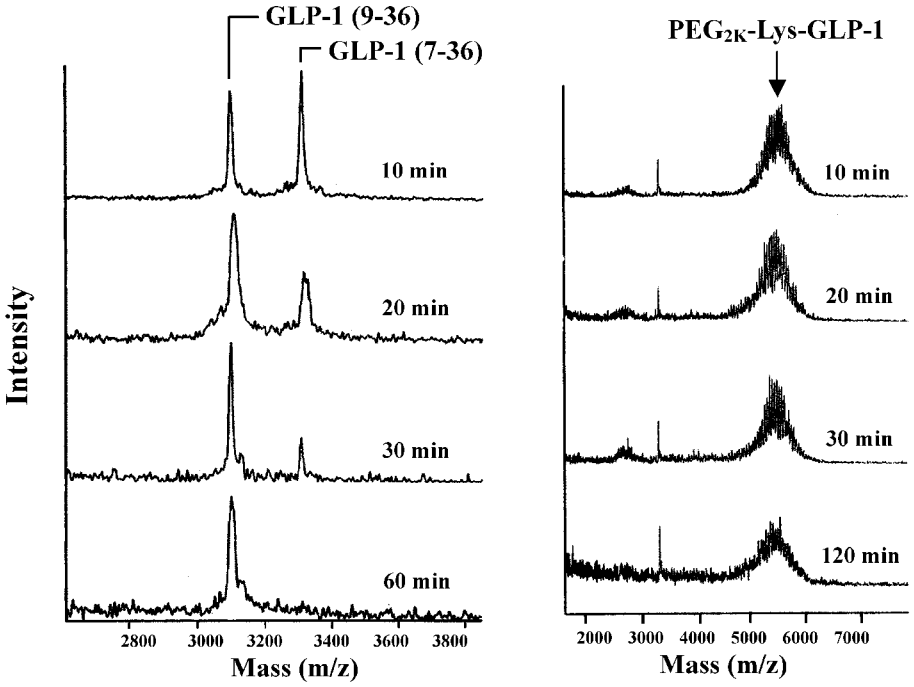

Figure 6. Mass spectra of DPP-IV-catalyzed (A) intact GLP-1 and (B) PEG_{2k}-Lys-GLP-1 upon degradation. Each peptide was incubated with purified DPP-IV, and reaction mixtures were monitored at different time intervals by MALDI-TOF MS over 2 h periods. GLP-1 (9−36) indicates the N-terminally truncated GLP-1 metabolite.

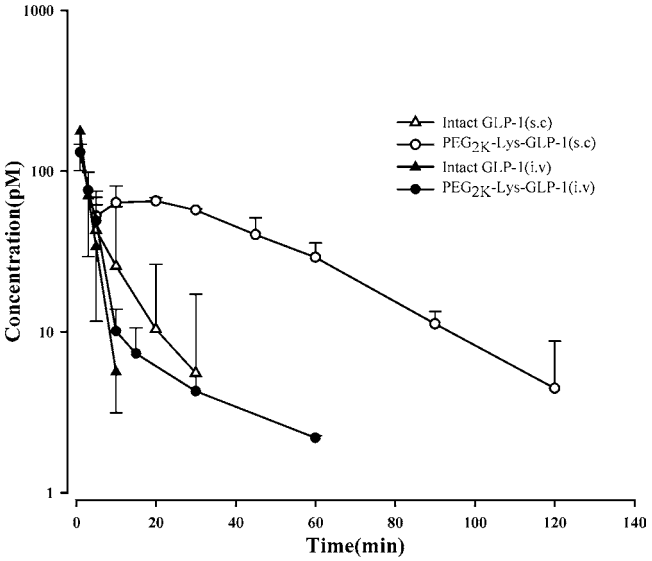

Figure 7. Plasma concentration of GLP-1 and PEG_{2k}-Lys-GLP-1 versus time after intravenous (1 μg/kg) and subcutaneous (10 μg/kg) injection in rats. Values are mean ± SD (n = 3).

biological activity, which is a decisive and potential advantage of our system in terms of efficiency.

Pharmacokinetics. The pharmacokinetic properties of GLP-1 and PEG_{2k}-Lys-GLP-1 were evaluated by non-compartmental and two-compartmental analysis following sc and iv administration in male SD rats, respectively. Figure 7 illustrates the plasma concentration profiles during 2 h experimental time periods, and pharmacokinetic parameters calculated from the data are summarized in Table 2. Plasma concentration of both intravenously administered GLP-1 and conjugate showed a biexponential disposition. Plasma activity of GLP-1 declined rapidly, with a half-life of 2.6 min, whereas the mono-PEGylated GLP-1 showed increased half-life by 10-fold, reduced clearance by 1.5-fold, and a 16-fold increase in mean residence time. Again, PEGylation had a profound effect on the pharmacokinetic parameters after sc administration as evident from the increase in the area under the curve (AUC) of the mono-PEGylated GLP-1. The plasma concentration of GLP-1 peaked 5 min after the sc injection; however, T_{max} of PEG_{2k}-Lys-GLP-1 observed 16 min after the injection. The pharmacokinetic profile of intact sc GLP-1 was unsuitable, showing a rapid peak followed by a fast decay in plasma, which is in accordance with human trials (*24*). In contrast, PEG_{2k}-Lys-GLP-1 showed a 2-fold increase in C_{max}, a 7.5-fold increase in AUC, and a 2.5-fold increase in half-life, noting a low variability among individuals. Consequently, PEG_{2k}-Lys-GLP-1 has a significantly improved plasma exposure and stability compared to intact GLP-1.

We have designed and characterized two series of mono-PEGylated GLP-1, PEG_{2k}-N^{ter}-GLP-1, and PEG_{2k}-

Table 2. Pharmacokinetic Parameters after GLP-1 and PEGylated GLP-1 Administration to SD Rats[a].

sc (10 μg/kg)	T_{max} (min)	C_{max} (ng/mL)	$T_{1/2}$ (min)	AUC (ng × min × mL^{-1})	MRT (min)
intact GLP-1	5.00 ± 0.00	0.14 ± 0.01	9.09 ± 3.49	1.73 ± 0.13	14.35 ± 3.66
PEG_{2k}-Lys-GLP-1	16.67 ± 5.77	0.22 ± 0.04	21.67 ± 9.36	12.63 ± 1.75	43.81 ± 5.90

iv (1 μg/kg)	$T_{1/2}$ (min)	MRT (min)	Cl (mL/min)	AUC (ng × min × mL^{-1})	AUMC (ng × min^2 × mL^{-1})
intact GLP-1	2.61 ± 0.82	3.34 ± 1.45	581.4 ± 339.8	2.11 ± 1.04	7.86 ± 6.85
PEG_{2k}-Lys-GLP-1	33.36 ± 20.84	54.21 ± 21.10	307.2 ± 64.06	3.35 ± 0.67	181.1 ± 76.69

[a] Data are means ± SD (n = 3). T_{max}, time to reach maximum plasma concentration; C_{max}, maximal plasma concentration;, $T_{1/2}$. half-life; AUC, area under the curve; MRT, mean residence time; Cl, clearance; AUMC; area under the moment curve. Individual data from sc and iv doses were analyzed by noncompartment and two-compartment models, respectively.

Lys-GLP-1. Biological activity was altered by site modification, in which PEG_{2k}-N^{ter}-GLP-1 showed a marked reduction in activity, whereas the PEG_{2k}-Lys-GLP-1 retained biological activity. The enzyme proteolytic stability of mono-PEGylated GLP-1 was significantly enhanced after PEGylation mainly by steric hindrance induced by the PEG molecule. When lead compound PEG_{2k}-Lys-GLP-1 was administered to rats, PEGylation improved the pharmacokinetic properties of the GLP-1. Increase in half-life and decrease in clearance resulted in substantial improvement in the plasma exposure of the mono-PEGylated GLP-1.

GLP-1 has been suggested to be a useful novel therapy in the treatment of NIDDM patients. However, the instability of GLP-1 against the proteolytic enzyme, DPP IV, is the most daunting factor for its therapeutic use as a new treatment modality. Although, the short metabolic stability of the native peptide can be offset by constant iv infusion, this does not fundamentally overcome the effect of proteolytic enzymes. Moreover, an iv infusion may constrain the potential use of GLP-1 in the clinical setting. Thus, the development of a prolonged-acting or slow release form of GLP-1 in vivo has been the focus of much recent research. In this respect, the enzyme-resistant form of site-specifically PEGylated PEG_{2k}-Lys-GLP-1 could serve as a potential GLP-1-based antidiabetic agent for clinical application.

While our prototype of PEGylated GLP-1 showed prolonged action in vivo compared with the native GLP-1, the total plasma residence time is still in the range of 1 to 2 h. Therefore, our further investigation will examine the effect of the molecular weight of PEG on extended metabolic stability of GLP-1 in vivo. In addition, pharmacodynamic responses using a NIDDM disease animal model are required to evaluate whether the improved half-life of PEGylated GLP-1 is sufficient for the treatment of diabetes.

ACKNOWLEDGMENT

This work was supported in part by a grant from the Korea Health 21 R&D Project, Ministry of Health & Welfare (02-PJ2-PG3-21701-0008), and a grant from the Ministry of Science and Technology, Republic of Korea.

LITERATURE CITED

(1) Kieffer, T. J., and Habener, J. F., (1999) The glucagon-like peptide. *Endocr. Rev. 20*, 876−913.

(2) Nathan, D. M., Schreiber, E., Fogel, H., Mojsov, S., and Habener, J. F. (1992) Insulinotropic action of glucagonlike peptide-I−(7−37) in diabetic and nondiabetic subjects. *Diabetes Care 15*, 270−276.

(3) Nauck, M. A., Wollschlager, D., Werner, J., Holst, J. J., Orskov, C., Creutzfeldt, W., and Willms, B. (1996) Effects of subcutaneous glucagon-like peptide 1 (GLP-1 [7−36 amide]) in patients with NIDDM. *Diabetologia 39*, 1546−1553.

(4) Carolyn, F. D. (2004) Therapeutic strategies based on glucagons-like peptide 1. *Diabetes 53*, 2181−2189.

(5) Xu, G., Stoffers, D. A., Habener, J. F., and Bonner-Weir, S. (1999) Exendin-4 stimulates both beta-cell replication and neogenesis, resulting in increased beta-cell mass and improved glucose tolerance in diabetic rats. *Diabetes 48*, 2270−2276.

(6) Stoffers, D. A., Kieffer, T. J., Hussain, M. A., Drucker, D. J., Bonner-Weir, S., Habener, J. F., and Egan, J. M. (2000) Insulinotropic glucagon-like peptide 1 agonists stimulate expression of homeodomain protein IDX-1 and increase islet size in mouse pancreas. *Diabetes 49*, 741−748.

(7) Deacon, C. F., Nauck, M. A., Toft-Nielsen, M., Pridal, L., Willms, B., and Holst, J. J. (1995) Both subcutaneously and intravenously administered glucagon-like peptide I are rapidly degraded from the NH2-terminus in type II diabetic patients and in healthy subjects. *Diabetes 44*, 1126−1131.

(8) Lotte, B. K. (2004) Glucagon-like Peptide-1: The basis of a new class of treatment for type 2 diabetes. *J. Med. Chem. 47*, 4128−4134.

(9) Knudsen, L. B., Nielsen, P. F., Huusfeldt, P. O., Johansen, N. L., Madsen, K., Pedersen, F. Z., Thogersen, H., Wilken, M., and Agerso, H. (2000) Potent derivatives of glucagon-like peptide-1 with pharmacokinetic properties suitable for once daily administration. *J. Med. Chem. 43*, 1664−1669.

(10) Kim, J. G., Baggio, L. L., Bridon, D. P., Castaigne, J. P., Robitaille, M. F., Jette, L., Benquet, C., and Drucker, D. J. (2003) Development and characterization of a glucagon-like peptide 1-albumin conjugate: the ability to activate the glucagon-like peptide 1 receptor in vivo. *Diabetes 52*, 751−759.

(11) Lee, K. C., Moon, S. C., Park, M. O., Lee, J. T., Na, D. H., Yoo, S. D., Lee, H. S., DeLuca, P. P. (1999) Isolation, characterization, and stability of positional isomers of mono-PEGylated salmon calcitonins. *Pharm. Res. 16*, 813−818.

(12) Na, D. H., Park, M. O., Choi, S. Y., Kim, Y. S., Lee, S. S., Yoo, S. D., Lee, H. S., Lee, K. C. (2001) Identification of the modifying sites of mono-PEGylated salmon calcitonins by capillary electrophoresis and MALDI-TOF mass spectrometry. *J. Chromatogr. B. 754*, 259−263.

(13) Lee, K. C., Park, M. O., Na, D. H., Youn, Y. S., Lee, S. D., Yoo, S. D., Lee, H. S., DeLuca, P. P. (2003) Intranasal delivery of PEGylated salmon calcitonins: hypocalcemic effects in rats. *Calcif. Tissue Int. 73*, 545−549.

(14) Na, D. H., Youn, Y. S., Park, E. J., Lee, J. M., Cho, O. R., Lee, K. R., Lee, S. D., Yoo, S. D., DeLuca, P. P., Lee, K. C. (2004) Stability of PEGylated salmon calcitonin in nasal mucosa. *J. Pharm. Sci. 93*, 256−261.

(15) Shin, B. S., Jung, J. H., Lee, K. C., and Yoo, S. D. (2004) Nasal absorption and pharmacokinetic disposition of salmon calcitonin modified with low molecular weight polyethylene glycol. *Chem. Pharm. Bull. 52*, 957−960.

(16) Roberts, M. J., Bentley, M. D., and Harris, J. M. (2002) Chemistry for peptide and protein PEGylation. *Adv. Drug Delivery Rev. 54*, 459−476.

(17) Caliceti, P., and Veronese, F. M. (2003) Pharmacokinetic and biodistribution properties of poly(ethylene glycol)-protein conjugates. *Adv. Drug Delivery Rev. 55*, 1261−1277.

(18) Bailon, P., Palleroni, A. Schaffer, C. A., Spence, C. L., Fung, W. J., Porter, J. E., Ehrlich, G. K., Pan, W., Xu, Z. X., Modi, M. W., Farid, A., Berthold, W., and Graves, M. (2001) Rational design of a potent, long-lasting form of interferon: A 40 kDa branched poly(ethylene glycol)-conjugated interferon α-2a for the treatment of hepatitis. *Bioconjugate Chem. 12*, 195−202.

(19) Na, D. H., and Lee, K. C. (2004) Capillary electrophoretic characterization of PEGylated human parathyroid hormone with matrix-assisted laser desorption/ionization time-of-flight mass spectrometry, *Anal. Biochem. 331*, 322−328.

(20) Lacy, P. E., and Kostianovsky, M. (1967) Method for the isolation of intact islets of Langerhans from the rat pancreas. *Diabetes 16*, 35−39.

(21) Na, D. H., DeLuca, P. P., and Lee, K. C. (2004) Direct Determination of the peptide content in microspheres by matrix-assisted laser desorption/ionization time-of-flight mass spectrometry. *Anal. Chem. 76*, 2669−2673.

(22) Siegel, E. G., Schulze, A., Schmidt, W. E., and Creutzfeldt, W. (1992) Comparison of the effect of GIP and GLP-1 (7−36 amide) on insulin release from rat pancreatic islets. *Eur. J. Clin. Invest. 22*, 154−157.

(23) Xiao, Q., Giguere, J., Parisien, M., Jeng, W., St-Pierre, S. A., Brubaker, P. L., and Wheeler, M. B. (2001) Biological activities of glucagon-like peptide-1 analogues in vitro and in vivo. *Biochemistry 40*, 2860−2869.

(24) Ritzel, R., Orskov, C., Holst, J. J., and Nauck, M. A. (1995) Pharmacokinetic, insulinotropic, and glucagonostatic properties of GLP-1 [7−36 amide] after subcutaneous injection in healthy volunteers. Dose−response-relationships. *Diabetologia 38*, 720−725.

BC049735+

Endowing RNase H-Inactive Antisense with Catalytic Activity: 2-5A-Morphants[⊥]

Longhu Zhou,[†] Edgar R. Civitello,[†] Nidhi Gupta,[†] Robert H. Silverman,[‡] Ross J. Molinaro,[‡,§] David E. Anderson,[∥] and Paul F. Torrence[†,*]

Department of Chemistry, Northern Arizona University, Box 5698, Flagstaff, Arizona 86011-5698, Department of Cancer Biology, Lerner Research Institute, Cleveland Clinic Foundation, 9500 Euclid Avenue, Cleveland, Ohio 44195, Department of Chemistry, Cleveland State University, Cleveland, Ohio 44115, and Structural Mass Spectrometry Facility, National Institute of Diabetes and Digestive and Kidney Diseases, National Institutes of Health, Bethesda, Maryland 20892. Received September 16, 2004; Revised Manuscript Received December 23, 2004

A convergent synthetic approach was used to conjugate 2′,5′-oligoadenylate (2-5A, p5′A2′ [p5′A2′]$_n$p5′A) to phosphorodiamidate morpholino oligomers (morphants). To provide requisite quantities of 2-5A starting material, commercially and readily available synthons for solid-phase synthesis were adapted for larger scale solution synthesis. Thus, the tetranucleotide 5′-phosphoryladenylyl(2′→5′)adenylyl-(2′→5′)adenylyl(2′→5′)adenosine (p5′A2′p5′A2′]$_2$p5′A2′, tetramer 2-5A, **9**) was synthesized starting with 2′,3′-*O*-dibenzoyl-N^6,N^6-dibenzoyl adenosine prepared from commercially available 5′-*O*-(4-monomethoxytrityl) adenosine. Coupling with N^6-benzoyl-5′-*O*-(4,4′-dimethoxytrityl)-3′-*O*-(*tert*-butyldimethylsilyl) adenosine-2′-(*N*,*N*-diisopropyl-2-cyanoethyl)phosphoramidite, followed by oxidization and deprotection, generated 5′-deprotected dimer 2-5A. Similar procedures lengthened the chain to form protected tetramer 2-5 A. The title product **9** p5′A(2′p5′A)$_3$ (tetramer 2-5A) was obtained through phosphorylation of the terminal 5′-hydroxy of the protected tetramer and removal of remaining protecting groups using concentrated ammonium hydroxide−ethanol (3:1, v/v) at 55 °C and tetrabutylammonium fluoride (TBAF) in THF at room temperature, respectively. The 2-5A-phosphorodiamidate morpholino antisense chimera **11** (2-5A-morphant) was synthesized by covalently linking an aminolinker-functionalized phosphorodiamidate morpholino oligomer with periodate oxidized 2-5A tetramer (p5′A2′[p5′A2′]$_2$p5′A). The resulting Schiff base was reduced with cyanoborohydride thereby transforming the ribose of the 2′-terminal nucleotide of 2-5A N-substituted morpholine. RNase L assays demonstrated that this novel 2-5A-antisense chimera had significant biological activity, thereby providing another potential tool for RNA ablation.

INTRODUCTION

RNA is being pursued ever more vigorously as a target for drug discovery. This pursuit has been buttressed by the realization that the decay of mRNA can be key in the posttranscriptional regulation of gene expression (*1*, *2*). Antisense oligonucleotides are one such class of RNA-targeting agent. Since the first reports that antisense oligonucleotides could inhibit gene expression in a sequence specific manner, there has been widespread interest in antisense oligonucleotides as therapeutic agents (*3*−*7*). One such drug, Vitravene for drug-resistant cytomegalovirus retinitis, has been FDA approved, and about 20 antisense drugs are in clinical development (*8*). Of the many modifications of antisense that have been introduced, we have focused on one that recruits the 2-5A-dependent RNase L to destroy targeted RNA (*9*−*21*).

2′,5′-Oligoadenylates (2-5A) are formed from ATP when viral double-stranded RNA binds to 2′,5′-oligoadenylate synthetase (OAS) in interferon-treated cells. 2-5A plays a key role in the mechanism of interferon antiviral activity (*22*), as it provides an unambiguous signal to initiate RNA decay in mammalian cells through its activation of the latent 2-5A-dependent RNase L which degrades viral mRNA, resulting in an inhibition of protein synthesis. However, RNase L may not distinguish well between viral and cellular RNA substrates (*23*). To overcome the nonspecific action of RNase L, a 3′,5′-antisense oligodeoxyribonucleotide was attached to the 2′,5′-oligoadenylate activator of the 2-5A dependent RNase L. This 2-5A-antisense composite nucleic acid (2-5A-antisense) could target a particular chosen mRNA sequence and then destroy it through localized activation of the latent 2-5A-dependent RNase L (*9*−*14*, *23*−*26*).

2-5A-Antisense oligonucleotides have been employed in vitro and in vivo (1) to block respiratory syncytial virus (RSV) replication through targeting of RSV genomic and mRNAs and (2) to halt tumor proliferation by destruction of telomerase template RNA (*9*−*21*).

The purpose of the present undertaking was 2-fold. First, to increase the efficacy of 2-5A-antisense, modifications are sought that would improve the biological half-life of such molecules and also perhaps endow them with different pharmacokinetic properties from the phospho-

[⊥] A preliminary account of this work was presented at the 227th American Chemical Society National Meeting in Anaheim, CA, March, 2004; abstract no. MEDI 308.

* To whom correspondence should be addressed. Phone (928) 523-0298; Fax (928) 523-8111; E-mail: Paul.Torrence@nau.edu.
[†] Northern Arizona University.
[‡] Lerner Research Institute, Cleveland Clinic Foundation.
[§] Cleveland State University.
[∥] NIDDK.

10.1021/bc049778q CCC: $30.25 © 2005 American Chemical Society
Published on Web 02/19/2005

rothioate analogues employed in a number of the documented examples above. Second, it is well established that the biological action of most antisense oligonucleotides involve either a passive mechanism of steric blocking of translation or else rely on intervention of RNase H to degrade the hybrid molecule formed between the antisense drug and the target RNA sequence. In one view, it might be expected that higher potency of antisense agent would be associated with the catalytic mode of action (RNase H-mediated) since theoretically one molecule of antisense drug could effect the turnover of multiple molecules of target RNA substrate. In other words, steric blocking antisense agents may not achieve the same efficacy of action, all other factors being equal. For instance, two analogues of deoxyribose phosphodiester backbone oligonucleotides have been described, and these have greatly improved properties in many respects compared to the parent DNAs. These include the peptide nucleic acids (PNAs) and the phosphorodiamidate morpholino oligomers (PMOs, morphants, morpholino oligos). Each of these modifications has certain considerable theoretical pharmacodynamic and pharmacokinetic advantages over their deoxyribose phosphodiester relatives; nonetheless, no viable drug has arisen so far form these promising structural modifications. Insofar as we had previously shown that PNAs could be converted to catalytically active molecules by conjugation to 2-5A, we have turned our attention to the phosphorodiamidate morpholino oligomers. These morpholino analogues are DNA mimetics in which the five-membered sugar−phosphate backbone is replaced by six-membered morpholine backbone moieties joined by nonionic phosphorodiamidate intersubunit linkages (*27*−*29*). Morpholino analogues (morphants) of oligonucleotides have demonstrated superior resistance to enzymatic degradation, and they obey the Watson−Crick rules binding complementary DNA and RNA with high affinity and long physiological half-lives (*27*−*29*). In a variety of systems, they have demonstrated substantial competence in RNA ablation (*30*−*34*). To apply these latter properties to 2-5A-antisense and to endow morphants with a catalytic mode of action, we have prepared 2-5A-morphants, a new class of 2-5A-antisense.

MATERIALS AND METHODS

Reagents. Sodium periodate, sodium cyanoborohydride, and 1*H*-tetrazole were purchased from Aldrich (Milwaukee, WI). ChemGenes (Wilmington, MA) was the source for N^6-benzoyl-5′-*O*-dimethoxytrityl-3′-*O*-*tert*-butyldimethylsilyladenosine 2′-(*N*,*N*-diisopropyl-2-cyanoethyl)phosphoramidite (ANP-5681) and bis-cyanoethyl-*N*,*N*-diisopropylphosphoramidite. Deblocking mix (3% trichloroacetic acid in dichloromethane) and oxidizing solution (0.10 M iodine in tetrahydrofuran/pyridine/water) were purchased from Glen Research (Sterling, VA). Antisense reagents **10a** and **10b** were purchased from Gene Tools (Philomath, OR). Anhydrous THF, DMF, CH_3CN, and pyridine were purchased from Aldrich and were dried using standard methods and distilled before use. TLC was carried out on precoated silica gel thin layer sheets 60 F_{254} from EMD (Darmstadt, Germany). Flash chromatography (FC) was carried out on silica gel 60 Å, 70−230 or 220−400 meshes from EM. ^{1}H NMR (400.14 MHz), ^{13}C NMR (100.62 MHz), and ^{31}P NMR (169.99 MHz) spectra were recorded on Varian VNMR 400 spectrometer in $CDCl_3$ as indicated below. Matrix-assisted laser desorption/ionization time-of-flight mass spectrometry (MALDI-TOF/MS) was carried out on a Kratos MALDI III instrument at HT laboratories (San Diego, CA) and a Voyager DE Pro instrument at the Structural Mass Spectrometry Facility, National Institute of Diabetes and Digestive and Kidney Diseases, National Institutes of Health (Bethesda, MD).

UV measurements were carried out on a HP 8452A spectrophotometer instrument. Concentrations of 2-5 A tetramer and 2-5 A-antisense were determined spectrophotometrically using the extinction coefficient ($\epsilon = 44.4 \times 10^3$). All reversed-phase HPLC analysis and purifications were conducted on a Varian Pro Star 210 and Beckman 406 instruments. Adsorbosphere ODS analytical (4.6 × 250 mm) and semipreparative (10 × 250 mm) C-18 and C-8 columns (Alltech Company) were used for the analysis and purification with the following respective buffers: A: 50 mM NH_4OAc or $NH_4H_2PO_4$ (pH 7.00); B: 50% MeOH/H_2O. Linear gradient elution was performed with flow rate of 1 mL/min for analytic and 5 mL/min for preparative application. For the purification of 2-5A tetramer, the deprotection mixture was pooled and evaporated in a Speedvac, and then the residue was desalted with a Sep-Pak C-18 cartridge (Waters).

Synthesis of 5′-Phosphoryladenylyl(2′→5′)adenylyl(2′→5′)adenylyl(2′→5′)adenosine (p5′A2′p5′A2′p5′A2′p5′A, 2-5A Tetramer). *N^6-Benzoyl-3′-O-(tert-butyl-dimethylsilyl)adenylyl-{2′-[O^P-(2-cyanoethyl)]-5′}-N^6,N^6-dibenzoyl-2′,3′-O-dibenzoyl adenosine (**3**).* 2′,3′-*O*-Dibenzoyl-*N*,*N*-dibenzoyladenosine (**1**, 150 mg, 0.22 mmol), N^6-benzoyl-5′-*O*-dimethoxytrityl-3′-*O*-*tert*-butyl-dimethylsilyl-adenosine 2′-(*N*,*N*-diisopropyl-2-cyanoethyl)phosphoramidite (ANP-5681, **2**, 500 mg, 0.5 mmol), and tetrazole (100 mg, 1.4 mmol) were added to a flask and then dried in a desiccator in vacuo overnight. The mixture was allowed to react in 1.5 mL of anhydrous acetonitrile under N_2 atmosphere for 6 h at room temperature followed by an additional 1 h in a water bath at 40−50 °C. The coupling product was oxidized with iodine reagent solution (8 mL), over 50 min at ambient temperature. The reaction mixture was then diluted with CH_2Cl_2 (45 mL) and washed with saturated $Na_2S_2O_3$ (60 mL). The aqueous phase was re-extracted with another aliquot of CH_2Cl_2 (6 × 25 mL), and the combined organic phase was dried (Na_2SO_4), evaporated, and then coevaporated with toluene (3 × 10 mL) and chloroform (3 × 10 mL) to remove residual pyridine. TLC analysis (CH_2Cl_2:MeOH, 30:1) indicated the starting material (**1**) had disappeared. The product was purified by column chromatography on silica gel (70−230 mesh, 60 Å) with a solvent gradient of hexane, CH_2Cl_2, and MeOH. A mixture of 250 mg 5′-dimethoxytritylated dimer and 5′-OH deprotected dimer was obtained. The above product mixture was deprotected with the deblocking solution (15 mL, 3% CCl_3COOH solution in CH_2Cl_2) at 0 °C for 15 min. The detritylation was stopped by the addition of saturated $NaHCO_3$ solution (75 mL), and the reaction mixture was extracted with dichloromethane (6 × 25 mL). The organic layer was dried ($MgSO_4$) and concentrated under reduced pressure. The crude product was purified by column chromatography on silica gel (70−230 mesh, 60 Å) with a solvent gradient of hexane, CH_2Cl_2, and CH_3OH to obtain pure 5′-OH dimer (**3**, 195 mg, 71%). Compound **3** on TLC gave an $R_f = 0.33$ (CH_2Cl_2:MeOH, 30:1).^{1}H NMR ($CDCl_3$): δ 0.01 (s, 3H, Si-CH_3), 0.02 (s, 3H, Si-CH_3), 0.78 (s, 3H, C-CH_3), 0.79 (s, 6H, 2 C-CH_3), 2.37−2.42 (m, 2H), 3.57−4.56 (m, 9H), 5.31−5.47 (m, 2H), 5.81−5.86 (m, 1H), 6.00−6.06 (m, 1H), 6.11 (dd, $J = 6.4$ Hz $J = 6.0$ Hz, 1H), 6.40 (d, $J = 5.2$ Hz, 1H), 7.16−7.39 (m, 15H, Bz-H), 7.71−7.83 (m, 10H, Bz-H), 8.14−8.55 (m, 4H, Ade-H), 9.16 (br, 1H, Ade-NH). ^{13}C NMR ($CDCl_3$): −5.1, −4.8, 17.8, 19.1, 19.2, 25.4, 25.5,

61.7, 62.4, 62.5, 66.9, 70.3, 71.9, 73.6, 73.7, 80.9, 86.2, 86.3, 87.7, 88.2, 116.0, 116.2, 124.2, 127.5−129.6 (m), 132.5, 132.8, 133.1, 133.5, 133.6, 133.7, 142.9, 143.5, 143.7, 149.9, 150.0, 150.8, 151.7, 151.8, 152.2, 152.5, 152.6, 164.6, 164.7, 164.8, 164.9, 165.1, 172.0, 172.1. ^{31}P NMR ($CDCl_3$): −0.86, 0.98. MALDI-TOF/MS (*m/z*): calcd for $C_{64}H_{62}N_{11}O_{15}PSi$: 1283.4; found 1283.4 ($M^+$).

*N^6-Benzoyl-3′-O-(tert-butyl-dimethylsilyl adenylyl-{2′-[O^P-(2-cyanoethyl)]-5′}-N^6-benzoyl-3′-O-(tert-butyl-dimethylsilyl)adenylyl-{2′-[O^P-(2-cyanoethyl)]-5′}-N^6,N^6-dibenzoyl-2′-O-,3′-O-dibenzoyladenosine (**4**)*. Compound **4** was obtained in a fashion similar to compound **3.** The 5′-OH dimer **3** (200 mg, 0.16 mmol) was coupled with N^6-benzoyl-5′-*O*-dimethoxytrityl-3′-*O*-*tert*-butyldimethylsilyladenosine 2′-(*N*,*N*-diisopropyl-2-cyanoethyl)phosphoramidite (**2**, 988 mg, 1.0 mmol) in the presence of tetrazole (143 mg, 2 mmol) under N_2. The resulting product then was oxidized with iodine solution and deprotected (dimethoxytrityl group removal) with 3% trichloroacetic acid in dichloromethane (18 mL). The product was purified by column chromatography on silica gel (200−400 mesh, 60 Å) employing a solvent gradient of hexane, CH_2Cl_2 and MeOH. The yield of trimer **4** was 254 mg (86.6%). ^{1}H NMR ($CDCl_3$): δ 0.00−0.07 (m, 12H, 4 Si-CH_3), 0.77−0.86 (m, 18H, 2 C$(CH_3)_3$), 2.49−2.56 (m, 4H), 3.60−4.08 (m, 11H), 4.38−4.62 (m, 4H), 5.39 (m, 3H), 5.92−6.42 (m, 5H), 7.17−7.43 (m, 21H), 7.72−7.86 (m, 11H), 8.29−8.58 (m, 4H), 9.00 (br, 1H, Ade-NH), 9.15 (br, 1H, Ade-NH). ^{31}P NMR ($CDCl_3$): −1.33 to −0.56 (m). MALDI-TOF/MS (*m/z*): calcd for $C_{90}H_{95}N_{17}O_{22}P_2Si_2$: 1883.5; found 1884.4 ($M^+ + 1$).

*N^6-Benzoyl-3′-O-(tert-butyl-dimethylsilyl) adenylyl-{2′-[O^P-(2-cyanoethyl)]-5′}-N^6-benzoyl-3′-O-(tert-butyl-dimethylsilyl)adenylyl-{2′-[O^P-(2-cyanoethyl)]-5′}-N^6-benzoyl-3′-O-(tert-butyl-dimethylsilyl)adenylyl-{2′-[O^P-(2-cyanoethyl)]-5′}-N^6,N^6-dibenzoyl-2′,3′-O-dibenzoyl adenosine (**5**)*. Following a procedure similar to the syntheses of compounds **3** and **4**, a dried mixture of 5′-OH trimer **4** (181 mg, 96 μmol), N^6-benzoyl-5′-*O*-dimethoxytrityl-3′-*O*-*tert*-butyldimethylsilyl-adenosine 2′-(*N*,*N*-diisopropyl-2-cyanoethyl)-phosphoramidite **2** (640 mg, 0.65 mmol), and tetrazole (100 mg, 1.4 mmol) was reconstituted with anhydrous acetonitrile (4.5 mL) under an N_2 atmosphere. After stirring for 6 h at room temperature, the reaction mixture was oxidized with the iodine solution (15 mL). The intermediate product was purified by column chromatography as described previously and then detritylated with 23 mL of cold 3% CCl_3COOH solution of dichloromethane in an ice−water bath. The product was again purified by column chromatography on silica gel (70−230 mesh, 60 Å) eluting with same solvent gradient. The final yield was 182 mg of solid product 5′-OH tetramer **5** (51% yield). ^{1}H NMR ($CDCl_3$): δ 0.01−0.07 (m, 18H, 6 Si-CH_3), 0.75−0.86 (m, 27H, 3 C$(CH_3)_3$), 2.40−2.59 (m, 6H), 3.82−4.67 (m, 21H), 5.35−6.43 (m, 10H), 7.19−8.60 (m, 43H), 9.35 (br, 3H, Ade-NH). ^{31}P NMR ($CDCl_3$): −1.63 to −0.56 (m). MALDI-TOF/MS (*m/z*): calcd for $C_{116}H_{128}N_{23}O_{29}P_3Si_3$: 2483.8; found 2484.8 ($M^+ + 1$).

*5′-O^P-Bis-(2-cyanoethyl)-N^6-benzoyl-3′-O-(tert-butyl-dimethylsilyl)adenylyl-{2′-[O^P-(2-cyanoethyl)]-5′}-N^6-benzoyl-3′-O-(tert-butyl-dimethylsilyl)adenylyl-{2′-[O^P-(2-cyanoethyl)]-5′}-N^6-benzoyl-3′-O-(tert-butyl-dimethylsilyl) adenylyl-{2′-[O^P-(2-cyanoethyl)]-5′}-N^6,N^6-dibenzoyl-2′,3′-O-dibenzoyadenosine (**7**)*. The coupling and oxidation procedure was very similar to synthesis of dimer **3**. 5′-OH-unprotected tetramer **5** (182 mg, 73 μmol) was coupled with bis-cyanoethyl-*N*,*N*-diisopropylphosphoramidite **6** (197 mg, 0.73 mmol) in anhydrous acetonitrile (0.9 mL) in the presence of tetrazole (110 mg, 1.5 mmol) as catalyst for 7 h at room temperature under N_2 atmosphere. After the coupling reaction was complete, the oxidation of the reaction mixture was carried out with iodine solution (11 mL) for 50 min. The reaction mixture was diluted with 40 mL CH_2Cl_2 and washed with saturated $Na_2S_2O_3$ (50 mL). The aqueous phase was re-extracted with another CH_2Cl_2 (6 × 30 mL), and the combined organic phase was dried, evaporated, and coevaporated with toluene to remove pyridine. The product of reaction was purified by column chromatography on silica gel by elution with a gradient of hexane, CH_2Cl_2, and MeOH, and 130 mg of solid product tetramer **7** (yield 66%) was collected. ^{1}H NMR ($CDCl_3$): δ 0.014−0.04 (m, 18H, 6 Si-CH_3), 0.78−0.82 (m, 27H, 3 C$(CH_3)_3$), 2.40−2.60 (m, 10H), 3.86−6.43 (m, 22H), 7.11−8.60 (m, 43H), 9.18 (br, 3H, Ade-NH). ^{31}P NMR ($CDCl_3$): −1.34 to −0.54 (m).

*5′-Phosphoryladenylyl(2′→5′)adenylyl(2′→5′)adenylyl-(2′→5′)adenosine (**9**) (2−5A tetramer, p5′A2′p5′A2′p5′A2′-p5′A)*. Protected tetramer **7** (110 mg, 41 μmol) was incubated with NH_4OH−EtOH solution (3:1, 24 mL) at 55 °C for 24 h to remove the cyanoethyl and benzoyl protecting groups. The reaction mixture was evaporated to dryness under reduce pressure (cold water bath), and tetrabutylammonium fluoride (TBAF) in THF solution (1M, 10.5 mL) was added to the residue. The mixture was incubated at room temperature for 24 h, and then the solvent was evaporated completely in vacuo using a cold water bath (10 °C). Sterile water (10 mL) was added to the residue, and the solution was loaded into a C-18 Sep-Pak Cartridge (prewashed with 10 mL of MeOH and 12 mL of sterile H_2O). The cartridge was washed with water until no salt detected by UV (200 mL of H_2O was used). Deprotected tetramer **9** was then eluted with 50 mL of MeOH−H_2O (1:1), and the solution was evaporated completely under reduced pressure. Sterile water (6 mL) was added to above residue to yield a clear solution. The total amount of 2-5A tetramer (1460 OD_{260}) was determined by UV (80% yield). The retention time and purity were determined by HPLC analysis with a Beckman 406 instrument employing an Adsorbosphere ODS analytical (4.6 × 250 mm) C-8 (Alltech Company) with the following buffers: A: 50 mM $NH_4H_2PO_4$ (pH 7.00); B: 50% MeOH/H_2O. Linear gradient elution was performed (0 min, 0% B; 25 min, 50% B; 40 min, 100% B; 45 min, 100% B; 50 min, 0% B; 60 min, 0% B) with a flow rate of 1 mL/min. The retention time of tetramer **9** was 12.5 min, and the purity was 98% assessed at by detection at 260 nm. MALDI-TOF/MS (*m/z*): calcd for $C_{40}H_{50}N_{20}O_{25}P_4$: 1334.2; found 1335.3 ($M^+ + 1$).

Synthesis of 2-5A-Morpholino Antisense Chimera 11a and 11b. Sodium periodate solution (2 μL of 0.1 M in water, total of 0.2 μmol) was added in one portion to a solution of 2-5A-tetramer **9** (40 μL of 2.5 mM in water, 0.1 μmol, Na^+ form), and the resulting mixture was stirred in the dark at 0 °C for 30 min. To destroy the excess periodate, a $Na_2S_2O_3$ solution (4 μL of 0.1 M, total of 4 μmol) was added, and the resultant solution was maintained at 0 °C for an additional 10 min in the dark. A solution of phosphorodiamidate morpholino oligomers **10a** (25 μL of 2 mM in water, total of 0.05 μmol) was added, and the pH of the reaction mixture was adjusted to 8.6 with 0.1 M NaOH. The resulting mixture was stirred at 0 °C for 2 h, and then a sodium cyanoborohydride solution (2 μL of 0.5 M in water, total of 1 μmol) was added. This reaction mixture was kept at 0 °C for 1 h during which time the pH was maintained at 6.6 by addition of 0.5% HOAc. The resulting reaction mixture was stirred at 4 °C overnight. The reaction mixture was

Scheme 1[a]

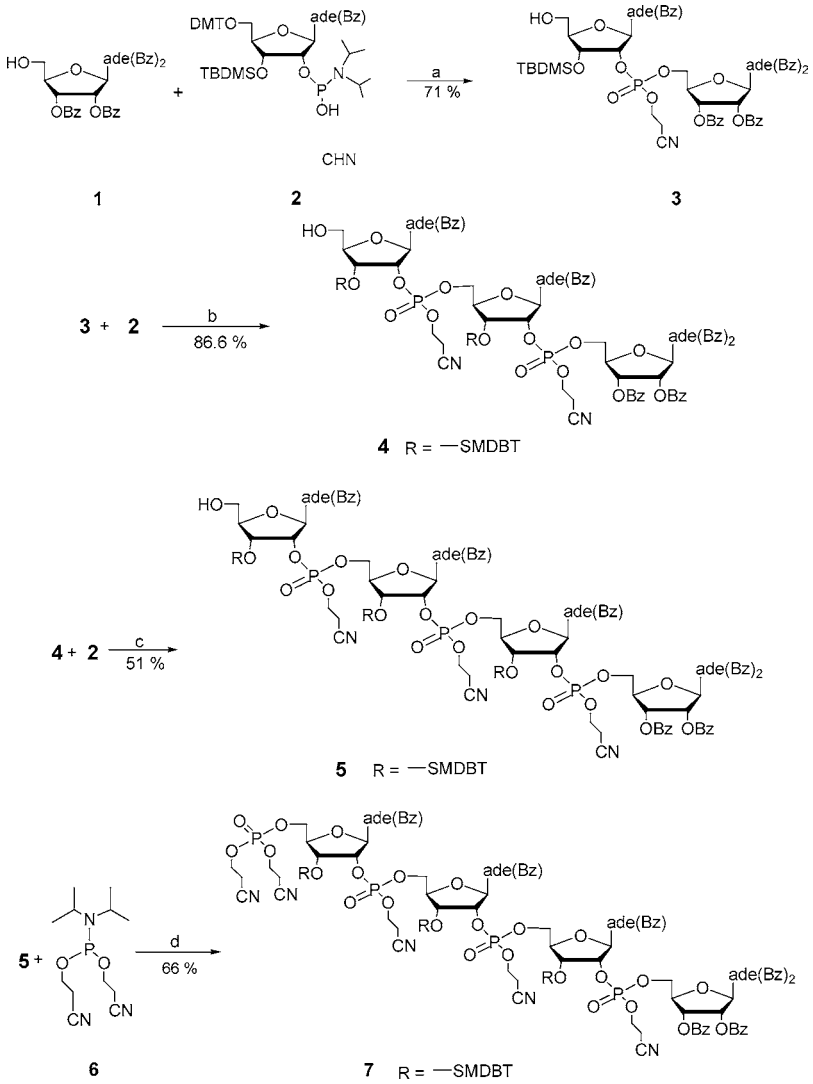

[a] Reaction conditions: (a) (i) 1*H*-tetrazole, anhydrous MeCN, N_2, rt; (ii) iodine solution, rt; (iii) 3% CCl_3COOH in CH_2Cl_2, 0 °C (three steps, 71% yield). (b) (i) 1*H*-tetrazole, anhydrous MeCN, N_2, rt; (ii) iodine solution, rt; (iii) 3% CCl_3COOH in CH_2Cl_2, 0 °C (three steps, 86.6% yield). (c) (i) 1*H*-tetrazole, anhydrous MeCN, N_2, rt; (ii) iodine solution, rt; (iii) 3% CCl_3COOH in CH_2Cl_2, 0 °C (three steps, 51% yield). (d) (i) 1*H*-tetrazole, anhydrous MeCN, N_2, rt; (ii) iodine solution, rt.

then diluted 10-fold with sterile water, and the conjugate product **11a** was purified by HPLC on an Adsorbosphere C-8 column (4.6 × 250 mm) (solvent A: 50 mmol $NH_4H_2PO_4$ (pH = 7.0); solvent B: MeOH/H_2O (1:1); 0 min, 0% B; 25 min, 50% B; 40 min, 100% B; 45 min, 100% B; 50 min, 0% B; 60 min, 0% B) at a flow rate of 1 mL/min. A total of 1.5 OD **11a** was obtained (A_{260}). The product was analyzed by MALDI-TOF mass spectrometry: (*m/z*, calcd for $C_{235}H_{360}N_{83}O_{101}P_{19}$: 6552.4; found 6552.5).

A similar procedure was employed in the synthesis of conjugate chimera **11b**. Purification of the product was performed on HPLC with adsorbosphere C-8 column using the same linear gradient program (A: 50 mmol NH_4OAc (pH = 7.0); B: MeOH/H_2O (1:1)). 1.01 OD of conjugate **11b** was obtained. The product was analyzed by MALDI-TOF mass spectrometry: (*m/z*, calcd for $C_{228}H_{349}N_{82}O_{100}P_{19}$: 6427.2; found 6427.2).

RNase L Activity. RNase L activity was determined by a fluorescence resonance energy transfer (FRET) method (*35*). The assay uses recombinant human RNase L produced in insect cells from a baculovirus vector and purified by FPLC columns (*36*). The cleavable substrate consists of a 36 nucleotide synthetic oligoribonucleotide sequence derived from respiratory syncytial virus with the fluorophore, FAM, at the 5′-terminus and black hole quencher-1 (BHQ-1), at the 3′-terminus (synthesized at Integrated DNA Technologies). The RNA sequence (6-FAM-UUA UCA AAU UCU UAU UUG CCC CAU UUU UUU GGU UUA-BHQ-1) contains several cleavage sites for RNase L (UU or UA). The test compounds or 2-5A were diluted to final concentrations of 1 nM, 3 nM, 10 nM, 30 nM, 100 nM, 300 nM, 1000 nM, and 3000 nM in DEPC treated water. Five microliters of each diluted sample was added in triplicate to 96-well black polystyrene microtiter plates (Corning) on ice. Forty-five microliters of the reaction mixture was added to each sample, and the plates were gently agitated for 10 s to mix and then were centrifuged briefly at 500 rpm. The assays contained 100 nM RNA probe, 25 nM RNase L, 25 mM Tris-HCl (pH7.4), 100 mM KCl, 10 mM $MgCl_2$, 50 μM ATP, and 7 mM 2-mercaptoethanol with and without 2-5A or analogues. RNase L was the last component added to the reaction mixtures. The plates were incubated at 20 °C protected from light. Fluorescence was measured at 5, 30, 60, and 90 min with a Wallac 1420 fluorimeter (Perkin-Elmer) (absorption 485 nm/emission 535 nm).

Scheme 2[a]

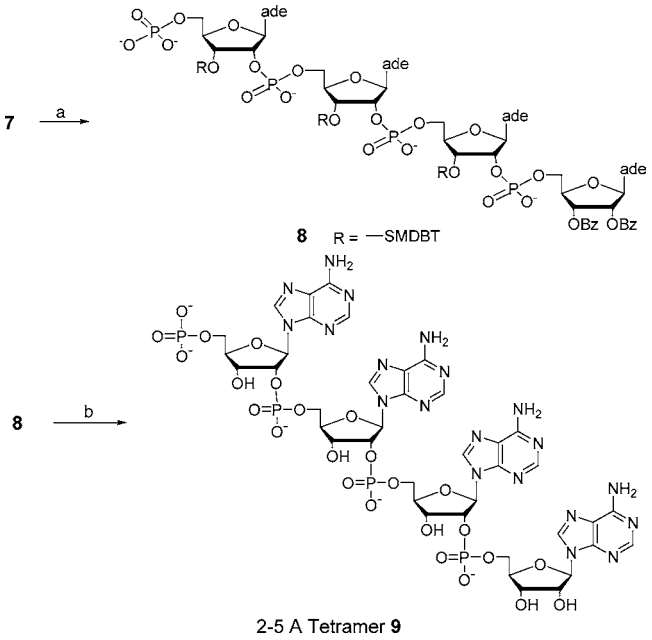

[a] Reaction conditions: (a) NH_4OH−EtOH (3:1), 55 °C; (b) 1 M tetrabutylammonium fluoride (TBAF) in THF, rt. (two steps of a and b, 80% yield).

RESULTS

Chemistry. *Synthesis of 2-5A Tetramer.* The target compound 2-5A tetramer **9** was synthesized by solution-phase phosphoramidite chemistry, and the synthesis, depicted in Schemes 1 and 2, was based upon a modified strategy of phosphoramidite methodology (*37*, *38*). 2′,3′-*O*-Dibenzoyl-N^6,N^6-dibenzoyl adenosine **1** was chosen as starting material for coupling with a commercially available N^6-benzoyl-5′-*O*-dimethoxytrityl-3′-*O*-*tert*-butyl-dimethylailyl-adenosine 2′-(*N*,*N*- diisopropyl-2-cyanoethyl)-phosphoramidite **2** at 5′-*O*-position in the presence of 1*H*-tetrazole in anhydrous acetonitrile at room temperature under nitrogen. Following oxidation by iodine solution and then detritylation with 3% CCl_3COOH in CH_2Cl_2, the corresponding dimer compound **3** was isolated in 71% yield. The deprotection of DMTr (dimethoxytrityl) group with 3% CCl_3COOH in CH_2Cl_2 was found to be much more effective than previous procedures using 80% acetic acid at room temperature (*38*). It was particularly important with relative higher concentration of reaction mixture in coupling step, because no reaction was observed with 10-fold less concentration, which was employed in the procedure for preparing the dimer **3**. Dinucleotide **3** was effectively coupled again with a higher mole ratio the building block **2** to yield the fully protected trinucleotide intermediate. After purified by flash column chromatography, the fully protected trimer was treated by 3% CCl_3COOH to produce trinucleotide **4** in 86.6% yield. The tetramer **5** was then prepared using the same coupling reaction, oxidation, and deprotection procedures from trimer **4** and phosphoramidite **2** with moderate yield (51.5%). The phosphorylation of the terminal 5′-hydroxy of tetramer **5** was also accomplished through the same coupling and oxidation procedure using commercially available bis-cyanoethyl-*N*,*N*-diisopropyl phosphoramidite **6** and afforded tetramer **7** with 66% yield (*39*). The deprotection of benzoyl and cyanoethyl groups was accomplished by treating of tetramer **7** with concentrated ammonium hydroxide−ethanol (3:1, v/v) at 55 °C for 9 h to produce tetramer **8** (Scheme 2). The *tert*-butyldimethylsily (TBDMS) silyl protection groups of **8** were removed by stirring with tetrabutylammonium fluoride (TBAF) solution in THF at room-temperature overnight (*33*). The final product was purified by a C-18 Sep-Pak Cartridge eluted with water and methanol−water (1:1) mixture to give a white solid **9** in 80% from

Scheme 3

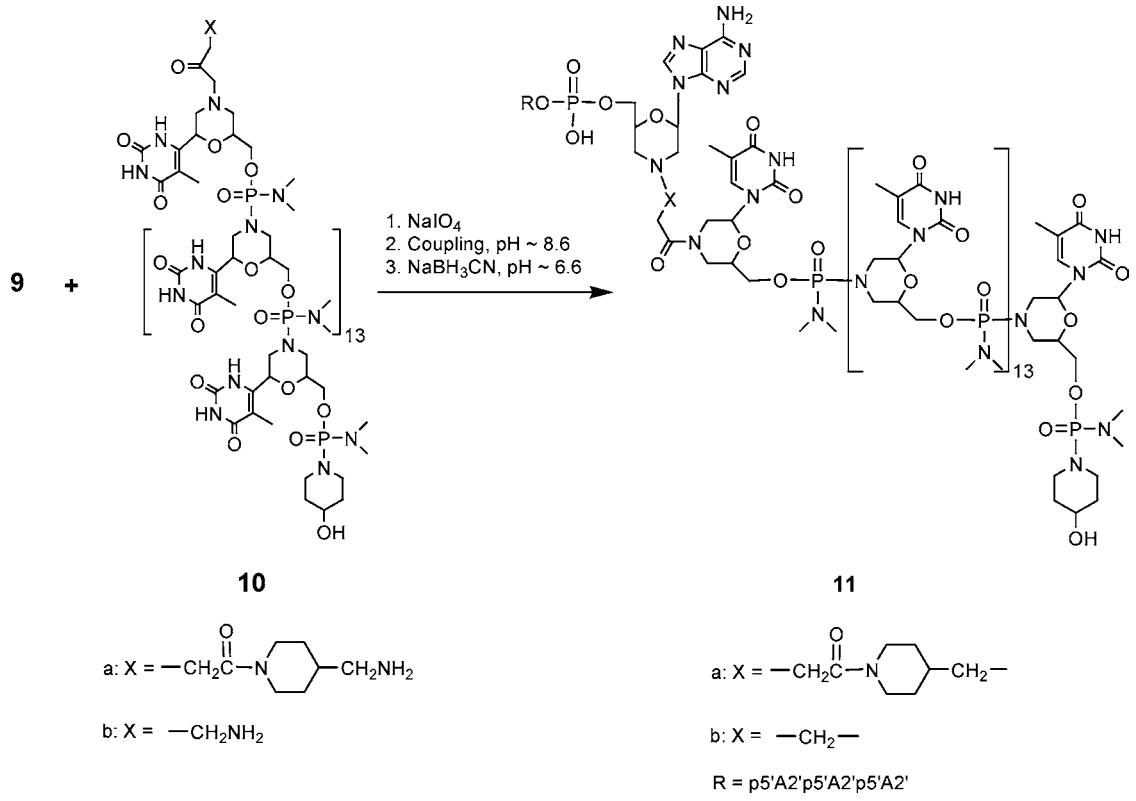

7. The overall yield from **1** was 16.5%. The product 2-5A tetramer **9** was analyzed by matrix-assisted laser desorption/ionization time-of-flight mass spectrometry (MALDI-TOF/MS), and the observed molecular weight supported its structure. It was only a single peak by HPLC analysis [Beckman 406 instrument and an Adsorbosphere ODS analytical (4.6 × 250 mm) C-8 column were used with the following buffers: A: 50 mM $NH_4H_2PO_4$ (pH 7.00); B: 50% MeOH/H_2O. Linear gradient elution was performed with a flow rate of 1 mL/min], and it had the same retention time on HPLC as a standard sample of **9** made from solid-phase method.

Synthesis of 2-5A-Morpholino Antisense Chimera. The morpholine ring has been used to form conjugates between RNAs and several of other molecules, such as peptides (*40*), peptide nucleic acids (PNAs) (*20*), fluorescent labels (*41*), and a half-ribozyme (*42*). Morpholino-based oligonucleotides also have been prepared as antisense oligo agents (*43*). Our route to the synthesis of a 2-5A-morpholino antisense chimera is based on the well-known oxidation−reductive amination conjugation method (*44*−*49*). Thus, the chimera can be prepared from 2-5A tetramer through the oxidative cleavage of the five-membered ribose ring with sodium periodate followed by reductive coupling of the resulting dialdehyde with 5′-aminotether thymine morphant 15-mer to give a six-membered morpholine ring. These three steps were carried out sequentially in a single step without intervening purifications. It was very important to destroy all of the excess periodate before addition of T_{15}-Morpholino antisense due to its high oxidation susceptibility (*49*). The conjugate product 2-5A-Morpholino antisense chimera **11** was synthesized (Scheme 3) by using two different kind of linkages and purified by HPLC using an adsorbosphere C-8 column (column 4.6 × 250 mm, Alltech Company) and recorded at 260 nm. However, it should be noted that an adsorbosphere C-18 column (column 4.6 × 250 mm, Alltech Company) cannot be used to purify the antisense chimeras, because the product **11** adhered very strongly on the C-18 column. The conjugate products were analyzed by MALDI-TOF mass spectrometry, and the observed molecular weight supported its structure.

Biological Assays. To determine the biological activity of the 2-5A-morphants, ability to activate RNase L was determined by a fluorescence resonance energy transfer (FRET) method similar to that published earlier (*35*). The assay used recombinant human RNase L produced in insect cells from a baculovirus vector and purified to homogeneity with three successive FPLC columns (*36*). The cleavable substrate consists of a 36-nucleotide synthetic oligoribonucleotide sequence derived from respiratory syncytial virus with the fluorophore, FAM, at the 5′-terminus and black hole quencher-1 (BHQ-1), at the 3′-terminus (synthesized at Integrated DNA Technologies). The RNA sequence contains several cleavage sites for RNase L (UU or UA). A typical assay results in shown in Figure 1 and 2. In these figures, relative fluorescence is plotted vs concentration of either pure 2-5A tetramer as a standard, or against the concentration of 2-5A-morphant. Increase of fluorescence corresponds to RNA cleavage as the Quencher moiety is released as one fragment of the RNA chain and cannot quench the fluorophore at the other end of the parent chain. Two completely separate experiments are shown, one in each figure. Figure 1 shows the results with 2-5A-morphant (**11a**). The 2-5A-morpholino antisense chimera displayed an EC_{50} of about 100 nM with the standard 2-5A tetramer showing an EC_{50} of about 3 nM. Thus, **11a** was about 30 times less effective as an RNAse L activator

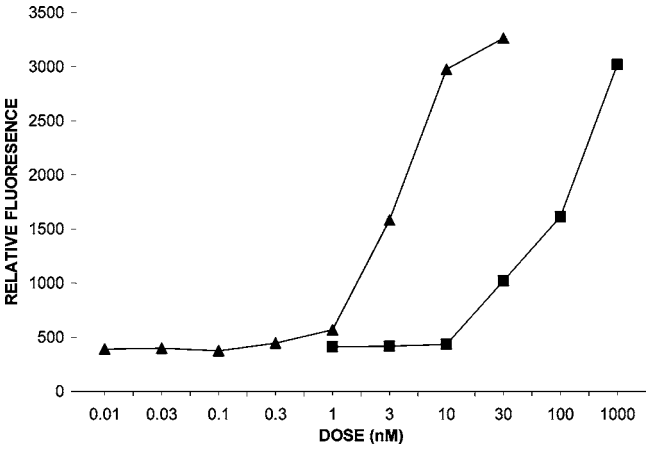

Figure 1. Standard curve dose−response of 2-5A tetramer **9** (▲) and 2-5A-T15-Morpholino antisense **11a** (■).

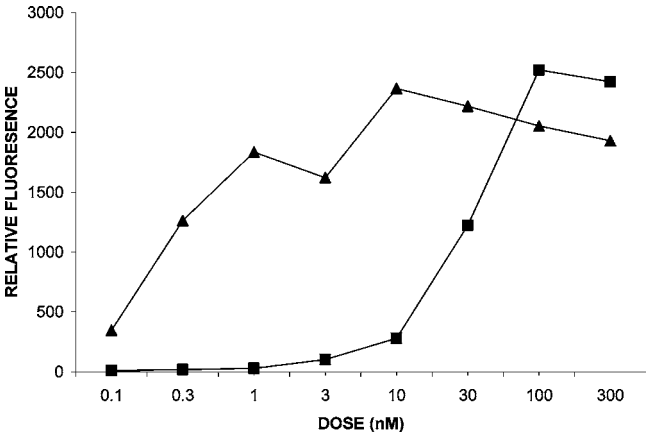

Figure 2. Standard curve dose−response at 90 min. 2-5A tetramer **9** (▲), 2-5A-T15-Morpholino antisense **11b** (■).

compared to parent 2-5A. In Figure 2 while 2-5A tetramer effected RNA substrate cleavage at an EC_{50} of approximately 0.3 nM, the 2-5A-morphant (**11b**) displayed an EC_{50} of about 30 nM.

DISCUSSION

To conjugate 2-5A to phosphorodiamidate morpholino oligomers, we first needed to prepare the 2-5A tetramer in reasonable amounts that would permit appropriate experimentation with development of conjugation chemistries and conditions. In fact, while various methodologies are reported in the literature, the generation of required synthons is no trivial procedure. Moreover, although synthons for solid-phase synthesis are commercially available, the overall yields of this solid-phase approach are only sub-micromoles using the presently available technology. Thus multiple solid-phase syntheses are required to provide a continual supply of 2-5A tetramer. We desired to develop a more practical approach to provide product 2-5A tetramer in a multiple micromole scale. We have successfully adapted synthetic conditions so that commercially available synthons can be used in solution phase to obviate the limitations of solid-phase synthesis. Herein we describe the synthesis of 2-5A tetramer on a multi-millimole scale in 98% purity.

The convergent synthesis strategy used to join 2-5A tetramer (**9**) to amino-derivatized phosphorodiamidate morpholino oligomers (**10a**, **10b**) was similar to that used to generate modified 2′,5′-oligoadenylates and 2-5A-PNAs. We employed an approach involving the periodate oxidation of 2′,5′-oligoadenylate to generate the terminal

dialdehyde, subsequent Schiff base formation with an aminolinker-bearing morpholino oligo, and finally reduction by cyanoborohydride. This route obviated the need for the development of a stepwise synthesis that would require synthons with RNA protecting groups compatible with morpholino oligo protection and coupling strategies.

We chose to synthesize prototype 2-5A-PMO conjugates with an all thymine PMO oligonucleotide analogue backbone in order to determine (a) if the PMO modification was compatible with RNase L activation and (b) the effect of linker variation on such activity if present. If the PMO and linkers were consistent with reasonable RNase L activation, then it would be possible to select specific virus- or cancer-related RNAs for 2-5A-PMO-antisense targeting. This investigational sequence is similar to that employed earlier to develop an effective inhibitor of respiratory syncytial virus (RSV) replication.

As is clear from Figures 1 and 2, both versions of the 2-5A-morpant conjugate are capable of activating RNase L albeit with reduced potency compared to parent 2-5A tetramer. These 30−100-fold reductions in RNase L activation ability, compared to unmodified 2-5A itself, are similar reductions in RNase L activation to that seen for other chimeric 2-5A-antisense constructs of similar chain length. This comparison is valid when evaluation was carried out against RNA substrates that were non-complementary to the antisense domain of 2-5A-antisense analogues. Thus for instance, in the case of the 2-5A-antisense chimera with an all DNA phosphodisester DNA antisense domain that did not complement the substrate RNA, RNase L activation ability was reduced by about 30-fold compared to parent 2-5A (*36*). When the antisense domain was a PNA that did not complement substrate RNA, then RNase L activation was reduced 60−100-fold (*20*). Greater activity has been observed when the antisense domain of the chimera targets specifically the RNA substrate. Thus a 2-5A-antisense molecule with an all phosphodiester DNA targeting a specific sequence of PKR RNA was only 3 times less active than parent 2-5A (*36*). This increase in activity against targeted substrate has been hypothesized to be related to a proximity effect due to creation of a new specific high affinity binding site (the antisense domain of the 2-5A-antisense chimera) on RNase L. In any case, it is clear from Figures 1 and 2 that 2-5A-morphants possess similar RNase L activation competence to previously described molecules of this genre. Furthermore, upon the basis of our experience with these assay determinations of EC_{50} and the fact that the experiments were completely independent, we do not ascribe any significant difference in RNase L activation competence to the two different 2-5A-morphants, **11a** and **11b**. Thus the linkage between the 2-5A and the morpholino antisense does not have a significant effect on biological activity, at least in this assay.

The results presented herein show that a convergent approach to 2-5A-phosphordiamidate morpholino oligomers (2-5A-morphants) is indeed possible. Moreover, the type of morpholino linkage generated by this periodate oxidation/Schiff base formation/cyanoborohydride reduction approach is compatible with reasonable activation of RNase L. Finally, these results suggest that the nature of the linker between the morpholino antisense domain and 2-5A moiety is likely of minimal importance.

These chimeric molecules, consisting of a 2′,5′-oligoadenylate activator of RNase L and a phosphordiamidate morpholino oligomer, combine the advantages of two previously separate strategies for RNA ablation. On one hand, the 2-5A domain of this conjugate recruits a constitutive cellular enzyme to the site of the targeted RNA molecule. On the other hand, the phosphordiamidate morpholino domain of the conjugate brings high resistance to degradation by enzymes of biological fluids, higher affinity for target RNAs, good water solubility, and greatly reduced synthetic production costs (*50*). In addition, morpholino oligos do not bind nonspecifically to many biological macromolecules, as do phosphorothioate oligos (*50*).

Ongoing studies will determine whether 2-5A-morphants have a significant future in antisense technology.

ACKNOWLEDGMENT

This research was supported in part by the US Department of Defense Congressionally Directed Medical Research Program on Prostate Cancer, Grant DAMD17-02-1-0255 (to P. F. T.), by State of Arizona Proposition 301 Funding (to P. F. T.) and by grant CA44059 from the National Cancer Institute, NIH (to R.H.S.). The expert technical assistance of Robert Smith is gratefully acknowledged.

LITERATURE CITED

(1) Williams, D. L., Sensel, M., McTigue, M., and Binder, R. (1993) Hormonal and developmental regulation of mRNA turnover. In *Control of Messenger RNA Stability* (Belasco, J., and Brawerman, G., Eds.) pp 161−197, Academic Press, San Diego.

(2) Torrence, P. F., Ed. (2000) *Biomedical Chemistry: Applying Chemical Principles to the Understanding and Treatment of Disease*, J. Wiley & Sons: New York.

(3) Stephenson, M. L., and Zamecnik, P. C. (1978) Inhibition of rous sarcoma viral replication and cell transformation by a specific oligondeoxyribonucleotide. *Proc. Natl. Acad. Sci. U.S.A. 75*, 285−288.

(4) Zamecnik, P. C., and Stephenson, M. L. (1978) Inhibition of rous sarcoma viral RNA translation by a specific oligondeoxyribonucleotide. *Proc. Natl. Acad. Sci. U.S.A. 75*, 280−284.

(5) Uhlmann, E., and Peyman, A. (1990) Antisense oligonucleotides: a new theraputic priciple. *Chem. Rev. 90,* 544−584.

(6) Milligan, J. F., Matteucci, M. D., and Martin, J. C. (1993) Current concepts in antisense drug design. *J. Med. Chem. 36*, 1923−1937.

(7) Chen, C. P., Zhang, L. R., Peng, Y. F., Wang, X. B., Wang, S. Q., and Zhang, L. H.. (2003) A concise method for the preparation of peptide and arginine-rich peptide-conjugated antisense oligonucleotide. *Bioconjugate Chem. 14*, 532-538.

(8) Crooke, S. T. (2004) Antisense strategies. *Curr. Mol. Med. 4*, 465−487.

(9) Torrence, P. F., Maitria, R., Lesiak, K., Khamnei, S., Zhou, A., and Silverman, R. H. (1993) Targeting RNA for destruction with a 2′, 5′-oligoadenylate-antisense chimera. *Proc. Natl. Acad. Sci. U.S.A. 90*, 1300−1304.

(10) Lesiak, K., Khamnei, S., and Torrence, P. F. (1993) 2′,5′-oligoadenylate-antisense chimera: synthesis and properties. *Biocojugate Chem. 4*, 467−472.

(11) Torrence, P. F., Xiao, W., Li, G., Gramer, H., Player, M. R., and Silverman, R. H. (1997) Recruiting the 2-5A System for antisense therapeutics. *Antisense Nucleic Acid Drug Dev. 7*, 203−206.

(12) Maitra, R. K., Li, G., Xiao, W., Dong, B., Torrence, P. F., and Silverman, R. H. (1995) Catalytic cleavage of an RNA Target by 2-5A-antisense and 2-5A-dependent RNase. *J. Biol. Chem. 270*, 15071−15077.

(13) Maran, A., Maitra, R. K., Kumar, A., Dong, B., Xiao, W., Li, G., Williams, B. R. G., Torrence, P. F., and Silverman, R. H. (1994) Blockage of NF-κB signaling by selection of an mRNA target by 2-5A antisense chimera. *Science 265*, 789−792.

(14) Maran, A., Waller, C. F., Paranjape, J. M., Li, G. Y., Xiao, W., Zhang, K., Kalaycio, M. E., Maitra, R. K., Lichtin, A. E., Brugger, W., Torrence, P. F., and Silverman, R. H. (1998)

2′,5′-oligoadenylate-antisense chimeras cause RNase L to selectively degrade bcr/abl mRNA in chronic myelogenous leukemia cells. *Blood 92*, 4336−4343.
(15) Kondo, S., Kondo, Y., Li, G., Silverman, R. H., and Cowell, J. K. (1998) Targeted therapy of human malignant glioma in a mouse model by 2-5A antisense directed against telomerase RNA. *Oncogene 16*, 3323−3330.
(16) Cirino, N. M., Li, G., Xiao, W., Torrence, P. F., and Silverman, R. H. (1997) Targeting RNA for decay in respiratory syncytial virus infected cells with 2′,5′-oligoadenylate-antisense, *Proc. Natl. Acad. Sci. U.S.A. 94*, 1937−1942.
(17) Player, M. R., Barnard, D., and Torrence, P. F. (1998) Potent inhibition of respiratory syncytial virus using a 2-5A-antisense chimera targeted to signals with the virus genomic RNA. *Proc. Natl. Acad. Sci. U.S.A. 95*, 8874−8879.
(18) Torrence, P. F. (1999) 2-5A-Antisense chimera: inhibitors of respiratory syncytial virus infection. *Curr. Opin. Mol. Ther. 1*, 307−315.
(19) Torrence, P. F. (2000) RSV Infections: Developments in the search for new drugs. *Drug News Perspect. 13*, 226−233.
(20) Wang, Z., Chen, L., Bayly, S. F., and Torrence, P. F. (2000) Convergent synthesis of Ribonucleae L-active 2′, 5′-oligoadenylate-peptide nucleic acids. *Bioorg. Med. Chem. Lett. 10*, 1357−1360.
(21) Ueno, Y., Kato, Y., Okatani, S., Ishida, N., Nakanishi, M., and Kitade, Y. (2003) Synthesis of antisense oligonucleotides carrying modified 2-5A molecules at their 5′-termini and their properties. *Bioconjugate Chem. 14*, 690−696.
(22) Player, M. R., and Torrence, P. F. (1998) The 2-5A system; modulation of viral and cellular processes through acceleration of RNA degradation. *Pharmacol. Ther. 78*, 55−113.
(23) Torrence, P. F., Xiao, W., Li, G., and Khamnei, S. (1994) Development of 2′, 5′-Oligonucleotides as Potential Therapeutic Agents. *Curr. Med. Chem. 1*, 176−191.
(24) Adah, S. A., Bayly, S. F., Cramer, H., Silverman, R. H., Torrence, P. F. (2001) Chemistry and biochemistry of 2′,5′-oligoadenylate-based antisense strategy. *Curr. Med Chem. 8*, 189−212.
(25) Imai, J., Johnston, M. I., and Torrence, P. F. (1982) Chemical modification potentiates the biological activities of 2-5A and its congeners. *J. Biol. Chem. 257*, 12739−12745.
(26) Torrence, P. F., Imai, J., Lesiak, K., Jamoulle, J. C., and Sawai, H. (1984) Oligonucleotide structural parameters that influence binding of 5′-*O*-triphosphoadenylyl-(2′→5′)-adenylyl-(2′→5′)-adenosine to the 5′-*O*-triphosphoadenylyl-(2′→5′)-adenylyl-(2′→5′)-adenosine dependent endoribonuclease: chain length, phosphorylation state, and heterocyclic base. *J. Med. Chem. 27*, 726−733.
(27) Summerton, J., and Weller, D. D. (1993) Uncharged Morpholino-based polymers having phosphorous linked chiral intersubunit linkages. US Patent 4123610.
(28) Partridge M., Vincent, A., Matthews, P., Puma, J., Stein, D., and Summerton, J. (1996) A simple method for delivering morpholino antisense oligos into the cytoplasm of cells. *Antisense Nucleic Acid Drug Dev. 6*, 169−175.
(29) Hudziak, R., Barofsky, E., Barofsky, D., Weller, D. L., Huang, S., and Weller, D. D. (1996) Resistance of morpholino phosphorodiamidate oligomers to enzymatic degradation. *Antisense Nucleic Acid Drug Dev. 6*, 267−272.
(30) Bakkers, J., Kramer, C., Pothof, J., Quaedvlieg, N. E., Spaink, H. P., Hammerschmidt, M. (2004) Has2 is required upstream of Rac1 to govern dorsal migration of lateral cells during zebrafish gastrulation. *Development 131*, 525−537.
(31) Ekker, S. C., Larson JD. (2001) Morphant technology in model developmental systems. *Genesis 30*, 89−93.
(32) Ekker, S. C. (2000) Morphants: a new systematic vertebrate functional genomics approach. *Yeast 17*, 302−306.
(33) Sumanas, S., Larson, J. D. (2002) Morpholino phosphorodiamidate oligonucleotides in zebrafish: a recipe forfunctional genomics? *Brief Funct. Genomic Proteomic. 1*, 239−256.
(34) Neuman, B. W., Stein, D. A., Kroeker, A. D., Paulino, A. D., Moulton, H. M., Iversen, P. L., Buchmeier, M. J. (2004) Antisense morpholino-oligomers directed against the 5′ end of the genome inhibit coronavirus proliferation and growth. *J Virol. 78*, 5891−5899.
(35) Geselowitz, D. A., Cramer, H., Wondrak, E. M., Player, M. R., Torrence, P. F. (2000) Fluorescence resonance energy transfer analysis of RNase L-catalyzed oligonucleotide cleavage. *Antisense Nucleic Acid Drug Dev. 10*, 45−51.
(36) Dong, B., Xu, L., Zhou, A., Hassel, B. A., Lee, X., Torrence, P. F., Silverman, R. H. (1994) Intrinsic molecular activities of the interferon-induced 2-5A-dependent RNase. *J. Biol. Chem. 269*, 14153−14158.
(37) Schirmeister, H., and Pfleiderer, W. (1994) Synthesis and characterization of modified 2′-5′ adenylate trimers-potential antiviral agents. *Helv. Chim. Acta 77*, 10−22.
(38) Zhang, B., Zhang, L., Sun, L., and Cui, Z. (2002) Synthesis of pCpCpA-3′-NH-phenylalanine as a ribosomal substrate. *Org. Lett. 4*, 3615−3618.
(39) Silverman, H., Maran, A., Maitra, R. K., Waller, C. F., Lesiak, K., Khamnei, S., Li, G., Xiao, W., and Torrence, (1997) P. F. 2-5A-antisense chimeras for targeted degradation of RNA. In *Antisense Technology: A Practical Approach* (Lichtensrein, C., and Nellen, W., Eds.) pp 127−155, IRL Press, New York.
(40) Gite, S., and RajBhandary, U. L. (1997) Lysine 207 as the site of cross-linking between the 3′-end of Escherichia coli initiator tRNA and methionyl-tRNA formyltransferase. *J. Biol. Chem. 272*, 5305−5312.
(41) Wu, T. P., Ruan, K. C., and Liu, W. Y. (1996) A fluorescence-labeling method for sequencing small RNA on polyacrylamide gel. *Nucleic Acids Res. 24*, 3472−3473.
(42) Bellon, L., Workman, C. T., Scherrer, J. Usman, N., and Wincott, F. E. (1996) Morpholino-Linked Ribozymes: A Convergent Synthetic Approach. *J. Am. Chem. Soc. 118*, 3771−3772.
(43) Summerton, J., and Weller, D. (1997) Morpholino antisense oligomers: design, preparation, and properties. *Antisense Nucleic Acid Drug Dev. 7*, 187−195.
(44) Brown, D. M., and Read, A. P. Nucleotide. Part XLIX. (1965) The reduction of the adduct of periodate-oxidized adenosine 5′-phosphate and methylamine. *J. Chem. Soc.* 5072-5074.
(45) Khym, J. X. (1963) The reaction of methylamine with periodate-oxidized adenosine 5′-phosphate. *Biochemistry 2*, 344−350.
(46) Jones, A. S., Markhan, A. F., and Walker, R. T. (1976) A simple method for the preparation of "ribonucleoside dialdehydes" and some comments on their structure. *J. Chem. Soc., Perkin Trans. 1* 1567−1570.
(47) RajBhandary, U. L. studied on polynucleotides. LXXVII. (1968) The labeling of end groups in polynucleotides chains: the selective modification of diol end groups in ribonucleic acids. *J. Biol. Chem. 243*, 556−564.
(48) Hansske, F., and Cramer, F. (1979) Modification of the 3′-terminus of tRNA by periodate oxidation and subsequent reaction with hydrazides. *Methods Enzymol. 59*, 172−181.
(49) Lesiak, K, and Torrence, P. F. (1997) Efficient functionalization of 2′,5′-oligoadenylates with sulfur. *Biocojugate Chem. 8*, 199−203.
(50) Summerton, J. (1999) Morpholino antisense oligomers: the case for an RNase H-independent structural type. *Biochim. Biophys. Acta 1489*, 141−158.

BC049778Q

Polymer–DNA Hybrid Nanoparticles Based on Folate–Polyethylenimine-*block*-poly(L-lactide)

Chau-Hui Wang[†,‡] and Ging-Ho Hsiue*[,†]

Department of Chemical Engineering, National Tsing Hua University, Hsinchu, 300 Taiwan, ROC, and Polymer Technology Division, Union Chemical Laboratories, Industrial Technology Research Institute, Hsinchu, 300 Taiwan, ROC. Received October 13, 2004; Revised Manuscript Received January 25, 2005

The ability of amphiphilic block copolymers that consist of polyethylenimine (PEI) and poly(L-lactide) (PLLA) to modulate the delivery of plasmid DNA was evaluated. Folate–polyethylenimine-*block*-poly(L-lactide) (folate–PEI-PLLA) was synthesized by linking folic acid and PLLA to PEI diamine. Water-soluble polycation PEI provides gene-loading capability. Additionally, PEI is considered to exhibit high transfection efficiency and endosomal disrupting capacity. Hydrophobic PLLA that is incorporated into the gene delivery vector is believed to enhance the cell interactions and tissue permeability of the delivery system. Polymeric carrier containing folic acid is expected to be able to identify tumor surface receptors and transfect cells by receptor-mediated endocytosis. The results of agarose retardation assay indicated that the folate–PEI-PLLA began to form polyplexes at a polymer/DNA weight ratio (P/D) of over 10, whereas branched polyethylenimine (B-PEI) formed polyplexes with DNA at a ratio of above 1. The spherical particle morphology was supplemented with a particle size of approximately 100 nm at 10 P/D ratio. The results indicated that folate–PEI-PLLA with proper PEI/PLLA ratio effectively reduced cytotoxicity and maintained acceptable transfection efficiency. Low cytotoxicity of the folate–PEI-PLLA gives an advantage to high-dose administration.

INTRODUCTION

Nonviral gene carriers are considered to be safer to administer and to be able to be designed with more versatility than viral-gene carriers. Nonviral gene vectors such as cationic lipids and cationic polymers have been employed to deliver DNA, RNA, and oligonucleotides (ODNs) into cells (*1*–*3*). Branched polyethylenimine (B-PEI) is a polycation often used to condense DNA through electrostatic interactions. B-PEI exhibited high transfection efficiency, probably because it has a high buffering capacity. The proton sponge effect of B-PEI gives the polyplexes an endosomal disrupting capability, thus enhancing gene expression (*4*). On the other hand, linear polyethylenimine (L-PEI), which is synthesized by hydrolyzing poly(2-substituted-2-oxazoline), has been shown to have lower cytotoxicity but higher transfection efficacy than B-PEI (*5*). Fully hydrolyzed L-PEI is water-insoluble because it is crystalline. The water-soluble L-PEI can be prepared by the controlled acid hydrolysis of poly(2-ethyl-2-oxazoline) (*6*). PEI was also modified to be multifunctional by introducing polymer segments or targeting moieties to extend and enhance the release of the gene (*7, 8*).

Biodegradable polyesters such as poly(lactide) (PLA) and poly(lactide-*co*-glycolide) (PLGA) have been demonstrated to encapsulate DNA for sustained gene expression (*9*–*11*). Park et al. conjugated antisense ODN to biodegradable PLGA to yield an amphiphilic structure, which could form micelles in the aqueous phase (*12*). Furthermore, hydrophobic moieties are considered to improve the cell interactions and increase the tissue permeability of delivery systems. Kissel et al. prepared hyperbranched polyethylenimine-*g*-poly(ϵ-caprolactone)-*b*-poly(ethylene glycol) (*hy*-PEI-*g*-PCL-*b*-PEG) as gene vectors, and a high gene transfection efficiency was obtained by properly controlling the compositions of copolymers (*13*). Pluronics could also be incorporated into cell membranes as a result of the presence of the hydrophobic poly(propylene oxide) (PPO) chain (*14, 15*).

In this study, folate–polyethylenimine-*block*-poly(L-lactide) (folate–PEI-PLLA) was prepared as a new gene carrier. Partial hydrolysis of poly(2-ethyl-2-oxazoline) (PEOz) yielded water-soluble L-PEI with a high buffering capacity. PLLA and folic acid were conjugated to L-PEI to increase the transfection efficiency and reduce the cytotoxicity. The amphiphilic folate–PEI-PLLA copolymers condensed plasmid DNA and formed micelles in aqueous solution. The micelle core comprised PLLA segments and hydrophobic complexes. Moreover, the folate receptors were overexpressed on carcinomas (*16, 17*). Polymeric carrier that contained folic acid was expected to be able to identify tumor surface receptors and transfect cells by receptor-mediated endocytosis (*18*). Receptor targeting, endosomal disruption, improved cell permeability, and reduced cytotoxicity were combined for designing this nonviral gene vector. Synthesis, electrophoresis, surface morphology, and luciferase gene expression of folate–PEI-PLLA polyplexes were investigated in this work.

EXPERIMENTAL SECTION

Materials. L-Lactide (Aldrich) and 1,4-dibromo-2-butene (Aldrich) were recrystallized from acetone and *n*-hexane, respectively. 2-Ethyl-2-oxazoline (Aldrich) was purified by vacuum distillation over CaH_2. Acetonitrile and benzyl alcohol were dried over CaH_2 and distilled under dry nitrogen. Folic acid and 3-(4,5-dimethylthiazol-

* To whom correspondence should be addressed. E-mail: ghhsiue@che.nthu.edu.tw.
† National Tsing Hua University.
‡ Industrial Technology Research Institute.

10.1021/bc049754j CCC: $30.25 © 2005 American Chemical Society
Published on Web 02/24/2005

2-yl)-2,5-diphenyltetrazolium bromide (MTT) were purchased from ICN Biomedicals, Inc. *N*,*N*′-Dicyclohexylcarbodiimide (DCC) was purchased from Lancaster Synthesis Ltd. Succinic anhydride and 4-(dimethylamino)pyridine (DMAP) were purchased from TCI Co., Ltd. pUHC 13-3 encoding for luciferase as a reporter gene was a gift from Prof. Jia-Ling Yang of National Tsing Hua University, Taiwan. Dulbecco's Modified Eagle's Medium (DMEM), fetal bovine serum (FBS), and trypsin−EDTA were the products of Gibco-BRL. Folate-free DMEM was purchased from Sigma. HeLa human adenocarcinoma cells were provided by Prof. Yu-Chen Hu of National Tsing Hua University, Taiwan. Dialysis tubing (MWCO 3500) was purchased from Spectrum Medical Industries, Inc.

Synthesis of Polyethylenimine (PEI) Diamine. Poly(2-ethyl-2-oxazoline) (PEOz) was synthesized by cationic ring-opening polymerization of 2-ethyl-2-oxazoline using 1,4-dibromo-2-butene as an initiator. A solution of 1,4-dibromo-2-butene (210 mg, 0.982 mmol) and 2-ethyl-2-oxazoline (10 mL, 98.86 mmol) in dry acetonitrile (30 mL) was heated to 100 °C and stirred for 16 h in an atmosphere of nitrogen. The living PEOz polymer chains were terminated by adding acetonitrile solution that contained NH_3 (0.12 N) at 0 °C; the solution was then stirred for 30 min. The polymer solution was filtered through the silica gel and was purified by precipitation in diethyl ether. After it had been completely dried, a powdery product was obtained. The molecular weight and polydispersity of PEOz diamine were analyzed by taking gel permeation chromatography (GPC) measurements.

PEOz diamine (2 g) was heated with a mixture of concentrated hydrochloric acid (11 mL, 35%) and water (16 mL) at 110 °C for 3 h. The pH of the polymer solution was adjusted to 9−10 by adding NaOH pellets. The product was then purified by dialysis for 3 days using cutoff dialysis tubing with a molecular weight of 3500. After it had been vacuum-dried, the product was stored at −20 °C. ^{1}H NMR (D_2O): δ 0.92 ($N(COCH_2CH_3)CH_2CH_2$), 2.25 ($N(COCH_2CH_3)CH_2CH_2$), 2.69 ($NHCH_2CH_2$), 3.40−3.50 ($N(COCH_2CH_3)CH_2CH_2$).

Synthesis of Monocarboxypoly(L-lactide) (PLLA-COOH). L-Lactide (4 g, 27.75 mmol) and benzyl alcohol (216 mg, 2 mmol) were polymerized with 1 wt % stannous octoate in dry toluene (2 mL) at 140 °C for 16 h under nitrogen. After being allowed to cool, the product was filtered using a syringe filter (0.22 μm) and then precipitated in *n*-hexane. The yielded PLLA-OH was vacuum-dried for 24 h.

PLLA-OH (1 g, 0.4 mmol), succinic anhydride (80 mg, 0.8 mmol), and DMAP (97.6 mg, 0.8 mmol) were dissolved in 1,4-dioxane (7 mL) and reacted in an atmosphere of nitrogen for 24 h at room temperature. The product was precipitated in *n*-hexane and reconstituted using tetrahydrofuran. After 0.1 N of HCl had been added, the polymer solution was poured into a large amount of distilled water. The precipitates were dissolved in tetrahydrofuran and then purified by precipitation in *n*-hexane. ^{1}H NMR ($CDCl_3$): δ 1.42 ($COCH(CH_3)O$), 3.75 ($COCH_2CH_2COOH$), 4.35 ($COCH_2CH_2COOH$) 5.19 ($COCH(CH_3)O$), 7.38 (C_6H_5).

Synthesis of Folate−Polyethylenimine-*block*-poly(L-lactide) (folate-PEI−PLLA). PEI diamine (500 mg, 0.167 mmol), PLLA-COOH (208 mg, 0.083 mmol), DMAP (40.8, 0.33 mmol), and DCC (69 mg, 0.33 mmol) were dissolved in DMSO (10 mL). The reaction was carried out in a nitrogen atmosphere at room temperature. After 24 h, folic acid (7.4 mg, 0.017 mmol), DMAP (40.8, 0.33 mmol), and DCC (69 mg, 0.33 mmol) were added into the mixture under nitrogen, and reacted at room temperature for a further 24 h. The unreacted PLLA-COOH and folic acid were purified by dialysis (with a molecular weight cutoff of 3500) in DMSO and distilled water for 3 days, respectively. Following lyophilization, the obtained folate−PEI-PLLA was stored at −20 °C.

Preparation of Polyplexes. A 5 μg amount of luciferase encoding plasmid pUHC-13-3 and the desired amount of polymer were each diluted in 100 μL of distilled water and gently mixed. The polyplex formulation was incubated at room temperature for 30 min before it was used. The particle size was analyzed by dynamic light scattering (DLS, Malvern Instrument Series 3000).

Gel Retardation Assay. Various formulations of polyplexes were prepared as previously described, before loading into the gel. The samples were electrophoresed on 1% agarose gel in 1X TRIS−boric acid−EDTA (TBE) buffer at 100 mV until the 1X loading dye ran through 80% of the gel. A 1 kb DNA marker (Violet) used for comparing the size of DNA was also run. The gel was stained with 0.5 μg/mL ethidium bromide for 45 min and analyzed using an UV transilluminator.

Atomic Force Microscopy. The surface morphology of polyplexes was analyzed by atomic force microscopy (AFM). The polyplex solution was diluted in 1 mL of distilled water and dropped on a silica wafer. After it was spin-coated with a spin coater, the sample was dried in the dry box for 2 days and in vacuo for 30 min before use.

Luciferase Transfection and Total Protein Assay. Human cervix carcinoma HeLa cells (2×10^5 cells/well) plated in six-well plates were incubated in DMEM media supplemented with 10% fetal bovine serum (FBS) in a humidified atmosphere of 5% CO_2 at 37 °C for 24 h. Transfection was conducted after the cells had become about 80% confluent. A 2 mL amount of growth medium that contained the DNA or polyplexes with a final amount of 5 μg of plasmid was incubated for 48 h at 37 °C. Following transfection, the cells were washed with cold PBS and then lysed with 400 μL of 1X cell lysis buffer. The cell lysate was then transferred into eppendorf tubes and centrifuged for 1 min at 12 000 rpm. Luciferase activity was measured in terms of relative light unit (RLU) using a 96-well plate luminometer (Wallac 1420 Multilabel Counter, Perkin-Elmer) and a luciferase assay kit (Promega). Total protein was measured at 595 nm using a BioRad protein assay.

In Vitro Cell Viability. Human cervix carcinoma HeLa cells (1×10^4 cells/well) were cultured onto a plate with 96 wells in DMEM media supplemented with 10% fetal bovine serum (FBS) in a humidified atmosphere of 5% CO_2 at 37 °C for 24 h. The growth medium was replaced with a medium that contained the desired amount of polymers. Cells were incubated for 24 h, and cell viability was assayed by adding 100 μL of medium that contained 10 μL of MTT PBS solution (5 mg/mL). After incubation for 4 h, the formazan crystals were dissolved in 100 μL of DMSO. The absorbance of each well was measured using a microplate reader (Stat Fax 2100, Awareness) at a test wavelength of 570 nm and a reference wavelength of 630 nm.

RESULTS AND DISCUSSION

Synthesis of Folate−PEI-PLLA. The PEOz was synthesized by cationic living polymerization with a bifunctional initiator 1,4-dibromo-2-butene (*19*). The reaction was terminated by adding NH_3 acetonitrile solution to introduce NH_2 functional groups to both ends

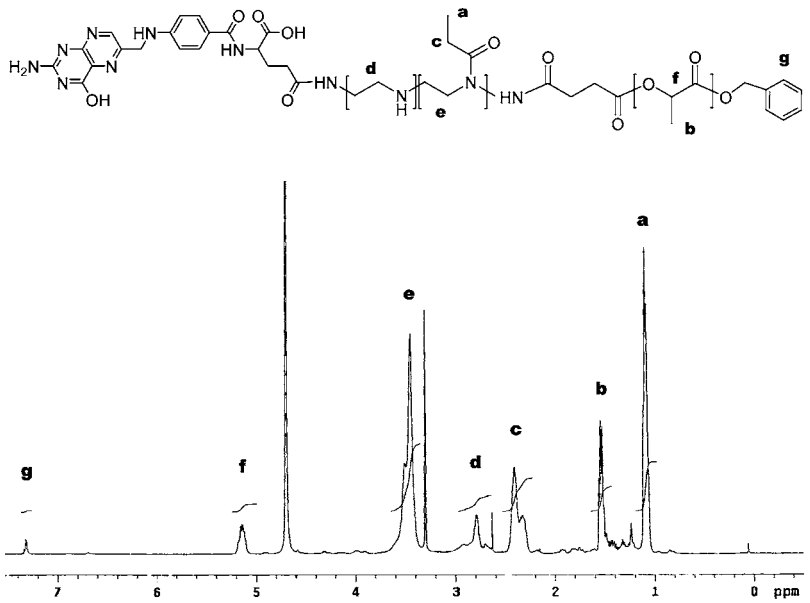

Figure 1. ^{1}H NMR spectrum of folate–PEI-PLLA.

Scheme 1. Synthesis of Folate–PEI-PLLA by the DCC-Mediated Polycondensation Reaction

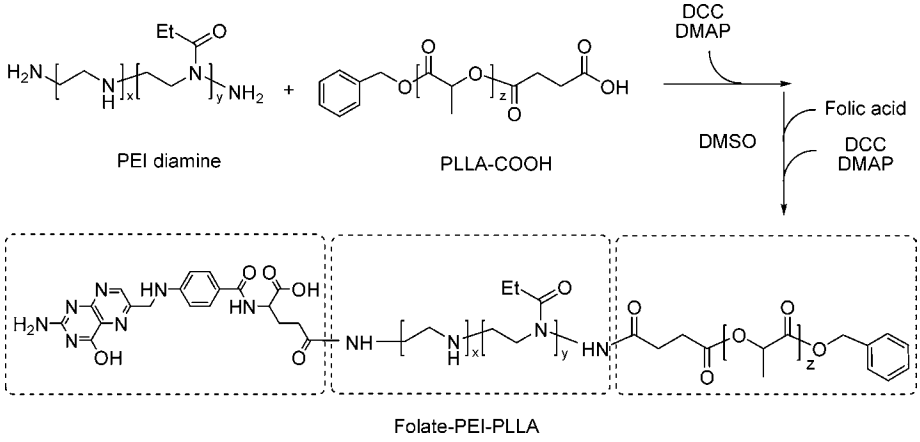

of polymer chains (*20*). The number average molecular weight (M_n) and polydispersity (PDI) determined by GPC were 9800 and 1.18, respectively.

Acid hydrolysis of the PEOz diamine was performed using hydrochloric acid. The percentage hydrolysis was estimated by comparing the integral peak area of the ethylenimine groups to *N*-propionylethylenimine groups. The molecular weight following hydrolysis was calculated from the percentage hydrolysis.

The L-lactide and benzyl alcohol were polymerized with stannous octoate. PLLA-OH was allowed to react with succinic anhydride in the presence of DMAP to prepare PLLA with a carboxyl group at the end of the chain (*21*). The M_n determined by GPC was 2500, and the PDI was 1.3.

The amphiphilic folate–PEI-PLLA copolymers were synthesized by the DCC-mediated polycondensation reaction of two oligomers: PEI diamine and PLLA-COOH (Scheme 1). The composition of folate–PEI-PLLA was varied to optimize the gene expression. Figure 1 presents the ^{1}H NMR spectrum of folate–PEI-PLLA. The molar ratio of PLLA to PEI was determined by the ratio between of the area under the peak of the methyl group in the PLLA block to that of the ethylene groups in the PEI block.

The folic acid content in folate–PEI-PLLA was measured using a UV/vis spectrophotometer. Folate–PEI-PLLA was dissolved in DMSO, and the absorbance at a wavelength of 289 nm was determined. The concentration of folic acid was calculated according to the calibration curve made from free folic acid. Both α- and γ-carboxyl groups on the folic acid have been reported to undergo coupling reactions, and only the γ-conjugate can bind to the folate receptor. The DCC-mediated polycondensation reaction involves about 80% γ-linked and 20% α-linked conjugates (*22*). Table 1 characterizes B-PEI, L-PEI, and folate–PEI-PLLA. The DLS analyses of the folate–PEI-PLLA and the DNA showed that no particle was formed before mixing them in solution.

Table 1. Characterizations of B-PEI, L-PEI, and Folate–PEI-PLLA

code	M_n (PEI)	hydrolysis (%)	PEI/PLLA (mol)	folic acid (mmol/g)	particle size (nm)
B-PEI	10000	–	–	–	68
L-PEI	5200	84	–	–	154
FEA1	5600	75	0.90	0.1100	156
FEA2	12600	66	0.93	0.0750	166
FEA3	3600	85	0.41	0.0421	110

Gel Retardation Assay. Agarose gel electrophoresis was performed to assess the influence of B-PEI, L-PEI, and folate–PEI-PLLA on DNA condensation. Figure 2 presents the gel retardation results for the polyplexes. Increasing the concentrations of the polymers reduced the electrophoretic mobility of the plasmid, by increasing

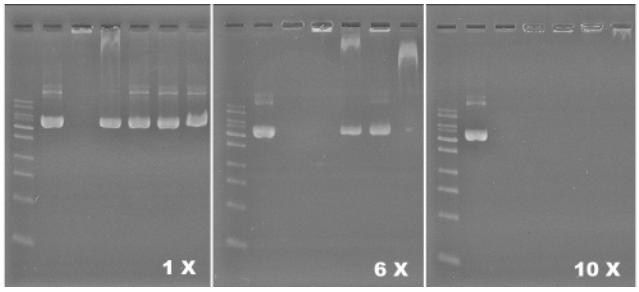

Figure 2. Gel retardation assay. Lane 1: DNA ladder, Lane 2: plasmid DNA, Lane 3: B-PEI/DNA polyplex, Lane 4: L-PEI/DNA polyplex, Lane 5: FEA1/DNA polyplex, Lane 6: FEA2/DNA polyplex, Lane 7: FEA3/DNA polyplex.

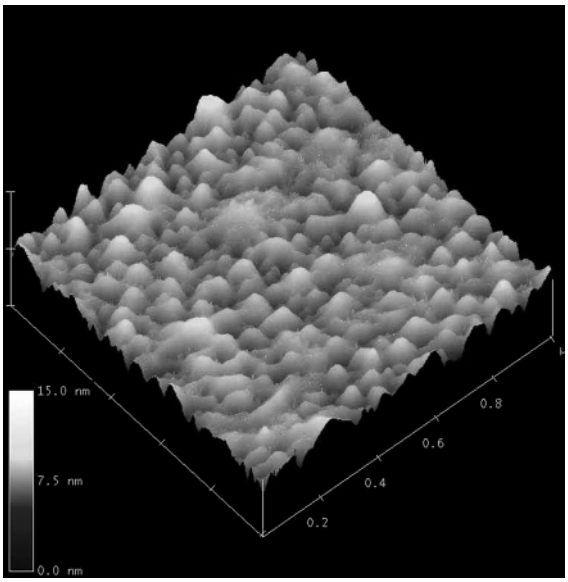

Figure 3. Atomic force microscopy (AFM) image of the folate−PEI-PLLA polyplexes (FEA3, P/D: 10).

DNA condensation and compaction. The B-PEI and L-PEI are completely retarded as can be seen as the polymer/DNA (P/D) ratio (w/w) approaches 1 and 6, respectively. The results of agarose retardation assay indicated that the DNA condensing capacity of folate−PEI-PLLA was slightly decreased. The folate−PEI-PLLA began to form polyplexes at a P/D ratio of above 10.

Atomic Force Microscopy. The surface morphology of folate−PEI-PLLA polyplex was determined by atomic force microscopy (AFM). Figure 3 shows an AFM image of folate−PEI-PLLA polyplexes (FEA3) spread on the silica wafer. The spherelike particles were around 100 nm in diameter at a P/D ratio of 10.

In Vitro Transfection. The transfection efficiencies of B-PEI, L-PEI, and folate−PEI-PLLA polyplexes prepared at various P/D ratios on HeLa human cervix carcinoma were evaluated. Transfection efficiency was determined by luciferase assay for the luciferase encoding plasmid. The total protein production, which was an indirect measure of induced toxicity, was analyzed to normalize the RLU. Figure 4 shows the luciferase gene expression of folate−PEI-PLLA at various P/D ratios on HeLa cells. The change in RLU is directly proportional to the amount of luciferase produced in the transfected cells. For a given amount of plasmid DNA (5 μg), increasing the amount of polymers increased the transfection efficiency. This result indicated that only FEA3 exhibited extensive luciferase gene expression. FEA1 and FEA2, which have relatively high PLLA contents, did not exhibit improved transfection efficiency. Figure 5 compares the luciferase gene expressions of B-PEI, L-PEI, and FEA3 polyplexes at various P/D ratios. For B-PEI and L-PEI polyplexes, luciferase expression in HeLa cells is stronger at a P/D ratio of above 3. FEA3 polyplex showed greater transfection at a P/D ratio of 7. Figure 6 shows the highest level of luciferase expression in naked DNA, B-PEI, L-PEI, and folate−PEI-PLLA. The results reveal that the appropriate gene carrier exhibited greater transfection efficacy than naked DNA. B-PEI and L-PEI

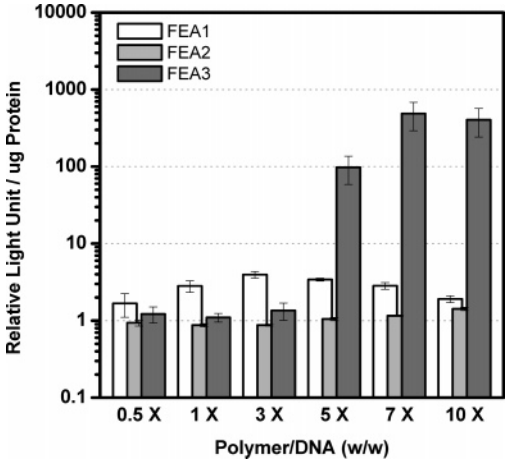

Figure 4. Luciferase gene expressions of FEA1, FEA2, FEA3 polyplexes at various P/D ratios (n = 3).

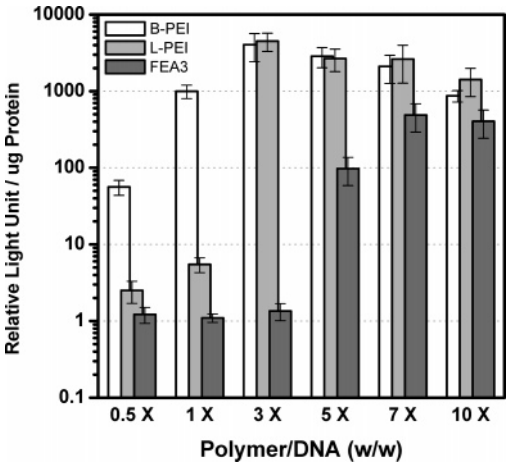

Figure 5. Luciferase gene expressions of the B-PEI, L-PEI, and FEA3 polyplexes at various P/D ratios (n = 3).

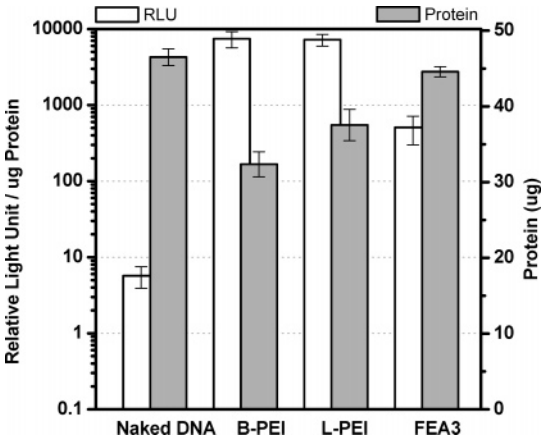

Figure 6. The highest level of luciferase expression in naked DNA, B-PEI, L-PEI, and folate−PEI-PLLA and their total protein productions (n = 3). B-PEI (P/D: 3), L-PEI (P/D: 3), FEA3 (P/D: 7).

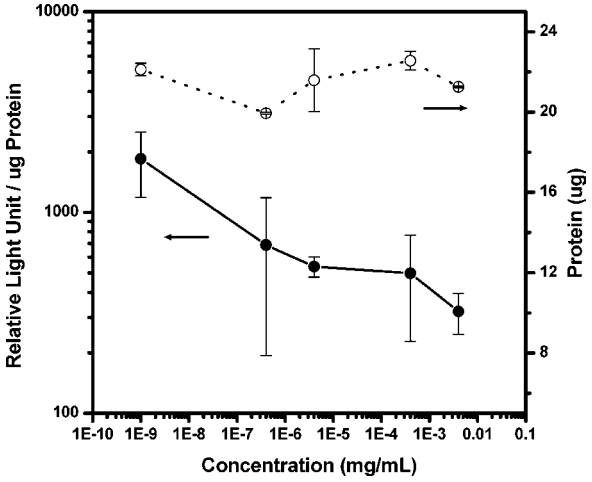

Figure 7. The luciferase gene expression of FEA3 polyplexes at different concentrations of free folic acid (n =3).

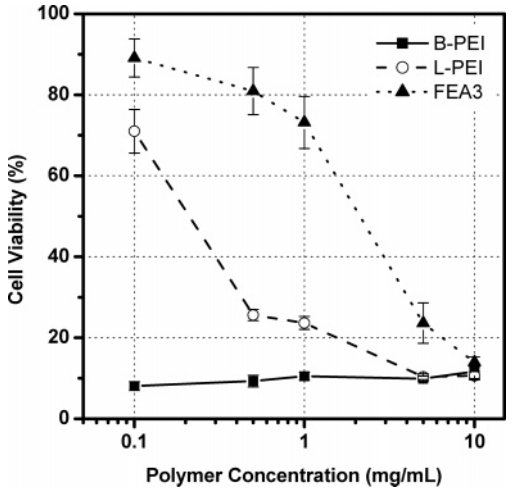

Figure 8. The cytotoxicity of B-PEI, L-PEI, and FEA3 on HeLa cells at various polymer concentrations (n = 6).

showed better gene expression than that of FEA3. In contrast, the protein production of FEA3 was similar to that of naked DNA, indicating that FEA3 had low cytotoxicity.

Folate−PEI-PLLA exhibited less transfection than B-PEI and L-PEI, so determining whether free folic acid suppresses transfection is important. It is not certain that HeLa cells have folate receptors. However, a number of publications have indicated that the folate receptors on HeLa cells are up-regulated ($>15 \times 10^6$ folate binding sites/HeLa cell) (*23*). As shown in Figure 7, free folic acid competed with FEA3 polyplexes in transfection. The common DMEM media contains 0.004 mg/mL of folic acid. The luciferase expression increased as the free folic acid concentration declined. The total protein production was maintained at about 22 μg, revealing that free folic acid did not affect cytotoxicity, and considerably inhibiting the endocytosis of FEA3.

Cell Viability. The in vitro cytotoxicity of B-PEI, L-PEI, and FEA3 at various concentrations was determined in the HeLa cell line by MTT assay. The wells that contained only the media and untreated polymer were regarded as positive controls, with a cell viability of 100%. The relative cell viability was determined as $[Abs]_{sample}/[Abs]_{control} \times 100$. Figure 8 reveals that B-PEI exhibited high toxicity, resulting in cell death. In contrast to B-PEI and L-PEI, the cell viability of FEA3 exceeded 80% at a concentration of 0.5 mg/mL. The efficacy of a gene carrier is depends partly on the corresponding toxicity of the polymer. The low cytotoxicity of folate−PEI-PLLA allows it to be safely administered.

CONCLUSION

In this work, a new polymeric gene carrier, folate−PEI-PLLA, was successfully synthesized. The introduction of PLLA and folic acid was expected to increase cell permeability and biocompatibility. However, polymers that contain relatively large amounts of high PLLA mediated gene transfer less efficiently than did B-PEI and L-PEI. Folate-PEI-PLLA effectively reduced toxicity on HeLa cells but also reduced the luciferase expression. Additionally, the morphology of folate−PEI-PLLA polyplex was spherical, thus unlike that obtained from the B-PEI polyplex. B-PEI formed a polyplex with DNA as an oblique sphere, which has been suggested to be able to enter the cell easily (*24*). Although biodegradable polyesters are commonly used to deliver plasmid DNA, their transfection efficiency compared with PEI has been rarely discussed. The results herein reveal that folate−PEI-PLLA with a proper PEI/PLLA ratio effectively reduced cytotoxicity and maintained an acceptable transfection efficiency. Low cytotoxicity of the folate−PEI-PLLA gives the advantage for the high dose amount of administration.

ACKNOWLEDGMENT

The authors thank Prof. Jia-Ling Yang at the Institute of Biotechnology of National Tsing Hua University for the assistance with luciferase expression assay and the Industrial Technology Research Institute of Taiwan (ITRI) for financial support.

LITERATURE CITED

(1) Lim, D. W., Yeom, Y. I., Park, and T. G. (2000) Poly(DMAEMA-NVP)-*b*-PEG-galactose as gene delivery vector for hepatocytes. *Bioconjugate Chem. 17*, 688−695.

(2) Mislick, K. A., Baldeschwielder, J. D., Kayyem, J. F., and Meade, T. J. (1995) Transfection of folate−polylysine DNA complexes: evidence for lysosomal delivery. *Bioconjugate Chem.* 6, 512−515.

(3) Choi, Y. H., Liu, F., Kim, J. S., Choi, Y. K., Park, J. S., and Kim, S. W. (1998) Poly(ethylene glycol)-grafted poly-L-lysine as polymeric gene carrier. *J. Controlled Release 54,* 39−48.

(4) Boussif, O., Lezoualc'h, H., Zanta, M. A., Mergny, M. D., Scherman, D., Demeneix, B., and Behr, J. P. (1995) A versatile vector for gene and oligonucleotide transfer into cells in culture and in vivo: polyethylenimine. *Proc. Natl. Acad. Sci. U.S.A.* 92, 7297−7301.

(5) Jeong, J. H., Song, S. H., Lim, D. W., Lee, H., and Park, T. G. (2001) DNA transfection using linear poly(ethylenimine) prepared by controlled acid hydrolysis of poly(2-ethyl-2-oxazoline). *J. Controlled Release 73*, 391−399.

(6) Brissault, B., Kichler, A., Guis, C., Leborgne, C., Danos, O., and Cheradame, H. (2003) Synthesis of linear polyethylenimine derivatives for DNA transfection. *Bioconjugate Chem. 14*, 581−587.

(7) Benns, J. M., Mahato, R. I., and Kim, S. W. (2002) Optimization of factors influencing the transfection efficiency of folate-PEG-folate-graft-polyethylenimine. *J. Controlled Release 79*, 255−269.

(8) Akiyama, Y., Harada, A., Nagasaki, Y., and Kataoka, K. (2000) Synthesis of poly(ethylene glycol)-*block*-poly(ethylenimine) possessing an acetal group at the PEG end. *Macromolecules 33,* 5841−5845.

(9) Perez, C., Sanchez, A., Putnam, D., Ting, D., Langer, R., and Alonso, M. J. (2001) Poly(lactic acid)-poly(ethylene glycol) nanoparticles as new carriers for the delivery of plasmid DNA. *J. Controlled Release 75*, 211−224.

(10) Cohen, H., Levy, R. J., Gao, J., Fishbein, I., Kousaev, V., Sosnoski, S., and Slomkowski, S. (2000) Sustained delivery and expression of DNA encapsulated in polymeric nanoparticles. *Gene Ther. 7*, 1896−1905.

(11) Maruyama, A., Ishihara T., Kim, J. S., Kim, S. W., and Akaike, T. (1997) Nanoparticle DNA carrier with poly(L-lysine) grafted polysaccharide copolymer and poly(D, L-lactic acid). *Bioconjugate Chem. 8*, 735−742.

(12) Jeong, J. H., and Park, T. G. (2001) Novel polymer-DNA polymeric micelles composed of hydrophobic poly(D, L-lactic-*co*-glycolic acid) and hydrophilic oligonucleotides. *Bioconjugate Chem. 12*, 917−923.

(13) Shuai, X., Merdan, T., Unger, F., Wittmar, M., and Kissel, T. (2003) Novel biodegradable ternary copolymers *hy*-PEI-*g*-PCL-*b*-PEG: synthesis, characterization, and potential as efficient nonviral gene delivery vectors. *Macromolecules 26*, 5751−5759.

(14) Batrakova, E. V., Miller, D. W., Li, S., Alakhov, V. Y., Kabanov, A. V., and Elmquist, W. F. (2001) Pluronic P85 enhances the delivery of digoxin to the brain: in vitro and in vivo studies. *J. Pharmacol. Exp. Ther. 296*, 551−557.

(15) Kabanov, A. V., Batrakova, E. V., and Alakhov, V. Y. (2002) Pluronic block coplymers as novel polymer therapeutics for drug and gene delivery. *J. Controlled Release 82*, 189−212.

(16) Lee, R. J., and Low, P. S. (1994) Delivery of liposomes into cultured KB cells via folate receptor-mediated endocytosis. *J. Biol. Chem. 269*, 3198−3204.

(17) Leamon, C. P., Weigl, D., and Hendren, R. W. (1999) Folate copolymer-mediated transfection of cultured cells. *Bioconjugate Chem.* 10, 947−957.

(18) Campbell, I. G., Jones, T. A., Foulkes, W. D., and Trowsdale, J. (1991) Folate-binding protein is a marker for ovarian cancer. *Cancer Res. 51*, 5329−5338.

(19) Wang, C. H., and Hsiue, G. H. (2003) New amphiphilic poly(2-ethyl-2-oxazoline)/poly(L-lactide) triblock copolymers. *Biomacromolecules 4*, 1487−1490.

(20) Kobayashi, S., Masuda, E., Shoda, S., and Shimano, Y. (1989) Synthesis of acryl- and methacryl-type macromonomers and telechelics by utilizing living polymerization of 2-oxazolines. *Macromolecules 22*, 2878−2884.

(21) Lee, S. C., Kang, S. W., Kim, C., Kwon, I. C., and Jeong, S. Y. (2000) Synthesis and characterization of amphiphilic poly(2-ethyl-2-oxazoline)/poly(ϵ-caprolactone) alternating multiblock copolymers. *Polymer 41*, 7091−7097.

(22) Gabizon, A., Horowitz, A. T., Goren, D., Tzemach, D., Mandelbaum-Shavit, F., Qazen, M. M., and Zalipsky, S. (1999) Targeting folate receptor with folate linked to extremities of poly(ethylene glycol)-grafted liposomes: in vitro studies. *Bioconjugate Chem. 10*, 289−298.

(23) Leamon, C. P., and Low, P. S. (1993) Membrane folate-binding proteins are responsible for folate-protein conjugate endocytosis into cultured cells. *Biochem. J. 291*, 855−860.

(24) Benns, J. M., Maheshwari, A., Furgeson, D. Y., Mahato, R. I., and Kim, S. W. (2001) Folate-PEG-Folate-Graft-Polyethylenimine-Based Gene Delivery. *J. Drug. Target. 9*, 123−139.

BC049754J

Synthesis and Evaluation of a Star Amphiphilic Block Copolymer from Poly(ϵ-caprolactone) and Poly(ethylene glycol) as a Potential Drug Delivery Carrier

Fei Wang,*,† Tatiana K. Bronich,‡ Alexander V. Kabanov,‡ R. David Rauh,† and Jacques Roovers§

EIC Laboratories, Inc., 111 Downey Street, Norwood, Massachusetts 02062, and Department of Pharmaceutical Science, University of Nebraska Medical Center, 986025 University Medical Center, Omaha, Nebraska 68198-6025. Received September 13, 2004; Revised Manuscript Received December 30, 2004

A star polymer composed of amphiphilic block copolymer arms has been synthesized and characterized. The core of the star polymer is polyamidoamine (PAMAM) dendrimer, the inner block in the arm is lipophilic poly(ϵ-caprolactone) (PCL), and the outer block in the arm is hydrophilic poly(ethylene glycol) (PEG). The star-PCL polymer was synthesized first by ring-opening polymerization of ϵ-caprolactone with a PAMAM-OH dendrimer as initiator. The PEG polymer was then attached to the PCL terminus by an ester-forming reaction. Characterization with SEC, ^{1}H NMR, FTIR, TGA, and DSC confirmed the star structure of the polymers. The micelle formation of the star copolymer (star-PCL−PEG) was studied by fluorescence spectroscopy. Hydrophobic dyes and drugs can be encapsulated in the micelles. A loading capacity of up to 22% (w/w) was achieved with etoposide, a hydrophobic anticancer drug. A cytotoxicity assay demonstrated that the star-PCL−PEG copolymer is nontoxic in cell culture. This type of block copolymer can be used as a drug delivery carrier.

INTRODUCTION

Micelles formed from amphiphilic block copolymers have recently attracted significant attention in diverse fields of medicine and biology. In particular, polymeric micelles have been developed as drug and gene delivery systems (*1*−*3*) as well as carriers for various contrasting agents in diagnostic imaging applications (*4*). In an aqueous environment, the hydrophobic blocks of the copolymer are expected to segregate into the core of the micelle, whereas the hydrophilic blocks form the corona or outer shell. Such a core−shell architecture of the polymeric micelles is essential for their utility as novel functional materials for pharmaceutical applications. The hydrophobic micelle core serves as a microenvironment for the incorporation of various therapeutic compounds; the corona, or outer shell, serves as a stabilizing interface between the hydrophobic core and the external medium. As a result, polymeric micelles can be used as efficient containers for reagents with poor solubility and/or low stability in physiological environments (*5*, *6*). Interest in polymeric micelles for drug delivery has increased rapidly since the late 1980s (*7*). Most of the work has focused on classical micelles formed by intermolecular aggregation of amphiphilic polymers as the drug delivery vehicle, and the advantages of using micelle structures as a drug delivery system have been demonstrated (*8*, *9*).

The major factors that influence the performance of polymeric micelles for drug delivery are loading capacity, release kinetics, circulation time, biodistribution, size, and stability (*2*). Micelle stability is particularly important. Recent studies have shown that the in vivo antitumor activity of a drug incorporated into the polymer micelles is positively correlated with the stability of micelles in vitro (*10*). The formation of classical micelles is thermodynamically favorable only above a specific concentration of the amphiphilic molecules (critical micelle concentration, cmc). Above the cmc, micelles are in dynamic equilibrium with the free copolymer molecules (unimers) in solution, continuously breaking and reforming (*11*). When the concentration of the copolymer is below the cmc, micelles tend to disassemble. Such thermodynamic instability of micelles below the cmc is one of the concerns for their application in vivo. A delivery system is subject to a severe dilution upon intravenous injection into an animal or human subject. In the bloodstream, under dilution, micelles begin to disassemble, causing changes in micelle structure and size. Therefore, controlling the release rate of drugs is difficult. Sudden dissociation of micelles may cause serious toxicity problems due to potentially large fluctuations in drug concentrations.

The problem associated with the classical micelle structure can be overcome by developing molecules in which the lipophilic components are covalently bound together within the micelle core. Core polymerization is an effective method to prevent dissociation of the block copolymer micelle. Kataoka's group has successfully employed this idea (*12*). In their study, the micelles were prepared from an amphiphilic block copolymer in which the hydrophobic block contained a polymerizable end group. After micellation, the end groups on the hydrophobic block were polymerized to form a stable core for the star-shaped polymer structure. The resulting micelles showed fairly high stability and maintained small size. As anticipated, the core polymerized micelle showed excellent solubilization of rather large molecules such as taxol (*13*).

* Author to whom correspondence should be addressed [telephone (781) 769-9450; fax (781) 551-0283; e-mail feiwang@eiclabs.com].

† EIC Laboratories.

‡ University of Nebraska Medical Center.

§ Present address: 21 Wren Rd., Gloucester, ON K1J 7H5, Canada.

10.1021/bc049784m CCC: $30.25 © 2005 American Chemical Society
Published on Web 02/23/2005

Another approach developed recently by Uhrich et al. (*14*) with a three-arm star polymer composed of mucic acid substituted with fatty acid as the lipophilic inner block and with PEG as the hydrophilic outer block. This new type of molecule was capable of encapsulating a hydrophobic model drug in aqueous media. However, due to the structural constraints, the free volume of the hydrophobic core was limited, and only one or two drug molecules could be encapsulated in each micelle. A series of star block copolymers with the number of arms ranging from three to eight has also been synthesized (*15*). The arms were composed of block copolymer with PEG as the inner hydrophilic block and PCL as the outer hydrophobic block. The application of this type of copolymer as an injectable drug delivery system was reported (*16*). It was found that a reversible sol−gel transition process exists for this system, which is useful for drug delivery. However, such star copolymers do not form micelles in aqueous media because the hydrophilic block is located in the interior of the star. A recent paper (*17*) described the synthesis of a four-arm star block copolymer of PCL and PEG by the same route and similar chemistry as reported in this paper. Another paper (*18*) described the preparation of a four-arm star PCL-*b*-PEG polymer with diethylzinc catalyst. However, the molecular weight distribution of the block copolymer was unacceptably wide.

Many studies have been carried out using dendrimers as drug delivery systems (*19*). Star polymers with a dendrimer as the hydrophobic core and multiple PEG chains as the hydrophilic arms have been synthesized and investigated as unimolecular micelles for drug delivery by Fréchet and Kono (*20*, *21*). It has been demonstrated that the micelles with larger dendrimer core have a higher encapsulation capability than those with smaller cores. However, due to the structural limitations involved in the synthesis of dendrimers of higher generation, and the relatively compact structure of the dendrimers, it is difficult to increase significantly the size of the hydrophobic dendritic core in the dendrimer−PEG star polymer. Therefore, such dendrimer systems have limitations in terms of drug-loading capacity and delivery of compounds of large size.

In this paper, we describe the synthesis and micellar characterization of a novel amphiphilic star polymer. The core of this star polymer is a polyamidoamine (PAMAM) dendrimer; the inner block in the arm is lipophilic poly(ϵ-caprolactone) (PCL), and the outer block in the arm is hydrophilic poly(ethylene glycol) (PEG). First, a star PCL polymer was synthesized using the PAMAM-OH dendrimer as the initiator for ring-opening polymerization of ϵ-caprolactone. A PEG polymer was then attached to the terminal group of PCL by an ester-forming reaction. In this star polymer the arms consist of polymers that are biocompatible and biodegradable. The star structure of the polymers was confirmed by several physicochemical methods. To establish this system as a suitable drug carrier, the micellar properties of the star amphiphilic polymer in aqueous media were studied by fluorescence techniques and dynamic light scattering. The solubilization capacity of star-PCL−PEG micelles was evaluated using several highly hydrophobic compounds, such as pyrene and water-insoluble dye molecules. A series of entrapment experiments showed that various drugs could be incorporated in such micelles. These results indicate that the star-PCL−PEG micelle system is a promising drug carrier for the delivery of lipophilic drugs.

EXPERIMENTAL SECTION

Materials and Methods. PEG (M_n = 5000) with methoxy and carboxymethyl terminal groups was used as received from Shearwater Polymers. 4-(Dimethylamino)pyridinium 4-toluenesulfonate (DPTS) was synthesized as described (*22*). Dichloromethane was dried by stirring over and distilling from P_2O_5. All other reagents and solvents were used as received from Aldrich Chemical. Indomethacin (IMC), doxorubicin hydrochloride (DOX), and etoposide were purchased from Sigma (St. Louis, MO) and were used without further purification.

^{1}H NMR spectra were recorded on a Hitachi R-1500 FT-NMR spectrometer at 60 MHz. Infrared spectra were recorded on a Nicolet 750 FTIR spectrometer. UV−vis spectra were recorded on a HP 8452A UV−vis diode array spectrophotometer. Size exclusion chromatography (SEC) was used to determine the molecular weights, polydispersity, and degree of branching of the synthesized polymers. SEC measurements were conducted using a Hewlett-Packard series 1050 HPLC equipped with one Polymer Laboratories PL gel 5μ mixed-D column and a Hewlett-Packard 1047A refractive index detector, Viscotek T60 light scattering (LS), and viscosity detectors. Chloroform was used as the eluting solvent at a flow rate of 1 mL/min. It was found that chloroform was the eluent of choice. The block copolymer is poorly soluble or is retained on the column as indicated by trailing elution profiles in other common SEC solvents. Data analysis was performed using Viscotek Trisec GPC software version 3.0.

The thermal transitions of the polymers were determined using a Perkin-Elmer DSC7 differential scanning calorimeter under nitrogen purge. The samples were heated at a rate of 10 °C/min. The thermal stability of the prepared polymers was evaluated using a Perkin-Elmer TGA7 thermogravimetric analyzer under nitrogen purge with a heating rate of 20 °C/min.

Synthesis of the Star-PCL. A 100 mL three-neck flask equipped with a condenser and an argon gas inlet was charged with PAMAM-OH dendrimer generation 2 with 16 terminal OH groups (20 wt % solution in methanol, 5.76 mL, 0.304 mmol). Methanol was then removed under vacuum. A predetermined amount of ϵ-caprolactone (14.42 g, 126 mmol) followed by 15 mL of benzene was added into the reaction flask. The mixture was heated to reflux using a Dean−Stark trap for 30 min, and benzene was distilled off. The heating of the reaction mixture to 140 °C resulted in the dissolution of the dendrimer in ϵ-caprolactone. Five milligrams (0.012 mmol) of tin(II) 2-ethylhexanoate [$Sn(Oct)_2$] was then introduced into the reaction mixture followed by stirring at 115−120 °C for 20 h. The reaction mixture was cooled to room temperature, dissolved in THF, and precipitated into cold methanol. After drying, 15.4 g (100% yield) of a white solid product was obtained. The polymer was further purified by fractionation. Three grams of star-PCL was dissolved in 60 mL of THF in a round-bottom flask, and methanol was added until the solution became cloudy. The solution was heated in a water bath at 60 °C and became clear. About 10 mL of methanol was added to reach a cloudy point, and the mixture was transferred into a hot separation funnel and allowed to stand at room temperature for 3 days. The polymer solution separated into two layers, and the top layer was removed without disturbing the lower layer. The lower layer was diluted with THF and precipitated into cold methanol; 1.47 g of polymer was obtained: ^{1}H NMR ($CDCl_3$) δ 4.07 (t, 2H, OCH_2), 2.31 (t, 2H, $COCH_2$), 1.1−2

[m, 6H, $(CH_2)_3$]. The characteristic peaks of dendrimer and polymer were overlapping, and peak integration was inconclusive.

Synthesis of the Linear-PCL. The linear PCL was synthesized in a similar procedure using ϵ-caprolactone (14.42 g, 126 mmol), ethylene glycol (0.098 g, 1.57 mmol), and a few drops of $Sn(Oct)_2$. Isolation was conducted with the same procedure as described previously.

Synthesis of the Star-PCL-PEG. Star-PCL (1.3 g, 0.0253 mmol), PEG (2.64 g, 0.527 mmol), and DPTS (0.155 g, 0.527 mmol) were dissolved in 80 mL of dry CH_2Cl_2 by stirring at room temperature. Then diisopropylcarbodiimide (DIPC) (0.2 g, 1.58 mmol) was added into the reaction mixture via syringe. The reaction mixture was stirred overnight at room temperature. An additional amount of DIPC (0.15 g) was added to the reaction mixture followed by stirring for 5 days. The reaction was stopped, and fractionation was used to purify the star-PCL−PEG. Briefly, 20 mL of CH_2Cl_2 was added to dilute the product. Hexane was slowly added to the resulting solution at 45 °C until the appearance of cloudiness. Then the mixture was transferred into a hot separation funnel and was allowed to stand at room temperature. The top layer was removed, and the lower layer was diluted with CH_2Cl_2 and precipitated into hexane. Analysis of the polymer by ^1H NMR indicated that the sample contained excess PEG and other impurities. The product was refractionated: the entire product (~3.5 g) was dissolved in 100 mL of CH_2Cl_2 followed by the gradual addition of hexane until the mixture became cloudy. The resulting mixture was then heated in a 45 °C bath followed by the addition of more hexane until a stable cloudy point was reached and transferred into a hot separation funnel. The lower layer was diluted with CH_2Cl_2 and precipitated into hexane. After drying, 3.04 g (91% yield) of white solid product was obtained: ^1H NMR ($CDCl_3$) δ 4.07 (t, 2H, $COOCH_2$), 3.64 (s, 18.8H, OCH_2CH_2O), 2.31 (t, 2H, $COCH_2$), 1.1−1.9 [m, 6H, $(CH_2)_3$].

Preparation of Star-PCL−PEG Micelles. The star-PCL−PEG polymer was dissolved in DMF at ~100 mg/mL and stirred overnight at room temperature. Water was added in a dropwise fashion to the star-PCL-PEG solution in DMF. The addition of water was continued until the desired water content was achieved (12.5−25 vol % of DMF in the final mixture). The obtained solution was stirred overnight and then dialyzed against Milli-Q distilled water using Membra-Cel MD-25-03.5 membrane tubing. The dialysate water was exchanged every hour for the first 4 h and then every 6 h for the next 12 h. The concentration of star-PCL−PEG solutions was determined by UV spectroscopy. The absorption spectrum of star-PCL−PEG in a DMF/water mixture (50 vol % DMF content) has a characteristic peak at 281.7 nm. The absorption maximum of star-PCL−PEG undergoes a bathochromic shift to 288.4 nm in pure aqueous solutions. A calibration curve of standard solutions of star-PCL−PEG from 0.1 to 1.5 mg/mL was constructed by monitoring UV absorbance at 288.4 nm and used to determine the star-PCL−PEG concentration in aqueous solutions after dialysis ($Y = 0.00006 + 0.1679\,X$, $r^2 = 1.0$).

Micelle Characterization. Dynamic laser light scattering (DLS) measurements on the star-PCL−PEG micelles were carried out using a "ZetaPlus" zeta potential analyzer (Brookhaven Instrument Co.) equipped with the multiangle sizing option (BI-MAS) and with a 15 mW solid-state laser operated at a wavelength of 635 nm. All measurements were performed at 23 °C and at scattering angle of 90°. Software provided by the manufacturer was used to calculate the effective hydrodynamic diameters of the micelles. The apparent critical micelle concentration (C_{app}) was determined using pyrene as a fluorescent probe. Sample solutions were prepared by adding known amounts of pyrene in acetone to each of a series of empty vials. The amount of pyrene was chosen so as to give a pyrene concentration in the final solution of 6×10^{-7} M. After the evaporation of acetone, solutions of star-PCL−PEG of various concentrations in phosphate buffer saline (10 mM, pH 7.4, 0.14 M NaCl) were added to the probe. Samples were equilibrated upon shaking overnight at the desired temperature. Steady-state fluorescence spectra were recorded using a Shimadzu RF5000U spectrofluorophotometer with bandwidths of 1.5 nm for excitation and 3 nm for emission, respectively. For fluorescence emission spectra, λ_{ex} was 336 nm, and for excitation spectra, λ_{em} was 390 nm.

Solubilization of Water-Insoluble Dyes. Oil Red O (ORO) and 1-(*m*-tolylazo)-2-naphthylamine (Yellow OB) were used as model hydrophobic molecules for solubilization experiments. Appropriate amounts of the copolymer solutions of various concentrations were added to the vials containing a given amount of solid dye and were equilibrated upon shaking for 2 days. Test solutions were centrifuged to remove the residual insoluble dye. The amount of dye entrapped in the micelles was determined by measuring the absorbance at 510 nm for ORO and at 450 nm for Yellow OB, respectively.

Preparation of Drug-Loaded Micelles. Indomethacin (IMC) was incorporated into the copolymer micelles either by dialysis or by an oil/water emulsion method.

(1) Dialysis Method. One hundred milligrams of IMC dissolved in 1 mL of DMF was added to 14 mg of polymer in 2 mL of a DMF/water mixture (50 vol % DMF). The solution was stirred for 4 h at room temperature and then dialyzed against 2 L of distilled water using Membra-Cel MD-25-03.5 membrane tubing. The precipitate of free IMC was removed by centrifugation at 15000 rpm for 30 min.

(2) Oil/Water (O/W) Emulsion Method. One milligram of IMC dissolved in 100 μL of chloroform was added dropwise to 4 mL of aqueous dispersion of copolymer (7 mg) with vigorous stirring. The mixture was stirred in an open-air system to remove chloroform by evaporation and then stirred overnight. The precipitate of unbound IMC was removed by centrifugation at 15000 rpm for 30 min. The amount of IMC entrapped into the polymer micelles was determined by measuring the absorbance at 320 nm in ethanol/water (1:1) mixtures using calibration curves generated from standard solutions.

Doxorubicin hydrochloride (DOX) loaded micelles were prepared according to a modified dialysis method. Specifically, 0.5 mL of aqueous star-PCL−PEG dispersion with a concentration of 15.3 mg/mL in dialysis tubing was placed in a beaker containing 100 mL of solution of DOX (0.1 mg/mL). The beaker was covered with Parafilm and wrapped in foil, and its content was allowed to equilibrate with continuous stirring for 24 h. At the end of the equilibration period, the sample in the dialysis tubing was placed into another beaker and dialyzed against 650 mL of a solution of DOX (0.46 μg/mL) for 24 h. Copolymer micelles loaded with DOX were further analyzed by SEC using a Shimadzu LC-10AT HPLC system equipped with a TSK-Gel G5000PWXL column (7.8 mm × 30 cm). NaCl (0.05 M) was used as the eluting solvent at a flow rate of 1.5 mL/min. Determination of the concentration of star-PCL−PEG copolymer and DOX was done by measuring the absorbance at 288 and 485 nm, respectively.

Etoposide was incorporated into the copolymer micelles according to two methods.

Scheme 1. Synthesis of Star-PCL−PEG Polymer

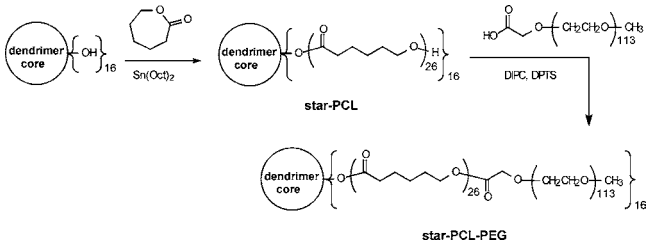

(1) Solid Extraction. A measured volume of a methanol solution of etoposide was added to a vial, and the solvent was removed under vacuum, leaving a solid film of etoposide. A polymer micelle solution was agitated with etoposide for 24 h. After filtration, the total etoposide concentration in the micelle solution was determined by UV spectroscopy

(2) Solution Extraction. The stock solution of etoposide (19.2 mg/mL) in 1:1 (vol) acetonitrile/methanol was added slowly with agitation to the polymer solutions of various concentrations to obtain the final concentration of etoposide of 1.8 mg/mL (final concentrations of polymer of 3.7, 7.6, and 15.1 mg/mL). The initially clear solutions were shaken overnight at 27 °C, and the next day some precipitate was observed. The precipitate was removed by filtration, and the etoposide concentration in the solutions was determined by UV spectroscopy. The total etoposide concentration in the polymer micelle solution was determined by measuring the absorbance at 284 nm using calibration curves generated from known methanol solutions of etoposide.

Cytotoxicity Assay. Porcine kidney epithelial cells (LLC-PK) were seeded into 96-well plates at a density of 5000 cells/well. Etoposide (0.95 mg/mL) was solubilized in the 7.6 mg/mL solution of polymer micelles as described above. Solutions were filtered through 22 μm filters, without loss of etoposide as determined by the absorbance intensity at 284 nm. The cells were exposed to etoposide alone, polymer micelles alone, or etoposide in polymer micelle compositions for 24 h, followed by washing with PBS and maintenance in the medium 199 for an additional 72 h. The cytotoxic effects were evaluated using a standard MTT assay (*23*). All experiments were performed in eight repeats.

RESULTS AND DISCUSSION

Synthesis of Star-PCL−PEG Copolymer. The synthesis of the star amphiphilic polymer was carried out as outlined in Scheme 1. The synthesis of the star PCL polymer was conducted with the PAMAM-OH generation 2 dendrimer as the initiator for the ring-opening polymerization of ϵ-caprolactone with $Sn(Oct)_2$ as the catalyst. The targeted molecular weight for each PCL arm is 3000 Da, which corresponds to a degree of polymerization of 26. Therefore, the feed molar ratio of ϵ-caprolactone to the hydroxyl groups of the dendrimer core was 26. The $Sn(Oct)_2$ catalyst was added in a concentration of 1/200 relative to the amount of initiating hydroxyl groups, which is the optimum catalyst amount reported in the literature (*24*, *25*). The reaction was carried out in neat ϵ-caprolactone at 115 °C for 20 h. In this way, the polymerization was well controlled, and the molecular weight of each arm in the product was determined by the monomer/initiator ratio.

The star-PCL product was obtained in quantitative yield. SEC analysis indicated the existence of a small amount of low molecular weight fraction. Fractionation was used to purify the polymer. The prepared star-PCL has a molecular weight of ~50000 Da and contains 16 terminal hydroxyl groups at the arm ends. To facilitate the star polymer structure characterization, a linear PCL polymer with a relatively broad molecular weight distribution was also synthesized according to the same method using ethylene glycol as the initiator. This polymer has been used as an auxiliary calibration tool of the SEC system.

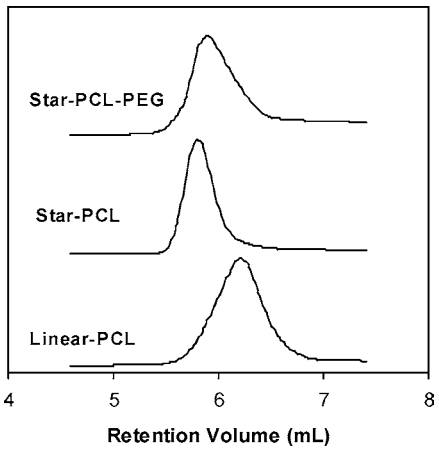

Figure 1. SEC chromatograms of linear-PCL, star-PCL, and star-PCL−PEG.

Table 1. SEC Results for the Polymers

	linear-PCL	star-PCL	star-PCL−PEG
theor mol wt	9200	51300	131300
wt-av mol wt, M_w	13000	53300	133000
no.-av mol wt, M_n	9500	49900	131000
polydispersity, M_w/M_n	1.37	1.07	1.02
intrinsic viscosity (dL/g)	0.362	0.303	0.489

The next step was to introduce hydrophilic PEG into the star-PCL polymer. A commercial PEG polymer with one end capped by a methoxy group and the other end by a carboxymethyl group was used. The carboxylic acid group in the PEG was used to react with the hydroxyl terminal groups of the star-PCL polymer to form the ester linkage and produce the desired final star-PCL−PEG. The coupling reaction was accomplished in dichloromethane at room temperature in the presence of DPTS and using DIPC as the activating agent for the carboxylic group (*22*). The advantages of this method are that reactions are conducted under very mild conditions, there is no need for preactivation of the carboxylic acid, and the product is formed in high yield. After the reaction was complete, the product was purified twice by fractionation to remove excess PEG and other impurities. The yield of the final star-PCL−PEG polymer was 91%.

Characterization of Star Polymers. The molecular weights of the synthesized polymers were determined by SEC and are summarized in Table 1. As can be seen, the molecular weight values of both star-PCL and star-PCL−PEG polymers agreed well with the calculated values (Table 1). The polydispersity of these star polymers was sufficiently narrow ($M_w/M_n < 1.07$).

The typical SEC chromatograms of the polymer samples are shown in Figure 1. The star-PCL sample is characterized by a narrower peak width when compared with linear PCL. This is consistent with the molecular weight distribution results for these two polymers. Comparison of the elution profiles for star-PCL and star-PCL−PEG samples revealed that star-PCL−PEG has a larger retention volume and a broader peak width compared with star-PCL. This is in apparent contradiction with the higher molecular weight and the narrow molecular

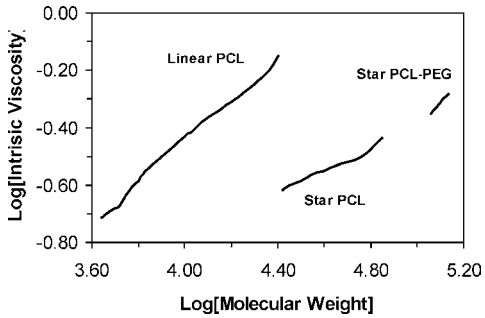

Figure 2. Log−log plot of intrinsic viscosities against molecular weight for linear and star polymers.

Table 2. g' Values Derived from Figure 2

	log[M]	$g' = [\eta]_{star}/[\eta]_{linear}$
star-PCL	4.60	0.32
	4.70	0.298
	4.80	0.285
star-PCL−PEG	5.06	0.259
	5.113	0.271

weight distribution determined for this polymer. We believe that the broader peak width and slower elution of star-PCL−PEG from the SEC column are probably due to the presence of PEG blocks in the arms of star-PCL−PEG copolymer. Indeed, PEG has a relatively high affinity to the column packing material, causing it to elute at higher retention times. Elution with other solvents (such as THF) showed severe trailing elution profiles, thus confirming the adsorptive interaction between the star-PCL−PEG copolymer and the column. However, the molecular weight determined from the analysis of data from the light scattering detector does not depend on the retention volume, and we are confident that the estimated molecular weight and polydispersity values for the star polymers are accurate.

In addition to the molecular characteristics, the analysis of the SEC data also provided information on the intrinsic viscosity ($[\eta]$) of the dilute solutions of the polymers studied (Table 1). These data are presented in the form of the Mark−Houwink plot for linear and star polymers in Figure 2. The solution of the branched star-PCL polymer had a lower $[\eta]$ than the linear polymer, which has a lower molecular weight. This result is consistent with the more compact structure of the star-shaped polymer. For star polymers and linear polymers with the *same molecular weight*, the ratio of their intrinsic viscosities, $g' = [\eta]_{star}/[\eta]_{linear}$, known as the *shrinking factor*, is a function of the number of arms (f) in the star polymer (*26*). Several theories have been developed to predict a relationship between g' and f (*26*). The theoretically predicted values of g' decrease with branching. Substantial experimental data have been collected for different molecular weights of star polymers in various solvent systems (*26*). The data of Figure 2 yield $[\eta] = 1.14 \times 10^{-3}\ M^{0.628}$ dL/g for linear PCL. Here we use the extrapolated $[\eta]_{linear}$ values from this equation to obtain calculated g' values for the star polymers. The ratios $[\eta]_{star}/[\eta]_{linear} = g'$ are shown in Table 2 for different molecular weights of star-PCL and star-PCL−PEG. Experimental g' values for three different model star polymer systems with various degrees of branching taken from the literature are summarized in Table 3 (*26*, *27*). A comparison of the data in Tables 2 and 3 reveals that the g' values calculated for star-PCL and star-PCL−PEG are close to the experimental g' values for model star polymers with $f = 16$. It is important to note that there are no data on g' values for the PCL-based polymer system. Also, one should be aware that the g' parameter for the star-PCL−PEG polymer is derived as the ratio between the $[\eta]$ of the star polymer with block copolymer arms and the $[\eta]$ of a pure PCL linear polymer (extrapolated values from equation). Therefore, the comparison presented herein is based on different polymer systems, and it can be used only for qualitative consideration.

Table 3. Literature Experimental g' Values

f	polyisoprene in θ solvent	polyisoprene in good solvent	PEG polymer
8	0.54	0.43	0.46
12	0.43	0.32	
16			0.26
18	0.30	0.23	

Table 4. TGA and DSC Result of Polymers

	T_{dec} (°C)	T_m (°C)	ΔH_m (J/g)
linear-PCL	283	57	68
star-PCL	266	54	65
PEG	260	62	164
star-PCL−PEG	362	57	82

Spectroscopic measurements also confirmed the structures of the star polymer products. In the ^{1}H NMR spectrum of star-PCL, three major resonances attributed to the oxycarbonyl-1,5-pentamethylene repeat unit of a PCL $[-O-CH_2-(CH_2)_3-CH_2-CO-]_n$ are observed: the triplet peak at 4.07 ppm is assigned to methylene protons in the $-OCH_2-$ group; the triplet at 2.32 ppm is assigned to methylene protons adjacent to the carbonyl group; and the $-(CH_2)_3-$ protons are shown as a multiple peak from 1.9 to 1.1 ppm. The dendrimer core contributes only minor peaks due to its relatively low content. In the ^{1}H NMR spectrum of star-PCL−PEG, in addition to the peaks from PCL blocks, the single peak at 3.65 ppm is observed due to the methylene protons of oxyethylene units of PEG. The integrated peak area ratio of PEG and PCL for the purified star-PCL−PEG sample is consistent with the expected structure.

The IR spectrum of the star-PCL had a band characteristic for the ester carbonyl at 1734 cm^{-1} and a band for hydroxyl at 3500 to 3200 cm^{-1}. There is only one hydroxyl group per PCL chain, so the intensity of the hydroxyl band was low, reflecting the low content of −OH in the sample. In the IR spectrum of star-PCL−PEG, this −OH band has disappeared, confirming the conjugation of PCL and PEG blocks. A stronger band at 1112 cm^{-1} for C−O−C appeared, consistent with the addition of PEG ether units.

Thermal Behavior. The thermal behavior of the synthesized copolymers as well as linear-PCL and PEG samples was investigated using thermogravimetric analysis (TGA) and differential scanning calorimetry (DSC). The results are summarized in Table 4. It is seen that both the linear polymers and the star-PCL are characterized by similar relatively low thermal stabilities due to the chain terminal groups (−OH and −COOH), which are subject to rapid thermal degradation. In contrast, star-PCL−PEG has stable chain terminal groups ($-OCH_3$), leading to a higher thermal stability. Therefore, the observed differences in the thermal stabilities of the synthesized polymers are consistent with their structures. The melting temperatures (T_m) and the heats of fusion (ΔH_m) of these polymers were determined from DSC data. The melting behavior of star-PCL, characterized by lower T_m and ΔH_m values compared to those of linear-PCL, probably reflected the branched nature of the star-PCL. Indeed, star branched polymers contain more defects caused by the core, which cannot be incorporated

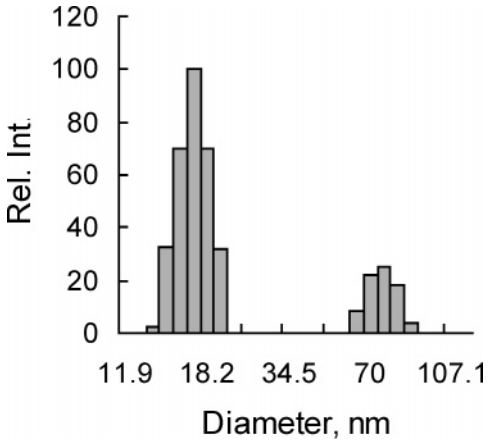

Figure 3. DLS graph of the micelle size distribution of star-PCL−PEG.

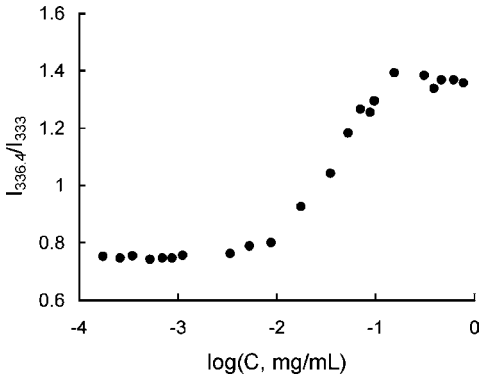

Figure 4. Dependence of intensity ratio $I_{336.4}/I_{333}$ (from pyrene excitation spectra) as a function of star-PCL−PEG concentration. [Py] = 6.0×10^{-7} M, λ_{em} = 390 nm, T = 37 °C.

in the crystallites. The DSC thermogram of star-PCL−PEG exhibited only a single melting peak characterized by T_m and ΔH_m values that were between those determined for star-PCL and PEG.

Micellar Properties of Star-PCL−PEG. The star-PCL−PEG polymer does not dissolve directly in water due to the hydrophobicity of the polycaprolactone core-forming block. For this reason, a dialysis method was employed to prepare polymeric micelles. The polymer was first dissolved in DMF, which is a good solvent for both PCL and PEG segments, and micellization was induced by the dropwise addition of water followed by dialysis.

The micelle size distribution of a polymer solution with a concentration of ~12 mg/mL was determined by DLS and is shown in Figure 3. It is a bimodal distribution with a smaller size component of ~16.9 nm (80%) and a large size component of ~75 nm (20%). These two components average to an overall effective hydrodynamic diameter of ~20.1 nm and a polydispersity index of 0.18. From the data presented in Table 1, the viscosity radius of the star-PCL−PEG can be calculated as R_v = 10.1 nm. Thus, the diameter determined from viscosity is 20.2 nm. Generally, the diameters determined from viscosity and DLS measurements are identical for star polymers (*26*). Because the SEC is performed in chloroform, both PCL and PEG segments are expanded. The DLS experiment is performed in water, however, and the PCL segment is contracted. Therefore, the nonaggregated star polymer in water should have a diameter of <20.2 nm. It appears thus that in all likelihood the small species in DLS with 16.9 nm diameter can be identified as the expected "unimolecular" micelle, and the large species with 70 nm diameter can be assigned to micelles formed from aggregated star polymers.

The association behavior of star-PCL−PEG copolymer in aqueous solutions was further characterized by a fluorescence technique using pyrene as a probe. This method is based on the sensitivity of the pyrene probe to the hydrophobicity and polarity of its microenvironment (*28*). In the presence of micelles or similar supramolecular aggregates, pyrene is solubilized within the interior of the hydrophobic core. As a result, significant changes in the spectroscopic properties are observed upon transfer of the probe from the aqueous environment to the nonpolar environment of the micelle core. First, the quantum yield of the fluorescence increases in the presence of the micelles. This effect is exhibited by an increase in the intensity of the fluorescence maximum at λ = 373 nm (I_1) in the emission spectrum of pyrene. Second, the vibrational fine structure of the emission spectrum undergoes changes. This effect is best characterized by the decrease in the ratio of the intensity of the vibrational band one to the vibrational band three (I_1/I_3), which is consistent with the decrease in polarity of the environment of the probe. Finally, the excitation spectra of pyrene are characterized by a red shift of the 333 nm (0,0) band. All of the key parameters characterizing the fluorescent properties of pyrene discussed above change sharply in a rather narrow range of star-PCL−PEG concentrations in aqueous solutions and then level off. Indeed, the (0,0) band in the excitation spectrum shifted from 333 to 336.4 nm, the total fluorescence intensity (I_1) increased, and the I_1/I_3 ratio decreased. For example, the change in the excitation spectrum of pyrene (characterized by a change of the $I_{336.4}/I_{333}$ intensity ratio) is presented in Figure 4 as a function of star-PCL−PEG concentration. It is seen that the $I_{336.4}/I_{333}$ values remain fairly constant below a certain concentration and then change substantially, reflecting the partitioning of the pyrene into the more hydrophobic environment. The onset of these changes can be considered as an apparent cmc (C_{app}) value. It is important to note that the analysis of all sets of data ($I_{336.4}/I_{333.2}$ ratio, I_1, and I_1/I_3 ratio) yielded essentially identical values for C_{app}, which is 3 mg/L. The determined C_{app} is in the same range as obtained for linear PCL−PEG copolymer (*29*) and the three- and four-arm star PCL−PEG copolymers (*17*). The existence of a C_{app} for star-PCL−PEG was consistent with the observation in the DLS data. This suggests that the larger associates composed of several copolymer molecules are formed in the aqueous dispersions of star-PCL−PEG. It is possible that such aggregates form as a result of the hydrophobic−hydrophobic interactions or van der Waals interactions between the exposed PCL cores of the individual star molecules.

A schematic picture of a possible aggregated micelle structure of star-PCL−PEG that may contribute to the existence of C_{app} is shown in Figure 5. Indeed, in the case of a star block copolymer with a low arm density (16 arms) the outer PEG shell most likely is too loose to outweigh the intermolecular association of the lipophilic PCL blocks. It is expected that when the number of arms in the star polymers increases significantly, the outer PEG blocks will form a tighter hydrophilic shell and reduce the tendency toward intermolecular micelle formation. The validation of this hypothesis is currently ongoing in our laboratories.

From the dependence of the fluorescence intensity of pyrene on star-PCL−PEG concentration the partitioning coefficient (P = 2410 ± 460) for pyrene in this micelle system was calculated as described (*30*). This value is 1

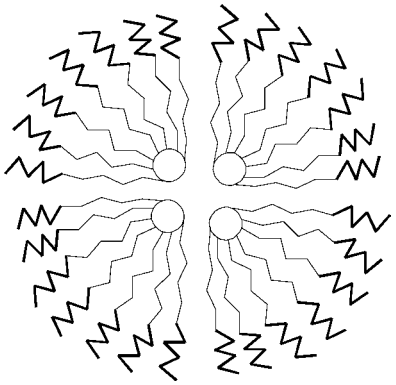

Figure 5. Possible aggregated micelle structure.

order of magnitude higher than was found for a linear PCL−PEG block copolymer system (*29*). The I_1/I_3 ratio was also used to characterize the polarity of the pyrene environment. The value measured for pyrene in a copolymer-free aqueous solution was ~1.8. As the concentration of the copolymer increased, the I_1/I_3 value decreased to ~1.49. This value corresponds to the polarity of ethyl acetate (I_1/I_3 = 1.45) (*28*) and seems to be reasonable for polyesters with moderate polarity, including PCL. These data suggest the preferential location of the pyrene probe in the hydrophobic environment of the PCL core of the micelles formed.

Evidence for excimer formation is another interesting feature of the pyrene fluorescence in the presence of star-PCL−PEG copolymer. At concentrations of star-PCL−PEG corresponding to C_{app}, there was an additional long-wavelength emission maximum of pyrene at $\lambda = 468$ nm. Excimer formation is rather unusual, taking into account the very low concentration (10^{-7} M) of the pyrene probe used in these experiments. Typically, such excimers can be observed at rather high concentrations (10^{-4}−10^{-3} M) of pyrene in aqueous media. A relatively high concentration of pyrene in the system is also needed to facilitate the formation of excimers in the micellar solutions (*31*). The excimer formation, which is a diffusion-limited process (*32*), suggests that the PCL core of star-PCL−PEG micelles probably afforded a rather small volume and that the PCL matrix is in the fluid (or liquid-crystalline) state.

Overall, the incorporation of a highly hydrophobic molecule, pyrene, reveals the suitability of this micelle system as a potential carrier for lipophilic compounds. Many experimental and theoretical studies have revealed that the greatest degree of solubilization of a compound within the micelle core will be reached when there is a close match between the degree of polarity and hydrophobicity of the compound and the micelle core (*2*). For this reason, we explored the incorporation of various hydrophobic substances, including drugs, into the star-PCL−PEG micelles.

Solubilization of Organic Dyes. The solubilization of water-insoluble dyes in the aqueous dispersions of star-PCL−PEG was studied in the range of concentration around the C_{app}. Figure 6 represents the data on solubilization of ORO dye as an example. It is important to note that even at a concentration of star-PCL−PEG lower than C_{app} the determined contents of dye in the test solutions were slightly higher compared to the polymer-free solutions. A similar behavior was also observed with Yellow OB dye. The solubilization of dyes in such dilute solutions of star-PCL−PEG copolymers is probably the result of incorporation of the dye in the PCL region of the intact star copolymer molecules. Therefore, this

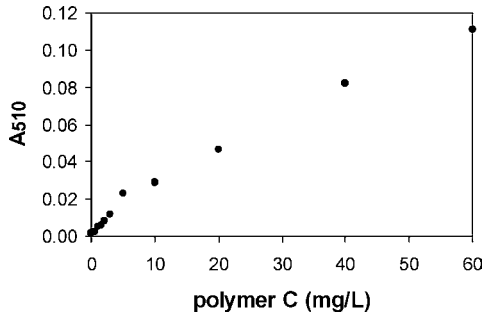

Figure 6. Absorbance of polymer/ORO solution at 510 nm against polymer concentration.

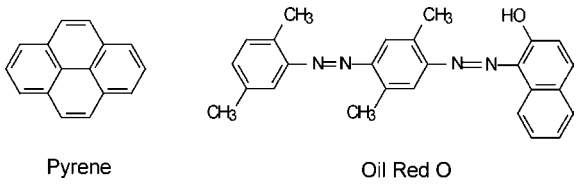

Figure 7. Structures of pyrene and Oil Red O.

observation confirmed the existence of a "unimolecular micelle." The amount of ORO detected in the solution increased almost monotonically as the concentration of star-PCL−PEG increased (Figure 6). In contrast to the pyrene solubilization experiments, the existence of C_{app} was not very pronounced in this study.

One of the possible explanations for such differences may be that the solubilization capacity of the PCL core with respect to pyrene is changing upon the transition from unimolecular micelle to multimolecular micelle. The hydrophobic core in the unimolecular micelle is smaller than the internal region of the multimolecular micelle. Therefore, a larger fraction of the core-forming chains in the unimolecular micelle will be exposed to the relatively hydrophilic environment. As a result, the volume of hydrophobic microphase that is available for partitioning of pyrene will be very small, and thus the concentration of pyrene in this phase would be too low to be detected. The association of several star molecules will cause an increase in the core size of the multimolecular micelle and thus provide for a larger loading capacity per micelle for pyrene. Furthermore, the compatibility between the solubilisate and the core-forming block should also be taken into account. It was shown previously that the partition coefficient for pyrene between micelles and water is higher in systems with cores of lower polarity (*33*). For instance, the partition coefficient of the order of 10^5 was reported for pyrene in polystyrene-*block*-PEG (*5*) and polystyrene-*block*-poly(acrylic acid) systems (*34*). Therefore, it is reasonable to expect that more polar compounds will be most easily loaded into micelles with more polar cores. Indeed, a comparison of the structures of ORO and pyrene (Figure 7) shows that the ORO molecule has more polar functional groups and should be more hydrophilic than pyrene. As a result, ORO may have a higher compatibility with the PCL core of the unimolecular micelle and incorporate into it more effectively than pyrene. Furthermore, it appears that the solubility of ORO in the PCL core of the micelle did not change drastically upon the transition from unimolecular micelle to multimolecular micelle. The apparent loading efficiency of star-PCL−PEG multimolecular micelles was ~6 wt % for both dyes studied.

Encapsulation of Drugs in Star-PCL−PEG Copolymer Micelles. The feasibility of using star-PCL−

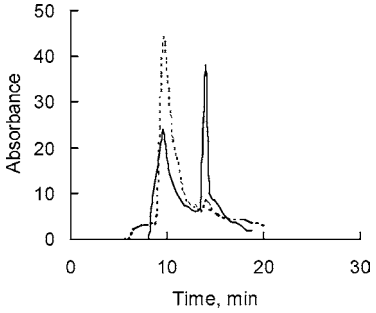

Figure 8. Chromatograms of the free (—) and DOX-loaded (· ··) star-PCL−PEG micelles. Eluent, 0.05 M NaCl; flow rate, 1.5 mL/min; detection wavelength, 288 nm.

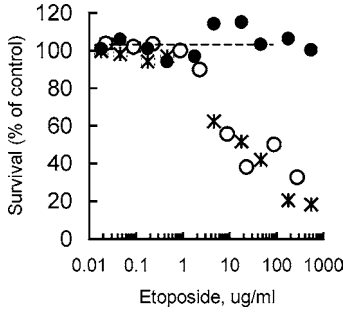

Figure 9. Cytotoxic effect of polymer micelles alone (●), free etoposide (∗), and etoposide in polymer micelles (○) in LLC-PK cells. Polymer concentrations in etoposide-free systems are the same as those at different etoposide dilutions.

Table 5. Loading of Etoposide in Star-PCL−PEG Micelle Systems

encapsulation method	polymer (mg/mL)	etoposide (mg/mL)	loading in polymer (% w/w)
solid extraction	0.38	0.15	7
solid extraction	3.7	0.92	22
solution extraction	7.6	0.95	11
solution extraction	15.1	0.95	6

PEG copolymer as a delivery carrier for lipophilic drugs was evaluated using IMC, DOX, and etoposide as the drug candidates. The IMC/star-PCL−PEG were obtained by dialysis and oil/water emulsion methods as described under Experimental Section. The experimentally determined IMC content entrapped into the star-PCL−PEG micelles was 5.4 wt % for the oil/water emulsion method and 9 wt % for the dialysis method. The loading capacity of 9 wt % corresponds to 33 IMC molecules per star copolymer molecule.

The encapsulation of DOX in star-PCL−PEG micelles was studied using SEC. The chromatograms of free and DOX-loaded star-PCL−PEG micelles are shown in Figure 8. The elution profile of free copolymer micelles revealed two sharp peaks (Figure 8, solid line). The peak at a retention time of ∼9.8 min was assigned to the aggregated polymer micelles, whereas the product eluting at 13.9 min was assigned to the intact unimolecular micelles. The ratio of the peak areas was ∼55:45. The chromatograms of DOX/copolymer samples detected at 288 nm (Figure 7, dotted line) were also characterized by two peaks (retention times of 9.5 and 13.8 min, respectively), but the peak areas ratio changed to ∼80:20. The elution profile of DOX/polymer samples detected at 485 nm, which is characteristic of DOX absorbance, was very similar, with a sharp peak at 9.7 min along with the small peak at 13.8 min (data not shown). These data indicated that DOX was incorporated into both types of star-PCL−PEG polymeric micelles. Furthermore, it is likely that incorporation of DOX enhanced the association of unimolecular micelles and that the majority of the drug was detected in the multimolecular copolymer micelles. The estimated amount of DOX encapsulated into copolymer micelles after elution from the column was ∼1.8 μg of DOX/mg of the copolymer. The contrast in loading level between IMC and DOX may be partially due to their acidity. IMC is an acid, DOX is a base, and the core of the star polymer is PAMAM, which contains 14 *tert*-amine bases. The acid−base interaction may contribute to the higher loading level for IMC.

A more hydrophobic anticancer drug, etoposide, was used to evaluate the encapsulation capacity of the star-PCL−PEG polymer. The results of different loading methods are summarized in Table 5. The etoposide concentrations in water and polymer micelle solutions were estimated by UV spectroscopy at 284 nm with the calibration curve obtained from methanol solution. We assume that the absorption coefficient of etoposide in water and in the micelle core is not very different from that in methanol solution. The saturated etoposide solubility in water was determined to be ∼0.12 mg/mL. The pure polymer solution has a small shoulder absorbance at 284 nm. The etoposide concentration loaded in micelles was determined from the absorbance at 284 nm after subtraction of the absorbance from the corresponding pure polymer solution and etoposide dissolved in water. A separate study determined that the organic solvent added (∼12 wt %) did not increase the solubility of etoposide in the absence of the polymer.

Significant amounts of etoposide can be incorporated in the polymer micelles. Interestingly, there is little dependence of etoposide solubility on the polymer concentration in the range studied, when the solution extraction method was used. Such behavior is typical for the incorporation of hydrophobic drugs in block copolymer micelles when there is a strong interaction between the drug and micelle core (*35*, *36*). The polymer micelle solutions remained stable over several days. Furthermore, they can be stored at 4 °C for at least 24 h without precipitation of etoposide.

Cytotoxicity Assay. This experiment examined whether etoposide incorporated in the polymer micelles can exhibit cytotoxic effects in cell culture. The results are presented in Figure 9. These data suggest that the polymer alone is not toxic, whereas etoposide incorporated in the micelles displays significant cytotoxic activity, comparable with that of the free etoposide (i.e., etoposide is released from the polymer micelles and acts on cells).

Concluding Remarks. In summary, we have successfully developed a high-yield, straightforward strategy for the synthesis of amphiphilic star-PCL−PEG polymers. The star structure was confirmed by SEC, spectroscopic, and thermal characterizations. The formation of unimolecular micelles from the 16-arm star polymer has been demonstrated by DLS and the dye solubilization study. The aggregation from unimolecular micelles into larger associated micelles has been observed in the DLS and pyrene fluorescence study. It is likely that the 16-arm star polymer forms a relatively loose outer PEG shell, which is not sufficient to hinder the intermolecular association of the inner hydrophobic PCL blocks. It is expected that more stable unimolecular micelles may be obtained when the number of arms in a star polymer increases to a higher number. It has been demonstrated that when the number of arms reaches 64, star polymers exhibit characteristics of a hard sphere, and the repulsion between the star molecules becomes much stronger (*37*).

We also demonstrated that lipophilic drugs can be encapsulated in the star-PCL−PEG micelles. A high loading level was achieved with more hydrophobic drugs, indomethacin and etoposide, whereas a relatively lower loading efficiency was achieved with a more hydrophilic drug, doxorubicin. A cytotoxicity assay demonstrated that the star-PCL−PEG polymer is nontoxic.

ACKNOWLEDGMENT

Funding of this work by the NIH (1R43GM62054-01) is gratefully acknowledged. F.W. thanks Dr. Savvas Makrides for help in proofreading the manuscript.

LITERATURE CITED

(1) Kwon, G. S., and Kataoka, K. (1995) Block copolymer micelles as long-circulating drug vehicles. *Adv. Drug Delivery Rev. 16*, 295.
(2) Allen, C., Maysinger, D., and Eisenberg, A. (1999) Nano-engineering block copolymer aggregates for drug delivery. *Colloids Surf. B: Biointerfaces 16,* 3.
(3) Kabanov, A. V., and Alakhov, V. Yu. (2002) Pluronic block copolymers in drug delivery: From micellar microcontainers to biological response modifiers. *Crit. Rev. Ther. Drug Carrier Systems 19*, 1.
(4) Torchilin, V. P. (1999) Polymeric micelles in diagnostic imaging. *Colloids Surf. B: Biointerfaces 16*, 305.
(5) Wilhelm, M., Zhao, C.; Wang, Y., Xu, R., Winnik, M. A., Mura, J., Reiss, G., and Croucher, M. D. (1991) Poly(styrene-ethylene oxide) Block Copolymer Micelle Formation in Water: A Fluorescence Probe Study. *Macromolecules 24*, 1033.
(6) Kwon, G. S., Naito, M., Yokoyama, M., Okano, T., Sakurai, Y., and Kataoka, K. (1993) Micelles Based on AB Block Copolymers of Poly(ethylene oxide) and Poly(β-benzyl L-aspartate). *Langmuir 9*, 945.
(7) Kabanov, A. V., Chekhonin, V. P., Alakhov, V. Yu., Batrakova, E. V., Lebedev, A. S., Melik-Nubarov, N. S., Arzhakov, S. A., Levashov, A. V., Morozov, G. V., Severin, E. S., and Kabanov, V. A. (1989) The neuroleptic activity of haloperidol increases after its solubilization in surfactant micelles. Micelles as microcontainers for drug targeting. *FEBS Lett. 258*, 343.
(8) Hagan, S. A., Coombes, A. G. A., Garnett, M. C., Dunn, S. E., Davies, M. C., Illum, L., Davis, S. S., Harding, S. E., Purkiss, S., and Gellert, P. R. (1996) Polylactide-Poly(ethylene glycol) Copolymers as Drug Delivery System. 1. Characterization of Water Dispersible Micelle-Forming Systems. *Langmuir 12*, 2153.
(9) Kataoka, K. (1993) Block copolymer micelles as vehicles for drug delivery. *J. Controlled Release 24*, 119.
(10) Yokoyama, M., Okano, T., Sakurai, Y., Okamptp, K., Fukushima, S., and Kataoka, K. (1996) Strategy and requirements of selective anticancer drug delivery to solid tumor with polymeric micelle. *Polym. Prepr. 27* (2)*,* 121.
(11) Hall, D. G., and Pethica, B. A. (1967) In *Nonionic Surfactants* (M. J. Schick, Ed.) p 516, Dekker, New York.
(12) Iijima, M., Nagasaki, Y., Okada, T., Kato, M., and Kataoka, K. (1999) Core-Polymerized Reactive Micelles from Heterotelechelic Amphiphilic Block Copolymers. *Macromolecules 32*, 1140.
(13) Kim, J.-H., Emoto, K., Iijima, M., Nagasaki, Y., Aoyagi, T., Okano, T., Sakurai, Y., and Kataoka, K. (1999) Core-Stabilized Polymeric Micelle as Potential Drug Carrier: Increased Solubilization of Taxol. *Polym. Adv. Technol. 10*, 647.
(14) Liu, H., Jiang, A., Guo, J., and Uhrich, K. E. (1999) Unimolecular Micelles: Synthesis and Characterization of Amphiphilic Polymer Systems. *J. Polym. Sci., Part A: Polym. Chem. 37*, 703.
(15) Choi, Y. K., Bae, Y. H., and Kim, S. W. (1998) Star-Shaped Poly(ether-ester) Block Copolymers: Synthesis, Characterization, and Their Physical Properties. *Macromolecules 31*, 8766.
(16) Jeong, B., Choi, Y. K., Bae, Y. H., Zentner, G., and Kim, S. W. (1999) New biodegradable polymers for injectable drug delivery systems. *J. Controlled Release 62*, 109.
(17) Kim, K. H., Cui, G. H., Lim, H. J., Huh, J., Ahn, C., and Jo, W. H. (2004) Synthesis and micellization of star-shaped poly(ethylene glycol)-*block*-poly(ϵ-caprolactone). *Macromol. Chem. Phys. 205*, 1684.
(18) Deng, M., Chen, X., Piao, L., Zhang, X., Dai, Z., and Jing, X. (2004) Synthesis of four-armed poly(ϵ-caprolactone)-block0poly(ethylene oxide) by diethylzinc catalyst. *J. Polym. Sci.: Part A: Polym. Chem. 42*, 950.
(19) Liu, M., and Fréchet, J. M. J. (1999) Designing dendrimers for drug delivery. *Pharm. Sci. Technol. Today 2*, 393.
(20) Liu, M., Kono, K., and Fréchet, J. M. J. (2000) Water-soluble dendritic unimolecular micelles: their potential as drug delivery agents. *J. Controlled Release 65*, 121.
(21) Kojima, C., Kono, K., Maruyama, K., and Takagishi, T. (2000) Synthesis of Polyamidoamine Dendrimers Having Poly(ethylene glycol) Graftes and Their Ability To Encapsulate Anticancer Drugs. *Bioconjugate Chem. 11*, 910.
(22) Moore, J. S., and Stupp, S. I. (1990) Room-Temperature Polyesterification. *Macromolecules 23*, 65.
(23) Ferrari, M., Fornasiero, M. C., and Isetta, A. M. (1990) MTT colorimetic assay for testing macrophage cytotoxic activity in vitro. *J. Immunol. Methods 131*, 165.
(24) Trollsås, M., Hedrick, J. L., Mecerreyes, D., Dubois, Ph., Jérôme, R., Ihre, H., and Hult, A. (1997) Versatile and Controlled Synthesis of Star and Branched Macromolecules by Dendritic Initiation. *Macromolecules 30*, 8508.
(25) Trollsås, M., Hedrick, J. L., Mecerreyes, D., Dubois, Ph., Jérôme, R., Ihre, H., and Hult, A. (1998) Highly Functional Branched and Dendri-Graft Aliphatic Polyesters through Ring Opening Polymerization. *Macromolecules 31*, 2756.
(26) Roovers, J. (1999) Dilute Solution Properties of Regular Star Polymers. Chapter 11 in *Star and Hyperbranched Polymers* (M. K. Mishra and S. Kobayashi, Eds.) Dekker, New York.
(27) Comanita, B., Noren, B., and Roovers, J. (1999) Star Poly(ethylene oxide)s from Carbosilane Dendrimers. *Macromolecules 32*, 1069.
(28) Kalayanasundaram, K., and Thomas, J. K. (1977) Environmental effects on vibronic band intensities of pyrene monomer fluorescence and their application in studies of micellar systems. *J. Am. Chem. Soc. 99*, 2039.
(29) Allen, C., Yu, Y., Maysinger, D., and Eisenberg, A. (1998) Polycaprolactone-*b*-poly(ethylene Oxide) Block Copolymer Micelles as a Novel Drug Delivery Vehicle for Neurotrophic Agents FK506 and L-685,818. *Bioconjugate Chem. 9*, 564.
(30) Kabanov, A. V., Nazarova, I. R., Astafieva, I. V., Batrakova, E. V., Alakhov, V. Yu., Yaroslavov, A. A., and Kabanov, V. A. (1995) Micelle formation and solubilization of fluorescent probes in poly(oxyethylene-*b*-oxypropylene-*b*-oxyethylene) solutions. *Macromolecules 28*, 2303.
(31) Lakowicz, J. R. (1983) *Principles of Fluorescence Spectroscopy*; Plenum Press, New York.
(32) Vanderkooi, J. M., and Callis, J. B. (1974) Pyrene. A probe of lateral diffusion in the hydrophobic region of membranes. *Biochemistry 13*, 4000.
(33) Kwon, G. S., Naito, M., Kataoka, K., Yokoyama, M., Sakurai, Y., and Okano, T. (1994) Block copolymer micelles as vehicles for hydrophobic drugs. *Colloids Surf. B: Biointerfaces 2*, 429.
(34) Astafieva, I., Zhong, X. F., and Eisenberg, A. (1993) Critical micellization phenomena in block polyelectrolyte solutions. *Macromolecules 26*, 7339.
(35) Xing, L., and Mattice, W. L. (1997) Strong solubilization of small molecules by triblock-copolymer micelles in selective solvents. *Macromolecules 30*, 1711.
(36) Gadelle, F., Koros, W. J., and Schechter, R. S. (1995) Solubilization of aromatic solutes in block copolymers. *Macromolecules 28*, 4883.
(37) Roovers, J., Toporowski, P. M., and Douglas, J. (1995) Thermodynamic Properties of Dilute and Semidilute Solutions of Regular Star Polymers. *Macromolecules 28*, 7064.

BC049784M

1-[3-(2-[^{18}F]Fluoropyridin-3-yloxy)propyl]pyrrole-2,5-dione: Design, Synthesis, and Radiosynthesis of a New [^{18}F]Fluoropyridine-Based Maleimide Reagent for the Labeling of Peptides and Proteins

Béatrice de Bruin,[†] Bertrand Kuhnast,[†] Françoise Hinnen,[†] Loïc Yaouancq,[‡] Mohamed Amessou,[§] Ludger Johannes,[§] Alain Samson,[‡] Raphaël Boisgard,[†,||] Bertrand Tavitian,[†,||] and Frédéric Dollé*[,†]

Service Hospitalier Frédéric Joliot, Département de Recherche Médicale, CEA/DSV, 4 place du Général Leclerc, F-91401 Orsay, France, Bionexis Pharmaceuticals, Paris-Biotech, 4 Avenue de l'Observatoire, F-75006 Paris, France, Laboratoire "Trafic et Signalisation", UMR144 Curie/CNRS, Institut Curie, 26 rue d'Ulm, F-75248 Paris Cedex 05, France, and INSERM ERM 0103, Service Hospitalier Frédéric Joliot, Département de Recherche Médicale, CEA/DSV, 4 place du Général Leclerc, F-91401 Orsay, France. Received October 22, 2004; Revised Manuscript Received January 7, 2005

FPyME (1-[3-(2-fluoropyridin-3-yloxy)propyl]pyrrole-2,5-dione) was designed as a [^{18}F]fluoropyridine-based maleimide reagent for the prosthetic labeling of peptides and proteins via selective conjugation with a thiol (sulfhydryl) function. Its pyridinyl moiety carries the radioactive halogen (fluorine-18) which can be efficiently incorporated via a nucleophilic *hetero*aromatic substitution, and its maleimido function ensures the efficient alkylation of a free thiol function as borne by cysteine residues. [^{18}F]-FPyME (HPLC-purified) was prepared in 17−20% non-decay-corrected yield, based on starting [^{18}F]-fluoride, in 110 min using a three-step radiochemical pathway. The developed procedure involves (1) a high-yield nucleophilic *hetero*aromatic ortho-radiofluorination on [3-(3-*tert*-butoxycarbonylamino-propoxy)pyridin-2-yl]trimethylammonium trifluoromethanesulfonate as the fluorine-18 incorporation step, followed by (2) rapid and quantitative TFA-induced removal of the *N*-Boc-protective group and (3) optimized maleimide formation using *N*-methoxycarbonylmaleimide. Typically, 4.8−6.7 GBq (130−180 mCi) of radiochemically pure [^{18}F]FPyME ([^{18}F]-**1**) could be obtained after semipreparative HPLC in 110 min starting from a cyclotron production batch of 33.3 GBq (900 mCi) of [^{18}F]fluoride (overall radiochemical yields, based on starting [^{18}F]fluoride: 28−37% decay-corrected). [^{18}F]FPyME ([^{18}F]-**1**) was first conjugated with a small model hexapeptide ((*N*-Ac)KAAAAC), confirming the excellent chemoselectivity of the coupling reaction (CH_2SH versus CH_2NH_2) and then conjugated with two 8-kDa proteins of interest, currently being developed as tumor imaging agents (c-AFIM-0 and c-STxB). Conjugation was achieved in high yields (60−70%, isolated and non-decay-corrected) and used optimized, short-time reaction conditions (a 1/9 (v/v) mixture of DMSO and 0.05 M aq Tris NaCl buffer (pH 7.4) or 0.1 M aq PBS (pH 8), at room temperature for 10 min) and purification conditions (a gel filtration using a Sephadex NAP-10 cartridge or a SuperDex Peptide HR 10/30 column), both compatible with the chemical stability of the proteins and the relatively short half-life of the radioisotope concerned. The whole radiosynthetic procedure, including the preparation of the fluorine-18-labeled reagent, the conjugation with the protein and the final purification took 130−140 min. [^{18}F]FPyME ([^{18}F]-**1**) represents a new, valuable, thiol-selective, fluorine-18-labeled reagent for the prosthetic labeling with fluorine-18 of peptides and proteins. Because of its excellent chemoselectivity, [^{18}F]FPyME offers an interesting alternative to the use of the nonselective carboxylate and amine-reactive [^{18}F]reagents and can therefore advantageously be used for the design and development of new peptide- and protein-based radiopharmaceuticals for PET.

INTRODUCTION

Positron emission tomography (PET) is a high-resolution, sensitive, molecular, and functional imaging technique. It permits repeated, noninvasive assessment and quantification of specific biological and pharmacological processes and is the most advanced technology currently available for studying in vivo molecular interactions. PET plays an increasing role in both drug discovery and development of radiopharmaceuticals, by assessing (once labeled with a positron-emitter) their in vivo distribution, pharmacokinetics, and dynamics.

Complex high-molecular-weight bioactive chemical structures, such as single-stranded oligonucleotides, peptides, and proteins are more and more often proposed as radiopharmaceuticals, and their applications are rapidly gaining importance in nuclear medicine (*1*−*4*). Over the past decades, these agents have evolved from large proteins (e.g. intact polyclonal antibodies with low specificity) to monoclonal antibodies and fragments (with relatively higher specificity), to smaller molecular recognition units such as single-chain antigen-binding domain fragments, and finally to receptor-specific peptides, which have emerged as one of the most promising classes of radiopharmaceuticals for both scintigraphic applications and therapeutic purposes (*2*, *4*).

* Corresponding author. Tel: + 33 1 69 86 77 04; Fax: + 33 1 69 86 77 49; e-mail: frederic.dolle@cea.fr.
[†] Service Hospitalier Frédéric Joliot.
[‡] Bionexis Pharmaceuticals.
[§] Institut Curie.
[||] INSERM ERM 0103.

10.1021/bc0497463 CCC: $30.25 © 2005 American Chemical Society
Published on Web 02/25/2005

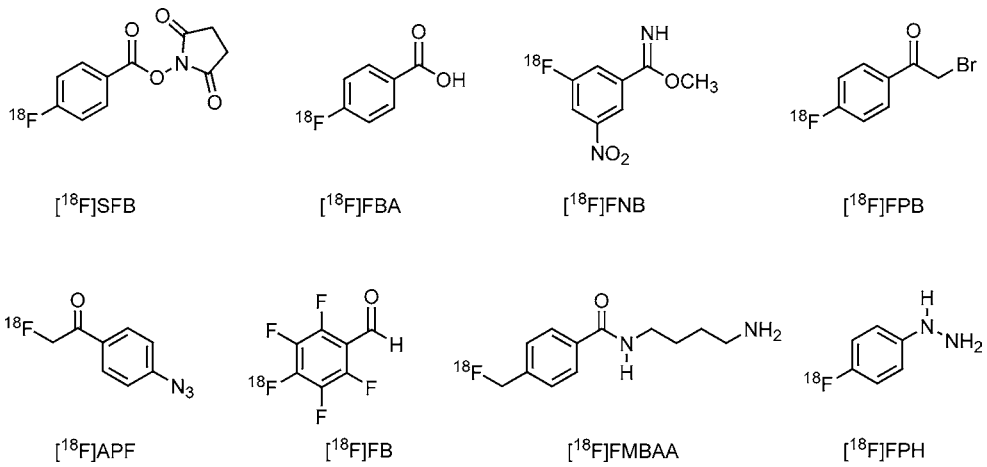

Figure 1. Chemical structures of *N*-succinimidyl 4-[18F]fluorobenzoate ([18F]SFB), 4-[18F]fluorobenzoic acid ([18F]FBA), 3-[18F]fluoro-5-nitrobenzimidate ([18F]FNB), 4-([18F]fluorophenacyl bromide ([18F]FPB), 4-azidophenacyl [18F]fluoride ([18F]APF), penta-[18F]-fluorobenzaldehyde ([18F]FB), 1-[4-([18F]fluoromethyl)benzoyl]-aminobutane-4-amine ([18F]FMBAA), and 4-[18F]fluorophenyl hydrazine ([18F]FPH),

Methods for radiolabeling these peptides and proteins have been of interest for several decades. Although many different radionuclides have been used to radiolabel proteins (*4*−*12*), the majority of labeled-protein studies have used radionuclides of iodine, principally iodine-125, iodine-123, and iodine-131. The latter radionuclides have properties which are adequate for a number of different applications (in vitro and in vivo imaging or therapy), are relatively easy to use, and are readily available at a nominal cost from commercial sources.

Peptides and proteins have also been labeled with positron-emitting radionuclides, even though fewer examples have been described in the literature. The short-lived positron-emitter fluorine-18 appears as the radionuclide of choice for the preparation of labeled bioactive peptides and proteins, as it is the case for conventional, low-molecular-weight radiotracers and radiopharmaceuticals (*13*−*16*). In regard of its physical and nuclear characteristics, fluorine-18 displays simple decay- and emission properties with a high positron abundance (97%). Compared with the other conventional short-lived positron-emitting radionuclides carbon-11, nitrogen-13, and oxygen-15, fluorine-18 has a relatively low positron emission energy (maximum 635 keV) and the shortest positron linear range in tissue (2.3 mm), resulting in the highest resolution in PET imaging. Its half-life (109.8 min) is long enough to give access to relatively extended imaging protocols compared to what is possible with carbon-11, therefore facilitating kinetic studies and high-quality metabolite and plasma analysis. Moreover, from a chemical point of view, it allows multistep synthetic approaches that can be extended over hours. These distinctive advantages, combined with its reliable multi-Curie production on widely implanted biomedical cyclotrons, have been effectively used for the labeling of various chemical structures (*13*−*16*).

Concerning peptides and proteins, the direct labeling of these macromolecules with fluorine-18 is, leaving aside some exceptions, not feasible and labeling is usually performed by conjugation of a prosthetic group, carrying the radioisotope, with a reactive function of the macromolecule. This strategy has the advantage of offering a wide choice of chemical routes, including drastic chemical conditions, for the preparation of the labeled prosthetic group entity, followed by the conjugation of the latter with a macromolecule using mild conditions needed to preserve the latter's integrity (*2*, *12*).

Several fluorine-18-labeled reagents have already been described in the literature (Figure 1). Most of them were designed for coupling to the peptide or protein via an amino function borne by an amino acid residue (*N*-terminus α-NH_2 or internal lysine ϵ-NH_2) or by an alkylamine linker. For example, the activated ester *N*-succinimidyl 4-[18F]fluorobenzoate ([18F]SFB) (*2*, *12*, *17*−*19*) is today probably the most often used prosthetic group introducing agent for the labeling of peptides and proteins via an acylation reaction, beside other carboxylic acids or esters, such as 4-[18F]fluorobenzoic acid ([18F]-FBA) (*20*), 2-[18F]fluoroacetic acid (*21*), or methyl 2-[18F]-fluoropropionate (*22*) (the latter two structures not shown). Other activated esters, such as *N*-succinimidyl 4-([18F]fluoromethyl)benzoate (*23*, *24*) and *N*-succinimidyl 8-[4′-[18F]fluorobenzyl)amino]suberate (*25*), have also been reported (structures not shown). Imidation reaction, using reagents such as 3-[18F]fluoro-5-nitrobenzimidate ([18F]FNB) (*26*), have been described. Finally, alkylation reactions using 4-[18F]fluorophenacyl bromide ([18F]FPB) (*26*) have been reported as well as photochemical conjugation using 4-azidophenacyl [18F]fluoride ([18F]APF) (*17*, *27*) and reductive amination using penta-[4-18F]fluorobenzaldehyde ([18F]FB) (*28*). A much smaller number of fluorine-18-labeled reagents for the coupling to the peptide or protein via another reactive function, the carboxylic acid function (*C*-terminus α-CO_2H or internal glutamic/aspartic acid α/β-CO_2H), have also been designed. To our knowledge, only two amines, 1-[4-([18F]-fluoromethyl)benzoyl]aminobutane-4-amine ([18F]FMBAA) (*29*) and 4-[18F]fluorophenylhydrazine ([18F]FPH) (*12*), have been described for these amidation reactions.

The free thiol function (also called sulfhydryl) is not very common in most peptides and proteins and is only present in cysteine residues (internal β-SH). Thiol-reactive agents have therefore been used to modify peptides and proteins at specific sites (*30*−*32*), providing a means of high chemoselectivity in contrast to the carboxylate and amine-reactive reagents described above. To our knowledge, to date, only two fluorine-18-labeled reagents have been described in an abstract by Shiue for the coupling to peptide or protein via alkylation of such a thiol function (*33*). In that work, the preparation of two *N*-substituted maleimides, 1-(4-[18F]fluorophenyl)pyrrole-2,5-dione ([18F]FPPD) and *N*-[3-(2,5-dioxo-2,5-dihydro-pyrrol-1-yl)phenyl]-4-[18F]fluorobenzamide ([18F]DDPFB),

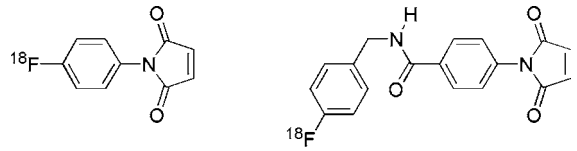

Figure 2. Chemical structures of 1-(4-[^{18}F]fluorophenyl)-pyrrole-2,5-dione ([^{18}F]FPPD) and *N*-[3-(2,5-dioxo-2,5-dihydro-pyrrol-1-yl)-phenyl]-4-[^{18}F]fluorobenzamide ([^{18}F]DDPFB).

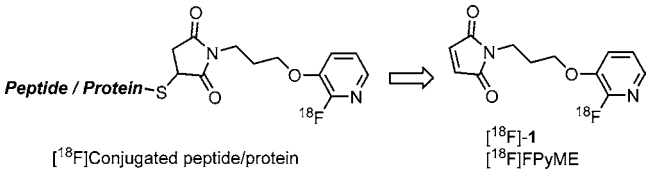

Figure 3. Fluorine-18-labeling design of peptide and protein via selective thiol alkylation using 1-[3-(2-[^{18}F]fluoropyridin-3-yloxy)propyl]pyrrole-2,5-dione ([^{18}F]FPyME, [^{18}F]-**1**).

was reported, and its coupling to proteins was briefly mentioned (Figure 2).

From a radiochemical point of view, all the above-mentioned fluorine-18-labeled reagents were prepared using the relatively restricted labeling strategies offered by *homo*aromatic and aliphatic nucleophilic substitution reactions (*14*, *15*). Recently, the scope of these nucleophilic radiofluorinations has been opened to *hetero*aromatic substitutions, particularly in the pyridine series (*34*). After evaluation and validation of the radiosynthesis of 2- and 4-[^{18}F]fluoropyridine as a model reaction (*35*, *36*), we and others have since applied successfully these nucleophilic *hetero*aromatic substitutions to the preparation of various PET radiotracers and radiopharmaceuticals (*34*), such as for example, the cholinergic $\alpha_4\beta_2$-subtype selective nicotinic radioligand 2-[^{18}F]fluoro-3-[2(*S*)-2-azetidinylmethoxy]pyridine (2-[^{18}F]F-A-85380) (*37*−*50*).

Considering chemical structures showing a fluoropyridinyl moiety, nucleophilic *hetero*aromatic substitution at the ortho-position with no-carrier-added [^{18}F]fluoride appears today as the more efficient method for the radiosynthesis of radiotracers and radiopharmaceuticals of high specific radioactivity when compared to *homo*aromatic or aliphatic nucleophilic radiofluorination. On the basis of these recent advances, we have designed a new [^{18}F]fluoropyridine-based maleimide reagent, [^{18}F]-**1** (1-[3-(2-[^{18}F]fluoropyridin-3-yloxy)propyl]pyrrole-2,5-dione, coded [^{18}F]FPyME, Figure 3) as a new fluorine-18-labeled reagent for the highly specific conjugation to peptides and proteins via thiol alkylation.

We herein report the design, selection, and synthesis of the nonlabeled fluoropyridinyl reagent (**1**, FPyME) as a reference, as well as the synthesis of the required nitro- and trimethylammonium trifluoromethanesulfonate derivatives as precursors for labeling with fluorine-18. We also present the radiosynthesis of [^{18}F]FPyME ([^{18}F]-**1**) using an efficient three-step radiosynthesis, involving a nucleophilic *hetero*aromatic ortho-radiofluorination as the fluorine-18 incorporation-step. In addition, we describe the conjugation of this maleimide reagent ([$^{18/19}$F]FPyME, [$^{18/19}$F]-**1**) with a small hexapeptide, (*N*-Ac)KAAAAC, chosen as a model peptide in order to confirm the chemoselectivity of the coupling reaction (CH_2SH versus CH_2NH_2). Finally, we present as applications to protein labeling, (a) the preparation of [^{18}F]c-AFIM-0, a selected 75-amino acid (∼ 8.8 kDa) mini-protein, derived from the specific binding domain of annexins for phosphatidylserine and (b) the preparation of [^{18}F]c-STxB, the nontoxic homopentameric B subunit (monomer size ∼ 8.0 kDa) of the bacterial (*Shigella dysenteriae*) Shiga toxin, both proteins being developed as tumor imaging agents.

EXPERIMENTAL SECTION

1. General. *Chemicals.* Chemicals were purchased from standard commercial sources (Aldrich, Fluka, or Sigma France) and were used without further purification, unless stated otherwise. Oxygen-18-enriched water ([^{18}O]H_2O, >95%) was purchased from CortecNet (Paris, France). (*N*-Ac)KAAAAC was custom-synthesized by Neosystem (France).

Analytical Methods. Thin layer chromatographies (TLCs) were run on precoated plates of silica gel $60F_{254}$ (Merck). The compounds were localized (1) when possible at 254 nm using a UV-lamp and/or (2) by dipping the TLC-plates in a 1% ethanolic ninhydrin solution and heating on a hot plate. Radioactive spots were detected using a Berthold TraceMaster 20 automatic TLC linear analyzer. Flash chromatographies were conducted on silica gel 63−200 μm (Merck) at 0.3 bar (Ar). High-pressure liquid chromatographies (HPLCs) were performed on Waters or Shimadzu systems: [HPLC A]: Equipment: a Waters 600 Pump, a Waters 600 Gradient Controller, a Shimadzu SPD10-AVP UV-multiwavelength spectrometer, and a Geiger-Müller detector; column: preparative SiO_2, Lichrosorb, Merck (250 × 27.0 mm; porosity: 7 μm); solvents and conditions: isocratic elution with heptane/EtOAc; temperature: RT; absorbance detection at λ = 254 nm. [HPLC B]: Equipment: a Waters 600 Pump, a Waters 600 Gradient Controller, a Shimadzu SPD10-AVP UV-multiwavelength spectrometer, and a Geiger-Müller detector; column: preparative C18, DeltaPak, Waters (300 × 19.0 mm; porosity: 15 μm); solvents and conditions: 0.1% aq TFA (v/v) and acetonitrile containing 0.1% TFA (v/v); linear gradient in 30 min from 100/0 to 65/35, flow rate: 10 mL/min; temperature: RT, absorbance detection at λ = 214 nm. [HPLC C]: Equipment: a Waters 600 Gradient Controller, a Waters 490E UV-multiwavelength spectrometer, and a Geiger-Müller detector; column: preparative Gel Filtration SuperDex Peptide HR 10/30, Amersham Pharmacia Biotech (300 × 10 mm); solvents and conditions: isocratic elution with aq PBS (20 mM KH_2PO_4; 150 mM NaCl) at pH 7.4; flow rate: 1 mL/min; temperature: RT; absorbance detection at λ = 214 nm. [HPLC D]: Equipment: a Waters 510 pump, a Shimadzu SPD10-AVP UV-multiwavelength spectrometer and a Geiger-Müller detector; column: semipreparative SiO_2 Zorbax Rx-SIL, Hewlett-Packard (250 × 9.4 mm; porosity: 5 μm); solvents and conditions: isocratic elution with heptane/EtOAc: 60/40 (v/v); flow rate: 5 mL/min; temperature: RT; absorbance detection at λ = 254 nm. [HPLC E]: Equipment: a Waters 600 Pump, a Waters 600 Gradient Controller, a Hewlett-Packard Series 1100 multiwavelength spectrometer and a Flow One Scintillation Analyzer Packard equipped with a positron dedicated cell for radioactivity monitoring; column: semipreparative C18, μBondapak, Waters (300 × 7.8 mm; porosity: 10 μm); solvents and conditions: 0.1% aq TFA (v/v) and acetonitrile containing 0.1% TFA (v/v); linear gradient in 15 min from 80/20 to 40/60, flow rate: 4 mL/min; temperature: RT, absorbance detection at λ = 214 nm. [HPLC F]: Equipment: a Waters 600 Gradient Controller, a Hewlett-Packard Series 1100 multiwavelength spectrometer and a Flow One Scintillation Analyzer Packard equipped with a positron-dedicated cell for radioactivity monitoring; column: preparative Gel Filtration SuperDex Peptide HR 10/30, Amersham Pharmacia Biotech (300 × 10 mm); solvents and conditions: isocratic elution with aq PBS

(20 mM KH_2PO_4; 150 mM NaCl) at pH 7.4; flow rate: 1 mL/min; temperature: RT; absorbance detection at λ = 214 nm. NMR spectra were recorded on a Bruker AMX (300 MHz) apparatus and on a Bruker Advance (400 MHz) apparatus using the hydrogenated residue of the deuterated solvents (CD_2Cl_2, δ = 5.32 ppm; DMSO-d_6, δ = 2.50 ppm and CD_3OD, δ = 3.35 ppm) and/or TMS as internal standards for ^{1}H NMR as well as the deuterated solvents (CD_2Cl_2, δ = 53.8 ppm; DMSO-d_6, δ = 39.5 ppm and CD_3OD, δ = 49.3 ppm) and/or TMS as internal standards for ^{13}C NMR. The chemical shifts are reported in ppm, downfield from TMS (s, d, t, q, q^5, dd, td, m, b for singlet, doublet, triplet, quadruplet, quintuplet, doublet of doublet, triplet of doublet, multiplet (or multi sharp-peak system), and broad, respectively). The mass spectra (MS) were measured on a Nermag R10−10 spectrometer (DCI/NH_4^+), a Quantum TCQ Discovery spectrometer (ES+), or a Perseptive Biosystem DE-RP MALDI-TOF Voyager spectrometer (ES+).

Miscellaneous. Radiosyntheses using fluorine-18, including the HPLC purifications, were performed in a 7.5-cm-lead shielded cell using a computer assisted Zymate robot system (Zymark corporation, USA).

Radioisotope Production. No-carrier-added aqueous [18F]fluoride ion was produced via the [^{18}O(p,n)^{18}F] nuclear reaction by irradiation of a 2 mL [^{18}O]water (>97%-enriched) target on a CGR-MeV 520 cyclotron (17 MeV proton beam) or on a IBA Cyclone-18/9 cyclotron (18 MeV proton beam) and was transferred to the appropriate hot cell. Target hardware: CGR-MeV 520 cyclotron: home-made, large volume, three-port, keyhole-shaped stainless steel/silver target holder (a complete description of this target hardware and -operation can be found in ref 81); IBA Cyclone-18/9 cyclotron: commercial, large volume, two-port, stainless steel target holder equipped with a domed-end niobium cylinder insert. Target to hot cell liquid-transfer system: 60 m PTFE line (0.8 mm internal diameter; 1/16 in. external diameter), 2.0 bar He drive pressure, transfer time 3−6 min). Typical production of [18F]fluoride at the end of bombardment for a 20 μA, 30 min (10 μA·h) irradiation: CGR-MeV 520 cyclotron: 550−650 mCi (20.3−24.0 GBq) and IBA Cyclone-18/9 cyclotron: 750−800 mCi (27.7−29.6 GBq).

2. Chemistry. Preparation of [(2-Nitropyridin-3-yloxy)alkyl]carbamic Acid *tert*-Butyl Esters (3a−e). *General Procedure.* To a solution of the appropriate (*N*-Boc-amino)alcohol (**2a−e**, 9−12 mmol) in THF (100−150 mL) were added 0.8 equiv of triphenylphosphine (MW: 262.29), 0.8 equiv of 3-hydroxy-2-nitropyridine (MW: 139.01), and dropwise 1.38 equiv of diisopropylazodicarboxylate (DIAD, MW: 202.21, d: 1.027). After stirring at room temperature for 24−28 h, the reaction mixture was concentrated to dryness and the residue was purified by column chromatography on silica gel. Elution with EtOAc/heptane (60/40 (v/v)) gave >90% pure [(2-nitropyridin-3-yloxy)alkyl]carbamic acid *tert*-butyl ester (**3a−e**). For analytical purposes only, an aliquot was further purified by preparative HPLC [HPLC A].

*[2-(2-Nitropyridin-3-yloxy)ethyl]carbamic Acid tert-Butyl Ester (**3a**).* The procedure described above was used with 2-(*N*-Boc-amino)ethanol (**2a**, 2.00 g) to give 1.35 g of **3a** as a pale-yellow oil (38%). R_f (EtOAc/heptane: 50/50 (v/v)): 0.74. t_R (HPLC A, EtOAc/heptane: 50/50 (v/v), flow rate: 25 mL/min): 10.3 min. ^{1}H NMR (CD_2Cl_2, 298 K): δ: 8.07 (bs, $w_{1/2}$ = 9.0 Hz, 1H); 7.55 (bs, $w_{1/2}$ = 7.0 Hz, 2H); 5.12 (b, 1H); 4.19 (t, J = 5.4 Hz, 2H); 3.52 (q, J = 5.4 Hz, 2H); 1.41 (s, 9H). ^{13}C NMR (CD_2Cl_2, 298 K): δ: 156.9 (C); 149.8 (C); 147.3 (C); 139.9 (CH); 129.3 (CH); 124.4 (CH); 79.9 (C); 69.6 (CH_2); 40.1 (CH_2); 28.5 (3×CH_3). MS (DCI/NH_4^+) $C_{12}H_{17}N_3O_5$: 284 [M + H$^+$].

*[3-(2-Nitropyridin-3-yloxy)propyl]carbamic Acid tert-Butyl Ester (**3b**).* The procedure described above was used with 3-(*N*-Boc-amino)propan-1-ol (**2b**, 2.00 g) to give 1.37 g of **3b** as a pale-yellow oil (40%). R_f (EtOAc/heptane: 50/50 (v/v)): 0.19. t_R (HPLC A, EtOAc/heptane: 50/50 (v/v), flow rate: 25 mL/min): 11.5 min. ^{1}H NMR (CD_2Cl_2, 298 K): δ: 8.06 (t, J = 3.3 Hz, 1H); 7.55 (d, J = 3.0 Hz, 2H); 4.20 (t, J = 5.7 Hz, 2H); 3.28 (q, J = 6.3 Hz, 2H); 2.03 (q^5, J = 6.3 Hz, 2H); 1.41 (s, 9H). ^{13}C NMR (CD_2Cl_2, 298 K): δ: 156.3 (C); 149.2 (C); 147.3 (C); 139.5 (CH); 129.2 (CH); 124.0 (CH); 79.2 (C); 68.3 (CH_2); 37.9 (CH_2); 29.5 (CH_2); 28.4 (3×CH_3). MS (DCI/NH_4^+) $C_{13}H_{19}N_3O_5$: 298 [M + H$^+$].

*[4-(2-Nitropyridin-3-yloxy)butyl]carbamic Acid tert-Butyl Ester (**3c**).* The procedure described above was used with 4-(*N*-Boc-amino)butan-1-ol (**2c**, 2.00 g) to give 1.19 g of **3c** as a pale-yellow oil (36%). R_f (EtOAc/heptane: 50/50 (v/v)): 0.42. t_R (HPLC A, EtOAc/heptane: 50/50 (v/v), flow rate: 25 mL/min): 11.4 min. ^{1}H NMR (CD_2Cl_2, 298 K): δ: 8.04 (t, $w_{1/2}$ < 2.0 Hz, 1H); 7.53 (bd, $w_{1/2}$ < 2.0 Hz, 2H); 4.73 (b, 1H); 4.15 (t, J = 6.6 Hz, 2H); 3.14 (q, J = 6.6 Hz, 2H); 1.84 (q^5, J = 6.6 Hz, 2H); 1.63 (q^5, J = 6.6 Hz, 2H); 1.41 (s, 9H). ^{13}C NMR (CD_2Cl_2, 298 K): δ: 156.2 (C); 149.8 (C); 147.3 (C); 139.3 (CH); 129.0 (CH); 123.9 (CH); 79.1 (C); 69.8 (CH_2); 40.2 (CH_2); 28.4 (3×CH_3); 26.8 (CH_2); 26.6 (CH_2). MS (DCI/NH_4^+) $C_{14}H_{21}N_3O_5$: 312 [M + H$^+$].

*[5-(2-Nitropyridin-3-yloxy)pentyl]carbamic Acid tert-Butyl Ester (**3d**).* The procedure described above was used with 5-(*N*-Boc-amino)pentan-1-ol (**2d**, 2.00 g) to give 0.93 g of **3d** as a pale-yellow solid (29%). R_f (EtOAc/heptane: 50/50 (v/v)): 0.35. t_R (HPLC A, EtOAc/heptane: 50/50 (v/v), flow rate: 25 mL/min): 10.0 min. ^{1}H NMR (CD_2Cl_2, 298 K): δ: 8.03 (t, J = 3.0 Hz, 1H); 7.53 (bd, 2H); 4.70 (b, 1H); 4.13 (t, J = 6.3 Hz, 2H); 3.09 (q, J = 6.3 Hz, 2H); 1.82 (q^5, J = 6.3 Hz, 2H); 1.60−1.40 (bm, 4H); 1.41 (s, 9H). ^{13}C NMR (CD_2Cl_2, 298 K): δ: 156.2 (C); 149.3 (C); 147.3 (C); 139.2 (CH); 128.9 (CH); 123.8 (CH); 78.9 (C); 70.0 (CH_2); 40.6 (CH_2); 30.0 (CH_2); 28.7 (CH_2); 28.4 (3×CH_3); 23.3 (CH_2). MS (DCI/NH_4^+) $C_{15}H_{23}N_3O_5$: 326 [M + H$^+$].

*[6-(2-Nitropyridin-3-yloxy)hexyl]carbamic Acid tert-Butyl Ester (**3e**).* The procedure described above was used with 6-(*N*-Boc-amino)hexan-1-ol (**2e**, 2.00 g) to give 1.25 g of **3e** as a pale-yellow solid (40%). R_f (EtOAc/heptane: 50/50 (v/v)): 0.17. t_R (HPLC A, EtOAc/heptane: 40/60 (v/v), flow rate: 30 mL/min): 8.6 min. ^{1}H NMR (CD_2Cl_2, 298 K): δ: 8.03 (t, J = 3.0 Hz, 1H); 7.52 (bd, 2H); 4.65 (b, 1H); 4.12 (t, J = 6.6 Hz, 2H); 3.07 (q, J = 6.6 Hz, 2H); 1.81 (q^5, J = 6.6 Hz, 2H); 1.70−1.30 (bm, 15H). ^{13}C NMR (CD_2Cl_2, 298 K): δ: 156.2 (C); 149.6 (C); 147.4 (C); 139.2 (CH); 128.9 (CH); 123.8 (CH); 78.9 (C); 70.1 (CH_2); 40.7 (CH_2); 30.3 (CH_2); 28.9 (CH_2); 28.5 (3×CH_3); 26.6 (CH_2); 25.8 (CH_2). MS (DCI/NH_4^+) $C_{16}H_{25}N_3O_5$: 340 [M + H$^+$].

Preparation of [(2-fluoropyridin-3-yloxy)alkyl]-carbamic Acid *tert*-Butyl Esters (4a−e). *General Procedure.* To a solution of the appropriate (*N*-Boc-amino)alcohol (**2a−e**, 9−12 mmol) in THF (100−150 mL) were added 0.8 equiv of triphenylphosphine (MW: 262.29), 0.8 equiv of 2-fluoro-3-hydroxypyridine (MW: 113.09), and dropwise 1.38 equiv of diisopropylazodicarboxylate (DIAD; MW: 202.21, d: 1.027). After addition, the reaction mixture was stirred at room temperature for 24−28 h. The reaction mixture was concentrated to dryness, and the residue was purified by column chromatography on silica gel. Elution with heptane/EtOAc (60/40 (v/v)) gave >90% pure [(2-fluoropyridin-3-yloxy)-

alkyl]carbamic acid *tert*-butyl ester (**4a**−**e**). For analytical purposes only, an aliquot was further purified by preparative HPLC [HPLC A].

*[2-(2-Fluoropyridin-3-yloxy)ethyl]carbamic Acid tert-Butyl Ester (**4a**).* The procedure described above was used with 2-(*N*-Boc-amino)ethanol (**2a**, 2.00 g) to give 0.86 g of **4a** as a pale-yellow solid (27%). R_f (EtOAc/heptane: 50/50 (v/v)): 0.55. t_R (HPLC A, EtOAc/heptane: 40/60 (v/v), flow rate: 25 mL/min): 8.1 min. ^{1}H NMR (CD_2Cl_2, 298 K): δ: 7.71 (bs, $w_{1/2}$ = 9.0 Hz, 1H); 7.32 (t, J = 8.7 Hz, 1H); 7.13 (dd, J = 7.8 and 4.8 Hz, 1H); 5.05 (b, 1H); 4.09 (t, J = 8.7 Hz, 2H); 3.54 (q, J = 5.4 Hz, 2H); 1.42 (s, 9H). ^{13}C NMR (CD_2Cl_2, 298 K): δ: 156.1 (C); 154.0 (d, J^1_{F-C} = 235 Hz, C); 142.3 (d, J^2_{F-C} = 26 Hz, C); 137.8 (d, J^3_{F-C} = 13 Hz, CH); 123.2 (CH); 122.3 (CH); 79.7 (C); 68.9 (CH_2); 40.2 (CH_2); 28.4 (3×CH_3). MS (DCI/NH_4^+) $C_{12}H_{17}F_1N_2O_3$: 257 [M + H$^+$].

*[3-(2-Fluoropyridin-3-yloxy)propyl]carbamic Acid tert-Butyl Ester (**4b**).* The procedure described above was used with 3-(*N*-Boc-amino)propan-1-ol (**2b**, 2.00 g) to give 1.51 g of **4b** as a pale-yellow oil (49%). R_f (EtOAc/heptane: 50/50 (v/v)): 0.44. t_R (HPLC A, EtOAc/heptane: 40/60 (v/v), flow rate: 25 mL/min): 10.2 min. ^{1}H NMR (CD_2Cl_2, 298 K): δ: 7.68 (dt, J = 3.0 and 1.5 Hz, 1H); 7.28 (td, J = 7.8 Hz and 1.5 Hz, 1H); 7.10 (dd, J = 8.1 and 5.1 Hz, 1H); 4.07 (t, J = 6.3 Hz, 2H); 3.27 (q, J = 6.3 Hz, 1H); 1.98 (q^5, J = 6.4 Hz, 2H); 1.39 (s, 9H). ^{13}C NMR (CD_2Cl_2, 298 K): δ: 156.3 (C); 154.1 (d, J^1_{F-C} = 237 Hz, C); 142.5 (d, J^2_{F-C} = 27 Hz, C); 137.5 (d, J^3_{F-C} = 15 Hz, CH); 123.0 (CH); 122.2 (CH); 79.2 (C); 67.3 (CH_2); 38.0 (CH_2); 29.8 (CH_2); 28.5 (3×CH_3). MS (DCI/NH_4^+) $C_{13}H_{19}F_1N_2O_3$: 271 [M + H$^+$].

*[4-(2-Fluoropyridin-3-yloxy)butyl]carbamic Acid tert-Butyl Ester (**4c**).* The procedure described above was used with 4-(*N*-Boc-amino)butan-1-ol (**2c**, 2.00 g) to give 1.14 g of **4c** as a pale-yellow oil (38%). R_f (EtOAc/heptane: 50/50 (v/v)): 0.36. t_R (HPLC A, EtOAc/heptane: 40/60 (v/v), flow rate: 20 mL/min): 5.9 min. ^{1}H NMR (CD_2Cl_2, 298 K): δ: 7.69 (td, J = 1.5 and 3.0 Hz, 1H); 7.30 (t, J = 8.7 Hz, 1H); 7.11 (dd, J = 7.8 and 5.1 Hz, 1H); 4.76 (b, 1H); 4.05 (t, J = 4.5 Hz, 2H); 3.16 (q, J = 6.6 Hz, 2H); 1.84 (q^5, J = 6.9 Hz, 2H); 1.66 (q^5, J = 6.7 Hz, 2H); 1.41 (s, 9H). ^{13}C NMR (CD_2Cl_2, 298 K): δ: 156.8 (C); 153.9 (d, J^1_{F-C} = 235 Hz, C); 142.9 (d, J^2_{F-C} = 26 Hz, C); 137.3 (d, J^3_{F-C} = 13 Hz, CH); 123.0 (CH); 122.2 (CH); 79.5 (C); 69.3 (CH_2); 40.4 (CH_2); 28.5 (3×CH_3); 27.0 (CH_2); 26.6 (CH_2). MS (DCI/NH_4^+) $C_{14}H_{21}F_1N_2O_3$: 285 [M + H$^+$].

*[5-(2-Fluoropyridin-3-yloxy)pentyl]carbamic Acid tert-Butyl Ester (**4d**).* The procedure described above was used with 5-(*N*-Boc-amino)pentan-1-ol (**2d**, 2.00 g) to give 0.90 g of **4d** as a pale-yellow solid (31%). R_f (EtOAc/heptane: 50/50 (v/v)): 0.43. t_R (HPLC A, EtOAc/heptane: 40/60 (v/v), flow rate: 20 mL/min): 5.4 min. ^{1}H NMR (CD_2Cl_2, 298 K): δ: 7.68 (bs, J < 1.5 Hz, 1H); 7.28 (t, J = 8.1 Hz, 1H); 7.10 (dd, J = 5.1 and 7.8 Hz, 1H); 4.61 (b, 1H); 4.02 (t, J = 6.6 Hz, 2H); 3.10 (q, J = 5.7 Hz, 2H); 1.83 (q^5, J = 6.6 Hz, 2H); 1.60−1.40 (bm, 4H); 1.40 (s, 9H). ^{13}C NMR (CD_2Cl_2, 298 K): δ: 155.8 (C); 154.1 (d, J^1_{F-C} = 235 Hz, C); 142.3 (d, J^2_{F-C} = 25 Hz, C); 136.8 (d, J^3_{F-C} = 13 Hz, CH); 122.4 (CH); 121.8 (CH); 79.8 (C); 69.5 (CH_2); 40.3 (CH_2); 29.8 (CH_2); 28.6 (CH_2); 28.1 (3×CH_3); 23.1 (CH_2). MS (DCI/NH_4^+) $C_{15}H_{23}F_1N_2O_3$: 299 [M + H$^+$].

*[6-(2-Fluoropyridin-3-yloxy)hexyl]carbamic Acid tert-Butyl Ester (**4e**).* The procedure described above was used with 6-(*N*-Boc-amino)hexan-1-ol (**2e**, 2.00 g) to give 0.90 g of the **4e** as a pale-yellow oil (31%). R_f (EtOAc/heptane: 50/50 (v/v)): 0.48. t_R (HPLC A, EtOAc/heptane: 40/60 (v/v), flow rate: 20 mL/min): 8.9 min. ^{1}H NMR (CD_2Cl_2, 298 K): δ: 7.68 (bs, 1H); 7.29 (t, J = 8.1 Hz, 1H); 7.11 (dd, J = 7.8 and 5.1 Hz, 1H); 6.82 (b, 1H); 4.02 (t, J = 6.6 Hz, 2H); 3.08 (q, J = 5.7 Hz, 2H); 1.83 (q^5, J = 6.6 Hz, 2H); 1.50 (bm, 6H); 1.41 (s, 9H). ^{13}C NMR (CD_2Cl_2, 298 K): δ: 156.0 (C); 154.4 (d, J^1_{F-C} = 235 Hz, C); 142.8 (d, J^2_{F-C} = 25 Hz, C); 137.2 (d, J^3_{F-C} = 13 Hz, CH); 122.9 (CH); 122.2 (CH); 79.0 (C); 70.1 (CH_2); 40.8 (CH_2); 30.3 (CH_2); 29.2 (CH_2); 28.5 (3×CH_3); 26.8 (CH_2); 25.9 (CH_2). MS (DCI/NH_4^+) $C_{16}H_{25}F_1N_2O_3$: 313 [M + H$^+$].

Preparation of [3-(2-Fluoro/nitro-pyridin-3-yloxy)]propylamines (5, 6). *General Procedure.* To a solution of the appropriate [3-(2- fluoro/nitro-pyridin-3-yloxy)propyl]carbamic acid *tert*-butyl ester (**3b** or **4b**, 0.5−5.0 mmol) in CH_2Cl_2 (1−10 mL) at 0−3 °C was added TFA (10−30% (v/v)). After stirring at room temperature for 1 h, the reaction mixture was concentrated to dryness to give the pure 3-(2- fluoro/nitro-pyridin-3-yloxy)propylamines (**5** and **6**, respectively) as their TFA salts (oils).

*[3-(2-Fluoropyridin-3-yloxy)]propylamine (**5**).* The procedure described above was used with [3-(2-fluoropyridin-3-yloxy)propyl]carbamic acid *tert*-butyl ester (**4b**, 0.40 g) to give 0.50 g of **5** as a pale-yellow oil (quantitative). ^{1}H NMR (CD_3OD, 298 K): δ: 7.51 (bs, $w_{1/2}$ = 5.0 Hz, 1H); 7.36 (bt, $w_{1/2}$ = 25.0 Hz, 1H); 7.04 (bd, $w_{1/2}$ = 15.0 Hz, 1H); 4.03 (bt, $w_{1/2}$ = 15.0 Hz, 2H); 2.99 (bt, $w_{1/2}$ = 15.0 Hz, 2H); 2.01 (bq, $w_{1/2}$ = 15.0 Hz, 2H). ^{13}C NMR (CD_3OD, 298 K): δ: 155.3 (d, J^1_{F-C} = 237 Hz, C); 144.3 (d, J^2_{F-C} = 24 Hz, C); 138.5 (d, J^3_{F-C} = 13 Hz, CH); 125.1 (CH); 123.8 (CH); 67.9 (CH_2); 38.6 (CH_2); 28.4 (CH_2). MS (DCI/NH_4^+) $C_8H_{11}F_1N_2O_1$: 171 [M + H$^+$].

*[3-(2-Nitropyridin-3-yloxy)]propylamine (**6**).* The procedure described above was used with [3-(2-nitropyridin-3-yloxy)propyl]carbamic acid *tert*-butyl ester (**3b**, 1.50 g) to give 2.00 g of **6** as a yellow oil (quantitative). ^{1}H NMR (CD_3OD, 298.0K): δ: 8.04 (d, J = 3.0 Hz, 1H); 7.82 (d, J = 9.0 Hz, 1H); 7.65 (dd, 9.0 and 3.0 Hz, 1H); 4.30 (t, J = 6.0 Hz, 1H); 3.12 (t, J = 6.0 Hz, 2H); 2.15 (q^5, J = 6.0 Hz, 2H). ^{13}C NMR (CD_3OD, 298.0K): δ: 149.8 (C); 148.5 (C); 140.8 (CH); 130.9 (CH); 126.6 (CH); 68.6 (CH_2); 38.7 (CH_2); 28.1 (CH_2). MS (DCI/NH_4^+) $C_8H_{11}N_3O_3$: 198 [M + H$^+$].

Preparation of 1-[3-(2-Fluoro/nitropyridin-3-yloxy)propyl]pyrrole-2,5-diones (1, 7). *General Procedure.* To a solution of the appropriate 3-(2-fluoro/nitropyridin-3-yloxy)propylamine (**5** or **6**, 3−5 mmol) in THF (100−170 mL) was added 5.0 equiv of *N*-methoxycarbonylmaleimide. The mixture was stirred at reflux overnight. A precipitate was formed and filtered. The obtained filtrate was concentrated to dryness, and the residue was purified by column chromatography on silica gel. Elution with heptane/EtOAc (50/50 (v/v)) gave pure 1-[3-(2-halogeno-pyridin-3-yloxy)propyl]pyrrole-2,5-dione (**1**,**7**) as a white powder.

*1-[3-(2-Fluoropyridin-3-yloxy)propyl]pyrrole-2,5-dione (**1**, FPyME).* The procedure described above was used with 3-(2-fluoropyridin-3-yloxy)propylamine (**5**, 0.50 g) to give 0.55 g of **1** (FPyME) as a white powder (75%). R_f (EtOAc/heptane: 50/50 (v/v)): 0.40. t_R (HPLC D): 10.2 min. ^{1}H NMR (CD_2Cl_2, 298.0K): δ: 7.69 (bd, J = 3.0 Hz, 1H); 7.27 (t, J = 9.0 Hz, 1H); 7.11 (dd, J = 9.0 and 3.0 Hz, 1H); 6.69 (s, 2H); 4.04 (t, J = 6.0 Hz, 2H); 3.72 (t, J = 6.0 Hz, 2H); 2.11 (q^5, J = 6.0 Hz, 2H). ^{13}C NMR (CD_2Cl_2, 298.0K): δ: 171.2 (2×C); 154.1 (d, J^1_{F-C} = 235 Hz, C); 142.4 (d, J^2_{F-C} = 25 Hz, C); 137.7 (d, J^3_{F-C} = 13 Hz, CH); 134.5 (2×CH); 123.2 (CH); 122.2 (CH); 67.5 (CH_2); 35.4 (CH_2); 28.4 (CH_2). MS (DCI/NH_4^+) $C_{12}H_{11}F_1N_2O_3$: 251 [M + H$^+$].

*1-[3-(2-Nitropyridin-3-yloxy)propyl]pyrrole-2,5-dione (**7**).* The procedure described above was used with 3-(2-nitropyridin-3-yloxy)propylamine (**6**, 1.00 g) to give 0.40

g of **7** as a white powder (28%). R_f (CH_2Cl_2/AcOEt: 60/40 (v/v)): 0.40. ^1H NMR (CD_2Cl_2, 298.0K): δ: 8.05 (bd, $w_{1/2}$ = 9.0 Hz, 1H); 7.51 (bd, J = 3.0 Hz, 2H); 6.67 (s, 2H); 4.13 (t, J = 6.0 Hz, 2H); 3.69 (q, J = 6.0 Hz, 2H); 2.11 (q^5, J = 6.0 Hz, 2H). ^{13}C NMR (CD_2Cl_2, 298.0K): δ: 171.1 (2xC); 149.5 (C); 147.5 (C); 139.6 (CH); 134.5 (2×CH); 129.0 (CH); 124.0 (CH); 68.0 (CH_2); 35.1 (CH_2); 28.4 (CH_2). MS (DCI/NH_4^+) $C_{12}H_{11}N_3O_5$: 278 [M + H^+].

*[3-(2-Dimethylaminopyridin-3-yloxy)propyl]carbamic Acid tert-Butyl Ester (**8**).* To a solution of 3-(*N*-Boc-amino)-propan-1-ol (**2b,** 0.31 g, 1.8 mmol) in THF (20 mL) were added 0.47 g of triphenylphosphine (MW: 262.29, 1.8 mmol, 1.0 equiv), 0.25 g of 2-(dimethylamino)-3-hydroxypyridine (MW: 138.00, 1.81 mmol, 1.0 equiv) and dropwise 0.35 mL of diisopropylazodicarboxylate (DIAD; MW: 202.21, d: 1.027, 1.8 mmol, 1.0 equiv). After stirring at room temperature for 24 h, the reaction mixture was concentrated to dryness and the residue was purified by column chromatography on silica gel. Elution with heptane/EtOAc (70/30 (v/v)) gave 0.23 g of **8** as a yellow oil (43%). For analytical purposes only, an aliquot was further purified by HPLC. R_f (EtOAc/heptane: 50/50 (v/v)): 0.35. t_R (HPLC A, EtOAc/heptane: 40/60 (v/v), flow rate: 35 mL/min): 8.6 min. ^1H NMR (CD_2Cl_2, 298 K): δ: 7.77 (dd, J = 4.8 Hz, 1H); 7.00 (dd, J = 7.8 Hz, J < 1.5 Hz, 1H); 6.72 (dd, J = 7.8 and 4.8 Hz, 1H); 4.02 (t, J = 6.0 Hz, 2H); 3.30 (q, J = 6.0 Hz, 2H); 2.93 (s, 6H); 2.00 (q^5, J = 6.0 Hz, 2H); 1.42 (s, 9H). ^{13}C NMR (CD_2Cl_2, 298 K): δ: 156.6 (C); 153.7 (C); 146.2 (C); 139.0 (CH); 118.8 (CH); 115.9 (CH); 79.1 (C); 67.4 (CH_2); 41.1 (2×CH_3); 38.8 (CH_2); 32.3 (CH_2); 28.5 (3×CH_3). MS (DCI/NH_4^+) $C_{15}H_{25}N_3O_3$: 296 [M + H^+].

*[3-(3-tert-Butoxycarbonylaminopropoxy)pyridin-2-yl]trimethylammonium Trifluoromethanesulfonate (**9**).* To a solution of [3-(2-dimethylaminopyridin-3-yloxy)propyl]-carbamic acid *tert*-butyl ester (8, 0.4 g, 1.35 mmol) in toluene was added 0.2 mL of methanetrifluoromethylsulfonate (MW: 164.10, d: 1.45, 1.77 mmol, 1.3 equiv) at 0 °C. After 3 min, a precipitate was obtained and the reaction mixture was stirred at room temperature for 1 h. The precipitate was filtered and washed with Et_2O to give 0.58 g of **9** as a white powder (93%). ^1H NMR (CD_2Cl_2, 298 K): δ: 8.10 (bd, J = 3.3 Hz, 1H); 7.66 (d, J = 8.1 Hz, 1H); 7.60 (dd, J = 6.1 and 4.2 Hz, 1H); 4.31 (t, J = 6.3 Hz, 2H); 3.71 (s, 9H); 3.31 (q, J = 6.3 Hz, 2H); 2.12 (q^5, J = 6.3 Hz, 2H); 1.38 (s, 9H).^{13}C NMR (CD_2Cl_2, 298 K): δ: 156.6 (C); 147.7 (C); 142.6 (C); 139.0 (CH); 129.0 (CH); 124.6 (CH); 121.2 (q, J = 319 Hz, CF_3); 79.3 (C); 68.1 (CH_2); 37.5 (CH_2); 30.0 (CH_2); 28.4 (3×CH_3).

3. Peptide/Protein Chemistry: Conjugation with 1-[3-(2-Fluoropyridin-3-yloxy)propyl]pyrrole-2,5-dione (1, FPyME). Conjugation of (*N*-Ac)KAAAAC (P1) with 1-[3-(2-Fluoropyridin-3-yloxy)propyl]pyrrole-2,5-dione (1, FPyME) at the Micromolar Scale. To 5.2 mg of (*N*-Ac)KAAAAC (**P1**, 9.0 μmol, MW: 575.69 g/mol), dissolved in a mixture of ethanol (450 μL), 50 mM aq phosphate buffer saline (PBS, at pH 6.5, 200 μL) and acetonitrile (450 μL), was added 4.5 mg of 1-[3-(2-fluoropyridin-3-yloxy)propyl]pyrrole-2,5-dione (**1**, FPyME, 18.0 μmol, 2 equiv). The reaction mixture was stirred at room temperature for 3 h and then purified by HPLC [HPLC B, t_R: 28.0 min]. The fractions containing the conjugated peptide, c-(*N*-Ac)KAAAAC (**c-P1**), were combined and then lyophilized, giving 2.0 mg of the conjugated peptide, c-(*N*-Ac)KAAAAC (**c-P1**). ^1H NMR (CD_3OD/D_2O, 50/50 (v/v)): δ: 7.65 (d, J: 4.8 Hz, 1H, Py); 7.53 (t, J: 9.6 Hz, 1H, Py); 7.27 (dd, J: 7.6 and 4.8 Hz, 1H, Py); 4.60 (m, 1H, α-CH-Lys); 4.31 (m, 1H, α-CH-Cys); 4.30−4.18 (4H, 4 × α-CH-Ala); 4.11 (m, 2H, CH_2O); 4.00 (ddd, J: 20.0 and 9.6 and 4.4 Hz, 1H, β-CH^1-Cys); 3.72 (m, 2H, CH_2N); 3.32 (m, 1H, β-CH^2-Cys); 3.25−3.10 (m, 2H, CH_2CO); 2.96 (m, 2H, ϵ-CH_2-Lys); 2.58 (m, 1H, CHCO); 2.09 (m, 2H, CH_2); 2.00 (s, 3H, *N*-Ac); 1.79 (m, 1H, β-CH^1-Lys); 1.74−1.60 (m, 3H, β-CH^2-Lys/δ-CH_2-Lys); 1.42 (m, 2H, γ-CH_2-Lys); 1.40−1.32 (m, 12H, 4 × β-CH_3-Ala). MS found: 826.3 (calcd: 825.91).

Conjugation of (*N*-Ac)KAAAAC (P1) with 1-[3-(2-Fluoropyridin-3-yloxy)propyl]pyrrole-2,5-dione (1, FPyME) at the Submicromolar Scale. *(A) Preparation of (N-Ac)KAAAAC (**P1**) for Conjugation.* To 0.126 μmol (72.5 μg) of (*N*-Ac)KAAAAC (**P1**, MW: 575.69 g/mol, 36 μL of a 2.0 mg/mL or 3.5 μmol/mL solution) in aq Tris NaCl (50 mM Tris-HCl; 150 mM NaCl) at pH 7.4 was added 0.193 μmol of TCEP (1.5 equiv, 7 μL of a 7.9 mg/mL or 27.6 μmol/mL solution) in solution in the same buffer. The resulting solution was left standing at room temperature for 5 min.

*(B) Conjugation of (N-Ac)KAAAAC (**P1**) with 1-[3-(2-Fluoropyridin-3-yloxy)propyl]pyrrole-2,5-dione (**1**, FPyME).* To 10 μL of DMSO containing 3−5 equiv of 1-[3-(2-fluoropyridin-3-yloxy)propyl]pyrrole-2,5-dione (**1**, FPyME, 190−315 μg) was added TCEP-treated (*N*-Ac)KAAAAC (**P1**, about 145 μg, without removal of the excess of TCEP) diluted in aq Tris NaCl, pH 7.4 (1 mL). The resulting solution was left standing at room temperature for 15 min, then the sample was purified by HPLC [HPLC B, t_R: 28.0 min].

Conjugation of AFIM-0 (P2) with 1-[3-(2-Fluoropyridin-3-yloxy)propyl]pyrrole-2,5-dione (1, FPyME) at the Submicromolar Scale. *(A) Preparation of AFIM-0 (**P2**) for Conjugation.* To a solution of AFIM-0 (**P2**, 1.0 mg; MW: 8576.78 g/mol) in 1 mL of aq Tris NaCl (50 mM Tris-HCl; 150 mM NaCl) at pH 7.4 was added TCEP (0.3 mg, 10 equiv) in solution in the same buffer (500 μL). The resulting solution was left standing at room temperature for 15 min. The excess of TCEP was removed from the solution by gel filtration using a NAP-10 G25 Sephadex cartridge (Amersham Pharmacia Biotech). The TCEP-treated (reduction of S−S bond, regeneration of free SH function) AFIM-0 (**P2**) was eluted from the cartridge in 1.5 mL of aq Tris NaCl buffer (according to manufacturer's instructions) and used within 15 min after purification.

*(B) Conjugation of AFIM-0 (**P2**) with 1-[3-(2-Fluoropyridin-3-yloxy)propyl]pyrrole-2,5-dione (**1**, FPyME).* To 100 μL of DMSO or acetonitrile containing 3−5 equiv of 1-[3-(2-fluoropyridin-3-yloxy)propyl]pyrrole-2,5-dione (**1**, FPyME, 42−71 μg) was added 750 μL of TCEP-treated AFIM-0 (**P2**, about 0.5 mg) in aq Tris NaCl, pH 7.4. The resulting solution was left standing at room temperature for 30 min, then the sample was purified by gel filtration using a NAP-10 G25 Sephadex cartridge (Amersham Pharmacia Biotech). The conjugated peptide, c-AFIM-0 (**c-P2**), was easily separated from nonreacted 1-[3-(2-fluoropyridin-3-yloxy)propyl]pyrrole-2,5-dione (**1**, FPyME) and was eluted from the cartridge in 1.5 mL of aq PBS (20 mM KH_2PO_4/150 mM NaCl; pH 7.4) according to manufacturer's instructions. For analytical purposes only, the conjugated peptide, c-AFIM-0 (**c-P2**), was further purified by chromatography on gel filtration [HPLC C, t_R: 14.5 min]. MS (ESI+): 8827.0 (theor.), 8830.5 (exp.).

*(C) Conjugation of STxB (**P3**) with 1-[3-(2-Fluoropyridin-3-yloxy)propyl]pyrrole-2,5-dione (**1**, FPyME).* To 10 μL of DMSO containing 1 equiv of 1-[3-(2-fluoropyridin-3-yloxy)propyl]pyrrole-2,5-dione (**1**, FPyME) was added 90 μL of STxB (**P3**, about 0.2 mg) in 0.1 M aq PBS at pH 8. The resulting solution was left standing at room temperature for 30 min, then the sample was purified by

dialysis against water. The conjugated peptide, c-STxB (**c-P3**), was characterized by RP-HPLC [HPLC E: t_R: 12.5 min] and gel filtration [HPLC F: t_R: 9.5 min]. MS (ESI+): 8043.0 (theor.), 8048.0 (exp.).

4. Radiochemistry. Preparation of the K[^{18}F]F-K_{222} Complex. To recover and recycle the [^{18}O]water target, 2 mL of aqueous [^{18}F]fluoride from the target holder was passed through an anion-exchange resin (Sep-Pak Light Waters Accell Plus QMA Cartridge in the chloride form, washed with 5 mL of 1M aq $NaHCO_3$, and then rinsed with 50 mL of water) by helium pressure (1.5−2.0 bar). Helium is blown through the column to maximally extract the [^{18}O]water. The [^{18}F]fluoride ion is then eluted from the resin using 1.0 mL of a 4.5 mg/mL aqueous K_2CO_3 solution into a Vacutainer tube containing 12.0 to 15.0 mg of Kryptofix222 (K_{222}: 4,7,13,16,21,24-hexaoxa-1,10-diazabicyclo[8.8.8]hexacosane). The resulting solution was then gently concentrated to dryness at 145−150 °C under a nitrogen stream for 10 min to give no-carrier-added K[^{18}F]F-K_{222} complex as a white semisolid residue.

If desired, the [^{18}F]fluoride ion production batch on the cartridge can also be divided into 2 to 12 aliquots in order to perform parallel syntheses. To do this, the [^{18}F]fluoride ion is eluted from the resin using 1.0 mL of a 4.5 mg/mL aqueous K_2CO_3 solution into an empty Vacutainer tube. To distribute equally this activity over n tubes (Vacutainer tube, $n = 2-12$), the quantity of K_2CO_3 was first adjusted to n times 4.5 mg with a 50.0 mg/mL aqueous K_2CO_3 solution and second, the total volume of the solution was adjusted to 2.0 mL with water. This new aqueous [^{18}F]fluoride solution was then equally distributed over the n tubes each containing 12.0 to 15.0 mg of Kryptofix222. Finally, the volume of each fraction was adjusted to 1.0 mL with water. The resulting solutions were then independently gently concentrated to dryness at 145−150 °C under a nitrogen stream for 10 min to give no-carrier-added K[^{18}F]F-K_{222} complex as a white semisolid residue.

[(2-[^{18}F]Fluoropyridin-3-yloxy)alkyl]carbamic Acid *tert*-Butyl Esters ([^{18}F]4a−e): Incorporation Studies with K[^{18}F]F-K_{222} Complex. *(A) General Procedure Using Conventional Heating.* A 600 μL amount of DMSO containing 10 to 17 μmol of the appropriate [(2-nitropyridin-3-yloxy)alkyl]carbamic acid *tert*-butyl ester **(3a−e)** as precursor for labeling was directly added into the Vacutainer tube containing the dried K[^{18}F]F-K_{222} complex. The tube (not sealed) was thoroughly vortexed (15 s) and then placed in a heating block (at 145 °C for 1 to 30 min) without stirring the contents. The reaction vessel was then cooled using an ice−water bath, and the remaining radioactivity was measured. A 90% to 95% level of the initial radioactivity placed in the vessel was still present. The resulting often dark-colored reaction mixture was then analyzed by radiochromatography. The reaction yield was calculated from the TLC-radiochromatogram and defined as the radioactivity area of the [(2-[^{18}F]fluoropyridin-3-yloxy)alkyl]carbamic acid *tert*-butyl ester ([^{18}F]**4a−e**) over total fluorine-18 radioactivity area ratio. (SiO_2-TLC: (A) eluent: EtOAc/heptane: 50/50 (v/v), R_f: [^{18}F]**4a−e**: 0.40−0.60 and R_f: [^{18}F]fluoride ion: 0.0; (B) eluent: EtOAc, R_f: [^{18}F]**4a−e**: 0.75−0.80 and R_f: [^{18}F]fluoride ion: 0.0).

(B) General Procedure Using Microwave Activation. A 600 μL amount of DMSO containing 10 to 17 μmol of the appropriate [(2-nitropyridin-3-yloxy)alkyl]carbamic acid *tert*-butyl ester **(3a−e)** as precursor for labeling was directly added into the Vacutainer tube containing the dried K[^{18}F]F-K_{222} complex. The tube (not sealed) was thoroughly vortexed (15 s) and then placed in a dedicated microwave oven (at 100 W, for 0.5 to 3 min) without stirring the contents. The remainder of the synthesis used the same procedure as described above.

Preparation of 1-[3-(2-[^{18}F]Fluoropyridin-3-yloxy)propyl]pyrrole-2,5-dione ([^{18}F]-1, [^{18}F]FPyME). *(A) Procedure Using 3-(2-Nitropyridin-3-yloxy)propyl]carbamic Acid tert-Butyl Ester (**3b**) as Precursor for Labeling.* A 600 μL amount of freshly distilled DMSO containing 5.0 mg of 3-(2-nitropyridin-3-yloxy)propyl]carbamic acid *tert*-butyl ester (**3b**) as the precursor for labeling was directly added into the Vacutainer tube containing the dried K[^{18}F]F-K_{222} complex. The tube (not sealed) was then thoroughly vortexed (15 s) and then placed in a heating block at 145 °C for 4 min without stirring the contents. The reaction mixture was diluted with 1 mL of water and transferred on a C18 Sep-pak cartridge (PrepSep R-C18, Fisher Scientific, activated beforehand with 2 mL of EtOH and then rinsed with 10 mL of water). The tube was rinsed twice with 1 mL of water which was also transferred and added to the diluted reaction mixture on the cartridge. After addition of another 2 mL of water, the whole was passed through the cartridge. The cartridge was washed with 1 mL of water and partially dried for 0.5 min by applying a nitrogen stream. The [3-(2-[^{18}F]fluoropyridin-3-yloxy)propyl]carbamic acid *tert*-butyl ester ([^{18}F]-**4b**) was eluted from the cartridge with 3 mL of CH_2Cl_2 into a 5 mL reaction vial containing 0.1 mL of TFA. Twice 1 mL of CH_2Cl_2 was used to wash the cartridge and to completely transfer [3-(2-[^{18}F]fluoropyridin-3-yloxy)propyl]carbamic acid *tert*-butyl ester ([^{18}F]-**4b**) (5% of the total radioactivity amount engaged in the fluorination process was left on the cartridge). The incorporation yield was also estimated after the C18 Sep-pak cartridge elution by the CH_2Cl_2 over total eluted radioactivity (DMSO/H_2O + CH_2Cl_2) ratio. The resulting CH_2Cl_2/TFA solution (50/1, v/v) was concentrated to dryness (at 65−75 °C under a gentle nitrogen stream for 4−6 min). The yield of deprotection was quantitative and no Boc-protected [^{18}F]-**4b** could be detected by radiochromatography (SiO_2-TLC, eluent: EtOAc, R_f: [^{18}F]-**4b**: 0.75 and R_f: [^{18}F]-**5**: 0.0). The above residue, containing 3-(2-[^{18}F]fluoropyridin-3-yloxy)propylamine ([^{18}F]-**5**) was redissolved in 2 mL of CH_2Cl_2 and concentrated again to dryness to minimize TFA presence (at 65−75 °C under a gentle nitrogen stream for another 2−3 min). The residue, containing [^{18}F]-**5**, was then redissolved in 0.25 mL of dioxane containing 25 mg of *N*-methoxycarbonylmaleimide. Aqueous sat. $NaHCO_3$ (0.75 mL) was then added to the solution, and the vessel was gently vortexed for 10 min at room temperature. The reaction mixture was diluted with 1 mL of aq 1M HCl and transferred onto a C18 Sep-pak cartridge (PrepSep R-C18, Fisher Scientific, activated beforehand with 2 mL of EtOH, rinsed with 10 mL of water, and loaded with 5 mL of water). The tube was rinsed twice with 1 mL of water which was also transferred and added to the diluted reaction mixture on the cartridge. The whole was passed through the cartridge. The cartridge was washed with 3 mL of water and partially dried for 0.5 min by applying a nitrogen stream. The 1-[3-(2-[^{18}F]fluoropyridin-3-yloxy)-propyl]pyrrole-2,5-dione ([^{18}F]-**1**, [^{18}F]FPyME) was eluted from the cartridge with 3 mL of CH_2Cl_2. Twice 1 mL of CH_2Cl_2 was used to wash the cartridge and to completely transfer [^{18}F]FPyME ([^{18}F]-**1**) (10−25% of the radioactivity amount was left on the cartridge). The resulting CH_2Cl_2 solution was partially (not to dryness) concentrated (at 65−75 °C under a gentle nitrogen stream for 2−4 min). The residue was diluted up to a volume of 1.0−1.5

mL with CH_2Cl_2 and HPLC-purified [HPLC D, t_R: 10.0−10.5 min] to give pure labeled [18F]FPyME ([18F]-**1**).

*(B) Procedure Using [3-(3-tert-Butoxycarbonylaminopropoxy)pyridin-2-yl]trimethylammonium Trifluoromethanesulfonate (**9**) as Precursor for Labeling.* A 600 μL amount of freshly distilled DMSO containing 4.0 mg of [3-(3-*tert*-butoxycarbonylaminopropoxy)pyridin-2-yl]trimethylammonium trifluoromethanesulfonate (**9**) as the precursor for labeling were directly added into the Vacutainer tube containing the dried K[18F]F-K_{222} complex. The tube (not sealed) was then thoroughly vortexed (15 s) and then placed in a heating block at 145 °C for 2 min without stirring the contents. The remainder of the preparation used the same procedure as described above.

Conjugation of (*N*-Ac)KAAAAC (P1) with 1-[3-(2-[18F]Fluoropyridin-3-yloxy)propyl]pyrrole-2,5-dione ([18F]-1, [18F]FPyME). Preparation of [18F]c-(*N*-Ac)KAAAAC ([18F]c-P1). To 50 μL of DMSO containing HPLC-purified [18F]FPyME ([18F]-**1**, freed from HPLC-solvents by concentration to dryness at 65−75 °C under a gentle nitrogen stream), was added TCEP-treated (*N*-Ac)KAAAAC (**P1**, about 72.5 μg, without removal of the excess of TCEP, see above) dissolved in aq Tris NaCl, pH 7.4 (1 mL). The resulting solution was left standing at room temperature for 10 min and then purified by HPLC [HPLC B, t_R: 28.0 min].

Conjugation of AFIM-0 (P2) with 1-[3-(2-[18F]Fluoropyridin-3-yloxy)propyl]pyrrole-2,5-dione ([18F]-1, [18F]FPyME). *(A) Preparation of [18F]c-AFIM-0 ([18F]**c-P2**).* To 100 μL of DMSO containing HPLC-purified [18F]FPyME ([18F]-**1**, freed from HPLC-solvents by concentration to dryness at 65−75 °C under a gentle nitrogen stream), was added 750 μL of TCEP-treated AFIM-0 (**P2**, about 0.5 mg, see above) in aq Tris NaCl, pH 7.4. The reaction mixture was gently vortexed for 5 min and then purified by gel filtration on a NAP-10 G25 Sephadex cartridge (Amersham Pharmacia Biotech). The conjugated and labeled peptide, [18F]c-AFIM-0 ([18F]**c-P2**), was easily separated from nonreacted [18F]FPyME ([18F]-**1**), if any, and was eluted from the cartridge in 1.5 mL of aq 0.9% NaCl according to manufacturer's instructions.

*(B) Formulation and Quality Control of Conjugated and Labeled [18F]c-AFIM-0 ([18F]**c-P2**).* The cartridge-fraction containing the conjugated and labeled peptide, [18F]c-AFIM-0 ([18F]**c-P2**), was diluted with physiological saline and finally sterile-filtrated on a 0.22 μm GS-Millipore filter (vented). As demonstrated by HPLC analysis [HPLC C], radiosynthesized conjugated and labeled [18F]c-AFIM-0 ([18F]**c-P2**) coeluted with an authentic sample of reference compound (fluorine-19-synthesized c-AFIM-0 (**c-P2**)). The radiolabeled product was found to be >90% radiochemically pure. The radiopharmaceutical preparation was shown to be free of nonreacted [18F]FPyME ([18F]-**1**) and radiochemically stable for at least 240 min.

Conjugation of STxB (P3) with 1-[3-(2-[18F]Fluoropyridin-3-yloxy)propyl]pyrrole-2,5-dione ([18F]-1, [18F]-FPyME). *(A) Preparation of [18F]c-STxB ([18F]**c-P3**).* To 100 μL of DMSO containing HPLC-purified [18F]FPyME ([18F]-**1**, freed from HPLC-solvents by concentration to dryness at 65−75°C under a gentle nitrogen stream), was added 330 μL of STxB (**P3**, about 1 mg) in aq 1.0 M PBS at pH 8. After addition of another 570 μL of 1.0 M aq PBS at pH 8, the reaction mixture was gently vortexed for 5 min and then purified by gel filtration on a NAP-10 G25 Sephadex cartridge (Amersham Pharmacia Biotech). The conjugated and labeled peptide, [18F]c-STxB ([18F]**c-P3**), was easily separated from nonreacted [18F]-FPyME ([18F]-**1**), if any, and was eluted from the cartridge in 1.5 mL of aq 0.9% NaCl according to manufacturer's instructions.

*(B) Formulation and Quality Control of Conjugated and Labeled [18F]c-STxB ([18F]**c-P3**).* The cartridge-fraction containing the conjugated and labeled peptide, [18F]c-STxB ([18F]**c-P3**), was diluted with physiological saline and finally sterile-filtrated on a 0.22 μm GS-Millipore filter (vented). As demonstrated by HPLC analysis [HPLC E and F], radiosynthesized conjugated and labeled [18F]c-STxB ([18F]**c-P3**) coeluted with an authentic sample of reference compound (fluorine-19-synthesized c-STxB (**c-P3**)). The radiolabeled product was found to be >95% radiochemically pure. The radiopharmaceutical preparation was shown to be free of nonreacted 1-[3-(2-[18F]fluoropyridin-3-yloxy)propyl]pyrrole-2,5-dione ([18F]-**1**, [18F]FPyME) and radiochemically stable for at least 400 min.

RESULTS AND DISCUSSION

Chemistry. The synthesis of FPyME (**1**) as well as that of the nitro derivatives **3b** and **7** and the trimethylammonium derivative **9** as the various selected precursors for fluorine-18 labeling is outlined in Schemes 1−4.

The [(2-nitropyridin-3-yloxy)alkyl]carbamic acid *tert*-butyl esters (**3a**−**e**) and [(2-fluoropyridin-3-yloxy)alkyl]-carbamic acid *tert*-butyl esters (**4a**−**e**) were all synthesized using the following general method. The nitro derivatives (**3a**−**e**) were prepared in 29−41% yield via a Mitsunobu coupling reaction (*51*) from the corresponding commercially available (hydroxyalkyl)carbamic acid *tert*-butyl esters (**2a**−**e**) and 2-nitro-3-hydroxypyridine (*37*, *40*), in THF at room temperature, using triphenylphosphine (0.8 equiv) and diisopropylazodicarboxylate (1.4 equiv) (Scheme 1).

Scheme 1. Preparation of [(2-Nitropyridin-3-yloxy)-alkyl]carbamic Acid *tert*-Butyl Ester (3a−e)

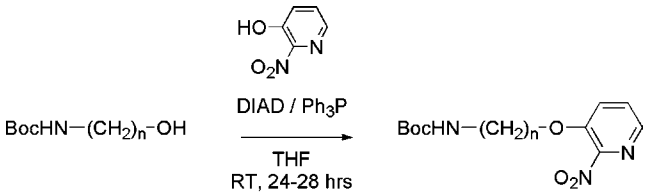

	n
2a	2
b	3
c	4
d	5
e	6

	n	yield
3a	2	38%
b	3	40%
c	4	40%
d	5	29%
e	6	41%

Analogously, the fluoro derivatives (**4a**−**e**) were prepared in 27−49% yield from the same corresponding (hydroxyalkyl)carbamic acid *tert*-butyl esters (**2a**−**e**) and 2-fluoro-3-hydroxypyridine (*37*, *40*) (Scheme 2).

The identification of the propyl chain as the most appropriate alkyl spacer and therefore the selection of the fluorinated derivative **1** (FPyME) (Scheme 3) as well as the selection of the nitro derivatives **3b** and **7** and the trimethylammonium derivative **9** (Schemes 3 and 4) as possible precursors for fluorine-18 labeling will be discussed in the radiochemistry part below. The choice of these functions (nitro and trimethylammonium) as leaving groups in the radiofluorination process will also be discussed in that section.

Removal of the *tert*-butoxycarbonyl function of the propyl derivatives **4b** and **3b** was performed with trifluoroacetic acid (TFA) in dichloromethane at room temperature and gave the desired free amines **5** and **6** in 90−95% yield (Scheme 3). Treatment of **5** and **6** with

Scheme 3. Preparation of 1-[3-(2-[^{18}F]Fluoropyridin-3-yloxy)propyl]pyrrole-2,5-dione (1, FPyME) and the Corresponding Nitro Derivative 7 as Precursor for Labeling

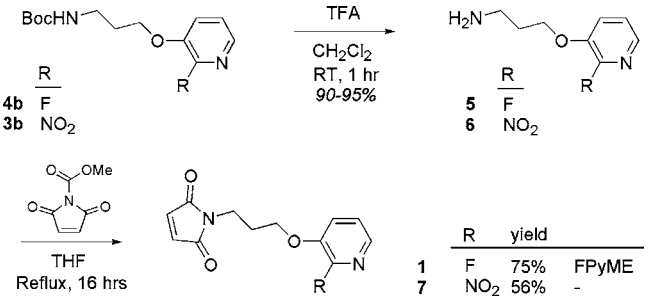

Scheme 2. Preparation of [(2-Fluoropyridin-3-yloxy)-alkyl]carbamic Acid *tert*-Butyl Ester (4a−e)

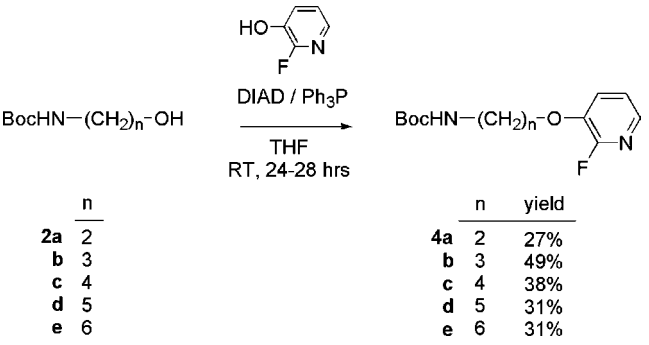

N-methoxycarbonylmaleimide in refluxing tetrahydrofuran gave the desired maleimides **1** (FPyME) and **7** in 75% and 56% yield, respectively (nonoptimized).

The dimethylamino derivative **8** was prepared in 58% yield, from the corresponding 2-(dimethylamino)-3-hydroxypyridine (*40*) under Mitsunobu conditions similar to those described above for the synthesis of **3a**−**e** and **4a**−**e** (Scheme 4). The trimethylammonium derivative **9** was cleanly obtained in 93% yield by methylation of the dimethylamine **8** using methyl trifluoromethanesulfonate (1.3 equiv) in toluene at 0 °C (Scheme 4).

Scheme 4. Preparation of [3-(3-*tert*-Butoxycarbonyl-aminopropoxy)pyridin-2-yl]trimethylammonium Trifluoromethanesulfonate (9)

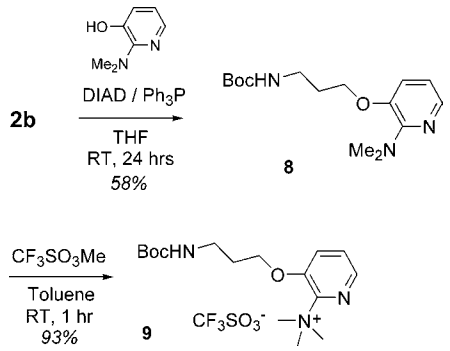

The synthetic procedure of conjugation of peptides and proteins described below is based on the efficient and highly selective coupling reaction of free thiol functions (cysteine β-SH) and *N*-substituted maleimides reagents (*30*−*32*). The reaction involves addition of the thiol across the double bond of the maleimide to yield a thioether (see Figure 3). In contrast to haloacetamides, the most frequently class of thiol-reactive reagents used, maleimides do not react with functions of other amino acid residues such as methionine, histidine, or tyrosine (*30*−*32*). These reagents react rapidly (2 to 3 orders of magnitude higher in terms of rate constants (*52*) at near-neutral pH and usually can be coupled selectively in the presence of free amine function (*N*-terminus α-NH_2 or internal lysine ϵ-NH_2), which are relatively unreactive below pH 8.

Table 1. Analytical Data Obtained for Peptide/Protein Conjugation with 1-[3-(2-Fluoropyridin-3-yloxy)propyl]-pyrrole-2,5-dione (1, FPyME)

			MS	
peptide/protein	chemistry	HPLC[a,b]	calcd[a,g]	found[a,g]
P1/c-P1	(*N*-Ac) KAAAAC (-SH)	28.0 min[c]	825.9	826.3
P2/c-P2	AFIM-0 (-SH)	14.5 min[d]	8827.0	8830.5
P3/c-P3	STxB (-SH)	12.5 min[e,f]	8043.0	8048.0

[a] Analytical data is given for the conjugated peptide/protein (**c-P1**, **c-P2**, and **c-P3**) only. [b] Analytical HPLC retention times. [c] HPLC B. [d] HPLC C. [e] HPLC E. [f] t_R: 9.5 min on HPLC F. [g] Mass spectrometry data (Perseptive Biosystem DE-RP MALDI-TOF Voyager spectrometer, ES+ mode).

Table 1 summarizes the principal characteristics of the peptide and proteins (**P1**, **P2**, and **P3**) used as starting material in the present study and the corresponding conjugated peptide and proteins (**c-P1**, **c-P2**, and **c-P3**) that we have synthesized. Analytical data obtained for these conjugated macromolecules are also indicated.

The (*N*-Ac)KAAAAC peptide (**P1**) was chosen as model peptide in order to confirm the chemoselectivity of the conjugation reaction of our maleimide reagent (**1**, FPyME). Conjugation of the (*N*-Ac)KAAAAC peptide (**P1**) at a micromolar scale was carried out using 3−5 equiv of FPyME (**1**) in a 1/9 (v/v) mixture of DMSO and 0.05 M aq Tris NaCl buffer (pH 7.4) at room temperature for 15−30 min (Scheme 5). The conjugation yields, based on starting peptide, were determined by HPLC (C18 Delta-Pak column, Waters) and were greater than 90%. Using preparative RP-HPLC (same column), the nonlabeled conjugated peptide (**c-P1**, t_R: 28.0 min) was easily separated from the nonreacted material such as the starting peptide (t_R: 13.0 min) and the maleimide reagent **1** (FPyME, t_R: 33.0 min). Mass spectrometry confirmed the identity of the conjugated peptide c-(*N*-Ac)KAAAAC (**c-P1**), giving the expected calculated mass (See Table 1). Higher molecular weight species could not be detected, clearly confirming the mono-conjugation with the maleimide reagent. ^{1}H NMR confirmed the chemoselectivity of the conjugation. Only the thiol (SH) function from the cysteine residue was conjugated with the maleimide reagent (**1**, FPyME), the amine (-ϵ-NH_2) function from the lysine residue being unaffected: in ^{1}H NMR experiments, the chemical shift of both β-CH_2 protons borne by the cysteine residue had moved from 3.00 and 3.35 ppm (CH_2SH) to 3.32 and 4.00 ppm (CH_2SR) respectively, after alkylation, whereas the chemical shift of both ϵ-CH_2 protons borne by the lysine residue were unchanged (2.96 ppm). The chemical shift of the α-CH proton borne by the cysteine residue was also slightly moved from 4.39 to 4.31 ppm.

Conjugation of the (*N*-Ac)KAAAAC peptide (**P1**) at a submicromolar scale however required preactivation of the thiol function (S−S bond reduction using tris(2-carboxyethyl)phosphine hydrochloride (TCEP) for 5 min at room temperature in 0.05 M aq Tris NaCl buffer at pH 7.4) prior to the formal coupling step with the maleimide reagent (**1**, FPyME). To this TCEP-treated peptide (**P1**) was then simply added FPyME (**1**, 3−5 equiv) in DMSO, and the mixture was left standing at room temperature for 15−30 min. Using these experimental conditions, RP-HPLC showed again almost com-

Scheme 5. Peptide/Protein Conjugation with 1-[3-(2-[19/18F]Fluoropyridin-3-yloxy)propyl]pyrrole-2,5-dione ([19/18F]-1, [19/18F]FPyME)

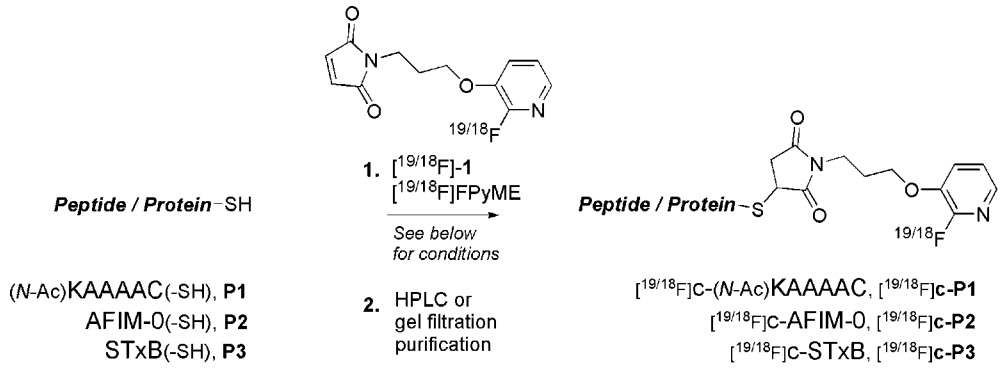

Conditions :
^{19}F : [^{19}F]-**1** (3-5 eq), aq. 50 mM Tris NaCl (pH 7.4) or aq. 0.1M PBS (pH 8.0) / DMSO : 9/1 (v/v), RT, 15-30 min
^{18}F : [^{18}F]-**1**, aq. 50 mM Tris NaCl (pH 7.4) or aq. 0.1M PBS (pH 8.0) / DMSO : 9/1 (v/v), RT, 5-10 min

plete consumption of starting peptide (t_R: 13.0 min), and the conjugation yields estimated both by HPLC and mass spectrometry analysis was greater than 90%.

The nonlabeled conjugated peptide (**c-P1**) was purified using preparative RP-HPLC and was easily separated from the nonreacted material (starting peptide at t_R: 13.0 min and excess of maleimide reagent at t_R: 33.0 min) as well as a new side-product at t_R: 26.0 min identified with mass spectrometry as TCEP-reduced FPyME (pyrrolidine-2,5-dione derivative, structure not shown). Mass spectrometry confirmed again the identity of the conjugated peptide c-(*N*-Ac)KAAAAC (**c-P1**).

The above-developed methodology was applied to the preparation of c-AFIM-0 (**c-P2**), a selected 75-amino acid (~ 8.8 kDa) miniprotein, derived from the specific binding domain of annexins for phosphatidylserine (*53*, *54*). This protein and its derivatives show high thermodynamic stability, reversible folding, and a high affinity for phosphatidylserine exposed at the external surface of biological membranes. They could be an interesting alternative to the use of fluorine-18-labeled annexin-V (*55*−*58*) and are currently developed by Bionexis Pharmaceuticals as selective fluorine-18-labeled imaging agents for the early detection of apoptosis (*53*, *54*, *59*−*62*).

Conjugation of the selected protein AFIM-0 (**P2**) was carried out using similar conditions to those described above (including a TCEP-treatment of the starting protein) with conjugation yields estimated quantitative by mass spectrometry analysis. The nonlabeled conjugated protein (**c-P2**) was separated from the nonreacted maleimide reagent (**1**, FPyME) by gel filtration using a Sephadex NAP-10 cartridge. Size-exclusion liquid chromatography on a Gel Filtration SuperDex Peptide HR 10/30 column showed a unique peak (t_R: 14.5 min) and absence of starting maleimide reagent (**1**, FPyME, t_R: 25.0 min). Mass spectrometry confirmed the identity of the conjugated protein c-AFIM-0 (**c-P2**), giving the expected calculated mass (see Table 1). Higher molecular weight species could also be detected, clearly confirming the mono-conjugation with the maleimide reagent.

The above-developed methodology was finally applied to the preparation of c-STxB (**c-P3**), the nontoxic homopentameric B subunit (monomer size ~ 8.0 kDa) of the bacterial (*Shigella dysenteriae*) Shiga toxin (*63*−*66*). This toxin is composed of two subunits, a catalytic A-subunit that inhibits protein biosynthesis by modifying ribosomal RNA, and a nontoxic homopentameric B-subunit. STxB binds to the cellular receptor of Shiga toxin, the glycosphingolipid globotriaosyl ceramide (Gb_3), that is expressed by human cancers, including a restricted set of lymphomas, and a wide range of solid tumors such as breast and ovarian carcinomas and testicular seminomas (*63*, *66*). STxB is currently developed by the Institut Curie as a selective tumor-targeting agent.

Conjugation of the selected protein STxB (**P3**) was carried out in a 1/9 (v/v) mixture of DMSO and 0.1 M aq phosphate buffer saline (PBS) at pH 8 (without TCEP pretreatment of the protein). Conjugation yields were estimated quantitative by mass spectrometry analysis. The nonlabeled conjugated protein (**c-P3**) was separated from the nonreacted maleimide reagent (**1**, FPyME) by dialysis against water. RP-HPLC on a C18 μBondapak column and size-exclusion liquid chromatography on a Gel Filtration SuperDex Peptide HR 10/30 column showed a unique peak (t_R: 12.5 min and 9.5 min, respectively) and absence of starting maleimide reagent (**1**, FPyME, t_R: 9.0 min and 45.3 min, respectively). Mass spectrometry confirmed the identity of the conjugated protein c-STxB (**c-P3**), giving the expected calculated mass (See Table 1). Higher molecular weight species could not be detected, clearly confirming the mono-conjugation with the maleimide reagent.

Radiochemistry. In a first set of experiments, the [(2-nitropyridin-3-yloxy)alkyl]carbamic acid *tert*-butyl esters (**3a**−**e**) were all evaluated for their effectiveness as precursors for fluorine-18-labeling using nucleophilic *hetero*aromatic fluorinations (Scheme 6) in order to

Scheme 6. Preparation of 2-[18F]Fluoropyridin-3-yloxy)alkyl]carbamic Acid *tert*-Butyl Ester ([18F]-4a−e)

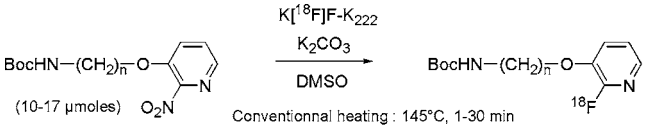

	n
3a	2
b	3
c	4
d	5
e	6

	n	yield*
[18F]-4a	2	07-13%
b	3	53-72%
c	4	41-57%
d	5	38-53%
e	6	17-35%

* Results at 5 min, 145°C, 17 µmoles of precursor (n=5)

determine the influence of the alkyl chain length on the incorporation of fluorine into the pyridine ring. These nucleophilic *hetero*aromatic substitutions, like the aliphatic nucleophilic radiofluorinations, only require a good

leaving group and there is no need for an additional strong electron-withdrawing substituent for activation of the aromatic ring such as in the *homo*aromatic nucleophilic radiofluorinations. The nitro function was therefore selected for its high potential as leaving group in comparison with the corresponding halo substituents (*35*, *36*) and for its ease of preparation from commercially available starting materials (see above). Introduction of the fluorine-18 as no-carrier-added naked [^{18}F]fluoride anion was performed in dimethyl sulfoxide (DMSO) with the activated K[^{18}F]F-Kryptofix222 complex (*67*) as the radiofluorinating reactant (Kryptofix222 (K_{222}): 4,7,13,16,-21,24-hexaoxa-1,10-diazabicyclo[8.8.8]hexacosane) by either conventional heating (at 145°C for 1 to 30 min) or microwave activation (at 100 W for 0.5 to 3 min). The radiochemical yields of fluorine-18 incorporation were calculated from the TLC-radiochromatogram and defined as the [^{18}F]fluoropyridine derivatives [^{18}F]-**4a**−**e** over total fluorine-18 activity area ratio.

A DMSO solution (600 μL) containing 17 μmol (4.8−5.8 mg) of the appropriate precursor for labeling **3a**−**e** was transferred to 30−60 mCi of the dried K[^{18}F]F-K_{222} complex in a reaction vial (Vacutainer tube). The tube (not sealed) was then placed in a heating block at 145 °C for 1 to 30 min without stirring the contents or in a dedicated microwave oven at 100 W for 0.5 to 3 min.

Using conventional heating at 145 °C, all nitro derivatives (**3a**−**e**) were reactive under the conditions described above. Whatever the precursor used (**3a**−**e**), the incorporation yields increased with the reaction time up to 5 min and then almost leveled (very slowly decrease). In each run, the remaining radioactivity at the end of the experiment was measured and 85% to 95% of the initial radioactivity placed in the vessel was still present. At 5 min, excellent incorporation yields were observed for the propyl derivative **3b** (53−72% yield). Good incorporation yields were also observed for the butyl and pentyl derivatives (**3c** and **3d**), 41−57% and 38−53%, respectively, whereas moderate incorporation yields were observed for the hexyl derivative (**3e**, 17−35%). Only low incorporation yields were observed for the ethyl derivative (**3a**, 7−13%). At 15 min and 30 min for example, the incorporation yields observed for the propyl derivative **3b** were still high (50−65% and 45−55% yields, respectively). Using only 10 μmol of the nitro derivatives (**3a**−**e**) resulted in slightly lower incorporation yields. Using microwave irradiations at 100 W, comparable results to those described above were obtained for all nitro derivatives (**3a**−**e**) with the highest incorporation yields observed at 2 min and again the propyl derivative **3b** being the more reactive precursor for labeling (50−75% yield). No further efforts were made at this stage to optimize and further increase the observed yields.

On the basis of these results, the propyl alkyl chain was selected for the design of the maleimide final reagent (**1**, FPyME).

A first dedicated maleimide-containing precursor for fluorine-18-labeling, the nitro derivative **7** (1-[3-(2-nitropyridin-3-yloxy)propyl]pyrrole-2,5-dione), was therefore designed and synthesized (see above), expecting the use of a one-step radiochemical process. Introduction of fluorine-18 was attempted in DMSO (600 μL) containing 17 μmol (4.7 mg) of the nitro derivative **7** with the activated K[^{18}F]F−Kryptofix222 complex as the radiofluorinating reactant, by conventional heating only (at 145°C for 1 to 10 min). However, no incorporation of fluorine-18 could be detected by TLC or HPLC using these radiochemical conditions (similar to those described for the preparation of the [(2-[^{18}F]fluoropyridin-3-yloxy)-

Scheme 7. Potential One-Step Process for the Preparation of 1-[3-(2-[^{18}F]Fluoropyridin-3-yloxy)propyl]pyrrole-2,5-dione ([^{18}F]-1, [^{18}F]FPyME)

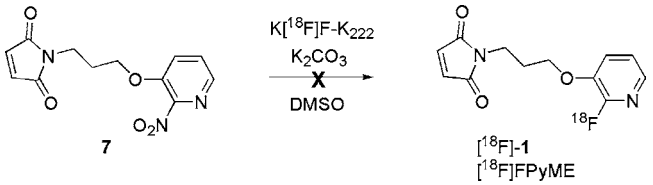

alkyl]carbamic acid *tert*-butyl ester ([^{18}F]-**4a**−**e**)) (Scheme 7), and the expected [^{18}F]FPyME ([^{18}F]-**1**) could not be isolated. This is probably due to the rapid decomposition of the maleimide ring (base-labile) to a mixture of nonreactive maleamic acids using the strong alkaline conditions required for the introduction of [^{18}F]fluorine as described above. A similar unsuccessful direct radiofluorination of a preformed maleimide was also reported by others (*33*). In view of these failures, the preparation of the corresponding *N*-trimethylammonium trifluoromethanesulfonate derivative ([3-[3-(2,5-dioxo-2,5-dihydropyrrol-1-yl)propoxy]pyridin-2-yl]trimethylammonium trifluoromethanesulfonate, structure not shown) was not attempted.

[^{18}F]FPyME ([^{18}F]-**1**) was therefore synthesized using the following three-step radiochemical process from the nitro derivative **3b** (Scheme 8).

Scheme 8. Preparation of 1-[3-(2-[^{18}F]Fluoropyridin-3-yloxy)propyl]pyrrole-2,5-dione ([^{18}F]-1, [^{18}F]FPyME) Using a Three-Step Process

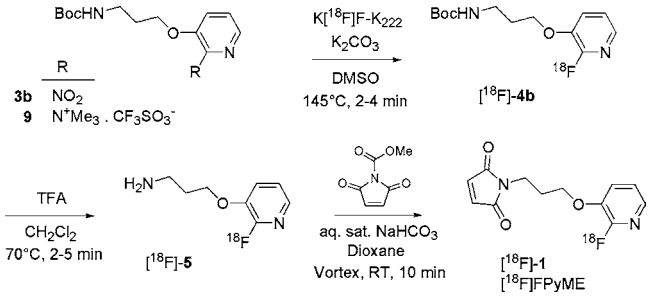

The first radiochemical step, the introduction of fluorine-18 into the pyridine ring, was performed as described above, in DMSO (600 μL) containing the nitro derivative **3b** (17 μmol) and the activated K[^{18}F]F-K_{222} complex, and by conventional heating at 145°C for 5 min, giving the desired [^{18}F]fluoropyridine derivative **4b** in 45−60% (decay-corrected) isolated radiochemical yields with respect to starting [^{18}F]fluoride after C-18 Sep-pak purification. The second radiochemical step, the removal of the *N*-Boc-protective group, was rapidly (2−5 min) performed in a mixture of TFA and dichloromethane (1/50 (v/v)) at room temperature, quantitatively yielding the free amine [^{18}F]-**5**. The third and final step, the maleimide ring formation, was first performed using maleic anhydride (25 mg to 50 mg) in *o*-xylene (at 180−190°C) for 10 to 20 min, based on literature procedures (see for example ref 68; over fifty references can be found in the literature via a bibliographic search using Beilstein Commander 2000 version 5.0, copyright 1995−2000, MDL Information Systems GmbH). On the basis of TLC analysis, the desired maleimide [^{18}F]-**1** ([^{18}F]FPyME) was obtained in 19−41% radiochemical yields. The use of other described solvents and experimental conditions using maleic anhydride, such as refluxing THF (*69*, *70*), acetic acid at 100 °C (*71*, *72*), refluxing dioxane containing triethylamine (*73*, *74*), or refluxing methanol containing sodium

hydroxyde (*75*), gave systematically lower radiochemical yields when the desired maleimide [18F]-**1** ([18F]FPyME) could be detected at all.

Using instead of maleic anhydride, *N*-methoxycarbonylmaleimide (25 mg) in *o*-xylene (at 180−190°C) gave higher radiochemical yields (46−77%, based on TLC analysis) for 5 min of reaction only. However, HPLC purification (semipreparative SiO_2 Zorbax Rx-SIL, Hewlett-Packard) led to [18F]-**1** ([18F]FPyME) with radiochemical purity of only about 90% and with systematically lower isolated radiochemical yields that expected from the TLC analysis. The maleimido ring formation was then investigated again, and the following optimal conditions, based on literature procedures, were found (*76*−*78*): the free amine [18F]-**5** (3-(2-[18F]fluoropyridin-3-yloxy)propylamine) was treated with *N*-methoxycarbonylmaleimide (25 mg) in a strongly vortexed 3/1 (v/v) solution (1 mL) of aqueous saturated bicarbonate and THF at room temperature for 10 min. On the basis of TLC analysis, the desired maleimide [18F]-**1** ([18F]FPyME) was obtained in >90% radiochemical yields and was practically the only detectable product on the TLC chromatogram. C-18 Sep-pak trapping, followed by HPLC purification (semipreparative SiO_2 Zorbax Rx-SIL, Hewlett-Packard), gave radiochemically pure [18F]-**1** ([18F]FPyME) in 64−77% isolated yields, confirming the excellent radiochemical yields of maleimido formation obtained from the TLC analysis.

Finally, the three-step radiochemical process for the preparation of [18F]FPyME ([18F]-**1**) was further optimized (Scheme 8) using a more efficient and attractive precursor for labeling, the *N*-trimethylammonium trifluoromethanesulfonate derivative **9** ([3-(3-*tert*-butoxycarbonylaminopropoxy)pyridin-2-yl]trimethylammonium trifluoromethanesulfonate). This type of precursor for labeling has been used extensively already in nucleophilic *homo*- and *hetero*aromatic radiofluorinations (*13*−*15*). It is particularly suitable for its expected superior separation (using HPLC or SPE-cartridge) from the reaction product (the fluoro derivative [18F]-**4b** in this case) due to the large differences in the physicochemical properties. Moreover, the trimethylammonium function possesses higher potential as leaving group (*79*) in comparison with the corresponding nitro and especially halo derivatives, giving usually higher incorporation yields under milder conditions. Introduction of the fluorine-18 was therefore performed using only 8.7 μmol of the *N*-trimethylammonium trifluoromethanesulfonate derivative **9** (4 mg) in DMSO (600 μL) containing the activated K[18F]F-K_{222} complex by conventional heating at 145 °C for 2 min, giving the desired [18F]fluoropyridine derivative **4b** in 64−76% (decay-corrected) isolated radiochemical yields with respect to starting [18F]fluoride after C-18 Sep-pak purification. The remainder of the radiosynthesis used the same procedures as described above.

Typically, 4.8−6.7 GBq (130−180 mCi) of radiochemically pure [18F]FPyME ([18F]-**1**) could be obtained after semipreparative HPLC in 110 minutes starting from a 33.3 GBq (900 mCi) cyclotron production batch of [18F]-fluoride (overall radiochemical yields, based on starting [18F]fluoride: 28−37% decay-corrected and 17−20% non-decay-corrected).

According to the available literature, only one report exists on two fluorine-18-labeled maleimide reagents that have been prepared and used for prosthetic conjugation of proteins (*33*). In that abstract, the authors described the preparation of 1-(4-[18F]fluorophenyl)pyrrole-2,5-dione ([18F]FPPD, see Figure 2) and *N*-[3-(2,5-dioxo-2,5-dihydropyrrol-1-yl)phenyl]-4-[18F]fluorobenzamide ([18F]-DDPFB, see Figure 2).

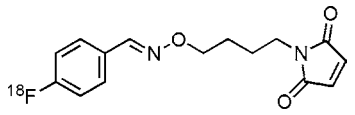

[18F]FBABM

Figure 4. Chemical structure of *N*-[4-[(4-[18F]fluorobenzylidene)aminooxy]butyl]maleimide ([18F]FBABM).

[18F]FPPD was synthesized in four radiochemical steps from 1,4-dinitrobenzene and cesium [18F]fluoride. It was obtained in 15% decay-corrected overall radiochemical yield in 100 min total synthesis time (*33*). [18F]DDPFB was synthesized in three radiochemical steps from 4-nitrobenzonitrile and cesium [18F]fluoride and was obtained in only 10% decay-corrected overall radiochemical yield in 70 min total synthesis time (*33*).

During the preparation of this manuscript, another fluorine-18-labeled maleimide reagent was published (*80*). *N*-[4-[(4-[18F]Fluorobenzylidene)aminooxy]butyl]-maleimide ([18F]FBABM, see Figure 4) was synthesized in only two steps, involving the preparation of 4-[18F]-fluorobenzaldehyde, followed by its aminooxy-aldehyde coupling reaction to the fluorine-18-labeled maleimide reagent, with an overall radiochemical yield of about 35% (decay-corrected) within 60 min of radiosynthesis time. This new fluorine-18-labeled maleimide reagent ([18F]-FBABM) is a valuable alternative to the use of our [18F]-FPyME ([18F]-**1**) and is the first reported example of an oxime-containing radiotracer for PET.

Conjugation of the (*N*-Ac)KAAAAC peptide (**P1**, TCEP-treated) with the HPLC-purified [18F]FPyME ([18F]-**1**) (Scheme 5) was carried out in a 1/9 (v/v) mixture of DMSO and 0.05 M aq Tris NaCl buffer (pH 7.4) at room temperature for 10 min. The labeled conjugated peptide [18F]**c-P1** was obtained in >90% yield, based on starting [18F]FPyME ([18F]-**1**), and determined both by radio-TLC analysis and radio-HPLC analysis (C18 DeltaPak column, Waters). [18F]c-(*N*-Ac)KAAAAC ([18F]**c-P1**) was purified by preparative HPLC (C18 DeltaPak column, Waters). It was easily separated from starting (*N*-Ac)-KAAAAC (t_R: 13.0 min), nonreacted [18F]FPyME ([18F]-**1**), if any (t_R: 33.0 min), and traces of a fluorine-18-labeled side product, associated with the TCEP-reduced-[18F]-FPyME species (t_R: 26.0 min, see above). [18F]c-(*N*-Ac)-KAAAAC ([18F]**c-P1**) coeluted with reference nonlabeled standard and was obtained with a radiochemical purity greater than 99%. Conjugation of AFIM-0 (**P2**) was carried out using similar conditions to those described above (including a TCEP-treatment, but including a removal step of this reducing agent by gel filtration prior to the use of the protein) with conjugation yields estimated quantitative by radio-TLC analysis. The labeled conjugated protein (**c-P2**) was separated from nonreacted [18F]FPyME ([18F]-**1**), if any, by gel filtration using a Sephadex NAP-10 cartridge. Size-exclusion liquid radiochromatography on a Gel Filtration SuperDex Peptide HR 10/30 column showed a unique peak (t_R: 14.5 min), which coeluted with reference standard. Conjugation of STxB (**P3**) was carried out in a 1/9 (v/v) mixture of DMSO and 0.1 M aq PBS at pH 8 (without TCEP-treatment of the starting protein), with conjugation yields estimated quantitative by radio-TLC analysis. The labeled conjugated protein (**c-P3**) was separated from nonreacted [18F]-FPyME ([18F]-**1**), if any, by gel filtration using a Sephadex NAP-10 cartridge. RP-HPLC on a C18 μBondapak column and size-exclusion liquid radiochromatography on a Gel Filtration SuperDex Peptide HR 10/30 column showed a unique peak (t_R: 12.5 and 9.5 min, respectively), which coeluted with reference standard.

Typically, 1.11−1.29 GBq (30−35 mCi) of pure conjugated [^{18}F]peptide or protein (specific radioactivity > 37 GBq/μmol) could be obtained in 25−30 min starting from 1.85 GBq (50 mCi) of [^{18}F]FPyME ([^{18}F]-**1**) (60−70% non-decay-corrected isolated yield). The whole synthetic procedure has been fully automated on our Zymate robot system and took 130−140 min. As demonstrated by LC analysis, radiosynthesized labeled conjugated peptide and protein ([^{18}F]**c-P1**, [^{18}F]**c-P2** and [^{18}F]**c-P3)** coeluted with the authentic synthesized reference compounds. The fluorine-18-labeled peptide and proteins were found to be more than 99%, 90%, and 97% radiochemically pure, respectively. The preparations were shown to be free of radioactive starting reagent ([^{18}F]FPyME, [^{18}F]-**1**) and radiochemically stable for at least 240 min.

The conjugation yields to the macromolecules obtained with [^{18}F]FPyME ([^{18}F]-**1**) are also higher than those obtained for the conjugation of the previously reported *N*-[3-(2,5-dioxo-2,5-dihydropyrrol-1-yl)phenyl]-4-[^{18}F]fluorobenzamide ([^{18}F]PPFB, see Figure 2). Therefore, about 50% yield could be obtained for the conjugation step with a protein part from a monoclonal antibody fragment (*33*). No complementary details, such as solvent, reagent, and conditions used for the conjugation, reaction time, and purification process, were given.

Conjugation to a protein of the recently published *N*-[4-[(4-[^{18}F]fluorobenzylidene)aminooxy]butyl]maleimide ([^{18}F]-FBABM, see Figure 4) has not been reported so far. Conjugation yields to a small tripeptide (GSH) were comparable to those obtained with [^{18}F]FPyME ([^{18}F]-**1**) (about 70% decay-corrected radiochemical yield).

CONCLUSION

The objective of the present work was to develop a [^{18}F]-fluoropyridine-based thiol (sulfhydryl)-selective reagent for the prosthetic labeling with fluorine-18 of peptides and proteins, offering a new alternative with improved chemoselectivity to the use of the nonselective carboxylate and amine-reactive [^{18}F]reagents already existing.

FPyME (**1**, 1-[3-(2-fluoropyridin-3-yloxy)propyl]pyrrole-2,5-dione) was designed as a radiochemically feasible reagent, its pyridinyl moiety carrying the radioactive halogen (fluorine-18) which can be efficiently incorporated via a nucleophilic *hetero*aromatic substitution, and its maleimido function ensuring the efficient alkylation of a free thiol function as borne by cysteine residues. [^{18}F]-FPyME ([^{18}F]-**1**, HPLC-purified) was efficiently prepared in 17−20% non-decay-corrected yield (based on starting [^{18}F]fluoride) in 110 min using a three-step radiochemical pathway. The developed procedure involves a high-yield nucleophilic *hetero*aromatic ortho-radiofluorination as the fluorine-18 incorporation step and uses a trimethylammonium trifluoromethanesulfonate as the most efficient precursor leaving group for labeling (when compared to the parallely tested nitro precursor). [^{18}F]FPyME ([^{18}F]-**1**) was first conjugated with a small hexapeptide ((*N*-Ac)-KAAAAC, **P1**), chosen as a model peptide, and the chemoselectivity of the coupling reaction (CH_2SH versus CH_2NH_2) was confirmed. The labeling strategy was then applied with success to the preparation of two 8-kDa proteins of interest, currently being developed as tumor imaging agents ([^{18}F]c-AFIM-0, [^{18}F]**c-P2**; [^{18}F]c-STxB, [^{18}F]**c-P3**). Conjugation was achieved in high yields (60−70%, isolated and non-decay-corrected yields) and uses optimized, short-time reaction and purification conditions, both compatible with the chemical stability of the proteins and the relatively short half-life of the radioisotope concerned. The whole radiosynthetic procedure, including the preparation of the fluorine-18-labeled reagent, the conjugation with the protein, and the final purification, took 130−140 min.

Given these high radiosynthetic yields, [^{18}F]FPyME ([^{18}F]-**1**) represents a new, valuable, thiol-selective, fluorine-18-labeled reagent and can advantageously be used for the design and development of peptide- and protein-based radiopharmaceuticals for PET.

ACKNOWLEDGMENT

The authors wish to thank the cyclotron operators Mr. Daniel Gouel, Mr. Christophe Peronne, and Mr. Christophe Lechêne for performing the irradiations, as well as Ms. Badia Amekraz (Laboratoire de Spéciation des Radionucléides et des Molécules, DEN/DPC/SECR, CEA-Saclay, F-91191 Gif-sur-Yvette, France) and Drs. Alain Pruvost and Eric Ezan (Laboratoire d'Études du Métabolisme des Médicaments, DSV/SPI, CEA-Saclay, F-91191 Gif-sur-Yvette, France) for recording the MS spectra and Drs Delphine Patin, Wolfgang Faigle and Damarys Loew (Institut Curie, F-75248 Paris Cedex, France) for expert help in some of the experiments. The authors also wish to thank Dr. Dirk Roeda for proofreading the manuscript and suggesting linguistic corrections. This work was supported by the OLIM European program QLG1-CT-2000-00562 and by the European Molecular Imaging Laboratories network (EMIL; LSH-2004-503569).

LITERATURE CITED

(1) Okarvi, S. M. (1999) Recent developments in ^{99}Tc^{m}-labelled peptide-based radiopharmaceuticals: an overview. *Nucl. Med. Commun. 20*, 1093−1112.
(2) Okarvi, S. M. (2001) Recent progress in fluorine-18 labeled peptide radiopharmaceuticals. *Eur. J. Nucl. Med. 28*, 929−938.
(3) Lundqvist, H., and Tolmachev, V. (2003) Targeting Peptides and Positron Emission Tomography. *Biopolymers 66*, 381−392.
(4) Okarvi, S. M. (2004) Peptide-Based Radiopharmaceuticals: Future Tools for Diagnostic Imaging of Cancers and Other Diseases. *Med. Res. Rev. 24*, 357−397.
(5) Eckelman, W. C., Paik, C. H., and Reba, R. C. (1980) Radiolabeling of Antibodies. *Cancer Res. 40,* 3036−3042.
(6) Kas, J., and Rauch, P. (1983) Labeled Proteins, Their Preparation and Applications. *Topics in Current Chemistry* (Boschke, F. L., Ed.) Vol. 112, pp 167−182, Springer-Verlag, New York.
(7) Regoeczi, E., Ed. (1984) *Iodine-Labeled Plasma Proteins,* Vols. I and II, CRC Press, Inc., New York.
(8) Osterman, L. A. (1984) Labeling of Proteins. *Methods of Protein and Nucleic Acid Research,* pp 131−143, Springer-Verlag, New York.
(9) Srivastava, S. C., Ed. (1988) *Radiolabeled Monoclonal Antibodies for Imaging and Therapy,* Part 111, pp 193−268, Plenum Press, New York.
(10) Fritzberg, A. R., Berninger, R. W., Hadley, S. W., and Wester, D. W. (1988) Approaches to Radiolabeling of Antibodies for Diagnosis and Therapy of Cancer. *Pharm. Res. 5*, 325−334.
(11) Magerstadt, M. (1991) *Antibody Conjugates and Malignant Disease,* pp 11−35, 79−93, CRC Press, Boca Raton, FL.
(12) Wilbur, D. S. (1992) Radiohalogenation of Proteins: An Overview of Radionucleides, Labeling Methods, and Reagents for Conjugate Labeling. *Bioconjugate Chem. 3*, 433−470.
(13) Kilbourn, M. R., and Welch, M. J. (1986) Fluorine-18 labeled receptor based radiopharmaceuticals. *Appl. Radiat. Isot. 37,* 677−683.
(14) Kilbourn, M. R. (1990) *Fluorine-18 labeling of radiopharmaceuticals − Nuclear Science Series* (Kilbourn, Ed.) pp 1−149, National Academy Press, Washington.
(15) Lasne, M. C., Perrio, C., Rouden, J., Barré, L., Roeda, D., Dollé, F., and Crouzel, C. (2002). Chemistry of β^{+}-emitting

compounds based on fluorine-18. *Topics in current chemistry* (Krause, Ed.) pp 201−211, Springer-Verlag, Berlin.
(16) Welch, M. J., and Redvanly, C. S. (2003) Radiochemistry and applications. *Handbook of radiopharmaceuticals* (Welch, M. J., Redvanly, C. S., Eds.) pp 1−848, Wiley-Interscience Publishers, New York.
(17) Wester, H. J., Hamacher, K., and Stöcklin, G. (1996) A comparative study of N.C.A. fluorine-18 labeling of proteins via acylation and photoactivation. *Nucl. Med. Biol. 23*, 365−372.
(18) Vaidyanathan, G., and Zalutsky, M. R. (1994) Improved synthesis of *N*-succinimidyl 4-[18F]fluorobenzoate and its application to the labeling of monoclonal antibody fragment. *Bioconjugate Chem. 5*, 352−356.
(19) Vaidyanathan, G., and Zalutsky, M. R. (1992) Labeling of proteins with fluorine-18 using *N*-succinimidyl 4-[18F]fluorobenzoate. *Nucl. Med. Biol. 19*, 275−281.
(20) Hostetler, E. D., Edwards, W. B., Anderson, C. J., and Welch, M. J. (1999). Synthesis of 4-[18F]fluorobenzoyl octreotide and biodistribution in tumor-bearing Lewis rats. *J. Labelled Compd. Radiopharm. 42*, S720−S722.
(21) Müller-Platz, C. M., Kloster, G., Legler, G., and Stöcklin, G. (1982) 18F−Fluoroacetate: an agent for introducing no-carrier-added fluorine-18 into urokinase without loss of biological activity. *J. Labelled Compd. Radiopharm. 19*, 1645−1646.
(22) Block, D., Coennen, H. H., and Stöcklin, G. (1988) N.c.a. 18F-fluoroacylation via fluorocarboxylic acid esters. *J. Labelled Compd. Radiopharm. 15*, 185−200.
(23) Lang, L., and Eckelman, W. C. (1994) One-step synthesis of 18F labeled [18F]-*N*-succinimidyl 4-(fluoromethyl)benzoate for protein labeling. *Appl. Radiat. Isot. 45*, 1155−1163.
(24) Lang, L., and Eckelman, W. C. (1997) Labeling proteins at high specific radioactivity using *N*-succinimidyl 4-([18F]-fluoromethyl)benzoate. *Appl. Radiat. Isot. 48*, 169−173.
(25) Garg, P. K., Garg, S., Bigner, D. D., and Zalutsky, M. R. (1991) Fluorine-18 labeling of monoclonal antibodies and fragments with preservation of immunoreactivity. *Bioconjugate Chem. 2*, 44−49.
(26) Kilbourn, M. R., Dence, C. S., Welch, M. J., and Mathias, M. J. (1987) Fluorine-18 labelling of proteins. *J. Nucl. Med 28*, 462−470.
(27) Wester, H. J., Hamacher, K., Guhlke, S., and Stöcklin, G. (1994) A simple and fast 18F-labeling of proteins by coupling with photogenerated [18F]arylnitrene. *J. Nucl. Med. 35*, 73P.
(28) Herman, L. W., Fischman, A. J., Tompkins, R. G., Hanson, R. N., Byon, C., Strauss, H. W., and Elmaleh, D. R. (1994) The use of pentafluorophenyl derivatives for the 18F labelling of proteins. *Nucl. Med. Biol. 21*, 1005−1010.
(29) Shai, Y., Kirk, L., Channing, M. A., Dunn, B. B., Lesniak, M. A., Eastman, R. C., Finn, R. D., Roth, J., and Jacobson, K. A. (1989) 18F-labeled insulin: a prosthetic group methodology for incorporation of a positron emitter into peptides and proteins. *Biochemistry 28*, 4801−4806.
(30) Brinkley, M. (1992) A brief survey of methods for preparing protein conjugates with dyes, haptens, and cross-linking reagents. *Bioconjugate Chem. 3*, 2−13.
(31) Wilbur, D. S. (1992) Radiohalogenation of proteins: an overview of radionuclides, labeling methods, and reagents for conjugate labeling. *Bioconjugate Chem. 3*, 433−470.
(32) Hermanson, G. T. (1996) *Bioconjugate Techniques*, Academic Press, San Diego, CA.
(33) Shiue C. Y., Wolf, A. P., and Hainfeld, J. F. (1998) Synthesis of 18F-labelled *N*-(*p*-[18F]fluorophenyl)maleimide and its derivatives for labelling monoclonal antibody with 18F. *J. Labelled Compd. Radiopharm. 26*, 287−289.
(34) Dollé, F. (2004) Fluorine-18-labeled fluoropyridines: Advances in radiopharmaceutical design. *Curr. Pharm. Des., in press.*
(35) Dolci, L., Dollé, F., Jubeau, S., Vaufrey, F., and Crouzel, C. (1999) 2-[18F]Fluoropyridines by no-carrier-added nucleophilic aromatic substitution with K[18F]F-K_{222} − A comparative study. *J. Labelled Compd. Radiopharm. 42,* 975−985.
(36) Karramkam, M., Hinnen, F., Vaufrey, F., and Dollé, F. (2003) 2-, 3- and 4-[18F]Fluoropyridines by no-carrier-added nucleophilic aromatic substitution with K[18F]F-K_{222} − A comparative study. *J. Labelled Compd. Radiopharm. 46,* 979−992.
(37) Dollé, F., Valette, H., Bottlaender, M., Hinnen, F., Vaufrey, F., Guenther, I., and Crouzel, C. (1998) Synthesis of 2-[18F]-fluoro-3-[2(*S*)-2-azetidinylmethoxy]pyridine, a highly potent radioligand for *in vivo* imaging central nicotinic acetylcholine receptors. *J. Labelled Compd. Radiopharm. 41,* 451−463.
(38) Liu, N., Ding, Y. S., Wang, T., Garza, V., and Fowler, J. S. (2002) Synthesis of 2-[18F]fluoro-3-[2(S)-2-azetidinylmethoxy]-pyridine as a radioligand for imaging nicotinic acetylcholine receptors. *Nucl. Sci. Technol. 13*, 92−97.
(39) Horti, A., Koren, A. O., Ravert, H. T., Musachio, J. L., Mathews, W. B., London, E. D., and Dannals, R. F. (1998) Synthesis of a radiotracer for studying nicotinic acetylcholine receptors: 2-[18F]fluoro-3-(2(S)-azetidinylmethoxy)pyridine (2-[18F]A-85380). *J. Labelled Compd. Radiopharm. 41*, 309−318.
(40) Dollé, F., Dolci, L., Valette, H., Hinnen, F., Vaufrey, F., Guenther, I., Fuseau, C., Coulon, C., Bottlaender, M., and Crouzel, C. (1999) Synthesis and nicotinic acetylcholine receptor in vivo binding properties of 2-fluoro-3-[2(*S*)-2-azetidinylmethoxy]pyridine: a new positron emission tomography ligand for nicotinic receptors. *J. Med. Chem. 42,* 2251−2259.
(41) Koren, A. O., Horti, A. G., Mukhin, A. G., Gündish, D., Kimes, A. S., Dannals, R. F., and London, E. D. (1998) 2-, 5-, and 6-Halo-3-(2(S)-azetidinylmethoxy)pyridines: Synthesis, affinity for nicotinic acetylcholine receptors, and molecular modeling. *J. Med. Chem. 41*, 3690−3698.
(42) Horti, A. G., Scheffel, U., Koren, A. O., Ravert, H. T., Mathews, W. B., Musachio, J. L., Finley, P. A., London, E. D., and Dannals, R. F. (1998) 2-[18F]fluoro-A-85380, an *in vivo* tracer for the nicotinic acetylcholine receptors. *Nucl. Med. Biol. 25*, 599−603.
(43) Valette, H., Bottlaender M., Dollé, F., Guenther, I., Coulon, C., Hinnen, F., Fuseau, C., Ottaviani, M., and Crouzel, C. (1999) Characterization of the nicotinic ligand 2-[18F]fluoro-3-[2(S)-2-azetidinylmethoxy]pyridine *in viv*o. *Life Sci 64*, 93−97.
(44) Valette, H., Bottlaender, M., Dollé, F., Guenther, I., Fuseau, C., Coulon, C., Ottaviani, M., and Crouzel, C. (1999) Imaging central nicotinic acetylcholine receptors in baboons with [18F]fluoro-A-85380. *J Nucl Med 40*, 1374−1380.
(45) Chefer, S. I., Horti, A. G., Koren, A. O., Gundisch, D., Links, J. M., Kurian, V., Dannals, R. F., Mukhin, A. G., and London, E. D. (1999) 2-[18F]F-A-85380: a PET radioligand for $\alpha_4\beta_2$ nicotinic acetylcholine receptors. *NeuroReport 10*, 2715−2721.
(46) Valette, H., Bottlaender, M., Dollé, F., Coulon, C., Ottaviani, M., and Syrota, A. (2003) Long-lasting occupancy of central nicotinic acetylcholine receptors after smoking: a PET study in monkeys. *J. Neurochem. 84*, 105−111.
(47) Chefer, S. I., London, E. D., Koren, A. O., Pavlova, O. A., Kurian, V., Kimes, A. S., Horti, A. G., and Mukhin, A. G. (2003) Graphical analysis of 2-[18F]FA binding to nicotinic acetylcholine receptors in rhesus monkey brain. *Synapse 48*, 25−34.
(48) Valette, H., Dollé, F., Bottlaender, M., and Marzin, D. (2002) Fluoro-A-85380 demonstrated no mutagenic properties in in vivo rat micronucleus and ames tests. *Nucl. Med. Biol. 29*, 849−853.
(49) Bottlaender, M., Valette, H., Roumenov, D., Dollé, F., Coulon, C., Ottaviani, M., Hinnen, F., and Ricard, M. (2003) Biodistribution and radiation dosimetry of [18F]fluoro-A-85380 in healthy volunteers. *J. Nucl. Med. 44*, 596−601.
(50) Kimes, A. S., Horti, A. G., London, E. D., Chefer, S. I., Contoreggi, C., Ernst, M., Friello, P., Koren, A. O., Kurian, V., Matochik, J. A., Pavlova, O., Vaupel, D. B., Mukhin, A. G. (2003) 2-[18F]F-A85380: PET imaging of brain nicotinic acetylcholine receptors and whole body distribution in humans. *FASEB J. 17*, 1331−1333.
(51) Mitsunobu, O. (1981) The use of diethyl azodicarboxylate and triphenylphosphine in synthesis and transformation of natural products. *Synthesis* 1−28.
(52) Schelte, P., Boeckler, C., Frisch, B., and Schuber, F. (2000) Differential Reactivity of Maleimide and Bromoacetyl Func-

tions with Thiols: Application to the Preparation of Liposomal Diepitope Constructs. *Bioconjugate Chem. 11*, 118−123.
(53) Sanson, A., Ochsenbein, F., and Dolle, F. (2004) Fluorine-18-marked peptides having affinity for negatively charged cell surfaces for use in diagnosis. PCT Int. Appl. WO 2004003016, 80 pp.
(54) Sanson, A., Ochsenbein, F., and Dolle, F. (2004) Peptides having affinity for phospholipids and their use in diagnosis, imaging, and separations. PCT Int. Appl. WO 2004003015, 57 pp.
(55) Zijlstra, S., Gunawan, J., and Burchert, W. (2003) Synthesis and evaluation of a 18F-labeled recombinant annexin-V derivative, for identification and quantification of apoptotic cells with PET. *Appl. Radiat. Isot. 58*, 201−207.
(56) Grierson, J. R., Yagle, K. J., Eary, J. F., Tait, J. F., Gibson, D. F., Lewellen, B., Link, J. M., and Krohn, K. A. (2004) Production of [F-18]Fluoroannexin for Imaging Apoptosis with PET. *Bioconjugate Chem. 15*, 373−379.
(57) Murakami, Y., Takamatsu, H., Taki, J., Tatsumi, M., Noda, A., Ichise, R., Tait, J. F., and Nishimura, S. (2004) 18F-labeled annexin V: a PET tracer for apoptosis imaging. *E. J. Nucl. Med. Mol. Imaging 31*, 469−474.
(58) Toretsky, J., Levenson, A., Weinberg, I. N., Tait, J. F., Uren, A., and Mease, R. C. (2004) Preparation of F-18 labeled annexin V: a potential PET radiopharmaceutical for imaging cell death. *Nucl. Med. Biol. 31*, 747−752.
(59) Dollé, F., Hinnen, F., Lagnel, B., Boisgard, R., Sanson, A., Russo-Marie, F., and Tavitian, B. (2003) Radiosynthesis of a [^{18}F]Fluoropyridine-Based Maleimide Reagent For Protein Labelling, *J. Labelled Compd. Radiopharm. 46*, S15.
(60) Boisgard, R., Blondel, A., Dollé, F., Hinnen, F., Tavitian, B., Turhan, A. G., Poupon, M. F., Kato, M., Nakashima, I., Syrota, A., Sanson, A., and Russo-Marie, F. (2003) A New ^{18}F Tracer for Apoptosis Imaging in Tumor Bearing Mice, *J. Nucl. Med. 44,* 49P.
(61) Boisgard, R., Vuillemard, C., Dollé, F., Blondel, A., Poupon, M. F., Sanson, A., Russo-Marie, F., and Tavitian, B. (2003) New ^{18}F and ^{99m}Tc Radiopeptides for Apoptosis Imaging in Tumour-Bearing Mice. *Cancer Biother. Radiopharm. 18,* 282.
(62) Dolle, F. (2004) Preparation of [^{18}F]-labeled maleimides, their use for marking macromolecules for medical imaging. PCT Int. Appl. WO 2004002984, 58 pp.
(63) Johannes, L. (2002) The Shiga Toxin B−Subunit System: Retrograde Transport, Intracellular Vectorization, and More. *Am. J. Physiol. Gastrointest. Liver Physiol. 283*, G1-G7.
(64) Hagnerelle, X., Plisson, C., Lambert, O., Marco, S., Rigaud, J. L., Johannes, L. and Levy, D. (2002) Two-Dimensional Structures of the Shiga Toxin B−Subunit and of a Chimera Bound to the Glycolipid Receptor Gb3. *J. Struct. Biol. 139*, 113-21.
(65) Pina, D. G., Gomez, J., Villar, E., Johannes, L., and Shnyrov, V. L. (2003) Thermodynamic Analysis of the Structural Stability of the Shiga Toxin B−Subunit. *Biochemistry 42*, 9498−9506.
(66) Smith, D. C., Lord, J. M., Roberts, L. M., and Johannes, L. (2004) Glycosphingolipids as Toxin Receptors. *Semin. Cell Dev. Biol. 15*, 397−408.
(67) Hamacher, K., Coenen, H. H., and Stöcklin, G. (1986) Efficient stereospecific synthesis of no-carrier-added 2-[^{18}F]-fluoro-2-deoxy-D-glucose using aminopolyether supported nucleophilic substitution. *J. Nucl. Med. Biol. 27,* 235−238.
(68) Coleman, L. E, Bork, J. F., and Dunn, H. (1959) Reaction of primary aliphatic amine with maleic anhydride. *J. Org. Chem. 24*, 135−136.
(69) Nielsen, O., and Buchardt, O. (1991) Facile synthesis of reagents containing a terminal maleimdo ligand linked to an active ester. *Synthesis 10*, 819−821.
(70) Al-Khathlan, H., and Zimmer, H. (1998) Dibromotriphenylphosphorane-promoted synthesis of condensed heterocyclic systems from aromatic diamines. *J. Heterocycl. Chem. 25*, 1047−1049.
(71) Manteca, I., Etxarri, B., Ardeo, A., Arrasate, S., Osante, I., Sotomayor, N., and Lete, E. (1998) Functionalized organolithium compounds: generation via reductive lithiation and nucleophilic addition to *N*-phenethylimides. Access to functionalized dihydropyrrolo[2,1-a]isoquinolinones. *Tetrahedron 54*, 12361−12378.
(72) Bennes, R., Babiloni, M. S., Hayes, W., and Philp, D. (2001) Recognition-induced control and acceleration of a pyrrole Diels−Alder reaction. *Tetrahedron Lett. 42*, 2377−2380.
(73) Brown, A. G., and Smale, T. C. (1972) Synthesis of (−)-versimide (methyl-(methylsuccinimido)acrylate) and related compounds. *J. Chem. Soc., Perkin Trans. 1,* 65−76.
(74) van Steen, B. J., van Wijngaarden, I., Tulp, M. Th. M., and Soudijn, W. A (1995) Series of *N*-4-Imidoethyl Derivatives of 1-(2,3-Dihydro-1,4-benzodioxin-5-yl)piperazine as 5-HT1A Receptor Ligands: Synthesis and Structure-Affinity Relationships. *J. Med. Chem. 38*, 4303−4308.
(75) Keana, J. F. W., Ogan, M. D., Lu, Y., Beer, M., and Varkey, J. (1986) Functionalized Keggin- and Dawson-type cyclopentadienyltitanium heteropolytungstate anions: small, individually distinguishable labels for conventional transmission electron microscopy. 2. Reactions. *J. Am. Chem. Soc. 108*, 7957−7963.
(76) Cheronis, J. C., Whalley, E. T., Nguyen, K. T., Eubanks, S. R., Allen, L. G., Duggan, M. J., Loy, S. D., Bonham, K. A., and Blodgett, J. K. (1992) A new class of bradykinin antagonists: synthesis and in vitro activity of bissuccinimidoalkane peptide dimers. *J. Med. Chem. 35*, 1563−1572.
(77) Cheronis, J. C., Whalley, E. T., Allen, L. G., Loy, S., Elder, M. W., Duggan, M. J., Gross, K. L., and Blodgett, J. K. (1994) Design, synthesis, and in vitro activity of bis(succinimido)-hexane peptide heterodimers with combined B1 and B2 antagonist activity. *J. Med. Chem. 37*, 348−355.
(78) Arano, Y., Uezono, T., Akizawa, H., Ono, M., Wakisaka, K., Nakayama, M., Sakahara, H., Konishi, J., and Yokoyama, A. (1996) Reassessment of Diethylenetriaminepentaacetic Dianhydride (DTPA) as a Chelating Agent for Indium-111 Labeling of Polypeptides Using a Newly Synthesized Monoreactive DTPA Derivative. *J. Med. Chem. 39*, 3451−3460.
(79) Haka, M. S., Kilbourn, M. R., Watkins, L., and Toorongian, S. A. (1989) Aryltrimethylammonium trifluoromethanesulfonates as precursors to aryl [^{18}F]fluorides: improved synthesis of [^{18}F]GBR-13119. *J. Labelled Compd. Radiopharm. 27*, 823−833.
(80) Toyokuni, T., Walsh, J. C., Dominguez, A., Phelps, M. E., Barrio, J. R., Gambhir, S. S., and Satyamurthy, N. (2003) Synthesis of a New Heterobifunctional Linker, *N*-[4-(Aminooxy)butyl]maleimide, for Facile Access to a Thiol-Reactive ^{18}F-Labeling Agent. *Bioconjugate Chem. 14*, 1253−1259.
(81) Dolci, L., Dollé, F., Valette, H., Vaufrey, F., Fuseau, C., Bottlaender, M., and Crouzel, C. (1999) Synthesis of a Fluorine-18 Labelled Derivative of Epibatidine for In Vivo Nicotinic Acetylcholine Receptor PET Imaging. *Bioorg. Med. Chem. 7*, 467−479.

BC0497463

Functionalization of Glucose at Position C-3 for Transition Metal Coordination: Organo-Rhenium Complexes with Carbohydrate Skeletons

Cécile Dumas,[†] Jeannine Petrig,[†] Luzia Frei,[†] Bernhard Spingler,[§] and Roger Schibli*[,†,‡]

Center for Radiopharmaceutical Science of the ETH-PSI-USZ, Paul Scherrer Institute, CH-5232 Villigen, Switzerland, Department of Chemistry and Applied Biosciences, ETH Zurich, CH-8093 Zurich, Switzerland, and Institute of Inorganic Chemistry, University of Zurich, CH-8057 Zurich, Switzerland. Received October 26, 2004

Novel 3-*O*-[1,2;5,6-di-*O*-isopropylidene-α-D-glucofuranose] and 3-*O*-[D-glucose] derivatives with an iminodiacetate (*N*,*O*,*O*), a histidinate, and an *N*-(acetetyl)picolylamine (*N*,*N*,*O*) chelating system for tridentate coordination of the organometallic $M(CO)_3$-fragment (M = Tc, Re) have been prepared. The chelates were introduced and assembled through reductive amination starting from 3-*O*-[1,2;5,6-di-*O*-isopropylidene-α-D-glucofuranose]-acetaldehyde. After deprotection, the pyranose derivatives were reacted with the precursor $[NEt_4]_2[ReBr_3(CO)_3]$ to afford the corresponding organometallic complexes in yields between 54% and 94%. The NMR, MS, and IR analyses corroborated the tridentate coordination of the organometallic metal center exclusively via the synthetic chelates. In the case of the *N*-(acetyl)picolylamine derivative, the coordinative properties were further confirmed by X-ray structure analysis of the first $Re(CO)_3$-D-glucofuranose complex. All glucose complexes unveiled good stability and solubility in organic and aqueous media.

INTRODUCTION

The coordination chemistry of carbohydrates with transition metal plays a significant role in processes such as transport and storage of metals as well as in the metabolism of toxic metals (*1*, *2*). However, from a coordination point of view, most of the native carbohydrate compounds possess functional groups with only weak donor capacities, which often can not effectively compete with, for example, water. Thus, functionalization with "artificial" chelating systems is necessary to produce more stable transition metal complexes. These features can be of pivotal importance for the development of novel pharmaceuticals with anti-proliferative and cytostatic properties displaying better biocompatibility and reduced side effects (*2*−*7*). Also, in the development of novel catalysts, carbohydrate-based ligand systems can lead to metal compounds with improved solubility in environmentally benign media (*8*). For both purposes (pharmaceuticals and catalysis), organometallic complexes with a carbohydrate skeleton are an interesting class of compound. Organometallic rhodium(III) and iridium(III) complexes of α-*N*-galactopyranose amino acids have been intensively investigated by Beck and co-workers (*9*, *10*). Dötz et al. have performed pioneering work on carbohydrate-based Fischer-type carbene complexes with a wide variety of transition metals (*11*−*14*).

We are interested in the development of novel, tumor-seeking (organometallic) compounds of technetium and rhenium for potential use in diagnostic and therapeutic radiopharmacy. For both elements, there exist radioactive isotopes (Tc-99m, and Re-186/188), which are very important in nuclear medicine. Recently, we have reported and structurally characterized the first examples of organo-technetium and -rhenium complexes of C-1 functionalized glucose derivatives (*15*). Experiments have shown that the complexes exhibit a high kinetic stability in human serum over a period of 24 h at 37 °C. Recently, other groups have described organometallic glucose and glucosamine complexes of technetium and rhenium, respectively, for potential use in radiopharmacy (*16*, *17*). However, our initial in vivo experiments have shown only low accumulation of the C-1 glucose complexes in cancer cells overexpressing Glut1 (the major transport system for glucose in humans) (*18*). This is presumably due to the fact that the hydroxyl group at the C-1 position is important for recognition and transport or glucose via Glut1. On the other hand, there is evidence that moderate modification at the C-3 and the C-6 positions is tolerated without complete loss of biological activity (*19*).

In the present work, we describe novel strategies for the syntheses of glucose derivatives functionalized at position C-3 with different tridentate metal chelating entities. The ligand systems are based on L-histidyl (**1**), iminodiacetic acid (**2**), and *N*-(acetyl)picolylamine (**3**) frameworks (Figure 1). The preparation, structural, and spectroscopic analyses of rhenium−tricarbonyl complexes of C-3 functionalized glucose derivatives are presented. The spectroscopic investigations of the stable and water-soluble fac-$Re(CO)_3$ complexes **13**−**15** have shown that in all of the cases the metal center coordinates tridentately via the chemically introduced anchor groups.

EXPERIMENTAL SECTION

Material and Methods. All chemicals were purchased of reagent grade and used without further purification. Dry THF was distilled from Na/benzophenone immediately before use. The precursor $(NEt_4)_2[ReBr_3(CO)_3]$ was synthesized according to the previously

* To whom correspondence should be addressed. Phone: +41-56-310-2837. Fax: +41-56-310-2849. E-mail: roger.schibli@psi.ch.
[†] Paul Scherrer Institute.
[‡] ETH Zurich.
[§] University of Zurich.

10.1021/bc049744i CCC: $30.25 © 2005 American Chemical Society
Published on Web 03/01/2005

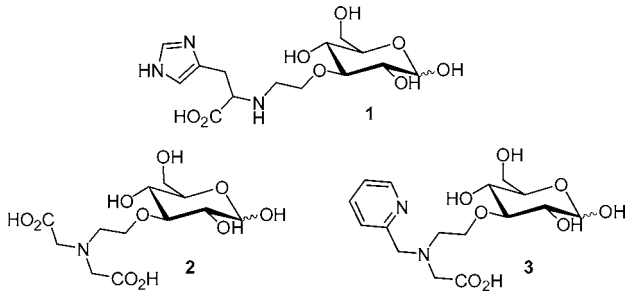

Figure 1. Structures of C-3 functionalized glucose derivatives for transition metal complexation.

published procedure (*20*). Tr-L-histidine methyl ester was synthesized according to the literature (*21*). Moisture-sensitive reactions were conducted in oven-dried glassware under a nitrogen atmosphere. All reactions were monitored by tin layer chromatography performed on Merck precoated silica gel (60 F254) plates and visualized using UV light and by applying a solution of potassium permanganate (1% in water). Amines were detected by ninhydrin (0.5% in methanol). Column chromatography was accomplished on Fluka silica gel 60 (0.062−200 mesh). HPLC analyses were performed on a Merck-Hitachi L-7000-system equipped with an L-7400 tunable absorption detector. A Macherey-Nagel C-18 reversed phase column (10 μm, 150 × 4.1 mm) was used. HPLC solvents consisted of aqueous 0.05 M TEAP (triethylammonium phosphate) buffer, pH = 2.25 (solvent A), and methanol (solvent B). The HPLC system started with 100% of A from 0 to 3 min. The eluent switched at 3 min to 75% A and 25% B and at 9 min to 66% A and 34% B followed by a linear gradient 66% A/34% B to 100% B from 9 to 20 min. The gradient remained at 100% B for 2 min before switching back to 100% A. The flow rate was 1 mL/min. The IR spectra were recorded on a Perkin-Elmer FT-IR 16PC. Mass spectra were measured on a Micromass VG Trio 2000 Operator. The NMR spectra were measured on a Varian Gemini 2000 (300 and 75 MHz for ^{1}H and ^{13}C, respectively). Unless otherwise specified, spectra were recorded in $CDCl_3$ as solvent, and chemical shifts were expressed in ppm relative to residual $CHCl_3$ at 7.27 ppm for ^{1}H and to $CDCl_3$ at 77.7 ppm for ^{13}C. The optical rotations were measured on a Polarimeter Perkin-Elmer 241. High-resolution mass spectroscopy and elemental analyses were performed at the Department of Organic Chemistry at the Federal Institute of Technology Zurich (ETHZ).

Synthesis of 3-*O*-[2-(L-Histidinato)ethyl]-α,*β*-D-glucopyranose, 1. Glucofuranose **8** (0.64 g, 0.92 mmol) was stirred at room temperature in H_2SO_4 (2 N, 3 mL) for 1 day. The solution was neutralized by addition of $Ba(OH)_2$, and the precipitate was separated by centrifugation. The ester was saponified by addition of NaOH (1 M, 1 mL) to the clear solution; after one night of stirring, the obtained solution was neutralized by addition of HCl (1 M, 1 mL). After evaporation of the water, the residual oil was dried in a desiccator. The solid was taken up in methanol (3 mL), and the insoluble particles were centrifuged. After evaporation to dryness of the supernatant, a white powder (0.24 g) was obtained. Yield 74%. ^{1}H NMR ([*d*^{6}]-DMSO, 50 °C): δ = 7.88 (s, 1H), 7.11 (s, 1H), 5.07 (d, *J* = 3.3 Hz, 0.5H), 4.46 (d, *J* = 7.5 Hz, 0.5H), 4.14−3.92 (m, 2H), 3.88−3.68 (m, 3H), 3.68−3.58 (m, 1H), 3.58−3.44 (m, 1H), 3.36 (t, *J* = 9.3 Hz, 1H), 3.29−3.13 (m, 4H), 3.08 (dd, *J* = 7.5, 15.0 Hz, 1H). IR (KBr): ν = 1632, 1384, 1038 cm^{-1}. MS (ES) *m/z* (%): 384 [M$^+$ + Na]. Anal. Calcd for $C_{14}H_{23}N_3O_8$: C, 46.53; H, 6.42; N, 11.63. Found: C, 46.81; H, 6.86; N, 11.23.

Synthesis of 3-*O*-[Bis(carboxymethyl)aminoethyl]-α,*β*-D-glucopyranose, 2. Compound **2** was prepared from **11** according to the preparation of **1**. Yield 60%. ^{1}H NMR ([*d*^{6}]DMSO, 60 °C): δ = 4.05 (d, *J* = 3.3 Hz, 0.4H), 4.44 (d, *J* = 6.9 Hz, 0.6H), 4.17−3.85 (m, 2H), 3.85−3.65 (m, 3H), 3.61 (s, 2H), 3.60 (s, 2H), 3.55−3.39 (m, 1H), 3.38−3.08 (m, 2H), 3.09−2.84 (m, 2H). IR ($CHCl_3$): ν = 1634, 1402, 1120, 1078, 1040 cm^{-1}. MS (ES) *m/z* (%): 338 [M$^+$ − H]. Analysis Calcd for $C_{12}H_{21}NO_{10}$: C, 42.48; H, 6.24; N, 4.13. Found: C, 42.51; H, 6.74; N, 3.93.

Synthesis of 3-*O*-[2-Carboxymethyl-2-(pyridin-2-ylmethyl)aminoethyl]-α,*β*-D-glucopyranose, 3. Compound **3** was prepared from **12** according to the preparation of **1**. Yield 95%. ^{1}H NMR ([*d*^{6}]DMSO, 50 °C): δ = 8.73−7.85 (m, 4H), 4.95 (s, 1H), 4.90−4.50 (m, 2H), 4.47−4.06 (m, 2H), 4.40 (s, 1H), 3.92−3.66 (m, 2H), 3.64−3.45 (m, 3H), 3.33 (s, 2H), 2.82−2.39 (m, 2H). IR ($CHCl_3$) ν = 1638, 1400, 1124, 1080 cm^{-1}. MS (ES) *m/z* (%): 373 (100) [M + H]$^+$, 395 (80) [M + Na]$^+$. Anal. Calcd for $C_{16}H_{24}N_2O_8$: C, 51.60; H, 6.50; N, 7.52. Found: C, 51.62; H, 7.08; N, 6.27.

Synthesis of 3-*O*-[2-(Methyl-N$_{im}$-triphenylmethyl-L-histidinato)ethyl]-1,2:5,6-(*O*-isopropylidene)-α-D-glucofuranose, 8. Aldehyde **7** (1.15 g, 3.8 mmol) dissolved in dry methanol (17 mL) and $NaBH_3CN$ (0.24 g, 3.3 mmol) were added to a solution of *N*-triphenylmethyl-L-histidine (1.56 g, 3.8 mmol) in dry methanol (17 mL) in the presence of molecular sieves. After the mixture was stirred for 24 h at room temperature, the molecular sieves were filtered over a Celite pad and the organic layer was evaporated to dryness. The resulting oil was diluted in chloroform (49 mL), extracted with water (20 mL), and the aqueous layer was back extracted with chloroform (30 mL). The combined organic layer was dried over Na_2SO_4 and evaporated. The crude was purified by chromatography on silica gel AcOEt/MeOH (14:1) to afford a pale yellow oil (0.64 g). Yield 24%. mp 82−83 °C; $[\alpha]^{24}_D$ = 3.50 (*c* = 0.371 in MeOH). ^{1}H NMR ([*d*^{6}]DMSO, 75 °C): δ = 7.54−7.49 (m, 1H), 7.49−7.37 (m, 9H), 7.29−7.17 (m, 6H), 6.71 (s, 1H), 5.96 (d, *J* = 3.3 Hz, 1H), 4.69 (d, *J* = 3.9 Hz, 1H), 4.48−4.38 (m, 1H), 4.24 (dd, *J* = 3.1, 7.6 Hz, 1H), 4.21−4.06 (m, 2H), 4.01 (d, *J* = 3.0 Hz, 1H), 3.99 (dd, *J* = 5.1, 6.6 Hz, 1H), 3.85−3.67 (m, 1H), 3.74 (s, 2H), 3.71 (s, 3H), 3.19−3.91 (m, 4H), 1.61 (s, 3H), 1.53 (s, 3H), 1.45 (s, 3H), 1.41 (s, 3H). ^{13}C NMR: δ = 174.4, 142.5 (2C), 142.3, 138.8, 137.1, 129.6 (8C), 128.2 (7C), 119.7, 111.8, 109.0, 105.4, 82.5, 81.2, 75.3, 72.7, 67.3, 61.8, 54.7, 51.8, 47.3, 32.2, 27.0 (2C), 26.4, 25.6. IR (KBr): ν = 1737, 1491, 1445, 1373, 1163, 1073 cm^{-1}. HRMS calcd for $C_{40}H_{47}N_3O_8$, 697.8165; found, 697.8170.

Synthesis of 3-*O*-[(1-Methoxycarbonyl)aminoethyl]-1,2:5,6-(*O*-isopropylidene)-α-D-glucofuranose, 9. Compound **9** was prepared from **7** and glycine methyl ester according to the preparation of **8**. The crude layer was purified by chromatography on silica gel AcOEt to afford a colorless oil (0.64 g). Yield 55%. $[\alpha]^{24}_D$ = −12.14 (*c* = 0.400 in MeOH). ^{1}H NMR: δ = 5.86 (d, *J* = 3.6 Hz, 1H), 4.55 (d, *J* = 3.6 Hz, 1H), 4.32−4.27 (m, 1H), 4.12−4.07 (m, 2H), 4.01−3.96 (m, 1H), 3.90 (d, *J* = 3.0 Hz, 1H), 3.8−3.72 (m, 1H), 3.71 (s, 3H), 3.66−3.59 (m, 1H), 3.43 (s, 2H), 2.83−2.75 (m, 2H) 2.03 (s, 1H), 1.48 (s, 3H), 1.40 (s, 3H), 1.32 (s, 3H), 1.30 (s, 3H). ^{13}C NMR: δ = 173.2, 112.4, 109.7, 105.9, 83.0, 82.9, 81.9, 73.1, 70.5, 68.1, 52.4, 51.3, 49.3, 27.5, 26.9, 25.9. IR ($CHCl_3$): ν = 1740, 1210, 1076 cm^{-1}. HRMS calcd for $C_{17}H_{29}NO_8$, 375.4141; found, 375.4136.

Synthesis of 3-*O*-[2-(Pyridin-2-ylmethyl)aminoethyl]-1,2:5,6-(*O*-isopropylidene)-α-D-glucofuranose,

10. Compound **10** was prepared from **7** and picolylamine according to the preparation of **8**. The crude was purified by chromatography on silica gel AcOEt/MeOH (1:1) to afford a pale yellow oil. Yield 22%. $[\alpha]^{24}_D = -20.4$ (c = 0.206 in MeOH). ^{1}H NMR: δ =8.55−8.53 (m, 1H), 7.66−7.60 (m, 1H), 7.33 (d, J = 7.7 Hz, 1H), 7.16−7.12 (m, 1H), 5.87 (d, J = 3.9 Hz, 1H), 4.56 (d, J = 3.6 Hz, 1H), 4.35−4.28 (m, 1H), 4.11−4.03 (m, 2H), 4.00−3.95 (m, 2H), 3.93 (s, 2H), 3.88−3.79 (m, 1H), 3.77−3.64 (m, 1H), 2.87−2.79 (m, 2H), 2.33 (br s, 1H), 1.48 (s, 3H), 1.38 (s, 3H), 1.30 (s, 3H), 1.26 (s, 3H). ^{13}C NMR: δ = 160.5, 150.0, 137.1, 122.7, 122.6, 112.4, 109.7, 106.0, 83.1, 82.9, 81.9, 73.2, 70.5, 68.1, 55.8, 49.3, 27.5, 26.9, 25.9. IR ($CHCl_3$): ν = 1594, 1378, 1252, 1076, 1018 cm^{-1}. HRMS calcd for $C_{20}H_{30}N_2O_6$, 394.4620; found, 394.4617.

Synthesis of 3-*O*-[Bis-*N*-[(1-methoxycarbonyl)-methyl]aminoethyl]-1,2:5,6-(*O*-isopropylidene)-α-D-glucofuranose, 11. Triethylamine (0.15 mL, 1.07 mmol) and methyl bromoacetate (0.1 mL, 1.07 mmol) were added to a solution of **9** (0.27 g, 0.71 mmol) in THF (7.5 mL), and the solution was refluxed overnight. After being cooled, the mixture was filtered; the filtrate was then diluted with CH_2Cl_2 (10 mL) and washed with water (15 mL). The organic layer was dried over Na_2SO_4, and the solvent was removed under reduced pressure. The crude product was purified by column chromatography on silica gel AcOEt/*n*-hexane (1:1). Yield 70%. $[\alpha]^{24}_D = -19.21$ (c = 0.400 in MeOH). ^{1}H NMR: δ = 5.83 (d, J = 3.6 Hz, 1H), 4.56 (d, J = 3.9 Hz, 1H), 4.28−4.22 (m, 1H), 4.12−4.04 (m, 2H), 4.01−3.96 (m, 1H), 3.96 (dd, J = 5.5, 8.5 Hz, 1H), 3.85 (d, J = 3.0 Hz, 1H), 3.81−3.74 (m, 1H), 3.69−3.65 (m, 1H), 3.69 (s, 6H), 3.61 (s, 4H), 3.03−2.90 (m, 2H), 1.48 (s, 3H), 1.40 (s, 3H), 1.32 (s, 3H), 1.30 (s, 3H). ^{13}C NMR: δ = 172.4, 112.4, 109.7, 105.9, 83.3, 82.9, 81.8, 73.1, 70.7, 68.0, 56.2, 54.7, 51.3, 27.2, 26.9, 26.0. IR ($CHCl_3$): ν = 1742, 1378, 1202, 1166, 1076, 1016 cm^{-1}. HRMS calcd for $C_{20}H_{33}NO_{10}$, 447.4767; found, 447.4759.

Synthesis of 3-*O*-[*N*-[(1-Methoxycarbonyl)methyl]-*N*-(pyridin-2-ylmethyl)aminoethyl]-1,2:5,6-(*O*-isopropylidene)-α-D-glucofuranose, 12. Compound **12** was prepared from **10** according to the preparation of **11**. AcOEt. Yield 81%. $[\alpha]^{24}_D = -21.6$ (c = 0.176 in MeOH). ^{1}H NMR: δ = 8.52−8.50 (m, 1H), 7.66−7.61 (m, 1H), 7.49 (d, J = 8.0 Hz, 1H), 7.16−7.12 (m, 1H), 5.80 (d, J = 3.6 Hz, 1H), 4.50 (d, J = 3.9 Hz, 1H), 4.28−4.22 (m, 1H), 4.11−4.01 (m, 2H), 3.98 (s, 2H), 3.98−3.92 (m, 1H), 3.66 (d, J = 2.8 Hz, 1H), 3.76−3.61 (m, 2H), 3.67 (s, 3H), 3.50 (s, 2H), 2.95−2.90 (m, 2H), 1.46 (s, 3H), 1.38 (s, 3H), 1.28 (s, 3H). ^{13}C NMR: δ = 172.5, 160.0, 149.9, 149.5, 137.2, 123.6, 122.9, 122.6, 112.4, 109.6, 105.7, 83.3, 83.0, 82.9, 82.0, 81.7, 73.1, 70.2, 68.0, 61.3, 56.0, 54.4, 52.2, 51.9, 27.6, 27.3, 27.0, 26.7, 25.8. IR ($CHCl_3$): ν = 1738, 1378, 1252, 1164, 1076, 1016 cm^{-1}. HRMS calcd for $C_{23}H_{34}N_2O_8$, 466.5247; found, 466.5247.

Preparation of 3-*O*-[2-[Tricarbonyl-(L-histidinato)rhenium(I)]ethyl]-α,β-D-glucopyranose, 13. To a methanolic solution (5 mL) of ligand **1** (31 mg, 0.09 mmol) was added $(NEt_4)_2[ReBr_3(CO)_3]$ (70 mg, 0.09 mmol). After 2 h of heating at 50 °C, the solvent was removed and the product was extracted into CH_2Cl_2, the insoluble residuals were filtered, the solvent was evaporated, and a white solid was dried in desiccator. Yield 57%. ^{1}H NMR ([d^6]-DMSO, 50 °C): δ = 8.26 (s, 1H), 7.23 (s, 1H), 5.70−5.61 (m, 1H), 5.07 (d, J = 3.3 Hz, 0.5H), 4.50−4.45 (m, 0.5H), 4.26−4.04 (m, 2H), 3.98−3.87 (m, 1H), 3.86−3.69 (m, 2H), 3.68−3.45 (m, 2H), 3.43−3.07 (m, 5H). IR (KBr): ν = 2018, 1886, 1632, 1036 cm^{-1}. MS (ES) m/z (%): 352 (60) $[M + Na]^+$, 354 (100) $[M + Na]^+$. Anal. Calcd for $C_{14}H_{23}N_3O_8$: C, 32.43; H, 3.36; N, 6.67. Found: C, 31.55; H, 3.12; N, 6.13.

Preparation of Tetraethylammonium 3-*O*-[2-(Iminodiacetic acid)ethyl]-D-glucopyranosyl Tricarbonyl Rhenat, 14. Complex **14** was prepared from **2** according to the preparation of **13**. Yield 94%. ^{1}H NMR ([d^6]DMSO): δ = 5.15−5.01 (m, 0.4H), 4.50−4.26 (m, 0.6H), 4.17−4.02 (m, 1H), 4.02−3.89 (m, 1H), 3.89−3.78 (m, 1H), 3.78−3.64 (m, 3H), 3.64−3.49 (m, 3H), 3.49−3.41 (m, 1H), 3.41−3.12 (m, 4H). MS (ES) m/z (%): 608 (24), 606 (18) [M$^-$], 432 (23), 430 (82), 428 (70), 426 (10), 388 (10), 386 (84), 384 (100), 382 (30), 343 (8), 341 (24). IR (KBr): ν = 2008, 1892, 1638, 1458, 1400, 1032 cm^{-1}. HRMS calcd for $C_{15}H_{19}NO_{13}Re$, 608.0419; found, 608.0409.

Preparation of 3-*O*-[2-Carboxymethyl-2-(pyridin-2-ylmethyl)aminoethyl]-α-D-glucopyranosyl Rhenium(I) Tricarbonyl, 15. Complex **15** was prepared from **3** according to the preparation of **14**. Yield 54%. ^{1}H NMR ([d^6]DMSO, 50 °C): δ = 8.88 (d, J = 5.4 Hz, 1H), 8.27 (dt, J = 1.2, 7.8 Hz, 1H), 7.90−7.78 (m, 1H), 7.75−7.66 (m, 1H), 5.28−5.02 (m, 3H), 4.83−4.69 (m, 1H), 4.56−4.43 (m, 2H), 4.28−4.15 (m, 1H), 4.06−3.72 (m, 4H), 3.71−3.60 (m, 2H), 3.47−3.21 (m, 2H). IR (KBr): ν = 2026, 1910, 1632, 1036 cm^{-1}. MS (ES) m/z (%): 663 (16) $[M + Na]^+$, 665 (20) $[M + Na]^+$. Anal. Calcd for $C_{19}H_{23}$-$N2O_{11}Re$: C, 35.57; H, 3.61; N, 4.37. Found: C, 35.50; H, 3.66; N, 4.35.

Synthesis of 3-*O*-[2-(N_{im}-Triphenylmethyl-L-histidinato)ethyl]-1,2:5,6-(*O*-isopropylidene)-α-D-glucofuranose, 16. Derivative **8** (851 mg, 1.22 mmol) was dissolved in NaOH (0.5M, 2.6 mL) and stirred overnight at room temperature. The solution was then neutralized with HCl (1 M), evaporated, and strongly dried. The obtained oil was solved in methanol, and the insolubles were centrifuged. The evaporation to dryness of the supernatant affords **16** as a pale yellow oil (751 mg). Yield 90%. $[\alpha]^{24}_D = +72.4$ (c = 0.500 in MeOH). ^{1}H NMR ([d^6]-DMSO, 75 °C): δ = 8.10−7.68 (m, 16H), 7.35 (s large, 1H), 6.40 (s large, 1H), 5.33−5.15 (m, 1H), 5.06−4.90 (m, 1H), 4.4.84−4.73 (m, 1H), 4.68−4.44 (m, 3H), 4.41−4.17 (m, 2H), 4.15−4.02 (m, 1H), 3.80−3.29 (m, 4H), 2.34 (s, 1H), 2.10 (s, 3H), 2.02 (s, 3H), 1.913 (s, 3H), 1.90 (s, 3H). ^{13}C NMR: δ = 178.7, 142.4 (3C), 138.2, 137.8, 129.9 (6C), 128.2 (9C), 119.3, 111.7, 109.1, 105.3, 82.4, 81.1, 75.4, 72.4, 67.3, 63.5, 55.8, 29.4, 27.0, 26.4, 25.5, 24.7. MS (ES) m/z (%): 707 $[M + Na]^+$. Anal. Calcd for $C_{39}H_{45}N_3O_8$: C, 68.50; H, 6.63; N, 6.15. Found: C, 68.51; H, 6.59; N, 6.18.

Preparation of 3-*O*-[2-(N_{im}-Triphenylmethyl-L-histidinato)ethyl]-1,2:5,6-(*O*-isopropylidene)-α-D-glucofuranosyl Rhenium(I)-tricarbonyl, 17. Complex **17** was prepared from **16** according to the preparation of **14**. Yield 97%. $[\alpha]^{22}_D = +17.3$ (c = 0.660 in MeOH). ^{1}H NMR ([d^6]DMSO, 500 MHz): δ = 7.70 (s, 0.33H), 7.61 (s, 0.33H), 7.57 (s, 0.33H), 7.49−7.41 (m, 7H), 7.38−7.1 (m, 2.67H), 7.28−7.24 (m, 0.67H), 7.16 (s, 0.67H), 7.14−7.08 (m, 5H), 6.00−5.90 (m, 0.33H), 5.88 (d, J = 3.5 Hz, 0.33H), 5.84 (d, J = 3.5 Hz, 0.33H), 5.85−5.75 (m, 0.33H), 5.20−5.10 (m, 0.33H), 4.70 (d, J = 4.0 Hz, 0.33H), 4.67 (d, J = 4.0 Hz, 0.33H), 4.35−4.20 (m, 0.67H), 4.10−3.85 (m, 3H), 3.81 (dd, J = 5.0, 8.5 Hz, 0.67H), 3.80−3.65 (m, 1H), 3.35−2.98 (m, 7H), 2.94 (s, 0.67H), 2.83−2.74 (m, 0.33H), 1.40 (s, 1H), 1.39 (s, 1H), 1.34 (s, 1H), 1.28 (s, 2H), 1.25 (s, 2.6H), 1.23 (s, 3.4H), 1.14 (s, 1H). ^{13}C NMR ([d^6]DMSO, 500 MHz): δ = 198.1, 197.3, 196.8, 179.9, 179.0, 178.7, 143.4, 141.4, 141.3, 141.1, 140.6, 140.6, 134.3, 133.0, 128.9, 128.8, 129.4, 128.3, 128.0, 127.5, 126.7, 120.4, 120.3, 120.3, 110.7, 110.6, 108.5, 108.0, 104.7, 104.6, 82.0, 81.5, 81.4, 81.3, 80.5, 80.3, 80.3, 76.1, 76.0, 72.1, 72.0, 67.7, 66.1, 66.0, 59.3, 57.9, 57.2, 51.4,

50.9, 49.0, 32.5, 31.0, 28.7, 28.6, 28.4, 28.3, 27.4, 27.1, 26.5, 26.4, 26.3, 25.9, 24.8, 24.5. IR (KBr): ν = 2021, 1893, 1657, 1016 cm^{-1}. MS (ES) *m/z* (%): 952 (28) $[M + H]^+$, 954 (64) $[M + H]^+$, 974 (61) $[M^+ + Na]$, 976 (100) $[M^+ + Na]$. Analysis Calcd for $C_{42}H_{44}N_3O_{11}Re$: C, 52.93; H, 4.65; N, 4.41. Found: C, 54.64; H, 4.69; N, 4.51.

Synthesis of 3-*O*-[2-Carboxymethyl-2-(pyridin-2-ylmethyl)aminoethyl]-1,2:5,6-(*O*-isopropylidene)-α-D-glucofuranose, 18. Compound **18** was prepared from **12** according to the preparation of **16**. Yield 98%. $[\alpha]^{24}_D$ = 3.1 (*c* = 0.100 in MeOH). ^1H NMR ([*d*^{6}]DMSO): δ = 8.58 (m, 1H), 7.88 (dt, *J* = 1.6, 7.7 Hz, 1H), 7.61 (m, 1H), 7.38 (m, 1H), 5.89 (d, *J* = 3.6 Hz, 1H), 4.69 (d, *J* = 3.8 Hz, 1H), 4.29 (q, *J* = 6.3 Hz, 1H), 4.06 (m, 2H), 4.05 (s, 2H), 3.85 (m, 3H), 3.65 (m, 1H), 3.52 (s, 2H), 2.96 (m, 2H), 1.84 (s, 3H), 1.40 (s, 3H), 1.34 (s, 3H), 1.32 (s, 3H). IR (KBr): ν = 1736, 1638, 1380, 1216, 1072 cm^{-1}. MS (ES) *m/z* (%): 475 $[M + Na]^+$. Anal. Calcd for $C_{22}H_{32}N_2O_8$: C, 58.39; H, 7.13; N, 6.19. Found: C, 58.49; H, 7.09; N, 6.25.

Preparation of 3-*O*-[2-(Picolylaminoacetic acid)-ethyl]-1,2-*O*-isopropyliden-α-D-glucofuranosyl Rhenium(I)-tricarbonyl, 19. Complex **19** was prepared from **18** according to the preparation of **14**. Yield 41%. ^1H NMR ([*d*^{6}]DMSO): δ = 8.86 (m, 1H), 8.25 (tt, *J* = 1.5, 7.5 Hz, 1H), 7.82 (m, 1H), 7.68 (m, 1H), 5.98 (d, *J* = 3.6 Hz, 1H), 4.84 (d, *J* = 3.8 Hz, 1H), 4.65 (d, *J* = 14.7 Hz, 1H), 4.56 (d, *J* = 14.7 Hz, 1H), 4.76−4.63 (m, 1H), 3.82 (d, *J* = 17.1 Hz, 1H), 3.54 (d, *J* = 17.1 Hz, 1H), 4.13−3.61 (m, 7H), 1.50 (s, 3H), 1.38 (s, 3H). IR (KBr): ν = 2024, 1888, 1632, 1454, 1378, 1068, 1018 cm^{-1}. MS (ES) *m/z* (%): 705 $[M + Na]^+$. Anal. Calcd (%) for $C_{22}H_{27}N_2O_{11}Re$ (681.67): C, 38.76; H, 3.99; N, 4.11. Found: C, 38.70; H, 3.97; N, 4.02.

RESULTS AND DISCUSSION

Syntheses of Glucose Derivatives. On the basis of our own and other groups experience about efficient and suitable ligand systems for stable, facial coordination of the $[M(CO)_3]$-moiety (M = ^{99m}Tc, ^{99}Tc, ^{188}Re, Re) (*22*−*25*), we were interested in C-3 functionalized glucose analogues with polyamino or polycarboxy functionalities. For the current studies, we recognized 3-*O*-acetaldehyde-1,2;5,6-di-*O*-isopropylidene-α-D-glucofuranose **7** as a versatile intermediate for the synthesis of C-3 derivatized glucose analogues in relatively good yields with the above-mentioned chelating systems via reductive amination. Compound **7** was prepared from the commercially available 1,2;5,6-di-*O*-isopropylidene-α-D-glucofuranose, diacetone-D-glucose **4**, in three steps similar to the previously published method by Zhong, with an overall yield of 51% (Scheme 1) (*26*). Compound **4** was converted in the first step to the allyl derivative **5** according to the method of Bessodes in the presence of KOH and the phase transfer catalyst 18-crown-6 in excellent yield (90%) (*27*). The diol **6** was prepared in the presence of *tert*-butyl-hydroperoxide with a catalytic amount of OsO_4. To remove OsO_4 from the reaction solution, silica gel was added. After purification, the product **6** was obtained in approximately 60% yield. If $NaHSO_3$ is used instead of silica gel, the protection groups of **6** are cleaved due to the low pH of the reaction after formation of the osmium sulfite adduct. After oxidative cleavage of the diol **6** with sodium periodate on silica gel, the aldehyde **7** could be isolated almost quantitatively.

Scheme 1[a]

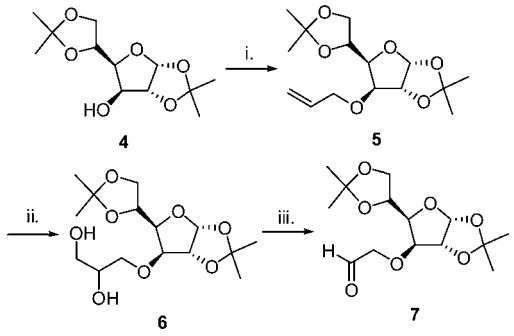

[a] Reagents and conditions: (i) allyl bromide, KOH, 18-crown-6, THF, room temperature, 1 h, 90%; (ii) OsO_4, *t*BuOOH, NEt_4OH, *t*BuOH, 0−5 °C, 16 h, 60%; (iii) $NaIO_4$, silica, CH_2Cl_2, room temperature, 30 min, 94%.

Scheme 2[a]

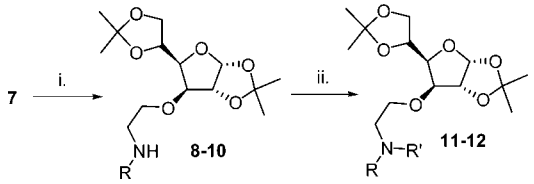

[a] Reagents and conditions: (i) amine, $NaBH_3CN$, MeOH, room temperature, 24 h; (ii) $BrCH_2CO_2Me$, NEt_3, THF, reflux, 16 h.

Table 1.

Product	Reactant	R	R'	Yield
8	H_3CO-His(τ-Tr)	H_3CO-Histamine(τ-Tr)	H	24 %
9	H_2N-CH_2-CO_2CH_3	CH_2-CO_2CH_3	H	55 %
10	H_2-NCH_2-(C_5H_4N)	CH_2-(C_5H_4N)	H	22 %
11	$BrCH_2$-CO_2CH_3	CH_2-CO_2CH_3	CH_2-CO_2CH_3	70 %
12	$BrCH_2$-CO_2CH_3	CH_2-(C_5H_4N)	CH_2-CO_2CH_3	81 %

For the three glucose derivatives **1**−**3**, the reductive amination was performed in dry methanol in the presence of $NaBH_3CN$ and molecular sieves (Scheme 2). The corresponding amines were used in a 4-fold excess. For the synthesis of the intermediate **8**, the N_ϵ-Tr-histidine methyl ester was used. We could show that the reaction works equally well for other ester protected amino acids such as L-methionine and N_ϵ-(Boc)-L-lysine (data not shown); however, for our radiopharmaceutical purpose, these derivatives were not suited. For the compounds **9** and **10**, the aldehyde **7** was reacted with glycine methyl ester or with 2-picolylamine, respectively. The Schiff's bases were in situ reduced with $NaBH_3CN$. After purification, the secondary amine functionalities of **9** and **10** were alkylated with methyl bromoacetate to afford the furanose intermediates **11** and **12** (Scheme 3 and Table 1). It is important to recognize that this efficient synthetic strategy can be applied to assemble a wide variety of other chelating systems, tailor-made for different transition metal centers and purposes.

The acetonide protecting groups in compounds **8**, **11**, and **12** were removed according to a modified procedure reported by Roberts in the presence of 2 N H_2SO_4 at room temperature (*28*). The trityl protection group was cleaved concomitantly under these conditions. After 24 h, the reaction solutions were neutralized with $Ba(OH)_2$. The suspensions were centrifuged to separate $BaSO_4$. Saponification of the remaining methyl ester has been accomplished with 1 N NaOH. After evaporation of the

Scheme 3[a]

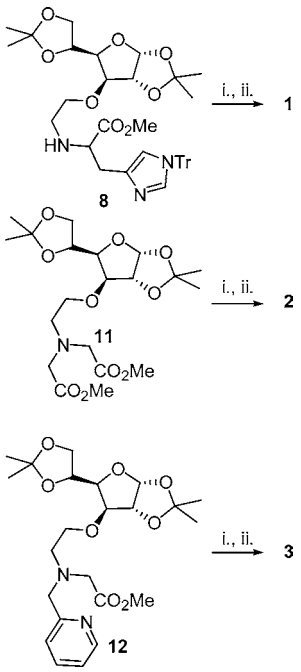

[a] Reagents and conditions: (i) H_2SO_4 (2 N), $Ba(OH)_2$, room temperature, 24 h; (ii) NaOH, HCl water, room temperature, 16 h, 60−95%.

Scheme 4[a]

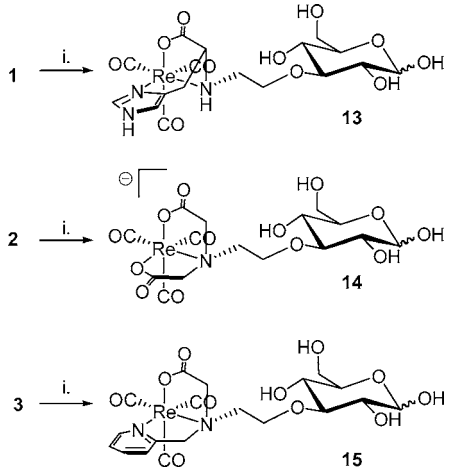

[a] Reagents and conditions: (i) $[NEt_4]_2[ReBr_3(CO)_3]$, MeOH, 50 °C, 2 h, 54−94%.

solvent, the final products **1**−**3** could be isolated with yields ranging from 60% to 95%.

In the ^{1}H NMR spectra of the deprotected ligands **1**−**3**, the signals in the region between 2.5 and 4.00 ppm are usually poorly resolved due to the presence of a mixture of α- and β-anomers. Only the signals of the H-1 proton and those in the aromatic region (compounds **1** and **3**) and the intense singlet at 3.61 ppm of the four protons of the iminodiacetic acid moiety (compound **2**) could be unambiguously attributed. However, mass spectrometric analyses provided in all of the cases evidence for the proposed composition and molecular structure.

Syntheses of Organometallic Glucose Complexes. The rhenium precursor $[NEt_4]_2[ReBr_3(CO)_3]$ reacted readily with the functionalized glucose derivatives **1**−**3** under mild and stoichiometric conditions in methanol (Scheme 4). All reactions have been monitored by means of HPLC. Thereby, complete consumption of the starting material has been observed after 2 h at 50 °C. The rhenium−tricarbonyl carbohydrate complexes **13**−**15** were isolated as pale yellow-brown, moisture- and air-stable powders in yields between 54% and 94%. Their proposed composition was confirmed by microanalysis, (high-resolution) mass spectrometry, IR, ^{1}H, and ^{13}C NMR spectroscopy.

The IR spectra of the anionic (**14**) and neutral (**13** and **15**) complexes revealed the typical fac-$Re(CO)_3$ pattern with sharp and intense absorption between 2008 and 2026 cm^{-1} and broad and intense absorption between 1886 and 1910 cm^{-1}. The wavelengths for the CO ligands are significantly blue shifted as compared to the starting material $[ReBr_3(CO)_3]^{2-}$ (2000, 1886 cm^{-1}). The mass spectra of the complexes were obtained via ESI-MS. The mass peak of the molecular anion of **14** was detected at 606/608 mass unit, showing the isotopic envelop characteristic (2/3) of a mono anion with one rhenium atom (isotopic composition ^{185}Re 40%:^{187}Re 60%). Further mass peaks at 428/430 mass units arose from fragments of complex **14** lacking the entire sugar entity. Complex **13** was measured in the negative and complex **15** in the positive mode, where their molecular mass at 628/630 $[M - 1]^-$ and 663/665 $[M + Na]^+$ mass units, respectively, could be detected.

The ^{1}H NMR spectra of the complexes **13**−**15**, recorded at room temperature, were very complex due the presence of mixtures of anomers and isomers, respectively. When recorded at 50 and 75 °C, the signals of the α- and β-anomeric protons collapse to give sharper signals; however, the attribution of the other proton signals became more difficult under these conditions because they formed broad and overlapped multiplets. Still, the spectra allowed determination of the coordinative preferences of the organometallic center to different functional groups of the sugar derivatives **1**−**3**. Generally, for the protons of the pyranose ring, a chemical shift of <0.3 ppm was detected. Thus, it can be concluded that the rhenium center does not coordinate to hydroxyl groups of the glucose moiety. On the other hand, most of the protons of the chelating systems (iminodiacetic acid, *N*-acetyl picolylamine, and L-histidyl) revealed significant shifts toward lower field and/or additional coupling patterns after coordination of the $[Re(CO)_3]^+$-moiety. Thus, it can be concluded that, due to the dominant donor characteristics of the anchoring groups, the glucose derivatives behaved coordinatively very much like the corresponding abiotic ligands without the glucose entity reported earlier (*22*, *24*, *29*).

Preparation of Complexes 17 and 19. More detailed NMR analyses have been performed with the furanose derivatives **17** and **19**, because this facilitated the attribution of ^{1}H NMR signals and differentiation of the isomers. The methyl ester derivatives **8** and **12** were saponified in the presence of sodium hydroxide, and the resulting acids **16** and **18** were labeled with the rhenium precursor $[NEt_4]_2[ReBr_3(CO)_3]$ according to the method described for complexes **13**−**15** (Scheme 5).

For complexes **17** and **19**, the formation of two diastereomers was expected with *S* or *R* configuration at the α-amino group and the tertiary amine, respectively. Thus, in the NMR spectrum of complex **17**, for all CH-protons two sets of signals with approximately a 1:1 intensity ratio were observed. In addition, two unresolved α-NH multiplets at 5.95 and 5.60 ppm with an identical intensity ratio were observed. ^{1}H NMR correlation experiments (COSY) revealed that these two multiplets coupled with the proton of the α carbon and the CH_2 of the neighboring ethylene spacer. It is noteworthy that the proton of the rhenium-coordinated α-NH group is detectable even after several days in deuterated, protic

Scheme 5[a]

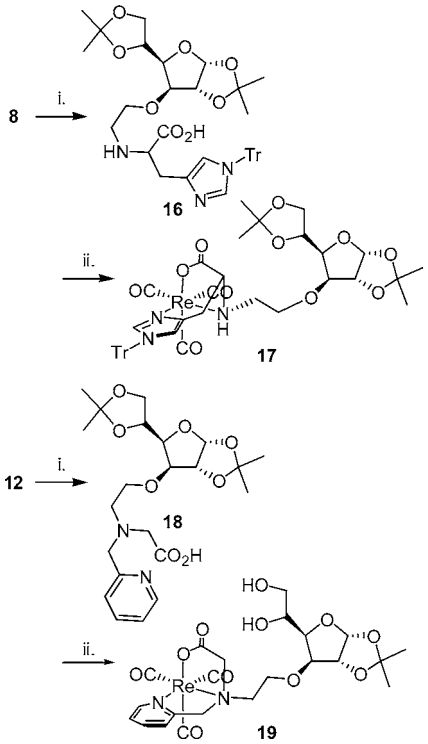

[a] Reagents and conditions: (i) NaOH, HCl water, room temperature, 16 h, 90−98%; (ii) $[NEt_4]_2[ReBr_3(CO)_3]$, MeOH, 50 °C, 2 h, 41−97%.

solvents. Surprisingly, only one set of ^{1}H NMR signals could be distinguished for complex **19**. Thus, it can be concluded that only one isomer has been formed. In addition, one of the two isopropylidene groups (facing the rhenium center) of ligand **18** has also been cleaved during the complex formation. This has been repeatedly observed for the reaction between $[ReBr_3(CO)_3]^{2-}$ and the ligand **18** under various conditions but never for compound **16** or, for example, **4** (performed as a control experiment). Whether this phenomenon is the reason for or is a consequence of the formation of a single diastereoisomer is unclear and debatable. However, the tridentate coordination of the metal core via the *N*-acetyl picolylamine chelate could be readily identified in the spectra. The singlets at 3.98 and 3.50 ppm of the two methylene protons of the pyridinyl group and the acetate protons in compound **12** converted into two AB spin systems detected at 4.65 and 4.56 ppm (methylene bridge of the pyridinyl group) and at 3.82 and 3.54 ppm (acetate group), which are partially overlaid by the other aliphatic protons. This feature can readily be explained be the nonequivalence of all four protons upon rigid coordination to the metal center, by virtue of their different chemical environment. This pattern is in accordance with the proposed tridentate coordination via the tertiary amine, the acetate function, and the pyridine nitrogen. Corresponding features have been previously reported by our group for the complex $[Tc(CO)_3(APPA)]$ (APPA = [(5-aminopentyl)pyridin-2-ylmethylamino]acetic acid) (*31*).

Crystal Structure of Complex 19. Because crystals of complexes **13**−**15** could not be obtained, attempts were undertaken to prepare the corresponding furanose complexes **17** and **19** in dry methanol. In the case of **19**, we could obtain crystals of X-ray quality. The colorless crystals of the *R*-N_α diastereoisomer were obtained by slow diffusion of ether into a methanolic solution of **19**. The molecular structure of compound **19** is shown in

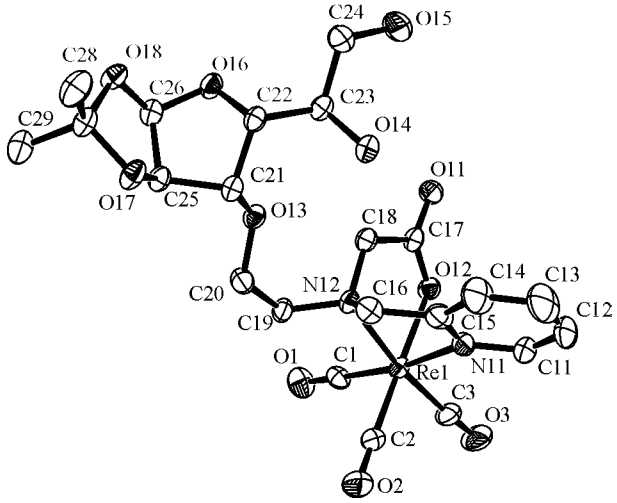

Figure 2. Molecular structure of complex **19** (*32*). Selected bond length and angles: Re(1)−C(2) 1.915(6) Å; Re(1)−C(1) 1.919(5) Å; Re(1)−C(3) 1.929(5) Å; Re(1)−O(12) 2.118(4) Å; Re(1)−N(11) 2.177(5) Å; Re(1)−N(12) 2.232(4) Å; C(2)−Re(1)−C(1) 88.6(2)°; C(2)−Re(1)−C(3) 88.7(2)°; C(1)−Re(1)−C(3) 89.3(3)°; C(2)−Re(1)−O(12) 174.8(2)°; C(1)−Re(1)−O(12) 95.79(19)°; C(3)−Re(1)−O(12) 94.2(2)°; C(2)−Re(1)−N(11) 93.5(2)°; C(1)−Re(1)−N(11) 170.5(2)°; C(3)−Re(1)−N(11) 100.0(2)°; O(12)−Re(1)−N(11) 81.71(16)°; C(2)−Re(1)−N(12) 97.79(19)°; C(1)−Re(1)−N(12) 94.71(18)°; C(3)−Re(1)−N(12) 172.4(2)°; O(12)−Re(1)−N(12) 79.02(14)°; N(11)−Re(1)−N(12) 75.83(17)°.

Figure 2 (*30*). The *N*-acetyl picolylamine ligand acts, as expected, as a tridentate *N*,*N*,*O* chelate coordinated to the rhenium−tricarbonyl center via the pyridine, the tertiary amine, and the deprotonated carboxylic acid functionality. The structure is in accordance with the ^{1}H NMR spectra of **19**. The complex reveals a distorted octahedral coordination sphere. Significant deviations can be found for the angles between the rhenium center and the coordinated heteroatoms (N(11)−Re(1)−N(12) 75.83(17)°; O(12)−Re(1)−N(11) 81.71(16)°; O(12)−Re(1)−N(12) 79.02(14)°), whereas the C−Re−C angles are close to the expected 90° (C(2)−Re(1)−C(1) 88.6(2)°; C(2)−Re(1)−C(3) 88.7(2)°; C(1)−Re(1)−C(3) 89.3(3)°). The three Re−C bond lengths are nearly equal within the standard deviation (1.92(7) Å). The same holds true for the two Re−N bond lengths (2.20(4) Å). The distance between Re(1) and O(12) is 2.118(4) Å long. The furanose ring adopts an envelope conformation. The remaining isopropylidene group points away from the metal center, whereas the diol functionality is oriented toward the metal center. However, no direct or indirect interaction of the furanose moiety with the metal chelate could be observed.

CONCLUSION

Due to the unique structural and chemical characteristics of carbohydrates, functionalized sugars can play an important role at the interface between transition metal chemistry and other disciplines of chemistry and biology. In this work, we could show that 3-*O*-acetaldehyde-1,2;5,6-di-*O*-isopropylidene-α-D-glucofuranose is a versatile intermediate for the development of different metal chelating moieties. The spectroscopic (NMR and IR) experiments revealed that the glucose derivatives coordinated readily and exclusively to the organometallic rhenium−tricarbonyl entity via the introduced tridentate chelates. This holds true for the compounds in solution as well as in the solid state. The first X-ray structure of a rhenium−tricarbonyl glucofuranoside complex could be elucidated during this project. In vitro and in vivo experiments with the corresponding organo-technetium

and -rhenium complexes are currently in progress to assess their potential in radiopharmacy.

ACKNOWLEDGMENT

We thank Mallinckrodt-Tyco Inc. for financial support of this work.

Supporting Information Available: Supplementary crystallographic data for compound **19**, ^{1}H NMR spectra of **1**−**3**, **8**, **13**−**15**, and **17**−**19**, ^{13}C NMR spectra of **8b**, **17**, and COSY NMR spectra of **17**, **18**, and **19**. This material is available free of charge via the Internet at http://pubs.acs.org.

LITERATURE CITED

(1) Chen, Y., Heeg, M. J., Braunschweiger, P. G., Xie, W., and Wang, P. (1999) A Carbohydrate-Linked Cisplatin Analogue Having Antitumor Activity. *Angew. Chem., Int. Ed. 38*, 1768−1769.

(2) Mikata, Y., Shinohara, Y., Yoneda, K., Nakamura, Y., Brudzinska, I., Tanase, T., Kitayama, T., Takagi, R., Okamoto, T., Kinoshita, I., Doe, M., Orvig, C., and Yano, S. (2001) Unprecedented sugar-dependent in vivo antitumor activity of carbohydrate-pendant cis-diamminedichloroplatinum(II) complexes. *Bioorg. Med. Chem. Lett. 11*, 3045−3047.

(3) Gyurcsik, B., Gajda, T., Nagy, L., Burger, K., Rockenbauer, A., and Korecz, L. (1993) Proton, Copper(Ii) and Nickel(Ii) Complexes of Some Amadori Rearrangement Products of D-Glucose and Amino-Acids. *Inorg. Chim. Acta 214*, 57−66.

(4) Kozelka, J., Legendre, F., Reeder, F., and Chottard, J.-C. (1999) Kinetic Aspects of Interactions between DNA and Platinum Complexes. *Coord. Chem. Rev. 61*, 190−192.

(5) Chen, J. T., Pill, T., and Beck, W. (1989) Metal-Complexes of Biologically Important Ligands. 50. Palladium(Ii), Platinum(Ii) and Copper(Ii) Complexes of Alpha- Amino Acid-*N*-Glycosides and of Fructose-Amino Acids (Amadori- Compounds). *Z. Naturforsch., B: Chem. Sci. 44*, 459−464.

(6) Junicke, H., Bruhn, C., Kluge, R., Serianni, A. S., and Steinborn, D. (1999) Novel platinum(IV)-carbohydrate complexes: Metal ion coordination behavior of monosaccharides in organic solvents. *J. Am. Chem. Soc. 121*, 6232−6241.

(7) Steinborn, D., and Junicke, H. (2000) Carbohydrate complexes of platinum-group metals. *Chem. Rev. 100*, 4283−4317.

(8) Shin, S., and RajanBabu, T. V. (1999) Water-soluble organometallic catalysts from carbohydrates. 1. diphosphinite-Rh complexes. *Org. Lett. 1*, 1229−1232.

(9) Malik, A., Ahmed, Z., Kazmi, N., and Khan, A. Q. (1987) Efficient Syntheses of a New Class of 6-Amino-6-Deoxy Sugars. *Z. Naturforsch., B: Chem. Sci. 42*, 514−515.

(10) Zhou, Y., Wagner, B., Polborn, K., Sünkel, K., and Beck, W. (1994) Metallkomplexe mit biologisch wichtigen Liganden, LXXIII; Komplexe von Palladium(II), Platin(II), Rhodium(III) und Iridium(III) mit N-6-Deoxy-galactopyranosyl-α-Aminosäuren. *Z. Naturforsch., B: Chem. Sci. 49*, 1193−1202.

(11) Dötz, K. H., Paetsch, D., and Le Bozec, H. (1999) Organotransition metal modified sugars 14. Activation of sugar-based alkynols at a metal carbonyl template: a metal vinyl carbene functionalization of carbohydrates and nonconventional route to organometallic disaccharides. *J. Organomet. Chem. 589*, 11−20.

(12) Dötz, K. H., Ehlenz, R., Straub, W., Weber, J. C., Airola, K., and Nieger, M. (1997) Organotransition metal modified sugars 4. Carbene complex functionalized acyclic carbohydrates. *J. Organomet. Chem. 548*, 91−98.

(13) Ehlenz, R., Neuss, O., Teckenbrock, M., and Dötz, K. H. (1997) Organometallic modified carbohydrates. 5. Carbohydrate functionalized oxacyclopentylidene complexes. *Tetrahedron 53*, 5143−5158.

(14) Janes, E., and Dötz, K. H. (2001) Organotransition metal modified sugars Part 21. Synthesis of organometallic disaccharides bearing two monosaccharide moieties linked by a chromium carbene spacer. *J. Organomet. Chem. 622*, 251−258.

(15) Petrig, J., Schibli, R., Dumas, C., Alberto, R., and Schubiger, P. A. (2001) Derivatization of glucose and 2-deoxyglucose for transition metal complexation: Substitution reactions with organometallic Tc-99m and Re precursors and fundamental NMR investigations. *Chem.-Eur. J. 7*, 1868−1873.

(16) Bayly, S. R., Fisher, C. L., Storr, T., Adam, M. J., and Orvig, C. (2004) Carbohydrate conjugates for molecular imaging and radiotherapy: Tc-99m(I) and Re-186(I) tricarbonyl complexes of N-(2′-hydroxybenzyl)-2-amino-2-deoxy-D-glucose. *Bioconjugate Chem. 15*, 923−926.

(17) Banerjee, S. R., Zubieta, J. A., and Babich, J. W. (2004) A new bifunctional amio acid chelator targeting glucose transporter. *J. Nucl. Med. 45*, 465P.

(18) Dumas, C., Petrig, J., Schibli, R., Stahel, J., Schubiger, A. P., Spadola, L., Scapozza, L., and Mertens, J. (2001) Functionalization of glucose for the labeling with 99mTc-tricarbonyl. *J. Labelled Compd. Radiopharm. 44 suppl. 1*, S57−S59.

(19) Halmos, T., Santarromana, M., Antonakis, K., and Scherman, D. (1996) Synthesis of glucose-chlorambucil derivatives and their recognition by the human GLUT1 glucose transporter. *Eur. J. Pharmacol. 318*, 477−484.

(20) Alberto, R., Schibli, R., Egli, A., Schubiger, P. A., Herrmann, W. A., Artus, G., Abram, U., and Kaden, T. A. (1995) Metal Carbonyl Syntheses XXII. Low-Pressure Carbonylation of $[MOCl_4]^-$ and $[MO_4]^-$: The Technetium(I) And Rhenium(I) Complexes $[NEt_4]_2[MCl_3(CO)_3]$. *J. Organomet. Chem. 493*, 119−127.

(21) Boger, D. L., Teramoto, S., and Cai, H. (1996) Synthesis and evaluation of deglycobleomycin A(2) analogues containing a tertiary *N*-methyl amide and simple ester replacement for the L-histidine secondary amide: Direct functional characterization of the requirement for secondary amide metal complexation. *Bioorg. Med. Chem. 4*, 179−193.

(22) Egli, A., Alberto, R., Tannahill, L., Schibli, R., Abram, U., Schaffland, A., Waibel, R., Tourwe, D., Jeannin, L., Iterbeke, K., and Schubiger, P. A. (1999) Organometallic Tc-99m-aquaion labels peptide to an unprecedented high specific activity. *J. Nucl. Med. 40*, 1913−1917.

(23) Schibli, R., La Bella, R., Alberto, R., Garcia-Garayoa, E., Ortner, K., Abram, U., and Schubiger, P. A. (2000) Influence of the denticity of ligand systems on the in vitro and in vivo behavior of Tc-99m(I)-tricarbonyl complexes: A hint for the future functionalization of biomolecules. *Bioconjugate Chem. 11*, 345−351.

(24) Schibli, R., Schwarzbach, R., Alberto, R., Ortner, K., Schmalle, H., Dumas, C., Egli, A., and Schubiger, A. P. (2002) Steps Toward High Specific Activity Labeling of Biomolecules for Therapeutic Application: Preparation of Precursor $[^{188}Re(H_2O)_3(CO)_3]^+$ and Synthesis of Tailor-Made Bifunctional Ligand Systems. *Bioconjugate Chem. 13*, 750−756.

(25) Banerjee, S. R., Levadala, M. K., Lazarova, N., Wei, L., Valliant, J. F., Stephenson, K. A., Babich, J. W., Maresca, K. P., and Zubieta, J. (2002) Bifunctional Single Amino Acid Chelates for Labeling of Biomolecules with the $\{Tc(CO)_3\}^+$ and $\{Re(CO)_3\}^+$ Cores. Crystal and Molecular Structures of $[ReBr(CO)_3(H_2NCH_2C_5H_4N)]$, $[Re(CO)_3\{(C_5H_4NCH_2)_2NH\}]Br$, $[Re(CO)_3\{(C_5H_4NCH_2)_2NCH_2CO_2H\}]Br$, $[Re(CO)_3\{X(Y)NCH_2CO_2CH_2CH_3\}]Br$ (X = Y = 2-pyridylmethyl; X = 2-pyridylmethyl, Y = 2-(1-methylimidazolyl)methyl; X = Y = 2-(1-methylimidazolyl)methyl), $[ReBr(CO)_3\{(C_5H_4NCH_2)NH(CH_2C_4H_3S)\}]$, and $[Re(CO)_3\{(C_5H_4NCH_2)N(CH_2C_4H_3S)(CH_2CO_2)\}]$. *Inorg. Chem. 41*, 6417−6425.

(26) Zhou, R., Wang, C., Hu, Y., and Flood, T. C. (1997) (1,4,7-Triazacyclononane)Rh(hydrocarbonyl)$_3$ Compounds and Their Derivatives. Strong Donor Labilization of RhCl Bonds toward Alkylation and Prepation of Unusually Stable Alkyl Hydride Complexes of Rhodium. *Organometallics 16*, 434−441.

(27) Bessodes, M., Shamsazar, J., and Antonakis, K. (1988) Crown Ether Catalyzed O-Alkylation of Carbohydrates and Nucleosides. *Synthesis* 560−562.

(28) Roberts, E. J., and Rowland, S. P. (1967) Synthesis of Mono-O-(2-Diethylaminoethyl)-D-Glucoses and Distribution of Substituent Groups in O-(2-Diethylaminoethyl)Cellulose. *Can. J. Chem. 45*, 261−265.

(29) Alberto, R., Schibli, R., Egli, A., Schubiger, A. P., Abram, U., and Kaden, T. A. (1998) A novel organometallic aqua complex of technetium for the labeling of biomolecules: Synthesis of $[^{99m}Tc(OH_2)_3(CO)_3]^+$ from $[^{99m}TcO_4]^-$ in aqueous solution and its reaction with a bifunctional ligand. *J. Am. Chem. Soc. 120*, 7987−7988.

(30) Crystal data for **19**: colorless plates, orthorhombic space group $P2_12_12_1$, $T = 183$ K, Mo Kα, $\lambda = 0.71073$ Å, $a = 7.2693(3)$ Å, $b = 9.9472(4)$ Å, $c = 34.2689(15)$ Å, $\alpha = 0°$, $\beta = 90°$, $\gamma = 90°$, $Z = 4$, R1 = 0.0344, wR2 = 0.0721, GOF = 0.975, structure solution (direct) with SHELXS97, full-matrix least squares refinement on F^2 (SHELXS97).

(31) Stichelberger, A., Waibel, R., Dumas, C., Schubiger, P. A., and Schibli, R. (2003) Versatile synthetic approach to new bifunctional chelating agents tailor-made for labeling with the *fac*-$[M(CO)_3]^+$ core (M = Tc, ^{99m}Tc, Re): synthesis, in vitro, and in vivo behavior of the model complex $[M(APPA)(CO)_3]$ (appa = [(5-amino-pentyl)-pyridin-2-yl-methyl-amino]-acetic acid). *Nucl. Med. Biol. 30*, 465−470.

(32) Farrugia, L. J. (1997) ORTEP-3 for Windows − a version of ORTEP-III with a Graphical User Interface (GUI). *J. Appl. Crystallogr. 30*, 565−566.

BC049744I

Modulation of Pharmacokinetics of Radioiodinated Sugar-Conjugated Somatostatin Analogues by Variation of Peptide Net Charge and Carbohydration Chemistry

Margret Schottelius,[†] Friederike Rau,[†] Jean Claude Reubi,[‡] Markus Schwaiger,[†] and Hans-Jürgen Wester*,[†]

Nuklearmedizinische Klinik und Poliklinik, Klinikum rechts der Isar, Technische Universität München, 81675 München, Germany, and Institute of Pathology, University of Berne, 3010 Berne, Switzerland. Received March 26, 2004; Revised Manuscript Received January 13, 2005

Sugar conjugation of biooactive peptides has been shown to be a powerful tool to modulate peptide pharmacokinetics. In the case of radiolabeled somatostatin analogues developed for in vivo scintigraphy of somatostatin receptor (sst) expressing tumors, it generally led to tracers with predominant renal excretion and low uptake in nontarget organs, and in some cases also with enhanced tumor accumulation. Especially with respect to endoradiotherapeutic applicability of these tracers, however, understanding the structural requirements for minimal kidney accumulation and maximal tumor uptake is important. The aim of this study was therefore the evaluation of the potential of specific glycoside structures in combination with reduced peptide net charge to reduce kidney accumulation without affecting tumor accumulation. Three glyco analogues of radioiodinated Tyr^3-octreotate (TOCA) with $z = 0$ were evaluated in a comparative study using [^{125}I]Mtr-TOCA ($z = +1$), the maltotriose-Amadori analogue of [^{125}I]TOCA, as a reference, [^{125}I]Glucuron-TOCA, the Amadori conjugate with glucuronic acid, and [^{125}I]Gluc-*S*- and [^{125}I]Gal-*S*-TOCA, the coupling products with glucosyl- and mannosyl-mercaptopropionate. In cells transfected with sst_1−sst_5, all three new analogues show sst-subtype binding profiles similar to I-Mtr-TOCA with high, but somewhat reduced, affinity for sst_2. In contrast, internalization into sst_2-expressing cells (in % of [^{125}I]Tyr^3-octreotide ([^{125}I]TOC)) as well as the $EC_{50,R}$ of unlabeled TOC for internalization determined in dual-tracer experiments are substantially enhanced for [^{123}I]Gal-*S*-TOCA and [^{123}I]Gluc-*S*-TOCA (internalization, 190% ± 12% and 265% ± 20%, respectively, vs 168% ± 6% of [^{125}I]TOC for [^{123}I]Mtr-TOCA; $EC_{50,R}$, 2.62 ± 0.07 and 2.96 ± 0.14, respectively, vs 1.81 ± 0.07 for [^{123}I]Mtr-TOCA). The tumor accumulation of [^{125}I]Gal-*S*-TOCA and [^{125}I]Gluc-*S*-TOCA in AR42J tumor-bearing nude mice 1 h p.i. is consequently very high (22.6 ± 2.2 and 26.2 ± 5.6%ID/g) and comparable to that of [^{125}I]Mtr-TOCA (25.1 ± 4.4%ID/g). [^{125}I]Glucuron-TOCA showed lower uptake in sst-expressing tissues than did [^{125}I]Mtr-TOCA, but considerably enhanced accumulation in nontarget organs such as liver, intestine, and kidney. Due to increased lipophilicity, hepatic and intestinal uptake 1 and 4 h p.i. of [^{125}I]Gal-*S*-TOCA and [^{125}I]Gluc-*S*-TOCA was also slightly higher than that of [^{125}I]Mtr-TOCA. Kidney accumulation, however, was reduced by approximately 50% for both compounds (2.6 ± 0.3 and 2.2 ± 0.4, respectively, vs 4.0 ± 0.7%ID/g at 1 h p.i.). Because no sugar-specific effect was detected in the latter case, it is concluded that general ligand pharmacokinetics and especially kidney accumulation of the tracers investigated are mainly determined by physicochemical characteristics such as lipophilicity, net charge, and also charge distribution ([^{125}I]Glucuron-TOCA vs [^{125}I]Gal-*S*- and [^{125}I]Gluc-*S*-TOCA). With respect to receptor targeting, however, the structure of the carbohydrate moiety plays an important role, leading to dramatically enhanced ligand internalization, especially in the case of [^{123}I]Gluc-*S*-TOCA. Taking into account the combined effects of the Gluc-*S*-moiety both on kidney and on tumor accumulation, this group seems to be a promising synthon for the synthesis of other radiolabeled peptide analogues with improved pharmacokinetics.

INTRODUCTION

That the introduction of carbohydrates into small bioactive peptides may have significant beneficiary impact on peptide pharmacokinetics has been demonstrated in a variety of studies. This approach has been successfully applied to improve drug delivery to the target tissues, either exploiting specific uptake mechanisms or enhanced peptide bioavailability. For example, enkephalin peptides glycosylated near or at the C-terminus were shown to elicit prolonged and profound analgesia in mice due to enhanced peptide delivery to the brain (*1*−*3*). Conjugation of Arg^8-vasopressin with alkyl-glucosides or -mannosides led to substantially enhanced and specific renal peptide uptake from blood (*4*). Furthermore, besides a stabilization toward enzymatic degradation in vivo, carbohydration of the tetrapeptide Gly−Gly−Tyr−Arg was shown to entail enhanced intestinal absorption of the peptide via the Na^+-dependent glucose transporter SGLT-1 (*5*). Enhanced bioavailability, both oral and intravenous, was observed for several other glycopeptides

* To whom correspondence should be addressed. Telephone: 49 89 4140 4586. Fax: 49 89 4140 4841. E-mail: h.j.wester@lrz.tum.de.

[†] Technische Universität München.

[‡] University of Berne.

10.1021/bc0499228 CCC: $30.25 © 2005 American Chemical Society
Published on Web 02/22/2005

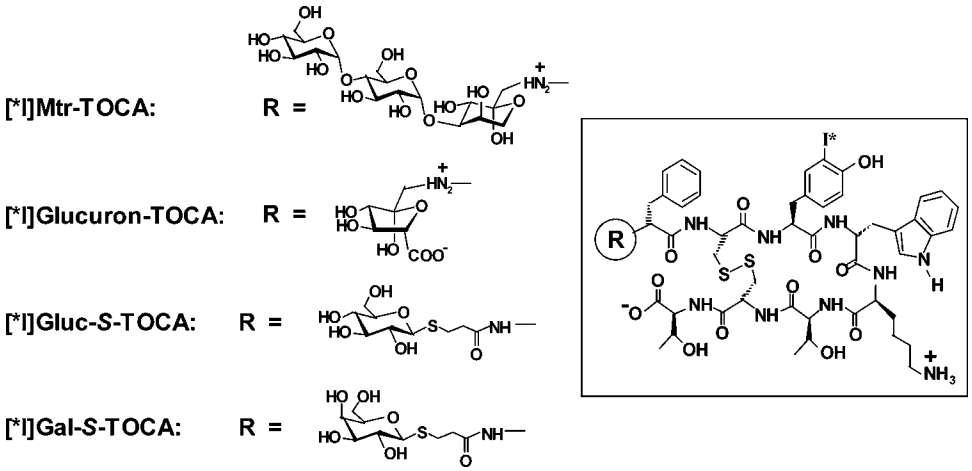

Figure 1. Structures of [^{125}I]Mtr-TOCA, [^{125}I]Glucuron-TOCA, [^{125}I]Gluc-*S*-TOCA, and [^{125}I]Gal-*S*-TOCA.

such as an N-linked glycopeptide renin inhibitor (*6*), glycosylated vasopressin analogues (*7*), and several Amadori sugar derivatives of octreotide (*8*). This effect was attributed to enhanced in vivo stability of the peptides, a shift from hepatobiliary toward renal excretion, leading to higher plasma levels of the drug (*6*, *8*), and to improved absorption from the small intestine (*7*).

These findings also constitute the basis of the recent development of a series of radiolabeled, glycosylated octreotide (*9*−*15*) and RGD analogues (*16*, *17*) as receptor ligands for the in vivo scintigraphic detection of somatostatin receptor (sst) and $\alpha v\beta 3$-integrin expressing human malignancies, respectively. Especially the sst-receptors are of high clinical relevance in nuclear oncology, because many tumors, predominantly those of neuroendocrine origin, show overexpression of somatostatin receptors (*18*), and especially of the sst_2-subtype (*19*, *20*). This overexpression allows high-level targeting of sst-expressing tumors both for scintigraphic and for endoradiotherapeutic applications. For these purposes, however, radiolabeled sst analogues need to meet certain prerequisites: fast clearance kinetics, predominant renal excretion, as well as high receptor affinity and selectivity, all of which lead to high target-to-nontarget tissue ratios (tumor-to-nontumor ratios).

That these can be substantially improved by glycosylation has been demonstrated in the case of various radiolabeled Tyr^3-octreotide (TOC) and Tyr^3-octreotate (TOCA) derivatives, which have been modified with different aldoses via Amadori reaction. As compared to their nonglycosylated counterparts, all showed substantially reduced hepatobiliary clearance in favor of fast renal excretion. This effect was found to correlate with increasing carbohydrate size, with the maltose derivatives showing the lowest extent of nonspecific accumulation in nontarget tissues such as liver and intestine (*9*−*15*).

Interestingly, the influence of carbohydration on the biodistribution of [^{125}I]TOC and [^{125}I]TOCA was not only limited to the above expected effect. For both glucose analogues, [^{125}I]Gluc-TOC and [^{125}I]Gluc-TOCA, ligand internalization into sst-expressing cells was significantly enhanced as compared to the nonmodified parent peptide (*14*, *15*). This effect was also reflected in the increased tumor accumulation of these radioligands. Despite an internalization efficiency comparable to that of [^{125}I]-TOCA, however, the maltotriose analogue [^{125}I]Mtr-TOCA (Figure 1) showed the highest tumor accumulation in AR42J tumor-bearing nude mice of all glyco derivatives investigated (25.1 ± 4.4%ID/g at 60 min p.i., *11*).

Furthermore, although the glucose- and maltose-Amadori derivatives of [^{125}I]TOC showed an increasing preference of renal over hepatobiliary excretion, their renal accumulation remained unaffected as compared to [^{125}I]-TOC (*10*). This finding suggested that, because the peptides investigated all bear approximately the same net charge under physiological conditions (+1.8 to +2 (positive charges on d-Phe^1 and Lys^5)), charge-dependent endocytosis into renal tubular cells may be the main contributor to kidney accumulation of these peptides, rendering an influence of carbohydrate structure on kidney accumulation improbable. The contrary, however, was observed in the case of [^{125}I]TOCA and its sugar analogues, where both the glucose and the maltose analogues showed a reduction of kidney accumulation by up to 50% as compared to [^{125}I]TOCA and its maltotriose analogue [^{125}I]Mtr-TOCA (*15*), indicating a certain influence of the sugar moiety on renal tracer accumulation in these cases.

It was therefore of interest to investigate in more detail the physicochemical and structural requirements for combined optimization of both receptor targeting and maximal reduction of kidney uptake of radiolabeled TOCA derivatives. As demonstrated in a previous study using different ^{111}In-DTPA-conjugated octreotide analogues, reduction of peptide net charge can lead to reduced renal tracer accumulation (*21*). This methodology was therefore chosen to attempt a further reduction of kidney uptake of radioiodinated, glycosylated TOCA analogues. Two approaches leading to glycopeptides with a net charge $z = 0$ instead of $z = 1$ were investigated: introduction of an additional negative charge by Amadori reaction of TOCA with glucuronic acid, leading to Glucuron-TOCA (Figure 1), and "removal" of the N-terminal positive charge via an alternative glycosylation route, that is, N-terminal acylation, leading to Gluc-*S*- and Gal-*S*-TOCA (Figure 1). In the latter case, the glycosylation method was based on results of Suzuki et al., who had demonstrated that kidney accumulation of Arg^8-vasopressin could not only be specifically enhanced by conjugation with certain O- and S-alkyl-glycosides, but could also be significantly reduced, depending on the length of the alkyl chain and the structure of the carbohydrate used (*4*, *22*). In this study, the structure of the alkylglycoside was chosen such that renal targeting via the basolateral membrane was highly improbable (*22*, *23*), that is, a very short alkyl chain (mercaptopropionyl). Due to the higher in vivo stability of S- versus O-glycosides, this spacer was used to link two different carbohydrates to [^{125}I]TOCA to study eventual influences of carbohy-

drate structure on the pharmacokinetics of the corresponding radiolabeled peptide. All three new compounds were evaluated in detail in vitro and in vivo, and data on receptor affinity, ligand internalization, and pharmacokinetics, especially with respect to renal uptake and tumor accumulation, were compared to those obtained with [^{125}I]Mtr-TOCA.

EXPERIMENTAL PROCEDURES

Peptide Synthesis. *General Conditions.* TCP-resin was obtained from PepChem (Tübingen, Germany). Fmoc- and other amino acids were supplied by Novabiochem or Bachem (Heidelberg, Germany). All other organic reagents were purchased from VWR (Darmstadt, Germany), Alexis (Grünberg, Germany), Aldrich, or Fluka (Neu-Ulm, Germany). Solvents were used without further purification.

Solid-phase peptide synthesis was carried out manually using a flask shaker (St. John Associates Inc., USA).

Thin-layer chromatography was performed using Kieselgel 60 F_{254} TLC plates from Merck (Darmstadt, Germany). UV absorption at 254 nm was detected using a Fluotest UV lamp. Compounds that showed no UV absorption were detected by treating the TLC plate with a solution of 0.5 mL of anisaldehyde and 1 mL of concentrated sulfuric acid in 50 mL of acetic acid and subsequent heating to 150−200 °C.

Flash-chromatographic separations were carried out using silica gel 60 (particle size 0.04−0.063 mm) with a mesh of 230−400 from Fluka (Neu-Ulm, Germany).

Analytic RP-HPLC was performed on Nucleosil 100 C18 (5 μm, 125 × 4.0 mm) columns (CS GmbH, Langerwehe, Germany) using a Sykam gradient HPLC System (Sykam, Fürstenfeldbruck, Germany). The peptides were eluted applying various gradients of 0.1% TFA (trifluoroacetic acid) in H_2O (solvent A) and 0.1% TFA in acetonitrile (solvent B) in 15 min at a constant flow of 1 mL/min. UV-Detection was performed at 220 nm in a 206 PHD UV−vis detector (Linear Instruments Corp., Reno, NV). For radioactivity measurement, the outlet of the UV-photometer was connected to a NaI(Tl) well-type scintillation counter from EG&G Ortec (München, Germany).

Preparative RP-HPLC was performed on the same HPLC system using a Multospher 100 RP 18-5 (250 × 10 mm) column (CS GmbH, Langerwehe, Germany) at a constant flow of 5 mL/min.

Mass spectra were recorded on the LC-MS system LCQ from Finnigan (Bremen, Germany) using the Hewlett-Packard series 1100 HPLC system.

Mtr-TOCA. Mtr-TOCA was synthesized as described previously (*11*). Briefly, the sequence H_2N−D-Phe−Cys(Trt)−Tyr(tBu)−D-Trp−Lys(Dde)−Thr(tBu)−Cys(Trt)−Thr(tBu) was assembled on TCP-resin using a standard Fmoc-protocol. After cleavage from the solid support using TFA/H_2O/TIBS (triisobutylsilane) (95/2.5/2.5 (v/v/v)), Lys^5(Dde)-TOCA (TOCA(Dde)) was cyclized using H_2O_2 in an aqueous THF (tetrahydrofurane) solution at pH 7. Derivatization with maltotriose was performed via Maillard reaction and subsequent Amadori rearrangement by treating the Lys^5(Dde)-protected peptide with 5 equiv of maltotriose in methanol/acetic acid (95/5) at 60 °C. Subsequent removal of the Lys^5(Dde) protecting group was carried out using 2% of hydrazine hydrate in DMF (dimethylformamide). After product isolation via preparative HPLC, Mtr-TOCA was obtained in 23% yield (based on Lys^5(Dde)-TOCA).

HPLC (15%→45% in 15 min): t_R = 7.88 min; K' = 3.52.

Calculated monoisotopic mass for Mtr-TOCA ($C_{67}H_{94}N_{10}O_{27}S_2$) = 1534.6;

found: m/z = 1535.2 $[M + H]^+$, m/z = 1557.2 $[M + Na]^+$.

Glucuron-TOCA. The synthesis of Glucuron-TOCA was performed according to the procedure described for Mtr-TOCA. For the conjugation of Lys^5(Dde)-TOCA with glucuronic acid, 10 equiv of the carbohydrate was used.

Yield after preparative HPLC: 24%.

HPLC (10%→60% in 15 min): t_R = 10.7 min; K' = 4.79.

Calculated monoisotopic mass for Glucuron-TOCA ($C_{55}H_{72}N_{10}O_{18}S_2$) = 1224.4;

found: m/z = 1225.3 $[M + H]^+$, 1247.3 $[M + Na]^+$, 1263.1 $[M + K]^+$.

Gluc-S-TOCA and Gal-S-TOCA. Both 1-*S*-(2,3,4,6-tetraacetyl-glucopyranosyl)-3-mercaptopropionate (Gluc(4Ac)-*S*-OH) and 1-*S*-(2,3,4,6-tetraacetyl-galactopyranosyl)-3-mercaptopropionate (Gal(4Ac)-*S*-OH) were prepared according to the literature (*24*). Synthesis of the corresponding pentafluorophenyl (Pfp) active esters Gluc(4Ac)-*S*-OPfp and Gal(4Ac)-*S*-OPfp was carried out as described previously using *N*,*N*′-diisopropyl carbodiimide (1.1 equiv) and pentafluorophenol (1.1 equiv) in THF (*13*). For sugar conjugation of TOCA(Dde), the peptide (50−100 mg, 1 equiv) and Gluc/Gal(4Ac)-*S*-OPfp (1.1 equiv) were dissolved in 1−2 mL of DMF and stirred at room temperature for 2 h in the presence of 1 equiv of Hünigs Base. After product precipitation using Et_2O and washing of the precipitate with Et_2O, the respective glycosylated peptides were obtained in 46−67% yield. Gluc(4Ac)-*S*-TOCA(Dde): HPLC (30%→80% B in 15 min): t_R = 12.1 min; K' = 6.31. Gal(4Ac)-*S*-TOCA(Dde): HPLC (30%→80% B in 15 min): t_R = 12.0 min; K' = 6.42.

After Dde-deprotection for 10 min at room temperature, the peptides were precipitated using Et_2O (diethyl ether). For subsequent sugar deacylation, peptides were redissolved in 1 mL of methanol containing 0.5 equiv of KCN (*25*). Deacylation was complete after stirring at room temperature for 4−48 h. The product was then precipitated using Et_2O and purified via preparative HPLC, yielding Gluc-*S*-TOCA and Gal-*S*-TOCA in yields of 12−15% (based on TOCA(Dde)).

Gluc-*S*-TOCA: HPLC (20%→70% B in 15 min): t_R = 8.2 min; K' = 3.99.

Gal-*S*-TOCA: HPLC (20%→70% B in 15 min): t_R = 8.3 min; K' = 3.96.

Calculated monoisotopic mass for Gluc-*S*-TOCA and Gal-*S*-TOCA ($C_{58}H_{78}N_{10}O_{18}S_3$)

found: m/z = 1299.3 $[M + H]^+$, 1321.3 $[M + Na]^+$, 1337.2 $[M + K]^+$.

3-Iodo-Tyr^3-Reference Compounds. For the synthesis of the 3-iodo-Tyr^3-reference compounds, Fmoc−Tyr(tBu)−OH was replaced by Fmoc−3-iodo-Tyr(tBu)−OH during SPPS. All other reaction steps were performed analogously to the syntheses presented in the previous section.

I-Mtr-TOCA. HPLC (10%→60% B in 15 min): t_R = 11.2 min; K' = 6.33.

Calculated monoisotopic mass for I-Mtr-TOCA ($C_{67}H_{93}N_{10}O_{27}S_2I$) = 1660.5;

found: m/z = 1661.2 $[M + H]^+$.

I-Glucuron-TOCA. HPLC (10%→60% B in 15 min): t_R = 11.1 min; K' = 6.41.

Calculated monoisotopic mass for I-Glucuron-TOCA ($C_{55}H_{71}N_{10}O_{18}S_2I$) = 1350.3;

found: m/z = 1351.3 $[M + H]^+$, 1373.3 $[M + Na]^+$, 1389.2 $[M + K]^+$.

I-Gluc-S-TOCA. HPLC (20%→70% B in 15 min): t_R = 9.2 min; K' = 4.72.

Calculated monoisotopic mass for I-Gluc-*S*-TOCA ($C_{58}H_{77}N_{10}O_{18}S_3I$) = 1424.4;
found: *m/z* = 1425.6 $[M + H]^+$, 1447.6 $[M + Na]^+$, 1463.5 $[M + K]^+$.

I-Gal-S-TOCA. HPLC (20%→70% B in 15 min): t_R = 9.1 min; K' = 4.79.

Calculated monoisotopic mass for I-Gal-*S*-TOCA ($C_{58}H_{77}N_{10}O_{18}S_3I$) = 1424.4;
found: *m/z* = 1425.6 $[M + H]^+$, 1447.6 $[M + Na]^+$, 1463.5 $[M + K]^+$.

Peptide Radioiodination. Radioiodination was generally performed using the Iodogen method.

A solution of 100−200 μg of peptide in 200 μL of PBS (phosphate buffered saline, 0.1 M, pH 7.4) was transferred to an Eppendorf cap coated with 30 μg of Iodogen (Pierce, Rockford, USA). After the addition of 5−20 μL of solution of radioiodide (Amersham, Buckinghamshire, UK) in 0.05 M NaOH ([^{125}I]NaI (n.c.a.), 18−74 MBq; [^{123}I]-NaI (c.a.), 37−185 MBq), the cap was vortexed and the labeling reaction was allowed to proceed for 20 min at room temperature. The peptide solution was then removed from the insoluble oxidizing agent.

The radioiodinated peptides were purified via RP-HPLC using an isocratic solvent mixture of 25% ([^{123}I]-Mtr-TOCA), 28% ([^{123}I]Glucuron-TOCA), or 33% ([^{123}I]-Gluc-*S*-TOCA and [^{123}I]Gal-*S*-TOCA) EtOH (0.5% AcOH) in water (0.5% AcOH).

For the biodistribution experiments, an excess of absolute ethanol was added to the collected fraction, and the solvents were evaporated to dryness. The radioiodinated product was reconstituted in PBS to yield a solution of radiolabeled peptide with an activity concentration of approximately 370 kBq/100 μL.

For the paired-label internalization experiments, [^{125}I]-TOC and the respective ^{123}I-labeled radioligand were each separately redissolved in assay medium (containing 5% BSA) and diluted to an activity concentration of approximately 200 000 cpm/10 μL. A 1:1 (v/v) mixture of both solutions containing approximately 100 000 cpm/10 μL of each radioligand was then used for the internalization experiment.

In Vitro Studies. *sst-Receptor Binding Affinities.* Cells stably expressing human sst_1, sst_2, sst_3, sst_4, and sst_5 were grown as described previously (*26*). Cell membrane pellets were prepared, and receptor autoradiography was performed on pellet sections (mounted on microscope slides), as described in detail previously (*26*). For each of the tested compounds, complete displacement experiments were performed with the universal somatostatin radioligand ^{125}I-[Leu^8, D-Trp^{22}, Tyr^{25}]-somatostatin 28 using increasing concentrations of the unlabeled peptide ranging from 0.1 to 1000 nM. Somatostatin 28 was run in parallel as control using the same increasing concentrations. IC_{50} values were calculated after quantification of the data using a computer-assisted image processing system. Tissue standards (autoradiographic [^{125}I]microscales Amersham), containing known amounts of isotopes, cross-calibrated to tissue equivalent ligand concentrations, were used for quantification (*26*).

Internalization and Determination of $EC_{50,R}$. CHO cells stably transfected with human sst_2 (epitope tagged at the N-terminal end) were kindly provided by Dr. Jenny Koenig, University of Cambridge, UK. Cells were grown in DMEM/Nutrition Mix F-12 with Glutamax-I (1:1) (Gibco BRL) supplemented with 10% FCS and 500 mg/L Geneticin (Gibco BRL). For the preparation of the solutions used for the internalization studies containing various concentrations of unlabeled TOC, FCS was replaced by 5% BSA (Sigma, St. Louis, MO).

For cell counting, a CASY1-TT cell counter and analyzer system (Schärfe System GmbH, Reutlingen, Germany) was used.

Internalization experiments were carried out as previously described in detail (*13*). Briefly, after preconditioning of the cells (approximately 100 000 cells/well) with 190 μL of unsupplemented medium for a minimum of 15 min, 50 μL (per well) of DMEM (5% BSA) containing increasing concentrations of unlabeled TOC (Tyr^3-octreotide) was added, followed by the addition of approximately 100 000 cpm of both the respective ^{123}I-labeled glycosylated peptide and the reference [^{125}I]TOC in 10 μL of DMEM (5% BSA). Final TOC concentrations in the incubation medium used for the determination of the $EC_{50,R}$ were 0.1, 0.2, 0.5, 0.8, 1, 2, 4, 6, 8, 10, 12, 15, 20, 50, 100, 500, and 1000 nM. In a control experiment (n.c.a. conditions), TOC-free DMEM (5% BSA) was added. Nonspecific internalization was determined by including 5 μM unlabeled TOC. Experiments were carried out in triplicate for each concentration.

After incubation at 37 °C (10 min), the incubation medium was removed, and cells were rinsed with 250 μL of fresh medium. The combined medium fractions represent the amount of free radioligand. Receptor bound (acid releasable) radioactivity was then removed using 2 × 250 μL of ice-cold acid wash buffer (0.02 M NaOAc buffered with AcOH to pH = 5). The internalized activity was released by incubation with 250 μL of 1 N NaOH, tranferred to vials, and combined with 250 μL of PBS used for rinsing the wells. Quantification of the amount of free, acid-releasable, and internalized activity was performed in a γ-counter.

For numerical analysis of the EC_{50} of TOC for internalization, data for both the ^{123}I-labeled compound of interest and the reference [^{125}I]TOC in the same experiment were first corrected by the amount of nonspecific internalization, respectively, and then each normalized to the amount of internalized ligand in the absence of unlabeled competitor (100%). Data were fitted with a weighted two-parameter logistic function using Sigma Plot. To eliminate the influence of cell count and cell viability on the absolute EC_{50}-values, data are expressed as the ratio ($EC_{50,R}$) of the EC_{50} observed for the compound of interest (COI) and the EC_{50} found for [^{125}I]TOC in the same experiment ($EC_{50,R} = EC_{50}(COI)/EC_{50}([^{125}I]\text{-TOC})$).

Biodistribution Experiments. *Tumor Model.* The AR42J cell line as a transplantable rat pancreatic tumor model with high sst_2 somatostatin receptor expression (*27*) was used. AR42J cells were obtained from ECACC (European Collection of Cell Cultures, Salisbury, UK). Cells were maintained in RPMI 1640 (Seromed, Berlin, Germany) supplemented with 10% FCS (Seromed) and 2 mM L-glutamine (Gibco BRL Life Technologies, Karlsruhe, Germany). To establish tumor growth, cells were detached from the surface of the culture flasks using 1 mM EDTA in PBS, centrifuged, and resuspended in serum-free culture medium. Concentration of the cell suspension was (2.5−5) × 10^6 cells/100 μL serum. Into nude mice (Swiss nu/nu, female, 6−8 weeks, from Charles River WIGA GmbH (Sulzfeld, Germany)) was injected 100 μL of the cell suspension subcutaneously into the flank. Ten days after tumor transplantation, all mice showed solid palpable tumor masses (tumor weight 20−200 mg) and were used for the experiments.

Biodistribution Studies. The radiolabeled peptides, 370 kBq (10 μCi) in 100 μL of PBS (pH 7.4), were injected i.v. into a tail vein of nude mice bearing an AR42J tumor. For competition studies, 10 μg TOC (0.4 mg/kg) was co-

Table 1. Affinity Profiles of Somatostatin 28 and the Compounds Investigated for Human sst_1−sst_5 Receptors Using ^{125}I-[Leu^8, D-Trp^{22}, Tyr^{25}]-Somatostatin 28 as the Radioligand (Values Are IC_{50} ± SD [nM], Number of Experiments in Parentheses)

peptide	hsst1	hsst2	hsst3	hsst4	hsst5
SS-28	3.6 ± 0.3 (5)	2.1 ± 0.3 (5)	3.2 ± 0.2 (5)	3 ± 0.3 (5)	2.5 ± 0.2 (5)
I-TOC	>10 000 (5)	1.3 ± 0.3 (5)	128 ± 22 (5)	867 ± 33 (5)	50 ± 12 (5)
I-TOCA	>10 000 (3)	0.47 ± 0.2 (3)	187 ± 38 (3)	337 ± 57 (3)	50 ± 5.8 (3)
I-Mtr-TOCA	>10 000 (3)	0.95 ± 0.3 (3)	823 ± 67 (3)	823 ± 87 (3)	327 ± 93 (3)
I-Glucuron-TOCA	>1 000 (2)	2.9 ± 1.3 (2)	>1000 (2)	220 ± 23 (2)	414 ± 160 (2)
I-Gluc-*S*-TOCA	>1 000 (3)	2.0 ± 0.7 (3)	398 ± 19 (3)	356 ± 60 (3)	310 ± 156 (3)
I-Gal-*S*-TOCA	>1 000 (3)	2.0 ± 0.8 (3)	491 ± 63 (3)	482 ± 134 (3)	413 ± 167 (3)

injected with the radioligands. The animals (groups of 3−4) were sacrificed 1 and 4 h postinjection, and the organs of interest were dissected. The radioactivity was measured in weighted tissue samples using a γ-Counter.

RESULTS

Peptide Synthesis. Solid-phase peptide synthesis using a standard Fmoc-protocol and HOBt/TBTU as coupling reagents yielded TOCA(Dde) and its 3-iodo-Tyr^3 analogue, I-TOCA(Dde), in 90−97% yield based on resin-bound Fmoc−Thr(tBu)−OH. Quantitative disulfide bridge formation was achieved within less than 30 min at room temperature using H_2O_2 in an aqueous THF-solution buffered to pH 7. While UV purity (220 nm) of crude cyclized TOCA(Dde) usually exceeded 93%, more side products were observed for the 3-iodo-Tyr^3-containing peptide (up to 20%). However, both peptides were used for the following reaction steps without further purification.

N-terminal glycosylation of the parent peptides with maltotriose (Mtr-) and glucuronic acid (Glucuron-) via Amadori reaction required reaction times of 16−20 h at 60 °C, and glycosylation yields usually did not exceed 85% (value based on the integration of product and precursor peaks in the reaction control RP-HPLC chromatograms (220 nm)). In contrast, N-terminal conjugation with the respective pentafluorophenyl active esters of (1-*S*-2,3,4,6-tetraacetyl-gluco/galactopyranosyl)-3-mercaptopropionate was quantitative within 30−45 min at room temperature.

Subsequent Dde-deprotection (and deacetylation in the case of Gluc-*S*- and Gal-*S*-TOCA), followed by preparative RP-HPLC purification, afforded all glycosylated TOCA derivatives as well as their 3-iodo-Tyr^3-counterparts in overall yields of 12−25% (based on nonglycosylated precursor) and in purities ≥98% (220 nm).

Radiolabeling. Due to the formation of radioiodinated side products, overall radiochemical yields of the ^{125}I- and ^{123}I-labeled peptides after RP-HPLC isolation were limited to 45−73%. Radiochemical purities of the isolated radioiodinated peptides, however, usually exceeded 98%.

The HPLC conditions applied allowed very efficient separation of the radioiodinated product from the unlabeled precursor ($\Delta t_R \geq 5$ min (*13*)) for all radioligands investigated. Thus, and because no coeluting carrier peak was observed in the labeled peptide peak in the quality control UV-chromatograms, the specific activity of the labeled peptides was assumed to be that of the radioiodide used for their preparation (≥2000 Ci/mmol for ^{125}I, ∼5000 Ci/mmol for ^{123}I).

In Vitro Studies. The affinities of I-Mtr-TOCA, I-Glucuron-TOCA, I-Gluc-*S*-TOCA, and I-Gal-*S*-TOCA to the five human sst-subtypes sst_1−sst_5 are summarized in Table 1 and compared to those of the reference I-TOC and of nonglycosylated I-TOCA. All sugar analogues show very high and comparable affinity to $hsst_2$, no affinity to $hsst_1$, and low to moderate affinity to $hsst_{3-5}$. As compared to I-TOCA, all glycosylated derivatives show significantly reduced affinities to $hsst_3$ and $hsst_5$. This effect, however, is more pronounced in the case of the Amadori analogues than for the two thioglycoside-modified peptides. Of the carbohydrated peptides investigated, I-Mtr-TOCA shows the highest $hsst_2$-specificity.

Table 2. Internalization (in % of the Reference [^{125}I]TOC) and Relative EC_{50} Values ($EC_{50,R}$) of Unlabeled TOC for Inhibition of the Internalization of [^{123}I]TOCA and the Sugar Analogues Investigated (CHO cells ($hsst_2$), 10 min Incubation, $n = 3$ in Three Separate Determinations, Mean ± SD)

	internalized [% of [^{125}I]TOC]	$EC_{50,R}$
[^{125}I]TOC	100	1
[^{123}I]TOCA	178.8 ± 6.9	1.70 ± 0.11
[^{123}I]Mtr-TOCA	168.0 ± 5.8	1.81 ± 0.07
[^{123}I]Gluc-*S*-TOCA	264.7 ± 20.3	2.96 ± 0.14
[^{123}I]Gal-*S*-TOCA	189.8 ± 11.7	2.62 ± 0.07

It has been shown in a previous study that the sst_2-affinity of radioiodinated sugar analogues of TOC and TOCA does not correlate with in vivo tumor accumulation (*13*). In contrast, both the internalization of a ligand in % of the reference [^{125}I]TOC, and the $EC_{50,R}$ of unlabeled TOC for ligand internalization ($EC_{50,R} = EC_{50}$(compound of interest):EC_{50}([^{125}I]TOC)) have been shown to be good predictive parameters for tumor uptake in vivo (*13*). Therefore, these two quantities have also been determined for the four compounds in this study (Table 2).

Internalization of all sugar analogues into $hsst_2$-expressing CHO cells was substantially increased as compared to the reference [^{125}I]TOC. For both [^{123}I]Mtr-TOCA and [^{123}I]Gal-*S*-TOCA, however, it remained almost unchanged as compared to nonmodified [^{123}I]TOCA (Table 2). Interestingly, the $EC_{50,R}$ of [^{123}I]Mtr-TOCA was also comparable to that of [^{123}I]TOCA, while it was significantly higher for [^{123}I]Gal-*S*-TOCA (2.6 vs 1.7). Only in the case of [^{123}I]Gluc-*S*-TOCA, however, was the very high $EC_{50,R}$ (3.0) also accompanied by dramatically enhanced ligand internalization (260% vs 170−190% of [^{125}I]TOC for all other TOCA analogues).

Biodistribution Studies. The biodistribution of [^{125}I]-Mtr-TOCA, [^{125}I]Glucuron-TOCA, [^{125}I]Gluc-*S*-TOCA, and [^{125}I]Gal-*S*-TOCA in AR42J tumor-bearing nude mice 1 and 4 h postinjection is shown in Table 3. Clearance of all four glycopeptides from the circulation is very rapid, resulting in low blood activity concentrations (0.47−0.75%ID/g) already 1 h p.i. Of the four compounds investigated, [^{125}I]Glucuron-TOCA showed the highest blood activity level, and also high nonspecific accumulation in kidney, liver, and intestine, the latter being nearly twice as high as that observed for [^{125}I]Mtr-TOCA. For both [^{125}I]Gluc-*S*-TOCA and [^{125}I]Gal-*S*-TOCA, almost identical biodistribution in nontarget organs was observed at all time points. As compared to [^{125}I]Mtr-TOCA, these two compounds show slightly increased hepatic and intestinal uptake, but also a reduction in renal activity

Table 3. Biodistribution of [^{123}I]Mtr-TOCA, [^{123}I]Glucuron-TOCA, [^{125}I]Gluc-*S*-TOCA, and [^{125}I]Gal-*S*-TOCA in AR42J Tumor-Bearing Nude Mice 1 and 4 h p.i. (Data Are %ID/g (mean ± SD, Groups of 3−4))

	[^{123}I]Mtr-TOCA		[^{123}I]Glucuron-TOCA		[^{125}I]Gluc-*S*-TOCA		[^{125}I]Gal-*S*-TOCA	
	1 h p.i.	4 h p.i.	1 h p.i.	4 h p.i.	1 h p.i.	4 h p.i.	1 h p.i.	4 h p.i.
blood	0.47 ± 0.10	0.26 ± 0.03	0.75 ± 0.08	0.34 ± 0.11	0.54 ± 0.13	0.28 ± 0.06	0.64 ± 0.09	0.30 ± 0.06
liver	0.43 ± 0.07	0.20 ± 0.03	0.95 ± 0.16	0.27 ± 0.06	0.61 ± 0.13	0.18 ± 0.05	0.80 ± 0.12	0.23 ± 0.04
intestine	4.29 ± 1.54	5.24 ± 0.56	8.05 ± 0.73	7.44 ± 2.91	5.23 ± 1.46	6.97 ± 1.30	5.53 ± 1.08	8.73 ± 3.73
kidney	3.98 ± 0.71	1.69 ± 0.21	4.34 ± 0.57	1.36 ± 0.29	2.24 ± 0.41	0.69 ± 0.13	2.58 ± 0.31	0.70 ± 0.07
lung	1.93 ± 1.04	0.90 ± 0.31	1.57 ± 0.50	0.68 ± 0.27	2.21 ± 1.32	0.77 ± 0.24	2.81 ± 1.26	0.79 ± 0.41
spleen	0.57 ± 0.10	0.31 ± 0.07	0.70 ± 0.21	0.34 ± 0.05	0.61 ± 0.12	0.28 ± 0.07	0.94 ± 0.46	0.49 ± 0.01
muscle	0.08 ± 0.02	0.08 ± 0.03	0.17 ± 0.02	0.09 ± 0.04	0.10 ± 0.02	0.09 ± 0.05	0.14 ± 0.03	0.07 ± 0.02
stomach	17.47 ± 2.78	5.92 ± 0.74	9.47 ± 0.98	3.30 ± 1.06	18.82 ± 3.39	4.24 ± 0.79	21.96 ± 1.61	3.93 ± 0.94
adrenals	5.30 ± 1.78	2.71 ± 0.07	3.65 ± 0.83	2.11 ± 0.60	4.98 ± 1.76	2.37 ± 0.15	6.29 ± 1.14	3.95 ± 0.88
pancreas	14.38 ± 4.39	3.93 ± 0.39	6.44 ± 2.58	1.37 ± 0.14	14.18 ± 4.57	3.35 ± 0.42	21.17 ± 6.57	2.87 ± 0.38
tumor	25.11 ± 4.40	12.80 ± 2.97	19.78 ± 3.12	5.87 ± 0.37	26.15 ± 5.56	7.54 ± 2.22	22.55 ± 2.16	6.35 ± 0.86

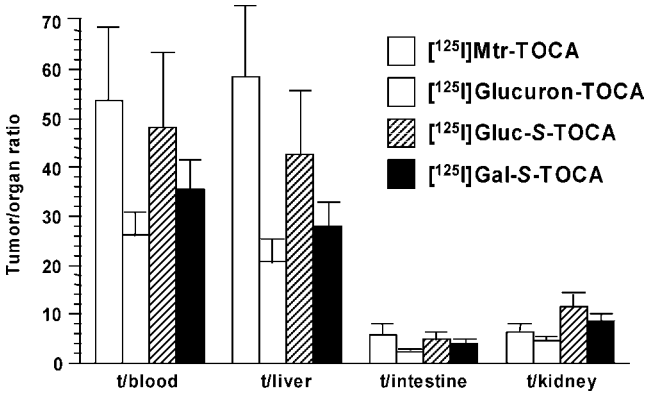

Figure 2. Tumor-to-organ ratios of [^{125}I]Mtr-TOCA, [^{125}I]-Glucuron-TOCA, [^{125}I]Gluc-*S*-TOCA, and [^{125}I]Gal-*S*-TOCA in AR42J tumor-bearing nude mice 60 min p.i. (mean ± SD, n = 3−4).

accumulation by up to 45% and 60% at 1 and 4 h p.i., respectively.

For all four peptides, the observed decrease in hepatic activity within the observation period was accompanied by an increase in intestinal activity accumulation, indicating a certain contribution of hepatobiliary excretion to overall tracer clearance. The substantial drop in kidney activity levels between 1 and 4 h p.i. detected for all four carbohydrated TOCA analogues indicates that, despite predominant renal excretion of the radiopeptides, no real tracer accumulation, that is, uptake and retention in renal tissue, occurs.

Of the glycopeptides investigated, [^{125}I]Glucuron-TOCA showed the lowest, albeit still very high, accumulation in sst-expressing tissues, that is, stomach, adrenals, pancreas, and tumor. Interestingly, tracer uptake in stomach and pancreas was highest for [^{125}I]Gal-*S*-TOCA, whereas tumor accumulation of this peptide was slightly lower than that of [^{125}I]Mtr-TOCA and [^{125}I]Gluc-*S*-TOCA (22.6 vs 25.2 and 26.2%ID/g at 1 h p.i., respectively). In most cases, tumor-to-organ ratios are therefore highest for these compounds, both 1 (Figure 2) and 4 h p.i. Due to their particularly low renal accumulation, however, tumor/kidney ratios are highest for [^{125}I]Gluc-*S*-TOCA and [^{125}I]Gal-*S*-TOCA (11.7 and 8.7 vs 6.3 and 4.6 for [^{125}I]-Mtr-TOCA and [^{125}I]Glucuron-TOCA, respectively, at 1 h p.i.).

As expected for radioiodinated tracers, washout of the four glycopeptides investigated from sst-expressing tissues between 1 and 4 h p.i. was considerable. Interestingly, tumor retention of [^{125}I]Mtr-TOCA was significantly higher than that of the other three peptides; that is, 50% instead of 28−30% of the tumor-localized activity at 1 h p.i. were still found inside the tumor at 4 h p.i. in the case of [^{125}I]Mtr-TOCA.

Receptor-specificity of ligand accumulation in sst-positive organs was demonstrated in a competition study (Figure 3). Co-injection of 10 μg unlabeled TOC per mouse led to a dramatic and comparable reduction of ligand accumulation in stomach, adrenals, pancreas, and tumor to 7−13%, 22−30%, 8−14%, and 18−31% of control (1 h p.i.) for all compounds investigated.

DISCUSSION

Maximizing tumor targeting and minimizing nonreceptor-mediated accumulation in excretion organs generally are the most important goals in the development of new receptor-targeted peptide tracers for application in nuclear oncology. The first can only be achieved by strutural modifications of the receptor ligand itself; for example, in the case of various radiometalated and radiohalogenated analogues of the somatostatin receptor ligand Tyr^3-octreotide (TOC), the desired improvement of receptor-mediated ligand accumulation was achieved by substitution of Thr(ol)^8 by Thr^8, leading to Tyr^3-octreotate (TOCA) (*13*−*15*, *28*, *29*). Furthermore, conjugation of [^{125}I]TOC and [^{125}I]TOCA with, for example, glucose via Amadori reaction (*10*, *14*, *15*) or the substitution of ^{111}In by ^{68}Ga in chelator-conjugated TOC and TOCA (*30*) also led to enhanced internalization in vitro and tumor uptake in vivo.

Of course, nonspecific radioligand uptake in the excretion organs is also mainly determined by the physicochemical properties of the molecule itself such as lipophilicity and net charge, which are dependent on the labeling method and/or the nature of further functionalities introduced into the peptide. In contrast to receptor targeting, however, radioligand accumulation in nontarget organs can also be influenced "externally". For example, the high kidney uptake of radiometalated TOC analogues, which leads to high nephrotoxicity and thus limits the applicable dose, has been efficiently reduced by coinfusion of basic amino acids (Lys/Arg) (*31*). This methodology relies on the assumption that the positively charged amino acids compete for charge-dependent endocytosis into the renal tubular cells.

Recent studies indicated that significantly reduced kidney accumulation may also be achieved by a reduction of peptide net charge by amino acid substitution in radiometalated octreotide (*21*) as well as by certain carbohydrates N-terminally linked to [^{125}I]TOCA (*15*).

To assess the relative impact of both of the above modifications in the same molecule, three new glycosylated [^{125}I]TOCA analogues, [^{125}I]Glucuron-TOCA, [^{125}I]-Gluc-*S*-, and [^{125}I]Gal-*S*-TOCA (Figure 1), were evaluated in vitro and in vivo with particular focus on the single and combined effects of carbohydrate structure, reduced net charge, and different charge distribution on receptor

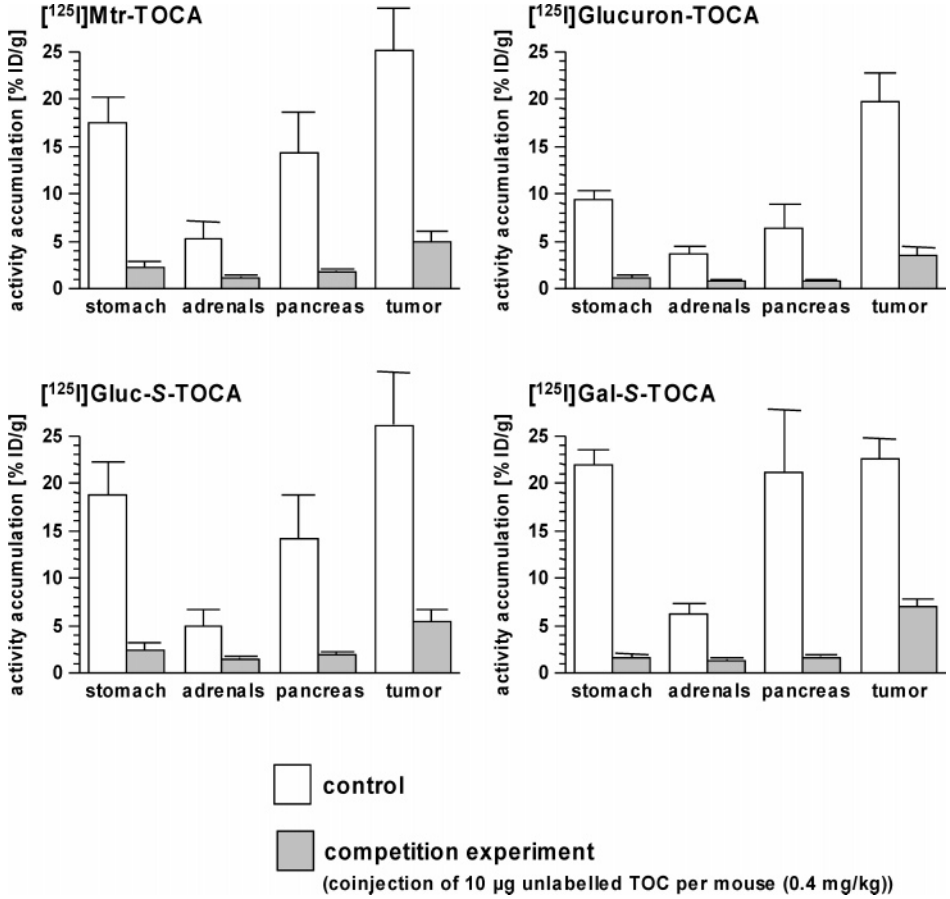

Figure 3. Effect of co-injection of 10 μg of unlabeled TOC per mouse (0.4 mg/kg) on the uptake of [^{125}I]Mtr-TOCA, [^{125}I]Glucuron-TOCA, [^{125}I]Gluc-*S*-TOCA, and [^{125}I]Gal-*S*-TOCA in stomach, adrenals, pancreas, and tumor of AR42J tumor-bearing nude mice 60 min p.i. (mean ± SD, $n = 3$).

affinity, ligand internalization, and pharmacokinetics, and compared to the reference [^{125}I]Mtr-TOCA. In this context, the potential identification of carbohydrate structures that might be generally applicable for a reduction of peptidic radiotracer accumulation in the kidney, ideally without affecting its receptor affinity and tumor accumulation, was of major interest.

So far, the differences in the sst-affinity profiles of I-Glucuron-TOCA, I-Gluc-*S*-, and I-Gal-*S*-TOCA as compared to I-Mtr-TOCA cannot be attributed unambiguously to the influence of either carbohydrate structure or a charge effect. However, one indicator for a charge-dependent effect is the slightly reduced sst_2-affinity of I-Glucuron-TOCA, I-Gluc-*S*-TOCA, and I-Gluc-*S*-TOCA ($z = 0$) as compared to I-Mtr-TOCA ($z = +1$). A detailed study including four octreotide analogues with net charges $z = +1$ to $z = +3$ demonstrated a strong correlation between peptide net charge and ligand receptor affinity. The more electropositive charges are on the peptide, the higher is the effective concentration of the peptide at the negatively charged membrane, and thus the higher are the receptor affinity and also functional activity observed for the respective peptide analogue (*32*). A second indicator for the (indirect) influence of peptide net charge on the sst-affinity profile is the reduced sst_2-specificity of the three new glyco-peptides with $z = 0$. In the case of radiometalated TOC analogues, a lower hydrophilicity (induced by reduced net charge) leads to increased affinity to sst-subtypes 3−5 (*26*). The same seems to be the case especially for I-Gluc-*S*-TOCA and I-Gluc-*S*-TOCA. Both peptides show a lower hydrophilicity than I-Mtr-TOCA (log $P_{ow} = -1.67 \pm 0.02$ vs -1.73 ± 0.04), and both show substantially increased $hsst_3$ and $hsst_4$ affinities.

It has already been demonstrated in several studies (*13*, *28*, *29*, *33*) that the sst_2-affinity of an octreotide analogue is of limited predictive value for the efficiency of ligand internalization into sst_2-expressing cells. The same was observed in this study. While both [^{123}I]Gluc-*S*- and [^{123}I]Gal-*S*-TOCA showed reduced sst_2-affinity as compared to [^{123}I]Mtr-TOCA (Table 1), they exhibited an increase in internalization by a factor of 1.57 and 1.13, respectively (Table 2). Furthermore, the effective concentration of unlabeled TOC needed to inhibit ligand internalization to 50% of maximum (normalized to the value found for the internal standard [^{125}I]TOC in the same experiment), the $EC_{50,R}$, of [^{123}I]Gluc-*S*- and [^{123}I]-Gal-*S*-TOCA was also substantially increased (Table 2). Thus, both compounds have an enhanced ability to compete with unlabeled competitor for receptor binding and subsequent endocytosis into the cell and thus a higher internalization potency than [^{123}I]Mtr-TOCA. So far, it remains unclear as to what extent either the reduced net charge or the change in carbohydrate structure or both are responsible for the divergence between data for [^{123}I]Mtr-TOCA and the two thioglycoside analogues. In contrast to the sst-affinity profiles, however, which were very similar for both [^{123}I]Gluc-*S*- and [^{123}I]-Gal-*S*-TOCA, both the internalization and the $EC_{50,R}$ determined for these two compounds with identical charge distribution differ significantly. This finding indicates that, although the structure of the carbohydrate (Gluc vs Gal) has no significant influence on the binding

affinity to immobilized receptors (Table 1), it does have substantial impact on ligand internalization into live cells. This is supported by data from a previous study in which the glucose-Amadori analogues of [^{123}I]TOC and [^{123}I]TOCA, [^{123}I]Gluc-TOC and [^{123}I]Gluc-TOCA, exhibited a considerable enhancement of ligand internalization and $EC_{50,R}$ as compared to their corresponding maltose- and maltotriose-counterparts (*13*), although the glycopeptides from each series (TOC and TOCA) had identical net charge ($z = +2$ and $z = +1$, respectively).

In the same study, it has been demonstrated that ligand internalization and also the $EC_{50,R}$ represent more reliable predictive parameters concerning the in vivo tumor accumulation of radiolabeled octreotide analogues in AR42J tumor-bearing mice than their sst_2-affinity. Also, in the case of [^{125}I]Mtr-TOCA, [^{125}I]Gluc-*S*-TOCA, and [^{125}I]Gal-*S*-TOCA, tumor accumulation (Table 3) rather reflects the tendencies found for ligand internalization than those for sst_2-affinity, but differences in tumor accumulation are by far not as pronounced as the observed variation in ligand internalization efficiency. This is not surprising, however, taking into account that tumor accumulation of the peptides investigated is very rapid and takes place early after ligand administration. The relatively fast blood clearance of the peptides, however, leads to rapidly decreasing tracer levels in blood and thus prevents optimal exploitation of the enhanced internalization efficiency of, for example, [^{125}I]Gluc-*S*-TOCA as compared to [^{125}I]Mtr-TOCA. Altogether, both in vitro uptake of [*I]Mtr-TOCA, [*I]Glucuron-TOCA, [*I]-Gluc-*S*-TOCA, and [*I]Gal-*S*-TOCA into sst-expressing cells as well as their in vivo accumulation in sst-positive tissues seem to be mainly determined by the structure of the carbohydrate-modification introduced into the molecule, and not by the net charge of the respective peptide. This is not true, however, for the biodistribution of these tracers in nontarget organs.

In the case of both [^{125}I]Gluc-*S*-TOCA and [^{125}I]Gal-*S*-TOCA, the reduced net charge leads to a loss in hydrophilicity as compared to [^{125}I]Mtr-TOCA ($\log P_{ow} = -1.67 \pm 0.02$ vs -1.73 ± 0.04), which is reflected in the slightly increased accumulation of these tracers in liver and intestine. These data are in accordance with results from a previous study, which demonstrated a correlation between the lipophilicity ($\log P_{ow}$) of radioiodinated, glycosylated TOC analogues with peptide accumulation in these organs (*10*). Interestingly, the data obtained for [^{125}I]Glucuron-TOCA are in contradiction to this correlation. Due to its higher charge density, the peptide has a nearly identical $\log P_{ow}$ as compared to [^{125}I]Mtr-TOCA ($\log P_{ow} = -1.74 \pm 0.04$ vs -1.73 ± 0.04). Both hepatic and intestinal uptake of [^{125}I]Glucuron-TOCA, however, are increased by a factor of ≥ 2 as compared to the maltotriose analogue. Furthermore, instead of the expected reduction of kidney uptake due to reduced positive net charge, [^{125}I]Glucuron-TOCA showed an increase in renal accumulation. In contrast, both [^{125}I]Gluc-*S*-TOCA and [^{125}I]Gal-*S*-TOCA having the same peptide net charge as [^{125}I]Glucuron-TOCA ($z = 0$), albeit a significantly different charge distribution within the peptide, showed the anticipated reduction in renal activity accumulation by up to 50% as compared to the reference peptide [^{125}I]Mtr-TOCA. The same had been observed for the L-Asp^1 analogue of [^{111}In]DTPA-L-Phe^1-octreotide, which showed an activity accumulation in the kidney of only approximately 7%ID/g at 1 h p.i. in normal mice as opposed to approximately 16%ID/g found for the L-Phe^1-parent peptide (*21*).

Thus, based on these findings and on the results obtained with the two thioglycoside analogues investigated in this study, modulating peptide net charge can be efficiently used to modify ligand accumulation in the kidney. The unexpected biodistribution pattern of [^{125}I]-Glucuron-TOCA as compared to the other two peptides with $z = 0$, however, indicates that not only peptide net charge, but also charge distribution may have a substantial impact on peptide uptake not only in the kidney, but also in the other excretion organs. Interestingly, and in contrast to the results obtained with respect to receptor targeting both in vitro and in vivo, the exact carbohydrate structure only seems to have secondary influence on general ligand biodistribution and excretion of radiolabeled sst-ligands. This is illustrated by the nearly identical pharmacokinetics of [^{125}I]Gluc-*S*-TOCA and [^{125}I]Gal-*S*-TOCA found in this study and is also supported by data from previous investigations comparing the pharmacokinetics of different sugar analogues of [^{125}I]TOC and [^{125}I]TOCA (*10*, *15*). Especially in the case of the [^{125}I]-Gluc-*S*-TOCA/[^{125}I]Gal-*S*-TOCA-pair, however, this finding was unexpected. A large variety of approaches for high-level (pre)targeting of bioactive molecules to the liver rely on the specific internalization of galactosyl-modified compounds into parenchymal liver cells via a high-affinity receptor for asialoglycoproteins (*34*). Surprisingly, because liver accumulation of [^{125}I]Gal-*S*-TOCA is very low at all time points investigated and nearly identical to that of [^{125}I]Gluc-*S*-TOCA, this specific transport system does not seem to be targeted by [^{125}I]Gal-*S*-TOCA.

In conclusion, both the reduction of peptide net charge as well as the methodology employed for N-terminal carbohydrate conjugation of radioiodinated TOCA have a significant impact on peptide pharmacokinetics. The excretion profile and especially kidney accumulation of the four analogues investigated, [^{125}I]Mtr-TOCA, [^{125}I]-Glucuron-TOCA, [^{125}I]Gluc-*S*-TOCA, and [^{125}I]Gal-*S*-TOCA, were found to be dominated by physicochemical characteristics such as lipophilicity, peptide net charge, and charge distribution within the peptide. A substantial influence of these factors on accumulation in sst-expressing cells and tissues, however, was not detectable, whereas it was greatly dependent on the structure of the N-terminal carbohydrate moiety. In this context, conjugation of TOCA with the Gluc-*S*-moiety allowed the most efficient optimization of peptide pharmacokinetics as compared to the reference [^{125}I]Mtr-TOCA, a reduction of kidney accumulation by approximately 50%, and a substantial increase of ligand internalization in vitro and also of tumor uptake in vivo. The Gluc-*S*-group therefore seems to be a promising synthon for the synthesis of a variety of other neuropeptide analogues with improved pharmacokinetics.

LITERATURE CITED

(1) Polt, R., Porreca, F., Szabo, L. Z., Bilsky, E. J., Davis, P., Abbruscato, T. J., Davis, T. P., Horcath, R., Yamamura, H. I., and Hruby, V. (1994) Glycopeptide enkephalin analogueues produce analgesia in mice: Evidence for penetration of the blood-brain barrier. *Proc. Natl. Acad. Sci. U.S.A. 91*, 7114−7118.

(2) Mitchell, S. A., Pratt, M. R., Hruby, V. J., and Polt, R. (2001) Solid-Phase Synthesis of O−Linked Glycopeptide Analogueues of Enkephalin. *J. Org. Chem. 66*, 2327−2342.

(3) Bilsky, E. J., Egleton, R. D., Mitchell, S. A., Palian, M. M., Davis, P., Huber, J. D., Jones, H., Yamamura, H. I., Janders, J., Davis, T. P., Porreca, F., Hruby, V. J., and Polt, R. (2000) Enkephalin glycopeptide analogueues produce analgesia with reduced dependence liability. *J. Med. Chem. 43*, 2586−2590.

(4) Suzuki, K., Susaki, H., Okuno, S., Yamada, H., Watanabe, H. K., and Sugiyama, Y. (1999) Specific renal delivery of sugar-modified low-molecular-weight peptides. *J. Pharmacol. Exp. Ther. 288*, 888−897.

(5) Nomoto, M., Yamada, K., Haga, M., and Hayashi, M. (1998) Improvement of Intestinal Absorption of Peptide Drugs by Glycosylation: Transport and Tetrapeptide by the Sodium Ion-Dependent D-Glucose Transporter. *J. Pharm. Sci. 87*, 326−332.

(6) Fisher, J. F., Harrison, A. W., Bundy, G. L., Wilkinson, K. F., Rush, B. D., and Ruwart, M. J. (1991) Peptide to glycopeptide: glycosylated oligopeptide renin inhibitors with attenuated in vivo clearance properties. *J. Med. Chem. 34*, 3140−3143.

(7) Kihlberg, J., Ahman, J., Walse, B., Drakenberg, T., Nilsson, A., Soderberg-ahlm, C., Begntsson, B., and Olsson, H. (1995) Glycosylated peptide hormones: pharmacological properties and conformational studies of analogueues of [1-desamino, 8-D-arginine]vasopressin. *J. Med. Chem. 38*, 161−169.

(8) Albert, R., Marbach, P., Bauer, W., Briner, U., Fricker, G., Bruns, C., and Pless, J. (1993) SDZ CO 611: A highly potent glycosylated analogue of somatostatin with improved oral acitivity. *Life Sci. 53*, 517−525.

(9) Leisner, M., Kessler, H., Schwaiger, M., and Wester, H. J. (1999) Synthesis of N_α-D-Phe^1-Amadori derivatives of Tyr^3-octreotide: Precursors for ^{123}I-/^{18}F-labeled sstr-binding SPECT/PET tracers with improved biodistribution. *J. Labelled Compd. Radiopharm. 42*, S549 (abstract).

(10) Schottelius, M., Wester, H. J., Reubi, J. C., Senekowitsch-Schmidtke, R., and Schwaiger, M. (2002) Improvement of Pharmacokinetics of radioiodinated Tyr^3-octreotide by Conjugation with Carbohydrates. *Bioconjugate Chem. 13*, 1021−1030.

(11) Wester, H. J., Schottelius, M., Scheidhauer, K., Reubi, J. C., Wolf, I., and Schwaiger, M. (2002) Comparison of radioiodinated TOC, TOCA and Mtr-TOCA: the effect of carbohydration on the pharmacokinetics. *Eur. J. Nucl. Med. Mol. Imaging 29*, 28−38.

(12) Wester, H. J., Schottelius, M., Scheidhauer, K., Meisetschläger, G., Herz, M., Rau, F., Reubi, J. C., Kimmich, T., Arnold, W., and Schwaiger, M. (2003) PET imaging of somatostatin receptors: design, synthesis and preclinical evaluation of a novel ^{18}F-labeled, carbohydrated analogue of octreotide. *Eur. J. Nucl. Med. 30*, 117−122.

(13) Schottelius, M., Reubi, J. C., Schwaiger, M., and Wester, H. J. (2005) N-terminal sugar conjugation and C-terminal Thr-for-Thr(ol) exchange in radioiodinated Tyr^3-octreotide: effect on cellular ligand trafficking in vitro and tumor accumulation in vivo. *J. Med. Chem.*, accepted.

(14) Vaidyanathan, G., Friedman, H. S., Schottelius, M., Wester, H. J., and Zalutsky, M. R. (2003) Specific and high-level targeting of radiolabeled octreotide analogueues to human medulloblastoma xenografts. *Clin. Cancer Res. 9*, 1868−1876.

(15) Wester, H. J., Schottelius, M., Poethko, T., Bruus-Jensen, K., and Schwaiger, M. (2004) Radiolabeled carbohydrated somatostatin analogues: a brief review of the current status. *Cancer Biother. Radiopharm. 19*, 231−244.

(16) Haubner, R., Wester, H. J., Burkhart, F., Senekowitsch-Schmidtke, R., Weber, W., Goodman, S., Kessler, H., and Schwaiger, M. (2001) Glycosylated RGD-containing peptides: tracer for tumor targeting and angiogenesis imaging with improved biokinetics. *J. Nucl. Med. 42*, 326−336.

(17) Haubner, R., Wester, H.-J., Weber, W., Mang, C., Ziegler, S. I., Senekowitsch-Schmidtke, R., Kessler, H., and Schwaiger, M. (2001) Non invasive imaging of $\alpha_v\beta_3$-integrin expression using a F-18-labeled RGD-containing glycopeptide and positron emission tomography. *Cancer Res. 61*, 1781−1785.

(18) Reubi, J. C., Krenning, E. P., Lamberts, S. W., and Kvols, L. (1990) Somatostatin receptors in malignant tissues. *J Steroid Biochem. Mol. Biol. 37*, 1073−1077.

(19) Reubi, J. C., Schaer, J. C., Laissue, J. A., and Waser, B. (1996) Somatostatin receptors and their subtypes in human tumors and peritumoral vessels. *Metabolism 45*, 39−41.

(20) Reubi, J. C., Waser, B., Schaer, J. C., and Laissue, J. A. (2001) Somatostatin receptor sst1-sst5 expression in normal and neoplastic human tissues using receptor autoradiography with subtype selective ligands. *Eur. J. Nucl. Med. 28*, 836−846.

(21) Akizawa, H., Arano, Y., Mifune, M., Iwado, A., Saito, Y., Mukai, T., Uehara, T., Ono, M., Fujioka, Y., Ogawa, K., Kiso, Y., and Saji, H. (2001) Effect of molecular charges on renal uptake of ^{111}In-DTPA-conjugated peptides. *Nucl. Med. Biol. 28*, 761−768.

(22) Suzuki, K., Susaki, H., Okuno, S., and Sugiyama, Y. (1999) Renal Drug targeting using a vector "alkylglycoside". *J. Pharmacol. Exp. Ther. 288*, 57−64.

(23) Suzuki, K., Ando, T., Susaki, H., Mimori, K., Nakabayashi, S., and Sugiyama, Y. (1999) Structural requirements for alkylglycoside-type renal targeting vector. *Pharm. Res. 16*, 1026−1034.

(24) Elofsson, M., Walse, B., and Kihlberg, J. (1991) Building blocks for glycopeptide synthesis: Glycosylation of 3-mercaptopropionic acid and Fmoc-amino acids with unprotected carboxyl groups. *Tetrahedron Lett. 32*, 7613−7616.

(25) Herzig, J., Nudelman, A., Gottlieb, H. E., and Fischer, B. (1986) Studies in sugar chemistry. 2. A simple method for O-deacylation of polyacylated sugars. *J. Org. Chem. 51*, 727−730.

(26) Reubi, J. C., Schär, J. C., Waser, B., Wenger, S., Heppeler, A., Schmitt, J. S., and Mäcke, H. R. (2000) Affinity profiles for human somatostatin receptor subtypes SST1-SST5 of somatostatin radiotracers selected for scintigraphic and radiotherapeutic use. *Eur. J. Nucl. Med. 27*, 273−282.

(27) Viguerie, N., Tahiri-Jouti, N., Esteve, J. P., Clerc, P., Logsdon, C., Svoboda, M., Susini, C., Vaysse, N., and Ribet, A. (1998) Functional somatostatin receptors on a rat pancreatic acinar cell line. *Am. J. Physiol.* 255, G113−G120.

(28) de Jong, M., Breeman, W. A., Bakker, W. H., Kooij, P. P., Bernard, B. F., Hofland, L. J., Visser, T. J., Srinivasan, A., Schmidt, M. A., Erion, J. L., Bugaj, J. E., Mäcke, H. R., and Krenning, E. P. (1998) Comparison of ^{111}In-labeled somatostatin analogueues for tumor scintigraphy and radionuclide therapy. *Cancer Res. 58*, 437−441.

(29) Lewis, J. S., Lewis, M. R., Srinivasan, A., Schmidt, M. A., Wang, J., and Anderson, C. J. (1999) Comparison of four ^{64}Cu-labeled somatostatin analogueues in vitro and in a tumor-bearing rat model: Evaluation of new derivatives for positron emission tomography imaging and targeted radiotherapy. *J. Med. Chem. 42*, 1341−1347.

(30) Froidevaux, S., Eberle, A. N., Christe, M., Sumanovski, L., Heppeler, A., Schmitt, J. S., Eisenwiener, K., Beglinger, C., and Mäcke, H. R. (2002) Neuroendocrine tumor targeting: study of novel gallium-labeled somatostatin radiopeptides in a rat pancreatic tumor model. *Int. J. Cancer 98*, 930−937.

(31) Rollemann, E. J., Valkema, R., de Jong, M., Kooij, P. P. M., and Krenning, E. P. (2003) Safe and effective inhibition of renal uptake of radiolabeled octreotide by a combination of lysine and arginine. *Eur. J. Nucl. Med. 30*, 9−15.

(32) Seelig, J., Nebel, S., Ganz, P., and Bruns, C. (1993) Electrostatic and nonpolar peptide-membrane interactions. Lipid binding and functional properties of somatostatin analogueues of charge $z = +1$ to $z = +3$. *Biochemistry 32*, 9714−9721.

(33) Hofland, L. J., Breeman, W. A., Krenning, E. P., de Jong, M., Waaijers, M., van Koetsveld, P. M., Mäcke, H. R., and Lamberts, S. W. (1999) Internalization of [DOTA^0, ^{125}I-Tyr^3]-octreotide by somatostatin receptor-positive cells in vitro and in vivo: implications for somatostatin receptor-targeted radioguided surgery. *Proc. Assoc. Am. Physicians 111*, 63−69.

(34) Ashwell, G., and Harford, J. (1982) Carbohydrate-specific receptors of the liver. *Annu. Rev. Biochem. 51*, 531−534.

BC0499228

Pyrazolyl Derivatives as Bifunctional Chelators for Labeling Tumor-Seeking Peptides with the *fac*-$[M(CO)_3]^+$ Moiety (M = ^{99m}Tc, Re): Synthesis, Characterization, and Biological Behavior

Susana Alves,[†] António Paulo,[†] João D. G. Correia,[†] Lurdes Gano,[†] Charles J. Smith,[‡] Timothy J. Hoffman,[‡] and Isabel Santos*,[†]

Departamento de Química, ITN, Estrada Nacional 10, 2686-953 Sacavém Codex, Portugal, The Harry S. Truman Memorial Veterans' Hospital, Columbia, Missouri 65201, Department of Radiology and Department of Internal Medicine, University of Missouri−Columbia School of Medicine, Columbia, Missouri 65211, and University of Missouri−Columbia Research Reactor Center, Columbia, Missouri 65211. Received August 26, 2004; Revised Manuscript Received January 6, 2005

Radiolabeling of biologically active molecules with the $[^{99m}Tc(CO)_3]^+$ unit has been of primary interest in recent years. With this in mind, we herein report symmetric (***L*^{1}**) and asymmetric (***L*^{2}**−***L*^{5}**) pyrazolyl-containing chelators that have been evaluated in radiochemical reactions with the synthon $[^{99m}Tc(H_2O)_3(CO)_3]^+$ (**1a**). These reactions yielded the radioactive building blocks $[^{99m}Tc(CO)_3(k^3\text{-L})]^+$ (L = ***L*^{1}**−***L*^{5}**, **2a**−**6a**), which were identified by RP-HPLC. The corresponding Re surrogates (**2**−**6**) allowed for macroscopic identification of the radiochemical conjugates. Complexes **2a**−**6a**, with log $P_{o/w}$ values ranging from −2.35 to 0.87, were obtained in yields of ≥90% using ligand concentrations in the 10^{-5}−10^{-4} M range. Challenge studies with cysteine and histidine revealed high stability for all of these radioactive complexes, and biodistribution studies in mice indicated a fast rate of blood clearance and high rate of total radioactivity excretion, occurring primarily through the renal-urinary pathway. Based on the framework of the asymmetric chelators, the novel bifunctional ligands 3,5-Me_2-pz$(CH_2)_2$N$((CH_2)_3$COOH$)(CH_2)_2NH_2$ (***L*^{6}**) and pz$(CH_2)_2$N$((CH_2)_3$COOH$)(CH_2)_2NH_2$ (***L*^{7}**) have been synthesized and their coordination chemistry toward $(NEt_4)_2[ReBr_3(CO)_3]$ (**1**) has been explored. The resulting complexes, *fac*-$[Re(CO)_3(k^3\text{-L})]Br$ (***L*^{6}** (**7**), ***L*^{7}** (**8**)), contain tridentate ancillary ligands that are coordinated to the metal center through the pyrazolyl and amine nitrogen atoms, as observed for the other related building blocks. ***L*^{6}** and ***L*^{7}** were coupled to a glycylglycine ethyl ester dipeptide, and the resulting functionalized ligands were used to prepare the model complexes *fac*-$[Re(CO)_3(\kappa^3\text{-3,5-}Me_2\text{-pz}(CH_2)_2N(glygly)(CH_2)_2NH_2)]^+$ (**9/9a**) and *fac*-$[Re(CO)_3(\kappa^3\text{-pz}(CH_2)_2N(CH_2)_3(glygly)(CH_2)_2NH_2)]^+$ (**10/10a**) (M = Re, ^{99m}Tc). These small conjugates have been fully characterized and are reported herein. On the basis of the in vitro/in vivo behavior of the model complexes (**2a**−**6a**, **9a**, **10a**), we chose to evaluate the in vitro/in vivo biological behavior of a new tumor-seeking Bombesin pyrazolyl conjugate, [(***L*^{6}**)-G-G-G-Q-W-A-V-G-H-L-M-NH_2], that has been labeled with the $[^{99m}Tc(CO)_3]^+$ metal fragment. Stability, in vitro cell binding assays, and pharmacokinetics studies in normal mice are reported herein.

INTRODUCTION

The most recent approaches for radiopharmaceutical development are mainly based on the search for target-specific radiopharmaceuticals (*1*−*4*). This strategy involves the labeling of biologically relevant molecules, somehow related to a certain disease or disease type, and intends to improve the specificity of diagnosis and therapy in nuclear medicine (*1*−*4*).

Most of the hormonal messengers are peptides, which are involved in more fundamental biological processes than any other class of molecules, including the regulation of cellular growth and proliferation in normal as well as in tumor cells (*4*−*7*). Moreover, most tumor cells overexpress receptors for regulatory peptides, which are often specific for a certain tumor type (*5*−*7*). Many peptide receptors have already been identified and associated with a specific tumor type, stressing the interest in radiolabeling regulatory peptide analogues. Furthermore, the success obtained with the labeling of some of these peptides, such as somatostatin analogues, has encouraged further work in this field (*5*−*8*).

A recently introduced organometallic aquaion *fac*-$[M(CO)_3(H_2O)_3]^+$, M = Re, $^{99/99m}$Tc, has opened new perspectives for the labeling of different biomolecules (*9*−*11*). The attractiveness of this low-valent precursor results from its particularly high thermodynamic stability, that is, high substitution stability of CO ligands and substitution lability of water molecules, which can be easily replaced by a variety of mono, bis, and tridentate ligands of different size, shape, and donor atom sets (*12*−*19*). This versatility allows for the synthesis of different building blocks with physicochemical properties matched to the biologically relevant molecule.

As part of our ongoing work on the search for bifunctional chelators suitable for the labeling of peptides with

* To whom correspondence should be addressed. Telephone: 351-21-994 6201. E-mail: isantos@itn.mces.pt.

[†] ITN.

[‡] The Harry S. Truman Memorial Veterans' Hospital, University of Missouri−Columbia School of Medicine, and University of Missouri−Columbia Research Reactor Center.

10.1021/bc0497968 CCC: $30.25 © 2005 American Chemical Society
Published on Web 03/01/2005

Chart 1. Pyrazolyl-Containing Ligands

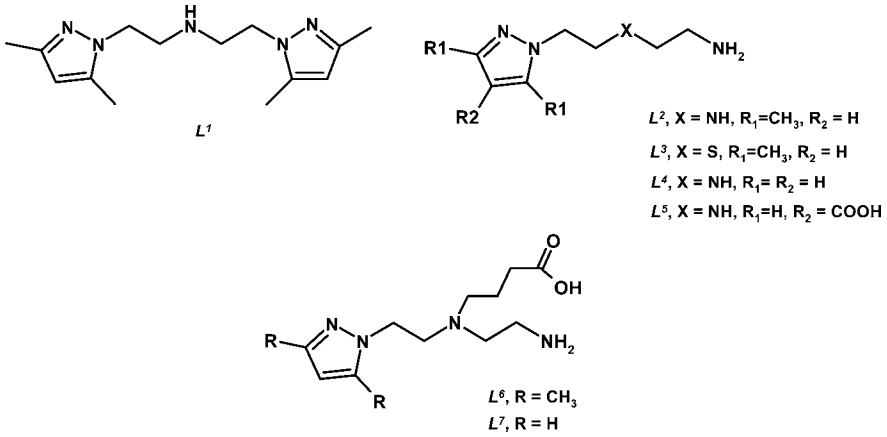

the *fac*-$[^{99m}Tc(CO)_3]^+$ moiety, we have previously synthesized a family of asymmetric and symmetric pyrazolyl-containing ligands (***L*^{1}**–***L*^{3}** and ***L*^{5}**) (Chart 1) and explored their chemistry with the precursor $(NEt_4)_2[ReBr_3(CO)_3]$ (**1**). This has led to the synthesis of different building blocks of the type *fac*-$[Re(CO)_3(k^3\text{-L})]^+$ (*20*–*22*).

As part of a study to select the most promising pyrazolyl-based chelators for further application on the labeling of biologically active peptides, we report herein on the synthesis, characterization, and biological evaluation of the corresponding ^{99m}Tc-building blocks, *fac*-$[^{99m}Tc(CO)_3(k^3\text{-L})]^+$. These complexes have been obtained by reaction of the *fac*-$[^{99m}Tc(H_2O)_3(CO)_3]^+$ precursor with ***L*^{1}**–***L*^{5}**. Taking advantage of the versatility of these systems, we also describe the synthesis and characterization of the novel bifunctional pyrazolyl-based chelators ***L*^{6}** and ***L*^{7}** (Chart 1), as well as the synthesis and characterization of the respective tricarbonyl rhenium complexes. The utility of the new ligand frameworks ***L*^{6}** and ***L*^{7}** is further demonstrated herein by radiolabeling and biological evaluation of [(***L*^{6}**)-G-G-G-Q-W-A-V-G-H-L-M-NH_2], a GRPr specific analouge with tumor-targeting capability.

Bombesin (BBN) is a 14 amino acid peptide with very high affinity for the gastrin-releasing peptide receptor (GRPr). The function and in vivo distribution of the GRPr has been well established, showing expression in the central nervous system (CNS) and in peripheral tissues such as the pancreas or intestinal tract (*23*–*28*). The GRPr is also expressed on a variety of tumors including breast, prostate, pancreatic, and small-cell lung cancer (*23*–*28*). Therefore, radiolabeled BBN/GRP analogues such as [(***L*^{6}**)-G-G-G-Q-W-A-V-G-H-L-M-NH2] hold some potential to be used as site-directed diagnostic and/or therapeutic targeting motifs when radiolabeled with the appropriate radionuclide.

MATERIALS AND METHODS

All chemicals and solvents were of reagent grade and were used without further purification unless stated otherwise. Reactions were monitored by thin-layer chromatography (TLC) carried out on 0.25 mm Merck silica gel aluminum plates, using UV light as visualizing agent. Silica gel was used for column chromatography. ^{1}H and ^{13}C NMR spectra were recorded on a Varian Unity 300 MHz spectrometer; ^{1}H and ^{13}C chemical shifts were referenced with the residual solvent resonances relative to tetramethylsilane. IR spectra were recorded as KBr pellets or in CsI cells on a Perkin-Elmer 577 spectrometer. The starting materials $(NEt_4)_2[ReBr_3(CO)_3]$ (**1**), $[^{99m}Tc(OH_2)_3(CO)_3]^+$ (**1a**), the ligands ***L*^{1}**–***L*^{3}** and ***L*^{5}**, and the complexes $[Re(CO)_3(k^3\text{-L})]Br$ (L = ***L*^{1}** (**2**), ***L*^{2}** (**3**), ***L*^{3}** (**4**), ***L*^{5}** (**6**)) were prepared according to published methods (*9*, *10*, *20*, *21*, *29*–*31*).

Peptide synthesis was performed on a Perkin-Elmer-Applied Biosystem model 432 automated peptide synthesizer employing traditional Fmoc chemistry. The preselected synthetic sequence was designed to produce the ***L*^{6}**-(X)-BBN conjugate with the following general structure ***L*^{6}**-X-Q-W-A-V-G-H-L-M-NH_2, where the spacer group, X = GlycylGlycylGlycine. The crude peptide was purified by HPLC, and the solvents were removed on a SpeedVac concentrator. Typical yields of the crude peptide were 80–85%. ES-MS was used to determine the molecular constitution of the ***L*^{6}**-(X)-BBN[7-14]NH_2 conjugate. Na[$^{99m}TcO_4$] was eluted from a ^{99}Mo/^{99m}Tc generator using 0.9% saline. HPLC analysis of the Re and ^{99m}Tc complexes was performed on a Shimadzu C-R4A chromatography system equipped with a Berthold-LB 505 γ-detector and with a tunable absorption UV detector. Separations were achieved on Nucleosil 250-4 100-10 C18 columns or on 250-4 100-5 C18 columns, using flows of 1 or 0.5 mL/min, respectively; UV detection, 254 nm; eluents, A-TFA 0.1%, B-MeOH; method, t = 0–3 min, 0% MeOH; 3–3.1 min, 0–25% MeOH; 3.1–9 min, 25% MeOH; 9–9.1 min, 25–34% MeOH; 9.1–20 min, 34–100% MeOH; 20–22 min, 100% MeOH; 22–22.1 min, 100–0% MeOH; 22.1–30 min, 0% MeOH. HPLC evaluation of the nonmetalated and metalated BBN-conjugate was performed using experimental conditions similar to those referenced above. However, the eluenting solvents were water with 0.1% TFA (A) and CH_3CN 0.1% TFA (B), and the wavelength of detection was 280 nm.

Synthesis of pz$(CH_2)_2$NH$(CH_2)_2NH_2$ (*L*^{4}). A solution of 1-(2-bromoethyl)pyrazole (*32*) (2.1 g, 12 mmol) in THF (10 mL) was added dropwise to a solution of ethylenediamine (14.4 g, 0.24 mol) in H_2O (20 mL). After refluxing for 4 h, the THF was removed under vacuum, and the residual water phase was washed with CH_2Cl_2. The aqueous phase was vacuum-dried with mild heating to eliminate some remaining ethylenediamine. Compound ***L*^{4}** was obtained as a yellow oil, which darkened to brown with heating. Yield: 924 mg, 50%. ^{1}H NMR (D_2O): 7.53 (d, H(3)pz, 1H); 7.45 (d, H(5)pz, 1H); 6.23 (t, H(4)pz, 1H); 4.14 (t, CH_2, 2H); 2.91 (t, CH_2, 2H); 2.77 (t, CH_2, 2H); 2.62 (t, CH_2, 2H). ^{13}C NMR (CD_3OD): 140.3 (C(3,5)pz); 131.9 (C(3,5)pz); 106.5 (C(4)pz); 52.48 (CH_2); 49.93 (CH_2); 41.60 (CH_2); 40.32 (CH_2). IR(ν/cm^{-1}) (CsI): 1651, 1094, 1034, 763.

Synthesis of 3,5Me$_2$-pz$(CH_2)_2$N$((CH_2)_3$COOH)$(CH_2)_2NH_2$ (*L*^{6}) and pz$(CH_2)_2$N$((CH_2)_3$COOH)$(CH_2)_2NH_2$ (*L*^{7}). *L*^{6}: An equimolar amount of BOC-ON in THF

was added dropwise to a solution of ***L²*** (4.0 g, 22.5 mmol) in THF (70 mL) at 0 °C, and the reaction mixture was left at this temperature for 3 h. A saturated aqueous solution of Na_2CO_3 and CH_2Cl_2 was added at room temperature, and the organic phase was separated, dried over anhydrous $MgSO_4$, and vacuum-dried. The yellow oil that was obtained, ***L²-Boc*** (5.7 g, 20 mmol), was dissolved in CH_3CN (60 mL), and an excess of K_2CO_3, KI, and ethyl 4-bromobutyrate was added. After 11 days at room temperature, the solution was filtered, vacuum-dried, and the residue was purified by column chromatography (ethyl acetate (50−100%)/hexane). The BOC protected derivative (4 g, 10.2 mmol) was dissolved in THF, and an excess of NaOH added and refluxed overnight, for saponification of the ethyl ester. The solution was neutralized with HCl (1 N), the solvents were removed, and the residue was extracted with CH_2Cl_2. The crude product was purified by column chromatography (MeOH (5−100%)/$CHCl_3$), and the pale yellow oil (2.2 g, 86%) was treated with an excess of TFA in CH_2Cl_2 to remove the BOC protecting group. Evaporation of the solvent, addition of H_2O, neutralization with 1 N HCl, and extraction with a small amount of MeOH led to a suspension, which, after being filtered off, was vacuum-dried yielding a pale yellow oil, which crystallizes upon standing. Yield: 2.07 g, 36%. ^{1}H NMR (CD_3OD): 5.83 (s, H(4)pz, 1H); 4.07 (t, CH_2, 2H); 2.98 (t, CH_2, 2H); 2.77 (t, CH_2, 2H); 2.70 (t, CH_2, 2H); 2.48 (t, CH_2, 2H); 2.26 (s, CH_3, 3H); 2.16 (s, CH_3, 3H); 2.00 (t, CH_2, 2H); 1.62 (q, CH_2, 2H). ^{13}C NMR (CD_3OD): 183.3 (COOH); 148.4 (C(3)pz); 141.0 (C(5)pz); 106.2 (C(4)pz); 54.1 (CH_2); 54.0 (CH_2); 52.0 (CH_2); 47.2 (CH_2); 38.5 (CH_2); 36.0 (CH_2); 24.8 (CH_2); 13.1 (CH_3); 10.9 (CH_3). IR (ν/cm^{-1}) (KBr): ν(C=O) 1694, 1559, 1442, 1210, 845, 804, 725.

L⁷*:** This compound was prepared as described for ***L⁶ (vide infra). Starting with 1.1 g (7 mmol) of ***L⁴*** in DMF, a brownish oil formulated as ***L⁷*** was obtained. Yield: 403 mg, 24%. ^{1}H NMR (D_2O): 7.58 (s, H(3)pz, 1H); 7.48 (s, H(5)pz, 1H); 6.25 (t, H(4)pz, 1H); 4.49 (t, CH_2, 2H); 3.64 (t, CH_2, 2H); 3.42 (t, CH_2, 2H); 3.25 (t, CH_2, 2H); 3.12 (t, CH_2, 2H); 2.30 (t, CH_2, 2H); 1.79 (q, CH_2, 2H). ^{13}C NMR (CD_3OD): 180.0 (COOH); 140.1 (C(3)pz); 131.8 (C(5)pz); 106.7 (C(4)pz); 54.9 (CH_2); 54.1 (CH_2); 52.0 (CH_2); 50.7 (CH_2); 38.6 (CH_2); 33.9 (CH_2); 23.9 (CH_2). IR (CsI) (ν/cm^{-1}): ν(C=O) 1685, 1442, 1209, 1138, 845, 803, 763.

Synthesis of 3,5Me₂-pz(CH₂)₂N(CH₂)₃(glygly-OEt)(CH₂)₂NH₂ (*L⁸*) and pz(CH₂)₂N(CH₂)₃(glygly-OEt)(CH₂)₂NH₂ (*L⁹*). Compounds ***L⁶-BOC*** or ***L⁷-BOC***, NEt_3 and HBTU, in the molar ratio 1:3:1, were dissolved in CH_3CN. To the resulting solutions were added equimolar amounts of glycylglycine ethyl ester (196 mg, 1 mmol). After reaction at room temperature, the solvent was evaporated and the residues were purified by column chromatography (MeOH (5−20%)/$CHCl_3$) or by dissolving the crude product in $CHCl_3$ and washing three times with H_2O. The BOC protecting group was removed with TFA. After 1 h at room temperature, the solvent was evaporated, and the residue was dissolved in H_2O and neutralized with NaOH(1N). Compound ***L⁸*** was obtained as a pale yellow oil upon evaporation of H_2O and purification by column chromatography (MeOH (20−50%)/$CHCl_3$). Compound ***L⁹*** was obtained as a yellow oil upon removal of H_2O and extraction with MeOH.

***L⁸*:** Yield: 179 mg, 45%. ^{1}H NMR (D_2O): 5.80 (s, H(4)pz, 1H); 4.04 (q, CH_2CH_3, 2H); 3.91 (t, CH_2, 2H); 3.85 (s, $NHCH_2$, 2H); 3.80 (s, $NHCH_2$, 2H); 2.81 (t, CH_2, 2H); 2.71 (t, CH_2, 2H); 2.59 (t, CH_2, 2H); 2.38 (t, CH_2, 2H); 2.10 (m, CH_2 + CH_3, 5H); 2.00 (s, CH_3, 3H); 1.53 (q, CH_2, 2H); 1.09 (t, CH_3, 3H). ^{13}C NMR (CD_3OD): 176.5 (CO); 172.3 (CO); 171.4 (CO); 148.5 (C(3)pz); 141.2 (C(5)pz); 106.3 (C(4)pz); 62.4 (CH_2); 54.0 (CH_2); 53.9 (CH_2); 52.0 (CH_2); 47.1 (CH_2); 43.2 (CH_2); 41.9 (CH_2); 38.6 (CH_2); 33.6 (CH_2); 23.8 (CH_2); 14.4 (CH_3); 13.2 (CH_3); 10.9 (CH_3). IR (CsI) (ν/cm^{-1}): ν(C=O) 1680, 1552, 1440, 1207, 1138, 1031, 842, 803, 724.

***L⁹*:** Yield: 121 mg, 33%. ^{1}H NMR (D_2O): 7.56 (d, H(3)pz, 1H); 7.46 (d, H(5)pz, 1H); 6.22 (t, H(4)pz, 1H); 4.46 (t, CH_2, 2H); 3.95 (m, CH_2CH_3, 2H); 3.72 (m, $2CH_2$, 4H); 3.59 (t, CH_2, 2H); 3.38 (t, CH_2, 2H); 3.22 (t, CH_2, 2H); 3.09 (t, CH_2, 2H); 2.25 (t, CH_2, 2H); 1.76 (m, CH_2, 2H); 1.02 (t, CH_3, 3H). ^{13}C NMR (CD_3OD): 176.2 (CO); 173.0 (CO); 172.0 (CO); 141.2 (C(3)pz); 132.3 (C(5)pz); 107.3 (C(4)pz); 62.4 (CH_2); 55.0 (CH_2); 54.6 (CH_2); 51.5 (CH_2); 47.8 (CH_2); 43.4 (CH_2); 41.7 (CH_2); 36.4 (CH_2); 33.5 (CH_2); 21.4 (CH_2); 14.4 (CH_3). IR (CsI) (ν/cm^{-1}): ν(C=O) 1677, 1426, 1202, 1135, 837, 800, 722.

Synthesis of the Re(I) Complexes (5 and 7−10). *General Method.* $(NEt_4)_2[ReBr_3(CO)_3]$ (**1**) (100 mg, 0.130 mmol) was reacted with equimolar amounts of the compounds ***L⁴*** and ***L⁶−L⁹*** in refluxing H_2O for 2 h or overnight. The complexes precipitate as white solids from the aqueous solutions upon concentration and cooling. Compounds **5** and **7−10** were obtained in yields between 75% and 85%. With the exception of **10**, the characterization of all complexes was achieved by IR, ^{1}H, and ^{13}C NMR spectroscopies and ES/MS. The identification of **10** involved only IR and ES/MS.

[Re(CO)3(κ³-pz(CH₂)₂NH(CH₂)₂NH₂)]Br (5). ^{1}H NMR (D_2O): 7.82 (d, H(3)pz, 1H); 7.76 (d, H(5)pz, 1H); 6.54 (s, br, NH, 1H); 6.39 (t, H(4)pz, 1H); 4.86 (s, br, NH_2, 1H); 4.43 (m, CH_2, 1H); 4.16 (m, CH_2, 1H); 3.94 (s, br, NH_2, 1H); 3.50 (m, CH_2, 1H); 2.87 (m, CH_2, 1H); 2.71 (m, CH_2, 2H); 2.48 (m, CH_2, 1H); 2.08 (m, CH_2, 1H). ^{13}C-RMN (CD_3OD): 198.2 (ReCO); 194.8 (ReCO); 194.7 (ReCO); 146.6 (C(3)pz); 135.6 (C(5)pz); 108.7 (C(4)pz); 56.0 (CH_2); 49.0 ($2CH_2$); 41.8 (CH_2). IV (cm^{-1}): ν(C≡O), 2020, 1920, 1890, 1599, 1461, 1283, 1197, 1078, 941, 758.

[Re(CO)₃(κ³-3,5Me₂-pz(CH₂)₂N((CH₂)₃COOH)-(CH₂)₂NH₂)]Br (7). ^{1}H NMR (CD_3OD): δ 6.20 (s, H(4)pz, 1H); 5.53 (s, br, NH_2, 1H); 4.58−4.52 (m, CH_2, 1H); 4.26−4.17 (m, CH_2, 1H); 4.10 (s, br, NH_2, 1H); 3.69 (m, CH_2, 1H); 3.53 (m, CH_2, 2H); 3.06 (m, CH_2, 1H); 2.90 (m, CH_2, 2H); 2.72 (m, CH_2, 1H); 2.55 (m, CH_2, 1H); 2.45 (s, CH_3, 3H); 2.38 (s, CH_3, 3H); 2.18 (m, CH_2, 2H); 2.04 (m, CH_2, 2H). ^{13}C-RMN (CD_3OD): 195.4 (3CO); 176.2 (COOH); 155.1 (C-pz); 145.3 (C-pz); 109.2 (C-pz); 67.1 (CH_2); 62.4 (CH_2); 53.7 (CH_2); 43.6 (CH_2); 31.5 (CH_2); 30.9 (CH_2); 20.5 (CH_2); 16.1 (CH_3); 11.6 (CH_3). IV (cm^{-1}): ν(C≡O), 2031, 1974, 1901; ν(C=O) 1686, 1432, 1205, 1143, 848, 800, 728, 588. ES/MS (+) (referenced to the species with ^{187}Re; relative abundance in parentheses): *m/z* 539 (100%) $[M]^+$.

[Re(CO)₃(κ³-pz(CH₂)₂N((CH₂)₃COOH)(CH₂)₂NH₂)]-Br (8). ^{1}H NMR (D_2O): δ 7.86 (t, H(3)pz, 1H); 7.81 (t, H(5)pz, 1H); 6.44 (s, H(4)pz, 1H); 5.07 (s br, NH_2, 1H); 4.52 (m, CH_2, 1H); 4.37 (m, CH_2, 1H); 4.10 (s br, NH_2, 1H); 3.58 (m, CH_2, 1H); 3.40 (m, CH_2, 2H); 2.89 (m, CH_2, 1H); 2.70 (m, CH_2, 1H); 2.40 (m, CH_2, 2H); 2.33 (m, CH_2, 1H); 2.13 (m, CH_2, 2H); 1.97 (m, CH_2, 2H). ^{13}C-RMN (CD_3OD): 198.2−193.8 (3CO); 185.3 (COOH); 146.6 (C-pz); 135.8 (C-pz); 108.9 (C-pz); 67.9 (CH_2); 63.0 (CH_2); 54.5 (CH_2); 52.0 (CH_2); 43.3 (CH_2); 31.6 (CH_2); 20.8 (CH_2). IR (KBr) (ν/cm^{-1}): ν(C≡O), 2023, 1901; ν(C=O), 1680, 1202, 1146, 1076, 852, 793, 762, 729. ES/MS (+) (referenced to the species with ^{187}Re; relative abundance in parentheses): *m/z* 511 (100%) $[M]^+$.

[Re(CO)₃(κ³-3,5Me₂-pz(CH₂)₂N(glygly)(CH₂)₂NH₂)]-Br (9). ^{1}H NMR (D_2O): δ 6.04 (s, H(4)pz, 1H); 5.05 (s, br, NH_2, 1H); 4.30 (m, CH_2, 1H); 4.05 (m, CH_2, 1H); 3.88

(s, NHCH_2CO, 2H); 3.84 (s, NHCH_2CO, 2H); 3.65 (s, br, NH_2, 1H); 3.53 (m, CH_2, 1H); 3.30 (m, CH_2, 2H); 2.86 (m, CH_2, 1H); 2.74 (m, CH_2, 2H); 2.57 (m, CH_2, 1H); 2.40 (m, CH_2, 1H); 2.73 (s, CH_3, 3H); 2.16 (s, CH_3, 3H); 2.10 (m, CH_2, 2H); 1.95 (m, CH_2, 2H).

^{13}C NMR (CD_3OD): 195.2 (ReCO); 194.8 (ReCO); 193.8 (ReCO); 175.2 (CO); 172.2 (CO); 171.3 (CO); 155.0 (C(3)pz); 145.3 (C(5)pz); 109.2 (C(4)pz); 67.1 (CH_2); 62.4 (CH_2); 53.8 (CH_2); 49.0 (CH_2); 43.7 (CH_2); 42.0 (CH_2); 33.3 (CH_2); 21.1 (CH_2); 16.2 (CH_3); 11.7 (CH_3). IR (KBr) (ν/cm^{-1}): ν(C≡O), 2015, 1876; ν (C═O) 1697, 1458, 1412, 1190, 1139, 850, 791, 729. ES/MS (referenced to the species with ^{187}Re; relative abundance in parentheses): *m/z* 653 (100%) $[M]^+$.

[Re(CO)$_3$(κ^3-pz(CH$_2$)$_2$N(CH$_2$)$_3$(glygly)(CH$_2$)$_2$NH$_2$)]-Br (10). IR (CsI) (ν/cm^{-1}): ν(C≡O) 2014, 1891; ν (C═O) 1689, 1460, 1397, 1204, 1136, 1003, 837, 800. ES/MS (referenced to the species with ^{187}Re; relative abundance in parentheses): *m/z* 625 (100%) $[M]^+$.

Synthesis of the ^{99m}Tc(I) Complexes (2a−6a, 9a−11a). *General Method.* In a nitrogen-purged glass vial, 100 μL of a 10^{-3} or 10^{-4} M solution of the compounds ***L*^{1}**−***L*^{6}**, ***L*^{9}**, ***L*^{10}**, and [***L*^{6}**-(GGG)-Bombesin(7−14)NH_2] were added to 900 μL of a solution of *fac*-[^{99m}Tc(OH$_2$)$_3$(CO)$_3$]$^+$ (1−2 mCi) in PBS. The reaction mixture was incubated at 100 °C for 30−60 min and then analyzed by HPLC.

Cysteine and Histidine Challenge. Aliquots of 100 μL of the ^{99m}Tc complexes were added to 900 μL of 10^{-3} M cysteine or histidine solutions in PBS (pH 7.4) (final ligand concentration 10^{-5} M). The solutions were incubated at 37 °C, and aliquots were removed at 1, 2, 4, and 6 h, at which time HPLC analysis was run.

Lipophilicity. The lipophilicity of the compounds was evaluated by determination of the partition coefficient (*P*) in physiological conditions (*n*-octanol/0.1 M PBS, pH 7.4).

Biodistribution Analysis of Complexes 2a−6a and 9a,10a in Normal, CD-1, Mouse Models. Biodistribution studies were performed using groups of five female CD-1 mice (randomly bred, Charles River) weighing approximately 20−25 g each. Prior to administration, complexes were diluted with PBS pH = 7.4. Animals were intravenously injected with 100 μL (2.5−12.5 MBq) of each preparation via the tail vein and were maintained on normal diet ad libitum. At 5 min, 30 min, 1 h, and 4 h, mice were sacrificed by cervical dislocation. The administered dose and the radioactivity in the sacrificed animals were measured in a dose calibrator (Aloka, Curiemeter IGC-3, Tokyo, Japan). The difference between the radioactivity in the injected and sacrificed animal was assumed to be due to excretion, mainly urinary excretion. Blood samples were taken by cardiac puncture at sacrifice. Tissue samples of the main organs were then removed, weighed, and counted in a gamma counter (Berthold, LB2111,Germany). Accumulation of radioactivity in the tissues was calculated and expressed as percentage of the injected dose per total organ (% ID/total organ) and/or per gram tissue (% ID/g organ). For blood, bone, and muscle, total activity was calculated assuming that these organs constitute 6%, 10%, and 40% of the total weight, respectively. Urine was also collected at the time of sacrifice.

The in vivo stability of the complexes was assessed by urine and murine serum HPLC analysis, using the above referenced experimental conditions. Urine: the urine was collected at sacrifice time and filtered through a Millex GV filter (0.22 μm) before RP-HPLC analysis. Serum: Blood collected from mice was immediately centrifuged for 15 min at 3000 rpm at 4 °C, and the serum was separated. Aliquots of 100 μL of serum were treated with 200 μL of ethanol to precipitate the proteins. Samples were centrifuged at 4000 rpm for 15 min, at 4 °C. Supernatant was collected and passed through a Millex GV filter (0.22 μm) prior to RP-HPLC analysis. Liver homogenate: After injection, animals were kept for 1 h on normal diet ad libitum, and, immediately after sacrifice, the liver was excised and rapidly rinsed and placed in chilled 50 mM TRIS/0.2 M sucrose buffer, pH = 7.4, wherein it was homogenized. Aliquots (in duplicate) of the liver homogenate were treated with ethanol in a 2:1 EtOH/aliquot v/v ratio. The samples were then centrifuged at 25 000 rpm for 15 min at 4 °C, filtered through Millex GV (0.22 μm), and analyzed by HPLC, following the experimental conditions referred above.

In Vitro Cell Binding Affinity Studies of [^{99m}Tc-*L*^{6}-(GGG)-Bombesin(7-14)NH_2] (11a). *In Vitro Receptor Binding.* The IC_{50} (inhibitory concentration 50%) value of [***L*^{6}**-(GGG)-Bombesin(7-14)NH_2] was determined by a competitive displacement cell binding assay using ^{125}I-Tyr^4-Bombesin as the radiolabel. Briefly, ∼3 × 10^6 cells (Suspended in D-MEM/F-12K media containing 0.01 M MEM and 2% BSA, pH = 5.5) were incubated at 37 °C for 1 h in the presence of 20 000 cpm ^{125}I-Tyr^4-Bombesin and increasing concentrations of nonradiolabeled conjugate. Upon completion of the incubation, the reaction medium was aspirated and the cells were washed four times with media. Cell-associated radioactivity was determined by counting in a Packard Riastar gamma counting system.

Internalization and Efflux Evaluation. In vitro internalization analysis of [^{99m}Tc(CO)$_3$-***L*^{6}**-(GGG)-Bombesin(7-14)NH_2] was carried out by incubation of ∼3 × 10^6 cells (in D-MEM/F-12K media containing 0.01 M MEM and 2% BSA, pH = 5.5) in the presence of 20 000 cpm labeled conjugate at 37 °C for selected timepoints of 15, 30, 45, 60, and 90 min. Upon completion of the incubation, the reaction medim was aspirated and the cells were washed four times with media. Surface-bound radioactivity was removed by washing the cells with 0.2 N acetic acid/0.5 M NaCl (pH = 2.5). The percent of internalized, cell-associated, radioactivity as a function of time was determined by counting in a Packard Riastar gamma counting system. Efflux evaluation was performed after a 45 min internalization period. The cellular medium was washed (3×) with buffer (room temperature) and resuspended for further incubation. Selected sampling at 0, 15, 30, 45, 60, and 90 min postinternalization was performed by an initial cold buffer wash of the cells, followed by washing with acetic acid/saline (pH = 2.5 at 4 °C).

Biodistribution Analysis of [^{99m}Tc-*L*^{6}-(GGG)-Bombesin(7-14)NH_2] in Normal, CF-1, Mouse Models. The biodistribution study of [^{99m}Tc-***L*^{6}**-(GGG)-Bombesin(7-14)NH_2] was determined in normal, CF-1 mice at the University of Missouri−Columbia. The mice were injected with 5 μCi (185 kBq) of the complex in 100 μL of isotonic saline via the tail vein. The mice were euthanized, and the tissues and organs were excised from the animals following at 1, 4, and 24 h postinjection (p.i.) Subsequently, the tissues and organs were weighed and counted in a NaI well counter and the percent injected dose (% ID) and % ID/g of each organ or tissue calculated. The % ID in whole blood was estimated assuming a whole-blood volume of 6.5% the total body weight.

RESULTS AND DISCUSSION

Pyrazolyl-Based ^{99m}Tc-Building Blocks. Following our previous work (*20*−*22*) and profiting from the ver-

Scheme 1. Synthesis of Metal Complexes (M = Re, X = Br (2−6) and M = ^{99m}Tc, X = H_2O (2a−6a))

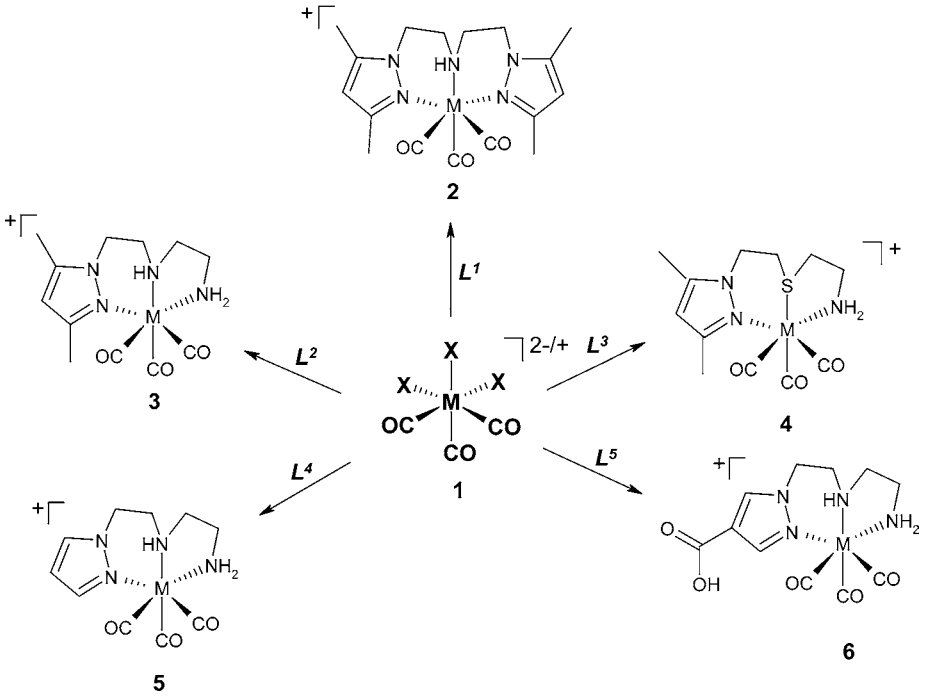

Table 1. Experimental Conditions for the Synthesis of Complexes 2a−6a and Characteristics of the Complexes

complex	yield [%]	*c* [M]	*t* [min]	*T* (°C)	RT (min)[a]	log $P_{o/w} \pm s$
2a (***L*^{1}**)	>90	10^{-4}	30	100	16.7 (16.2)[b]	0.87 ± 0.03
3a (***L*^{2}**)	>99	10^{-5}	30	100	24.2 (23.4)[c]	−0.24 ± 0.03
4a (***L*^{3}**)	>95	10^{-5}	30	100	19.8 (19.4)[b]	−0.07 ± 0.01
5a (***L*^{4}**)	>95	10^{-5}	30	100	16.9 (16.5)[c]	−0.93 ± 0.01
6a (***L*^{5}**)[20b]	>95	10^{-4}	30	100	18.8 (18.2)[b]	−2.35 ± 0.01

[a] The values in parentheses are for the Re complexes. [b] Nucleosil 250-4 100-10 C18 columns, flow of 1 mL/min. [c] Nucleosil 250-4 100-5 C18 columns, flow of 0.5 mL/min.

satility of the symmetric (***L*^{1}**) and asymmetric (***L*^{2}**−***L*^{5}**) pyrazolyl-containing ligands, we evaluated the behavior of these compounds toward the *fac*-[^{99m}Tc(CO)$_3$]$^+$ moiety. We intended to assess the influence of using symmetric and asymmetric ligands, having different pyrazolyl substituents (−H, −CH_3, −COOH) and/or donor atom sets, on the physicochemical and biological properties of the corresponding ^{99m}Tc complexes.

The ligands ***L*^{1}**−***L*^{3}** and ***L*^{5}**, as well as the corresponding tricarbonyl rhenium complexes **2**−**4** and **6**, were already available, and their synthesis and characterization has been previously reported by our group (*20*, *21*). In contrast, the lighter member of this family of ligands, compound ***L*^{4}**, which was not described previously, has been obtained by refluxing 1-(2-bromoethyl)pyrazole with an excess of ethylenediamine in a mixture of THF/H_2O, and its characterization was done by ^{1}H and ^{13}C NMR spectroscopy. Reaction of the mixed halide-carbonyl $(NEt_4)_2[ReBr_3(CO)_3]$ (**1**) with ***L*^{4}** in water yielded $[Re(CO)_3(k^3$-***L*^{4}**$)]$Br (**5**) (Scheme 1). The IR, ^{1}H, and ^{13}C NMR spectroscopic data obtained for **5** are compatible with the tridentate coordination mode of ***L*^{4}** and compare well with the results previously found for the complexes $[Re(CO)_3(k^3$-L$)]$Br (L = ***L*^{2}** (**3**), ***L*^{3}** (**4**)), which were characterized both in the solid state and in solution (Scheme 1) (*20*, *21*).

The ^{99m}Tc-building blocks $[^{99m}Tc(CO)_3(k^3$-L$)]^+$ (L = ***L*^{1}**−***L*^{5}** (**2a**−**6a**)) have been obtained by reacting $[^{99m}Tc(CO)_3(OH_2)_3]^+$ (**1a**) with aliquots of standard solutions of the corresponding pyrazolyl ligands, in a total volume of 1 mL (Scheme 1). The compounds formed were identified by comparing their HPLC chromatograms with the HPLC profiles of the analogues Re complexes, fully characterized either in the solid state and/or in solution (*20*, *21*).

The labeling conditions, the labeling yields, the log $P_{o/w}$, and the retention times for the ^{99m}Tc complexes are shown in Table 1. Under optimized labeling conditions, all complexes were obtained in almost quantitative yield (≥90%), with final concentration of the ligands (L) spanning from 10^{-4} to 10^{-5} M.

Complexes **2a**−**6a** were challenged in 1 mM cysteine and histidine solutions at 37 °C. The samples were analyzed by HPLC at 1, 2, 4, and 6 h, and the results obtained have confirmed a high stability for the complexes. Even for the less stable complex **2a**, almost no degradation or trans-chelation was observed, as can be confirmed by the data shown in Figure 1.

The biological distribution of the tricarbonyl complexes **2a**−**6a** was assessed in CD-1 mice at 5 min, 1 h, and 4 h after administration. Tissue distribution data of these complexes were expressed as the percentage of injected dose per gram of organ, and the uptake and clearance from most relevant organs can be overviewed in the histogram shown in Figure 2. Just for comparison, we also present in Table 2 the biodistribution of these complexes 4 h after administration. Total excretion of radioactivity over time is graphically represented in Figure 3.

The data show that all of the ^{99m}Tc-tricarbonyl complexes under study were rapidly cleared from blood and other main organs, primarily the renal-urinary pathway with a small portion retained in the hepatobiliary tract. The main differences in the biodistribution of the differ-

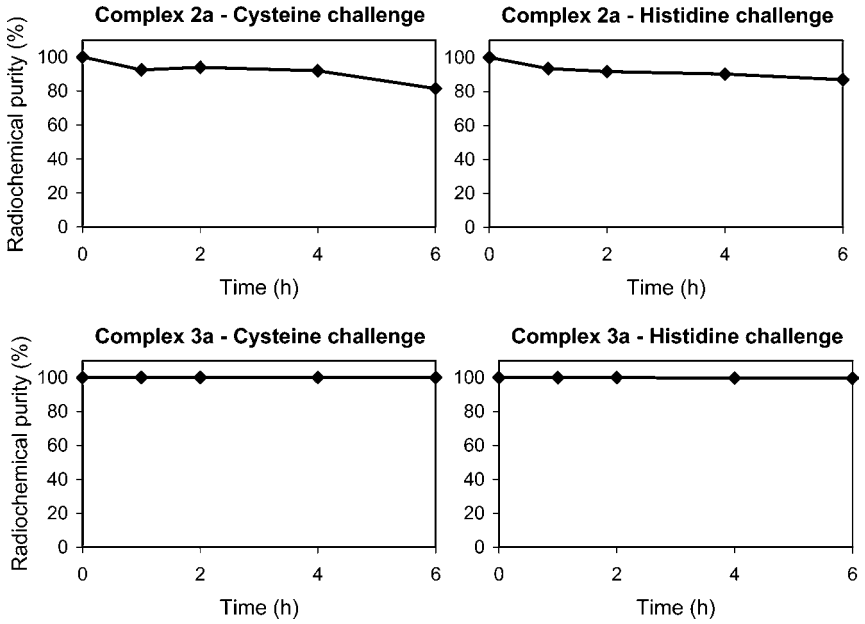

Figure 1. Stability of **2a** and **3a** in 1 mM cysteine and histidine solutions, at 37 °C.

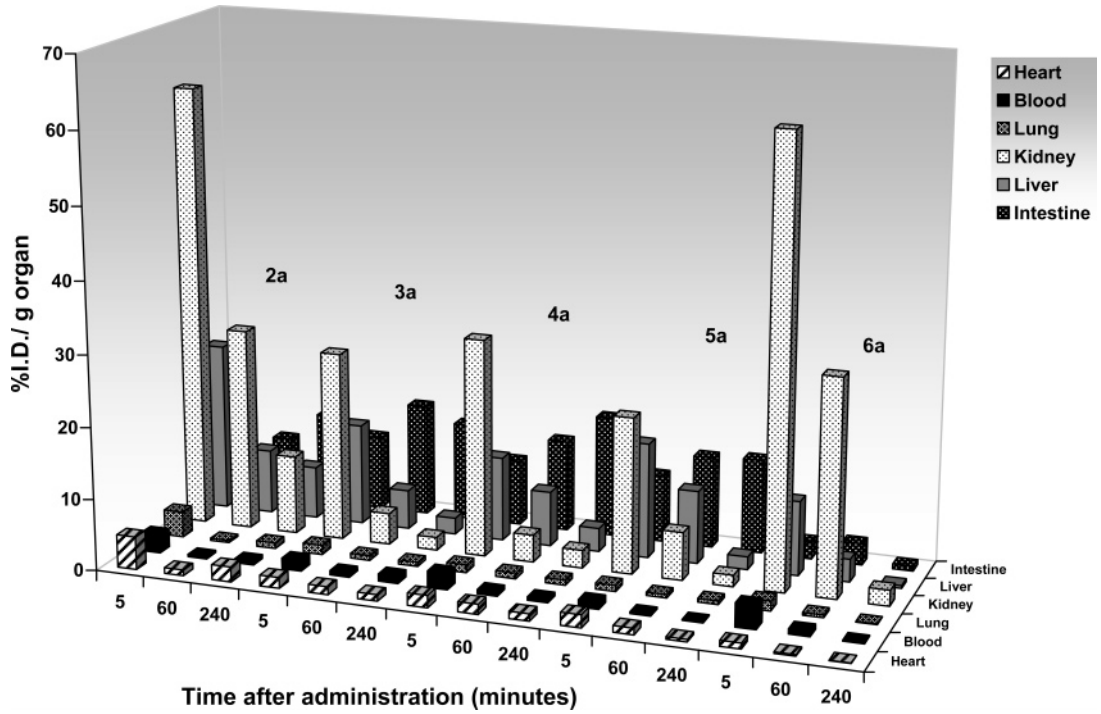

Figure 2. Histogram (% ID/g) for complexes **2a**−**6a** in CD-1 Charles River, as a function of time after IV administration.

Table 2. Biodistribution (% ID/g) of ^{99m}Tc Complexes 2a−6a in CD/1 Charles River, 4 h after IV Administration

organ	**2a**	**3a**	**4a**	**5a**	**6a**
blood	0.5 ± 0.1	1.0 ± 0.2	0.5 ± 0.2	0.10 ± 0.01	0.13 ± 0.01
liver	7.3 ± 1.8	2.3 ± 0.4	3.3 ± 0.6	1.8 ± 0.2	0.4 ± 0.1
intestine	12.8 ± 2.8	13.7 ± 3.5	16.9 ± 2.2	13.2 ± 1.6	0.7 ± 0.3
spleen	2.1 ± 0.5	0.47 ± 0.09	0.4 ± 0.1	0.11 ± 0.04	0.07 ± 0.01
pancreas	1.8 ± 0.1	1.9 ± 0.4	2.0 ± 0.3	2.0 ± 0.2	0.06 ± 0.01
heart	2.1 ± 0.3	0.9 ± 0.2	1.0 ± 0.2	0.35 ± 0.05	0.06 ± 0.02
lung	0.8 ± 0.1	0.59 ± 0.08	0.7 ± 0.1	0.5 ± 0.1	0.09 ± 0.03
kidney	11.0 ± 3.4	1.8 ± 0.2	2.5 ± 0.5	1.6 ± 0.1	2.2 ± 0.4
muscle	0.7 ± 0.1	0.15 ± 0.03	0.29 ± 0.04	0.08 ± 0.02	0.02 ± 0.01
bone	0.5 ± 0.1	0.15 ± 0.02	0.24 ± 0.01	0.2 ± 0.1	0.04 ± 0.01
stomach	2.4 ± 0.4	1.4 ± 0.4	2.4 ± 0.1	1.5 ± 0.2	0.08 ± 0.01

ent complexes are related to the clearance from tissues as well as to the rate of overall excretion. The highest retention of activity in all organs was observed for complex **2a** with most of the radioactivity retained in kidneys, liver, and intestines. The rate of injected dose cleared via the liver into the intestines is also slightly slower for **2a**, and consequently the total radioactivity excretion from whole animal body is significantly slower

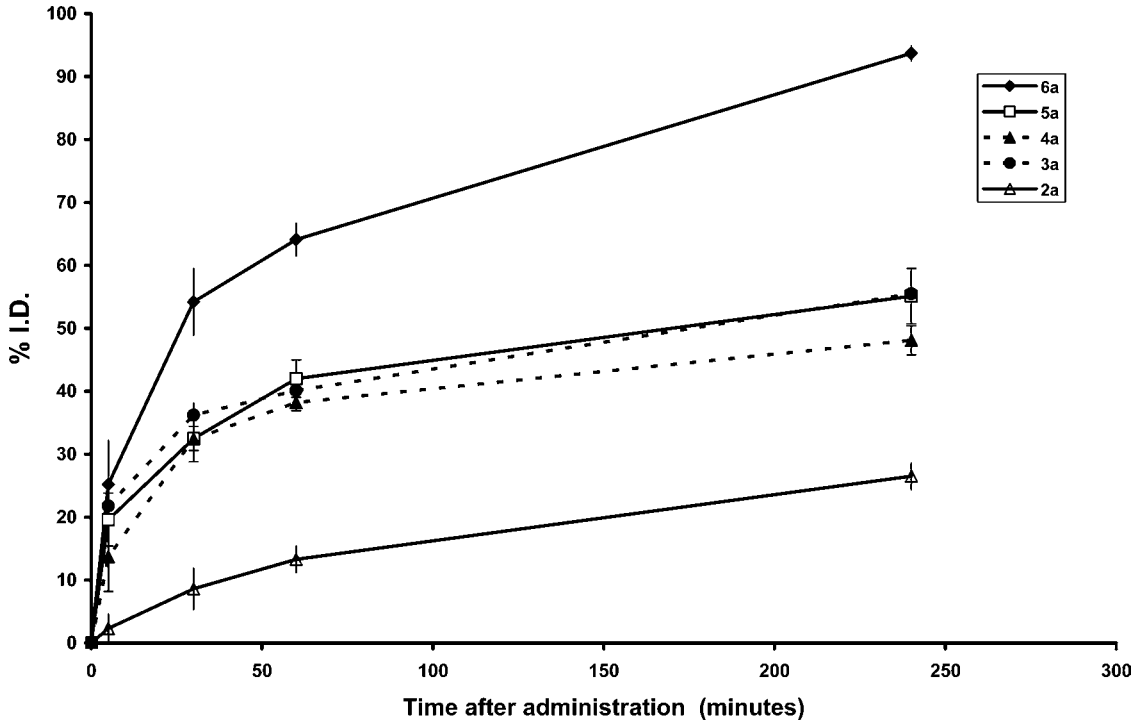

Figure 3. Total excretion for the tricarbonyl complexes **2a**−**6a**.

than for the other complexes (Figure 3). Complexes **3a**−**5a** have similar biological behavior in mice with few significant differences in their pharmacokinetics. As compared to these complexes, **6a** shows a faster clearance from the main organs and the total radioactivity excretion was relatively enhanced while the hepatic retention was reduced. Despite knowing that parameters other than lipo(hydro)philicity can affect the biodistribution profile, the predominant route of excretion, the urinary tract, seems to correlate with the log $P_{o/w}$ values found for the complexes (Table 1). The highest hepatic retention was found for **2a**, which has a log $P_{o/w}$ value of 0.87, while for **6a** which has a log $P_{o/w}$ value of −2.35 was observed a more rapid clearance and total excretion. The high hydrophilicity of **6a** and the rapid total radioactivity excretion may be related to the presence of the carboxylate group introduced in the 4-position of the pyrazolyl ring.

Bifunctional Pyrazolyl Chelators for the Labeling of Peptides. Taking into account the in vitro stability, lipophilicity, and biological profile of the building blocks previously described, we consider that all of the ligands, except for ligand **2a**, are very promising for labeling biologically active peptides. To have better insight into this aspect, we have decided to evaluate the possibility of preparing bifunctional chelators based on the ***L²*** and ***L⁴*** lead structures. By choosing these ligand frameworks, we also took into account that ***L²*** and ***L⁴*** allowed the synthesis of the ^{99m}Tc-building blocks with high specific activity (Table 1), being very similar in terms of biological profile and only slightly different in terms of molecular weight and lipophilicity.

The synthesis of the bifunctional pyrazolyl chelators involved the selective BOC protection of the primary amine functions of ***L²*** and ***L⁴***, followed by alkylation of the secondary amine with ethyl 4-bromobutyrate. 3,5-Me_2-pz$(CH_2)_2$N$((CH_2)_3$COOH$)(CH_2)_2NH_2$ (***L⁶***) and pz$(CH_2)_2$N$((CH_2)_3$COOH$)(CH_2)_2NH_2$ (***L⁷***), having a carboxylate group suitable for conjugation of tumor-seeking peptides, were finally obtained as yellow oils, after ester hydrolysis and removal of the BOC protecting group (Scheme 2).

Considering that the introduction of a pendant carboxylate group could modify the coordination mode of the pyrazolyl derivatives, we decided to study reactions of $(NEt_4)_2[ReBr_3(CO)_3]$ (**1**) with ***L⁶*** and ***L⁷***. Both ligands react promptly with **1**, leading to the formation of complexes $[Re(CO)_3(k^3$-L$)]$ (L = ***L⁶*** (**7**), ***L⁷*** (**8**)). On the basis of the splitting and chemical shifts of the ^{1}H and ^{13}C NMR resonances (vide experimental data), we concluded that in **7** and **8** the chelators ***L⁶*** and ***L⁷*** act as tridentate through the nitrogen atoms, similarly to the coordination mode found for the parent ligands ***L²*** and ***L⁴*** in complexes **3** and **5**, respectively (Scheme 1). These results prompted the coupling of the ***L⁶*** and ***L⁷*** to glycylglycine used as a peptide model, to prove the utility of these bifunctional chelators for labeling biologically relevant molecules.

The coupling of the dipeptide to ***L⁶*** and ***L⁷*** was achieved by reacting ***L⁶-BOC*** or ***L⁷-BOC*** with ethyl glycylglycine ester in the presence of HBTU and NEt_3, followed by deprotection of the primary amine and hydrolysis of the ester (Scheme 2). The coordination capability of the resulting functionalized ligands ***L⁸*** and ***L⁹*** toward the *fac*-$[M(CO)_3]$ (M = Re, ^{99m}Tc) moiety was evaluated by reacting these ligands with **1/1a** under aqueous conditions (Scheme 3). These reactions are accompanied by hydrolysis of the ester function of the glycylglycine fragment, and the complexes synthesized were *fac*-$[M(CO)_3(\kappa^3$-3,5-Me_2-pz$(CH_2)_2$N(glygly$)(CH_2)_2NH_2)]^+$ (**9/9a**) and *fac*-$[M(CO)_3(\kappa^3$-pz$(CH_2)_2$N$(CH_2)_3$(glygly$)(CH_2)_2NH_2)]^+$ (**10/10a**) (M = Re, ^{99m}Tc) (Scheme 3).

Compound **9** was characterized by ES/MS, IR, ^{1}H, and ^{13}C NMR spectroscopy, while the formulation of **10** was only established by ES/MS. The ^{99m}Tc complexes were characterized by comparing their radioactive traces on the HPLC with the UV traces of the analytically pure Re analogues.

The ^{99m}Tc-complexes **9a** and **10a** were obtained in high radiochemical purity, using final ligand concentrations

Scheme 2.[a] Synthesis of *L*[6]–*L*[9]

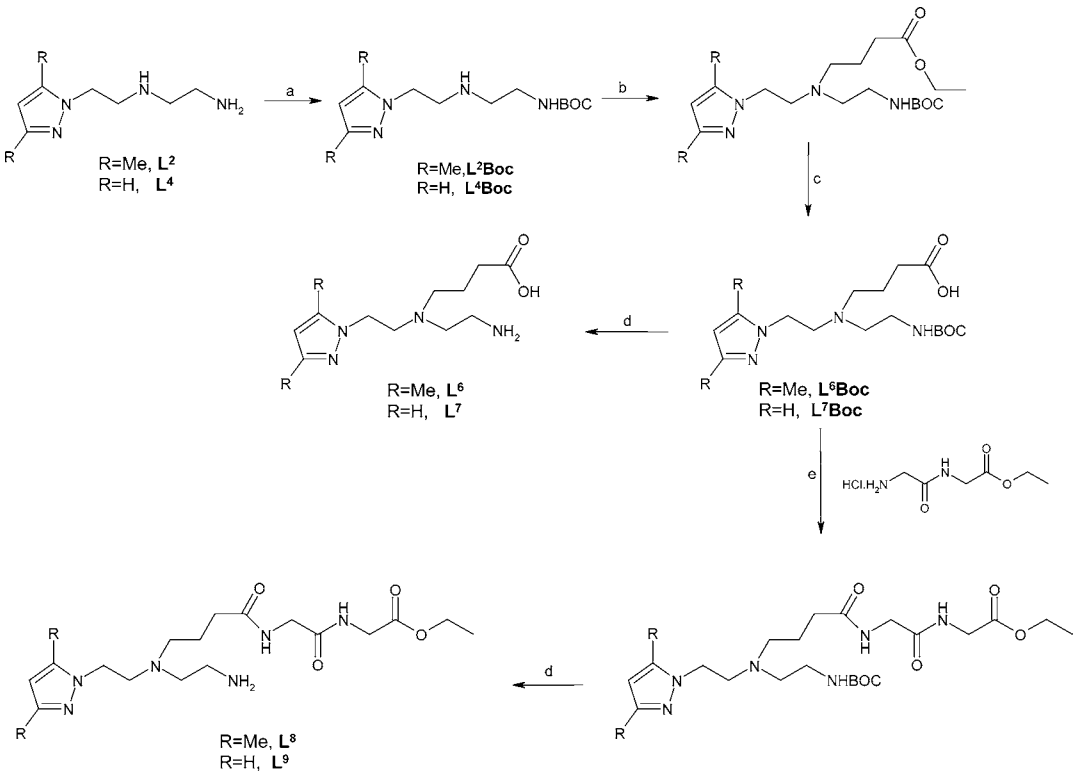

[a] (a) BOC-ON, THF/DMF, 0 °C, 2 h; (b) ethyl 1-bromobutyrate/K_2CO_3/Ki/CH_3CN; (c) NaOH, H_2O, THF, reflux, o.n.; (d) TFA, CH_2Cl_2, room temperature, 1 h; (e) HBTU, NEt_3, CH_3CN, room temperature, 4 h.

Scheme 3. Reactions of *fac*-$[Re(CO)_3Br_3]^{2-}$ and *fac*-$[^{99m}Tc(H_2O)_3(CO)_3]^{+}$ with *L*[8] and *L*[9]

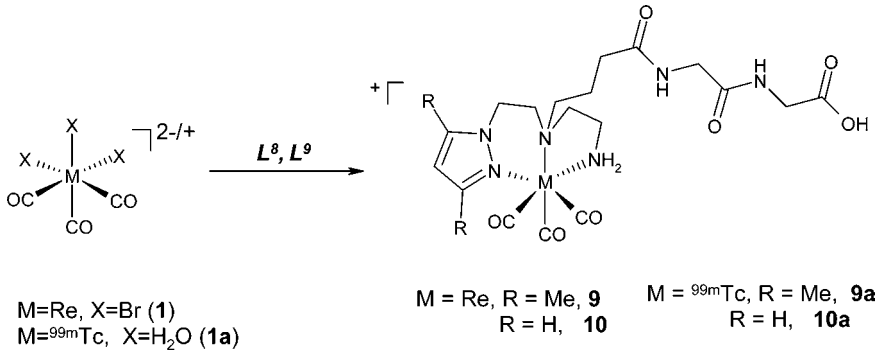

Table 3. Experimental Conditions for the Synthesis of Complexes 9a and 10a and Characteristics of the Complexes

complex	yield [%]	*c* [M]	*t* [min]	*T* (°C)	RT (min)[a]	log $P_{o/w} \pm s$
9a (***L*[8]**)	≥95	$(3-5) \times 10^{-5}$	60/30	100	19.2 (18.7)[b]	-1.12 ± 0.20
10a (***L*[9]**)	≥90	$(3-5) \times 10^{-5}$	60/30	100	17.2 (16.8)[b]	-2.11 ± 0.02

[a] The values in parentheses are for the rhenium complexes. [b] Nucleosil 250-4 100-10 C18 columns, flow of 1 mL/min.

in the $(3-5) \times 10^{-5}$ M range (Table 3), which are not significantly higher than the concentrations of ***L*[1]** and ***L*[4]** used to prepare the parent building blocks **3a** and **5a**. Hence, the attachment of the pendant arm at the central nitrogen does not strongly affect the coordination capability of these pyrazolyl-based chelators. Consistently, as complexes **3a** and **5a**, the glycylglycine functionalized complexes **9a** and **10a** also displayed a high robustness in cysteine and histidine challenge experiments.

In Table 4 are presented the biodistribution data of complexes **9a** and **10a** in CD-1 mice as percentage of injected dose per gram of organ, as well as the total radioactivity excretion as a function of time.

These results clearly indicate a biodistribution and pharmacokinetics for the glycylglycine functionalized complexes that are comparable to those found for building blocks **3a** and **5a**. However, for **9a** and **10a**, the enhanced urinary excretion, due to a lower retention of radioactivity in the kidneys over time, increased the percentage of overall excretion. To verify the in vivo stability of complexes **9a** and **10a**, serum, liver homogenate, and urine of the murines were also analyzed by radiometric HPLC. The murine serum, isolated from blood collected 30 min after i.v. administration, shows no pertechnetate, and more than 98% of the radioactivity could be assigned to complexes **9a** and **10a**. Furthermore, HPLC analysis of liver homogenate, from mice sacrificed 1 h after administration, also revealed that more than 98% of the radioactivity could be assigned to the ^{99m}Tc-tricarbonyl complexes **9a** and **10a**, indicating their resistance to

Table 4. Biodistribution (% ID/g) of ^{99m}Tc Complexes 9a and 10a in CD/1 Charles River, as a Function of Time after IV Administration

	9a				10a			
organ	5 min	30 min	60 min	240 min	5 min	30 min	60 min	240 min
blood	9.1 ± 1.3	1.7 ± 0.2	0.88 ± 0.04	0.39 ± 0.03	5.0 ± 0.9	0.9 ± 0.1	0.45 ± 0.06	0.06 ± 0.02
liver	17.1 ± 0.6	10.2 ± 1.2	4.8 ± 1.3	5.4 ± 0.8	19.8 ± 2.5	22.6 ± 3.1	14.7 ± 2.7	2.9 ± 0.8
intestine	2.7 ± 0.4	11.0 ± 2.1	7.7 ± 1.2	9.6 ± 1.7	1.7 ± 0.2	4.5 ± 0.9	7.5 ± 2.2	14.2 ± 2.0
spleen	2.5 ± 0.8	1.2 ± 0.2	0.5 ± 0.2	1.8 ± 0.4	0.7 ± 0.1	0.14 ± 0.04	0.08 ± 0.01	0.03 ± 0.02
pancreas	1.1 ± 0.1	0.4 ± 0.1	0.24 ± 0.04	0.16 ± 0.01	1.0 ± 0.1	0.3 ± 0.1	0.3 ± 0.1	0.08 ± 0.03
heart	1.8 ± 0.2	0.4 ± 0.1	0.24 ± 0.02	0.25 ± 0.04	1.1 ± 0.2	0.25 ± 0.06	0.12 ± 0.02	0.03 ± 0.00
lung	12.3 ± 0.9	1.5 ± 0.1	0.94 ± 0.05	3.8 ± 0.9	2.1 ± 0.3	0.49 ± 0.04	0.19 ± 0.05	0.05 ± 0.02
kidney	9.6 ± 0.4	2.9 ± 0.5	1.7 ± 0.2	1.0 ± 0.1	11.2 ± 1.3	3.1 ± 0.9	1.2 ± 0.2	0.26 ± 0.03
muscle	1.2 ± 0.2	0.25 ± 0.06	0.14 ± 0.03	0.08 ± 0.01	1.1 ± 0.3	0.18 ± 0.05	0.08 ± 0.01	0.02 ± 0.01
bone	1.6 ± 0.2	0.30 ± 0.07	0.15 ± 0.01	0.14 ± 0.01	1.2 ± 0.3	0.21 ± 0.04	0.08 ± 0.01	0.05 ± 0.03
stomach	1.0 ± 0.5	1.2 ± 0.3	0.4 ± 0.2	0.4 ± 0.1	0.7 ± 0.6	0.6 ± 0.3	0.7 ± 0.2	0.3 ± 0.1
excretion (% I.D./organ)	16.9 ± 1.4	46.8 ± 5.8	57.7 ± 2.2	59.5 ± 2.6	24.6 ± 3.9	40.2 ± 6.1	55.2 ± 9.6	63.1 ± 6.0

metabolic degradation. Analysis of urine collected at sacrifice time demonstrated again high in vivo stability of the complexes, because no metabolites could be detected. As an example, the HPLC chromatograms of biological samples collected from mice injected with **9a** are shown in Figure 4. The resistance to metabolic degradation in blood and liver, an organ rich in enzymes such as peptidases, and the excretion of the ^{99m}Tc tricarbonyl complexes intact into the urine demonstrate their high in vivo robustness.

To further demonstrate the utility of this family of bifunctional chelators in synthesizing receptor-avid peptide pyrazolyl conjugates, a GRP receptor-specific peptide (G-G-G-Q-W-A-V-G-H-L-M-NH_2) was chosen for coupling to ***L*^{6}**. The new conjugate was synthesized by SPPS and characterized by electrospray ionization mass spectrometry. The radiolabeled peptide conjugate [^{99m}Tc(CO)$_3$-***L*^{6}**-(GGG)-Bombesin(7-14)NH_2] (**11a**) was obtained in high yield (≥95%) upon addition of 100 μL of a solution of the conjugate ($(3-5) \times 10^{-5}$ M) to a vial containing 900 μL of the precursor [^{99m}Tc(CO)$_3$(H_2O)$_3$], with heating (Figure 5). Radiochemical yields of the new ^{99m}Tc-conjugates were monitored by RP-HPLC. The chromatographic profile of metalated conjugate is shown in Figure 6. The chromatogram displays a single peak with a retention time of 14.6 min. This conjugate is stable in aqueous solution for time periods of ≥24 h.

Competitive binding displacement studies of [***L*^{6}**-(GGG)-Bombesin(7-14)NH_2] demonstrated an IC_{50} value of 0.7 ± 0.2 nM. This value is very much comparable to

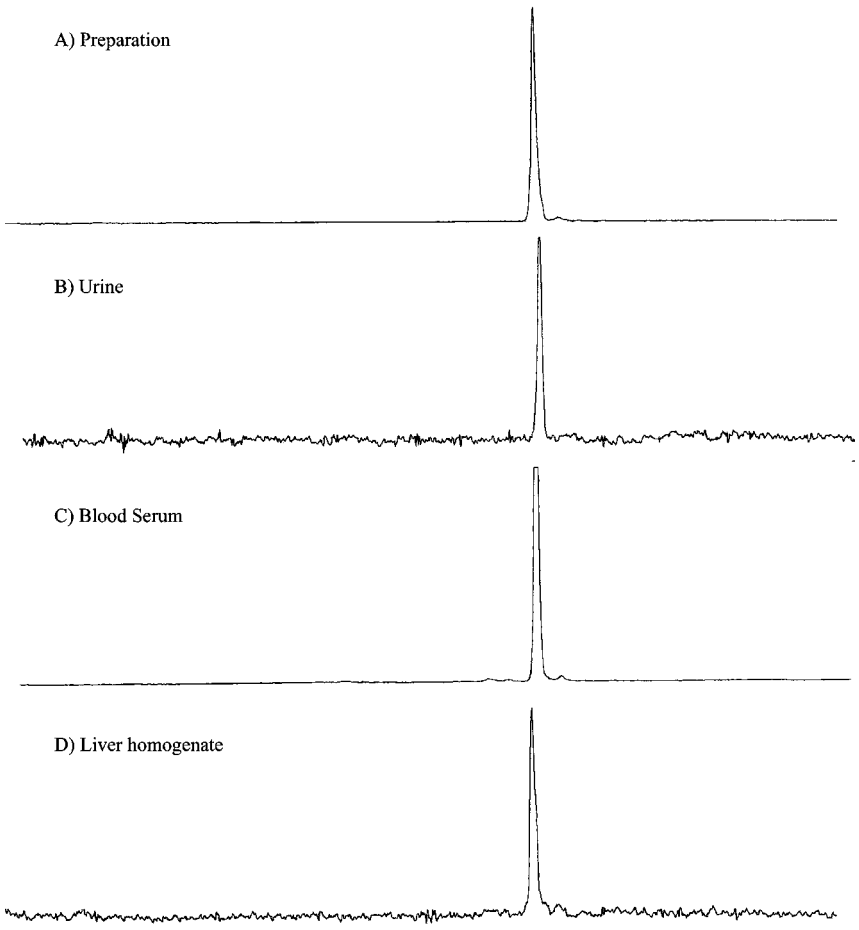

Figure 4. HPLC chromatogram for complex **10a**: (A) preparation, (B) urine, (C) blood serum, and (D) liver homogenate.

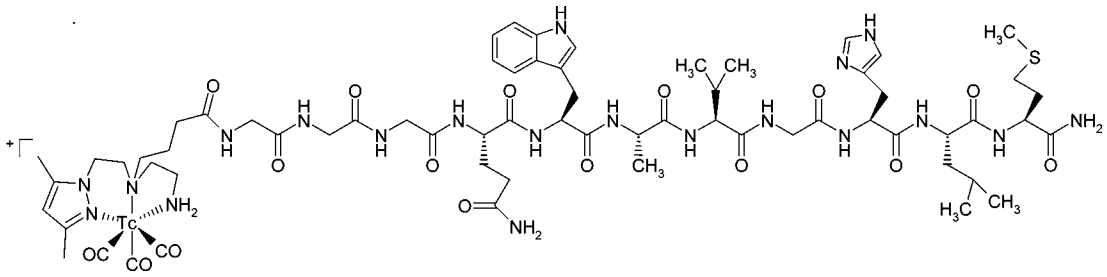

Figure 5. Metalated BBN analogue (**11a**).

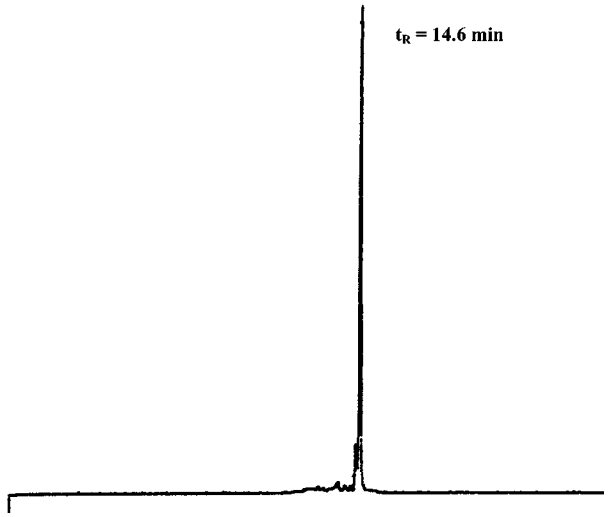

Figure 6. HPLC elution profile of the metalated BBN analogue [^{99m}Tc(CO)$_3$-***L*^{6}**-(GGG)-Bombesin(7-14)NH$_2$] (**11a**) (t_R, 14.6 min).

those previously reported for conjugates of this type (*33*−*36*).

Figure 7 summarizes the results of studies to assess the degree of uptake (internalization) of the new conjugate in PC-3 cells. At 90 min postincubation, the amout of internalized activity is ∼60% of the total activity administered. These data are considerably lower when compared to other conjugates of this type (*35*, *36*). Figure 8 summarizes the results of studies to assess the degree of trapping (efflux) of the [^{99m}Tc(CO)$_3$-***L*^{6}**-(GGG)-Bombesin(7-14)NH$_2$] (**11a**) in PC-3 cells. The total ^{99m}Tc activity associated with the cells after the 45 min incubation was measured following washing of the cells with the pH 7.4 incubation media. After washing these cells with the pH 2.5 buffer to remove surface-bound ^{99m}Tc activity, approximately 60% remained trapped by the cells. Results of measurements at 15, 30, 45, 60, and 90 min show that

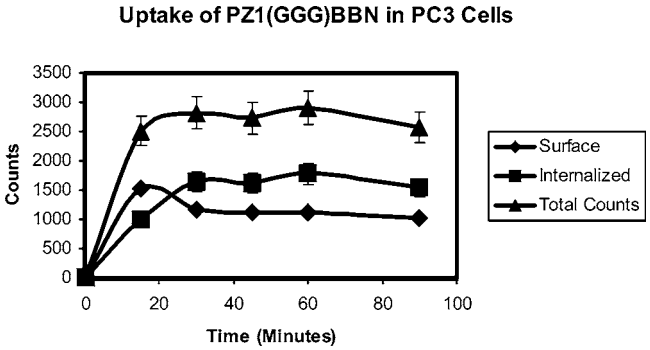

Figure 7. Internalization of [^{99m}Tc(CO)$_3$-***L*^{6}**-(GGG)-Bombesin(7-14)NH$_2$] (**11a**) in human prostate (PC-3) cancerous cells.

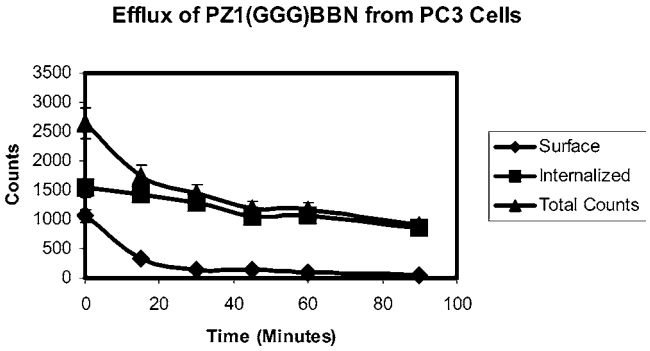

Figure 8. Efflux of [^{99m}Tc(CO)$_3$-***L*^{6}**-(GGG)-Bombesin(7-14)NH$_2$] (**11a**) in human prostate (PC-3) cancerous cells.

radioactivity does remain trapped by the cells, with approximately 45% of the ^{99m}Tc-activity associated with the cells at $t = 0$ remaining residualized at 90 min. Thus, at 90 min, approximately 66% of the activity remains residualized when normalized to the 60% trapped in the cells at $t = 0$. Efflux of this conjugate from PC-3 prostate tumor cells is comparable to other ^{99m}Tc(I)-conjugates of this type (*35*, *36*). The introduction of the pyrazolyl ligand

Table 5. Biodistribution of [^{99m}Tc(CO)$_3$-*L*^{6}**-(GGG)-Bombesin(7-14)NH$_2$] (11a) in CF-1 Normal Mice as a Function of Time after IV Administration**

	% ID/organ			% ID/g organ		
organ	1 h	4 h	24 h	1 h	4 h	24 h
blood	1.35 ± 0.06	0.76 ± 0.20	0.23 ± 0.07	0.80 ± 0.04	0.45 ± 0.12	0.14 ± 0.04
liver	5.73 ± 1.10	2.43 ± 0.79	1.88 ± 0.27	3.77 ± 0.80	1.64 ± 0.55	1.17 ± 0.11
intestine	24.3 ± 3.92	18.3 ± 6.62	0.49 ± 0.05	16.2 ± 1.70	19.0 ± 6.54	0.38 ± 0.04
spleen	0.05 ± 0.02	0.02 ± 0.01	0.01 ± 0.00	1.17 ± 1.72	0.34 ± 0.30	0.17 ± 0.05
pancreas	1.05 ± 0.20	0.09 ± 0.03	0.03 ± 0.01	5.80 ± 0.87	0.46 ± 0.01	0.15 ± 0.04
heart	0.05 ± 0.01	0.03 ± 0.01	0.02 ± 0.01	0.42 ± 0.14	0.23 ± 0.12	0.13 ± 0.05
lung	0.12 ± 0.01	0.10 ± 0.03	0.05 ± 0.01	0.54 ± 0.11	0.54 ± 0.31	0.20 ± 0.03
kidney	0.87 ± 0.09	0.59 ± 0.18	0.34 ± 0.03	2.20 ± 0.30	1.77 ± 0.57	0.91 ± 0.17
muscle	0.02 ± 0.00	0.01 ± 0.01	0.01 ± 0.01	0.10 ± 0.02	0.14 ± 0.16	0.06 ± 0.03
bone	0.03 ± 0.00	0.01 ± 0.01	0.01 ± 0.01	0.31 ± 0.14	0.25 ± 0.22	0.35 ± 0.50
stomach	0.30 ± 0.12	0.13 ± 0.04	0.09 ± 0.05	0.72 ± 0.26	0.21 ± 0.14	0.12 ± 0.07
carcass	5.24 ± 0.79	4.15 ± 2.40	1.45 ± 0.29	5.24 ± 0.79	5.24 ± 0.79	5.24 ± 0.79
bladder	0.06 ± 0.03	0.01 ± 0.01	0.01 ± 0.00	3.32 ± 1.47	0.53 ± 0.50	0.29 ± 0.22
urine	60.7 ± 2.94	73.3 ± 9.27	67.3 ± 7.28			

onto BBN[7-14]NH_2 has little or no effect on the efflux properties of the ^{99m}Tc-conjugate in GRP receptor-specific PC-3 cells as this new conjugate demonstrates uptake comparable to other ^{99m}Tc(I)-conjugates of this type (*35*, *36*).

Table 5 summarizes the results of the biodistribution studies in normal CF-1 mice at 1 h postintravenous injection for the [^{99m}Tc$(CO)_3$-***L*^{6}**-(GGG)-Bombesin(7-14)NH_2] conjugate. The conjugate was surprisingly hydrophilic with 71.9 ± 2.49% ID clearing via the renal-urinary pathway at 4 h p.i. The remainder of the radioactivity was cleared via the hepatobiliary pathway. There is no significant uptake or retention in the stomach, indicating that there is minimal, if any, in vivo dissociation of ^{99m}Tc from the pyrazolyl ligand to produce $^{99m}TcO_4^-$. Pancreatic tissue expresses the GRPr in high density. Therefore, the accumulation of ^{99m}Tc-activity in pancreatic tissue reflects the ability of these derivatives to target GRP receptor-expressing cells in vivo. Receptor-mediated pancreatic uptake of this ^{99m}Tc-conjugate was noticeably lower (i.e., 5.8 ± 0.87% ID/g at 1 h p.i.) when compared to other BBN conjugates designed and developed in our laboratory. This is presumably due to an increased rate of clearance from serum into the hepatobiliary system as compared to other more hydrophilic conjugates of similar structure (*33*−*36*). Kidney retention for the ^{99m}Tc-conjugate was found to be ∼2% ID/g. Blocking studies in which high levels of cold BBN[1-14] was administered 30 min prior to the ^{99m}Tc-ligands reduced the % ID/g uptake/retention in the pancreas at 1 h p.i. significantly, demonstrating the in vivo receptor specificity of this analogue for GRP-receptor expressing cells (data not shown).

CONCLUSION

The pyrazolyl-based chelators ***L*^{1}**−**L*^{5}** react with $(NEt_4)_2$-[$ReBr_3(CO)_3$] (**1**) and [^{99m}Tc$(H_2O)_3(CO)_3]^+$ (**1a**) forming well-defined complexes of the type [$M(CO)_3(k^3$-L)$]^+$. The ^{99m}Tc complexes are obtained in high yield, with high radiochemical purity, and are stable against cysteine and histidine exchange reactions. The biological profile and pharmacokinetics of these building blocks indicate that they were rapidly cleared from blood and other main organs into urine, mainly the renal-urinary pathway, with a small portion retained in the hepatobiliary tract. Most of these ligands can be functionalized through the primary or secondary amine as well as through the pyrazolyl ring. In this report, we have explored functionalization through the secondary amine. We have shown that the introduction of a pendant carboxylate arm on ***L*^{2}** and ***L*^{4}** does not change the coordination mode of the final bifunctional chelators. Furthermore, coupling of this ligand to a small peptide such as BBN(7-14)NH_2 does not change the high in vitro and in vivo stability of the metalated conjugates. This important requirement together with the favorable tissue distribution profile of the complexes/conjugate (i.e., rapid clearance from nontarget tissue, rapid urinary excretion, and low retention of radioactivity in the kidneys) are quite attractive features of these pyrazolyl derivatives. In summary, these results can be seen as proof-of-principle of the utility of tridentate and asymmetric pyrazolyl-based ligands as bifunctional chelators for labeling tumor-seeking peptides with the *fac*-[^{99m}Tc$(CO)_3]^+$ moiety. Moreover, the characteristics of the ligands are expected to allow a fine-tuning of the biological properties of the labeled tumor-seeking peptides.

ACKNOWLEDGMENT

We thank Mallinckrodt-Tyco Inc. for financial support. S.A. thanks Fundação para a Ciência e Tecnologia for a Ph.D. grant (BD/3052/2000). We would also like to acknowledge the research group of Dr. Timothy J. Hoffman at the Harry S. Truman Memorial Veterans' Hospital and the University of Missouri−Columbia for contributing effort toward the biodistribution analysis of the bombesin conjugates.

LITERATURE CITED

(1) Hom, R. K., and Katzenellenbogen, J. A. (1997) Technetium-99m.-Labeled Receptor-Specific Small-Molecule Radiopharmaceuticals: Recent Development and Encouraging Results *Nucl. Med. Biol*. *24*, 485−498.

(2) Dilworth, J. R., and Parrott, S. J. (1998) The Biomedical Chemistry of Technetium and Rhenium. *Chem. Soc. Rev*. *27*, 43.

(3) Jurisson, S. S., and Lydon, J. D. (1999) Potential technetium small molecules radiopharmaceuticals. *Chem. Rev*. *99*, 2205−2218.

(4) Liu, S., and Edwards, D. S. (1999) ^{99m}Tc-labeled small petides as diagnostic radiopharmaceuticals. *Chem. Rev*. *99*, 2235−2268.

(5) Heppeler, A., Froidevaux, S., Eberle, A. N., and Maecke, H. R. (2000) Receptor Targetting for Tumor Localisation and Therapy with Radiopeptides. *Curr. Med. Chem*. *7*, 971−994.

(6) Behr, T. M., Gotthardt, M., Barth, A., and Béhé, M. (2001) Imaging tumors with peptide-based radioligands. *Q. J. Nucl. Med*. *45*, 189−200.

(7) Okarvi, S. M. (2004) Peptide-Based Radiopharmaceuticals: Future Tools for Diagnostic Imaging of Cancers and Other Diseases. *Med. Res. Rev. 24*, 357−397.

(8) Kwekkeboom, D., Krenning, E. P., and de Jong, M. (2000) Peptide Receptor Imaging and Therapy. *J. Nucl. Med*. *41*, 1704−1713.

(9) Alberto, R., Schibli, R., Egli, A., Schubiger, P. A., Herrmann, W. A., Artus, G., Abram, U., and Kaden, T. A. (1995) Metal−carbonyl syntheses. Low-pressure carbonylation of $MOCl_4^-$ and MO_4^--the technetium(I) and rhenium(I) complexes $[NEt_4]_2$-$[MCl_3(CO)_3]$. *J. Organomet. Chem. 493*, 119−127.

(10) Alberto, R., Schibli, R., Egli, A., Schubiger, P. A., Abram, U., and Kaden, T. A. (1998) A novel organometallic aqua complex of technetium for the labeling of biomolecules: synthesis of [^{99m}Tc$(H_2O)_3(CO)_3]^+$ from [$^{99m}TcO_4]^-$ in aqueous solution and its reaction with a bifunctional ligand. *J. Am. Chem. Soc. 120*, 7987−7988.

(11) Metzler-Nolte, N. (2001) Labeling of Biomolecules for Medicinal Applications − Bioorganometallic Chemistry at Its Best. *Angew. Chem., Int. Ed*. *40*, 1040−1043.

(12) Schibli, R., La Bella, R., Alberto, R., Garcia-Garayoa, E., Ortner, K., Abram, U., and Schubiger, P. A. (2000) Influence of the Denticity of Ligand Systems on the in Vitro and in Vivo Behaviour of ^{99m}Tc(I) Tricarbonyl Complexes: A Hint for the Future Functionalization of Biomolecules. *Bioconjugate Chem*. *11*, 345−351.

(13) Garcia, R., Paulo, A., Domingos, A., Santos, I, Ortner, K., and Alberto, R., (2000) Re and Tc Complexes Containing B−H...M Agostic Interactions as Building Blocks for the Design of Radiopharmaceuticals. *J. Am. Chem. Soc*. *122*, 11240−11241.

(14) Wald, J., Alberto, R., Ortner, K., and Candreia, L. (2001) Aqueous One-Pot Synthesis of Derivatized Cyclopentadienyl − Tricarbonyl Complexes of ^{99m}Tc with an In Situ CO Source: Application to a Serotonergic Receptor Ligand. *Angew. Chem., Int. Ed. 40*, 3062−3066.

(15) Correia, J. D. G., Domingos, A., Santos, I, Alberto, R., and Ortner, K. (2001)Re Tricarbonyl Complexes with Ligands Containing P, N, N and P, N, O Donor Atom Set: Synthesis and Structural Characterization. *Inorg. Chem*. *40*, 5147−5151.

(16) Garcia, R., Paulo, A., Domingos, A., and Santos, I. (2001) Rhenium(I) Organometallic Complexes with Novel Bis(mercaptoimidazolyl)borates and with Hydrotris(mercaptoimid-

azolyl)borate: Chemical and Structural Studies. *J. Organomet. Chem*. *632*, 41.
(17) Sogbein, O. O., Merdy, P., Morel, P., and Valliant, J. F. (2004) Preparation of Re(I)- and ^{99m}Tc(I)-Metallocarboranes in Water under Weakly Basic Reaction Conditions. *Inorg. Chem*. *43*, 3032−3034.
(18) Bernard, J., Ortner, K., Spingler, B., Pietzsch, H.-J., and Alberto, R. (2003) Aqueous Synthesis of Derivatized Cyclopentadienyl Complexes of Technetium and Rhenium Directed toward Radiopharmaceutical Application. *Inorg. Chem*. *42*, 1014−1022.
(19) Pak, J. K., Benny, P., Spingler, B., Ortner, K., and Alberto, R. (2003) N^{ϵ} Functionalization of Metal and Organic Protected L-Histidine for a Highly Efficient, Direct Labeling of Biomolecules with $[Tc(OH_2)_3(CO)_3]^+$. *Chem.-Eur. J. 9*, 2053−2061.
(20) Alves, S., Paulo, A., Correia, J. D. G., Domingos, Â., and Santos, I. (2002) Coordination Capabilities of Pyrazolyl Containing Ligands Towards the *fac*-$[Re(CO)_3]^+$ Moiety. *J. Chem. Soc., Dalton Trans*. *24*, 4714−4719.
(21) Vitor, R., Alves, S., Correia, J. D. G., Paulo, A., and Santos, I. (2004)Rhenium(I)- and Technetium(I) Tricarbonyl Complexes Anchored by Bifunctional Pyrazole-Diamine and Pyrazole-Dithioether Chelators. *J. Organomet. Chem*. *689*, 4764−4774.
(22) Alves, S., Paulo, A., Correia, J. D. G., Gano, L. Â., and Santos, I. (2002) New Building Blocks for Labeling Peptides with the $[^{99m}Tc(CO)_3]^+$ Core. *Technetium, Rhenium and Other Metals in Chemistry and Nuclear Medicine 6* (Nicolini, M., Mazzi, U., Eds.) pp 139−142, SGEditoriali, Padova.
(23) Mahmoud, S., Staley, J., Taylor, J., Bogden, A., Moreau, J.-P., Coy, D., Avis, I., Cuttitta, F., Mulshine, J. L., and Moody, T. W. (1985) [Psi^{13,14}] Bombesin Analogues Inhibit Growth of Small Cell Lung Cancer In Vitro and In Vivo. *Life Sci*. *37*, 105−113.
(24) Qin, Y., Ertl, T., Cai, R.-Z., Halmos, G., and Schally, A. V. (1994) Inhibitory Effect of Bombesin Receptor Antagonist RC-3095 on the Growth of Human Pancreatic Cancer Cells In Vivo and In Vitro. *Cancer Res*. *54*, 1035−1041.
(25) Qin, Y., Ertl, T., Cai, R.-Z., Horvath, J. E., Groot, K., and Schally, A. V. (1995) Antagonists of Bombesin/Gastrin-releasing Peptide Inhibit Growth of SW-1990 Human Pancreatic Adenocarcinoma and Production of Cyclic AMP. *Int. J. Cancer 63*, 257−262.
(26) Plonowski, A., Nagy, A., Schally, A. V., Sun, B., Groot, K., and Halmos, G. (2000) In Vivo Inhibition of PC-3 Human Androgen-independent Prostate Cancer by a Targeted Cytotoxic Bombesin Analogue, AN-215. *Int. J. Cancer 88*, 652−657.
(27) Breeman, W. A. P., Hofland, L. J., De Jong, M., Bernard, B. F., Srinivasan, A., Kwekkeboom, D. J., Visser, T. J., and Krenning, E. P. (1999) Evaluation of Radiolabeled Bombesin Analogues for Receptor-targeted Scintigraphy and Radiotherapy. *Int. J. Cancer 81*, 658−665.
(28) Breeman, W. A. P., De Jong, M., Bernard, B. F., Kwekkebom, D. J., Srinivasan, A., van der Pluijm, M. E., Hofland, L. J., Visser, T. J., and Krenning, E. P. (1999) Pre-clinical Evaluation of [^{111}In-DTPA-Pro^1, Tyr^4]Bombesin, a New Radioligand for Bombesin-receptor Scintigraphy. *Int. J. Cancer 83*, 657−663.
(29) Sorrel, T. N., and Malachowski, M. R. (1983) Mononuclear Three-Coordinate Copper (I) Complexes: Synthesis, Structure and Reaction with Carbon Monoxide. *Inorg. Chem*. *22*, 1883−1887.
(30) Haanstra, W. G., Driessen, W. L., Van Roon, M., Stoffels, A. L. E., and Reedijk, J. (1989) Unusual Chelating Properties of the Ligand 1,8-Bis (3, 5-dimethyl-1-pyrazolyl)-3,6-dithiaoctane (bddo). Crystal Structures of Ni(bddo)(NCS)2, Zn(bddo)(NCS)2 and Cd2(bddo9(NCS)4. *J. Chem. Soc., Dalton Trans*. 2309−2314.
(31) Van Berkel, P. M., Driessen, W. L., Parlevliet, F. J., Reedijk, J., and Sherrington, D. C. (1997) Metal-uptake Behaviour by a Novel Pyrazole-Containing Ligand Immobilised on to Poly(Glycidylmethacrylate-*co*-trimethylolpropane-trimethacrylate). *Eur. Polym. J*. *33*, 129−135.
(32) Lopez, P., Seipelt, G., Merkling, P., Sturz, L., Alvarez, J., Dolle, A., Zeidler, M. D., Cerdan, S., and Ballesteros, P. (1999) N-2-(Azol-1(2)yl)ethyliminodiacetic acids: A novel Series of Gd(III) Chelators as T2 Relaxation Agents for Magnetic Resonance Imaging. *Bioorg. Med. Chem. 7*, 517−527.
(33) Smith, C. J., Gali, H., Sieckman, G. L., Hayes, D. L., Owen, N. K., Mazuru, D. G., Volkert, W. A., and Hoffman, T. J. (2003) Radiochemical Investigations of ^{177}Lu-DOTA-8-Aoc-BBN[7−14]NH_2: An In vitro/in vivo assessment of the Targeting Ability of this New Radiopharmaceutical for PC-3 Human Prostate Cancer Cells. *Nucl. Med. Biol*. *30*, 101−109.
(34) Smith, C. J., Volkert, W. A., and Hoffman, T. J. (2002) Gastrin Releasing Peptide (GRP) Receptor Targeted Radiopharmaceuticals: A Concise Update. *Nucl. Med. Biol*. *30*, 861−868.
(35) Smith, C. J., Sieckman, G. L., Owen, N. K., Hayes, D. L., Mazuru, D. L., Volkert, W. A., and Hoffman, T. J. (2003) Radiochemical Investigations of [$^{188}Re(H_2O)(CO)_3$-Dpr-SSS−Bombesin(7−14)NH_2]: Syntheses, Radiolabeling, and In Vitro/In Vivo Studies Where Dpr = Diaminopropionic Acid. *Anticancer Res. 23*, 63−70.
(36) Smith, C. J., Sieckman, G. L., Owen, N. K., Hayes, D. L., Mazuru, D. G., Kannan, R., Volkert, W. A., and Hoffman, T. J. (2003) Radiochemical Investigations of GRP Receptor-specific [$^{99m}Tc(X)(CO)_3$- Dpr-Ser-Ser-Ser-Gln-Trp-Ala-Val-Gly-His-Leu-Met-(NH_2)] in PC-3, Tumor-bearing, Rodent Models: Syntheses, Radiolabeling, and In Vitro/In Vivo Studies Where Dpr = 2,3-Diaminopropionic acid and X = H_2O or $P(CH_2OH)_3$. *Cancer Res. 63*, 4082−4088.

BC0497968

TECHNICAL NOTES

Anchorage of Synthetic Peptides onto Liposomes via Hydrazone and α-Oxo Hydrazone Bonds. Preliminary Functional Investigations

Line Bourel-Bonnet,*,† Eve-Isabelle Pécheur,‡,|| Cyrille Grandjean,†,⊥ Annick Blanpain,† Thorsten Baust,§,▽ Oleg Melnyk,† Bernard Hoflack,‡,§,▽ and Hélène Gras-Masse†

UMR 8525 CNRS, Institut Pasteur de Lille et Université de Lille 2, France, FRE 2377 CNRS, Institut de Biologie de Lille, 1 rue du Pr. Calmette, 59021 Lille, France, and Biotec, Proteomics, TU Dresden, Max-Planck-Institute for Molecular Cell Biology and Genetics, Pfotenhauerstrasse 108, 01307 Dresden, Germany. Received April 13, 2004; Revised Manuscript Received January 6, 2005

Synthetic peptidoliposomes have been designed and prepared according to a chemoselective ligation. Two aldehyde-functionalized lipidic anchors were synthesized and incorporated into the lipidic bilayers of unilamellar liposomes during their preparation. Complementary hydrazino acetyl peptides were synthesized on the solid phase using *N*,*N*′,*N*′-tri(*tert*-butyloxycarbonyl)-hydrazino acetic acid and further coupled to the aldehyde groups displayed at the surface of the vesicles. Coupling yields were measured by amino acid hydrolysis following total acid hydrolysis. The ligation methodology proved superior to the simple insertion of lipopeptides, which was performed for comparison in terms of yields, implementation, and reproducibility. To check whether the grafted-peptides were accessible and functional, cytoplasmic sequences of LAMP protein (lysosomal associated membrane protein), which is involved in intracellular membrane trafficking, have been selected. Using this model, we demonstrated in vitro the specific interaction of the synthetic LAMP-peptidoliposomes with the cytoplasmic adaptor protein AP-3, a result that contributes to the understanding of protein sorting in cells. Thus, these results clearly indicate the usefulness of such peptidoliposomes, easily prepared by hydrazone chemoselective ligation, as a tool for biological investigation.

INTRODUCTION

The modification of the surface properties of liposomes by peptides or proteins has been extensively studied (*1*−*3*). Considering peptides, most of the time, their stable anchorage into the phospholipid bilayers requires their derivatization by a lipidic foot (*4*, *5*) composed of at least two alkyl chains (*6*, *7*). However, it is a challenging task due to the generally low solubility of the resulting conjugates. To circumvent these difficulties, alternative strategies have been developed where the purified peptide is ligated to a functionalized lipidic anchor already inserted in the membrane (*8*). In these strategies, the chemical bond between anchor and peptide is often chosen among the amide (*9*) or thioether bonds (*3*, *5*, *10*−*12*), disulfide bridge (*13*), and, sometimes, imine bond (*14*). However, peptides are randomly oriented, usually by more than one side chain if their sequence comprises more than one lysine and/or cysteine.

Alternatively, the hydrazone bond has been proposed by some authors to site-specifically immobilize peptides or proteins onto vesicles or microspheres (*15*). Conjugates are prepared by mild periodate oxidation of N-terminus Seryl or Threonyl peptides (*16*) or sugar of antibodies' Fc fragment (*17*) followed by the incubation of the product with hydrazide-phosphatidylethanolamine (*18*) contained in the bilayers. Advantageously, this method does not require any activating agent, nor does it generate any side-product. The reverse reaction consisting of the coupling of amphiphilic aldehyde-like anchors with synthetic hydrazino acetyl peptides remains unprecedented (Scheme 1).

This strategy can now be envisaged because of the recent progress concerning the preparation of the latter compounds. In particular, the use of the *N*,*N*′,*N*′-tri(*tert*-butyloxycarbonyl)-hydrazino acetic acid allows the facile introduction of the hydrazino-group on peptides using solid-phase peptide synthesis (*19*, *20*). Notably, this approach does not require extra steps to functionalize the peptides after cleavage from the resin and purification as compared to the synthesis of glyoxyl-peptides. Moreover, sulfur-containing peptides are more easily accessible because no deleterious periodate oxidation is performed. At any case, this reverse strategy will probably complement and reinforce the attractiveness of the hydrazone chemoselective ligation.

* To whom correspondence should be addressed. Phone: 00 33 (0)3 20 96 49 49. Fax: 00 33 (0)3 20 96 47 09. E-mail: lbourel@pharma.univ-lille2.fr.

† UMR 8525 CNRS.

‡ FRE 2377 CNRS.

§ Max-Planck-Institute for Molecular Cell Biology and Genetics.

|| Present address: Structural NMR and Bioinformatics, UMR 5086 CNRS, IBCP, Lyon, France.

⊥ Present address: Unité de Chimie Organique, URA CNRS 2128, Institut Pasteur, Paris, France.

▽ Present address: Biotechnologisches Zentrum der TU-Dresden, BioInnovationsZentrum, Dresden, Germany.

10.1021/bc049908v CCC: $30.25 © 2005 American Chemical Society
Published on Web 02/25/2005

Scheme 1. α-Oxo Hydrazone (A) or Hydrazone Ligation Principles (B), and Corresponding Peptido Liposomes

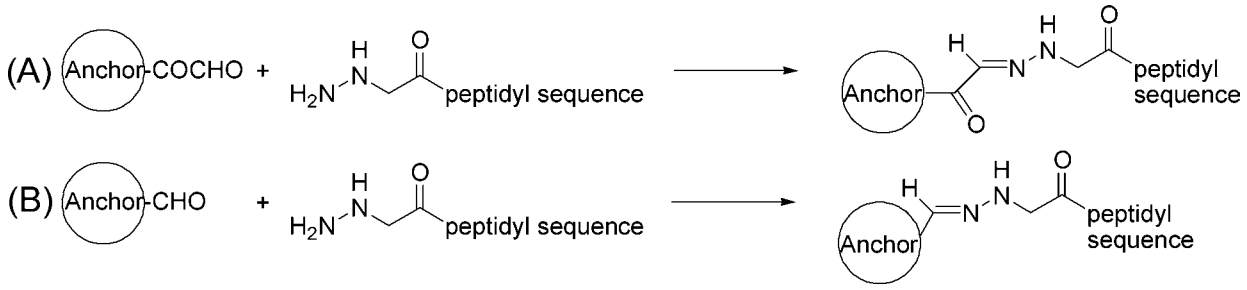

To test its feasability, we recently reported the solid-phase synthesis of an α-oxo aldehyde anchor **1a** (Figure 1), within 25% overall yield. As expected, **1a** was successfully coupled to a model hydrazino acetyl peptide within 81% RP-HPLC conversion and 41% isolated yield in an organic-aqueous solution (*21*). Moreover, we recently performed a comprehensive physicochemical study of **1a** reactivity to form hydrazone bonds on colloids just as the stability of the latter (*22*). Briefly, we demonstrated in that paper that hydrazone ligation offered high chemoselectivity and versatility. As we intended to use the hydrazone ligation to target the controlled release of therapeutic agents by vesicles, an accurate measure of the ligation bond stability was performed to ensure it would stand long exposures to physiological conditions. The mechanism of the reaction in solution as well as in different self-organized systems (micelles, liposomes, and multilamellar vesicles) was investigated. In solution, submicromolar stability was achieved as well as half-lives of several weeks (as an example, the hydrolysis rate constants estimated at pH 7.4 and 25 °C gave for our ligation products half-lives of 23 to 800 days and should be long enough at 37 °C to touch and attach their cell target in vivo). The kinetics and stability were both enhanced in colloidal media thanks to autoassociation effects. Finally, the grafting of synthetic mannose receptor−ligands onto onion-like vectors to target human dendritic cells provided a first example of the efficiency of this strategy (*23*).

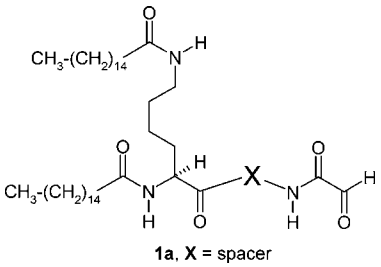

Figure 1. Amphiphilic α-oxo aldehyde **1a** (with X = Tyr−NH−$(CH_2)_3O[(CH_2)_2O]_2-(CH_2)_3$−NH−$COCH_2OCH_2CO$−Gly−NH−$(CH_2)_3$−).

To further demonstrate the usefulness and the versatility of our strategy, and particularly for probing biological processes, we describe herein the synthesis of a second aldehyde anchor (**1b**, Scheme 2), the inclusion of **1a** and **1b** into liposomes, and their reaction with hydrazino acetyl peptides, via α-oxo hydrazone (A) or hydrazone (B) bonds, respectively, to obtain peptidoliposomes (Scheme 1).

Peptido- or proteoliposomes have been used for various purposes in the cell biology of membranes, in particular to reconstitute in vitro several aspects of intracytoplasmic membrane trafficking. In eukaryotes, vesicular intracellular transport is mediated by several coat components (COPs) and adaptor proteins (APs), the latter functioning with clathrin (*32*−*35*). These cytosolic coat components bind to cytoplasmic domains of transmembrane proteins to segregate them into transport vesicles. Previously, the interaction of COPs had been reconstituted in vitro using chemically defined proteoliposomes (*36*−*38*).

The AP-3 complex interacts in vivo with a tyrosine-based sorting motif in the cytoplasmic domain of transmembrane LAMP (lysosomal-associated membrane protein) (*39*). We show here that AP-3 can specifically interact in vitro with liposomes onto which a synthetic cytoplasmic domain of LAMP has been coupled.

To demonstrate this, hydrazone-based peptidoliposomes were incubated with pig brain cytosol. These peptidoliposomes bore either the wild-type sequence of the LAMP cytoplasmic domain (wt) or a mutated sequence in which the key tyrosine residue of the sorting motif had been replaced by an alanine, thereby producing a nonfunctional sorting signal. In this context, AP-3 was specifically recruited onto wt LAMP-bearing liposomes, demonstrating that synthetic peptidoliposomes are excellent versatile tools for the in vitro study of membrane trafficking. More generally, in a context of reconstituted conditions in vitro, the necessity or the role of each partner, reagent, and/or condition can be studied.

EXPERIMENTAL PROCEDURES

Chemicals and Antibodies. All Fmoc protected amino acids (L-Arg(Pmc),[1] L-Asn(Trt), L-Asp(O*t*Bu), L-Gln(Trt), L-Glu(O*t*Bu), L-His(Trt), L-Lys(Boc), L-Lys(Fmoc), L-Ser(*t*Bu), L-Thr(*t*Bu), L-Tyr(*t*Bu)), coupling agents (HOBt, HBTU, BOP), and resins (Wang, Novasyn) were purchased from Novabiochem. Chemicals were from Sigma-Aldrich except cyanuric fluoride, which was from Lancaster. Solvents were from Acros.

Lipids (phosphatidylcholine (PC), phosphatidylethanolamine (PE), phosphatidylserine (PS), and cholesterol (chol)) were from Avanti Polar Lipids. The antiprotease cocktail, GTP, and GTP-γ-S (the nonhydrolyzable GTP analogue) were from Roche Biochemicals, and reagents

Scheme 2. Solution-Phase Synthesis of Anchor 1b[a]

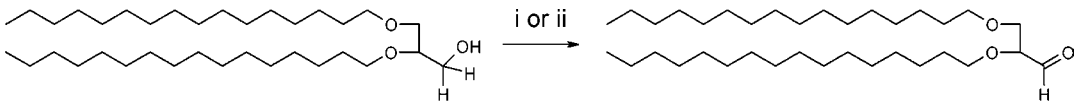

[a] Conditions and reagents: (i) Swern oxidation (35%); (ii) Dess−Martin oxidation (86%).

for chemiluminescence detection were from Pierce. The antibodies used in this study were as follows: affinity-purified rabbit polyclonal 2583 against the σ subunit of AP-3, recognizing a doublet on Western blots (the σ3 A and B isoforms); monoclonal antibody 100/3 against the γ-subunit of AP-1 (Sigma Immunochemicals); monoclonal antibody maD against the β subunit of COP I (Sigma Immunochemicals). The secondary antibodies used were goat anti-mouse and goat anti-rabbit conjugated to horseradish peroxidase (Sigma Immunochemicals).

RP-HPLC Eluents. **A**: TFA 0.05% in H_2O. **B**: TFA 0.05% in CH_3CN/H_2O 80/20 (v/v). **C**: TFA 0.05% in propan-2-ol/H_2O 40/60 (v/v). **D**: CH_3CN/potassium phosphate buffer 50 mM, pH 7.21 20/80 (v/v). **E**: CH_3CN/potassium phosphate buffer 50 mM, pH 7.21 75/25 (v/v).

Buffers for Biological Experiments. F: 1.79 mL of citric acid 0.1 M + 3.21 mL of Na_2PO_4 0.2 M + 5 mL of water to reach 100 mM, pH 6.4. **G**: 25 mM Hepes-KOH pH 7.2 + 125 mM KOAc + 2.5 mM MgOAc + 1 mM DTT.

Synthesis of anchor 1a was performed as described in ref *21*.

Synthesis of Anchor 1b. Di-*O*-hexadecyl-rac-glyceraldehyde was obtained using Dess−Martin's oxidation reagent. CH_2Cl_2 was distilled over P_2O_5. Dess−Martin periodinane, 15% weight solution in CH_2Cl_2 (287 mg, 0.10 mmol), was added to a solution of di-*O*-hexadecyl-rac-glycerol (50 mg, 0.09 mmol) in CH_2Cl_2 (2 mL) under N_2, with stirring. After 30 min, the resulting suspension was diluted with 9 mL of CH_2Cl_2/heptane 2/1 (v/v) and added to 10 mL of 1 M NaOH. After 10 min of stirring, the organic layer was washed with water, dried over Na_2SO_4, and concentrated under reduced pressure. The white residue was purified by chromatography on silica gel (eluent: heptane/AcOEt 95/5 (v/v)) to give **1b** (43 mg, 86%) as a white solid. ^{1}H NMR (300 MHz, $CDCl_3$) δ ppm: 9.24 (d, 1H, J = 1.4 Hz), 3.81 (ddd, 1H, J = 1.4, 4.0 and 5.4 Hz), 3.71 (dd, 1H, J = 4.0 and 10.5 Hz), 3.68 (dd, 1H, J = 5.4 and 10.5 Hz), 3.63 (dt, 1H, J = 6.7 and 9.2 Hz), 3.56 (dt, 1H, J = 6.6 and 9.2 Hz), 3.48 (dt, 1H, J = 6.5 and 9.3 Hz), 3.40 (dt, 1H, J = 6.6 and 9.3 Hz), 1.64 (q, CH_2, J = 6.6 Hz), 1.55 (q, CH_2, J = 6.9 Hz), 1.25 (br s, 26CH_2), 0.88 (t, 2 × 3H, J = 6.4 Hz, 2CH_3). ^{13}C NMR (75 MHz, $CDCl_3$) δ ppm: 203.3, 84.0, 72.1, 71.5, 70.0, 32.1, 29.9, 29.8, 29.6, 29.4, 26.2, 22.9, 14.3. TOF-PDMS: m/z 539 $[M + H]^+$.

Synthesis of the Dipalmitoyl Peptides 2a and 2b. A Fmoc/*t*Bu peptide synthesis was performed on 0.25 mmol of Wang resin in a 431A syntheziser (Applied Biosystems, UK) with a double coupling 4 equiv in situ activation of amino acid in the presence of HBTU (4 equiv), HOBt (4 equiv), DIEA (16 equiv), and Fmoc-protected amino acids to obtain the two expected Fmoc peptidyl resins. The last Fmoc was removed manually by a piperidine/NMP treatment 2/8 (v/v) within 2 and 20 min, and the resin was washed with NMP. Fmoc−Lys-(Fmoc)−OH was introduced manually as above. Following an ultimate deprotection, palmitic acid (8 equiv) reacted first under HBTU (8 equiv), HOBt (8 equiv) activation with DIEA (32 equiv) onto the deprotected diamino peptidyl resin. To prepare the second acylation, palmitic acid (8 equiv) was activated by cyanuric fluoride (32 equiv) in the presence of pyridine (8 equiv) under argon for 2 h in CH_2Cl_2/*t*BuOMe 4/1 (v/v) (*24*). Following an aqueous washing, CH_2Cl_2 was evaporated, and the fluoride was solubilized in DMF and reacted in parallel on the resins in the presence of DIEA (16 equiv) for 3 h. A total acid hydrolysis of the peptidyl resin conducted with HCl/propionic acid 1/1 (v/v) at 130 °C for 3 h gave quantification results as expected. The dipalmitoyl peptidyl resins were cleaved by TFA in the presence of H_2O/phenol/ethanedithiol/thioanisole: 0.5 mL/0.75 g/0.25 mL/0.5 mL in 10 mL of TFA for 2 h. Small amounts (37 mg out of 600 mg) of crude lipopeptides **2a** and **2b** were purified by preparative RP-HPLC (C3 Zorbax column, 300 Å, 1.8 μm, 15 × 500 mm, 4 mL min^{-1}, λ = 225 nm, 50 °C, eluents **A** and **B**, **B** 0 to 100% in 30 min, 100% **B** for 10 min). 7 mg of **2a** (19%) and 14 mg of **2b** (38%) were obtained. Identity was controlled by MALDI-TOF mass spectrometer and purity by RP-HPLC (C3 Zorbax, 4.6 × 200 mm, 1 mL min^{-1}, λ = 215 nm, 50 °C, eluents **A** and **B**, **B** 0 to 100% in 30 min, 100% **B** for 10 min). Total acidic hydrolyses in evacuated sealed tubes with 6 N HCl/phenol 10/1 (v/w) at 110 °C for 24 h followed by amino acid analysis were in agreement with expected results.

The synthesis of hydrazino acetyl peptides 3 was reported in refs *19*, *20* for other applications. Briefly, Fmoc−*t*Bu peptide syntheses were performed on 0.1 mmol of Wang resin in a Pioneer syntheziser (Applied Biosystems, UK) with a 10 equiv in situ activation of amino acid in the presence of HBTU, HOBt, DIEA, and protected amino acids to obtain the Fmoc peptidyl resins. Fmoc was removed automatically, and the deprotected N-terminal amine was acylated by *N*,*N*′,*N*′-tri(*tert*-butyloxycarbonyl)-hydrazino acetic acid using a HBTU/HOBt activation. TFA/H_2O/TIS 9.5/0.25/0.25 (v/v/v) allows the deprotection and cleavage of peptides **3** then precipitated in cold Et_2O, washed and purified by preparative RP-HPLC (C18 Nucleosil column, 15 × 500 mm, 4 mL·min^{-1}, λ = 225 nm, 50 °C, eluents **A** and **C**, **C** 0 to 100% in 30 min, 100% **C** for 10 min). The peptides' purities were controlled by RP-HPLC, and their identities were controlled on a MALDI-TOF spectrometer. **3a**: >95%, m/z observed 1446.6 ($[M + H]^+$). **3b**: >97%, m/z observed 1353.82 ($[M + H]^+$).

Chemoselective ligation between anchor 1a and LAMP wt peptide 3a in solution was performed as reported in ref *21*. Briefly, 4.5 mg of anchor **1a** (3.5 μmol) in $CHCl_3$/MeOH 1/1 (v/v) (105 μL) was added to 6.6 mg of hydrazino acetyl peptide **3a** (3.5 μmol) solubilized in propan-2-ol/acetate buffer 10 mM pH 5:8/2 (v/v) (500 μL) at 37 °C. For a better stirring of the suspension, 1.3 mL of propan-2-ol/acetate buffer 1/1 (v/v) was added. RP-HPLC analyses were performed on a C3 Zorbax column (4.6 × 300 mm, 1 mL·min^{-1}, λ = 215 nm, 70 °C, eluents **A** and **B**, gradient: 0−100% **B** over 30 min, 100% **B** for 5 min, 0% **B** for 10 min). After 3 h, the RP-HPLC conversion could be calculated as high as 81% on the basis of peptide **3a** disappearance. The crude compound was purified on a C3 Zorbax column, (15 × 500 mm, 4 mL·min^{-1}, λ = 225 nm, 50 °C, same eluents and gradients) to obtain 41% isolated yield.

Chemoselective Ligation between Di-*O*-hexadecyl-rac-glyceraldehyde 1b and LAMP wt Peptide 3a in Solution. 1b (1 mg, 1.8 μmol) and **3a** (3.53 mg, 1.8 μmol) were added to 330 μL of a mixture of $CHCl_3$/2-

[1]Abbreviations: Boc, tertiobutyloxycarbonyl; BOP, benzotriazole-1-yl-oxy-tris-(dimethylamino)-phosphonium hexafluorophosphate; DBU, 1,8-diazabicyclo [5,4,0]undec-7-ene; DIEA, diisopropylethylamine; DMAP, 4-*N*,*N*-(dimethylamino)pyridine; DMF, *N*,*N*-dimethylformamide; DMSO, dimethyl sulfoxide; DTT, dithiothreitol; ES-MS, electrospray mass spectrometry; Fmoc, 9-fluorenylmethyloxycarbonyle; HBTU, 2-(1H-benzotriazole-1-yl)-1,1,3,3-tetramethyluronium hexafluorophosphate; HOBt, *N*-hydroxybenzotriazole; IPT, isopropylidene tartrate; Mtt, 4-methyltrityl; NMP, *N*-methyl pyrrolidone; OSu, *N*-hydroxysuccinimide ester; Pam, palmitoyl; PE, phosphatidyl ethanolamine; *t*Bu, tertiobutyl; TFA, trifluoroacetic acid; TIS, triisopropyl silane; TNBS, 2,4,6-trinitrobenzenesulfonic acid.

Table 1. Peptide Sequences, Synthesis Yields, and Insertion (I) or Ligation (L) to Liposomes Yields (Measured by the Same Quantitative Method, by Amino Acid Analysis, Mean of Three Experiments)[a]

	name	sequence	synthesis yield	insertion or ligation to liposomes yield
2a	$(Pam)_2$-LAMP wild type (wt)	Pam−K(Pam)−GRKRSHAG**Y**QTI−OH	19%	<3% (I)
2b	$(Pam)_2$-LAMP mutant (Y-A)	Pam−K(Pam)−GRKRSHAG**A**QTI−OH	38%	<3% (I)
3a	LAMP wild type (wt)	H_2N−GGRKRSHAG**Y**QTI−OH	35%	44% (L)
3b	LAMP mutant (Y-A)	H_2N−GGRKRSHAG**A**QTI−OH	40%	58% (L)

[a] Liposomes compositions were as follows: (I) PC/PE/PS/chol 50/30/10/10 (by mol.); (L) PC/PE/PS/chol/anchor **1b** 40/30/10/10/10 (by mol.). Pam = palmitoyl.

methyl-2-propanol/citrate-phosphate buffer 10 mM, pH 5.19, 8/10/15 (v/v/v). The suspension was stirred at room temperature for 4 h and at 37 °C overnight. Conversion was estimated to 60% from analytical RP-HPLC. The resulting mixture was then diluted with water and lyophilized. The pale yellow powder was purified by RP-HPLC on a C3 Zorbax column (15 × 500 mm, 4 mL·min^{-1}, λ = 225 nm, 50 °C, eluents **D** and **E**, gradient: 0−100% over 40 min) to give the expected compound in about 15% isolated yield.

Functionalized Liposomes Preparation. Anchors **1a** or **1b** were solubilized in $CHCl_3$/MeOH 1/1 (v/v) at a 10 mM final concentration. A mixture of PC/PE/PS/chol/anchor **1a** or **1b** 40/30/10/10/10 (by mole) in a $CHCl_3$/MeOH 1/1 (v/v) solution was evaporated to dryness under a stream of nitrogen and resuspended in buffer **F** for further coupling to peptides such as 1 mL of suspension contains 5 μmol of total lipids and, among them, 0.5 μmol of anchor. After vigorous vortexing, the lipid suspension was submitted to 10 freeze-and-thaw cycles in liquid nitrogen and in a 37 °C water bath, respectively, and filtered through polycarbonate 400 nm-membranes to size the liposomes homogeneously. In control liposomes, anchor was replaced by PC.

Next, 0.5 μmol·mL^{-1} (1 equiv considering total anchor) of hydrazino acetyl peptide solution (3 mM in buffer **F**) was reacted to the suspension. The liposome/peptide mixture was left overnight at room temperature for coupling to occur, and unbound peptide was removed by gel filtration over a Sephadex G-25 column with buffer **G** (NAP 5 columns, Amersham Pharmacia Biotech).

Amino Acid Analysis. 100 μL of liposome suspensions was submitted to a 48 h total acid hydrolysis with 1 mL of HCl 6 N/phenol 10/1 (v/w) at 110 °C in the presence of 10 μL of norleucine 0.5 mM in evacuated sealed tubes. The quantification of each immobilized peptide was achieved by the determination of the subsequent amino acid composition using a Beckman amino acid analyzer model 7300 with ninhydrin detection.

Coat Protein Recruitment Assay. Pig brain cytosol was prepared from fresh brains obtained at the local slaughterhouse. Brain slices were transferred to homogenization buffer (25 mM Hepes-KOH pH 7.4, 250 mM sucrose, 1 mM EDTA supplemented with an antiprotease cocktail) on ice. Homogenization was done with a Waring blender in a 2-to-1 buffer-to-tissue (w/w) ratio. The crude homogenate was centrifuged at 4 °C at 3000*g* for 10 min, then at 10 000*g* for 20 min, and finally at 100 000*g* for 60 min. The final supernatant served as the cytosolic fraction and was flash-frozen in liquid nitrogen before storage at −80 °C. Before use, cytosol was rapidly thawed and desalted over Sephadex G-25 (PD-10) columns previously equilibrated with buffer **G**. Any aggregated material was then removed by centrifugation at 250 000*g* for 30 min at 4 °C.

Recruitment reactions were performed in siliconized microfuge tubes in a total volume of 200 μL. Typical recruitment reaction mixtures contained buffer **G** and a combination of gel-filtered cytosol (5 mg·mL^{-1} final), liposomes (200 μg·mL^{-1}), GTP (1 mM) or GTP-γ-S (0.1 mM), and/or ARF1 (ADP Ribosylation Factor-1, a myristoylated G-protein that acts as membrane anchor for the assembly of protein coats, 3 μg·mL^{-1} final). Tubes were kept on ice, and binding reactions were initiated by transfer at 37 °C. After 20 min, reactions were stopped on ice, and membranes were recovered by centrifugation at 4 °C for 15 min at 20 000*g*. Pellets were solubilized in SDS sample buffer, boiled for 5 min, and analyzed by SDS-PAGE followed by immunoblotting using the relevant antibodies. Visualization was performed by chemiluminescence, and quantitation was obtained by scanning and spot analysis with the NIH software version 1.60/PPC.

RESULTS AND DISCUSSION

Ligation versus Incorporation of Lipopeptides into Preformed Vesicles. In a first strategy, we envisaged the preparation of synthetic peptidoliposomes by mixing all liposomal components including the peptides as lipopeptides. To this aim, we envisaged the synthesis of peptidic sequences modified at the N-terminus position by two palmitoyl (Pam) groups using standard solid-phase protocols (*25*, *26*). The RP-HPLC purification of lipopeptides is often difficult due to their generally low solubility and to the line broadening induced by the fatty acid chain(s). Thus, the major difficulty we encountered during the lipopeptides' production was associated with the preparative RP-HPLC steps. The overall yields were modest and hardly reproducible. Thus, synthetic dipalmitoyl-peptides corresponding to the intracytoplasmic LAMP sequences **2a**, and its control **2b** where the tyrosine residue was replaced by alanine, were produced as Pam−L-Lys(Pam)-peptides under moderate to average yields (19% for **2a** and 38% for **2b**, Table 1).

Once obtained, **2a** and **2b** lipopeptides were inserted into preformed liposomes. No more than 3% insertion was reached, calculated by amino acid analysis following total acid hydrolysis (Table 1). This phenomenon was previously reported by Elliott and Prestwich (*27*). In their case, as much as 90% lipopeptide was aggregated in a micellar form rather than inserted into liposomes. A weak solubility and a propensity to aggregate are responsible for the bad insertion of lipopeptides into liposomes. Thus, due to synthetic difficulties, this strategy turned out to be unapplicable to systematic and iterative studies.

We then envisaged a second strategy based on the chemical ligation principle, where peptides are selectively attached onto liposomes. In a project aimed at anchoring various and sometimes complex polyfunctional molecules to lipid membranes, we have examined the utility of the hydrazone and α-oxo hydrazone bonds. The hydrazone link was chosen because it could be achieved in the absence of activating agent and did not generate any toxic

or remaining side-product. We immobilized synthetic hydrazine-like peptides onto aldehyde or α-oxo aldehyde-liposomes, a strategy that was unprecedented. This strategy not only required the design and synthesis of amphiphilic aldehyde-like anchors to be manipulated as lipids when preparing the liposome suspension (Figure 1), but also those of hydrazino acetyl peptides (Scheme 1). Concerning the ligation process, a first and comprehensive work had been performed on the thermodynamic and kinetic parameters of the reaction (*22*, see Introduction). In this study, the α-oxo hydrazone bond formed between vesicles and hydrazino compounds in aqueous buffer was found to be totally chemoselective and quantitative. Its stability in physiological conditions was in the submicromolar range, and nonspecific adsorption could be diminished to 10−15% on average. These results formed the basis of our present work.

Anchors' Design and Synthesis. A first anchor **1a** of type Pam−L-Lys(Pam)−spacer−CO−CHO was prepared as previously described (Figure 1 (*21*)). The difficulty in preparing amphiphilic compounds such as **1a** resides in the fine-tuning of the physicochemical properties to allow their solubilization, purification, and characterization. In addition, depending on the biomolecular interactions studied, the anchored peptide should be close to or distant from the membrane surface. Thus, to allow the spacer arm to be easily modulated, anchors of the type **1a** were elaborated on solid phase using standard Fmoc/*t*Bu protocols (*28*, *29*). Compound **1a** was isolated with a 25% overall yield.

A further anchor **1b** presenting the basic elements required for this application was synthesized in solution (Scheme 2). It contained a double hexadecyl arm to be inserted among liposome phospholipids and an aldehyde reactive head. Di-*O*-hexadecyl-rac-glyceraldehyde **1b** was first obtained starting from di-*O*-hexadecyl-rac-glycerol following Swern's oxidation procedure (*30*). **1b** was obtained after purification together with unreacted di-*O*-hexadecyl-rac-glycerol (35%). The reaction did not come to its completion, which was assigned to the poor solubility of the lipophilic molecules in cold CH_2Cl_2. Indeed, as high as 86% isolated yield could be obtained when the oxidation was performed at room temperature using Dess−Martin's reagent (*31*).

To summarize, two types of synthetic anchors are now available. Those of the type **1a** are versatile in such a way that four analogues were synthesized (10−50% overall yield according to the spacer X in 100−500 mg scale). Anchor **1b** is simple and cheap and was also obtained in a 100 mg scale. Some PE derivatives are currently under investigation. This should reinforce the interest of using a hydrazone bond in the preparation of peptidoliposomes.

Hydrazino Acetyl Peptides' Synthesis. In parallel, α-hydrazino acetyl peptides were automatically produced. Their sequences corresponded to a part of the cytoplasmic domain of the lysosome-associated membrane protein LAMP (wild-type LAMP, wt) or to a mutated sequence where the tyrosine sorting motif was replaced by an alanine (Table 1, entries **3a**,**b**). A conventional Fmoc/*tert*-butyl solid-phase peptide strategy (*28*, *29*) and our recently described tri-protected compound *N*,*N*′,*N*′-tri-(*tert*-butyloxycarbonyl)-hydrazino acetic acid, $(Boc)_2N-N(Boc)-CH_2-COOH$, were employed for the unambiguous introduction of the hydrazino acetyl group upon the selectively deprotected α-amino group of the N-terminal amino acyl resins (*19*, *20*). Each crude α-hydrazino acetyl peptide was easily purified by RP-HPLC, freeze-dried as a TFA salt, and could be thoroughly characterized by amino acid analysis, RP-HPLC, and MALDI-TOF-MS (yields **3a**, 35%, **3b**, 40%, amino acid analyses in accordance with expected results, RP-HPLC purity superior to 95%). It is noteworthy that hydrazino acetyl peptides are unstable in the presence of acetonitrile and should be purified with RP-HPLC eluents containing 2-propanol as was exposed in ref *19*.

Thus, the solid-phase synthesis of hydrazino acetyl peptides requires fewer steps than that of N-terminus glyoxylyl peptides, where a deleterious periodic oxidation and a second purification are necessary. Here, hydrazino acetyl peptides were readily obtained after cleavage from the resin and RP-HPLC purification. Moreover, in our hands, hydrazino acetyl peptide synthesis offered a total flexibility, and as many as 10 sequences from three models were easily assembled and functionalized in good yields.[2] These advantages are good reasons for applying the hydrazone chemical ligation.

In-Solution Ligation. 1a and **1b** were engaged in a chemoselective hydrazone ligation in solution with hydrazino acetyl peptide **3a** to control both the accessibility and the reactivity of the functional groups. The reaction of **1a** or **1b** with **3a** led to the formation of the corresponding α-oxo hydrazone with 81% and 60% RP-HPLC conversion and 41% and 15% isolated yield following RP-HPLC purification, respectively. Although successful, these two reactions remained very difficult to handle and required heating and a mixture of organo-aqueous solvents.

Ligation onto Liposomes. Ligation of hydrazino acetyl peptides proved to be more convenient and efficient onto vesicles, as anchors **1a** and **1b**'s aldehyde head seemed to be more "available" in liposomes than in organo-aqueous solution. These results are consistent with what we reported in our physicochemical study: when the ligation was performed in self-organized media, its speed and its stability were enhanced due to autoassociation of the reagents.

The liposomes were prepared by integrating 10% (mol/mol) of one of the anchors **1a** or **1b**. Assuming that the vesicles were unilamellar, 0.25 mM aldehyde functions could be reacted on the outer membrane (see Experimental Procedures for further numerical data). The proteoliposomes were obtained by simple stirring of the functionalized liposomes with the α-hydrazino acetyl peptides **3** (1 equiv toward total aldehydes, i.e., 2 equiv toward outer exposed aldehydes, Scheme 3). The incubation mixture was left overnight for the reaction to be completed. However, we routinely observed that 5 h were sufficient for a total conversion.

Unbound peptide was removed by gel filtration. The addition of the peptidic reagent and the workup imposed a 2.5-fold dilution of the liposome suspension. Thus, 0.1 μmol of peptides was the maximum to be anchored per milliliter of recovered liposome suspension.

Quantification of the amount of peptide associated to liposomes was performed by amino acid analysis following total acid hydrolysis using norleucine as an internal standard. As the medium was not totally homogeneous, the acidolysis was left over 48 h to be as complete as possible and the analyses were performed three times (three samples) for more accuracy.

[2]Baust, T., Bourel-Bonnet, L., Gras-Masse, H., and Hoflack, B. (2004) Selective assembly of AP-1 and AP-3 coats onto synthetic membranes: Requirement for ARF1, sorting signals of specific cargo transmembrane proteins and phosphatidylinositol-phosphates. Unpublished results.

Scheme 3. Onto-Liposome Ligation of Anchor 1b to Peptides 3a or 3b

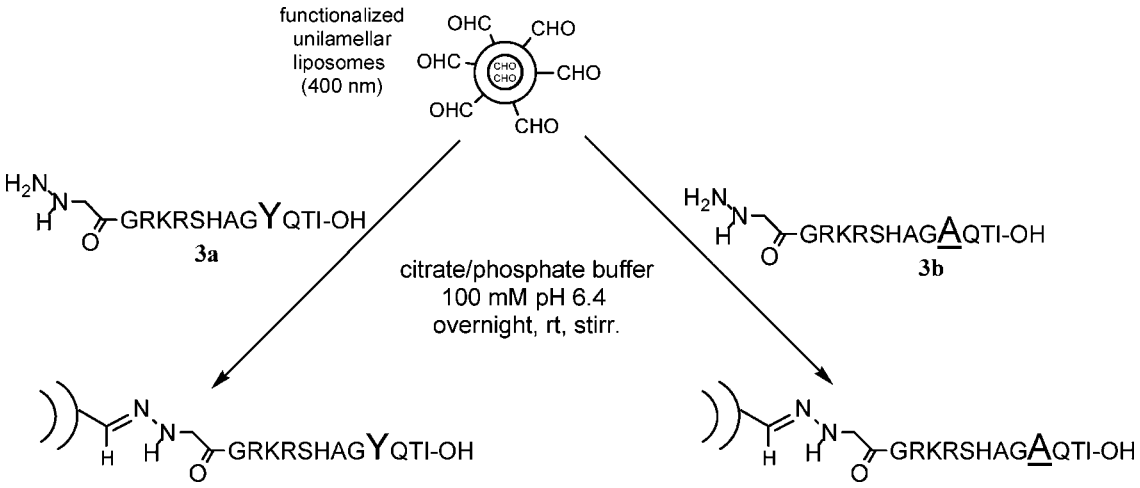

Liposomes containing anchor **1b** (**1b**-liposomes) were first coupled to hydrazino peptide **3a**, and a reproducible 44% ± 3% coupling yield was measured (mean 44%, Table 1). When these vesicles were coupled to hydrazino peptide **3b**, the coupling yield was comprised between 49% and 70% (mean 58%, Table 1). Apart from uncomplete amino acid hydrolysis, these variations may be due to the dilution of the suspensions occurring during the purification by gel filtration.

Therefore, to further confirm these results, the peptide remaining in the supernatants after ligation onto **1b**-liposomes was quantified by RP-HPLC. The amount of recovered peptide was measured (assuming that the peptide amount that was not recovered was anchored onto the liposome) and was compared to the amino acid analyses of the suspensions. A good correlation could be established between the average amount of peptide remaining in the supernatant and that of the peptide present in the suspension (51% against 50%). Obtained either by RP-HPLC quantification or by amino acid analysis, these results demonstrate that ligation is greatly superior to insertion of lipopeptides for the preparation of peptidoliposomes. These results are reported in Table 1 (lanes **2a** and **2b** as compared to lanes **3a** and **3b**).

Biological Evaluation of the Vesicles. The scope of our strategy stretches to ligand/receptor interactions. We chose to illustrate it in the field of cellular biology. Precisely, our peptidoliposomes were used to reconstitute in vitro a particular aspect of membrane trafficking. In this work, we demonstrated that AP-3 complex can specifically interact in vitro with liposomes onto which the cytoplasmic domain of LAMP has been coupled.

Coat Recruitment Assay with the Peptidoliposomes. **1b**-Liposomes were coupled to **3a** or **3b**, two hydrazino acetyl dodecapeptides displaying either the tyrosine sorting motif of LAMP cytoplasmic tail or an alanine, respectively (Scheme 3). After the free peptide was eliminated by gel filtration, the suspensions were incubated with pig brain cytosol. Vesicles were recovered after centrifugation at high speed. After washing, specific monoclonal antibodies were used to detect and identify which cytosolic proteins were immobilized (in other words, "recruited") onto the liposomes by western blotting (Figure 2).

When comparing lanes (a) and (b) (LP control with no anchor and LP-LAMP Y-A exposing the anchored mutated peptide, respectively) to lane (c) (LP-LAMP wt exposing the anchored wt LAMP peptide), it becomes clear that AP-3 recruitment is higher when liposomes bear an intact LAMP cytosolic domain with a tyrosine-based sorting signal. Most notably, no AP-3 was recruited onto liposomes bearing the mutated LAMP peptide lacking the tyrosine sorting motif, emphasizing the specificity of our recruitment reaction. LP control represents liposomes without anchor (**1b** was replaced by PC, see Experimental Procedures) exposed to peptide **3a** and gel-filtered. For this type of suspension, the amino acid quantification was not reproducible, and peptide amounts wavered between 10% and 40%, due to peptide adsorption in a nonspecific manner. Because we observed that AP-3 could not be efficiently recruited onto these liposomes, we concluded that covalent binding of the peptide was necessary for the peptide to interact with the AP-3 coat. These results are consistent with some previously reported work. As an example, Pécheur and Hoekstra showed that liposomes' fusion could only happen when a fusion-inducing peptide was covalently bound to the lipid bilayer and not when it was adsorbed to the surface (*40*). We suggest that, in our case, this covalent binding allowed a correct exposition of the peptide to the cytosol, thus presenting the sorting motif in a proper way. Additional controls showed that, in the absence of peptide, even when the anchor **1b** was present, AP could not

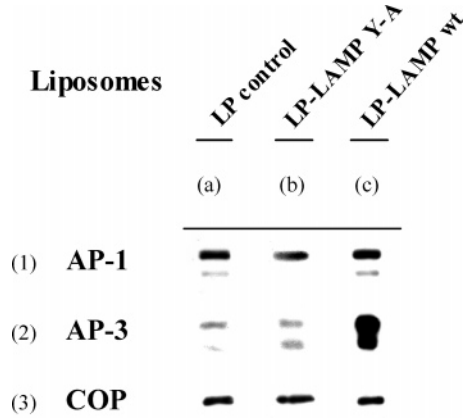

Figure 2. AP-3 membrane recruitment is LAMP-dependent. (a) LP control represents liposomes containing no anchor exposed to peptide **3a**. (b) LP-LAMP Y-A and (c) LP-LAMP wt were prepared with peptides **3b** and **3a**, respectively. After incubation with a pig brain cytosol, AP-1, AP-3, and COP bound to liposomes were detected by western blotting using specific antibodies.

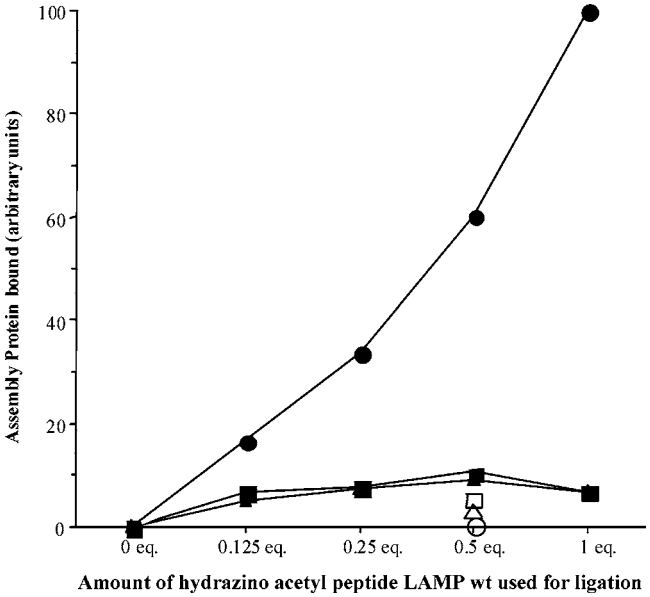

Figure 3. AP-3 membrane recruitment is dependent on the amount of peptide LAMP wt bound. Recruited protein detected: AP-3 (●), AP-1 (■), COP (▲). Open symbols correspond to the amount of AP-3 (○), AP-1 (□), and COP (△) recruited in the presence of 0.5 equiv of LAMP mutant (**3b**). Data are representative of duplicate experiments.

get recruited onto the liposomes, reinforcing the specificity of our recruitment reaction (see Supporting Information).

Selective AP-3 Recruitment onto LAMP-Peptidoliposomes Is a Function of LAMP Coupling Yield. 1b-Liposomes containing a fixed amount of lipidic anchor (10 mol %) were incubated with increasing amounts of LAMP wt peptide **3a**, and 1 equiv means 1 equiv toward the overall anchor (see experimental conditions for ligation). Figure 3 shows that AP-3 binding depends on the concentration of LAMP wt peptide present on liposomes. AP-3 binding onto liposomes exposing the mutated LAMP peptide was not observed, whatever the amount of mutated peptide was. This confirmed the specificity of our in vitro system.

CONCLUSION

We successfully prepared hydrazone-based peptidoliposomes. We designed and synthesized two different aldehyde-functionalized anchors able to covalently immobilize hydrazino acetyl peptides onto liposomes. This ligation strategy was more efficient and versatile than the direct insertion of lipopeptides into liposomes. Several types of peptidoliposomes could be prepared in parallel. As an example to illustrate the functionality of the vesicles, we have successfully reconstituted the selective interaction of the AP-3 coat with cytoplasmic domains of transmembrane proteins covalently immobilized on liposomes. This methodology can be applied to different coat components involved in different aspects of membrane trafficking and in a more general manner to any biological problem into which transmembrane or membrane-associated proteins are implicated.

ACKNOWLEDGMENT

We thank Dr. Pascale Chenevier for fruitful scientific discussions, and Frédéric Malingue, Eric Diesis, and Hervé Drobecq (UMR 8525) for technical assistance. We gratefully acknowledge financial support from the Ministère de la recherche (L.B.-B. received a young scientist "ACI jeune chercheur" financial support in 2001), Université de Lille 2, Centre National de la Recherche Scientifique (CNRS), Institut Pasteur de Lille, Agence pour la Recherche contre le Cancer (ARC), and Agence Nationale de Recherche sur le SIDA (ANRS).

Supporting Information Available: Additional experimental data. This material is available free of charge via the Internet at http://pubs.acs.org.

LITERATURE CITED

(1) For adhesion motifs, see, for example: Hojo, H., Kojima, T., Yamauchi, K., and Kinoshita, M. (1996) Synthesis and liposome-formation of a thermostable lipid bearing cell adhesion peptide sequence. *Tetrahedron Lett. 37*, 7391−7394.

(2) For synthetic antigens, see, for example: Boeckler, C., Frisch, B., and Schuber, F. (1998) Design and synthesis of thiol-reactive lipopeptides. *Bioorg. Med. Chem. Lett. 8*, 2055−2058.

(3) Schelré, P., Boeckler, C., Frisch, B., and Schuber, F. (2000) Differential reactivity of maleimide and bromoacetyl functions with thiols: Application to the preparation of liposomal diepitope constructs. *Bioconjugate Chem. 11*, 118−123.

(4) Sankaram, M. B. (1994) Membrane interaction of small N-myristoylated peptides: implications for membrane anchoring and protein−protein association. *Biophys. J. 67*, 105−112.

(5) Silvius, J. R., and l'Heureux, F. (1994) Fluorimetric evaluation of the affinities of isoprenylated peptides for lipid bilayers. *Biochemistry 33*, 13093−13101.

(6) Epand, R. M. (1997) Biophysical studies of lipopeptide−membrane interactions. *Biopolymers 43*, 15−24.

(7) Shahinian, S., and Sivius, J. R. (1995) Doubly lipid-modified protein sequence exhibit long-lived anchorage to lipid bilayer membranes. *Biochemistry 34*, 3813−3822.

(8) Martin, F. J., and Papahadjopoulos, D. (1982) Irreversible coupling of Immunoglobuline fragment to preformed vesicles − an improved method for liposome targeting. *J. Biol. Chem. 257*, 286−288.

(9) Kung, V. T., and Redemann, C. T. (1986) Synthesis of carboxyacyl derivatives of phosphatidylethanolamine and use as an efficient method for conjugaison of protein to liposomes. *Biochim. Biophys. Acta 862*, 435−439.

(10) Heeremans, J., Kraaijenga, J., Los, P., Kluft, C., and Crommelin, D. (1992) Development of a procedure for coupling the homing device Glu-Plasminogen to liposomes. *Biochim. Biophys. Acta 1117*, 258−264.

(11) Fleiner, M., Benzinger, P., Fichert, T., and Massing, U. (2001) Studies on protein-liposome coupling using novel thiol-reactive coupling lipids: influence of spacer length and polarity. *Bioconjugate Chem. 12*, 470−475.

(12) Kamps, J., Swart, P., Morselt, H., Pauwels, R., De Béthune, M.-P., De Clerck, E., Meijer, D., and Scherphof, G. (1996) Preparation and characterization of conjugates of (modified) human serum albumin and liposomes: Drug carriers with an intrinsic anti-HIV activity. *Biochim. Biophys. Acta 1278*, 183−190.

(13) Barbet, J., Machy, P., and Leserman, L. (1981) Monoclonal antibody covalently coupled to liposomes − specific targeting to cells. *J. Supramol. Struct. Cell. Biochem. 16*, 243−258.

(14) Nakano, Y., Mori, M., Nishinohara, S., Takita, Y., Naito, S., Kato, H., Taneichi, M., Komuro, K., and Uchoda, T. (2001) Surface linked liposomal antigen induces IgE-selective unresponsiveness regardless of the lipid components of liposomes. *Bioconjugate Chem. 12*, 391−395.

(15) Horak, D., Karpisek, M., Turkova, J., and Benes, M. (1999) Hydrazide-functionalized poly(2-hydroxyethyl methacrylate) microspheres for immobilization of horseradish peroxidase. *Biotechnol. Prog. 15*, 208−215.

(16) Zalipsky, S., Puntambekar, B., Boulikas, P., Engbers, C. M., and Woodle, M. C. (1995) Peptide attachment to extremities of liposomal surface PEG chains: preparation of the long-circulating form of laminin pentapeptide, YIGSR. *Bioconjugate Chem. 6*, 705−708.

(17) Harding, J. A., Engbers, C. M., Newman, M. S., Goldstein, N. I., and Zalipsky, S. (1997) Immunogenicity and pharmacokinetics attributes of poly(ethylene glycol)-grafted immunoliposomes. *Biochim. Biophys. Acta 1327*, 181−192.
(18) Zalipsky, S. (1993) Synthesis of an end-group functionalized polyethylene glycol−lipid conjugate for preparation of polymer-grafted liposomes. *Bioconjugate Chem. 4*, 296−299.
(19) Bonnet, D., Grandjean, C., Rousselot-Pailley, P., Joly, P., Bourel-Bonnet, L., Santraine, V., Gras-Masse, H., and Melnyk, O. (2003) Solid-phase functionalization of peptides by an alpha-hydrazinoacetyl group. *J. Org. Chem. 68*, 7033−7040.
(20) Bonnet, D., Ollivier, N., Gras-Masse, H., and Melnyk, O. (2001) Chemoselective acylation of fully deprotected hydrazino acetyl peptides. Application to the synthesis of lipopeptides. *J. Org. Chem. 66*, 443−446.
(21) Bourel-Bonnet, L., Gras-Masse, H., and Melnyk, O. (2001) A novel family of amphiphilic α-oxo aldehydes for the site-specific modification of peptides by two palmitoyl groups in solution or in liposome suspension. *Tetrahedron Lett. 42*, 6851−6853.
(22) Chenevier, P., Bourel-Bonnet, L., and Roux, D. (2003) Chemical characterization of alpha-oxo hydrazone ligation on colloids: toward grafting molecular addresses onto biological vectors. *J. Am. Chem. Soc. 125*, 16261−16270.
(23) Chenevier, P., Grandjean, C., Loing, E., Malingue, F., Angyalosi, G., Gras-Masse, H., Roux, D., Melnyk, O., and Bourel-Bonnet, L. (2002) Grafting of synthetic mannose receptor−ligands onto onion vectors for the human dendritic cells' targeting. *Chem. Commun*. 2446−2447.
(24) Olah, G. A., Nojima, M., and Kerekes, I. (1973) Synthetic methods and reactions; IV. Fluorination of carboxylic acids with cyanuric fluoride. *Synthesis* 487.
(25) Wiesmüller, K.-H., Bessler, W. G., and Jung, G. (1992) Solid-phase peptide synthesis of lipopeptide vaccines eliciting epitope-specific B-, T-helper and T-killer cell response. *Int. J. Pept. Protein Res. 40*, 255−260.
(26) Seitz, O., Heinemann, I., Mattes, A., and Waldmann, H. (2001) Synthetic conjugates. Tailor-made probes for the biology of protein modification and protein processing. *Tetrahedron 57*, 2247−2277.
(27) Elliott, J. T., and Prestwich, G. D. (2000) Maleimide-functionalized lipids that anchor polypeptides to lipid bilayers and membranes. *Bioconjugate Chem. 11*, 832−841.
(28) Fields, G. B., and Noble, R. L. (1990) Solid-phase peptide synthesis utilizing 9-fluorenylmethoxycarbonyl amino acids. *Int. J. Pept. Protein Res. 35*, 161−214.
(29) Chan, W. C., and White, P. D. (2000) *Fmoc Solid-Phase Synthesis, A Practical Approach* (Chan, W. C., and White, P. D., Eds.) pp 9−76 and 277−302, Practical Approach Series, Oxford University Press, Oxford.
(30) Mancuso, A. J., and Swern, D. (1981) Activated dimethyl sulfoxide: useful reagents for synthesis. *Synthesis* 165−185.
(31) Dess, D. B., and Martin, J. C. (1983) Readily accessible 12-I-5 oxidant for the conversion of primary and secondary alcohols to aldehydes and ketones. *J. Org. Chem. 48*, 4155−4156.
(32) Schekman, R., and Orci, L. (1996) Coat proteins and vesicle budding. *Science 271*, 1525−1533.
(33) Rothman, J. E., and Wieland, F. T. (1996) Protein sorting by transport vesicles. *Science 272*, 227−234.
(34) Kirchhausen, T. (2000) Three ways to make a vesicle. *Nat. Rev. Mol. Cell. Biol. 1*, 187−198.
(35) Robinson, M. S. (2004) Adaptable adaptors for coated vesicles. *Trends Cell. Biol. 14*, 167−174.
(36) Matsuoka, K., Orci, L., Amherdt, M., Bednarek, S., Hamamoto, S., Schekman, R., and Yeung, T. (1998) COPII-coated vesicle formation reconstituted with purified coat proteins and chemically defined liposomes. *Cell 93*, 263−275.
(37) Matsuoka, K., Morimitsu, Y., Uchida, K., and Schekman, R. (1998) Coat assembly directs v-SNARE concentration into synthetic COPII vesicles. *Mol. Cell 2*, 703−708.
(38) Bremser, M., Nickel, W., Schwelkert, M., Ravazzola, M., Amherdt, M., Hughes, C., Sollner, T., Rothman, J., and Wieland, F. (1999) Coupling of coat assembly and vesicle budding to packaging of putative cargo receptors. *Cell 96*, 495−506.
(39) Le Borgne, R., Alconada, A., Bauer, U., and Hoflack, B. (1998) The mammalian AP-3 adaptor-like complex mediates the intracellular transport of lysosomal membrane glycoproteins. *J. Biol. Chem. 273*, 29451−29461.
(40) Pécheur, E. I., Hoekstra, D., Sainte-Marie, J., Maurin, L., Bienvenue, A., and Philippot, J. R. (1997) Membrane anchorage brings about fusogenic properties in a short synthetic peptide. *Biochemistry 36*, 3773−3781.

BC049908V

Synthesis and Self-Alkylation of Isotope-Coded Affinity Tag Reagents

Zhidong Zhang, Patrick J. Edwards, Roger W. Roeske, and Lili Guo*

Department of Biochemistry and Molecular Biology, School of Medicine, Indiana University, Indianapolis, Indiana 46202. Received September 16, 2004

A pair of ICAT reagents, *N*-(13-iodoacetamido-2,2,3,3,11,11,12,12-octadeutero-4,7,10-trioxa-tridecanyl)-biotinamide (**8d**, ICAT-d_8) and *N*-(13-iodoacetamido-4,7,10-trioxa-tridecanyl)biotinamide (**8c**, ICAT-d_0), and an alternative pair of ICAT reagents, *N*-(10-iodoacetamido-2,5,5,6,6,9-hexadeutero-4,7-dioxa-decanyl)biotinamide (**8b**, s-ICAT-d_6) and *N*-(10-iodoacetamido-4,7-dioxa-decanyl)biotinamide (**8a**, s-ICAT-d_0), were successfully synthesized. A mixture of sodium borohydride and cobalt(II) chloride reduced the intermediate dinitrile to the diamine without loss of the deuterium labels, which occurred when Raney nickel was the reducing agent. The problem caused by unsymmetrical biotinylation of the intermediate diamine was solved by using the solid-phase method in which one end of the diamine was attached to a chlorotrityl chloride resin, followed by biotinylation of the resin-bound amine. The self-alkylation of ICAT reagents that accounted for their instability and their limitations in the applications was also studied.

INTRODUCTION

Quantitative proteomics has become very important because of its potential to determine properties of biological systems that are not determined by DNA or mRNA sequence analysis alone, but related to protein expression, subcellular location, posttranslational modification, and interactions, as well as the rate of change of these properties under specific conditions. This information can aid in the discovery of diagnostic or prognostic protein markers, therapeutic targets in understanding the initiation and progression of disease states (*1*−*4*).

One of the approaches in quantitative proteomics is based on stable isotope labeling of proteins or peptides and automated tandem mass spectrometry (MS/MS) (*5*, *6*). The isotope-coded affinity tag (ICAT) method developed by Aebersold and co-workers (*7*) is a pioneering step in this field. The ICAT reagents have three elements: an affinity tag (biotin), a linker containing stable isotopes (either eight H atoms (d_0) or eight deuterium atoms (d_8)), and a reactive moiety to react with sulfhydryl groups of cysteines in proteins. The protein mixtures from two sets of cell states (or tissue extracts) are independently labeled with the d_0 and d_8 ICAT reagents; the samples are combined, and then proteolytically cleaved. The ICAT labeled peptides are isolated by affinity chromatography on an avidin column and analyzed by microcapillary liquid chromatography-electrospray ionization-tandem mass spectrometry (LC-ESI-MS/MS). Peptide sequence information is obtained by tandem mass spectrometry and computer searches of protein data banks. Quantification of proteins in two cell states is performed by comparing the intensity of the identical peptide peak pair from the two samples defined by the isotopic difference in the light and heavy reagent.

Although the ICAT reagent has been widely used in quantitative proteomics (*8*−*13*), synthesis of the ICAT reagent was not adequately described in the original papers (*7*, *14*). Our first attempt to reproduce the published synthesis resulted in considerable loss of the deuterium labels. Another problem was biotinylation of the diamines, in which a large excess of ether diamine was required to avoid formation of bis-biotinylation. Recently, a seven-step alternative synthesis of ICAT-d_8 was published by Perrin (*15*). Their orthogonal protection strategy overcame deuterium loss and allowed effective mono-biotinylation. We also like to report here our successful resolution of these problems to obtain the pair of pure ICAT reagents, *N*-(13-iodoacetamido-2,2,3,3,11,-11,12,12-octadeutero-4,7,10-trioxa-tridecanyl)bio tinamide (Scheme 1, **8d**, ICAT-d_8) and *N*-(13-iodoacetamido-4,7,10-trioxa-tridecanyl)biotinamide (Scheme 1, **8c**, ICAT-d_0), in reasonable yields. The synthetic scheme was also used to synthesize alternative ICAT reagents, *N*-(10-iodoacetamido-2,5,5,6,6,9-hexadeutero-4,7-dioxa-decanyl-)biotinamide (Scheme 1, **8b**, s-ICAT-d_6) and *N*-(10-iodoacetamido-4,7-dioxa-decanyl)biotinamide (Scheme 1, **8a**, s-ICAT-d_0). We also studied the self-alkylation of ICAT reagents, which accounted for their instability and their limitations in the applications.

EXPERIMENTAL PROCEDURES

General. Most of the reagents and solvents were obtained from Sigma-Aldrich (MO) or Fisher Scientific (NJ). 2-(1H-Benzotriazol-1-yl)-1,1,3,3-tetramethyluronium hexafluorophosphate (HBTU), 1-hydroxybenzotriazole (HOBt), and *N*,*N*-diisopropylethylamine (DIEA) were purchased from Applied Biosystems (Warrington, UK). 2-Chlorotrityl chloride resin was from Novabiochem (CA). Trifluoroacetic acid (TFA) was obtained from Halocarbon (NJ) and distilled before use. Triisopropylsilane (TIS) was obtained from Sigma-Aldrich (MO).

Analytical reverse-phase HPLC was performed on a Varian model 5000 liquid chromatograph with a UV-100 detector unless otherwise specified. A Vydac C_{18} column (218TP54, 4.6 × 250 mm) was used at a flow rate of 1 mL/min. Preparative reverse-phase HPLC was carried out on a Waters-600E HPLC system fitted with a 486

* To whom correspondence should be addressed. Phone: (317) 274-7507. Fax: (317) 274-4686. E-mail: lguo@iupui.edu.

10.1021/bc049777y CCC: $30.25 © 2005 American Chemical Society
Published on Web 02/23/2005

Scheme 1

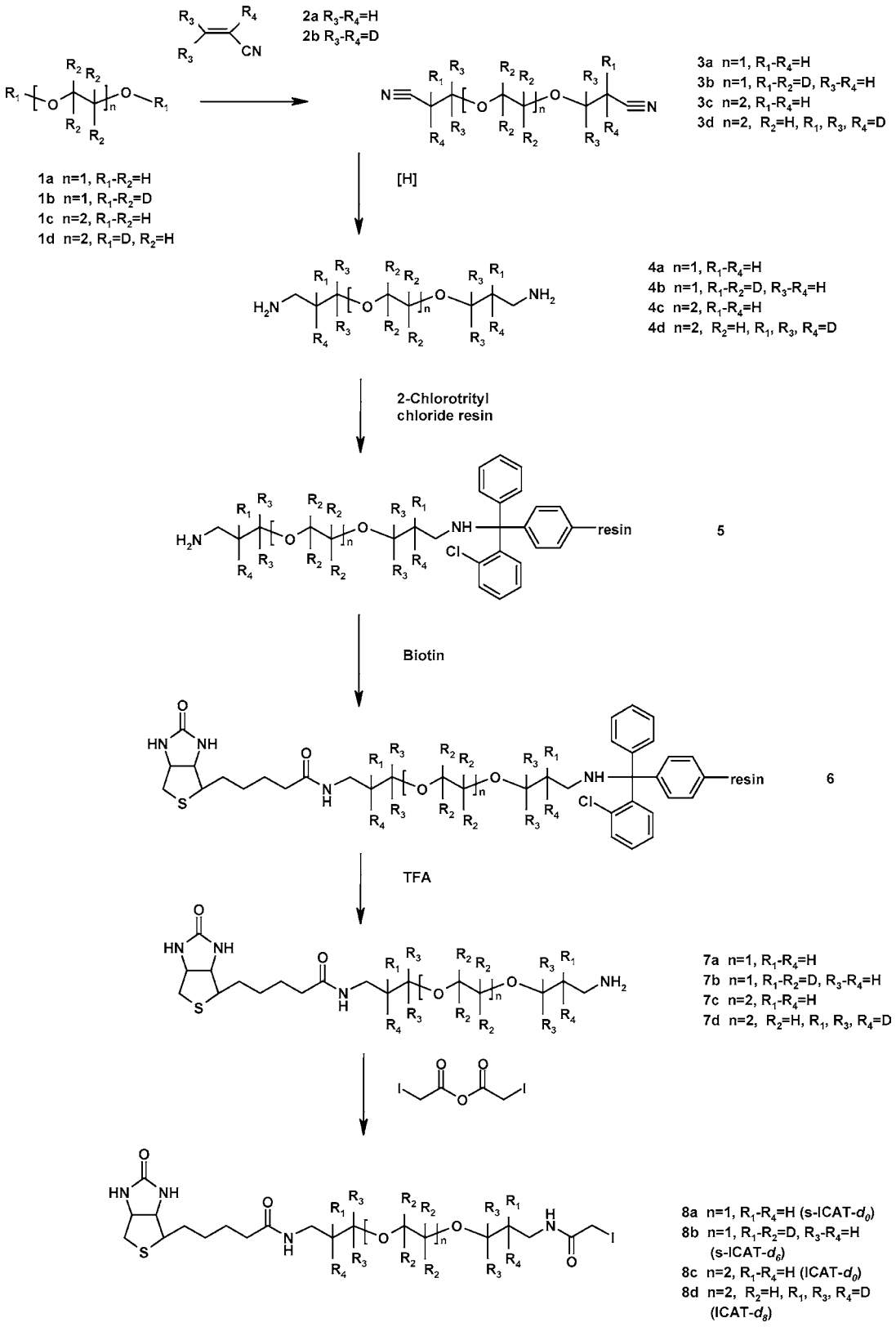

tunable absorbance detector using a Vydac C_{18} column (218TP101550, 50 × 250 mm) at a flow rate of 15 mL/min. The absorbance was recorded at 214 nm wavelength, and a solvent system of A, 0.1% TFA in water, and B, 70% acetonitrile in water containing 0.09% TFA, was used both for analytical and for preparative HPLC. Flash chromatography was performed on a 5 × 60 cm column packed with Baker silica gel (40 μm average particle diameter) using 2% MeOH in $CHCl_3$ as eluting solvent. Electrospray ionization mass spectra (ESI-MS) were obtained on a Finigan LCQ LC/MS system. TLC was carried out on Merck Kieselgel 60 precoated plates and visualized by iodine absorption. 1-Butanol/acetic acid/water/pyridine (4/1/2/1 vol) was used as development solvent.

For study of self-alkylation of ICAT compounds, the solid samples of ICAT compounds were flushed with

nitrogen and stored at −20 °C. The solution samples were made in a concentration of 1 mg/mL solvent mixture and stored at room temperature. The reaction of self-alkylation was monitored by HPLC and ESI-MS. HPLC analysis was conducted on a Varian Prostar 210 system fitted with a Prostar 320 UV/vis detector using a Vydac C_{18} 218TP54 column at a flow rate of 1 mL/min. Solvent gradient was an isocratic 5% B for 5 min, then a linear gradient 5% to 60% B for 25 min.

Synthesis of Ether Dinitriles. *2,2,3,3,11,11,12,12-Octadeutero-4,7,10-trioxa-1,13-tridecanedinitrile (**3d**).* To a stirred solution of di(ethylene glycol-d_2) (**1d**) (2.54 mL, 26.7 mmol) in benzene (3 mL) was added sodium deuterioxide (4 drops of 40% solution in D_2O), followed by dropwise addition of a solution of acrylonitrile-d_3 (**2b**) (3.52 mL, 53.5 mmol) in benzene (3 mL) at room temperature over 20 min. After being stirred for 1 h, the reaction mixture was filtered and the solvent was removed by rotary evaporation. The residue was purified by flash chromatography, and a clear oil (4.85 g) was obtained in 82% yield. TLC: only one spot, R_f = 0.65. ESI-MS m/z = 221.1 $[M + H]^+$ (calc. 221.2).

Ether dinitriles **3a**, **3b**, and **3c** were prepared as **3d** from the appropriate glycol and acrylonitrile. The crude products were obtained in 96% or higher yields, and TLC showed only one spot with R_f at 0.65.

Reduction of Ether Dinitriles. *Synthesis of 2,2,3,3,-11,11,12,12-Octadeutero-4,7,10-trioxa-1,13-tridecanediamine (**4d**) with $NaBH_4$-Raney Nickel Catalyst.* To a stirred solution of **3d** (4.8 g, 21.8 mmol) in MeOH (20 mL) was added Raney 2800 nickel (8.5 g) followed by dropwise addition of a solution of $NaBH_4$ (1.76 g 46.5 mmol) in 8 M NaOH (40 mL) over 2.5 h. The reaction temperature was kept between 15 and 25 °C with a water bath, and the reaction was stopped 5 min after the H_2 bubbles ceased. The catalyst was filtered off and washed with MeOH (50 mL × 2). Washing and mother liquor were combined and concentrated in a vacuum. Solid KOH (19 g) was added to the residue, and the diamine product was salted out of solution as a light yellow oil. Crude product was separated and purified by vacuum distillation. Diamine (**4d**) (2.61 g, yield 52%) was collected at 150−152 °C/0.75 mmHg. TLC R_f = 0.22. ESI-MS m/z = 227.3 (main peak) $[M + H]^+$ (calc. 229.2).

4,7,10-Trioxa-1,13-tridecanediamine **4c** was prepared as for **4d** using **3c** as starting ether dinitrile and $NaBH_4$-Raney nickel as reducing reagent. Crude product was obtained in 79% yield. TLC R_f = 0.22. ESI-MS m/z = 221.2 $[M + H]^+$ (calc. 221.2).

*Synthesis of 2,2,3,3,11,11,12,12-Octadeutero-4,7,10-trioxa-1,13-tridecanediamine (**4d**) with $NaBH_4$−$CoCl_2$·6H_2O Catalyst.* To a stirred mixture containing **3d** (1.32 g, 6 mmol), $CoCl_2$·6H_2O (5.71 g, 24 mmol), and MeOH (60 mL) was added $NaBH_4$ (4.54 g, 120 mmol) in portions at room temperature over 15 min. The mixture was allowed to stir for 1 h. 6 N hydrochloric acid (15 mL) was added to dissolve the black precipitate formed (Co_2B), and then the mixture was made basic with 8 N NaOH (8 mL). The $Co(OH)_2$ precipitate and MeOH were removed by filtration and rotary evaporation, respectively. To the residue was added solid KOH (16 g), and the slurry was extracted with ether (40 mL × 4). The combined extracts were dried over Na_2SO_4 and evaporated to remove ether. A light yellow oil (1.0 g, 73%) was obtained. TLC R_f = 0.22. ESI-MS m/z = 229.3 $[M + H]^+$ (calc. 229.2). There were two impurity peaks, m/z = 212.3 and 440.6 $[M + H]^+$, which corresponded to the cyclic amine $O(CH_2CH_2OCD_2CD_2CH_2)_2NH$ (calc. 212.2), and the dimer of ether diamine **4d** $[H_2NCH_2CD_2CD_2O(CH_2CH_2O)_2CD_2CD_2CH_2]_2NH$ (calc. 440.5). The crude product was used for the next step of synthesis without vacuum distillation because the sample was too small to distill.

Ether diamines **4c**, **4a**, and **4b** were prepared by the same procedure as **4d** using $NaBH_4$−$CoCl_2$·6H_2O catalyst in yields 61−65%. TLC showed all three diamines had similar R_f values (0.22). ESI-MS m/z: for **4c**, 221.2 $[M + H]^+$ (calc. 221.2); for **4a**, 177.2 $[M + H]^+$ (calc. 177.2); for **4b**, 182.8 $[M + H]^+$ (calc. 183.2). ESI-MS also showed two impurities in the reduction products, which were cyclic amines and dimers of the ether diamine.

Solid-Phase Synthesis of *N*-(Amino-oxa-alkyl)-biotinamide. *N-(13-Amino-2,2,3,3,11,11,12,12-octadeutero-4,7,10-trioxatridecanyl)biotinamide (**7d**).* A solution of **4d** (0.99 g, 4.3 mmol) in 4 mL of CH_2Cl_2 was added to 254 mg, 0.43 mmol of 2-chlorotrityl chloride resin in a 30 mL reaction vessel having a glass frit (Peptides International, Inc., KY). The vessel was flushed with N_2 and then shaken at room temperature for 2 h. The reaction mixture was filtered, and the diamine-loaded resin was washed with CH_2Cl_2, MeOH, 20%DIEA in NMP, and NMP (15 mL × 4, each). The filtrate and CH_2Cl_2 washings were collected and treated with solid KOH followed by rotary evaporation to recover the unreacted **4d**. To the washed resin were added 2 M DIEA in NMP (1.29 mL, 2.58 mmol), 0.45 M HBTU/HOBt in DMF (4.5 mL, 2 mmol), and biotin (0.525 g, 2.15 mmol) in a mixed solvent of DMSO and NMP (vol ratio 1:1, 12 mL). The reaction vessel was flushed with N_2 and shaken at room temperature for 24 h, after which the Kaiser test was negative. The resin was separated by filtration and washed with a 1:1 (vol) solution of DMSO and NMP, NMP and CH_2Cl_2 (15 mL × 3, each). Compound **7d** was cleaved from resin with 20 mL of a cocktail solution containing TFA, CH_2Cl_2, and TIS in a volume ratio of 16:4:1. The reaction mixture was flushed with N_2 followed by shaking at room temperature for 2 h. The resin was removed by filtration, and the solvents were evaporated. The residue was extracted with ether (100 mL × 2), dissolved in H_2O (50 mL), and lyophilized. The crude **7d** was purified by preparative HPLC, using isocratic 5% solvent B for 30 min, then a linear gradient from 5% to 30% B in 330 min at a flow rate of 15 mL/min. After lyophilization, a colorless viscous liquid (57 mg) was obtained in 24% yield. HPLC showed only one peak at retention time (R_t) 18.65 min using isocratic 5% solvent B for 2.5 min, then a linear gradient from 5% to 30% B in 27.5 min at a flow rate of 1 mL/min. TLC R_f = 0.36. ESI-MS m/z = 455.4 $[M + H]^+$ (calc. 455.3).

N-(Amino-oxa-alkyl)biotinamides **7c**, **7a**, and **7b** were also prepared as **7d** with the above procedure using diamines **4c**, **4a**, and **4b** as starting materials, respectively. For **7c**: yield 18%, HPLC R_t = 18.65 min, TLC R_f = 0.38. ESI-MS m/z = 447.4 $[M + H]^+$ (calc. 447.3). For **7a**: yield 22%, HPLC R_t =16.88 min (obtained on a 130A Separation System of Applied Biosystems using Vydac 218TP52 column; running isocratic 10% B for 16 min and then a linear gradient 10−70% B for 30 min at a flow rate of 0.2 mL/min). TLC R_f = 0.37. ESI-MS m/z = 403.3 $[M + H]^+$ (calc. 403.2). For **7b**: yield 16%, HPLC R_t = 16.71 min (as done previously for **7a**), TLC R_f = 0.36. ESI-MS m/z = 409.5 $[M + H]^+$ (calc. 409.3).

Iodoacetylation of *N*-(Amino-oxa-alkyl) Biotinamide. *N-(13-Iodoacetamido-2,2,3,3,11,11,12,12-octadeutero-4,7,10-trioxa-tridecanyl)biotinamide (**8d**, ICAT-d_8).* To a solution of **7d** (55 mg, 0.097 mmol) in DMF (1 mL) was added DIEA (37 μL, 0.213 mmol) and a solution of

iodoacetic anhydride (37.7 mg, 0.107 mmol) in DMF (2 mL). The mixture was flushed with N_2 and stirred at room temperature for 3 h. The solvent was removed by rotary evaporation. The crude product was purified by preparative HPLC using isocratic 5% B for 50 min, then a linear gradient of 5−50% solvent B in 340 min at a flow rate of 15 mL/min. A light yellow solid was collected in a yield of 63% after lyophilization of the peak fractions. Analytical HPLC showed only one peak with a $R_t = 15.55$ min using isocratic 5% solvent B for 2.5 min, then a linear gradient of 5−60% solvent B for 27.5 min at a flow rate of 1 mL/min. TLC $R_f = 0.60$. ESI-MS $m/z = 623.3$ $[M + H]^+$ (calc. 623.2).

8c (ICAT-d_0), **8a** (s-ICAT-d_0), and **8b** (s-ICAT-d_6) were also prepared as **8d** (ICAT-d_8) with the above procedure using **7c**, **7a**, and **7b** as starting materials, respectively. For **8c**: yield 57%, HPLC $R_t = 15.61$ min, TLC $R_f = 0.60$, ESI-MS $m/z = 637.3$ $[M + Na]^+$ (calc. 637.2). For **8a**: yield 55%, HPLC $R_t = 22.78$ min (obtained on a 130A Separation System of Applied Biosystems using a Vydac 218TP52 column; running isocratic 10% B for 16 min and then a linear gradient 10−70% B for 30 min at a flow rate of 0.2 mL/min). TLC $R_f = 0.61$, ESI-MS $m/z = 571.3$ $[M + H]^+$ (calc. 571.1). For **8b**: yield 50%, HPLC $R_t =$ 22.56 min (as done previously for **8a**), TLC $R_f = 0.61$, ESI-MS $m/z = 599.4$ $[M + Na]^+$ (calc. 599.2).

RESULTS AND DISCUSSION

Synthesis of ICAT Compounds. As shown in Scheme 1, two pairs of ICAT compounds were prepared: one is compounds **8c** and **8d**, the classic ICAT-d_0 and ICAT-d_8 (*7*); the ICAT-d_8 was prepared from acrylonitrile-d_3 and di(ethylene glycol-d_2). Another pair is compounds **8a** and **8b**, termed s-ICAT-d_0 and s-ICAT-d_6 as they have a shorter linker than the classic one. The s-ICAT-d_6 was prepared with nondeuterated acrylonitrile and fully deuterated ethylene glycol as starting materials. The preparation of s-ICAT-d_0 and s-ICAT-d_6 was intended to lower the cost of the procedure. The use of acrylonitrile instead of its fully deuterated analogue may reduce the cost of starting materials by about 5-fold.

Synthesis of ICAT compounds began with the reaction of ethylene glycol or di(ethylene glycol) **1a**, **1b**, **1c**, and **1d** with acrylonitrile **2a** and **2b** to form ether dinitrile **3a**, **3b**, **3c**, and **3d** by Michael addition in benzene (*16*). After removal of solvent, the desired compounds were obtained in yield of 96% or higher and with good purity as shown on TLC (only one spot with R_f values around 0.65). These ether dinitriles were used in the next reaction without further purification.

Reduction of deuterated ether dinitrile to diamine is one of the crucial reactions in the synthesis because it may involve loss of deuterium by exchange with hydrogen. Gerber et al. prepared ether diamine **4d** by hydrogenation of ether dinitrile **3d** with Raney Ni catalyst (*14*). They found that the product was obtained in very low yield and with considerable exchange of deuterium (*17*). We also tried a mixture of Raney Ni and $NaBH_4$ to reduce **3d** to **4d**. The product was obtained in 53% yield after vacuum distillation. However, ESI-MS showed the main peak was diamine-d_6 ($m/z = 227.3$ $[M + H]^+$); about one-fourth of deuterium on the molecule was replaced by hydrogen during reduction. When the ratios of Ni and $NaBH_4$ to dinitrile were increased by 50%, the main peak in ESI-MS was diamine-d_4; the deuterium loss increased to 35%. These results of reduction and hydrogenation catalyzed by Raney Ni indicated that nickel may be responsible for deuterium loss in the reactions. Horner (*18*) investigated the H−D exchange process on Raney nickel in toluene. When Raney nickel was shaken for 16 h with a solution of toluene in cyclohexane under a deuterium atmosphere, hydrogen atoms both in the aromatic ring and in the methyl group of toluene could be exchanged by deuterium.

To overcome the problem, we tried several non-nickel-catalyzed reduction systems such as $LiAlH_4$ (*19*), AlH_3 (*20*), $H_3B{\cdot}S(CH_3)_2$ (*21*), and $NaBH_4-CoCl_2$ (*22*). We found that the best result was obtained with $NaBH_4-CoCl_2$. Satoh et al. first reported that nitriles could be easily reduced to primary amines with sodium borohydride-transition metal salts (e.g., $CoCl_2$) systems in MeOH (*22*). Ganem et al. studied the mechanism of $NaBH_4-CoCl_2$ reduction and concluded that the Cobalt boride formed in situ served as a true catalyst, strongly coordinating nitriles and activating them toward reduction by $NaBH_4$ (*23*, *24*). Dinitriles **3a**, **3b**, **3c**, and **3d** were reduced to diamines **4a**, **4b**, **4c**, and **4d** with $NaBH_4-CoCl_2$ in MeOH at room temperature. The reaction gave the desired products in 61−74% yields, and ESI-MS showed appropriate molecular weight with little loss of incorporated deuterium from deuterated diamines. Two impurities in the crude products were identified by ESI-MS as cyclic amines and dimers of diamine. These secondary amine byproducts are often seen in the reduction of nitriles when the reactions proceed stepwise (*19*, *25*). The crude diamines were used in the next step of synthesis without distillation.

Biotinylation of the symmetrical diamines is another crucial step in ICAT synthesis. Wilbur et al. prepared *N*-(13-amino-4,7,10-trioxatridecanyl)biotinamide, compound **7c**, by acylation of ether diamine **4c** with biotin tetrafluorophenyl ester in DMF in the presence of triethylamine (*26*). Aebersold et al. used this method to prepare its deuterated analogue **7d** in their study of ICAT reagent (*7*). A large excess of ether diamine must be used in this method to minimize formation of bis-biotin derivative of diamine. The excess of unreacted diamine is difficult to recover from the reaction mixture and results in a significant loss of diamine. Recently, Patel and Perrin described a new method to prepare **7d** (*15*). An orthogonally protected di(ethylene glycol)-d_8 linker was first prepared, and the linker was then extended by successive introduction of protected propylamine fragments. A monoamine was obtained by chemoselective deprotection and coupled with biotin pentafluorophenyl ester in DMF in the presence of DIEA. This method overcame the problem associated with the bis-biotinylation of diamine. However, the process involved a large number of reaction steps.

We wish to report a solid-phase biotinylation of diamine compounds. A 2-chlorotrityl chloride resin is loaded with 10 equiv of diamine relative to the resin in CH_2Cl_2. The reaction mixture was filtered, and the unreacted diamine was recovered by treatment of the filtrate with solid KOH to remove HCl followed by rotary evaporation to remove CH_2Cl_2. Because the loading reaction involved only resin, diamine, and CH_2Cl_2, the diamine could be recovered in quantitative yield. Biotinylation of the resin-bound amine was effected with 5 equiv of biotin relative to the resin in a solvent mixture of NMP, DMF, and DMSO in the presence of DIEA and HBTU/HOBt. The biotinylated amine was cleaved from resin with a cocktail containing TFA, CH_2Cl_2, and TIS in a volume ratio of 16:4:1. The crude product was purified by preparative HPLC. The biotin derivative of diamines **7a**, **7b**, **7c**, and **7d** were prepared by this

Scheme 2

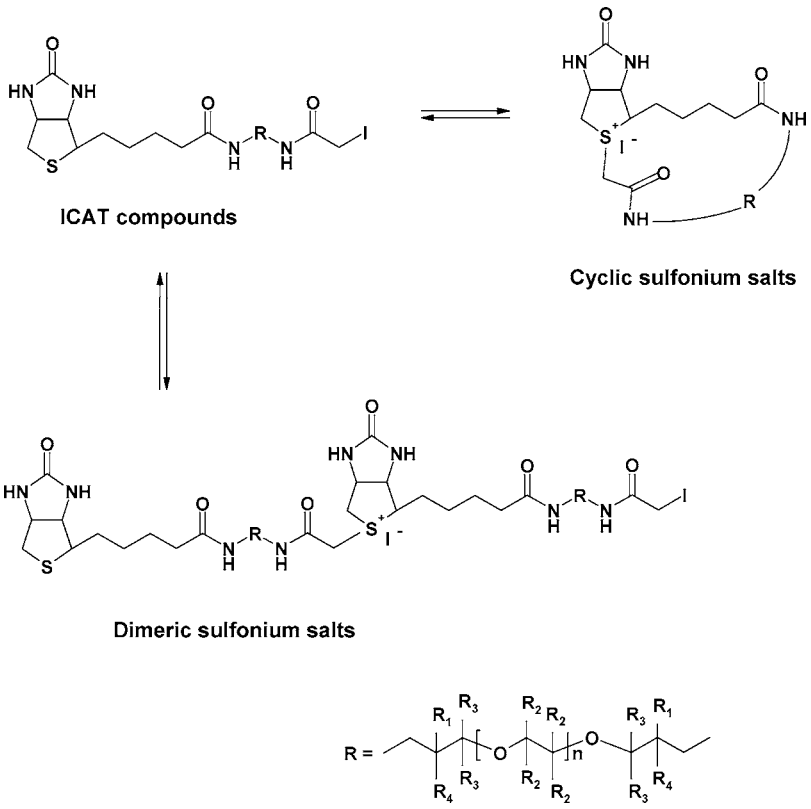

Table 1. HPLC and ESI-MS Analysis of Aged ICAT Reagents[a]

	ICAT				dimeric sulfonium salt				cyclic sulfonium salt	
	HPLC		ESI-MS $[M + H]^+$, *m/z*		HPLC		ESI-MS $[M + H]^+$, *m/z*		ESI-MS $[M + H]^+$, *m/z*	
	R_t, min	%	exp.	calc.	R_t, min	%	exp.	calc.	exp.	calc.
ICAT-d_8	22.4	59.9	623.1	623.2	23.3	40.1	1117.3	1117.5	495.3	495.3
ICAT-d_0	22.4	63.3	615.1	615.2	23.2	36.7	1101.1	1101.5	487.1	487.3
s-ICAT-d_6	21.6	52.3	577.1	577.1	22.2	47.7	1025.1	1025.3	449.3	449.2
s-ICAT-d_0	21.6	67.4	571.3	571.1	22.1	32.6	1013.1	1013.3	443.4	443.2

[a] The samples were stored under a nitrogen atmosphere at −20 °C for 1 year.

method from **4a**, **4b**, **4c**, and **4d**, respectively, in overall yields of 16−24% for the three steps of solid-phase synthesis. The low yield was caused by use of crude diamine in the synthesis. Compound **7c** was obtained in 43% yield if reagent diamine (Aldrich) was used. Analysis by HPLC, TLC, and ESI-MS showed the compounds to be quite pure and to have the correct molecular weight. Solid-phase synthesis overcame the problem of formation of bis-biotin derivative and difficult recovery of diamine and made the synthetic process simpler and easier.

Iodoacetylation of mono-biotinylated amine, the last step of ICAT synthesis, was carried out with iodoacetic anhydride in DMF in the presence of DIEA (*7*). After purification by HPLC, compounds **8d** (ICAT-d_8), **8c** (ICAT-d_0), **8b** (s-ICAT-d_6), and **8a** (s-ICAT-d_0) were obtained from **7d**, **7c**, **7b**, and **7a**, respectively, in yields of 50−63%. ESI-MS gave appropriate molecular weights with little loss of incorporated deuterium. TLC and HPLC analysis showed good purity for **8d** and **8**c and **a** considerable amount of dimeric sulfonium salts in **8a** and **8b**, which were formed during HPLC purification.

Self-Alkylation of ICAT Compounds. There are two functional groups in an ICAT molecule, dialkyl sulfide of biotin on one end and iodoalkyl of iodoacetamide on another end. Dialkyl sulfides are sufficiently nucleophilic to react with primary alkyl halides under mild conditions, frequently simply by mixing the reagents at room temperature (*27*). Thus, ICAT compounds may undergo self-alkylation between the dialkyl sulfide and iodoalkyl group, to give dimeric sulfonium salt by intermolecular alkylation and cyclic sulfonium salt by intramolecular alkylation (Scheme 2).

The self-alkylation of ICAT compounds results in a stability problem of the ICAT reagent. No dimeric or cyclic sulfonium salts were found by HPLC and ESI-MS in the crude product, most likely because the last step of ICAT synthesis was carried out in a nonaqueous medium and in the presence of a base (DIEA). Some dimeric sulfonium salts were formed during HPLC purification in a mixed solvent of acetonitrile and water with 0.1% TFA. The two s-ICAT compounds formed dimeric sulfonium salts more readily than the longer one, and it was difficult to obtain a pure product by HPLC in this solvent system. The undesired self-alkylation reaction proceeded not only in an aqueous solution but also in their solid state. Table 1 shows the analysis of ICAT samples which were stored at −20 °C for about 1 year. The HPLC and ESI-MS data demonstrated that about one-third to one-half of ICAT compounds were converted into dimeric sulfonium salts and a tiny amount of cyclic sulfonium salts.

The stability of ICAT compounds in different solvent systems was examined using s-ICAT-d_0 as an example.

Table 2. Effect of Different Solvent Systems on Stability of s-ICAT-d_0

days of storage at room temp	dimeric sulfonium salt %, HPLC				
	water 75% CH_3CN 25% TFA 0.1%	water 75% CH_3CN 25% NH_4OAc 0.01 M	water 67% MeOH 33% NH_4OAc 0.01 M	water 67% MeOH 33%	MeOH
0	32.1	32.4	34.3	33.1	32.6
4	39.3	37.9	36.7	36.5	20.0
14	57.4	54.9	46.3	47.9	11.5

Table 3. Regeneration of ICAT Compounds from Their Dimeric Sulfonium Salts (DSS) in MeOH

days of storage at room temp	composition %, HPLC							
	ICAT-d_8		ICAT-d_0		s-ICAT-d_6		s-ICAT-d_0	
	ICAT	DSS	ICAT	DSS	ICAT	DSS	ICAT	DSS
0	59.9	40.1	63.3	36.7	52.3	47.7	67.4	32.6
5	78.0	22.0	86.1	13.9	69.0	31.0	83.2	16.8
11	83.4	16.6	89.1	10.9	75.3	24.7	87.2	12.8
19	85.4	14.6	91.5	8.5	78.8	21.2	90.7	9.3
34	88.8	11.2	93.7	6.3	85.5	14.5	92.9	7.1
70	93.0	7.0	95.6	4.4	89.6	10.4	94.4	5.6

The results are in Table 2. The content of dimeric sulfonium salt was increased by 12.0−25.3% in all of the solvent systems containing water during 2 weeks of storage at room temperature. Neither the acidic buffer nor the neutral buffer showed any significant effect on reaction rates of self-alkylation in the mixed solvents used. The most interesting observation was the behavior of s-ICAT-d_0 in pure MeOH. Instead of self-alkylation, its dimeric sulfoniun salt was dealkylated into its monomer form at a quite rapid rate. The content of dimeric sulfonium salt was decreased from 32.6% to 11.5% in 2 weeks of storage in MeOH. This fact demonstrates that the self-alkylation reaction of ICAT compounds is reversible; the sulfonium salt can be dealkylated by the iodide ion, leading to the regeneration of ICAT compounds.

Both self-alkylation of ICAT compounds and dealkylation of its sulfonium salt are nucleophilic substitution reactions. The solvent that is used in a nucleophilic substitution reaction can have a profound effect on the rate of the reaction (*28*). In reactions in which product formation is favored by charge development in the transition state, solvents of high dielectric constant favor the process; conversely, in reactions in which reduction or dispersal of charge in the transition state favors product formation, solvents of low dielectric constant will favor the process. Thus, self-alkylation of ICAT compounds is greatly accelerated by solvents of high dielectric constant because charge is developed in the transition state and product; the dealkylation of ICAT sulfonium salts involving negatively charged nucleophiles, on the other hand, takes place more rapidly in solvents of low dielectric constant. Water has a much higher dielectric constant than MeOH (78 vs 33). Therefore, the equilibrium of the reversible reaction of ICAT self-alkylation will shift in favor of formation of the sulfonium salt in the solvent systems containing water and shift in favor of dealkylation in MeOH.

The conversion of ICAT sulfonium salts into their monomer forms in MeOH was further demonstrated by all four ICAT compounds studied (Table 3). The contents of dimeric sulfonium salt in the aged ICAT samples were reduced from 32.6% to 47.7% to about 5−10% in 70 days of storage in MeOH at room temperature. The regeneration treatment by MeOH or other solvents of low dielectric constant may provide a useful method for purification of ICAT compounds contaminated by their sulfonium salts.

LITERATURE CITED

(1) Blackstock, W. P., and Weir, M. P. (1999) Proteomics: quantitative and physical mapping of cellular proteins. *Trends Biotechnol. 17*, 121−127.

(2) Gabor Miklos, G. L., and Maleszka, R. (2001) Integrating molecular medicine with functional proteomics: realities and expectations. *Proteomics 1*, 30−41.

(3) Witzmann, F. A., and Li, J. (2002) Cutting-edge technology. II. Proteomics: core technologies and applications in physiology. *Am. J. Physiol. Gastrointest. Liver Physiol. 282*, G735−G741.

(4) Figeys, D. (2002) Proteomics approaches in drug discovery. *Anal. Chem. 74*, 412A−419A.

(5) Goshe, M. B., and Smith, R. D. (2003) Stable isotope-coded proteomic mass spectrometry. *Curr. Opin. Biotechnol. 14*, 101−109.

(6) Tao, W. A., and Aebersold, R. (2003) Advances in quantitative proteomics via stable isotope tagging and mass spectrometry. *Curr. Opin. Biotechnol. 14*, 110−118.

(7) Gygi, S. P., Rist, B., Gerber, S. A., Turecek, F., Gelb, M. H., and Aebersold, R. (1999) Quantitative analysis of complex protein mixtures using isotope-coded affinity tags. *Nat. Biotechnol. 17*, 994−999.

(8) Zhang, R., Sioma, C. S., Wang, S., and Regnier, F. E. (2001) Fractionation of isotopically labeled peptides in quantitative proteomics. *Anal. Chem. 73*, 5142−5149.

(9) Yu, L. R., Johnson, M. D., Conrads, T. P., Smith, R. D., Morrison, R. S., and Veenstra, T. D. (2002) Proteome analysis of camptothecin-treated cortical neurons using isotope-coded affinity tags. *Electrophoresis 23*, 1591−1598.

(10) Shiio, Y., Donohoe, S., Yi, E. C., Goodlett, D. R., Aebersold, R., and Eisenman, R. N. (2002) Quantitative proteomic analysis of Myc oncoprotein function. *EMBO J. 21*, 5088−5096.

(11) Lee, H., Griffin, T. J., Gygi, S. P., Rist, B., and Aebersold, R. (2002) Development of a multiplexed microcapillary liquid chromatography system for high-throughput proteome analysis. *Anal. Chem. 74*, 4353−4360.

(12) Guina, T., Wu, M., Miller, S. I., Purvine, S. O., Yi, E. C., Eng, J., Goodlett, D. R., Aebersold, R., Ernst, R. K., and Lee, K. A. (2003) Proteomic analysis of *Pseudomonas aeruginosa* grown under magnesium limitation. *J. Am. Soc. Mass Spectrom. 14*, 742−751.

(13) Oda, Y., Owa, T., Sato, T., Boucher, B., Daniels, S., Yamanaka, H., Shinohara, Y., Yokoi, A., Kuromitsu, J., and Nagasu, T. (2003) Quantitative chemical proteomics for identifying candidate drug targets. *Anal. Chem. 75*, 2159−2165.

(14) Gerber, S. A., Scott, R., Turecek, F., and Gelb, M. H. (1999) Analysis of rates of multiple enzymes in cell lysates by electrospray ionization mass spectrometry. *J. Am. Chem. Soc. 121*, 1102−1103.

(15) Patel, A., and Perrin, D. M. (2004) Efficient synthesis of isotopically pure isotope-coded affinity tagging reagents. *Bioconjugate Chem. 15*, 224−230.
(16) Ashikaga, K., Ito, S., Yamamoto, M., and Nishijima, Y. (1988) Intramolecular end-to-end reactions of photoactive terminal groups linked by poly(oxyethylene) chains. *Bull. Chem. Soc. Jpn. 61*, 2443−2449.
(17) Gerber, S. A., Turecek, F., and Gelb, M. H. (2001) Design and synthesis of substrate and internal standard conjugates for profiling enzyme activity in the sanfilippo syndrome by affinity chromatograghy/electrospray ionization mass spectrometry. *Bioconjugate Chem. 12*, 603−615.
(18) Horner, L. (1969) Competing processes on the surface of Raney nickel during the hydrogenation of olefins. *Ann. N.Y. Acad. Sci. 158*, 456−470.
(19) Hazzard, B. J. (1973) *Organicum*, Chapter 7, Addison-Wesley Publishing Co., Inc., Reading, MA.
(20) Yoon, N. M., and Brown, H. C. (1968) Selective reductions. XII. Explorations in some representative applications of aluminum hydride for selective reductions. *J. Am. Chem. Soc. 90*, 2927−2938.
(21) Brown, H. C., Choi, Y. M., and Narasimhan, S. (1981) Improved procedure for borane-dimethyl sulfide reduction of nitriles. *Synthesis* 605−606.
(22) Satoh, T., Suzuki, S., Suzuki, Y., Miyaji, Y., and Imai, Z. (1969) Reduction of organic compounds with sodium borohydride-transition metal salt systems (1). Reduction of organic nitrile, nitro and amide compounds to primary amines. *Tetrahedron Lett. 52*, 4555−4558.
(23) Heinzman, S. W., and Ganem, B. (1982) The mechanism of sodium borohydride-cobaltous chloride reductions. *J. Am. Chem. Soc. 104*, 6801−6802.
(24) Osby, J. O., Heinzman, S. W., and Ganem, B. (1986) Studies on the mechanism of transition-metal-assisted sodium borohydride and lithium aluminum hydride reductions. *J. Am. Chem. Soc. 108*, 67−72.
(25) Egli, R. A. (1970) Katalysierte Nitrilreduktionen mit natriumborhydrid. *Helv. Chim. Acta 53*, 47−53.
(26) Wilbur, D. S., Hamlin, D. K., Vessella, R. L., Stray, J. E., Buhler, K. R., Stayton, P. S., Klumb, L. A., Pathare, P. M., and Weerawarna, S. A. (1996) Antibody fragments in tumor pretargeting. Evaluation of biotinylated Fab' colocalization with recombinant streptavidin and avidin. *Bioconjugate Chem. 7*, 689−702.
(27) Lowe, P. A. (1981) Synthesis of sulfonium salts. *The chemistry of the sulfonium group*: *part 1* (Stirling, C. J. M., Ed.) pp 267−312, Chapter 11, John Wiley & Sons, Chichester-New York-Brisbane-Toronto.
(28) Gutsche, C. D., and Pasto, D. J. (1975) *Fundamentals of Organic Chemistry*, pp 600−647, Chapter 21, Prentice-Hall, Inc., NJ.

BC049777Y

Optimized Synthesis of Functionalized Fluorescent Oligodeoxynucleotides for Protein Labeling

Charles Goussu,[†,‡] Jean-Jacques Vasseur,[†] Hervé Bazin,[‡] Eric Trinquet,[‡] Fabrice Maurin,[‡] and François Morvan*[,†]

Laboratoire de Chimie Organique Biomoléculaire de Synthèse, UMR 5625 CNRS-UM II, Université de Montpellier II, CC008, Place E. Bataillon, 34095 Montpellier Cedex 5, France, and CIS Biointernational, Marcoule, BP 84 175, 30204 Bagnols/Cèze Cedex, France. Received October 18, 2004; Revised Manuscript Received January 31, 2005

Phthalimido-alkanol solid supports were rapidly prepared from solid supported phthalic anhydride and amino alcohol condensation induced by microwaves. These supports were used to synthesize 5′-fluorescent 3′-aminoalkyl oligodeoxynucleotides allowing a two-step deprotection necessary to avoid aminolink alkylation. After conversion into an NHS derivative using dissuccinimidyl suberate and an optimized isolation, they were conjugated with a protein.

INTRODUCTION

Although the labeling of proteins with fluorescent dyes is well documented and many prelabeled proteins are commercially available, it appears that the quality of the conjugates is not always satisfactory. The most common labeling method involves a selective acylation of an amino function (reaction of activated esters on ϵ-NH_2 from lysines). Since several reactive sites are available on a given protein, the reaction leads to a "statistical labeling" (*1*) resulting in a population of multiple labeled molecules (*2, 3*). The labeling ratio (number of dyes per protein) usually measured from the UV−visible spectrum of the purified conjugate is a macroscopic value corresponding to the average ratio for the population. Organic dyes such as fluoresceins, cyanines, or Alexa are often preferred since they have a minimum impact on the biological properties (e.g. immunoreactivity for a antibody) and the labeling process is straightforward. The state of the art in immunochemistry is to develop, in a reproducible manner, a conjugate in which the unlabeled protein is largely in the minority and most of the molecules bear two or more labels. This has an important impact on the fluorescent properties of the conjugates, since most of fluorescent dyes undergo fluorescence quenching due to the proximity between two dye molecules (*4, 5*). Although some sulfonated Cy5 are claimed to yield conjugates presenting a low level of dye dimerization (*6*) characterized by a reduced hypochromic D-band, we observed a 50% decrease in the quantum yield even at a dye/protein ratio of two for the labeling of IgG with commercial Cy5 *N*-hydroxysuccinimidyl (NHS) ester, following the recommended protocol (Amersham Biosciences) as previously observed by others (*7*) who reported that for a ratio of 2 to 3 Cy5 labels per IgG, some moderate fluorescence was obtained and IgG bearing six Cy5 label was almost nonfluorescent. Furthermore, overlabeling should be avoided since it also has a negative impact on the biological activity (binding constants) of macromolecules.

For all these reasons, it is highly desirable to find a way to avoid any detrimental interaction between individual fluorophores coupled to the same molecule. A few methods are known to ensure the controlled labeling of native proteins as antibodies, one possibility being the use of cyclodextrin−dye complex which allow multiple labeling with minimum fluorescence quenching (*8*). An alternative is the use of a fluorescent dye substituted by an oligonucleotide (ODN) moiety bearing a reactive linker enabling the conjugation of this probe to a target protein (*9*). For this unconventional application of ODNs, one needs is an efficient way to obtain doubly modified ODN bearing for example a Cy5 dye on its 5′-end and an aminoalkyl linker on its 3′-end. For routine labeling, these doubly modified ODNs should be readily available and it should be confirmed that the amino group is indeed fully unprotected and free of side-products. A linker bearing a primary amino group was chosen since it is the most versatile and can be converted into many reactive groups used in immunochemistry (e.g. NHS ester, maleimide, thiol, etc.) through the use of a panoply of homobifunctional reagents (e.g. dissuccinimidyl suberate, DSS) (*10*) or heterobifunctional reagents (e.g. succinimidyl *trans*-4-(*N*-maleimidylmethyl)cyclohexane-1-carboxylate: SMCC) which are widely used in immunochemistry and are commercially available.

ODNs with 3′-aminoalkyl arms are conveniently prepared through standard solid-phase synthesis on a 3′-amino-protected support which releases the free 3′-amino during the final deprotection (*11*−*15*). The 3′-amino support based on an immobilized 3-nitro-6-succinyloxymethylbenzoyl group (*15*) or an immobilized phthalimido protective group (*16*) is particularly attractive since it releases an enantiomerically pure ODN (as compared to some amino links (*12*) which give rise to resolvable diastereoisomers). Unfortunately, the former was synthesized with a very low yield from 6-nitrophthalide and *O*-(4,4′-dimethoxytrityl)-1-hexanol-6-amine. A solid support from phthalimido groups exhibits two main advantages: it cannot react with acetic anhydride during the capping step of the elongation process, and furthermore, the cyanoethyl groups can be removed from the support before the phthamilido cleavage, avoiding the reaction

* Corresponding author. Telephone +33/ 467 144 961, fax +33/ 467 042 029, e-mail morvan@univ-montp2.fr.
† Université de Montpellier II.
‡ CIS Biointernational.

10.1021/bc049752z CCC: $30.25 © 2005 American Chemical Society
Published on Web 02/24/2005

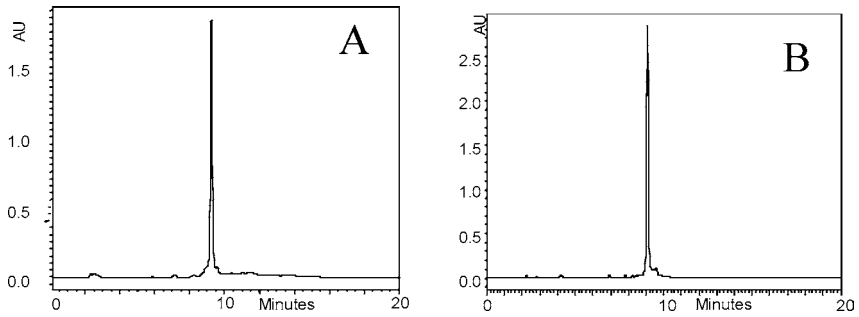

Figure 1. Crude HPLC profiles of (A) T_6-$(CH_2)_6$-NH_2 and (B) T_{15}-$(CH_2)_3$-NH_2 on column C_{18} nucleosil, gradient 5 to 36% acetonitrile in 50 mM TEAAc in 20 min.

Table 1. Reagents and Conditions for the Preparation of Phthalimido Alkanols Solid Support 3a–c Using Microwaves

entry	reagents	time (s)	temperature or watt	solid support & loading	
1	**2**+ $NH_2(CH_2)_6OH$	120 (6 × 20 s)	650 W	**3a**	49 μmol/g
2	**2**+ $NH_2(CH_2)_6OH$	150	200 °C	**3a**	62 μmol/g
3	**2**+ $NH_2(CH_2)_2OH$	150	150 °C	**3b**	67 μmol/g
4	**2**+ $NH_2(CH_2)_3OH$	150	150 °C	**3c**	59 μmol/g

of acrylonitrile with the free amine (*17*). Unfortunately, this support is expensive and its preparation requires three steps, with a crystallization and a chromatography step, to obtain the *p*-nitrophenyl active ester in 47% yield after which then reacts poorly with LCAA CPG (long chain aminoalkyl-controlled pore glass) to give a loading of only 20 μmol/g (*16*).

We developed a very convenient, rapid, and efficient synthesis of phthalimido alkyl alcohol solid supports. All the reactions were performed on the solid support; hence, workups consisted of only filtrations and washes. Several free alkyl alcohols reacted on the immobilized phthalic anhydride to give the corresponding solid supports with high loading (~60 μmol/g). Indeed, the hydroxyl function does not need to be protected since the reaction is chemoselective. From the solid support, 5′-fluorescent 3′-alkylamino ODN was synthesized, and by an optimized procedure it was conjugated with an antibody.

EXPERIMENTAL SECTION

Measurement of Cy5 Dye Concentrations. For sulfonated Cy5 dye and conjugates, the concentration were measured from the absorbance values at λ_{max} assuming a molar extinction coefficient of 250 000 M^{-1} cm^{-1} according to the product data sheet (Amersham Biosciences Cy5 monoreactive dye # PA25001) and literature (*18*). For nonsulfonated Cy5 dye linked to oligonucleotides, the concentrations was measured at λ_{max} assuming a molar extinction coefficient of 250 000 M^{-1} cm^{-1} according to the product data sheet (Amersham Biosciences Cy5 phosphoramidite).

Preparation of Phthalimido Alkyl Alcohol Solid Supports. One gram of LCAA-CPG (Sigma), pretreated for 2 h with 3% TCA in CH_2Cl_2 (*19*), was gently shaken with 63.2 mg (0.3 mmol) of 1,2-anhydrotrimellitic chloride and 105 μL (0.6 mmol) of diisopropylethylamine in 5 mL of CH_2Cl_2 for 3 h. The resin was filtered off, washed with CH_2Cl_2 and ether, and dried under vacuum. The resin was treated for 2 h with 10 mL of a mixture of Ac_2O, pyridine, THF (1:1:8, v/v/v) (Cap A) and 10% *N*-methylimidazole in THF (Cap B). The resin was filtered off, washed with CH_2Cl_2 and ether, and dried under vacuum. The resulting resin was mixed with 0.3 mmol of amino alcohol in 5 mL of DMF and heated in a microwave synthesizer (Discover from CEM Corporation) set at 300 W and 200 °C for 150 s, or in a domestic MW oven at 650 W for 6 × 20 s with a cooling of the mixture between two runs. The resin was filtered off, washed with CH_2Cl_2 and ether, and dried. Approximately 20 mg of the solid support was poured into a column, and then a standard thymidine phosphoramidite was incorporated and detritylated. The loading was determined at 498 nm by the assay of the dimethoxytrityl cation released. (Table 1).

Synthesis of 5′-Cy5,3′-Aminoalkyl Oligonucleotides. From the phthalimido alkyl alcohol solid support (1 μmol), the ODN was synthesized on a ABI 394 DNA synthesizer using standard reagents and 15 equiv of commercially available phosphoramidites. A standard elongation cycle was applied except that the first detritylation step was omitted since the solid support is hydroxyl free. Then, the Cy5 phosphoramidite (Amersham Biosciences) was incorporated using a coupling step of 120 s to ensure optimum coupling. Next, a treatment with a solution of 10% piperidine in CH_3CN was applied for 10 min to remove the cyanoethyl groups. After washes with CH_3CN, the supported ODN was treated overnight with aqueous concentrated ammonia in the dark. Ammonia was removed by evaporation under reduced pressure to yield a dark blue solution. Finally, the fluorescent aminoalkyl ODN was purified by HPLC on a Delta Pak column (Waters) 15 μm, C18, 100 Å, 7.8 × 300 mm, using a gradient of CH_3CN in 50 mM TEAAc, pH 7, 2 mL/min (Figure 2). UV-visible spectrum for Cy5-T_{15}-$(CH_2)_6$ NH_2 (0.1 M phosphate buffer, pH 7) λ_{max} = 265 600 (sh), 646 nm, $A_{265}/A_{646} = 0.639$, $A_{280}/A_{650} = 0.417$, $A_{600}/A_{650} = 0.38$.

MALDI-TOF Mass Spectrometry. MALDI-TOF mass spectra were recorded on a Voyager DE mass spectrometer (Perseptive Biosystems, Framingham, MA) equipped with an N_2 laser (337 nm). MALDI conditions are as follows: laser power 2400 (arbitrary units); accelerating voltage 24 000 V; guide wire 0.05% of accelerating voltage; grid voltage 94% of accelerating voltage; delay extraction time 550 ns and 100 scans averaged. All reported spectra here were obtained in negative ion mode and were not smoothed. THAP (trihydroxyacetophenone) as matrix; T_6-$(CH_2)_6$ NH_2 *m/z* for $C_{66}H_{92}N_{13}O_{43}P_6$: Calcd 1941.38; Found 1941.82; T_{15}-$(CH_2)_3NH_2$ *m/z* for $C_{153}H_{203}N_{31}O_{106}P_{15}$: Calcd 4637.08; Found 4633.78; Cy5-17mer-$(CH_2)_6$ NH_2: *m/z* for $C_{204}H_{258}N_{79}O_{98}P_{18}$: Calcd 5941.33; Found 5942.40.

Labeling of Antibody with Reference Cy5 Dye. The antibody to be labeled was dialyzed against pH 9 0.1 M carbonate–bicarbonate buffer and the concentra-

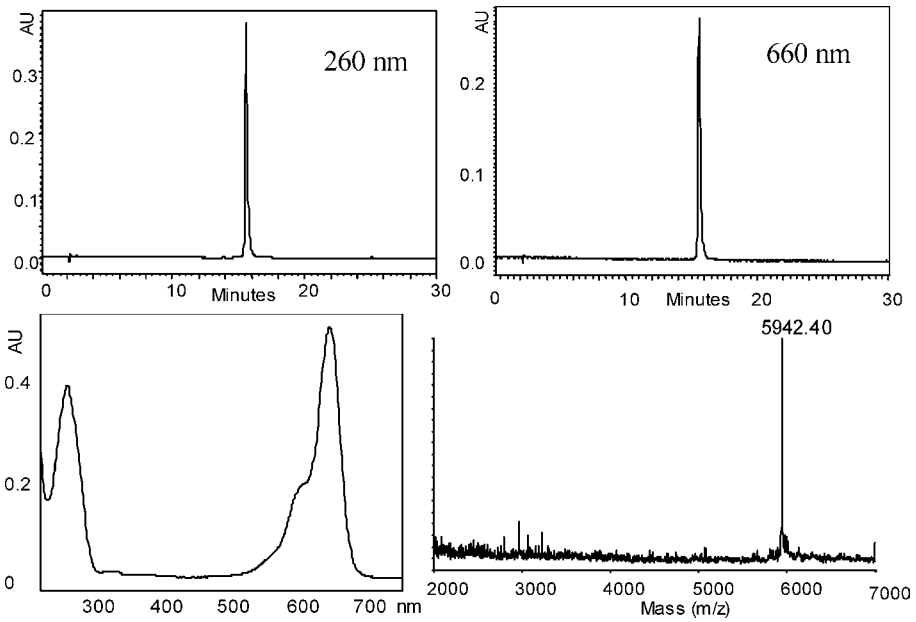

Figure 2. HPLC profiles at 260 and 660 nm of purified Cy5-GCG AAA AAA AAA AGC TC-$(CH_2)_6$-NH_2, UV/visible spectrum and MALDI-TOF mass spectrometry.

tion adjusted to 1 mg/mL. The NHS-activated Cy5 dye ('to label 1 mg of protein" Amersham Biosciences kit) was dissolved in DMSO, and several labeling reactions were performed, varying the number of equivalents of Cy5 added. After 30 min, the reaction mixture was separated by gel filtration over SD 200 in an HR10/30 column (Amersham Biosciences), eluting at 1 mL/min in 0.1 M phosphate buffer, pH 7. The protein concentrations in the void volume were calculated from A_{280} according to ϵ_{280} = 210 000 M^{-1} cm^{-1} for the antibody, taking into account the contribution of the Cy5 dye at 280 nm (0.05 × A_{650}) according to the manufacturer's instruction and literature (*18*). The dye over protein ratio (D/P) and the A_{600}/A_{650} ratio were calculated as previously described (*7*).

Conjugation of Cy5-oligonucleotides with Antibody. Starting with the 5′-Cy5 labeled ODN bearing a 3′ aminolinker (10 nmol) in 12 μL of 50 mM N−(3-sulfopropyl) morpholine (MOPS) pH 7.0, we added 4 μmol of DSS in 28 μL of DMF (Fluka), and the mixture was kept under vigorous mixing (Eppendorf vortexer) either at 20 °C for 5 h or at 4 °C for 16 h. The conversion into active ester was monitored by RP-HPLC for example the 5′-Cy5-$(dT)_{15}$-3′-hexylamine (Rt = 15 mn) gave the corresponding NHS-suberate derivative (Rt = 16.1 mn). Column Lichrospher RP-18 E 5 μm 125 × 4 mm, elution 1 mL/min, gradient 9.5% to 50% of CH_3CN in 25mM TEAAc in 30 min. The reaction mixture was then loaded on a NAP 5 column (Amersham Biosciences) equilibrated in 10 mM MOPS pH 6.0 (4 °C) to remove the excess DSS, and the exclusion fraction (1 mL) collected in a 2 mL eppendorf was then extracted by 1 mL of *n*-Butanol (vortexing, centrifuging and pipeting off the upper phase). The process was repeated three times and a fourth time after the addition of 1.5 mL *n*-Butanol and 2 min centrifuging (14 000 rpm) the Cy5-ODN-NHS ester was precipitated as a blue spot. The supernatant was removed and the precipitate was dried under vacuum (5 min, speed-Vac). This Cy5-ODN-NHS ester can be kept dried at −80 °C (or even −20 °C) for a few days with limited decomposition. The antibody (300 μg, 2 nmol) was added to the Cy5-ODN-NHS in 35 μL of 0.1 M sodium carbonate buffer pH 9, the reaction mixture was kept at room temperature for 30 min and then loaded on an HR10/30 Superdex 200 column (Amersham Biosciences). The elution was carried out with 0.1 M phosphate buffer pH 7, the fastest blue band (t_R = 10 min) containing the conjugate was collected and was well resolved from the excess of Cy5-ODN (t_R = 17 min). An initial Cy5-ODN-NHS/IgG ratio of 4 gave a conjugate (62% yield) for which the UV−visible spectrum (A_{650} = 0.286, A_{600} = 0.103, A_{280} = 0.236) indicated the conjugate contained an average of two cyanines (Cy5) per antibody. An initial Cy5-ODN-NHS/IgG ratio of 12 gave a conjugate (49% yield) for which the UV−visible spectrum (A_{650} = 0.463, A_{604} = 0.168, A_{280} = 0.283) indicates that the conjugate contained an average of five cyanines (Cy5) per antibody. The contribution at 280 nm due to the Cy5-T_{15} moiety is 0.435 × A_{650}. For long-term storage, 0.1% BSA (Sigma Bovine Serum Albumin "protease free") was added as stabilizer, and aliquots were stored at −20 °C. The conjugates (ca. 150 pmol) were analyzed on a Superdex 200 column connected to a diode array detector, and a single peak was detected for the conjugates in both conditions (t_R = 12 min for 5(Cy5-T_{15})−Ab and t_R = 12.7 min for 5(Cy5-T_{15})−Ab), the native antibody being eluted at t_R = 13.6 min. The conjugates were well resolved from the excess of hydrolyzed Cy5-ODN labeling reagent, so the A_{650}/A_{280} ratio could be used with confidence to assess the average number of Cy5 moieties covalently bound to the antibody. Furthermore, analysis of the conjugates by size exclusion chromatography showed a single species absorbing at 650 nm, and although the population of labeled antibodies was not resolved, the retention time (centroid of the population) had a tendency to become shorter when increasing the number of Cy5 moieties bound to antibodies.

Fluorescence Measurements. All measurements were performed in 0.1 M phosphate buffer, pH 7, at 20 °C. The Cy5-T_{15} used as reference and the two conjugates 2(Cy5-T_{15})−Ab and 5(Cy5-T_{15})−Ab obtained above were diluted (triplicates) to 100 nM chromophore concentration (A_{650} = 0.025) according to the A_{650} measured for the mother solutions. The fluorescence spectra were recorded on a LS50 fluorimeter, the excitation being set at 640 nm (10 nm slit), and scanning at 650−750 nm (5 nm slit). For each compound, the acquired spectra (triplicates) were averaged.

Scheme 1. Synthesis of Phthalimido Alkyl Solid Support[a]

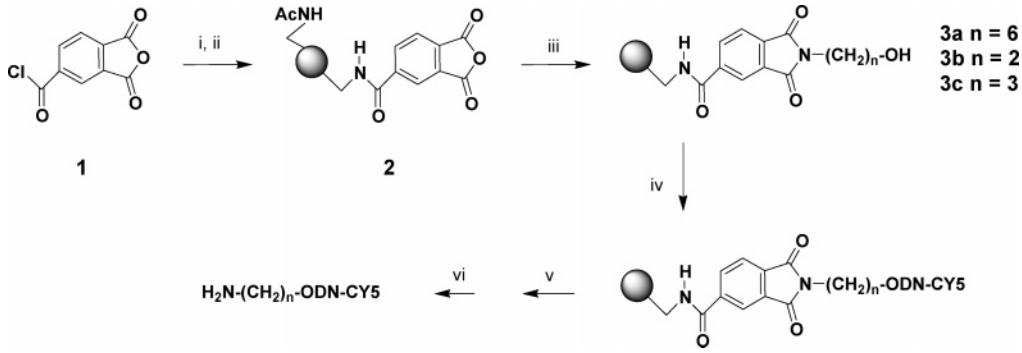

[a] Reagents and conditions: i: LCAA CPG, 1,2-anhydrotrimellitic chloride, CH_2Cl_2, iPr_2EtN 3 h; ii: CAP A: Ac_2O, pyridine, THF (10/10/80) + CAP B: 10% *N*-methylimidazole, THF 2 h; iii: amino alcohol, DMF, MW 150 s; iv: classic ODN synthesis; v: 10% piperidine/ CH_3CN 10 min; vi: aq NH_3 16 h rt.

RESULTS AND DISCUSSION

Since solution-phase synthesis requires time-consuming workup and purification, we developed a strategy on solid support using only commercially available reagents. Thus, the preparation of the phthalimido solid supports was convenient, easy, inexpensive, fast, and also versatile since any aminoalkyl alcohol or amino-PEG-alcohol (e.g. 2-(2-aminoethoxy)ethanol)) could be anchored. This method was applied to the preparation of phthalimido-ethyl, -propyl, and -hexanyl alcohol solid supports. Finally, using the phthalimido-hexanol solid support, a 5′-fluorescent 3′-amino ODN was synthesized, converted into an NHS derivative, and then conjugated with an antibody.

The solid supports **3a**−**c** were prepared in two steps (Scheme 1). The first step was the reaction of 1,2-anhydrotrimellitic acid chloride **1** (0.3 mmol) on CPG-LCAA (*19*) (1 g) to yield the phthalic anhydride CPG **2** within 3 h (*14, 20*). The resin was filtered off, washed, and dried. Unreacted amines were capped with commercial Cap A and Cap B solutions for 2 h. The resin was filtered off, washed, and dried. The key step was the formation of a phthalimido function which was performed under microwave irradiation (MW). It should be noted that a partial reaction yielding an amide linkage must be avoided since its hydrolysis under basic conditions is very long ($t_{1/2}$ = 17 500 h at 0.1 M NaOH at 30 °C) (*21*). Reactions of phthalic anhydride with amine occur with or without solvent by conventional heating (175−225 °C) (*16*) or by MW (*22, 23*). Note that the reaction is chemoselective since it occurs specifically with the amino moiety. In addition it was reported that reaction of phthalic anhydride with 6-amino-1-hexanol is faster when it occurred by MW than under conventional heating (*23*). Theoretically, since 6-amino-1-hexanol is a solid with a low melting point (56−58 °C), it could be used without solvent. In our case, to optimize the interaction between the solid supported phthalic anhydride and the 6-amino-1-hexanol, and later with the other alkylamino alcohol, DMF was selected as solvent. Reactions were performed with 0.3 mmol of alkylamino alcohol per gram of solid-supported phthalic anhydride **2** in 5 mL of dry DMF.

The reaction was first performed using a domestic MW oven (650W full power) by 6 × 20 s with a cooling of the mixture between two runs (to avoid bumping and spillage), yielding the expected solid support **3a** with a fairly high loading of 49 μmol per gram of resin (Table 1, entry 1). Initially, the loading was determined by dimethoxytritylation of a support sample followed by its detritylation and assay of the trityl cation at 498 nm. This method was deemed inefficient, because it was time-consuming and poorly reproducible. Thus, a coupling with commercial thymidine cyanoethyl diisopropylphosphoramidite was preferred, and the loading was determined from the cation released during a detritylation step. This method is fast and gives reproducible values. The reaction was also performed in a sealed tube using a microwave synthesizer with the temperature set at 200 °C, 300 W for 150 s (Table 1, entry 2).

Next, the reaction was extended to ethanolamine and 3-amino-1-propanol, setting the microwave synthesizer at 150 °C, 300 W for 150 s (Table 1, entries 3 and 4). For all the solid supports, a similar loading was obtained around 60 μmol/g, demonstrating that reaction is fast and efficient.

The use of a microwave synthesizer for the preparation of the phthalimido-alkanol solid support is convenient and gives reproducible results and high loading. However, this solid support could also be prepared using a common domestic MW oven with a slightly lower but still high loading (49 μmol/g). Using this procedure, all the steps were performed on solid supports that allow rapid and easy workups. The use of MW speeds up the reaction, and several new solid supports were prepared in less than 1 day using inexpensive, commercially available reagents.

To evaluate the properties of the resins, a few short ODN T_6-NH_2 were synthesized on these various supports (Figure 1A), and for each the same trend was observed in the HPLC profiles. Longer ODNs were synthesized as T_{15}-$(CH_2)_3$-NH_2 (Figure 1B) and also a hetero ODN [5′-Cy5-d(GCG AAA AAA AAA AGC TC_3-$(CH_2)_6$-NH_2)], labeled with the cyanine Cy5 on its 5′ position (Figure 2). The syntheses were carried out on a 1 μmol scale using 15 equiv of phosphoramidite and regular reagents on an ABI 394 DNA synthesizer. The first detritylation step was omitted. The average yield was better than 98.5%. ODNs were deprotected by a two-step procedure. First, cyanoethyl groups were removed by a piperidine treatment (*24*) (10% piperidine in acetonitrile for 10 min at room temperature and washing) to remove the resulting acrylonitrile that could further react with the amino function (*17*). Then, on the partially deprotected ODN still attached to the CPG, a treatment with concentrated ammonia at 55 °C for 17 h for unlabeled ODN or 16 h at room temperature in the dark for the Cy5 ODN yielded the fully deprotected 3′-amino ODNs in solution (Figures 1 and 2), which were purified by HPLC. ODNs were characterized by MALDI-TOF MS (see Experimental Section).

The activation of amine-tethered ODN by homobifunctional reagents such as DSS (dissuccinimidyl suberate)

Scheme 2. Conjugation of Fluorescent Alkylamino ODN to Antibody[a]

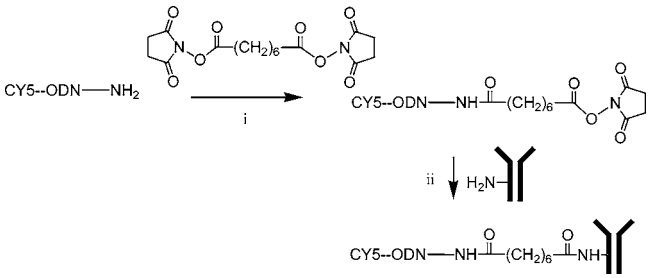

[a] Reagents and conditions: i: 50 mM MOPS buffer, pH 7, DMF; ii: antibody, $NaHCO_3$ pH 9.

Table 2. A_{600}/A_{650} Ratios of Cy5 Dye−Antibody Conjugates

	Cy5/Ab ratio				
	0.73	1.32	2.64	3.56	5.40
A_{600}/A_{650}	0.353	0.394	0.490	0.592	0.613

[a] For free sulfonated Cy5 the A_{600}/A_{650} ratio is 0.315 (0.1 M phosphate buffer pH 7).

(*10*) or EGS (ethylene glycol−bis-succinic acid NHS ester) (*25*) is reported for the preparation of ODN−enzyme conjugates. However, the protocols described were not found to be satisfactory since the diafiltration process to remove reagent excesses was too slow, and extensive breakdown of the NHS ester was observed by HPLC monitoring. DSS was preferred (Scheme 2) since it is less reactive than EGS. It therefore leads to a more stable and storable ODN-NHS ester, and, as an intermediary, allows conjugation to proteins in a short time at pH 9. Thus, the Cy5-ODN-NH_2 in DMF and MOPS buffer, pH 7, was reacted with DSS. The isolation protocol combines the use of a fast size exclusion column and simple *n*-butanol extractions to yield an Cy5-ODN-NHS ester in a dry state allowing its storage and later use. The overall process can be easily scaled up and is highly reproducible. Finally, the Cy5-ODN-NHS ester was conjugated with antibody (Ab) in a pH 9 sodium carbonate buffer, and the Cy5-ODN−Ab conjugates were isolated by size exclusion chromatography. As reference compounds we prepared several conjugates using commercially available sulfonated Cy5 dye, for the free Cy5 dye in phosphate buffer we observed a A_{600}/A_{650} ratio of 0.315 which is in agreement with previous data (*7*), and as shown in Table 2 this ratio increased with the number of Cy5 dyes bound per antibody as previously reported (*7*). In contrast with the appearance of a higher 600 nm absorbance, increasing with the number of bound Cy5 dyes observed for antibodies labeled with sulfonated Cy5 and the concomitant loss of fluorescence efficiency (*7*), in the labeling strategy presented here we do not observe such a phenomenom. Ideally, the spectrophotometric properties of the dye in Cy5-ODN−antibodies should be compared with the nonsulfonated dye; unfortunately, this one is only available as a phosphoramidite and is not soluble in aqueous buffers, therefore the Cy5-ODN which is the closest related compound available is used as reference. The UV−visible spectrum of the commercial Cy5-phosphoramidite in acetonitrile showed a $\lambda_{max} = 644$ nm which is close to $\lambda_{max} = 645$ nm observed for the Cy5-ODNs in water or buffer; for the Cy5-phosphoramidite, the A_{600}/A_{650} ratio was 0.35 in acetonitrile solution. The UV−visible spectra of a conjugate containing two Cy5-ODN moieties per antibody displayed a A_{600}/A_{650} ratio of 0.36 which is very close to the value of 0.38 measured on a "free" Cy5-ODN molecule in which the cyanine dye was in a monomeric form. For a conjugate containing an average of five Cy5-ODN moieties per antibody, we observed that the A_{600}/A_{650} ratio was 0.37; again, this value was close to the one observed for the monomeric Cy5. The measured fluorescence intensity was $I_{665} = 140.9 \pm 4.3$ a.f.u. (arbitrary fluorescence units) for the 2(Cy5-T_{15})−Ab conjugate, $I_{665} = 141.1 \pm 3.8$ a.f.u. for 5(Cy5-T_{15})−Ab, and $I_{665} = 163.1 \pm 3.8$ a.f.u. for the reference Cy5-T_{15} oligodeoxynucleotide. These measurements performed at a constant chromophore concentration (100 nM) showed that the relative quantum yields of the Cy5 moieties were almost the same for both conjugates and only about 15% lower than compound Cy5-T_{15} taken as reference. This shows that using the new labeling strategy results in no loss of fluorescence efficiency, by increasing the number of bound Cy5-T_{15} units.

CONCLUSION

We developed a convenient, easy, inexpensive, fast, and versatile protocol for the preparation of phthalimido alkanol solid supports used for the synthesis of 3′ aminoalkyl-ODNs which can be labeled on their 5′ position with classic fluorescent dyes or other tags. This was exemplified on the 5′-Cy5-labeled ODN. After release from the solid support, the Cy5-labeled ODN was converted into an activated NHS ester and was conjugated with an antibody. By adjusting the molar excess of the reactive Cy5-ODN, conjugates exhibiting a dye-to-protein ratio up to five were isolated. Using this labeling strategy and in contrast with classical Cy5 antibody labeling, no decrease of the fluorescence efficiency was observed by increasing the number of dyes per antibody. This should ensure a higher brightness using the conjugates, for example as acceptors in fluorescent resonance energy transfer (FRET)-based immunoassays.

ACKNOWLEDGMENT

We thank CIS Biointernational for financial support.

LITERATURE CITED

(1) Weber, G., and Daniel, E. (1966) Cooperative effects in binding by bovine serum albumin. II. The binding of 1-anilino-8-naphthalenesulfonate. Polarization of the ligand fluorescence and quenching of the protein fluorescence *Biochemistry 5*(6), 1900−1907.

(2) Adamczyk, M., Buko, A., Chen, Y. Y., Fishpaugh, J. R., Gebler, J. C., and Johnson, D. D. (1994) Characterization of protein-hapten conjugates. 1. Matrix-assisted laser desorption ionization mass spectrometry of immuno BSA-hapten conjugates and comparison with other characterization methods *Bioconjugate Chem. 5*(6), 631−635.

(3) Adamczyk, M., Gebler, J. C., and Mattingly, P. G. (1996) Characterization of protein-hapten conjugates. 2. Electrospray mass spectrometry of bovine serum albumin-hapten conjugates *Bioconjugate Chem. 7*(4), 475−481.

(4) Haugland, R. P. (1995) Coupling of monoclonal antibodies with fluorophores *Methods Mol. Biol. 45*, 205−221.

(5) Midoux, P., Roche, A. C., and Monsigny, M. (1987) Quantitation of the binding, uptake, and degradation of fluoresceinylated neoglycoproteins by flow cytometry *Cytometry 8*, 327−334.

(6) Mujumdar, R. B., Ernst, L. A., and Waggoner, A. S. (1993) Method for labeling and detecting materials employing arylsulfonate cyanine dyes US5268486.

(7) Gruber, H. J., Hahn, C. D., Kada, G., Riener, C. K., Harms, G. S., Ahrer, W., Dax, T. G., and Knaus, H.-G. (2000) Anomalous fluorescence enhancement of Cy3 and Cy3.5 versus anomalous fluorescence loss of Cy5 and Cy7 upon covalent linking to IgG and noncovalent binding to avidin *Bioconjugate Chem. 11*, 696−704.

(8) Aspe, D. (1998) Nonaggregated fluorescent conjugates and method for obtaining them WO9826287.
(9) Bazin, H., Mathis, G., Trinquet, E., and Maurin, F. (2003) Fluorescent entity, useful as fluorescent tracer, comprises fluorophore and functional group, introduced or generated on the fluorophore or an oligonucleotide or oligonucleotide analogue WO03104685.
(10) Ruth, J. L. In *Protocols for Oligonucleotide conjugates*, Agrawal, S., Ed., Humana Press Inc: Totowa, NJ, 1994; Vol. 26, p 167−185.
(11) Asseline, U., and Thuong, N. T. (1990) New solid-phase for automated synthesis of oligonucleotides containing an amino-alkyl linker at their 3′-end *Tetrahedron Lett. 31*, 81−84.
(12) Nelson, P. S., Kent, M., and Muthini, S. (1992) Oligonucleotide Labeling Methods. 3. Direct Labeling of Oligonucleotides Employing a Novel, Nonnucleosidic, 2-Aminobutyl-1,3-Propanediol Backbone *Nucleic Acids Res. 20*, 6253−6259.
(13) Kumar, P., Gupta, K. C., Rosch, R., and Seliger, H. (1996) Universal Polymer Support For the Synthesis Of 3′-End Modified Oligonucleotides *Bioorg. Med. Chem. Lett. 6*, 2247−2252.
(14) Lyttle, M. H., Adams, H., Hudson, D., and Cook, R. M. (1997) Versatile Linker Chemistry For Synthesis Of 3′-Modified DNA *Bioconjugate Chem. 8*, 193−198.
(15) Leuck, M., Giare, R., Paul, M., Zien, N., and Wolter, A. (2004) A novel solid support for the synthesis of 3′-aminoalkylated oligonucleotides *Tetrahedron Lett. 45*, 317−320.
(16) Petrie, C. R., Reed, M. W., Adams, A. D., and Meyer, R. B. (1992) An improved CPG support for the synthesis of 3′-amine-tailed oligonucleotides *Bioconjugate Chem. 3*, 85−87.
(17) Griffey, R. H., Monia, B. P., Cummins, L. L., Freier, S., Greig, M. J., Guinosso, C. J., Lesnik, E., Manalili, S. M., Mohan, V., Owens, S., Ross, B. R., Sasmor, H., Wancewicz, E., Weiler, K., Wheeler, P. D., and Cook, P. D. (1996) 2′−O−Aminopropyl Ribonucleotides − a Zwitterionic Modification That Enhances the Exonuclease Resistance and Biological Activity Of Antisense Oligonucleotides *J. Med. Chem. 39*, 5100−5109.
(18) Mujumdar, R. B., Ernst, L. A., Mujumbar, S. R., Lewis, C. J., and Waggoner, A. S. (1993) Cyanine dye labeling reagents: Sulfoindocyanine succinimidyl esters *Bioconjugate Chem. 4*, 105−111.
(19) Pon, R. T., Usman, N., and Ogilvie, K. K. (1988) Derivatization of controlled pore glass beads for solid-phase oligonuclzotide synthesis *Biotechniques 6*, 768−775.
(20) Bauer, J., and Rademann, J. (2003) Trimellitic anhydride linker (TAL)- -highly orthogonal conversions of primary amines employed in the parallel synthesis of labeled carbohydrate derivatives *Tetrahedron Lett. 44*, 5019−5023.
(21) Khan, M. N. (1996) Suggested Improvement in the Ing-Manske Procedure and Gabriel Synthesis of Primary Amines: Kinetic Study on Alkaline Hydrolysis of N−Phthaloylglycine and Acid Hydrolysis of N−(o-Carboxybenzoyl)-glycine in Aqueous Organic Solvents *J. Org. Chem. 61*, 8063−8068.
(22) Peng, Y., Song, G., and Qian, X. (2001) Imidation of cyclic carboxylic anhydrides under microwave irradiation *Synthetic Com. 31*, 1927−1931.
(23) Vidal, T., Petit, A., Loupy, A., and Gedye, R. N. (2000) Reexamination of Microwave-Induced Synthesis of Phthalimides *Tetrahedron 56*, 5473−5478.
(24) Meyer, A., Debart, F., Imbach, J. L., and Vasseur, J. J. (2001) Step-by-step control by MALDI-TOF MS of an oligonucleotide synthesis on standard CPG solid-support *Nucleosides Nucleotides and Nucleic Acids 20*, 951−954.
(25) Reyes, R. A., and Cockerell, G. L. (1993) Preparation of Pure Oligonucleotide-Alkaline Phosphatase Conjugates *Nucleic Acids Res. 21*, 5532−5533.

BC049752Z

MAY/JUNE 2005
Volume 16, Number 3

© Copyright 2005 by the American Chemical Society

Bioconjugate Chemistry

REVIEWS

Use of Carbonyl Group Addition−Elimination Reactions for Synthesis of Nucleic Acid Conjugates

Timofei S. Zatsepin,[†] Dmitry A. Stetsenko,[‡,§] Michael J. Gait,[‡] and Tatiana S. Oretskaya[†,*]

Department of Chemistry, M. V. Lomonossov Moscow State University, 1 Leninskie Gory, Moscow, 119992, Russia, and Medical Research Council, Laboratory of Molecular Biology, Hills Road, Cambridge CB2 2QH, UK.
Received December 2, 2004; Revised Manuscript Received March 3, 2005

This review outlines the synthesis of covalent conjugates of oligonucleotides and their analogues that are obtained by reactions of carbonyl compounds with various nucleophiles such as primary amines, *N*-alkoxyamines, hydrazines, and hydrazides. The products linked by imino, oxime, hydrazone, or thiazolidine groups are shown to be useful intermediates for a wide range of chemical biology applications. Methods for their preparation, isolation, purification, and analysis are highlighted, and the comparative stabilities of the respective linkages are evaluated. The relative merits of incorporation of a carbonyl group, particularly an aldehyde group, into either the oligonucleotide or the ligand parts are considered. Examples of harnessing of aldehyde−nucleophile coupling for the labeling of nucleic acids are given, as well as their conjugation to various biomolecules (e.g. peptides and small molecule ligands), site-specific cross-linking of oligonucleotides to nucleic acid-binding proteins, assembly of multibranched supramolecular structures, and immobilization on functionalized surfaces. Future perspectives of bioconjugation and complex molecular engineering via carbonyl group addition−elimination reactions in nucleic acids chemistry are discussed.

INTRODUCTION

Structurally diverse conjugates of oligonucleotides have found numerous applications in different fields of molecular and cell biology. Molecules attached to oligonucleotides are often used as reporter groups, e.g. fluorescent (*1*, *2*), electrochemical (*3*, *4*), or spin (*5*−*7*) labels, for stabilization of double- or triple-helical structures, e.g. intercalators (*8*) and minor groove binders (*9*, *10*), and for increase of cellular uptake of conjugates, e.g. peptides (*11*−*13*), hydrophobic molecules (*14*), and certain carbohydrates (*15*).

There are two alternative approaches to the synthesis of modified nucleic acids: (a) automated solid-supported phosphoramidite or H-phosphonate oligonucleotide assembly using appropriately modified nucleoside or non-nucleoside derivatives (*16*−*18*), and (b) enzymatic incorporation of a 5′-triphosphate of a modified nucleoside (*19*).

* To whom correspondence should be addressed. Phone: +7(095) 939-5411. Fax: +7(095) 939-3181. E-mail: oretskaya@belozersky.msu.ru.
[†] MSU, Russia.
[‡] MRC, UK.
[§] Present address: School of Pharmacy and Pharmaceutical Sciences, University of Manchester, Oxford Road, Manchester M13 9PT, UK.

10.1021/bc049712v CCC: $30.25 © 2005 American Chemical Society
Published on Web 05/04/2005

Scheme 1. Reductive Amination: Schiff Base (imine) Formation Followed by Reduction

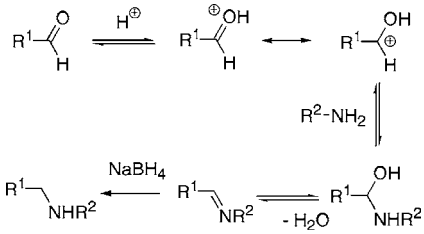

Chemically synthesized oligonucleotides may be extended by polymerase chain reaction (PCR) or joined by chemical (*20*) or enzymatic (*21*) ligation. The triphosphate approach provides an opportunity for multiple incorporation of modified nucleoside 5′-triphosphate derivatives into either DNA or RNA. Unfortunately, this method is limited mainly to base-modified nucleoside derivatives, since most nucleoside modifications lead to an inability of the corresponding 5′-triphosphate to be incorporated by polymerases (*22*).

Three strategies are generally used for synthesis of oligonucleotide conjugates. The first approach requires synthesis of a nucleoside or non-nucleoside synthon followed by appropriate protection and phosphitylation. The phosphoramidite or H-phosphonate derivative is then incorporated into an oligonucleotide chain during solid-phase synthesis. The conjugated molecule needs to be stable during oligonucleotide synthesis and deprotection. A limitation of this approach is that a reasonably large-scale and multistep synthesis of a modified monomer is required. It seems to be optimal only for incorporation of those reporter or marker groups that are chemically robust and easily accessible synthetically.

The second approach employs fragment conjugation of a target molecule to fully protected support-immobilized oligonucleotide containing a free reactive group. This reactive function must be blocked with a protecting group that can be removed without affecting other protecting and anchoring groups of the oligonucleotide. Selective deprotection of the reactive group is followed by conjugation and then by cleavage and deprotection of the conjugate. Only certain selectively removable protecting groups/conditions for their removal have been used for preparation of oligonucleotide conjugates, such as allyloxycarbonyl (Alloc[1])/Pd (0) (*23*, *24*), fluorenylmethyloxycarbonyl (Fmoc)/morpholine (*25*, *26*), levulinoyl (Lev), and phthaloyl (Phth)/hydrazinium acetate (*24*, *27*), and photolabile protecting groups of the 2-nitrobenzyl type (*28*, *29*). In some cases, preliminary deblocking of internucleoside phosphates is needed to increase the solvation of the oligonucleotide chain and to remove reactive acrylonitrile that sometimes causes side-reactions. The approach is indispensable for synthesis of combinatorial libraries, especially in the case of hydrophobic ligands, since a large excess of the ligand can be used (*30*). However, the resultant conjugate also needs to be stable under the deprotection conditions.

[1] Alloc, allyloxycarbonyl; AP site, abasic, or apurinic/apyrimidinic, site; Bn, benzyl; Boc, *tert*-butoxycarbonyl; Bz, benzoyl; DBU, 1,8-diazabicyclo[5.4.0]undec-7-ene; DEAD, diethyl 1,1′-azodicarboxylate; DEC, 1-(3-dimethylaminopropyl)-3-ethylcarbodiimide; DMTr, 4,4′-dimethoxytrityl; Fmoc, 9-fluorenylmethoxycarbonyl; Lev, levulinoyl (4-oxopentanoyl); MMTr, 4-methoxytrityl; OSu, *N*-hydroxysuccinimide ester; Phth, phthaloyl; Py, pyridine; RP-HPLC -reverse-phased HPLC; SNP, single nucleotide polymorphism; TBDMS, *tert*-butyldimethylsilyl; Tf, trifluoromethanesulfonyl; Tr, trityl (triphenylmethyl).

Scheme 2. Reductive Amination of an Apurinic Site with an Amine under Neutral or Acidic pH

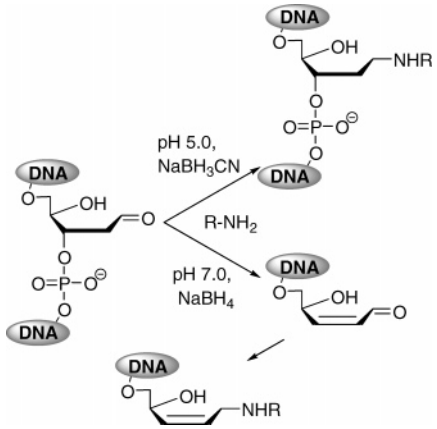

In the third approach, conjugation of a deprotected and (if necessary) purified oligonucleotide is carried out in solution. This approach seems to be the most flexible, since no harsh treatment is required after the reaction. The main problem is the need for isolation of the conjugate from the reaction mixture. There are many different types of chemistry available for fragment coupling in solution. Oligonucleotides with amino or thiol groups are conjugated by amide, disulfide, or thioether bond formation (*16*), while those with electrophilic groups are rarely used because of the complicated synthesis of the appropriate derivatives (*31*). However in the case of complex biomolecules, regio- and chemoselectivity are the main concerns in the reaction. Chemoselective conjugation is widely used in peptide chemistry (*32*, *33*), carbohydrate chemistry (*34*), chemistry of nucleic acids (*35*), and steroids (*36*−*38*). During the past decade, a number of classical organic reactions, such as the Staudinger (*39*, *40*), Diels−Alder (*41*−*43*), and 1,3-dipolar cycloaddition reactions (*44*−*46*), have been applied successfully to the bioconjugation of nucleic acids. Extraordinary regioselectivity and high yields of the reactions make this approach the method of choice for biomolecular conjugation.

Here we describe the application of addition−elimination reactions of a carbonyl group, mainly an aldehyde group, with various nitrogen nucleophiles for chemoselective conjugation of the appropriately modified oligonucleotides. We discuss both the introduction of an aldehyde group into an oligonucleotide as well as into the molecule to be conjugated.

CONJUGATION VIA IMINE, OR SCHIFF BASE FORMATION FOLLOWED BY BOROHYDRIDE REDUCTION

Schiff base, or imine, formation followed by reduction, i.e. reductive amination, is widely used in total synthesis of natural products. The reaction is slower at low pH due to protonation of the amino group but may be carried out at neutral or mildly basic conditions. However, the reaction is reversible, so the imine should be reduced in situ to the secondary amine to drive it to completion (Scheme 1). Various borohydride reagents are used for the reduction, but sodium borohydride and sodium cyanoborohydride are by far the most common. Sodium cyanoborohydride is more stable in aqueous solution and is a milder reductant and thus is used more frequently.

Methods of synthesis of both amino (*16*, *18*) and aldehyde (*31*) oligonucleotides are reviewed elsewhere. Here we would like to outline the conditions of the

Scheme 3. 1,4-Addition of 3-Aminocarbazole to 2,3-Dideoxy-2,3-dehydroribose Residue at the 3′-End

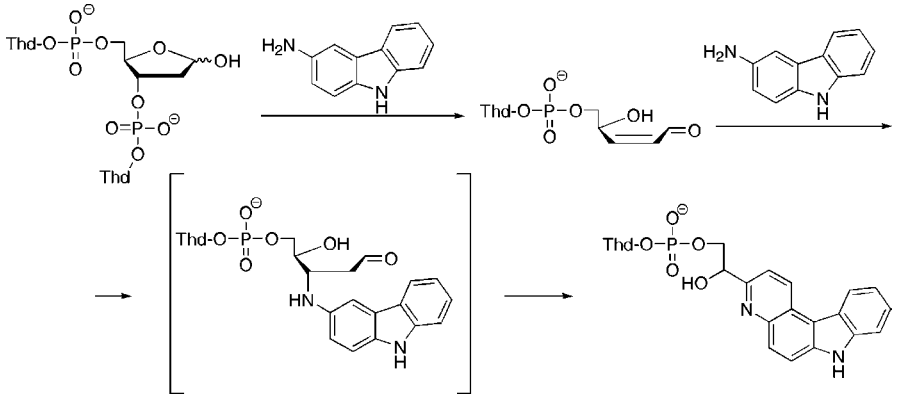

Scheme 4. Reductive Amination of 3′-Terminal Periodate-Cleaved RNA

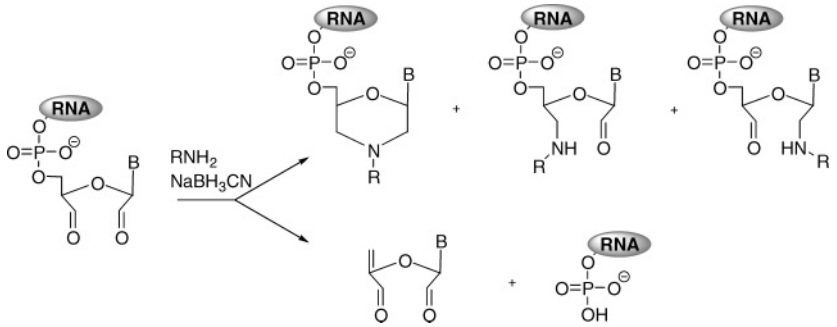

Scheme 5. Aldehyde Derivatives of Oligonucleotides That Have Been Used for Reductive Amination

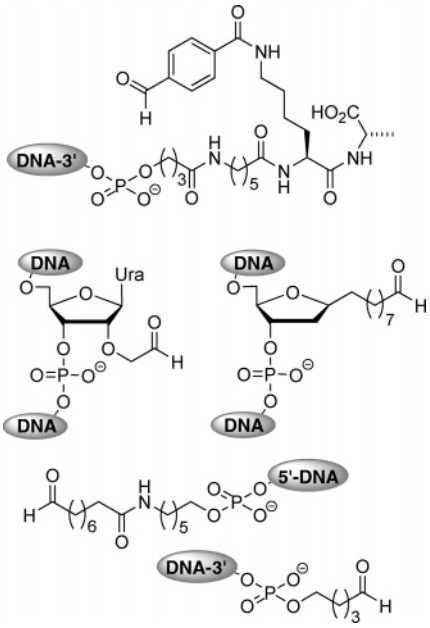

Scheme 6. Aldehyde Derivatives of Oligonucleotides Used for Affinity Modification of DNA-Binding Proteins via Reductive Amination

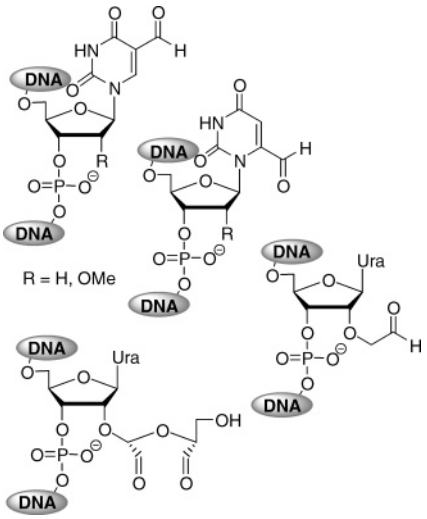

Scheme 7. Modified Nucleoside and Dinucleosides Used for Template-Directed Polymerization

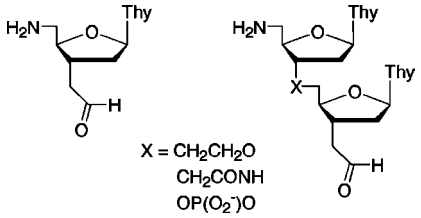

reaction and emphasize the influence of both the nature and placement of an aldehyde group on the conjugate yield.

Probably, the most common example of reductive amination via Schiff base formation is aminooligonucleotide immobilization on various aldehyde-coated surfaces for DNA chip fabrication (*47*). This combination of reactive groups is more effective then the opposite due to nonspecific interactions between anionic oligonucleotides and positively charged surface (*48*). However in the case of aldehyde-coated surfaces, blocking of the unreacted aldehyde groups by aminooligoethyleneglycol decreases nonspecific oligonucleotide binding and provides better sensitivity during hybridization assays (*49*−*50*). Another reason for immobilization of aminooligonucleotides on the aldehyde surfaces has been the lack until recently of commercial availability of aldehyde phosphoramidites. Nevertheless, two common methods for the

Scheme 8. C-Terminal PNA Aldehyde

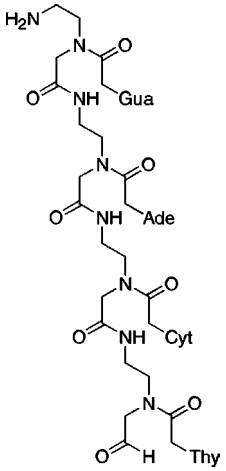

introduction of an aldehyde group into nucleic acids have been used.

The most popular method for generation of an aldehyde group in native DNA is partial acidic depurination. Proudnikov et al. (*51*) demonstrated that DNA that contains apurinic, or AP, sites undergoes facile β-elimination under neutral conditions. However, reductive amination proceeds smoothly under slightly acidic pH (Scheme 2).

Vasseur et al. (*52*) demonstrated that reaction of the AP site with 3-aminocarbazole leads to a chain break followed by nucleophilic addition to α,β-unsaturated aldehyde (Scheme 3). Such complex processes have not been followed step by step by others, but Greenberg et al. (*53*) later observed an analogous process during interactions of a lysine residue of DNA glycosylase with ribonolactone at the 3′-end of an oligonucleotide. Later Manoharan et al. (*54*) conjugated a number of amines, including tripeptides and aminophenanthroline, to an AP site in oligodeoxyribonucleotides under reductive conditions, without giving the yields of the conjugates.

Another common method for generation of an aldehyde group in nucleic acids is periodate oxidation of the 3′-terminal ribonucleotide in native RNA, synthetic oligoribo- or oligodeoxyribonucleotides 3′-modified with a single ribonucleotide residue. Apart from conjugation of the resulting dialdehyde derivatives with amines, some β-elimination also takes place (*55*) (Scheme 4).

These approaches may be useful for immobilization of nucleic acids on a surface or on beads, where a large excess of oligonucleotide is normally used, but they are far from optimal for the synthesis of various oligonucleotide conjugates. However, Schiff base formation has been used to synthesize conjugates of oligonucleotides that contain an aldehyde group (Scheme 5) with alkaline phosphatase (*56*), methionine (*57*), 1-aminomethylpyrene, aminooligoethyleneglycol (*58*), and an aminoalkyl derivative of biotin (*59*, *60*). Sando et al. (*61*) applied a different approach, the conjugation of 5′-amino oligonucleotides with reducing carbohydrates. Phosphate and borate buffers that cover a wide basic pH range (6.8−9.5) were used. The yields of the conjugates varied from 50% to

Scheme 9. Oligonucleotide Ligation by Metal-Directed Salen Complex Formation

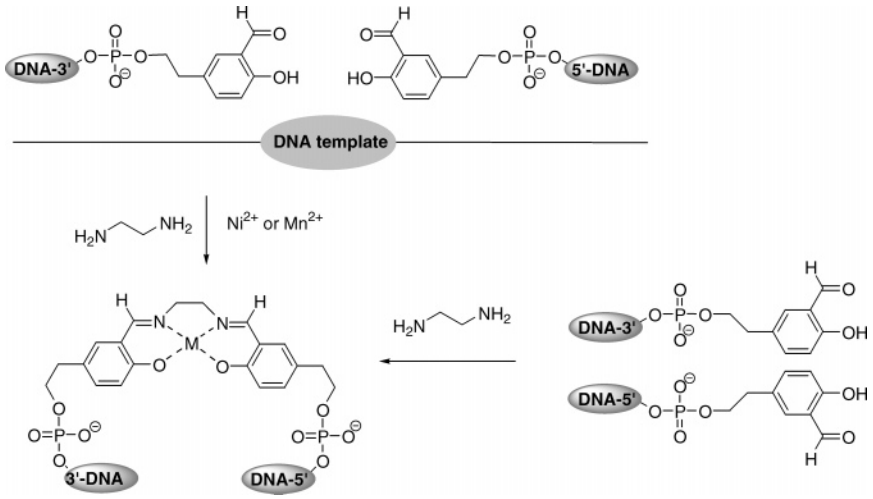

Scheme 10. Phosphoramidites Used for Synthesis of Supramolecular Structures

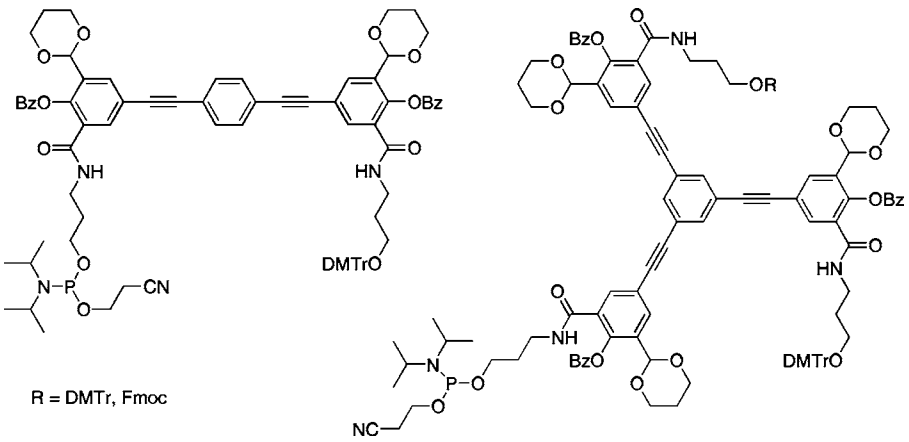

Scheme 11. Synthesis of *N*-Hydroxyphthalimide Derivatives

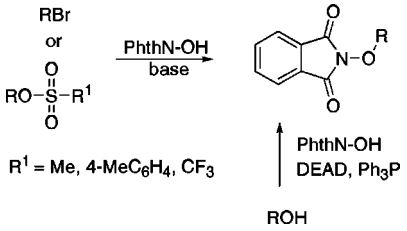

quantitative, but a large excess of the amine is usually used. Sando et al. (*61*) emphasized the superiority of the borate buffer due to an increase in the reaction rate.

Kittaka et al. used modified oligonucleotides bearing aldehyde groups (Scheme 6) in the heterocyclic base for affinity modification of Rel/NF-kB (*62*−*64*), c-Myb (*65*), or RecA proteins (*66*, *67*). Schiff base formation with lysine residues significantly increased binding to the protein. However, oligonucleotides containing 6-formyl-2′-deoxy- and 6-formyl-2′-*O*-methyluridine were found to be ineffective due to significant duplex disturbance and low binding to proteins. The duplex structure was somewhere between A- and B-forms, as judged by CD-spectroscopy (*65*, *68*). More recently, oligonucleotides containing an aldehyde group at the 2′-position of a sugar residue were used for affinity modification of NF-kB protein (*69*, *70*) and DNA-methyltransferase SsoII (Vorobjeva, Zatsepin, Kubareva, Oretskaya, unpublished results). Also oligonucleotides with 2′-dialdehyde group were used in affinity modification of methyltransferases (*71*) and T7 RNA polymerase (*72*).

Recently Bugaut et al. (*73*) used oligonucleotides containing 2′-amino-2′-deoxyuridine for identification of duplex-stabilizing ligands bearing an aldehyde group by a dynamic combinatorial library approach. A number of aromatic aldehydes were added to DNA duplexes containing a 2′-amino-2′-deoxyuridine residue at the 3′- or 5′-terminus or in the middle of an oligonucleotide chain. The ratio of conjugates as a function of time was monitored by HPLC. Imines formed were reduced to the corresponding amines, which are analyzed more easily. It was demonstrated that the portion of product containing the most stable conjugate is increased, and that the rate of change of that portion is proportional to duplex stability.

During the past decade, interest in DNA template-directed organic synthesis has increased significantly (*21*, *74*−*77*). Earlier the main efforts were centered on chemical ligation of short oligonucleotides or monomeric nucleotides on a DNA template. Today DNA template-directed synthesis allows for regioselective chemical reactions, otherwise ineffective or even impossible in aqueous solution.

Lynn et al. (*78*, *79*) used Schiff base formation to ligate modified oligonucleotides. It was demonstrated that the imine reduction shifts the equilibrium toward products and allows the reaction to function in a catalytic mode due to significant destabilization of the duplex (*79*). Later Lynn et al. demonstrated oligomerization of a modified thymidine or thymidine dinucleoside that carry 5′-amino and 3′-aldehyde groups (Scheme 7) on an oligoadenylate template (*80*, *81*). It should be noted that the process was effective only if the template was in solution or immobilized on a polystyrene support, and was very sensitive to mismatches.

Liu et al. (*82*−*86*) used 5′- or 3′-aldehyde oligonucleotides for ligation on a DNA template with aminooligonucleotides or cross-linking to a modified matrix. The authors studied the dependence of the reaction yield on the structure of the template i.e. its length, presence of loops and reactive groups. Reductive amination showed a pronounced distance-dependence in the case of linear templates, but a lower distance-dependence was observed for a looped template. A number of subsequent ligations and cross-linkings with different templates allowed the synthesis of rather complex molecules conjugated to DNA (e.g. macrocyclic compounds (*85*, *86*)). Later Rosenbaum and Liu (*87*) carried out oligomerization of a PNA tetramer containing a C-terminal aldehyde group (Scheme

Scheme 12. Phosphoramidite Derivatives Obtained via Mitsunobu Reaction That Were Used for Synthesis of Aminooxyoligonucleotides

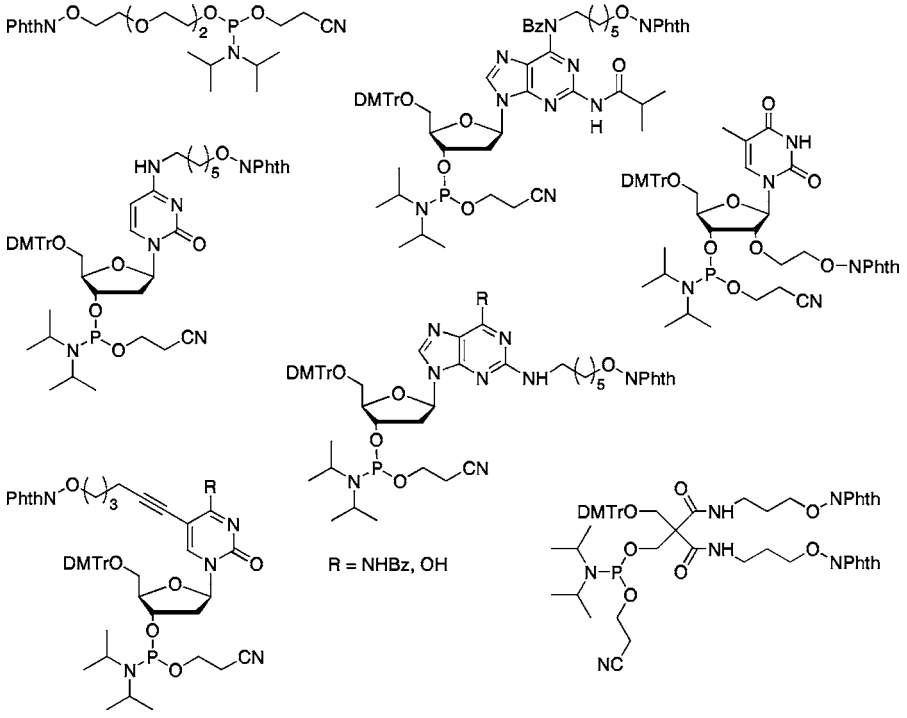

Scheme 13. Synthesis of a Protected Aminooxy Building Block by Nucleophilic Subsitution

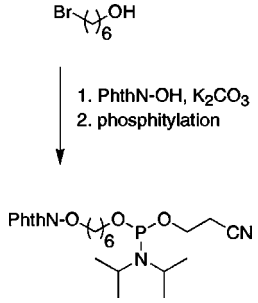

8) on a long DNA template (40 nt). The process could be described as an artificial DNA replication.

Czlapinski and Sheppard (*88*, *89*) applied metal−salen complex formation for oligonucleotide ligation on a DNA template or ligation of self-complementary oligonucleotides (Scheme 9). Oligonucleotides containing 5′- or 3′-salicylaldehyde moieties, respectively, were ligated on a DNA template by ethylenediamine in the presence of Mn^{2+} or Ni^{2+}. The yields were up to 74% (compared with <4% in the absence of a template or metal ions). The ligation of self-complementary oligonucleotides did not depend on the presence of a metal ion or pH, probably due to preorganization of fragments because of salicylaldehyde participation in stacking interactions. Later, Ni−salen DNA derivatives were used for site-specific oxidative cleavage of DNA (*90*).

Later Gothelf et al. (*91*−*93*) synthesized a set of non-nucleoside phosphoramidites (Scheme 10) that may be used to construct 2D or 3D supramolecular structures containing metal−salen complex at a branching point. The distinct feature of the approach is a possibility of nanostructures formation followed by DNA removal. This may be used for preparation of novel 3D catalysts e.g. asymmetric catalysts (*94*, *95*).

CONJUGATION VIA OXIME FORMATION

Since Schiff bases are unstable under acidic or basic conditions, use of stronger nucleophiles and weaker bases such as *O*-alkyl hydroxylamines is preferred over the use of amines due to greater stability of the oximes formed (*96*, *97*). The increased nucleophilicity of an aminooxy group is determined by an α-effect, or the presence of a lone electron pair on the adjacent heteroatom (*98*). The weak basicity of an aminooxy group allows for its chemoselective conjugation in the presence of protonated amino groups at low pH. Here we will discuss methods for incorporation of an aminooxy group into oligonucleotides or conjugated molecules.

Synthesis of Oligonucleotides Containing an Aminooxy Group and Their Conjugation with Aldehydes. Incorporation of an aminooxy group into oligonucleotides requires synthesis of the appropriately blocked nucleoside or non-nucleoside phosphoramidite. The simplest way to incorporate an aminooxy group is through nucleophilic displacement of a primary hydroxylic group by *N*-hydroxyphthalimide under conditions of Mitsunobu reaction (*99*) or through alkylation of *N*-hydroxyphthalimide by aliphatic bromides/iodides or alkane/arene sulfonates (Scheme 11).

An approach based on a Mitsunobu reaction was applied by Lönnberg, Manoharan and others (*100*−*103*) (Scheme 12). Such a scheme seems to be preferable, since hydroxy derivatives of nucleosides are more available synthetically than the corresponding halo or sulfonate derivatives.

Some authors used nucleophilic substitution of an alkyl bromide for synthesis of a 5′-aminooxy-modifier (*104*, *105*) (Scheme 13). Easily accessible 6-bromohexanol was used as the starting material. However, a Mitsunobu reaction with *N*-hydroxyphthalimide proceeds smoothly only in the case of a primary hydroxyl group. Beigelman et al. (*106*) demonstrated that the yield of a 2′-substitution for a 5′,3′-blocked uridine is about 10%, while nucleophilic substitution of 2′-triflate derivatives of blocked arabinonucleosides by *N*-hydroxyphthalimide/DBU leads to 90% yields (Scheme 14).

An alternative approach was developed by Trevisiol et al. (*107*). A presynthesized aminooxy derivative was coupled to base-modified nucleosides either by a Sonogashira−Heck reaction or by acylation (Scheme 15).

Scheme 14. Synthesis of Blocked 2′-Aminooxynucleosides by Nucleophilic Subsitution

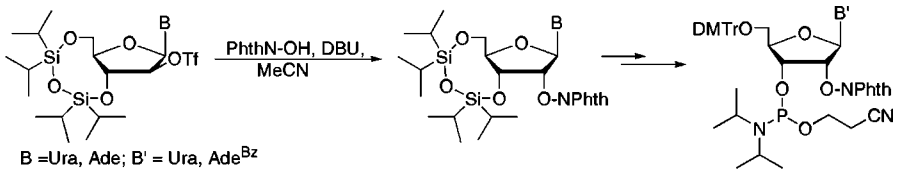

Scheme 15. Synthesis of Ribonucleoside 5′-Triphosphates Containing an Aminooxy Group in the Heterocyclic Base

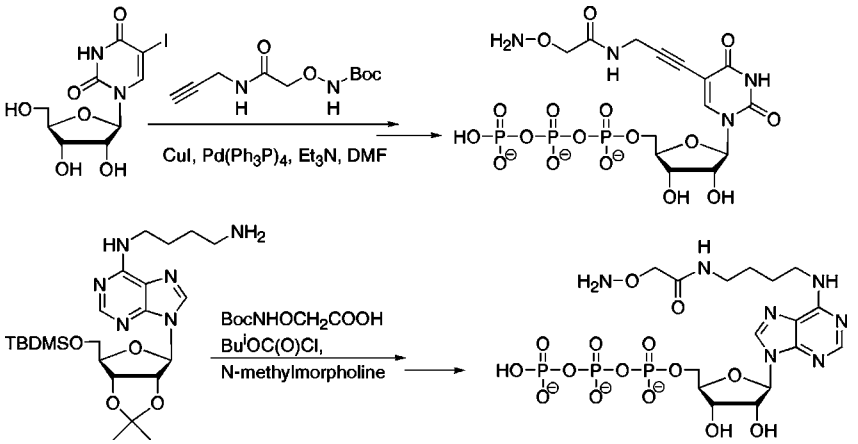

Scheme 16. Synthesis of Quinoline Phosphoramidite Derivative with Blocked Aminooxy Group

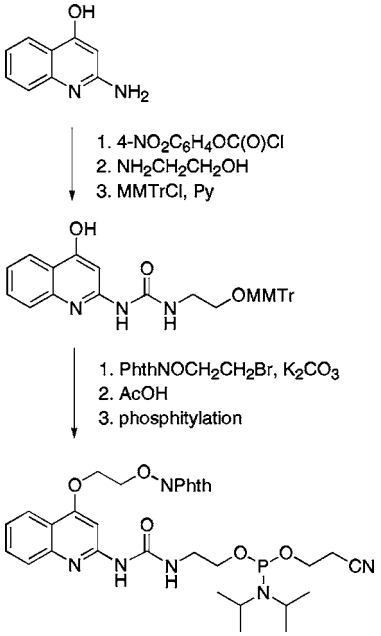

Commercial availability of *N*-Boc-aminooxyacetic acid makes this approach rather straightforward. The nucleosides were then converted into their corresponding 5′-triphosphates and introduced into RNA enzymatically.

A similar approach was applied by Miller et al. (*108*, *109*), who synthesized a quinoline-based phosphoramidite, which contains a blocked aminooxy group (Scheme 16) that has been introduced via a presynthesized alkyl bromide.

Although a phthaloyl protecting group is compatible with automated phosphoramidite oligonucleotide synthesis, substituted trityl groups have been used as an alternative in the synthesis of 5′-aminooxy oligonucleotides (Scheme 17). Deprotection of the 5′-phthaloyl group during ammonolysis makes reverse-phase (RP)-HPLC purification difficult and leads to side reactions with traces of aldehydes and ketones present in solution (*110*). A number of authors demonstrated formation of unidentified compounds under standard ammonolytic conditions (*101*, *108*). Preliminary deblocking of an aminooxy group by hydrazinolysis or ethylenediamine treatment is thus required. Cebon et al. (*104*) compared phthaloyl and trityl protecting groups for 5′-modification and demonstrated that detritylation was partial and depurination was observed under harsher conditions. N-Tritylated derivatives were obtained from *N*-phthalimido derivatives. Later, Defrancq and Lhomme (*105*) successfully used *N*-tritylaminooxy phosphoramidite for the 5′-modification. No depurination was observed under deprotection conditions (80% AcOH, 7 h). Despite the contradicting data, most authors prefer to use the phthaloyl group for aminooxy group protection.

Forget et al. (*111*) synthesized oligonucleotide−peptide conjugates via oxime formation. In this case an aminooxy group was introduced into the oligonucleotide and an aldehyde into the peptide or vice versa. As we emphasized earlier, an aminooxy group easily reacts with traces of aldehydes or ketones in buffers, so having the aminooxy group on the peptide seems to be preferable, due to the availability of peptides in larger quantities than oligonucleotides. In general, an excess of the aminooxy component is needed during oxime synthesis, since even distilled water contains traces of aldehydes (*112*, *113*). However, oligonucleotides containing an aminooxy group have been used successfully for conjugation with a number of carbonyl compounds including a fluorescein derivative (*105*) and peptides (*104*, *108*, *109*) (Scheme 18).

Scheme 18. Carbonyl Compounds Used for Conjugation with Aminooxy Oligonucleotides

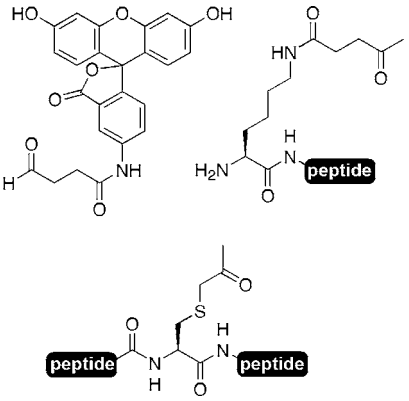

More recently, Edupuganti et al. (*114*) have used intramolecular oxime formation for cyclization of an oligonucleotide (Scheme 19). An aldehyde group was incorporated on the 3′-end and an aminooxy group on the 5′-end. Cyclization occurs spontaneously under mild acidic conditions. It should be noted that formation of concatemers was not observed.

Lönnberg et al. (*101*, *102*) developed a solid-phase conjugation method by oxime formation of immobilized aminooxy oligonucleotides (Scheme 20). The phthaloyl protecting group was selectively removed by hydrazinium acetate followed by conjugation with retinal or 1-pyrenecarboxaldehyde. The resultant oximes were claimed to be stable during ammonolysis. Later the same methodology was applied for multiple conjugations with a mannose derivative (*102*).

Oligonucleotides bearing an aminooxy group at the 5′-end were used for immobilization on aldehyde-modified glass or gold surfaces (*101*, *115*, *116*) (Scheme 21). This method provides higher density and homogeneity of the

Scheme 17. Synthesis of N-Tritylated 5′-Aminooxy Phosphoramidite Series

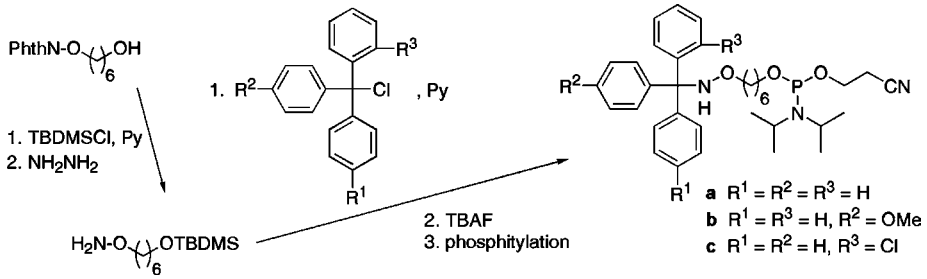

Scheme 19. Synthesis of Cyclooligonucleotides by Oxime Formation

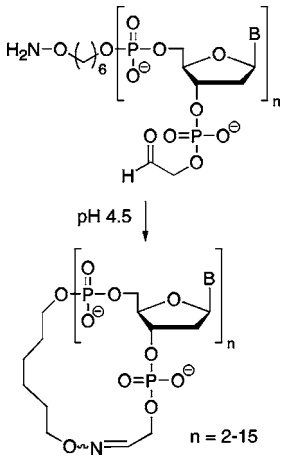

oligonucleotide array than traditional reductive amination (*117*) or de novo synthesis (*48*).

Conjugation of *O*-Alkylhydroxylamines with Aldehyde Oligonucleotides. This method was first used for qualitative or quantitative detection of abasic sites in DNA (Scheme 22). This DNA damage is a result of spontaneous acidic depurination or incomplete enzymatic repair (*118*). ^{14}C-Methoxyamine (*119*, *120*), aminooxyacetic acid (*121*), derivatives of 4-nitrophenol (*122*, *123*), biotin (*124*), or a number of dyes (*125*−*129*) bearing an aminooxy group were used in the assay. The reaction was usually carried out under neutral conditions to avoid additional depurination. Chakrabarti et al. (*130*, *131*) used a FRET technique to detect abasic sites proximal to each other. Also a synthetic AP site was used by Ito and Rokita (*132*−*134*) to attach an aminooxy derivative of *N*,*N*,*N*′,*N*′-tetramethyl-1,5-diaminonaphthalene. The conjugate was used for photoinduced cleavage of complementary DNA containing 5-bromo-2′-deoxyuridine. This assay was developed to screen aromatic amines for their ability to initiate charge transfer by reductive electron donation.

Later, aminooxy derivatives of a dansyl group or rhodamine were conjugated to aldehyde oligonucleotides

Scheme 20. Solid-Phase Oxime Conjugation of Immobilized Aminooxy Oligonucleotides

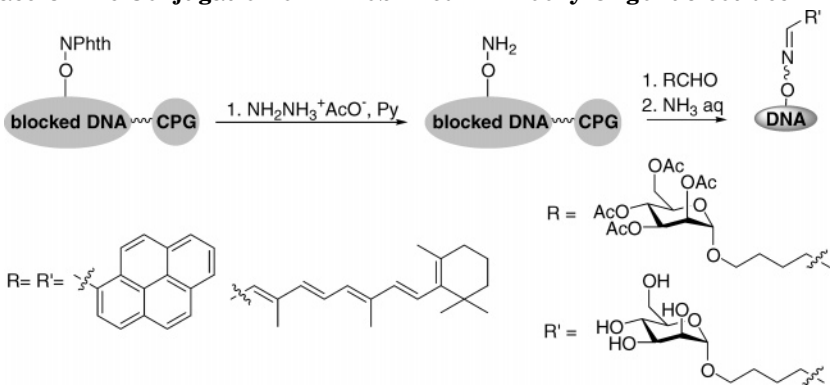

Scheme 21. Immobilization of Aminooxy Oligonucleotides on Aldehyde-Coated Surface

Scheme 22. Aminooxy Reagents for Modification of Abasic Sites

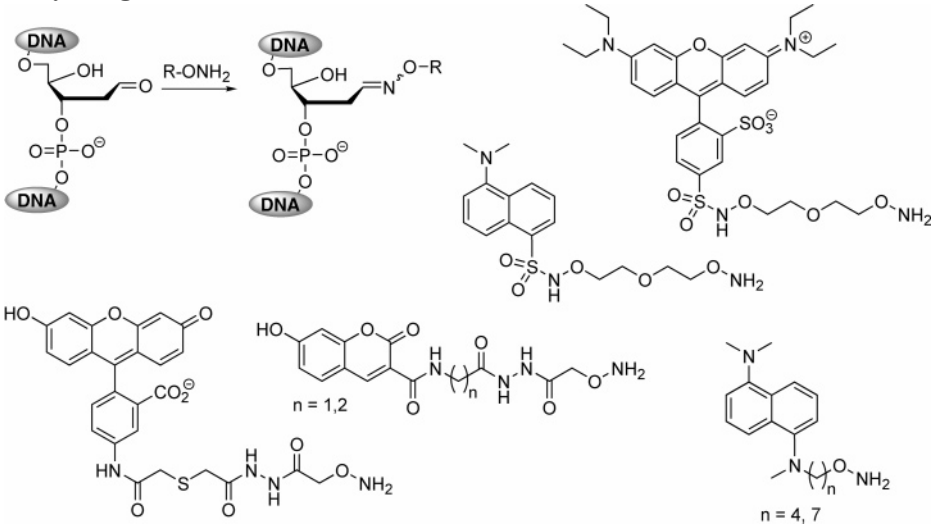

Scheme 23. Aldehyde Oligonucleotides Used for Oxime Formation

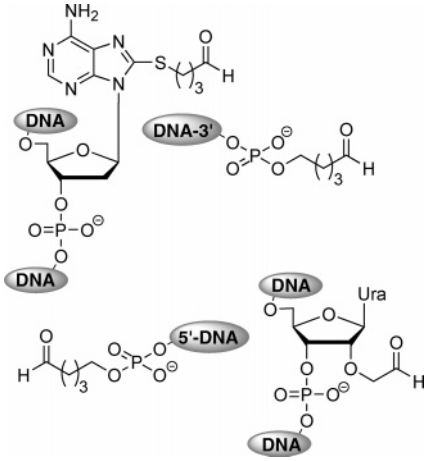

Scheme 24. Aminooxy Compounds Used for Oxime Formation

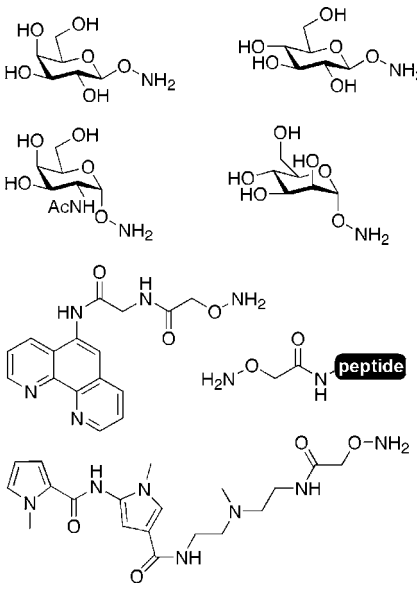

(Scheme 23) (*135*−*137*). 2D ^{1}H NMR spectra demonstrated that the oxime formed is a mixture of isomers (*Z*:*E* = 1:1) (*136*). 2′-Aldehydo oligonucleotides were applied to conjugation with peptides (*138*). Multiple incorporation of the 2′-modified nucleotides has been used to attach several peptide moieties. The same approach has been applied to conjugation with aminooxy carbohydrates (*136*, *139*), 1,10-phenanthroline (*140*), distamycin (*141*), and peptides (*111*, *138*) (Scheme 24).

Very recently Edupuganti et al. (*142*) developed a method for sequential conjugation of two different molecules (e.g. two peptides or fluorescent derivatives) to a modified oligonucleotide via an oxime linkage (Scheme 25). 3′,5′-Dialdehyde (Scheme 25A) or 3′-aldehyde, 5′-aminooxy (Scheme 25B) oligonucleotides were used for double conjugation.

A number of authors used ketones as the electrophilic components. Both keto group-modified oligonucleotides (*143*) and peptides (*104*) have been applied. In both cases the yields were good, but the reaction time was increased to 12−48 h compared to 1−3 h for aldehydes. Trevisiol et al. (*143*) used a number of the 5′-triphosphates (Scheme 26) for synthesis of modified RNAs followed by multiple labeling with an aminooxy fluorescein derivative.

Dey and Sheppard also used a similar approach (*144*). A wide range of compounds has been conjugated both to single- and double-stranded DNA (Scheme 27).

An oxime conjugation was used for synthesis of PNA−peptide conjugates (*145*). Ketone bis-PNA was conjugated with peptides bearing an aminooxy group either at the *N*-terminus or coupled to the ϵ-amino group of a lysine residue (Scheme 28). The reaction was carried out for 12 h with isolated yields for the conjugates of 15−20%.

CONJUGATION VIA HYDRAZONE FORMATION

Hydrazone formation seems to be the oldest method for coupling in biomolecular chemistry. The reaction of a hydrazino or hydrazido group with an aldehyde leads to hydrazone formation. Usually hydrazones are rather stable but in some cases reduction to hydrazine is needed. Sayer et al. (*146*) studied the rate of hydrazone hydrolysis as a function of the R^1 substituent (Scheme 29). It was demonstrated that an increase in electronegativity of R^1 leads to a decrease in hydrazone stability under acidic and basic conditions. Thus the stability of the hydrazone decreases in the order: aromatic hydrazine > aliphatic hydrazine > hydrazides.

Scheme 25. Double Conjugation to 3′,5′-Bis-Modified Oligonucleotides

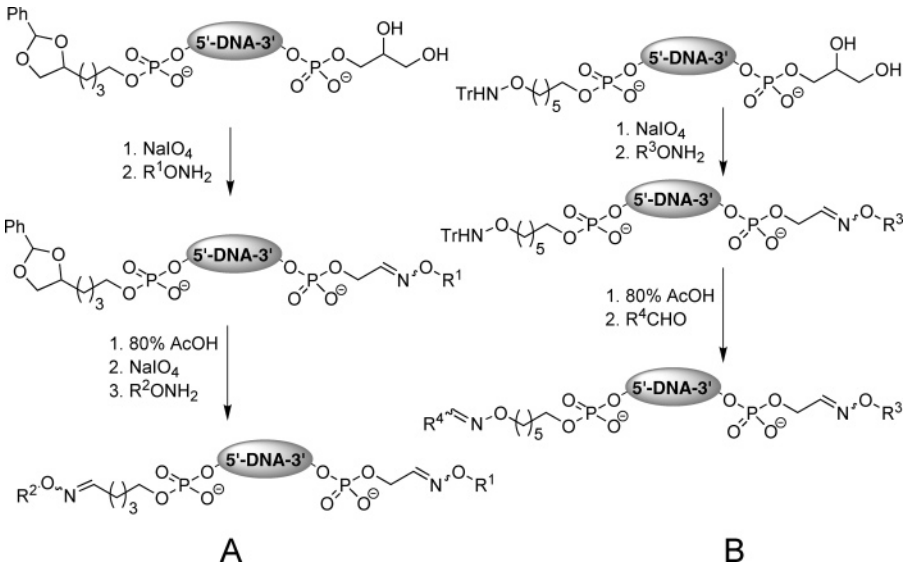

Scheme 26. 5′-Triphosphates of Ketonucleosides Used for Incorporation into RNA and the Aminooxy Fluorescein Derivative for Subsequent Labeling via Oxime Formation

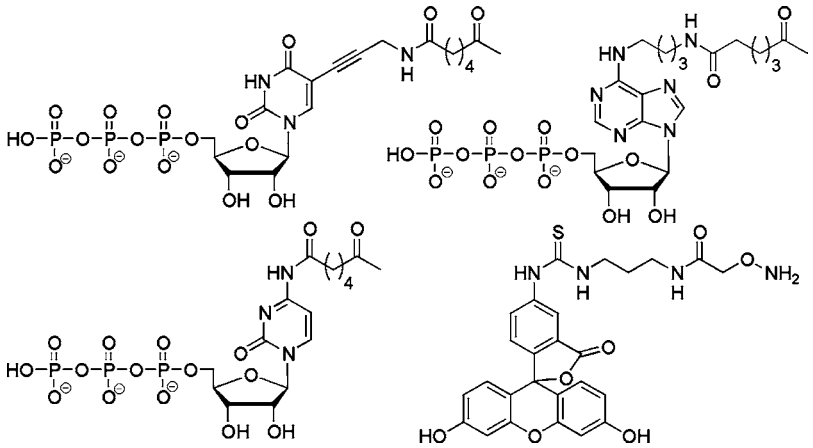

Scheme 27. Keto Oligonucleotides and Aminooxy Compounds Used for Conjugation (*144*)

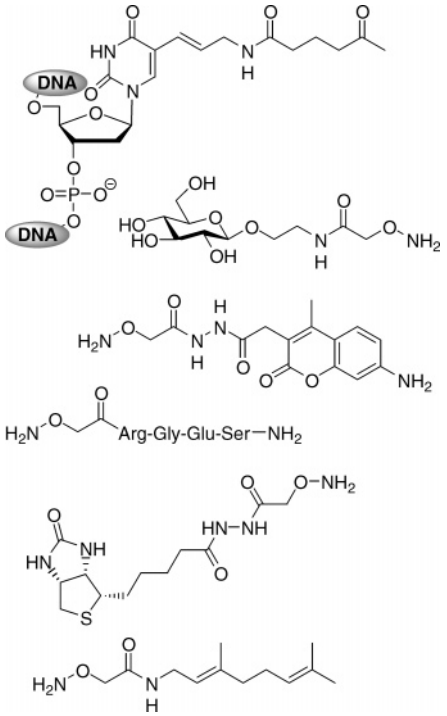

Scheme 28. Conjugation of a Keto Bis-PNA with an Aminooxypeptide

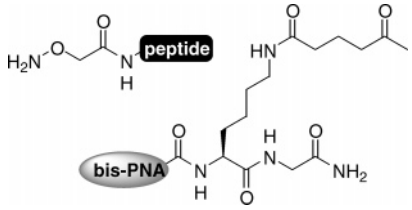

Since hydrazino/hydrazido group may be incorporated into either an oligonucleotide or a ligand, this section is divided into two parts covering both possible cases.

Synthesis of Hydrazido Oligonucleotides and Their Conjugation with Aldehydes. Most of the oligonucleotides containing hydrazide groups have been synthesized by hydrazinolysis of ester groups in nucleosides or oligonucleotides during a hydrazine-mediated deblocking reaction. In 1989 Ghosh et al. (*147*) synthesized a 5′-hydrazide derivative by coupling carbohydrazide to an activated 5′-phosphate group of an oligonucleotide

Scheme 29. Hydrolysis of a Hydrazone Linkage

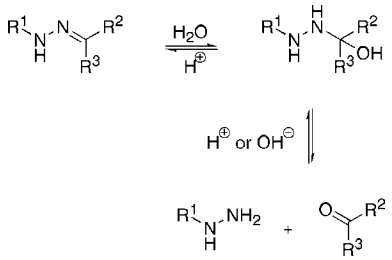

(Scheme 30). These oligonucleotides have been used to conjugate 2,4-dinitrobenzaldehyde hapten and aldehyde-modified alkaline phosphatase. In the latter case, several oligonucleotides were attached to the enzyme.

Oshevski (*148*) described synthesis of a 3′-hydrazide by phosphoramidate formation. The oligonucleotide containing a 4-aminomethylbenzhydrazide residue was ligated to a 5′-aldehyde oligonucleotide on a DNA template (Scheme 31). Usually the yields did not exceed 20% under optimal conditions, and no ligation was observed in the case of mismatches in a DNA template close to the ligation point. The system was proposed for SNP detection.

Raddatz et al. (*149*) synthesized a series of blocked hydrazide phosphoramidites by hydrazinolysis of esters followed by phosphitylation (Scheme 32). Also several phosphoramidites containing ester groups were prepared, and hydrazide formation was carried out during oligonucleotide deblocking step. Some of the derivatives carried two or four hydrazide moieties. The hydrazide oligonucleotides were conjugated to a peptide and used for DNA array preparation. It was shown that effectiveness of immobilization increased as the number of hydrazide groups per oligonucleotide increased.

Later von Kiedrowski et al. (*150*) prepared a branched oligonucleotide with a defined structure by hydrazone formation with 1,3,5-benzenetricarboxaldehyde on a branched DNA template (Scheme 33). Sodium cyanoborohydride reduction slightly increased the yield. No reaction occurred without template.

Zubin et al. (*151*) attempted a synthesis of oligonucleotides containing a hydrazide group at the 2′-position of a sugar residue via a blocked uridine 2′-hydrazido phosphoramidite (Scheme 34). However, the authors reported only a conversion of the hydrazide group into the amide during ammonia treatment, even under milder conditions. This may be ascribed to the more electrophilic nature of the hydrazide.

Scheme 30. Oligonucleotides Containing 5′-Carbohydrazide and Their Conjugation to Aldehydes

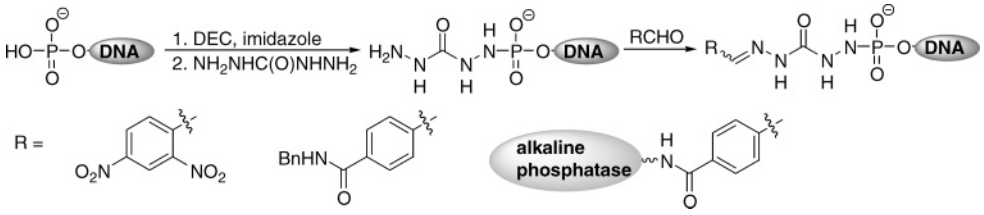

Scheme 31. Template-Directed Ligation of the 3′-Hydrazide and 5′-Aldehyde Oligonucleotides

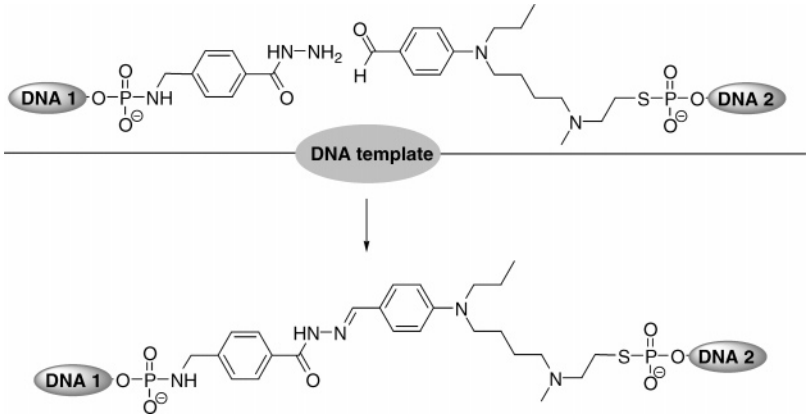

Scheme 32. Phosphoramidite Building Blocks Used for Synthesis of Hydrazide Oligonucleotides. Generation of a Hydrazide Group in the Modified Oligonucleotides

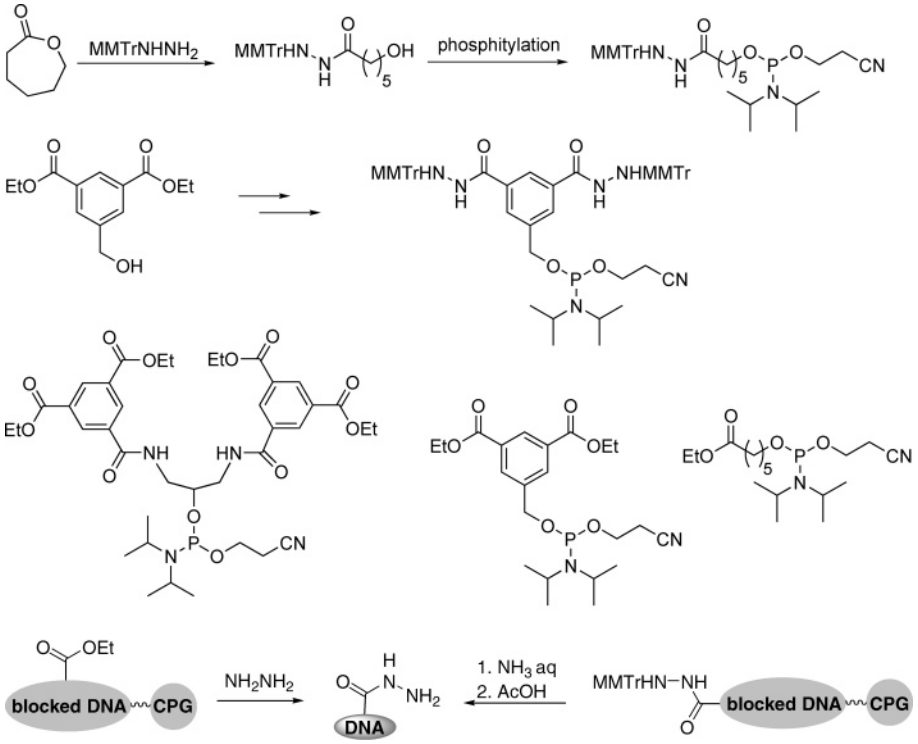

Gao and Orgel (*152*) used hydrazone formation for the synthesis of a rigidly cross-linked base pair within an oligonucleotide sequence (Scheme 35). Introduction of a hydrazino group into the 4-position of a cytosine residue by transamination in the presence of bisulfite was followed by conjugation with the modified nucleoside containing a malondialdehyde group. Heterocyclic bases of the cross-linked pair are coplanar, and the geometry of the pair resembles that of native double-stranded DNA. These properties allow the oligomerization of activated nucleotides on a template cross-linked to the starting nucleoside. The product of the oligomerization reaction could be detached by an excess of hydrazine. Hydrazone reduction leads to a significant decrease in the yield of the ligation product.

Zhao et al. (*153*, *154*) demonstrated the application of commercially available 5′- and 3′-aldehydo or hydrazino oligonucleotides for DNA ligation, conjugation to modified antibodies or for immobilization on a modified glass surface (Scheme 36). This method for oligonucleotide immobilization was further used by Zhong et al. (*155*).

The commercial availability (Solulink, San Diego, CA) of *N*-hydroxysuccinimide esters of 6-hydrazinonicotinic acid and 4-formylbenzoic acid and the corresponding

Scheme 33. Ligation of Hydrazide Oligonucleotides with 1,3,5-Benzenetricarboxaldehyde on a Branched Tris-Oligonucleotide Template

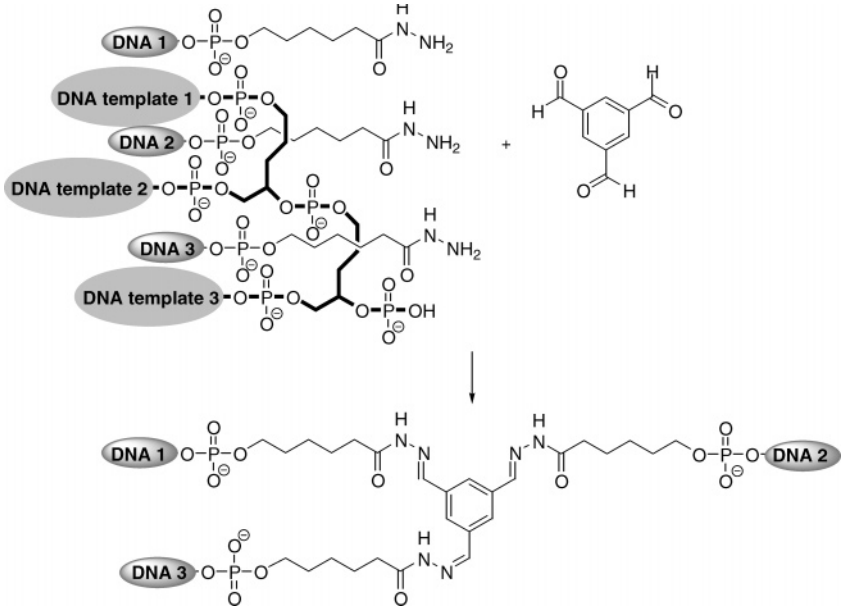

Scheme 34. An Attempt To Prepare the 2′-Hydrazide Oligonucleotides via a Presynthesized 2′-Hydrazide Synthone

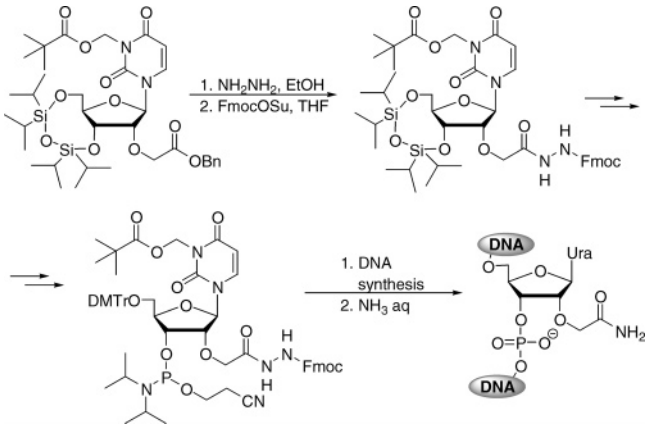

phosphoramidites that can be used for incorporation of an aldehyde or hydrazine group into oligonucleotides and other biomolecules may add significantly to the popularity of hydrazone coupling in nucleic acid chemistry.

Conjugation of Aldehyde Oligonucleotides with Hydrazines and Hydrazides. A number of publications describe conjugation of aldehyde oligonucleotides to hydrazines and hydrazides. Kremsky et al. (*156*) biotinylated a 5′-aldehyde oligonucleotide by hydrazone formation with biotin hydrazide. Later Sonveaux et al. (*59*, *60*) used the same scheme for oligonucleotides containing an aldehyde group in the middle of a sequence. In both cases the conversion was quantitative under reducing conditions. Melnyk et al. (*157*) used 5′-glyoxylyl oligonucleotides for conjugation with a hydrazino peptide (Scheme 37). A 5′-amino oligonucleotide was acylated by *O*,*O*′-diacetyl tartaric anhydride on solid phase. A glyoxylyl group was generated by periodate oxidation after oligonucleotide deprotection. Very recently a different scheme was used for the synthesis of 5′-glyoxylyl oligonucleotides by Defrancq et al. (*158*). An O,N-blocked serine residue was introduced into oligonucleotides by use of a phosphoramidite during standard DNA synthesis, followed by ammonolysis and periodate oxidation (Scheme 37). The presence of an electron-withdrawing amide group placed α to the aldehyde increases its reactivity and the stability of the resultant hydrazone. It was shown that ca. 50% conversion occurs in a few seconds and the reaction was complete in 15 min (*157*). However, the stability of the aldoxime linkage

Scheme 35. Conjugation of *N*-Aminocytosine Oligonucleotide with Malondialdehyde Nucleoside

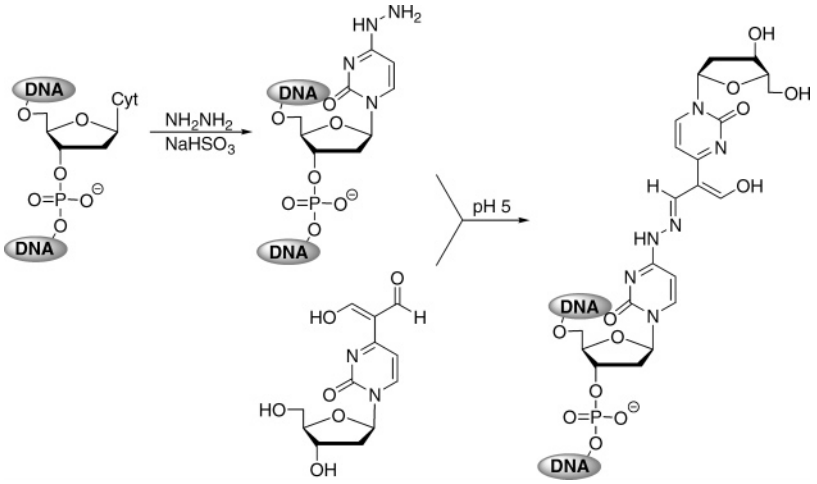

Scheme 36. Conjugation Reactions of Hydrazino and Aldehydo Oligonucleotides Prepared from a Commercially Available Set of Reagents

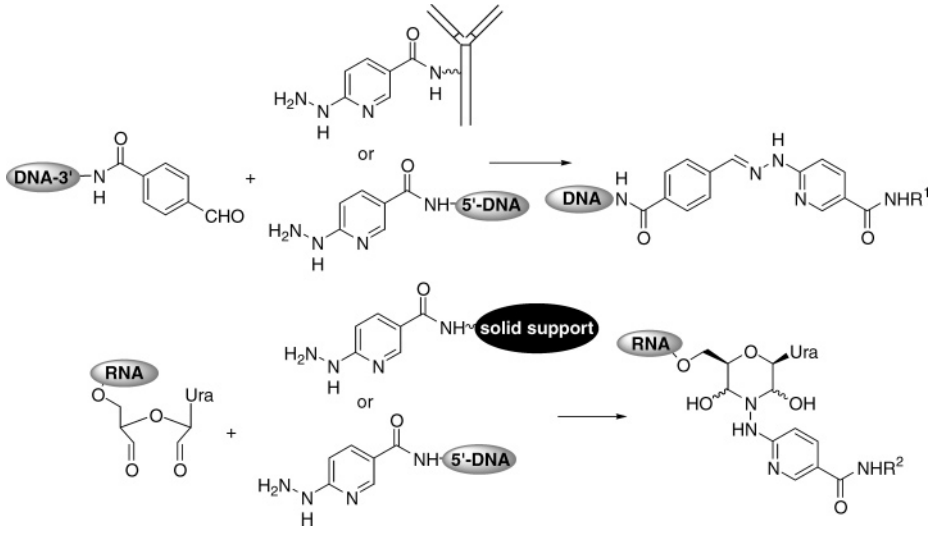

Scheme 37. Synthesis of 5′-Glyoxylyl Oligonucleotides and Conjugation with N-Terminal Hydrazino and Aminooxy Peptides

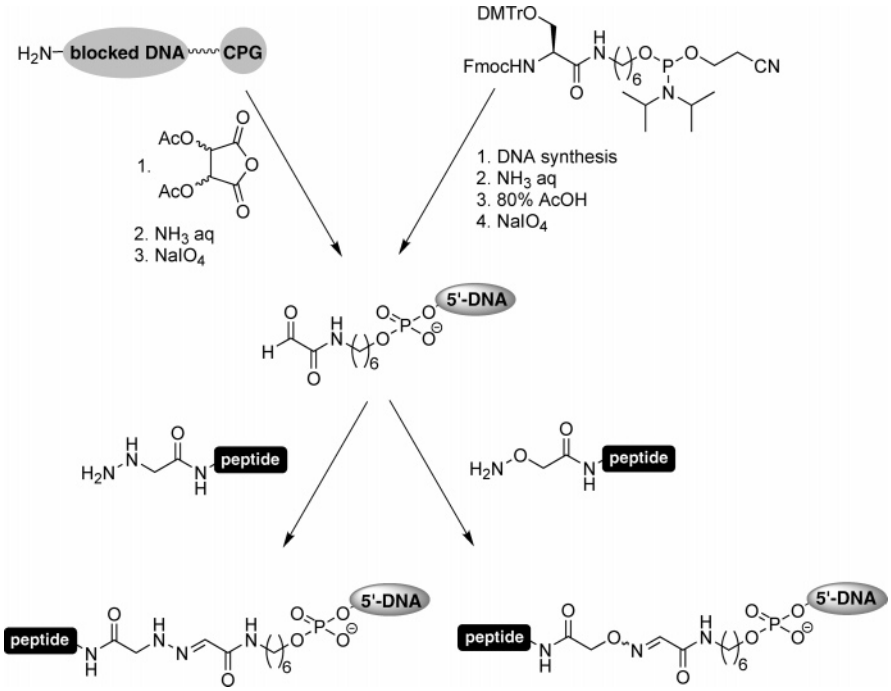

is lower at basic pH compared to other oxime linkages (*158*).

Incorporation of an aldehyde group onto the 5′-end of an oligonucleotide limits the number and position of conjugated moieties. An aldehyde group in the 2′-position of ribose provides an opportunity for multiple conjugation of hydrazides and hydrazines, as has been shown by Zatsepin et al. (*138*). However, the hydrazones formed were prone to hydrolysis in the neutral and basic pH range, and borohydride reduction was required (Scheme 38). More recently, oligonucleotide-containing aldehyde groups in the 2′-position of one or more arabinouridine residues have been prepared (*159*). It was demonstrated that a hydrazone formed by an aromatic hydrazine, 9-hydrazinoacridine, is more stable in comparison to hydrazones of aliphatic hydrazides and does not need reduction in order to be purified by HPLC.

Tetramethylrhodamine (TAMRA) hydrazine (Scheme 39) was used for DNA or RNA labeling through an AP site or through a 3′-periodate-oxidized ribose (*160*), respectively, as described previously for aminooxy derivatives. Labeling was carried out under acidic pH followed by sodium cyanoborohydride reduction. Later Manoharan et al. (*54*) also used an AP site to incorporate hydrazide derivatives of biotin, pyrene, and fluorescein. These authors generated an AP site enzymatically by treatment of DNA with uracil-DNA glycosylase.

Aldehyde oligonucleotides have been used many times for immobilization on hydrazide-modified surfaces. Kremsky et al. (*156*) and Schluep and Cooney (*161*, *162*) used aldehyde oligonucleotides for immobilization on hydrazide-modified latex or glass, respectively (Scheme 40). Hydrazone reduction led to an increase in the extent of immobilization.

Later glyoxylyl (*163*) and benzaldehyde (*164*) oligonucleotides were used for immobilization on a semicarbazide-modified glass (Scheme 41). Semicarbazide glass was synthesized either by hydrazine addition to the

Scheme 38. Synthesis of Oligonucleotide−Peptide Conjugates via Hydrazone Formation Followed by Reduction

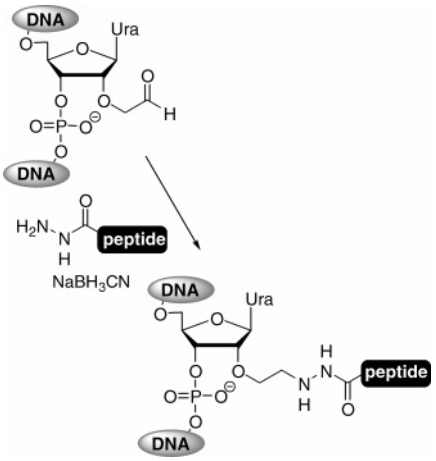

Scheme 39. TAMRA Hydrazine

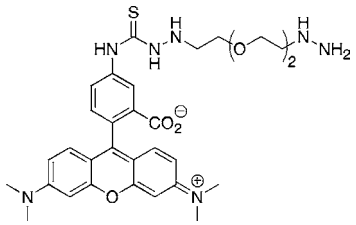

Scheme 40. Immobilization of the 5′-Aldehyde Oligonucleotides on Hydrazide Surfaces

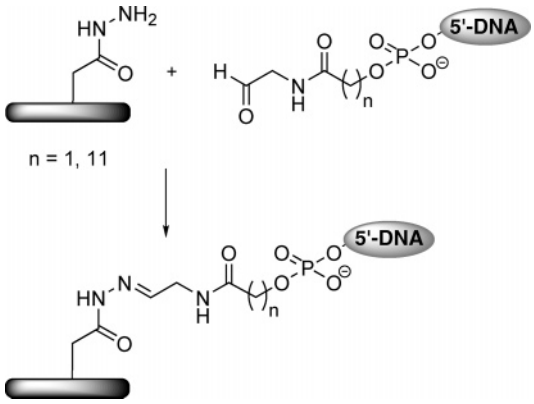

isocyanate glass (*163*) or via a direct silylation by the silane containing a blocked (*163*) or even a free (*164*) semicarbazide group. The first approach gave better homogeneity and higher density of the array. The hydrazones were rather stable over a wide pH range, but borohydride reduction again increased the shelf life of the DNA chips obtained.

CONJUGATION VIA REACTIONS OF ALDEHYDE OLIGONUCLEOTIDES WITH MISCELLANEOUS NUCLEOPHILES

As it was discussed above, reaction of a side-chain amino group in amino acids with aldehydes leads to an imine formation. However in the case of cysteine, the reaction is followed by intramolecular addition of the thiol group with concomitant thiazolidine formation (Scheme 42). This approach was used to synthesize a number of oligonucleotide−peptide conjugates (*111*, *138*, *141*). An aldehyde group was introduced onto the 5′-end of an oligonucleotide or into the 2′-position of a sugar moiety.

Zatsepin et al. (*165*) introduced a 2,3-diaminopropoxy group into the 2′-position of a sugar moiety and demonstrated a model conjugation with benzaldehyde via imidazolidine formation (Scheme 43). However, the imidazolidine is less stable than a thiazolidine both in basic and acidic conditions, so the application of the former has less general utility than that of the latter.

Liu et al. published a number of inspiring contributions (*82*−*84*, *166*, *167*) on use of DNA as a template for organic reactions. These authors explored Wittig reaction, nitroaldol condensation (Henry reaction), or oxazolidine formation (Scheme 44). The reactions were carried out in aqueous medium. The driving force seems to be a spatial proximity of the reactive groups on oligonucleotides. The groups were incorporated at adjacent positions on complementary oligonucleotides or in contiguous oligonucleotides bound to a DNA template. It is evident that these methods would allow for adaptation of many types of reaction from classical organic chemistry for modification of nucleic acids.

CONCLUSIONS

Analysis of the literature demonstrates that the most widely used approach that involves carbonyl group addition−elimination reactions for synthesis of oligonucleotide conjugates is still Schiff base (imine) formation followed by borohydride reduction. Usually the yields are not quantitative and a number of side reactions occur, but the accessibility of starting materials makes this approach rather popular. The method is especially effective for conjugation or immobilization of native DNA and RNA. However, in the case of chemically synthesized oligonucleotides the oxime and hydrazone formation are

Scheme 41. Synthesis of the Semicarbazide Glass and Immobilization of the 5′-Benzaldehyde or Glyoxylyl Oligonucleotides on It

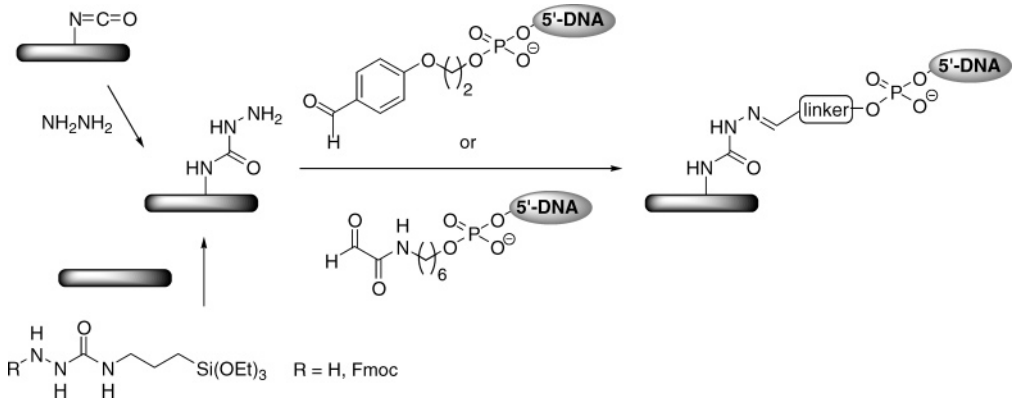

Scheme 42. Conjugation of Aldehyde Oligonucleotides with Cysteine Derivatives via Thiazolidine Formation

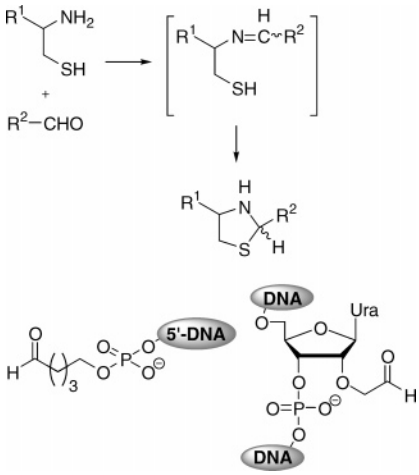

Scheme 43. Conjugation of the 2′-(2,3-Diaminopropoxy) Oligonucleotides with Benzaldehyde

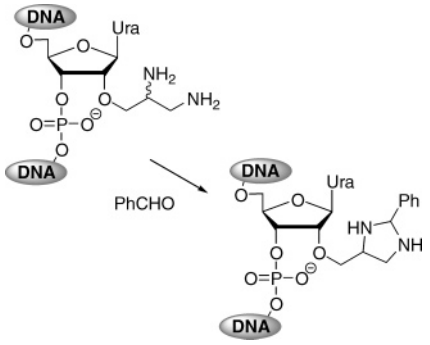

evident alternatives. As emphasized above, in most cases the compounds are stable enough and no reduction is needed. Only a small excess of the nucleophilic component is required during oxime or hydrazone synthesis, which makes the approach cost-effective. Side-reactions of *O*-alkyl hydroxylamines with traces of aldehydes and ketones in water are avoided by use of a small excess of aminooxy compound. Due to such considerations, the incorporation of an aldehyde group into the oligonucleotide chain seems to be the best route, because the molecules to be conjugated can normally be used in excess. Aminooxy oligonucleotides are more attractive for immobilization on aldehyde-coated surfaces, since the density of the array is higher compared to reductive amination. Aromatic hydrazines seem to be a good choice for hydrazone conjugation, since these form the most stable linkages in comparison to aliphatic hydrazines or hydrazides. However, in some cases a borohydride reduction is mandatory, e.g. when basic treatment is involved. Ketones are generally a poorer alternative to aldehydes. Although ketones are more stable to oxidants and milder reductants, and keto-derivatives of the oligonucleotides can be synthesized more easily, the lower reactivity of ketones makes their conjugation with amino compounds less practical. The possibility of conjugation with double-stranded nucleic acids could find broad application in the case of siRNA modification.

In this review we highlighted the most significant contributions published to date in the field of application of addition−elimination reactions of a carbonyl group with nitrogen nucleophiles for nucleic acid chemistry. It is evident that there are now much more numerous

Scheme 44. DNA Ligation via Wittig or Henry Reaction or Oxazolidine Formation

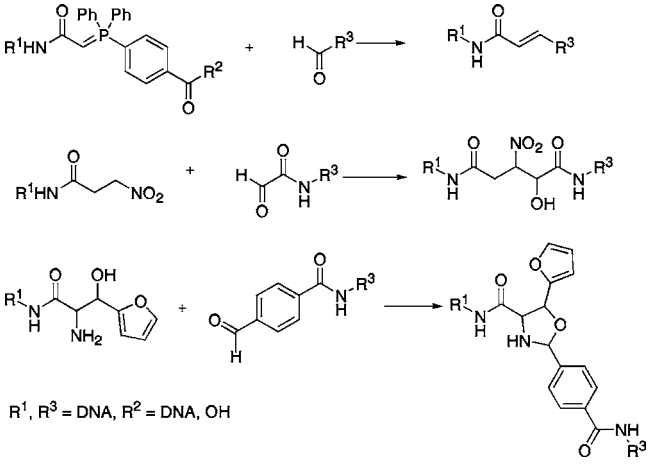

choices either in reagents or in chemical methods available to prepare nucleic acids conjugates that are purposefully constructed to meet the requirements of any particular biological application.

ACKNOWLEDGMENT

The authors thank Drs. A. Yu. Tomashevsky, University of Virginia, Charlottesville, VA, and A. Zamyatnin, Swedish University of Agricultural Sciences, Uppsala, Sweden, for their valuable assistance in preparation of this review for publication. The review has been written within the framework of the Program "Universities of Russia", Project No. UR.05.02.547, and with the financial support of the Wellcome Trust CRIG 069419 and the Russian Foundation for Basic Research Project 03-04-48957.

LITERATURE CITED

(1) Kricka, L. J. *Nonisotopic DNA Probe Technique*, Academic Press, New York, 1992.

(2) Davies, M. J., Shah, A., and Bruce, I. J. (2000) Synthesis of fluorescently labelled oligonucleotides and nucleic acids. *Chem. Soc. Rev. 29*, 97−107.

(3) Drummond, T. G., Hill, M. G., and Barton, J. K. (2003) Electrochemical DNA sensors. *Nat. Biotechnol. 21*, 1192−1199.

(4) Zatsepin, T. S., Andreev, S. Yu., Hianik, T., and Oretskaya, T. S. (2003) Ferrocene-containing nucleic acids. Synthesis and electrochemical properties. *Russ. Chem. Rev. 72*, 537−554.

(5) Edwards, T. E., Okonogi, T. M., Robinson, B. H., and Sigurdsson, S. T. (2001) Site-specific incorporation of nitroxide spin-labels into internal sites of the TAR RNA.; structure-dependent dynamics of RNA by EPR spectroscopy. *J. Am. Chem. Soc. 123*, 1527−1528.

(6) Hester, J. D., Bobst, E. V., Kryak, D. D., and Bobst, A. M. (2002) Identification of a single genome by electron paramagnetic resonance (EPR) with nitroxide−labeled oligonucleotide probes. *Free Radic. Res. 36*, 491−498.

(7) Schiemann, O., Piton, N., Mu, Y., Stock, G., Engels, J. W., and Prisner, T. F. (2004) A PELDOR-based nanometer distance ruler for oligonucleotides. *J. Am. Chem. Soc. 126*, 5722−5729.

(8) Hoshika, S., Ueno, Y., and Matsuda, A. (2003) Nucleosides and nucleotides. 218. Alternate-strand triple-helix formation by the 3′-3′-linked oligodeoxynucleotides using a purine motif. *Bioconjugate Chem. 14*, 607−613.

(9) Lukhtanov, E. A., Kutyavin, I. V., Gamper, H. B., and Meyer, R. B., Jr. (1995) Oligodeoxyribonucleotides with conjugated dihydropyrroloindole oligopeptides: preparation and hybridization properties. *Bioconjugate Chem. 6*, 418−426.

(10) Levina, A. S., Metelev, V. G., Cohen, A. S., and Zamecnik, P. C. (1996) Conjugates of minor groove DNA binders with oligodeoxynucleotides: synthesis and properties. *Antisense Nucleic Acid Drug Dev. 6*, 75−85.

(11) Gait, M. J. (2003) Peptide-mediated cellular delivery of antisense oligonucleotides and their analogues. *Cell Mol. Life Sci. 60*, 844−853.

(12) Moulton, H. M., and Moulton, J. D. (2003) Peptide-assisted delivery of steric-blocking antisense oligomers. *Curr. Opin. Mol. Ther. 5*, 123−132.

(13) Zatsepin, T. S., Turner, J. J., Oretskaya, T. S., Gait, M. J. (2005) Conjugates of oligonucleotides and analogues with cell penetrating peptides as gene silencing agents. *Curr. Pharm. Des.*, in press.

(14) Manoharan, M. (2002) Oligonucleotide conjugates as potential antisense drugs with improved uptake, biodistribution, targeted delivery, and mechanism of action. *Antisense Nucleic Acid Drug Dev. 12*, 103−128.

(15) Zatsepin, T. S., and Oretskaya, T. S. (2004) Synthesis and applications of oligonucleotide-carbohydrate conjugates. *Chem. Biodiversity 1*, 1401−1417.

(16) Beaucage, S. L., and Iyer, R. P. (1993) The functionalization of oligonucleotides via phosphoramidite derivatives. *Tetrahedron 49*, 1925−1963.

(17) Venkatesan, N., Kim, S. J., and Kim, B. H. (2003) Novel phosphoramidite building blocks in synthesis and applications toward modified oligonucleotides. *Curr. Med. Chem. 10*, 1973−1991.

(18) Virta, P., Katajisto, J., Niittymäki, T., and Lönnberg, H. (2003) Solid-supported synthesis of oligomeric bioconjugates. *Tetrahedron 59*, 5137−5174.

(19) Verma, S., Jäger, S., Thum, O., and Famulok, M. (2003) Functional tuning of nucleic acids by chemical modifications: Tailored oligonucleotides as drugs, devices, and diagnostics. *Chem. Rec. 3*, 51−60.

(20) Dolinnaya, N. G., and Shabarova, Z. A. (1995) Chemical reaction in double helical nucleic acids: modelling the action of DNA ligases. *Sov. Sci. Rev. D*, *Physicochem. Biol. 13*, 1−49.

(21) Leitzel, J. C., and Lynn, D. G. (2001) Template-directed ligation: From DNA towards different versatile templates. *Chem. Rec. 1*, 53−62.

(22) Eaton, B. E., and Pieken, W. A. (1995) Ribonucleosides and RNA. *Annu. Rev. Biochem.*, *64*, 837−863.

(23) Maier, M. A., Barber−Peoc′h, I., and Manoharan, M. (2002) Postsynthetic guanidilation of primary amino groups in the minor and major grooves of oligonucleotides. *Tetrahedron Lett.* 43, 7613−7616.

(24) Kachalova, A. V., Zubin, E. M., Zatsepin, T. S., Agapkina, Yu. V., Ivanova, Yu. M., Stetsenko, D. A., Gait, M. J., and Oretskaya, T. S. (2004) Chemoselective Ligation of Oligonucleotides Modified with Reactive Groups. In *Innovation & Perspectives in Solid-Phase Synthesis & Combinatorial Libraries* (Epton, R., Ed.) pp 255−260, Mayflower Worldwide, Kingswinford.

(25) Zubin, E. M., Romanova, E. A., Volkov, E. M., Tashlitsky, V. N., Korshunova, G. A., Shabarova, Z. A., and Oretskaya, T. S. (1999) Oligonucleotide−peptide conjugates as potential antisense agents. *FEBS Lett. 456*, 59−62.

(26) Dobson, N., McDowell, D. G., French, D. J., Brown, L. J., Mellor, J. M., and Brown, T. (2003) Synthesis of HyBeacons and dual-labeled probes containing 2′-fluorescent groups for use in genetic analysis. *Chem. Commun.* 1234−1235.

(27) Meldgaard, M., Nielsen, N. K., Bremner, M., Pedersen, O. S., Olsen, C. E., and Wengel, J. (1997) Automated synthesis of branched oligodeoxynucleotide analogues using arabinouridine as branching nucleotide. *J. Chem. Soc.*, *Perkin Trans. 1* 1951−1956.

(28) Kahl, J. D., and Greenberg, M. M. (1999) Introducing structural diversity in oligonucleotides via photolabile, convertible *C*5-substituted nucleotides. *J. Am. Chem. Soc. 121*, 597−604.

(29) Hwang, J.-T., and Greenberg, M. M. (2001) Synthesis of 2′-modified oligodeoxynucleotides via on-column conjugation. *J. Org. Chem. 66*, 363−369.

(30) Dombi, K. L., Steiner, U. E., and Richert, C. (2003) Rapidly measuring reactivities of carboxylic acids to generate equireactive building block mixtures: a spectrometric assay. *J. Comb. Chem. 5*, 45−60.

(31) Kachalova, A. V., Zubin, E. M., and Oretskaya, T. S. (2002) Methods for the synthesis of oligonucleotides containing reactive electrophilic groups. *Russ. Chem. Rev. 71*, 1041−1059.

(32) Tam, J. P., Xu, J., and Eom, K. D. (2001) Methods and strategies of peptide ligation. *Biopolymers 60*, 194−205.

(33) Tam, J. P., and Spetzler, J. C. (1995) Chemoselective approaches to the preparation of peptide dendrimers and branched artificial proteins using unprotected peptides as building blocks. *Biomed. Pept. Proteins Nucleic Acids 1*, 123−132.

(34) Peri, F., and Nicotra F. (2004) Chemoselective ligation in glycochemistry. *Chem. Commun.* 623−627.

(35) Stetsenko, D. A., and Gait, M. J. (2000) Efficient conjugation of peptides to oligonucleotides by "native ligation". *J. Org. Chem. 65*, 4900−4908.

(36) Adamczyk, M., Chen, Y. Y., Grote, J., and Mattingly, P. G. (1999) *O*-(fluoresceinylmethyl)hydroxylamine (OFMHA): a reagent for the preparation of fluorescent *O*-(fluoresceinylmethyl)oxime (FMO)-steroid conjugates. *Steroids 64*, 283−290.

(37) Adamczyk, M., Grote, J., Mattingly, P. G., and Pan, Y. (2000) *O*-(Acridinium)hydroxylamine (AHA): a reagent for the preparation of chemiluminescent acridinium oxime (AO)-steroid conjugates. *Steroids 65*, 387−394.

(38) Peuralahti, J., Suonpää, K., Blomberg, K., Mukkala, V. M., and Hovinen, J. (2004) Labeling of steroids on solid phase. *Bioconjugate Chem. 15*, 927−930.

(39) Wang, C. C., Seo, T. S., Li, Z., Ruparel, H., and Ju, J. (2003) Site-specific fluorescent labeling of DNA using Staudinger ligation. *Bioconjugate Chem. 14*, 697−701.

(40) Köhn, M., and Breinbauer, R. (2004) The Staudinger ligation-a gift to chemical biology. *Angew. Chem.*, *Int. Ed. 43*, 3106−3116.

(41) Jaschke, A., and Seelig, B. (1997) Site−specific modification of enzymatically synthesized RNA: transcription initiation and Diels−Alder reaction. *Tetrahedron Lett. 38*, 7729−7732.

(42) Hill, K. W., Taunton−Rigby, J., Carter, J. D., Kropp, E., Vagle, K., Pieken, W., McGee, D. P. C., Husar, G. M., Leuck, M., Anziano, D. J., and Sebesta, D. P. (2001) Diels−Alder bioconjugation of diene−modified oligonucleotides. *J. Org. Chem. 66*, 5352−5358.

(43) Graham, D., Grondin, A., McHugh, C., Fruk, L., and Smith, W. E. (2002) Internal labeling of oligonucleotide probes by Diels−Alder cycloaddition. *Tetrahedron Lett. 43*, 4785−4788.

(44) Breinbauer, R., and Köhn, M. (2003) Azide−alkyne coupling: a powerful reaction for bioconjugate chemistry. *ChemBioChem 4*, 1147−1149.

(45) Seo, T. S., Li, Z., Ruparel, H., and Ju, J. (2003) Click chemistry to construct fluorescent oligonucleotides for DNA sequencing. *J. Org. Chem. 68*, 609−612.

(46) Seo, T. S., Bai, X., Ruparel, H., Li, Z., Turro, N. J., and Ju J. (2004) Photocleavable fluorescent nucleotides for DNA sequencing on a chip constructed by site−specific coupling chemistry. *Proc. Natl. Acad. Sci. U.S.A. 101*, 5488−5493.

(47) Beaucage, S. L. (2001) Strategies in the preparation of DNA oligonucleotide arrays for diagnostic applications. *Curr. Med. Chem. 8*, 1213−1244.

(48) Zammatteo, N., Jeanmart, L., Hamels, S., Courtois, S., Louette, P., Hevesi, L., and Remacle J. (2000) Comparison between different strategies of covalent attachment of DNA to glass surfaces to build DNA microarrays. *Anal. Biochem. 280*, 143−150.

(49) Dombi, K. L., Griesang, N., and Richert, C. (2002) Oligonucleotide arrays from aldehyde-bearing glass with coated background. *Synthesis* 816−824.

(50) Kottysch, T., Ahlborn, C., Brotzel, F., and Richert, C. (2004) Stabilizing or destabilizing oligodeoxynucleotide duplexes containing single 2′-deoxyuridine residues with 5-alkynyl substituents. *Chem. Eur. J. 10*, 4017−4028.

(51) Proudnikov, D., Timofeev, E., and Mirzabekov, A. (1998) Immobilization of DNA in polyacrylamide gel for the manufacture of DNA and DNA-oligonucleotide microchips. *Anal. Biochem. 259*, 34−41.
(52) Vasseur, J. J., Rayner, B., Imbach, J. L., Verma, S., McCloskey, J. A., Lee, M., Chang, D. K., and Lown, J. W. (1987) Structure of the adduct formed between 3-aminocarbazole and the apurinic site oligonucleotide model d(Tp(Ap)pT). *J. Org. Chem. 52*, 4994−4998.
(53) Kroeger, K. M., Hashimoto, M., Kow, Y. W., and Greenberg M. M. (2003) Cross-linking of 2-deoxyribonolactone and its beta-elimination product by base excision repair enzymes. *Biochemistry 42*, 2449−2455.
(54) Manoharan, M., Andrade, L. K., Mohan, V., Freier, S. M., and Cook, P. D.(1997) Oligonucleotide conjugates derived from an electrophilic site: conjugation to baseless carbohydrate residue. Synthesis, hybridization and modeling studies. *Nucleosides*, *Nucleotides 16*, 1741−1744.
(55) Timofeev, E., Kochetkova, S. V., Mirzabekov, A. D., and Florentiev, V. L. (1996) Regioselective immobilization of short oligonucleotides to acrylic copolymer gels. *Nucleic Acids Res. 24*, 3142−3148.
(56) Haralambidis, J., Lagniton, L., and Tregear, G. W. (1994) The preparation of enzyme-labelled oligonucleotides by reductive amination. *Bioorg. Med. Chem. Lett. 4*, 1005−1010.
(57) Kachalova, A. V., Zatsepin, T. S., Romanova, E. A., Stetsenko, D. A., Gait, M. J., and Oretskaya, T. S. (2000) Synthesis of modified nucleotide building blocks containing electrophilic groups in the 2′-position. *Nucleosides*, *Nucleotides*, *Nucleic Acids 19*, 1693−1707.
(58) Skrzypczynski, Z., and Wayland, S. (2003) New reagents for the introduction of reactive functional groups into chemically synthesized DNA probes. *Bioconjugate Chem. 14*, 642−652.
(59) Dechamps, M., and Sonveaux, E. (1998) Aldehydo-oligonucleotides for bioconjugation. *Nucleosides*, *Nucleotides 17*, 697−709.
(60) Tilquin, J. M., Dechamps, M., and Sonveaux, E. (2001) Incorporation of an aldehyde function in oligonucleotides. *Bioconjugate Chem. 12*, 451−457.
(61) Sando, S., Matsui, K., Niinomi, Y., Sato, N., and Aoyama, Y. (2003) Facile preparation of DNA-tagged carbohydrates. *Bioorg. Med. Chem. Lett. 13*, 2633−2636.
(62) Kittaka, A., Kuze, T., Asakura, T., Ito, K., and Miyasaka, T. (1998) Oligonucleotides bearing 5-formyl-2′-O-methyluridine: preference in binding affinity to the NF-kappa B (p50)2 homo- and p50/p65 heterodimers. *Bioorg. Med. Chem. Lett. 8*, 3207−3210.
(63) Kittaka, A., Horii, C., Kuze, T., Asakura, T., Ito, K., Nakamura, K. T., Miyasaka, T., and Inoue, J. (1999) Introduction of 5-formyl-2′-deoxyuridine into a κB site: critical discrimination of a base structure in the major groove by NF-κB p50 homodimer. *Synlett*. 869−872.
(64) Kittaka, A., Takayama, H., Kurihara, M., Horii, C., Tanaka, H., Miyasaka, T., and Inoue, J. (2001) DNA sequence recognition by NF kappa B p50 homodimer: strict and obscure recognition sites in the binding sequence. *Nucleosides*, *Nucleotides*, *Nucleic Acids 20*, 669−672.
(65) Kittaka, A., Kuze, T., Amano, M., Tanaka, H., Miyasaka, T., Hirose, K., Yoshida, T., Sarai, A., Yasukawa, T., and Ishii, S. (1999) Introduction of 6-formylcytidine into a Myb binding sequence. *Nucleosides*, *Nucleotides 18*, 2769−2783.
(66) Sugiyama, T., Kittaka, A., Takayama, H., Tomioka, M., Ida, Y., and Kuroda, R. (2001) Chemical cross-linking of peptides derived from RecA with single-stranded oligonucleotides containing 5-formyl-2′-deoxyuridine. *Nucleosides*, *Nucleotides*, *Nucleic Acids 20*, 1079−1083.
(67) Sugiyama, T., Kittaka, A., Tomioka, M., Ida, Y., and Kuroda, R. (2003) Aggregation of RecA-derived peptides on single-stranded oligonucleotides triggered by Schiff base-mediated crosslinking. *Bioorg. Med. Chem. Lett. 13*, 2847−2851.
(68) Kittaka, A., Kuze, T., Sarai, A., Takayama, H., Tanaka, H., Miyasaka, T., Inoue, J., and Ishii, S. (2003) Synthesis of oligonucleotides with 6-formyl-2′-*O*-methyluridine and thermal stability of their duplexes. *Heterocycles 59*, 207−215.
(69) Turutin, D. V., Zatsepin, T. S., Timchenko, M. A., Kubareva, E. A., and Oretskaya, T. S. (2002) Cross-linking of transcription factor NF-kappaB with a DNA ligand bearing the 2′-aldehyde group. *Mol. Biol. (Russ.) 36*, 877−879.
(70) Romanenkov, A. S., Ustyugov, A. A., Zatsepin, T. S., Nikulova, A. A., Kolesnikov, I. V., Metelev, V. G., Oretskaya, T. S., and Kubareva, E. A. (2005) Analysis of DNA-protein interactions in complexes of transcription factor NF−κB with DNA target sites. *Biochemistry (Moscow)*, in press.
(71) Brevnov, M. G., Gritsenko, O. M., Mikhailov, S. N., Efimtseva, E. V., Ermolinsky, B. S., Van Aerschot, A., Herdewijn, P., Repyk, A. V., Gromova, E. S. (1997) DNA duplexes with reactive dialdehyde groups as novel reagents for cross−linking to restriction−modification enzymes. *Nucleic Acids Res. 25*, 3302−3309.
(72) Tunitskaya, V. L., Rusakova, E. E., Memelova, L. V., Kochetkov, S. N., Van Aerschot, A., Herdewijn, P., Efimtseva, E. V., Ermolinsky, B. S., Mikhailov, S. N. (1999) Mapping of T7 RNA polymerase active site with novel reagents—oligonucleotides with reactive dialdehyde groups. *FEBS Lett. 442*, 20−24.
(73) Bugaut, A., Toulmé, J.-J., and Rayner, B. (2004) Use of dynamic combinatorial chemistry for the identification of covalently appended residues that stabilize oligonucleotide complexes. *Angew. Chem.*, *Int. Ed. 43*, 3144−3147.
(74) Gat, Y., and Lynn, D. G. (1998) Reading DNA differently. *Biopolymers 48*, 19−28.
(75) Summerer, D., and Marx, A. (2002) DNA-templated synthesis: more versatile than expected. *Angew. Chem.*, *Int. Ed. 41*, 89−90.
(76) Li, X., and Liu, D. R. (2004) DNA-templated organic synthesis: nature's strategy for controlling chemical reactivity applied to synthetic molecules. *Angew. Chem.*, *Int. Ed. Engl. 43*, 4848−4870.
(77) Calderone, C. T., and Liu, D. R. (2004) Nucleic−acid−templated synthesis as a model system for ancient translation. *Curr. Opin. Chem. Biol. 8*, 645−653.
(78) Goodwin, J. T., and Lynn, D. G. (1992) Template-directed synthesis: use of a reversible reaction. *J. Am. Chem. Soc. 114*, 9197−9198.
(79) Zhan, Z.-Y. J., and Lynn, D. G. (1997) Chemical amplification through template-directed synthesis. *J. Am. Chem. Soc. 119*, 12420−12421.
(80) Li, X., Zhan, Z.-Y. J., Knipe, R., and Lynn, D. G. (2002) DNA-catalyzed polymerization. *J. Am. Chem. Soc. 124*, 746−747.
(81) Li, X., and Lynn, D. G. (2002) Polymerization on solid supports. *Angew. Chem.*, *Int. Ed. Engl. 41*, 4567−4569.
(82) Gartner, Z. J., Kanan, M. W., and Liu, D. R. (2002) Expanding the reaction scope of DNA-templated synthesis. *Angew. Chem.*, *Int. Ed. 41*, 1796−1800.
(83) Calderone, C. T., Puckett, J. W., Gartner, Z. J., and Liu, D. R. (2002) Directing otherwise incompatible reactions in a single solution by using DNA-templated organic synthesis. *Angew. Chem.*, *Int. Ed. 41*, 4104−4108.
(84) Gartner, Z. J., Grubina, R., Calderone, C. T., and Liu, D. R. (2003) Two enabling architectures for DNA-templated organic synthesis. *Angew. Chem.*, *Int. Ed. 42*, 1370−1375.
(85) Gartner, Z. J., Tse, B. N., Grubina, R., Doyon, J. B., Snyder, T. M., Liu, D. R. (2004) DNA-templated organic synthesis and selection of a library of macrocycles. *Science 305*, 1601−1605.
(86) Kanan, M. W., Rozenman, M. M., Sakurai, K., Snyder, T. M., Liu, D. R. (2004) Reaction discovery enabled by DNA-templated synthesis and in vitro selection. *Nature 431*, 545−549.
(87) Rosenbaum, D. M., and Liu, D. R. (2003) Efficient and sequence-specific DNA-templated polymerization of peptide nucleic acid aldehydes. *J. Am. Chem. Soc. 125*, 13924−13925.
(88) Czlapinski, J. L., and Sheppard, T. L. (2001) Nucleic acid template-directed assembly of metallosalen-DNA conjugates. *J. Am. Chem. Soc. 123*, 8618−8619.
(89) Czlapinski, J. L., and Sheppard, T. L. (2004) Template-directed assembly of metallosalen-DNA hairpin conjugates. *ChemBioChem 5*, 127−129.

(90) Czlapinski, J. L., and Sheppard, T. L. (2004) Site-specific oxidative cleavage of DNA by metallosalen-DNA conjugates. *Chem. Commun.* 2468−2469.
(91) Gothelf, K. V., Thomsen, A., Nielsen, M., Clo, E., and Brown, R. S. (2004) Modular DNA-programmed assembly of linear and branched conjugated nanostructures. *J. Am. Chem. Soc. 126*, 1044−1046.
(92) Nielsen, M., Thomsen, A. H., Clo, E., Kirpekar, F., and Gothelf, K. V. (2004) Synthesis of linear and tripoidal oligo-(phenylene ethynylene)-based building blocks for application in modular DNA-programmed assembly. *J. Org. Chem. 69*, 2240−50.
(93) Brown, R. S., Nielsen, M., and Gothelf, K. V. (2004) Self-assembly of aluminium-salen coupled nanostructures from encoded modules with cleavable disulfide DNA-linkers. *Chem. Commun.* 1464−1465.
(94) Jacobsen, E. N. (2000) Asymmetric catalysis of epoxide ring-opening reactions. *Acc. Chem. Res. 33*, 421−431.
(95) Gothelf, K. V., and Brown, R. S. (2005) A modular approach to DNA-programmed self-assembly of macromolecular nanostructures. *Chem. Eur. J. 11*, 1062−1069.
(96) Jencks, W. P. (1959) Studies on the mechanism of oxime and semicarbazone formation. *J. Am. Chem. Soc. 81*, 475−481.
(97) Jencks, W. P. (1964) Mechanism and catalysis of simple carbonyl group reactions. *Prog. Phys. Org. Chem. 2*, 63−128.
(98) Um, I. H., and Buncel, E. (2000) The origin of the alpha-effect: dissection of ground-state and transition-state contributions. *J. Org. Chem. 65*, 577−582.
(99) Mitsunobu, O. (1981) The use of diethyl azodicarboxylate and triethenylphosphine in synthesis and transformation of natural products. *Synthesis* 1−28.
(100) Kawasaki, A. M., Casper, M. D., Prakash, T. P., Manalili, S., Sasmor, H., Manoharan, M., and Cook, P. D. (1999) Synthesis, hybridization, and nuclease resistance properties of 2′-*O*-aminooxyethyl (2′-*O*-AOE) modified oligonucleotides. *Tetrahedron Lett. 40*, 661−664.
(101) Salo, H., Virta, P., Hakala, H., Prakash, T. P., Kawasaki, A. M., Manoharan, M., and Lönnberg, H. (1999) Aminooxy functionalized oligonucleotides: preparation, on-support derivatization, and postsynthetic attachment to polymer support. *Bioconjugate Chem. 10*, 815−823.
(102) Manoharan, M., Lonnberg, H., Salo, H., Virta, P., ISIS Pharmaceuticals, Inc. (Carlsbad, CA) (2003) U.S. Patent 6,576,752 B1.
(103) Katajisto, J., Virta, P., and Lönnberg, H. (2004) Solid-phase synthesis of multiantennary oligonucleotide glycoconjugates utilizing on-support oximation. *Bioconjugate Chem. 15*, 890−896.
(104) Cebon, B., Lambert, J. N., Leung, D., Mackie, K., McCluskey, K. L., Nguyen, H., and Tassone, C. (2000) New DNA modification strategies involving oxime formation. *Austr. J. Chem. 53*, 333−340.
(105) Defrancq, E., and Lhomme, J. (2001) Use of an aminooxy linker for the functionalization of oligodeoxyribonucleotides. *Bioorg. Med. Chem. Lett. 11*, 931−933.
(106) Karpeisky, A., Gonzalez, C., Burgin, A. B., and Beigelman, L. (1998) Highly efficient synthesis of 2′-*O*-amino nucleosides and their incorporation in hammerhead ribozymes. *Tetrahedron Lett. 39*, 1131−1134.
(107) Trevisiol, E., Defrancq, E., Lhomme, J., Laayoun, A., and Cros, P. (2000) Synthesis of nucleoside triphosphates that contain an aminooxy function for "post-amplification labelling". *Eur. J. Org. Chem.*, 211−217.
(108) Hamma, T., and Miller, P. S. (2003) 4-(2-aminooxyethoxy)-2-(ethylureido)quinoline-oligonucleotide conjugates: synthesis, binding interactions, and derivatization with peptides. *Bioconjugate Chem. 14*, 320−330.
(109) Prater, C. E., and Miller, P. S. (2004) 3′-methylphosphonate-modified oligo-2′-*O*-methylribonucleotides and their Tat peptide conjugates: uptake and stability in mouse fibroblasts in culture. *Bioconjugate Chem. 15*, 498−507.
(110) Buré, C., Lelièvre, D., and Delmas, A. (2000) Identification of by-products from an orthogonal peptide ligation by oxime bonds using mass spectrometry and tandem mass spectrometry. *Rapid Commun. Mass Spectrom. 14*, 2158−2164.
(111) Forget, D., Boturyn, D., Defrancq, E., Lhomme, J., and Dumy, P. (2001) Highly efficient synthesis of peptide−oligonucleotide conjugates: chemoselective oxime and thiazolidine formation. *Chem. Eur. J. 7*, 3976−3984.
(112) Legrand, M., Defrancq, E., Houdier, S., Croze, S., Lhomme, J., and Boturyn, D. (1999) A new fluorescent probe for sensitive detection of carbonyl compounds. *Anal. Chim. Acta 382*, 253−263.
(113) Houdier, S., Perrier, S., Defrancq, E., and Legrand, M. (2000) A new fluorescent probe for sensitive detection of carbonyl compounds: sensitivity improvement and application to environmental water samples. *Anal. Chim. Acta 412*, 221−233.
(114) Edupuganti, O. P., Defrancq, E., and Dumy, P. (2003) Head-to-tail oxime cyclization of oligodeoxynucleotides for the efficient synthesis of circular DNA analogies. *J. Org. Chem. 68*, 8708−8710.
(115) Boncheva, M., Scheibler, L., Lincoln, P., Vogel, H., and Akerman, B. (1999) Design of oligonucleotide arrays at interfaces. *Langmuir 15*, 4317−4320.
(116) Defrancq, E., Hoang, A., Vinet, F., and Dumy, P. (2003) Oxime bond formation for the covalent attachment of oligonucleotides on glass support. *Bioorg. Med. Chem. Lett. 13*, 2683−2686.
(117) Schena, M., Shalon, D., Heller, R., Chai, A., Brown, P., and Davie, R. (1996) Parallel human genome analysis: microarray-based expression monitoring of 1000 genes. *Proc. Natl. Acad. Sci. U.S.A. 93*, 10614−10619.
(118) Lhomme, J., Constant, J. F., and Demeunynck, M. (1999) Abasic DNA structure, reactivity, and recognition. *Biopolymers 52*, 65−83.
(119) Talpaert-Borlé, M., and Liuzzi, M. (1983) Reaction of apurinic/apyrimidinic sites with ^{14}C-methoxyamine. A method for the quantitative assay of AP sites in DNA. *Biochim. Biophys. Acta 740*, 410−416.
(120) Liuzzi, M., and Talpaert-Borlé, M. (1988) Characterization of damage in gamma-irradiated and OsO_4-treated DNA using methoxyamine. *Int. J. Radiat. Biol. 54*, 709−722.
(121) Angeloff, A., Dubey, I., Pratviel, G., Bernadou, J., and Meunier, B. (2001) Characterization of a 5′-aldehyde terminus resulting from the oxidative attack at *C*5′ of a 2-deoxyribose on DNA. *Chem. Res. Toxicol. 14*, 1413−1420.
(122) Kow, Y. W. (1989) Mechanism of action of *Escherichia coli* exonuclease III. *Biochemistry 28*, 3280−3287.
(123) Chen, B. X., Kubo, K., Ide, H., Erlanger, B. F., Wallace, S. S., and Kow. Y. W. (1992) Properties of a monoclonal antibody for the detection of abasic sites, a common DNA lesion. *Mutat. Res. 273*, 253−261.
(124) Kubo, K., Ide, H., Wallace, S. S., and Kow, Y. W. (1992) A novel, sensitive, and specific assay for abasic sites, the most commonly produced DNA lesion. *Biochemistry 31*, 3703−3708.
(125) Boturyn, D., Boudali, A., Constant, J. F., Defrancq, E., and Lhomme, J. (1997) Synthesis of fluorescent probes for the detection of abasic sites in DNA. *Tetrahedron 53*, 5485−5492.
(126) Boturyn, D., Constant, J. F., Defrancq, E., Lhomme, J., Barbin, A., and Wild, C. P. (1999). A simple and sensitive method for in vitro quantitation of abasic sites in DNA. *Chem. Res. Toxicol. 12*, 476−482.
(127) Adamczyk, M., Mattingly, P. G., and Moore, J. A. (1998) *O*-(fluoresceinylmethyl)hydroxylamine (OFMHA): a fluorescent reagent for detection of damaged nucleic acids. *Bioorg. Med. Chem. Lett. 8*, 3599−3602.
(128) Adamczyk, M., Mattingly, P. G., Moore, J. A., and Pan, Y. (1999) Synthesis of a chemiluminescent acridinium hydroxylamine (AHA) for the direct detection of abasic sites in DNA. *Org. Lett. 1*, 779−781.
(129) Maulik, G., Botchway, S., Chakrabarti, S., Tetradis, S., Price, B., and Makrigiorgos, G. M. (1999) Novel nonisotopic detection of MutY enzyme-recognized mismatches in DNA via ultrasensitive detection of aldehydes. *Nucleic Acids Res. 27*, 1316−1322.
(130) Makrigiorgos, G. M., Chakrabarti, S., and Mahmood, A. (1998) Fluorescent labeling of abasic sites: a novel methodol-

ogy to detect closely spaced damage sites in DNA. *Int. J. Radiat. Biol. 74*, 99−109.
(131) Chakrabarti, S., Mahmood, A., and Makrigiorgos, G. M. (1999) Fluorescent labeling of closely spaced aldehydes induced in DNA by bleomycin-Fe(III). *Int. J. Radiat. Biol. 75*, 1055−1065.
(132) Ito, T., and Rokita, S. E. (2003) Excess electron transfer from an internally conjugated aromatic amine to 5−bromo−2′−deoxyuridine in DNA. *J. Am. Chem. Soc. 125*, 11480−11481.
(133) Ito, T., Rokita, S. E. (2004) Criteria for efficient transport of excess electrons in DNA. *Angew. Chem. Int. Ed. 43*, 1839−1842.
(134) Ito, T., and Rokita, S. E. (2004) Reductive electron injection into duplex DNA by aromatic amines. *J. Am. Chem. Soc. 126*, 15552−15559.
(135) Trevisiol, E., Renard, A., Defrancq, E., and Lhomme, J. (1997) The oxyamino-aldehyde coupling reaction: an efficient method for the derivatization of oligonucleotides. *Tetrahedron Lett. 38*, 8687−8690.
(136) Forget, D., Renaudet, O., Boturyn, D., Defrancq, E., and Dumy, P. (2001) 3′-Oligonucleotides conjugation via chemoselective oxime bond formation. *Tetrahedron Lett. 42*, 9171−9174.
(137) Trevisiol, E., Renard, A., Defrancq, E., and Lhomme, J. (2000) Fluorescent labeling of oligodeoxyribonucleotides by the oxyamino-aldehyde coupling reaction. *Nucleosides*, *Nucleotides*, *Nucleic Acids 19*, 1427−1439.
(138) Zatsepin, T. S., Stetsenko, D. A., Arzumanov, A. A., Romanova, E. A., Gait, M. J., and Oretskaya, T. S. (2002) Synthesis of peptide−oligonucleotide conjugates with single and multiple peptides attached to 2′-aldehydes through thiazolidine, oxime, and hydrazine linkages. *Bioconjugate Chem. 13*, 822−830.
(139) Forget, D., Renaudet, O., Defrancq, E., and Dumy P. (2001) Efficient preparation of carbohydrate-oligonucleotide conjugates (COCS) using oxime bond formation. *Tetrahedron Lett. 42*, 7829−7832.
(140) Deroo, S., Defrancq, E., Moucheron, C., Mesmaeker, K., and Dumy, P. (2003) Synthesis of an oxyamino-containing phenantroline derivative for the efficient preparation of phenantroline oligonucleotide oxime conjugates. *Tetrahedron Lett. 44*, 8379−8382.
(141) Ghosh, S., Defrancq, E., Lhomme, J. H., Dumy, P., and Bhattacharya, S. (2004) Efficient conjugation and characterization of distamycin-based peptides with selected oligonucleotide stretches. *Bioconjugate Chem. 15*, 520−529.
(142) Edupuganti, O. P., Singh, Y., Defranq, E., and Dumy, P. (2004) New strategy for the synthesis 3′,5′-bifunctionalized oligonucleotide conjugates through sequential formation of chemoselective oxime bonds. *Chem. Eur. J. 10*, 5988−5995.
(143) Trevisiol, E., Defrancq, E., Lhomme, J., Laayoun, A., and Cros, P. (2000) Synthesis of methyl ketone containing nucleoside triphosphates for RNA labelling. *Tetrahedron 56*, 6501−6510.
(144) Dey, S., and Sheppard, T. L. (2001) Ketone-DNA: a versatile postsynthetic DNA decoration platform. *Org. Lett. 3*, 3983−3986.
(145) Neuner, P., Gallo, P., Orsatti, L., Fontana, L., and Monaci, P. (2003) An efficient and versatile synthesis of bisPNA-peptide conjugates based on chemoselective oxime formation. *Bioconjugate Chem. 14*, 276−281.
(146) Sayer, J. M., Peshkin, M., and Jencks, W. P. (1973) Imine-forming elimination reactions. I. General base and acid catalysis and influence of the nitrogen substituent on rates and equilibria for carbinolamine dehydration. *J. Am. Chem. Soc. 95*, 4277−4287.
(147) Ghosh, S. S., Kao, M. P., and Kwoh, D. Y. (1989) Synthesis of 5′-oligonucleotide hydrazide derivatives and their use in preparation of enzyme-nucleic acid hybridization probes. *Anal. Biochem. 178*, 43−51.
(148) Oshevski, S. I. (1998) Concept of "Binary oligonucleotide reagent". *Nucleosides*, *Nucleotides 17*, 1969−1975.
(149) Raddatz, S., Mueller-Ibeler, J., Kluge, J., Burdinski, G., Havens, J. R., Onofrey, T. J., Wang, D., and Schweitzer, M. (2002) Hydrazide oligonucleotides: new chemical modification for chip array attachment and conjugation. *Nucleic Acids Res. 30*, 4793−4802.
(150) Eckardt, L. H., Naumann, K., Pankau, W. M., Rein, M., Schweitzer, M., Windhab, N., and von Kiedrowski, G. (2002) DNA nanotechnology: chemical copying of connectivity. *Nature 420*, 286.
(151) Zubin, E., Stetsenko, D., Oretskaya, T. S., and Gait, M. (2003) 1,2-Diol and hydrazide phosphoramidites for solid-phase synthesis and chemoselective ligation of 2′-modified oligonucleotides. *Nucleotides*, *Nucleosides*, *Nucleic Acids 22*, 1375−1378.
(152) Gao, K., and Orgel, L. E. (1999) Nucleic acid duplexes incorporating a dissociable covalent base pair. *Proc. Natl. Acad. Sci. U.S.A. 96*, 14837−14842.
(153) Kozlov, I. A., Melnyk, P. C., Stromsborg, K. E., Chee, M. S., Barker, D. L., and Zhao, C. (2004) Efficient strategies for the conjugation of oligonucleotides to antibodies enabling highly sensitive protein detection. *Biopolymers 73*, 621−630.
(154) Steinberg, G., Stromsborg, K., Thomas, L., Barker, D. L., and Zhao, C. (2004) Strategies for covalent attachment of DNA to beads. *Biopolymers 73*, 597−605.
(155) Zhong, X. B., Reynolds, R., Kidd, J. R., Kidd, K. K., Jenison, R., Marlar, R. A., and Ward, D. C. (2003) Single-nucleotide polymorphism genotyping on optical thin−film biosensor chips. *Proc. Natl. Acad. Sci. U.S.A. 100*, 11559−11564.
(156) Kremsky, J. N., Wooters, J. L., Dougherty, J. P., Meyers, R. E., Collins, M., and Brown, E. L. (1987) Immobilization of DNA via oligonucleotides contaning an aldehyde or carboxylic acid group at the 5′−terminus. *Nucleic Acids Res. 15*, 2891−2909.
(157) Ollivier, N., Olivier, C., Gouyette, C., Huynh-Dinh, T., Gras-Masse, H., and Melnik, O. (2002) Synthesis of oligonucleotide−peptide conjugates using hydrazone chemical ligation. *Tetrahedron Lett. 43*, 997−999.
(158) Singh, Y., Defrancq, E., Dumy, P. (2004) New method to prepare peptide−oligonucleotide conjugates through glyoxylic oxime formation. *J. Org. Chem. 69*, 8544−8546.
(159) Zatsepin, T. S., Ivanova, Yu. M., Stetsenko, D. A., Gait, M. J., and Oretskaya, T. S. (2004) Efficient conjugation and preferential DNA binding of oligonucleotides containing 2′-*O*-(2-oxoethyl)arabinouridine. *Tetrahedron Lett. 45*, 7327−7330.
(160) Proudnikov, D., and Mirzabekov, A. (1996) Chemical methods of DNA and RNA fluorescent labeling. *Nucleic Acids Res. 24*, 4535−4532.
(161) Schluep, T., and Cooney, C. L. (1998) Purification of plasmids by triplex affinity interaction. *Nucleic Acids Res. 26*, 4524−4528.
(162) Schluep, T., and Cooney, C. L. (1999) Immobilization of oligonucleotides on a large pore support for plasmid purification by triplex affinity interaction. *Bioseparation 7*, 317−326.
(163) Olivier, C., Hot, D., Huot, L., Ollivier, N., Mahdi, Q., Guyette, C., Huynh-Dinh, T., Gras-Masse, H., Lemoine, Y., and Melnyk, O. (2003) α-Oxo semicarbazone peptide or oligodeoxynucleotide microarrays. *Bioconjugate Chem. 14*, 430−439.
(164) Podyminogin, M. A., Lukhtanov, E. A., and Reed, M. W. (2001) Attachment of benzaldehyde-modified oligodeoxynucleotide probes to semicarbazide-coated glass. *Nucleic Acids Res. 29*, 5090−5098.
(165) Zatsepin, T. S., Romanova, E. A., Stetsenko, D. A., Gait, M. J., and Oretskaya, T. S. (2003) Synthesis of 2′-modified oligonucleotides containing aldehyde or ethylenediamine groups. *Nucleosides*, *Nucleotides*, *Nucleic Acids 22*, 1383−1385.
(166) Garther, Z. J., Kanan, M. W., and Liu, D. R. (2002) Multistep small-molecule synthesis programmed by DNA templates. *J. Am. Chem. Soc. 124*, 10304−10306.
(167) Li, X., Gartner, Z. J., Tse, B. N., and Liu, D. R. (2004) Translation of DNA into synthetic *N*-acyloxazolidines. *J. Am. Chem. Soc. 126*, 5090−5092.

BC049712V

COMMUNICATIONS

Inhibition of Membrane-Associated Methyltransferases by a Cholesterol-Based Metal Chelator

Heather B. Hodges, Mingkang Zhou, Saubhik Haldar, Jessica L. Anderson, David H. Thompson,* and Christine A. Hrycyna*

Department of Chemistry and Purdue Cancer Center, Purdue University, 560 Oval Drive, West Lafayette, Indiana 47907. Received February 1, 2005

We have designed, synthesized, and characterized a metal chelating compound that is based on the structure of cholesterol and contains the high affinity metal chelating group, lysine nitrilotriacetic acid (Lys-NTA). Using the enzyme isoprenylcysteine carboxylmethyltransferase (Icmt) from yeast as a model integral membrane metalloenzyme, we find that this agent potently inhibits Icmt activity with an IC_{50} value between 35 and 75 μM, which is at least 40 times more potent than the best known Icmt metal chelating inhibitor, Zincon. We propose that the rigid hydrophobic cholesterol moiety promotes partitioning into the membrane, enabling the metal-binding NTA group(s) to inactivate the enzyme by metal chelation. Because this compound is based on a naturally occurring membrane lipid and appears to chelate metals buried deeply within water insoluble environments, this agent may also be useful as a general tool for identifying previously unappreciated metal dependencies of other classes of membrane proteins.

Metalloproteins are essential to biological systems, playing critical roles in processes ranging from oxygen transport to signal transduction. The metals within these proteins can serve as structural components or as active site catalytic centers. Although many identified metalloproteins are membrane-spanning proteins, possessing one or more hydrophobic domains, the relative water solubility of standard metal chelators used to probe membrane protein function suggests that many other membrane proteins may have gone unrecognized as metalloproteins. In this study, we report the development of a cholesterol-based chelator that may serve as an excellent tool for identifying the metal dependence of membrane proteins. This molecule (**7**) contains the high affinity metal chelating group, lysine nitrilotriacetic acid (Lys-NTA), covalently linked via an N^{ϵ}-carbamoyl linkage to cholesterol through the 3-hydroxyl on ring A (Chart 1). Other classes of chelator lipids coupled to Lys-NTA, such as NTA-dioctadecylamine (NTA-DODA) (*1*) or imidodiacetic acid (IDA) (*2*), have been synthesized and used previously for targeting biomolecules to artificial membranes and for organizing both soluble and membrane-associated histidine-tagged biomolecules at lipid interfaces to form two-dimensional arrays (*1*–*15*).

We used the isoprenylcysteine carboxylmethyltransferase (Icmt) from *S. cerevisiae*, Ste14p, as the model enzyme for this study. Ste14p is a 26 kDa endoplasmic reticulum (ER) membrane-spanning enzyme responsible for the posttranslational carboxylmethylation of CaaX motif proteins (*16*–*19*). Preliminary evidence suggests that Ste14p and its mammalian Icmt counterparts are dependent upon metals for activity (*20*, *21*). Although concentrations of EDTA up to 100 mM have no effect on activity, treatment of crude membranes with relatively high concentrations (10–50 mM) of *o*-phenanthroline eliminate the catalytic activity, presumably by chelation and perhaps removal of the metal from the enzyme (*20*, *21*). Lower concentrations of the more hydrophobic chelator compound 2-[5-(2-hydroxy-5-sulfophenyl)-3-phenyl-1-formazyl]benzoate (Zincon) were more effective, demonstrating 50% inhibition at approximately 3 mM (*21*). Taken together, these data suggest that more membrane-permeable, polycyclic, hydrophobic chelators would be increasingly effective at inhibiting these methyltransferases. In particular, we hypothesized that chelating moieties linked to naturally occurring membrane components may be most efficacious.

The compounds shown in Chart 1 were synthesized (*22*) to determine the molecular properties that are required to successfully inhibit Ste14p activity (see Supporting Information for the detailed synthesis of cholesterol-Lys-NTA (**7**)). Methyltransferase assays were performed essentially as described (*23*–*26*) with minor modifications. The assay mixture contained a total volume of 60 μL and a final Tris-HCl concentration of 100 mM, pH 7.5. All reactions contained 20 μM *S*-adenosyl-[^{14}C-*methyl*]-methionine (SAM) and 5 μg of membrane protein from Ste14p-overexpressing yeast strains (*21*). Inhibition curves were generated by varying the amount of potential inhibitor compound in each reaction

* Corresponding authors: Christine A. Hrycyna, Ph.D., Phone: 765-494-7322. Fax: 765-494-0239. e-mail: hrycyna@purdue.edu. David H. Thompson, Ph.D., Phone: 765-494-0386. Fax: 765-494-0239. e-mail: davethom@purdue.edu.

10.1021/bc050027d CCC: $30.25 © 2005 American Chemical Society
Published on Web 04/30/2005

Chart 1. Metal-Chelating Organic Compounds Tested as Inhibitors on Ste14p Activity in Vitro[a]

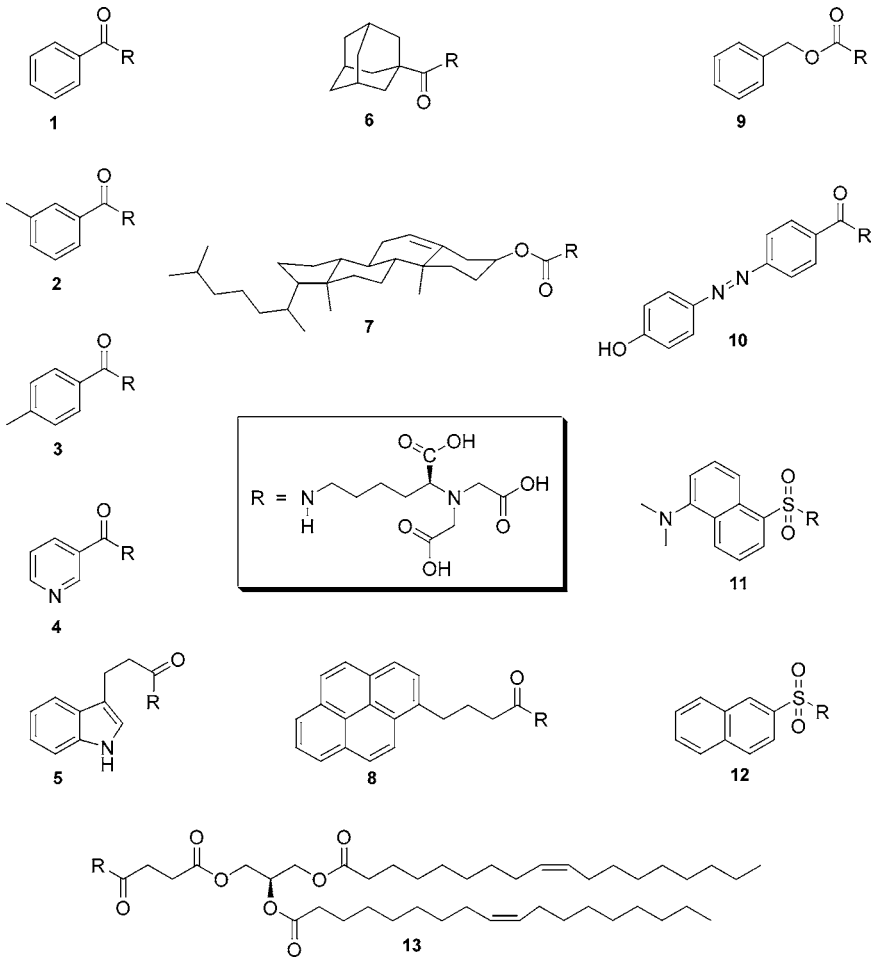

[a] Benzoic-Lys-NTA (**1**); *m*-toluic-Lys-NTA (**2**); *p*-toluic-Lys-NTA (**3**); nicotinic-Lys-NTA (**4**); indole-3-acetic-Lys-NTA (**5**); adamantane-Lys-NTA (**6**); cholesterol-Lys-NTA (**7**); 1-pyrenebutyric-Lys-NTA (**8**); benzylcarbamoyl-Lys-NTA (**9**); azo-Lys-NTA (**10**); dansyl-Lys-NTA (**11**); 2-naphthalenesulfonyl-Lys-NTA (**12**); 1,2-dioleoyl-sn-glycero-3-[*N*-(5-amino-1-carboxypentyl)iminodiacetic acid)succinyl] (DOGS)-NTA (**13**) (Avanti Polar Lipids, Inc.)

in the presence of *N*-acetyl-*S*-farnesyl-L-cysteine (AFC), the methyl accepting substrate, at 33 μM, which is twice the K_m for the yeast Ste14p enzyme in membranes. Membranes were preincubated for ~5 min with inhibitor compounds on ice prior to the addition of AFC and SAM. The reactions were then incubated at 30 °C for 30 min and stopped with the addition of 50 μL of 1 M NaOH/1% (v:v) SDS. One hundred microliters of this mixture was spotted on folded filter paper (5.5 cm × 1.5 cm) and lodged in the neck of a scintillation vial containing 10 mL of scintillation fluid. Hydroxide ion forms a tetrahedral intermediate with the newly formed ^{14}C-methyl ester on the methyl acceptor. This intermediate then eliminates ^{14}C-methanol that diffuses into the scintillation fluid below. The filters were pulled out after 2−3 h, and the vials were shaken well and counted in a liquid scintillation analyzer.

In this study, we found that only cholesterol-Lys-NTA (**7**) was effective in inhibiting the in vitro methyltransferase activity of Ste14p (Table 1, Figure 1). The Ste14p protein used in these experiments contains a 10 histidine repeat at the N-terminus followed by a triply iterated *myc* epitope tag (His-Ste14p) (*21*). These tags were engineered to aid in purification and identification of Ste14p by immunoblot analysis. The inhibition by each compound is shown in Table 1 and is represented as the percent methyltransferase activity remaining upon treatment with 1 mM of the respective compound compared

Table 1. Percent Activity of Ste14p in Vitro in the Presence and Absence of 1 mM Inhibitor Compounds

compound no.	percent activity	compound no.	percent activity
no inhibitor	100 ± 2.6	**7**	5.8 ± 2.5
1	108 ± 2.2	**8**	108 ± 1.2
2	111 ± 1.9	**9**	112 ± 1.3
3	108 ± 1.7	**10**	112 ± 4.1
4	111 ± 2.2	**11**	104 ± 1.9
5	108 ± 3.4	**12**	122 ± 4.6
6	107 ± 1.8	**13**	76.2 ± 4.6

to the untreated control reaction. We further examined the concentration dependence of inhibition by **7** on methyltransferase activity and determined the IC_{50} value to be ~75 μM (Figure 1), which is nearly 40 times more potent than the best known Icmt inhibitor, Zincon. The relative potency of this compound compared to EDTA and *o*-phenanthroline can be attributed to both the hydrophobicity of the cholesterol moiety ligated to the chelating agent Lys-NTA and the rigidity of the fused ring system. We propose that the rigid hydrophobic cholesterol moiety promotes partitioning into the membrane, enabling the metal-binding NTA groups to inactivate the enzyme by metal chelation. The only other compound that demonstrated any inhibitory ability (~25% inhibition; Table 1) was the commercially available DOGS−NTA (**13**), another compound that resembles a naturally occurring membrane lipid. The relative ineffectiveness of DOGS−NTA as an inhibitor may be due to the flexibility of this

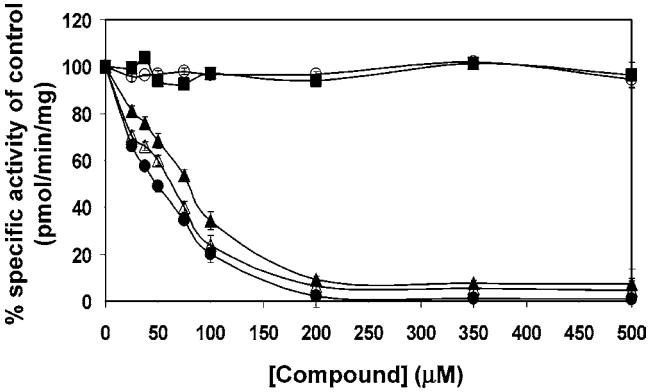

Figure 1. Concentration dependent inhibition of Ste14p-dependent methyltransferase activity by compound **7** and related compounds. Three Ste14p variants were used: His-Ste14p, untagged Ste14p and Ste14p^{C99S,C121S,C126S}. Assays were performed with 5 μg crude membrane protein expressing one of these variants in the presence of 33 μM *N*-acetyl-S-farnesyl-L-cysteine (AFC) and the activity was quantified by the in vitro vapor diffusion methyltransferase assay (*23, 26, 28*). To normalize for batch to batch and variant to variant differences in enzymatic activity, the inhibition data is presented as the percent of the control reactions that lacked inhibitor. His-Ste14p in the presence of **7** (▲); Cholesterol-Lys-NTA trimethyl ester (○); or cholesterol (■). Compound **7** incubated with untagged Ste14p (●) or Ste14p^{C99S,C121S,C126S} (△). Each experiment was performed in duplicate a minimum of two times. Error bars report standard error.

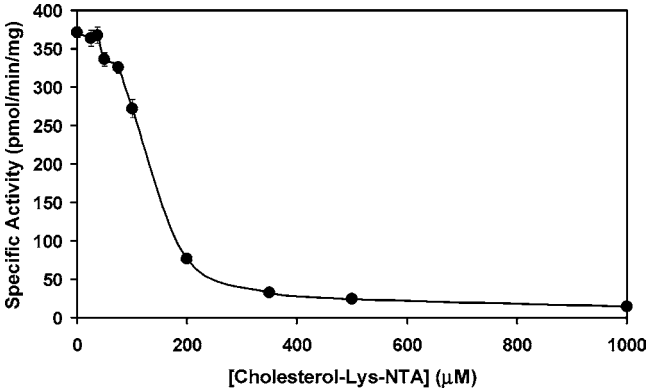

Figure 2. Concentration dependent inhibition of His-hIcmt-dependent methyltransferase activity by compound **7**. Assays were performed with 5 μg of crude membrane protein expressing His-hIcmt in the presence of 33 μM AFC, and the activity was quantified by the in vitro vapor diffusion methyltransferase assay. Each experiment was performed in duplicate a minimum of two times. Error bars are reported as standard error.

compound that may preclude access of the NTA group to the hydrophobic metal binding region of the protein.

Because the Ste14p protein used in these experiments contains a 10 histidine repeat at the N-terminus followed by a triply iterated *myc* epitope tag, we needed to ensure that the inhibition we observed with the cholesterol-Lys-NTA compound (**7**) was not due to interaction with the tags on Ste14p. Therefore, we constructed and expressed an untagged version of the Ste14p protein and performed similar methyltransferase assays in the presence and absence of **7**. These results demonstrated that the untagged wild-type protein is also inhibited by **7** in a concentration dependent manner with an IC_{50} of ~45 μM (Figure 1), suggesting that interaction of **7** with the tags is not responsible for the inhibition.

To further substantiate our hypothesis that **7** is inhibiting via metal chelation, we examined the effects of unmodified cholesterol and cholesterol-Lys-NTA trimethyl ester as inhibitors. In the latter compound, the carboxylic acids in the NTA portion of the molecule are methyl-esterified and thus unable to engage in metal chelation. The addition of increasing concentrations of either cholesterol or cholesterol-Lys-NTA trimethyl ester to the reaction had no inhibitory effect on Ste14p methyltransferase activity (Figure 1). These data further support the hypothesis that the inhibition mechanism of **7** is via metal chelation. An alternative hypothesis suggesting that Ste14p methyltransferase inhibition arises from a detergent effect of the hydrophobic NTA derivatives is not supported by our findings since the DOGS−NTA compound, a superior detergent to cholesterol-Lys-NTA, only inhibits ~25% of the methyltransferase enzymatic activity at 1 mM (Table 1).

Cysteine and histidine residues are common chelating ligands in proteins. To assess the importance of cysteines in the activity of Ste14p as well as in the ability of **7** to inhibit activity, a mutant of Ste14p was constructed that had all three naturally occurring cysteines mutagenized to serine (Ste14p^{C99S,} Ste14p^{C121S,} Ste14p^{C126S}). This cysteine-less Ste14p variant was expressed equally to the untagged wild-type protein as determined by immunoblot analysis (see Supporting Information). Our data further demonstrate that **7** inhibits the cysteine-less mutant with an IC_{50} of ~35 μM, a value comparable to that for the untagged wild-type enzyme (Figure 1). Taken together, these data suggest that the cysteine residues in Ste14p are not essential for activity and that other amino acids in Ste14p must be ligated to the metal ion in the protein structure.

We further examined the ability of **7** to inhibit the activity of the human homologue of Ste14p, hIcmt. Ste14p and hIcmt share 41% identity and 63% similarity overall, suggesting that their three-dimensional structures and mechanisms of action are similar. In fact, human Icmt expressed in yeast functionally complements a Δ*ste14* deletion strain (*27*). By analogy to the His-Ste14p experiments, an epitope tagged variant of hIcmt (His-hIcmt) containing a 10 histidine repeat at the N-terminus followed by a triply iterated *myc* epitope tag was expressed in *S. cerevisiae* and assayed for activity in the presence and absence of increasing concentrations of **7** (Figure 2) (*21*). The calculated IC_{50} for inhibition of His-hIcmt with **7** is ~135 μM (Figure 2). These data not only suggest that the human and yeast enzymes both have similarly accessible metal ions and, thus, three-dimensional structures, they also show that **7** should prove to be a excellent tool for studying the metal dependence of other members of the Icmt family of enzymes.

We report here that the novel compound cholesterol-Lys-NTA (**7**) exhibits great potential as a tool for characterizing the metal dependence of the Icmt family of enzymes. Although outside the scope of this initial study, complete certainty of the efficacy of **7** as a membrane metalloenzyme probe will come with the successful identification of the chelated metal. We are currently developing a strategy to extract the cholesterol−Lys-NTA−metal complex from reconstituted vesicles containing purified Ste14p (*21*) and are seeking to identify the metal by inductively coupled plasma mass spectrometry. Because **7** is based on a naturally occurring membrane lipid and appears to chelate metals buried deeply within water insoluble environments, this agent may also be useful as a general tool for identifying previously unappreciated metal dependencies of other classes of membrane proteins.

ACKNOWLEDGMENT

We would like to thank Kathryn Solka and Hilary Frase for preliminary data and Olvia C. Colon-Villafane for plasmid construction and protein expression. This work was supported by a grant from the National Pancreas Foundation (to C.A.H) and the Indiana 21st Century Fund (to C.A.H, and D.H.T).

Supporting Information Available: The chemical synthesis of the compound **7** as well as a description of the cloning procedures, immunoblot assays, and enzymatic assay is available free of charge via the Internet at http://pubs.acs.org.

LITERATURE CITED

(1) Schmitt, L., Dietrich, C., and Tampe, R. (1994) Synthesis and Characterization of Chelator-Lipids for Reversible Immobilization of Engineered Proteins at Self-Assembled Lipid Interfaces. *J. Am. Chem. Soc. 116*, 8485−8491.

(2) Shnek, D. R., Pack, D. W., Sasaki, D. Y., and Arnold, F. H. (1994) Specific Protein Attachment to Artificial Membranes via Coordination to Lipid-Bound Copper(II). *Langmuir 10*, 2382−2388.

(3) Gritsch, S., Neumaier, K., Schmitt, L., and Tampe, R. (1995) Engineered fusion molecules at chelator lipid interfaces imaged by reflection interference contrast microscopy (RICM). *Biosens Bioelectron 10*, 805−812.

(4) Dietrich, C., Boscheinen, O., Scharf, K. D., Schmitt, L., and Tampe, R. (1996) Functional immobilization of a DNA-binding protein at a membrane interface via histidine tag and synthetic chelator lipids. *Biochemistry 35*, 1100−1105.

(5) Dietrich, C., Schmitt, L., and Tampe, R. (1995) Molecular organization of histidine-tagged biomolecules at self-assembled lipid interfaces using a novel class of chelator lipids. *Proc. Natl. Acad. Sci. U.S.A. 92*, 9014−9018.

(6) Busch, K., and Tampe, R. (2001) Single molecule research on surfaces: from analytics to construction and back. *J. Biotechnol. 82*, 3−24.

(7) Levy, D., Mosser, G., Lambert, O., Moeck, G. S., Bald, D., and Rigaud, J. L. (1999) Two-dimensional crystallization on lipid layer: A successful approach for membrane proteins. *J. Struct. Biol. 127*, 44−52.

(8) Kubalek, E. W., Le Grice, S. F., and Brown, P. O. (1994) Two-dimensional crystallization of histidine-tagged, HIV-1 reverse transcriptase promoted by a novel nickel-chelating lipid. *J. Struct. Biol. 113*, 117−123.

(9) Barklis, E., McDermott, J., Wilkens, S., Schabtach, E., Schmid, M. F., Fuller, S., Karanjia, S., Love, Z., Jones, R., Rui, Y., Zhao, X., and Thompson, D. (1997) Structural analysis of membrane-bound retrovirus capsid proteins. *EMBO J. 16*, 1199−1213.

(10) Chiu, W., Avila-Sakar, A. J., and Schmid, M. F. (1997) Electron crystallography of macromolecular periodic arrays on phospholipid monolayers. *Adv. Biophys. 34*, 161−172.

(11) Kornberg, R. D., and Darst, S. A. (1991) Two-dimensional crystals of proteins on lipid layers. *Curr. Op. Struct. Biol. 1*, 642−646.

(12) Uzgiris, E. E., and Kornberg, R. D. (1983) Two-dimensional crystallization technique for imaging macromolecules, with application to antigen−antibody−complement complexes. *Nature 301*, 125−129.

(13) Bischler, N., Balavoine, F., Milkereit, P., Tschochner, H., Mioskowski, C., and Schultz, P. (1998) Specific interaction and two-dimensional crystallization of histidine tagged yeast RNA polymerase I on nickel-chelating lipids. *Biophys. J. 74*, 1522−1532.

(14) Celia, H., Wilson-Kubalek, E., Milligan, R. A., and Teyton, L. (1999) Structure and function of a membrane-bound murine MHC class I molecule. *Proc. Natl. Acad. Sci. U.S.A. 96*, 5634−5639.

(15) Venien-Bryan, C., Balavoine, F., Toussaint, B., Mioskowski, C., Hewat, E. A., Helme, B., and Vignais, P. M. (1997) Structural study of the response regulator HupR from Rhodobacter capsulatus. Electron microscopy of two-dimensional crystals on a nickel-chelating lipid. *J. Mol. Biol. 274*, 687−692.

(16) Zhang, F. L., and Casey, P. J. (1996) Protein prenylation: molecular mechanisms and functional consequences. *Annu. Rev. Biochem. 65*, 241−269.

(17) Young, S. G., Ambroziak, P., Kim, E., and Clarke, S. (2000) in *The Enzymes,* 3rd ed.; pp 155−213, Academic Press, San Diego, CA.

(18) Hrycyna, C. A., and Clarke, S. (1993) Modification of eukaryotic signaling proteins by C-terminal methylation reactions. *Pharmacol. Ther. 59*, 281−300.

(19) Clarke, S. (1992) Protein isoprenylation and methylation at carboxyl-terminal cysteine residues. *Annu. Rev. Biochem. 61*, 355−386.

(20) Desrosiers, R. R., Nguyen, Q. T., and Beliveau, R. (1999) The carboxyl methyltransferase modifying G proteins is a metalloenzyme. *Biochem. Biophys. Res. Commun. 261*, 790−797.

(21) Anderson, J. L., Frase, H., Michaelis, S., and Hrycyna, C. A. (2005) Purification, functional reconstitution and characterization of the Saccharomyces Cerevisiae isoprenylcysteine carboxyl methyltransferase Ste14p. *J. Biol. Chem. 280*, 7336−7345.

(22) Zhou, M. H., Haldar, S., Franses, J., Kim, J. M., and Thompson, D. H. (2005) Synthesis and self-assembly properties of acylated cyclodextrins and nitrilotriacetic acid (NTA)-modified ligands for interfacial protein crystallization. *Supramol. Chem. 17*, 101−111.

(23) Hrycyna, C. A., Wait, S. J., Backlund, P. S., Jr., and Michaelis, S. (1995) Yeast STE14 methyltransferase, expressed as TrpE-STE14 fusion protein in Escherichia coli, for in vitro carboxylmethylation of prenylated polypeptides. *Methods Enzymol. 250*, 251−266.

(24) Ota, I. M., and Clarke, S. (1989) Enzymatic methylation of 23−29-kDa bovine retinal rod outer segment membrane proteins. Evidence for methyl ester formation at carboxyl-terminal cysteinyl residues. *J. Biol. Chem. 264*, 12879−12884.

(25) Stephenson, R. C., and Clarke, S. (1990) Identification of a C-terminal protein carboxyl methyltransferase in rat liver membranes utilizing a synthetic farnesyl cysteine-containing peptide substrate. *J. Biol. Chem. 265*, 16248−16254.

(26) Hrycyna, C. A., and Clarke, S. (1990) Farnesyl cysteine C-terminal methyltransferase activity is dependent upon the STE14 gene product in Saccharomyces cerevisiae. *Mol. Cell Biol. 10*, 5071−5076.

(27) Dai, Q., Choy, E., Chiu, V., Romano, J., Slivka, S. R., Steitz, S. A., Michaelis, S., and Philips, M. R. (1998) Mammalian prenylcysteine carboxyl methyltransferase is in the endoplasmic reticulum. *J. Biol. Chem. 273*, 15030−15034.

(28) Hrycyna, C. A., Sapperstein, S. K., Clarke, S., and Michaelis, S. (1991) The Saccharomyces cerevisiae STE14 gene encodes a methyltransferase that mediates C-terminal methylation of a-factor and RAS proteins. *EMBO J. 10*, 1699−1709.

BC050027D

Transferrin-Mediated Gold Nanoparticle Cellular Uptake

Pei-Hui Yang,[†,§] Xuesong Sun,[†] Jen-Fu Chiu,[‡] Hongzhe Sun,*[,†] and Qing-Yu He*[,†]

Department of Chemistry and Open Laboratory of Chemical Biology, and Institute of Molecular Biology, University of Hong Kong, Hong Kong . Received September 18, 2004; Revised Manuscript Received February 10, 2005

Targeted drug delivery is an important research area in specific therapy. Transferrin-conjugated nanoparticles are an attractive formulation as a vehicle for specific cellular uptake and targeted drug delivery. In this report, atomic force microscopy imaging was used to visualize the process of cellular uptake of transferrin-coupled gold nanoparticles on the surfaces of live cells for the first time. High-resolution images were captured, showing the endocytosis of transferrin-conjugated nanoparticles taking place during the process of internalization. This specific transferrin-mediated nanoparticle uptake was validated by confocal scanning imaging and transferrin competition experiments.

Targeted entry into cells is an important area of research in drug delivery and therapy (*1*–*4*). Site-specific delivery of drugs and therapeutics can significantly reduce drug toxicity and increase therapeutic effects. To realize efficient and specific cellular drug delivery, one strategy is to modify or conjugate drug with a ligand that can be efficiently taken up by target cells via receptor-mediated endocytosis (*5*). Transferrin (TF)[1] is such a suitable "ligand" for conjugating drugs, since it can be specifically recognized and taken up by TF receptors actively expressed on the surface of various tumor cells (*6*). The transferrin−receptor interaction has therefore been exploited as a potential efficient pathway for the cellular uptake of drugs and genes (*7*–*9*).

Nanoparticles have also been considered as effective delivery vehicles and extensively studied for delivering drugs, genes, diagnostics, and vaccines into cells of interest (*10*–*12*). Nanoparticles cross-linking with proteins have demonstrated better stability and efficiency for cellular uptake. Nanoparticle−TF conjugation is thus an attractive formulation for specific cellular uptake and targeted drug delivery.

Atomic force microscopy (AFM) is a surface analytical technique that can generate nanoscale topography by scanning a fine silicon tip across the surface. Because it can perform high-resolution imaging under physiological conditions in a nondestructive manner, AFM has developed into a powerful tool for studying the structural details of biological systems (*13, 14*). While the use of AFM to characterize the morphology of nanoparticles and biophysical properties of cells has previously been reported, the imaging of the nanoparticle uptake into cells is a rarely studied area. In this report we used AFM to visualize the process of cellular uptake of TF-conjugated gold nanoparticles on the surfaces of live cells for the first time.

Gold nanoparticles were synthesized according to a modified literature method (*15*). These nanoparticles were characterized by transmission electron micrography and powder X-ray diffraction. They were then covalently coupled to TF molecules by mercaptoacetic acid (*16*). Measurements with dynamic laser light scattering showed that these nanoparticles have sizes of 20.2 ± 0.6 nm for Au alone and 96.7 ± 2.0 for TF-derivatized Au−TF particles, indicating that multiple coupling of Au to TF or aggregation for some of the Au−TF particles occurred. When the Au−TF nanoparticles were incubated with human nasopharyngeal carcinoma cells (NPC, SUNE1) (*17*) under physiologically relevant conditions, a phenomenon of nanoparticle internalization into cells was visualized by a multimode AFM with a Nanoscopy IIIa controller (Veeco/Digital Instruments, Santa Barbara, CA) (Figure 1). The AFM image captured after 5-h incubation shows that cellular uptake was partially proceeding, leading to a "bumpy" surface (Figure 1C). The process of the nanoparticle uptake by NPC cells can be further observed by AFM imaging in a "zoom in" scale. The high-resolution image in Figure 1D demonstrated how the endocytosis is taking place. While a couple of clear holes indicated that the endocytosis may be just completed in these areas, cellular uptake halfway through the internalization process for some of the Au−TF nanoparticle cluster was vividly visualized. To our knowledge, this is the first time that the cellular process of nanoparticle uptake has been observed by AFM.

To validate the nanoparticle internalization into NPC cells, a Zeiss 410 (Germany) confocal laser scanning microscope (excitation at wavelength 488 nm and emission at wavelength 515 nm) was utilized to capture the fluorescence images of the cells after incubation with fluorescence-labeled Au−TF nanoparticles. The emission of the labeled TF nanoparticles produces green fluorescence. Its position and intensity represent the location

* Correspondence to Dr. Qing-Yu He, Department of Chemistry, University of Hong Kong, Pokfulam, Hong Kong, China. Tel: (852)2299-0787, Fax: (852)2817-1006, E-mail: qyhe@hku.hk.

† Department of Chemistry and Open Laboratory of Chemical Biology.

‡ Institute of Molecular Biology.

§ A visiting scholar from the Department of Chemistry, Jinan University, Guangzhou, China, and registered Ph.D. student in the Anhui Institute of Optics and Fine Mechanics, Chinese Academy of Sciences.

[1] Abbreviations: TF, transferrin; Au−TF, transferrin-conjugated gold nanoparticles; holo-TF, natural full-length transferrin; AFM, atomic force microscopy; NPC, nasopharyngeal carcinoma cells; ICP-MS, inductive coupled plasma mass spectroscopy.

10.1021/bc049775d CCC: $30.25 © 2005 American Chemical Society
Published on Web 04/12/2005

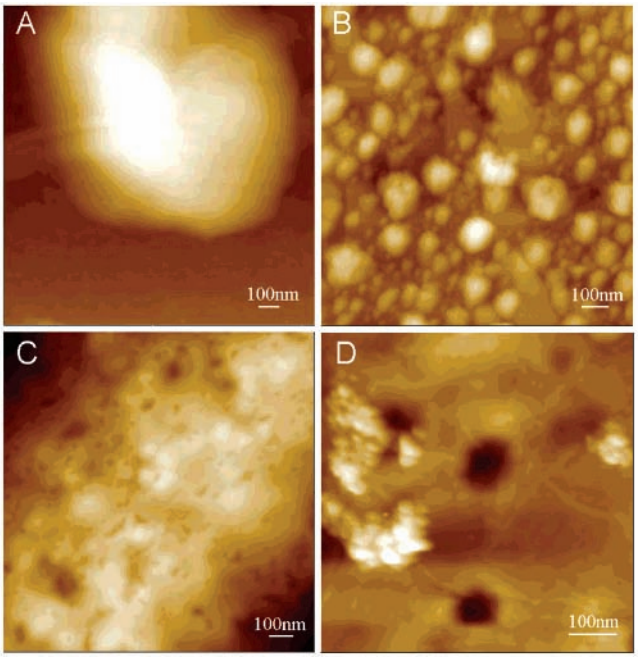

Figure 1. AFM images demonstrate Au−TF nanoparticle uptake by NPC cells. (A) A single NPC cell; (B) Au−TF nanoparticles on a NPC cell surface at the beginning of incubation; (C) NPC cell surface after incubation with Au−TF nanoparticles for 5 h; and (D) "zoom in" AFM image of cell surface after incubation with Au−TF for 5 h, showing nanoparticle uptake during the process of endocytosis.

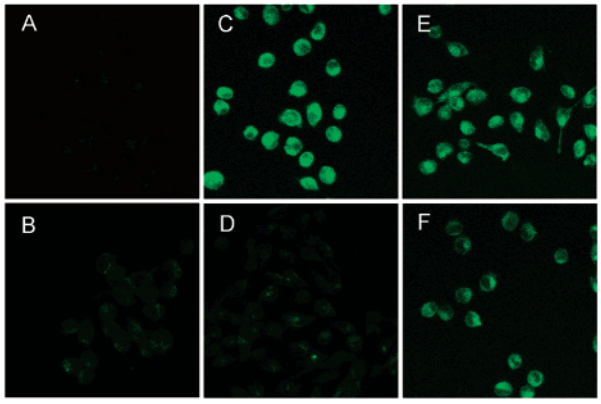

Figure 2. Confocal cell images show that Au−TF nanoparticles were internalized into the cellular plasma of NPC cells via TF−receptor interaction pathway (5-h treatment). (A) Control cells without Au−TF nanoparticles; (B) cells treated with Au nanoparticles alone; (C) cells incubating with Au−TF nanoparticles; (D) cells treated with Au−albumin nanoparticles; (E and F) cells cotreated with different proportions of Au−TF verses holo-TF (1:2 and 1:5, respectively).

and relative concentration of the labeled TF nanoparticles. Figure 2 shows confocal images for cells treated under different conditions for 5 h. Control cells (Figure 2A) and cells treated with Au nanoparticles alone (Figure 2B) reasonably displayed little fluorescence. In contrast, very bright fluorescence was observed in cells incubated with Au−TF (Figure 2C), clearly indicating that alot of Au−TF nanoparticles were taken up into cells, with most of the internalized nanoparticles localizing in the cytoplasm compartment. At the same time, the NPC cells were still healthy after taking up the nanoparticles. Moreover, a control study showed that the fluorescence-labeled Au−TF particles did not have detectable changes

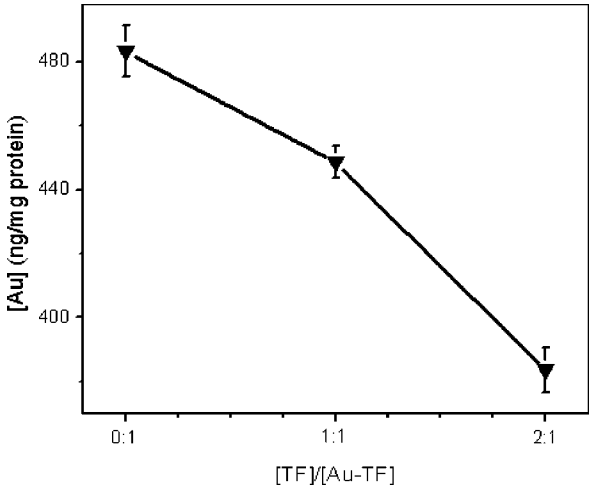

Figure 3. Nanoparticle concentrations at different ratio of holo-TF verses Au−TF. [Au−TF] were fixed at 10 μM.

in sizes after incubation with the cell culture medium for 24 h, revealing the high stability of the covalently TF-derivatized particles during the experiments.

Since nanoparticle uptake into cells could go through different processes including phagocytosis, fluid-phase endocytosis, and receptor-mediated endocytosis, we performed control studies with fluorescence-labeled Au−albumin and competition experiments with natural full-length transferrin (holo-TF) to verify whether the internalization of the TF-coupled nanoparticles was mediated via the specific TF−receptor interaction pathway. As shown in Figure 2D, cells incubated with Au−albumin displayed only little minor fluorescence, and compared to that in Figure 2C, fluorescence intensities significantly decreased in the cells cotreated with Au−TF and excess holo-TF (Figure 2E,F). These results evidently implicate the specific nanoparticle cellular uptake through TF−receptor interaction.

Other supporting evidence was derived from ICP-MS measurements of the nano−Au contents in cells treated with different proportions of holo-TF/Au−TF. Three different concentration ratios (0:1, 1:1, and 2:1) of holo-TF verses Au−TF were introduced into the cell culture. Total cell lysates digested from the harvested NPC cells were used for determination of Au concentration in cells by ICP-MS (7500 series, Agilent). Figure 3 clearly shows that the Au concentration in the cells significantly decreased with regard to the increase of holo-TF concentration in the cell culture. These data, together with the above confocal results, strongly suggest that at least part of the TF-coupled nanoparticles were internalized into cells via TF-receptor mediated endocytosis.

The TF−receptor cycling pathway has long been considered to be an effective "delivery system" into cells, and many cytotoxic agents have been conjugated to TF as potential anticancer therapeutics (*6, 9*). Our present data demonstrated that TF−receptor-mediated nanoparticle delivery into cells really occurred, and that the endocytosis process can be directly visualized through AFM imaging. In light of a recent study showing that TF binds the receptor ectodomain to form the TF−receptor complex (*18*), it is possible that TF conjugation with nanoparticles at certain positions is tolerable for the endocytosis, since the ectal binding mode of TF−receptor reduces space restrictions. That being the case, our present observations provide useful information for better design of nanodrugs and their targeted delivery.

ACKNOWLEDGMENT

This work was partially supported by Hong Kong Research Grants Council Grants HKU 7227/02M (to Q.Y.H.), the Department of Chemistry, and the Areas of Excellence scheme of Hong Kong University Grants Committee. We thank Mr. Rong Chen for providing Au nanoparticles.

Supporting Information Available: Experimental details. This material is available free of charge via the Internet at http://pubs.acs.org.

LITERATURE CITED

(1) Finley, R. S. (2003) Overview of targeted therapies for cancer. *Am. J. Health Syst. Pharm. 60*, S4−10.
(2) Portlock, J. L., and Calos, M. P. (2003) Site-specific genomic strategies for gene therapy. *Curr. Opin. Mol. Ther. 5*, 376−382.
(3) Abou-Jawde, R., Choueiri, T., Alemany, C., and Mekhail, T. (2003) An overview of targeted treatments in cancer. *Clin. Ther. 25*, 2121−2137.
(4) Weissig, V. (2003) Mitochondrial-targeted drug and DNA delivery. *Crit. Rev. Ther. Drug Carrier Syst. 20*, 1−62.
(5) Russell-Jones, G. J. (2001) The potential use of receptor-mediated endocytosis for oral drug delivery. *Adv. Drug Delivery Rev. 46*, 59−73.
(6) Qian, Z. M., Li, H., Sun, H., and Ho, K. (2002) Targeted drug delivery via the transferrin receptor-mediated endocytosis pathway. *Pharmacol. Rev. 54*, 561−587.
(7) Li, H., and Qian, Z. M. (2002) Transferrin/transferrin receptor-mediated drug delivery. *Med. Res. Rev. 22*, 225−250.
(8) Li, H., Sun, H., and Qian, Z. M. (2002) The role of the transferrin-transferrin-receptor system in drug delivery and targeting. *Trends Pharmacol. Sci. 23*, 206−209.
(9) Widera, A., Norouziyan, F., and Shen, W. C. (2003) Mechanisms of TfR-mediated transcytosis and sorting in epithelial cells and applications toward drug delivery. *Adv. Drug Delivery Rev. 55*, 1439−1466.
(10) Rao, G. C., Kumar, M. S., Mathivanan, N., and Rao, M. E. (2004) Nanosuspensions as the most promising approach in nanoparticulate drug delivery systems. *Pharmazie 59*, 5−9.
(11) Cui, Z., and Mumper, R. J. (2003) Microparticles and nanoparticles as delivery systems for DNA vaccines. *Crit Rev. Ther. Drug Carrier Syst. 20*, 103−137.
(12) Panyam, J., and Labhasetwar, V. (2003) Biodegradable nanoparticles for drug and gene delivery to cells and tissue. *Adv. Drug Deliv. Rev. 55*, 329−347.
(13) Horber, J. K., and Miles, M. J. (2003) Scanning probe evolution in biology. *Science 302*, 1002−1005.
(14) Allen, S., Rigby-Singleton, S. M., Harris, H., Davies, M. C., and O'Shea, P. (2003) Measuring and visualizing single molecular interactions in biology. *Biochem. Soc. Trans. 31*, 1052−1057.
(15) Sun, Y., and Xia, Y. (2002) Shape-controlled synthesis of gold and silver nanoparticles. *Science 298*, 2176−2179.
(16) Chan, W. C., and Nie, S. (1998) Quantum dot bioconjugates for ultrasensitive nonisotopic detection. *Science 281*, 2016−2018.
(17) Wang, X., Masters, J. R., Wong, Y. C., Lo, A. K., and Tsao, S. W. (2001) Mechanism of differential sensitivity to cisplatin in nasopharyngeal carcinoma cells. *Anticancer Res. 21*, 403−408.
(18) Cheng, Y., Zak, O., Aisen, P., Harrison, S. C., and Walz, T. (2004) Structure of the human transferrin receptor-transferrin complex. *Cell 116*, 565−576.

BC049775D

The Peptide Route to Multifunctional Gold Nanoparticles

Zhenxin Wang,[†] Raphaël Lévy,[†,‡] David G. Fernig,[‡] and Mathias Brust[†,*]

Centre for Nanoscale Science, Department of Chemistry and School of Biological Sciences, The University of Liverpool, Liverpool, UK. Received February 21, 2005; Revised Manuscript Received April 8, 2005

Extremely stable, peptide-capped gold nanoparticles with two different biomolecular recognition motifs expressed on their surface have been prepared, and their specific and selective binding to artificial, DNA-modified target particles and to DNA and protein microarrays has been demonstrated. Stabilization and biofunctionalization has been achieved in a single preparative step starting with citrate-stabilized gold hydrosols and a derivatization cocktail of peptide-capping ligands, which carry the functionalities of choice.

Exploiting the optical properties of nanoparticles for the development of ultrasensitive detection and imaging methods in the biomedical sciences is becoming increasingly important (*1*−*3*). Particularly attractive is the use of Au and Ag nanoparticles in resonant light scattering (RLS) and photothermal microscopy, which are able to image single particles (*4*−*7*). The latter technique is capable of detecting particles at least as small as 2 nm in complex biological environments. For these applications, attaching the biomolecular recognition motif of interest to the nanoparticles has to be readily achieved, and, most importantly, the probes must not bind nonspecifically to each other or to anything else present in the system under investigation. In addition, introducing multiple functionalities would be of great value, as it provides more flexibility for multiplexing in bioanalytical applications and new tools to control the bottom-up assembly of nanostructures.

Here we demonstrate that multiply functional peptide-stabilized gold nanoparticles are readily obtained in a one-step surface coating procedure and that the respective surface functionalities can be selectively addressed on a microarray. The particles are of the stability typical for peptide capping (*8*) and show no indication of nonspecific binding as established by transmission electron microscopy (TEM), UV−vis spectroscopy, and microarray imaging even under testing conditions of ionic strength (see Supporting Information). In contrast to most previously reported approaches, stabilization and functionalization of the particles are independent of each other, while both are achieved in a single step. Functionality is simply introduced by including a proportion of stabilizing peptide to which a functionality of choice has been attached. Therefore, the number of recognition functions present on each particle could be altered and even reduced to a single or very few moieties without compromising the stability of the particles.

We have previously reported the preparation of peptide-capped gold nanoparticles and their functionalization with biotin (see also Supporting Information) (*8*). We now take advantage of the generality of the peptide route and demonstrate that it provides a fast and simple approach to DNA functionalization and to bifunctional nanoparticles carrying both DNA and biotin moieties. These functionalities were chosen for being already well established in nanoparticle systems and thus predictable in their recognition properties (*1*−*7*, *9*−*26*).

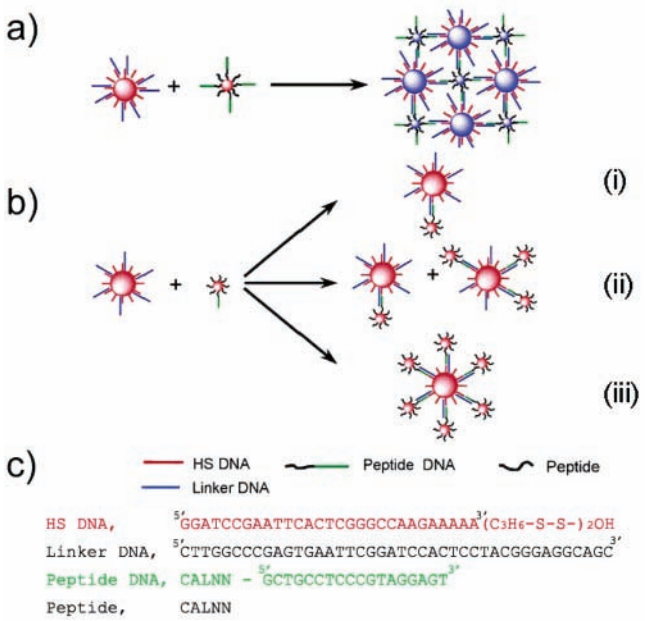

Figure 1. Nanoparticle binding scenarios and sequences of DNA and functionalized peptides. (a) 13 nm DNA-functionalized small particles with high DNA loading (>3%) binding to 40 nm DNA-stabilized large particles to form extended aggregates. (b) 13 nm DNA functionalized small particles with intermediate DNA loading (0.3−1%) binding to DNA-stabilized 40 nm large particles at a small particle to large particle ratio of (i) 10:1, (ii) 30:1, and (iii) 100:1. (c) Sequences of DNA and functionalized peptides used. Peptides are in the conventional N- to C-terminal orientation.

Thirteen nanometer gold nanoparticles were prepared via the classical citrate reduction route (*27*, *28*). Stabilization and DNA functionalization was achieved by adding an aqueous mixture of the CALNN (cysteine, alanine, leucine, asparagine, asparagine) capping peptide and a CALNN−DNA conjugate (18 base single-stranded DNA) followed by centrifugation to purify the material.

* Corresponding author. E-mail: M.Brust@liv.ac.uk; Fax: (+44) 151-794-3588.

[†] Centre for Nanoscale Science, Department of Chemistry.

[‡] Centre for Nanoscale Science, School of Biological Sciences.

10.1021/bc050047f CCC: $30.25 © 2005 American Chemical Society
Published on Web 04/26/2005

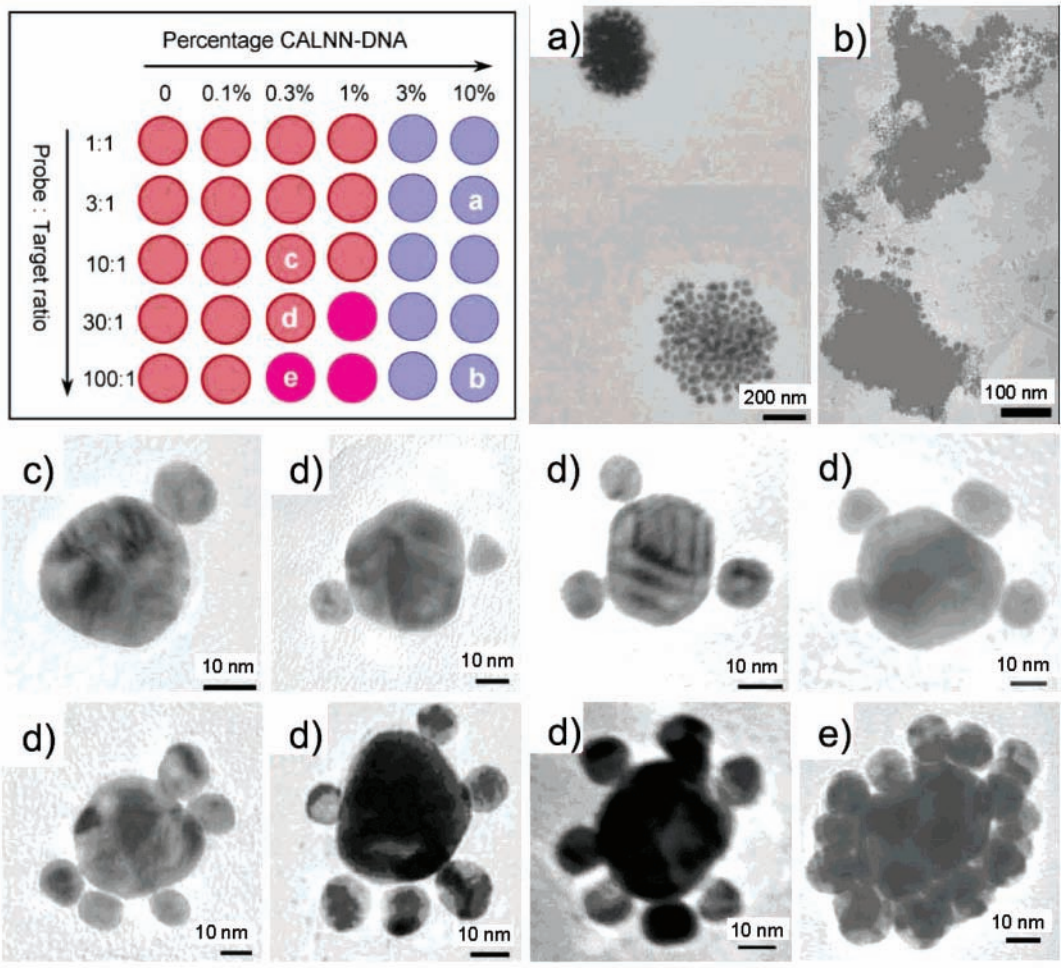

Figure 2. Dependence of the aggregation of small (probe) and large (target) particles on the experimental conditions. Varying both the DNA loading of the small particles and the small particle to large particle ratio affects the perceived color of the solutions (top left panel) and the type of aggregates formed (see selected TEM images, labels correspond to those in the top left panel). Blue color indicates the formation of extended aggregates (a and b), red indicates either no aggregation or the formation of large particles labeled by a small number of small particles (c and d), and purple indicates the formation of a dense shell of small particles around individual large particles (e).

The specific recognition properties of these particles were investigated by binding to standard Mirkin-type (*9*) 40 nm gold nanoparticles via a three-strand system. The 40 nm particles were stabilized by a shell of thiol-modified (ss) DNA, which was then hybridized to a linker strand of 42 bases to leave 18 bases as an overhanging recognition sequence. This sequence was chosen to be complementary to the DNA on the peptide-capped particles. DNA hybridization then leads to particle aggregation, demonstrating the successful DNA functionalization of the peptide-capped particles.

In an attempt to control the number of DNA molecules per nanoparticle, we systematically varied the proportion of CALNN−DNA in the stabilization mixture. We also changed the relative abundance of 40 and 13 nm particles in the hybridization buffer. Possible binding scenarios for these different experimental conditions are schematically suggested in Figure 1, and the range of different nanostructures found experimentally by TEM is shown in Figure 2. It was found that the formation of very different aggregated structures was controlled by these two parameters. At a glance, this is best confirmed by optical spectroscopy or simply by visual inspection of the aqueous reaction mixtures. The formation of extended aggregates is observed already for relatively low DNA loadings, i.e., whenever the concentration of CALNN−DNA in the stabilizing mixture reaches 3% in total ligands (40 nM) or more. This aggregation behavior has been confirmed from a one-to-one ratio to a 100-fold excess of complementary particles in the solution. The transition from a well-dispersed system to complete aggregation happens rather suddenly. Close to the proportion of CALNN−DNA in the stabilization mixture required for the formation of precipitates, structures, in which two or more large particles were bound to each other via small particles were regularly observed. The formation of extended aggregates is readily monitored by a clearly perceptible color change of the solutions from red to blue followed by the slow precipitation of the material. On the contrary, at a CALNN−DNA concentration of 1.4 nM (0.1% of total number of ligands) or less no specific binding was observed in the system, even with a 100-fold excess of small particles. The parameter space in which pairs between large and small particles were obtained was remarkably narrow. Isolated aggregated structures of a discrete number of small particles bound to a single large particle were obtained only for intermediate concentrations (4−14 nM, i.e., 0.3−1% of total number of ligands) of CALNN−DNA in the stabilizing mixture. Within this narrow range the binding number of small particles per large particle is chiefly determined by the relative proportion of small particles in the system, as illustrated by the bar diagrams in Figure 3. Depending on the relative excess of small particles, aggregates with binding

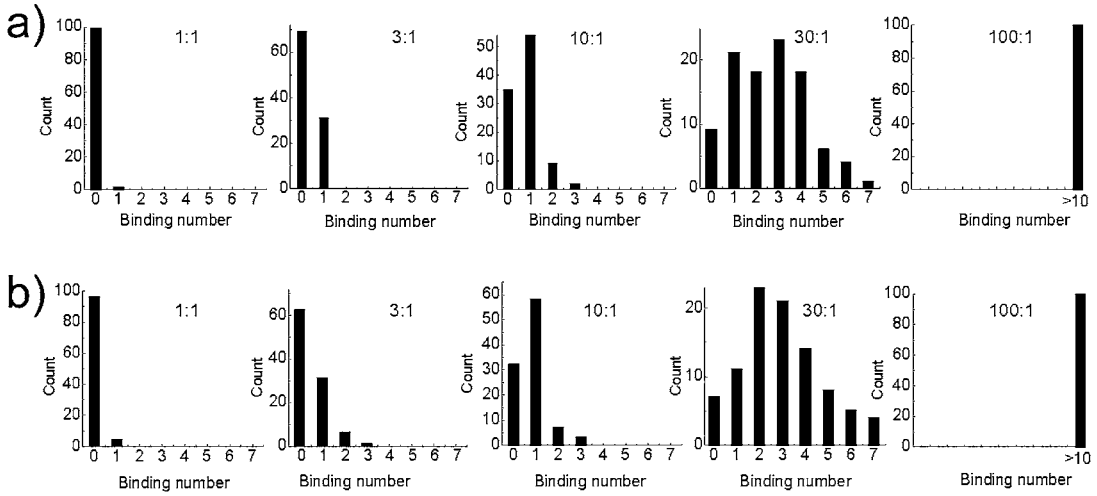

Figure 3. Dependence of small particle to large particle binding numbers on the applied small particle to large particle ratio. Experimentally found binding number distributions (by TEM) are shown for small particle to large particle ratios from 1:1 to 100:1 for a DNA loading of the small particles of (a), 0.3% and (b), 1%.

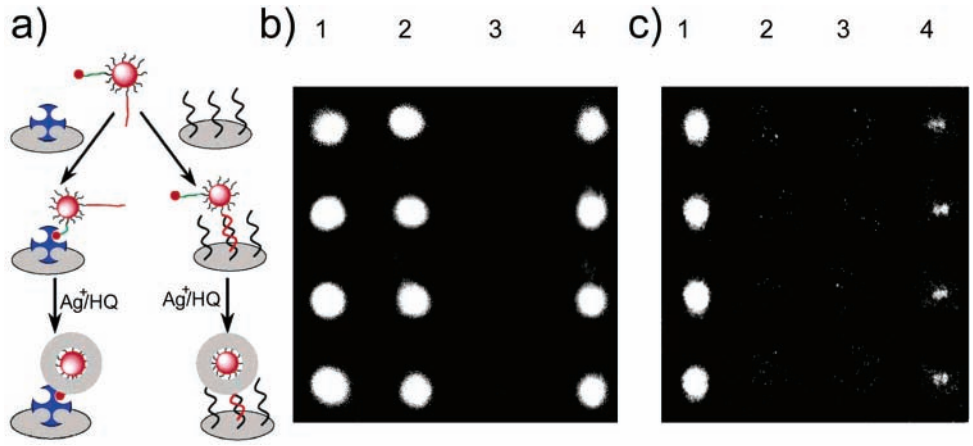

Figure 4. Schematic representation of DNA and protein microarrays labeled with bifunctional gold nanoparticles followed by silver enhancement (a). Light scattering images of protein microarray (b) and DNA microarray (c) after silver enhancement. In b, avidin was spotted on column 1, 2, and 4, while protein A was spotted as a nonspecific control on column 3; in c, perfectly matched DNA was spotted on column 1, three-base-mismatched DNA was spotted on column 2, two-base-mismatched DNA was spotted on column 3, and one-base-mismatched DNA was spotted on column 4.

numbers from 1 to ca. 100 small particles per large particle could be prepared. The limiting case is the formation of a complete shell of small particles around each large particle as shown in Figure 2e. Aggregates with such high binding numbers also led to a perceptible color change of the solution from red to purple without subsequent precipitation. Core−shell nanostructures of large particles surrounded by small particles are stable in solution for weeks and are readily isolated from excess small particles by centrifugation.

These experiments may mimic the attachment of gold nanoparticle probes to target structures in biological systems and map out the conditions required to achieve effective labeling. More importantly, they provide guidance for the preparation of nanoparticles with two or more different specific recognition groups attached. Such multifunctionality of nanoparticles has been reported previously for nonbiomolecular functionalities on monolayer protected clusters (MPCs) (*18*, *29*−*31*). Niemeyer et al. have shown that multifunctionality can be achieved by the use of different DNA sequences on one particle and also reported that a relatively low loading of the particles with DNA is sufficient to achieve very efficient specific binding (*19*). Here we demonstrate that different types of biomolecular recognition groups, i.e., biotin and DNA, can be readily incorporated in a single stabilization/functionalization step via our peptide route. Guided by the results obtained for the DNA only system we have chosen to include 70 nM (5% of total number of ligands) CALNN-DNA (18 base recognition sequence) and 70 nM (5% of total number of ligands) CALNNGK(biotin)G in the stabilization mixture. This should lead to high reactivity of the particles toward both complementary DNA and avidin. To demonstrate the binding specificity of these bifunctional particles, we prepared a protein microarray containing spots with avidin as well as control spots with protein A, and a DNA microarray containing spots with complementary DNA, as well as control spots with DNA possessing mismatches of one, two, and three bases. After binding of the particles the microarrays were exposed to a silver enhancement step, i.e., electroless deposition of metallic silver on the gold particles, which act as nucleation sites (*32*). The microarrays were read by measuring the intensity of scattered light using a Qiagen High-light System. The results of specific binding of the bifunctional particles to these microarrays are shown in Figure 4. It was found that the particles bind to both avidin and to complementary DNA with high specificity. Importantly, no evidence for significant nonspecific binding was found (detailed data in Supporting

Information). DNA with a one base mismatch is still weakly detected, which is consistent with the expected remaining recognition properties of this DNA. No binding to DNA with a mismatch of two or more bases is detected.

In conclusion, we have developed a straightforward route to stable gold nanoparticles, both with single and with dual biological functionality. The particles exhibit the specific recognition properties of the biological functionalities they carry without any indication of nonspecific binding or particle aggregation. While the stability of the particles does not depend on the number of functional groups introduced, functionalization and stabilization are achieved in a single step where the relative abundance of functional peptides in the stabilization mixture appears to control the number of functionalities introduced into the peptide ligand shell of the particles. The large difference in the chemical nature of the recognition motifs used in this study suggests that this approach should be easily extended to a variety of peptide and peptide conjugate labels, including the large number of peptides recognizing with high specificity and affinity biological and nonbiological structures.

ACKNOWLEDGMENT

The authors thank the BBSRC (Centre for BioArray Innovation), the Cancer and Polio Research Fund, the European Union, and the North West Cancer Research Fund for financial support.

Supporting Information Available: Experimental details. This material is available free of charge via the Internet at http://pubs.acs.org.

LITERATURE CITED

(1) Alivisatos, A. P. (2004) The use of nanocrystals in biological detection. *Nature Biotechnol*. *22*, 47−52.
(2) Liz-Marzán, L. M. (2004) Nanometals: formation and color. *Mater. Today 7* (2), 26−31.
(3) Katz, E., and Willner, I. (2004) Integrated Nanoparticle-Biomolecule Hybrid Systems: Synthesis, Properties, and Applications. *Angew. Chem., Int. Ed. 43*, 6042−6108.
(4) Yguerabide, J., and Yguerabide, E. E. (2001) Resonance light scattering particles as ultrasensitive labels for detection of analytes in a wide range of applications. *J. Cell. Biochem. 37* (Suppl.), 71−81.
(5) Sonnichsen, C., Franzl, T., Wilk, T., von Plessen, G., Feldmann, J., Wilson, O., and Mulvaney, P. (2002) Drastic reduction of plasmon damping in gold nanorods. *Phys. Rev. Lett*. *88*, art. no. 077402.
(6) Boyer, D., Tamarat, P., Maali, A., Lounis, B., and Orrit, M. (2002) Photothermal imaging of nanometer-sized metal particles among scatterers. *Science 297*, 1160−1163.
(7) Berciaud, S., Cognet, L., Blab, G. A., and Lounis, B. (2004) Photothermal heterodyne imaging of individual nonfluorescent nanoclusters and nanocrystals. *Phys. Rev. Lett. 93*, art. no. 257402.
(8) Levy, R., Thanh, N. T. K., Doty, R. C., Hussain, I., Nichols, R. J., Schiffrin, D. J., Brust, M., and Fernig, D. G. (2004) Rational and combinatorial design of peptide capping ligands for gold nanoparticles. *J. Am. Chem. Soc. 126*, 10076−10084.
(9) Mirkin, C. A., Letsinger, R. L., Mucic, R. C., and Storhoff, J. J. (1996) A DNA-based method for rationally assembling nanoparticles into macroscopic materials. *Nature 382*, 607−609.
(10) Alivisatos, A. P., Johnsson, K. P., Peng, X., Wilson, T. E., Loweth, C. J., Bruchez, M. P., Jr., and Schultz, P. G. (1996) Organization of 'nanocrystal molecules' using DNA. *Nature 382*, 609−611.
(11) Mucic, R. C., Storhoff, J. J., Mirkin, C. A., and Letsinger, R. L. (1998) DNA-directed synthesis of binary nanoparticle network materials. *J. Am. Chem. Soc. 120*, 12674−12675.
(12) Loweth, C. J., Caldwell, W. B., Peng, X., Alivisatos, A. P., and Schultz, P. G. (1999) DNA-based assembly of gold nanocrystals. *Angew. Chem., Int. Ed. 38*, 1808−1812.
(13) Storhoff, J. J., and Mirkin, C. A. (1999) Programmed materials synthesis with DNA. *Chem. Rev. 99*, 1849−1862.
(14) Mann, S., Shenton, W., Li, M., Connolly, S., and Fitzmaurice, D. (2000) Biologically programmed nanoparticle assembly. *Adv. Mater. 12*, 147−150.
(15) Taton, T. A., Mirkin, C. A., and Letsinger, R. L. (2000) Scanometric DNA array detection with nanoparticle probes. *Science 289*, 1757−1760.
(16) Niemeyer, C. M. (2001) Nanoparticles, proteins, and nucleic acids: Biotechnology meets materials science. *Angew. Chem., Int. Ed. 40*, 4128−4158.
(17) Zanchet, D., Micheel, C. M., Parak, W. J., Gerion, D., and Alivisatos, A. P. (2001) Electrophoretic isolation of discrete Au nanocrystal/DNA conjugates. *Nano Lett. 1*, 32−35.
(18) Sastry, M., Rao, M., and Ganesh, K. N. (2002) Electrostatic assembly of nanoparticles and biomacromolecules. *Acc. Chem. Res. 35*, 847−855.
(19) Niemeyer, M., Ceyhan, B., and Hazarika, P. (2003) Oligofunctional DNA-Gold Nanoparticle Conjugates. *Angew. Chem., Int. Ed., 42*, 5766−5770.
(20) Fu, A., Micheel, C. M., Cha, J., Chang, H., Yang, H., and Alivisatos, A. P. (2004) Discrete nanostructures of quantum dots/Au with DNA. *J. Am. Chem. Soc. 126*, 10832−10833.
(21) Li, M., and Mann, S. (2004) DNA-directed assembly of multifunctional nanoparticle networks using metallic and bioinorganic building blocks. *J. Mater. Chem. 14*, 2260−2263.
(22) Gourishankar, A., Shukla, S., Ganesh, K. N., and Sastry, M. (2004) Isothermal titration calorimetry studies on the binding of DNA bases and PNA base monomers to gold nanoparticles. *J. Am. Chem. Soc. 126*, 13186−13187.
(23) Wessels, J. M., Nothofer, H. G., Ford, W. E., von Wrochem, F., Scholz, F, Vossmeyer, T., Schroedter, A., Weller, H., and Yasuda, A. (2004) Optical and electrical properties of three-dimensional interlinked gold nanoparticle assemblies. *J. Am. Chem. Soc. 126*, 3349−3356.
(24) Kanaras, A. G., Wang, Z., Bates, A. D., Cosstick, R., and Brust, M. (2003) Towards multistep nanostructure synthesis: Programmed enzymatic self-assembly of DNA/gold systems. *Angew. Chem., Int. Ed. 42*, 191−194.
(25) Wang, Z., Kanaras, A. G., Bates, A. D., Cosstick, R., and Brust, M. (2004) Enzymatic DNA processing on gold nanoparticles. *J. Mater. Chem*. *14*, 578−580.
(26) Niazov, T., Pavlov, V., Xiao, Y., Gill, R., and Willner, I. (2004)DNAzyme-functionalized Au nanoparticles for the amplified detection of DNA or telomerase activity. *Nano Lett. 4*, 1683−1687.
(27) Turkevich, J., Stevenson, P. C., and Hillier, J. (1951) Astudy of the nucleation and growth processes in the synthesis of colloidal gold. *Discuss. Faraday Soc. 11*, 55−75.
(28) Frens, G. (1973) Controlled nucleation for the regulation of the particle size in monodisperse gold suspensions. *Nature Phys. Sci. 241*, 20−22.
(29) Ingram, R. S., Hostetler, M. J., and Murray, R. W. (1997) Poly-hetero-ω-functionalized Alkanethiolate-Stabilized Gold Cluster Compounds. *J. Am. Chem. Soc*. *119*, 9175−9178.
(30) Templeton, A. C., Hostetler, M. J., Warmoth, E. K., Chen, S. W., Hartshorn, C. M., Krishnamurthy, V. M., Forbes, M. D. E., and Murray, R. W. (1998) Gateway Reactions to Diverse, Polyfunctional Monolayer-Protected Gold Clusters. *J. Am. Chem. Soc*. *120*, 4845−4849.
(31) Templeton, A. C., Wuelfing, W. P., and Murray, R. W. (2000) Monolayer-Protected Cluster Molecules. *Acc. Chem. Res. 33*, 27−36.
(32) Holgate, C. S., Jackson, P. I., Cowen, P. N., and Bird, C. C. (1983) Immunogold silver staining- new method of immunostaining with enhanced sensitivity. *J. Histochem. Cytochem. 31*, 938−944.

BC050047F

Enhanced Oligonucleotide Binding to Self-Assembled Nanofibers

Mustafa O. Guler,[†] Jonathan K. Pokorski,[†] Daniel H. Appella,[†] and Samuel I. Stupp*[,†,‡,§]

Department of Chemistry, Department of Materials Science and Engineering, and Feinberg School of Medicine, Northwestern University, 2220 Campus Drive, Evanston, Illinois 60208 . Received February 24, 2005; Revised Manuscript Received March 23, 2005

A peptide nucleic acid/peptide amphiphile conjugate (PNA−PA) that self-assembles into fiber-shaped nanostructures was designed to bind oligonucleotides with high affinity and specificity. Oligonucleotide binding to PNA−PA nanofibers was studied using fluorescence polarization, and thermal stability was examined by UV−vis measurement of duplex melting temperatures. The self-assembled PNA−PA DNA system was observed to bind more strongly than the corresponding DNA−DNA duplex. We also observed single base specificity with a 16 °C in thermal stability. As expected from the previous PNA studies, PNA−PA RNA binding is also stronger than the corresponding RNA−RNA duplex.

Recent developments in molecular biology demonstrate the importance of RNA isolation and detection experiments such as Northern analysis (*1*, *2*), nuclease protection assays (*3*), RT-PCR (reverse transcription−polymerase chain reaction) (*4*), RNA mapping (*5*), and in vitro translation (*6*). Among the different methodologies used to separate and purify RNA sequences for genetic research, isolation of mRNA containing polyadenylic (poly A) regions plays an important role in detection and quantification of low-copy mRNAs (*7*). Therefore, developing isolation tools for poly A-containing mRNAs using thymine-functionalized high molecular weight polymers (e.g. cellulose, polystyrene beads) has been an active area of research (*8*, *9*). Hydrogels derived from self-assembled molecules that specifically bind oligonucleotides are interesting targets for new biomaterials (*10*). In this study, we exploit the nanoscale structure of self-assembled nanofiber networks as an approach to bind poly A sequences.

We have designed and synthesized a novel peptide nucleic acid/peptide amphiphile conjugate (PNA−PA). These molecules contain a peptide nucleic acid segment followed by a peptide sequence terminated by an alkyl segment. The PNA−PA molecules self-assemble upon increasing pH to above pH 7 to form a self-supporting gel consisting of a network of nanofibers. This behavior is similar to that of peptide amphiphiles (PAs) reported previously by our laboratory which self-assemble after pH changes or electrolyte neutralize or shield molecular charges (*11*−*16*). The PNA−PA was designed to contain a KGGGAAAK peptide sequence since nanofiber formation is promoted by intermolecular β-sheets among peptide amphiphiles (*17*). Branching at one of the lysine residues was used to provide an attachment point for the PNA recognition unit on the self-assembled nanofibers and also to increase water solubility (see Figure 1). PNA was chosen over DNA for several reasons (*18*−*23*). First, the uncharged PNA backbone results in thermally stronger PNA−DNA and PNA−RNA duplexes and triplexes than DNA-DNA and RNA-RNA counterparts, especially at very low ionic strength. Second, PNA synthesis is compatible with solid-phase peptide synthesis (SPPS) used for PAs.

The PNA−PA was synthesized by SPPS. Branching of the peptide headgroup was achieved by using orthogonal protecting group chemistry for the amines at the α and ϵ positions of a lysine residue. A poly-thymine PNA heptamer was then built on the PA. The PNA−PA was found to be soluble in water at pH 4. Solutions with concentrations over 1 wt % were observed to form self-supporting gel by increasing the pH above 7. Gel formation was found to be reversible when pH was reduced to 4. Transmission electron microscopy (TEM) and circular dichroism (CD) spectroscopy were used to characterize the supramolecular structure of the PNA−PA. TEM micrographs of the PNA−PA revealed formation of uniform nanofibers with a diameter of 8 ± 1 nm and lengths ranging from 100 nm to several micrometers, as shown in Figure 2 and also in Supporting Information. Circular dichroism spectra of the self-assembled PNA−PA revealed a β-sheet signal at 215 nm ($n\pi^*$ transition) resulting from hydrogen bonding between the peptide segments (see Supporting Information) (*24*). As expected, the PNA segment did not show any CD signal given its achiral structure.

The thermal stability of duplexes formed by nucleotide oligomers and PNA−PA nanofibers was determined by their melting temperature (T_m) using UV to detect their thermal denaturation (*25*). Compared to previous work with PNAs, the PNA−PA nanofibers formed stronger complexes with both polyadenylic DNA and RNA heptamers (*26*, *27*). This resulted in a ca. 25 °C increase in T_m over the corresponding polythymine PNA heptamer (Table 1). Furthermore, the PNA−PA retained sequence specificity when tested with 5′-AAATAAA-3′ single strand DNA (ssDNA). This complex melted at 55.5 °C, which is ca. 16 °C lower than the melting temperature of the fully matched sequence when bound to PNA−PA nanofibers.

Oligonucleotide binding to the PNA−PA was also tested with fluorescence polarization with 5′-AAAAAAA-3′-fluorescein ssDNA. The fluorescence polarization of

* To whom correspondence should be addressed. E-mail: s-stupp@northwestern.edu.
[†] Department of Chemistry.
[‡] Department of Materials Science and Engineering.
[§] Feinberg School of Medicine.

10.1021/bc050053b CCC: $30.25 © 2005 American Chemical Society
Published on Web 04/20/2005

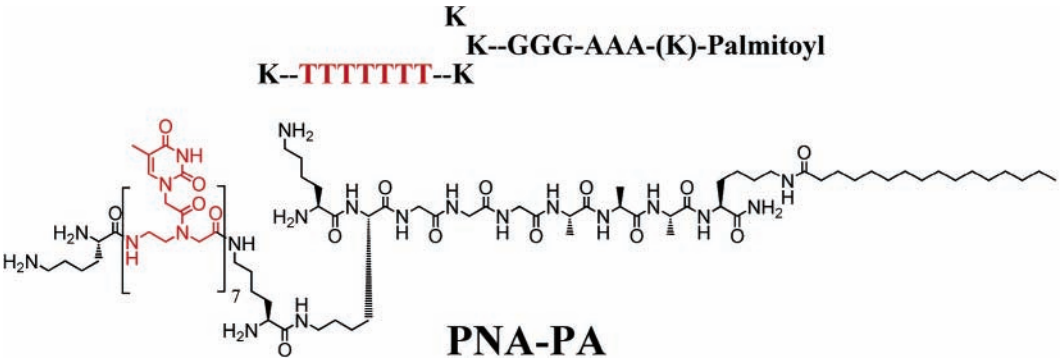

Figure 1. Structure of peptide nucleic acid/peptide amphiphile conjugate (PNA−PA). The thymine nucleic acid base was attached through an acetyl linker to an *N*-(2-aminoethyl)glycine PNA derivative, shown in red.

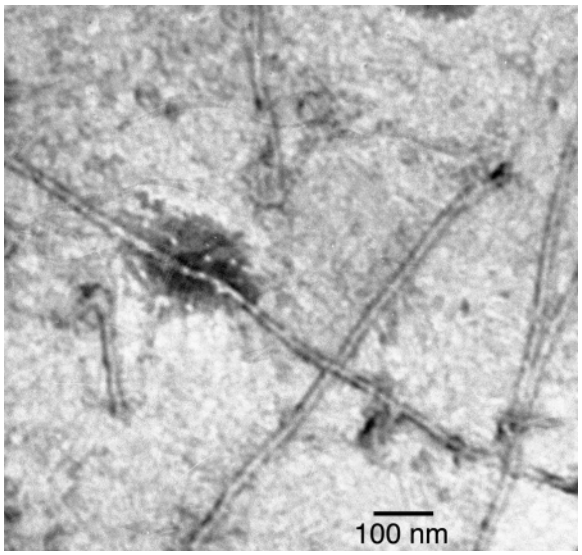

Figure 2. TEM micrograph of negatively stained PNA−PA nanofibers.

Table 1. T_m Data for PNA−PA/Oligonucleotide Complexes[a]

T_m (°C)	PNA_2DNA	PNA_2RNA	mismatch	ΔT_m (°C)
PNA−PA	71.4	73.8	55.5	−15.9
PNA[b]	44.4[b]	48.3[b]		

[a] Conditions for T_m measurement: 10 mM TAPS, 0.1 mM EDTA, and 150 mM NaCl, pH 8.5, UV measured at 260 nm from 90 °C to 25 °C, in 1 °C increments. Strand concentrations were 5.0 μM in PNA and 2.5 μM in the complementary oligonucleotide. ΔT_m represents the difference in melting temperature between the complementary DNA and the DNA with the indicated mismatch. Mismatch represents 5′-AAATAAA-3′ ssDNA. [b] Data adopted from ref (*26*).

fluorescein-tagged polyadenylic ssDNA heptamer was measured to be 0.4 ± 2 milli-Polarization (mP), with an increase to 33 ± 2 mP observed in the presence of self-assembled PNA−PA nanofibers. We attribute this increase to reduced rotational freedom of the tagged DNA sequence, indicative of binding to the self-assembled nanofibers. Fluorescence polarization of fluorescein alone in the presence of the PNA−PA was measured as 0.1 ± 2 mP, indicating an absence of nonspecific binding of the dye to the PNA-PA nanofibers.

We have reported a peptide nucleic acid/peptide amphiphile conjugate that binds to oligonucleotides with high affinity and specificity after self-assembly into nanostructures. Because the nanostructures are easily endocytosed by cells (*28*), this type of hybrid material could be attractive in biomedical research for applications such as RNA interference studies and gene silencing, mRNA separation and purification, as well as potential sensor applications that require strong and specific binding to oligonucleotides. Longer peptide nucleic acid sequences could be of interest for RNA interference applications; however, further study will be necessary to determine if these sequences can be incorporated without distrupting peptide amphiphile self-assembly. Small interfering RNAs (siRNAs) incorporate into protein complexes that are critical in mRNA destruction and translation regulation (*29*). The self-assembling nanostructures described here can be potentially useful in this context, however the siRNA sequence presented on the nanostructures must be released in cytoplasm and be able to complex to proteins without affecting their functions. Further studies are underway to explore other PNA−PA sequences and their behavior under physiological conditions.

ACKNOWLEDGMENT

This work was funded by the US Department of Energy (DoE) under award No. DE-FG02-00ER54810, NSF Nanoscale Science and Engineering Center (NSEC) (EEC-0118025), and J.K.P. was supported by Northwestern University's NIH Biotechnology Training Grant (T32GM008449). We thank the Electron Probe Instrumentation Center for use of its Hitachi H-8100 transmission electron microscope and the Keck Biophysics Facility for use of its Jasco J-715 CD spectrometer and Beacon 2000 fluorescence polarization system at Northwestern University. We also thank Mukti Rao and Liang-Shi Li for TEM and James Hulvat for his helpful discussions.

Supporting Information Available: Experimental protocols, circular dichroism spectrum, and additional TEM images. This material is available free of charge via the Internet at http://pubs.acs.org.

LITERATURE CITED

(1) Alwine, J. C., Kemp, D. J., and Stark, G. R. (1977) Method for Detection of Specific RNAs in Agarose Gels by Transfer to Diazobenzyloxymethyl-Paper and Hybridization with DNA Probes. *Proc. Natl. Acad. Sci. U.S.A. 74*, 5350−5354.

(2) Ahlquist, P. (2002) RNA-dependent RNA polymerases, viruses, and RNA silencing. *Science 296*, 1270−1273.

(3) Calzone, F. J., Britten, R. J., and Davidson, E. H. (1987) Mapping of Gene Transcripts by Nuclease Protection Assays and Cdna Primer Extension. *Methods Enzymol. 152*, 611−632.

(4) Erlich, H. A., Gelfand, D., and Sninsky, J. J. (1991) Recent Advances in the Polymerase Chain-Reaction. *Science 252*, 1643−1651.

(5) Paterson, B. M., Roberts, B. E., and Kuff, E. L. (1977) Structural Gene Identification and Mapping by DNA-Mes-

senger-RNA Hybrid-Arrested Cell-Free Translation. *Proc. Natl. Acad. Sci. U.S.A. 74*, 4370−4374.
(6) Ling, M. L., Risman, S. S., Klement, J. F., McGraw, N., and McAllister, W. T. (1989) Abortive Initiation by Bacteriophage-T3 and Bacteriophage-T7 Rna-Polymerases under Conditions of Limiting Substrate. *Nucleic Acids Res. 17*, 1605−1618.
(7) Wang, L. T., Eckmann, C. R., Kadyk, L. C., Wickens, M., and Kimble, J. (2002) A regulatory cytoplasmic poly(A) polymerase in Caenorhabditis elegans. *Nature 419*, 312−316.
(8) Smolenski, A., Schultess, J., Danielewski, O., Arguinzonis, M. I. G., Thalheimer, P., Kneitz, S., Walter, U., and Lohmann, S. M. (2004) Quantitative analysis of the cardiac fibroblast transcriptome-implications for NO/cGMP signaling. *Genomics 83*, 577−587.
(9) Jacobsen, N., Nielsen, P. S., Jeffares, D. C., Eriksen, J., Ohlsson, H., Arctander, P., and Kauppinen, S. (2004) Direct isolation of poly(A)(+) RNA from 4 M guanidine thiocyanate-lysed cell extracts using locked nucleic acid-oligo(T) capture. *Nucleic Acids Res. 32*, e64.
(10) Lee, K. Y., and Mooney, D. J. (2001) Hydrogels for tissue engineering. *Chem. Rev. 101*, 1869−1879.
(11) Hartgerink, J. D., Beniash, E., and Stupp, S. I. (2001) Self-assembly and mineralization of peptide-amphiphile nanofibers. *Science 294*, 1684−1688.
(12) Hartgerink, J. D., Beniash, E., and Stupp, S. I. (2002) Peptide-amphiphile nanofibers: A versatile scaffold for the preparation of self-assembling materials. *Proc. Natl. Acad. Sci. U.S.A. 99*, 5133−5138.
(13) Niece, K. L., Hartgerink, J. D., Donners, J., and Stupp, S. I. (2003) Self-assembly combining two bioactive peptide-amphiphile molecules into nanofibers by electrostatic attraction. *J. Am. Chem. Soc. 125*, 7146−7147.
(14) Silva, G. A., Czeisler, C., Niece, K. L., Beniash, E., Harrington, D. A., Kessler, J. A., and Stupp, S. I. (2004) Selective differentiation of neural progenitor cells by high-epitope density nanofibers. *Science 303*, 1352−1355.
(15) Guler, M. O., Soukasene, S., Hulvat, J. F., and Stupp, S. I. (2005) Presentation and recognition of biotin on nanofibers formed by branched peptide amphiphiles. *Nano Lett. 5*, 249−252.
(16) Bull, S. R., Guler, M. O., Bras, R. E., Meade, T. J., and Stupp, S. I. (2005) Self-assembled peptide amphiphile nanofibers conjugated to MRI contrast agents. *Nano Lett. 5*, 1−4.
(17) Behanna, H. A., Donners, J., Gordon, A. C., and Stupp, S. I. (2005) Coassembly of amphiphiles with opposite peptide polarities into nanofibers. *J. Am. Chem. Soc. 127*, 1193−1200.
(18) Nielsen, P. E. (2001) Peptide nucleic acid: a versatile tool in genetic diagnostics and molecular biology. *Curr. Opin. Biotechnol. 12*, 16−20.
(19) Doyle, D. F., Braasch, D. A., Simmons, C. G., Janowski, B. A., and Corey, D. R. (2001) Inhibition of gene expression inside cells by peptide nucleic acids: Effect of mRNA target sequence, mismatched bases, and PNA length. *Biochemistry 40*, 53−64.
(20) Kuhn, H., Demidov, V. V., Coull, J. M., Fiandaca, M. J., Gildea, B. D., and Frank-Kamenetskii, M. D. (2002) Hybridization of DNA and PNA molecular beacons to single-stranded and double-stranded DNA targets. *J. Am. Chem. Soc. 124*, 1097−1103.
(21) Okamoto, A., Tanabe, K., and Saito, I. (2002) Site-specific discrimination of cytosine and 5-methylcytosine in duplex DNA by peptide nucleic acids. *J. Am. Chem. Soc. 124*, 10262−10263.
(22) Nielsen, P. E., Egholm, M., Berg, R. H., and Buchardt, O. (1991) Sequence-Selective Recognition of DNA by Strand Displacement with a Thymine-Substituted Polyamide. *Science 254*, 1497−1500.
(23) Demidov, V. V., Potaman, V. N., Frankkamenetskii, M. D., Egholm, M., Buchard, O., Sonnichsen, S. H., and Nielsen, P. E. (1994) Stability of Peptide Nucleic-Acids in Human Serum and Cellular-Extracts. *Biochem. Pharmacol. 48*, 1310−1313.
(24) Greenfield, N., and Fasman, G. D. (1969) Computed Circular Dichroism Spectra for Evaluation of Protein Conformation. *Biochemistry 8*, 4108−4116.
(25) Warshaw, M. M., and Tinoco, I. (1966) Optical Properties of 16 Dinucleoside Phosphates. *J. Mol. Biol. 20*, 29−38.
(26) Myers, M. C., Witschi, M. A., Larionova, N. V., Franck, J. M., Haynes, R. D., Hara, T., Grajkowski, A., and Appella, D. H. (2003) A cyclopentane conformational restraint for a peptide nucleic acid: Design, asymmetric synthesis, and improved binding affinity to DNA and RNA. *Org. Lett. 5*, 2695−2698.
(27) Pokorski, J. K., Witschi, M. A., Purnell, B. L., and Appella, D. H. (2004) (*S*,*S*)-trans-cyclopentane-constrained peptide nucleic acids. A general backbone modification that improves binding affinity and sequence specificity. *J. Am. Chem. Soc. 126*, 15067−15073.
(28) Beniash, E., Storrie, H, and Stupp, S. I. Manuscript under preparation.
(29) Hutvagner, G., Simard, M. J., Mello, C. C., and Zamore, P. D. (2004) Sequence-specific inhibition of small RNA function. *PLoS Biol. 2*, 465−475.

BC050053B

ARTICLES

Structural and Biophysical Characterization of the 40 kDa PEG−Interferon-α_{2a} and Its Individual Positional Isomers

Christophe Dhalluin, Alfred Ross, Luc-Alexis Leuthold, Stefan Foser, Bernard Gsell, Francis Müller, and Hans Senn*

F. Hoffmann-La Roche AG Department of Pharma Research CH-4070 Basel, Switzerland Received September 15, 2004; Revised Manuscript Received March 8, 2005

The human recombinant Interferon-α_{2a} (IFNα_{2a}) is a potent drug (Roferon-A) to treat various types of cancer and viral diseases including Hepatitis B/C infections. To improve the pharmacological properties of the drug, a new pegylated form of IFNα_{2a} was developed (PEGASYS). This 40 kDa PEG-conjugated IFNα_{2a} (^{40}PEG−IFNα_{2a}) is obtained by the covalent binding of one 40 kDa branched PEG-polymer to a lysine side chain of IFNα_{2a}. ^{40}PEG−IFNα_{2a} is a mixture of mainly six monopegylated positional isomers modified at K31, K134, K131, K121, K164, and K70, respectively. Here we report the detailed structural and biophysical characterization of ^{40}PEG−IFNα_{2a} and its positional isomers, in comparison with IFNα_{2a}, using NMR spectroscopy, analytical ultracentrifugation, circular dichroism, fluorescence spectroscopy, and differential scanning calorimetry. Our results show that the three-dimensional structure of IFNα_{2a} is not modified by the presence of the polymer in all positional isomers constituting ^{40}PEG−IFNα_{2a}. Regardless of where the PEG-polymer is attached, it adopts a very mobile and flexible random coil conformation, producing a shield for the protein without a permanent coverage of the protein surface. Hydrodynamic data indicate that the protein-attached PEG has a slightly more compact random-coil structure than the free PEG-polymer. Our results also provide evidence of significant structural and physicochemical advantages conferred by the pegylation: increase of the effective hydrodynamic volume and modification of the molecular shape, higher temperature stability, and reduced tendency for aggregation. These results are of tremendous pharmacological interest and benefit as was clinically shown with PEGASYS. This study constitutes a new standard for the characterization of pegylated proteins and enables an important step toward the understanding on a molecular level of the binding of ^{40}PEG−IFNα_{2a} and its positional isomers to its cellular receptors.

INTRODUCTION

In the 1970s, pegylation was developed to enhance the bioavailability of therapeutic proteins (*1*). In this process, an inert, nontoxic, and water-soluble poly(ethylene glycol) (PEG)-polymer,[1] linear or branched, is attached to a therapeutic protein via a covalent linkage, mostly at lysine or histidine residues located on the surface of the native protein (*2*−*4*). This process has been shown to alter the biochemical and pharmacological properties of the resulting PEG-conjugated proteins (*5*, *6*). It leads to a protein with improved solubility and temperature stability (*7*), enhanced stability against enzymatic degradation (*8*, *9*), increased serum half-life (*10*), decreased renal clearance (*11*), and immunogenicity (*12*, *13*) and thus enhanced biological effectiveness (*14*, *15*) when compared with the unmodified protein.

Today one of the major health concerns worldwide is the chronic Hepatitis C Virus (HCV) infection. It is estimated that 180 million people are infected with HCV (*16*). This infection is the leading cause of chronic liver disease and hepatocellular carcinoma, and the main indication for liver transplantation in the United States and Western Europe (*17*). Until recently the primary therapy for the treatment of chronic HCV infection remained subcutaneous injections of recombinant human Interferon-α (IFNα) in combination with the oral antiviral agent ribavirin (*14*, *18*). It was realized that the pharmacokinetic properties of IFNα proteins are the major factors limiting the efficacy of the treatment: the protein is rapidly degraded, diffuses widely throughout the entire body and has a high rate of renal clearance (*19*, *20*). As a result, after one subcutaneous injection the serum half-life of Interferon-α_{2a} (IFNα_{2a}) is short (ranging from 4 to 8 h) and the serum concentration decreases

* To whom correspondence should be addressed. Tel: +41 (0)-61 68 82028; fax: +41 (0)61 68 87408; e-mail: hans.senn@roche.com.

[1] Abbreviations: HCV, Hepatitis C Virus; IFNα, Interferon-α; IFNα_{2a}, Interferon-α_{2a} (Roferon-A); ^{15}N-IFNα_{2a}, uniformly ^{15}N-labeled Interferon-α_{2a}; PEG, poly(ethylene glycol); ^{40}PEG−IFNα_{2a}, (PEGASYS) 40 kDa branched PEG-conjugated Interferon-α_{2a}, composed of monopegylated positional isomers; monopegylated positional isomer, one 40 kDa branched PEG molecule covalently attached at a lysine residue of Interferon-α_{2a}; ^{15}N-isomer, uniformly^{15}N-labeled isomer; pegylated lysine, lysine residue of Interferon-α_{2a} linking the PEG-polymer to the protein; PEG-linker lysine, lysine molecule linking two PEG branches of 20 kDa each; NMR, nuclear magnetic resonance; AUC, analytical ultracentrifugation; CD, circular dichroism; DSC, differential scanning calorimetry; SAW, Self-Avoiding-Walk; r.c., random-coil.

10.1021/bc049781+ CCC: $30.25 © 2005 American Chemical Society
Published on Web 05/03/2005

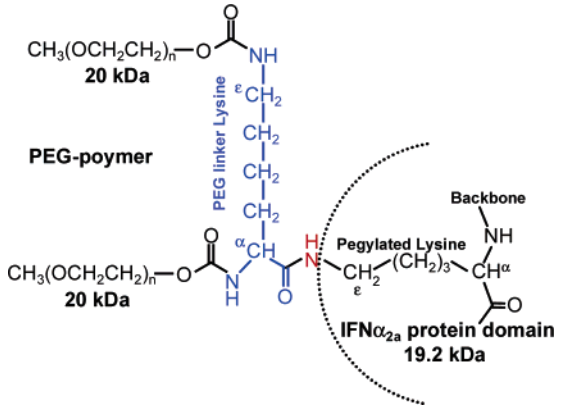

Figure 1. Schematic representation of a monopegylated positional isomer molecule of ^{40}PEG–IFNα_{2a}: one 40 kDa branched PEG-polymer is covalently attached to IFNα_{2a} by an amide bond at the ϵ-amino group (in red) of a lysine residue of IFNα_{2a}. The IFNα_{2a} protein and the PEG-polymer are schematically separated by a dotted line. In the PEG-polymer, the two 20 kDa PEG branches (n = 420–510) are linked by a lysine molecule (in blue), also called PEG-linker lysine, via urethane bonds, one at the α-amide group and the other at the ϵ-amide group of the PEG-linker lysine. IFNα_{2a} contains 11 lysine residues (K23, K31, K49, K70, K83, K112, K121, K131, K133, K134, and K164). Potentially 11 monopegylated positional isomers plus one at the N-terminus may be formed. However, only six positional isomers constitute more than ~98% of the mixture (*28*). In the ^{15}N-labeled positional isomer samples, the nitrogen nuclei of the protein domain including the $N_\epsilon H$ group of the pegylated lysine are ^{15}N, whereas the one of the PEG-linker lysine are ^{14}N.

below its detection limit after 24 h (*21*, *22*). Thus, even though the current HCV treatment requires up to three subcutaneous injections weekly, the virus has extended periods when it is not exposed to a therapeutic concentration of the drug (*14*, *15*). This results in a treatment regimen that places a significant burden on the patient, negatively impacting quality of life and often interfering with compliance.

In the early 1990s, the pegylation of IFNα_{2a} for the HCV treatment was first attempted with a 5 kDa linear PEG-polymer linked by a urea bond to lysine side chains of the protein.[23] However, the pharmacological properties and efficacy of this first generation of pegylated IFNα_{2a} were not significantly improved over that obtained with unmodified protein (*24*).

Within the past several years, the influence of various PEG structures on the in vitro biological activity have been investigated (*2*, *25*, *26*). These results showed an important correlation between the PEG-polymer characteristics and the pharmacological properties. On the basis of this knowledge, second-generation pegylated IFNα drugs were developed by two companies. The biophysical charactersation for a 12 kDa PEG IFNα_{2b} construct (Intron A) was reviewed by Wang et al. (*27*). Here we focus on the ^{40}PEG–IFNα_{2a} (PEGASYS) construct recently developed (*24*) in house. It is obtained by covalent binding of one 40 kDa branched PEG-polymer via an amide bond to a lysine side chain of the protein (Figure 1). ^{40}PEG–IFNα_{2a} is a mixture of mainly six monopegylated positional isomers (*28*). It exhibits a superior efficacy over IFNα_{2a} with significantly increased serum half-life, and because of its increased size a reduced renal clearance, resulting in a strong antiviral response throughout a once weekly dosing schedule (*29*, *30*). In patients with chronic HCV and liver cirrhosis, ^{40}PEG–IFNα_{2a} monotherapy achieves a sustained virological response close to four times higher than conventional IFNα_{2a} (*14*). In late 2002, PEGASYS was approved by the FDA for HCV treatment.

On a structural level, the molecular bulk conferred by the PEG-polymer may effectively shield the protein surface (*9*). On one hand, these effects enhance serum half-life and reduce renal clearance, which in turn tend to potentiate the biological efficacy of the pegylated protein versus the unmodified form (*10*). On the other hand, the attached PEG may sterically and thermodynamically interfere with the ability of the protein to interact with its cellular receptors, which exert the biological effectiveness (*9*, *31–33*). The overall biological response to the pegylated protein is consequently dependent upon a balance of these competing factors.

Previous studies reporting biological activities showed an unavoidable reduction in specific activities upon pegylation (*23*, *32*, *34*). As far as ^{40}PEG–IFNα_{2a} is concerned, it exhibits an approximately 30-fold reduced in vitro biological activity in the antiviral assays relative to IFNα_{2a} (*24*). However, substantial variations in the in vitro antiviral activity were observed when the individual positional isomers were isolated and compared (*28*). It is anticipated that these activity variations are due to differences in the kinetics and thermodynamics of the interaction between each positional isomer and Interferon receptors. These observations clearly highlight the need to investigate the structural, kinetic, and thermodynamic properties of ^{40}PEG–IFNα_{2a} and its positional isomers, that influence the interaction with its cellular receptors and therefore its biological activity (*35*). In view of the tremendous value of pegylated therapeutic proteins in medicine, it is quite surprising that few data are available on their structure, stability, and interaction with their receptors (*23*, *31–34*). In this study we report the detailed structural and biophysical characterization of ^{40}PEG–IFNα_{2a} and its positional isomers using NMR spectroscopy, analytical ultracentrifugation (AUC), circular dichroism (CD), fluorescence spectroscopy, and differential scanning calorimetry (DSC). The results are also compared with those obtained with unmodified IFNα_{2a}. These data constitute the basis and form an essential collection of knowledge, on which the interaction of ^{40}PEG–IFNα_{2a} with its cellular receptors can be understood. The results of the study of the interaction between ^{40}PEG–IFNα_{2a} and its individual positional isomers with the extracellular domain of the receptor IFNAR2 are reported in the accompanying publication (*36*).

Further improvements in the development of medically relevant therapeutic proteins critically depend on this type of knowledge and may lead to a third generation of structurally modified pegylated protein drugs.

MATERIALS AND METHODS

Materials. The standard material of the recombinant human Interferon-α_{2a}, Roferon-A (IFNα_{2a}) (19.2 kDa, 165 amino acids) (*37*, *38*) and the 40 kDa branched PEG-conjugated-IFNα_{2a}, PEGASYS (^{40}PEG–IFNα_{2a}) (*24*), and the *N*-hydroxysuccinimide ester derivative of a 40 kDa branched PEG-polymer reagent (*39*) used for the pegylation reaction were obtained from the Biopharmaceuticals Production Department of Hoffmann-La Roche Inc.. For the purpose of the NMR analysis, uniformly ^{15}N-labeled IFNα_{2a} (^{15}N-IFNα_{2a}) was produced in *E. coli* expression system and purified as previously reported (*37*, *40*). The ^{15}N-IFNα_{2a} was subsequently pegylated using the standard pegylation procedure (*24*) that is only summarized here: ^{15}N-IFNα_{2a} is reacting with the 40 kDa branched PEG-polymer reagent. The PEG molecule

is attached on surface exposed ϵ-amino group of lysine residues via an amide bond. The pegylation reaction product is subsequently purified to remove the excess of PEG-reagent, reaction byproducts, and pegylated ^{15}N-IFNα_{2a} oligomers. This procedure results in a mixture of monopegylated ^{15}N-IFNα_{2a} conjugates (one IFNα_{2a} molecule with one 40 kDa PEG molecule). As the PEG-reagent is reacting nonspecifically with any of the IFNα_{2a} lysine side chains, the pegylation reaction results in potentially 11 positional isomers (plus the N-terminus) with different yield. Very recently, a combination of an analytical ion exchange separation procedure, peptide mapping and MALDI-TOF (matrix-assisted laser desorption/ionization time-of-flight) mass spectrometric analyses showed that ^{40}PEG−IFNα_{2a} is composed mainly of nine bioactive positional isomers of monopegylated IFNα_{2a}: four major isomers modified at K31, K134, K131, K121; two minor isomers modified at K164 and K70; three very minor isomers modified at K83, K49, and K112 (*28*).

The reaction product of monopegylated positional ^{15}N-isomers, as well as the ^{40}PEG−IFNα_{2a} standard product, was subjected to preparative ion-exchange (IEX) separation methods that enabled the isolation of the four major and two minor unlabeled and ^{15}N-labeled positional isomers. First, a cation exchange FPLC (fast-protein liquid chromatography) method (100 mg of material injected) was applied to separate pure positional isomers modified at K31, K134, and K70, respectively. With this method, an elution peak containing the positional isomers modified at K131, K121, and K164 was also collected. This elution peak was then further purified by a preparative (IEX) separation method (3 mg injected material per run). In final, the four major and two minor positional unlabeled and ^{15}N-labeled isomers modified at K31, K134, K131, K121, K164, and K70, respectively, were separated in milligram amount (varying from 2 to 20 mg) with a purity over 97% as checked by analytical ion-exchange HPLC. The molecular weight of IFNα_{2a} protein, based on the amino acid content, is 19241.28 Da. IFNα_{2a} and ^{40}PEG−IFNα_{2a} extinction coefficient is 1.00 mL·mg^{-1}·cm^{-1} and 1.05 mL·mg^{-1}·cm^{-1}, respectively. Sample concentrations for ^{40}PEG−IFNα_{2a} are given in mass of protein per unit of volume. In the manuscript, IFNα_{2a} and ^{40}PEG−IFNα_{2a} are referring to standard materials (see above) and the positional isomers to the four major and two minor monopegylated positional isomers modified at K31, K134, K131, K121, K164, and K70, respectively.

Analytical Ultracentrifugation. Prior to the AUC measurement, IFNα_{2a} and ^{40}PEG−IFNα_{2a} solutions were dialyzed in 10 mM potassium phosphate 0.02% NaN_3 pH 3.7 and subjected to a preparative centrifugation (Beckman UZ Kontron apparatus, 2 h, 300 000 g, 6 °C) to ensure the removal of aggregates. The protein concentration was measured by UV absorbance (280 nm) as being 0.80 mg·mL^{-1} and 1.60 mg·mL^{-1} for IFNα_{2a} and ^{40}PEG−IFNα_{2a}, respectively. A solution of 40 kDa branched PEG-polymer 1.00 mg·mL^{-1} was equally dialyzed against the buffer solution specified above.

The knowledge of the partial specific volume v_{bar} (mL·gr^{-1}) of IFNα_{2a} and ^{40}PEG−IFNα_{2a} was required for the evaluation of the AUC data. In principle v_{bar} for a protein can be calculated from its amino acid sequence (*41*), but for ^{40}PEG−IFNα_{2a} the presence of the PEG-polymer does not allow this calculation. v_{bar} of IFNα_{2a}, ^{40}PEG−IFNα_{2a}, and the 40 kDa branched PEG-polymer was experimentally determined by measurement of the density of the solute and the buffer solution. Measurements were performed using a five-digit precision density-meter DMA-4500 Anton Paar at 20 °C (±0.01 °C). The eq 1 allowed the determination of v_{bar} with c the total material concentration (g·mL^{-1}), ρ and ρ_0 the density (g·mL^{-1}) of the solute and dialysis buffer solution, respectively.

$$v_{bar} = \frac{1}{\rho_0}\left(1 - \frac{\rho - \rho_0}{c}\right) \quad (1)$$

Sedimentation equilibrium experiments were performed with a XL-A AUC apparatus (Beckman Instruments, Palo Alto, CA) at 20 °C equipped with UV absorption optics on IFNα_{2a} and ^{40}PEG−IFNα_{2a} to determine the molecular weight MW and second virial coefficient B. The data were analyzed using the DISCREEQ (*42*) and Beckman software packages. The molecular weight of a protein can be determined in a sedimentation equilibrium experiment independently of the protein shape (*43*, *44*). At the equilibrium between sedimentation and diffusion a radial gradient of concentration in the measurement cell is formed. By radial scanning (r = 5.8−7.2 cm) of the sample UV absorbance at 280 nm, the molecular weight MW (Da) of the solute in an ideal and noninteracting system can be extracted from the eq 2,

$$\mathrm{MW} = \frac{2RT}{(1 - \rho_0 v_{bar})\omega^2}\frac{\partial(\ln c)}{\partial r^2} \quad (2)$$

with c the concentration, R (8.31 J·K^{-1}·mol^{-1}) the gas constant, T (K) the absolute temperature, v_{bar} (mL·g^{-1}) the partial specific volume of the solute, ρ_0 (g·mL^{-1}) the solvent density, and ω (rpm) the rotor angular velocity (22 000 rpm and 12 000 rpm for IFNα_{2a} and ^{40}PEG−IFNα_{2a}, respectively).

The second virial coefficient B (L·mol·g^{-2}) of IFNα_{2a} and ^{40}PEG−IFNα_{2a} was evaluated as well. In solution the solute molecules can interact with one another (also called nonideality) (*43*, *44*), because of the finite size and the charges they carry. With a real solution of a single solute, the measured molecular weight obtained from the slope of (ln c) versus r^2 is an apparent molecular weight $MW_{app.}$. The dependency on the solute concentration is given in eq 3,

$$\mathrm{MW}_{app.} = \frac{\mathrm{MW}}{\left(1 + c\frac{\partial(\ln \gamma)}{\partial c}\right)} \quad (3)$$

with MW the true molecular weight and (ln γ) the logarithm of the activity expressed as polynomial of c with ($\ln \gamma = B \times \mathrm{MW} \times c + C \times \mathrm{MW} \times c^2 + \ldots$). For the low concentration range, higher orders can be neglected therefore the eq 3 becomes:

$$\mathrm{MW}_{app.} \approx \frac{\mathrm{MW}}{1 + B \times \mathrm{MW} \times c} \quad (4)$$

The apparent molecular weight $MW_{app.}$ was measured at different solute concentration c (0.1, 0.2, 0.4, 1.0, 1.5, and 1.9 mg·mL^{-1}) of IFNα_{2a} and ^{40}PEG−IFNα_{2a}. By the measurement of the second virial coefficient B of the solute, relevant information about the strength of intermolecular interaction is revealed. The sign of B discriminates repulsive from attractive interaction and describes the strength of the solute−solute interactions (*45*). For a solute with B positive, solute−solvent interactions are

preferred over solute−solute contacts. In contrast for a negative B the opposite holds true.

The sedimentation coefficient S of IFNα_{2a} and ^{40}PEG−IFNα_{2a} was measured at 20 °C by AUC sedimentation velocity experiment using the apparatus as described above. S (in Svedberg unit [10^{-13} s]) represents the speed at which solute molecules are sedimenting to the bottom of the centrifuge cell under the influence of a strong force field during the experiment. The net sedimentation behavior of macromolecules in the centrifugal force is described by the Svedberg equation:

$$S = \frac{\partial r}{\partial t}\left(\frac{1}{r\omega^2}\right) = \frac{MW \times (1 - \rho_0 v_{bar})}{N_{av} f} = \frac{MW \times D_T \times (1 - \rho_0 v_{bar})}{RT} \quad (5)$$

The rate of sedimentation dr/dt is dependent on the centrifugal force $r\omega^2$. S is expressed with the partial specific volume of the molecule v_{bar}, the molecular weight MW, the Avogadro number N_{av}, the shape of the macromolecule by its frictional coefficient f, the density of the buffer ρ_0, the gas constant R, the absolute temperature T, and the translational diffusion coefficient D_T. The Stokes−Einstein relationship (*46*) (eq 6) was used to derive the right-hand term in the Svedberg equation.

$$D_T = RT/N_{av} f \quad (6)$$

Upon high angular velocity of the rotor (40 000 rpm), the sedimentation leads to formation of a solute concentration gradient in the form of boundaries recorded in UV absorbance at 280 nm by successive radial scanning in time (r = 5.8−7.2 cm). For an ideal and noninteracting system, the sedimentation coefficient S can be extracted, using the second moment boundary spreading method with the Beckman software package, by the analysis of the rate of movement of the midpoint of the boundaries (*43*, *44*). S of the 40 kDa branched PEG-polymer was measured at 20 °C by sedimentation velocity experiment using the apparatus as described above equipped with an interference optical device under an angular rotor velocity of 60 000 rpm.

The sedimentation coefficient S provides a description of the hydrodynamic shape of the molecule by the frictional coefficient f. Using the Stokes−Einstein relationship (eq 6), the frictional coefficient for a sphere, f_0, can be calculated with:

$$f_0 = 6\pi\eta R_0 = 6\pi\eta\left(\frac{3 \times MW \times v_{bar}}{4\pi N_{av}}\right)^{1/3} \quad (7)$$

with η the viscosity of the solution and R_0 the radius of the sphere defined with:

$$\frac{4\pi}{3}R_0^{\,3} = \frac{MW \times v_{bar}}{N_{av}} \quad (8)$$

Thus, the Svedberg relationship (eq 5) can be used to calculate the sedimentation coefficient of a sphere, S_0, as function of MW, v_{bar}, ρ_0, and η to obtain:

$$S_0 = \frac{MW \times (1 - \rho_0 v_{bar})}{6\pi\eta N_{av}\left(\frac{3 \times MW \times v_{bar}}{4\pi N_{av}}\right)^{1/3}} \quad (9)$$

Substituting the values of all the constants (η for water at 20 °C) using eq 9 yields the sedimentation value for a sphere in terms of MW, v_{bar}, ρ_0, and η.

$$S_0 = 0.012 \times (1 - \rho_0 v_{bar}) \times \left(\frac{MW^2}{v_{bar}}\right)^{1/3} \quad (10)$$

S_0 is the maximum sedimentation coefficient that can be obtained for a molecule of a given mass, because a sphere has the minimum surface area in contact with solvent. Consequently a spherical molecule has a minimum frictional coefficient f_0. The ratio of the sedimentation coefficient predicted for a sphere, S_0, to the experimental S is f/f_0 which can be interpreted for the molecule like its maximum shape asymmetry from a sphere.

Differential Scanning Calorimetry. The DSC method was used to monitor the thermal unfolding transition of IFNα_{2a} and ^{40}PEG−IFNα_{2a}. Prior to the measurement, the protein solutions were dialyzed in 20 mM sodium acetate/50 mM NaCl/0.02% NaN_3, pH 5.0, and subjected to a preparative centrifugation (as described above) to ensure the removal of aggregates. The protein concentration was measured by UV absorbance (280 nm) as being 0.82 mg·mL^{-1} and 0.60 mg·mL^{-1} for IFNα_{2a} and ^{40}PEG−IFNα_{2a}, respectively. DSC experiments were conducted with a MicroCal (Northampton, MA) microcalorimeter by measuring the difference of energy uptake between the sample cell and a reference cell that contains only dialysis buffer upon an increase of the temperature by 1 °C per minute from 20 °C to 85 °C. The denaturation melting temperature T_m was determined at the maximum of the heat capacity.

Circular Dichroism. The CD measurements were performed for IFNα_{2a} and ^{40}PEG−IFNα_{2a} using a Jobin-Yvon CD-6 spectrometer equipped with a temperature-controlled water bath. Prior to the measurement, the protein solutions were dialyzed in 10 mM potassium phosphate/0.02% NaN_3, pH 3.7, and subjected to a preparative centrifugation (as described above) to ensure the removal of aggregates. The protein concentration was measured by UV absorbance (280 nm) as being 0.80 mg·mL^{-1} and 1.60 mg·mL^{-1} for IFNα_{2a} and ^{40}PEG−IFNα_{2a}, respectively. The protein backbone absorption band (195−260 nm) and the protein aromatic absorption band (250−350 nm) were recorded at 20 °C in 0.05 and 1.00 cm path length cylindrical cell, respectively. The Cotton effect was plotted as $\Delta\epsilon$ that is related to the mean molecular ellipticity Θ [deg·cm^2·dmol^{-1}] by the relationship $\Theta = 3298.8 \times \Delta\epsilon$. Buffer baseline recorded prior the CD measurement of the protein solution was subtracted from the protein data to minimize the effects of UV lamp drifts. The secondary structure content of the proteins was estimated from the absorption band (195−240 nm) using the Provencher method (*47*). It involves the simulation of the CD spectrum of the protein of interest as a linear combination of the CD spectra of 16 proteins whose secondary structures are known from X-ray crystallography.

Fluorescence Spectroscopy. The fluorescence measurements were performed for IFNα_{2a} and ^{40}PEG−IFNα_{2a} at room temperature with a SLM 8100 fluorometer. Prior to the measurement, the protein solutions were dialyzed in 10 mM potassium phosphate 0.02% NaN_3 pH 3.7 and subjected to a preparative centrifugation (as described above) to ensure the removal of aggregates. The protein concentration was measured by UV absorbance (280 nm) as being 0.80 mg·mL^{-1} and 1.60 mg·mL^{-1} for IFNα_{2a} and ^{40}PEG−IFNα_{2a}, respectively. The fluorescence emission

spectra were recorded between 300 and 450 nm, with excitation at 283 nm.

NMR Spectroscopy. NMR measurements were performed at 25 °C on a Bruker DRX-800 MHz spectrometer, equipped with *xyz*-axis pulse field gradient triple resonance probe-head, and on a DMX-600 MHz spectrometer, equipped with *z*-axis pulse field gradient triple resonance cryo-probe-head. Data were processed and analyzed with XWIN NMR 2.6 and NMRPipe (*48*).

NMR samples of the following materials were prepared: ^{15}N-labeled and unlabeled IFNα_{2a}; ^{40}PEG−IFNα_{2a}; the ^{15}N-labeled and unlabeled positional isomers modified at K31, K134, K131, K121, K164, and K70, respectively. The NMR samples were prepared using the following procedure: preparative centrifugation (as described above); dialysis in 50 mM acetic acid, pH 3.5, 0.02% NaN_3, at 6 °C; concentration to 1 mL volume; dialysis in H_2O, pH 3.5 (HCl), 0.02% NaN_3, at 6 °C; dialysis in an aqueous solution containing protease inhibitors (H_2O/D_2O, 9/1) pH 3.5 (HCl), 0.02% NaN_3, at 6 °C; preparative centrifugation for 1 h at 185 000 g at 6 °C; readjustment of the pH to 3.5 (HCl). The final concentration of the samples ranged from 0.35 mM to 0.60 mM in 5 mm NMR sample tubes. A NMR sample of the 40 kDa branched PEG-polymer was prepared. An amount of 8.5 mg of *N*-hydroxysuccinimide ester derivative of the 40 kDa branched PEG-polymer reagent used for the pegylation reaction was diluted in 550 μL of H_2O, pH 12 (NaOH), 0.02% NaN_3, and stirred overnight at 6 °C to hydrolyze the *N*-hydroxysuccinimide ester derivative. The solution was subsequently dialyzed in (H_2O/D_2O, 9/1) pH 3.5 (HCl), 0.02% NaN_3, overnight at 6 °C. The resulting dialyzed solution of PEG-polymer free of *N*-hydroxysuccinimide derivative was then transferred with a concentration of ~0.38 mM to a 5 mm NMR tubes.

In all the NMR experiments the water signal suppression was performed using the WATERGATE scheme (*49*). For all the samples, a 1D ^{1}H NMR spectrum was acquired at 600 MHz with 8990 Hz sweep-width (1024 scans) and 2048 acquisition points zero-filled to 4096 points and subjected to a squared sine-bell window function shifted by 60°.

For the samples of PEG-polymer and the positional ^{15}N-isomers, 2D ^{1}H-DQ and 2D ^{15}N-filtered ^{1}H-TOCSY were acquired at 600 MHz to derive the ^{1}H assignment of the linker lysine in the PEG-polymer (Figure 1) (*50*, *51*). The linker lysine remains unlabeled (^{14}N) at the Nα and Nϵ positions, as only IFNα_{2a} was labeled with ^{15}N. 2D ^{1}H-DQ was recorded with 1536 t_2 acquisition points (96 scans) and 512 t_1 increments and spectral width of 14 and 24 ppm in F2 and F1 dimensions, respectively. ^{15}N-Decoupling was performed by a 180° pulse (carrier frequency at 118 ppm for ^{15}N) and the GARP scheme (*52*) during t_1 and t_2 evolution period, respectively. 2D ^{15}N-filtered ^{1}H-TOCSY with DIPSI-2 (*53*) for spin-lock (52 ms for mixing time) was recorded with 1536 t_2 acquisition points (64 scans) and 512 t_1 increments with a spectral width of 12 ppm in both dimensions. A postacquisition ^{15}N-filtration was performed by the implementation of a ^{15}N-filter during the experiment (carrier frequency at 118 ppm for ^{15}N) combined with an interleaved acquisition method (*54*). Because of the ^{15}N-filter, only ^{14}N- and carbon-attached proton resonances are visible along the F2-dimension in the aromatic region of the spectrum. For the 2D ^{1}H-DQ, ^{15}N-filtered ^{1}H-TOCSY and 2D [^{1}H−^{15}N]-TROSY-HSQC (see below), the t_2 and t_1 time domains were zero-filled to the next power of two and subjected to a squared sine-bell window function shifted by 60°.

For the samples of ^{15}N-IFNα_{2a} and the positional ^{15}N-isomers, 2D [^{1}H−^{15}N]-TROSY-HSQC was acquired at 800 MHz to derive the ^{1}H and ^{15}N chemical shift of the amides in the positional isomers (*55*). The experiments were recorded with 1536 t_2 acquisition points (96 scans) and 512 t_1 increments spectral width of 15 and 24 ppm in ^{1}H and ^{15}N (carrier frequency at 118 ppm), respectively. The ^{1}H and ^{15}N chemical shift of the ϵ-amide group N$_\epsilon$H of the pegylated lysine in the protein domain of the positional isomers was derived from these experiments. The chemical shift perturbation Δppm of the backbone amides due to the PEG-polymer in each positional isomers was evaluated as follows (eq 11) where $\Delta(^1\mathrm{H})$ and $\Delta(^{15}\mathrm{N})$ are the backbone amide chemical shift differences in ^{1}H and ^{15}N, respectively, between ^{15}N-IFNα_{2a} and the positional ^{15}N-isomers.

$$\Delta\mathrm{ppm} = 1/2[(\Delta(^1\mathrm{H}))^2 + (\Delta(^{15}\mathrm{N}))^2/25]^{1/2} \qquad (11)$$

To assess the shielding effect of the PEG-polymer on ^{1}H/^{2}H exchange of the protein, NMR saturation transfer experiments (*56*) were acquired by recording 2D [^{1}H−^{15}N]-TROSY-HSQC spectra with and without presaturation (50 Hz) of the water signal during 3 s.

For ^{15}N-IFNα_{2a} and the positional ^{15}N-isomers, 3D ^{15}N-edited [^{1}H−^{1}H]-NOESY (*57*) was acquired to derive the NOE internuclear distance connectivities within the protein and between the former and the PEG-polymer. 3D ^{15}N-edited [^{1}H−^{1}H]-NOESY were recorded at 800 MHz using 100 ms mixing time, 2048 acquisition points (8 scans), 90 increments for ^{1}H and 40 increments for ^{15}N (carrier frequency at 118 ppm) with spectral widths of 15, 12, and 24 ppm, respectively. The indirect time dimension in ^{1}H and ^{15}N were doubled by linear prediction and zero-filled to the next power of two and subjected to a squared sine-bell window function shifted by 60° and 90°, respectively.

For IFNα_{2a}, ^{40}PEG−IFNα_{2a} and the 40 kDa branched PEG-polymer samples pulse field gradient−(longitudinal eddy current) PFG-(LED) (*58*) NMR experiment was recorded to derive the translational diffusion coefficient D_T. Self-diffusion is defined as translational motion reflecting the random motions (Brownian movement) of a molecule in the absence of a concentration gradient. D_T is indicative of hydrodynamic properties and molecular size. The PFG-(LED) NMR method is suitable for D_T measurements of macromolecules because it is designed to minimize the T_2 relaxation effects by storing the magnetization along the *z*-axis during the translational diffusion period, so that relaxation depends primarily on T_1 which is much longer than T_2 for macromolecules. The experiment was acquired with 1D ^{1}H-spectra recorded at 600 MHz with 12000 Hz sweep-width (64 scans) and 32 k acquisition points zero-filled to 64 k and subjected to an exponential window function (line-broadening factor of 1 Hz) before FT. In the experiment the magnitude of *z*-gradient pulses is increased in successive 1D ^{1}H-spectra where the signal intensity is attenuated due to the translational diffusion. The decrease in signal intensity I, normalized to the signal in the absence of gradient I_o, is given by (*59*):

$$\frac{I}{I_o} = \exp(-\gamma^2 G^2 \delta^2 D_T(\Delta - \delta/3)) \qquad (12)$$

with γ the ^{1}H gyromagnetic ratio (2.68 10^4 Gauss^{-1}·s^{-1}), Δ the diffusion period (300 ms), δ the gradient duration (2 ms), and G the gradient magnitude varying from 0% to 100% (calibrated to 57.6 G·cm^{-1}). The determination of D_T (cm^2·s^{-1}) allows the calculation of a hydrodynamic

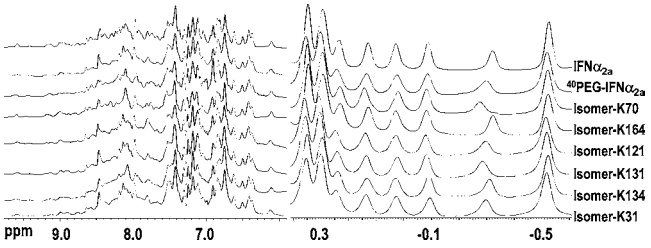

Figure 2. Aromatic (left) and aliphatic (right) regions of the 1D ^{1}H NMR spectra recorded at 600 MHz for IFNα_{2a}, ^{40}PEG–IFNα_{2a} and the positional isomers modified at K31, K134, K131, K121, K164, and K70, respectively. In this representation, amplitudes in the aliphatic region are rescaled, with respect to the aromatic region, by a factor ~4.

radius R_H (nm) of a sphere with equivalent translational diffusion constant using the Stokes–Einstein equation:

$$R_H = \frac{k_B T}{6\pi\eta D_T} \qquad (13)$$

with k_B the Boltzmann constant, T (K) the absolute temperature, and η the viscosity taken to be that of water at 25 °C (*46*, *60*).

RESULTS

NMR Structural Analysis of the Protein Domain of Pegylated IFNα_{2a}s. The 1D ^{1}H NMR spectra of IFNα_{2a} and ^{40}PEG–IFNα_{2a} are extremely well superimposable in the resolved regions (Figure 2). The ^{1}H linewidth for ^{40}PEG–IFNα_{2a} is broader (+5 Hz) as compared to IFNα_{2a}, but much less broad than expected for a 60 kDa protein (*61*). The spectral identity in the 2D ^{1}H-NOESY spectra of the two samples is also remarkable. However, because ^{40}PEG–IFNα_{2a} is a mixture of positional isomers, NMR data do not resolve structural differences that may exist. Detailed NMR based structural comparison was achieved using NMR data of isolated positional isomers.

The individual 1D ^{1}H NMR spectra of the six isolated positional isomers of ^{40}PEG–IFNα_{2a} display a similar dispersion of signals in the aromatic and aliphatic regions with broader ^{1}H-line-width (+5 Hz) as compared to IFNα_{2a} (Figure 2). The perturbation of the PEG-polymer on the IFNα_{2a} protein structure (*40*) was evaluated by the mapping of the chemical shift perturbation Δppm (eq 11) of the backbone amide ^{1}H- and ^{15}N-resonances for each amino acid derived from 2D ^{15}N-TROSY-HSQC spectra for the positional ^{15}N-isomers as compared to ^{15}N-IFNα_{2a}. This is illustrated in Figure 3 for the ^{15}N-Isomer-K31. The chemical shift perturbation plotted for all the amino acid sequence shows that the perturbation is small (maximum 0.12 ppm in the Isomer-K31) and localized to the attachment site of the PEG-polymer at K31 and surface regions close by in space (Figure 4). The same holds true for most of the positional isomers, as shown in Figure 4. Only the Isomer-K164 displays a chemical shift perturbation spread more widely over the protein surface. K164 is located at the C-terminal end of the polypeptide chain which is known to be highly flexible (*40*).

For each positional ^{15}N-isomer, a 3D ^{15}N-edited [^{1}H–^{1}H]-NOESY spectrum was recorded. The analysis of the 3D spectra showed that all amino acid residues experiencing chemical shift perturbation display unaltered NOE internuclear ^{15}NH-based distance connectivities when compared with IFNα_{2a}. The same also holds true, as expected, for all the nonshifted ^{15}NH resonances. This is illustrated in Figure 5 for the ^{15}N-Isomer-K31 for which the residue H34 displays chemical shift perturbation because it is close to the pegylated lysine K31. The ^{1}H-resonance of this amide displays the same NOE internuclear distance connectivities as in ^{15}N-IFNα_{2a}: the long-range NOE connectivity cross-peak between the resonance of the amide proton of H34 and the degenerated resonances of the two methyl groups of V142 is shown. For no positional isomer could a NOE internuclear distance connectivity be detected between the ethylene glycol units (OCH_2CH_2) or the two terminal groups (OCH_3) of the PEG-polymer and the amides of the protein backbone.

NMR Structural Analysis of the Pegylated Protein-lysine and the 40 kDa Branched PEG-polymer. For all the positional ^{15}N-isomers, the ^{1}H and ^{15}N chemical shift of the ϵ-amide group of the pegylated lysine of the protein domain (Figure 1) was unambiguously assigned by the identification of additional cross-peaks ($^{15}N_\epsilon/^{15}N_\epsilon H$) in the 2D ^{15}N-TROSY-HSQC spectra when compared to the IFNα_{2a} reference spectrum (Figure 3 and

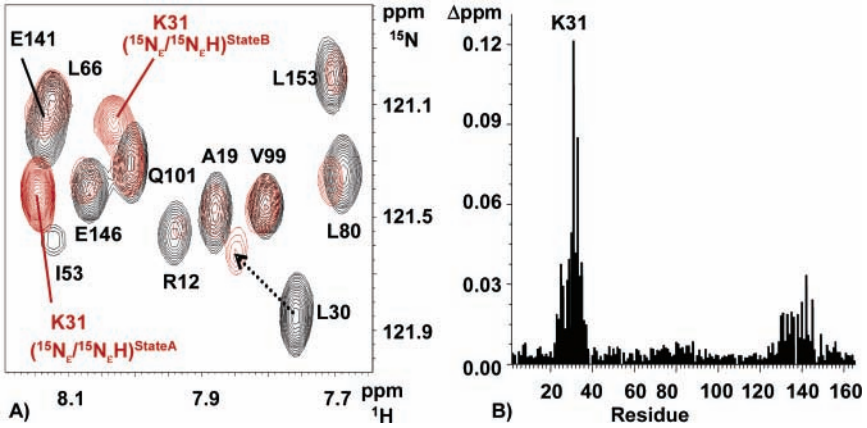

Figure 3. (A) Section of the superimposed 2D ^{15}N-TROSY-HSQC spectra recorded at 800 MHz for ^{15}N-IFNα_{2a} (black) and the positional ^{15}N-Isomer-K31 (red). As an example the amide of L30 close to the pegylated lysine K31 shows significant ^{1}H and ^{15}N chemical shift changes (black dotted arrow) whereas residues far away from the pegylated site do not display chemical shift perturbation. Two cross-peaks ($^{15}N_\epsilon/^{15}N_\epsilon H$) are observed for the ϵ-amide group of the pegylated lysine K31. Based on the relative intensity ratio (Table 1), these cross-peaks are assigned as the conformational State-A and State-B of the ϵ-amide group of the pegylated lysine. At the contour level of the spectrum for the positional ^{15}N-Isomer-K31 the existing cross-peak for I53 is not visible. (B) Chemical shift perturbation Δppm (eq 11) of the backbone amides due to the PEG-polymer for the Isomer-K31 as a function of the amino acid sequence.

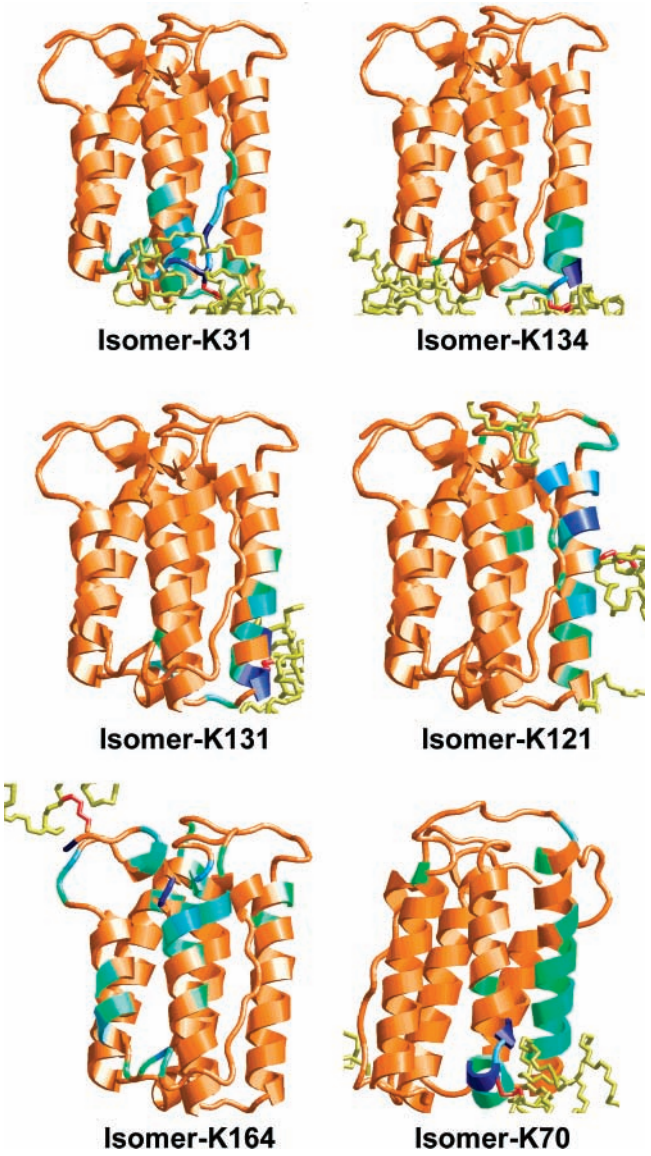

Figure 4. Ribbon representation of IFNα_{2a} structure (*40*) in the positional isomers modified at K31, K134, K131, K121, K164, K70, respectively. Amino acid residues that experience backbone amide chemical shift perturbation Δppm (eq 11) due to the PEG-polymer, are color-coded from dark blue for the most pronounced changes (0.12 ppm ≥ Δppm ≥ 0.08 ppm) gradually to light green for the small changes (0.04 ppm ≥ Δppm ≥ 0.01 ppm). The side chain of the pegylated lysine is colored in red. For each positional isomer, one possible r.c. conformation of the 40 kDa branched PEG-polymer (in yellow) was calculated but only partly represented for clarity. The polymer conformation was calculated as an on-lattice SAW (see also Figure 8).

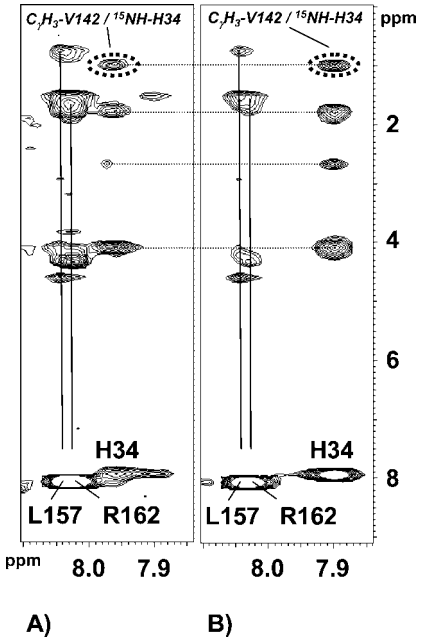

Figure 5. Region of a selected [^{1}H−^{1}H]-plane from the 3D ^{15}N-edited [^{1}H−^{1}H]-NOESY spectra recorded at 800 MHz for ^{15}N-Isomer-K31 (A), and ^{15}N-IFNα_{2a} (B). The planes correspond to the ^{15}N-shift (120.3 ppm) of the residue H34. This residue that is close to the pegylated lysine in the Isomer-K31 showed backbone amide chemical shift perturbation in ^{1}H but no change in ^{15}N. The ^{1}H-resonance of the amide of H34 displays the same NOE internuclear distance connectivities in both molecules: a long-range NOE connectivity between the amide of H34 and the degenerated resonances of the two methyl groups of V142 is circled as an example.

Table 1). The ^{1}H assignment to this position was further confirmed by the observation of direct and remote cross-peaks for $^{15}N_\epsilon H$ in the 2D ^{1}H-DQ spectra (*50*) (data not shown): these cross-peaks are again missing in the 2D ^{1}H-DQ reference spectrum of ^{15}N-IFNα_{2a}. As shown in Figure 3, two ($^{15}N_\epsilon/^{15}N_\epsilon H$) cross-peaks are observed for the ϵ-amide group of the pegylated lysine K31 with a ∼6.5:3.5 relative intensity ratio. The same holds true for the ^{15}N-Isomer-K134 and -K121 with a ∼5.5:4.5 relative intensity ratio in both isomers (Table 1). No correlation cross-peak is observed between the two $^{15}N_\epsilon H$ signals in the 3D ^{15}N-edited [^{1}H−^{1}H]-NOESY spectra. The structural origin of this peak duplication indicates a highly localized conformational heterogeneity of the pegylated lysine of the protein domain. For the ^{15}N-Isomer-K131, -K164, -K70 only one ($^{15}N_\epsilon/^{15}N_\epsilon H$) cross-peak is observed for the ϵ-amide group of the pegylated lysine (Table 1). The peak duplication is here either not resolved or not occurring (see Discussion).

For all the positional ^{15}N-isomers and the free PEG-polymer samples, the 1D ^{1}H NMR spectra display for the two 20 kDa PEG branches of the polymer (Figure 1) a unique, very intense, and sharp resonance line (∼5 Hz) at 3.60 ppm for the ethylene-glycol units (OCH_2CH_2) and a sharp but much less intense resonance line at 3.27 ppm for the two terminal groups (OCH_3).

The ^{1}H chemical shifts of the PEG-linker lysine for all the samples were obtained from analysis of the 2D ^{1}H-DQ and ^{15}N-filtered ^{1}H-TOCSY spectra. In the aromatic region of the ^{15}N-filtered ^{1}H-TOCSY spectra along the F2-dimension, only the ^{14}N-attached proton resonances, namely $N_\alpha H$ and $N_\epsilon H$ of the amide groups of the PEG-linker lysine, are seen. For all the samples, two ^{1}H-resonances are observed for $N_\alpha H$ and $N_\epsilon H$ of the PEG-linker lysine (Table 1 and Figure 6). They derive from a cis/trans isomerization of the urethane bond (*62*−*64*) at the α- and ϵ-amide groups of the PEG-linker lysine (Figure 6). This isomerization was confirmed by the observation of conformational exchange cross-peaks between both conformations of the amide groups in 2D-^{1}H-NOESY (*65*) and 2D-^{1}H-ROESY (*66*) spectra (data not shown). The isomerization rate was estimated on the PEG-polymer sample from the signal separation (∼240 Hz) as lying in the millisecond time range (∼5 ms < $1/k_{ex}$ < ∼50 ms). The trans and cis conformations of each of the urethane bond at the α- and ϵ-positions were assigned to be populated in the ratio ∼9:1, based on the relative intensity ratio of ($N_\alpha H/C_\alpha H$) and ($N_\epsilon H/C_\epsilon H_2$) cross-peaks, respectively (Table 1). This ratio is substantially different from the ratio derived from the localized conformational

Table 1. ^{1}H Chemical Shift (ppm) of $N_\alpha H$, $C_\alpha H$, $N_\epsilon H$, and $C_\epsilon H_2$ from the α- and ϵ-Amide Groups of the Linker Lysine in the 40 kDa Branched PEG-polymer and the Positional Isomers[a]

	pegylated lysine in the protein domain		linker lysine in the PEG-polymer domain							
	$^{15}N_\epsilon/^{15}N_\epsilon H$		$N_\alpha H$		$C_\alpha H$		$N_\epsilon H$		$C_\epsilon H_2$	
compound	State-A	State-B	trans[d]	cis[d]	trans[d]	cis[d]	trans[d]	cis[d]	trans[d]	cis[d]
40 kDa branched PEG polymer			7.07	6.64	3.88	3.92	6.76	6.40	2.99,2.97	3.01,3.01
Isomer-K31	121.4/8.14 ~65%[b]		7.15	6.77	3.89	3.91	6.75	6.37	3.02,2.98	3.01,3.01
		121.1/8.03 ~35%[b]	7.22	6.77	3.91	3.91	6.75	6.37	3.02,2.98	3.01,3.01
Isomer-K134	121.9/8.08 ~55%[b]		7.15	6.76	3.89	3.89	6.76	6.39	3.00,2.97	3.00,3.00
		121.1/8.08 ~45%[b]	7.18	6.76	3.89	3.89	6.76	6.39	3.00,2.97	3.00,3.00
Isomer-K131	121.1/8.07[e]		7.13[e]	6.74[e]	3.84[e]	3.87[e]	6.76	6.40	2.99,2.99	2.99,2.9
Isomer-K121	121.2/8.10 ~55%[c]		7.13	6.77	3.89	3.89	6.74	6.37	2.97,2.96	2.98,2.9
		121.2/8.08 ~45%[c]	7.16	6.72	3.89	3.89	6.74	6.37	2.97,2.96	2.98,2.9
Isomer-K164	120.8/8.05[e]		7.14[e]	6.74[e]	3.87[e]	3.87[e]	6.74	6.38	2.99,2.96	2.98,2.9
Isomer-K70	121.2/8.10[e]		7.16[e]	6.75[e]	3.85[e]	3.87[e]	6.73	6.37	3.00,2.96	2.98,2.9

[a] Measured from 2D ^{15}N-filtered ^{1}H-TOCSY and 2D ^{1}H-DQ spectra. ^{15}N and ^{1}H chemical shift (ppm) of $^{15}N_\epsilon$ and $^{15}N_\epsilon H$, respectively, from the ϵ-amide group of the pegylated lysine in the protein domain of the positional isomers identified from 2D ^{15}N-TROSY-HSQC and 2D ^{1}H-DQ spectra. [b] Populations based on the relative intensity ratio of the two cross-peaks for ($^{15}N_\epsilon/^{15}N_\epsilon H$) in the 2D ^{15}N-TROSY-HSQC spectra: the cross-peaks with the highest and lowest intensity were assigned as deriving from the two conformational states called State-A and State-B, respectively, of the ϵ-amide group of the pegylated lysine. [c] Populations based on the relative intensity ratio of the two cross-peaks for ($N_\alpha H/C_\alpha H$)^{trans} observed at the α-amide group of the PEG linker lysine in the 2D ^{15}N-filtered ^{1}H-TOCSY spectrum. [d] Trans and cis populations are in the ratio (~9:1), respectively, according to the relative intensity ratio of the cross-peaks ($N_\alpha H/C_\alpha H$) and ($N_\epsilon H/C_\epsilon H_2$) of the PEG linker lysine observed in the 2D ^{15}N-filtered ^{1}H-TOCSY spectra. [e] Only one set of cross-peaks is observed. The signals are not split in the 2D ^{15}N-TROSY-HSQC and 2D ^{15}N-filtered ^{1}H-TOCSY spectra.

heterogeneity of the pegylated lysine, where the conformational exchange is also slow.

An additional duplication of ^{1}H-resonances of the linker lysine of the polymer for $N_\alpha H$ is also observed for the Isomer-K31, -K134, and -K121. This is illustrated in Figure 6 with the ^{15}N-filtered ^{1}H-TOCSY spectrum of ^{15}N-Isomer-K121: doubling of both $N_\alpha H^{trans}$ and $N_\alpha H^{cis}$ is observed with a relative intensity ratio ~5.5:4.5 in both cases. This ratio is identical to the one observed at the neighboring group $^{15}N_\epsilon H$ of the pegylated K121 of the protein. For the Isomer-K31 and -K134 this doubling is observed only for the ^{1}H-resonance of $N_\alpha H^{trans}$ with a relative intensity ratio ~6.5:3.5 and ~5.5:4.5, respectively. For the Isomer-K131, -K164, and -K70, the ^{1}H-resonance of $N_\alpha H^{trans}$ and $N_\alpha H^{cis}$, respectively does not show any doubling.

Biophysical Characterization of IFNα$_{2a}$, ^{40}PEG–IFNα$_{2a}$ and the 40 kDa Branched PEG-polymer. The data reflecting the biophysical characterization of IFNα$_{2a}$, ^{40}PEG–IFNα$_{2a}$ and the free 40 kDa branched PEG-polymer are collected in Table 2. They are derived from the determination of the following parameters: the partial specific volume v_{bar} by densitometry; the molecular weight MW, the second virial coefficient B, and the sedimentation coefficient S by AUC; the denaturation melting temperature T_m by DSC; the secondary structure content by CD; the translational diffusion coefficient D_T by PFG-(LED) ^{1}H NMR spectroscopy.

The partial specific volume v_{bar} of IFNα$_{2a}$ and the 40 kDa branched PEG-polymer (Table 2) are in good agreement with the value calculated from the amino acid content (0.739 mL·gr^{-1}) (*41*) and values reported for other PEG-polymers (*67*), respectively. ^{40}PEG–IFNα$_{2a}$ presents a v_{bar} that corresponds approximately to the mass weighted average of v_{bar} of IFNα$_{2a}$ and the PEG-polymer. The knowledge of v_{bar} for IFNα$_{2a}$ and ^{40}PEG–IFNα$_{2a}$ allowed the determination of the molecular weights, by AUC to be 19.2 kDa and 58.9 kDa, respectively.

The second virial coefficients B for IFNα$_{2a}$ and ^{40}PEG–IFNα$_{2a}$ are of opposite sign with a negative and positive value, respectively (Table 2). It is interesting to note that literature values of B for PEG-polymers are positive as well (*68*, *69*), indicative that the B value of ^{40}PEG–IFNα$_{2a}$ is dominated by the properties of the PEG-polymer rather than IFNα$_{2a}$.

The sedimentation coefficient S of IFNα$_{2a}$ and the 40 kDa branched PEG-polymer are in the range of S values for globular proteins (*43*, *44*) and other PEG-polymers (*70*, *71*) of similar size. ^{40}PEG–IFNα$_{2a}$ presents a S value between, but closer to, the one of the PEG-polymer than of IFNα$_{2a}$ (Table 2). For the positional isomers modified at K31, K134, K131, and K121, the sedimentation coefficient S was also measured and gave values comparable to ^{40}PEG–IFNα$_{2a}$ (data not shown).

The thermal unfolding transition from the native to the denaturated state monitored by DSC (Figure 7.A) is, for IFNα$_{2a}$ and ^{40}PEG–IFNα$_{2a}$, an irreversible process. For ^{40}PEG–IFNα$_{2a}$, the baseline of the DSC scan displays a normal profile. In contrast, the strongly dropping baseline observed for IFNα$_{2a}$ highlights an aggregation process that starts in the early phase of the unfolding transition and dominates beyond the denaturation melting temperature T_m. As compared to IFNα$_{2a}$, ^{40}PEG–IFNα$_{2a}$ is more stable throughout the thermal denaturation with a slightly elevated T_m and a substantially reduced tendency for aggregation. This is indicated by the difference of the shape of the denaturation curve. The extraction of the enthalpy of unfolding is not possible due to the irreversibility of the denaturation process.

The CD spectra for IFNα$_{2a}$ and ^{40}PEG–IFNα$_{2a}$ recorded in the backbone and aromatic absorption region are identical over a broad range of pH values (pH 3.5 to 8). One example for sample conditions close to those of the NMR samples is shown in Figure 7, parts C and D, respectively. The same holds true for the fluorescence spectra (Figure 7B). Analysis of the CD spectra in the backbone absorption region shows that IFNα$_{2a}$ and ^{40}PEG–IFNα$_{2a}$ present ~75% of α-helix secondary structure (*40*, *47*). The unfolding and refolding process was monitored by the acquisition of CD spectra in the backbone absorption region during a thermal denaturation-renaturation cycle from 20 °C to 80 °C and back. These CD spectra showed ~41% and ~61% of α-helix secondary structure for IFNα$_{2a}$ and ^{40}PEG–IFNα$_{2a}$ respectively, after completing the cycle. It must be noted

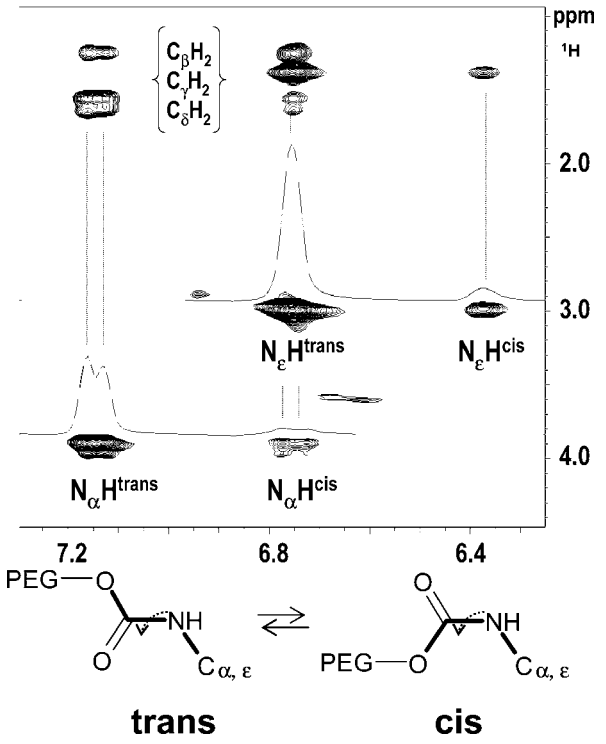

Figure 6. Section of the 2D ^{15}N-filtered ^{1}H-TOCSY spectrum for the positional^{15}N-Isomer-K121 recorded at 600 MHz. In this region of the spectrum along the F2-dimension only the ^{14}N-attached $N_\alpha H$ and $N_\epsilon H$ proton resonances of the amide groups of the unlabeled PEG-linker lysine are seen. Because of the cis/trans isomerization of the urethane bond (in bold) at the α- and ϵ-amide groups of the PEG-linker lysine, two resonances for $N_\alpha H$ and $N_\epsilon H$ are observed: namely $N_\alpha H^{trans}$, $N_\alpha H^{cis}$ and $N_\epsilon H^{trans}$, $N_\epsilon H^{cis}$, respectively. The cis/trans assignment is based on the relative intensity ratio of the cross-peaks ($N_\alpha H/C_\alpha H$) and ($N_\epsilon H/C_\epsilon H_2$). Because of the concomitant existence of two conformational states for the neighboring ϵ-amide group of the pegylated lysine, an additional doubling is observed for $N_\alpha H^{trans}$ resonance of the PEG-linker lysine as shown with the 1D trace at $\delta(C_\alpha H) = 3.89$ ppm: the two peaks have a relative intensity ratio ~5.5:4.5. The same observation holds true for the resonance $N_\alpha H^{cis}$. In contrast the 1D trace at $\delta(C_\epsilon H_2) = 2.96$ ppm does not show any doubling for the resonance $N_\epsilon H^{trans}$ and $N_\epsilon H^{cis}$. This group is structurally more remote than the ϵ-amide group of the pegylated lysine. The chemical shift region for the ^{1}H-resonances of $C_\beta H_2$, $C_\gamma H_2$ and $C_\delta H_2$ is reported with a bracket. Below the spectrum the cis/trans isomerization of the urethane bond at the α- and ϵ-amide groups of the PEG-linker lysine is schematically shown.

however that α-helical recovery does not necessarily imply a return to correctly folded protein.

The NMR-measured translational diffusion coefficients D_T of IFNα$_{2a}$ and the 40 kDa branched PEG-polymer (Table 2) are in agreement with values reported for globular proteins and other PEG-polymers (*72*−*74*). In contrast, D_T of ^{40}PEG−IFNα$_{2a}$ corresponds, neither to a 60 kDa globular protein nor to a 60 kDa PEG-polymer. The D_T of ^{40}PEG−IFNα$_{2a}$ lies much closer to that of the 40 kDa branched PEG-polymer.

The hydrodynamic parameters v_{bar}, S and D_T experimentally determined by independent methods for IFN-α$_{2a}$, ^{40}PEG−IFNα$_{2a}$ and the 40 kDa branched PEG-polymer (Table 2) are consistent with the corresponding molecular weight calculated using the Svedberg and Stokes−Einstein relationships (eqs 5 and 6 in Materials and Methods, respectively).

The calculation of the hydrodynamic radius R_H of the sphere with equivalent translational diffusion coefficient and the maximum shape asymmetry from a sphere f/f_0 reveals important differences of hydrodynamic properties, i.e., molecular size and shape, between IFN-α$_{2a}$, ^{40}PEG−IFNα$_{2a}$ and the 40 kDa branched PEG-polymer (Table 2). Surprisingly, R_H of the 60 kDa pegylated protein is smaller than the one observed for the free 40 kDa PEG-polymer.

DISCUSSION

Overall Structure of the Protein Domain in Pegylated IFNα$_{2a}$. The 1D ^{1}H NMR spectra of the six isolated positional isomers and IFNα$_{2a}$ are fully superimposeable and almost identical in the resolved regions. The integrity of the IFNα$_{2a}$ fold in the positional isomers was also confirmed by fluorescence and CD spectra (data not shown). For each positional isomer, the chemical shift perturbation Δppm (eq 11) induced by the PEG-polymer on the IFNα$_{2a}$ protein structure is small and localized to the PEG-polymer attachment site and surface regions close by in space. Only the Isomer-K164 displays Δppm changes which are more spread over the protein surface (Figure 4). This may be caused by the higher flexibility of the PEG-attachment site at K164 that is located in the most mobile part of the protein at the C-terminus (*40*). The observed chemical shift perturbations on the protein structure probably do not reflect structural changes or differences to IFNα$_{2a}$ for any of the positional isomers. No structural differences in IFNα$_{2a}$ could be detected among the positional isomers, as the same NOE internuclear distance connectivities in the 3D ^{15}N-edited [^{1}H−^{1}H]-NOESY spectra of the positional isomers are observed as in IFNα$_{2a}$. This also holds true for the residues displaying PEG-polymer induced chemical shift perturbations. The NOE spectral analysis for all the positional isomers further showed that no NOEs could be identified between the PEG-polymer and the amides of the protein backbone, indicative that there is no stable contact between the protein surface and the two branches of the PEG-polymer.

As no experimental result so far was found that indicates resolvable structural differences among and between the positional isomers and IFNα$_{2a}$, the alteration of the protein structure by the attached 40 kDa branched PEG-polymer is very minor if at all. Nevertheless, the physical bulk of the PEG-polymer, although not interacting in a defined and stable manner, produces a shield around some areas of the protein merely by its exclusion volume. This shielding effect may interfere with the ability of the protein to bind to its cellular receptors (*9*, *31*−*33*, *36*). Indeed, the antiviral activity of the individual positional isomers of ^{40}PEG−IFNα$_{2a}$ is reduced to various degrees depending on the PEG-attachment site (*28*).

The acidic pH (3.5) of all the NMR samples causes a slow exchange rate, of the order of minutes, for the surface and solvent exposed amide protons of the IFNα$_{2a}$ protein domain with water (*61*). An acidic pH is needed to obtain resolved NMR spectra. These conditions do not allow the assessment of the differential shielding by the PEG-polymer of the protein surface by ^{1}H/^{2}H exchange NMR experiments (*56*).

The moderately broader lines (+5 Hz) of the ^{1}H-resonances for the positional isomers, when compared to IFNα$_{2a}$, indicate that the molecular tumbling of the positional isomers does not at all correspond to that of a 60 kDa protein. With respect to ^{1}H-dipolar relaxation, these pegylated IFNα$_{2a}$ isomers behave like a protein with ~25 kDa apparent molecular weight. The modest line-broadening can be explained only by a highly independent motion of both the protein domain and the PEG-polymer (see below).

Table 2. Hydrodynamic Properties and Thermal Stability of IFNα2a, ^{40}PEG–IFNα2a and the 40 kDa Branched PEG-polymer

properties	IFNα_{2a}	^{40}PEG–IFNα_{2a}	40 kDa branched PEG-polymer
partial specific volume, v_{bar}[a] (ml·g^{-1})	0.737 ± 0.002	0.806 ± 0.002	0.824 ± 0.002
molecular weight, MW[b] (kDa)	19.2 ± 0.9	58.9 ± 2.9	37.3–45.2[h]
second virial coefficient, B[b] (10^{-6} L·mol·g^{-2})	−1.49 ± 0.07	2.71 ± 0.13	2.21[i]
sedimentation coefficient, S[b] (Sevdberg, 10^{-13}s)	2.45 ± 0.10	1.46 ± 0.06	0.70 ± 0.03
maximum shape asymmetry from a sphere, f/f_0[c]	1.02	2.59	3.76
hydrodynamic radius, R_H[d] (nm)	2.73 ± 0.01	9.46 ± 0.09	10.65 ± 0.39
translational diffusion coefficient, D_T[e] (10^{-7} cm^2·s^{-1})	8.95 ± 0.03	2.59 ± 0.02	2.30 ± 0.08
secondary structure content (α-helix)[f] (%)	75 ± 3	74 ± 3	–
α-helix content after thermal denaturation[f] (%)	~41	~61	-
denaturation melting temperature, T_m[g] (°C)	66.1 ± 0.3	67.4 ± 0.3	-

[a] Determined by densitometry. v_{bar} for IFNα_{2a} was also calculated based on the amino acid sequence to 0.739 mL·g^{-1} (*41*). [b] Determined by AUC. [c] Ratio of frictional coefficients f/f_0 equal to the ratio of S_0/S, with S_0 the calculated value for a sphere with corresponding mass and S the experimental value (*44*). [d] Determined by PFG-(LED) ^{1}H NMR spectroscopy (*57*). [e] Hydrodynamic radius of the sphere with equivalent translational diffusion coefficient D_T calculated using the Stokes–Einstein equation. [f] Determined by analysis of the CD spectra at 20 °C (*47*). [f] Protein solutions experienced a thermal denaturation cycle from 20 °C to 80 °C and back to 20 °C monitored by CD. At this latter temperature the amount of α-helix content was evaluated (*47*). [g] Determined by DSC. [h] From ref 24. [i] From ref 68.

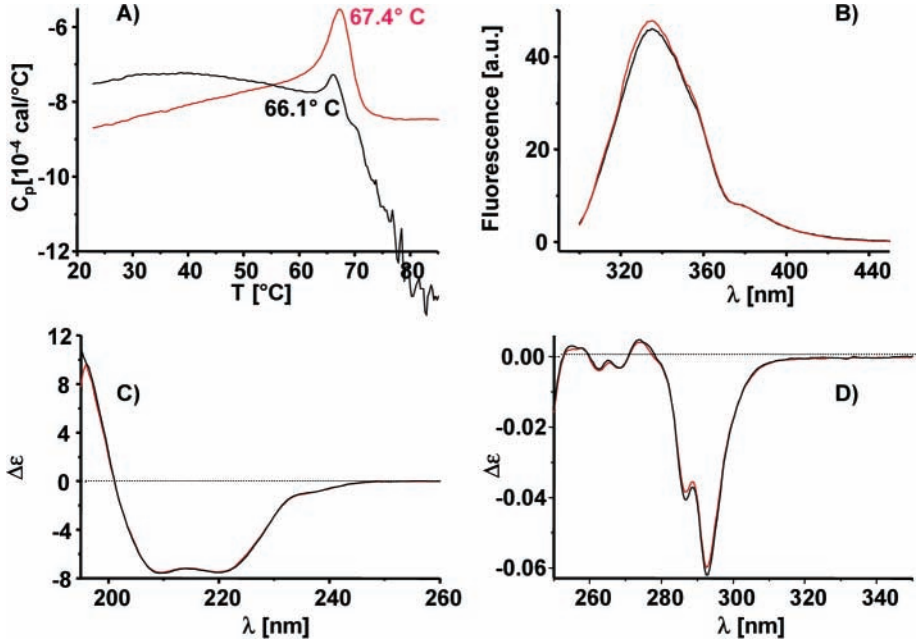

Figure 7. (A) DSC scans of the unfolding transition of IFNα_{2a} (black) and ^{40}PEG–IFNα_{2a} (red). The denaturation melting temperature T_m is evaluated at the maximum of the heat capacity. (B) Fluorescence emission spectra recorded at room temperature after excitation at 283 nm of IFNα_{2a} (black) and ^{40}PEG–IFNα_{2a} (red). (C) CD spectra recorded at 20 °C of IFNα_{2a} (black) and ^{40}PEG–IFNα_{2a} (red) in the backbone absorption region, and (D) in the aromatic absorption region. Optical spectra as shown in B and C were also acquired for the individual positional isomers modified at K31, K134, K131, and K121, leading to identical results (data not shown).

Structure of the 40 kDa Branched PEG-polymer and the Pegylated Lysine. Weak coupling of motions of the protein domain and the PEG-polymer is further supported by the observation of an unique set of sharp resonance lines in the 1D ^{1}H NMR spectra for the PEG-units and the two terminal groups (OCH_3) with identical line-widths and chemical shifts in all the samples including free PEG-polymer. This shows that the polymer molecule adopts a very flexible and mobile random coil (r.c.) conformation, that seems neither to be influenced by IFNα_{2a} nor depends on the pegylation site. Hydrodynamic data indicate, however, that the protein attached-PEG seems to be slightly more compact than the free PEG-polymer (see below). A snapshot of such a highly dynamic system is shown in Figure 8 based on the IFNα_{2a} structure and Self-Avoiding-Walk (SAW) (*75*) model for the polymer conformation.

Despite the very flexible structure of the PEG-polymer, local points of rigidity exist. In all the positional isomers and the free PEG-polymer a cis/trans isomerization was observed at the urethane bonds, one at the α- and the other at the ϵ-position of the PEG-linker lysine (Figure 1). The same ratio ~9:1 of trans and cis populations, respectively was observed in free PEG-polymer and for all the positional isomers independently of the pegylation site. Interestingly, in the Isomer-K121 an additional conformational heterogeneity was indicated by a doubling of the ^{1}H-resonance for $N_\alpha H^{trans}$ and $N_\alpha H^{cis}$ with relative intensity ratio of ~5.5:4.5 reflected in both signals. For the Isomer-K31 and -K134, only the doubling of the ^{1}H-resonance for $N_\alpha H^{trans}$ was observed with the relative intensity ratio of ~6.5:3.5 and ~5.5:4.5, respectively. For the Isomer-K131, -K164, and -K70, the signal splitting is not resolved or not present. For all the three positional isomers which showed the additional splitting of the $N_\alpha H$ linker signal, a corresponding doubling with identical intensity ratio was observed for the cross-peaks of the neighboring $^{15}N_\epsilon H$ of the pegylated lysine (Figure 3). These cross-peaks could be assigned to two conformational states, arbitrarily called State-A and State-B, according to their higher and lower intensity, respectively. The observation of two ($^{15}N_\epsilon/^{15}N_\epsilon H$) cross-peaks for

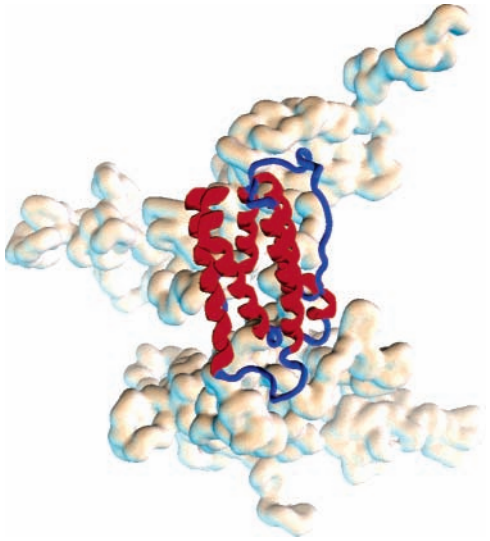

Figure 8. Three-dimensional model of one positional isomer pegylated at K164 of ^{40}PEG−IFNα_{2a}. The model is based on the NMR solution structure of IFNα_{2a} which is shown as a ribbon with α-helices in red and connecting loops and turns in blue (*40*). The r.c. conformation of the two 20 kDa branches of the PEG-polymer was calculated as an on-lattice SAW (*75*) using the molecular modeling package MOLOC (*84, 85*). It must be noted that the polymer molecule experiences a very high number of conformations, therefore this representation is only one snapshot of a single possible conformation. The polymer is reported as a solid Gaussian−Connolly molecular surface in white-grey computed with the MOE software (Chemical Computing Group Inc., Montreal, Canada). The impact of the time-averaged structural envelope of the ensemble of r.c. conformations for the polymer is further evaluated in the accompanying publication with respect to the binding to the extracellular domain of the receptor

the ϵ-amide group of the pegylated lysine coincides with the duplication of the ^{1}H-resonance for N_αH of the PEG-linker lysine. The same relative intensity for the split lines of N_αH of the PEG-linker lysine and of the neighboring $^{15}N_\epsilon$H of the pegylated lysine indicates that a common conformational process is responsible for both duplication of signals. As no conformational exchange was observed between State-A and -B on the time scale accessible by NMR, these two states are either in a very slow dynamic exchange or stable over time. This is in contrast with the cis/trans isomerization of the two neighboring urethane bonds, where for both α- and ϵ- positions, a conformational exchange takes place within the millisecond time range ($\sim$5 ms < $1/k_{ex}$ < $\sim$50 ms). State-A and -B may be caused by a slow cis/trans isomerization of the peptide bond linking the IFNα_{2a} protein to the polymer (Figure 1).

Hydrodynamic Properties of ^{40}PEG−IFNα_{2a} As Compared To IFNα_{2a} and the 40 kDa Branched PEG-polymer. The favorable pharmacological properties of ^{40}PEG−IFNα_{2a} are intimately related to the molecular structure and thermodynamic properties of the branched PEG, as discussed here and in the accompanying publication (*36*). The pegylation of the protein with the 40 kDa branched PEG-polymer alters the hydrodynamic properties of IFNα_{2a} dramatically (Table 2): both sedimentation S and translational diffusion D_T coefficients are substantially smaller in the modified protein. The hydrodynamic radius R_H expands three to four times and the overall shape of the pegylated molecule becomes highly asymmetric (see f/f_0 values). By the same token, the conformation of the protein domain remains unchanged, as was shown by detailed NMR structural analysis of the positional ^{15}N-isomers as compared to IFNα_{2a}.

The size difference of the pegylated protein when compared with the unmodified IFNα_{2a} is clearly reflected in the change of D_T. The observed decrease in the D_T value, however, is much higher than expected from MW consideration alone. The 60 kDa pegylated IFNα_{2a} shows diffusion properties very similar to globular proteins with MW's of approximately 300 kDa (*72*, *73*). If the effective hydrodynamic volumes are compared, the 40 kDa branched PEG-polymer is approximately 60 times larger ($R^3_H{}^{PEG}/R^3_H{}^{IFN\alpha 2a}$) and less densely packed ($1/\upsilon_{bar}$) than IFNα_{2a}. As the polymer has the unique property to 'bind' two to three water molecules per ethylene glycol unit (*76*), its r.c. structure is dynamically associated with a large cloud of water molecules. These hydrodynamic properties of the PEG-polymer are effectively transferred to IFNα_{2a} upon pegylation, leading to a molecular particle with an effective hydrodynamic volume that has increased approximately 40 times. Unexpectedly, however, the 40 kDa PEG-polymer is self-diffusing $\sim$1.1 times slower than ^{40}PEG−IFNα_{2a} that is 1.5 times higher in molecular weight. Attaching the polymer to the protein can be interpreted as leading to a reduction of the effective hydrodynamic volume of the PEG molecule by $\sim$30%. The protein attached-PEG, while keeping its very flexible and mobile r.c. conformation, seems to adopt a slightly more compact conformation than the free PEG-polymer in solution. Polymer branching can lead to compaction for entropic reasons (*77*, *78*). In our case, attaching a protein to the two PEG-chains at its 'branching' site could be formally viewed as increasing the branching of the polymer. However, the compaction can also be explained enthalpically by assuming a small attractive interaction between the polymer and the protein. To decide between the two compaction mechanisms is not possible based on our current experimental evidence.

The significant differences for the sedimentation coefficient S measured by AUC further show that pegylation changes the hydrodynamic shape of the pegylated protein. As expected, ^{40}PEG−IFNα_{2a} sediments faster than the 40 kDa PEG-molecule but, surprisingly, slower than IFNα_{2a}, despite its bigger molecular weight. Therefore, the overall shapes, of IFNα_{2a} and ^{40}PEG−IFNα_{2a} must be very different. In the sedimentation experiment with ^{40}PEG−IFNα_{2a}, the PEG-moiety can be envisaged as a 'parachute' slowing down the sedimentation rate. The changes in hydrodynamic shape can be assessed from S by the ratio f/f_0 that gives a measure of the maximum shape asymmetry from a sphere (*44*). The value f/f_0 of 1.02 for IFNα_{2a} indicates that the hydrodynamic shape of the protein is very close to a sphere. In contrast, the value f/f_0 of 3.76 for the 40 kDa branched PEG-polymer shows that the hydrodynamic shape of the polymer alone is very asymmetric. This is in agreement with theoretical calculations of polymer structures by SAW showing highly asymmetric molecular shapes (*79*, *80*). The attachment of the PEG to the protein creates a molecule with a hydrodynamic shape less asymmetric than the free PEG-polymer with a f/f_0 value of 2.59. Further experimental evidence based on hydrodynamic modeling might allow a tentative approximation of the molecular shape of the 40 kDa branched PEG-polymer and ^{40}PEG−IFNα_{2a} to a hydrodynamic equivalent oblate or prolate ellipsoid of revolution.

The uniquely tailored hydrodynamic properties and shape of ^{40}PEG−IFNα_{2a} are of extreme pharmacological interest and benefit as clinically shown with PEGASYS. The shielding of the protein by the polymer may effectively prevent, by steric hindrance, large molecules such as antibodies (*9*) or receptors (*33*, *36*) from reaching

the protein surface. The recognition of pegylated proteins by the immune system is reduced, and in parallel also the immunogenicity of the protein drug (*9*, *81*). Similarly, the increased resistance of pegylated proteins toward proteolytic degradation (*9*) is mediated by PEG through its large volume close to the protein surface which excludes other large molecules. Pegylation makes the molecular shape of a protein looks much larger than the actual MW of the pegylated protein might suggest. In this way, pharmacological properties related to size, e.g. the renal clearance of the drug, can critically be modulated and tuned. It is known that the size cutoff for a protein to be filtered out from the blood circulation by the kidney, is lower than 300 kDa (*11*, *82*). The enhanced and prolonged bioavailability of the ^{40}PEG–IFNα_{2a} drug in the body (*83*) can thus be directly related to hydrodynamic properties of the pegylated protein.

The second virial coefficient B is a description of the solute–solute interaction strength in solution. The opposite sign of B for IFNα_{2a} and ^{40}PEG–IFNα_{2a} shows that the molecules have a completely different aggregation behavior (*45*). For IFNα_{2a}, intermolecular solute–solute interactions are preferred, i.e., they are attractive, whereas for ^{40}PEG–IFNα_{2a} these interactions are repulsive, as solvent–solute interactions prevail. Again, these favorable properties are caused by the highly hydrated polymer and are effectively transferred to ^{40}PEG–IFNα_{2a}, creating a molecule with reduced tendency for aggregation. This becomes noticeable if the thermal unfolding of ^{40}PEG–IFNα_{2a} is compared with IFNα_{2a}. As shown by DSC and CD, ^{40}PEG–IFNα_{2a} has a significantly reduced tendency for heat induced irreversible aggregation, coupled with a slightly elevated denaturation melting temperature T_m (Table 2). At 20 °C, IFNα_{2a} and ^{40}PEG–IFNα_{2a} present ~75% of α-helix secondary structure. After a melting (80 °C) and cooling (20 °C) cycle, more α-helix secondary structure is recovered for ^{40}PEG–IFNα_{2a} (~61% α-helix) than for IFNα_{2a} (~41% α-helix). The prevention of aggregation in protein drugs is crucial for the preservation of the native protein fold. The increased stability contributes to the favorable pharmacokinetic and immunological properties that are a consequence of the improved hydrodynamic properties of the pegylated protein.

Summarizing the hydrodynamic properties (v_{bar}, B, S, f/f_0, D_T, and R_H), one can see that the covalent attachment of an unstructured, mobile, and highly flexible PEG-polymer molecule of appropriate size on a compact structured protein causes an efficient transfer of favorable hydrodynamic properties of the PEG-polymer to the pegylated protein. The modification of IFNα_{2a} by the 40 kDa branched PEG-polymer provides a shield for the protein domain without changing the three-dimensional structure and conformation of the protein. The pegylation does alter the size and shape of the molecule, significantly increasing the effective hydrodynamic volume. It also improves the physicochemical properties of the protein, resulting in higher temperature stability and reduced tendency for aggregation. The small changes of the NMR ^{1}H-resonance line-width of IFNα_{2a} and the unchanged line-width observed for PEG in ^{40}PEG–IFNα_{2a} show that the protein and PEG domains behave independently.

CONCLUSION

Here, we reported the detailed structural and biophysical characterization by NMR spectroscopy, AUC, CD, fluorescence spectroscopy, and DSC of ^{40}PEG–IFNα_{2a} and its positional isomers modified at K31, K134, K131, K121, K164, and K70, respectively, as compared to IFNα_{2a}. Our results show that the three-dimensional structure of IFNα_{2a} is not modified by the presence of the attached 40 kDa branched PEG-polymer in any positional isomer of ^{40}PEG–IFNα_{2a}. Regardless of where the PEG-polymer is attached, it adopts a very mobile and flexible r.c. conformation, producing a shield for the protein without a permanent coverage of the protein surface. This shield can be best envisaged by a large excluded volume close to the protein surface. This volume is visible to other large molecules, e.g. antibodies, proteases or receptors, approaching this part of space. Our results also provide evidence of significant structural and physicochemical advantages conferred by the pegylation to IFNα_{2a}: alteration of the hydrodynamic properties by increase of the effective hydrodynamic volume and modification of the molecular shape, higher temperature stability, and reduced tendency for aggregation. These properties are of tremendous pharmacological interest and benefit as clinically shown with PEGASYS.

Finally, our work represents a new standard for the characterization and quality-control of pegylated proteins, and it can be foreseen that this will have a significant impact in the pegylation area which plays an increasingly important role in new pharmaceutical applications. In the future, further investigations, particularly IFNα_{2a} receptor binding studies, are clearly needed for a better understanding of the relationship between the structure and the biological function of ^{40}PEG–IFNα_{2a} and its positional isomers. Ultimately, this knowledge might lead to selectively engineered positional pegylated IFNα_{2a} with unique and optimized properties.

ACKNOWLEDGMENT

We would like to thank D. Brugger, Dr. F. Danel, J. Kohler, E. Kusznir, and A. Schacher for their help in obtaining materials and for experimental work. We gratefully acknowledge Drs. T. Schreitmüller, K. Weyer, and B. Wipf for constant support. For stimulating discussions and help many thanks to Drs. P. Gerber, S. E. Harding (Nothingham University), W. Huber, W. Klaus, and T. Schulz-Gasch. We thank Dr. D. Banner for a careful reading of the manuscript.

LITERATURE CITED

(1) Abuchowski, A., Van Es, T., Palczuk, N., and Davis, F. (1977) Alteration of immunological properties of bovine serum albumin by covalent attachment of poly-ethylene-glycol. *J. Biol. Chem. 252*, 3578–3581.

(2) Bailon, P., and Berthold, W. (1998) Poly(ethylene glycol)-conjugated pharmaceuticals proteins. *Pharm. Sci. Technol. Today 1*, 352–356.

(3) Wang, Y. S., Youngster, S., Bausch, J., Zhang, R., McNemar, C., and Wyss, D. F. (2000) Identification of the major positional isomer of pegylated Interferon alpha-2b. *Biochemistry 39*, 10634–10640.

(4) Harris, J. M., and Chess, R. B. (2003) Effect of pegylation on pharmaceuticals. *Nat. Rev. Drug Discovery 2*, 214–221.

(5) Fuerteges, F., and Abuchowski, A. (1990) The clinical efficacy of poly-(ethylene-glycol)-modified proteins. *J. Controlled Release 11*, 139–148.

(6) Inada, I., Matsushima, A., Kodera, Y., and Nishimura, H. (1990) Polyethylene-Glycol (PEG)-proteins conjugates: applications to biomedical and biotechnological processes. *J. Bioact. Compat. Polym. 5*, 343–364.

(7) Katre, N. V., Knauf, M. J., and Laird, W. (1987) Chemical modification of Interleukin-2 by polyethylene glycol increases its potency in the murine Meth A Sarcoma model. *Proc. Natl. Acad. Sci. U.S.A. 84*, 1487–1491.

(8) Lisi, P. L., Van Es, T., Palczuk, N. C., and Davis, F. F. (1982) Enzyme therapy: Polyethylene-Glycol, α-glucuronidase conjugates as potential therapeutic agents in acid mucopolysacchararidosis. *J. Appl. Biochem. 4*, 19−33.

(9) Veronese, F. M., Caliceti, P., and Schiavon, O. (1997) Branched and linear poly(ethylene glycol): influence of the polymer structure on enzymological, pharmacokinetic, and immunological properties of proteins conjugates. *J. Bioact. Comput. Polym. 12*, 196−207.

(10) Knauf, M. J., Bell, D. P., Hirtzer, P., Luo, Z. P., Young, J. D., and Katre N. V. (1988) Relationship of effective molecular size to systemic clearance in rats of recombinant interleukin-2 chemically modified with water-soluble polymers. *J. Biol. Chem. 263*, 15064−15070.

(11) Yamaoka, T., Tabata, Y., and Ikada, Y. (1994) Distribution and tissue uptake of poly(ethylene-glycol) with different molecular weights after intravenous administration to mice. *J. Pharm. Sci. 4*, 601−606.

(12) Abuchowski, A., McCoy, J., Palczuk, N., Van Es, T., and Davis, F. (1977) Effect of covalent attachment of polyethylene-glycol on immunogenicity and circulating life of bovine liver catalase. *J. Biol. Chem. 252*, 3582−3586.

(13) Katre, N. V. (1990) Immunogenicity of recombinant IL-2 modified by covalent attachment of polyethylene glycol. *J. Immunol. 144*, 209−213.

(14) Heathcote, E. J., Shiffman, M. L., Cooksley, W. G., Dusheiko, G. M., Lee, S. S., Luis Balart, L., Reindollar, R., Reddy, R. K., Wright, T. L., Lin, A., Hoffman, J., and De Pamphilis, J. (2000) Peginterferon Alfa-2a in Patients with Chronic Hepatitis C and Cirrhosis. *N. Engl. J. Med. 343*, 1673−1680.

(15) Zeuzem, S., Feinman, S. V., Rasenack, J., Heathcote, E. J., Lai, M.-Y., Gane, E., O'Grady, J., Reichen, J., Diago, M., Lin, A., Hoffman, J., and Brunda, M. J. (2000) Peginterferon Alfa-2a in Patients with Chronic Hepatitis C. *N. Engl. J. Med. 343*, 1666−1672.

(16) Cohen, J. (1999) The Scientific Challenge of Hepatitis, C. *Science. 285*, 26−30.

(17) Liang, T. J., Rehermann, B., Seeff, L. B., and Hoofnagle, J. H. (2000) Pathogenesis, natural history, treatment, and prevention of Hepatitis C. *Ann. Intern Med. 132*, 296−305.

(18) Pol, S., Couzigou, P., Berliere, M., Abergel, A., Combis, J. M., Larrey, D., Tran, A., Moussali, J., Moussali, J., Poupon, R., Berthelot, P., and Brechot, C. (1999) A randomized trial of ribavirin and Interferon-α vs Interferon-α alone in patients with chronic Hepatitis C who were not responders to previous treatment. *J. Hepatol. 31*, 1−7.

(19) Rostaing, L., Chatelut, E., Payen, J. L., Izopet, J., Thalamas, C., Ton-That, H., Pascal, J. P., Duramd, D., and Canal, P. (1998) Pharmacokinetics of alphaIFN-2b in chronic Hepatitis C virus patients undergoing hemodialysis or with normal renal function: clinical implications. *J. Am. Soc. Nephrol. 9*, 2344−2348.

(20) Zeuzem, S. (1999) Clinical implications of Hepatitis C viral kinetics. *J. Hepatol. 31*, Sup. 1, 61−64.

(21) Barouki, F. M., Witter, F. R., Griffin, D. E., Nadler, P. I., Woods, A., Wood, D. E., and Lietman, P. S. (1987) Time course for virus for 24 weeks following the completion of treatment of interferon levels, antiviral state, 2′,5′-oligoadenylate synthetase and side effects in healthy men. *J. Interferon Res. 7*, 29−39.

(22) Wills, R. J. (1990) Clinical pharmacokinetics of Interferons. *Clin. Pharmacokinet. 19*, 390−399.

(23) Monkarsh, S. P., Ma, Y., Aglione, A., Bailon, P., Ciolek, D., DeBarbieri, B., Graves, M. C., Hollfelder, K., Michel, H., Palleroni, A., Porter, J. E., Russoman, E., Roy, S., and Pan, Y. C. (1997) Positional isomers of monopegylated Interferonα-2a: isolation, characterization, and biological activity. *Anal. Biochem. 247*, 434−440.

(24) Bailon, P., Palleroni, A., Schaffer, C., Spence, C., Fung, W., Porter, J., Ehrlich, G., Pan, W., Xu, Z. X., Modi, M., Farid, A., and Berthold, W. (2001) Rational design of a potent, long lasting form of Interferon: a 40 kDa branched Polyethylene Glycol-conjugated Interferonα-2a for the treatment of Hepatitis C. *Bioconjugate Chem. 12*, 195−202.

(25) Fung, W. J., Porter, J. E., and Bailon, P. (1997) Strategies for the preparation and characterization of poly-(ethylene glycol) (PEG) conjugated pharmaceutical proteins. *Polym. Prepr. 38*, 565−566.

(26) Caliceti, P., Schiavon, O., and Veronese, F. M. (1999) Biopharmaceutical properties of urecase conjugated to neutral and amphiphilic polymers. *Bioconjugate Chem. 10*, 638−646.

(27) Wang, Y. S., Youngster, S., Grace, M., Bausch, J., Bordens, R., Wyss, D. F. (2002) Structural and biological characterization of pegylated recombinant interferon alpha-2b and ist therapeutic implications. *Adv. Drug Delivery Rev. 54*, 547−570.

(28) Foser, S., Schacher, A., Weyer, K. A., Brugger, D., Dietel, E., Marti, S., and Schreitmüller, T. (2003) Isolation, structural characterization, and antiviral activity of positional Isomers of monopegylated Interferon alpha-2a. *J. Prot. Exp. Purif. 30*, 78−87.

(29) Perry, M. C., and Jarvis, B. (2001) Peginterferon-α-2a (40 kD): a review of its use in the management of chronic Hepatitis C. *Drugs 15*, 2263−2288.

(30) Lamb, M. V., and Martin, E. N. (2002) Weight-based versus fixed dosing of Peginterferon-α-2a (40 kDa). *Ann. Pharmacother. 36*, 933−938.

(31) Roseng, L., Tolleshaug, H., and Berg, T. (1992) Uptake, intracellular transport, and degradation of polyethyleneglycol-modified Asialofetuin in hepatocytes. *J. Biol. Chem. 267*, 22987−22993.

(32) So, T., Ueda, T., Yoshito, A., Nakamata, T., and Imoto, T. (1996) Situation of monomethoxypolyethylene glycol covalently attached to lyzozyme. *J. Biochem. 119*, 1086−1093.

(33) Pradhananga, S., Wilkinson, I., and Ross, R. J. M. (2002) Receptor antagonists, Pegvisomant: structure and function. *J. Mol. Endocrinol. 29*, 11−14.

(34) Youngster, S., Wang, Y. S., Grace, M., Bausch, J., Bordens, R., and Wyss, D. F. (2002) Structure, biology, and therapeutic implications of pegylated interferon alpha-2b. *Curr. Pharm. Des. 8*, 2139−2157.

(35) Piehler, J., Roisman, L. C., and Schreiber, G. (2000) New structural and functional aspects of the type-I Interferon-receptor interaction revealed by comprehensive mutational analysis of the binding interface. *J. Biol. Chem. 275*, 40425−40433.

(36) Dhalluin, C., Ross, A., Huber, W., Gerber, P., Brugger, D., Gsell, B., and Senn, H. (2005) Structural, kinetic and thermodynamic analysis of the binding interaction of the 40 kDa PEG-Interferon-α_{2a} (PEGASYS) and its individual positional isomers to the extracellular domain of the receptor IFNAR2. *Bioconjugate Chem. 16*, 518−527.

(37) Hochuli, E. (1986) Large-scale recovery of Interferonα-2a synthesized in bacteria. *Chimia 40*, 408−412.

(38) Baron, S., Tyring, S. K., Fleischmann, W. R., Coppenhaver, D. H., Niesel, D. W., Klimpel, G. R., Stanton, J., and Hughes, T. K. (1991) The interferons, mechanisms of action and clinical applications. *JAMA 266*, 1375−1383.

(39) Kozlowski, A., and Harris, J. M. (2001) Improvements in protein PEGylation: pegylated interferons for treatment of Hepatitis C. *J. Controlled Release 72*, 217−224.

(40) Klaus, W., Gsell, B., Labhardt, A., Wipf, B., and Senn, H. (1997) The three-dimensional high-resolution structure of human Interferonα-2a determined by heteronuclear NMR spectroscopy in solution. *J. Mol. Biol. 374*, 661−675.

(41) Edsall, J. T. (1943) *Protein, amino acids and peptides as ions and dipolar ions* (Cohn, E. J., and Edsall, J. T., Eds.) pp 370−381, Reinhold, New York.

(42) Schuck, P. (1994) Simultaneous radial and wavelength analysis with the Optima XL-A analytical ultracentrifuge. *Prog. Colloid Polym. Sci. 94*, 1−13.

(43) Laue, T. M., and Stafford, W. F., III (1999) Modern Applications of Analytical Ultracentrifugation. *Annu. Rev. Biophys. Biomol. Struct. 28*, 75−100.

(44) Lebowitz, J., Lewis, M. S., and Schuck, P. (2002) Modern analytical ultracentrifugation in protein science: A tutorial review. *Prot. Sci.*, *11*, 2067−2079.

(45) George, A., Chiang, Y., Guo, B., Arabshahi, A., Cai, Z., and Wilson, W. (1997) Second virial coefficient as predictor in protein crystal growth. *Methods Enzymol. 276*, 100−110.

(46) Berne, B. J., and Pecora, R. (1976) *Dynamic Light Scattering*, John Wiley and Sons, New York.
(47) Provencher, S., and Glöckner, J. (1981) Estimation of globular protein secondary structure from circular dichroism. *Biochemisty 20*, 33−37.
(48) Delaglio, F., Grzesiek, S., Vuister, G. W., Zhu, G., Pfeifer, J., and Bax, A. (1995) NMRPipe: a multidimensional spectral processing system based on UNIX pipes. *J. Biomol. NMR 6*, 277−293.
(49) Piotto, M., Saudek, V., and Sklenar, V. (1992) Gradient-tailored excitation for single-quantum NMR spectroscopy of aqueous solutions. *J. Biomol. NMR 2*, 661−665.
(50) Wagner, G., and Zuiderweg, E. R. P. (1983) Two-dimensional double quantum ^{1}H NMR spectroscopy of proteins. *Biochem. Biophys. Res. Commun. 113*, 854−860.
(51) Braunschweiler, L., and Ernst, R. R. (1983) Coherence transfer by isotropic mixing: application to proton correlation spectroscopy. *J. Magn. Reson. 53*, 521−528.
(52) Shaka, A. J., Barker, P. B., and Freeman, R. (1985) Computer-optimized decoupling scheme for wideband applications and low level operation. *J. Magn. Reson. 64*, 547−552.
(53) Shaka, A. J., Lee, C. J., and Pines, A. (1988) Iterative schemes for bilinear operators; application to spin decoupling. *J. Magn. Reson. 77*, 274−293.
(54) Sattler, M., Schleucher, J., and Griesinger, C. (1999) Heteronuclear multidimensional NMR experiments for the structure of proteins in solution employing pulsed field gradients. *Prog. NMR Spectrosc. 34*, 93−158.
(55) Pervushin, K., Riek, R., Wider, G., and Wüthrich, K. (1997) Attenuated T2 relaxation by mutual cancellation of dipole−dipole coupling and chemical shift anisotropy indicates an avenue to NMR structures of very large biological macromolecules in solution. *Proc. Natl. Acad. Sci. U.S.A. 94*, 12366−12371.
(56) Takahashi, H., Nakanishi, T., Kami, K., Arata, Y., and Shimada, I. (2000) A novel NMR method for determining the interfaces of large protein−protein complexes. *Nat. Struct. Biol. 7*, 220−223.
(57) Marion, D., Driscoll, P. C., Kay, L. E., Wingfield, P. T., Bax, A., Gronenborn, A. M., and Clore, G. M. (1989) Overcoming the overlap problem in the assignment of ^{1}H NMR spectra of larger proteins by the use of three-dimensional heteronuclear ^{1}H−^{15}N Hartmann−Hahn multiple quantum coherence and Nuclear Overhauser multiple quantum coherence spectroscopy. *Biochemistry 28*, 6150−6156.
(58) Gibbs, S. J., and Johnson, C. S. (1991) A PFG NMR experiment for accurate diffusion and flow studies in the presence of eddy currents. *J. Magn. Reson. 93*, 395−402.
(59) Stejskal, E. O., and Tanner, J. E. (1965) Spin diffusion measurements: spin−echoes in the presence of a time dependent field gradient. *J. Chem. Phys. 42*, 288−292.
(60) Weast, R. C. (1984) CRC *Handbook of Chemistry and Physics*, 64th ed., CRC Press, Boca Raton, FL.
(61) Wüthrich, K. (1986) *NMR of proteins and nucleic acids*, John Wiley and Sons, New York.
(62) Kessler, H., and Molter, M. (1976) Conformation of protected amino acids. V. Application of lanthanide-shift reagents for conformatiopnal studies of *tert*-butoxycarbonyl α-amino acid esters: equilibrium changes and kinetics of the isomerization. *J. Am. Chem. Soc. 98*, 5969−5973.
(63) Jaikaran, D. C. J., and Wooley, G. A. (1995) Characterization of thermal isomerization at the single molecule level. *J. Phys. Chem. 99*, 13352−13355.
(64) Wooley, G. A., Jaikaran, D. C. J., Zhang, Z., and Peng, S. (1995) Design of regulated Ion channels using measurements of cis/trans isomerization in single molecules. *J. Am. Chem. Soc. 117*, 4448−4454.
(65) Kumar, A., Ernst, R. R., and Wüthrich, K. (1980) Two-dimensional nuclear Overhauser enhancement (2D NOE) experiment for the elucidation of complete proton−proton cross-relaxation networks in biological macromolecules. *Biochem. Biophys. Res. Commun. 95*, 1−6.
(66) Bothner-By, A. A., Stephens, R. L., Lee, J. M., Warren, C. D., and Jeanloz, R. W. (1984) Structure determination of a tetrasaccharide: transient Nuclear Overhauser effects in the rotating frame. *J. Am. Chem. Soc. 106*, 811−813.
(67) Lepori, L., and Mollica, V. (1978) Volumetric properties of dilute aqueous solutions of poly(ethylene glycols). *J. Polym. Sci., Polym. Phys. Ed. 16*, 1123−1134.
(68) Devanand, K., and Selser, J. C. (1991) Asymptotic behavior and long-range interactions in aqueous solutions of Poly(ethylene oxide). *Macromolecules 24*, 5943−5947.
(69) Kawaguchi, S., Imai, G., Suzuki, J., Miyahara, A., Kitano, T., and Ito, K. (1997) Aqueous solution properties of oligo- and poly(ethylene oxide) by static light scattering and intrinsic viscosity. *Polymer 38*, 2885−2891.
(70) Chew, B., and Couper, A. (1973) Diffusion, viscosity and sedimentation of poly(ethylene oxide) in water. *J. Chem. Soc., Faraday Trans. 1 72*, 382−386.
(71) Brown, W., Stilbs, P., and Johnsen, R. M. (1983) Friction coefficients in self-diffusion, velocity sedimentation, and mutual diffusion for poly(ethylene oxide) in aqueous solution. *J. Polym. Sci. Polym. Phys. Ed. 21*, 1029−1039.
(72) Tanford, C. (1961) *Physical Chemistry of Macromolecules*, John Wiley and Sons, New York.
(73) Wilkins, D. K., Grimshaw, S. B., Receveur, V., Dobson, C., Jones, J. A., and Smith, L. J. (1999) Hydrodynamic radii of native and denatured proteins measured by pulse field gradient NMR techniques. *Biochemistry 38*, 16424−16431.
(74) Waggoner R. A., Blum, F. D., and Lang, J. C. (1995) Diffusion in aqueous solutions of Poly(ethylene glycol) at low concentrations. *Macromolecules 28*, 2658−2664.
(75) Flory, P. J. (1969) *Statistical mechanics of chain molecules*, Wiley-Interscience, New York.
(76) Maxfield, J., and Shepherd, T. J. (1975) Conformation of polyethylene-glycol oxide in the solid-state, melt, and solution measured raman scattering. *Polymer 16*, 505−512.
(77) Vlahos, C. H., Horta, A., Hadjichristidis, N., and Freire, J. J. (1995) Monte Carlo calculations of $A_\alpha B_{f-x}$ Miktoarm star copolymers. *Macromolecules 28*, 1500−1505.
(78) Aerts, J. (1998) Prediction of intrinsic viscosities of dendritic, hyperbranched and branched polymers. *Comput. Theor. Polym. Sci. 8*, 49−54.
(79) Mazur, J., Guttman, C. M., and McCrackin, F. L. (1973) Monte Carlo studies of self-interacting polymer chains with excluded volume II Shape of a chain. *Macromolecules 6*, 872−874.
(80) Rudnick, J., and Gaspari, G. (1987) The shapes of random walk. *Science 237*, 384−389.
(81) Harris, J. M., Martin, N. E., and Modi, M. (2001) Pegylation, a novel process for modifying pharmacokinetics. *Clin. Pharmacokinet. 40*, 539−551.
(82) Karnam, U. S., and Reddy, K. R. (2003) Pegylated Interferons. *Clin. Liver Dis. 7*, 139−148.
(83) Algranati, N. E., Sy, S., and Modi, M. (1999) A branched methoxy 40 kDa polyethylene glycol (PEG) moiety optimizes the pharmacokinetics (PK) of peginterferon α-2a (PEG-IFN) and may explain its enhanced efficacy in chronic Hepatitis C (CHC). *Hepatology 30*, 4 Pt 2, 190A.
(84) Müller, K., Ammann, H. J., Doran, D. M., Gerber, P. G., Gubernator, K., and Schrepfer, G., (1988) Complex heterocyclic structures: a challenge for computer assisted molecular modeling. *Commun. Soc. Chim. Belg. 97*, 655−667.
(85) Gerber, P. G., and Müller (1995) MAB, a generally applicable molecular force field for structure modelling in medicinal chemistry. *J. Comput.-Aided Mol. Des. 9*, 251−268.

BC049781+

Structural, Kinetic, and Thermodynamic Analysis of the Binding of the 40 kDa PEG−Interferon-α_{2a} and Its Individual Positional Isomers to the Extracellular Domain of the Receptor IFNAR2

Christophe Dhalluin,‡ Alfred Ross,‡ Walter Huber, Paul Gerber, Doris Brugger, Bernard Gsell, and Hans Senn*

F. Hoffmann-La Roche AG Department of Pharma Research CH-4070 Basel, Switzerland. Received September 15, 2004; Revised Manuscript Received March 8, 2005

Type-I Interferons exert antiviral and antiproliferative activities through the binding to a common cell surface receptor comprising two subunits, IFNAR1 and IFNAR2. Human recombinant Interferon-α_{2a} (IFNα_{2a}) is a potent drug (Roferon-A) used to treat various cancers and viral diseases including Hepatitis B/C infections. To significantly improve the pharmacological properties of the drug, a pegylated form of IFNα_{2a} was developed (PEGASYS). This 40 kDa PEG-conjugated IFNα_{2a} (^{40}PEG−IFNα_{2a}) is obtained by the covalent binding of one 40 kDa branched PEG-polymer to a lysine side-chain of IFNα_{2a}. Here, we report the detailed structural, kinetic, and thermodynamic analysis of the binding to the extracellular domain of the receptor IFNAR2 of ^{40}PEG−IFNα_{2a} and its isolated positional isomers modified at K31, K134, K131, K121, K164, and K70, respectively, in comparison with unmodified IFNα_{2a}. Our binding studies, using the surface plasmon resonance technique, show that the pegylation does not abolish the binding to the receptor, but significantly reduces the affinity mainly due to a change of the association rate. The results are supported by modeling and simulation of the binding, using Self-Avoiding-Walk calculations for the polymer conformations. A correlation between the structural parameters and the kinetic and thermodynamic parameters of the binding of the positional isomers could be established. For the Isomer-K31 and -K164, the PEG-polymer attachment point is located in proximity to the binding interface, and the isomers display affinity in the range 150−520 nM in an enthalpy-driven binding process. In contrast for the Isomer-K134, -K131, -K121, and -K70, the PEG-polymer is attached remotely from the binding interface, and the isomers exhibit a higher affinity (32−76 nM) in an entropy-driven binding process. This study constitutes an essential collection of knowledge on which the interaction of ^{40}PEG−IFNα_{2a} and its positional isomers with its cellular receptors can be better understood.

INTRODUCTION

Type-I Interferons (IFNs)[1] are a family of homologous cytokines that potently elicit an antiviral and antiproliferative state in cells (*1*). Human type-I IFN α/β bind to a common cell surface receptor consisting of two transmembrane subunits, IFNAR1 and IFNAR2 (*2*, *3*), to form a ternary complex (Figure 1). IFNAR2 is the major ligand binding component of the receptor complex, exhibiting nanomolar affinity to both IFNα and IFNβ (*4*). While IFNAR2 binds IFNs, such as Interferon-α_{2a} (IFNα_{2a}) with high affinity ($K_D \sim 2-10$ nM), the intrinsic binding affinity of IFNAR1 to IFNα_{2a} is low ($K_D > 100$ nM). The ternary complex mediates activation of numerous genes

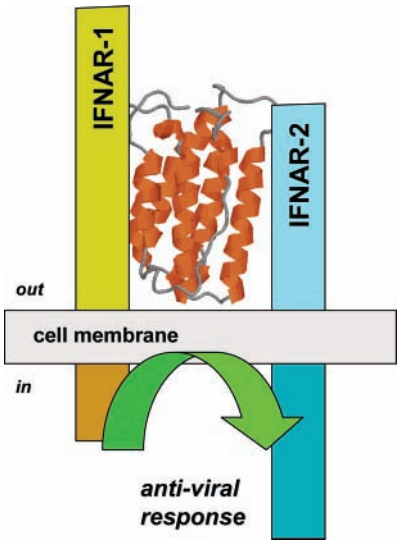

Figure 1. Schematic diagram showing the ternary complex formed by the binding of INFα_{2a} to the human IFN α/β receptor comprising two transmenbrane subunits, IFNAR1 and IFNAR2. The IFNα_{2a} structure (*35*) is reported as a ribbon with α-helices in orange and connecting loops and turns in light gray.

* To whom correspondence should be addressed. Tel: +41 (0)61 68 82028; fax: +41 (0)61 68 87408; e-mail: hans.senn@roche.com.

‡ These authors contributed equally to this work.

[1] Abbreviations: IFN, Interferon; HCV, Hepatitis C Virus; IFNα_{2a}, Interferon-α_{2a}; IFNAR2^{EC}, extracellular domain of the receptor IFNAR2; PEG, poly(ethylene glycol); ^{40}PEG−IFNα_{2a} (PEGASYS) 40 kDa branched PEG-conjugated Interferon-α_{2a}, composed of monopegylated positional isomers; monopegylated positional isomer, one Interferon-α_{2a} molecule with one 40 kDa branched PEG molecule covalently attached at the ϵ-amino group of a lysine residue of Interferon-α_{2a}; ^{5}PEG−IFNα_{2a}, Interferon-α_{2a} modified at the ϵ-amino group of a lysine residue with a 5 kDa linear PEG-polymer; SAW, Self-Avoiding-Walk; SEC, size-exclusion chromatography; LS, light-scattering; RP-HPLC, reverse-phase high-performance liquid chromatography; SPR, surface plasmon resonance; NMR, nuclear magnetic resonance.

10.1021/bc049780h CCC: $30.25 © 2005 American Chemical Society
Published on Web 05/03/2005

through different transduction pathways (*5*). Various expression profiles are induced by IFNs, apparently through the same receptor with particular differences between IFNα and IFN*β*. However, the molecular mechanisms underlying the functional differences between IFNs remain elusive.

IFNs are currently one of the classes of human proteins most widely used as therapeutic agents, approved to treat various types of cancer and viral diseases. Since 1986, the medical potential of recombinant human IFNα_{2a} has been recognized and the drug (Roferon-A) approved for the treatment of malignant melanoma, renal cell carcinoma, chronic myelogenous leukaemia, non-Hodgkin's lymphoma, and Hepatitis B/C infections (*8*, *9*). Today, a major worldwide health concern is infection by Hepatitis C Virus (HCV). The factors limiting the efficacy of IFNα in the treatment of HCV are the pharmacokinetic properties of IFNα, that lead to a short serum half-life of the drug: the protein is rapidly degraded, diffuses widely throughout the entire body, and has a high rate of renal clearance (*10*, *11*).

One successful way to overcome these limitations has been the use of pegylation, the process by which an inert, nontoxic, and water soluble poly(ethylene glycol) (PEG)-polymer is covalently attached to a therapeutic protein (*12*–*15*).

An earlier developed pegylated IFNα_{2a} was obtained with a 5 kDa linear PEG-polymer (*16*). However, this first generation of pegylated IFNα_{2a}, ^{5}PEG–IFNα_{2a}, did not exhibit significant improvements, in terms of pharmacological properties and efficacy, with respect to unmodified IFNα_{2a} (*13*). Based on the latest advancements in pegylation technology and a better empirical basis of the correlation existing between the PEG-polymer characteristics and the resulting pharmacological properties of the modified protein (*12*, *17*, *18*), a second generation of pegylated IFNα_{2a} drug was developed, ^{40}PEG–IFNα_{2a} (PEGASYS) (*13*). Here, by the covalent binding of one 40 kDa branched PEG-polymer to a lysine side-chain of the protein, a mixture of mainly six monopegylated positional isomers with distinct in vitro antiviral activity is obtained (*19*). The drug has a superior efficacy over IFNα_{2a}, with increased serum half-life and reduced renal clearance (*9*, *20*). PEGASYS received FDA approval for the HCV treatment in late 2002.

Understanding the molecular basis of the in vitro biological activity of ^{40}PEG–IFNα_{2a} requires quantitative and qualitative interpretation of the structural, kinetic, and thermodynamic binding parameters for the interaction of the individual positional isomers with the receptors IFNAR1 and IFNAR2.

Very recently, the NMR solution structure of the extracellular domain of the receptor IFNAR2 (IFNAR2^{EC}) has been solved and a model of the IFNα_{2a}/IFNAR2^{EC} complex reported, presenting a molecular basis for the IFN binding mechanism (*21*). The IFNAR2^{EC} binding site is formed by an extensive and predominantly hydrophobic patch, which interacts with a matching hydrophobic surface of IFNα_{2a}, while complementary adjacent motifs of alternating charged side-chains provide specific recognition.

In an accompanying publication we present the structural and biophysical characterization of the individual positional isomers of ^{40}PEG–IFNα_{2a} (*22*). In this study, we establish the correlation between the structural parameters and the kinetic and thermodynamic parameters of the binding of the positional isomers to IFNAR2^{EC}. The results are compared to those obtained for IFNα_{2a} and ^{5}PEG–IFNα_{2a}. In addition, we present results on the time-course of the digestion of IFNα_{2a} and ^{40}PEG–IFNα_{2a} by trypsin that provide evidence for the PEG-polymer protection against proteolytic degradation. The interpretation of the experimental results is supported by modeling and simulation of the binding of the positional isomers with the polymer conformations mimicked as Self-Avoiding-Walk (SAW) constructs (*23*). The data presented here constitute an important step toward understand the rules that govern the in vitro antiviral activity of the different positional isomers of ^{40}PEG–IFNα_{2a} and may support in the future the development of a third generation of pegylated IFNα_{2a} or other pegylated proteins.

MATERIALS AND METHODS

IFNα_{2a}, Pegylated IFNα_{2a} and Polymer Materials. The standard recombinant human Interferon-α_{2a}, Roferon-A (IFNα_{2a}) (19.2 kDa, 165 amino acids) (*8*, *24*), the 40 kDa branched PEG-conjugated IFNα_{2a}, PEGASYS (^{40}PEG–IFNα_{2a}), and the 5 kDa linear PEG-conjugated IFNα_{2a} (^{5}PEG–IFNα_{2a}) were obtained from the Biopharmaceuticals Production Department of Hoffmann-La Roche Inc., as well the PEG-polymer reagents used for the pegylation reactions, the *N*-hydroxysuccinimide ester derivative of a 40 kDa branched PEG-polymer, and the pyridinyl carbamate derivative of a 5 kDa linear PEG-polymer (*13*, *16*, *25*). In ^{5}PEG–IFNα_{2a} and ^{40}PEG–IFNα_{2a}, the PEG-polymer is attached nonspecifically on surface exposed ϵ-amino group of lysine residues via an urea bond and an amide bond, respectively (*13*, *16*). The final product of the respective pegylation reactions is a mixture of monopegylated IFNα_{2a} conjugates with potentially 11 lysine positions of modification (plus the N-terminus).

Very recently, an ion-exchange HPLC separation procedure of the positional isomers of ^{40}PEG–IFNα_{2a} has been developed, and it has been shown that ^{40}PEG–IFNα_{2a} is composed of nine bioactive isomers (*19*). Using this isolation method, the four major isomers modified at K31, K134, K131, K121 and the two minor isomers modified at K164 and K70 were separated with a purity of over 97% as determined by analytical ion-exchange HPLC. These six positional isomers have been extensively analyzed structurally (*22*) and constitute approximately ~98% of the protein mixture.

The molecular weight of IFNα_{2a} protein, based on the amino acid content, is 19241 Da. The calculated extinction coefficients of IFNα_{2a} and ^{40}PEG–IFNα_{2a} are 1.00 mL·mg^{-1}·cm^{-1} and 1.05 mL·mg^{-1}·cm^{-1}, respectively. The sample concentration for the pegylated IFNα_{2a}s is given in mass of protein per unit of volume. In this work, the positional isomers refer to the four major and two minor monopegylated positional isomers of ^{40}PEG–IFNα_{2a} modified at K31, K134, K131, K121, K164, and K70, respectively.

Production of the Extracellular Domain of IFNAR2 Receptor and Complex Formation with IFNα_{2a}. IFNAR2^{EC} was produced in an *E. coli* expression system and purified by ion-exchange and size-exclusion chromatography as previously described (*26*). The expression yield was ~5 mg of protein per gram of biomass. The molecular weight of IFNAR2^{EC} protein (216 amino acids ending with the sequence SESAES) determined by electro-spray-ionization mass specrometry was 24621 Da. This is in agreement with the expected mass of 24628 Da. Analytical Size-Exclusion Chromatography (SEC) on a Superdex-75 HR10/30 (Pharmacia Biotech) in 20 mM TRIS/HCl, 100 mM NaCl at pH 8.4 coupled to a Minidawn

Light-Scattering (LS) detector system (Wyatt Technology, Germany) showed that IFNAR2^{EC} was monomeric and aggregate-free in solution.

As previously described (*27*), a (1:1) stoichiometric complex IFNα_{2a}/IFNAR2^{EC} was prepared and purified by SEC-LS with a molecular weight of ~44.5 kDa. By performing an analytical RP-HPLC run of the complex IFNα_{2a}/IFNAR2^{EC}, the activity of IFNAR2^{EC} was determined to be over 95%.

Experimental Details of Surface Plasmon Resonance. The binding affinity of IFNα_{2a}, ^{5}PEG−IFNα_{2a}, ^{40}PEG−IFNα_{2a}, and its positional isomers for IFNAR2^{EC} was determined by SPR measurements on a Biacore-3000 (Biacore, Sweden) instrument at 10, 17, 25, 30, and 37 °C. For all the samples, the measurement was repeated in duplicate or triplicate at nine different concentrations ranging from 0.6 nM to 1500 nM. The BIAevaluation program (Biacore, Sweden) was used to analyze and fit the experimental data to a (1:1) biomolecular interaction model with mass transport limitation. The binding affinity of the free 5 kDa linear and 40 kDa branched PEG-polymers was evaluated at 25 °C.

The receptor IFNAR2^{EC} was labeled with biotin before being immobilized on a streptavidin containing sensor surface (SA sensor, Biacore-3000). Biotinylation was performed by mixing a 0.8 mM solution of biotinamidocaproate-*N*-hydrosuccinimide ester (Fluka) in DMSO to the IFNAR2^{EC} solution (0.1 mg·mL^{-1} in 10 mM HEPES buffer at pH 8.4) to get a final concentration of 20 μM of biotinylated reagent. After 1 h of reaction, the solution was dialyzed overnight in 10 mM HEPES buffer at pH 8.4 to remove excess biotin. Immobilization was performed by contacting the biotinylated protein solution, diluted to 0.01 mg·mL^{-1}, with the SA sensor surface. For the binding experiments, the amount of immobilized protein was controlled via the contact time: 200 RU were immobilized, corresponding to approximately 0.2 ng·mm^{-2} of IFNAR2^{EC}. The sample and running buffer for the binding experiments was 10 mM HEPES, 150 mM NaCl, 3 mM $CaCl_2$, 0.005% polysorbate-20 at pH 8.4 with a flow velocity of 50 μL·min^{-1}. The acquisition sampling rate was 5 points per second. Between the measurements no regeneration of the sensor surface was needed because of the fast dissociation process. Typical sensorgram responses are shown in Figure 2.

Data Analysis of SPR: Equilibrium Binding and Kinetic Rate Constants. The equilibrium dissociation constant $K_{Deq.}$ was determined after analysis of the equilibrium SPR response with the Scatchard analysis: the ratio of the sensor response to the ligand concentration was plotted versus the sensor response, and the resulting slope of the straight line provided the equilibrium association constant $K_{Aeq.} = 1/K_{Deq.}$. The association and dissociation rates, k_{on} and k_{off}, were determined by fitting the time dependent association and dissociation phases with a mathematical model for a (1:1) complex formation. $K_{Dkin.}$ was calculated as k_{off}/k_{on}. In case of fast association, k_{on} could not be evaluated with a reliable fitting of the association phase. In such a case, only k_{off} was obtained by the fitting of the dissociation phase by a monoexponential decay curve. The $K_{Deq.}$ value determined by the Scatchard analysis of the equilibrium sensor response was then used to calculate k_{on} via the expression $k_{on} = k_{off}/K_{Deq.}$. Results obtained are presented in Table 1.

Equilibrium Thermodynamics of the Binding to IFNAR2^{EC}. Upon binding of IFNα_{2a} and the pegylated IFNα_{2a}s to IFNAR2^{EC}, the change in free energy $\Delta G°$ is related to the enthalpy change $\Delta H°$, the entropy change

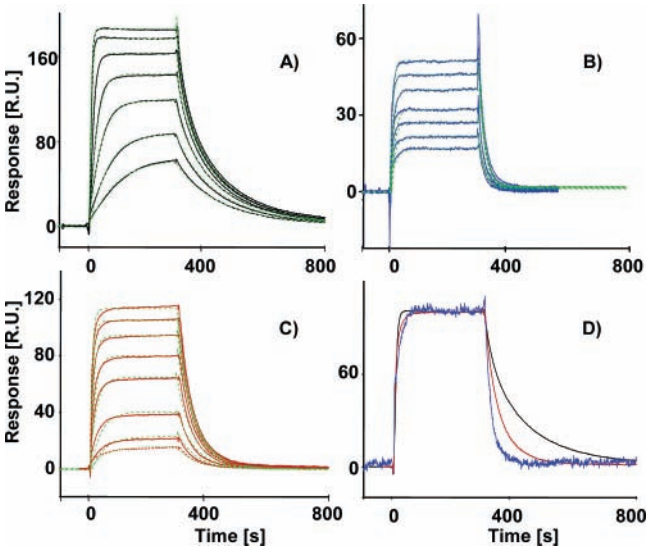

Figure 2. Sensorgram response of binding affinity measured by SPR with immobilized IFNAR2^{EC} at 25 °C in contact with: (A) IFNα_{2a} at concentrations 100, 80, 40, 20, 10, 5, and 2.5 nM, respectively (black line); (B) Isomer-K31 at concentrations 1000, 800, 600, 400, 300, 200 and 150 nM, respectively (blue line); (C) Isomer-K70 at concentrations 300, 290, 150, 120, 70, 40, 15, and 7.5 nM, respectively (red line). For panels A, B, and C, the green dashed lines represent the result of global fits using a (1:1) biomolecular interaction model. Panel D presents the overlay of the 100 nM sensorgram response of binding kinetics with immobilized IFNAR2^{EC} in contact with IFNα_{2a}, the Isomer-K31 and -K70, colored in black, blue, and red lines, respectively. For comparison, the maximum sensorgram response at equilibrium was adjusted to the same level.

Table 1. Kinetic Parameters k_{on}, k_{off}, $K_{Dkin.}$ (= k_{off}/k_{on}), and $K_{Deq.}$ of the Binding to IFNAR2^{EC} of IFNα_{2a}, ^{40}PEG−IFNα_{2a} and Its Individual Positional Isomers, and ^{5}PEG−IFNα_{2a}[a]

	k_{on} 10^5 M^{-1}·s^{-1}	k_{off} 10^{-2} s^{-1}	$K_{Dkin.}$, nM	$K_{Deq.}$, nM
IFN$_{\alpha 2a}$	27.0	1.3	5.0	5.5
^{40}PEG−IFNα_{2a}[b]	1.6	2.0	121	124
Low Affinity (LA) Isomer				
Isomer-K31	1.0	5.2	520	500
Isomer-K164	2.3	3.3	150	150
High Affinity (HA) Isomer				
Isomer-K134	2.7	2.1	76	77
Isomer-K131	4.8	1.9	40	43
Isomer-K121	5.3	2.1	39	40
Isomer-K70	5.5	1.8	32	32
^{5}PEG−IFNα_{2a}[c]	7.4	1.3	17	17

[a] SPR measurements were done at 25 °C. For all the values, the standard error is ±10%. [b] ^{40}PEG−IFNα_{2a} is a mixture of mainly six monopegylated positional isomers modified at K31, K134, K131, K121, K164, and K70, respectively, representing ~98% of the mixture (*19*). [c] ^{5}PEG−IFNα_{2a} is a mixture of 11 monopegylated positional isomers modified at all the lysine positions (*16*).

$\Delta S°$, and the equilibrium association constant $K_{Aeq.}$ according to the eq 1 with R the gas constant (1.99 × 10^{-3} kcal·K^{-1}·mol^{-1}).

$$\Delta G° = \Delta H° - T\Delta S° = -RT \ln K_{Aeq.} \quad (1)$$

If the enthalpy change does not vary with the temperature, the van't Hoff plot of ln $K_{Aeq.}$ versus 1/T results in a straight line of slope $\Delta H°/R$.

$$\ln K_{Aeq} = -\Delta H°/RT + \Delta S°/R \quad (2)$$

Although the intercept, $\Delta S°/R$, provides the entropy, a better alternative is to use eq 1. However $\Delta H°$ and $\Delta S°$

Table 2. Thermodynamic Parameters $\Delta G°$, $\Delta H°$, and $T\Delta S°$, for the Binding to IFNAR2^{EC} of IFNα_{2a}, ^{40}PEG–IFNα_{2a} and Its Individual Positional Isomers, and ^{5}PEG–IFNα_{2a}[a]

	$\Delta G°$, kcal·mol^{-1}	$\Delta H°$, kcal·mol^{-1}	$T\Delta S°$, kcal·mol^{-1}	ΔCp°, kcal·mol^{-1}·K^{-1}
IFNα_{2a}	−11.2	−5.7	5.5	−0.2
^{40}PEG–IFNα_{2a}[b]	−9.4	−3.7	5.7	n.d.[d]
Low Affinity (LA) Isomer				
Isomer-K31	−8.6	−6.5	2.1	−0.5
Isomer-K164	−9.3	−6.0	3.3	−0.6
High Affinity (HA) Isomer				
Isomer-K134	−9.7	−3.0	6.7	−0.2
Isomer-K131	−10.0	−4.6	5.4	−0.5
Isomer-K121	−10.1	−3.6	6.5	−0.1
Isomer-K70	−10.2	−4.6	5.6	−0.4
^{5}PEG–IFNα_{2a}[c]	−10.6	−5.4	5.2	−0.4

[a] The values were derived from the van't Hoff analysis of the temperature dependence of the binding affinity data at equilibrium. $T\Delta S°$ is calculated at 25 °C. The temperature dependence of the enthalpy and entropy was evaluated by the determination of ΔCp°. The standard errors for $\Delta G°$, $\Delta H°$, TΔS° were estimated to be in the 10% range, and that of ΔCp° was estimated to be in the 100% range. This estimated was done by a replicate of the K_d(T) series of IFN$_{\alpha 2a}$ which showed a experimental error on K_d in the 10% range. This experimental error was used as noise in a Monte Carlo simulation of the fit parameters of the van't Hoff equation. [b] ^{40}PEG–IFNα_{2a} is a mixture of mainly six monopegylated positional isomers modified at K31, K134, K131, K121, K164, and K70, respectively, representing ~98% of the mixture (*19*). [c] ^{5}PEG–IFNα_{2a} is a mixture of 11 monopegylated positional isomers modified at all the lysine positions (*16*). [d] n.d. = not determined.

very often show temperature variations, resulting in a non-zero value of the heat capacity change ΔCp°. Within the temperature range relevant for the study of such associations, ΔCp° itself does not vary with temperature. The temperature dependence of the equilibrium association constant, $K_{Aeq.}$, is then taken into account by introducing ΔCp° in the integrated van't Hoff eq 3.

$$\ln(K_{Aeq.}/K°) = [(\Delta H° - T_o.\Delta Cp°) \times (1/T_o - 1/T) + \Delta Cp° \ln(T_o/T)]/R \quad (3)$$

Here, a nonlinear fitting of the experimental data provides $\Delta H°$ and ΔCp°. Thus, ΔG° and $\Delta S°$ were calculated using eq 1. The standard temperature T_o was taken to 25 °C. Thermodynamic parameters are summarized in Table 2.

Monitoring of the in Vitro Digestion of IFNα_{2a} and ^{40}PEG–IFNα_{2a} by Trypsin. The in vitro digestion of IFNα_{2a} and ^{40}PEG–IFNα_{2a} by trypsin at room temperature was monitored by successive RP-HPLC runs spaced in time. RP-HPLC experiments were conducted with a Hewlett-Packard 1050 HPLC system equipped with a Supelco-C5 column (4.6 mm inner diameter × 150 mm length) from Sigma-Aldrich. Proteins were eluted using a gradient of acetonitrile in 0.08% trifluoroacetic acid and water in 0.1% trifluoroacetic acid at a flow rate of 0.25 mL·min^{-1} and monitored by absorbance at 214 nm.

Prior to measurement, IFNα_{2a} and ^{40}PEG–IFNα_{2a} solutions were dialyzed in 20 mM TRIS 0.02% NaN_3 at pH 7.4 and subjected to a preparative centrifugation to ensure the removal of aggregates. The protein solutions were subsequently diluted to a concentration of 0.25 mg·mL^{-1} measured by UV absorbance (280 nm). Bovine pancreas trypsin of sequencing grade quality was purchased from Roche Diagnostics (Penzberg, Germany). This serine protease specifically cleaves peptide bonds at C-terminally arginine and lysine at an optimum working pH of 8.0. A stock solution of 1 mg·mL^{-1} of trypsin was prepared in the buffer specified above. In individual sealed vials, the digestion was triggered by mixing a specific amount of trypsin solution to 1 mL of IFNα_{2a} and ^{40}PEG–IFNα_{2a} solutions at 0.25 mg·mL^{-1}, respectively, to make a molar ratio (1:40; trypsin:protein). After 1 h of incubation, the first RP-HPLC chromatogram was recorded by injecting an aliquot of 60 μL from the vials. The monitoring of the in vitro digestion of IFNα_{2a} and ^{40}PEG–IFNα_{2a} by trypsin was subsequently performed by time-spaced injections of 60 μL from the content of the vials over the time-course of the digestion. Each chromatogram provided a snapshot of the digestion at different times with decreasing signals derived from intact IFNα_{2a} and ^{40}PEG–IFNα_{2a}, respectively, and new increasing signals derived from peptide fragments. IFNα_{2a} and ^{40}PEG–IFNα_{2a} proteins displayed the same retention times in all their respective chromatograms. Digestive time-courses are shown in Figure 3.

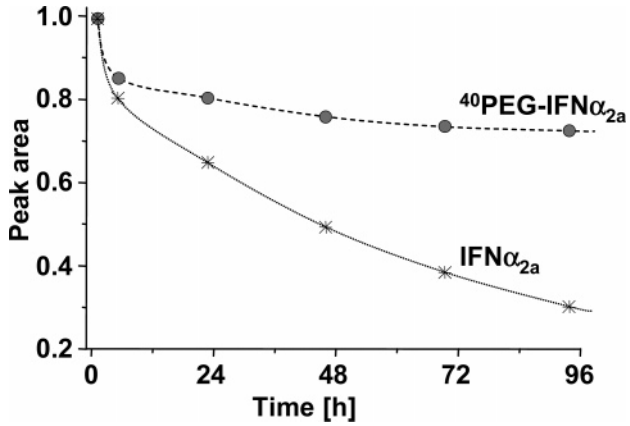

Figure 3. Time-course of the in vitro digestion of INFα_{2a} and ^{40}PEG-INFα_{2a}, respectively by trypsin monitored with successive RP-HPLC runs. For each time point, an aliquot (60 μL) of the incubation solution was injected. For both proteins tested, the concentration was 0.25 mg·mL^{-1} in 20 mM TRIS 0.02% NaN_3 at pH 7.4. The molar ratio (trypsin:protein) was (1:40). In the RP-HPLC chromatograms, the area of the elution peak, derived from the intact protein, was normalized with respect to the area of elution peak for the first time-point, i.e., 1 h after incubation.

Self-Avoiding-Walk and Simulation of the Binding to IFNAR2^{EC}. To structurally understand the differences observed for IFNAR2^{EC} binding data of ^{40}PEG–IFNα_{2a} and its positional isomers with respect to IFNα_{2a}, a simple kinetic model (*28*) and numerical simulations of the protein-polymer construct were used. In the simulation, proteins are modeled as hard spheres of defined radii and the polymer-chains represented as an ensemble of on-lattice SAWs. All molecular modeling calculations were performed using the molecular modeling package MOLOC on a PC-workstation (*29*, *30*).

In a brute force on-lattice representation of a single PEG-polymer chain the grid in use has to encompass as many shells as there are bonds in the chain to prevent undesired compaction of the SAW. This requires, for a 40 kDa single PEG chain of ^{40}PEG–IFNα_{2a} a grid dimension of 465 (units) × 3 (bonds) = 1395 shells, not tractable by use of the computational power available. Basic polymer theory (*31*) shows that a long polymer-chain can be represented by a much smaller number of nodes if the unit length of the grid is defined by a properly selected statistical length that is related to the typical direction correlation distance of the polymer.

To define this statistical length, 1000 SAWs of 72 steps were enumerated on a diamond lattice (dmd) of 72 shells;

thus, the SAWs are never restricted by hitting the boundary as they start at the origin. Artifactual compaction of SAWs is excluded.

Direction correlation distance was extracted from distance, i.e., number of steps, dependent walk direction correlation function, evaluated from the SAW ensemble. The number of steps over which these correlation functions decayed to e^{-1} was 1.163.

For the definition of the statistical length needed, connection with real PEG chain was made by the experimental finding that the ratios for populations of gauche and trans steps is 90% for the O−C−C−O conformation and 10% for the C−O−C−C links (*32*). Thus, the real PEG chain loses its direction of propagation approximately every third step, i.e., every monomer. From this estimate and the direction correlation length of 1.163, diamond lattice walks of ∼465 steps (equal to the mean number of units in a 20 kDa PEG-chain) were considered. Thus, a reduction in the number of lattice shells by a factor of 3, corresponding to a reduction in computational time by a factor of 3^3 was achieved. The size of the SAWs is well below the dimension of the corresponding lattices. Errors introduced from walks bouncing off the lattice surface are prevented.

Due to the scaling of lengths described above, IFNα_{2a} has to be represented by a sphere of size 4.36 lattice bond distances. The spheres were placed such that the lattice origin was at the surface of the sphere. All walks started from this origin and could not penetrate to lattice vertexes inside the sphere. 4000 SAWs were generated.

To evaluate the activation entropic contribution to the free energy of protein−protein association, a purely entropic model was used. In this model, a test sphere representing an approaching protein, e.g. a receptor or a protease, of varying radius was placed in the lattice box in surface-contact with IFNα_{2a} sphere. This was done at various azimuth angles θ with respect to the starting point of the SAWs at the surface of the IFNα_{2a} sphere. Sphere size and angle dependent contributions were obtained by counting the fraction of SAWs that did not penetrate the test sphere. Thus, the likelihood that a protein in surface-contact with the protein part of the pegylated construct intersects with the polymer was evaluated. This measure was calculated as the fraction of an ensemble of SAWs intersecting with a test sphere in contact with the pegylated protein but positioned at different locations with respect to the origin of the SAWs. The result can be displayed as an intersection probability $p(\theta)$ expressed as an activation entropic contribution $\Delta S^{\ddagger}(\theta)$ to the free energy of association by a simple Boltzmann like relationship given by $p(\theta) \propto \exp(-\Delta S^{\ddagger}(\theta)/k_B)$, with k_B the Boltzmann constant. To test the influence of the lattice type used, we repeated all simulations with a simple (sc) a body (bcc) and a face-centered (fcc) cubic lattice. It turned out that the type of lattice has only a minor influence on the fraction of intersecting walks. Averages over all lattice types were used for further discussion. Results are shown in Figures 4 and 5.

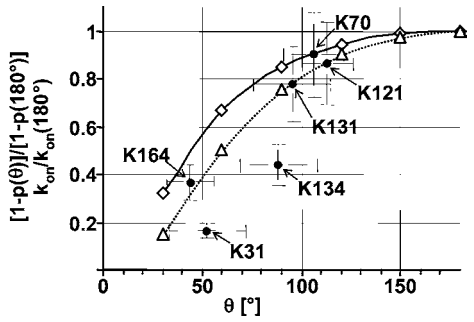

Figure 4. Normalized probability of nonintersection $[1 - p(\theta)]$ of an ensemble of SAWs of the PEG-chains with a test sphere positioned in surface contact with the INFα_{2a} sphere at an azimuth angle θ with respect to the origin of the SAW (see Materials and Methods). The origin is defined at the center of the INFα_{2a} binding epitopes of IFNAR2^{EC} (see text). The normalization is done with respect to a SAW starting on the opposite side of the sphere contact point given by $[1 - p(180°)]$. Two simulations are included: diamond-shaped points connected by a solid line, the diameter of the test sphere was the same as the INFα_{2a} sphere; triangles connected by a dashed line, the diameter of the test sphere was doubled. Lines are shown to guide the eye. Filled circles represent angle corrected ratios $k_{on}/k_{on}(180°)$ of experimental k_{on} values of the positional isomers. $k_{on}(180°)$ is defined by $k_{on}(180°) = {}^{121}k_{on} \times p(113°)/p(180°)$, with ${}^{121}k_{on}$ the association rate of the Isomer-K121. The θ-angles are extracted from the literature (*21*). The definition of the *x*- and *y*-error bars is given in the text.

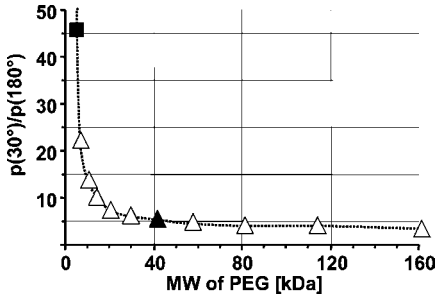

Figure 5. Simulation of the intersection probability $p(30°)$ of an ensemble of SAWs of various PEG-polymers with a test sphere (same radius as the INFα_{2a} sphere) positioned in surface-contact with the INFα_{2a} sphere at an azimuth angle of 30° normalized to $p(180°)$ in dependence on the molecular weight of a PEG-polymer (see Materials and Methods). Clearly seen is the plateau of this ratio for a molecular weight beyond 20 kDa. Line is shown to guide the eye. The filled square and triangle correspond to a 5 kDa and 40 kDa PEG-polymer, respectively.

RESULTS AND DISCUSSION

Experimental Results: Kinetics and Thermodynamics of the Binding to IFNAR2^{EC}. SPR experiments provided essential data for dissecting out the kinetics and mechanisms involved in the binding of IFNα_{2a}, ^{5}PEG−IFNα_{2a}, ^{40}PEG−IFNα_{2a}, and its positional isomers to IFNAR2^{EC}. All the proteins, including the receptor IFNAR2^{EC}, were obtained and used in a highly pure monomeric and aggregate-free form (see Materials and Methods section) (*22*). For all the samples, the SPR sensograms displayed a very good signal-to-noise ratio with an increase in the rate and extent of the binding with increasing protein concentrations. Typical sensorgrams for the binding to IFNAR2^{EC} of varying concentrations of IFNα_{2a} and the positional isomers modified at −K31 and −K70 are illustrated in Figure 2. For all the samples, $K_{Dkin.}$, k_{on}, and k_{off} could be calculated. The binding affinity data extracted from the SPR measurements at 25 °C for IFNα_{2a}, ^{5}PEG−IFNα_{2a}, ^{40}PEG−IFNα_{2a}, and its individual positional isomers are reported in Table 1. Neither the free 5 kDa linear PEG-polymer nor the free 40 kDa branched PEG-polymer displayed any SPR response indicative of an affinity to the receptor (data not shown).

IFNα_{2a} binds to IFNAR2^{EC} with a very high affinity ($K_{Dkin.}$ = 5 nM). This is in agreement with previously reported values and the model recently proposed for the complex IFNα_{2a}/IFNAR2^{EC} (*21*, *27*, *33*, *34*). Here, the binding involves hydrophobic patches of IFNα_{2a} interacting with matching hydrophobic surfaces of IFNAR2^{EC},

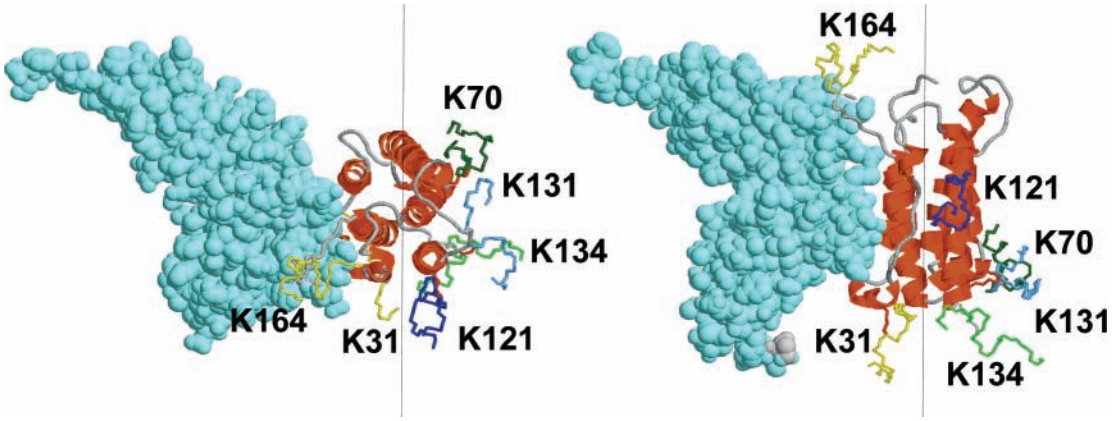

Figure 6. Representation of the complex structure INFα_{2a}/IFNAR2^{EC} obtained by the docking of the two individual NMR structures (*21*, *35*). The model has been described and documented in ref 21. The IFNAR2^{EC} structure is reported as a space-fill representation. The IFNα_{2a} structure is reported as a ribbon with α-helices in orange and connecting loops and turns in light gray. At the lysine positions known to be pegylated in the positional isomers of ^{40}PEG-INFα_{2a}, two short PEG-chains are represented as on-lattice SAWs of 20 steps using the molecular modeling package MOLOC (*29*, *30*). The PEG-chains of the class-LA isomers at K31 and K164 are colored in yellow. The PEG-chains of the class-HA isomers at K134, K131, K121, and K70 are colored in light green, light blue, dark blue, and dark green, respectively. Separation between the class-LA and -HA isomers is indicated by a dashed line. These figures were generated using the RasMol program (*48*).

while complementary adjacent motifs of alternating charged side-chains guide the two proteins in a fast association to form a tight complex.

Compared to IFNα_{2a}, the binding affinity of ^{5}PEG–IFNα_{2a} to the receptor is ~3.4-fold reduced, mainly due to a ~3.6-fold decrease of the association rate. This must be attributed to the 5 kDa linear PEG-polymer. Once bound, ^{5}PEG–IFNα_{2a} dissociates with the same k_{off} as IFNα_{2a}. For ^{40}PEG–IFNα_{2a}, the binding affinity for the receptor is ~24-fold reduced with respect to IFNα_{2a}. Again, this is mainly due to a change of the association rate: k_{on} decreases by ~16.8-fold while k_{off} remains essentially unaltered. All these results clearly show that the pegylation significantly reduces the affinity of the pegylated IFNα_{2a} for IFNAR2^{EC} without abolishment of the binding, and that the affinity is PEG-size dependent. However, as ^{40}PEG–IFNα_{2a} as well as ^{5}PEG–IFNα_{2a} is a mixture of monopegylated positional isomers (*16*, *19*), the kinetic parameters extracted results from the weighted contributions of all the components in the mixture. Therefore, only a careful analysis of the binding of the individual isomers to the receptor can provide a clear interpretation of the kinetic binding parameters for ^{40}PEG–IFNα_{2a} (see below). For ^{5}PEG–IFNα_{2a}, the isolated positional isomers were not available.

Each positional isomer of ^{40}PEG–IFNα_{2a} exhibits different binding affinity for IFNAR2^{EC}, ranging from 32 nM to 520 nM (Table 1). The losses of binding affinity are clearly attributable to the 40 kDa branched PEG-polymer and are dependent on the pegylation site. One can identify among the positional isomers two classes with respect to the kinetic binding process. The first class, called the class-LA (LA for low affinity), comprises the Isomer-K31 and -K164, that bind to the receptor with lower affinities (150–520 nM). In contrast, the second class, called the class-HA (HA for high affinity), comprises the Isomer-K134, -K131, -K121, and -K70, that interact with the receptor with higher affinities (32–76 nM). The two classes are directly related to two different areas of location of the pegylation sites (Figure 6). For the class-LA isomers, the PEG-polymer attachment point is located in proximity to the IFNAR2^{EC} binding interface (*21*). A high steric hindrance of the protein–protein contacts due to the PEG-polymer seems therefore to be responsible for the reduced binding affinity of these isomers. This especially holds true for the Isomer-K31 that carries the polymer close to a hot-spot region for the interaction with IFNAR2^{EC} (*33*, *34*). For the class-HA isomers, the PEG-polymer is attached remotely with respect to the binding interface. This leads to lower reduction of binding affinities, certainly due to lower steric hindrance by the polymer.

In all the isomers, the affinity losses are controlled by a substantial change of the association rate combined with a moderate change of the dissociation rate. The models, presented in the molecular modeling and simulation section, explain nicely the reduction in k_{on} experimentally observed for the class-LA and -HA isomers by ~16-fold and ~6-fold, respectively. As far as the dissociation rate k_{off} is concerned, only the class-LA isomers present notable differences with respect to IFNα_{2a}: the Isomer-K31 and -K164 are released from the complex ~4-fold and ~2.5-fold faster than IFNα_{2a}, respectively. Again these differences are attributed to the location sites of the PEG-polymer. The attachment of the PEG-polymer at the binding interface may favor a faster release of the isomer than in the case where the polymer is located on the opposite side of the interface (Figure 6). Moreover, it is known that the charges contribute to the binding affinity to IFNAR2^{EC} (*21*, *33*, *34*). Thus for the Isomer-K31, the removal of one charge by pegylation of K31 might increase the dissociation rate. In the Isomer-K164, the high mobility of the C-terminal segment of IFNα_{2a} (*35*) may bring the pegylated residue K164 near to the binding interface. Thus, the removal of one charge might also contribute in this isomer to increase k_{off}.

Experimental Results: Temperature Dependence of the Equilibrium Thermodynamics of the Binding to IFNAR2^{EC}. The thermodynamic analysis of the temperature dependence of the binding affinity data at equilibrium, derived from SPR measurements, was performed using the van't Hoff analysis. The free energy ΔG°, the enthalpy change $\Delta H°$, the entropy change $\Delta S°$, and the specific heat capacity ΔCp° of the binding of IFNα_{2a} and pegylated IFNα_{2a}s to IFNAR2^{EC} at equilibrium could be determined. The thermodynamic parameters at equilibrium ΔG°, $\Delta H°$, $\Delta S°$, and ΔCp° are reported in Table 2.

The high affinity binding of IFNα_{2a} to IFNAR2^{EC} is a slightly enthalpy-driven process as the free energy of binding, $\Delta G° = -11.2$ kcal·mol^{-1}, results from an enthalpy contribution of $\Delta H° = -5.7$ kcal·mol^{-1}. The

formation of electrostatic and hydrophobic contacts and hydrogen bonds between the two molecules account for this exothermic interaction ($\Delta H° < 0$), accompanied by an increase of entropy $\Delta S°$ also favorable for binding. This large entropy contribution suggests that the binding may involve a burial of hydrophobic surface, an increase in the conformation freedom of the proteins and/or a release of bound water molecules (*36*, *37*). Water release is consistent with a charge compensation occurring at the binding interface upon complex formation. In the IFNα_{2a}/IFNAR2^{EC} model, important electrostatic contacts are responsible for driving the two proteins in a tight complex (*21*).

The binding of ^{5}PEG−IFNα_{2a} to IFNAR2^{EC} is also a slightly enthalpy-driven process, with enthalpy and entropy losses of ∼5% and ∼10%, respectively, when compared to IFNα_{2a}. These low $\Delta H°$ and $\Delta S°$ variations show the similarities of the thermodynamic binding process. In contrast for ^{40}PEG−IFNα_{2a}, the binding to IFNAR2^{EC} is entropy-driven. But it must be noted that this change in character is mostly caused by a loss of enthalpy by ∼35% while the entropy remains unaltered. To provide a detailed description of the thermodynamics of binding of ^{40}PEG−IFNα_{2a}, each individual positional isomer was analyzed (see below).

Upon binding to IFNAR2^{EC}, all the positional isomers of ^{40}PEG−IFNα_{2a} gained enthalpy and entropy. With respect to the relative importance of electrostatic and hydrophobic contacts involved, this suggests that the isomers interact with IFNAR2^{EC} globally in a similar manner as IFNα_{2a}. Interestingly, the class-LA binds to the receptor, like IFNα_{2a}, in an enthalpy-driven binding process. In contrast the binding for the class-HA members, like ^{40}PEG−IFNα_{2a}, is entropy-driven. As compared to IFNα_{2a}, the class-LA isomers present a mean enthalpy gain of ∼10%. In contrast, the class-HA isomers display a mean enthalpy loss of ∼30%. Whether these trends of $\Delta H°$ change are due to alterations of remotely located surface charges and/or charges involved in the binding cannot be decided with the data available. The differences in $\Delta H°$ can also be attributed to differences in the details of the hydration of the proteins and the PEG-polymer involved (*38*, *39*). An obvious possibility to explain the significant loss of entropy by ∼50% for the class-LA isomers, is the reduced number of conformations accessible to the PEG-polymer due to the steric hindrance of mobility arising from IFNα_{2a} and IFNAR2^{EC}, and vice-versa (*36*, *40*).

Experimental Results: PEG-Polymer Protection against Proteolytic Degradation. To evaluate the PEG-polymer protection against proteolytic degradation, the in vitro digestion of IFNα_{2a} and ^{40}PEG−IFNα_{2a} by trypsin was monitored by RP-HPLC. As illustrated in Figure 3, the area of the normalized signal of intact ^{40}PEG−IFNα_{2a} in the chromatograms decreases ∼7-fold slower than IFNα_{2a}. This shows a reduction of the in vitro proteolytic degradation due to the pegylation of IFNα_{2a}. By imposing a steric hindrance on the protein, the PEG-polymer limits with a large excluded volume the accessibility for protease. The increased stability against proteolytic degradation was also reported for other pegylated proteins (*41*, *42*).

Molecular Modeling and Simulation of Binding to IFNAR2^{EC}. The reduction in binding affinity by a factor of ∼24 observed for the ^{40}PEG−IFNα_{2a}/IFNAR2^{EC} complex, as compared to its IFNα_{2a} counterpart, is mainly determined by a corresponding difference in the association rate k_{on} (Table 1). In general the kinetics of the formation of a protein−protein complex can be explained by the following determinants. The collision rate, at which two partners meet, is controlled by the concentration of the two molecules. Under diffusion-limited conditions, the collision rate is independent of the molecular weight of the partners and their relative orientation. This rate constitutes an upper limit and is defined in water at 300 K by $k_{collision} \approx 6.6 \times 10^9$ $M^{-1}\cdot s^{-1}$ (*28*). If each hit of two molecules would lead to a complex, this value is the expected k_{on} of the binding process. However, k_{on} values for real proteins are often substantially lower, as productive complex formation depends on a correct position and relative orientation of the two partners with respect to each other. A correct preorientation of the binding partners can, for example, be achieved by long-range electrostatic interactions assuming a freely accessible binding area. In this case, the two binding partners can interact and lower the free-energy of the complex compared to the unbound state. In the case of the IFNα_{2a}/IFNAR2^{EC} complex, it is estimated that only one out of approximately 2400 collisions leads to an active complex. This reduction is related to the ratio of the interaction surface to the overall surface of the proteins involved. It has been shown that k_{on} scaling is expected to be proportional to R_H^{-2}, with R_H being the hydrodynamic radius (*28*). With the R_H scaling argument given above and using experimental R_H values, k_{on} for ^{40}PEG−IFNα_{2a} was estimated to be reduced ∼10-fold compared to IFNα_{2a} (*22*). Thereby, it is assumed that the size of the contact area and the long-range interactions between the proteins are not altered by the presence and location of the PEG-polymer. Already, this simple kinetic model provides a rough estimate for the expected drop of k_{on} and K_D for pegylated proteins. It has to be emphasized that this reduction in k_{on} proportional in R_H^{-2} cannot be circumvented by optimized positioning of the polymer with respect to the binding interface.

Further reduction of k_{on} is expected if the polymer is attached near to or at the edge of the binding interface, due to steric hindrance of the formation of specific protein−protein contacts. This holds true in the case of the class-LA isomers (Table 1). But also the variations in k_{on} between all the isomers in both cases can be rationalized as a consequence of different steric interactions in the process of complex formation due to spatial differences among the positional isomers. In our model elaborated in this work, hindrance is represented as the likelihood that a protein, e.g. IFNAR2^{EC}, in surface-contact with the protein domain of the pegylated construct intersects with the polymer. This likelihood was calculated as the fraction of an ensemble of SAWs intersecting with a test sphere in contact with the pegylated protein. The test sphere is positioned at different locations defined by an azimuth angle θ with respect to the origin of the SAWs. The result is displayed as an intersection probability $p(\theta)$ expressed as an activation entropic contribution $\Delta S^{\ddagger}(\theta)$ to the free energy of association (see Materials and Methods). Thus $[1 - p(\theta)]$ defines the fraction of an approaching protein that can form an active complex.

Pictorially, it is clear that the protection of a surface-element located on the surface of the IFNα_{2a} sphere against a contact with an approaching protein is more pronounced if the PEG-polymer attachment point is located close in space. The normalized function $[1 - p(\theta)]/[1 - p(180°)]$ is reported for two test sphere radii in Figure 4. It is a measure to rate the additional repulsive effect of the different isomers of ^{40}PEG−IFNα_{2a} as compared to the hypothetical most remotely attached polymer position, i.e., for $\theta = 180°$. In the complex of

IFNAR2^{EC} with the positional isomers, the starting points for the SAWs are defined by the azimuth angle θ between the PEG-polymer attachment point and the center of the binding interface (*21*). The reference k_{on} value for the hypothetical isomer at $\theta = 180°$, $k_{on}(180°)$, was calculated by scaling k_{on} of the Isomer-K121 ($\theta = 113°$) by the factor $p(113°)/p(180°)$. A relative contribution for the destabilization of the complex is reported for each individual positional isomer with k_{on} in Figure 4 by $k_{on}/k_{on}(180°)$. It must be noted that the definition of the center of the binding interface is somewhat arbitrary. This reflects itself in angular θ-error bars given for the experimental data points in Figure 4. This SAW based-model can semiquantitatively explain the experimental differences in k_{on} observed for the various isomers (Table 1). Especially, the experimental factor ~5.5 for the isomer dependent k_{on} variations is nicely reproduced with this simulation. In addition, the model predicts that only a factor below ~10 in k_{on} can be gained for hypothetical pegylation at θ ~180° compared to pegylation at the rim (θ ~30°) of the binding interface. Of high importance is the finding that if the pegylation is performed at an angle of at least ~40° away from the ridge of the binding interface, i.e., θ ~70°, only a ~2-fold reduction in k_{on} is expected compared to the sterically most favorable case with $\theta = 180°$ (Figure 4). The azimuth angles of all the isomers, with the exception of the Isomer-K31 and -K164, lie in this range. These two isomers display a small θ angle, as their pegylation sites are located at or close to the rim of the binding interface. However, for the Isomer-K164, it must be noted that the pegylation site resides in the highly flexible C-terminal region of the protein (*35*); therefore, it is not clear whether the extracted angle really represents an accurate value valid for the complex. One is tempted to increase the θ-angle for the Isomer-K164 by approximately ~15° still representing a conformation accessible for the flexible C-terminus without steric clash.

Only the Isomer-K31 and -K134 experience a k_{on} reduced by a factor ~2.0 compared to the prediction of the SAW model (Figure 4). For the Isomer-K31, the deviation is in line with the argument that the removal of a charge on the side-chain influences the long-range interactions needed for the prepositioning of the proteins to support complex formation. Whether the same holds true for the Isomer-K134 is not clear.

To summarize, the variations in k_{on} observed for IFNα_{2a} and the individual positional isomers of ^{40}PEG–IFNα_{2a} (Table 1) can be explained with reasonable accuracy by taking into account (a) the size (R_H) of the unpegylated and pegylated IFNα_{2a} (*22*) and (b) the differences in steric hindrance encountered between IFNAR2^{EC} and the positional isomers in the process of complex formation. The first effect can be semiquantitatively explained by the rigid-body association model (*28*), and the second effect by the SAW based-model elaborated above. Only this latter model can convincingly explain the observed variations in binding affinities and association rates for the positional isomers.

The SAW based-model can also make a prediction of the steric effect for different sizes of PEG-polymer attached at various θ-angles on intermolecular interaction. Figure 5 shows the ratio $p(30°)/p(180°)$, expressing the relative hindrance at two extreme angles of PEG attachment site (see above) in dependence on the polymer molecular weight. This dependence becomes independent of the molecular weight of the polymer above 20 kDa. Therefore, very similar if not identical angle dependencies are expected for k_{on} of proteins modified with polymer-chains larger than 20 kDa. For smaller PEG-chains a more pronounced θ-dependence is observed (Figure 5). A substantially higher reduction of k_{on} relative to the relaxed position at $\theta = 180°$ is expected, if PEG-chains smaller than 20 kDa were attached close to the binding interface, e.g. in case of a ~5 kDa PEG-chain, the variations $p(30°)/p(180°)$ are ~6-times larger than that expected for a 20 kDa PEG-chain.

In all the positional isomers investigated here, the PEG-polymer attachment site lies well outside or close to the rim of the binding epitopes of IFNα_{2a}. If the attachment site were to be within the binding region, very pronounced effects on the binding affinity, association and dissociation rates would be expected. In this particular case, the flexible polymer-chain would severely prevent the correct alignment and interaction of the two binding partners, by its steric bulk. In IFNα_{2a}, no lysine (with the exception of K31 known to lie close to a hot-spot region of binding) is directly within this critical region (*27*, *33*). For the stability and endurance of the complex, the strength of the electrostatic, hydrogen bond, van der Waals and hydrophobic (dehydration) interactions are of high importance. These effects, however, have only a minor effect on k_{on} (see above), having a higher importance once the complex is formed.

Pharmacological Effects and Molecular Properties. The reduction in receptor binding affinity of pegylated IFNα_{2a} has direct implications on the in vitro biological activity. In the in vitro antiviral assay an approximately ~3-fold and ~30-fold lower specific activity was observed for ^{5}PEG–IFNα_{2a} and ^{40}PEG–IFNα_{2a}, respectively (*16*, *19*). In the in vivo situation, this PEG-size dependent effect is more than counterbalanced by the two following positive findings: (a) the prolongation of PEG-chains goes in hand with an increase in stability and protection against proteolytic degradation, and (b) bigger particles experience a reduction in renal clearance by glomerular filtration (*41*–*43*). Both effects also depend critically on the size of the attached-PEG-polymer. The size of the pegylated protein particle is given by the hydrodynamic radius R_H, and as it is dominated by a long polymer chain, it increases with MW$^{3/5}$, with MW the polymer molecular weight (*22*, *31*, *44*). The simple kinetic model described above predicts a increased protection against proteolytic degradation roughly proportional in ~R_H^2 (~MW$^{1.2}$). An estimate of the protection against the proteolytic degradation thus predicts a decrease of the digestion rate of ^{40}PEG–IFNα_{2a} by a factor ~10 as compared to IFNα_{2a}, in good agreement with the experimentally observed reduction of the in vitro digestion rate by a factor of ~7 (Figure 3). Previously, it has been shown that the pegylation of IFN$_{\alpha 2a}$ reduces the tendency of the protein for aggregation (*22*). Here, the same rigid-body association model predicts that the self-aggregation of pegylated IFN$_{\alpha 2a}$ by protein–protein interactions is reduced by a scaling factor ~R_H^{-4}. This remains to be confirmed experimentally. Due to the low concentration of the drug in the body, aggregation is expected to be of minor importance after the substance is administered. However, reduced aggregational property is essential while the protein is maintained in its formulation at higher concentration. It is well conceivable that this R_H^{-4} dependence also relates to the substantially reduced rate of self-digestion if a polymer is attached on proteases (*45*, *46*). Steric hindrance of protein approach brought about by the large hydrodynamic volume of the PEG-polymer (*22*) can also account for the significantly improved immunological properties of ^{40}PEG–IFNα_{2a} (*9*), as the immune system requires the recognition of the antigen.

Clinical data show that the half-life of ^{40}PEG−IFNα_{2a} in the blood is at least by a factor of ∼8 longer than IFNα_{2a} (*20*). The new drug PEGASYS has superior efficacy over IFNα_{2a}. The reduced receptor affinity of ^{40}PEG−IFNα_{2a} and its correspondingly reduced in vitro antiviral activity is thus more than compensated by the dramatically increased efficacy due to the significantly improved half-life in the blood.

Impact for Future Molecular Design of Pegylated Proteins. The data, presented in this work and the accompanying paper (*22*), provide a solid collection of knowledge on variously pegylated IFNα_{2a}. They contribute to a better understanding of the molecular framework responsible for improved structural stability, binding interaction, and pharmacological properties of pegylated proteins in general. Thus, future research and technology to optimize and tailor the pharmacological properties of proteins by pegylation may be rationally guided. Some of the methods presented already constitute new indispensable tools in the quality control of pegylated IFNα_{2a}s (*22*). For design purposes, the dependence of the intermolecular association rate k_{on} on polymer size found ($\sim 1/R_H^2 \propto 1/MW^{1.2}$), and its modulation by the spatial location of the PEG attachment site are of great interest. If possible the PEG-polymer attachment sites should be located as remotely as possible from the protein binding interface, but angles above ∼40° away from the rim of the binding interface already lead to only a minor decrease of the association rate k_{on} as compared to the maximum value achievable by a given size of the PEG-polymer. The angle dependent effect is expected to be more pronounced for polymer chains of lower molecular weight (<20 kDa). If the size of proteins that interact with the pegylated-protein drugs increases, the angular dependencies of k_{on} become more pronounced (Figure 4), but the dependency on PEG-size decreases (data not shown). Thus, the θ-dependent shielding is more critical in the case of interaction with large protein-receptors than with smaller proteins or enzyme substrates. The simulations presented may also help to decide about the feasibility of single versus multiple pegylation sites in dependence of PEG-polymer MW and structural details of molecular recognition.

Conclusion. Here, we report a detailed analysis of the binding to IFNAR2^{EC} of ^{40}PEG−IFNα_{2a} and its positional isomers modified at K31, K134, K131, K121, K164, and K70 respectively, as compared to IFNα_{2a} and ^{5}PEG−IFNα_{2a}. Our results clearly show that the affinity for the receptor is PEG-size dependent with no abolishment of the binding, and that the pegylation significantly reduces the affinity mainly due to a change of the association rate k_{on}. These results are in agreement with modeling and simulation of the binding, based on SAW calculation. A correlation between the structural parameters and the kinetic and thermodynamic parameters of the binding of the positional isomers could be established. For the Isomer-K31 and -K164, the PEG-polymer attachment point is located in proximity of the binding interface, and the isomers display the lower affinity in an enthalpy-driven binding process. In contrast, for the Isomer-K134, -K131, -K121, and -K70, the PEG-polymer is attached remotely from the binding interface and the isomers exhibit the higher affinity in an entropy-driven binding process. With the RP-HPLC monitoring of the time-course in vitro digestion of IFNα_{2a} and ^{40}PEG−IFNα_{2a} by trypsin, we also provided evidence for a decrease of the proteolytic degradation due to pegylation.

With the work presented in this study we compiled a solid collection of knowledge regarding the structural, kinetic, and thermodynamic parameters of the binding of ^{40}PEG−IFNα_{2a} and its positional isomers to IFNAR2^{EC}. This constitutes a molecular basis for a better understanding of receptor binding mechanisms and the relationship between the structure and the biological function of the positional isomers.

At this level of the knowledge, relating the variations in the in vitro antiviral activity (Foser 2003) of the positional isomers with the structural, kinetic, and thermodynamic parameters of their binding to IFNAR2^{EC} is highly speculative and out of scope of this study. Indeed even if the putative binding interface between IFNα_{2a} and the receptor IFNAR1 could be postulated (*21*, *47*), essential binding affinity data defining the interaction to the second receptor IFNAR1 and other data are yet to be determined. All these data taken together will help in the future to potentially identify pegylation sites of enhanced in vitro biological activity where the PEG-polymer is most remotely attached with respect to both IFNAR1 and IFNAR2 binding sites. This could lead to a third generation of pegylated IFNα_{2a}.

ACKNOWLEDGMENT

We would like to thank J. Kohler for her help in experimental work, Drs. P. Bailon and G. Ehrlich for giving us the 5 kDa PEG-conjugated IFNα_{2a} material, and Drs. J. Anglister and J. Chill for providing us the coordinates of the IFNα_{2a}/IFNAR2^{EC} complex structure prior to publication. We acknowledge Drs. S. Foser, W. Klaus, T. Schreitmüller, R. Thoma, and K. Weyer for fruitful discussions and Dr. H. Jacobsen for his help and advice to produce and cleave the receptor protein. We thank Dr. D. Banner for a careful reading of the manuscript.

LITERATURE CITED

(1) Isaacs, A., and Lindenmann J. (1957) Virus interference I: the interferon. *Proc. R. Soc. Ser. B 147*, 258−267.
(2) Uze, G., Lutfalla, G., and Gresser, I. (1990) Genetic transfer of a functional human interferon-α receptor into mouse cells: cloning and expression of its cDNA. *Cell 60*, 225−234.
(3) Novick, D., Cohen, B., and Rubinstein, M. (1994) The human interferon-α/β receptor: characterization and molecular cloning. *Cell 77*, 391−400.
(4) Cohen, B., Novick, D., Barak, S., and Rubinstein, M. (1995) Ligand induced association of the type-I receptor components. *Mol. Cell. Biol. 15*, 4208−4214.
(5) Stark, G., Kerr, I., Williams, B. R. G., Silverman, R., and Schreiber, R. (1998) How cells respond to interferons. *Annu. Rev. Biochem. 67*, 225−264.
(6) Rani, M. R. S., Foster, G. R., Leung, S., Leaman, D., Stark, G. R., and Ransohoff, R. M. (1996) Characterization of β-R1, a gene that is selectively induced by Interferon β (IFN- β) compared with IFN-α. *J. Biol. Chem. 271*, 22878−22884.
(7) Der, S. D., Zhou, A., Williams, B. R., and Silverman, R. H. (1998) Identification of genes differentially regulated by Interferon α, β or γ using oligonucleotide arrays. *Proc. Natl. Acad. Sci. U.S.A. 95*, 15623−15628.
(8) Baron, S., Tyring, S. K., Fleischmann, W. R., Coppenhaver, D. H., Niesel, D. W., Klimpel, G. R., Stanton, J., and Hughes, T. K. (1991) The interferons, mechanisms of action and clinical applications. *JAMA 266*, 1375−1383.
(9) Harris, J. M., Martin, N. E., and Modi, M. (2001) Pegylation, a novel process for modifying pharmacokinetics. *Clin. Pharmacokinet. 40*, 539−551.
(10) Rostaing, L., Chatelut, E., Payen, J. L., Izopet, J., Thalamas, C., Ton-That, H., Pascal, J. P., Duramd, D., and Canal, P. (1998) Pharmacokinetics of alphaIFN-2b in chronic Hepatitis C virus patients undergoing hemodialysis or with normal renal function: clinical implications. *J. Am. Soc. Nephrol. 9*, 2344−2348.

(11) Zeuzem, S. (1999) Clinical implications of Hepatitis C viral kinetics. *J. Hepatol. 31*, 61−64.
(12) Bailon, P., and Berthold, W. (1998) Poly(ethylene glycol)-conjugated pharmaceuticals proteins. *Pharm. Sci., Technol. Today 1*, 352−356.
(13) Bailon, P., Palleroni, A., Schaffer, C., Spence, C., Fung, W., Porter, J., Ehrlich, G., Pan, W., Xu, Z. X., Modi, M., Farid, A., and Berthold, W. (2001) Rational design of a potent, long lasting form of Interferon: a 40 kDa branched Polyethylene Glycol-conjugated Interferonα-2a for the treatment of Hepatitis C. *Bioconjugate Chem. 12*, 195−202.
(14) Youngster, S., Wang, Y. S., Grace, M., Bausch, J., Bordens, R., and Wyss, D. F. (2002) Structure, biology, and therapeutic implications of pegylated interferon alpha-2b. *Curr. Pharm. Des. 8*, 2139−2157.
(15) Harris, J. M., and Chess, R. B. (2003) Effect of pegylation on pharmaceuticals. *Nat. Rev. Drug Discovery 2*, 214−221.
(16) Monkarsh, S. P., Ma, Y., Aglione, A., Bailon, P., Ciolek, D., DeBarbieri, B., Graves, M. C., Hollfelder, K., Michel, H., Palleroni, A., Porter, J. E., Russoman, E., Roy, S., and Pan, Y. C. (1997) Positional isomers of monopegylated Interferonα-2a: isolation, characterization, and biological activity. *Anal. Biochem. 247*, 434−440.
(17) Fung, W. J., Porter, J. E., and Bailon, P. (1997) Strategies for the preparation and characterization of poly-(ethylene glycol) (PEG) conjugated pharmaceutical proteins. *Polym. Prepr. 38*, 565−566.
(18) Caliceti, P,. Schiavon, O., and Veronese, F. M. (1999) Biopharmaceutical properties of urecase conjugated to neutral and amphiphilic polymers. *Bioconjugate Chem. 10*, 638−646.
(19) Foser, S., Schacher, A., Weyer, K. A., Brugger, D., Dietel, E., Marti, S., and Schreitmüller, T. (2003) Isolation, structural characterization, and antiviral activity of positional Isomers of monopegylated Interferon alpha-2a. *J. Prot. Exp. Purif. 30*, 78−87.
(20) Algranati, N. E., Sy, S., and Modi, M. (1999) A branched methoxy 40 kDa polyethylene glycol (PEG) moiety optimizes the pharmacokinetics (PK) of peginterferon α-2a (PEG−IFN) and may explain its enhanced efficacy in chronic Hepatitis C (CHC). *Hepatology 30*, 4 Pt 2, 190A.
(21) Chill, J., Quadt, S., Levy, R., Schreiber, G. and Anglister, J. (2003) The human type I Interferon receptor: NMR structure reveals the molecular basis of ligand binding. *Structure 11*, 791−802.
(22) Dhalluin, C., Ross, A., Leuthold, L. A., Foser, S., Gsell, B., Müller, F., and Senn, H. (2005) Structural and biophysical characterization of the 40 kDa PEG-Interferon-α_{2a} (PEGASYS) and its individual positional isomers. *Bioconjugate Chem. 16*, accompanying paper in this issue.
(23) Flory, P. J. (1969) *Statistical mechanics of chain molecules*, Wiley-Interscience, New York.
(24) Hochuli, E. (1986) Large-scale recovery of Interferonα-2a synthesized in bacteria. *Chimia 40*, 408−412.
(25) Kozlowski, A., and Harris, J. M. (2001) Improvements in protein PEGylation: pegylated interferons for treatment of Hepatitis C. *J. Controlled Release 72*, 217−224.
(26) Chill, J., Nivasch, R., Levy, R., Albeck, S., Schreiber, G. and Anglister, J. (2002) The human Interferon receptor: NMR-based modeling, mapping of IFN-α2 binding site, and observed ligand induced tightening. *Biochemistry 41*, 3575−3585.
(27) Piehler, J., and Schreiber, G. (1999a) Biophysical analysis of the interaction of human Ifnar2 expressed in E. Coli with IFNα2. *J. Mol. Biol. 289*, 57−67.
(28) Janin, J. (1997) The kinetics of protein−protein recognition. *Proteins*: *Struct., Funct., Genet. 28*, 153−161.
(29) Müller, K., Ammann, H. J., Doran, D. M., Gerber, P. G., Gubernator, K., and Schrepfer, G., (1988) Complex heterocyclic structures: a challenge for computer assisted molecular modeling. *Com. Soc. Chim. Belg. 97*, 655−667.
(30) Gerber, P. G., and Müller (1995) MAB, a generally applicable molecular force field for structure modeling in medicinal chemistry. *J. Comput.-Aided Mol. Des. 9*, 251−268.
(31) Tanford, C. (1961) *Physical Chemistry of Macromolecules*, John Wiley and Sons, New York.
(32) Yoshida, H., Takikawa, K., Kaneko, I., and Matsuura, H. (1994) Conformational analysis of model compounds of nonionic surfactants in aqueous solution: Raman spectroscopy and ab initio MO calculations. *J. Mol. Struct. 311*, 205−210.
(33) Piehler, J., and Schreiber, G. (1999b) Mutational and structural analysis of the binding interface between type I Interferons and their receptor IFNAR2. *J. Mol. Biol. 294*, 223−237.
(34) Piehler, J., Roisman, L. C., and Schreiber, G. (2000) New structural and functional aspects of the type-I Interferon-receptor interaction revealed by comprehensive mutational analysis of the binding interface. *J. Biol. Chem. 275*, 40425−40433.
(35) Klaus, W., Gsell, B., Labhardt, A., Wipf, B., and Senn, H. (1997) The three-dimensional high-resolution structure of human Interferonα-2a determined by heteronuclear NMR spectroscopy in solution. *J. Mol. Biol. 374*, 661−675.
(36) Brady, G. P., and Sharp K. A. (1997) Entropy in protein folding and in protein−protein interactions. *Curr. Opin. Struct. Biol. 7*, 215−221.
(37) Roos, H., Karlsson, R., Nilshans, H., and Persson, A. (1998) Thermodynamic analysis of protein interactions with biosensor technology. *J. Mol. Recogn. 11*, 204−211.
(38) Ito, W., Yasui, H., and Kurasawa, Y. (1995) Mutations in the complementary-determining regions do not cause differences in free energy during the process of formation of the activated complex between an antibody and the corresponding protein antigen. *J. Mol. Biol. 248*, 729−732.
(39) Maxfield, J., and Shepherd, T. J. (1975) Conformation of polyethylene-glycol oxide in the solid-state, melt, and solution measured raman scattering. *Polymer 16*, 505−512.
(40) Farooq, A., Plotnikova, O., Zeng, L., and Zhou, M.-M. (1999) Phosphotyrosine binding domains of Shc and insulin receptor substrate 1 recognize the NPXpY motif in a thermodynamically distinct manner. *J. Biol. Chem. 274*, 6114−6121.
(41) Delgado, C., Francis, G. E., and Fischer, D. (1982) The uses and properties of PEG-linked proteins. *Crit. Rev. Ther. Drug. Carrier Syst. 9*, 219−304.
(42) Veronese, F. M., Caliceti, P. and Schiavon, O. (1997) Branched and linear poly(ethylene glycol): influence of the polymer structure on enzymological, pharmacokinetic, and immunological properties of proteins conjugates. *J. Bioact. Comput. Polym. 12*, 196−207.
(43) Yamaoka, T., Tabata, Y., and Ikada, Y. (1994) Distribution and tissue uptake of poly(ethylene-glycol) with different molecular weights after intraveneous administration to mice. *J. Pharm. Sci. 4*, 601−606.
(44) Kawaguchi, S., Imai, G., Suzuki, J., Miyahara, A., Kitano, T., and Ito, K. (1997) Aqueous solution properties of oligo- and poly(ethylene oxide) by static light scattering and intrinsic viscosity. *Polymer 38*, 2885−2891.
(45) Abuchowski, A., and Davis, F. (1979) Preparation and properties of polyethylene glycol-trypsin adducts. *Biochim. Biophys. Acta 578*, 41−46.
(46) Rajagopalan, S., Gonias, S. L., and Pizzo, S. V. (1985) A nonantigenic covalent streptokinase-polyethylene glycol complex with plasminogen activator function. *J. Clin. Invest. 75*, 413−419.
(47) Deonarain, R., Chan, D. C. M., Platanias, L. C., and Fish, E. N. (2002) Interferonα/β receptor interactions: a complex story unfolding. *Curr. Pharm. Des. 8*, 2131−2137.
(48) Sayle, R., and Milner-White, J. (1995) RasMol: Biomolecular graphics for all. *Trends Biol. Sci. 20*, 374−375.

BC049780H

Oligomeric Fluorescent Labels for DNA

Andrea Cuppoletti, Younjin Cho, Jin-Seong Park, Christoph Strässler, and Eric T. Kool*

Department of Chemistry, Stanford University, Stanford, California 94305-5080. Received September 17, 2004; Revised Manuscript Received March 21, 2005

In an effort to find fluorescent labels that have large Stokes shifts and increased emission intensity, a strategy for fluorescence labeling of DNA was explored in which multiple individual fluorophores are incorporated at adjacent positions at the end of a DNA probe. To encourage close interactions, hydrocarbon and heterocycle fluorophores were substituted at C-1 of deoxyribose, replacing the DNA base. The C-glycosides studied contained the well-known fluorophores terphenyl, pyrene, and terthiophene. For comparison, a commercial fluorescein−dU nucleotide was examined. Oligomeric labels containing up to five fluorophores were tested. Interestingly, all four dyes behaved differently on multiple substitution. Fluorescein displayed strong self-quenching properties, with the quantum yield dropping severalfold with each additional substitution and with a constant, small Stokes shift. In contrast, pyrene showed increases in quantum yield on addition of more than one fluorophore and yielded efficient long-wavelength emission on multiple substitution, with Stokes shifts of >130 nm. Oligomeric terphenyl labels gave a small progressive red shift in absorption and a marked red shift in emission wavelength and showed a strong increase in brightness with more monomers. Finally, terthiophene oligomers showed self-quenching combined with increasing Stokes shifts. Overall, the results suggest that some oligomeric fluorescent labels exhibit properties not available in common fluorescein class (or other commercial) labels, such as large Stokes shifts and increasing brightness with increasing substitution.

INTRODUCTION

Because of the expanding demands placed on fluorescent labels, there has been a growing interest in finding ways to make new fluorescent molecules and to expand the properties of existing ones. Among the properties that are desirable in various applications are emission intensity, ease of preparation and conjugation, water solubility, varied excitation and emission wavelengths, and large Stokes shifts (*1*, *2*).

We have adopted a new strategy for the discovery of fluorescent labels for biomolecules that, in principle, may favorably affect these properties. This strategy involves the synthesis of oligomeric strings of fluorophores on a DNA-like phosphodiester scaffold. In these oligomeric molecules the fluorophores replace the DNA bases (*3*−*5*). This has the effect of encouraging close physical and electronic interactions, including face-to-face stacked interactions, such as commonly occur in DNA itself. In principle, such a close arrangement may enhance electronic communication between the individual fluorophores, resulting in useful changes in fluorescence characteristics in the oligomeric dye as a whole (*4*, *5*). In addition, these molecules are simple to assemble, because DNA synthesizers can place them in varied number and ordering using well-optimized chemistry and with automated methodology. Moreover, the charged nature of the DNA backbone encourages water solubility, and many conjugates can be prepared using commercial chemistry and reagents.

Previous studies have explored combinations of oligomeric fluorescent deoxyribosides and did not involve conjugation to nucleic acids (*4*, *5*). Here we report an exploratory study of such oligomeric dyes in the DNA context, using four different fluorophores as monomers and using only homooligomers to avoid mixed effects. Three of the monomers are nucleoside-like molecules in which fluorophores (terphenyl, pyrene, terthiophene) replace the DNA base (*3*). For comparison we also studied oligomers of fluorescein in a commercial conjugate with deoxyuridine. All were studied as conjugates adjacent to the same DNA probe sequence. We found a surprising variation in fluorescence properties, both with different fluorophores and with different numbers of the same fluorophore. Some of the new properties observed in the oligomeric dyes are not present in commercially available monomeric labels, and so such fluorescent oligomers may have potentially useful applications in labeling of biomolecules.

MATERIALS AND METHODS

Preparation of Deoxyribosides. Terphenyl, pyrene, and terthiophene α-deoxyribosides and their 5′-dimethoxytrityl-3′-phosphoramidite derivatives were prepared as previously described (*3*, *6*). Fluorescein−dT-phosphoramidite was purchased from Glen Research.

Synthesis of Oligonucleotides. DNA oligonucleotides were synthesized on an Applied Biosystems 392 synthesizer using standard β-cyanoethylphosphoramidite chemistry. Natural β-cyanoethylphosphoramidites were purchased from Glen Research or ABI and used as received. The solid support used was 3′-phosphate-ON support (Glen Research), which allows for 3′ placement of nonnatural nucleosides. After synthesis, oligonucleotides were deprotected and removed from the solid support with concentrated ammonia at 55 °C for 12 h. Oligomers were then purified by preparative denaturing polyacrylamide gel electrophoresis. The DNA was visualized by UV shadowing, and the bands containing the

* Author to whom correspondence should be addressed [fax (650) 725-0259; e-mail kool@stanford.edu].

10.1021/bc0497766 CCC: $30.25 © 2005 American Chemical Society
Published on Web 04/26/2005

desired product were excised, crushed with a glass rod, and soaked in 0.2 M NaCl for 12 h. The solution was then filtered and placed in dialysis tubing (VWR, Spectra/Por MWCO 1000, or 500, as appropriate.). The solution was dialyzed for 24 h, in 6 h periods, with 2 L of Millipore water. Most of the samples were then further purified by HPLC, column PRP-1 Hamilton, C18 reverse phase, acetonitrile/K_2PO_4 buffer as the eluent, with a gradient from 9:1 to 75:25. The samples were again dialyzed against water, lyophilized, and redissolved in a Tris−boric−EDTA (TBE) buffer solution (pH 7.0).

Absorption Spectra. Absorption spectra were measured on a Cary 1 UV−visible spectrophotometer. In a general experiment a quartz cuvette with a 1 cm length path, equipped with a Teflon stopper, was charged with 0.5−1.0 mL of a solution of the oligonucleotide in TBE buffer (pH 7.0). All spectra collected were corrected for background and solvent absorption.

Fluorescence Spectra. Fluorescence spectra were measured on a Spex Fluorolog-3 spectrophotometer. In a general experiment a quartz cuvette with a 1 cm length path, equipped with a Teflon stopper, was charged with 0.5−1.0 mL of a solution of the oligonucleotide in TBE buffer (pH 7.0). All slits were set to 1 nm except in photobleaching experiments (20 nm), and all spectra collected were corrected for instrument response, background, and solvent emission. The samples were prepared to have an optical density (OD) of ≤0.05 at the excitation wavelength, to minimize internal absorption. Fluorescence quantum yields, ϕ_f, were calculated according to the equation $\phi_f = \phi_s(I_0 OD_s \eta_0^2)/(I_s OD_0 \eta_s^2)$, where the subscript s refers to the standard, the subscript 0 refers to the sample, η is the refractive index of the medium, I is the corrected integrated fluorescence, OD is the optical density at the excitation wavelength, and ϕ_s is the fluorescence quantum yield of the standard [fluorescein, quantum yield = 0.90 in 0.1 N NaOH (*7*)].

Thermal Denaturation Studies. The solution for the thermal denaturation studies contained a one-to-one ratio of the two complementary oligomers in 1× TBE buffer at pH 7.0 containing 0.1 mM EDTA, 200 mM KCl, and 5 mM $MgCl_2$. The solution was heated at 90 °C and allowed to cool slowly at room temperature prior to the melting experiment. The studies were carried out in a Teflon-stopped quartz cuvette with a 1 cm length path, under nitrogen atmosphere on a Cary 1 UV−visible spectrophotometer equipped with a thermoprogrammer. Absorbance was monitored while the temperature was raised from 5 to 80 °C at a rate of 0.5 °C/min.

RESULTS

Structures and Design. The structures of the four fluorescent monomers in this study are shown in Figure 1, and the absorption and emission spectra for these are given in Figures 2 and 3. Data are presented in Table 1. The three fluorophore deoxyribosides have been prepared previously (3) but were not incorporated into DNA, nor have they been studied as homooligomers. Also studied for comparison was a fluorescein dye conjugate of dU, which (like the above) can be incorporated into DNA at any position. Fluorescein was chosen for comparison because it is probably the most commonly used fluorescent dye in DNA conjugates. As reported previously (*3*), the fluorescence characteristics of the monomeric fluorescent deoxyribosides are very similar to those of published data for the dyes without attachment to deoxyribose. One significant difference, however, is that fluorescein has a molar absorptivity approximately twice

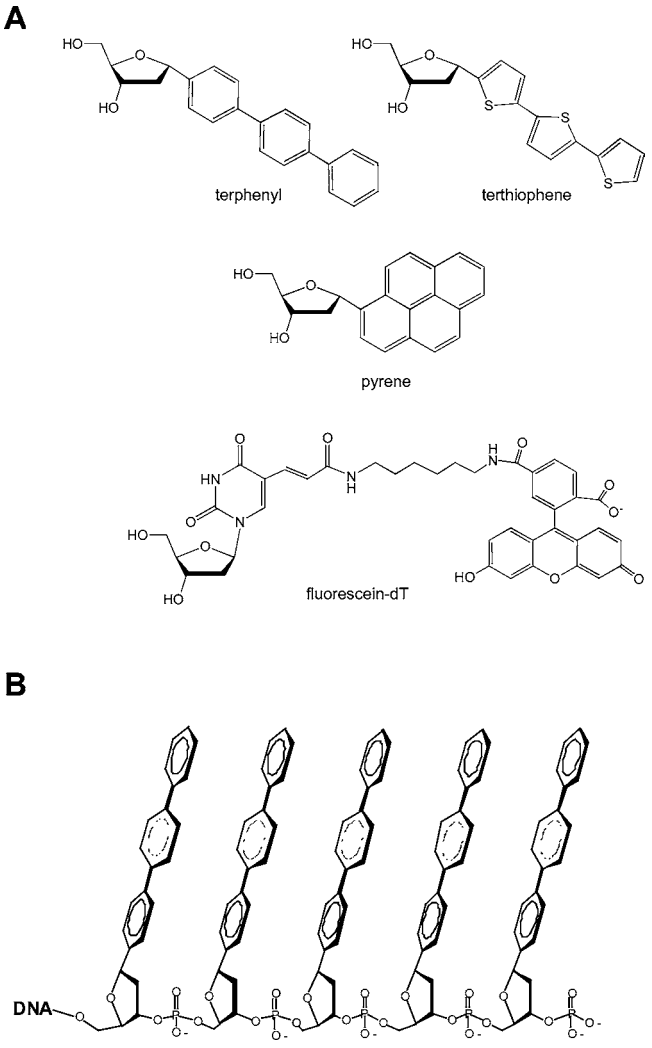

Figure 1. Structures of fluorescent deoxyribosides in this study (a) and example of an oligofluor label (b), showing the structure of a penta (terphenyl) label conjugated to DNA.

those of the other monomeric dyes. In addition, the quantum yields for fluorescein and pyrene are quite high, whereas those of terphenyl and terthiophene are moderate in air-saturated methanol (3).

Short octamer DNA sequences (5′-dTCAGGTTC) were prepared with the dyes placed at the 3′ end. This sequence was chosen because it previously has been useful in fluorescence hybridization studies in our laboratory (8). We prepared oligomers containing either one, two, or three fluoresceins or one through five fluorophore deoxyribosides containing terphenyl, pyrene, or terthiophene. The conjugated DNAs were purified by gel electrophoresis. Intact incorporation of each new dye into DNA was confirmed by mass spectrometry.

Absorption and Emission Properties. Studies of the fluorescence properties of these labels were then carried out in this single-stranded DNA sequence. Special care was taken (by varying the concentration) to study the properties under conditions at which no significant aggregation was taking place. It was found that at high concentrations (i.e., >50 μM) there was concentration dependence of the fluorescence emission for some of the more hydrophobic cases (for example, five pyrenes or five terthiophenes), which suggests interstrand aggregation behavior. At the low concentrations at which fluorescence was characterized (ca. <1.0 μM) we saw no such concen-

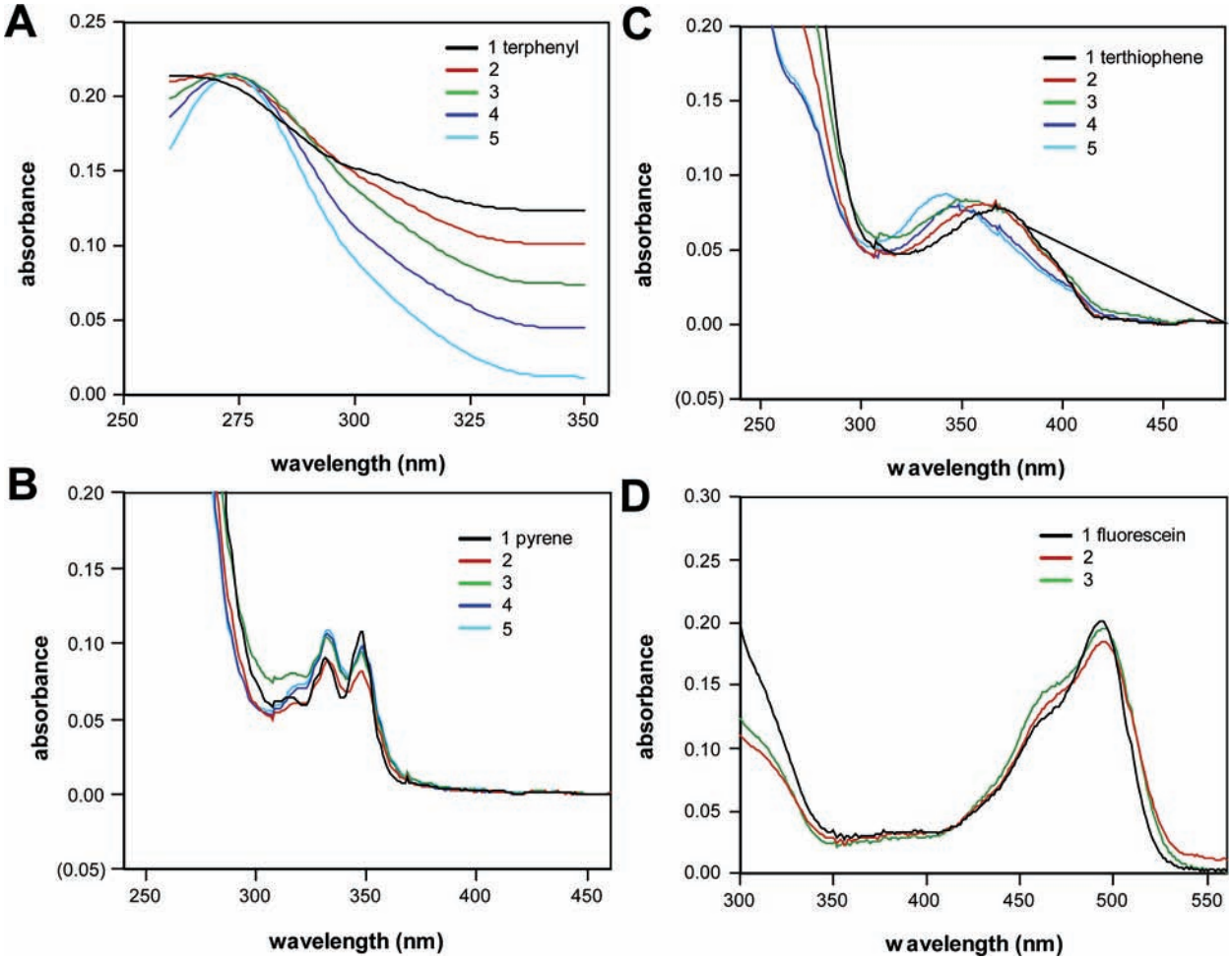

Figure 2. Absorption spectra of the oligofluors in this study conjugated to an octamer oligonucleotide. Spectra for increasing numbers of dyes are shown at matched absorbance to aid in comparison of peak shapes and wavelengths. Data were taken in water.

tration dependence, establishing that these are properties of single-strand species.

Absorption spectra (in water) for each dye series are shown in Figure 2. In the three fluorophore deoxyriboside series there was significant evidence of ground-state electronic interactions between the dyes. The terphenyl series showed a significant red shift with increasing monomer number, from 264 to 273 nm, although overlap with the normal DNA absorption at 260 nm interfered with analysis somewhat. The pyrene series showed a small red shift with increasing numbers and a decreasing peak-to-valley ratio, both of which lend evidence of ground-state association between pyrenes (9). The terthiophene series, by contrast, displayed a marked blue shift with increasing numbers of monomers, from 373 to 342 nm, suggesting significant structural organization in the oligomer (see Supporting Information). Finally, the fluorescein control showed no significant change in absorption wavelength or peak shape with increasing numbers, thus providing no evidence of organized ground-state structure.

The temperature dependence of absorption was also measured for these single-stranded oligomers (Figure S1 in the Supporting Information). In general, we found a small increase in absorption (at the peak maximum) for the three fluorophore deoxyriboside monomer series. However, the effect was small, showing <5% hyperchromicity on increasing temperature over the range from 10 to 80 °C.

The steady-state fluorescence properties of the same four oligomeric series were then characterized in water. The full data are listed in Table 1, and emission spectra are plotted in Figure 3. We took no steps to deoxygenate the solutions because our long-term goal is the development of fluorescent properties that can be applied without the exclusion of air. The data for the terphenyl series showed increasing fluorescence intensity (on an equal absorbance basis) and a large red shift with increasing numbers of monomers (from 344 to 383 nm). The excitation spectra showed a progressively larger red shift with increasing number of dyes, suggestive of a cooperative effect among the dyes in the oligomer (*10*, *11*). The overall Stokes shift increased markedly from 80 to 110 nm over the series with one to five dyes (Figure 4).

The pyrene series was markedly different than the terphenyl series and showed long-wavelength emission, suggestive of excimer emission (*9*, *12*) in all cases with two or more units. As the number of monomers increased, the excimer-to-monomer ratio increased markedly, and the cases with four and five pyrenes showed little remaining monomer emission (Table S1). The Stokes shift abruptly jumped from 28 nm (when only monomer fluorescence is observed) to ~133 nm through the series (Figure 4).

Finally, the terthiophene series showed a different behavior from either of the above two series. Substantial quenching was observed with increasing numbers (Figure 3) (although not as marked as for fluorescein, see below), a phenomenon that partially compensated for the increase in absorbance as the numbers of dyes increased. As with terphenyl we observed a red shift with increasing

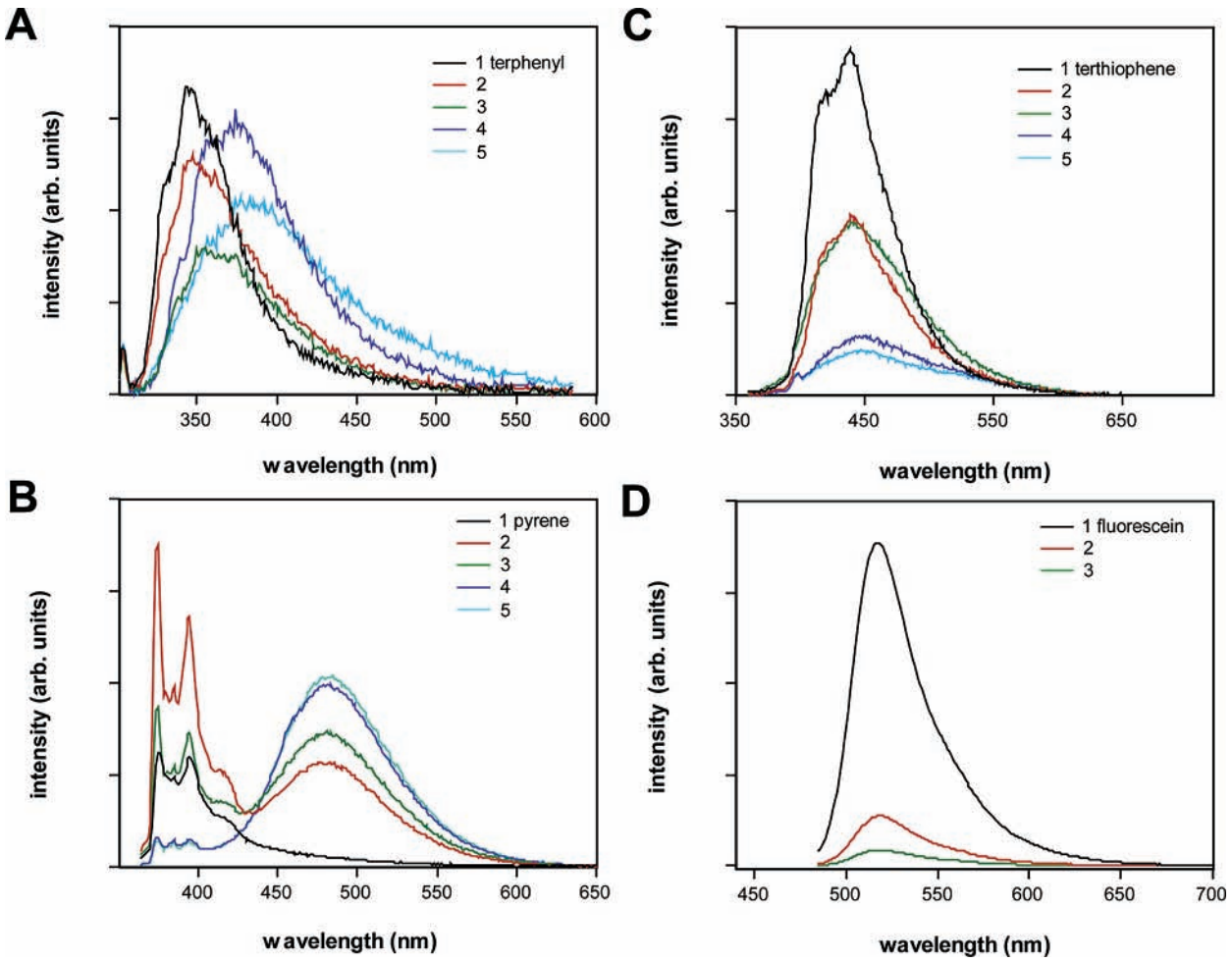

Figure 3. Emission spectra in water for oligofluors conjugated to DNA. Data are shown for matching absorbance at the excitation wavelength. Excitation wavelengths were 275 nm (terphenyl series), 340 nm (pyrene series), 350 nm (terthiophene series), and 480 nm (fluorescein series).

Table 1. Photophysical Data for Oligomers of Three Fluorophore Deoxyribosides with Comparison to Fluorescein-dU[a,b]

fluorescent species	absorption λ_{max} (nm)	absorptivity ϵ^b (μmol cm^{-1})	emission λ_{max} (nm)	Φ	brightness $\epsilon \times \Phi$	Stokes shift (nm)
pyrene	347	34400	375	0.026	890	28
(pyrene)$_2$	348	68800	375, 480	0.083	5700	27
(pyrene)$_3$	348	103000	375, 481	0.076	7800	27
(pyrene)$_4$	348	138000	481	0.077	11000	133
(pyrene)$_5$	348	172000	483	0.081	14000	135
terthiophene	373	31400	440	0.126	4000	67
(terthiophene)$_2$	362	62800	441	0.079	5000	79
(terthiophene)$_3$	352	94200	441	0.086	8100	89
(terthiophene)$_4$	347	126000	446	0.037	4800	99
(terthiophene)$_5$	342	157000	447	0.031	4900	105
terphenyl	264	40100	344	0.108	4300	80
(terphenyl)$_2$	270	80200	347	0.095	7600	77
(terphenyl)$_3$	271	120000	355	0.081	9700	84
(terphenyl)$_4$	273	160000	374	0.200	32000	99
(terphenyl)$_5$	273	201000	383	0.206	41000	110
fluorescein	495	75000	517	0.440	33000	22
(fluorescein)$_2$	495	150000	517	0.069	10000	22
(fluorescein)$_3$	495	225000	519	0.023	5200	24

[a] Fluorophores (X) are present in the DNA sequence 5′-dTCAGGTTC(X). [b] Conditions: oligonucleotide dissolved in 1× Tris−borate−EDTA buffer, pH 7.0, 25 °C. [c] Absorptivities are estimates based on addition of absorptivities of the individual chromophores and do not take into account hypochromicity (which is observed to be <5%, see Figure 3).

numbers of monomers, although the total shift in fluorescence maximum was significantly smaller, at ~7 nm (from 440 to 447 nm). Combined with the strong blue shift in absorbance, however (see above), this resulted in large Stokes shifts that increased strongly [from 67 to 105 nm over the series (Figure 4)].

For comparison, the results with multiple substitution of fluorescein are also plotted (Figure 3). Consistent with

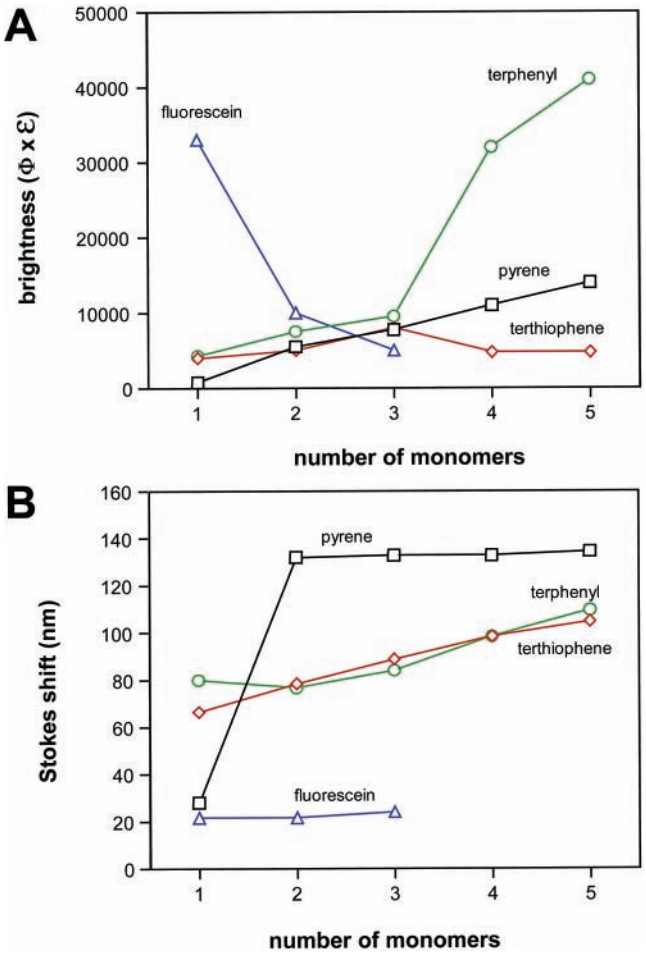

Figure 4. Trends with increasing numbers of monomer fluorophores conjugated to DNA: (a) relative emission intensity of the labels ("brightness" is calculated as quantum yield multiplied by molar absorptivity); (b) changes in Stokes shifts with increasing numbers of monomer fluorophores. See Table 1, note *b* for conditions.

earlier observations (*12*), strong quenching of emission was observed with the adjacent substitution of more than one fluorophore. Thus, as the numbers of dyes increased, quantum yield dropped markedly (Figure 3 and Table 1). There was little or no associated red or blue shift.

CD Spectra. More evidence of structural and electronic interactions was obtained from CD spectra of the DNA-conjugated oligomeric dyes in the series. Figure S2 shows the data for the three fluorescent deoxyriboside series. For the terphenyl series, the CD measurements revealed a strong exciton splitting with four and five monomers, suggesting an organized structure in the oligomeric dyes (see Supporting Information for details). The terthiophene series showed a similar behavior (Figure S2), but with maximum structural organization seen at three dyes. The oligomeric pyrene series displayed a different behavior in the CD spectra, with a general lack of exciton splitting except with two chromophores.

Effects of Buffer Conditions. Recent experiments have suggested that oligomeric fluorophores might be able to respond to varying physical conditions in solution with changes in fluorescence (*5*). We therefore explored the effects of varying environment (buffer pH and ionic strength) on oligomers of the two most promising new fluorophores, terphenyl and pyrene, with comparison to fluorescein as the FAM−thymidine conjugate. We tested monomeric, dimeric, and trimeric labels. Data at varied ionic strength for the trimers are shown in Figure S3, using sodium chloride concentrations ranging from 0 to 1000 mM. Results showed that there was essentially no change in emission for any of the trimeric fluorophores.

Data for varied pH are shown in Figure S4. The effects of pH were tested at values of 4, 7, and 11; results showed that all three oligomeric dyes gave greatest emission intensity at pH 7 and 11, but all three sets showed lower emission intensity at pH 4. Cases with one to three fluorescein labels gave no apparent change in emission spectrum with lowered pH, save for markedly lowered emission intensity (see data for trimer; data for monomer and dimer are not shown but are similar). Pyrene labels also gave no change in emission wavelength, but excimer emission bands were less intense at pH 7 than at pH 11, and at pH 4 the excimer band (490 nm) was nearly completely lost, whereas the monomer emission (380 nm) appeared to be unaffected. Finally, terphenyl oligomers (particularly the trimer) gave an increasing red shift, and moderately increasing intensity, with increasing pH from 4 to 7 to 11.

Photobleaching and Wavelength Shifts with Light Exposure. We also evaluated the response of trimeric dyes involving terphenyl, pyrene, and fluorescein to long-term light exposure, to measure their susceptibility to photobleaching in air-saturated buffer. The labels were excited at their absorption maxima over a period of hours in a fluorescence spectrometer, and emission intensity was measured over time (Figure S5). Results showed that the FAM−T trimer gave the slowest photobleaching under these conditions, with a half-life of ~7.5 h. Both the terphenyl and pyrene oligomers showed similar bleaching rates at their emission maxima, with half-lives of 2.8 and 3.3 h, respectively. However, the three trimers were markedly different in their wavelength responses: fluorescein simply dropped in emission intensity while keeping its spectral shape and wavelength constant. In contrast to this, the pyrene trimer shifted its spectrum markedly, losing its excimer band and keeping its monomer emission band intact. Thus, the pyrene trimer changed its color from green to blue, similar to what was observed recently for certain combinatorial fluorophores (5). The terphenyl trimer, in contrast to the above two results, shifted its emission to the red (from 355 to 390 nm) after the long-term UV exposure. Thus, all three oligomeric labels behaved differently during long-term irradiation.

Stabilization of DNA Hybridization. Finally, to evaluate how the attachment of such nonnatural α-oriented deoxyribosides might affect the hybridization properties of DNA, we carried out a simple duplex hybridization between the octamer DNA sequence and its complement, with a single overhanging fluorescent residue to evaluate inherent properties with the shortest variants of the labels. We tested dyes at the 3′ end and 5′ end of the DNA. Interestingly, the data showed (Table 2) that all cases increased the stability of hybridization. The order of stabilization at the 3′ end was α-pyrene > α-terphenyl > α-terthiophene. Like the previously studied pyrene β-deoxyriboside in 5′-end substitutions (*14*), the 3′-α-pyrene increased T_m markedly, in this case by 11.4 °C for a single substitution and giving 2.3 kcal/mol of thermodynamic stabilization. This is a greater stabilization than previously reported for the naturally oriented β isomer of the pyrene nucleoside at the 5′ end of DNA (albeit in a different sequence context) (*14*). At the 5′ end, the order of stabilization was terphenyl > pyrene; in this case, terphenyl added 10.3 °C of thermal stability, similar to the large stabilization by pyrene at the opposite end.

Table 2. Stabilization of Duplexes by Single Fluorescent Nucleosides in a 5′ or 3′ Dangling Position

fluorescent nucleoside (X)	T_m (°C)[b,c]	$\Delta G°_{37}$ (kcal/mol)	$\Delta H°$ (kcal/mol)	$\Delta S°$ (cal/mol·K)	$\Delta\Delta G°_{37}$ (kcal/mol)
5′ end					
none	31.9 ± 0.5	−7.4 ± 0.2	−63 ± 8	−180 ± 30	
α-pyrene	38.4 ± 0.5	−8.1 ± 0.1	−54 ± 4	−147 ± 12	0.7 ± 0.3
α-terphenyl	43.0 ± 0.5	−9.0 ± 0.1	−63 ± 4	−173 ± 12	1.6 ± 0.3
FAM-T	32.5 ± 0.5	−7.0 ± 0.1	−59 ± 5	−169 ± 18	−0.4 ± 0.3
3′ end					
none	31.9 ± 0.5	−7.4 ± 0.2	−63 ± 8	−180 ± 30	
α-pyrene	43.3 ± 0.5	−9.7 ± 0.1	−63 ± 1	−171 ± 4	2.3 ± 0.3
α-terphenyl	38.1 ± 0.5	−8.6 ± 0.1	−81 ± 6	−230 ± 20	1.2 ± 0.3
α-terthiophene	35.9 ± 0.5	−8.4 ± 0.2	−57 ± 5	−156 ± 17	1.0 ± 0.4

[a] Sequences: 5′-(X)TCA GGT TC(X)-3′. Complementary strand: 5′-GAA CCT GA-3′. [b] Conditions: 1× TBE buffer (pH 7.0) with 0.1 mM EDTA, 200 mM KCl, and 5 mM $MgCl_2$. [c] T_m values are at 5.0 μM.

DISCUSSION

One of the major goals of this study was to evaluate whether pure oligomeric labels composed of terphenyl, pyrene, or terthiophene might offer potentially useful properties in nucleic acid labeling that single or multiple standard labels (such as fluoresceins) do not. Clearly the answer to this question is positive, in several respects. First, fluorescein and other common commercial dyes are known to self-quench in multiple DNA substitutions (*13*), and thus incorporation of multiple fluorescein labels into a biomolecule does not lead to increased detection sensitivity, unless the labels are separated by relatively large distances to ameliorate quenching (*15*). The current experiments with fluorescein confirmed this. In the present molecular design, the distance between fluorophores is minimized and the molecules are small. We find, not surprisingly, that this close arrangement has different effects on the quantum yield (and, thus, overall brightness, defined as quantum yield multiplied by molar absorptivity), depending on the fluorophore. The plots in Figure 4 show clearly that two of the new oligomeric labels (containing pyrene or terphenyl) exhibit increasing brightness with increasing numbers; the terphenyl labels emit more intensely than can be achieved in this system with the very successful and widely used dye fluorescein. It remains to be seen whether further increasing numbers could yield still further enhancements. Of course, the emission intensity of the label is directly related to the sensitivity of detection of biomolecules at low concentrations. It is also an important issue in single-molecule fluorescence studies.

Another practical issue in the intensity of labeling of nucleic acids is the fact that nucleobases themselves often quench fluorescence. For example, the above oligomeric pyrene labels are significantly quenched by attachment to DNA, consistent with previous studies of pyrene conjugates (*16*). Our experiments showed that quantum yields were higher by ∼30-fold for the oligomeric labels alone (data not shown). On the other hand, the present terphenyl labels are not markedly quenched by attachment to DNA. Interestingly, even for cases that are markedly quenched we have observed that certain spacer molecules can help "insulate" such oligomeric fluorophores from quenching by DNA (A. Cuppoletti et al., manuscript in preparation). Nevertheless, in a practical sense one must consider the effect of the molecule being labeled on the fluorescence characteristics of the reporter molecule.

Beyond the relative brightness of the labels, the oligomeric fluorophores in this study also offer other potentially useful differences in comparison to commercial fluorescein labels. Stokes shifts in this series are all markedly increased relative to that of fluorescein. Indeed, Stokes shifts are often small (∼20−30 nm) for most commercial monomer dye molecules. This small separation between excitation and emission often causes interference between the excitation source and the light being observed, and one often must work on the shoulders of the absorption and emission peaks to avoid such difficulties. In the cases of the oligomeric dyes containing pyrene or terphenyl, one has examples of bright labels with Stokes shifts of >100 nm. Thus, in a practical sense one can easily avoid interference between excitation and emission light.

In a different approach for the use of multiple labels for DNA, recent work in other laboratories has shown that fluorescence resonance energy transfer (FRET) can occur through more than two fluorophores (*17*−*19*). As with the current approach, the multi-FRET approach uses three or more dyes and yields large Stokes shifts. One advantage of the current strategy is that the labels are incorporated alone, whereas multi-FRET requires separation between the dyes and thus larger molecules.

Some of the current fluorophores have been examined previously in aggregated states or in other situations in which they are interacting closely with another of the same fluorophore. The aggregation of pyrenes has been extensively studied in many molecular settings and has been reviewed (*9*). The main difference between the present oligomeric pyrene dyes and previous cases is the high efficiency of excimer formation using the DNA backbone. A number of other cases of multiple pyrenes in DNA or peptides are known (*20*−*23*).We know of few other cases in which excimer/monomer ratios are this high, except in pyrene crystals and polymers (*9*, *23*). For one comparison, a dimeric pyrene molecule is offered commercially as a label (*24*), but it has an excimer-to-monomer ratio of ∼1 , well below those described here. We surmise that the DNA backbone is especially well suited to arranging these aromatic molecules in a stacked arrangement, and the spectroscopic data add support to this notion.

Whitten and co-workers (*25*) have shown in non-nucleic acid systems that weak $\pi-\pi$ stacking interactions among terphenyl groups are nevertheless responsible for the generation of large and well-ordered structures. Saturated fatty acids or phospholipids functionalized with terphenyl groups were found to generate supramolecular aggregates where the dyes assumed a pinwheel structure to maximize an edge-to-face interaction, resulting in an H-type aggregation. Other studies have also reported on the hydrophobic aggregation of terphenyl (*26*, *27*).

We know of only one previous case of terthiophene being used as a nucleic acid label (*3*) and no cases of its multiple use. However, in solids and in polymers, workers have observed a blue shift of the terthiophene absorption maxima and quenching of the fluorescence (*28*−*31*), similar to the effects observed here.

In a practical sense, we expect that oligomeric labels such as those containing pyrene or terphenyl may be useful for their large Stokes shifts and their emission intensity. They can, of course, be used in labeling of DNAs and RNAs by direct addition on a synthesizer. However, we anticipate that they also may be useful in labeling other biomolecules such as proteins or antibodies. There are several commercially available chemical conjugating groups (usually applied to oligonucleotides) that should allow the ready functionalization of these molecules for attachment to other species.

ACKNOWLEDGMENT

This work was supported by grants from the U.S. Army Research Office and the U.S. National Institutes of Health (GM067201). The Swiss National Science Foundation is acknowledged for a Stipendium für Angehende Forschende to C.S., and the KOSEF Foundation for a postdoctoral fellowship to J.S.P.

Supporting Information Available: Figure and tables showing effects on absorption and emission for oligomeric labels. This material is available free of charge via the Internet at http://pubs.acs.org.

LITERATURE CITED

(1) Mayer, A., and Neuenhofer, S. (1994) Luminescent labels—more than just an alternative to radioisotopes? *Angew. Chem., Int. Ed. 33*, 1044−1072.
(2) Zimmer, M. (2002) Green fluorescent protein (GFP): applications, structure, and related photophysical behavior. *Chem. Rev. 102*, 759−781.
(3) Strässler, C., Davis, N. E., and Kool, E. T. (1999) Novel nucleoside analogues with fluorophores replacing the DNA base. *Helv. Chim. Acta 82*, 2160−2171.
(4) Gao, J., Strässler, C., Tahmassebi, D. C., and Kool, E. T. (2002) Libraries of composite polyfluors built from fluorescent deoxyribosides. *J. Am. Chem. Soc. 124*, 11590−11591.
(5) Ren, R. X.-F., Chaudhuri, N. C., Paris, P. L., Rumney IV, S., and Kool, E. T. (1996) Naphthalene, phenanthrene, and pyrene as DNA base analogues: synthesis, structure, and fluorescence in DNA. *J. Am. Chem. Soc. 118*, 7671−7678.
(6) Crosby, G. A., and Demas, J. N. (1971) Measurement of photoluminescence quantum yields. Review. *J. Phys. Chem. 75*, 991.
(7) Xu, Y., Karalkar, N. B., and Kool, E. T. (2001) Nonenzymatic autoligation in direct three-color detection of RNA and DNA point mutations. *Nat. Biotechnol. 19*, 148−152.
(8) Winnik, F. M. (1993) Photophysics of preassociated pyrenes in aqueous polymer solutions and in other organized media. *Chem. Rev. 93*, 587−614.
(9) Place, I., Perlstein, J., Penner, T. L., and Whitten, D. G. (2000) Stabilization of the aggregation of cyanine dyes at the molecular and nanoscopic level. *Langmuir 16*, 9042−9048.
(10) Wang, M., Silva, G. L., and Armitage, B. A. (2000) DNA-templated formation of a helical cyanine dye J-aggregate. *J. Am. Chem. Soc. 122*, 9977−9986.
(11) Forster, T., and Kasper, K. (1955) Concentration reversal of the fluorescence of pyrene. *Z. Elektrochem. 59*, 976−980.
(12) Haralambidis, J., Angus, K., Pownall, S., Duncan, L., Chai, M., and Tregear, G. W. (1990) The preparation of polyamide-oligonucleotide probes containing multiple non-radioactive labels. *Nucleic Acids Res. 18*, 501−505.
(13) Guckian, K. M., Ren, R. X.-F., Chaudhuri, N. C., Tahmassebi, D. C., and Kool, E. T. (2000) Factors contributing to aromatic stacking in water: evaluation in the context of DNA. *J. Am. Chem. Soc. 122*, 2213−2222.
(14) Wang, J., Jiang, M., Nilsen, T. W., and Getts, R. C. (1998) Dendritic nucleic acid probes for DNA biosensors. *J. Am. Chem. Soc. 120*, 8281−8282.
(15) Telser, J., Cruickshank, K. A., Morrison, L. E., and Netzel, T. L. (1989) Synthesis and characterization of DNA oligomers and duplexes containing covalently attached molecular labels: comparison of biotin, fluorescein, and pyrene labels by thermodynamic and optical spectroscopic measurements. *J. Am. Chem. Soc. 111*, 6966−6976.
(16) Tong, A. K., Jackusch, S., Li, Z., Zhu, H.-R., Akins, D. L., Turro, N. J., and Ju, J. (2001) Triple fluorescence energy transfer in covalently trichromophore-labeled DNA. *J. Am. Chem. Soc. 123*, 12923−12924.
(17) Ohya, Y., Yabuki, K., Hashimoto, M., Nakajima, A., and Ouchi, T. (2003) Multistep fluorescence resonance energy transfer in sequential chromophore array constructed on oligo-DNA assemblies. *Bioconjugate Chem. 14*, 1057−1066.
(18) Ohya, Y., Yabuki, K., Tokuyama, M., and Ouchi, T. (2003) Construction of sequential chromophore arrays on oligo-DNA assembly and their energy transfer behavior. *Supramol. Chem. 15*, 45−54.
(19) Erikkson, M., Norden, B., Jernström, B., Gräslund, A., and Lycksell, P.-O. (1988) Observation of excimer formation in the covalent adducts of 9,10-epoxy-7,8,9,10-tetrahydrobenzo-[*a*]pyrene-7,8-diol with poly(dG-dC). *J. Chem. Soc., Chem. Commun*. 211−212.
(20) Kitamura, M., Nimura, A., Yamana, K., and Shimidzu, T. (1991) Oligonucleotides with bis-pyrene adduct in the backbone: synthesis and properties of intramolecular excimer forming probe. *Nucleic Acids Res. Symp. Ser. 25*, 67−68.
(21) Tong, G., Lawlor, J. M., Tregear, G. W., and Haralambidis, J. (1995) Oligonucleotide−polyamide hybrid molecules containing multiple pyrene residues exhibit significant excimer fluorescence. *J. Am. Chem. Soc. 117*, 12151−12158.
(22) Shoji, O., Okumura, M., Kuwata, H., Sumida, T., Kato, R., Annaka, M., Yoshikuni, M., and Nakahira, T. (2001) Secondary structure and side-chain chromophore orientation in poly(L-glutamines) having pyrene chromophores in the side chains. *Macromolecules 34*, 4270−4276.
(23) Molecular Probes catalog (Molecular Probes Inc., Eugene, OR), item B-311.
(24) Geiger, H. C., Perlstein, J., Lachicotte, R., Wyrozebski, R., and Whitten, D. G.(1999) Self-assembly of aromatic-derivatized amphiphiles: phenyl, biphenyl, and terphenyl fatty acids and phospholipids. *Langmuir 15*, 5606−5616.
(25) Whitten, D. G., Chen, L., Geiger, H. C., Perlstein, J., and Song, X. (1998) Self-assembly of aromatic-functionalized amphiphiles: the role and consequences of aromatic−aromatic noncovalent interactions in building supramolecular aggregates and novel assemblies. *J. Phys. Chem. B 102*, 10098−10111.
(26) Dutta, A. K., and Misra, T. N. (1994) Aggregation-induced reabsorption of *p*-terphenyl in Langmuir−Blodgett films: a spectral study. *J. Phys. Chem. 98*, 12844.
(27) DiCesare, N., Belletete, M., Marrano, C., Leclerc, M., and Durocher, G. (1999) Intermolecular interactions in conjugated oligothiophenes. 1. Optical spectra of terthiophene and substituted terthiophenes recorded in various environments. *J. Phys. Chem. A 103*, 795−802.
(28) Bosiso, R., Botta, C., Colombo, A., Destri, S., Porzio, W., Grilli, E., Tubino, R., Bongiovanni, G., Mura, A., and Di Silvestro, G. (1997) Excitonic effects in thiophene oligomers. *Synth. Met. 87*, 23−29.
(29) Feast, W. J., Goldoni, F., Kilbinger, A. F. M., Meijer, E. W., Petty, M. C., and Schenning, A. P. H. (2001) Synthesis and properties of self-organizing semiconducting and luminescent polymers and model compounds. *Macromol. Symp. 175*, 151−158,
(30) Kilbinger, A. F. M., and Feast, W. J. (2000) Solution processable alternating oligothiophene-PEO-*block-co*-polymers: synthesis and evidence for solvent dependent aggregation. *J. Mater. Chem. 10*, 1777−1784.
(31) Berova, N., and Nakanishi, K. (2000) *Circular Dichroism: Principles and Applications*, 2nd ed., pp 337−382 (Berova, N., Nakanishi, K., Woody, R. W., Eds.) Wiley, New York.
(32) Lightner, D. A., and Gurst, J. E. (2000). *Organic Conformational Analysis and Stereochemistry from Circular Dichroism Spectroscopy*, pp 423−457, Wiley-VCH, Weinheim, Germany.

BC0497766

In Vitro and in Vivo Evaluation of Hydrophilic Dendronized Linear Polymers

Cameron C. Lee,[†] Masaru Yoshida,[†,§] Jean M. J. Fréchet,[†] Edward E. Dy,[‡] and Francis C. Szoka*[,‡]

Center for New Directions in Organic Synthesis, Department of Chemistry, University of California, Berkeley, California 94720-1460, and Department of Biopharmaceutical Sciences & Pharmaceutical Chemistry, University of California, San Francisco, California 94143-0446. Received September 23, 2004; Revised Manuscript Received April 8, 2005

Rigid-rod dendronized linear polymers consisting of a poly(4-hydroxystyrene) backbone and fourth-generation polyester dendrons were evaluated in vitro and in vivo to determine their suitability as drug delivery vectors. Cytotoxicity assays indicated that the polymers were well tolerated by cells in vitro. Biodistribution studies of the polymers in both nontumored and tumored mice revealed that as for random coil linear polymers, renal clearance was a function of polymer size, with significant urinary excretion observed for a 67 kDa dendronized polymer. High accumulation in organs of the reticuloendothelial system was exhibited by a dendronized polymer with a very high molecular weight (M_n = 1740 kDa), but was not as significant for smaller polymers with M_n = 67 kDa and M_n = 251 kDa. The rank order for tumor accumulation of the polymers on a percent injected dose per gram tumor basis was 251 kDa ~ 1740 kDa > 67 kDa. These data will help guide the selection of highly functionalizable rigid-rod dendronized polymers with pharmacokinetic properties appropriate for use as drug carriers.

INTRODUCTION

Polymers, both natural and synthetic in origin, have attracted attention as drug delivery vehicles due to their ability to favorably alter the biological properties of attached therapeutic agents (*1*). For example, polymer–drug conjugates may have increased blood circulation half-lives, reduced toxicities, and increased solubilities relative to the parent drugs (*2*). In addition, high molecular weight (MW) polymers can exhibit enhanced accumulation in tumor tissues relative to normal tissues. This phenomenon is termed the enhanced permeation and retention effect (EPR effect), and its occurrence is attributed to the "leaky" blood vessels and poorly developed lymphatic drainage system present within tumor tissues (*3*).

To date, the carriers that have been most extensively investigated for drug delivery applications are linear polymers such as poly(ethylene oxide) (PEO) (*4*) and poly(*N*-(2-hydroxypropylmethacrylamide)) (HPMA) (*5*, *6*). However, increasing attention is being given to new, more highly branched structures such as dendrimers and star polymers with the hope that interesting effects of architecture on biological properties may be discovered (*7*–*14*). Dendronized linear polymers, a recent addition to the branched polymer family, are linear polymers that bear dendrons at each repeat unit along their backbones (Figure 1). It is believed that as the sizes of the pendant dendrons increase, so do the interactions between adjacent dendrons, and at higher generations these macromolecules attain extended conformations and can be described as somewhat rigid, cylindrical rods (*15*). Dendronized polymers may be interesting scaffolds for drug delivery as the large number of functionalizable peripheral groups on the dendrons should allow for very high levels of drug loading, and furthermore it has been suggested that the shape and multivalency of a macromolecule can influence its biological properties (*16*–*20*). However, in contrast to dendrimers, few biological studies of dendronized linear polymers have been reported to date (*21*–*23*). Here we describe the cytotoxicity, biodistribution, and pharmacokinetics of synthetic, water-soluble, rigid-rod dendronized linear polymers consisting

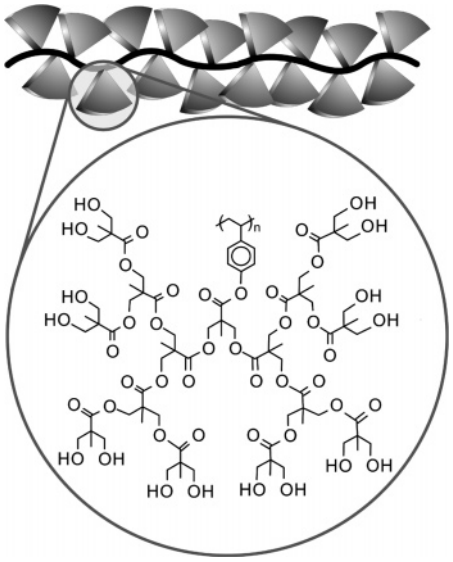

Figure 1. Schematic representation of a dendronized linear polymer and the molecular structure of generation-four dendronized poly(4-hydroxystyrene).

* To whom correspondence should be addressed: School of Pharmacy S-926, University of California, San Francisco, CA 94143-0446. Tel (415) 476–3895, Fax (415) 476–0688, E-mail szoka@cgl.ucsf.edu.

[†] University of California, Berkeley.

[‡] University of California, San Francisco.

[§] Permanent address: Nanotechnology Research Institute, National Institute of Advanced Industrial Science and Technology (AIST), 1-1-1 Higashi, Tsukuba, Ibaraki 305-8565, Japan.

10.1021/bc0497665 CCC: $30.25 © 2005 American Chemical Society
Published on Web 04/29/2005

of a poly(4-hydroxystyrene) backbone and fourth-generation polyester dendrons in normal and tumored mice (Figure 1). To the best of our knowledge, this constitutes the first report on the in vivo biodistribution of dendronized polymers.

MATERIALS AND METHODS

Materials. Unless otherwise noted, reagents and solvents were obtained from commercial suppliers and used without further purification. Polymers **1**−**3** were prepared as previously reported (*24*, *25*).

Characterization. Analytical size exclusion chromatography (SEC) in *N*,*N*-dimethylformamide (DMF) with 0.2% LiBr was performed at 70 °C at a nominal flow rate of 1.0 mL/min on a chromatography line calibrated with linear poly(ethylene oxide) (PEO) standards (6450−529500 Da) and fitted with two 7.5 × 300 mm PLgel mixed-bed C columns (5-μm particle size). The SEC system used when determining PEO-equivalent MWs consists of a Waters 510 pump, a Waters U6K injector, and a Waters 410 differential refractive index detector thermostated at 35 °C. The SEC system for determining absolute MWs consists of a Waters 510 pump, a 7125 Reodyne injector, a Wyatt DAWN-EOS multi-angle laser light scattering detector (laser of λ = 690 nm), and a Wyatt Optilab differential refractive index detector. Light scattering data were analyzed using Astra software from Wyatt, and SEC data using the differential refractive index detector were analyzed using Millennium software from Waters.

Volume-average particle diameters were determined using dynamic light scattering. Experiments were performed at least three times at 25 °C in saline solution with a Zetasizer Nano ZS (Malvern Instruments) equipped with a 4 mW He−Ne laser at 633 nm.

Radioactivity from ^{125}I was quantified with a 1480 Wallac Wizard 3 Automatic Gamma Counter. Counts emitted from samples contained in screw-cap scintillation vials were measured over the course of one minute and were recorded as counts per minute (cpm).

Cytotoxicity of 1−3. Cell toxicity studies were performed at the UC Berkeley Tissue Culture Facility. MDA-MB-231 human breast cancer cells were seeded in 96-well plates at a density of 1.6×10^4 cells per well in 100 μL of DMEM with 10% FBS (DMEM + FBS). After incubation overnight (37 °C, 5% CO_2), the medium was removed by aspiration and replaced with fresh medium (100 μL) containing 0−3.0 mg/mL of polymers **1**−**3**. These solutions also contained antibiotics (1% penicillin−streptomycin). (Each of the polymers used in these experiments was purified prior to use by size exclusion chromatography on a PD-10 column, followed by lyophilization.) Following incubation for 48 h, the medium was aspirated off and replaced with 100 μL of fresh medium and 20 μL of a 5 mg/mL MTT solution. The cells were incubated for 4 h, after which time the medium was removed, leaving behind purple crystals. These crystals were dissolved in 200 μL of DMSO and 25 μL of glycine buffer (0.1 M glycine, 0.1 M NaCl, pH 10.5). The absorbance values at 520 nm were measured using a SpectraMAX 190 microplate reader. (Molecular Devices). The percent viability of cells in treated wells relative to nontreated cells was calculated and represents the average value over four wells (Figure 2).

Synthesis of Tyramine-Functionalized Dendronized Polymers 1−3. 1, **2**, or **3** was dissolved in 1 mL of anhydrous pyridine and reacted overnight with a solution containing 5−7 mol % (relative to hydroxyls) of 4-nitrophenyl chloroformate in 1 mL of CH_2Cl_2. The solvent was evaporated, and the polymer was dissolved in 2 mL of anhydrous *N*,*N*-dimethylformamide. An excess of 4-(2-aminoethyl)phenol (tyramine) and 1 mol equiv of anhydrous triethylamine was added to the solution and was stirred overnight. The polymers were purified of low MW contaminants by dialysis in Spectra/Por regenerated cellulose membranes (MWCO = 8000, Spectrum Laboratories) against distilled water. The presence of tyramine groups was confirmed by ^{1}H NMR analysis of a lyophilized aliquot of the solution retained in the dialysis membrane. The aromatic protons appear at 6.6 and 6.9 ppm, and the benzylic protons appear at 2.6 ppm.

Table 1. Molecular Weights, Sizes, and Pharmacokinetic Parameters for 1−3 Measured in Mice.

	SEC-MALLS[a] (kDa)		SEC[b] (kDa)			DLS
	M_n	M_w	M_n	M_w	PDI	D[c] (nm)
1	67.0	69.0	13.7	16.0	1.16	5.8
2	251	260	38.2	45.2	1.18	10.0
3	1,740	1,890	190.0	242.0	1.27	15.7

[a] Absolute MWs. [b] Relative PEO MWs from SEC in DMF. [c] Mean volume-average diameter.

Radioiodination of Tyramine-Functionalized Polymers 1−3. Tyramine functionalized **1**, **2**, or **3** were iodinated as previously described (*8*, *26*), resulting in solutions of radiolabeled polymer in HBS (10 mM HEPES/Cl, 140 mM NaCl, pH 7.4). Non-polymer-bound ^{125}I was removed by ion exchange chromatography on Bio-Rad AG 1-X-2 resin (chloride form), and polymers were separated from residual low MW radioactive contaminants by size exclusion chromatography on Bio-Rad 10DG desalting columns that had been equilibrated with HBS. The initial, high-MW fractions were collected and pooled. The specific activities of the solutions for the biodistribution experiments in nontumored mice were measured to be 23, 3, and 35 μCi/mL for polymers **1**, **2**, and **3**, respectively, and for the biodistribution experiments in tumored mice the activities were 15, 26, and 16 μCi/mL, respectively. The final concentration of polymer in the solutions was 0.8 mg/mL.

Biodistribution of 1−3 in Nontumored Mice. Polymer solutions (200 μL) were administered intravenously to 6−8 week-old CD-1 female mice (three mice per experimental group). The mice were sacrificed at six different times following injection for biodistribution analyses: 10, 30, 90, 540, 1440, and 2880 min postinjection. The blood (collected by heart puncture), heart, lungs, liver, stomach, spleen, intestines, kidney, and carcass (divided into three portions) were weighed, and the amount of radioactivity present in each organ was quantified. For the 24- and 48-h time points, mice were housed in metabolic cages to allow for the collection of urine and feces. The amount of radioactivity recovered was on average 86 ± 9% of that injected; we attribute the nonquantitative recoveries to injection variability. The data were corrected for radioactive decay and plotted as % of injected dose per gram of organ versus time and as % of injected dose per organ versus time for each organ (Figure 3).

The % of the injected dose per gram (% ID/g) of blood versus time curve was analyzed using a two-compartment model, since ln[% ID/g] versus time curves clearly displayed two different rates of decay for early and late time points. The pharmacokinetic parameters for the two-compartment model were estimated using the residuals method (*27*). A complete list of pharmacokinetic parameters is presented in Table 2.

For urine analysis at 24 h, 1.0 mL of urine was loaded onto a PD-10 column and eluted in 1.0 mL fractions to

Table 2. Pharmacokinetic Parameters for 1−3[a]

	1	2	3
$t_{1/2,\beta}$ (h)	14 ± 2	19 ± 2	44 ± 9
$t_{1/2,\alpha}$ (h)	0.9 ± 0.2	1.3 ± 0.9	1.1 ± 0.6
k_{21} (min^{-1})	0.0040 ± 0.0003	0.0054 ± 0.0005	0.0055 ± 0.0007
k_{12} (min^{-1})	0.007 ± 0.002	0.003 ± 0.006	0.004 ± 0.006
k_{el} (min^{-1})	0.0025 ± 0.0006	0.0010 ± 0.0007	0.0005 ± 0.0003
C_o (% ID/g)	40 ± 3	41 ± 4	38 ± 5
V_1 (g blood)	2.5 ± 0.2	2.5 ± 0.2	2.6 ± 0.3
$AUC_{0-\infty}$ (% ID·min·g^{-1})	16000 ± 3000	40000 ± 4000	80000 ± 20000

[a] Parameters were extracted from %ID/g blood curves assuming a two-compartment model, where the concentration of radioactivity in the blood is represented by the equation: $C = Ae^{-\alpha t} + Be^{-\beta t}$. Values for A, α, B, and β were calculated using the residuals method (*27*). Definitions: $t_{1/2,\beta}$, elimination half-life; $t_{1/2,\alpha}$, distribution half-life; k_{21}, rate of polymer loss from central to peripheral compartment; k_{12}, rate of polymer loss from peripheral to central compartment; k_{el}, rate of elimination from the central compartment; C_o, concentration of polymer in central compartment after injection but before clearance or loss to peripheral compartments; V_1, apparent volume of the central compartment; $AUC_{0-\infty}$, area under the % ID/g blood curves from zero to infinity.

separate high MW components from lower ones by size exclusion chromatography. Radioactivity was found to elute from the column in two major fractions. The first fractions (1−6) contained high MW species, and the second fractions (7 and above) contained low MW species. The recovery of radioactivity from the columns was quantitative. The percent of the recovered radioactivity found in the high MW fractions for mice given polymers **1**, **2**, and **3**, were 99%, 85%, and 76%, respectively.

For feces analysis at 24 h, ∼400 mg of feces were weighed into a tube containing zirconia beads and 1.0 mL of HBS. The tube was capped, and the feces were homogenized using a Bead Beater (Biospec) for 200 s at 5000 rpm. The solids were centrifuged out, and 50−250 μL of the supernatant was removed, loaded onto a PD-10 column, and eluted in 1.0 mL fractions in the same manner as for the urine analysis. The recovery of radioactivity from the column was quantitative. Again, the first fractions (1−8) contained high MW species, and the second fractions (9 and above) contained low MW species. The percent of the recovered radioactivity found in the high MW fractions in the feces for mice given polymers **1**, **2**, and **3**, was 97%, 91%, and 95%, respectively.

Biodistribution of 1−3 in Tumored Mice. Female 8-week old BALB/c mice were inoculated with C26 tumor cells via subcutaneous injection in the right hind flank on day zero (1×10^6 cells in 50 μL of cell media). On the twelfth day postinoculation, when the tumors were ∼5 mm in diameter, polymer solutions (200 μL) were administered intravenously to the mice (three mice per experimental group). The mice were housed in metabolic cages to allow for the collection of urine and feces, and at 24 h postinjection the mice were sacrificed and the blood (collected by heart puncture), heart, lungs, liver, stomach, spleen, intestines, kidney, tumor, leg muscle, and carcass (divided into three portions) were weighed, and the amount of radioactivity present in each tissue type was quantified. The amount of radioactivity recovered was on average 80 ± 9% of that injected; we attribute the nonquantitative recoveries to injection variability. The data were corrected for radioactive decay and plotted as % of injected dose per gram of organ and as % of injected dose per organ for each organ (Figure 5).

RESULTS AND DISCUSSION

Polymer Synthesis and Characterization. Three dendronized polymers were prepared starting with poly(4-hydroxystyrene) having different backbone lengths (5, 17, and 130 kDa) and low polydispersity indices (PDIs < 1.3). Dendronization was carried out using the previously reported divergent route up to the fourth-generation polyester dendron in each case (Figure 1) (*24*, *25*). The absolute and relative MWs of each polymer, as measured by size exclusion chromatography (SEC), are given in Table 1. The MWs measured by SEC relative to PEO calibration standards are much lower than their absolute MWs measured using an online multiangle laser light scattering (MALLS) detector; PEO-equivalent MWs are reported here because they provide an estimate of the hydrodynamic sizes of the dendronized polymers. The dimensions of the polymers were also measured using dynamic light scattering (DLS) and are presented in Table 1.

In Vitro Cytotoxicity Studies. To determine the biocompatibility of the dendronized polymers, toxicity experiments were performed in vitro with MDA-MB-231 human breast cancer cells. After a 48 h incubation period, cell viability was evaluated using the MTT assay (Figure 2). Over the concentration range investigated, the polymers did not exhibit high levels of toxicity, with greater than 85% cell viability at a concentration of 0.25 mg/mL and greater than 70% viability at the highest concentration tested (3.00 mg/mL).

In Vivo Biodistribution Studies in Nontumored Mice. After determining that cells were viable in the presence of the dendronized polymers, in vivo experiments were performed to determine their time-dependent biodistribution profiles in mice. To track the polymers in vivo, a small fraction of the peripheral hydroxyl groups of each dendronized polymer were statistically converted to tyramine carbamates, and the polymers were then radiolabeled with ^{125}I as previously described (*8*, *26*).

Polymer solutions were administered intravenously to 6−8 week-old CD-1 female mice, and their tissue distribution profiles were monitored over time. Polymer **1** showed little tissue-specific accumulation as a function of time (Figures 3a,b). The kidney was the only organ having elevated polymer levels relative to other den-

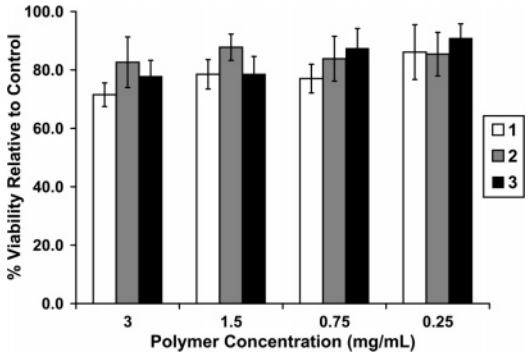

Figure 2. Toxicity of polymers **1**−**3** toward MDA-MB-231 cells.

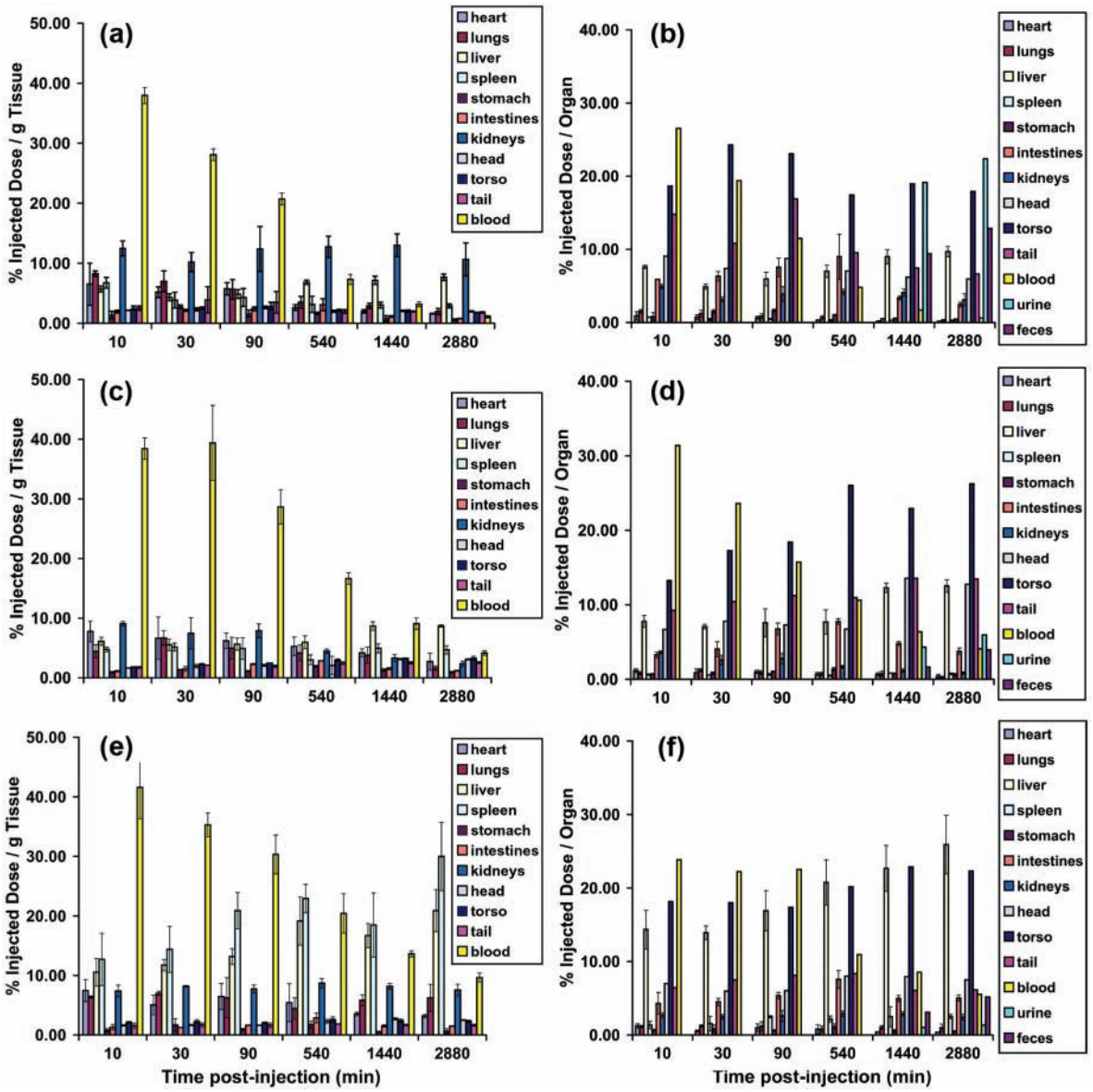

Figure 3. Biodistribution of (a−b) **1**, (c−d) **2**, and (e−f) **3** in CD-1 mice, plotted as % injected dose per gram of tissue versus time and % injected dose per organ versus time. The values at 10 min in (a) and the values at 30 min in (e) are averages for two mice, and the error bars therefore represent the range of two values. In b, d, and f, error bars have been omitted from the head, torso, tail, and blood values because the volume/mass recovered from these tissues can vary widely from mouse to mouse. Error bars have been omitted from the feces and urine values because the respective excrements for each time point were not collected individually but were pooled together.

dronized polymers studied (% injected dose/g (%ID/g) > 10%). This kidney accumulation was accompanied by substantial renal clearance, with 19% and 22% of the injected radioactivity excreted into the urine after 24 and 48 h. The small increase in the amount of radioactivity present in the urine 48 h postinjection when compared to the amount present 24 h postinjection indicates that the majority of the polymer was excreted within the initial 24 h. After determining that the data was best described by a two-compartment distribution model, the elimination half-life of **1** was calculated to be 14 h (Table 2).

A notable feature of this experiment is the lack of significant liver accumulation. Previous biodistribution experiments in which the radiolabel was placed at the periphery of a PEO star polymer suffered from rapid accumulation in the liver, a finding that was attributed to the interaction of exposed iodophenols with complementary receptors (*26*). In the present case, however, the radiolabeled phenols are likely shielded within the dense branches of the dendronized structure. It is also possible that a small number of defects (lack of dendron growth) along the poly(4-hydroxystyrene) backbone lead to iodination of the highly encapsulated phenolic backbone itself.

As shown in Figures 3c,d, polymer **2** showed no unusual tissue accumulation. Compared to polymer **1**, the amount of radioactivity lost in the urine was significantly lower for polymer **2**, with only 6% of the initial dose present in the urine after 48 h. Consequently, the lack of renal clearance resulted in increased blood concentrations of radioactivity for **2** throughout the experiment, with an elimination half-life of 19 h, and in total only 10% of the initial dose was excreted in the urine and feces combined after 48 h.

The biodistribution profile of the largest evaluated dendronized polymer **3** differed significantly from that of the previous two polymers (Figures 3e,f). Like **2**, polymer **3** was cleared very slowly from the body, with only 6.5% excreted after 48 h (urine + feces). The elimination half-life for this high MW polymer was 44 h. Most striking was the steady increase in polymer concentra-

tions in the liver and spleen with time. In these organs, maximum polymer concentrations of 21% ID/g in the liver and 30% ID/g in the spleen were reached 48 h after injection. In comparison, mice given polymers **1** or **2** had 3% or 5%, respectively, in the spleen, and 8% or 9%, respectively, in the liver. Previous studies have shown that as polymer MW increases PEO is taken up by Kupffer cells (*28*) and poly(vinylpyrrolidone) is taken up by macrophages (*29*) to a greater extent, and a high level of uptake in reticuloendothelial cell-rich organs is not uncommon for large particles such as liposomes and nano/microparticles (*30*).

In the case of particles, uptake is believed to be caused either by filtration in the spleen if their diameters are greater than 200 nm, or by opsonization (absorption of phagocytosis-stimulating proteins) (*31*). If we consider that the size of **3** measured by DLS is ~16 nm, it seems unlikely that splenic filtration is occurring, unless polymer aggregation occurs in vivo. However, filtration should not be ruled out, as this polymer is expected to be much less flexible than a nondendronized polymer of an equivalent hydrodynamic size, and its end-to-end dimensions might not be accurately represented in DLS measurements (*25*). While opsonization is another possibility, it would be surprising, as this behavior was not observed for the two other polymers that have the same surface functionality. Further examination will be necessary to deduce the source of the high reticuloendothelial system accumulation of **3**, and to determine whether this uptake is caused by the molecular size, shape, surface chemistry, or some combination of the three.

It is important to note that in the urine, SEC analysis revealed that for mice given polymers **1**, **2**, and **3**, 99%, 85%, and 76% of the total excreted radioactivity was associated with high MW species (Figure 4a), respectively, while in the feces, greater than 90% of water-soluble radioactivity was attributable to high MW compounds (Figure 4b). We were unable to assess the high/low MW nature of the radioactivity that remained insoluble in the feces by this method; however, we were able to estimate the amount of radioactivity that was made soluble as ~100%, ~60%, and ~20% from the feces of mice given polymers **1**, **2**, and **3**, respectively. Since the water solubilities of the dendronized polymers decrease as the polymer chain length increases, and because we would expect small molecule radioactive components to have good water solubility, we believe that the low solubility of radioactivity found in the feces of mice treated with larger polymers indicates that the insoluble radioactivity is associated with high MW material. The small quantity of low MW species excreted by the mice does not amount to more than a few percent of the total injected dose, and therefore we are confident that our data reflects the biodistribution behavior of the polymers and not that of free iodine.

Overall, the results indicate that polymer **1** was small enough to pass through pores of the renal membrane, while polymers **2** and **3** were too large to undergo this process (*32*). Therefore, the apparent MW cutoff for glomerular filtration is between 67 and 251 kDa (M_n) for these fourth-generation dendronized polymers. If the hydrodynamic sizes of these polymers relative to PEO (as measured by SEC, Table 1) are considered, their blood clearance rates are consistent with the reported nominal MW cutoff for PEO of 30−40 kDa (*33*).

In Vivo Biodistribution Studies in Tumored Mice. Recently, Uzgiris has speculated that due to enhanced reptation, linear polymers with extended backbone conformations may be able to more easily traverse the porous capillary walls found in tumor tissues than would a linear polymer in a predominantly coiled conformation (*19*, *20*). Since the dendronized linear polymers presently under study have been shown to have extended conformations in solution (*25*), preliminary biodistribution experiments were performed in BALB/c mice bearing subcutaneous C26 tumors at a single 24 h time point to determine their propensity for tumor accumulation. Polymers **1**, **2**, and **3** were found to be present in the excised tumors at concentrations of 6%, 18%, and 14% ID/g, respectively (Figure 5). The significantly lower concentration of **1** found in the tumor is likely a consequence of its shorter blood circulation half-life. In contrast, **2** and **3** have increased access to the tumor vasculature due to their long-circulating nature and thus have sufficient time for the EPR effect to take place (*34*), resulting in higher concentrations of polymer in the tumors. Interestingly, the polymer concentration in the tumor for **3** was not statistically different from that of **2**, even though it is 7-fold larger in mass and has a 2-fold longer blood elimination half-life. The levels of tumor accumulation found for **2** and **3** are comparable with those of drug carriers based on liposomes (*35*) and are among the highest published values for this tumor model. At present we are unable to determine whether the conformations of the polymers have any effect on their ability to access the interstitial space of the tumor due to a lack of relevant model polymers. Studies seeking to answer this question are underway.

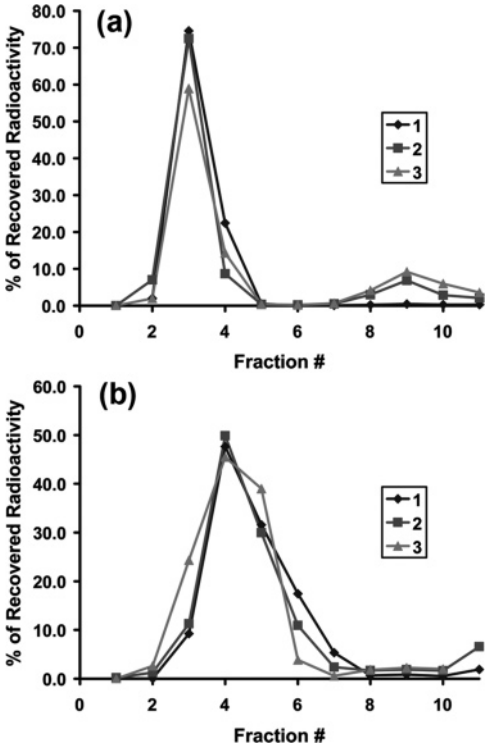

Figure 4. (a) Size exclusion chromatography of urine collected from mice 24 h postinjection. Fraction no. 11 is actually the sum of fractions 11−20. (b) Size exclusion chromatography of the soluble materials from homogenized feces collected from mice 24 h postinjection. For polymers 1 and 2, fraction no. 11 is actually the sum of fractions 11−20. For polymer 3, fraction no. 10 is actually the sum of fractions 10−19.

Conclusions. In conclusion, we have shown that highly functionalizable, nontoxic, dendronized polymers represent a promising new scaffold for polymeric drug delivery systems. As with linear polymers, a positive correlation was observed between the size of the dendronized polymer and its blood circulation time. The long-

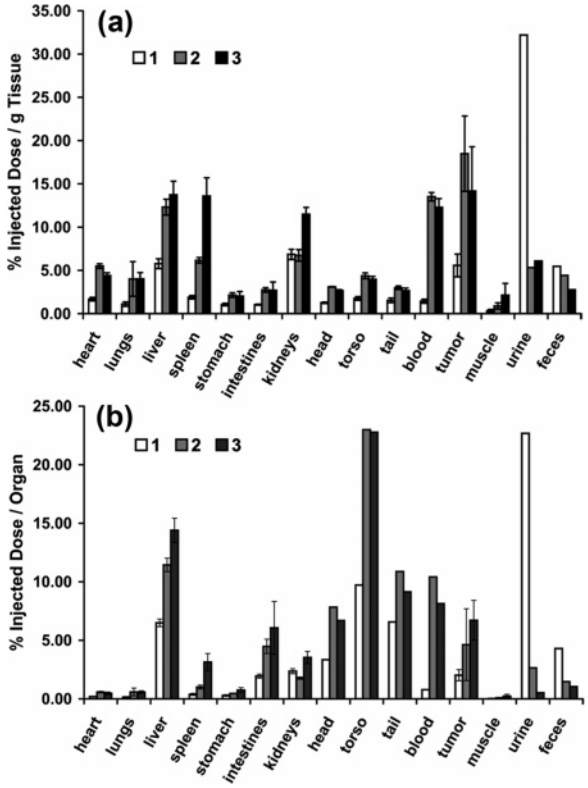

Figure 5. Biodistribution of **1**, **2**, and **3** in BALB/c mice bearing subcutaneous C26 tumors, plotted as (a) % injected dose per gram of tissue versus time and (b) % injected dose per organ versus time. Error bars have been omitted from the head, torso, tail, and blood values because the volume/mass recovered from these tissues can vary widely from mouse to mouse. Error bars have been omitted from the feces and urine values because the respective excrements for each time point were not collected individually but were pooled together. In a, the mean concentrations of radioactivity in the tumor were significantly different between **1** and **2** and **1** and **3** ($P < 0.05$) but not **2** and **3** ($P = 0.16$).

circulating nature of these high MW polymers is advantageous for their development as drug carriers since it has been shown that enhanced tumor accumulation is observed for polymers with long circulation half-lives, a feature that was successfully demonstrated in our preliminary biodistribution experiments. Therefore, future work will focus on the application of these novel polymers as carriers of anticancer drugs. In addition, as total body clearance of the higher MW polymers was low (≤10%), future studies will utilize polymers with degradable backbones to prevent long-term accumulation (*36*).

ACKNOWLEDGMENT

Financial support of this research by the National Institutes of Health (GM 65361 and EB 002047) is acknowledged with thanks. Fellowship support for M.Y. from the Japan Society for the Promotion of Science (JSPS) is gratefully acknowledged. We thank De Li for assistance with size exclusion chromatography studies, and we also thank Ann Fischer at the University of California Tissue Culture Facility for assistance with cell studies.

LITERATURE CITED

(1) Duncan, R. (2003) The dawning era of polymer therapeutics. *Nat. Rev. Drug Discovery* 2, 347−360.

(2) Maeda, H., Seymour, L. W., and Miyamoto, Y. (1992) Conjugates of anticancer agents and polymers: Advantages of macromolecular therapeutics in vivo. *Bioconjugate Chem. 3*, 351−362.

(3) Maeda, H., Wu, J., Sawa, T., Matsumura, Y., and Hori, K. (2000) Tumor vascular permeability and the EPR effect in macromolecular therapeutics: A review. *J. Controlled Release 65*, 271−284.

(4) Greenwald, R. B., Choe, Y. H., McGuire, J., and Conover, C. D. (2003) Effective drug delivery by PEGylated drug conjugates. *Adv. Drug Delivery Rev. 55*, 217−250.

(5) Kopecek, J., Kopeckova, P., Minko, T., and Lu, Z. (2000) HPMA copolymer-anticancer drug conjugates: Design, activity, and mechanism of action. *Eur. J. Pharm. Biopharm. 50*, 61−81.

(6) Rihova, B. and Kubackova, K. (2003) Clinical implications of *N*−(2-hydroxypropyl)methacrylamide copolymers. *Curr. Pharm. Biotechnol. 4*, 311−322.

(7) Ihre, H. R., Padilla de Jesús, O. L., Szoka, F. C., Jr., and Fréchet, J. M. J. (2002) Polyester dendritic systems for drug delivery applications: Design, synthesis, and characterization. *Bioconjugate Chem. 13*, 443−452.

(8) Padilla de Jesús, O. L., Ihre, H. R., Gagne, L., Fréchet, J. M. J., and Szoka, F. C., Jr. (2002) Polyester dendritic systems for drug delivery applications: In vitro and in vivo evaluation. *Bioconjugate Chem. 13*, 453−461.

(9) Gillies, E. R. and Fréchet, J. M. J. (2002) Designing macromolecules for therapeutic applications: Polyester dendrimer-poly(ethylene oxide) "bow-tie" hybrids with tunable molecular weight and architecture. *J. Am. Chem. Soc. 124*, 14137−14146.

(10) Malik, N., Wiwattanapatapee, R., Klopsch, R., Lorenz, K., Frey, H., Weener, J. W., Meijer, E. W., Paulus, W., and Duncan, R. (2000) Dendrimers: relationship between structure and biocompatibility in vitro, and preliminary studies on the biodistribution of 125I-labeled polyamidoamine dendrimers in vivo. *J. Controlled Release 65*, 133−148.

(11) Shamis, M., Lode, H. N., and Shabat, D. (2004) Bioactivation of self-immolative dendritic prodrugs by catalytic antibody 38C2. *J. Am. Chem. Soc. 126*, 1726−1731.

(12) Stiriba, S. E., Frey, H., and Haag, R. (2002) Dendritic polymers in biomedical applications: From potential to clinical use in diagnostics and therapy. *Angew. Chem., Int. Ed. 41*, 1329−1334.

(13) DeNardo, S. J., Yao, Z., Lam, K. S., Song, A., Burke, P. A., Mirick, G. R., Lamborn, K. R., O'Donnell, R. T., and DeNardo, G. L. (2003) Effect of molecular size of pegylated peptide on the pharmacokinetics and tumor targeting in lymphoma-bearing mice. *Clin. Cancer Res. 9*, 3854S−3864S.

(14) Gillies, E. R., Dy, E., Fréchet, J. M. J., and Szoka, F. C. (2005) Biological evaluation of polyester dendrimer: poly(ethylene oxide) "bow-tie" hybrids with tunable molecular weight and architecture. *Mol. Pharm. 2*, 129−138.

(15) Schlüter, A. D. and Rabe, J. P. (2000) Dendronized polymers: Synthesis, characterization, assembly at interfaces, and manipulation. *Angew. Chem., Int. Ed. 39*, 864−883.

(16) Bohrer, M. P., Deen, W. M., Robertson, C. R., Troy, J. L., and Brenner, B. M. (1979) Influence of molecular configuration on the passage of macromolecules across the glomerular capillary wall. *J. Gen. Physiol. 74*, 583−593.

(17) Ohlson, M., Sorenson, J., Lindstrom, K., Blom, A. M., Fries, E., and Haraldsson, B. (2001) Effects of filtration rate on the glomerular barrier and clearance of four differently shaped molecules. *Am. J. Physiol. Renal Physiol. 281*, F103−F113.

(18) Mammen, M., Choi, S. K., and Whitesides, G. M. (1998) Polyvalent interactions in biological systems: Implications for design and use of multivalent ligands and inhibitors. *Angew. Chem., Int. Ed. 37*, 2755−2794.

(19) Uzgiris, E. (2004) The role of molecular conformation on tumor uptake of polymeric contrast agents. *Invest. Radiol. 39*, 131−137.

(20) Uzgiris, E. E., Cline, H., Moasser, B., Grimmond, B., Amaratunga, M., Smith, J. F., and Goddard, G. (2004) Conformation and structure of polymeric contrast agents for medical imaging. *Biomacromolecules 5*, 54−61.

(21) Grayson, S. M. Ph.D. Dissertation, University of California, Berkeley, CA, 2002.

(22) Gossl, I., Shu, L. J., Schluter, A. D., and Rabe, J. P. (2002) Molecular structure of single DNA complexes with positively charged dendronized polymers. *J. Am. Chem. Soc. 124*, 6860−6865.

(23) Ghosh, S. (2004) Novel poly(ethylene glycol) embedded polyamidoamine side chain dendritic polyurethane architecture: Synthesis and preliminary studies on the cytotoxicity and interaction with tryptophan molecule. *Biomacromolecules 5*, 1602−1605.

(24) Grayson, S. M., and Fréchet, J. M. J. (2001) Divergent synthesis of dendronized poly(p-hydroxystyrene). *Macromolecules 34*, 6542−6544.

(25) Yoshida, M., Fresco, Z. M., Ohnishi, S., and Fréchet, J. M. J. (2005) Efficient divergent synthesis of dendronized polymers with extremely high molecular weight: Structural characterization by SEC-MALLS and SFM and novel organic gelation behavior. *Macromolecules 38*, 334−344.

(26) Larwood, D. J., and Szoka, F. C. (1984) Synthesis, characterization, and in vivo disposition of iodinatable polyethyleneglycol derivatives: Differences in vivo as a function of chain-length. *J. Labelled Compd. Radiopharm. 21*, 603−614.

(27) Welling, P. G. (1986) The two-compartment open model with intravenous or oral administration. *Pharmacokinetics*, pp 213−240, Chapter 14, American Chemical Society, Washington, DC.

(28) Yamaoka, T., Tabata, Y., and Ikada, Y. (1994) Distribution and tissue uptake of poly(ethylene glycol) with different molecular weights after intravenous administration to mice. *J. Pharm. Sci. 83*, 601−606.

(29) Duncan, R., Pratten, M. K., Cable, H. C., Ringsdorf, H., and Lloyd, J. B. (1981) Effect of molecular size of I-125-labeled poly(vinylpyrrolidone) on its pinocytosis by rat visceral yolk sacs and rat peritoneal macrophages. *Biochem. J. 196*, 49−55.

(30) Barratt, G. (2003) Colloidal drug carriers: Achievements and perspectives. *Cell. Mol. Life Sci. 60*, 21−37.

(31) Moghimi, S. M., Hunter, A. C., and Murray, J. C. (2001) Long-circulating and target-specific nanoparticles: Theory to practice. *Pharmacol. Rev. 53*, 283−318.

(32) Drobnik, J., and Rypacek, F. (1984) Soluble synthetic polymers in biological systems. *Adv. Polym. Sci. 57*, 1−50.

(33) Murakami, Y., Tabata, Y., and Ikada, Y. (1997) Tumor accumulation of poly(ethylene glycol) with different molecular weights after intravenous injection. *Drug Delivery 4*, 23−31.

(34) Maeda, H. (2001) The enhanced permeability and retention (EPR) effect in tumor vasculature: The key role of tumor-selective macromolecular drug targeting. *Adv. Enzyme Regul. 41*, 189−207.

(35) Huang, S. K., Mayhew, E., Gilani, S., Lasic, D. D., Martin, F. J., and Papahadjopoulos, D. (1992) Pharmacokinetics and therapeutics of sterically stabilized liposomes in mice bearing C-26 colon carcinoma. *Cancer Res. 52*, 6774−6781.

(36) Lee, C. C., Grayson, S. M., and Fréchet, J. M. J. (2004) Synthesis of narrow-polydispersity degradable dendronized aliphatic polyesters. *J. Polym. Sci., Part A: Polym. Chem. 42*, 3563−3578.

BC0497665

Near-Infrared Optical Imaging of B16 Melanoma Cells via Low-Density Lipoprotein-Mediated Uptake and Delivery of High Emission Dipole Strength Tris[(porphinato)zinc(II)] Fluorophores

Sophia P. Wu,[†] Intae Lee,[‡] P. Peter Ghoroghchian,[†,§] Paul R. Frail,[†] Gang Zheng,[‡] Jerry D. Glickson,[‡] and Michael J. Therien*[,†]

Department of Chemistry, University of Pennsylvania, 231 South 34th Street, Philadelphia, Pennsylvania 19104-6323, Department of Radiology, University of Pennsylvania, 423 Guardian Drive, Philadelphia, Pennsylvania 19104, and Department of Bioengineering, University of Pennsylvania, 3320 Smith Walk, Philadelphia, Pennsylvania 19104-6392. Received October 28, 2004; Revised Manuscript Received March 17, 2005

Meso-to-*meso* ethyne-bridged tris[(porphinato)zinc(II)] (**PZn$_3$**) near-infrared (NIR) fluorophores (λ_{em}^{max} ~800 nm) can be rendered sufficiently amphiphilic to enable their facile incorporation into the hydrophobic core of the apo form of low-density lipoprotein (apo-LDL). These NIR fluorophores are notable in that they manifest low energy excited states polarized exclusively along the long axis of the supermolecule, broad spectral coverage of the visible and high energy NIR spectral domains, intense $S_0 \rightarrow S_1$ transition moments, and comparably large $S_1 \rightarrow S_0$ emission dipole strengths. The reconstituted LDL(**PZn$_3$**) proteins can be used to deliver rapidly hundreds of copies of **PZn$_3$** to a given murine B16 melanoma cell via LDL receptor-mediated endocytosis. **PZn$_3$**-based NIRFs and their corresponding LDL(**PZn$_3$**) proteins have been shown to display minimal cytotoxicity. Confocal NIR fluorescence microscopy evinces that B16 cells can be imaged at very low doses (~nM) of NIRF. The highly attractive photophysical properties of **PZn$_3$** and closely related chromophores, coupled with their lack of toxicity and compatibility with uptake into apo-LDL and subsequent rapid delivery to B16 cells via LDLr-mediated endocytosis, suggest the potential utility of this platform for NIR optical imaging of cancer cells in vivo.

INTRODUCTION

The utilization of near-infrared (NIR) probes in cancer prevention/detection strategies has attracted attention due to the facts that (i) light scattering in tissue decreases with the reciprocal of the fourth power of wavelength (λ^{-4}), (ii) the NIR spectral domain provides a substantial optical window where hemoglobin and water absorption are minimal, and (iii) such optically based imaging technology, if realized, would presumably be inexpensive, mobile, and free of the biological effects associated with radiological probes (*1*, *2*). Key to making such a modality a viable means to image deep tissue is the development of strategies that enable adequate NIR optical signal output per cellular recognition event.

Deep tissue optical imaging requires both delineation of drastically superior fluorescent probes and delivery platforms that guarantee emissive signatures orders of magnitude greater than that provided by a single NIR fluorophore (NIRF). With respect to conventional NIRFs, indocyanine green (ICG), currently the only FDA-approved NIR imaging dye, suffers from both a modest fluorescence quantum yield (*3*) and a dominance of nonradiative excited state dynamics in physiological environments (*4*, *5*). Fluorescence-based optical imaging within the NIR spectral window (~710−950 nm) thus requires the development of new classes of biologically compatible chromophores that emit at long wavelengths with high emission dipole strengths; ideally, such NIRFS should possess emission maxima (λ_{em}^{max}) ≥ 800 nm to permit maximal photon penetration of living tissues (*6*−*8*).

Targeted NIR contrast agent delivery for in vivo optical imaging has exploited NIRF coupling to (i) peptide conjugates preferentially activated by cancer cells (*9*, *10*), (ii) receptor specific peptides that include somatostatin analogues (*11*−*14*), and (iii) monoclonal antibodies (*15*, *16*). While successful targeting and imaging of neoplastic tissue via each of these approaches has been demonstrated, these methods typically rely upon cell surface receptor recognition events involving conjugates featuring a single NIRF.

A promising method for packaging and delivery of multiple fluorophores involves reconstitution of NIRFs into the core of low-density lipoprotein (LDL) (*17*−*20*). LDL, an endogenous constituent of blood, is a particle 20−30 nm in diameter containing a core of neutral cholesterol esters and triglycerides surrounded by a polar shell of phospholipids, unesterified cholesterol, and apolipoprotein B100 that is recognized by the LDL receptor (LDLr) (*21*). Because of the high cholesterol demand of rapidly dividing cells, a number of tumor cells, such as acute myeloid leukemia, epidermoid cervical cancer, and squamous lung tumor, overexpress LDLr (*22*). This fact, coupled with the observation that LDL, due to its nanoscale dimensions, penetrates even solid tumors (*17*), has made it an attractive platform for delivery of a wide range of hydrophobic compounds (*23*, *24*) that include antitumoral drugs (*20*, *25*−*28*), photodynamic therapy

* To whom correspondence should be addressed. Tel: 215-898-0087. Fax: 215-898-6242. E-mail: therien@sas.upenn.edu.
[†] Department of Chemistry.
[‡] Department of Radiology.
[§] Department of Bioengineering.

10.1021/bc0497416 CCC: $30.25 © 2005 American Chemical Society
Published on Web 04/30/2005

agents (*18*, *19*, *29*, *30*), and imaging dyes (*31*, *32*) to neoplastic tissues.

We report herein the reconstitution of LDL with *meso*-to-*meso* ethyne-bridged tris[(porphinato)zinc(II)] (**PZn_3**) fluorophores. These NIRFs and their structurally related analogues manifest low energy excited states polarized exclusively along the long axis of the supermolecule (*33*−*42*), intense $S_0 \rightarrow S_1$ transition moments, and comparably large $S_1 \rightarrow S_0$ emission dipole strengths (*33*, *36*, *37*, *40*). We show further via in vitro experiments that **PZn_3**-containing LDL particles deliver the core NIRFs to murine B16 melanoma cells via the LDLr pathway, which can be subsequently imaged using scanning fluorescence confocal microscopy.

EXPERIMENTAL PROCEDURES

Synthesis. All manipulations were carried out under nitrogen previously passed through an O_2 scrubbing tower (Schweitzerhall R3-11 catalyst) and a drying tower (Linde 3 Å molecular sieves) unless otherwise stated. Air sensitive solids were handled in a Braun 150-M glovebox. Standard Schlenk techniques were employed to manipulate air sensitive solutions. CH_2Cl_2 and tetrahydrofuran (THF) were distilled from CaH_2 and K/4-benzoylbiphenyl, respectively, under N_2. *N*,*N*-Dimethylformamide (DMF) and triethylamine (TEA) were dried over $MgSO_4$ and KOH, respectively, and distilled under reduced pressure. Absolute ethanol was used as received from Fisher Scientific. All NMR solvents were used as received. The catalysts tris(dibenzylideneacetone)dipalladium(0) and triphenylarsine ($AsPh_3$) were purchased from Strem Chemicals and used as received. 1-Hydroxybenzotriazole (HoBt) and *N*-methylmorpholine (NMM) (Acros) as well as (benzotriazol-1-yloxy)tripyrrolidinophosphonium hexafluorophosphate (PyBOP) (Nova Biochem) were used as received. 5,15-Bis[[5′,10′,20′-bis[3,5-di(3,3-dimethyl-1-butyloxy)phenyl]porphinato)zinc(II)]ethynyl]-10,20-bis-[3,5-di(9-methoxy-1,4,7-trioxanonyl)phenyl]porphinato)-zinc(II) (**PZn_3a**), (5-ethynyl-10,20-bis[3′,5′-bis(3,3-dimethyl-1-butyloxy)phenyl]porphinato)zinc(II) (**1**), (5,15-dibromo-10,20-bis[3′,5′-bis(3,3-dimethyl-1-butyloxy)-phenyl]-porphinato)zinc(II) (**2**) (*38*), [5-ethynyl-10,20-diphenyl-porphinato]zinc(II) (**3**) (*34*, *43*), and 5-androsten-17β-amino-3β-yl oleate (**4**) (*29*) were synthesized according to literature procedures.

Chemical shifts for ^{1}H NMR spectra are reported relative to residual protium in the deuterated solvents ($CDCl_3$, $\delta = 7.24$ ppm; DMF-d_7, $\delta = 8.03$ ppm; pyridine-d_5, $\delta = 8.74$ ppm; and DMSO-d_6, $\delta = 2.50$ ppm). The number of attached protons is found in parentheses following the chemical shift value. Flash and size exclusion column chromatography were performed on the benchtop, using, respectively, silica gel (EM Science, 230−400 mesh) and Bio-Rad Bio-Beads SX-1 as media. Electrospray ionization (ESI-MS) data were obtained in the University of Pennsylvania Chemistry Mass Spectrometry Facility. Fast atom bombardment (FAB) mass spectrometry was performed at the Mass Spectrometry Center of Drexel University, while matrix-assisted laser desorption/ionization time-of-flight (MALDI-TOF) mass spectra were obtained using a Perspective Voyager DE instrument in the Laboratory of Dr. William DeGrado (Department of Biophysics and Biochemistry, University of Pennsylvania). Samples for MALDI-TOF mass spectra were prepared as micromolar solutions in THF; dithranol or 1,4-bis(5-phenyoxazol-2-yl)benzene (Aldrich) was utilized as the matrix.

Instrumentation. Electronic spectra were recorded on an OLIS UV−vis/NIR spectrophotometry system that is based on the optics of a Cary 14 spectrophotometer. Emission spectra were recorded on a SPEX Fluorolog luminescence spectrophotometer that utilized a T-channel configuration with a red sensitive R2658 Hamamatsu PMT and liquid nitrogen-cooled InGaAs and extended InGaAs detectors; these spectra were corrected using a calibrated light source supplied by the National Bureau of Standards. NMR spectra were recorded on either 250 MHz AC-250 or 360 MHz DMX-360 Brüker spectrometers. Confocal microscopy experiments were performed at the Bioengineering Confocal and Multiphoton Core Facilities at the University of Pennsylvania using a Biorad Radiance 2000-MP laser scanning confocal microscope and a Nikon Eclipse TE-300 CCD camera.

(4-Formyl-phenoxy)acetic Acid Ethyl Ester (5). The reaction conditions for this precursor are analogous to those reported in the literature (*44*). A 200 mL round-bottom flask was charged with of 4-hydroxybenzaldehyde (6.5 g, 53 mmol), ethyl bromoacetate (9.78 g, 58.5 mmol), potassium carbonate (8.08 g, 58.5 mmol), and 100 mL of acetone. The reaction mixture was brought to a gentle reflux overnight. It was then diluted with water and extracted thrice with ethyl ether. The combined ether layers were then washed three times with 2 M KOH solution and once with water. The organic layer was then dried over Na_2SO_4 and evaporated to yield a yellow oil (15.3 g, 90% yield based on mass of 4-hydroxybenzaldehyde). ^{1}H NMR (250 MHz, $CDCl_3$): δ 9.88 (s, 1 H), 7.82 (d, 2 H, $J = 4.6$ Hz), 7.0 (d, 2 H, $J = 4.6$ Hz), 4.69 (s, 2 H), 4.25 (q, 2 H, $J = 7.0$ Hz), 1.25 (t, 3 H, $J = 7.0$ Hz) ppm. HRMS (M^+): 208.0734 (calcd 208.0735).

5,15-Di[((4-ethyl ester)methyleneoxy)phenyl]porphyrin (6). 2,2′-Dipyrrylmethane (*45*, *46*) (1.54 g, 10.5 mmol) and **5** (2.19 g, 10.5 mmol) were brought together in a 2 L round-bottom flask containing 1.5 L of dry methylene chloride and a magnetic stir bar under N_2. Triflouroacetic acid (0.16 mL, 2.1 mmol) was added to this mixture; the flask was then covered with aluminum foil and stirred at room temperature for 14 h. 2,3-Dichloro-4,5-dicyanoquinone (3.58 g, 15.75 mmol) was added to the methylene chloride solution, and the mixture was allowed to stir for 15 min before the solvent was removed under reduced pressure. The reaction mixture was then purified by silica chromatography using 99:1 CH_2Cl_2:methanol as the eluant, to give 1.5 g of the isolated product (43% yield based on 1.54 g of the dipyrrylmethane starting material). Vis (CH_2Cl_2) λ_{max} nm (log ϵ): 408 (5.37), 504 (4.17), 539 (3.79), 577 (3.75), 632 (3.37). ^{1}H NMR (250 MHz, $CDCl_3$): δ 10.29 (s, 2 H), 9.37 (d, 4 H, $J = 4.65$ Hz), 9.07 (d, 4 H, $J = 4.65$ Hz), 8.16 (d, 4 H, $J = 7.95$ Hz), 7.28 (d, 4 H, $J = 7.95$ Hz) 5.53 (s, 4 H), 4.40 (q, 4 H, $J = 7.28$ Hz), 1.42 (t, 6 H, $J = 7.30$ Hz), −3.02 (broad s, 2 H) ppm. HRMS (MH^+): 667.2573 (calcd 667.2537).

5,10-Dibromo-10,20-di[((4-ethyl ester)methyleneoxy)phenyl]porphyrin (7). In a 1.0 L round-bottomed flask, **6** (600 mg, 0.9 mmol) was dissolved in 500 mL of methylene chloride. *N*-Bromosuccinimide (320 mg, 1.8 mmol) was then added to the stirring porphyrin solution. The reaction was allowed to proceed for 15 min and quenched by the addition of 30 mL of acetone. The solvents were removed, and the recovered reaction mixture was purified by silica chromatography using methylene chloride as the eluent. Three bands were isolated; the fastest moving band was isolated as the title compound (590 mg, 80% yield based on 600 mg of **6**). Vis ($CHCl_3$) λ_{max} (log ϵ): 415 (5.05), 510 (4.10), 545 (3.78), 586 (3.58) 642 (3.18) nm. ^{1}H NMR (250 MHz, $CDCl_3$): δ 9.60 (d, 2 H, $J = 4.7$ Hz), 8.83 (d, 2H, $J = 4.6$), 8.16 (d,

4H, $J = 7.95$ Hz), 7.28 (d, 4H, $J = 7.95$ Hz) 4.92 (s, 4H), 4.40 (q, 4 H, $J = 7.28$ Hz), 1.42 (t, 6 H, $J = 7.30$ Hz), −2.75 (broad s, 2 H).

[5,10-Dibromo-10,20-di[((4-ethyl ester)methyleneoxy)phenyl]porphinato]zinc(II) (8). Compound **7** (500 mg, 0.6 mmol) and zinc acetate (658 mg, 3 mmol) were refluxed in 400 mL of chloroform in a 1 L round-bottom flask equipped with a magnetic stir bar and a reflux condenser. The reaction was monitored by optical spectroscopy and was complete within 2 h. Once the solvents were evaporated, the reaction mixture was passed down a short silica column with methylene chloride as the eluent. The first band to elute is the desired product (506 mg, 95% yield based on 500 mg of **7**). Vis ($CHCl_3$) λ_{max} (log ϵ): 420 (5.38), 550 (4.10), 590 (3.33) nm. ^{1}H NMR (250 MHz, $CDCl_3$): δ 9.60 (d, 2H, $J = 4.7$ Hz), 8.83 (d, 2H, $J = 4.6$ Hz), 8.0 (d, 4H, $J = 7.95$ Hz), 7.26 (d, 4H, $J = 7.95$ Hz), 4.89 (s, 4H), 4.40 (q, 4 H, $J = 7.28$ Hz), 1.39 (t, 6 H, $J = 7.30$ Hz).

[5,10-Dibromo-10,20-di[((4-carboxy)methyleneoxy)phenyl]porphinato]zinc(II) (9). A 100 mL round-bottom flask was charged with **8** (100 mg, 0.112 mmol) and dissolved in 80 mL of 3:1 THF:EtOH solution. An aqueous solution of KOH (63 mg, 1.12 mmol, 5 mL) was added to the stirred solution. The reaction mixture was refluxed for 2 h, following which the solvents were removed under reduced pressure. The resulting mixture was dissolved in ~20 mL of water and acidified by dropwise addition of concentrated HCl to pH 3. The resulting purple precipitate was filtered and dried to give the desired product (86 mg, 92% yield, based on 100 mg of the dihalogenated (porphinato)zinc(II) starting material). Vis (DMSO) λ_{max} (log ϵ): 435 (5.44), 571 (4.11), 614 (4.07) nm. ^{1}H NMR (250 MHz, DMF-d_6): δ 9.70 ppm (d, 4 H, $J = 4.65$ Hz), 8.90 (d, 4 H, $J = 4.63$ Hz), 8.17 (d, 4 H, $J = 8.4$ Hz), 7.45 (d, 4 H, $J = 8.6$ Hz), 5.09 (s, 4 H) ppm. ESI-MS (MH^+): 830.3 (calcd for $C_{36}H_{22}Br_2N_4O_6Zn$, 830.9). FAB-MS (M^+): 829.6 (calcd 829.9).

[5,10-Dibromo-10,20-di[((4-5-androsten-17β-amino-3β-yl oleate)methyleneoxy)phenyl]porphinato]zinc-(II) (10). [5,10-Dibromo-10,20-di[((4-carboxy)methyleneoxy)phenyl]porphinato]zinc(II) (**9**) (31 mg, 0.0373 mmol), PyBOP (43 mg, 0.0821 mmol), HoBt (11 mg, 0.0821 mmol), and NMM (25 μL, 0.224 mmol) were dissolved in 5 mL of DMF at room temperature and stirred under argon for 30 min. 5-Androsten-17β-amino-3β-yl oleate (**4**) (47 mg, 0.078 mmol), dissolved in approximately 10 mL of DMF, was transferred under Ar to the porphyrin-containing solution. The reaction mixture was stirred at ambient temperature and allowed to proceed until the TLC showed that all of the porphyrin starting material had been consumed (~22 h). The mixture was then diluted with ethyl acetate and washed three times with brine. The combined organic phases were dried over $MgSO_4$ and evaporated. The residue was chromatographed on silica gel using 3:2 hexanes:THF as the eluant, following which it was rechromatographed on silica gel using 99:1 CH_2Cl_2:MeOH as the eluant. The product was isolated as a green solid (12 mg, 38% yield based on 31 mg of **9**). Compound **10** was used immediately in the subsequent cross-coupling reaction described below. Vis (CH_2Cl_2) λ_{max}(log ϵ): 420 (5.38), 550 (4.16), 590 (3.69) nm. ^{1}H NMR (250 MHz, $CDCl_3$): 9.71 (d, 4 H, $J = 4.75$ Hz), 8.84 (d, 4 H, $J = 4.66$ Hz), 8.00 (d, 4 H, $J = 8.41$ Hz), 6.80 (d, 4 H, $J = 7.92$ Hz), 5.40 (s, 4 H), 5.34 (m, 6 H), 5.05 (m, 2 H), 4.65 (m, 2 H), 2.28 (m, 12 H), 1.98 (m, 22 H), 1.3−0.8 (m, cholesteryl oleate alkyl H) ppm. MALDI-TOF MS (M^+): 1936.2 (calcd for $C_{112}H_{152}Br_2N_6O_8Zn$, 1935.6).

5,15-Bis[[5′,-10′,20′-bis((4-5-androsten-17β-amino-3β-yl oleate)methyleneoxy)phenyl]porphinato)-zinc(II)ethynyl]-10,20-(diphenyl)porphinato)zinc-(II)(PZn_3b). Compound **10** (22 mg, 0.0116 mmol), **3** (14 mg, 0.0243 mmol), Pd_2dba_3 (2.7 mg, 0.0029 mmol), $AsPh_3$ (7.1 mg, 0.0232 mmol), and TEA (0.3 mL) were dissolved in THF (20 mL) in a 50 mL Schlenk tube and subjected to three freeze−pump−thaw degas cycles. The mixture was heated at 40 °C under Ar overnight, during which time the solution changed from purple to brown. The solution was then diluted with ethyl acetate, washed three times with water, dried over $MgSO_4$, and evaporated. The residue was purified by flash chromatography on silica gel, using 3:2 hexanes:THF as the eluant, following which it was rechromatograhed on silica gel using CH_2Cl_2 as the eluant. The isolated product was recrystallized from THF/hexanes to give 12 mg of the product (38% yield, based on 22 mg of compound **10**). Vis (CH_2Cl_2) λ_{max} (log ϵ): 421 (5.06), 489 (4.93), 768 (4.61) nm. ^{1}H NMR (99:1 $CDCl_3$:pyridine-d_5): δ 10.44 (d, 4 H, $J = 4.65$ Hz), 10.37 (d, 4 H, $J = 4.65$ Hz), 10.09 (s, 2 H), 9.27 (d, 4 H, $J = 4.43$ Hz), 9.13 (d, 4 H, $J = 4.63$ Hz), 9.01 (d, 4 H, $J = 4.50$ Hz), 8.96 (d, 4 H, $J = 4.43$ Hz), 8.27 (m, 8 H), 7.78 (m, 12 H), 7.36 (d, 4 H, $J = 8.58$ Hz), 6.72 (d, 4 H, $J = 9.18$ Hz), 5.31 (br s, 4 H), 4.84 (s, 6 H), 4.10 (m, 2 H), 3.83 (m, 2 H), 2.30 (m, 12 H), 2.0−0.8 (m, cholesteryl oleate alkyl H) ppm. MALDI-TOF MS (M^+): 2894.0 (calcd for $C_{180}H_{190}N_{14}O_8Zn_3$, 2894.3).

5,15-Bis[(5′,-10′,20′-diphenyl)porphinato)zinc(II)-ethynyl]-10,20-bis[(4-ethyl ester)methyleneoxy)phenyl]porphinato)zinc(II) (PZn_3c). [5-Ethynyl-10,20-diphenylporphinato]zinc (II) (**3**) (50 mg, 0.0885 mmol), **8** (38 mg, 0.0421 mmol), Pd_2dba_3 (9.6 mg, 0.0105 mmol), $AsPh_3$ (26 mg, 0.0842 mmol), THF (20 mL), and TEA (0.1 mL) were brought together in a 50 mL Schlenk tube under Ar and stirred overnight at 50 °C. The reaction mixture was diluted with ethyl acetate, washed three times with water, dried over $MgSO_4$, and evaporated. The residue was chromatographed on silica gel using 3:2 hexanes:THF as the eluant, following which the product was recrystallized from THF/hexanes to yield **PZn_3c** (66 mg, 83% yield based on 38 mg of **8**). Vis (THF) λ_{max} (log ϵ): 412 (5.42), 494 (5.51), 548 (4.34), 576 (4.33), 776 (5.07) nm. ^{1}H NMR (360 MHz, 50:1 $CDCl_3$:pyridine-d_5): 10.46 (d, 2H, $J = 4.7$ Hz), 10.36 (d, 2H, $J = 4.5$ Hz), 10.05 (s, 2H), 9.26 (d, 2H, $J = 4.2$ Hz), 9.13 (d, 2H), 9.04 (d, 2H, $J = 4.5$ Hz), 8.96 (d, 2H, $J = 4.8$ Hz), 8.27 (m, 10H), 7.78 (m, 8H), 4.95 (s, 2H), 4.43 (q, 4H, $J = 7.2$ Hz), 1.43 (t, 6H, $J = 7.1$ Hz). MALDI-TOF MS (M^+): 1826.0 (calcd for $C_{108}H_{68}N_{12}O_6Zn_3$, 1826.0).

5,15-bis[[(5′,-10′,20′-bis[3,5-di(3,3-dimethyl-1-butyloxy)phenyl]porphinato)zinc(II)]ethynyl]-10,20-bis-[(3,5-di(3,3-dimethyl-1-butyloxy)phenyl)porphinato]zinc(II) (PZn_3d). Compounds **1** (84 mg, 0.0885), **2** (46 mg, 0.0421 mmol), Pd_2dba_3 (9.6 mg, 0.0105 mmol), $AsPh_3$ (26 mg, 0.0842 mmol), and TEA (0.1 mL) were dissolved in THF (20 mL) in a 50 mL Schelnk tube and reacted overnight under Ar at 60 °C. The reaction mixture was then diluted with $CHCl_3$, washed three times with water, dried over $CaCl_2$, and evaporated. The residue was chromatographed on silica gel using 17:3 hexanes:THF as the eluant. Trace amounts of a butadiyne-bridged bis-[(porphinato)zinc(II)] contaminant were removed via size exclusion chromatography using THF as the eluant to give 97 mg of the product (82% yield based on 46 mg of **2**). Vis (THF) λ_{max} (log ϵ): 416 (4.85), 493 (4.99), 542 (4.00), 563 (3.97), 760 (4.54) nm. ^{1}H NMR (250 MHz, 50:1 $CDCl_3$:pyridine-d_5): 10.41 (d, 4H, $J = 4.75$ Hz), 10.34 (d, 4H, $J = 4.25$ Hz), 10.03 (s, 2H), 9.23 (d, 8H, $J = 4.5$ Hz),

Scheme 1. Synthetic Route to NIRFs

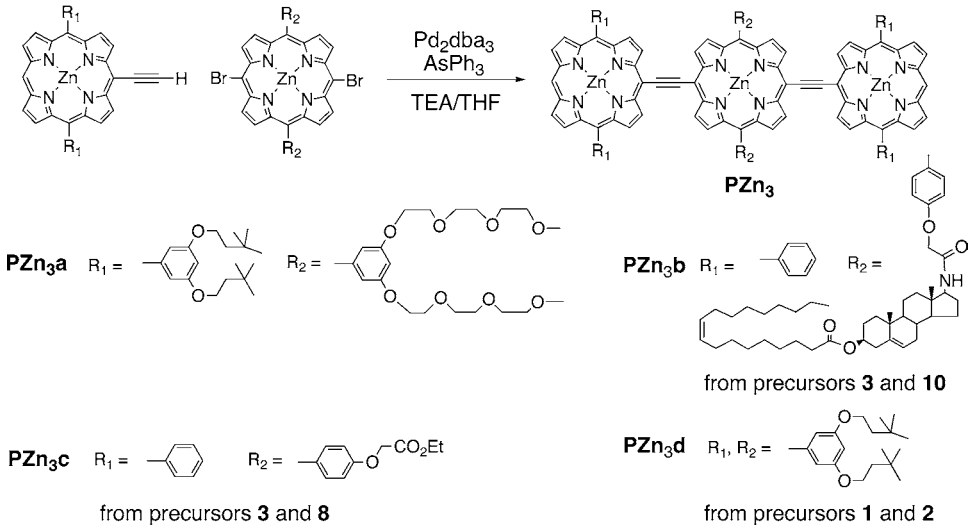

9.13 (d, 4H, $J = 4.5$ Hz), 9.05 (d, 4H, $J = 4.0$ Hz), 7.45 (m, 12H), 6.87 (s, 6H), 4.19 (t, 24H, $J = 7.4$ Hz), 4.16 (s, 6H), 1.83 (t, 24H, $J = 7.4$ Hz), 0.96 (s, 108H). MALDI-TOF MS (M^+): 2823.7 (calcd for $C_{112}H_{200}N_{12}O_{12}Zn_3$, 2823.4).

LDL Reconstitution. A modified version of the classic Krieger reconstitution procedure (*47*) was used. Human LDL was purchased from either Dr. Sissel Lund-Katz, who purified it from serum of patients with familial hypercholesteremia at the Children's Hospital of Philadelphia (*48*), or from Intracel Corporation (Frederick, Maryland). Prior to reconstitution, 1.9 mg of LDL, stored in 150 mM NaCl with 0.01% EDTA at pH 7.2, was dialyzed at 4 °C against a PBS buffer (137 mM NaCl, 2.7 mM KCl, 10 mM phosphate, pH 7.4) containing 0.3 mM EDTA, following which it was lyophilized in the presence of 25 mg of starch in a test tube pretreated with an antiwetting agent (Sigmacote). Endogeneous lipids were extracted by vortexing the lyophilized apoprotein/starch mixture with 5 mL of heptanes. The LDL-containing suspension was centrifuged at 2000 rpm for 10 min, and the supernatant was discarded. This procedure to extract LDL core lipids was repeated two more times. After the heptanes layer was removed for the final time, 6 mg of the appropriate **PZn$_3$**-based NIRF dissolved in 200 μL of benzene was added to the LDL pellet and incubated at 4 °C for 90 min. The organic solvents were then removed under a stream of Ar at −15 °C over a 30 min period. The reconstituted LDL was solubilized by briefly sonicating the residue in 2 mL of tricine buffer (10 mM, pH 8.4); this solution was incubated at 4 °C for 24 h. Starch and excess protein were removed by low-speed centrifugation (2000 rpm) at 4 °C for 10 min. The supernatant was collected and further clarified by centrifuging at 9000 rpm for two 10 min periods. The concentration of the reconstituted LDL solutions was determined by the Lowry method (*49*). Reconstituted LDL was stored under a nitrogen atmosphere at 4 °C. The integrity of the LDL(**PZn$_3$**) protein solutions, as determined from measurements of fluorescence intensity, remained constant over 8 weeks.

Cytotoxicity Experiments. The in vitro cytotoxicities of **PZn$_3$a**, **PZn$_3$b**, and their corresponding reconstituted LDL(**PZn$_3$**) protein solutions [LDL(**PZn$_3$a**) and LDL(**PZn$_3$b**)] were determined using a clonogenic assay. B16 melanoma cells from a cell line that overexpresses LDLr (generously provided by Dr. Theodore van Berkel, Leiden University, The Netherlands) were plated on six well plates overnight for cell attachment. Cells were exposed to DMSO solutions of **PZn$_3$a**, **PZn$_3$b**, and solutions (10 mM tricine, pH = 8.4) containing the analogous reconstituted LDL(**PZn$_3$**) proteins for 3 h, 24 h, and 8 days (no rinse). After exposure, the cells were twice rinsed with HBSS and then added to DMEM media supplemented with 10% fetal bovine serum and 25 mM HEPES buffer. After incubation for 8 days, the media were discarded and the cells were fixed with 5 mL of 99.5% ethanol for 10 min, rinsed three times with water, stained with 2% crystal violet for 10 min, and rinsed again with water. Clones with more than 50 cells were counted as survivors. The surviving fraction was calculated for the clonogenic assay.

Cellular Uptake and Imaging. B16 murine melanoma cells (2×10^4) were plated into two well chamber slides and incubated for 3 days at 37 °C prior to treatment with LDL(**PZn$_3$a**) and LDL(**PZn$_3$b**). The cells were incubated with the reconstituted dye solutions (1 μg/mL) for 1 h and subsequently washed twice with HBSS prior to fixing with absolute EtOH for 10 min at ambient temperature. The slides were then sealed and mounted for confocal imaging.

RESULTS AND DISCUSSION

Synthesis. The synthesis of **PZn$_3$**-based NIRFs is outlined in Scheme 1 (*33*, *38*, *50*). Because of the oxidative instability of cholesteryl oleate, reactions involving 5-androsten-17β-amino-3β-yl oleate-modified (porphinato)zinc(II) species proceeded in lower yields relative to analogous syntheses of **PZn$_3$** NIRFs lacking ancillary steroidal groups (**PZn$_3$a**, **PZn$_3$c**, and **PZn$_3$d**). Because endogeneous LDL lipids are completely displaced during its reconstitution, the NIRFs utilized for LDL reconstitution reactions must be sufficiently lipophilic in order to circumvent nonspecific leakage and aggregation of the reconstituted LDL (*22*). Furthermore, solubility of the **PZn$_3$**-based NIRFs in apolar organic solvents is also crucial for incorporation into the LDL interior. All the **PZn$_3$** ancillary substituents highlighted in Scheme 1 satisfy these constraints.

Note that the 4′-arylester groups of **PZn$_3$c** provide functionality for conjugation to moieties that engender augmented lipophilic character. **PZn$_3$b**, which bears two 5-androsten-17β-amino-3β-yl oleate esters, was synthesized from synthetic precursors to **PZn$_3$c** to determine the extent to which such modifications impact LDL

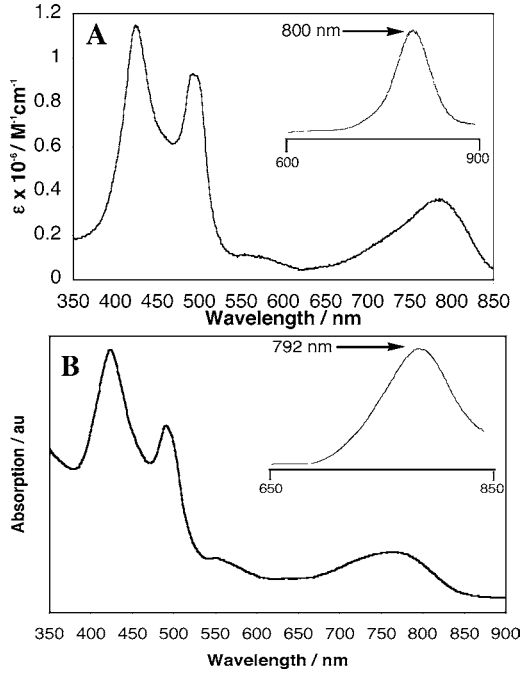

Figure 1. Electronic absorption and emission spectra of tris[(porphinato)zinc(II)] fluorophores. (A) Cholesteryl oleate-conjugated NIRF **PZn$_3$b** in benzene solvent. (B) Reconstituted LDL(**PZn$_3$a**) in tricine buffer (10 mM, pH 8.4). Corrected emission spectra, labeled with the emission wavelength maximum, are shown in the insets.

reconstitution with these tris[(porphinato)zinc(II)] species and affect subsequent cellular uptake by B16 murine melanoma cells. Previous studies demonstrated the utility of this approach for driving incorporation of cytotoxic and phototoxic agents into the LDL interior and facilitating their respective release into cells via LDLr-mediated endocytosis (*17*, *25*, *29*, *31*, *51*, *52*), consistent with the fact that oleoyl residues are abundant components of native LDL (*53*).

LDL Reconstitution. Following the modified Krieger protocol for LDL reconstitution outlined above (see Experimental Procedures) (*47*), NIRFs **PZn$_3$a** and **PZn$_3$b** were successfully incorporated into the LDL lipid core. Neither **PZn$_3$c** nor **PZn$_3$d** was taken up into apo-LDL under these conditions. These experiments suggest that without the cholesteryl oleate lipid anchor, **PZn$_3$c** lacks the hydrophobicity necessary to drive LDL incorporation; furthermore, it is apparent that the increased **PZn$_3$d** hydrophobicity relative to that of successfully-incorporated **PZn$_3$a** neither enhances nor guarantees successful reconstitution. This result may indicate that **PZn$_3$d** amphiphilicity has decreased below the threshold required for LDL compatibility; qualitatively similar observations emerge from structure−activity relationships delineated for amphiphilic drugs, which often show that potency is parabolically related to lipophilicity (*54*−*56*). Alternatively, disparate NIRF solvational environments that trace their genesis to the nature of the **PZn$_3$** *meso*-aryl-pendant solubilizing groups may serve as a key determinant of the extent to which **PZn$_3$a** and **PZn$_3$d** are taken up into apo-LDL under these conditions (*53*).

Figure 1 displays representative optical spectra of **PZn$_3$**-based NIRFs in low dielectric strength solvent and for reconstituted LDL(**PZn$_3$**) proteins. These optical spectra display absorptive and emissive signatures characteristic of extensive π conjugation and exciton coupling, similar to those elucidated for closely related compounds in higher dielectric strength media (*33*−*42*). These features include substantial B-state ($S_0 \rightarrow S_2$ absorption) domain spectral breadths, high oscillator strength, low energy Q-derived $S_0 \rightarrow S_1$ transitions, and correspondingly intense $S_1 \rightarrow S_0$ fluorescence emission bands. Assuming that the electronic absorption extinction coefficients of these NIRFs within the LDL hydrophobic core are similar to those determined previously in hydrophobic solvents, we estimate that ~30 chromophores are incorporated per LDL protein; note that this result is consistent with previous data that show that similar copy numbers of a range of amphipathic drugs are internalized into LDL using analogous reconstitution methodologies (*25*, *27*, *52*, *57*).

With respect to other classes of NIRFs that have been incorporated into the LDL core (*29*, *31*), note that the electronic absorption characteristics of these **PZn$_3$**-based chromophores include unusually comprehensive coverage of the UV, visible, and high energy NIR regions of the solar spectrum. Because **PZn$_3$** and related chromophores exhibit rapid $S_2 \rightarrow S_1$ internal conversion rate constants ($\tau_{ic} \sim 150$ fs), which are 1 order of magnitude faster than that manifested by conventional porphyrin monomers, formation of the low energy emitting state thus occurs within the ultrafast time domain, regardless of whether these species are excited within their lowest energy absorption band or within the higher lying B-state manifold (*36*, *40*); hence, optical excitation of the dyes could be performed at any wavelength between 400 and 800 nm.

Cytotoxicity of PZn$_3$a, PZn$_3$b, and Their Corresponding Reconstituted LDL(PZn$_3$) Proteins. The in vitro cytotoxicities of **PZn$_3$a**, **PZn$_3$b**, and their corresponding reconstituted LDL(**PZn$_3$**) proteins [LDL(**PZn$_3$a**) and LDL(**PZn$_3$b**)] were determined using a clonogenic assay. These data show that these conjugates display no apparent toxicity to murine B16 cells, as evident from the respective cellular survival rates determined as a function of time following exposure (Figure 2).

Murine B16 melanoma cells have been shown to bind LDL with affinity similar to human parenchymal cells and are thus good models for evaluating the effectiveness of LDLr-mediated delivery (*58*, *59*). Note that the Figure 2 data do not allow determination of IC_{50} values for **PZn$_3$a**, **PZn$_3$b**, LDL(**PZn$_3$a**), or LDL(**PZn$_3$b**) at 3 or 24 h of exposure, due to their apparent relative nontoxicity. The IC_{50} value determined for **PZn$_3$a** at 8 days of exposure was ~70 μg/mL, while that for **PZn$_3$b** was 45 μg/mL. The cytotoxicities for both **PZn$_3$a** and **PZn$_3$b** increased slightly as a function of exposure time. Note that the toxicity profiles of **PZn$_3$a** and **PZn$_3$b** contrast with that determined for tetrakis[(4-sulfonatophenyl)-porphinato]zinc(II) on G361 human melanoma cells (IC_{50} > 125 μg/mL, $t_{exposure}$ = 60 min) (*60*). Furthermore, the 50% inhibitory concentrations for both LDL(**PZn$_3$a**) and LDL(**PZn$_3$b**) were greater than 1000 ng/mL at 8 days of exposure. The benign nature of these fluorophore-reconstituted lipoproteins is similar to that established previously for in vitro toxicity studies of 3,3′-dioctadecylindocarbocyanine-labeled LDL (DiI-LDL) on MRC^5 human fetal fibroblasts (*61*).

Recent cytotoxicity studies of the FDA-approved NIR contrast agent, ICG, on human retinal pigment epithelium cells (RPE) showed that exposure to ICG at 100 μg/mL for 3 h resulted in approximately 20% cell death (*62*). After exposure to ICG at 5 mg/mL for the same amount of time, no cells survived. Even at a very short exposure time of 3 min at 0.5 mg/mL of ICG, RPE cell survival rate was modestly reduced to 92.8% (*63*). In contrast, no

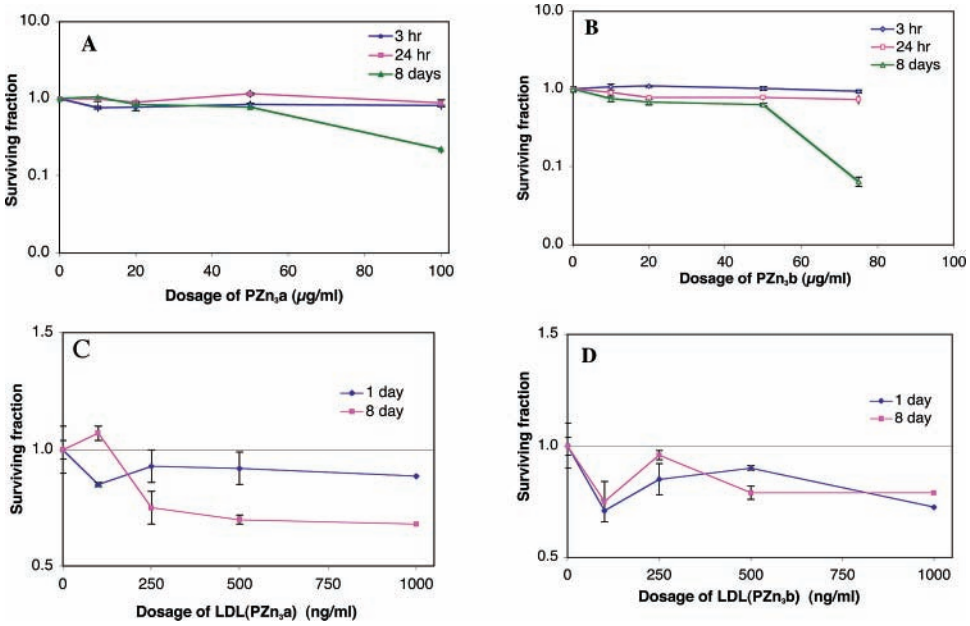

Figure 2. Time-dependent cytotoxicity of **PZn$_3$**-based NIRFs on B16 melanoma cells determined by a clonogenic assay for (A) **PZn$_3$a**, (B) **PZn$_3$b**, (C) LDL(**PZn$_3$a**), and (D) LDL(**PZn$_3$b**). Clones with more than 50 cells were counted as survivors. Data points represent means ± standard errors and were obtained from at least four independent experiments.

Table 1. Qualitative Comparison of in Vitro Experimental Conditions Required to Generate NIR Confocal Fluorescence Microscope Images of Tumor Cells Qualitatively Similar to that Depicted in Figure 3B as a Function of NIRF, Delivery Platform, Dose, Exposure Time, and Emission Wavelength

Entry	Contrast Agents	Delivery Platform	Tumor Cell Line	Dose of Dye	Exposure Time	λ_{emit} (nm)	Ref.
A	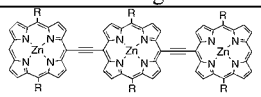	LDL	B16 Melanoma	60 nM	1 h	792	*This Work*
B	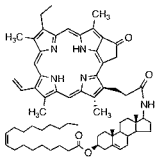	LDL	Hepato-blastoma G2	3 μM[a]	3 h	720	29, 64
C	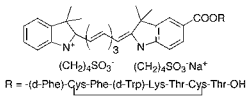	Somatostatin Receptor	RIN38 SSTR2[b]	1 μM[c]	1 h	780	11, 13
D	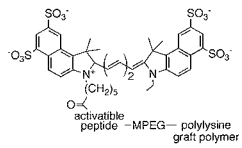	Proteolytic Enzyme Activation[d]	LX-1[e]	3.5 μM	15 min	700	9
E	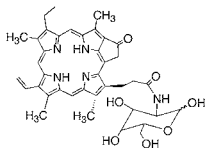	Glucose Transporter	9L Glioma	50 μM	30 min	720	50

[a] Calculated from a cell culture treatment using [LDL(dye)] = 20 μg/mL, in which each reconstituted LDL protein is calculated to contain ~75 dye molecules (*29*, *64*). [b] Somatostatin receptor subtype 2 transfected rat insulinoma pancreatic tumor. [c] Incubation of dye–peptide conjugate was performed at 4 °C. [d] Fluorescence signal generated through the action of proteolytic enzymes preferentially expressed in tumor tissues that release cyanine dyes from a protein/polymer matrix in which NIR fluorescence was previously quenched. [e] XG human lung carcinoma.

significant toxicity can be detected for either **PZn$_3$a** or **PZn$_3$b** on B16 cells even after 24 h of exposure at 100 and 80 μg/mL concentrations, respectively. These data suggest that the **PZn$_3$** family of fluorophores, as well as related structural analogues of these species, may prove suitable for in vivo studies.

Confocal Microscopy. Cellular uptake of the LDL reconstituted dye solutions was visualized using laser scanning confocal fluorescence microscopy (Figure 3). Figure 3A,C,E shows transmission images of B16 melanoma cells, while panels B, D, and F illustrate their corresponding cellular NIR fluorescence images. As

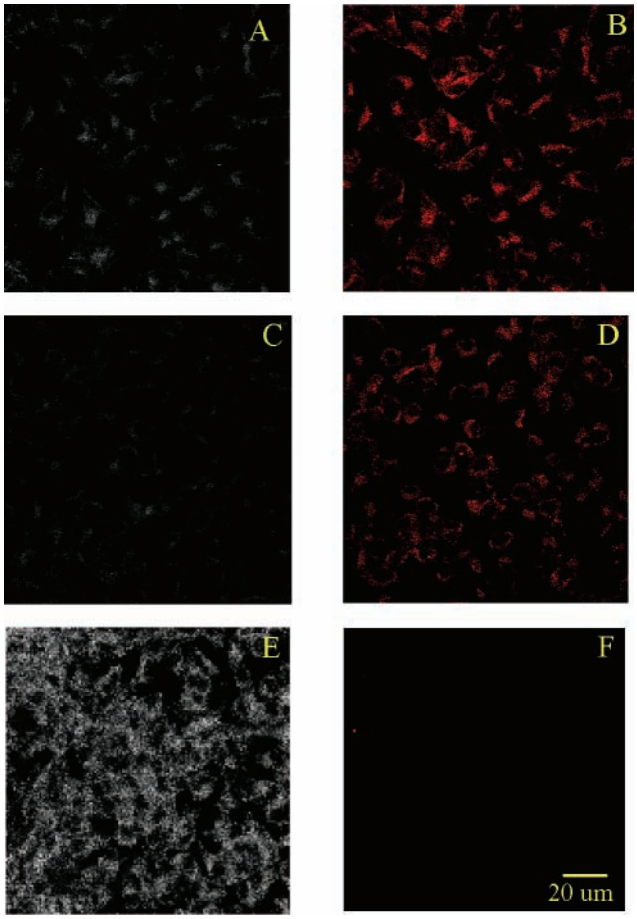

Figure 3. Confocal microscope images of B16 cells. (A) Transmission image of B16 cells treated with LDL(**PZn$_3$a**). (B) Fluorescence image of panel A. (C) Transmission microscopy image of B16 cells treated with LDL(**PZn$_3$b**). (D) Fluorescence image of panel C. (E) Transmission microscopy image of B16 cells incubated in culture medium to which aliquots of DMSO solutions of **PZn$_3$a** (1 μg/mL) were added. (F) Fluorescence image of panel E. Experimental conditions: B16 cells (2.5×10^4) were incubated at 37 °C for 3 days and then treated with solutions of LDL(**PZn$_3$**) (1 μg/mL; 10 mM tricine buffer, pH 8.4) for 1 h at ambient temperature. Following cellular washing and fixing with EtOH (see Experimental Procedures), slides were sealed and mounted. All images were taken at the same magnification using $\lambda_{ex} = 488$ nm and a 700 nm long pass filter.

Figure 3 clearly demonstrates, both LDL(**PZn$_3$a**) and LDL(**PZn$_3$b**) were internalized by B16 cells within 1 h; intense fluorescence signals were detected throughout the cellular membranes of the B16 cells. When B16 cells were incubated in culture medium to which aliquots of DMSO solutions of **PZn$_3$a** and **PZn$_3$b** (1 μg/mL) were added, no emission was detected from the cells (Figure 3E,F), indicating that the NIRF uptake highlighted by the Figure 3 data is mediated solely via LDLr-mediated endocytosis.

The low doses of dye ([LDL(**PZn$_3$**)] = 1 μg/mL = 2 nM protein; [NIRF] = 60 nM) used to obtain the confocal images highlight the emissive characteristics of the **PZn$_3$**-based NIRFs and the utility of LDL as an efficient vehicle for delivery of multiple copies of these fluorophores to a single cell. The short incubation time required for fluorophore uptake in these experiments demonstrates the rapid internalization of LDL through the B16 cells' overexpressed LDLrs, a characteristic displayed by many tumor types (*22*).

Table 1 highlights treatment conditions required for previously studied biomolecule−dye conjugates to obtain qualitatively similar confocal NIR fluorescence images of in vitro-targeted cancer cells. In vitro cellular delivery of the NIRF pyropheophorbide via the glucose transporter (Table 1, entry E) requires 20-fold greater concentration of fluorophore to generate a confocal image similar in quality to that obtained for delivery of the same dye via LDL reconstitution and subsequent LDLr-mediated endocytosis (Table 1, entry B) (*50*). Note that the amount of LDL-reconstituted pyropheophorbide necessary to generate NIR fluorescence confocal images similar to that shown in Figure 3B,D is at least 50 times higher than that used in this study (Table 1, entry A) (*29*). Because (i) dye doses cited in Table 1 do not necessarily correspond to the minimal amount necessary for obtaining a suitable fluorescence image and (ii) parameters such as instrument sensitivity, imaging acquisition times, and camera settings cannot be directly compared, we emphasize that the experimental data comparisons highlighted Table 1 are qualitative in nature. Nonetheless, the small concentration of **PZN$_3$** fluorophore required to obtain the in vitro images shown in Figure 3B,D underscore the promise of this NIR emissive platform for imaging applications.

CONCLUSIONS

We have shown that *meso*-to-*meso* ethyne-bridged tris-[(porphinato)zinc(II)] (**PZn$_3$**) NIRFs can be rendered sufficiently amphiphilic to enable their facile incorporation into the hydrophobic core of apo-LDL. These reconstituted LDL(**PZn$_3$**) proteins can be used to deliver rapidly hundreds of copies of **PZn$_3$** to a given B16 melanoma cell via LDLr-mediated endocytosis. **PZn$_3$**-based NIRFs and their corresponding LDL(**PZn$_3$**) proteins display minimal cytotoxicity. Confocal NIR fluorescence microscopy evinces that B16 cells can be imaged at very low doses (~nM) of NIRF. The highly attractive photophysical properties of **PZn$_3$** and closely related chromophores, coupled with their lack of toxicity and compatibility with uptake into apo-LDL and subsequent rapid delivery to B16 cells via LDLr-mediated endocytosis, suggest the potential utility of this platform for NIR optical imaging of cancer cells in vivo.

ACKNOWLEDGMENT

This research was supported by the National Cancer Institute (N01-CO-29008). J.D.G. acknowledges support from the National Cancer Institute (R24-CA83105-05 and P20-CA86255), and G.Z. thanks NASA and NCI (N01-CO-37119) for funding. S.P.W. is grateful to the National Science Foundation for an Access Science Predoctoral Fellowship. P.P.G. acknowledges predoctoral fellowship support from the NIH Medical Scientist Training Program (MSTP) and the Whitaker Foundation. We are indebted to Gladys Gray-Board for her assistance with the confocal microscopy experiments, to Dr. Sissel Lund-Katz of the Children's Hospital of Philadelphia for LDL, to Dr. Hui Li for guidance in the LDL reconstitution experiments, and to Dr. Theo van Berkel of Leiden University for providing the B16 melanoma cell line that overexpresses LDLr.

LITERATURE CITED

(1) Hawrysz, D. J., and Sevick-Muraca, E. M. (2000) Developments toward diagnostic breast cancer imaging using near-infrared optical measurements and fluorescent contrast agents. *Neoplasia 2*, 388−417.

(2) Weissleder, R. (2001) A clearer vision for in vivo imaging. *Nat. Biotechnol. 19*, 316−317.

(3) Reindl, S., Penzkofer, A., Gong, S.-H., Landthaler, M., Szeimies, R. M., Abels, C., and Baumler, W. (1997) Quantum yield of triplet formation for indocyanine green. *J. Photochem. Photobiol. A: Chem. 105*, 65−68.
(4) Landsman, M. L. J., Kwant, G., Mook, G. A., and Zijlstra, W. G. (1976) Light-absorbing properties, stability, and spectral stabilization of indocyanine green. *J. Appl. Physiol. 40*, 575−583.
(5) Philip, R., Penzkofer, A., Baumler, W., Szeimies, R. M., and Abels, C. (1996) Absorption and fluorescence spectroscopic investigation of indocyanine green. *J. Photochem. Photobiol. A: Chem. 96*, 137−148.
(6) Licha, K. (2002) Contrast agents for optical imaging. *Top. Curr. Chem. 222*, 1−29.
(7) Quaresima, V., Matcher, S. J., and Ferrari, M. (1998) Indentification and quantificaion of instrinsic optical contrast for near-infrared mammography. *Photochem. Photobiol. 67*, 4−14.
(8) Zaheer, A., Lenkinski, R. E., Mahmood, A., Jones, A. G., Cantley, L. C., and Frangioni, J. V. (2001) In vivo near-infrared fluorescence imaging of osteoblatic activity. *Nat. Biotechnol. 19*, 1148−1154.
(9) Weissleder, R., Tung, C.-H., Mahmood, U., and Bagdanov, A. J. (1999) In vivo imaging of tumors with protease-activated near-infrared fluorescent probes. *Nat. Biotechnol. 17*, 375−378.
(10) Bremer, C., Tung, C.-H., and Weissleder, R. (2001) In vivo molecular target assessment of matrix metalloproteinase inhibition. *Nat. Med. 7*, 743−748.
(11) Licha, K., Hessenius, C., Becker, A., Henklein, P., Bauer, M., Wisniewski, S., Wiedenmann, B., and Semmler, W. (2001) Synthesis, characterization and biological properties of cyanine-labeled somatostatin analogues as receptor-targeted fluorescent probes. *Bioconjugate Chem. 12*, 44−50.
(12) Grotzinger, C., and Wiedenmann, B. (2004) Somatostatin receptor targeting for tumor imaging and therapy. *Ann. N. Y. Acad. Sci. 1014*, 258−264.
(13) Becker, A., Hessenius, C., Licha, K., Ebert, B., Sukowski, U., Semmler, W., Wiedenmann, B., and Grotzinger, C. (2001) Receptor-targeted optical imaging of tumors with near-infrared fluorescent ligands. *Nat. Biotechnol. 19*, 327−331.
(14) Achilefu, S. A., Jimenez, H. N., Dorshow, R. B., Bugaj, J. E., Webb, E. G., Wilhelm, R. R., Rajagopalan, R., Johler, J., and Erion, J. L. (2002) Synthesis, in vitro receptor binding, and in vivo evaluation of fluorescein and carbocyanine peptide-based optical contrast agents. *J. Med. Chem. 45*, 2003−2015.
(15) Ballou, B., Fisher, G. W., Waggoner, A. S., Farkas, D. L., Rieland, J. M., Jaffee, R., Mujumdar, R. B., Mujumdar, S. R., and Hakala, T. R. (1995) Tumor labeling in vivo using cyanine-conjugated monoclonal antibodies. *Cancer Immunol. Immunother. 41*, 257−263.
(16) Folli, S., Wagnieres, G., Pelegrin, A., Calmes, J.-M., Braichotte, D., Buchegger, F., Chalandon, Y., Hardman, N., Heusser, C., Givel, J.-C., Chapuis, G., Chatelain, A., van der Bergh, H., and Mach, J.-P. (1992) Immunophotodiagnosis of colon carcinomas in patients injected with fluoresceinated chimeric antibodies against carcinoembryonic antigen. *Proc. Natl. Acad. Sci. U.S.A. 89*, 7973−7977.
(17) Kader, A., Davis, P. J., Kara, M., and Liu, H. (1998) Drug targeting using low-density lipoprotein (LDL): Physicochemical factors affecting drug loading into LDL particles. *J. Controlled Release 55*, 231−243.
(18) Reddi, E. (1997) Role of delivery vehicles for photosensitizers in the photodynamic therapy of tumours. *J. Photochem. Photobiol. B: Biol. 37*, 189−195.
(19) Konan, Y. N., Gurny, R., and Allemann, E. (2002) State of the art in the delivery of photosensitizers for photodynamic therapy. *J. Photochem. Photobiol. B: Biol. 66*, 89−106.
(20) Shaw, J. M., Shaw, K. V., Yanovich, S., Iwanik, M., Futch, W. S., Rosowsky, A., and Schook, L. B. (1987) Delivery of lipophilic drugs using lipoproteins. *Ann. N. Y. Acad. Sci. 507*, 252−271.
(21) Brown, M. S., Kovanen, P. T., and Goldstein, J. L. (1980) Evolution of the LDL-receptor concept—Cultured cells to intact animal. *Ann. N. Y. Acad. Sci. 348*, 48−68.
(22) Firestone, R. A. (1994) Low-density lipoprotein as a vehicle for targeting antitumor compounds to cancer cells. *Bioconjugate Chem. 5*, 105−113.
(23) Krieger, M., Goldstein, J. L., and Brown, M. S. (1978) Receptor-mediated uptake of low-density lipoprotein reconstituted with 25-hydroxycholesteryl oleate suppresses 3-hydroxy-3-methylglutaryl-coenzyme A reductase and inhibits growth of human fibroblasts. *Proc. Natl. Acad. Sci. U.S.A. 75*, 5052−5056.
(24) Krieger, M., Brown, M. S., Faust, J. R., and Goldstein, J. L. (1978) Replacement of endogenous cholesteryl esters of low-density lipoprotein with exogenous cholesteryl linoleate. *J. Biol. Chem. 253*, 4093−4101.
(25) Masquelier, M., Vitols, S., and Peterson, C. (1986) Low-density lipoprotein as a carrier of antitumoral drugs: In vivo fate of drug-human low-density lipoprotein complexes in mice. *Cancer Res. 46*, 3842−3847.
(26) Lundberg, B. (1987) Preparation of drug-low-density lipoprotein complexes for delivery of antitumoral drugs via the low-density lipoprotein pathway. *Cancer Res. 47*, 4105−4108.
(27) de Shmidt, P. C., and van Berkel, T. J. C. (1990) Prolonged serum half-life of antineoplastic drugs by incorporation into low-density lipoprotein. *Cancer Res. 50*, 7476−7482.
(28) Vitols, S. (1991) Uptake of low-density lipoprotein by maglignant cells—Possible therapeutic applications. *Cancer Cells 3*, 488−495.
(29) Zheng, G., Li, H., Zhang, M., Lund-Katz, S., Chance, B., and Glickson, J. D. (2002) Low-density lipoprotein reconstituted by pyropheophorbide cholesteryl oleate as target-specific photosensitizer. *Bioconjugate Chem. 13*, 392−396.
(30) de Shmidt, P. C., Versluis, A. J., and van Berkel, T. J. C. (1993) Properties of incorporation, redistribution, and integrity of porphyrin-low-density lipoprotein complexes. *Biochemistry 32*, 2916−2922.
(31) Zheng, G., Li, H., Yang, K., Blessington, D., Licha, K., Lund-Katz, S., Chance, B., and Glickson, J. D. (2002) Tricarbocyanine cholesteryl laurates labeled LDL: New near-infrared fluorescent probes (NIRFs) for monitoring tumors and gene therapy of familial hypercholesterolemia. *Bioorg. Med. Chem. Lett. 12*, 1485−1488.
(32) Craig, I. F., Via, D. P., Mantulin, W. W., Pownall, H. J., Gotto, A. M., Jr., and Smith, L. C. (1981) Low-density lipoproteins reconstituted with steroids containing the nitrobenzoxadiazole fluorophore. *J. Lipid Res. 22*, 687−696.
(33) Lin, V. S.-Y., DiMagno, S. G., and Therien, M. J. (1994) Highly conjugated, acetylenyl bridged porphyrins: New models for light-harvesting antenna systems. *Science 264*, 1105−1111.
(34) Lin, V. S.-Y., and Therien, M. J. (1995) The role of porphyrin-to-porphyrin linkage topology in the extensive modulation of the absorptive and emissive properties of a series of ethynyl- and butadiynyl-bridged bis- and tris-(porphinato)zinc chromophores. *Chem. Eur. J. 1*, 645−651.
(35) Angiolillo, P. J., Lin, V. S.-Y., Vanderkooi, J. M., and Therien, M. J. (1995) EPR spectrocsopy and photophysics of the lowest photoactivated triplet state of a series of highly conjugated (porphinato)zinc arrays. *J. Am. Chem. Soc. 117*, 12514−12527.
(36) Kumble, R., Palese, S., Lin, V. S.-Y., Therien, M. J., and Hochstrasser, R. M. (1998) Ultrafast dynamics of highly conjugated porphyrin arrays. *J. Am. Chem. Soc. 120*, 11489−11498.
(37) Shediac, R., Gray, M. H. B., Uyeda, H. T., Johnson, R. C., Hupp, J. T., Angiolillo, P. J., and Therien, M. J. (2000) Singlet and triplet excitated states of emissive, conjugated bis-(porphyrin) compounds probed by optical and EPR spectroscopic methods. *J. Am. Chem. Soc. 122*, 7017−7033.
(38) Susumu, K., and Therien, M. J. (2002) Decoupling optical and potentiometric band gaps in π-conjugated materials. *J. Am. Chem. Soc. 124*, 8550−8552.
(39) Fletcher, J. T., and Therien Michael, J. (2002) Extreme electronic modulation of the cofacial porphyrin structural motif. *J. Am. Chem. Soc. 124*, 4298−4311.
(40) Rubtsov, I. V., Susumu, K., Rubtsov, G. I., and Therien, M. J. (2003) Ultrafast singlet excitated-state polarization in

electronically asymmetric ethyne-bridged bis[(porphinato)-zinc(II)] complexes. *J. Am. Chem. Soc. 125*, 2687−2696.
(41) Ostrowski, J. C., Susumu, K., Robinson, M. R., Therien M. J., and Bazan, G. C. (2003) Near-infrared electroluminescent light-emitting devices based on ethyne-based porphyrin fluorophores. *Adv. Mater. 15*, 1296−1300.
(42) Angiolillo, P. J., Uyeda, H. T., Duncan, T. V., and Therien M. J. (2004) Impact of electronic asymmetry on photoexcited triplet-state spin distributions in conjugated oligomers probed via EPR spectroscopy. *J. Phys. Chem. B 108*, 11893−11903.
(43) DiMagno, S. G., Lin, V. S.-Y., and Therien, M. J. (1993) Facile elaboration of porphyrins via metal-mediated cross-coupling. *J. Org. Chem. 58*, 5983−5993.
(44) Lottner, C., Bart, K.-C., Bernhardt, G., and Brunner, H. (2002) Soluble tetraarylporphyrin-platinum conjugates as cytotoxic and phototoxic antitumor agents. *J. Med. Chem. 45*, 207−289.
(45) Lin, V. S.-Y., Iovine, P. M., DiMagno, S. G., and Therien, M. J. (2002) Dipyrryl and porphyrinic precursors to supramolecular conjugated (porphinato)metal arrays: Synthesis of dipyrrylmethane and (5,15-diphenylporphinato)zinc(II). *Inorg. Synth. 33*, 55−61.
(46) Littler, B. J., Miller, M. A., Hung, C.-H., Wagner, R. W., O'Shea, D. F., Boyle, P. D., and Lindsey, J. S. (1999) Refined synthesis of 5-substituted dipyrromethanes. *J. Org. Chem. 64*, 1391−1396.
(47) Krieger, M. (1986) Reconstitution of the hydrophobic core of low-density lipoprotein. *Methods Enzymol. 128*, 608−613.
(48) Lund-Katz, S., Laplaud, P. M., Phillips, M. C., and Chapman, M. J. (1998) Apolipoprotein B-100 conformation and particle surface charge in human LDL subspecies: Implication for LDL receptor interaction. *Biochemistry 37*, 12867−12874.
(49) Lowry, O. H., Rosebrough, N. J., Farr, A. L., and Randall, R. J. (1951) Protein measurement with the Folin phenol reagent. *J. Biol. Chem. 193*, 265−275.
(50) Zhang, M., Zhang, Z., Blessington, D., Li, H., Busch, T. M., Madrak, V., Miles, J., Chance, B., Glickson, J. D., and Zheng, G. (2003) Pyropheophorbide 2-deoxyglucosamide: A new photosensitizer targeting glucose transporters. *Bioconjugate Chem. 14*, 709−714.
(51) Ji, B., Peacock, G., and Lu, D. R. (2002) Synthesis of cholesterol-carborane conjugate for targeted drug delivery. *Bioorg. Med. Chem. Lett. 12*, 2455−2458.
(52) Hammel, M., Laggner, P., and Prassl, R. (2003) Structural characterization of nucleoside loaded low-density lipoprotein as a main criterion for the applicability as drug delivery system. *Chem. Phys. Lipids 123*, 193−207.
(53) Krieger, M., McPhaul, M. J., Goldstein, J. L., and Brown, M. S. (1979) Replacement of neutral lipids of low-density lipoprotein with esters of long chain unsaturated fatty acids. *J. Biol. Chem. 254*, 3845−3853.
(54) Aarons, L., Bell, D., Waigh, R., and Ye, Q. (1982) Parabolic structure−activity relationships: A simple pharmacokinetic model. *J. Pharm. Pharmacol. 34*, 746−749.
(55) Henderson, B. W., Bellnier, D. A., Greco, W. R., Sharma, A., Pankey, R. K., Vaughan, L. A., Wieshaupt, K. R., and Dougherty, T. J. (1997) An in vivo quantitative structure−activity relationship for a congeneric series of pyropheophorbide derivatives as photosensitizer for photodynamic therapy. *Cancer Res. 57*, 4000−4007.
(56) Kang, J.-H., Kim, S. Y., Lee, J., Marquez, V. E., Lewin, N. E., Pearce, L. V., and Blumberg, P. M. (2004) Macrocyclic diacylglycerol-bis-lactones as conformationally constrained analogues of diacylglycerol-lactones. Interactions with protein kinase C. *J. Med. Chem. 47*, 4000−4007.
(57) Iwanik, M. J., Shaw, K. V., Ledwith, B. J., Yanovich, S., and Shaw, J. M. (1984) Preparation and interaction of a low-density lipoprotein: Daunomycin complex with P388 leukemic cells. *Cancer Res. 44*, 1206−1215.
(58) Versluis, A. J., van Geel, P. J., Oppelaar, H., van Berkel, T. J. C., and Bijsterbosch, M. K. (1996) Receptor-mediated uptake of low-density lipoprotein by B16 melanoma cells in vitro and in vivo in mice. *Br. J. Cancer 74*, 525−532.
(59) Kamps, J. A. A. M., Kuiper, J., Kruijt, J. K., and van Berkel, T. J. C. (1991) Complete down regulation of low-density lipoprotein receptor activity in human liver parenchumal cells by β-very low-density lipoprotein. *FEBS Lett. 287*, 34−38.
(60) Kolarova, H., Mosinger, J., Lenobel, R., Kejlova, K., Jirova, D., and Strnad, M. (2003) In vitro toxicity testing of supramolecular sensitizers for photodynamic therapy. *Toxicol. in Vitro 17*, 775−778.
(61) Crawford, J. M., and Braunwald, N. S. (1991) Toxicity in vital fluorescence microscopy: Effect of dimethyl sulfoxide, rhodamine-123, and DiI-low-density lipoprotein on fribroblast growth in vitro. *In Vitro Cell. Dev. Biol.: Anim. 27A*, 633−638.
(62) Ho, J.-D., Tsai, R. J.-F., Chen, S.-N., and Chen, H.-C. (2003) Cytotoxicity of indocyanine green on retinal pigment epithelium. *Arch. Ophthalmol. 121*, 1423−1429.
(63) Gale, J. S., Proulx, A. A., Gonder, J. R., Mao, A. J., and Hutnik, C. M. L. (2004) Comparison of the in vitro toxicity of indocyanine green to that of trypan blue in human retinal pigment epithelium cell cultures. *Am. J. Ophthalmol. 138*, 64−69.
(64) Zheng, G. Personal communication.

BC0497416

Development of Polymer Latex Particles for Selective Cleavage of Mismatched DNA and Their Application for DNA Diagnosis

Shinsuke Oba,[†] Mamoru Hatakeyama,[†] Hiroshi Handa,[‡] and Haruma Kawaguchi*[,†]

Department of Applied Chemistry, Faculty of Science and Technology, Keio University, 3-14-1 Hiyoshi, Kouhoku-ku, Yokohama 223-8522, Japan, and Department of Biomolecular Engineering, Faculty of Bioscience and Biotechnology, Tokyo Institute of Technology, 4259 Nagatsuta-cho, Midori-ku, Yokohama 226-8501, Japan.
Received November 11, 2004; Revised Manuscript Received March 27, 2005

We developed functional polymer latex particles that can catch and cleave mismatched DNA selectively and propose a new mismatch detection system using the functional particles. The aimed particles possess two functional units composed of mismatch binding protein (MutS) and an anthraquinone derivative (AQ), a light-activated agent that photocleaves dsDNA. Use of the functional particles made it possible to discriminate complementary and mismatched DNAs and photocleave mismatched DNA selectively. The efficiency of photocleavage of mismatched DNA by the functional particles increased with UV irradiation time. It was also found that the functional particles were reusable and had dissociation constants (K_d) of 1000 and 68.5 nM for G/C homoduplex and G/T heteroduplex, respectively. Using the functional partcles and a dsDNA-binding fluorescent dye, SYBR-Gold, we could construct the system for detection of mismatched DNA that was 40 base pairs. The functional particles prepared in this study will be an absolutely new tool for mismatch detection in DNA diagnosis.

1. INTRODUCTION

A large number of human genetic diseases and single-nucleotide polymorphisms (SNPs) are caused by gene mutations including single-base substitutions and small additions or deletions (*1*, *2*). Therefore it is very meaningful to detect such gene mutations as early as possible, and rapid, easy to handle, and high-throughput mismatch detection methods are urgently demanded. To date, different approaches for constructing mismatch detection systems that are useful and unique have been reported (*3*−*7*). In our previous study, we proposed an application of affinity latex particles for efficient purification of several DNA binding proteins (*8*, 9), single-stranded DNA and RNA (*10*), and for constructing a DNA diagnosis system (*11*−*13*). Also, we developed protein- and peptide-carrying affinity latex particles and purified several proteins by using the particles (*14*). In this study, we developed functional polymer latex particles that can catch and cleave mismatched DNA selectively and propose a new mismatch detection system using the functional particles. These functional particles need to have functional units to discriminate complementary and mismatched DNAs and to cleave mismatched DNA that is caught. As the unit of discriminating complementary and mismatched DNAs, MutS protein was selected. The MutS protein is a crucial element of DNA mismatch repair (MMR) system in many organisms such as *Escherichia coli* (*15*). MutS is the 97 kDa protein that can specifically recognize and bind all possible single-base mismatches, as well as 1−4 base insertion or deletion loops (*16*, *17*). On the other side, as the unit for cleaving mismatched DNA, an anthraquinone derivative (AQ) is selected. AQ is a light-activated agent that cleaves double-stranded DNA (*18*, *19*). AQ has two separate oxidative pathways: electron transfer from a nearby base and hydrogen atom abstraction from the deoxyribose component of the nucleic acid backbone. The former leads to GG-selective cleavage of dsDNA by intercalated AQ, and the latter leads to non-sequence-selective cleavage of dsDNA by nonintercalated AQ. In this report, we present the preparative method of the functional particles that are composed of polymer latex particles, MutS protein, and AQ and the characterization results. The intended functional particles offer several distinct advantages: (1) Composed of polymer latex particles, they are easy to handle, separate, and collect compared to other devices such as hybrid enzyme. (2) The extremely small diameter of the particles (200 nm) provides a large surface area, giving the particles a relatively high capacity (*20*). (3) MutS protein is expected to be more stable because of being immobilized on the particle surface. (4) By means of photocleavage of mismatched DNA by AQ, a mismatch detection system constructed using the functional particles is easy and simple. These functional particles carrying AQ-MutS hybrid on their surface will be an absolutely new device for mismatch detection, as shown in Figure 1.

2. EXPERIMENTAL PROCEDURE

2.1. Materials. For preparation of polymer latex particles, styrene (St), glycidyl methacrylate (GMA), divinylbenzene (DVB), and 2,2′-azobis(2-amidinopropane-)HCl (V-50) were purchased from Wako Pure Chemicals Co. (Tokyo, Japan). St and GMA were distilled at 46 °C/21.5 mmHg and 33 °C/2 mmHg, respectively. DVB was used without further purification. Ethyleneglycol diglycidyl ether (EGDE), *p*-toluenesulfonyl chloride (TsCl), and pyridine for improvement of the particle surface were purchased from Wako Pure Chemicals Co. (Tokyo, Japan). Histidine-tagged MutS protein (MutS-$(His)_6$) was

* To whom correspondence should be addressed. Tel: +81-45-566-1563. Fax: +81-45-564-5095. Email: haruma@applc.keio.ac.jp.
[†] Keio University.
[‡] Tokyo Institute of Technology.

10.1021/bc049728l CCC: $30.25 © 2005 American Chemical Society
Published on Web 05/03/2005

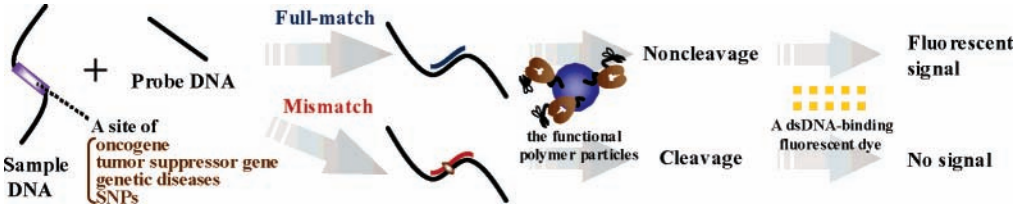

Figure 1. Schematic representation of a new mismatch detection system using the functional polymer latex particles.

expressed from *E. coli*. For quantification of protein, the BCA protein assay reagent kit was purchased from Pierce (USA).

Oligonucleotides 5′-ACTTGTGTTAGTTCGAGCTGGT-TGCGTACTCAAGAGTGAT-3′(RM40N-GG), 5′-ATCACT-CTTGAGTACGCAACCAGCTCGAACTAACACAAGT-3′-(RMc40N-CC), 5′-ATCACTCTTGAGTACGCAACTAGCTC-GAACTAACACAAGT-3′(RMc40M-CT), and 5′-ATC-ACTCTTGAGTACGCAACTCAGCTCGAACTAA-CACAAGT-3′(RMc41M-CTC) were chemically synthesized by JBios (Japan). The picogreen dsDNA quantification reagent kit and SYBR-Gold nucleic acid gel stain were purchased from Molecular Probes (The Netherlands). As an anthraquinone derivative (AQ), 2-hydroxymethylanthraquinone (AQ-CH_2OH) was purchased from Tokyo Kasei Kogyo (Japan). Lumi-Phos530, a formulation of the dioxetane substrate 4-methoxy-4-(3-phosphonophenyl)spiro[1,2-dioxetane-3,2′-adamantane] and streptavidin-alkalinephosphatase conjugate (SA-AP) were purchased from Wako Pure Chemicals Co. (Tokyo, Japan) for the chemiluminescence assay.

2.2. Buffers. The following buffers were prepared and used for each process. Immobilization buffer: 10 mM sodium phosphate buffer (pH 7.5), 150 mM NaCl, and 5% (v/v) glycerol. Washing buffer: 10 mM sodium phosphate buffer (pH7.5), 500 mM NaCl, and 5% (v/v) glycerol. DNA-binding buffer: 10 mM sodium phosphate buffer (pH 7.5), 150 mM NaCl, 5% (v/v) glycerol, 5 mM $MgCl_2$, and 0.005% (w/v) tween20. DNA-releasing buffer: 10 mM sodium phosphate buffer (pH 7.5), 150 mM NaCl, 5% (v/v) glycerol, 5 mM EDTA, and 0.005% (w/v) tween20.

2.3. Preparation of Polymer Latex Particles. Basic polymer latex particles (SG particles) were prepared by soap-free emulsion polymerization. St, GMA, and DVB were copolymerized in a soap-free aqueous medium using V-50. Ammonia was reacted with the epoxy groups of the SG particles as a joint, at 70 °C, pH 11 for 24 h. The resulting particles carrying amino groups were reacted with EGDE at 30 °C, pH 11 for 24 h to give a spacer on the particle surface. Then epoxy groups of the ends of the EGDE spacers were hydrolyzed to hydroxyl groups at 40 °C, pH 2 for 24 h. Finally, we introduced tosyl(*p*-toluene sulfonyl) groups according to the method described previously (*21*). The hydrodynamic size of these particles was measured by photon correlation spectroscopy (PCS), using PA3000 from Ohtsuka Electronics Co., Ltd. (Japan). The size and appearance of these particles were observed by transmission electron microscopy (TEM).

2.4. Immobilization of MutS Protein onto Tosylated Particles. Tosylated particles (5 mg) were washed three times with 400 μL of immobilization buffer and mixed with 40, 100, 200, 400, and 800 μg of MutS-$(His)_6$ in 400 μL of immobilization buffer. The coupling reaction was carried out at 4 °C for 4 h. The particles were collected by brief centrifugation in a microcentrifuge at 12 000*g* for 10 min and washed with 400 μL of washing buffer three times. The amount of immobilized MutS-$(His)_6$ was determined by quantifying the MutS in the supernatant and three consecutive wash solutions by using the BCA protein assay reagent kit. This protein assay reagent enables the quantification of as little as 10 μg/mL MutS-$(His)_6$. Remaining active tosyl groups were blocked and deactivated with 1 mL of immobilization buffer containing 2 mM 2-amino-2-hydroxymethyl-1,3-propanediol (Tris) and were then stored at 4 °C (MutS-immobilized particles).

2.5. Ability of MutS-Immobilized Particles to Discriminate Complementary and Mismatched DNA. MutS-immobilized particles (1 or 0.5 mg) were washed three times with 200 μL of DNA-binding buffer and mixed with various amouns of dsDNAs; RM40N-GG/RMc40N−CC (G/C complementary DNA), RM40N-GG/RMc40M-CT (G/T mismatched DNA) or RM40N-GG/RMc41M-CTC (T-bulge DNA) in 200 μL of DNA-binding buffer (*11*). The binding reaction was carried out at 37 °C for 24 h. The particles were collected by brief centrifugation in a microcentrifuge at 12 000*g* for 10 min. The amount of dsDNA binding to MutS-immobilized particles was determined by quantifying dsDNA remaining in the supernatant using the picogreen dsDNA quantification reagent kit. The reagent enables the quantification of as little as 25 pg/mL for dsDNA.

2.6. Affinity Elution of dsDNA Bound to MutS-Immobilized Particles. After the binding reaction, MutS-immobilized particles were suspended in DNA-releasing buffer at 37 °C for 24 h. Then the particles were collected by brief centrifugation in a microcentrifuge at 12 000*g* for 10 min and washed three times with 200 μL of DNA-releasing buffer. The amount of dsDNA eluting from MutS immobilized on the particle surface was determined by quantifying the dsDNA in the supernatant and three consecutive wash solutions using the picogreen dsDNA quantification reagent kit.

2.7. AQ Conjugation to MutS-Immobilized Particles. 2-Hydroxymethylanthraquinone was activated with *p*-toluenesulfonyl chloride to conjugate with MutS-immobilized particles. AQ conjugation to MutS-immobilized particles was carried out at 4 °C for 4 h in immobilization buffer. After conjugation, AQ-MutS-immobilized particles were centrifuged in a microcentrifuge at 12 000*g* for 10 min and washed three times with immobilization buffer. The amount of binding AQ was determined by its maximum absorption with $\lambda_{max} = 330$ nm of the supernatant and three consecutive wash solutions.

2.8. Ability of AQ-MutS-Immobilized Particles To Photocleave Mismatched DNA Selectively. AQ-MutS-immobilized particles (0.5 mg) were washed three times with 200 μL of DNA-binding buffer and mixed with various amount of G/C complementary DNA or G/T mismatched DNA in 200 μL of DNA-binding buffer. The binding reaction was carried out at 37 °C for 24 h. The particles were collected by brief centrifugation in a microcentrifuge at 12 000*g* for 10 min. The amount of dsDNA binding to AQ-MutS-immobilized particles was determined by quantifying dsDNA remaining in the supernatant using the picogreen dsDNA quantification reagent kit. Additionally, the particles were redespersed

Table 1. Diameter and Transmission Electron Micrograph (TEM) Image of a Series of the Particles

Particle codes	Diamters (nm) PCS	Diamters (nm) TEM	TEM views
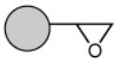	204.4	174.9	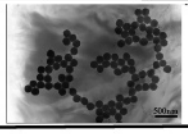
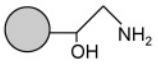	223.0	191.0	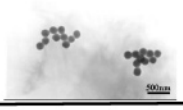
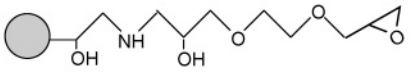	216.8	185.4	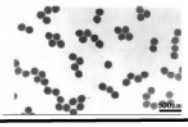
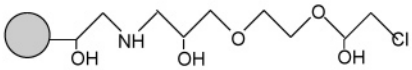	222.7	195.3	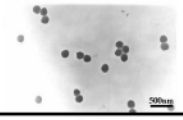
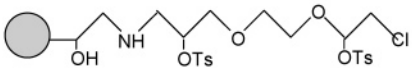	226.2	190.3	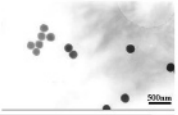

in 200 μL of DNA-binding buffer and irradiated with 365 nm UV light for 30 or 60 min. Then the particles were suspended in 200 μL of DNA-binding buffer at 85 °C for 2 h to denature MutS immobilized on the particle surface. After denaturation, the particles were collected by brief centrifugation in a microcentrifuge at 12 000*g* for 10 min and washed three times with 200 μL of DNA-binding buffer. The amount of dsDNA detached from AQ-MutS immobilized on the particle surface was determined by quantifying the dsDNA in the supernatant and three consecutive wash solutions using the picogreen dsDNA quantification reagent kit.

2.9. **Chemiluminescence Assay.** Biotinylated RM40N-GG was purchased and hybridized with RMc40N-CC or RM40N-CT (Bio-G/C complementary DNA or Bio-G/T mismatched DNA). After the binding and photocleaving reactions of it with AQ-MutS-immobilized particles, 200 μL of 20mU/ml SA-AP solution was added and incubated for 30 min at room temperature to complete the biotin−avidin reaction. Then the particles were collected by brief centrifugation in a microcentrifuge at 12 000*g* for 10 min and washed three times with 200 μL of DNA-binding buffer. After the dispersion of the particles was diluted, a 120 μL aliquot of Lumi-Phos530 was added to the Bio-DNA and SA-AP complex. The alkalinephosphatase-catalyzed dephosphorylation of the dioxetane substrate was followed to proceed in the dark for 1 h at room temperature. The mixture was then transferred to a cuvette and the chemiluminescent signal (CL signal) was measured by a luminometer.

2.10. Construction of Mismatch Detection System using AQ-MutS-Immobilized Particles. AQ-MutS-immobilized particles (40 μg) and various amounts of G/C complementary DNA or G/T mismatched DNA were added in 200 μL of DNA-binding buffer. The mixture was kept standing at 37 °C for 6 h and irradiated with 365 nm UV light for 60 min. Then a dsDNA-binding fluorescent dye, SYBR-Gold, was added to the mixture, and the mixtue was dropped in a 96-well microtiter to measure the fluorescence with a spectrometer.

3. RESULTS AND DISCUSSIONS

3.1. Preparation of Tosylated Particles and Immobilization of MutS Protein onto the Particles. We had previously developed affinity latex particles composed of a poly(glycidyl methacrylate) (polyGMA)-covered GMA-styrene (St) copolymer core (SG particles) that were originally used for affinity purification (*8*, *9*). To reduce steric hindrance, we introduced ethyleneglycol diglycidyl ether (EGDE) as a spacer after aminolysis of the epoxy groups on the particle surface. For protein immobilization, we introduced tosyl groups after hydrolysis of epoxy groups of the ends of EGDE spacers on the particle surface. The diameters of initial, intermediate, and final particles by PCS and TEM are shown in Table 1. SG particles and the series of modified SG particles were monodisperse. The fact that the final particles were monodisperse indicated EGDE was immobilized without interparticle cross-linking (*14*). Introducing the EGDE spacer makes the particle surface hydrophilic, thus minimizing nonspecific protein binding (*8*) and also gives the particle chemical and physical stability in organic solvents (*14*). According to the elementary analysis, the tosylated particles had 456 μmol of tosyl groups/g particles (11 units/nm^2) on the surface.

In this study, there are two possible ways to prepare the functional particles. One way is to immobilize MutS onto the polymer latex particles first and then to conjugate AQ to MutS-immobilized particles, and the other is to immobilize AQ-MutS hybrid prepared beforehand onto the polymer latex particles. In the latter way the AQ-MutS hybrid after being immobilized on the particles had lost its mismatch binding activity (data not shown), so that we decided to adopt the former way. Immobilization of MutS onto tosylated particles was carried out at pH 7.5 and 4 °C for 4 h. The coupling of protein with the tosyl group has some advantages: (1) The coupling reaction can be performed at neutral pH and at 4 °C. (2) The amino, thiol, and imidazole groups of protein directly react with the carbon atoms of the tosyl end of the spacer, so that side reactions hardly occur during the coupling

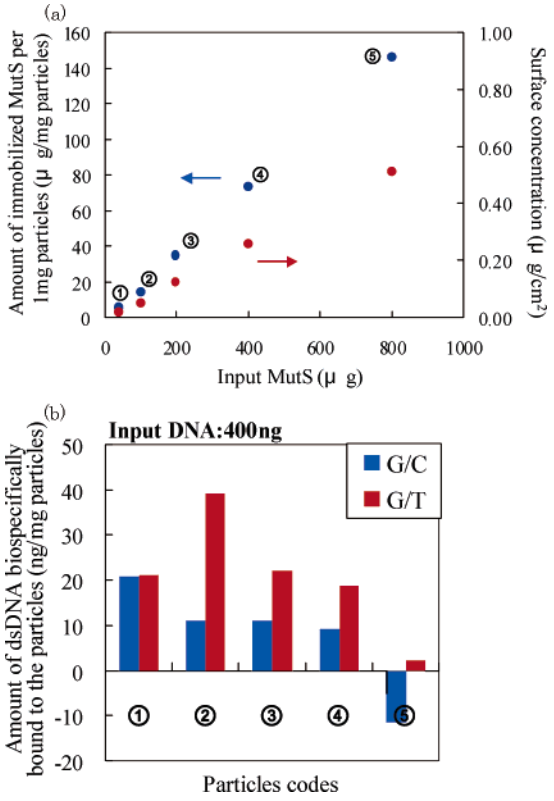

Figure 2. (a) Immobilization of MutS onto tosylated particles. (b) Amount of dsDNA bound to various MutS-immobilized particles. Binding reaction was performed at 37 °C for 30 min in IB containing 5 mM $MgCl_2$. (Amount of dsDNA biospecifically bound to MutS = amount of dsDNA adsorbed on MutS-immmobilized particles − amount of dsDNA adsorbed on bare particles.)

reaction. (3) Protein is covalently coupled to spacers through a carbon−nitrogen or a carbon−sulfur bond, which is expected not to be broken by hydrolysis (*22*). Figure 2a shows that the amount of MutS immobilized onto the particles increased proportionally to the charged amount. Amount of MutS immobilized on the particles was ① 5.5, ② 14.3, ③ 34.9, ④ 73.1, and ⑤ 145.7μg/mg particles, which corresponds to ① 0.02, ② 0.05, ③ 0.12, ④ 0.26, and ⑤ 0.51μg/cm^2, respectively. The apparent density of MutS molecules on the particle was calculated to be ① 0.3, ② 0.8, ③ 1.8, ④ 3.8, and ⑤ 7.5 molecules/nm^2, assuming that the surface is flat. The values of the latter two, 3.8 and 7.5 molecules/nm^2, are too large to imagine the presence of MutS immobilized on the particle in a single layer. Using the series of MutS-immobilized particles, an experiment of discriminating complementary and mismatched DNAs was carried out. Figure 2b shows amounts of dsDNA biospecifically bound to MutS-immobilized particles at 37 °C for 30 min. It is clear that the difference in the amounts between complementary and mismatched DNA binding to code- ② particles was highest among the series of MutS-immobilized particles. That is, code- ② particles had the highest ability to discriminate complementary and mismatched DNA. It is concluded that there is an appropriate amount of MutS immobilized on the particles. If the amount of MutS immobilized on the particles is low, fewer DNA binding sites are present on the particles, so less DNA is captured. On the other hand, if amount of MutS immobilized on the particles is high, MutS molecules are too close to each other to allow DNA binding to all MutS molecules. Therefore the highest ability of MutS-immobilized particles to discriminate complementary and mismatched DNA would be obtained by immobilizing MutS with the density at which it retain its natural conformation.

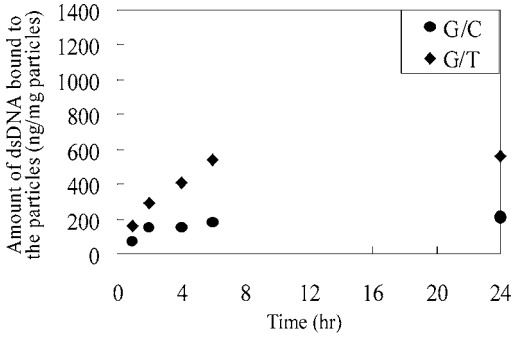

Figure 3. Time dependence of binding reaction of dsDNA with MutS-immobilized particles. Binding reaction was performed at 37 °C for 1, 2, 4, 6, and 24 h in DNA-binding buffer.

3.2. Improvement of MutS-Immobilized Particles. To improve the ability of MutS-immobilized particles to discriminate complementary and mismatched DNA, some of active tosyl groups of tosylated particles were reacted with 2-amino-2-hydroxymethyl-1,3-propanediol (Tris) before immobilization of MutS onto tosylated particles. Masking of some of the active tosyl groups with Tris before immobilization caused an increase in the amount of mismatched DNA caught by MutS on the particles, as well as the ability of MutS-immobilized particles to discriminate complementary and mismatched DNA. This would be because MutS was prevented from being immobilized at multiple points on the particles by the Tris-masking treatment before immobilization, so its native conformation remained, and/or the surface of MutS-immobilized particles was positively charged owing to Tris-masking treatment, so anionic dsDNA was easy to interact with the particles electrostatically. Therefore we prepared MutS-immobilized particles in this way afterward.

Figure 3 shows time dependence of the binding reaction of dsDNA with MutS-immobilized particles at 37 °C. The result indicates that MutS-immobilized particles caught more dsDNA, both G/C complementary and G/T mismatched DNAs, with increasing binding reaction time, and the amounts of dsDNA bound to the particles became a plateau within 24 h. From this result, we adopted 24 h as the sufficient binding reaction time at which binding reaction of dsDNA with MutS-immobilized particles was considered to be at equilibrium at 37 °C.

3.3. Ability of MutS-Immobilized Particles To Discriminate Complementary and Mismatched DNAs and Affinity Elution of dsDNA Bound to MutS-Immobilized Particles. In the experiment for discriminating complementary and mismatched DNAs using MutS-immobilized particles, the ability of MutS-immobilized particles to discriminate complementary and mismatched DNAs (DM) was defined as follows:

$$\mathrm{DM}\ (\%) = \left(1 - \frac{\text{amount of particle-bound complementary DNA}}{\text{amount of particle-bound mismatched DNA}}\right) \times 100 \quad (1)$$

Figure 4a shows the amount of dsDNA bound to MutS-immobilized particles at 37 °C for 24 h and DMs calculated by eq 1. DMs were 79% and 86% for G/T mismatched DNA and T-bulge DNA, respectively. The difference between the two can be explained by the reported property of MutS that the order of its binding

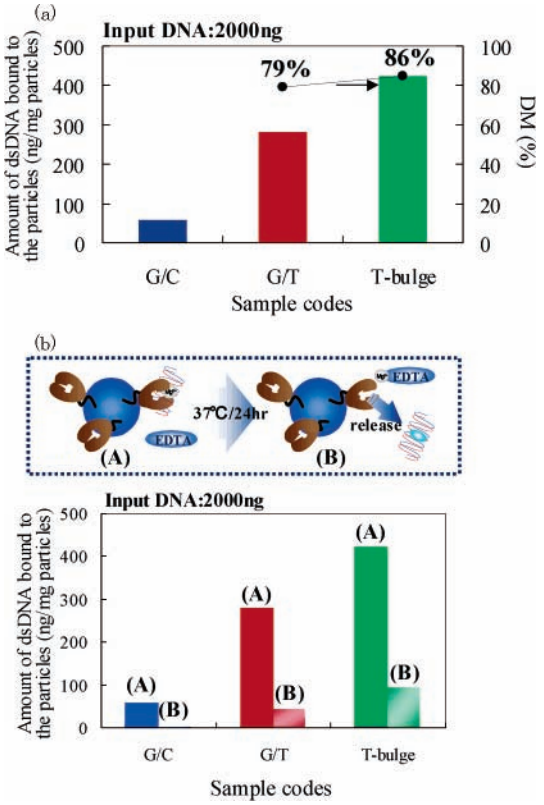

Figure 4. (a) Amount of dsDNA bound to MutS-immobilized particles and ability to discriminate complementary and mismatched DNAs (DM) of MutS-immobilized particles. Binding reaction was performed at 37 °C for 24 h in DNA-binding buffer. (b) Amount of dsDNA bound to MutS-immobilized particles before and after elution.

affinity to different mismatches is ΔT > GT > GG > AA ≈ TT ≈ TC > CA > GA > CC > GC (*23*). The result indicates that MutS immobilized on the particles could have similar relative binding affinity to free MutS. The experiments were carried out using MutS-immobilized particles on which MutS was immobilized to the particle through the EGDE spacer. The spacer could afford MutS immobilized on the particles to act freely, so MutS-immobilized particles could retain their mismatch binding activity as described in other reports; MutS immobilized by binding to nitrocellulose (*24*) or Trx-His_6-Linker peptide-Strep-tag II-Linker peptide-MutS (THLSLM) immobilized on the chip matrix coated with streptavidin through the Strep-tag II-streptavidin binding reaction (*25*). The EGDE spacer is considered to have the appropriate chain length and hydrophilicity for protein immobilization.

Figure 4b shows the amount of dsDNA bound to MutS-immobilized particles before and after elution using EDTA; the amount of dsDNA bound to the particles after elution has obviously decreased. This result means that dsDNA bound to MutS-immobilized particles was eluted by chelating effect of EDTA. That is, Mg^{2+} contributes to the formation of dsDNA and MutS hybrid (*26*), and the above-mentioned affinity elution was due to a drastic decrease of binding affinity for dsDNA of MutS owing to chelation of Mg^{2+} with EDTA.

Taking advantage of this affinity elution using EDTA, we tried reusing MutS-immobilized particles. A series of binding and eluting treatment was performed three times, and the amount of dsDNA bound to MutS-immobilized particles and DMs in each cycle are shown in Figure 5. It is found from Figure 5 that MutS-

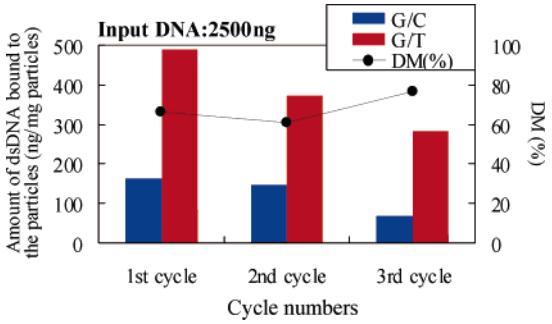

Figure 5. Comparison of ability (DM) to discriminate complementary and mismatched DNAs of MutS-immobilized particles for each cycle. Binding reaction was performed at 37 °C for 24 h in DNA-binding buffer.

immobilized particles were reusable for three continuous uses. In each cycle DM was about 70% but the amount of dsDNA bound to the particles decreased as the number of times increased. This is due to incompleteness of affinity elution using EDTA, shown in Figure 4b. That is, some of MutS immobilized on the particles was occupied by dsDNA remaining after elution, and consequently the substantial amount of MutS immobilized on the particles that was expected to be usable in next cycle had decreased.

3.4. Preparation and Characterization of AQ-MutS-Immobilized Particles. Conjugation of AQ to MutS-immobilized particles was carried out at 4 °C through tosyl chloride activation (*22*). A series of hybrid particles, AQ-MutS-immobilized particles carrying different amounts of AQ, were prepared, and first their ability to discriminate complementary and mismatched DNAs was examined at 37 °C for 24 h. Figure 6a and b shows the number of bound AQ per MutS immobilized on the particles and the amount of dsDNA bound to AQ-MutS-immobilized particles and DMs calculated by eq 1. It is found from Figure 6a and b that the amount of binding AQ had little effect on the DM. The series of AQ-MutS-immobilized particles had the same DMs as MutS-immobilized particles. That is, there is retention of mismatch binding activity of MutS immobilized on the particles after conjugation of AQ.

Second, the activity of AQ-MutS-immobilized particles to photocleave mismatched DNA was assessed by using the series of AQ-MutS-immobilized particles mentioned above. The results in Figure 7 show us that AQ-MutS-immobilized particles with more AQ cleaved more mismatched DNA and suggest that AQs bound to MutS immobilized on the particles retained their activity to photocleave dsDNA. This cleavage of mismatched DNA occurred upon irradiation with 365 nm light. There are two mechanisms in the cleavage of mismatched DNA by AQ on UV irradiation. The one is base selective cleavage and the other is nonselective. The fomer takes place with the aid of piperidine, which contributes electron transfer to AQ from a base near the intercalated AQ, whereas the latter takes place through hydrogen atom abstraction from the deoxyribose component of the nucleic acid backbone by nonintercalated AQ (*18*, *19*). The spontaneous cleavage of mismatched DNA in the present system suggested that the cleavage was the nonselective mechanism by the nonintercalated AQ. Using the AQ-MutS-immobilized particles that had the highest activity to photocleave mismatched DNA, time dependence of the binding reaction of dsDNA with the particles at 37 °C was also examined. The results in Figure 8 indicate that the particles caught more dsDNA with increasing binding reaction time, and the amounts of dsDNA bound to the

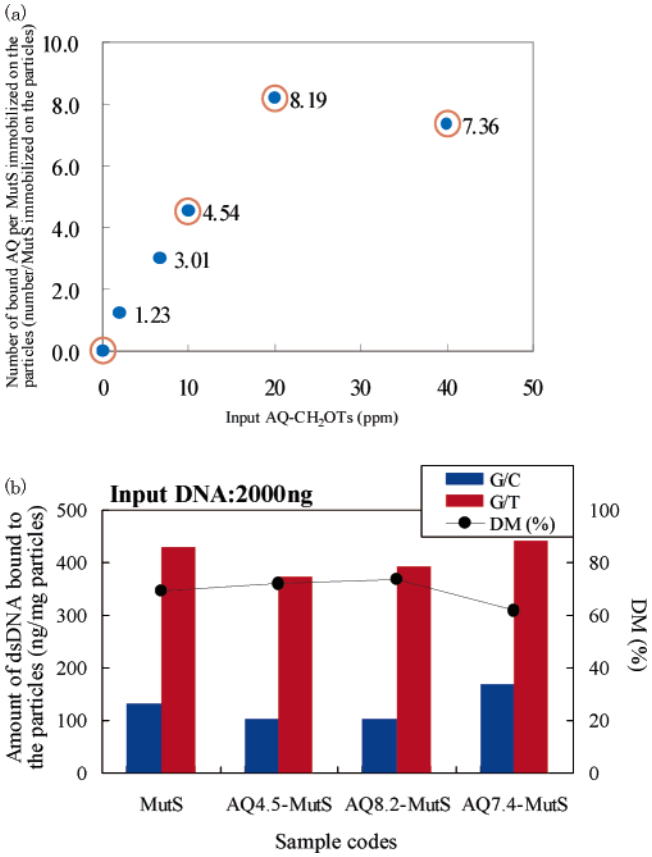

Figure 6. (a) AQ conjugation to MutS-immobilized particles. (b) Comparison of ability (DM) to discriminate complementary and mismatched DNAs among AQ-MutS-immobilized particles with different amount of AQ. Binding reaction was performed at 37 °C for 24 h in DNA-binding buffer.

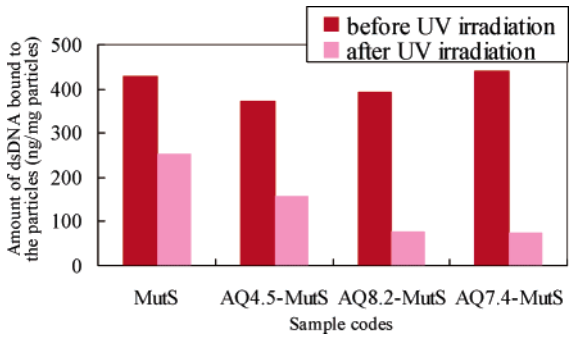

Figure 7. Comparison of ability to photocleave mismatched DNA among a series of AQ-MutS-immobilized particles.Photocleaving reaction was performed at 25 °C for 30 min in DNA-binding buffer. After photocleaving reaction, reaction buffer was treated at 85 °C for 2 h to denature MutS immobilized on the particles.

particles became a plateau within 24 h. From this results, as the sufficient binding reaction time we adopted 24 h, when the binding reaction of dsDNA with the AQ-MutS-immobilized particles was considered to be at equilibrium at 37 °C like MutS-immobilized particles. Then values for the dissociation constant (K_d) for the G/C homoduplex and G/T heteroduplex of AQ-MutS-immobilized particles were determined by Scatchard analysis. The K_d values were 1000 and 68.5 nM for the G/C homoduplex and G/T heteroduplex, respectively. These results indicate that the particles had a high affinity for G/T heteroduplex, and the specificity value corresponding to the quotient $K_{d(G/C)}/K_{d(G/T)}$ was 14.6 (*27*). On the other hand, K_d values of MutS-immobilized particles were 909.1 and 65.4 nM

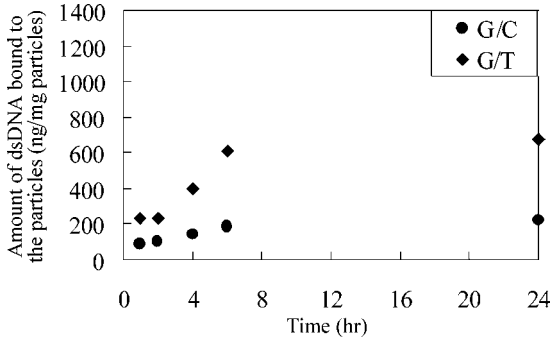

Figure 8. Time dependence of binding reaction of dsDNA with AQ-MutS-immobilized particles. Binding reaction was performed at 37 °C for 1, 2, 4, 6, and 24 h in DNA-binding buffer.

for for G/C homoduplex and G/T heteroduplex, respectively. The K_d values of AQ-MutS-immobilized particles were as same as those of MutS-immobilized particles. In this experiment we evaluated AQ-MutS-immobilized particles using a fluorescence assay that was indirect. Therefore we needed to revaluate the particles using another assay, that is, the chemiluminescence assay mentioned below.

3.5. Chemiluminescence Assay for Characterization of AQ-MutS-Immobilized Particles. The chemiluminescence assay was composed of biotinylated DNA, streptavidin-alkalinephosphatase conjugate (SA-AP), and Lumi-Phos530. In this assay a chemiluminescent reaction is triggered by enzymatic reaction by SA-AP bound to biotinylated DNA through biotin−avidin interaction. It was reported that as little as mamoles (10^{-21} mol) of alkalinephosphatase was detected without particle influence on chemiluminescent signals under a low particle concentration using Lumi-Phos530 (*28*). Therefore the chemiluminescence assay is considered to be a highly sensitive and direct method that can detect dsDNA caught by MutS immobilized on the particles. The results in Figure 9 show that AQ-MutS-immobilized particles could discriminate G/C complementary and G/T mismatched DNAs and cleave G/T mismatched DNA caught by MutS selectively upon UV irradiation. It is also found that the DM of AQ-MutS-immobilized particles was 96.9%, the same as that of MutS-immobilized particles, and the efficiency of photocleavage of G/T mismatched DNA increased with UV irradiation time. That is, AQ-MutS-immobilized particles retained the mismatch binding activity of MutS and photocleaving activity of AQ. It is due to washing of the particles for elimination of nonspecific adsorbed SA-AP in the chemiluminescence assay that the DM calculated in the chemiluminescence assay was higher than in the fluorescence assay. It is confirmed that DM increased because the amount of dsDNA nonspecifically bound to the particles decreases as time of washing increases (data not shown). Fluorescence and chemiluminescence assays proved that AQ-MutS-immobilized particle could catch and cleave mismatched DNA selectively.

3.6. Construction of Mismatch Detection System using AQ-MutS-Immobilized Particles. Finally we tried to construct a new mismatch detection system using AQ-MutS-immobilized particles. The mismatch detection system consisted of AQ-MutS-immobilized particles, and a dsDNA-binding fluorescent dye, SYBR-Gold, was tested. Figure 10 shows relative fluorescence intensity of G/C complementary and G/T mismatched DNAs before and after UV irradiation. Only the spot of G/T mismatched DNA caught by AQ-MutS-immobilized particles and UV irradiated was bright, that is, weak in fluorescence. The

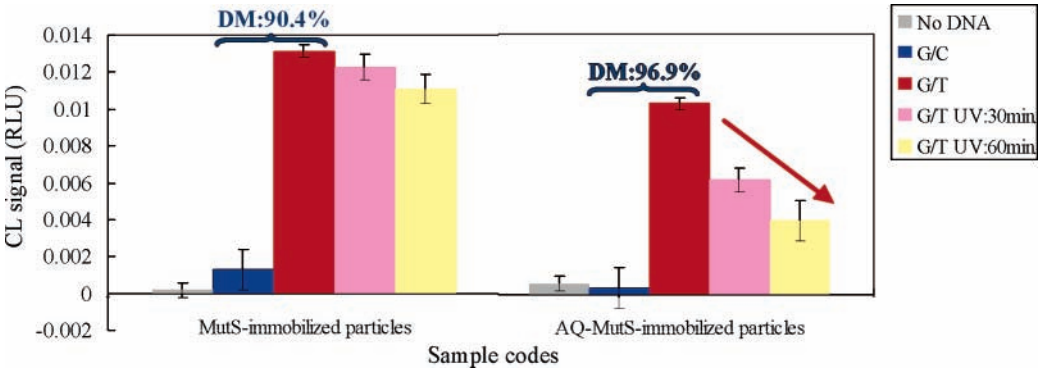

Figure 9. Ability to discriminate complementary and mismatched DNAs and photocleave mismatched DNA using AQ-MutS-immobilized particles. Binding reaction was performed at 37 °C for 24 h in DNA-binding buffer. Photocleaving reaction was performed at 25 °C for 30 and 60 min in the same buffer.

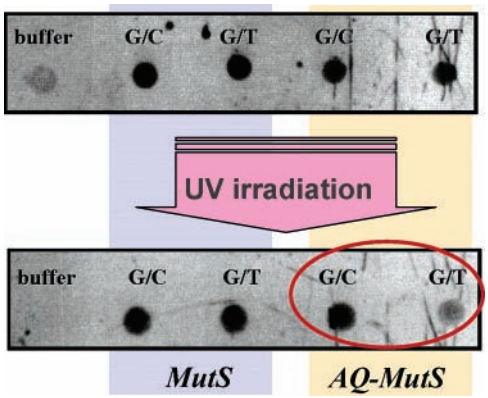

Figure 10. Relative fluorescence intensity of G/C complementary and G/T mismatched DNAs (2.22 nM) before and after UV irradiation in the mismatch detection system using AQ-MutS-immobilized particles (200 ng/μL) and a dsDNA-binding fluorescent dye, SYBR-Gold. Binding reaction was performed at 37 °C for 6 h in DNA-binding buffer and photocleaving reaction was performed at 25 °C for 60 min in the same buffer.

results in Figure 10 suggest that AQ-MutS-immoblized particles cleaved G/T mismatched DNA selectively upon UV irradiation for 60 min. This system enables the detection of mismatched DNA with 40 base pairs by decrease of relative fluorescence intensity after UV irradiation. Clearer all-or-none detection could be done if we carried out the experiment using more AQ-MutS-immobilized particles, although in such a case a step to separate the particles from supernatant should be necessary before measurement. Our system is expected to be practically usable even in diluted dispersion when the 40-mer DNA amplified by PCR is applied. In comparison with other methods to discriminate mismatch DNA (*3*−*7*), our method is simple, regardless of the chain length of sample DNA in theory, and needs no large-scaled instruments. The storage stability of the dispersion of AQ-MutS-immobilized particles was guaranteed for more than 3 months judging from the reproducible results obtained after long storage. In conclusion, we could propose a new mismatch detection system and show that AQ-MutS-immobilized particles would be a useful tool for mismatch detection in DNA diagnosis.

4. CONCLUSIONS

This work proposes a new mismatch detection system by the usage of functional polymer latex particles that can catch and cleave mismatched DNA selectively. We showed that the functional polymer latex particles carrying MutS, mismatch binding protein, and anthraquinone derivative (AQ), a light-activated agent that photocleaves dsDNA, could discriminate G/C complementary and G/T mismatched DNAs and cleave G/T mismatched DNA selectively upon irradiation with 365 nm light. The efficiency of photocleavage of G/T mismatched DNA increased as the number of AQ bound to MutS immobilized on the particles increased and as UV irradiation time extended. In this paper the system consisting of AQ-MutS-immobilized particles and a dsDNA-binding fluorescent dye, SYBR-Gold, was able to detect mismatched DNA with 40 base pairs. The functional particles developed in this work are an absolutely new tool for mismatch detection in DNA diagnosis.

ACKNOWLEDGMENT

This work was supported by the Grant-in-Aid for the 21st Century COE program "KEIO Life Conjugated Chemistry" and the project on "Molecules, Supra-Molecules and Supra-Structured Materials" from the Ministry of Education, Culture, Sports, Science and Technology, Japan.

LITERATURE CITED

(1) Stewart, P. R., EL-Adhami, W., Inglis, B., and Franklin, J. C. (1993) Analysis of an outbreak of variably methicillin-resistant Staphylococcus aureus with chromosomal RFLPs and mec region probes. *J. Med. Microbiol. 38*, 270−277.

(2) Everett, L. A., Glaser, B., Beck, J. C., Idol, J. R., Buchs, A., Heyman, M., Adawi, F., Hazani, E., Nassir, E., Baxevanis, A. D., Sheffield, V. C., and Green, E. D. (1997) Pendred syndrome is caused by mutations in a putative sulphate transporter gene (PDS). *Nat. Genet. 17*, 411−422.

(3) Mirkin, C. A., Letsinger, R. L., Mucic, R. C., and Storhoff, J. J. (1996) A DNA-based method for rationally assembling nanoparticles into macroscopic materials. *Nature 382*, 607−609.

(4) Anada, T., Ogawa, M., Yokomizo, H., Ozaki, Y., Takarada, T., Katayama, Y., and Maeda, M. (2003) Oligodeoxynucleotide-modified capillary for electrophoretic separation of single-stranded DNAs with a single-base difference. *Anal. Sci. 19*, 73−77.

(5) Sato, Y., Ikegaki, S., Suzuki, K., and Kawaguchi, H. (2003) Hydrogel-microsphere-enhanced surface plasmon resonance for the detection of a K-ras point mutation employing peptide nucleic acid. *J. Biomater. Sci., Polym. Ed. 14* (8), 803−820.

(6) Kim, W. J., Akaike, T., and Maruyama, A. (2002) DNA strand exchange stimulated by spontaneous complex formation with cationic comb-type copolymer. *J. Am. Chem. Soc. 124*, 12676−12677.

(7) Komiyama, M., Ye, S., Liang, X., Yamamoto, Y., Tomita, T., Zhou, J. M., and Aburatani, H. (2003) PNA for one-base differentiating protection of DNA from nuclease and its use for SNPs detection. *J. Am. Chem. Soc. 125*, 3758−3762.

(8) Inomata, Y., Kawaguchi, H., Hiramoto, M., Wada, T., and Handa, H. (1992) Direct purification of multiple ATF/E4TF3

polypeptides from HeLa cell crude nuclear extracts using DNA affinity latex particles. *Anal. Biochem. 206*, 109−113.
(9) Inomata, Y., Wada, T., Handa, H., Fujimoto, K., and Kawaguchi, H. (1994) Preparation of DNA-carrying affinity latex and purification of transcription factors with the latex. *J. Biomater. Sci., Polym. Ed. 5*, 293−302.
(10) Imai, T., Sumi, Y., Hatakeyama, M., Fujimoto, K., Kawaguchi, H., Hayashida, N., Shiozaki, K., Terada, H., Yajima, H., and Handa, H. (1996) Selective isolation of DNA or RNA using single-stranded DNA affinity latex particles. *J. Colloid Interface Sci. 177*, 245−249.
(11) Hatakeyama, M., Iwato, S., Fujimoto, K., Handa, H., and Kawaguchi, H. (1998) DNA-carrying latex particles for DNA diagnosis. 1. Separation of normal and point mutant DNAs according to difference in hybridization efficiency. *Colloids Surf., B 10*, 161−169.
(12) Hatakeyama, M., Nakamura, K., Iwato, S., Handa, H., Fujimoto, K., and Kawaguchi, H. (1998) DNA-carrying latex particles for DNA diagnosis. 2. Distinction of normal and point mutant DNA using S1 nuclease. *Colloids Surf., B 10*, 171−178.
(13) Hatakeyama, M., Iwato, S., Hanashita, H., Nakamura, K., Fujimoto, K., and Kawaguchi, H. (1999) DNA-carrying latex particles for DNA diagnosis. 3. Detection of point mutant DNA using an indirect labeled probe.*Colloids Surf., A 153*, 445−451.
(14) Inomata, Y., Kasuya, Y., Fujimoto, K., Handa, H., and Kawaguchi, H. (1995) Purification of membrane receptors with peptide-carrying affinity latex particles. *Colloids Surf., B 4*, 231−241.
(15) Marti, T. M., Kunz, C., and Fleck, O. (2002) DNA mismatch repair and mutation avoidance pathways. *J. Cell. Physiol. 191*, 28−41.
(16) Obmolova, G., Ban, C., Hsieh, P., and Yang, W. (2000) Crystal structures of mismatch repair protein MutS and its complex with a substrate DNA. *Nature 407*, 703−710.
(17) Lamers, M. H., Perrakis, A., Enzlin, J. H., Winterwerp, H. H. K., Wind, N. D., and Sixma, T. K. (2000) The crystal structure of DNA mismatch repair protein MutS binding to a GT mismatch. *Nature 407*, 711−717.
(18) Armitage, B., Yu, C., Devadoss, C., and Schuster, G. B. (1994) Cationic anthraquinone derivatives as catalytic DNA photonucleases: Mechanisms for DNA damage and quinone recycling. *J. Am. Chem. Soc. 116*, 9847−9859.
(19) Breslin, D. T., and Schuster, G. B. (1996) Anthraquinone photonucleases: Mechanisms for GG-selective and nonselective cleavage of double-stranded DNA. *J. Am. Chem. Soc. 118*, 2311−2319.
(20) Shimizu, N., Sugimoto, K., Tang, J., Nishi, T., Sato, I., Hiramoto, M., Aizawa, S., Hatakeyama, M., Ohba, R., Hatori, H., Yoshikawa, T., Suzuki, F., Oomori, A., Tanaka, H., Kawaguchi, H., Watanabe, H., and Handa, H. (2000) High-performance affinity beads for identifying drug receptors. *Nat. Biotechnol. 18*, 877−881.
(21) Hatakeyama, M., Ogura, Y., Sawada, J., Fujimoto, K., Handa, H., and Kawaguchi, H. (1997) Preparation of dimerized polypeptide-carrying microspheres and purification of specific protein bound to these microspheres. *Colloids Surf., B 10*, 41−49.
(22) Nilsson, K., and Mosbach, K. (1981) Immobilization of enzymes and affinity ligands to various hydroxyl group carrying supports using highly reactive sulfonyl chlorides. *Biochem. Biophys. Res. Commun. 102*, *1*, 449−457.
(23) Brown, J., Brown, T., and Fox, K. R. (2001) Affinity of mismatch-binding protein MutS for heteroduplexes containing different mismatches. *Biochem. J. 354*, 627−633.
(24) Wagner, R., Debbie, P., and Radman, M. (1995) Mutation detection using immobilized mismatch binding protein (MutS). *Nucleic Acid Res. 23* (19), 3944−3948.
(25) Bi, L. J., Zhou, Y. F., Zhang, X. E., Deng, J. Y., Zhang, Z. P., Xie, B., and Zhang, C. G. (2003) A MutS-based protein chip for detection of DNA mutations. *Anal. Chem. 75*, 4113−4119.
(26) Obmolova, G., Ban, C., Hsieh, P., and Yang, W. (2000) Crystal structures of mismatch repair MutS and its complex with a substrate DNA. *Nature* 407, 703−710
(27) Blackwell, L. J., Bjornson, K. P., Allen, D. J., and Modrich, P. (2001) Distinct MutS DNA-binding modes that are differentially modulated by ATP binding and hydrolysis. *J. Biol. Chem. 276* (36), 34339−34347.
(28) Ishii, J. K., and Ghosh, S. S. (1993) Beads-based sandwich hybridization characteristics of oligonucleotide-alkaline phosphatase conjugates and their potential for quantitating target RNA sequences. *Bioconjugate Chem. 4*, 34−41.

BC049728L

Pegylated, Steptavidin-Conjugated Quantum Dots Are Effective Detection Elements for Reverse-Phase Protein Microarrays

David Geho,[†] Nicholas Lahar,[†] Prem Gurnani,[‡] Michael Huebschman,[‡] Paul Herrmann,[†] Virginia Espina,[†] Alice Shi,[†] Julia Wulfkuhle,[§] Harold Garner,[‡] Emanuel Petricoin, III,[§] Lance A. Liotta,[†] and Kevin P. Rosenblatt*[,‡]

FDA-NCI Clinical Proteomics Program, Laboratory of Pathology, National Cancer Institute, National Institutes of Health, Bethesda, Maryland 20892, Office of Cellular and Gene Therapy, Center for Biologics Evaluation and Research, Food and Drug Administration, Bethesda, Maryland 20892, and Department of Pathology, Division of Translational Pathology, University of Texas Southwestern, Dallas, Texas 75390. Received December 2, 2004; Revised Manuscript Received March 24, 2005

Protein microarray technologies provide a means of investigating the proteomic content of clinical biopsy specimens in order to determine the relative activity of key nodes within cellular signaling pathways. A particular kind of protein microarray, the reverse-phase microarray, is being evaluated in clinical trials because of its potential to utilize limited amounts of cellular material obtained through biopsy. Using this approach, cellular lysates are arrayed in dilution curves on nitrocellulose substrates for subsequent probing with antibodies. To improve the sensitivity and utility of reverse-phase microarrays, we tested whether a new reporter technology as well as a new detection instrument could enhance microarray performance. We describe the use of an inorganic fluorescent nanoparticle conjugated to streptavidin, Qdot 655 Sav, in a reverse-phase protein microarray format for signal pathway profiling. Moreover, a pegylated form of this bioconjugate, Qdot 655 Sav, is found to have superior detection characteristics in assays performed on cellular protein extracts over the nonpegylated form of the bioconjugate. Hyperspectral imaging of the quantum dot microarray enabled unamplified detection of signaling proteins within defined cellular lysates, which indicates that this approach may be amenable to multiplexed, high-throughput reverse-phase protein microarrays in which numerous analytes are measured in parallel within a single spot.

INTRODUCTION

The pathophysiology of cancer is effected, in part, by proteins elaborated by diseased and normal cells within the tumor microenvironment (*1*). An important milestone in understanding tumorigenic processes is uncovering the nature of tumor cell signaling pathways (*2*). Certain classes of proteins form noncovalent associations, or networks, that comprise signaling pathways. With each association, one protein (a kinase) confers a posttranslational modification such as phosphorylation on its binding partner. This type of interaction is a fundamental means of cellular communication in a cellular environment and underlies the development of malignancy through potentiation of cellular motility, invasiveness, motility, proliferation, and evasion of apoptosis.

Reverse-phase protein microarrays (RPMAs; Figure 1) are an emerging high-throughput technology that offer a means to quantitatively measure both protein levels and posttranslational modifications of signaling proteins in clinical specimens (*3*−*6*). Current genomic techniques are unable to measure such modifications, which are important determinants of protein activity. In this assay, the lysates contain heterogeneous protein mixtures, or analytes, obtained from laser capture microdissected tumor cells extracted from individual patient specimens.

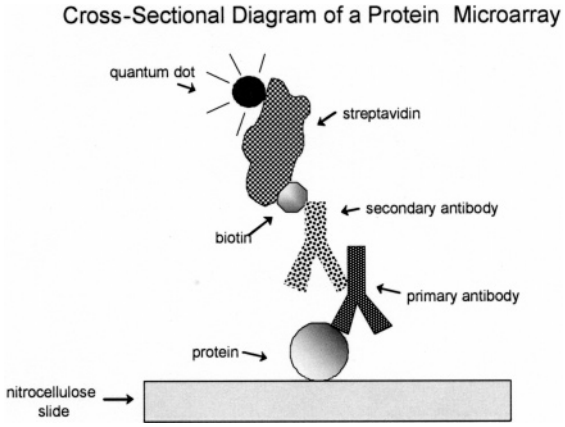

Figure 1. Reverse-phase microarray. In the RPMA, proteins extracted from cellular lysates are arrayed onto a nitrocellulose substrate and probed with a primary antibody. In turn, a biotinylated secondary antibody recognizes the presence of the primary antibody. The biotinyl groups are then detected by streptavidin linked to reporter molecules such as quantum dots or enzymes such as HRP that carry out catalyzed reporter deposition for signal amplification.

These lysates are noncovalently immobilized onto an array surface such as nitrocellulose and then probed by a variety of techniques. This reverse-phase format enables the measurement of low-abundance proteins from a minute amount of scarce clinical samples (on the order of nanoliters) and allows the clinical investigator or clinical lab specialist to compare numerous distinct patient samples, various clinical stages of cancer, mor-

[†] National Institutes of Health.
[‡] University of Texas Southwestern.
[§] Food and Drug Administration.
* Corresponding author. E-mail: kevin.rosenblatt@utsouthwestern.edu.

10.1021/bc0497113 CCC: $30.25 © 2005 American Chemical Society
Published on Web 05/04/2005

phological subtypes, and uninvolved tissues in parallel for side-by-side comparisons of protein activity and signal pathway analysis.

The analytes are detected using an interacting molecule such as a recombinant protein, an antibody, small molecules such as drugs, DNA aptamers, or phage display libraries. Because the analytes can be analyzed in a denatured or native protein format, antibodies useful for western blotting to detect sequential epitopes can be utilized in addition to antibodies employed in ELISAs for conformational epitopes. In fact, RPMAs are especially useful in measuring phospho-specific events since these epitopes are usually masked and require denaturation of the target molecule prior to analysis. The presence of a bound primary antibody can then be visualized through the use of several technologies. For example, the presence of a bound biotinylated antibody can in turn be detected by streptavidin linked to a reporter molecule. This allows a single reporter system to be applied to various, different primary probes. Whereas DNA microarrays benefit from nucleic acid amplification for increased sensitivity, proteins cannot be similarly amplified. Therefore, the detection systems for protein arrays must have a built-in signal enhancement step. A variety of conventional labeling techniques, including radioactivity (*7*), chromagens, and fluorescence (*8*, *9*), have been used to report the presence of proteins on arrays. However, in their current forms, they often have significant limitations in terms of their sensitivity, dynamic range, durability, speed, safety, and ability for multiplexing.

When investigating clinical specimens, a reporter system with a broad dynamic range is required so that disparate quantities of input material can be effectively measured under a single format or experiment in which detection saturation is not easily achieved. A common means of expanding the dynamic range of a protein assay is through the use of fluorescent reporter molecules, and there is an abundance of commercially available organic fluorophores that have been used to tag biological molecules. Unfortunately, many organic fluorescent molecules lack the sensitivity of amplified chromogenic systems and are highly susceptible to photobleaching. Application of emerging nanotechnologies to biology and medicine has produced an alternative class of fluorescently labeled probes through the conjugation of inorganic fluorophores called quantum dots (QDs) to biological interacting molecules (*10*−*12*). QDs are fluorescent, semiconducting nanocrystals, ranging in size from 1 to 10 nm. These nanoparticle labeling agents possess broadband excitation bandwidths with narrow emission bandwidths, large extinction coefficients, and very high quantum yields that result in bright fluorescence. Because of these factors, QDs have distinct advantages over organic fluorescent reporter molecules. Moreover, due to their resistance to photobleaching, QDs produce signals that can be time averaged.

To evaluate methods that could increase the sensitivity and potential for multiplexing the reverse-phase microarray technology, we tested whether QDs could be used as reporter agents using this methodology. Further, we investigated the utility of hyperspectral image analysis in detecting primary, unamplified QD signals (*13*, *14*), which could dramatically improve the chances for high-throughput and rapid analysis. We report here the coupling of QD reporter molecules and hyperspectral imaging techniques that results in the detection of primary, unamplified signals in assays probing for the presence of signaling proteins present in cellular extracts. The detection of numerous unamplified signals within the same protein spot heralds the approach of truly multiplexed quantitative microarray assays for protein activity. This approach has potential utility in clinical settings, enabling selection of personalized therapeutic regimes (*15*).

MATERIAL AND METHODS

Cellular Lysate Preparation. Whole cell lysates were prepared in the following manner. Jurkat cells (clone E6-1, ATCC, Manassas, VA) were grown in RPMI 1640 media (Invitrogen, Carlsbad, CA) supplemented with 10% heat inactivated fetal bovine serum supplemented with 1 mM L-glutamine. Jurkat cells (3×10^6) were then treated with 0.5 μg/mL anti-Fas antibody (Upstate, Waltham, MA) per 1 mL of media at 37 °C in 5% CO_2 for 6 h in order to induce apoptosis. Treated Jurkat cells were harvested by centrifuging the cells at 4 °C for 10 min at 1000 rpm. Subsequently, the cells were washed twice in cold phosphate buffered saline (PBS). The cell pellets were then lysed in a buffer consisting of T-PER (Pierce, Rockford, IL), 2x Tris-glycine SDS loading buffer (Invitrogen, Carlsbad, CA), and β-mercaptoethanol (Sigma, St. Louis, MO). The cellular lysates were vortexed, centrifuged, and stored at −20 °C. A431 cell lysates generated from cells treated with EGF were purchased from a commercial source (BD Biosciences, Chicago, IL).

Reverse-Phase Microarrays. The reverse-phase microarrays were generated as previously described (*6*). Lysates, diluted 1:1 in sample buffer (1 mL of T-PER extraction buffer added to 950 μL of 2x SDS sample buffer and 50 μL of β-mercaptoethanol), were arrayed on nitrocellulose-coated FAST glass slides (Schleicher & Schuell Bioscience, Keene, NH) using a GMS 417 pin-and-ring arrayer (Affymetrix, Santa Clara, CA) that utilizes 500 μm^2 pins. The lysates were arrayed in serial dilutions with a negative control (sample buffer only) included. Approximately 1.5 nL per spot was arrayed, and the slides were stored at −20 °C in a desiccated environment (Dreirite, W. A. Hammond, Xenia, OH) or used immediately.

Immunostaining Procedure. Once the slides were arrayed, they were placed into 1X Re-Blot, mild solution (Chemicon, Temecula, CA), for 15 min to relax protein structure. After the Re-Blot was removed, the slides were washed two times for 5 min each in PBS. The slides were placed into I-Block dissolved in PBS/0.1% Tween-20 for at least 2 h (Applied Biosystems, Foster City, CA) and were then immunostained using an automatic slide stainer (Autostainer Dako Cytomation, Carpinteria, CA) using manufacturer-supplied reagents. Briefly, the slides were incubated for 5 min with hydrogen peroxide and then rinsed with high-salt Tris-buffered saline (CSA Buffer, Dako) supplemented with 0.1% Tween-20. The slides were blocked with avidin block solution for 10 min, rinsed with CSA buffer, and then incubated with biotin block solution for 10 min. After another CSA buffer rinse, a 5 min incubation with Protein Block solution was followed with air-drying. The slides were then incubated with either a specific primary antibody diluted in Dako Antibody Diluent or, as a control, only DAKO Antibody Diluent for 30 min. The primary polyclonal antibodies used in the study were specific for ERK and phosphoERK (Cell Signaling Technology, Inc., Beverly, MA) at dilutions of 1:2000 as demonstrated by western blots (data not shown). The slides were washed with CSA buffer. A secondary biotinylated goat anti-rabbit IgG H+L antibody (1:5000) (Vector Labs, Burlingame, CA) was incubated with the arrays for 15 min. For amplification

purposes, the slides were washed with CSA buffer and incubated with streptavidin−biotin complex for 15 min. After another wash with CSA buffer, the Amplification Reagent was added and incubated for 15 min.

For slides developed using the chromogen system, after washing with CSA buffer, streptavidin−horseradish peroxidase (HRP) was added for 15 min, followed by a CSA buffer rinse; slides were incubated in diaminobenzidine (DAB) chromogen diluted in Dako DAB diluent for 5 min. After the chromogen incubation, the slides were washed in deionized water and imaged using a text scanner. For slides developed using QDs and catalyzed reporter amplification instead of streptavidin HRP, pegylated-Qdot 655-PEG-Sav or nonpegylated-Qdot 655-Sav diluted in QD Buffer was incubated for 15 min on the slides (QD reagents obtained from Quantum Dot Corporation, Hayward, CA). The slides probed with QDs were visualized using 254 nm epifluorescent UV lamps in a FluorChem cabinet system (Alpha Innotech, San Leandro, CA). The emission signal was visualized using a 655 nm narrow bandwidth emission filter (Omega Optical, Brattleboro, VT). Signal intensities for both the chromogen and fluorescent systems were measured and quantified using ImageQuant (version 5.2) (Molecular Dynamics) data analysis software.

A noncommercial hyperspectral imaging microscope was used for detecting proteins labeled without the use of catalyzed reporter amplification (*13*). Arrayed slides were pretreated with 1X Re-Blot and I-Block as described above followed by avidin and biotin blocking and then incubation with the DAKO Protein Block solution. After a 30 min incubation with the primary antibodies and subsequent incubation with the biotinylated secondary antibody, the slides were then exposed directly to the pegylated-Qdot 655-PEG-Sav reagent for 15 min. After being washed, the slides were dried and analyzed on the hyperspectral imaging system using a spectrophotometer coupled to a CCD camera. The slit width was 50 μm, and a 100 W Hg lamp was used for excitation. Continuous spectra between 549 and 666 nm were collected for each array.

Calibration of Hyperspectral Imaging System. During the imaging of the unamplified slides on the hyperspectral imaging system, slightly shorter wavelengths were observed from those reported by the manufacturer. To determine whether those values were a result of our imaging system or image analysis package, we calibrated our system using two monochromatic light sources. Briefly, the hyperspectral imaging microscope was configured with the *f*/6.5, $^1/_2$ meter spectrometer and cooled CCD camera. (For the original slide measurements, it was configured with a *f*/1.2 holographic spectrometer, photointensifier, and cooled CCD camera.) The measurement was made by first illuminating an unamplified specimen slide and recording the fluorescence emitted by the QDs used in the labeling reactions. The excitation illumination was provided via an Olympus U-MWIB filter cube (excitation 460−490 nm and emission LP 515 nm). Next, red (632.8 nm) and green (532 nm) lasers were directed through the microscope objective lens and similarly recorded on the same CCD camera array. The QD and laser spectra are overlayed pixel by pixel (Figure 5A). The wavelength scale calibration is provided by the known laser wavelengths. The wavelength measurement of the QD peak was determined from a simple Gaussian fit of the peak. The instrument function of the spectrometer was not subtracted from the spectra before a fit was made, but a spectral image of a non-QD region was subtracted from the data image before fitting the spectra. Ten peaks were measured from different areas of the image cube acquisition. An error of ~1 nm from the measurements and an estimated QD product uncertainty of ~1 nm give a combined error of ~1.414 nm.

RESULTS

Streptavidin-conjugated quantum dots were incorporated into a standard reverse-phase microarray assay to determine their utility as reporter molecules for this type of high-throughput proteomic test (*3*, *6*, *16*). Qdot 655 streptavidin conjugates were used to detect the presence of bound primary antibody/biotinylated secondary antibody complexes on protein lysates arrayed on nitrocellulose surfaces using an Affymatrix robotic arrayer. As a test system, a Jurkat T-cell population was treated with anti-FAS antibody, which induces apoptosis (*17*). This population of induced cells expresses detectable levels of activated ERK signaling protein based on previous laboratory experience and provided an excellent testing system for phosphoactivation of signaling proteins (data not shown).

Scanning/Detection Modalities. After blocking unbound nitrocellulose sites, arrays bearing immobilized cellular lysates were incubated with a rabbit anti-human ERK antibody. Following the washing steps, a biotinylated goat anti-rabbit secondary antibody was incubated for detection of bound anti-ERK primary antibody. To serve as background controls, identical slides were incubated without primary antibody (antibody diluent only). A secondary biotinylated anti-rabbit antibody was then incubated with the arrays. After washing, signal enhancement utilizing catalyzed signal amplification (CSA) was performed. Signal amplification via catalyzed biotinyl tyramide deposition is an effective tool for enhancing the sensitivity of immunoassays and has been previously shown to be useful in detecting intracellular signaling proteins using reverse-phase microarrays (*18*). Subsequently, the arrays were incubated with the Qdot 655 streptavidin reagent. The QD-probed array was scanned using an Alpha Innotech FluorChem imager using an excitation wavelength of 254 nm and emission measured at 655 nm (Figure 2A,C). Several scanning modalities were employed (data not shown), with the most effective signal-to-noise achieved using an Omega Optical filter made for assessment of 655 nm fluorescent emissions (20 nm bandwidth centered at 655 nm with added heavy blocking of wavelengths in the IR and UV ranges).

Nonspecific QD Interactions. While strong signals were observed within the protein spots after incubation with the primary, secondary, and streptavidin reagents, a similar signal was also present on spots incubated only with secondary reagent and the Qdot 655 streptavidin conjugate (Figure 2A). A similar level of background staining was not found in assays performed with the same secondary antibody reagent and a streptavidin-horseradish peroxidase conjugate followed by chromagen deposition with DAB (data not shown). The Qdot 655 streptavidin conjugate signal was restricted to the protein spots and was not present on the blocked nitrocellulose surface, indicating that molecular constituents of the cellular protein extracts were strongly binding to the QD conjugates in a dose-dependent manner.

Reduction of Nonspecific Binding Using Pegylated QD Conjugate. To decrease nonspecific binding, a modified form of streptavidin-conjugated QDs, Qdot 655-PEG-Sav, was used as the detection molecule in the

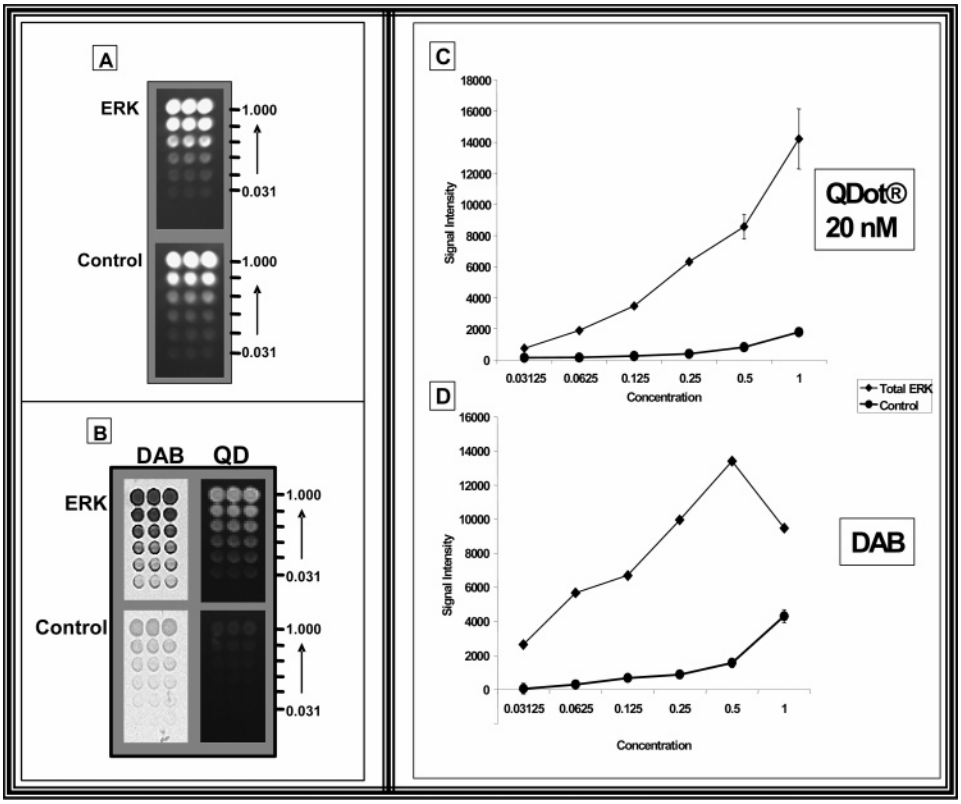

Figure 2. Protein extract binding properties of Qdot-655-SAV conjugates. Jurkat cell lysates, from cells treated with anti-FAS antibody, were arrayed upon nitrocellulose slides in serial dilutions. The array surfaces were then probed with anti-Erk antibody and subjected to biotinyl tyramide amplification. (A) Qdot-655-SAV conjugate (10 nM) was incubated on the arrays. The Qdot-655-SAV conjugate bound equally well to protein spots incubated with anti-ERK antibody or with buffer alone. (B−D) Then, either streptavidin-HRP (B, D) or Qdot 655-PEG-Sav (B, C) (20 nM) were incubated on the arrays. The signal produced by the amplified QDs resulted in a signal intensity per protein spot comparable to that of the standard colorimetric signal (DAB). Low background binding by the pegylated QD was observed. For visualization, the slides probed with QDs were excited using 254 nm UV light for 2 min and visualized using a 655 nm narrow-bandwidth (20 nm) emission filter.

RPMA format. This modification involved the introduction of poly(ethylene glycol) groups onto the streptavidin−quantum dot conjugates. In contrast to the nonpegylated form of the streptavidin-quantum dot conjugate, Qdot 655-PEG-Sav markedly improved the assay by decreasing the intrinsic binding characteristics of the streptavidin QDs to the protein spots (Figure 2B). Only in the presence of a bound primary antibody did Qdot 655-PEG-Sav bind strongly to the protein spots, indicating that the QD signals were limited to the presence of exogenously added biotinylated secondary antibody. Moreover, an identical array was concomitantly analyzed using the chromogen-based assay with DAB deposition as the reporter mechanism, and this also showed a similar staining pattern. The chromogen-based assay was scanned for quantitation using a standard 12-bit text scanner (Figure 2B), while the Qdot-probed array was scanned using an Alpha Innotech FluorChem imager using an excitation wavelength of 254 nm and emission measured at 655 nm (Figure 2C). The QD assay produced an antigen-dependent signal that was linear with a wide dynamic range. Detectable signal was present within the same analyte concentration range observed with the DAB-based chromogenic system; however, the text imaging system was unable to effectively measure the relative amount of chromagen that was deposited at higher protein concentrations due to saturation of the chromagen signal. The QD reporting system, on the other hand, performed well at higher signal intensities, and the dynamic range was significantly broader than the colorimetric method.

Generation of Time-Averaged Signals. One limitation of chromogen-based microarray assays is that only one time period for the development of signal through chromagen deposition can be chosen, and it must be committed to prior to assay performance. This can be a complicating factor in complex assays wherein multiple cellular lysates are arrayed on the same substrate with varying amounts of target proteins present in different dilution curves. The stability of QDs, in addition to their resistance to photobleaching, allows them to be imaged multiple times, for extended periods of time, to capture the linear portions of markedly different dilution curves located on the same array surface. To demonstrate the time-dependence of the quantum dot signal, Jurkat cell lysates, from cells treated with anti-FAS antibody (Figure 3A,B), were arrayed in serial dilutions. The array surfaces were then probed with the anti-ERK antibody. An amplification step followed with deposition of biotinyl tyramide. Qdot 655-PEG-Sav (10 nM) was then incubated on the arrays. The same slide was exposed to UV excitation (254 nm) at 30, 45, and 60 s time intervals. Increasing excitation times increased the signal emission by the QDs, while the background produced by the controls did not increase significantly. This experiment demonstrates the versatility of QDs in generating time-averaged signals. The titration of exposure times allowed the linear portions of various dilution curves to be elucidated in the same assay. Such control over the exposure time cannot be achieved with chromogenic assays, where only one development time is possible.

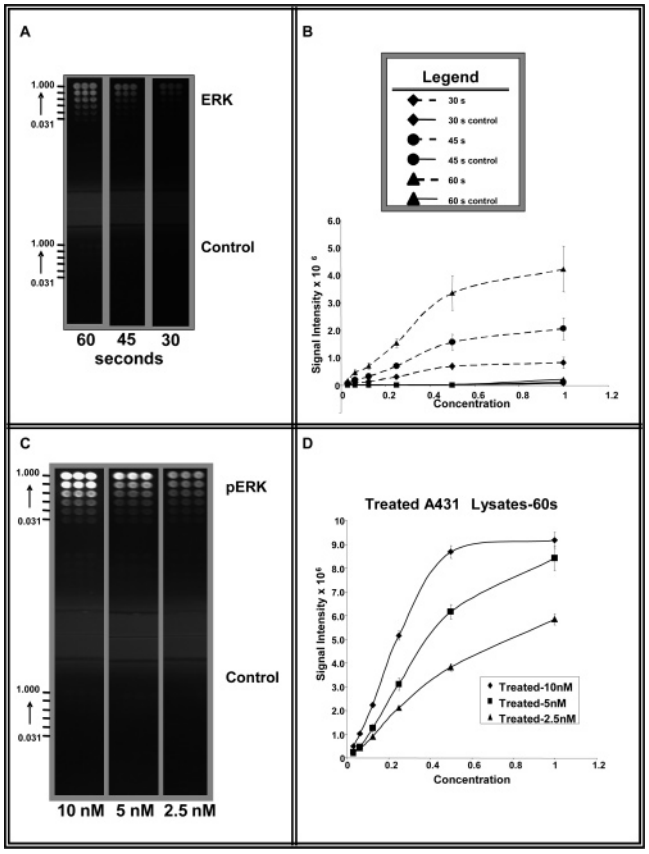

Figure 3. Concentration and time dependence of quantum dot reporter reagents. (A, B) Jurkat cell lysates, from cells treated with anti-FAS antibody, were arrayed upon nitrocellulose slides using serial 1:1 dilutions, probed with an anti-ERK antibody, and subjected to biotinyl tyramide amplification. For background controls, identical slides were incubated without antibody (antibody diluent only). Following the antibody probes, either streptavidin−HRP or Qdot 655-PEG-Sav (10 nM) were then incubated on the arrays. Flourescent slides were exposed to UV excitation (254 nm) at 30, 45, and 60 s time intervals. Increasing excitation times increased the signal emission by the QDs, while the background produced by the controls did not increase significantly. (C, D) EGF-treated A431 lysates were arrayed upon nitrocellulose slides in 1:1 serial dilutions and probed with anti-phosphorylated ERK antibody. For background controls, identical slides were incubated without antibody (antibody diluent only). Following the antibody probes, the slides were then incubated with either streptavidin−HRP or Qdot 655-PEG-SAv. The QD reagent was used at concentrations of 10, 5, and 2.5 nM. A clear dose dependence, based on the amount of QD conjugate added to the system, was observed.

Application of QDs to Alternative Cellular Lysates. To demonstrate the broader applicability of QD detection reagents in reverse-phase arrays, an alternative cellular lysate population was chosen. An epidermal growth factor-treated A431 epidermoid tumor cell line was arrayed on nitrocellulose slides in serial dilutions. The immobilized lysates were then probed with a rabbit anti-human polyclonal antibody that detects phosphorylated ERK (pERK), an activated form of the ERK signaling protein. A secondary biotinylated anti-rabbit antibody was then incubated with the arrays. Again, for the background control, no primary antibody was incubated on the array prior to the addition of a biotinylated anti-rabbit secondary antibody. After an amplification step using the biotinylated tyramide system, the slides were then incubated with Qdot 655-PEG-SAv at varying concentrations (10, 5, and 2.5 nM). The QD-treated slides were then subjected to 254 nm UV excitation, and a 655 nm narrow bandwidth filter was used during imaging (Figure 3C,D). While treated A431 cells did not reveal large increases in total ERK protein levels compared to untreated controls, a large increase in pERK levels was detected after exposure of the cells to EGF (data not shown). EGF is known to lead to phosphorylation of ERK protein (19); this demonstrates the utility of the assay for measuring posttranslational modifications and, thus, protein activation, which is not possible with genomic assays such as DNA microarrays. This experiment also demonstrated that the Qdot 655-PEG-SAv reagent could be applied to an alternative cellular lysate. Furthermore, the dose dependence of the QD signal was demonstrated by greater signal production, with increasing concentration, for a given protein.

Hyperspectral Imaging of QD Microarrays. With present imaging modalities, QD signals are undetectable when used in an unamplified system in RPMAs (data not shown). Hyperspectral imaging enables high-sensitivity scanning for the presence of multiple fluorophores (*13*, *14*). To this end, we tested whether the hyperspectral imager could detect significant signals from unamplified QD RPMA (Figure 4A−D). Indeed, a clear, significant QD signal above background was detected on an unamplfied microarray surface. Further, this measurement was performed on a microarray experiment that had been performed over six months previously, demonstrating the long life of these reporter molecules. Of note, the imaging analysis from our wavelength-calibrated system revealed that the peak emission spectrum was located at 648 nm, rather than the 655 nm emission specified by the supplier, indicating a slight blue-shift in the emission spectrum in our assays (Figure 4E).

Because of the stability of QD emissions over time, several different measurements of the microarrays can be taken at different times to enable optimization of the measurements or for verification of the measurements by different researchers. The hyperspectral image shown below (Figure 4), which had better S/N than at other dates of scanning, revealed a lower-than-expected emission maximum for the QDs (Figure 4E). This experiment indicated that the peak fluorescence of the 655-PEG-SAv reagent, when scanned at that date, was approximately 648 nm. The calculated combined error in our system due to an error of measurement of ~1 nm and an estimated QD product uncertainty of ~1 nm was ~1.414 nm, suggesting a true decrease in the emission wavelength from that reported by the company. To determine whether those measured values resulted from errors in the detection system, a two-laser calibration was performed (Figure 5A). Interestingly, a time-dependent decrease in peak maximum is apparent from the different measurements (Figure 5B).

DISCUSSION

One fundamental goal of clinical proteomics is the development of high-throughput tools that enable limited amounts of patient tissue specimens to be probed for the presence of molecular derangements. RPMAs represent one type of several high-throughput proteomic platforms currently being developed for use in clinical trials. This array format has shown great promise for phosphoproteomic profiling by effectively measuring cellular signaling events. Given the limited amount of material available in biopsy tissue specimens, there is an ongoing effort to improve the sensitivity, robustness, and versatility of RPMAs, so that the maximum amount of information can be extracted from patient specimens. The development of more sensitive detection technologies for

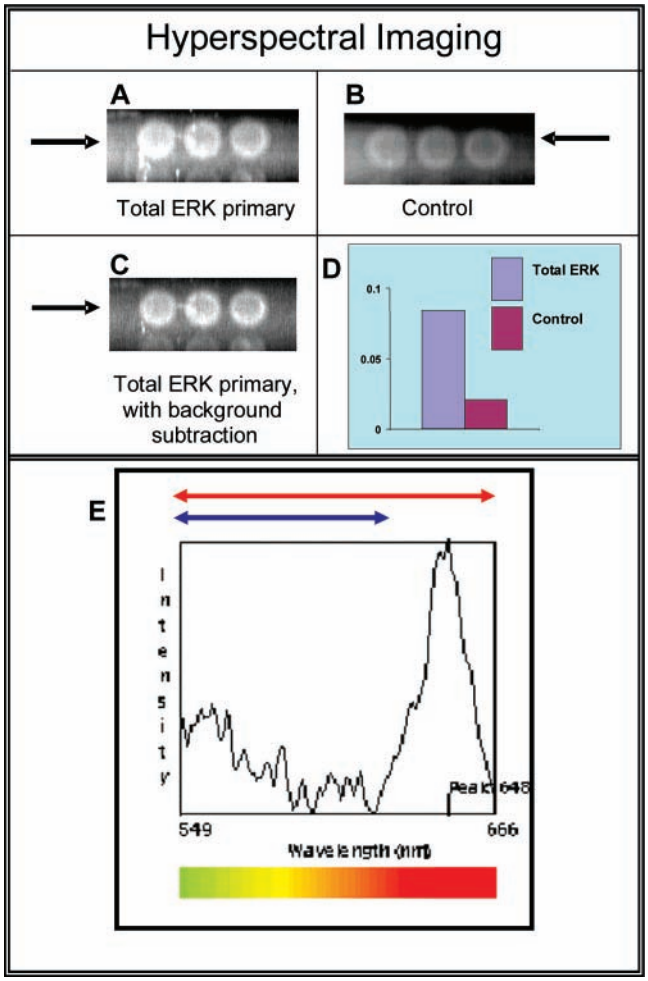

Figure 4. Hyperspectral imager detection of unamplified QD signal. Jurkat cell lysates, from cells treated with anti-FAS antibody, were arrayed upon nitrocellulose slides in a serial dilution. The array surfaces were then probed with anti-ERK antibody. As a background control, an identical slide was incubated without antibody (buffer only). A secondary biotinylated goat anti-rabbit antibody was then incubated with the arrays. Then, Qdot 655-PEG-Sav (20 nM) was incubated with the arrays. The signal produced by the unamplified QDs resulted in a signal detectable by hyperspectral imaging (A, C). Low background binding by the pegylated QD was observed (B). Relative fluorescence intensity is plotted in (D) to compare the signal from the array probed with the primary antibody (A) and the array without the primary antibody (B). The background, non-QD-dependent fluorescence (blue arrow in Figure 4E) was subtracted from the entire continuous spectrum (red arrow in Figure 4E) collected between 549 and 666 nm, resulting in an image signal mostly comprised of QD 655 nm-dependent light. Note, the peak emission spectrum was at 648 nm, an apparent blue-shift from the reported 655 nm peak from the commercial source (E).

protein arrays is being aided by recent developments in nanotechnology.

QDs are a recent example of an emerging nanotechnology. These nanoparticle-scale semiconductor crystals have wide excitation properties and narrow bandwidth emissions, which are generated primarily from elements in Groups II−VI or III−V of the periodic table (*20*, *21*). The emission wavelength can be tuned from the blue to the near-infrared by varying the size and chemical composition of QDs. Also for the same composition of QDs, the smaller the QD, the shorter its emitted wavelength. QDs have higher molar extinction coefficients when excited in the lower wavelength region of the spectrum. For example, QD 605 streptavidin conjugates (by Quantum Dots Corporation, Hayward, CA) have extinction coefficients ranging from 650 000 M^{-1} cm^{-1} at 600 nm to 3 500 000 M^{-1} cm^{-1} at 400 nm and even higher coefficients when excited with higher energy photons. In contrast, fluorescein has a maximum extinction coefficient of 80 000 M^{-1} cm^{-1} (*22*).

Coupled with their dimensional similarity to biomacromolecules, QD conjugates have been shown to be well suited as potential agents for molecular profiling and imaging (*10*, *11*, *20*−*22*). The quantum yields of most organic dye molecules are often decreased upon conjugation to biomolecules. However, higher quantum yields of QD conjugates (up to 80%) that remain unaffected by conjugation to biomolecules have been reported (*22*). Of note, QDs have been used in the development of a filtration-based protein microarray technique that can overcome the diffusion limit and enhance the overall performance of protein microarrays (*23*). The arrays used in that study consisted of an immobilized protein that bound a labeled analyte. Such an array, a forward-phase array, is not optimal for the analysis of heterogeneous clinical specimens and can suffer from lack of unmatched antibody affinities on a single array. The RPMA, as used in our present study, may be a more clinically applicable assay system in that the proteins from cellular lysates are arrayed directly onto a substrate, and since each analyte is measured one at a time, a direct comparison between patients, cell types, or therapeutic response can be evaluated. Direct immobilization of limited target proteins is required in order to realize protein microarrays in a clinical setting. This heterogeneous protein mixture requires a much more sensitive assay than is required for the capture (or forward-phase array) format.

One of the challenges in using QDs for biological studies is the design of hydrophilic QDs that can adapt to various biological environments. Surface coatings such as poly(ethylene glycol) and peptides have been used to decrease nonspecific binding, in the case of PEG, and to provide targeting motifs, in the case of peptides (*24*). QDs coated using an amphiphilic poly(acrylic acid) polymer or PEG are stable in vivo yet have different circulating half-lives (*25*). In the present study, pegylation of streptavidin-conjugated QDs improved the specificity of the binding interactions. Nonpegylated conjugates demonstrated high background binding to protein spots, which was not found with the pegylated conjugate.

QDs have symmetrical, narrow emission peaks unlike organic dyes, which possess asymmetrical and wider emission peaks, especially in the red region of the spectrum. Moreover, the large Stokes shifts between the excitation and emission spectra result in little autofluorescence when using a single common excitation wavelength in the high-UV range for all the different QD colors used in the same assay. These properties lead to minimal overlap, reducing spectral cross-talk between adjacent colors and enabling the possibility of simultaneous analysis of multicolor QDs with multiple narrow bandwidth filters. However, hyperspectral imaging tolerates overlapping spectral signatures. The characteristic property of simultaneous excitation of multicolor QDs with a single light source without appreciable energy transfer among different molecules makes them attractive for numerous biological applications. As it is possible to produce QDs with various emission wavelengths, one potential use of this reporter system is for highly parallel multiplex probing of numerous proteins on a single array. An important step forward toward this goal is the integration of hyperspectral imaging, which enables the detection of mutltiple unamplified QD wavelengths in

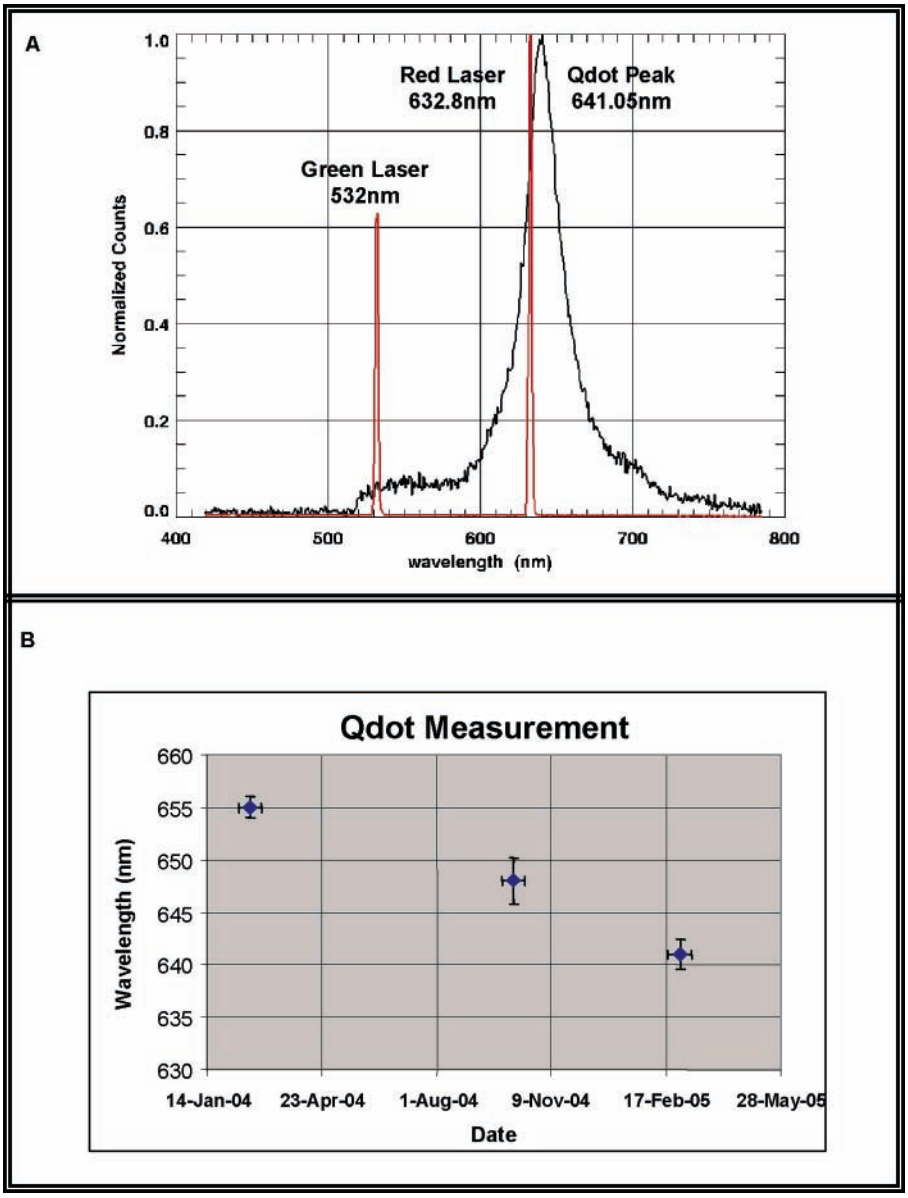

Figure 5. Overlay of laser calibration with the pixel to pixel Qdot signal measurement with the hyperspectral imaging microscope. Green (532 nm) and red (632.8 nm) lasers were used to calibrate the hyperspectral imaging microscope. The figure displays a pixel by pixel overlay of the QD and laser spectra (A). Multiple peaks were measured from different areas of the image acquisition cube. From the figure, the peak intensity of the QD is at 641 nm, which indicates a slight blue-shift of the 655 nm reported by the manufacturer when taking into account a combined error of ~1.414 nm. A plot of the measurements of the maximum wavelength vs time of measurement indicates a time-dependent decrease in the wavelength, possibly revealing erosion of the outer QD shell (B).

parallel. Because this imaging technique measures spectral signatures over a given bandwidth and does not simply count photons passed through a narrow-bandwidth filter, overlapping fluorescent spectra can be read in parallel on a single protein spot in our assay format. One can now envision the multiplexed analysis of the same area of a microarray probed with various QD-conjugated biomolecules, each with a distinct emission peak. Thus, the amount of information that can be gleaned from a single RPMA is dramatically enhanced. Integration of QD technology into protein microarray platforms will likely provide a means for subtle measurements of intracellular signaling pathways while surveying multiple molecular targets simultaneously through multiplexing at subcellular localization resolution.

QDs have remarkably high photochemical stability and can withstand numerous illumination cycles compared to organic fluorophores that get bleached much more rapidly, as exemplified by the extended analytical shelf life of our protein arrays. Extended integration times are thus possible, as are improved signal-to-noise ratios, enhanced sensitivity, enhanced quantitation, and increased assay reliability. For clinical samples in which the concentrations of target proteins may vary considerably, one array may need to be exposed multiple times in order to image widely varying concentrations of analytes. The QDs promote tailored imaging at multiple time intervals for each array on the basis of the signal level present within each sample. Chromogenic arrays do not permit this flexibility, and organic fluorophores rapidly degrade upon repeated imaging. Of note in this study, the QD signal showed remarkable longevity, with unamplified signal present over six months after the initial testing using a hyperspectral imager analyzer. This quality is a very attractive attribute as the protein microarray moves toward clinical usage; however, there may be a time-dependent change in wavelength associated with this signal.

A change in QD wavelength has been reported before, and a mechanism has been suggested. Ballou et al. (2004) pointed out that QD coatings do break down and do remain fluorescent for at least four months (*25*). If the PEG shell of the Qdot 655-PEG-Sav reagent erodes and the ZnS shell is breached or eroded, the Cd and Se atoms could wear down in addition. One report described ZnS shell erosion of QDs with a resultant blue-shift of the emission wavelength (*26*). However, this change was not described for the 655 nm quantum dot, and the shift shown is not large enough to account for the 14 nm we see in our last microarray scan by hyperspectral imaging. On the basis of published data (*26*), the wavelength changes ~43 nm for each 1 nm diameter change of CdSe. Our 14 nm change corresponds to a reduction in diameter of 3.2 Å; such a depth of erosion could be due to the removal of just 3 Cd and/or Se atoms from the surface of the core.

In conclusion, the potential for multiplexed assays, detection of unamplified signals, expanded dynamic range, and robustness under repeated and varying exposure periods makes QD nanoparticles especially suitable for clinical proteomics applications. The hyperspectral image analyzer enables a broadened use of QDs in RPMAs because of its sensitivity and multiplexing characteristics. Technological advances such as integration of QDs and hyperspectral imaging into RPMAs for molecular network analysis will hasten the advance of personalized assessments of patient tumor cells.

ACKNOWLEDGMENT

The authors wish to thank Theresa Harper (Quantum Dot Corporation) for her input into this study. Also, they wish to thank Mary Winters for providing Jurkat cell lysates. Animesh Nandi and Johanne Pastor provided insightful critiques of the manuscript. This work was supported by the University of Texas Southwestern Center for Proteomics Research contract from the NHLBI and the Hudson Foundation.

LITERATURE CITED

(1) Liotta, L. A., and Kohn, E. C. (2001) The microenvironment of the tumour-host interface. *Nature 411*, 375.
(2) Hunter, T. (2000) Signaling—2000 and beyond. *Cell 100*, 113.
(3) Liotta, L. A., Espina, V., Mehta, A. I., Calvert, V., Rosenblatt, K., Geho, D., Munson, P. J., Young, L., Wulfkuhle, J., and Petricoin, E. F., 3rd. (2003) Protein microarrays: meeting analytical challenges for clinical applications. *Cancer Cell 3*, 317.
(4) Grubb, R. L., Calvert, V. S., Wulkuhle, J. D., Paweletz, C. P., Linehan, W. M., Phillips, J. L., Chuaqui, R., Valasco, A., Gillespie, J., Emmert-Buck, M., Liotta, L. A., and Petricoin, E. F. (2003) Signal pathway profiling of prostate cancer using reverse phase protein arrays. *Proteomics 3*, 2142.
(5) Wulfkuhle, J. D., Aquino, J. A., Calvert, V. S., Fishman, D. A., Coukos, G., Liotta, L. A., and Petricoin, E. F., 3rd. (2003) Signal pathway profiling of ovarian cancer from human tissue specimens using reverse-phase protein microarrays. *Proteomics 3*, 2085.
(6) Paweletz, C. P., Charboneau, L., Bichsel, V. E., Simone, N. L., Chen, T., Gillespie, J. W., Emmert-Buck, M. R., Roth, M. J., Petricoin, I. E., and Liotta., L. A. (2001) Reverse phase protein microarrays which capture disease progression show activation of pro-survival pathways at the cancer invasion front. *Oncogene 20*, 1981.
(7) Morozov, V. N., Gavryushkin, A. V., and Deev, A. A. (2002) Direct detection of isotopically labeled metabolites bound to a protein microarray using a charge-coupled device. *J. Biochem. Biophys. Methods 51*, 57.
(8) Wiese, R. (2003) Analysis of several fluorescent detector molecules for protein microarray use. *Luminescence 18*, 25.
(9) Kukar, T., Eckenrode, S., Gu, Y., Lian, W., Megginson, M., She, J. X., and Wu, D. (2002) Protein microarrays to detect protein−protein interactions using red and green fluorescent proteins. *Anal. Biochem. 306*, 50.
(10) Alivisatos, P. (1996) Perspectives on the physical chemistry of semiconductor nanocrystals. *J. Phys. Chem. 100*, 13226.
(11) Alivisatos, P. (2004) The use of nanocrystals in biological detection. *Nat. Biotechnol. 22*, 47.
(12) Bruchez, M., Moronne, M., Gin, P., Weiss, S., and Alivisatos, A. (1998) Semiconductor nanocrystals as fluorescent biological labels. *Science 281*, 2013.
(13) Huebschman, M. L., Schultz, R. A., and Garner, H. R. (2002) Characteristics and capabilities of the hyperspectral imaging microscope. *IEEE Eng. Med. Biol. Mag. 21,* 104.
(14) Schultz, R. A., Nielsen, T., Zavaleta, J. R., Ruch, R., Wyatt, R., and Garner, H. R. (2001) Hyperspectral imaging: a novel approach for microscopic analysis. *Cytometry 43*, 239.
(15) Petricoin, E. F., Zoon, K. C., Kohn, E. C., Barrett, J. C., and Liotta, L. A. (2002) Clinical proteomics: translating benchside promise into bedside reality. *Nat. Rev. Drug Discovery 1*, 683.
(16) Espina, V., Mehta, A. I., Winters, M. E., Calvert, V., Wulfkuhle, J., Petricoin, E. F., 3rd, and Liotta, L. A. (2003) Protein microarrays: molecular profiling technologies for clinical specimens. *Proteomics 3*, 2091.
(17) Boise, L. H., and Thompson, C. B. (1997) Bcl-x(L) can inhibit apoptosis in cells that have undergone Fas-induced protease activation. *Proc. Natl. Acad. Sci. U.S.A. 94*, 3759.
(18) Bobrow, M. N., Harris, T. D., Shaughnessy, K. J., and Litt, G. J. (1989) Catalyzed reporter deposition, a novel method of signal amplification application to immunoassays. *J. Immunol. Methods 125*, 279.
(19) Marshall, C. J. (1995) Specificity of receptor tyrosine kinase signaling: transient versus sustained extracellular signal-regulated kinase activation. *Cell 80*, 179.
(20) Chan, W., Maxwell, D., Gao, X., Bailey, R., Han, M., and Nie, S. (2002) Luminescent quantum dots for multiplexed biological detection and imaging. *Curr. Opin. Biotechnol. 13*, 40.
(21) Han, M., Gao, X., Su, J. Z., and Nie., S. (2001) Quantum-dot-tagged microbeads for multiplexed optical coding of biomolecules. *Nat. Biotechnol. 19*, 631.
(22) Watson, A., Wu, X., and Bruchez, M. (2003) Lighting up cells with quantum dots. *Biotechniques 34*, 296.
(23) Xu, Y., and Bao, G. (2003) A filtration-based protein microarray technique. *Anal. Chem. 75,* 5345.
(24) Akerman, M., Chan, W., Laakkonen, P., Bhatia, S., and Ruoslahti, E. (2002) Nanocrystal targeting in vivo. *Proc. Natl. Acad. Sci. U.S.A. 99*, 12617.
(25) Ballou, B., Lagerholm, B., Ernst, L., Bruchez, M., and Waggoner, A. (2004) Noninvasive imaging of quantum dots in mice. *Bioconjugate Chem. 15*, 79.
(26) Dabbousi, B. O., Rodriguez-Viejo, J., Mikulec, F. V., Heine, J. R., Mattoussi, H., Ober, R., Jensen, K. F., and Bawendi, M. G. (1997) (CdSe)ZnS core−shell quantum dots: synthesis and characterization of a size series of highly luminescent nanocrystrallites. *J. Phys. Chem. B 101*, 9463.

BC0497113

Selective Cell Attachment to a Biomimetic Polymer Surface through the Recognition of Cell-Surface Tags

Yasuhiko Iwasaki,*,† Emi Tabata,†,§ Kimio Kurita,§ and Kazunari Akiyoshi†,‡

Institute of Biomaterials and Bioengineering, Tokyo Medical and Dental University, 2-3-10, Kanda-surugadai, Chiyoda-ku, Tokyo 101-0062, Japan, Center of Excellence Program for Frontier Research on Molecular Destruction and Reconstruction of Tooth and Bone, Tokyo Medical and Dental University, 2-3-10, Kanda-surugadai, Chiyoda-ku, Tokyo 101-0062, Japan, and Department of Materials and Applied Chemistry, College of Science and Technology, Nihon University, 1-8-14, Kanda-surugadai, Chiyoda-ku, Tokyo 101-8308, Japan. Received December 7, 2004; Revised Manuscript Received March 18, 2005

Reactive phosphorylcholine polymers, which can recognize biosynthetic cell-surface tags, were synthesized to control cell attachment. Human promyelocytic leukemia cells (HL-60) with unnatural carbohydrates as cell-surface tags were harvested by treatment with *N*-levulinoylmannosamine (ManLev). The attachment of ManLev-treated HL-60 cells to 2-methacryloyloxyethyl phosphorylcholine (MPC) polymers with hydrazide groups was studied. HL-60 cells, which are nonadhesive, did not attach to any polymer surface without ManLev treatment. In contrast, ManLev-treated HL-60 cells attached to a poly[MPC-*co*-*n*-butyl methacrylate (BMA)-*co*-methacryloyl hydrazide (MH)] (PMBH) surface following 15 min of incubation. The cells that attached to the PMBH surface retained their native morphology and viability for 24 h of incubation. On the other hand, approximately half of the HL-60 cells that attached to the poly(BMA-*co*-MH) (PBH) surface died. These results suggest that MH units in the polymer act as anchors for cell attachment and MPC units help to preserve cell viability on a polymer surface. The coculture of ManLev-treated HL-60 and fluorescence-stained human uterine cervical cancer cells (HeLa) was carried out on polymer surfaces. ManLev-treated HL-60 cells specifically attached to the PMBH surface. In contrast, both HL-60 and HeLa cells were observed on the PBH surface. The control of cellular interactions with synthetic polymers may be useful for the future development of cell-integrated biosensors and biomedical devices.

INTRODUCTION

Synthetic polymers capable of selectively recognizing proteins or cells play important roles in cell separation, biosensors, and the development of biomedical materials (*1*, *2*). In general, few synthetic polymers can recognize a specific biomolecule or cell in vivo because of the complexity of the environment.

Using physicochemical and biological approaches, various surface conditions, such as a wettability gradient (*3*), topological patterns (*4*, *5*), and peptide-immobilization (*6*−*13*) have been applied to control cell attachment. Particularly, Arg-Gly-Asp (RGD)-immobilized surfaces have been extensively studied to control cell adhesion with ligand−receptor interactions (*6*, *11*−*13*). While these approaches have been quite successful, the selectivity of RGD is limited because the RGD sequence is not unique for a specific cell. Moreover, the control of cell attachment to a solid surface has been mainly studied with adhesive cells, and there have been few reports on systems for nonadhesive cells such as leukemia cells (*14*).

Synthetic polymers with an affinity for a cell surface at a submolecular level may be useful for controlling cell/polymer interactions (*15*). Most of these polymers are water-soluble and are used to immobilize the cell surface. For example, lipophilic anchors (*14*), chemical immobilization (*16*, *17*), and ligand−receptor interactions (*18*) have been studied. Through fixation of these polymers on solid surfaces, controlled cell attachment can be achieved. However, the recognition of a specific cell by a synthetic polymer is still limited because most of the cell/polymer interactions proposed are seen with a wide variety of cells, in contrast to unique interaction with a specific cell type. Also, some approaches cannot be applied under physiological conditions because nonspecific interaction with plasma protein often interferes with the specificity of materials for a cell membrane.

In a living cell, carbohydrates on the cell surface contribute to most communications between the cell and its environment (*19*). Therefore, it may be possible to control cell functions with polymers, which can affect carbohydrate interaction with a cell surface. For the recognition of a specific cell, tagging of carbohydrates on the cell membrane, as well as the polymer design, may be effective.

The incorporation of unnatural carbohydrates into living cells provides an opportunity to study the specific contributions of sialic acid and its *N*-acyl side chains to sialic acid-dependent ligand−receptor interactions at a submolecular level. Bertozzi and co-workers have expressed unnatural functional groups, i.e., acetyl, levulinoyl, and azideacetyl groups, on living cell surfaces through the glycosylation of unnatural monosaccharides (*20*−*23*). Since the initial demonstration of cell-surface engineering with *N*-levulinoylmannosamine (ManLev),

* Corresponding author. Phone: +81-3-5280-8026. Fax: +81-3-5280-8027. E-mail: yasu.org@tmd.ac.jp.

† Institute of Biomaterials and Bioengineering, Tokyo Medical and Dental University.

‡ Center of Excellence Program for Frontier Research on Molecular Destruction and Reconstruction of Tooth and Bone, Tokyo Medical and Dental University.

§ Nihon University.

10.1021/bc049707r CCC: $30.25 © 2005 American Chemical Society
Published on Web 04/16/2005

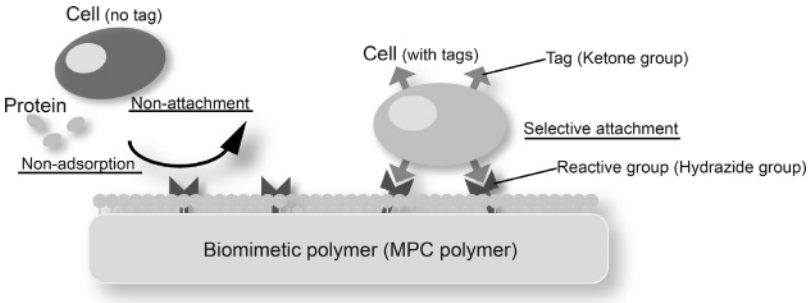

Figure 1. Schematic representation of specific cell attachment to a nonfouling MPC polymer surface through cell-surface tags.

Table 1. Results of Polymer Synthesis

abbrev	molar fraction of units (MPC/BMA/MH) in feed	molar fraction of units (MPC/BMA/MH) in copolymer	conversion,[a] %	M_w[b] ($\times 10^{-4}$)	M_w/M_n[b]	surface mole fraction of coating sample[c] (MPC/BMA/MH)
PMB	0.30/0.70/-	0.30/0.70/-	–	–	–	0.37/0.63/-
PMBH0.5	0.295/0.70/0.005	0.287/0.71/0.003	48.0	–	–	0.34/0.64/0.02
PMBH2	0.28/0.70/0.02	0.26/0.73/0.01	47.8	13.9	2.4	0.13/0.82/0.05
PMBH5	0.20/0.70/0.10	0.18/0.77/0.05	18.3	4.6	2.4	0.25/0.71/0.04
PMBH10	0.25/0.70/0.05	−0.19/0.74/0.07	80.6	8.2	2.9	0.22/0.74/0.04
PBH2	−/0.98/0.02	−/0.98/0.02	64.6	5.9	1.9	−/0.95/0.05
PBH5	−/0.95/0.05	−/0.98/0.02	58.5	5.1	1.6	−/0.94/0.06
PBMA[d]	−/1.00/−	−/1.00/−	–	33.7	–	−/1.00/−

[a] [monomer] = 1.0 M, [AIBN] = 0.5 mM, polymerization temperature 60 °C. [b] Determined by GPC. [c] Determined by XPS. [d] Purchased from Aldrich.

this technique has been applied to the development of targeted imaging reagents (*24*) and methods for gene transfer (*25*). This tagging technique has led to great progress in cell biology and biomedical science (*26*). Sadamoto and co-workers immobilized the cell surface of bacteria using an unnatural cell-surface precursor (*27*). The adhesion of surface-engineered bacteria onto a concanavalin A-immobilized substrate has also been enhanced (*28*). The ability of noncanonical amino acids to introduce novel chemical functionalities into proteins and cells has been explored by Tirrell and co-workers (*29*−*31*). They recently reported an alternate strategy for the detection of noncanonical amino acids, in which azidohomoalanine is incorporated into the *Escherichia coli* outer membrane protein OmpC (*32*, *33*).

We have been studying 2-methacryloyloxyethyl phosphorylcholine (MPC) polymers synthesized as biomimetics of biomembrane structures (*34*−*37*). MPC polymers have a surface that resists nonspecific protein adsorption and cell adhesion, i.e., "biofouling" (*38*, *39*). Biofouling reduces the functionality of a material and can induce an unexpected bioreaction. Further, it has been shown that cells in contact with MPC polymers do not exhibit activation or an inflammatory response (*40*, *41*). However, an MPC polymer has not yet been used as a substrate for a biorecognition surface.

We report here a novel strategy for controlling selective cell attachment and detachment even in nonadhesive cells by using biomimetic polymer surface engineering and cell-surface engineering. To this end, we designed reactive biomimetic MPC polymer surfaces with hydrazide groups, which can react selectively with unnatural ketone-containing carbohydrate as a cell surface tag. Figure 1 shows a schematic representation of selective cell attachment through the recognition of a cell-surface tag. The MPC polymer surface prohibits nonspecific interaction with plasma protein that often interferes with the specificity of the interaction of materials with a cell membrane. Hydrazide groups on the MPC polymer surface react with ketone groups on the cell surface even in cell culture medium. The surface tags on living cells can be introduced in the presence of ManLev by surface engineering (*20*−*25*). In this study, we synthesized MPC polymers with hydrazide groups, prepared and characterized the polymer surface, and controlled cell attachment onto their surfaces.

MATERIALS AND METHODS

Polymer Synthesis. Methyl methacrylate and *n*-butyl methacrylate (BMA) were purified by conventional distillation. Other reagents and solvents were obtained commercially in extra-pure grade and used without further purification. 2-Methacryloyloxyethyl phosphorylcholine (MPC) was synthesized as previously reported (*42*). Methacryloyl hydrazide (MH) was synthesized by reacting methyl methacrylate (0.25 mol, 25 g) and hydrazine monohydrate (0.15 mol, 7.5 g) at 0 °C. Unreacted MMA was removed at 0 °C/10 mmHg, and MH was purified by recrystallization from toluene. ^{1}H NMR (500 MHz, ppm in $CDCl_3$) MH: 6.90 (s; NH, 1H), 5.70, 5.30(s; CH═, 1H), 3.90 (s; NH_2, 2H), 1.90 (s; CH_3, 3H).

N-Levulinoylmannosamine (ManLev) was synthesized as previously described (*21*).

Poly(MPC-*co*-BMA) (PMB), poly(BMA-*co*-MH) (PBH), and poly(MPC-*co*-BMA-*co*-MH) (PMBH) were synthesized by radical polymerization using 2,2′-azobisisobutyronitrile (AIBN) as an initiator (*38*, *42*). BMA was used as a comonomer because it makes it possible to process a polymer membrane. The mole fraction of monomer units in the polymer was determined by phosphorus analysis and elemental analysis. The number-averaged and weight-averaged molecular weight of polymers were determined with a Tosoh gel-permeation chromatography (GPC) system with a refractive index detector and size-exclusion columns (Polymer Laboratories Ltd.), MIXED-C with a poly(ethylene glycol) standard (PEG, Tosoh standard sample) in CH_3Cl/methanol (6/4,vol/vol). The results of polymerization are summarized in Table 1.

Preparation of Sample Plates for the Cell Culture Experiment. The poly(ethylene terephthalate) (PET) plates (14 mm in diameter; Wako Pure Chemical Industries, Ltd., Osaka, Japan) were immersed in an ethanol or chloroform solution of the polymer (0.5 wt %) and dried

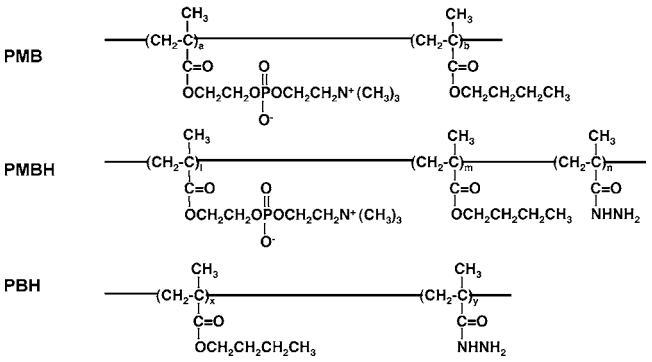

Figure 2. Chemical structures of polymers synthesized in this study.

under a vapor atmosphere of the solvent at room temperature for 30 min. This procedure was repeated twice, and the plates were then dried in vacuo. The surface properties of polymer-coated PET plates were analyzed by surface contact angle measurement (G-1; Erma, Tokyo, Japan) and X-ray photoelectron spectroscopy (XPS) (ESCA-200; Scienta, Uppsala, Sweden) with AlKα (takeoff angle 90°). Survey scan spectra of C_{1s}, O_{1s}, N_{1s}, and P_{2p} were taken.

Cell Culture Experiment. Human promyelocytic leukemia cells (HL-60) were purchased from Health Science Research Resources Bank and maintained in RPMI1640 with 10% fetal bovine serum at 37 °C in a humidified atmosphere of air containing 5% CO_2. The concentration of HL-60 was adjusted to 1.5×10^5 cells/mL. The medium was changed with that containing 10 mM ManLev, and the cells were stored for 3 days. The cells were then washed with fresh medium and centrifuged to remove free ManLev in the medium. The expression of ketones on the cell membrane was confirmed by fluorescence staining with 5 mM Alexa Fluor 350 hydrazide (Molecular Probes, OR).

ManLev-treated HL-60 cells were resuspended with fresh medium, and the concentration was adjusted to 1.0×10^5 cells/mL. The suspension (1 mL) was seeded on PMB, PMBH, and PBH and incubated for 15 min, 2, 4, and 24 h. The cells were then washed twice with fresh medium and observed by phase-contrast microscopy.

To investigate the stability of cells attached to the surface, the surface was rinsed twice with culture medium after a 2-h incubation of ManLev-treated cells on a polymer surface, and cell culture was continued for various periods.

The density of cells attached to the surface was counted in five randomly chosen areas on each polymer surface. A statistical analysis was performed with Student's *t*-test.

Sialidase Treatment. ManLev-treated HL-60 cells were in contact with PMBH5 as mentioned above. After a 2-h incubation of ManLev-treated HL-60 cells on a polymer surface, the surface was rinsed twice with fresh medium to remove nonattached cells. The polymer sample was soaked in 900 μL of fresh medium. Sialidase buffer (20mM HEPES, 140 mM NaCl, pH 6.8) was prepared, and the concentration of sialidase was adjusted to 1 U/mL. The sialidase buffer (100 μL) was added to each medium and stored at 37 °C for 30 min. The surface of the polymer was observed by phase-contrast microscopy. To identify the density of ketones on the cell membrane, cells were stained with 5 mM Alexa Fluor 488 hydrazide (Molecular Probes, Eugene, OR) and analyzed by flow cytometry (Becton Dickinson FACSCalibur).

Cytotoxicity Test. The viability of adherent HL-60 cells on a polymer surface was investigated with a LIVE/DEADViability/Cytotoxicity kit (Molecular Probes, OR). After a 2-h incubation of ManLev-treated HL-60 cells on a polymer surface, the surface was rinsed twice with fresh medium to remove nonattached cells. The cell culture was then continued for various durations. The cells attached to the polymer surface were then stained with 1 μM calcein dye and 2 μM ethidium homodimer-1 (EthD-1) dye. The samples were incubated for 15 min at 37 °C and observed by phase-contrast and fluorescence microscopy (IX-70, OLYMPUS, Tokyo, Japan). The number of attached cells and the percentage of live cells were determined in five randomly chosen areas on each polymer surface. A statistical analysis was performed with Student's *t*-test.

Coculture Experiment. Human uterine cervical cancer cells (HeLa) were purchased from Riken Cell Bank and maintained in RPMI1640 with 10% fetal bovine serum at 37 °C in a humidified atmosphere of air containing 5% CO_2. The contents of the flasks for cell maintenance were detached by trypsin treatment and a cell suspension containing 1.0×10^5 cells/mL in D-PBS was prepared. 5-(and-6)-Carboxyfluorescein diacetate, succinimidyl ester (CFSE, 50 μM) was added to the suspension, and the cells were stored for 15 min. The suspension was then centrifuged to remove free CFSE. CFSE-stained HeLa cells and ManLev-treated HL-60 cells were mixed in fresh medium, and their concentrations were adjusted to 1.0 X 10^4 and 1.0×10^5 cells/mL, respectively. The mixed cells were seeded on polymer surfaces and cocultured for 24 h. After being rinsed with the culture medium, the polymer surfaces were immediately observed by phase-contrast and fluorescence microscopy.

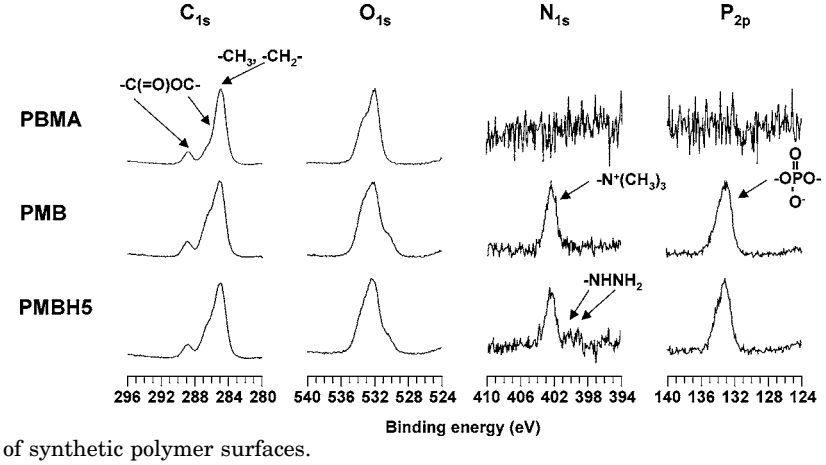

Figure 3. XPS spectra of synthetic polymer surfaces.

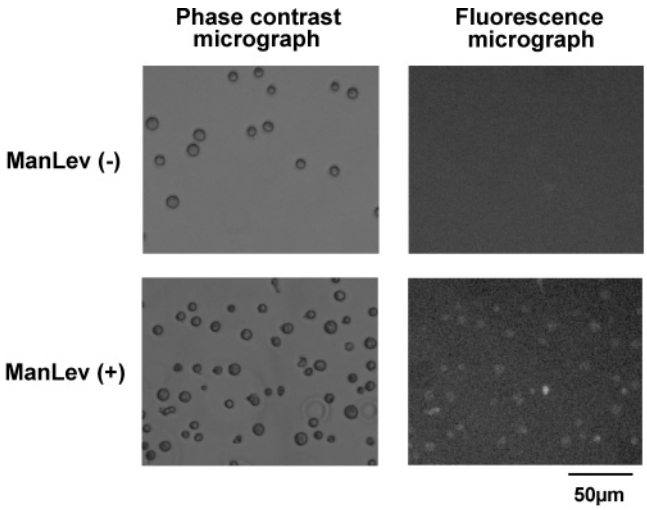

Figure 4. Fluorescence micrographs of ManLev-treated HL-60 cells stained with Alexa Fluor 350 hydrazide.

Table 2. Contact Angle Data for Polymer Surfaces

	θ_A (deg)	θ_A (deg)
PMB	92	8
PMBH0.5	87	22
PMBH2	83	16
PMBH5	93	26
PMBH10	85	25
PBH2	92	78
PBH5	92	85
PBMA	92	77

Detection of Fibronectin Adsorbed onto the Surface. The adsorption of bovine serum fibronectin from the cell culture medium onto the polymer surface was detected by a method based on the antigen/antibody reaction with enzyme-labeled immunoglobulin (*37*). Briefly, polymer-coated PET plates were placed in a 24-well tissue culture plate and secured with a silicone rubber ring. They were left in contact with PBS overnight at room temperature for equilibration of the surface. The cell culture medium was added to each well after the removal of PBS and kept there for 1 h at 37 °C; the PET plates were then rinsed with PBS. A bovine serum albumin (BSA, Sigma Chemical, St. Louis, MO) solution (1 wt % BSA in PBS) was used as a blocking reagent to inhibit any undesirable reactions and nonspecific adsorption with the following antibodies. The PET plates were kept at 4 °C for 3 h and then rinsed with PBS. After the BSA solution was removed, the plates were incubated with the primary antibodies [1 wt % BSA solution containing rabbit immunoglobulin of anti-bovine fibronectin (polyclonal, TELIOS, Pharmaceutical Inc., San Diego, CA)] for 60 min at 37 °C. The plate was rinsed with PBS. The secondary antibody (goat anti-rabbit immunoglobulin, Sigma Chemicals, St. Louis, MO) labeled with horseradish peroxidase (HRP) was then poured into each well, and the wells were stored for 60 min at 37 °C. The plates were transferred to new wells and placed in contact with 3,3′,5,5′-tetramethylbentizine (TMBZ) solution (Color formation kit, SUMILON, Tokyo, Japan) at 25 °C for 10 min in the dark. Absorbance of the TMBZ solution at 450 nm was measured using a microplate reader (Model 450, BIO-RAD Laboratories, Richmond, CA). A statistical analysis was performed with Student's *t*-test.

RESULTS AND DISCUSSION

Characterization of Polymers and Polymer Surfaces. To control cell-attachment, polymer surfaces with reactive units in a phosphorylcholine surface were designed. The hydrazide group was selected as a reaction site for a ketone group on the cell surface. Figure 2 shows the structures of polymers synthesized in this study. The polymerization of 2-methacryloyloxyethyl phosphorylcholine (MPC), *n*-butyl methacrylate (BMA), and methacryloyl hydrazide (MH) occurred in ethanol or ethanol/tetrahydrofuran (THF) mixture. As indicated in Table 1, the composition of each monomer unit could be controlled with the feed. Amphiphilic copolymers containing various amounts of hydrazide groups were obtained. PET plates coated with the synthesized polymers were prepared by the solvent evaporation technique. Elemental analysis of polymer-coated PET surfaces was performed by X-ray photoelectron spectroscopy (XPS). In the case of PET plates coated with MPC polymers, nitrogen and phosphorus peaks were observed at 402.5 and 133.0 eV, respectively (Figure 3). These are attributed to the phosphorylcholine group in the MPC units. Moreover, nitrogen peaks at 399.0 and 400.0 eV due to hydrazide groups were also observed on the surface of PMHB. The

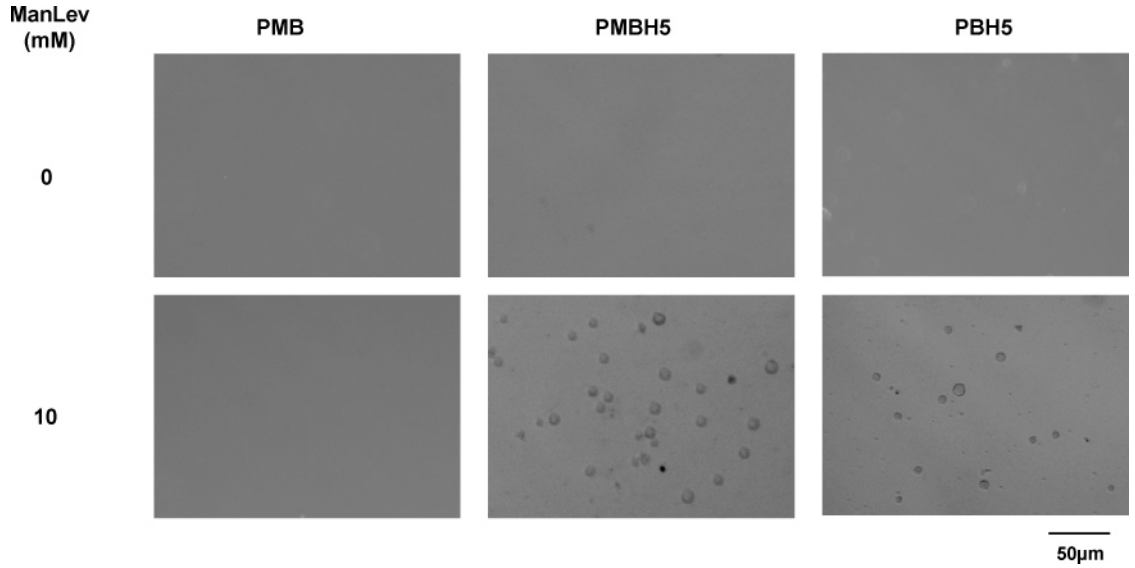

Figure 5. Phase-contrast microscopy images of polymer surfaces after contact with native and ManLev-treated HL-60 cells for 2 h.

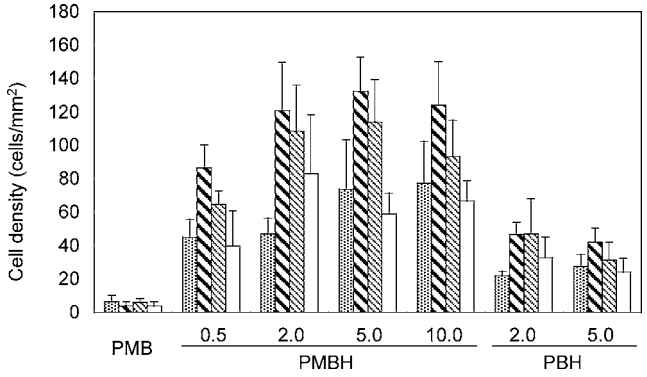

Figure 6. Surface density of ManLev-treated HL-60 cells adhered to polymer surfaces. Filled column: 15 min, deep stripe column: 2 h, light stripe column: 4 h, open column: 24 h.

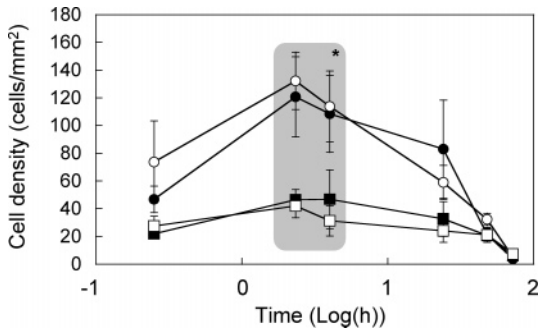

Figure 7. Time-dependence of cell density on PMHB and PBH. Filled circle: PMBH2, open circle: PMBH5, filled square: PBH2, open square: PBH5. * $p < 0.01$ PMBH vs PBH.

surface mole fraction of MH units was determined from the XPS elemental concentration, and the amount was almost constant regardless of the bulk concentration when the MH unit mole fraction in the feed was more than 2 mol %, as shown in Table 1. The water contact angles of the polymer surface are summarized in Table 2. The receding contact angle for the MPC polymers was lower than those for PBH and PBMA. MH unit mole fractions within the range of 2−5 mol % did not affect the water contact angles.

A phosphorylcholine surface with hydrazide groups was prepared by coating a PET plate with PMBH.

Attachment of HL-60 Cells to a Polymer Surface. In this study, HL-60 cells were used as typical nonadhesive cells. The expression of ketone groups on the cell surface was confirmed by treatment with Alexa Fluor 350 hydrazide. This compound stained the cell membrane of ManLev-treated HL-60 cells, but not that of ManLev-untreated HL-60 cells, as shown in Figure 4.

Figure 5 shows phase-contrast micrographs of the polymer surfaces after incubation (2 h) with HL-60 cells that had been pretreated with or without ManLev. ManLev-untreated HL-60 cells did not attach to any of the polymer surfaces. ManLev-treated HL-60 cells did not attach to the control PMB surface. In contrast, ManLev-treated HL-60 cells attached to both the PMBH and PBH surfaces.

The surface densities of adherent cells on polymer surfaces as a function of time after incubation are summarized in Figures 6 and 7. On polymer surfaces with hydrazide groups, cell attachment occurred after 15 min of incubation and the density was stable for 2 h. The density of cells attached to PMBH surfaces increased with an increase in the surface mole fraction of MH units.

The number of HL-60 cells attached to PMBH decreased after 24 h of incubation, as shown in Figure 7.

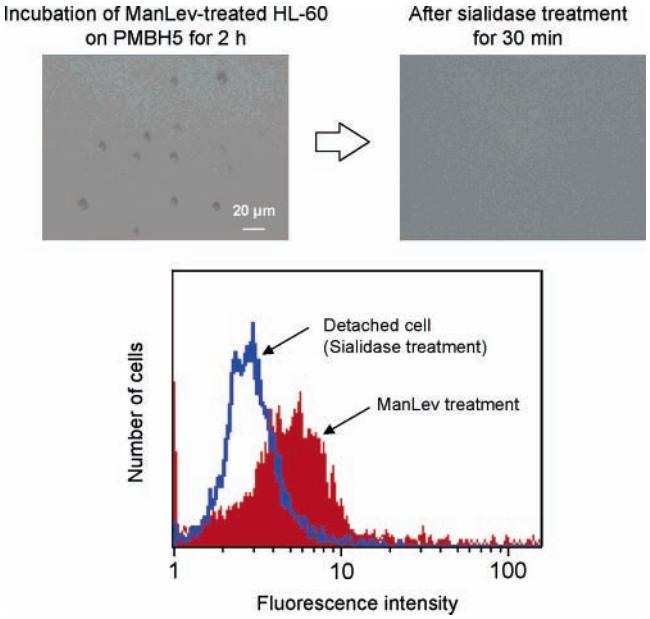

Figure 8. Effect of sialidase treatment on ManLev-treated HL-60 cells attached on PMBH5.

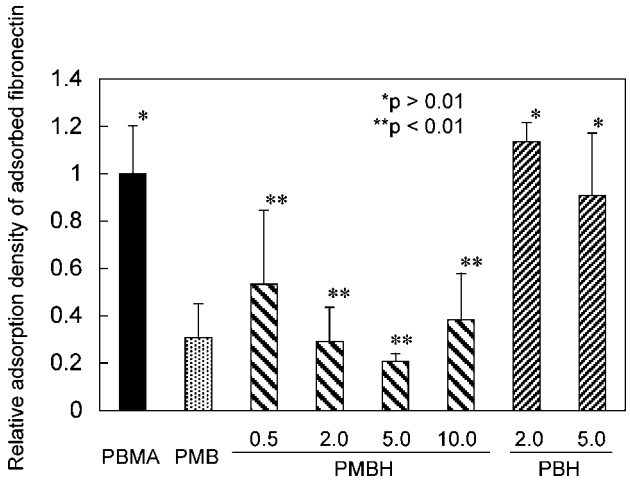

Figure 9. Relative density of fibronectin adsorbed on polymer surfaces from 10% FBS. PBMA = 1.0.

The cell-surface ketone groups decreased to 50% of their initial level at 48 h (*21*). Cell attachment was affected by the density of cell-surface ketone groups. On the other hand, the detachment of cells from the PBH surface was not observed until 48 h of incubation. The metabolic function of HL-60 cells attached to PBH may be affected by the surface. After 72 h of incubation, almost all of the attached cells were detached from the polymer surfaces.

The reactivity of ketone groups on a cell surface with hydrazide groups was confirmed in previous reports (*20*, *43*). In addition, ManLev-treated HL-60 cells did not attach to PMBH or PBH upon further incubation in fresh medium (without ManLev) for 3 days before contact with the polymers (data not shown) because of the depletion of ketone groups from the cell surfaces. The detachment of cells from PMBH by enzyme treatment for 30 min, every cell was detached from the PMBH5 surface as shown in Figure 8. The surface density of ketone groups on the cell membrane of cells detached from a polymer surface was lower than that of ManLev-treated cells. All of these results suggest that cells attached to polymer surfaces through the reaction of ketone groups in carbo-

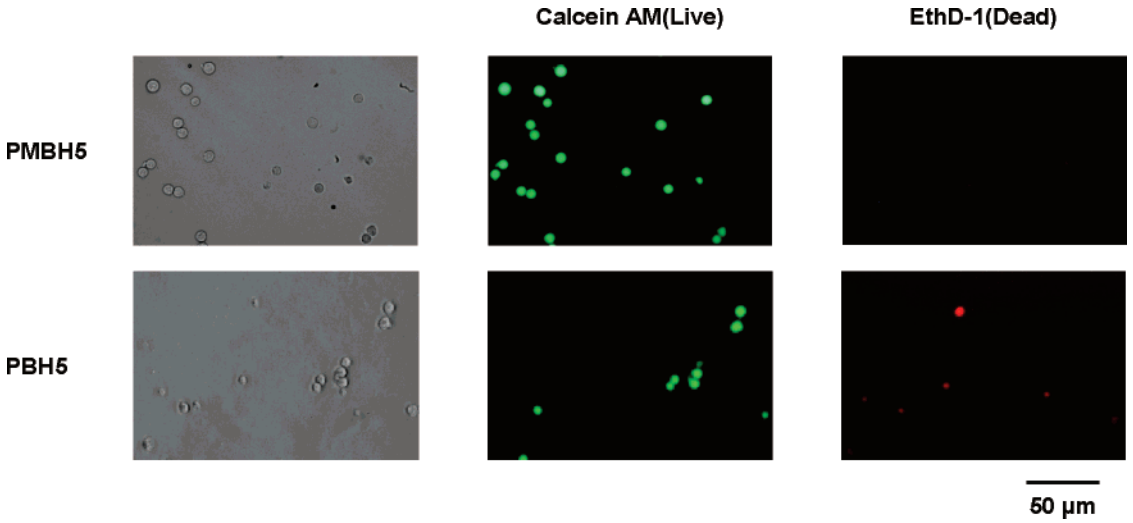

Figure 10. Micrographs of viability of adherent cells on polymer surfaces.

hydrates on the cell surface and hydrazide groups on the polymer surface.

The PMBH surface showed a much greater attachment of cells than the PBH surface, even with the same amount of hydrazide groups. The density on PMBH was approximately three times greater ($p < 0.01$ at 2 and 4 h of incubation) than that on PBH, as shown in Figure 7.

We also studied interaction between MPC polymer and plasma protein. When the mole fraction of MPC units in a polymer was around 0.3, nonspecific protein adsorption was effectively reduced and the extent of adsorption from human plasma was approximately 0.4 μg/cm^2, which is lower than the extent of monolayer adsorption of albumin (lit. 0.9 μg/cm^2) (*38*, *44*). In contrast, the amount of protein adsorbed on PBMA was more than 1.0 μg/cm^2. It has also been clarified that protein in contact with MPC polymer does not undergo denaturation (*39*). We measured the amount of serum protein adsorbed on polymer surfaces to better understand the difference in cell adhesion on PMBH and PBH. As shown in Figure 9, the amount of fibronectin adsorbed onto PBH was the same as that adsorbed onto PBMA, but was significantly greater than that on PMBH. Thus, on the PBH surface, the amount of adsorbed serum proteins would be greater than the amount of monolayer adsorption.

The hydrazide groups on the PMBH surface were not covered with serum protein, and these groups are effective for recognition of the cell surface. On the other hand, the adsorbed proteins on PBH hid hydrazide groups on the polymer, which resulted in a decrease in the density of cell attachment because the surface properties of PBH were similar to those of PBMA (Table 2), which shows a large amount of protein adsorption from plasma (*38*). The PMBH surface could effectively catch HL-60 cells and did not have an adverse effect on cell function.

Viability of Cells Attached to a Polymer Surface. Figure 10 shows phase-contrast and fluorescence microscopy images of polymer surfaces after incubation with HL-60 cells for 24 h. On the PMBH surface, almost all of the adherent cells were stained with calcein (green image) and keep their spherical shape. On the other hand, some of the adherent cells on PBH were stained with EthD-1 (red image) and were deflated. The percentage of live cells attached to the polymer surface is summarized in Figure 11. On the PMBH surface, more than 80% of the cells were alive. However, about 50% of the cells that adhered to PBH were dead. The biological

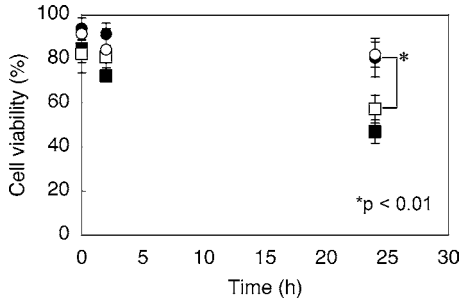

Figure 11. Time-dependence of viability of adherent cells on polymer surfaces. Open circle: PMBH2, filled circle: PMBH5, open square: PBH2, filled square: PBH5.

functions of HL-60 cells in contact with polymer surfaces were retained.

When we previously measured the cytoplasmic free calcium concentration in platelets in contact with an MPC polymer surface, the calcium concentration was unaffected and stayed at its native value (*34*). Moreover, the inflammatory response of differentiated HL-60 cells that adhered to the MPC polymer surface was investigated by the determination of IL-1β mRNA (*41*). While the expression of IL-1β mRNA from adherent cells was observed on conventional polymer materials, secreted mRNA was not observed on the MPC polymer surface, which has an MPC unit mole fraction of more than 0.2. MPC units on a polymer surface probably act to maintain the native condition of attached cells.

Coculture of HL-60 and HeLa Cells on a Polymer Surface. To clarify the possibility of using a polymer surface to recognize specific cells with cell-surface tags, the coculture of ManLev-treated HL-60 cells with native HeLa cells was examined. HeLa cells are a typical cancer cell and nonspecifically adhere to a conventional polymer surface through cell-binding proteins adsorbed on the surface. Figure 12 shows phase-contrast and fluorescence microscopy images of polymer surfaces after the coculture experiment. Cell adhesion was completely suppressed on the PMB surface. On the other hand, both HL-60 and HeLa cells were observed on PBH. HL-60 cells selectively attached to PMBH, while HeLa cells did not. The adhesion of HeLa to a polymer surface is closely associated with the adsorption of cell-binding proteins, such as fibronectin, fibrinogen, and vitronectin, on the surface because these proteins have an RGD binding site for integrin of the cell membrane (*45*). On PMBH, the

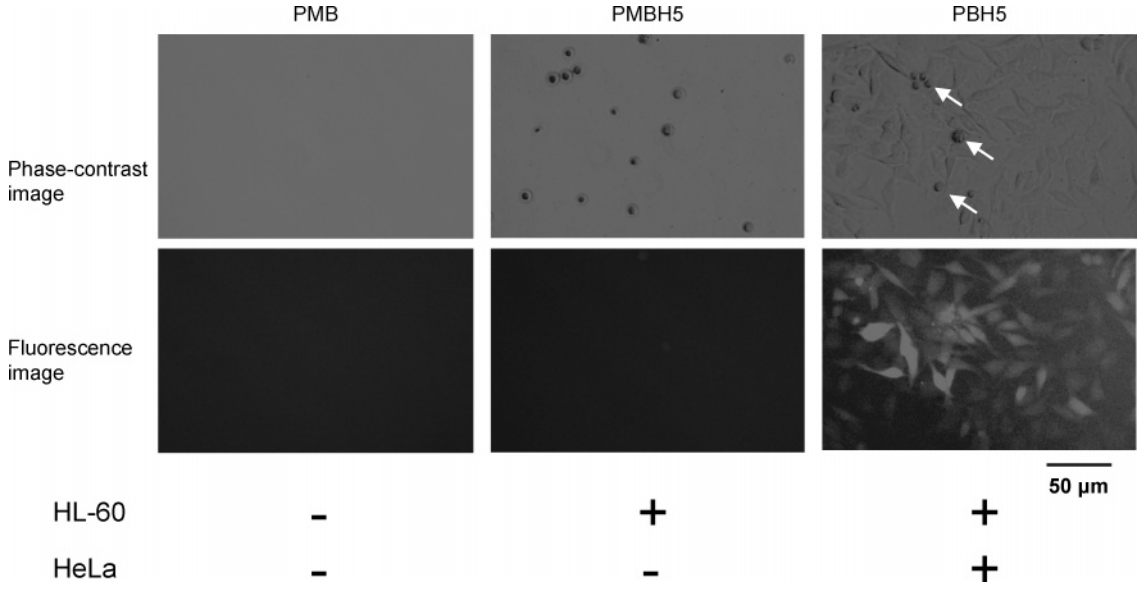

Figure 12. Phase-contrast and fluorescence micrographs of polymer surfaces after the coculture experiment. White arrows represent HL-60.

adhesion of HeLa cells was reduced due to fibronectin-resistance, as shown in Figure 9. It has been previously reported that MPC polymer can nonspecifically reduce plasma protein adsorption (*46*). The nonfouling property of the MPC polymer surface is quite important for achieving specific interaction with a cell.

These results indicate that cell-surface recognition by a polymer surface is evident in both single- and two-cell systems. Such recognition on an MPC polymer surface was effective in a multiple-cell system because the MPC polymer surface rejects the adhesion of cells without tags. Moreover, the control of cell attachment can be applied to a wide variety cells because the expression of unnatural carbohydrates on cell surfaces has been observed on various types of cells (*21*).

CONCLUSION

The present work describes a new cell-recognition surface that works through the coupling of ketone groups on the cell membrane with hydrazide groups on the phosphorylcholine polymer. This cell attachment was specific, and cells were recovered by the depletion of cell-surface tags. On a phosphorylcholine polymer surface, cell viability was effectively retained. Moreover, controlled cell attachment was not affected by the presence of serum protein. The control of cell attachment in a multicellular system was also demonstrated.

Prescher and co-workers recently reported that cell-surface modification with monosaccharides could be applied in a living animal (*47*). Tagging of cancer cells in vivo may be possible through cell-surface engineering because cancer cells have a higher metabolic flux than normal cells (*26*). It has been reported that nanoparticles coated with MPC polymer were not recognized by macrophages (*48*), and they could be used as long-term circulating drug carriers in the blood stream. It may be possible to develop a novel drug targeting system if the functionalities for recognizing cell-surface tags of a cancer cell or a specific tissue can be put on nanoparticles. Moreover, various types of polymer materials using MPC, such as films (*49*), fibers (*50*), nanoparticles (*51*), and micelles (*52*), can be prepared. Cell-surface recognition with MPC polymer promises to be an important technology in drug delivery and bioreactor systems.

ACKNOWLEDGMENT

We thank the New Energy and Industrial Technology Development Organization (NEDO) Japan (Industrial Technology Research Grant in '04, 04A02025) for financial support.

LITERATURE CITED

(1) Ratner, B. D. (1996) The engineering of biomaterials exhibiting recognition and specificity. *J. Mol. Recognit. 9*, 617−625.

(2) Ratner, B. D. (1993) New ideas in biomaterials science—a path to engineered biomaterials. *J. Biomed. Mater. Res. 27*, 837−850.

(3) Lee, J. H., and Lee, H. B. (1993) A wettability gradient as a tool to study protein adsorption and cell adhesion on polymer surfaces. *J. Biomater. Sci. Polym. Ed. 4*, 467−481.

(4) Mrksich, M., Chen, C. S., Xia, Y., Dike, L. E., Ingber, D. E., and Whitesides, G. M. (1996) Controlling cell attachment on contoured surfaces with self-assembled monolayers of alkanethiolates on gold. *Proc. Natl. Acad. Sci. 93*, 10775−10778.

(5) Ito, Y. (1999) Surface micropatterning to regulate cell functions. *Biomaterials 20*, 2333−2342.

(6) Massia, S. P., and Hubbell, J. A. (1991) Human endothelial cell interactions with surface-coupled adhesion peptides on a nonadhesive glass substrate and two polymeric biomaterials. *J. Biomed. Mater. Res. 25*, 223−242.

(7) Lin, H. B., Garcia-Echeverria, C., Asakura, S., Sun, W., Mosher D. F., and Cooper, S. (1992) Endothelial cell adhesion on polyurethanes containing covalently attached RGD-peptides. *Biomaterials 13*, 905−914.

(8) Sugawara, T., and Matsuda, T. (1995) Photochemical surface derivatization of a peptide containing Arg-Gly-Asp (RGD). *J. Biomed. Mater. Res. 29*, 1047−1052.

(9) Shakesheff, K., Cannizzaro, S., and Langer R. (1998) Creating biomimetic micro-environments with synthetic polymer-peptide hybrid molecules. *J. Biomater. Sci. Polym. Ed. 9*, 507−518.

(10) VandeVondele, S., Voros, J., and Hubbell, J. A. (2003) RGD-grafted poly-L-lysine-graft-(poly(ethyleneglycol)) copolymers block non-specific protein adsorption while promoting cell adhesion. *Biotechnol. Bioeng. 82*, 784−90.

(11) Murphy, W. L., Mercurius, K. O., Koide, S., and Mrksich, M. (2004) Substrates for cell adhesion prepared via active site-directed immobilization of a protein domain. *Langmuir 20*, 1026−1030.

(12) Hersel, U., Dahmen, C., and Kessler, H. (2003) RGD modified polymers: biomaterials for stimulated cell adhesion and beyond. *Biomaterials 24*, 4385−4415.

(13) Massia, S. P., and Hubbell, J. A. (1991) An RGD spacing of 440 nm is sufficient for integrin alpha V beta 3-mediated fibroblast spreading and 140 nm for focal contact and stress fiber formation. *J. Cell Biol. 114*, 1089−1100.

(14) Kato, K., Umezawa, K., Funeriu D. P., Miyake, M., Miyake, J., and Nagamune, T. (2003) Immobilized culture of nonadherent cells on an oleyl poly(ethylene glycol) ether-modified surface. *Biotechniques 35*, 1014−1021.

(15) Fujimoto, K. (2002) Supramolecular approaches for cellular modulation. *Supramolecular Design for Biological Applications* (Yui, N., Ed.) pp 343−369, Chapter 17, CRC Press, New York.

(16) Armstrong, J. K., Meiselman, H. J., and Fisher, T. C. (1997) Covalent binding of poly(ethylene glycol) (PEG) to the surface of red blood cells inhibits aggregation and reduces low shear blood viscosity. *Am. J. Hematol. 56*, 26−28.

(17) Panza, J. L., Wagner, W. R., Rilo, H. L., Rao, R. H., Beckman, E. J., and Russell, A. J. (2000) Treatment of rat pancreatic islets with reactive PEG. *Biomaterials 21*, 1155−1164.

(18) Fujimoto, K., Ito. K., and Kawaguchi, H. (1998) Modification and functionalization of cell surface by polymer chains with cell-adhesive ligands. *Abstr. Pap. Am. Chem. Soc. 216*, 318.

(19) Dwek, R. A. (1996) Glycobiology: Toward Understanding the Function of Sugars. *Chem. Rev. 96*, 683−720.

(20) Mahal, L. K., Yarema, K. J., and Bertozzi, C. R. (1997) Engineering chemical reactivity on cell surfaces through oligosaccharide biosynthesis. *Science 276*, 1125−1128.

(21) Yarema, K. J., Mahal, L. K., Bruehl, R. E., Rodriguez, E. C., and Bertozzi, C. R. (1998) Metabolic delivery of ketone groups to sialic acid residues. Application To cell surface glycoform engineering. *J. Biol. Chem. 273*, 31168−31179.

(22) Saxon, E., and Bertozzi, C. R. (2000) Cell surface engineering by a modified Staudinger reaction. *Science 287*, 2007−2010.

(23) Yarema, K. J., and Bertozzi, C. R. (2001) Characterizing glycosylation pathways. *Genome Biol. 2*, REVIEWS0004.

(24) Lemieux, G. A., Yarema, K. J., Jacobs, C. L., and Bertozzi, C. R. (1999) Exploiting differences in sialoside expression for selective targeting of MRI contrast reagents. *J. Am. Chem. Soc. 121*, 4278−4279.

(25) Lee, J. H., Baker, T. J., Mahal, L. K., Zabner, J., Bertozzi, C. R., Wiemer, D. F., and Welsh, M. J. (1999) Engineering novel cell surface receptors for virus-mediated gene transfer. *J. Biol. Chem. 274*, 21878−21884.

(26) Keppler, O. T., Horstkorte, R., Pawlita, M., Schmidt, C., and Reutter, W. (2001) Biochemical engineering of the N-acyl side chain of sialic acid: biological implications. *Glycobiology 11*, 11R−18R.

(27) Sadamoto, R., Niikura, K., Sears, P. S., Liu, H., Wong, C. H., Suksomcheep, A., Tomita, F., Monde, K., and Nishimura, S. (2002) Cell-wall engineering of living bacteria. S. *J. Am. Chem. Soc. 124*, 9018−9019.

(28) Sadamoto, R., Niikura, K., Ueda, T., Monde, K., Fukuhara, N., and Nishimura, S. (2004) Control of bacteria adhesion by cell-wall engineering. *J. Am. Chem. Soc. 126*, 3755−3761.

(29) Datta, D., Wang, P., Carrico, I. S., Mayo, S. L., and Tirrell, D. A. (2002) A designed phenylalanyl-tRNA synthetase variant allows efficient in vivo incorporation of aryl ketone functionality into proteins. *J. Am. Chem. Soc. 124*, 5652−5653.

(30) Kirshenbaum, K., Carrico, I. S., and Tirrell, D. A. (2002) Biosynthesis of proteins incorporating a versatile set of phenylalanine analogues. *ChemBioChem 3*, 235−237.

(31) Kiick, K. L., Saxon, E., Tirrell, D. A., and Bertozzi, C. R. (2002) Incorporation of azides into recombinant proteins for chemoselective modification by the Staudinger ligation. *Proc. Natl. Acad. Sci. U.S.A. 99*, 19−24.

(32) Link, A. J., and Tirrell, D. A. (2003) Cell Surface Labeling of *Escherichia coli* via Copper(I)-Catalyzed [3 + 2] Cycloaddition. *J. Am. Chem. Soc. 125*, 11164−11165.

(33) Link, A. J., Vink, M. K. S., and Tirrell, D. A. (2004) Presentation and Detection of Azide Functionality in Bacterial Cell Surface Proteins. *J. Am. Chem. Soc. 126*, 10598−10602.

(34) Iwasaki, Y., Mikami, A., Kurita, K., Yui, N., Ishihara, K., and Nakabayashi, N. (1997) Reduction of surface-induced platelet activation on phospholipid polymer. *J. Biomed. Mater. Res. 36*, 508−515.

(35) Iwasaki, Y., Sawada, S., Nakabayashi, N., Khang, G., Lee, H. B., and Ishihara, K. (1999) The effect of the chemical structure of the phospholipid polymer on fibronectin adsorption and fibroblast adhesion on the gradient phospholipid surface. *Biomaterials 20*, 2185−2191.

(36) Ishihara, K., Ishikawa, E., Iwasaki, Y., and Nakabayashi, N. (1999) Inhibition of fibroblast cell adhesion on substrate by coating with 2-methacryloyloxyethyl phosphorylcholine polymers. *J. Biomater. Sci. Polym. Ed. 10*, 1047−1061.

(37) Iwasaki, Y., Nakabayashi, N., and Ishihara, K. (2001) Preservation of platelet function on 2-methacryloyloxyethyl phosphorylcholine-graft polymer as compared to various water-soluble graft polymers *J. Biomed. Mater. Res. 57*, 72−78.

(38) Ishihara, K., Oshida, H., Endo, Y., Ueda. T., Watanabe, A., and Nakabayashi, N. (1992) Hemocompatibility of human whole blood on polymers with a phospholipid polar group and its mechanism. *J. Biomed. Mater. Res. 26*, 1543−1552.

(39) Ishihara, K., Nomura, H., Mihara, T., Kurita, K., Iwasaki. Y., and Nakabayashi, N. (1998) Why do phospholipid polymers reduce protein adsorption? *J. Biomed. Mater. Res. 39*, 323−330.

(40) Iwasaki, Y., Sawada, S., Ishihara, K., Khang, G., and Lee, H. B. (2002) Reduction of surface-induced inflammatory reaction on PLGA/MPC polymer blend. *Biomaterials 23*, 3897−3903.

(41) Sawada, S., Sakaki, S., Iwasaki, Y., Nakabayashi, N., and Ishihara, K. (2003) Suppression of the inflammatory response from adherent cells on phospholipid polymers. *J. Biomed. Mater. Res. 64A*, 411−416.

(42) Ishihara, K., Ueda, T., and Nakabayashi, N. (1990) Preparation of phospholipid polymers and their properties as polymer hydrogel membrane. *Polym. J. 22*, *355−360*.

(43) Saxon, E., Luchansky, S. J., Hang, H. C., Yu, C., Lee, S. C., and Bertozzi, C. R. (2002) Investigating cellular metabolism of synthetic azidosugars with the Staudinger ligation. *J. Am. Chem. Sci. 124*, 14893−14902.

(44) Baszkin, A., and Lyman, D. J. (1980) The interaction of plasma proteins with polymers. I. Relationship between polymer surface energy and protein adsorption/desorption. *J. Biomed. Mater. Res. 14*, 393−403.

(45) Hirano, Y., Okuno, M., Hayashi, T., Goto, K., and Nakajima, A. (1993) Cell-attachment activities of surface immobilized oligopeptides RGD, RGDS, RGDV, RGDT, and YIGSR toward five cell lines. *J. Biomater. Sci. Polym. Ed. 4*, 235−243.

(46) Ishihara, K., Ziats, N. P., Tierney, B. P., Nakabayashi, N., and Anderson, J. M. (1991) Protein adsorption from human plasma is reduced on phospholipid polymers. *J. Biomed. Mater. Res. 25*, 1397−1407.

(47) Prescher, J. A., Duhe, D. H., and Bertozzi, C. R. (2004) Chemical remodelling of cell surfaces in living animals. *Nature 430*, 873−877.

(48) Konno, T., and Ishihara K. (2001) Blood Compatible Nanoparticles Immobilized with 2- Methacryloyloxyethyl Phosphorylcholine Polymer. *Trans. Mater. Res. Soc. Jpn. 26*, 897−900.

(49) Iwasaki, Y., Uchiyama, S., Kurita, K., Morimoto, N., and Nakabayashi, N. (2002) A nonthrombogenic gas-permeable membrane composed of a phospholipid polymer skin film

adhered to a polyethylene porous membrane. *Biomaterials 23*, 3421−3427.
(50) Hasegawa, T., Iwasaki, Y., and Ishihara, K. (2001) Preparation and performance of protein-adsorption-resistant asymmetric porous membrane composed of polysulfone/phospholipid polymer blend. *Biomaterials 22*, 243−51.
(51) Konno, T., Kurita, K., Iwasaki, Y., Nakabayashi, N., and Ishihara, K. (2001) Preparation of nanoparticles composed with bioinspired 2-methacryloyloxyethyl phosphorylcholine polymer. *Biomaterials 22*, 1883−1889.
(52) Ishihara, K., Iwasaki, Y., and Nakabayashi, N. (1999) Polymeric lipid nanosphere consisting of water-soluble poly(2-methacryloyloxyethyl phosphorylcholine-*co*-*n*-butyl methacrylate). *Polym. J. 31*, 1231−1236.

BC049707R

In Vivo Imaging of Activated Endothelium Using an Anti-VCAM-1 Magnetooptical Probe

Andrew Tsourkas,† Vivek R. Shinde-Patil,† Kimberly A. Kelly, Pratik Patel, Allison Wolley, Jennifer R. Allport, and Ralph Weissleder*

Center for Molecular Imaging Research, Department of Radiology, Massachusetts General Hospital and Harvard Medical School, 149 13th Street, Charlestown, Massachusetts 02129-2060. Received January 7, 2005; Revised Manuscript Received March 25, 2005

It has been suggested that vascular cell adhesion molecule-1 (VCAM-1) could serve as an early marker for inflammation of the endothelium. The ability to noninvasively image VCAM-1 could thus be a useful tool to diagnose a number of inflammatory diseases at early stages. Here we demonstrate that magnetooptical nanoparticles conjugated to anti-VCAM-1 antibodies can be used to specifically detect VCAM-1 expression on endothelial cells in culture and in vivo. Elevated VCAM-1 expression was detected on cultured murine heart endothelial cells by both fluorescence and magnetic resonance, while only basal expression levels were detected on murine dermal endothelial cells. Intravital microscopy of a murine inflammatory model injected with the VCAM-1 targeted nanoparticles revealed specific labeling of the activated endothelium, with labeling kinetics yielding a maximum vessel wall signal 6 h after injection. In contrast, nontargeted nanoparticles did not exhibit any specific labeling of the endothelium. These studies suggest that the developed nanoparticle would be useful for MR and optical detection of activated endothelium.

INTRODUCTION

The ability to noninvasively image cell surface receptors in vivo provides a promising approach for the early detection and characterization of disease (*1*–*5*). One particularly appealing application is the imaging and identification of host response biomarkers. An inflammatory response of the endothelium is characterized by the expression of a repertoire of inducible adhesion molecules that are tightly regulated both spatially and temporally (*6, 7*). Thus, cell surface molecules that have a significant role in the adhesion of mononuclear leukocytes to sites of inflammation could serve as imaging targets for contrast reagents. Potential candidates include vascular cell adhesion molecule-1 (VCAM-1), P-selectin, and E-selectin (*3, 8*–*11*). VCAM-1 is of particular interest, because it has been found to selectively bind to classes of leukocytes found predominately during the early stages of inflammation (*7, 12*). To date, several attempts have been made to image VCAM-1 expression with radiolabeled antibodies; however, these methods have been limited by low target-to-background ratios (*9, 13*). Therefore, there is a need to develop alternative methods for imaging VCAM-1, ideally with improved sensitivity and resolution.

In this study, we tested whether cross-linked dextran-coated iron oxide (CLIO) nanoparticles labeled with the near-infrared fluorochrome Cy5.5 and conjugated with an anti-VCAM-1 antibody (VCAM−NP) could be used to image TNF-α activated endothelium in an inflammatory murine ear model. Analogous nanoparticles with rat IgG substituted for anti-VCAM-1 antibodies were used as controls for nonspecific labeling. Magnetic resonance and optical imaging of two murine primary endothelial cell types with different VCAM-1 expression levels validated the applicability and targeting specificity of VCAM−NP in vitro. Furthermore, intravital microscopy and subsequent immunohistochemistry on a murine inflammatory model demonstrated the potential for imaging VCAM-1 expression using antibody-conjugated nanoparticles in vivo.

EXPERIMENTAL PROCEDURES

Synthesis and Characterization of Nanoparticles. Superparamagnetic monocrystalline nanoparticles consisting of an iron oxide core and an aminated cross-linked dextran coating (CLIO) were synthesized as previously described (*14, 15*). The iron oxide core size was 3−5 nm in diameter (approximately 9000 Fe centers per particle, assuming a spherical geometry), as previously determined (*16*). The average nanoparticle diameter was determined to be 32.5 nm by laser light scattering (Zetasizer 3000, Malvern Instruments Inc.). The relaxivity of the nanoparticles (R1 = 21.53 mM^{-1} s^{-1}, R2 = 54.2 mM^{-1} s^{-1}) was measured using a 0.47 T tabletop minispec (NMS120, Bruker). The number of amines per nanoparticle was approximately 40, as quantified by methods described previously (*17*).

Cy5.5 (0.5 mg) was suspended in 50 μL of DMSO and added dropwise to 1 mL of CLIO (5 mg of Fe) in PBS, pH 7.4, to yield fluorescent CLIO. The sample was mixed overnight at room temperature and in the dark. The CLIO−Cy5.5 conjugate was purified by extensive dialysis against PBS, pH 7.4, at 4 °C. The Cy5.5 concentration was determined according to the manufacturer's instructions (ϵ = 250 000 at 674 nm). The final iron concentration was determined by dissolution of the iron oxide core in 6 N HCl and 0.03% hydrogen peroxide and comparing absorbance measurements at 410 nm (minus the contri-

* To whom correspondence should be addressed. Tel: 617-726-8226. Fax: 617-726-5708, E-mail: weissleder@helix.mgh.harvard.edu.

† Authors contributed equally.

10.1021/bc050002e CCC: $30.25 © 2005 American Chemical Society
Published on Web 04/28/2005

bution from Cy5.5) to known standards. The total iron content was determined by comparing the measured absorbance (minus the contribution from Cy5.5) to known standards. On the basis of the measurement of 9000 Fe centers per nanoparticle, the number of Cy5.5 molecules per nanoparticle was determined to be approximately 10.

Synthesis of NHS−COOH. Suberic acid (1.742 g, 10 mmol) was added to 0.61 mL of trimethylacetyl chloride (5 mmol). To this was added 20 mL of anhydrous dichloromethane. The solution was stirred on ice for 5 min. Then 0.73 mL of triethylamine (5.25 mmol) was added, and the solution was mixed for 2 h on ice under nitrogen (flask 1). In a separate flask, 0.575 g of NHS (5 mmol) was suspended in 10 mL of tetrahydrofuran and mixed under nitrogen (flask 2). After the contents of flask 1 had mixed for 2 h, the two flasks were combined. The solution was mixed on ice until cool (approximately 5 min). Then, 0.73 mL of triethylamine (5.25 mmol) was added and the solution was mixed for 2 h on ice under nitrogen. The sample was centrifuged at 2500 rpm for 10 min and allowed to stand for 30 min. The sample separated into two phases, and the bottom phase was collected and filtered through a 0.45 μm syringe filter. Aliquots of the product were placed in 1.5 mL tubes, desiccated overnight, and subsequently stored at −20 °C.

Carboxylating CLIO (CLIO−COOH). Amine-containing CLIO−Cy5.5 (0.5 mg) was diluted into a 1 mL 50/50 mixture of PBS (pH 7.4) and DMF. This was added to approximately 50 μmol of dry NHS−COOH. The sample was vortexed until the NHS−COOH was completely suspended, and it was then incubated overnight in the dark. Four volumes of 2-propanol were then added, and the sample was centrifuged at 2000*g* for 2 min. The supernatant was removed, and the pellet was resuspended in DMF. The 2-propanol precipitation procedure was repeated two more times, but the pellet was resuspended in PBS (pH 7.4). Additional purification was performed by repeatedly filtering the nanoparticles on a Microcon YM-50 centrifugation column (Millipore) and resuspending in PBS (pH 7.4).

Antibodies. M/K-2.7 hybridoma cells (ATCC, Catalog No. CRL-1909) that secrete rat anti-mouse anti-VCAM-1 monoclonal antibodies were batch cultured in a CellLine Apparatus (BD Biosciences) according to the manufacturer's instructions. Antibody secreted into the media (2−20 mg/culture batch) was recovered and concentrated by affinity purification using IgG purification columns (Pierce Chemical), dialyzed into PBS, and stored at −20 °C. Rat IgG control antibody was purchased from Sigma.

CLIO-Antibody Conjugation. Purified carboxylated nanoparticles (0.1 mg) were precipitated in four volumes of 2-propanol. The suparnatant was removed, and the pellet was resuspended in 50 μL of MES buffer (pH 6.0) (50 mM MES, 0.5 M NaCl). To this were added 10 μL of 200 mM EDC and 10 μL of 500 mM Sulfo-NHS. The sample was mixed at room temperature for 1 h. Then the nanoparticles were precipitated in four volumes of 2-propanol and resuspended in 100 μL of 5 mg/mL anti-VCAM-1 antibody or rat IgG. The sample was mixed overnight at 15 °C in the dark. Nanoparticle−antibody conjugates (VCAM−NP and IgG−NP, respectively) were purified from unbound antibodies by isolating the conjugates by magnetic separation on a MACs MS column (Miltenyi Biotech). The nanoparticle−antibody conjugates were eluted in PBS (pH 7.4). The nanoparticle concentration was determined as described above, and the antibody concentration was determined by performing a BCA assay according to the manufacturer's instructions. Labeling ratios of 0.63 mg of IgG per mg of Fe and 0.87 mg of anti-VCAM per mg of Fe were measured.

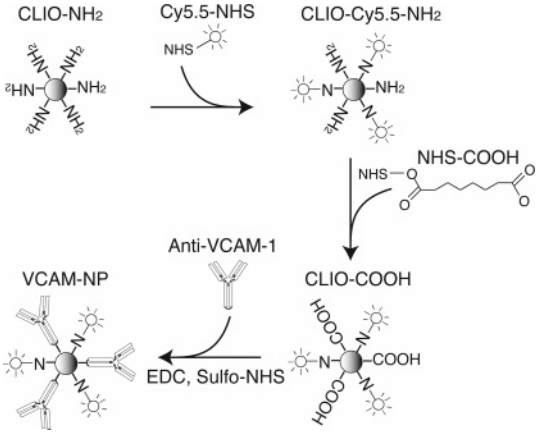

Figure 1. Schematic of VCAM−NP synthesis. Superparamagnetic monocrystalline nanoparticles consisting of an iron-oxide core and an aminated cross-linked dextran coating (CLIO−NH_2) were labeled with the near-infrared fluorochrome Cy5.5. Next the remaining free amines were converted to carboxyls (CLIO−COOH). Anti-VCAM-1 antibodies were then attached using EDC/Sulfo-NHS chemistry (VCAM−NP).

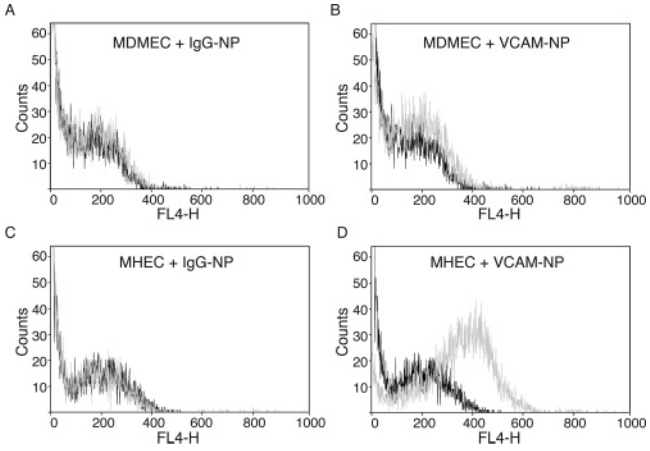

Figure 2. FACS analysis of murine dermal endothelial cells (MDMEC) and murine heart endothelial cells (MHEC). A suspension of each endothelial cell phenotype was incubated with IgG−NP or VCAM−NP for 30 min. Positive labeling was determined by detecting of Cy5.5 fluorescence in the FL4-H channel. Cells labeled with either IgG−NP or VCAM−NP (as indicated in the figure) are represented by the gray lines. Unlabeled cells are represented by the black lines. High expression levels of VCAM-1 expression were only evident on the MHEC (panel D). Cells labeled with IgG−NP (panels A and C) did not exhibit any fluorescence, indicating the absence of nonspecific labeling/uptake.

Cell Culture and Flow Cytometry (FACS). Murine heart endothelial cells (MHEC) and murine dermal endothelial cells (MDMEC) were isolated and propagated as described previously (*18*). Cells were grown to confluence on gelatin-coated six-well plates (six wells each) and then incubated with either murine tumor necrosis factor-α (mTNF-α, 120 ng/mL) or vehicle for 4.5 h. Endothelial monolayers were washed 3× with HBSS (prewarmed to 37 °C), harvested by brief (30 s) trypsinization, and recovered in ice-cold FACS buffer (RPMI containing 5% FCS). Endothelial cells were washed by centrifugation at 4 °C for 5 min and then incubated in either 25 μg/mL anti-VCAM-1 (on 100 μL of VCAM−NP), 25 μg/mL IgG (on 100 μL IgG−NP), or vehicle (control) for 30 min at 37 °C. Analogous control experiments were performed with 10 μg/mL anti-VCAM-1 antibody and 10 μg/mL IgG

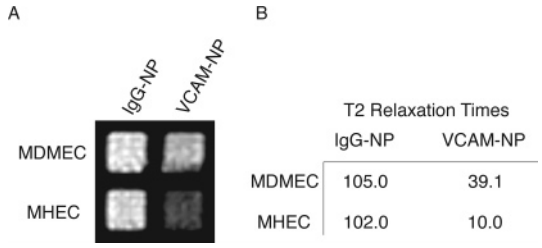

Figure 3. MR analysis of MDMEC and MHEC labeled with either VCAM−NP or IgG−NP. (A) Cross-sectional MR image of MDMEC and MHEC lysates in 384-well plates. MDMEC and MHEC were incubated with either VCAM−NP or IgG−NP for 30 min. Following a 3× wash in PBS, the cells were lysed and pipetted into a 384-well plate and T2-weighted images were acquired. MR images were obtained using a 4.7 T superconducting magnet (Bruker) and performing multiecho spin−echo sequences (TR/Te = 2000/3.5 ms × 40). (B) T2 relaxation times (21 °C; 4.7 T) determined for the MDMEC and MHEC lysates.

directly labeled with Cy5.5 (i.e. without nanoparticle) to confirm the level of VCAM-1 expression on each cell type. Incubated cells were washed 2× in cold FACS buffer and 1× in cold DPBS alone, fixed in 100 μL of 2% paraformaldehyde (in DPBS) and stored at 4 °C in the dark. Samples were analyzed by flow cytometry (10 000 cells/sample) on a Becton Dickinson FACSCalibur (San Jose, CA) using the FL-4 channel to detect the Cy5.5 label on the nanoparticles. Cell isolation, labeling, and FACS analysis were performed in duplicate.

MR Imaging. MHEC and MDMEC were grown to confluence in six-well plates and then harvested as described above. MHEC and MDMEC were pooled separately into two tubes, centrifuged at 4 °C for 10 min, and resuspended in 500 μL of DMEM containing 5% FCS. Each cell suspension was then split into two 250 μL aliquots. One pair of MHEC and MDMEC aliquots were incubated in 100 μL of 100 μg/mL IgG on IgG−NP, while the second pair were incubated in 100 μL of 100 μg/mL anti-VCAM-1 on VCAM−NP for 30 min at 37 °C. Following incubation, the cells were washed three times in DMEM containing 5% FCS, lysed, and pipetted into 4 wells of a 384-well plate. MR images of the wells were obtained on a 4.7 T superconducting magnet (Bruker) using multiecho spin−echo sequences (96 × 96 matrix, 3.0 cm FOV, 1 mm slice thickness, TR 2000 ms, Te_1 = 3.5 ms × 40 echoes). The T2 relaxation time of each sample was determined as previously described (*19*).

Intravital Confocal Microscopy and Immunohistochemistry. C57B1/6 mice (n = 6) were injected subcutaneously in the left ear with 5 ng of mTNF-α in 10 μL of saline. After 24 h, the animals were anesthetized with isoflurane (1−2%) and injected intravenously (retino-orbital) with either VCAM−NP (n = 2) or IgG−NP (n = 2) at a dosage of 165 μg of Fe in 150 μL of PBS (pH 7.4). The ears of each animal were imaged on a Nikon EF600N microscope equipped with a BioRad Radiance 2100 confocal system at 1, 6, and 24 h following nanoparticle injection using a 40× water immersion objective. Fluorescence images of the vasculature were acquired with a z resolution of 1 μm and a depth of 25 μm in the Cy5.5 channel. Identical settings were used for the acquisition of all confocal images. Images used in the figures represent the brightest cross-sectional image of the stack of images. The two animals that were not injected with nanoparticles were sacrificed by CO_2 asphyxiation at the 6 h time point for histology. The other four animals were sacrificed upon completion of imaging at the 24 h time point. The ears were removed from each of the animals and sections stained for CD31 and VCAM-1. Digital images were acquired on a Nikon Eclipse E400 upright microscope equipped with an Insight color camera using a 40× objective.

RESULTS AND DISCUSSION

Endothelial host response is one of the earliest and most consistent biomarkers of many diseases. One promising molecular marker for identifying sites of early-stage inflammation is VCAM-1. Here, we developed a magnetofluorescent nanoparticle capable of detecting VCAM-1 expression by both magnetic resonance and optical imaging. This would allow disease screening by MR imaging and after surgical identification of diseased areas by intraoperative fluorescence imaging. Specifically, we coupled a near-infrared fluorochrome (Cy5.5) and an anti-VCAM-1 antibody to cross-linked dextran-coated iron oxide (CLIO) nanoparticles (Figure 1). CLIO nanoparticles provide an attractive platform for creating targeted imaging probes because of their high stability, superparamagnetic properties for MR contrast, and their controllable chemistry for surface modification. The CLIO nanoparticles utilized in this study were synthesized with aminated functional groups introduced onto the dextran to facilitate bioconjugation. Each nanoparticle was labeled with approximately 10 Cy5.5 fluorochromes. The remaining unconjugated amines were converted to carboxyl groups, and rat anti-mouse anti-VCAM-1 antibodies were covalently conjugated to the nanoparticles using carbodiimide (EDC) and sulfo-NHS chemistry (VCAM−NP). In parallel, Cy5.5 labeled CLIO nanoparticles were

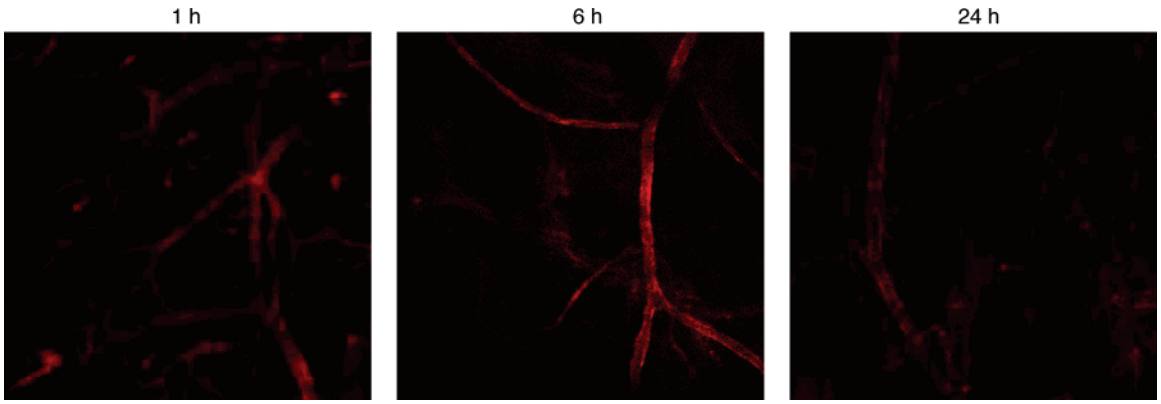

Figure 4. Fluorescence confocal microscopy images of mTNF-α activated endothelium in a C57B1/6 mouse 1, 6, and 24 h after injection of VCAM−NP. The left ears of C57B1/6 mice were injected with mTNF-α. After 24 h, VCAM−NP was introduced via retino-orbital injection. Representative fluorescence images of the left ear at 1, 6, and 24 h postinjection are shown. At 1 h, most of the nanoparticles still appear to be in circulation; however, by 6 h VCAM−NP is clearly localized at the endothelial wall.

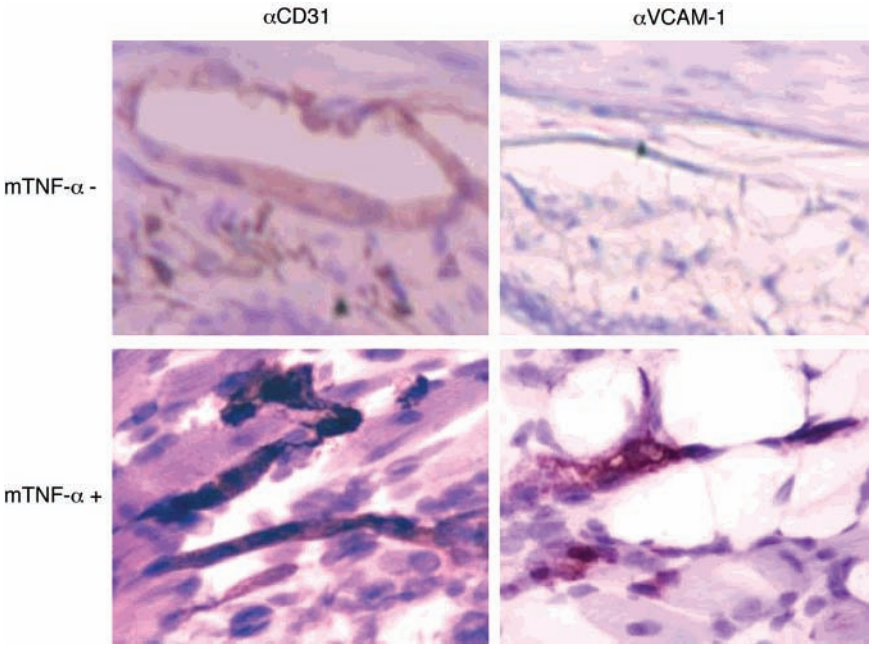

Figure 5. Immunohistochemical analysis of normal and mTNF-α activated ears. Adjacent serial sections of ears 30 h following mTNF-α treatment revealed the up-regulation of VCAM-1 in endothelial cells. Endothelial cells from untreated ears did now show any appreciable VCAM-1 staining.

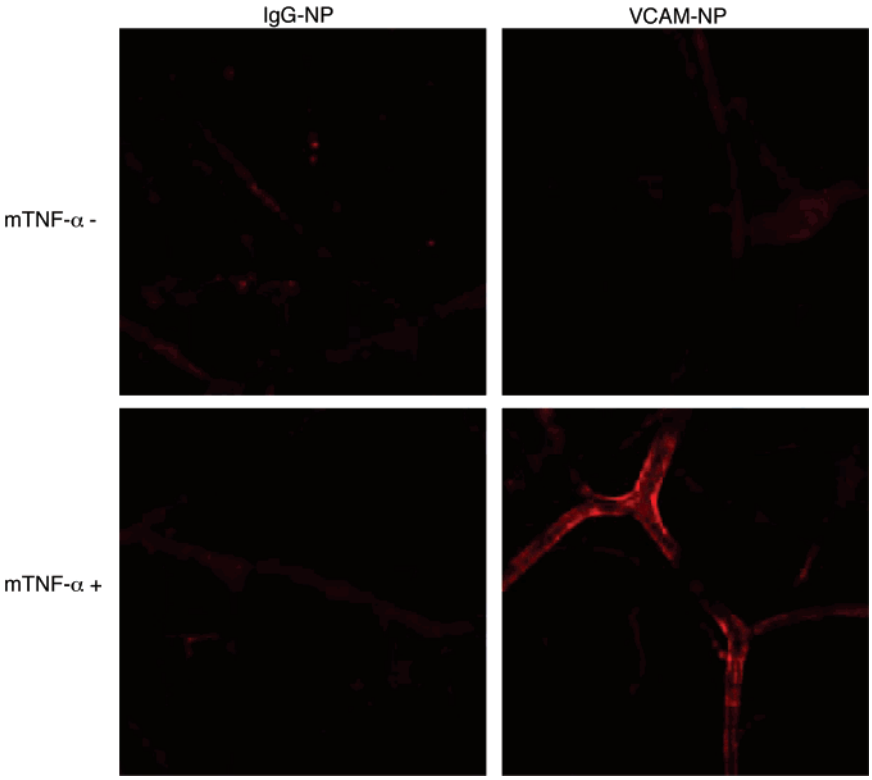

Figure 6. Fluorescence confocal images of normal and mTNF-α activated ears 6 h following administration of either IgG−NP or VCAM−NP. Specific staining of the endothelium is only seen in the activated ear of animals injected with VCAM−NP. Small amounts of IgG−NP can be detected in circulation, but no fluorescence appears to be localized to the endothelium.

similarly labeled with rat IgG (IgG−NP), as a negative control. Labeling ratios of 0.63 mg of IgG per mg of Fe and 0.87 mg of anti-VCAM-1 per mg of Fe were measured.

To evaluate the ability of the targeted nanoparticles to detect the expression of VCAM-1 on endothelial cells, a model system was established using primary cultures of MDMEC and MHEC. MDMEC has previously been shown to naturally express low levels of VCAM-1 in culture unless activated by agents such as TNF-α, while MHEC expresses constitutively high levels of VCAM-1 in culture (*20*). Each cell line was grown to confluence in culture and labeled with either VCAM−NP or IgG−NP. FACS analysis demonstrated a significant shift in fluorescence solely for the MHEC labeled with VCAM−NP (Figure 2). No shift was evident for either cell line when labeled with IgG−NP, indicating little cell uptake and nonspecific binding during the 30 min labeling procedure.

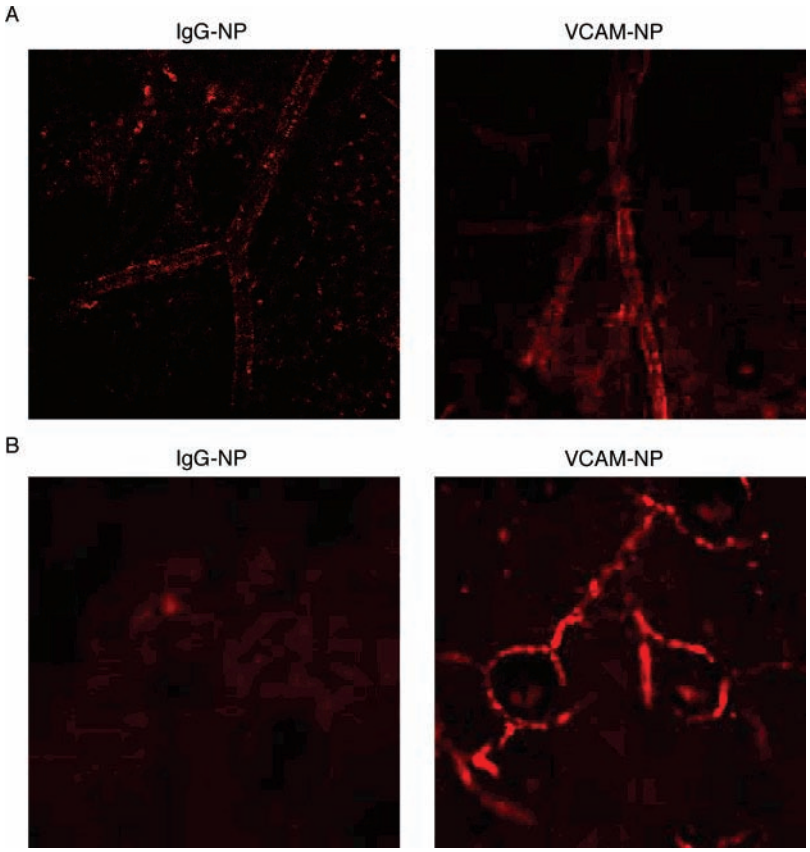

Figure 7. Fluorescence confocal images of mTNF-α activated ears 24 h following administration of either IgG−NP or VCAM−NP. (A) At 24 h postinjection of IgG−NP, nonspecific uptake of the nanoparticles along the activated endothelium can be detected in some of the larger vessels by fluorescence confocal microscopy. Activated endothelium targeted with VCAM−NP, however, still maintains a greater level of labeling, as exhibited by the brighter fluorescence signal. (B) IgG−NP cannot be detected in the microvasculature of the mTNF-α activated endothelium (at 24 h), while VCAM−NP still elicits a bright fluorescence signal, particularly in the microvasculature surrounding hair follicles.

A statistically insignificant shift in fluorescence was observed with MDMEC labeled with VCAM−NP, which could be attributed to low levels of VCAM-1 expression, but is at the fringe of the detection limit of this system. Similar results were seen in analogous experiments conducted with anti-VCAM-1 antibody and IgG directly labeled with Cy5.5 (i.e. without nanoparticle).

In addition to detecting VCAM-1 expression by flow cytometry, we also detected endothelial VCAM-1 expression by MRI. Specifically, following the labeling of MDMEC and MHEC with VCAM−NP or IgG−NP in culture, the cells were lysed and the extracts imaged in a 384-well plate using a 4.7 T MR scanner (Figure 3). MHEC labeled with VCAM−NP exhibited a substantially reduced T2 relaxation time (T2 = 10.0 ms, 21 °C, 4.7 T) compared with MDMEC and MHEC incubated with IgG−NP (T2 = 105.0 ms, 21 °C, 4.7 T). A low T2 relaxation time is indicative of superparamagnetic nanoparticles present in the sample. The MDMEC that were labeled with VCAM−NP also demonstrated a reduced relaxation time (T2 = 39.1 ms, 21 °C, 4.7 T), which could, again, be attributed to low levels of VCAM-1 expression. Although this VCAM-1 expression on MDMEC was far less evident by FACS analysis, it should be noted that FACS records fluorescence on a per cell basis, most likely resulting in a higher threshold for detection than in pooled cell samples and making it difficult to detect low levels of bound contrast agents (i.e. VCAM−NP).

The ability of VCAM−NP to detect activated endothelium in vivo was evaluated by intravenously administering the nanoparticles in a murine inflammatory model. Specifically, the endothelium in the left ear of C57B1/6 mice was activated by injection of mTNF-α. After 24 h, either VCAM−NP or IgG−NP was introduced intravenously by retino-orbital injection. The vasculature of the left (mTNF-α positive) and right ear (mTNF-α negative) was then imaged at 1, 6, and 24 h postinjection via intravital confocal microscopy. The greatest degree of cell surface labeling with VCAM−NP in the mTNF-α activated ear was observed at the 6 h time point (Figure 4). Fluorescence from VCAM−NP clearly localized to the endothelium. Conversely, at 1 h most of the nanoparticles were still in the circulation and there was no clear sign of cell surface receptor labeling. At 24 h, the VCAM−NP was localized at the endothelium, but the signal had grown faint, most likely from dissociation of the anti-VCAM-1 antibodies from their target. Immunohistochemistry confirmed the upregulation of VCAM-1 expression at 6 h (Figure 5).

Analysis of all the fluorescent confocal images of the vasculature at 6 h postinjection demonstrate the specific binding of VCAM−NP only to the endothelium of the mTNF-α activated ear (Figure 6). VCAM−NP did not appear to bind to the endothelial surface of the vasculature in the unactivated ear, while IgG−NP did not label the vasculature in either ear. However, a low fluorescent signal was detected within the vessel lumen in all acquired images, indicative of residual circulating nanoparticles at this time point. Nonetheless, activated endothelium could easily be identified with VCAM−NP.

It should be noted that, at 24 h postinjection, IgG−NP also localized to the mTNF-α activated vasculature

to a small extent (Figure 7A). This is in agreement with previous reports of the nonspecific uptake and accumulation of CLIO at sites of inflammation by 24 h postinjection (*21*−*23*). However, a brighter signal still existed along the activated endothelium of animals injected with VCAM−NP.

Another interesting observation at 24 h was the extensive labeling, with VCAM−NP, of the mTNF-α activated microvasculature surrounding the hair follicles (Figure 7B). This could be the result of improved binding efficiency at the lower flow rates in the microvasculature or possibly an increased level of VCAM-1 expression per endothelial cell in the microvasculature. Surprisingly, however, there was no indication of fluorescence due to nonspecific uptake of IgG−NP in the activated microvasculature, in contrast to what was observed in some of the larger vessels. Further, no fluorescent signal was detected from IgG−NP in either ear (data not shown).

In conclusion, we have demonstrated a simple method for the attachment of near-infrared fluorochromes and whole antibodies to nanoparticles for intravital use. The anti-VCAM-1 antibodies retained activity following conjugation and were shown to specifically target endothelial cells expressing high levels of VCAM-1 by both FACS analysis and MR imaging of cell lysates. Further, effective delivery and labeling of activated endothelium was demonstrated in vivo using a murine inflammatory model. The VCAM−NP localized specifically to regions of the vasculature overexpressing VCAM-1, as determined by intravital microscopy and immunohistochemistry. The acquisition of bright fluorescent images suggests that fluorescently labeled CLIO nanoparticles could provide an alternative to other fluorescent tags for in vivo optical imaging. CLIO nanoparticles, however, also maintain the unique ability to provide MR contrast for deep tissue imaging, and their nontoxicity makes them a viable option for clinical applications.

ACKNOWLEDGMENT

We acknowledge NCI T32 CA79443 for supporting A.T. and P50 CA86355. Work was partly funded by a grant from the Reynolds Foundation.

LITERATURE CITED

(1) Dayton, P. A., and Ferrara, K. W. (2002) Targeted imaging using ultrasound. *J. Magn. Reson. Imaging 16*, 362−377.
(2) Jaffer, F. A., and Weissleder, R. (2004) Seeing within: molecular imaging of the cardiovascular system. *Circ. Res. 94*, 433−445.
(3) Kang, H. W., Josephson, L., Petrovsky, A., Weissleder, R., and Bogdanov, A., Jr. (2002) Magnetic resonance imaging of inducible E-selectin expression in human endothelial cell culture. *Bioconjug. Chem. 13*, 122−127.
(4) Li, K. C., and Bednarski, M. D. (2002) Vascular-targeted molecular imaging using functionalized polymerized vesicles. *J. Magn. Reson. Imaging 16*, 388−393.
(5) Artemov, D., Mori, N., Ravi, R., and Bhujwalla, Z. M. (2003) Magnetic resonance molecular imaging of the HER-2/neu receptor. *Cancer Res. 63*, 2723−2727.
(6) Cybulsky, M. I., and Gimbrone, M. A., Jr. (1991) Endothelial expression of a mononuclear leukocyte adhesion molecule during atherogenesis. *Science 251*, 788−791.
(7) Libby, P. (2002) Inflammation in atherosclerosis. *Nature 420*, 868−874.
(8) Koskinen, P. K., and Lemstrom, K. B. (1997) Adhesion molecule P-selectin and vascular cell adhesion molecule-1 in enhanced heart allograft arteriosclerosis in the rat. *Circulation 95*, 191−196.
(9) McHale, J. F., Harari, O. A., Marshall, D., and Haskard, D. O. (1999) Vascular endothelial cell expression of ICAM-1 and VCAM-1 at the onset of eliciting contact hypersensitivity in mice: evidence for a dominant role of TNF-alpha. *J. Immunol. 162*, 1648−1655.
(10) Molenaar, T. J., Twisk, J., de Haas, S. A., Peterse, N., Vogelaar, B. J., van Leeuwen, S. H., Michon, I. N., van Berkel, T. J., Kuiper, J., and Biessen, E. A. (2003) P-selectin as a candidate target in atherosclerosis. *Biochem. Pharmacol. 66*, 859−866.
(11) Nakashima, Y., Raines, E. W., Plump, A. S., Breslow, J. L., and Ross, R. (1998) Upregulation of VCAM-1 and ICAM-1 at atherosclerosis-prone sites on the endothelium in the ApoE-deficient mouse. *Arterioscler. Thromb. Vasc. Biol. 18*, 842−851.
(12) Iiyama, K., Hajra, L., Iiyama, M., Li, H., DiChiara, M., Medoff, B. D., and Cybulsky, M. I. (1999) Patterns of vascular cell adhesion molecule-1 and intercellular adhesion molecule-1 expression in rabbit and mouse atherosclerotic lesions and at sites predisposed to lesion formation. *Circ. Res. 85*, 199−207.
(13) Sans, M., Fuster, D., Vazquez, A., Setoain, F. J., Piera, C., Pique, J. M., and Panes, J. (2001) 123Iodine-labeled anti-VCAM-1 antibody scintigraphy in the assessment of experimental colitis. *Eur. J. Gastroenterol. Hepatol. 13*, 31−38.
(14) Josephson, L., Tung, C. H., Moore, A., and Weissleder, R. (1999) High-efficiency intracellular magnetic labeling with novel superparamagnetic-Tat peptide conjugates. *Bioconjug. Chem. 10*, 186−191.
(15) Perez, J. M., Josephson, L., O'Loughlin, T., Hogemann, D., and Weissleder, R. (2002) Magnetic relaxation switches capable of sensing molecular interactions. *Nat. Biotechnol. 20*, 816−820.
(16) Reynolds, F., O'Loughlin, T., Weissleder, R., and Josephson, L. (2005) Method for determining nanoparticle core weight. *Anal. Chem. 77*, 814−817.
(17) Tsourkas, A., Hofstetter, O., Hofstetter, H., Weissleder, R., and Josephson, L. (2004) Magnetic relaxation switch immunosensors detect enantiomeric impurities. *Angew. Chem., Int. Ed. 43*, 2395−2399.
(18) Allport, J. R., Lim, Y. C., Shipley, J. M., Senior, R. M., Shapiro, S. D., Matsuyoshi, N., Vestweber, D., and Luscinskas, F. W. (2002) Neutrophils from MMP-9- or neutrophil elastase-deficient mice show no defect in transendothelial migration under flow in vitro. *J. Leukoc. Biol. 71*, 821−828.
(19) Hogemann, D., Ntziachristos, V., Josephson, L., and Weissleder, R. (2002) High throughput magnetic resonance imaging for evaluating targeted nanoparticle probes. *Bioconjug. Chem. 13*, 116−121.
(20) Jiang, M. Z., Tsukahara, H., Ohshima, Y., Todoroki, Y., Hiraoka, M., Maeda, M., and Mayumi, M. (2004) Effects of antioxidants and nitric oxide on TNF-alpha-induced adhesion molecule expression and NF-kappaB activation in human dermal microvascular endothelial cells. *Life Sci. 75*, 1159−1170.
(21) Kooi, M. E., Cappendijk, V. C., Cleutjens, K. B., Kessels, A. G., Kitslaar, P. J., Borgers, M., Frederik, P. M., Daemen, M. J., and van Engelshoven, J. M. (2003) Accumulation of ultrasmall superparamagnetic particles of iron oxide in human atherosclerotic plaques can be detected by in vivo magnetic resonance imaging. *Circulation 107*, 2453−2458.
(22) Litovsky, S., Madjid, M., Zarrabi, A., Casscells, S. W., Willerson, J. T., and Naghavi, M. (2003) Superparamagnetic iron oxide-based method for quantifying recruitment of monocytes to mouse atherosclerotic lesions in vivo: enhancement by tissue necrosis factor-alpha, interleukin-1beta, and interferon-gamma. *Circulation 107*, 1545−1549.
(23) Ruehm, S. G., Corot, C., Vogt, P., Kolb, S., and Debatin, J. F. (2001) Magnetic resonance imaging of atherosclerotic plaque with ultrasmall superparamagnetic particles of iron oxide in hyperlipidemic rabbits. *Circulation 103*, 415−422.

BC050002E

Cell Uptake and Radiotoxicity Studies of an Nuclear Localization Signal Peptide–Intercalator Conjugate Labeled with $[^{99m}Tc(CO)_3]^+$

Pascal Haefliger,[†] Nikos Agorastos,[†] Annabelle Renard,[‡] Guya Giambonini-Brugnoli,[||] Cornelia Marty,[§] and Roger Alberto*,[†]

Institute of Inorganic Chemistry, University of Zürich, Winterthurerstrasse 190, 8057 Zürich, Switzerland, Institute of Organic Chemistry, University of Zürich, Winterthurerstrasse 190, 8057 Zürich, Switzerland, Molecular Cell Biology, Paul Scherrer Institute, 5232 Villigen-PSI, Switzerland, and Institute of Cell Biology, ETH Hönggerberg, Schafmattstrasse 18, 8093 Zürich. Received January 13, 2005; Revised Manuscript Received April 1, 2005

A trifunctional bioconjugate consisting of the SV40 nuclear localization signal (NLS) peptide, an aliphatic triamine ligand, and the DNA intercalating pyrene has been synthesized and quantitatively labeled with $[^{99m}Tc(OH_2)_3(CO)_3]^+$. The radiotoxicity of the resulting nucleus-targeting radiopharmaceutical on B16F1 mouse melanoma cells has been investigated to evaluate the activity of Auger and Coster–Kronig electrons on the viability of cells. We found a dose-dependent significant radiotoxicity of the nucleus-targeting radiopharmaceutical clearly related to the low energy decay of ^{99m}Tc. These principal results imply a possible therapeutic strategy based on the use of the low-energy Auger electron-emitting ^{99m}Tc radionuclide attached to nucleus-targeting molecules and comprising an intercalator. Highly efficient DNA targeting vectors could complement the usual role of ^{99m}Tc in diagnostic applications. The Auger electrons emitted by the ^{99m}Tc nuclide induce DNA damage leading ultimately, through a mitotic catastrophe pathway, to necrotic cell death. Non-DNA-targeting ^{99m}Tc complexes display much lower radiotoxicity.

INTRODUCTION

Targeted radionuclide therapy is a very attractive strategy that specifically delivers therapeutic radiation doses to tumors without causing significant toxicity to normal tissue. Still, in reality this approach is often limited by the inevitable damage induced to healthy untargeted tissues such as bone marrow, liver, and kidneys by the high-energy particles commonly employed (*1*–*5*). In addition to α- or β^--emitters, the application of low-energy high-LET (linear energy transfer) Auger electron emitters has been proposed. This approach requires the radionuclide to be conjugated to carriers that specifically internalize and reach the DNA of targeted cancer cells to induce lethal DNA damage (*6*–*8*). Respective studies have been published in this context, in particular with ^{125}I and ^{111}In but also other radionuclides (*9*–*13*). The short path length of low-energy Auger electrons reduces the overall damage caused in nontargeted tissue. Moreover, in radiodrug metabolites DNA targeting and binding properties are often affected or lost; thus, they will display a lower radiotoxicity, damage to kidney and liver (*10*). The therapeutic advantage of Auger electron- versus α^- or β^--emitting radionuclides has been demonstrated clinically for several nuclides but only in theory for ^{99m}Tc (*2*, *14*–*17*). This radionuclide emits besides its well-known γ-radiation an average of four Auger or Coster–Kronig electrons per decay, according to the radiation spectra calculated by Howell (*18*). These data provide more complete Auger electron spectra than the ones given by MIRD and ICRP which do not consider the very low-energy N- and O-shell electrons. We recently demonstrated that ^{99m}Tc induces in vitro double-strand breaks in circular dsDNA when carried in its direct vicinity by DNA binding moieties such as intercalators (*19*). These results were the first experimental evidence that ^{99m}Tc possesses an unexpected potential for systemic radiotherapy, complementing its widely known diagnostic applications. As an extension of this study, it was intriguing to confirm the radiotoxic potential of DNA targeting ^{99m}Tc complexes also on the cellular level.

Scheme 1. Structures of Compounds 1 and 3

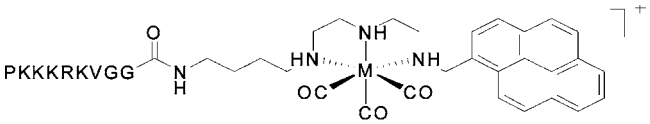

1 (M = ^{99m}Tc)
3 (M = Re)

P = Proline, K = Lysine, R = Arginine, V = Valine, G = Glycine

We present in this paper the first in vitro experimental evidence that ^{99m}Tc complexes with nuclear targeting and DNA binding functionalities such as compound **1** (Scheme 1) have a pronounced radiotoxic effect on cultured mouse melanoma B16F1 cells. The nucleus targeting property has been analyzed by single cell fluorescence microscopy (with its nonradioactive Re analogue **3**) as well as with radioactivity-based cell uptake experiments.

EXPERIMENTAL PROCEDURES

Chemicals and solvents were purchased from Fluka AG Buchs Switzerland or Aldrich and used without further

* To whom correspondence should be addressed. E-mail: ariel@aci.unizh.ch.
[†] Institute of Inorganic Chemistry, University of Zürich.
[‡] Institute of Organic Chemistry, University of Zürich.
[§] Paul Scherrer Institute.
[||] ETH Hönggerberg.

10.1021/bc0500084 CCC: $30.25 © 2005 American Chemical Society
Published on Web 04/26/2005

purification. All reactions were performed under N_2 or Ar. $Na^{99m}TcO_4$ was eluted from a $^{99}Mo/^{99m}Tc$ Generator (Mallinckrodt) in 0.9% saline.

^1H and ^{13}C NMR spectra were recorded on Varian Gemini 300 or Bruker DRX500 spectrometers at 300 and 75 MHz, or 500 and 125 MHz, respectively. The reported chemical shifts (in ppm) are relative to solvent protons as reference.

Fluorescence Microscopy. Single cell fluorescence microscopy was performed on a Zeiss Axiovert microscope equipped with Hamamatsu camera. Costaining was performed by mounting the cells on a glass plate with glycerol/PBS (phosphate buffer in 0.9% NaCl) containing 1 μg/mL of DAPI (4′,6-diamidino-2-phenylindole).

Cell Uptake Experiments. About 10^6 exponentially growing B16F1 melanoma cells were incubated in six-well plates in a humidified 5% CO_2 atmosphere at 37° in DME medium (supplemented with 10% FBS, 100 U/mL of penicillin, and 100 g/mL of streptomycin) containing 10 MBq of the carrier-free compound of interest. After 5 h, the medium was removed and the cells rinsed with 3 mL of PBS. The cells were then incubated on ice for 5 min with 3 mL of NP-40 lysis buffer (10 mM Tris, pH 7.4; 10 mM NaCl; 5 mM $MgCl_2$; 0.5% NP-40). This solution was then transferred to an Eppendorf tube and gently vortexed to prevent the formation of cell aggregates. The nuclei were collected by centrifugation at 500*g* for 5 min at 4 °C. The nuclear pellet was resuspended in 3 mL of NP-40 lysis buffer as previously described (*20*). The nuclei were again collected by centrifugation at 500*g* for 5 min at 4 °C. All fractions (wells, growth medium, lysis buffer, and nuclei pellet) were assayed for radioactivity using a Veenstra VDC-304 ionization chamber.

HPLC was performed on a Merck L7000 system using a Macherey-Nagel EC 250/3 Nucleosil 100−5 C18HD column for nonradioactive and a Macherey-Nagel EC 250/3 Nucleosil 100−5 C18 column for radioactive compounds. HPLC solvents were 0.1% trifluoroacetic acid (solvent A) and MeOH HPLC grade (solvent B). Gradient: 0−3 min: 100% A; 3.1−9 min: 75% A, 25% B; 9.1−20 min: linear gradient from 66% A (34% B) to 0% A (100% B); 20−28 min: 100% B; 28.1−30: 100% A. Flow rate: 0.5 mL/min, detection at 250 nm and/or with a γ-detector for the radiolabeled compounds.

Radiotoxicity Experiments. About 2000 exponentially growing B16F1 melanoma cells per well were incubated in 96-well plates in a humidified 5% CO_2 atmosphere at 37° in 100 μL of DME medium (supplemented with 10% FBS, 100 U/mL of penicillin, and 100 g/mL of streptomycin) containing the desired amount of the carrier-free compound of interest. After 5 to 9 days, the supernatant was removed and 100 μL of freshly diluted WST-1 (4-[3-(4-iodophenyl)-2-(nitrophenyl)-2*H*-5-tetrazolio]-1,3-bezene disulfonate) solution was added. The plates were incubated for 30−60 min at 37° in a humidified 5% CO_2 atmosphere. Cell viability was evaluated by measurement of the absorption at 450 nm using a Dynatech MR5000 plate reader.

***N*-(2-Aminoethyl)-*N*′-pyrene-1-ylmethylethane-1,2-diamine (4).** Pyrene-1-carbaldehyde (1.08 g, 4.69 mmol) and diethylenetriamine (1.452 g, 1.528 mL, 14.07 mmol) were dissolved in 50 mL of EtOH. About 25 mL of CH_2Cl_2 was added until the solution became clear. After addition of 5 g of molecular sieves of 3 Å pore diameter, and stirring for 36 h at r.t., the solution was cooled to 0 °C, and $NaBH_4$ (355 mg, 9.38 mmol) was added in small portions. After 12 h, excess of $NaBH_4$ was quenched with a few drops of H_2O. The solution was filtered, and the solvents from the filtrate were evaporated under vacuum. The resulting oil was purified by flash chromatography (CH_2Cl_2/MeOH/25% NH_4OH, 10:3:0.3) to afford 649 mg (2.06 mmol) (44%) of a light yellow oil. ^1H NMR ($CDCl_3$, 300 MHz): δ 8.22 (d, 1H), 8.07 (d, 2H), 8.01 (m, 2H), 7.90 (m, 4H), 4.34 (s, 2H), 2.99 (s, 4H), 2.74 (t, 2H), 2.66 (t, 2H), 2.60 (t, 2H), 2.51 (t, 2H). ^{13}C NMR ($CDCl_3$, 75 MHz): δ 133.4, 131.1, 130.6, 130.5, 128.9, 127.5, 127.3, 126.9, 125.8, 125.0, 124.9, 124.8, 124.6, 124.5, 123.0, 51.1, 50.6, 48.5, 40.6. MS (ESI): *m/z* 318.27 [$(M + H^+)$, calcd for $C_{21}H_{24}N_3^+$ 318.20]. HPLC t_R = 17.8 min. TLC R_f = 0.15 (CH_2Cl_2/MeOH/25% NH_4OH, 100:30:3).

(2-Aminoethyl)-[2-(*tert*-butoxycarbonylpyrene-1-ylmethylamino)ethyl]carbamic Acid *tert*-Butyl Ester (5). 2-Acetyl-5,5-dimethylcyclohexane-1,3-dione (Dde) (316 mg, 1.73 mmol) was added to a solution of **4** (500 mg, 1.58 mmol) in 20 mL of EtOH. The solution was stirred at r.t. for 3 h. Di-*tert*-butyl pyrocarbonate ($(BOC)_2O$) (759 mg, 3.48 mmol) was added to the solution, and stirring was continued for 5 h. A 5 mL amount of a 25% aqueous hydrazine solution was added to the reaction mixture. After 2 h the solvent was removed in vacuo. The resulting oil was dissolved in 15 mL of CH_2Cl_2, filtered, and dried again. Purification by flash chromatography (CH_2Cl_2/MeOH, 10:1) yielded 752 mg (1.45 mmol) (92%) of a light brown slightly sticky solid. ^1H NMR ($CDCl_3$, 300 MHz) δ 8.30−7.70 (m, 9H), 5.23 (s, 2H), 3.47−3.10 (br, 10H), 1.43 (s, 18 H). ^{13}C NMR ($CDCl_3$, 75 MHz) δ 155.4, 131.1−130.6 (br), 129.2, 128.9, 128.1, 127.2, 125.9, 125.1, 124.8, 124.6, 123.3−122, 80.6, 48.7−42.9 (br), 39.6, 28.4. MS (ESI) *m/z* (%) 518.00 (100) [$(M + H)^+$], 417.96 (10) [$(M + H)^+$-BOC], calcd 518.29, 418.24. HPLC t_R = 23.5 min. TLC R_f = 0.15 (CH_2Cl_2/MeOH, 10:1).

[2-(*tert*-Butoxycarbonylpyren-1-ylmethylamino)-ethyl]-{2-[4-(1,3-dioxo-1,3-dihydroisoindol-2-yl)butylamino]ethyl}carbamic Acid *tert*-Butyl Ester (6). A 20 mL aqueous suspension containing 2 g of KF and 2 g of Celite was stirred for 1 h at room temperature. The solvent was then removed under vacuo. The resulting powder was subsequently resuspended in acetonitrile and dried in high vacuum several times to remove any trace of water. The KF/Celite mixture obtained was then added to a solution containing 820 mg (1.59 mmol) of **5** in 25 mL of dried acetonitrile. After 1 h stirring at room temperature, the suspension was heated until reflux. *N*-(4-Bromobutyl)phthalimide (305 mg, 1.08 mmol) of and 178 mg (1.19 mmol) of NaI were then added to the boiling solution, which was then further refluxed in the dark for 14 h. The reaction mixture was then filtered and cooled. After removal of the solvent, the product was purified by flash chromatography (CH_2Cl_2/MeOH/25% NH_4OH, 100:3:0.5) to yield 503 mg (0.72 mmol) (65%) of a light yellow solid.^1H NMR ($CDCl_3$, 300 MHz) δ, 8.09 (m, 5H), 7.91 (m, 4H), 7.67 (m, 2H), 7.53 (m, 2H), 5.21 (s, 2H), 3.60 (m, 2H), 3.38 (br, 2H), 3.19 (br, 2H), 3.06 (br, 1H), 2.79−2.66 (m, 4H), 2.45 (s, 2H), 1.54 (s, 9H), 1.43 (s, 13H). ^{13}C NMR ($CDCl_3$, 75 Hz) δ 168.4, 155.7, 133.9, 132.0, 131.3, 131.0, 130.8, 127.9, 127.4, 126.1, 125.3, 125.0, 124.7, 123.1, 79.9, 77.4, 61.9, 53.4, 48.7, 47.7, 47.5, 37.6, 37.5, 30.8, 29.7, 28.3, 27.0, 26.1, 25.0, 24.5. MS (ESI) *m/z* (%) 719.80 (100) [$(M + H)^+$], calcd 719.37. HPLC t_R = 24.3 min. TLC R_f = 0.52 (CH_2Cl_2/MeOH/25% NH_4OH, 10:1:0.1).

{2-[(4-Aminobutyl)-*tert*-butoxycarbonylamino]-ethyl}-[2-(*tert*-butoxycarbonylpyrene-1-ylmethylamino)ethyl]carbamic Acid *tert*-Butyl Ester (7). Di-*tert*-butyl-pyrocarbonate (77 mg, 0.35 mmol) in 3 mL of absol ethanol was slowly added to an ice-cooled solution of **6** (169 mg, 0.23 mmol) in 3 mL of abs. ethanol. The

Scheme 2. Synthesis of 2 from Pyrene-1-carbaldehyde[a]

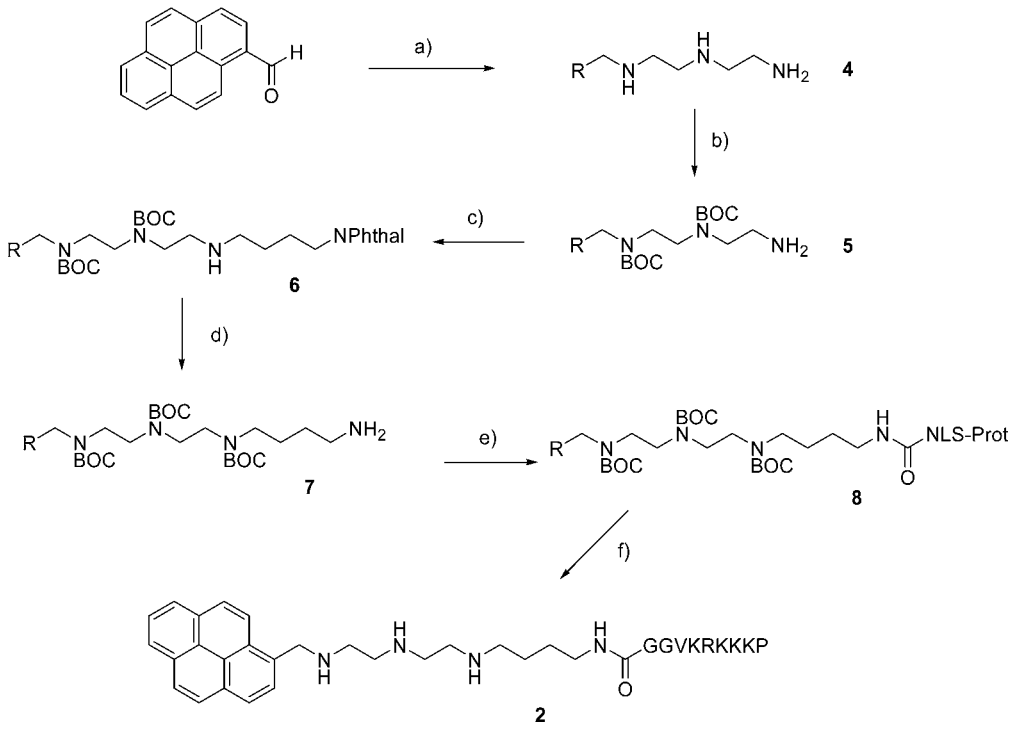

[a] Reagents and conditions: (a) 3 equiv of diethylenetriamine, EtOH/CH_2Cl_2, r.t., 36 h/$NaBH_4$, EtOH, r.t., 12 h; 44%; (b) Dde-OH, EtOH, r.t./$(BOC)_2O$, EtOH, r.t./hydrazine, EtOH, r.t., 92%; (c) bromobutylphthalimide, KF/Celite, CH_3CN, reflux, 65%; (d) $(BOC)_2O$, EtOH, r.t., hydrazine, EtOH, r.t; 78%. (e) Prot-NLS-COOH, BOP, NEt_3, CH_2Cl_2, r.t. 29%; (f) CF_3COOH, CH_2Cl_2, r.t./piperidine 20%, DMF, r.t., 9%.

reaction mixture was then stirred overnight at room temperature. Excess $(BOC)_2O$ was then hydrolyzed by adding a few drops of water. A 25% hydrazine aqueous (1 mL) solution was added to the reaction mixture. After a further 3 h of stirring, the solvent was removed in vacuo and the resulting crude product was purified by flash chromatography (CH_2Cl_2/MeOH/25% NH_4OH, 10:1:0.1) to afford 126 mg (0.18 mmol) (78%) of the compound **7** as a light yellow oil. ^1H NMR ($CDCl_3$, 300 MHz) δ 8.20−8.06 (m, 5H), 8.0−7.92 (m, 4H), 5.23 (s, 2H), 3.44−3.0 (br m, 10H), 2.93 (s, 2H), 2.71 (s, 2H), 1.55 (s, 4H), 1.45 (s, 9H), 1. 40 (s, 18H). ^{13}C NMR ($CDCl_3$, 75 MHz) δ 155.1, 155.0, 130.2, 130.1, 130.0, 129.5, 127.8, 127.3, 126.1, 125.2, 125.1, 124.6, 80.3, 80.0, 77.3, 47.5, 46.9, 45.5, 45.3, 44.9, 44.5, 43.8, 41.5, 41.3, 30.0, 29.8, 29.4, 29.1, 28.3, 25.8, 25.0. MS (ESI) *m/z* (%) 689.30 (100) [$(M + H)^+$], 1376.43 (22) [$(M_2)^{+\cdot}$], calcd 689.42, 1376.84. HPLC t_R = 23.8 min. TLC R_f = 0.24 (CH_2Cl_2/MeOH/25% NH_4OH, 10:1:0.1).

Compound 8. A solution containing 20 mg (0.0107 mmol) of $PZ_1-KZ_2-KZ_2-KZ_2-RZ_3-KZ_2-V-G-G$ (Z_1 = Fmoc, Z_2 = BOC, Z_3 = Pbf), 11 mg (0.016 mmol) of **7**, and 17 mg (0.0321 mmol) of PyBOP in 3 mL of dichloromethane was stirred for 8 h at room temperature. After addition of 3 μL (2.2 mg) (0.0217 mmol) of triethylamine, the solution was further stirred for 8 h. After removal of the solvent in vacuo, the crude product was purified by preparative HPLC to afford 8 mg (0.005 mmol) (29%) of compound **8** as a light yellow oil. MS (ESI): 1272.47 (100) [$(M + 2H)^{2+}$], calcd 1272.22. HPLC: t_R = 28.3

Compound 2. A solution containing 8 mg (0.005 mmol) of **8** in 2 mL of TFA/TIS/water (95%/2.5%/2.5%) was stirred for 2 h at room temperature. After removal of the solvent in vacuo, the resulting crude product was dissolved in 2 mL of 20% piperidine in DMF. This solution was stirred for 45 min at room temperature. After removal of the solvent in vacuo, the resulting crude product was purified by preparative HPLC to afford 400 μg (0.4 μmol) (9%) of compound **2**. MS (ESI): 1367.8 (100) [$(M + H)^+$], calcd 1367.92. HPLC: t_R = 18.1.

Radiolabeling. The precursor $[^{99m}Tc(OH_2)_3(CO)_3]^+$ was prepared as described elsewhere (*21*). Compound **1** was prepared from **2** and $[^{99m}Tc(OH_2)_3(CO)_3]^+$ as follows: 100 μL of a 10^{-4} M solution of **2** was added to a saline solution (900 μL) containing the radiolabeling precursor $[^{99m}Tc(OH_2)_3(CO)_3]^+$ in a sealed vial under N_2. The vial was heated to 90 °C for 30 min and cooled in an ice bath. Radiochemical yield was better than 95%; quality control was performed by HPLC with a gradient as described in the beginning, t_R = 22.5 min.

RESULTS AND DISCUSSION

The trifunctional compound **2** (Scheme 2) comprises a SV40 nuclear localizing signal (NLS) peptide known to carry cargo molecules to the nucleus of living cells, a pendant DNA-intercalating pyrene moiety, and a triamine tridentate ligand which is used for later labeling with $[^{99m}Tc(OH_2)_3(CO)_3]^+$ or its rhenium surrogate to yield compounds **1** and **3**, respectively (*21*−*25*). According to the biological properties of SV40, this conjugate is expected to cross the cellular and nuclear membranes of any type of cell and to bind through the pyrene functionality to cellular DNA. The Auger electrons emitted by the ^{99m}Tc nuclide in the direct vicinity of cellular DNA would then induce enough DNA damage, and in particular double-strand breaks, to lead to the death of the cell.

Synthesis. The bioconjugate **2** comprising the SV40 NLS peptide, a pendant DNA-intercalating pyrene moiety, and a triamine tridentate ligand was synthesized with standard protecting group procedures according to Scheme 2. Compound **2** reacts in water with $[M(OH_2)_3(CO)_3]^+$ (M = ^{99m}Tc (*21*), Re (*26*)) to form the ^{99m}Tc-labeled complex **1** and nonradioactive Re complex **3** in quantita-

Scheme 3. Structure of Compound [Re(4)(Co)3]$^+$

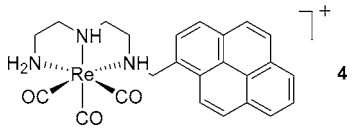

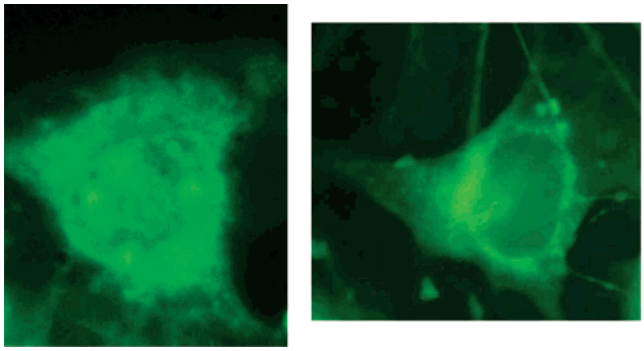

Figure 1. Cellular distribution of compound **3** (left) and **4** (right) observed with a fluorescence microscope after 5 h incubation. Only compound **3**, which is a bioconjugate with the SV40 NLS peptide, accumulates in the nucleus.

tive yields. The aliphatic triamine ligand has been chosen since it forms a small monopositively charged complex supporting electrostatic interaction to the negatively charged DNA backbone. Compounds **1** and **3** possess a rather rich stereochemistry since they exist as four diastereomeric pairs of enantiomers. The structure of the complex will influence the biological behavior of the bioconjugate; however, since it is not a direct part of the targeting portion, we expected the influence to be rather small. The d^6 low spin nature of the M(I) center renders the complex very robust, and no decomposition was observed at low pH values or under physiological conditions.

Nuclear Localization. The ability of complex **3** to target nuclear DNA of cultured cells was determined by single cell fluorescence microscopy, making use of the strong fluorescing emission properties of pyrene. A negative control experiment was performed with the cationic complex [Re(**4**)(CO)3]$^+$ (*19*) which bears the pyrene moiety and the ^{99m}Tc tricarbonyl core but lacks the NLS peptide required for nuclear localization (Scheme 3). Thus, this compound should not enter the cellular nucleus. Figure 1 shows the images of single B16F1 mouse melanoma cells taken after 5 h of incubation in the growth medium containing compounds **3** and **4** in a concentration of 10^{-5} M. Expectedly, the images reveal that complex **3** accumulates in the nucleus while compound **4** does not.

Besides qualitative visualization, we also aimed at quantification of cell uptake in the nucleus with the ^{99m}Tc compound **1**. About 10^6 B16F1 adherent cells were incubated in 3 mL of growth medium containing 5 MBq (8×10^{-11} M) of **1**. As is the case for all cell studies described herein, compound **1** was purified by HPLC after synthesis and before incubation. Therefore, so-called no carrier added radiopharmaceutical was applied and no cold, unlabeled material was present. After 5 h, cell membranes were lysed under mild conditions, and intact nuclei were separated by centrifugation. The radioactivity present in the different fractions (growth medium, cell membrane and cytoplasm, nuclei, and well plastic walls) was measured. About $3.5 \pm 0.5\%$ of **1** was present in the nucleus while $14.0 \pm 0.9\%$ was found in the cytoplasm and/or the cell membrane. The remaining 82% stayed in the growth medium or bound to the vial. According to

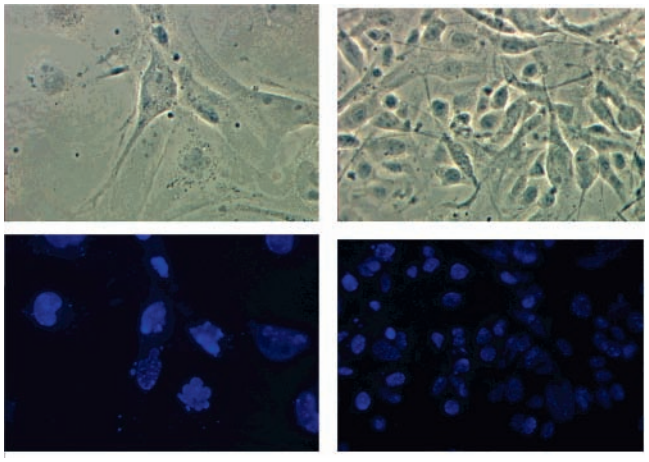

Figure 2. White light (top) and DAPI staining fluorescence (bottom) images of mouse melanoma B16F1 cells after 5 days incubation with compound **1** (left) and [^{99m}TcO$_4$]$^-$ (right) (same enlargement). Micronuclei are clearly visible after incubation with compound **1**.

the initial concentration of bioconjugate and with the specific activity of ^{99m}Tc, an average of about 5×10^3 molecules or ^{99m}Tc radionuclides did, thus, reach every nucleus.

The nucleus uptake is related to the presence of the SV40 peptide. Under the same conditions, less than 1% of [^{99m}TcO$_4$]$^-$ or the cationic complex [^{99m}Tc(diethylenetriamine)(CO)$_3$]$^+$ were found in the cytoplasm and the cell membrane, while for both no significant amount was detected in the nucleus.

Radiotoxicity. Radiotoxicity of ^{99m}Tc based on its Auger electron emission has been described only punctually (*27*, *28*). The radiotoxic effect of ^{99m}Tc complex **1** was studied by incubating cells (about 3000 cells per well in a 96-well plate) in 100 μL of growth medium containing different activities of this compound. To avoid any chemical effect or saturation of the cells with unlabeled trifunctional ligand **2**, complex **1** was purified by HPLC prior to addition to the cells. As control experiments, non-DNA-targeting [^{99m}TcO$_4$]$^-$ and [^{99m}Tc(diethylenetriamine)(CO)$_3$]$^+$ were used as references in the same experimental setup. Furthermore, to rule out any chemical cytotoxicity induced by the pyrene unit or the technetium tricarbonyl complex, cells were incubated with the same concentration of the nonradioactive Re complex **3**. Overall concentrations of the hot and cold compounds are in the nanomolar range. After 36 h of incubation, the growth medium was removed and replaced by fresh medium to allow the cells to recover. After 5 and 9 days, images of the cells were taken (Figures 2 and 3) and the fraction of surviving cells was determined by WST-1 based colorimetric assay (Figure 4).

At a radioactivity concentration of 35 MBq/100 μL (1.75×10^{-8} M) of complex **1**, virtually 100% of the cells died within 9 days; no outgrowth of viable cells could be seen anymore. Interestingly, the cell death process was very slow. It has to be considered at this point, that the radioactivity ^{99m}Tc ($T_{1/2} = 6$ h) approaches zero after 48 h (8 half-life times). Cells gradually increased in size about 24 h after beginning of incubation. These cells were no longer capable of division, but colorimetric assays showed that they were still viable. They continued to increase in size, becoming huge, and then gradually began to die after about 5 days. At that time, staining with (4′,6-diamidino-2-phenylindole) clearly showed nuclear damage and in some cells formation of micronu-

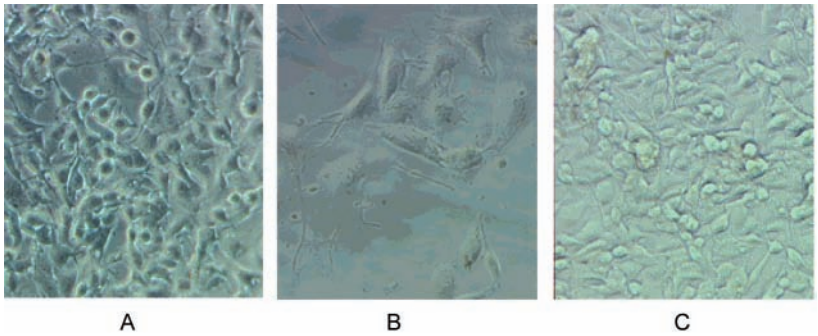

Figure 3. Images (same enlargement) of cells taken 5 days after incubation with 10 MBq/100 μL of (A) $[^{99m}TcO_4]^-$, (B) complex **1**. (C) Untreated cells. While cells treated with $[^{99m}TcO_4]^-$ are healthy and reproductively active, those treated with **1** show typical swelling and micronuclei formation and are also no longer capable of division.

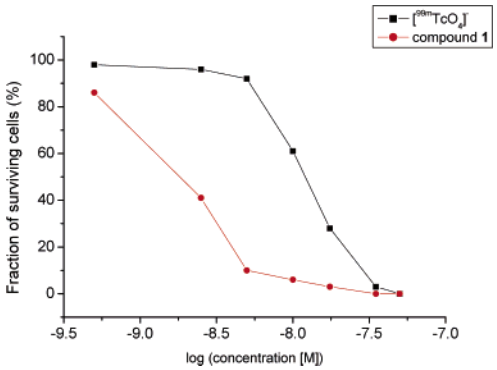

Figure 4. Dose−response for compound **1** and $[^{99m}TcO_4]^-$.

clei (Figure 2). These observations (cell swelling, micronuclei formation) are typical of either radiation-induced mitosis-linked death or radiation-induced cell senescence. Both mechanisms, which usually result from radiation-induced DNA damage, ultimately lead to cell necrosis (*29*, *30*). With the same radioactivity (35 MBq/100 μL), non-nucleus-targeting $[^{99m}TcO_4]^-$ and $[^{99m}Tc(diethylenetriamine)(CO)_3]^+$ displayed a much lower radiotoxic effect than compound **1**. Cellular division was delayed, probably due to cell cycle arrest, but recovery with exponential growth was observed within a few days. The same concentration (1.75×10^{-8} M) of nonradioactive Re complex **3** displayed no cytotoxicity at all, which clearly rules out any chemotoxic effect.

The radiotoxic effect reduces with decreasing amount of ^{99m}Tc radioactivity. Cells incubated with 10 MBq/100 μL (5×10^{-9} M) of compound **1** also displayed typical cell swelling and formation of micronuclei (Figure 3). After 5 days of incubation, about 6% of the cells, as compared to untreated cells, were still viable. After day 6, a few cells recovered and regrew in an exponential way. Incubation with 10 MBq/100μL of non-nuclear-targeting $[^{99m}TcO_4]^-$ and $[^{99m}Tc(diethylenetriamine)(CO)_3]^+$ did not induce any cell swelling at all (Figure 3). After 5 days about 60% of the cells were found to be viable. Concentrations as low as 1.4 MBq/100 μL (7×10^{-10} M) of either compound **1** or $[^{99m}TcO_4]^-$ and $[^{99m}Tc(diethylenetriamine)(CO)_3]^+$ had almost no effect on cell proliferation.

Figure 4 shows the dose−response relationship for compound **1** and $[^{99m}TcO_4]^-$. From these curves, LD_{50} values of about 1.8×10^{-9} M in and 1.2×10^{-8} M, respectively, can be estimated. This demonstrates that the radiotoxicity of the nuclear targeting compound **1** is about 10 times higher as compared to $[^{99m}TcO_4]^-$. This factor can be significantly higher, if a more efficient nuclear targeting agent is found.

CONCLUSION

In conclusion, we have demonstrated with single cell fluorescence microscopy and distribution assays that trifunctional complex **1** targets and accumulates in the nucleus of B16F1 mouse melanoma cells. We further showed that, at equal doses, compound **1** has a much stronger radiotoxic effect than non-nuclear-localizing ^{99m}Tc complexes. Morphological changes of the dying cells, such as cell swelling and formation of micronuclei, are typical of either radiation-induced mitosis-linked cell death or radiation-induced cell senescence, both phenomena resulting from DNA damage. The radiotoxic effect of **1** is most likely due to the induction of DNA strand breaks by the Auger electrons of ^{99m}Tc and is, thus, the first experimental evidence on the cellular level that ^{99m}Tc possesses a potential for systemic radionuclide therapy, complementing its widely known diagnostic application.

The amount of ^{99m}Tc radioactivity applied in our experiments was still relatively large or, in other words, the uptake of ^{99m}Tc too small or too slow to become therapeutically relevant. On the other hand, we could show that a small number of ^{99m}Tc radionuclides taken up in the nucleus leads to cell death. In our current work, we are studying nucleus targeting compounds which have a very high and fast uptake in order to reduce the radioactivity needed to achieve a site-specific, therapeutic effect. Combination of such labeled compounds with cell receptor targeting molecules aims at tumor cell-specific uptake.

ACKNOWLEDGMENT

We thank Tyco-Mallinckrodt Med. BV Petten/The Netherlands for financial support.

LITERATURE CITED

(1) Behr, T. M., Sgouros, G., Vougioukas, V., Memtsoudis, S., Gratz, S., Schmidberger, H., Blumenthal, R. D., Goldenberg, D. M., and Becker, W. (1998) Therapeutic efficacy and dose-limiting toxicity of auger-electron vs beta emitters in radioimmunotherapy with internalizing antibodies: Evaluation of I-125- vs I-131-labeled CO17−1A in a human colorectal cancer model. *Int. J. Cancer 76*, 738−748.

(2) Behr, T. M., Behe, M., Jungclas, H., Jungclas, H., Becker, W., and Sgouros, G. (2001) Higher relative biological efficiency of alpha-particles: in vitro veritas, in vivo vanitas? *Eur. J. Nucl. Med. 28*, 1435−1436.

(3) Blumenthal, R. D., Sharkey, R. M., and Goldenberg, D. M., (1995) Overcoming dose-limiting, radioantibody-induced myelotoxicity. *Cancer therapy with radiolabeled antibodies*, pp 295−314, CRC Press, Boca Raton.

(4) Behr, T. M., Sharkey, R. M., Juweid, M. E., Dunn, R. M., Vagg, R. C., Ying, Z. L., Zhang, C. H., Swayne, L. C., Vardi,

Y., Siegel, J. A., and Goldenberg, D. M. (1997) Phase I/II clinical radioimmunotherapy with an iodine-131-labeled anti-carcinoembryonic antigen murine monoclonal antibody IgG. *J. Nucl. Med. 38*, 858−870.
(5) Behr, T. M., Behe, M., Lohr, M., Sgouros, G., Angerstein, C., Wehrmann, E., Nebendahl, K., and Becker, W. (2000) Therapeutic advantages of Auger electron- over beta-emitting radiometals or radioiodine when conjugated to internalizing antibodies. *Eur. J. Nucl. Med. 27*, 753−765.
(6) O'Donoghue, J. A., and Wheldon, T. E. (1996) Targeted radiotherapy using Auger electron emitters. *Phys. Med. Biol. 41*, 1973−1992.
(7) Sastry, K. S. R. (1992) Biological effects of the Auger emitter I-125 − a review − Report No 1 of Aapm-Nuclear-Medicine-Task-Group No 6. *Med. Phys. 19*, 1361−1370.
(8) Ftacnikova, S., and Bohm, R. (2000) Monte Carlo calculations of energy deposition in DNA for Auger emitters. *Radiat. Prot. Dosim. 92*, 269−278.
(9) Griffiths, G. L., Govindan, S. V., Sgouros, G., Ong, G. L., Goldenberg, D. M., and Mattes, M. J. (1999) Cytotoxicity with Auger electron-emitting radionuclides delivered by antibodies. *Int. J. Cancer 81*, 985−992.
(10) Karamychev, V. N., Panyutin, I. G., Kim, M. K., Le, N., Paik, C. H., Carrasquillo, J. A., Reed, M. W., and Neumann, R. D. (2000) DNA cleavage by ^{111}In-labeled oligodeoxyribonucleotide. *J. Nucl. Med. 41*, 1093−1101.
(11) Sedelnikova, O. A., Rogakou, E. P., Panyutin, I. G., and Bonner, W. M. (2002) Quantitative detection of (125) IdU-induced DNA double-strand breaks with gamma-H2AX antibody. *Radiat. Res. 158*, 486-492.
(12) Sedelnikova, O. A., Karamychev, V. N., Panyutin, I. G., and Neumann, R. D. (2002) Sequence-specific gene cleavage in intact mammalian cells by I-125-labeled triplex-forming oligonucleotides conjugated with nuclear localization signal peptide. *Antisense Nucleic A 12*, 43−49.
(13) Sedelnikova, O. A., Luu, A. N., Karamychev, V. N., Panyutin, I. G., and Neumann, R. D. (2001) Development of DNA-based radiopharmaceuticals carrying Auger-electron emitters for antigene radiotherapy. *Int. J. Radiat. Oncol. 49*, 391−396.
(14) Desombre, E. R., Shafii, B., Hanson, R. N., Kuivanen, P. C., and Hughes, A. (1992) Estrogen Receptor-Directed Radiotoxicity with Auger Electrons − Specificity and Mean Lethal Dose. *Cancer Res. 52*, 5752−5758.
(15) Ochakovskaya, R., Osorio, L., Goldenberg, D. M., and Mattes, M. J. (2001) Therapy of disseminated B-cell lymphoma xenografts in severe combined immunodeficient mice with an anti-CD74 antibody conjugated with ^{111}In, ^{67}Ga, or ^{90}Y. *Clin. Cancer Res. 7*, 1505−1510.
(16) Mattes, M. J. (2002) Radionuclide-antibody conjugates for single-cell cytotoxicity. *Cancer 94*, 1215−1223.
(17) Goddu, S. M., Rao, D. V., and Howell, R. W. (1994) Multicellular dosimetry for micrometastases − dependence of self-dose versus cross-dose to cell-nuclei on type and energy of radiation and subcellular-distribution of radionuclides. *J. Nucl. Med. 35*, 521−530.
(18) Howell, R. W. (1992) Radiation Spectra for Auger-Electron Emitting Radionuclides − Report No 2 of Aapm-Nuclear-Medicine-Task-Group No 6. *Med. Phys. 19*, 1371−1383.
(19) Haefliger, P., Agorastos, N., Spingler, B., Georgiev, O., Viola, G., and Alberto, R. (2005) Induction of DNA-double-strand breaks by Auger electrons from ^{99m}Tc complexes with DNA-binding ligands. *ChemBioChem. 6*, 414−421.
(20) Sambrook, J., and Russell, D. W., (2001) *Molecular Cloning*, Chapter 17.26, Cold Spring Harbor Laboratory Press, Cold Spring Harbor, NY.
(21) Alberto, R., Schibli, R., Egli, A., Schubiger, A. P., Abram, U., and Kaden, T. A. (1998) A novel organometallic aqua complex of technetium for the labeling of biomolecules: Synthesis of $[^{99m}Tc(OH_2)_3(CO)_3]^+$ from $[^{99m}TcO_4]^-$ in aqueous solution and its reaction with a bifunctional ligand. *J. Am. Chem. Soc. 120*, 7987−7988.
(22) Boulikas, T. (1994) Putative Nuclear-Localization Signals (Nls) in Protein Transcription Factors. *J. Cell Biochem. 55*, 32−58.
(23) Adam, S. A., and Gerace, L. (1991) Cytosolic Proteins That Specifically Bind Nuclear Location Signals Are Receptors for Nuclear Import. *Cell 66*, 837−847.
(24) Zanta, M. A., Belguise-Valladier, P., and Behr, J. P. (1999) Gene delivery: A single nuclear localization signal peptide is sufficient to carry DNA to the cell nucleus. *Proc. Natl. Acad. Sci. U.S.A. 96*, 91−96.
(25) Alberto, R., Schibli, R., Egli, A., Schubiger, A. P., Abram, U., and Kaden, T. A. (1998) A novel organometallic aqua complex of technetium for the labeling of biomolecules: Synthesis of $[^{99m}Tc(OH_2)_3(CO)_3]^+$ from $[^{99m}TcO_4]^-$ in aqueous solution and its reaction with a bifunctional ligand. *J. Am. Chem. Soc. 120*, 7987−7988.
(26) Schibli, R., Thesis, Universität Basel, 1996, Basel.
(27) Pedraza-Lopez, M., Ferro-Flores, G., Mendiola-Cruz, T., and Morales-Ramirez, P. (2000) Assessment of radiation-induced DNA damage caused by the incorporation of Tc-99m-radiopharmaceuticals in murine lymphocytes using single cell gel electrophoresis. *Mutat. Res. 465*, 139−144.
(28) Silva, C. R., Valsa, J. O., Canine, M. S., Caldeira-de-Araujo, A., and Bernardo-Filho, M. (1998) Evaluation of technetium-99m decay on Escherichia coli inactivation: Effects of physical or chemical agents. *Yale J. Biol. Med. 71*, 7−14.
(29) Roninson, I. B., Broude, E. V., and Chang, B. D. (2001) If not apoptosis, then what? − Treatment-induced senescence and mitotic catastrophe in tumor cells. *Drug Resist. Update 4*, 303−313.
(30) Cohen-Jonathan, E., Bernhard, E. J., and McKenna, W. G. (1999) How does radiation kill cells? *Curr. Opin. Chem. Biol. 3*, 77−83.

BC0500084

Cross-Linking between Thymine and Indolyl Radical: Possible Mechanisms for Cross-Linking of DNA and Tryptophan-Containing Peptides

Petar M. Mitrasinovic*

Department of Chemistry, Dalhousie University, Halifax, Nova Scotia, Canada B3H 4J3. Received February 22, 2005; Revised Manuscript Received March 31, 2005

As experimentally observed in γ-irradiated aqueous solutions of tryptophan-containing peptides in the presence of DNA, a fast electron (or hydrogen atom) transfer from the DNA restores an intact tryptophan residue at the expense of the DNA integrity. Alternatively, addition of the deprotonated electron-deficient indolyl radical to the DNA, followed by subsequent rearrangement, may lead toward DNA/tryptophan-containing peptide cross-linking. Herein, possible reaction mechanisms for thymine−indolyl radical cross-linking are proposed. The consistent use of the contact spin density distribution is the key virtue of this work. The Becke 3, Lee, Yang, and Parr (B3LYP) density functional theory (DFT) method is employed to investigate the feasibility of the proposed cross-linking mechanisms. A possible complete reaction mechanism consists of a combination of the C_5-hydroxylated thymine and indolyl radicals forming the initial cross-linked product, a hydrogen transfer within the initial cross-linked product by use of a bridging water molecule, and a dehydration step. The overall thermodynamics of the free energy profiles at 0 and 298 K are similar and display differences of magnitude for the hydrogen-transfer reaction. Temperature may be a key factor influencing the overall mechanism. The skeletal structures and contact spin densities on the heavy atoms of the tryptophan side chain and indolyl radicals are essentially equal. Hence, it is believed that a direct combination of the C_5-hydroxylated thymine and tryptophan radicals should form the initial cross-linked product, as far as addition of the tryptophan radical to the DNA is concerned.

INTRODUCTION

Various agents and processes such as drugs (*1*), ionizing radiation (*2*), and autoxidation (*3*) induce damage to DNA in vitro and in vivo. Reactive oxygen species (ROSs), such as singlet oxygen ($^1O_2$), hydrogen peroxide (H_2O_2), superoxide anion ($O_2^{\bullet -}$), hydroxyl radical ($^\bullet$OH), and hydroperoxyl radical (HOO$^\bullet$), are able to disturb the oxidant−antioxidant balance, influencing many pathological conditions, such as cancer (*4*−*8*), Alzheimer's disease (*9*, *10*), and Parkinson's disease (*11*). Up to 10^3 oxidative damaging events upon the DNA of each cell in the human body can occur every day (*12*). Presumably, the $^\bullet$OH radical is the most damaging (*12*, *13*). The importance of radiation biology to probe the oxidative effects of hydroxyl radicals has been recognized by biologists and chemists (*14*, *15*). ROSs attack DNA bases and proteins inside the nucleus and generate bioradicals, protein and DNA (sugar or base) radicals, as primary products that may lead to chain breaks and DNA−DNA or DNA−protein cross-links. DNA−protein cross-links have been observed in living cells and isolated chromatin (*16*−*18*). However, in the overall consideration of DNA damage and its consequences, cross-linking is by no means a minor process.

Several model systems (*19*−*25*), composed of pyrimidine bases and various amino acids in aqueous solution, have been separated and characterized via capillary gas chromatography−mass spectrometry. Hydroxyl radical-induced cross-links between cytosine and tyrosine (*22*), between thymine (Thym) and tyrosine (*19*), and between thymine and lysine (*23*) have been investigated in greater detail. The final step in possible reaction mechanisms is unknown for the cytosine (or thymine)/tyrosine system. On the basis of the identified final products, possible reaction pathways have been hypothesized (*20*, *22*, *25*). The energetic and thermodynamic arguments have been used to investigate the formation of cytosine−tyrosine cross-links (*26*). There are indications that ionizing radiation-induced cross-linking occurs most likely between DNA bases and the aromatic or positively charged amino acids of histone (*27*). These specific amino acids have been singled out because they participate in the formation of the DNA−protein complex (*28*). Physically, negatively charged amino acids, such as glutamic and aspartic acids, are expected to be far away from the negatively charged DNA strand in the DNA−histone complex. Consequently, the probability of a cross-link formation is minimal. In general, the kinetics and mechanisms of the cross-linking reactions have not received their deserved attention and are currently little understood.

The fundamental idea behind this study is as follows. The question of how DNA binding affects the formation and reactions of the tryptophan (indolyl) radicals in peptides and proteins has been previously addressed via pulse radiolysis technique (*29*). The pulse radiolysis study of a γ-irradiated aqueous solution of tryptophan (Trp) peptides in the presence of DNA has revealed that the kinetics of the oxidized Trp residue is best described by the first-order decay rationalized by a fast electron (or hydrogen atom) transfer from DNA to the oxidized Trp. This mechanism is formally identical to the electron transfer observed in proteins from tyrosine residues to oxidized Trp (*30*). Alternatively, addition of the deprotonated electron-deficient indolyl radical (Ind$^\bullet$) to the DNA, followed by subsequent rearrangement, may be

* E-mail pmitrasinovic@yahoo.ca.

10.1021/bc0500490 CCC: $30.25 © 2005 American Chemical Society
Published on Web 05/03/2005

Scheme 1. Proposal of the Cross-Linking Reaction Mechanisms of Thymine, C_5-Hydroxylated Thymine Radical, C_6-Hydroxylated Thymine Radical, and Indolyl Radical

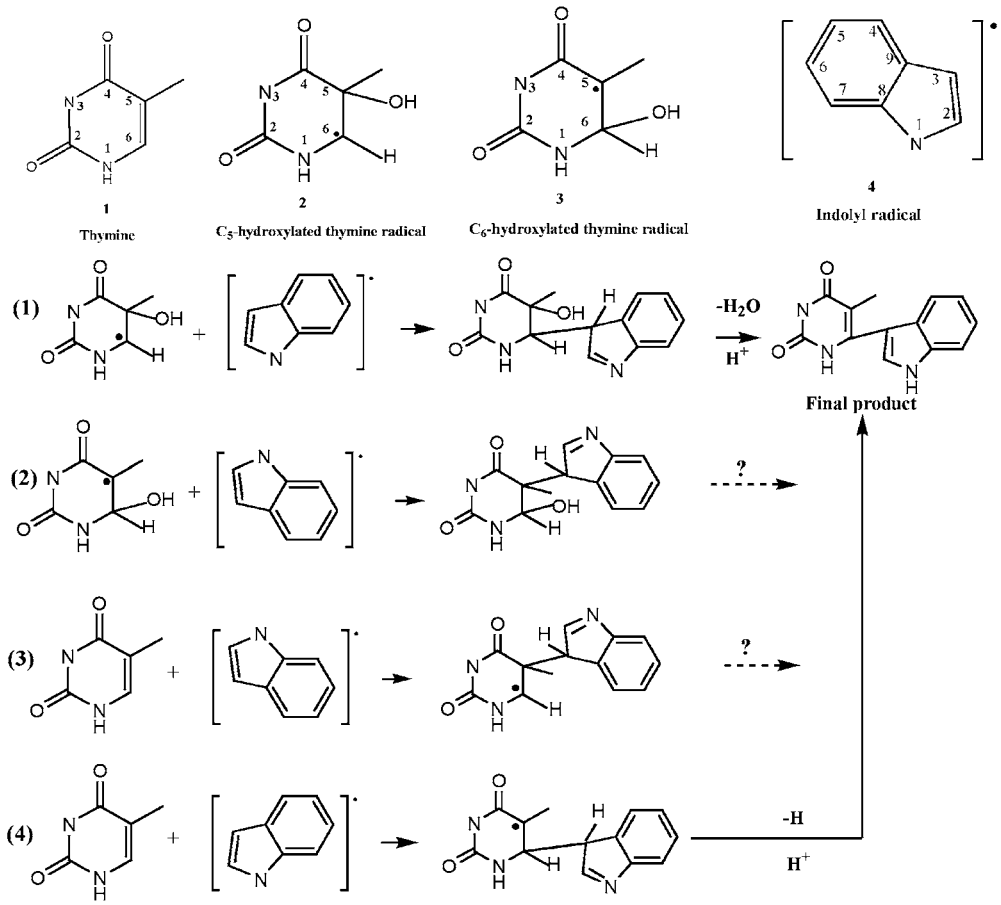

proposed, leading to DNA/tryptophan-containing peptide cross-linking.

Several computational chemistry methods have been contrasted to density functional theory methods in terms of whether DFT is able to predict reliable geometries (*31*) and reaction barriers (*32*). The unrestricted Hartree−Fock (UHF) and MP2 levels of theory, if employed to study free radicals, show spin contamination problems. Although the B3LYP method may have some problems in locating transition structures (TSs) when the reaction barrier is very low, the B3LYP method is able to describe potential energy surfaces (*33*). In this context, DFT methods are well established to the study of large biological systems (*34*−*39*).

This paper is outlined as follows. First, possible reaction mechanisms for the formation of cross-links between thymine and the indolyl radical are proposed (Scheme 1). Second, DFT methods are employed to investigate the feasibility of the proposed reaction pathways. Finally, the nature of the cross-link-bonded interaction in the final product is explored by use of the topological features of the electron density. A slanted prime has been used throughout the text to denote atoms originally on the indolyl radical moiety.

PROPOSAL OF REACTION MECHANISMS

Radiation-generated hydroxyl radicals have been experimentally established by pulse radiolysis to react rapidly with thymine (*40*). The prevailing mode of this interaction is addition to the C_5-C_6 double bond of thymine with a preference for C_5 (*41*). Abstraction of hydrogen at the methyl group, bonded to C_5 of thymine, is preferable to a much lesser extent (*42*, *43*). The majority contact spin density at C_3' of the indolyl radical (Figure 1c) is consistent with the observed site for radical attack on Ind• (*44*, *45*). Therefore, thymine, C_5-hydroxylated thymine radical [denoted C(C_5OH)], C_6-hydroxylated thymine radical [denoted C(C_6OH)], and indolyl radical can be considered as being the most likely reactants participating in the formation of the Thym−Ind• cross-links. We propose four possible reaction steps (Scheme 1) leading to the initial cross-linked products: (1) the combination of the C(C_5OH) and indolyl radicals, (2) the combination of the C(C_6OH) and indolyl radicals, (3) the addition of the indolyl radical to C_5 of thymine, and (4) the addition of the indolyl radical to C_6 of thymine. In each of the mechanisms, the final cross-linked product is presumably formed via several steps of the reaction.

METHODOLOGY

All geometry optimizations were carried out with the B3LYP/6-31G(d,p) hybrid DFT method using the GAUSSIAN 98 suite of programs (*46*). A combination of Becke's three-parameter hybrid exchange functional (*47*), as implemented in GAUSSIAN 98 (*48*), and the Lee−Yang−Parr correlation functional (*49*) gives the B3LYP functional. The restricted (RB3LYP) and unrestricted (UB3LYP) B3LYP procedures were used for closed-shell and open-shell systems, respectively. Vibrational frequencies and zero-point vibrational energies (ZPVEs) were computed at the same level of theory. Relative energies were determined by both performing single-point calculations at the B3LYP/6−311(2df,p) level using the optimized geometries and including the zero-point vibrational energy, that is, B3LYP/6-311(2df,p)//B3LYP/

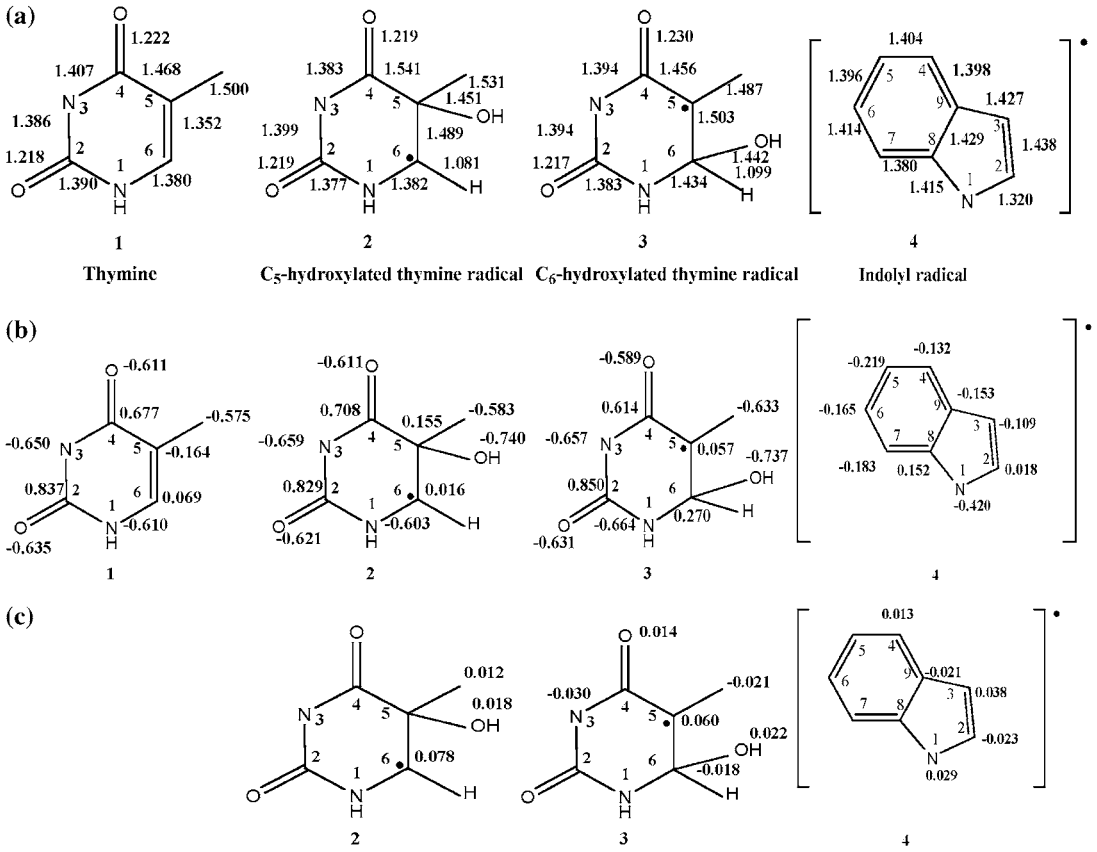

Figure 1. (a) B3LYP/6-31G(d,p) optimized structures (bond lengths) of thymine (**1**), C_5-hydroxylated thymine radical (**2**), C_6-hydroxylated thymine radical (**3**), and indolyl radical (**4**). (b) Natural charges on the heavy atoms of **1**−**4**. (c) Contact spin densities on the heavy atoms of **2**−**4**. Only values numerically larger than 0.01 and less than −0.01 are shown.

6-31G(d,p) + ZPVE. The potential energy profiles were constructed along the lowest energy pathways in redundant internal coordinates (*50*). The points on the path were generated by two successive linear interpolations, first between the reactant and transition structure and then between the transition structure and product. The central point is optimized to the transition structure. The entropy contribution to the free energy at 298 K was extracted from frequency calculations. All energies are given in kilojoules per mole (kJ mol^{-1}). All bond lengths are expressed in angstroms (Å).

The solvent effect on the reaction mechanisms was treated by way of the polarizable dielectric model (DPCM) (*51*) as implemented in GAUSSIAN 98 with a dielectric constant of 78.39 for H_2O and by performing single-point calculations at the B3LYP/6-311(2df,p) level on the optimized gas-phase structures.

The calculations pertaining to the topological features of the total electron density were carried out by use of the program EXTREM (*52*). The contact spin densities were calculated by the program EXTREM. The natural charges were computed by GAUSSIAN 98. The natural charges obtained in this way were shown to be both sufficiently stable to computational parameters (*53*) and insensitive to the particular basis set (*54*). Figures were generated using the program MOLEKEL (*55*). Figure 5 only was generated using the program MOLDEN (*56*). The consistent use both of the physically meaningful natural charges and of the contact spin density throughout the paper makes our work fundamentally different from that reported in ref *26*. The previously reported strategy is based upon the Mulliken charges and spin density having a nonphysical background. Table 1 is a clear indicator speaking in favor of the present approach.

Table 1. Contact Spin Density Partitioning between the Thymine and Indolyl Radical Moieties in Compounds 3a, 3b, 3c, 4a, 4b, and 4c

moiety	3a	3b	3c	4a	4b	4c
Contact Spin Density						
thymine	0.001	0.038	0.076	−0.002	0.013	0.047
indolyl radical	0.012	0.074	0.051	0.018	0.057	0.037
Mulliken Spin Density[a]						
thymine	−0.002	0.511	0.921	−0.004	0.512	0.946
indolyl radical	1.002	0.489	0.079	1.004	0.488	0.054

[a] From left to right, note a decreasing trend of the Mulliken spin densities for the indolyl radical moiety, in contrast to the trend of the contact spin densities. Most importantly, the trends of the contact and Mulliken spin densities, associated with the changes in the molecular energy along the reaction pathways, do not agree. A similar trend of the Mulliken spin densities previously reported speaks in favor of the arbitrary (nonphysical) background of that analysis (*26*).

FEASIBILITY OF THE CROSS-LINKING MECHANISMS

Reactivity of the Reactants. The B3LYP/6-31G(d,p) optimized structures of thymine (**1**), C_5-hydroxylated thymine radical (**2**), C_6-hydroxylated thymine radical (**3**), and indolyl radical (**4**) are given in Figure 1a. The natural charges and contact spin densities on the heavy atoms of **1**−**4** are shown in Figure 1b,c, respectively.

The C_5−C_6 bond (1.352 Å) of thymine is much shorter than the C−C bond in benzene (1.396 Å) (*57*) and has a more localized double-bond character. The natural charge at C_5 is negative (−0.164), whereas that at C_6 is slightly positive (+0.069). The natural charge separation is a consequence of the heteroatom positions within the thymine molecule. As a substantial selectivity toward an electron-rich center determines the addition of the •OH

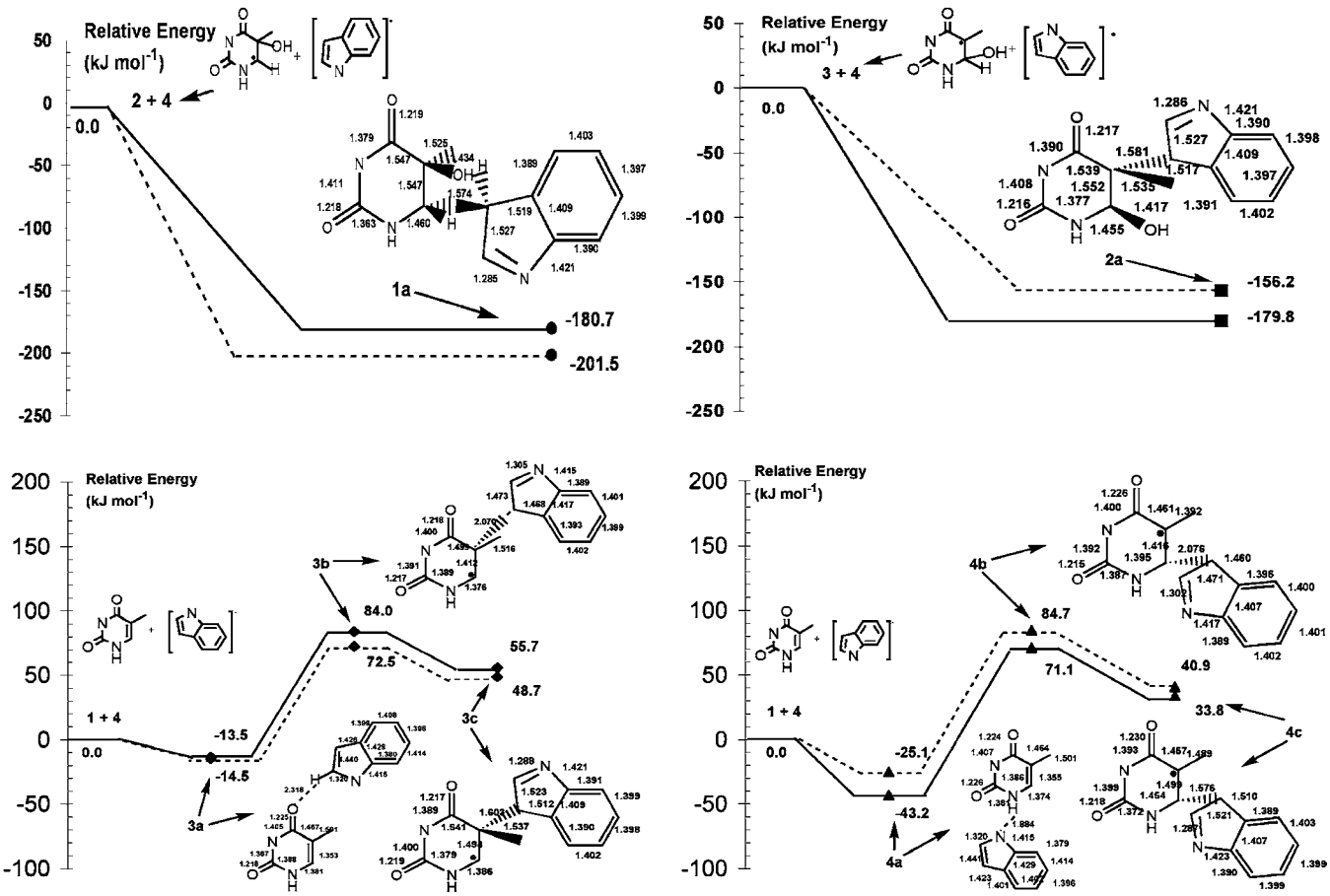

Figure 2. Calculated energy profiles for the initial reaction steps of (a, top left) mechanism 1 (**2** + **4**), (b, top right) mechanism 2 (**3** + **4**), (c, bottom left) mechanism 3 (**1** + **4**), addition to C_5 of thymine, and (d, bottom right) mechanism 4 (**1** + **4**), addition to C_6 of thymine, in the gas phase (solid line) and in aqueous solution (dashed line) at 298 K and 1 atm.

radical to a polarizable double bond (*58*), the C_5 site can be viewed as favorable for the •OH addition to thymine (*59*). The C_5 atom of thymine is methyl (Me) group-substituted with the ∠(C_4−C_5−methyl C) of 117.7°. The C_5 site, as less accessible, is expected to affect the energetics of the •OH addition reaction. Thus, a bulky substituent needs to be forced into an out-of-plane position.

The OH group at C_5 of **2** is pushed away from the ring plane with the C_5−O bond distance being 1.451 Å. The geometry of **2** displays a half-chair conformation with C_5 being the chair-back. The formation of a tetrahedral C_5 center in **2** weakens the N_1−C_6 and C_2−N_3 bonds and strengthens the N_1−C_2 and N_3−C_4 bonds with respect to those in **1**. At the same time, the C_6 atom becomes both pyramidal by ∼20° [∠(N_1−C_6−C_5−H on C_6) = 159.9°] and a localized radical center with a contact spin density of 0.078.

The six-membered ring of **3** shows a half-chair conformation with C_6 being the chair-back. The OH group is pushed behind the ring with the C_6−O bond distance being 1.442 Å. The formation of a tetrahedral C_6 center in **3** weakens the C_2−N_3 bond and strengthens the N_1−C_2, N_3−C_4, and C_4−C_5 bonds with respect to those in **1**. Consequently, C_5 is both pyramidal by ∼9° [∠(C_4−C_5−C_6-methyl C) = 171.2°] and a localized radical center with a contact spin density of 0.060.

On the basis of pulse radiolysis measurements (*60*, *61*), possible reactions of the C(C_5OH) and C(C_6OH) radicals were generally proven to be very fast.

To the best of my knowledge, experimental geometries and spin densities for the indolyl radical are unknown. The skeletal structure of **4** is planar. The structure of **4** has been previously investigated by use of the Slater (*62*), Vosko, Wilk, and Nusair (*63*) (SVWN)/6-31G(d) and B (*64*) LYP (*65*)/6-31G(d) DFT methods (*36*). The B3LYP/6-31G(d,p) geometry used in this paper shows satisfactory agreement with the BLYP/6-31G(d) geometry, with the bonds in Figure 1a being shorter by ∼0.01 Å than those previously reported (*36*). The N_1'−C_2' and C_4'−C_5' bonds show the largest shortenings of 0.018 and 0.012 Å, respectively. Besides, the geometry of the indolyl radical can be considered as being unique in some respect. By both removing a hydrogen atom from indole to form the indolyl radical and removing an electron from indole to form the indolyl radical cation, I have attempted to investigate the changes experienced by the optimized structure of indole. Although a pattern of the changes of interatomic distances for the indolyl radical has been similar to that for the indolyl radical cation, removing a hydrogen atom from indole alters both σ bonding and the identity of the singly occupied molecular orbital. Although the elongation and contraction of most bond distances for the indolyl radical cation with respect to those of indole are predictable on the basis of the nodal structure of indole's highest occupied molecular orbital, the structural changes for the indolyl radical are not predictable from the π orbitals of indole (*36*). Hence, the changes in the electron density distribution appear to be of vital importance for the understanding of the structural changes displayed by Ind• with respect to indole.

The majority contact spin density (0.038) at C_3' of **4** is consistent with the observed site for radical attack on the indolyl radical (*44*, *45*) and contrasts with the

extremely large spin density on N_1' obtained by use of the restricted open-shell Hartree−Fock effective core potential (ROHF-ECP) method (*65*). This supports our proposal that the C_3' site of **4** is the most likely reactive site for the addition of **2** or **3** to **4**.

Initial Step of the Cross-Linking Mechanisms. Hereafter, the proposed reaction pathways are considered as competitive reactions. The energy profiles for the direct combination of **2** and **4** in forming **1a** and for the direct combination of **3** and **4** in forming **2a** are shown schematically in Figure 2a,b, respectively. The B3LYP/6-31G-(d,p) optimized structures (bond lengths) of **1a** and **2a** are given in the same figures. Including scans of the singlet and triplet energy surfaces, all attempts to locate transition structures for the formation of **1a** and **2a** were unsuccessful. The radical combination forming the product **1a** is energetically favorable by 180.7 kJ mol^{-1}, whereas that forming the product **2a** is energetically favorable by 179.8 kJ mol^{-1}. Thus, product **1a** is slightly more energetically favorable by ∼0.9 kJ mol^{-1} than product **2a**. The direct combination of the C(C_5OH) and indolyl radicals occurs with a small or effectively no barrier.

The energy profile for the addition of **4** to C_5 of **1** to form the most stable conformer of the product **3c** is shown schematically in Figure 2c. The B3LYP/6-31G(d,p) optimized structures (bond lengths) of **3a**, **3b**, and **3c** are shown in the same figure. The resulting reactant complex **3a** is 13.5 kJ mol^{-1} lower in energy than the isolated reactants. The formation of the cross-linked product **3c** involves an activation barrier of 97.5 kJ mol^{-1} via TS **3b**. Product **3c** lies 55.7 kJ mol^{-1} higher in energy than the reactant system.

The spin partitioning between the thymine and indolyl radical moieties of **3a**, **3b**, and **3c** is shown in Table 1. The thymine ring has a contact spin density of 0.038 in **3b** and of 0.076 in **3c**, 0.035 and 0.083 of which is localized at C_6, respectively. Due to the formation of a localized C_6 radical center, **3b** and **3c** are higher in energy than the isolated reactants. Whereas the C_5-C_3' bond length in TS **3b** is 2.070 Å, the C_5-C_3' bond length in **3c** is 1.603 Å. However, the Mulliken spin densities given in Table 1 need to be viewed with more care. Following the data (from **3a** to TS **3b)** in Table 1, the contact spin densities show an increase of the spin over both thymine (from 0.001 to 0.038) and the indolyl radical (from 0.012 to 0.074), whereas the Mulliken spin densities show an increase of the spin over the thymine moiety (from −0.002 to 0.511) and a decrease of the spin over the indolyl radical moiety (from 1.002 to 0.489). The contact spin density of thymine moiety in **3c** is larger by 0.038 than that in **3b**, whereas the contact spin density of the indolyl radical moiety in **3c** is smaller by 0.023 than that in **3b**. In contrast to the trend (from **3a** to **3c** via **3b**) of the contact spin densities for the indolyl radical moiety, the Mulliken spin densities show a decreasing (and nonphysical) trend because of known difficulties (*66*, *67*) with this method for determining spin population.

The energy profile for the addition of the indolyl radical to C_6 of thymine to form the most stable conformer **4c** of the product is given schematically in Figure 2d. The B3LYP/6-31G(d,p) optimized structures (bond lengths) of **4a**, **4b**, and **4c** are shown in the same figure. The resulting reactant complex **4a** lies 43.2 kJ mol^{-1} lower in energy than the isolated reactants. The formation of the cross-linked product **4c** involves an activation barrier of 114.3 kJ mol^{-1} via TS **4b**. Product **4c** lies 33.8 kJ mol^{-1} higher in energy than the isolated reactants. The contact spin density over the thymine moiety is 0.013 in **4b** and 0.047 in **4c**, 0.036 and 0.058 of which is localized at C_5, respectively. Due to the formation of a localized C_5 radical center, **4b** and **4c** are higher in energy than the reactant system. Whereas the C_6-C_3' bond length in TS **4b** is 2.076 Å, the C_6-C_3' bond length in **4c** is 1.576 Å. Because there is a free N−H in thymine that may interfere with the reaction mechanisms, the use of thymine to mimic DNA is questionable in some respects. As a matter of fact, this interference is seen in Figure 2d, where a hydrogen bond formation involving N−H is proposed. Although an N-1 methylated thymine may be a better candidate, some activation barrier will remain and will not affect the conclusion on the most likely reaction pathway leading to the initial cross-linked product.

Table 2. Calculated Entropy, Free Energy, and Enthalpy Changes for Various Reaction Steps at 298 K and 1 atm

starting point	final point	ΔS_{298K} (kJ mol^{-1} K^{-1})	ΔG_{298K} (kJ mol^{-1})	ΔH_{298K} (kJ mol^{-1})
2 + **4**	**1a**	−0.203	−125.4	−185.9
3 + **4**	**2a**	−0.218	−120.8	−185.8
1 + **4**	**3a**	−0.117	24.4	−10.5
1 + **4**	**3b**	−0.181	136.8	82.9
1 + **4**	**3c**	−0.179	109.5	56.2
1 + **4**	**4a**	−0.138	0.0	−41.1
1 + **4**	**4b**	−0.171	122.9	71.9
1 + **4**	**4c**	−0.163	82.7	34.1
1a	**1b**	−0.003	142.1	141.2
1a	**1c**	−0.001	−74.6	−74.9
1a + H_2O	**1d**	−0.129	7.6	−30.8
1a + H_2O	**1e**	−0.146	144.4	100.9
1a + H_2O	**1f**	−0.092	−76.9	−104.3
1c	**1g** + H_2O	0.167	−86.4	−36.6

It is noted that product **4c** is ∼21.9 kJ mol^{-1} lower in energy than product **3c** and that TS **4b** is ∼12.9 kJ mol^{-1} lower in energy than TS **3b** (see Figure 2). More importantly, the formation of the cross-linked product **3c** involves an activation barrier of 97.5 kJ mol^{-1} via TS **3b**, whereas the formation of the cross-linked product **4c** involves an activation barrier of 114.3 kJ mol^{-1} via TS **4b** (see Figure 2). Thus, the computed energy surfaces suggest that the addition of the indolyl radical to thymine prefers the C_5 site over C_6.

The effects of the solvent on the potential energy surface were investigated by single-point DPCM/B3LYP/6-311G(2df,p) calculations with a dielectric constant of 78.39 for water. The energy profiles of the four mechanisms including solvation are shown in Figure 2 by a dashed line. Solvation reduces the activation energy barriers of mechanisms 3 and 4 from 97.5 and 114.3 to 87.0 and 109.8 kJ mol^{-1}, respectively. The solvated products **1a** and **3c** have lower relative energies (−201.5 and 48.7 kJ mol^{-1}) than in the gas phase (−180.7 and 55.7 kJ mol^{-1}), whereas the solvated products **2a** and **4c** have higher relative energies (−156.2 and 40.9 kJ mol^{-1}) than in the gas phase (−179.8 and 33.8 kJ mol^{-1}).

The calculated entropy changes (Table 2) of the initial steps of the four mechanisms are negative, and the calculated free energy changes (Table 2) of the reactions at 298 K suggest that the reactions are more favorable at 0 K than at 298 K. The initial steps of mechanisms 3 and 4 have larger barriers than the initial steps of

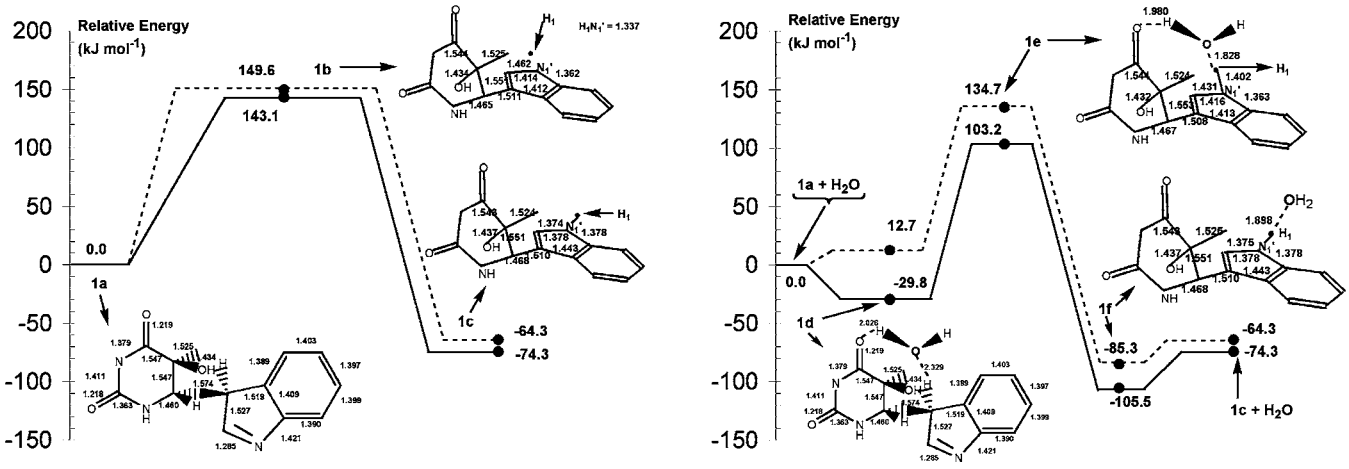

Figure 3. Calculated energy profiles of the hydrogen (H_1) transfer from C_3' to N_1' (a, top) for mechanism A and (b, bottom) for mechanism B in the gas phase (solid line) and in aqueous solution (dashed line) at 298 K and 1 atm.

mechanisms 1 and 2, both in the gas phase and in solution, are thermodynamically unfavorable, and their possible diastereomers have not been considered. Of mechanisms 3 and 4, mechanism 3 is thermodynamically more favorable both in the gas phase and in solution. The initial step of mechanism 1 is energetically more favorable both in the gas phase and in solution than that of mechanism 2. These high-energy, short-lived radicals (**2** and **4**) are supposed to exist next to each other at exactly the same time and in the correct orientation for their combination. Although the intermediates for the radical recombination mechanism contain three chiral centers, the formation of other diastereomers has not been considered due to its nonsubstantial impact (within 1 kcal mol^{-1}) on the solvated relative energies. Thus, the possible reaction steps proceeding from intermediate product **1a** are considered below.

Hydrogen Transfer. Two possible reaction mechanisms (Figure 3) for an internal hydrogen (denoted H_1) transfer from carbon (denoted C_3') to nitrogen (denoted N_1') within the initial cross-linked product **1a** are considered: (A) direct hydrogen transfer from C_3' to N_1' and (B) hydrogen transfer from C_3' to N_1' by way of a bridging water molecule. I have attempted to consider a concerted reaction mechanism for a hydrogen transfer from C_3' to N_1' within **1a**, but all attempts to locate a TS linking **1d** and **1f** (see Figure 3) were unsuccessful. Because the OH group at C_5 of the thymine moiety in **1d** is in an out-of-plane position, the hydroxyl group does not seem to be able to partake in a possible concerted hydrogen-transfer reaction occurring on the opposite side of the ring plane between C_3' and N_1'.

The calculated potential energy surface of mechanism A is shown in Figure 3a. The formation of the hydrogen-transferred product **1c** via TS **1b** can occur with an activation barrier of 143.1 kJ mol^{-1}. **1c** is 74.3 kJ mol^{-1} lower in energy than **1a**. Due to the high barrier, this pathway is unlikely. The distance between H_1 and N_1' in **1a** is ~3.025 Å. It would be difficult for the direct transfer of H_1 from C_3' to N_1' to take place over such a distance. As the reaction is supposed to be carried out in aqueous solution, water molecules may be involved in the hydrogen-transfer reaction. Hence, mechanism B is proposed to explore the role of a water molecule in the hydrogen transfer.

The calculated energy profile of mechanism B is shown in Figure 3b. Initially, **1a** interacts with a water molecule, forming hydrogen-bonded complex **1d** that lies 29.8 kJ mol^{-1} lower in energy than the isolated reactants. The oxygen atom at C_4 of the thymine moiety and the H−O part of the water molecule form a hydrogen bond in **1d** with a length of 2.026 Å. Product complex **1f** can form via TS **1e** with an activation barrier of 133.0 kJ mol^{-1}. The barrier of mechanism B is lower than the barrier of 143.1 kJ mol^{-1} of mechanism A. Two hydrogen bonds are present in TS **1e**. First, the hydrogen bond of 2.026 Å in **1d** gets stronger in TS **1e** with a bond length of 1.980 Å. Second, the oxygen atom of the water molecule and H_1−N_1' form a hydrogen bond having a length of 1.828 Å. The H_1−N_1' distance in **1e** is 1.402 Å. **1f** is 105.5 kJ mol^{-1} lower in energy than the isolated reactants. The hydrogen bond length between N_1'−H_1 and OH_2 in **1f** is 1.898 Å. The cost for isolating **1c** + H_2O from **1f** is 31.2 kJ mol^{-1}. It is clear that the water molecule acts as a catalyst in this particular situation. It is concluded that mechanism B is preferred over mechanism A. In addition, hydrogen-bonding interactions play a key role in the hydrogen-transfer reaction step.

The calculated entropy changes at 298 K of the two hydrogen-transfer reactions are given in Table 2. The calculated free energy changes of the reactions at 298 K (Table 2) suggest that the reactions are less favorable at 298 K than at 0 K.

Single-point DPCM/B3LYP/6-311G(2df,p) calculations with a dielectric constant of 78.39 for water have been employed to investigate solvent effects. The barriers for mechanisms A and B in aqueous solution are 149.6 and 122.0 kJ mol^{-1}, respectively. The solvation-included barrier of mechanism A is higher than the barrier of 143.1 kJ mol^{-1} of mechanism A in the gas phase. The barrier of mechanism B in aqueous solution is lower than the barrier of 133.0 kJ mol^{-1} of mechanism B in the gas phase. It is concluded that mechanism B is the preferred pathway both in the gas phase and in solution.

Dehydration of Intermediate 1c. Dehydration of **1c** leads to the final cross-linked product **1g**, as given in Figure 4. The oxygen atom of the OH group at C_5 of the thymine moiety is denoted by O_1. The dehydration step proceeds by a standard reaction sequence, such as protonation at O_1, loss of water at C_5, and deprotonation at C_6. This is an acid-catalyzed reaction. The formation of the final product **1g** at 298 K via dehydration of **1c** is energetically favored by 42.9 kJ mol^{-1}, whereas the computed entropy change is 0.167 kJ mol^{-1} K^{-1} (Table 2). The free energy difference from 0 to 298 K is favorable for the dehydration step.

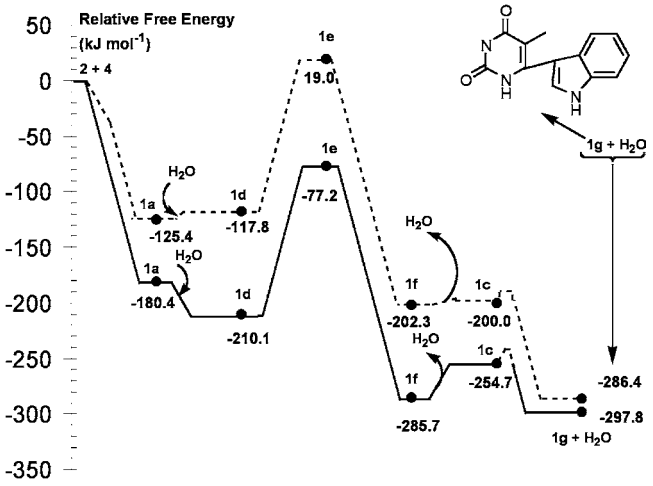

Figure 4. Calculated free energy profiles of the complete reaction mechanism at 0 K (solid line) and 298 K (dashed line) in the gas phase at 1 atm.

Complete Cross-Linking Mechanism at 0 and 298 K. The free energy profile at 0 and 298 K of the most favorable energy surface for the complete reaction mechanism is shown in Figure 4. In the segment of **1d** → **1f**, the water is partaking in the complexes. Although the free energy profiles at the two temperatures display differences of magnitude in the segment of **1d** → **1c**, the overall thermodynamics at 0 and 298 K are similar. Because of the entropy contribution to the free energy, temperature may be a central factor influencing the overall mechanism.

NATURE OF THE CROSS-LINK IN FINAL PRODUCT **1g**

I will begin with the natural charges of C_6 and C_3'. The C_6 atom of the thymine moiety has a natural charge of +0.212 and is quite positive. The C_3' atom of the indolyl radical moiety has a natural charge of −0.036 and is slightly negative or essentially neutral. The picture, which emerges from the natural charges of the atoms, is that the C_6-C_3' bond is not charge-separated to a great extent. It is also possible to determine charge separation between the two moieties by summing the corresponding natural charges of atoms. The natural charge partitioning between the thymine and indolyl radical moieties in **1g** is Thym(−0.077)−Ind•(+0.077). Clearly, the cross-link between the two moieties is not substantially charge-separated in its nature, but shows an inclination toward a mild electrostatic character. In this particular situation, the indolyl radical acts as a donor while thymine acts as an acceptor. According to the quantum theory of atoms in molecules (QTAIM), a necessary and sufficient condition for the existence of a through-space-bonded interaction is the existence of a bond path (*68*). A bond path is defined as a line of the highest electron density linking a pair of atoms. The AIM analysis confirms the existence of a C_6-C_3' bond path with the C_6-C_3' bond path length (1.4710 Å) being in agreement with the geometric C_6-C_3' bond length (1.4709 Å) in the final cross-linked product. The point of a line of the highest electron density, determined by the condition that the gradient of the electron density is equal to zero, is the bond critical point. The topological features of the electron density at this point provide quantitative information on the characteristics of a bond. The position of the C_6-C_3' BCP is shown in Figure 5. A small electron density of 1.8569 eÅ^{-3} at the BCP between C_6 and C_3' in **1g** is slightly larger than those (0.7−0.9 eÅ^{-3}) typically associated with weak bonds in donor−acceptor complexes. The second derivative or Laplacian of the electron density, $\nabla^2\rho(r)$, shows where the electron density is locally concentrated [$\nabla^2\rho(r) < 0$] and depleted [$\nabla^2\rho(r) > 0$] and contains a large amount of chemical information. The Laplacian has a value of −17.9232 eÅ^{-5}, indicating a local charge concentration at the BCP between C_6 and C_3' in the final cross-linked product.

TRYPTOPHAN SIDE CHAIN AND INDOLYL RADICALS

The calculated structures and contact spin densities on the heavy atoms of the tryptophan side chain and

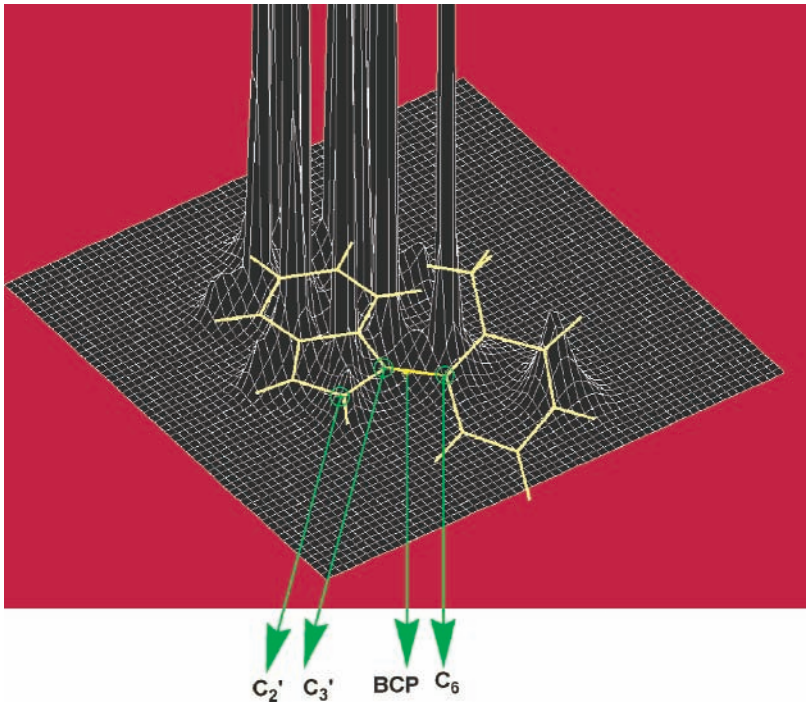

Figure 5. Cut of the electron density in the final product **1g**. C_6, C_3', and C_2' are in the plane of the cut. The position of the C_6-C_3' bond-critical point (BCP) is nicely visible. The C_6-C_3' bond path length is 1.4710 Å. The C_6−BCP distance is 0.7518 Å.

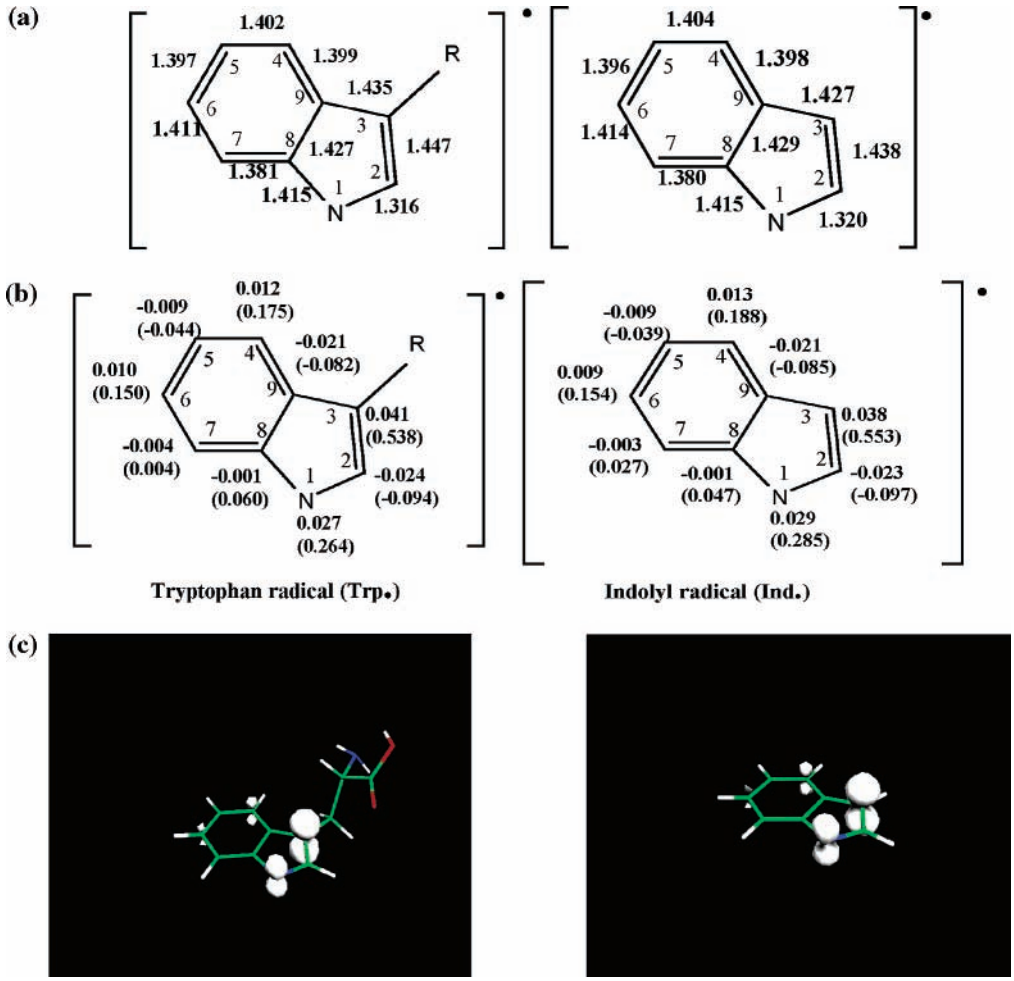

Figure 6. Tryptophan side chain and indolyl radicals: (a) B3LYP/6-31G(d,p) optimized structures (bond lengths); (b) contact spin densities on the heavy atoms [the Mulliken spin densities (in parentheses) show substantial discrepancies (note carbon 7) for the two radicals due to a nonphysical background of the method (*66*, *67*) for determining spin population]; (c) isosurface plots of the contact spin densities.

indolyl radicals are shown schematically in Figure 6. The side chain on the carbon C_3' of the tryptophan radical is $-CH_2-CH(NH_2)-COOH$. Clearly, the optimized geometries and contact spin density distributions of the two radicals are essentially equal. Thus, we believe that the direct combination of the C_5-hydroxylated thymine and tryptophan radicals should form the initial cross-linked product, as far as a chiral addition of the tryptophan radical to the DNA is concerned. It is also important to note the Mulliken spin densities given in parentheses in Figure 6. Several substantial discrepancies between the values are quite obvious, of which that at carbon 7 is the most conspicuous. Whereas the contact spin densities indicate a vanishing spin down at nucleus 7 in either case, the Mulliken spin densities show a vanishing spin up of 0.004 for the tryptophan radical and a substantially larger spin up of 0.027 for the indolyl radical. The Mulliken spin densities confirm the arbitrary (nonphysical) background of this population analysis (*66*, *67*).

CONCLUSIONS

The reaction mechanisms for the cross-linking of thymine and indolyl radical have been proposed.

The direct combination of the C_5-hydroxylated thymine and indolyl radicals is suggested to be the preferred mechanism in aqueous solution with a small or effectively no barrier in forming the initial cross-linked product, which is energetically more favorable by 45.3 kJ mol^{-1} than that formed by the direct combination of the C_6-hydroxylated thymine and indolyl radicals. The indolyl radical additions to C_5 and C_6 of thymine are suggested to be thermodynamically unfavorable in forming the initial cross-linked product.

Hydrogen-bonding interactions are suggested to play a key role in the hydrogen-transfer reaction by way of a bridging water molecule within the initial cross-linked product.

The formation of the final product **1g** via dehydration of **1c** is energetically favorable by 42.9 kJ mol^{-1}. The calculated entropy change at 298 K is 0.167 kJ mol^{-1} K^{-1}, and the free energy difference from 0 to 298 K is favorable for the dehydration reaction step.

Although bulk solvation has significant impact on the energetics of the cross-linking mechanisms, the preferred mechanism is suggested to be the same both in the gas phase and in solution.

The cross-link between the indolyl radical (donor) and thymine (acceptor) moieties in the final product is not substantially charge-separated in its nature, but shows an inclination toward a mild electrostatic character.

ACKNOWLEDGMENT

This work was supported by the Killam Trust. I thank the reviewers for valuable comments.

LITERATURE CITED

(1) (a) Kohn, K. W. (1977) Interstrand cross-linking of DNA by 1,3-bis(2-chloroethyl)-1-nitrosourea and other 1-(2-haloethyl)-1-nitrosoureas. *Cancer Res. 37*, 1450−1454. (b) Kohn, K. W., and Ewig, R. A. G. (1979) DNA-protein crosslinking by *trans*-platinum(II) diamminedichloride in mammalian-cells: a new method of analysis. *Biochim. Biophys. Acta 562*, 32−40.

(2) (a) Fornace, A. J., Jr., and Little, J. B. (1977) DNA cross-linking induced by x-rays and chemical agents. *Biochim. Biophys. Acta 477*, 343−355. (b) Mee, L. K., and Adelstein, S. J. (1981) Predominance of core histones in formation of DNA−protein cross-links in gamma-irradiated chromatin. *Proc. Natl. Acad. Sci. U.S.A. 78*, 2194−2198. (c) Bowden, G. T., Kasunic, M., and Cress, A. E. (1982) Thermal enhancement of x-ray-induced DNA crosslinking. *Radiat. Res. 83*, 203−208.

(3) Reiss, U. M., and Tappel, A. L. (1973) Fluorescent product formation and changes in structure of DNA reacted with peroxidizing arachidonic acid. *Lipids 8*, 199−203.

(4) Malins, D. C., Polissar, N. L., and Gunselman, S. J. (1996) Progression of human breast cancers to the metastatic state is linked to hydroxyl radical-induced DNA damage. *Proc. Natl. Acad. Sci. U.S.A. 93*, 2557−2563.

(5) Ames, B. N., Shigenaga, M. K., and Hagen, T. M. (1993) Oxidants, antioxidants, and the degenerative diseases of aging. *Proc. Natl. Acad. Sci. U.S.A. 90*, 7915−7922.

(6) Loft, S., and Poulsen, H. E. (1996) Cancer risk and oxidative DNA damage in man. *J. Mol. Med. 74*, 297−312.

(7) Totter, J. R. (1980) Spontaneous cancer and its possible relationship to oxygen metabolism. *Proc. Natl. Acad. Sci. U.S.A. 77*, 1763−1767.

(8) Ohshima, H., and Bartsch, H. (1994) Chronic infections and inflammatory processes as cancer risk-factors—possible role of nitric-oxide in carcinogenesis. *Mutat. Res. 305*, 253−264.

(9) Hsiao, K., Chapman, P., Nilsen, S., Eckman, C., Harigaya, Y., Younkin, S., Yang, F. S., and Cole, G. (1996) Correlative memory deficits, a beta elevation, and amyloid plaques in transgenic mice. *Science 274*, 99−103.

(10) Selkoe, D. J. (1994) Cell biology of the amyloid beta-protein precursor and the mechanism of Alzheimer's disease. *Annu. Rev. Cell Biol. 10*, 373−403.

(11) Youdim, M. B. H., and Riederer, P. (1997) Understanding Parkinson's disease. *Sci. Am. 276*, 52−59.

(12) de Lara, C. M., Jenner, T. J., Townsend, K. M. S., Marsden, S. J., and O'Neill, P. (1995) The effect of dimethyl-sulfoxide on the induction of DNA double-strand breaks in v79-4 mammalian-cells by alpha-particles. *Radiat. Res. 144*, 43−49.

(13) Chapman, J. D., Reuvers, R. P., Borsa, J., and Grrenstock, C. L. (1973) Chemical radioprotection and radiosensitization of mammalian-cells growing in-vitro. *Radiat. Res. 56*, 291−306.

(14) von Sonntag, C. (1997) *The Chemical Basis of Radiation Biology*, Taylor and Francis, London, U.K.

(15) Tyrrell, R. M. (2000) Role for singlet oxygen in biological effects of ultraviolet A radiation. *Methods Enzymol. 319*, 290−296. Kvam, E., Hejmadi, V., Ryter, S., Pourzand, C., and Tyrrell, R. M. (2000) Heme oxygenase activity causes transient hypersensitivity to oxidative ultraviolet A radiation that depends on release of iron from heme. *Free Radical Biol. Med. 28*, 1191−1196.

(16) Ramakrishnan, N., Chiu, S. M., and Oleinick, N. L. (1987) Yield of DNA-protein cross-links in gamma-irradiated Chinese-hamster cells. *Cancer Res. 47*, 2032−2035.

(17) Mee, L. K., and Adelstein, S. J. (1979) Radiolysis of chromatin extracted from cultured mammalian cells: formation of DNA-protein cross links. *Int. J. Radiat. Biol. 36*, 359−366.

(18) Yamamoto, O. (1976) In *Aging, Carcinogenesis, and Radiation Biology* (Smith, K. C., Ed.), Plenum Press, New York.

(19) Gajewski, E., Fuciarelli, A. F., and Dizdaroglu, M. (1988) Structure of hydroxyl radical-induced DNA-protein crosslinks in calf thymus nucleohistone invitro. *Int. J. Radiat. Biol. 54*, 445−459.

(20) (a) Dizdaroglu, M., Gajewski, E., Reddy, P., and Margolis, S. A. (1989) Structure of a hydroxyl radical-induced DNA-protein cross-link involving thymine and tyrosine in nucleohistone. *Biochemistry 28*, 3625−3628. (b) Margolis, S. A., Coxon, B, Gajewski, E., and Dizdaroglu, M. (1988) Structure of a hydroxyl radical-induced cross-link of thymine and tyrosine. *Biochemistry 27*, 6353−6359.

(21) Dizdaroglu, M., and Gajewski, E. (1989) Structure and mechanism of hydroxyl radical-induced formation of a DNA-protein cross-link involving thymine and lysine in nucleohistone. *Cancer Res. 49*, 3463−3467.

(22) Gajewski, E., and Dizdaroglu, M. (1990) Hydroxyl radical induced cross-linking of cytosine and tyrosine in nucleohistone. *Biochemistry 29*, 977−980.

(23) Nackerdien, Z., Rao, G., Cacciuttolo, M. A., Gajewski, E., and Dizdaroglu, M. (1991) Chemical nature of DNA-protein cross-links produced in mammalian chromatin by hydrogen-peroxide in the presence of iron or copper ions. *Biochemistry 30*, 4873−4879.

(24) Morimoto, S., Hatta, H., Fujita, S., Matsuyama, T., Ueno, T., and Nishimoto, S. (1998) Hydroxyl radical-induced cross-linking of thymine and lysine: identification of the primary structure and mechanism. *Bioorg. Med. Chem. Lett. 8*, 865−870.

(25) Charlton, T. S., Ingelse, B. A., Black, D. StC., Craig, D. C., Mason, K. E., and Duncan, M. W. (1999) A covalent thymine-tyrosine adduct involved in DNA-protein cross-links: synthesis, characterization, and quantification. *Free Radical Biol. Med. 27*, 254−261.

(26) Ban, F., Lundqvist, M. J., Boyd, R. J., and Eriksson, L. A. (2002) Theoretical studies of the cross-linking mechanisms between cytosine and tyrosine. *J. Am. Chem. Soc. 124*, 2753−2761.

(27) Simic, M. G., and Dizdaroglu, M. (1985) Formation of radiation-induced cross-links between thymine and tyrosine—possible model for cross-linking of DNA and proteins by ionizing radiation. *Biochemistry 24*, 233−236.

(28) Takeda, Y., Ohlendorf, D. H., Anderson, W. F., and Matthews, B. W. (1983) DNA-binding proteins. *Science 221*, 1020−1026.

(29) Casas-Finet, J. R., Toulme, J. J., Santus, R., Butler, J., Land, E. J., and Swallow, A. J. (1984) Influence of DNA binding on the formation and reactions of tryptophan and tyrosine radicals in peptides and proteins. *Int. J. Radiat. Biol. 45*, 119−132.

(30) Prutz, W. A., Butler, J., Land, E. J., and Swallow, A. J. (1980) Direct demonstration of electron transfer between tryptophan and tyrosine in proteins. *Biochem. Biophys. Res. Commun. 96*, 408−414.

(31) Curtiss, L. A., Redfern, P. C., Raghavachari, K., and Pople, J. A. (2001) Gaussian-3X (G3X) theory: use of improved geometries, zero-point energies, and Hartree−Fock basis sets. *J. Chem. Phys. 114*, 108−117.

(32) Lynch, B. J., and Truhlar, D. G. (2001) How well can hybrid density functional methods predict transition state geometries and barrier heights? *J. Phys. Chem. A 105*, 2936−2941.

(33) Wetmore, S. D., Boyd, R. J., Llano, J., Lundqvist, M. J., and Eriksson, L. A. (2000) Hydroxyl radical reactions in biological media. *Recent Advances in Density Functional Theory Methods*, *Vol. 3* (Barone, V., Bencini, A., and Fantucci, P., Eds.), World Scientific, Singapore.

(34) Himo, F., and Siegbahn, P. E. M. (2000) Very stable ribonucleotide substrate radical relevant for class I ribonucleotide reductase. *J. Phys. Chem. B 104*, 7502−7509.

(35) Ban, F. Q., Gauld, J. W., and Boyd, R. J. (2001) Modeling the action of an antitumor drug: A density functional theory study of the mechanism of tirapazamine. *J. Am. Chem. Soc. 123*, 7320−7325.

(36) Walden, S. E., and Wheeler, R. A. (1996) Distinguishing features of indolyl radical and radical cation: implications for tryptophan radical studies. *J. Phys. Chem. 100*, 1530−1535.

(37) Reha, D., Kabelac, M., Ryjacek, F., Sponer, J., Sponer, J. E., Elstner, M., Suhai, S., and Hobza, P. (2002) Intercalators. 1. Nature of stacking interactions between intercalators (ethidium, daunomycin, ellipticine, and 4′,6-diaminide-2-

phenylindole) and DNA base pairs. Ab initio quantum chemical, density functional theory, and empirical potential study. *J. Am. Chem. Soc. 124*, 3366−3376.
(38) Yekeler, H., and Ozbakir, D. (2001) Concerning the solvent effect in the tautomerism of uracil, 5-fluorouracil, and thymine by density-functional and ab initio calculations. *J. Mol. Mod. 7*, 103−111.
(39) Ban, F., Rankin, K. N., Gauld, J., and Boyd, R. J. (2002) Recent applications of density functional theory calculations to biomolecules. *Theor. Chem. Acc. 108*, 1−11.
(40) Farhataziz, and Ross, A. B. (1977) Selected and specific rates of reactions of transients from water in aqueous solutions. Hydroxyl radical and perhydroxyl radical and their radical ions. *Reference Data System−National Bureau of Standards NSRDS-NBS*, U.S. Department of Commerce, Washington, DC.
(41) Huttermann, J., Herak, J. N., and Westhof, E. (1978) In *Effects of Ionizing Radiation on DNA* (Huttermann, J., Kohnlein, W., and Teoule, R., Eds.), Springer-Verlag, Berlin.
(42) Scholes, G. (1978) In *Effects of Ionizing Radiation on DNA* (Huttermann, J., Kohnlein, W., and Teoule, R., Eds.), Springer-Verlag, Berlin.
(43) Fujita, S., and Steenken, S. (1981) Pattern of OH radical-addition to uracil and methyl-substituted and carboxyl-substituted uracils−electron-transfer of OH adducts with *N*,*N*,*N*′,*N*′-tetramethyl-*p*-phenylenediamine and tetranitromethane. *J. Am. Chem. Soc. 103*, 2540−2545.
(44) Remers, W. A. (1972) *Heterocyclic Compounds. Indoles I. Vol. 25* (Houlihan, W. J., Ed.), Wiley, New York.
(45) Shen, X., Lind, J., Eriksen, T. E., and Merenyi, G. (1980) The reactions of indoles in aqueous solution initiated by one-electron oxidation. *J. Chem. Soc., Perkin Trans. 2*, 597−603.
(46) Frisch, M. J., Trucks, G. W., Schlegel, H. B., Scuseria, G. E., Robb, M. A., Cheeseman, J. R., Zakrzewski, V. G., Montgomery, J. A., Stratmann, R. E., Burant, J. C., Dapprich, S., Millam, J. M., Daniels, A. D., Kudin, K. N., Strain, M. C., Farkas, O., Tomasi, J., Barone, V., Cossi, M., Cammi, R., Mennucci, B., Pomelli, C., Adamo, C., Clifford, S., Ochterski, J., Petersson, G. A., Ayala, P. Y., Cui, Q., Morokuma, K., Malick, D. K., Rabuck, A. D., Raghavachari, K., Foresman, J. B., Cioslowski, J., Ortiz, J. V., Baboul, A. G., Stefanov, B. B., Liu, G., Liashenko, A., Piskorz, P., Komaromi, I., Gomperts, R., Martin, R. L., Fox, D. J., Keith, T. A., Al-Laham, M. A., Peng, C. Y., Nanayakkara, A., Challacombe, M., Gill, P. M. W., Johnson, B., Chen, W., Wong, M. W., Andres, J. L., Gonzalez, C., Head-Gordon, M., Replogle, E. S., and Pople, J. A. (1998) *GAUSSIAN 98*, Gaussian, Inc., Pittsburgh, PA.
(47) Becke, A. D. (1993) A new mixing of Hartree−Fock and local density-functional theories. *J. Chem. Phys. 98*, 1372−1377.
(48) Stephens, P. J., Devlin, F. J., Chabalowski, C. F., and Frisch, M. J. (1994) Ab-initio calculation of vibrational absorption and circular-dichroism spectra using density-functional force-fields. *J. Phys. Chem. 98*, 11623−11627.
(49) Lee, C. T., Yang, W. T., and Parr, R. G. (1988) Development of the Cole-Salvetti correlation energy formula into a functional of the electron density. *Phys. Rev. B 37*, 785−789.
(50) Ayala, P. Y., and Schlegel, H. B. (1997) A combined method for determining reaction paths, minima, and transition state geometries. *J. Chem. Phys. 107*, 375−384.
(51) (a) Miertus, S., Scrocco, E., and Tomasi, J. (1981) Electrostatic interaction of a solute with a continuum−a direct utilization of ab initio molecular potentials for the prevision of solvent effects. *Chem. Phys. 55*, 117−129. (b) Miertus, S., and Tomasi, J. (1982) Approximate evaluations of the electrostatic free-energy and internal energy changes in solution processes. *Chem. Phys. 65*, 239−245. (c) Cossi, M., Barone, V., Cammi, R., and Tomasi, J. (1996) Ab initio study of solvated molecules: a new implementation of the polarizable continuum model. *Chem. Phys. Lett. 255*, 327−335.
(52) Biegler-Konig, F. W., Bader, R. F. W., and Tang, T. H. (1982) Calculation of the average properties of atoms in molecules. 2. *J. Comput. Chem. 3*, 317−352.
(53) (a) Reed, A. E., Curtiss, L. A., and Weinhold, F. (1988) Intermolecular interactions from a natural bond orbital, donor−acceptor viewpoint. *Chem. Rev. 88*, 899−926. (b) Glendening, E. D., Reed, A. E., and Weinhold, F. NBO version 3.1.
(54) Mo, Y., Song, L., Wu, W., and Zhang, Q. (2004) Charge transfer in the electron donor−acceptor complex BH_3NH_3. *J. Am. Chem. Soc. 126*, 3974−3982.
(55) (a) Flukiger, P., Luthi, H. P., Portmann, S., and Weber, J. (2000) MOLEKEL 4.3, Swiss Center for Scientific Computing, Manno, Switzerland. (b) Portmann, S., and Luthi, H. P. (2000) MOLEKEL: an interactive molecular graphics tool. *CHIMIA 54*, 766−769.
(56) Schaftenaar, G. (2000) MOLDEN 3.7, CAOS/CAMM Center Nijmegen, The Netherlands.
(57) Cabana, A., Bachand, J., and Giguere, J. (1974) The equilibrium structure of benzene. *Can. J. Phys. 52*, 1949−1955.
(58) (a) Steenken, S., and O'Neill, P. (1978) Selectivity of addition of the hydroxyl radical to ring positions of pyridine and pyridine mono- and dicarboxylic acids. An electron spin resonance investigation. *J. Phys. Chem. 82*, 372−374. (b) Anbar, M., Meyerstein, D., and Neta, P. (1966) The reactivity of aromatic compounds toward hydroxyl radicals. *J. Phys. Chem. 70*, 2660−2662.
(59) Dizdaroglu, M., and Simic, M. G. (1984) Radiation-induced formation of thymine-thymine crosslinks. *Int. J. Radiat. Biol. 46*, 241−246.
(60) Myers, L. S., Jr., Hollis, M. L., Theard, L. M., Peterson, F. C., and Warnick, A. (1970) Pulse radiolysis of nucleic acid constituents and related compounds. III. Optical spectra and reactivity of organic free radicals formed by reaction of hydroxyl free radicals with pyrimidine bases. *J. Am. Chem. Soc. 92*, 2875−2882.
(61) Hayon, E., and Simic, M. G. (1973) Addition of hydroxyl radicals to pyrimidine bases and electron-transfer reactions of intermediates to quinone. *J. Am. Chem. Soc. 95*, 1029−1035.
(62) Slater, J. C. (1951) A simplification of the Hartree−Fock method. *Phys. Rev. 81*, 385−390.
(63) Vosko, S. H., Wilk, L., and Nusair, M. (1980) Accurate spin-dependent electron liquid correlation energies for local spin-density calculations−a critical analysis. *Can. J. Phys. 58*, 1200−1211.
(64) Becke, A. D. (1988) Density-functional exchange-energy approximation with correct asymptotic-behavior. *Phys. Rev. B 38*, 3098−3100.
(65) Krauss, M., and Garmer, D. R. (1993) Assignment of the spectra of protein radicals in cytochrome-*c* peroxidase *J. Phys. Chem. 97*, 831−836.
(66) Mulliken, R. S. (1955) Electronic population analysis on LCAO-MO molecular wave functions. I. *J. Chem. Phys. 23*, 1833−1840.
(67) Mulliken, R. S., and Ermler, W. C. (1977) *Diatomic Molecules*, Academic Press, New York.
(68) Bader, R. F. W. (1990) *Atoms in Molecules*, Clarendon Press, Oxford, U.K.

BC0500490

N-(2-Hydroxypropyl)methacrylamide Copolymers of a Glutathione (GSH)-Activated Glyoxalase I Inhibitor and DNA Alkylating Agent: Synthesis, Reaction Kinetics with GSH, and in Vitro Antitumor Activities

Zhe-Bin Zheng,[†] Guozhang Zhu,[†] Heekyung Tak,[†] Erin Joseph,[‡] Julie L. Eiseman,[‡] and Donald J. Creighton*,[†]

Department of Chemistry and Biochemistry, University of Maryland, Baltimore County, Baltimore, Maryland 21250, and University of Pittsburgh Cancer Center, Pittsburgh, Pennsylvania 15213. Received February 13, 2004; Revised Manuscript Received March 28, 2005

The incorporation of anticancer prodrugs into polyacrylamide conjugates has been shown to improve tumor targeting via the so-called "enhanced permeability and retention" effect. This strategy has now been expanded to include two different classes of glutathione (GSH)-activated antitumor agents prepared by radical polymerization of *N*-(2-hydroxypropyl)methacrylamide (HPMA) with 2-methacryloyloxy-methyl-2-cyclohexenone (**7**) and/or with *S*-(*N*-4-chlorophenyl-*N*-hydroxycarbamoyl-thioethyl)-methacrylamide (**8**), followed by treatment with 3-chloroperoxybenzoic acid, to give the HPMA copolymers of **7** and the **8**-sulfoxide, respectively. In aqueous-buffered solution at pH 6.5, GSH reacts rapidly with poly-HPMA-**8**-sulfoxide ($k \approx 2.3$ mM^{-1} min^{-1}) to give *S*-(*N*-4-chlorophenyl-*N*-hydroxycarbamoyl)glutathione (**1**), a tight-binding transition state analogue inhibitor of the antitumor target enzyme glyoxalase I ($K_i = 46$ nM), or with poly-HPMA-**7** ($k \approx 0.02$ mM^{-1} min^{-1}) to give the electrophilic antitumor agent 3-glutathio-2-methylenecyclohexenone (**4**). Indeed, B16 melanotic melanoma in culture is inhibited by poly-HPMA-**8**-sulfoxide and by poly-HPMA-**7** with IC_{50} values of 168 ± 8 and 284 ± 5 μM, respectively. These values are significantly greater than those of the unpolymerized prodrugs suggesting that the cytotoxicity of the polymer prodrugs might be limited by slow cellular uptake via pinocytosis. This prodrug strategy should be applicable to a range of different GSH-based antitumor agents.

INTRODUCTION

A conceptually important strategy for improving tumor targeting during cancer chemotherapy is to use high molecular weight copolymer prodrugs to better direct the drug to tumor tissue via the so-called "enhanced permeability and retention" (EPR)[1] effect (for reviews, see ref *1*). This effect arises, in part, from the tendency of high molecular weight copolymer prodrugs (>70 000 Da) to remain in circulating plasma longer than low molecular weight drugs and from the fact that blood vessels in rapidly growing tumors are more permeable to high molecular weight species than are blood vessels in normal, established tissues. Once concentrated in tumor tissue, the copolymer prodrug can then enter tumor cells by endocytosis.

The challenge is to design copolymer prodrugs that will release the antitumor agents into the cell cytosol after endocytosis. A frequently used design strategy is to covalently attach the drug to the polymer via a peptide linkage, which will undergo catalyzed hydrolysis when the copolymer prodrug-filled endosomes fuse with the peptidase-filled lysosomes. The free drug is then available to diffuse out of the lysosomes into the cell cytosol. Indeed, prodrug conjugates of poly-*N*-2-(hydroxypropyl)-methacrylamide (HPMA) have been designed to deliver the anticancer drugs doxorubicin (*2*), daunomycin (*3*), and 5-fluorouracil (*4*) and the DNA alkylating agent melphalan (*5*) into tumor cells. Moreover, some of these conjugates are now entering phase I/II clinical trials (*6*). Nevertheless, a potential limitation of this approach is that cleavage of the peptide bond in the linker tends to be a slow process taking several hours (*2*).

An alterative strategy that avoids reliance on lysosomal peptidases is to use lysosomal thiols such as GSH and/or cysteine as cleaving agents after endocytotic uptake of appropriately designed copolymer prodrugs (*7*). This approach is particularly interesting because GSH concentrations are often elevated by as much as 2-fold in tumor tissues (*8*−*10*) vs normal tissues, which are in the range of 2−8 mM (*10*, *11*). Moreover, some drug resistant tumors overexpress GSH by as much as 10-fold (*12*). Thus, these concentration differences could give rise to preferential activation of the copolymer prodrug in tumor cells vs normal cells. The adventitious activation of the copolymer prodrug in circulating human plasma should be minimal, as GSH concentrations are typically 1−2 μM (*13*). To test the feasibility of this strategy, we have been working to prepare copolymer prodrugs that will react with GSH to give two different classes of GSH

* To whom correspondence should be addressed. Tel: 410-455-2518. Fax: 410-455-2608. E-mail: creighto@umbc.edu.
[†] University of Maryland.
[‡] University of Pittsburgh Cancer Center.

[1] Abbreviations: EPR, enhanced permeability and retention; GPC, gel permeation chromatography; AIBN, azobisisobutylnitrile; HPMA, *N*-2-(hydroxypropyl)methacrylamide; M_n, number average molecular weight; M_w, weight average molecular weight; GlxI, glyoxalase I.

10.1021/bc0499634 CCC: $30.25 © 2005 American Chemical Society
Published on Web 04/19/2005

Scheme 1

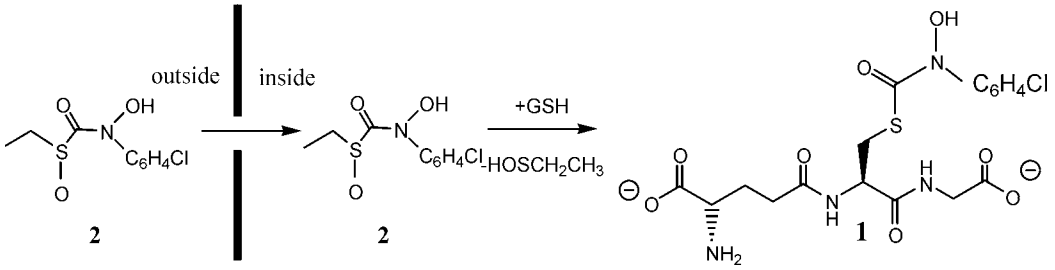

Scheme 2

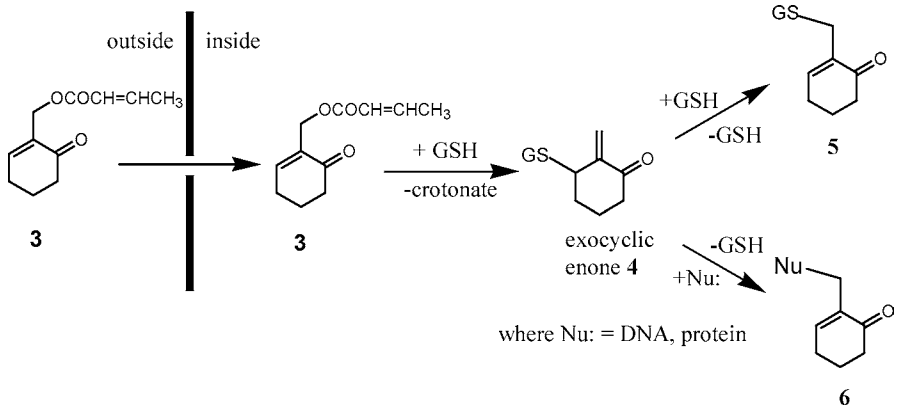

derivatives currently undergoing development as a new generation of antitumor agents (*14*−*17*).

The first class of antitumor agents are transition state analogue inhibitors of the human methylglyoxal-detoxifying enzyme glyoxalase I (hGlxI) (*18*); e.g., *S*-(*N*-4-chlorophenyl-*N*-hydroxycarbamoyl)glutathione (**1**, K_i = 46 nM) (*19*). Previous work has shown that this compound can be delivered into tumor cells either as a [glycyl, glutamyl] diethyl ester prodrug **1**$(Et)_2$ (*20*) or as the membrane permeable sulfoxide prodrug *S*-(*N*-4-chlorophenyl-*N*-hydroxycarbamoyl)ethyl sulfoxide **2**, which undergoes an acyl interchange reaction with GSH to give **1** (Scheme 1) (*21*).

Both prodrugs are cytostatic and cytotoxic to several different tumor cell lines in vitro, apparently because inhibition of GlxI by the enediol analogue **1** results in the accumulation of cytotoxic methylglyoxal. The basis of the exceptional sensitivity of tumors to methylglyoxal toxicity is not well-understood but appears to arise, in part, from extensive covalent modification of heat shock protein 27 (Hsp27), which induces caspase-dependent differentiation and apoptosis (programmed cell death) in tumor cells (*22*). Methylglyoxal is also potentially genotoxic, as methylglyoxal has been demonstrated to covalently modify nucleotide bases (*23*, *24*).

The second class of antitumor agents includes electrophilic endocyclic enones such as 2-crotonyloxymethyl-2-cyclohexenone (**3**), which rapidly diffuses across cell membranes and, once inside the cell, undergoes a Michael addition reaction with intracellular GSH to give the reactive exocyclic enone **4** (Scheme 2) (*25*, *26*).

This species can potentially react with either free GSH to give **5** or form covalent adducts with proteins and/or nucleic acids (**6**) critical to cell viability. Indeed, mass spectral studies show that in the presence of GSH compound **3** alkylates the exocyclic amino groups of nucleotide bases composing single-stranded oligonucleotides (*27*).

However, neither of the prodrug strategies described above is designed to deliver antitumor agents specifically to tumor tissue. For example, in vivo efficacy studies show that intravenous administration of **1**$(Et)_2$ to tumor-bearing mice inhibits the growth of B16 melanotic melanoma, PC3 prostate tumors, and HT29 human colon tumors (*28*). While there were no significant side effects detected in these short-term efficacy studies, intravenous administration of **1**$(Et)_2$ results in the appearance of **1** in all major organs of tumor-bearing mice. This could give rise to significant side effects during long-term administration of drug.

Here, we describe for the first time the synthesis, physicochemical properties, and in vitro antitumor activities of two lead HPMA copolymer prodrugs, which rapidly release **1** and/or the reactive exocyclic enone **4** in neutral aqueous solutions of GSH.

EXPERIMENTAL PROCEDURES

Analytical Instrumentation. NMR spectra were taken on a GE QE-300 NMR spectrometer. IR spectra measured with a ThermoNicolet Avatar 370 FTIR spectrometer using a Pike MIRacle ATR accessory (AMTIR crystal). Mass spectral data were obtained at the Center for Biomedical and Bio-organic Mass Spectrometry, Washington University. UV spectra were recorded using a Beckman DU 640 spectrophotometer. High-performance liquid chromatography (HPLC) was carried out using a Waters HPLC System composed of a 600 Controller, Delta 600 Pumps, and 996 photodiode array detector. Analytical HPLC was performed using a Waters Nova-Pak C_{18}, 4 μm, 3.9 mm × 150 mm column or Symmetry C_{18}, 5 μm, 4.6 mm × 150 mm column. Preparative HPLC was performed using a SymmetryPrep C_{18}, 7 μm, 19 mm × 150 mm column. The molecular weights of the HPMA copolymers were estimated by gel permeation chromatography (GPC) using a high-performance gel permeation column (Tricorn Superose 12 10/300 GL) from Amersham Biosciences.

Materials. Dextran molecular weight standards were purchased from Sigma Chem. Co. (1000, 5000, and 12 000

Scheme 3. Mechanism for Generating t.s. Analogue 1 and Exocyclic Enone 4 from Copolymer−Prodrug Conjugate in the Presence of GSH

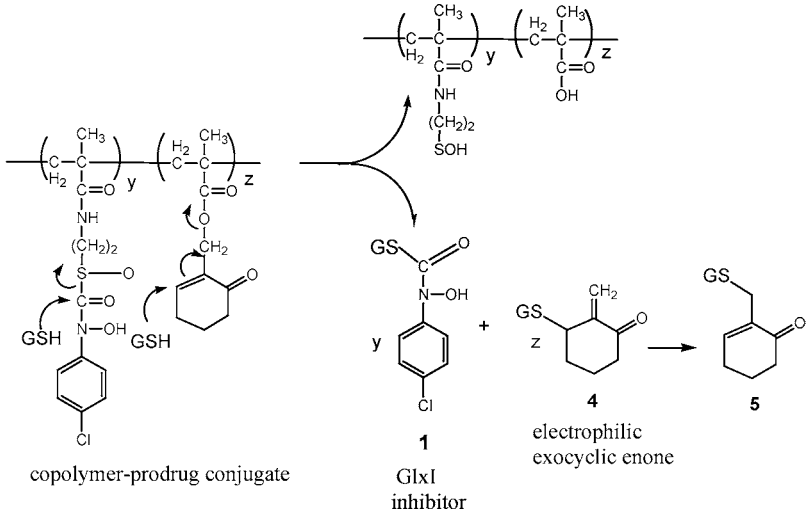

Da) and Polysciences, Inc. (40 000 Da). Lyophilized human serum and GSH were purchased from Sigma Chem. Co. HPMA was purchased from Polysciences, Inc. Azobisisobutylnitrile (AIBN), methacryloyl chloride, 4-methylmorpholine, and 3-chloroperoxybenzoic acid (80−85% pure) were purchased from Aldrich Chem. Co. All other reagents were of the highest purity commercially available.

***S*-(*N*-4-Chlorophenyl-*N*-hydroxycarbamoyl)thioethylamine (9).** To a solution of *S*-(*N*-4-chlorophenyl-*N*-hydroxycarbamoyl)ethyl sulfoxide (**2**) (*21*) (495 mg, 2 mmol) in a mixture of 12 mL of methanol and 12 mL of phosphate buffer (0.1 M, pH 7.5) was added a solution of cysteamine (990 mg, 12.9 mmol) in 5 mL of phosphate buffer (0.1 M, pH 7.5). The mixture was stirred at 0 °C for 1 h. The precipitate was collected by filtration, washed with water, and dried under vacuum to give the final product as a white solid; yield 86% (424 mg). ^{1}H NMR (300 MHz, methanol-d_4/TMS): δ 3.01 (2H, t, J = 6.6 Hz), 3.50 (2H, t, J = 6.6 Hz), 7.32 (2H, d, J = 9.2 Hz), 7.61 (2H, d, J = 9.2 Hz). HRMS (ESI): *m/z* 247.0294 (calcd for $C_9H_{12}N_2O_2SCl$: 247.0308). [Note added in proof: This procedure must form the thiol ester and not the amide because the "sulfoxide"-containing copolymers (synthesized using **9**; Scheme 4) react with free GSH to give the enediol analogue **1** at rates similar to those observed for the reaction of GSH with the simple sulfoxide **2** to give **1** (Scheme 1); see Discussion.]

***S*-(*N*-4-Chlorophenyl-*N*-hydroxycarbamoylthioethyl)methacrylamide (8).** To a stirring solution of **9** (410 mg, 1.66 mmol) in 26 mL of anhydrous dimethyl formamide and 13 mL of pyridine at 0 °C was added slowly over 30 min methacryloyl chloride (318 μL, 3.29 mmol), and the reaction mixture was stirred at room temperature for an additional 20 min. The solvent was removed in vacuo, and the residue was fractionated by reverse-phase HPLC, using 50% acetonitrile in water, containing 0.1% trifluoroacetic acid, as a running solvent. The product peak was collected and dried under vacuum overnight to give the final product as a white solid; yield 51% (269 mg). ^{1}H NMR (300 MHz, methanol-d_4/TMS): δ 1.90 (3H, s), 3.00 (2H, t, J = 6.6 Hz), 3.45 (2H, t, J = 6.6 Hz), 5.34 (1H, br s), 5.67 (1H, br s), 7.32 (2H, d, J = 9.2 Hz), 7.59 (2H, d, J = 9.2 Hz). HRMS (ESI): *m/z* 337.0379 (calcd for $[M + Na]^+$, $C_{13}H_{15}N_2O_3NaSCl$: 337.0390).

2-Methacryloyloxymethyl-2-cyclohexenone (7). To a stirring solution of 2-hydroxymethyl-2-cyclohexenone

Scheme 4. Synthesis of HPMA Polyacrylamide Conjugates of 7- and 8-Sulfoxide[a]

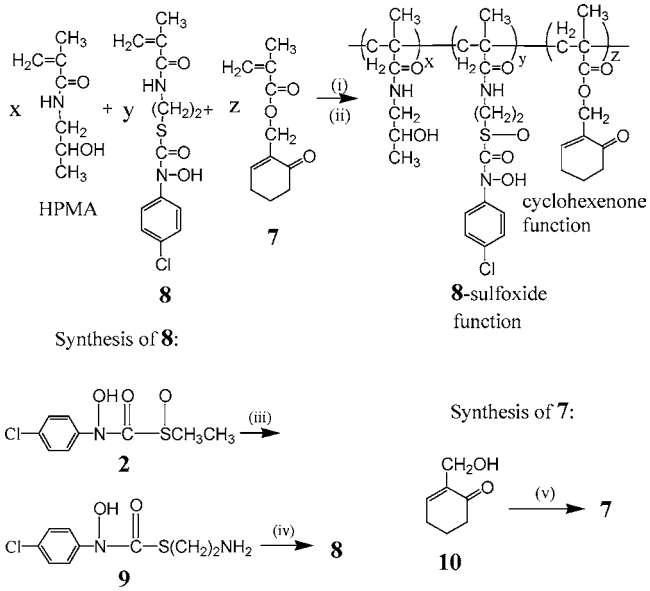

[a] Reagents and conditions: (i) AIBN/acetone, 55 °C; (ii) 3-chloroperoxybenzoic acid; (iii) mercaptoethylamine/methanol−phosphate buffer (pH 7.5); (iv) methacryloyl chloride/pyridine; and (v) methacryloyl chloride/4-methylmorpholine.

10 (*29*) (504 mg, 4 mmol) and 4-methylmorpholine (1 mL, 9 mmol) in 10 mL of CH_2Cl_2 at 0 °C was added methacryloyl chloride (0.79 mL, 8 mmol) dropwise over about 30 min. The reaction mixture was allowed to stir for an additional 20 min. The solvent was removed in vacuo, and the crude product was fractionated by preparative reverse phase HPLC using 40% acetonitrile in water, containing 0.1% trifluoroacetic acid, as a running solvent. The product peak was collected and brought to dryness under vacuum to give the final product as a colorless oil; yield 66% (515 mg). ^{1}H NMR (300 MHz, acetone-d_6): δ 1.96 (3H, s), 2.03 (2H, p, J = 6.2), 2.48 (2H, t, J = 7.33 Hz), 2.42−2.60 (2H, m), 4.84 (2H, s), 5.58 (1H, br s), 6.13 (1H, br s), 7.01 (1H, t, J = 4.3 Hz). HR-FABMS (3-NBA/Li): *m/z* 201.1100 (calcd for $[M + Li]^+$, $C_{11}H_{14}O_3Li$: 201.1103).

Copolymer P1. The methacryloyl derivative **8** (41 mg, 0.13 mmol), HPMA (110 mg, 0.77 mmol), and AIBN (6 mg) were dissolved in 0.75 mL of acetone under argon in

a closed vial and incubated at 50−55 °C for 24 h. The white precipitate was recovered by filtration and was dried under vacuum for 30 min. The crude product was dissolved in 0.25 mL of methanol and then precipitated by the slow addition of excess acetone:diethyl ether (3:1). The precipitation procedure was repeated, and the precipitate was dried under vacuum overnight; yield 63 mg. A portion of the residue (30 mg) was dissolved in 1 mL of methanol at 0 °C, and 3-chloroperoxybenzoic acid (5.6 mg, 0.017 mmol) in 0.05 mL of diethyl ether was slowly added dropwise to this solution. The reaction mixture was allowed to stir for an additional 1 h at 0 °C. The solvent was removed in vacuo, the residue was dissolved in 0.2 mL of methanol, and the desired product precipitated by the slow addition of 5 mL of excess diethyl ether. The precipitation procedure was repeated twice more, and the product was dried under vacuum overnight to give the final product; yield overall from **8** and HPMA, 12 mg. IR (ATR, AMTIR): br 3352, 2973, 2934, 2907, s 1636, s 1526, s 1487 (S−O), 1202 cm^{-1}.

Copolymers P2 and P3. These copolymers were prepared by the same general procedure used to prepare **P1**, with reaction mixtures having the following composition. **P2**: **8** (21 mg, 0.067 mmol), HPMA (76 mg, 0.53 mmol), and AIBN (2 mg) dissolved in 0.4 mL of acetone. Acetone was used as a precipitant during the precipitation procedures; mass yield 29%. IR (ATR, AMTIR): br 3349, 2972, 2930, 2886, s 1636, s 1527, 1487 (S−O), 1203 cm^{-1}. **P3**: **8** (42 mg, 0.13 mmol), HPMA (282 mg, 2 mmol), and AIBN (18 mg) dissolved in 1.6 mL of acetone; yield 32 mg. IR (ATR, AMTIR): br 3353, 2972, 2934, 2905, s 1638, s 1527, 1487 (S−O), 1202 cm^{-1}.

^{1}H NMR (300 MHz, Methanol-d_4/TMS) Spectra of P1−P3. The spectra were all very similar to one another, with significant line broadening due to the high molecular weights of the copolymers. The chemical shift assignments were based on comparisons with the NMR spectra of poly-HPMA and **8**; relative integrated intensities varied as a function of the mol % of the **8**-sulfoxide function: δ 1.01 [s, $CH_3C(C)_3$], 1.16 (d, CH_3CO-), 1.6−2.0 [m, $-(CH_2)-$HPMA], 2.9−3.3 (m, $-NCH_aH_bCO-$; $N-CH_2CH_2-S$), 3.87 (m, −HCO−), 7.40 (d, arom. H, meta to Cl), 7.70 (d, arom. H, ortho to Cl). The mol % of the **8**-sulfoxide function in the different polymers was estimated from the integrated intensities of the aromatic ring protons (δ 7.40, 7.70) vs that of H−C−O (δ 10.02): **P1**, ∼10; **P2**, ∼9; and **P3**, ∼5.

Copolymers P4−P6. These copolymers were prepared by the same general procedure used to prepare **P1** with the exception that the oxidation step with 3-chloroperoxybenzoic acid was not used. **P4**: **7** (68 mg, 0.351 mmol), HPMA (100 mg, 0.702 mmol), and AIBN (9 mg) dissolved in 0.8 mL of acetone; yield 38 mg. IR (ATR, AMTIR): br 3366, 2970, 2931, m 1723 (C=O, cyclohexenone function), s 1639, s 1527, 1175, 1138 cm^{-1}. **P5**: **7** (44 mg, 0.227 mmol), HPMA (130 mg, 0.907 mmol), and AIBN (9 mg) dissolved in 0.7 mL of acetone; yield 112 mg. IR (ATR, AMTIR): br 3362, 2970, 2929, m 1724 (C=O, cyclohexenone function), s 1639, s 1528, 1199, 1138 cm^{-1}. **P6**: **7** (15 mg, 0.076 mmol), HPMA (87 mg, 0.61 mmol), and AIBN (5 mg) dissolved in 0.5 mL of acetone; yield 52 mg. IR (ATR, AMTIR): br 3354, 2971, 2931, m 1721 (C=O, cyclohexenone function), s 1637, s 1527, 1201, 1137 cm^{-1}.

^{1}H NMR (300 MHz, Methanol-d_4/TMS) Spectra of P4−P6. The spectra were all very similar to one another, with significant line broadening due to the high molecular weights of the copolymers (Figure 1). The chemical shift assignments were based on comparisons with the NMR spectra of poly-HPMA, **7**, and **8**; relative integrated intensities varied as a function of the mol % of the cyclohexenone function derived from **7**: δ 1.01 [s, $CH_3C(C)_3$], 1.16 (d, CH_3CO-), 1.6−2.0 [m, $-(CH_2)-$HPMA], 2.0−2.15 [m, $-(C(4)H_2)-$cyclohex-2-enone ring], 2.45−2.60 [m, $-(C(5)H_2, C(6)H_2)-$cyclohex-2-enone ring], 2.9−3.3 (m, $-NCH_aH_bCO-$; $N-CH_2CH_2-S$), 3.87 (m, −HCO−), 7.2−7.3 (t, vinyl-H). The mol % of the cyclohexenone function was estimated from the integrated intensities of the cyclohexenone ring protons $C(5)H_2$, $C(6)H_2$ (δ 9.85), vs that of H−C−O (δ 10.02): **P4**, ∼27; **P5**, ∼20; and **P6**, ∼12.

Copolymer P7. A solution of **7** (15 mg, 0.076 mmol), **8** (24 mg, 0.076 mmol), HPMA (87 mg, 0.61 mmol), and AIBN (6 mg) in 0.6 mL of acetone under argon in a closed vial was heated at 50−55 °C for 24 h. The white precipitate was recovered by filtration and brought to dryness to give 70 mg of crude product. The crude product was dissolved in 2 mL of methanol at 0 °C, and 3-chloroperoxybenzoic acid (9.1 mg, 0.042 mmol) in 0.1 mL of diethyl ether was added dropwise. The reaction mixture was allowed to stir for an additional 1 h, the solvent was removed in vacuo, and the residue was dissolved in 0.4 mL of methanol. The product was precipitated by the dropwise addition of acetone:diethyl ether (3:1). The precipitation procedure was repeated, and the final copolymer product was dried under vacuum overnight; yield 52 mg. IR (ATR, AMTIR): br 3364, 2970, 2930, m 1721(C=O, cyclohexenone function), 1638, 1527, s 1487 (S−O), 1200, 1137 cm^{-1}.

Copolymer **P8** was prepared by the same general procedure used to prepare **P7** starting with a reaction mixture composed of **7** (16 mg, 0.084 mmol), **8** (26 mg, 0.084 mmol), HPMA (191 mg, 1.336 mmol), and AIBN (12 mg) dissolved in 1.2 mL of acetone; yield 91 mg. IR (ATR, AMTIR): br 3365, 2971, 2931, m 1723(C=O, cyclohexenone function), 1639, 1527, s 1482 (S−O), 1201, 1138 cm^{-1}.

^{1}H NMR (300 MHz, Methanol-d_4/TMS) Spectra of P7 and P8. The spectra were both similar to one another, with significant line broadening due to the high molecular weights of the copolymers (Figure 1). The chemical shift assignments were based on comparisons with the NMR spectra of poly-HPMA, **7**, and **8**; relative integrated intensities varied as a function of the mol % cyclohexenone and **8**-sulfoxide functions: δ 1.01 [s, $CH_3C(C)_3$], 1.16 (d, CH_3CO-), 1.6−2.0 [m, $-(CH_2)-$HPMA], 2.0−2.15 [m, $-(C(4)H_2)-$cyclohex-2-enone ring], 2.45−2.60 [m, $-(C(5)H_2, C(6)H_2)-$cyclohex-2-enone ring], 2.9−3.3 (m, $-NCH_aH_bCO-$), 3.87 (m, −HCO−), 7.2−7.3 (t, vinyl-H), 7.40 (d, arom. Hs, meta to Cl), 7.70 (d, arom. Hs, ortho to Cl). The mol % of the **8**-sulfoxide and the cyclohexenone functions were estimated from the integrated intensities of the aromatic ring protons (δ 7.40, 7.70) and cyclohexenone ring protons $C(5)H_2$, $C(6)H_2$ (δ 2.5), vs that of H−C−O (δ 3.9). For **P7**: mol % **8**-sulfoxide, ∼2%; cyclohexenone function, ∼2%. For **P8**: mol % **8**-sulfoxide, ∼6%; cyclohexenone function, ∼6%.

***S*-(*N*-4-Chlorophenyl-*N*-hydroxycarbamoyl)propylsulfoxide (2a).** To *S*-(*N*-4-chloro-phenyl-*N*-hydroxycarbamoyl)ethylsulfoxide (**2**) (*21*) (150 mg, 0.61 mmol) in 3 mL of pyridine on ice was added thiopropane (138 mg, 1.187 mmol). The reaction mixture was brought to room temperature and stirred for 30 min, and aqueous 1.6 N HCl (15 mL) was slowly added to the stirring reaction mixture. The reaction mixture was extracted with methylene chloride (3 × 10 mL), the organic layer was dried over sodium sulfate, and the solvent was removed in vacuo. The residue was crystallized from hexane to give the synthetic intermediate *S*-(*N*-4-chlorophenyl-*N*-hy-

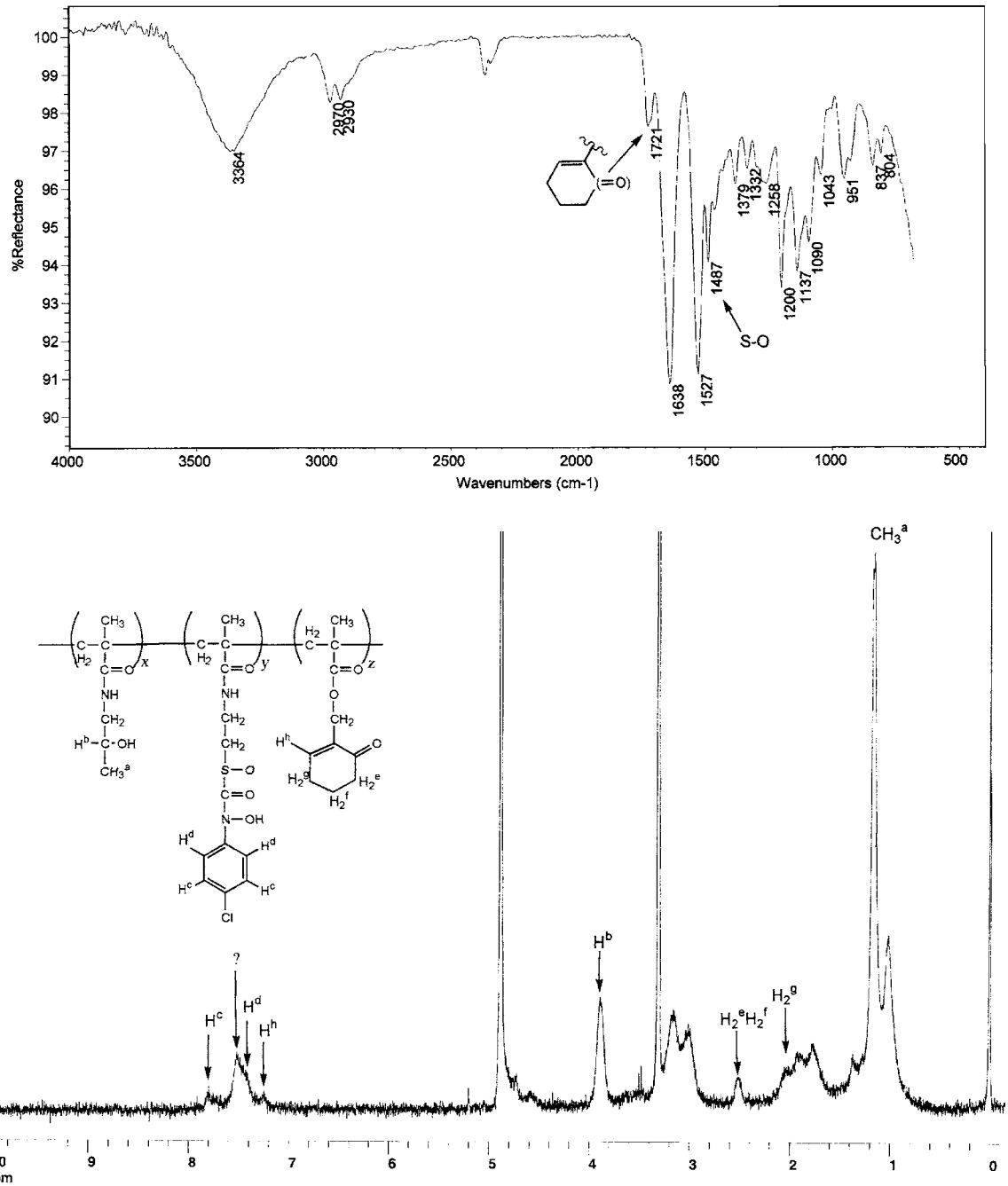

Figure 1. Spectral data for HPMA-copolymer P7 containing both the sulfoxide and the 2-methylenecyclohexenone functions: (top) IR (ATR, AMTIR); (bottom) ^{1}H NMR 300 MHz (methanol-d_4/TMS) spectra. Spectral lines unique to the three functional groups in the copolymers are indicated in the spectra. Other assignments may be found in the Experimental Procedures.

droxycarbamoyl)thiopropyl ester as light brown crystals (yield 41%). The ester (0.252 mmol) was dissolved in 2 mL of diethyl ether to which was added dropwise 3-chloroperoxybenzoic acid (0.248 mmol) in 2 mL of diethyl ether. The white precipitate was collected and washed with diethyl ether to give the final product; the yield from the intermediate ester was 48%. ^{1}H NMR (300 MHz, methanol-d_4/TMS): δ 0.99 (3 H, t, J = 7.3 Hz), 1.73 (2 H, m), 3.04 (2 H, m), 7.37 (2 H, d, J = 9.2 Hz), 7.68 (2 H, d, J = 9.2 Hz).

***S*-(*N*-4-Chlorophenyl-*N*-hydroxycarbamoyl)butylsulfoxide (2b).** This compound was prepared by a procedure analogous to that used to prepare **2a**; yield 29%. ^{1}H NMR (300 MHz, $CDCl_3$/TMS): δ 0.87 (3 H, t, J = 7.3 Hz), 1.40 (2 H, m), 1.70 (2 H, m), 3.08 (2 H, m), 7.37 (2 H, d, J = 8.8 Hz), 7.69 (2 H, d, J = 8.8 Hz).

Determination of the Molecular Weights of the Copolymer Prodrugs. The number average molecular weight (M_n), weight average molecular weight (M_w), and polydispersity (M_w/M_n) of the HPMA copolymers were obtained by high-performance GPC (*30*). The gel permeation column was eluted with 50 mM sodium phosphate buffer (pH 7.0) containing 0.25 M NaCl at a flow rate of 1 mL/min. Molecular weights were interpolated from standard curves (log M_n and log M_w vs retention time) obtained using polydextran molecular weight standards.

Determination of mol % Sulfoxide and Cyclohexenone Functions in the Copolymers. Ethanolic solutions of copolymer were prepared, and 20 μL aliquots were mixed with 80 μL of 10 mM GSH in potassium phosphate buffer (0.1 M, pH 7.5) and incubated at room temperature for 10 min to convert the **8**-sulfoxide and/

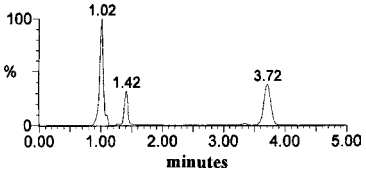

Figure 2. Elution profile from a reverse phase HPLC column (Waters Symmetry C_{18} 5 μm column, 4.6 mm $\times$ 150 mm) of a reaction mixture obtained after incubating **P8** (Table 1) with 10 mM GSH in potassium phosphate buffer (0.1 M, pH 6.5) for 15 min. Abscissa: percent total absorbency (200−400 nm). Peaks at 1.02, 1.42, and 3.72 min correspond to GSH, the GSH-2-methylcyclohexenone adduct **5**, and the transition state analogue **1**, respectively. Running solvent: 25% acetonitrile in water containing 0.1% TFA.

or cyclohexenyl functions to **1** and the GSH adduct **5**, respectively. A 10 μL aliquot of this solution was then fractionated by reverse phase HPLC (Nova-Pak C_{18}, 4 μm, 3.9 mm $\times$ 150 mm column). For the analysis of **1**, the running solvent was 25% acetonitrile in water, containing 0.1% trifluoroacetic acid; for **5**, the running solvent was 13% acetonitrile in water, containing 0.1% trifluoroacetic acid. The areas under the peaks corresponding to **1** and **5** were converted to mole quantities by comparison with standard curves of peak areas vs moles of authentic **1** and **5** injected onto the same column. The amounts of **1** and **5** were then used to calculate mol fractions of **8**-sulfoxide and cyclohexenyl groups in the original copolymer.

Kinetics of Drug Release. Reactions were initiated by the introduction of ethanolic solutions of copolymer into cuvettes containing at least a 20-fold excess of GSH over the equivalents of **8**-sulfoxide and/or cyclohexenyl groups in degassed/N_2-saturated potassium phosphate buffer (0.1 M), pH 6.5, 25 °C. Rate constants were calculated from the first-order decrease in absorbency at 305 and 235 nm resulting from the loss of **8**-sulfoxide and cyclohexenyl groups, respectively (Figure 3).

Stability of Copolymers in Human Serum. To 0.45 mL of human serum at 37 °C was added **P8** to an initial concentration of approximately 1 mM in **8**-sulfoxide and cyclohexenyl groups. As a function of time, 30 μL aliquots of the incubation mixture were transferred to 20 μL of potassium phosphate buffer (0.1 M, pH 7.5) containing 1.6 mM GSH to convert the **8**-sulfoxide and cyclohexenyl functions to **1** and **5**, respectively. After incubation at room temperature for 5 min, the samples were deproteinized by the addition of 100 μL of ethanol. The protein precipitate was sedimented by centrifugation at 13000*g*, and the supernatant was fractionated by reverse phase

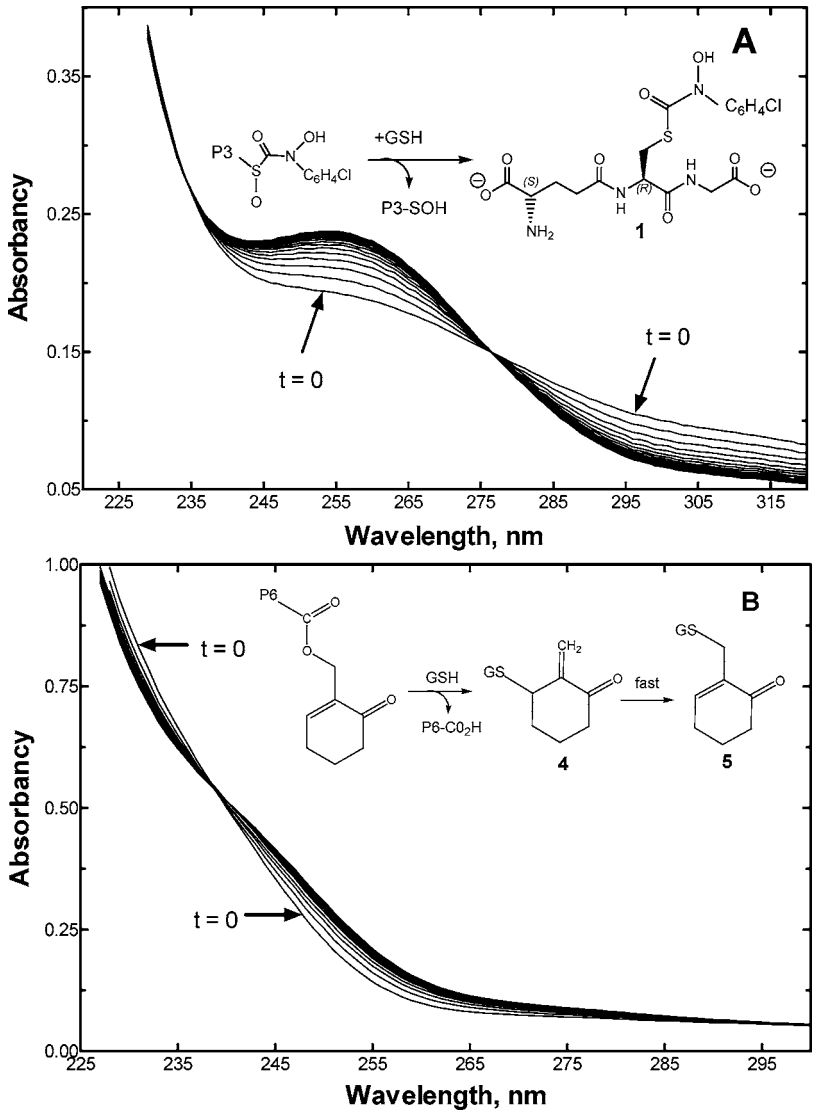

Figure 3. Time-dependent change in the UV spectrum of (A) **P2** (0.025 mM in **8**-sulfoxide) in potassium phosphate buffer (0.1 M, pH 6.5), GSH (0.5 mM), EDTA (0.05 mM), and 2.5 vol % ethanol at 25 °C (spectral scans taken every 25 s) and of (B) **P6** (0.05 mM in **7**) in potassium phosphate buffer (0.1 M, pH 6.5), GSH (1.0 mM), and 5 vol % ethanol at 25 °C (spectral scans taken every 10 min).

HPLC, as described above. The transition state analogue **1** and the GSH adduct **5** were quantitated, as described above. The rate constants were calculated from the first-order rate of loss of **8**-sulfoxide or cyclohexenyl groups as a function of the time.

In Vitro Cytotoxicity Studies. Murine B16 melanotic melanoma was obtained from the DCT Tumor Repository (NCI—Cancer Research and Development Center, Frederick, MD) and was maintained in RPMI 1640 medium containing L-glutamate (Gibco, BRL, Gaithersburg, MD), supplemented with 10% heat-inactivated fetal calf serum and gentamycin (10 μg/mL), under 37 °C humidified air containing 5% CO_2. Under these conditions, B16 cells have a doubling time of about 26 h. For the toxicity studies, cells in logarithmic growth were introduced into 24 well plates at a density of 2×10^4 cells/mL in the absence and presence of drug spanning the IC_{50} values. After 72 h, the cells were washed with Hank's balanced salt solution without Ca^{2+}, treated with trypsin for 10 min at 37 °C, and concentrated by centrifugation, and cell densities were determined with a Coulter Counter. Cell viabilities were determined by the trypan blue exclusion method (*31*).

Reported IC_{50} values (mean ± standard deviation of triplicate determinations carried out in three separate assays on different days) were calculated using the Hill equation and the program Adapt (*32*).

RESULTS

Synthetic Methods. Two new classes of HPMA copolymer prodrugs have been prepared, which employ the same prodrug chemistry previously used to generate the transition state analogue inhibitor of GlxI (**1**) and exocyclic enone **4** in the presence of GSH (Scheme 3).

The prodrugs were prepared by radical polymerization of variable amounts of 2-methacryloylmethyl-2-cyclohexenone **7** and *N*-(4-chlorophenyl-*N*-hydroxycarbamoylthioethyl)methacrylamide **8** with HPMA, followed by treatment with 3-chloro-peroxybenzoic acid to oxidize the thioester function to a sulfoxide (Scheme 4).

Repeated precipitation from methanol/diethyl ether solution gave copolymer preparations that were free of unreacted **8**-sulfoxide and/or **7** by HPLC. The yields were in the range of 28−64%. The polyacrylamide monomers were prepared by an extension of published procedures (*21*, *25*). IR and NMR spectroscopy (e.g., Figure 1) confirmed the chemical identities of the polymers.

The 1487 and 1721 cm^{-1} bands were assigned to the S−O and C=O stretching frequencies of the **8**-sulfoxide and cyclohexenenone functions, respectively, on the basis of comparisons with the IR spectra of **2** and **10**. The integrated intensities of the resonances shown in the NMR spectrum could be used to calculate approximate values for the mol % compositions of the copolymers. However, more precise values were obtained by reacting the copolymers with GSH and quantitating the GSH adducts **1** and **5** after isolation by HPLC (see the Experimental Procedures).

Kinetics of Drug Release. Incubation of the HPMA copolymers with GSH produced a time-dependent increase in product species, which comigrated with authentic samples of transition state analogue **1** and GSH-2-methylcyclohexenone adduct **5** monitored by reverse phase HPLC; e.g., Figure 2.

The rate constants for formation of these species correlated well with the first-order rate of decrease in absorbency at 305 and 235 nm, corresponding to the loss of the sulfoxide and cyclohexenone functions of the copolymers, respectively (Figure 3).

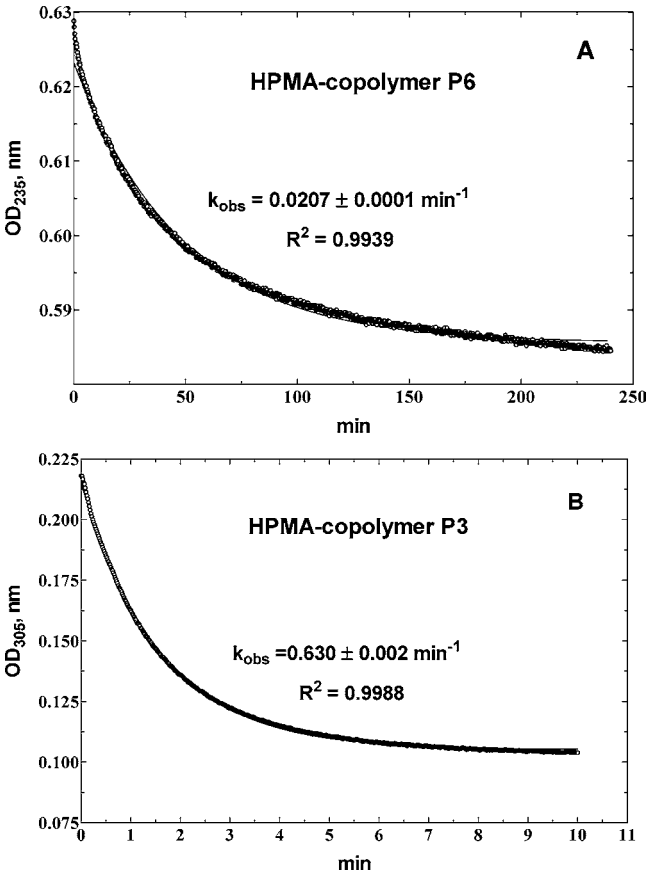

Figure 4. Rate profiles for the reaction of (A) copolymer **P6** (0.05 mM in cyclohexenyl equivalents) with GSH (1 mM) and of (B) copolymer **P3** (0.025 mM in **8**-sulfoxide equivalents) with GSH (0.5 mM). Conditions: Potassium phosphate buffer (0.1 M, pH 6.5), 25 °C. The rate constants given in the figures are the best-fit values to the expression for a first-order exponential decay (solid line through the data).

These wavelengths were selected for the kinetic analyses, as they permit the independent assessment of the rates of loss of each functional group in copolymers containing both functional groups. The rates of formation of **5** and **1** from copolymers containing variable amounts of either the cyclohexenyl and/or the **8**-sulfoxide groups conform to first-order kinetics over 4−5 half-lives (e.g., Figure 4) (Table 1).

Stabilities in Human Plasma. The likely chemical stabilities of the **8**-sulfoxide and cyclohexenyl groups in the copolymers under physiological conditions were estimated by determining the time-dependent loss of these groups from **P8** during incubation human serum at 37 °C. The half-lives for loss of the **8**-sulfoxide and cyclohexenyl groups were determined to be 6.6 ± 0.7 and 37.5 ± 7.5 min (n = 3), respectively.

In Vitro Efficacy Studies. Both the HPMA-**8**-sulfoxide copolymer and the HPMA-**7** copolymer inhibit the growth of B16 in a concentration range where the HPMA polymer alone shows no activity (Figure 5).

Therefore, growth inhibition must result from the prodrug component of the copolymer. Not unexpectedly, the in vitro efficacies of the unpolymerized prodrugs exceed those of the copolymer prodrugs (Table 2).

The simple ethyl, propyl, and butyl sulfoxide prodrugs (**2**−**2b**) have IC_{50} values that are roughly 5−10-fold lower than that of HPMA-**8**-sulfoxide (**P1**), while the IC_{50} value of **3** is over 7000-fold lower than that of HPMA-**7** (**P4**).

Table 1. Mol % Compositions and Spectrophotometrically Determined Second-Order Rate Constants (k_2) for the Reaction of GSH with the Sulfoxide and Cyclohexenone Functions of Different Copolymer Prodrugs[a]

copolymer designation	sulfoxide (mol %)	cyclohexenone (mol %)	M_n (Da) $\times 10^{-3}$	M_w/M_n	k_2 (−sulfoxide) (mM^{-1} min^{-1})	k_2 (−cyclohexenone) (mM^{-1} min^{-1})
P1	8.7 ± 0.30		2.80	1.41	1.85 ± 0.12	
P2	5.2 ± 0.03		7.44	1.47	2.54 ± 0.04	
P3	1.5 ± 0.04		26.5	1.55	2.38 ± 0.07	
P4		19.4 ± 0.7	13.5	1.51		0.015 ± 0.001
P5		12.0 ± 0.4	30.0	1.56		0.015 ± 0.002
P6		6.4 ± 0.1	31.5	1.57		0.021 ± 0.003
P7	4.3 ± 0.03	4.6 ± 0.2	15.4	1.52	2.49 ± 0.051	0.021 ± 0.001
P8	3.6 ± 0.04	1.9 ± 0.01	26.9	1.55	2.11 ± 0.074	0.021 ± 0.001

[a] Kinetic constants were calculated from the first-order rate of loss of the functional group under pseudo-first-order conditions (>20-fold excess of GSH) and are the average of triplicate determinations ± standard deviation. Conditions: potassium phosphate buffer (0.1 M, pH 6.5), 25 °C.

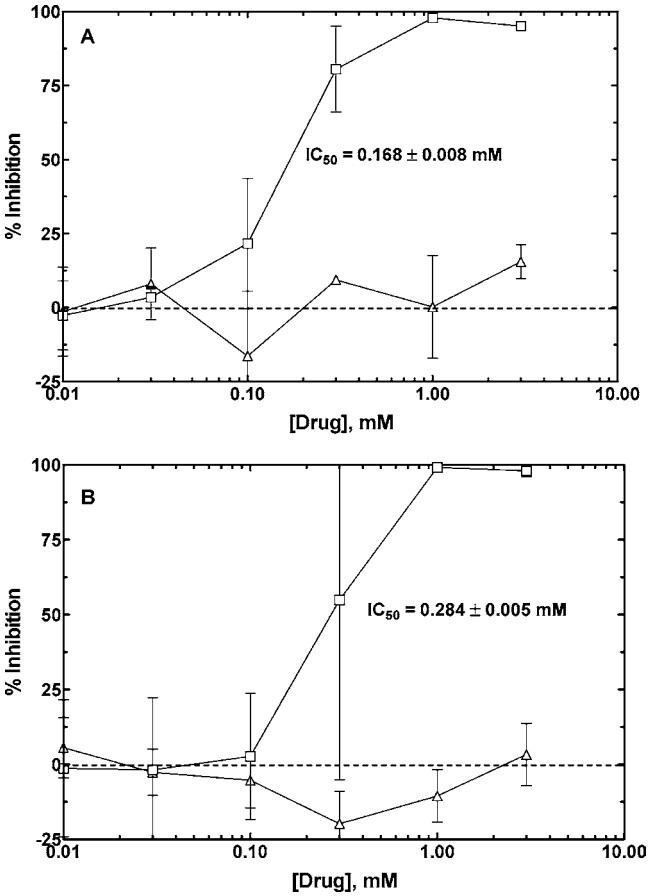

Figure 5. Growth inhibition of B16 melanoma in the presence of (A) **P1** or (B) **P4**. Data for copolymer drug conjugates are indicated by squares; data for polymer controls with no appended drugs are indicated by triangles. The drug concentration is calculated, on the basis of equivalents of drug/L. For conditions, see the Experimental Procedures.

In contrast, the IC_{50} values for **P1**, **P4**, and the copolymer containing both prodrugs (**P7**) differ by no more than a factor of 3.

DISCUSSION

The central outcome of this work is that the kinetic properties and antitumor activities of the lead compounds described here support the feasibility of using HPMA copolymers to deliver cytotoxic GSH derivatives into tumor cells.

Kinetic Properties of the HPMA Copolymers. HPMA copolymers are well-designed to serve as platforms for delivering GSH-activated prodrugs into cells via endocytosis. The reaction between excess GSH and the copolymers to form the GlxI inhibitor **1** or the alkylating agent **4** follows simple first-order kinetic behavior over several half-lives (e.g., Figure 4). This indicates that the copolymers exist primarily in an open or extended conformation in solution, which allows free access of GSH to the reactive groups appended to the copolymers. Moreover, the polyacrylamide backbone does not interfere significantly with the reaction between the GSH and the **8**-sulfoxide function, as the rate constants for reaction of GSH with copolymers **P1**−**P3** (Table 1) are at least as large as that reported for the reaction of GSH with the simple sulfoxide derivative **2** (Scheme 1): $k = 1.84 \pm 0.07$ mM^{-1} min^{-1}, potassium phosphate buffer (0.1 M, pH 7.5), 25 °C (*21*). Indicative of a small steric effect on the reaction of GSH with the cyclohexenone functions of **P4**−**P6**, the rate constants are about 3-fold smaller than that reported for the reaction of GSH with the crotonate ester **3** (Scheme 2): $k = 0.068 \pm 0.001$ mM^{-1} min^{-1}, potassium phosphate buffer (0.1 M, pH 6.5), 25 °C (*17*). Therefore, the ~100-fold greater reactivities of the sulfoxide- vs cyclohexenone-containing copolymers reflect primarily the different intrinsic chemical reactivities of the functional groups with GSH and not the steric properties of the polymer backbone.

Finally, there is little difference in the kinetic properties of the copolymers having either different molecular weights or different mole fractions of the appended sulfoxide or cyclohexenone functions (Table 1). Therefore, loading of the HPMA polymer with high levels of prodrug will not adversely affect the kinetic properties of the copolymers. Not surprisingly, the sulfoxide and cyclohexenone functions in the mixed function copolymers **P7** and **P8** independently react with free GSH, as the rate constants for the individual reactive groups are similar in magnitude to those for the copolymers containing only one of the reactive groups (Table 1).

Model for Endocytotic Drug Delivery. There is a substantial body of evidence indicating that endocytosis is the dominant mechanism for delivering HPMA copoly-

Table 2. In Vitro Inhibition of B16 Melanotic Melanoma by Different HPMA Copolymer−Prodrug Conjugates vs the Monomeric Prodrugs

compound	IC_{50}[a] (μM)
Copolymer Prodrugs	
HPMA-**8** sulfoxide (**P1**)	168 ± 8
HPMA-**7** (**P4**)	284 ± 5
HPMA-(**8**-sulfoxide/**7**) (**P7**)	107 ± 9
Monomer Prodrugs	
cyclohexenone **3**[b] (Scheme 2)	0.04 ± 0.01
ethyl sulfoxide **2** (Scheme 1)	35 ± 8
propyl sulfoxide **2a**	29 ± 5
butyl sulfoxide **2b**	15 ± 2

[a] Values are means (± SD) of three experiments each of which was carried out in triplicate. [b] Value taken from ref *26*.

mers into tumor cells (*1*). In the past, HPMA copolymers were designed to depend on intralysosomal peptidases to cleave the linker between the HPMA and the drug to allow the drug to diffuse into the cytoplasm of the tumor cell. In the present study, thiols rather than peptidases function to liberate the drugs into the cytoplasm of the tumor cell. While there are no good estimates of the steady state concentrations of specific thiols inside the lysosomes of mammalian cells, there is ample evidence to indicate that lysosomes contain highly specific transporter systems for importing cysteine and cysteinyl dipeptides such as cysteinyl-glycine into lysosomes (*33*). For example, a highly specific cysteine-dependent transporter has been found in human fibroblast lysosomes with a $K_m = 0.5$ mM, and evidence has been presented for the efflux of cystine and cysteine from these lysosomes (*34*). An important role of cysteine is to activate intralysosomal thiol-dependent proteases that function to breakdown proteins taken up by endocytosis. Early evidence that GSH also stimulates intralysosomal protein breakdown was attributed to a GSH transporter in the lysosomal membrane (*35*). However, subsequent studies indicate that some or perhaps all of the activation is due to breakdown of GSH to cysteinylglycine, which is subsequently transported into the lysosomes (*36*). Therefore, the presence of a GSH transport system in lysosomes has not been firmly established at this time.

In Vitro Efficacy. The antitumor activities of the HPMA copolymer prodrugs listed in Table 2 are most likely due to the copolymers themselves and not to toxic contaminants in the copolymer preparations. Antitumor activity is unlikely to arise from unreacted sulfoxide-**8** and/or **7** (Scheme 4), as neither NMR nor HPLC analysis of the copolymer preparations indicates that these species are present. Conceivably, **1** and/or **4** might form in the growth medium during the efficacy studies, due to reaction of the copolymers with contaminating GSH (arising from cell lysis). However, this is an unlikely source of antitumor activity, because highly charged S-substituted GSH derivatives such as **1** and **4** do not readily diffuse across cell membranes near neutral pH (*20*). Thus, the observed antitumor activities most likely result from processing of the HPMA copolymers inside tumor cells, during endocytosis.

The in vitro antitumor activity of sulfoxide copolymer **P1** (Table 2) implies the presence of intralysosomal GSH to react with **P1** to give the cytotoxic transition state analogue inhibitor **1**. This follows from reports that yeast GlxI is highly specific for GSH and will not use cysteine or cysteinylglycine as cofactors (*37*). Conceivably, the cysteine and/or cysteinylglycine homologues of **1** might form inside the lysosomes, diffuse across the lysosomal membrane into the cytosol, and then form **1** via acyl interchange with cytosolic GSH. This kind of cofactor specificity is not required to explain the cytotoxicity of the cyclohexenone-containing copolymer **P7**, as intralysosomal GSH, cysteine, or cysteinylglycine could all react with **P7** to give cytotoxic exocyclic enones.

Both the sulfoxide- and the cyclohexenone-containing copolymer prodrugs are significantly less potent than the low molecular weight prodrugs designed to enter cells by diffusion across the cell membrane. HPMA-**8** sulfoxide **P1** is about 6.5-fold less potent than sulfoxides **2**, **2a**, and **2b**, and HPMA-**7** (**P4**) is about 7×10^3-fold less potent that the simple substituted cyclohexenone **3**. This is not a new phenomenon. For example, the HPMA copolymer of 6-(3-aminopropyl)ellipticine (APE) is >75-fold less potent than APE with B16F10 melanoma in vitro, although the copolymer is significantly more potent in tumor-bearing mice (*38*). This has been attributed to the slow rate of endocytotic uptake of the copolymer and the slow rate of peptide hydrolysis of the linker, which can have half-lives on the order of many hours. Likewise, endocytotic uptake of the copolymers described in the current study might be a slow process; the rate constants for formation of **1** and **4** at pH 5.3 will be approximately 50-fold smaller than the rate constants that apply in the cytosol with a pH of 7. Moreover, efficacy might also be limited by the rate of expulsion of the prodrugs from the lysosomes into the cytoplasm of the cell. Thus, the chemotherapeutic potential of the copolymer prodrugs is difficult to appreciate prior to completion of in vivo efficacy studies.

Drug Delivery Strategies. The stability of the copolymer prodrugs in circulating human plasma is another important aspect of drug efficacy in humans. The approximate half-lives for the reaction of the sulfoxide- and cyclohexenone-containing copolymers with free GSH (~2 μM) (*13*) that applies in circulating human plasma at pH 7.5 are estimated to be about 175 and 17400 min, respectively, using the rate constants in Table 1. However, these half-lives are significantly longer than the half-lives of 7 and 38 min determined for the loss of the sulfoxide and cyclohexenone functions, respectively, when the copolymers are incubated in noncirculating human plasma. Therefore, the chemistry associated with the latter process is most significant in determining the bioavailability of the copolymer prodrugs to tumor cells. Compounds with such short half-lives in circulating plasma would be poor candidates for optimizing drug pharmacokinetics via controlled release. The HPMA copolymer prodrugs undergoing clinical evaluation at this time have half-lives in circulating plasma on the order of hours (*39*). However, continuous infusion might still be used to optimize the plasma pharmacokinetics of less stable copolymer prodrug conjugates and allow tumor targeting via the EPR effect. Finally, the lead compounds containing mixed functional groups (**P7**, **P8**) provide a precedent for the application of copolymer prodrugs in combination chemotherapy.

ACKNOWLEDGMENT

This work was supported by a grant from the NCI (CA 59612) and a grant from Maryland Technology Development Corporation. We thank Diana S. Hamilton and Ellyn Sharkey of this laboratory for preparing the starting materials for the syntheses of **8** and **7**.

LITERATURE CITED

(1) (a) Brocchini, S., and Duncan, R. (1999) Pendent drugs, release from polymers. In *Encyclopedia of Controlled Drug Delivery* (Mathiowitz, E., Ed.) pp 786−816, John Wiley and Sons: New York. (b) Duncan, R. (2003) The dawning era of polymer therapeutics. *Nat. Rev. Drug Discovery 2*, 347−360. (c) Thanou, M., and Duncan, R. (2003) Polymer-protein and polymer-drug conjugates in cancer therapy. *Curr. Opin. Invest. Drugs 4*, 701−709. (d) Duncan, R. (1992) Drug-polymer conjugates for improving chemotherapy. *Anti-Cancer Drugs 3*, 175−210.

(2) Seymour, L. W., Ulbrich, K., Wedge, S. R., Hume, I. C., Strohalm, J., and Duncan, R. (1991) *N*-(2-Hydroxypropyl)-methacrylamide copolymers targeted to the hepatocyte galactose-receptor: Pharmacokinetics in DBA mice. *Br. J. Cancer 63*, 859−866.

(3) Duncan, R., Kopeckova, P., Strohalm, J., Hume, I. C., Lloyd, J. B., and Kopecek, J. (1988) Anticancer agents coupled to *N*-(2-hydroxypropyl)methacrylamide copolymers. II. Evaluation of daunomycin conjugates in vivo against L1210 leukaemia. *Br. J. Cancer 57*, 147−156.

(4) Putnam, D., and Kopecek, J. (1995) Enantioselective release of 5-fluorouracil from *N*-(2-hydroxypropyl)methacrylamide-based copolymers via lysosomal enzymes. *Bioconjugate Chem. 6*, 483−492.
(5) Duncan, R., Hume, I. C., Yardley, H. J., Flanagan, P. A., Ulbrich, K., Subr, V., and Strohalm, J. (1991) Macromolecular prodrugs for use in targeted cancer chemotherapy: Melphalan covalently coupled to *N*-(2-hydroxypropyl)methacrylamide copolymers. *J. Controlled Release 16*, 121−136.
(6) Duncan, R. (2003) Polymer-drug conjugates. In *Handbook of Anticancer Drug Development* (Budman, H., Calvert, H., and Rowinsky, E., Eds.) pp 230−260, Lippinott Williams and Wilkins: Baltimore.
(7) Wang, L., Kristensen, J., and Ruffner, D. E. (1998) Delivery of antisense oligonucleotides using HPMA polymer: Synthesis of a thiol polymer and its conjugation to water-soluble molecules. *Bioconjugate Chem. 9*, 749−757.
(8) Cook, J. A., Pass, H. I., Iype, S. N., Friedman, N., Degraff, W., Russo, A., and Mitchell, J. B. (1991) Cellular glutathione and thiol measurements from surgically resected human lung tumor and normal lung tissue. *Cancer Res. 51*, 4287−4294.
(9) Blair, S. L., Heerdt, P., Sacher, S., Abolhoda, A., Hochwald, S., Cheng, H., and Burt, M. (1997) Glutathione metabolism in patients with nonsmall cell lung cancers. *Cancer Res. 57*, 152−155.
(10) Kosower, N. S., and Kosower, E. M. (1978) The glutathione status of cells. *Int. Rev. Cytol. 54*, 109−160.
(11) Meister, A. (1983) Metabolism and transport of glutathione and other γ-glutamyl compounds. In *Functions of Glutathione*: *Biochemical, Physiological, Toxicological, and Clinical Aspects* (Larsson, et al., Eds.) pp 1−22, Raven Press: New York.
(12) Britten, R. A., Green, J. A., and Warenius, H. M. (1992) Cellular glutathione and glutathione *S*-transferase activity in human ovarian tumor biopsies following exposure to alkylating agents. *Int. J. Radiat. Oncol. Biol. Phys. 24*, 527−531.
(13) Anderson, M. E. (1989) Enzymatic and chemical methods for determination of glutathione. In *Glutathione: Chemical, Biochemical, and Medical Aspects* (Dolphin, D., Avramovic, O., and Poulson, R., Eds.) Vol. IIIA, John Wiley and Sons: Toronto.
(14) Creighton, D. J., Hamilton, D. S., Kavarana, M. J., Sharkey, E. M., and Eiseman, J. L. (2000) Glyoxalase enzyme system as a potential target for antitumor drug development. *Drugs Future 25*, 385−392.
(15) Creighton, D. J., Zheng, Z.-B., Holewinski, R. J., Hamilton, D. S., and Eiseman, J. L. (2003) Glyoxalase I inhibitors in cancer chemotherapy. *Biochem. Soc. Trans. 31*, 1378−1382.
(16) Hamilton, D. S., and Creighton, D. J. (1992) Inhibition of glyoxalase I by the enediol mimic *S*-(*N*-hydroxy-*N*-methylcarbamoyl)glutathione: The possible basis of a tumor-selective anticancer strategy. *J. Biol. Chem. 267*, 24933−24936.
(17) Hamilton, D. S., Ding, Z., Ganem, B., and Creighton, D. J. (2002) Glutathione *S*-transferase-catalyzed addition of glutathione to COMC: A new hypothesis for antitumor activity. *Org. Lett. 4*, 1209−1212.
(18) Creighton, D. J., and Pourmotabbed, T. (1988) Glutathione-dependent aldehyde oxidation reactions. In *Molecular Structure and Energetics: Principles of Enzyme Activity* (Liebman, J. F., and Greenberg, A., Eds.) Vol. 9, pp 353−386, VCH Publishers: New York.
(19) Murthy, N. S. R. K., Bakeris, T., Kavarana, M. J., Hamilton, D. S., Lan, Y., and Creighton, D. J. (1994) *S*-(*N*-Aryl-*N*-hydroxycarbamoyl)glutathione derivatives are tight-binding inhibitors of glyoxalase I and slow substrates for glyoxalase II. *J. Med. Chem. 37*, 2161−2166.
(20) Kavarana, M. J., Kovaleva, E. G., Creighton, D. J., and Eiseman, J. L. (1999) Mechanism based competitive inhibitors of glyoxalase I: Membrane transport properties, in vitro antitumor activities, and stabilities in human serum and mouse serum. *J. Med. Chem. 42*, 221−228.
(21) Hamilton, D. S., Kavarana, M. J., Sharkey, E. M., Creighton, D. J., and Eiseman, J. L. (1999) A new method for generating inhibitors of glyoxalase I inside tumor cells using *S*-(*N*-aryl-*N*-hydroxycarbamoyl)ethylsulfoxide. *J. Med. Chem. 42*, 1823−1827.
(22) Tsuruo, T., Naito, M., Tomida, A., Fujita, N., Mashima, T., Sakamoto, H., and Haga, N. (2003) Molecular targeting therapy of cancer: Drug resistance, apoptosis and survival signal. *Cancer Sci. 94*, 15−21.
(23) White, J. S., and Rees, K. R. (1982) Inhibitory effects of methylglyoxal on DNA, RNA, and protein synthesis in cultured guinea pig karatocytes. *Chem-Biol. Interact. 38*, 339−347.
(24) Papoulis, A., Al-Abed, Y., and Bucala, R. (1995) Identification of N^2-(1-carboxyethyl)guanine (CEG) as a guanine advanced glycosylation end product. *Biochemistry 34*, 648−655.
(25) Hamilton, D. S., Zhang, X., Ding, Z., Hubatsch, I., Mannervik, B., Houk, K. N., Ganem, B., and Creighton, D. J. (2003) Mechanism of the glutathione transferase-catalyzed conversion of antitumor 2-crotonyloxymethyl-2-cycloalkenones to GSH adducts. *J. Am. Chem. Soc. 125*, 15049−15058.
(26) Joseph, E., Eiseman, J. L., Hamilton, D. S., Wang, H., Tak, H., Ganem, B., and Creighton, D. J. (2003) Molecular basis of the antitumor activities of crotonyloxymethyl-2-cyclohexenones. *J. Med. Chem. 46*, 194−196.
(27) Zhang, Q., Ding, Z., Creighton, D. J., Ganem, B., and Fabris, D. (2002) Alkylation of nucleic acids by the antitumor agent COMC. *Org. Lett. 4*, 1459−1462.
(28) Sharkey, E. M., O'Neill, H. B., Kovaleva, E. G., Kavarana, M. J., Wang, H., Creighton, D. J., Sentz, D. L., and Eiseman, J. L. (2000) Pharmacokinetics and antitumor properties in tumor bearing mice of an enediol analogue inhibitor of glyoxalase I. *Cancer Chemother. Pharmacol. 46*, 156−166.
(29) Rezgui, F., and Gaied, M. E. (1998) DMAP-catalyzed hydroxymethylation of 2-cyclohexenones in aqueous medium through the Baylis-Hillman reaction. *Tetrahedron Lett. 39*, 5965−5966.
(30) Strohalm, J., and Kopecek, K. (1978) Poly *N*-(2-hydroxypropyl)methacrylamide IV. Heterogeneous polymerization. *Angew. Makromol. Chem. 70*, 109−118.
(31) Kaltenbach, J. P., Kaltenbach, M. H., and Lyons, W. B. (1958) Nigrosin for differentiating live and dead cells. *Exp. Cell Res. 15*, 112−117.
(32) D'Argenio, D. Z., and Schumitzky, A. (1979) A package program for simulation and parameter estimation in pharmacokinetic systems. *Comput. Methods Programs Biomed. 9*, 115−134.
(33) Foster, S., and Lloyd, J. B. (1988) Solute translocation across the mammalian lysosome membrane. *Biochim. Biophys. Acta 947*, 465−491.
(34) Pisoni, R. L., Acker, T. L., Lisowski, K. M., Lemmons, R. M., and Thoene, J. G. (1990) A cysteine-specific lysosomal transport system provides a major route for delivery of thiol to human fibroblast lysosomes: Possible role in supporting lysosomal proteolysis. *J. Cell Biol. 110*, 327−335.
(35) Mego, J. L. (1984) Role of thiols, pH and cathepsine D in the lysosomal catabolism of serum albumin in kidney lysosomes. *Biochem. J. 218*, 775−783.
(36) Mego, J. L. (1985) Stimulation of intralysosomal proteolysis by cysteinyl-glycine, a product of the action of γ-glutamy transpeptidase on glutathione. *Biochim. Biophys. Acta 841*, 139−144.
(37) Kermack, W. O., and Matheson, N. A. (1957) The effects of some analogues of glutathione on the glyoxalase system. *Biochem. J. 65*, 48−58 and references therein.
(38) Searle, F., Gac-Breton, S., Keane, R., Dimitrijevic, S., Brocchini, S., Sausville, E. A., and Duncan, R. (2001) *N*-(2-Hydroxypropyl)methacrylamide copolymer-6-(3-amino-propyl)ellipticine conjugates. Synthesis, in vitro, and preliminary in vivo evaluation. *Bioconjugate Chem. 12*, 711−718.
(39) Duncan, R. (1992) Drug-polymer conjugates: Potential for improved chemotherapy. *Anti-Cancer Drugs 3*, 175−210.

BC0499634

Neutral Postgrafted Colloidal Particles for Gene Delivery

B. Thompson,[†] N. Mignet,[†,*] H. Hofland,[‡] D. Lamons,[‡] J. Seguin,[†] C. Nicolazzi,[†] N. de la Figuera,[†] R. L. Kuen,[§] X. Y. Meng,[‡] D. Scherman,[†] and M. Bessodes[†]

CNRS-UMR7001/ENSCP/Gencell S.A., Aventis Pharma, 13 Quai Jules Guesdes, 94403 Vitry-Seine, France, Gencell, Aventis Pharma, 3825 Bay Center Place, Hayward, California, 94545, and Cellular and Molecular Imagery Service, Faculté de Pharmacie, 4 avenue de l'Observatoire, 75270 Paris Cedex 06, France. Received March 28, 2004; Revised Manuscript Received December 3, 2004

Surface modification of cationic lipoplexes has been carried out by means of a postgrafting reaction. The original lipoplexes described comprise a cationic lipid, a neutral lipid, poly(ethylene glycol)–cholesterol (with or without a targeting ligand) and DNA. Modifying their surface via a chemical, postgrafting reaction did not alter their size (~100 nm) nor their ability to compact DNA, but did give a reduced zeta potential (~0 mV) to afford surface neutral particles. With the modified lipoplexes nonspecific NIH3T3 cell surface binding in vitro was inhibited. Intravenous injection of the neutralized lipoplexes in mice showed decreased accumulation of the particles in the lung as compared to PEGylated cationic lipoplexes. Tumor targeting was also achieved in vivo by the addition of an RGD-PEG-Cholesterol as a lipid-ligand in the postgrafted lipoplex formulation.

INTRODUCTION

Liposomes have been widely investigated for their potential clinical use, as they can be used as vectors for a various range of compounds. To allow them to efficiently associate with DNA, cationic lipids have been introduced to form the lipid bilayer. Cationic lipoplexes have been part of an expanding research area over the past decade due to their favorable DNA association as well as their cellular interactions (*1*). However, while they have proven very efficient in vitro they have suffered from problems in vivo, namely rapid elimination from the circulation due to interactions with proteins, opsonins, and the reticuloendothelial system (RES)[1] (*2*).

Methods to help alleviate these problems have included the incorporation of poly(ethylene glycol) (PEG) in liposome preparation. PEG, when grafted onto a lipid or cholesterol moiety and included in liposome preparation, offers colloidal stability due to its bulky, hydrophilic chain (*3*). Lipid-PEG has also shown to be useful at masking some of the positive charges on the surface of cationic lipoplexes. However, while PEG does indeed mask some of the positive charges, it has been found that the particles are still subject to unfavorable interactions with blood components and continue to suffer from rapid elimination from the circulation (*4*). The reduction of positive charges has been achieved by the addition of negatively charged PEG–lipids which helps to afford a more neutral surface charge and allows for enhanced stability in serum (*5*).

Other methods employed to increase the efficacity of lipoplexes in vivo have been to include a targeting moiety in conjunction with PEG–lipids in liposome preparation. One recent example includes the addition of a PEGylated, folate-bearing lipid into liposome formulation, in which folate-targeted complexes restored gene transfer activity in tumors but where the activity in the lung was reduced as compared to nontargeted lipoplexes (*6*). In the case of immunoliposomes, it was found that coupling an antibody to the distal ends of PEG allowed for improved target binding ability (*7*). Some of the more recent and efficient models have involved the preparation of PEG derivatives that are available for surface functionalization by a coupling reaction with target-specific antibodies after liposome formation. Several different chemistries have been used with success for such "postgrafting" strategies (*8*–*11*).

In our case, taking advantage of the lipid cationic charges to associate DNA, grafting was carried out postlipoplex formation. Our goal was to prepare surface neutral particles by means of a "postgrafting" reaction on the surface of preformed lipoplexes. The neutrality of the lipoplexes was expected to render the particles more stable with regard to their blood circulation lifetime, which would then lead to their passive accumulation in tumor tissue.

MATERIALS AND METHODS

Materials. L-α-Dioleoylphosphatidylethanolamine (DOPE), L-α-dioleoylphosphatidylethanolamine–lissamine rhodamine B (DOPE–lissamine rhodamine B), and 1,2-dipalmitoyl-*sn*-glycero-3-phosphocholine (DPPC) were purchased from Avanti Polar Lipids. Cationic lipid 2-(3-[bis(3-aminopropyl)amino]propylamino)-*N*-ditetradecylcarbamoylmethylacetamide (RPR209120B) (*12*), cholesteryl carbonate–poly(ethylene glycol)$_{42}$-OH (Chol-PEG$_{42}$),

* Corresponding author. Unité de Pharmacologie Chimique et Génétique, Inserm U640 – CNRS UMR 8151, Faculté de Pharmacie, 4 avenue de l'Observatoire, 75270 Paris cedex 06, France. nathalie.mignet@univ-paris5.fr; Tel +33 (0)1 53 73 95 81; Fax +33 (0)1 43 26 69 18.

[†] CNRS-UMR7001/ENSCP/Gencell S.A., Aventis Pharma.

[‡] Gencell, Aventis Pharma.

[§] Cellular and Molecular Imagery Service.

[1] Abbreviations: CAT, chloramphenicol acetyltransferase; Chol, cholesterol; DOPE, dioleoylphosphatidylethanolamine; DPPC, 1,2-dipalmitoyl-*sn*-glycero-3-phosphatidylcholine; DSPE, 1,2-distearoyl-*sn*-glycero-3-phosphoethanolamine; ELISA, enzyme-linked immunosorbent assay; EtBr, ethidium bromide; NHS, *N*-hydroxysuccinimide; PEG, poly(ethylene glycol); RES, reticuloendothelial system; RPR209120B, 2-(3-[bis(3-aminopropyl)-amino]propylamino)-*N*-ditetradecylethanolamine; TEM, transmission electron microscopy.

10.1021/bc040244z CCC: $30.25 © 2005 American Chemical Society
Published on Web 04/30/2005

and cholesteryl carbamate−poly(ethylene glycol)$_{75}$−(ACDCRGDCFCG)-COOH (Chol−PEG$_{75}$−RGD-4C) (*13*) were synthesized as described in the Supporting Information. Organic solvents chloroform and ethanol were purchased from Merck. H_2O for injection was purchased from Cooperative Pharmaceutique Française. HEPES was purchased from Sigma. Sulfo-NHS acetate and Slide-A-Lyzer dialysis cassettes were purchased from Pierce.

Preparation of Cationic Liposomes (thin-film method). The cationic lipid RPR209120B (16.82 mg, 20 μmol), DOPE (14.88 mg, 20 μmol), and DOPE−lissamine rhodamine B (0.52 mg, 0.4 μmol, 1% total lipid) were dissolved in chloroform, and the solvent was removed under reduced pressure on a rotary evaporator. The resulting thin film was further dried on the rotary evaporator at 5 mbar for 2 h in order to remove any remaining solvent. The film was rehydrated in 2 mL of H_2O for injection by gentle rotation overnight at room temperature to afford a final concentration of 10 mM. The particles were sonicated to afford a homogeneous size distribution of approximately 100−150 nm as measured by dynamic light scattering on a Coulter N4 Plus (Coulter, Beckman).

Preparation of Cationic Liposomes (ethanol injection method). The cationic lipid RPR209120B (16.82 mg, 20 μmol), DPPC (14.68 mg, 20 μmol), and DOPE−lissamine rhodamine B (0.52 mg, 0.4 μmol, 1% total lipid) were dissolved in absol ethanol. Their total volume was adjusted to 3.5 mL by the further addition of ethanol. This mixture was then added dropwise to 35 mL of H_2O with vigorous stirring and left to stir overnight. The excess solvent was removed under reduced pressure on a rotary evaporator until only a 2 mL quantity remained (corresponding to a concentration of 10 mM). The size of the resulting lipoplexes is of the order of 90−100 nm.

Postinsertion of Chol−PEG$_{42}$ in Cationic Liposomes. To functionalize the surface of the liposomes, all of the PEG−lipids were introduced via a postinsertion method. The Chol−PEG$_{42}$ (105 μL, 0.125 μmol) was dissolved in 40 mM HEPES pH 7.5 and added to the cationic liposomes (295 μL, 2.5 μmol) mixture dropwise with vortexing and left to incubate at 37 °C for 2 h.

Preparation of DNA/Vector Lipoplexes. Lipoplexes were prepared in 5% glucose with a charge ratio (+/−) = 5. Plasmid DNA (pCMVCAT) (500 μL, 0.5 g/L, 10% glucose) was added to RPR209120B/DOPE/Chol−PEG$_{42}$ or RPR209120/DPPC/Chol−PEG$_{42}$ cationic liposomes (400 μL, 5 mM total lipids) dropwise with constant vortexing. HEPES (100 μL, 1 M, pH 7.5) was then added to the complex with rapid vortexing, and the samples were left to incubate for 24 h at room temperature.

The insertion of lipid−PEG into the cationic liposome prior to DNA addition was assessed by an indirect method: indeed, if the lipid−PEG was not inserted into the outer bilayer of the liposome, the complex would aggregate upon the addition of 10 mol equiv of sulfo-NHS acetate per mole of RPR209120B (i.e. 5 equiv of sulfo-NHS acetate per primary amine of RPR209120B).

Reaction of the Lipoplexes with Sulfo-NHS Acetate. Sulfo-NHS acetate (3.24 mg, 10 equiv, 12.5 μmol) was added to lipoplex RPR209120B/DOPE/Chol−PEG$_{42}$/DNA or RPR209120B/DPPC/Chol−PEG$_{42}$/DNA (1 mL, 1 equiv, 1.25 μmol RPR209120B) buffered with 100 mM HEPES at pH 7.5. The reagent was added as a powder, and the resulting mixture was gently mixed by inverting the reaction tube several times to aid dissolution. The reaction mixture was left to incubate for 1 h at room temperature with occasional gentle mixing. The reaction complex was then transferred to Slide-A-Lyzer dialysis cassettes and dialyzed overnight against 5% glucose and 100 mM HEPES.

Preparation of Targeting Postgrafted Lipoplexes. First, Chol−PEG$_{42}$ lipids (105 μL, 0.125 μmol) were dissolved in 40 mM HEPES pH 7.5 and added to the cationic liposomes (190 μL, 2.5 μmol) mixture dropwise with vortexing and left to incubate at 37 °C for 2 h. Then, plasmid DNA (pCMVCAT) (500 μL, 0.5 g/L, 10% glucose) was added to RPR209120B/DOPE/Chol−PEG$_{42}$ or RPR209120/DPPC/Chol−PEG$_{42}$ cationic liposomes (295 μL, 5 mM total lipids) dropwise with constant vortexing. HEPES (100 μL, 1 M, pH 7.5) was then added to the complex with rapid vortexing, and the samples were left to incubate for 24 h at room temperature. Sulfo-NHS acetate (3.24 mg, 10 equiv, 12.5 μmol) was added to the lipoplex (895 μL, 1 equiv, 1.25 μmol of RPR209120B) buffered with 100 mM HEPES at pH 7.5; the lipoplexes were incubated and purified as described above. Finally, to prepare the RGD lipoplexes, the Chol−PEG$_{75}$−RGD-4C was dissolved in 40 mM HEPES pH 7.5 (105 μL, 0.125 μmol) and was added to postgrafted lipoplexes (895 μL) with vortexing, and the samples were left to incubate for 24 h at room temperature. The Chol−PEG$_{75}$−RGD-4C was inserted postacetate reaction and postdialysis in order to avoid any unwanted side-reactions taking place.

Size of Complexes/Zeta Potential of Complexes. The size of the complexes was determined by dynamic light scattering on a Coulter N4 Plus. Typically 10 μL of complex was added to 800 μL of H_2O for injection for each sample measured, mean value are given for 90°, 1 min equilibration, 3 min run.

The zeta potential measurements were performed on a Malvern Zetasizer 3000. Samples of 1 mL containing 100 μL of complex (5 mM) in 20 mM NaCl were injected in the cell and subjected to 5 × 8 s measurements.

Transmission Electronic Microscopy. The lipoplexes prepared as described (Concentration divided by 10) were loaded on a Formvar/carbon copper grid 200 mesh from Agar Scientific. Uranyl acetate was used to stain the samples. Analyses were performed on a microscope JEOL, JEM 100S.

In Vivo Distribution in Normal or Tumor-Bearing Mice. Six-week-old female C57B1/6 mice (Charles River) were anesthetized by intraperitoneal injection of a mix of ketamine (85.8 mg/kg; Merial) and xylazine (3.1 mg/kg; Bayer) diluted in 150 mM NaCl. A 200 μL volume of rhodamine-labeled lipoplexes (50 μg of DNA, 250 nmol cationic lipids in 5% glucose) was injected into the mouse tail vein. Blood was collected by cardiac puncture at appropriate intervals (30 min, 1, 2, and 6 h after injection), and mice were euthanized at the end of the sample taking. In the distribution study, mice were sacrificed at 30 min and at 1, 2, and 6 h after injection and the liver, spleen, and lungs were removed, weighed, and homogenized in pH 7.4 phosphate-buffered saline (PBS, 5 mL/g tissue). Experiments were conducted following NIH recommendations for animal experimentation and Aventis local ethic committee on animal care and experimentation.

Rhodamine-labeled lipids were extracted according to Takeuchi et al. (*14*) from 100 μL of blood or tissue homogenates with 3 mL of $CHCl_3$−MeOH (1:1, v/v) by vigorous mixing during 30 min for blood and 40 min for tissue homogenates followed by centrifugation (3000 rpm, 10 min). The fluorescence intensity corresponding to DOPE−rhodamine was assayed on the supernatant with a fluorospectrophometer (Fluoromax 2, Jobin Yvon, λ_{exc} 550 nm/λ_{em} 590 nm). The amount of lipoplexes in the blood or tissue homogenates was evaluated with a

Scheme 1. Illustration of the Postgrafting Strategy with Sulfo-NHS Acetate

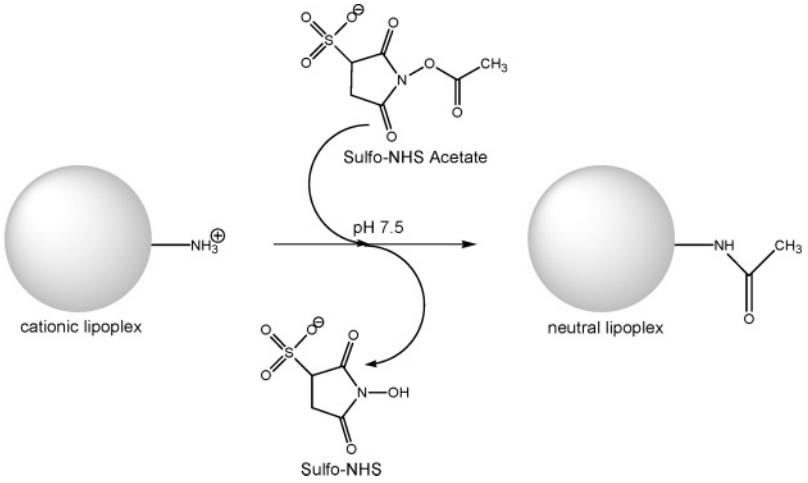

calibration curve of the initial lipoplexes containing 1% DOPE−rhodamine and expressed as the remaining percentage of injected dose.

Lewis lung and colon carcinoma tumors kindly provided by Aventis Pharma (Vitry/Seine, France) were implanted subcutaneously in the right flank of six-week-old female C57B1/6 mice (Charles River), and 10−14 days later, biodistribution studies were undertaken as previously described.

Reporter Gene Expression in Lungs and PO_2 Colon Carcinoma. Six-week-old female C57B/16 mice (Charles River) were anesthetized by intraperitoneal injection of a mix of ketamine (85.8 mg/kg) and xylazine (3.1 mg/kg) diluted in 150 mM NaCl. A 200 μL volume of rhodamine-labeled lipoplexes (50 μg of DNA, 250 nmol of cationic lipids in 5% glucose) was injected into the mouse tail vein. Mice were sacrificed at 24 h postinjection, and lungs and PO_2 colon carcinoma were harvested, weighed, and homogenized in 1 mL of PBS using an Ultra Thurax (Diax 600, Heidolph, Fisher). The samples were centrifuged (1000 rpm, 30 min, 4 °C), and the amount of Chloramphenicol acetyl transferase (CAT) transgene expressed was determined using a standard enzyme-linked immunosorbent assay (ELISA) kit (Roche Diagnostics).

RESULTS

Postgrafting Method. Reaction of Cationic PEGylated Lipoplexes with Sulfo-NHS Acetate. Sulfo-NHS acetate is traditionally used on proteins to irreversibly block primary amines and form stable amides; it is very reactive toward primary amines between pH 7−9 and less reactive toward secondary amines. The postgrafting method consists of DNA/vector lipoplex preformation followed by reaction with an excess of sulfo-NHS acetate to mask the cationic charges (Scheme 1). One can predict that masking all cationic charges on the lipoplex will lead to particle aggregation due to a lack of electrostatic repulsion. The insertion of a PEG−lipid in lipoplex formulation is therefore necessary to maintain particles with a small diameter, and we have used cholesterol−PEG_{42} (Chol−PEG_{42}) in the present study. The pH at which the postgrafting experiments are carried out is low enough to prevent the acetylation of DNA (a pH between 8.5 and 9.0 is required for DNA acylation). Reactions can be carried out in a buffered medium, and they proceed readily at room temperature. The successive steps involved in lipoplex preparation used in the present postgrafting study are shown (Scheme 2), and the non-commercial lipids used in their formulation are illustrated (Scheme 3).

To optimize the reaction conditions for postgrafting sulfo-NHS acetate on lipoplexes, initial experiments were carried out with various molar ratios. The following molar equivalents (1:1, 5:1, 10:1, and 50:1) of sulfo-NHS acetate versus cationic lipid were investigated (Table 1).

The size of the unreacted PEGylated particles, prepared by the thin-film method, was approximately 131 nm, and their zeta potential was +16.42 mV. These results are in good agreement with previous reports. It can be shown that while the addition of PEG−lipid in lipoplex preparation does reduce the zeta potential of the particles, it does not completely mask the surface charges, and residual positive charges can still be measured (*5*). The size of the postgrafted particles gradually increased to approximately 189 nm (with 50 mol of sulfo-NHS acetate per mole of RPR209120B), and their zeta potential was reduced to approximately zero. In the case where lipoplexes were reacted with 50 equiv of sulfo-NHS acetate, the zeta potential of the particles was reversed to −15 mV, and we could see a partial DNA release on agarose gel electrophoresis as indicated by the ethidium bromide (EtBr) fluorescence increase (Table 1).

The particles, both modified and unmodified, were stable for more than 60 days with respect to their size (approximately 150 nm for both types of particles) and their zeta potential (approximately +5 mV for particles modified with 10 mol of sulfo-NHS acetate per mole of RPR209120B and approximately +12 mV for unmodified particles) (data not shown).

Acetylation Yield of Postgrafted Complexes. The lipids of postgrafted complexes were extracted and subjected to analysis (experimental details can be found in the Supporting Information). The degree of acetylation of lipid RPR209120B in the complexes was evaluated by LC-MS and it was found that the postgrafting procedure produced a mixture of compounds. Two corresponding peaks were determined, of which the major peak (65%) contained a mixture of both the starting lipid and the diacetate. The minor peak (35%) was found to be the triacetate. These results are in good agreement with the results above. A certain amount of unreacted starting lipid in the postgrafted complex is required to continue to compact DNA, and the ethidium bromide assay shows that this is indeed the case (Table 1). The proportions of diacetate and triacetate found in the extracted mixture are also what would be expected due to their reactivities and relative position within the complexes.

Scheme 2. Illustration of the Successive Lipoplex Preparation Steps Used in the Present Postgrafting Study

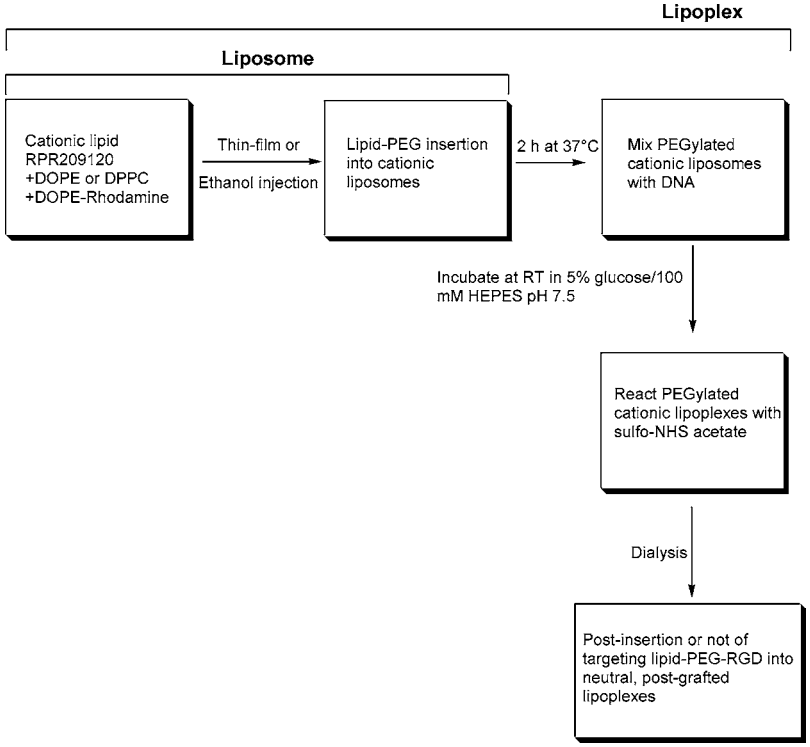

Scheme 3. The Cationic Lipid RPR209120B, Cholesterol−PEG_{42} (Chol−PEG_{42}) and Cholesterol−PEG_{75}−RGD-4C (Chol−PEG_{75}−RGD-4C)

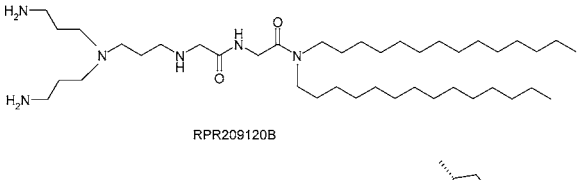

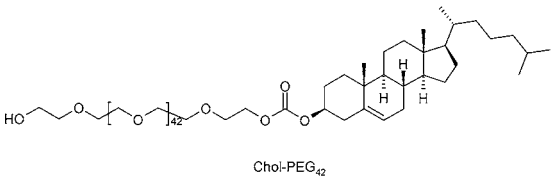

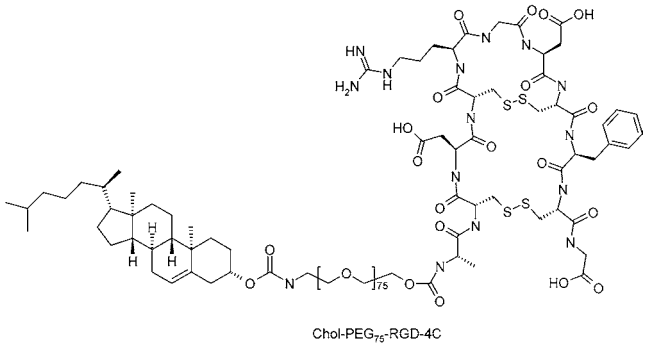

Characterization of the Postgrafted Lipoplexes for Both in Vitro and in Vivo Experiments. From these results above, it was established that postgrafting up to 10 mol of sulfo-NHS acetate per mole of cationic lipid RPR209120B on the surface of preformed lipoplexes did not alter their size nor their ability to compact DNA, yet it did afford surface-neutral particles as demonstrated by their zeta potential. For biological studies, we chose to use these conditions, and we prepared postgrafted lipoplexes containing or not containing a Cholesterol−PEG_{75}−RGD-4C (Chol−PEG_{75}−RGD-4C) targeting lipid.

Table 1. Physicochemical Data Corresponding to the Reaction of Different Amounts of Sulfo-NHS Acetate on PEGylated Cationic Lipoplexes[a]

molar ratio sulfo-NHS acetate/ cationic lipid	zeta potential (mV)	EtBr (relative fluorescence)	particle size (nm)
0	16.42	4.6	131
1	−2.19	5.7	151
5	−0.36	10.2	168
10	−2.09	11.0	169
50	−15.0	13.1	189

[a] The molar equivalents (1:1, 5:1, 10:1, and 50:1) of sulfo-NHS acetate versus cationic lipid RPR209120B were investigated. Lipoplexes comprised RPR209120B/DSPE−PEG_{42}(10%)/DNA with a charge ratio (+/−) = 5 and were prepared by the thin-film method.

It was necessary to use a HEPES buffer concentration of 100 mM in order to maintain the pH at ∼7.4 during and after the reaction with sulfo-NHS acetate since it is subject to hydrolysis, which releases acetic acid and sulfo-*N*-hydroxysuccinimide.

Liposomes were prepared either by film formation followed by rehydration or by the ethanol injection method (see Materials and Methods and Scheme 2). While Chol−PEG_{42} was inserted in the cationic liposomes before sulfo-NHS acetate postgrafting in order to maintain the colloidal stability of the neutralized lipoplexes, the targeting lipid, Chol−PEG_{75}−RGD-4C, was inserted after the postgrafting reaction. Size and zeta potential of the final complexes for in vivo studies were measured (Table 2).

Cationic lipoplexes, prepared by the ethanol injection method, gave a measured zeta potential of +39.7 ± 1.1 mV, which was reduced to +12.5 ± 0.9 mV by addition of 5% Chol−PEG_{42} in the formulation. Insertion of lipid−PEG_{42} in the film during the preparation of the liposomes led to similar results (+16 mV, Table 1).

By reacting sulfo-NHS acetate with the surface amine moieties of preformed PEGylated lipoplexes, neutral

Table 2. Size and Zeta Potential Data of Non-targeted and Targeted Lipoplexes Used for Biological Experiments[a]

type of complex	size (nm)	zeta potential (mV)
cationic lipoplex	109.8 ± 24.1	+39.7 ± 1.1
lipoplex + 5%Chol−PEG_{42}	125.2 ± 50.9	+12.5 ± 0.9
lipoplex + 5%Chol−PEG_{42} + postgrafting	96.9 ± 29.6	+1.2 ± 0.9
lipoplex + 5%Chol−PEG_{42} + postgrafting + 5%Chol−PEG_{75}−RGD-4C	211 ± 89.9	−3.4 ± 1.0

[a] Liposomes were prepared by the ethanol injection method. Cationic lipoplex comprised RPR209120B/DPPC/DNA; lipoplex + 5%Chol−PEG_{42} comprised RPR209120B/DPPC/Chol−PEG_{42}(5%)/DNA; lipoplex + 5%Chol−PEG_{42} + postgrafting comprised RPR209120B/DPPC/Chol−PEG_{42}(5%)/DNA and was reacted with sulfo-NHS acetate; lipoplex + 5%Chol−PEG_{42} + postgrafting + 5%Chol−PEG_{75}−RGD-4C comprised RPR209120B/DPPC/Chol−PEG_{42}(5%)/DNA, was reacted with sulfo-NHS acetate followed by insertion of Chol−PEG_{75}−RGD-4C (5%). All above lipoplexes were prepared with a charge ratio (+/−) = 5.

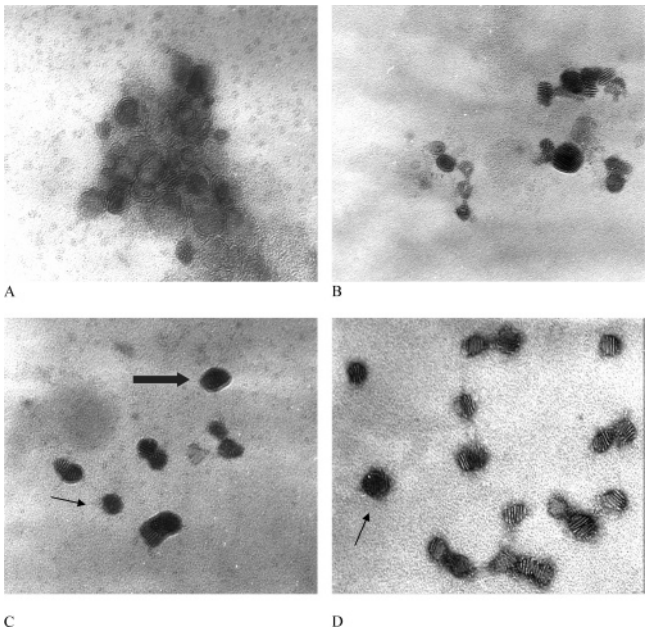

Figure 1. TEM pictures of lipoplexes obtained by negative staining. A. Liposomes (film) RPR209120B/DOPE/Chol−PEG_{42}-(5%)/DNA B. Same liposomes as in A + sulfo-NHS acetate postgrafting; C. Liposomes (ethanolic injection) RPR209120B/DPPC/Chol−PEG_{42}(5%)/DNA. D. Same liposomes as in C + sulfo-NHS acetate postgrafting.

particles were obtained (zeta potential = +1.2 ± 0.9 mV). When lipoplexes were reacted with sulfo-NHS acetate, and Chol−PEG_{75}−RGD-4C was further added to the preformed complexes, the zeta potential was reduced to −3.4 ± 1.0 mV (Table 2); this value is in agreement with the presence of two aspartic acids and a free C-terminal carboxylate function in the RGD moiety.

Electronic transmission microscopy was carried out for acetylated and nonacetylated particles prepared by the thin-film and the ethanolic injection methods (Figure 1).

No structural differences between postgrafted and non postgrafted particles were observed, indicating that the postgrafting process does not alter the particle structures. However, the surface of postgrafted particles appears slightly changed with enhanced lamellas. By laser diffraction size measurement, postgrafted particles appeared larger than the non postgrafted ones (within 10−20 nm increase), and we obtained smaller particles by the ethanol injection method as compared to the film-hydration method. As an example, the isolated particles in C and D represent 20 and 40 nm in diameter, respectively. On some of the particles, an outer layer probably corresponding to the PEG shielding was clearly visualized (large gray arrow on C).

Lipoplex Pharmacokinetics after iv Injection. Intravenous injections of PEGylated cationic lipoplexes versus PEGylated postgrafted lipoplexes were performed in mice bearing subcutaneous 3LL Lewis Lung tumors. The postgrafted complexes, where the liposome component was prepared via the thin-film method, showed an increased amount of postgrafted complex in the circulation by a factor of 7 at the end of 30 min and by a factor of 5 after 1 h. There was also a marked decrease in the uptake of acetylated, postgrafted particles in the lung. However, there was no significant passive accumulation in the tumor (Figure 2). As already observed, most of the rhodamine signal was recovered in the RES (5).

The postgrafted complexes, where the liposome component was prepared via the ethanol injection method, did not show as dramatic a difference in circulation time as compared to nonacetylated particles. The smaller size achieved with these particles might be the main reason for this. A different liposome flexibility due to the preparation might also influence this difference (*15*). Nevertheless, there was again a decrease in lung uptake of the acetylated particles (data not shown).

Targeting with RGD−PEG−Lipid. The postgrafting strategy afforded lipoplexes with a longer circulation lifetime, but at the same time, as could be expected, diminished their cell membrane interactions required for transfection. We thus postulated that the addition of an integrin-targeting ligand in lipoplex formulation may help to restore their accumulation in the tumor. Experiments were performed on mice bearing PO_2 tumors validated for their $\alpha v \beta 3$ integrin expression in the tumor vasculature.

An increased trend of lipoplex accumulation in the tumor when an RGD-4C ligand was added to the formulation was noted as compared to the same formulation of postgrafted complexes without RGD (Figure 3). Taking the Chol−PEG_{75}−RGD-4C liposome as a control, an increase of 5- and 2-fold in the tumor were measured, 30 min and 1 h postinjection, respectively, for the liposome + Chol−PEG-RGD-4C + postgrafting particles. This increased liposome accumulation was reflected in an increased gene expression for both cationic PEGylated lipoplexes and PEGylated postgrafted lipoplexes bearing a Chol−PEG-RGD-4C targeting moiety (Figure 4). However, no statistically significant difference was observed for transgene expression between the nonneutralized or acetate-neutralized targeted lipoplexes.

DISCUSSION AND CONCLUSIONS

Improving the circulation lifetime of iv injected cationic lipid/DNA complexes is of great interest. Cationic lipids are excellent vectors for DNA due to both their ability to efficiently compact negatively charged DNA at a certain charge ratio, as well as their favorable cellular interactions which lead to transfection in vitro. However, in vivo cationic lipid efficacy is hampered by their nonspecific interactions with blood components and their rapid elimination from the circulation (*4*). The addition of PEG in lipoplex formulation has achieved less positively charged particles, with respect to their surface charge (i.e. their zeta potential), but this has been found to be insufficient to completely mask any residual cationic charges on the lipoplex surface, which are still subject to unfavorable blood component interactions.

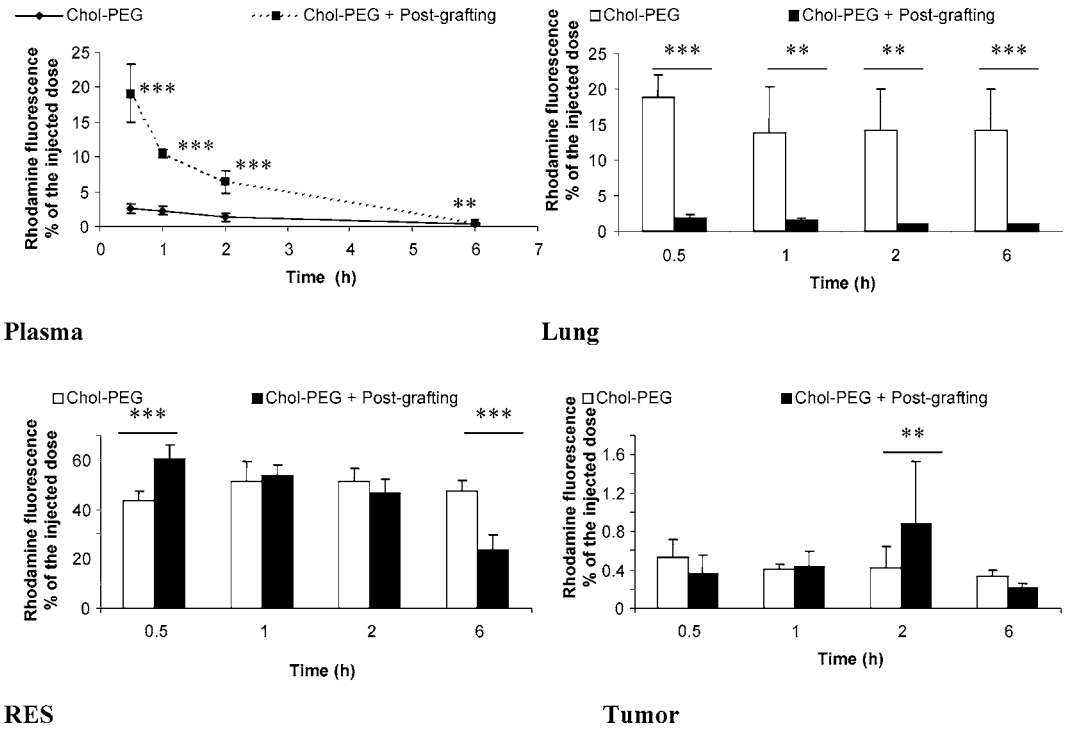

Figure 2. Blood, lung, RES, and tumor concentration of modified (postgrafting) versus unmodified lipoplexes. Rhodamine−lipid levels in the plasma, lung, RES, and 3LL tumor of tumor-bearing mice after systemic injection. Results are expressed as the mean ± SD. Significant difference: **: $P < 0.01$ and ***: $P < 0.001$

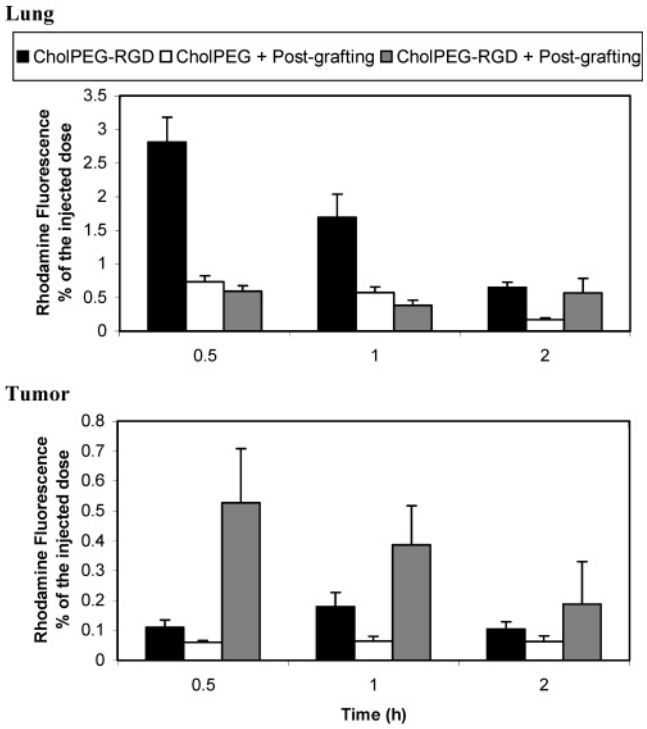

Figure 3. Lung and PO_2 tumor concentration of targeting-neutral versus targeting-PEGylated lipoplexes and neutral nontargeting lipoplexes. Rhodamine−lipid levels in the lungs and PO_2 tumor of tumor-bearing mice after systemic injection. Results are expressed as the mean of five values; error bars indicate standard error of the mean.

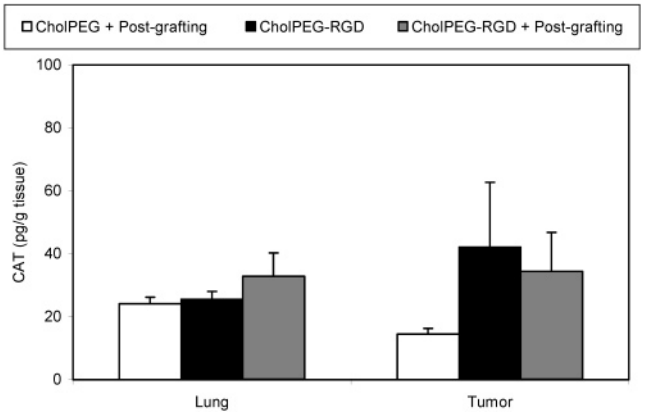

Figure 4. CAT expression in lung and PO_2 colon carcinoma. Results are expressed as the mean of five values; error bars indicate standard error of the mean.

The original postgrafting method presented here was validated as a way to compact DNA and obtain neutral particles while maintaining their size. Binding experiments performed at 4 °C on NIH3T3 cells with fluorescent particles showed no fluorescence for postgrafted complexes while nonspecific fluorescence was observed for nonacetylated complexes (data not shown) (*16*). This confirmed the potential of sulfo-NHS acetate lipoplex neutralization to decrease nonspecific cell interaction.

Our postgrafted formulations included PEG−lipids for steric stabilization of the particles. This strategy allowed the incorporation of a lipid−PEG-ligand without protocol modification. Incorporation of Chol−PEG_{75}−RGD-4C into the formulation increased lipoplex tumor delivery. Although an increase in tumor transfection was observed in RGD-targeted formulations, neutralized particles were not superior to nonneutralized ones. This might result from incomplete DNA release or less efficient transfection by neutralized particles. The use of a cytotoxic drug or an antiangiogenic plasmid (*17*) instead of a DNA model would be an alternative and a more straightforward manner to assay the potential advantage of the present formulation for therapeutic use, as only a release at the level of the vessels would be required to starve the tumor. Integrins have been shown to be overexpressed by the inflammed endothelium (*18*), which would be easier to

reach for particles. It has been reported that RGD-targeted liposomes can act as a site-specific drug delivery system to tumor endothelial cells in vitro, which was demonstrated by increased binding, as well as redirecting targeted liposomes containing doxorubicin to angiogenic endothelial cells in vivo which led to inhibited tumor growth (*19*). Thus, in the present case, the targeted particles possibly accessed the tumoral endothelium without reaching the tumor cells. Experiments are currently being undertaken to determine the localization of the particles in and around the tumor.

The postgrafting strategy reported here has succeeded in further reducing the zeta potential of cationic lipoplexes (to approximately 0 mV) to afford surface neutral particles and has allowed for a longer lifetime of the complexes in vivo. Despite increased circulation time in the blood, no passive accumulation in 3LL tumors was measured. Insertion of a targeting Chol−PEG_{75}−RGD-4C succeeded in PO_2 tumor targeting and increased DNA expression. Ways of triggering DNA release in the target are now in process.

ACKNOWLEDGMENT

B. Thompson thanks the European Community for the Pierre and Marie Curie grant. We thank P. Wils for very helpful discussions. We also thank S. Sable and B. Monegier (Aventis Pharma) for structural analyses.

Supporting Information Available: Experimental details. This material is available free of charge via the Internet at http://pubs.acs.org.

LITERATURE CITED

(1) Felgner, P. L., Gadek, T. R., Holm, M., Roman, R., Chan, H. W., Wenz, M., Northrop, J. P., Ringold, G. M., and Danielsen, M. (1987) Lipofection: a highly efficient, lipid-mediated DNA-transfection procedure. *Proc. Natl. Acad. Sci. U.S.A. 84*, 7413−7417.

(2) Maurer, N., Mori, A., Palmer, L., Monck, M., Mok, K., Mui, B., Akhong, Q., and Cullis, P. (1999) Lipid-based systems for the intracellular delivery of genetic drugs. *Mol. Membr. Biol. 16*, 129−140.

(3) Papahadjopoulos, D., Allen, T. A., Gabizon, A., Mayhew, E., Matthay, K., Huang, S., Lee, K., Woodle, M., Lasic, D., Redemann, C., and Martin, F. (1991) Sterically stabilized liposomes: improvements in pharmacokinetics and antitumor therapeutic efficacy. *Proc. Natl. Acad. Sci. U.S.A. 88*, 11460−11464.

(4) Song, L., Ahkong, Q., Rong, Q., Wang, Z., Ansell, S., Hope, M., and Mui, B. (2002) Characterization of the inhibitory effect of PEG-lipid conjugates on the intracellular delivery of plasmid and antisense DNA mediated by cationic lipid liposomes. *Biochim. Biophys. Acta 1558*, 1−13.

(5) Nicolazzi, C., Mignet, N., de la Figuera, N., Cadet, M., Torero Ibad, R., Seguin, J., Scherman, D., and Bessodes, M. (2003) Anionic poly(ethylene glycol) lipids added to cationic lipoplexes increase their plasmatic circulation time. *J. Controlled Release 88*, 429−443.

(6) Hofland H., Masson, C., Iginla, S., Osetinsky, I., Reddy, J. A. Leamon, C. P., Scherman, D., Bessodes, M., and Wils, P. (2002) Folate-Targeted Gene Transfer in Vivo. *Mol. Ther. 5*, 739−744.

(7) Allen, T. (1994) Long-circulating (sterically stabilized) liposomes for targeted drug delivery. *Trends Pharmacol. Sci. Rev. 15*, 215−220.

(8) Maruyama, K., Takizawa, T., Yuda, T., Kennel, S., Huang, L., and Iwatsuru, M. (1995) Targetability of novel immunoliposomes modified with amphipathic poly(ethylene glycol)s conjugated at their distal terminals to monoclonal antibodies. *Biochim. Biophys. Acta 1234*, 74−80.

(9) Hansen, C., Kao, G., Moase, E., Zalipsky, S., and Allen, T. (1995) Attachment of antibodies to sterically stabilized liposomes: evaluation, comparison and optimization of coupling procedures. *Biochim. Biophys. Acta 1239*, 133−144.

(10) Blume, G., Cevc, G., Crommelin, M., Bakker-Woudenberg, I., Kluft, C., and Storm, G. (1993) Specific targeting with poly(ethylene glycol)-modified liposomes: coupling of homing devices to the ends of the polymeric chains combines effective target binding with long circulation times. *Biochim. Biophys. Acta 1149*, 180−184.

(11) Bendas, G., Krause, A., Bakowsky, U., Vogel, J., and Rothe, U. (1999) Targetability of novel immunoliposomes prepared by a new antibody conjugation technique. *Int. J. Pharm. 181*, 79−93.

(12) Byk, G., Scherman, D., Schwartz, B., Dubertret, C. (1997) Lipopolyamines as transfection agents and pharmaceutical uses thereof. Rhone-Poulanc Rorer, S.A., WO97/18185, 81 pp.

(13) Koivunen, E., Wang, B., and Ruoslahti, E. (1995) Phage libraries displaying cyclic peptides with different ring sizes: ligand specificities of the RGD-directed integrins. *BioTechnology 13*, 265−70.

(14) Takeuchi, H., Kojima, K., Yamamoto, H., and Kawashima, Y. (2000) Polymer coating of liposomes with a modified poly(vinyl alcohol) and their systemic circulation and RES uptake in rats. *J. Controlled Release 68*, 195−205.

(15) Templeton, N. (2003) Cationic liposomes as in vivo delivery vehicles. *Curr. Med. Chem. 10*, 1279−1287.

(16) Shi, F., Wasungu, L., Nomden, A., Stuart, M., Polushkin, E., Engberts, J., and Hoekstra, D. (2002) Interference of poly(ethylene glycol)-lipid analogues with cationic-lipid-mediated delivery of oligonucleotides; role of lipid exchangeability and non-lamellar transitions. *Biochem. J. 366*, 333−341.

(17) Blezinger, P., Yin, G., Xie, L., Wang, J., Matar, M., Bishop, J., and Min, W. (1999) Intravenous delivery of an endostatin gene complexed in cationic lipid inhibits systemic angiogenesis and tumor growth in murine models. *Angiogenesis 3*, 205−210.

(18) Brooks, P., Clarck, R., and Cheresh, D. (1994) Requirement of vascular integrin $\alpha_v\beta_3$ for angiogenesis. *Science 264*, 569−571.

(19) Schiffelers, R., Koning, G., ten Hagen, T., Frens, M., Schraa, A., Janssen, A., Kok, R., Molema, G., and Storm, G. (2003) Antitumor efficacy of tumor vasculature-targeted liposomal doxorubicin. *J. Controlled Release 91*, 115−58.

BC040244Z

Synthesis and Biological Properties of Insulin−Deoxycholic Acid Chemical Conjugates

Seulki Lee, Kwangmeyung Kim, Tadiparthi Suresh Kumar, Jisook Lee, Sang Kyoon Kim, Dong Yun Lee, Yong-kyu Lee, and Youngro Byun*

Department of Materials Science and Engineering, Gwangju Institute of Science and Technology, 1 Oryong-dong, Buk-gu, Gwangju, 500-712, Korea. Received June 2, 2004; Revised Manuscript Received March 23, 2005

Bile acids have been considered very useful in the preparation of new pharmaceuticals, and more recently in the preparation of peptide and protein drugs because of their natural chemical and biological properties. In this study, we modified recombinant human insulin by covalently attaching deoxycholic acid (DOCA) derivatives in order to synthesize orally active insulin analogues. DOCA derivatives, namely succinimido deoxycholate and succinimido bisdeoxycholyl-L-lysine were prepared and site specifically conjugated at Lys^{B29} of insulin. The resultant insulin conjugates, [N^{B29}−deoxycholyl] insulin (Ins−DOCA) and [N^{B29}−bisdeoxycholyl-L-lysil] insulin (Ins−bisDOCA), were studied for their chemical, structural, and biological properties. Their chemical properties were determined by HPLC, MALDI-TOF mass spectroscopy, and dynamic light scattering. Lipophilicity and self-aggregation behavior of insulin conjugates were enhanced with increasing number of labeled bile acid. The far-ultraviolet region of circular dichroism spectra showed no significant change of the tertiary structure of insulin in aqueous solution due to conjugation. Competitive insulin binding assay with HepG2 cells revealed that monosubstituted insulin conjugates still retained high binding affinity to the insulin receptor. When the insulin conjugates were intravenously administered (0.33 IU/kg) to streptozotocin (STZ)-induced diabetic rats, the conjugates showed sustained biological activity for a longer period with the similar lowest blood glucose level (glucose nadir), compared to native insulin. In further studies, the resulting new insulin conjugates will be investigated for their oral efficiency as a long-acting insulin formulation for the treatment of diabetic patients.

INTRODUCTION

Insulin is the primary hormone utilized for treatment of virtually all types of diabetic patients. Insulin can be administered only by parenteral injection; however, conventional injectable insulin replacement therapy has several therapeutic risk factors, such as poor compliance and unsatisfactory metabolic regulation in diabetic patients (*1*, *2*). Many attempts have therefore been made to enhance therapeutic performance of insulin using various delivery systems (*3*−*5*). However, these alternative delivery methods of insulin still have many problems mainly due to natural characteristics of insulin such as physicochemical instability, increased susceptibility to proteolysis, solubility, large molecular weight, and limited ability to traverse biological barriers (*6*, *7*).

To overcome these limitations, several kinds of chemical modifications of insulin have been proposed. For instance, lipid modification of insulin could improve solubility and showed extended-action via binding to an existing serum protein (*8*−*10*). In addition, poly(ethylene glycol), 9-fluorenylmethoxycarbonyl, transferrin, polysialic acid, and poly(ethylene glycol)-alkyl linker chemically conjugated insulin derivatives showed improved therapeutic profiles, such as solubility, enzymatic stability, circulation half-life, or permeability against mucosal membrane (*11*−*16*).

Among all the different alternative route of insulin delivery, peroral formulation is the most preferable for its significantly pronounced therapeutic and patient acceptability. In our previous study, deoxycholic acid (DOCA)-conjugated heparin was highly absorbed in the intestine without damaging the tissue structure of the mucous membrane (*17*, *18*). More recently, we have prepared a new oral delivery carrier based on bile acid which improves the oral bioavailability of human insulin (*19*). Based on substantiated observations that associated bile acids could enhance the absorption of poorly permeable macromolecules in the intestine, we have designed site-specific DOCA-conjugated insulin analogues. DOCA is one of the bile acids which are natural compounds consisting of a facially amphiphilic steroid nucleus with a hydrophobic β-side and a hydrophilic α-side. They are synthesized from cholesterol in the liver, released in the small intestine, and returned to the liver by absorption through the bile acid transporter (*20*, *21*). Bile acids have been considered in the preparation of new drugs because bile acid-conjugated materials can retain the properties of bile acids, such as amphiphilicity, capacity of self-assembling, high chemical stability, and binding ability to bile acid transporters in the intestine (*22*, *23*). Taken together, this spectrum of properties gives the therapeutic peptide a unique pharmacological profile that is attractive for developing new orally active formulations.

In this respect, we hypothesized that covalent coupling of bile acid to a specific site of insulin may improve the therapeutic profiles of insulin while maintaining its biological activity. We synthesized, in this study, site specifically labeled insulin−DOCA conjugates and char-

* To whom correspondence should be addressed: Youngro Byun, Ph.D., Department of Materials Science and Engineering, Gwangju Institute of Science and Technology, 1 Oryong-dong, Buk-gu, Gwangju, 500-712, Korea. Phone, 82-62-970-2312; fax, 82-62-970-2354; e-mail, yrbyun@gist.ac.kr.

10.1021/bc049871e CCC: $30.25 © 2005 American Chemical Society
Published on Web 04/19/2005

acterized their biological activity in vitro and in vivo, respectively.

EXPERIMENTAL PROCEDURES

Materials. Human crystalline zinc insulin (Zn^{2+} insulin) was purchased from Serologicals Corp. (Norcross, GA) and used without further purification. (3-[^{125}I]-Iodotyrosyl^{A14})-insulin (human recombinant) was obtained from Amersham Biosciences Corp. (Piscataway, NJ). Deoxycholic acid (DOCA), L-lysine ethyl ester, *N*,*N*′-dicyclohexylcarbodiimide (DCC), *N*-hydroxysuccinimide (NHS), tetrahydrofuran (THF), anhydrous *N*,*N*-dimethylformamide (DMF), triethylamine (TEA), ethyl acetate (EtOAc), absolute ethanol (EtOH), ammonium bicarbonate (NH_4HCO_3), magnesium sulfate anhydrous ($MgSO_4$), and streptozotocin (STZ) were purchased from Sigma-Aldrich Co. (St. Louis, MO). Before use, THF was distilled from sodium benzophenone. All reagents and organic solvents used were at least ACS grade.

Preparation of DOCA Derivatives. *Succinimido Deoxycholate*. DOCA (200 mg, 0.5 mmol) and NHS (76 mg, 0.67 mmol) were dissolved in anhydrous THF (20 mL). DCC (136 mg, 0.67 mmol) was added and stirred at 4 °C for 6 h. After urea derivatives were filtered, the filtrate was poured into cold *n*-hexane (120 mL) and the precipitate was dried in a vacuum. The synthesized succinimido deoxycholate was obtained as white powder. ^{1}H NMR, 350 MHz, $CDCl_3$: 0.59 (s, 3H, 18-Me); 0.86 (s, 3H, 19-Me); 0.91 (d, 3H, 21-Me); 1.03−2.50 (25H, steroidal H); 2.81 (s, 4H, CH_2CH_2); 3.78 (m, 1H, 3β-H); 4.06 (br s, 1H, 12β-H). MALDI-MS: calcd MW, 489.6; found, 490.

Succinimido Bisdeoxycholyl-L-lysine. A suspension of L-lysine ethyl ester HCl (50 mg, 0.24 mmol) in anhydrous DMF (15 mL) containing TEA (140 μL, 1 mmol) was stirred at room temperature for 30 min, followed by addition of DOCA (190 mg, 0.48 mmol) and NHS (71 mg, 0.62 mmol). DCC (129 mg, 0.62 mmol), dissolved in anhydrous DMF (5 mL), was added dropwise to the mixture and then stirred at room temperature for 12 h. The mixture was filtered, and the filtrate was diluted with EtOAc (40 mL). The organic mixture was successively washed with 15 mL of 0.5 N HCl, distilled water, 0.5 N NaOH, and distilled water. The dried products were dissolved in EtOH (10 mL) containing saturated NaOH and allowed reaction followed by refluxing on a stream bath at 60 °C for 6 h. After filtration at room temperature, the filtrate was added dropwise to a cold acid solution (pH 3). The precipitates were filtered, washed, and dried in a vacuum. Finally, bisdeoxycholyl-L-lysine was obtained as white powder. The carboxylic group of bisdeoxycholyl-L-lysine was activated by NHS as described above to obtain succinimido bisdeoxycholyl-L-lysine. ^{1}H NMR, 350 MHz, $CDCl_3$−CD_3OD: 0.58 (s, 6H, 2 × 18-Me); 0.84 (s, 6H, 2 × 19-Me); 0.92 (d, 6H, 2 × 21-Me); 1.05−2.40 (56H, steroidal 50H, 3 × CH_2); 2.75 (s, 4H, CH_2CH_2); 2.98 (m, 2H, CH_2−NHCO); 3.61 (m, 2H, 2 × 3β-H); 4.16 (br s, 1H, 2 × 12β-H); 4.47 (s, 1H, C*H*-NHCO); 7.73 (br s, 1H, CH_2−N*H*CO); 7.96 (br s, 1H, CH−N*H*CO). MALDI-MS: calcd MW, 992.4; found, 991.

Preparation of Insulin Conjugates. *[N^{B29}−Deoxycholyl] Insulin*. This conjugate was synthesized according to a modified method used for the acylation of insulin with fatty acid (*9*). Briefly, Zn^{2+} insulin (100 mg, 17 μmol) was dissolved in DMF/H_2O (6 mL, 3/2 v/v, pH 10) at room temperature. Succinimido deoxycholate (12.6 mg, 25.8 μmol) was dissolved in anhydrous DMF (1 mL) and added to the insulin solution. Apparent pH was adjusted constantly by the addition of 1 N NaOH. After 30 min, the reaction was quenched by addition of distilled water, and the pH was adjusted to 2 with 1 N HCl. The reaction mixture was immediately filtered, dialyzed against 0.01% of NH_4HCO_3, and lyophilized. The lyophilized sample was further purified by preparative reversed-phase HPLC (Shimadzu, Tokyo, Japan) with a Shim-pack Prep-ODS column (20 mm × 250 mm). The mobile phase consisted of 0.1% TFA in distilled water (eluent A) and acetonitrile containing 0.1% TFA (eluent B). The mobile phase was run with a linear gradient from 35 to 45% eluent B for 15 min at a flow rate of 10 mL/min, and the UV absorbance of the eluent was monitored at 280 nm.

[N^{B29}−Bisdeoxycholyl-L-lysil] Insulin. Zn^{2+} insulin (100 mg, 17 μmol) and succinimido bisdeoxycholyl-L-lysine (25.7 mg, 25.8 μmol) were treated and purified as described above. The mobile phase of preparative reversed-phase HPLC was run with a linear gradient from 45 to 55% eluent B for 15 min at a flow rate of 10 mL/min.

Characterization. *MALDI-TOF Mass Spectroscopy*. Molecular weight was obtained from MALDI-TOF mass spectrometry using a Voyager Biospectrometry Workstation (PerSeptive Biosystem, Framingham, MA). Samples were prepared by mixing 2 μL of aliquot with 2 μL of the matrix solution, a saturated solution of α-CHCA in 50% of water/acetonitrile with 0.3% TFA. One microliter of the sample mixture was spotted into a well of the sample plate and dried by vacuum prior to mass spectrometry. Data for 2 ns pulses of the 337 nm nitrogen laser were averaged for each spectrum in a linear mode, and positive ion TOF detection was performed using an accelerating voltage of 25 kV.

Structural Verification. Insulin and the conjugates were incubated with trypsin (1 mg/mL) at 37 °C for 2 h. This treatment was expected to cleave the Arg−Gly bond in the β-chain of insulin. After incubation, the mixture was acidified with 0.1% TFA to quench the reaction and the mass of resulting proteolytic fragment was determined by using MALDI-TOF mass spectrometry.

Circular Dichroism. All samples were prepared in 10 mmol HCl at concentrations of 0.1 mmol and filtered through a 0.2 μm syringe filter. A Jasco J-720 spectropolarimeter (Tokyo, Japan) was used, and three to five scans were averaged before the final spectrum was acquired. The data (ellipticity in mdeg) was then transformed to mean residue ellipticity (θ_m) using the expression, $\theta_m = (\theta M)/(Cl)$, where θ is the observed ellipticity (mdeg), M is the mean residue molecular weight (g/mol), C is the protein concentration (g/mL), and l is the optical path length (cm).

Dynamic Light Scattering. The characteristics of self-aggregates of insulin analogues in PBS (pH 7.4) were investigated by dynamic light scattering at a wavelength of 488 nm with an Ar ion laser (Cyonics, San Jose, CA). The scattered light was measured at an angle of 90° and was collected with Multi-8 correlator (Malvern Instruments Ltd., U.K.). The hydrodynamic radius was analyzed by using the PCS software provided by the same company.

Competitive Insulin Receptor-Binding Assay. The biological activities of the insulin conjugates were determined using a competitive receptor-binding assay at steady state (*24*). HepG2 human hepatoma cell line (ATCC, Rockville, MD) were cultured at 37 °C in a 5% CO_2-humidified atmosphere in culture flasks with Dulbecco's modified Eagle's Medium (DMEM) supplemented with 10% fetal calf serum, 2 mM glutamine, 50 μg/mL streptomycin, and 50 U/mL penicillin. For binding stud-

ies, cells were seeded on 24-well plates at a density of 4×10^5 cells/well. Cells were used after 3 days when confluence was reached. Cells were washed twice with cell-binding media (DMEM containing 20 mM Hepes and 0.1% human albumin, pH 7.4), and competitive binding of unlabeled insulin and conjugates at steady state was measured by 2 h incubation at 4 °C with 1 mL binding media containing 25 pM [^{125}I]-insulin as the radio ligand in the presence of various concentrations of unlabeled insulin and the conjugates. Incubation was performed at 4 °C to inhibit endocytosis of receptor-bound insulin and the conjugates. After incubation, cells were washed twice with cold PBS, extracted with 1 mL of 1 N NaOH, and an aliquot of 100 μL was transferred into a glass tube for γ-radiation counting. All assays were made in triplicate. Nonspecific binding was determined in the presence of 10^{-6} M unlabeled insulin. The results were analyzed according to the four-parameter logistic model, and the affinity of the each conjugate was expressed relative to that of native insulin. The concentration giving half-maximal inhibition of receptor-bound tracer (IC_{50}) was also estimated.

In Vivo Hypoglycemic Effect. We followed the National Institutes of Health (NIH) guidelines for the care and use of laboratory animals (NIH publication 85-23 Rev. 1985). After an initial 3-day acclimation period, male Sprague−Dawley rats weighing from 230 to 250 g were fasted for 12 h before inducing diabetes mellitus. Diabetes was induced by a single intraperitoneal injection of STZ (in citrate buffer, pH 4.5) at 70 mg/kg. Five days after the STZ treatment, the test solutions (insulin, 0.33 IU/kg, 0.4 mL/kg and the equivalent amount of the conjugates) were administered intravenously into the tail vain. Blood samples for the analysis of blood glucose were taken from the tail veins and determined immediately on fresh samples by using a one touch blood glucose monitoring system (Glucocard II, Arkray, Kyoto, Japan).

Binding of Insulin Conjugates to Serum Albumin. Binding of insulin conjugates to serum albumin was assessed using size exclusion chromatography (7.8 mm $\times$ 300 mm Ultrahydrogel 250, Waters). Elution profiles were obtained for insulin and the conjugates (both 5 μmol) in the absence and presence of bovine serum albumin (BSA; 25 μmol; Sigma). The mobile phase was run with distilled water for 20 min at a flow rate of 0.5 mL/min, and the UV absorbance of the eluent was monitored at 280 nm.

Statistical Analysis. Data are expressed as mean $\pm$ SE. Student's t-test was performed, and a value of $p < 0.05$ was considered to be statistically significant.

RESULTS AND DISCUSSION

Synthesis and Characterization of Insulin Conjugates. The succinimidyl ester of two kinds of DOCA derivatives, succinimido deoxycholate and succinimido bisdeoxycholyl-L-lysine, were synthesized and conjugated to the ϵ-amino group of Lys^{B29} insulin. Since the pK_a's of two N-terminal α-amino groups of insulin are reported as 8.4 and 7.1 for Gly^{A1} and Phe^{B1}, respectively, and above 9.8 for ϵ-amino group of Lys^{B29}, insulin could be selectively labeled to Lys^{B29} in a base condition (*9*, *11*, *25*). Conjugates were prepared in a basic (pH 10) 60% DMF solution, where the amino groups of Lys^{B29} are most reactive.

The conjugate was obtained with above 99% purity (Figure 2) with above 45% product yield. The molecular weight of conjugates analyzed by MALDI-TOF mass spectroscopy (calculated molecular weight/measured molecular weight; for insulin, Ins−DOCA and Ins−bisDOCA were 5807/5805.2, 6181.6/6176.3 and 6679.4/6679.7, respectively) clearly indicated that both conjugates were purely monosubstituted. Native insulin and purified insulin conjugates were subjected to the trypsin digestion to determine the positional substitution of DOCA derivatives. It was expected that proteolytic fragment with a DOCA derivative attached to it should result in a shift in retention time compared to the respective unlabeled fragment. By peptide mapping using HPLC and MALDI-TOF, it was confirmed that both bile acid derivatives were labeled at Lys^{B29} of insulin (Table 1).

Retention time in HPLC profiles of insulin, Ins−DOCA, and Ins−bisDOCA was 22.87, 28.13, and 33.83 min, respectively. Calculated lipophilic index (lipophilic index = $\log((t_R - t_0)/t_0)$; t_0, retention time of solvent) of insulin,

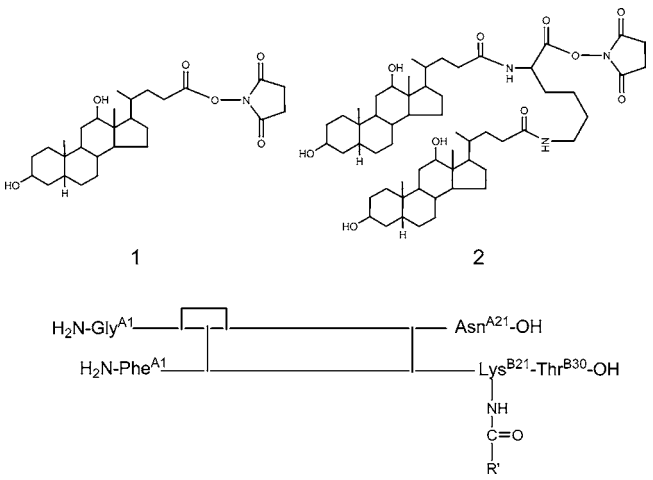

Figure 1. Chemical structures of succinimido deoxycholate **1** and succinimido bisdeoxycholyl-L-lysine **2** and insulin conjugates. R′ = deoxycholyl and bisdeoxycholyl-L-lysil, respectively.

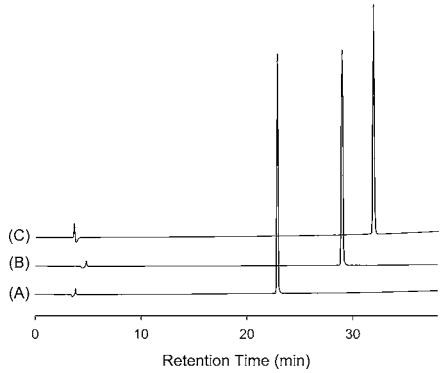

Figure 2. Reversed-phase HPLC chromatograms (detection at 280 nm): (A) human insulin, (B) [N^{B29}−deoxycholyl] insulin, and (C) [N^{B29}−bisdeoxycholyl-L-lysil] insulin.

Table 1. HPLC Retention Times (the Last Three Columns) and Molecular Mass of Insulin and Their Conjugate Fragments after Trypsin Protease Digestion of the HPLC-Purified Peak[a]

proteolytic fragment	insulin standard	Ins−DOCA	Ins−bisDOCA
A(1−21)−B(1−22)	22.0 min (4865.5/4864.5)	21.96 min (4865.5/4864.8)	21.96 min (4865.5/4865.0)
B(23−29)	19.39 min (859.0/863.4)		
B(23−30)		31.1 min (1334.7/1336.5)	40.95 min (1836.8/1837.9)

[a] Parentheses indicate mass; calculated molecular weight/measured molecular weight.

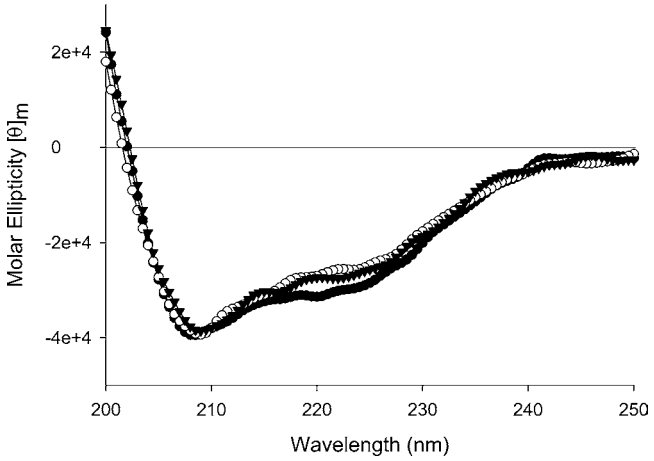

Figure 3. Far-UV−CD spectra of Zn^{2+} insulin (○), Ins−DOCA (●), and Ins−bisDOCA (▼). Solutions were prepared in 10 mmol HCl to a protein concentration of 0.1 mmol.

Ins−DOCA, and Ins−bisDOCA was 0.701, 0.806, and 0.898, respectively. The lipophilic indices of conjugates were higher than that of native insulin, indicating that these derivatives were more lipophilic compared to native insulin. In addition, the lipophilicity of the conjugates increased with increasing number of DOCA molecules that were chemically attached.

Circular dichroism (CD) spectroscopy has been applied to evaluate the conformational change of insulin conjugates (Figure 3). Because insulin conjugates showed higher self-aggregation behavior mainly due to the labeled bulky hydrophobic DOCA derivatives, insulin conjugate samples for CD analysis were prepared in acid condition to maintain a monomeric form and clear solution. The far-UV−CD band at 208 nm primarily arises from α-helix structure, and 223 nm is for component of the β-structure. The ratio between both bands ($[\phi]_{208}/[\phi]_{223}$) can be used to inform a qualitative measure of overall conformation structure of insulin and conjugates. The $[\phi]_{208}/[\phi]_{223}$ ratio value for insulin, Ins−DOCA, and Ins−bisDOCA was 1.32, 1.49, and 1.38, respectively. The spectral characteristics of the conjugates indicated that conjugation of DOCA derivatives to insulin does not alter the overall tertiary structure of native peptide.

Competitive Insulin Receptor-Binding Assay. Human hepatoma cell line HepG2 has been chosen as a model for the in vitro studies of insulin-receptor binding of insulin conjugates. The HepG2 cells maintain the function of differentiated liver cells, and the relative binding affinities for the insulin receptor in HepG2 cells are consistent with the relative metabolic potencies shown by fat cells (*26*, *27*). The competition curves of insulin or the conjugates to insulin receptors on intact HepG2 cells are shown in Figure 4. The absolute mean value of IC_{50} for the insulin receptor was 1.28×10^{-9} M for insulin, 3.37×10^{-9} M for Ins−DOCA, and 2.24×10^{-9} M for Ins−bisDOCA. Therefore, monosubstituted insulin conjugates still retained high binding affinity to the insulin receptor.

In Vivo Hypoglycemic Effect. The pharmacodynamic activity of insulin conjugates was evaluated in STZ-induced diabetic rats. Figure 5 illustrates the blood glucose level following intravenous injection of insulin and the conjugates. Reduction in glucose level for insulin, Ins−DOCA, and Ins−bisDOCA was 46.1 ± 7.9%, 41.1 ± 8.7%, 39.0 ± 11.1%, respectively. Compared to native insulin, insulin conjugates did not show any differences in glucose nadir. Although the glucose nadir was similar

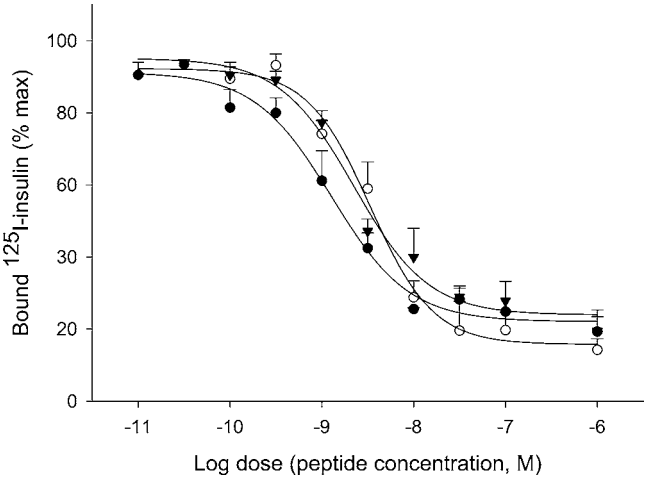

Figure 4. Inhibition of ^{125}I-insulin binding to HepG2 cells by native insulin and synthetic insulin conjugates. Insulin and conjugates were incubated with HepG2 cells as described under Experimental Procedures. Zn^{2+} insulin (●), Ins−DOCA (○), and Ins−bisDOCA (▼). Results are mean ± SE (n = 3).

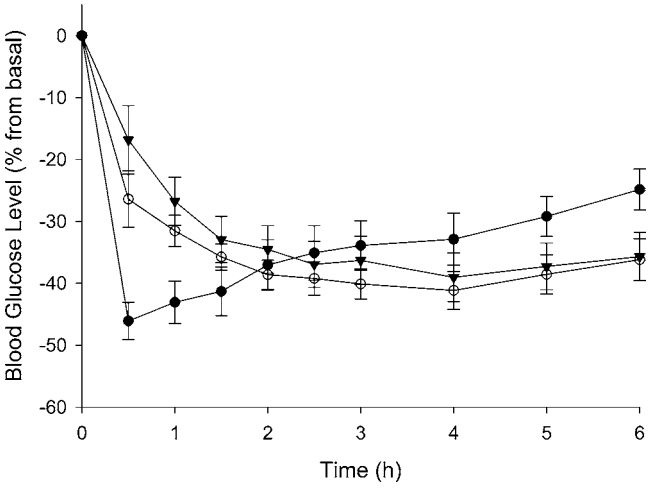

Figure 5. Blood glucose response following intravenous administration of insulin (0.33 IU/kg, ●, n = 5) and an equivalent amount of Ins−DOCA (○, n = 8) and Ins−bisDOCA (▼, n = 8) prepared in 10 mmol PBS. Samples were injected into the tail vein of STZ-induced diabetic rats. Results are mean ± SE.

to that of native insulin, the conjugates induced a slower rate of the blood glucose levels for Ins−DOCA and Ins−bisDOCA, were slowly reduced, and were maintained at low level for about 6 h, while the blood glucose level of native insulin was rapidly decreased after insulin injection and increased again. Therefore, the duration of the blood glucose lowering effect of the conjugates seemed to be sustained compared to native insulin.

To evaluate whether sustained biological action of the conjugates is responsible for existing serum protein (e.g., albumin) binding ability derived by conjugated DOCA, the binding affinity of insulin conjugates to serum albumin was evaluated using a size exclusion chromatography. Figure 6 illustrates the elution profiles of BSA, human insulin, and the conjugates in the absence (Figure 6A) and presence (Figure 6B) of BSA. It was hypothesized that, if insulin conjugates could bind to the BSA, the elution position of the conjugates would be identical to that of BSA. As shown in Figure 6, the elution position of insulin and the conjugates changed slightly; however, it was nearly unaffected by the presence of BSA. This result confirmed that the insulin conjugates did not bind

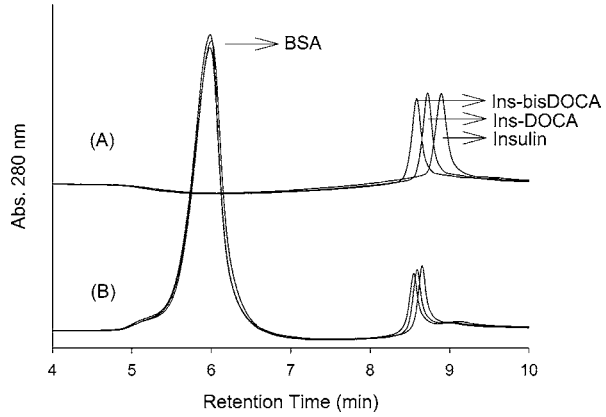

Figure 6. Size exclusion chromatography assessment of binding of insulin and insulin conjugates to bovine serum albumin (BSA). (A) Insulin and insulin conjugates (5 μmol), run separately, and (B) insulin and insulin conjugates (5 μmol) + BSA (25 μmol), run separately.

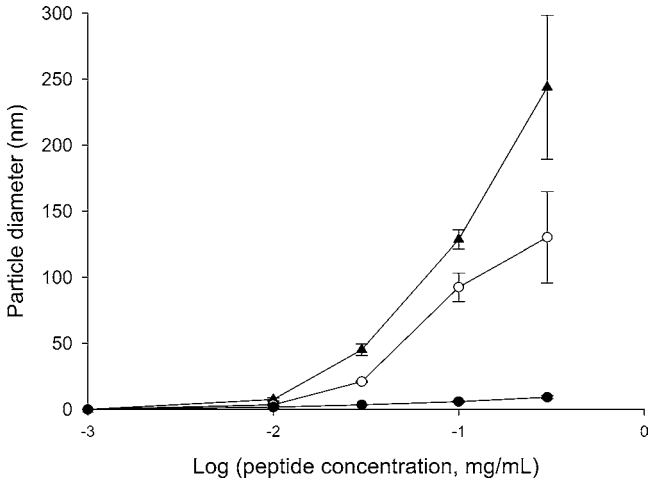

Figure 7. Size distribution profiles of insulin and conjugates at various concentrations determined by dynamic light scattering. Solutions were prepared in 10 mmol PBS at 25 °C for insulin (●), Ins−DOCA (○), and Ins−bisDOCA (▼).

to serum albumin, and the sustained action of the conjugate was not related to the binding affinity with albumin.

On the other hand, the sustained biological action of the insulin conjugates could be explained by the self-association profile of the conjugates. We introduced bulky hydrophobic region to the surface of the peptide. Labeled DOCA derivatives have high capacity of self-assembling (by combining an amphiphilic steroid nucleus with the reactivity of the side groups of DOCA), and these could increase hydrophobic aggregation behavior above a certain concentration. Consequently, different physical states of insulin in solution might impact its pharmacological profile. In view of the degree of aggregation of insulin conjugates in PBS, DLS measurement was selected to characterize self-association properties.

As illustrated in Figure 7, insulin conjugates showed higher aggregation behavior compared to insulin and possessed mean hydrodynamic diameter of 130 and 240 nm for Ins−DOCA and Ins−bisDOCA, while native insulin showed negligible size distribution. The tendency of aggregation was reversible and decreased by dilution. As the mole ratio of the conjugated DOCA molecules to insulin was increased, the aggregate size of insulin conjugates increased. Self-aggregated states correspond to unusual micelle-like structures that result biologically inactive. However, when the aggregate form slowly gets dissociated due to dilution in the blood stream, the conjugate's biological activity would gradually appear. Therefore, different glucodynamic profiles of insulin conjugates in vivo could be explained by the aggregation property of the insulin conjugates.

In conclusion, we have successfully conjugated two different kinds of DOCA derivatives to Lys^{B29} of insulin. The lipophilicity and self-aggregation behavior of insulin were enhanced by increasing the number of conjugated bile acid. The overall tertiary structure of insulin was preserved after conjugation, and it still retained high binding strength to the insulin receptor despite the fact that a bulky group of bile acid derivatives was attached to it. The insulin conjugates showed a gradual biological response, increased duration of action, and increased residence time compared to native insulin due to the high order of aggregation properties.

Beyond the development of orally active insulin formulation based on bile acid acylation techniques, our concern was to develop site-specific bile acid-conjugated insulin analogues which can maintain their biological activity while bearing the properties of bile acid. To this end, we have designed and prepared biologically active DOCA-conjugated insulin analogues. Furthermore, we have found that chemically bound bile acid could prolong the biological activity of native insulin in the physiological condition. The potential of our DOCA−insulin conjugates for oral delivery is under evaluation using in vivo models, and we anticipate that our new insulin conjugates would be applied to enhance the clinical efficiency of the present treatment for diabetic patients.

ACKNOWLEDGMENT

This study was supported by National Research Laboratory (NRL) Project from the Ministry of Science and Technology in Korea.

Supporting Information Available: The HPLC and mass spectrometry data of insulin and their conjugates after trypsin protease digestion. This material is available free of charge via the Internet at http://pubs.acs.org.

LITERATURE CITED

(1) Skyler, J. S. (1986) Lessons from studies of insulin pharmacokinetics. *Diabetes Care 9*, 666−668.
(2) Binder, C., Lauritzen, T., Faber, O., and Pramming, S. (1984) Insulin pharmacokinetics. *Diabetes Care 7*, 188−199.
(3) Owens, D. R. (2002) New horizons−alternative routes for insulin therapy. *Nat. Rev. Drug Discovery 1*, 529−540.
(4) Cefalu, W. T. (2004) Concept, strategies, and feasibility of noninvasive insulin delivery. *Diabetes Care 27*, 239−46.
(5) Gordberg, M., and Gomez-Orellana, I. (2003) Challenges for the oral delivery of macromolecules. *Nat. Rev. Drug Discovery 4*, 289−295.
(6) Wearley, L. L. (2001) Recent progress in protein and peptide delivery by noninvasive routes. *Crit. Rev. Ther. Drug Carrier Syst. 8*, 331−394.
(7) Banga, A. K., and Chien, Y. W. (1988) Systemic delivery of therapeutic peptides and proteins. *Int. J. Pharmacol. 48*, 15−50.
(8) Markussen, J., Havelund, S., Kurtzhals, P., Andersen, A. S., Halstrom, J., Hasselager, E., Larsen, U. D., Ribel, U., Schaffer, L., Vad, K., and Jonassen, I. (1996) Soluble, fatty acid acylated insulins bind to albumin and show protracted action in pigs. *Diabetologia 39*, 281−288.
(9) Myers, S. R., Yakubu-Madus, F. E., Johnson, W. T., Baker, J. E., Cusick, T. S., Williams, V. K., Tinsley, F. C., Kriauciunas, A., Manetta, J., and Chen, V. J. (1997) Acylation of human insulin with palmitic acid extends the time action of human insulin in diabetic dogs. *Diabetes 46*, 637−642.

(10) Mei, H., Yu, C., and Chan, K. K. (1999) NB1-C16−insulin: site-specific synthesis, purification, and biological activity. *Pharm. Res. 16*, 1680−1686.
(11) Hinds, K., Koh, J. J., Joss, L., Liu, F., Baudys, M., and Kim, S. W. (2000) Synthesis and characterization of poly(ethylene glycol)−insulin conjugates. *Bioconjugate Chem. 11*, 195−201.
(12) Gershonov, E., Shechter, Y., and Fridkin, M. (1999) New concept for long-acting insulin: spontaneous conversion of an inactive modified insulin to the active hormone in circulation: 9-fluorenylmethoxycarbonyl derivative of insulin. *Diabetes 48*, 1437−1442.
(13) Xia, C. Q., Wang, J., and Shen, W. C. (2000) Hypoglycemic effect of insulin−transferrin conjugate in streptozotocin-induced diabetic rats. *J. Pharmacol. Exp. Ther. 295*, 594−600.
(14) Jain, S., Hreczuk-Hirst, D. H., McCormack, B., Mital, M., Epenetos, A., Laing, P., and Gregoriadis, G. (2003) Polysialylated insulin: synthesis, characterization and biological activity in vivo. *Biochim. Biophys. Acta 1622*, 42−49.
(15) Clement, S., Dandona, P., Still, J. G., and Kosutic, G. (2004) Oral modified insulin (HIM2) in patients with type 1 diabetes mellitus: results from a phase I/II clinical trial. *Metabolism 53*, 54−58.
(16) Kipnes, M., Dandona, P., Tripathy, D., Still, J. G., and Kosutic, G. (2003) Control of postprandial plasma glucose by an oral insulin product (HIM2) in patients with type 2 diabetes. *Diabetes Care 26*, 421−426.
(17) Lee, Y., Nam, J. H., Shin, H. C., and Byun, Y. (2001) Conjugation of low-molecular-weight heparin and deoxycholic acid for the development of a new oral anticoagulant agent. *Circulation 104*, 3116−3120.
(18) Lee, Y., Kim, S. H., and Byun, Y. (2000) Oral delivery of new heparin derivatives in rats. *Pharm. Res. 17*, 1259−1264.
(19) Lee, S., Lee, J., Lee, D. Y., Kim, S. K., Lee, Y., and Byun Y. (2005) A new drug carrier, N^{α}-deoxycholyl-L-lysil-methylester, for enhancing insulin absorption in the intestine. *Diabetologia 48*, 405−411.
(20) Matern, S., and Gerok, W. (1979) Pathophysiology of the enterohepatic circulation of bile acids. *Rev. Physiol. Biochem. Pharmacol. 85*, 125−204.
(21) Danilson, H., and Sjovall, J. (1985) *Steroids and Bile Acids: New Comprehensive Biochemistry*, Vol. 12, Elsevier Publishing Inc.: Amsterdam, The Netherlands.
(22) Kramer, W., Wess, G., Neckermann, G., et al. (1994) Intestinal absorption of peptides by coupling to bile acids. *J. Biol. Chem. 269*, 10621−10627.
(23) Zhu, X. X., and Nichifor, M. (2002) Polymeric materials containing bile acids. *Acc. Chem. Res. 35*, 539−546.
(24) Drejer, K., Kruse, V., Larsen, U. D., Hougaard, P., Bjorn, S., and Gammeltoft, S. (1991) Receptor binding and tyrosine kinase activation by insulin analogs with extreme affinities studied in human hepatoma HepG2 cells. *Diabetes 40*, 1488−1495.
(25) Gao, J., Mrksich, M., Gomez, F. A., and Whitesides, G. M. (1995) Using capillary electrophoresis to follow the acetylation of the amino groups of insulin and to estimate their basicities. *Anal. Chem. 67*, 3093−3100.
(26) Podskalny, J. M., Takeda, S., Silverman, R. E., Tran, D., Carpentier, J. L., Orci, L., and Gorden, P. (1985) Insulin receptors and bioresponses in a human liver cell line HepG2. *Eur. J. Biochem. 150*, 401−407.
(27) Brange, J., Owens, D. R., Kang, S., and Volund, A. L. (1990) Monomeric insulins and their experimental and clinical implications. *Diabetes Care 13*, 923−954.

BC049871E

Detection of Lipopolysaccharide and Lipid A Employing a Spermine–Pyrene Conjugate

Guilford Jones II* and Hui Jiang

Department of Chemistry and Photonics Center, Boston University, Boston, Massachusetts 02215
Received October 18, 2004; Revised Manuscript Received March 3, 2005

An amphiphilic fluorescent spermine–pyrene conjugate (Sp–Py) is shown to interact with lipopolysaccharide (LPS) or lipid A in aqueous solution. This complexation was studied by UV/visible absorption and steady-state fluorescence spectroscopy. In the presence of LPS or lipid A, Sp–Py displayed self-aggregation, resulting in the appearance of chromophore dimer absorption and fluorescence at the expense of probe monomer features. The equivalent weight of LPS or lipid A and the binding constants for Sp–Py complexation were estimated. The change of the ratio of monomer to dimer emission with concentration of LPS or lipid A indicated that Sp–Py is a sensitive fluorescence probe for the endotoxins in aqueous media.

INTRODUCTION

Lipopolysaccharides (LPS) are the integral constituents of the outer membrane of Gram-negative bacteria. In nature, they are amphiphilic, consisting of hydrophilic polysaccharide and lipophilic lipid moieties. The polysaccharide region is composed of three separate domains: an inner core, an outer core, and an O-specific chain or O-polysaccharide (*1*–*3*). The lipid moiety, or lipid A, consists of diphosphorylated glucosamine disaccharide, carrying a number of higher fatty acid chains. Lipid A is the cause of most of the toxic effects associated with the endotoxins (*1*–*3*). The presence of covalently bound phosphate groups and acidic sugars in lipid A and in the core renders LPS a highly anionic polyelectrolyte (*3*). On the basis of the amphiphilic and anionic properties of LPS, David et al. proposed that cationic amphiphilic molecules represent potentially ideal ligands for complexation with LPS and studied the interactions of LPS with a number of classes of structures, including proteins (*4*), peptides (*5*), pharmaceuticals (*6*), and other synthetic polycationic amphiphiles (*7*). Among these compounds, lipopolyamines elicit special interest, since at physiological pH, polyamines (e.g. spermine and spermidine) exist as polyammonium ions and play many important biological roles (*8*). In fact, lipopolyamines have been used in gene transfer (*9*) and complexation with DNA (*10*, *11*), as well as LPS or lipid A (*7*, *12*).

There are few reports that deal with the interaction of dyes with LPS or lipid A. Such studies have the purpose of probing the properties of LPS molecules in solution or developing simple and sensitive detection methods. Most of the studies have focused on cationic cyanine dyes (*13*–*15*), because the absorption spectra for their complexes with LPS undergo shifts to shorter wavelengths. Pinacyanol chloride shows a similar shift upon LPS binding (from 600 to 495 nm) (*16*). Little work has been reported on the characterization of the interactions between dyes and LPS using fluorescence spectroscopy (*16*).

* To whom correspondence should be addressed. Tel.: +1 617 3538656. Fax: +1 617 3537271. E-mail: giljones@chem.bu.edu.

Chart 1. Structure of Sp–Py (Protonated Form)

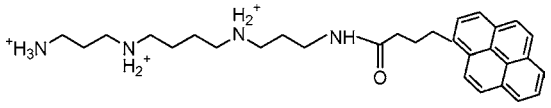

There are a number of biochemically based assays for LPS or lipid A in different environments, among which *Limulus* amebocyte lysate (LAL) and enzyme-linked immunosorbent assay (ELISA) are the most common and useful ones. However, these methods are generally time-consuming and labor-intensive. The absorption spectral blue shifts of certain compounds upon LPS binding (*13*–*17*) can provide a simple and fast alternative. Recently, fluorescent proteins have also been developed as biosensors for bacterial endotoxins (*18*, *19*).

Here we report the characterization of an amphiphilic spermine–pyrene conjugate (Sp–Py; Chart 1) for LPS or lipid A binding and detection studies. The cationic spermine moiety provides three positive charges near neutral pH, whereas the 1-pyrenebutyric acid amide (PBA) moiety serves as both a lipophilic pendant and chromophore. Sp–Py is shown to be a sensitive fluorescent indicator for LPS or lipid A in aqueous solution.

MATERIALS AND METHODS

Spermine, ethyl trifluoroacetate, di-*tert*-butyl dicarbonate (Boc), 1-pyrenebutyric acid *N*-hydroxysuccinimide ester (PBA-HSIE), trifluoroacetic acid (TFA), lipopolysaccharides (LPS) (rough strains) from *Salmonella minnesota* Re 595 (Re mutant), and lipid A (diphosphoryl form) from *Escherichia coli* F583 (Rd mutant) were all purchased from Sigma-Aldrich and used without further purification.

Synthesis and Characterization of Sp–Py. The synthesis of Sp–Py is shown in Scheme 1. The unsymmetrically protected spermine intermediate **1** was synthesized by following a reported procedure (*10*, *11*) and characterized by ^{1}H NMR and HRMS. 1-Pyrenebutyric acid *N*-hydroxysuccinimide ester (PBA-HSIE) (120 mg, 0.31 mmol) and **1** (120 mg, 0.24 mmol) were dissolved in

10.1021/bc0497517 CCC: $30.25 © 2005 American Chemical Society
Published on Web 04/26/2005

Scheme 1. Synthesis of Sp−Py

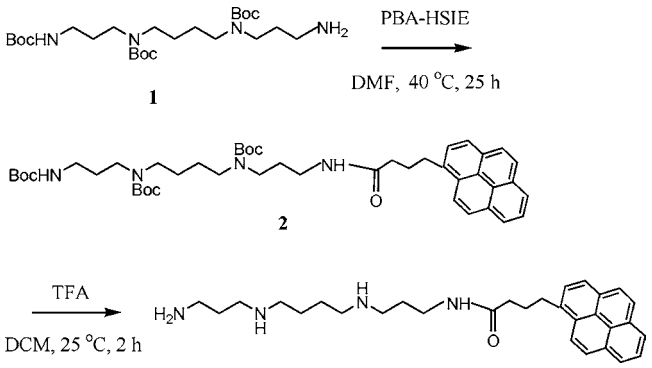

2 mL of distilled DMF, and the reaction mixture was stirred at 40 °C for 25 h. The crude product was purified by flash chromatography (SiO_2, petroleum ether−ethyl acetate gradient from 70:30 to 0:100), and a light yellow oil of **2** was obtained (60 mg, yield 33%). To **2** (60 mg, 0.078 mmol) in 2 mL of dichloromethane (DCM) was added 2 mL of trifluoroacetic acid (TFA), and the solution was stirred at room temperature for 2 h (*10*, *11*). A brown oily residue was obtained after the solution was concentrated and lyophilized. The crude product was purified by preparative RP-HPLC over a Vydac C_{18} column using a water (0.05% TFA)−acetonitrile (0.05% TFA) gradient to afford the final product Sp−Py (35 mg, yield 95%). Matrix-assisted laser desorption/ionization (MALDI) MS: found 473.961 ($M^+ + 1$); calcd for $C_{30}H_{41}N_4O$ 473.673 ($M^+ + 1$). ^{1}H NMR (400 MHz, DMSO-d_6): δ 1.58 (4H, s, CH_2); 1.74 (2H, t, CH_2); 1.86 (2H, t, CH_2); 2.03 (2H, t, CH_2); 2.25 (2H, t, CH_2); 2.87 (10H, s, CH_2); 3.14 (2H, d, CH_2); 3.32 (2H, CH_2, overlap with H_2O); 7.90−8.40 (9H, m, Ar *H*). ^{13}C NMR (300 MHz, D_2O): δ 17.74 (*C*H_2); 18.86 (*C*H_2); 20.65 (*C*H_2); 21.61 (*C*H_2); 27.32 (*C*H_2); 30.42 (*C*H_2); 30.79 (*C*H_2); 31.65 (*C*H_2); 39.64 (*C*H_2); 41.64 (*C*H_2); 41.99 (*C*H_2); 118.54 (Ar *C*); 119.34 (Ar *C*); 120.20 (Ar *C*); 121.60 (Ar *C*); 121.91 (Ar *C*); 122.46 (Ar *C*); 122.76 (Ar *C*); 123.01 (Ar *C*); 123.40 (Ar *C*); 124.80 (Ar *C*); 125.78 (Ar *C*); 126.32 (Ar *C*); 131.13 (Ar *C*); 172.44 (*C*═O).

Sp−Py and buffer stock solutions were prepared in Milli-Q water. LPS and lipid A stock solutions were prepared in 4:1 (v:v) THF/CH_3OH. Absorption spectra were recorded on a Beckman DU-640B spectrophotometer. Steady-state fluorescence emission and excitation spectra were obtained using a PTI (Photon Technology International, Inc.) fluorimeter equipped with Felix software.

RESULTS AND DISCUSSION

Complexation of Sp−Py with LPS or Lipid A. In phosphate buffer solution (pH 7.4), 5.0 μM Sp−Py shows only monomer absorption and fluorescence (Figure 1), indicating that conjugation with spermine does not appreciably affect the photophysical properties of the parent 1-pyrenebutyric acid (PBA). With the choice of a low concentration of Sp−Py (e.g. micromolar), and consistent with the electrostatic repulsion expected for the charged spermine moiety at pH 7.4, ground-state Sp−Py dimer or excimer formation is not observed. In the presence of 3.75 μg/mL of LPS or 5.00 μg/mL of lipid A, both absorption and emission spectra change. The absorption spectrum shows band broadening and a small shift to the red of peak absorptivity. The fluorescence spectrum shows both weaker monomer emission and a broad structureless band centered at about 474 nm, which is ascribed to pyrene excimer or dimer fluorescence

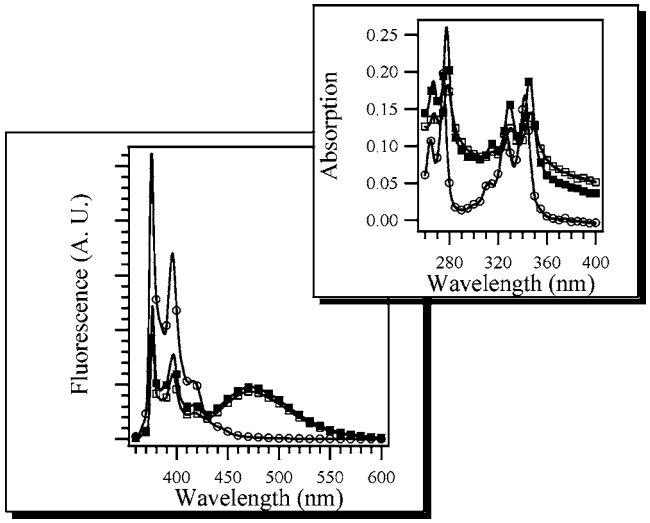

Figure 1. Absorption and emission spectra obtained for 5.0 μM Sp−Py in the absence (○) and presence of 3.75 μg/mL of LPS (■) or 5.00 μg/mL of lipid A (□) in 2 mM pH 7.4 phosphate buffer solution (excitation at 347 nm).

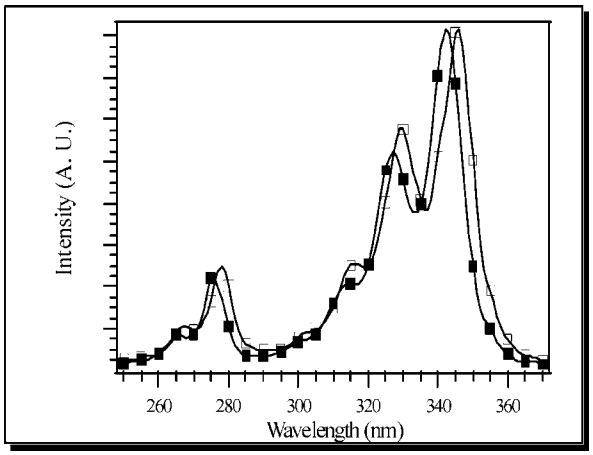

Figure 2. Uncorrected excitation spectra obtained for 5.0 μM Sp−Py in the presence of 3.75 μg/mL of LPS or 5.00 μg/mL of lipid A: (■) monitored at 376 nm; (□) monitored at 474 nm.

(*20*−*22*). However, the absorption and excitation (Figure 2) spectral change excludes the possibility of excimer formation via a bimolecular encounter of a ground-state Sp−Py and the excited state of the conjugate.

These spectral changes reflect the ground-state aggregation of pyrene chromophores in LPS or lipid A microdomains. Due to the binding of Sp−Py to LPS or lipid A, the electrostatic repulsion between spermine moieties is diminished and the local concentration is enhanced, so that two pyrene moieties (2 Sp−Py) can aggregate. This feature is clearly shown in the fluorescence spectra, which display increasing dimer emission at the expense of monomer emission. Since the intensity ratio of monomer to dimer emission (I_{376}/I_{474}, see below) shows a limiting value, it appears that not all bound Sp−Py can achieve chromophore stacking; thus, there is residual monomer fluorescence. As the absorption spectra indicate, there is some light scattering observed (turbidity is visible) for moderately concentrated solutions (e.g., 6 μg/mL). When higher concentrations of LPS or lipid A are utilized (e.g., 10 μg/mL), precipitation occurs (observable loss of chromophore).

If the Sp−Py monomer emission monitored at 376 nm is plotted against volume of added LPS or lipid A stock solution (2.5 mg/mL), an equivalent point is obtained

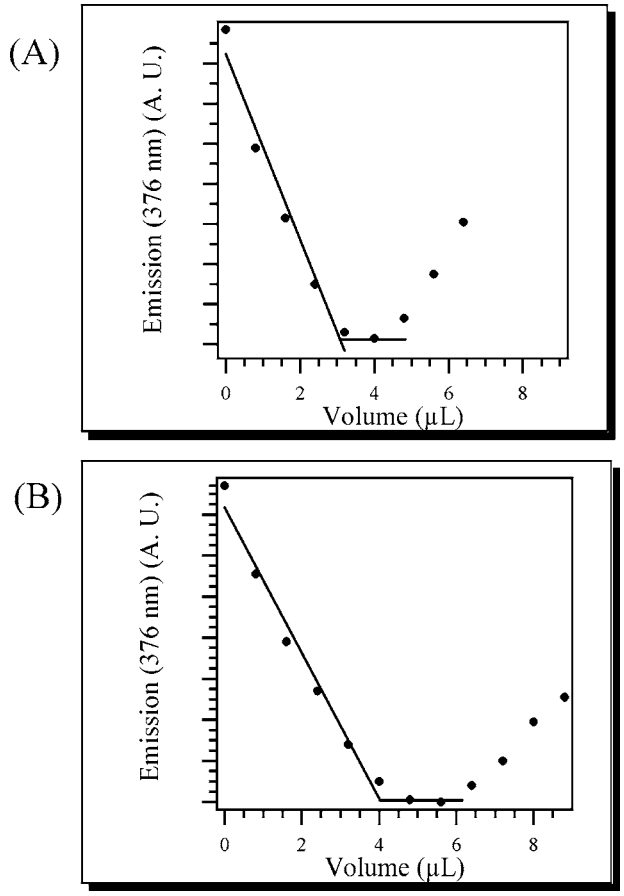

Figure 3. Fluorimetric titration of Sp−Py with LPS or lipid A (A): [Sp−Py] = 9.8 μM, [LPS] = 2.5 mg/mL; (B) [Sp−Py] = 7.4 μM, [lipid A] = 2.5 mg/mL.

(Figure 3). Before this point, the monomer fluorescence decreases progressively upon addition of an increasing amount of LPS or lipid A. Beyond the equivalent point, the monomer fluorescence is partially restored, consistent with the provision of an increased number of available interaction sites and a redistribution of the bound monomer vs dimer probe species. If the equivalent weight for LPS or lipid A is defined as the average mass of LPS or lipid A corresponding to 1 mol of bound Sp−Py, the equivalent weight can be determined using this equivalent point: i.e., the total mass of added LPS or lipid A divided by the moles of the chromophore conjugate. From the data in Figure 3, the equivalent weights are found to be about 400 Da for LPS and 700 Da for lipid A, respectively. Because lipid A is only one of the two moieties of LPS, LPS should have a higher molecular weight than lipid A. The opposite pattern of equivalent weights found for LPS and lipid A indicates that one LPS molecule binds more Sp−Py counterions than lipid A does. For comparison, using a similar treatment, the equivalent weight of *Klebsiella O3* LPS was found to be 830 Da for several dye−LPS complexes (*16*). The calculated equivalent weight of lipid A (700 Da) for Sp−Py is less than half of the approximate molecular weight provided by the supplier (about 1700−1800 Da), which indicates that two or more Sp−Py molecules can interact with one lipid A molecule. This finding is consistent with the formation of Sp−Py dimers in the presence of LPS or lipid A. One should note that the equivalent weight deduced by this spectroscopic titration method is phenomenological and does not provide specific information regarding binding site structure.

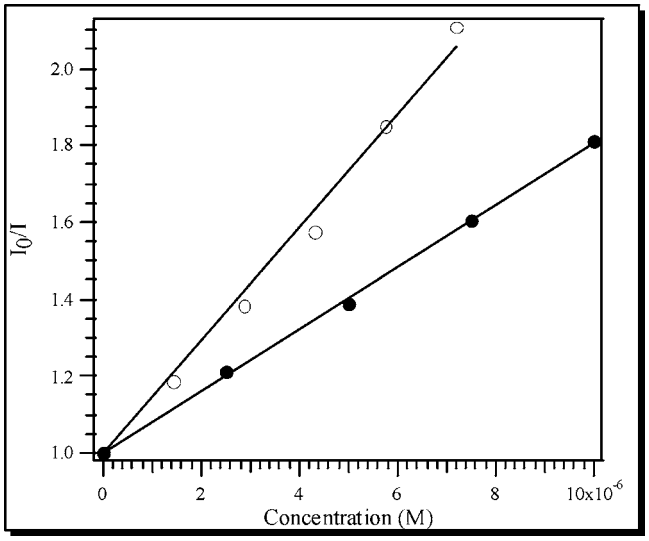

Figure 4. Stern−Volmer plot for the quenching of Sp−Py fluorescence (monitored at 376 nm) with LPS (●) or lipid A (○).

A similar dye aggregation phenomenon, on binding to polyelectrolytes, has been observed frequently and interpreted using cooperative binding theory (*23*, *24*). The elementary binding process can be expressed as

$$\mathrm{D} + \bullet\bullet\mathrm{U}\bullet\bullet \leftrightarrows \bullet\bullet\mathrm{O}\bullet\bullet \qquad (1)$$

where D stands for free dye monomers, U for unoccupied binding sites, and O for occupied binding sites. For the initial nucleation of binding, namely

$$\mathrm{D} + \mathrm{UUU} \leftrightarrows \mathrm{UDU} \qquad (2)$$

the intrinsic binding constant can be expressed as

$$K^{\ddagger} = [\mathrm{UDU}]/([\mathrm{D}][\mathrm{UUU}]) \qquad (2a)$$

For the binding of a second dye molecule in the nearby site, namely

$$\mathrm{D} + \mathrm{UDU} \leftrightarrows \mathrm{DDU} \qquad (3)$$

the cooperative binding constant can be expressed as

$$K = [\mathrm{DDU}]/([\mathrm{D}][\mathrm{UDU}]) \qquad (3a)$$

Since dye aggregation can promote the binding, K is generally larger than $K^{\ddagger}$. The ratio of the two binding constants reflects the degree of cooperativity (*23*). In the current case, since the absorption and emission spectral changes are induced by the Sp−Py dimer formation after binding to LPS or lipid A, the cooperative binding theory can be applied, provided that one Sp−Py is assumed to interact with one binding site (consequently, 1 equiv of LPS or lipid A corresponds to 1 mol of binding sites as well) and that two binding sites are close enough so that two pyrene moieties on two different Sp−Py molecules can interact with each other.

The cooperative binding constants associated with Sp−Py and LPS or lipid A interactions can be determined by Stern−Volmer analysis of the monomer fluorescence data (*25*). As shown in Figure 4, the ratio of the fluorescence intensity of the dye solution (I_0) to the intensity of the dye−target (LPS or lipid A) mixture (I) is plotted against the concentration (evaluated on the basis of the equivalent weight data above) of the added target which acts as the quencher (Q). Using the

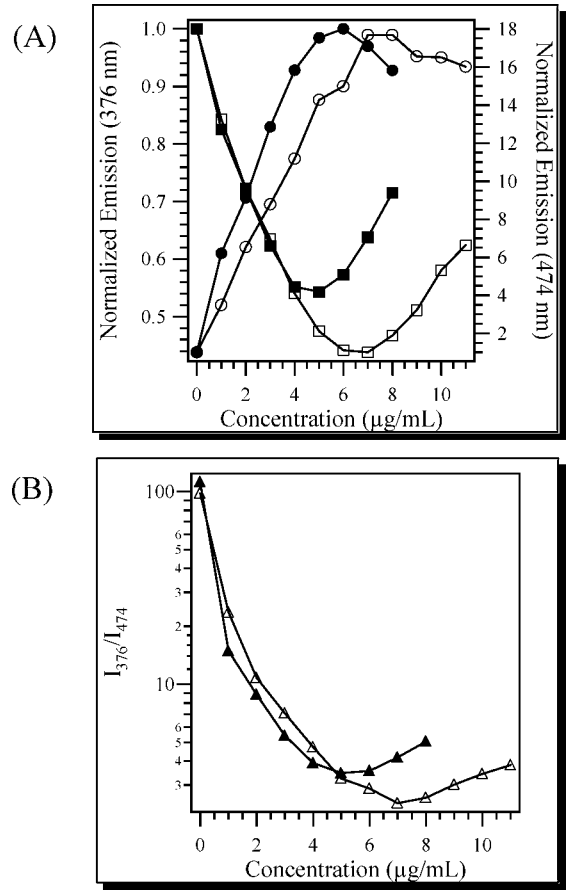

Figure 5. Fluorescence changes obtained for Sp−Py in the presence of LPS ([Sp−Py] = 9.8 μM) or lipid A ([Sp−Py] = 7.4 μM) in 2 mM pH 7.4 phosphate buffer: (A) Sp−Py monomer (■) and dimer (●) in the presence of LPS and Sp−Py monomer (□) and dimer (○) in the presence of lipid A; (B) Sp−Py monomer/dimer ratio in the presence of LPS (▲) and in the presence of lipid A (△).

Stern−Volmer equation

$$I_0/I = 1 + K_{sv}[Q] \quad (4)$$

the cooperative binding constants ($K = K_{sv}$, the slope of the best linear fit) are determined to be 8.1×10^4 M^{-1} for LPS and 1.5×10^5 M^{-1} for lipid A. These values are somewhat higher than the binding constants evaluated using a similar method for two other dye−LPS complexes (5.1×10^4 and 2.6×10^4 M^{-1} found for LPS complexes with acridine orange and safranin O, respectively) (*16*).

Application of Sp−Py to LPS or Lipid A Detection. The decrease of Sp−Py monomer emission or increase of the dimer emission in the presence of LPS or lipid A can be used for the detection of these endotoxins in aqueous solution. Figure 5A shows the normalized emissions of Sp−Py monitored for monomer (at 376 nm) and dimer (at 474 nm) versus LPS or lipid A concentration. For both LPS and lipid A, the normalized monomer emission decreases with increased target concentration until the equivalent point is reached. The dimer emission shows the opposite trend. About 0.5 μg/mL of target can induce a 10% change in monomer emission. If the ratio of monomer to dimer emission (I_{376}/I_{474}) is plotted against the target concentration, higher sensitivity can be achieved. As shown in Figure 5B, both LPS and lipid A induce a similar change. However, 0.5 μg/mL of target can induce a 50% alteration in the emission ratio. In particular, the change is dramatic with the initial addition of analyte. This method can provide a sensitive ratiometric fluorescence detection assay for LPS or lipid A in aqueous solution, with a limit of detection estimated to be in the 10−100 ng/mL (ppb) range.

CONCLUSION

The amphiphilic fluorescent spermine-pyrene conjugate (Sp−Py), in the presence of LPS or lipid A in aqueous solution, shows chromophore ground-state aggregation, resulting in dimer absorption and fluorescence emission at the expense of monomer spectral features. From fluorimetric titration data, the equivalent weights for LPS and lipid A were determined to be 400 and 700 Da, respectively. Binding constants were estimated by Stern−Volmer analysis of the monomer fluorescence quenching. For detection purposes, either the pyrene monomer fluorescence decrease or the dimer fluorescence increase can be used. The change of the ratio of the monomer to dimer emission was shown to be an especially sensitive parameter, with a limit of detection estimated in the range 10−100 ng/mL (ppb).

ACKNOWLEDGMENT

We acknowledge with thanks support of this work by the U.S. Army Research Laboratory.

LITERATURE CITED

(1) Raetz, C. R. (1990) Biochemistry of endotoxins. *Annu. Rev. Biochem. 59*, 129−170.

(2) Nikaido, H., and Nakase, T. (1979) The outer membrane of Gram-negative bacteria. *Adv. Microb. Physiol. 20*, 163−250.

(3) Williams, K. L. (2001) *Endotoxins: Pyrogens, LAL Testing, and Depyrogenation*, 2nd ed.; Marcel Dekker: New York.

(4) David, S. A., Balaram, P., and Mathan, V. I. (1995) Characterization of the interaction of lipid A and lipopolysaccharide with human serum albumin: Implications for an endotoxin carrier function for albumin. *J. Endotoxin Res. 2*, 99−106.

(5) David, S. A., Balaram, P., and Mathan, V. I. (1993) Interaction of basic amphiphilic polypeptide antimicrobials, gramicidin S, tyrocidine and efrapeptin, with endotoxic lipid A. *Med. Microbiol. Lett. 2*, 42−47.

(6) David, S. A., Bechtel, B., Annaiah, C., Mathan, V. I., and Balaram, P. (1994) Interaction of cationic amphiphilic drugs with lipid A: implications for development of endotoxin antagonists. *Biochim. Biophys. Acta 1212*, 167−175.

(7) David, S. A., Silverstein, R., Amura, C. R., Kielian, T., and Morrison, D. C. (1999) Lipopolyamines: novel antiendotoxin compounds that reduce mortality in experimental sepsis caused by gram-negative bacteria. *Antimicrob. Agents Chemother. 43*, 912−919.

(8) Heby, O. (1986) Putrescine, spermidine, and spermine. *News Physiol. Sci. 1*, 12−15.

(9) Behr, J. P., Demeneix, B., Loeffler, J. P., and Perez-Mutul, J. (1989) Efficient gene transfer into mammalian primary endocrine cells with lipopolyamine-coated DNA. *Proc. Natl. Acad. Sci. U.S.A. 86*, 6982−6986.

(10) Geall, A. J., and Blagbrough, I. S. (1998) Homologation of polyamines in the synthesis of lipo-spermine conjugates and related lipoplexes. *Tetrahedron Lett. 39*, 443−446.

(11) Geall, A. J., and Blagbrough, I. S. (2000) Homologation of polyamines in the synthesis of lipo-spermine conjugates and related lipoplexes. *Tetrahedron 56*, 2449−2460.

(12) Blagbrough, I. S., Geall, A. J., and David, S. A. (2000) Lipopolyamines incorporating the tetraamine spermine, bound to an alkyl chain, sequester bacterial lipopolysaccharide. *Bioorg. Med. Chem. Lett. 10*, 1959−1962.

(13) Janda, J., and Work, E. (1971) Colorimetric estimation of lipopolysaccharides. *FEBS Lett. 16*, 343−345.

(14) Zey, P., and Jackson, S. (1973) Conditions that affect the colorimetric analysis of lipopolysaccharide from *Escherichia coli* and *Treponema palladium*. *Appl. Microbiol. 26*, 129−133.
(15) Ogawa, Y., and Kanoh, S. (1984) Enhancement of endotoxicity and reactivity with carbocyanine dye by sonication of lipopolysaccharide. *Microbiol. Immunol. 28*, 1313−1323.
(16) Panda, A. K., and Chakraborty, A. K. (1997) Studies on the interaction of bacterial lipopolysaccharide with cationic dyes by absorbance and fluorescence spectroscopy. *J. Photochem. Photobiol. A 111*, 157−162.
(17) Rangin, M., and Basu, A. (2004) Lipopolysaccharide identification with functionalized polydiacetylene liposome sensors. *J. Am. Chem. Soc. 126*, 5038−5039.
(18) Goh, Y. Y., Frecer, V., Ho, B., and Ding, J. L. (2002) Rational design of green fluorescent protein mutants as biosensor for bacterial endotoxin. *Protein Eng. 15*, 493−502.
(19) Goh, Y. Y., Ho, B., and Ding, J. L. (2002) A novel fluorescent protein-based biosensor for gram-negative bacteria. *Appl. Environ. Microbiol. 68*, 6343−6352.
(20) Jones, G., II, and Vullev, V. I. (2001) Ground- and excited-state aggregation properties of a pyrene derivative in aqueous media. *J. Phys. Chem. A 105*, 6402−6406.
(21) Vullev, V. I., Jiang, H., and Jones, G., II. Excimer Sensing. *Advanced Concepts in Fluorescence Sensing. Part B: Macromolecular Sensing*. (Geddes, C. D., and Lakowicz, J. R., Eds.) Kluwer Academic/Plenum Press: New York, in press.
(22) Jones, G., II, and Vullev, V. I. (2001) Contribution of a pyrene fluorescence probe to the aggregation propensity of polypeptides. *Org. Lett. 3*, 2457−2460.
(23) Schwarz, G. (1970) Cooperative binding to linear biopolymers. 1. Fundamental static and dynamic properties. *Eur. J. Biochem. 12*, 442−453.
(24) Bradley, D. F., and Wolf, M. K. (1959) Aggregation of dues bound to polyanions. *Proc. Natl. Acad. Sci. U.S.A. 45*, 944−952.
(25) Lakowicz, J. R. (1999) *Principles of Fluorescence Spectroscopy*; Kluwer Academic/Plenum Publishers: New York.

BC0497517

Polycationic Block Copolymers of Poly(ethylene oxide) and Poly(propylene oxide) for Cell Transfection

Lev Bromberg,[†] Smeet Deshmukh,[†] Marina Temchenko,[†] Ludmila Iourtchenko,[‡] Valery Alakhov,[‡] Carmen Alvarez-Lorenzo,[§] Rafael Barreiro-Iglesias,[§] Angel Concheiro,[§] and T. Alan Hatton*,[†]

Department of Chemical Engineering, Massachusetts Institute of Technology, Cambridge, Massachusetts 02139, Supratek Pharma, Inc., 531 Boulevard des Prairies, Building 18, Laval, Québec, Canada H7V 1B7, and Departamento de Farmacia y Tecnología Farmacéutica, Facultad de Farmacia, Universidad de Santiago de Compostela, 15872 Santiago de Compostela, Spain. Received October 19, 2004; Revised Manuscript Received March 18, 2005

A facile, one-step synthesis of cationic block copolymers of poly(2-*N*-(dimethylaminoethyl) methacrylate) (pDMAEMA) and copolymers of poly(propylene oxide) (PPO) and poly(ethylene oxide) (PEO) has been developed. The PEO−PPO−PEO−pDMAEMA (L92−pDMAEMA) and PEO−pDMAEMA copolymers were obtained via free radical polymerization of DMAEMA initiated by polyether radicals generated by cerium(IV). Over 95% of the copolymer fraction was of molecular mass ranging from 6.9 to 7.1 kDa in size, indicating the prevalence of the polyether-monoradical initiation mechanism. The L92−pDMAEMA copolymers possess parent surfactant-like surface activity. In contrast, the PEO−pDMAEMA copolymers lack significant surface activity. Both copolymers can complex with DNA. Hydrodynamic radii of the complexes of the L92−pDMAEMA and PEO−pDMAEMA with plasmid DNA ranged in size from 60 to 400 nm, depending on the copolymer/DNA ratio. Addition of Pluronic P123 to the L92−pDMAEMA complexes with DNA masked charges and decreased the tendency of the complex to aggregate, even at stoichiometric polycation/DNA ratios. The transfection efficiency of the L92−pDMAEMA copolymer was by far greater than that of the PEO−pDMAEMA copolymer. An extra added Pluronic P123 further increased the transfecton efficacy of L92−pDMAEMA, but did not affect that of PEO−pDMAEMA.

INTRODUCTION

The development of gene therapy relies on designing optimal systems for nucleic acid transfer and expression, cationic polymers being a promising alternative to viral vectors (*1*). Because the latter are toxic and immunogenic, nonviral strategies toward gene transfection are becoming more and more attractive. A variety of synthetic, polycationic polymers have become available; they demonstrate adequate safety profiles and can complex large plasmids, forming polymer−DNA complexes (polyplexes). Some of the polyplexes have superior transfection efficiency and serum sensitivity compared to the lipid−DNA complexes (lipoplexes) (*2*−*4*). These considerations make polycations a compelling target for future exploration in nonviral gene delivery (*5*). Polycations bind to nucleic acids due to the formation of cooperative systems of salt bonds between the cationic groups of the polycation and phosphate groups of the DNA. Great efforts have been undertaken to improve the efficiency of the polycations, but, as yet, satisfactorily effective polymer systems have still to be achieved. One of the promising strategies toward creating more effective polycationic systems that complex DNA forming polyplexes (*6*) involves attachment of hydrophilic polymers such as poly(ethylene oxide) (PEO) (*7*, *8*). The modification of the polyplexes with PEO shields positive surface charges and creates a steric barrier against self-aggregation and unfavorable interactions with albumin, complement factors, or cellular components in the bloodstream. The modification of such polyplexes may reduce the potential of nonspecific interactions, such as opsonization or deposition due to cationic surface charges. Block copolymers of cationic polymers and PEO form complexes with DNA that are more acceptable to systemic administration than complexes of the unmodified polycations and DNA (*9*, *10*). Furthermore, copolymers of PEO and poly(propylene oxide) (PPO) such as PEO−PPO−PEO (tradename Pluronic), when bonded to polycations, provide additional advantages to the resulting copolymers from the efficiency standpoint (*11*−*15*).

The Pluronic−polycation copolymers and oligonucleotides spontaneously associate into polyion complex micelles with a hydrophobic core formed by neutralized polyions and a hydrophilic shell formed by PEO. Such complexes are sufficiently stable in solution despite complete neutralization of charge and exhibit elevated levels of transgene expression (*12*). Thus far, the synthetic route toward the polycation−Pluronic copolymers involved chemical activation of the hydroxyl termini of Pluronic followed by conjugation with the primary amino groups of the polycation and separation of the conjugated copolymer from the parent Pluronic (*7*). Such a synthetic route involves several steps, each followed by purification of products, and results in fairly polydisperse copolymers. In the present work, we aimed at development of a more straightforward synthetic route that would enable one-step synthesis of a wide range of polyether−polycation copolymers, wherein the polycation may be optionally

* Author to whom correspondence should be addressed [telephone (617) 253-4588; e-mail tahatton@mit.edu].
[†] Massachusetts Institute of Technology.
[‡] Supratek Pharma, Inc.
[§] Universidad de Santiago de Compostela.

10.1021/bc049749f CCC: $30.25 © 2005 American Chemical Society
Published on Web 04/26/2005

devoid of the primary amino groups. The synthesis we opted to use involved the generation of polyether radicals that act as an initiator for the free radical polymerization of a cationic monomer, 2-(dimethylamino)ethyl methacrylate (DMAEMA). The DMAEMA possesses tertiary amino groups, and its polymers are known for their capacity to complex and transfect DNA (*16*). An analogous "oxyanionic polymerization" involving the use of potassium alcoholates such as monohydroxy-capped poly(alkylene oxide)s in the role of macroinitiators for the polymerization of DMAEMA resulting in PEO−pDMAEMA copolymers has been reported (*17*). Such a polymerization proceeds in rigorously dry THF, which is oftentimes an experimental hurdle. Instead, in the synthetic route explored herein we used free radical polymerization of DMAEMA initiated by the Pluronic radicals generated by the redox reaction of the Pluronic with cerium(IV) in water. The major thrust of the present work has been the development of a facile, one-step synthetic route resulting in desired block copolymers of well-defined molecular weight. This synthetic route is applicable to a variety of vinyl monomers as well as hydroxyl-terminated polyethers. Herein, a relatively hydrophobic Pluronic L92 (PPO content of 80%) was chosen as a representative example of the Pluronic family of the surface-active copolymers because of its high modification activity toward cell membranes. The resulting L92−pDMAEMA copolymers were demonstrated to possess a good transfection capability for plasmid DNA when compared with a routinely used Lipofectamine and were much more active compared to their PEO−pDMAEMA counterparts.

EXPERIMENTAL PROCEDURES

Materials. Pluronic L92 (average composition, EO_8-$PO_{52}EO_8$) and P123 (average composition, $EO_{19}PO_{69}EO_{19}$) were received from BASF Corp. (Mount Olive, NJ) and used without further treatment. 2-(Dimethylamino)ethyl methacrylate (DMAEMA, 98%), ammonium cerium(IV) nitrate (98.5%), 2,2′-azobisisobutyronitrile (AIBN, 98%), nitric acid (70%), poly(ethylene glycol) (average M_n = 3350) were all obtained from Sigma-Aldrich Co. (St. Louis, MO) and were used without further purification. Plasmid DNA encoding β-galactosidase (pCMV-β) was obtained from Clontech BD Biosciences (Palo Alto, CA), whereas Lipofectamine 2000 reagent was purchased from Invitrogen (Carlsbad, CA). Deuterated solvents were obtained from Cambridge Isotope Laboratories (Andover, MA), and all other chemicals were received from commercial sources and were of the highest purity available.

Methods. *Polymer Synthesis.* The polymerization with the cerium ion redox system and DMAEMA monomer was carried out in a three-neck flask equipped with a stirrer, a reflux condenser, and a nitrogen inlet/outlet. In a typical polymerization procedure, DMAEMA (5.0 g), Pluronic L92, or poly(ethylene glycol) (5.0 g) and 1 mL of 70% nitric acid were dissolved in 70 mL of deionized water, and the solution was deoxygenated by nitrogen flow and thermostated at 55 °C with stirring for 1 h. The reaction was started by injecting 3.278 g (6 mmol) of cerium(IV) ammonium nitrate dissolved in 3 mL of 0.5 M HNO_3. The reaction was allowed to proceed for 4 h under nitrogen flow and stirring. The resulting polymer was repeatedly precipitated by the addition of 1 M NaOH, redissolved in 0.01 M HCl, and dialyzed against a large excess of 0.01 M HCl solution in deionized water using dialysis tubing (Spectrum Laboratories, Inc., molecular weight cutoff, 3500). The overall yields of the polyether copolymer were 91 and 94% in the cases of L92−pDMAEMA and PEO−pDMAEMA, respectively. To prove the suggested mechanism of polymerization via formation of polyether radicals due to the presence of cerium(IV), a control experiment without Ce^{4+} was conducted. Namely, polymerization in a mixture of DMAEMA and Pluronic L92 identical to the described above was induced by the addition of 1 mmol of AIBN in acetone. A viscous solution was obtained after the polymerization conducted at 55 °C for 8 h. The solution was precipitated using 1 M NaOH, and the precipitate and the supernatant were separated. The precipitated polymer was dissolved in 0.1 M HCl, and the procedure of precipitation was repeated twice. The resulting polymer was analyzed by ^{1}H NMR, which found no presence of the polyether. This proved that to obtain the L92−pDMAEMA copolymer the Pluronic radicals must be generated. It was also observed that on the addition of Ce^{4+} solution to DMAEMA in the same range of concentrations used in the above polymerization, no polymer was formed within 8 h at 55 °C, indicating the absence of homopolymerization.

Copolymer Characterization. Proton NMR spectra of polymer solutions in D_2O/DCl were acquired on a Bruker AMX400 spectrometer. To obtain the apparent pK_a of the polymers, a titration was performed at 25 ± 1 °C using a 736 GP Titrino potentiometric titration system (Metrohm Ltd., Herisau, Switzerland). Titration of the copolymers in their acidic form was carried out in a degassed 75 mM NaCl solution with 0.1 M NaOH as a titrant, at 0.5 wt % polymer concentration. The titration was carried out slowly for several hours to allow for proper equilibration. The apparent dissociation constant (pK_a) and the degree of ionization (α) were calculated from experimental potentiometric titration data using the Henderson−Hasselbach expression (*18*). Surface tension measurements of the copolymer solutions at certain pH values were accomplished using a Kruss USA model K11 tensiometer applying the Wilhelmy plate method. In the surface tension measurements, the L92−pDMAEMA copolymers were additionally purified by repeated precipitation in 1 M NaOH followed by the removal and drying of the polymer and redissolution in deionized water. No traces of unattached Pluronic copolymers in these species was detected by HPLC. Molecular weight (MW) determination was accomplished using size exclusion chromatography. Polymer samples were precipitated in 1 M NaOH, dried, and redissolved in dimethylformamide (DMF) at 1 mg/mL. The MW of the copolymers was measured in DMF using a Hewlett-Packard series 1100 HPLC system with a refractive index detector and two PLgel Mixed E columns (Polymer Laboratories, Inc., Amherst, MA). Run parameters were as follows: injection volume, 100 μL; flow rate, 1 mL/min; temperature, 40 °C. Calibration curves were developed using a PEG calibration kit (Polymer Laboratories, Inc.).

Preparation and Characterization of Copolymer/Plasmid DNA Complexes. The DNA/copolymer complexes were prepared by adding 3.1 μL of 3.2 mg/mL pCMV-βgal plasmid DNA solution in water to 997 μL of an appropriate copolymer solution in 10 mM *N*-2-hydroxyethylpiperazine-*N*′-2-ethanesulfonic acid (HEPES) buffer (pH 7.0) followed by vortexing and equilibration of a sample overnight. Series of samples containing L92−pDMAEMA and PEO−pDMAEMA copolymers, as well as L92−pDMAEMA+Pluronic P123 (1:5 weight ratio), were thus prepared. The resulting DNA/copolymer solution was filtered using a 0.2 μm membrane filter (Pall Gelman Labs). The ratio of the copolymer to DNA in the complex (N/P) was expressed via the ratio of equivalents of DMAEMA units to the number of nucleotides in DNA.

The nucleotide average molecular mass was assumed to be 324 g/mol (*19*).

Measurements of the potential at the surface of shear (ζ-potential) and dynamic light scattering experiments of the copolymer as well as DNA/copolymer complex solutions were performed at 25 ± 0.1 °C using a ZetaPals zeta potential analyzer and a BI-200SM goniometer, a BI-9000 correlator, and a Spectra Physics He−Ne model 127 laser operating at a scattering angle of 90° and a wavelength of incident light of 633 nm at a power of 50 mW. All of the above instruments were from Brookhaven Instruments Co. Measurements were performed at least in triplicate, and intensity-average hydrodynamic diameter (D_h) and Smoluchowski ζ-potential values calculated by the built-in software are reported herein.

Cell Transfection. Chinese hamster ovary cells (CHO-K1) obtained from the American Type Culture Collection (Manassas, VA) were grown in F-12 nutrient mixture supplemented by 10% FCS (both from Invitrogen). The cells were seeded in a 24-well plate (Nunc, Roskilde, Denmark) 1 day prior to the transfection at a density of 1×10^5 cells/cm^2 in 500 μL of the growth medium. The cells were 90−95% confluent at the time of transfection. The cells were then transfected with a pCMV-β for the β-galactosidase expression following the manufacturer's protocol developed for Lipofectamine 2000. Lipofectamine 2000 is a liposome-containing formulation combining two lipids such as cationic (2,3-dioleyloxy-*N*-[2(sperminecarboxamide)ethyl]-*N*,*N*-dimethyl-1-propanaminium trifluoroacetate) (DOSPA) and neutral dioleyl phosphatidylethanolamine (DOPE). Lipofectamine is frequently used as an industry standard to compare transfection efficiencies of synthetic vectors (*20*). The L92−pDMAEMA and PEO−pDMAEMA were used at different copolymer/DNA weight ratios ranging from 0.6 to 35. The complex of L92−pDMAEMA with Pluronic P123 was also used as a transfection reagent at a ratio of copolymer to P123 of 1:5, 1:50, or 1:500 (w/w). This complex was prepared by mixing (1:1 dilution, v/v) L92−pDMAEMA, 0.1% aqueous solution (pH 7.5), with an aqueous solution of P123, pH 7.5. Dilution of copolymers and copolymer−Pluronic complexes was performed in microcentrifuge tubes of a serum-free medium (50 μL), so that concentration of the transfection reagents ranged from 10 μg/mL to 1 mg/mL. Plasmid DNA solution was also diluted in serum-free medium to a concentration of 16 μg/mL. After a 5-min incubation at room temperature, the DNA solution (50 μl) was added to each tube containing solution of transfection reagents and mixed gently, and after 20 min of equilibration at room temperature, 100 μL of either Lipofectamine/DNA, polycation/DNA, or polycation and P123/DNA complexes was added to each well containing cells with 500 μL of fresh growth medium supplemented with the appropriate amount of FCS. The cells were exposed to the transfection mixture for 3 h. The transfection medium was then removed and replaced with F12 supplemented with 5% FCS. Cells were incubated at 37 °C in a CO_2 incubator (Revco Technologies, Asheville, NC) for 24−72 h.

The effects of the L92−pDMAEMA and Pluronic P123 on the CHO cell growth were further examined by the cell viability tests. The 50% confluent CHO cells were incubated with polymer at final concentrations ranging from 1 μg/mL to 10 mg/mL. After 3 days of incubation at 37 °C, the number of viable cells was measured to determine the concentration of L92−pDMAEMA or Pluronic P123 leading to the death of 50% of the cell population (LD_{50}). The LD_{50} determined for the L92−pDMAEMA was 50 μg/mL, whereas the Pluronic P123 did not show any toxic effects on the CHO cells even at concentrations up to 10 mg/mL. All of the experiments described herein were conducted at polycation concentrations below the LD_{50}.

The β-galactosidase Enzyme Assay System kit (Promega, Madison, WI) combined with a BCA Protein Assay Reagent kit (Bio-Rad Laboratories, Inc., Richmond, CA) was used for assaying β-galactosidase activity in lysates prepared from the transfected cells following the assay protocol from the manufacturer. In brief, after 24−72 h of transfection, the cells were rinsed twice with PBS and lysed for 15 min at room temperature by a lysis buffer, containing 25 mM Tris (pH 7.8), 2 mM CDTA, 2 mM dithiothreitol, 10% glycerol, and 1% Triton X-100. The resulting cell lysate was scraped from all areas of the plate surface, transferred to a microcentrifuge tube, vortexed, and centrifuged at top speed (20000*g*) for 2 min at 4 °C. The cell lysate (150 μL) was then mixed with 150 μL of Assay 2X buffer, containing 200 mM sodium phosphate (pH 7.3), 2 mM $MgCl_2$, 100 mM β-mercaptoethanol, and 1.33 mg/mL of *o*-nitrophenyl-β-D-galactopyranoside (ONPG) substrate. β-Galactosidase converts the colorless ONPG substrate into galactose and the chromophore *o*-nitrophenol, yielding a bright yellow solution. The mixtures were incubated at 37 °C until a yellow color developed (within ~1 h), and then the reaction was stopped by the addition of 1 M sodium carbonate solution (500 μL). Electronic absorbance was read at 420 nm in a quartz spectrophotometer cuvette using a SpectraMax Plus^{384} high-throughput microplate spectrophotometer (Molecular Devices Corp., Sunnyvale, CA). The β-galactosydase activity was calculated as nanomoles of β-galactose formed per minute per milligram of lysate at 37 °C, according to the instruction manual. The electronic absorbance units were also used as a measure of the β-galactosidase expression. All data were obtained in triplicate.

RESULTS AND DISCUSSION

Polymer Synthesis and Structure. The polymerization of DMAEMA was carried out using a redox system consisting of Ce^{4+} ions and Pluronic or PEG. The cerium ion−alcohol redox reaction leads to the formation of a radical on the carbon atom linked with the hydroxyl group (*21*). It has been shown that in the case of a polymeric alcohol, PEG, as a reducing agent, the formation of the radicals takes place at the terminal carbon atom and not along the polyether chain (*22*). Drawing an analogy between PEG and PEO−PPO−PEO copolymers, we depicted the polymerization as shown in Scheme 1. In the first step, a redox reaction occurs between Ce^{4+} and the $-CH_2OH$-terminal group of the PEO segment, generating a free radical in a position of the hydroxide. The radical thus formed is transferred from the polymer chain to the DMAEMA monomer, and the polymerization propagates. Formation of diradicals is possible, but their relative content is minor, according to the literature data (*10*, *21*−*23*). The presence of diradicals, if any, can lead to the formation of copolymers of higher molecular weight. In the present study, we were able to validate the polymerization mechanism by size exclusion chromatography (SEC) and NMR.

Figure 1 depicts typical SEC chromatograms of L92−pDMAEMA and PEO−pDMAEMA copolymer samples, calibrated in molecular weights. Peaks centered at 7100 (94.7% total area) and 10500 (5.3%) Da as well as 6950 (94.7%) and 10100 (5.2%) Da were observed in the case of the L92−pDMAEMA and PEO−pDMAEMA copoly-

Scheme 1. Initiation and Propagation Steps in the Free Radical Polymerization Leading to pDMAEMA−Pluronic Block Copolymers

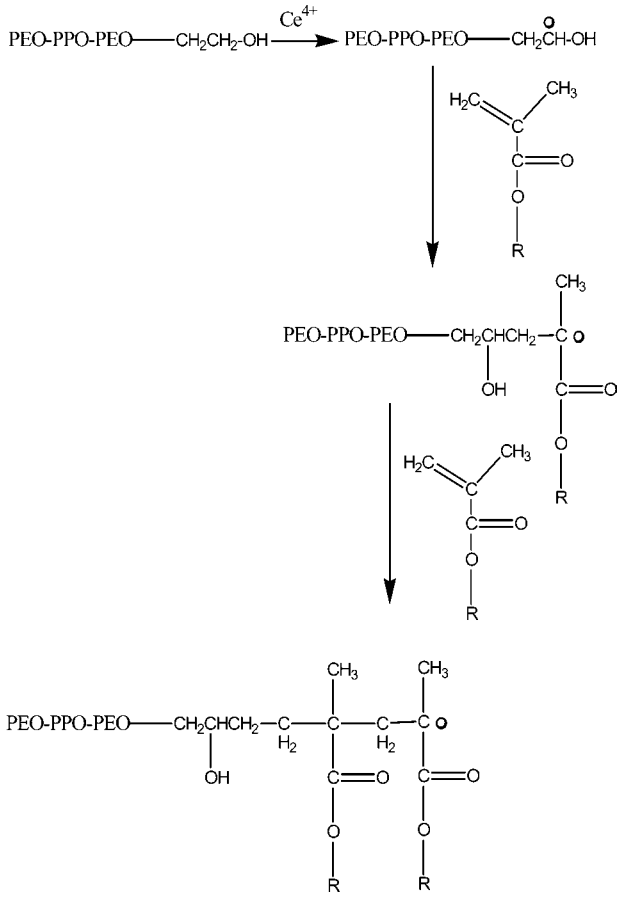

mers, respectively. The polydispersity index calculated by the instrument's software using an absolute MW calibration curve was in the range of 1.22−1.25, in accord with the previously observed formation of relatively monodisperse copolymers resulting from polyoxyethylene-radical-induced polymerization of DMAEMA (*10*, *17*, *24*). On the basis of the average MW of the Pluronic L92 and PEG being 3720 and 3350 Da, respectively, ∼95% of either copolymer is a product of polyether-monoradical formation, resulting in "diblock" Pluronic−pDMAEMA or PEG−pDMAEMA structure. About 5% of the resulting polymers of either species are the result of the polyether-diradical formation, resulting in the bonding of two polyether segments to the forming pDMAEMA chain, with corresponding peaks observed in the 10 kDa area in the SEC chromatograms (Figure 1). The length of the pDMAEMA block is 22 or 23 units in L92−pDMAEMA or PEO−pDMAEMA, respectively, in the main fractions of these copolymers. These calculations are supported by the nitrogen content measurements: N, found, 4.15% (calcd, 4.26%) for the L92−pDMAEMA and N, found, 4.75% (calcd, 4.61%) for the PEO−pDMAEMA copolymer, respectively.

Using ^{1}H NMR spectroscopy, we were able to verify the structure of the pDMAEMA−L92 copolymers resulting from polymerization (Scheme 1, Figure 2). As is seen in Table 1, the proton ratios measured by NMR corresponded to the proposed structure quite well. The average number of DMAEMA units bonded to the one L92 segment was calculated from the ratio of the backbone methylene protons in these units, respectively (Table 1). At $y = 1$ (one Pluronic segment), we obtained

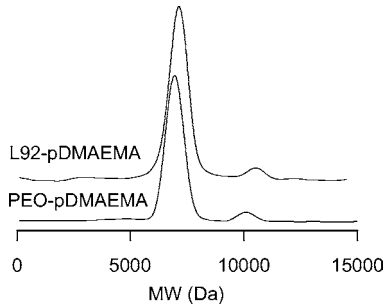

Figure 1. Typical size exclusion chromatographs of L92−pDMAEMA and PEO−pDMAEMA copolymers in DMF. For SEC conditions, see Experimental Procedures.

Chart 1. Structure of the pDMAEMA-L92 Copolymer

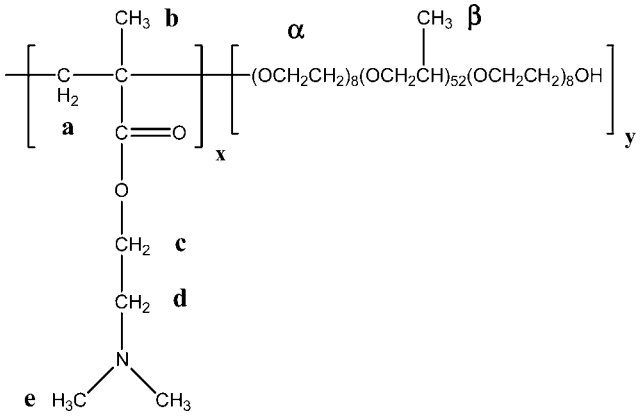

Table 1. Structure of Copolymers Obtained from ^{1}H NMR

structural element	protons[a]	calcd	found from NMR
DMAEMA	a:b:c:d:e	1.0:1.5:1.0:1.0:3.0	1.0:1.1:1.1:1.0:3.2
L92	α:*β*	1.08:1.00	1.06:1.00
DMAEMA/L92, mol/mol	a:α	*x*:84*y*	0.9:3.3 *x* = 22.9 *y* = 1

[a] For proton designations, see Chart 1.

the expression $x/84 = 0.9/3.3$, and thus $x = 23$; that is, 1 Pluronic segment is bound to 23 DMAEMA units on average. This is in excellent agreement with the $x = 22$ found from SEC. Importantly, no protons belonging to the methylene or methyl groups of the polyether were observed in the NMR spectrum of the sample synthesized in the absence of Ce^{4+} followed by the Pluronic removal by dialysis (see spectrum C in Figure 2). These observations further confirm the mechanism of the copolymer formation via cerium(IV)-induced initiation (Scheme 1).

Self-Assembling Properties of the Copolymers. Having confirmed the structure of the copolymers resulting from the cerium-initiated copolymerization of polyethers with DMAEMA, we embarked on the study of their properties that are of importance for complexation with DNA and transfection. To assess the polyelectrolyte properties of the novel copolymers, potentiometric titration of their aqueous solutions was conducted. The titration curves yielded the apparent pK_a and ionization degree (α) of the titratable (tertiary amino) groups. The intrinsic dissociation constant (K_0) was found by extrapolating pK_a to $\alpha = 0$ in the pK_a versus α curves. (*18*). The pK_0 values of the L92−pDMAEMA and PEO-DMAEDMA were found to be 7.1 and 7.4, respectively. A shift to lower pK_0 in the case of the L92−pDMAEMA can be explained by the effect of Pluronic lowering the dielectric constant

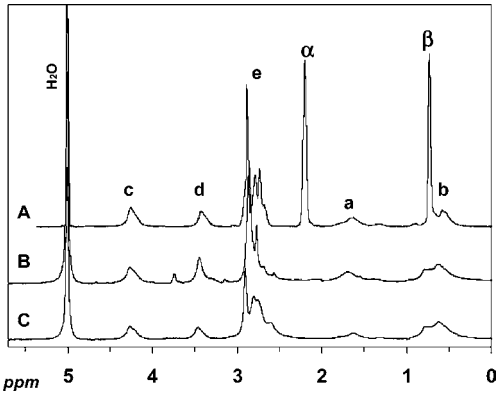

Figure 2. ^{1}H NMR (400 MHz) spectra of pDMAEMA−L92 (A), pDMAEMA (B), and pDMAEMA/L92 blend after dialysis (C) in D_2O/5 mM DCl. Protons are labeled as shown in Scheme 1.

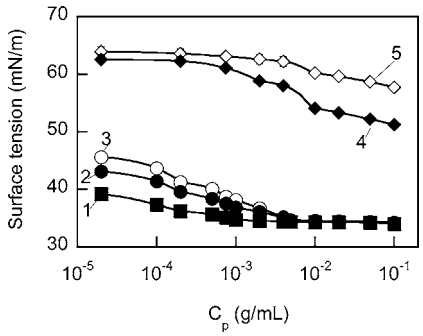

Figure 3. Equilibrium surface tension of the Pluronic L92 (1), L92−pDMAEMA (2, 3), and PEO−pDMAEMA (4, 5) copolymers as a function of the copolymer concentration (C_p) at 25 °C. Dependencies 1, 3, and 5 were obtained at pH 5.0, and dependencies 2 and 4 were measured at pH 7.0, in triplicate. Standard deviations are shown.

of the microenvironment of the amino groups. In contrast, the pK_o of the PEO−pDMAEMA copolymer roughly corresponded to the pK_a = 7.4−7.8 reported for the pDMAEMA polymer (*16*), indicating that PEO block alone has a lesser effect on the ionization of the pDMAEMA than PEO−PPO−PEO when bonded with the polycation. The DMAEMA monomer possesses a notably higher pK_a of 8.0−8.4 than its homo- and copolymers because of the neighboring effect (*25*); that is, the presence of some protonated side chains reduces the ability of the remaining dimethylamino groups to become protonated.

The presence of the hydrophobic PPO segments in the structure of the polyether segments of the copolymers leads to profound differences in the surface activity of the L92−pDMAEMA and PEO−pDMAEMA copolymers in aqueous solutions (Figure 3). The surface activity of the L92−pDMAEMA copolymers was comparable to that of the parent L92 surfactant, with the critical micellization concentrations (cmc) of 5×10^{-3} and 2×10^{-3} g/mL measured for the L92−pDMAEMA and L92 copolymers, respectively. The obtained cmc of the Pluronic L92 corresponded well with the literature data, previously reported for 37 and 15 °C (*26*−*28*). Higher ionization of the copolymer at pH 5.0 resulted in lower surface activity than at pH 7.0 throughout the concentration range. The PEO−pDMAEMA copolymers possessed dramatically lower surface activity than their L92−pDMAEMA counterparts at both pH values studied. At pH 5.0, where the copolymer is highly ionized, a very minimal surface activity was observed. At pH 7.0, which is closer to pK_a of the copolymer, the pDMAEMA segment becomes more

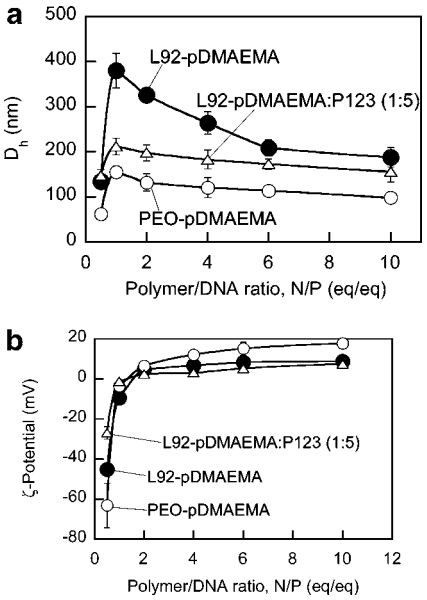

Figure 4. Hydrodynamic diameter (D_h) (a) and ζ-potentials (b) of the complexes formed between pCMV-βgal plasmid DNA and polycationic copolymers L92−pDMAEMA and PEO−pDMAEMA as well as a mixture of L92−pDMAEMA and Pluronic P123 (1:5 wt/wt) as a function of the polymer/DNA (N/P) ratio. The N/P ratio is expressed via the ratio of the equivalents of DMAEMA units in the copolymer to the nucleotide units in the DNA. Measurements were conducted in triplicate at 25 °C in 10 mM HEPES solution at pH 7.0. Standard deviations are shown.

hydrophobic and, thus, more of the copolymer adheres to the air−water interface, lowering the measured surface tension. Similar effects of pH on surface activity have been observed with block copolymers of DMAEMA and methyl methacrylate (*29*). The apparent cmc of the PEO−pDMAEMA was ∼0.01 g/mL at pH 7.0 and could not be measured at pH 5.0. We hypothesized that the observed differences in the surface activity of the PEO- and Pluronic-based polycations could have an effect on the ability of the copolymers to serve as nonviral transfection agents, because surfactants such as Pluronics can fuse with the cell membranes, thus decreasing their microviscosity, which leads to an enhancement of the transmembrane transport that is likely involved in the transfection mechanism (*30*). As shown in the forthcoming parts of the work, we indeed observed enhanced transfection with the L92−pDMAEMA copolymers.

Complexation of the polycationic copolymers with plasmid DNA was studied by assessing the average hydrodynamic diameter as well as ζ-potential of the particles of the formed complexes (Figure 4). Within the range of concentrations studied, no precipitation was observed at any N/P ratio. A significant increase in the average particle size was observed upon neutralization of the complexes when a 1:1 stoichiometry was reached, and then the particle size gradually decreased and leveled off as particles became positively charged. The complexes of the L92−pDMAEMA with pCMV-βgal plasmid DNA had larger hydrodynamic diameters than any other complexes throughout the N/P range studied (Figure 4), with the solution at N/P = 1.0 being faintly opaque. Intermolecular associations of the hydrophobic segments of the complexes were evidently more prevalent with the L92−pDMAEMA copolymer. Notably, the addition of the relatively hydrophilic Pluronic P123, which forms mixed micelles with L92, reduced the size of the aggregates and their electrokinetic mobility (Figure 4). The excess of

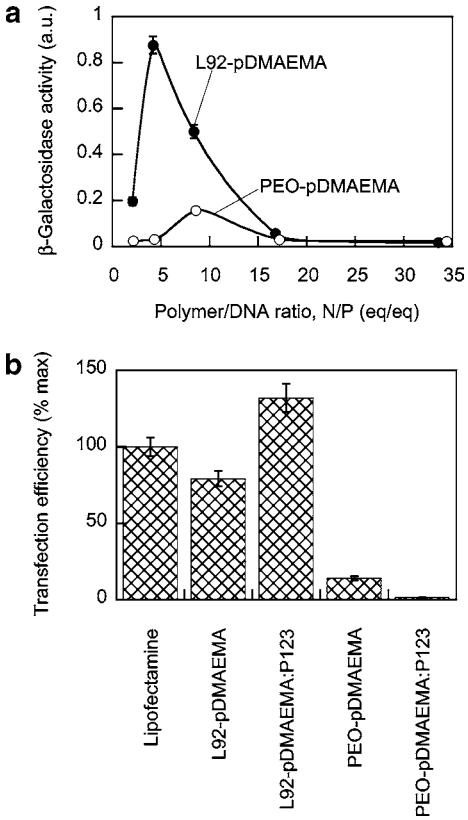

Figure 5. Transfection of CHO cells by pCMV-βgal using L92−pDMAEMA and PEO−pDMAEMA copolymers, mixtures of L92−pDMAEMA or PEO−pDMAEMA with 0.005% Pluronic P123 and Lipofectamine as transfection agents (TA). In (a), the 95% confluent CHO cells were transfected with the complexes of L92−pDMAEMA and plasmid DNA at different polymer/DNA (N/P) ratios, expressed in equivalents of charged groups in the copolymer and DNA. The β-galactosidase activity was assayed 48 h after the transfection using the ONPG assay. In (b), the effect of the transfection agents was calculated as the maximum β-galactosidase activity relative to the maximum enzyme activity achieved with the Lipofectamine. All assays were conducted under identical conditions 72 h after the transfection. Measurements were performed in triplicate, and standard deviations are shown. Statistical significance of the results for each experiment was calculated using Student's t test (all reported data were characterized by $P < 0.01$).

Pluronic P123 masked the charges of the particles as compared to the L92−pDMAEMA/DNA complexes without Pluronic addition. No opacity in the solutions with P123 was observed, even at the stoichiometric N/P = 1.0. Such a stabilizing effect of the presence of the Pluronic P123 on the stabilization of the polycation/DNA complex has been previously reported with other polycationic systems (*7*, *12*).

Cell Transfection. As shown in Figure 5, the L92−pDMAEMA copolymer significantly enhances cell transfection in the N/P ratio ranging from 2 to 34, exhibiting a maximum level of β-gal expression at the N/P ratio of 4. Pluronic P123 significantly increased the level of transfection when added to the L92−pDMAEMA composition, resulting in 1.7- and 1.3-fold higher β-gal expressions when compared to the effects of L92−pDMAEMA alone and Lipofectamine, respectively.

In contrast to the effects of the L92−pDMAEMA copolymer, the PEO−pDMAEMA copolymer resulted in only very weak β-galactosidase expression, and Pluronic 123 when added to this formulation did not increase the transfection efficacy (Figure 5b).

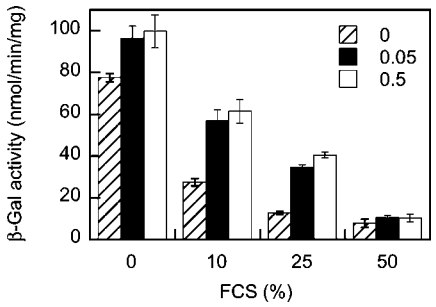

Figure 6. Effect of FCS concentration in the medium on β-galactosidase transfection activity. The CHO cells were transfected with L92−pDMAEMA/pCMV β-gal (4:1, w/w) complexes with or without Pluronic P123, added at 0.05 or 0.5%. The media contained increasing levels of serum from 0 to 50% FCS. The β-galactosidase activity was calculated as nanomoles of β-galactose formed per minute per milligram of lysate at 37 °C by using ONPG as a substrate. All data were obtained in triplicate. Numbers stand for 0, 0.05, and 0.5% of Pluronic P123 added.

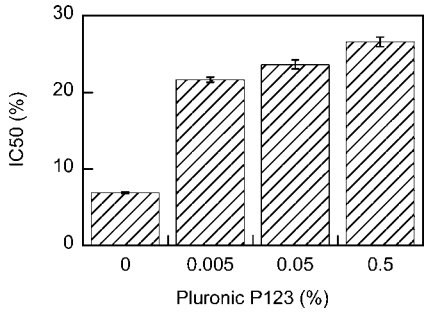

Figure 7. Effect of Pluronic P123 on reduction of the serum-mediated inhibition of transfection. The CHO cells were transfected with L92−pDMAEMA/pCMV β-gal (4:1, w/w) complexes with or without added Pluronic P123 (0.005, 0.05, or 0.5%). The results are presented via FCS concentration resulting in 50% inhibition of transfection activity of L92−pDMAEMA−pCMV−β-gal complex without the addition of P123 in serum-free conditions (IC_{50}, percent). All data were obtained in triplicate.

The efficacy of cell transfection by means of cationic polymers is often diminished by serum. However, it has been demonstrated (*7*) that conjugation of polycations such as poly(ethylene imine) (PEI) with polyethers results in copolymers capable of forming stable complexes in serum. Furthermore, addition of Pluronics to PEI−DNA complexes has been shown to alleviate the reduction of serum-mediated gene transfer to murine fibroblasts (*31*). We reasoned that the addition of Pluronic P123 that we observed to significantly enhance the efficiency of transfection (Figure 5b) can help in reducing the deleterious effects of serum. Therefore, the ability of L92−pDMAEMA to mediate DNA transfer at various serum concentrations in the transfection medium was studied. The media tested contained increasing levels of serum from 0 to 50% and Pluronic P123 from 0 to 0.5%. As is seen in Figure 6, the L92−pDMAEMA copolymer alone is more serum-sensitive than the L92−pDMAEMA-P123 complex, when used as a transfection reagent. Addition of FCS to the transfection medium at a 10% level resulted in 2.8- and 1.3-fold lower β-gal expressions when compared to the serum-free medium, when L92−pDMAEMA alone or L92−pDMAEMA−P123 complex was used, respectively. Pluronic P123 increased the transfection activity dramatically and at the same time reduced the serum-mediated inhibition of the DNA transfer.

Figure 7 shows the effect of Pluronic P123 on the transfection activity of the L92−pDMAEMA−DNA complex in the serum-containing medium. The results were

reported as the percentage of FCS in the transfection medium necessary to cause 50% inhibition of the transfection activity of L92−pDMAEMA−DNA without Pluronic in serum-free conditions (IC_{50}). Remarkably, as little as 0.005% Pluronic P123 helped to increase the IC_{50} from 7 to 22%. This certainly proves shielding of the copolymer−DNA complexes from the serum by added Pluronic species. One might attribute this protective effect to a steric barrier that Pluronic assemblies with the copolymer−DNA complex create toward the complex−serum interaction (*31*).

CONCLUDING REMARKS

A simple synthetic procedure for the free radical polymerization of DMAEMA initiated by polyether radicals that are generated by cerium(IV) has been developed. The procedure results in block copolymers of pDMAEMA and polyethers with high yields. The copolymers of Pluronic L92 with pDMAEMA are highly surface-active at pH 5.0 and 7.0, whereas the PEO−pDMAEMA copolymer is slightly surface-active only at pH 7.0, at which it is sufficiently hydrophobic. The complexes of the L92−pDMAEMA are larger than those of the PEO−pDMAEMA throughout the polymer/DNA range studied. The results shown in Figure 5 demonstrate that the L92−pDMAEMA enables transfection efficacy of the plasmid DNA comparable to that achieved with lipid-based formulations such as Lipofectamine. Furthermore, the addition of Pluronic P123 further increases the carrier efficacy and reduces serum-mediated inhibition of DNA transfer. We have previously reported that cationic polymers conjugated with nonionic amphiphilic polymers such as PEI−Pluronic provide plasmid DNA with transfection efficiency similar to that achieved using lipid-based systems in in vitro settings. Such copolymers are quite beneficial when used for systemic administration. The new L92−pDMAEMA carrier evaluated in this study has demonstrated analogous in vitro properties. This polymer, however, is a product of a one-step, robust polymerization procedure, which represents a significant advantage compared to the PEI−Pluronic carriers that are produced by a complex and poorly controlled conjugation chemistry.

The ability of Pluronic P123 added to the L92−pDMAEMA/DNA complex to further enhance the transfection efficacy is likely related to the above-described stabilizing effect of this polymer leading to a reduction in the particle size of the L92−pDMAEMA/DNA (see Figure 4). This benefit, although well seen in the in vitro system, may be much more pronounced upon a systemic administration of the formulation.

The in vivo performance of L92−pDMAEMA and its combination with Pluronic P123 and other similar block copolymers as DNA delivery systems is presently being evaluated in our laboratories.

LITERATURE CITED

(1) Ilies, M. A., Seitz, W. A., and Balaban, A. T. (2002) Cationic lipids in gene delivery: principles, vector design and therapeutical applications. *Curr. Pharm. Des. 8* (27), 2441−2473.

(2) Gebhart, C. L., and Kabanov, A. V. (2001) Evaluation of polyplexes as gene transfer agents. *J. Controlled Release 73*, 401−416.

(3) Merdan, T., Kopecek, J., and Kissel, T. (2002) Prospects for cationic polymers in gene and oligonucleotide therapy against cancer. *Adv. Drug Deliv. Rev. 54* (5), 715−758.

(4) Kabanov, A. V., and Kabanov, V. A. (1998) Interpolyelectrolyte and block ionomer complexes for gene delivery: physiochemical aspects. *Adv. Drug Deliv. Rev. 30* (1−3), 49−60.

(5) Thomas, M., and Klibanov, A. M. (2003) Non-viral gene therapy: polycation-mediated DNA delivery. *Appl Microbiol Biotechnol. 62*, 27−34.

(6) Wagner, E. (2004) Strategies to improve DNA polyplexes for in vivo gene transfer: will "artificial viruses" be the answer? *Pharm. Res. 21* (1), 8−14.

(7) Nguyen, H. K., Lemieux, P., Vinogradov, S. V., Gebhart, C. L., Guerin, N., Paradis, G., Bronich, T. K., Alakhov, V. Y., and Kabanov, A. V. (2000) Evaluation of polyether−polyethyleneimine graft copolymers as gene transfer agents. *Gene Ther. 7* (2), 126−138.

(8) Tan, J. F., Ravi, P., Too1, H. P., Hatton, T. A., and Tam, K. C. (2005) Association behavior of biotinylated and non-biotinylated poly(ethylene oxide)−*b*-poly(2-(diethylamino)-ethyl methacrylate). *Biomacromolecules* (in press).

(9) Toncheva, V., Wolfert, M. A., Das, P. R., Oupicky, D., Ulbrich, K., Seymour, L. W., and Schacht, E. H. (1998) Novel vectors for gene delivery formed by self-assembly of DNA with poly-(lysine) grafted with hydrophilic polymers. *Biochim. Biophys. Acta 1380*, 354−368.

(10) Dubruel, P., and Schacht, E. H. (2000) Effect of polyethylene oxide blocks or grafts on the physicochemical properties of poly-(2-*N*-(dimethylaminoethyl)methacrylate) DNA complexes of polycations and DNA. *Bioact. Compat. Polym. 15*, 279−296.

(11) Lemieux, P., Vinogradov, S. V., Gebhart, C. L., Guerin, N., Paradis, G., Nguyen, H. K., Ochietti, B., Suzdaltseva, Y. G., Baratakova, E. V., Bronich, T. K., St-Pierre, Y., Alakhov, V. Y., and Kabanov, A. V. (2000) Block and graft copolymers and NanoGel copolymer networks for DNA delivery into cell. *J. Drug Target. 8* (2), 91−105.

(12) Gebhart, C. L., Sriadibhatla, S., Vinogradov, S., Lemieux, P., Alkahov, V., and Kabanov, V. A. (2002) Design and formulation of polyplexes based on Pluronic−polyethyleneimine conjugates for gene transfer. *Bioconjugate Chem. 13* (5), 937−944.

(13) Ochietti, B., Lemieux, P., Kabanov, A. V., Vinogradov, S., St-Pierre, Y., and Alakhov, V. (2002) Inducing neutrophil recruitment in the liver of ICAM-1-deficient mice using polyethyleneimine grafted with Pluronic P123 as an organ-specific carrier for transgenic ICAM-1. *Gene Ther. 14*, 939−945.

(14) Ochietti, B., Guerin, N., Vinogradov, S. V., St-Pierre, Y., Lemieux, P., Kabanov, A. V., and Alakhov, V. Y. (2002) Altered organ accumulation of oligonucleotides using polyethyleneimine grafted with poly(ethylene oxide) or pluronic as carriers. *J. Drug Target. 2*, 113−121.

(15) Belenkov, A. I., Alakhov, V. Y., Kabanov, A. V., Vinogradov, S. V., Panasci, L. C., Monia, B. P., and Chow, T. Y. (2004) Polyethyleneimine grafted with pluronic P85 enhances Ku86 antisense delivery and the ionizing radiation treatment efficacy in vivo. *Gene Ther. 11* (22), 1665−1672.

(16) van de Wetering, P., Zuidam, N. J., van Steenbergen, M. J., van der Houwen, O. A. G. J., Underberg, M. J. M., and Hennink, W. E. (1998) A mechanistic study of hydrolytic stability of poly(2-(dimethylamino)ethyl methacrylate). *Macromolecules 31*, 8063−8068.

(17) Vamvakaki, M., Billingham, N. C., and Armes, S. P. (1999) Synthesis of controlled structure water-soluble diblock copolymers via oxyanionic polymerization. *Macromolecules 32* (6), 2088−2090.

(18) Bromberg, L., Temchenko, M., and Hatton, T. A. (2003) Smart microgel studies. Polyelectrolyte and drug-absorbing properties of microgels from polyether-modified poly(acrylic acid). *Langmuir 19* (21), 8675−8684.

(19) Deshpande, M. C., Garnett, M. C., Vamvakaki, M., Bailey, L., Armes, S. P., and Stolnik, S. (2002) Influence of polymer architecture on the structure of complexes formed by PEG-tertiary amine methacrylate copolymers and phosphorothioate oligonucleotide. *J. Controlled Release 81* (1−2), 185−199.

(20) Lampela, P., Soininen, P., Urtti, A., Männistö, P. T., and Raasmaja, A. (2004) Synergism in gene delivery by small PEIs and three different nonviral vectors. *Int. J. Pharm. 270*, 175−184.

(21) Tauer, K., Antonietti, M., Rosengarten, L., and Miller, H. (1998) Initiators based on poly(ethylene glycol) for starting

heterophase polymerizations: generation of block copolymers and new particle morphologies. *Macromol. Chem. Phys. 199*, 897−890.

(22) Tauer, P., Westbroek, J., De Strycker, P., Dubruel, P., Temmerman, E., and Schacht, E. H. (2002) Flow-through cell for on-line amperometric determination of Ce(IV) during polymerization reactions. *Anal. Chem. 74*, 915−920.

(23) Nagarajan, S., Sabdham, K., and Spinivasan, V. (1995) Redox polymerization process: an efficient tool for the synthesis of block copolymers. *J. Polym. Sci., Polym. Chem. 33*, 2925−2933.

(24) Rungsardthong, U., Deshpande, M., Bailey, L., Vamvakaki, M., Armes, S. P., Garnett, M. C., and Stolnik, S. (2001) Copolymers of amine methacrylate with poly(ethylene glycol) as vectors for gene therapy. *J. Controlled Release 73* (2−3), 359−380.

(25) Přádny, M., and Ševčik, S. (1987) Precursors of hydrophilic polymers, 7. Potentiometric properties and structure of copolymers of 2-dimethylaminoethyl methacrylate. *Makromol. Chem. 188* (2), 227−238.

(26) Batrakova, E., Lee, S., Li, S., Venne, A., Alakhov, V., and Kabanov, A. (1999) Fundamental relationships between the composition of pluronic block copolymers and their hypersensitization effect in MDR cancer cells. *Pharm. Res. 16* (9), 1373−1379.

(27) Kozlov, M. Y., Melik-Nubarov, N. S., Batrakova, E. V., and Kabanov, A. V. (2000) Relationship between pluronic block copolymer structure, critical micellization concentration and partitioning coefficients of low molecular mass solutes. *Macromolecules 33* (9), 3305−3313.

(28) Zhang, R., Liu, J., Han, B., He, J., Liu, Z., and Zhang, J. (2003) Recovery of nanoparticles from (EO)8(PO)50(EO)8/*p*-xylene/H_2O microemulsions by tuning the temperature. *Langmuir 19* (21), 8611−8614.

(29) An, S. W., Thomas, R. K., Baines, F. L., Bullingham, N. C., Armes, S. P., and Penfold, J. (1998) Neutron reflectivity of an adsorbed water-soluble block copolymer at the air/water interface: the effects of pH and ionic strength. *J. Phys. Chem. B 102*, 5120−5126.

(30) Krylova, O. O., Melik-Nubarov, N. S., Badun, G. A., Ksenofontov, A. L., Menger, F. M., and Yaroslavov, A. A. (2003) Pluronic L61 accelerates flip-flop and transbilayer doxorubicin permeation. *Chemistry 9* (16), 3930−3936.

(31) Kuo, J.-H. S. (2003) Effect of Pluronic block copolymers on the reduction of serum-mediated inhibition of gene transfer of polyethyleneimine-DNA complexes. *Biotechnol. Appl. Biochem. 37*, 267−271.

BC049749F

Mixed-Ligand Rhenium-188 Complexes with Tetradentate/Monodentate NS_3/P ('4 + 1') Coordination: Relation of Structure with Antioxidation Stability

Eik Schiller,[†] Sepp Seifert,[†] Francesco Tisato,[‡] Fiorenzo Refosco,[‡] Werner Kraus,[§] Hartmut Spies,[†] and Hans-Juergen Pietzsch*[,†]

Forschungszentrum Rossendorf, Institut für Bioanorganische und Radiopharmazeutische Chemie, 510119, D-01314 Dresden, Germany, Consiglio Nazionale delle Ricerche, Istituto di Chimica Inorganica e delle Superfici, Corso Stati Uniti 4, I-35127 Padova, Italy, and Bundesanstalt für Materialforschung und -pruefung, Richard-Willstaetter-Strasse 11, D-12489 Berlin, Germany. Received October 26, 2004; Revised Manuscript Received February 10, 2005

Development of new radiopharmaceuticals based on rhenium-188 depends on finding appropriate ligands able to give complexes with high in vivo stability. Rhenium(III) mixed-ligand complexes with tetradentate/monodentate ('4 + 1') coordination of the general formula [Re(NS_3)(PRR′R″)] (NS_3 = tris-(2-mercaptoethyl)amine and derivatives thereof, PRR′R″ = phosphorus(III) ligands) appear to be among the promising tools to achieve this goal. According to this approach, we synthesized and characterized a series of rhenium model complexes. In vitro stabilities of the corresponding rhenium-188 complexes were determined by incubating 2−3 MBq or alternatively 37 MBq of the complexes in phosphate buffer, human plasma, and rat plasma, respectively, at 22 °C or 37 °C, followed by checking the amount of $^{188}ReO_4^-$ formed after 1 h, 24, and 48 h by thin-layer chromatography. The rate of perrhenate formation varied over a wide range, depending primarily on the nature of the phosphorus(III) ligand. Physicochemical parameters of the corresponding nonradioactive rhenium complexes were analyzed in detail to find out the factors influencing their different stability and furthermore to design new substitution-inert '4 + 1' complexes. Tolman's cone angle of phosphorus(III) ligands and the lipophilic character of the inner coordination sphere were found to be crucial factors to build up stable rhenium '4 + 1' complexes. Additional information useful to describe electronic and steric properties of these compounds were selected from electronic spectra (wavelength of the Re→S charge-transfer band), cyclovoltammetric measurements ($E°$ of the Re^{III}/Re^{IV} couple), and NMR investigations (^{31}P chemical shift of coordinated P(III) ligands).

INTRODUCTION

Rhenium-188 is an attractive candidate for therapeutic applications in oncology due to its nuclide properties ($E_{\beta max}$ = 2.1 MeV, $t_{1/2}$ = 16.9 h) and its daily availability from a $^{188}W/^{188}Re$ generator (*1*−*3*). To exploit the potencies of this nuclide, target-specific radiotherapeuticals must be developed to accumulate the radioactivity in the tumor and to spare healthy tissue from radiation. This can be achieved by linking a radionuclide-bearing chelate to a target-seeking biomolecule. Being capable to control the biodistribution requires kinetically inert and metabolically stable complexes. Despite some rhenium-188 tricarbonyl complexes with tridentate ligands (*4*) and in some cases $^{188}Re(O)MAG_3$ that show fairly good stability both in vitro and in vivo (*5*−*7*), antioxidation stability at high level of radioactivity remains one of the most important questions in rhenium radiopharmacology.

A promising approach for attaching rhenium-188 to biomolecules is the so-called '4 + 1' mixed ligand system (*8*). Here a rhenium(III) center is coordinated by the tetradentate tris(2-mercaptoethyl)amine chelator (NS_3) or a derivative thereof and a phosphorus(III) compound or an isocyanide as monodentate ligand. The latter also serves as a linker for coupling target-specific biomolecules such as peptides, antibodies, and oligonucleotides (Figure 1).

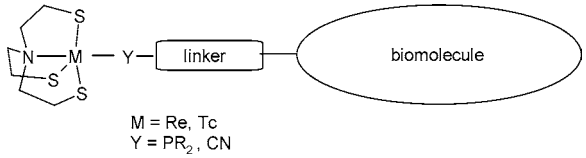

Figure 1. The '4 + 1' mixed ligand approach.

Until now, '4 + 1' complexes of technetium and rhenium with the NS_3 chelator tris(2-mercaptoethyl)-amine and several isocyano or phosphine ligands were predominantly of lipophilic character (*9*, *10*). Development of more hydrophilic rhenium complexes may help to minimize exposure of radiation-sensitive organs by fast excretion of radioactive metabolites and furthermore enables radiolabeling of water-soluble biomolecules such as antibodies and peptides in aqueous solution. A first attempt to produce more hydrophilic '4 + 1' complexes was published recently by our group, involving the preparation of a tetradentate NS_3 ligand bearing a carboxyl group (*11*).

In the present work we report on the extension of the '4 + 1' system using different monodentate phosphorus-

* To whom correspondence should be addressed. Fax: +49 351 260 3232. E-mail: h.j.pietzsch@fz-rossendorf.de.

[†] Institut für Bioanorganische und Radiopharmazeutische Chemie.

[‡] Istituto di Chimica Inorganica e delle Superfici.

[§] Bundesanstalt für Materialforschung und -pruefung.

10.1021/bc049745a CCC: $30.25 © 2005 American Chemical Society
Published on Web 04/14/2005

Scheme 1. Reaction Routes to Re(III) '4 + 1' Complexes

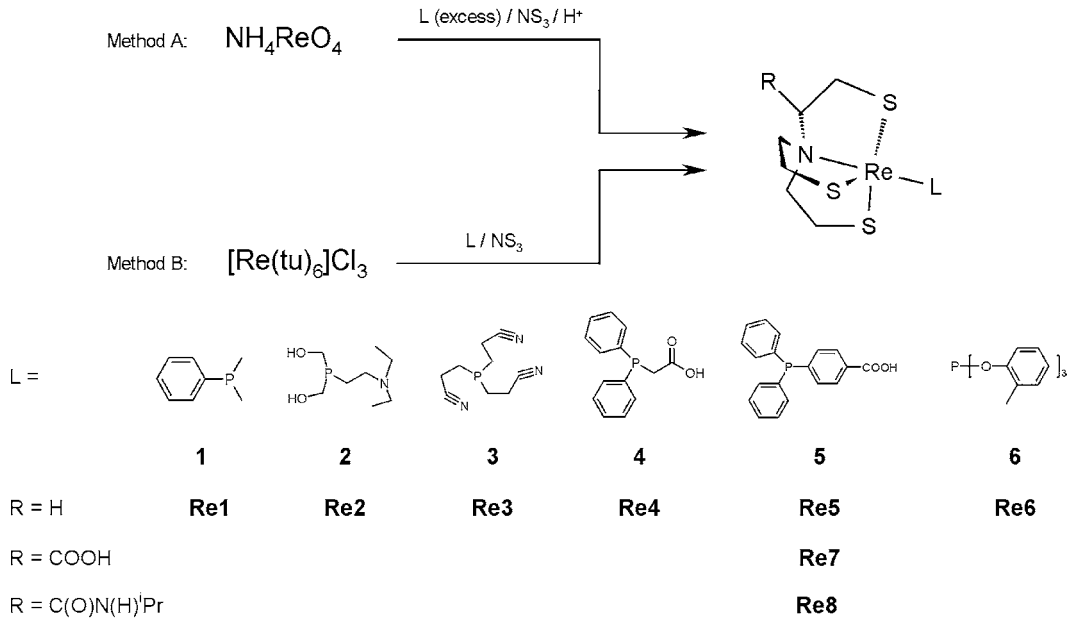

(III) ligands, including both lipophilic and hydrophilic tertiary phosphines and phosphites (see Scheme 1). Moreover, the use of the unsubstituted NS_3 chelator compared with substituted NS_3 ligands bearing a carboxyl group (NS_3COOH) and an isopropyl amide (NS_3-$CONH^iPr$), respectively, offers the possibility of fine-tuning the system. We evaluated the potentials of the resulting complexes as tools for therapeutic purposes. Therefore, in vitro stabilities, which we defined as the amount of perrhenate formed after incubation of the rhenium-188 complexes at low (2−3 MBq) or medium (37 MBq) activity level in phosphate buffer, human plasma, and rat plasma, were determined. Physicochemical parameters of the corresponding nonradioactive rhenium complexes were analyzed in detail to find out trends useful to explain the different in vitro stabilities of various rhenium-188 complexes. Results of this analysis were used to design complexes of superior in vitro stability.

EXPERIMENTAL PROCEDURES

General. All solvents and commercially available substances were of reagent grade and used without further purification. Commercially available phosphines and phosphites are dimethylphenylphosphine **1** and 4-(diphenylphosphino)benzoic acid **5** (Aldrich), tris(2-cyanoethyl)phosphine **3** and tris(*o*-tolyl)phosphite **6** (Alfa Aesar). Diphenylphosphino acetic acid **4** was synthesized according to the method described by Jarolim et al. (*12*). Syntheses of the tetradentate ligand tris(2-mercaptoethyl)amine (NS_3) and rhenium complex **Re1** were reported elsewhere (*8*). Tris(2-mercaptoethyl)amine was isolated and applied as the oxalate. 2-[Bis(2-mercaptoethyl)amino]-3-mercaptopropionic acid (NS_3COOH) was prepared as hydrochloride salt by double N-alkylation of *S*-benzylcysteine (*11*). $^{188}ReO_4^-$ was eluted from a $^{188}W/^{188}Re$ generator (Oak Ridge National Laboratories, Oak Ridge, TN).

Instrumentation. Nuclear magnetic resonance spectra were recorded on a 400 MHz Varian Inova 400 spectrometer. The ^1H and ^{13}C chemical shifts are reported relative to residual solvent signals or TMS as reference. ^{31}P chemical shifts are reported relative to H_3PO_4 as external reference. Mass spectrometric measurements were performed with a Micromass Tandem Quadropole Mass Spectrometer (Quadro LC) operating in the MS mode. Mass spectral data were recorded in the positive ESI mode. About 10^{-4} mol of the sample dissolved in 1.0 mL of methanol or acetonitrile were injected at a flow rate of 5 μL/min.

Elemental analyses were performed on a LECO Elemental Analyzer CHNS-932. Cyclic voltammetry was carried out in dichloromethane solutions (1×10^{-3} mol dm^{-3}) with [n-Bu_4N][ClO_4] (0.1 mol dm^{-3}) as supporting electrolyte, at a stationary platinum-disk electrode (area ca. 1.28 mm^2), which was cleaned after each run, with scan rate 0.2 V s^{-1} at 293 K. Potentials were measured relative to an Ag-wire pseudoelectrode using the Fc/Fc^+ couple as internal reference. Controlled potential coulometries of dichloromethane solutions were performed using an Amel model 721 integrator, in a H-shaped cell containing, in arm 1, a platinum-gauzed working electrode, and an Ag/Ag^+ reference isolated inside a salt bridge by a medium glass frit and, in arm 2, an auxiliary platinum-foil electrode. UV/vis spectra were recorded on a SPECORD S10 spectrometer (Carl Zeiss Jena).

HPLC analysis and purification of rhenium-188 complexes were performed using a Perkin-Elmer instrument consisting of a Turbo LC System with a quaternary pump (Series 200 LC Pump) and a programmable absorbance detector model 785A.

Nonradioactive rhenium complexes were monitored by their UV absorption at 254 nm, and rhenium-188 complexes by γ-ray detection (Bohrloch, NaI(Tl) crystal).

Synthesis of {[2-(Diethylamino)ethyl]phosphinediyl}dimethanol 2. To a solution of 0.001 mol of diethyl [2-(diethylamino)ethyl]phosphonate, synthesized according to the method of Kosolapoff et al. (*13*), in 5 mL of dry diethyl ether, at 0 °C, was added 1.5 mL of a 1 mol/L $LiAlH_4$ solution (diethyl ether) dropwise via syringe. After the mixture was stirred at 0 °C under an argon atmosphere for 0.5 h about 3 mL of H_2O was added. The organic layer was separated, and the aqueous layer was extracted two times each with 3 mL of diethyl ether. The solvent of the combined organic solutions was removed in an argon stream. To the remaining oil were added 3 mL of degassed EtOH, 250 μL (0.003 mol) of a formaldehyde solution (37% in H_2O/MeOH), and 0.5 mL of 3 N

aq HCl. After being stirring at room temperature overnight, the solvent was stripped in vacuo, yielding 88% of a colorless viscous oil. Phosphine **2** was liberated in situ during the complex synthesis step.

General Synthesis Procedure for the Preparation of Rhenium Complexes Re3, Re4, Re6. To a solution of 0.1 mmol of tris(2-mercaptoethyl)ammonium oxalate (NS_3) and 0.3 mmol of the phosphine/phosphite in 5 mL of methanol (for **Re3**) or acetonitrile (for **Re4** and **Re6**) was added 0.1 mmol (26.8 mg) of NH_4ReO_4 (dissolved in ca. 200 μL of concentrated HCl for **Re3** and **Re4**). The reaction mixture was refluxed under an argon atmosphere for 2 h. The solvent was removed in vacuo and the residue purified by column chromatography (silica). Eluents were chloroform/ethyl acetate (90:10) for **Re3**, chloroform/ethyl acetate/TFA (90:10:0.1) for **Re4**, and *n*-hexane/ethyl acetate (50:50) for **Re6**. Crystals suitable for X-ray structure analysis were obtained by slow solvent evaporation of chloroform solutions of **Re3**, **Re4**, or **Re6.**

Re3. Yield: 64% dark-green crystals. Mp: >210 °C (decomp). Anal. ($C_{15}H_{24}N_4S_3PRe$) Calcd: C 31.40%, H 4.22%, N 9.77%, S 16.76%. Found: C 31.01%, H 4.36%, N 9.72%, S 16.77%. UV/vis (CH_2Cl_2): $\lambda_{max}(\log \epsilon) = 344$ (3.0), 450 (3.1), 577 (2.4). ^{1}H NMR (DMSO-d_6): 2.29 (m, 6 H, PCH_2), 2.61 (m, 6 H, CH_2CN), 2.90 (bs, 12 H). ^{13}C NMR (DMSO-d_6) 13.50 (d, J = 6.10 Hz, 3 C, CH$_2$CN), 31.60 (d, J = 26.70 Hz, 3 C, PCH$_2$), 46.60 (d, J = 5.34 Hz, 3 C, SCH$_2$), 59.36 (s, 3 C, NCH$_2$), 121.55 (s, 3 C, CN). ^{31}P NMR (DMSO-d_6) 18.42 (s). ESI-MS (*m/z*): 574 $[M]^+$.

Re4. Yield: 34% dark-green crystals. Mp: >215 °C (decomp). Anal. ($C_{20}H_{25}NO_2S_3PRe$) Calcd: C 38.45%, H 4.03%, N 2.24%, S 15.39%. Found: C 37.90%, H 4.13%, N 1.92%, S 13.84%. UV/vis (CH_2Cl_2): $\lambda_{max}(\log \epsilon) = 455$ (2.9), 590 (2.2). ^{1}H NMR ($CDCl_3$) 2.80 (bs, 12 H), 3.64 (d, J = 7.87 Hz, 2 H, CH_2), 7.17 (m, 2 $H_{arom.}$), 7.24 (m, 4 $H_{arom.}$), 7.62 (m, 4 $H_{arom.}$). ^{13}C NMR ($CDCl_3$) 46.38 (d, J = 4.58 Hz, 3 C, SCH$_2$), 48.86 (d, J = 16.79 Hz, 1 C, PCH$_2$), 60.00 (s, 3 C, NCH$_2$), 127.51 (d, J = 9.92 Hz, 4 $C_{arom.}$), 128.99 (s, 2 $C_{arom.}$), 133.06 (d, J = 11.44 Hz, 4 $C_{arom.}$), 144.03 (d, J = 45.78 Hz, 2 $C_{arom.}$), 172.47 (s, 1 C, C(O)). ^{31}P NMR ($CDCl_3$) 18.20 (s).

Re6. Yield: 24% brownish-red crystals. Mp: 225−233 °C. Anal. ($C_{27}H_{33}NO_3S_3PRe$) Calcd: C 44.25%, H 4.54%, N 1.91%, S 13.12%. Found: C 44.16%, H 4.53%, N 1.82%, S 13.24%. UV/vis (CH_2Cl_2): $\lambda_{max}(\log \epsilon) = 356$ (3.0), 418 (3.2), 524 (2.4). ^{1}H NMR ($CDCl_3$) 2.17 (s, 9 H, CH_3), 2.91 (bs, 12 H), 6.95 (m, 3 $H_{arom.}$), 7.05 (m, 3 $H_{arom.}$), 7.11 (d, J = 7.32 Hz, 3 $H_{arom.}$), 7.55 (d, J = 8.06 Hz, 3 $H_{arom.}$). ^{13}C NMR ($CDCl_3$) 17.22 (s, 9 C, CH$_3$), 44.08 (d, J = 6.10 Hz, 3 C, SCH$_2$), 59.06 (s, 3 C, NCH$_2$), 121.40 (d, J = 3.82 Hz, 3 $C_{arom.}$), 123.33 (s, 3 $C_{arom.}$), 126.42 (s, 3 $C_{arom.}$), 130.65 (d, J = 4.58 Hz, 3 $C_{arom.}$), 130.80 (s, 3 $C_{arom.}$), 151.99 (d, J = 8.39 Hz, 3 $C_{arom.}$). ^{31}P NMR ($CDCl_3$) 115.54 (s). ESI-MS (*m/z*): 733 $[M]^+$.

General Synthesis Procedure for the Preparation of Re2, Re5, Re7, Re8. The rhenium precursor $[Re(tu)_6]Cl_3 \times H_2O$ was synthesized by the method described by Gambino et al. (*14*). The monodentate ligand, tris(2-mercaptoethyl)ammonium oxalate (NS_3) (0.1 mmol, 28.6 mg), and $[Re(tu)_6]Cl_3 \times H_2O$ (0.1 mmol, 76.7 mg) were dissolved in 10 mL of methanol. For the synthesis of **Re2**, 100 μL triethylamine was added to the mixture to convert the phosphonium salt into the corresponding tertiary phosphine **2**. The solution was refluxed under an argon atmosphere for 3 h. After being cooling to room temperature, the reaction mixture was filtered and the solvent stripped in vacuo. **Re2** was purified by column chromatography (silica, acetone/chloroform/triethylamine (66:33:0.1)). In the case of **Re5**, **Re7**, and **Re8**, the crude product, which was impured by its methyl ester derivatives, was dissolved in a mixture of 3 mL of dioxane and 1 mL of 1 N NaOH and refluxed for 3 h. The reaction mixture was then acidified with 0.1 N HCl and the product extracted with chloroform. After evaporation of the solvent, the complex was further purified by silica column chromatography (*n*-hexane/ethyl acetate/TFA (50:50:0.1). Crystals of **Re2** suitable for X-ray structure analysis were obtained by slow solvent evaporation of a solution of **Re2** in methylenchloride/*n*-hexane.

Re2. Yield: 31% dark-green crystals. Mp: 159−162 °C. UV/vis (CH_2Cl_2): $\lambda_{max}(\log \epsilon) = 340$ (2.9), 461 (3.0), 592 (2.2). ^{1}H NMR ($CDCl_3$) 1.19 (t, J = 7.33 Hz, 6 H, CH_3), 2.59 (m, 2 H, PCH_2CH$_2$), 2.87 (q, J = 7.33 Hz, 4 H, NCH_2-CH$_3$), 2.90 (bs, 12 H), 3.06 (m, 2 H, NCH_2CH$_2$), 4.22 (m, 4 H, CH_2OH). ^{13}C NMR ($CDCl_3$) 8.90 (s, 2 C, CH$_3$), 21.64 (d, J = 26.70 Hz, 1 C, PCH$_2$, 46.18 (s, 2 C, NCH$_2$), 47.32 (d, J = 4.58 Hz, 3 C, SCH$_2$), 50.21 (d, J = 12.17 Hz, 1 C, NCH$_2$), 59.74 (s, 3 C, NCH$_2$), 73.17 (d, J = 28.23 Hz, 2 C, CH$_2$OH). ^{31}P NMR ($CDCl_3$) 16.50 (s). ESI-MS (*m/z*): 575 $[M + H]^+$.

Re5. Yield: 25% dark-green crystals. Mp: >120 °C (decomp). UV/vis (CH_2Cl_2): $\lambda_{max}(\log \epsilon) = 457$ (3.3), 591 (2.6). ^{1}H NMR ($CDCl_3$) 2.87 (bs, 12 H), 7.28 (m, 6 $H_{arom.}$), 7.45 (m, 4 $H_{arom.}$), 7.53 (d, J = 7.51 Hz, 2 $H_{arom.}$), 7.98 (d, J = 8.24 Hz, 2 $H_{arom.}$). ^{13}C NMR ($CDCl_3$) 47.12 (s, 3 C, SCH$_2$), 60.54 (s, 3 C, NCH$_2$), 128.04 (d, J = 6.87 Hz, 4 $C_{arom.}$),129.15 (s, 1 $C_{arom.}$),129.42 (m, 4 $C_{arom.}$), 134.02 (d, J = 9.16 Hz, 2 $C_{arom.}$), 134.46 (d, J = 9.15 Hz, 4 $C_{arom.}$), 143.31 (d, J = 47.30 Hz, 2 $C_{arom.}$), 151.56 (d, J = 54.93 Hz, 1 $C_{arom.}$), 171.00 (s, 1 C, C(O)). ^{31}P NMR ($CDCl_3$) 30.68 (s).

Re7. Yield: 36% dark-green crystals. Mp: >145 °C (decomp). UV/vis (CH_2Cl_2): $\lambda_{max}(\log \epsilon) = 455$ (3.0), 586 (2.2). ^{1}H NMR ($CDCl_3$) 2.47 (m, 1 H), 2.76 (m, 3 H), 3.09 (m, 2 H), 3.22 (m, 1 H), 3.40 (dd, J = 13.64, 4.85 Hz, 1 H), 3.51 (m, 1 H), 3.63 (m, 2 H), 7.30 (m, 6 $H_{arom.}$), 7.44 (m, 6 $H_{arom.}$), 7.93 (dd, J = 8.24, 1.28 Hz, 2 $H_{arom.}$). ^{13}C NMR ($CDCl_3$) 46.46 (d, J = 3.05 Hz, 1 C, SCH$_2$), 48.96 (d, J = 5.34 Hz, 1 C, SCH$_2$), 50.53 (d, J = 4.58 Hz, 1 C, SCH$_2$), 55.85 (s, 1 C, NCH$_2$), 57.25 (s, 1 C, NCH$_2$), 70.44 (s, 1 C, NCH), 128.13 (d, J = 9.92 Hz, 4 $C_{arom.}$), 129.05 (d, J = 1.53 Hz, 1 $C_{arom.}$), 129.55 (m, 4 $C_{arom.}$), 134.10 (d, J = 11.44 Hz, 2 $C_{arom.}$), 134.47 (d, J = 11.44 Hz, 4 $C_{arom.}$), 142.69 (d, J = 47.30 Hz, 2 $C_{arom.}$), 151.83 (d, J = 41.96 Hz, 1 $C_{arom.}$), 171.82 (s, 1 C, C(O)), 175.23 (s, 1 C, C(O)). ^{31}P NMR ($CDCl_3$) 29.94 (s).

Re8. Yield: 29% dark-green crystals. Mp: >155 °C (decomp). UV/vis (CH_2Cl_2): $\lambda_{max}(\log \epsilon) = 457$ (3.2), 590 (2.4). ^{1}H NMR ($CDCl_3$) 1.16 (d, J = 6.59 Hz, 3 H, CH_3), 1.22 (d, J = 6.59 Hz, 3 H, CH_3), 2.51 (m, 1 H), 2.81 (m, 3 H), 3.22 (m, 5 H), 3.44 (m, 1 H), 3.78 (m, 1 H), 4.15 (m, 1 H), 5.52 (m, 1 H, NH), 7.35 (m, 6 $H_{arom.}$), 7.47 (m, 4 $H_{arom.}$), 7.55 (dd, J = 9.98, 8.52 Hz, 2 $H_{arom.}$), 8.02 (dd, J = 8.15, 1.37 Hz, 2 $H_{arom.}$). ^{13}C NMR ($CDCl_3$) 22.66 (s, 1C, CH$_3$), 23.23 (s, 1C, CH$_3$), 42.53 (s, 1 C, CH(CH$_3$)$_2$), 57.00 (m), 73.50 (m), 128.15 (s), 129.20 (s), 129.56 (s), 134.17 (s), 134.57 (s), 168.35 (s, 1 C, C(O)), 171.35 (s, 1 C, C(O)). ^{31}P NMR ($CDCl_3$) 29.85 (s). ESI-MS (*m/z*): 772 $[M]^+$.

X-ray Data Collection and Processing. The X-ray data were collected at room temperature (293 K) on a SMART-CCD diffractometer (SIEMENS), using graphite monochromatized Mo K_α radiation (λ = 0.71073 Å). A summary of the crystallographic data of **Re2**, **Re3**, **Re4**, and **Re6** is given in Table 1. The positions of the non-hydrogen atoms were determined by the heavy atom technique. After anisotropic refinement of these positions,

Table 1. Crystallographic Data of X-ray Diffraction Studies of Rhenium Complexes Re2, Re3, Re4, and Re6

	Re2	Re3	Re4	Re6
formula	$C_{14}H_{32}N_2O_2PReS_3$	$C_{15}H_{24}N_4PReS_3$	$C_{20}H_{25}NO_2PReS_3$	$C_{27}H_{33}NO_3PReS_3$
formula wt	573.77	573.73	624.78	732.89
crystal system	monoclinic	monoclinic	orthorhombic	monoclinic
space group	*P*2(1)/*c*	*P*2(1)/*c*	*Pbca*	*P*2(1)/*n*
a (Å)	10.646(6)	22.313(8)	14.436(18)	9.716(4)
b (Å)	12.198(7)	12.791(4)	12.568(16)	12.182(5)
c (Å)	16.203(10)	14.924(5)	29.67(3)	24.439(10)
α (deg)	90.00	90.00	90.00	90.00
β (deg)	91.699(12)	97.063(7)	90.00	100.508(8)
χ (deg)	90.00	90.00	90.00	90.00
volume (Å^3)	2103(2)	4227(2)	5383(12)	2844(2)
Z	4	8	8	4
T (K)	273(2)	273(2)	273(2)	273(2)
ρ (g/cm^3)	1.812	1.803	1.836	1.712
absorption coeff (mm^{-1})	6.160	6.126	5.124	4.578
F(000)	1136	2240	2912	1456
λ (Mo K$_\alpha$) (Å)	0.71073	0.71073	0.71073	0.71073
crystal size (mm^3)	0.8 × 0.024 × 0.016	0.25 × 0.07 × 0.015	0.85 × 0.5 × 0.15	0.5 × 0.25 × 0.2
θ-range from data collection	1.91−25.00	0.92−25.00	1.97−25.00	2.38−29.00
index ranges	$-12 \le h \le 12$	$-26 \le h \le 21$	$-17 \le h \le 9$	$-12 \le h \le 12$
	$-14 \le k \le 14$	$-14 \le k \le 15$	$-14 \le k \le 14$	$-16 \le k \le 9$
	$-12 \le l \le 19$	$-17 \le l \le 17$	$-37 \le l \le 27$	$-31 \le l \le 32$
reflections collected	10212	20443	24134	17707
independent reflections	3703	7421	4740	7195
goodness-of fit of F^2	0.634	0.977	0.877	0.974
R [$I > 2\sigma$ (I)]	R1 = 0.0398	R1 = 0.0587	R1 = 0.0555	R1 = 0.0388
	wR2 = 0.0950	wR2 = 0.1205	wR2 = 0.1202	wR2 = 0.0958
R (all data)	R1 = 0.0778	R1 = 0.1503	R1 = 0.1094	R1 = 0.0501
	wR2 = 0.1098	wR2 = 0.1393	wR2 = 0.1410	wR2 = 0.0983

Table 2. Selected Bond Lengths (Å) and Angles (deg) of Re2, Re3, Re4, and Re6

	Re2	Re3	Re4	Re6
Re−N(1)	2.207(7)	2.202(11)	2.179(10)	2.207(4)
Re−S(1)	2.226(3)	2.235(4)	2.257(4)	2.2292(14)
Re−S(2)	2.230(3)	2.212(4)	2.252(4)	2.2321(14)
Re−S(3)	2.234(3)	2.227(4)	2.260(4)	2.2317(13)
Re−P	2.297(2)	2.291(4)	2.301(4)	2.2228(13)
N(1)−Re−S(1)	85.5(2)	85.6(3)	86.4(2)	85.17(9)
N(1)−Re−S(2)	84.5(2)	84.9(4)	85.1(2)	85.03(11)
N(1)−Re−S(3)	85.6(2)	85.8(3)	84.2(2)	85.98(10)
S(1)−Re−S(2)	119.00(11)	118.71(19)	118.60(12)	119.12(5)
S(1)−Re−S(3)	118.95(11)	118.50(19)	119.81(14)	119.09(6)
S(2)−Re−S(3)	119.98(12)	120.92(19)	119.56(12)	119.88(5)
N(1)−Re−P	177.9(2)	178.7(3)	177.4(2)	177.84(9)
S(1)−Re−P	93.24(9)	93.21(15)	94.63(11)	92.75(4)
S(2)−Re−P	97.59(8)	95.18(15)	96.42(11)	95.51(6)
S(3)−Re−P	93.53(9)	95.23(14)	93.23(12)	95.54(4)

the hydrogen positions were calculated according to ideal geometries. Empirical absorption corrections were made using psi scans. Most of the calculations were carried out in the SHELXTL system with some local modifications. Selected bond lengths and angles are reported in Table 2.

CCDC 253461 (**Re2**), CCDC 253462 (**Re3**), CCDC 253463 (**Re4**), and CCDC 253464 (**Re6**) contain the supplementary crystallographic data for this paper.

These data can be obtained free of charge via http://www.ccdc.cam.ac.uk/data_request/cif, by emailing data_request@ccdc.cam.ac.uk, or by contacting The Cambridge Crystallographic Data Centre, 12, Union Road, Cambridge CB2 1EZ, UK; fax: +44 1223 336033.

Synthesis Procedure for ^{188}Re Complexes. Synthesis was carried out via the EDTA intermediate as previously described by Seifert and co-workers (*11*).

^{188}Re-EDTA. 3−5 mL of perrhenate eluate from a ^{188}W/^{188}Re generator were added together with 0.5 mL of 0.1 N HCl to a kit vial containing 5 mg of EDTA, 5 mg of mannitol, and 1.0 mg of $SnCl_2$ in freeze-dried form under nitrogen. After 20−30 min at room temperature the complex formation is finished. Yield: >95% (TLC).

'4 + 1' ^{188}Re Complexes. A 0.3 mg amount of the appropriate NS_3 derivative and 0.05−0.20 mg of phosphine, dissolved in a mixture of 0.5 mL of water and 0.5 mL of methanol, were added with a syringe to the ^{188}Re-EDTA preparation, and the solution was heated at 50 °C (**Re4**, **Re5**, **Re6**) or 75 °C (**Re1**, **Re2**, **Re3**, **Re7**, **Re8**) for 30 min. Radiochemical yield: 50−90% (TLC), except **Re6**: 20−30%. The preparations were purified for stability studies by HPLC using the following methods.

*Method 1 (**Re1, Re2, Re3, Re5**)*: Hypersil ODS (10 μm, 250 × 8 mm, Knauer), 3 mL/min; solvent A: methanol; solvent B: 0.01 M phosphate buffer pH 7.4 (PBS); gradient elution: 0−10 min 0 to 100% A (**Re1**, **Re3**) or 0−10 min 30 to 100% A (**Re2, Re5**).

*Method 2 (**Re4, Re7, Re8**)*: PRP-1 (10 μm, 250 × 10 mm, Hamilton); 3 mL/min; solvent A: acetonitrile + 0.1% trifluoro acetic acid (TFA); solvent B: water + 0.1% TFA; gradient elution: 0−10 min 30 to 100% A.

*Method 3 (**Re6**)*: Zorbax 300 SB−C18 (5 μm, 250 × 9.4 mm, Agilent); 3 mL/min; solvent A: acetonitrile + 0.1% TFA; solvent B: water + 0.1% TFA; gradient elution: 0−10 min 30 to 100% A.

Thin-layer chromatography (TLC) was performed using RP-18 silica gel strips (Merck) and methanol/0.01 M phosphate buffer pH 7.4 (90:10) for **Re1**−**Re3** or acetonitrile/water/TFA (80:20:0.1) for **Re4**−**Re8** as mobile phases. All compounds show R_f values between 0.4 and 0.6. The strips were scanned with a raytest Rita radioanalyzer.

Stability Studies. The in vitro stability was determined by adding 2−3 MBq or 37 MBq of the relevant pure ^{188}Re complex, dissolved in 100 μL of propylene glycol, to (i) 400 μL of phosphate buffer (PBS) pH = 7.4; (ii) 200 μL of human plasma + 200 μL of phosphate buffer (PBS) pH = 7.4; (iii) 200 μL of rat plasma + 200 μL of phosphate buffer (PBS) pH = 7.4. The samples containing 2−3 MBq were incubated at room temperature (22 °C), the 37 MBq samples at 37 °C.

All compounds were investigated at low activity level due to the low radiation exposure and easy performance

Table 3. In Vitro Stabilities of ^{188}Re Complexes Re1−Re8 (% $^{188}ReO_4^-$, values are presented as mean ± SD, n = 3)

	phosphate buffer			human plasma			rat plasma		
	1 h	24 h	48 h	1 h	24 h	48 h	1 h	24 h	48 h
Re1	100 ± 0	100 ± 0	100 ± 0	100 ± 0	100 ± 0	100 ± 0	100 ± 0	100 ± 0	100 ± 0
Re2	65 ± 7	100 ± 0	100 ± 0	84 ± 2	100 ± 0	100 ± 0	100 ± 0	100 ± 0	100 ± 0
Re3	11 ± 4	49 ± 1	67 ± 2	5 ± 1	15 ± 1	22 ± 3	16 ± 2	33 ± 3	42 ± 2
Re4	1 ± 1	15 ± 1	32 ± 6	1 ± 1	27 ± 3	33 ± 8	1 ± 1	28 ± 4	30 ± 5
Re5	3 ± 0	3 ± 1	4 ± 1	3 ± 1	6 ± 1	6 ± 0	3 ± 1	7 ± 2	9 ± 4
Re6	1 ± 1	10 ± 3	17 ± 8	0 ± 0	0 ± 1	0 ± 0	2 ± 1	9 ± 2	26 ± 3
Re7	7 ± 1	16 ± 2	16 ± 1	8 ± 1	13 ± 2	13 ± 3	6 ± 2	9 ± 2	9 ± 3
Re8	4 ± 2	8 ± 2	10 ± 1	1 ± 1	2 ± 1	3 ± 1	2 ± 1	3 ± 0	3 ± 0

of the experiments. Only stable complexes have been investigated under harsher conditions. We chose the same conditions as those published by Schibli et al. (*4*), enabling the comparison of the results.

RESULTS

Rhenium Chemistry. *Synthesis*. As outlined in Scheme 1, the nonradioactive Re(III) '4 + 1' model complexes can be prepared using two different methods: (A) reduction−substitution reactions starting from ammonium perrhenate (*8*) or (B) ligand-exchange reactions starting from the hexakisthiourea Re(III) precursor. In the first case, an equimolar amount of NS_3 and an excess of phosphorus(III) ligand, dissolved in methanol (or acetonitrile for carboxyl group-bearing ligands and phosphites), react under reflux (2 h) with an acidic solution of perrhenate (without addition of HCl for phosphite ligand **6**) under an argon atmosphere to afford stable Re(III) '4 + 1' complexes.

Alternatively, equimolar amounts of $[Re(tu)_6]Cl_3$, NS_3 and phosphine react in refluxing methanol to give analogous Re(III) '4 + 1' complexes in moderate yields. Both procedures are characterized by a typical change in color from colorless perrhenate to green or reddish, indicating the reduction from Re(VII) to Re(III) (method (A)), or from brownish to yellow-green in the case of ligand-exchange reactions (method (B)).

Characterization. The Re(III) complexes have been characterized by means of (i) elemental analyses, which are in good agreement with the proposed formulation, (ii) cyclic voltammetry, (iii) spectroscopic measurements, comprising UV/vis and multinuclear NMR, (iv) mass spectrometry, and (v) X-ray structure analyses of four representative complexes including unsubstituted NS_3 and phosphines **2**, **3**, or **4** and phosphite **6** (complexes **Re2**, **Re3**, **Re4**, and **Re6**).

The diamagnetism shown by this class of Re(III) complexes is in agreement with low-spin d^4 trigonal bipyramidal configuration (vide infra, X-ray description). Thus, NMR spectra of **Re1**−**8** exhibit a sharp ^{31}P singlet, which moves significantly downfield, by 30−40 ppm, upon coordination in phosphine containing complexes **Re1**−**5** and **Re7**−**8** compared to the values shown by uncoordinated ligands (see Table 4). On the contrary, such a singlet moves upfield by 16 ppm in the unique case of the coordinated phosphite in **Re6**. ^{1}H and ^{13}C spectra of Re(III) '4 + 1' complexes show signals both in the aromatic and in the aliphatic regions, consistent with the formulation. In particular, proton spectra of complexes comprising the unsubstituted NS_3 ligand (**Re1**−**6**) are dominated by a broad signal at δ 2.9 ppm, characteristic for the NS_3 ethylene arms. Incorporation of a carboxyl group or a substituted carboxyl function in the NS_3 framework causes such a signal to become a series of multiplets falling in the 2.4−3.7 ppm region (complexes **Re7** and **Re8**; see Figure 2).

Table 4. Physicochemical Parameters vs in Vitro Stability of Complexes Re1−Re8

	cone angle θ of the free P(III) ligand,[a] deg	$E°$ [V]	λ [nm][b]	δ $^{31}P_{complex}$ [ppm]	% $^{188}ReO_4^-$ in human plasma after 24 h
Re1	122	−0.05	464	−13	100 ± 0
Re2	∼115	+0.04	461	+16	100 ± 0
Re3	∼140[c]	+0.19	450	+20	15 ± 1
Re4	∼140	−0.02	455	+18	27 ± 3
Re5	∼145	+0.05	457	+31	6 ± 1
Re6	141	+0.37	418	+116	0 ± 0
Re7	∼145	+0.13	455	+30	13 ± 2
Re8	∼145	+0.04	457	+30	2 ± 1

[a] Taken or estimated from ref 18. [b] Most intensive band in the vis region. [c] Data estimated from Rahman (*19*) who corrected the 132° value reported by Tolman (*18*).

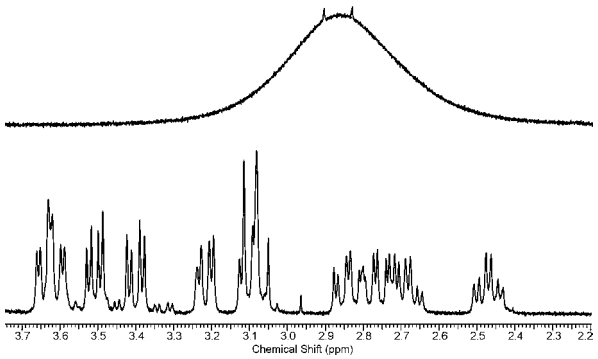

Figure 2. ^{1}H NMR spectra of **Re5** (above) and **Re7** (below) in the region 2.2−3.7 ppm.

The UV/vis spectra of **Re1**−**8** are characterized by intense absorption bands at approximately 420−460 nm (ϵ approximately 1000), and less intense absorptions (ϵ approximately 250) in the 520−590 nm region. The energy associated with these absorptions indicates that the former bands correspond to metal to ligand (Re→S) charge-transfer transitions, whereas less intense bands correspond to d−d transitions. Both absorption bands are responsible for the green or reddish color of these complexes and move to shorter wavelengths in the phosphite-containing complex **Re6** (see Table 4), indicating that the energy involved in the transfer for **Re6** is higher compared to the energy implicated in phosphine complexes.

The molecular structure of four representative examples of five-coordinate Re(III) '4 + 1' complexes, **Re2**, **Re3**, **Re4**, and **Re6**, were investigated in the solid state by X-ray diffraction methods. A summary of the crystallographic data is given in Table 1, and selected bond lengths and angles are reported in Table 2. As outlined in Figures 3−6, the four complexes adopt a trigonal-bipyramidal geometry. The three NS_3 thiolate sulfurs form the trigonal plane, and the amine nitrogen of the chelate ligand and the phosphine phosphorus occupy the apical positions. These structures strictly resemble those

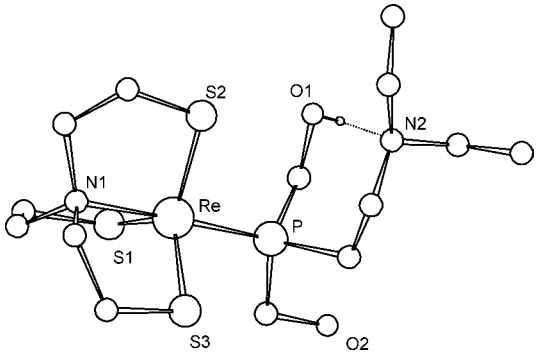

Figure 3. Molecular structure of **Re2**.

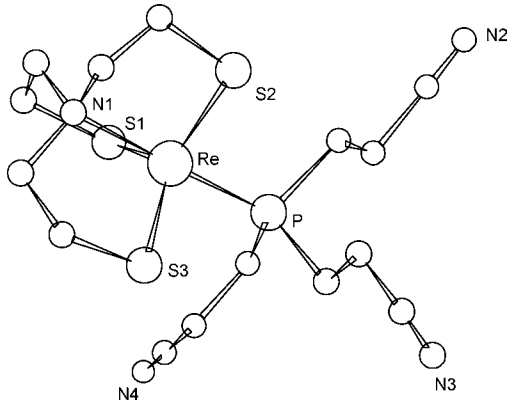

Figure 4. Molecular structure of **Re3**.

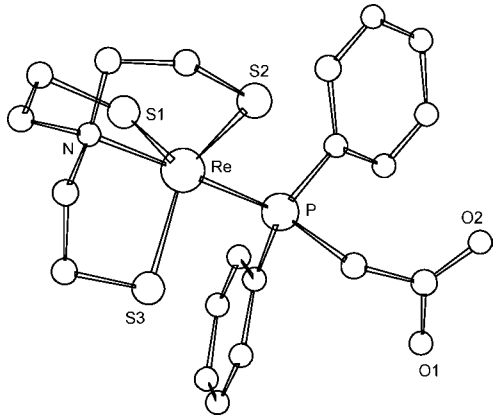

Figure 5. Molecular structure of **Re4**.

of rhenium complexes and its second-row congener technetium, in which the monodentate phosphine ligand has been replaced by various isocyanide groups (*8*−*10*). Angles and bond distances comprising the [Re(NS_3)] fragment, as well as the linearity of the N−Re−P spin, compare well with those reported in technetium complexes and do not deserve further comment. The Re−P bond distance elongates going from phosphite (**Re6**, Re−P = 2.2228(13) Å) to phosphine complexes (**Re3**, Re−P = 2.291(4); **Re2**, Re−P = 2.297(2); **Re4**, Re−P = 2.301(4) Å). For **Re2**, a hydrogen bond between one of the hydroxyl groups and the nitrogen in the backbone of the monodentate P(III) ligand is observed (see Figure 3). This additional contact may further diminish the steric hindrance of this ligand (vide infra). For **Re3**, both Δ and Λ conformers were found. For clarity reasons, only the latter is displayed in Figure 4.

The cyclovoltammetric profile of each complex recorded in CH_2Cl_2 shows only a reversible one-electron process in the anodic region which can be assigned, by coulometric experiments, to the formation of Re(IV), presumably accessing the $5d^3$ system. The oxidation process occurs in the region from −0.05 to +0.19 V for phosphine-containing complexes. The unique phosphite complex **Re6** is more difficult to oxidize by approximately 200−400 mV than similar phosphine complexes, corroborating the view that phosphite-containing compounds could be more stable toward reoxidation to perrhenate.

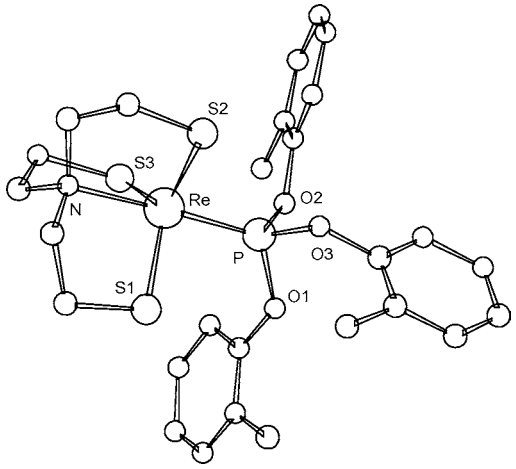

Figure 6. Molecular structure of **Re6**.

Scheme 2. Carrier-Free Preparation of ^{188}Re '4 + 1' Complexes

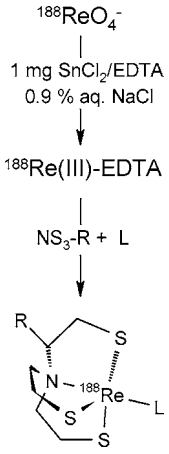

Rhenium-188 Chemistry and Stability Studies. *Preparation of the ^{188}Re Complexes.* A two-step procedure was used for the synthesis of '4 + 1' ^{188}Re complexes. At first a ^{188}Re(III)-EDTA intermediate complex was formed by reduction of $^{188}ReO_4^-$ with 1 mg of $SnCl_2$ in acidic solution (pH < 3). This labile intermediate species was converted to the '4 + 1' complex in a second step by contemporary addition of the NS_3/P ligands (Scheme 2). The yields were not optimized and were between 50 and 90% for phosphine complexes and 20−30% for phosphite complex **Re6**, as assessed by TLC. Comparison of retention times obtained by means of parallel radiometric and photometric detection of nonradioactive rhenium complexes and rhenium-188 complexes established the identity of the complexes prepared at millimolar and nanomolar concentrations.

Stability Studies. In vitro stabilities were determined by incubating 2−3 MBq of rhenium-188 complexes in phosphate buffer, human serum, and rat serum at room temperature. The amount of formed $^{188}ReO_4^-$ was determined by TLC analysis. Stabilities for **Re1**−**Re8** are shown in Table 3 and graphically illustrated in Figure 7.

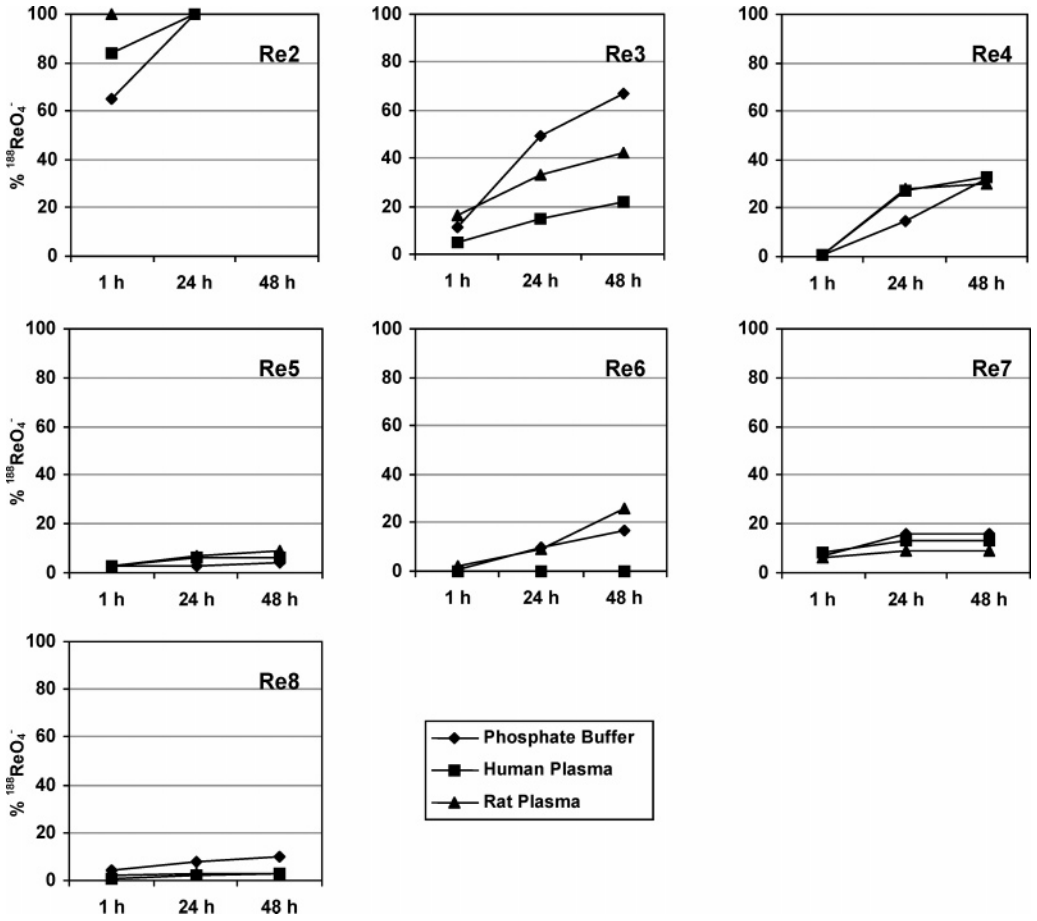

Figure 7. In vitro stabilities of ^{188}Re complexes **Re2**−**Re8** (standard deviations are omitted for clarity).

Re 5, which can be easily attached to biomolecules via an amide bond, was one of the most stable compounds at low activity level. Its in vitro stability was therefore further investigated under harsher conditions using 37 MBq of the complex and incubation at 37 °C in human plasma. The following amounts of $^{188}ReO_4^-$ were found (% $^{188}ReO_4^-$, means ± SD, $n = 3$): 9 ± 1 (1 h); 16 ± 1 (24 h); 19 ± 2 (48 h).

DISCUSSION

M(III) '4 + 1' complexes (M = Tc, Re) with NS_3 and isocyano ligands synthesized so far were predominantly lipophilic compounds (*9*, *10*). Development of more hydrophilic '4 + 1' species would be an important result (i) to favor renal excretion of radioactive metabolites in order to minimize exposure of radiation-sensitive organs and (ii) to open the possibility for labeling of antibodies and peptides in aqueous media. By using phosphorus(III) compounds (tertiary phosphines and phosphites of different size and lipophilicity, see Scheme 1) instead of isocyano ligands, another class of stable Re(III) '4 + 1' complexes was easily accessible.

Nonradioactive rhenium complexes were synthesized either starting from perrhenate or by using a prereduced rhenium(III) thiourea precursor, whereas rhenium-188 complexes were prepared using a method recently described by Seifert and co-workers (*11*). Since the direct reduction of $^{188}ReO_4^-$ with NS_3 and phosphorus(III) ligands in the presence of $SnCl_2$ led to a large amount of reduced/hydrolyzed rhenium-188 compounds, we preferred an alternative way based on the formation of a prereduced ^{188}Re(III)-EDTA complex as a labile intermediate. Following ligand-exchange with the contemporary addition of NS_3/P(III) ligands, '4 + 1' complexes were obtained with up to 90% radiochemical purity.

In vitro stability of these ^{188}Re '4 + 1' agents was found to be very unpredictable, but strongly dependent on the nature of the monodentate P(III) coligand (Figure 7). For example, lipophilic **Re1** was completely reoxidized to $^{188}ReO_4^-$ within 1 h. Similarly, the most hydrophilic complexes **Re2** bearing the hydroxymethyl phosphine and **Re3** comprising the cyanoethyl phosphine were not stable as well, giving large amounts of perrhenate. Conversely, more lipophilic complexes such as **Re5** and **Re6** were found to produce only little amounts of $^{188}ReO_4^-$ in all investigated media. Differences between stabilities of **Re3** and **Re6** in human plasma, rat plasma, and phosphate buffer give rise to the assumption that the in vitro stability is influenced by both biological and chemical factors. The former can be specific enzymes responsible for the cleavage of chemical bonds and/or the free radicals scavenger capability of plasma components such as human serum albumin (*15*−*17*).

With the aim of understanding the strikingly different in vitro stability of these ^{188}Re '4 + 1' compounds, we prepared the corresponding nonradioactive rhenium complexes **Re1**−**Re8**, collected a series of significant physicochemical parameters (compiled in Table 4), and tried to find out which factors may govern the production of substitution-inert or hydrolyzable species. In this connection, we evidently focused our attention on the coordinated P(III) ligand.

The influence of steric and electronic properties of phosphorus(III) ligands on complex reactivity has been investigated over the past decades (see a comprehensive review article published by Tolman (*18*)) according to the

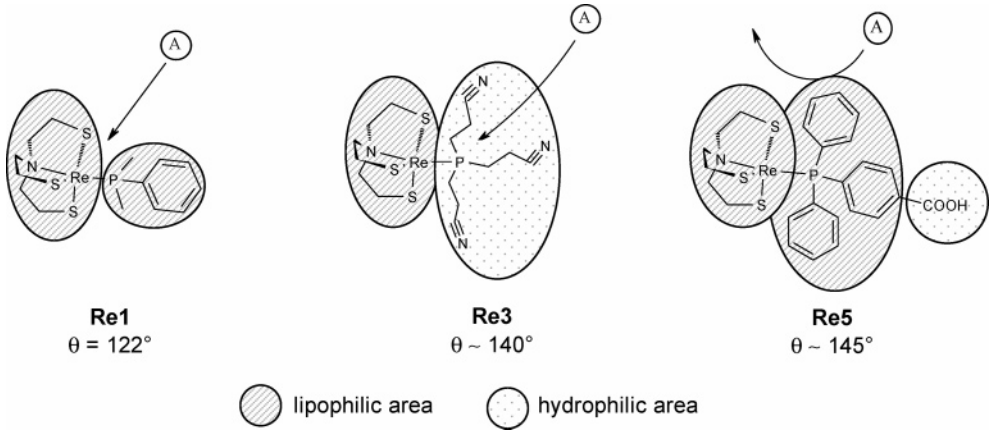

Figure 8. Possible attack of a reactive water-derived species (A) on Re '4 + 1' complexes of varying steric properties.

essential role played by transition metal−phosphorus(III) ligand complexes in homogeneous catalysis. Even if steric and electronic effects are always synergistically related and their individual analysis is difficult to perform, we tried to examine physicochemical parameters one at a time.

Considering the ^{31}P NMR shift ongoing from noncoordinated to coordinated P(III) ligands in the '4 + 1' rhenium complexes, we observed that the electron density at the P atom decreases in the case of tertiary phosphines (downfield shift) and increases in the case of phosphites (upfield shift). This electron delocalization directly influenced the $E°$ of the Re^{III}/Re^{IV} couple: for example, the phosphite complex **Re6** was harder to oxidize by 200−400 mV compared to all of the phosphine complexes. In principle, this property could be associated with the high in vitro stability exhibited by phosphite-containing **Re6**, even if complexes showing $E°$ values approaching the Fc/Fc^+ reference couple (ca. 0.00 mV, for instance **Re5** and **Re8**) were quite stable in vitro as well. The analysis of the electronic spectra confirms the difference between phosphine and phosphite complexes regarding their electron-withdrawing ability, but does not provide unambiguous information to discriminate between complexes of high and low in vitro stability. The observation that complexes showing better resistance to oxidation (higher $E°$ values) are more stable in vitro toward oxidation to perrhenate appears rather obvious and seems to be only one of the factors influencing the in vitro stability.

Much more information comes out from the analysis of steric factors. As pointed out by Tolman (*18*), the thermodynamic stability and kinetic inertness of most transition metal complexes including phosphorus(III) ligands is dominated by steric effects. The Tolman's cone angle θ (*18*, *20*) is the parameter utilized to describe the steric hindrance of these ligands. θ is the interior linear angle of a cone centered 2.28 Å from the center of the P atom and the edges of the cone tangential to the outermost van der Waals radii of the ligand. If we correlate θ with the amount of $^{188}ReO_4^-$ formed (Table 4), it can be seen that the in vitro stability of **Re1**−**Re8** strongly depends on this parameter. In fact, only P(III) ligands with θ values comprised in the 140−145° range afforded stable, sterically tight rhenium-188 compounds. In contrast, complexes including both lipophilic or hydrophilic phosphine ligands with smaller cone angles (**Re1**, **Re2**) were thermodynamically accessible in the sense that they formed in a good yield and could be completely characterized at macroscopic level with cold rhenium from common organic solutions, but were labile and gave rise to complete reoxidation to perrhenate in the presence of water. For **Re2**, it has to be considered that the hydrogen bond in the phosphine's backbone (see Figure 3) may induce a further decrease of the cone angle supporting further its instability in vitro. Analogously, phosphite ligands $P(OEt)_3$ (θ = 109°) and $P(O^iPr)_3$ (θ = 130°) taken from ref 18, which were expected to yield more stable Re '4 + 1' complexes on the basis of electronic considerations, showed high instability with reoxidation to perrhenate in water solutions, either at macroscopic and carrier-free levels. These findings indicate that, despite the thermodynamic stability exhibited by this class of trigonal bipyramidal Re '4 + 1' compounds, the inertness in aqueous solution appeared to be the critical factor to consider for their overall stability.

As sketched in Figure 8, only complexes incorporating a tailored P(III) ligand are able to generate, along with the thiolate sulfurs of the NS_3 ligand, an appropriate hydrophobic core around the rhenium. Only these complexes (i.e. **Re5** or **Re8**) are kinetically inert in aqeous solution. Less encumbering P(III) ligands (smaller θ) produced instead complexes (i.e. **Re1**) amenable to attack for steric reasons, and, analogously, more hydrophilic Re '4 + 1' species (i.e. **Re3**) with a suitable P(III) cone angle were subjected to hydrolysis for solubility reasons. Despite this speculation, the mechanism could be tentatively assigned as associative: the attack of a reactive water-derived species, formed under the influence of radiation, was followed by the release of the P(III) ligand, crumbling of the $Re(NS_3)$ moiety, and reoxidation to perrhenate. Radiation and formation of radicals should be considered for causing instability of rhenium-188 complexes in vitro. The fact that the amount of perrhenate is increasing with increasing activity concentration (see **Re5** in Figure 9) supports our interpretation.

On the opposite side, P(III) ligands with larger cone angles such as the lipophilic triisopropylphosphine (θ = 160°) or the hydrophilic triphenylphosphine-3,3′,3″-trisulfonic acid (θ ~155°) did not form Re '4 + 1' compounds, indicating that overencumbered ligands cannot efficiently reach the $Re(NS_3)$ moiety.

According to the above data, hydrophilicity of the whole complex, which still remained an important goal of this study, had to be introduced by means of suitable functional groups on the periphery of the molecule, either on the monodentate phosphine and/or on the chelate NS_3 framework. The increase of the overall hydrophilicity in '4 + 1'-type compounds has already been demonstrated in analogous Tc complexes (*11*) by insertion of a carboxyl group into the NS_3 chelate. The incorporation of a carboxyl group could also serve for the conjugation of

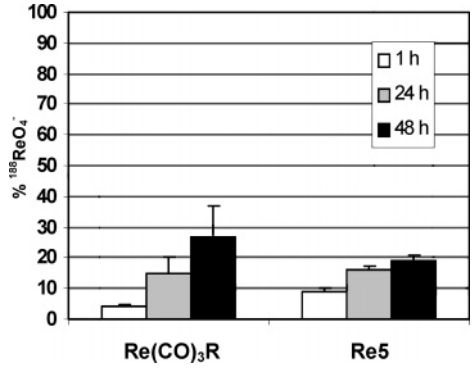

Figure 9. Comparison of in vitro stabilities of $^{188}Re(CO)_3$\{[(di-1*H*-imidazol-2-ylmethyl)amino] acetic acid\} (*4*) and **Re5** after incubation in human plasma at 37 °C.

biomolecules. Such peripheral variation does not affect the in vitro stability of the complexes. For example, **Re7** and **Re8**, carrying a free carboxyl group or an amide group onto the NS_3 backbone exhibited higher hydrophilicity (**Re7** ≫ **Re8** > **Re5**) but comparable in vitro stability than their unsubstituted analogue **Re5**.

Only few and mostly imprecise data on the stability of ^{188}Re complexes are found in the literature. Complexes with mercaptoacetyl triglycine ($^{188}Re(O)MAG_3$) and those of the HYNIC system were found to be unstable in vitro and in vivo by our and other groups (*21*−*23*). Contrarily, some groups found high in vitro and in vivo stability of $^{188}Re(O)MAG_3$ even at high activity concentration (*5*−*7*). Schibli and co-workers reported on the in vitro stability of ^{188}Re-tricarbonyl complexes incorporating different tridentate ligands (*4*), but utilizing higher activity and higher temperature (37 MBq, 37 °C). We compared the in vitro stability of **Re5** under these conditions with that displayed by the most stable tricarbonyl complex having [(di-1*H*-imidazol-2-ylmethyl)amino]-acetic acid as tridentate ligand and found similar in vitro stabilities (Figure 9).

CONCLUSION

A series of Re(III) '4 + 1' complexes, [$ReNS_3$)(PRR′R″)], containing a tetradentate NS_3 chelator and a monodentate phosphorus(III) coligand (tertiary phosphine or phosphite) has been prepared both at macroscopic level with nonradioactive rhenium and at carrier-free level with ^{188}Re. In vitro stabilities of ^{188}Re '4 + 1' complexes in human plasma, rat plasma, and in phosphate buffer depend primarily on the nature of the phosphorus(III) coligand. Several physicochemical parameters of homologous rhenium complexes including Re^{III}/Re^{IV} redox potentials and electronic and NMR spectra, together with scrutiny of the steric hindrance of P(III) ligands, were consequently analyzed in order to rationalize the in vitro behavior. The Tolman's cone angle θ was found to be the crucial factor in the formation of substitution-inert Re(III) '4 + 1' complexes. Only tertiary phosphines and phosphites with cone angles in the range between 140 and 145° gave rise to agents stable in vitro. Obviously, the steric hindrance of these P(III) coligands along with the lipophilic nature of the three coordinated thiolate sulfurs generates a hydrophobic area around the Re(III) center which prevents hydrolysis and reoxidation to perrhenate. Hence, the initial idea to synthesize overall hydrophilic Re '4 + 1' compounds was changed, and, while preserving a lipophilic core in the inner coordination sphere, hydrophilicity was introduced into the periphery of the complex by insertion of carboxylic functions, either at the NS_3 framework and/or at the monodentate phosphine ligand. ^{188}Re '4 + 1' complexes of this formulation were found to be sufficiently stable toward reoxidation in phosphate buffer as well as in rat plasma and human plasma, both at low and high activity levels. Therefore, we consider these agents as promising candidates for the development of ^{188}Re radiotherapeutics.

ACKNOWLEDGMENT

We thank G. Wunderlich (Klinik und Poliklinik für Nuklearmedizin, TU Dresden) for providing a $^{188}W/^{188}Re$ generator and the Deutscher Akademischer Austauschdienst (DAAD) for financial support.

LITERATURE CITED

(1) Knapp, F. F. (1998) Rhenium-188 − A generator-derived radioisotope for cancer therapy. *Cancer Biother. Radiopharm. 13*, 337−349.

(2) Knapp, F. F., Beets, A. L., Guhlke, S., Zamora, P. O., Bender, H., Palmedo, H., and Biersack, H.-J. (1997) Availability of rhenium-188 from the alumina-based tungsten-188/rhenium-188 generator for preparation of rhenium-188-labeled radiopharmaceuticals for cancer treatment. *Anticancer Res. 17*, 1783−1796.

(3) Jeong, J. M., and Chung, J.-K. (2003) Therapy with ^{188}Re-labeled radiopharmaceuticals: An overview of promising results from initial clinical trials. *Cancer Biother. Radiopharm. 5*, 707−717.

(4) Schibli, R., Schwarzbach, R., Alberto, R., Ortner, K., Schmalle, H., Dumas, C., Egli, A., and Schubiger, P. A. (2002) Steps toward high specific activity labeling of biomolecules for therapeutic application: Preparation of precursor ($^{188}Re(H_2O)_3(CO)_3)^+$ and synthesis of tailor-made bifunctional ligand systems. *Bioconjugate Chem. 13*, 750−756.

(5) Lin, W. Y., Tsai, S. C., Hsieh, B. T., Lee, T. W., Ting, G., and Wang, S. J. (2000) Evaluation of three rhenium-188 candidates for intravascular radiation therapy with liquid-filled balloons to prevent restenosis. *J. Nucl. Cardiol. 7*, 37−42.

(6) Guhlke, S., Schaffland, A., Zamora, P. O., Sartor, J., Diekman, D., Bender, H., Knapp, F. F., and Biersack, H.-J. (1998) ^{188}Re- and ^{99m}Tc-MAG_3 as prosthetic groups for labeling amines and peptides: Approaches with pre- and postconjugate labeling. *Nucl. Med. Biol. 25*, 621−631.

(7) Oh, S. J., Moon, D. H., Ha, H. J., Park, S. W., Hong, M. K., Park, S. J., Choi, T. H., Lim, S. M., Choi, C. W., Knapp, F. F., and Lee, H. K. (2001) Automation of the synthesis of highly concentrated ^{188}Re-MAG_3 for intracoronary radiation therapy. *Appl. Radiat. Isot. 54*, 419−427.

(8) Spies, H., Glaser, M., Pietzsch, H.-J., Hahn, F. E., and Lügger, T. (1995) Synthesis and reactions of trigonal-bipyramidal rhenium and technetium complexes with a tripodal, tetradentate NS_3 ligand. *Inorg. Chim. Acta 240*, 465−478.

(9) Drews, A., Pietzsch, H.-J., Syhre, R., Seifert, S., Varnäs, K., Hall, H., Halldin, C., Kraus, W., Karlsson, P., Johnsson, C., Spies, H., and Johannsen, B. (2002) Synthesis and biological evaluation of technetium(III) mixed-ligand complexes with high affinity for the cerebral 5-HT_{1a} receptor and the alpha1-adreneric receptor. *Nucl. Med. Biol. 29*, 389−398.

(10) Pietzsch, H.-J., Gupta, A., Syhre, R., Leibnitz, P., and Spies, H. (2001) Mixed-ligand technetium(III) complexes with tetradentate/monodentate NS_3/isocyanide coordination: A new nonpolar technetium chelate system for the design of neutral and lipophilic complexes stable in vivo. *Bioconjugate Chem. 12*, 583−544.

(11) Seifert, S., Künstler, J.-U., Schiller, E., Pietzsch, H.-J., Pawelke, B., Bergmann, R., and Spies, H. (2004) Novel procedures for preparing ^{99m}Tc complexes with tetradentate/monodentate coordination of varying lipophilicity and adaption to ^{188}Re analogues. *Bioconjugate Chem. 15*, 856−863.

(12) Jarolim, T., and Podlahova, J. (1976) Coordinating behaviour of diphenylphosphineacetic acid. *J. Inorg. Nucl. Chem. 38*, 125−129.
(13) Kosolapoff, G. M. (1948) Isomerization of trialkyl phosphites. Some derivatives of 2-bromoethane phosphonic acid. *J. Am. Chem. Soc. 70*, 1971−1972.
(14) Gambino, D., Otero, L., Kremer, E., Piro, O. E., and Castellano, E. E. (1997) Synthesis, characterization and crystal structure of hexakis-(thiourea-S)-rhenium(III) trichloride tetrahydrate: A potential precursor to low-valent rhenium complexes. *Polyhedron 16*, 2263−2270.
(15) Chakrabarti, M. C., Le, N., Paik, C. H., de Graff, W. G., and Carrasquillo, J. A. (1996) Preventions of radiolysis of monoclonal antibody during labeling. *J. Nucl. Med. 37*, 1384−1388.
(16) Salako, Q. A., O'Donell, R. T., and DeNardo, S. J. (1998) Effects of radiolysis on yttrium-90-labeled Lym-1 antibody preparations. *J. Nucl. Med. 39*, 667−670.
(17) Iznaga-Escobar, N. (2001) Direct radiolabeling of monoclonal antibodies with rhenium-188 for radioimmunotheraphy of solid tumors − A review of radiolabeling characteristics, quality control and in vitro stability studies. *Appl. Radiat. Isot. 54*, 399−406.
(18) Tolman, C. A. (1977) Steric effects of phosphorus ligands in organometallic chemistry and homogeneous catalysis. *Chem. Rev. 77*, 313−348.
(19) Rahman, M., Liu, H. Y., Prock, A., and Giering, W. (1987) Steric and electronic factors influencing transition-metal-phosphorus(III) bonding. *Organometallics 6*, 650−658.
(20) Tolman, C. A. (1970) Phosphorus ligand exchange equilibria on zerovalent nickel. A dominant role for steric effects. *J. Am. Chem. Soc. 92*, 2956−2965.
(21) He, J., Liu, C., Venderheyden, J. L., Liu, G., Dou, S., Ruschkowski, M., and Hnatowich, D. J. (2003) Radiolabeling morpholinos with ^{188}Re carbonyl provides improved in vitro and in vivo stability to re-oxidation. *J. Nucl. Med. 44*, 100P.
(22) Liu, C.-B., Liu, G.-B., Liu, N., Zhang, Y.-M., He, J., Rusckowski, M., and Hnatowich, D. J. (2003) Radiolabeling morpholinos with ^{90}Y, ^{111}In, ^{188}Re, ^{99m}Tc. *Nucl. Med. Biol. 30*, 207−214.
(23) Seifert, S., Künstler, J.-U., and Johannsen, B. (2002) Stability of ^{99m}Tc and ^{188}Re labelled HYNIC−IVIG. *Wissenschaftlich-Technische Berichte FZR-340, Annual Report 2001*; p 42.

BC049745A

Radioiodinated Azide and Isothiocyanate Derivatives of Cocaine for Irreversible Labeling of Dopamine Transporters: Synthesis and Covalent Binding Studies

John R. Lever,[†,*] Mu-Fa Zou,[‡] M. Laura Parnas,[§] Romain A. Duval,[†] Sara E. Wirtz,[∥] Joseph B. Justice,[∥] Roxanne A. Vaughan,[§] and Amy Hauck Newman[‡]

Departments of Radiology, and Medical Pharmacology and Physiology, University of Missouri—Columbia, Columbia, Missouri 65212 and Research Service, Harry S. Truman Veterans Administration Medical Center, Columbia, Missouri 65201, Medicinal Chemistry Section, National Institute on Drug Abuse, Intramural Research Program, Baltimore, Maryland 21224, Department of Biochemistry and Molecular Biology, University of North Dakota, Grand Forks, North Dakota 58203, and Department of Chemistry, Emory University, Atlanta, Georgia 30322. Received November 19, 2004; Revised Manuscript Received February 15, 2005

Two novel N-substituted-3β-phenyltropane alkaloids have been labeled with iodine-125 for use as irreversible probes of dopamine transporter (DAT) binding sites. One contains an iodoaryl azide moiety for photolabeling, while the other bears an iodoaryl isothiocyanate for direct conjugation. Both radioligands were prepared in a one-flask procedure by electrophilic radioiodination of the corresponding aniline under no-carrier-added conditions, followed either by diazotization and treatment with sodium azide, or by addition of thiophosgene under basic conditions. Specifically, (−)-*N*-[4-(3-[^{125}I]iodo-4-azidophenyl)butyl]-2β-carbomethoxy-3β-(4-chlorophenyl)tropane ([^{125}I]MFZ-2-24) and (−)-*N*-[4-(3-[^{125}I]iodo-4-isothiocyanophenyl)butyl]-2β-carbomethoxy-3β-(4-chlorophenyl)tropane ([^{125}I]MFZ 3-37) were synthesized. Isolation by reversed-phase HPLC and solid-phase extraction gave good average yields of [^{125}I]MFZ-2-24 (67%, $n = 5$) and [^{125}I]MFZ-3-37 (45%, $n = 3$) with high radiochemical purities (96−99%) and specific radioactivities (>2000 mCi/μmol). The utility of the radioligands was demonstrated by their covalent linkage to rat striatal membranes, and immunoprecipitation of a single radiolabeled band at 80 kDa corresponding to the full-length DAT.

INTRODUCTION

The dopamine transporter (DAT)[1] is an 80 kDa phosphoprotein, thought to have 12 transmembrane domains (TMs), that is regulated by protein kinases, controls synaptic dopamine concentrations, and plays a pivotal role in locomotion (*1*, *2*). Inhibition of dopamine uptake also is recognized as a critical determinant of the reinforcing properties and abuse liability of cocaine and other stimulants (*3*, *4*). Thus, the identification of therapeutic DAT inhibitors that block the actions of stimulant drugs of abuse with minimal disruption of normal dopaminergic function is a topic of current interest (*5*, *6*). In fact, dopamine, cocaine, amphetamine, and other structural classes of DAT ligands bind to recognition sites that seem to be at least partially discrete based upon functional, chimera, and mutagenesis studies.

Accordingly, we have been developing irreversible ligands to assess and differentiate the features of DAT binding domains at the molecular level. These ligands include several radioiodinated photoaffinity probes: [^{125}I]RTI-82 (*7*, *8*), a tropane alkaloid congener of cocaine; [^{125}I]DEEP (*7*,*9*) and [^{125}I]AD-96-129 (*10*) which are based upon GBR12,909; and [^{125}I]GA-2-34 (*11*), a benztropine with key pharmacophores drawn from both of the other structural classes (Figure 1). Studies to date confirm that distinct regions of the DAT primary sequence are labeled covalently depending upon ligand framework. In brief, [^{125}I]RTI-82 becomes incorporated specifically in TMs 4−6, [^{125}I]DEEP and [^{125}I]GA-2-34 preferentially attach to TMs 1−2, and [^{125}I]AD-96-129 labels TMs 1−2 and 4−6 to about the same extent (*12*, *13*). The data for [^{125}I]AD-96-129 suggests that TMs 1−2 and 4−6 should be close together in the three-dimensional structure of the DAT and, by comparison to the results from [^{125}I]DEEP, demonstrates the sensitivity of DAT binding to modest structural modifications (*13*).

Interestingly, [^{125}I]GA-2-34 and [^{125}I]RTI-82 attach covalently to different TMs even though they both have a tropane ring system (*12*). This finding is consistent with work showing that benztropines exhibit potent DAT binding but do not display a behavioral profile like that

* Address correspondence to John R. Lever, Ph.D., Department of Radiology, M292 Medical Sciences Bldg., University of Missouri—Columbia, One Hospital Dr., Columbia, MO 65212. Phone: 573-814-6000 ext. 3686. FAX: 573-814-6551. E-mail: leverj@health.missouri.edu.

† University of Missouri—Columbia and Harry S. Truman Veterans Administration Medical Center.

‡ National Institute on Drug Abuse.

§ University of North Dakota.

∥ Emory University.

[1] Abbreviations: AD-96-129, 4-[2-(diphenylmethoxy)ethyl]-1-[(4-azido-3-iodophenyl)methyl]piperidine; DAT, dopamine transporter; DEEP, 1-[2-(diphenylmethoxy)ethyl]-4-[2-(4-azido-3-iodophenyl)ethyl]piperazine; DTT, dithiothreitol; GA-2-34, *N*-[*n*-butyl-4-(4-azido-3-iodophenyl)]-4,4-difluoro-3-(diphenylmethoxy)tropane; GBR 12 ,909, 1-{2-[bis(4-fluorophenyl)methoxy]ethyl}-4-(3-phenylpropyl)piperazine; HEK, human embryonic kidney; IP, immunoprecipitated; MFZ-2-24, (−)-*N*-[4-(3-iodo-4-azidophenyl)butyl]-2β-carbomethoxy-3β-(4-chlorophenyl)tropane; MFZ 3-37, (−)-*N*-[4-(3-iodo-4-isothiocyanophenyl)butyl]-2β-carbomethoxy-3β-(4-chlorophenyl)tropane; RTI-82, 3-(4-chlorophenyl)tropane-2-carboxylic acid, 4-azido-3-iodophenylethyl ester; TM, transmembrane domain; WIN 35, 428, (−)-2-carbomethoxy-3-(4-fluorophenyl)tropane.

10.1021/bc0497214 CCC: $30.25 © 2005 American Chemical Society
Published on Web 04/15/2005

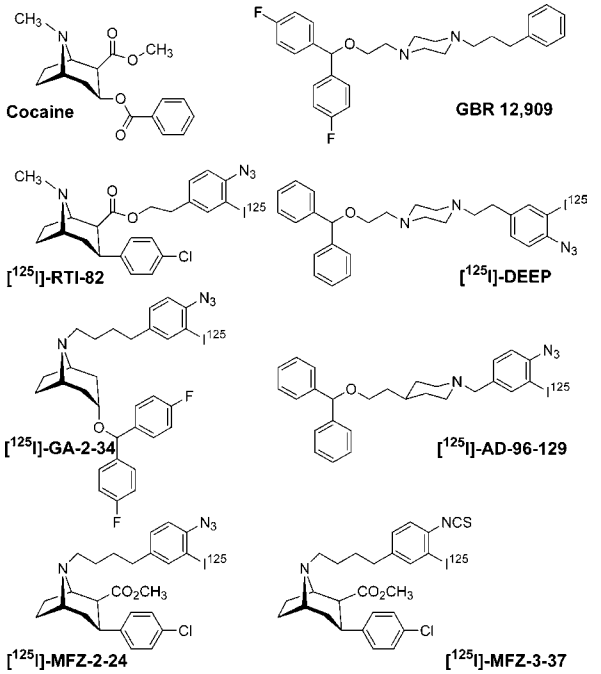

Figure 1. Structures of the cocaine and GBR 12 909 scaffolds, the DAT photoaffinity labels whose sites of incorporation have been identified, and the new irreversible ligands, [^{125}I]MFZ-2-24 and [^{125}I]MFZ-3-37.

of cocaine (*14*, *15*) and comparative molecular field analyses indicating different DAT binding requirements for benztropines and cocaine (*16*, *17*). As discussed by Zou et al. (*18*), [^{125}I]GA-2-34 and [^{125}I]RTI-82 might bind to discrete DAT recognition sites or might bind to the same site but covalently label different domains because of differing spatial orientations of the aryl azide substituents (cf. Figure 1). Therefore, a complementary RTI-82 analogue, MFZ-2-24, was prepared where the *N*-methyl was replaced by a butyl linker to an aryl azide moiety as found in GA-2-34. Nonradioactive MFZ-2-24 displayed high, reversible binding affinity (IC_{50} 33 nM vs [3H]-WIN35,428) for the human DAT expressed in mammalian cell line HEK 293 and the structurally related isothiocyanate, MFZ-3-37, covalently bound to human DAT in washout experiments (*18*). In the present study, we report the synthesis of [^{125}I]MFZ-2-24, MFZ-3-37, and [^{125}I]MFZ-3-37 (Figure 1). We also demonstrate, by photoaffinity and direct labeling of rat striatal DAT, their potential as tools for molecular characterization of DAT binding domains.

EXPERIMENTAL PROCEDURES

General. Fully characterized, nonradioactive samples of tropane alkaloids were prepared as previously described (*18*). Other chemicals and solvents were the best grade available and were used as received from commercial sources. No-carrier-added [^{125}I]NaI was obtained from Amersham Corp. (1 mCi/10 μL; NaOH solution, pH 8−12). HPLC equipment consisted of a Rheodyne 7125 injector, Waters 510EF pumps, Waters 490 UV absorbance detector (λ 254 nm), a flow-through NaI(Tl) crystal scintillation detector comprised of EG&G Ortec components, Shimadzu CR-3A integrating recorders, and a Rainan Dynamax system for digital recording. Waters C-18 Nova-Pak columns, protected by matching guard columns, were used for preparative and analytical HPLC. Activated Waters SEP−PAK Light *t*-C-18 cartridges were employed for solid-phase extraction. Radioactivity was measured with a radioisotope dose calibrator (Capintec CRC-15W) using similar counting geometries or correction factors for each reading. ^{1}H and ^{13}C NMR spectra were recorded on a Bruker AC-300 instrument. Proton chemical shifts are reported as parts per million (δ) relative to internal tetramethylsilane (δ = 0.00 ppm). Carbon chemical shifts are reported as parts per million (δ) relative to deuterated chloroform (δ = 77.0 ppm). Infrared spectra were recorded as a neat film on NaCl plates using a Perkin-Elmer 1600 FTIR spectrometer. Microanalyses were performed by Atlantic Microlab, Inc. (Norcross, GA) and agree within 0.4% of calculated values.

(−)-*N*-[4-(3′-Iodo-4′-isothiocyanophenyl)butyl]-2β-carbomethoxy-3β-(4-chlorophenyl)tropane (MFZ-3-37). (−)-*N*-[4-(3′-Iodo-4′-aminophenyl)butyl]-2β-carbomethoxy-3β-(4-chlorophenyl)tropane (*18*) (0.24 g, 0.43 mmol) was dissolved in a biphasic mixture of $CHCl_3$ (25 mL) and water (10 mL) containing $NaHCO_3$ (0.16 g). The mixture was cooled to 0 °C, and freshly distilled thiophosgene (0.56 mmol, 1.3 equiv) was added with vigorous stirring. After 3 h, the reaction was brought to ambient temperature, the layers were separated, and the aqueous phase was extracted with $CHCl_3$ (3 × 10 mL). The combined organic extracts were dried (K_2CO_3) and concentrated in vacuo. The residue was purified by flash column chromatography ($CHCl_3$/MeOH/NH_4OH; 98:2:1) to afford 0.22 g (84%) of product that was converted to the salt with methanolic HCl. $[\alpha]^{25}_D$ −22.7 (*c* 1.1, $CHCl_3$); ^{1}H NMR ($CDCl_3$) δ 7.60 (s, 1H), 7.26−7.10 (m, 6H), 3.68 (m, 1H), 3.46 (s, 3H), 3.35 (m, 1H), 3.00−2.82 (m, 2H), 2.60−2.50 (m, 3H), 2.27−1.95 (m, 4H), 1.78−1.55 (m, 5H), 1.37 (m, 2H); ^{13}C NMR ($CDCl_3$) δ 26.0, 28.8, 34.2, 34.5, 35.3, 51.4, 523.2, 53.6, 61.8, 63.2, 94.4, 127.0, 128.4, 129.1, 129.7, 131.8, 132.9, 139.6, 142.2, 144.2, 172.2; IR (neat): 2076 (br, s), 1744.7(s) cm^{-1}; Anal. ($C_{26}H_{28}N_2O_2$-ClIS·HCl·2H_2O) C, H, N.

(−)-*N*-[4-(3′-[^{125}I]Iodo-4′-azidophenyl)butyl]-2β-carbomethoxy-3β-(4-chlorophenyl)tropane ([^{125}I]MFZ-2−24). In a representative procedure, (−)-*N*-[4-(4′-aminophenyl)butyl]-2β-carbomethoxy-3β-(4-chlorophenyl)tropane (*18*) (50 μL, 3.0 mM) in NaOAc buffer (pH 4.0; 0.3 M) containing MeOH (33%, *v*/*v*) was added to a glass vial and sealed with a Teflon-faced septum. [^{125}I]NaI (20 μL, 2.09 mCi; ca. 1.0 nmol) was added, followed by aqueous *N*-chloro-4-toluenesulfonamide (Chloramine-T) trihydrate (10 μL, 3.5 mM). The mixture was incubated for 30 min at ambient temperature, chilled in an ice/methanol bath, and then diluted with cold HOAc (50 μL, 3.0 M) followed by cold $NaNO_2$ (25 μL, 0.5 M). After 15 min at −10 °C, NaN_3 (25 μL, 0.5 M) was added, and the mixture was allowed to warm to ambient temperature and stand for 15 min before a $Na_2S_2O_5$ (5 μL, 50 mM) quench. The contents were withdrawn by syringe, and combined with MeOH (2 × 100 μL) rinses of the reaction vessel for HPLC purification using a C-18 column (Waters Nova-Pak, radial compression module, 8 × 100 mm, 6 μm). Using a mobile phase of MeOH (21%), CH_3CN (21%), and a water (58%) solution containing Et_3N (2.1% *v*/*v*) and HOAc (2.8% *v*/*v*) at a flow rate of 5 mL/min, [^{125}I]MFZ-2-24 eluted with a retention time (t_R = 34.3 min, k' = 56) corresponding to nonradioactive MFZ-2-24 and was resolved from radioactive and nonradioactive side products. The radioligand was collected in a 22.5 mL volume, diluted to 50 mL with distilled water, and passed through an activated solid-phase extraction cartridge that was flushed with water (2.5 mL), to remove salts, and then with air. Elution of the cartridge with MeOH (1.1 mL) provided 1.49 mCi (71%) of [^{125}I]MFZ-2-24. Analytical

Scheme 1. Synthesis of [^{125}I]MFZ-2-24

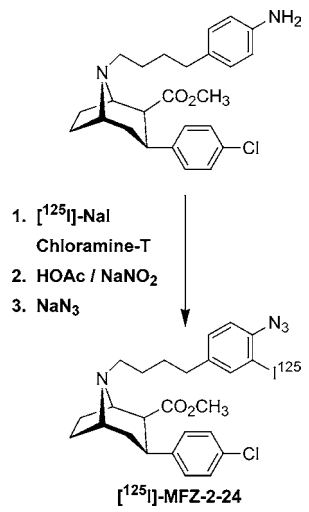

HPLC of 0.20 mCi aliquots, taken from the HPLC mobile phase after the preparative collection, used the same HPLC column with a mobile phase of MeOH (30%), CH_3CN (30%) and the aqueous mixture (40%) at 4 mL/min. [^{125}I]MFZ-2-24 ($t_R = 5.1$ min, $k' = 12$) had no radiochemical impurities, and specific radioactivities up to 2104 mCi/μmol were calculated based upon comparisons with standard samples. The relation of mass to the HPLC UV response was validated by a six-point linear curve ($r^2 = 0.99$) for nonradioactive MFZ-2-24 that bracketed the region of interest (0.036−1.8 nmol). Only minor decomposition (ca. 5%) was noted after storage at −20 °C in the dark for 19 weeks.

(−)-*N*-[4-(3′-[^{125}I]Iodo-4′-isothiocyanophenyl)butyl]-2β-carbomethoxy-3β-(4-chlorophenyl)tropane ([^{125}I]-MFZ-3-37). As described above, *N*-[4-(4′-aminophenyl)-butyl]-2β-carbomethoxy-3β-(4-chlorophenyl)tropane (50 μL, 3.0 mM) was treated with [^{125}I]NaI (25 μL, 2.81 mCi) and Chloramine-T trihydrate (10 μL, 7.0 mM) for 30 min at ambient temperature and then chilled in an ice/methanol bath. The mixture was made basic with $NaHCO_3$ (50 μL, 0.5 M), and thiophosgene (1.14 μL, 15 μmol) in $CHCl_3$ (50 μL) was added. After vortex mixing, the vessel was incubated at −20 °C for 120 h in a freezer and then warmed to ambient temperature. A homogeneous solution was obtained by adding 1.0 mL of the mobile phase to be used for HPLC: MeOH (25%), CH_3CN (25%), and a water (50%) solution containing Et_3N (2.1% *v*/*v*) and HOAc (2.8% *v*/*v*). Using a flow rate of 8 mL/min and a semipreparative C-18 column (Waters Nova-Pak, 7.8 mm × 30 cm, 6 μm), [^{125}I]MFZ-3-37 eluted with an appropriate retention time ($t_R = 53.8$ min, $k' = 52$), and was resolved from radioactive and nonradioactive side products. The radioligand (1.90 mCi) was collected in a 40 mL volume, diluted to 133 mL with distilled water, and passed through an activated solid-phase extraction cartridge that was flushed with water (2.5 mL), and then with air. Elution of the cartridge with MeOH (1.5 mL) provided 1.53 mCi (54%) of [^{125}I]MFZ-3-37. Analytical HPLC (Waters Nova-Pak, radial compression module, 8 × 100 mm, 6 μm) using a mobile phase of MeOH (30%), CH_3CN (30%), and a water (40%) solution containing Et_3N (2.1% *v*/*v*) and HOAc (2.8% *v*/*v*) at a flow rate of 4 mL/min showed a high degree of chemical and radiochemical purity (>96%) for the radioligand ($t_R = 10.6$ min, $k' = 26$). The specific radioactivity was estimated as 2000 mCi/μmol based upon comparisons with standard samples of nonradioactive material. The MeOH was removed by evaporation under a stream of argon at 45 °C, and replaced with CH_3CN.

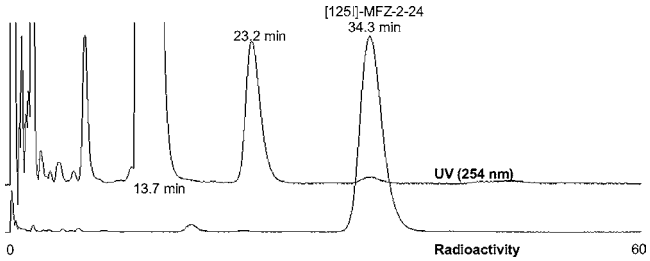

Figure 2. HPLC chromatogram for isolation of [^{125}I]MFZ-2-24.

Covalent Labeling and Immunoprecipitation of DAT. Covalent labeling and immunoprecipitation of DAT with [^{125}I]MFZ-2-24 and [^{125}I]MFZ-3-37 were performed, with minor modifications, as previously described for other irreversible labels (*12*, *13*). Briefly, male Sprague Dawley rats were decapitated, and striatal tissue was removed from the brain, weighed, and homogenized (Polytron) in sucrose-phosphate (SP) buffer (10 mM sodium phosphate, 0.32 M sucrose; pH 7.4). Homogenates were centrifuged (20 000*g*, 12 min; 4 °C), and the pellet was washed twice and resuspended to 20 mg/mL, original wet weight, in ice-cold SP buffer. Radioligands were added to the membrane suspension at a final concentration of 5 nM, and then incubated for 2 h at 0 °C. Aryl azide [^{125}I]MFZ-2-24 was covalently attached to DAT by irradiating the sample with ultraviolet light for 45 s. This step was omitted for the isothiocyanate [^{125}I]MFZ-3-37. Membranes were washed twice with SP buffer, and the final pellet was resuspended to 20 mg/mL in sample buffer (50 mM Tris-HCl, pH 6.8, containing 2% sodium dodecyl sulfate (SDS), 0.60 M dithiothreitol (DTT), 30% glycerol, and 0.001% bromphenol blue) for immunoprecipitation and electrophoresis. DTT and other reducing agents were omitted from samples labeled with [^{125}I]-MFZ-3-37. The solubilized DATs were immunoprecipitated with antiserum 16 as previously described in detail (*12*, *13*). Total binding and immunoprecipitated samples were subjected to electrophoresis on a 10% SDS-polyacrylamide gel, followed by autoradiography using Hyperfilm MP film for 1 to 4 days at −80 °C. Animals were housed and cared for in accordance with guidelines established by the Institutional Animal Care and Use Committees, and the National Institutes of Health.

RESULTS AND DISCUSSION

The radiosynthesis of [^{125}I]MFZ-2-24 proved straightforward (Scheme 1). We followed the three-step, one-flask methodology developed by Wilson (*9*) for production of [^{125}I]DEEP that has been applied successfully to several radioiodinated photoaffinity labels for the DAT (*8*, *10*, *11*). In brief, electrophilic radioiodination of the aniline (*18*) was accomplished by treatment with [^{125}I]NaI under no-carrier-added conditions at ambient temperature for 30 min using chloramine-T as oxidant at pH 4. The incorporation of radioiodine was >90%. Acidification with HOAc, followed by treatment with $NaNO_2$ at −10 °C, formed the diazonium salt in situ. A solution of NaN_3 was added and the mixture warmed to ambient temperature to liberate the aryl cation. Trapping of this reactive intermediate by azide concluded the sequence.

One major radioiodinated product was formed that displayed a chromatographic profile on reversed-phase, ion-pair HPLC ($t_R = 34.3$ min, $k' = 56$; Figure 2) that was identical to that of a characterized sample of

Scheme 2. Synthesis of MFZ-3−37

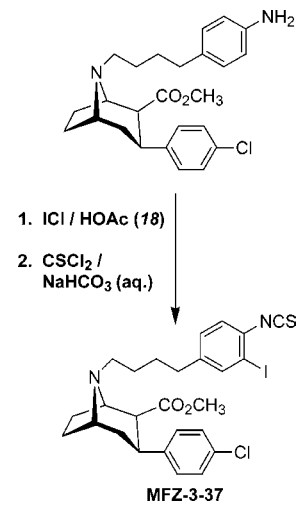

Scheme 3. Synthesis of [^{125}I]MFZ-3-37

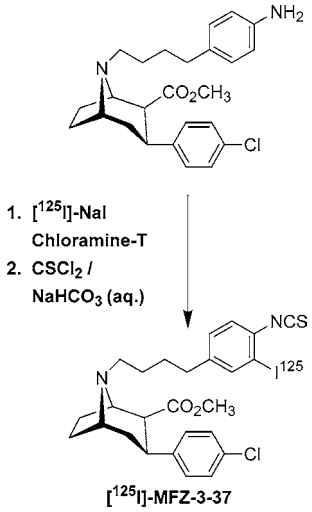

nonradioactive MFZ-2-24 prepared as previously described (*18*). Conditions for purification on an analytical column were chosen so the [^{125}I]MFZ-2-24 was resolved fully from radioactive and nonradioactive side products. The major nonradioactive materials were assigned as the corresponding azide (t_R = 13.7 min, k' = 22) and chloroazide (t_R = 23.2 min, k' = 38) taking into consideration the synthetic route, relative HPLC retention profiles and data from previous studies (*8*, *9*). Model reactions conducted without radioiodine showed that the putative azide was the sole product in the absence of chloramine-T, and that the proportion of the putative chloroazide grew with increasing amounts of chloramine-T. The amount of chlorination is relatively small and is a common side reaction when *N*-chloroamine oxidants are used for radioiodinations (*19*).

Over a series of runs, isolated yields of [^{125}I]MFZ-2-24 ranged from 58 to 73%, and averaged 67% (n = 5). Specific radioactivities were near the theoretical value (2175 mCi/μmol) for the radioiodine employed. Calculations were based upon comparisons of HPLC UV absorbance peak areas for aliquots of [^{125}I]MFZ-2-24 having known radioactivity to that of standards of nonradioactive material. The [^{125}I]MFZ-2-24 was radiochemically pure by HPLC, and found to be stable in buffered methanol during prolonged storage (>2 half-lives) at −20 °C in the dark.

To expand the scope of possible DAT labeling experiments, we also chose a radioiodinated isothiocyanate as a target ligand. A tropane-based isothiocyanate with appropriate properties would not require photoactivation for irreversible DAT binding and would covalently label nucleophilic amino acid residues in close proximity to the binding site(s). As shown in Scheme 2, we prepared MFZ-3-37, the isothiocyanate congener of MFZ-2-24, by treatment of the known iodoaniline (*18*) with thiophosgene in a biphasic mixture of $CHCl_3$ and aqueous $NaHCO_3$. Extractive work up, followed by column chromatography and formation of the HCl salt, gave MFZ-3-37 in 84% yield.

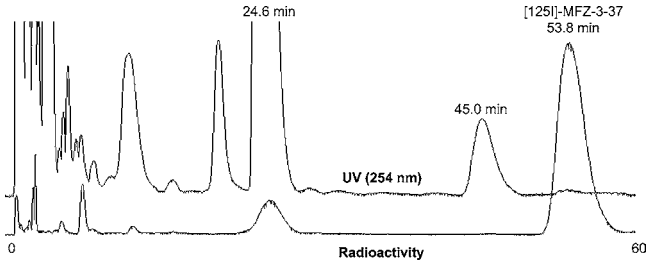

Figure 3. HPLC chromatogram for isolation of [^{125}I]MFZ-3-37.

Despite the high yields often noted for this transformation on a macroscopic scale, yields at the no-carrier-added level can be quite low, and there are relatively few examples of radiolabeled isothiocyanates. For instance, de Costa and colleagues obtained only a 13% yield for conversion of a tritiated aniline to an isothiocyanate for irreversible radiolabeling of kappa-opioid receptors (*20*). Moreover, isothiocyanate and thiourea functionalities are known to interfere with various radiohalogenation techniques (*21*). Even with a highly activated substrate, *p*-methoxyphenyl isothiocyanate, carefully optimized yields for chloramine-T-promoted radioiodination were only 15−20%, and the reaction required ultrasonication for 2 h (*22*). Nonetheless, the radioiodinated *p*-methoxyphenyl isothiocyanate developed by Dewanjee et al. proved useful for conjugation with oligonucleotides (*22*). Thus, there are certain general constraints on the preparation of radiolabeled isothiocyanates. However, our present case logically calls for simple radioiodination of an activated aromatic system as the first step, and we further planned to minimize synthetic manipulations over the two-step process to reduce mechanical losses. In practice, we developed a one-flask method where electrophilic radioiodination (vide supra) of the anilino precursor was followed by basification of the chilled reaction mixture with aqueous $NaHCO_3$ and treatment with a solution of thiophosgene in $CHCl_3$ at −20 °C for 120 h (Scheme 3).

After warming to room temperature, the biphasic mixture was made homogeneous by adding the mobile phase to be used for semipreparative, reversed-phase HPLC. The major radioactive material, assigned as [^{125}I]-MFZ-3-37, eluted with an appropriate retention time (t_R = 53.8 min, k' = 52) and was resolved from radioactive and nonradioactive side products (Figure 3). The two major nonradioactive materials observed are likely to be the isothiocyanate (t_R = 24.6 min, k' = 23) and the chlorinated isothiocyanate (t_R = 45.0 min, k' = 43) (vide supra). The radioligand was isolated in up to 54% yield with high specific radioactivity and >96% radiochemical purity. The average yield for three runs was 45%; thus, sufficient [^{125}I]MFZ-3-37 is available for various DAT studies. An aprotic solvent, acetonitrile, was used for extended storage to minimize potential hydrolysis.

With radioligands in hand, we turned our attention to a set of experiments designed to demonstrate covalent

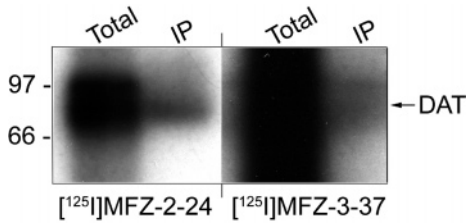

Figure 4. Irreversible labeling of rat striatal DAT with [^{125}I]-MFZ-2-24 and [^{125}I]MFZ-3-37. Membranes were incubated with the indicated compounds and irradiated in the case of [^{125}I]MFZ-2-24. The solubilized proteins were subjected to electrophoresis directly (Total) or immunoprecipitated (IP) with serum 16, followed by autoradiography. The arrow indicates the migration of the DAT at about 80 kDa based upon molecular mass standards.

radiolabeling of rat striatal DAT. Incubation of membranes with either [^{125}I]MFZ-2-24 followed by ultraviolet irradiation, or with [^{125}I]MFZ-3-37 treatment alone, resulted in incorporation of the radioligands into membrane proteins (Figure 4). Levels of total binding similar to that displayed by the aryl azide, [^{125}I]MFZ-2-24, are routinely found for other DAT photoaffinity labels (*7*, *11*−*13*). Much higher levels of total binding, involving numerous proteins, were noted for [^{125}I]MFZ-3-37. This result is in accord with the more indiscriminate nature of covalent labeling of an isothiocyanate to various biological nucleophiles.

For both radioligands, immunoprecipitation of the solubilized membranes with an antibody, serum 16, that is highly specific for amino acids 42 to 59 in the N-terminal DAT tail (*23*, *24*) resulted in the extraction of a single radioactive band. This band migrates at about 80 kDa, a molecular mass appropriate for the full-length rat striatal DAT. Other studies using a nonimmunogenic serum (*24*) that does not precipitate the radiolabeled DAT band, as well as pharmacology studies using specific peptide blockers, are consistent with the identity of the radiolabeled protein as the DAT (data not shown). Together, the results demonstrate that both [^{125}I]MFZ-2-24 and [^{125}I]MFZ-3-37 become attached covalently to the DAT and can be used as tools to help elucidate DAT binding domains. In fact, recent trypsin proteolysis and detailed epitope-specific immunoprecipitation studies show that [^{125}I]MFZ-2-24 is complementary to [^{125}I]RTI-82 and primarily labels N-terminal TMs 1−2 accompanied by only a small fraction, <5%, of covalent labeling of TMs 4−6 of rat striatal DAT (*25*, *26*). [^{125}I]MFZ-2-24 also labels the human DAT stably expressed by HEK 293 cells, and HPLC and mass spectrometry studies are underway in an effort to identify the specific amino acid residues that are photolabeled (*26*, *27*).

ACKNOWLEDGMENT

We thank the National Institute on Drug Abuse, Grants DA15175 (R.A.V.) and DA11176 (J.B.J.), and the National Institute on Drug Abuse, Intramural Research Program (A.H.N.), for the support of this research.

LITERATURE CITED

(1) Foster, J. D., Pananusorn, B., and Vaughan, R. A. (2002) Dopamine transporters are phosphorylated on N-terminal serines in rat striatum. *J. Biol. Chem*. *277*, 25178−25186.

(2) Uhl, G. R. (2003) Dopamine transporter: basic science and human variation of a key molecule for dopaminergic function, locomotion, and Parkinsonism. *Mov. Disord. 18*, S71−S80.

(3) Kuhar, M. J., Boja, J. W., Patel, A., Pilotte, N., Cerruti, C., and Lever, J. (1995) Cocaine and Dopamine Transporters, in *The Neurobiology of Cocaine: Cellular and Molecular Mechanisms* (Hammer, R. P., Jr., Ed.) pp 201−213, CRC Press, Inc., Boca Raton.

(4) Kahlig, K. M., and Galli, A. (2003) Regulation of dopamine transporter function and plasma membrane expression by dopamine, amphetamine, and cocaine. *Eur. J. Pharmacol. 479*, 153−158.

(5) Newman, A. H., and Kulkarni, S. (2002) Probes for the dopamine transporter: new leads toward a cocaine-abuse therapeutic- -A focus on analogues of benztropine and rimcazole. *Med. Res. Rev. 22*, 429−464.

(6) Dutta, A. K., Zhang, S., Kolhatkar, R., and Reith, M. E. (2003) Dopamine transporter as target for drug development of cocaine dependence medications. *Eur. J. Pharmacol. 479*, 93−106.

(7) Patel, A., Boja, J. W., Lever, J., Lew, R., Simantov, R., Carroll, F. I., Lewin, A. H., Philip, A., Gao, Y., and Kuhar, M. J. (1992) A cocaine analog and a GBR analog label the same protein in rat striatal membranes. *Brain Res. 576*, 173−174.

(8) Lever, J. R., Carroll, F. I., Patel, A., Abraham, P., Boja, J., Lewin, A., and Lew, R. (1993) Radiosynthesis of a photoaffinity probe for the cocaine receptor of the dopamine transporter: 3β-(*p*-chlorophenyl)tropan-2β-carboxylic acid *m*-([^{125}I]-iodo)-p-azidophenethyl ester ([^{125}I]-RTI-82). *J. Labelled Compd. Radiopharm*. *33*, 1131−1137.

(9) Wilson, A. A., Grigoriadis, D. E., Dannals, R. F., Ravert, H. T., and Wagner, H. N., Jr. (1989) A one-pot radiosynthesis of [^{125}I]iodoazido photoaffinity labels. *J Labelled Compd. Radiopharm*. *27*, 1299−1305.

(10) Dutta, A. K., Fei, X. S., Vaughan, R. A., Gaffaney, J. D., Wang, N., Lever, J. R., and Reith, M. E. (2001) Design, synthesis, and characterization of a novel, 4-[2-(diphenylmethoxy)ethyl]-1-benzyl piperidine-based, dopamine transporter photoaffinity label. *Life Sci. 68*, 1839−1849.

(11) Agoston, G. E., Vaughan, R., Lever, J. R., Izenwasser, S., Terry, P. D., and Newman, A. H. (1997) A novel photoaffinity label for the dopamine transporter based on N-substituted-4′,4″-difluoro-3α-(diphenylmethoxy)tropane. *Bioorg. Med. Chem. Lett. 7*, 3027−3032.

(12) Vaughan, R. A., Agoston, G. E., Lever, J. R., and Newman, A. H. (1999) Differential binding of tropane-based photoaffinity ligands on the dopamine transporter. *J. Neurosci. 19*, 630−636.

(13) Vaughan, R. A., Gaffaney, J. D., Lever, J. R., Reith, M. E., and Dutta, A. K. (2001) Dual incorporation of photoaffinity ligands on dopamine transporters implicates proximity of labeled domains. *Mol. Pharmacol. 59*, 1157−1164.

(14) Katz, J. L., Agoston, G. E., Alling, K. L., Kline, R. H., Forster, M. J., Woolverton, W. L., Kopajtic, T. A., and Newman, A. H. (2001) Dopamine transporter binding without cocaine-like behavioral effects: synthesis and evaluation of benztropine analogs alone and in combination with cocaine in rodents. *Psychopharmacol*. *154*, 362−374.

(15) Katz, J. L., Kopajtic, T. A., Agoston, G. E., and Newman, A. H. (2004) Effects of N-substituted analogs of benztropine: diminished cocaine-like effects in dopamine transporter ligands. *J. Pharmacol. Exp. Ther. 309*, 650−660.

(16) Newman, A. H., Izenwasser, S., Robarge, M. J., and Kline, R. H. (1999) CoMFA study of novel phenyl ring-substituted 3α-(diphenylmethoxy)tropane analogues at the dopamine transporter. *J. Med. Chem. 42*, 3502−3509.

(17) Kulkarni, S. S., Grundt, P., Kopajtic, T., Katz, J. L., and Newman, A. H. (2004) Structure−activity relationships at monoamine transporters for a series of N-substituted 3α-(bis-[4-fluorophenyl]methoxy)tropanes: comparative molecular field analysis, synthesis, and pharmacological evaluation. *J. Med. Chem. 47*, 3388−3398.

(18) Zou, M. F., Kopajtic, T., Katz, J. L., Wirtz, S., Justice, J. B., Jr., and Newman, A. H. (2001) Novel tropane-based irreversible ligands for the dopamine transporter. *J. Med. Chem*. *44*, 4453−4461.

(19) Lever, J. R. (1995) Radioiodinated Compounds, in *Principles of Nuclear Medicine* (Wagner, H. N., Jr., Szabo, Z., and Buchanan, J. W., Eds.) pp 199−213, W.B. Saunders Company, Philadelphia.

(20) De Costa, B. R., Thurkauf, A., Rothman, R. R., Jacobson, A. E., and Rice, K. C. (1990) Synthesis of high specific activity tritium labeled 1S, 2S−(−)-*trans*-2-isothiocyanato-N-methyl-N-[2-(1-pyrrolidinyl)-cyclohexyl]benzeneacetamide, a specific irreversible ligand for kappa opioid receptors. *J. Labelled Compd. Radiopharm. 28*, 1257−1264.

(21) Wilbur, D. S., Chyan, M. K., Hamlin, D. K., Kegley, B. B., Risler, R., Pathare, P. M., Quinn, J., Vessella, R. L., Foulon, C., Zalutsky, M., Wedge, T. J., and Hawthorne, M. F. (2004) Reagents for astatination of biomolecules: comparison of the in vivo distribution and stability of some radioiodinated/astatinated benzamidyl and nido-carboranyl compounds. *Bioconjugate Chem. 15*, 203−223.

(22) Dewanjee, M. K., Ghafouripour, A. K., Werner, R. K., Serafini, A. N., and Sfakianakis, G. N. (1991) Development of sensitive radioiodinated anti-sense oligonucleotide probes by conjugation technique. *Bioconjugate Chem. 2*, 195−200.

(23) Vaughan, R. A. (1995) Photoaffinity-labeled ligand binding domains on dopamine transporters identified by peptide mapping. *Mol. Pharmacol. 47*, 956−964.

(24) Vaughan, R. A., and Kuhar, M. J. (1996) Dopamine transporter ligand binding domains. Structural and functional properties revealed by limited proteolysis. *J. Biol. Chem. 271*, 21672−21680.

(25) Parnas, M. L., Gaffaney, J. D., Newman, A. H., Zou, M. F., Lever, J. R., and Vaughan, R. A. (2003) Irreversible cocaine analogues map to multiple sites on the dopamine transporter. *Soc. Neurosci. Abstr. 33*, 253.18.

(26) Vaughan, R. A, Parnas, M. L., Gaffaney, J. D., Lowe, M. J., Wirtz, S., Pham, A., Reed, B., Dutta, S. M., Murray, K. K., and Justice, J. B. (2005) Affinity labeling the dopamine transporter ligand binding site. *J. Neurosci. Methods 143*, 33−40.

(27) Wirtz, S. E., Parnas, L., Jackson, T. V., Danilenko, U., Pham, A. T., Zou, M. F., Newman, A. H., Lever, J. R., Vaughan, R. A., and Justice, J. B. (2004) Identification of an MFZ 2-24 photoaffinity labeling site on the human dopamine transporter. *Soc. Neurosci. Abstr. 33*, 53.19.

BC0497214

Adenosine 2′-Monophosphate, 5′-*O*-[*S*-(4-Succinimidylbenzophenone)-thiophosphate]: A New Photoaffinity Label for the Coenzyme Site of Porcine NADP-Specific Isocitrate Dehydrogenase

Peychii Lee and Roberta F. Colman*

Department of Chemistry and Biochemistry, University of Delaware, Newark, Delaware 19716.
Received November 19, 2004; Revised Manuscript Received February 16, 2005

A new photoaffinity label, adenosine 2′-monophosphate, 5′-*O*-[*S*-(4-succinimidyl-benzophenone)-thiophosphate] (2′-P-AMPS-Succ-BP), has been synthesized by an initial thiophosphorylation of 2′-AMP with $PSCl_3$ to form 2′-AMP-5′-thiophosphate (2′-AMP-5′-SP), followed by a coupling reaction of 2′-AMP-5′-SP with benzophenone-4-maleimide to produce 2′-P-AMPS-Succ-BP. This product and its precursor were characterized by thin-layer chromatography, ^{31}P NMR, phosphorus analysis, and electron-spray mass spectroscopy. 2′-P-AMPS-Succ-BP functions as a photoaffinity label of porcine NADP-specific isocitrate dehydrogenase. To obtain reaction with other amino acids, Cys269 and Cys379, the most reactive cysteines of this enzyme, were mutated to yield a double mutant enzyme (C269A/C379S) exhibiting comparable activity and kinetic parameters to those of wild-type enzyme. 2′-P-AMPS-Succ-BP inactivates C269A/C379S enzyme upon UV irradiation. The reaction exhibits a nonlinear relationship of k_{inact} versus [2′-P-AMPS-Succ-BP] with $K_R = 12\ \mu M$ and $k_{max} = 0.0275\ min^{-1}$. NADP, NADPH, or 2′-monophospho-adenosine 5′-diphosphoribose protects the enzyme against 2′-P-AMPS-Succ-BP inactivation. The ligand protection studies suggest that 2′-P-AMPS-Succ-BP binds to the porcine enzyme at the site best occupied by NADP/NADPH. The dimeric C269A/C379S isocitrate dehydrogenase incorporates 1.0 mol of 2′-P-[^{35}S]AMPS-Succ-BP/mol enzyme dimer concomitant with *complete* loss of enzyme activity. The new photoaffinity label may be generally useful to identify important amino acid residues of NADP-specific enzymes.

INTRODUCTION

Locating enzyme active sites is critical in understanding the relationship between enzymes' structures and their functions and in designing potential drug candidates. Recent advances in bioinformatics provide tools such as sequence homology analysis and protein structure prediction to identify critical amino acids involved in enzyme functions. However, these computational predictions may not be effective in comparing enzymes isolated from distant sources (such as prokaryotes vs eukaryotes). Affinity labels are reagents which are structurally similar to enzyme ligands but contain a reactive functional group (*1*). The affinity label initially forms a reversible enzyme−reagent complex which mimics the enzyme−ligand complex. Subsequently, the reactive functional group of the affinity label forms a covalent bond with the side chain of an adjacent amino acid. Unlike X-ray crystallography which determines enzyme structure in crystalline state, affinity labeling is conducted in solution, where enzymatic catalysis occurs in nature. On the basis of their chemical structures, NAD(P) affinity labels can be categorized into three groups: analogues based on the entire nicotinamide adenine dinucleotide structure, on the nicotinamide mononucleotide moiety alone, or on the adenine nucleotide fragment of the coenzyme (*2*). 8-(4-Bromo-2,3-dioxobutylthio)NAD (8-BDB-TNAD),[1] periodate-oxidized NADPH, and 2-azido-NAD are compounds that belong to the first group. 8-BDB-TNAD, synthesized previously in this laboratory, contains a bromodioxobutyl group that can react with nucleophilic side chains of lysine, tyrosine, cysteine, glutamate, aspartate, histidine, methionine, and arginine (*3*). The compound 5′-*p*-(fluorosulfonyl)benzoyl-8-azidoadenosine (5′-FSBAzA), a bifunctional affinity label with a structure similar to adenosine, is capable of interacting with amino acids through its sulfonyl group or photoreactive azido group (*4*).

Here, we report the synthesis of a new photoaffinity labeling reagent, adenosine 2′-monophosphate, 5′-*O*-[*S*-(4-succinimidyl-benzophenone)thiophosphate] (2′-P-AMPS-Succ-BP), which is structurally similar to NADP, as shown in Figure 1. 2′-P-AMPS-Succ-BP contains the same adenosine 2′-monophosphate moiety as in NADP and thus should be effective for NADP-specific (in contrast to NAD-specific) dehydrogenases. When compared with the extended form of NADP, the 5′-thiophos-

* To whom correspondence should be addressed. Phone: (302) 831-2973. Fax: (302) 831-6335. Email: rfcolman@udel.edu.

[1] Abbreviations used: 2′-AMP, adenosine 2′-monophosphate; $PSCl_3$, thiophosphoryl chloride; 2′-AMP-5′-SP, adenosine 2′-monophosphate, 5′-thiophosphate; 2′-P-AMPS-Succ-BP, adenosine 2′-monophosphate 5′-*O*-[*S*-(4-succinimidyl-benzophenone)-thiophosphate]; AMPS-Succ-BP, adenosine 5′-*O*-[*S*-(4-succinimidyl-benzophenone)thiophosphate; ATPR, 2′-monophospho-adenosine 5′-diphosphoribose; BP-MAL, benzophenone-4-maleimide; IPTG, isopropylthiogalactoside; 2-BDB-TA-2′,5′-DP, 2-[(4-bromo-2,3-dioxobutyl)thio]adenosine 2′,5′-bisphosphate; 8-BDB-TNAD, 8-(4-bromo-2,3-dioxobutylthio)NAD; TEMED, *N*,*N*,*N*′,*N*′-tetramethylethylenediamine; SDS−PAGE, sodium dodecyl sulfate−polyacrylamide gel electrophoresis; TLC, thin-layer chromatography; *E. coli*, *Escherichia coli*; *A. vinelandii*, *Azotobacter vinelandii*; *B. subtilis*, *Bacillus subtilis*; CD, circular dichroism; Tris, tris(hydroxymethyl)aminomethane.

10.1021/bc049722w CCC: $30.25 © 2005 American Chemical Society
Published on Web 04/26/2005

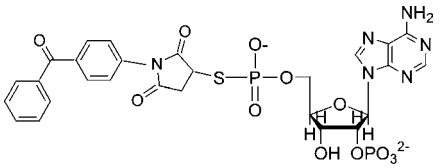

Figure 1. Chemical structure of adenosine 2′-monophosphate, 5′-*O*-[*S*-(4-succinimidyl-benzophenone)thiophosphate] (2′-P-AMPS-Succ-BP).

phoryl group and one of the carbonyls of the succinimidyl ring of 2′-P-AMPS-Succ-BP occupies the same position as the α- and β-phosphoryl groups of NADP, respectively. One of the phenyl rings of the affinity compound is located in the vicinity of the nicotinamide ribose, and the second phenyl group may correspond to or be close to the position of the nicotinamide of NADP. The phenyl rings of 2′-P-AMPS-Succ-BP can interact with amino acids of the enzyme through hydrophobic interaction or an aromatic ring stacking interaction (*5*). The carbonyl group of benzophenone can covalently react with a C−H side chain of any amino acid near the functional group (*6*). In contrast to affinity labels with 4-bromo-2,3-dioxobutyl functional groups, which react only with nucleophilic amino acids, the new affinity label can react photochemically with the side chain of any amino acid that is located near its carbonyl group. We have previously used photoaffinity labels with benzophenone groups, such as glutathionyl *S*-[4-(succinimidyl)benzophenone (GS-Succ-BP) to identify catalytically important methionine residues in rat liver glutathione S-transferase (*7*) and adenosine 5′-*O*-[*S*-(4-succinimidyl-benzophenone)thiophosphate] (AMPS-Succ-BP) to reveal a critical arginine residue at the allosteric ADP site of bovine liver glutamate dehydrogenase (*5*).

Isocitrate dehydrogenase catalyzes the oxidative decarboxylation of isocitrate to α-ketoglutarate. The proposed catalytic mechanism of isocitrate dehydrogenase involves an initial oxidation of isocitrate to oxalosuccinate by the removal of a proton from the C-2 hydroxyl of isocitrate, followed by the transfer of a C-2 hydride to the nicotinamide ring of NADP. In the second step of the reaction, the β-carboxylate of oxalosuccinate is released as CO_2, which is followed by a protonation of its β-carbon to form α-ketoglutarate (*8, 9*). NADP-specific porcine heart mitochondrial isocitrate dehydrogenase (EC1.1.1.42) is a homodimer. Each monomer is composed of 413 amino acids with a subunit molecular weight of 46 600 Da (*10*−*12*).

The X-ray crystal structure of porcine mitochondrial NADP-dependent isocitrate dehydrogenase, complexed with the substrates isocitrate and Mn^{2+}, has been solved at a resolution of 1.85 Å (*13, 14*). However, since the enzyme was not crystallized with coenzyme, there is little direct information regarding the coenzyme site of this porcine enzyme. Here, we describe the specific covalent reaction of 2′-P-AMPS-Succ-BP with porcine isocitrate dehydrogenase in the region of the active site best occupied by the coenzymes NADP/NADPH.

EXPERIMENTAL PROCEDURES

Materials. Yeast adenosine 2′-monophosphate (free acid), 4-(*N*-maleimido)benzophenone, triethanolamine hydrochloride, NADP, Sephadex G-50, ampicillin, trimethyl phosphate, thiophosphoryl chloride, trifluoroacetic acid, and isobutyric acid were purchased from Sigma-Aldrich Chemical Corporation. Triethylamine, sodium sulfate, manganous sulfate, maltose, acrylamide/bisacrylamide mixture, glycine, acetonitrile, DNA grade agarose, sodium acetate, barium acetate, ethanol, EDTA, boric acid, Tris, ethidium bromide, IPTG, tryptone, yeast extract, and agar were from Fisher Scientific. AG 50W−X4 cation-exchange resin, concentrated Protein Dye Reagent, Coomassie blue, and TEMED were from Bio-Rad Laboratories. DL-Isocitrate was obtained from USB. Deuterium oxide was from Cambridge Isotope Laboratories, Inc. QIA prep spin miniprep kit and QIAquick gel extraction kit were purchased from Qiagen. Amylose resin, *Escherichia coli* TB1 cells, Vent DNA polymerase, T4 DNA ligase, BamHI, and BlpI were obtained from New England Biolabs. Matrex Gel Red A resin and Amicon YM-10 filtration membrane were from Millipore. SDS−PAGE low molecular weight markers were purchased from Pharmacia Biotech. [^{35}S]Sulfur in toluene was obtained from Amersham Pharmacia Biotech. DEAE-cellulose anion-exchange resin (DE52) was from Whatman. Human plasma thrombin was from Enzyme Research Laboratories. QuikChange XL site-directed mutagenesis kit was purchased from Stratagene. Oligonucleotides for site-directed mutagenesis and sequencing were purchased from Biosynthesis Incorporated.

Synthesis of Adenosine 2′-Monophosphate, 5′-Thiophosphate. Adenosine 2′-monophosphate, 5′-thiophophate (2′-AMP-5′-SP) was synthesized by thiophosphorylation of the 5′-hydroxyl group of adenosine 2′-monophosphate with thiophosphoryl chloride. The free acid of adenosine 2′-monophosphate (2′-AMP; 0.24 mmol) was dissolved in 3.2 mL of trimethyl phosphate, and the pH of the solution was adjusted to 5.0 with triethylamine. Thiophosphoryl chloride ($PSCl_3$, 2.4 mmol) was gradually added to the reaction mixture. Periodically, the pH of the reaction mixture was checked by pH paper and readjusted to 5.0 by addition of triethylamine. 2′-AMP was completely dissolved in 15 min. The reaction was allowed to proceed at room temperature for 3 h. At the end of the reaction, thiophosphorylated 2′-AMP was converted to its barium salt by adding 1 mL of 0.4 M barium acetate per 0.4 mL of reaction mixture, followed by the addition of 4 mL of ethanol containing 200 μL of triethylamine (*15*). The precipitate was washed once with 4 mL of 70% ethanol and dried overnight. Barium was removed from the thiophosphorylated 2′-AMP precipitate by a method described previously (*16*). Briefly, the barium salts of thiophosphorylated 2′-AMP were dissolved in 4 mL of 1 M acetic acid. Concentrated sulfuric acid was added to the solution to convert barium to barium sulfate precipitate and this salt was separated by centrifugation from the thiophosphorylated 2′-AMP. The pH of the supernatant was adjusted to 8.0 with concentrated ammonium hydroxide. The supernatant was diluted 100-fold with distilled water and applied to a DE52 column (1.5 cm × 50 cm), which had previously been equilibrated with 10 mM NH_4HCO_3, pH 8.0. 2′-AMP-5′-SP was separated from other thiophosphorylation byproducts by a linear gradient formed by 350 mL of 10 mM NH_4HCO_3, pH 8.0 and 350 mL of 0.5 M NH_4HCO_3, pH 8.0. Gradient separation was monitored both by absorbance at 260 nm and thin-layer chromatography (TLC). Samples from fractions and a standard 2′-AMP solution were applied to a Kodak polyester TLC plate coated with cellulose containing fluorescent indicator. The mobile phase for TLC separation was isobutyric acid/H_2O/NH_4OH (66/33/1). 2′-AMP-5′-SP was eluted by the NH_4HCO_3 gradient from the DE52 column as the last of the three peaks. Fractions containing adenosine 2′-AMP-5′-SP were pooled and dried using a rotary evaporator. The 2′-AMP-5′-SP was dissolved in 5 mL of 1 M acetic acid, applied to an AG 50W X-4 column (H^+ form, 1 cm × 40 cm), and eluted with

distilled H_2O. The fractions with high absorbance at 260 nm were collected and dried using a rotary evaporator.

Synthesis of Adenosine 2′-Monophosphate, 5′-*O*-[*S*-(4-Succinimidyl-benzophenone)thiophosphate]. Adenosine 2′-monophosphate, 5′-*O*-[*S*-(4-succinimidyl-benzophenone)thiophosphate] (2′-P-AMPS-Succ-BP) was synthesized by a method similar to that described previously for adenosine 5′-*O*-[*S*-(4-succinimidyl-benzophenone)thiophosphate] (AMPS-Succ-BP) which lacks the 2′-phosphate (*5*). 2′-AMP-5′-SP (10 μmol) was dissolved in 0.4 mL of distilled H_2O, and the pH of the solution was adjusted to 5.0 with triethylamine. The 2′-AMP-5′-SP solution was gradually added to benzophenone-4-maleimide (BP-MAL, 11 μmol), which had been dissolved in 0.6 mL of acetonitrile. The coupling reaction was allowed to proceed at room temperature in an aluminum foil-covered vial with constant stirring for 5 h. The reaction mixture was lyophilized, redissolved in 1 mL of distilled H_2O, and centrifuged to remove any insoluble BP-MAL. The supernatant was subjected to reversed-phase high-performance liquid chromatography (HPLC) purification. The chromatography was conducted using a Varian model 5000 system equipped with a Vydac C_{18} column (0.46 × 25 cm). The column was equilibrated with H_2O (solvent A) at a flow rate of 1 mL/min. After the sample injection, the column was further washed with H_2O for 30 min to remove unreacted 2′-AMP-5′-SP, followed by a linear gradient from 0 to 40% acetonitrile (solvent B) for 80 min, and finally a linear gradient from 40 to 90% solvent B for 50 min. Fractions containing 2′-P-AMPS-Succ-BP (eluted from the HPLC column at 10−15% acetonitrile) were pooled, lyophilized, and dissolved in a small volume of 10 mM triethanolamine hydrochloride, pH 7.4 buffer for storage at −80°C.

Synthesis of Radioactive 2′-P-[^{35}S]AMPS-Succ-BP. Radioactive sulfur was introduced into thiophosphoryl chloride ($PSCl_3$) by a modification of the method of Slama et al. (*17*). Briefly, 2.5 mCi of [^{35}S]sulfur in toluene was pipetted into a glass vial with a Teflon screw cap and dried using argon gas. $PSCl_3$ (50 μL, 0.49 mmol) was added to the dried [^{35}S]sulfur, and the mixture was sealed and heated at 110 °C in a sand bath for 48 h. A 1.91 mmol (195 μL) amount of nonradioactive $PSCl_3$ was added to the reaction mixture, and the synthesis of radioactive 2′-P-AMPS-Succ-BP was carried out using the same procedures described above for the nonradioactive 2′-P-AMPS-Succ-BP.

Phosphorus Analysis. The organic phosphorus content of 2′-P-AMPS-Succ-BP was determined chemically by the method described previously (*18*). Briefly, 100 μL phosphorus standard solutions, ranging from 2 nmol to 20 nmol, or 100 μL 2′-P-AMPS-Succ-BP samples, were first hydrolyzed by 20 μL of 10 N H_2SO_4 at 190 °C for 2 h. After 2 h of hydrolysis, 50 μL of 30% H_2O_2 was added to the sample and incubated at 190 °C for 1 h. The hydrolyzed samples were mixed with 800 μL freshly prepared malachite green and ammonium molybdate solution, and the absorbance at 600 nm was measured using a Bio-Rad titer plate reader.

Site-Directed Mutagenesis of Porcine Isocitrate Dehydrogenase. It is known that porcine mitochondrial NADP-specific isocitrate dehydrogenase has reactive cysteines (*8*). To facilitate reaction of 2′-P-AMPS-Succ-BP with other amino acids, the reactive cysteines were replaced by the non reactive alanine or serine. Site-directed mutagenesis to obtain mutants C74A, C115A, C269A, and C379S was performed by a two-stage PCR megaprimer method as described previously (*19, 20*). The oligonucleotides used for site-directed mutagenesis were C74A forward primer: 5′-GTGGCTGTCAAGGCGGC-CACCATCACC-3′, C115A reverse primer: 5′-GTGG-GATGTTCTTCGCGATGATGGGC-3′, C269A forward primer: 5′-CGTGTGGGCCGCGAAGAACTACGATG-3′, and C379S forward primer: 5′-ACCTGGCGGGCTCTAT CCATGGCCT-3′, where the mutated sequences are underlined. The BlpI forward primer sequence is 5′-GGC-GTGCTGAGCGCAGGTATTAACGCCGCCAGTCCG-3′ and the BamHI reverse primer sequence is 5′-CTAGAGGATCCTTACTACTGCCGGCCCAGAG-CTCTGTC-3′. C269A/C379S double mutant was generated using a QuikChange XL site-directed mutagenesis kit. Plasmid isolated from the C379S mutant was used as the DNA template for a PCR reaction. A pair of complementary primers, C269A forward primer (sequence as shown above) and C269A reverse primer: 5′-CGTAG TTCTTCGCGGCCCACACGAAG-3′, were used to introduce the mutation sequence at residue 269 to the plasmid C379S. All mutants were confirmed by BigDye terminator cycle sequencing performed at the DNA Sequencing Facility, University of Delaware.

Enzyme Expression and Purification. Wild-type, C115A, C269A, and C379S isocitrate dehydrogenases were expressed in *E. coli* TB1 cells and purified to homogeneity by amylose column chromatography, thrombin digestion, Matrex Gel Red column chromatography, and by a second amylose column (*19, 20*). Mutants C74A and C269A/C379S enzymes were purified to homogeneity by amylose column chromatography, thrombin digestion, and DE52 column chromatography, as described (*21*). The purity of wild-type and mutant isocitrate dehydrogenase was determined by electrophoresis on a 10% polyacrylamide gel containing 0.1% SDS as denaturant (*22*). N-Terminal sequencing of the purified enzyme was performed on an Applied Biosystems gas-phase sequenator (Model Procise) equipped with an on-line microgradient delivery system (Model 140C) and a computer (Model 610 Macintosh).

Circular Dichroism of Wild-type and Cysteine Mutant Enzymes. The secondary structure of cysteine mutants was measured using a Jasco model J-710 spectropolarimeter as described previously (*20*). The purified enzymes (~0.3 mg/mL) were first dialyzed against 25 mM triethanolamine hydrochloride, pH 7.7 buffer containing 75 mM sodium sulfate and 10% glycerol. The final concentrations of the enzymes were determined by a Coomassie blue dye binding assay (*23*), using wild-type porcine isocitrate dehydrogenase as the protein standard. Each sample (350 μL) was pipetted into a 0.1 cm path length quartz cuvette. The ellipticity of each sample was measured by scanning the sample 5 times between 200 and 250 nm at 0.1 nm increments. The molar ellipticity, $[\theta]$, was calculated from the equation: $[\theta] = \theta/(10nCl)$, where θ is the measured ellipticity, n is the number of amino acids per enzyme subunit (413 for porcine isocitrate dehydrogenase), C is the molar concentration of the enzyme, and l is the cell path length in cm.

Enzyme Activity Assay and Determination of Kinetic Parameters. The specific activity of isocitrate dehydrogenase was determined at 25 °C by measuring the time-dependent increase in absorbance at 340 nm which results from the reduction of NADP to NADPH. The standard assay solution contained 4 mM DL-isocitrate, 100 μM NADP, and 2 mM $MnSO_4$ in 30 mM triethanolamine hydrochloride, pH 7.4 buffer in a total volume of 1 mL. To determine the K_m for NADP of wild-type and mutant enzymes, DL-isocitrate and $MnSO_4$ concentrations were fixed at 4 mM and 2 mM, respec-

tively. To determine the K_m for isocitrate, NADP was fixed at 100 μM and $MnSO_4$ at 2 mM. The K_m for $MnSO_4$ was determined using an assay solution containing 4 mM DL-isocitrate and 100 μM NADP. The 2′-P-AMPS-Succ-BP was evaluated as a reversible inhibitor of isocitrate dehydrogenase by measuring the K_m for NADP and isocitrate of C269A/C379S enzyme in the presence of a constant 2′-P-AMPS-Succ-BP (150 μM) without UV irradiation. The data were analyzed by a Lineweaver−Burk plot to obtain K_m and V_{max} values.

Inactivation of Mutant Isocitrate Dehydrogenase C269A/C379S with 2′-P-AMPS-Succ-BP. Mutant isocitrate dehydrogenase C269A/C379S (0.1 mg/mL, 2.15 μM enzyme subunit) was preincubated in 30 mM triethanolamine hydrochloride, pH 7.4 buffer for 15 min prior to the addition of 5−205 μM 2′-P-AMPS-Succ-BP. An aliquot of the inactivation mixture (0.3 mL) was pipetted into each well of a microtiter plate, which had been placed on top of an ice bed, and irradiated with long-wave (365 nm) UV light generated by a Spectroline, model ENF-240C lamp which had been placed directly on the top of the microtiter plate. At various times, 2 μL aliquots of the inactivation mixture were withdrawn and added to 1 mL of standard assay solution to measure the residual enzyme activity. An enzyme incubated and irradiated in the absence of 2′-P-AMPS-Succ-BP was used as a control. To study the ability of active site ligands to protect C269A/C379S enzyme against inactivation by 20 μM 2′-P-AMPS-Succ-BP, the enzyme was preincubated with ligands for 15 min in 30 mM triethanolamine HCl, pH 7.4 buffer, prior to the addition of 2′-P-AMPS-Succ-BP.

Incorporation of 2′-P-[^{35}S]AMPS-Succ-BP into Mutant Isocitrate Dehydrogenase C269A/C379S. Isocitrate dehydrogenase C269A/C379S (0.1 mg/mL, 2.15 μM enzyme subunit) was incubated with 40 μM 2′-P-[^{35}S]-AMPS-Succ-BP in 30 mM triethanolamine hydrochloride, pH 7.4 buffer and irradiated by a UV lamp at 365 nm, as described above. At various times, 2 μL aliquots of the inactivation mixture were withdrawn to test for residual enzyme activity and another 0.5 mL were pipetted onto a 5-mL Sephadex G50 spin column, which had previously been equilibrated with 0.1 M triethanolamine hydrochloride, pH 7.7 buffer containing 300 mM Na_2SO_4 and 10% glycerol, to remove excess 2′-P-[^{35}S]AMPS-Succ-BP by the gel centrifugation method (*24*). The incorporation of 2′-P-[^{35}S]AMPS-Succ-BP into C269A/C379S enzyme at time zero was determined by addition of the compound without any UV irradiation. The enzyme concentration was determined by a dye-binding Bradford method (*23*). The incorporation of 2′-P-[^{35}S]AMPS-Succ-BP into the enzyme was determined by measuring the radioactivity of enzyme aliquots using a Packard Tri-Carb liquid scintillation counter (Model 4640).

Ultrafiltration Measurements. The binding stoichiometry of native and 2′-P-AMPS-Succ-BP-modified C269A/C379S for NADPH or isocitrate was determined by an ultrafiltration method described previously (*25*−*27*). Briefly, native or modified C269A/C379S (1.0−1.3 mg/mL, 22−28 μM enzyme subunit) in 100 mM triethanolamine hydrocholoride, pH 7.7 buffer, containing 300 mM Na_2SO_4 and 10% glycerol, were mixed with either NADPH (63−97 μM) or isocitrate solution (90−140 μM) in a total volume of 1 mL. The binding mixture was incubated at 25 °C for 15 min prior to being transferred to an Amicon centricon YM-10 (molecular weight cutoff: 10 000 Da). Ultrafiltration was conducted at 3000*g* for 1 h and 0.5 mL of the filtrate was collected for measurements. The initial NADPH concentration and the free NADPH in the filtrate were measured spectrophotometrically by using an extinction coefficient of 6200 M^{-1} cm^{-1} for NADPH at 340 nm. The concentrations of isocitrate in the initial incubation mixture and the filtrate were determined indirectly by measuring the maximum change in $A_{340\,nm}$ generated by wild-type isocitrate dehydrogenase in a total of 1 mL assay solution containing 50−100 μL of the initial incubation mixture or the free isocitrate filtrate, 100 μM NADP, and 2 mM $MnSO_4$ in 30 mM triethanolamine hydrochloride, pH 7.4; no other isocitrate was added. The bound isocitrate (or NADPH) was calculated from the difference between total and free isocitrate (or NADPH).

RESULTS

Characterization of Adenosine 2′-Monophosphate, 5′-*O*-[*S*-(4-succinimidyl-benzophenone)thiophosphate] and Its Precursors. The synthesis of 2′-P-AMPS-Succ-BP was accomplished by initial thiophosphorylation of 2′-AMP with $PSCl_3$ to yield 2′-AMP-5′-SP, followed by coupling of 2′-AMP-5′-SP with BP-MAL to generate the final product, 2′-P-AMPS-Succ-BP. 2′-AMP-5′-SP was separated from its precursor and reaction byproducts by applying the thiophosphorylation mixture on a DE52 anion exchange column. Three peaks were eluted from the DE52 column using an NH_4HCO_3 gradient elution. The first peak has an R_f value of 0.46 on a cellulose TLC sheet with isobutyric acid/H_2O/ammonium hydroxide as the mobile phase; the second peak has an R_f value of 0.33, and the third peak has an R_f value of 0.13. The precursor, 2′-AMP, has an R_f value of 0.49. Phosphorus determinations indicated that the second and third peaks from the DE52 column each contains 2 mol of phosphorus per mole compound, with the compound's concentration being determined spectrophotometrically ($\epsilon_{259\,nm}$ = 15 400 M^{-1} cm^{-1}).

The ^{31}P NMR spectrum of the third eluted peak has two dominant peaks centered at 43.6 and 4.2 ppm, while the second eluted peak has two dominant peaks centered at 2.1 and 7.4 ppm. Adenosine 5′-*O*-thiomonophosphate (5′-AMPS) obtained from commercial sources exhibits a single peak at 43.8 ppm in its ^{31}P NMR spectrum. The reported chemical shifts of the phosphorus of 2′-AMP and 5′-AMPS were 4.34 and 42.93 ppm, respectively (*28*). Thus, the TLC, phosphorus determination, and ^{31}P NMR results indicate that the third peak eluted from the DE52 column is the thiophosphorylation product, 2′-AMP-5′-SP.

2′-P-AMPS-Succ-BP was synthesized by a reaction of 2′-AMP-5′-SP with BP-MAL at room temperature for 5 h, and was purified using reversed phase HPLC. The ^{31}P NMR spectrum of 2′-AMP−5′-S-Succ-BP shows, in addition to 2′-phosphate peak of 4.2 ppm, a new chemical shift of 16.7 ppm, as compared to 43.6 ppm for its precursor 2′-AMP-5′-SP, and this value is close to the reported chemical shifts of the 5′-phosphorus of adenosine 5′-*O*-(*S*-methyl thiophosphate) ($AMPSCH_3$) (22.9 ppm) and AMPS-Succ-BP (22.6 ppm) (*5, 28*). The reversed-phase HPLC-purified 2′-AMP-5′-S-Succ-BP (in H_2O containing 0.1% TFA) exhibits a mass of 721.1 when subjected to electron-spray mass spectroscopy (Thermo Finnigan model LCQ Advantage). This determined mass is close to the calculated formula weight of 720.5. Thus, the results from NMR and electron-spray mass spectrometry demonstrate that the fractions collected from the HPLC separation contain the final product, 2′-P-AMPS-Succ-BP, shown in Figure 1. The phosphorus content of 2′-P-AMPS-Succ-BP was determined chemically after hydrolysis by H_2SO_4 (2 mol of phosphorus/mol of reagent, consistent with

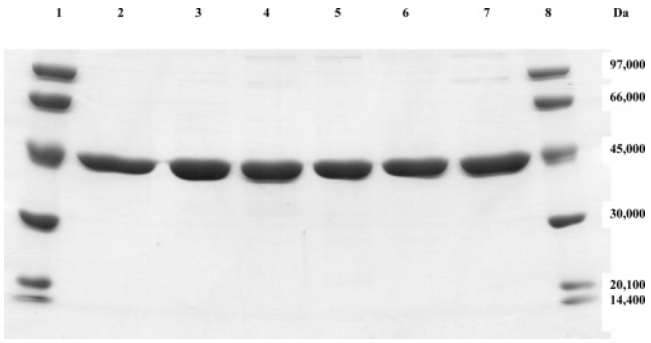

Figure 2. SDS−PAGE of purified wild-type and cysteine mutant isocitrate dehydrogenases. Lanes 1 and 8 are molecular weight markers, which contains trypsin inhibitor (20.1 KDa), carbonic anhydrase (30 KDa), ovalbumin (45 KDa), albumin (66 KDa), and phosphorylase b (97 KDa). Lane 2: wild-type; Lane 3: C74A; Lane 4: C115A; Lane 5: C269A; Lane 6: C379S; and Lane 7: C269A/C379S.

that of its precursor, 2′-AMP-5′-SP), and this value was used to calculate the extinction coefficient of the photoaffinity reagent. 2′-P-AMPS-Succ-BP exhibits maximum absorbance at 259 nm with an extinction coefficient of 28 000 M^{-1} cm^{-1} as measured in 10 mM triethanolamine hydrochloride, pH 7.4, which is close to the reported extinction coefficient for AMPS-Succ-BP (30,700 M^{-1} cm^{-1}) in 50 mM PIPES, pH 7.0 (*5*).

Purification of Wild-type and Mutant Porcine Isocitrate Dehydrogenases. Wild-type and mutant enzymes were expressed in *E. coli* TB1 cells and purified as described in Experimental Procedures. The purified enzymes were homogeneous, as shown by SDS−PAGE (Figure 2). Both wild-type and mutant enzymes exhibit a single band on 10% SDS−PAGE gel with a molecular weight of about 45 kDa, which is close to the calculated subunit molecular weight of porcine isocitrate dehydrogenase based on its amino acid sequence (46.6 kDa) (*11*). The purity of the prepared enzymes was further confirmed by N-terminal sequencing. All enzymes contain the correct N-terminal sequence of porcine isocitrate dehydrogenase, which is distinguished from *E. coli* isocitrate dehydrogenase in 9 out of the first 10 amino acids.

Secondary Structures of Wild-type and Mutant Porcine Isocitrate Dehydrogenases. The secondary structures of wild-type and cysteine mutant enzymes were determined using circular dichroism. All of the cysteine mutants have CD spectra similar to that of wild-type enzyme (data not shown). Wild-type and mutant enzymes all exhibit minima of molar ellipticity at 210 and 225 nm, indicating appreciable α-helix in their structures. The CD results indicate that mutations at selected cysteine residues do not cause significant change in the enzyme's secondary structure.

Specific Activities and Kinetic Parameters of Wild-type and Mutant Isocitrate Dehydrogenases. We have previously used *N*-ethylmaleimide (NEM) to label four cysteines of porcine isocitrate dehydrogenase: Cys74, Cys115, Cys269, and Cys379 (*29*). In the presence of isocitrate and Mn^{2+}, only Cys379 was modified by NEM and the modified enzyme retained its full activity, suggesting that Cys379 is not required for enzyme function. On the contrary, modifying Cys269 by NEM greatly reduces the enzyme activity, suggesting that Cys269 is involved in enzyme function. To evaluate the importance of these four cysteines in the function of porcine isocitrate dehydrogenase, each cysteine was replaced either by alanine or serine. The specific activities of wild-type and mutant enzymes were determined using

Table 1. Specific Activities and Kinetic Parameters of Wild-type and Mutant Isocitrate Dehydrogenases[a]

enzyme	specific activity[b] (μmol/min/mg protein)	K_m (NADP)[b] (μM)	K_m (isocitrate)[b] (μM)	K_m (Mn^{2+})[b] (μM)
wild-type[c]	38.6 ± 2.8	8.8 ± 0.3	7.4 ± 0.9	0.3 ± 0.1
C74A	21.2 ± 1.8	10.1 ± 0.4	15.3 ± 2.2	0.3 ± 0.1
C115A	28.3 ± 1.4	7.8 ± 1.8	8.2 ± 1.2	0.3 ± 0.1
C269A	35.1 ± 2.9	6.7 ± 1.3	8.9 ± 2.5	0.4 ± 0.0
C379S	37.8 ± 1.4	7.9 ± 0.9	10.4 ± 1.7	0.2 ± 0.0
C269A/C379S	39.2 ± 1.4	9.4 ± 0.4	9.7 ± 1.3	0.4 ± 0.0

[a] The standard assay solution contained 4 mM DL-isocitrate, 100 μM NADP, and 2 mM $MnSO_4$ in 30 mM triethanolamine hydrochloride, pH 7.4 buffer in a total volume of 1 mL. The specific activity and kinetic parameters were measured as described in Experimental Procedures. [b] Specific activities and kinetic parameters are expressed as mean ± standard deviation (SD). [c] The specific activity and kinetic parameters for the wild-type enzyme were determined previously (*21*).

substrate concentrations which saturate their individual sites, as described in Experimental Procedures. Table 1 shows the specific activities and K_m values for isocitrate, NADP, and Mn^{2+} of wild-type and cysteine mutant enzymes. C269A, C379S, and C269A/C379S mutant enzymes exhibit comparable specific activities to that of wild-type enzyme. Mutations at Cys74 or Cys115 result in a small decrease in mutant enzyme specific activity; they retain 55% and 73%, respectively, of wild-type enzyme residual activity. Replacement of cysteine at positions 74, 115, 269, or 379 does not markedly alter the K_m values for NADP, isocitrate, or Mn^{2+}. These results indicate that none of these four cysteine residues is directly involved in porcine isocitrate dehydrogenase catalysis or substrate binding.

To evaluate whether the new nucleotide analogue binds to NADP-specific isocitrate dehydrogenase, 2′-P-AMPS-Succ-BP was tested (without UV irradiation) as an inhibitor of the conversion of isocitrate to α-ketoglutarate catalyzed by the C269A/C379S enzyme. Measurement of the initial velocity as a function of the NADP concentration in the presence of the constant concentration of 150 μM 2′-P-AMPS-Succ-BP yields the same V_{max} but an increase in the apparent K_m for NADP to 47.7 μM, as compared to 9.4 μM (Table 1, last line) in the absence of 2′-P-AMPS-Succ-BP. Thus, 2′-P-AMPS-Succ-BP exhibits the characteristics of a competitive inhibitor with respect to NADP, with a K_I of 36.9 μM. Since the presence of 150 μM 2′-P-AMPS-Succ-BP increased the apparent K_m value for NADP of C269A/C379S enzyme, subsequent measurements for the apparent K_m value for isocitrate in the presence of the affinity reagent were conducted in assay solution containing 400 μM NADP. Measurement of the initial velocity as a function of the isocitrate concentration in the presence of the constant concentration of 150 μM 2′-P-AMPS-Succ-BP gave the comparable V_{max} and apparent K_m for isocitrate as those in the absence of the photoaffinity compound (K_m=13.8 μM in the presence of 2′-P-AMPS-Succ-BP versus K_m = 9.7 μM in the absence of the affinity label). Thus, 2′-P-AMPS-Succ-BP is not a competitive inhibitor with respect to isocitrate.

Photoinactivation of C269A/C379S Enzyme by 2′-P-AMPS-Succ-BP. Irradiation of the C269A/C379S enzyme (0.1 mg/mL, 2.15 μM enzyme subunit) in the presence of 10 μM 2′-P-AMPS-Succ-BP in 30 mM triethanolamine hydrochloride, pH 7.4 at 0 °C, results in a time-dependent inactivation of the enzyme, as shown in Figure 3 (○). In contrast, control enzyme, irradiated under the same conditions but in the absence of 2′-P-

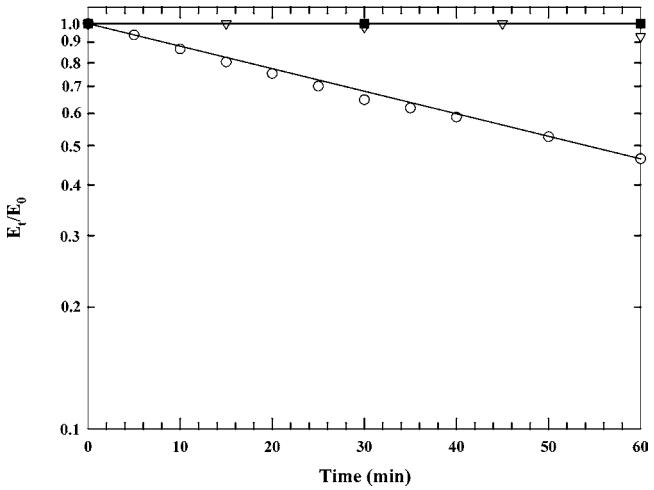

Figure 3. Photoinactivation of C269A/C379S enzyme by 2′-P-AMPS-Succ-BP. 0.1 mg/mL of C269A/C379S was either incubated on ice in the presence of 10 μM 2′-P-AMPS-Succ-BP (○) or in the absence of reagent (▽) during UV irradiation at 365 nm. The enzyme was also incubated with 10 μM 2′-P-AMPS-Succ-BP in the absence of UV irradiation (■). At various times, small aliquots were withdrawn and assayed for residual enzyme activity.

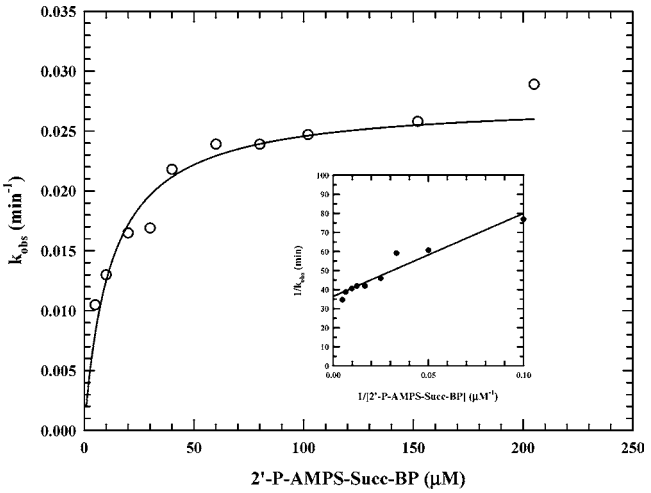

Figure 4. Dependence of inactivation rate constant of C269A/C379S mutant isocitrate dehydrogenase on the concentration of 2′-P-AMPS-Succ-BP. C269A/C379S mutant (0.1 mg/mL) was incubated with 5−205 μM 2′-P-AMPS-Succ-BP in 30 mM trithanolamine HCl, pH 7.4. The rate constants were determined from the first 60 min of reaction. Inset is the double reciprocal plot of $1/k_{obs}$ against 1/[2′-P-AMPS-Succ-BP].

AMPS-Succ-BP, shows no activity loss over the same incubation time (Figure 3, ▽). In the absence of UV light, the enzyme also retains its activity completely, even in the presence of 2′-P-AMPS-Succ-BP (Figure 3, ■). These results indicate that 2′-P-AMPS-Succ-BP acts as a photoaffinity label for porcine isocitrate dehydrogenase, requiring UV light to produce inactivation. 2′-P-AMPS-Succ-BP, which had been UV-irradiated for 3 h prior to addition to the inactivation mixture, produced comparable time-dependent inactivation of porcine isocitrate dehydrogenase to that seen with "fresh" 2′-P-AMPS-Succ-BP. This result indicates that 2′-P-AMPS-Succ-BP still retains its ability to function as a photoaffinity label during the 3 h irradiation period.

Isocitrate dehydrogenase C269A/C379S (0.1 mg/mL, 2.15 μM enzyme subunit) was incubated on ice with 5 to 205 μM 2′-P-AMPS-Succ-BP. The apparent rate constant (k_{obs}) of photoinactivation was calculated from the slope of $\ln(E_t/E_0)$ versus time, where E_t is the enzyme activity at time t and E_0 is the enzyme activity at time zero. A nonlinear relationship is observed when the inactivation rate constant (k_{obs}) is plotted versus the concentration of 2′-P-AMPS-Succ-BP (Figure 4), suggesting the initial formation of a reversible enzyme-ligand complex, prior to the irreversible modification. At high concentrations of 2′-P-AMPS-Succ-BP, the mutant enzyme is saturated with the reagent and the rate constant approaches a maximum (k_{max}). This type of inactivation kinetics can be described by the equation (*2*):

$$1/k_{obs} = 1/k_{max} + K_R/k_{max}\,(1/[2'\text{-P-AMPS-Succ-BP}]) \quad (1)$$

The maximum rate of inactivation (k_{max}) is 0.0275 min^{-1} and the apparent dissociation constant (K_R) is 12 μM. We had previously synthesized AMPS-Succ-BP, a similar photoaffinity label, but which lacks the 2′-phosphate of its adenosine ribose (*5*). AMPS-Succ-BP inactivates wild-type NADP-specific isocitrate dehydrogenase upon UV irradiation, but only at much higher concentrations; it has a higher K_R value as compared to 2′-P-AMPS-Succ-BP (K_R = 870 μM for AMPS-Succ-BP). The results indicate the required presence of a 2′-phosphate at the adenosine ribose for proper binding of the reagent to NADP-specific porcine isocitrate dehydrogenase.

Table 2. Effect of Active Site Ligands on Photoinactivation of C269A/C379S Mutant Isocitrate Dehydrogenase by 20 μM 2′-P-[^{35}S]AMPS-Succ-BP[a]

ligand added to incubation mixture	k_{obs} (min^{-1})	k_+/k_-
(1) None	0.0179	1.00
(2) 10 μM NADPH	0.0023	0.13
(3) 50 μM NADPH	0.0000	0.00
(4) 50 μM NADH	0.0211	1.18
(5) 100 μM NADP	0.0056	0.31
(6) 200 μM NADP	0.0025	0.14
(7) 100 μM ATPR	0.0000	0.00
(8) 100 μM isocitrate + 100 μM $MnSO_4$	0.0000	0.00

[a] Reaction was conducted on ice in 30 mM triethanolamine hydrochloride, pH 7.4, as described in Experimental Procedures. The value of k_+/k_- is the ratio of the rate constant for photoinactivation in the presence of an active site ligand to that in its absence.

Effect of Ligands on the Inactivation Rate of C269A/C379S Mutant Enzyme by 20 μM 2′-P-AMPS-Succ-BP. The ability of active site ligands to protect C269A/C379S isocitrate dehydrogenase (0.1 mg/mL, 2.15 μM enzyme subunit) against inactivation by 20 μM 2′-P-AMPS-Succ-BP is recorded in Table 2. The concentrations of NADP, NADPH, and isocitrate plus Mn^{2+} used in the studies were high compared to their K_m values determined in this study (K_m = 9.4 μM for NADP, K_m = 9.7 μM for isocitrate, and K_m = 0.4 μM for Mn^{2+} of C269A/C379S enzyme, Table 1). Both NADP and NADPH protect C269A/C379S enzyme against 2′-P-AMPS-Succ-BP inactivation, and the protection is concentration dependent (Table 2, lines 2, 3 and lines 5, 6). NADPH, which has a higher affinity for porcine isocitrate dehydrogenase (*32*), protects the cysteine mutant enzyme against inactivation at lower ligand concentration than does NADP. NADH (50 μM), which has the same maximum absorbance at 340 nm as does 50 μM NADPH but binds weakly to porcine isocitrate dehydrogenase, does not provide any protection to C269A/C379S enzyme against inactivation (line 4). This result indicates that the observed protection by enzyme active site ligands is due to the competitive binding of ligands with 2′-P-

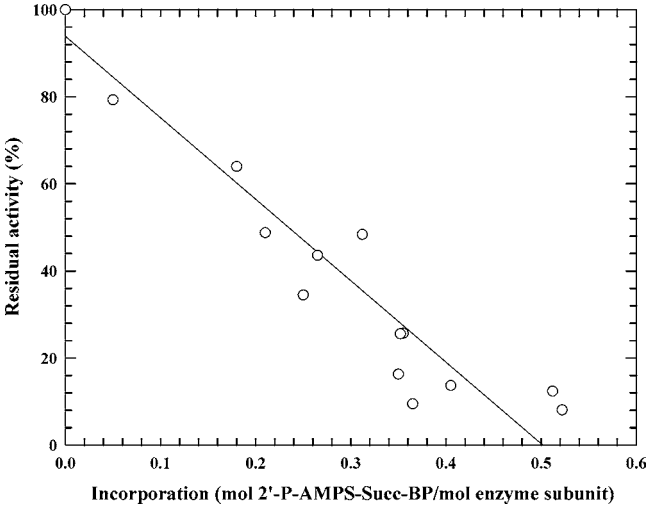

Figure 5. The incorporation of 2′-P-[^{35}S]AMPS-Succ-BP into C269A/C379S mutant enzyme as a function of the percentage of residual activity. The enzyme was incubated with 40 μM reagent, as described in Experimental Procedures. Aliquots were removed at various times for measurement of residual activity and amount of reagent incorporation. Extrapolation to complete inactivation of the enzyme yields 0.5 mol of reagent incorporation per mol of enzyme subunit.

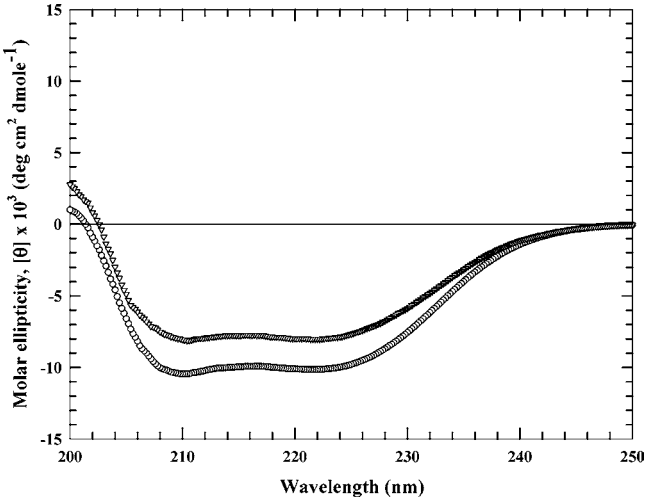

Figure 6. Circular diochroism (CD) spectra of isocitrate dehydrogenase. The CD spectra of C269A/C379S (○) and 2′-P-AMPS-Succ-BP-modified C269A/C379S (▽) were measured and the molar ellipticity was calculated as described in Experimental Procedures.

AMPS-Succ-BP for the enzyme site and is not due to the absorbance of UV light at 340 nm by the reduced coenzyme. 2′-Monophospho-adenosine 5′-diphosphoribose (ATPR), an NADP analogue which lacks the nicotinamide ring of NADP, has previously been shown to bind tightly to isocitrate dehydrogenase (*33*). ATPR completely protects the enzyme against inactivation (line 7). These protection studies suggest that 2′-P-AMPS-Succ-BP acts as a photoaffinity label and that it binds to the mutant enzyme in the region of the active site best occupied by coenzyme, NADP/NADPH. The enzyme also retains its full activity when 100 μM isocitrate plus 100 μM Mn^{2+} are present in the inactivation mixture (line 8). The complete protection provided by isocitrate and Mn^{2+} may be due to the proximity between the isocitrate and NADP sites of the porcine enzyme as well as the previously reported weakened binding of NADPH by the porcine enzyme in the presence of isocitrate and Mn^{2+} (*8, 9, 32*).

Incorporation of 2′-P-[^{35}S]AMPS-Succ-BP into C269A/C379S Enzyme. A time-dependent incorporation of 2′-P-[^{35}S]AMPS-Succ-BP into the C269A/C379S enzyme was observed concomitant with the decrease in enzyme activity. Figure 5 shows a plot of percentage of residual activity versus 2′-P-[^{35}S]AMPS-Succ-BP incorporation. The line can be extrapolated to 0% residual activity to yield 0.5 mol of 2′-P-[^{35}S]AMPS-Succ-BP incorporated per mol of enzyme subunit (or 1 mol of reagent/mol enzyme dimer) when the enzyme loses all activity.

Characteristics of 2′-P-AMPS-Succ-BP-Modified Enzyme. The CD spectrum of 2′-P-AMPS-Succ-BP inactivated C269A/C379S enzyme (~17% residual activity and 0.4 mol reagent incorporated/mol enzyme subunit) is shown in Figure 6. The shape of the CD spectrum of the modified C269A/C379S enzyme is very similar to that of unmodified C269A/C379S enzyme. However, the magnitude of the molar ellipticity of the modified enzyme is much less than that of unmodified enzyme, indicating that the modified enzyme contains less α-helical structure as compared to that of unmodified enzyme.

The binding stoichiometry for NADPH or isocitrate of native and 2′-P-AMPS-Succ-BP-modified C269A/C379S isocitrate dehydrogenases determined by ultrafiltration are compared in Table 3. Native C269A/C379S isocitrate dehydrogenase binds 0.97 mol of NADPH or D-isocitrate/mol of enzyme subunit (or 1.94 mol of NADPH or D-isocitrate/mol of enzyme dimer), which is in agreement with the binding stoichiometry of wild-type enzyme determined previously by fluorescence titration and ultrafiltration (*27, 33*). 2′-P-AMPS-Succ-BP-modified C269A/C379S enzyme is capable of binding 0.41 mol of D-isocitrate/mol enzyme subunit and 0.51 mol of NADPH/mol enzyme subunit (or 0.82 mol of D-isocitrate/mol enzyme dimer and 1.02 mol of NADPH/mol enzyme dimer). These ligand binding results for the 2′-P-AMPS-Succ-BP-modified C269A/C379S enzyme are similar to those of wild-type enzyme modified with 2-BDB-TA-2′,5′-DP or 2-BDB-TϵA-2′,5′-DP (*25, 26*) and implies that 2′-P-AMPS-Succ-BP occupies only one of the two active sites of isocitrate dehydrogenase dimer.

Table 3. Binding Stoichiometry of D-Isocitrate and NADPH to Native C269A/C379S and 2′-P-AMPS-Succ-BP-Modified C269A/C379S Isocitrate Dehydrogenases[a,b]

enzyme	mol of bound D-isocitrate/mol of enzyme subunit	mol of bound NADPH/mol of enzyme subunit
native	0.97	0.97
modified	0.41	0.51

[a] Isocitrate dehydrogenase was modified as described in Experimental Procedures. The modified enzyme had 20−23% residual activity. The ultrafiltration experiments were performed at 25 °C in 50 mM triethanolamine hydrocholoride, pH 7.7 buffer, containing 150 mM Na_2SO_4 and 10% glycerol. [b] Wild-type NADP-dependent isocitrate dehydrogenase has previously been shown to bind 0.98 mol of D-isocitrate/mol of enzyme subunit and 1.00 mol of NADPH/mol of enzyme subunit under the same conditions (*27*).

DISCUSSION

The coenzyme site of porcine mitochondrial isocitrate dehydrogenase has been studied previously using the affinity labels, 2-(4-bromo-2,3-dioxobutylthio)-1, N^6-ethenoadenosine 2′,5′-bisphosphate (2-BDB-TϵA-2′,5′-DP), 2-[(4-bromo-2,3-dioxobutyl)thio]adenosine 2′,5′-bisphosphate (2-BDB-TA-2′,5′-DP), and 2-[(3-bromo-2-oxopropyl)thio]adenosine 2′,5′-bisphosphate (2-BOP-TA-

2′,5′-DP) (*10, 25, 26, 31*). Each of these affinity labels is an adenosine analogue with a reactive bromoketo group linked to the C2 position of adenine and is capable of revealing active site residues in the vicinity of the nicotinamide ring of NADP. 2-BDB-TϵA-2′,5′-DP causes rapid inactivation of the porcine isocitrate dehydrogenase which is prevented by NADP or NADPH, and Cys379 is the residue modified by the compound (*10, 31*). The results suggested that Cys379 is involved in isocitrate dehydrogenase catalysis and it is located at the NADP site of the enzyme. In contrast, modification of the porcine enzyme with the small NEM indicates that Cys379 is not essential for catalysis while Cys269 may be involved in enzyme catalysis (*29*). To clarify the roles of Cys269 and Cys379 in isocitrate dehydrogenase catalysis, we replaced these cysteines with alanine and serine, respectively. Cys74 and Cys115, which have been partially modified by NEM, were also chosen for site-directed mutagenesis. C74A, C115A, C269A, and C379S mutant enzymes all exhibited comparable activity and kinetic parameters to those of wild-type enzyme, which suggest that none of the four cysteines is involved in the porcine enzyme catalytic function, but that they may reside close to the enzyme active sites. The nucleotide affinity label still may occupy the active site even though it modifies a proximal but nonessential cysteine(s), which may explain the previously observed inactivation by the large reagents (*30*). In this study, we generated a double mutant (C269A/C379S) by replacing the two most reactive nonessential cysteine residues with either alanine or serine. The resulting double mutant enzyme has similar specific activity as well as kinetic parameters to those of wild-type enzyme. However, the C269A/C379S mutant enzyme, similar to the NEM-modified porcine isocitrate dehydrogenase (*30*), is not inactivated by 2-BDB-TA-2′,5′-DP (data not shown). The results indicate that the two mutated cysteines had been the targets of 2-BDB-TA-2′,5′-DP. We have used C269A/C379S enzyme in our photoaffinity labeling experiments to promote reaction with other amino acids.

Here, we describe a new affinity label, 2′-P-AMPS-Succ-BP, which modifies the active site of porcine isocitrate dehydrogenase. 2′-P-AMPS-Succ-BP is structurally similar to 2′-AMP and contains a succinimidyl benzophenone thiophosphate moiety adjacent to the C5′ position of the adenosine ribose. The approximate length of the benzophenone moiety is about 10Å (*6*), which is close to the distance (14 Å) between the adenine and nicotinamide rings of NADP in the *E. coli* isocitrate dehydrogenase crystal structure (*34*). Although more than one conformation is possible of 2′-P-AMPS-Succ-BP, in the extended form shown in Figure 1 the photoreactive carbonyl oxygen would be positioned toward the nicotinamide site. Upon UV irradiation, the reactive carbonyl group can react indiscriminately with any amino acid in its vicinity. Our results show that 2′-P-AMPS-Succ-BP functions as an affinity label for the coenzyme site of porcine isocitrate dehydrogenase.

Porcine isocitrate dehydrogenase reacted with by 2-BDB-TA-2′,5′-DP, 2-BOP-TA-2′,5′-DP or 2-BDB-TϵA-2′,5′-DP exhibits a biphasic inactivation: a fast inactivation protected by NADP followed by a slow inactivation which is prevented by isocitrate and Mn^{2+}. This indicates that the affinity labels bind to the enzyme at more than one region of the active site (*10, 26*). In contrast, the photoinactivation of the porcine enzyme by 2′-P-AMPS-Succ-BP shows a monophasic inactivation, implying that the new affinity label targets a single active site on the porcine enzyme. Actually, our active site ligand protection studies and kinetic parameters determined in the presence of 2′-AMP-5′-S-Succ-BP further suggest that the photoaffinity label competes with NADP for the coenzyme site of the porcine enzyme. The nonlinear relationship between the initial inactivation rate constant and the 2′-P-AMPS-Succ-BP concentration indicates the reversible binding of 2′-P-AMPS-Succ-BP to C269A/C379S enzyme (with a K_R of 12 μM) prior to irreversible inactivation. This K_R value (obtained at ice temperature) is comparable in magnitude to the K_m value for NADP (9.4 μM, determined in this study) of C269A/C379S enzyme, suggesting that the enzyme has similar affinity for the reagent as for its natural substrate, NADP. The coenzyme preference of dehydrogenases is determined by the interaction between the enzyme and the 2′-phosphate of NADP and the 2′- and 3′-hydroxyls of NAD (*35*). The ^{31}P NMR studies on the porcine enzyme indicate that the 2′-phosphate of enzyme-bound NADP is present in its dianionic form and likely interacts with a nearby positively charged amino acid(s) (*36*). Previous site-directed mutagenesis studies of porcine isocitrate dehydrogenase reveal that Arg314 and His315 may interact with the 2′-phosphate of NADP via electrostatic interaction (*21, 27*). Similar electrostatic interactions between the 2′-phosphate of NADP and positively charged side chains (His and Arg) were also observed in *E. coli* and *A. vinelandii* isocitrate dehydrogenases (*9, 34, 37*).

Porcine isocitrate dehydrogenase has very low affinity for NAD (K_m = 12.2 mM) as compared to its preferred coenzyme, NADP (K_m = 8.8 μM) (*21, 38*). AMPS-Succ-BP, which contains a hydroxyl group at the C2′ position of the adenosine ribose similar to that of NAD, would be expected to bind poorly to this porcine enzyme. Our studies did show that AMPS-Succ-BP exhibits a much higher K_R value (870 μM) for the porcine enzyme as compared to that of 2′-P-AMPS-Succ-BP (12 μM), which further implies the contribution of the 2′-phosphate of the reagent to the binding of the compound to the NADP-specific porcine enzyme.

The target site of 2′-P-AMPS-Succ-BP is revealed by examining the protective effects of active site ligands against inactivation by the compound. The complete protection by NADP, NADPH, and ATPR indicate that 2′-P-AMPS-Succ-BP occupies the coenzyme site of porcine isocitrate dehydrogenase, as might be expected from the striking similarity in structures between the coenzymes and the reagent. Alternatively, the porcine isocitrate dehydrogenase may adopt a closed active site structure upon NADP binding, similar to that of the *A. vinelandii* enzyme crystal structure complexed with NADP and the active site conformational changes may prevent the binding of 2′-P-AMPS-Succ-BP to the porcine enzyme (*37*). However, our kinetic studies conducted in the presence of 2′-P-AMPS-Succ-BP suggest that the affinity reagent competes with NADP for the same region on the porcine enzyme, consistent with the conclusion that 2′-P-AMPS-Succ-BP targets the coenzyme site of porcine isocitrate dehydrogenase.

The complete protection provided by isocitrate and Mn^{2+} against inactivation by a *nucleotide* analogue may appear to be anomalous. However, the proposed mechanisms for isocitrate dehydrogenase suggest that the nicotinamide ring of NADP must be close to the isocitrate site in order to extract a hydride from isocitrate (*8, 9*). A conformational change near the coenzyme site upon NADP binding and a 45° rotation of the bond between C4 and C5 of isocitrate in order to accommodate the NADP binding are observed in the *E. coli* isocitrate dehydrogenase crystal structure (*34*). Additionally, isoci-

trate and Mn^{2+} have been shown to weaken the binding of NADPH to the porcine enzyme (*32*); the substrate and coenzyme sites appear to interact, although they clearly cannot be identical. In our studies, the higher K_I (36.9 μM) for 2′-P-AMPS-Succ-BP determined in the complete assay as a competitive inhibitor with respect to NADP, as compared with the K_R (12 μM) for 2′-P-AMPS-Succ-BP determined from the photoinactivation in the absence of isocitrate and Mn^{2+}, is in agreement with the previously observed inhibition by substrates of the binding of NADPH by the porcine enzyme. The K_m for isocitrate in the current studies (measured with 2′-P-AMPS-Succ-BP present) was determined at elevated concentrations of NADP (400 μM), which would have excluded the binding of 2′-P-AMPS-Succ-BP and yielded the result that 2′-P-AMPS-Succ-BP did not compete kinetically with isocitrate. Thus, the proximity between the NADP and isocitrate sites and the inhibitory effects of isocitrate and Mn^{2+} upon the binding of NADPH to the porcine enzyme may account for the observed protection by isocitrate and Mn^{2+} against 2′-P-AMPS-Succ-BP inactivation of isocitrate dehydrogenase. We consider that the affinity label 2′-P-AMPS-Succ-BP reacts at the coenzyme site.

Incorporation measurements indicate that only one of the two active sites of the isocitrate dehydrogenase dimer is occupied by 2′-P-AMPS-Succ-BP concomitant with complete loss of enzymatic activity. The active site located in the other subunit of the inactivated enzyme is still capable of binding D-isocitrate or NADPH, as demonstrated by the ligand binding stoichiometry studies. The X-ray crystal structures of several isocitrate dehydrogenases reveal that the enzyme active sites consist of residues from both subunits of the homodimer (*9, 14, 34*). Modification of one active site of the porcine enzyme with 2′-P-AMPS-Succ-BP may introduce conformational changes to the other active site. Our CD studies reveal that modified enzyme does contain less α-helical structure than that of native enzyme. An increase in protein fluorescence was reported previously when porcine isocitrate dehydrogenase bound NADP, adenosine 2′,5′-bisphosphate or 2′-phosphoadenosine 5′-diphosphoribose, reflecting a conformational change (*33*). The maximum fluorescence enhancement was observed when one coenzyme site per enzyme dimer was occupied; addition of more NADP did not further change the protein fluorescence (*33*). Similar conformational changes may prevent the productive catalysis by the other active site on the enzyme modified by 2′-P-AMPS-Succ-BP, even though it can still bind ligands. In our reagent incorporation studies, the enzyme was incubated with 40 μM of 2′-P-AMPS-Succ-BP for 80 min, sufficient to almost completely abolish enzyme activity. Under these conditions, 2′-P-AMPS-Succ-BP occupies only one of the active sites per enzyme dimer; these results do not exclude the possibility that the compound can react with the half unmodified subunit, but it could not further inactivate an already inactive enzyme.

Previously synthesized affinity labels for the coenzyme site of porcine NADP-specific isocitrate dehydrogenase either contain only the adenosine ribose fragment of the coenzyme (e.g., 2-BDB-TA-2′,5′-DP, 2-BOP-TA-2′,5′-DP, and 2-BDB-TϵADP), have limited reactivities with amino acid side chains (e.g., periodate-oxidized NADP), or lack the 2′-phosphate for proper coenzyme binding (e.g., 8-BDB-TNAD) (*3, 10, 26*). In contrast, 2′-P-AMPS-Succ-BP contains the critical 2′-phosphate at its adenosine ribose ring and a succinimidyl-benzophenone thiophosphate to structurally mimic the nicotinamide moiety of coenzyme, NADP. 2′-P-AMPS-Succ-BP can covalently react with any amino acid through its carbonyl group of benzophenone upon UV irradiation (*6*). The new photoaffinity label thus complements the existing NADP affinity labels and has potential applications in other NADP-specific enzymes.

ACKNOWLEDGMENT

This work was supported by NIH Grant R01 HL 67774. The authors would like to thank Drs. Yu-Chu Huang and Melissa Vargo for performing N-terminal sequencing, Dr. Shi Bai for determining the ^{31}P NMR of 2′-P-AMPS-Succ-BP, and Dr. John Dykins for his help in acquiring the mass spectrum of the affinity label.

LITERATURE CITED

(1) Colman, R. F. (1997) Chemical arrows for enzymatic targets. *FASEB J.* 217−226.
(2) Colman, R. F. (1997) Affinity labels for NAD(P)-specific sites. *Methods in Enzymology*, vol. 280, pp 186−203, Academic Press, New York.
(3) Kumar, A., and Colman, R. F. (1994) 8-(4-Bromo-2,3-dioxobutylthio)NAD: a new affinity label for NAD-specific isocitrate dehydrogenase. *Arch. Biochem. Biophys. 308*, 357−366.
(4) Dombrowski, K. E., and Colman, R. F. (1989) 5′-p-(Fluorosulfonyl)benzoyl-8-azidoadenosine: a new bifunctional affinity label for nucleotide binding sites in proteins. *Arch. Biochem. Biophys. 275*, 302−308.
(5) Madhusoodanan, K. S., and Colman, R. F. (2001) Adenonsine 5′-*O*-[*S*-(4-succinimidyl-benzophenone)thiophosphate]: a new photoaffinity label of the allosteric ADP site of bovine liver glutamate dehydrogenase. *Biochemistry 40*, 1577−1586.
(6) Dorman, G., and Prestwich, G. D. (1994) Benzophenone photophores in biochemistry. *Biochemistry 33*, 5661−5673.
(7) Wang, J., Bauman, S., and Colman, R. F. (1998) Photoaffinity labeling of rat liver glutathinone S-transferase, 4−4, by glutathionyl S-[4-(succinimidyl)-benzophenone]. *Biochemistry 37*, 15671−15679.
(8) Colman, R. F. (1983) Aspects of the structure and function of the isocitrate dehydrogenases. *Peptide and Protein Review*, vol. 1, pp 41−69, Marcel Dekker, Inc. New York.
(9) Hurley, J. H., Dean, A. M., Koshland, D. E. Jr., and Stroud, R. M. (1991) Catalytic mechanism of $NADP^+$-dependent isocitrate dehydrogenase: implication from the structures of magnesium-isocitrate and $NADP^+$ complexes. *Biochemistry 30*, 8671−8678.
(10) Bailey, J. M., and Colman, R. F. (1985) Affinity labeling of NADP+-specific isocitrate dehydrogenase by a new fluorescent nucleotide analogue, 2-[(4-bromo-2,3-dioxobutyl)thio]-1,N^6-ethenoadenosine 2′,5′-bisphosphate. *Biochemistry 24*, 5367−5377.
(11) Haselbeck, R. J., Colman, R. F., and McAlister-Henn, L. (1992) Isolation and sequence of a cDNA encoding porcine mitochondrial NADP-specific isocitrate dehydrogenase. *Biochemistry 31*, 6219−6223.
(12) Kelly, J. H., and Plaut, G. W. E. (1981) Physcial evidence for the dimerization of the triphosphorylpyridine-specific isocitrate dehydrogenase from pig heart. *J. Biol. Chem. 256*, 330−334.
(13) Endrizzi, J., Zhang, G., Xiong, W. C., Hurley, J. H., Remington, S. J., and Colman, R. F. (1996) Crystallization and preliminary diffraction analysis of porcine heart mitochondrial $NADP^+$-dependent isocitrate dehydrogenase. *Acta Crystallogr. D52*, 1024−1026.
(14) Ceccarelli, C., Grodsky, N. B., Ariyaratne, N., Colman, R. F., and Bahnson, B. J. (2002) Crystal structure of porcine mitochondrial $NADP^+$-dependent isocitrate dehydrogenase complexed with Mn^{2+} and isocitrate. *J. Biol. Chem. 277*, 43454−43462.
(15) Lee, T. T., Worby, C., Dixon, J. E., and Colman, R. F. (1997) Identification of His^{141} in the active site of *Bacillus subitilis* adenylosuccinate lyase by affinity labeling with 6-(4-bromo-2,3-dioxobutyl)thioadenosine 5′-monophosphate. *J. Biol. Chem. 272*, 458−465.

(16) Deutsch, D. H., and Phillips, R. E. (1957) Preparation of tricarboxylic acids. *Methods in Enzymology*, vol. 3, pp 421−425, Academic Press, New York.
(17) Slama, J. T., Simmons, A. M., Hernandez, T. M., and Keenan, R. W. (1993) Synthesis of [^{35}S]thiophosphoryl adenylic acid, utilizing a general procedure for [^{35}S]thiophosphoryl chloride production. *Anal. Biochem. 209*, 143−149.
(18) Lee, P., Gorrell, A., Fromm, H. J., and Colman, R. F. (1999) 8-(4-Bromo-2,3-dioxobutylthio)guanosine 5′-triphosphate: a new affinity label for purine nucleotide sites in proteins. *Arch. Biochem. Biophys. 372*, 205−213.
(19) Soundar, S., Danek, B. L., and Colman, R. F. (2000) Identification by mutagenesis of arginines in the substrate binding site of the porcine NADP-dependent isocitrate dehydrogenase. *J. Biol. Chem. 275*, 5606−5612.
(20) Grodsky, N. B., Soundar, S., and Colman, R. F. (2000) Evaluation by site-directed mutagenesis of aspartic acid residues in the metal site of pig heart NADP-dependent isocitrate dehydrogenase. *Biochemistry 39*, 2193−2200.
(21) Lee, P., and Colman, R. F. (2002) Implication by site-directed mutagensis of Arg^{314} and Tyr^{316} in the coenzyme site of pig mitochondrial NADP-dependent isocitrate dehydrogenase. *Arch. Biochem. Biophys. 401*, 81−90.
(22) Laemmli, U. K. (1970) Cleavage of structural proteins during the assembly of the head of bacteriophage T4. *Nature 227*, 680−685.
(23) Bradford, M. M. (1976) A rapid and sensitive method for the quantitaion of microgram quantities of protein utilizing the principle of protein-dye binding. *Anal. Biochem. 72*, 248−254.
(24) Penefsky, H. S. (1979) A centrifuged-column procedure for the measurement of ligand binding by beef heart F1. *Methods in Enzymology*, vol. 56, pp 527−530, Academic Press, New York.
(25) Bailey, J. M., and Colman, R. F. (1987) Distances among coenzyme and metal sites of NADP$^+$-dependent isocitrate dehydrogenase using resonance energy transfer. *Biochemistry 26*, 4893−4900.
(26) Bailey, J. M., and Colman, R. F. (1987) 2[(4-bromo-2,3-dioxobutyl)thio]- and 2-[(3-bromo-2-oxopropyl)thio]adenosine 2′,5′-bisphosphate: new nucleotide analogue that act as affinity labels of nicotinamide adenine dinucleotide phosphate specific isocitrate dehydrogenase. *Biochemistry 26*, 6858−6869.
(27) Huang, Y. C., and Colman, R. F. (2002) Evaluation by mutagenesis of the roles of His^{309}, His^{315}, and His^{319} in the coenzyme site of pig heart NADP-dependent isocitrate dehydrogenase. *Biochemistry 41*, 5637−5643.
(28) Connolly, B. A., and Eckstein, F. (1982) S-methylated nucleoside phosphorothioates as probes of enzyme metal-nucleotide binding sites. *Biochemistry 21*, 6158−6167.
(29) Smyth, G. E., and Colman, R. F. (1991) Cysteinyl peptides of pig heart NADP-dependent isocitrate dehydrogenase that are modified upon inaction by *N*-ethylmaleimide. *J. Biol. Chem. 266*, 14918−14925.
(30) Smyth, G. E., and Colman, R. F. (1992) Inactivation of pig heart NADP-specific isocitrate dehydrogenase by two affinity reagents is due to reaction with a cysteine not essential for function. *Arch. Biochem. Biophys. 293*, 356−361.
(31) Bailey, J. M., and Colman, R. F. (1987) Isolation of the glutamyl peptide labeled by the nucleotide analogue 2-(4-bromo-2,3-dioxobutylthio)-1,N^6-ethenoadenosine 2′,5′-bisphophate in the active site of NADP$^+$-specific isocitrate dehydrogenase. *J. Biol. Chem. 262*, 12620−12626.
(32) Ehrlich, R. S., and Colman, R. F. (1975) Coenzyme binding by native and chemically modified pig heart triphosphopyridine nucleotide dependent isocitrate dehydrogenase. *Biochemistry 14*, 5008−5016.
(33) Mas, M. T., and Colman, R. F. (1985) Spectroscopic studies of the interactions of coenzymes and coenzyme fragments with pig heart, oxidized triphosphopyridine nucleotide specific isotictrate dehydrogenase. *Biochemistry 24*, 1634−1646.
(34) Stoddard, B. L., Dean, A., and Koshland, D. E. Jr. (1993) Structure of isocitrate dehydrogenase with isocitrate, nicotinamide adenine dinucleotide phosphate, and calcium at 2.5-Å resolution: a pseudo-Michaelis ternary complex. *Biochemistry 32*, 9310−9316.
(35) Chen, R., Greer, A., and Dean, A. M. (1995) A highly active decarboxylating dehydrogenase with rationally inverted coenzyme specificity. *Proc. Natl. Acad. Sci. U.S.A. 92*, 11666−11670.
(36) Mas, M. T., and Colman, R. F. (1984) Phosphorus-31 nuclear magnetic resonance studies of the binding of nucleotides to NADP$^+$-specific isocitrate dehydrogenase. *Biochemistry 23*, 1675−1683.
(37) Yasutake, Y., Watanabe, S., Yao, M., Takada, Y., Fukunaga, N., and Tanaka, I. (2003) Crystal structure of the monomeric isocitrate dehydrogenase in the presence of NADP$^+$. *J. Biol. Chem. 278*, 36897−36904.
(38) Ehrlich, R. S., and Colman, R. F. (1978) Histidine in the nucleotide-binding site of NADP-linked isocitrate dehydrogenase from pig heart. *Eur. J. Biochem. 89*, 575−587.

BC049722W

Dramatic Effect of the Tridentate Ligand on the Stability of ^{99m}Tc "3 + 1" Oxo Complexes Bearing Arylpiperazine Derivatives

C. Fernandes,[†] J. D. G. Correia,[†] L. Gano,[†] I. Santos,*[,†] S. Seifert,[‡] R. Syhre,[‡] R. Bergmann,[‡] and H. Spies[‡]

Departamento de Química, ITN, Estrada Nacional 10, 2686-953, Sacavém Codex, Portugal, and Institute of Bioinorganic & Radiopharmaceutical Chemistry, Forschungszentrum Rossendorf, D-01314 Dresden, Germany.
Received November 22, 2004; Revised Manuscript Received March 28, 2005

Mixed − ligand model complexes of general formula [^{99m}Tc(O)(κ^3-PNX)(κ^1-SPh))] [X = O (**1a**), S (**2a**)] were prepared in a one-step procedure from [$^{99m}TcO_4^-$] using stannous chloride as reducing agent. Stability studies and challenge experiments with glutathione showed that complex **2a** presented promising features for pursuing animal studies. The activity in the brain (% dose injected/organ) at 5 min (0.14% ± 0.03) and 120 min (0.11% ± 0.02) pi encouraged the synthesis of several mixed-ligand "3 + 1" oxo complexes of general formula [M(O)(κ^3-PNS)(κ^1-SL))] (M = ^{99m}Tc, **3a**−**6a**, Re, **3**−**6**), in which the tridentate ligand is the heterofunctionalized phosphine 2-(diphenylphosphanyl)-*N*-(2-thioethyl)benzamide (PNS) and the co-ligands are different arylpiperazine derivatives (HSL1−HSL4). The ^{99m}Tc complexes have been characterized by comparison of their retention times in the HPLC chromatogram (γ-detection) with the retention times of the analogous Re complexes (UV detection at 254 nm). The ^{99m}Tc complexes, obtained with radiochemical purity higher than 95%, after HPLC purification, are stable in saline, 0.01 M PBS (pH 7.4), rat plasma (4 h, 37 °C), and glutathione (10 mM solutions, 2h, 37 °C). Binding affinity and selectivity for 5-HT_{1A} receptors (relative to the 5-HT_{2A} receptor) were determined, complex **5** demonstrating the best values (IC_{50} for the 5-HT_{1A} 2.35 ± 0.02 nM; competitor 5-HT_{2A} 372 ± 11 nM). Biodistribution and stability studies in mice indicated a preferred hepatobiliary excretion, a high in vivo stability, but a poor brain uptake.

INTRODUCTION

One of the major challenges in the development of new specific radiopharmaceuticals based on ^{99m}Tc, the radionuclide of choice in nuclear medicine, is to bind a biomolecule to the metal center without drastically modifying its biological activity and metabolism. The development of ^{99m}Tc-based radiopharmaceuticals for studying the receptor function in the central nervous system (CNS) requires neutral and lipophilic complexes to facilitate their penetration through the blood−brain barrier (BBB), maintaining the affinity and selectivity for the neuroreceptor. Despite the difficulties, several approaches have been investigated to achieve that purpose (*1*−*3*). The successful development of [^{99m}Tc]TRODAT-1 as a ^{99m}Tc-radiopharmaceutical for imaging the dopamine transporters in the human brain was a very encouraging result (*4*, *5*).

The so-called "3 + 1" approach has been thoroughly investigated in the past few years for the design and preparation of specific radiopharmaceuticals of rhenium and technetium (*6*−*10*). This method uses tridentate dithiolate ligands HSESH (E = S; NR; O) and monodentate thiolate (HSR) co-ligands to stabilize the core $[Tc(O)]^{3+}$ and to form neutral and lipophilic complexes of general formula [Tc(O)(SES)(SR)].

However, one of the problems associated with the use of such systems is the low stability of these complexes against thiolated nucleophiles such as glutathione. In fact, although stable in PBS solutions, they presented low stability in vivo. Challenge experiments against glutathione (GSH) showed that their in vivo instability is mediated by the nucleophilic substitution of the monodentate co-ligand by glutathione with formation of the hydrophilic complex [^{99m}Tc(O)(SES)(SG)] (E = S, NR). Such instability was considered to be strongly dependent on the nature of the tridentate/monodentate ligands but, so far, no tri/monodentate pair has been found to overcome this problem (*11*−*13*).

Scheme 1

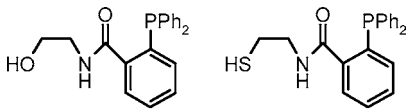

H_2PNO H_2PNS

The (tri)bidentate heterofunctionalized phosphines, 2-(diphenylphosphanyl)-*N*-(2-hydroxyethyl)benzamide (H_2-PNO) and 2-(diphenylphosphanyl)-*N*-(2-thioethyl)benzamide (H_2PNS) (Scheme 1), which are quite versatile in terms of charge and denticity toward the $[M{=}O]^{3+}$ core, form "3 + 1" mixed-ligand oxo complexes of general formula [Re(O)(PNX)(SR)] (X = O, S) with different thiolated monodentate co-ligands, some of them presenting a high stability (*14*−*16*).

Visualization of brain serotonin receptors, particularly the 5-HT_{1A} subtype, is of great interest since these receptors are implicated in various neuropsychiatric diseases (*17*, *18*). The aim of our work is the preparation of novel mixed-ligand ^{99m}Tc oxo complexes with potential for in vivo assessment of 5-HT_{1A} receptors.

* To whom correspondence should be addressed. E-mail: isantos@itn.mces.pt.
[†] Estrada Nacional 10.
[‡] Institute of Bioinorganic & Radiopharmaceutical Chemistry.

10.1021/bc049718k CCC: $30.25 © 2005 American Chemical Society
Published on Web 04/29/2005

Herein we report on the synthesis, characterization, and biological evaluation of mixed-ligand model complexes of general formula [^{99m}Tc(O)(κ^3-PNX)(κ^1-SPh))] [X = O (**1a**), S (**2a**)]. The complexes [M(O)(κ^3-PNS)(κ^1-SL)] (M = ^{99m}Tc, **3a**−**6a**, Re, **3**−**6**), anchored by the H_2PNS ligand and by several thiolated arylpiperazine derivatives (HSL1-HSL4) will also be described (Scheme 4). The binding affinity and specificity of **3**−**6** for the $5HT_{1A}$ receptors, the in vitro and in vivo stability, and the biokinetics of **3a**−**6a** are also reported.

EXPERIMENTAL SECTION

Materials and Methods. Unless otherwise stated, all chemicals were of reagent grade and were used without further purification. The heterofunctionalized phosphines, 2-(diphenylphosphanyl)-*N*-(2-hydroxyethyl)benzamide (H_2PNO), 2-(diphenylphosphanyl)-*N*-(2-thioethyl)-benzamide (H_2PNS), and succinimido 3-[(triphenylmethyl)-thio]propionate, were prepared as previously reported (*14*, *15*, *19*). The monothiols, thiophenol, *p*-aminothiophenol, mercaptopropionic acid, benzylmercaptane, cyclohexanethiol, and L-glutathione (GSH), were commercially available. [^{n}Bu$_4$N][Re(O)Cl$_4$], [Re(O)Cl$_3$(PPh$_3$)] and [Re(O)(κ^3-PNX)(κ^1-SPh))] (X = O (**1**), = S (**2**)) were prepared according to literature methods (*20*, *21*, *14*, *15*). Sodium pertechnetate was obtained in saline solution from a commercial ^{99}Mo/^{99m}Tc generator (MDS Nordion S.A., Belgium or Mallinckrodt).

Elemental analysis was performed on a Perkin-Elmer automatic analyzer. Infrared spectra were recorded in the range 4000−200 cm^{-1} on a Perkin-Elmer 577 spectrometer from KBr pellets. The ^{1}H and ^{31}P NMR spectra were recorded on a Varian Unity 300 MHz spectrometer; ^{1}H chemical shifts were referenced relative to tetramethylsilane and the ^{31}P chemical shifts to external 85% H_3PO_4 solution. The NMR samples were prepared in $CDCl_3$, chemical shifts are given in ppm. Mass spectrometric analyses were carried out on a Micromass Tandem Quadrupole Mass Spectrometer (Quattro LC) operating in the MS mode. Mass spectral data were recorded at the negative and positive ESI mode using a cone voltage of 20 or 60 V. About 0.1 mg of the sample dissolved in 1.0 mL methanol/water (50/50), and 0.05% formic acid was infused at a flow rate of 5 μL/min.

Chemical reactions were monitored by thin-layer chromatography (TLC) on Merck plates precoated with silica gel 60 F_{254}. Spots were visualized either by UV light and/or Ellman's reagent for thiols. Column chromatography was performed in silica gel 60 (Merck). High performance liquid chromatography (HPLC) analysis was performed on a Perkin-Elmer system coupled with two detectors: a UV−Vis detector, LC 290, Perkin-Elmer (UV detection for ligands and Re complexes at 254 nm) and a γ-detector (LB 509, Berthold) for ^{99m}Tc compounds. Separations were achieved on a reversed phase (RP) Hypersil ODS column (4.0 × 250 mm, 10 μm) eluted with a binary gradient system with a flow rate of 1.0 mL/min. Mobile phase A is methanol while mobile phase B is 0.01 M phosphate buffer (pH 7.4). The elution profile used was a linear gradient starting with 75% A/25% B to 95% A/5% B in 10 min, and this composition was held for 5 min. The ^{99m}Tc model complexes were analyzed by TLC using two different chromatographic systems: (a) Silufol/(BuOH/MeOH/water/ammonia) (60/20/20/1); (b) Silufol/saline.

Synthesis of Monodentate Thiolate Ligands Bearing Arylpiperazine Derivatives. *3-Mercapto-1-[4-(2-methoxyphenyl)-piperazin-1-yl]propan-1-one (HSL2).* Ph$_3$CSCH$_2$CH$_2$C(O)PIP (where PIP is 4-(2-methoxyphenyl)-piperazin-1-yl): 1-(2-Methoxyphenyl)piperazine (0.29 g, 1.5 mmol) was dissolved in 5 mL of dichloromethane and stirred at room temperature (r.t.) under a nitrogen atmosphere. A solution of succinimido 3-[(triphenylmethyl)thio]propionate (0.67 g, 1.5 mmol) dissolved in the same solvent (10 mL) and triethylamine (110 μL, 1.5 mmol) was added dropwise. After 22 h the reaction was completed, a diluted solution of HCl was added, and the reaction mixture was extracted three times with dichloromethane. The organic phase was collected, washed with water, dried over $MgSO_4$, filtered, and vacuum-dried. A viscous oil, which afforded a white solid after being vacuum-dried, was obtained (0.70 g, 90%). IR (cm^{-1}, KBr): 1635 (C═O), 1490, 1240, 1200, 750, 700. ^{1}H NMR (δ, ppm, $CDCl_3$): 2.14 (t, 2H, CH_2), 2.56 (t, 2H, CH_2), 2.94 (br s, 4H, CH_2), 3.34 (br s, 2H, CH_2), 3.70 (br s, 2H, CH_2), 3.85 (s, 3H, OCH_3), 7.03−6.85 (m, 4H, CH_{ar}), 7.42−7.14 (m, 15H, CH_{ar}). Elemental analysis: $C_{33}H_{34}O_2N_2S$ calcd, C 75.83, H 6.56, N 5.36. found, C 75.14, H 8.30, N 4.96.

Ph$_3$CSCH$_2$CH$_2$C(O)PIP (0.30 g, 0.58 mmol) was dissolved in 10 mL of trifluoroacetic acid (TFA) and cooled in an ice bath, and triethylsilane (0.2 mL 1.2 mmol) was added. The color of the initial solution (yellow) discharged, and a white precipitate was formed. After stirring for 15 min more, the solution was diluted with a mixture of hexane/water. The aqueous phase was separated, washed three times with hexane, and extracted three times with dichloromethane (25 mL). The organic phase was collected, washed with a saturated solution of sodium bicarbonate and water, and finally dried over $MgSO_4$. After filtration, the solvent was evaporated and the colorless oil obtained became a white solid on standing. This compound was formulated as HSL2 based on the analytical data (0.12 g, 74%). IR (cm^{-1}, KBr): 1635 (C═O), 1490, 1240, 1200, 750, 700. ^{1}H NMR (δ, ppm, $CDCl_3$): 1.75 (t, 1H, SH), 2.68 (t, 2H, CH_2), 2.82 (q, 2H, CH_2), 3.05−2.99 (m, 4H, CH_2), 3.63 (t, 2H, CH_2), 3.79 (t, 2H, CH_2), 3.85 (s, 3H, OCH_3), 7.03−6.86 (m, 4H, CH_{ar}). Elemental analysis: $C_{14}H_{20}O_2N_2S$ calcd, C 59.99, H 7.19, N 9.99 S 11.43, found, C 58.99, H 6.80, N 9.92 S 11.04.

Synthesis of 3-[4-(2-Methoxyphenyl)piperazin-1-yl]propane-1-thiol (HSL3). To a solution of Ph$_3$CSCH$_2$CH$_2$C(O)PIP (346 mg, 0.66 mmol) in dichloromethane (10 mL) was added dropwise 1 M borane−methyl sulfide solution (2.6 mL, 2.6 mmol) and the mixture stirred for 18 h at room temperature, under nitrogen atmosphere. The reaction mixture was cooled and methanol added dropwise until gas formation was ceased. The solvent was evaporated under vacuum, dichloromethane was added, and the mixture was refluxed for 15 min. After removal of the solvent, the crude product obtained was purified by column chromatography (silica gel), using as eluent dichloromethane/methanol (9:1). Ph$_3$CSCH$_2$CH$_2$CPIP was obtained as a white solid, after removing the solvent under vacuum (0.24 g, 72%). After deprotection, as above-described for HSL2, compound HSL3 was obtained as a white solid (0.12 g, 74%). IR (cm^{-1}, KBr): 1490, 1240, 1200, 750, 700. ^{1}H NMR (δ, ppm, $CDCl_3$): 1.40 (t, 1H, SH), 1.83 (q, 2H, CH_2), 2.51 (t, 2H, CH_2), 2.57 (t, 2H, CH_2), 2.64 (br s, 4H, CH_2), 3.01 (br s, 4H, CH_2), 3.84 (s, 3H, OCH_3), 6.95−6.82 (m, 4H, CH_{ar}). Elemental analysis: $C_{14}H_{22}ON_2S$ calcd, C 63.12, H 8.32, N 10.52, S 12.03, found, C 62.99, H 9.10, N 9.92 S 11.04.

Synthesis of 4-Mercapto-N-{3-[4-(2-methoxyphenyl)piperazin-1-yl]propyl}benzamide (HSL4). Triphenylmethylmercaptobenzoic Acid*:* Triphenylmethanol (1,04 g, 4 mmol) was added to a suspension of mercaptobenzoic acid (0.62 g, 4 mmol) in TFA yielding a yellow solution. After 1 h at room temperature, under stirring, the solution was

evaporated to dryness. The resulting yellow solid was dissolved with ethyl acetate and washed with 3 N NaOH solution, water, a saturated solution of sodium bicarbonate, and finally with brine. The organic phase was dried over $MgSO_4$, filtered, and after vacuum-drying, triphenylmethylmercaptobenzoic acid was obtained as a solid (1.54 g, 97%). The compound was used without any further purification.

Triphenylmethyl(mercaptobenzoyloxy)succinimide: Triphenylmethylmercaptobenzoic acid (1.41 g, 3.55 mmol) and *N*-hydroxysuccinimide (0.87 g, 7.4 mmol) were dissolved in dichloromethane (20 mL), and dicyclohexylcarbodiimide (1.54 g, 7.4 mmol) dissolved in the same solvent was added dropwise. After 4 h the reaction was complet (TLC/ethyl acetate/hexane (1:1)) and the urea formed was removed by filtration through Celite. The solution was vacuum-dried and the solid obtained recrystallized from ethyl acetate. The white solid obtained was formulated as triphenylmethyl(mercaptobenzoyloxy)succinimide, based on analytical data (1.48 g (85%). ^{1}H NMR (δ, ppm, $CDCl_3$): 2.85 (s, 4H, CH_2), 7.00 (d, $J = 8.1$ Hz, 2H, CH_{ar}), 7.24−7.38 (m, 15H, CH_{ar}), 7.70 (d, $J = 8.1$ Hz, 2H, CH_{ar}). Elemental analysis: $C_{30}H_{23}O_4NS$ calcd, C 73.02, H 4.66, N 2.83 S 6.49, found, C 72.21, H 5.47, N 2.24, S 7.07.

Triphenylmethyl(mercaptobenzoyloxy)succinimide (0.25 g, 0.5 mmol), 4-(3-aminopropyl)-1-(methoxyphenyl)piperazine (0.13 g, 0.5 mmol), and triethylamine (50 μL) reacted in dichloromethane (30 mL) at room temperature, under nitrogen atmosphere. After 18 h, the reaction was complete. A diluted solution of HCl was added and the aqueous phase extracted three times with dichloromethane. The organic phase was collected, washed with water, and dried over $MgSO_4$. After evaporation of the solvent a white solid was obtained, which after deprotection of the thiol group was formulated as HSL4 (0.11 g, 75%). IR (cm^{-1}, KBr): 1630 (C=O), 1590, 1240, 740, 695. ^{1}H NMR (δ, ppm, $CDCl_3$): 2.00 br s, 2H, CH_2), 2.85 (br s, 2H, CH_2), 2.99 (br s, 4H, CH_2), 3.26 (br s, 4H, CH_2),), 3.60 (br s, 2H, CH_2), 3.84 (s, 3H, OCH_3), 7.85−6.86 (m, 8H, CH_{ar}), 8.41 (t, 1H, NH). Elemental analysis: $C_{21}H_{27}O_2N_3S$ calcd, C 65.45, H 7.01, N 10.91 S 8.31, found, C 64.95, H 8.02, N 10.77, S 9.16.

General Procedure for the Preparation of Re Complexes. To a stirred suspension of $[Re(O)Cl_3(PPh_3)_2]$ in a 0.15 M methanolic solution of sodium acetate (10 mL) was added a mixture of H_2PNS with the corresponding thiolated aryl piperazine derivative in the same solution (5 mL). The suspension was stirred and refluxed for 1 h, yielding a dark brown solution. After cooling to room temperature, the reaction mixture was diluted with dichloromethane and with a 0.01 M HCl solution. The aqueous phase was then extracted three times with dichloromethane, and the organic phases were collected. After drying over magnesium sulfate, the solution was filtered and the solvent evaporated. The dark brown residue obtained was washed three times with diethyl ether and purified by chromatography using a silica gel column and a mixture of methanol−chloroform as eluent.

[Re(O)(PNS)(SL2)] (4). IR (cm^{-1}, KBr): 1630 (C=O), 1600 (C=O), 970 (Re=O), 745, 690. ^{1}H NMR (δ, ppm, $CDCl_3$): 8.13 (m, 1H, CH_{ar}), 7.67−7.18 (m, 12H, CH_{ar}), 7.03−6.85 (m, 4H, CH_{ar}), 6.79−6.73 (m, 1H, CH_{ar}), 5.05 (m, 1H, CH of tridentate ligand), 4.15 (m, 2H, SCH_2), 3.84 (s, 3H, OCH_3), 3.73 (br s, 4H, CH_2 of piperazine), 3.01−2.92 (m, 2H, CH_2 of piperazine, CH_2 of monodentate ligand, CH of tridentate ligand), 2.78−2.69 (m, 1H, CH of tridentate ligand), 2.19 (m, 1H, CH of tridentate ligand); ^{31}P NMR (δ, ppm, $CDCl_3$): 20.0. Elemental analysis: $C_{35}H_{37}O_4N_3PS_2Re$ calcd, C 49.75, H 4.41, N 4.97 S 7.59, found, C, H, N, S.

[Re(O)(PNS)(SL3)] (5). IR (cm^{-1}, KBr): 1590 (C=O), 970 (Re=O), 750, 690. ^{1}H NMR (δ, ppm, $CDCl_3$): 8.15−8.11 (m, 1H, CH_{ar}), 7.67−7.22 (m, 12H, CH_{ar}), 6.92−6.71 (m, 5H, CH_{ar}), 5.06 (m, 1H, CH of tridentate ligand), 3.83 (s, 3H, OCH_3), 3.59 (m, 2H, CH_2 of propyl), 3.07 (br s, 4H, CH_2 of piperazine), 2.97 (2.73−2.61 (m, 6H, CH_2 of piperazine, CH_2 of propyl), 2.60−2.55 (m, 1H, CH of tridentate ligand), 2.20 (m, 1H, CH of tridentate ligand), 1.83 (m, 2H, CH_2 of propyl); ^{31}P NMR (δ, ppm, $CDCl_3$): 19.9. Elemental analysis: $C_{35}H_{39}O_3N_3PS_2Re$ calcd, C 50.59, H 4.73, N 5.06, S 7.72, found, C, H, N, S.

[Re(O)(PNS)(SL4)] (6). IR (cm^{-1}, KBr): 1640 (C=O), 1590 (C=O), 975 (Re=O), 750, 700. ^{1}H NMR (δ, ppm, $CDCl_3$): 8.37 (t, 1H, NH), 8.17−8.13 (m, 1H, CH_{ar}), 7.87−7.24 (m, 16H, CH_{ar}), 6.92−6.71 (m, 5H, CH_{ar}), 5.05 (m, 1H, CH of tridentate ligand), 3.83 (s, 3H, OCH_3), 3.59 (m, 2H, CH_2 of propyl), 3.09 (br s, 4H, CH_2 of piperazine), 2.73−2.61 (m, 6H, CH_2 of piperazine, CH_2 of propyl), 2.60−2.55 (m, 1H, CH of tridentate ligand), 2.20 (m, 1H, CH of tridentate ligand), 1.83 (m, 2H, CH_2 of propyl); ^{31}P NMR (δ, ppm, $CDCl_3$): 19.6. Elemental analysis: $C_{42}H_{44}O_4N_4PS_2Re$ calcd, C 53.09, H 4.60, N 5.90 S 6.75, found, C, H, N, S.

^{99m}Tc Complexes. *[^{99m}Tc(O)(PNO)(SPh)] (**1a**).* The preparation of the complexes at the tracer level was accomplished in a one step procedure, starting with [$^{99m}TcO_4^-$] and using stannous chloride as reducing agent. The following general procedure was used: A mixture of propylene glycol (50 μL), ethanol or acetonitrile (1300 μL), 0.5 mg (4.5×10^{-6} mol) of thiophenol, 0.05 mg (1.43×10^{-7} mol) of H_2PNO, 0.1 N NaOH (200 μL), 20 μL of a $SnCl_2$ solution (1.0−2.0 mg $SnCl_2$ dissolved in 5 mL 0.1 N HCl), and 0.5 mL of [^{99m}Tc]pertechnetate eluate (100−200 MBq) was heated at 37 °C over 20 min. The reaction mixture was analyzed by HPLC, using the conditions described above and also by TLC using two different chromatographic systems: (a) Silufol/(BuOH/MeOH/water/ammonia) (60/20/20/1); (b) Silufol/saline. Yields > 90% were obtained.

The complexes were purified by HPLC on a semi-preparative Hypersil ODS column (Hypersil 120 ODS, 250 × 8 mm, 10 μm, flow rate 2.0 mL/min) using a linear gradient (t[min]/%A: (5/75), (10/95), (10/95) of methanol (A)/0.01 M phosphate buffer (pH 7.4) (B).

Characterization of the ^{99m}Tc complexes was accomplished by chromatographic correlation (HPLC) with the corresponding rhenium complexes, previously described (*14*, *15*).

*[^{99m}Tc(O)(PNS)(SPh)] (**2a**).* In the case of the H_2PNS ligand, the "3 + 1" mixed-ligand complex is not formed under alkaline conditions. So, the same procedure described above was used but in the absence of NaOH. Compound [^{99m}Tc(PNS)(SPh)] was obtained in relatively good yield (>90%).

[$^{99/99m}$TcO(PNS)(SPh)]. Complex [$^{99/99m}$TcO(PNS)(SPh)] was prepared as described for **2a,** using a [$^{99m}TcO_4^-$] eluate enriched with ^{99}Tc (10^{-8} or 10^{-7} mol $^{99}TcO_4^-$). The characterization was done by HPLC using the Re complex as a surrogate and also by mass spectrometry.

General Procedure for the Preparation of ^{99m}Tc Complexes (3a−6a). The ^{99m}Tc complexes were prepared by direct reduction of pertechnetate with stannous chloride. The following general procedure was used: 50 μL of propylene glycol (PG), 1300 μL of ethanol, 0.03−0.05 mg of the monodentate ligand, 0.001 mg (1.4×10^{-6} mol) of H_2PNS, and 20 μL of a $SnCl_2$ solution (2.0−3.0 mg of $SnCl_2$ dissolved in 5 mL of 0.1 N HCl) were added

to 0.5 mL (100−200 MBq) of [^{99m}Tc]pertechnetate eluate. The reaction mixture was heated at 40−50 °C for 20 min. The ^{99m}Tc complexes were analyzed by HPLC using a reversed-phase Hypersil 120 ODS column (250 × 4 mm, 10 μm). The column was eluted using methanol/water as mobile phase at 1.0 mL/min flow rate and with a linear gradient of 70−100% methanol over 10 min followed by 10 min at 100% of methanol. These complexes were also analyzed by TLC using two different chromatographic systems: (a) silica gel/acetone; (b) silica gel/saline.

The compounds were purified on a semipreparative Hypersil ODS column (250 × 8 mm, 10 μm) using methanol/water as mobile phase (flow rate: 2 mL/min) and with a linear gradient of 70−100% methanol over 10 min followed by 10 min at 100% of methanol. The fractions were collected and analyzed in the analytical column. The purified complexes, after removal of the organic solvent, were reconstituted with 0.1 M PBS 7.4, and 100 μL of PG was added. The characterization of the ^{99m}Tc complexes was accomplished by chromatographic correlation (HPLC) with the corresponding rhenium complexes.

General Procedures for Stability Studies in Vitro. *Challenge with GSH*. 100 μL (approximately 10 MBq) of the purified ^{99m}Tc complex was mixed with 100 μL of a 2 mM or 20 mM solution of GSH in 0.1 M phosphate buffer (pH 7.4). The mixture was incubated at 37 °C for 5−120 min and analyzed by HPLC. Samples without GSH were also analyzed and used for comparison. HPLC analyses were carried out using the experimental conditions above-described.

Stability in Rat Plasma. Blood collected from mice in heparinized polypropylene tubes was immediately centrifuged for 15 min at 2000 rpm at 4 °C and the plasma collected. The ^{99m}Tc complex (100 μL, ≈10 MBq) was added to fresh rat plasma (1 mL), and the mixture was incubated at 37 °C. At appropriate periods of time (5 min, 30 min, 1, 2, and 4 h), 100 μL aliquots (in duplicate) were sampled and treated with 200 μL of ethanol to precipitate the proteins. Samples were then cooled at 4 °C and centrifuged at 3000 rpm for 15 min at 4 °C. The supernatant was separated from the precipitate, and the sediment was washed twice with ethanol (1 mL) and counted in a gamma counter. The activity in the sediment was compared with the total activity used, and the percent of complex bound to proteins was calculated. The supernatant was analyzed by HPLC, using the experimental conditions above-described.

Stability in Whole Human Blood. To whole human blood (1 mL), collected in heparinized polypropylene tubes, was added a solution of the ^{99m}Tc-complex (≈10 MBq), and the mixture was incubated at 37 °C. Samples were taken 5 min, 1 h, and 4 h after incubation and centrifuged 15 min at 2000 rpm at 4 °C. The plasma was separated and ethanol was added in a 2:1 (v/v) ratio. The samples were centrifuged at 3000 rpm, and the supernatant was analyzed by HPLC.

Receptor Binding Assays on Rat Brain Homogenates. The $5HT_{1A}$ receptor binding assays were performed using [^{3}H]-8-OH-DPAT as radioligand and rat hippocampus homogenate. The binding assay was carried out in a final volume of 2.5 mL of Tris-HCl buffer (50 mM, pH 7.4, 0.1% ascorbic acid, 2 mM $CaCl_2$) containing 0.10 nM [^{3}H]-8-OH-DPAT, membrane homogenate (about 20 μg/mL protein), and various concentration of the rhenium complexes **3**−**6.** The complexes were dissolved in DMSO up to 1 nM and then diluted with buffer. Nonspecific binding was defined as the amount of [^{3}H]-8-OH-DPAT bound in the presence of serotonin (Sigma). The samples were incubated in triplicates at 20 °C for 120 min. The incubation was terminated by rapid filtration through GF/B glass fiber filters (Whatman) using a 30-port Brandel Cell Harvester. The filters were rapidly washed with four portions of ice-cold buffer, transferred into 10 mL of scintillation fluid (Ultima-Gold, Packard), and analyzed for radioactivity.

The $5HT_{2A}$ receptor binding assays: The cortex of rat brain was homogenized in ice-cold buffer (50 mM tris-HCl, pH 7.6) with an Ultra-Turrax T 25. The homogenate was centrifuged at 20 000*g* for 10 min. The resulting pellet was resuspended and centrifuged under the above conditions. After repeating the same procedure, the pellet was resuspended in 10 mL of buffer and stored at −20 °C.

[^{3}H]Ketanserin (from NEN) was used as a radioligand. The binding assay was carried out in a final volume of 5 mL of Tris-HCl buffer, pH 7.6, containing 0.12 nM [^{3}H]-ketanserin, membrane homogenate (about 20 μg/mL protein), and various concentrations of the Re complexes. The complexes were dissolved in DMSO up to 1 nM and then diluted with buffer. Nonspecific binding was defined as the amount of [^{3}H]ketanserin bound in the presence of 1 μM mianserin (Sigma). The samples were incubated in triplicates at 20 °C for 60 min. Incubation, filtration, and counting of the samples were the same as described above.

General Procedures for in Vivo Studies. *Biodistribution Studies.* The in vivo behavior of the ^{99m}Tc complexes was evaluated in groups of 3−5 female CD-1 mice (randomly bred, Charles River) weighing approximately 20−25 g each. Animals were intravenously injected with 100 μL (1−3 MBq) of each preparation via the tail vein and were maintained on normal diet ad libitum. At 5 min and 1 h mice were killed by cervical dislocation. The radioactive dosage administered and the radioactivity in the sacrificed animal were measured in a dose calibrator (Aloka, Curiemeter IGC-3, Tokyo, Japan). The difference between the radioactivity in the injected and sacrificed animal was assumed to be due to excretion, mainly urinary excretion. Blood samples were taken by cardiac puncture at sacrifice. Tissue samples of the main organs were then removed and counted in a gamma counter (Berthold). Biodistribution results were expressed as percent of injected dose per organ (% I.D./total organ). For blood, bone, and muscle, total activity was calculated assuming that these organs constitute 6, 10, and 40% of the total weight, respectively. The remaining activity in the carcass was also measured in a dose calibrator. In vivo stability was just assessed by murine serum RP-HPLC analysis. For that, blood was centrifuged and serum separated and analyzed by HPLC after treatment with ethanol, as described above for the stability in whole human blood.

RESULTS AND DISCUSSION

Preparation of [^{99m}Tc(O)(PNX)(SPh)] (X = O, 1a; X = S, 2a). For the introduction of stable mixed-ligand oxometal complexes with ^{99m}Tc/Re, namely those of the "3 + 1" type, with adequate physicochemical and biological characteristics for CNS receptor targeting, we have prepared oxorhenium complexes of the type [Re(O)-(κ^2-PNX)(κ^1-SR)] (X = O, S) anchored by the heterofunctionalized phosphines H_2PNO and H_2PNS, and by different monodentate thiol co-ligands (*14*). To check whether this type of approach could be extended to the no carrier added level, we have used complexes [^{99m}Tc(O)(PNX)-(SPh)] (X = O, **1a**; X = S, **2a**) as models. These ^{99m}Tc

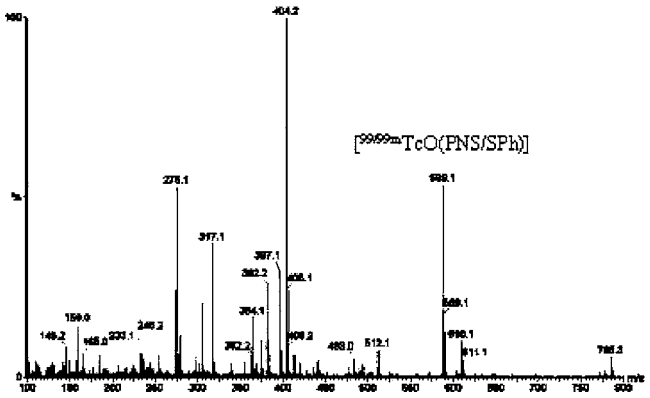

Figure 1. ES/MS of [99/99mTcO(PNS/PhS)]: *m/z* (found) 588 (M + 1), *m/z* (calcd) 587 for [TcO(PNS/PhS)] ($C_{27}H_{23}NO_2PS_2Tc$).

Scheme 2. Synthesis of the Complexes 1, 1a and 2, 2a

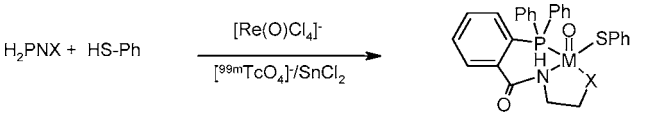

X = O, M = Re (**1**), ^{99m}Tc (**1a**)
X = S, M = Re (**2**), ^{99m}Tc (**2a**)

complexes have been prepared in a one-step procedure, by direct reduction of $[^{99m}TcO_4]^-$ with stannous chloride in the presence of thiophenol and of the corresponding tridentate H_2PNO or H_2PNS ligands (Scheme 2).

To maximize the radiochemical yield of **1a** and **2a**, the labeling conditions were optimized, namely the concentration, tridentate/monodentate ligand molar ratios, and pH. When dealing with H_2PNS, the main radiochemical impurity was the complex $[^{99m}Tc(O)(\kappa^3\text{-PNS})(\kappa^1\text{-HPNS})]$, formed due to the κ^3,κ^1-coordination versatility of PNS. This radiochemical impurity has been identified by comparing its retention time in the HPLC with that of the fully characterized analogue Re complex [Re(O)-(κ^3-PNS)(κ^1-HPNS)] (*14*). Although being a less critical factor, the concentration of thiophenol also has to be controlled in order to minimize the formation of the homoleptic complex $[^{99m}Tc(O)(SPh)_4]^-$. Regarding pH, **1a** requires alkaline conditions for its formation, while **2a** is formed at a lower pH value (pH ~ 6).

After optimization of the labeling conditions, complexes **1a** and **2a** were obtained in yields higher than 90%, with only 1−3% of reduced hydrolyzed technetium and with no free pertechnetate, as indicated by TLC and HPLC.

Characterization of [99mTc(O)(PNX)(SPh)] (X = O, 1a; X = S, 2a). The characterization of **1a** and **2a** was done by comparing their retention times in the HPLC (γ detection: **1a**, 6.3 min; **2a**, 9.1 min) with the corresponding retention times of the analogous Re complexes **1** and **2** (UV detection − 254 nm, **1**: 6.3 min, **2**: 9.0 min). For unambiguous identification of **2a**, the complex [99/99mTc(O)(PNS)(SPh)] was synthesized using a $[^{99m}TcO_4]^-$ eluate enriched with 10^{-8} or 10^{-7} mol of $[^{99}TcO_4]^-$. As can be seen in the ES/MS spectrum shown (Figure 1) a significant peak appears at *m/z* 588 (M + 1), which correlates well with the value *m/z* of 587 calculated for [99TcO(PNS)(SPh)].

Stability and in Vivo Behavior of [99mTc(O)(PNX)-(SPh)] (X = O, 1a; X = S, 2a). The in vitro stability of the model complexes **1a** and **2a** was evaluated in physiological solutions (saline, 0.01 M PBS pH 7.4, at 37 °C) and in the presence of glutathione (1 and 10 mM solutions, 37 °C).

Complex **1a** decomposes to more hydrophilic species during incubation in saline or PBS at 37 °C, and only

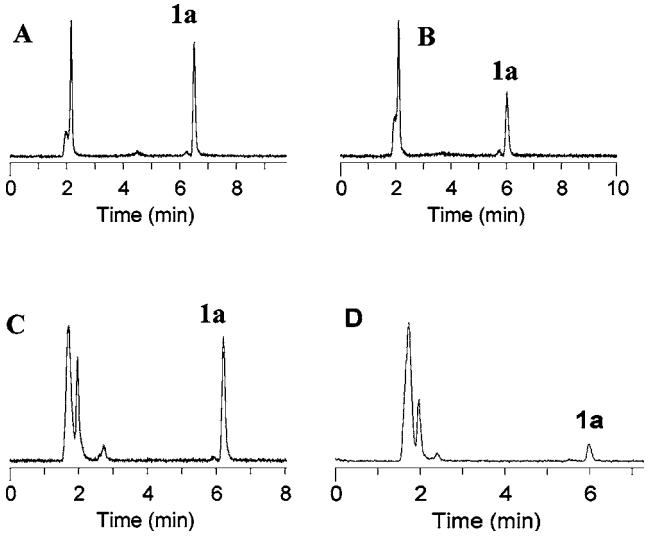

Figure 2. Stability studies of [99mTcO(PNO/SPh)] (**1a**) by HPLC. In saline at 37 °C: A, after 30 min; B, after 60 min; against 1 mM glutathione solution at 37 °C: C, after 30 min; D, after 60 min;

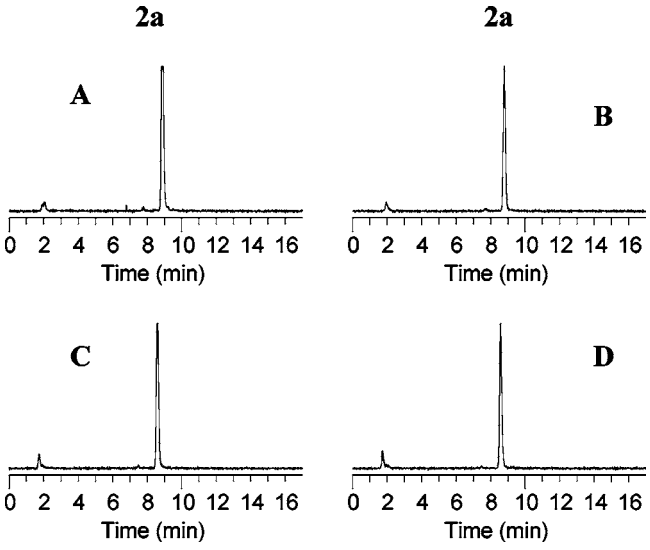

Figure 3. Stability studies of [99mTcO(PNS/SPh)] (**2a**) by HPLC. In saline at 37 °C: A, 30 min; B, 120 min; against 1 mM glutathione solution, at 37 °C: C, 5 min; D, 120 min.

43% or 33% of **1a** remains intact after 30 or 60 min incubation, respectively (Figure 2). Challenge experiments against glutathione revealed that **1a** decomposes also to more hydrophilic unknown radiochemical species even faster than in saline or PBS solutions.

On the contrary, complex [99mTc(O)(PNS)(SPh)] (**2a**) is stable in saline, in 0.01 M PBS pH 7.4 (1:1 dilutions), and also in the presence of glutathione (1 and 10 mM solutions, 2 h, 37 °C) (Figure 3). On the basis of these results, which confirm clearly the importance of the donor atom sets on the stabilization of the "3 + 1" mixed-ligand complexes, complex **2a** was chosen to pursue our studies.

The overall general biodistribution profile for **2a** is shown in Table 1. This complex, despite presenting a high liver uptake, also shows some initial brain uptake (0.14 ± 0.03% ID/organ, 5 min. pi), which does not decrease significantly with time (2 h after injection: 0.11 ± 0.02% ID/organ).

These results, encouraged the use of the tridentate H_2PNS ligand for the preparation of ^{99m}Tc mixed-ligand complexes bearing antagonists of the 5-HT_{1A} receptors.

Table 1. Biodistribution of ^{99m}TcO(PNS/SPh) in Wistar Rats (n = 5) at 5 and 120 min pi (%ID/organ ± SD)

	% injected dose/organ ± SD	
organ	5 min pi	120 min pi
brain	0.14 ± 0.03	0.11 ± 0.02
spleen	0.95 ± 0.25	0.35 ± 0.11
kidney	4.16 ± 0.22	7.52 ± 0.41
heart	0.93 ± 0.08	0.46 ± 0.03
lung	1.88 ± 0.16	0.80 ± 0.11
liver	51.30 ± 1.40	26.60 ± 1.60

To achieve this goal, several thiolated arylpiperazine derivatives containing the 1-(2-methoxyphenyl)piperazine unit, a fragment of the potent and selective 5-HT_{1A} antagonist WAY 100635 moiety, were prepared and used as monodentate co-ligands (Scheme 3).

Syntheses and Characterization of the Ligands HSL2−HSL4. The ligand HSL1 was prepared as previously described (*14*). The monothiolates HSL2 and HSL3 were synthesized by a coupling reaction between 3-[(triphenylmethyl)thio]propionate and 1-(2-methoxyphenyl)piperazine, followed by deprotection of the thiol group or by reduction of the amide group with borane−methyl sulfide followed by deprotection, respectively.

The synthesis of HSL4 involved the activation of the protected mercaptobenzoic acid with *N*-hydroxysuccinimide in the presence of *N*,*N*′-dicyclohexylcarbodiimide and conjugation of the resulting compound with 4-(3-aminopropyl)-1-(methoxyphenyl)piperazine. Deprotection of the thiol group with triethylsilane in trifluoroacetic acid afforded HSL4.

Compounds HSL2−HSL4 have been thoroughly characterized by the usual analytical techniques. The main feature of the IR spectra of HSL2 and HSL4 is the presence of a strong band at 1635 cm^{-1} (HSL2) and 1630 cm^{-1} (HSL4) assigned to the carbonyl amide stretching vibration. This band is absent in the IR spectrum of HSL3, confirming the reduction of the carbonyl group. The ^{1}H NMR spectra of HSL2−HSL4 present all the expected resonances, including a triplet which appears at δ 2.58 in the NMR spectrum of HSL3, confirming the presence of the methylene group formed due to the reduction of the carbonyl function. In the ^{1}H NMR spectrum of HSL2 and HSL3 also appears a triplet at 1.75 and 1.40, respectively, assigned to the thiol group.

Syntheses and Characterization of the Complexes [Re(O)(PNS)(SL)] (4−6). The "3 + 1" mixed-ligand oxorhenium complexes (**4**−**6**) were synthesized by reacting $[Re(O)Cl_3(PPh_3)_2]$ with the tridentate ligand H_2-PNS in the presence of HSL2−HSL4, as previously described for compound **3** (Scheme 4) (*14*). The synthesis was carried out under nitrogen atmosphere, to avoid the oxidation of the thiol or of the phosphine ligands.

The molar ratio $[Re(O)Cl_3(PPh_3)_2]/H_2$PNS/HSL has to be maintained at 1:1:1 to minimize the formation of the subproduct [Re(O)(κ^3-PNS)(κ^1-HPNS)] (*14*). All the complexes were fully characterized by elemental analysis, IR, ^{1}H and ^{31}P NMR spectroscopy, and HPLC.

The IR spectra of compounds **4**−**6** exhibit strong bands in the range 970−975 cm^{-1} assigned to the ν(Re=O) stretching vibration. These values compare well with the values found for the same stretching vibration in compound **3** and also in other compounds of the "3 + 1" type stabilized by the PNS tridentate ligand and different monodentate co-ligands (970−980 cm^{-1}) (*14*, *16*). Another common feature to all the IR spectra is the presence of two strong absorption bands, typical of the phenylphosphine moiety, which appear in the range 745−750 and 690−700 cm^{-1} (*22*, *14*). In the IR spectra of **4** and **6** also appears a strong band at ν 1630 cm^{-1} and ν 1640 cm^{-1}, respectively, assigned to the carbonyl group of the monodentate co-ligand.

The ^{31}P NMR spectra of complexes **4**−**6** present only one singlet, which appears in the range δ 19.6−20.0 ppm, being comparable with the values previously reported for other "3 + 1" oxo complexes with the [PNS/S] donor atom set (*14*−*16*). These resonances, assigned to the tridentate ligand H_2PNS, are low-field shifted relative to the value found for the corresponding free ligand (δ −9.4 ppm), clearly indicating that the phosphorus atom is involved in the coordination to the metal.

The ^{1}H NMR spectra of complexes **4**−**6** reveal four sets of multiplets, integrating for one proton each, due to the methylenic protons of the H_2PNS ligand, which are diastereotopic due to the asymmetry introduced in the molecule by the oxo group. The resonances due to the aromatic rings of the H_2PNS and of the co-ligand appear in the expected range.

Preparation of the Complexes [^{99m}Tc(O)(PNS)(SL)] (3a−6a). Complexes **3a**−**6a** were synthesized using the procedure described for the model complex **2a.** After optimizing the concentration of the tridentate ligand, **3a**−**6a** were obtained in relatively high yields (80−95%) and were identified by comparing their retention times (γ detection) with the retention times of the well-characterized analogous rhenium complexes (**3**−**6**) (Table 2).

Stability of the ^{99m}Tc Complexes (3a−6a). Complexes **3a** −**6a** are stable in saline and in 0.01 M PBS (pH 7.4) solutions at least for 6 h (both at room temperature and at 37 °C). As mentioned above, the main drawback associated with the "3 + 1" complexes of the type [TcO(SES)(SR)] (E = S, O, NR) is their instability toward the presence of thiolated nucleophiles, like glutathione (*11*−*13*). For the first time, we found that complexes of the "3 + 1" type (**3a**−**6a**) do not exchange with glutathione, even in the presence of concentrated solutions (1 mM and 10 mM GSH), also remaining intact in fresh rat plasma and in whole human blood (37 °C, 4 h) (Figure 4). Comparing our results with others previously reported, the high stability found for **2a**−**6a** can only be assigned to the electronic and/or steric factors imposed by the tridentate PNS ligand. However, as referred to above, complex **1a** is not stable in the presence of GSH, despite being anchored by the analogous tridentate PNO ligand. This finding led us to conclude that the stability found for complexes **2a**−**6a** is certainly due to the electronic properties of the PNS ligand. The combination of a soft π-donor, like sulfur, and a soft π-acceptor, like phosphorus, most probably promotes a strong bond between the metal center and the sulfur atom of the co-ligand, leading to a less electrophilic and more stable complex. Nevertheless, a better understanding of these results would need MO theoretical calculations.

Lipophilicity. The lipophilicity of all the complexes was evaluated by determination of the partition coefficient (P) in physiological conditions (n-octanol/0.1 M phosphate buffer pH 7.4). The results obtained, expressed as log $P_{o/w}$, are presented in Table 2. All the compounds are lipophilic and the values found (log $P_{o/w}$ = 1.70−2.01) are in the range normally accepted for the complexes to be able to cross the BBB (log $P_{o/w}$ = 0.5−2.5) (*3*). The lipophilicity found for **3a** (1.70) and for **6a** (2.01) relates well with the presence of an aliphatic and an aromatic group in **3a** and **6a**, respectively.

In Vitro Receptor Binding Studies. To evaluate the effect of the chemical modifications introduced in the monodentate ligand, and the effect of the chelate unit,

Scheme 3. Synthesis of the Arylpiperazine Derivatives (R = *N*-succinimido)

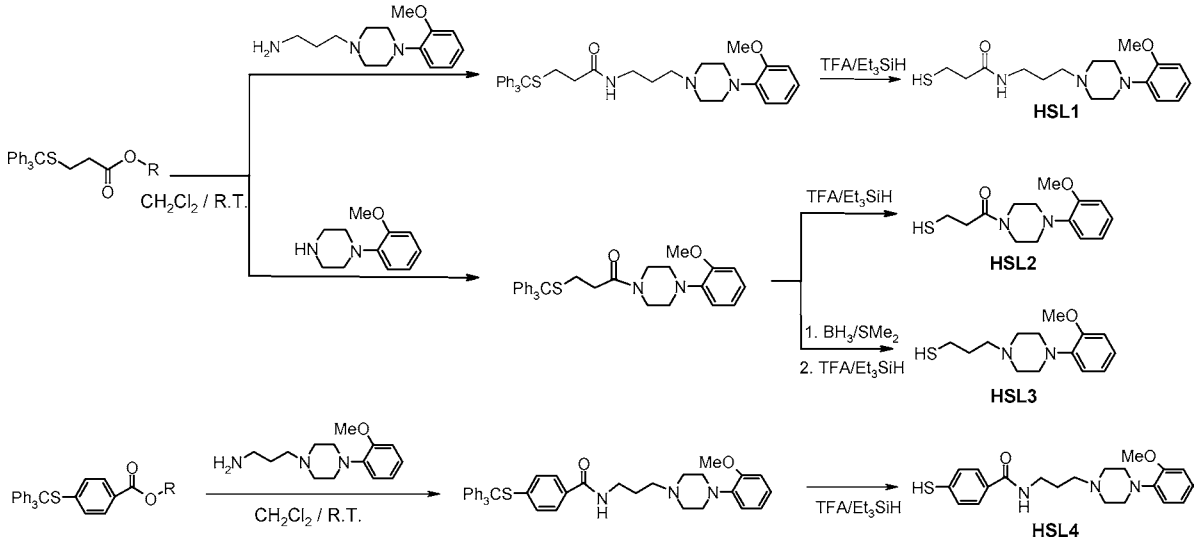

Scheme 4. Synthesis of the Re Complexes 3−6

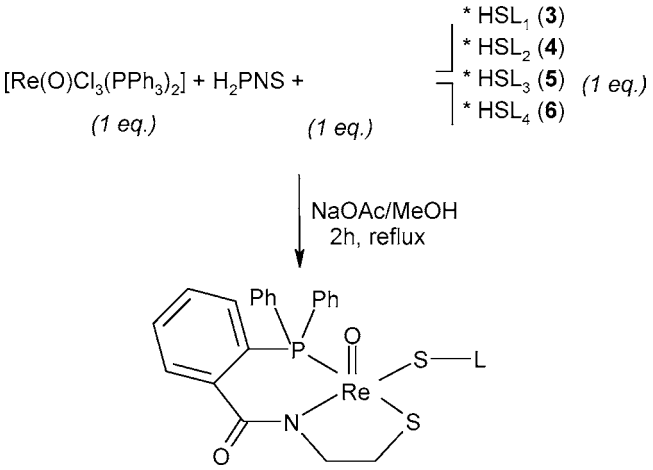

Table 2. Properties of Compounds 3a−6a

compound	labeling yield (%)	t_R (min) HPLC	log $P_{o/w}$	protein binding (%) 5 min	protein binding (%) 1 h
3/3a	70−90	8.2/8.1	1.70	2.4	8.7
4/4a	60−90	8.3/8.1	1.98	2.3	9.8
5/5a	60−70	6.3/6.1 11.8/11.7[a]	1.99	2.0	6.3
6/6a	85−90	5.5/5.5 11.9/11.7[a]	2.01	12.8	20.2

[a] Other HPLC conditions: column Hypersil 120 ODS (250 × 4 mm, 10 μm,1 mL/min); mobile phase methanol/0.02% Et_3N in water; gradient: 50−100% methanol over 10 min followed by 10 min at 100% methanol.

the binding affinity of the complexes **3**−**6** for the 5-HT_{1A} and 5-HT_{2A} receptors was determined. Their affinity for the 5-HT_{1A} receptor subtype was assessed in vitro on the basis of their ability to displace [^{3}H]-8-OH-DPAT, a potent and specific 5-HT_{1A} receptor agonist, from 5-HT_{1A} binding sites in rat hippocampal homogenates.

The IC_{50} values for the tested compounds are presented in Table 3. The Re complexes **3** and **6** had moderate affinity for the 5-HT_{1A} receptors (**3**, IC_{50} 120 ± 1.1 nM **6**, 79.3 ± 11 nM). Substitution of the ethylenic chain of complex **3** (in HSL1) by the aromatic ring in complex **6** (in HSL4) increased the affinity for the 5-HT_{1A} receptors. Complex **5** presents the highest affinity and selectivity for the 5-HT_{1A} receptors (IC_{50} for 5-HT_{1A} 2.35 ± 0.02 nM; competitor 5-HT_{2A} 372 ± 11 nM). This value is similar to the reported value for the parent compound WAY 100635 (IC_{50} = 2.2 nM), suggesting that the affinity of the *o*-methoxyphenylpiperazine moiety for 5-HT_{1A} receptors is not reduced by its functionalization with a thiol group and by the presence of the $[Re(O)(PNS)]^+$ metal fragment (*18*). A further important criterion for the potential application of this type of *biocomplexes* is the selectivity of the pharmacophore for the 5-HT_{1A} receptors. According to Halldin et al., ideally the affinity of a radioligand should be highest for the site of interest by more than 1 order of magnitude (*23*). Compound **5** presents a selectivity toward the 5-HT_{2A} receptors which is over 150-fold. Complex **4** completely lost affinity for the 5-HT_{1A} receptors**,** must probably due to the presence of the carbonyl function in the monodentate ligand, which seems to prevent the access to the receptor-binding site.

Biodistribution. The in vivo behavior of the ^{99m}Tc complexes (**3a**−**6a**) was evaluated in mice at 5 and 60 min post intravenous injection. Figure 5 shows the tissue distribution results expressed as % I.D./total organ in the most relevant organs. These results indicate a similar pattern for all the complexes under study, showing a slow clearance from organs such as blood and muscle and a slow rate of total radioactivity excretion from whole animal body (less than 12% of total injected dose 1 h after administration). All the complexes have high initial blood and muscle uptake that slowly clear, mainly via the hepatobiliary pathway. Complex **4a** presents a quite fast blood and muscle clearance when compared to **3a**, **5a**, and **6a**. As expected for lipophilic compounds, there is a very high and rapid liver uptake that decreases over the time with a significant amount of injected dose cleared into the intestines. The low kidney uptake associated to the low total radioactivity excretion indicates that those complexes are mainly eliminated through the hepatobiliary tract with quite low urinary elimination.

Despite being neutral and lipophilic, all the complexes (**3a**−**6a**) present low brain uptake (%I.D./organ ≤ 0.2%, 5 min after administration) and no significant retention of the radioactivity is observed. HPLC analysis of the murine serum collected after 5 min and 1 h postinjection indicated that all the complexes remain intact in circulation, confirming their high in vivo stability.

Despite the good perspectives related to the charge, lipophilicity, and in vitro and in vivo stability of the complexes, they are not able to cross the BBB, which would enable the in vivo assessment of 5-HT_{1A} receptors.

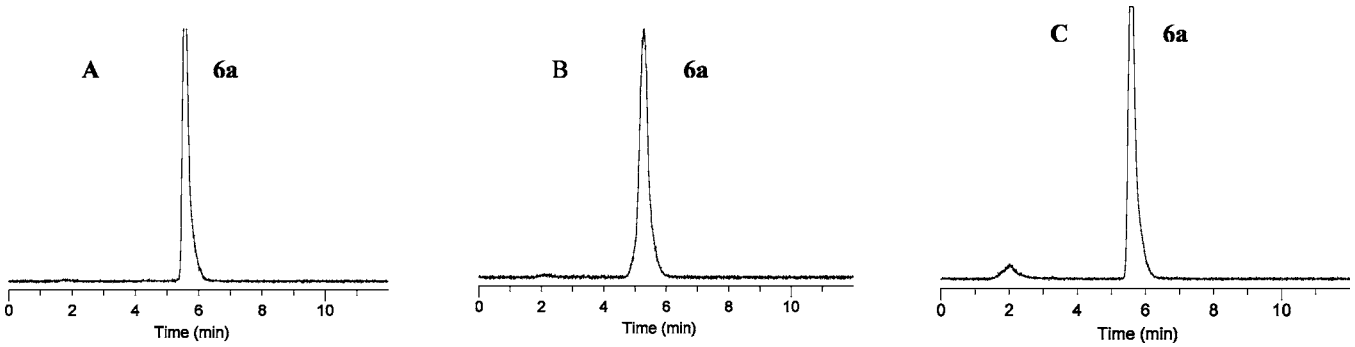

Figure 4. HPLC chromatograms of **6a** (A); (B) after incubation with rat serum, 37 °C, 4 h; (**C**) after incubation with 10 mM gluthathione solution, 2 h, 37 °C.

Table 3. IC_{50} (nM) Values for the Tested Compounds 3a−6a

	IC_{50} (nM)		
complex	5-HT_{1A} ([^{3}H]OH-DPAT)	5-HT_{2A} ([^{3}H]-ketanserin)	5-HT_{2A}/5HT_{1A}
3a	120 ±1.1	860 ± 51	7.16
4a	15170 ± 532	148 ± 50	< 0.01
5a	2.35 ± 0.02	372 ± 11	158.3
6a	79.3 ±1.2	542 ± 15	6.8

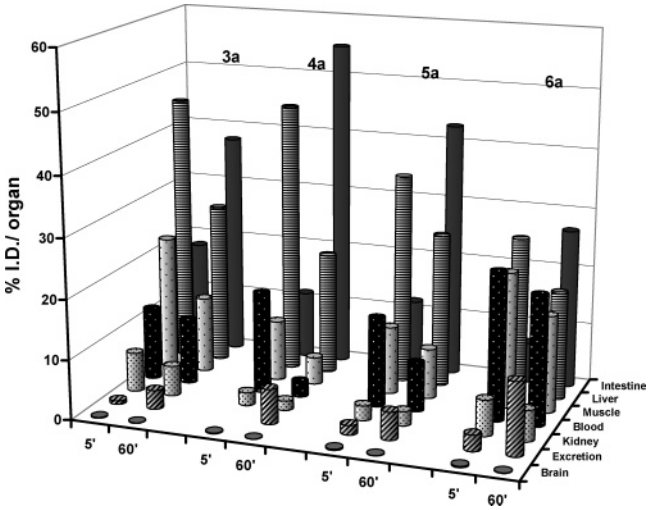

Figure 5. Biodistribution results in mice (% injected dose/ organ) for complexes **3a**−**6a**.

This can be due to the presence of the chelate moiety that influences the properties of the whole molecule in an unclear manner. Finding rules for or, better, relations between structure parameters of metal complexes to allow passage through the BBB is an important goal but has hardly been investigated so far. Attempts to interpret the BBB transport of Tc complexes on the basis of rough physicochemical parameters such as lipophilicity and basicity have not been successful.

CONCLUDING REMARKS

We were able to prepare the "3 + 1" oxotechnetium(V) complexes **1a** and **2a** at the nca level, using the heterofunctionalized phosphines H_2PNO and H_2PNS as tridentate ligands, and thiophenol as monodentate co-ligand. These model complexes present different in vitro stability, confirming the importance of the donor atom set.

Using the tridentate H_2PNS ligand, several "3 + 1" oxotechnetium(V) complexes bearing 5-HT_{1A} receptor-binding ligands have been prepared in good yields and high radiochemical purity (>95%). All are stable in saline, PBS pH 7.4, rat plasma, and human serum. No exchange with glutathione was observed, even when high concentrations of this nucleophile are used. This is a remarkable feature for this type of complex, and these are the first examples of "3 + 1" complexes presenting no transchelation toward glutathione. One of the complexes (**5/5a**) also showed a remarkable affinity and selectivity for the 5-HT_{1A} receptors (IC_{50} for 5-HT_{1A} 2.35 ± 0.02 nM; competitor 5-HT_{2A} 372 ± 11 nM; 5-HT_{1A}/5-HT_{2A} = 158.3), comparable to the corresponding values found for the [^{11}C]-WAY 100635 (IC_{50} for 5-HT_{1A} 2.2 nM). These results confirmed the possibility of preparing metal complexes without affecting the affinity and selectivity of the biomolecules for the corresponding receptors. Unfortunately, despite displaying adequate characteristics, such as neutrality, high lipophilicity, and high in vitro and in vivo stability, none of the complexes cross the BBB, as demonstrated by biodistribution studies in mice. This topic is an open field and deserves considerable attention. Such work is of the highest importance, when aiming at the development of brain-related metallo-(radio)pharmaceuticals.

ACKNOWLEDGMENT

This work has been partially supported by a bilateral project ICCTI/DAAD and by COST Action B12.

LITERATURE CITED

(1) Hom, R. K., and Katzenellenbogen, J. A. (1997) Technetium-99m-Labeled Receptor-Specific Small-Molecule Radiopharmaceuticals: Recent Developments and Encouraging Results. *Nucl. Med. Biol. 24*, 485−498.

(2) Jurisson, S. S., and Lydon, J. D. (1999) Potential Technetium Small Molecule Radiopharmaceuticals. *Chem. Rev*. *99*, 2205−2218.

(3) Johannsen, B., and Pietzsch, H. (2002) Development of technetium-99m-based CNS receptor ligands: have there been any advances?. *Eur. J. Nucl. Med. 29*, 263−275.

(4) Meegalla, S., Plossl, K., Kung, M. P., and Stevenson, D. A. (1995) First example of a ^{99m}Tc Complex as a Dopamine Transporter Imaging Agent. *J. Am. Chem. Soc*. *117*, 11037−11038.

(5) Kung, H. F., Kim, H.-J., Kung, M. P., Meegalla, S., Plossl, K., and Lee, H.-K. (1996) Imaging of dopamine transporters in humans with technetium-99m TRODAT-1. *Eur. J. Nucl. Med. 23*, 1527−1530.

(6) Spies, H., Fietz, T., Pietzch, H.-J., Johannsen, B., Leibnitz, P., Reck, G., Scheller, D., and Klostermann, K. (1995) Neutral Oxorhenium(V) Complexes with Tridentate Dithiolates and Monodentate Alkane- or Arene-thiolate Coligands. *J. Chem. Soc., Dalton Trans*. 2277−2280.

(7) Johannsen, B., Scheunemann, M., Spies, H., Brust, P., Wober, J., Syhre, R., and Pietzch, H.-J. (1996) Technetium-(V) and Rhenium(V) Complexes for 5-HT_{2A} Serotonin Receptor Binding: Structure-Affinity Considerations. *Nucl. Med. Biol*. *23*, 429−438.

(8) Mastrostamis, S. G., Papadopoulos, M. S., Pirmettis, I. C., Paschali, E., Varvarigou, A. D., Stassinopoulou, C. I., Raptopoulou, C. P., Terzis, A., and Chiotellis, E. (1994) Tridentate Ligands Containing the SNS Donor Atom Set as a Novel Backbone for the Development of Technetium Brain-Imaging Agents. *J. Med. Chem. 37*, 3212−3218.

(9) Papagiannopoulou, D., Pirmettis, I., Maina, T., Pelecanou, M., Nikolopoulou, A., Chiotelis, E., Raptopoulou, C. P., Vlahos, A. T., Terzis, A., Papadopoulos, M., and Chiotelis, E. (2001) Development of novel mixed-ligand oxotechnetium [SNS/S] complexes as potencial 5-HT_{1A} receptor imaging agents. *J. Biol. Inorg. Chem. 6*, 256−265.

(10) Fernandes, C., Patrício, L., Moreira, R., Cantinho, G., Pena, H., Campello, P. C., and Santos, I. (2004) Novel 3+1 Mixed-Ligand Technetium-99m Complexes Carrying Dipeptides as Monodentate Ligands. *Nucl. Med. Biol. 31*, 139−145.

(11) Gupta, A., Seifert, S., Syhre, R., Scheunemann, P., Brust, P., and Johannsen, B. (2001) Reactivity of ^{99m}Tc(V) "3 + 1" mixed-ligand complexes towards glutathione. *Radiochim. Acta 89*, 43−49.

(12) Syhre, R., Seifert, S., Spies, H., Gupta, A., and Johannsen, B. (1998) Stability versus reactivity of "3 + 1" mixed-ligand technetium-99m complexes in vitro and in vivo. *Eur. J. Nucl. Med. 25*, 793−796.

(13) Seifert, S., Gupta, A., Syhre, R., Spies, H., and Johannsen, B. (2001) Ligand-exchange reaction of labile "3 +1" ^{99m}Tc(V) complexes with SH group-containing proteins. *Appl. Radiat. Isot. 54*, 637−644.

(14) Correia, J. D. G., Domingos, A., Santos, I., and Spies, H. (2001) Synthesis and characterization of mixed-ligand oxorhenium(V) complexes with new [(PNO/S)/(S)] donor atom sets. *J. Chem. Soc., Dalton Trans.* 2245−2250.

(15) Correia, J. D. G., Domingos, A., and Santos, I. (2000) Neutral Trichlorooxorhenium(V) complexes containing phosphane ligands of the type PN_2 and PNO. *Eur. J. Inorg. Chem.* 1523−1529.

(16) Kniess, T., Fernandes, C., Santos, I., Spies, H., and Kraus, W. (2003) Silylated mixed-ligand rhenium complexes with the [PNS/S] donor atom set. *Inorg. Chim. Acta 348*, 237−241.

(17) Passchier, J., and Waarde, A. V. (2001) Visualisation of serotonin-1A (5-HT1A) receptors in the central nervous system. *Eur. J. Nucl. Med. 28*, 113−129.

(18) Pike, V. W., Halldin, C., Wikstrom, H., Marchais, S., McCarron, J. A., Sandell, J., Nowicki, B., Swahn, C.-G., Osman, S., Hume, S. P., Constantinou, M., Anfrée, B., and Farde, L. (2000) Radioligands for the study of brain 5-HT_{1A} receptors in vivo-development of some new analogues of WAY. *Nucl. Med. Biol. 27*, 449−455.

(19) Brenner, D., Davison, A., Lister-James, J., and Jones, A. G. (1984) Synthesis and characterization of a series of isomeric oxotechnetium(V) diamido dithiolates. *Inorg. Chem. 23*, 3793−3797.

(20) Alberto, R., Schibli, A., Egli, A., Schubiger, P., Herrmann, W. A., Artus, G., Abram, U., and Kaden, T. A. (1995) Metal carbonyl synthesis XXII. Low-pressure carbonylation of $[MOCl_4]^-$ and $[MO_4]^-$: the Technetium(I) and Rhenium(I) complexes $[NEt_4][MCl_3(CO)_3]$. *J. Organomet. Chem. 493*, 119−127.

(21) Ram, M. S., and Hupp, J. T. (1991) Generalized synthesis of cis- and trans-dioxorhenium(V) (bi)pyridyl complexe. *Inorg. Chem. 30*, 130−133.

(22) Nakamoto, K. (1970) *Infrared Spectra of Inorganic and Coordination Compounds*, 2nd ed., pp 205−209, Chapter 3. Wiley-Interscience, New York.

(23) Halldin, C., Gulyás, B., Langer, O., and Farde, L. (2001) Brain radioligands − State of the art and new trends. *Q. J. Nucl. Med. 45*, 139−152.

(24) Fernandes, C., Correia, J. D. G., Gano, L., Santos, I., Seifert, S., Spies, H., and Syhre, R. (2001) Tc oxocomplexes with the PNO/S and PNS/S donor atom sets: labelling of a 5HT_{1A} receptor-binding ligand. *J. Labelled Comp. Radiopharm. 44*, S518−S520.

BC049718K

Synthesis and Activity of C11-Modified Wortmannin Probes for PI3 Kinase

Hushan Yuan,[†] Ji Luo,[‡] Seth Field,[‡] Ralph Weissleder,[†] Lewis Cantley,[‡] and Lee Josephson*,[†]

Center for Molecular Imaging Research, Massachusetts General Hospital, Building 149, 13th Street, 5403, Charlestown, Massachusetts 02129, and Department of Systems Biology, Harvard Medical School, 77 Avenue Louis Pasteur, Boston, Massachusetts. Received November 29, 2004; Revised Manuscript Received March 21, 2005

The key role played by PI3 kinase in cancer, hormone action, and a host of other biological functions suggests that specific inhibitors whose disposition could be ascertained in vivo would be useful in biological research or, potentially, for imaging PI3K in a clinical setting. Wortmannin (Wm, **1**) is an inhibitor of PI3 kinase with high specificity for this enzyme. We synthesized three modified Wm probes, a biotinylated Wm (**7a**), a 4-hydroxy-3-iodophenylated Wm, which was obtained both unlabeled (**7b**) and labeled with ^{125}I (**8**), and a fluoresceinated Wm (**7c**), through modification at C-11, and evaluated their inhibitive activity as inhibitors of PI3 kinase. Biotinylated (**7a**) and 4-hydroxy-3-iodophenylated Wm's (**7b**) had IC_{50}s for PI3K of 6.11 and 11.02 nM, respectively, compared to an IC_{50} for Wm of 1.63 nM. Fluoresceinated Wm (**7c**) lost considerably more activity than the other derivatives, with an IC_{50} of 64.9 nM. The ^{125}I labeled 4-hydroxy-3-iodophenylated Wm (**8**) could be detected after reaction with an immunoprecipitate of PI3 kinase. The activity of these reporter Wm's is discussed in relationship to earlier findings on the pharmacological activity of Wm derivatives and the ability of inhibitors to fit into the ATP pocket of PI3 kinase.

INTRODUCTION

Specific inhibitors of enzymes whose position can be monitored in cells have been widely used to elucidate the role an enzyme plays in biological processes (*1*−*5*). The key role played by PI3 kinase in cancer (*6*−*8*), hormone action (*9*, *10*), and a host of other biological functions (*11*−*14*) suggests that specific inhibitors, whose disposition could be ascertained, would be useful in biological or pharmaceutical research or, potentially, for imaging PI3 kinase in a clinical setting. Wortmannin (Wm) is a fungal product that is a specific inhibitor of PI3 kinase which can covalently react with a lysine in the ATP binding site of the enzyme (Figure 1) (*15*−*17*). Wm consists of a steroid-like ring system with two features that make the synthesis of Wm derivatives a challenging task. First, the furan ring, subject to attack by the epsilon amino group of lysine in the active site of PI3 kinase, can react with other nucleophiles (*18*), and this can occur in an unintended fashion. Second, the six-membered lactone ring of Wm, roughly comparable to the A ring of steroid ring system (Figure 1), is extremely sensitive to base (*19*).

Our goal was therefore to overcome these challenging features of Wm chemistry and synthesize Wm derivatives modified at C11 that might serve as "reporter Wm's," that is compounds that retained the ability of the parent Wm to inhibit PI3 kinase but with the potential to detect their position after application to a biological system. Three approaches to reporter Wm's were investigated: (i) biotinylated Wm (**7a**) was synthesized that might be detected by the Western blot method; (ii) a 4-hydroxy-3-iodophenyl Wm (**7b**) was synthesized, with nonradioactive iodine for enzyme inhibition studies and as an ^{125}I labeled (**8**) compound for autoradiography, and (iii) a fluorescent Wm (**7c**) was synthesized, for detection by fluorescence microscopy. All were made by selective modification at C-11 of Wm that had previously been shown to have little effect on the ability of Wm to inhibit PI3K (*20*). Our results show that biotinylated (**7a**) and 4-hydroxy-3-iodophenylated (**7b**) Wm's retained a good inhibitory activity for PI3K compared to the parent, but the inhibitory activity of fluoresceinated Wm (**7c**) was reduced. The relationship of these findings to earlier pharmacological and crystallographic studies of Wm's interaction with PI3 kinase are discussed.

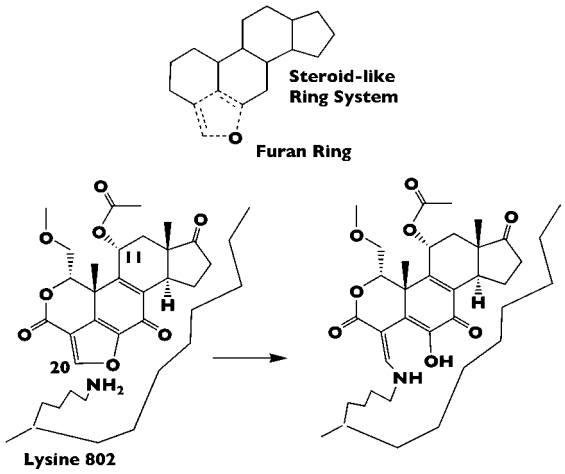

Figure 1. Wortmannin structure and reaction with PI3 kinase. Wortmannin is a steroid-like compound with a furan ring (top) that reacts with a lysine in the active site of PI3 Kinase (bottom). The positions of C-11 and C-20 on wortmannin are shown.

* To whom correspondence should be addressed. Tel: (617) 726-6478. Fax: (617) 726-5708. E-mail: ljosephson@partners.org.
[†] Center for Molecular Imaging Research, Massachusetts General Hospital and Harvard Medical School.
[‡] Department of Systems Biology, Harvard Medical School.

10.1021/bc049714f CCC: $30.25 © 2005 American Chemical Society
Published on Web 04/29/2005

Scheme 1. Synthesis of Intermediates Used To Obtain C11-Modified Wm Probes[a]

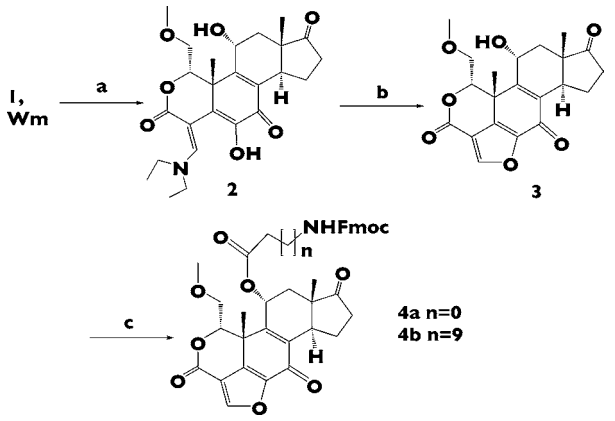

[a] Reagents and conditions: (a) **1**, diethylamine, methanol, room temperature, 20 h; (b) 1,4-dioxane, 1 N HCl, room temperature, 22 h (75% based on wortmannin); (c) *N*-Fmoc glycine chloride (for **4a**) or *N*-Fmoc-11-aminoundecanoyl chloride (for **4b**), pyridine, dichloromethane, room temperature, overnight, (94.6% for **4a**, 89.0% for **4b**).

EXPERIMENTAL METHODS

General. Wortmannin was a gift of the Natural Products Branch of the NCI. All reagents (Aldrich, or NovaBiochem) and solvents (Aldrich) were of standard quality and used without further purification unless indicated. Acetonitrile for HPLC analysis was obtained as HPLC grade from Fisher Scientific. Silica gel for column chromatography was conducted with 60−200 mesh silica gel (J. T. Baker Inc.). FITC was from Molecular Biosciences. Iodogen was purchased from Pierce and $Na^{125}I$ was from Amersham Bioscience. NMR was performed on a Varian 400 MHz instrument with $CDCl_3$ as solvent, while mass spectra were obtained on a Micromass LCT instrument with time-of-flight ESI technique. HPLC separations were accomplished on a Varian ProStar 210 gradient pumping system with a variable-wavelength PDA 330. HPLC separations were carried out on reversed-phase C18 column (VYDAC, Millipore) with water (0.1% trifluoroacetic acid,) (buffer A) and acetonitrile (containing 20% buffer A) (buffer B) as elution buffer. Three variations of this were employed. *System 1*: buffer A/buffer B (80:20) for 5 min, then linear gradient of buffer A/buffer B (80:20−0:100) over 30 min and then isocratic for 5 min, flow: 6.0 mL/min, λ_{max}: 255 nm; *System 2*: buffer A/buffer B (50:50) for 5 min, linear gradient of buffer A/buffer B (50:50−25:75) over 25 min and then isocratic for 5 min, flow: 4.9 mL/min, λ_{max}: 255 nm. *System 3*: buffer A/buffer B (70:30) for 5 min, linear gradient of buffer A/buffer B (70:30−0:100) over 45 min and then isocratic for 5 min, flow: 4.9 mL/min, λ_{max}: 440 nm.

The C11-modified Wm's were synthesized in two steps. First the Fmoc-protected intermediates **4a** or **4b** were synthesized, which were stable when stored at −20 °C for at least 3 months (Scheme 1). In a second step, the Fmoc group was removed, and the amino group was modified by the attachment of biotin (**7a**, Scheme 2), 4-hydroxy-3-iodophenylacetic acid (**7b**, Scheme 3), or FITC (**7c**, Scheme 4). The potency of the three C11-modified Wm probes as inhibitors for PI3 K was then ascertained. We also synthesized a ^{125}I version of C11 4-hydroxy-3-iodophenyl Wm (**8**) as shown in Scheme 5.

Synthesis of Intermediates 4a or 4b. *Steps a and b, Scheme 1*, were accomplished by slight modifications of published procedures (*20*). Wm (0.107 g, 0.25 mmol) was dissolved in anhydrous methanol (6 mL) with diethylamine (0.1 mL) and the furan ring opened within 10 min as indicated by the yellowish color appearance. A second portion of diethylamine (0.5 mL) was added for desacetylation of C-11 at room temperature for 20 h. After removal of methanol and diethylamine by evaporation under reduced pressure, the residue was dissolved in 1,4-dioxane (10 mL) and the furan ring closed to obtain compound (**3**). This was accomplished with 1.6 mL of aqueous 1 N HCl at room temperature in 22 h. Compound **3** was purified by silica gel column chromatography eluting with a gradient ethyl acetate/hexane with a yield of 75%. *Step c, Scheme 1*. The acylation of the C11-hydroxy group was accomplished by dissolving **3** (0.077 g, 0.2 mmol) in dichloromethane (2 mL) and anhydrous pyridine (1 mL) and using a 4-fold excess of either *N*-Fmoc glycine chloride (0.252 g, 0.8 mmol, for **4a**) or a 3-fold excess of *N*-Fmoc-11-amino-undecanoyl chloride (0.264 g, 0.6 mmol for **4b**), stirring at room temperature for overnight. **4a** and **4b** were purified by silica gel column chromatography as above. A sticky solid was obtained after the solvent was removed by evaporation. Both products were obtained by the addition of sufficient hexane to the dichloromethane solution to induce precipitation and were off-white solids for long-term storage (**4a**: 0.126 g, 94.6% and **4b**: 0.14 g, 89.0%). The structures of **4a** and **4b** were identified by NMR and HR-MS spectrometry. Selected data: **4a**: HR-MS: $C_{38}H_{35}NO_{10}$, calcd 666.2339 ($M + H^+$), found: 666.2342; ^1H NMR ($CDCl_3$, 400 MHz): 0.95 (3H, s, C*H*$_3$-13), 1.50−1.60 (1H, m, *H-12*), 1.74 (3H, s, C*H*$_3$-10), 2.01−2.07(1H, m, *H-16*), 2.20−2.30 (1H, m, *H-15*), 2.56−2.66 (2H, m, *H-12*, *H-16*), 2.81−2.88 (2H, m, *H-14*, OC*H*$_2$), 3.13 (3H, s, C*H*$_3$O), 3.14−3.21 (1H, m, *H-15*), 3.39 (1H, d, $J = 12$ Hz, OC*H*$_2$), 3.84, 3.89 (1H, dd, $J_1 = 6$ Hz, $J_2 = 18.4$ Hz, NHC*H*$_2$CO), 4.13, 4.18(1H, dd, $J_1 = 6$ Hz, $J_2 = 18.4$ Hz, NHC*H*$_2$CO), 4.22 (1H, t, $J = 6.4$ Hz, COOCH$_2$C*H*), 4.48 (2H, d, $J = 6.4$Hz, COOC*H*$_2$CH), 4.72(d, $J = 7.2$ Hz, *H-1*), 5.63 (1H, t, $J = 6$ Hz, N*H*), 6.21(1H, dt, $J_1 = 8.4$ Hz, $J_2 = 2.8$ Hz, *H-11*), 7.27−7.41 (4H, m), 7.58 (2H, t, $J = 7.6$ Hz, Ar*H*), 7.74 (1H, dd, $J_1 = 3.2$ Hz, $J_2 = 7.2$ Hz, Ar*H*), 8.28 (1H, s, *H-21*); ^{13}C NMR ($CDCl_3$, 100 MHz): 14.5, 22.9, 26.5, 35.7, 35.0, 40.7, 43.0, 44.0, 47.1, 49.2, 59.6, 67.0, 71.2, 72.9, 88.8, 114.1, 120.0, 124.8, 124.9, 127.0, 127.1, 127.7, 127.7, 140.9, 141.3, 141.4, 142.6, 143.7, 144.8, 148.8, 150.2, 156.4, 157.4, 169.0, 172.5, 215.9. **4b**: HR-MS: $C_{47}H_{53}NO_{10}$, calcd 792.3747 ($M + H^+$), found: 792.3746. ^1H NMR($CDCl_3$, 400 MHz): 0.98 (3H, s, C*H*$_3$-13), 1.28−1.67 (17H, m, OOCCH$_2$(C*H*$_2$)$_8$CH$_2$NH, *H-12*), 1.73 (3H, s, C*H*$_3$-10), 1.99−2.14 (1H, m, *H-16*), 2.20−2.31 (1H, m, *H-15*), 2.33−2.42 (2H, m, OOCC*H*$_2$), 2.56−2.63 (2H, m, *H-12*, *H-16*), 2.86−2.98 (1H, m, *H-14*), 3.00−3.12 (1H, dd, $J_1 = 6.8$ Hz, $J_2 = 11.2$ Hz, CH$_3$OC*H*$_2$), 3.17 (6H, b, OC*H*$_3$, NHC*H*$_2$, *H-15*), 3.45 (1H, dd, $J_1 = 11.2$ Hz, $J_2 = 2$ Hz, CH$_3$OC*H*$_2$), 4.22 (1H, t, $J = 6.8$ Hz, OCH$_2$C*H*Ar), 4.40 (2H, d, $J = 6.8$ Hz, OC*H*$_2$CHAr), 4.76 (1H, dd, $J_1 = 6.8$ Hz, $J_2 = 2$ Hz, *H-1*), 4.81 (1H, b, N*H*), 6.18 (1H, dt, $J_1 = 9.2$ Hz, $J_2 = 2.4$ Hz, *H-11*), 7.31 (2H, t, $J = 7.2$ Hz, Ar*H*), 7.40 (2H, t, $J = 7.2$ Hz, Ar*H*), 7.60 (2H, d, $J = 7.2$ Hz, Ar*H*), 7.77 (2H, d, $J = 7.2$ Hz, Ar*H*), 8.24 (1H, s, *H-21*); ^{13}C NMR: 14.6, 22.9, 24.7, 26.5, 26.7, 29.0, 29.2, 29.2, 29.3, 29.4, 30.0, 34.4, 35.7, 36.1, 40.7, 41.1, 44.1, 47.3, 49.2, 59.4, 66.5, 69.9, 72.8, 88.5, 114.3, 120.0, 125.0, 127.0, 127.6, 140.2, 141.3, 142.9, 144.0, 144.8, 149.7, 150.0, 156.4, 157.7, 172.2, 172.7, 216.3.

Synthesis of C11 Biotinylated Wm (7a): *For step a, Scheme 2*, a solution of **4a** (6.7 mg, 0.01 mmol) in anhydrous dichloromethane (1 mL) was added diethylamine (0.2 mL, 1.9 mmol). After stirring for 6 h at room

Scheme 2. Synthesis of C11 Biotinylated Wm (7a)[a]

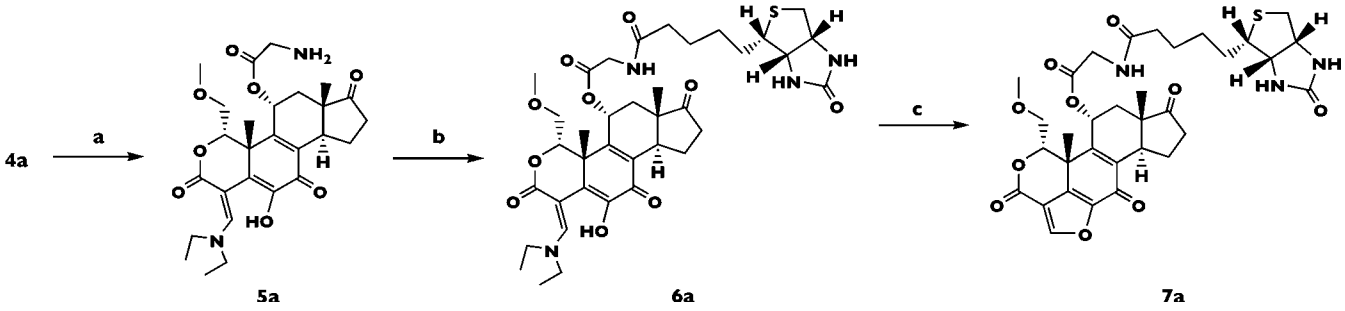

[a] Reagents and conditions: (a) **4a**, diethylamine, dichloromethane, room temperature, 6 h (58.2% for **5a**); (b) **5a**, biotin, HATU, HOBT, DMF, CH_2Cl_2, r. t.; (c) 1 N HCl, DMF, 1,4-dioxane, 48 h (total yield 28.5%, based on 41.9 μmol of **4a**).

Scheme 3. Synthesis of C11 4-Hydroxy-3-iodophenyl Wm (7b)[a]

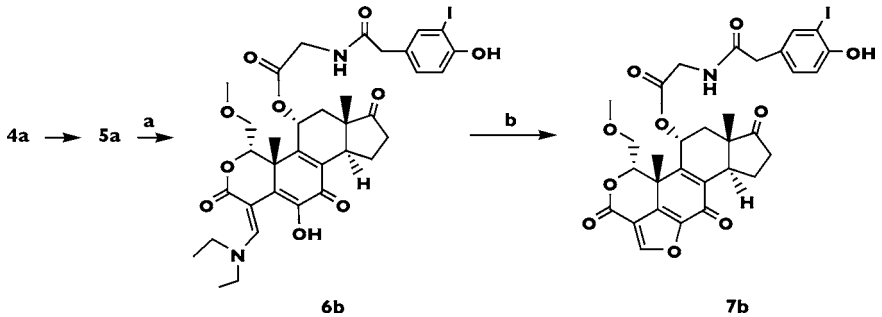

[a] Reagents and conditions: (a) **5a**, EDC, 4-hydroxy-3-iodophenylacetic acid, room temperature, 20 min; (b) 1,4-dioxane, 1 N HCl, 24 h (17.3%, overall, 0.01 mmol **4a** based).

temperature, a single major spot was obtained by silica gel TLC (CH_2Cl_2:MeOH/100:5). The solution containing **5a** was extracted with an acidic aqueous phase (3 × 5 mL 1 N HCl) and followed by the removal of impurities in the aqueous phase with dichloromethane (2 × 2 mL) extraction. The aqueous layer was then brought to pH 8 with $NaHCO_3$ powder, followed by extraction of **5a** into dichloromethane (3 × 5 mL). The solution was then dried over Na_2SO_4, and the volume was reduced to 0.5 mL with N_2 stream. Compound **5a** was characterized by HR-MS: $C_{27}H_{36}N_2O_8$, calcd 517.2550 ($M + H^+$), found 517.2552. *For step b, Scheme 2*, HATU (24.3 mg, 0.0639 mmol) and biotin (15.4 mg, 0.0633 mmol) were dissolved in anhydrous dichloromethane (3 mL) and DMF (2 mL), and the mixture was stirred at room temperature for 20 min. To this was added **5a** dissolved in 0.5 mL of anhydrous dichloromethane (0.0419 mmol based on **4a**). The mixture was stirred for 72 h at room temperature. *For step c, Scheme 2*, for the closure of the furan ring, dichloromethane was removed by evaporation and 1,4-dioxane (2 mL) was added to the remaining DMF solution. This was followed by addition of 1 N HCl in water (5 mL), and the mixture, which consisted of a single phase, was stirred at room temperature for 48 h. The mixture was extracted with dichloromethane (4 × 5 mL), and the organic layer was washed by water (2 × 5 mL). The organic layer was then dried over Na_2SO_4, and the volume was reduced by vacuum, followed by a final purification with RP-HPLC by System 1. An off-white solid was obtained by precipitation with hexane from a solution of dichloromethane. (8 mg, 28.5% overall, 0.0419 mmol based on **4a**). Selected data for compound **7a**: HR-MS: $C_{33}H_{39}N_3O_{10}S$, calcd 670.2434 (M + 1), found: 670.2435. ^{1}H NMR ($CDCl_3$, ppm): 0.96 (3H, s, C*H*$_3$-13), 1.26 (2H, m, $COCH_2CH_2CH_2CH_2CH_2$), 1.63−1.75 (8H, m, CH_3-13, H-12, $COCH_2CH_2CH_2CH_2CH_2$), 2.01−2.10 (1H, m, H-16), 2.18−2.38 (3H, H-15, CH_2CO), 2.52−2.68 (2H, m, H-12, H-16), 2.76−2.79 (1H, d, J = 12 Hz, SCH_2), 2.86−2.98 (2H, m, H-14, SCH_2), 2.95−3.08 (1H, b, SC*H*), 3.19 (5H, b, OCH_3, OCH_2, H-15), 3.50 (1H, d, J = 7.2 Hz, OCH_2), 3.92−4.13 (2H, m, COCH_2NH), 4.42 (1H, b, NHC*H*CH), 4.61 (1H, b, H-12), 5.02 (1H, b, NHC*H*CH_2), 6.00−6.20 (2H, b, NH, H-11), 6.54 (1H, b, NH), 7.08 (1H, b, NH), 8.27 (1H, s, H-21). ^{13}C NMR ($CDCl_3$, ppm): 14.8, 23.2, 25.5, 26.6, 28.1, 31.2, 35.2, 36.0, 40.6, 41.0, 41.9, 44.2, 49.4, 55.6, 59.8, 60.8, 62.2, 71.8, 73.2, 88.7, 114.5, 140.8, 143.2, 145.0, 149.2, 150.4, 158.0, 164.7, 169.6, 172.8, 174.3, 216.7.

Synthesis of C11 4-Hydroxy-3-iodophenylated Wm (7b). Compound **5a** was prepared as above. *For step a, Scheme 3*, EDC (1-[3-(dimethylamino)propyl]-3-ethylcarbodiimide hydrochloride) (3.8 mg, 0.02 mmol) and 4-hydroxy-3-iodophenyl acetic acid (5.4 mg, 0.02 mmol) were dissolved in anhydrous dichloromethane (0.5 mL) and stirred for 10 min. To this solution was added **5a** (0.01 mmol based on **4a**), prepared in anhydrous dichloromethane (0.5 mL). The mixture was stirred at room temperature for 20 min. *Step b, Scheme 3*, furan ring closure, was performed as above. The final product was purified with RP-HPLC by *system 2*. An off-white solid was obtained by precipitation with hexane from a solution of dichloromethane. (1.6 mg, 22.7% for **7b** overall, 0.01 mmol **4a** based). Selected data for **7b**: HR-MS: $C_{31}H_{30}INO_{10}{\cdot}NH_4^+$, calcd 721.1258, found 721.1262. ^{1}H NMR (CDCl3, 400 MHz): 0.92 (3H, s, C*H*$_3$-13), 1.41−1.47 (1H, m, *H-12*), 1.72 (3H, s, C*H*$_3$-10), 1.97−2.08 (1H, m, *H-16*), 2.23−2.33 (1H, m, *H-15*), 2.55−2.62 (2H, m, *H-12, H-16*), 2.79−2.83 (1H, m, *H-14*), 2.87−2.91 (1H, m, OCH_2), 3.15−3.22 (1H, m, *H-15*), 3.27 (3H, s, CH_3O), 3.29−3.58 (3H, m, OCH_2, ArCH_2CO), 3.85 (1H, dd, J_1 = 5.6 Hz, J_2 = 18 Hz, NHCH_2CO), 4.18(1H, dd, J_1 = 5.6 Hz, J_2 = 18 Hz, NHCH_2CO), 4.73 (1H, d, J = 6.4 Hz, *H-1*), 5.64 (1H, broad, O*H*), 6.15 (1H, td, J_1 = 8 Hz, J_2 = 2.4 Hz, *H-11*), 6.32 (1H, t, J = 5.6 Hz, N*H*), 6.91 (1H, d, J = 8.4 Hz, Ar*H*), 7.17 (1H, dd, J_1 = 3 Hz, J_2 = 8.4 Hz Ar*H*), 7.54 (1H, d, J = 3 Hz, ArH) and 8.27 (1H, s, *H-21*). ^{13}C NMR: ($CDCl_3$, 100 MHz): 14.7, 23.1, 26.6, 35.9, 36.3, 40.5, 41.0, 42.0, 44.2, 49.3, 60.2, 71.3, 73.3, 77.4, 86.0,

Scheme 4. Synthesis of C11 Fluorescein Wm (7c)[a]

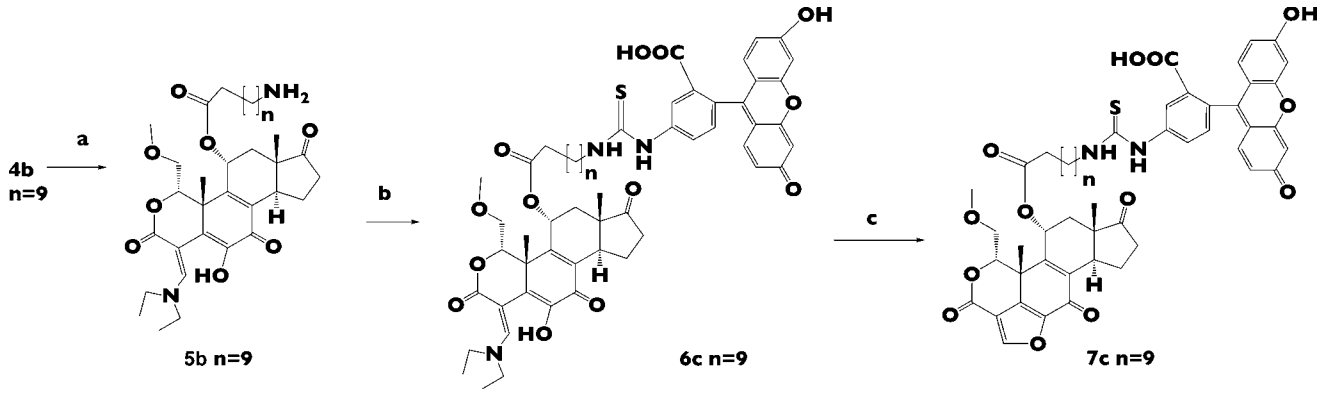

[a] Reagents and conditions: (a) **4b**, diethylamine, dichloromethane, room temperature, 6 h (35.3%). (b) **5b**, fluorescein 5(6)-isothiocyanate, DMF, DIPEA, room temperature, overnight; (c) 1 N HCl, 1,4-dioxane, room temperature, 24 h, (8.9%, overall, 0.02 mmol **4b** based).

Scheme 5. Synthesis of ^{125}I Labeled C11 4-Hydroxy-3-iodophenylated Wm (8)[a]

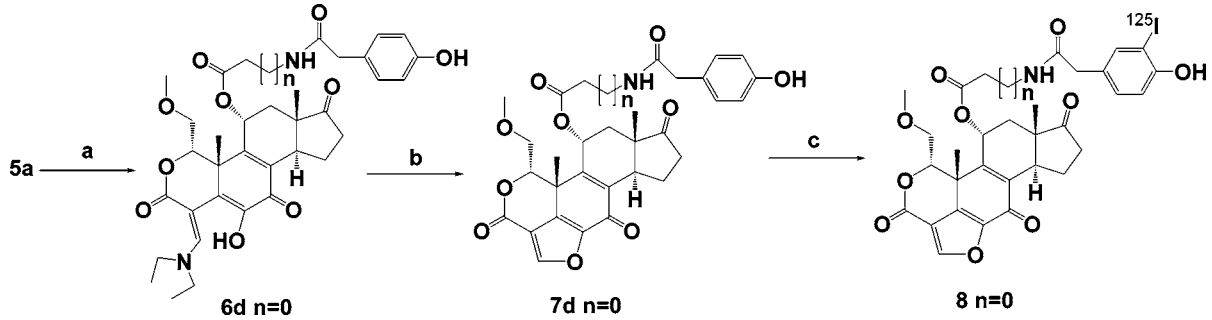

[a] Reagents and conditions: (a) **5a**, EDC, 4-hydroxyphenylacetic acid, room temperature, 20 min; (b) 1,4-dioxane, 1 N HCl, 24 h (17.3%, overall, 0.01 mmol **4a** based); (c) **7d**, NaI-125, iodogen, phosphate buffer (0.5 M, pH 7.4), room temperature, 1−2 min, (more than 85% based on NaI-125).

89.4, 114.3, 115.3, 115.7, 128.6, 130.9, 131.4, 138.5, 139.1, 141.2, 142.8, 145.0, 149.0, 150.4, 154.7, 157.6, 168.8, 171.4, 172.8, and 216.0 (rotomer could be observed).

Synthesis of C11 Fluorescein Wm (7c). The reaction of **5a** with FITC and NHS esters of fluorescein was unsuccessful, presumably on steric grounds, so **5b** with an 11-carbon spacer between the primary amine and Wm was synthesized for fluorescein attachment (Scheme 4). *Fmoc Deprotection of 4b*. To **4b** (9.6 mg, 0.01 mmol) in anhydrous dichloromethane (1 mL) was added diethylamine (0.2 mL). After stirring for 6 h at room temperature, the solvent was evaporated under reduced pressure. The residue was fractioned by preparative silica gel TLC plate (dichloromethane:MeOH:triethylamine = 100:10:1). A yellow foam was obtained after the purification which contains trace amount of impurities generated during the concentration (2.3 mg, 35.3%). Compound **5b** was characterized by HR-MS: $C_{36}H_{54}N_2O_8$, calcd 643.3958 ($M + H^+$), found 643.3943.

For step b, Scheme 4, **5b** (0.02 mmol based on **4b**) and fluorescein 5(6)-isothiocyanate (15.6 mg, 0.04 mmol) were dissolved in DMF (1 mL) with diisopropylethylamine (0.05 mL) and stirred at room temperature for overnight. The closure of the furan ring (step c) was as above, with a final purification by HPLC with System 3. A brown solid was obtained (1.7 mg, 8.9% overall yield, based on 0.02 mmol **4b**). The proton NMR of **7c** lacked some structural detail due to the mixture of 6(5)-isomers in the starting FITC. However, key structural information was obtained confirming the structure **7c**: (1) a singlet at 11.94 ppm indicated the hydroxyl proton on the carboxylic acid fragment of fluorescein; (2) a singlet at 8.27 ppm indicated the furan ring was closed as in Wm; (3) a broad peak at 6.18 ppm indicated that C-11 hydroxy group was acylated; (4) strong peaks at the higher field overlapped with each other, indicating the existence of the 11-amino-undecanoyl ester linkage between Wm and fluorescein. The HR-MS supported the structure **7c**: $C_{53}H_{54}N_2O_{13}S$: calcd 959.3427 ($M + H^+$), found, 959.3434. UV absorbance (λ_{max} = 449.79 nm in methanol) and fluorescence spectra (λ_{ex} = 450 nm, λ_{em} = 515.9 nm in methanol) further indicated the presence fluorescein.

Synthesis of ^{125}I Labeled C11 4-Hydroxy-3-iodophenylated Wm (8). Compound **5a** was converted to **7d** with the similar procedures as **7b** without the isolation of **6d** except the application of 4-hydroxyphenyl acetic acid as one of the reactants (Scheme 5). **7d** was purified by reverse-phase HPLC (system 2) and identified by NMR and MS techniques**.** Iodination of the **7d** was accomplished by using iodogen (1,3,4,6-tetrachloro-3α,6α-diphenylglycoluril) as the oxidant in the precoated tubes for 1−2 min. A stock solution of iodogen in dichloromethane with 0.5 μg/μL concentration (10 μL) was transferred to a V-shape vial. An iodogen precoated tube was made by blowing the above vial to dry with N_2 flow. Then phosphate buffer (0.5 M, pH 7.0) (10 μL) was added to the vial. A solution of 125-NaI (1 μL, 400−500 μCi) and a solution of **7d** in DMSO (1 μg/μL) (1 μL) were added sequentially. The mixture was vortexed for 1−2 min.

PI3 Kinase Assay. The assay was that of Cantley and co-workers with minor modifications (*21*). Briefly, CHO-K1 cells were lysed with lysis buffer (25 mM Tris-HCl pH 7.4, 150 mM NaCl, 1% NP-40, 1 mM EDTA, 20 mM NaF, 10 mM NaPPi, 50 mM β-glycerophosphate, 1 mM DTT, 1 mM Na_3VO_4, 1 mM PMSF, 4 μg/mL each of leupeptin, aproteinin, and pepstatin). The lysate was

clarified by centrifugation, and PI3K was immunoprecipitated overnight at 4 °C with a rabbit polyclonal antiserum against the p85 regulatory subunit of PI3K. The immunoprecipitate was captured on protein-A Sepharose beads and washed thrice with IP wash buffer (25 mM Tris-HCl pH 7.4, 150 mM NaCl, 1% NP-40, 1 mM EDTA, 20 mM NaF, 10 mM NaPPi, 50 mM β-glycerophosphate) and thrice with kinase assay buffer (20 mM Tris-HCl pH 7.4, 100 mM NaCl, 0.5 mM EGTA). The immunoprecipitated PI3K was preincubated with a lipid substrate mix of phosphatidylserine, phosphatidylinositol, pnosphatidylinositol 4-phosphate, and phosphatidylinositol 4,5-bisphosphate (in HEPES pH 7.4 30 mM, EGTA 1 mM) at room temperature for 10 min with or without the presence of Wm. Kinase reaction was initiated with the addition of γ-[32]P-ATP (in HEPES pH 7.4 30 mM, $MgCl_2$ 10 mM and ATP 0.5 mM) and allowed to proceed for 10 min at room temperature before termination with 4 M HCl. The phospholipid products were extracted with MeOH:$CHCl_3$ (1:1). The organic fraction contained the phospholipids that were separated by TLC with 2 M acetic acid:*n*-propanol (35:65) as solvent. Phospholipid signal was quantified using a phosphoimager screen. The percent inhibition of enzyme activity as a function of Wm concentration was analyzed to yield IC_{50}s using a four-parameter fit on GraphPad Prism software.

Reaction of C11-Modified Wm's with Proteins. ^{125}I labeled C11 4-hydroxy-3-iodophenylated Wm (**8**) was reacted with PI3K purified by immunoprecipitation as above. Briefly, 300 μg lysate was incubated with 1000 nM **8** (250 μCi) for 30 min at 4 °C. Proteins were then solubilized in reducing SDS sample buffer and resolved by SDS−PAGE. Gels were dried and visualized by exposure to a phosphorimager cassette for 18 h. For the reaction of C11 biotinylated Wm with BSA, 10 mg/mL in PBS was reacted with 10 or 100 μM of either C11 biotin Wm or as a positive control the *N*-hydroxysuccinimide ester of biotin (Pierce Chemical, Rockford IL) for 1 h at 37 °C. Two micrograms of protein was then subjected to SDS−PAGE followed by reaction with avidin-horseradish peroxidase (Pierce Chemical) diluted 1/20 000 in PBS containing 0.05% Tween 20 (2 h, RT, shaking). Visualization was with 3,3′-diaminobenzidine and 4-chloro-1-naphthol (Sigma-Aldrich, St. Louis, MO) at 20 mg of each, in 100 mL of PBS with 20 μL of 30% hydrogen peroxide.

RESULTS

The synthetic strategy of C11 reporter Wm's has several key features. Wm was reacted in a polar solvent methanol with diethylamine to form a C20-modified and C-11-desacetylated adduct (**2**) which was converted to the furan ring-closed derivative **3** according to the method of Creemer et al. (*20*). Compound **3** was reacted with *N*-Fmoc-glycyl acid chloride or *N*-Fmoc-11-aminododecanoyl acid chloride to yield **4a** and **4b**, respectively, with decent yields, quality, and stability. These compounds were stable during storage at −20 °C for at least 3 months and were obtained in high yield (50−70%). An instability was noted when the storage of **5a** and **5b** was attempted. Due to the base sensitivity of the compound, Fmoc deprotection was accomplished with milder base diethylamine in nonpolar solvent dichloromethane, which removed the Fmoc group and opened the furan ring in a useful manner. Reaction of FITC with **4a** was unsuccessful, presumably on steric grounds, so **4b** was synthesized with an 11-carbon spacer between the primary amine and Wm structures. The furan ring reformed readily in acidic conditions.

Table 1. Inhibition of PI3 Kinase by C11 Reporter Wm's

compound	IC_{50} (nM)[a]
Wm (**1**)	1.63 (1.52−1.75)
C11 biotinylated Wm (**7a**)	6.11 (5.31−7.03)
C11 4-hydroxy-3-iodophenylated Wm (**7b**)	11.02 (9.95−12.2)
C11 fluoresceinated Wm (**7c**)	64.9 (54.2−77.8)

[a] 95% confidence intervals within parentheses.

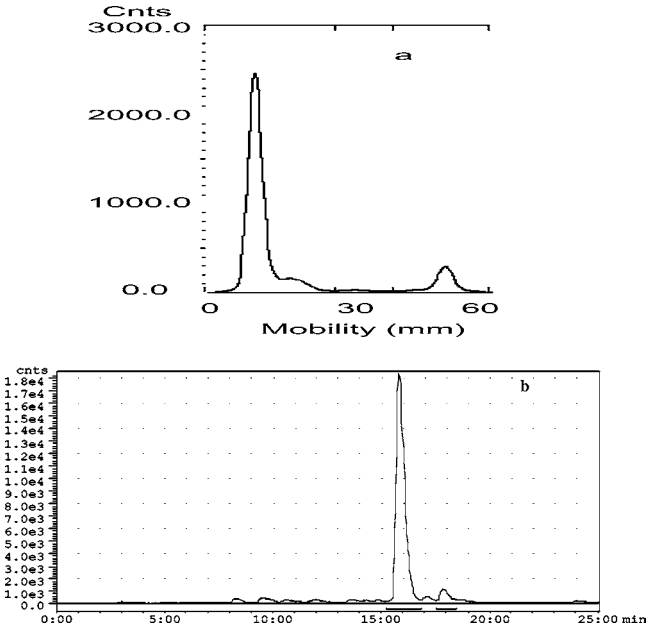

Figure 2. Iodination of C11−4-hydroxyphenylated Wm (**7d**). (a) TLC scan after iodination of **7d**. A reverse phase-TLC with C18-modified silica gel was developed with a mixture of PBS and methanol (2:1). (b) HPLC of the iodination of **7d** with γ-ray detector, C18-modified silica gel column (4.6 × 250 mm), and gradient was from water:acetonitrile 80:20 to 15:85 in 25 min. The peak of radioactivity at 15.48 min corresponded to the peak of C11 4-hydroxy-3-iodophenylate Wm (**7b**) as the internal standard with UV detector at 15.50 min.

The three C11 reporter Wm's were then analyzed for their ability to inhibit PI3 kinase as summarized in Table 1. An IC_{50} of 1.63 nM for Wm (**1**) was obtained, in good agreement with the IC_{50} of 1.8 nM reported earlier (*20*). The C11 biotinylated Wm (**7a**) and C11 4-hydroxy-3-iodophenyl Wm (**7b**) had IC_{50}s of 6.11 and 11.02 nM, respectively, modestly higher than Wm, while the C11 FITC Wm (**7c**) had an IC_{50} to 64.9 nM.

We used a C11 4-hydroxyphenyl Wm (**7d**) as substrate for iodination with 125-NaI by the iodogen method as shown in Scheme 5. About 85−100% of iodine reacted with **7d** as shown by the larger peak of low mobility in Figure 2a. The smaller peak of high mobility was identified as radioactive iodide. The iodinated mixture was further characterized by HPLC using a radioactive detector as shown in Figure 2b. The major peak at 15.48 min had been verified with the retention time consistency with **7b** at 15.50 min by using **7b** as an internal standard with a UV detector.

We next examined whether our C11 ^{125}I labeled 4-hydroxy-3-iodophenyl Wm (**8**) could be detected after reaction with proteins, and whether it could indicate the molecular weight of the protein with which it reacted. C11 ^{125}I labeled 4-hydroxy-3-iodophenyl Wm (**8**) was reacted with a p85 immunoprecipitate from CHO cells as shown in Figure 3. After reaction, radioactivity was

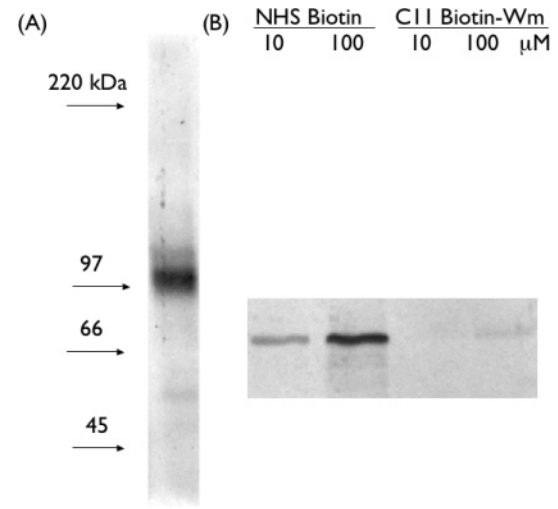

Figure 3. Visualization of the reaction of C11-modified Wm's with proteins. (A) The C11 ^{125}I 3-iodo-4-hydroxyphenyl Wm (**8**) was reacted with purified PI3K, subjected to SDS−PAGE and visualized by autoradiography. Molecular markers were myosin, phosphorylase, bovine serum albumin, and ovalbumin. (B) The C11 biotinylated Wm (**7a**) or the *N*-hydroxysuccinimide ester of biotin at 10 or 100 μM was reacted with purified bovine serum albumin at 10 mg/mL (2 h, 37 °C), subjected to SDS−PAGE and visualized with an avidin-horseradish peroxidase and substrate.

detectable and was associated with a band of about 100 kDa, which is a mobility similar to that expected for p110 catalytic subunit of PI3K (Figure 3A). We also examined the ability of our C11 biotinylated Wm (**7a**) to be detected after exposure to a non-PI3K protein, bovine serum albumin (BSA), under conditions of high protein (20 mg/mL) which would favor this reaction. As a positive control, BSA was reacted with the *N*-hydroxysuccinimide (NHS) ester of biotin. As shown in Figure 3B, only a trace amount of biotinylated BSA was seen with 100 μM C11 biotinylated Wm. Thus both C11 ^{125}I labeled 4-hydroxy-3-iodophenyl Wm (**8**) and the C11 biotinylated Wm (**7a**) are Wm probes that can be used to monitor the reactivity of Wm with proteins.

DISCUSSION

The inhibition of PI3 kinase with C11-modified Wm's can be evaluated in light of previous studies of Wm-based PI3 kinase inhibitors. Creemer et al. found that the replacement of the C11 acetyl group (CH_3COO) with a variety of modestly larger functional groups yield compounds with lower IC_{50}s than Wm (**1**). For example replacement of the C11 acetyl with a propyl group (CH_3-CH_2COO) yielded an IC_{50} of 0.38 nM, while removal of the acetyl group (11-*O*-desacetylwortmannin) had an IC_{50} of 10 nM (Wm IC_{50} = 1.8 nM). These results are supported by the crystal structure of the Wm binding in the ATP site of PI3 kinase, indicating hydrophobic amino acid side chains in the vicinity of the C11 interact favorably with small hydrophobic groups and unfavorably with the hydrophilic hydroxyl group of 11-*O*-desacetylwortmannin (*16*). The modest increase in IC_{50}s we obtained for the C11 biotinylated (**7a**) and 4-hydroxy-3-iodophenyl Wm's (**7b**), 3.7 and 6.8-fold respectively, suggest these compounds slightly exceed the constraints of the PI3 kinase Wm binding site for C11 modifications. The larger C11-fluorescein-modified Wm (**7c**) we synthesized appears to exceed the constraints of the C11 pocket, evident by a 39.8-fold increase in IC_{50}. Thus PI3 kinase binds C11-modified Wm's, provided the modification remains about the size of a biotin moiety or smaller and suggest that future C11 Wm probes must utilize small and hydrophobic modifications at C11, to maximize their interaction with ATP site of PI3 kinase.

A goal of this work was to determine whether various reporter Wm's might inhibit PI3 kinase sufficiently to permit their use with in vivo systems. It would be reasonable to evaluate these probes in vivo, in light of the affinities and losses in affinity often associated with the synthesis of radioactive steroids (*22*−*24*). In addition, our results suggest that the design of further fluorescent C11 Wm's that have a high affinity for PI3 kinase might be possible, but that the size of the modification and fluorochrome should be kept as small as possible.

ACKNOWLEDGMENT

Work was supported NIH grants RO1 EB00662-A01, GM41890, CA89021, and P50CA86355 and by the Dana Farber Harvard Cancer Center Healthcare Molecular Imaging Initiative.

LITERATURE CITED

(1) Kumar, S., Zhou, B., Liang, F., Wang, W. Q., Huang, Z., and Zhang, Z. Y. (2004) Activity-based probes for protein tyrosine phosphatases. *Proc. Natl. Acad. Sci. U.S.A. 101*, 7943−8.
(2) Deigner, H. P., Kinscherf, R., Claus, R., Fyrnys, B., Blencowe, C., and Hermetter, A. (1999) Novel reversible, irreversible and fluorescent inhibitors of platelet-activating factor acetylhydrolase as mechanistic probes. *Atherosclerosis 144*, 79−90.
(3) Melrose, J., Ghosh, P., and Patel, M. (1995) Biotinylated aprotinin: a versatile probe for the detection of serine proteinases on western blots. *Int. J. Biochem. Cell Biol. 27*, 891−904.
(4) Saltmarsh, J. R., Boyd, A. E., Rodriguez, O. P., Radic, Z., Taylor, P., and Thompson, C. M. (2000) Synthesis of fluorescent probes directed to the active site gorge of acetylcholinesterase. *Bioorg. Med. Chem. Lett. 10*, 1523−6.
(5) Gehring, M. E., and Koty, P. P. (2004) Detection of programmed cell death in cells exposed to genotoxic agents using a caspase activation assay. *Methods Mol. Biol. 291*, 465−72.
(6) Vivanco, I., and Sawyers, C. L. (2002) The phosphatidylinositol 3-Kinase AKT pathway in human cancer. *Nat. Rev. Cancer 2*, 489−501.
(7) Luo, J., Manning, B. D., and Cantley, L. C. (2003) Targeting the PI3K-Akt pathway in human cancer: Rationale and promise. *Cancer Cell 4*, 257−262.
(8) Brader, S., and Eccles, S. A. (2004) Phosphoinositide 3-kinase signaling pathways in tumor progression, invasion and angiogenesis. *Tumori 90*, 2−8.
(9) Evans, J. L., Honer, C. M., Womelsdorf, B. E., Kaplan, E. L., and Bell, P. A. (1995) The effects of wortmannin, a potent inhibitor of phosphatidylinositol 3-kinase, on insulin-stimulated glucose transport, GLUT4 translocation, antilipolysis, and DNA synthesis. *Cell Signal 7*, 365−76.
(10) Okada, T., Kawano, Y., Sakakibara, T., Hazeki, O., and Ui, M. (1994) Essential role of phosphatidylinositol 3-kinase in insulin-induced glucose transport and antilipolysis in rat adipocytes. Studies with a selective inhibitor wortmannin. *J. Biol. Chem. 269*, 3568−73.
(11) Fruman, D. A., and Cantley, L. C. (2002) Phosphoinositide 3-kinase in immunological systems. *Semin. Immunol. 14*, 7−18.
(12) Nakanishi, S., Yano, H., and Matsuda, Y. (1995) Novel functions of phosphatidylinositol 3-kinase in terminally differentiated cells. *Cell Signal 7*, 545−57.
(13) Okarvi, S. M. (2001) Recent progress in fluorine-18 labeled peptide radiopharmaceuticals. *Eur. J. Nucl. Med. 28*, 929−38.
(14) Habeck, M. (2003) Knocking down the PI3 kinase pathway. *Targets 2*, 38−39.
(15) Thelen, M., Wymann, M. P., and Langen, H. (1994) Wortmannin binds specifically to 1-phosphatidylinositol 3-kinase while inhibiting guanine nucleotide-binding protein-

coupled receptor signaling in neutrophil leukocytes. *Proc. Natl. Acad. Sci. U.S.A. 91*, 4960−4.
(16) Walker, E. H., Pacold, M. E., Perisic, O., Stephens, L., Hawkins, P. T., Wymann, M. P., et al. (2000) Structural determinants of phosphoinositide 3-kinase inhibition by wortmannin, LY294002, quercetin, myricetin, and staurosporine. *Mol. Cell 6*, 909−19.
(17) Ui, M., Okada, T., Hazeki, K., and Hazeki, O. (1995) Wortmannin as a unique probe for an intracellular signaling protein, phosphoinositide 3-kinase. *Trends Biochem. Sci. 20*, 303−7.
(18) Norman, B. H., Shih, C., Toth, J. E., Ray, J. E., Dodge, J. A., Johnson, D. W., et al. (1996) Studies on the mechanism of phosphatidylinositol 3-kinase inhibition by wortmannin and related analogues. *J. Med. Chem. 39*, 1106−11.
(19) Holleran, J. L., Egorin, M. J., Zuhowski, E. G., Parise, R. A., Musser, S. M., and Pan, S. S. (2003) Use of high-performance liquid chromatography to characterize the rapid decomposition of wortmannin in tissue culture media. *Anal. Biochem. 323*, 19−25.
(20) Creemer, L. C., Kirst, H. A., Vlahos, C. J., and Schultz, R. M. (1996) Synthesis and in vitro evaluation of new wortmannin esters: potent inhibitors of phosphatidylinositol 3-kinase. *J. Med. Chem. 39*, 5021−4.
(21) Fruman, D. A., Snapper, S. B., Yballe, C. M., Davidson, L., Yu, J. Y., Alt, F. W., et al. (1999) Impaired B cell development and proliferation in absence of phosphoinositide 3-kinase p85alpha. *Science 283*, 393−7.
(22) Seimbille, Y., Rousseau, J., Benard, F., Morin, C., Ali, H., Avvakumov, G., et al. (2002) 18F-labeled difluoroestradiols: preparation and preclinical evaluation as estrogen receptor-binding radiopharmaceuticals. *Steroids 67*, 765−75.
(23) Pomper, M. G., VanBrocklin, H., Thieme, A. M., Thomas, R. D., Kiesewetter, D. O., Carlson, K. E., et al. (1990) 11β-methoxy-, 11β-ethyl- and 17α-ethynyl-substituted 16-α-fluoroestradiols: receptor-based imaging agents with enhanced uptake efficiency and selectivity. *J. Med. Chem. 33*, 3143−55.
(24) Kochanny, M. J., VanBrocklin, H. F., Kym, P. R., Carlson, K. E., O'Neil, J. P., Bonasera, T. A., et al. (1993) Fluorine-18-labeled progestin ketals: synthesis and target tissue uptake selectivity of potential imaging agents for receptor-positive breast tumors. *J. Med. Chem. 36*, 1120−7.

BC049714F

Example of Fatty Acid-Loaded Lipoplex in Enhancing in Vitro Gene Transfer Efficacies of Cationic Amphiphile[§]

Bharat Kumar Majeti,[†] Priya Prakash Karmali,[†] Sunkara Sakunthala Madhavendra,[‡] and Arabinda Chaudhuri*,[†]

Division of Lipid Science and Technology, and Electron Microscopy Center, Indian Institute of Chemical Technology, Hyderabad 500 007, India. Received December 31, 2004; Revised Manuscript Received April 5, 2005

Herein, we report on the design and synthesis of a novel nontoxic cationic amphiphile *N*,*N*-di-n-tetradecyl-*N*-[2-[*N*′,*N*′-bis(2-hydroxyethyl)amino]ethyl]-*N*-(2-hydroxyethyl)ammonium chloride (lipid **1**) whose in vitro gene transfer efficacies in CHO, COS-1, MCF-7, and HepG2 cells are remarkably enhanced when used in combination with 30 mole percent added myristic acid. Reporter gene expression assay using *p*-CMV-SPORT-*β*-gal reporter gene revealed poor gene transfer properties of the cationic liposomes of lipid **1** and cholesterol (colipid). However, the in vitro gene delivery efficacies of lipid **1** were found to be remarkably enhanced when the cationic liposomes of lipid **1** and cholesterol were prepared in the presence of 30 mole percent added myristic acid (with respect to lipid **1**) as the third liposomal ingredient. The whole cell histochemical X-gal staining of representative CHO cells further confirmed the significantly enhanced gene transfer properties of the fatty acid-loaded cationic liposomes of lipid **1** and cholesterol. Electrophoretic gel patterns in the gel mobility shift assay supports the notion that better DNA release from fatty acid lipoplexes might play a role in their enhanced gene transfer properties. In addition, such myristic acid-loaded lipoplexes of lipid **1** were also found to be serum-compatible up to 30% added serum. Taken together, our present findings demonstrate that the transfection efficacies of fatty acid-loaded lipoplexes are worth evaluating particularly when traditional cationic liposomes prepared with either cholesterol or DOPE colipids fail to transfect cultured cells.

INTRODUCTION

Designing safe and efficacious reagents for transferring genes into body cells continue to remain as the key challenge in gene therapy. Contemporary gene transfection vectors are broadly classified into two categories: viral and nonviral. Viral vectors, although remarkably efficient, suffer from numerous biosafety-related disadvantages including generation of replication-competent virus, possible inflammatory and immunogenic responses against the virus structural components, etc. (*1*−*8*). In addition, viral vectors have a low insert-size limit for the therapeutic genes they can pack inside. Conversely, because of their least immunogenic nature, robust manufacture, ability to deliver large pieces of DNA, and ease of handling and preparation techniques, cationic amphiphiles are increasingly being demonstrated as the alternative nonviral transfection vectors of choice (*9*−*39*), our own work included (*31*−*39*). However, a major limitation of cationic transfection lipids is their poor transgene expression efficacies. To this end, previously reported structure−activity investigations have demonstrated that presence of one or two 2-hydroxyethyl functionalities in the polar headgroup regions of cationic amphiphiles, in general, imparts high in vitro gene transfer properties to cationic amphiphiles (*33*, *36*, *39*−*40*). Inspired by these early reports, in the present investigation, we designed and synthesized a novel cationic lipid *N*,*N*-di-n-tetradecyl-*N*-[2-[*N*′,*N*′-bis(2-hydroxyethyl)amino]ethyl]-*N*-(2-hydroxyethyl)ammonium chloride (lipid **1**, Figure 1) and evaluated its in vitro gene transfer efficacies in multiple cultured cells including CHO, COS-1, MCF-7, and HepG2 using pCMV-SPORT-*β*-gal plasmid as the reporter gene. As delineated below, except in CHO cells at lipid:DNA charge ratio of 0.3:1, lipid **1** was found to be poorly transfecting when used in combination with equimolar cholesterol as co-lipid in COS-1, MCF-7, and HepG2 cells across the entire lipid:DNA charge ratios of 9:1 to 0.3:1. Electrophoretic gel patterns in the gel mobility shift assay indicated the

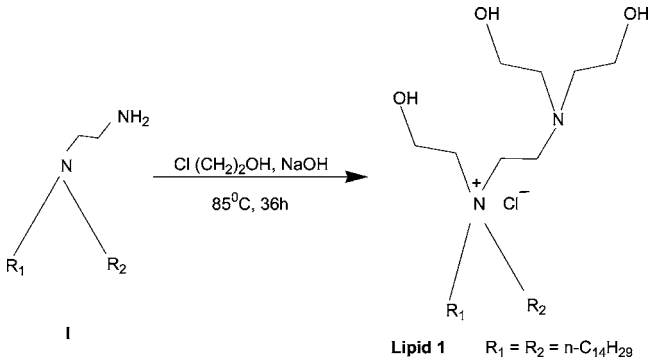

Figure 1. Synthesis of cationic lipid **1**.

* Corresponding author. Tel: 91 40 27193201. Fax: 91 40 27160757. E-mail: arabinda@iict.res.in.

† Division of Lipid Science and Technology.

‡ Electron Microscopy Center.

§ IICT Communication No. 041108.

[1] Abbreviations: DMEM, Dulbecco's modified Eagle's medium; ONPG, *o*-nitrophenyl-*β*-D-galactopyranoside; Chol, cholesterol; DOPE, 1,2-dioleoyl-*sn*-glycero-3-phosphoethanolamine; FBS, fetal bovine serum; PBS, phosphate-buffered saline; MTT, 3-(4,5-dimethylthiazol-2-yl)-2,5-diphenyltetrazolium bromide; NP-40, Nonidet P-40.

10.1021/bc049687t CCC: $30.25 © 2005 American Chemical Society
Published on Web 04/26/2005

existence of strong binding interactions between DNA and the cationic liposomes of lipid **1** and equimolar cholesterol across the lipid:DNA charge ratios of 9:1 to 1:1 and existence of moderate binding interactions even at the low lipid:DNA charge ratio of 0.3:1. In other words, the findings in the gel mobility shift assay hinted that poor gene transfer efficacies of lipid **1** might originate due to such strong lipid:DNA interactions. Toward reducing strong binding interactions between the cationic liposomes of lipid **1** and DNA, we decided to use myristic acid as an additional liposome ingredient with the assumption that the negatively charged carboxyl group of the added myristic acid would be able to reduce the overall positive charge of the resulting liposome. Consistent with such a rationale, not only the in vitro gene transfer efficacies of such myristic acid-loaded lipoplexes of lipid **1** were observed to be remarkably enhanced in all four cell lines, but the enhanced gene transfer properties of the resulting fatty acid-loaded lipoplexes were also found to be serum-compatible in the presence of up to 30% added serum. Herein, we report on the enhanced gene transfer efficacies and serum compatiblity of the myristic acid-loaded lipoplexes of lipid **1** compared to their acid-lacking counterparts in CHO, COS-1, MCF-7, and HepG2 cells. Taken together, our present findings demonstrate that the transfection efficacies of fatty acid-loaded lipoplexes are worth evaluating particularly where traditional cationic liposomes prepared with either cholesterol or DOPE colipids fail to transfect cultured cells.

EXPERIMENTAL PROCEDURES

Materials and Methods. The FABMS analyses were performed on a Micromass AUTOSPEC-M mass spectrometer (Manchester, UK) with OPUS V3, 1X data system. Data were acquired by liquid secondary ion mass spectrometry (LSIMS) using *m*-nitrobenzyl alcohol as the matrix. ^{1}H NMR spectra were recorded on a Varian FT 200 MHz or AV 300 MHz. 1-Bromotetradecane and n-tetradecylamine were procured from Lancaster (Morecambe, England). Column chromatography was performed with silica gel (Acme Synthetic Chemicals, India, 60−120 mesh), and Amberlyst A-26 was purchased from Lancaster (Morecambe, UK). Cell culture media, fetal bovine serum, 3-(4,5-dimethylthiazol-2-yl)-2,5-diphenyltetrazolium bromide (MTT), poly(ethylene glycol) 8000, *o*-nitrophenyl-*β*-D-galactopyranoside(ONPG), agarose, cholesterol, and cell culture lysis buffer were purchased from Sigma, St. Louis, MO. Lipofectamine 2000 was purchased from invitrogen. NP-40 and antibiotics were purchased from Hi-media, India. Unless otherwise stated, all reagents were purchased from local commercial suppliers and were used without further purification. Purity of the final lipid (**1**) was determined by analytical HPLC (Shimadzu Model LC10A) using a PARTISIL 5 ODS-3 WCS analytical column (4.6 × 250 mm, Whatman Inc., Clifton, NJ) in two different mobile phases. One solvent system (A) was methanol**:**water in the ratio 98:2 (v/v) for 20 min with a flow rate of 0.9 mL/min. The other solvent system (B) was methanol (100%) for 20 min with a flow rate of 0.9 mL/min. Peaks were detected by UV absorption at 219 nm. The target lipid (**1**) showed more than 95% purity. The retention times for lipid **1** in mobile phase A and B were 2.75 min and 2.27 min, respectively.

Synthesis of *N*,*N*-Di-n-tetradecyl-*N*-[2-[*N*′,*N*′-bis-(2-hydroxyethyl)amino]ethyl]-*N*-(2-hydroxyethyl)-ammonium Chloride (Lipid 1, Figure 1). *N*-(aminoethyl)-*N*,*N*-di-n-tetradecylamine (**I**, 1 g, 2.212 mmol, prepared as described previously (*35*)) was stirred at room temperature with an excess amount of chloroethanol (3 mL) for 5 min. NaOH (885 mg, 22.12 mmol) dissolved in water (3 mL) was added to the reaction mixture, and it was heated at 85 °C for 36 h. Excess 2-chloroethanol was removed on a rotary evaporator by repeated addition of methanol. Column chromatographic purification using 60−120 mesh silica gel and 5−7% methanol in chloroform as eluent afforded 260 mg (19%) of the title compound as a white solid. ^{1}H NMR (300 MHz, $CDCl_3$) δ/ppm = 0.90 [t, 3H, C*H*$_3$(CH$_2$)$_{13}$], 1.20−1.45 [bs, 44H, (C*H*$_2$)$_{11}$], 1.60−1.80 [m, 4H, N(CH$_2$C*H*$_2$)], 2.65−2.80 [bs, 4H, N(C*H*$_2$CH$_2$OH)], 3.00−3.15 [bs, 2H, NCH$_2$C*H*$_2$N], 3.30−3.50 [bs, 4H, NC*H*$_2$(CH$_2$)$_{12}$], 3.60−3.80 [bs, 8H, NCH$_2$C*H*$_2$-OH, NC*H*$_2$CH$_2$N, quaternary NC*H*$_2$CH$_2$OH], 4.00−4.15 [bs, 2H, quaternary NCH$_2$C*H*$_2$OH]. FABMS (LSIMS)**:** *m*/*z*: 586 [M + 1]$^+$ for $C_{36}H_{77}O_3N_2$.

Plasmids. pCMV-SPORT-*β*-gal plasmid was amplified in DH5α strain of *Escherichia coli*, isolated by an alkaline lysis procedure and finally purified by PEG-8000 precipitation as described previously (*41*). The purity of plasmid was checked by A_{260}/A_{280} ratio (around 1.9) and 1% agarose gel electrophoresis.

Cells and Cell Culture. COS-1 (SV 40 transformed African green monkey kidney cells)**,** CHO (Chinese hamster ovary), MCF-7 (human breast adenocarcinoma cell), and HepG2 (human hepatocarcinoma) cell lines were procured from the National Centre for Cell Sciences (NCCS), Pune, India. Cells were cultured at 37 °C in Dulbecco's modified Eagle's medium (DMEM) with 10% fetal bovine serum, 50 *μ*g /mL penicillin, 50 *μ*g/mL streptomycin, and 20 *μ*g/mL kanamycin in a humidified atmosphere containing 5% CO_2.

Preparation of Liposomes and Lipid−DNA Complexes. The cationic lipid and cholesterol in 1:1 mole ratio or the cationic lipid, cholesterol, and myristic acid in 1:1:0.3 mole ratio were dissolved in chloroform in a glass vial. The solvent was removed with a thin flow of moisture-free nitrogen gas, and the dried lipid film was then kept under high vacuum for 8 h. The dried lipid film was hydrated in sterile deionized water in a total volume of 3 mL at cationic lipid concentration of 1 mM for a minimum of 12 h. Liposomes were vortexed for 1−2 min to remove any adhering lipid film and sonicated in a bath sonicator (ULTRAsonik 28X) for 2−3 min at room temperature to produce multilamellar vesicles (MLV). MLVs were then sonicated with a Ti-probe (using a Branson 450 sonifier at 100% duty cycle and 25 W output power) for 1−2 min to produce small unilamellar vesicles (SUVs) as indicated by the formation of a clear translucent solution.

Transfection Biology. Cells were seeded at a density of 20000 cells (for CHO, MCF-7, HepG2) and 15000 cells (for COS-1) per well in a 96-well plate 18−24 h before the transfection. 0.30 *μ*g of pDNA was complexed with varying amounts of lipids (to give ± ratios of 0.3:1, 1:1, 3:1, and 9:1) in plain DMEM (total volume made up to 100 *μ*L) for 20−30 min. While evaluating the transfection efficiencies of the lipids in the presence of serum, the complexes were diluted with 100 *μ*L of DMEM containing either 20% or 60% FBS to give a final concentration of 10% and 30% serum, respectively. After 3 h of incubation, the medium was replaced by 200 *μ*L of DMEM containing 10% FBS. The medium was changed to complete medium containing 10% FBS after 24 h, and the reporter gene activity was estimated after 48 h. Cells were washed with PBS (100 *μ*L) and lysed in 50 *μ*L lysis buffer [0.25 M Tris-HCl (pH 8.0), 0.5% NP40]. The *β*-galactosidase activity per well was estimated by adding 50 *μ*L of 2×-substrate solution [1.33 mg/mL of ONPG, 0.2 M sodium phosphate

(pH 7.3) and 2 mM magnesium chloride] to the lysate in a 96-well plate. Absorbance of the product *o*-nitrophenol at 405 nm was converted to β-galactosidase units by using the calibration curve constructed using the pure commercial β-galactosidase enzyme. The transfection values reported are the average values from two replicate experiments performed in the same plate on the same day. The values of β-galactosidase units for duplicate experiments carried out on the same day varied within 20−30%. Each transfection experiment was performed two times on two different days. The day to day variation in transfection efficiency was mostly within 2−3-fold and was dependent on the cell density and condition of the cells. The transfection profiles obtained on different days were identical.

Toxicity Assay. Cytotoxicity of lipid **1** was assessed by the 3-(4,5-dimethylthiazol-2-yl)-2,5-diphenyltetrazolium bromide (MTT) reduction assay as described earlier (*42*)**.** The cytotoxicity assay was performed in a 96-well plate by maintaining the same ratio of number of cells to amount of cationic lipid, as used in the transfection experiments. MTT was added 3 h after addition of cationic lipid to the cells. Results were expressed as percent viability = [A_{540}(treated cells) − background/ A_{540}(untreated cells) − background] × 100.

Gel Mobility Shift Assay. The DNA binding ability of the cationic lipid **1** was assessed by the gel mobility shift assay on a 1% agarose gel. 0.60 μg of pCMV-β-gal was complexed with varying amounts of cationic lipids (using the indicated lipid:DNA charge ratios in Figure 6) in a total volume of 40 μL in HEPES buffer, pH 7.40, and incubated at room temperature for 20−25 min. 8 μL of 6× loading buffer (0.25% bromophenol blue, 40% sucrose) was added to it, and 20 μL of the resultant solution was loaded in each well. The samples were electrophoresed at 90 V for approximately 3 h, and the DNA bands were visualized by staining for 30 min with ethidium bromide solution.

X-Gal Staining. Cells expressing β-galactosidase were histochemically stained with the substrate 5-bromo-4-chloro-3-indolyl-β-D-galactopyranoside (X-gal) (Figure 3) as described previously (*34*). Briefly, 48 h after transfection with lipoplexes in 96-well plates, the cells were washed two times (2 × 100 μL) with phosphate-buffered saline (PBS, 137 mM NaCl, 2.7 mM KCl, 10 mM Na_2HPO_4, 2 mM KH_2PO_4, pH 7.4) and fixed with 0.5% glutaraldehyde in PBS (225 μL). After 15 min incubation at room temperature, the cells were washed again with PBS three times (3 × 250 μL) and subsequently were stained with 1.0 mg/mL X-gal in PBS containing 5.0 mM $K_3[Fe(CN)_6]$, 5.0 mM $K_4[Fe(CN)_6]$, and 1 mM $MgSO_4$ for 2−4 h at 37 °C. Blue colored cells were identified by a light microscope (Leica, Germany).

Transmission Electron Microscopy. Transmission electron microscopy was performed on a FEI Tecnai 12 TEM apparatus operated at 100 KV. Liposomes or lipoplex samples were transferred onto an ultrathin carbon-coated copper grid by placing the grid on top of a 10 μL drop of the sample for 1 min. After removing the excess fluid from one side, the grid was placed on a 20 μL water drop for a 30 s wash. The excess fluid was removed, and the grid was placed for 1 min on a 20 μL drop of freshly filtered uranyl acetate (1.33%). Once again, the excess fluid was wicked away, and the grid was air-dried.

RESULTS

Chemistry. The mixed tertiary-primary amine precursor (**I**, Figure 1) was prepared by reacting *N*,*N*-di-n-tetradecylamine with *N*-*tert*-butyloxycarbonyl-2-bromoethylamine in ethyl acetate in the presence of anhydrous potassium carbonate followed by acid deprotection as described previously (*35*). Lipid **1** was synthesized by quaternizing the mixed tertiary-primary amine precursor (**I**, Figure 1) with excess 2-chloroethanol. The unreacted 2-chloroethanol was removed under vacuum, and the column chromatographic purification of the residue afforded pure target lipid **1**. Presence of quaternized nitrogen center in lipid **1** was confirmed from the disappearance of the two triplet peaks in the ^{1}H NMR spectrum of precursor **I** (Figures S1 and S2, Supporting Information) associated with the three methylene units directly attached to its tertiary nitrogen atom. The molecular ion peak in FAB mass spectrum (M + 1 586, Figure S3, Supporting Information) and the relative integration peak areas in the ^{1}H NMR spectrum of lipid **1** (Figure S2, Supporting Information) clearly showed that the primary amine group of precursor **I** was covalently modified with only two 2-hydroxyethyl groups when treated with excess 2-chloroethanol. Purity of lipid **1** was confirmed by reversed phase HPLC analysis using two different mobile phases (Figure S4, Supporting Information).

Contrasting Transfection Efficacies of Fatty Acid-Loaded Lipoplexes and Their Acid-Lacking Counterparts. The in vitro gene transfer efficacies of lipid **1** were first measured by the reporter gene expression assay using equimolar cholesterol as colipid, and pCMV-SPORT-β-gal plasmid as the reporter gene, in COS-1, CHO, MCF-7, and HepG2 cells across the lipid:DNA charge ratios 9:1−0.3:1 in the absence of any added fatty acids. Except in CHO cells at lipid:DNA charge ratio of 0.3:1, the gene transfer efficacies of lipid **1** were found to be significantly less than that of LipofectAmine 2000, one of the most widely used commercially available liposomal transfection kits (Figure 2, parts A−D, open bars). Contrastingly, the efficacies of lipid **1** in transfecting all four cell lines were remarkably enhanced when 30 mole percent myristic acid (with respect to lipid **1**) was used as an added liposomal ingredient (Figure 2, parts A−D, filled bars). While in both MCF-7 and COS-1 cells, myristic acid-loaded liposomes of lipid **1** were found to be optimally transfection efficient around 0.3:1 lipid **1**:DNA charge ratio (Figure 2, parts A and C, filled bars), the highest efficacies of the acid-loaded liposomes of lipid **1** in transfecting CHO and HepG2 cells were found to be at lipid **1**:DNA charge ratios of 1:1 and 3:1, respectively (Figure 2, parts B and D, filled bars). In all four cell lines, the optimal transfection efficiencies of fatty acid-loaded liposomes of lipid **1** were observed to be better than or comparable to that of LipofectAmine 2000 (Figure 2, parts A−D, filled bars). Interestingly, the most extensively used colipid in cationic lipid-mediated gene delivery, namely 1,2-dioleyol-*sn*-glycerophosphatidylethanolamine (DOPE), was found to be ineffective in imparting any gene transfer properties to lipid **1** (data not shown). The superior transfection profile of fatty acid-loaded liposomes of lipid **1** was further confirmed by the whole cell histochemical X-gal staining of the representative CHO cells. Consistent with the findings in the reporter gene expression assays as summarized in part B of Figure 2, the number of transfected X-gal stained cells at lipid **1**:DNA charge ratio of 1:1 was found to be significantly higher with fatty acid-loaded liposomes of lipid **1** (Figure 3).

Serum-Compatible Transfection Properties of Fatty Acid-Loaded Lipoplexes of Lipid 1. In stark contrast to the commonly observed serum incompatibility

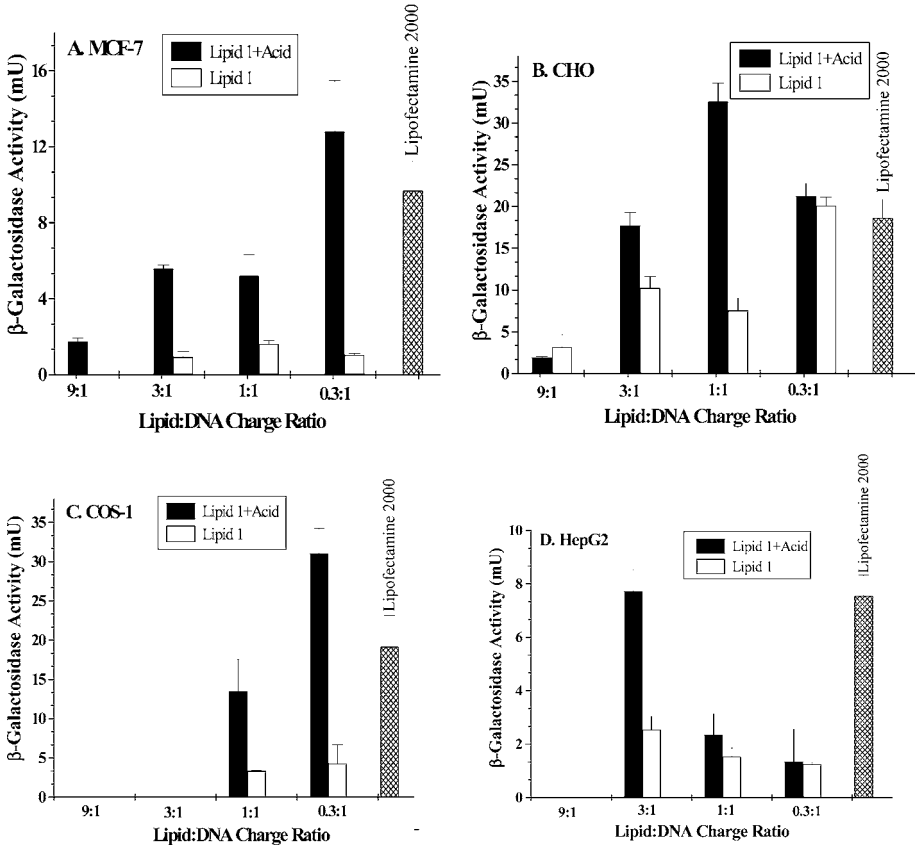

Figure 2. In vitro transfection efficiencies of lipid **1** using reporter gene expression assays. MCF-7 (A), CHO (B), COS-1 (C), and HepG2 (D) cells were transfected with lipid **1** and cholesterol (as colipid) both in the presence and in absence of added myristic acid at lipid:colipid:myristic acid mole ratio of 1:1:0.3 and 1:1:0, respectively. The transfection efficiencies of the lipid **1** were compared to that of commercially available Lipofectamine 2000. Units of β-galactosidase activity were plotted against the varying lipid to DNA (+/−) charge ratios. The transfection values shown are average of duplicate experiments performed on the same day. Details of transfection assays are as described in the text.

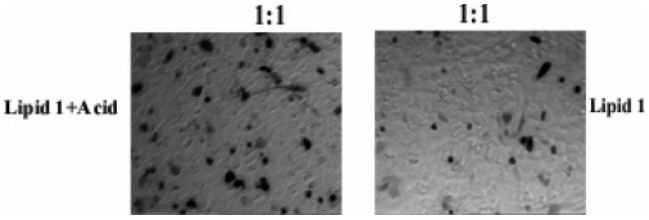

Figure 3. The whole cell histochemical X-gal staining of transfected CHO cells. CHO cells were transfected with lipid **1** (both in the presence and in absence of added myristic acid at lipid:cholesterol:myristic acid mole ratio of 1:1:0.3 and 1:1:0, respectively) at lipid:DNA charge ratio of 1:1. Cells expressing β-galactosidase were stained with X-gal as described in the text.

of cationic transfection lipids, myristic acid-loaded liposomes of lipid **1** were found to be serum-compatible (up to 30% added serum). The most encouraging serum-compatible transfection profiles were observed in MCF-7 and CHO cells at lipid **1**:DNA charge ratios of 9:1 and 3:1. In MCF-7 cells, at both the lipid:DNA charge ratios, the fatty acid-loaded liposomes remained remarkably transfection efficient up to 30% added fetal bovine serum practically without any loss of transfection efficiency (Figure 4, parts A and B). However, transfection efficacies were compromised with more than 30% added serum (data not shown). Most notably, at the high lipid **1**:DNA charge ratio of 9:1, the transfection efficacies of fatty acid-loaded liposomes of lipid **1** were found to be remarkably enhanced compared to their non-fatty acid counterparts in the presence of 30% added serum in both MCF-7 and CHO cells (Figure 4, parts A and C). Interestingly, the serum-compatible high transfection efficacies of fatty acid-loaded liposomes of lipid **1** (compared to their non-fatty acid counterparts) in COS-1 cells were observed only at lower lipid:DNA charge ratios of 0.3:1 up to 30% added serum and in HepG2 cells at 9:1 lipid:DNA charge ratios up to 10% added serum (data not shown).

Physicochemical Characterizations of Liposomes and Lipoplexes. Sizes and Zeta Potentials. Toward gaining insights into whether varying sizes and global surface charges of both the fatty acid-loaded of liposomes of lipid **1** and its non-fatty acid counterparts might play some role behind their contrasting transfection profiles, lipoplex sizes and surface potentials were measured in the presence of DMEM by dynamic laser light scattering instrument equipped with zeta-sizing capacity. Interestingly, the average sizes of both the lipoplexes (fatty acid-loaded lipoplexes and lipoplexes with no added fatty acids) were found to be within the range 200−270 nm for lipid:DNA charge ratios 0.3:1 and 1:1 (detail size data of lipoplexes measured across the lipid:DNA charge ratios are provided in Table 1). However, at 3:1 lipid:DNA charge ratio, lipoplexes with no fatty acid ingredient were found to be significantly bigger (>900 nm) than those containing fatty acids (about 260 nm, Table 1). At 9:1 lipid:DNA charge ratios, both the lipoplexes (with and without added fatty acids) grew big in size (>950 nm, Table 1).

Transmission Electron Microscopy. With a view to gaining insights into whether the fatty acid-loaded lipoplexes as wells as their acid-lacking counterparts

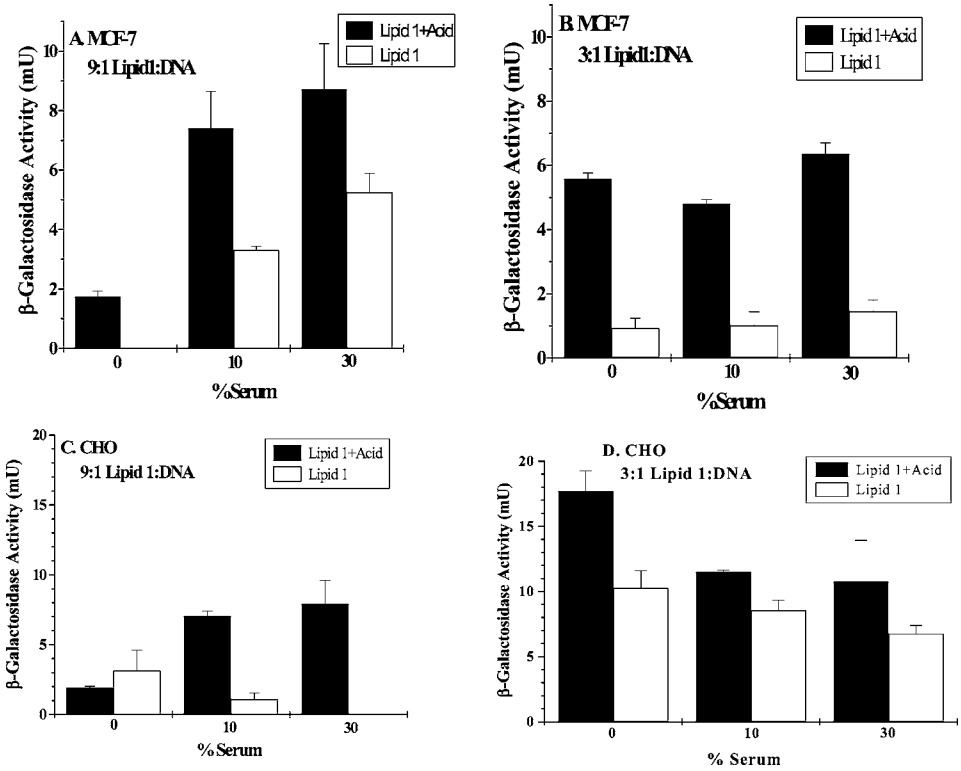

Figure 4. Serum-compatible transfection efficacies of fatty acid-loaded liposomes. In vitro transfection efficiencies of lipid **1** both in the presence and in absence of added myristic acid were measured with 10% and 30% added serum in MCF-7 and CHO cells at lipid:cholesterol:myristic acid mole ratio of 1:1:0.3 or 1:1:0 at lipid:DNA charge ratio of 9:1 (A and C) and 3:1 (B and D). Details of transfection experiments are as described in the text.

Table 1. Hydrodynamic Diameters and Zeta Potentials of Liposomes and Lipoplexes for Lipid 1 in DMEM[a]

Lipids		lipid:DNA (1:0)	lipid:DNA (0.3:1)	lipid:DNA (1:1)	lipid:DNA (3:1)	lipid:DNA (9:1)
Lipid **1**	size (nm)	119.6 ± 0.2	247.2 ± 1.9	207.9 ± 5.1	911.8 ± 77.6	960.3 ± 54.1
	zeta potential (mV)	31.3 ± 0.9	−8.1 ± 3.5	−36.1 ± 1.2	22.3 ± 3.4	27.7 ± 4.6
Lipid **1** + Acid	size (nm)	117.5 ± 3.1	269.6 ± 3.5	204.5 ± 3.7	261.1 ± 8.6	1022.8 ± 107
	zeta potential (mV)	27.9 ± 2.3	−29.5± 2.1	−35.1± 1.6	−18.7 ± 3.2	17.6 ± 3.7

[a] Sizes and Zeta potentials were measured by laser light scattering technique using Zetasizer 3000HS_A (Malvern Instruments, UK) in DMEM. Values shown are the averages obtained from three (size) and ten (zeta potential) measurements.

possess distinctly different morphologies that could possibly play important role behind their contrasting transfection profiles (Figures 2 and 3), we carried out negative staining transmission electron microscopic investigation. The transmission electron micrographs (TEM) of the representative acid-loaded and acid-lacking liposomes and lipoplexes (prepared using lipid: DNA charge ratio of 3:1) indeed revealed some distinct morphological differences. Although fatty acid-loaded liposomes revealed the existence of the usual closed lamellar morphologies (part A, Figure 5), the TEM picture of their acid-lacking counterparts, in addition to showing such regular closed lamellar structures (micrograph not shown), showed the presence of stacked sheets of bilayers containing channel-like structures between (part B, Figure 5). Most notably, the lipid:DNA complexes (lipoplexes) prepared from both these acid-lacking liposomes showed the presence of neither any aggregated sheets of bilayers nor any regular closed bilayer structures. The transmission electron micrographs of the acid-lacking lipoplexes displayed the presence of non-bilayer clustered complexes (Figure 5, part D). Existence of such clustered structures for lipoplexes have previously been reported in the cryo-TEM studies on lipoplexes by Smisterova et al. (*43*). Interestingly, the TEM picture of the fatty acid-containing lipoplexes showed the presence of extensive network of non-bilayer structures (Figure 5, part C).

Gel Mobility Shift Assay. Toward understanding the role of lipid:DNA electrostatic binding interactions (if any) in modulating the in vivo transfection efficacies of fatty acid-loaded liposomes of lipid **1** and their acid-lacking counterparts, gel mobility shift assays were performed using lipoplexes prepared across the wide range of lipid:DNA charge ratios of 9:1 to 0.1:1. The band intensities of the free DNA (unassociated or loosely bound with lipoplexes) particularly for acid-loaded lipoplexes with lipid:DNA charge ratios 1:1 and 0.3:1 were found to be significantly higher than the corresponding bands for acid-lacking lipoplexes (Figure 6)

Cell Viabilities. With a view to understand whether varying cell viabilities could be responsible behind the remarkably superior transfection profiles of myristic acid-loaded liposomes of lipid **1** compared to its acid-lacking counterpart liposomes, cell viabilities of both the lipoplexes were measured using MTT-based cell viability assays in representative MCF-7 cells across the lipid:DNA charge ratios of 9:1 to 0.3:1. Interestingly, both the lipoplexes showed more than 90% cell viabilities up to lipid:DNA charge ratios of 3:1 and slightly reduced cell viabilities (more than 75%) at lipid:DNA charge ratio of 9:1 (Figure 7). Thus, varying cell viabilities of the acid-loaded and acid-lacking lipoplexes were ruled out as a possible cause for their contrasting gene delivery efficacies.

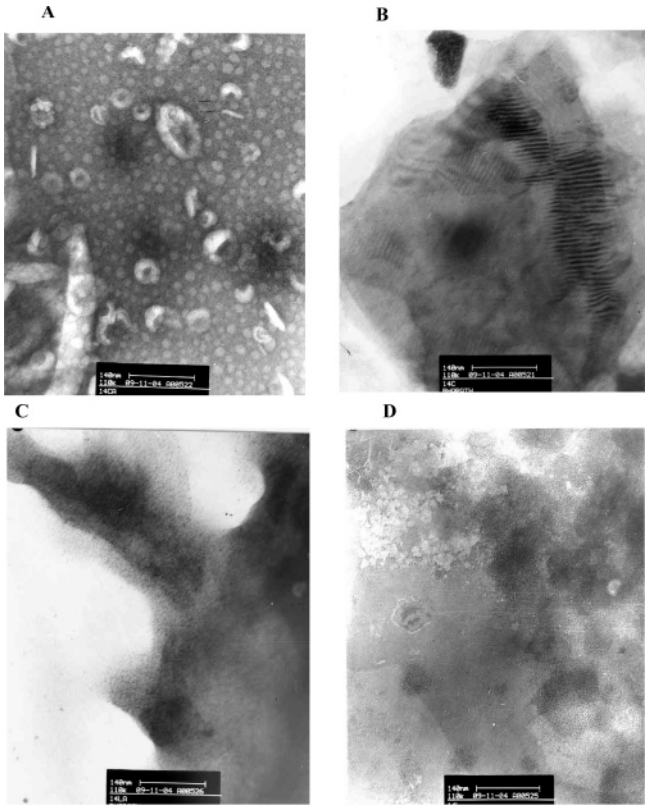

Figure 5. Transmission electron micrographs of liposomes and lipoplexes. Liposomes with loaded fatty acid (A), liposomes without added fatty acid (B), myristic acid-loaded lipoplex of lipid **1** (C), and acid-lacking lipoplex of lipid **1** (D). Lipoplexes were prepared at lipid:DNA charge ratio of 3:1 as described in text. Bars correspond to 140 nm.

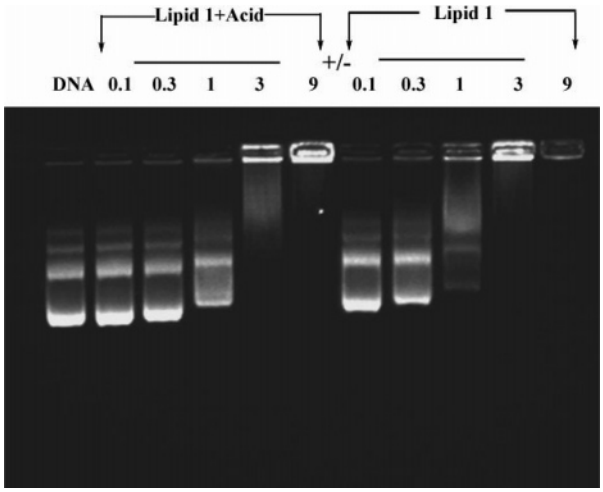

Figure 6. Gel retardation assay. Electrophoretic gel patterns for DNA associated with lipoplexes of lipid **1** prepared from myristic acid-loaded liposomes and liposomes containing no added acid. The lipid:DNA charge ratios are indicated at the top of each lane. The details of treatment are as described in the text.

DISCUSSION

In the present investigation, we report on the remarkably enhanced in vitro gene transfer properties of a novel cationic amphiphile namely, *″ N*,*N*-di-n-tetradecyl-*N*-[2-[*N*′,*N*′-bis(2-hydroxyethyl)amino]ethyl]-*N*-(2-hydroxyethyl)ammonium chloride (lipid **1**, Figure 1) when used in combination with 30 mole percent added myristic acid.

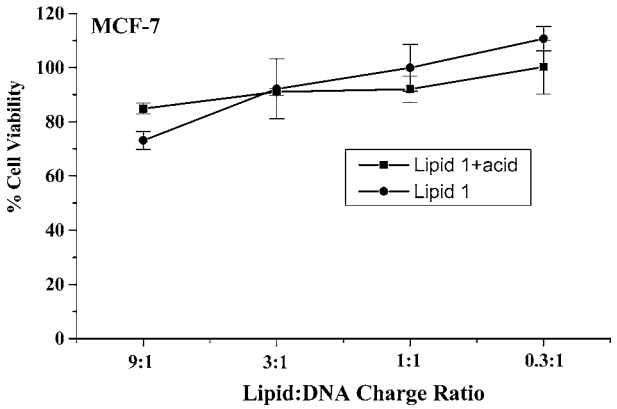

Figure 7. MTT assay-based percent cell viabilities of both acid-loaded and acid-lacking lipoplexes in representative MCF-7 cells. The percent cell viability values shown are average of triplicate experiments performed on the same day. Details of treatment are described in the text.

Except in CHO cells, in the absence of added myristic acid, lipid **1** essentially failed to transfect COS-1, HepG2, and MCF-7 cells (Figure 2) when used in combination with cholesterol. The electrophoretic gel pattern observed in the gel mobility shift assay revealed strong DNA-binding characteristics of cationic liposomes prepared with lipid **1** and equimolar cholesterol (Figure 6). We reasoned that the compromised transfection properties of lipid **1** used in combination with cholesterol might, in part, originate from such strong lipid **1**:DNA electrostatic interactions (capable of preventing optimal DNA release from the lipoplexes inside the cell cytoplasm). With such a rationale in mind, we decided to reduce the overall positive surface charge of cationic liposomes prepared with lipid **1** and cholesterol by using myristic acid as an additional third liposomal ingredient (hoping that the negatively charged carboxylate headgroup of the added fatty acid might be able to reduce the overall positive surface charge of the liposomes and thereby would be able to weaken the strong electrostatic interaction between acid-lacking liposomes and DNA). The transfection results summarized in Figures 2 and 3, taken together, convincingly demonstrated that 30 mole percent added myristic acid was indeed capable of imparting high gene transfer properties to the poorly transfecting acid-lacking liposomes of lipid **1**. Not only were the in vitro gene transfer efficacies of such myristic acid-loaded lipoplexes of lipid **1** observed to be remarkably enhanced in all four cell lines at optimal lipid:DNA charge ratios, but the enhanced gene transfer properties of the resulting fatty acid-loaded lipoplexes were also found to be serum-compatible in the presence of up to 30% added serum (Figure 4). Keeping in view the commonly used high lipid:DNA charge ratios (6:1 to 12:1) in systemic applications of cationic transfection lipids, the remarkably enhanced transfection efficacies of the fatty acid-loaded liposomes of lipid **1** in MCF-7 and CHO cells at 9:1 lipid:DNA charge ratio in the presence of 30% added serum (Figure 4, parts A and C) justifies future studies aimed at exploring the in vivo potential of the presently described myristic acid-loaded lipoplex of lipid **1**.

In presence of serum, the high transfection profiles of cationic amphiphiles are, in general, found to be severely compromised (*44*−*50*). The usual serum incompatibility of cationic transfection lipids are believed to begin via adsorption of negatively charged serum proteins onto the positively charged cationic liposome surfaces (*48*, *50*−*52*). The serum-compatible transfection properties of the present fatty acid-loaded lipoplexes of lipid **1** may partly

originate from their overall reduced positive surface charge. Clearly, future studies aimed at probing serum protein binding with both fatty acid liposomes as well as with their acid-lacking counterparts will be needed to gather further mechanistic insights into the origin of the serum compatibility of the presently described myristic acid-loaded lipoplexes.

The size data support the notion that the poorly transfecting or essentially transfection-incompetent nature of acid-lacking lipoplexes at 3:1 and 9:1 lipid:DNA charge ratios (Figure 2) as well as the transfection incompetent nature of the fatty acid-loaded lipoplexes with 9:1 lipid:DNA charge ratios in absence of serum in all four cell lines (Figure 2) might be related to their big sizes (difficult for the cells to endocytose). Except for lipoplexes with 1:1 lipid:DNA charge ratio, the global surface charges of the fatty acid-loaded lipoplexes were found to be significantly lower than those of the acid-lacking lipoplexes (Table 1). Such lower surface potentials of the fatty acid-loaded lipoplexes up to 3:1 lipid:DNA charge ratios (compared to their acid lacking counterparts) strongly support our above-mentioned rationale of using fatty acid as an additional liposomal ingredient toward imparting enhanced transfection efficacies of lipid **1** lipoplexes.

A possible origin of the extensive network structure of fatty acid-loaded lipoplexes as revealed in its transmission electron micrograph (Figure 5, part C) could be that the fatty acid's negatively charged carboxylate headgroup functionality, in addition to neutralizing the positive charge of cationic amphiphiles, may get involved in the formation of an extensive hydrogen-bonding network with the multiple hydroxyl headgroup functionalities of the neighboring cationic lipids. Such an extensive network of non-bilayer structures might reduce the extent of negatively charged serum proteins adsorption onto the lipoplex surface and thereby imparting serum-compatibility to fatty acid loaded liposomes of lipid **1**. However, details of how such subtle ultrastructural differences between the non-bilayer morphologies of fatty acid-loaded and acid-lacking lipoplexes contribute to their contrasting gene transfer profiles remain unclear at this point of investigation.

The electrophoretic gel pattern observed in the gel mobility shift assay (Figure 6) are consistent with the notion that fatty acid-loaded lipoplexes are more DNA-releasing than their acid-lacking counterparts. This observation is consistent with the superior transfection properties of the fatty acid-loaded lipoplexes partly originating from the enhanced DNA release. In summary, our present findings demonstrate that use of fatty acid-loaded lipoplexes containing low mole percent added fatty acid (with respect to cationic lipid) holds promise toward overcoming the usual serum incompatibity of cationic lipids in nonviral gene therapy.

In conclusion, we have designed a novel nontoxic cationic amphiphile whose in vitro gene transfer efficacies in CHO, COS-1, MCF-7, and HepG2 cells are remarkably enhanced when used in combination with 30 mole percent added myristic acid. In addition, such myristic acid-loaded lipoplexes of lipid **1** were also found to be serum-compatible up to 30% added serum. Taken together, our present findings demonstrate that the transfection efficacies of fatty acid-loaded lipoplexes are worth evaluating particularly when traditional cationic liposomes prepared with either cholesterol or DOPE colipids fail to transfect cultured cells.

ACKNOWLEDGMENT

Financial support received from the Department of Biotechnology, Government of India (to A.C.), is gratefully acknowledged. B.K.M. and P.P.K. acknowledge the Senior Research Fellowships received from the Council of Scientific and Industrial Research and University Grant Commission, Government of India, respectively.

Supporting Information Available: ^{1}H NMR (300 MHz) and FAB mass spectra of lipid **1**, ^{1}H NMR (300 MHz) of the precursor **I**, reverse phase HPLC chromatograms of lipid **1**, and HPLC conditions. This material is available free of charge via the Internet at http://pubs.acs.org.

LITERATURE CITED

(1) Verma, I. M., and Somina, M. (1997) Gene Therapy-Promises, Problems and Prospects. *Nature 389*, 239−242.
(2) Anderson, W. F. (1998) Human Gene Therapy. *Nature 392*, 25−30.
(3) Yla-Herttuala, S., and Martin, J. F. (2000) Cardiovascular Gene Therapy. *Lancet 355*, 213−222.
(4) Yang, Y., Nunes, F. A., Berencsi, K., Furth, E. E., Gonczol, E., and Wilson, J. M. (1994) Cellular Immunity to Viral Antigens Limits E1-Deleted Adenoviruses for Gene Therapy. *Proc. Natl. Acad. Sci. 91*, 4407−4411.
(5) Knowles, M. R., Hohneker, K. W., Zhou, Z.; Olsen, J. C., Noah, T. L., Hu, P. C., Leigh, M. W., Engelhardt, J. F., Edwards, L. J., Jones, K. R., and Boucher, R. A. (1995) Controlled Study of Adenoviral-Vector mediated Gene Transfer in the Nasal Epithelium of Patients with Cystic Fibrosis. *New Engl. J. Med. 333*, 823−831.
(6) Crystal, R. G., McElvaney, N. G., Rosenfeld, M, A., Chu, C. S., Mastrangeli, A., Hay, J. G., Brody, S. L., Jaffe, H. A., Eissa, N. T., and Danel, C. (1994) Administration of an Adenovirus containing the Human CFTR cDNA to the Respiratory Tract of Individuals with Cystic Fibrosis. *Nat. Genet. 8*, 42−51.
(7) Yang, Y., Nunes, F. A., Berencsi, K., Gonczol, E., Engelhardt, J. F., and Wilson, J. (1994) Inactivation of E2a in Recombinant Adenoviruses Improves the Prospect for Gene Therapy in Cystic Fibrosis. *Nat. Genet. 7*, 362−369.
(8) Lehrman, S. (1999) Virus Treatment Questioned after Gene Therapy Death. *Nature 401*, 517−518.
(9) Ilies, M. A., Seitz, W. A., Ghiviriga, I., Johnson, B. H., Miller, A., Thompson, E. B., and Balaban, A. T. (2004) Pyridinium Cationic Lipids in Gene Delivery: A Structure−Activity Correlation Study. *J. Med. Chem. 15*, 3744−3754.
(10) Lee, Y., Koo, H., Lim, Y. B., Lee, Y., Mo, H., and Park, J. S. (2004) New Cationic Lipids for Gene Transfer with High Efficiency and Low Toxicity: T-shape Cholesterol Ester Derivatives. *Bioorg. Med. Chem. Lett. 14*, 2637−2641.
(11) Bell, P. C., Bergsma, I. P., Bras, W., Stuart, M. C. A., Rowan, M. C., Feiters, M. C., and Engberts, J. B. F. N. (2003) Transfection mediated by Gemini Surfactants: Engineered Escape from Endosomal Compartment. *J. Am. Chem. Soc. 125*, 1551−1558.
(12) Kirby, A. J., Carmilleri, P., Engberts, J. B. F. N., Feiters, M. C., Nolte, R. J. M., Soderman, O., Bergsma, M., Bell, P. C., Fielden, M. L., Garcia Rodriguez. C. L., Guedat, P., Kremer, A., McGregor, C., Perrin, C., Ronsin, G., and Van Eijik, M. C. P. (2003) Gemini Surfactants: New Synthetic Vectors for Gene Transfection. *Angew. Chem., Int. Ed.. 42*, 1448−1457.
(13) Leclercq, F., Cohen-Ohana, M., Mignet, N., Sbarbati, A., Herscovici, J., Scherman, D., and Byk, G. (2003) Design, Synthesis and Evaluation of Gadolinium Cationic Lipids as Tools for Biodistribution Studies of Gene Delivery Complexes. *Bioconjugate Chem. 14*, 112−119.
(14) Fabio, K., Gaucheron, J., Giorgio, C. D., and Vierling, P. (2003) Novel Galactosylated Polyamine Bolaamphiphiles for Gene Delivery. *Bioconjugate Chem. 14*, 358−367.
(15) Heyes, J. A., Duvaz, D. N., Cooper, R. G., and Springer, C. J. (2002) Synthesis of Novel Cationic Lipids: Effect of

Structural Modification on the Efficiency of Gene Transfer. *J. Med. Chem. 45*, 99−114.
(16) Ewert, K., Ahmed, A., Evans, H. M., Schmidt, H. W., and Safinya, C. R. (2002) Efficient Synthesis and Cell-transfection Properties of a New Multivalent Cationic Lipid for Non-Viral Gene Delivery. *J. Med. Chem. 45*, 5023−5029.
(17) McGregor, C., Perrin, C., Monck, M., Camilleri, P., Anthony., and Kirby, J. (2001) Rational Approaches to the Design of Cationic Gemini Surfactants for Gene Delivery. *J. Am. Chem. Soc. 123*, 6215−6220.
(18) Guenin, E., Herve, A. C., Floch, V., Loisel, S., Yaounac, J. J., Clement, J. C., Ferec, C., and des Abbayas, H. (2000) Cationic Phosphonolipids containing Quaternary Phosphonium and Arsonium Groups for DNA Transfection with Good Efficiency and Low Cellular Toxicity. *Angew. Chem., Int. Ed. 39*, 629−631.
(19) Floch, V., Loisel, S., Guenin, E., Herve, A. C., Clement, J. C., Yaouanc, J. J., des Abbayes, H., and Ferec, C. (2000) Cation Substitution in Cationic Phosphono lipids: A New Concept To Improve Transfection Activity and Decrease Cellular Toxicity. *J. Med. Chem. 43*, 4617−4628.
(20) Fichert, T., Regelin, A., and Massing, U. (2000) Synthesis and Transfection Properties of Novel Nontoxic Monocationic Lipids: Variations of Lipid Anchor, Spacer and Headgroup Structure. *Bioorg. Med. Chem. Lett. 10*, 787−791.
(21) Choi, J. S., Lee, E. J., Jang, H. S., and Sang, J. P. (2001) New. Cationic Liposomes for Gene Transfer into Mammalian Cells with High Efficiency and Low Toxicity. *Bioconjugate Chem. 12*, 108−113.
(22) Byk, G., Wetzer, B., Frederic, M., Dubertret, C., Pitard, B., Jaslin, G., and Scherman, D. (2000) Reduction-Sensitive Lipopolyamines as a Novel Nonviral Gene Delivery System For Modulated Release of DNA with Improved Transgene Expression. *J. Med. Chem. 43*, 4377−4387.
(23) Byk, G., Dubertret, C., Escriou, V., Frederic, M., Jaslin, G., Rangara, R., Pitard, B., Crouzet, J., Wils, P., Schwartz, B., and Scherman, D. (1998) Synthesis, Activity, and Structure−Activity Relationship Studies of Novel Cationic Lipids for DNA Transfer *J. Med. Chem. 41*, 224−235.
(24) Wang, J., Guo, X.; Xu, Y., Barron, L., and Szoka, F. C., Jr. (1998) Synthesis and Characterization of Long Chain Alkyl Acyl Carnitine Esters. Potentially Biodegradable Cationic Lipids for Use in Gene Delivery. *J. Med.Chem. 41*, 2207−2215.
(25) Miller, A. D. (1998) Cationic Liposomes in Gene Therapy. *Angew. Chem., Int. Ed. 37*, 1768−1785 and references therein.
(26) Floch V., Bolc'h G. L., Gable-Guillaume, C., Bris, N. L., Yaouanc, J−J., Abbayes, H., Ferec, C., and Clement, J−C. (1998) Phosphonolipids as Non-Viral Vectors for Gene Therapy. *Eur. J. Med. Chem. 33*, 923−934.
(27) Byk, G., Dubertret, C., Escriou, V., Frederic, M., Jaslin, G., Rangara., Pitard B., Crouzet, J., Wils, P., Schwartz, B., and Scherman, D. (1998) Synthesis, Activity and Structure−Activity Relationship Studies of Novel Cationic Lipids for DNA Transfer. *J. Med. Chem. 41*, 224−235.
(28) Ghosh, Y. K., Visweswariah, S. S., and Bhattacharya, S. (2002) Advantage of the Ether Linkage between the Positive Charge and the Cholesteryl Skeleton in Cholesterol-Based Amphiphilkes as Vectors for Gene Delivery. *Bioconjugate Chemistry*, *13*, 378−384.
(29) Gaucheron J., Wong T., Wong K. F., Maurer N., and Cullis P. R. (2002) Synthesis and Properties of Novel Tetraalkyl Cationic Lipids. *Bioconjugate Chemistry*, *13*, 671−675.
(30) Kim, H. S., Moon, J., Kim, K. S., Choi, M. M., Lee, J. E., Heo, Y., Cho, D. H., Jang, D. O., and Park, Y. S. (2004) Gene-transferring efficiencies of novel diamino cationic lipids with varied hydrocarbon chains. *Bioconjugate Chem. 15*, 1095−1101.
(31) Karmali, P. P., Kumar, V. V., and Chaudhuri, A. (2004) Design, Syntheses and In Vitro Gene Delivery efficacies of Novel Mono-, Di-, and Tri-lysinated Cationic Lipids: A Structure Activity Investigation. *J. Med. Chem. 47*, 2123−2132.
(32) Mahidhar, Y. V., Rajesh, M., and Chaudhuri, A. (2004) Strikingly Spacer-Arm Modulated Gene Delivery Efficacies of Novel Cationic Glycolipids: Design, Synthesis and In Vitro Transfection Biology. *J. Med. Chem. 47*, 3938−3948.
(33) Majeti, B. K., Singh, R. S., Yadav, S. K., Reddy, S. B., Ramkrishna, S., Diwan, P. V., Madhavendra, S. S., and Chaudhuri, A. (2004). Enhanced Intravenous Transgene Expression in Mouse Lung using Cyclic-head Cationic Lipids. *Chem. Biol. 11*, 427−437.
(34) Singh, R. S., and Chaudhuri, A. (2004) Single Additional Methylene Group in the Headgroup region Imparts High Gene Transfer Efficacy to a Transfection-Incompetent Cationic Lipid. *FEBS Lett. 556*, 86−90.
(35) Kumar, V. V., Pichon, C., Refregiers, M., Guerin, B., Midoux, P., and Chaudhuri, A. (2003) Single Histidine Residue in Headgroup Region is Sufficient to Impart Remarkable Gene Transfection Properties to Cationic Lipids: Evidence for Histidine-mediated Membrane Fusion at Acidic pH. *Gene. Ther. 10*, 1206−1215.
(36) Singh, R. S., Mukherjee, K., Banerjee, R., Chaudhuri, A., Hait, S. K., Moulik, S., Ramadas, Y., Vijayalakshmi, A., and Rao, N. M. (2002) Anchor-dependency for Non- glycerol based Cationic Lipofectins: Mixed Bag of Regular and Anomalous Transfection Profiles. *Chem. Eur. J. 8*, 900−909.
(37) Srilakshmi, G. V., Sen, J., Chaudhuri, A., Ramdas, Y., and Rao, N. M. (2002) Anchor-dependent Lipofection with Non-glycerol based Cytofectins containing Single 2-Hydroxyethyl Headgroups. *Biochim. Biophys. Acta 1559*, 87−95.
(38) Banerjee, R., Mahidhar, Y. V., Chaudhuri, A., Gopal, V., and Rao, N. M. (2001) Design, Synthesis and Transfection Biology of Novel Cationic Glycolipids for Use in Liposomal Gene Delivery. *J. Med. Chem. 44*, 4176−4185.
(39) Banerjee, R., Das, P. K., Srilakshmi, G. V., Chaudhuri, A., and Rao, N. M. (1999) A Novel Series of Nonglycerol based Cationic Transfection Lipids for Use in Liposomal Gene Delivery. *J. Med. Chem. 42*, 4292−4299.
(40) Felgner, J. H., Kumar, R., Sridhar, C. N., Wheeler, C. J., Tsai, Y.-J., Border, R., Ramsey, P., Martin, M., and Felgner, P. L. (1994) Enhanced gene delivery and mechanism studies with a novel series of cationic lipid formulations. *J. Biol. Chem. 269*, 2550−2561.
(41) Sambrook, J., Fritsch, E. F., and Maniatis, T. (2001) *Molecular Cloning: A Laboratory Manual*, 3rd Ed. Vol. 1. Cold Spring Harbor Laboratory Press: New York).
(42) Hansen, M.-B., Neilson, S. E., and Berg, K. (1989) Reexamination and further development of a precise and rapid dye method for measuring cell growth/cell kill. *J. Immunol.. Methods 119*, 203−210.
(43) Smisterova, J., et al. Smisterova, J., Wagenaar, A., Stuart, M. C. A., Polushkin, E., Brinke, G. T., Hulst, R., Engberts, J. B. F. N., and Hoekstra, D. (2001) Molecular shape of the cationic lipid controls the structure of cationic lipid/dioleylphosphatidylethanolamine-DNA complexes and the efficiency of gene delivery. *J. Biol. Chem. 276*, 47615−47622.
(44) Thierry, A. R., Rabinovich, P., Peng, B., Mahan, L. C., Bryant, J. L., and Gallo, R. C. (1997) Characterization of liposome-mediated gene delivery: expression, stability and pharmacokinetics of plasmid DNA. *Gene Ther. 4*, 226−237.
(45) Trivedi, R. A., and Dickson, G. (1995) Liposome-mediated gene transfer into normal and dystrophin-deficient mouse myoblasts. *J. Neurochem. 64*, 2230−2238.
(46) Zelphati, O., Uyechi, L. S., Barron, L. G., and Szoka, F. C., Jr. (1998) Effect of serum components on the physicochemical properties of cationic lipid/oligonucleotide complexes and on their interactions with cells. *Biochim. Biophys. Acta 1390*, 119−133.
(47) Farhood, H., Bottega, R., Epand, R. M., and Huang, L. (1992) Effect of cationic cholesterol derivatives on gene transfer and protein kinase C activity. *Biochim. Biophys. Acta 1111*, 239−246.
(48) Yang, J. P., and Huang, L. (1998) Time-dependent maturation of cationic liposome-DNA complex for serum resistance. *Gene Ther. 5*, 380−387.
(49) Yang, J. P., and Huang, L. (1997) Overcoming the inhibitory effect of serum on lipofection by increasing the charge ratio of cationic liposome to DNA. *Gene Ther. 4*, 950−960.
(50) Li, S., Tseng, W. C., Stolz, D. B., Wu, S. P., Watkins, S. C., and Huang, L. (1999) Dynamic changes in the characteristics

of cationic lipidic vectors after exposure to mouse serum: implications for intravenous lipofection. *Gene Ther. 6*, 585−594.

(51) Li, S., Rizzo, M. A., Bhattacharya, S., and Huang, L. (1998) Characterization of cationic lipid-protamine-DNA (LPD) complexes for intravenous gene delivery. *Gene Ther. 5*, 930−937.

(52) Crook, K., Stevenson, B. J., Dubouchet, M., and Porteous, D. J. (1998) Inclusion of cholesterol in DOTAP transfection complexes increases the delivery of DNA to cells in vitro in the presence of serum. *Gene Ther. 5*, 137−143.

BC049687T

Sulfhydryl-Reactive, Cleavable, and Radioiodinatable Benzophenone Photoprobes for Study of Protein−Protein Interaction

Lian-Wang Guo,*[,†,§] Abdol R. Hajipour,[†,∥,§] Monica L. Gavala,[†] Marty Arbabian,[†] Kirill A. Martemyanov,[‡] Vadim Y. Arshavsky,[‡] and Arnold E. Ruoho[†]

Department of Pharmacology, University of Wisconsin Medical School, Madison, Wisconsin 53706, Pharmaceutical Laboratory, College of Chemistry, Isfahan University of Technology, Isfahan, 84156, I.R., Iran, and Department of Ophthalmology, Harvard Medical School and the Massachusetts Eye and Ear Infirmary, Boston, Massachusetts 02114. Received January 24, 2005; Revised Manuscript Received March 17, 2005

The major task in proteomics is to understand how proteins interact with their partners. The photo-cross-linking technique enables direct probing of protein−protein interaction. Here we report the development of three novel sulfhydryl-reactive benzophenone photoprobes of short "arm" length, each with a substitution of either amino, iodo, or nitro at the para-position, rendering the benzophenone moiety directly radioiodinatable. Their potential for study of protein−protein interaction was assessed using the inhibitory subunit of rod cGMP phosphodiesterase (PDEγ) and the activated transducin α subunit (Gαt-GTPγS) as a model system. These photoprobes proved to be stable at neutral pH and dithiothreitol-cleavable in addition. The PDEγ constructs derivatized at the C-terminal positions with these probes could be readily purified, had unaltered PDEγ functional activity, and were shown to photo-cross-link to Gαt-GTPγS with an efficiency as high as 40%. Additionally, the amino benzophenone probe was radioiodinated, facilitating sensitive detection of label transfer. The uniquely combined features of these benzophenone photoprobes promise robust and flexible methods for characterization of protein−protein interaction, either by mass spectrometry when a nonradioactive label is available or by autoradiography when using radioiodinated derivatives.

INTRODUCTION

The signaling pathway for visual excitation in rod photoreceptors represents a prototypical G-protein cascade comprising the seven-transmembrane receptor (rhodopsin), the heterotrimeric G-protein (transducin), and the effector (phosphodiesterase, PDE6[1]). The interaction between the trandsducin α subunit (Gαt) and the inhibitory γ subunit of PDE6 (PDEγ or Pγ) is a key step. Upon activation by photoexcited rhodopsin, GTP-loaded Gαt activates PDE6 by binding to PDEγ. This signaling event eventually leads to the generation of the electrical response of the photoreceptor cell (*1*). On the other hand, the Gαt/PDEγ interaction is also required for rapid termination of the rod photoresponse (*2*). The conversion of the activated transducin to its inactive state is greatly accelerated by the ninth member of the regulators of G-protein signaling family (RGS9), whose action requires the association of transducin with PDEγ (*2*, *3*). Therefore, information concerning the Gαt/PDEγ interaction is critical for understanding the molecular mechanisms of visual transduction, and, most likely, other G-protein pathways.

Much has been learned about regulation of visual transduction. The atomic structures of activated Gαt alone (*4*, *5*) and complexed with the PDEγ C-terminal half and the catalytic domain of RGS9 (*6*) have greatly enriched our knowledge about interactions of these two signaling proteins. However, due to a lack of atomic structure of the complex of Gαt and full-length PDEγ, it remains a challenging task to uncover important details of a "real" signaling state of the Gαt/PDEγ interaction. While X-ray crystallography and nuclear magnetic resonance (NMR) can offer detailed information about protein−protein interactions, the stability issue and large size of a protein complex add extra difficulty for solving its atomic structure. Some alternative approaches such as photo-cross-linking, however, offer a powerful approach for discovering the missing pieces of the puzzle.

A radiolabeled cleavable photoprobe, [^{125}I]-ACTP ([^{125}I]-*N*-[(3-iodo-4-azidophenyl propionamido-*S*-(2-thiopyridyl)]-cysteine), which contains an azide photophore, has been applied for the structural study of Gαt (*7*), Gαt/PDEγ interaction (*8*), and PDE6 $\alpha\beta$ subunits/PDEγ interaction (*9*). Azides have been conventionally taken as the primary choice of photoreactive group by many researchers since it can be prepared very easily. However, shorter UV wavelengths required for activation of azide photoprobes sometimes cause significant damage to proteins, and azide photoprobes are not efficient since the singlet phenylnitrenes are short-lived (*10*). A photoprobe with an aryldiazonium moiety is more efficient than its azide

* To whom correspondence should be addressed. Tel: 608 263 3980. Fax: 608 262 1257. E-mail: Lianwangguo@wisc.edu.
† University of Wisconsin.
§ Both authors have equally contributed to this work.
∥ Isfahan University of Technology.
‡ Harvard Medical School.

[1] Abbreviations: PDE6, rod phosphodiesterase; PDEγ, PDE6 inhibitory subunit; Gαt, transducin α subunit; MTS, methanethiosulfonate; MS, mass spectrometry; NMR, nuclear magnetic resonance; ABM, 4-methanethiosulfinate methyl-4′-aminobenzophenone; IBM, 4-methanethiosulfinate methyl-4′-iodobenzophenone; NBM, 4-methanethiosulfinate methyl-4′-nitrobenzophenone; DTT, dithiothreitol; PAGE, polyacrylamide gel electrophoresis; HPLC, high-performance liquid chromatography.

10.1021/bc050016k CCC: $30.25 © 2005 American Chemical Society
Published on Web 04/29/2005

derivative but less stable (*11*). In contrast, the benzophenone photophore has distinct advantages. It can be activated in a reversible manner via excitation−relaxation cycles at 350−360 nm, avoiding UV damage, and only C−H bonds within 3.1 Å of the carbonyl oxygen are modified. Moreover, the benzophenone group is stable to common protic solvents, reacts only with target proteins, and generally leads to highly efficient single-site photocovalent modification (*12*). Noncleavable benzophenone photoprobes have been used for defining protein−protein interactions of Gαt/PDEγ (*13*, *14*) and other proteins (*15*−*18*) by photo-cross-linking and mass spectrometry (MS). The proteins cross-linked with the noncleavable photoprobes cannot be separated, resulting in complexity in identification of photoinsertion sites. Cleavable benzophenone photoprobes suited for photo-cross-linking/label transfer experiments are therefore highly desirable.

Here we report the development of three cleavable benzophenone photoprobes each with a methanethiosulfonate (MTS) group, which is highly sulfhydryl-reactive (Figure 1). To illustrate the use of these probes, they were employed to derivatize the single-cysteine PDEγ constructs for cross-linking with Gαt-GTPγS. Their potential for study of protein−protein interactions was assessed using PDEγ/Gαt-GTPγS as a model system. As an additional feature, the amino-benzophenone probe was shown to be radioiodinatable. A noniodinatable benzophenone derivative has been reported for immobilization of ion channels (*19*, *20*), but it is not suitable for radiolabel transfer. To our knowledge, the photoprobes developed in this study are the only reported sulfhydryl-reactive, cleavable, and radioiodinatable benzophenone photoprobes that are optimized for protein−protein interaction studies through a photo-cross-linking/label transfer methodology.

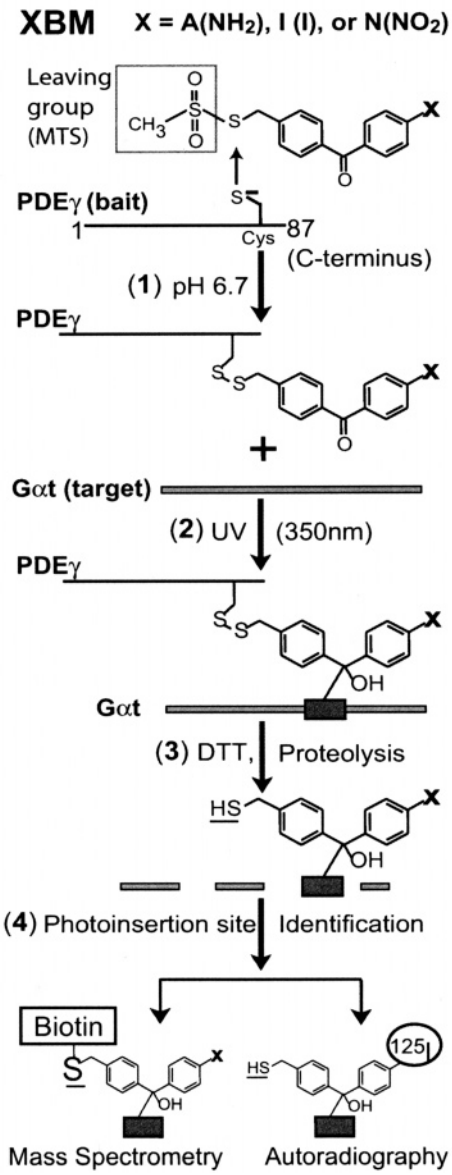

Figure 1. Schematic strategy of protein−protein interaction analysis by photo-cross-linking/label transfer using cleavable benzophenone photoprobes. PDEγ/Gαt interaction is presented as a model system. Solid line, PDEγ. Bar, Gαt. Box, photoinsertion-containing proteolytic fragment of a target protein. DTT-reversed sulfhydryl (underlined) can be made available for addition of a biotin or fluorescent tag.

EXPERIMENTAL PROCEDURES

General. All yields refer to isolated products after purification. Products were characterized by spectroscopy data (IR, ^{1}H NMR spectrum, CHN analyses, melting and boiling point). ^{1}H NMR spectra were recorded at 300 MHz. The spectra were measured in $CDCl_4$ unless otherwise stated, relative to TMS (0.00 ppm). BPMTS (benzophenone-4-carboxamidocysteine methanethiosulfonate) was purchased from Toronto Research Chemicals. Na^{125}I was from Perkin-Elmer as carrier-free radioiodide (2200 Ci/mmol, 5 mCi/20 μL in 0.1 N NaOH). All other chemicals and reagents were from Sigma-Aldrich unless stated elsewhere.

Synthesis of 4-Methyl-4′-nitrobenzophenone (1). In a 500 mL round-bottomed flask to a stirred solution of toluene (300 mL) and 4-nitrobenzoyl chloride (20 g, 108 mmol) was added aluminum chloride (18.7 g, 140 mmol). The resulting red solution was stirred at room temperature for 90 min, and then 5 mL of water was added dropwise and the mixture was stirred for 20 min. The reaction mixture was washed with water (2 × 100 mL) and 10% $NaHCO_3$ (2 × 100 mL) and dried ($Mg SO_4$). The solvent was evaporated under reduced pressure with a rotary evaporator to a pale yellow solid (22.3 g). The resulting residue was recrystallized from methylenechloride/hexane to produce 19.8 g of compound **1** (80%) as light yellow needles. Mp: 119−120 °C. ^{1}H NMR: δ 8.36 (d, J = 8.8 Hz, 2 H), 7.9 (d, J = 8.1 Hz, 2 H), 7.70 (d, J = 8.0 Hz, 2 H), 7.31 (d, J = 8.0 Hz, 2 H), 2.50 (s, 3 H). Anal. Calcd for $C_{14}H_{11}NO_3$: C, 69.70; H, 4.60; N, 5.81. Found: C, 69.80; H, 4.70; N, 5.80.

Synthesis of 4-Bromomethyl-4′-nitrobenzophenone (2). In a 250 mL round-bottomed flask to a stirred solution of CCl_4 (100 mL) and compound **1** (2.4 g, 10 mmol) were added *N*-bromo succinimide (NBS) (2.0 g, 11 mmol) and 2,2′-azobisisobutyronitrile (AIBN) (10 mg). The resulting mixture was refluxed for 38 h. After cooling, the white precipitate of succinimide was filtered and the solvent was evaporated to a brown solid. The resulting residue was purified by column chromatography on silica gel (CH_2Cl_2/hexane, 1:1 v/v) to produce 2.1 g of compound **2** (66%). Mp: 124−125 °C. ^{1}H NMR: δ 8.40 (d, J = 8.8 Hz, 2 H), 7.9 (d, J = 7.9 Hz, 2 H), 7.70 (d, J = 8.1 Hz, 2 H), 7.55 (d, J = 8.1 Hz, 2 H), 4.54 (s, 2 H). Anal. Calcd for $C_{14}H_{10}BrNO_3$: C, 52.52; H, 3.15; N, 4.38. Found: C, 52.60; H, 3.20; N, 4.30.

Synthesis of Sodium Methanethiosulfonate ($MeSO_2SNa$). A mixture of sodium methanesulfonate ($MeSO_2Na$) (5 g, 42.0 mmol) and sulfur (1.56 g, 48.8 mmol) in methanol (300 mL) was treated under reflux conditions for 30 min, at which time all of the sulfur had

dissolved. Removal of the solvent gave sodium methanethiosulfonate as a white powder. IR (KBr): 1320, 1220, and 1100. ^{1}H NMR (D_2O): δ 3.30 (s, 3 H).

Synthesis of 4-Methanethiosulfinate Methyl-4′-nitrobenzophenone (NBM) (3). In a 100 mL round-bottomed flask to a stirred solution of methanol (30 mL) and compound **2** (0.44 g, 1.46 mmol) was added sodium methanethiosulfonate (0.2 g, 1.7 mmol). The resulting mixture was refluxed for 3 h until compound **2** disappeared on TLC (toluene/diethylamine, 20:1 v/v). After cooling, the precipitate was filtered and the solvent was evaporated under reduced pressure. The resulting residue was purified by column chromatography on silica gel (toluene/diethylamine, 20:1) to produce 0.39 g of compound **3** (80%). Mp: 156−158 °C. ^{1}H NMR: δ 8.40 (d, J = 8.8 Hz, 2 H), 7.9 (d, J = 7.9 Hz, 2 H), 7.70 (d, J = 8.1 Hz, 2 H), 7.55 (d, J = 8.1 Hz, 2 H), 4.42 (s, 2 H). Anal. Calcd for $C_{15}H_{13}NO_5S_2$: C, 51.28; H, 3.70; N, 3.99; S, 18.23. Found: C, 51.20; H, 3.80; N, 4.10; S, 18.30.

Synthesis of 4-Methanethiosulfinate Methyl-4′-aminobenzophenone (ABM) (4). In a 100 mL round-bottomed flask a stirred solution of methanol (30 mL) and compound **3** (0.35 g, 1.0 mmol) and 10% Pd−C (80 mg) was reduced with hydrogen gas at room temperature for 10 h until compound **3** disappeared on TLC (toluene/diethylamine, 4:1). After cooling, the precipitate was filtered and the solvent was evaporated under reduced pressure. The resulting residue was purified by column chromatography on silica gel (toluene/diethylamine, 4:1) to produce 0.31 g of compound **4** (98%). Mp: 178−180 °C. ^{1}H NMR: δ 7.9 (d, J = 7.9 Hz, 2 H), 7.55 (d, J = 8.1 Hz, 2 H), 7.30 (d, J = 8.1 Hz, 2 H), 6.90 (d, J = 8.8 Hz, 2 H), 4.42 (s, 2 H), 3.52 (s, 2 H, NH_2). Anal. Calcd for $C_{15}H_{15}NO_3S_2$: C, 56.07; H, 4.67; N, 4.36; S, 19.94. Found: C, C, 56.20; H, 4.60; N, 4.50; S, 20.10.

Synthesis of 4-Methanethiosulfinate Methyl-4′-iodobenzophenone (IBM) (5). In a 50 mL round-bottomed flask a cooled stirred solution of water (30 mL) and compound **4** (0.16 g, 0.5 mmol) was treated with $NaNO_2$ (52 mg, 0.75 mmol) and 1 mL of concentrated HCl. The resulting mixture was stirred at 0 °C for 30 min and then with NaI (113 mg, 0.75 mmol). After 30 min the product was extracted with ethyl acetate (3 × 10 mL). The extracts were pooled and dried with $MgSO_4$, and the solvent was evaporated into an orange oil with a rotary evaporator. The resulting residue was purified by column chromatography on silica gel (toluene/diethylamine, 4:1) to produce 140 mg of compound **5** (65%), as an oil. ^{1}H NMR: δ 7.9 (d, J = 7.9 Hz, 2 H), 7.55 (d, J = 8.1 Hz, 2 H), 7.30 (d, J = 8.1 Hz, 2 H), 7.25 (d, J = 8.8 Hz, 2 H), 4.42 (s, 2 H). Anal. Calcd for $C_{15}H_{13}IO_3S_2$. C, 41.67; H, 3.01; S, 14.81. Found: C, 41.80; H, 3.20; S, 14.70.

Preparation of the Benzophenone−PDEγ Photoprobes. The constructs for expressing the full-length wild type (wt) PDEγ (single cysteine at position 68) (*14*) and the single-cysteine mutants were generated as described previously (*9*). The plasmids were transformed into *E.coli* strain BL21 DE3 cells (Novagen) for overexpression. Induction by 1 mM IPTG was initiated at an optical cell density of ∼1.5 (OD_{600}) and continued for an additional 4−6 h at 30 °C. Expressed PDEγ constructs were first purified through a column of chitin beads (New England Biolabs), and then further purification was achieved (>95%) by reversed-phase HPLC (Waters) using a self-packed column of POROS 20 R2 resin (PerSeptive Biosystems).

The lyophilized pure PDEγ after POROS column purification was used for derivatization. Benzophenone photoprobes were dissolved in acetonitrile to prepare stock solutions immediately before the derivatization reactions. A typical reaction includes 150 μM PDEγ, 50 mM NaH_2PO_4, pH 6.7, 60% acetonitrile, and 3 mM benzophenone compound. The reaction was incubated at room temperature under argon for 1 h and quenched with 0.1% TFA, then loaded to a Vydac C4 column for reversed-phase HPLC. A gradient of 1% acetonitrile per 8 min with 0.1% TFA was used to separate the derivatized PDEγ from the underivatized population at a flow rate of 1 mL/min. All the steps were carried out in dim room light. The benzophenone−PDEγ product eluted at ∼47% acetonitrile was lyophilized and stored at −80 °C.

Functional Assay of the Benzophenone−PDEγ Photoprobes. Transducin GTPase activity was determined by using a single-turnover technique as described previously (*21*). The assays were conducted at room temperature (22−24 °C) in a buffer containing 25 mM Tris-HCl (pH 8.0), 140 mM NaCl, and 8 mM $MgCl_2$. The urea-treated ROS membranes, lacking endogenous activity of RGS9, were used as a source for the photoexcited rhodopsin required for transducin activation. The reactions were initiated by the addition of 10 μL of 0.6 μM [^{32}P] GTP (∼10^5 dpm/sample) to 20 μL of urea-treated ROS membranes (20 μM final rhodopsin concentration) reconstituted with transducin heterotrimer (1 μM) and recombinant RGS9-Gβ5 complex (0.5 μM). The reactions were performed in either the absence or presence of PDEγ derivatives (1 μM). The reaction was stopped by the addition of 100 μL of 6% perchloric acid. The ^{32}Pi formation was measured with activated charcoal. The assays were conducted in the absence of reducing agent because of the disulfide linkage between the benzophenone group and PDEγ.

Photo-Cross-Linking of the Benzophenone−PDEγ Photoprobes with Gαt-GTPγS. Gαt-GTPγS was prepared as previously described (*8*). Briefly, rod outer segment membranes were prepared from frozen dark-adapted bovine retinas (from J. A. & W. L. Lawson Co.), and the Gαt-GTPγS subunit was released using GTPγS and purified on Blue Sepharose CL-6B, as described by Kroll et al. (*22*). Coomassie Blue staining demonstrated that the Gαt subunit was more than 95% pure on SDS-polyacrylamide gel electrophoresis (PAGE).

Photo-cross-linking reactions were carried out in HEPES buffer (10 mM HEPES pH 7.5, 100 mM NaCl, 5 mM $MgCl_2$) containing Gαt-GTPγS (5 μM) and benzophenone−PDEγ derivative at a desired concentration. The reaction mixture contained in a 1.7 mL ultraclear microcentrifuge tube (Axygen) was dark-incubated on ice for 15 min and then illuminated at 350 nm and ∼4 °C in a RPR-100 Rayonet photochemical reactor (Southern New England Ultraviolet) for various times (5 min dark interval after each 10 min UV light). The cross-linked proteins were separated from the un-cross-linked by nonreducing 15% SDS-PAGE.

Preparation of Radioiodinated Benzophenone−PDEγ Photoprobes. [^{125}I] IBM was synthesized based on the Sandmeyer method for preparation of [^{127}I] IBM (compound **5**) as described above. In standard scale reactions, $NaNO_2$ (3 mg, 43 μmol) was dissolved in 20 μL of H_2O, and 6 μL of HCl (1 N) was added. Into this solution was added ABM (0.3 mg, 1.0 μmol) in acetonitrile immediately after HCl addition. The mixture was stirred at room temperature for 10 min, and then a 15 μL NaOH solution (0.1 N) containing Na^{127}I (0.3 mg, 2 μmol) and 0.5 mCi Na^{125}I was added and incubated for 30 min at room temperature with occasional vortexing. The reaction mixture was then extracted three times with 200 μL of

ethyl acetate. The extracts were pooled and purified by TLC (silica gel, toluene/diethylamine, 20:1 v/v). The radioactive band that comigrated with [^{127}I] IBM on the TLC plate was extracted with ethyl acetate, dried under N_2 gas, and redissolved in 50 μL of acetonitrile. A 10 μL portion of this solution was used to derivatize wt-PDEγ (50 μg, 5 nmol) in 50 mM phosphate buffer for 1.5 h at pH 6.7 and room temperature. The [^{125}I] IBM−PDEγ derivative was purified using an AutoSeq G50 spin column (Pharmacia).

An alternative radioiodination that yields ^{125}I-ABM was carried out using chloramine T. For a standard reaction, ABM (1 mg, 3 μmol) in 30 μL of methanol was mixed with 20 μL of sodium acetate (0.5 M, pH 5.6). Into this solution was added 2 μL of Na^{125}I (0.5 mCi) followed by 2 μL of HCl (0.1 N), and then 30 μL of chloramine T (30 μg, 0.13 μmol) was immediately added. The reaction was incubated at room temperature for 10 min and then stopped by adding 100 μL of $Na_2S_2O_5$ (0.5 mg, 2.6 μmol). Product extraction, purification, and PDEγ derivatization were performed as described in the above [^{125}I] IBM−PDEγ preparation. Photolabeling of Gαt-GTPγS by ^{125}I-ABM, as essentially described in "Photo-Cross-Linking of the Benzophenone−PDEγ Photoprobes with Gαt-GTPγS" above, was detected on a reducing SDS-PAGE 15% gel by PhosphorImager (445 SI, Molecular Dynamics).

Other Methods. Electrospray ionization mass spectrometry (ESI MS) of the HPLC-purified PDEγ samples was performed in the Mass Spectrometry Facility of the Chemistry Department at the University of Wisconsin−Madison. The mass spectra were obtained with a Micromass (Beverly, MA) LTC mass spectrometer. This instrument uses a time-of-flight analyzer. Aliquots with added methanol were sprayed with a sample cone set at 20 V. The samples in a piece of glass capillary were inserted directly into the source, and the resulting vapor was bombarded with 70 eV electrons. Perfluorokerosene was used for calibration.

For Western blotting, proteins were separated by nonreducing 15% SDS-PAGE and transferred to a PVDF membrane (Millipore, 0.45 μm) and analyzed using anti-PDEγ (N-terminus) (Affinity BioReagents), horseradish peroxidase (HRP)-conjugated IgG, and enhanced chemiluminescence (ECL) reagents obtained from Pierce. The same blot was stripped and reprobed using anti-Gαt (N-terminus) (Affinity BioReagents).

Gαt concentration was measured by the Bradford method using BSA as a standard. PDEγ concentration was also measured by the Bradford method but corrected based on the 280 nm spectrophotometric measurement and extinction coefficient of 6990. Protein amount on the scanned Coomassie gels was quantified using NIH Image 1.62.

RESULTS AND DISCUSSION

Practical Considerations. Photo-cross-linking is a straightforward technique to investigate protein (or peptide)−protein interaction. In recent years, the interest in this technique has been raised again as a result of the development of more efficient photophores and the emergence of proteomics (*10, 12, 23*−*25*). Combined with other techniques such as modern mass spectrometry, the photo-cross-linking technique is useful not only for identifying protein interaction sites but also for obtaining structural information of proteins (*26*−*29*).

The principle of a photo-cross-linking/label transfer approach for characterization of protein−protein interaction is illustrated in Figure 1, using PDEγ/Gαt as a model system. A benzophenone probe is used to derivatize a single cysteine that is site-specifically engineered on a bait protein, PDEγ (Step 1). The benzophenone-derivatized bait protein is mixed with its interaction target protein, Gαt, to form a complex, and subjected to UV light to cross-link the two proteins (Step 2). The photoinserted target protein is separated from the bait protein by reducing with DTT (dithiothreitol) and then proteolyzed (Step 3). The photoinsertion site on the target protein is identified, either by MS when a nonradioactive label is available or by autoradiography when using a radiolabeled photoprobe (Step 4). In this strategy, label transfer following photo-cross-linking is advantageous because the bait protein that is cross-linked to the target protein can be removed by DTT reversal, and the contamination of the bait protein in the analysis of the photoinsertion site on the target protein can thus be avoided. Furthermore, the free sulfhydryl of the photoprobe released by DTT reversal can be used for adding a tag, such as a biotin group, permitting affinity purification of the photoinserted proteolytic fragments for MS analysis (*30*) (Grant, J. E. and Ruoho, A. E., 2005, unpublished data obtained using IBM-derivatized PDEγ). Since the tag is added to the photoprobe after photolabel transfer, a possible impairment of the tag on the function of bait protein can be avoided.

Therefore, a photoprobe favored for protein−protein interaction studies is expected to be not only stable and efficient but also sulfhydryl-reactive, cleavable, and tagged with a label convenient for purification or detection yet exerting minimum impairment on the function of bait protein. Several comparative studies have shown that reliable and reproducible high-efficiency labeling of target proteins is obtained using tetrafluorophenyl azides, trifluoromethylphenyl diazirines, and benzophenone photoprobes, but the benzophenone photophore performs the best (*12*, *25*, *31*). We thus have chosen benzophenone as the photophore for our photoprobes. Of the sulfhydryl-reactive groups, MTS is the most rapidly reacting. MTS is also distinguished by its high selectivity for cysteinyl sulfhydryls, its ability to effect quantitative and complete conversion to the mixed disulfide, and the general reversibility of the disulfide bond (*32*). For radiolabel transfer experiments, an ^{125}I-labeled benzophenone photoprobe may be prepared since ^{125}I has often been used as a radiolabel due to its high sensitivity and relatively small size. Since the PDEγ C-terminal half has been suggested to be the major domain interacting with activated Gαt (*6*, *8*, *13*, *33*−*35*), we linked the benzophenone probes to single cysteines engineered at the PDEγ C-terminal positions for cross-linking with Gαt-GTPγS.

High-Yield Chemical Synthesis of the Bezophenone Photoprobes. As shown in Scheme 1, 4-methyl-4′-nitrobenzophenone (compound **1**) was prepared by Friedel−Crafts reaction of 4-nitrobenzoyl chloride with toluene in the presence of $AlCl_3$ at room temperature with an 80% yield. Compound **1** was converted to 4-bromomethyl-4′-nitrobenzophenone (compound **2**) by NBS in CCl_4 in the presence of a catalytic amount of AIBN as a free radical initiator. Reaction of compound **2** with sodium methanethiosulfinate in refluxing methanol produced NBM (compound **3**) with an 80% yield. NBM was reduced to the corresponding amine derivative ABM (compound **4**) by Pd−C in methanol at room temperature with a 98% yield and then converted to IBM (compound **5**) with a 65% yield by treating with $NaNO_2$/HCl and then with NaI at room temperature.

Scheme 1. Synthetic Scheme of the Benzophenone−MTS Photoprobes[a]

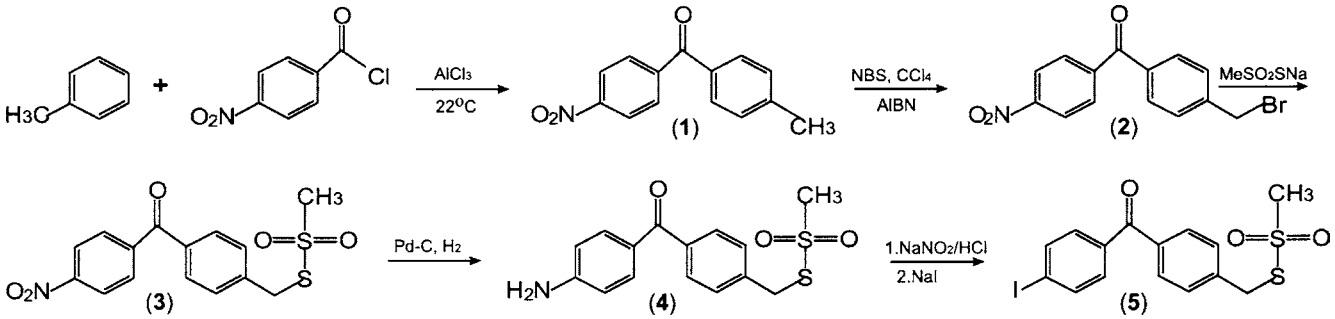

[a] NBS: *N*-bromo succinimide; AIBN: 2,2′-azobisisobutyronitrile.

The Benzophenone−PDEγ Photoprobes Were Readily Prepared, Purified, and Fully Functionally Active. Stability of photoprobes is an important issue for their biochemical applications. Importantly, all three benzophenone−MTS compounds with a para-position substitution of an amino (ABM), iodo (IBM), and nitro (NBM) group, respectively (Figure 1), were found to be stable at pH 6.7; for example, IBM stayed as a single peak on the HPLC chromatogram even after overnight incubation in phosphate buffer at pH 6.7 and room temperature. BPMTS, however, showed a significant breakdown product after 1 h incubation (data not shown). We thus carried out the PDEγ derivatization reactions using the benzophenone compounds at pH 6.7, taking advantage of their superb stability. As indicated by the chromatograms in Figure 2A, B, and C, after a 1 h room-temperature incubation with PDEγ (73C), reactions were ~70% completed with all three compounds, as estimated by the underivatized and derivatized PDEγ peaks. In fact, the derivatization reaction can be 100% completed after 2.5 h at room temperature, as demonstrated by the reaction using wt-PDEγ and IBM (Figure 2E). The benzophenone−PDEγ derivatives were well separated from the underivatized PDEγ population and unreacted free compounds by reversed-phase HPLC with a Vydac C4 column. Derivatization of PDEγ with all three benzophenone compounds shifted the PDEγ peak to ~4 min later than underivatized PDEγ, although these compounds have different hydrophobicity, as evidenced by different HPLC retention times (Figure 2A, B, and C).

An additional beneficial feature of the benzophenone probes is their UV absorption property, which is very different than PDEγ. As is evident in the HPLC chromatograms (Figure 2), the ratio of absorption by the benzophenone group at 215 nm versus 280 nm was approximately 1. In contrast, the 215 nm/280 nm absorption ratio of PDEγ was greater than 20, but the benzophenone adduct to PDEγ molecule changed this ratio to <10. The benzophenone-derivatized PDEγ peak can thus be easily recognized by its 215 nm/280 nm absorption ratio even without additional characterization following DTT reversal or MS determination.

However, since the linkage between the benzophenone moiety and the single cysteine of PDEγ is a mixed disulfide, we have further confirmed the mixed disulfide derivatized PDEγ samples by a DTT reversal reaction. After 1 h incubation of IBM-73C with 50 mM DTT, the PDEγ peak was shifted back to the exact position of underivatized PDEγ, and the 215 nm/280 nm absorption ratio was also converted back to >20 (Figure 2D). Furthermore, when the molecular mass of the derivatized PDEγ products was determined by ESI MS, the major population, as shown in the mass spectrum of either IBM-73C or IBM-87C, was highly consistent with the predicted mass (Figure 3A). A minor population, with the measured mass lower than the major population by 131, is very likely the PDEγ population with the N-terminal methionine excised by the ribosome-associated methionyl-aminopeptidase during the posttranslational processing in *E.coli* (*36*). The N-terminal methionine-removed PDEγ population had unaltered function (data not shown). Taken together, the ESI MS data further verified that

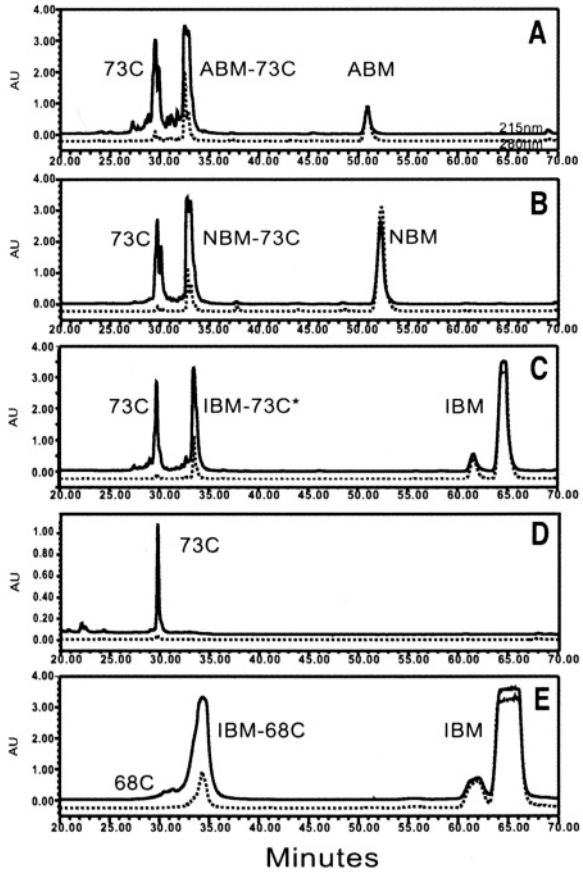

Figure 2. HPLC purification of PDEγ derivatized with the benzophenone photoprobes. The HPLC (Vydac C4 column) chromatograms are shown as absorptions at 215 nm (upper, solid) and 280 nm (lower, dashed). AU, relative absorption unit. A, B, and C: Purification of PDEγ (73C) derivatized with ABM, NBM, and IBM, respectively. The underivatized PDEγ (73C) fractions were eluted at 29.5 min; the derivatized products were at ~33.5 min. D: DTT reversal of IBM-73C, which was taken from a portion of the 33.5 min peak in C (asterisk-marked). IBM-73C was incubated with 50 mM DTT at room temperarure and pH 7.5 for 1 h and then applied to HPLC under the same conditions as in C. E: Purification of the IBM-68C derivative. The derivatization reaction was conducted at room temperature for 2.5 h, with 150 μM PDEγ, 50 mM NaH_2PO_4, pH 6.7, 60% acetonitrile, and 3 mM benzophenone compound.

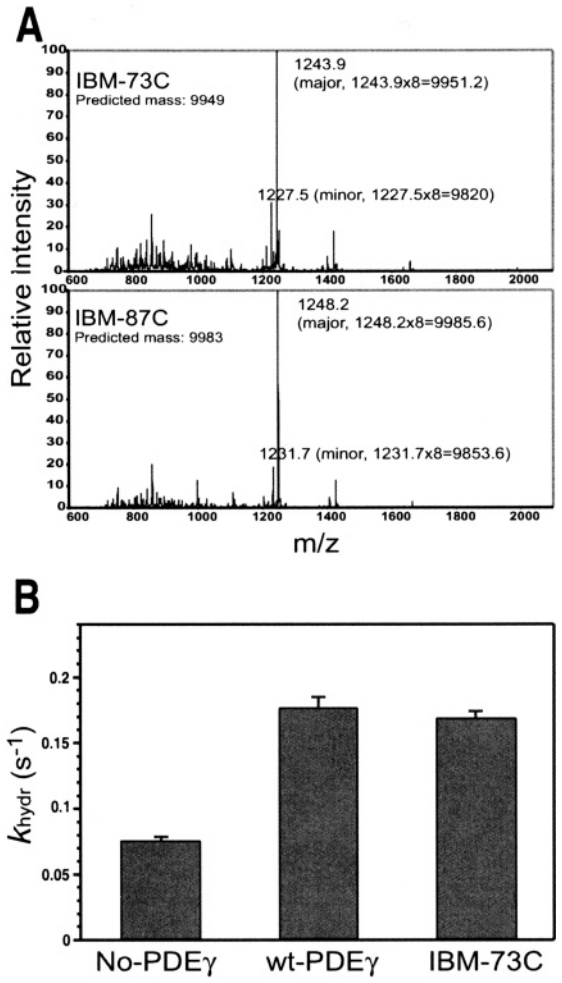

Figure 3. Characterization of the benzophenone−PDEγ photoprobes. A: ESI mass spectra of IBM-73C (upper panel) and IBM-87C (lower panel). The intensity of the major MS peak is taken as 100%. The predicted masses were calculated using PeptideMass of ExPASy (Swiss Institute of Bioinformatics). A measured mass is an *m/z* value multiplied by charge, as indicated in parentheses. B: Functional activity of IBM-73C. The RGS9 stimulated GTPase activity of transducin was measured in single-turnover assays in the absence of PDEγ (No-PDEγ) and in the presence of either wild-type PDEγ (wt-PDEγ) or IBM-derivatized PDEγ (IBM-73C). The rate constants of GTP hydrolysis (k_{hydr}) were determined from the single-exponential fits of the reaction time course and plotted as bars. Error bars represent SE of exponential analysis.

the benzophenone−PDEγ derivatives were highly purified and homogeneous.

One great concern for the application of photoprobes is whether the addition of a photoreactive group to a bait protein affects its function. Since PDEγ is known to be an essential component for accelerating the GTP hydrolysis activity of Gαt (*1*, *37*), the functional integrity of the benzophenone-derivatized PDEγ preparations was assayed by analyzing their abilities to potentiate the activity of RGS9/Gβ5 in stimulating Gαt-GTPase. Our data indicate that the derivatization of PDEγ at position 73 with IBM did not affect the function of PDEγ (Figure 3B). This was most likely due to the short length of the benzophenone photoprobe and the structural similarity of the benzophenone moiety to the phenylalanine residue at position 73 on wt-PDEγ.

The Benzophenone−PDEγ Photoprobes Specifically Cross-Linked to Gαt-GTPγS with High Efficiency. The photo-cross-linking reactions using benzophenone−PDEγ photoprobes and Gαt-GTPγS were

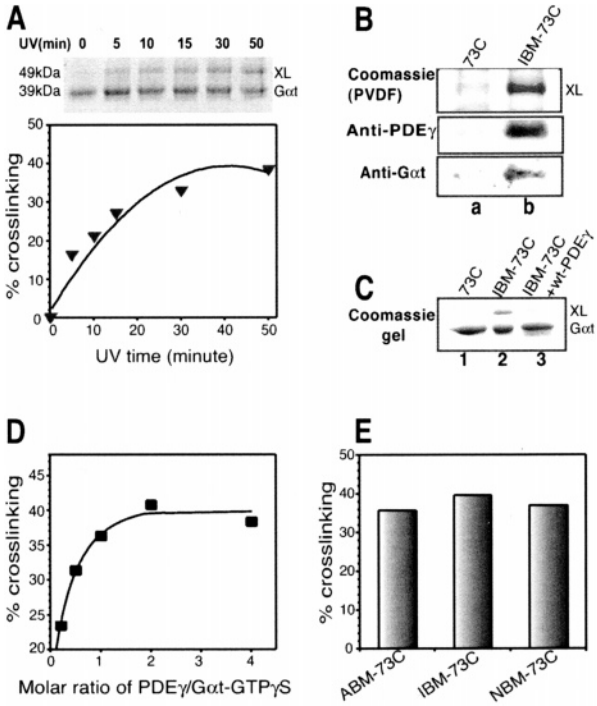

Figure 4. Specific photo-cross-linking of the benzophenone−PDEγ photoprobes with Gαt-GTPγS. Following UV photolysis, the reaction contents were separated by 15% SDS-PAGE in the absence of DTT and then stained with Coomassie Blue R-250. Percentage of cross-linking was calculated as the ratio of the protein amount in the cross-linked band versus total protein present in both the cross-linked and the un-cross-linked bands. A: Photo-cross-linking time course. The cross-linking reactions were performed with IBM-73C and Gαt-GTPγS (molar ratio 1.5:1) under UV light (as described in the "Experimental Procedures") for various times as indicated on top of the Coomassie-stained SDS-PAGE. The background from the dark control (0 min) is subtracted. XL, cross-linking. B: Western blotting of the cross-linked Gαt/PDEγ complex. Photo-cross-linking reactions were performed under conditions similar to A, using PDEγ that was not derivatized (lane a) or derivatized (lane b) with IBM. After 20 min UV photolysis, the reaction was subjected to Western blotting, as described in the "Experimental Procedures". C: Photo-cross-linking was conducted under UV for total 30 min with Gαt and 73C (lane 1), IBM-73C (lane 2), and IBM-73C after 10 min preincubation (on ice) of wt-PDEγ in 5-fold excess (lane 3). The ratio of IBM-73C/Gαt was 1.5:1. D: PDEγ/Gαt molar ratio dependence of photo-cross-linking. The cross-linking reactions were performed at various IBM-87C/Gαt-GTPγS ratios under UV light for a total of 30 min. E: Photo-cross-linking of Gαt-GTPγS with different benzophenone-73C photoprobes. The cross-linking reactions were performed under UV for a total of 30 min with a PDEγ/Gαt-GTPγS molar ratio of ~1.5:1.

conducted to test the specificity and cross-linking efficiency of the photoprobes (Figure 4). As shown in Figure 4A, UV photolysis of the Gαt/PDEγ reaction mixture generated a band on the Coomassie-stained gel with a molecular size of approximately 50 kDa, the sum of Gαt (~40 kDa) and PDEγ (~10 kDa). This cross-linked complex was confirmed to contain both Gαt and PDEγ by Western blotting (Figure 4B). The cross-linked species was not observed in the dark control (0 min) (Figure 4A), nor with the underivatized 73C construct (Figure 4B), and was inhibited by preincubation of wt-PDEγ with Gαt (Figure 4C), indicating specificity of cross-linking. Moreover, the cross-linking of IBM-73C with Gαt-GTPγS was saturable with regard to photolysis time (Figure 4A) and photoprobe concentration (Figure 4D), further demonstrating the cross-linking specificity.

The maximum efficiency of cross-linking between the benzophenone−PDEγ photoprobes and Gαt-GTPγS was as high as 40% (Figure 4A and D); a comparison of the 73C derivatives of the three benzophenone photoprobes indicated similar cross-linking efficiencies (Figure 4E). The efficient cross-linking of the PDEγ C-terminal positions with Gαt-GTPγS further supports the previous observations that the PDEγ C-terminal half is a major domain interacting with Gαt-GTPγS (*33*−*35*).

The high efficiency of specific photo-cross-linking of the benzophenone photoprobes is a valuable feature, since a common problem using the photo-cross-linking approach is the low efficiency of the photolysis event that produces only trace amounts of labeled peptides after proteolysis. This often means that a number of unlabeled fragments mask the specifically labeled fragments and result in difficult purification of these complex digestion mixtures (*10*). The exceptionally high cross-linking efficiency of the benzophenone probes used in this study is likely to circumvent this problem. Besides the high photoreactivity of the benzophenone photophore, the short arm length (estimated 8−10 Å from the modified cysteinyl α-carbon) of these photoprobes is likely to be an additional factor leading to high cross-linking efficiency. These probes are probably the shortest stable benzophenone photoprobes that can be synthesized, considering that they have only one carbon between the disulfide bond and the benzophenone moiety. A similar but shorter benzophenone compound that we synthesized with no carbon between the sulfur and the benzophenone moiety (4-methanethiosulfonate benzophenone) turned out to be unstable at neutral pH (data not shown). A shorter arm length is usually favorable for cross-linking studies since the photoinsertion site reflects a more precise protein−protein interaction position, a property not held by BPMTS, which has a longer arm length.

The Directly Radioiodinated Amino-Benzophenone Photoprobe Offered a Sensitive Detection of Label Transfer to Gαt-GTPγS. While the benzophenone photoprobes proved to be substantially useful in probing photoinsertion sites on Gαt-GTPγS from derivatized PDEγ, through a biotin tag added to the photoprobe after photolysis (Grant, J. E. and Ruoho, A. E., 2005, unpublished data), detection of label transfer through autoradiography is a convenient approach under some circumstances. We therefore explored this possibility for extended applications of these benzophenone photoprobes.

Since the nonradiolabeled iodobenzophenone photoprobe ([^{127}I] IBM) was synthesized using ABM as starting material, we radioiodinated ABM in order to generate a radiolabeled benzophenone photoprobe. One approach that was used was to follow the [^{127}I] IBM synthesis protocol described in the Experimental Procedures to generate [^{125}I] IBM (Figure 5A). As shown in Figure 5B, the purified radiolabeled product comigrated on TLC with the standard [^{127}I] IBM control, indicating the product to be [^{125}I] IBM. In addition, PDEγ derivatized with the radioiodinated IBM was disulfide cleavable by DTT (Figure 5C), further characterizing it as [^{125}I] IBM. A second approach was through the use of a mild oxidizing agent, chloramine T, by which Na^{125}I was "activated" and added ortho to the amino-benzophenone group of ABM, yielding the product ^{125}I-ABM (Figure 5D). This probe derivatized a single-cysteine PDEγ construct in a manner that was sensitive to DTT reversal (data not shown). The PDEγ derivatives of the ^{125}I-labeled benzophenone probes were readily purified from free Na^{125}I by size-exclusion

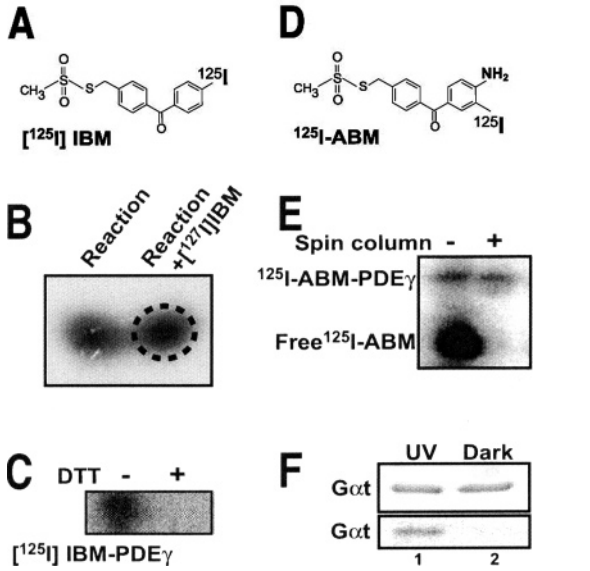

Figure 5. Preparation of radioiodinated benzophenone−PDEγ photoprobes. A: Molecular structure of [^{125}I] IBM. B: Autoradiogram of TLC purification of [^{125}I] IBM. Left lane, [^{125}I] IBM reaction; right lane, comigration of the [^{125}I] IBM reaction and the pure [^{127}I] IBM control whose position is indicated by the dashed ring. C: Autoradiogram of [^{125}I] IBM-PDEγ in the dark on a SDS-PAGE gel run without and with DTT. D: Molecular structure of ^{125}I-ABM. E: Autoradiogram of a SDS-PAGE gel showing the purification of ^{125}I-ABM-PDEγ with a spin column (right lane) as compared with the sample before purification (left lane). F: Photolabel transfer to Gαt-GTPγS (2 μM) from ^{125}I-ABM-68C (3 μM). The proteins after photolysis (lane 1) or dark incubation on ice (lane 2) were separated by 15% reducing SDS-PAGE. Upper panel, Coomassie-stained gel; lower panel, autoradiogram.

chromatography using spin columns (Figure 5E), which offers a sensitive detection of label transfer to Gαt-GTPγS from derivatized PDEγ (see Figure 5F).

An indirect way of photoprobe radiolabeling has been reported previously which involved derivatization of the DTT-reversed sulfhydryl of a reversible thiol-reactive photoprobe using [^{3}H]-*N*-ethylmaleimide, but this method suffers from the need to block unlabeled free sulfhydryls first and an unfortunate problem involving a high radioactive background (*11*). Another way of indirect photoprobe radiolabeling was to radioiodinate a peptide at a site away from a benzophenone photoprobe incorporated in the peptide, as previously reported (*38*). The radiolabel, however, can be lost if unwanted proteolytic cleavage separates the radioiodinated residue from the benzophenone cross-linking site. The direct radiolabeling of benzophenone reported here is therefore advantageous.

While biotin and fluorescent groups may provide alternate labeling approaches, their bulkiness often greatly impairs the function of derivatized bait proteins, thus limiting their applications. The ^{125}I radiolabel, on the other hand, is exceptionally sensitive yet relatively small and can be directly added to the benzophenone moiety with minimal effects on the function of PDEγ.

Summary. The data presented in this study indicate that the novel benzophenone photoprobes that have been developed in our laboratory are suitable for protein−protein interaction analysis through a photo-cross-linking/label transfer strategy. These probes are short in length, stable at neutral pH, and DTT-cleavable. The PDEγ constructs derivatized with these probes could be readily purified and had unaltered function (as demonstrated by the IBM-73C derivative). Photo-cross-linking of PDEγ and Gαt-GTPγS through these photoprobes was

highly efficient. In addition, the amino-benzophenone photoprobe (ABM) was radioiodinatable, facilitating sensitive detection of photoinserted proteins, and this probe is potentially a module for adding additional functional groups to the amino on benzophenone. These combined features favor convenient identification of photoinsertion sites. Since these benzophenone probes can be linked through a disulfide bond to an engineered cysteine on a given protein in a site-specific manner, they may have broad applications for investigation of protein−protein interactions.

ACKNOWLEDGMENT

This work was supported by an NIH Grant (NIH GM33138) to A.E.R. and an NIH Grant (EY12859) to V.Y.A. We thank Dr. Martha M. Vestling, director of the Mass Spectrometry Facility, Department of Chemistry, University of Wisconsin−Madison, for performing ESI MS and data processing. Thanks also go to Dr. Jennifer E. Grant in the laboratory of A.E.R. for the wt-PDEγ/intein construct.

LITERATURE CITED

(1) Arshavsky, V. Y., Lamb, T. D., and Pugh, E. N., Jr. (2002) G proteins and phototransduction. *Annu. Rev. Physiol. 64*, 153−187.

(2) Tsang, S. H., Burns, M. E., Calvert, P. D., Gouras, P., Baylor, D. A., Goff, S. P., and Arshavsky, V. Y. (1998) Role for the target enzyme in deactivation of photoreceptor G protein in vivo. *Science 282*, 117−121.

(3) Chen, C. K., Burns, M. E., He, W., Wensel, T. G., Baylor, D. A., and Simon, M. I. (2000) Slowed recovery of rod photoresponse in mice lacking the GTPase accelerating protein RGS9-1. *Nature 403*, 557−560.

(4) Noel, J. P., Hamm, H. E., and Sigler, P. B. (1993) The 2.2 A crystal structure of transducin-alpha complexed with GTP gamma S. *Nature 366*, 654−663.

(5) Sondek, J., Lambright, D. G., Noel, J. P., Hamm, H. E., and Sigler, P. B. (1994) GTPase mechanism of G proteins from the 1.7-A crystal structure of transducin alpha-GDP-AlF_4^-. *Nature 372,* 276−279.

(6) Slep, K. C., Kercher, M. A., He, W., Cowan, C. W., Wensel, T. G., and Sigler, P. B. (2001) Structural determinants for regulation of phosphodiesterase by a G protein at 2.0 A. *Nature 409,* 1071−1077.

(7) Dhanasekaran, N., Wessling-Resnick, M., Kelleher, D. J., Johnson, G. L., and Ruoho, A. E. (1988) Mapping of the carboxyl terminus within the tertiary structure of transducin's alpha subunit using the heterobifunctional cross-linking reagent, ^{125}I-N-(3-iodo-4-azidophenylpropionamido-S-(2-thiopyridyl) cysteine. *J. Biol. Chem. 263*, 17942−17950.

(8) Liu, Y., Arshavsky, V. Y., and Ruoho, A. E. (1996) Interaction sites of the COOH-terminal region of the gamma subunit of cGMP phosphodiesterase with the GTP-bound alpha subunit of transducin. *J. Biol. Chem. 271,* 26900−26907.

(9) Guo, L.-W., Grant, J. E., Hajipour, A. R., Muradov, K., Arbabian, M., Artemyev, N. O., and Ruoho, A. E. (2005) Asymmetric interaction between the rod phosphodiesterase inhibitory gamma subunits and the alpha and beta catalytic subunits. *J. Biol. Chem.* In press.

(10) Hatanaka, Y. and Sadakane, Y. (2002) Photoaffinity labeling in drug discovery and developments: chemical gateway for entering proteomic frontier. *Curr. Top. Med. Chem. 2*, 271−288.

(11) Teixeira-Clerc, F., Michalet, S., Menez, A., and Kessler, P. (2003) A cysteine-linkable, short cleavable photoprobe with dual functionality to explore protein−protein interfaces. *Bioconjug. Chem. 14*, 554−562.

(12) Dorman, G. and Prestwich, G. D. (2000) Using photolabile ligands in drug discovery and development. *Trends Biotechnol. 18*, 64−77.

(13) Artemyev, N. O., Mills, J. S., Thornburg, K. R., Knapp, D. R., Schey, K. L., and Hamm, H. E. (1993) A site on transducin alpha-subunit of interaction with the polycationic region of cGMP phosphodiesterase inhibitory subunit. *J. Biol. Chem. 268*, 23611−23615.

(14) Grant, J. E., Guo, L.-W., Vestling, M. M., Martemyanov, K. A., Arshavsky, V. Y., and Ruoho, A. E. (2005) The N-terminus of GTPγS-activated transducin α subunit interacts with the C-terminus of the cGMP phosphodiesterase γ subunit. *J. Biol. Chem.* Submitted

(15) Artemyev, N. O., Natochin, M., Busman, M., Schey, K. L., and Hamm, H. E. (1996) Mechanism of photoreceptor cGMP phosphodiesterase inhibition by its gamma-subunits. *Proc. Natl. Acad. Sci. U.S.A. 93*, 5407−5412.

(16) Muradov, K. G., Granovsky, A. E., Schey, K. L., and Artemyev, N. O. (2002) Direct interaction of the inhibitory gamma-subunit of Rod cGMP phosphodiesterase (PDE6) with the PDE6 GAFa domains. *Biochemistry 41*, 3884−3890.

(17) Luo, Y., Leszyk, J., Li, B., Li, Z., Gergely, J., and Tao, T. (2002) Troponin-I interacts with the Met47 region of skeletal muscle actin. Implications for the mechanism of thin filament regulation by calcium. *J. Mol. Biol. 316,* 429−434.

(18) Wahlstrom, J. L., Randall, M. A. Jr., Lawson, J. D., Lyons, D. E., Siems, W. F., Crouch, G. J., Barr, R., Facemyer, K. C., and Cremo, C. R. (2003) Structural model of the regulatory domain of smooth muscle heavy meromyosin. *J. Biol. Chem. 278,* 5123−5131.

(19) Horn, R., Ding, S., and Gruber, H. J. (2000) Immobilizing the moving parts of voltage-gated ion channels. J. *Gen. Physiol. 116*, 461−476.

(20) Nguyen, T. P., and Horn, R. (2002) Movement and crevices around a sodium channel S3 segment. *J. Gen. Physiol. 120,* 419−36.

(21) Martemyanov, K. A., and Arshavsky, V. Y. (2004) Kinetic approaches to study the function of RGS9 isoforms. *Methods Enzymol.* (Siderovski, D. Ed.) 390, 196−209.

(22) Kroll, S., Phillips, W. J., and Cerione, R. A. (1989) The regulation of the cyclic GMP phosphodiesterase by the GDP-bound form of the alpha subunit of transducin. *J. Biol. Chem. 264*, 4490−4497.

(23) Brunner, J. (1993) New photolabeling and crosslinking methods. *Annu. Rev. Biochem. 62*, 483−514.

(24) Dorman, G., and Prestwich, G. D. (1994) Benzophenone photophores in biochemistry. *Biochemistry. 33*, 5661−5673.

(25) Fleming, S. A. (1995) Chemical reagents in photoaffinity labeling. *Tetrahedron 51*, 12479−12520.

(26) Jahn, O., Eckart, K., Brauns, O., Tezval, H., and Spiess, J. (2002) The binding protein of corticotropin-releasing factor: ligand-binding site and subunit structure. *Proc. Natl. Acad. Sci. U.S.A. 99,* 12055−12060.

(27) Alami, M., Luke, I., Deitermann, S., Eisner, G., Koch, H. G., Brunner, J., and Muller, M. (2003) Differential interactions between a twin-arginine signal peptide and its translocase in *Escherichia coli*. *Mol. Cell. 12,* 937−946.

(28) Jahn, O., Eckart, K., Tezval, H., and Spiess, J. (2004) Characterization of peptide−protein interactions using photoaffinity labeling and LC/MS. *Anal. Bioanal. Chem. 378*, 1031−1036.

(29) Junge, H. J., Rhee, J. S., Jahn, O., Varoqueaux, F., Spiess, J., Waxham, M. N., Rosenmund, C., and Brose, N. (2004) Calmodulin and Munc13 form a Ca^{2+} sensor/effector complex that controls short-term synaptic plasticity. *Cell 118*, 389−401.

(30) Cai, K., Itoh, Y., and Khorana, H. G. (2001) Mapping of contact sites in complex formation between transducin and light-activated rhodopsin by covalent crosslinking: use of a photoactivatable reagent. *Proc. Natl. Acad. Sci. U.S.A. 98*, 4877−4882.

(31) Weber, P. J. A., and Beck-Sickinger, A. G. (1997) Comparison of the photochemical behavior of four different photoactivable probes. *J. Pept. Res. 49,* 375−383.

(32) Kenyon, G. L., and Bruice, T. W. (1977) Novel sulfhydryl reagents. *Methods Enzymol. 47*, 407−430.
(33) Slepak, V. Z., Artemyev, N. O., Zhu, Y., Dumke, C. L., Sabacan, L., Sondek, J., Hamm, H. E., Bownds, M. D., and Arshavsky, V. Y. (1995) An effector site that stimulates G-protein GTPase in photoreceptors. *J. Biol. Chem. 270,* 14319−14324.
(34) Skiba, N. P., Artemyev, N. O., and Hamm, H. E. (1995) The carboxyl terminus of the gamma-subunit of rod cGMP phosphodiesterase contains distinct sites of interaction with the enzyme catalytic subunits and the alpha-subunit of transducin. *J. Biol. Chem*. *270*, 13210−13215.
(35) Granovsky, A. E., and Artemyev, N. O. (2001) A conformational switch in the inhibitory gamma-subunit of PDE6 upon enzyme activation by transducin. *Biochemistry 40*, 13209−13215.
(36) Hirel, P. H., Schmitter, M. J., Dessen, P., Fayat, G., and Blanquet, S. (1989) Extent of N-terminal methionine excision from *Escherichia coli* proteins is governed by the side-chain length of the penultimate amino acid. *Proc. Natl. Acad. Sci. U.S.A. 86*, 8247−8251.
(37) Arshavsky, V. Y. and Bownds, M. D. (1992) Regulation of deactivation of photoreceptor G protein by its target enzyme and cGMP. *Nature 357*, 416−417.
(38) Yahalom, D., Wittelsberger, A., Mierke, D. F., Rosenblatt, M., Alexander, J. M., and Chorev, M. (2002) Identification of the principal binding site for RGD-containing ligands in the alpha(V)beta(3) integrin: a photoaffinity cross-linking study. *Biochemistry 41*, 8321−8331.

BC050016K

Effects of Side Chain Configuration and Backbone Spacing on the Gene Delivery Properties of Lysine-Derived Cationic Polymers

Sarah E. Eldred,[‡] Margaret R. Pancost,[‡] Karin M. Otte,[‡] David Rozema,[§,*] Shannon S. Stahl,[‡,*] and Samuel H. Gellman[‡,*]

Department of Chemistry, University of Wisconsin—Madison, 1101 University Ave., Madison, Wisconsin 53706, and Mirus Corporation, 505 S. Rosa Road, Madison, Wisconsin 53719. Received January 25, 2005; Revised Manuscript Received April 3, 2005

A series of lysine-based oligomers (18 residues) that differ in side chain configuration or side chain spacing along the backbone was tested for DNA transfection activity. Although materials constructed from lysine are not the most effective polymeric transfection agents, we have chosen L-lysine-based molecules as a starting point because this system allows us to examine the functional effects of incremental changes in polycation structure. The oligomer constructed from β^3-homolysine (β^3-hLys) and that from α-D-lysine were superior to an α-L-lysine 18-mer in gene delivery assays. This improved activity is attributed to the fact that the α-L-peptide is a protease substrate while the other 18-mers are not. This conclusion is supported by the effects of chloroquine on transfection activity, based on the protease inhibition activity of chloroquine. To our knowledge, these results represent the first direct comparison of a D-lysine oligomer with an L-lysine oligomer in the context of gene delivery. Poly(β^3-hLys) was synthesized from the ring opening polymerization of the corresponding lactam. The DNA transfection ability of this polymer was compared with that of commercially available poly(L-lysine) (PLL). In each case the polymer was more active than the corresponding oligomer.

INTRODUCTION

Techniques for efficient delivery of foreign DNA into cells could lead to gene therapies for many human disorders, but realizing this potential will require improvement relative to current gene delivery methods (*1*). Injection of naked DNA into the body results in its rapid clearance and degradation, which precludes therapeutic efficacy (*2*–*3*). A further problem is that naked DNA is only poorly taken up by cells because of the large persistent length (stiffness) of this anionic biopolymer. Therefore, a delivery vehicle or "vector" is required. Viral vectors are among the most efficient gene delivery vehicles, but concerns about their safety have curtailed their use in clinical trials (*1*, *3*). Nonviral vectors are safer, but they suffer from lower transfection efficiencies (*4*).

Two classes of nonviral vectors are being investigated for gene delivery: cationic lipids and cationic polymers. Neutral polymers have been used in transfections but only when coupled to adenoviruses (*5*). The lipids can be effective, but inconsistencies in their preparation and difficulties in their purification have led to irreproducible transfection results in some cases (*4*, *6*). Additionally, minor lipid modifications, desirable in terms of analyzing structure–activity relationships, can be difficult to achieve. A further problem is that lipid–DNA interactions are relatively weak and unstable in the presence of serum proteins (*2*). Polycations, on the other hand, are relatively easy to prepare, modify, and formulate with DNA. Thus, polycationic gene delivery vectors have received widespread attention (*7*–*14*). Much research has focused on increasing the uptake of vector–DNA complexes ("polyplexes") by attaching cell-adhesive ligands to the vectors in order to take advantage of receptor-mediated endocytosis. Another common transfection strategy has been to enhance endosomolysis (following polyplex uptake) by the incorporation of pH buffering or membrane-lytic agents into the vector. Less studied are the factors that control the intracellular dissociation of DNA from the cationic polymer, which is ultimately required for transcription and which may be important for transfection (*15*–*22*).

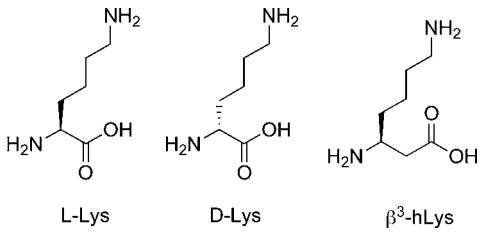

Figure 1. Amino acid building blocks.

We have undertaken a fundamental study of the effects of cationic polymer structure on transfection efficiency, using several lysine-based oligomers and analogous polymers. Poly(L-lysine) (PLL) and L-lysine oligomers are well-known to condense DNA, and to provide modest gene delivery to cells in culture (*23*–*25*). Although the activity of L-lysine-based polycations is inferior to that of other cationic polymers, we have chosen L-lysine-based molecules as a starting point because this system allows us to examine incremental changes in polycation structure. We have examined both the effect of changing the configuration of the side chain attachment point (use of D-lysine in place of L-lysine) and the effect of altering the backbone (use of β^3-homolysine (β^3-hLys) in place of lysine) on gene delivery activity (Figure 1).

* To whom correspondence should be addressed. E-mail addresses: stahl@chem.wisc.edu, gellman@chem.wisc.edu, dave.rozema@mirusbio.com.

‡ University of Wisconsin—Madison.

§ Mirus Corporation.

10.1021/bc050017c CCC: $30.25 © 2005 American Chemical Society
Published on Web 05/03/2005

Oligomers and polymers of L-Lys are substrates for proteolytic enzymes, while polycations comprising D-Lys or β^3-hLys are not (*26*−*28*). Therefore, comparisons among these three polycations should indicate whether proteolytic degradation is favorable or unfavorable with regard to delivery efficacy. (Comparisons among the Lys- and β^3-hLys-derived cations probe more subtle effects of polymer structure on delivery.) Polymer degradation too early in the uptake process would presumably be detrimental to transfection efficiency, but such degradation in later stages might enhance the necessary DNA unpacking. The effect of delivery vehicle degradation has received relatively little attention, even though poly(D-lysine) is commonly used in gene delivery studies instead of poly(L-lysine) (*29*). Side chain configuration effects have been examined elsewhere to track the intracellular fate of plasmid DNA during transfection (*30*), but to our knowledge the present study is unique in comparing the transfection efficacy of well-defined enantiomeric lysine oligomers and in extending the comparison from side chain configuration to side chain spacing along the backbone.

EXPERIMENTAL PROCEDURES

General. All commercially available compounds were purchased from Aldrich and used as received unless otherwise noted. Fmoc-Lys(Boc)-OH (D and L versions) was purchased from Nova Biochem. Anhydrous CH_2Cl_2 was obtained from Fisher Scientific in FisherPak containers. It was passed through a solvent purification system prior to use (*31*). ^{1}H and ^{13}C NMR spectra were recorded on Bruker AC-300 MHz (75 MHz for ^{13}C) spectrometers, and $CDCl_3$ was purchased from both Cambridge Isotope Laboratories, Inc., and Aldrich. The chemical shifts (δ) are given in parts per million relative to internal TMS (0 ppm for ^{1}H) and $CDCl_3$ (77.23 ppm for ^{13}C). IR spectra were recorded on a Bruker Tensor 27 IR instrument with an ATR attachment (Pike Technologies). MALDI-TOF-MS was performed using a Bruker REFLEX II spectrometer with a 337 nm laser using the α-cyano-4-hydroxycinnamic acid matrix. HPLC purification was performed using a Shimadzu instrument equipped with a reverse phase C_4-silica column. Flash chromatography was performed on silica gel 60 (particle size 0.040−0.063 nm, 200−400 mesh ASTM, purchased from Sorbent Technology). Polymer molecular weight was determined by Dr. Michelle Chen at Wyatt Technologies using GPC with Shodex SB guard columns along with a Wyatt DAWN EOS multiangle light scattering detector and a Wyatt Optilab rEX concentration detector.

Oligomer Synthesis. β-Amino acid residues were synthesized according to literature procedures (*32*−*34*). Peptide oligomers were synthesized using standard Fmoc solid-phase peptide synthesis techniques with HBTU activation on Rink amide resin (Applied BioSystems) on a Synergy automated synthesizer (Applied Biosystems). The resin-bound peptides were cleaved from the solid support and deprotected simultaneously by using trifluoroacetic acid. The peptides were precipitated by evaporation of the deprotection solution and addition of excess cold anhydrous diethyl ether. The peptide products were purified by reverse-phase HPLC and analyzed using MALDI-TOF-MS.

Lactam 7. β^3-hLys (*32*−*33*) **5** (1 equiv) was cyclized following the general procedure of Huang and co-workers (*35*). Briefly, **5** was placed in a round-bottomed flask with 2-chloro-1-methylpyridinium iodide (1.1 equiv), and CH_3CN was added to make the reaction 0.01 M in substrate. Triethylamine (2.2 equiv) was then added, and the reaction was refluxed under nitrogen for 24 h. The solvent was then removed by rotary evaporation, and the residue was purified by column chromatography in ethyl acetate/hexanes. ^{1}H NMR ($CDCl_3$) δ 1.33−1.81, m, 15H; 2.57, dq J = 14.7, 1.2 Hz, 1H; 3.06, ddd J = 15.0, 5.1, 2.4 Hz, 1H; 3.13, q J = 6.6 Hz, 2H; 3.61, qd J = 4.8, 2.4 Hz, 1H; 4.51, br s, 1H; 6.0, br s, 1H. ^{13}C NMR ($CDCl_3$) δ 23.62, 28.63, 30.08, 35.23, 43.72, 48.21, 77.66, 156.24, 168.14. FTIR (ATR): 1518 cm^{-1} (amide II); 1689 cm^{-1} (carbamate); 1791 cm^{-1} (amide I); 3366 cm^{-1} (N−H). MS-ESI: m/z = 265.1 $[M + Na]^+$ (Calculated m/z = 242.2 $[M]^+$.)

Poly(β^3-hLys). In the glovebox, lactam **7** (1 equiv) was placed in a round-bottomed flask with $Sc(NTMS_2)_3(THF)_3$ (2.5%) and anhydrous CH_2Cl_2 to make the reaction 0.02 M in substrate. The flasks were sealed, removed from the glovebox, and stirred at RT for 24 h. After 24 h the flasks were opened, and the contents were poured into diethyl ether to precipitate the polymer. The polymer was collected by filtration. Deprotection was accomplished by stirring in trifluoroacetic acid until the polymer dissolved (usually 2−3 days). The deprotected polymer was dialyzed against DI H_2O with MW 1000 cutoff membranes and then lyophilized. ^{1}H NMR (D_2O) δ 1.33−1.66, br m, 6H; 2.38, br s, 2H; 2.96, t J = 7.5 Hz, 2H; 4.10, br s, 1H. FTIR (ATR): 1561 cm^{-1} (amide II); 1646 cm^{-1} (amide I); 1676 cm^{-1} (TFA); 3280 cm^{-1} (N−H). Molecular weight was determined using GPC. M_n = 62 000, M_w = 93 000, PDI = 1.5.

Transfections. Plasmid DNA pCIluc (10 μg/mL, pCIluc is prepared according to a published procedure (*36*) where the luciferase reporter gene was under the cytomegalovirus promoter) in 0.25 mL of 5 mM HEPES pH 7.5 was complexed with polymers at a weight ratio of 1:2.66 DNA:polymer (N:P ratio of 1:3.5 using the TFA salt molecular weight for the polycation). Other weight ratios were tested and gave similar results. The DNA complexes were then added (100 μL) to wells containing cultured cells (mouse hepatoma Hepa-1clc7 cells or monkey kidney COS-7 cells, obtained from the American Type Culture Collection (ATCC)) in Dulbecco's modified Eagle Media containing 10% fetal bovine serum. The cells were allowed to incubate for 48 h. The percentages of well surface area covered with cells were then determined using an Olympus CK2 inverted microscope. We have previously found (*37*) that assays of cell toxicity using confluency and methylthiazolyldiphenyltetrazolium bromide (MTT) give, within error, equivalent results. Due to the ease of measurement and the ability to assay toxicity and transfection using the same sample, confluency was used as a measure of toxicity in our studies. Cells in each well were 85−100% confluent at the time of the assay, indicating that the oligomers and polymers tested were noncytotoxic at the levels used for transfection. The cells were harvested and assayed for luciferase expression as previously reported (*38*) using a Lumat LB 9507 (EG&G Berthold, Bad-Wildbad, Germany) luminometer. Reported data is an average of at least six trials.

Chloroquine Studies. Transfection studies with chloroquine were performed in a manner identical to that used in the non-chloroquine studies, save for the addition of 80 μM chloroquine to the wells along with the polyplexes. In these cases, the medium was changed after 2 h, and the cells were allowed to incubate for 46 h more.

DNA Titration Assays. The collapse of TMR-labeled DNA was assessed using a quantitative assay based on condensation-induced quenching of a fluorophore covalently attached to DNA (*39*). Briefly, tetramethyl rhodamine-labeled DNA (TMR-DNA) was synthesized

using tetramethyl rhodamine LabelIT (Mirusbio Corp) according to manufacturer's protocol at a 1:1 DNA:TMR weight ratio. TMR-DNA (10 μg) was mixed with increasing quantities of polymers in 0.5 mL of 10 mM HEPES, pH 7.5. After addition of the polymer, TMR fluorescence of the samples was measured using a Cary spectrofluorometer (excitation wavelength (λ_{ex}) of 546 nm; emission wavelength (λ_{em}) of 576 nm) at room temperature. A similar method was used to carry out the NaCl titration study. Polyplexes were generated using a 1:2.66 TMR-DNA:oligomer ratio, and the TMR fluorescence was measured following NaCl additions.

Particle Sizing. Particles comprised of DNA and polycations were formulated in 20 mM HEPES buffer pH 7.5 at a DNA:polycation ratio of 1:2.66 at a DNA concentration of 10 μg/mL. The size of the particles was assayed by light scattering at 532 nm using a Brookhaven Instruments Corporation, ZetaPlus Particle Sizer, I90.

RESULTS AND DISCUSSION

Activity Comparisons among 18-Mers. Our studies compared (α-L-Lys)$_{18}$ (**1**), which is known to be modestly active in gene delivery (*23*−*25*), with (α-D-Lys)$_{18}$ (**2**), and the homologue of (**1**), (β^3-hLys)$_{18}$ (**3**). We also examined β-peptide **4**, the analogue of **3**, in which β^3-hLys at one-third of the positions is replaced with a more rigid but still cationic residue, *trans*-4-aminopiperidine-3-carboxylic acid (APiC (*34*)). Transfection assays with hepa cells indicated that the β-oligomers (**3** and **4**) and (α-D-Lys)$_{18}$ (**2**) outperformed (α-L-Lys)$_{18}$, but that the two β-peptides were comparable to one another (Table 1). Because the APiC monomer is more difficult to prepare than is β^3-hLys (*34*), subsequent β-peptide studies were limited to molecules containing exclusively β^3-hLys.

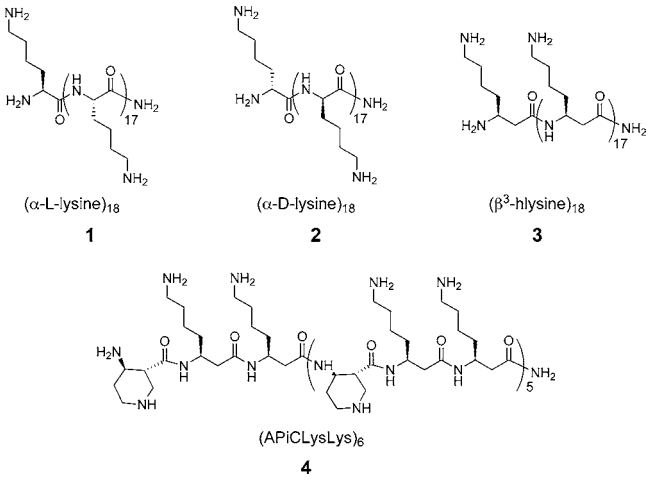

Transfections of both hepa and COS cells showed enhanced activity for both **2** and **3** relative to **1** (Table 1). The hepa cell line was chosen because of long-term interest in gene delivery to hepatocytes, while the COS cell line was selected to demonstrate generality (COS cells are not hepatocytes) and because the transfection properties of COS cells are well-known. In the transfection assays, cells were plated into wells at 40−50% confluency, as determined by light microscopy. At the conclusion of the 48-h incubation period, the confluency of the cells was again determined by light microscopy. Previous work (*37*) has shown that any toxic effects of transfection agents will be manifested as low confluency after the incubation period, and that confluency is comparable to an MTT assay as an indicator of toxicity (or lack thereof). In our studies, all cells were between 85 and 100% confluent at the end of the 48-h incubation period, indicating that the oligomers used were not cytotoxic at the levels employed for transfection.

Table 1. DNA Transfection Activity of Oligomers 2−4 Relative to 1[a]

entry	oligomer	cell line	transfection relative to **1** (no chloroquine)	transfection relative to **1** (with 80 μM chloroquine)
1	**2**	hepa	2.3 ± 0.6	0.5 ± 0.2
2	**3**	hepa	4.1 ± 1.5	0.6 ± 0.5
3	**4**	hepa	4.2 ± 1.9	−
4	**2**	COS	24 ± 10	1.1 ± 0.2
5	**3**	COS	32 ± 10	1.3 ± 0.04

[a] Transfections were performed at a DNA:oligomer ratio of 1:2.66. Data reported is an average of at least six trials. Errors are one standard deviation from the mean.

Our primary goal was to determine the relative transfection efficiencies of a set of related lysine-based oligocations. This information is intended to illuminate the relationship between polycation structure and transfection efficacy and thereby provide a basis for developing more effective transfection agents in the future. Since the crucial observations in this case are the *relative* transfection efficiencies among oligomers **1**−**4**, and not the absolute transfection results, the data have been normalized to the transfection efficiency of oligomer **1**.

The results in Table 1 show that **2** and **3** are superior to **1** for both hepa cells (entries 1 and 2) and COS cells (entries 4 and 5), but that the advantage is larger for COS cells. We cannot explain this difference. The most important point, however, is that for both cell types (α-D-Lys)$_{18}$ and (β^3-hLys)$_{18}$ display enhanced activity relative to (α-L-Lys)$_{18}$.

Chloroquine Effects. Chloroquine is a well-known transfection-boosting reagent that has been used to promote endosomal escape by DNA−cation polyplexes (*40*). It is hypothesized that chloroquine's favorable effect derives from its buffering activity, which prevents the normal endosomal acidification process and causes release of the endosomal contents into the cytoplasm (*4*, *40*, *41*). Not surprisingly, transfection assays of 18-mers **1**−**3** conducted in the presence of chloroquine led to overall activity enhancements relative to assays conducted without chloroquine. More interesting is the observation that the transfection ability of protease-sensitive L-Lys 18-mer **1** has a significantly greater enhancement relative to those of **2** or **3** in the presence of chloroquine. The activity of **1** is greater than or equal to the activity of enantiomer **2** or β-peptide **3** when chloroquine is used with either hepa cells (Table 1, entries 1−2) or COS cells (Table 1, entries 4−5). As in the absence of chloroquine, cells were 85−100% confluent at the completion of the 48 h incubation period; thus, the chloroquine concentration we used does not exert significant toxic effects.

Chloroquine acts as a protease inhibitor in addition to its buffering ability (*16*, *42, 43*). We attribute chloroquine's greater enhancement of transfection by **1**, relative to the effects on **2** or **3**, to the protease inhibition activity of chloroquine. L-Lys 18-mer **1** should be readily degraded by cellular proteases while D-Lys 18-mer **2** and β^3-hLys 18-mer **3** should be intrinsically resistant to proteolysis. Previous research has shown that L-Lys oligomers shorter than 18 units are not effective for DNA transfection (*44*); therefore, it is reasonable to assume that the fragments of oligomer **1** would not be effective for transfection. Our observations concerning chloroquine's enhancement suggest that in the case of protease-labile delivery vectors,

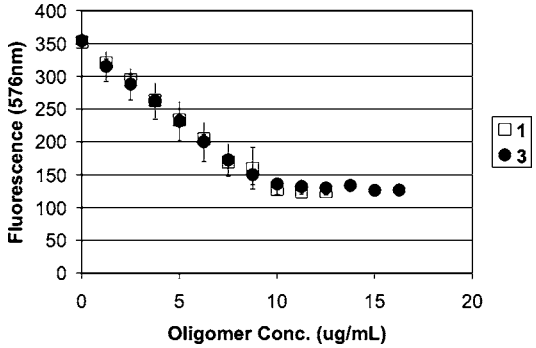

Figure 2. Quenching of fluorescent DNA as a function of amount of added oligomer for **1** and **3**. Error bars are one standard deviation from the mean. Full condensation was reached at a DNA:oligomer weight ratio of 1:1.

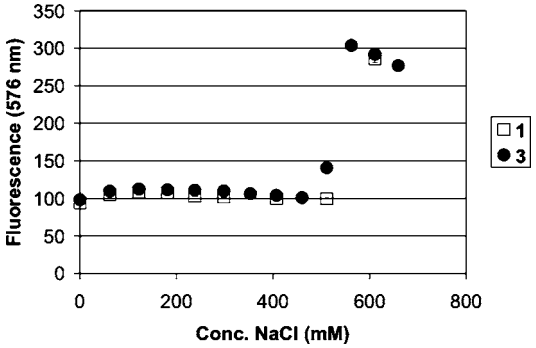

Figure 3. Effect of NaCl concentration on polyplex stability for polyplexes formed between fluorescently labeled DNA and **1** or **3**. Error bars are one standard deviation from the mean.

pH-buffering is not the only activity of chloroquine responsible for increased transfection activity. The differential effect of chloroquine within polycation series **1**−**3** is consistent with our hypothesis that the superior gene delivery activity of **2** and **3** relative to **1** in the absence of chloroquine stems from the chemical instability of **1** in cellular fluids. Since the polycation must dissociate from the DNA at some point within the cell to allow transcription, and since cleavage of the polycation should encourage dissociation from the DNA, it is not obvious a priori whether proteolytic degradation of the cationic vector would enhance or diminish delivery efficiency. Our results suggest that breakdown of a polycationic delivery vector can impede transfection.

Evaluation of DNA−Oligocation Interactions. In an effort to elucidate the origin of the difference in gene delivery activity among 18-mers **1**−**3**, we compared DNA polyplex formation with these oligomers. Complexes formed at a 1:2.66 DNA:oligomer ratio (effective for transfection) were found to be indistinguishable in size. Polyplexes generated from **1** had an average diameter of 48 nm, polyplexes from **2** had an average diameter of 60 nm, and polyplexes from **3** had an average diameter of 58 nm. These differences are not significant.

We used titration experiments to probe the efficiency of DNA-polycation complexation (*39*). In these experiments, varying amounts of polycation are added to fluorescently labeled DNA. Polycation-induced condensation of the DNA is detected as a decrease in fluorescence. When the fluorescence reaches a steady minimum, we assume that the DNA is fully condensed. Figure 2 shows that the results for **1** and **3** are identical; results for **2** (not shown) were also indistinguishable. These findings indicate that the DNA−polycation ratios in these polyplexes are not altered by backbone spacing or side chain configuration. In addition, the observation that the same level of quenching is reached for both polycations indicates that the average distance between flourophores is the same, which implies that the condensed-DNA particles have very similar packing and structure.

A third experiment was performed in order to compare the stabilities of the polyplexes. Polyplexes formed between fluorescently labeled DNA and oligocation **1**, **2**, or **3** were exposed to increasing concentrations of NaCl in order to determine the salt concentration required to "unpack" the polyplex (as indicated by an increase in fluorescence). In the absence of polycation, high salt concentrations result in a nominal increase in fluorescence; however, this increase is gradual as a function of salt concentration, unlike the sharp rise seen in Figure 3 at approximately 550 mM NaCl. The magnitude of the change is much smaller in the absence of polycation than in its presence. Figure 3 shows that the results for **1** and **3** are identical; results for **2** (not shown) were indistinguishable. Thus, the strength of DNA−oligocation association is not influenced by the variation in backbone spacing of side chains or side chain configuration. Overall, we find no significant differences among polyplexes formed between DNA and 18-mers **1**−**3** can be detected by three distinct measurements.

Scheme 1

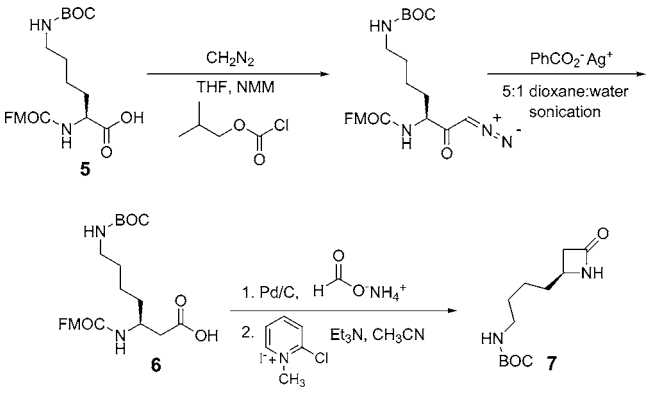

Scheme 2

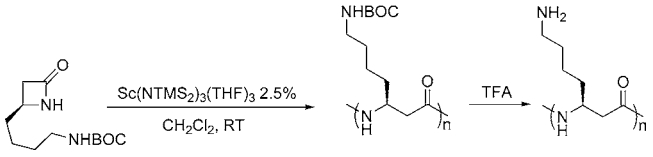

Cationic Polymers. The transfection efficacy for lysine polymers depends on molecular weight, and an oligomer containing only 18 residues is expected to be less effective on a weight basis than are longer polymers (*23*−*25*). We examined higher molecular weight polymers of β^3-hLys in order to determine whether a similar trend would be observed in these cases as well. Commercially available poly(L-lysine) (PLL) was used as a positive control for comparison with poly(β^3-hLys) prepared in our laboratory. We selected 70 and 188 K PLL as our control polymers in order to bracket the molecular weight of the poly(β^3-hLys) (93 K).

The poly-β-peptide was synthesized by metal-catalyzed ring-opening polymerization of a protected β-lactam (*45*). Synthesis of this β-lactam begins with a commercially available protected form of amino acid L-lysine (**5**), which is homologated using the Arndt−Eistert sequence to provide β-amino acid **6** (Scheme 1) (*32*−*33*).

Table 2. DNA Transfection Activity of Poly(β^3-hLys) Relative to PLL[a]

entry	polycation	cell line	relative transfection
1	poly(β^3-hLys)	hepa	13 ± 8 (relative to 70 K PLL)
2	poly(β^3-hLys)	hepa	18 ± 5 (relative to 188 K PLL)
3	poly(β^3-hLys)	COS	11 ± 3 (relative to 70 K PLL)
4	poly(β^3-hLys)	COS	9 ± 7 (relative to 188 K PLL)

[a] Transfections performed at a DNA: oligomer ratio of 1:2.66. Data reported is an average of at least six trials. Errors are one standard deviation from the mean.

Deprotection and cyclization then yield β-lactam **7** (*35*). Polymerization of **7** leads to the side chain-protected polymer (Scheme 2).

Deprotection with trifluoroacetic acid followed by dialysis provides poly(β^3-hLys) with M_n = 62 000 and M_w = 93 000 (PDI = 1.5). Transfection assays with hepa cells (Table 2, entries 1−2) show that poly(β^3-hLys) outperforms both PLL controls. Studies with COS cells (Table 2, entries 3−4) indicate superiority of poly(β^3-hLys) over both 70 and 188 K PLL.

CONCLUSIONS

We have shown that oligomers or polymers of D-Lys or β^3-hLys are more effective gene delivery agents than are analogous oligomers or polymers of L-Lys for cultured cells. This difference in activity appears to result from the fact that proteases can degrade vectors composed of L-Lys, while vectors composed of D-Lys or β^3-hLys are not susceptible to proteolysis. By several measures, the polyplexes formed between DNA and 18-mers of L-Lys, D-Lys or β^3-hLys do not differ significantly from one another. Our results indicate that premature breakdown of a cationic oligomer or polymer used to package DNA for delivery can diminish gene transfer activity.

ACKNOWLEDGMENT

This work was supported in part by the NSF Collaborative Research in Chemistry Program (CHE-0404704). Initial phases of the research were supported by seed funding (UW-Madison MRSEC) and by an Industrial and Economic Development Research grant from UW-Madison. We thank Dr. Michelle Chen of Wyatt Technologies for polymer molecular weight characterization.

LITERATURE CITED

(1) Mulligan, R. C. (1993) The basic science of gene therapy. *Science 260*, 926−932.
(2) Langner, M. (2000) The intracellular fate of non-viral DNA carriers. *Cell. Mol. Biol. Lett. 5*, 295−313.
(3) Piskin, E., Dinçer, S., and Türk, M. (2004) Gene delivery: intelligent but just at the beginning. *J. Biomater. Sci. Polym. Ed. 15*, 1181−1202.
(4) Pouton, C. W., Lucas, P., Thomas, B. J., Uduehi, A. N., Milroy, D. A., and Moss, S. H. (1998) Polycation−DNA complexes for gene delivery: A comparison of the biopharmaceutical properties of cationic polypeptides and cationic lipids. *J. Controlled Release 53*, 289−299.
(5) Bellocq, N. C., Kang, D. W., Wang, X., Jensen, G. S., Pun, S. H., Schluep, T., Zepeda, M. L., and Davis, M. E. (2004) Synthetic biocompatible cyclodextrin-based constructs for local gene delivery to improve cutaneous wound healing. *Bioconjugate Chem. 15*, 1201−1211.
(6) Guo, X., and Szoka, F. C., Jr. (2003) Chemical approaches to triggerable lipid vesicles for drug and gene delivery. *Acc. Chem. Res. 36*, 335−341.
(7) Wolfert, M. A., Dash, P. R., Nazarova, O., Oupicky, D., Seymour, L. W., Smart, S., Strohalm, J., and Ulbrich, K. (1999) Polyelectrolyte vectors for gene delivery: Influence of cationic polymer on biophysical properties of complexes formed with DNA. *Bioconjugate Chem. 10*, 993−1004.
(8) Roufaí, M. B., and Midoux, P. (2001) Histidylated polylysine as DNA vector: Elevation of the imidazole protonation and reduced cellular uptake without change in the polyfection efficiency of serum stabilized negative polyplexes. *Bioconjugate Chem. 12*, 92−99.
(9) Reschel, T., Koňák, C., Oupicky, D., Seymour, L. W., and Ulbrich, K. (2002) Physical properties and in vitro transfection efficiency of gene delivery vectors based on complexes of DNA with synthetic polycations. *J. Controlled Release 81*, 201−217.
(10) Putnam, D., Gentry, C. A., Pack, D. W., and Langer, R. (2001) Polymer-based gene delivery with low cytotoxicity by a unique balance of side-chain termini. *Proc. Natl. Acad. Sci., U.S.A. 98*, 1200−1205.
(11) Boussif, O., Lezoualc'h, F., Zanta, M. A., Mergny, M. D., Scherman, D., Demeneix, B., and Behr, J.-P. (1995) A versatile vector for gene and oligonucleotide transfer into cells in culture and in vivo: Polyethylenimine. *Proc. Natl. Acad. Sci., U.S.A. 92*, 7297−7301.
(12) Midoux, P., and Monsigny, M. (1999) Efficient gene transfer by histidylated polylysine/pDNA complexes. *Bioconjugate Chem. 10*, 406−411.
(13) Liu, Y., Wenning, L., Lynch, M., and Reineke, T. M. (2004) New poly(D-glucaramidoamine)s induce DNA nanoparticle formation and efficient gene delivery into mammalian cells. *J. Am. Chem. Soc. 126*, 7422−7423.
(14) Park, Y., Kwok, K. Y., Boukarim, C., and Rice, K. G. (2002) Synthesis of sulfhydryl cross-linking poly(ethylene glycol)-peptides and glycopeptides as carriers for gene delivery. *Bioconjugate Chem. 13*, 232−239.
(15) Varga, C. M., Wickham, T. J., and Lauffenburger, D. A. (2000) Receptor-mediated targeting of gene delivery vectors: Insights from molecular mechanisms for improved vehicle design. *Biotech. Bioeng. 70*, 593−605.
(16) Cotten, M., Längle-Rouault, F., Kirlappos, H., Wagner, E., Mechtler, K., Zenke, M., Beug, H., and Birnstiel, M. L. (1990) Transferrin-polycation-mediated introduction of DNA into human leukemic cells: Stimulation by agents that affect the survival of transfected DNA or modulate transferrin receptor levels. *Proc. Natl. Acad. Sci., U.S.A. 87*, 4033−4037.
(17) Cartier, R., and Reszka, R. (2002) Utilization of synthetic peptides containing nuclear localization signals for nonviral gene transfer systems. *Gene Ther. 9*, 157−167.
(18) Wagner, E., Zatloukal, K., Cotten, M., Kirlappos, H., Mechtler, K., Curiel, D. T., and Birnstiel, M. L. (1992) Coupling of adenovirus to transferrin-polylysine/DNA complexes greatly enhances receptor-mediated gene delivery and expression of transfected genes. *Proc. Natl. Acad. Sci., U.S.A. 89*, 6099−6103.
(19) Curiel, D. T., Agarwal, S., Wagner, E., and Cotten, M. (1991) Adenovirus enhancement of transferrin-polylysine-mediated gene delivery. *Proc. Natl. Acad. Sci., U.S.A. 88*, 8850−8854.
(20) Schaffer, D. V., Fidelman, N. A., Dan, N., and Lauffenburger, D. A. (2000) Vector unpacking as a potential barrier for receptor-mediated polyplex gene delivery. *Biotech. Bioeng. 67*, 598−606.
(21) Wen, J., Mao, H.-Q., Li, W., Lin, K. Y., and Leong, K. W. (2004) Biodegradable polyphosphoester micelles for gene delivery. *J. Pharm. Sci. 93*, 2142−2157.
(22) Forrest, M. L., Koerber, J. T., and Pack, D. W. (2003) A degradable polyethylenimine derivative with low toxicity for highly efficient gene delivery. *Bioconjugate Chem. 14*, 934−940.
(23) McKenzie, D. L., Collard, W. T., and Rice, K. G. (1999) Comparative gene transfer efficiency of low molecular weight polylysine DNA-condensing peptides. *J. Pept. Res. 54*, 311−318.
(24) Kwoh, D. Y., Coffin, C. C., Lollo, C. P., Jovenal, J., Banaszczyk, M. G., Mullen, P., Phillips, A., Amini, A., Fabrycki, J., Bartholomew, R. M., Brostoff, S. W., and Carlo, D. J. (1999) Stabilization of poly-L-lysine/DNA polyplexes for in vivo gene delivery to the liver. *Biochim. Biophys. Acta 1444*, 171−190.

(25) Read, M. L., Etrych, T., Ulbrich, K., and Seymour, L. W. (1999) Characterisation of the binding interaction between poly(L-lysine) and DNA using the fluorescamine assay in the preparation of nonviral gene delivery vectors. *FEBS Lett. 461*, 96−100.
(26) Frackenpohl, J., Arvidsson, P. I., Schreiber, J. V., and Seebach, D. (2001) The outstanding biological stability of β- and γ-peptides toward proteolytic enzymes: An in vitro investigation with fifteen peptidases. *Chembiochem 2*, 445−455.
(27) Seebach, D., Abele, S., Schreiber, J. V., Martinoni, B., Nussbaum, A. K., Schild, H., Schulz, H., Hennecke, H., Woessner, R., and Bitsch, F. (1998) Biological and pharmacokinetic studies with β-peptides. *Chimia 52*, 734−739.
(28) Hintermann, T., and Seebach, D. (1997) The biological stability of β-peptides: No interactions between α- and β-peptidic structures? *Chimia 50*, 244−247.
(29) Kim, T.-G., Kang, S.-Y., Kang, J.-H., Cho, M.-Y., Kim, J.-I., Kim, S.-H., and Kim, J.-S. (2004) Gene transfer into human hepatoma cells by receptor-associated protein/polylysine conjugates. *Bioconjugate Chem. 15*, 326−332.
(30) Laurent, N., De Connick, S. W., Mihaylova, E., Leontieva, E., Warnier-Pirotte, M.-T., Wattiaux, R., and Jadot, M. (1999) Uptake by rat liver and intracellular fate of plasmid DNA complexed with poly-L-lysine or poly-D-lysine. *FEBS Lett. 443*, 61−65.
(31) Pangborn, A. B., Giardello, M. A., Grubbs, R. H., Rosen, R. K., and Timmers, F. J. (1996) Safe and convenient procedure for solvent purification. *Organometallics 15*, 1518−1520.
(32) Guichard, G., Abele, S., and Seebach, D. (1998) Preparation of N−Fmoc-protected β^2- and β^3-amino acids and their use as building blocks for the solid-phase synthesis of β-peptides. *Helv. Chim. Acta 81*, 187−206.
(33) Müller, A., Vogt, C., and Sewald, N. (1998) Synthesis of Fmoc-β-homoamino acids by ultrasound-promoted Wolff rearrangement. *Synthesis*, 837−841.
(34) Schinnerl, M., Murray, J. K., Langenhan, J. M., and Gellman, S. H. (2003) Asymmetric synthesis of a new helix-forming β-amino acid: *trans*-4-aminopipridine-3-carboxylic acid. *Eur. J. Org. Chem.*, 721−726.
(35) Huang, H., Iwasawa, N., and Mukaiyama, T. (1984) A convenient method for the construction of β-lactam compounds from β-amino acids using 2-chloro-1-methyl pyridinium iodide as condensing reagent. *Chem. Lett.* 1465−1466.
(36) Danko, I., Williams, P., Herweijer, H., Zhang, G., Latendresse, J. S., Bock, I., and Wolff, J. A. (1997) High expression of naked plasmid DNA in muscles of young rodents. *Hum. Mol. Genet. 6*, 1435−1443.
(37) Wakefield, D. H., Klein, J. J., Wolff, J. A., Rozema, D. B. Membrane activity and transfection ability of amphipathic polycations as a function of alkyl group size. Submitted for publication.
(38) Wolff, J. A., Malone, R. W., Williams, P., Chong, W., Acsadi, G., Jani, A., and Felgner, P. L. (1990) Direct gene transfer into mouse muscle in vivo. *Science 247*, 1465−1468.
(39) Trubetskoy, V. S., Slattum, P. M., Hagstrom, J. E., Wolff, J. A., and Budker, V. G. (1999) Quantitative assessment of DNA condensation. *Anal. Biochem. 267*, 309−313.
(40) Pack, D. W., Putnam, D., and Langer, R. (2000) Design of imidazole-containing endosmolytic biopolymers for gene delivery. *Biotech. Bioeng. 67*, 217−223.
(41) Hellgren, I., Gorman, J., and Sylvén, C. (2004) Factors controlling the efficiency of Tat-mediated plasmid DNA transfer. *J. Drug Target. 12*, 39−47.
(42) Luthman, H., and Magnusson, G. (1983) High efficiency polyoma DNA transfection of chloroquine treated cells. *Nucleic Acids Res. 11*, 1295−1308.
(43) Coonrod, A., Li, F.-Q., and Horwitz, M. (1997) On the mechanism of DNA transfection: Efficient gene transfer without viruses. *Gene Ther. 4*, 1313−1321.
(44) Wadhwa, M. S., Collard, W. T., Adami, R. C., McKenzie, D. L., and Rice, K. G. (1997) Peptide-mediated gene delivery: Influence of peptide structure on gene expression. *Bioconjugate Chem. 8*, 81−88.
(45) Cheng, J., and Deming, T. J. (2001) Controlled polymerization of β-lactams using metal-amido complexes: Synthesis of block copoly(β-peptides). *J. Am. Chem. Soc. 123*, 9457−9458.

BC050017C

Solid-Phase Synthesis of Oligonucleotides Labeled with Luminescent Lanthanide(III) Chelates

Lassi Jaakkola,[†] Jari Peuralahti,[†] Harri Hakala,[†] Jenni Kunttu,[†,‡] Pekka Tallqvist,[†,‡] Veli-Matti Mukkala,[†] Alice Ylikoski,[†] and Jari Hovinen*[,†]

PerkinElmer Life and Analytical Sciences, Wallac Oy, P.O. Box 10, FIN-20101 Turku, Finland, and Department of Chemistry, University of Turku, FIN-20014 Turku, Finland. Received January 26, 2005; Revised Manuscript Received March 23, 2005

The synthesis of phosphoramidite building blocks that allow introduction of luminescent europium(III), terbium(III), dysprosium(III), and samarium(III) chelates to oligonucleotides on the solid phase is described. Several labeled oligonucleotides using these building blocks were prepared, and the photophysical properties of these bioconjugates were investigated.

INTRODUCTION

The development of stable and luminescent lanthanide(III) chelates has enabled the use of homogeneous assay technologies based on time resolution (*1*). Thus, time-resolved fluorescence quenching assays based on energy transfer from a lanthanide(III) chelate to a nonfluorescent quencher have been applied in various assays of hydrolyzing enzymes (*2*−*4*) as well as for nucleic acid detection (*5*, *6*). The different photochemical properties of europium, terbium, dysprosium, and samarium chelates enable development of even multiparametric homogeneous assays (*4*, *6*).

The biomolecule conjugates used in the homogeneous quenching assays have to be extremely pure, since even small amounts of fluorescent impurities considerably increase the luminescence backround and reduce the detection sensitivity. Thus, it is highly desirable to perform the biomolecule conjugation on the solid phase, since most of the impurities can be removed by washings when the biomolecule is still anchored to the solid support, and after release to the solution, only one chromatographic purification is required.

We have already reported a solid-phase method for the labeling of oligopeptides (*7*) and oligonucleotides (*8*, *9*). The approach involves synthesis of oligonucleotide and oligopeptide building blocks, which can be introduced to the biomolecule structure using commercial oligonucleotide and oligopeptide synthesizers by phosphoramidite and Fmoc chemistries, respectively. Upon completion of the chain assembly, the oligomers are deprotected and finally treated with the appropriate lanthanide(III) citrate producing the desired biomolecule conjugates. We report here the synthesis of various building blocks which extend our labeling strategy to the preparation of synthetic oligonucleotides labeled with photoluminescent europium, terbium, samarium, and dysprosium chelates. The photophysical properties of these biomolecule conjugates are also presented.

* To whom correspondence should be addressed. Tel: + 358 2 2678 111. Fax: + 358 2 2678 380. E-mail: jari.hovinen@perkinelmer.com.

[†] PerkinElmer Life and Analytical Sciences.

[‡] University of Turku.

EXPERIMENTAL PROCEDURES

General Methods. Adsorption column chromatography was performed on columns packed with silica gel 60 (Merck) or basic aluminum oxide (Aldrich; 150 mesh, Brockmann I). Reagents for oligonucleotide synthesis were purchased from Proligo. 2-Acetyl-6-methylpyridine was purchased from HetCat (Switzerland). NMR spectra were recorded on a Bruker 250 spectrometer operating at 250.13 MHz for ^{1}H and on a JEOL LA 400 spectrometer operating at 161.9 MHz for ^{31}P. The signal of TMS was used as an internal (^{1}H) and H_3PO_4 as an external (^{31}P) reference. Coupling constants are given in hertz. ESI-TOF mass spectra were recorded on an Applied Biosystems Mariner instrument. Luminescence measurements were measured with a PerkinElmer LS-55 luminescence spectrometer equipped with a Hamamatsu R928 red-sensitive photomultiplier tube. IR and UV spectra were recorded on a PerkinElmer Spectrum One and a Shimazu UV-2100 instrument, respectively. Melting points were analyzed on a Gallenkamp apparatus and are uncorrected.

(*E*)-3-(Dimethylamino)-1-(6-methylpyridin-2-yl)-prop-2-en-1-one, 1. A mixture of 2-acetyl-6-methylpyridine (10.0 g, 74.0 mmol) and *N*,*N*-dimethylformamide dimethyl acetal (10.5 mL, 74.0 mmol) was heated at 105 °C for 7 h. The mixture was allowed to cool to room temperature, and all volatiles were removed in vacuo. The residue was suspended in petroleum ether (bp 40−60 °C), filtered, washed with petroleum ether, and dried. Yield: 10.63 g (75%). Mp: 100 °C. ^{1}H NMR ($CDCl_3$): δ 7.93 (2H, 2d, J 6.4 and 12.9); 7.90 (1H, d, J 12.5); 7.67 (1H, t, J 7.6); 7.22 (1H, d, J 7.6); 6.47 (1H, d, J 12.9) 3.16 (3H, br s); 3.00 (3H, br s); 2.61 (3H, s). ESI-TOF-MS for $C_{11}H_{15}N_2O$ $(M + H)^+$: calcd 191.12, found 191.11. λ_{max}/nm (EtOH): 254, 355.

2-Methyl-6-(1*H*-pyrazol-3-yl)pyridine, 2. Compound **1** (5.97 g, 31.4 mmol) was dissolved in ethanol (35 mL). Hydrazine monohydrate (1.80 mL, 36.9 mmol) was added, and the mixture was stirred at ambient temperature for 20 h. The mixture was concentrated in vacuo and diluted with water (25 mL). The precipitate formed was filtered, washed twice with water, and dried. Yield: 4.41 g (87%). Mp: 115 °C. ^{1}H NMR ($CDCl_3$): δ 11.46 (1H, br); 7.64 (1H, d, J 1.8); 7.62 (1H, t, J 7.6); 7.51 (1H, d, J 7.6); 7.09 (1H, d, J 7.7); 6.76 (1H, d, J 2.1); 2.59 (3H, s). ESI-TOF-MS

10.1021/bc050019x CCC: $30.25 © 2005 American Chemical Society
Published on Web 04/27/2005

for $C_9H_{10}N_3$ $(M + H)^+$: calcd 160.09, found 160.09. λ_{max}/nm (EtOH): 248, 285.

2,2′-(1*H*-Pyrazole-1,3-diyl)bis(6-methylpyridine), 3. A mixture of compound **2** (4.57 g, 28.7 mmol) and 2-bromo-6-methylpyridine (3.34 mL, 28.7 mmol) was heated at 190 °C for 15 h. The mixture was then cooled to room temperature and diluted with water (25 mL). The mixture was warmed to 50 °C, and the pH of the solution was adjusted to 9 with solid sodium carbonate. The solution was cooled on an ice bath, and the precipitate formed was collected by filtration and washed with cold water. The precipitate was redissolved in the mixture of ethanol (7 mL) and water (25 mL) and allowed to cool on an ice bath. The precipitate formed was filtered and washed with cold water and dried in vacuo over silica gel. The crude product was purified by silica gel column chromatography (eluent petroleum ether, bp 40−60 °C/ethyl acetate 5:1 v/v). Yield: 4.81 g (67%). Mp: 151 °C. ^{1}H NMR ($CDCl_3$): δ 8.67 (1H, d, *J* 2.4); 7.92 (2H, dd, *J* 3.3 and 7.9); 7.67 (2H, m); 7.13 (1H, br d, *J* 7.6); 7.12 (1H, d, *J* 2.7); 7.06 (1H, br d, *J* 7.6); 2.65 (3H, s); 2.58 (3H, s). ESI-TOF-MS for $C_{15}H_{15}N_4$ $(M + H)^+$: calcd 251.13, found 251.11. λ_{max}/nm (EtOH): 300.

2,2′-(1*H*-Pyrazole-1,3-diyl)bis(6-methylpyridine) 1,1′-Dioxide, 4b. Compound **3** (6.40 g, 44.0 mmol) was dissolved in acetic acid (50 mL). Magnesium monoperoxyphthalate hexahydrate (80%; 18.15 g) was added, and the mixture was stirred at 80 °C for 8 days. The mixture was cooled to room temperature, and the precipitate formed was removed by filtration. The solution was evaporated to dryness and coevaporated with butanol. The residue was suspended in CH_2Cl_2 (400 mL) and washed with saturated $NaHCO_3$. The organic phase was dried over Na_2SO_4 and concentrated. Purification on silica gel column chromatography (eluent from 3.5 to 15% (v/v) of MeOH in CH_2Cl_2) gave 7.66 g (62%) of compound **4b** as a solid. Mp: 188 °C. ^{1}H NMR ($CDCl_3$): δ 9.38 (1H, d, *J* 2.7); 8.16 (1H, dd, *J* 2.9 and 7.6); 8.02 (1H, dd, *J* 2.2 and 8.3); 7.83 (1H, d, *J* 2.7); 7.35−7.19 (4H, m). 2.63 (3H, s); 2.61 (3H, s). ESI-TOF-MS for $C_{15}H_{15}N_4O_2$ $(M + H)^+$: calcd 283.12, found 283.14. λ_{max}/nm (EtOH): 224, 256, 273, 310.

2,2′-(4-Iodo-1*H*-pyrazole-1,3-diyl)bis(6-methylpyridine) 1,1′-Dioxide, 5. Compound **4b** (2.0 g, 7.09 mmol) was dissolved in the mixture of water (5 mL) and nitric acid (5 mL). Iodine (1.86 g, 7.33 mmol) was added, and the mixture was heated at reflux for 4 h before being cooled to ambient temperature. Chloroform (20 mL) was added, and the solution was basified with 1 M NaOH. The organic phase was separated, and the aqueous phase was washed with ethanolic chloroform (1:4, v/v; 3 × 15 mL). The combined organic layers were dried over Na_2SO_4. The product was purified by silica gel column chromatography (eluent MeOH in CH_2Cl_2, from 3:97 to 15:100, v/v). Yield: 1.27 g (80%). Mp: 226 °C dec. ^{1}H NMR ($CDCl_3$): δ 9.48 (1H, s); 7.95 (1H, dd, *J* 2.4 and 7.8); 7.40−7.19 (5H, m); 2.61 (6H, 2 s). ESI-TOF-MS for $C_{15}H_{14}IN_4O_2$ $(M + H)^+$: calcd 409.02, found 409.05. λ_{max}/nm (EtOH): 244, 295.

6,6′-(4-Iodo-1*H*-pyrazole-1,3-diyl)bis(pyridine)-2,2′-bis(methanol), 6. Compound **5** (2.33 g, 5.7 mmol) was dissolved in acetic anhydride (15 mL), and the mixture was heated at reflux for 2.5 h, cooled to room temperature, and concentrated. The residue was dissolved in methanolic potassium hydroxide (1 M, 15 mL) and was stirred for 45 min at room temperature and concentrated. The residue was partitioned between water (20 mL) and 10% methanolic dichloromethane (100 mL). The organic phase was separated, and the aqueous phase was extracted twice with dichloromethane. The combined organic phases were dried and concentrated to give 1.40 g (63%) of compound **6**. It was used for the next step without further purification. An analytical sample was purified on silica gel (eluent 10% MeOH in CH_2Cl_2, v/v). Compound **6**. Mp: 164 °C. ^{1}H NMR (DMSO-d_6): δ 8.84 (1H, s); 8.08−7.84 (5H, m); 7.54 (1H, d, *J* 7.0); 7.48 (1H, d, *J* 7.3); 5.56 (1H, t, *J* 5.8); 5.47 (1H, t, *J* 5.8); 4.69 (2H, d, *J* 5.8); 4.63 (2H, d, *J* 5.7). ESI-TOF-MS for $C_{15}H_{14}IN_4O_2$ $(M + H)^+$: calcd 409.02, found 409.00. λ_{max}/nm (EtOH): 204, 229, 300.

2,2-(4-Iodo-1*H*-pyrazole-1,3-diyl)bis(4-chloro-6-methylpyridine), 7. Compound **5** (0.15 g, 0.37 mmol) was dissolved in anhydrous dioxane (10 mL). Phosphorus oxychloride (0.6 mL, 17.8 mmol) was added, and the mixture was heated overnight at reflux, cooled to room temperature, and concentrated in vacuo. Purification on silica gel (eluent petroleum ether, bp 40−60 °C/ethyl acetate, 5:1, v/v) gave 0.11 g (65%) of compound **7**. Mp: 160 °C. ^{1}H NMR ($CDCl_3$): δ 8.73 (1H, s); 7.90 (1H, d *J* <1); 7.88 (1H, d, *J* 1.8); 7.29 (1H, d, *J* 1.7); 7.09 (1H, d, *J* 1.7); 2.65 (3H, s); 2.54 (3H, s). ESI-TOF-MS for $C_{15}H_{12}Cl_2IN_4$ $(M + H)^+$: calcd 444.95, found 444.99.

2,2′-(4-Iodo-1*H*-pyrazole-1,3-diyl)bis(6-bromomethylpyridine), 8. Phosphorus tribromide (0.21 mL; 2.2 mmol) was added in dry DMF (15 mL) on an ice−water bath, and the mixture was stirred for 10 min. Compound **6** (0.42 g, 1.0 mmol) was added, and the mixture was stirred for 30 min at room temperature. All volatiles were removed in vacuo. The residue was dissolved in dichloromethane, washed with satd $NaHCO_3$, and dried over Na_2SO_4. Purification on silica gel using dichloromethane as the eluent yielded 0.5 g of compound **7** (94%). ^{1}H NMR ($CDCl_3$): δ 8.79 (1H, s); 7.99 (1H, d, *J* 8.0); 7.96 (1H, d, *J* 7.6); 7.84 (1H, t, *J* 7.5); 7.80 (1H, t, *J* 7.6); 7.49 (1H, d, *J* 7.6); 7.37 (1H, d, *J* 7.6); 4.68 (2H, s); 4.54 (2H, s). ESI-TOF-MS for $C_{15}H_{12}Br_2IN_4$ $(M + H)^+$: calcd 532.85, found 532.87.

Tetramethyl 2,2′,2″,2‴-{[6,6′-(4-Iodo-1*H*-pyrazole-1,3-diyl)bis(pyridine)-2,2′-diyl]bis(methylenenitrilo)}tetrakis(acetate) 9. *Method A*. Compound **8** (0.47 g, 0.88 mmol) was dissolved in dry acetonitrile (20 mL). Anhydrous potassium carbonate (1.2 g) and iminoacetic acid methyl ester (0.31 g, 1.94 mmol) were added, and the mixture was heated at reflux for 2.5 h, cooled to room temperature, and filtered. The filtrate was concentrated in vacuo, and the product was purified on silica gel (eluent petroleum ether, bp 40−60 °C/ethyl acetate, from 5:1 to 10:7; v/v). Yield: 0.45 g (74%). *Method B.* Compound **12** (10.5 g, 26.4 mmol) was suspended in dry THF (300 mL). Borane−THF complex (300 mL, 1 M in THF) was added, and the mixture was stirred overnight at room temperature. The excess of borane was destroyed with methanol (*caution*: foaming), and all volatiles were removed in vacuo. The residue was dissolved in methanolic hydrochloric acid (450 mL, 1.25 M), stirred for 2 h at room temperature, and concentrated. The residue was suspended in dry THF, filtered, and dried to give the amine **13** as pentahydrochloride. It was then suspended in dry acetonitrile (200 mL). Anhydrous K_2CO_3 (84 g) and methyl bromoacetate (12.4 mL, 0.13 mol) were added, and the mixture was heated overnight at 60 °C. The mixture was cooled to room temperature, filtered, and washed with acetonitrile. The filtrate was concetrated in vacuo, dissolved in dichloromethane, washed with satd $NaHCO_3$, dried over Na_2SO_4, and concentrated. Purification on silica gel (eluent MeOH/CH_2Cl_2, 3:97, v/v) gave 12.5 g (68%) of compound **9**. ^{1}H NMR ($CDCl_3$): δ 8.72 (1H, s); 7.94 (2H, 2 d, *J* 7.6); 7.83 (1H, t, *J* 7.4); 7.79 (1H, t, *J*

7.6); 7.63 (1H, dd, *J* 7.7 and < 1); 7.49 (1H, dd, *J* 7.3 and < 1); 4.18 (2H, s); 4.08 (2H, s); 3.73 (6H, s); 3.72 (6H s and 4H, s); 3.68 (4H, s). ESI-TOF-MS for $C_{27}H_{32}IN_6O_8$ $(M + H)^+$: calcd 695.13, found 695.12. λ_{max}/nm (EtOH): 228, 302.

2,2′-(1*H*-Pyrazole-1,3-diyl)bis(pyridine) 1,1′-Dioxide, 10. Oxidation of 2,2′-(1*H*-pyrazole-1,3-diyl)bis(pyridine) (*10*) with magnesium monoperoxyphthalate hexahydrate yielded the title compound (62%). It was spectroscopically identical with material synthesized according to ref 10.

2,2′-(4-Iodo-1*H*-pyrazole-1,3-diyl)bis(pyridine) 1,1′-Dioxide, 11. Iodination of compound **10** (13.4 g, 52.7 mmol) as described above for compound **4b** yieded 14.3 g (71%) of compound **11**. Mp > 250 °C. ^{1}H NMR ($CDCl_3$): δ 9.49 (1H, s); 8.34 (2H, m); 8.06 (1H, dd, *J* 1.9 and 8.5); 7.50 (1H, dd, *J* 2.7 and 7.3); 7.35 (4H, m); 7.22 (1H, m). ESI-TOF-MS for $C_{13}H_{11}IN_4O_2$ $(M + H)^+$: calcd 380.98, found 380.98. λ_{max}/nm (EtOH): 291, 264 (sh), 246. ν_{max} (film)/cm^{-1}: 1251 (N → O).

2,2′-(4-Iodo-1*H*-pyrazole-1,3-diyl)bis(pyridine)-6,6′-dicarbonitrile, 12. Compound **11** (13.2 g, 34.7 mmol) was suspended in dry dichloromethane (350 mL). Trimethylsilyl cyanide (46 mL, 0.35 mol) was added during 5 min, and the mixture was stirred for an additional 10 min at room temperature. Benzoyl chloride (16 mL, 0.14 mol) was added dropwise, and the mixture was stirred overnight at room temperature and concentrated to half volume. K_2CO_3 (10%, 400 mL) was added, and the mixture was stirred for 2 h at room temperature. The precipitate formed was filtered, washed with cold water, and dried in vacuo. Yield: 11.6 g (84%). ^{1}H NMR ($CDCl_3$): δ 8.79 (1H, s); 8.31 (1H, d, *J* 8.5 and <1); 8.30 (1H, dd, *J* 8.1 and < 1); 8.02 (1H, dd, *J* 7.5 and 8.5); 7.95 (1H, dd, *J* 7.7 and 8.1); 7.73 (1H, dd, *J* 7.7 and 1.0); 7.66 (1H, dd, *J* 7.5 and <1). ESI-TOF-MS for $C_{15}H_9IN_6$ $(M + H)^+$: calcd 398.99, found 398.98. λ_{max}/nm (EtOH): 306, 245. ν_{max} (film)/cm^{-1}: 2235 (C≡N).

Tetramethyl 2,2′,2″,2‴-{[6,6′-[(4-(3-hydroxy-1-propyn-1-yl)-1*H*-pyrazole-1,3-diyl)bis((pyridine)-2,2′-diyl]bis(methylenenitrilo)}tetrakis(acetate), 14. Compound **9** (0.44 g, 0.63 mmol) was dissolved in dry DMF (5 mL) and deaerated with argon. $Pd(PPh_3)_2Cl_2$ (9 mg, 0.013 mmol), CuI (5 mg, 0.026 mmol), propargyl alcohol (43 μL, 0.76 mmol), and piperidine (2 mL) were added, and the mixture was deaerated for an additional 10 min before being heated overnight at 40 °C in dark. All volatiles were removed in vacuo, and the residue was dissolved in dichloromethane, washed with water, dried (Na_2SO_4), and purified on silica gel (eluent MeOH/CH_2Cl_2, 1:9, v/v). Yield: 0.34 g (85%). ^{1}H NMR ($CDCl_3$): δ 8.74 (1H, s); 8.02 (1H, d, *J* 7.9); 7.99 (1H, d, *J* 7.9); 7.83 (1H, t, *J* 8.0); 7.78 (1H, t, *J* 7.6); 7.54 (1H, d, *J* 7.9); 7.49 (1H, d, *J* 7.5); 4.54 (2H, s); 4.19 (2H, s); 4.08 (2H, s); 3.73 (6H, s); 3.71 (6H, s and 4H, s); 3.69 (4H, s). ν_{max} (film)/cm^{-1}: 2243w (C≡C). ESI-TOF-MS for $C_{30}H_{35}N_6O_9$ $(M + H)^+$: calcd 623.25, found 623.27.

Tetramethyl 2,2′,2″,2‴-{[6,6′-[(4-(3-hydroxy-1-propyl)-1*H*-pyrazole-1,3-diyl)bis((pyridine)-2,2′-diyl]bis(methylenenitrilo)}tetrakis(acetate), 15. Compound **14** (0.32 g, 0.51 mmol) was dissolved in methanol (30 mL) and deaerated with argon for 5 min. Pd/C (10%; 40 mg) was added, and then the mixture hydrogenated at atmospheric pressure for 7 h. (Note: The use of higher pressure caused the decomposition of the desired product.) The mixture was filtered through Celite and concentrated in vacuo. Purification on silica gel (eluent MeOH/CH_2Cl_2, 1:9, v/v) yielded 0.20 g (63%) of the title compound. ^{1}H NMR ($CDCl_3$): δ 8.44 (1H, s); 7.99 (1H, dd, *J* 6.7 and <1); 7.94 (1H, d, *J* 8.0); 7.81 (1H, t, *J* 7.7); 7.80 (1H, t, *J* 7.6); 7.62 (1H, dd, *J* 7.6 and <1); 7.44 (1H, d, *J* 7.0); 4.11 (2H, s); 4.09 (2H, s); 3.72 (6H, s); 3.71 (6H, s); 3.69 (4H, s); 3.65 (4H, s); 3.62 (2H, t, *J* 5.2); 3.05 (2H, t, *J* 6.7); 1.91 (2H, p). ESI-TOF-MS for $C_{30}H_{39}N_6O_9$ $(M + H)^+$: calcd 627.28, found 627.28.

5′-*O*-(4,4′-Dimethoxytrityl)-2′-deoxy-3-{tetramethyl 2,2′,2″,2‴-{[6,6′-[(4-(3-propyl)pyrazole-1″,3″-diyl)-bis(pyridine)-2,2′-diyl]bis(methylenenitrilo)}tetrakis-(acetato)}uridine, 17. Compound **15** (0.46 g, 0.73 mmol), 5′-*O*-(4,4′-dimethoxytrityl)-2′-deoxyuridine (0.50 g, 0.95 mmol), and triphenylphosphine (0.23 g, 0.88 mmol) were dissolved in dry THF (5 mL). Diethyl azodicarboxylate (170 μL, 1.07 mmol) was added dropwise, and the mixture was stirred for 2 h at room temperature before being concentrated in vacuo. Purification on silica gel (eluent: petroleum ether, bp 40−60 °C: ethyl acetate/triethylamine, 1:5:1, v/v/v) gave 0.80 g (97%) of compound **17**. ^{1}H NMR ($CDCl_3$): δ 8.74 (1H, s); 7.95−7.22 (tot. 12H); 6.83 (4H, d, *J* 8.9); 6.35 (1H, t, *J* 6.7); 5.46 (1H, d, *J* 7.9); 4.54 (1H, m); 4.13 (2H, s); 4.09 (2H, s); 4.06 (1H, m); 3.78 (3H, s); 3.71 (12H, s); 3.69 (2 · 4H s); 3.42 (2H, m); 3.00 (2H, t, *J* 7.6); 2.60 (2H, m); 2.51 (1H, m); 2.22 (1H, m); 2.06 (2H, m). ESI-TOF-MS for $C_{60}H_{67}N_8O_{15}$ $(M + H)^+$: calcd 1139.47, found 1139.45.

4′-(6-Hydroxyhexyl-1-oxy)-2,2′:6′,2″-terpyridine 1,1″-Dioxide, 20. Compound **19** (2.62 g, 7.5 mmol) was dissolved in dichloromethane (100 mL). 3-Chloroperbenzoic acid (6.50 g, 37.5 mmol; 55%) was added, and the mixture was stirred overnight at room temperature. The mixure was dried over Na_2SO_4 and concentrated. Purification on basic alumina using dichloromethane containing 3% methanol (v/v) as the eluent followed by precipitation from diethyl ether gave the bis-*N*-oxide **20** (2.2 g, 77%). Mp: 168 °C. ^{1}H NMR ($CDCl_3$): δ 8.58 (2H, s); 8.33 (2H, dd, *J* < 1 and 6.6); 8.24 (2H, dd, *J* 2.2 and 7.8); 7.39 (2H, dt, *J* 1.2 and 7.5); 7.33 (2H, dt; *J* 2.4 and 7.5); 4.17 (2H, t, *J* 6.6); 3.62 (2H, t, *J* 6.1); 3.17 (1H, br. s); 1.84 (2H, p, *J* 6.8); 1.59 (2H, p, *J* 6.8); 1.47 (4H, m). ESI-TOF MS for $C_{21}H_{24}N_3O_4^+$ $(M + H)^+$: calcd 382.18, obsd 382.18.

4′-(6-Hydroxyhexyl-1-oxy)-2,2′:6′,2″-terpyridine 2,6″-Dicarbonitrile, 21. Compound **20** (2.25 g, 5.9 mmol) was dissolved in dichloromethane (120 mL). Trimethylsilyl cyanide (5.95 g, 60 mmol) was added, and the mixture was stirred for 5 min at room temperature, after which time benzoyl chloride (3.37 g, 24 mmol) was added dropwise during 20 min and the mixture was stirred for 1 h at room temperature. An aqueous 10% solution of K_2CO_3 (80 mL) was added, and stirring was continued for 1 h. The organic layer was separated, and the aqueous phase was extracted twice with dichloromethane. The combined dichloromethane layers were dried over Na_2SO_4 and concentrated. Purification on silica gel (eluent 5% MeOH in CH_2Cl_2, v/v) followed by precipitation from diethyl ether yielded the title compound (1.9 g, 81%). Mp: 169−170 °C. ^{1}H NMR ($CDCl_3$): δ 8.81 (2H, dd, *J* <1 and 8.0); 8.08 (2H, s); 8.00 (2H, t, *J* 7.8); 7.75 (2H, dd, *J* 1 and 7.5); 4.26 (2H, t, *J* 6.4); 3.71 (2H, t, *J* 6.3); 1.93 (2H, p, *J* 6.5); 1.64 (5H, m and br s). ESI-TOF MS for $C_{23}H_{22}N_5O_2$ $(M + H)^+$: calcd 400.18, obsd 400.18. ν_{max} (KBr)/cm^{-1}: 2237 (C≡N). λ_{max}/nm (EtOH): 213, 250, 386.

Tetramethyl 2,2′,2″,2‴-{[4′-(6-Hydroxyhexyl-1-oxy)-2,2′:6′,2″-terpyridine-6,6″-diyl]bis(methylenenitrilo)}-tetrakis(acetate), 23. Compound **21** (1.0 g, 2.5 mmol) was dissolved in dry THF (20 mL), and the mixture was deaerated with argon. Borane−THF complex (24 mL; 1 M) was added during 5 min, and the mixture was stirred overnight at room temperature. The excess of borane was destroyed by careful addition of methanol (100 mL).

When the foaming had ceased, all volatiles were removed in vacuo. The residue was dissolved in satd methanolic HCl (50 mL), stirred for 2 h at room temperature and concentrated. The residue was triturated with diethyl ether and filtered to give compound **22** as pentahydrochloride (ESI-TOF MS for $C_{23}H_{30}N_5O_2$ $(M + H)^+$ calcd 408.24, found 408.21). The residue was dissolved in dry DMF (15 mL). Anhydrous K_2CO_3 (1.0 g) and methyl bromoacetate (0.89 mL, 6.0 mmol) were added, and the mixture was stirred for 2 h at room temperature and concentrated. The residue was suspended in dichloromethane, washed with water, and dried over Na_2SO_4. Purification was performed on silica gel (eluent petroleum ether bp 40−60 °C/ethyl acetate/triethylamine 2:5:1, v/v/v). ESI-TOF MS for $C_{35}H_{46}N_5O_{10}$ $(M + H)^+$: calcd 696.32, found 696.31. ^{1}H NMR ($CDCl_3$): δ 8.50 (2H, d, *J* 7.9); 8.00 (2H, s); 7.83 (2H, t, *J* 7.8);7.58 (2H, d, *J* 7.5); 4.24 (2H, t, *J* 6.3); 4.16 (4H, s); 3.72 (12H, s); 3.71 (8H, s); 3.69 (2H, t); 1.90 (4H, m); 1.54 (4H, m).

Diethyl 2,2′-(4-Bromo-6-bromomethyl-2-pyridylmethylenenitrilo)bis(acetate), 26. 4-Bromo-2,6-bis(bromomethyl)pyridine (**25**; 3.10 g, 9.0 mmol) was dissolved in dry acetonitrile (80 mL). Potassium carbonate (6.2 g) and iminodiacetic acid methyl ester (0.77 g, 4.8 mmol) were added, and the mixture was stirred for 3.5 h at 60 °C, filtered, and concentrated. Purification was performed on silica gel (eluent petroleum ether, bp 40−60 °C/ethyl acetate from 15:1 to 2:5, v/v). Yield: 1.65 g (43%). ^{1}H NMR ($CDCl_3$): δ 7.76 (1H, s); 7.51 (1H, s); 4.46 (2H, s); 4.04 (2H, s); 3.72 (6H, s); 3.63 (4H, s). ESI-TOF-MS for $C_{13}H_{17}Br_2N_2O_4$ $(M + H)^+$: calcd 422.96, found 422.94.

Tetramethyl 2,2′,2″,2‴-{[6-(Hydroxyhex-1-ylimino]bis(methylene)bis(4-bromopyridine-6,2-diyl)bis(methylenenitrilo)}tetrakis(acetate), 27. Compound **26** (1.60 g, 3.77 mmol) and 6-aminohexan-1-ol (0.46 g, 3.96 mmol) were dissolved in dry DMF (35 mL). *N,N*-Diisopropylethylamine (3.3 mL) was added, and the mixture was stirred for 3 h at 60 °C before being cooled to room temperature and concentrated in vacuo. The residue was dissolved in dichloromethane, washed with water, and dried over Na_2SO_4. Purification on silica gel (eluent 10% MeOH in CH_2Cl_2, v/v) yielded the title compound (1.0 g, 66%) as an oil. Compound **27**. ^{1}H NMR ($CDCl_3$): δ 7.66 (2H, s); 7.58 (2H, s); 7.52 (2H, d, *J* 1.8); 4.00 (4H, s); 3.73 (4H, s); 3.70 (12H, s); 3.61 (8H, s); 3.60 (2H, m); 2.51 (2H, t, *J* 6.6); 1.54 (4H, m); 1.30 (4H, m). ESI-TOF-MS for $C_{32}H_{45}Br_2N_5O_9$ $(M + H)^+$: calcd 802.19, found 802.19.

Tetramethyl 2,2′,2″,2‴-{[6-(hydroxyhex-1-ylimino]bis(methylene)bis[4-(2-furyl)pyridine-6,2-diyl)]bis(methylenenitrilo)}-tetrakis(acetate), 28. Compound **27** (0.53 g, 0.66 mmol) and 2-(tributylstannyl)furan (0.44 mL, 1.39 mmol) were dissolved in dry DMF, and the mixture was deaerated with argon for 15 min. $(Ph_3P)_4Pd$ (76 mg, 0.066 mmol) was added, and the mixture was stirred at 90 °C for 3.5 h, allowed to cool to room temperature, and concentrated. The residue was dissolved in dichloromethane, washed twice with 1 M Na_2CO_3, dried, and concentrated. Purification on silica gel (eluent 10% MeOH in CH_2Cl_2, v/v) yielded the title compound (0.44 g, 86%) as an oil. Compound **28**. ^{1}H NMR ($CDCl_3$): δ 7.81 (2H, s); 7.68 (2H, s); 7.52 (2H, d, *J* 1.8); 6.92 (2H, d, *J* 3.2); 6.51 (2H, dd, *J* 1.8 and 3.2); 4.06 (4H, s); 3.82 (4H, s); 3.70 (12H, s); 3.65 (8H, s); 3.57 (2H, t, *J* 6.6); 2.60 (2H, t, *J* 6.6); 1.80 (1H, br s); 1.54 (4H, m); 1.33 (4H, m). ESI-TOF-MS for $C_{40}H_{52}N_5O_{11}$$(M + H)^+$: calcd 778.40, found 778.40.

Tetramethyl 2,2′,2″,2‴-{{[6-(4-Methoxytrityloxy)hex-1-ylimino]bis(methylene)bis(4-bromopyridine-6,2-diyl)}bis(methylenenitrilo)}tetrakis(acetate), 30. Compound **27** (0.46 g, 0.6 mmol) was dried by coevaporation with dry pyridine and dissolved in the same solvent (15 mL). MMTr-chloride (0.28 g, 0.9 mmol) was added, and the mixture was stirred overnight at room temperature and concentrated in vacuo. The residue was dissolved in dichloromethane, washed with satd $NaHCO_3$, and dried over Na_2SO_4. Purification on silica gel (eluent petroleum ether/ethyl acetate, from 5:1 to 1:1, v/v) yielded 0.44 g (59%) of compound **30**. ^{1}H NMR ($CDCl_3$): δ 7.66 (2H, d, *J* 1.4); 7.58 (2H, d, *J* 1.4); 7.43 (4H, m); 7.44 (4H, m); 7.28 (8H, m); 6.82 (2H, d, *J* 8.3); 4.00 (4H, s); 3.79 (3H, s); 3.72 (4H, s); 3.70 (12H, s); 3.60 (8H, s); 3.02 (2H, t, *J* 6.6); 2.49 (2H, t, *J* 7.3); 1.61 (2H, m); 1.51 (2H, m); 1.28 (4H, m). ESI-TOF-MS for $C_{52}H_{62}Br_2N_5O_{10}$ $(M + H)^+$: calcd 1074.28, found 1074.26.

Tetramethyl 2,2′,2″,2‴-{{[6-(4-Methoxytrityloxy)hex-1-ylimino]bis(methylene)bis[4-(2,4,6-trimethoxyphenyl)pyridine-6,2-diyl]}bis(methylenenitrilo)}-tetrakis(acetate), 31. Compound **30** (0.39 g, 0.38 mmol) and 2,4,6-trismethoxyphenylboronic acid (0.24 g, 1.14 mmol) were dissolved in dry DMF, and the mixture was deaerated with argon. $(Ph_3P)_4Pd$ (17 mg, 0.015 mmol) and Cs_2CO_3 (0.42 g, 1.3 mmol) were added, and the mixture was heated overnight at 95 °C. The cooled mixture was concentrated in vacuo, and the residue was dissolved in dichloromethane, washed with satd $NaHCO_3$, and dried over Na_2SO_4. Purification on silica gel (eleuent 10% MeOH in CH_2Cl_2) yielded the title compound. ^{1}H NMR (DMSO-d_6): δ 7.63 (2H, s); 7.35 (2H, s); 7.32−7.17 (12H, m); 6.86 (2H, d, *J* 8.9); 6.25 (4H, s); 3.90 (4H, s); 3.81 (4H, s); 3.71 (3H, s); 3.57 (18H, s) 3.49 (12H, s); 3.34 (8H, s); 2.87 (2H, t, *J* 5.2); 2.44 (2H, t, *J* 6.4); 1.44 (4H, m); 1.18 (4H, m). ESI-TOF-MS calcd for $C_{70}H_{84}N_5O_{16}^+$ 1250.59, found 1250.54.

Tetramethyl 2,2′,2″,2‴-{{(6-Hydroxyhex-1-ylimino)bis(methylene)bis[4-(2,4,6-trimethoxyphenyl)pyridine-6,2-diyl]}bis(methylenenitrilo)}tetrakis(acetate), 32. Compound **31** (0.14 g, 0.11 mmol) was dissolved in dichloromethane (5 mL). Trifluoroacetic acid (0.25 mL) was added, and the mixture was strirred for 3 h at room temperature. Methanol (10 mL) was added, and all volatiles were removed in vacuo. Purification on silica gel (eluent MeOH/CH_2Cl_2, from 1:9 to 1:5, v/v) yielded compound **32**. ^{1}H NMR ($CDCl_3$) δ 7.52 (2H, s); 7.32 (2H, s); 4.06 (4H, s); 3.85 (8H, s); 3.68 (18H, s); 3.66 (4H, s); 3.53 (12H, s); 3.52 (2H, m); 2.58 (2H, m); 1.52 (8H, m).

Synthesis of the Phosphoramidites. General Procedure. The predried alcohol (**15**, **17**, **23**, **28**, and **32**) and 2-cyanoethyl *N,N,N′,N′*-tetraisopropylphosphordiamidite (1.5 equiv) were dissolved in dry acetonitrile. 1*H*-Tetrazole (1 equiv; 0.45 M in acetonitrile) was added, and the mixture was stirred for 30 min at room temperature before being poured into 5% $NaHCO_3$ and extracted with dichloromethane and dried over Na_2SO_4. Purification on silica gel (eluent: petroleum ether, bp 40−60 °C: ethyl acetate/triethylamine, 2:5:1, v/v/v) yielded the desired phosphoramidites. Compound **18** was a solid, and the non-nucleosidic phosphoramidites were oils. Compound **16**. ^{31}P NMR ($CDCl_3$): δ 149.3. ESI-TOF-MS for $C_{39}H_{56}N_8O_{10}P$ $(M + H)^+$: calcd 827.39, found 827.37. Compound **18**. ^{31}P NMR ($CDCl_3$): δ 152.5 (0.5 P), 152.1 (0.5 P). ESI-TOF-MS for $C_{69}H_{84}N_{10}O_{16}P$ $(M + H)^+$: calcd 1339.58, found 1339.85. Compound **24**. ^{31}P NMR ($CDCl_3$): δ 147.7. ESI-TOF-MS for $C_{44}H_{64}N_7O_{11}P$ $(M + H)^+$: calcd 896.43, found 896.32. Compound **29**: ^{31}P NMR ($CDCl_3$): δ 148.6. ESI-TOF-MS for $C_{49}H_{69}N_7O_{12}P$ $(M + H)^+$: calcd 978.47, found 978,32. **33**: ^{31}P NMR ($CDCl_3$):

δ 149.0. ESI-TOF-MS for $C_{59}H_{85}N_7O_{16}P$ $(M + H)^+$: calcd 1178.58, found 1178.43.

Synthesis and Purification of the Oligonucleotide Conjugates. The oligonucleotides were assembled on an Applied Biosystems 3400 instrument on a 1.0 μmol scale using phosphoramidite chemistry and recommended protocols. The phosphoramidites (**16**, **24**, **29**, and **33**) were coupled to the 5′-terminus of the oligonucleotide sequence (coupling time 10 min, concentration 0.2 M). As the chain assembly was completed, the oligonuleotides were deprotected by first treating the solid support with 0.1 M NaOH for 4 h at room temperature. Ammonium chloride (1.0 M) was then added, and the solution was concentrated in vacuo. The residue was treated with concentrated ammonia for 16 h at 55 °C, after which time aqueous lanthanide citrate (5 equiv per ligand) was added, and the mixture was kept for 90 min at room temperature. Desalting by gel filtration followed by denaturing PAGE yielded the oligonucleotide conjugates (**35**−**41**). The following oligonucleotides were synthesized

5′-X-AAT CAG ACT GTT CAA GAC-3′ (**35**)
5′-X TGA CAG CGA CGT GGA T-3′ (**36**, **37**)
5′-X TCT CCA TCA AAT TCA TTT-3′ (**38**)
5′-X ATC TTC TAA ATC TGC GTT-3′ (**39, 41**)
5′-XAAT GTA GTC CCT GGA A-3′ (**40**)

where X is the position of the label (for structures of X, see Table 1).

RESULTS AND DISCUSSION

Synthesis of the Oligonucleotide Labeling Reactants. Preparation of the phosphoramidite building blocks that enable introduction of luminescent europium(III), terbium(III), samarium(III), and dysprosium(III) chelates to synthetic oligonucleotides on solid phase is outlined in Schemes 1-4. The key steps are discussed below.

The terbium(III) chelate based on 2-(3-(pyridin-2-yl)-1*H*-pyrazol-1-yl)pyridine (**A**, Chart 1) has excellent photophysical properties including high luminescent quantum yield and relatively high energy of its lowest triplet state (*10*). To use this chelate for biomolecule derivatization, the synthetic route had to be modified. Several approaches were investigated, and the most useful ones are demonstrated in Scheme 1. Accordingly, 6-methyl-2-acetylpyridine was initially converted to (*E*)-3-(dimethylamino)-1-(6-methylpyridin-2-yl)prop-2-en-1-one (**1**) by treatment with *N,N*-dimethylformamide dimethyl acetal. It was then cyclized to **2** with hydrazine hydrate followed by reaction with 2-bromo-6-methylpyridine giving rise to **3**, which was subsequently oxidized to the corresponding di-*N*-oxide with magnesium monoperoxyphthalate in glacial acetic acid (*11*). Interestingly, while the mono-*N*-oxide **4a** was formed readily, a prolonged reaction time (8 days at 80 °C) was required for the preparation of the di-*N*-oxide **4b**. The use of *m*-chloroperbenzoic acid as the oxidant (*10*) resulted in even longer reaction times.

To attach linker arms to the pyrazole moiety, a method for the preparation of the corresponding 4-halogenated precursor is needed. While iodination of **4b** with KI/I_2 (*12*) was not successful, the classical HIO-assisted iodination (*13*) occurred readily giving rise to **5**. It was essential to convert **3** to **4b** prior to iodination, since the 4-iodo derivative of **3** was not stable during the rather drastic conditions needed for oxidation. Treatment of **5** with acetic anhydride followed by base-catalyzed hydrolysis (*14*) gave the dimethanol **6**, which was converted almost quantitatively to the corresponding dibromide **8** by reaction with PBr_3 in dry DMF. It is worth noting that reaction of **4b** with $POBr_3$ or the free-radical bromination with NBS (*15*) were not successful. Reaction of **4b** with phosphorus oxychloride (*15, 16*), in turn, did not yield the corresponding 6,6″-bis(chloromethyl) derivative, but the undesired dichloride **7** (*11*). Reaction of **7** with iminodiacetic acid dimethyl ester gave **9** in high yield.

An alternative route for the preparation of the key intermediate **9** involves iodination of 1,3-di(pyridyl)-pyrazole *N,N*″-dioxide, **5** (*10*) and its conversion to the corresponding 6,6′-dicarbonitrile **12** by treatment with trimethylsilylcyanide and benzoyl chloride followed by borane reduction. Reaction of the amine **13** with methyl bromoacetate in acetonitrile in the presence of potassium carbonate gave **9** in high yied.

The rest of the synthesis was straightforward. Reaction of **9** with propargyl alcohol in the presence of copper(I) iodide and $Pd(Ph_3P)_2Cl_2$ as catalysts gave **14**. The highest coupling yield was obtained using DMF as the solvent and piperidine as the base. The reaction could be performed at ambient temperature demonstrating the power of iodine as the leaving group in Sonogashira reaction. Catalytic hydrogenation over Pd/C yielded **15**. It was then phosphitylated to **16** by treatment with 2-cyanoethyl *N,N,N′,N′*-tetraisopropylphosphordiamidite in dry acetonitrile using 1*H*-tetrazole as the catalyst. Alternatively, **15** was initially converted to the nucleoside **17** by reaction with 2′-deoxy-5′-*O*-(4,4′-dimethoxytrityl)-uridine in the presence of triphenylphosphine and diisopropylazodicarboxylate (*8*) and then phosphitylated to give **18**, a nucleosidic phosphoramidite designed for multilabeling of oligonucleotides.

Terpyridine-based lanthanide(III) chelates are among the best luminescent europium(III) chelates used as nonradioactive markers in a wide variety of routine and research applications (*10, 15*−*19*). One of the structures is shown in Chart 1. We have also synthesized the corresponding nucleosidic and non-nucleosidic phosphoramidites and oligopeptide building blocks and demonstrated their suitability to the preparation of labeled oligonucletides and oligopeptides (*7*−*9*). Here, we wanted to simplify the synthetic procedure by omitting the central phenyl ring from the structure by connecting the linker arm to 4′-positon via an ether linkage. The ether function, in turn, is known to increase the energy of the lowest triplet state of the ligand (*10*), an important parameter effecting on the luminescent quantum yield of the europium(III) chelate. Accordingly, the terminal pyridine moieties of 4′-(6-hydroxyhexyloxy)-2,2′:6′,2″-terpyridine **19** (*20*) were oxidized with *m*-chloroperbenzoic acid to give the *N,N*″-dioxide **20** in high yield. In strict contrast to the oxidation of **3**, the reaction was completed in few hours at ambient temperature. The modified Reissert−Henze reaction (*21*) converted **20** to the 6,6″-dicarbonitrile **21**. The reaction was completed in 1 h at room temperature. Prolonged reaction time caused partial benzoylation of the ω-hydroxy group. However, this side reaction was not crucial, since the ω-benzoyl group was cleaved during borane reduction to give **22**, followed by carboxymethylation to the tetraester **23** with methyl bromoacetate in the presence of potassium carbonate as the base. Phosphitylation as described above yielded the corresponding phosphoramidite, **24**.

Certain ligands with furylpyridine and trismethoxyphenylpyridine subunits form highly luminescent chelates with europium as well as with terbium and dys-

Table 1. Photophysical Properties of the Oligonucleotide Conjugates Prepared (for Oligonucleotide Sequences See the Experimental Procedures)

Compound	Structure	Excitation wavelength (nm)	Emission wavelength (nm)	τ (ms)	εΦ
35	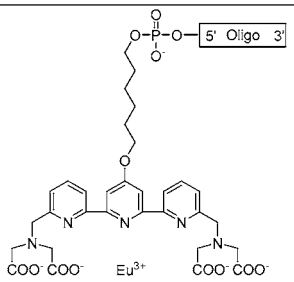	328	596 (16%) 616 (37%) 650 (4%) 695 (43%) 765 (0.6%)	1.40	3300
36	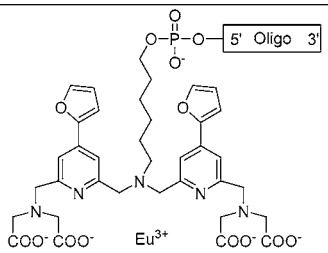	315	593 (9%) 617 (53%) 654 (3%) 698 (33%) 750 (1%)	1.16	14000
37	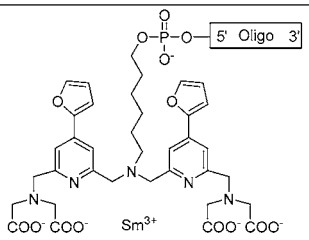	318	564 (8%) 599 (36%) 645 (38%) 709 (14%) 784 (4%)	0.0192	160
38	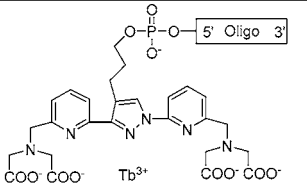	331	491 (21%) 544 (50%) 587 (15%) 622 (9%) 649 (3%) 681 (3%)	2.20	7200
39	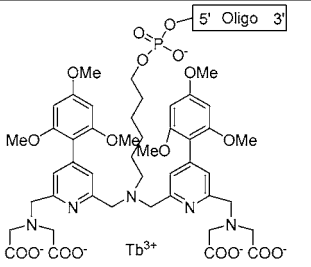	310	490 (19%) 545 (58%) 586 (12%) 621 (8%) 649 (3%) 670 (1%)	2.12	15000
40	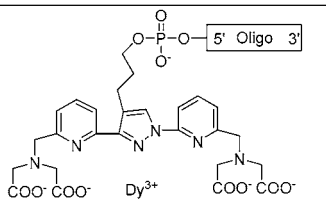	328	478 (37%) 574 (49%) 658 (6%) 759 (8%)	0.0049	260
41	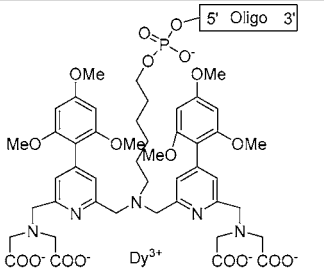	310	480 (31%) 575 (59%) 661 (5%) 750 (5%)	0.0216	330

Scheme 1. Synthesis of the Oligonucleotide-Labeling Reactant Based on 2-(3-(Pyridin-2-yl)-1*H*-pyrazol-1-yl)-pyridine

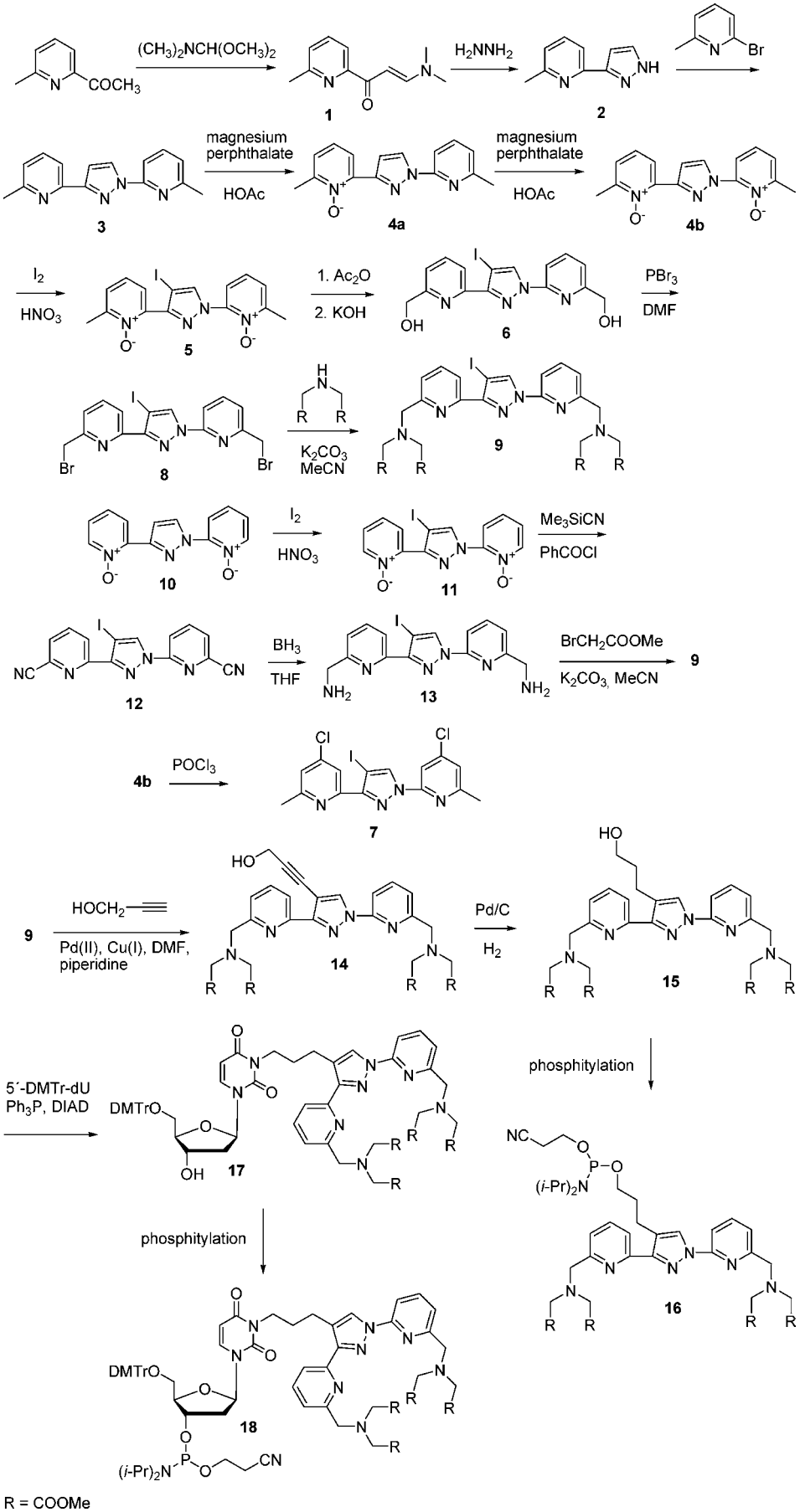

Scheme 2. Synthesis of the Oligonucleotide-Labeling Reactant Based on Terpyridine

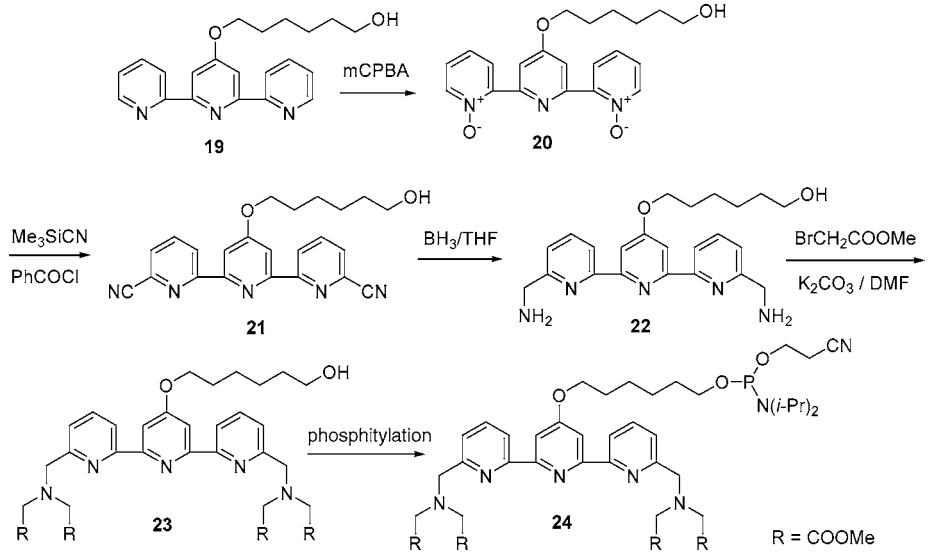

Scheme 3. Synthesis of the Oligonucleotide-Labeling Reactant Based on Furylpyridine Subunits

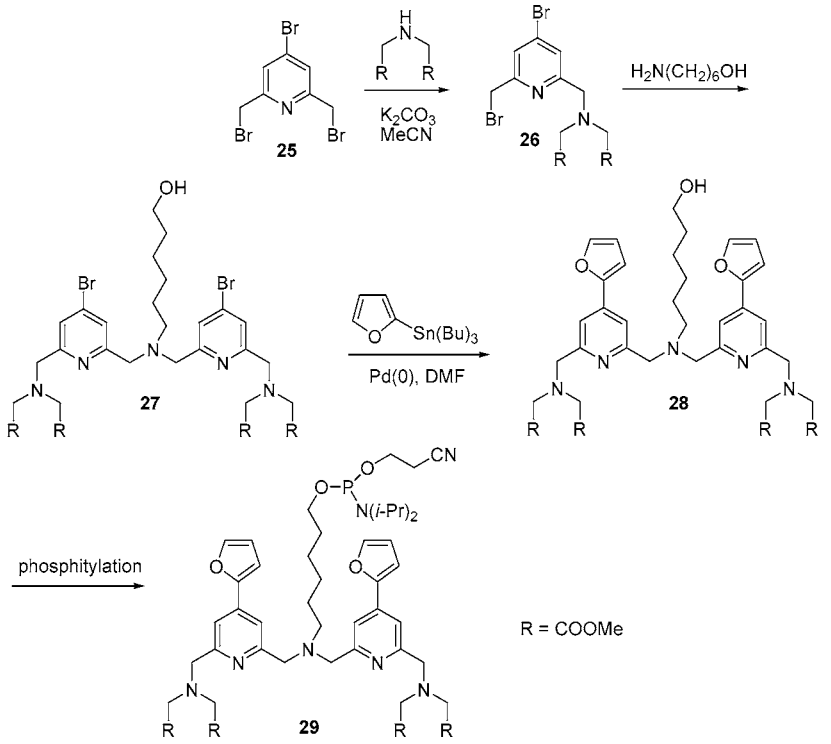

prosium, respectively (structures **C** (*22*) and **D** (*23*) in Chart 1). Thus, these chromophores were chosen as key elements of the next oligonucleotide labeling reactants. Their syntheses are desribed in Schemes 3 and 4. Initially, 4-bromo-2,6-bis(bromomethyl)pyridine, **25** (*24*), was allowed to react with an equimolar amount of iminodiacetic acid dimethyl ester to yield the monobromide **26**, which was further allowed to react with 0.5 equiv of 6-aminohexan-1-ol giving **27** in moderate yield. The palladium(0)-catalyzed Stille reaction of **27** with tributylstannylfuran gave **28**, which was finally converted to the corresponding phosphoramidite **29** as above. The corresponding trismethoxyphenyl derivative **33** was obtained analogously, but the ω-hydroxy group of **27** was protected as a MMTr-ether prior to coupling to 2,4,6-trimethoxybenzeneboronic acid in the presence of cesium carbonate and tetrakis(triphenylphosphine)palladium(0). Without protection, formation of the ester derivative **34** (structure tentatively assigned based on MS analysis) was a serious side reaction in the Suzuki reaction.

Syntheses of the Oligonucleotide Conjugates. Syntheses of the oligonucleotide conjugates were performed with a standard oligonucleotide synthesizer using phosphoramidite chemistry (*8*, *9*). Upon completion of the syntheses, the conjugates were deprotected and converted the corresponding lanthanide(III) chelates by treatment with appropriate lanthanide(III) salts. The oligonucleotides were purified on gel electrophoresis. According to mass spectrometric analyses, the observed molecular weights of the biomolecule conjugates were in accordance with the proposed structures.

Photophysics. The measured excitation and emission wavelengths as well as the decay times (τ) and luminescence yields ($\epsilon\Phi$) of chelates coupled to oligonucleotides (**35**−**41**) are shown in Table 1. The measurements were carried out in Tris buffer containing 0.9% NaCl at pH

Scheme 4. Synthesis of the Oligonucleotide-Labeling Reactant Based on Trismethoxyphenylpyridine Subunits

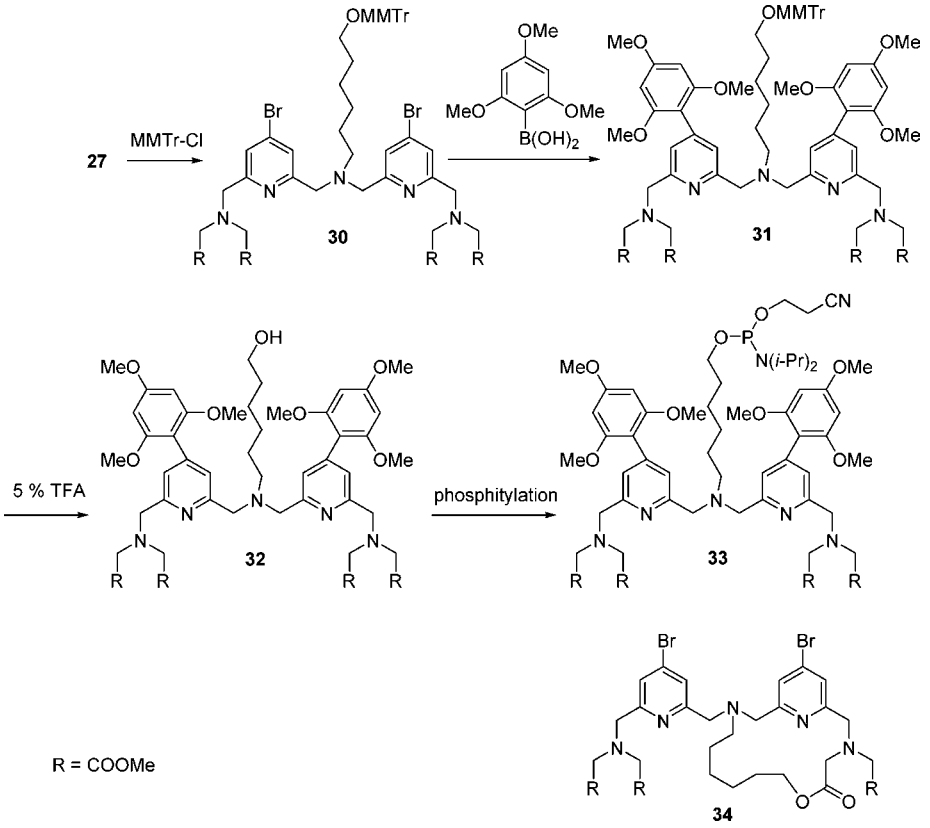

7.75. The luminescence yields were measured by a relative method described earlier (*10*, *26*). The observed emission spectra were typical for lanthanide chelates corresponding to the $^5D_0 \rightarrow {}^7F_j$, $^4G_{5/2} \rightarrow {}^6H_j$, $^5D_4 \rightarrow {}^7F_j$, and $^4F_{9/2} \rightarrow {}^6H_j$ transitions for Eu^{3+}, Sm^{3+}, Tb^{3+}, and Dy^{3+}, respectively. The main emission lines of chelates were centered as usual around 617 (Eu^{3+}), 645 (Sm^{3+}), 544 (Tb^{3+}), and 575 nm (Dy^{3+}). The only exception was **35**, which has 695 nm peak slightly more intense than that of 617 nm. The decay times were normal for nonadentate chelates except that of chelate **40**, which has surprisingly short decay time. The luminescence yields of studied chelates were high compared to earlier published results. The ether function of **35** decreased the excitation wavelength and increased the luminescence yield compared to parent compound (*10*). Although the luminescence yield of **35** was high, the luminescence yield of **36** was still over four times higher. Therefore, the **36** is the brightest stable, directly luminescent europium(III) chelate published, according to our knowledge. When the ligand of **36** was used with samarium(III) ion, i.e., compound **37**, the luminescence yield obtained was high compared to earlier published results (*18*, *26*, *27*). The terbium(III) chelates **38** and **39** also had high luminescence yields, **39** having two times higher than **38**. The ligand structures of **38** and **39** were applied also with dysprosium(III) ion (**40** and **41**). The luminescence yields obtained were high, although the decay time of **40** was surprisingly short. It is worth noting that although the decay times are shorter and luminescence yields much lower in the case of samarium and dysprosium chelates than in the case of europium and terbium chelates, they are valuable when multiparametric assays are developed (*4*, *6*, *28*).

We are currently studying the use of the biomolecule conjugates synthesized in multiparametric TruPoint assays. These results will be published in due course.

Chart 1

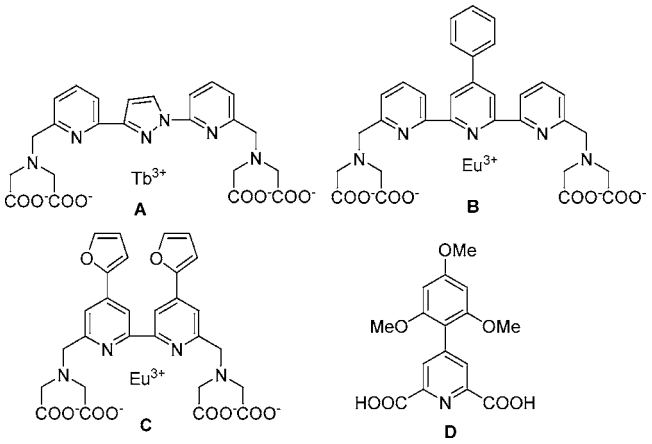

LITERATURE CITED

(1) Hemmilä, I., and Mukkala, V.-M. (2001) Time-resolution in fluorometry technologies, labels, and applications in bioanalytical assays. *Crit. Rev. Clin Lab. Sci. 38*, 441−519.

(2) Karvinen, J., Hurskainen, P., Gopalakrishnan, S., Burns, D., Warrior, U., and Hemmilä, I. (2002) Homogeneous time-resolved fluorescence quenching assay (LANCE) for caspase-3. *J. Biomol. Screening 7*, 223−231.

(3) Karvinen, J., Laitala, V., Mäkinen, M.-L., Mulari, O., Tamminen, J., Hermonen, J., Hurskainen, P., and Hemmilä, I. (2004) Fluorescence quenching-based assays for hydrolyzing enzymes. Application of time-resolved fluorometry in assays for caspase, helicase and phosphatase. *Anal. Chem. 76*, 1429−1436.

(4) Karvinen, J., Elomaa, A., Mäkinen, M.-L., Hakala, H., Mukkala, V.-M., Peuralahti, J., Hurskainen, P., Hovinen, J., and Hemmilä, I. (2004) Caspase multiplexing: simultaneous homogeneous time-resolved quenching assay (TruPoint) for caspases 1, 3, and 6. *Anal. Biochem. 325*, 317−325.

(5) Nurmi, J., Ylikoski, A., Soukka, T., Karp, M., and Lövgren, T. (2000) A new label technology for the detection of specific polymerase chain reaction products in a closed tube. *Nucleic Acids Res. 28*, E28.
(6) Ylikoski, A., Elomaa, A., Ollikka, P., Hakala, H., Mukkala, V.-M., Hovinen, J., and Hemmilä, I. (2004) Homogeneous time-resolved fluorescence quenching assay (TruPoint) for nucleic acid detection. *Clin. Chem. 50*, 1943−1947.
(7) Peuralahti, J., Hakala, H., Mukkala, V.-M., Hurskainen, P., Mulari, O., and Hovinen, J. (2002) Introduction of lanthanide-(III) chelates to oligopeptides on solid phase. *Bioconjugate Chem. 13*, 870−875.
(8) Hovinen, J. and Hakala, H. (2001) Versatile strategy for oligonucleotide derivatization. Introduction of lanthanide(III) chelates to oligonucleotides. *Org. Lett. 3*, 2473−2476.
(9) Hakala, H., Ollikka, P., Degerholm, J., and Hovinen, J. (2002) Oligonucleotide conjugates based on acyclonucleotides and their use in DNA hybridization assays. *Tetrahedron*, *58*, 8771−8777.
(10) Latva, M., Takalo, H., Mukkala, V.-M., Matachescu, C., Rodríquez-Ubis, J. C. and Kankare, J. (1997) Correlation between the lowest triplet state energy level of the ligand and lanthanide(III) luminescence quantum yield. *J. Lumin. 75*, 149−169.
(11) Katritzky, A. R., and Lagowski, J. M. (1971) *Chemistry of the Heterocyclic N-oxides* Academic Press Inc.: London.
(12) Holzer, W., and Gruber, H. (1995) *N*1-substituted 3,5-dimethoxy-4-halogeno-1*H*-pyrazoles: synthesis and NMR study. *J. Heterocycl. Chem. 21*, 1351−1354.
(13) Lew, Y., and Noller, C. R. (1963) 2-Iodothiophene. *Organic Syntheses* Collect. Vol. IV, pp 545−547, Wiley: New York.
(14) Newkome, G. R., Puckett, W. E., Kiefer, G. E., Gupta, V. K., Xia, Y., Coreil, M., and Hackney, M. A. (1982) α-Methyl functionalization of electron-poor heterocycles: chloromethyl derivatives of 2, 2′-bipyridines. *J. Org. Chem. 47*, 4116−4119.
(15) Mukkala, V.-M., Sund, C., Kwiatkowski, M., Pasanen, P., Högberg, M., Kankare, J., and Takalo, H. (1992) New heteroaromatic complexing agents and luminescence of their europium(III) and terbium(III) chelates. *Helv. Chim. Acta 75*, 1621−1632.
(16) Sakamoto, T., Kaneda, S., Hama, Y., Yoshizawa, H., and Yamanaka, H. (1983) Studies on pyrimidine derivatives XXXI. Synthesis of chloromethylpyridimidines by reaction of monomethylpyridine *N*-oxides with phosphoryl chloride. *Heterocycles 20*, 991−995.
(17) Mukkala, V.-M., Helenius, M., Hemmilä, I., Kankare, J., and Takalo, H. (1993) Development of luminescent europium-(III) and terbium(III) chelates of 2,2′:6′,2″-terpyridine derivatives for protein labeling. *Helv. Chim. Acta 76*, 1361.
(18) Galaup, C., Couchet, J. M., Picard, C., and Tisnes, P. (2001) Novel terpyridine macrocyclic complexing agent and luminescence of its neutral Ln(III) complexes (Ln = Eu, Tb, Sm, Dy) in aqueous solution. *Tetrahedron Lett. 42*, 6275−6278.
(19) Cooper, M. E. and Sammes, P. G. (2000) Synthesis and spectral properties of a new luminescent europium(III) terpyridyl chelate. *J. Chem. Soc., Perkin Trans. 2* 1695−1700.
(20) Sampath, U., Putnam, W. C., Osiek, T. A., Touami, S., Xie, J., Cohen, D., Cagnolini, A., Droege, P., Klug, D., Barnes, C. L., Modak, A., Bashkin, J. K., and Jurisson, S. S. (1999) Terpyridyl derivatives as bifunctional chelates: synthesis and crystal structures of 4′-[2-(1,3-dioxolan-2-yl)ethylsulfanyl]-2,2′:6′,2″-terpyridine and chloro(4′-methylsulfanyl-2,2′:6′,2″-terpyridine)gold(II) bis(trifluoromethanesulfonate). *J. Chem. Soc., Dalton Trans*. 2049−2058.
(21) Fife, W. K. (1983) Regioselective cyanation of pyridine 1-oxides with trimethylsilanecarbonitrile: a modified Reissert-Henze reaction. *J. Org. Chem. 48*, 1375−1377.
(22) Mukkala, V.-M. and Kankare, J. (1992) New 2,2′-bipyridine derivatives and their luminescence properties with europium-(III) and terbium(III). *Helv. Chim. Acta 75*, 1578−1592.
(23) Hemmilä, I., Mukkala, V.-M., Latva, M., and Kiilholma, P. (1993) Di- and tetracarboxylate derivatives of pyridines, bipyridines and terpyridines as luminogenic reagents for time-resolved fluorometric determination of terbium and dysprosium. *J. Biochem. Biophys. Methods 26*, 283−290.
(24) Takalo, H., Pasanen, P., and Kankare, J. (1988) Synthesis of 4-(phenylethynyl)-2,6-bis[N,N-bis(carboxymethyl)aminomethyl]pyridine. *Acta Chem. Scand. B42*, 373−377.
(25) von Lode, P., Rosenberg, J., Pettersson, K., and Takalo, H. (2003) A europium chelate for quantitative point-of-care immunoassays using direct surface measurement. *Anal. Chem. 75*, 3193−3201.
(26) Hakala, H., Liitti, P., Puukka, K., Peuralahti, J., Karvinen, J., Ollikka, P., Ylikoski, A., Mukkala, V.-M., and Hovinen, J. (2002) Novel Luminescent Samarium(III) Chelates. *Inorg. Chem. Commun. 5*, 1059−1062.
(27) Gonçalves e Silva F. R., Malta, O. L., Reinhard, C., Güdel, H.-U., Piguet, C., Moser, J. E., and Bünzli, J.-C. G. (2002) Visible and near-infrared luminescence of lanthanide-containing dimetallic triple-standarded helicates: energy transfer mechanism in Sm^{III} and Yb^{III} molecular edifices. *J. Phys. Chem. A 106*, 1670−1677.
(28) Rodríquez-Ubis, J. C., Sedano, R., Barroso, G., Juanes, O., and Brunet, E. (1997). Lanthanide complexes of polyacid ligands derived from 2,6-bis(pyrazol-1-yl)pyridine, pyrazine, and 6,6′-bis(pyrazol-1-yl) 2,2′-bipyridine: synthesis and luminescence properties. *Helv. Chim. Acta 80*, 86−96.

BC050019X

Identification of a UDP-Glucose-Binding Site of Human UDP-Glucose Dehydrogenase by Photoaffinity Labeling and Cassette Mutagenesis

Jae-Wan Huh,[†] Hyun-Ju Lee,[†] Myung-Min Choi,[†] Seung-Ju Yang,[†] Seung Yong Yoon,[‡] Dae Won Kim,[§] So Young Kim,[§] Soo Young Choi,[§] and Sung-Woo Cho*[,†]

Department of Biochemistry and Molecular Biology and Department of Anatomy and Cell Biology, University of Ulsan College of Medicine, Seoul 138-736, Korea, and Department of Genetic Engineering, College of Life Sciences, Hallym University, Chuncheon 200-702, Korea. Received February 12, 2005; Revised Manuscript Received March 29, 2005

We have identified a UDP-glucose-binding site within human UDP-glucose dehydrogenase (hUGDH) by photoaffinity labeling with a specific probe, [^{32}P]5N$_3$UDP-glucose, and cassette mutagenesis using a synthetic hUGDH gene. Photolabel-containing peptides were generated by photolysis followed by tryptic digestion and isolated using the phosphopeptide isolation kit. Photolabeling of these peptides was effectively prevented by the presence of UDP-glucose during photolysis, demonstrating a selectivity of the photoprobe for the UDP-glucose-binding site. Amino acid sequencing and compositional analysis identified the UDP-glucose-binding site of hUGDH as the region containing the sequence, ASVGFGGSXFQK, corresponding to A268−K279 of the amino acid sequence of hUGDH. The unidentified residue, X, can be designated as a photolabeled C276 because the sequences including the cysteine residue in question have a complete identity with those of other UGDH species known. The importance of the C276 residue in the binding of UDP-glucose was further examined with mutant proteins at the C276 site. The mutagenesis at C276 has no effect on the expression of the mutants (C276G, C276K, C276E, C276L, and C276Y). Enzyme activities of the C276 mutants were not measurable under normal assay conditions, suggesting an important role for the C276 residue. No incorporation of [^{32}P]5N$_3$UDP-glucose was also observed for the mutants. These results indicate that C276 plays an important role for efficient binding of UDP-glucose to hUGDH.

INTRODUCTION

UDP-glucose dehydrogenase (UGDH;[1] EC 1.1.1.22) is an NAD$^+$-linked oxidoreductase that catalyzes, in vertebrates, the unique pathway forming UDP-glucuronate from UDP-glucose. UDP-glucuronate is one of the main substrates in glycosaminoglycan synthesis. Because the UDP-glucuronate supply is a limiting step in glycosaminoglycan synthesis, it was recently postulated that any modification of UGDH activity may influence the proteoglycan structure and function (*1*). For example, the mutation inactivation of the *Drosophila* gene (*sugarless* or *suppenkasper*) suppresses the Wingless activity in developing pups (*2*), confirming the role of glycosaminoglycans in growth-factor-signaling mechanisms. In addition to providing the glucuronate and iduronate moieties of glycosaminoglycans, UDP-glucuronate is the required substrate for glucuronidation of many substances, including xenobiotics, opioids, androgens, and heme proteins, through the action of UDP-glucuronosyl transferases in the liver (*3*).

Among UGDH, the most information is known regarding the bovine liver UGDH. This protein is proposed to act as a homohexamer of 52-kDa subunits, described as a "trimer of dimers" (*4*, *5*). The human enzyme cDNA codes for 494 amino acids and has 27% homology to its *Escherichia coli* ortholog, with identical consensus sequence for the NAD$^+$-binding site (*6*). The cloned murine and bovine cDNAs share over 97% identity with the human sequence (*7*, *8*). Recently, the recombinant human UGDH has been cloned, expressed, and affinity-purified (*9*). The enzyme is active as a hexamer with some evidence for assembly in a trimer of dimers as has been proposed for the bovine enzyme. Steady-state kinetic constants were established and found to be comparable with previously published data in the bovine system (*4*, *10*−*12*).

All forms of the enzyme are known to catalyze the same reaction. The mechanism used by the bovine liver UGDH is thought to involve an initial oxidation of the C-6 hydroxy of UDP-glucose to form an aldehyde intermediate and NADH (*10*, *11*). It has been suggested that the aldehyde is bound via an imine linkage with a lysine residue (*10*). The second oxidation is initiated by the addition of an active-site cysteine thiol to the aldehyde to form a thiohemiacetal intermediate (*11*). A hydride transfer from the intermediate to NAD$^+$ then takes place to produce an enzyme-bound thioester intermediate and a second molecule of NADH. In a final irreversible step, the thioester is hydrolyzed to give the product UDP-glucuronate. The streptococcal enzyme is believed to form a covalent intermediate specifically between the product of the first oxidation and C260 within the active site, which is required for the second oxidation. This residue

* To whom correspondence should be addressed. Telephone and Fax: 82 2 30104278. E-mail: swcho@amc.seoul.kr.

[†] Department of Biochemistry and Molecular Biology, University of Ulsan College of Medicine.

[‡] Department of Anatomy and Cell Biology, University of Ulsan College of Medicine.

[§] Hallym University.

[1] Abbreviations: UGDH, UDP-glucose dehydrogenase.

10.1021/bc0500387 CCC: $30.25 © 2005 American Chemical Society
Published on Web 04/15/2005

Chart 1. Structure of $5N_3$UDP-Glucose

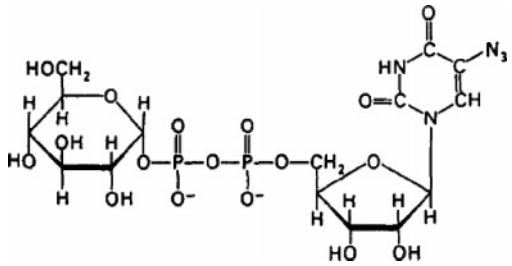

is uniformly conserved across all species and corresponds to C276 in the human enzyme (*9*). However, direct evidence for the binding of C276 with UDP-glucose has not been reported.

Identification of the nucleotide binding sites of a variety of proteins has been advanced by the use of nucleotide photoaffinity analogues that selectively insert into a site upon photoactivation with ultraviolet light (*13*−*16*). The 5-azidopyrimidine analogues of both uridine and deoxyuridine were synthesized and used in the study of UTP and dTTP binding proteins and in the production of 5-azidodeoxyuridine-containing DNA used for investigations on protein−DNA interactions (*17*). Because of the role of nucleotide diphosphate sugars in several aspects of metabolism and in the synthesis of important macromolecules, a model azidonucleotide sugar analogue, [^{32}P]5-azidouridine 5′-diphosphoglucose ([^{32}P]$5N_3$UDP-glucose) (Chart 1), has been widely used to identify and characterize UDP-glucose-binding proteins (*18*−*21*).

In the present work, we have identified the UDP-glucose-binding site of human UGDH using a photoaffinity labeling with $5N_3$UDP-glucose and cassette mutagenesis using a synthetic hUGDH gene (*22*). This study shows that C276 is an active catalytic residue and critically involved in the substrate binding in the human UGDH.

EXPERIMENTAL PROCEDURES

Materials. UDP-glucose, NAD^+, ampicillin, isopropyl thio-β-D-galactoside, phenylmethanesulfonyl fluoride, and L-1-tosylamido-2-phenylethyl chloromethyl ketone-treated trypsin were purchased from Sigma Chemical Co. Human UGDH gene (pHUGDH) has been chemically synthesized and expressed in *E. coli* as a soluble protein in our laboratory (*22*). $5N_3$UDP-glucose was purchased from ALT, Inc. (Lexington, KY). [β-^{32}P]$5N_3$UDP-glucose (specific activity, 24 mCi/μmol) was synthesized by a procedure described elsewhere (*23*). Pre-cast gels for SDS−PAGE were purchased from Novex. All other chemicals and solvents were of reagent grade or better.

Bacterial Strains. *E. coli* DH5α (*24*) was used as the host strain for plasmid-mediated transformations during the assembly of the synthetic *hUGDH* gene (pHUGDH) and for cassette mutagenesis. *E. coli* BL21 (DE3) (*25*) was used for high level expression of the recombinant hUGDH.

Photoaffinity Labeling of hUGDH. Photoaffinity labeling of wild-type hUGDH and mutant proteins were performed as described elsewhere with a slight modification (*14*, *22*). For saturation studies, 100 μg of the wild-type hUGDH in 10 mM Tris-acetate at pH 8.0 was incubated with various concentrations of [^{32}P]$5N_3$UDP-glucose in Eppendorf tubes for 5 min. For competition studies, 100 μg of enzyme was incubated with various concentrations of UDP-glucose for 10 min in the same buffer prior to the addition of 120 μM [^{32}P]$5N_3$UDP-glucose and then allowed to incubate with the photoprobe for 5 min as described above. The samples were irradiated with a handhold 254-nm UV lamp for 90 s twice at 4 °C. The reaction was quenched by the addition of ice-cold trichloroacetic acid (final 7%). The reaction mixtures were kept on the ice bath for 30 min and centrifuged at 10 000*g* for 15 min at 4 °C. The pellets were resuspended with SDS−PAGE sample buffer. After SDS−PAGE, the gels were dried and subjected to autoradiography at −80 °C followed by densitometry scanning of labeled bands.

Tryptic Digestion and Isolation of Photolabeled Peptide. To determine the site modified by [^{32}P]$5N_3$UDP-glucose, 1.0 mg of wild-type hUGDH and mutant proteins in 10 mM Tris acetate at pH 8.0 was incubated with 120 μM [^{32}P]$5N_3$UDP-glucose for 5 min at 4 °C. The mixtures were irradiated twice for 90 s. The reaction was quenched by the addition of ice-cold trichloroacetic acid (final 7%) and kept at 4 °C for 15 min. The protein was precipitated by centrifugation at 10 000*g* for 15 min at 4 °C, and the pellet was resuspended in 75 mM NH_4HCO_3 at pH 8.5 containing 2 M urea. The enzymes were proteolyzed by the addition of 30 μg of trypsin and kept at room temperature for 3 h after which 30 μg of trypsin was added again. After 3 more hours at room temperature, 40 μg of trypsin was added, and the digestion mixture was kept at 25 °C overnight. To validate that the isolated peptide was specific for the UDP-glucose-binding site and could be protected from photomodification, the hUGDH proteins were separately photolyzed in the presence of 150 μM UDP-glucose and proteolyzed as described above. The tryptic-digested peptides were separated by the "Phosphopeptide Isolation Kit" from Pierce Biotechnology (Rockford, IL) following the protocol of the manufacturer and sequenced by the Edman degradation method.

Construction and Characterization of C276 Mutants. Cassette mutagenesis at the C276 site was performed using a synthetic human hUGDH gene, pHUGDH. The plasmid DNA was digested with *Nhe*I and *Eco*NI to remove a 60 base-pair fragment that encodes amino acids 269−287, and vector DNA was purified by electrophoresis using 1% low melting point agarose. The 60 base-pair *Nhe*I/*Eco*NI fragment was replaced with five 60 base-pair synthetic DNA duplexes containing a substitution on both DNA strands at positions encoding C276 to make C276G, C276K, C276E, C276L, and C276Y mutants. Mutagenic oligonucleotides were annealed, ligated, and transformed into DH5α as described above, and C276 mutants were identified by DNA sequencing using plasmid DNA as a template. Each of these mutants has been expressed in *E. coli* strain DE3, purified to homogeneity as described above, and has had its steady-state kinetic parameters determined. The gene expression level of C276 mutant proteins in the crude extracts was examined by Western blot using monoclonal antibodies against the hUGDH and compared with that of wild-type hUGDH.

Protein Purification and Enzyme Assay. For purification of the wild-type and mutant enzymes, fresh overnight cultures of DE3/pHUGDH were used to inoculate 1 L of Luria−Bertani (LB) containing 100 μg of ampicillin/mL. DE3/pHUGDH was grown at 37 °C until the A_{600} reached 1.0, and then isopropyl thio-β-D-galactoside was added to a final concentration of 1 mM. After isopropyl thio-β-D-galactoside induction, DE3/pHUGDH was grown for an additional 3 h at 37 °C and then harvested by centrifugation. Cell pellets were suspended in 100 mL of 100 mM Tris-HCl at pH 7.4, 1 mM EDTA, and 5 mM dithiothreitol and lysed with a sonicator. Cellular debris was removed by centrifugation, and the

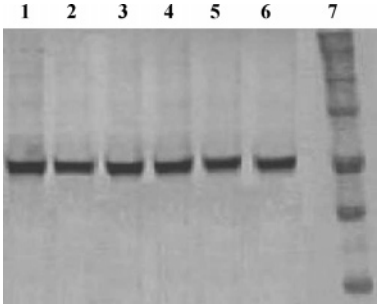

Figure 1. Western blot analysis of wild-type and C276 mutants. The supernatants of the crude extracts were submitted to SDS−PAGE and immunoblotted as described under the Materials and Methods. The final amount of total proteins loaded on each lane was 0.1 mg. Lane 1, wild-type hUGDH; lanes 2−6, C276G, C276K, C276E, C276L, and C276Y, respectively; lane 7, prestained marker proteins.

crude extract was loaded onto a Blue Sepharose CL-6B column that was equilibrated with buffer A (20 mM Tris/HCl at pH 6.5, 5 mM $MgCl_2$, and 10 mM β-mercaptoethanol). The column was washed with buffer A until the breakthrough peak of protein had been eluted. The enzyme was then eluted by a gradient up to 500 mM NaCl. The fractions containing hUGDH were pooled and concentrated, and the buffer changed to buffer B (50 mM Tris/HCl at pH 8.0, 0.5 mM EDTA, and 10 mM β-mercaptoethanol) using Amicon concentrator and then applied to a FPLC Resource-Q column equilibrated with buffer B. The enzyme was then eluted using a linear gradient made with buffer B in an increasing concentration of NaCl (from 0 to 300 mM) at 3 mL/min. The fractions containing hUGDH were pooled and concentrated. The purified enzymes were analyzed by SDS−PAGE and recognized by Western blot using monoclonal antibodies against the hUGDH.

hUGDH activity was performed spectrophotometrically by measuring the reduction of NAD^+ in the presence of UDP-glucose at 340 nm as described previously (*22*). Reactions were performed in a total volume of 1 mL with hUGDH adjusted to give a measured rate of less than 0.04 absorbance units/min. One unit of hUGDH activity was defined as the amount of enzyme required to reduce 2 μmol of NAD^+/min at pH 8.7 at room temperature.

RESULTS

Construction and Characterization of C276 Mutants. In this work, the functional role of C276 residue was examined by cassette mutagenesis using a synthetic human UGDH gene. For this study, the mutant human UGDHs containing Gly, Lys, Glu, Leu, or Tyr at the cysteine 276 site have been expressed in *E. coli* as a soluble protein, purified, and characterized. The 60 base-pair *Nhe*I/*Eco*NI fragment was replaced with five 60 base-pair synthetic DNA duplexes containing a substitution on both DNA strands at positions encoding C276. These substitutions made the mutant hUGDHs C276G, C276K, C276E, C276L, and C276Y. These mutants were designed to have different sizes, hydrophobicities, and ionizations of the side chains at each position. Analysis of crude cell extracts by Western blot showed that C276 mutant plasmids encoding an amino acid substitution at position 276 directed the synthesis of a 57-kDa protein that interacted with monoclonal antibodies raised against hUGDH at almost identical levels for all mutant hUGDHs and wild-type hUGDH (Figure 1). These results indicate that the mutagenesis at the C276 site has no effects on expression of the different mutant hUGDHs. Catalytic activity of hUGDH point mutants was measured under standard reaction conditions and found to be negligible, suggesting an important role for the C276 residue (Table 1). This observation is consistent with results of the analogous C260S streptococcal point mutant, which lacked activity to an unquantified degree (*26*, *27*). In addition, no incorporation of [^{32}P]5N_3UDP-glucose was also observed for the C276E mutant. These results indicate that C276 plays an important role for efficient binding of UDP-glucose to human UGDH.

Table 1. Kinetic Properties of Wild-Type and C276 Mutants Observed with UDP-Glucose and 5N_3UDP-Glucose

	UDP-glucose		5N_3UDP-glucose	
	specific activity[a] (nmol min^{-1} mg^{-1})	K_m (μM)	specific activity[a] (nmol min^{-1} mg^{-1})	K_m (μM)
wild type	157.22	17.03	108.42	56.17
C276G	0.36	nd[b]	nd	nd
C276K	0.34	nd	nd	nd
C276E	0.47	nd	nd	nd
C276L	0.68	nd	nd	nd
C276Y	0.34	nd	nd	nd

[a] Specific activities of the mutants were not detectable under standard reaction conditions and found less than 1% activity relative to the wild-type enzyme after measuring activity for 3 h. [b] nd = not detectable because of the extremely low activities.

Table 2. Photoinactivation of the Enzyme by 5N_3UDP-Glucose[a]

additions	hv	relative activity[b] (%)
no addition	−	100 ± 2[c]
5N_3UDP-glucose	−	68 ± 3
UDP-glucose	+	95 ± 2
5N_3UDP-glucose	+	11 ± 3
UDP-glucose and 5N_3UDP-glucose	+	89 ± 4

[a] A total of 3 μM enzyme, 120 μM 5N_3UDP-glucose, 1 mM NAD^+, and 1 mM UDP-glucose were used. The data represent the mean of three independent experiments with the difference expressed as a ±deviation. [b] Mean of triplicates. [c] The activity of the untreated control was equal to 157 nmol min^{-1} (mg of protein)$^{-1}$.

Photoaffinity Labeling of hUGDH. The reactive amino acid involved in the direct binding of UDP-glucose to hUGDH was identified by photoaffinity labeling with [^{32}P]5N_3UDP-glucose. The ability of a nucleotide analogue to mimic the natural nucleotide in its binding properties to the enzyme is essential to secure the specificity of photoinsertion into the active site. To show that 5N_3UDP-glucose could mimic the stimulatory properties of UDP-glucose, the photoanalogue should be able to activate hUGDH in the absence of activating light. When assayed with NAD^+ as a coenzyme, 5N_3UDP-glucose was able to activate the wild-type hUGDH, although maximal activity with 5N_3UDP-glucose (108 nmol min^{-1} mg^{-1}) was ~70% of the maximal activity obtained with UDP-glucose (157 nmol min^{-1} mg^{-1}) (Table 1). The K_m for 5N_3UDP-glucose was 56 μM, which was also comparable with the K_m value for UDP-glucose (17 μM). These results show that the azidonucleotide, 5N_3UDP-glucose, is able to elicit biological effects on the wild-type hUGDH as the natural nucleotide, UDP-glucose. The ability to mimic a native compound before photolysis has an advantage over determination of the enzyme function after modification. The ability of 5N_3UDP-glucose to inhibit hUGDH activity by photoinsertion upon irradiation under different conditions was investigated (Table 2). hUGDH activity was slightly affected by UV light under these conditions. In the presence of 120 μM 5N_3UDP-glucose, 89% of the enzyme activity was lost after 5 min of photolabeling.

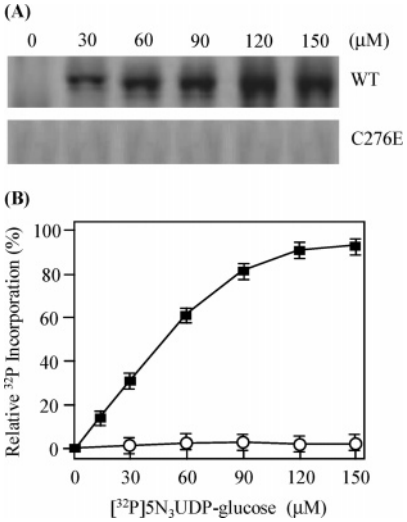

Figure 2. Saturation of photoinsertion of [^{32}P]5N$_3$UDP-glucose into hUGDH. Wild-type hUGDH and C276E mutant in the reaction buffer were separately photolabeled with the indicated concentrations of [^{32}P]5N$_3$UDP-glucose subjected to SDS−PAGE. (A) Autoradiograph. (B) Densitometry readings of the resulting autoradiograph. ^{32}P incorporations into proteins were expressed in autoradiograph. Data are expressed relative to the value in the absence of [^{32}P]5N$_3$UDP-glucose (control) being assigned 100%. Wild-type (■). C276E mutant (○).

When the enzyme was photolyzed in the presence of 1 mM UDP-glucose, only 11% of the enzyme activity was lost. These results suggest that the 5N$_3$UDP-glucose was photoinserting into a UDP-glucose-binding site on hUGDH in a specific manner.

To show specificity of the photoprobe−protein interaction, saturation of photoinsertion should be observed. For demonstrating saturation effects with the photoprobe, the purified enzymes were photolabeled with increasing concentrations of [^{32}P]5N$_3$UDP-glucose (Figure 2A). Under the experimental conditions described, saturation of photoinsertion with [^{32}P]5N$_3$UDP-glucose occurred at around 120 μM photoprobe (Figure 2B). The data in Figure 2 demonstrate the apparent K_d value of approximately 45 μM, which is in reasonably good agreement with the K_m value (56 μM) for 5N$_3$UDP-glucose (Table 1). The results in Figure 2 indicate the saturability of the UDP-glucose-specific site of hUGDH with this photoprobe and therefore decrease the possibility of nonspecific photoinsertion. No photoaffinity labeling of [^{32}P]5N$_3$UDP-glucose was measured for C276 mutants under the same experimental conditions for the wild-type enzyme (parts A and B of Figure 2). Because almost identical results were obtained with all five different mutants at the position of C276, only the results obtained with C276E are shown. These results are consistent with the postulated role of C276 in UDP-glucose binding and support its position in the reaction mechanism for the human enzyme.

Prevention of [^{32}P]5N$_3$UDP-Glucose Photoinsertion into hUGDH by Various Competitors. The studies were performed to examine the ability of the constituents of the sugar nucleotide to compete with [^{32}P]5N$_3$UDP-glucose for photolabeling of the UDP-glucose-binding site of hUGDH (Figure 3). The results show that uracil, uridine, and glucose had a poor protective effect on the labeling, while UDP and UDP-glucose strongly inhibited photoinsertion (Figure 3).

To further demonstrate specific labeling of hUGDH, the wild-type hUGDH was photolabeled with [^{32}P]5N$_3$-UDP-glucose in the presence of increasing UDP-glucose

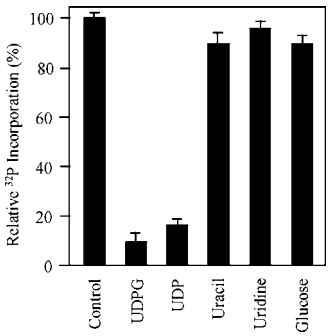

Figure 3. Prevention of [^{32}P]5N$_3$UDP-glucose photoinsertion into hUGDH by various competitors. Wild-type hUGDH and C276E mutant in the reaction buffer were separately photolabeled with 120 μM [^{32}P]5N$_3$UDP-glucose in the presence of competitors (200 μM) and subjected to SDS−PAGE. Densitometry readings of the resulting autoradiograph to quantitate the labeling of hUGDH was carried out as indicated in Figure 2. Because no photolabeling was observed with C276 mutants even in the absence of competitors, only the results obtained with the wild-type enzyme are expressed.

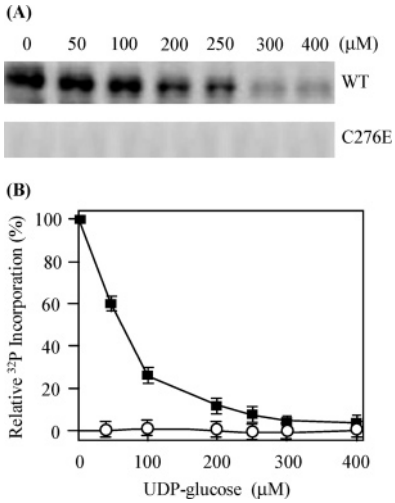

Figure 4. Effect of UDP-glucose on photoinsertion of [^{32}P]5N$_3$-UDP-glucose into hUGDH. Wild-type hUGDH and C276E mutant in the reaction buffer were separately photolabeled with 120 μM [^{32}P]5N$_3$UDP-glucose in the presence of the indicated concentrations of UDP-glucose and subjected to SDS−PAGE. (A) Autoradiograph. (B) Densitometry readings of the resulting autoradiograph. ^{32}P incorporations into proteins were expressed in autoradiograph. Data are expressed relative to the value in the absence of UDP-glucose (control) being assigned 100%. Wild-type (■). C276E mutant (○).

concentrations. As shown in the results of the competition experiments, UDP-glucose was able to protect photolabeling from [^{32}P]5N$_3$UDP-glucose (Figure 4A). As competitor concentrations increased from 50 to 400 μM in the presence of 120 μM [^{32}P]5N$_3$UDP-glucose, the photoinsertion of the probe into the hUGDH became reduced (Figure 4B) with a K_d value of approximately 60 μM, which is in reasonably good agreement with the K_m value for UDP-glucose (Table 1). These results of photoinsertion studies (Figures 2−4) show the specificity and utility of [^{32}P]5N$_3$UDP-glucose as a good probe for determining the UDP-glucose-binding site.

Identification of the UDP-Glucose-Binding Site. To identify the peptides modified by [^{32}P]5N$_3$UDP-glucose, the enzymes were photolabeled twice in the absence or presence of 150 μM UDP-glucose and digested with trypsin. [^{32}P]5N$_3$UDP-glucose is a probe that, on photolysis, generates a very reactive nitrene that has the capacity of photoinserting into any residue. The photo-

Table 3. Alignment of [^{32}P]5N$_3$UDP-Glucose-Labeled Peptides with Homologous Sequence from Various UGDHs

source	reference	amino acid sequence[a]
human (wild type)	this paper	A S V G F G G S X F Q K
human (C276E)	this paper	not detected
Streptococcus pyogenes	*36*	P S F G Y G G Y C L P K D T K
Streptococcus pneumoniae	*37*	P S F G Y G G Y C L P K D T K
bovine	*35*	A S V G F G G S C F Q K D V L
Cryptococcus neoformans	*38*	A S V G F G G S C F Q K D I L
fruitfly	*39*	A S V G F G G S C F Q K D I L
mouse	*7*	A S V G F G G S C F Q K D V L
poplar	*40*	A S V G F G G C F S Q K D I L
		268[b] 282

[a] The amino acids are denoted by the single-letter code. [b] The amino acid numbering is that of the mature human UGDH (*7*).

labeled hUGDH was separated from most of the noncovalently bound nucleotide by acid precipitation and proteolyzed by trypsin. After overnight trypsin digestion of hUGDH modified with [^{32}P]5N$_3$UDP-glucose, the digested samples were purified by the "Phosphopeptide Isolation Kit" from Pierce Biotechnology (Rockford, IL). The radioactive peptides were eluted with 100 mM ammonium bicarbonate at pH 9 containing 0.3 M ammonium hydroxide and 20% acetonitrile. Photolabeling of the peptide was prevented by the presence of UDP-glucose during photolysis. When 150 μM UDP-glucose was originally present in the incubation mixture, ~95% of the radioactivity of the eluent was eliminated. These results demonstrate a selectivity of the photoprobe and suggest that the radioactive fractions represent a peptide in the UDP-glucose-binding domain of the hUGDH. The radioactive fractions were collected and identified by amino acid sequence analysis.

The amino acid sequence analysis revealed that the radioactive eluent contained the amino acid sequence ASVGFGGSXFQK. As judged by comparison with the amino acid sequence of various UGDHs (Table 3), this peptide was identified as residues 268−279 of hUGDH. The symbol X indicates a position for which no phenylthiohydantoin-amino acid could be assigned. The missing residue, however, can be designated as a photolabeled cysteine because the sequences including the cysteine residue in question have a complete identity with those of the other UGDH species known. Because the photolabeled peptides are tryptic digests, it was expected to produce a sequence ending with Arg or Lys. The amino acid composition of the photolabeled peptide revealed that the peptide had a composition that was compatible with that of the tryptic peptide spanning residues Ala268−Lys279 with an exception that there was a significant reduction in cysteine (data not shown). On the basis of information obtained on the amino acid sequence determination and composition analysis of the isolated peptide, we suggest that the attachment site of [^{32}P]5N$_3$-UDP-glucose is C276. Unlike the wild-type hUGDH, no peptides containing amino acids around the 276 position were detected with the C276E mutant. Once again, these results demonstrate selectivity of the photoprobe for the UDP-glucose-binding site and suggest that C276 is critically involved in the binding of [^{32}P]5N$_3$UDP-glucose to human UGDH.

DISCUSSION

The majority of previous studies on UGDH have focused on the bovine liver enzyme, and until recently very little was known about the human enzyme. The structure of the enzyme is well-conserved between the species and phyla. The cloned mammalian proteins from different species showed an overall 97% identity (*8*). The human enzyme cDNA codes for 494 amino acids and has 27% homology to the *E. coli* ortholog. The conserved amino acids are uniformly distributed along the molecule. Very recently, mechanistic details for the human enzyme were acquired by a combination of site-directed mutagenesis, activity measurements, and homology modeling (*9*, *22*). On the basis of the model of the active site of *Streptococcus pyrogenes* UGDH, Sommer et al. (*9*) have reported that C276 of human UGDH is essential for the second oxidation and suggested its role as a catalytic residue. However, direct evidence for the involvement of the C276 residue in substrate binding has not been addressed yet. In the present work, we have identified an amino acid residue in the UDP-glucose-binding domain of hUGDH by cassette mutagenesis and photoaffinity labeling with [^{32}P]5N$_3$UDP-glucose. The azidosugar nucleotide has the distinct advantage over a classic chemical probe in that the photoactive group is not reactive without exposure to the proper wavelength of light (Table 2). As it has been described (*28*), the 5-azidouridine derivative of UDP-glucose did not produce long-lived reactive intermediates in aqueous solutions. The result, showing no labeling of hUGDH when the probe is subjected to photolysis before the addition of the enzyme (data not shown), eliminates the existence of any long-lived chemically reactive intermediate that could be involved in covalently modifying enzymes. The selectivity and specificity has been successfully utilized to locate the specific base-binding domains of nucleotide-binding site peptides of many proteins (*13*−*22*).

The specificity of [^{32}P]5N$_3$UDP-glucose and the utility of this probe as a good candidate for determining the UDP-glucose-binding site were further supported by the following. First, in the absence of activating light, 5N$_3$UDP-glucose is a substrate for hUGDH (Table 2). The ability to mimic a native compound before photolysis has an advantage over determination of the enzyme function after modification. Second, the photoinsertion into hUGDH was saturated with [^{32}P]5N$_3$UDP-glucose. Saturation of photoinsertion with [^{32}P]5N$_3$UDP-glucose occurred at around 120 μM photoprobe (Figure 2). Third, the prevention of photoinsertion of [^{32}P]5N$_3$UDP-glucose by UDP-glucose demonstrates that the photoprobe is inserting into a specific UDP-glucose site within hUGDH (Table 2 and Figure 4). In addition, the sites of attachment of the photoaffinity label were more precisely defined by generating small peptide fragments of the labeled protein and separating the labeled peptides. For separation of the ^{32}P-labeled peptide fragments generated in the proteolytic digest, the "Phosphopeptide Isolation Kit" from Pierce Biotechnology was successfully carried out.

There were differences in the biochemical properties between wild-type hUGDH and C276 mutants. Catalytic activities of the hUGDH point mutant at the 276 site were not measurable under normal assay conditions and found less than 0.1% activity relative to wild-type enzyme

after measuring activity for 3 h (Table 1). This result suggests a possibility that the loss of enzymatic activity is due to a change in binding of UDP-glucose in the C276 mutants. In addition, no detectable amounts of photoaffinity labeling (Figure 2 and Figure 3) and no photolabeled peptides (Table 3) were observed for C276 mutants when treated with [^{32}P]5N$_3$UDP-glucose both in the presence and absence of UDP-glucose under the same experimental conditions as the wild-type enzyme. The results from the Western blot analysis show that the mutagenesis at the C276 site has no effects on expression or stability of the mutant (Figure 1). Therefore, the results with cassette mutagenesis and photoaffinity labeling techniques suggest that the loss of enzyme activities of C276 mutants is mainly caused by its inability to bind UDP-glucose and C276 is required for efficient base binding of UDP-glucose to hUGDH.

Both C276 and D280 are situated in the strictly conserved active-site signature sequence, GGxCxxxD (Table 3), that is characteristic of UGDH. The strictly conserved glycine pair preceding C276 suggests that main-chain conformations inaccessible to nonglycine residues are required for proper orientation of the catalytic nucleophile during catalysis. This is well-precedented within the aldehyde dehydrogenase extended family where a strictly conserved glycine residue precedes the catalytic cysteine and is necessary to allow the polypeptide chain to "twist back on itself" (*29*). The existence of an active-site cysteine residue has been well-documented in the case of UGDH from beef liver. Thiol modification studies using iodoacetate (*30*), 5-[[(iodoacetamido)ethyl]amino]naphthalene-1-sulfonic acid (*31*), 5,5′-dithiobis-(2-nitrobenzoate] (*11*), iodoacetamidofluorescein (*32*), and 6,6′-dithionicotinate (*33*) all indicate that a cysteine is required for catalysis. The observation that the cysteine is protected from modification by the addition of UDP-glucose or UDP-xylose suggests that it is located in the active site (*30*, *34*). The iodoacetate-labeling experiments clearly indicate that one thiol has been modified during the inactivation process and support the notion that a cysteine is in the proper vicinity to participate in covalent catalysis. Proteolytic digestion and sequencing studies on the iodoacetate-labeled bovine enzyme have indicated that C275 (C276 in the human enzyme) supplies the reactive thiol (*32*, *35*). This C276 thiol is within hydrogen-bonding distance of the 6′-hydroxyl of UDP-glucose and is located approximately for catalysis. When the protein sequence of the bovine enzyme is compared with that of the other known UGDHs, the cysteine is strictly conserved. This observation strongly indicates that C276 is the active-site thiol.

Competitive binding experiments showed that the substrate UDP-glucose protected against photolabeling of hUGDH (Figures 3 and 4). The inhibitor substrate UDP showed a similar protection against insertion, while uridine, uracil, and glucose were poor competitors (Figure 3). These results indicate that, although the interaction of the position 5 of the uridine ring with a neighboring amino acid residue at the UDP-glucose-binding site allows the specific photolabeling, the other interaction may occur between the pyrophosphate or a phosphate moiety of UDP-glucose and another amino acid residue at the binding site. Further studies using various mutated forms of hUGDH should make it possible to identify the residues involved in the binding of the sugar nucleotide phosphate.

The construction of a synthetic gene encoding hUGDH and the high level of hUGDH expression as a soluble protein in *E. coli* will enable us to generate a large number of site-directed mutations at several positions in the coding region and facilitate the purification of large quantities of mutant proteins for biochemical and structural studies. The combination of genetic and photolabeling techniques could be used to address a broad range of questions relating to the structure and function of human UGDH.

ACKNOWLEDGMENT

This work was supported by grants from the Korea Research Foundation (KRF-2004-005-C00008) and the Korea Health 21 R&D Project from the Ministry of Health and Welfare (03-PJ1-PG3-20900-0047) to S.-W. C.

LITERATURE CITED

(1) Cumberledge, S., and Reichsman, F. (1997) Glycosaminoglycans and WNTs: Just a spoonful of sugar helps the signal go down. *Trends Genet. 13*, 421−423.
(2) Hacker, U., Lin, X., and Perrimon, N. (1997) The *Drosophila* sugarless gene modulates Wingless signaling and encodes an enzyme involved in polysaccharide biosynthesis. *Development 124*, 3565−3573.
(3) Jansen, P. L., Mulder, G. J., Burchell, B., and Bock, K. W. (1992) New developments in glucuronidation research: Report of a workshop on "glucuronidation, its role in health and disease". *Hepatology 15*, 532−544.
(4) Franzen, J., Marchetti, P. S., and Feingold, D. S. (1980) Resonance energy transfer between catalytic sites of bovine liver uridine diphosphoglucose dehydrogenase. *Biochemistry 19*, 6080−6089.
(5) Jaenicke, R., Rudolph, R., and Feingold, D. S. (1986) Dissociation and *in vitro* reconstitution of bovine liver uridine diphosphoglucose dehydrogenase. The paired subunit nature of the enzyme. *Biochemistry 25*, 7283−7287.
(6) Wegrowski, Y., Perreau, C., Bontemps, Y., and Maquart, F. X. (1998) Uridine diphosphoglucose dehydrogenase regulates proteoglycan expression: cDNA cloning and antisense study. *Biochem. Biophys. Res. Commun. 250*, 206−211.
(7) Spicer, A. P., Kaback, L. A., Smith, T. J., and Seldin, M. F. (1998) Molecular cloning and characterization of the human and mouse UDP-glucose dehydrogenase genes. *J. Biol. Chem. 273*, 25117−25124.
(8) Lind, T., Falk, E., Hjertson, E., Kusche-Gullberg, M., and Lidholt, K. (1999) cDNA cloning and expression of UDP-glucose dehydrogenase from bovine kidney. *Glycobiology 9*, 595−600.
(9) Sommer, B. J., Barycki, J. J., and Simpson, M. A. (2004) Characterization of human UDP-glucose dehydrogenase. CYS-276 is required for the second of two successive oxidations. *J. Biol. Chem. 279*, 23590−23596.
(10) Ordman, A. B., and Kirkwood, S. (1977) Mechanism of action of uridine diphoglucose dehydrogenase. Evidence for an essential lysine residue at the active site. *J. Biol. Chem. 252*, 1320−1326.
(11) Ridley, W. P., Houchins, J. P., and Kirkwood, S. (1975) Mechanism of action of uridine diphosphoglucose dehydrogenase. Evidence for a second reversible dehydrogenation step involving an essential thiol group. *J. Biol. Chem. 250*, 8761−8767.
(12) Franzen, J. S., Kuo, I., Eichler, A. J., and Feingold, D. S. (1973) UDP-glucose dehydrogenase: Substrate binding stoichiometry and affinity. *Biochem. Biophys. Res. Commun. 50*, 517−523.
(13) Kon, N., and Suhadolnik, R. J. (1996) Identification of the ATP binding domain of recombinant human 40-kDa 2′,5′-oligoadenylate synthetase by photoaffinity labeling with 8-azido-[α-^{32}P]ATP. *J. Biol. Chem. 271*, 19983−19990.
(14) Lee, E. Y., Yoon, H. Y., Ahn, J. Y., Choi, S. Y., and Cho, S.-W. (2001) Identification of GTP binding site of human glutamate dehydrogenase using cassette mutagenesis and photoaffinity labeling. *J. Biol. Chem. 276*, 47930−47936.
(15) Yoon, H.-Y., Lee, E.-Y., and Cho, S.-W. (2002) Cassette mutagenesis and photoaffinity labeling of adenine binding

domain of ADP regulatory site within human glutamate dehydrogenase. *Biochemistry 41*, 6817−6823.
(16) Dezhurov, S. V., Khodyreva, S. N., Plekhanova, E. S., and Lavrik, O. I. (2005) A new highly efficient photoreactive analogue of dCTP. Synthesis, characterization, and application in photoaffinity modification of DNA binding proteins. *Bioconjugate Chem. 16*, 215−222.
(17) Evans, R. K., Johnson, J. D., and Haley, B. E. (1986) 5-Azido-2′-deoxyuridine 5′-triphosphate: A photoaffinity-labeling reagent and tool for the enzymatic synthesis of photoactive DNA. *Proc. Natl. Acad. Sci. U.S.A. 83*, 5382−5386.
(18) Carrizo, M. E., and Curtino, J. A. (1998) Identification of two uridine binding domain peptides of the UDP-glucose-binding site of rabbit muscle glycogenin. *Biochem. Biophys. Res. Commun. 253*, 786−789.
(19) Drake, R. R., Igari, Y., Lester, R., Elbein, A. D., and Radominska, A. (1992) Application of 5-azido-UDP-glucose and 5-azido-UDP-glucuronic acid photoaffinity probes for the determination of the active site orientation of microsomal UDP-glucosyltransferases and UDP-glucuronosyltransferases. *J. Biol. Chem. 267*, 11360−11365.
(20) Frost, D. J., Read, S. M., Drake, R. R., Haley, B. E., and Wasserman, B. P. (1990) Identification of the UDP-glucose-binding polypeptide of callose synthase from *Beta vulgaris* L. by photoaffinity labeling with 5-azido-UDP-glucose. *J. Biol. Chem. 265*, 2162−2167.
(21) Lin, F. C., Brown, R. M., Drake, R. R., and Haley, B. E. (1990) Identification of the uridine 5′-diphosphoglucose (UDP-Glc) binding subunit of cellulose synthase in *Acetobacter xylinum* using the photoaffinity probe 5-azido-UDP-Glc. *J. Biol. Chem. 265*, 4782−4784.
(22) Huh, J.-W., Yoon, H.-Y., Lee, H.-J., Choi, W.-B., Yang, S.-J., and Cho, S.-W. (2004) Importance of Gly-13 for the coenzyme binding of human UDP-glucose dehydrogenase. *J. Biol. Chem. 279*, 37491−37498.
(23) Drake, R. R., Jr., Evans, R. K., Wolf, M. J., and Haley, B. E. (1989) Synthesis and properties of 5-azido-UDP-glucose. Development of photoaffinity probes for nucleotide diphosphate sugar binding sites. *J. Biol. Chem. 264*, 11928-1933.
(24) Hanahan, D. (1983) Studies on transformation of *Escherichia coli* with plasmids. *J. Mol. Biol. 166*, 557−580.
(25) Studier, F. W., and Moffatt, B. A. (1986) Use of bacteriophage T7 RNA polymerase to direct selective high-level expression of cloned genes. *J. Mol. Biol. 189*, 113−130.
(26) Campbell, R. E., Sala, R. F., van de Rijn, I., and Tanner, M. E. (1997) Properties and kinetic analysis of UDP-glucose dehydrogenase from group A streptococci. Irreversible inhibition by UDP-chloroacetol. *J. Biol. Chem. 272*, 3416−3422.
(27) Campbell, R. E., Mosimann, S. C., van de Rijn, I., Tanner, M. E., and Strynadka, N. C. (2000) The first structure of UDP-glucose dehydrogenase reveals the catalytic residues necessary for the two-fold oxidation. *Biochemistry 39*, 7012−7023.
(28) Drake, R. R., and Elbein, A. D. (1992) Photoaffinity labelling of glycosyltransferases. *Glycobiology 2*, 279−284.
(29) Perozich, J., Nicholas, H., Lindahl, R., and Hempel, J. (1999) In *Enzymology and Molecular Biology of Carbonyl Metabolism 7* (Weiner, H., Maser, E., Crabb, D. W., and Lindahl, R., Eds.) pp 1−7, Kluwer Academic/Plenum Publishers, New York.
(30) Franzen, J. S., Ishman, R., and Feingold, D. S. (1976) Half-of-the-sites reactivity of bovine liver uridine diphosphoglucose dehydrogenase toward iodoacetate and iodoacetamide. *Biochemistry 15*, 5665−5671.
(31) Franzen, J. S., Ashcom, J., Marchetti, P., Cardamone, J. J., Jr., and Feingold, D. S. (1980) Induced versus pre-existing asymmetry models for the half-of-the-sites reactivity effect in bovine liver uridine diphosphoglucose dehydrogenase. *Biochim. Biophys. Acta 614*, 242−255.
(32) Franzen, B., Carrubba, C., Feingold, D. S., Ashcom, J., and Franzen, J. S. (1981) Amino acid sequence of the tryptic peptide containing the catalytic-site thiol group of bovine liver uridine diphosphate glucose dehydrogenase. *Biochem. J. 199*, 599−602.
(33) Franzen, J. S., Marchetti, P., Ishman, R., Ashcom, J., and Feingold, D. S. (1978) Half-sites oxidation of bovine liver uridine diphosphate glucose dehydrogenase. *Biochem. J. 173*, 701−704.
(34) Gainey, P. A., Pestell, T. C., and Phelps, C. F. (1972) A study of the subunit structure and the thiol reactivity of bovine liver uridine diphosphate glucose dehydrogenase. *Biochem. J. 129*, 821−830.
(35) Hempel, J., Perozich, J., Romovacek, H., Hinich, A., Kuo, I., and Feingold, D. S. (1994) UDP-glucose dehydrogenase from bovine liver: Primary structure and relationship to other dehydrogenases. *Protein Sci. 3*, 1074−1080.
(36) Dougherty, B. A., and van de Rijn, I. (1993) Molecular characterization of hasB from an operon required for hyaluronic acid synthesis in group A streptococci. Demonstration of UDP-glucose dehydrogenase activity. *J. Biol. Chem. 268*, 7118−7124.
(37) Arrecubieta, C., Lopez, R., and Garcia, E. (1994) Molecular characterization of cap3A, a gene from the operon required for the synthesis of the capsule of *Streptococcus pneumoniae* type 3: Sequencing of mutations responsible for the unencapsulated phenotype and localization of the capsular cluster on the pneumococcal chromosome. *J. Bacteriol. 10*, 6375−6383.
(38) Bar-Peled, M., Griffith, C. L., Ory, J. J., and Doering, T. L. (2004) Biosynthesis of UDP-GlcA, a key metabolite for capsular polysaccharide synthesis in the pathogenic fungus *Cryptococcus neoformans*. *Biochem. J. 381*, 131−136.
(39) Benevolenskaya, E. V., Frolov, M. V., and Birchler, J. A. (1998) The sugarless mutation affects the expression of the white eye color gene in *Drosophila melanogaster*. *Mol. Gen. Genet. 260*, 131−143.
(40) Johansson, H., Sterky, F., Amini, B., Lundeberg, J., and Kleczkowski, L. A. (2002) Molecular cloning and characterization of a cDNA encoding poplar UDP-glucose dehydrogenase, a key gene of hemicellulose/pectin formation. *Biochim. Biophys. Acta 1576*, 53−58.

BC0500387

Generation of an Intensely Potent Anthracycline by a Monoclonal Antibody–β-Galactosidase Conjugate

Michael Y. Torgov,[†] Stephen C. Alley,[†] Charles G. Cerveny,[†] David Farquhar,[‡] and Peter D. Senter[†,*]

Seattle Genetics, 21823 30th Drive SE, Bothell, Washington 98021, and University of Texas M.D. Anderson Cancer Center, Houston, TX, 77025. Received February 14, 2005; Revised Manuscript Received April 1, 2005

The L49 monoclonal antibody against the p97 antigen on melanomas and carcinomas was chemically conjugated to *E. coli* β-galactosidase (β-gal), forming a largely monomeric conjugate with preserved enzymatic activity. The resulting L49–β-gal conjugate was used to activate (*N*-[(4″*R*,*S*)-4″-hexyloxy-4″-(1‴-*O*-β-D-galactopyranosyl)butyl]daunorubicin) (**1**), a derivative of daunorubicin that has low cytotoxicity and high chemical stability. Addition of the conjugate to the prodrug resulted in an increase in cytotoxicity of approximately 10^5-fold, a level of activation that is higher than any mAb–enzyme/prodrug combination yet described. Furthermore, the released drug had an IC_{50} value of approximately 10 pM, making it significantly more potent than the vast majority of clinically approved anticancer drugs. The potential of this enzyme/prodrug combination for cancer therapy is discussed.

INTRODUCTION

A considerable amount of research has surrounded the use of monoclonal antibody (mAb)–enzyme conjugates for the activation of anticancer prodrugs (*1, 2*). This approach to cancer chemotherapy, referred to as ADEPT (antibody-directed enzyme prodrug therapy) involves two separate steps to achieve therapeutic efficacy. Initially, a mAb–enzyme conjugate is administered, which localizes within the tumor mass and clears from the systemic circulation over time. In the second step an anticancer prodrug is administered, which circulates throughout the body and is converted to active drug by the mAb–enzyme conjugate. Depending on the tumor to nontumor conjugate ratio, the prodrug can be very well-tolerated, and high intratumoral drug concentrations are obtained (*1–4*). The strength of this approach is evident from not only the large number of mAb–enzyme/prodrug combinations that have preclinical activity, but also from the indications of efficacy in early-stage clinical trials (*1, 5*).

One of the interesting aspects of ADEPT is that it allows not only for intratumoral generation of clinically approved drugs such as doxorubicin (*6*), paclitaxel (*7*), etoposide (*8*), 5-fluorouracil (*4*), and melphalan (*9*) but also of drugs that would be too toxic for use in a nontargeted form. Such drugs include potent minor groove binders (*10*), bis-iodomustards (*11*), cyanide (*12*), and the marine natural product palytoxin (*13*). The rationale for generating highly potent drugs is that the amount of localized enzyme within solid tumors is likely to be very low (*14*), and this will restrict the number of drug molecules that are generated. Therefore, maximal therapeutic efficacy is likely to be obtained through the intratumoral generation of highly potent cytotoxic agents. ADEPT systems that lead to such drugs would not only require a high tumor to nontumor conjugate ratio, but also a prodrug with greatly attenuated toxicity.

In this paper, we describe a mAb–β-galactosidase (β-gal[1]) conjugate for the activation of an intensely potent daunorubicin derivative. Previous studies have shown that treatment of a galactosyl derivative of daunorubicin (**1**, Figure 1A) with unconjugated β-gal released a daunorubicin derivative that was 100–1000 times more potent than unmodified daunorubicin (*15, 16*). This enzyme has also been used to release such agents as CC-1065 derivatives (*10, 17*) and daunorubicin (*18*). The only mAb-conjugated form of β-gal used for prodrug activation involved a derivative of 5-fluorouridine (*19*). Here, we extend these findings by demonstrating that **1** can be activated by as much as 10^5-fold by a mAb–β-gal conjugate that binds to the p97 antigen on melanomas and some carcinomas. This represents one of the highest cytotoxic differentials between a prodrug and potent drug for application in ADEPT.

EXPERIMENTAL PROCEDURES

General Analytical Methods and Materials. The murine L49 mAb was obtained as previously described (*20*). *E. coli* β-gal was purchased from Calbiochem (San Diego, CA). *N*-(ε-maleimidocaproic acid)hydrazide (EMCH), DTNB, and the BCA protein assay reagent were from Pierce (Rockford, IL). (*N*-[(4″*R*,*S*)-4″-Hexyloxy-4″-(1‴-*O*-β-D-galactopyranosyl)butyl]daunorubicin) (**1**) and (*N*-(5,5-diacetoxypent-1-yl)doxorubicin) (**5**) were prepared as previously described (*15, 16*). Protein concentrations of unmodified L49 and β-gal were determined by UV absorption spectrometry at 280 nm, and those of conjugated enzyme were determined using the BCA protein assay reagent. All measurements were made against known concentrations of β-gal as a reference standard.

Oxidation of L49 and Conjugation to β-Gal. $NaIO_4$ (final concentration 12.5 mM) was added to L49 in 50 mM sodium acetate (pH 5.5) and 50 μM methionine. The reaction was allowed to proceed in the dark for 50 min at ambient temperature. The oxidized L49 was desalted and buffer exchanged into PBS using a PD-10 column (Amersham Biosciences, Piscataway, NJ). EMCH was

* To whom inquiries should be directed at psenter@seagen.com.
† Seattle Genetics.
‡ University of Texas M.D. Anderson Cancer Center.

[1] Abbreviations used: EMCH, *N*-(ε-maleimidocaproic acid)-hydrazide; β-gal, β-galactosidase; 4-MUG, 4-methylumbelliferyl-β-D-galactopyranoside.

10.1021/bc050039z CCC: $30.25 © 2005 American Chemical Society
Published on Web 04/27/2005

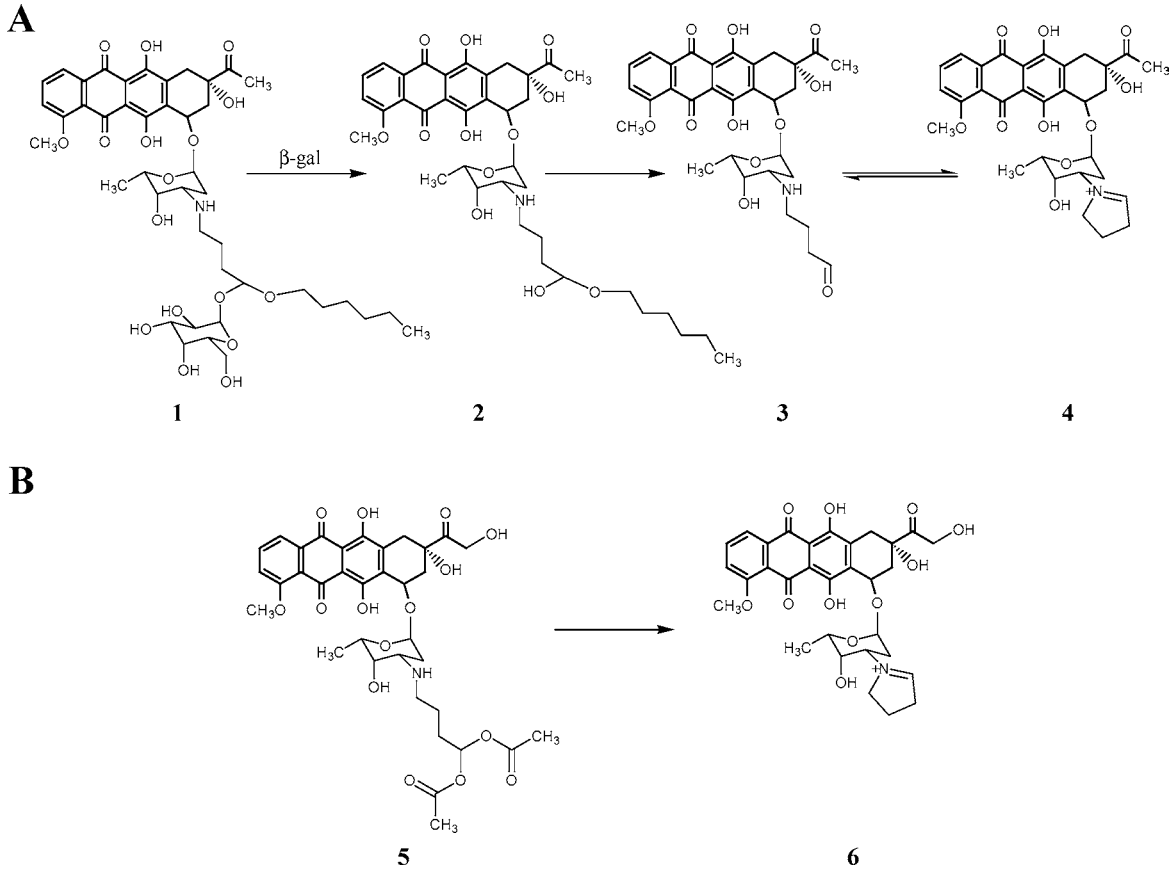

Figure 1. A. Mechanism of activation of **1** by β-gal. B. Formation of the analogous iminium ion **6** by **5**.

then added at a 50-fold molar excess over L49 and allowed to react for 4 h at ambient temperature with 10% DMSO present to ensure the solubility of EMCH. L49−EMCH was then purified using a PD-10 column pre-equilibrated with PBS. The number of the introduced maleimide residues was determined by treating with 50 μM cysteine and quantitating the remaining unreacted cysteine with DTNB. β-Gal was added to L49−EMCH at 0.5:1 enzyme to antibody molar ratio, and the reaction was allowed to incubate overnight at 4 °C. The conjugate was purified from unreacted L49 by SEC HPLC on a TSKgel G3000SW column (Tosoh Bioscience, Montgomeryville, PA) using PBS containing 10 mM $MgSO_4$ as the mobile phase. After concentration, the L49−β-gal conjugate was stored at 4 °C.

Amino Acid Analysis for the Determination of Conjugation Ratio. Amino acid analysis was performed on the L49−β-gal conjugate by the molecular structure facility at the University of California at Davis. The experimental mole fraction of each amino acid in the conjugate (MF_{AAA}) was determined from these data. The theoretical mole fraction of each amino acid was calculated from the primary amino acid sequence of L49 (MF_{L49}) and β-gal ($MF_{\beta-gal}$). The stoichiometry of the L49−β-gal conjugate (X moles of L49 per 1 mole of β-gal) is related to the experimental and theoretical mole fraction by eq 1:

$$MF_{AAA} = \frac{Xm MF_{L49} + 1n MF_{\beta-gal}}{Xm + 1n} \quad (1)$$

where m and n are the number of occurrences of the amino acid in L49 and β-gal, respectively. Solving for X for each amino acid yielded an average value of 0.7 mol of L49 per mole of β-gal.

Enzyme Activity Assays. β-Gal activity of the conjugate was measured using 4-methylumbelliferyl-β-D-galactopyranoside (4-MUG) or **1** as substrates. Dilutions of the enzyme or the conjugate (1 μg per data point) in 25 μL of PBS with 10 mM $MgSO_4$ were incubated for 5 min at 37 °C and then mixed with an equal volume of the substrate in the same buffer. The final substrate concentration varied from 80 to 8 μM. During a 20 min incubation course at 37 °C, 50 μL aliquots were taken and quenched with an equal volume of methanol. Aliquots (100 uL) were analyzed by HPLC on a 4.6 × 150 mm, 4u Synergi MAX-RP 80 column (Phenomenex, Torrance, CA) using the following gradient at 1 mL min^{-1}: solvent A 0.1% trifluoroacetic acid in H_2O; solvent B 0.1% trifluoroacetic acid in acetonitrile; a 10-min linear gradient from 10% A to 90% A. Peak areas at 495 or 315 nm for **1** and 4-MUG, respectively, were used to calculate concentrations of the product based on the peak area at time infinity. Eady−Hofstee plots of velocity versus the ratio of velocity and substrate concentration were used to calculate V_{max} and K_m.

In Vitro Cytotoxicity Assay. H3677 melanoma cell line seeded at a density of 2×10^3 per well in a 96-well plate and allowed to adhere overnight in RPMI 1640 medium containing 10% FBS in the absence of antibiotics. Serial dilutions of the L49−β-gal conjugate and an L49 control were added, incubated for 1 h at room temperature, and then washed. The prodrugs **1** or **5** were then added for 24 h. Cultures were washed and grown for an additional 92 h, at which point Alamar Blue (Biosource International, Camarillo, CA) was added to 10% of the total culture volume. Cells were incubated for 4 h, and dye reduction was measured on a Fusion HT fluorescent plate reader (Packard Instruments, Meriden, CT).

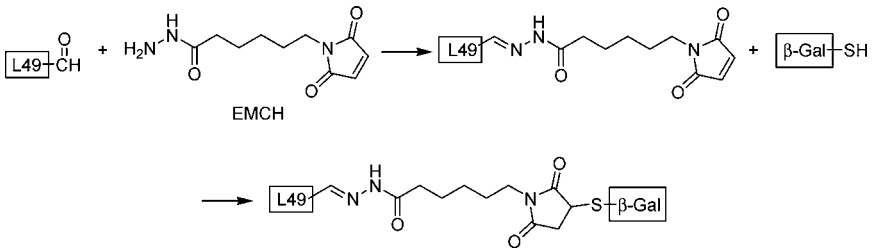

Figure 2. Mechanism of conjugate formation. L49 oxidized with sodium periodate (L49-CHO) reacts with EMCH to form L49–EMCH. The endogenous thiols of β-gal (β-gal-SH) then reacts with the maleimide to form the L49–β-gal conjugate.

RESULTS AND DISCUSSION

Prodrug Design. The structure of the known daunorubicin analogue **1** (*16*) is shown in Figure 1. This previously reported compound has been shown to give rise to an intensely potent metabolite in the presence of β-gal. In phosphate buffer at 37 °C, **1** is slowly degraded with a half-life of 49 h (*16, 21*). The proposed mechanism of action is that hemiacetal **2**, formed by the cleavage of the glycosyl bond of **1**, spontaneously loses hexanol to form aldehyde **3,** which then spontaneously cyclizes leading to the generation of iminium ion **4** (Figure 1A). Figure 1B shows the mechanism of formation of **6**, a compound related in structure to **4**, from *N*-(5,5-diacetoxypent-1-yl)doxorubicin (**5**) (*15*). Thus, compound **5**, which was designed to be hydrolyzed by cellular esterases, can be used to gauge the potential differences in cytotoxic activities between **1** and the unstable hydrolysis product **4**. DNA interstrand cross-links in HL-60 human leukemia cells have been shown and proposed for compound **5** and **1**, respectively (*15, 22*). Thus, these compounds differ mechanistically from the topoisomerase II inhibitor daunorubicin.

L49–β-Gal Conjugate Preparation. *E. coli*-derived β-gal is a tetrameric enzyme composed of 116 kDa monomers that has previously been used successfully for anticancer prodrug activation (*19, 23*). The enzyme has a neutral pH optimum while mammalian β-gal has optimal activity under acidic conditions (*24, 25*). Bacterial and mammalian β-gal activities have been successfully distinguished in transgenic mice by carefully controlling pH (*26*). Because of these differences in pH optima, it was anticipated that the prodrugs would undergo minimal nonspecific activation when administered in vivo.

To prepare the L49–β-gal conjugate, the carbohydrates of L49 were oxidized with sodium periodate, generating aldehydes on the heavy chain in the vicinity of the hinge region. The aldehydes were subsequently reacted with *N*-(ε-maleimidocaproic acid)hydrazide (EMCH) to yield a maleimide-activated antibody. These were coupled with β-gal, which contains endogenous sulfhydryl groups (Figure 2). L49 was added in a 2-fold excess with respect to the enzyme to minimize the amount of unreacted enzyme remaining after the conjugation reaction. The resulting conjugate, whose formation was manifested by the forward shift relative to the β-gal peak, was purified from unreacted L49 by size-exclusion HPLC (Figure 3A).

SDS–PAGE analysis further confirmed the presence of the cross-linked material (Figure 3B). β-gal is a tetramer composed of 116 kDa monomers. The conjugation conditions were targeted toward 1:1 cross-linking ratio, e.g. a single antibody molecule per enzyme tetramer. Therefore, under both reducing and nonreducing conditions, a dominant 116 kDa β-gal band is present that corresponds to the non-cross-linked subunit in the enzyme tetramer. A cross-linked product represented by two bands of approximately 160 kDa is consistent with

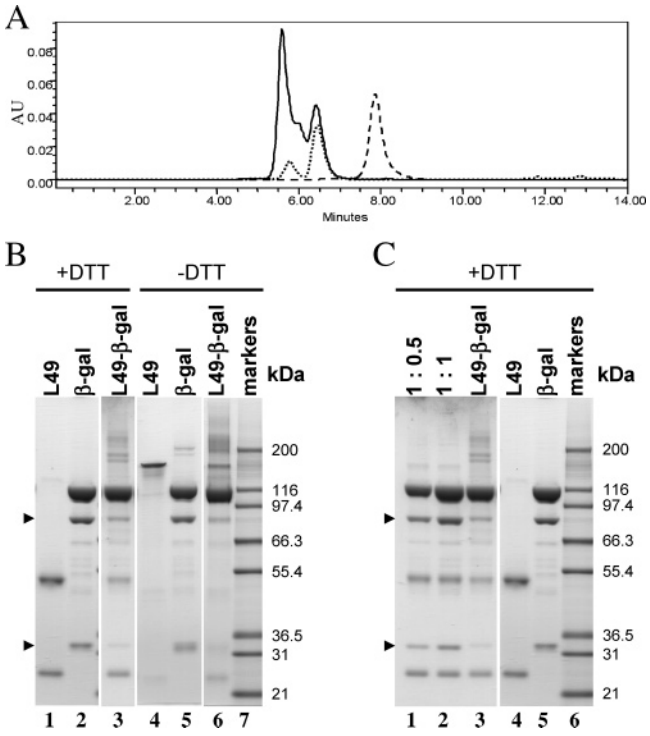

Figure 3. A. Size-exclusion chromatography HPLC traces for L49–β-gal conjugate (solid line), β-gal (dotted line), and L49 (dashed line) using PBS with 10 mM $MgSO_4$ as a mobile phase. B. SDS–PAGE (4–12%) of L49, β-gal, and L49–β-gal conjugate under reducing (with DTT) and nonreducing (without DTT) conditions. The arrowheads represent a contaminant present in the enzyme preparation. Lane 1, L49 with DTT; lane 2, β-gal with DTT; lane 3, L49–β-gal conjugate with DTT; lane 4, L49 without DTT; lane 5, β-gal without DTT; lane 6, L49–β-gal conjugate without DTT; and lane 7, molecular weight markers. C. SDS–PAGE (4–12%) of authentic mixtures of β-gal and L49 compared to L49–β-gal conjugate. All lanes are under reducing conditions. The arrowheads represent a contaminant present in the enzyme preparation. Lane 1, 1:0.5 mixture of β-gal and L49; lane 2, 1:1 mixture of β-gal and L49; lane 3, L49–β-gal conjugate; lane 4, L49; lane 5, β-gal; lane 6, molecular weight markers.

the expected combined size of a single enzyme subunit and a L49 heavy chain. In addition, under reducing conditions both heavy and light antibody chains are present in the lane with conjugate. However, their relative intensities are skewed toward the light chain due to sequestration of the heavy chain into conjugate (compare lane 1 and 3).

Amino acid analysis performed to assess the antibody-to-enzyme ratio revealed that the conjugate is composed of 0.7 mole of L49 per 1 mole of enzyme. When L49 and β-gal were mixed at different molar ratios and compared by SDS PAGE to the conjugate, it was confirmed that the composition of the conjugate lies between 0.5 and 1 molecule of L49 per molecule of the enzyme tetramer, consistent with the amino acid analysis data (Figure 3C).

Table 1. Enzyme Kinetic Parameters of L49 and L49−β-Gal[a]

		β-gal activity	
compound	substrate	K_m (μM)	V_{max} (μM·min^{-1}·mg^{-1})
β-gal	**1**	38 ± 22	0.052 ± 0.025
	4-MUG	22	89.6
L49−β-gal	**1**	60 ± 16	0.035 ± 0.01
	4-MUG	21.4	78.4

[a] Values shown are the average of a minimum of two independent experiments, except for 4-MUG (performed once).

Enzyme Activity. To test the enzyme activity, either **1** or 4-methylumbelliferyl-β-D-galactopyranoside (4-MUG) was added at concentrations ranging from 8 to 80 μM to β-gal or the L49−β-gal conjugate. Aliquots were precipitated with methanol and the substrate conversion was monitored by reversed-phase HPLC. The results, summarized in Table 1, demonstrate that the K_m and V_{max} values on both substrates were similar for the conjugate and free enzyme. This indicates that the conjugation chemistry did not impair the enzymatic activity of β-gal in the L49−β-gal conjugate. It should be noted that the specific activity values are in good agreement with those reported for a related molecule, gal−DNC4 (*21*). The slow rate of drug release most likely involves hydrolysis of the glycosidic bond as the rate limiting step, as significantly improved release kinetics were obtained using 4-MUG, which incorporates a better leaving group.

In Vitro Studies. The cytotoxic activities of L49−β-gal in combination with **1** were determined using the p97 positive H3677 human melanoma cell line. Cells were preincubated with the conjugate for 1 h, washed to remove the unbound material, and then exposed to **1** for a total of 24 h. Following the drug removal, the cytotoxic effects relative to untreated cells were determined using Alamar Blue as an indicator of cell viability. *N*-(5,5-Diacetoxypent-1-yl)doxorubicin (**5**) was used as a control in the assay since it generates the active doxorubicin iminium ion **6**, analogous to the daunorubicin iminium ion **4** generated from **1**. The difference in cytotoxicity between **5** and **1** was approximately 10^5-fold. Consistent with published data (*15*), **5** had an IC_{50} value of 20 pM (Figure 4A). In contrast, the IC_{50} of prodrug **1** alone was 0.8 μM. Preincubation of cells with L49 in the presence of prodrug **1** did not have any effect on the cytotoxicity of **1**. However, when the L49−β-gal conjugate was used, **1** exhibited cytotoxicity similar to **5**. These data are consistent with the conclusions that **4** is generated as a result of galactoside cleavage, and that the galactoside of **1** is completely cleaved by β-gal.

Next, we sought to establish the minimal concentration of the conjugate required to attain complete prodrug activation. Serial dilutions of the conjugate were incubated with the cells as described above, and any unbound conjugate was removed by washing. The prodrug **1** was then added at a constant concentration of 10 nM, significantly lower than its IC_{50} value. The assay demonstrated that a conjugate concentration of 40 nM (6 μg/mL) led to 50% cell kill (Figure 4B). Thus, the two assays show that efficient prodrug activation is achieved and that the difference in prodrug and drug toxicity is pronounced.

CONCLUSIONS

We have demonstrated that a chemical conjugate of L49−β-gal activates **1**, with a cytotoxic differential of approximately 5 orders of magnitude. This degree of prodrug activation has not been demonstrated previously

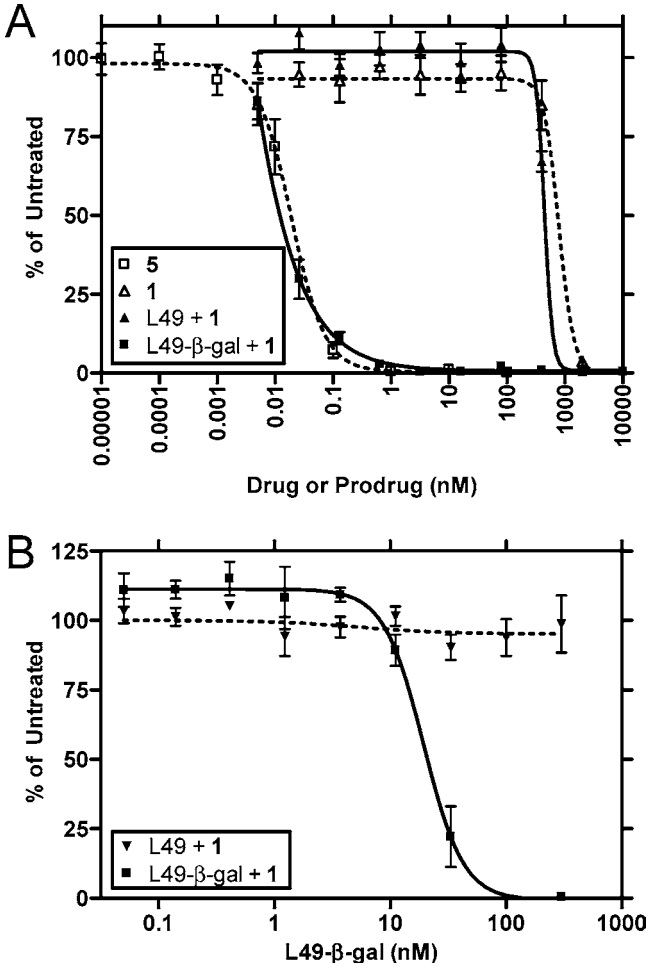

Figure 4. In vitro cytotoxicity of **1** and **5** on H3677 cells detected by Alamar Blue reduction. Cells were treated with L49 or L49−β-gal conjugate for 1 h, washed, and then treated with **1** or **5**. A. Cells were treated with 100 nM of L49 or L49−β-gal conjugate and the concentration of **1** or **5** varied. Open squares, **5**; open triangles, **1**; closed triangles, L49 plus **1**; closed squares, L49−β-gal plus **1**. B. Cells were treated with varied concentration of L49 or L49−β-gal conjugate and then 10 nM **1**. Open squares, **1** plus L49; closed squares, **1** plus L49−β-gal.

in other ADEPT systems, which typically provide differences in the range of 10 to 100-fold (*1, 2*). The results reported here strongly suggest that attachment of the β-gal residue to daunorubicin leads to almost complete drug inactivation, and that the glycosidic bond is highly stable under the conditions used in the in vitro assay. These are necessary requirements in developing an ADEPT system involving a highly potent drug component. An additional feature of this system that distinguishes it from many other ADEPT systems is that the released drug is capable of circumventing the MDR phenotype (*15*). This latter property is critical, since it is highly likely that most patients who receive mAb−enzyme/prodrug combinations will have already been treated extensively with conventional chemotherapy. While drug potency has not yet been shown to be a critical parameter for therapeutic efficacy in ADEPT, it may well be if, as expected, very small percentages of the injected conjugate accumulate within solid tumor masses.

The results reported here justify future studies surrounding the in vivo activities of L49−β-gal/galactosyl−daunorubicin combinations. It is expected that optimization will require the development of an engineered fusion protein containing an L49 fragment, since such

molecules have demonstrated much higher tumor to normal tissue ratios than chemically derived conjugates (*20, 27*). In addition, forms of β-gal that are minimally immunogenic will be of greatest clinical utility. The development of molecules such as these will be the subject of future investigations.

LITERATURE CITED

(1) Bagshawe, K. D., Sharma, S. K., and Begent, R. H. (2004) Antibody-directed enzyme prodrug therapy (ADEPT) for cancer. *Expert Opin. Biol. Ther. 4*, 1777−89.
(2) Senter, P. D., and Springer, C. J. (2001) Selective activation of anticancer prodrugs by monoclonal antibody-enzyme conjugates. *Adv. Drug Delivery Rev. 53*, 247−64.
(3) Bosslet, K., Czech, J., and Hoffmann, D. (1994) Tumor-selective prodrug activation by fusion protein-mediated catalysis. *Cancer Res. 54*, 2151−9.
(4) Wallace, P. M., MacMaster, J. F., Smith, V. F., Kerr, D. E., Senter, P. D., and Cosand, W. L. (1994) Intratumoral generation of 5-fluorouracil mediated by an antibody-cytosine deaminase conjugate in combination with 5-fluorocytosine. *Cancer Res. 54*, 2719−23.
(5) Francis, R. J., Sharma, S. K., Springer, C., Green, A. J., Hope-Stone, L. D., Sena, L., Martin, J., Adamson, K. L., Robbins, A., Gumbrell, L., O'Malley, D., Tsiompanou, E., Shahbakhti, H., Webley, S., Hochhauser, D., Hilson, A. J., Blakey, D., and Begent, R. H. (2002) A phase I trial of antibody directed enzyme prodrug therapy (ADEPT) in patients with advanced colorectal carcinoma or other CEA producing tumours. *Br. J. Cancer 87*, 600−7.
(6) HariKrishna, D., Rao, A. R., and Krishna, D. R. (2003) Selective activation of anthracycline prodrugs for use in conjunction with ADEPT. *Drug News Perspect. 16*, 309−18.
(7) Rodrigues, M. L., Carter, P., Wirth, C., Mullins, S., Lee, A., and Blackburn, B. K. (1995) Synthesis and beta-lactamase-mediated activation of a cephalosporin-taxol prodrug. *Chem. Biol. 2*, 223−7.
(8) Senter, P. D., Saulnier, M. G., Schreiber, G. J., Hirschberg, D. L., Brown, J. P., Hellstrom, I., and Hellstrom, K. E. (1988) Antitumor effects of antibody-alkaline phosphatase conjugates in combination with etoposide phosphate. *Proc. Natl. Acad. Sci. U. S. A. 85*, 4842−6.
(9) Vrudhula, V. M., Kerr, D. E., Siemers, N. O., Dubowchik, G. M., and Senter, P. D. (2003) Cephalosporin prodrugs of paclitaxel for immunologically specific activation by L-49-sFv-beta-lactamase fusion protein. *Bioorg. Med. Chem. Lett. 13*, 539−42.
(10) Tietze, L. F., Herzig, T., Fecher, A., Haunert, F., and Schuberth, I. (2001) Highly selective glycosylated prodrugs of cytostatic CC-1065 analogues for antibody-directed enzyme tumor therapy. *Chembiochem 2*, 758−65.
(11) Niculescu-Duvaz, D., Niculescu-Duvaz, I., Friedlos, F., Martin, J., Lehouritis, P., Marais, R., and Springer, C. J. (2003) Self-immolative nitrogen mustards prodrugs cleavable by carboxypeptidase G2 (CPG2) showing large cytotoxicity differentials in GDEPT. *J. Med. Chem. 46*, 1690−705.
(12) Kousparou, C. A., Epenetos, A. A., and Deonarain, M. P. (2002) Antibody-guided enzyme therapy of cancer producing cyanide results in necrosis of targeted cells. *Int. J. Cancer 99*, 138−48.
(13) Bignami, G. S., Senter, P. D., Grothaus, P. G., Fischer, K. J., Humphreys, T., and Wallace, P. M. (1992) *N*-(4′-hydroxyphenylacetyl)palytoxin: a palytoxin prodrug that can be activated by a monoclonal antibody-penicillin G amidase conjugate. *Cancer Res. 52*, 5759−64.
(14) Batra, S. K., Jain, M., Wittel, U. A., Chauhan, S. C., and Colcher, D. (2002) Pharmacokinetics and biodistribution of genetically engineered antibodies. *Curr Opin. Biotechnol. 13*, 603−8.
(15) Farquhar, D., Cherif, A., Bakina, E., and Nelson, J. A. (1998) Intensely potent doxorubicin analogues: structure−activity relationship. *J Med Chem 41*, 965−72.
(16) Bakina, E., and Farquhar, D. (1999) Intensely cytotoxic anthracycline prodrugs: galactosides. *Anticancer Drug Des. 14*, 507−15.
(17) Tietze, L. F., Feuerstein, T., Fecher, A., Haunert, F., Panknin, O., Borchers, U., Schuberth, I., and Alves, F. (2002) Proof of principle in the selective treatment of cancer by antibody-directed enzyme prodrug therapy: the development of a highly potent prodrug. *Angew. Chem., Int. Ed. 41*, 759−61.
(18) Gesson, J. P., Jacquesy, J. C., Mondon, M., Petit, P., Renoux, B., Andrianomenjanahary, S., Dufat-Trinh Van, H., Koch, M., Michel, S., Tillequin, F., and et al. (1994) Prodrugs of anthracyclines for chemotherapy via enzyme-monoclonal antibody conjugates. *Anticancer Drug Des. 9*, 409−23.
(19) Abraham, R., Aman, N., von Borstel, R., Darsley, M., Kamireddy, B., Kenten, J., Morris, G., and Titmas, R. (1994) Conjugates of COL-1 monoclonal antibody and beta-D-galactosidase can specifically kill tumor cells by generation of 5-fluorouridine from the prodrug beta-D-galactosyl-5-fluorouridine. *Cell Biophys. 24−25*, 127−33.
(20) Siemers, N. O., Kerr, D. E., Yarnold, S., Stebbins, M. R., Vrudhula, V. M., Hellstrom, I., Hellstrom, K. E., and Senter, P. D. (1997) Construction, expression, and activities of L49−sFv-beta-lactamase, a single-chain antibody fusion protein for anticancer prodrug activation. *Bioconjugate Chem. 8*, 510−9.
(21) Farquhar, D., Pan, B. F., Sakurai, M., Ghosh, A., Mullen, C. A., and Nelson, J. A. (2002) Suicide gene therapy using E. coli beta-galactosidase. *Cancer Chemother. Pharmacol. 50*, 65−70.
(22) Zwelling, L. A., Altschuler, E., Cherif, A., and Farquhar, D. (1991) N-(5,5-diacetoxypentyl)doxorubicin: a novel anthracycline producing DNA interstrand cross-linking and rapid endonucleolytic cleavage in human leukemia cells. *Cancer Res. 51*, 6704−7.
(23) Leenders, R. G., Damen, E. W., Bijsterveld, E. J., Scheeren, H. W., Houba, P. H., van der Meulen-Muileman, I. H., Boven, E., and Haisma, H. J. (1999) Novel anthracycline-spacer-beta-glucuronide,-beta-glucoside, and -beta-galactoside prodrugs for application in selective chemotherapy. *Bioorg. Med. Chem. 7*, 1597−610.
(24) Cohen, R. B., Tsou, K. C., Rutenburg, S. H., and Seligman, A. M. (1952) The colorimetric estimation and histochemical demonstration of beta-d-galactosidase. *J. Biol. Chem. 195*, 239−49.
(25) Tenu, J. P., Viratelle, O. M., Garnier, J., and Yon, J. (1971) pH dependence of the activity of beta-galactosidase from Escherichia coli. *Eur. J. Biochem. 20*, 363−70.
(26) Weiss, D. J., Liggitt, D., and Clark, J. G. (1999) Histochemical discrimination of endogenous mammalian beta-galactosidase activity from that resulting from lac-Z gene expression. *Histochem. J. 31*, 231−6.
(27) Bhatia, J., Sharma, S. K., Chester, K. A., Pedley, R. B., Boden, R. W., Read, D. A., Boxer, G. M., Michael, N. P., and Begent, R. H. (2000) Catalytic activity of an in vivo tumor targeted anti-CEA scFv:: carboxypeptidase G2 fusion protein. *Int. J. Cancer 85*, 571−7.

BC050039Z

A Single-Step Method for the Production of Sugar Hydrazides: Intermediates for the Chemoselective Preparation of Glycoconjugates

Nicholas S. Flinn,* Martin Quibell, Tracy P. Monk, Manoj K. Ramjee, and Christopher J. Urch†

Amura Therapeutics Limited, Horizon Park, Barton Road, Comberton, CB3 7AJ, United Kingdom. Received February 15, 2005; Revised Manuscript Received March 10, 2005

The ability to selectively conjugate carbohydrate molecules to a protein is a key step in the preparation of conjugate vaccines, while facile methods for linking carbohydrates to polymers or solid surfaces to produce diagnostic probes and functional microarrays are also sought. Here, we describe a simple, single-step method of producing glycosylhydrazides from unprotected sugars, which were then linked in a controlled manner to a desired carrier, through an appropriate linker. The method was chemoselective and did not require coupling reagents, and the native pyranose form of the reducing end residue was retained. Initially, mono- and disaccharide hydrazides were produced from the corresponding reducing sugars and linked to BSA through a bifunctional linker. Final exemplification of the procedure was demonstrated by the preparation of a LewisY tetrasaccharide protein conjugate, which was recognized by a LewisY monoclonal antibody indicating the preservation of the natural conformation of the tetrasaccharide in the final construct. It is envisaged that this method will have general applicability to a variety of functionally diverse reducing sugars and provide a route to highly defined glycoconjugates, without the need for elaborate synthetic strategies.

INTRODUCTION

Bacterial derived polysaccharides presented as vaccines have already been effective in controlling certain types of pneumonia and meningitis (*1*, *2*), while "tumor-associated" carbohydrates unique to certain cancers, have also proved attractive as candidates for incorporation into therapeutic cancer vaccines (*3*−*7*). The promise of such subunit vaccines has been limited by their low immunogenicity, and to make polysaccharide vaccines broadly more effective, the polysaccharides require conjugation to "carrier proteins" (*8*), which are often prepared from bacterial sources themselves. The resultant conjugate vaccines tend to be highly immunogenic and confer long-lasting protection.

Conjugation of polysaccharides to a carrier protein, however, is by no means a simple task, given the polyfunctional nature and complexity of the molecules. Nonspecific approaches include the use of cyanogen bromide (CNBr) (*9*, *10*) and 1-cyano-4-dimethylamino-pyridinium tetrafluoroborate (CDAP) (*11*, *12*), which involve activation of hydroxyl groups on the polysaccharide and result in attachment through multiple sites. More controlled methods of conjugation utilize reductive amination, whereby the reducing end of the polysaccharide is reacted with an amine present on a bifunctional spacer molecule or on a protein to form a Schiff adduct, which is then reduced with sodium cyanoborohydride to form a physiologically stable bond (*13*, *14*). However, the ring opening of the reducing end residue, which occurs during reductive amination, may have a detrimental effect on the biological activity or immunogenicity of the carbohydrate, because the loss of structure ultimately equates to the loss of function (*15*).

A much improved approach involves the introduction of a primary amine at the reducing end terminus of an unprotected carbohydrate (*16*). The pyranose form of the reducing end terminus monosaccharide is preserved, and the new amine provides a useful handle for further elaboration that may lead to selectively defined glycoconjugates (*15*, *17*, *18*). Obviously, defined sugar conjugates may be obtained from a wholly synthetic approach; however, this chemistry is complex and is limited to short-chain-length oligosaccharides (<10 residues).

We have developed a chemoselective linker for controlled conjugation, particularly in the preparation of constructs where retention of structure and function is paramount (e.g., vaccines, functional arrays, etc.) (*19*). The methodology, which has already been applied to peptides, proteins, and small molecules, requires a hydrazide to be present, because conjugation proceeds through hydrazone formation (*20*). Herein, we describe a one-step method for the preparation of glycosylhydrazides directly from reducing sugars, without the need for elaborate synthetic manipulation or initial conversion to an amino derivative. Reaction of model mono- and disaccharides with the homobifunctional spacer adipic dihydrazide, produced the desired glycosylhydrazides in predominantly the β-pyranose form. These hydrazide-modified sugars were then conjugated to bovine serum albumin (BSA) in a selective manner, using our previously described linker technology (*20*). In a further exemplification of the methodology, a BSA conjugate of the LewisY tetrasaccharide (*21*, *22*) was also prepared and the conjugate was recognized by a LewisY-specific monoclonal antibody, demonstrating the retention of the native LewisY structure during the process. It is envisaged that the chemistries derived for these model systems could be extended to more complex saccharides and

* To whom correspondence should be addressed. E-mail: nick.flinn@amura.co.uk. Telephone: +44(0)1223-264211. Fax: +44(0)01223-265662.

† Current address: Glycoform Limited, Unit 44C, Milton Park, Abingdon, Oxon, OX14 4RU, U.K.

10.1021/bc050041q CCC: $30.25 © 2005 American Chemical Society
Published on Web 04/20/2005

provide a generalized method for the prederivatization of a range of complex glycans ready for chemoselective glycoconjugate production.

EXPERIMENTAL PROCEDURES

General Biochemistry. All reagents were of the highest commercially available quality and were used as received. Unless otherwise stated all chemicals and biochemicals were purchased from the Sigma Chemical Company (Poole, Dorset, U.K.). Unless otherwise stated, routine protocols were carried out at ambient temperature and kinetic experiments were carried out at 25 °C. Protein concentrations were determined using the Bradford reagent (Sigma) according to the instructions of the manufacturer using BSA as the standard. Absorbance measurements were either carried out in 384-well microtiter plates (Corning Costar 3702 plates, Fisher Scientific, Loughborough, U.K.), flat-bottomed 96-well plates (Spectra; Greiner Bio-One Ltd., Stonehouse, Gloucestershire, U.K.) or standard 1 mL quartz cuvettes, using a SpectraMax PLUS384 plate reader (Molecular Devices, Crawley, U.K.). Fluorescence measurements were carried out in either 384-well microtiter plates (Corning Costar 3705 plates, Fisher Scientific) or 96-well "U" bottomed Microfluor W1 microtiter plates (Thermo Labsystems, Ashford, Middlesex, U.K.). Fluorescence assays were monitored using a SpectraMax Gemini fluorescence plate reader (Molecular Devices). In all cases, SOFTmax Pro 3.1.2 software was used for data collection and handling (Molecular Devices). All spectra were collected at a resolution of 2 nm. Gel and membrane images were captured using a Hewlett−Packard C7710A scanner employing HP Precision ScanPro 3.02 software on default settings. Images were routinely scanned at a minimum resolution of 600 dpi in gray scale mode (32 bit). Images were marked with legends employing Powerpoint (Microsoft Corp., Seattle, WA). Image analysis and processing was carried out using ImageJ software (*23*).

General Chemistry. All solid-phase synthesis was performed using an "Fmoc/tBu" procedure (*24*) invoking standard solid-phase synthesis resin washing protocols. Standard Fmoc amino acids were obtained from Chem-Impex International (Wood Dale, IL) and Merck Biosciences (Nottingham, U.K.) with the exception of Fmoc *N*-ϵ-trimethyllysine, which was purchased from Bachem U.K. Ltd. (St. Helens, U.K.). 2-Chlorotrityl-resin (Product 04-12-2800) was obtained from Merck Biosciences (Nottingham, U.K.). PS-carbodiimide resin was obtained from Argonaut Technologies (Muttenz, Switzerland). All solvents were purchased from Romil (Cambridge, U.K.). Solid-phase syntheses were performed manually in a polypropylene syringe fitted with a polypropylene frit to allow filtration under vacuum. Analytical HPLC was performed on Agilent 1100 series instruments including a G1311A quaternary pumping system, with a G1322A degassing module and a G1365B multiple wavelength UV−vis detector. Data were collected and integrated with Chemstation 2D software. The analyses were performed on a Zorbax, 5 μm, C8 reverse-phase column (150 × 4.6 mm i.d.), at a flow rate of 1.5 mL/min, monitoring at 215 and 254 nm. Eluents used were (A) 0.1% trifluoroacetic acid in water and (B) 90% acetonitrile/10% eluent A and used to run a gradient starting at 10% B, increasing to 90% B over 7 min, holding for 1 min, returning to 10% B over 1 min, and then remaining at initial conditions for a further 4 min to allow column re-equilibration. Compounds were purified by semipreparative HPLC, using a Phenomenex Jupiter C4 reverse-phase column (250 × 10 mm i.d.) at a flow rate of 4 mL/min, using the equipment and eluents described above or by gel filtration, using BioGel P-2 resin (extra fine in 0.02 M ammonium bicarbonate, Bio-Rad Laboratories). The molecular ions of compounds were determined on an Agilent 1100 series LC/MSD electrospray mass spectrometer (ESI−MS). ^{1}H NMR was performed on a Bruker Avance (500 MHz, TXI probe with ATM) at 300 K.

Amine Determination. The amine concentrations were determined using fluorescamine (Fluram; Fluka) (*25*), employing Ac-Lys-NH_2 (Bachem) as the calibration control. Routinely, 10 μL of test sample was diluted into 85 μL of 100 mM sodium phosphate at pH 10 and 5 μL of 10 mM Fluram (in 100% acetonitrile) added. The Fluram solutions were freshly prepared prior to use. The reactions were mixed and incubated at ambient temperature for 30 min prior to measuring the fluorescence (390 nm, excitation; 460 nm, emission).

SDS−PAGE and Western Blot Analysis. The SDS−PAGE and Western blot components were obtained from Invitrogen, Paisley, U.K. For denatured protein analysis, samples were routinely analyzed by SDS−PAGE using the NuPAGE system employing 4−12% bis-tris NuPAGE gels and, unless otherwise stated, all gels were run in MES or MOPS running buffer. The POWEREASE system was used to carry out electrophoresis employing protocols embedded in the software of the unit. Proteins were visualized with SimplyBlue stain or SilverExpress stain kits according to protocols of the manufacturers. After staining, gels were dried using DryEase gel-drying solution and cellophane membranes.

For Western blot analysis of conjugates, the proteins were transferred from the gel onto PVDF membrane using the reagents and protocols of the manufacturer (Invitrogen). The PVDF membranes were blocked by gentle agitation in 50 mL phosphate-buffered saline containing 1% Tween 20 (PBST; Sigma) plus 1% (w/v) casein for 60 min. The recovered membranes were washed 3 times, by gentle agitation, in 50 mL of PBST for 5 min per cycle. After this, the membranes were incubated in 30 mL of PBST containing 1:100 dilution of mouse IgM LewisY monoclonal antibody (Alexis Corporation, SIG-317) for 60 min. After washing as before, the membranes were incubated in 30 mL of PBST containing 1:1000 dilution goat anti-mouse IgM, HRP conjugated antibody (Alexis Corporation, A90-101P) for 60 min, washed as before in PBST, and allowed to partially drip dry. Regions of peroxidase activity were visualized by addition of a 3,3′,5,5′-tetramethylbenzidine (TMB) liquid substrate (Sigma) onto the static membrane. After appropriate exposure, the membrane was recovered, washed in water, and air-dried prior to scanning, analysis, and storage.

ELISA assays were performed in immulon 2HB 96-well plates (Thermo Labsystems). Samples were introduced in PBS buffer and incubated overnight at 37 °C. Washing was performed 3 times with 200 μL of PBST, and the plate was blocked with 100 μL of PBST containing 1% casein (w/v) for 60 min. Primary and secondary antibodies (100 μL) were the same as those used for the Western blot analysis, both being incubated for 60 min at 37 °C with a PBST wash step in between. After a final PBST wash, peroxidase activity was visualized by addition of 100 μL of *o*-phenylenediamine (OPD; Sigma) and the reaction was quenched with 100 μL of 0.1 M sulfuric acid. Quantitation was by absorbance at 490 nm.

Diafiltration. Routinely, Amicon Ultra-4 ($\leq$4 mL) or Ultra-15 ($\leq$15 mL) centrifugal filter units (10 000 mwco; Millipore, Watford, U.K.) were used for diafiltration. Each cycle consisted of diluting the protein sample approxi-

mately 10-fold with exchange buffer and concentrating the sample by centrifugation back to its original volume. Cycles were repeated as required for quick and highly efficient equilibration/washing of protein samples. Routinely, six cycles were completed for each diafiltration step.

Synthesis of 5-[*N*′-(3,4,5-Trihydroxy-6-hydroxymethyltetrahydropyran-2-yl)-hydrazinocarbonyl] Pentanoic Hydrazide (3a). A mixture of glucose **1a** (90 mg, 0.5 mmol) and adipic dihydrazide **2** (recrystallized from water−acetonitrile) (870 mg, 5 mmol) in water (5 mL) and acetonitrile (5 mL) was heated at 80 °C. After 8 h, the mixture was evaporated under reduced pressure, water (2 mL) was added, and the mixture was evaporated under reduced pressure. Gel-filtration chromatography was performed twice to give **3a** (22 mg, 13%) as a white solid, following lyophilisation. ^{1}H NMR (D_2O) δ: 3.96 (d, 1H, J = 9.0 Hz), 3.77 (dd, 1H, J = 12.2, 2.1 Hz), 3.58 (dd, 1H, 12.2, J = 5.8 Hz), 3.38 (t, 1H, J = 9.1 Hz), 3.28 (ddd, 1H, J = 9.8, 5.9, 2.3 Hz), 3.22 (t, 1H, J = 9.3 Hz), 3.14 (t, 1H, J = 9.0 Hz), 2.11 (m, 4H), 1.47 (m, 4H). MS *m/z*: 337.2 (M + H^+), 359.2 (M + Na^+). Exact mass calculated for $C_{12}H_{24}N_4O_7$ (MH+), 337.1718; found, 337.1710 (δ −2.19 ppm).

Synthesis of 5-{*N*′-[3,4-Dihydroxy-6-hydroxymethyl-5-(3,4,5-trihydroxy-6-hydroxymethyltetrahydropyran-2-yloxy)tetrahydro-pyran-2-yl]hydrazinocarbonyl} Pentanoic Hydrazide (3b). A mixture of α-D-lactose monohydrate **1b** (180 mg, 0.5 mmol) and **2** (recrystallized from water−acetonitrile) (870 mg, 5 mmol) was heated in water (5 mL) and acetonitrile (5 mL) at 80 °C. After 8 h, the mixture was evaporated under reduced pressure, water (2 mL) was added, and the mixture was evaporated under reduced pressure. Gel-filtration chromatography was performed twice to give **3b** (182 mg, 73%) as a white solid, following lyophilisation. ^{1}H NMR (D_2O) for β isomer δ: 4.35 (d, 1H, J = 7.9 Hz), 4.03 (d, 1H, J = 9.0 Hz), 3.87 (dd, 1H, J = 12.2, 2.1 Hz), 3.83 (d, 1H, J = 3.3 Hz), 3.75−3.50 (m, 7H), 3.45 (m, 2H), 3.25 (t, 1H, J = 9.0 Hz), 2.14 (m, 4H), 1.51 (m, 4H). MS *m/z*: 499.2 (M + H^+), 521.2 (M + Na^+), 1019.3 (2M + Na^+). Exact mass calculated for $C_{18}H_{34}N_4O_{12}$ (MH^+), 499.2246; found, 499.2252 (δ +1.25 ppm).

Synthesis of *N*-[2-(*N*′-Acetylhydrazino)-5-[4,5-dihydroxy-6-hydroxymethyl-3-(3,4,5-trihydroxy-6-methyltetrahydropyran-2-yloxy)tetrahydropyran-2-yloxy]-6-hydroxymethyl-4-(3,4,5-trihydroxy-6-methyltetrahydropyran-2-yloxy)tetrahydropyran-3-yl]-5-hydrazinocarbonylpentamide (3c). A mixture of LewisY tetrasaccharide **1c** (3 mg as supplied by Sigma, 0.0044 mmol) and adipic dihydrazide **2** (recrystallized from water−acetonitrile) (7.7 mg, 0.044 mmol) in pH 4.75 sodium formate buffer (0.1 mL) was heated at 30 °C, and the reaction was monitored for product formation. After 6 days, the mixture was diluted with water (0.1 mL), frozen, and lyophilized. Gel-filtration chromatography (Bio-Gel P-2 Gel, extra fine, 0.02 M ammonium bicarbonate) gave the LewisY tetrasaccharide-adipic dihydrazide adduct **3c** (1.66 mg, 45%) as a white solid, following lyophilisation. ^{1}H NMR (D_2O) major isomer δ: 5.15 (d, 1H, J = 3.5 Hz), 4.97 (d, 1H, J = 3.9 Hz), 4.76 (brq, 1H, J = 6.0 Hz), 4.37 (d, 1H, J = 7.8 Hz), 4.13 (d, 1H, J = 4.6 Hz), 4.11 (brs, 1H), 3.86 (d, 1H, J = 10.3 Hz), 3.80−3.40 (m, 19H), 3.30 (m, 1H), 2.25−2.05 (m, 4H), 1.89 (s, 3H), 1.55−1.40 (m, 4H), 1.13 (d, 3H, J = 6.6 Hz), 1.10 (d, 3H, J = 6.6 Hz). MS *m/z*: 832.3 (M + H^+), 854.3 (M + Na^+). Exact mass calculated for $C_{32}H_{57}N_5O_{20}$ (MNa+), 854.3495; found, 854.3470 (δ −2.92 ppm).

Synthesis of 5-(4-Formyl-3-hydroxyphenoxy)pentanoic Acid 2,5-Dioxo-pyrrolidin-1-yl Ester (4) (AmLinker *N*-Hydroxysuccinimide Ester). Compound **4** was prepared as described previously (*20*).

Preparation of AmLinker−BSA (5). BSA (2 mg, 29 nmol) was dissolved in 0.1 M sodium acetate (1 mL, pH 7.25), to which 500 μL of a 15 mM solution of **4** (in 100% DMSO) was added, and the reaction was stirred at ambient temperature. The disappearance of free amine was monitored using Fluram titration and once complete (∼2−3 h) the reaction mixture was purified by diafiltration using 10 mM ammonium bicarbonate (pH 8) and the product analyzed by SDS−PAGE.

Preparation of Glucose, Lactose, and LewisY BSA Conjugates (6a−c, Respectively). The glucose, lactose, and LewisY conjugates (**6a−c**) were produced by stirring AmLinker−BSA (**5**) (1 mg, 14 nmol) with sugar hydrazides **3a**, **3b**, and **3c** in sodium formate (0.1 M; pH 4: 1 mL) containing between 10 and 30% DMSO (v/v) at room temperature, using 3−5 molar equivalents of sugar hydrazide over the molar equivalents of AmLinker coupled to the surface of the BSA. The reactions were monitored by UV at 318 nm and allowed to run until deemed completed (by the UV profile), which in general was 5−6 h. The conjugates were purified by diafiltration and characterized by SDS−PAGE.

RESULTS AND DISCUSSION

Synthesis of Hydrazide-Modified Sugars. We recently reported the development of a charge-balanced linker for the chemoselective conjugation of proteins, peptides, and small molecules (*20*) and were attracted by the potential wider application of the linkage technology to include the preparation of defined glycoconjugates. Because the linkage chemistry relies on hydrazone formation, it is necessary to introduce a hydrazide moiety into the carbohydrate of interest, before conjugation to a carrier or solid surface can be performed. With this in mind, a simple method of glycosylhydrazide production was sought that was selective, did not require elaborate synthetic protocols, and had the potential for application to increasingly complex saccharides. It was deemed imperative that the procedure should leave the pyranose form of the sugar intact and not disrupt its native ring conformation, and herein, we report our results.

Given the success of the well-precedented selective preparation of β-glycosylhydrazines from reducing sugars by treatment with hydrazine (*26*) and hydrazine derivatives (*27*), we sought to replicate the process replacing hydrazine with a hydrazide. Simple mono- and disaccharide sugars (**1a** and **1b**) were reacted with the commonly used bifunctional spacer adipic dihydrazide **2** (in excess) to yield the corresponding hydrazide-modified sugars (**3a** and **3b**) (Scheme 1).

For sugars **1a** and **1b**, the reaction was performed at 80 °C for 8 h in a 50:50 mixture of water and acetonitrile (acetonitrile could be replaced with DMSO, without any detrimental effect), which usually resulted in a near quantitative yield of the hydrazide adduct. Further examples of glycosylhydrazides were also prepared from glucosamine, *N*-acetyl glucosamine, and glucuronic acid, to demonstrate the broad applicability of the method to structurally diverse sugars, although in these latter examples, the products were not isolated (*28*).

As a result of very high water solubility and the small differences in molecular weight between product and reactants, purification of the glucose monoglycosylhydrazide (**3a**) proved troublesome by gel-filtration chro-

Scheme 1

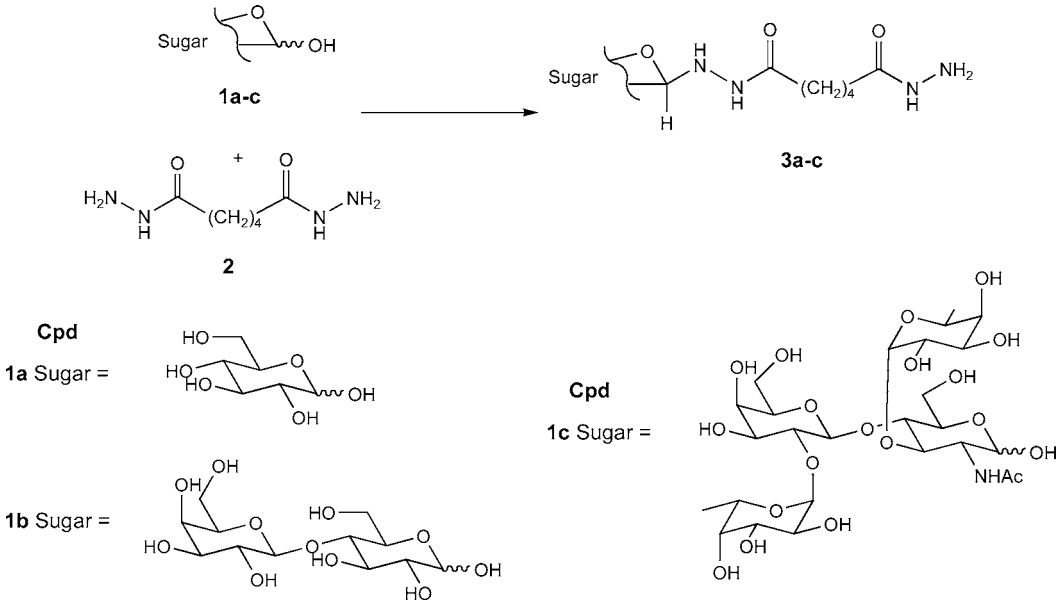

Scheme 2. Proposed Mechanism for the Glycosylhydrazide Formation

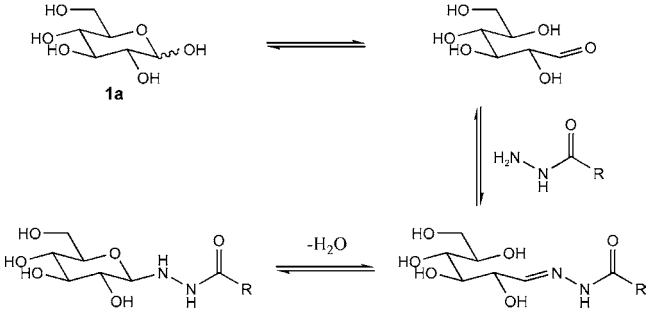

matography, with an isolated yield of only 13% being obtained despite the reaction being near quantitative. However, the higher molecular weight sugars were more amenable to gel-filtration chromatography. For example, when the lactose and LewisY derivatives (**3b** and **3c**) were purified by gel filtration, much higher isolated yields (73 and 45%, respectively) were obtained. In each reaction, the β isomer was the major product estimated at about 90% (but because of the proximity of the anomeric proton of the α isomer to the water signal in the NMR spectra, greater accuracy was not possible).

This selectivity of a reaction for an anomeric position bearing a hydroxyl group is important because it means that sugar conjugates can be made without the risk of decomposition of the saccharide. It also implies that the mechanism of reaction is via the open-chain sugar and is reinforced by the fact that the open imine form of the product can be identified in some cases by NMR, particularly before the reaction has gone to completion (shown in Scheme 2 for glucose **1a**).

After we demonstrated the feasibility of glycosylhydrazide preparation from simple unprotected sugars, a more complex and biologically relevant carbohydrate was sought as a final exemplification. Of particular interest was the LewisY tetrasaccharide (**1c**, Scheme 1), a carbohydrate specificity belonging to the A, B, and H Lewis blood group family, which is overexpressed on many carcinomas, including ovary, pancreas, prostate, breast, colon, and nonsmall cell lung cancers (*4*, *29*, *30*) and has been highlighted as a possible tumor vaccine candidate. A further attraction was the fact that monoclonal antibodies (mAb) specific for LewisY were commercially available, which was useful for determining whether the structural conformation of the LewisY was retained during the derivatization procedure and final conjugation process, because the LewisY mAb would presumably only recognize the native structure.

In the case of the Lewis Y tetrasaccharide, it was not possible to form the glycosylhydrazide under the conditions previously employed because of the practical difficulties of maintaining a small volume (0.1 mL) at 80 °C. Thus, it was necessary to find conditions that allowed equilibrium to be reached at a lower temperature on a reasonable time scale. This was accomplished by performing the reaction under mildly acidic conditions. Trial reactions using *N*-acetyl glucosamine and adipic dihydrazide **2** at 30 °C were essentially complete after 5 days. Thus, the Lewis Y tetrasaccharide **1c** and 10 equiv of adipic dihydrazide **2** were heated at 30 °C in pH 4.75 formate buffer for 6 days, at which point TLC (SiO_2 and MeOH) indicated complete conversion to the glycosylhydrazide. Characterization of the crude reaction mixture by ESI−MS and NMR indicated one major product. Gel-filtration chromatography gave the desired product **3c** in an isolated yield of 45%.

Because glycosylhydrazide formation can occur at mildly acidic to neutral pH, it is possible to modify reaction conditions such as pH and temperature to achieve optimal reaction rates while maintaining a stable environment for the reactants and product. This versatility should render the process applicable to a diverse array of complex carbohydrates, some of which may be chemically sensitive.

Carrier Protein Conjugation. With the glycosylhydrazides prepared, we next sought to use these derivatized sugars to produce protein−sugar conjugates. Thus, BSA, which is often exploited as a carrier protein for experimental conjugate vaccines, was derivatized by acylation with the *N*-hydroxysuccinimide ester of our linker **4** (AmLinker-NHS) to produce a BSA−AmLinker-derived carrier protein **5** (Scheme 3).

Using a modification of the general coupling conditions elucidated previously for peptide hydrazides (*19*, *20*), conjugation reactions were attempted with the AmLinker-modified BSA **5** and hydrazide sugars **1a** and **1b** to produce BSA−sugar conjugates of glucose and lactose

Scheme 3. Preparation of BSA Glycoconjugates via AmLinker

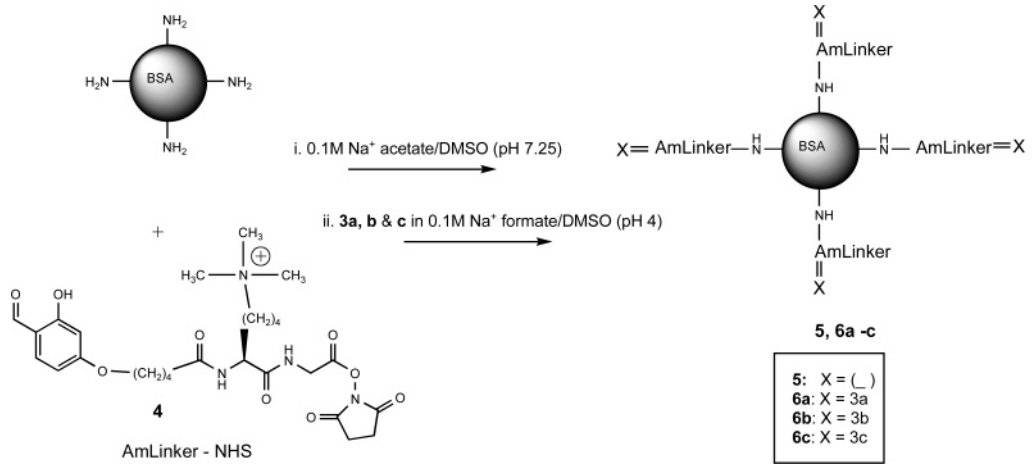

(**6a** and **6b** respectively). The process was monitored by the increase in absorbance at 318 nm, as described previously (*20*) (Figure 1A).

Characterization of the conjugates was accomplished by gel electrophoresis, which was employed to give an estimation of molecular weight. Figure 1B shows the slight increase in molecular weight between BSA and conjugates **6a** and **6b**.

Conjugation of **3c** to BSA−AmLinker **5** was carried out and monitored by UV at 318 nm (Figure 2) as stated previously for conjugates **6a** and **6b**, with the exception that only 3 molar equivalents of **3c** was used over **5**, because of the limited availability of the LewisY starting material.

After purification of the product by diafiltration, the LewisY−BSA conjugate (**6c**) was initially characterized by gel electrophoresis to assess molecular weight and loading (Figure 3A). Figure 3A clearly shows that the BSA−LewisY conjugate **6c** has an increased molecular weight of approximately 25 kDa when compared to the unmodified BSA protein. Modification of the BSA with 1 AmLinker molecule and the LewisY tetrasaccharide would lead to an increase of a little over 1 kDa. Thus, a molecular weight increase of 25 kDa would suggest a loading of ∼22−24 molecules of LewisY on every molecule of BSA (which represents the majority of surface-available linkage points). It was also observed that the glycoconjugate remained soluble in the buffer solution even though the protein had undergone substantial surface modification, indicating the benefits of the charge

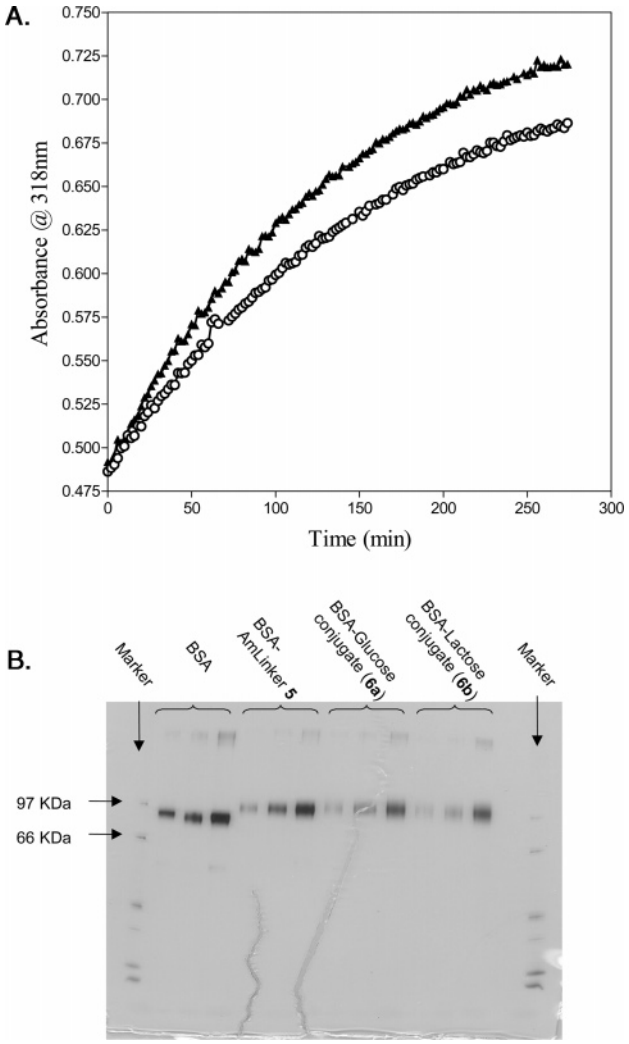

Figure 1. (A) Production of BSA glycoconjugates **6a** (○) and **6b** (▲). Glucose hydrazide (**3a**) and lactose hydrazide (**3b**) conjugation, to BSA−AmLinker (**5**) in 100 mM formate at pH 4.0 (with 20% v/v DMSO), monitored by a change in absorbance at 318 nm. (B) Characterization of conjugates **6a** and **6b** by SDS−PAGE.

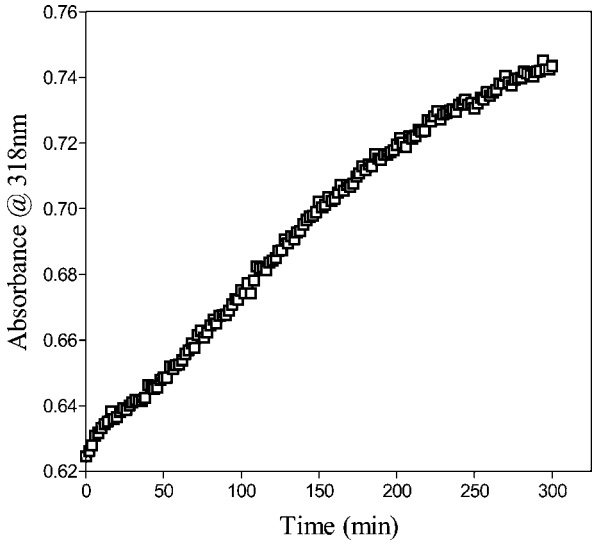

Figure 2. Production of BSA−LewisY conjugate (**6c**) (□). LewisY hydrazide (**1c**) conjugation to BSA−AmLinker (**5**) in 100 mM sodium formate at pH 4.0 (with 20% v/v DMSO), monitored by a change in absorbance at 318 nm.

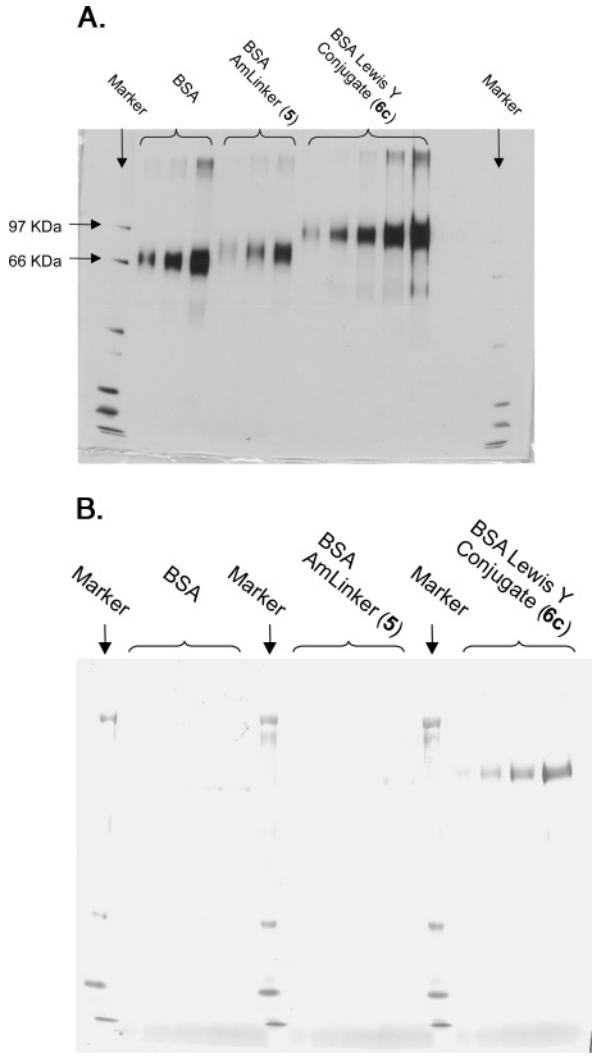

Figure 3. (A) Increase in molecular weight of BSA−LewisY conjugate (**6c**) shown by SDS−PAGE: The single band suggests an homogeneous conjugate preparation. (B) Western blot of BSA, BSA−AmLinker (**5**), and BSA−LewisY conjugate (**6c**) using a LewisY specific mAb and an anti-mouse IgM HRP labeled secondary antibody. Visualization was achieved with ″TMB. Rainbow markers were used to give molecular weight estimates.

compensation mechanism built into AmLinker, which replenishes the positive charge of the surface amine lost during its covalent modification (*20*).

To further characterize the conjugate, binding assays were performed using a LewisY-specific mAb to demonstrate that the LewisY tetrasaccharide was conjugated in a selective manner and remained structurally unperturbed. In the first experiment, a Western blot of a gel similar to that in Figure 3A was produced and exposed to the LewisY-specific mAb. After the blot was developed, it was clear that the mAb recognized the BSA−LewisY conjugate **6c** alone and not the BSA or the BSA−AmLinker **5** intermediate (Figure 3B).

To confirm that the LewisY-specific mAb recognized only the LewisY and not the BSA or AmLinker, an ELISA immunoassay was performed, whereby the BSA−LewisY conjugate **6c** was treated with 1 N hydrochloric acid (HCl) and then repurified by ultradiafiltration. Because one aspect of AmLinker is its reversibility (*20*), treatment with acid will remove any conjugated molecule while leaving the BSA−AmLinker preparation intact. Thus, the LewisY-specific mAb should no longer recognize this acid-treated sample after removal of the LewisY tetrasaccharide.

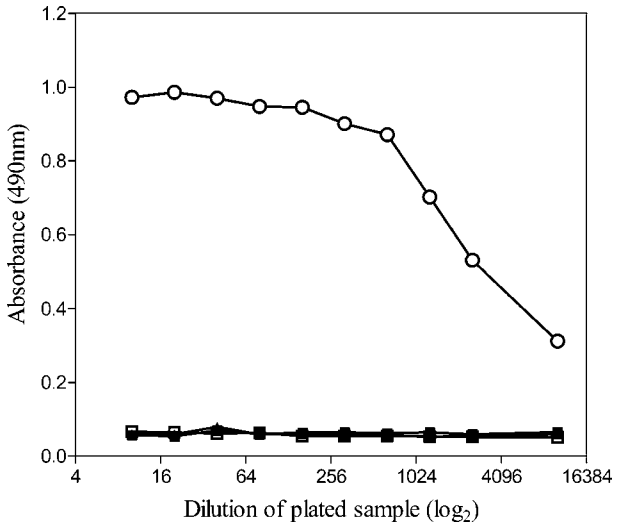

Figure 4. ELISA shows the specific recognition of the BSA−LewisY conjugate (**6c**) (○) with the LewisY specific mAb, whereas BSA (■), BSA−AmLinker (**5**) (▲), and the post-acid-treated BSA−LewisY conjugate (□) display no reaction. Visualization was achieved with an anti-mouse IgM HRP labeled secondary antibody and OPD and quantified by absorbance at 490 nm.

The samples were added to a microtiter plate and double-diluted in PBS, while PBS alone was used as the blank. After exposure to the LewisY-specific mAb, only the BSA−LewisY conjugate **6c** displayed binding, while the other samples, including the acid-treated BSA−LewisY conjugate, were not recognized by the mAb, as quantified by absorbance readings at 490 nm (Figure 4).

CONCLUSION

The synthetic study described herein successfully demonstrates that glycosylhydrazides can be prepared from their unprotected precursor reducing sugars in a single step reaction, employing simple solvents and without the need for aggressive activating reagents. These stable glycosylhydrazides may then be conjugated, via our proprietary linkage technology (AmLinker) (*20*) to any amine functionalized surface. The uncomplicated and selective manner in which the derivitisation and conjugation is performed permits the retention of the native pyranose structure of the reducing end sugar and leads to the enhanced prospect of producing functional conjugates. This is a primary consideration when designing and developing glycoconjugates for use as vaccines, diagnostic tools, or in high throughput screening strategies, where the loss of native conformation ultimately leads to an attenuation of biological activity.

Although exemplification of this feasibility study culminated in the production of glycoprotein conjugates, our AmLinker technology has already demonstrated applicability to the construction of functional peptide and small molecule arrays and protein conjugates (*19*). Thus, it is envisaged that the simple preparation of unprotected sugar hydrazides, described herein, utilizing an established dihydrazide spacer molecule, may be employed over a wide range of applications, where conjugation of mono-, di-, oligo-, or polysaccharides to a carrier molecule or solid surface would be desirable.

ACKNOWLEDGMENT

This work was supported by funding from a SMART Award (SEC 117/381) from the Department of Trade and

Industry. We thank staff at Amura Therapeutics Limited for technical assistance, advice, and manuscript review.

LITERATURE CITED

(1) Zielen, S., Buhring, I., Strnad, N., Reichenbach, J., and Hofmann, D. (2000) Immunogenicity and tolerance of a 7-valent pneumococcal conjugate vaccine in nonresponders to the 23-valent pneumococcal vaccine. *Infect. Immun. 68*, 1435−1440.

(2) Jin, Z., Chu, C., Robbins, J. B., and Schneerson, R. (2003) Preparation and characterization of group A meningococcal capsular polysaccharide conjugates and evaluation of their immunogenicity in mice. *Infect. Immun. 71*, 5115−5120.

(3) Ko, B. K., Kawano, K., Murray, J. L., Disis, M. L., Efferson, C. L., Kuerer, H. M., Peoples, G. E., and Ioannides, C. G. (2003) Clinical studies of vaccines targeting breast cancer. *Clin. Cancer Res. 9*, 3222−3234.

(4) Kudryashov, V., Glunz, P. W., Williams, L. J., Hintermann, S., Danishefsky, S. J., and Lloyd, K. O. (2001) Toward optimized carbohydrate-based anticancer vaccines: Epitope clustering, carrier structure, and adjuvant all influence antibody responses to Lewis(y) conjugates in mice. *Proc. Natl. Acad. Sci. U.S.A. 98*, 3264−3269.

(5) Ragupathi, G., Coltart, D. M., Williams, L. J., Koide, F., Kagan, E., Allen, J., Harris, C., Glunz, P. W., Livingston, P. O., and Danishefsky, S. J. (2002) On the power of chemical synthesis: immunological evaluation of models for multiantigenic carbohydrate-based cancer vaccines. *Proc. Natl. Acad. Sci. U.S.A. 99*, 13699−13704.

(6) Chapman, P. B., Morrissey, D. M., Panageas, K. S., Hamilton, W. B., Zhan, C., Destro, A. N., Williams, L., Israel, R. J., and Livingston, P. O. (2000) Induction of antibodies against GM2 ganglioside by immunizing melanoma patients using GM2-keyhole limpet hemocyanin + QS21 vaccine: A dose−response study. *Clin. Cancer Res. 6*, 874−879.

(7) Gilewski, T., Ragupathi, G., Bhuta, S., Williams, L. J., Musselli, C., Zhang, X. F., Bornmann, W. G., Spassova, M., Bencsath, K. P., Panageas, K. S., Chin, J., Hudis, C. A., Norton, L., Houghton, A. N., Livingston, P. O., and Danishefsky, S. J. (2001) Immunization of metastatic breast cancer patients with a fully synthetic globo H conjugate: A phase I trial. *Proc. Natl. Acad. Sci. U.S.A. 98*, 3270−3275.

(8) Avery, O. T., and Goebel, W. F. (1929) Chemo-immunological studies on conjugated carbohydrate-proteins. II. Immunological specificity of synthetic sugar−protein antigens. *J. Exp. Med. 50*, 533−550.

(9) Axen, R., Porath, J., and Ernback, S. (1967) Chemical coupling of peptides and proteins to polysaccharides by means of cyanogen halides. *Nature 214*, 1302−1304.

(10) Kohn, J., and Wilchek, M. (1982) A new approach (cyano-transfer) for cyanogen bromide activation of Sepharose at neutral pH, which yields activated resins, free of interfering nitrogen derivatives. *Biochem. Biophys. Res. Commun. 107*, 878−884.

(11) Kohn, J., and Wilchek, M. (1983) 1-Cyano-4-dimethylamino pyridinium tetrafluoroborate as a cyanylating agent for the covalent attachment of ligand to polysaccharide resins. *FEBS Lett. 154*, 209−210.

(12) Shafer, D. E., Toll, B., Schuman, R. F., Nelson, B. L., Mond, J. J., and Lees, A. (2000) Activation of soluble polysaccharides with 1-cyano-4-dimethylaminopyridinium tetrafluoroborate (CDAP) for use in protein−polysaccharide conjugate vaccines and immunological reagents. II. Selective crosslinking of proteins to CDAP-activated polysaccharides. *Vaccine 18*, 1273−1281.

(13) Gray, G. R. (1974) The direct coupling of oligosaccharides to proteins and derivatized gels. *Arch. Biochem. Biophys. 163*, 426−428.

(14) Hase, S., Ikenaka, T., and Matsushima, Y. (1979) Analyses of oligosaccharides by tagging the reducing end with a fluorescent compound. II. Linkage point analyses. *J. Biochem. 85*, 995−1002.

(15) Prasad, A. V., and Richards, J. C. (1997) Method for producing synthetic N-linked glycoconjugates. WO9702277.

(16) Lubineau, A., Auge, J., and Drouillat, B. (1995) Improved synthesis of glycosylamines and a straightforward preparation of *N*-acylglycosylamines as carbohydrate-based detergents. *Carbohydr. Res. 266*, 211−219.

(17) Oberg, C. T., Carlsson, S., Fillion, E., Leffler, H., and Nilsson, U. J. (2003) Efficient and expedient two-step pyranose-retaining fluorescein conjugation of complex reducing oligosaccharides: Galectin oligosaccharide specificity studies in a fluorescence polarization assay. *Bioconjugate Chem. 14*, 1289−1297.

(18) Dwek, R. A., Manger, I. D., Rademacher, T. W., and Wong, S. Y. C. (1992) Method for producing synthetic N-linked glycoconjugates. EP0538230.

(19) Flinn, N. S., Quibell, M., Turnell, W. G., and Ramjee, M. K. (2003) Organic molecules. WO03087824.

(20) Flinn, N. S., Quibell, M., Turnell, W. G., Monk, T. P., and Ramjee, M. K. (2004) Novel chemoselective linkage chemistry toward controlled loading of ligands to proteins through in situ real-time quantification of conjugate formation. *Bioconjugate Chem. 15*, 1010−1020.

(21) Cordon-Cardo, C., Lloyd, K. O., Sakamoto, J., McGroarty, M. E., Old, L. J., and Melamed, M. R. (1986) Immunohistologic expression of blood-group antigens in normal human gastrointestinal tract and colonic carcinoma. *Int. J. Cancer 37*, 667−676.

(22) Sakamoto, J., Furukawa, K., Cordon-Cardo, C., Yin, B. W., Rettig, W. J., Oettgen, H. F., Old, L. J., and Lloyd, K. O. (1986) Expression of Lewisa, Lewisb, X, and Y blood group antigens in human colonic tumors and normal tissue and in human tumor-derived cell lines. *Cancer Res. 46*, 1553−1561.

(23) http://rsb.info.nih.gov/ij/index.html.

(24) Atherton, E., and Sheppard, R. C. (1989) *Solid-Phase Peptide Synthesis: A Practical Approach*, IRL Press, Oxford, U.K.

(25) Udenfriend, S., Stein, S., Bohlen, P., Dairman, W., Leimgruber, W., and Weigele, M. (1972) Fluorescamine: A reagent for assay of amino acids, peptides, proteins, and primary amines in the picomole range. *Science 178*, 871−872.

(26) Tweeddale, H. J., Batley, M., and Redmond, J. W. (1994) Binding of carbohydrates to solid supports, Part 2: Reaction of sugar hydrazones with isothiocyanate-substituted polystyrene. *Glycoconjugate J. 11*, 586−592.

(27) John, C. M., and Gibson, B. W. (1990) Amino and hydrazino alkyl benzoates as derivatizing agents for the separation and mass spectrometric analysis of oligosaccharides from bacterial lipooligosaccharides. *Anal. Biochem. 187*, 281−291.

(28) Krug, L. M., Ragupathi, G., Hood, C., Kris, M. G., Miller, V. A., Allen, J. R., Keding, S. J., Danishefsky, S. J., Gomez, J., Tyson, L., Pizzo, B., Baez, V., and Livingston, P. O. (2004) Vaccination of patients with small-cell lung cancer with synthetic fucosyl GM-1 conjugated to keyhole limpet hemocyanin. *Clin. Cancer Res. 10*, 6094−6100.

(29) Sabbatini, P. J., Kudryashov, V., Ragupathi, G., Danishefsky, S. J., Livingston, P. O., Bornmann, W., Spassova, M., Zatorski, A., Spriggs, D., Aghajanian, C., Soignet, S., Peyton, M., O'Flaherty, C., Curtin, J., and Lloyd, K. O. (2000) Immunization of ovarian cancer patients with a synthetic Lewis(y)-protein conjugate vaccine: A phase 1 trial. *Int. J. Cancer 87*, 79−85.

(30) Hellstrom, I., Garrigues, H. J., Garrigues, U., and Hellstrom, K. E. (1990) Highly tumor-reactive, internalizing, mouse monoclonal antibodies to Le(y)-related cell surface antigens. *Cancer Res. 50*, 2183-2190.

BC050041Q

TECHNICAL NOTES

Probing for Integrin $\alpha_v\beta_3$ Binding of RGD Peptides Using Fluorescence Polarization

Wei Wang,[†] Qingping Wu,[†] Marites Pasuelo,[†] John S. McMurray,[‡] and Chun Li*,[†]

Department of Experimental Diagnostic Imaging and Department of Neuro-oncology, The University of Texas M. D. Anderson Cancer Center, Houston, Texas 77030. Received September 29, 2004; Revised Manuscript Received March 1, 2005

Integrin $\alpha_v\beta_3$ is an adhesion molecule involved in tumor invasion, angiogenesis, and metastasis. There is substantial interest in developing novel agents that bind to integrin $\alpha_v\beta_3$. Here we report the synthesis and characterization of a fluorescent integrin $\alpha_v\beta_3$ probe and its use in a nonradioactive, simple, sensitive fluorescence polarization (FP) assay to quantify binding to integrin $\alpha_v\beta_3$. For assay validation, the FP assay was compared to a cell adhesion assay. In the two assays, probe binding to integrin $\alpha_v\beta_3$ showed a similar dependence on probe concentration. The FP assay was successfully applied to measure the binding affinity to integrin $\alpha_v\beta_3$ of several cyclic peptides containing the Arg-Gly-Asp (RGD) motif. The FP assay we describe here may be appropriate for high-throughput screening for integrin $\alpha_v\beta_3$-binding ligands used for anti-integrin therapy or noninvasive imaging of integrin expression.

INTRODUCTION

Integrins are heterodimeric transmembrane proteins that function principally as receptors for spatially restricted extracellular ligands (*1*). The α_v-integrins ($\alpha_v\beta_3$, $\alpha_v\beta_5$) play a critical role in tumor angiogenesis and are associated with tumor progression and metastasis (*2*−*4*). They are overexpressed on brain and melanoma tumor cells and newly formed tumor microvessels but not on normal cells and quiescent endothelial cells (*5*−*7*). Antibody, peptide, and peptidomimetic integrin $\alpha_v\beta_3$ antagonists have been shown to impair angiogenesis, growth, and metastasis of solid tumors (*8*−*10*). Furthermore, imaging the expression of α_v-integrins may allow determination of the optimal biological dose and schedule of integrin-targeted therapeutics and may allow monitoring of tumor responses to such therapeutics. Thus, there is substantial interest in developing novel agents that bind to α_v-integrins for both therapeutic and diagnostic purposes.

Existing in vitro methods for detecting integrin $\alpha_v\beta_3$ binding include a binding assay that uses immobilized integrin and a radiolabeled tracer (*11*, *12*), a competitive enzyme-linker immunosorbent assay (*13*), and surface plasma resonance (*14*). All of these methods, however, require immobilization of integrins on a solid surface.

A fluorescence polarization (FP) assay would be a more suitable assay for detecting integrin $\alpha_v\beta_3$ binding because FP is a homogeneous technology requiring only simple mix reagents and read format that can be easily automated (*15*). The technique has recently been introduced for high-throughput screening in the drug discovery process (*16*). FP depends on the excitation of a fluorescent molecule with plane-polarized light. This results in the emission of photons in the planes parallel and perpendicular to the excitation plane and confers information about the local environment of the fluorophore. Smaller molecules rotate faster and hence have smaller polarization values. Conversely, larger molecules (e.g., fluorescent probe bound to target) rotate more slowly and thus have bigger polarization values. Thus, the observed polarization value gives a direct measure of the molecular size of the analyte and the extent of tracer binding to macromolecules at constant temperature and viscosity. FP assays work well in colored and cloudy solutions. There is no need for radioisotopes, and there are no solid-phase artifacts. The technique does not require washing steps, and the system is easily automated.

To our knowledge, no fluorescence-labeled integrin $\alpha_v\beta_3$ ligands that could be used in an FP assay have previously been validated. Here we report the synthesis and characterization of a fluorescent derivative of the cyclic pentapeptide cyclo(Lys-Arg-Gly-Asp-phe) [c(KRGDf)]. We show that this probe tightly bound integrin $\alpha_v\beta_3$ and that its interaction with integrin $\alpha_v\beta_3$ was competed with by integrin ligands containing the Arg-Gly-Asp (RGD) motif.

EXPERIMENTAL PROCEDURES

Materials. All N^{α}-Fmoc-amino acids, 1-hydroxybenzotriazole (HOBt), benzotriazol-1-yl-oxy-tris-pyrrolidino-phosphonium hexafluorophosphate (PyBOP), and solid support linker [4-(4-hydroxymethyl-3-methoxyphenoxy)-acetic acid] (HMPA) were purchased from Novabiochem (San Diego, CA). Trifluoroacetic acid (TFA) was purchased from Chem-Impex International, Inc. (Wood Dale, IL). PL-DMA resin was purchased from Polymer Labo-

* To whom correspondence should be addressed. Mailing address: Department of Experimental Diagnostic Imaging—Unit 59, The University of Texas M. D. Anderson Cancer Center, 1515 Holcombe Blvd., Houston, TX 77030. Phone: (713) 792-5182. Fax: (713) 794-5456. E-mail address: cli@di.mdacc.tmc.edu.

[†] Department of Experimental Diagnostic Imaging.

[‡] Department of Neuro-oncology.

10.1021/bc049763s CCC: $30.25 © 2005 American Chemical Society
Published on Web 04/29/2005

ratories (Amherst, MA). *N,N*-Diisopropylethylamine (DIPEA), triethylsilane (TES), 5(6)-carboxyfluorescein, tetrakis(triphenylphosphine)palladium ($Pd^0[P(C_6H_5)_3]_4$), *N*-methylmorpholine (NMP), and 1,3-diisopropylcarbodiimide (DIPCDI) were purchased from Aldrich Chemical Co. (St. Louis, MO). Integrin $\alpha_v\beta_3$ was purchased from Chemicon International, Inc. (Temecula, CA). All solvents were purchased from VWR (San Dimas, CA). A 96-well flat-bottom assay plate (black polystyrene) was purchased from Corning, Inc. (Corning, NY).

Analysis. Products were purified by reverse-phase high-performance liquid chromatography (HPLC), eluted with H_2O/acetonitrile containing 0.1% TFA, and validated by analytical HPLC and matrix-assisted laser desorption ionization (MALDI) mass spectrometry. Analytical HPLC was carried out on an Agilent 1100 system (Wilmington, DE) equipped with a Vydac peptide and protein analytical C-18 column (Anaheim, CA). Preparative HPLC was carried out on a Rainin Rabbit HP system (Walnut Creek, CA) equipped with a 25 × 2.5 cm Vydac C-18 column. MALDI was performed in the proteomics laboratory in the Department of Molecular Pathology at The University of Texas M. D. Anderson Cancer Center (Houston, TX).

Synthesis of Cyclic Peptides. RGD peptides were synthesized on a solid support. Briefly, PL-DMA resin (1 g) was treated with ethylenediamine (30 mL) overnight. HMPA linker (3 equiv) was attached to resin in the presence of DIPCDI (3 equiv) and HOBt (3 equiv). Peptides Fmoc-phe-X-Arg(Pbf)-Gly-Asp(resin)OAll, where X represents Lys(Boc), Glu(OBut), or Lys(Mtt), were synthesized using Fmoc solid-phase chemistry. The protecting groups of the amino acid side chains were *N-tert*-butoxycarbonyl (Boc) or 4-methyltrityl (Mtt) for Lys, *tert*-butyl (But) for Glu, 2,2,4,6,7-pentamethyldihydrobenzofuran-5-sulfonyl (Pbf) for Arg, and allyl (All) for Asp. Amino acids (3 equiv) were coupled stepwise in the presence of DIPCDI (3 equiv) and HOBt (3 equiv) coupling reagents. After removal of All and Fmoc protecting groups using $Pd^0[P(C_6H_5)_3]_4$ (3 equiv) in dichloromethane(DCM)/NMP/AcOH (37/1/2) and 20% piperidine in dimethylformamide (DMF), respectively, the cyclization was carried out on the solid support using PyBOP (3 equiv), HOBt (3 equiv), and DIPEA (6 equiv) as coupling agents to afford cyclo-[Lys(Boc)-Arg(Pbf)-Gly-Asp(resin)-phe], cyclo-[Glu(OBut)-Arg(Pbf)-Gly-Asp(resin)-phe), and cyclo-[(Lys(Mtt)-Arg(Pbf)-Gly-Asp(resin)-phe]. Mtt protecting group was removed by treatment with TFA/TES/DCM (1/2/97). To synthesize dimeric RGD peptide, Lys(Boc), Glu(OAll), phe, Asp(OBut), Gly, and Arg(Pbf) were successively attached to cyclo-[Lys-Arg-(Pbf)-Gly-Asp(resin)-phe] to form an undecapeptide Fmoc-Arg(Pbf)-Gly-Asp(OBut)-phe-Glu(OAll)-Lys(Boc)-cyclo-[Lys-Arg(Pbf)-Gly-Asp(resin)-phe]. After removal of All and Fmoc protecting groups, the second cyclization was carrier out on the solid support. Deprotection and cleavage of all these compounds from the solid support were carried out simultaneously by treatment with TFA/H_2O/TES (95/1/4) to afford c(KRGDf), cyclo(Glu-Arg-Gly-Asp-phe) [c(ERGDf)], or c(RGDfE)-K-c(KRGDf). All products were purified by reverse-phase HPLC and validated by MALDI mass spectrometry.

To synthesize the cyclic pentapeptide Ac-Ala-c(Cys-Asn-Gly-Arg-Cys)-Gly [Ac-A-c(CNGRC)-G], linear peptide Ac-ACNGRCG was first prepared using Fmoc solid-phase peptide synthesis. After removal of the peptide from the solid support by TFA/H_2O/TES (95/1/4), cyclization was achieved in NH_4OH aqueous solution (pH 9). The product was purified by reverse-phase HPLC and validated by MALDI mass spectrometry.

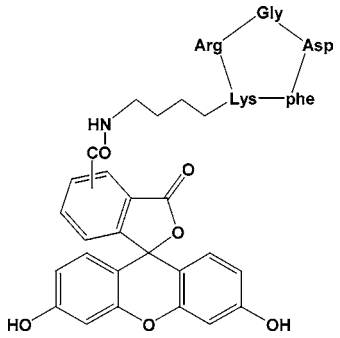

Figure 1. Structure of 5(6)-carboxyfluorescein−c(KRGDf) conjugate.

Conjugation of Fluorescein to c(KRGDf). Carboxyfluorescein (3 equiv) was coupled to c[Lys-Arg(Pbf)-Gly-Asp(resin)-phe] using DIPCDI (3 equiv) and HOBt (3 equiv) as the coupling agents. Deprotection and cleavage from the solid support were carried out simultaneously by treatment with TFA/H_2O/TES (95/1/4) to afford the target compound carboxyfluorescein-c(KRGDf) (FL-RGD) (Figure 1). The product was purified by reverse-phase HPLC and validated by MALDI mass spectrometry.

Fluorescence Polarization Assay. A solution of 200 μM FL-RGD or fluorescein in phosphate-buffered saline was diluted with Tris buffer (50 mM Tris, pH 7.4, 1 mM $CaCl_2$, 10 μM $MnCl_2$, 1 mM $MgCl_2$, 100 mM NaCl) to give a 100 nM stock solution. The reaction mixture (100 μL) in each well was composed of 10 nM FL-RGD probe (10 μL of 100 nM stock solution) and different concentrations of integrin $\alpha_v\beta_3$ (0 to 650 nM) in Tris buffer. The microwell assay plate was incubated at 29 °C for 0.5 h. Fluorescein alone (10 nM) and FL-RGD alone (10 nM) served as controls. FP was measured with a Tecan Polarion reader (Research Triangle Park, NC). The polarization value was expressed in millipolarization units (mP). The integrin titration data were analyzed using Graph-Pad PRISM software (GraphPad Software, Inc., San Diego, CA) with the one-site binding equation $FP = FP_{max}C/(K_d + C)$, where FP_{max} is the maximal FP value, C is the concentration of the protein, and K_d represents the dissociation constant.

Competitive displacement studies were performed with the integrin ligands c(KRGDf), c(ERGDf), and c(RGDfE)-K-c(KRGDf). The cyclic pentapeptide containing the Asn-Gly-Arg (NGR) motif, Ac-A-c(CNGRC)-G, was used as a negative control. Stocks of these compounds were made in phosphate-buffered saline at a concentration of 500 μM. The ligands were serially diluted in the assay buffer to concentrations ranging from 0.01 to 5 μM. The FL-RGD probe and $\alpha_v\beta_3$ were added at concentrations of 10 nM and 290 nM, respectively. The reaction mixture was shaken, and the FP values in mP were recorded. The mP values were plotted against the ligand concentration. The Polarion data were analyzed using Graph-Pad PRISM software with linear regression to obtain the concentration at which 50% inhibition of FL-RGD's binding to integrin $\alpha_v\beta_3$ was achieved (IC_{50} values).

Cell Adhesion Assay. Human melanoma M21 cells were obtained from Dr. David Cheresh (Scripps Research Institute, San Diego, CA). The cells were seeded in Dulbecco's modified Eagle's medium/F12 culture medium supplemented with 10% fetal bovine serum for 24 h. Cells (1×10^5) with different concentrations of c(KRGDf), c(ERGDf), c(RGDfE)-K-c(KRGDf), FL-RGD, or Ac-A-c(CNGRC)-G were added to vitronectin-coated microtiter wells under serum-free conditions and incubated at 37

Scheme 1. Synthesis of RGD Derivatives and RGD Fluorescent Probe[a]

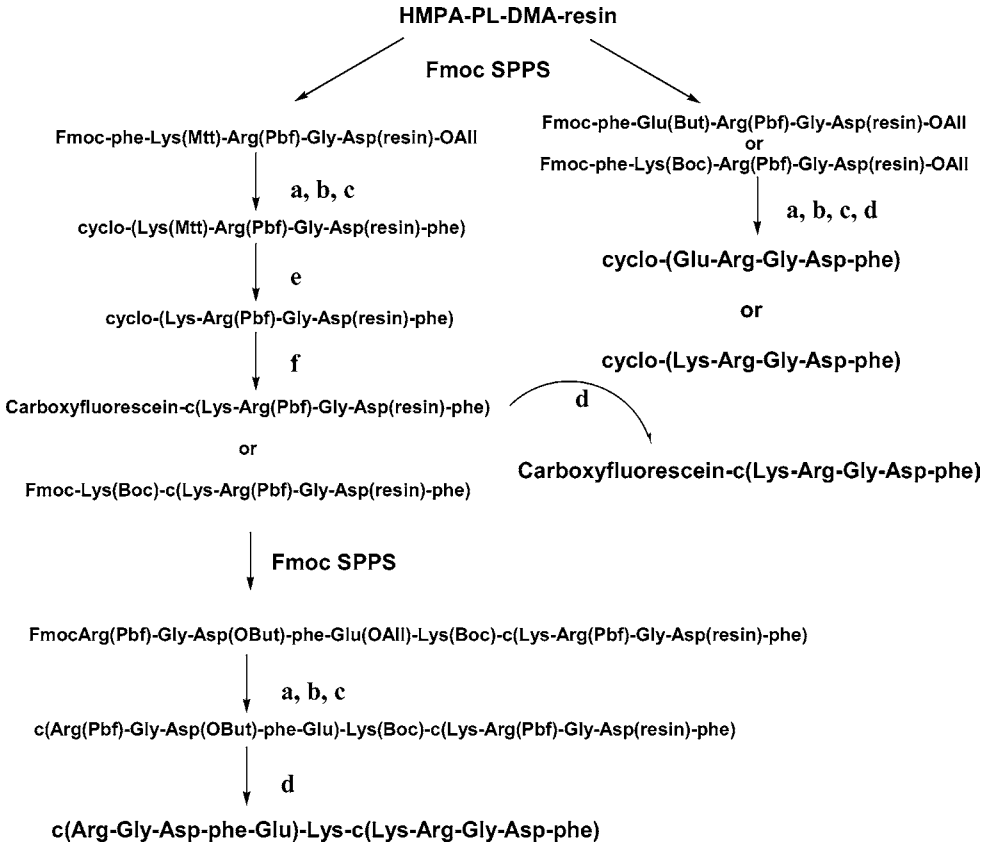

[a] Reagents and conditions: (a) $Pd^0[P(C_6H_5)_3]_4$ (3 equiv), $CHCl_3$/AcOH/NMM (37/2/1, v); (b) 20% piperidine, DMF; (c) PyBOP/HOBt/DIPEA (3/3/6 equiv) in DMF; (d) TFA/H_2O/TES (95/1/4, v); (e) TFA/DCM/TES (1/97/2, v); (f) 5(6)-carboxyfluorescein (3 equiv) or Fmoc-Lys(Boc) (3 equiv), DIPCDI (3 equiv), HOBt (3 equiv) in DMF and DCM (1/1, v); (g) *p*-succinicamido-benzyl-DTPA penta-*tert*-butyl ester (2 equiv), PyBOP (3 equiv), HOBt (3 equiv), DIPEA (6 equiv) in DMF. SPPS, solid-phase peptide synthesis.

°C for 1 h. After washing steps, the bound cells were stained with 5% crystal violet, and then 0.1 M HCl was added to each well. The concentrations of crystal violet were determined by UV/Vis absorption at 627 nm. IC_{50} values were estimated from the dose−activity curves.

RESULTS AND DISCUSSION

Chemistry. Integrins bind extracellular matrix factors, such as vitronectin, that contain the RGD amino acid sequence, which appears to be critical in mediating the ligation signal, allowing endothelial cells to attach to the extracellular matrix and thus support endothelial survival and growth (*5*, *6*, *17*). Integrin antagonists and imaging agents are generally developed on the basis of cyclic peptides composed of five amino acids. One such agent, Cilengitide (c[RGDf(NMe)V]), has entered clinical phase II studies as a potent and selective integrin peptidic antagonist (*18*). Several radiolabeled peptides containing the RGD motif plus various combinations of two additional amino acids have been used for custom-made purposes such as iodination (tyrosine) or linkage of chelators (lysine) (*12*, *19*−*22*). Thus we selected c(KRGDf) peptide as the ligand for FP probe development.

We synthesized fluorescein-conjugated c(KRGDf) to use this agent as a probe for our FP assay. In addition, we synthesized the unconjugated monomeric peptides c(KRGDf) and c(ERGDf) and the dimeric cyclic peptide c(RGDfE)-K-c(KRGDf). All of these compounds were prepared by solid-phase peptide synthesis (Scheme 1). Starting from Asp attached to PL-DMA resin with HMPA linker coupled to the side chain of Asp, linear peptides were synthesized using an Fmoc strategy. The cyclization of pentapeptides was achieved on the solid support after selective removal of the N-terminal Fmoc and C-terminal All protecting groups to afford cyclo[X-Arg(Pbf)-Gly-Asp(resin)-phe], where X represents Lys(Boc), Glu(OBut), or Lys(Mtt). For the preparation of c(KRGDf), Boc was used as a protecting group for Lys. TFA was used to simultaneously cleave the peptide from the resin and remove the side chain protecting groups, yielding cyclic pentapeptides c(KRGDf) and c(ERGDf) (Scheme 1).

For preparation of the dimer c(RGDfE)-K-c(KRGDf) and FL-RGD, Mtt was used as the protecting group for Lys for the construction of cyclo[Lys(Mtt)-Arg(Pbf)-Gly-Asp(resin)-phe]. The side chain protecting group Mtt on Lys was selectively removed in diluted TFA without peptide cleaved from the resin. This allowed further elaboration for the second cyclic peptide or conjugation of carboxyfluorescein through the Lys unit on the solid support (Scheme 1). The physicochemical properties of the peptides synthesized are summarized in Table 1.

Fluorescence Polarization Assay. To demonstrate that the FP signal was a result of binding of FL-RGD with integrin, the FP assay was performed as a function of integrin concentrations with 10 nM probe in the assay. The FP signal rose from 40 mP (background mP value due to intrinsic polarization of the probe) to about 140 mP when the concentrations of integrin increased from 0 to 650 nM (Figure 2). This finding was expected because addition of more integrin would make more integrin available for complexing with the probe. The titration curve showed that the FL-RGD probe bound to integrin $\alpha_v\beta_3$. The dissociation constant (K_d) for FL-RGD−integrin

Table 1. Physicochemical Property of the Fluorescent RGD Probe and Testing Compounds

cyclic peptides	molecular formula	mass spectrometry: calculated MW	mass spectrometry: observed (M + 1)	retention time (min)
c(KRGDf)	$C_{27}H_{41}N_9O_7$	603.313	604.356	10.97[a]
c(ERGDf)	$C_{26}H_{36}N_8O_9$	604.261	605.210	13.93[a]
FL-c(KRGDf)	$C_{48}H_{51}N_9O_{13}$	961.361	962.310	24.94[a]
c(RGDfE)-K−c(KRGDf)	$C_{59}H_{87}N_{19}O_{16}$	1317.658	1318.645	10.24[b]
Ac-A-c(CNGRC)-G	$C_{25}H_{41}N_{11}O_{10}S_2$	719.248	720.225	7.77[a]

[a] Sample was eluted with H_2O and acetonitrile containing 0.1% TFA varying from 0% to 40% over 30 min. [b] Sample was eluted with H_2O and acetonitrile containing 0.1% TFA varying from 10% to 50% over 30 min.

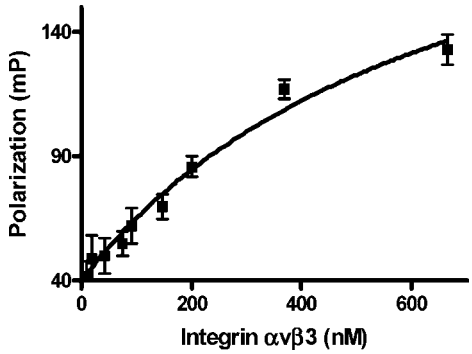

Figure 2. Titration curve for binding of FL-RGD probe to integrin $\alpha_v\beta_3$ as a function of $\alpha v\beta 3$ concentration. FP values (mP) were measured after incubation of FL-RGD (10 nM) and $\alpha_v\beta_3$ (0−650 nM) mixture at 29 °C for 30 min. The mP value obtained in the absence of $\alpha_v\beta_3$ (40 mP) represents the background mP value due to intrinsic polarization of the probe. Data are presented as mean values ± standard deviations from 3 independent experiments.

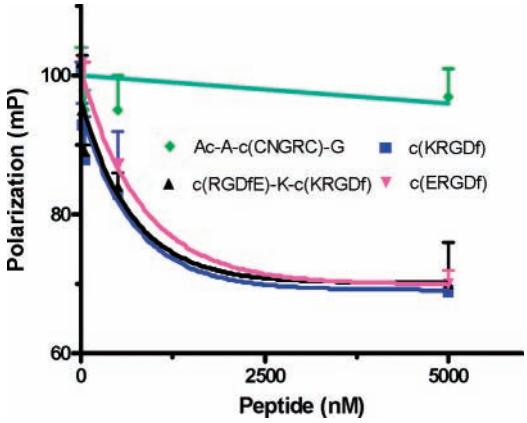

Figure 3. Titration curve for binding of FL-RGD probe (10 nM) to integrin $\alpha_v\beta_3$ (290 nM) in the presence of increasing concentrations of $\alpha_v\beta_3$ inhibitors. The NGR peptide [Ac-A-c(CNGRC)-G] is a negative control that does not bind $\alpha_v\beta_3$.

complex was 0.67 ± 0.15 μM as determined using GraphPad PRISM software with the one-site binding equation $FP = FP_{max}C/(K_d + C)$. The binding was fast; increasing the incubation time beyond 5 min did not have any effect on the FP signal (data not shown). These results showed that the FP assay with FL-RGD as a probe can be used to measure the binding affinity of ligands to integrin $\alpha_v\beta_3$.

To further demonstrate that the FP signal was dependent on formation of the RGD−integrin complex, the FP assay was performed as a function of concentration for several integrin inhibitors containing the RGD motif. Increasing the amounts of RGD peptides at fixed probe and integrin concentrations result in a decreased FP signal (Figure 3). The FP signal fell from about 105 mP to about 70 mP when the concentrations of the RGD peptide competitors increased from 0 to 5 μM. A window

Table 2. Comparison of IC_{50} Values Obtained from FP Assay and Cell Adhesion Assay[a]

cyclic peptides	FP IC_{50} (μM)	cell adhesion IC_{50} (μM)
carboxyfluorescein-c(KRGDf)		4.2 ± 0.27
c(KRGDf)	0.11 ± 0.003	5.0 ± 0.77
c(ERGDf)	0.28 ± 0.004	3.2 ± 0.16
c(RGDfE)-K-c(KRGDf)	0.11 ± 0.003	4.0 ± 0.32
Ac-A-c(CNGRC)-G	not available	not available

[a] Data are presented as mean values ± standard deviations from three independent experiments.

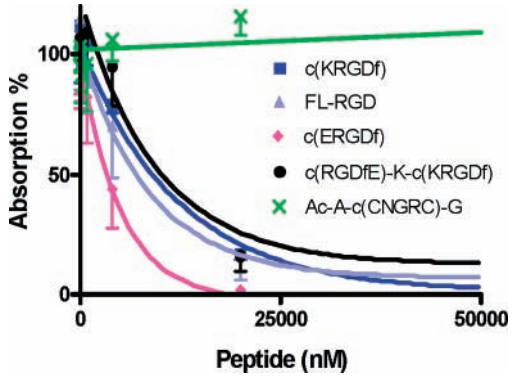

Figure 4. Adhesion of M21 human melanoma cells to vitronectin-coated microtiter wells in the presence of increasing concentrations of $\alpha_v\beta_3$ inhibitors. After washing steps, the bound cells were stained with 5% crystal violet, and then 0.1 M HCl was added to each well. The concentrations of crystal violet were determined by UV/Vis absorption at 627 nm. The percentage absorption values reported on the *y*-axis are relative to the absorption value measured in the absence of RGD peptides.

of about 35 mP was observed with peptide concentrations from 0 to 5 μM. Because of nonspecific binding, the FP value never dropped to the 40-mP background value observed in the absence of integrin inhibitors. IC_{50} values derived from linear regression of the competition curves for c(KRGDf), c(ERGDf), and c(RGDfE)-K-c(KRGDf) were 0.11, 0.28, and 0.11 μM, respectively. The NGR control peptide could not displace fluorescent probe from binding to integrin even at the maximal tested concentration of 5 μM (Figure 3; Table 2).

Cell Adhesion Assay. To validate the FP-integrin assay procedure, the FP assay was compared to a more standard functional assay that measures the inhibition of M21 tumor cell adhesion to extracellular matrix proteins. FL-RGD and the parent peptide c(KRGDf) gave similar IC_{50} values of 4.2 μM and 5.0 μM, respectively. These values are within the range of 3.2−5.0 μM for other RGD peptides, suggesting that FL-RGD is as efficacious as the parent peptide in inhibiting adhesion of tumor cells to vitronectin-coated microwells (Table 2). The number of attached cells decreased in a dose-dependent manner for all three unconjugated cyclic peptides containing the RGD motif as well as for FL-RGD (Figure 4). No inhibitory activity was observed for the NGR control peptide

(Figure 4). The IC_{50} values obtained from the FP assay paralleled the IC_{50} values obtained from the cell adhesion assay, albeit IC_{50} for integrin binding was approximately 10-times lower than IC_{50} for bioactivity. These data suggest that RGD peptides may possess nonspecific interaction with vitronectin in cell based adhesion assay. Nevertheless, both assays showed no significant differences among the three cyclic peptides containing RGD motif in their ability to bind integrin and inhibit cell adhesion (Table 2). We interpreted these findings as indicating that a similar binding affinity to integrin $\alpha v\beta 3$ resulted in a similar biological activity.

Binding Affinity of Various Cyclic RGD Peptides to Integrin $\alpha_v\beta_3$. The observation of no difference in integrin binding between c(KRGDf) and c(ERGDf) by FP assay confirms a previously reported finding that changing the amino acid X in c(XRGDf) does not significantly affect the binding affinity of cyclic RGD peptide to integrin (*23*). It has been proposed that multimeric constructs based on RGD peptide may lead to ligands with substantially increased binding affinity for integrin $\alpha_v\beta_3$ owing to the multivalency effect. Thumshirn et al. (*24*) observed 2.3- to 22-fold increases in IC_{50} values when monomeric peptides were compared to dimeric peptides linked together through a flexible oligomeric ethylene oxide linker. Janssen et al. (*25*) compared the IC_{50} of the radiolabeled monomer c(RGDfK) and dimeric E-[c(RGDfK)]$_2$ determined in immobilized human $\alpha_v\beta_3$ using an enzyme-linked immunosorbent assay. The affinity of the dimer for $\alpha_v\beta_3$ was 10 times the affinity of the monomer. In our hands, the dimeric peptide c(RGDfE)-K-c(KRGDf) did not show increased integrin binding as compared to the integrin binding of its individual monomers c(ERGDf) and c(KRGDf). It is possible that the distance and orientation between the two cyclic peptide rings could have affected the binding of the dimer to integrin receptors. With the integrin-binding FP assay validated, it is now possible to systematically investigate the effect of linker molecule on the binding of dimeric RGD peptide to integrin $\alpha_v\beta_3$. Work along this line is in progress.

Summary. In summary, the FP assay method should be advantageous compared to other methods reported in the literature for the measurement of integrin binding because the FP assay is a simple, one-step, nonradioactive assay that is performed in solution. We found that a fluorescent integrin $\alpha_v\beta_3$ probe based on the cyclic pentapeptide c(KRGDf) tightly bound integrin $\alpha_v\beta_3$ and that the probe's interaction with integrin $\alpha_v\beta_3$ was competed with by integrin ligands containing the RGD motif. The FP assay we describe here may be appropriate for high-throughput screening for integrin $\alpha_v\beta_3$-binding ligands used for anti-integrin therapy or noninvasive imaging of integrin expression.

ACKNOWLEDGMENT

Supported in part by NCI grants R01 EB000174 and U54 CA90810 and by the John S. Dunn Foundation. MALDI mass spectrometry was done by the Proteomics Core Laboratory in the Department of Molecular Pathology at M. D. Anderson Cancer Center.

LITERATURE CITED

(1) Hynes, R. O. (1992) Integrins: Versatility, modulation, and signaling in cell adhesion. *Cell 69*, 11−25.

(2) van Muijen, G. N., Jansen, K. F., Cornelissen, I. M., Smeets, D. F., Beck, J. L., and Ruiter, D. J. (1991) Establishment and characterization of a human melanoma cell line (mv3) which is highly metastatic in nude mice. *Int. J. Cancer 48*, 85−91.

(3) Felding-Habermann, B., Mueller, B. M., Romerdahl, C. A., and Cheresh, D. A. (1992) Involvement of integrin alpha v gene expression in human melanoma tumorigenicity. *J. Clin. Invest. 89*, 2018−2022.

(4) Mitjans, F., Sander, D., Adan, J., Sutter, A., Martinez, J. M., Jaggle, C. S., Moyano, J. M., Kreysch, H. G., Piulats, J., and Goodman, S. L. (1995) An anti-alpha v-integrin antibody that blocks integrin function inhibits the development of a human melanoma in nude mice. *J. Cell Sci. 108 (Pt 8)*, 2825−2838.

(5) Brooks, P. C., Clark, R. A., and Cheresh, D. A. (1994) Requirement of vascular integrin alpha v beta 3 for angiogenesis. *Science 264*, 569−571.

(6) Eliceiri, B. P., and Cheresh, D. A. (1999) The role of alpha v integrins during angiogenesis: Insights into potential mechanisms of action and clinical development. *J. Clin. Invest. 103*, 1227−1230.

(7) Brooks, P. C., Stromblad, S., Klemke, R., Visscher, D., Sarkar, F. H., and Cheresh, D. A. (1995) Antiintegrin alpha v beta 3 blocks human breast cancer growth and angiogenesis in human skin. *J. Clin. Invest. 96*, 1815−1822.

(8) Varner, J. A., Nakada, M. T., Jordan, R. E., and Coller, B. S. (1999) Inhibition of angiogenesis and tumor growth by murine 7e3, the parent antibody of c7e3 fab (abciximab; reopro). *Angiogenesis 3*, 53−60.

(9) Buerkle, M. A., Pahernik, S. A., Sutter, A., Jonczyk, A., Messmer, K., and Dellian, M. (2002) Inhibition of the alpha-nu integrins with a cyclic RGD peptide impairs angiogenesis, growth and metastasis of solid tumours in vivo. *Br. J. Cancer 86*, 788−795.

(10) MacDonald, T. J., Taga, T., Shimada, H., Tabrizi, P., Zlokovic, B. V., Cheresh, D. A., and Laug, W. E. (2001) Preferential susceptibility of brain tumors to the antiangiogenic effects of an alpha(v) integrin antagonist. *Neurosurgery 48*, 151−157.

(11) Boger, D. L., Goldberg, J., Silletti, S., Kessler, T., and Cheresh, D. A. (2001) Identification of a novel class of small-molecule antiangiogenic agents through the screening of combinatorial libraries which function by inhibiting the binding and localization of proteinase mmp2 to integrin alpha(v)beta(3). *J. Am. Chem. Soc. 123*, 1280−1288.

(12) Haubner, R., Wester, H. J., Reuning, U., Senekowitsch-Schmidtke, R., Diefenbach, B., Kessler, H., Stocklin, G., and Schwaiger, M. (1999) Radiolabeled alpha(v)beta3 integrin antagonists: A new class of tracers for tumor targeting. *J. Nucl. Med. 40*, 1061−1071.

(13) Kling, A., Backfisch, G., Delzer, J., Geneste, H., Graef, C., Hornberger, W., Lange, U. E. W., Lauterbach, A., Seitz, W., and Subkowski, T. (2003) Design and synthesis of 1,5- and 2,5-substituted tetrahydrobenzazepinones as novel potent and selective integrin [alpha]v[beta]3 antagonists. *Bioorg. Med. Chem. 11*, 1319−1341.

(14) Hu, B., Finsinger, D., Peter, K., Guttenberg, Z., Barmann, M., Kessler, H., Escherich, A., Moroder, L., Bohm, J., Baumeister, W., Sui, S. F., and Sackmann, E. (2000) Intervesicle cross-linking with integrin alpha iib beta 3 and cyclic-rgd-lipopeptide. A model of cell-adhesion processes. *Biochemistry 39*, 12284−12294.

(15) Lakowicz, J. (1999) *Principles of fluorescence spectroscopy*, 2nd ed., Kluwer Academic/Plenum, New York.

(16) Nasir, M. S., and Jolley, M. E. (1999) Fluorescence polarization: An analytical tool for immunoassay and drug discovery. *Comb. Chem. High Throughput Screen. 2*, 177−190.

(17) Cheresh, D. A. (1987) Human endothelial cells synthesize and express an arg-gly asp-directed adhesion receptor involved in attachment to fibrinogen and von willebrand factor. *Proc. Natl. Acad. Sci. U. S. A. 84*, 6471−6475.

(18) Dechantsreiter, M. A., Planker, E., Matha, B., Lohof, E., Holzemann, G., Jonczyk, A., Goodman, S. L., and Kessler, H. (1999) N-Methylated cyclic rgd peptides as highly active and selective alpha(v)beta(3) integrin antagonists. *J. Med. Chem. 42*, 3033−3040.

(19) Haubner, R., Wester, H. J., Weber, W. A., Mang, C., Ziegler, S. I., Goodman, S. L., Senekowitsch-Schmidtke, R., Kessler, H., and Schwaiger, M. (2001) Noninvasive imaging of alpha(v)beta3 integrin expression using 18f-labeled rgd-containing

glycopeptide and positron emission tomography. *Cancer Res. 61*, 1781−1785.
(20) Janssen, M. L., Oyen, W. J., Dijkgraaf, I., Massuger, L. F., Frielink, C., Edwards, D. S., Rajopadhye, M., Boonstra, H., Corstens, F. H., and Boerman, O. C. (2002) Tumor targeting with radiolabeled alpha(v)beta(3) integrin binding peptides in a nude mouse model. *Cancer Res. 62*, 6146−6151.
(21) Chen, X., Park, R., Tohme, M., Shahinian, A. H., Bading, J. R., and Conti, P. S. (2004) Micropet and autoradiographic imaging of breast cancer alpha v-integrin expression using 18f- and 64cu-labeled RGD peptide. *Bioconjugate Chem. 15*, 41−49.
(22) Haubner, R., Bruchertseifer, F., Bock, M., Kessler, H., Schwaiger, M., and Wester, H. J. (2004) Synthesis and biological evaluation of a (99m)tc-labeled cyclic rgd peptide for imaging the alphavbeta3 expression. *Nuklearmedizin. 43*, 26−32.
(23) Xiong, J. P., Stehle, T., Zhang, R., Joachimiak, A., Frech, M., Goodman, S. L., and Arnaout, M. A. (2002) Crystal structure of the extracellular segment of integrin alpha vbeta3 in complex with an Arg-Gly-Asp ligand. *Science 296*, 151−155.
(24) Thumshirn, G., Hersel, U., Goodman, S. L., and Kessler, H. (2003) Multimeric cyclic RGD peptides as potential tools for tumor targeting: Solid-phase peptide synthesis and chemoselective oxime ligation. *Chemistry 9*, 2717−2725.
(25) Janssen, M., Oyen, W. J. G., Massuger, L. F. A. G., Frielink, C., Dijkgraaf, I., Edwards, D. S., Radjopadhye, M., Corstens, F. H. M., and Boerman, O. C. (2002) Comparison of a monomeric and dimeric radiolabeled RGD-peptide for tumor targeting. *Cancer Biother. Radiopharm. 17*, 641−646.

BC049763S

Synthesis and Application of a Water-Soluble Near-Infrared Dye for Cancer Detection Using Optical Imaging

Wellington Pham, Zdravka Medarova, and Anna Moore*

Athinoula A. Martinos Center for Biomedical Imaging, Department of Radiology, Massachusetts General Hospital, Room 2301, Building 149, 13th Street, Charlestown, Massachusetts 02129.
Received December 15, 2004; Revised Manuscript Received March 14, 2005

A novel water-soluble 2-[2-(2-chloro-3-{2-[3,3-dimethyl-5-sulfo-1-(4-sulfo-butyl)-3*H*-indol-2-yl]-vinyl}-cyclohex-2-enylidene)-ethylidene]-3,3-dimethyl-1-(4-sulfo-butyl)-2,3-dihydro-1*H*-indole-5-carboxylic acid (dye **2**) was developed via an asymmetric approach. With an additional sulfonate group, the near-infrared feature of this dye exhibited a 2-fold increase in quantum yield compared to the previous generation. The current synthetic strategy provided a single carboxylic group as a handle for conjugation, thus allowing selectivity for bioconjugation. The stability of this dye was demonstrated by labeling peptides via solid-phase peptide chemistry. The in vivo optical imaging showed potential and broad applications of this dye in developing molecular-based beacons for cancer detection.

INTRODUCTION

The development of highly sensitive fluorescent dyes in combination with innovative optical techniques plays a pivotal role in the advancement of noninvasive imaging of human pathologic conditions. Fluorochromes attached to various ligands have been used for detecting nucleic acid hybridization, in drug discovery for sensing molecular interactions, and for deciphering biological pathways (*1*). Cyanine fluorochromes belong to a super-family of dyes that have attracted the most attention in molecular imaging recently, given the fact that the near-infrared (NIR) feature of the dye could theoretically be predicted and designed based on the length of the polymethine chain connecting the heterocyclic rings (*2*). The delocalization of a pair of electrons on an indole ring across the polymethine unsaturated bridge system defines the absorption maximum that corresponds to the transition from a ground state to an excited electronic state. For every double bond increase in the methine chain, there would be a 100 nm bathochromic shift as opposed to only 20 nm for every additional aromatic ring (*3*). Therefore, the absorption and emission wavelength of the cyanine dye can be tuned several hundred nanometers in the far-red region, though still maintain its compact structure compared to other types of dyes.

Optical imaging in the NIR region (700−900 nm) has a low absorption by intrinsic photoactive biomolecules and allows light to penetrate several centimeters into the tissue, a depth that is sufficient to image practically all small animal models (*1*). This technique, in conjunction with the development of a specific targeted molecular probe, not only allows detection of the enhanced contrasting signal, but also reveals specific molecular events associated with the disease state. Necessary features of fluorochromes for NIR in vivo imaging include water solubility, detectability in the NIR region, good quantum yield, stability in an array of different environments, and the availability of a handle for bioconjugation. Recently, we have described the development of cyclic polymethine dye **1**, in which the stability was remarkably improved by partially rigidizing two of the methine groups into a ring system (Figure 1). In addition, it has been observed that the ring not only increased the stability but also advanced the absorbance of the dye in the NIR region (*4*). The stability and diversity of dye **1** has been demonstrated in a first proof-of-concept study where it was used to label peptides and proteins in solid- and solution-phase chemistry, respectively (*5*, *6*). During the course of work, however, we realized that this first generation cyclic polymethine dye **1** had a few limitations. First, due to its intrinsic hydrophobicity, at the high concentrations needed for in vivo application (10−20 μM), a significant amount of organic solvent such as DMSO has to be applied in order to generate a homogeneous solution, thus becoming toxic to testing subjects. Second, despite the straightforwardness of the chemistry used to develop a symmetrical dye, the presence of two activated carboxylic acid moieties could easily lead to a cross-link reaction with amino groups on peptides or proteins. Third, the intrinsic hydrophobicity of the dye led to aggregation in an aqueous environment, which, in turn, caused fluorescence quenching and as a consequence a reduced quantum yield (*7*). We report herein on our efforts to overcome the above-mentioned obstacles and further optimize the optical properties of lead compound **1** for in vivo imaging.

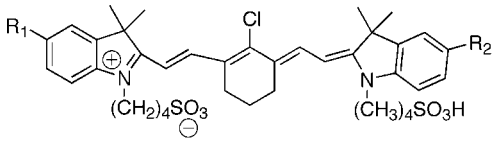

1. $R_1 = R_2 = COOH$
2. $R_1 = SO_3H$, $R_2 = COOH$
3. $R_1 = SO_3H$, $R_2 = CONH(CH_2)_6$AREPPTRTFAYWG

Figure 1. Chemical structures of dye **1**, second generation dye **2**, and the peptide-based probe **3**.

* Correspondence should be addressed to Anna Moore, Ph.D., MGH/MIT/HMS Athinoula A. Martinos Center for Biomedical Imaging, Department of Radiology, Massachusetts General Hospital/Harvard Medical School, Rm. 2301, Bldg.149, 13th St., Charlestown, MA 02129. Tel: (617)724−0540. Fax: (617)726-7422. E-mail: amoore@helix.mgh.harvard.edu.

10.1021/bc049700+ CCC: $30.25 © 2005 American Chemical Society
Published on Web 04/14/2005

MATERIALS AND METHODS

Apparatus and Reagents. Unless otherwise stated, reagents and solvents were obtained from commercial sources without further purification. Thin layer chromatography (TLC) was obtained from Polygram SIL G/UV_{254} plates (Bodman, Aston, PA) using reagent-graded solvents. Flash column chromatography was performed on silica gel 60 (230−400 mesh, Bodman). Reverse phase TLC was performed on Whatman KC 18F silica gel 60 Å (10 × 10 cm, Cat # 4803-425). All moisture- or air-sensitive reactions were carried out under a static argon atmosphere. Nuclear magnetic resonance (NMR) spectra were obtained with a Varian 400 MHz NMR in CD_3OD, DMSO-d_6 with TMS as an internal standard. The NMR signals were described with symbols s for singlet, d for doublet, t for triplet, m for multiplet, and br for broad. The chemical shifts are reported in parts per million downfield from tetramethylsilane, and coupling constants are reported in hertz. High performance liquid chromatography (HPLC) was performed on the Hitachi chromatograph equipped with diode array detector L-2450 and the LaChrom Elite software for performing 2-D intepretation. MALDI-TOF mass spectroscopy was performed by Tufts Core Mass Spectrometry Facility (Tufts University Medical School, Boston, MA). Absorption and emission spectra were determined using a Biomate spectrophotometer (Thermo Electron Spectroscopy Ltd, Cambridge, UK) and a Spex FluoroLog-3 spectrophotometer (Horiba Jobin Yvon, NJ) respectively. The molar extinction coefficient was obtained from HPLC-purified compound using Beer's law at 0.1−1.0 μM concentration of the dye. The relative fluorescence quantum yield was determined using the model:

$$\phi_{F(X)} = (A_s/A_x)\,(F_x/F_s)\,(n_x/n_s)^2\phi_{F(s)}$$

where ϕ_F is the fluorescence quantum yield, A is the absorbance, F is the area under the emission curve, and n is the refractive index of the solvents using in measurement (*8*). The subscripts s and x represent the standard and the unknown, respectively. Isocyanine green (ICG, Akorn, Inc. Decatur, IL) was used as a reference standard.

2,3,3-Trimethyl-3*H*-indole-5-sulfonic Acid (5). Glacial acetic acid (30 mL) was added to a mixture of 4-hydrazino-benzenesulfonic acid **4** (5.6 g, 30 mmol), methyl isopropyl ketone (4.6 mL, 43 mmol), and sodium acetate (5.0 g, 60 mmol) in a flame-dried round-bottom flask fitted with a reflux condenser. The brown suspension was refluxed for 18 h, the hot solution was filtered through the sintered glass filter to remove undissoved material followed by cooling to room temperature, and the brown solid product was precipitated in ether (70%); TLC: (2/1) CH_2Cl_2:CH_3OH, R_f = 0.53; λ_{max} (water) = 275 nm; ^{1}H NMR (DMSO-d_6, 400 MHz): δ 7.63 (1H, s, ArH), 7.56 (1H, d, J = 8.0 Hz, ArH), 7.34 (1H, d, J = 8.0 Hz, ArH), 2.20 (3H, s, CH_3), 1.82 (1H, s SO_3H), 1.23 (6H, s, $2CH_3$); ^{13}C NMR δ 189.1, 153.7, 145.2, 144.8, 125.2, 119.2, 118.2, 53.3, 22.5, 15.2

2,3,3-Trimethyl-5-sulfo-1-(4-sulfo-butyl)-3*H*-indolium (6). 1,2-Dichlorobenzene (50 mL) was added to a mixture of compound **5** (11.0 g, 46 mmol) and 1,4-butane sultone (4.9 mL, 48 mmol), and the mixture was heated to 110 °C for 12 h. The solid was triturated with 2-propanol triturate to provide a fine powder (68%), TLC: (2/1) CH_2Cl_2:CH_3OH, R_f = 0.18; λ_{max} (water) = 275 nm; ^{1}H NMR (CH_3OH, 400 MHz): δ 8.12 (1H, s, ArH), 8.04 (1H, d,d, J = 1.6, 7.0 Hz, ArH), 7.98 (1H, d, J = 8.4 Hz, ArH), 4.56 (2H, t, J = 8.0 Hz, CH_2N), 2.89 (2H, t, J = 7.4 Hz, CH_2SO_3), 2.13 (2H, m, CH_2), 1.85 (2H, m CH_2), 1.62 (6H, s, $2CH_3$); ^{13}C NMR δ 160.5, 145.7, 138.6, 136.0, 125.5, 119.5, 103.9, 74.6, 51.2, 43.5, 41.4, 29.8, 24.9, 22.7

5-Carboxy-2,3,3-trimethyl-1-(4-sulfo-butyl)-3*H*-indolium (7). 1,2-Dichlorobenzene (20 mL) was added to a mixture of 2,3,3-trimethyl-3*H*-indole-5-carboxylic acid (2.72 g, 13.4 mmol) and 1,4-butane sultone (3.2 mL, 31 mmol), and the mixture was heated to reflux for 5 h. The solution was cooled to room temperature, and the solids were collected by filtration and washed with acetone to provide the brown product (2.7 g, 60%), TLC (2/1) CH_2Cl_2:CH_3OH, R_f = 0.25; λ_{max}(water) = 325 nm; ^{1}H NMR (DMSO-d_6, 400 MHz): δ 8.36 (1H, s, ArH), 8.14 (2H, s, ArH), 4.50 (2H, m, NCH_2), 2.88 (3H, s, CH_3), 2.52 (2H, t, J = 6.4 Hz, CH_2SO_3), 1.94 (2H, m, CH_2), 1.75 (2H, m, CH_2), 1.54 (6H, s, $2CH_3$); ^{13}C NMR δ 199.6, 166.4, 144.4, 142.3, 131.6, 130.7, 130.5, 124.9, 115.9, 54.5, 50.1, 47.6, 26.0, 22.0, 14.3

NIR Dye 2. A suspension of intermediate **6** (100 mg, 0.27 mmol), *N*-[(3-(anilinomethylene)-2-chloro-1-cyclohexen-1-yl)methylene]aniline monhydrochloride (109.6 mg, 0.31 mmol), and sodium acetate (44.3 mg, 0.54 mmol) in absolute ethanol was refluxed for 4 h. The progress of the reaction was monitored by the disappearance of the absorption peak at 275 nm and the appearance of a strong peak at 650 nm. Intermediate **7** (92 mg, 0.27 mmol) was quickly added to the reaction flask and continued to reflux for 1 h. The solvent was reduced by using the rotor vapor. The residue was redissolved in water and purified by HPLC to provide the green, lyophilized solid (21.4 mg, 9.3%). Reversed phase TLC (1/1) water:CH_3OH, R_f = 0.72; λ_{max} (water) = 790 nm; ^{1}H NMR (DMSO-d_6, 400 MHz): δ 8.39 (1H, d, J = 14.8 Hz, CH of the bridge), 8.09 (1H, d, J = 13.6 Hz, CH of the bridge), 8.03 (1H, s, ArH of disulfonated indole ring), 7.93 (1H, d, J = 8.4 Hz, ArH of disulfonated indole ring), 7.85 (1H, s, ArH of monosulfonated indole ring), 7.70 (1H, d, J = 8.4 Hz, ArH of monosulfonated indole ring), 7.60 (1H, d, J = 8.4 Hz, ArH of disulfonated indole ring), 7.36 (1H, d, J = 8.8 Hz, ArH of monosulfonate indole ring), 6.66 (1H, d, J = 14.8 Hz, CH of the bridge), 6.20 (1H, d, J = 13.6 Hz, CH of the bridge), 2.75 (4H, br, $2(CH_2SO_3H)$), 2.50 (4H, partial overlapped by DMSO, 4H of cyclohexene), 1.7−19 (10H, br, m, CH_2CH_2, cyclohexene CH_2), 1.70 (6H, s, $2CH_3$ of disulfonated indole ring), 1.65 (6H, s, $2CH_3$ of monosulfonated indole ring). MS (MALDI-TOF) calcd (MH^+) 852.45, found 852. 42.

Synthesis of Probe 3. The peptide substrate, AREPPTRTFAYWG, with an aminohexanoic acid (AHA) moiety as a spacer on the N-terminus was synthesized using an automatic peptide synthesizer (PS 3, Protein Technologies, Inc.) by conventional Fmoc chemistry (0.1 mmol) using Rink amide resin (0.43 mmol/g) and HBTU/HOBT as the activating reagents. After completion of the peptide synthesis, the NIR dye **2** was coupled to the N-terminus of the AHA group. NIR dye **2** (71.3 mg, 0.084 mmol) was first initially activated with HBTU (44.6 mg, 0.12 mmol) and HOBT (16.2 mg, 0.12 mmol) in 1:10 of pyridine/DMF in the presence of argon for 2 h. The labeling product was charged with TFA/thioannisole/ethandithiol/anisole (90/5/3//2) to deprotect the acid-labile protective groups as well as the resin followed by C18 reversed-phase 2D-HPLC purification to afford a green product.

In Vivo Optical Imaging. Two million human pancreatic adenocarcinoma CAPAN-2 cells were implanted subcutaneously into athymic nude mice on the back adjacent to the upper thigh. When the tumors reached

Scheme 1. Synthesis of Asymmetric Water-Soluble NIR Dye 2[a]

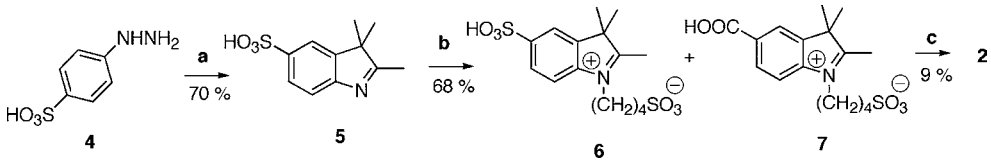

[a] Reagents and conditions: (a) $(CH_3)_2CHCOCH_3$, acetic acid; (b) 1,4-butane sultone, 1,2-dichlorobenzene; (c) *N*-[(3-(anilinomethylene)-2-chloro-1-cyclohexen-1-yl)methylene]aniline monohydrochloride, NaOAc, EtOH.

3−4 mm in diameter, the in vivo NIR fluorescence imaging experiments were performed. Animals were anesthetized with isoflurane and injected intravenously in the tail vein with 10 μM of probe **3** in Hanks Balanced Salt Solution (HBSS), pH 7.2, and subjected to NIR imaging 0.4, 0.2, 1, 2, 3, 6, 10, and 24 h postinjection. Imaging was performed using a whole-mouse imaging system (Imaging Station IS2000MM, Kodak Scientific Imaging System, New Haven, CT), equipped with a band-pass filter at 720 nm and a long-pass filter at 790 nm (Chroma Technology Corporation, Rockingham, VT). Images were analyzed using Kodak ID3.6.3 network version imaging software.

Fluorescence Microscopy. After completion of the in vivo imaging experiments, animals were sacrificed, and tumors were excised, snap frozen in liquid nitrogen, cut into 7 μm sections, and fixed in 2% paraformaldehyde. Sections were counterstained with DAPI to depict cell nuclei. Microscopy was performed using a Nikon Eclipse 50i fluorescence microscope equipped with an appropriate filter set (Chroma Technology Corporation, Rockingham, VT). Images were acquired using a CCD camera with near-infrared sensitivity (SPOT 7.4 Slider RT_{KE}; Diagnostic Instruments, Sterling Heights, MI) and analyzed using SPOT 4.0 advanced version software (Diagnostic Instruments, Sterling Heights, MI).

RESULTS AND DISCUSSION

Synthesis. To improve the limited physical properties of **1**, we performed the following modifications. First, to avoid cross-reaction with amino groups from targeted labeling entities and to increase water solubility, we replaced one of the carboxylic groups on the indole ring system by a sulfonic version (Scheme 1). Second, to produce the asymmetric dye, we employed a known procedure for a sequential, one-pot synthesis in the final step (*9*). It has been shown that an additional sulfonic group incorporated on the aromatic nucleus of the cyanine fluorophore not only enhanced water solubility, but also improved the quantum yield of the dye in a biological environment (*9*). The synthesis was commenced with Fischer indole condensation between hydrazino-benzene-sulfonic acid **4** and an isopropyl methyl ketone in acetic acid to yield intermediate **5** followed by alkylation of the indole ring with butane sultone in refluxing 1,2-dichlorobenzene to provide the water-soluble sulfonate analogue **6**. Finally, intermediate **6** was heated to reflux with *N*-[(3-(anilinomethylene)-2-chloro-1-cyclohexen-1-yl)methylene]aniline in ethanol in the presence of sodium acetate for 4 h, followed by an addition of intermediate **7** (*6*) to afford **2** in a modest yield (Scheme 1). During the course of work, we found that compound **7** was very susceptible to the condensation reaction, probably due to its better solubility in ethanol, and as a consequence, there was an equal formation of **1** as determined by 2-D HPLC and analyzed by matrix-assisted laser desorption/ionization time-of-flight (MALDI-TOF) spectrometry.

As we anticipated, the polarity of dye **2** was enhanced significantly by the incorporation of an additional sulfonate group while the absorption and emission maxima remained unchanged compared to the previous generation. The solubility of dye **2** was tested against former dye **1** at a high concentration (1 mg/100 μL) using solvents with a high dielectric constant such as DMSO, DMF, and water. Furthermore, the difference in polarity was confirmed by reverse phase HPLC where the retention time of dye **2** was 5 min earlier compared to that of **1**. We did not observe any new absorption band as an indication of dimerization or dye−dye interaction in addition to the major absorbance wavelength at 790 nm of the monomers (*7*) (Figure 2). The dye solutions in water followed Beer's law at a wide concentration range. NIR dye **2** in water had a molar extinction coefficient and quantum yield of 200 000 M^{-1} cm^{-1} and 0.18, respectively, compared to 180 000 M^{-1} cm^{-1} and 0.08 of compound **1** (*6*). The broad absorbance spectrum of dye **2** enabled excitation of the molecule several nanometers prior to the maximum excitation peak (λ_{max} = 790 nm) using a commercially available 720 nm excitation filter and collecting the emission light 50 nm away from the excitation wavelength by using a narrow-band emission filter at 790 nm. This strategy could eventually diminish the high background resulting from the cross-talk when the excitation and emission filters' wavelengths are too close (*10*).

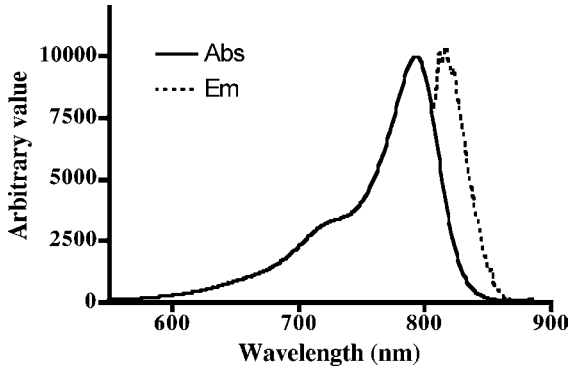

Figure 2. A normalized absorption and emission spectra of NIR dye **2** in water at 42 μM.

To prove the utility of the newly synthesized dye in vivo, we performed experiments that were based on our continued work toward the development of optical probes for early cancer detection. Underglycosylated mucin-1 tumor antigen (uMUC-1) is one of the early hallmarks of tumorogenesis in a wide variety of tumors. MUC-1 is overexpressed and underglycosylated on almost all human epithelial cell adenocarcinomas, including more than 90% of human breast cancers (*11*−*14*), ovarian (*15*−*17*), pancreatic (*18*), colorectal (*18*−*20*), lung (*21*, *22*), prostate (*23*), and gastric carcinomas (*24*, *25*). Moreover, MUC-1 expression has been demonstrated in nonepithelial cancer cell lines (astrocytoma, melanoma, and neuroblastoma (*19*)) as well as in hematological malignancies such as multiple myeloma and some B-cell non-Hodgkin lymphomas (*26*−*29*), constituting more than 50% of all cancers

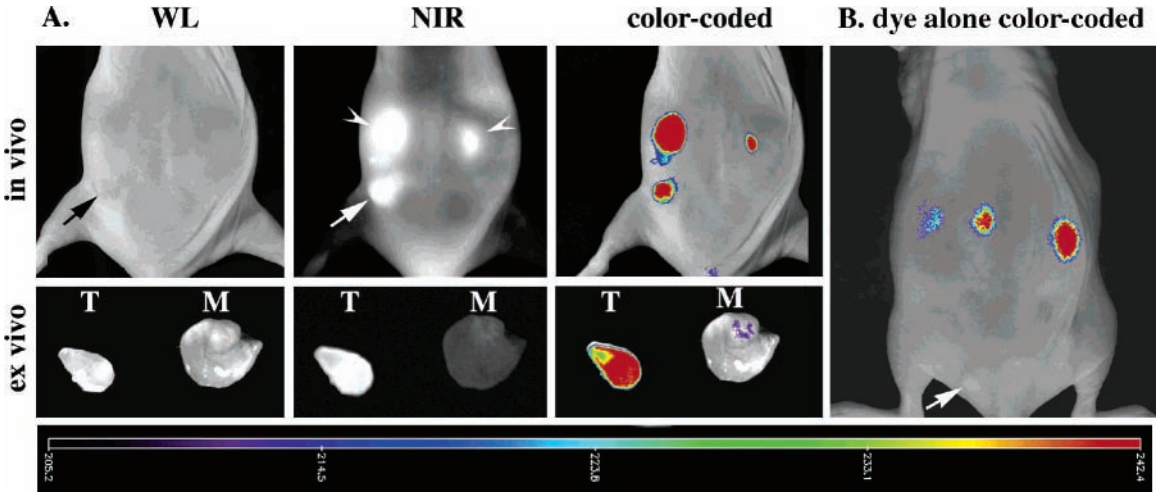

Figure 3. A. White light (WL), near-infrared (NIR), and color-coded map of mice bearing human pancreatic adenocarcinoma CAPAN-2 in vivo (top) and ex vivo (bottom). NIR fluorescence imaging was performed 24 h postinjection of 10 μM of probe **3**. Bright NIR fluorescence in the tumor (arrow) is the result of the accumulation of the probe labeled with dye **2**. Kidneys (arrowheads) showed systemic accumulation followed by clearance. Ex vivo images confirmed the signal coming from the excised tumor (T) compared to control muscle tissue (M). B. Color-coded map of tumor-bearing mice injected with unconjugated dye **2.** No accumulation of the unconjugated dye in the tumor (arrow) was detected.

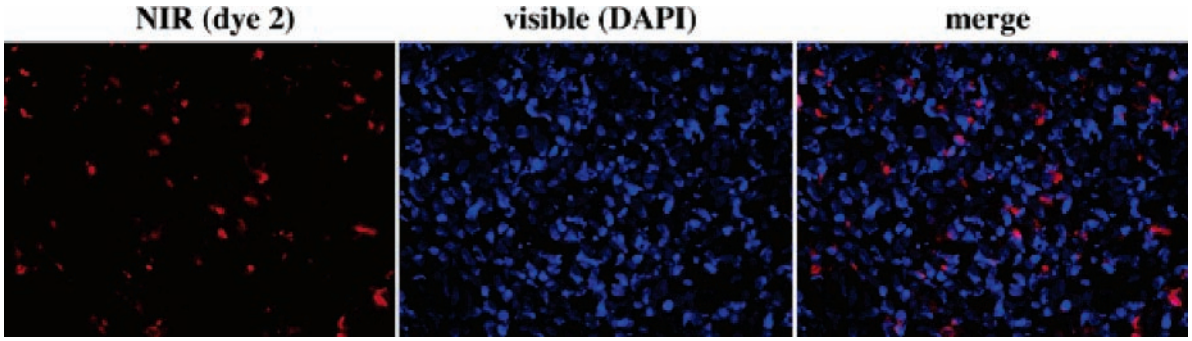

Figure 4. Dual channel fluorescence microscopy of the sections of excised tumor isolated from mouse 24 h after iv injection. Nuclear staining with DAPI was detected with a visible channel, while dye **2** as a component of probe **3** projected a strong signal in the NIR channel.

in humans (*30*). We have previously reported on the development of a multimodal (fluorescent and MRI) peptide-based imaging probe, targeting the uMUC-1 tumor antigen in a mouse model of human cancer (*31*). The peptide (EPPT peptide) targeting the uMUC-1 antigen was derived from the CDR3V$_\beta$ region of a monoclonal antibody raised against human epithelial cancer cells (*32*, *33*), and its sequence was determined (AREPPTRTFAYWG). The NIR fluorescence imaging experiments in our previous studies were performed on tumor-bearing mice using a Cy5.5-labeled probe. In the present study we used our newly developed dye **2** conjugated to an EPPT peptide, which showed specific accumulation in tumors expressing the uMUC-1 antigen (*31*). The peptide was derivatized with an aminohexanoic acid spacer (AHA), which concomitantly provided a sole amino terminal moiety for dye conjugation in solid-phase synthesis (*5*). The dye, activated in situ with *N*-hydroxybenzotriazole and 2-(1*H*-benzotriaole-1-yl)-1,1,3,3-tetramethyluronium (HOBT/HBTU) reacted with the aminated AHA-A-R(Pbf)-E(OtBu)-P-P-T(tBu)-R(Pbf)-T(tBu)-F-A-Y(tBu)-W(Boc)-G peptide with selectivity. During the course of our work, it turned out that the limited reagent of green color dye **2** could be used as an indicator to monitor the progress of the reaction; when the coupling reaction finished, the green color of the solution faded, while the resin turned green. The resin as well as the acidic labile side chain protection groups was deprotected in trifluoroacetic acid in the presence of scavengers to provide probe **3**. We observed no physical change in the dye property after peptide labeling.

In Vivo NIR Imaging and ex Vivo Microscopy. Tumor bearing animals were subjected to NIR imaging after intravenous injection of probe **3**. We detected a strong NIR fluorescent signal in the tumor 10 h after injection, and the signal continued to accumulate 24 h postinjection (Figure 3A). The NIR signal depicted from the tumor was of high intensity, readily distinguished from the background. After systemic distribution of the probe, there was a noticeable accumulation in the peripheral tissues (kidneys, spleen) followed by eventual clearance. Ex vivo images of the excised tumor (left) and muscle tissues (right) were obtained immediately after in vivo imaging. We observed a bright NIR signal coming from the tumors, whereas there was little signal from the muscle tissue. The ratio of fluorescence signal of the tumor versus muscle was 2.5 as determined by ROI analysis (Figure 3A). In contrast, animals injected with the same amount of unconjugated dye **2** did not show any signal in the tumors (Figure 3B). Other organs showed distribution similar to the conjugated dye. To confirm the presence of the probe in the tumor, we correlated our macroscopic observations with dual-channel fluorescence microscopy. NIR fluorescence was detected in tumor cell cytoplasm confirming the presence of the probe in the tumor tissue (Figure 4).

Overall, in this study we performed an improved development of NIR fluorescent dye **2** with enhanced

physical properties for in vivo imaging. First, we increased the overall hydrophilicity of the dye by adding a sulfonic moiety to its structure. Second, we eliminated the possibility of cross-linking with peptides/proteins during conjugation by removing one of the activated carboxylic acid group. Finally, we improved the quantum yield more than two times compared to the original dye **1**. Furthermore, we showed the suitability of dye **2** for in vivo NIR fluorescence optical imaging in a mouse model of human cancer. We confirmed our in vivo results with fluorescence microscopy where the dye was readily detectable on a cellular level. We anticipate that this modification of the NIR dye will be further used for conjugation with targeting molecules for in vivo optical imaging.

ACKNOWLEDGMENT

This work was supported in part by NIH grant EB001727-02 to A.M.

LITERATURE CITED

(1) Lewis, J. S., Achilefu, S., Garbow, J. R., Laforest, R., and Welch, M. J. (2002) Small animal imaging. Current technology and perspectives for oncological imaging. *Eur. J. Cancer 38*, 2173−88.

(2) Levine, I. N. (1984) *Quantum Chemistry,* 3rd ed., pp 463−466, Allyn and Bacon, Boston.

(3) Benson, R. C., and Kues, H. A. (1977) Absorption and fluorescence properties of cyanine dyes. *J. Chem. Eng. Data 22*, 379−83.

(4) Reynolds, G. A., and Drexhage, K. H. (1977) Stable heptamethine pyrylium dyes that absorb in the infrared. *J. Org. Chem. 42*, 885−8.

(5) Pham, W., Yongdoo, C., Weissleder, R., and Tung, C. H. (2004) Developing a Peptide-Based Near-Infrared Molecular Probe for Protease Sensing. *Bioconjugate Chem 15*, 1403−1407.

(6) Pham, W., Lai, W. F., Weissleder, R., and Tung, C. H. (2003) High efficiency synthesis of a bioconjugatable near-infrared fluorochrome. *Bioconjugate Chem 14*, 1048−51.

(7) West, W., and Pearce, S. (1965) The dimeric state of cyanine dyes. *J. Phys. Chem. 69*, 1894−903.

(8) Fery-Forgues, S., and Lavabre, D. (1999) Are fluorescence quantum yields so tricky to measure? A demonstration using familiar stationery products. *J. Chem. Educ. 76*, 1260−1264.

(9) Mujumdar, R. B., Ernst, L. A., Mujumdar, S. R., Lewis, C. J., and Waggoner, A. S. (1993) Cyanine dye labeling reagents: sulfoindocyanine succinimidyl esters. *Bioconjugate Chem 4*, 105−11.

(10) Zhang, Z., and Achilefu, S. (2004) Synthesis and evaluation of polyhydroxylated near-infrared carbocyanine molecular probes. *Org. Lett. 6*, 2067−70.

(11) Xing, P., Tjandra, J., Stacker, S., Teh, J., Thompson, C., McLaughlin, P., and McKenzie, I. (1989) Monoclonal antibodies reactive with mucin expressed in breast cancer. *Immunol. Cell Biolol. 67 (Pt 3)*, 183−195.

(12) Hayes, D., Mesa-Tejada, R., Papsidero, L., Croghan, G., Korzun, A., Norton, L., Wood, W., Strauchen, J., Grimes, M., Weiss, R., Ree, H., Thor, A., Koerner, F., Rice, M., Barcos, M., and Kufe, D. (1991) Prediction of prognosis in primary breast cancer by detection of a high molecular weight mucin-like antigen using monoclonal antibodies DF3, F36/22, and CU18: a Cancer and Leukemia Group B study. *J. Clin. Oncol. 9*, 1113−1123.

(13) Perey, L., Hayes, D., Maimonis, P., Abe, M., O'Hara, C., and Kufe, D. (1992) Tumor-specific reactivity of a monoclonal antibody prepared against a recombinant peptide derived from the D3 human breast carcinoma-associated antigen. *Cancer Res. 52*, 2563−2568.

(14) Nacht, M., Ferguson, A., Zhang, W., Petroziello, J., Cook, B., Hong Gao, Y., Maguire, S., Riley, D., Coppola, G., Landes, G., Madden, S., and Sukumar, S. (1999) Combining serial analysis of gene expression and array technologies to identify genes differentially expressed in breast cancer. *Cancer Res. 59*, 5464−5470.

(15) van Hof, A., Molthoff, C., Davies, Q., Perkins, A., Verheijen, R., Kenemans, P., den Hollander, W., Wilhelm, A., Baker, T., Sopwith, M., Frier, M., Symonds, E., and Roos, J. (1996) Biodistribution of (111)indium-labeled engineered human antibody CTMO1 in ovarian cancer patients: influence of protein dose. *Cancer Res. 56*, 5179−5185.

(16) Avichezer, D., Taylor-Papadimitriou, J., and Arnon, R. (1998) A short synthetic peptide (DTRPAP) induces anti-mucin (MUC-1) antibody, which is reactive with human ovarian and breast cancer cells. *Cancer Biochem. Biophys. 16*, 113−128.

(17) Hough, C., Sherman-Baust, C., Pizer, E., Montz, F., Im, D., Rosenshein, N., Cho, K., Riggins, G., and Morin, P. (2000) Large-scale serial analysis of gene expression reveals genes differentially expressed in ovarian cancer. *Cancer Res. 60*, 6281−6287.

(18) Budrick, M., Harris, A., Reid, C., Iwamura, T., and Hollingsworth, M. (1997) Oligosaccharides expressed on MUC1 produced by pancreatic and colon tumour cell lines. *J. Biol. Chem. 272*, 24198−24202.

(19) Aoki, R., Tanaka, S., Haruma, K., Yoshihara, M., Sumii, K., Kajiyama, G., Shimamoto, F., and Kohno, N. (1998) MUC-1 expression as a predictor of the curative endoscopic treatment of submucosally invasive colorectal carcinoma. *Dis. Colon. Rectum 41*, 1262−1272.

(20) Oosterkamp, H., Scheiner, L., Stefanova, M., Lloyd, K., and Finstad, C. (1997) Comparison of MUC-1 mucin expression in epithelial and nonepithelial cancer cell lines and demonstration of a new short variant form (MUC-1/Z). *Int. J. Cancer 72*, 87−94.

(21) Willsher, P., Xing, P., Clarke, C., Ho, D., and McKenzie, I. (1993) Mucin 1 antigens in the serum and bronchial lavage fluid of patients with lung cancer. *Cancer 72*, 2936−2942.

(22) Maeshima, A., Miyagi, A., Hirai, T., and Nakajima, T. (1997) Mucin-producing adenocarcinoma of the lung, with special reference to goblet cell type adenocarcinoma: immunohistochemical observation and Ki-ras gene mutation. *Pathol. Int. 47*, 454−460.

(23) Zhang, S., Zhang, S., Reuter, V., Slovin, S., Scher, H., and Livingston, P. (1998) Expression of potential target antigens for immunotherapy on primary and metastatic prostate cancers. *Clin. Cancer Res. 4*, 295−302.

(24) Strous, G., and Dekker, J. (1992) Mucin-like glycoproteins. *Crit. Rev. Biochem. Mol. Biol. 27*, 57−92.

(25) Medina, M., Velez, D., Asenjo, J., Egea, G., Real, F., Gil, J., and Subiza, J. (1999) Human colon adenocarcinomas express a MUC1-associated novel carbohydrate epitope on core mucin glycans defined by a monoclonal antibody (A10) raised against murine Ehrlich tumor cells. *Cancer Res. 59*, 1061−1070.

(26) Burton, J., Mishina, D., Cardillo, T., Lew, K., Rubin, A., Goldenberg, D., and Gold, D. (1999) Epithelial mucin-1 (MUC1) expression and MA5 anti-MUC1 monoclonal antibody targeting in multiple myeloma. *Clin. Cancer Res. 5*, 3065s−3072s.

(27) Treon, S., Mollick, J., Urashima, M., Teoh, G., Chauhan, D., Ogata, A., Raje, N., Hilgers, J., Nadler, L., Belch, A., Pilarski, L., and Anderson, K. (1999) Muc-1 core protein is expressed on multiple myeloma cells and is induced by dexamethasone. *Blood 93*, 1287−1298.

(28) Dyomin, V., Palanisamy, N., Lloyd, K., Dyomina, K., and Jhanwar, S. (2000) MUC1 is activated in a B-cell lymphoma by the t(1:14)(q21;q32) translocation and is rearranged and amplified in B-cell lymphoma subsets. *Blood 95*, 2666−2671.

(29) Brossart, P., Schneider, A., Dill, P., Schammann, T., Grunebach, F., Wirths, S., Kanz, L., Buhring, H., and Brugger, W. (2001) The epithelial tumor antigen MUC1 is expressed in hematological malignancies and is recognized by MUC1-specific cytotoxic T-lymphocytes. *Cancer Res. 61*, 6846−6850.

(30) Greenlee, R., Murray, T., Bolden, S., and Wingo, P. (2000) Cancer statistics. *CA Cancer J. Clin. 50*, 7.
(31) Moore, A., Medarova, Z., Potthast, A., and Dai, G. (2004) In vivo targeting of underglycosylated MUC-1 tumor antigen using a multimodal imaging probe. *Cancer Res. 64*, 1821−7.
(32) Sivolapenko, G., Douli, V., Pectasides, D., Skarlos, D., Sirmalis, G., Hussain, R., Cook, J., Courtenay-Luck, N., Merkouri, E., Konstantinides, K., and Epenetos, A. (1995) Breast cancer imaging with radiolabelled peptide from complementary-determining region of antitumour immunity. *Lancet 346*, 1662−1666.
(33) Hussain, R., Courtenay-Luck, N., and Siligardi, G. (1996) Structure−function correlation and biostability of antibody CDR-derived peptides as tumor imaging agents. *Biomed. Pept., Proteins Nucleic Acids 2*, 67−70.

BC049700+

JULY/AUGUST 2005
Volume 16, Number 4

© Copyright 2005 by the American Chemical Society

Bioconjugate Chemistry

REVIEWS

Identification and Mapping of Protein−Protein Interactions by a Combination of Cross-Linking, Cleavage, and Proteomics

Michael A. Trakselis,[†] Stephen C. Alley,*[,‡] and Faoud T. Ishmael[§]

Medical Research Council, Cancer Cell Unit, Hutchison MRC Research Centre, Hills Road, Cambridge CB2 2XZ, United Kingdom, Seattle Genetics, Inc., 21823 30th Drive Southeast, Bothell, Washington 98021, and The Pennsylvania State University, College of Medicine, Department of Medicine, H039, 500 University Drive, P.O. Box 850, Hershey, Pennsylvania 17033-0850. Received February 15, 2005; Revised Manuscript Received May 2, 2005

Protein−protein interactions are vital for almost all cellular functions, and many require the formation of multiprotein complexes. Identification of the macroscopic and microscopic protein interactions within these complexes is essential in understanding their mechanisms, both under physiologic as well as pathologic conditions. This review describes the current technology available to investigate interactions between proteins utilizing chemical cross-linking and site-directed cleavage reagents, outlining the necessary steps involved in identifying interacting proteins both in vitro and in vivo. Once interacting proteins are identified, more information about the architecture of the assemblies is necessary. Unique separation techniques coupled with cross-linking and mass spectrometry can now identify specific interaction sites and lead to the development of quaternary structural protein models. Furthermore, combination of these methods with proteomic approaches enables the identification and analysis of complex interactions in vivo. Finally, future directions in cross-linking methodologies are discussed.

INTRODUCTION

Protein−protein interactions are of extraordinary importance in biology. From multiprotein complexes, such as those found in DNA replication and RNA transcription, to transient interactions, such as those found in signal transduction networks, biological systems contain interaction networks that are critical for their function. The completed sequence information of a significant number of genomes and the availability of an increasing number of X-ray and NMR structures of key individual proteins have precipitated many advances in describing protein−protein interactions.

Numerous techniques have been developed to probe protein−protein interactions, with some methods providing very high structural resolution with low throughput, such as X-ray crystallography and multidimensional NMR, while others offer very high throughput with low structural resolution, such as phage display, yeast two-hybrid screens, and protein microarrays. Quantitative descriptions of the strength of protein−protein interac-

* To whom correspondence should be addressed: Tel: 425-527-4752; fax: 425-527-4001; e-mail: SAlley@seagen.com.
[†] Hutchison MRC Research Centre.
[‡] Seattle Genetics, Inc.
[§] The Pennsylvania State University.

10.1021/bc050043a CCC: $30.25 © 2005 American Chemical Society
Published on Web 07/01/2005

tions with low structural resolution can be determined by methods such as gel filtration, Biacore, and fluorescence spectroscopy. Chemical cross-linking does not have the throughput of techniques such as phage display or yeast two-hybrid systems, where libraries of interacting partners can be rapidly screened, nor does it provide information about the strength of an interaction, but it does allow higher resolution structural data to be generated where protein−protein interactions can be mapped to specific domains or amino acids. Most importantly, cross-linking allows noncovalent protein−protein interactions, which may be transient or dependent on specific physiological conditions, to be captured into long-lived covalent complexes that maintain structural information during subsequent purification, enrichment, and analysis.

Many protein cross-linking tools are commercially available, enabling wide access to investigation of protein−protein interactions. New reagents and mass spectrometry (MS)[1] have significantly increased the power of these tools and the ability to investigate more complicated systems, including protein−protein interactions in vivo. Interestingly, the two areas of protein cross-linking and proteomics have taken inspiration from each other, and several hybrid tools have emerged.

The investigation of protein−protein interactions may have several goals. The first may simply be the identification of two proteins that interact and may start with the two proteins in either purified form or in more complex mixtures. Detecting a new, higher molecular-weight band on an SDS−PAGE gel after cross-linking and Coomassie or silver staining is sufficient to identify an interaction between two purified proteins. However, the absence of a new band is not sufficient to exclude the possibility that two proteins do interact. This limitation is identical for many other techniques for investigating protein−protein interactions, in that the absence of a signal only excludes protein−protein interactions under the specific set of conditions used, which may be very different from those in vivo or lack additional factors necessary for forming the interaction. Detection of cross-links in the presence of many other proteins requires affinity tagging the protein or using antibodies against the protein for visualization. In the absence of these reagents, more sophisticated separation and/or visualization techniques, such as using affinity handles on the cross-linker or tandem mass spectrometry, will be required for identification of cross-linked proteins. Once interacting partners have been identified, the next goal may be to map the location of the interaction, which may also employ these sample visualization and identification tools with MS. Importantly, the yield from cross-linking and any separation technique employed must be high enough so that the subsequent MS analysis will be successful in identifying points of interaction. Significant effort in the choice of cross-linking reagent, scale-up, and/or cross-linking reaction optimization may be necessary in advance of MS investigation. Ultimately, sophisticated

[1] Abbreviations: ANB-NOS, *N*-5-azido-2-nitrobenzoyloxysuccinimide; BMHT, betaine-homocysteine methyltransferase; DSP, dithiobis[succinimidylpropionate]; DSS, disuccinimidyl suberate; DTT, dithiothreitol; ECAT, element-encoded affinity tag; FeBABE, 1-(*p*-bromoacetmidobenzyl)-EDTA; IAC, *N*-(3-iodo-4-azidosalicyl)cysteine; ICAT, isotope-coded affinity tag; MBP, 4-maleimidobenzophenone; MS, mass spectrometry, SAED, sulfosuccinimidyl 2-[7-amino-4-methylcoumarin-3-acetamido]-ethyl-1,3′dithiopropionate; sulfo-SBED, sulfosuccinimidyl[2-6-(biotinamido)-2-(*p*-azidobenzamido)-hexanoamido]-ethyl-1,3′-dithiopropionate; VICAT, visible isotope-coded affinity tag.

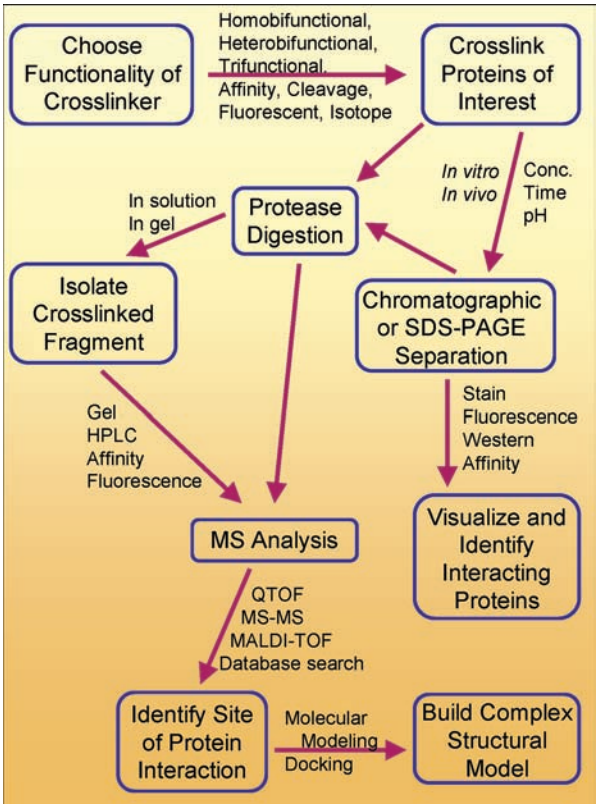

Figure 1. Cross-linking methodology flowchart demonstrating the procedures involved in identification of the specific site of cross-linking between two or more proteins and construction of quaternary complex models.

models of multiprotein complexes can be assembled from these results. Figure 1 characterizes the uses of cross-linking discussed above and outlines general strategies for the identification of specific protein interaction sites that can be used to develop quaternary protein models.

This review will illustrate the techniques that are currently being used in the identification of protein−protein interactions. Many commercially available reagents have been used in these studies, and novel probes and mass spectrometry techniques have come into play as the complexity of the multiprotein complexes under investigation have increased. Figure 2 provides an overview of the types of protein modification groups that are available. Modern mass spectrometry and proteomics techniques have significantly increased the scope of these studies and have begun to allow investigation of protein−protein interactions under more physiologically relevant conditions than for two purified and isolated proteins, including cell lysates and in vivo.

IDENTIFYING PROTEIN−PROTEIN INTERACTIONS

Homobifunctional and Heterobifunctional Cross-Linkers. The most common type of protein−protein interaction is the interaction of a protein with itself to form multimers. Often this can regulate the activity of the protein and provide a powerful switch between active and inactive forms. There are numerous techniques for studying oligomerization, and cross-linking provides the ability both to determine the degree of oligomerization and to map the network of interactions at the protein−protein interface. Many commercially available reagents can facilitate these studies by forming cross-links in proteins between pairs of lysines, lysines and aspartic or glutamic acids, lysines and cysteines, or pairs of

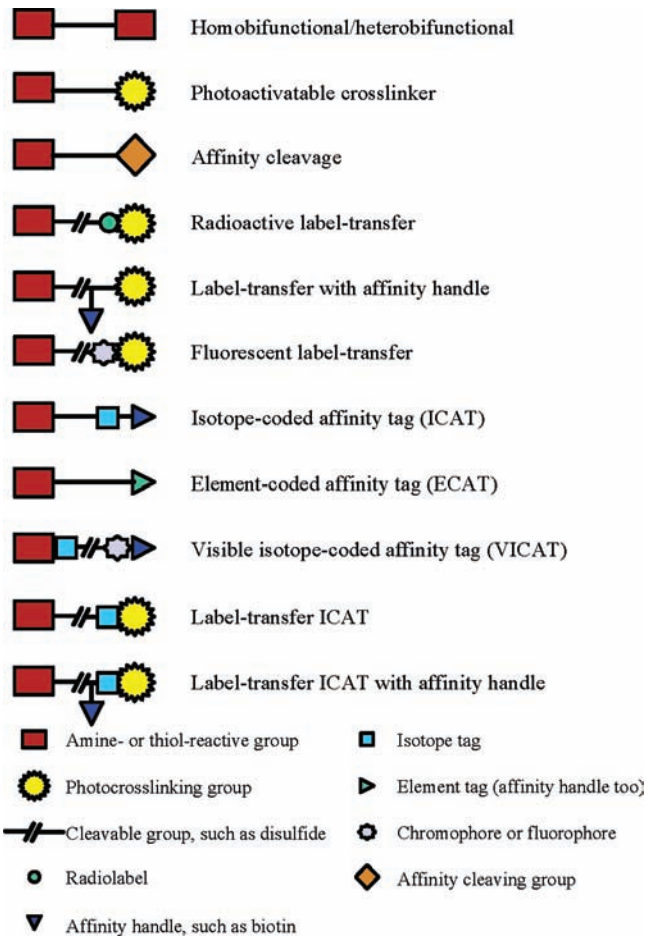

Figure 2. Schematic structures of the protein modification groups discussed in this review.

cysteines. The following examples show that these types of cross-links can be formed under a variety of biologically relevant conditions, including inside of cells and membrane preparations.

Cross-linking through the ϵ-amino group of lysines can demonstrate oligomerization due to the large number of lysines present on the surface of most proteins. It is highly likely that two lysines will be close to each other at the protein−protein interface and form cross-links. Szegedi and Garrow (*1*) used a 30-min incubation with glutaraldehyde to cross-link betaine-homocysteine methyltransferase (BHMT). Coupled with gel filtration, the oligomeric state of BHMT and several mutants could be assigned. Wild-type BHMT and some mutants were tetramers, while other mutants were dimers. Dimeric mutants were enzymatically inactive, demonstrating that the tetrameric form is required for activity.

Cysteines are less common on the surface of proteins, but can provide a higher resolution investigation of the protein−protein interface. Bunn and Ordal (*2*) made 30 single cysteine mutants (2 runs of 15 contiguous amino acids) of the homodimeric *Bacillus subtilis* chemoreceptor McpB, a member of a two-component signal transduction cascade. Using a 5-min incubation with copper-phenanthroline to oxidize properly orientated cysteines from each monomer to disulfides (a zero-length and reversible cross-link), contacts within the two α-helical transmembrane domains were mapped. Cross-linking was carried out using cells transformed with plasmids containing mutant *mcpB* and cross-links visualized by Western blots probed with anti-McpB antibodies. As would be expected for an α-helical bundle, cross-linking was maximized (up to 100% yield) at a spacing of n to n+3/n+4 in each domain, establishing the dimerization interface. However, cross-linking was also observed at amino acids on the opposite side of the α-helical bundle from the dimerization interface, leading the authors to suggest that in vivo, McpB can also exist as trimers of dimers.

The tether length of the cross-linker can be varied to map the distance between two cross-linked cysteines. Kaback and co-workers used 5 and 21 Å tether length bis-methane thiosulfonates to cross-link single cysteine mutants of *Escherichia coli* lactose permease (LacY). LacY is a membrane protein with 12 transmembrane helices and loops on the periplasmic and cytoplasmic sides of the membrane. Two hundred fifty transmembrane mutants (*3*) and 143 extramembrane mutants (*4*) were investigated for their importance in homodimer formation. Cross-linking was carried out for 3 min to 1 h using sonicated *E. coli* membrane suspensions made from cells transformed with plasmids containing mutant *lacY*, with anti-C-terminal antibodies used for visualization of cross-links on Western blots. Cross-linking yields of greater than 40% were observed for some mutants. Only 4% of the transmembrane mutants formed cross-links with the 5 Å cross-linker, while 53% of the extramembrane mutants formed cross-links with the 5 and 21 Å cross-linkers. Just over half of the extramembrane cross-links formed with only the 21 Å cross-linker. An interaction map of the homodimer interface was constructed from these results, with domains from both the periplasmic and cytoplasmic faces contributing significant contacts.

Photoactivatable Cross-Linking. Cross-links can also be formed between proteins using reagents that are activated by light. Heterobifunctional benzophenones and aryl azides can first be attached to proteins through lysines or cysteines, and then multiprotein complexes can be assembled under safe lighting conditions. Cross-links are only formed upon exposure to highly intense, short wavelength (250−350 nm) light. This offers the researcher a significant advantage, in that there is very good control for the start and end of cross-linking since light is the exclusive trigger for the cross-linking reaction. Photo-cross-linking times are generally shorter (5−15 min with aryl azides) than chemical cross-linking times, sometimes significantly shorter (down to 1 s with metal catalysis). However, photo-cross-linking can often be a process with poor yields and a diversity of possible products, especially with aryl azides, potentially making the identification of the location of photo-cross-linking very difficult. Numerous commercially available reagents, such as 4-maleimidobenzophenone (MBP) and *N*-5-azido-2-nitrobenzoyloxysuccinimide (ANB-NOS) (Figure 3), have been used to form photo-cross-links.

Giron-Monzon and co-workers (*5*) investigated the ATP-dependent activation of the *E. coli* mismatch repair exonuclase MutH by MutL by photo-cross-linking. MutL has 7 native cysteines, and these were first mutated to serine, leucine, or phenylalanine. Thirteen single cysteine mutants were then constructed and labeled with MBP. Complexes with MutH in the presence or absence of ATP, the nonhydrolysable ATP analogue ADPnP, and DNA were formed and then photolyzed for 10−30 min. An interaction map was then constructed, and a mechanism for the ATP dependence of the MutH-MutL complex formation could be determined.

Protein−protein interactions can also be studied by metal-catalyzed chemical- and photo-cross-linking. Chelated Ni(II) can be used to introduce zero-length cross-links by treating with an oxidant such as magnesium

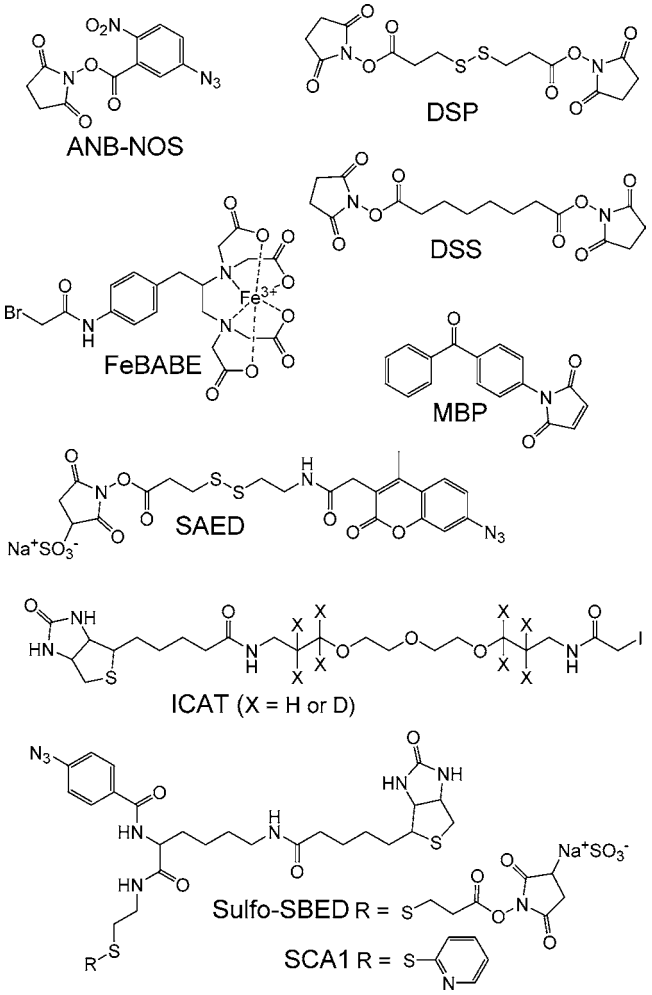

Figure 3. A selection of the structures of commonly used cross-linkers discussed in this review: *N*-5-azido-2-nitrobenzoyl-oxysuccinimide (ANB-NOS), dithiobis(succinimidyl propionate) (DSP), disuccinimidyl suberate (DSS), 1-(*p*-bromoacetmidobenzyl)-EDTA (FeBABE), 4-maleimidobenzophenone (MBP), sulfosuccinimidyl 2-(7-azido-4-methylcoumarin-3-acetamido)-ethyl-1,3′-dithiopropionate (SAED), isotope-coded affinity tag (ICAT), sulfosuccinimidyl 2-[6-(biotinamido)-2-(*p*-azidobenzamido)-hexanoamido]-ethyl-1,3′-dithiopropionate (Sulfo-SBED), and 1-[6-(biotinamido)-2-(*p*-azidobenzamido)-hexanoamido]-2-(2′-pyridyldithio)ethane (SCA1).

monoperoxyphthalic acid (*6*), while chelated Ru(II) (*7*) or Pd(II) (*8*) can introduce zero-length cross-links by photolysis in the presence of persulfate. Genetically encoded His_6-tags have been used for protein-bound Ni(II) chelators, while bodipy and porphyrins have been used for nonprotein bound chelation of Ru(II) and Pd(II), respectively. Depending on the system, photo-cross-linking times can be less than 1 s, and yields tend to be very high. Cross-linked amino acids are commonly tyrosines. These cross-linking reagents can also be used for affinity labeling with biotin-tyramine (*9*, *10*), which is chemically similar to tyrosine. The mechanisms of cross-linking and the protein complexes investigated with these reagents have been described in two excellent reviews (*11*, *12*).

Site-Directed Cleavage Agents. Instead of producing covalent cross-links, site-directed cleavage agents can be used to cleave a target protein at the point of protein−protein interactions. Iron-EDTA complexes have been used to generate hydroxyl radicals via a Fenton reaction and cleave both nucleic acids (*13*) and proteins. 1-(*p*-Bromoacetmidobenzyl)-EDTA (FeBABE) (Figure 3) can be attached to protein cysteines or 2-iminothiolane-modified amino groups and activated with iron, sodium ascorbate, and hydrogen peroxide. First demonstrated by internally cleaving bovine serum albumin (*14*), this technique generates peptide fragments that are not chemically damaged at their termini and can be Edman-sequenced to identify the location of cleavage. This site-directed cleavage agent can cleave peptide bonds within a protein or on interacting proteins as well as phosphodiester bonds of polynucleotides (Figure 4).

FeBABE has been used to study protein−protein interactions in the *E. coli* RNA polymerase holoenzyme. The stationary phase σ factor (σ^s) was mutated such that unique cysteines were independently placed at nine locations. The FeBABE−σ^s conjugates were assembled into the $\alpha_2\beta\beta'$ RNA polymerase holoenzyme, and cleavage was observed on the β and β' subunits, but not on the α subunit (*15*). In this study, visualization of the individual RNA polymerase subunits was accomplished by probing a Western blot with antibodies to the N-termini of each of the subunits.

In an extension of this method, FeBABE was used to map interactions between *S. cerevisiae* TFIIB and RNA ploymerase II. Five mutants of TFIIB containing unique, alkylatable cysteines were labeled with FeBABE and incubated with yeast nuclear extracts containing RNA polymerase II subunits individually genetically flag-tagged. The location of cleavage was determined using flag-tagged size standards from in vitro transcription/translation reactions of truncated RNA polymerase II subunit genes as templates (*16*). The use of genetically encoded flag tags removed the requirement for production of antibodies against all of the potentially cleaved proteins. In principle, any type of genetically encoded affinity tag, such as His-tags, GST-tags, or peptide sequences that are biotinylated during expression (*17*), could provide both purification and visualization handles for any recombinant proteins without the need to produce antibodies to these proteins.

Visualization Techniques: Label Transfer Agents. Tracking changes by mobility shift on by SDS−PAGE with Coomassie or silver staining to identify interacting proteins becomes quickly intractable as the number of proteins in the reaction mixture increases. Protein−protein interactions found within large complexes, such as those found in DNA replication and RNA transcription complexes, often occur in the presence of up to 50 polypeptides. To study these interactions, researchers have developed novel reagents to monitor protein−protein interactions. These reagents incorporate isotope or element tags to allow identification by mass spectrometry, radiolabels or fluorophores to enable identification of interaction partners, or affinity tags to allow both purification and identification. One powerful application of these techniques is label transfer (Figure 5).

Label transfer requires that a single protein of interest (A in Figure 5) is first modified with the label transfer agent. Second, the multiprotein complex is assembled in the presence of the labeled protein and cross-links are formed, typically by photolysis of reactive groups such as benzophenones or aryl azides. The identification of the interacting protein or proteins (B in Figure 5) is accomplished by separation by SDS−PAGE followed by autoradiography or visualization of the affinity tag (for instance, probing a gel with streptavidin−horseradish peroxidase to identify biotinylated proteins). The resolution of these techniques can be significantly enhanced by coupling with molecular biology: engineering of unique cysteines allows the label to be incorporated site-

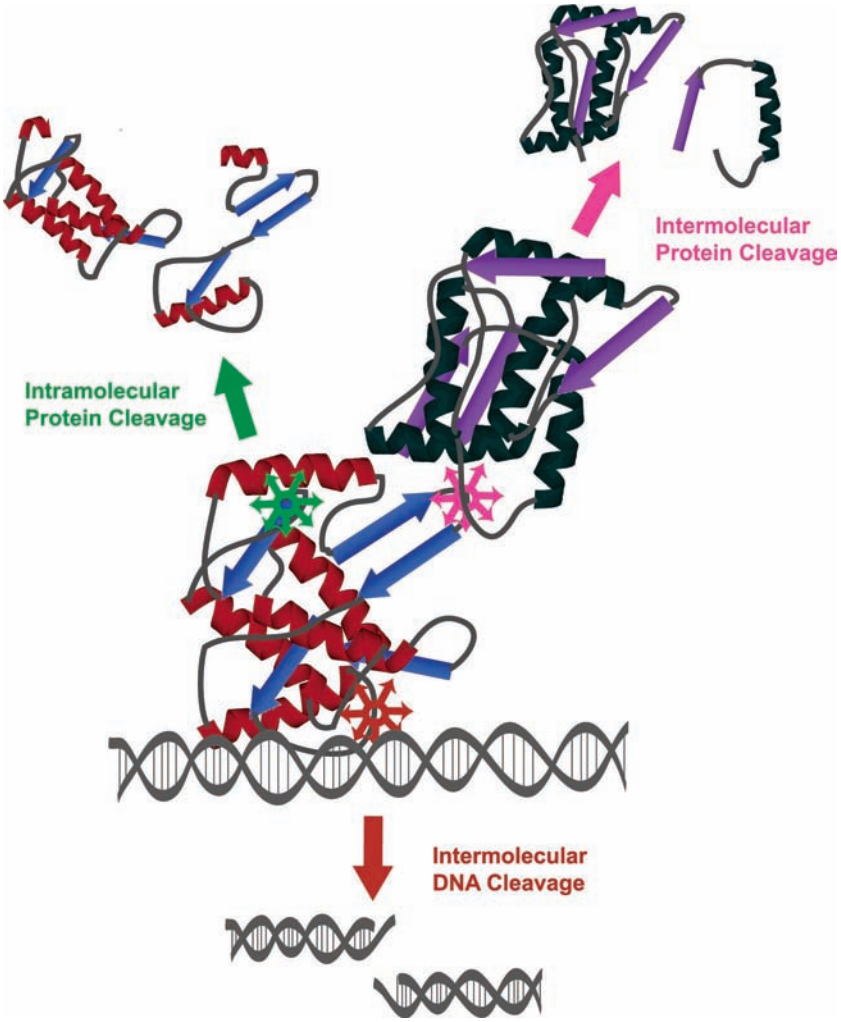

Figure 4. Site-directed cleavage agents such as FeBABE can be attached at site-specific cysteines or modified amines within a bait protein to detect intra- or intermolecular interactions. In the presence of ascorbate and peroxide, Fe^{3+} is reduced to Fe^{2+} and radicals cleave peptide bonds or phosphodiester bonds that are close in space. Detection of the resulting peptide or nucleic acid pattern can be analyzed by electrophoresis, Western blot, sequencing, or mass spectrometry and can provide information relating to the region of contact within the protein or the interacting complex.

specifically, and moving this unique cysteine around the protein enables interaction mapping.

Classically, label transfer used ^{125}I- (protein A-IgG) or ^{35}S- (gelatin-fibronectin) labeled reagents on lysine-reactive probes (*18*, *19*). Cleavage of the cross-linking group transfers the label to the interacting partner and was affected with DTT to cleave a disulfide or sodium dithionite to cleave an azo linkage. These early studies were enhanced when cysteine reactive probes were introduced. Chen and co-workers (*20*) incorporated ^{125}I-labeled *N*-(3-iodo-4-azidosalicyl)cysteine (IAC) into an engineered form of the catabolite gene activator protein (CAP). Following photo-cross-linking, label transfer, and DTT cleavage, the interaction of CAP, labeled in a region important for activation, was mapped to the carboxyl-terminal region of the α-subunit of RNA polymerase (RNAP) within the four-polypeptide RNAP. In the absence of the lac promoter DNA and/or CAP, no cross-linking or label transfer was observed, demonstrating the high specificity of the technique.

As an alternative to radioactive visualization, an affinity label-transfer reagent, sulfo-SBED (Figure 3) was developed at Pierce (*21*). This reagent transfers biotin from the labeled protein to the cross-linked interaction partner. Biotin is then used as a visualization reagent: Western blots of cross-linking mixtures following label transfer are probed with horseradish peroxidase to reveal cross-linked proteins. Sulfo-SBED is lysine reactive and has been used to study many protein−protein interactions. To increase the utility of this reagent, it has been converted to cysteine-reactive reagent by attaching a thiopyridyl group (SCA1, Figure 3) (*22*). This modified reagent has been used to track protein−protein interactions in the bacteriophage T4 DNA replication complex (four polypeptides in a ca. 350 kDa complex with DNA) (*22*) and a 1.8 MDa RNA transcription complex with at least 14 unique polypeptides (*23*). The benefit of these trifunctional reagents is the rapid identification of interacting proteins which only require photo-cross-linking and Western blotting with a universal reagent, without resorting to having to raise antibodies to every potential protein in the complex and running multiple Western blots with these custom reagents.

Sample Preparation: Proteomics and ICAT. The investigations described above involve labeling or making a mutant of a protein of interest before cross-linking. Studying protein−protein interactions in vivo generally does not allow for such modifications before crosslinking. Using these highly complex mixtures of proteins requires significant effort in sample preparation to identify interacting proteins. This can be accomplished after cross-linking by electrophoresis or chromatography, either with

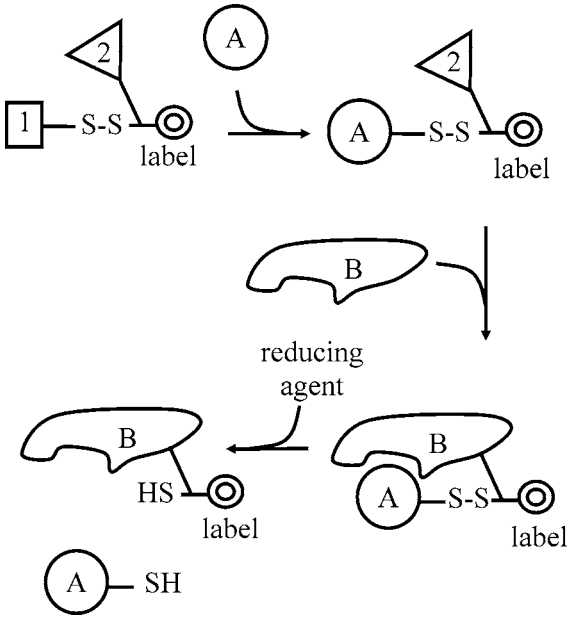

Figure 5. Label transfer cross-linking. Cross-linker consists of an amine or thiol reactive group (1), a photactivatable group (2), and a label (typically either a radioactive or biotin moiety). Protein A is first conjugated to the cross-linker at site 1. Protein B is then added and photo-cross-linked at site 2. Reduction of the disulfide bond with DTT results in the transfer of the label to protein B liberating free protein A. Separation of the protein mixture is performed by SDS−PAGE. Detection of the transferred label then occurs either by autoradiography or probing with streptavidin−horseradish peroxidase.

or without the benefit of affinity handles for enrichment and visualization.

The emergence of matrix-assisted laser desorption/ionization time-of-flight (MALDI-TOF) mass spectrometry within the past decade has greatly simplified the ability to identify proteins using an approach termed proteomics. Proteomics generally involves separating a mixture of proteins in a given system using techniques such as 2D gel electrophoresis followed by staining to detect protein bands. These bands are then excised, digested with a protease in-gel, and subjected to mass spectrometry. Each protein exhibits a specific digestion pattern with a given protease, which is manifested on MALDI as a specific mass fingerprint. This allows the identification of unknown proteins by comparing its digestion pattern to a database containing the proteolytic masses of known proteins. A variety of databases and algorithms have been constructed and developed to search for corresponding fragments within an organism's genome (*24*). The combination of these techniques with cross-linking has provided a powerful methodology to quickly determine interacting proteins in a complex.

This approach was exemplified by Bernhard et al. in the study of the transmembrane CD4 receptor (*25*). The authors used the homobifunctional lysine-lysine cross-linker DSP (Figure 3) to cross-link the proteins at the cell surface. Study of cell surface proteins and their associations with other proteins has traditionally been very difficult. In vitro analyses usually require removal of the protein from the membrane by proteolyitc cleavage, detergent-mediated release, or removal of the transmembrane domain by mutagenesis, all of which may alter its structure and function. However, the utilization of this cross-linker was beneficial because it allowed the protein to be studied in an in vivo setting, and the abundance of lysines on proteins in general allows for the maximal amount of cross-links between proteins in the complex. DSP also contains a disulfide linkage enabling cleavage of the linker if desired. The cross-linked proteins were released from the cell membrane and immunopreciptated using an antibody against the CD4 receptor to isolate only the cross-linked complex of interest. The cross-linker was then cleaved with a reducing agent to release the covalently linked complex, and the proteins were separated by SDS−PAGE. Individual bands were excised and digested, and the proteins were identified using MALDI MS. The authors were able to identify interacting proteins, including a trasferrin receptor, and a protein phosphatase, which provided valuable information about the function of the protein.

A similar technique was employed by Meunier and coworkers (*26*) in the study of chaperone proteins within the ER of mammalian cells. This group also used DSP to cross-link the proteins and followed with isolation by affinity purification, separation by 2D gel electrophoresis, and identification with MS. The interaction of an immunoglobulin with a chaperone complex was probed. These studies recognized a novel organization of chaperone proteins in a preformed complex and gave insight into its interaction with unfolded proteins. Because of the ability of DSP to cross the cell surface and permeate cells, these experiments were conducted in intact cells, further delineating the importance of this technique in studying in vivo systems.

Proteomics and mass spectrometry also benefit from enrichment and visualization tools. The first tools designed for these purposes include isotope-coded affinity tags (ICAT) (Figure 3) (*27*), which were designed to modify proteins with noncleavable biotin groups containing isotopic labels. Biotin allows enrichment of the sample before analysis, and the use of multiple isotope labels allows different states of the biological system to be encoded with each label. Mass spectrometry enables rapid identification of labeled proteins from their unique masses. Extensions of this method include element-encoded affinity tags (ECAT) (*28*) and visible isotope-coded affinity tags (VICAT) (*29*). ECAT reagents combine the element tag and affinity handle into a single DOTA functional group (anti-DOTA antibodies can be used for sample enrichment), while VICAT incorporates a visual chromophore for tracking during chromatography.

To extend these techniques for the investigation of protein−protein interactions, Trester-Zedlitz and coworkers (*30*) combined label transfer and ICAT in a modular system. Label-transfer reagents were built such that spacer lengths, chemical reactivities, affinity handles, cleavage sites, and isotope tags were varied so that they could be optimized to the multiprotein complex to be studied. The authors point out that a general method of interaction identification is probably not achievable due to the diversity of protein structure and reactive groups for label attachment. Building a modular toolbox will extend these techniques to a much greater number of proteins.

MAPPING SPECIFIC PROTEIN−PROTEIN CONTACT POINTS

Once two proteins have been identified as interacting partners by cross-linking, the specific site of interaction can be determined through mass spectrometry. MS analysis can be simplified exponentially if the digested cross-linked peptide can be isolated and purified first. Incorporation of either fluorescent probes or affinity handles into traditional cross-linkers aid tremendously in the isolation of the suitable adducts. Once the peptide of interest is isolated, analysis by a variety of MS

techniques reduce the old saying of "finding a needle in a haystack" to just finding the hay. An important caveat to this approach is that significant amounts of cross-linked products are needed for MS analysis. Therefore, efficient cross-linking and/or enrichment of a cross-linked species are necessary for successful identification. Various techniques including cross-linking conditions, fluorescent cross-linkers, affinity labels, and the ever increasing sensitivity of mass spectrometers all help to overcome this limitation.

Bromobimanes are the most widely used fluorescent cross-linkers. They are thiol−thiol cross-linkers and have the advantage that they only fluoresce upon conjugation. Therefore, the reaction progress can be monitored directly, simplifying analysis. They are also extremely stable in solution and have high thiol selectivity (*31*). Dibromobimane has been used successfully to cross-link and identify intramolecular thiols in myosin (*32*), lactose permease (*33*), and ATPase (*34*). A cleavable, fluorescent, photoactive cross-linking agent, sulfosuccinimidyl-2-(7-azido-4-methylcoumarin-3-acetamido)-ethyl-1,3′-dithiopropionate (SAED, Figure 3) has also been used to identify specific protein cross-links (*35*, *36*). The cross-linker is initially attached to amino groups of the protein of interest, then photo-cross-linked via an azide to residues on an interacting protein. The complex is then reduced, cleaving the disulfide within the cross-linker and transferring the fluorescent group to the interacting protein in a label transfer reaction (Figure 4). Protease digestion will then liberate a peptide with the fluorescent group identifying the interacting site. Other fluorescent dyes can be incorporated into trifunctional cross-linkers as the third arm to provide a tracer for peptide isolation. After digestion with trypsin or other proteases, these fluorescent protein fragments can be separated chromatographically or by SDS−PAGE and specifically analyzed by MS.

Another method of identification of cross-linked products is the use of affinity handles for enrichment of cross-linked products. The most common affinity handle is biotin, which can be specifically isolated using an affinity column composed of monomeric avidin or streptavidin beads. The previously described biotin cross-linkers, typically used in a label transfer reaction for visualization (*21*, *22*), can be used in addition to other trifunctional reagents (*30*, *37*) as affinity purification tools. After cross-linking two proteins, the biotin moiety is transferred to the cross-linked interacting protein with addition of a reducing agent. After protease digestion, isolation of a cross-linked fragment occurs by passing the entire protease digestion over an avidin affinity column. After washing, the cross-linked peptide with the biotin moiety is eluted with free biotin and isolated for MS analysis.

Upon isolation and purification of the cross-linked fragment, the mass of the individual peptide can be easily identified by MS through a single peak (*38*). Then the composition of the cross-linked peptide can be determined by comparison with the known sequence of the two interacting proteins. Advances in mass spectrometry have led to new methods of analysis including tandem mass spectrometry (*39*, *40*). This technique combines two rounds of MS analysis to identify the specific composition of a component. The first round separates the components based on mass, and the second round of MS breaks apart the individual peptides one amino acid at a time to yield a ladder of peaks identifying the sequence of a peptide. The mapping of specific protein−protein contact points by cross-linking along with individual structures of proteins and computer modeling will allow scientists to piece together protein complexes from a limited number of interaction points. As the sensitivity of MS detection and analysis increases, specific interactions in transient protein complexes should also become more clear.

USING CROSS-LINKING TO CREATE PROTEIN COMPLEX MODELS

Once interacting proteins in a complex are identified, with or without the determination of specific interaction points as described above, additional structural relationships and information about the architecture of the complex are necessary for a complete understanding of biological function. Sites of interaction or interfaces formed can be important in structure and function, and thus may be important in normal physiologic as well as pathologic processes, and generation of therapeutic agents. To reduce the bias and improve the resolution of the final model, a large number of cross-links should be formed across the interaction interface. Use of a homobifunctional lysine-lysine cross-linker allows the maximal amount of cross-linking due to the large number of lysines in proteins. Not only is there a greater chance that at least one of these lysines lie in or close to an interface, but the likelihood of multiple lysines at this site allows a map to be created of the interaction interface. In this way, unexpected or multiple modes of interaction may also be observed.

Young et al. (*41*) examined the intramolecular cross-links of fibroblast growth factor (FGF-2) which has a known three-dimensional structure. They were able to separate intramolecular cross-links from intermolecular cross-links by column chromatography or SDS−PAGE. Chromatographically separated fractions of the peptide digest of the intramolecular cross-links were then analyzed by MS. Cross-links were identified by analyzing the MS data with a custom software program, ASAP, and a model of the protein was generated. The data obtained were consistent with the crystal structure of FGF-2, with the interatomic distances experimentally determined by cross-linking close to the predicted distances. The structure of ubiquitin was also probed using a modified procedure in which the cross-linked protein was injected into an electrospray ionization (ESI)−Fourier transform (FT) mass spectrometer, and the cross-link positions were localized by multiple stages of fragmentation and mass spectrometry, instead of proteolysis followed by column chromatography and then MS (*42*). This approach, which yielded similar data, provided a simpler and quicker approach, which facilitates the application to high throughput experiments.

The structure of the yeast prohibin complex, a large multimeric assembly with chaperone-like activity was investigated without chromatographic separation techniques (*43*). The oligomer, which is composed of repeating heterodimers of a PHB1 and PHB2 subunits was cross-linked with DSP, digested with trypsin, and analyzed by either MALDI MS or ESI MS. The authors used a custom-made software tool, FindLink, to filter the data and identify cross-linked peptides. Since each protein contained multiple lysine residues close to the subunit interface, a total of nine heterodimeric cross-links were identified. This allowed a map of the subunit interface to be generated, and a model of the dimer was generated.

Similarly, a model of the signal recognition particle (FfH) and its receptor (FtsY) was built by chemical cross-linking with disuccinimydyl suberate (DSS, Figure 3) or bis(sulfosuccinimidyl) adipate (BSSA), proteolytic digestion, and tandem MS (*44*). In this study, they identified a total of nine separate intermolecular cross-linked

peptides. Using a novel model building approach which included geometric restraint optimization and macromolecular docking, they were able to identify a best fit for this complex based on the cross-linking data. After these findings, a partial crystal structure of the FfH−FtsY complex was determined and found to be in good agreement with the cross-linking model but lacked the M domain of FfH. Interestingly, four out of the nine cross-linked fragments provided information of the FfH M domain and provided new insights into its conformation relative to the rest of the complex which could not be determined in the crystal structure complex.

In a final example, the binding of calmodulin to mettilin, a polypeptide and principal component of honeybee venom, was also investigated without chromatographic separation techniques (*45*). The proteins were cross-linked with a number of different length amine−amine and amine−carboxylic acid cross-linkers, digested with trypsin, and analyzed by HPLC equipped with a high-resolution FT ion cyclotron resonance (ICR) mass spectrometer. The authors used distance constraints derived from the chemical cross-linking data in combination with computational methods three-dimensional structure models of the calmodulin−mettilin complex. From the numerous points of cross-linking obtained, an interface between the two proteins was mapped. The authors demonstrated for the first time that mettilin could bind to calmodulin in two different orientations (Figure 6).

The combination of cross-linking with mass spectrometric techniques used in proteomic identification has provided a powerful new tool to study the quaternary structure of multiprotein complexes. The development of tandem MS has allowed for more accurate identification and sequencing of peptides and the ability to detect femtomolar to nanomolar amounts of material, and increasingly sophisticated software tools may ultimately allow determination of cross-linking locations without the need for enrichment or separation techniques.

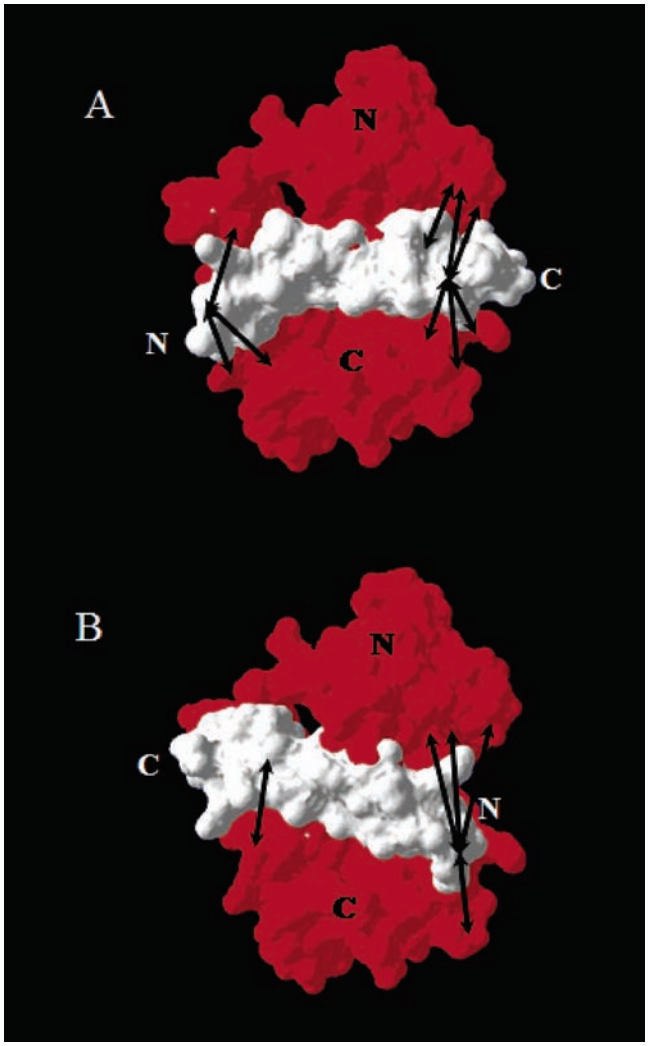

Figure 6. The complex between calmodulin (red) and mettilin (white) was analyzed using cross-linkers of different lengths. The arrows represent cross-links that were obtained and mapped. Calmodulin was found to bind mettilin in two different orientations, as shown in panels A and B. The amino- and carboxyl-terminal domains of calmodulin are labeled N and C, respectively. The amino and carboxyl termini of mettilin are similarly labeled.

FUTURE DIRECTIONS

Genetically Encoded Cross-Linking Agents. One of the challenges of site-specific modification of proteins with cross-linking agents is the necessity for a single alkylatable amino acid, typically cysteine. This can be accomplished by mutagenesis, but large proteins with numerous cysteines pose a significant challenge for constructing genes with multiple mutations. The alternative is to genetically incorporate noncanonical amino acids into proteins to provide the cross-linking group. Incorporation of noncanonical amino acids has been an accessible technology for decades, such as the incorporation of selenocysteine by adding this amino acid to the growth medium during protein expression. The native cysteine-tRNA synthetase can aminoacylate $tRNA_{cys}$ with selenocysteine under conditions when intracellular cysteine concentrations are low. The diversity of noncanonical amino acids that can be mischarged is low and unfortunately does not include cross-linking groups.

In the past few years, tRNA synthetases have been engineered to be able to aminoacylate tRNAs with an impressive number of noncanonical amino acids (*46*), including photo-cross-linking amino acids. Benzophenone is a very high efficiency photo-cross-linker and can be incorporated into proteins with the amino acid *p*-benzoyl-L-phenylalanine (pBpa). A library of *Methanococcus jannaschii* tyrosyl-tRNA synthetases was selected for the ability to aminoacylate a mutant tyrosine amber suppressor tRNA with pBpa. By engineering an amber codon into glutathione S-transferase and expressing in the presence on the mutant tRNA synthetase/tRNA pair and pBpa, site-specific incorporation of a benzophenone group was accomplished (*47*).

Alternatively, a mutant *E. coli* phenylalanine-tRNA synthetase has been engineered to allow incorporation of *p*-azidophenylalanine. Incorporation of this photo-cross-linking amino acid was accomplished using an *E. coli* phenylalanine auxotroph. Dihydrofolate reductase was successfully expressed with *p*-azidophenylalanine in place of phenylalanine (*48*). The disadvantage of this system is that all of the phenylalanines in the protein will be replaced, which is no more desirable than chemical modification of multiple cysteines. It has been shown, however, that the *E. coli* phenylalanine codon degeneracy can be broken with a mutant yeast phenylalanine tRNA specific for only one of the two phenylalanine codons (*49*). Site-specific incorporation of *p*-azidophenylalanine could be accomplished after making a mutant gene encoding for only one copy of the target codon, similar to the amber suppressing method above.

Expressing site-specific photo-cross-linking amino acids in proteins opens up the possibility of probing protein−

protein interactions in vivo without having to purify a target protein, incorporate the cross-linker, and reconstitute the protein complex. Expression of proteins with noncanonical amino acids in yeast (*50*) may also enable the opportunity of studying eukaryotic protein complexes using these technologies.

Identification of Variable Protein Complex Interactions. Rearrangements of protein complex composition are known to occur in response to extremes that alter the cellular environment, during normal processes throughout the cell cycle of an organism, or in the presence of pathologic disease. Already, microarray technology has detected these phenomena at the mRNA level, but this technology does not demonstrate what happens at the functional protein level. Assembly and disassembly of protein complexes occur in response to cellular signals. Formation of DNA replication factories, modulation of signal transduction complexes, transcriptional activation and repression, and translational protein/RNA complexes, as well as other multiprotein enzymatic machines, are all assembled and disassembled in response to cellular signaling. In vivo cross-linking in combination with antibody arrays designed for a specific biological area of interest coupled with mass spectrometry will provide a way to monitor changes in protein−protein interactions in response to certain cellular signals.

The ability to detect complex networks of interacting proteins has been limited in the past to focusing on single pairs of interacting proteins or a limited study of single branches of pathways. With the advances in the sensitivity, accuracy, and speed of mass spectrometers, there has been a trend toward automation of gathering and analyzing data. Mass spectrometers equipped with robotic machinery can prepare, process, and analyze a vast number of samples, enabling the development of high throughput approaches to proteomic analysis. These advances, combined with current experimental techniques including cell cycle synchrony, in vivo cross-linking, and immunoprecipitation arrays will allow for study of large complexes and protein networks.

The benefit of this combination of techniques is that it will provide for complete protein complex analysis in response to a variety of cellular signals. Protein complex assembly and disassembly can be followed over time. Most interestingly, promiscuous proteins involved in a number of protein complexes can be specifically examined to determine their appropriate complex association under various conditions or times. The results of these studies will produce a complex traffic map of protein interactions during normal cellular function as well as in response to changing cellular conditions. This map can then be exploited in the development of therapeutics designed to disrupt or alter the assembly or disassembly of specific protein complexes in response to specific cellular signals.

ACKNOWLEDGMENT

The authors are grateful to Stephen J. Benkovic at The Pennsylvania State University for seeding our interest and knowledge of this topic. M.A.T. acknowledges the Royal Society for generous funding. We thank Nicole Okeley for critically reading this manuscript.

LITERATURE CITED

(1) Szegedi, S. S., and Garrow, T. A. (2004) Oligomerization is required for betaine-homocysteine S-methyltransferase function. *Arch. Biochem. Biophys. 426*, 32−42.

(2) Bunn, M. W., and Ordal, G. W. (2003) Transmembrane organization of the Bacillus subtilis chemoreceptor McpB deduced by cysteine disulfide crosslinking. *J. Mol. Biol. 331*, 941−9.

(3) Guan, L., Murphy, F. D., and Kaback, H. R. (2002) Surface-exposed positions in the transmembrane helices of the lactose permease of Escherichia coli determined by intermolecular thiol cross-linking. *Proc. Natl. Acad. Sci. U.S.A. 99*, 3475−80.

(4) Ermolova, N., Guan, L., and Kaback, H. R. (2003) Intermolecular thiol cross-linking via loops in the lactose permease of Escherichia coli. *Proc. Natl. Acad. Sci. U.S.A. 100*, 10187−92.

(5) Giron-Monzon, L., Manelyte, L., Ahrends, R., Kirsch, D., Spengler, B., and Friedhoff, P. (2004) Mapping protein−protein interactions between MutL and MutH by cross-linking. *J. Biol. Chem. 279*, 49338−45.

(6) Brown, K. C., Yang, S. H., and Kodadek, T. (1995) Highly specific oxidative cross-linking of proteins mediated by a nickel-peptide complex. *Biochemistry 34*, 4733−9.

(7) Fancy, D. A., and Kodadek, T. (1999) Chemistry for the analysis of protein−protein interactions: rapid and efficient cross-linking triggered by long wavelength light. *Proc. Natl. Acad. Sci. U.S.A. 96*, 6020−4.

(8) Kim, K., Fancy, D. A., Carney, D., and Kodadek, T. (1999) Photoinduced Protein Cross-Linking Mediated by Palladium Porphyrins. *J. Am. Chem. Soc. 121*, 11896−11897.

(9) Amini, F., Denison, C., Lin, H. J., Kuo, L., and Kodadek, T. (2003) Using oxidative crosslinking and proximity labeling to quantitatively characterize protein−protein and protein-Peptide complexes. *Chem. Biol. 10*, 1115−27.

(10) Amini, F., Kodadek, T., and Brown, K. C. (2002) Protein affinity labeling mediated by genetically encoded peptide tags. *Angew. Chem., Int. Ed. 41*, 356−9.

(11) Fancy, D. A. (2000) Elucidation of protein−protein interactions using chemical cross-linking or label transfer techniques. *Curr. Opin. Chem. Biol. 4*, 28−33.

(12) Melcher, K. (2004) New chemical crosslinking methods for the identification of transient protein−protein interactions with multiprotein complexes. *Curr. Protein Pept. Sci. 5*, 287−96.

(13) Tullius, T. D., and Dombroski, B. A. (1986) Hydroxyl radical "footprinting": high-resolution information about DNA-protein contacts and application to lambda repressor and Cro protein. *Proc. Natl. Acad. Sci. U.S.A. 83*, 5469−73.

(14) Rana, T. M., and Meares, C. F. (1990) Specific cleavage of a protein by an attached iron chelate. *J. Am. Chem. Soc. 112*, 2457−2458.

(15) Colland, F., Fujita, N., Ishihama, A., and Kolb, A. (2002) The interaction between sigmaS, the stationary phase sigma factor, and the core enzyme of *Escherichia coli* RNA polymerase. *Genes Cells 7*, 233−47.

(16) Chen, H. T., and Hahn, S. (2003) Binding of TFIIB to RNA polymerase II: Mapping the binding site for the TFIIB zinc ribbon domain within the preinitiation complex. *Mol. Cell 12*, 437−47.

(17) Schatz, P. J. (1993) Use of peptide libraries to map the substrate specificity of a peptide-modifying enzyme: a 13 residue consensus peptide specifies biotinylation in Escherichia coli. *Biotechnology (NY) 11*, 1138−43.

(18) Schwartz, M. A., Das, O. P., and Hynes, R. O. (1982) A new radioactive cross-linking reagent for studying the interactions of proteins. *J. Biol. Chem. 257*, 2343−9.

(19) Denny, J. B., and Blobel, G. (1984) 125I-labeled crosslinking reagent that is hydrophilic, photoactivatable, and cleavable through an azo linkage. *Proc. Natl. Acad. Sci. U.S.A. 81*, 5286−90.

(20) Chen, Y., Ebright, Y. W., and Ebright, R. H. (1994) Identification of the target of a transcription activator protein by protein−protein photocrosslinking. *Science 265*, 90−2.

(21) Hermanson, G. (1996) *Bioconjugate Techniques*, Academic Press, San Diego.

(22) Alley, S. C., Ishmael, F. T., Jones, A. D., and Benkovic, S. J. (2000) Mapping Protein−Protein Interactions in the Bacteriophage T4 DNA Polymerase Holoenzyme Using a Novel Trifunctional Photo-cross-linking and Affinity Reagent. *J. Am. Chem. Soc. 122*, 6126−6127.

(23) Brown, C. E., Howe, L., Sousa, K., Alley, S. C., Carrozza, M. J., Tan, S., and Workman, J. L. (2001) Recruitment of HAT

complexes by direct activator interactions with the ATM-related Tra1 subunit. *Science 292*, 2333−7.
(24) Sadygov, R. G., Cociorva, D., and Yates, J. R. (2004) Large-scale database searching using tandem mass spectra: Looking up the answer in the back of the book. *Nature Methods 1*, 195−202.
(25) Bernhard, O. K., Sheil, M. M., and Cunningham, A. L. (2004) Lateral membrane protein associations of CD4 in lymphoid cells detected by cross-linking and mass spectrometry. *Biochemistry 43*, 256−64.
(26) Meunier, L., Usherwood, Y. K., Chung, K. T., and Hendershot, L. M. (2002) A subset of chaperones and folding enzymes form multiprotein complexes in endoplasmic reticulum to bind nascent proteins. *Mol. Biol. Cell 13*, 4456−69.
(27) Gygi, S. P., Rist, B., Gerber, S. A., Turecek, F., Gelb, M. H., and Aebersold, R. (1999) Quantitative analysis of complex protein mixtures using isotope-coded affinity tags. *Nat. Biotechnol. 17*, 994−9.
(28) Whetstone, P. A., Butlin, N. G., Corneillie, T. M., and Meares, C. F. (2004) Element-coded affinity tags for peptides and proteins. *Bioconjugate Chem. 15*, 3−6.
(29) Lu, Y., Bottari, P., Turecek, F., Aebersold, R., and Gelb, M. H. (2004) Absolute quantification of specific proteins in complex mixtures using visible isotope-coded affinity tags. *Anal.Chem 76*, 4104−11.
(30) Trester-Zedlitz, M., Kamada, K., Burley, S. K., Fenyo, D., Chait, B. T., and Muir, T. W. (2003) A modular cross-linking approach for exploring protein interactions. *J. Am. Chem. Soc. 125*, 2416−25.
(31) Kim, J. S., and Raines, R. T. (1995) Dibromobimane as a fluorescent crosslinking reagent. *Anal. Biochem 225*, 174−6.
(32) Konno, K., Ue, K., Khoroshev, M., Martinez, H., Ray, B., and Morales, M. F. (2000) Consequences of placing an intramolecular crosslink in myosin S1. *Proc. Natl. Acad. Sci. U.S.A. 97*, 1461−6.
(33) Wu, J., Voss, J., Hubbell, W. L., and Kaback, H. R. (1996) Site-directed spin labeling and chemical crosslinking demonstrate that helix V is close to helices VII and VIII in the lactose permease of Escherichia coli. *Proc. Natl. Acad. Sci. U.S.A. 93*, 10123−7.
(34) Bhattacharjee, H., and Rosen, B. P. (1996) Spatial proximity of Cys113, Cys172, and Cys422 in the metalloactivation domain of the ArsA ATPase. *J. Biol. Chem. 271*, 24465−70.
(35) Sharma, K. K., Kaur, H., and Kester, K. (1997) Functional elements in molecular chaperone alpha-crystallin: identification of binding sites in alpha B-Crystallin. *Biochem. Biophys. Res. Commun. 239*, 217−22.
(36) Wine, R. N., Dial, J. M., Tomer, K. B., and Borchers, C. H. (2002) Identification of components of protein complexes using a fluorescent photo-cross-linker and mass spectrometry. *Anal. Chem 74*, 1939−45.
(37) Alley, S. C., Trakselis, M. A., Mayer, M. U., Ishmael, F. T., Jones, A. D., and Benkovic, S. J. (2001) Building a replisome solution structure by elucidation of protein−protein interactions in the bacteriophage T4 DNA polymerase holoenzyme. *J. Biol. Chem. 276*, 39340−9.
(38) Hurst, G. B., Lankford, T. K., and Kennel, S. J. (2004) Mass spectrometric detection of affinity purified crosslinked peptides. *J. Am. Soc. Mass. Spectrom. 15*, 832−9.
(39) Heck, A. J., and Van Den Heuvel, R. H. (2004) Investigation of intact protein complexes by mass spectrometry. *Mass Spectrom. Rev. 23*, 368−89.
(40) Gorman, J. J., Wallis, T. P., and Pitt, J. J. (2002) Protein disulfide bond determination by mass spectrometry. *Mass Spectrom. Rev. 21*, 183−216.
(41) Young, M. M., Tang, N., Hempel, J. C., Oshiro, C. M., Taylor, E. W., Kuntz, I. D., Gibson, B. W., and Dollinger, G. (2000) High throughput protein fold identification by using experimental constraints derived from intramolecular cross-links and mass spectrometry. *Proc. Natl. Acad. Sci. U.S.A. 97*, 5802−6.
(42) Kruppa, G. H., Schoeniger, J., and Young, M. M. (2003) A top down approach to protein structural studies using chemical cross-linking and Fourier transform mass spectrometry. *Rapid. Commun. Mass Spectrom. 17*, 155−62.
(43) Back, J. W., Sanz, M. A., De Jong, L., De Koning, L. J., Nijtmans, L. G., De Koster, C. G., Grivell, L. A., Van Der Spek, H., and Muijsers, A. O. (2002) A structure for the yeast prohibitin complex: Structure prediction and evidence from chemical crosslinking and mass spectrometry. *Protein Sci. 11*, 2471−8.
(44) Chu, F., Shan, S. O., Moustakas, D. T., Alber, F., Egea, P. F., Stroud, R. M., Walter, P., and Burlingame, A. L. (2004) Unraveling the interface of signal recognition particle and its receptor by using chemical cross-linking and tandem mass spectrometry. *Proc. Natl. Acad. Sci. U.S.A. 101*, 16454−9.
(45) Schulz, D. M., Ihling, C., Clore, G. M., and Sinz, A. (2004) Mapping the topology and determination of a low-resolution three-dimensional structure of the calmodulin-melittin complex by chemical cross-linking and high-resolution FTI-CRMS: direct demonstration of multiple binding modes. *Biochemistry 43*, 4703−15.
(46) Link, A. J., Mock, M. L., and Tirrell, D. A. (2003) Non-canonical amino acids in protein engineering. *Curr. Opin. Biotechnol. 14*, 603−9.
(47) Chin, J. W., Martin, A. B., King, D. S., Wang, L., and Schultz, P. G. (2002) Addition of a photocrosslinking amino acid to the genetic code of Escherichiacoli. *Proc. Natl. Acad. Sci. U.S.A. 99*, 11020−4.
(48) Kirshenbaum, K., Carrico, I. S., and Tirrell, D. A. (2002) Biosynthesis of proteins incorporating a versatile set of phenylalanine analogues. *Chembiochem 3*, 235−7.
(49) Kwon, I., Kirshenbaum, K., and Tirrell, D. A. (2003) Breaking the degeneracy of the genetic code. *J. Am. Chem. Soc. 125*, 7512−3.
(50) Chin, J. W., Cropp, T. A., Anderson, J. C., Mukherji, M., Zhang, Z., and Schultz, P. G. (2003) An expanded eukaryotic genetic code. *Science 301*, 964−7.

BC050043A

ARTICLES

Development of a Rhenium-186-Labeled MAG3-Conjugated Bisphosphonate for the Palliation of Metastatic Bone Pain Based on the Concept of Bifunctional Radiopharmaceuticals

Kazuma Ogawa,[†,‡,§] Takahiro Mukai,[†,∥] Yasushi Arano,[⊥] Masahiro Ono,[†] Hirofumi Hanaoka,[†] Seigo Ishino,[†] Kazuyuki Hashimoto,[#] Hiroshi Nishimura,[§] and Hideo Saji*[,†]

Department of Patho-Functional Bioanalysis, Graduate School of Pharmaceutical Sciences, Kyoto University, Yoshida Shimoadachi-cho, Sakyo-ku, Kyoto 606-8501, Japan, Central Institute of Radioisotopes Science, Division of Tracer Kinetics, Advanced Science Research Center, Kanazawa University, 13-1 Takara-machi, Kanazawa 920-8640, Japan, Radioisotope Laboratory, Kyoto Prefectural University of Medicine, 465 Kajii-cho, Kamigyo-ku, Kyoto 602-0841, Japan, Department of Biomolecular Recognition Chemistry, Graduate School of Pharmaceutical Sciences, Kyushu University, 3-1-1 Maidashi, Higashi-ku, Fukuoka 812-8582, Japan, Department of Molecular Imaging and Radiotherapy, Graduate School of Pharmaceutical Sciences, Chiba University, 1-8-1 Inohana, Chuo-ku, Chiba 260-8675, Japan, and Japan Atomic Energy Research Institute, Tokai-mura, Ibaraki 319-1195, Japan. Received July 10, 2004; Revised Manuscript Received May 20, 2005

Rhenium-186-1-hydroxyethylidene-1,1-diphosphonate (^{186}Re-HEDP) has been used for the palliation of metastatic bone pain. Delayed blood clearance and high gastric uptake of radioactivity have been observed upon injection, due to the instability of ^{186}Re-HEDP in vivo. In this study, on the basis of the concept of bifunctional radiopharmaceuticals, we designed a stable ^{186}Re-mercaptoacetylglycylglycylglycine (MAG3) complex-conjugated bisphosphonate, [[[[(4-hydroxy-4,4-diphosphonobutyl)carbamoylmethyl]carbamoylmethyl]carbamoylmethyl]carbamoylmethanethiolate]oxorhenium(V) (^{186}Re-MAG3-HBP). As a precursor, [1-hydroxy-1-phosphono-4-[2-[2-[2-(2-tritylmercaptoacetylamino)acetylamino]acetylamino]acetylamino]butyl]phosphonic acid (Tr-MAG3-HBP) was synthesized by the conjugation of *N*-[(tritylmercapto)acetyl]glycylglycylglycine (Tr-MAG3) with the bisphosphonate analogue. After deprotection of the trityl group of Tr-MAG3-HBP, ^{186}Re-labeling was performed by reacting $^{186}ReO_4^-$ with $SnCl_2$ in citrate buffer. After purification by HPLC, ^{186}Re-MAG3-HBP showed a radiochemical purity of over 95%. To compare the stability of ^{186}Re-MAG3-HBP and ^{186}Re-HEDP, these ^{186}Re complexes were incubated in phosphate buffer. No measurable decomposition of ^{186}Re-MAG3-HBP occurred over a 24-h period, while only approximately 30% of ^{186}Re-HEDP remained intact 24 h postincubation. In biodistribution experiments, the radioactivity level of ^{186}Re-MAG3-HBP in bone was significantly higher than that of ^{186}Re-HEDP. Blood clearance of ^{186}Re-MAG3-HBP was faster than that of ^{186}Re-HEDP. In addition, the gastric accumulation of ^{186}Re-MAG3-HBP radioactivity was lower than that of ^{186}Re-HEDP. In conclusion, ^{186}Re-MAG3-HBP is expected to be a useful radiopharmaceutical for the palliation of metastatic bone pain.

INTRODUCTION

Malignant tumors, especially breast and prostate carcinomas, frequently metastasize to the bone (*1*). A prominent symptom caused by these metastases is pain, which has a significant impact on the patients' quality of life. Localized radiation therapy is an effective method for the treatment of bone pain (*2*); however, a common problem in patients with bone metastases is the development of multiple sites of metastasis, and so internal radiotherapy using specifically localized beta emitters is preferable. Recently, $^{89}SrCl_2$ has been used as a palliative agent for painful osseous metastases (*3*, *4*). However, ^{89}Sr is a pure beta emitter and has a relatively long half-life (50.5 d). These physical properties could be a disadvantage for clinical use.

Rhemium-186-1-hydroxyethylidene-1,1-diphosphonate (^{186}Re-HEDP) has also been proposed for the palliation of metastatic bone pain (*5*−*7*). ^{186}Re is a Group VII metal that decays with the emission of a beta particle with a maximal energy of 1.07 MeV. A 9% abundance gamma ray with energy of 137 keV is also produced in the decay process, enabling correlative imaging to be performed. Its relatively short physical half-life of 90.6 h accounts for high dose rates and allows for repeated treatments at short time intervals. Moreover, problems of radioactive waste handling and storage are

* To whom correspondence should be addressed. Telephone: 81-75-753-4556; fax: 81-75-753-4568; e-mail: hsaji@pharm.kyoto-u.ac.jp.
† Kyoto University.
‡ Kanazawa University.
§ Kyoto Prefectural University of Medicine.
∥ Kyushu University.
⊥ Chiba University.
Japan Atomic Energy Research Institute.

10.1021/bc040249w CCC: $30.25 © 2005 American Chemical Society
Published on Web 07/01/2005

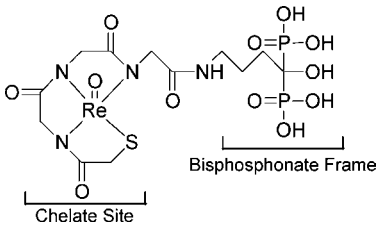

Figure 1. Chemical structure of Re-MAG3-HBP.

reduced. However, ^{186}Re-HEDP has showed delayed blood clearance and high gastric uptake. It has been reported that the unnecessary radiation in patients is due to the poor stability of the ^{186}Re complex in vivo leading to the generation of $^{186}ReO_4^-$ (*8*–*10*). Furthermore, a marked accumulation in bone is also a definitive requirement for a therapeutic drug in the palliation of metastatic bone pain. The accumulation of bisphosphonate analogues in the bone is responsible for the binding of hydroxyl groups of their phosphonate group to Ca^{2+} of hydroxyapatite (*11*). In the case of ^{186}Re-HEDP, since it is reasonable that some hydroxyl groups of HEDP bind to Ca^{2+} of hydroxyapatite and the rest coordinate rhenium, it is predictable that the coordination will reduce the inherent accumulation in bone of HEDP.

Thus, we planned the development of a novel ^{186}Re-labeled compound with a high affinity for bone and low accumulation of radioactivity in other organs. For this purpose, on the basis of the concept of bifunctional radiopharmaceuticals, we designed a stable ^{186}Re-mercaptoacetylglycylglycylglycine (MAG3) complex-conjugated bisphosphonate, [[[[(4-hydroxy-4,4-diphosphonobutyl)carbamoylmethyl]carbamoylmethyl]carbamoylmethyl]carbamoylmethanethiolate]oxorhenium(V) (^{186}Re-MAG3-HBP) (Figure 1). In this study, ^{186}Re-MAG3-HBP was synthesized and its stability and biodistribution were studied in comparison to ^{186}Re-HEDP.

MATERIALS AND METHODS

General. Proton nuclear magnetic resonance (^{1}H NMR) spectra were recorded on a Bruker AC-200 spectrometer (JEOL Ltd., Tokyo, Japan), and the chemical shifts were reported in ppm downfield from an internal tetramethylsilane standard. Fast atom bombardment mass spectra (FAB-MS) were obtained with a JMS−HX/HX 110 A (JEOL Ltd.). Ionspray mass spectra (IS-MS) were obtained with an API*III*E (Parkin-Elmer Sciex Instruments, Toronto, Canada). Electrospray ionization mass spectra (ESI-MS) were obtained with a LCMS-QP8000α (Shimadzu, Kyoto, Japan). ^{186}Re was supplied by the Japan Atomic Energy Research Institute (Tokai-mura, Japan) as perrhenate ($^{186}ReO_4^-$) (*12*). Cellulose acetate electrophoresis (CAE, Separax-SP; Joko Co. Ltd., Tokyo, Japan) was run in an electrostatic field of 0.8 mA/cm for 20 min in veronal buffer (I = 0.06, pH 8.6). TLC analyses were performed with silica plates (Merck Art 5553) using acetone as a developing solvent. Benzoyl-mercaptoacetylglycylglycylglycine (Bz-MAG3) was supplied by Daiich Radioisotopes Labs (Chiba, Japan). Other reagents were of reagent grade and used as received.

Synthesis of ^{186}Re-MAG3-HBP. ^{186}Re-MAG3-HBP (**10**) was synthesized according to the procedure outlined in Scheme 1.

Tritylmercaptoacetic Acid (3). Mercaptoacetic acid (8.3 g, 90 mmol) and trityl chloride (25.0 g, 90 mmol) were dissolved in 45 mL of dimethylformamide (DMF). After the reaction mixture had been stirred at room temperature for 48 h, the solvent was removed in vacuo. The residue was dissolved in 100 mL of chloroform, and then 6 N NaOH was gradually added to the solution. The precipitated white crystals were collected and washed with distilled water to obtain compound **3** (22.3 g, 74.3%). ^{1}H NMR ($CDCl_3$): δ 7.43−7.19 (overlapped m, 15H), 3.03 (s, 2H). FAB-MS calcd for $C_{21}H_{18}O_2S$ $(M - H)^-$: *m/z* 333. Found: 333.

***N*-[(Tritylmercapto)acetyl]glycylglycylglycine (Tr-MAG3) (5).** Compound **3** (10.0 g, 30 mmol) was dissolved in 150 mL of chloroform, and *N*-hydroxysuccinimide (NHS) (3.45 g, 30 mmol) was added to the solution. Dicyclohexylcarbodiimide (DCC) (7.40 g, 36 mmol) in 25 mL of chloroform was added dropwise to the reaction mixture at room temperature. The reaction solution was stirred at room temperature for 18 h. The solvent was removed in vacuo. The residue was suspended in ethyl acetate. After filtration, the filtrate was evaporated in vacuo, and the residue was washed with hexane to obtain compound **4** (3.64 g) as the crude product. Glycylglycylglycine (0.73 g, 3.87 mmol) was dissolved in 22 mL of distilled water, and the solution was adjusted to pH 8.8 with 1 N NaOH. Compound **4** (2.00 g) was dissolved in 20 mL of DMF and was added dropwise to the glycylglycylglycine aqueous solution. After 3 h of stirring at 40 °C, the solvent was removed in vacuo. The residue was suspended in 30 mL of dilute hydrochloric acid (pH 2−3), and the aqueous mixture was extracted with chloroform. The organic layer was dried over anhydrous $CaSO_4$, and the solvent was removed in vacuo. The residue was purified by chromatography on silica gel using chloroform−methanol−acetic acid (50:10:1) as the eluent to obtain compound **5** (501 mg, 21.3%) as white crystals. ^{1}H NMR ($CDCl_3$): δ 7.23−7.44 (overlapped m, 15H), 4.13 (s, 4H), 3.65 (s, 2H), 3.47 (s, 2H). FAB-MS calcd for $C_{27}H_{27}N_3O_5S$ $(M + H)^+$: *m/z* 506. Found: 506.

4-Amino-1-hydroxybutylidene-1,1-bisphosphonate (7). Compound **7** was synthesized according to the procedure of Kiecykowski (*13*). Briefly, phthalic anhydride (29.6 g, 0.2 mol) was reacted with 4-aminobutyric acid (20.6 g, 0.2 mol) in 50 mL of acetic acid at 120 °C for 2 h. The reaction solution was cooled, and 300 mL of distilled water was gradually added to the solution. The precipitated white crystals were collected and washed with distilled water to obtain 4-phthalimidobutyric acid (40.5 g, 86.9%). ^{1}H NMR ($CDCl_3$): δ 7.82−7.89 (overlapped m, 2H), 7.76−7.65 (overlapped m, 2H), 3.77 (t, 2H), 2.43 (t, 2H), 2.02 (quin, 2H). FAB-MS calcd for $C_{12}H_{11}NO_4$ $(M + H)^+$: *m/z* 234. Found: 234.

4-Phthalimidobutyric acid (11.7 g, 50 mmol) was reacted with thionyl chloride (7.37 g, 62 mmol) in 50 mL of toluene and 50 μL of DMF at 50 °C for 1 h. The excess thionyl chloride was removed by distillation. The volume of the reaction mixture was reduced to 25 mL by distillation under a house vacuum (100 mmHg) at 80 °C. An additional 50 mL of toluene was added, and the mixture was distilled. The clear, colorless solution was used in the next reaction without further purification. Trimethyl phosphate (6.50 g, 53 mmol) was added, and the reaction solution was stirred at room temperature for 18 h. The reaction solution was used in the next reaction without further purification. Dimethyl phosphite (5.80 g, 53 mmol) was added to the reaction solution. Triethylamine (5.00 g, 50 mmol) was then added dropwise at 20 °C. During the addition of triethylamine, there was a rapid crystallization. After stirring for an additional 1 h, the reaction mixture was allowed to stand at 4 °C for 1 h. The precipitated white crystals were collected and washed with toluene to obtain tetramethyl 4-phthalimido-1-hydroxybutylidene-1,1-bisphosphonate

Scheme 1. Synthesis of ^{186}Re-MAG3-HBP[a]

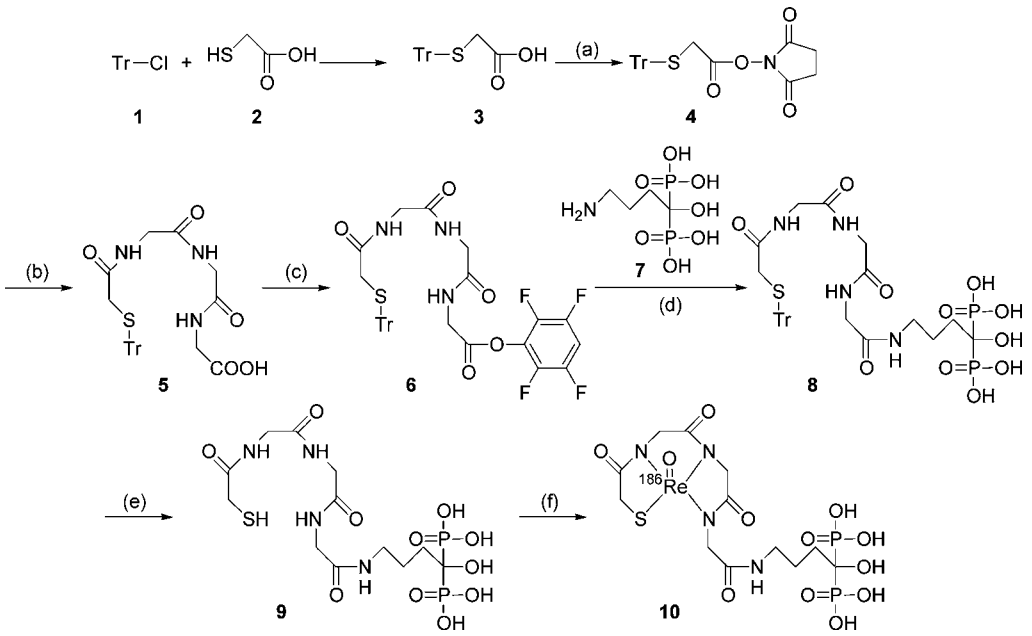

[a] Reagents: (a) NHS, DCC; (b) glycylglycylglycine; (c) TFP, DCC; (d) Et_3N; (e) TFA, triethylsilane; (f) $^{186}ReO_4^-$, $SnCl_2$/citrate.

(10.2 g, 46.9%). ^{1}H NMR ($CDCl_3$): δ 7.81−7.86 (overlapped m, 2H), 7.70−7.75 (overlapped m, 2H), 3.81−3.89 (overlapped m, 12H), 3.72 (t,2H), 2.00−2.14 (overlapped m, 4H). FAB-MS calcd for $C_{16}H_{23}NO_9P_2$ $(M + H)^+$: *m/z* 436. Found: 436.

Tetramethyl 4-phthalimido-1-hydroxybutyliden-1, 1-bisphosphonate (1.00 g, 2.3 mmol) was hydrolyzed by the reflux in 5 mL of 6 N HCl for 18 h. The resulting suspension was cooled to 0 °C, and the phthalic acid was removed by filtration. The filtrate was concentrated. Compound **7** was crystallized by the addition of 1.25 mL of water and 1.88 mL of ethanol. After the suspension was cooled at 4 °C for 2 h, compound **7** (430 mg, 75.1%) was obtained by filtration and washing with 95% ethanol as white crystals. ^{1}H NMR ($NaOD/D_2O$): δ 2.88 (m, 2H), 1.85 (m, 4H). FAB-MS calcd for $C_4H_{13}NO_7P_2$ $(M + Na)^+$: *m/z* 272. Found: 272.

[1-Hydroxy-1-phosphono-4-[2-[2-[2-(2-tritylmercaptoacetylamino)acetylamino]acetylamino]acetylamino]butyl]phosphonic Acid (8) (Tr-MAG3-HBP). Tr-MAG3 (**5**) (100 mg, 0.198 mmol) and tetrafluorophenol (TFP) (38.8 mg, 0.220 mmol) were dissolved in 14 mL of chloroform. DCC (45.8 mg, 0.220 mmol) in 6 mL of chloroform was added dropwise to the reaction mixture at room temperature. After 1 h of stirring at room temperature, the solvent was removed in vacuo. The residue was then suspended in an adequate volume of ethyl acetate, DCC urea was removed by filtration, and the filtrate was evaporated in vacuo to obtain crude compound **6**. Compound **6** was used in the next reaction without further purification. Compound **7** (57.0 mg, 0.229 mmol) was suspended in 3 mL of distilled water, and triethylamine (139 mg, 1.37 mmol) was added to the suspension. After a few seconds of stirring at room temperature, the suspension became clear. Compound **6** was dissolved in 4 mL of acetonitrile and then added to the reaction mixture. Triethylamine (23.1 mg, 0.229 mmol) was then added, and the reaction mixture was stirred for 3 h at room temperature. This mixture was purified by reversed phase (RP)-HPLC performed with a Cosmosil $5C_{18}$-AR 300 column (10 × 150 mm; Nacalai Tesque, Kyoto, Japan) at a flow rate of 4.7 mL/min with a gradient mobile phase of 25% acetonitrile in water with 0.1% trifluoroacetic acid (TFA) to 40% acetonitrile in water with 0.1% TFA for 30 min. Chromatograms were obtained by monitoring the UV adsorption at a wavelength of 254 nm. The fraction containing compound **8** was determined by mass spectrometry and collected. The solvent was removed by lyophilization to provide compound **8** (50.3 mg, 34.5%) as white crystals. ^{1}H NMR (DMSO-d_6): δ 8.22 (t,1H), 8.18 (t, 1H), 8.10 (t, 1H), 7.81 (t, 1H), 7.25−7.36 (overlapped m, 15H), 3.63−3.76 (overlapped m, 6H), 2.98 (q, 2H), 2.85 (s, 2H), 1.67−1.85 (overlapped m, 4H). IS-MS calcd for $C_{31}H_{38}N_4O_{11}P_2S$ $(M + H)^+$: *m/z* 737. Found: 737.

[[[[(4-Hydroxy-4,4-diphosphonobutyl)carbamoylmethyl]carbamoylmethyl]carbamoylmethyl]carbamoylmethanethiolate]oxorhenium(V) (10) (^{186}Re-MAG3-HBP). The trityl group of Tr-MAG3-HBP was deprotected just before radiolabeling. Tr-MAG3-HBP (0.1 mg) was dissolved in 190 μL of TFA and 10 μL of triethylsilane and gently shaken. After removal of the solvent under a stream of N_2, 0.1 mL of 0.2 M acetate buffer (pH 3.0) was added to the residue. Stannous chloride (0.3 mg) in 0.1 mL of 0.1 M citrate-buffer (pH 5.0), and 0.1 mL of $^{186}ReO_4^-$ solution, were added to the MAG3-HBP ligand solution. The reaction mixture was vigorously stirred and allowed to react at 90 °C for 1 h. After the reaction mixture had cooled to room temperature, ^{186}Re-MAG3-HBP (**10**) was purified by RP-HPLC performed with a Cosmosil $5C_{18}$-AR-300 column (4.6 × 150 mm) at a flow rate of 1 mL/min with a mixture of 0.2 M phosphate buffer (pH 6.0) and ethanol (90:10) containing 10 mM tetrabutylammoniumhydroxide.

Synthesis of Nonradioactive Re-MAG3-HBP. Nonradioactive Re-MAG3-HBP (**14**) was synthesized according to the procedure outlined in Scheme 2.

[Mercaptoacetylglycylglycylglycine]oxorhenium-(V) (12) (Re-MAG3). A procedure reported previously was employed with slight modification (*14*). Bz-MAG3 (**11**) (300 mg, 817 μmol) was dissolved in 50 mL of acetonitrile−water (6:4). Stannous chloride (616 mg, 2.73 mmol) in 50 mL of 0.1 M citrate buffer (pH 5.0) and $KReO_4$ (228 mg, 789 μmol) in 50 mL of water were added to the Bz-MAG3 solution. The reaction mixture was stirred and refluxed for 1 h. After the reaction mixture

Scheme 2. Synthesis of Re-MAG3-HBP[a]

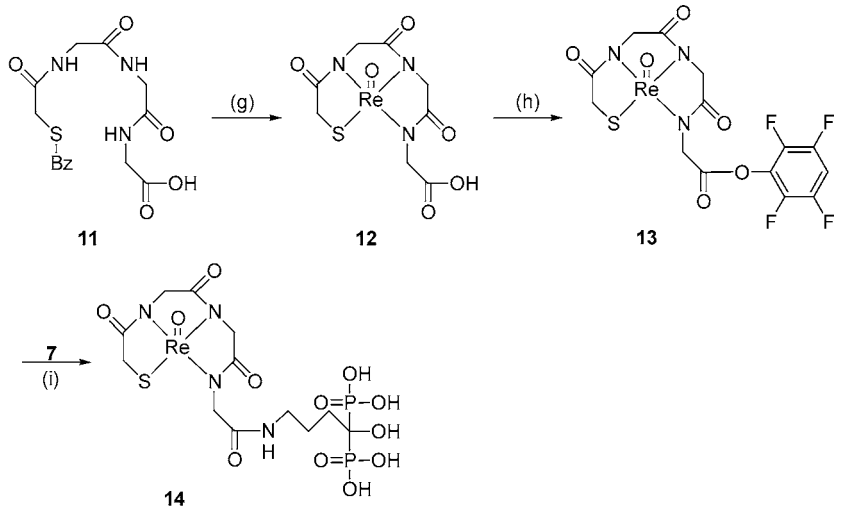

[a] Reagents: (g) $KReO_4$, $SnCl_2$/citrate; (h) TFP, DCC; (i) Et_3N.

had cooled to room temperature, Re-MAG3 was purified by RP-HPLC performed with a Cosmosil $5C_{18}$-AR300 column (20 × 150 mm) at a flow rate of 12 mL/min with a gradient mobile phase of 5% acetonitrile in water with 0.1% TFA to 30% acetonitrile in water with 0.1% TFA for 30 min. Chromatograms were obtained by monitoring the UV adsorption at a wavelength of 254 nm. The fraction containing compound **12** was determined by mass spectrometry and collected. The solvent was removed by lyophilization to provide Re-MAG3 (**12**) (70.8 mg, 18.7%) as purple crystals. ESI-MS calcd for $C_8H_9N_3O_6{}^{187}ReS$ $(M - H)^-$: *m/z* 461. Found: 461, $C_8H_9N_3O_6{}^{185}ReS$ $(M - H)^-$: *m/z* 459. Found: 459.

[[[[(4-Hydroxy-4,4-diphosphonobutyl)carbamoylmethyl]carbamoylmethyl]carbamoylmethyl]-carbamoylmethanethiolate]oxorhenium(V) (14) (Re-MAG3-HBP). To synthesize compound **13**, a procedure reported previously was employed with slight modifications (*15*, *16*). After Re-MAG3 (**12**) (10.0 mg, 21.6 μmol) was dissolved in 1 mL of acetate buffer (0.1 M, pH 6.0), TFP (4.15 mg, 25.0 μmol) in 100 μL of acetonitrile was added to the solution. HCl salt of 1-ethyl-3-(3-dimethylaminopropyl)carbodiimide (48.5 mg, 25.1 μmol) and triethylamine (35.0 μL, 25.2 μmol) was added to the reaction mixture. After the pH was adjusted to about 6.0 with 1 N HCl, the mixture was stirred for 30 min at room temperature. The reaction mixture was diluted with water to a volume of 8 mL and purified on two conditioned Sep-Pak C18 cartridges (Waters, Milford, MA). For washing, 20 mL of water for injection, 30 mL of 20% ethanol in 0.01 M phosphate buffer (pH 7.0), 10 mL of water and 0.5 mL of ether were used. The active ester (**13**) was eluted with 2.5 mL of acetonitrile. Compound **7** (5.38 mg, 21.6 μmol) in 1 mL of 0.1 M borate buffer (pH 9.5), and triethylamine (15.0 μL), were added to the active ester solution. After the pH was adjusted to 9.0 with 1 N NaOH, the reaction mixture was stirred for 3 h at room temperature. This reaction mixture was purified by RP-HPLC performed with a Hydrosphere C18 column (20 × 150 mm, YMC, Kyoto, Japan) at a flow rate of 14 mL/min with a gradient mobile phase of 20% acetonitrile in water with 1% formic acid to 50% acetonitrile in water with 1% formic acid for 30 min. Chromatograms were obtained by monitoring the UV adsorption at a wavelength of 254 nm. The fraction containing compound **14** was determined by mass spectrometry and collected. The solvent was removed by lyophilization to provide Re-MAG3-HBP (**14**) (1.86 mg, 12.4%) as light purple crystals. ESI-MS calcd for $C_{12}H_{20}N_4O_{12}P_2{}^{187}ReS$ $(M - H)^-$: *m/z* 692. Found: 692 $C_{12}H_{20}N_4O_{12}P_2{}^{185}ReS$ $(M - H)^-$: *m/z* 690. Found: 690.

Preparation of ^{186}Re-HEDP. ^{186}Re-HEDP was prepared according to a published procedure (*9*) and used after confirmation of its radiochemical purity by TLC ($R_f = 0$) and CAE (3.5 cm anode from the origin).

In Vitro Stability. To evaluate the stability of ^{186}Re complexes in buffered solution, ^{186}Re-labeled compounds were diluted with 0.1 M phosphate buffer (pH 7.0) saturated with 95% O_2/5% CO_2, and the solutions were incubated at 37 °C. After 1, 3, and 24 h of incubation, the samples were drawn and the radioactivity was analyzed by RP-HPLC or TLC.

Biodistribution. After HPLC purification of ^{186}Re-MAG3-HBP, solvent exchange was performed using Sep-pak C18 cartridges eluted with ethanol. The ethanol was evaporated with a stream of N_2 gas, and the residue was dissolved in saline.

Biodistribution experiments were performed by intravenously administering ^{186}Re-labeled compounds into 6-week-old male ddY mice (27−30 g). Groups of five mice were administered 100 μL of each ^{186}Re-labeled compound prior to sacrifice at 10 and 30 min, and 1, 3, 6, and 24 h postinjection. Tissues of interest were removed and weighed, and radioactivity counts were determined with an auto well gamma counter (ARC-2000; Aloka, Tokyo, Japan).

Statistical Evaluation. Biodistribution data were compared using Students' *t* test; $p = 0.05$ was defined as the limit of significance.

RESULTS

^{186}Re-MAG3-HBP (**10**) was prepared according to the method shown in Scheme 1. The precursor (Tr-MAG3-HBP (**8**)) of ^{186}Re-MAG3-HBP was synthesized by coupling the carboxyl group of Tr-MAG3 (**5**) with the amino group of a bisphosphonate derivative (**7**). The trityl group of Tr-MAG3-HBP was deprotected by treatment with TFA and triethylsilane just before radiolabeling, and ^{186}Re-MAG3-HBP (**10**) was prepared by complexation with ^{186}Re using citrate/$SnCl_2$ as a reducing system. The radiochemical yield of ^{186}Re-MAG3-HBP was 76%. After purification by RP-HPLC, ^{186}Re-MAG3-HBP showed a radiochemical purity of over 95%.

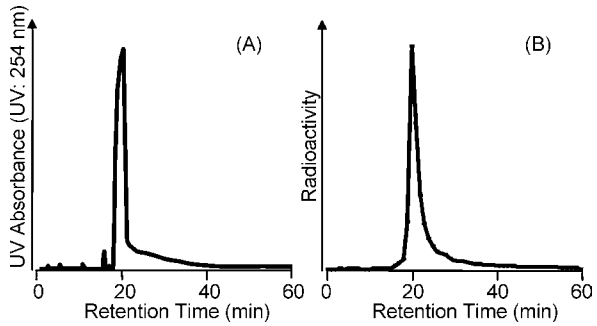

Figure 2. RP−HPLC chromatograms of (A) Re-MAG3-HBP and (B) ^{186}Re-MAG3-HBP after purification. Conditions: A flow rate of 1 mL/min with 10% ethanol in 200 mM phosphate buffer pH 6.0 containing 10 mM tetrabutylammoniumhydroxide.

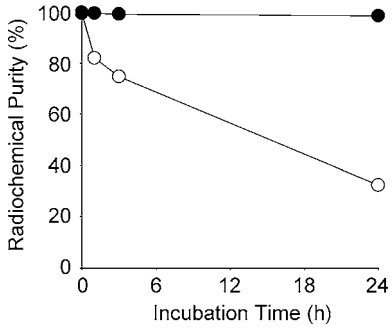

Figure 3. Stability of ^{186}Re-MAG3-HBP (closed circles) and ^{186}Re-HEDP (open circles) in buffered-solution.

Nonradioactive Re-MAG3-HBP (**14**) was synthesized by the coupling of Re-MAG3 (**12**) complexed previously with the bisphosphonate derivative (**7**), to exclude the possibility of complexation between rhenium or tin and the bisphosphonate structure (Scheme 2). Each RP-HPLC analysis of ^{186}Re-MAG3-HBP and Re-MAG3-HBP showed the same retention time (Figure 2). This indicates that the radiolabeled product proved identical to an authentic nonradioactive counterpart, and that ^{186}Re was chelated only with the MAG3 site.

Figure 3 shows the stability of ^{186}Re-MAG3-HBP and ^{186}Re-HEDP in buffered solution. After 24 h of incubation, about 95% of ^{186}Re-MAG3-HBP remained intact, whereas about 30% was intact in the case of ^{186}Re-HEDP.

The biodistributions of ^{186}Re-MAG3-HBP and ^{186}Re-HEDP in normal mice are presented in Tables 1 and 2, respectively. ^{186}Re-MAG3-HBP showed a rapid accumulation and long residence in the bone, and its uptake by the bone was significantly higher than that of ^{186}Re-HEDP. Furthermore, ^{186}Re-MAG3-HBP showed a faster clearance from the blood than did ^{186}Re-HEDP. Therefore, ^{186}Re-MAG3-HBP showed significantly higher bone:blood ratios of radioactivity than ^{186}Re-HEDP (Figure 4). Meanwhile, ^{186}Re-MAG3-HBP showed a significantly lower uptake by the stomach than ^{186}Re-HEDP.

DISCUSSION

The basic requirements of internal radiotherapeutic agents for the palliation of metastatic bone pain include excellent stability in vivo and marked accumulation in bone.

On the basis of the concept of bifunctional radiopharmaceuticals, we designed a ^{186}Re-labeled MAG3-conjugated bisphosphonate derivative (^{186}Re-MAG3-HBP, Figure 1). MAG3 was selected as the ^{186}Re-chelating group because it could form a stable, compact, and hydrophilic complex with ^{186}Re in high yield (*15*, *16*).

Table 1. Biodistribution of Radioactivity after Intravenous Administration of ^{186}Re-MAG3-HBP in Mice[a]

tissue	10 min[b]	30 min[b]	1 h[b]	3 h[b]	6 h[b]	24 h[b]
blood	3.05	0.68[d]	0.15[d]	0.05[d]	0.04[d]	0.01[d]
	(0.32)	(0.16)	(0.03)	(0.01)	(0.01)	(0.00)
liver	0.91[d]	0.40[d]	0.30[d]	0.22[d]	0.25[d]	0.12[d]
	(0.09)	(0.15)	(0.07)	(0.06)	(0.06)	(0.01)
kidney	5.40	4.35	2.42	1.30[d]	1.32	0.56
	(1.05)	(2.30)	(0.84)	(0.13)	(0.28)	(0.07)
intestine	0.70	0.44[d]	0.51[d]	0.59[d]	0.73	0.09
	(0.12)	(0.05)	(0.14)	(0.15)	(0.19)	(0.03)
spleen	0.74	0.26	0.14[d]	0.10[d]	0.10	0.08
	(0.23)	(0.09)	(0.07)	(0.02)	(0.05)	(0.02)
pancreas	0.77	0.23	0.12[d]	0.07[d]	0.08	0.05[d]
	(0.07)	(0.03)	(0.05)	(0.04)	(0.05)	(0.02)
lung	2.20	0.66	0.26[d]	0.21	0.20	0.08
	(0.51)	(0.18)	(0.06)	(0.06)	(0.03)	(0.03)
stomach[c]	0.46[d]	0.38[d]	0.25[d]	0.23[d]	0.21[d]	0.14
	(0.22)	(0.11)	(0.07)	(0.10)	(0.11)	(0.08)
femur	18.51[d]	27.19[d]	26.65[d]	28.78[d]	27.65[d]	24.51[d]
	(2.02)	(4.40)	(2.91)	(3.41)	(2.04)	(2.83)
muscle	0.84	0.23	0.45	0.09	0.06	0.18
	(0.55)	(0.14)	(0.37)	(0.06)	(0.04)	(0.16)

[a] Expressed as % injected dose per gram. Each value represents the mean (SD) for five animals at each interval. [b] Time after administration. [c] Expressed as % injected dose. [d] Significant difference.

Table 2. Biodistribution of Radioactivity after Intravenous Administration of ^{186}Re-HEDP in Mice[a]

tissue	10 min[b]	30 min[b]	1 h[b]	3 h[b]	6 h[b]	24 h[b]
blood	2.82	1.28	0.78	0.36	0.24	0.04
	(0.38)	(0.26)	(0.11)	(0.04)	(0.03)	(0.02)
liver	1.19	0.81	0.75	0.51	0.42	0.08
	(0.24)	(0.11)	(0.11)	(0.09)	(0.06)	(0.01)
kidney	6.38	6.78	5.40	1.60	1.27	0.36
	(1.50)	(5.49)	(3.79)	(0.24)	(0.04)	(0.13)
intestine	0.62	0.71	0.88	0.86	0.96	0.15
	(0.10)	(0.20)	(0.14)	(0.17)	(0.15)	(0.08)
spleen	0.70	0.31	0.25	0.15	0.09	0.06
	(0.15)	(0.05)	(0.05)	(0.02)	(0.01)	(0.04)
pancreas	1.02	0.28	0.21	0.13	0.07	0.02
	(0.38)	(0.04)	(0.02)	(0.03)	(0.02)	(0.02)
lung	1.90	0.72	0.60	0.27	0.19	0.06
	(0.36)	(0.16)	(0.19)	(0.04)	(0.03)	(0.02)
stomach[c]	0.98	1.31	1.70	1.38	0.70	0.39
	(0.10)	(0.35)	(0.37)	(0.15)	(0.19)	(0.42)
femur	12.71	14.67	17.47	13.60	14.87	11.78
	(2.05)	(1.82)	(2.82)	(2.26)	(1.29)	(3.67)
muscle	0.88	0.41	0.20	0.07	0.04	0.04
	(0.36)	(0.29)	(0.15)	(0.07)	(0.04)	(0.04)

[a] Expressed as % injected dose per gram. Each value represents the mean (SD) for five animals at each interval. [b] Time after administration. [c] Expressed as % injected dose.

The result of in vitro stability experiments indicates that ^{186}Re-MAG3-HBP is more stable than ^{186}Re-HEDP. This result was reflected in the biodistribution. Namely, since accumulation in the stomach is an index of the decomposition of a Re-complex in biodistribution studies (*17*, *18*), a low level of ^{186}Re-MAG3-HBP in the stomach indicates good stability in vivo. The blood clearance could be also influenced by this stability. When calculated from the results of the biodistribution experiments, the rate of blood clearance of ^{186}Re-MAG3-HBP and ^{186}Re-HEDP was 49.7 mL/h and 15.6 mL/h, respectively. ^{186}Re-HEDP complex gave rise to $^{186}ReO_4^-$ in vivo, and the clearance from blood of $^{186}ReO_4^-$ was slower than that of ^{186}Re-HEDP (*9*). It is suggested that the more rapid clearance from the blood of ^{186}Re-MAG3-HBP is responsible for its stability, when compared with ^{186}Re-HEDP. This rapid clearance could lead to a decrease in the level of unnecessary radiation.

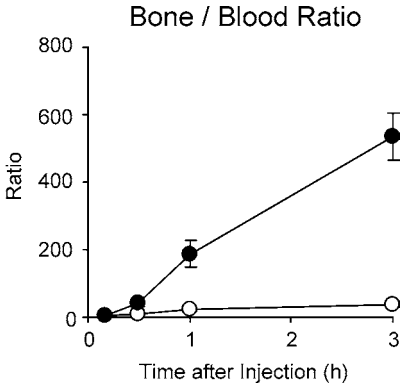

Figure 4. Bone blood ratios of radioactivity after injection of ^{186}Re-MAG3-HBP (closed circles) and ^{186}Re-HEDP (open circles) in mice.

The bone uptake of ^{186}Re-MAG3-HBP was compared with ^{186}Re-HEDP in mice. When expressed as %dose/g tissue × body weight in order to correct the difference in weight of the animals (*19*, *20*), the uptake of ^{186}Re-MAG3-HBP and ^{186}Re-HEDP in the femur 24 h after injection was 711% and 342%, respectively, while the uptake of ^{186}Re-MAG3-HBP was more than twice that of ^{186}Re-HEDP. Furthermore, bone uptake of ^{186}Re-MAG3-HBP was almost the same as that of ^{131}I-labeled arylalkylidenebisphosphonate reported recently (850%) (*19*). This ^{131}I-labeled bisphosphonate analogue was designed based on the same concept as ^{186}Re-MAG3-HBP, i.e., both compounds have a stable labeling site distinct from the bisphosphonate frame. Thus, the results obtained with the ^{131}I-labeled bisphosphonate support the usefulness of the drug design of ^{186}Re-MAG3-HBP based on bifunctional radiopharmaceuticals. In addition, $^{89}SrCl_2$ and ^{153}Sm-EDTMP were approved by the Food and Drug Administration for the treatment of painful osseous metastases, and the uptake value was 354% ($^{89}SrCl_2$, 24 h, mice) (*21*) and 580% (^{153}Sm-EDTMP, 24 h, rats) (*22*), respectively. Since the value of ^{186}Re-MAG3-HBP is higher than each of the values of $^{89}SrCl_2$ and ^{153}Sm-EDTMP, it is expected that ^{186}Re-MAG3-HBP will be of clinical use.

In conclusion, we developed a highly stable ^{186}Re-labeled bisphosphonate, ^{186}Re-MAG3-HBP. This agent showed a marked accumulation in bone and rapid clearance from other tissues. Thus, ^{186}Re-MAG3-HBP is expected to be a useful radiopharmaceutical for the palliation of metastatic bone pain.

ACKNOWLEDGMENT

This work was supported in part by Grants-in-Aid for Young Scientists (13770500 and 15790665) and Exploratory Research (13877381) from the Ministry of Education, Culture, Sports, Science and Technology of Japan.

LITERATURE CITED

(1) Yoneda, T., Sasaki, A., and Mundy, G. R. (1994) Osteolytic bone metastasis in breast cancer. *Breast Cancer Res. Treat. 32*, 73−84.

(2) Arcangeli, G., Giovinazzo, G., Saracino, B., D'Angelo, L., Giannarelli, D., and Micheli, A. (1998) Radiation therapy in the management of symptomatic bone metastases: the effect of total dose and histology on pain relief and response duration. *Int. J. Radiat. Oncol. Biol. Phys. 42*, 1119−1126.

(3) Silberstein, E. B., and Williams, C. (1985) Strontium-89 therapy for the pain of osseous metastases. *J. Nucl. Med. 26*, 345−348.

(4) Robinson, R. G., Preston, D. F., Schiefelbein, M., and Baxter, K. G. (1995) Strontium 89 therapy for the palliation of pain due to osseous metastases. *JAMA 274*, 420−424.

(5) Elder, R. C., Yuan, J., Helmer, B., Pipes, D., Deutsch, K., and Deutsch, E. (1997) Studies of the structure and composition of rhenium-1,1-hydroxyethylidenediphosphonate (HEDP) analogues of the radiotherapeutic agent ^{186}ReHEDP. *Inorg. Chem. 36*, 3055−3063.

(6) Kolesnikov-Gauthier, H., Carpentier, P., Depreux, P., Vennin, P., Caty, A., and Sulman, C. (2000) Evaluation of toxicity and efficacy of ^{186}Re-hydroxyethylidene diphosphonate in patients with painful bone metastases of prostate or breast cancer. *J. Nucl. Med. 41*, 1689−1694.

(7) Limouris, G. S., Shukla, S. K., Condi-Paphiti, A., Gennatas, C., Kouvaris, I., Vitoratos, N., Manetou, A., Dardoufas, C., Rigas, V., and Vlahos, L. (1997) Palliative therapy using rhenium-186-HEDP in painful breast osseous metastases. *Anticancer Res. 17*, 1767−1772.

(8) de Klerk, J. M., van Dijk, A., van het Schip, A. D., Zonnenberg, B. A., and van Rijk, P. P. (1992) Pharmacokinetics of rhenium-186 after administration of rhenium-186-HEDP to patients with bone metastases. *J. Nucl. Med. 33*, 646−651.

(9) Arano, Y., Ono, M., Wakisaka, K., Uezono, T., Akizawa, H., Motonari, Y., Makata, Y., Konishi, J., and Yokoyama, A. (1995) Synthesis and biodistribution studies of ^{186}Re complex of 1-hydroxyethylidene-1,1-diphosphonate for treatment of painful osseous metastases. *Radioisotopes 44*, 514−522.

(10) De Winter, F., Brans, B., Van De Wiele, C., and Dierckx, R. A. (1999) Visualization of the stomach on rhenium-186 HEDP imaging after therapy for metastasized prostate carcinoma. *Clin. Nucl. Med. 24*, 898−899.

(11) Rogers, M. J., Watts, D. J., and Russell, R. G. (1997) Overview of bisphosphonates. *Cancer 80*, 1652−1660.

(12) Kobayashi, K., Motoishi, S., Terunuma, K., Rauf, A. A., and Hashimoto, K. (2000) Production of $^{186/188}$Re and recovery of tungsten from spent ^{188}W/^{188}Re generator. *Radiochemistry 42*, 551−554.

(13) Kieczykowski, G. R. (1992) New process for preparing an antihypercalcemic agent. UK Patent GB 2248061A.

(14) Guhlke, S., Schaffland, A., Zamora, P. O., Sartor, J., Diekmann, D., Bender, H., Knapp, F. F., and Biersack, H. J. (1998) ^{188}Re- and ^{99m}Tc-MAG3 as prosthetic groups for labeling amines and peptides: approaches with pre- and postconjugate labeling. *Nucl. Med. Biol. 25*, 621−631.

(15) Visser, G. W., Gerretsen, M., Herscheid, J. D., Snow, G. B., and van Dongen, G. (1993) Labeling of monoclonal antibodies with rhenium-186 using the MAG3 chelate for radioimmunotherapy of cancer: a technical protocol. *J. Nucl. Med. 34*, 1953−1963.

(16) van Gog, F. B., Visser, G. W., Klok, R., van der Schors, R., Snow, G. B., and van Dongen, G. A. (1996) Monoclonal antibodies labeled with rhenium-186 using the MAG3 chelate: relationship between the number of chelated groups and biodistribution characteristics. *J. Nucl. Med. 37*, 352−362.

(17) Lin, W. Y., Hsieh, J. F., Tsai, S. C., Yen, T. C., Wang, S. J., and Knapp, F. F., Jr. (2000) A comprehensive study on the blockage of thyroid and gastric uptakes of ^{188}Re-perrhenate in endovascular irradiation using liquid-filled balloon to prevent restenosis. *Nucl. Med. Biol. 27*, 83−87.

(18) Deutsch, E., Libson, K., Vanderheyden, J. L., Ketring, A. R., and Maxon, H. R. (1986) The chemistry of rhenium and technetium as related to the use of isotopes of these elements in therapeutic and diagnostic nuclear medicine. *Nucl. Med. Biol. 13*, 465−477.

(19) Årstad, E., Hoff, P., Skattebøl, L., Skretting, A., and Breistøl, K. (2003) Studies on the synthesis and biological properties of noncarrier-added [^{125}I and ^{131}I]-labeled arylalkylidenebisphosphonates: potent bone-seekers for diagnosis and therapy of malignant osseous lesions. *J. Med. Chem. 46*, 3021−3032.

(20) Larsen, R. H., Murud, K. M., Akabani, G., Hoff, P., Bruland, O. S., and Zalutsky, M. R. (1999) ^{211}At- and

^{131}I-labeled bisphosphonates with high in vivo stability and bone accumulation. *J. Nucl. Med. 40*, 1197−1203.
(21) Henriksen, G., Fisher, D. R., Roeske, J. C., Bruland, O. S., and Larsen, R. H. (2003) Targeting of osseous sites with alpha-emitting ^{223}Ra: comparison with the beta-emitter ^{89}Sr in mice. *J. Nucl. Med. 44*, 252−259.
(22) Laznicek, M., Laznickova, A., Budsky, F., Prokop, J., and Kopicka, K. (1994) Comparison of biological characteristics of EDTMP complexes with ^{99m}Tc, ^{111}In and ^{153}Sm in rats. *Appl. Radiat. Isot. 45*, 949−953.

BC040249W

A New Platform for Oligonucleotide Delivery Utilizing the PEG Prodrug Approach

Hong Zhao,* Richard B. Greenwald, Prasanna Reddy, Jing Xia, and Ping Peng

Enzon Pharmaceuticals Inc., 20 Kingsbridge Road, Piscataway, New Jersey 08854. Received August 16, 2004; Revised Manuscript Received May 24, 2005

The oligonucleotide (oligo, ODN), Genasense (GS), an ODN currently waiting for FDA approval, was chosen as a model and modified with a 5′ or 3′ aminohexyl functionality (**1** and **4**, respectively) using solid-state synthesis. These amino derivatives were reacted with different releasable PEGs (rPEGs). The in vitro results of the PEG-modified oligos (Table 1) clearly show a substantial increase in rat plasma half-life and enhanced stability against a variety of nucleases, especially the predominant nuclease (PEII) in mammals, which is the main source of oligo degradation in cells. The advantage of using a PEG prodrug approach was further demonstrated by the pharmacokinetic (PK) results, which exhibited much greater C_{max}, plasma half-life, and area under the curve (AUC) for **3** compared to unmodified GS. A key step in the synthesis of ODN prodrug conjugates with a dye label was also accomplished successfully by employing dihydropyran derivatives of alcohols and acids as orthogonal protecting groups during the synthesis.

INTRODUCTION

Poly(ethylene glycol) (PEG) permanently bonded to oligodeoxynucleotides, generally as phosphate esters, has been synthesized by Bonora (*1*), Burchovich (*2*), Drioli (*3*) and several other groups to stabilize the rapidly metabolized oligo while enhancing, hopefully, cellular uptake (for reviews on this subject see Chirila (*4*) and Bonora (*5*)). PEG coupling to the 3′ and 5′ terminal positions showed more than a 10-fold increase in exonuclease stability, while maintaining in vitro activity (*6*). However anti-sense activity in vivo has yet to be demonstrated. This may in part be due to the inability of solid-phase methods to produce sufficient quantities of materials to test.

Other cases of oligos with 3′ or 5′ modifications including dyes, cholesterol (*7*), or other polymers (*8*) have shown enhanced antisense binding activities in vitro (*9*−*12*). Recently Agrawal et al. (*13*) have shown that conjugation of dyes, nucleotides, or oligomers through the 5′-position suppresses immunostimulatory activity of CpG containing ODNs, while conjugation at the 3′-position does not.

Construction of a pure, high molecular weight PEG prodrug by using the available NH_2 moiety obtained by introduction of an amino alkyl side chain at either the 3′ or 5′ terminal positions should provide a long-lived species and enhance oligo bioavailability using this long-circulating prodrug form. Kawaguchi (*14*) used a hexylamine linker at the 5′ terminus during the automated synthesis of a 15 base pair ODN and then permanently conjugated the basic NH_2 group to a low molecular weight (10 000 Da) branched PEG derivative, 2,4-(*O*-methoxypoly(ethylene glycol))-6-chloro-*S*-triazine. Unfortunately, purity was not defined, and a comparison of half-lives in human plasma in the presence of S1 nuclease demonstrated that the PEGylated mixture had marginally greater stability, while the free oligo with a phosphorothioate backbone showed the greatest stability. No PEGylation of the latter was reported.

* To whom correspondence should be addressed. Phone: (732) 980-4902. Fax: (732) 885-2950. E-mail: hong.zhao@enzon.com.

PEG conjugation has been shown to enhance cellular uptake in vitro (*15*), thus making a PEG prodrug strategy particularly appealing since the native drug can be generated after cellular accumulation. The use of high molecular weight PEG (>20 000 Da) can control circulating half-life in plasma, while the linkage can be designed to release native oligo into the cell. In fact, application of this concept using phosphorothioate-based ODNs conceivably can provide constructs with outstanding stability. Therefore, to evaluate the effect of ODN−PEG conjugation on circulating half-life, drug delivery, and cellular uptake, we initiated a program that was based on the use of an aminohexyl modification at the 3′- and 5′-postions of different oligos to facilitate the reaction sequences. Preparation for future cellular uptake investigations of these PEG conjugates was also addressed by synthesizing a heterobifunctional rPEG with a releasable FITC conjugated oligo on one terminus and a fluorescent dye (Texas Red) on the distal end.

CHEMISTRY

The oligo, Genasense (GS), an ODN currently waiting for FDA approval, was chosen as a model and modified with a 5′ or 3′ aminohexyl functionality (**1** and **4**) using a solid-state synthesis. This amino derivative was reacted with releasable PEG (rPEG) based on 1,6-benzyl elimination (BE) (*16*) as shown in Schemes 1−3, and this reaction resulted in 50−80% isolated yield of the desired PEG prodrugs, **3**, **5**, **7**, **9**, and **11**. Conjugation with the bicin aliphatic linker (**16**) (*17*) proceeded readily and also gave similar yields to the BE aromatic product, **17** (Scheme 5). Unreacted oligo is easily recovered from these conjugation reactions and can be recycled to increase the overall yield. This is in contrast to the liquid-phase synthesis of a PEGylated mercaptoalkyl ester where the final yield of substituted oligo was reported (*11*) to be only 3%. As was the case with other small molecules, by variation of the trigger different rates of release could be obtained (*16*). In addition to **1**, which contains a phosphorothioate backbone, another model 4-mer oligo

10.1021/bc049804k CCC: $30.25 © 2005 American Chemical Society
Published on Web 06/30/2005

Scheme 1

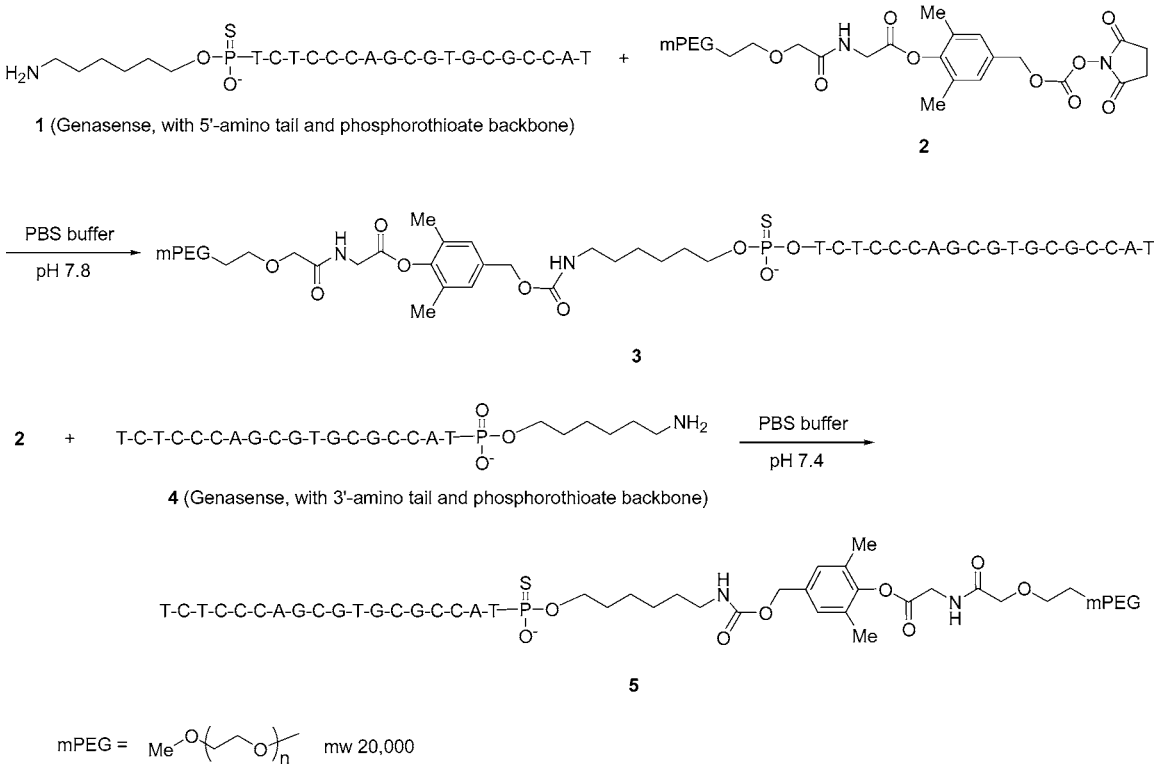

Scheme 2

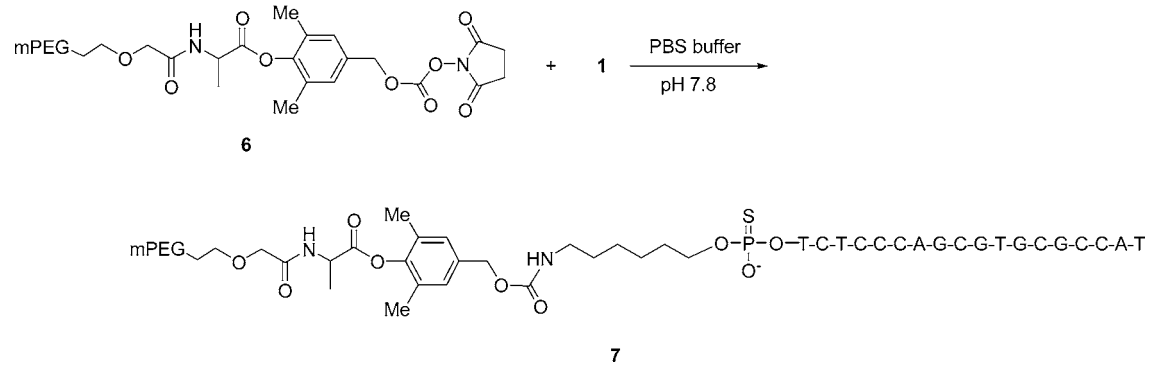

was prepared with a normal phosphate ester backbone, modified as the PEG prodrug (**15**, Scheme 4), and encouragingly, also demonstrated much greater in vitro stabilities (Table 1).

Cellular uptake studies of an rPEG−oligo conjugate should characterize the species produced using confocal microscopy analysis. To accomplish such a study, a heterobifunctional molecule would be required to provide two different types of substitutions at the termini of the PEG linker. Since the rPEG that was used in the first part of this investigation had a MW of 20 000 Da, it was decided to fix the variable of MW so that direct comparisons could be made. The synthesis of **35**, the first example of a high molecular weight (hMW) PEG heterobifunctional prodrug, was accomplished by the series of reactions shown in Schemes 6−8. Noteworthy in these sequences is the use of dihydropyran to form orthogonal protecting groups for the distal hydroxy and carboxy groups. The hMW α,ω-amino carboxy PEG derivative **24** was prepared by condensing the commercially available 3400 Da heterobifunctional derivatives **18** and **19** in the presence of DMAP to give heterobifunctional 6800 Da **20**, which was divided into two separate portions. The first segment was treated with TFA freeing the distal amino group and producing the amino acid salt **21**. The other functional unit was activated at the carboxy functionality by reaction with 2-mercaptothiazolidine (2-MT) to yield **22** in 90% yield. Reaction of **21** and **22** in the presence of DMAP resulted in the Boc-protected amino acid, **23**, which had a MW of 13 600Da. Compound **23** was deblocked with TFA and then reacted with **22**, which resulted in the hMW amino acid **24** (20 400 Da). It can be appreciated not only that further symmetrical condensations will double the MW each time but that the use of unequal MW portions will result in amino acids of intermediate molecular weights (MW). The introduction of the unsubstituted 1, 6-BE system was done as described earlier (*18*) for 2,6-dimethyl-4-hydroxybenzyl alcohol as shown in Scheme 7. Reaction of the carbonate *of p*-hydroxy benzaldehyde (**25**) with **24** formed the PEG aldehyde (**26**), which was reduced to the desired alcohol acid, **27**, with sodium borohydride.

Hussain and Truelove (*19*) have shown that the acyloxy derivatives of vinyl ethers (2-tetrahydropyranyl benzoate) undergo first-order hydrolysis with respect to the compound, independent of pH. However acetal derivatives of dihydropyran are only susceptible to acid-catalyzed hydrolysis (*20*). Since both types of dihydropyran deriva-

Scheme 3

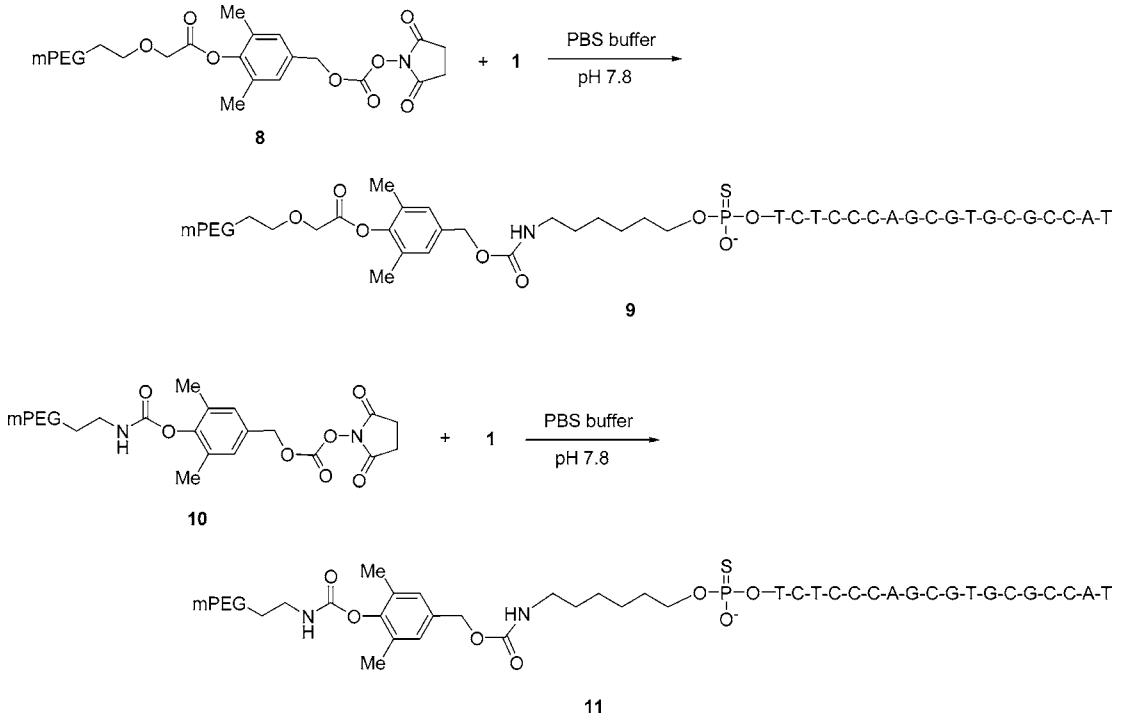

Scheme 4

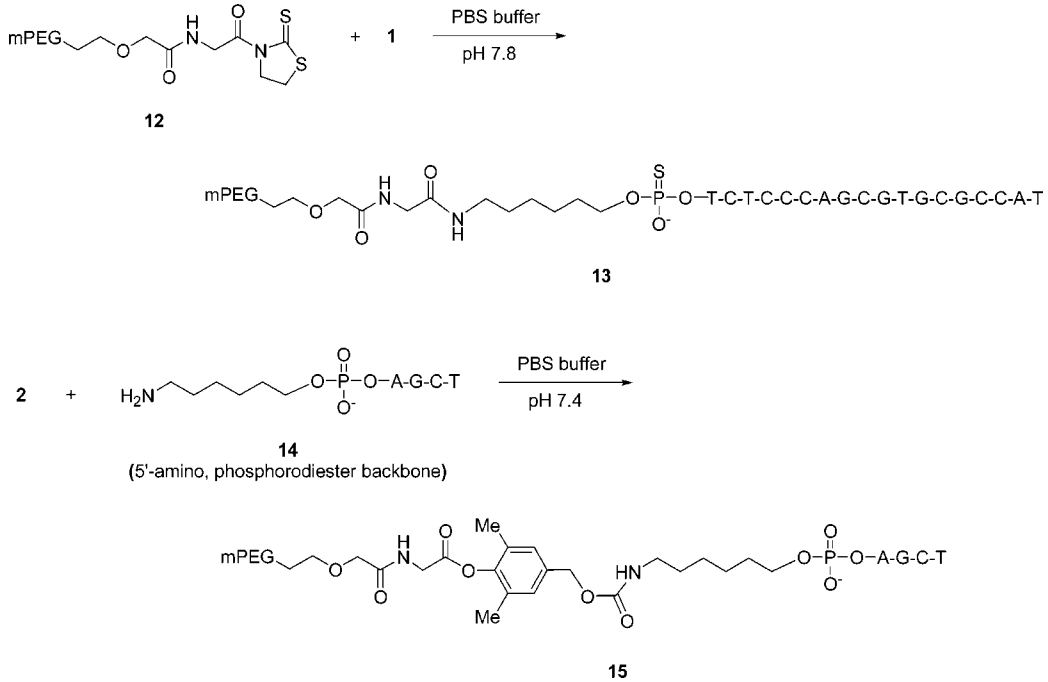

tives are formed under the same conditions, we reasoned that reaction of the heterobifunctional PEG alcohol acid (**27**) with dihydropyran should form both types of protecting groups simultaneously. With dry DCM and TsOH as catalyst, **27** provided the desired di-protected PEG species, **28**, in 95% yield. Dissolution of **28** in water at room temperature for 1 h removed the acyloxy ether but not the acetal moiety and provided an 88% yield of the desired monoprotected PEG acid, **29**. Conjugation of the free carboxyl group with Texas Red (**30**) in the presence of EDC resulted in the formation of the stable amide (**31**) in quantitative yield (Scheme 8). Finally, removal of the acetal from **31** was done with 50% acetic acid and gave the 1,6-benzyl alcohol−Texas Red derivative **32** in 89% yield. Activation of the OH group was done as described previously (*16*) by reaction with DSC to give **33**, followed by condensation with the aminohexyl derivative of GS with FITC labeling at the 3′ terminus resulting in the desired bifunctional substituted **35**. Inspection of **35** pinpoints the trigger (*16*) as an enzymatically labile phenolic carbamate (*21*, *22*). The ODN is attached distally as a stable aliphatic carbamate that releases only after the trigger hydrolyzes.

EXPERIMENTAL SECTION

General Procedures. All the conjugation reactions between PEG linkers and oligonucleotides were carried out in PBS buffer systems at various temperatures.

Scheme 5

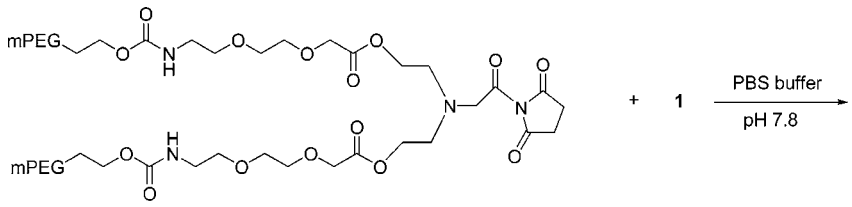

16 (PEG mw 12,000)

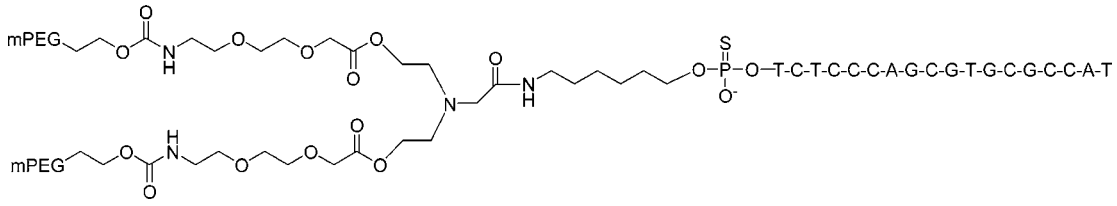

17

Table 1. In Vitro Properties of PEG−Oligo Conjugates[a]

compd	$t_{1/2}$ (buffer), h	$t_{1/2}$ (rat plasma), h	$t_{1/2}$ (PEI), h	$t_{1/2}$ (PEII), h	$t_{1/2}$ (nuclease P1), min
1	>48	1.3	1.5	>24	<1
3	>48	14.7	>24	>48	<5
5	>48	13.8	>24	>48	<5
7	>48	>24	>24	>48	<5
9	>48	6.5	>24	>48	<5
11	>48	4.1	5.6	>48	<5
13	>48	>48	>24	>48	<5
15	>48	2.3	0.25	>48	<5
17	>48	11	18.7	>24	<5

[a] PEI = phosphodiesterase I, 5′-exonuclease, kinetics done in pH 8.8 TEAA buffer at 37 °C; PEII = phosphodiesterase II, 3′-exonuclease, kinetics done in pH 6.5 TEAA buffer at 37 °C; nuclease P1 = endonuclease, kinetics done in pH 5.3 TEAA buffer at 37 °C. For all enzymes, 1 unit releases 1 μmol of oligonucleotide.

Extraction with organic solvents in general removed the unreacted oligonucleotides; further anion-exchange chromatography separated PEG−oligo conjugates from nonreacted excess PEG linkers to give pure products.

HPLC Methods. The reaction mixtures and the purity of intermediates and final products were monitored by a Beckman Coulter System Gold HPLC instrument employing a ZORBAX 300 SB C-8 reversed phase column (150 mm × 4.6 mm) or a Phenomenex Jupiter 300A C18 reversed phase column (150 mm × 4.6 mm) with a multiwavelength UV detector, using a gradient of 30−90% of acetonitrile in 0.5% trifluoroacetic acid (TFA) and 25−35% acetonitrile in 50 mM TEAA buffer with 4 mM TBACl at a flow rate of 1 mL/min. The anion-exchange chromatography was run on Bio-Cad 700E perfusion chromatography workstation from Applied Biosystems using either Poros 50HQ strong anion-exchange resin from Applied Biosystems or DEAE Sepharose fast-flow weak anion-exchange resin from Amersham Biosciences packed in an AP-Empty glass column from Waters. Desalting was achieved by using HiPrep 26/10 or PD-10 desalting columns from Amersham Biosciences.

ESI-MS Analysis. The composition and integrity of oligonucleotide (Genasense, **1**) in PEG−oligo conjugates were confirmed by electrospray ionization mass analysis using negative ion mode (Novatia LLC, Inc. Princeton, NJ) after base hydrolysis of each PEG−oligo conjugate. Releasable PEG−oligo conjugates were hydrolyzed using aqueous NH_3, lyophilized, and then sent for analysis. The samples containing released full-length oligonucleotide were flow-injected, and the obtained MS spectra were deconvoluted using ProMass software.

Compound 3. To a solution of compound **1** (25 mg, 3.9 μmol) in PBS buffer (5 mL, pH 7.8) was added **2** (600 mg, 39 μmol), and the mixture was stirred at room temperature for 5 h. The reaction solution was extracted with DCM (3 × 10 mL), the combined organic layers were dried ($MgSO_4$) and filtered, and the solvent was evaporated under reduced pressure. The residue was dissolved in double distilled water (5 mL) and loaded on a DEAE fast-flow weak anion-exchange column (27 mm × 250 mm, bed volume ≈ 50 mL), which was preequilibrated with 20 mM Tris-HCl buffer, pH 7.4. The unreacted PEG linkers were eluted with water (3−4 column volumes), and the product then eluted with a gradient of 0−100% 1 M NaCl in 20 mM Tris-HCl buffer, pH 7.4, in 10 min, followed by 100% 1 M NaCl in 20 mM Tris-HCl buffer, pH 7.4, for 10 min at a flow rate of 3 mL/min. The fractions containing pure product were pooled and desalted with an Amicon stirred cell concentrator using Ultracell membrane with a molecular weight cutoff of 5000, and the resulting solution was lyophilized to yield pure **3** (63 mg, 2.42 μmol, 60%). The analytical HPLC profile for purified compound **3** is shown in Figure 1; no free oligo impurity was detected. ESI-MS for released oligonucleotide: *m/z* 586.9 (42%) $[M - 10H]^{10-}$, 652.2 (100%) $[M - 9H]^{9-}$, 733.9 (88%) $[M - 8H]^{8-}$, 838.9 (68%) $[M - 7H]^{7-}$, 978.8 (46%) $[M - 6H]^{6-}$. M_{obsd} 5879.1; M_{calcd} 5879.8.

Compound 5. Compound **5** was made and purified in a similar way as **3** at a yield of 65%. Similar to **3**, analytical HPLC showed no impurity. ESI-MS for released oligonucleotide: *m/z* 586.9 (16%) $[M - 10H]^{10-}$, 652.2 (100%) $[M - 9H]^{9-}$, 733.9 (90%) $[M - 8H]^{8-}$, 838.8 (40%) $[M - 7H]^{7-}$, 978.8 (22%) $[M - 6H]^{6-}$. M_{obsd} 5879.0; M_{calcd} 5879.8.

Compound 7. Compound **7** was made and purified in a similar way as **3** at a yield of 80%. Analytical HPLC showed no impurity. ESI-MS for released oligonucleotide: *m/z* 586.9 (54%) $[M - 10H]^{10-}$, 652.3 (100%) $[M - 9H]^{9-}$, 733.9 (59%) $[M - 8H]^{8-}$, 838.9 (30%) $[M - 7H]^{7-}$, 978.8 (27%) $[M - 6H]^{6-}$. M_{obsd} 5879.5; M_{calcd} 5879.8.

Compound 9. Compound 9 was made and purified in a similar way as **3** at a yield of 62%. Analytical HPLC showed no impurity. ESI-MS for released oligonucleotide: *m/z* 587.0 (39%) $[M - 10H]^{10-}$, 652.3 (100%) $[M - 9H]^{9-}$, 733.9 (76%) $[M - 8H]^{8-}$, 838.9 (61%) $[M - 7H]^{7-}$, 978.9 (41%) $[M - 6H]^{6-}$. M_{obsd} 5879.6; M_{calcd} 5879.8.

Scheme 6

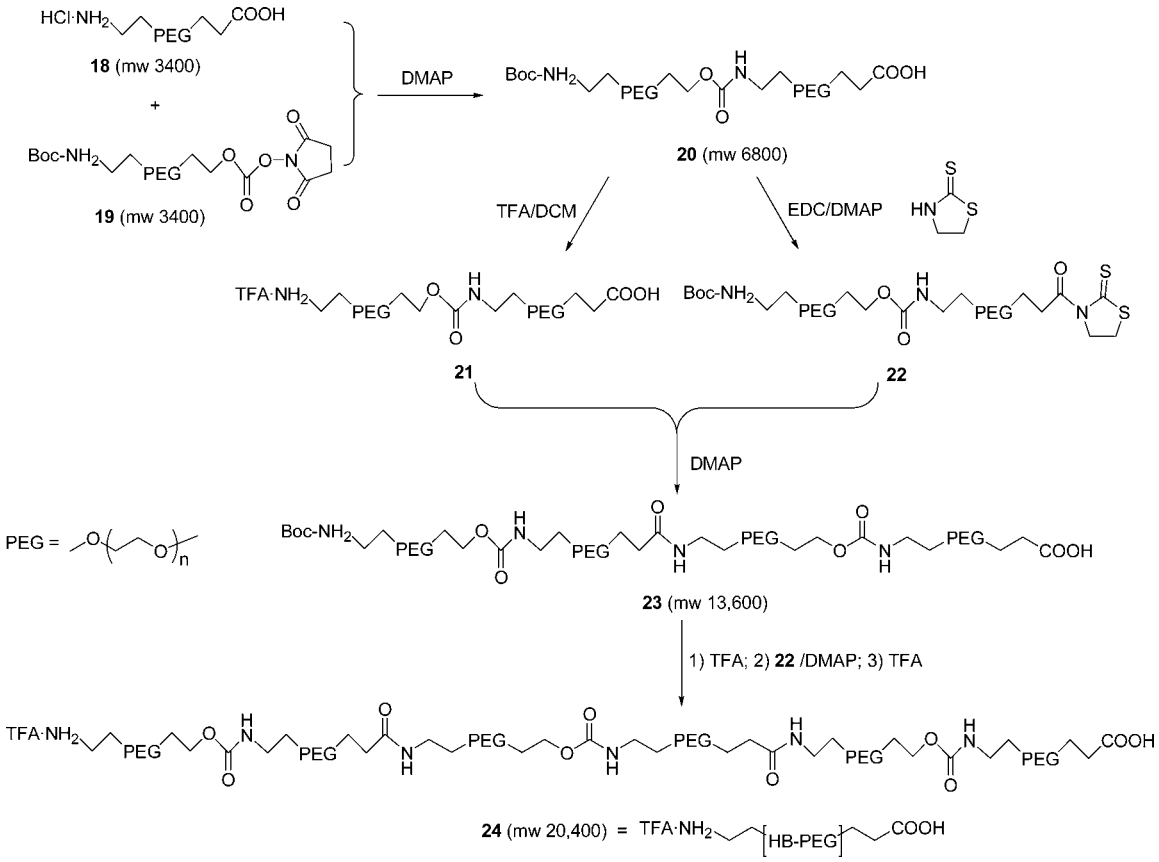

Scheme 7

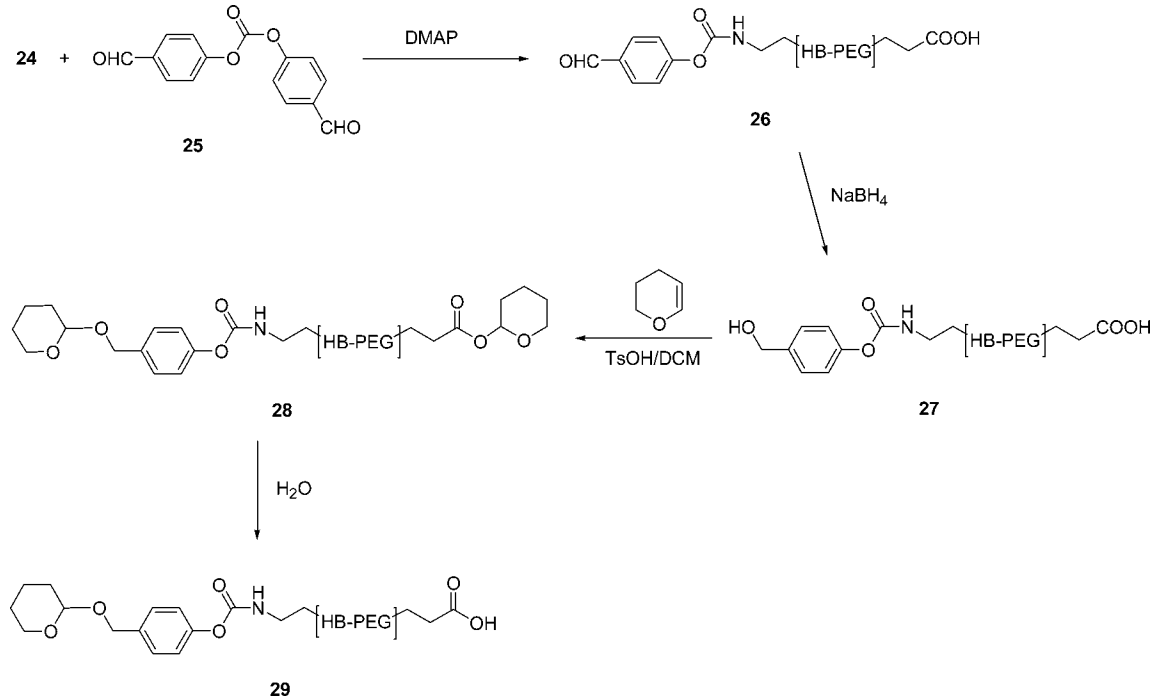

Compound 11. Compound **11** was made and purified in a similar way as **3** at a yield of 50%. Analytical HPLC showed no impurity. ESI-MS for released oligonucleotide: *m/z* 586.9 (60%) $[M - 10H]^{10-}$, 652.3 (100%) $[M - 9H]^{9-}$, 733.9 (58%) $[M - 8H]^{8-}$, 838.9 (34%) $[M - 7H]^{7-}$, 978.8 (26%) $[M - 6H]^{6-}$. M_{obsd} 5879.5, M_{calcd} 5879.8.

Compound 13. Compound **13** was made and purified in a similar way as **3** at a yield of 55%. Analytical HPLC showed no impurity. Hydrolysis study could not release free oligo due to the nature of permanent bonding in this compound.

Compound 15. Compound **15** was made and purified in a similar way as **3** at a yield of 50%. Analytical HPLC showed no impurity.

Compound 17. Compound **17** was made and purified in a similar way as **3** at a yield of 50%. Analytical HPLC

Scheme 8

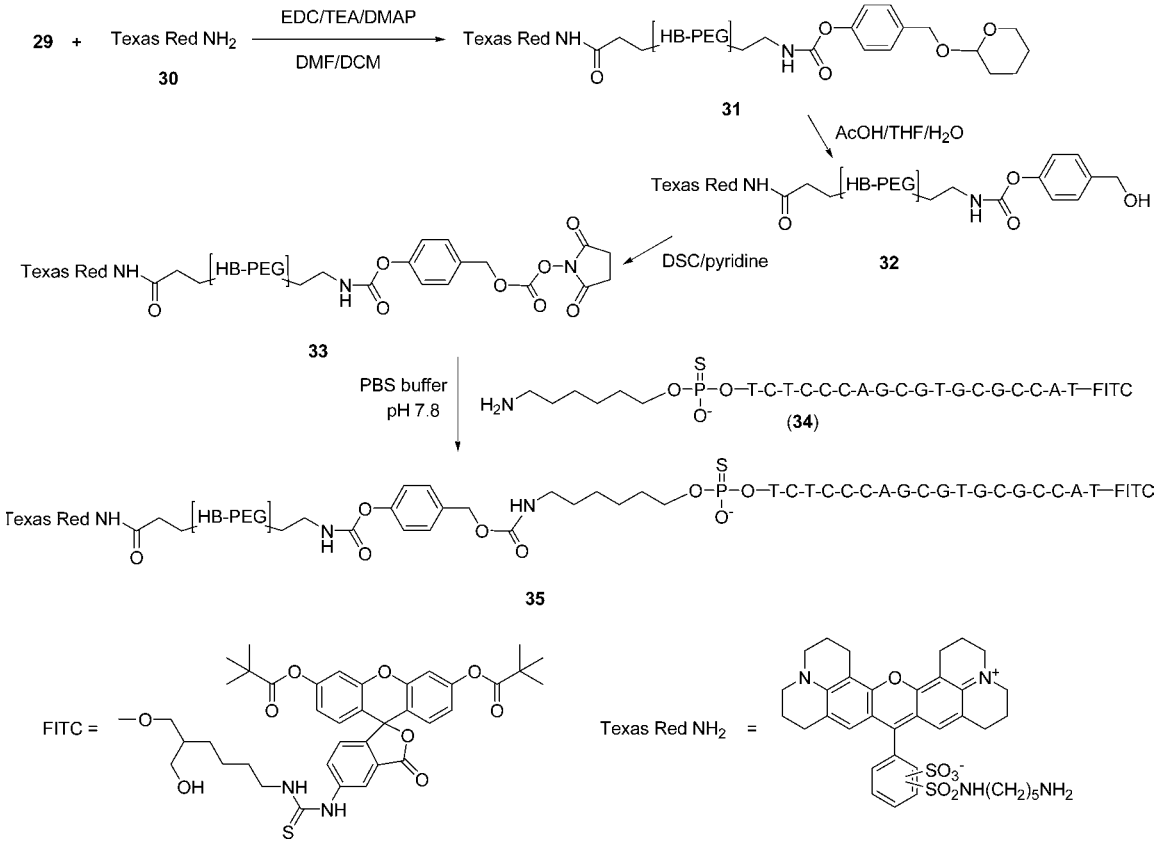

showed no impurity. ESI-MS for released oligonucleotide: *m/z* 587.0 (65%) $[M - 10H]^{10-}$, 652.2 (100%) $[M - 9H]^{9-}$, 734.2 (45%) $[M - 8H]^{8-}$, 838.7 (31%) $[M - 7H]^{7-}$, 979.3 (10%) $[M - 6H]^{6-}$. M_{obsd} 5879.5, M_{calcd} 5879.8.

Compound 20. A solution of **18** (0.623 g, 0.180 mmol), **19** (0.623 g, 0.180 mmol), and *N,N*-(dimethylamino)-pyridine (DMAP, 0.110 g, 0.90 mmol) in dichloromethane (DCM, 20 mL) was stirred at room temperature for 12 h. The solution was washed with 0.1 N HCl (2 × 20 mL), dried ($MgSO_4$), and filtered, and the solvent was removed under reduced pressure; The product was crystallized from isopropyl alcohol (IPA, 25 mL) to give **20** (0. 910 g, 0.134 mmol, 74.3%). ^{13}C NMR (67.8 MHz, $CDCl_3$) δ 171.91, 155.79, 155.30, 66.15, 63.32, 40.34, 39.91, 34.26, 28.02.

Compound 21. A solution of **20** (0.707 g, 0.104 mmol) in DCM/trifluoroacetic acid (TFA) (8 mL/4 mL) was stirred at room temperature for 3.5 h. The solvents were removed under reduced pressure, and the resulting solid was washed with ether to yield **21** (0.707 g, 0.104 mmol, 100%). ^{13}C NMR (67.8 MHz, $CDCl_3$) δ 172.18, 155.94, 66.62, 66.32, 63.49, 40.49, 39.71, 34.46.

Compound 22. To a solution of **20** (0.910 g, 0.134 mmol), 2-mecaptothiazoline (2-MT, 0.0 319 g, 0.268 mmol), and DMAP (0.032.7 g, 0.268 mmol) in DCM (15 mL) cooled at 0 °C for 15 min was added 1-[3-(dimethylamino)-propyl]-3-ethylcarbodiimide hydrochloride (EDC, 0.0513 g, 0.268 mmol), and the reaction solution was allowed to gradually warm to room temperature and then stirred for 12 h. The PEG derivative was precipitated with ethyl ether, collected by filtration, and crystallized from IPA (19 mL) to give **22** (0.820 g, 0.121 mmol, 90.0%). ^{13}C NMR (67.8 MHz, $CDCl_3$) δ 200.94, 171.73, 155.85, 155.36, 65.75, 63.37, 55.54, 40.37, 39.94, 38.73, 28.08.

Compound 23. To a solution of **21** (0.668 g, 0.098 mmol) in DCM (15 mL) was added DMAP to adjust the pH to 7.0. Compound **22** (0.677 g, 0.098 mmol) was added, and the reaction mixture was stirred at room temperature for 12 h. The solution was washed with 0.1 N HCl (2 × 20 mL), dried ($MgSO_4$) and filtered, solvent was removed under reduced pressure, and the residue was crystallized from IPA (25 mL) to give **23** (1.05 g, 0.077 mmol, 79.0%). ^{13}C NMR (67.8 MHz, $CDCl_3$) δ 171.97, 170.72, 155.87, 155.36, 66.83, 66.24, 63.39, 40.40, 39.99, 38.74, 36.50, 34.34, 28.08.

Compound 24. A solution of **23** (4.50 g, 0.335 mmol) in DCM/TFA (30 mL/15 mL) was stirred at room temperature for 3.5 h. The solvents were removed under reduced pressure, and the resulting solid was washed with ether. The solid (4.30 g, 0.320 mmol) was dissolved in DCM (50 mL). To this solution was added DMAP (to achieve pH 7.0) and compound **22** (2.20 g, 0.320 mmol); the reaction mixture was stirred at room temperature for 12 h. The solution was washed with 0.1 N HCl (2 × 30 mL), dried ($MgSO_4$), and filtered, the solvent was removed under reduced pressure, and the residue was crystallized from IPA (25 mL) to yield BOC-protected PEG-acid (MW 20 400, 5.30 g, 0.260 mmol), which was treated with DCM/TFA (30 mL/15 mL) at room temperature for 3.5 h. The solvents were removed under reduced pressure, and the resulting solid was washed with ether to yield **24** (5.30 g, 0.260 mmol, 78%). ^{13}C NMR (67.8 MHz, $CDCl_3$) δ 171.77, 170.60, 155.75, 66.73, 66.12, 63.28, 40.29, 39.86, 38.66, 36.41, 34.19.

Compound 26. To a solution of **24** (2.7 g, 0.134 mmol) in DCM (25 mL) was added DIEA until it reached pH 7.0. Compound **25** (72.6 mg, 0.269 mmol) was added, and the reaction mixture was stirred at room temperature for 12 h. The solution was washed with 0.1 N HCl (2 × 20 mL), dried ($MgSO_4$), and filtered, solvent was removed under reduced pressure, and the residue was crystallized from IPA (90 mL) to give **26** (2.11 g, 0.105 mmol, 78.1%).

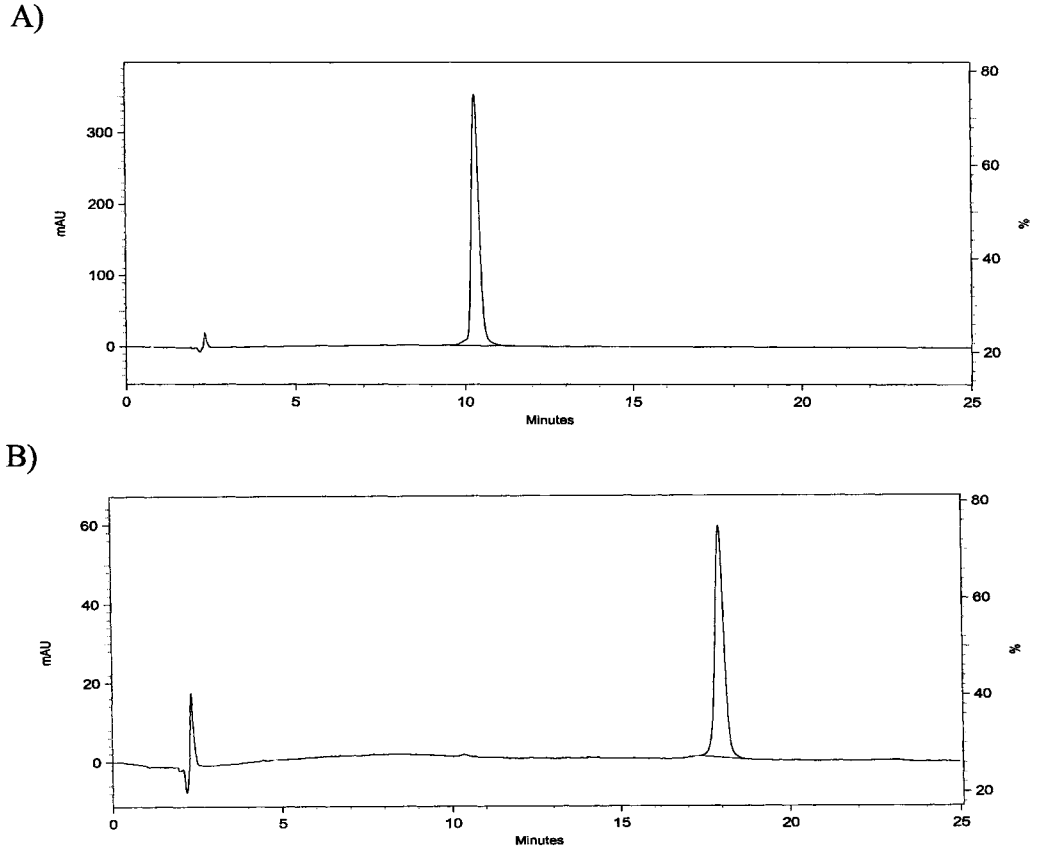

Figure 1. Analytical HPLC profile for (A) compound **1**, retention time 10.3 min, and (B) compound **3** (purified), retention time 17.9 min (UV detection at 260 nm).

^{13}C NMR (67.8 MHz, $CDCl_3$) δ *190.18*, 171.80, 170.63, 155.76, 155.36, 153.01, 130.74, 130.45, 121.40, 66.76, 66.15, 63.32, 40.61, 40.32, 38.69, 36.45, 34.23.

Compound 27. To a solution of **26** (2.1 g, 0.104 mmol) in MeOH (30 mL) cooled at 15 °C was added sodium borohydride (6.31 mg, 0.167 mmol), and the reaction solution was gradually warmed to room temperature and stirred for 2 h. This solution was treated with 1 N HCl to bring the pH to 6.5, the solvent was removed under reduced the pressure, and the residue was redissolved in about 20 mL of water. After the pH was adjusted to 2 with 1 N HCl, the aqueous solution was extracted three times with DCM. The organic fractions were combined, dried ($MgSO_4$), and filtered, solvent was removed partially under reduced pressure, and the residue was precipitated by addition of ether to give **27** (1.5 g, 0.074 mmol, 71.8%). ^{13}C NMR (67.8 MHz, $CDCl_3$) δ 171.57, 170.40, 161.58, 155.61, 153.91, 149.4, 137.84, 126.79, 120.59, 66.58, 66.00, 63.23, 60.81, 40.34, 40.14, 38.51, 36.22, 34.08.

Compound 28. To a solution of **27** (1.56 g, 0.0774 mmol) and 3,4-dihydro-2*H*-pyran (DHP, 283 μL, 3.10 mmol) in DCM (20 mL) was added toluenesulfonic acid (TsOH, 3.68 mg, 0.019 mmol), and the reaction solution was stirred for 12 h at room temperature. The solution was filtered, and ethyl ether was added to precipitate the product. The crude product was crystallized from DMF/IPA (1:4, v/v) and DCM/ether (1:4, v/v) to yield **28** (1.49 g, 0.073 mmol, 95%). ^{13}C NMR (67.8 MHz, $CDCl_3$) δ 170.37, 169.22, 155.56, 153.87, 149.64, 134.19, 127.81, 120.65, 97.94, 96.64, 91.70, 63.90, 63.02, 62.19, 61.25, 40.29, 40.08, 38.44, 36.16, 34.60, 29.87, 28.98, 28.45, 24.81, 24.54, 24.28, 22.77, 18.68, 17.82.

Compound 29. A solution of **28** (1.4 g, 0.073 mmol) in water (20 mL) was stirred for 1 h at room temperature. The solvent was removed under reduced pressure, and the residue was crystallized from DMF/IPA (1:4, v/v) and DCM/ether (1:4, v/v) to yield **29** (1.3 g, 0.064, 87.8%). ^{13}C NMR (67.8 MHz, $CDCl_3$) δ 171.56, 170.35, 155.55, 153.85, 149.62, 134.18, 127.80, 120.64, 97.91, 96.63, 63.92, 63.00, 61.22, 40.26, 40.06, 38.43, 36.12, 34.00, 29.85, 29.00, 24.78, 24.51, 22.74, 18.66.

Compound 31. To a solution of **29** (1.2 g, 0.059 mmol) in DCM (10 mL) was added the DMF solution (10 mL) of **30** (47 mg, 0.068 mmol) and 4 Å molecular sieves (1 g), and the reaction mixture was stirred for about 30 min before being cooled to 0 °C. Then TEA (179 μL, 1.29 mmol), DMAP (157 mg, 1.29 mmol), and EDC (200 mg, 1.05 mmol) were added, and the reaction mixture was stirred at room temperature for an additional 12 h. The solution was filtered, diluted with DCM, washed with water (2 × 20 mL) and 0.01 N $NaHCO_3$ (3 × 20 mL), dried ($MgSO_4$), and filtered, the solvent was removed under reduced pressure, and the residue was crystallized from 20% DMF in IPA three times to yield **31** (1.23 g, 0.059 mmol, 99%).

Compound 32. A solution of **31** (1.23 g, 0.059 mmol) in AcOH/THF/water (20:10:5 mL) was stirred for 12 h at room temperature. The solvents were removed under reduced pressure, and the residue was redissolved in DCM (20 mL). The solution was washed with water, dried ($MgSO_4$), and filtered, solvent was removed under reduced pressure, and the product was crystallized from 20% DMF in IPA to yield **32** (1.10 g, 0.053 mmol, 89%).

Compound 33. To a solution of **32** (1.1 g, 0.53 mmol) and DSC (0.108 g, 0.424 mmol) in DCM (20 mL) cooled to 0 °C was added pyridine (0.033 mL, 0.424 mmol), and the mixture was slowly warmed to room temperature and stirred for 12 h. The solvent was partially removed under reduced pressure, and the PEG compound was precipi-

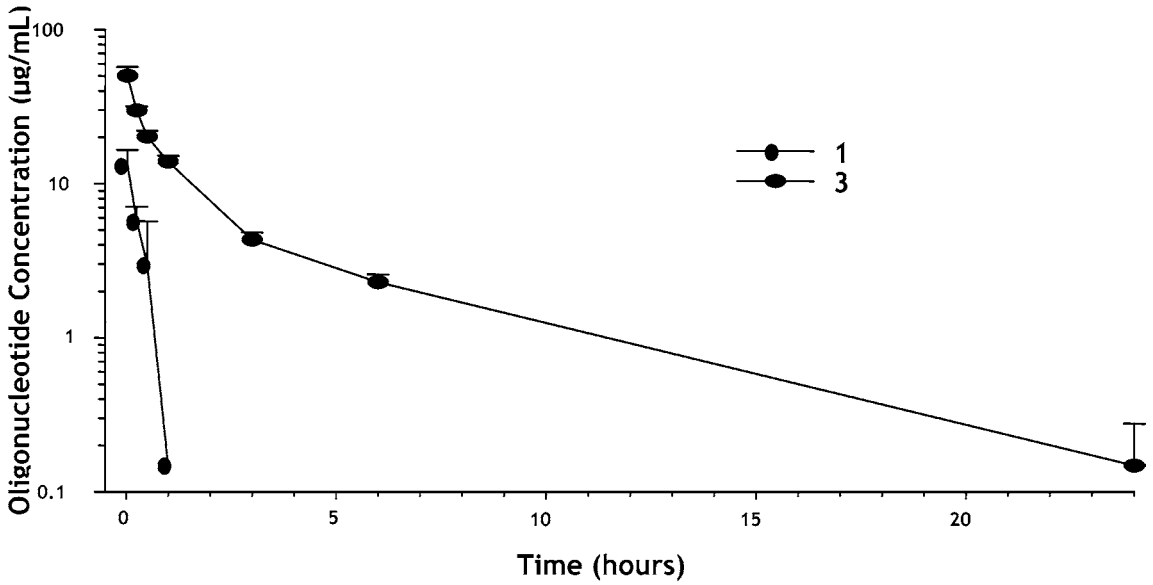

Figure 2. In vivo pharmacokinetic analysis of compounds **1** and **3**. A single iv bolus administration of 5 mg/kg native oligo (**1**) equivalents of PEGylated oligo conjugate (**3**) in mice.

tated with ethyl ether (50 mL). The crude product was crystallized from DMF/IPA (4 mL/30 mL) to give **33** (0.9 g, 0.43 mmol, 81%).

Compound 34. Compound **34** was made and purified in a similar way as **3** at a yield of 40%. Similar to **3**, analytical HPLC showed no free oligo impurity.

RESULTS AND DISCUSSION

The objectives of this study were to attempt to increase circulating half-life, drug delivery, and cellular uptake of ODNs aminohexyl-modified at the 3′- and 5′-positions by the synthesis of releasable PEG−ODN conjugates. To do so, we have developed a highly efficient method to synthesize and purify PEG−oligonucleotide conjugate. As illustrated by the synthesis of compound **3**, the purity of the final compound was checked both by analytical HPLC and by ESI-MS methods. From the HPLC chromatogram of both native oligonucleotide (Genasense) and PEG−oligo conjugate, we can clearly see that there is no free oligo in the final product (Figure 1). We then hydrolyzed the PEG−oligo conjugate to release the oligo and analyzed the mixture by ESI-MS. The data clearly show that full-length Genasense molecule was detected, which indicates that the Genasense in the PEG−oligo conjugate is intact. This was proven true for the rest of the PEG−oligo conjugates. The in vitro results of the PEG-modified oligos are summarized in Table 1 and clearly show a substantial increase in rat plasma half-life and enhanced stability against a variety of nucleases, especially the predominant nuclease (PEII) in mammals, which is the main source of oligo degradation in cells. The advantage of using an rPEG prodrug approach, resulting in a controlled continuous release of oligo and thus greater bioavailability, was further demonstrated by the pharmacokinetic (PK) results (performed using a previously described method) (*16*), which exhibited a much greater C_{max}, plasma half-life, and area under the curve (AUC) for prodrug **3** compared to non-PEGylated GS (Figure 2 and Table 2). Permanent PEG-conjugated oligo **13** showed greater PK results, as expected, but was not active in vivo (*23*).

Complete in vitro and in vivo activity test results derived from the PEG-conjugated oligos synthesized in this study will be reported in greater detail in a separate publication (*23*).

Table 2. Pharmacokinetics of PEG−Oligo Conjugate in ICR Mice[a]

compd	C_{max} (μg/mL)	plasma half-life (h)	AUC (h·μg/mL)
1	14.9	0.19	4.1
3	54.8	0.66	51.8
13[b]	491.2	1.05	730.6

[a] A single iv bolus administration of 5 mg/kg of native oligo (**1**) equivalents of PEGylated oligo conjugate (**3**) in mice. [b] Separate study at 50 mg/kg dose.

The availability of a heterobifunctional rPEG with a releasable FITC-conjugated oligo on one terminus and a fluorescent dye (Texas Red) on the distal end now enables the question of cellular uptake of these compounds to be addressed. The results of this study will be presented shortly (*23*). These types of compounds or other nonpolymeric prodrug conjugates, which possess a permanent and a releasable dye at the distal termini, can be used for cellular uptake studies of ODNs providing detailed internalization information of delivered ODNs at subcellular levels.

CONCLUSIONS

rPEG linkers can be easily conjugated to aminoalkyl-ODNs in high yield to provide prodrugs that increase the stability of the oligo and provide a controlled release of the native drug. The facile purification of the rPEG conjugate makes this a very practical approach for prodrug scale-up, especially for (animal) studies that require large amounts of drug. The ease of variation of $t_{1/2}$ for the BE and bicin rPEG systems provides a versatile delivery platform for the intravenous administration of oligo drugs that addresses the issue of the low bioavailability of the ODN usually encountered and theoretically should permit PEG−ODN conjugates to be given at a lower dosage, thus avoiding spiking and subsequent toxicity problems. Synthesis of high MW heterobifunctional rPEG can also be done by a series of chain condensations starting from the more easily prepared low MW heterobifunctional compounds. Acetals

and acyl vinyl ethers (prepared simultaneously) can be employed as orthogonal protecting groups in PEG and other heterobifunctional molecules, thus permitting selective substitutions to be done at will.

LITERATURE CITED

(1) Bonora, M., Ivanova, E., Zarytova, V., Burchovich, B., and Veronese, F. (1997) Synthesis and characterization of High-Molecular Mass Poly(ethylene glycol)-conjugated Oligonucleotides. *Bioconjugate Chem. 8*, 793−797.

(2) Burchovich, B., Veronese, F., Zarytova, V., and Bonora G. (1998) Branched Poly(ethylene glycol) (bPEG) Conjugated Antisense Oligonucleotides. *Nucleosides Nucleotides 17*, 1567−1570.

(3) Drioli, S., Adamo, I., Ballico, M., Morvan, F., and Bonora. G. (2002) Liquid-Phase Synthesis and Characterization of a Conjugated Chimeric Oligonucleotide-PEG-Peptide. *Eur. J. Org. Chem.*, 3473−3480.

(4) Chirila, T., Rakoczy, P., Garrett, K., Xia, L., and Constable. I. (2002) The use of synthetic polymers for delivery of therapeutic antisense oligodeoxynucleotides. *Biomaterials 23*, 321−342.

(5) Bonora, G. (2002) Polymer-conjugated Bioactive Oligonucleotides. *J. Bioact. Compat. Polym. 17*, 375−389.

(6) Jaschke, A., Furste, J., Nordhoff, E., Millenkamp, F., Cech, D., and Erdman, V. (1994) Synthesis and properties of oligodeoxynucleotide − poly(ethylene glycol) conjugates. *Nucleic Acids Res. 22*, 4810−4817.

(7) Letsinger, R., Zhang, G., Sun, D., Ikeuchi, T., and Sarin, P. (1989) Cholesterol-conjugated oligonucleotides: Synthesis, properties, and activity as inhibitors of replication of human immunodeficiency virus in cell culture. *Proc. Natl. Acad. Sci. U.S.A. 86*, 6553−6556.

(8) Jensen, K. D., Kopeckova, P., and Kopecek, J. (2002) Antisense Oligonucleotides Delivered to the Lysosome Escape and actively inhibit the Hepatitus B Virus. *Bioconjugate Chem. 13*, 975−984.

(9) Saison-Behmoaras, T., Duroux, I., Thuong, N., Asseline, U., and Helene, C. (1997) Antisense Properties of End-Modified Oligonucleotide Targeted to Ha-ras Oncogene. *Antisense Nucleic Acid Drug Dev. 7*, 361−368.

(10) Godard, G., Bourtorine, A., Saison-Behmoaras, E., and Helene, C. (1995) Antisense effects of cholesterol-oligodesoxynucleotide conjugates associated with poly (alkylcyanoacrylate) nanoparticles. *Eur. J. Biochem. 232*, 404−410.

(11) Jones, D., Hachmann, J., Osgood, S., Hayag, M., Barsad, P., Iverson, G., and Coutts, S. (1994) Conjugates of Double-Stranded Oligonucleotides with Poly (ethylene glycol) and Keyhole Limpet Hemocyanin: A Model for Treating Systemic Lupus Erythematosus. *Bioconjugate Chem. 5*, 390−399.

(12) Dheur, S., et al. (1999) Poly ethyleneimine but not cationic lipid improves antisense activity of 3′-capped phosphodiester oligonucleotides. *Antisense Nucleic Acid Drug Dev. 9*, 515−525.

(13) Kandimalla, E. R., Bhagat, L., Yu, D., Cong, Y., Tang, J., and Agrawal, S. (2002) Conjugation of Ligands at the 5′-End of CpG DNA Affects Immunostimulatory Activity. *Bioconjugate Chem. 13*, 966−974.

(14) Kawaguchi, T., Asakawa, H., Tashiro, Y., Juni, K., and Sueishi, T. (1995) Stability, Specific Binding Activity, and Plasma Concentration in Mice of a Oligodeoxynucleotide Modified at 5′-erminal with Poly (ethylene glycol). *Biol. Pharm. Bull. 3*, 474−476.

(15) Rapozzi, V., Cogoi, S., Spessotto, P., Risso, A., Bonora, G., Quadrifoglio, F., and Xodo, L. (2002) Antigene Effect in K562 Cells of a PEG-Conjugated Triplex-Forming Oligonucleotide Targeted to the *bcr/abl* Oncogene. *Biochemistry 41*, 502−510.

(16) Greenwald, R, Pendri, A., Conover, C., Zhao, H., Choe, Y., Martinez, A, Shum, K., and Guan, S. (1999) Drug delivery systems employing 1,4- or 1,6-elimination: poly(ethylene glycol) prodrugs of amine containing compounds. *J. Med. Chem. 42*, 3657−3667.

(17) Greenwald, R., Zhao, H., Yang, K., Reddy, P., and Martinez, A. (2004) A New Aliphatic Amine Prodrug System for the Delivery of Small Molecules and Proteins Utilizing Novel PEG Derivatives. *J. Med. Chem. 47*, 726−734.

(18) Greenwald, R. B., Zhao, H., Xia, J., and Martinez. A. (2003) Poly (ethylene glycol) Transport Forms of Vancomycin: A Long-Lived Continuous Release Delivery System. *J. Med. Chem. 46*, 5021−5030.

(19) Hussain, A., and Trulove, J. (1979) Effect of Hydroxyl Group Substituents on Pyran Ring on Hydrolysis Rate of Benzoates: 2-Tetrahydopyranyl Benzoate. *J. Pharm. Sci. 68*, 235−236.

(20) Greene, T. W., and Wuts, P. G. M. (1999) Protective Groups in Organic Synthesis, Third Edition., *Tetrahydropyranyl Ethers*, pp 49−53. John Wiley & Sons, New York.

(21) Christenson, I. (1964) Alkaline Hydrolysis of Some Carbamic Acid Esters. *Acta Chem. Scand. 18*, 904−922.

(22) Bender, M. L., and Homer, R. B. (1965) The Mechanism of the Alkaline Hydrolysis of *p*-Nitrophenyl *N*-Methylcarbamate. *J. Org. Chem. 30*, 3975−3978.

(23) Zhao, H, Reddy, R., Zhang, Y., Borowski, V., Mehlig, M., Peng, P., Lipman, J., Benimetskaya, L., and Stein, C. A. (2005) Delivery of Antisense Oligonucleotides using releasable Poly(ethylene glycol) linkers: Control of the Pharmacokinetic Profile and Impact on Efficacy. *Bioconjugate Chem.*, manuscript in preparation.

BC049804K

Enzymatic Degradation of Liposome-Grafted Poly(hydroxyethyl L-glutamine)

Birgit Romberg,[†] Josbert M. Metselaar,[†] Tom deVringer,[§] Kei Motonaga,[§] J. Jantina Kettenes-van den Bosch,[‡] Christien Oussoren,[†] Gert Storm,[†] and Wim E. Hennink*,[†]

Departments of Pharmaceutics and Biomedical Analysis, Utrecht Institute for Pharmaceutical Sciences (UIPS), Utrecht University, Sorbonnelaan 16, 3584 CA Utrecht, The Netherlands, and Yamanouchi Europe B.V., Leiderdorp, The Netherlands. Received September 21, 2004; Revised Manuscript Received April 18, 2005

Liposomes coated with poly(hydroxyethyl L-glutamine) (PHEG) show prolonged circulation times and biodistribution patterns comparable to PEG-coated liposomes. While PEG is a nondegradable polymer, PHEG is expected to be hydrolyzed by proteases. In this study the enzymatic degradability of PHEG both in its free form and grafted onto liposomes was investigated, using the proteases papain, pronase E, and cathepsin B. Enzymatic action was monitored with a ninhydrin assay, which quantifies amine groups formed due to hydrolysis of amide bonds, and the degradation products were characterized by MALDI-ToF mass spectrometry. PHEG, both in its free form and when grafted onto liposomes, showed degradation into low molecular weight peptides by the enzymes. Thus, we present a polymer-coated long-circulating liposome with an enzymatically degradable coating polymer, avoiding the risk of cellular accumulation.

INTRODUCTION

Liposomes are nanosized particles consisting of an aqueous volume enclosed by one or more phospholipid bilayers. Because of their biocompatibility and versatility they have been extensively studied as systems for the (targeted) delivery of small conventional drugs but also of macromolecules such as antigens, proteins, and DNA. Both lipophilic and hydrophilic compounds can be incorporated into liposomes, either in or absorbed to the lipid bilayer or in the aqueous compartment(s) (*1*–*4*). Intravenously injected liposomes are generally rapidly removed from the circulation, often hampering their ability to reach the aimed target site. This rapid elimination is due to recognition and capture by macrophages of the mononuclear phagocyte system (MPS), particularly those present in liver and spleen (*2, 3*). Surface modification with the hydrophilic polymer poly(ethylene glycol) (PEG) results in a decrease in uptake by the MPS and consequently in a prolonged circulation time (*2, 5*). Due to this MPS avoidance ('stealth') effect, PEG-liposomes are able to extravasate at pathological sites with areas of leaky endothelium, e.g. in tumors and inflamed tissues (so-called EPR effect (*6, 7*)). Besides PEG, several other polymers have been investigated for prolonging the circulation times of liposomes. Torchilin et al. studied vinyl-based liposome coatings (*8*), Woodle et al. studied poly(oxazoline) conjugates (*9*), and Maruyama et al. studied polyglycerol (*10*). Intravenously injected low molecular weight PEG (MW < 20 kDa) is rapidly cleared by the kidney (*11, 12*). However, its intracellular fate after uptake of PEG-coated liposomes is not known. PEG and the other polymers mentioned are not degradable by mammalian enzymes and therefore there is a risk of accumulation in cells in which the liposomes localize (e.g. macrophages), which in turn can lead to cell function impairment.

In a previous study we reported on two poly(α-amino acid)−lipid conjugates, namely poly(hydroxyethyl L-glutamine)−*N*-succinyldioctadecylamine (PHEG−DODASuc) and poly(hydroxyethyl L-asparagine)−DODASuc (PHEA−DODASuc), as stealth coatings for liposomes (structures shown in Figure 1). Indeed, liposomes coated with these polymers showed circulation kinetics and biodistribution patterns comparable to PEG-liposomes (*13*). The conjugates are based on modified L-α-amino acids and therefore have the potential to be degraded in vivo by proteases and peptidases. Poly(hydroxyethyl L-glutamine) (PHEG) has been investigated as biomaterial for different applications, and its enzymatic degradability has already been demonstrated (*14*–*21*). Relatively high molecular weight PHEG (MW = 25000−75000 Da) is cleaved into low molecular weight peptides by several proteolytic enzymes (e.g. papain, pepsin, pronase E, cathepsin B) of which the cysteine protease papain showed the highest activity (*17, 19*). Besides that enzymatic degradation reduces the risk of polymer accumulation inside cells, an enzymatically degradable coating polymer can also be used to trigger cellular uptake of the liposomes and/or release of the entrapped biologically active agent. To be more precise, in the extracellular space of tumors and inflamed tissues relatively high concentrations of proteases are present (*22, 23*). As just pointed out, long-circulating liposomes preferentially accumulate in such pathological tissues and 'stripping' of the polymer coating by enzymatic action can occur. As a result of the stripping process, surface properties (e.g. charge) and surface-associated targeting moieties that were initially shielded by the polymer coating become exposed (sheddable shielding) which may induce cellular binding and internalization.

In contrast to high molecular weight PHEG, the enzymatic degradation of low molecular PHEG as well

* To whom correspondence should be addressed. Tel: +31-(0)30−2536964. Fax: +31-(0)-2517839. E-mail: W.E.Hennink@pharm.uu.nl.
[†] Department of Pharmaceutics, Utrecht University.
[‡] Department of Biomedical Analysis, Utrecht University.
[§] Yamanouchi Europe B.V.

10.1021/bc0497719 CCC: $30.25 © 2005 American Chemical Society
Published on Web 06/11/2005

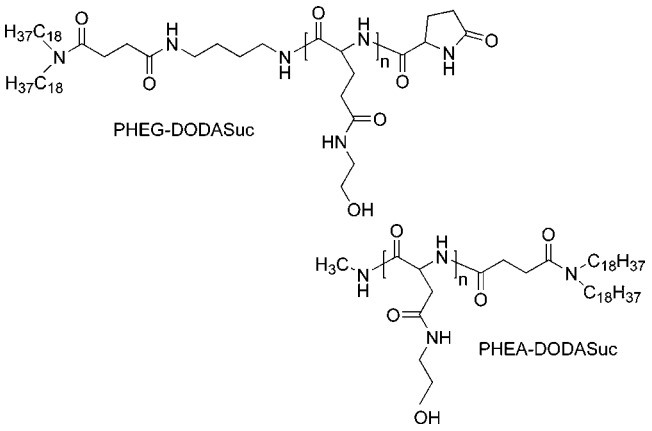

Figure 1. Structures of PHEG−DODASuc and PHEA−DODASuc.

as liposome-grafted PHEG has not been studied so far. The purpose of the present study was to investigate the enzymatic degradability of PHEG−DODASuc used as a coating for long-circulating liposomes and to identify the degradation products. Model enzymes, papain and pronase E, with specificities comparable to those of intra- and extracellular proteases, and the lysosomal cysteine protease cathepsin B, were used. All three enzymes are known to be capable of cleaving high molecular weight PHEG. Papain is a well-studied cysteine endopeptidase from *Carica papaya* latex with a broad catalytic specificity and is frequently used as a substitute for cathepsin B in degradation studies (*20, 21*). Pronase E, isolated from *Streptomyces griseus*, is composed of endo- and exopeptidases and therefore represents a natural mixture of proteases (*24*). Cathepsin B is a cysteine protease, which is present, for example, in mammalian lysosomes and is involved in protein turnover (*25*). It is also extracellularly present in pathological tissues such as tumors and sites of inflammation (*22, 23*).

The PHEG-conjugate was evaluated for enzymatic degradability both in its free form and grafted onto the surface of liposomes. Poly-L-glutamic acid was used as a control. Degradation of the free and grafted conjugate was assessed using a ninhydrin assay. Degradation products were analyzed by matrix-assisted laser desorption/ionization mass spectrometry (MALDI-ToF MS).

MATERIALS AND METHODS

Materials. PHEG−DODASuc (average MW = 3500 Da, determined by NMR and MALDI-ToF MS, corresponding with an average degree of polymerization of 16) was used in this study. Papain from papaya latex (33 units/mg in suspension, 28 mg protein/mL), cathepsin B from bovine spleen (lyophilized powder, 5.6 units/mg solid, 14 units/mg protein), Z-L-Lys-ONp hydrochloride, poly-L-glutamic acid (sodium salt, MW 1500−3000), ninhydrin, hydridantin, 2-methoxyethanol, α-cyano-hydroxycinnaminic acid, *n*-octylglucoside, and cholesterol were all purchased from Sigma-Aldrich Chemie BV, Zwijndrecht, The Netherlands. *N*-α-Benzoyl-D,L-arginine-*p*-nitroanilide (D,L-BAPNA) was obtained from ICN Biomedicals BV, Zoetermeer, The Netherlands. Pronase E (from *Streptomyces griseus*, 6−8 U/mg, lyophilized powder) was a product of Serva Electrophoresis GmbH, Heidelberg, Germany. Dipalmitoylphosphatidylcholine (DPPC) and poly(ethylene glycol)-distearylphosphatidylethanolamine (PEG2000-DSPE) were purchased from Lipoid GmbH, Ludwigshafen, Germany. All other reagents were of analytical grade.

Degradation with Papain. Thirty five microliters of the papain suspension was added to 965 μL of buffer (50 mM KH_2PO_4, 2.5 mM EDTA, 15 mM dithiothreitol, pH 6.5) to give a clear solution (32 U papain/mL). The solution was incubated for 1 h at 37 °C to activate the enzyme (*26*). The enzyme concentration was determined by UV spectroscopy at 278 nm (specific extinction coefficient $\epsilon_{\%} = 25.0$) (*27*). To determine the activity of papain, 50 μL of activated papain solution was added to 950 μL of 2 mM N-α-benzoyl-D,L-arginine-*p*-nitroanilide (D,L-BAPNA) solution in phosphate buffer (50 mM KH_2PO_4, 2.5 mM EDTA, pH 6.5). The formation of the product, 4-nitroaniline, was monitored spectroscopically at 410 nm.

The stability of papain was assessed by incubating the enzyme (400 μL of activated papain solution in 7.6 mL of phosphate buffer) at 37 °C for 120 h. At different time points the activity of papain was determined by mixing 500 μL of this solution with 500 μL of 2 mM D,L-BAPNA followed by the spectrophotometric analysis as described above. PHEG−DODASuc and poly-L-glutamic acid (pGlu) were dissolved in phosphate buffer (50 mM KH_2PO_4, 2.5 mM EDTA, pH 6.5) to a final concentration of 1 mg/mL. Activated papain (150 μL) was added to 2850 μL of the polymer solution. The mixtures were incubated at 37 °C. At different time points samples of 250 μL for ninhydrin analysis and of about 50 μL for mass spectrometric analysis were withdrawn. To inactivate the enzyme, the tubes were closed, heated for 5 min at 100 °C, and stored at −20 °C until analysis.

Degradation with Pronase E. Pronase E was dissolved to a concentration of 1 mg/mL in 10 mM HEPES (*N*-(2-hydroxyethyl)piperazine-*N*′-2-ethanesulfonic acid), 5 mM $CaCl_2$, pH 7.5. PHEG−DODASuc and pGlu were dissolved in the same buffer to a final concentration of 1 mg/mL. The pronase E solution (150 μL) was added to 2850 μL of the polymer solutions, which were subsequently incubated at 37 °C for 216 h. At different time points samples of 250 μL for the ninhydrin assay and samples for mass spectrometric analysis were withdrawn and heat inactivated as described for the papain samples. The samples were stored at −20 °C until further analysis.

Degradation with Cathepsin B. To assess the activity of cathepsin B, 1 mg of the enzyme was dissolved in 300 μL buffer (20 mM sodium acetate, 1 mM EDTA, 5 mM cysteine, pH 5). The substrate Z-L-Lys-ONp hydrochloride was dissolved in DMSO to a concentration of 2.3 mg/mL. Substrate solution (50 μL) and enzyme solution (10 μL) were added to 3 mL of acetate buffer. The generation of 4-nitrophenol was monitored spectroscopically over 5 min at 326 nm.

For studying the degradation of PHEG−DODASuc, cathepsin B was dissolved to a concentration of 16.5 mg/mL in buffer (50 mM sodium acetate, 1 mM EDTA, 10 mM dithiothreitol, pH 5.5). PHEG−DODASuc was dissolved in the same buffer without dithiothreitol to a final concentration of 1 mg/mL. Cathepsin B (150 μL) was added to 2850 μL of the polymer solution. The mixture was incubated at 37 °C for 144 h. Samples for ninhydrin and mass spectrometric analysis were withdrawn at different time points, and the enzyme was inactivated as described above. Samples were stored at −20 °C before analysis.

The activity of cathepsin B was also followed in time. Cathepsin B was incubated at 37 °C in buffer (50 mM sodium acetate, 1 mM EDTA, 10 mM dithiothreitol, pH 5.5) at a concentration of 0.825 mg/mL for 144 h. Samples of 10 μL were withdrawn at different time points and added to a mixture of 50 μL of the substrate solution and

3 mL of buffer (50 mM sodium acetate, 1 mM EDTA, pH 5.5). Formation of 4-nitrophenol was monitored spectroscopically at 326 nm.

Liposome Preparation. PHEG−DODASuc- and PEG−DSPE-liposomes were prepared by a film-extrusion method (*28*). In a typical experiment, a lipid mixture composed of DPPC/cholesterol/coating polymer (1,85:1:0.15 molar ratio; total lipid ≈100 mg) was dissolved in about 2 mL of a mixture of chloroform/methanol (1:1 v/v) in a 50 mL round-bottom flask. A lipid film was obtained by evaporation of the solvent under reduced pressure at 50 °C. After being flushed with nitrogen, the lipid film was hydrated in 4 mL of phosphate buffer (50 mM KH_2PO_4, 2.5 mM EDTA, pH 6.5), yielding a phospholipid concentration of 18.5 μmol/mL for the PHEG-liposomes and 20 μmol/mL for the PEG-liposomes. Liposomes were sized by sequential extrusion through two stacked polycarbonate filters (Poretics, 400, 200, 100, and 50 nm) with a high-pressure extrusion device. The liposomes were subjected to ultracentrifugation at 200000*g* (2 × 30 min, 4 °C) using a Beckman LE-80K Ultracentrifuge and redispersed in 4 mL of buffer (50 mM KH_2PO_4, 2.5 mM EDTA, pH 6.5).

Liposome Characterization. The mean particle size and polydispersity index of the liposome dispersions (10 times diluted with phosphate buffer) were determined by dynamic light scattering using a Malvern 4700 spectrometer. The zeta potential of the liposomes (diluted 1:100 in 5 mM HEPES buffer, pH 7.0) was determined using a Malvern Zetasizer 2000. Phospholipids were quantified spectrophotometrically according to Rouser et al. (*29*) after extraction of the lipids from the phosphate buffer with chloroform (*30*).

Degradation of Liposome-Grafted Poly(amino acid)−Lipid Conjugates with Papain. Activated papain in phosphate buffer (450 μL, 32 U/mL) was added to 8.55 mL of the dispersions of PEG−DSPE- and PHEG−DODASuc-liposomes. The dispersions were incubated at 37 °C and samples (250 μL) were taken periodically. The size and zeta potential of the liposomes were measured as described above. To separate the liposomes from the soluble degradation products, they were spun down by ultracentrifugation. In detail, 5 mL of phosphate buffer was added to the samples. Ultracentrifugation was done for 30 min at 200,000 g at 4 °C. The supernatant was collected, freeze-dried, stored at −20 °C and subsequently analyzed for degradation products by the ninhydrin assay. After 48 h of incubation, *n*-octylglucoside (150 mg) was added to 3 mL of the PHEG−liposome dispersion. Next, fresh papain (150 μL to 2850 μL of solution) was added. Samples of 250 μL were withdrawn at different time points, heat inactivated, stored at −20 °C and subsequently analyzed by the ninhydrin assay.

Quantitative ^{1}H NMR analysis of Papain-Treated PHEG-liposomes. PHEG-liposomes were incubated with papain as described above. After 48 h the papain-treated liposomes were separated from the soluble degradation products by ultracentrifugation (1 mL of liposome dispersion diluted with 5 mL of 5 mM NaCl, 200000*g*, 30 min, 4 °C). Next, the liposome pellet was dispersed in 1 mL of 5 mM NaCl and freeze-dried. The cake was dissolved in a mixture of $CDCl_3/d_6$-DMSO (2:1) and subsequently analyzed by ^{1}H nuclear magnetic resonance spectroscopy (NMR). Spectra were recorded with a Varian G-300 spectrometer (Varian, Palo Alto, CA) at 300 MHz. The number of accumulated transients was 32; the relaxation delay D1 was 10 s. The signals of the liposome mixture were assigned on the basis of chemical shift and intensity data and confirmed by homonuclear double resonance experiments. The relative amount of PHEG−DODASuc was quantified by comparing the integral values of proton signals of cholesterol and PHEG−DODASuc. The cholesterol signal chosen for calculation was at δ 5.2 (position: C6 at the double bond, corresponding to one proton) and the PHEG−DODASuc signal was at δ 3.45 (position: side chain-CH_2 next to OH, corresponding to 16 × 2 protons for $n = 16$). As a control formulation a sample of PHEG-liposomes that were not incubated with papain was prepared and analyzed as described above. A detailed description of this analytical method and its validation will be published elsewhere.

Ninhydrin Assay. When peptide bonds in peptides are cleaved due to action of the enzymes, primary amines are formed. The concentration of amines in the different samples was determined spectrophotometrically by the use of ninhydrin (*31*). The samples were thawed, and 1 M sodium acetate buffer (pH 5.5) was added to give a final volume of 1 mL. Next, 1 mL of freshly prepared ninhydrin solution (2.0 g ninhydrin and 0.3 g hydridantin dissolved in 75 mL of 2-methoxyethanol and 25 mL of 4 M sodium acetate buffer, pH 5.5) was added. The mixtures were vortexed and incubated for 15 min at 100 °C. After being cooled to room temperature, the samples were diluted with 5 mL of 50% ethanol in water, and the absorbance was read at 570 nm with a Perkin-Elmer Lambda 2 UV/vis spectrophotometer. Glycine (in 1 M acetate buffer) was used for calibration. The calibration curve was linear up to 0.5 μmol glycine/mL. Suitable controls containing only substrate or papain were run in parallel, and their readings were subtracted for plotting the degradation of the polymer-conjugates and controls.

MALDI-ToF Mass Spectrometry. α-Cyano-4-hydroxycinnaminic acid was used as a matrix and dissolved to a concentration of 10 mg/mL in 50% acetonitrile in water containing 0.1% trifluoroacetic acid. The samples were mixed with the matrix solution in a volume ratio of 1:3. Three times 1 μL of this mixture was put on a single position of the sample deposition plate and left at room temperature to allow solvent evaporation. Spectra of samples incubated with papain, pronase E, and cathepsin B were acquired with a Voyager-DE STR MALDI-ToF mass spectrometer (Applied Biosystems, Foster City, CA) operated in positive ion mode. Ionization was initiated with a nitrogen laser operating at 337 nm with a repetition rate of 7.6 Hz. Delayed extraction linear mode with an accelerating voltage of 20 kV was used and the acquisition mass range was 700−7000 Da. Calibration was done with a peptide mixture (900−3700 Da). MALDI-ToF spectra were analyzed with the Applied Biosystems Data Explorer Software.

RESULTS AND DISCUSSION

Enzymatic Degradation of PHEG−DODASuc Followed by the Ninhydrin Assay. *Papain Incubation.* The stability of papain was established using *N*-α-benzoyl-D,L-arginine-*p*-nitroanilide as substrate. It was shown that papain retained 50% of its activity after 72 h of incubation at pH 6.5 and 37 °C. The decrease in activity is likely caused by self-destruction, a phenomenon frequently observed for proteolytic enzymes with a broad specificity (*17*). The degradation PHEG−DODASuc and the control pGlu by papain was monitored by determination of the formed primary amine groups using the ninhydrin assay. The results are presented in Figure 2. During the first 10 h of incubation a strong increase

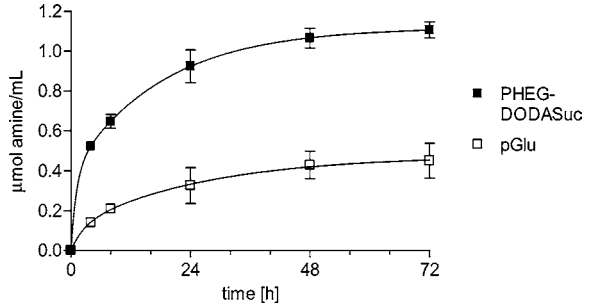

Figure 2. Time course of the concentration of primary amines in papain-incubated samples of PHEG−DODASuc (■) and poly-L-glutamic acid (□) as determined by the ninhydrin assay (average ± SD of three experiments). PHEG−DODASuc incubated in buffer without papain shows a constant concentration of amines in time.

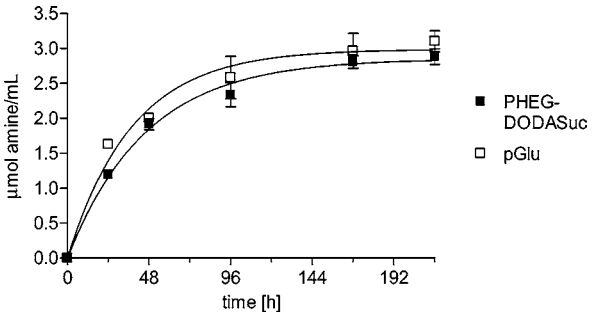

Figure 3. Time course of the concentration of primary amines in pronase E-incubated samples of PHEG−DODASuc (■) and poly-L-glutamic acid (□) as determined by the ninhydrin assay (average ± SD of three experiments).

in free amine concentration was observed for PHEG−DODASuc and pGlu, demonstrating that both relatively low molecular weight polymers are degraded by papain, as previously reported for their high molecular weight counterparts (*14*−*21*, *32*). Figure 2 also shows that a plateau value in amine concentration was obtained after 48−72 h. As mentioned, papain was still active after 72 h indicating that the degradation process did not stop due to inactivity of the enzyme. However, the activity of the enzyme might be inhibited by the formed degradation products. To investigate this, fresh papain was added after 48 h of incubation. No further increase in amine concentration was found, which shows that the obtained fragments cannot be further cleaved by the enzyme. The concentration of the formed amine groups in the PHEG−DODASuc sample after 72 h incubation (1.1 μmol amine/mL) corresponds with about four hydrolysis sites per molecule, yielding fragments with 3−4 amino acids. Fragments of 8−9 amino acids were formed after 72 h incubation of pGlu with papain. The modification of the glutamic acid side chain in PHEG with hydroxyalkylamine can be responsible for its higher enzymatic susceptibility (*16*).

Pronase E Incubation. Figure 3 shows the degradation profiles obtained when PHEG−DODASuc and pGlu were incubated with pronase E. This figure demonstrates that, in agreement with the findings of Pytela et al. for relatively high molecular weight PHEG (*19, 20*), the PHEG−conjugate as well as poly-L-glutamic acid are cleaved by this enzyme. On the basis of the plateau values of the amine concentrations, it is calculated that PHEG and pGlu are finally degraded into fragments of 1−2 and 2−3 amino acids, respectively. The higher susceptibility of PHEG for pronase E (final degradation fragments of 1−2 amino acids) as compared to papain (3−4 amino acids) is likely due to the fact that pronase E contains a cocktail of both endo- and exopeptidases.

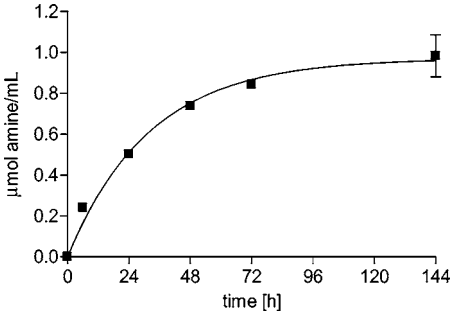

Figure 4. Time course of the concentration of primary amines in cathepsin B-incubated samples of PHEG−DODASuc as determined by the ninhydrin assay (average ± SD of three experiments).

Cathepsin B Incubation. Figure 4 demonstrates the degradability of PHEG−DODASuc by cathepsin B. The number of amine groups increases upon incubation, reaching its maximum value after 144 h. Unfortunately, the final fragment size could not be calculated since the concentration of primary amine groups in a control solution of cathepsin B only increased in time. Likely due to autodigestion, some of the peptide bonds in the enzyme are hydrolyzed, and the formed amine groups give a signal in the ninhydrin assay. In line herewith, an activity assay with a low molecular weight substrate showed that under the selected conditions the activity half-life of cathepsin B was about 30 h. Nevertheless, the concentration of amines in the samples with PHEG−DODASuc was always greater than in the control solution, demonstrating that this conjugate is a substrate for this enzyme. To get insight into the extent of PHEG−DODASuc degradation by cathepsin B, mass spectrometric analysis was done.

Mass Spectrometric Analysis of Enzymatically Degraded PHEG−DODASuc. Figure 5, 6, and 7 show representative mass spectra of papain-, pronase E-, and cathepsin B-degraded PHEG−DODASuc; Table 1 gives the peak assignments. In the spectrum of the nondegraded PHEG−DODASuc (Figure 5a), the peak distributions of the K^+- and the Na^+-adducts are present. The K^+-adduct is abundant since KH_2PO_4 was used in the degradation buffer. In the spectra of PHEG−DODASuc incubated with papain (Figure 5b and 5c), the high mass peaks originating from the nondegraded conjugate disappeared in time, and new peaks were observed. These new peaks have relatively lower masses and increase in their relative abundance in time (most pronounced at $t = 72$ h). A lactam group forms the terminus of the peptide chain in the native conjugate (Figure 1). The observed peaks in the degraded samples can be assigned to degradation fragments of the PHEG-conjugate without this lactam end group and a lower degree of polymerization. For example in the spectrum of the sample incubated for 8 h with papain (Figure 5b), masses of these fragments were between 1400 and 3000 Da, corresponding to fragment size of 4−13 amino acid residues. The observation that the resulting conjugates do not carry a lactam group indeed demonstrates that the peptide chain was hydrolytically cleaved, yielding PHEG−DODASuc (with an NH_2 terminus) and PHEG with COOH and lactam termini as degradation products. The latter products were not detected due to their low molecular weight. In the spectrum of the papain-degraded conjugate after 72 h incubation (Figure 5c) the peak population shifted to low masses of 1000−2300 Da, corresponding

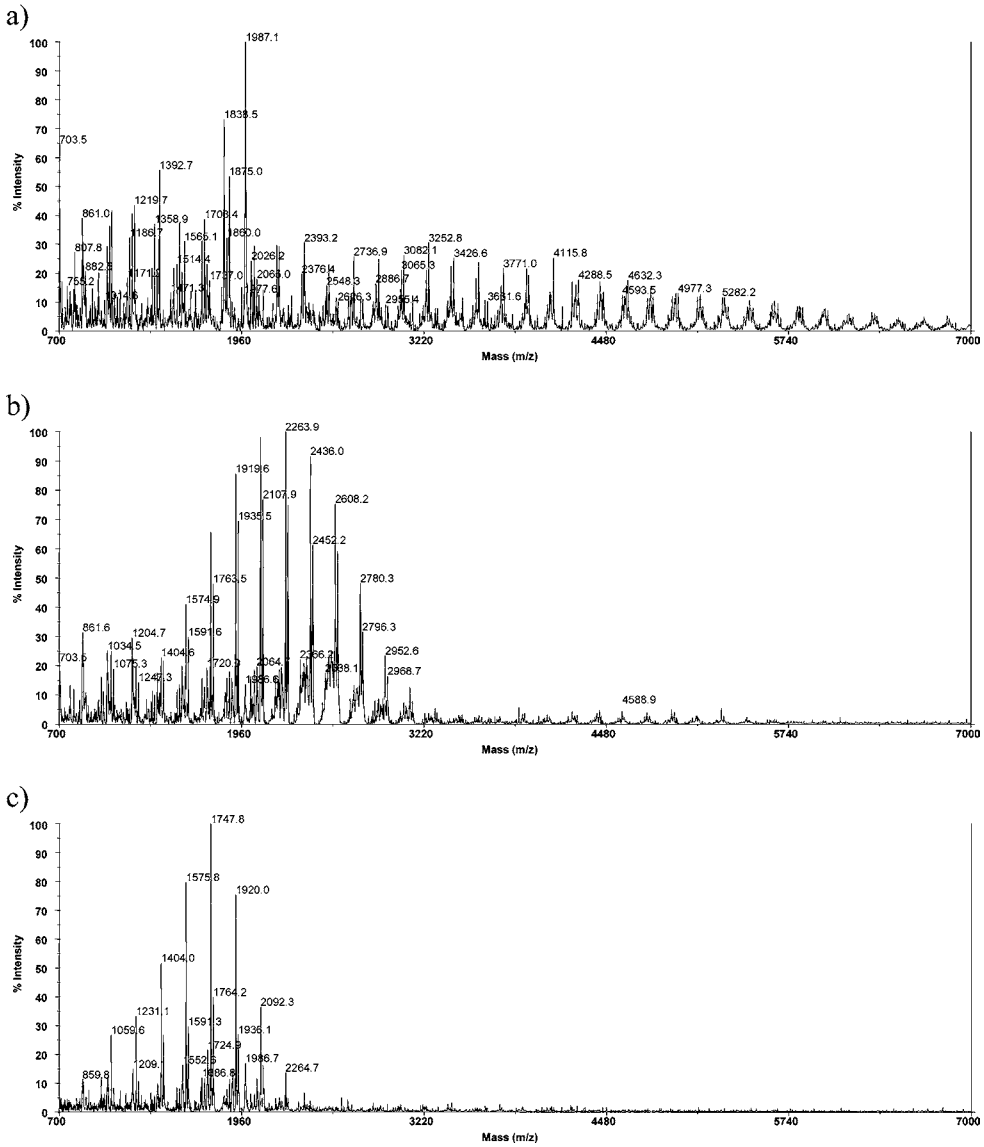

Figure 5. Mass spectra of PHEG−DODASuc (a) and after incubation with papain for 8 h (b) and 72 h (c).

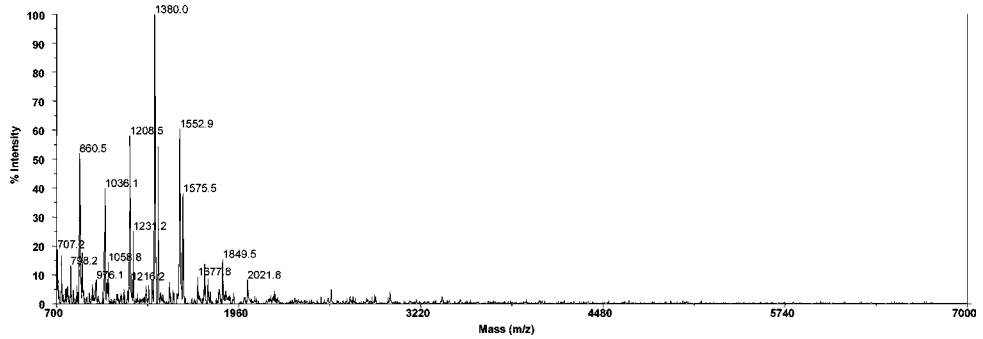

Figure 6. Mass spectrum of PHEG−DODASuc after incubation with pronase E for 216 h.

with fragments of 2−9 amino acids. Figure 6 shows the mass spectrum of PHEG−DODASuc incubated with pronase E. The peak population of the original conjugate disappeared, and peaks of Na^+-adducts of conjugate molecules without the lactam end group appear. Here the Na^+-adducts are the most abundant due to the choice of the buffer. The highest peak represents a fragment size of the DODASuc-anchor with 4 amino acids. Mass spectrometric analysis suggests a lower extent of degradation than the ninhydrin analysis (pronase E-catalyzed degradation of PHEG−DODASuc: compare fragments of 1−2 amino acids based on ninhydrin assay with those found with mass spectrometry analysis (2−5 amino acids)). It should be noted, however, that with the ninhydrin assay both fragments with and without the DODASuc-anchor are detected, whereas in the mass spectrum only the fragments with the anchor were observed. Obviously, the DODASuc-anchor prevents binding of the conjugate to the enzyme when a certain fragment size is achieved. Figure 7 shows the mass spectrum of PHEG−DODASuc degraded by cathepsin B after 144 h of incubation. The highest population of peaks

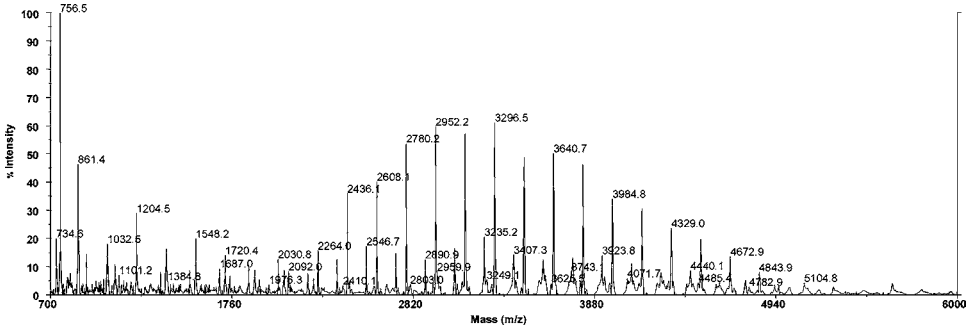

Figure 7. Mass spectrum of PHEG−DODASuc after incubation with cathepsin B for 144 h.

Table 1. Peak Assignment in Mass Spectra of PHEG−DODASuc Incubated with Papain, Pronase E, and Cathepsin B, as Shown in Figures 5, 6, and 7, Respectively

incubation	*m/z*	assignment
papain (t = 0 h)	1186.7	[DODASuc−$(PHEG)_2$-lactam+K]$^+$
	1875.0	[DODASuc−$(PHEG)_6$-lactam+K]$^+$
	2548.3	[DODASuc−$(PHEG)_{10}$-lactam+Na]$^+$
	3252.8	[DODASuc−$(PHEG)_{14}$-lactam+K]$^+$
	4632.3	[DODASuc−$(PHEG)_{22}$-lactam+K]$^+$
	5282.2	[DODASuc−$(PHEG)_{26}$-lactam+Na]$^+$
papain (t = 8 h)	4588.9	[DODASuc−$(PHEG)_{22}$-lactam+H]$^+$
	1075.3	[DODASuc−$(PHEG)_2$+K]$^+$
	1574.9	[DODASuc−$(PHEG)_5$+Na]$^+$
	2107.9	[DODASuc−$(PHEG)_8$+K]$^+$
	2263.9	[DODASuc−$(PHEG)_9$+Na]$^+$
	2796.3	[DODASuc−$(PHEG)_{12}$+K]$^+$
	2952.6	[DODASuc−$(PHEG)_{13}$+Na]$^+$
papain (t = 72 h)	1059.6	[DODASuc−$(PHEG)_2$+Na]$^+$
	1591.3	[DODASuc−$(PHEG)_5$+K]$^+$
	1747.8	[DODASuc−$(PHEG)_6$+Na]$^+$
	1936.1	[DODASuc−$(PHEG)_7$+K]$^+$
	2264.7	[DODASuc−$(PHEG)_9$+Na]$^+$
pronase E (t = 216 h)	1036.1	[DODASuc−$(PHEG)_2$+H]$^+$
	1058.8	[DODASuc−$(PHEG)_2$+Na]$^+$
	1380.0	[DODASuc−$(PHEG)_4$+H]$^+$
	1552.9	[DODASuc−$(PHEG)_5$+H]$^+$
	1575.5	[DODASuc−$(PHEG)_5$+Na]$^+$
cathepsin B (t = 144 h)	2546.7	[DODASuc−$(PHEG)_{10}$-lactam+Na]$^+$
	3235.2	[DODASuc−$(PHEG)_{14}$-lactam+Na]$^+$
	4782.9	[DODASuc−$(PHEG)_{23}$-lactam+Na]$^+$
	2264.0	[DODASuc−$(PHEG)_9$+Na]$^+$
	3296.5	[DODASuc−$(PHEG)_{15}$+Na]$^+$
	4843.9	[DODASuc−$(PHEG)_{24}$+Na]$^+$

can be assigned to Na^+-adducts of degradation fragments without lactam endgroup. The peak population of the Na^+-adduct of the nondegraded conjugate is also present; however, their peak intensities are much lower than those of the degraded conjugate. Masses of the degraded fragments are between 1500 and 5000 Da, corresponding with conjugates of DODASuc with 5 to 25 hydroxylethyl L-glutamine residues. These results demonstrate that under the selected conditions PHEG−DODASuc is degraded by cathepsin B, however, not as considerable as observed with papain or pronase E. Because cathepsin B is rather unstable under the experimental condtions ($t_{1/2}$ = approximately 30 h), maximal fragmentation of PHEG−DODASuc is not achieved. It is therefore expected that under physiological conditions where the enzyme concentration is substantially higher (10−40 mg/mL in lysosomes (*25*), as compared to 0.8 mg/mL in this study) and its turnover is high, PHEG−DODASuc can be degraded further.

Degradation of PHEG Conjugate Grafted onto a Liposome Surface. Polymer-coated (PHEG/PEG) liposomes were prepared by the film-extrusion method. The loss of phospholipids during liposome preparation was approximately 30%; Table 2 shows the physical characteristics (size and charge) of the different liposome preparations. The PHEG-coated liposomes were slightly bigger than the PEG-liposomes. This is probably due to aggregate formation during the ultracentrifugation step (UC induced size increase of ≈30 nm, increase in polydispersity of ≈0.2). The negative values of the zeta potential of the different liposomes are probably due to the low ionic strength (5 mM HEPES, pH 7.0) at which the measurements were done (*33*).

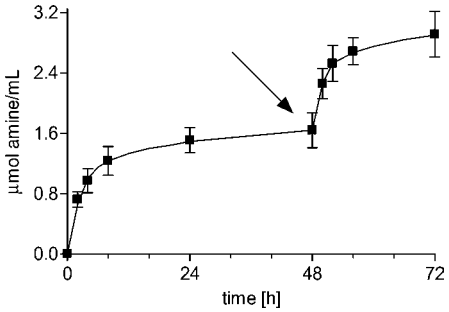

Figure 8. Time course of the concentration of amines in the papain-incubated samples of PHEG−DODASuc-coated liposomes as determined by the ninhydrin assay (average ± SD of three experiments). The arrow indicates the time point when liposomes were solubilized with *n*-octylglucoside and fresh papain was added.

Table 2. Liposome Characteristics

liposome type	mean diameter [nm]	polydispersity index	zeta potential [mV]
PHEG−DODASuc	158 ± 1	0.31 ± 0.03	−29 ± 1
PEG−DSPE	127 ± 1	0.07 ± 0.02	−35 ± 5

Figure 8 shows that the concentration of amines increased in time when liposomes grafted with PHEG−DODASuc were incubated with papain. This means that PHEG−DODASuc grafted onto a liposomal surface is still susceptible for degradation by papain and probably by other proteolytic enzymes. In agreement with expectations, PEG−DSPE coated on the liposomes was not degraded by this enzyme. For PHEG−DODASuc, a plateau in amine concentration was reached after approximately 24−40 h of incubation. In Figure 9 the size and zeta potential of the liposomes as a function of incubation time with papain are shown. For the PEG−DSPE coated liposomes, no significant changes in size and zeta potential upon incubation were observed. However, the PHEG−DODASuc-coated liposomes decreased around 20 nm in size during the first 5−10 h of degradation. The degradation of the conjugate on the liposome surface results in a smaller hydrodynamic diameter and is therefore a possible explanation, but this alone cannot be the reason for the observed drop in size. The end-to-end distance of the peptide part of the conjugate is approximately 6.5 nm; thus, a complete shedding of the peptide would result in a maximum size decrease of ≈13

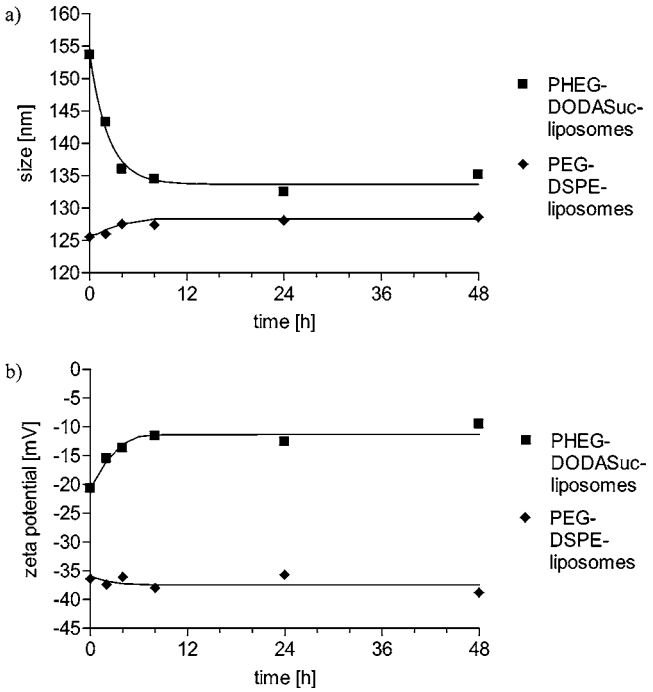

Figure 9. Size (a) and zeta potential (b) of PHEG−DODASuc liposomes (■) and PEG−DSPE liposomes (◆) as a function of incubation time with papain.

nm. As the polydispersity index of the PHEG-coated liposomes decreased from 0.3 to around 0.2 upon incubation with the enzyme, a dissociation of the aggregates, which were formed during ultracentrifugation, is likely to occur as well. The zeta potential of the PHEG-liposomes goes from −20 mV to about −10 mV. Mass spectrometry (Figure 5b/5c) demonstrates that after enzymatic digestion the formed DODASuc-peptide fragment has a terminal amine group (instead of the neutral lactam group of the nondegraded conjugate). This amine group is protonated at pH of 7.0 and likely responsible for the less negative zeta-potential. The progression of changes in size and zeta potential in time are in very good agreement with the progression of the amine content of the samples as seen in the ninhydrin degradation assay (compare Figures 8 and 9). The preparation method applied will result in the formation of unilamellar liposomes (*34*), with polypeptide conjugate present at both the inner and outer layer. It is likely that only the polypeptide present at the outside of the liposomal bilayer is accessible for enzymatic attack. When the liposomes were destabilized by *n*-octylglucoside after 48 h incubation with papain, formation of amines continued (Figure 8). This indicates that indeed only the polypeptide present at the outside of intact liposomes is degraded by papain.

According to the phosphate determination 70% of the initial phospholipid amount is recovered in the final dispersion. Assuming that therefore around 70% of the initial PHEG-conjugate amount is remaining in the liposome dispersions after preparation, the extent of degradation of surface grafted PHEG is the same as that of the conjugate in solution (final degradation products contain 3−4 amino acids). ^{1}H NMR-analysis of the liposome dispersion incubated with papain for 48 h showed that 63 ± 10% of the PHEG was still associated with the liposomal bilayer. As concluded from the data presented in Figure 8, PHEG present at the inside the liposome (≈50% of the totally present polymer) is not accessible for enzymatic attack. From the ^{1}H NMR analysis it can be derived that the PHEG fragment present at the outer layer of the liposomal membrane after enzymatic degradation contains 4−5 amino acid residues. This is in excellent agreement with the data of the enzymatic degradation of the PHEG-conjugate after mass spectrometric analysis.

In conclusion, this paper demonstrates that PHEG−DODASuc is enzymatically degradable even when it is attached to a liposomal surface, avoiding the risk of intracellular accumulation and making liposomes with a sheddable coating feasible.

ACKNOWLEDGMENT

The authors thank Mirjam Damen of the Department of Biomedical Analysis for her valuable assistance with mass spectrometry analysis.

LITERATURE CITED

(1) Sharma, A., and Sharma, U. S. (1997) Liposomes in drug delivery: progress and limitations. *Int. J. Pharm. 154*, 123−140.

(2) Torchilin, V. P., and Trubetskoy, V. S. (1995) Which polymers can make nanoparticulate drug carriers long-circulating? *Adv. Drug Delivery Rev. 16*, 141−155.

(3) Marjan, J. M., and Allen, T. M. (1996) Long circulating liposomes: past, present and future. *Biotechnol. Adv. 14*, 151−175.

(4) Lasic, D. D. (1994) Sterically stabilized vesicles. *Angew. Chem., Int. Ed. Engl. 33*, 1685−1698.

(5) Woodle, M. C., and Lasic, D. D. (1992) Sterically stabilized liposomes. *Biochim. Biophys. Acta 1113*, 171−199.

(6) Maeda, H., Wu, J., Sawa, T., Matsumura, Y., and Hori, K. (2000) Tumor vascular permeability and the EPR effect in macromolecular therapeutics: a review. *J. Controlled Release 65*, 271−284.

(7) Gabizon, A., Catane, R., Uziely, B., Kaufman, B., Safra, T., Cohen, R., Martin, F., Huang, A., and Barenholz, Y. (1994) Prolonged circulation time and enhanced accumulation in malignant exudates of doxorubicin encapsulated in polyethylene-glycol coated liposomes. *Cancer Res. 54*, 987−992.

(8) Torchilin, V. P., Shtilman, M. I., Trubetskoy, V. S., Whiteman, K., and Milstein, A. M. (1994) Amphiphilic vinyl polymers effectively prolong liposome circulation time in vivo. *Biochim. Biophys. Acta 1195*, 181−184.

(9) Woodle, M. C., Engbers, C. M., and Zalipsky, S. (1994) New amphipatic polymer−lipid conjugates forming long-circulating reticuloendothelial system-evading liposomes. *Bioconjugate Chem. 5*, 493−496.

(10) Maruyama, K., Okuizumi, S., Ishida, O., Yamauchi, H., Kikuchi, H., and Iwatsuru, M. (1994) Phosphatidylpolyglycerols prolong liposome circulation in vivo. *Int. J. Pharm. 111*, 103−107.

(11) Mehvar, R. (2000) Modulation of the pharmacokinetics and pharmacodynamics of proteins by polyethylene glycol conjugation. *J Pharm. Pharm. Sci. 3*, 125−136.

(12) Caliceti, P., and Veronese, F. M. (2003) Pharmacokinetic and biodistribution properties of poly(ethylene glycol)-protein conjugates. *Adv. Drug Delivery Rev. 55*, 1261−1277.

(13) Metselaar, J. M., Bruin, P., de Boer, L. W., de Vringer, T., Snel, C., Oussoren, C., Wauben, M. H., Crommelin, D. J., Storm, G., and Hennink, W. E. (2003) A novel family of L-amino acid-based biodegradable polymer−lipid conjugates for the development of long-circulating liposomes with effective drug-targeting capacity. *Bioconjugate Chem. 14*, 1156−1164.

(14) Rypacek, F. (1998) Structure-to-function relationships in the biodegradation of poly(amino acids)s. *Polym. Deg. Stab. 59*, 345−351.

(15) Dickinson, H. R., and Hiltner, A. (1981) Biodegradation of a poly-(alpha-amino acid) hydrogel. II. In vitro. *J. Biomed. Mater. Res. 15*, 591−603.

(16) Chiu, H. C., Kopeckova, P., Deshmane, S. S., and Kopecek, J. (1997) Lysosomal degradability of poly(a-amino acids). *J. Biomed. Mater. Res. 34*, 381−392.
(17) Rypacek, F., Pytela, J., Kotva, R., and Skarda, V. (1997) Biodegradation of poly(amino acid)s: evaluation methods and structure-to-function relationships. *Macromol. Symp. 123*, 9−24.
(18) Yaacobi, Y., Sideman, S., and Lotan, N. (1985) A mechanistic model for the enzymic degradation of synthetic biopolymers. *Life Support Syst. 3*, 313−326.
(19) Pytela, J., Saudek, V., Drobnik, J., and Rypacek, F. (1989) Poly(N5-hydroxyalkylglutamines). IV. Enzymatic degradation of N5-(2-hydroxyethyl)-L-glutamine homopolymers and copolymers. *J. Controlled Release 10*, 17−25.
(20) Pytela, J., Kotva, R., and Rypacek, F. (1998) Enzymatic degradation of poly[N5-(2-hydroxyethyl)-L-glutamine] and poly[N5-(2-hydroxyethyl)-L-glutamine-stat-L-glutamic acid]: analysis of final degradation products. *J. Bioact. Compat. Pol. 13*, 198−209.
(21) Hayashi, T., Tabata, Y., and Nakajima, A. (1985) Biodegradation of poly(a-amino acid) in vitro. *Polymer J. 17*, 463−471.
(22) Koblinski, J. E., Ahram, M., and Sloane, B. F. (2000) Unraveling the role of proteases in cancer. *Clin. Chim. Acta 291*, 113−135.
(23) Trabandt, A., Gay, R. E., Fassbender, H. G., and Gay, S. (1991) Cathepsin B in synovial cells at the site of joint destruction in rheumatoid arthritis. *Arthritis Rheum. 34*, 1444−1451.
(24) Awad, W. M., Jr., Soto, A. R., Siegel, S., Skiba, W. E., Bernstrom, G. G., and Ochoa, M. S. (1972) The proteolytic enzymes of the K-1 strain of Streptomyces griseus obtained from a commercial preparation (pronase). I. Purification of four serine endopeptidases. *J. Biol. Chem. 247*, 4144−4154.
(25) Otto, H. H., and Schirmeister, T. (1997) Cysteine Proteases and Their Inhibitors. *Chem. Rev. 97*, 133−172.
(26) Zhao, G., and Zhou, Z. S. (2001) Vinyl sulfonium as novel proteolytic enzyme inhibitor. *Bioorg. Med. Chem. Lett. 11*, 2331−2335.
(27) Mitchel, R. E., Chaiken, I. M., and Smith, E. L. (1970) The complete amino acid sequence of papain. Additions and corrections. *J. Biol. Chem. 245*, 3485−3492.
(28) Amselem, S., Gabizon, A., and Barenholz, Y. (1993) *Liposome Technology* (Gregoriadis, G., Ed.) pp 501−525, CRC press, Boca Raton, FL.
(29) Rouser, G., Fleischer, S., and Yamamoto, A. (1970) Two-dimensional thin layer chromatographic separation of polar lipids and determination of phospholipids by phosphorus analysis of spots. *Lipids 5*, 494−496.
(30) Bligh, E. G., and Dyer, W. J. (1959) A rapid method of total lipid extraction and purification. *Can. J. Med. Sci. 37*, 911−917.
(31) Prochazkova, S., Varum, K. M., and Ostgaard, K. (1999) Quantitative determination of chitosans by ninhydrin. *Carbohydr. Polym. 38*, 115−122.
(32) Miller, W. G. (1961) Degradation of poly-a, L-glutamic acid. I. Degradation of high molecular weight PGA by papain. *J. Am. Chem. Soc. 83*, 259−265.
(33) Moribe, K., Maruyama, K., and Iwatsuru, M. (1997) Estimation of surface state of poly(ethylene glycol)-coated liposomes using an aqueous two-phase partitioning technique. *Chem. Pharm. Bull. (Tokyo) 45*, 1683−1687.
(34) Jousma, H., Talsma, T., Spies, F., Joosten, J. G. H., Junginger, H. E., and Crommelin, D. J. A. (1987) Characterization of liposomes. The influence of extrusion of multilamellar vesicles through polycarbonate membranes on particle size, particle size distribution and number of bilayers. *Int. J. Pharm. 35*, 263−274.

BC0497719

PEG–Doxorubicin Conjugates: Influence of Polymer Structure on Drug Release, in Vitro Cytotoxicity, Biodistribution, and Antitumor Activity

Francesco M Veronese,*,⊥ Oddone Schiavon,⊥ Gianfranco Pasut,⊥ Raniero Mendichi,† Lars Andersson,‡ Anders Tsirk,‡ Jayne Ford,§ Gefei Wu,§ Samantha Kneller,§ John Davies,‖ and Ruth Duncan*,§

Department of Pharmaceutical Science, University of Padua, Via F. Marzolo 5, 35100 Padua, Italy, Istituto per lo Studio delle Macromolecole (CNR), Via E. Bassini 15, 20133, Milano, Italy, PolyPeptide Laboratories (Sweden) AB, PO Box 30089, SE-200 61 Limhamn, Sweden, Centre for Polymer Therapeutics, Welsh School of Pharmacy, Cardiff University, Redwood Building, King Edward VII Avenue, Cardiff, Wales, U.K., and Polymer Laboratories Ltd, Unit 4/5, The Mynd Industrial Estate Church Stretton, Shropshire, SY6 6EA, U.K.
Received November 13, 2004

Polymer–drug conjugates (polymer therapeutics) are finding increasing use as novel anticancer agents. Here a series of poly(ethylene glycol) PEG–doxorubicin (Dox) conjugates were synthesized using polymers of linear or branched architecture (molecular weight 5000–20000 g/mol) and with different peptidyl linkers (GFLG, GLFG, GLG, GGRR, and RGLG). The resultant conjugates had a drug loading of 2.7–8.0 wt % Dox and contained <2.0% free drug (% total drug). All conjugates containing a GFLG linker showed ~30% release of Dox at 5 h irrespective of PEG molecular weight or architecture. The GLFG linker was degraded more quickly (~57% Dox release at 5 h), and the other linkers more slowly (<16% release at 5 h), by lysosomal enzymes in vitro. In vitro there was no clear relationship between cytotoxicity toward B16F10 cells and the observed Dox release rate. All PEG conjugates were more than 10-fold less toxic (IC_{50} values > 2 μg/mL) than free Dox (IC_{50} value = 0.24 μg/mL). Biodistribution in mice bearing sc B16F10 tumors was assessed after administration of PEGs (5000, 10000, or 20000 g/mol) radioiodinated using the Bolton and Hunter reagent or PEG–Dox conjugates by HPLC. The ^{125}I-labeled PEGs showed a clear relationship between Mw and blood clearance and tumor accumulation. The highest Mw PEG had the longest plasma residence time and consequently the greatest tumor targeting. The PEG–Dox conjugates showed a markedly prolonged plasma clearance and greater tumor targeting compared to free Dox, but there was no clear molecular weight-dependence on biodistribution. This was consistent with the observation that the PEG–Dox conjugates formed micelles in aqueous solution comprising 2–20 PEG–Dox molecules depending on polymer Mw and architecture. Although PEG–Dox showed greater tumor targeting than free Dox, PEG conjugation led to significantly lower anthracycline levels in heart. Preliminary experiments to assess antitumor activity against sc B16F10 in vivo showed the PEG_{5000}linear (L)–GFLG–Dox and PEG_{10000}branched (B)–GLFG–Dox (both 5 mg/kg Dox-equiv) to be the most active with T/C values of 146 and 143%, respectively. Free Dox did not show significant activity in this model (T/C = 121%). Dose escalation of PEG_{5000}(L)–GFLG–Dox to 10 mg/kg Dox-equiv prolonged further animal survival (T/C = 161%). Using the Dox-sensitive model ip L1210 (where Dox displayed a T/C = 150% after single ip dose), the PEG_{5000}(L)–GFLG–Dox displayed a maximum T/C of 141% (10 mg/kg Dox-equiv) using a once a day (×3) schedule. Further studies are warranted with PEG_{5000}(L)–GFLG–Dox to determine its spectrum of antitumor activity and also the optimum dosing schedule before clinical testing.

INTRODUCTION

Early efforts to capitalize on lysosomotropic drug delivery (*1*) and tumor-specific uptake by the enhanced permeability and retention (EPR) effect (*2*) has generated antitumor polymer conjugates that have progressed into clinical trial (*3*–*6*). These first successes have led to an exponentially growing interest in the field of drug–polymer conjugates (polymer therapeutics) particularly as Phase I clinical studies with *N*-(2-hydroxypropyl)-methacrylamide (HPMA) copolymer–doxorubicin (Dox) showed a 4–5-fold decrease in Dox toxicity together with antitumor activity of the conjugate in chemotherapy refractory patients (*3*).

For many years, poly(ethylene glycol)s (PEGs) have been used to modify peptides and proteins (reviewed in refs 7, 8) in order to increase solubility, reduce immunogenicity, increase resistance to proteolysis and, in addition, provide a means to modulate pharmacokinetics (*8*). More recently, PEG conjugates containing antitumor drugs such as paclitaxel, camptothecin, and Dox have been described (reviewed in ref 9). A PEG–camptothecin conjugate has progressed to clinical trial (*10*).

To identify a PEG–Dox conjugate with improved tumor targeting and efficacy, a series of monomethoxy-PEG–peptide–Dox conjugates were prepared. PEGs of different (linear (L) or branched (B)) architecture and Mw (5000,

* Corresponding authors. francesco.veronese@unipd.it (F.M.V.) or duncanr@cf.ac.uk (R.D.).
⊥ University of Padua.
† Istituto per lo Studio delle Macromolecole (CNR).
‡ PolyPeptide Laboratories (Sweden) AB.
§ Cardiff University.
‖ Polymer Laboratories Ltd.

10.1021/bc040241m CCC: $30.25 © 2005 American Chemical Society
Published on Web 05/14/2005

10000, or 20000 g/mol) were used together with a library of peptidyl linkers (GFLG, GLFG, GLG, Nle-GGRR, or Nle-RGLG) for covalent attachment of Dox to the carrier. The resultant conjugates were characterized in respect of their total and free Dox content and tendency to form micelles in aqueous solution. To aid selection of compounds for in vivo evaluation, the rate of Dox release by isolated lysosomal enzymes was established in vitro, and also their cytotoxicity was determined in vitro using a murine melanoma B16F10 model. To establish the effect of PEG molecular weight on tumor targeting, the biodistribution of ^{125}I-labeled PEGs of Mw 5000, 10000, and 20000 g/mol was studied at various times after intravenous (iv) administration to mice bearing established subcutaneous (sc) B16F10 tumors. Additionally, the biodistribution of PEG−Dox conjugates was followed using an HPLC method to detect Dox in tissues. Finally, the antitumor activity of the conjugates was investigated in a Dox-resistant model (sc B16F10) and a Dox-sensitive model (ip L1210). These models were chosen as they have been widely used to evaluate PK1 and other polymeric antitumor conjugates (*11*, *12*) and the mechanism of EPR-mediated targeting has been widely studied in the B16F10 model (*13*).

MATERIAL AND METHODS

Materials and Equipment. Linear monomethoxy-PEG of weight average molecular mass (Mw) 5000 and 10000 g/mol, linear PEG−norleucine-OSu (PEG−Nle-OSu) Mw = 5000 g/mol, branched PEG-OSu Mw = 10000 and 20000 g/mol were obtained from Shearwater Polymers (Huntsville, AL). Dox·HCl was purchased from Tide International LTD (China). 4-Nitrophenyl chloroformate, 1-cyclohexyl-3-(2-morpholinoethyl)carbodiimide methyl *p*-toluensulfonate (CMC), and *N*-hydroxybenzotriazole (HOBT) were obtained from Aldrich Chemie (Steinnheim, Germany). The solvents and other chemicals were of analytical grade from Merk (Darmstadt, Germany). 3-[4,5-Methylthiazol-2-yl]-2,5-diphenyltetrazolium bromide (MTT), optical grade DMSO, and Bz-PVR-*p*-nitroanilide (NAp) were from Sigma, UK. The B16F10 cell line was kindly donated by Professor Ian Hart, St Thomas Hospital, London.

For pH titration, a radiometer autoburet ABU 80 (Copenhagen, Denmark) with titration TTT 80 and titrigraph REA 160 was used. UV−visible analyses were performed on a Perkin-Elmer Lamba 5 spectrophotometer. Analytical chromatography was performed using a liquid chromatograph LC 10 AS−SPD 10A VP UV−Vis detetctor (Shimadzu). Preparative size exclusion chromatography or ion exchange chromatography was carried out using Sephadex LH-20 or QAE-Sephadex A-50 columns (Pharmacia Biotech, Sweden), respectively. ^{1}H (200 Mz) NMR spectra were recorded in DMSO-*d*6 (Varian Gemini-200).

Solid-Phase Synthesis of Peptides. Peptides H-GFLG-OH·TFA, H-GLPG-OH·TFA, and HGLG- OH·TFA were synthesized by solid-phase peptide synthesis (SPPS) using the Merrifield procedure (*14*). Merrifield resin containing the first amino acid, Boc-G-OH, was preattached to the support (degree of substitution 1.04 mmol/g) and was used for synthesis of the desired peptide on a 5 mmol scale. Addition of the remaining amino acids was accomplished by repeated cycles of coupling and deprotection. Boc-amino acids (2-fold molar excess) were coupled to the peptide resin employing DCC as a condensation reagent. The peptides obtained were cleaved from the resin and deprotected by treatment with liquid HF and purified by preparative C_{18} reverse phase HPLC. Absorbed peptide was eluted by gradient elution. Eluant A was 0.1% TFA, and eluant B was acetonitrile. The gradient was run from 100% A to 60% B over 60 min. Fractions containing pure peptide were pooled and lyophilized.

Solution Synthesis of Hydrophobic Peptides. Boc-G-OSu was coupled to H-LG-OH in an active ester coupling to give Boc-GLG-OH. The tripeptide obtained was deprotected by treatment with 50% TFA/DCM (v/v) for 30 min. After evaporation of the solvents, the residue obtained was precipitated by addition of diethyl ether, and the precipitate was filtered. The tripeptide H-GLG-OH·TFA was purified as described above for the solid-phase produced peptides.

The tetrapeptide H-GLFG-OH·TFA was synthesized by reaction of Boc-GL-OSu with H-FG-OH using an active ester coupling to give Boc-GLFG-OH. The tetrapeptide obtained was deprotected by treatment with 50% TFA/DCM (v/v) for 30 min. After solvent evaporation the residue obtained was precipitated by addition of diethyl ether, and the precipitate was filtered. The product was purified as described above.

The tetrapeptide H-GFLG-OH·TFA was assembled by reaction of Boc-GP-OSu and HLG-OH in an active ester coupling to give Boc-GPLG-OH. The product was deprotected by treatment with 50% TFA/DCM (v/v) for 30 min. After solvent evaporation, the residue obtained was precipitated by addition of diethyl ether and the precipitate was filtered, and the product was purified as described above. The arginine-containing peptides H-GGRR-OH and H-RGLG-OH were also prepared by solid-phase synthesis in the same manner as described for the hydrophilic peptides, but in this case the side chain protection of arginine was achieved using a tosyl group.

Hydroxy-Terminated PEG−Peptide Conjugates. Linear monomethoxy-PEG-OH (Mw = 5000 g/mol or 10000 g/mol) (1 g, 0.2 mmol or 2 g, 0.2 mmol) was dissolved in 20 mL of toluene and dried by water−toluene distillation. To the water-free PEG-OH toluene solution were added ethylene chloride (2 mL) and 4-nitrophenyl chloroformate (80.6 mg, 0.4 mmol). The pH was brought to 8.0 by TEA (56 μL, 0.4 mmol). The obtained PEG-*p*-nitrophenyl carbonate was recovered by ether addition (300 mL) and the precipitate purified by crystallization from ethyl acetate. The peptide H-GFLG-OH (236 mg, 0.6 mmol) were dissolved in 4 mL of CH_3CN/H_2O (1:1) in the presence of TEA (84 μL, 0.6 mmol) and PEG-*p*-nitrophenyl carbonate (0.52 mg, 0.1 mmol) was added. The mixture was maintained at room temperature, under constant stirring of the solution, for 12 h. The pH of the solution was brought to 3.0, and the product was extracted into chloroform (five times, 50 mL each), concentrated, and precipitated with diethyl ether. The white solid product was collected by filtration and dried in vacuo (yield 467.3 mg, 0.086 mmol, 86%).

To characterize the product in respect to the carboxylic groups, the peptide was titrated with 0.01 N NaOH. The homogeneity was also assessed by HPLC chromatography using a Vydac C_{18} (250 mm × 4.6 mm) reverse phase column with UV detection at 226 nm. The gradient used water (A) and acetonitrile (B) as eluants (both containing 0.05% TFA) and was run from 10%(B) to 80%(B) over 40 min, and then the elution was maintained as isocratic for a further 10 min.

Carboxy-Terminated PEG−Peptide Conjugates. Branched monomethoxyPEG activated as succinimidyl ester (PEG-OSu) (Mw 10000 g/mol or 20000 g/mol) (1.03 g, 0.1 mmol or 2.03 g, 0.1 mmol) was added under stirring

to H-GPLG-OH (58.9 mg, 0.15 mmol.), H-GLPG-OH (58,9 mg, 0.15 mmol), or H-GLG-OH (36.8 mg, 0.15 mmol), dissolved in 2 mL of anhydrous DMSO. TEA 21 mL (0.15 mmol) was added to reach pH 8, and the reaction mixture was maintained under stirring at room temperature for 12 h. The solution was cooled, diluted with water, brought to pH 3 with 0.1 N HCl, and extracted with chloroform (five times, 50 mL each). After concentration under vacuum, the solution was precipitated with diethyl ether and dried. The precipitate was collected, dried in vacuo, and crystallized from ethanol (yield 467.3 mg, 0.086 mmol, 86%). The product was characterized by titration and by reverse phase HPLC as reported above.

In the case of peptides H-GGRR-OH and H-RGLG-OH the solvent of coupling was H_2O/acetonitrile (2:1) and the peptide was added at a molar excess, PEG−Nle-OSu:H-peptide-OH molar ratio = 1:6).

Synthesis of PEG−Peptide−Dox. Linear or branched PEG−peptides (526.5 mg,0.05 mmol) were dissolved in 2 mL of anhydrous DMF. Dox·HCl (43.5 mg, 0.075 mmol) and TEA (26 mL, 0.184 mmol) were dissolved separately in anhydrous DMF (3 mL), and the mixture was added to the PEG−peptide solution. 1-Cyclohexyl-3-(2-morpholinoethyl)carbodiimide methyl *p*-toluensolfonate (CMC) (63.5 mg, 0.15 mmol) in 1 mL of DMF and *N*-hydroxybenzotriazole (HOBT) (6.7 mg, 0.05 mmol) were added to the ice-cooled reaction mixture. The reaction mixture was left under constant stirring for 24 h at room temperature. After evaporation of the DMF, the residue was purified by gel filtration chromatography using a Sephadex LH20 resin with DMF as eluant. The fractions were analyzed for Dox by measuring absorption at 480 nm and using an iodine assay for free PEG (*15*). The PEG−Dox-containing fractions were pooled, and the solvent was evaporated. The red solid residue was redissolved in dichloromethane and added dropwise into diethyl ether (200 mL). The precipitate was collected and dried in vacuo, yielding the final conjugate (460 mg, 0.0415 mmol, 83%).

Measurement of Total Dox Content in PEG−Peptide−Dox Conjugates. PEG−peptide−Dox (8.4×10^{-4}) conjugates were dissolved in 1 mL of 1 N HCl and heated in a water bath at 50 °C for 2 h to yield doxorubicinone. The solution was cooled at room temperature, diluted by addition of 3 mL of DMSO, and analyzed within 2 h by HPLC using a Vydac C_{18} reverse phase column (250 mm × 4.6 mm) with UV detection at 480 nm. A gradient elution was used with water as eluant (A) and acetonitrile as eluant (B) (both containing 0.05% TFA). The gradient was run from 25% B to 30% B over 10 min, and then to 80% B over 5 min. Isocratic elution was then maintained for a further 15 min. Doxorubicinone was used as reference standard.

Solution Properties of PEG−Peptide−Dox Conjugates. A multiangle laser light scattering (MALS) photometer Dawn DSP-F from Wyatt (Santa Barbara, CA) was used in off-line batch mode to study the molecular properties (molecular weight, dimension, and aggregation number) of the PEG−peptide−Dox conjugates. The MALS photometer uses a vertically polarized laser, 632.8 nm of wavelength, and measures simultaneously by an array of photodiodes the intensity of the scattered light at 15 fixed angular locations ranging in aqueous solvent from 14.5° to 151.3°. Even though measurements were performed in static off-line mode a K5 flow cell was preferred to reduce the scattering volume. The solvent used was 0.15 M NaCl, and analyses were performed at room temperature. The calibration constant used to transform the photodiode voltage, i.e., the Rayleigh Factor $R(\theta)$, was calculated using toluene as a standard ($R(\theta)=1.406 \times 10^{-5}$ cm^{-1}), where θ denotes the angle between the detector and the primary incident light. The angular normalization of the different photodiodes was undertaken using a concentrated solution of bovine serum albumin (BSA) assumed to be an isotropic scatterer. Details of the MALS photometer have been described in detail elsewhere (*16*). It is well-known that three important parameters could be obtained from a MALS experiment in batch mode (Zimm plot): the weight-average molar mass M_w, the second virial coefficient A_2, and the *z*-average of the root-mean squares radius $\langle s^2 \rangle_z$, which denotes the gyration radius R_g. The specific refractive index increment, d*n*/d*c*, with respect to the solvent was measured by a KMX-16 differential refractometer from LDC Milton Roy (Riviera Beach, FL). The d*n*/d*c* value for the conjugates ranged from 0.131 to 0.135 mL/g. Each solution was filtered through a 0.2 μm filter.

Evaluation of Dox Release by Isolated Lysosomal Enzymes. Experiments were carried out as described previously (*17*, *18*). Briefly, rat liver lysosomal enzymes (Tritosomes) were isolated according to the method of Trouet (*19*) and were standardized for activity by measuring their ability to degrade the substrate Bz-PVR-*p*-nitroanilide (NAp). Protein content of the tritosomes was also measured. The batch used here contained 0.96 mg protein/mL and had an activity 24.7 nmol NAp release/min/mg protein.

PEG−Dox conjugates were dissolved in 0.2 M citrate-phosphate buffer pH 5.5 containing Triton x-100 (0.2%v/v), reduced glutathione (5 mM), and EDTA (1 mM) to give a final concentration of 100 μg Dox-equiv/mL. Tritosomes (400 μL per mL of incubation mixture) were added to start the assay, and the sample was thoroughly mixed. All reagents were maintained at 37 °C throughout. Samples (100 μL) were taken over 5 h and immediately frozen in liquid nitrogen and stored frozen until analysis by HPLC.

A method previously described (*20*, *21*) was used as an initial step to extract free Dox from the PEG−Dox samples. However, some PEG−Dox was also transferred into the extraction solvent using this procedure. Therefore, after solvent evaporation, 0.5 mL of ethanol was added to the dry Dox residue in a 15 mL polypropylene centrifuge tube. After 30 s at 45 °C, the samples were vortexed for 5 s and placed on ice overnight to precipitate contaminating PEG−Dox conjugate. After this time, the sample was centrifuged (2000*g* for 15 min at 4 °C) and the supernatant containing Dox and the internal standard daunomycin (Dnm) was analyzed by HPLC. Isoproanol (29% in water) adjusted to pH 3.2 was used as a mobile phase, flow rate 1 mL/min, with a C_{18} Bondapack column (3.9 × 150 mm) using fluorescence detection. The free Dox recovery using this procedure was 85%, and the limit to detection for free Dox was ~10 ng.

Evaluation of in Vitro Cytotoxicity. The cytotoxicity of the PEG−Dox conjugates was assessed using the adherent murine B16F10 melanoma cell line as previously described (*22*). Cells were grown in RPMI medium supplemented with 10% fetal calf serum and seeded at a density of 10^4 cells per well in 96-well tissue culture plates. After 24 h, the medium was replaced and with serial dilutions of either Dox or the PEG−Dox added in fresh medium (100 μL). All stock solutions were filtered through a 0.22 μm membrane filter to ensure sterility. The cells were then incubated for 67 h at 37 °C. Then 20 μL of sterile MTT solution (0.5% w/v in PBS) was added to each well. After an additional 5 h incubation, the

Scheme 1

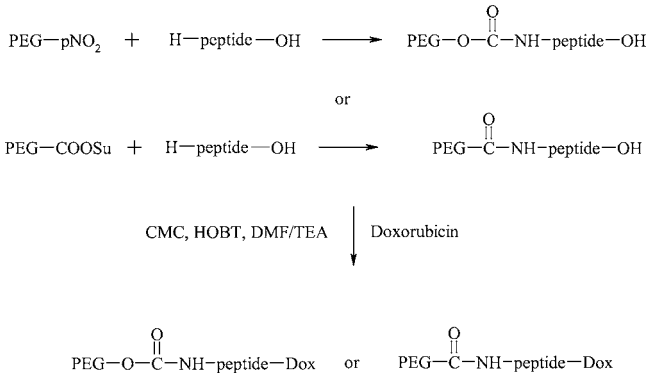

medium was removed and optical grade DMSO added to dissolve the insoluble formazan dye formed. Absorbance at 550 nm was measured using a microtiter plate reader and cell viability expressed as a percentage viability of cells incubated with medium alone.

Biodistribution of ^{125}I-Labeled PEGs and PEG−Dox in Mice Bearing sc B16F10 Tumors. *Tumor Model.* All animal experiments were conducted according to the United Kingdom Coordinating Committee on Cancer Research (UKCCCR) Guidelines (*23*). C57 black male mice were inoculated with 10^5 B16F10 tumor cells sc behind the neck. Once the tumor was palpable (∼50 mm^2), approximately 11 days later, ^{125}I-labeled PEGs or PEG−Dox was administered iv.

^{125}I-Labeled PEGs. Mono-amine-PEG 5000 g/mol (Shearwater), bis-amine-PEG 10, 000 g/mol (Fluka) and bis-amine-PEG 20 000 g/mol (Fluka) were labeled with [^{125}I]iodide using Bolton Hunter reagent. The crude reaction mixture was purified by elution through Sephadex G-25 gel filtration medium, and the purity in respect of free [^{125}I]iodide was assessed by paper electrophoresis. The specific activity of the products was 44, 50, and 42 μCi/mg for PEG 5000, 10000, and 20000 g/mol, respectively, and their purity > 99%. The ^{125}I-labeled PEGs were each diluted to give 5×10^6 cpm/mL before iv injection (dose ∼ 1.4 mg/kg). The mice were killed after 1 h, 5 h, or 24 h ($n = 3$), and a blood sample was taken before the tumor and organs were dissected. Blood and organs (after homogenization) were made up to a known volume and assayed for radioactivity. The biodistribution was expressed as a percentage of dose administered.

PEG−Dox Conjugates. Once the sc tumors had become palpable, PEG−Dox conjugates were injected iv at a dose of 5 mg/kg (Dox-equiv). After 1 h, the animals were killed and the organs were dissected as above. In this case an HPLC method (as described above) was used to quantify the total Dox content of blood and tissues. In this case the samples were subjected to acid hydrolysis before extraction and quantitation of Dox aglycone.

Antitumor Activity of PEG−Dox in the sc B16F10 and ip L1210 Models. *B16F10 Model.* C57 black male mice were injected with 1×10^5 B16 F10 murine melanoma cells sc as described above. They were then left for 10−12 days until tumor size reached between 9 and 25 mm^2. Animals were randomized into control and treatment groups ($n = 5$) and injected intraperitoneally (ip) with saline, Dox, or PEG−Dox according to the schedules and doses shown in the Results section.

L1210 Model. On day 0, 1×10^5 L1210 cells were injected ip into DBA2 mice. On day 1, the mice were randomized into control and treatment groups ($n = 5$). They were injected ip (either on day 1 only or on days 1, 2, and 3) with saline, free Dox or the PEG−Dox conjugate. The precise dose and schedule is shown in the Results section. In both cases animals were monitored daily for weight change, and for the B16F10 tumor model the tumor size was measured. Animals were humanely killed when their tumor burden reached the maximum allowable size according to the UKCCCR Guidelines (*23*).

Table 1. Structure and Composition of the PEG−Peptide−Dox Conjugates (a typical conjugate structure is shown)

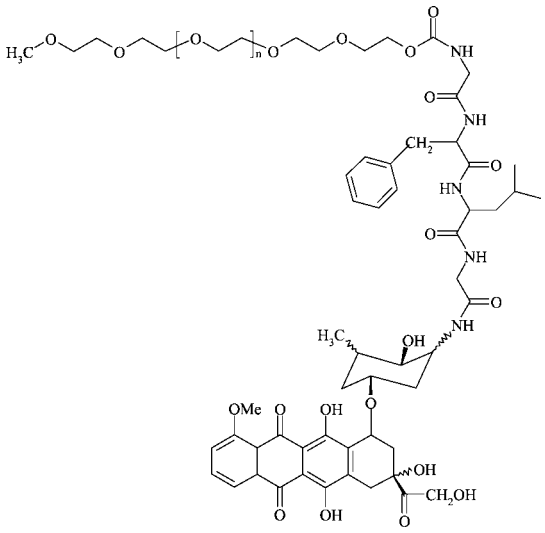

compd	structure	total Dox content[a] (wt %)	free Dox content[a] (% total Dox)
1	linear PEG_{5000}−GFLG−Dox	3.0−7.4	0.53−1.41[a]
2	branched PEG_{10000}−GFLG−Dox	5.0	0.99
3	linear PEG_{10000}−GFLG−Dox	4.3	1.47
4	branched PEG_{20000}−GFLG−Dox	2.7	0.56
5	branched PEG_{10000}-GLFG−Dox	5.2	0.24
6	branched PEG_{10000}-GLG−Dox	5.8	0.62
7	linear PEG_{5000}−Nle-GGRR−Dox	8.0	1.57
8	linear PEG_{5000}−Nle-RGLG−Dox	6.4	0.89

[a] Varied in different batches. Total Dox content was evaluated by HPLC on the basis of doxorubicinone released after acid hydrolysis, while free Dox was evaluated on the HPLC of the untreated sample. The amount of unconjugated free PEG remaining in samples was not evaluated.

RESULTS AND DISCUSSION

Synthesis and Characterization of PEG−Peptide−Dox Conjugates. Three peptides H-GFLG-OH·TFA, H-GLFG-OH·TFA, and H-GLG-OH·TFA were synthesized using solid-phase and solution synthesis. The crude products were purified to homogeneity by preparative HPLC using a C_{18} derivatized silica column, and each peptide was characterized by analytical HPLC, amino acid analysis, and mass spectroscopy (MS). These analyses confirmed the proposed structure and also demonstrated that the two synthetic methods (solid phase and solution) were equally effective in giving pure products (by HPLC purity ranged between 99.3 −100%). The two hydrophilic arginine-containing peptides HGGRR-OH·TFA and H-RGLG-OH·TFA were synthesized using solid-phase synthesis only. Again purification was facilitated by reverse phase chromatography as described above. Analysis (HPLC, MS, and amino acid analysis) confirmed peptide structure, and the purity as assessed by analytical HPLC was >97%. Both hydrophobic and the more hydrophilic arginine-containing peptides were prepared in good yield (∼80% yield) using the methods described. Whereas solid-phase synthesis is preferred for rapid

synthesis of peptides on a small scale, in contrast, for large scale preparation, solution synthesis is frequently used as a less expensive alternative.

To prepare PEG−peptide−Dox conjugates, a sequential synthetic procedure was adopted. First the desired peptide linker was bound to PEG, and then Dox was conjugated via the amino glycoside to the peptide carboxylic group using CMC and HOBT as coupling agents (Scheme 1). This method was preferred to conventional PEG-supported liquid-phase synthesis in which the amino acids are added sequentially, as it allows the use of the same stock of peptide for binding to PEGs of different structure. Eight different conjugates were thus synthesized that differ in molecular weight and shape of the polymer (linear or branched PEG) and in composition of the peptide arm (Table 1).

In the first group of compounds (PEG−Dox **1**−**4**) the peptide H-GFLG-OH was retained, but PEGs with a linear or a branched form of Mw 5000 g/mol or 10000 g/mol were used (Table 1). In the second group of compounds (PEG−Dox **5**, **6**) the peptide composition was changed: First by reversal of FL to give LF (compare PEG−Dox **5** and PEG−Dox **1**−**4**) and then by deletion of F completely (PEG−Dox **6**). Finally two conjugates containing arginine in the linker were synthesized (PEG−Dox **7**, **8**). Arginine was inserted to increase the linker hydrophilicity with the aim of decreasing the tendency of Dox-induced micelle formation in water.

Different activation conditions were used when binding the various PEGs to peptides. For linear PEG terminating with an hydroxyl group, chloroformate activation was used to give a stable carbamate linkage between PEG and peptide (PEG−Dox **1** and **3**). In this case, aqueous−organic reaction conditions were used to give better dissolution of the peptide. However, it should be noted that a molar excess of peptide was needed to overcome the partial hydrolysis of the nitrophenyl group that takes place simultaneously to the aminolysis. The advantage of this procedure lies in the fact that unreacted PEG is hydrolyzed back to hydroxyl PEG and thus it cannot react with Dox in the following synthetic step. In contrast the branched PEGs had terminal COOH groups due to their unique method of synthesis (*24*). These PEGs were activated as hydroxysuccinimidyl esters and, since they are easily hydrolyzed by water, the reaction with the peptides was carried out in DMSO. Under these conditions, a large molar excess of peptide was not needed.

For the synthesis of the two arginine-containing peptides, a special Nle-containing PEG was used (*25*). The Nle residue is particularly useful, as it allows an easy analytical characterization of the products by amino acid analysis after acid hydrolysis. Arginine peptides were linked to the terminal COOH group of PEG−Nle-OH previously activated as succinimidyl ester. An aqueous−organic solution was needed since these peptides possess very low solubility in organic solvents. Also in this case a large molar excess of peptide over PEG was used to overcome the hydrolysis of the succinimidyl ester in this solvent mixture. In the PEG−Nle conjugates, the conjugate composition could be confirmed precisely by measuring the Nle:arginine ratio after acid hydrolysis, and the observed ratios were consistent with the theoretical. Dox conjugation to PEG−peptides was carried out in DMF also using CMC in the presence of HOBT (Scheme 1). Excess Dox was used to achieve complete reaction with the PEG−peptides. It is easier to separate the low molecular mass Dox from the large conjugate PEG−peptide−Dox than to remove excess PEG reagent of a similar molecular weight. Free Dox was removed using

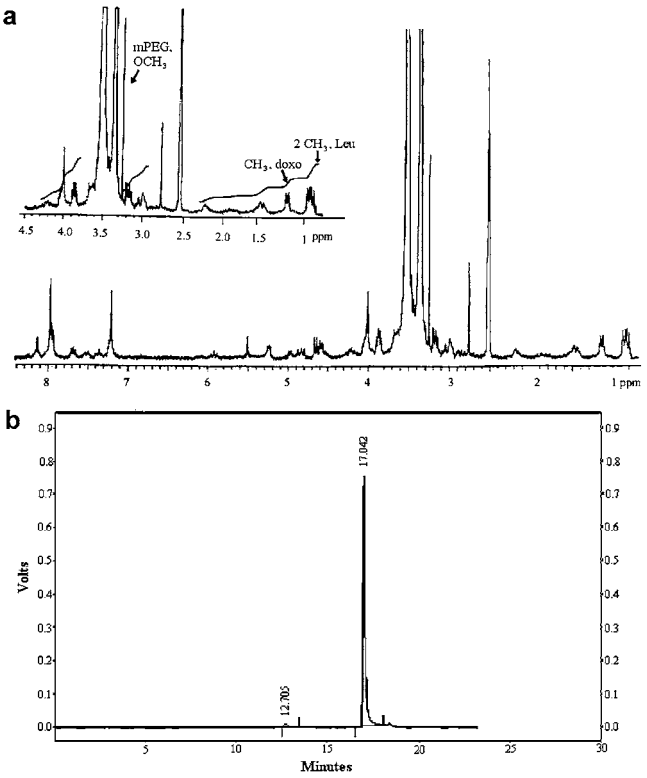

Figure 1. Characterization of PEG−Dox conjugates. Panel a shows an ^{1}H NMR spectrum of the linear PEG_{5000}−GFLG−Dox conjugate. The chemical shifts are shown in Table 2. Panel b shows a C_{18}-HPLC chromatogram of PEG−Dox 1 (UV = 226 nm). The major peak at t_R = 17.04 min is PEG−Dox 1 and free Dox is at t_R = 12.71 min. The chromatogram indicates the absence of unreacted PEG−AA (no peak at t_R = 16.01 min).

LH-20 Sephadex column chromatography with DMF as eluant. Only occasionally did a small amount of free Dox remain, and in this case a second chromatography run was needed to reduce the percentage free Dox in the product below 2.0% the total Dox content. The purity of the conjugates was assayed by C_{18}HPLC which could resolve conjugated and free Dox and any residual unreacted PEG−peptide. For example, the elution pattern of the PEG−Dox 1 is reported in Figure 1b. A trace of free Dox (∼0.5%) can be seen at t_R = 12.71 min and the major peak at t_R = 17.04 min corresponds to the conjugate. No evidence of unreacted PEG−AA (t_R = 16.01 min) could be seen.

The total and free Dox content of all conjugates is shown in Table 1. The peptide composition of each conjugate was confirmed by quantitative amino acid analysis after acid hydrolysis, and the amino acid ratios seen corresponded to the expected within the experimental error of the methods. ^{1}H NMR in DMSO was used to confirm product identity. A typical ^{1}H NMR spectrum (for the linear PEG_{5000}−GFLG−Dox conjugate) is shown in Figure 1a, and the chemical shifts ascribed to the polymer chain, Dox, and the spacer arm protons are reported in Table 2. The integral values of the methoxy group protons of the polymer chain and 2-methyl proton of leucine and 5′-methyl protons of Dox again support the assignment of a 1:1:1 composition of the PEG:peptide:Dox. For in vitro and in vivo experiments, total Dox content of the conjugates was calculated by UV absorption, since PEG has such as a high hydration tendency and it is not possible to remove the strongly bound water by azeotropic distillation due to the instability of Dox under these conditions. The presence of unreacted PEG would also have added to the error if weight % had been used.

Table 2. Proton Shifts Seen for the Linear PEG_{5000}−GFLG−Dox Conjugate during ^1H NMR (see also Figure 1)

δ	^1H NMR signals	descriptor
0.82	6H, q, $2CH_3$	Leu
1.13	3H, d, CH_3-C-5′	Dox
1.47	2H, d, CH_2	Phe
1.85	2H, m, H_2C-2′	Dox
2.20	2H, m, H_2C-9	Dox
2.75	2H, s, CH_2	Dox
3.24	3H, s, OCH_3	H-PEG
3.99	3H, s, H_3C-O-C-1	Dox
4.20	1H, m, HC-5′	Dox
4.59	2H, d, H_2C-14	Dox
4.70−4.90	2H, m, OH-C-8 and OH-C-4′	Dox
4.92	1H, m, HC-10	Dox
5.25	1H, m, HC-1′	Dox
5.92	1H, t, HO-C-14	Dox
7.20	5H, m, arom	Phe
7.69	1H, t, HC-3	Dox
7.92	2H, d, HC-2 and HC-4	Dox

Table 3. Determination of the Solution Properties of the PEG−Dox Conjugates Using Light Scattering

compound	apparent Mw (g/mol × 10^{-3})	R_g[a] (nm)	aggregation number[b]
PEG−Dox-1	120.0	23.3	20.1
PEG−Dox-2	33.6	29.7	3.0
PEG−Dox-3	33.1	15.6	3.0
PEG−Dox-5	28.4	13.0	2.6
PEG−Dox-6	30.6	16.8	2.8
PEG−Dox-7	54.7	45.6	9.1
PEG−Dox-8	35.2	21.3	5.9

[a] R_g gives the average radius of the molecule or aggregate. [b] The aggregation number indicates the approximate number of PEG−Dox molecules in the surpramolecular assembly.

Solution Properties of PEG−Dox Conjugates. Evaluation of the properties of the PEG−peptide−Dox conjugates in aqueous solution by light scattering showed clear evidence of conjugate aggregation (Table 3). The extent of aggregation was dependent on conjugate structure, and the linear PEG_{5000}−GFLG−Dox conjugate had by far the greatest tendency to form micelles that had an apparent Mw of 120000 g/mol which is equivalent to an aggregation number of ∼20. In general the other hydrophobic conjugates showed much lower aggregation tendency with an aggregation number of ∼3. Contrary to expectation, however, the more hydrophilic arginine-containing conjugates displayed a relatively high tendency to form micelles. These were composed of ∼6−9 PEG_{5000}−NleRGLG−Dox or PEG_{5000}−NleGGRR−Dox molecules, respectively. The tendency of polymer−drug conjugates to form unimolecular micelles (with bound hydrophobic drug forming the intramolecular core) or multimolecular micellar aggregates is important to note. It has been clearly shown that this phenomenon can limit access of activating enzyme and thus often determines the biological activity of these macromolecular prodrugs (*26*).

Lysosomal Enzyme-Mediated Release of Dox from PEG−Dox Conjugates. Incubation of the PEG−peptide−Dox conjugates **1**−**6** with tritosomes led to a linear initial release of Dox over 5 h (Figure 2; Table 3). It was evident that the amino acid sequence of the peptide spacer rather than PEG structure had the strongest influence on Dox release since conjugates **1**−**4**, which bore very different PEGs but had identical spacers, released similar quantities of Dox over 5 h. Branched PEG_{10000}-GLFG−Dox (conjugate **5**) displayed the fastest initial release rate. The tripeptide-containing linear PEG_{5000}-GLG−Dox (conjugate **6**) displayed a slower release rate. This pattern of degradation corresponds to the known susceptibilities of these linkers to degradation by lysosomal thiol-dependent proteases when the same sequences were used as side-chains in *N*-(2-hydroxypropyl)methacrylamide (HPMA) copolymer conjugates containing Dox (*27*). Interestingly, linear PEG_{5000}−GFLG−Dox released drug at the same rate as HPMA copolymer−GFLG−Dox when incubated with tritosomes, but much more quickly than a PEG−peptide block copolymer bearing GFLG−Dox side chains (*28*).

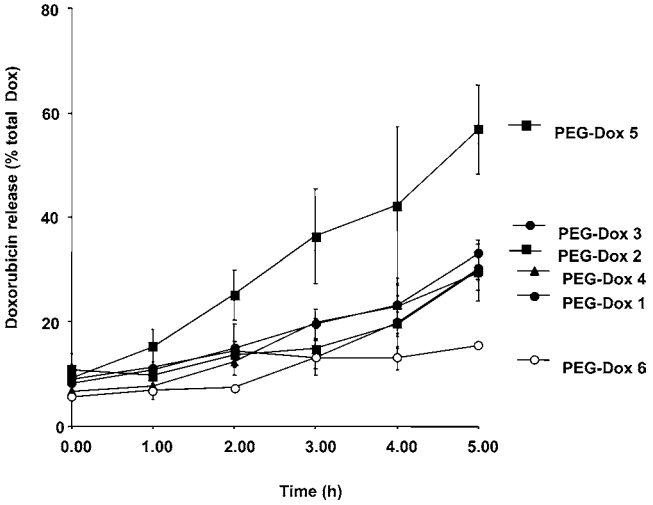

Figure 2. Release of Dox from PEG−peptide−Dox conjugates during incubation with isolated rat liver lysosomal enzymes (tritosomes). Each data point represents the mean ± SD of three separate experiments.

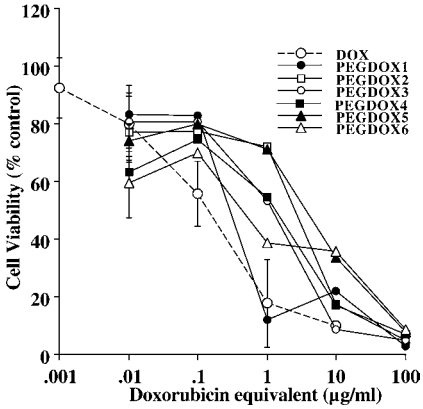

Figure 3. In vitro cytotoxicity of the PEG−Dox conjugates assessed using B16 F10 cells (MTT assay) after a 72 h incubation. Error bars represent the mean ± SD and $n = 4$−6.

The arginine-containing linkers displayed the lowest rate of release of free Dox, but this is most likely due to the specificity of the predominant lysosomal proteases rather than the micellerization of these conjugates.

In Vitro Cytotoxicity. The in vitro cytotoxicity tests (Figure 3; Table 4) showed the PEG−peptide−Dox conjugates to be 10−100 fold less toxic than free Dox (0.24 μg/mL) against B16F10 cells, an observation consistent with the slower rate of endocytic uptake and lysosomotropic activation as the rate-limiting step. Conjugates **1**−**4** having the GFLG linker displayed the greatest cytotoxicity ($IC_{50} = 4.6$−8.3 μg/mL). The low cytotoxicity of PEG−GLG−Dox conjugate **6** correlates well with its poor rate of enzymatic activation. However, it is difficult to explain the relatively low cytotoxicity of PEG−GLFG−Dox conjugate **5** as this contains the linker most susceptible to enzyme attack. Throughout the in vitro testing

Table 4. Summary of the Biological Properties of the PEG−Dox Conjugates

compound	release of Dox during incubation with tritosomes (% total Dox liberated) 5 h	24 h	IC_{50} (μg/mL)[a]	B16F10 model T/C (%)
Dox	N/A	N/A[b]	0.2	121
PEG−Dox 1	30.22 ± 2.19	75.9	5.2	146
PEG−Dox 2	29.74 ± 3.70	48.4	8.3	134
PEG−Dox 3	33.07 ± 2.40	51.4	4.6	113
PEG−Dox 4	29.31 ± 5.48	60.6	6.7	130
PEG−Dox 5	56.89 ± 8.54	72.1	72	143
PEG−Dox 6	15.50 ± 0.53	37.6	105	N/A
PEG−Dox 7	3.08 ± 0.90	N/A	2.4	N/A
PEG−Dox 8	4.00 ± 1.03	N/A	3.8	N/A

[a] Assessed against B16 F10 cells over 72 h using the MTT assay. [b] N/A; not undertaken.

there seemed to be no clear correlation between PEG structure and cytotoxicity, and this is noteworthy that the free Dox content in each conjugate, even though the levels are low, can influence in vitro cytoxicity.

Biodistribution of ^{125}I-Labeled PEGs and PEG−Dox Conjugates. As would be predicted for water-soluble macromolecules (*29, 30*), the higher molecular weight ^{125}I-labeled PEGs remained circulating in the blood for longer due to decreased renal clearance after iv injection (Figure 4a; Table 5). This longer plasma residence time led to increased tumor targeting (Figure 4a; Table 5), but in many cases also gave increased normal tissue exposure (Table 5). Although the highest molecular weight PEG showed greatest tumor levels, comparison of the area under the curve values for each polymer indicated that PEG_{5000} had the most favorable

Table 5. Body Distribution of ^{125}I-Labeled PEGs of Mw 10000 g/mol and 20000 g/mol after iv Injection

organ	time (h)	PEG 5K[a]	PEG 10K[a]	PEG 20K[a]
blood	1	0.48 ± 0.05	2.7 ± 0.54	10.68 ± 1.02
	5	0.39 ± 0.05	1.22 ± 0.30	5.59 ± 0.90
	24	0.26 ± 0.06	0.57 ± 0.13	1.45 ± 0.21
tumor	1	0.36 ± 0.02	1.19 ± 0.20	1.96 ± 0.77
	5	0.57 ± 0.65	1.06 ± 0.31	2.01 ± 0.62
	24	0.11 ± 0.04	0.26 ± 0.07	0.81 ± 0.11
liver	1	5.11 ± 0.50	4.34 ± 0.38	4.20 ± 0.55
	5	4.75 ± 0.70	3.89 ± 0.69	3.56 ± 0.78
	24	3.75 ± 0.76	1.79 ± 0.53	1.60 ± 0.33
heart	1	0.10 ± 0.03	0.58 ± 0.12	1.90 ± 0.30
	5	0.10 ± 0.02	0.18 ± 0.06	1.19 ± 0.14
	24	0.03 ± 0.02	0.08 ± 0.03	0.23 ± 0.04
spleen	1	0.29 ± 0.03	0.47 ± 0.12	1.16 ± 0.15
	5	0.23 ± 0.05	0.26 ± 0.08	0.90 ± 0.15
	24	0.08 ± 0.03	0.16 ± 0.05	0.37 ± 0.07
lungs	1	0.32 ± 0.16	0.90 ± 0.05	2.43. ± 0.33
	5	0.18 ± 0.08	0.39 ± 0.04	1.73 ± 0.64
	24	0.09 ± 0.02	0.19 ± 0.06	0.54 ± 0.16
kidneys	1	0.87 ± 0.09	1.57 ± 0.40	3.00 ± 0.30
	5	0.62 ± 0.15	0.74 ± 0.21	1.61 ± 0.34
	24	0.20 ± 0.07	0.20 ± 0.03	0.44 ± 0.06

[a] Results represent the mean ± SD. $n = 3$.

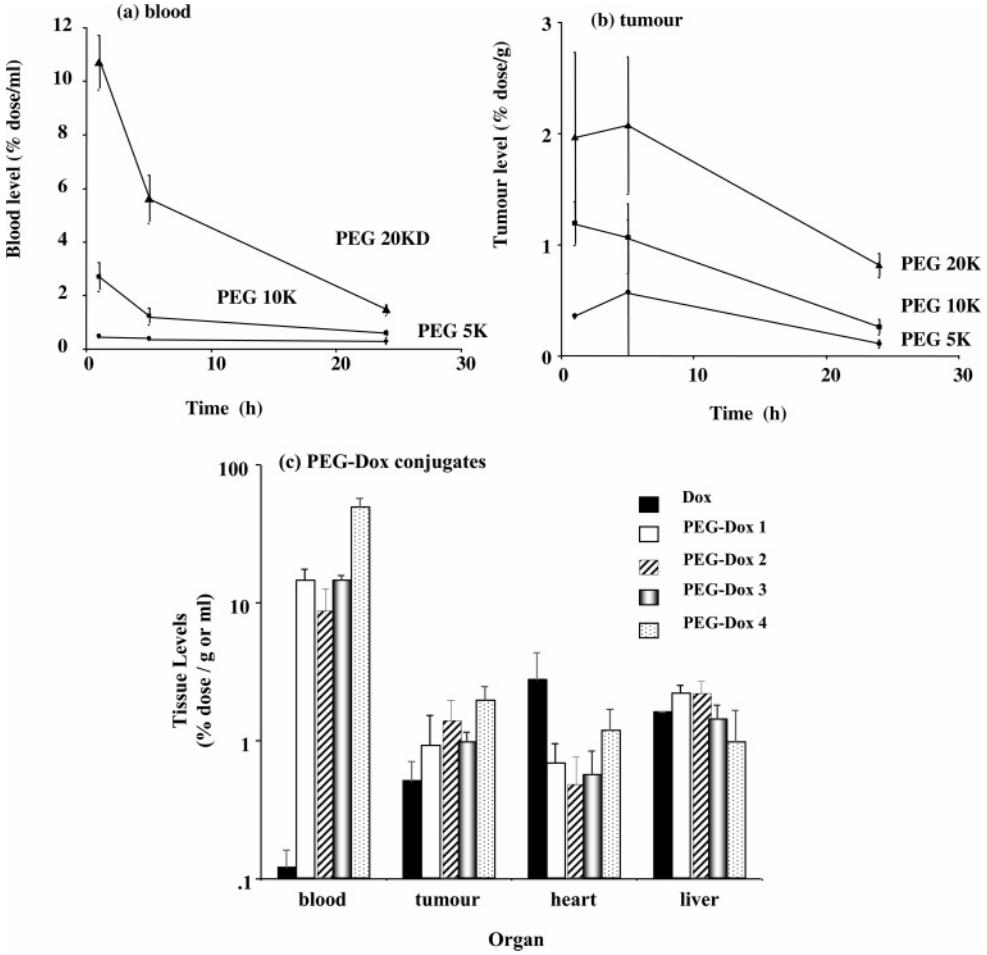

Figure 4. Biodistribution of ^{125}I-labeled PEGs and PEG−Dox conjugates after iv administration to mice bearing sc B16F10 tumors. Panel a shows the time-course of radioactivity detected in blood after administration of ^{125}I-labeled PEGs, panel b shows the time-course of radioactivity detected in tumor tissue and panel c shows the total Dox recovered in all tissues at 1 h after administration of PEG−Dox conjugates. (Analysis by HPLC). The data representmean ± SD where $n = 3-5$.

Table 6. Treatment of Mice Bearing sc B16F10 Murine Melanoma with Various PEG−DOX Conjugates

group	mean survival time (days)[a]	T/C × 100
saline	5.6	100
Dox	6.8	121
PEG−Dox 1	8.2	146[a]
PEG−Dox 2	7.5	132[a]
PEG−Dox 3	6.3	113
PEG−Dox 4	7.3	130[a]
PEG−Dox 5	8.0	143[a]

[a] In this aggressive B16F10 model it is usual to have statistical significance when T/C is greater than 125% and when the group size is $n = 5$, as was the case here.

tumor:heart ratio. Considering the known dose-limiting toxicity of Dox, this may be important. The radioactivity associated with ^{125}I-labeled PEGs in the liver were similar for PEG 10000 and 20000 g/mol, but were higher for PEG 5000 g/mol. and did not decrease in the same manner as in other tissues. Nevertheless, for all PEGs investigated, liver uptake was never more than 6% which is only a little higher than other water soluble polymeric drug carriers such as HPMA copolymers, for example. The variability in tumor accumulation of ^{125}I-labeled PEGs may be explained by the tendency of small tumors to accumulate more polymer than large tumors, a phenomenon shown previously with HPMA copolymer−Dox (*31*). Scatter plots of tumor uptake per gram against tumor weight showed that accumulation at 1 h was higher in smaller tumors (data not shown).

As a preliminary study, the biodistribution of the PEG−Dox conjugates, the levels of total Dox in blood, tumor, and the other principal organs, was examined at 1 h after iv injection. All the PEG−Dox conjugates showed a significantly longer plasma half-life than free Dox (Figure 4c). PEG−Dox 4 showed significantly higher blood levels than the other conjugates at 1 h. This is perhaps surprising as light scattering experiments suggested that PEG−Dox 1 had the highest apparent size and would suggest that the micellar aggregate of PEG−Dox 1 rapidly dissociates in blood. All PEG−Dox conjugates showed higher tumor Dox concentrations than free Dox and importantly lower heart levels (Figure 4c). It is important to note that the blood clearance and tumor targeting of the PEG−Dox conjugates was markedly different than seen for the corresponding molecular weight ^{125}I-labeled PEGs. This emphasizes the importance of monitoring biodistribution of each polymer−drug conjugate as well as the parent polymeric carrier.

Antitumor Activity of PEG−Dox Conjugates. An important factor leading to improved efficacy of polymer conjugates is tumor targeting by the EPR effect. Thus it is important to use solid tumor models to evaluate therapeutic potential of polymer conjugates. As we have used the B16F10 melanoma model to compare the activity of other anticancer conjugates that we have subsequently progressed into clinical trial (*32*−*34*), the antitumor activity of PEG−Dox conjugates was assessed using this model. It should be noted that this is a very aggressive tumor, and animals not treated usually die within 6−10 days of the tumor becoming palpable. First studies compared the activity of PEG−Dox conjugates 1−5 at a Dox dose of 5 mg/kg (Dox-equiv). Although Dox showed no significant antitumor activity, both PEG−Dox 1 and PEG−Dox 5 were active although the increase in survival was modest (T/C ∼ 145%) (Table 6). Antitumor activity would appear to correlate with the highest rate of Dox release in the presence of lysosomal enzymes (Table 4). Activity of PEG−Dox 1 was confirmed in a second experiment designed to examine the dose-dependency of activity. Although no clear dose−response was observed antitumor activity was evident, in this case a T/C of ∼ 160% was observed (Table 7).

The mouse leukemia L1210, grown as an ip ascites, is classically used to establish the activity of anthracycline derivatives. When PEG−Dox-1 was evaluated in this model, antitumor activity was observed, but survival was reduced in comparison to treatment with Dox alone (Table 8). Considering the differential pharmacokinetics of free Dox and PEG−DOX conjugates at the whole organism and cellular level, this observation is consistent with the need for EPR-mediated targeting to allow polymer conjugates to show therapeutic benefit. Additionally it is noteworthy throughout these experiments that the PEG−Dox conjugates were less toxic as evidenced by their lesser effect on animal weight loss (Figure 5).

CONCLUSIONS

Structure of PEG−peptide−Dox conjugates can be tailored to give a 1:1:1 stoichiometry of PEG chain, amino acid spacer, and anthracycline. This offers a unique

Table 7. Treatment of Mice Bearing sc B16F10 Murine Melanoma with PEG_{5000}−GLFG−Dox (PEG−Dox-1). Effect of Dose

treatment	dose (mg/kg Dox-equiv)	dosing schedule[a]	survival (mean ± SD)	T/C (%)[b]	number of toxic deaths
Saline	-	day 1	8.75 ± 1.9	100	0/4
PEG−Dox-1	10	day 1	10.6 ± 2.1	161**	0/5
PEG−Dox 1	5	day 1	8.6 ± 1.34	130^{NS}	2/5
PEG−Dox 1	1	day 1	8.25 ± 1.71	161^{NS}	0/4

[a] Single dose given after tumor reaches palpable size. [b] Statistical significance was calculated using a Student's *t* test for small sample sizes. ** = $p > 0.01$. NS = not significant.

Table 8. Effect of ip PEG_{5000}−GLFG−Dox (PEG−Dox 1) Administration on the Survival of DBA2 Mice Bearing ip L1210 Leukaemia. Animals Were Treated on Day 1 or Day 1, 2, and 3 after Tumor Inoculation

treatment	dose[a]	dosing schedule	survival days	survival days (mean ± SD)[b]	T/C (mean ± SD)	toxic deaths
saline	-	1	18, 18, 18, 18, 18	18	100	0/5
Dox	5	1	27, 15, 32, 29, 32	27 ± 7.0*	150 ± 39	0/5
PEG−Dox 1	10	1	15, 28, 24, 24, 25	23.2 ± 4.87^{NS}	129 ± 27	0/5
PEG−Dox 1	1	1, 2, 3	22, 24, 21, 22, 23	22.4 ± 1.14**	124 ± 6	0/5
PEG−Dox 1	5	1, 2, 3	15, 22, 24, 21, 26	21.6 ± 4.16^{NS}	120 ± 23	0/5
PEG−Dox 1	10	1, 2, 3	25, 27, 22, 28, 25	25.4 ± 2.3**	141 ± 13	0/5

[a] Dose expressed as Dox-equiv (mg/kg). [b] Statistical significance was calculated using a Student's *t* test for small sample sizes. * = $p > 0.05$ and ** = $p > 0.001$. NS = not significant.

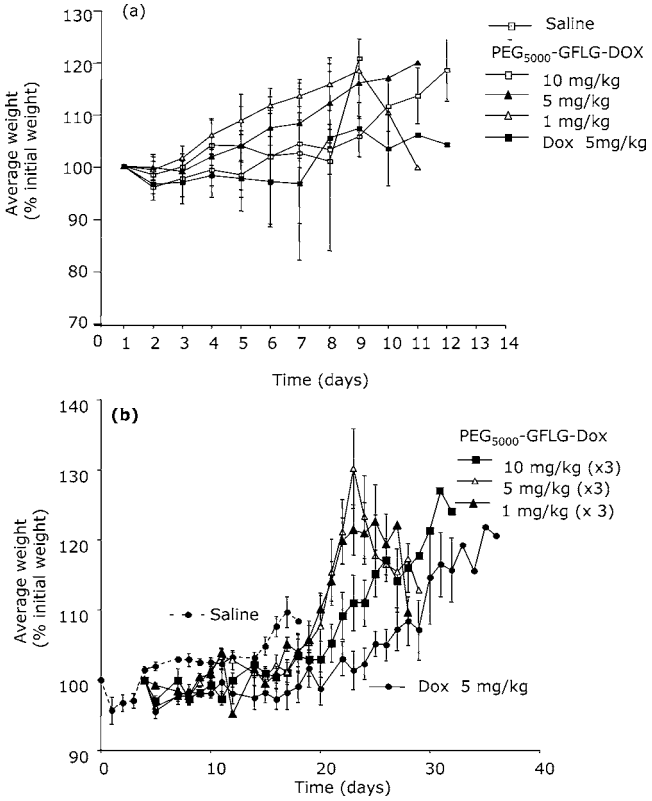

Figure 5. Effect of PEG–Dox conjugates on animal weight. The effect of PEG–Dox-1 and free Dox on the weight of mice during antitumor experiment. Panel a shows the weight change in C57 mice bearing a sc B16F10 tumor, and panel b shows the weight change in DBA2 mice bearing ip L1210.

opportunity to prepare anticancer polymeric conjugates of low polydispersity, which is advantageous compared to other pendant polymer conjugates. Solution properties are however complicated by the tendency of PEG–Dox conjugates to form multimolecular aggregates. The aggregation number was dependent on the nature of the PEG used (Mw and architecture), and further study of micellar stability is warranted before further development of such conjugates. The rate of Dox release on exposure to lysosomal enzymes was controlled by the peptidyl linker used, but the nature of the PEG carrier had little influence on this process. In vivo studies confirmed the effect of PEG Mw on the biodistribution of ^{125}I-labeled PEGs. However, the biodistribution of PEG–Dox conjugates was not clearly related to Mw or architecture of the carrier, but was probably governed by the nature and stability of the PEG–Dox aggregates formed. In all cases the PEG–Dox conjugates displayed greater tumor targeting than free Dox and also lower heart levels of the bound anthracycline. This justified evaluation of their antitumor activity in vivo. Experiments in mice bearing either a sc B16F10 tumor or and ip L1210 tumor confirmed the activity of selected PEG–Dox conjugates and also underlined the importance of the EPR effect as a means to enhance tumor targeting. PEG_{5000}–GFLG–Dox was selected as the lead candidate for further preclinical evaluation.

ACKNOWLEDGMENT

This work was supported by BE Project 97- 4133. We would like to thank Dr. Steve Stribbling for technical help with the in vivo experiments.

LITERATURE CITED

(1) Duncan, R. (1992) Drug-polymer conjugates: potential for improved chemotherapy. *Anti-Cancer Drugs 3*, 175–210.
(2) Matsumara, Y., and Maeda, H. (1986) A new concept for macromolecular therapeutics in cancer chemotherapy; mechanism of tumoritropic accumulation of proteins and the antitumor agent SMANCS. *Cancer Res. 6*, 6387–6392.
(3) Vasey, P., Twelves, C., Kaye, S., Wilson, P., Morrison, R., Duncan, R., Thomson, A., Hilditch, T., Murray, T., Burtles, S., and Cassidy, J. (1999) Phase I clinical and pharmacokinetic study of PKI (HPMA copolymer doxorubicin): first member of a new class of chemotherapeutic agents: drug-polymer conjugates. *Clin. Cancer Res. 5*, 83- 94.
(4) Seymour, L. W., Ferry, D. R., Anderson, D., Hesslewood, S., Julyan, P. J., Payner, R., Doran, J., Young, A. M., Burtles, S., and Kerr, D. J. (2002) Hepatic drug targeting: Phase I evaluation of polymer bound doxorubicin. *J. Clin. Oncol*. 20, 1668.
(5) Duncan, R. (2003) The Dawning Era of Polymer Therapeutics. *Nature Rev. Drug Discov. 2*, 347–360.
(6) Thanou, M., and Duncan, R. (2003) Polymer-protein and polymer-drug conjugates in cancer therapy. *Cur. Opin. Invest. Drugs 4*, 701–709.
(7) Harris, J. M., and Chess, R. B. (2003) Effect of pegylation on pharmaceuticals. *Nature Rev. Drug Discov. 2*, 214–221.
(8) Veronese, F. M., and Harris, J. M. (2002) Peptide and protein PEGylation. *Adv. Drug Delivery Systems 54* (no. 4) whole issue.
(9) Greenwald, R. B., Choe, Y. H., McGuire, J., and Conover, R. C. D. (2003) Effective drug delivery by pegylated drug conjugates. *Adv. Drug Delivery Rev. 55*, 217–250.
(10) Greenwald, R., Pendri, A., Conover, C., Gilbert, C., Yang, R., and Xia, J. (1996) Drug delivery systems. 2 Camptothecin 20-O-poly(ethylene glycol) ester transport forms. *J. Med. Chem. 39*, 1938–1940.
(11) Duncan, R., Hume, I. C., Kopeckova, P., Ulbrich, K., Strohalm, J., and Kopecek, J. (1989) Anticancer agents coupled to *N*-(2-hydroxypropyl)methacrylamide copolymers, 3. Evaluation of adriamycin conjugates against mouse leukaemia L1210 in vivo. *J. Controlled Release 10*, 51–63.
(12) Duncan, R., Seymour, L. W., O'Hare, K. B., Flanagan, P. A., Wedge, S., Hume, I. C., Ulbrich, K., Strohalm, J., Subr, V., Spreafico, F., Grandi, M., Ripamonti, M., Farao, M. and Suarato, A. (1992) Preclinical evaluation of polymer-bound doxorubicin. *J. Controlled Release 19*, 331–346.
(13) Seymour, L. W., Ulbrich K., Styger, P. S., Brereton, M., Subr V., Strohalm, J., and Duncan, R. (1994) Tumoritropism and anticancer efficacy of polymer-based doxorubicin prodrugs in the treatment of subcutaneous murine B16F10 melanoma. *Br. J. Cancer 70*, 636–641.
(14) Jones, J. (1992) *Amino Acid and Peptide Synthesis* (Davies, S. G., Ed.) pp 94, Oxford University Press, Oxford.
(15) Sims, G. E. C., and Snape, T. J. (1980) A method for the estimiation of polyethyleneglycol in plasma protein fraction. *Anal. Biochem. 107*, 60–63.
(16) Wyatt, P. J. (1993) Light Scattering and absolute characterization of macromolecules. *Anal. Chim. Acta 272*, 1–40.
(17) Duncan, R., Cable, H. C., Lloyd, J. B., Rejmanova, P., and Kopecek, J. (1983) Degradation of side-chains of N–(2-hydroxypropyl)methacrylamide copolymers by lysosomal thiol-proteinases. *Biosci. Rep. 2*, 1041–1046.
(18) Duncan, R., Cable, H. C., Lloyd, J. B., Rejmanova, P., and Kopecek, J. (1984) Polymers containing enzymatically degradable bonds, 7. Design of oligopeptide side chains in poly N-(2-hydroxypropyl)methacrylamide copolymers to promote efficient degradation by lysosomal enzymes. *Makromol. Chem. 184*, 1997–2008.
(19) Trouet, A. (1974) Isolation of modified liver lysosomes. *Methods in Enzymology XXXI* (Fleischer, S., Packer, L., Eds.) pp 323–329, Academic Press, New York.
(20) Wedge, S. (1990) Mechanism of action of polymer anthracyclines: potential to overcome multidrug resistance. Ph.D. Thesis, Keele University.
(21) Fraier, D. D., Fraier, E., Frigerio, E., Pianezzola, M., Strolin Benedetti, J., Cassidy and Vasey, P. (1995) A sensitive

procedure for the quantitation of free and N−(2-hydroxypropyl)methacrylamide polymer-bound doxorubicin (PK1) and some of its metabolites, 13-dihydrodoxorubicin, 13-dihydrodoxorubicinone and doxorubicinone, in human plasma and urine by reverse phase HPLC with fluorimetric detection. *J. Pharm. Biomed. Anal. 13*, 625−633.

(22) Sgouras, D., and Duncan, R. (1990) Methods for the evaluation of Biocompatibility of Soluble Synthetic Polymers which have potential for Biomedical Use. 1 Use of a tetrazolium-based colorimetric assay (MTT) as a preliminary screen for evaluation of in vitro cytotoxicity. *J. Mater. Sci.: Mater. Med. 2*, 61−68.

(23) United Kingdom Coordinating Committee on Cancer Research (UKCCCR) (1998) Guidelines for the welfare of animals in experimental neoplasia, 2nd ed.. *Br. J. Cancer 77*, 1−10.

(24) Monfardini, C., Schiavon, O., Caliceti, P., Morpurgo, M., Harris, J. M., and Veronese, F. M. (1995) A branched monomethoxypoly(ethylene glycol) for protein modification. *Bioconjugate Chem. 6*, 62−69.

(25) Sartore, L. Caliceti, P. Schiavon, O., and Veronese, F. M. (1991) Enzyme modification by mPEG with amino acid and peptide as spacer arm. *Appl. Biochem. Biotechnol. 27*, 55−63.

(26) Searle, F., Gac-Breton, S., Keane, R., Dimitrijevic, S., Brocchini, S., and Duncan, R. (2001) *N*-(2-hydroxypropyl)-methacrylamide copolymer-6-(3-aminopropyl)-ellipticine conjugates, synthesis, characterisation and preliminary in vitro and in vivo studies. *Bioconjugate Chem. 12*, 711−718.

(27) Subr, V., Strohalm, J., Ulbrich, K., and Duncan, R. (1992) Polymers containing enzymatically degradable bonds, XII. Release of daunomycin and adriamycin from poly[N−(2-hydroxypropyl)methacrylamide] copolymers. *J. Controlled Release 18*, 123−132.

(28) Pechar, M., Ulbrich, K., Subr, V., Seymour, L. W., and Schacht, E. H. (2000) *Bioconjugate Chem. 11*, 131−139.

(29) Seymour, L. W., Duncan, R., Strohalm, J., and Kopecek, J. (1987) Effect of molecular weight (Mw) of *N*-(2-hydroxypropyl)methacrylamide copolymers on body distribution and rate of excretion after subcutaneous, intraperitoneal and intravenous administration to rats. *J. Biomed. Mater. Res. 21*, 1341−1358.

(30) Seymour, L. W., Miyamoto, Y., Maeda, H., Brereton, M, Srohalm, J., Ulbrich, K., and Duncan, R. (1995) Influence of molecular weight on passive tumor accumulation of a soluble macromolecular drug carrier. *Eur. J. Cancer 31*, 766−770.

(31) Duncan, R., and Sat, Y. (1998) Tumor targeting by enhanced permeability and retention (EPR) effect. *Ann. Oncol. 9* (S2), 149.

(32) Duncan, R., Seymour, L. W., O'Hare, K. B., Flanagan, P. A., Wedge, S., Hume, I. C., Ulbrich, K., Strohalm, J., Subr, V., Spreafico, F., Grandi, M., Ripamonti, M., Farao, M., and Suarato, A. (1992) Preclinical evaluation of polymer-bound doxorubicin, *J. Controlled Release 19*, 331−346.

(33) Gianasi, E., Wasil M., Evagorou, E. G., Keddle, A., Wilson, G., and Duncan, R. (1999) HPMA copolymer platinates as novel antitumor agents: *in-vitro* properties, pharmacokinetics and antitumor activity in vivo. *Eur. J. Cancer 35*, 994−1002.

(34) Gianasi, E., Buckley, R. G., Latigo, J., Wasil, M., and Duncan, R. (2002) HPMA copolymers platinates containing dicarboxylato ligands. Preparation, characterisation and *in vitro* and *in vivo* evaluation. *J. Drug Target. 10*, 549−556.

BC040241M

PEGylation of Poly(ethylene imine) Affects Stability of Complexes with Plasmid DNA under in Vivo Conditions in a Dose-Dependent Manner after Intravenous Injection into Mice

Thomas Merdan,[†] Klaus Kunath,[†] Holger Petersen,[†] Udo Bakowsky,[†] Karl Heinz Voigt,[‡] Jindrich Kopecek,[§] and Thomas Kissel*,[†]

Department of Pharmaceutics and Biopharmacy, Philipps-University of Marburg, Ketzerbach 63 , D-35032 Marburg, Germany, Department of Physiology, Philipps-University of Marburg, Pilgrimstein, D-35037 Marburg, Germany, Department of Pharmaceutics and Pharmaceutical Chemistry, The University of Utah, 30 South, 2000 East, Salt Lake City, Utah 84112.. Received October 26, 2004; Revised Manuscript Received April 8, 2005

The influence of PEGylation on polyplex stability from poly(ethylene imine), PEI, and plasmid DNA was investigated both in vitro and after intravenous administration in mice. Polyplexes were characterized with respect to particle size (dynamic light scattering), zeta-potential (laser Doppler anemometry), and morphology (atomic force microscopy). Pharmacokinetics and organ accumulation of both polymers and pDNA were investigated using ^{125}I and ^{32}P radioactive labels, respectively. Furthermore gene expression patterns after 48 h were measured in mice. To elucidate the effect of different doses, all experiments were performed using ca. 1.5 μg and 25 μg of pDNA per mouse. Our studies demonstrated that both PEI and PEG−PEI form stable polyplexes with DNA with similar sizes of 100−130 nm. The zeta potential of PEI/pDNA polyplexes was highly positive, whereas PEG−PEI/pDNA showed a neutral surface charge as expected. The pharmacokinetic and organ distribution profiles after 2 h show similarities for both PEI and pDNA blood-level time curves from polyplexes at both doses indicative for significant stability in the bloodstream. A very rapid clearance from the bloodstream was observed and as major organs of accumulation liver and spleen were identified. PEG−PEI/pDNA complexes at a dose of ∼25 μg exhibit similar profiles except a significantly lower deposition in the lung. At the lower dose of ∼1.5 μg pDNA, however, for polyplexes from PEG−PEI, significant differences in blood level curves and organ accumulation of polymer and pDNA were found. In this case PEG−PEI shows a greatly enhanced circulation time in the bloodstream. By contrast, pDNA was rapidly cleared from circulation and significant amounts of radioactivity were found in the urine, suggesting a rapid degradation possibly by serum nucleases after complex separation. Regarding in vivo gene expression, no luciferase expression could be detected at ∼1.5 μg dose in any organ using both types of complexes. At 25 μg only in the case of PEI/pDNA complexes were significant levels of the reporter gene detected in lung, liver, and spleen. This coincided with high initial accumulation of pDNA complexed with PEI and a high acute in vivo toxicity. For PEG−PEI, initial accumulation was much lower and no gene expression as well as a low acute toxicity was found. In summary, our data demonstrate that PEG−PEI used in this study is not suitable for low dose gene delivery. At a higher dose of ∼25 μg, however, polyplex stability is similar to PEI/pDNA combined with a more favorable organ deposition and significantly lower acute in vivo toxicity. These findings have consequences for the design of PEG−PEI-based gene delivery systems for in vivo application.

INTRODUCTION

Nonviral gene delivery has proven its efficiency in numerous in vitro studies (*1*). The use of genes as therapeutic agents offers tremendous potential for the causal treatment of yet incurable diseases, especially viral infections and cancer (*2*). For systemic gene therapy, however, it is necessary to develop vectors with a low toxicity and sufficient stability and circulation time in the bloodstream in order to reach remote sites of the body, e.g. disseminated metastases. With cationic polymers, such as linear poly(ethylene imine), PEI (*3*, *4*), or methacrylates (*5*), in vivo transfection experiments have been reported using primarily luciferase encoding reporter genes. Also pharmacokinetic and organ distribution data have been obtained for different nonviral vectors, demonstrating rapid clearance of positively charged polyplexes from circulation (*6*−*8*).

To extend the blood circulation times of nonviral vectors, hydrophilic polymers, such as poly(ethylene glycol), PEG, or poly(*N*-(2-hydroxypropyl)methacrylamide) (pHPMA), have been coupled to polycations (*9*−*11*) to achieve hydrophilic shielding ("stealth" effect) similar to PEGylated liposomes (*12*). PEG-modified polycations have shown promising biophysical properties after complexation with p-DNA, such as a neutral zeta potential, very low cytotoxicity, and little or no tendency for aggregation (*9*, *11*, *13*). While the stability of polyplexes under in vitro conditions is well documented (*11*,

* To whom correspondence should be addressed. Tel.: (0049)-6421-282-5881. Fax: (0049)-6421-282-7016. E-mail: kissel@mailer.uni-marburg.de.

[†] Department of Pharmaceutics and Biopharmacy, Philipps-University of Marburg.

[‡] Department of Physiology, Philipps-University of Marburg.

[§] The University of Utah.

10.1021/bc049743q CCC: $30.25 © 2005 American Chemical Society
Published on Web 06/14/2005

14), relatively little is known about polyplex stability in an in vivo situation.

Promising results have been obtained in animal studies with loco-regional administration of PEG-modified polymer/DNA complexes (*15*, *16*). Also repeated administration of PEG−PEI/DNA polyplexes led to a more prolonged transgene expression in the spinal cord as compared to PEI (*17*). By contrast, the fate of the constituents of polyplexes in the bloodstream after intravenous injection is incompletely understood, especially the influence of hydrophilic polymers, such as PEG. A comparison of poly(L-lysine) and PEGylated poly(L-lysine)/DNA complexes revealed significant DNA degradation in vivo for the PEGylated polymer indicative of polyplex disintegration (*7*). Further studies addressed pharmacokinetic profiles and organ distribution of either plasmid DNA *or* polymer after intravenous injection in mice (*9*, *11*). However, little is known about the quantitative distribution and blood level profiles of both complex constituents determined under the same experimental conditions and to what extent polyplexes retain their integrity in the bloodstream.

In this study we investigated blood level profiles and organ distributions of PEI/pDNA and PEG−PEI/pDNA polyplexes after intravenous injection into mice. To trace both complex constituents separately, two different radioactive labels for plasmid (^{32}P) and polymers (^{125}I) were used. To determine the influence of pDNA dose on blood level profiles and organ accumulation, we applied a total dose of 1.5 μg (0.075 mg/kg) and 25 μg (1.25 mg/kg) of plasmid DNA plus the corresponding amount of polymer per animal. Furthermore, we investigated gene expression profiles at both doses for PEI/plasmid and PEG−PEI/plasmid complexes, and we compared these with accumulation data of plasmid in major organs 30 min after injection and after 2 h.

EXPERIMENTAL SECTION

Materials and Animals. Endotoxin-free luciferase-encoding plasmid (pCMV-luc) was purchased from Plasmid Factory, Bielefeld, Germany. PEI 25 kDa was obtained from Sigma-Aldrich, Germany. PEI(25k)-*g*-PEG-$(2k)_{10}$ was synthesized as previously described (*18*). Male balb/c mice were purchased from Charles River, Germany.

Preparation of Polyplexes. Polymer solutions for complex formation were prepared in 79 μL of 150 mM NaCl with 10 mM HEPES buffer pH 7.4 and 36 μL glucose 5% pH 7.4. These mixtures were added to solutions of plasmid in 115 μL glucose 5% pH 7.4. All complexes used in this study were prepared at an N/P ratio of six.

Dynamic Light Scattering. Hydrodynamic diameters of polymer/pDNA polyplexes were determined by photon correlation spectroscopy. Plasmid (0.5 μg pCMV-Luc) in 25 μL of glucose 5%, pH 7.4 were complexed with the appropriate amount of polymer in 25 μL of glucose 5%, pH 7.4 each, as described above. Measurements were performed on a Zetasizer 3000 HS from Malvern Instruments, Germany (10 mW HeNe laser, 633 nm). Scattering light was detected at 90° angle through a 400 μm pinhole. For data analysis, the viscosity (0.88 mPa s) and the refractive index (1.33) of distilled water at 25 °C were used. The instrument was routinely validated using Standard Reference latex particles (AZ 55 Electrophoresis Standard Kit, Malvern Instruments). Each experiment was performed in quintuplet.

Measurement of Zeta Potential. Zeta-potential measurements were carried out in the standard capillary electrophoresis cell of the Zetasizer 3000 HS from Malvern Instruments at position 17.0. Measurements were performed in glucose 5%, pH 7.4, and all experiments were performed in quintuplet.

Radioactive Labeling of Polymers. Polymers were labeled employing *N*-succinimidyl-3-(4-hydroxy-3-[^{125}I]-iodo-phenyl)propionate (Amersham Pharmacia Biotech, Germany) according to the method of Bolton and Hunter as described earlier (*9*, *19*). Briefly: Polymers were dissolved in 0.1 M borate buffer pH 8.5, and the Bolton Hunter reagent was dissolved in DMSO. The polymer solution was added to the Bolton Hunter reagent solution, and the reaction was carried out for 60 min at room temperature. Purification was performed on a Sephadex G-25 column (PD10, Pharmacia, Germany), using an elution buffer containing 150 mM NaCl and 10 mM HEPES at pH 7.4.

Radioactive Labeling of DNA. Plasmid (pCMV-Luc) was radioactively labeled by incorporation of ^{32}P-dCTP (Readivue, Amersham Pharmacia, Germany) using a nick translation kit (Amersham Pharmacia, Germany) following a protocol provided by the manufacturer. Unincorporated nucleotides were carefully removed using Autoseq spin columns containing Sephadex G50 (Amersham Pharmacia, Germany) in two subsequent purification runs. Plasmid purity was verified via size exclusion chromatography using a PD-10 column and via ultracentrifugation using Microcon 10 spin columns (Amicon) via verification of absence of low molecular weight radioactive compounds. No significant amounts of free ^{32}P-dCTP were detected.

Pharmacokinetic Analysis and Organ Distribution. All animal experiments followed the "Principles of Laboratory Animal Care" (NIH publication #85-23, revised 1985) and were approved by an external review committee for laboratory animal care. Male balb/c mice with a body weight of 20−25 g were anaesthetized using Ketamine (Ketavet, Pharmacia & Upjohn, Germany) and Xylazine (Rompun, Bayer AG, Germany). Complexes of either ^{125}I-poylmer/plasmid or polymer/^{32}P-plasmid were injected as a bolus of approximately 100μL through the jugular vein. Two different doses, 1.5 μg of pDNA and 25 μg of pDNA, complexed with the corresponding amount of polymer to give a nitrogen-to-phosphate ratio of 6 were administered. Blood samples were obtained via a catheter in the common carotid artery, and urine was sampled by flushing the bladder with sodium chloride solution through a two-way catheter. After 30 or 120 min, mice were sacrificed and organs (liver, kidneys, lungs, spleen, cortex, heart, fatty tissue, vena jugularis, and cortex) were weighed and assayed for radioactivity. Radioactivity of the ^{125}I-polymer was measured on a 1277 Gammamaster (Perkin-Elmer Wallac, Germany). To assess the radioactivity from ^{32}P-pCMV-Luc, organs and blood samples were dissolved in 1 mL of Soluene 350 (Amersham Pharmacia, Germany). Subsequently, 200 μL of 30% sodium peroxide was incubated with the mixture for 30 min and then added to 15 mL of HionicFluor (Perkin-Elmer, Germany). Measurements were performed using a TriCarb liquid scintillation counter (Perkin-Elmer, Germany) with a counting time of 15 min and 1 min precount delay. Measurements of aliquots of complex solutions were used for both tracers to determine the injected dose of radioactivity. All experiments at low dose were performed in quadruplet; those at high dose were performed using eight animals.

In the case of PEI/pDNA complexes at both doses and PEG−PEI/pDNA complexes at ~25 μg dose, concentration−time curves from polymer and pDNA were fitted

to a two-compartmental model with the Software Kinetica 1.1 from Simed. The model used was $C(t) = Ae^{-\alpha t} + Be^{-\beta t}$, and the weighting applied was $1/(c_{calcd})^2$. Polymer concentrations in the samples were then calculated as percent of injected dose (%ID) or %ID/mL, respectively. Unpaired *t*-test was performed using Microcal Origin version 6.0 to compare blood levels of different polymers at corresponding time points. Differences were considered significant if two-tail $P \leq 0.05$.

Luciferase Expression in Vivo. Mice were anaesthetized as described above, and complexes containing either 1.5 or 25 μg of pCMV-luc were injected through the jugular vein in the same volume as described above. After 48 h mice were sacrificed and subsequently organs were removed. Liver, lung, spleen, kidneys, vena jugularis, cortex, and heart were dissolved in Lysis Buffer provided by Promega, Germany, and after centrifugation an aliquot of the supernatant was assayed for luciferase using a commercial kit and photon counting with a luminometer (Sirius Berthold, Germany). In vivo gene expression studies were performed in quadruplet.

RESULTS AND DISCUSSION

Size and Zeta Potential Measurements. At an N/P ratio of 6, both PEI 25 kDa and PEI(25k)-*g*-PEG(2k)$_{10}$ were capable of forming complexes with plasmid DNA. Polyplexes prepared with PEI 25 kDa displayed a size of 106 (±7) nm and a zeta potential of +26 (±2) mV. By contrast, PEG–PEI/DNA complexes reached a size of approximately 127 (±6) nm and a neutral zeta potential (0.5 ± 0.9 mV), indicating an efficient shielding of the cationic charge by grafted linear PEG chains. Compared to measurements obtained in 150 mM sodium chloride (*20*), complexes were significantly smaller when prepared in 5% glucose.

Atomic Force Microscopy (AFM). AFM images shown in Figure 1 as three-dimensional plots illustrate that both PEI and PEG–PEI formed defined, spherical complexes with plasmid DNA. Shape and size for both polyplex types appear to be similar and are in good agreement with previously published data (*18*, *20*). However, PEI/pDNA complexes seemed to be more uniform, more spherical, more compact, and smoother. PEG–PEI/DNA complexes were found to be flatter, and they showed a more irregular shape, suggesting that grafted PEG chains affected condensation of pDNA No free or only loosely complexed pDNA could be observed as described in earlier studies (*18*). Furthermore, DNA binding studies have been performed which indicated an efficient complexation of pDNA by PEI(25k)-*g*-PEG(2k)$_{10}$ (*20*). These observations suggest that these polyplexes could be suitable for in vivo evaluation.

Pharmacokinetic Analysis and Organ Distribution. Blood level profiles of polymers and pDNA are depicted in Figures 2–7. At a dose of approximately 1.5 μg of pDNA, none of the animals died during the experiments and no signs of acute toxicity were observed. Also at the higher dose of approximately 25 μg of pDNA, in the case of PEG–PEI/DNA complexes all animals survived without any signs of acute toxicity. However, after administration of unmodified PEI/pDNA complexes at a dose of 25μg of pDNA, two out of eight animals died within 30 min after injection, confirming previously published observations (*21*).

PEI/plasmid Polyplexes at Low Dose (Figure 2). Pharmacokinetic profiles obtained with PEI and plasmid DNA at a 1.5 μg dose displayed a very rapid clearance from the bloodstream. Curves fitted to a biexponential disposition equation by nonlinear curve fitting (Figure 2A) showed very steep alpha phases with a $t_{1/2\ alpha}$ of 4.9 min for the polymer and 3.4 min for pDNA (see Table 1). Subsequent beta elimination phases were very flat with $t_{1/2\ beta}$ of 120.0 and 132.6 min, respectively. After 30 min, less than 3% of the injected dose (polymer, as well as pDNA) per milliliter blood remained in blood circulation, approaching levels of approximately 1% ID/ml blood after 2 h. Comparison of pharmacokinetic data from plasmid DNA and PEI at 1.5 μg (Table 1) revealed very similar behavior especially within the first 30 min suggesting that PEI/DNA polyplexes remained intact to a substantial degree during blood circulation.

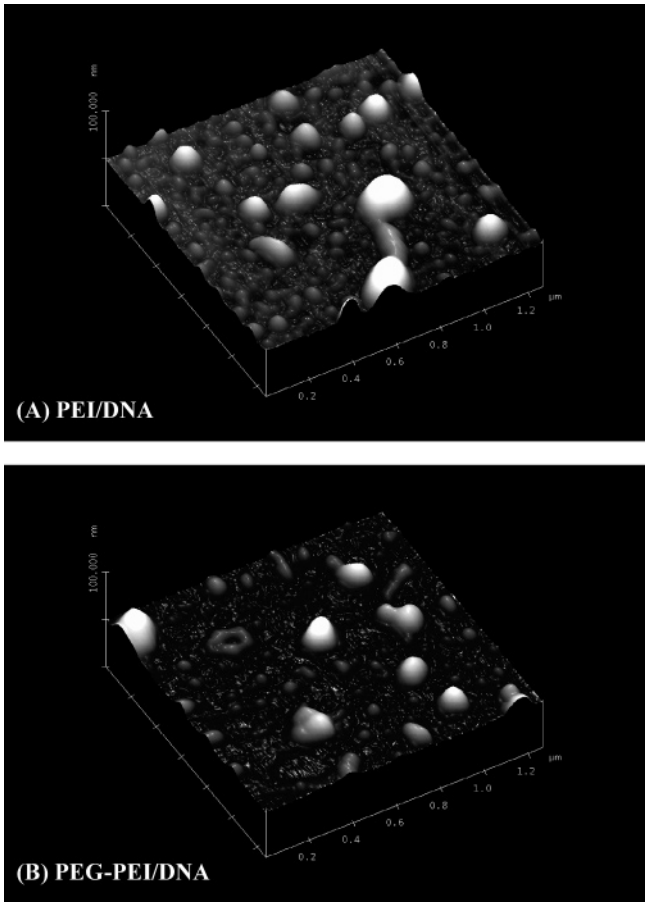

Figure 1. Complexes of PEI/DNA (A) and PEG–PEI/DNA (B) visualized by atomic force microscopy at N/P = 6 in 5% glucose. Images display defined structures of both complex types, and no free DNA could be observed in any image. Some larger aggregates are visible in both preparations.

The organ distribution of both PEI and pDNA at a 1.5 μg dose reached similar levels of radioactivity after 2 h in major organs, such as liver, kidney and lung (Figure 2B). These similarities provided additional evidence for polyplex stability in the bloodstream with concomitant uptake of both PEI and pDNA into tissues. Highest levels for polymer and pDNA were detected in the liver. Uptake probably occurred after opsonization of polyplexes as suggested by Planck et al. (*22*) with a subsequent rapid capture by mononuclear phagocytic cells. Organ deposition in the spleen showed approximately 3-fold higher accumulation of ^{125}I compared to ^{32}P. This fairly high accumulation in the spleen has been reported earlier for PEI 25 kDa polymer at a low dose (*9*) and was possibly caused by free polymer present at the N/P ratio used (*23*) or a minor degree of polyplex separation in the bloodstream.

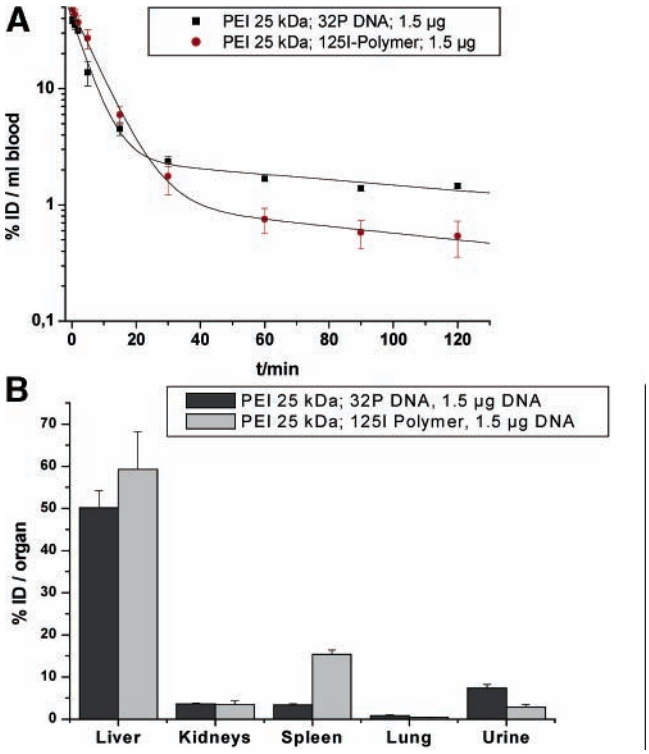

Figure 2. Blood level curves and organ accumulation after 2 h of PEI/pDNA at ~1.5 μg of pCMV-luc per mouse. A very rapid clearance of polymers and DNA from the bloodstream can be observed for polymer and pDNA.

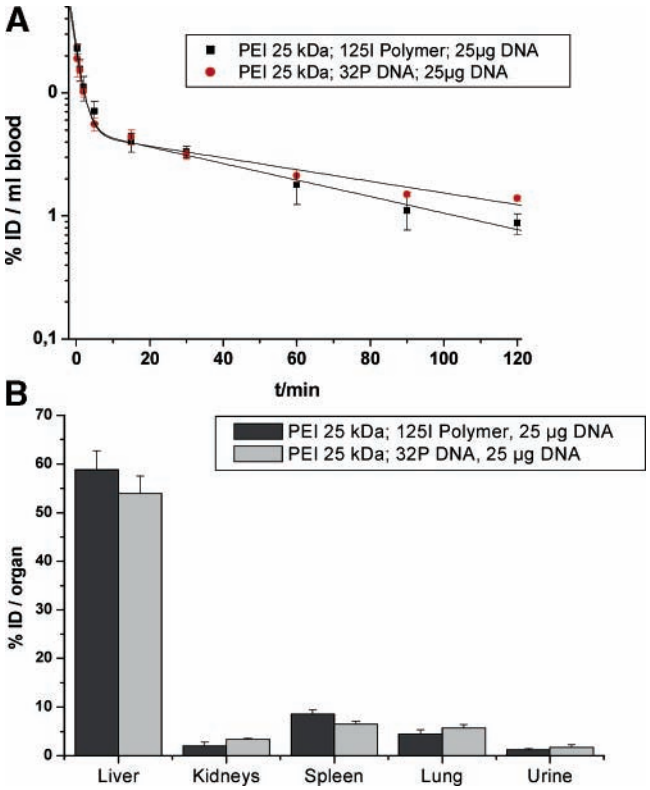

Figure 3. Blood level curves and organ accumulation after 2 h of PEI/pDNA at ~25 μg of pCMV-luc per mouse. Again a very rapid clearance from the blood stream can be observed for both complex constituents. Organ accumulation displays similar levels for pDNA and polymer. Compared to the low dose, a significantly higher level of accumulation was found in the lung.

Significant levels of radioactivity from ^{32}P were detected in the urine, in contrast to ^{125}I from the polymer. This difference most likely occurred as a result of polyplex separation followed by rapid pDNA degradation as described earlier (*24*). Uptake into the lungs is fairly low at 1.5 μg dose after 2 h (Figure 2B) and even at a 30 min no elevation in radioactivity were observed (data not shown). Due to the low dose formation of aggregates with e.g. erythrocytes was possibly reduced (*18*). Other tissues, such as heart, cortex, fatty tissue or the injection site in the jugular vein, did not exhibit significant levels of radioactivity from either polymer or pDNA after application of both PEI/DNA complexes (<1.5% ID). These findings were in good agreement with earlier studies (*9*, *25*).

PEI/plasmid Polyplexes at High Dose (Figure 3). At a 25 μg dose of DNA blood level profiles and organ distribution were rather similar to that at lower doses. Again a biphasic profile was found with $t_{1/2}$ alpha of 1.5 min and $t_{1/2\ \mathrm{beta}}$ of 45.9 min for polymer and $t_{1/2\ \mathrm{alpha}}$ of 1.4 min and $t_{1/2\ \mathrm{beta}}$ of 64.1 min for DNA (see Table 2). Clearance from the bloodstream occurred even more rapidly at the high dose. Furthermore, a significantly lower value for the area under the curve was found for polymer and pDNA compared to the lower dose (Tables 1 and 2). With respect to organ distribution, higher accumulation of radioactivity in the lung was detectable after 2 h for both pDNA and polymer (Figure 3B), possibly due to aggregate formation and subsequent entrapment in capillary bed of the lungs (*26*). After 30 min even higher accumulation of plasmid DNA in the lungs was found (Figure 6), compatible with initial accumulation and subsequent redistribution to the liver. This initial accumulation of polyplexes in the lung seemed to be responsible for the rapid death of about one-

Table 1. Biopharmaceutical Data for PEI/DNA and PEG−PEI/DNA Complexes at a Dose of ~1.5 μg of pDNA per Mouse[a]

1.5 μg data	AUC [%ID mL^{-1} min^{-1}]	*A* [%ID/mL]	$t_{1/2,\mathrm{alpha}}$ [min]	B [%ID/mL]	$t_{1/2,\mathrm{beta}}$ [min]
PEI 25 kDa ^{125}I polymer	527 ± 76	48.0 ± 7.8	4.9 ± 0.7	1.1 ± 0.2	120.0 ±57.6
PEI 25 kDa ^{32}P DNA	668 ± 26	38.9 ± 3.5	3.4 ± 0.3	2.5 ± 0.3	132.6 ± 21.2
PEG−PEI ^{125}I polymer	8891 ± 2418	n/a[a]	n/a	n/a	n/a
PEG−PEI ^{32}P DNA	2752 ± 1595	n/a	n/a	n/a	n/a

[a] All curves could be fitted to a two-compartment model. [b] n/a means that these curves could not be fitted to a two-compartment model.

Table 2. Biopharmaceutical Data for PEI/DNA and PEG−PEI/DNA Complexes at a Dose of ~25 μg pDNA per Mouse[a]

25 μg data	AUC [%ID mL^{-1} min^{-1}]	*A* [%ID/mL]	$t_{1/2,\mathrm{alpha}}$ [min]	*B* [%ID/mL]	$t_{1/2,\mathrm{beta}}$ [min]
PEI 25 kDa ^{125}I polymer	366 ± 59	19.5 ± 0.4	1.5 ± 0.6	5.0 ± 0.6	45.9 ± 7.3
PEI 25 kDa ^{32}P DNA	451 ± 19	17.8 ± 6.9	1.4 ± 0.4	4.6 ± 0,6	64.1 ± 9.1
PEG−PEI ^{125}I polymer	289 ± 91	15.1 ± 0.4	1.3 ± 0.5	4.2 ± 1.6	46.0 ± 16.2
PEG−PEI ^{32}P DNA	531 ± 118	11.6 ± 1.2	3.6 ± 2.4	3.9 ± 0.5	86.5 ± 24.6

[a] PEI/DNA data could be fitted to a two-compartment model. PEG−PEI/DNA, however, showed a different profile indicating complex separation.

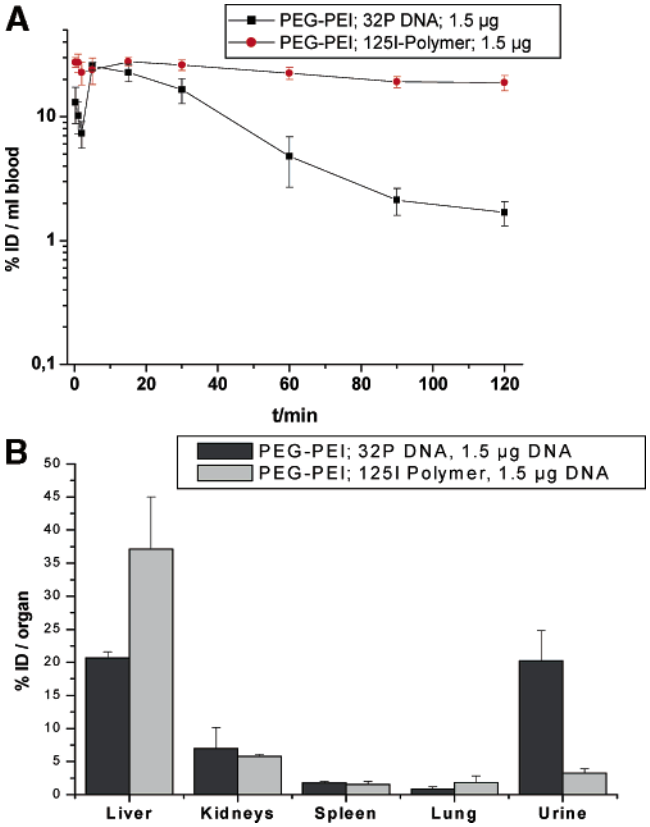

Figure 4. Blood level profiles and organ accumulation after application of PEG–PEI/pDNA complexes at a dose of ~1.5 μg of pDNA. Significant differences can be observed in blood level curves and organ depositions after 2 h, indicating a rapid separation of complex constituents at this low dose.

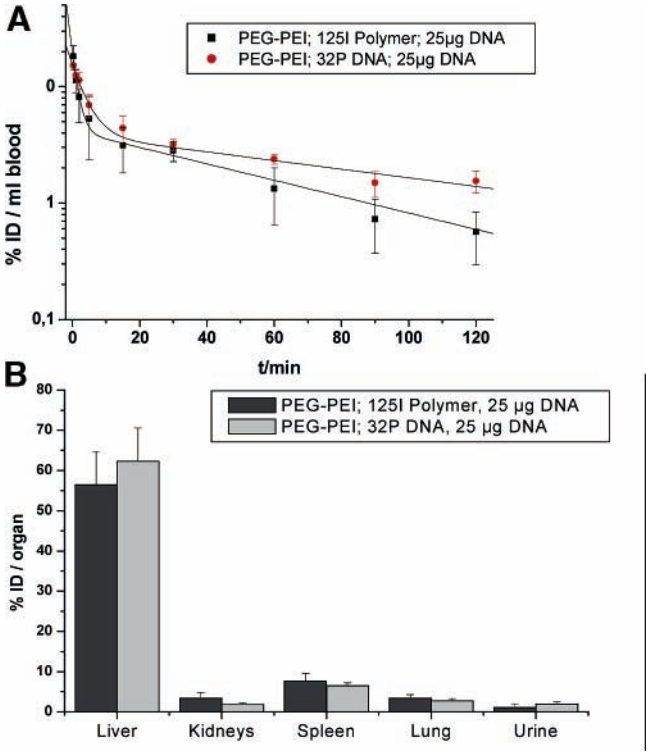

Figure 5. Blood level profiles and organ accumulation at 2 h from injection after application of PEG–PEI/pDNA complexes at a dose of 25 μg of pDNA per mouse. No enhancement of circulation time could be observed by using a PEGylated polymer; however, a significantly lower accumulation in the lung was observed compared to PEI/pDNA complexes at the same dose

fourth of laboratory animals. Measurements of radioactivity revealed enormous amounts of polymer and pDNA in the lungs of these animals, suggesting lung embolism as the most likely cause of death.

PEG–PEI/Plasmid Polyplexes at Low Dose (Figure 4). Blood level profiles and organ distribution data from PEG–PEI/DNA complexes at 1.5 μg yielded different results for the radioactive labels attached to the polymer (^{125}I) and plasmid DNA (^{32}P) (Figure 4A). While PEG–PEI displayed a rapid elimination phase initially, after approximately 5 min a plateau was reached at ~25 (% ID/mL). Blood level of PEG–PEI decreased marginally over the following 2 h. This long circulation of the PEG–PEI is thought to be caused by an efficient steric stabilization against opsonization by PEG and thus reduced uptake into the reticuloendothelial system of the liver. Another, less likely explanation could be the attachment of the PEG–PEI to, for example, cellular blood components as described earlier for cationic structures (*27*). Whereas the pharmacokinetic profile of PEG–PEI labeled with ^{125}I seemed to be attractive for intravenous delivery, the comparison with kinetic profile of ^{32}P labeled pCMV-Luc suggested a rapid dissociation of pDNA from polyplexes. After a maximum at 5 min at approximately 25% ID/mL, rapid clearance was observed. This maximum was possibly caused by an initial entrapment of pDNA or PEG–PEI/pDNA in the lung microvasculature with a subsequent time-delayed redistribution into the bloodstream as described earlier (*28*). After the maximum, the blood level of DNA decreased rapidly, reaching levels of less than 2% after 120 min.

Also organ distribution after 2 h showed differences between PEG–PEI and ^{32}P from pDNA (Figure 4B). While radioactivity from the polymer accumulated predominantly in the liver, reaching approximately 40% of injected dose, ^{32}P appeared in the liver at a significantly lower level (~20% ID). A high level of radioactivity of more than 20% ID from ^{32}P was found in the urine after 2 h. Since the size of plasmid DNA is far above the kidney threshold, this increase in urine levels was probably caused by degradation of pDNA or the ^{32}P label (*24*). Both pharmacokinetic profiles and organ accumulation support the conclusion that PEG–PEI/DNA polyplexes very likely undergo a rapid separation of polymer and DNA at this low dose. After separation, the PEG–PEI is taken up by the liver as described earlier (*9*) and a substantial amount of the injected dose circulates in the bloodstream, possibly attached to cellular blood components (*27*). Plasmid DNA, however, is probably degraded by serum nucleases rapidly after separation and degradation products are excreted.

PEG–PEI/Plasmid Complexes at High Dose (Figure 5). At a dose of 25 μg, DNA blood level profiles and organ distribution after 2 h are similar for PEG–PEI and pDNA. Again biphasic profiles were observed with a very rapid clearance from the bloodstream, displaying a $t_{1/2\ \mathrm{alpha}}$ of 1.3 min for the polymer and 3.6 min for the pDNA. Again a flat beta elimination phase follows with $t_{1/2\ \mathrm{beta}}$ of 46.0 min for the polymer and 86.5 min for pDNA. Interestingly there is no significant enhancement of the area under the curve for polymer or pDNA when PEG–PEI/pDNA complexes are compared to PEI/pDNA complexes (Table 2). Actually one intention of using PEG–PEI was to enhance circulation time. This effect could not be observed in this study with PEI(25k)-*g*-PEG(2k)$_{10}$. Organ distribution was similar at 25 μg for PEG–PEI and pDNA (Figure 5B). The majority of polymer and

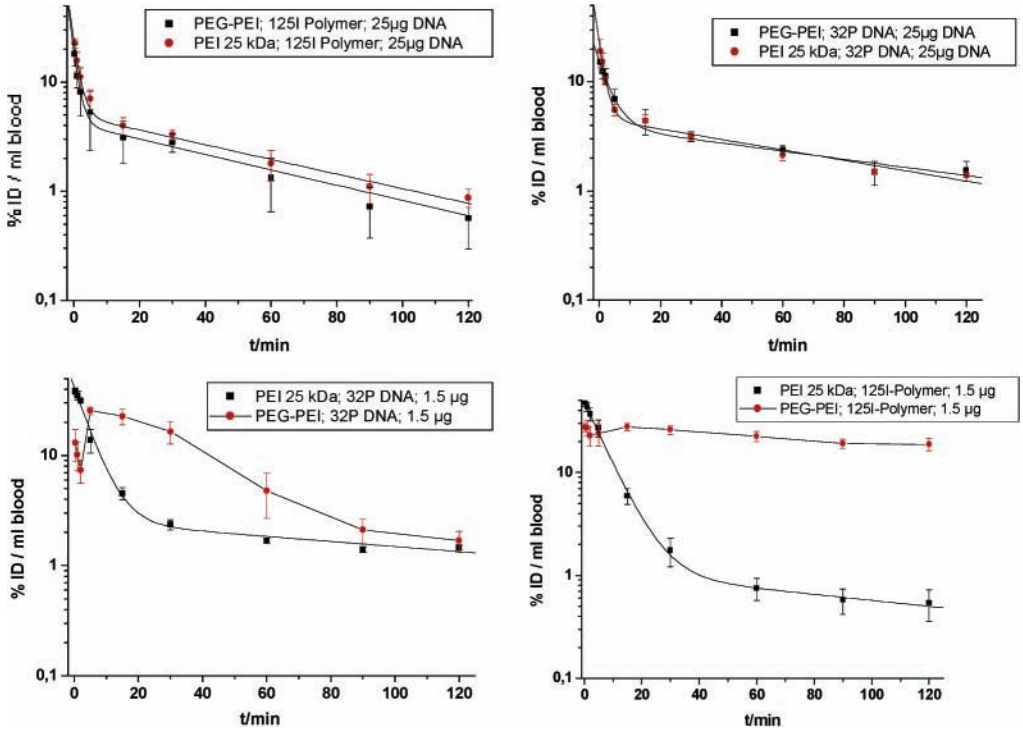

Figure 6. Comparison of blood level curves of PEI with PEG−PEI at two different doses and plasmid DNA complexed to PEI and PEG−PEI at two different doses.

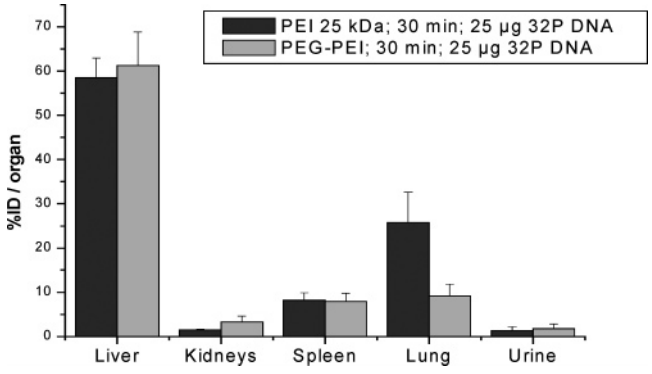

Figure 7. Organ accumulation of ^{32}P pCMV-luc from PEI/DNA and PEG−PEI/DNA complexes after 30 min using 25 μg of pDNA per mouse. A very high accumulation of pDNA can be observed for PEI/DNA complexes.

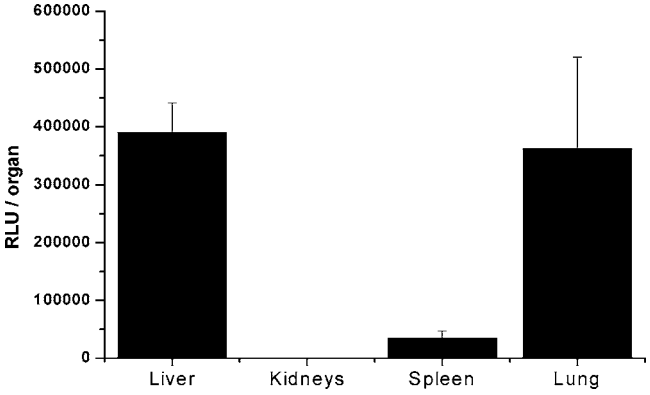

Figure 8. Gene expression pattern from PEI/pCMV-luc complexes after 48 h using ~25 μg of DNA. In the case of PEG−PEI/DNA complexes at ~25 μg and for both polymers at ~1.5 μg, no luciferase expression could be observed.

pDNA are sequestered into the liver very rapidly. Accumulation in the lung is significantly lower than that observed for PEI 25 kDa at 25 μg (Figures 3B and 7) possibly due to a lower level of aggregate formation caused by steric stabilization of complexes and a neutral surface charge provided by PEG-shielding. At this high dose much lower amounts of radioactivity were found in the kidneys and in the urine in contrast to the 1.5 μg data with PEG−PEI.

Comparisons of blood level profiles of PEI to PEG−PEI at two different doses and comparison of respective plasmid DNA curves are shown in Figure 6. At a high dose no significant differences were detected when comparing blood level profiles of pDNA complexed to either PEI or PEG−PEI. Polymer curves were very similar as well; however, in this case significant but not relevant differences were detected after 60 min. Again this indicates that PEGylation obviously does not extend circulation time of the polymer at this high dose. Concerning the low doses, however, blood level profiles were entirely different when comparing polymers among each other and respective pDNA levels such as previously described probably due to complex separation.

In Vivo Gene Expression in Mice (Figure 8). No gene expression could be detected in any organ for PEI and PEG−PEI at the low dose of 1.5 μg of DNA. This was not unexpected from results in the literature obtained with linear PEI (*26*). With the higher dose of 25 μg of pDNA, no luciferase expression was detected using PEG−PEI as a polycation. Using PEI 25 kDa, however, significant levels of luciferase expression were found in liver, spleen, and lung in accordance with the literature (*4*). Analysis of gene expression after 24 h revealed similar degrees of expression and profiles (data not shown).

Blood level profiles of polyplexes and organ distribution suggest that transfection of lung tissue is tightly associated with polyplex accumulation in the lung (*26*). Aggregates formed with cellular blood components or plasma proteins (*18*) obstructed fine lung capillaries, thus leading to a higher pressure in the microvasculature. This effect

may facilitate penetration of polyplexes across the endothelial barrier, leading to transfection of lung tissue even beyond the endothelia as described earlier (*29*, *30*). PEG−PEI/pDNA showed little or no tendency for aggregation with erythrocytes due to their neutral surface charge (*18*) and consequently accumulated to a lesser extent in the lung, preventing transfection of lung tissue in mice. This effect is expected and a prerequisite for active drug targeting.

Transfection using unmodified PEIs was accompanied by acute signs of toxicity, such as obstruction of lung vasculature (*21*, *26*). Massive damage in lung and liver tissue occurred as demonstrated by Chollet et al. (*26*). Therefore, unmodified PEI does not seem to be suitable for systemic transfection under in vivo conditions. Lung accumulation and toxicity of PEG−PEI/DNA complexes are much lower; therefore, this type of polymers appears to be more appropriate for in vivo use. A targeting moiety needs to be coupled to the polyplex to provide uptake into tumor tissues, e.g. transferrin (*31*) or epidermal growth factor for tumors (*32*).

Our data suggest that polyplexes of PEG−PEI and pDNA show a dose-dependent stability in circulation after intravenous injection. Rapid separation of pDNA from PEG−PEI polyplexes with subsequent degradation of DNA was not entirely unexpected, since PEGylated poly(L-lysine)/pDNA complexes were less stable against enzymatic degradation of DNA in vivo (*7*). The mechanism by which polyplexes are destabilized in a dose-dependent manner requires further investigations, especially to probe if there are threshold levels above which destabilization does not occur and to verify scalability across different species.

Also complexation and condensation of DNA by electrostatic interactions using polycations seemed to be influenced by the chain mobility of the polymer. This finding has consequences for the design of targetable nonviral vectors based upon polycations in which PEGylation is a requirement to avoid unspecific interaction with blood components. High grafting densities of PEG chains and relatively long PEG chains as in this case both destabilize PEGylated polyplexes under in vivo conditions. It worth mentioning that these instabilities were not detected with in vitro assays. Possibly high shear stress in the capillary beds of the lung compressed the hydrophilic coating layer leading to interactions of the positively charged core with blood components and the endothelial surface (*14*). Why separation of PEG−PEI polyplexes occurred as a saturable process merits further investigations. At higher doses PEG−PEI and pDNA remain associated and display a lower in vivo toxicity which suggests that optimization of polyplex composition, PEG−PEI structure, and the careful design of animal experiments could be promising strategies to exploit sterically shielded polyplexes for gene delivery.

Moreover, prolongation of PEG−PEI circulation in the bloodstream remains to be improved. In publications with PEGylated PEI, transfection under in vivo conditions was demonstrated; however, no pharmacokinetic evaluation was perfomed (*32*). Furthermore, all of these studies used doses of pDNA of 25 μg and above in mice (*21*, *31*, *32*). This translates into doses of almost 100 mg pDNA in humans, raising questions of practicability and potential safety of polyplexes. Therefore, polyplex formulations, which are effective at lower doses, remain an objective of high priority. A lateral stabilization of polyplexes, as described by Oupicky et al. (*33*), could improve the stability of PEG−PEI/pDNA to intravenous application of lower doses.

Apart from the obvious need to further optimize PEG−PEI polyplexes, this study highlights the necessity for more detailed mechanistic investigations of the behavior of "stealth" polyplexes under in vivo conditions. Testing of cytotoxicity in cell cultures is an important prerequisite to characterize polyplexes prior to animal studies. The lack of predictive power of in vitro assays for the performance of polyplexes in animals needs to be taken into account for further development of nonviral gene delivery systems. Moreover, the dose-dependent stability of polyplexes after intravenous injection raises questions about the possibility to separate transfection efficiency from toxic effects of polycations. Clearly more research into these issues and a standardization of animal protocols would be desirable.

ACKNOWLEDGMENT

We would like to thank Gudrun Hohorst and Eva Mohr for excellent technical assistance.

LITERATURE CITED

(1) Brown, M. D., Schatzlein, A. G., and Uchegbu, I. F. (2001) Gene delivery with synthetic (non viral) carriers. *Int. J. Pharm. 229*, 1−21.

(2) Merdan, T., Kopecek, J., and Kissel, T. (2002) Prospects for cationic polymers in gene and oligonucleotide therapy against cancer. *Adv. Drug. Delivery Rev. 54*, 715−758.

(3) Ferrari, S., Moro, E., Pettenazzo, A., Behr, J. P., Zacchello, F., and Scarpa, M. (1997) ExGen 500 is an efficient vector for gene delivery to lung epithelial cells in vitro and in vivo. *Gene Ther. 4*, 1100−1106.

(4) Zou, S. M., Erbacher, P., Remy, J. S., and Behr, J. P. (2000) Systemic linear polyethylenimine (L-PEI)-mediated gene delivery in the mouse. *J. Gene Med. 2*, 128−134.

(5) van de Wetering, P., Schuurmans-Nieuwenbroek, N. M., Hennink, W. E., and Storm, G. (1999) Comparative transfection studies of human ovarian carcinoma cells in vitro, ex vivo and in vivo with poly(2-(dimethylamino)ethyl methacrylate)-based polyplexes. *J. Gene Med. 1*, 156−165.

(6) Verbaan, F. J., Oussoren, C., van Dam, I. M., Takakura, Y., Hashida, M., Crommelin, D. J., Hennink, W. E., and Storm, G. (2001) The fate of poly(2-dimethyl amino ethyl)-methacrylate-based polyplexes after intravenous administration. *Int. J. Pharm. 214*, 99−101.

(7) Mullen, P. M., Lollo, C. P., Phan, Q. C., Amini, A., Banaszczyk, M. G., Fabrycki, J. M., Wu, D., Carlo, A. T., Pezzoli, P., Coffin, C. C., and Carlo, D. J. (2000) Strength of conjugate binding to plasmid DNA affects degradation rate and expression level in vivo. *Biochim. Biophys. Acta 1523*, 103−110.

(8) Oupicky, D., Ogris, M., Howard, K. A., Dash, P. R., Ulbrich, K., and Seymour, L. W. (2002) Importance of lateral and steric stabilization of polyelectrolyte gene delivery vectors for extended systemic circulation. *Mol. Ther. 5*, 463−472.

(9) Kunath, K., von Harpe, A., Petersen, H., Fischer, D., Voigt, K., Kissel, T., and Bickel, U. (2002) The structure of PEG-modified poly(ethylene imines) influences biodistribution and pharmacokinetics of their complexes with NF-kappaB decoy in mice. *Pharm. Res. 19*, 810−817.

(10) Nguyen, H. K., Lemieux, P., Vinogradov, S. V., Gebhart, C. L., Guerin, N., Paradis, G., Bronich, T. K., Alakhov, V. Y., and Kabanov, A. V. (2000) Evaluation of polyether-polyethyleneimine graft copolymers as gene transfer agents. *Gene Ther. 7*, 126−138.

(11) Oupicky, D., Howard, K. A., Konak, C., Dash, P. R., Ulbrich, K., and Seymour, L. W. (2000) Steric stabilization of poly-L-Lysine/DNA complexes by the covalent attachment of semitelechelic poly[*N*-(2-hydroxypropyl)methacrylamide]. *Bioconjugate Chem. 11*, 492−501.

(12) Woodle, M. C. (1998) Controlling liposome blood clearance by surface-grafted polymers. *Adv. Drug Delivery Rev.* 32, 139−152.

(13) Sung, S. J., Min, S. H., Cho, K. Y., Lee, S., Min, Y. J., Yeom, Y. I., and Park, J. K. (2003) Effect of polyethylene glycol on gene delivery of polyethylenimine. *Biol. Pharm. Bull. 26*, 492−500.

(14) Oupicky, D., Konak, C., Dash, P. R., Seymour, L. W., and Ulbrich, K. (1999) Effect of albumin and polyanion on the structure of DNA complexes with polycation containing hydrophilic nonionic block. *Bioconjugate Chem. 10,* 764−772.

(15) Tang, G. P., Zeng, J. M., Gao, S. J., Ma, Y. X., Shi, L., Li, Y., Too, H. P., and Wang, S. (2003) Poly(ethylene glycol) modified polyethylenimine for improved CNS gene transfer: effects of PEGylation extent. *Biomaterials 24*, 2351−2362.

(16) Kichler, A., Chillon, M., Leborgne, C., Danos, O., and Frisch, B. (2002) Intranasal gene delivery with a polyethylenimine-PEG conjugate. *J. Controlled Release 81*, 379−388.

(17) Shi, L., Tang, G. P., Gao, S. J., Ma, Y. X., Liu, B. H., Li, Y., Zeng, J. M., Ng, Y. K., Leong, K. W., and Wang, S. (2003) Repeated intrathecal administration of plasmid DNA complexed with polyethylene glycol-grafted polyethylenimine led to prolonged transgene expression in the spinal cord. *Gene Ther. 10*, 1179−1188.

(18) Petersen, H., Fechner, P. M., Martin, A. L., Kunath, K., Stolnik, S., Roberts, C. J., Fischer, D., Davies, M. C., and Kissel, T. (2002) Polyethylenimine-graft-poly(ethylene glycol) copolymers: influence of copolymer block structure on DNA complexation and biological activities as gene delivery system. *Bioconjugate Chem.13,* 845−854.

(19) Bolton, A. E., Hunter, W. M. (1973) The labelling of proteins to high specific radioactivities by conjugation of ^{125}I-containing acylating agent. *Biochem. J. 133*, 519−539.

(20) Merdan, T., Callahan, J., Petersen, H., Kunath, K., Bakowsky, U., Kopeckova, P., Kissel, T., and Kopecek, J. (2003) Pegylated polyethylenimine-Fab′ antibody fragment conjugates for targeted gene delivery to human ovarian carcinoma cells. *Bioconjugate Chem. 14,* 989−996.

(21) Ogris, M., Brunner, S., Schuller, S., Kircheis, R., and Wagner, E. (1999) PEGylated DNA/transferrin-PEI complexes: reduced interaction with blood components, extended circulation in blood and potential for systemic gene delivery. *Gene Ther. 6*, 595−605.

(22) Plank, C., Mechtler, K., Szoka, F. C., Jr., and Wagner, E. (1996) Activation of the complement system by synthetic DNA complexes: a potential barrier for intravenous gene delivery. *Hum. Gene Ther.* 7, 1437−1446.

(23) Clamme, J. P., Azoulay, J., and Mely, Y. (2003) Monitoring of the formation and dissociation of polyethylenimine/DNA complexes by two photon fluorescence correlation spectroscopy. *Biophys. J. 84*, 1960−1968.

(24) Kawabata, K., Takakura, Y., and Hashida, M. (1995) The fate of plasmid DNA after intravenous injection in mice: involvement of scavenger receptors in its hepatic uptake. *Pharm. Res. 12*, 825−830.

(25) Oh, Y., Kim, J., Yoon, H., Kim, J., Yang, J. and Kim, C. (2001) Prolonged organ retention and safety of plasmid DNA administered in polyethylenimine complexes. *Gene Ther. 8*, 1587−1592.

(26) Chollet, P., Favrot, M. C., Hurbin, A., and Coll, J. L. (2002). Side-effects of a systemic injection of linear polyethylenimine-DNA complexes. J Gene Med*4*, 84−91.

(27) Ward, C. M., Read, M. L., and Seymour, L. W. (2001) Systemic circulation of poly(L-lysine)/DNA vectors is influenced by polycation molecular weight and type of DNA: differential circulation in mice and rats and the implications for human gene therapy. *Blood 97,* 2221−2229.

(28) Ishiwata, H., Suzuki, N., Ando, S., Kikuchi, H., and Kitagawa, T. (2000) Characteristics and biodistribution of cationic liposomes and their DNA complexes. *J. Controlled Release 69*, 139−148.

(29) Goula, D., Benoist, C., Mantero, S., Merlo, G., Levi, G., and Demeneix, B. A. (1998) Polyethylenimine-based intravenous delivery of transgenes to mouse lung. *Gene Ther. 5,* 1291−1295.

(30) Zou, S. M., Erbacher, P., Remy, J. S., and Behr, J. P. (2000) Systemic linear polyethylenimine (L-PEI)-mediated gene delivery in the mouse. *J. Gene Med. 2*, 128−134.

(31) Kircheis, R., Blessing, T., Brunner, S., Wightman, L., and Wagner, E. (2001) Tumor targeting with surface-shielded ligand−polycation DNA complexes. *J. Controlled Release 72*, 165−170.

(32) Ogris, M., Walker, G., Blessing, T., Kircheis, R., Wolschek, M., and Wagner, E. (2003) Tumor-targeted gene therapy: strategies for the preparation of ligand-poly(ethylene glycol)-polyethylenimine/DNA complexes. *J. Controlled Release 91*, 173−181.

(33) Oupicky, D., Ogris, M., and Seymour, L. W. (2002) Development of long-circulating polyelectrolyte complexes for systemic delivery of genes. *J. Drug Target. 10*, 93−98.

BC049743Q

Polypeptide Point Modifications with Fatty Acid and Amphiphilic Block Copolymers for Enhanced Brain Delivery

Elena V. Batrakova,[†] Serguei V. Vinogradov,[†] Sandra M. Robinson,[‡] Michael L. Niehoff,[‡] William A. Banks,[‡] and Alexander V. Kabanov*[,†]

Department of Pharmaceutical Sciences and Center for Drug Delivery and Nanomedicine, College of Pharmacy, University of Nebraska Medical Center, 985830 Nebraska Medical Center, Omaha, Nebraska 68198, and GRECC Veterans Affairs Medical Center-St. Louis and Division of Geriatrics, Department of Internal Medicine, Saint Louis University School of Medicine, 915 North Grand Boulevard, St. Louis, MO 63104. Received November 9, 2004; Revised Manuscript Received April 29, 2005

There is a tremendous need to enhance delivery of therapeutic polypeptides to the brain to treat disorders of the central nervous system (CNS). The brain delivery of many polypeptides is severely restricted by the blood−brain barrier (BBB). The present study demonstrates that point modifications of a BBB-impermeable polypeptide, horseradish peroxidase (HRP), with lipophilic (stearoyl) or amphiphilic (Pluronic block copolymer) moieties considerably enhance the transport of this polypeptide across the BBB and accumulation of the polypeptide in the brain in vitro and in vivo. The enzymatic activity of the HRP was preserved after the transport. The modifications of the HRP with amphiphilic block copolymer moieties through degradable disulfide links resulted in the most effective transport of the HRP across in vitro brain microvessel endothelial cell monolayers and efficient delivery of HRP to the brain. Stearoyl modification of HRP improved its penetration by about 60% but also increased the clearance from blood. Pluronic modification using increased penetration of the BBB and had no significant effect on clearance so that uptake by brain was almost doubled. These results show that point modification can improve delivery of even highly impermeable polypeptides to the brain.

INTRODUCTION

Efficient delivery of therapeutic polypeptides across the blood−brain barrier (BBB) could result in improved diagnostics and treatment of diseases of central nervous system (CNS). Some examples include Parkinson's and Alzheimer's diseases (*1*−*3*), stroke (*4*, *5*), lysosomal storage diseases (*6*−*8*), and human obesity (*9*, *10*). The BBB is one of the most restrictive barriers in biology, which provides a formidable impediment for delivery of many polypeptides to the brain. Some peptides and regulatory proteins cross the BBB by saturable or nonsaturable mechanisms, whereas others cannot cross. Artificial hydrophobization of polypeptides with a small number of fatty acid residues (e.g., stearate or palmitate) was shown to enhance cellular uptake of these polypeptides in vitro (*11*). As a result of such modification, the polypeptide molecule remains water-soluble but also acquires lipophilic anchors that can target even very hydrophilic molecules to cell surfaces (*12*). The studies carried out in Russia over a decade ago have shown that modification of the Fab fragments of antibodies against gliofibrillar acid protein (GFAP) and brain-specific α-2-glycoprotein (α-2GP) with stearate moieties led to an increased accumulation of the modified Fab fragments in the brains of rats (*13*, *14*). Furthermore, a neuroleptic drug conjugated with stearoylated antibody Fab fragments was much more potent compared to the free drug. In comparison, fatty acylated Fab fragments of nonspecific antibodies did not accumulate in the brain but instead accumulated in the liver, while stearoylated Fab fragments of brain-specific antibodies displayed preferential accumulation in the brain. Subsequent studies using bovine brain microvessel endothelial cells (BBMEC) as an in vitro model of BBB demonstrated that stearoylation of ribonuclease A (approximately 13.6 kDa) increases the passage of this enzyme across the BBB by almost 9-fold (*15*).

Based on this foundation the present work focused on the development of optimal modifications of polypeptides to enhance their delivery to the brain. The studies reported here show that chemical modification of polypeptides with lipophilic and amphiphilic groups can increase the permeability of a model polypeptide, horseradish peroxidase (HRP), 40 kDa, across the BBB in vitro and in vivo. More specifically, modification of HRP with (1) stearoyl chloride or (2) Pluronic block copolymers (poly(ethylene oxide)-*b*-poly(propylene oxide)-*b*-poly(ethylene oxide)) increased the rate of transport of HRP across the BBB and enhanced accumulation of HRP within the brain. The paper reports for the first time conjugation of a protein with amphiphilic block copolymer moieties via biodegradable disulfide links and demonstrates that such a modification is most successful for enhanced polypeptide delivery to the brain.

EXPERIMENTAL PROCEDURES

Materials. Horseradish peroxidase type VI, MW 44 kDa (HRP), stearoyl chloride, sulfosuccinic acid bis(2-ethylhexyl)ester (AOT), dithiobis(succinimidylpropionate) (DSP), disuccinimidylsuberate (DSS), 4-methoxytrityl chloride (MTr-CL), 1,1′-carbonyldiimidazole, ethylendiamine, 2,4,6-trinitrobenzenesulfonic acid (TNBS), trifluoroacetic acid, acetone, dichloromethane, dimethylform-

* To whom correspondence should be addressed. Tel: (402) 559-9364. Fax (402) 559-9365. akabanov@unmc.edu.

[†] University of Nebraska Medical Center.

[‡] Saint Louis University School of Medicine.

10.1021/bc049730c CCC: $30.25 © 2005 American Chemical Society
Published on Web 06/24/2005

Scheme 1. Synthesis of Pluronic−HRP Conjugates[a]

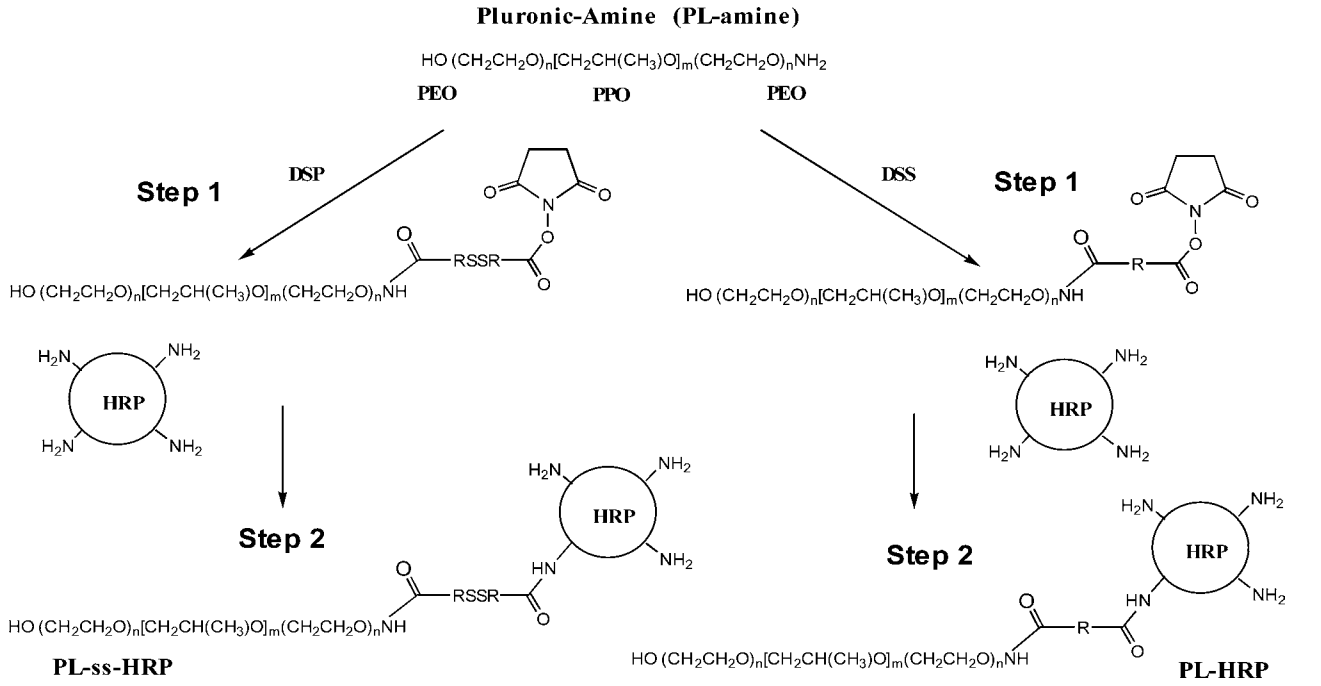

[a] Step 1: Pluronic-amine is activated by bifunctional reagents (DSP or DSS) to obtain hydroxysuccinimide derivatives of Pluronic capable of reacting with the protein amino groups. Step 2: the excess of the reagents was removed by gel filtration, and the activated polymers were immediately reacted with HRP.

amide, anhydrous acetonitrile, and pyridine were obtained from Sigma-Aldrich Co. (St-Louis, MO). Pluronic P85 (lot no. WPOP-587A) and Pluronic L121 (lot no. WPAC-550B) were kindly provided by BASF Corp. (Parispany, NJ). All other reagents were of analytical grade.

Chemical Modification of HRP with Stearic Acid Chloride in Reverse Micelles. Modification of amino groups of HRP by stearoyl chloride was performed in the reverse micelle system of AOT in octane as described earlier (*12*). Briefly, HRP solution (2.5 mg/mL) in 0.1 M sodium borate buffer (pH 9.5) was mixed with a 10-fold volume excess of 0.3 M AOT solution in octane. The emulsion was vigorously shaken for 10 min until an optically transparent solution was obtained. Following a 2-hour incubation at room temperature, the protein was precipitated in a 5-fold volume excess of cold acetone (−20 °C) with subsequent centrifugation at 2000 rpm. The precipitate was washed three times with cold acetone, dried, and dissolved in 0.1 M borate buffer (pH 9.5). The product was purified of low molecular residuals by gel-permeation chromatography on a Sephadex G25 column (Amersham, Piscataway, NJ). The protein recovery was determined by BCA Pierce method (*16*). The modification degree (the number of fatty residues introduced in a protein molecule) of HRP was determined by titration of free amino groups with TNBS as described below.

Conjugation of HRP with Pluronic Block Copolymers. *Preparation of Monoamino Derivatives of Pluronics P85 and L121.* A Pluronic molecule contains two terminal hydroxyl groups, both of which can be used for conjugation with proteins. To obtain the monoamino derivative of Pluronic, one of the hydroxyl functions was protected with a 4-methoxytrityl (MTr) group. For this purpose, Pluronics (P85 or L121) were dried by coevaporation with anhydrous pyridine in vacuo at 50 °C. Then, the dried polymer was mixed with an equimolar amount of MTr-CL in anhydrous pyridine, and the obtained mixture was incubated at room temperature for 3 h. The reaction was stopped by addition of methanol, and pyridine was removed in vacuo by coevaporation with toluene. The monosubstituted product, MTr-Pluronic, was purified from nonmodified polymer and traces of bis-MTr-Pluronic by absorption chromatography on a Silicagel column (4.5 cm × 10 cm) in dichloromethane using stepwise elution with dichloromethane containing 2%, 5%, or 10% of methanol. Mono-MTr-Pluronic was dried by coevaporation with anhydrous acetonitrile in vacuo, and then incubated with 3-fold molar excess of 1,1′-carbonyldiimidazole in anhydrous acetonitrile for 4 h at 40 °C. Activated Pluronic was dissolved in ethanol and added dropwise to 10-fold excess of ethylenediamine in ethanol to obtain polymer with one side amino group as described elsewhere (*17*). The product was dialyzed against 10% ethanol to remove low molecular weight compounds. Removal of the MTr group from the polymer was achieved with 2% trifluoroacetic acid in dichloromethane. All synthetic steps have been controlled by thin-layer chromatography on Silicagel-coated plates using a dichloromethane/methanol (9:1) mixture as an eluent. Monoamino derivatives of Pluronics have been isolated by gel-permeation chromatography on the Sephadex LH-20 column (2.5 cm × 45 cm) in methanol as eluent. Colorimetric analysis of fractions with ninhydrine detected the presence of amino groups in the product. Amino-group content was analyzed by titration of the polymers with TNBS (*18*) and was equivalent to >45% substitution of all hydroxyl groups in Pluronics.

Conjugation of HRP with Monoamino Derivatives of Pluronics P85 and L121 via a Biodegradable Link (DSP method). To obtain a biodegradable link, HRP was conjugated with Pluronics through a reducible disulfide bond (Scheme 1). Pluronic-amine is activated by a bifunctional reagent, DSP, to obtain a hydroxysuccinimide derivative of Pluronic capable of reacting with the protein amino groups (step 1). Excess of the reagent was removed by gel filtration, and the activated polymers were immediately reacted with HRP (step 2). Briefly, monoamino derivatives of Pluronics were first dissolved

in methanol (70 μmol) and added dropwise to a stirred solution of DSP (0.2 mmol) in dimethylformamide at 25 °C. Following the 30-min reaction at room temperature, the DSP-modified Pluronic was purified by gel-filtration chromatography on a Sephadex LH 20 column in methanol. The product was concentrated in vacuo and dissolved in 20% ethanol. A solution of HRP (2 μmol) in 0.1 M borate (pH 9.5) was mixed with a DSP-modified Pluronic solution prepared earlier, and the homogeneous reaction mixture was incubated overnight at 4 °C. Modified HRP was precipitated in cold (−10 °C) ethanol, incubated at 4 °C for 30 min, and separated from the excess of DSP-modified Pluronic by centrifugation at 3000 rpm for 20 min at 4 °C. Brown precipitate was washed with cold ethanol and dried in vacuo. Pluronic−HRP conjugate was purified by cation-exchange chromatography on TSK CM-650M resin with 10 mM sodium acetate (pH 4.4), 10 mM NaCl, and 5% ethanol as an eluent. First, elution of Pluronic−HRP was performed with this eluent, and then a gradient of NaCl (from 0.01 to 0.15 M) was used for elution of residual (unconjugated) HRP. Collected fractions were desalted in dialysis tubes with a molecular weight cutoff of 20 kDa (SpectroPor, Fisher Scientific, Pittsburg, PA) against water overnight at 4 °C and freeze-dried. The obtained conjugate was analyzed for protein and salt contents using the analytical procedures described below.

Conjugation of HRP with Monoamino Derivatives of Pluronics P85 and L121 by Nonbiodegradable Bond (DSS method). To obtain a nonbiodegradable link, monoamino derivatives of Pluronics were conjugated with HRP similar to the method described above except using DSS, instead of DSP (Scheme 1).

Analysis of HRP Conjugates. *Protein Assay*. The BCA Kit from Pierce (Rockford, IL) was used to measure protein content in the obtained HRP conjugates. The obtained conjugates (1.0 mg/mL) were dissolved in water and mixed with coloring solutions according to the manufacturer's protocol. Mixtures were incubated for 30 min at 37 °C, and absorbance values were measured at 550 nm using a microplate reader Multiskan MCC/340 (Fisher Scientific, Pittsburgh, PA) as described elsewhere (*16*).

HRP Enzymatic Activity. The enzymatic activity of HRP in the obtained conjugates was assessed with *o*-phenylenediamine as described earlier (*12*). Briefly, conjugate solutions (0.1 mg/mL) were mixed in a 96-well plate with the solution of *o*-phenylenediamine (5 mg/mL) in 0.1 M citrate buffer (pH 5) containing 1 mg/mL bovine serum albumin (BSA), 0.1% Triton, and hydrogen peroxide solution (0.02%). After incubating the mixture for 5 min at 37 °C, the reaction was stopped by the addition of 0.5% sodium sulfite in 2 M sulfuric acid, and absorbance was measured at 550 nm using the microplate reader Multiskan MCC/340. The activities were related to HRP concentration in the sample.

Modification Degree. The modification degree of HRP (the number of fatty residues or Pluronic molecules introduced in a protein molecule) was determined by titration of the free amino groups of the protein with TNBS as described elsewhere (*18*). Briefly, solutions of native and modified protein (1 mg/mL) were mixed with 5% TNBS solution in 0.1 M sodium borate buffer (pH 9.5) in 96-well plate. Reaction mixtures were incubated for 1 h at 25 ° C, and absorbance was measured at 405 nm using the microplate reader. The degree of modification was calculated using following equation:

$$S_i = 4N_o(A_oN_o - A_i/N_i)/A_o \quad (1)$$

where N_o and N_i were protein content and A_o and A_i were amino group content in native and modified protein, respectively.

Binding of HRP Conjugates to the Brain Endothelial Cells. BBMEC were used as an in vitro model of the BBB in these studies. BBMEC were isolated from cow brains using mechanical and enzymatic disruption of brain matter coupled with gradient separation as described earlier (*19*). Cells were seeded onto collagen-coated, fibronectin-treated 24-well culture plates at a density of 50 000 cells/cm^2 and grown using media consisting of 45% minimum essential medium (MEM), 45% Ham's F-12 (F12), and 10% horse serum supplemented with antibiotics and heparin sulfate and used after reaching confluency (typically 10−12 days). All tissue culture media was obtained from Gibco Life Technologies, Inc. (Grand Island, NY). The BBMEC monolayers were incubated with unmodified HRP or the conjugates for various time points up to 120 min. Then, the cell monolayers were washed with 1% BSA in phosphate-buffered saline (PBS) and then washed in BSA-free PBS. The cells were then lysed in 1% Triton X100, and the net amount of the cell-bound enzyme was determined by colorimetric reaction with *o*-phenylenediamine in 0.1 M citrate buffer (pH 5) containing 0.1% Triton X100, 1 mg/mL BSA, and 0.02% hydrogen peroxide as described above. The amount of HRP was normalized by the amount of cell protein as determined by the Pierce BCA assay.

Transport of HRP Conjugates across BBMEC Monolayers. Isolated BBMEC were seeded on fibronectin- and collagen-coated polycarbonate membrane inserts (Transwell, Costar Permeability Supports, Cole-Parmer Instruments Co, Vernon Hills, IL, Contd.; pore size 0.4 μm; diameter 24.0 mm) at a density of 250 000 cells per insert and allowed to grow and differentiate for up to complete maturation of the monolayers (typically within 14 days). The trans-epithelial electrical resistance (TEER) of the monolayers was recorded as an index of cell viability and monolayer integrity. The TEER values of the confluent BBMEC monolayers were no less than 130.0 Ω·cm^2. Polycarbonate membrane inserts with confluent BBMEC monolayers were placed in Side-Bi-Side diffusion cells from Crown Bio Scientific, Inc. (Somerville, NJ) maintained at 37 °C, and the transport of HRP conjugates across cell monolayers was determined as described earlier (*20*). Briefly, for luminal to abluminal transport studies, the assay buffer at the luminal (apical) side was removed and replaced with the assay buffer containing solutions of the modified or native HRP (40 μg/mL). The solutions in the donor chamber also contained 1 nM H^3-mannitol as a paracellular marker (DuPont Corp., Boston, MA). At various time points, the solutions in the receiver chamber (at the basolateral side of the monolayers) and aliquots (20 μL) from the donor chamber (at the apical side of the monolayers) were removed for the determination of the HRP concentration. The enzyme activity of HRP was measured using the *o*-phenylenediamine method as described above. ^{3}H-mannitol concentrations were determined using Beckman LS 6000 IC liquid scintillation counter (Beckman Counter, Inc., Fullerton, CA). All transport experiments were conducted in triplicate. Apparent permeability coefficients (P_{app}) of the polypletides were calculated using the following equation:

$$P_{app} = \frac{1}{AC_0}\frac{dQ}{dt} \quad (2)$$

where dQ/dt is the flux across the cell monolayers, A is the surface area of the membrane, and C_0 is the initial concentration of the drug.

Localization of HRP Conjugates in BBMEC Monolayers. For this study, HRP conjugated with Pluronic P85 via the biodegradable DSP bond (Scheme 1) was used. The native and modified proteins were labeled with Alexa Fluor 594 protein labeling kit (Molecular Probes Inc., Eugene, OR) according to the manufacture's protocol. BBMEC grown on chamber slides (Fisher, St. Louis, MO) were incubated with Alexa-labeled native or P85-modified HRP (1 mg/mL) in assay buffer for 2 h at 37 °C. Following incubation, the loading solutions were removed, and cell monolayers were washed three times with ice-cold PBS containing 1% BSA and examined with a Zeiss LSM 410 confocal laser scanning microscope, CLSM (Goettinger, Germany). All pictures were taken at the same brightness and contrast.

In Vivo Transport of St−HRP and Pluronic−HRP Conjugates to the Brain. *Radioactive Labeling of HRP.* Native, Pluronic P85-modified, or stearoyl-modified HRP were labeled by the chloramine-T method (i.e., excluding the sodium metabisulfite treatment) (*21*). Briefly, 1 mCi of ^{131}I (New England Nuclear, Boston, MA), 10 μg of chloramine T, and 5.0 μg of protein were incubated together for 60 s. The reaction was halted by adding 10 μg of sodium metabisulfite. The iodinated materials were purified by filtration on Sephadex G10 (Sigma Chemical Co., St. Louis, MO) columns. Incorporation of the radioactive ^{131}I, as determined by TCA/brine precipitation, was greater than 90% for all materials, and the specific activities were estimated to be between 50 and 150 Ci/g of protein. Albumin was labeled with ^{99m}Tc with stannous tartrate (*22*) and purified on a column of Sephadex G-10.

Measurement of Unidirectional Influx Rates. Male CD-1 mice (Charles River Labs, Wilmington, MA) weighing 20−30 g were anesthetized with an ip injection of 40% ethyl carbamate. The left jugular vein and right carotid artery were isolated. A volume of 0.2 mL of 1% BSA in lactated Ringer's solution was injected into the jugular vein. The injection contained 1×10^5 cpm of a radioactively iodinated native or Pluronic- or stearoyl-modified HRP. Between 2 and 180 min after injection, blood was obtained from the carotid artery, and the mouse was decapitated. The brain was removed, the pineal and pituitaryglands were discarded, the remainder of the brain was weighed, and the levels of radioactivity were determined in a γ counter that could simultaneously count ^{131}I. The whole blood was centrifuged at 5000g for 10 min at 4 °C, and the level of radioactivity was determined in the resulting serum. The brain/serum ratio was calculated with the equation

$$\text{brain/serum ratio } (\mu\text{L/g}) = (\text{cpm/g of brain})/(\text{cpm}/\mu\text{L of serum}) \quad (3)$$

To adjust for clearance of the protein from the blood, exposure time (expt) was calculated from the equation

$$\text{expt} = [I_0^{\,t}\text{Cp}(J)\text{d}J]/\text{Cpt} \quad (4)$$

where Cpt is the level of radioactivity in serum at time t, and J is the dummy variable for time (*23*, *24*). Brain/serum ratios of the protein content were plotted against expt, and the regression line for the linear portion of the relation was calculated. The slope of this relation measures K_i and the intercept measures the distribution volume within brain at $t = 0$ (V_i in units of μL/g). Lack of a statistically significant relation between the brain/serum ratios and expt indicates either that the protein does not cross the BBB or that a steady state between the rate of influx and efflux has already been reached.

Calculation of the Percent of Injected Proteins Taken up by Brain. The clearance of the radioactively labeled native, Pluronic-modified, or stearoyl-modified HRP from blood was first characterized. The amount of radioactivity injected intravenously was divided by the level of radioactivity in serum to yield the percent of injected radioactivity present in 1 mL of serum (% inj/mL):

$$\%\ \text{inj/mL} = 100(\text{cpm of injected radioactivity})/(\text{cpm/mL of serum}) \quad (5)$$

To calculate the percent of the injected dose of the protein entering a gram of brain (% inj/g), % inj/mL was divided by 1000 to convert it to units of % inj/μL. The brain/serum ratios for the HRPs were corrected for vascular contamination by subtracting10 μL/g. The resulting brain/serum ratio was then multiplied by % inj/μL to yield % inj/g. The area under the curve (AUC) was calculated with Prism 4.0 software, which uses the trapezoidal method.

Capillary Depletion. To distinguish whether the native, stearoyl-modified, or Pluronic-modified HRP taken up by brain tissue was sequestered by the brain endothelial cells, which comprise the BBB or was transported fully across them into brain tissue, we performed capillary depletion with the protocol adapted to mice (*25*) from rats (*26*). CD-1 male mice anesthetized with ip ethyl carbamate received an iv injection of 0.2 mL of lactated Ringer's solution containing 1% BSA, 1×10^6 cpm of a radioactively labeled native, stearoyl-modified, or Pluronic-modified HRP, and 1×10^6 of ^{99m}Tc-labeled albumin. Blood from the abdominal aorta was collected. The thorax was then opened to expose the heart, both jugular veins were severed, the descending thoracic aorta was clamped, and 20 mL of lactated Ringer's solution was injected into the left ventricle of the heart within about 1 min. The cerebral cortex was removed 30 or 120 min after iv injection. The cerebral cortex was weighed and emulsified with a glass homogenizer (10 strokes) in 0.8 mL of physiological buffer (10 mM HEPES, 141 mM NaCl, 4 mM KCl, 2.8 mM $CaCl_2$, 1 mM $MgSO_4$, 1 mM NaH_2PO_4, and 10 mM D-glucose adjusted to pH 7.4). Dextran solution (1.6 mL of a 26% solution) was added to the homogenate, and the suspension was vigorously mixed and homogenized again (3 strokes). Homogenization was performed at 4 °C in less than 1 min. An aliquot of the homogenate was centrifuged at 5400g for 15 min at 4 °C in a Beckman TL-100 ultracentrifuge with a TLS-55 swinging bucket rotor. The pellet containing the brain vasculature and the supernatant containing the brain parenchyma were carefully separated. The levels of radioactivity in these fractions and in the aortic serum were determined in a γ counter. The fractions were expressed as volumes of distribution in μL/g, and the parenchymal fraction for HRP was corrected for vascular contamination by subtracting the value for the parenchymal fraction for albumin (P_v). The amount of HRP retained by brain capillaries (*5*) was measured by the volume of distribution for the vascular fraction from this experiment.

Statistical Analysis. All statistical tests were performed by Microsoft Excel XP program using the two-tailed heteroscedastic t-tests. A minimum p value of 0.05 was estimated as the significance level for all tests. SEM values for modified and native HRP accumulation and transfer levels were less than 10% of the mean.

RESULTS

Chemical Modification of HRP with Stearic Acid Chloride in Reverse Micelles. The HRP contains six amino groups available for chemical modification. To modify these groups with stearic acid residues, the enzyme was reacted with stearoyl chloride in the reverse micelle system of AOT in octane (*12*). Based on the titration of the remaining free amino groups of the protein with TNBS (see Experimental Procedures section), an average of 1.1 stearic acid residues per protein molecule was introduced onto HRP under these conditions. The solubility of the stearoylated HRP (St−HRP) was approximately 1 mg/mL, its RZ (absorbance ratio A_{403}/A_{280}) was 2.7, and the catalytic activity was 50% of the native HRP activity (RZ of native HRP was 3.0).

Conjugation of HRP with Pluronic Block Copolymers. Pluronics have a three-block ABA structure, where the A block is hydrophilic poly(ethylene oxide) (PEO) and the B block is a lipophilic poly(propylene oxide) (PPO) chain. Variations in the length of the blocks result in copolymers with different molecular masses and hydrophilic−lipophilic balances (HLB). We synthesized conjugates of HRP with Pluronic P85, a copolymer of intermediate lipophilicity, and Pluronic L121, a highly lipophilic copolymer. Initially monoamino derivatives of P85 and L121 were prepared as described in the Experimental Procedures section. These derivatives, "Pluronic-amine" were then conjugated to HRP using a two-step procedure shown in Scheme 1. First, Pluronic-amines were activated with DSP or DSS reagents. Second, the products of these reactions were linked to the amino groups of HRP. The DSP reagent was used to introduce a degradable disulfide linkage between the HRP and Pluronic molecules, while the DSS linkage was not degradable. To vary the number of copolymer chains per protein molecule, different excesses of activated Pluronic were used. The conjugation steps are described in greater detail in the Experimental Procedures section. The modified proteins were isolated by precipitation in cold ethanol and then purified by ion-exchange chromatography (Figure 1). TNBS analysis demonstrated that the products contained mainly mono- and bis-substituted protein. The fractions of unmodified HRP did not exceed 25%. The unmodified HRP was discarded, while the fractions of modified protein (peaks 1 and 2) were combined for each conjugate and used in subsequent studies. Overall, four conjugates with stable or degradable linkages and different modification degrees were synthesized as shown in Table 1. Residual activity of modified proteins was about 90−100%.

Binding and Transport of Stearoyl-Modified HRP across BBMEC Monolayers. The stearic acid was conjugated to the HRP molecule via a nonbiodegradable bond. The effect of this modification on the binding of HRP with brain endothelial cells was studied using BBMEC monolayers. The results are presented in Figure 2. Modification of HRP resulted in about a 3-fold increase of its binding with the BBMEC.

Figure 3 shows the effect of stearoyl modification on HRP transport across BBMEC monolayers from the apical to the basolateral side. As is seen in Figure 3, HRP modification increased the apparent permeability coefficient (P_{app}) about 1.6 times (3.8×10^{-7} cm/s) when compared with the nonmodified HRP (2.4×10^{-7} cm/s). Equally important, there were no changes in TEER or permeability of a paracellular marker, ^{3}H-mannitol, demonstrating that the integrity of the monolayers was not altered.

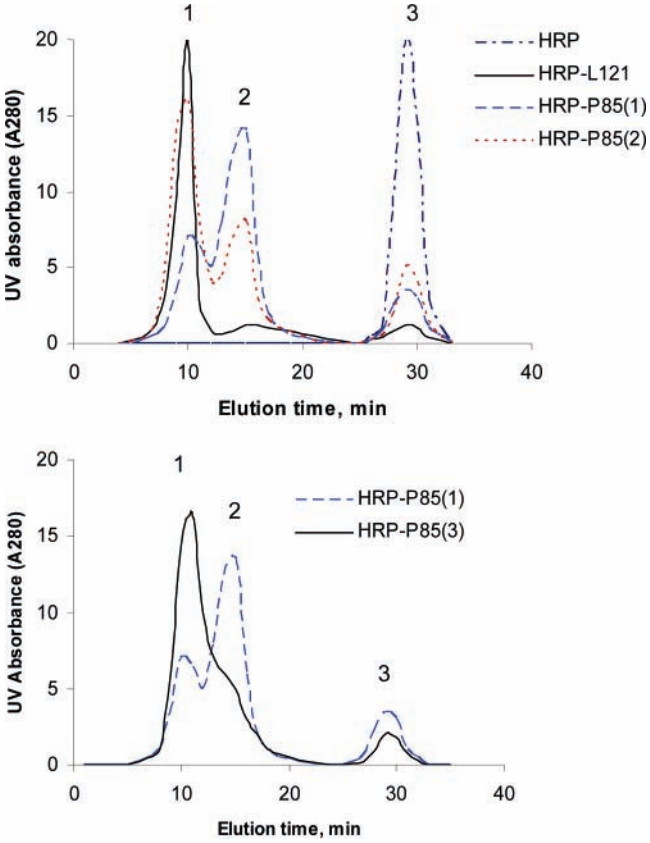

Figure 1. Chromatographic isolation of the HRP−Pluronic conjugates using TSK CM-650 column (2 cm × 15 cm) in NaCl salt gradient (0.01−0.2 M) (pH 4.5, elution rate 2 mL/min, detection at 280 nm). The peaks correspond to (1) bis-substituted HRP, (2) monosubstituted HRP, and (3) unmodified HRP. The substitution degree in each fraction was confirmed by the TNBS assay.

Table 1. Characteristics of HRP−Pluronic Conjugates

conjugate	Pluronic excess	type of link	modification degree[a]	residual activity, %[b]
HRP−P85 (1)	50	degradable	1.4	97
HRP−P85 (2)	50	stable	1.6	100
HRP−P85 (3)	70	degradable	2.0	89
HRP-L121	70	degradable	2.1	95

[a] Average number of Pluronic chains per HRP molecule determined using TNBS titration assay. [b] Compared to the native HRP, *o*-phenylenediamine reaction.

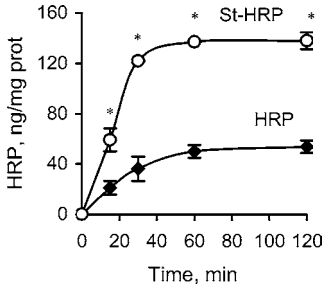

Figure 2. Binding of unmodified HRP and St−HRP with BBMEC monolayers. Data are mean ± SEM ($n = 4$). Asterisk (*) shows significant difference between HRP and St−HRP groups. Modification of HRP resulted in about a 3-fold increase of its binding with the cells.

Binding and Transport of Pluronic−HRP Conjugates across BBMEC Monolayers. Figure 4 presents the results of the study of binding of various Pluronic−HRP conjugates with BBMEC monolayers. The cells were

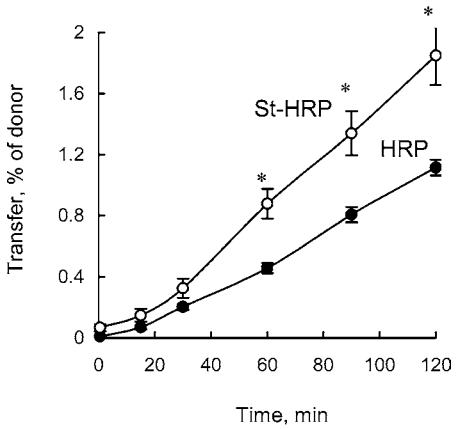

Figure 3. Apical to basolateral permeability of HRP and St−HRP in BBMEC monolayers. Data are mean ± SEM ($n = 4$). Asterisk (∗) shows a significant difference between HRP and St−HRP. Stearoyl modification of the protein results in about a 1.6-fold increase in its transport across the BBMEC.

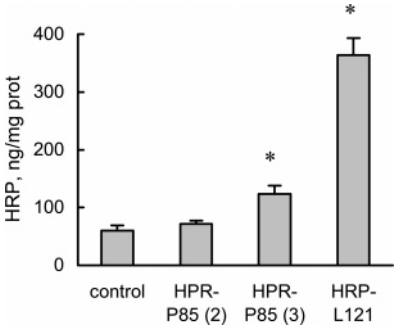

Figure 4. Binding of unmodified HRP and Pluronic−HRP conjugates (described in Table 1) with BBMEC monolayers at 60 min incubation. Results are mean ± SEM ($n = 4$). Asterisk (∗) shows a significant difference compared to HRP. Modification of HRP with Pluronic increases the binding (about 6 times for HRP−L121) of this protein with BBMEC.

incubated with unmodified HRP or the conjugates for 60 min, and the net amount of the cell-bound enzyme was determined as described above. There was practically no difference in binding between the unmodified HRP and the HRP−P85 (2) containing a nondegradable link. However, binding of conjugates containing the cleavable disulfide link, HRP−P85 (3) and HRP−L121, was increased significantly. The most pronounced effect (over 6-fold increase in binding) was observed in the case of the lipophilic Pluronic L121 conjugate. This result was consistent with our earlier report suggesting strong binding of this lipophilic block copolymer with the BBMEC membranes (*27*). HRP−P85 (3) displayed a only a 2-fold increase in cell binding compared to HRP.

The study of the permeability of various Pluronic−HRP conjugates across BBMEC was carried out in two steps. The initial experiment compared Pluronic−HRP conjugates with nondegradable and degradable links and unmodified HRP (data not shown). Modification of HRP with P85 via nondegradable link, HRP−P85 (2) resulted in about a 2-fold increase in the HRP transport. The conjugate containing a cleavable link, HRP−P85 (3), was transported almost 6 times faster than the unmodified HRP. Finally, the conjugate with the lipophilic Pluronic L121, also containing a cleavable linkage, displayed the highest rates of transport across the BBMEC monolayers. The rate of its transport was over 10-times higher than that of the unmodified HRP. Noteworthy, the amount of HRP transported across the BBMEC monolayers was determined using enzymatic reaction with the HRP

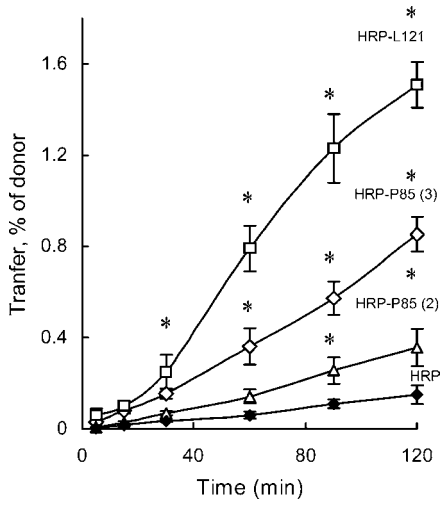

Figure 5. Apical to basolateral permeability of HRP and Pluronic−HRP in BBMEC monolayers. Data are mean ± SEM ($n = 4$). Asterisk (∗) shows significant difference between HRP and Pluronic−HRP groups. Conjugation of HRP with Pluronics via the biodegradable linkage resulted in the greatest increase (over 10-fold for HRP−L121) in permeability across the BBMEC.

substrate, *o*-phenylenediamine, suggesting that enzymatic activity of the protein was preserved during the transport across the cellular monolayers. Based on this experiment, Figure 5 compared conjugates of HRP with degradable links, HRP−L121 and HRP−P85 (3), as well as St-HRP and unmodified HRP. There were no changes in ^{3}H-mannitol permeability (not shown). At the same time, there were substantial differences in the permeability of different HRP samples increasing in the order HRP < HRP−St < HRP−P85 (3) < HRP−L121. Overall, conjugation of the enzyme with the highly hydrophobic Pluronic L121 via the biodegradable link resulted in the greatest increase in its transport across BBMEC monolayers. The P_{app} values were as follows: HRP 1×10^{-7} cm/s; St−HRP 3×10^{-7} cm/s; HRP−P85 (3) 7.8×10^{-7} cm/s; HRP−L121 10.4×10^{-7} cm/s. A separate experiment using HRP−P85 (3) labeled with Alexa FLUOR 594 determined that the amount of HRP associated with BBMEC monolayers was approximately 11.8% ± 0.3% at 60 min and 12.1% ± 0.4% at 120 min, while the amount of transferred enzyme was increasing in time reaching 3.6% ± 0.4% at 120 min.

Localization of HRP Conjugates in BBMEC Monolayers. Figure 6 shows confocal microscopy images of intracellular localization of a nonmodified protein, HRP (A, B), and HRP conjugated with Pluronic block copolymer P85 (C, D) in BBMEC monolayers. Pictures B and D represent fluorescent images; A and C represent differential interference contrast (DIC) and fluorescence images combined. HRP was linked to Pluronic P85 by a biodegradable disulfide linkage (conjugate HRP−P85 (3)). As is seen in the figure, unmodified HRP does not enter the barrier cells (A, B). Modification of the protein with Pluronic block copolymer drastically enhanced transport of HRP into the cells with accumulation in the cytoplasm, nuclei, and other cellular organelles (C, D).

Transport of St−HRP into the Brains of Mice. Figure 7 shows that linear relations existed between brain/serum ratios and exposure times for St−HRP ($r = 0.979$, $n = 7$, $p \ll 0.001$) to about 100 min and for HRP ($r = 0.959$, $n = 10$, $p \ll 0.001$) for over 250 min. This indicates passage across the BBB for both compounds and allows computation of K_i for those time periods. The K_i for St−HRP was 0.192 ± 0.018 μL/(g·min) and for HRP

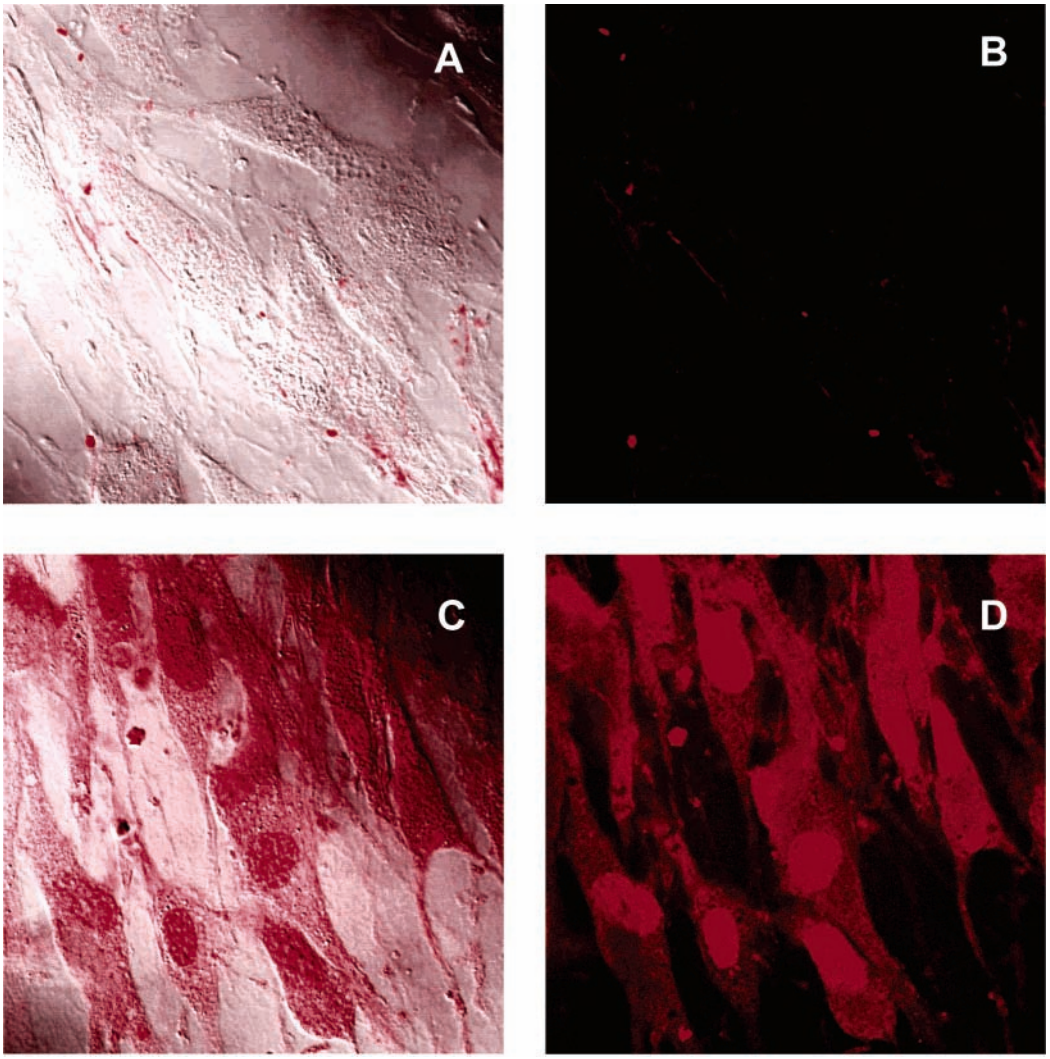

Figure 6. The confocal microscopy images showing the intracellular localization of Alexa-HRP (A, B), and Alexa-P85−HRP (C, D) in BBMEC monolayers. Pictures B and D represent fluorescent images; A and C represent differential interference contrast (DIC) and fluorescence images combined. HRP was linked to Pluronic P85 via a biodegradable disulfide linkage. The cells were exposed to Alexa-labeled native and modified HRP solutions for 2 h and washed with PBS. Modification of the protein with Pluronic L121 drastically enhanced transport of HRP into the cells with accumulation in the cytoplasm, nuclei, and other cellular organelles.

was 0.079 ± 0.008 μL/(g·min), a 2.4-fold difference. The two values differed from each other at the $p < 0.001$ level. The rate for HRP is only a little faster than the upper range usually measured for the entry of albumin.

Figure 8A shows the clearance of St−HRP and HRP from the blood. The half-time clearance (calculated with the first time point excluded for each compound) was 89.5 min for St-HRP and 79.6 min for HRP. The volume of distribution for St-HRP was 7.67 mL and for HRP was 5.93 mL. Statistical analysis showed that the slopes (half-time clearance rates) of these lines were not different, but that the intercepts (volume of distribution) were different: $F(1,1) = 7.65$, $p < 0.05$.

The percent of the injected dose taken up by brain (%inj/g) depends on two factors: the rate of entry into brain and the peripheral pharmacokinetics (such as half-time clearance rate and volume of distribution). Figure 9A shows the %inj/g for the first 180 min after injection of these compounds. St−HRP peaked higher and sooner. The ratio of the AUC for stearoyl-modified protein vs native protein (St−HRP/HRP) was 1.6 for the first 90 min of the experiment, but only 1.13 for the entire 180 min.

Figure 10 A,B shows results for capillary depletion after vascular washout and correction for albumin space with Tc−albumin for St−HRP and HRP. As is seen in Figure 10A (performed at 30 min), little or no St−HRP or HRP taken up by brain had been retained by capillaries but had all entered the brain parenchymal space. Two-way ANOVA showed significant effects for compound ($p < 0.001$), region ($p < 0.001$), and interaction ($p < 0.001$). Figure 10B shows parenchymal levels at 30 and 120 min. More HRP and St−HRP was found in the parenchymal compartment at 120 than 30 min, but at both times, entry favored St−HRP. A two-way ANOVA was significant for compound ($p < 0.05$) and time ($p < 0.05$) but not interaction.

Transport of HRP−P85 Conjugate into the Brain of Mice. Pluronic block copolymer with intermediate hydrophilic−lipophilic properties, P85, conjugated with HRP by biodegradable linkage (conjugate HRP−P85 (3), Table 1) was used for these studies. The unidirectional influx rate (K_i) for HRP−P85 was 0.0800 ± 0.0173 μL/(g·min) (regression line based on $n = 10$, $r = 0.853$, $p < 0.005$), and the K_i for HRP was 0.0206 ± 0.0081 μL/(g·min) ($n = 10$, $r = 0.669$, $p < 0.05$), a 3.9-fold increase, Figure 7B. The significant p values show that there was a statistically significant correlation between brain/serum ratios and exposure time and so indicates that both compounds crossed the BBB. The line for HRP−P85 was linear for about 180 min and for HRP for about

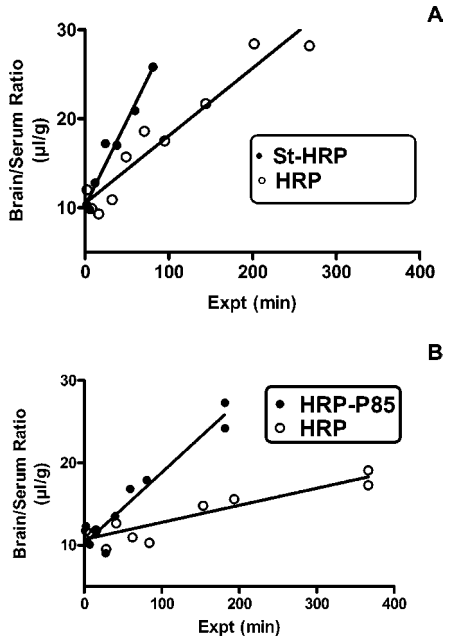

Figure 7. Comparison of blood-to-brain transport for St−HRP (A) and HRP−P85 (B) vs HRP. Modification of HRP increased K_i by 2.4-fold for St−HRP and by 3.9-fold for HRP−P85.

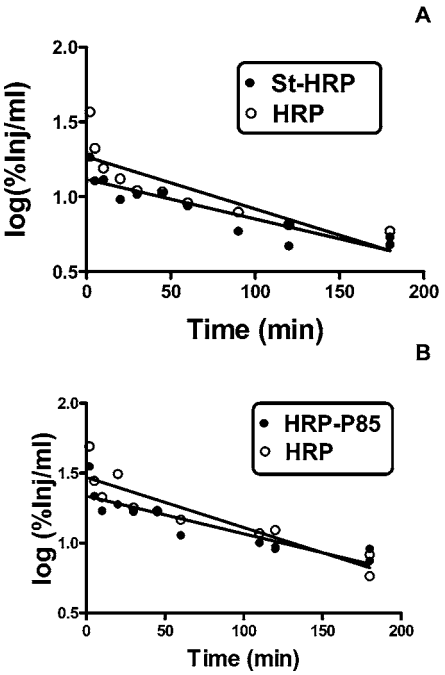

Figure 8. The percent of injected radioactivity present in 1 mL of serum (%inj/g) following injection of St−HRP and HRP (A) or HRP−P85 and HRP (B).

360 min. The K_i for HRP−P85 was about 3.9 times higher than the K_i for HRP, and this was significantly different: $F(1,16) = 9.27$, $p < 0.01$.

The half-time clearance from blood did not differ between the two compounds (Figure 8B), being 131 min for HPR−P85 and 94.5 min for HRP (2 min time points excluded). The volume of distribution after iv injection also did not differ between HPR−P85 (5.17 mL) and native HRP (3.82 mL).

Figure 9B compares the values for %inj/g for HRP−P85 and HRP. The curves differed little for the first 30 min, but thereafter, uptake of HRP−P85 exceeded that

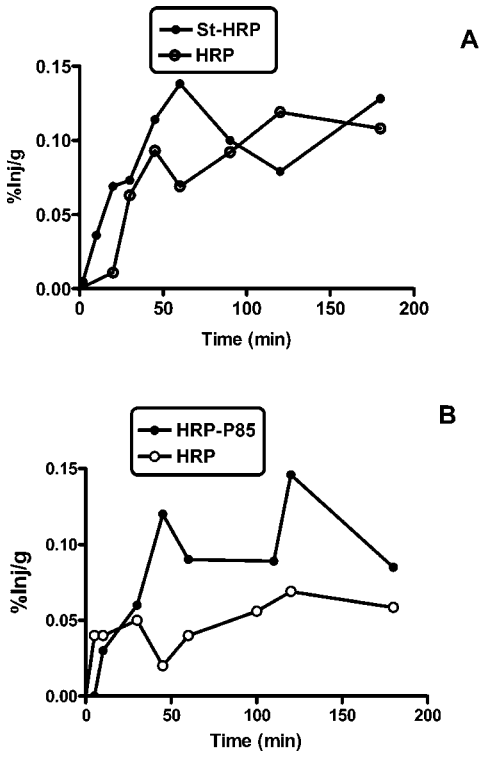

Figure 9. Modification of the protein with stearoyl or Pluronic moiety increased the AUC for brain uptake by 13% (St−HRP) and 82% (HRP−P85) during the 180 min of the experiment.

of HRP. The ratio of the area under the curve (HRP−P85/HRP) was 1.82.

Figure 10 shows results for capillary depletion after vascular washout and correction for albumin space with Tc−albumin. Figure 10C shows that at 30 min little or no HRP−P85 or HRP taken up by brain had been retained by capillaries but had all entered the brain parenchymal space. Two-way ANOVA test showed significant effects for region ($p < 0.05$) but not for compound or interaction. The lack of difference between these compounds is consistent with the %inj/g results, which showed HRP−P85 and HRP similar at that time point. Figure 10D shows parenchymal levels at 30 and 120 min. More HRP and HRP−P85 was found in the parenchymal compartment at 120 than 30 min, but at 120 min, entry favored HRP−P85. A two-way ANOVA test was significant for compound, time, and interaction all at the $p <$ 0.001 level.

DISCUSSION

Strategies for improving transport of therapeutic polypeptides to the brain are crucial for the successful applications of polypeptides for diagnostics and treatment of CNS diseases. The present in vitro and in vivo study demonstrates that point modifications of a model polypeptide, HRP, with lipophilic or amphiphilic groups greatly enhance the transport and accumulation of HRP in the brain. The key for such modifications is to achieve a delicate balance in hydrophilic−lipophilic properties of the modified polypeptides. On one hand, the modified polypeptide should be lipophilic to interact with and incorporate into the membranes of microvessel endothelial cells, but on the other hand, the protein should retain its high solubility in the blood stream. To accomplish this goal for stearoylated polypeptide, we used reverse micelles of a surfactant, AOT, producing microreactors and allowing a point conjugation of each polypeptide molecule

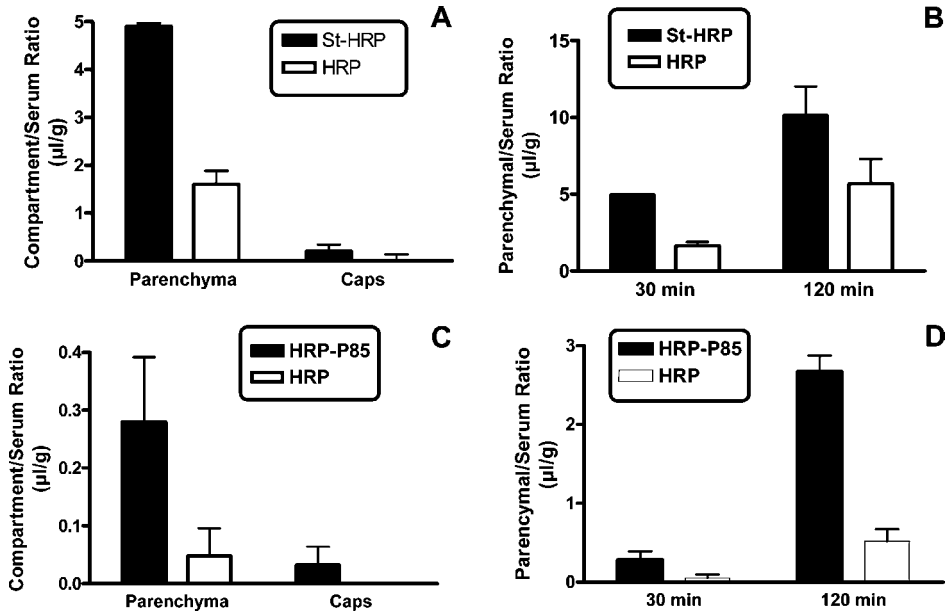

Figure 10. Capillary depletion compared for HRP and St-HRP (A,B) or HRP and HRP−P85 (C,D) 30 min after injection. Results show that all studied proteins crossed the BBB to enter the parenchymal compartment of the brain. The amount of native HRP (white bars, A−D), St−HRP (black bars, A and B), or HRP−P85 (black bars, C and D) retained in the brain is shown for capillaries and parenchyma (30 min after iv injection, A and C) or for parenchyma only (30 and 120 min after iv injection, B and D). Modification of HRP with stearoyl or Pluronic moiety significantly increased protein accumulation in the brain.

with 1−2 strearic acid residuals of the aliphatic chain. Based on the earlier reports (*11*, *15*, *28*), a stearic derivative was chosen as the most appropriate for this purpose. Consequently, total binding and transport of the stearoyl-modified HRP was increased about 2−3 times in the brain microvessel endothelial cells in vitro.

A similar principle was used in the case of a protein modification with Pluronic block copolymers; the designed conjugates had different balances between hydrophilic and lipophilic properties. Modification of HRP with Pluronic L121 was the most promising for the CNS delivery of the conjugate. The total binding and transport of Pluronic P85 and L121 modified HRP were increased up to 6 and 10 times, respectively, compared with the native HRP. A method of conjugation using biodegradable and nonbiodegradable links was also varied. As expected, the modification of the protein via a biodegradable link resulted in the most effective transport of the protein across the brain microvessel endothelial cell monolayers. We speculate that being highly hydrophilic the HRP molecule requires a highly lipophilic moiety to obtain the optimal hydrophilic−lipophilic balance of the conjugate. Such a lipophilic group has a tendency to remain associated with the cellular membrane as an anchor. Therefore, a biodegradable link allowed the polypeptide molecule to separate from its lipophilic moiety and enter the brain after the conjugate passed membranes of the barrier cells. Data obtained by confocal microscopy visualizes this effect. Modification of the protein with Pluronic P85 via biodegradable link drastically enhanced transport of HRP into the cells and its accumulation in the cytoplasm, nuclei, and other cellular organelles. We suggest that the protein conjugate was initially bound to the cellular membrane through the Pluronic moiety incorporated into the lipid bilayer followed by cleavage of the HRP molecule from the Pluronic anchors.

Another crucial point is to preserve the function of the modified protein (1) after the modification and (2) after the transport across the BBB. From this prospective, modification of HRP with Pluronic block copolymers was more preferable than conjugation with stearoyl moiety; Pluronic-based conjugates retained 90−100% of the native enzyme activity, whereas St−HRP retained only 50%. A considerable decrease in the enzymatic activity of St−HRP could be a result of the last step of the synthesis, when obtained conjugate was precipitated by ice-cold acetone. Nevertheless, all obtained conjugates retain their enzymatic activity during their transport across the BBMEC monolayers in vitro, as was detected by an HRP substrate, *o*-phenylenediamine.

In vivo studies found that (1) hydrophobization with stearoyl group or (2) amphiphilic modification with a Pluronic block copolymer had increased the rate of HRP penetration across the BBB and increased accumulation of HRP by the brain. In vivo studies of BBB permeability can differ from in vitro studies because clearance, serum protein binding, and tissue sequestration are factors that can influence in vivo results. Lipophilic modifications are especially notorious for increasing the ability of compounds to cross the BBB while decreasing the amount of compound accumulated by brain. This paradoxical effect occurs because lipophilic modification increases uptake by all tissues, not just brain, and so reduces the amount of the compound available for transport across the BBB. If the decrease in the amount of compound available for transport exceeds the increase in transport rate, the net effect is to decrease the amount of compound taken up by brain. Here we found that, in comparison to HRP, St−HRP had an increase in transport rate of 2.4-fold. However, volume of distribution as measured in Figure 8A was increased, indicating that there was increased uptake by other tissues. These two factors resulted in a net uptake by brain of St−HRP as measured by %inj/g of about 60% for the first 90 min after injection and an increase of about 13% over the entire study period.

Another problem with lipid modification as discussed above is that compounds can partition into cell membranes and become trapped there. For in vivo BBB, this results in material being retained by the capillaries and not being able to enter the brain parenchymal space. Here, the capillary depletion method was used to assess this possibility. It was found that although more St−HRP

than HRP was retained by capillaries, the vast majority of St−HRP entered brain parenchyma.

Overall modification with Pluronic block copolymers appeared to be more promising for HRP delivery to the brain. Permeation of the BBB in vivo was increased almost 4-fold with no statistically significant effects on peripheral pharmacokinetics or entry into the parenchymal space. The %inj/g was almost twice as great for HRP−P85 as for HRP.

CONCLUSIONS

This study indicates that simple and straightforward modification of polypeptides with lipophilic or amphiphilic groups can considerably increase the transport of HRP into the brain, while preserving the enymatic activity of HRP. A delicate balance between lipophilic and hydrophilic properties of the conjugate should be achieved to accomplish its efficient delivery into the brain. To achieve this balance, each unique polypeptide may require tailoring of the lipophilic moiety to match the hydrophilic−lipophilic characteristics of the native polypeptide.

ACKNOWLEDGMENT

This work was supported by National Institutes of Health Grants R01 NS36229, R01 NS41863, and R01 AA12743 and VA Merit Review.

LITERATURE CITED

(1) Brinton, R. D. (1999) A women's health issue: Alzheimer's disease and strategies for maintaining cognitive health. *Int. J. Fertil. Women's Med. 44*, 174−185.

(2) Gozes, I. (2001) Neuroprotective peptide drug delivery and development: potential new therapeutics. *Trends Neurosci. 24*, 700−705.

(3) Kroll, R. A., and Neuwelt, E. A. (1998) Outwitting the blood-brain barrier for therapeutic purposes: osmotic opening and other means. *Neurosurgery 42*, 1083−1099; discussion 1099−1100.

(4) Koliatsos, V. E., Clatterbuck, R. E., Nauta, H. J., Knusel, B., Burton, L. E., Hefti, F. F., Mobley, W. C., and Price, D. L. (1991) Human nerve growth factor prevents degeneration of basal forebrain cholinergic neurons in primates. *Ann. Neurol. 30*, 831−840.

(5) Dogrukol-Ak, D., Banks, W. A., Tuncel, N., and Tuncel, M. (2003) Passage of vasoactive intestinal peptide across the blood-brain barrier. *Peptides 24*, 437−444.

(6) Desnick, R. J., and Schuchman, E. H. (2002) Enzyme replacement and enhancement therapies: lessons from lysosomal disorders. *Nat. Rev. Genet. 3*, 954−966.

(7) Downs-Kelly, E., Jones, M., Alroy, J., Cavanagh, K., King, B., Lucas, R., Baker, J., Kraemer, S., and Hopwood, J. (2000) Caprine mucopolysaccharidosis IIID: a preliminary trial of enzyme replacement therapy. *J. Mol. Neurosci. 15*, 251−262.

(8) Urayama, A., Grubb, J. H., Sly, W. S., and Banks, W. A. (2004) Developmentally regulated mannose 6-phosphate receptor-mediated transport of a lysosomal enzyme across the blood-brain barrier. *Proc. Natl. Acad. Sci. U.S.A. 101*, 12658−12663.

(9) Banks, W. A., and Farrell, C. L. (2003) Impaired transport of leptin across the blood-brain barrier in obesity is acquired and reversible. *Am. J. Physiol. Endocrinol. Metab. 285*, E10−15.

(10) Banks, W., and Lebel, C. (2002) Strategies for the delivery of leptin to the CNS. *J. Drug Target 10*, 297−308.

(11) Kabanov, A., Levashov, A., and Alakhov, V. (1989) Lipid modification of proteins and their membrane transport. *Protein Eng. 3*, 39−42.

(12) Slepnev, V., Phalente, L., Labrousse, H., Melik-Nubarov, N., Mayau, V., Goud, B., Buttin, G., and Kabanov, A. (1995) Fatty acid acylated peroxidase as a model for the study of interactions of hydrophobically modified proteins with mammalian cells. *Bioconjugate Chem. 6*, 608−615.

(13) Chekhonin, V., Kabanov, A., Zhirkov, Y., and Morozov, G. (1991) Fatty acid acylated Fab-fragments of antibodies to neurospecific proteins as carriers for neuroleptic targeted delivery in brain. *FEBS Lett. 287*, 149−152.

(14) Chekhonin, V., Ryabukhin, I., Zhirkov, Y., Kashparov, I., and Dmitriyeva, T. (1995) Transport of hydrophobized fragments of antibodies through the blood-brain barrier. *Neuroreport 7*, 129−132.

(15) Chopineau, J., Robert, S., Fenart, L., Cecchelli, R., Lagoutte, B., Paitier, S., Dehouck, M., and Domurado, D. (1998) Monoacylation of ribonuclease A enables its transport across an in vitro model of the blood-brain barrier. *J. Controlled Release 56*, 231−237.

(16) Smith, P. K., Krohn, R. I., Hermanson, G. T., Mallia, A. K., Gartner, F. H., Provenzano, M. D., Fujimoto, E. K., Goeke, N. M., Olson, B. J., and Klenk, D. C. (1985) Measurement of protein using bicinchoninic acid. *Anal. Biochem. 150*, 76−85.

(17) Nguyen, H. K., Lemieux, P., Vinogradov, S. V., Gebhart, C. L., Guerin, N., Paradis, G., Bronich, T. K., Alakhov, V. Y., and Kabanov, A. V. (2000) Evaluation of polyether-polyethyleneimine graft copolymers as gene transfer agents. *Gene Ther. 7*, 126−138.

(18) Friser, H. (1975) An improved 2,4,6-trinitrobenzenesulfonic acid method for the determination of amines. *Anal. Biochem. 64*, 284−288.

(19) Miller, D., Audus, K., and Borchardt, R. (1992) Application of cultured bovine brain endothelial cells of the brain microvasiculature in the study of the blood-brain barrier. *J. Tissue Cult. Methods 14*, 217−224.

(20) Batrakova, E., Li, S., Miller, D., and Kabanov, A. (1999) Pluronic P85 increases permeability of a broad spectrum of drugs in polarized BBMEC and Caco-2 cell monolayers. *Pharm. Res. 16*, 1366−1372.

(21) Banks, W. A., Kastin, A. J., Brennan, J. M., and Vallance, K. L. (1999) Adsorptive endocytosis of HIV-1gp120 by blood-brain barrier is enhanced by lipopolysaccharide. *Exp. Neurol. 156*, 165−171.

(22) Banks, W. A., Goulet, M., Rusche, J. R., Niehoff, M. L., and Boismenu, R. (2002) Differential transport of a secretin analogue across the blood-brain and blood-cerebrospinal fluid barriers of the mouse. *J. Pharmacol. Exp. Ther. 302*, 1062−1069.

(23) Blasberg, R. G., Fenstermacher, J. D., and Patlak, C. S. (1983) Transport of alpha-aminoisobutyric acid across brain capillary and cellular membranes. *J. Cereb. Blood Flow Metab. 3*, 8−32.

(24) Patlak, C. S.,Blasberg, R. G., and Fenstermacher, J. D. (1983) Graphical evaluation of blood-to-brain transfer constants from multiple-time uptake data. *J. Cereb. Blood Flow Metab. 3*, 1−7.

(25) Gutierrez, E. G., Banks, W. A., and Kastin, A. J. (1993) Murine tumor necrosis factor alpha is transported from blood to brain in the mouse. *J. Neuroimmunol. 47*, 169−176.

(26) Triguero, D., Buciak, J., and Pardridge, W. M. (1990) Capillary depletion method for quantification of blood-brain barrier transport of circulating peptides and plasma proteins. *J. Neurochem. 54*, 1882−1888.

(27) Batrakova, E., Li, S., Alakhov, V., Miller, D., and Kabanov, A. (2003) Optimal structure requirements for pluronic block copolymers in modifying P-glycoprotein drug efflux transporter activity in bovine brain microvessel endothelial cells. *J. Pharmacol. Exp. Ther. 304*, 845−854.

(28) Kabanov, A., Levashov, A., and Martinek, K. (1987) Transformation of water-soluble enzymes into membrane active form by chemical modification. *Ann. N. Y. Acad. Sci. 501*, 63−66.

BC049730C

Synthesis and Biological Evaluation of EC72: A New Folate-Targeted Chemotherapeutic

Christopher P. Leamon,* Joseph A. Reddy, Iontcho R. Vlahov, Marilynn Vetzel, Nikki Parker, Jeffrey S. Nicoson, Le-Cun Xu, and Elaine Westrick

Endocyte, Inc., 3000 Kent Avenue, West Lafayette, Indiana 47906. Received December 6, 2004; Revised Manuscript Received April 14, 2005

A novel folate conjugate of mitomycin C, herein referred to as EC72, was designed and evaluated for biological activity against FR-positive cells and tumors. EC72 was produced by coupling folic acid-γ-cysteine to 7-N-modified MMC via a disulfide bond. This water soluble conjugate was found to retain high affinity for FR-positive cells, and it produced dose responsive activity in vitro against a panel of folate receptor (FR)-positive cell lines. EC72's activity was considered to be targeted and specific for the FR since (i) excess folic acid blocked biological activity, and (ii) FR-negative cell lines were unresponsive to this drug. Initial in vivo tests confirmed EC72's activity in both syngeneic and xenograft models, and this activity occurred in the apparent absence of gross or pathological toxicity. These results are significant, since daily dosing of EC72 for more than 30 consecutive days yielded no evidence of myelosuppression or toxicity to major organs, including the FR-positive kidneys. The latter observation supports published data, indicating that the apically oriented kidney proximal tubule FRs function to salvage folates prior to their excretion and to return these molecules back into systemic circulation. Overall, EC72's performance in vitro and in vivo warrants further preclinical study before this novel targeted chemotherapeutic is considered for clinical investigation.

INTRODUCTION

Notwithstanding the noteworthy advances in its treatment, cancer persists as the second largest cause of death in America, with one in four deaths being caused by this disease (*1*). Chemotherapy remains the primary method of treatment for metastasized or disseminated cancers. Traditionally, chemotherapy regimens have been designed to administer the untargeted drug intermittently (e.g. once every three to six weeks) at its maximum tolerated dose followed by a recovery period. This approach has been used for over 50 years with dismal improvements in patient cure rates. One reason for this apparent failure is that this method of treatment is plagued by toxicity resulting from the nondiscriminate uptake of these poisons into proliferating cells of both normal and neoplastic tissue. Second, the kinetics of tumor tissue recovery is much faster than the kinetics of normal tissue recovery, thus making tumor elimination highly unlikely in response to infrequent drug administration. In theory, the normal tissue toxicity manifested by any drug should be decreased or eliminated if the pharmacophore were specifically targeted to the diseased cells. This alternative approach might also enable a more aggressive metronomic-style of dosing, which would be expected to produce better therapeutic outcomes because the tumor would never have the opportunity to "recover". As such, tumor-specific targeting of drugs remains one of the most important goals in cancer treatment today.

The vitamin folic acid is a ligand capable of targeting covalently attached bioactive agents quite specifically to folate receptor (FR)-positive tumors. The FR, which is a well-known tumor associated protein, can actively internalize bound folates via endocytosis (*2, 3*). It has been detected at very high levels in >90% of ovarian and other gynecological cancers, as well as at high to moderate levels in kidney, brain, lung, and breast carcinomas (*4*–*14*). Not surprisingly, the concept of "folate–drug targeting" has been effectively exemplified over the past 14 years using payloads as diverse as small radiopharmaceutical agents to large DNA-containing formulations (see (*15*) for a comprehensive overview of this technology).

Recent efforts from a small molecule research project led to the creation of a folate–mitomycin C (MMC) conjugate. This novel FR-targetable chemotherapeutic, named EC72, was constructed using disulfide linker technology to afford molecular separation of MMC from folate once this conjugate enters the endosomes of FR-positive cancer cells. As reported below, EC72 was found to produce encouraging in vitro and in vivo therapeutic activity in multiple FR-positive models, and these data warrant further preclinical study of this new investigational agent.

EXPERIMENTAL PROCEDURES

Materials. N^{10}-Trifluoroacetylpteroic acid was purchased from Eprova AG, Schaffhausen, Switzerland. Peptide synthesis reagents were purchased from Nova-Biochem (La Jolla, CA) and Bachem (San Carlos, CA). Folate-free RPMI media (FFRPMI) and PBS were obtained from Gibco, Grand Island, NY. ^{3}H-Thymidine and N^{1a}-(^{3}H-methyl)mitomycin K were purchased from Moravek Biochemicals, Brea, CA.

Synthesis, Purification, and Analytical Characterization of EC72 and ^{3}H-Methyl-EC72. Construction of EC72 began with the synthesis of the thiol containing folate linker, Pte-γGlu-Cys-OH, using a preloaded Fmoc-Cys(Trt) Wang resin and standard solid-phase techniques. The linker was purified on a preparative RP-HPLC system connected to a Novapak HR C18 19 × 300

* To whom correspondence should be addressed. Phone (765) 463-7175; fax (765) 463-9271; e-mail chrisleamon@endocyte.com.

10.1021/bc049709b CCC: $30.25 © 2005 American Chemical Society
Published on Web 06/11/2005

mm column. A gradient method was used, starting with 99% mobile phase A (10 mM ammonium acetate buffer, pH 5.5) and 1% mobile phase B (acetonitrile) and reaching 50% B within 30 min at a flow rate of 15 mL/min. Fractions corresponding to the main peak (UV monitoring at 280 nm) were combined, and the acetonitrile was removed under reduced pressure. The rest was subjected to freeze-drying for 48 h to give the folate linker at >94% purity based on analytical HPLC (RT = 10 min) on NovaPak C18 3.9 × 150 mm column and using a gradient of solvents, starting with 99% mobile phase A (1 mM phosphate buffer, pH 6.5) and 1% mobile phase B (acetonitrile) and reaching 50% B within 30 min at a flow rate of 1.0 mL/min. ^{1}H NMR (300 MHz, DMSO-d_6): 1.87−2.93 (m,1H), 1.98−2.04 (m,1H), 2.10−2.15 (m, 2H), 2.54−2.68 (dd, J = 13.5 Hz, J = 5.6 Hz, 1H), 2.71−2.82 (dd, J = 13.5 Hz, J = 4.7 Hz, 1H), 4.05−4.08 (dd, J = 5.6 Hz, J = 4.7 Hz, 1H), 4.15−4.20 (dd, J = 8.2 Hz, J = 4.4 Hz, 1H), 6.61−6.63 (d, J = 8.7 Hz, 2H), 7.60−7.62 (d, J = 8.7 Hz, 2H), 8.61 (s, 1H).

The other reaction partner, pyridyldithioethylmitomycin C, was prepared by treating the commercially available 2-pyridyldithioethylamine with the vinylogous methyl ester in the quinone moiety of mitomycin A (*16*). The resulting 2-pyridyldithiol derivative was used for sulfenylation of the thiol group in Pte-γGlu-Cys-OH to provide EC72 (Pte-γGlu-Cys-SS-MMC). In brief, 100 mg (0.21 mmol) of Pte-γGlu-Cys-OH were mixed with 4.0 mL of HPLC-grade water, and the resulting suspension was bubbled with argon. While purging, the mixture was treated with 0.1 N sodium bicarbonate until the pH reached 7.0, at which time the solution turned clear yellow. One hundred twenty milligrams (0.24 mmol) of pyridyldithioethylmitomycin C dissolved in 3.0 mL of methanol was then added to the reaction vessel. The reaction mixture was stirred under argon for 1 h, after which methanol and some of the water were removed under reduced pressure. The resulting dark green suspension was filtered through a 0.45 μm filter to give a dark green solution; the sample was then loaded onto a preparative RP-HPLC system connected to a Novapak HR C18 19 × 300 mm column. A gradient method was used starting with 99% mobile phase A (10 mM ammonium acetate buffer, pH 6.3) and 1% mobile phase B (acetonitrile) and reaching 50% B within 30 min at a flow rate of 15 mL/min. Fractions corresponding to the main peak (UV monitoring at 280 nm) were combined, and the acetonitrile was removed under reduced pressure. The remaining material was subjected to freeze-drying for 48 h to yield 68 mg of final EC72 conjugate. EC72's analytical HPLC profile revealed 93% purity (t_R = 16.5 min) on a NovaPak C18 3.9 × 150 mm column, using a gradient of solvents starting with 99% mobile phase A (1 mM phosphate buffer, pH 6.5) and 1% mobile phase B (acetonitrile) while reaching 50% B within 30 min at a flow rate of 1.0 mL/min. The structure of EC72 was characterized by ^{1}H NMR (500 MHz, D_2O): δ 1.73 (s, 3H), 2.07−2.13 (m,1H), 2.28−2.32 (m,1H), 2.46−2.53 (m, 2H), 2,56−2.61 (m, 1H), 2.64−2.73 (m,1H), 2.90−2.96 (dd, J = 14.0 Hz, J = 8.3 Hz, 1H), 2.97−2.99 (m, 2H), 3.08−3.11 (dd, J = 14.0 Hz, J = 1.7 Hz, 1H), 3.25 (s, 3H), 3.46−3.49 (dd, J = 10.6 Hz, J = 4.4 Hz, 1H), 3.50−3.64 (m, 3H), 4.07−4.10 (d, J = 13.3 Hz, 1H), 4.16−4.21 (t, J = 10.6 Hz, 1H), 4.38−4.43 (m, 2H), 4.50 (s, 2H), 6.68−6.70 (d, J = 8.7 Hz, 2H), 7.62−76.4 (d, J = 8.7 Hz, 2H), 8.66 (s, 1H) and ES MS: $(m-H)^-$ 935.6, $(m+H)^+$ 937.4.

The synthesis of ^{3}H-methyl-EC72 was performed as described above except that N^{1a}-(^{3}H-methyl)mitomycin K (Moravek Biochemicals) was substituted for mitomycin A. The reaction mixture was condensed to 0.5 mL under reduced pressure, and the residue was purified by HPLC using the aforementioned conditions. The eluates containing ^{3}H-methyl-EC72 were collected and condensed to 1 mL under reduced pressure. The radiochemical purity was 98.5%, and the specific activity was 3.2 Ci/mmol.

Cell Culture. Cells were grown continuously as a monolayer using folate-free RPMI medium (FFRPMI) containing 10% heat-inactivated fetal calf serum (HIFCS) at 37 °C in a 5% CO_2/95% air-humidified atmosphere with no antibiotics. The HIFCS contained its normal complement of endogenous folates which enabled the cells to sustain growth in this more physiologically relevant medium (*3*). All cell experiments were performed using FFRPMI containing 10% HIFCS (FFRPMI/HIFCS) as the growth medium, except where indicated.

Folate Receptor Assay. A folate receptor (FR) assay was performed as previously described by Parker et al. (*14*), and all sample preparation procedures were performed at 4 °C. Briefly, tissue samples were homogenized in homogenization buffer (10 mM Tris, pH 8.0, 0.02 mg/mL each of leupeptin and aprotinin; 1 mL buffer per 50 mg of tissue). Membrane pellets were collected by centrifugation (40 000*g* for 60 min. at 4 °C) and resuspended in solubilization buffer (50 mM Tris, pH 7.4, 150 mM NaCl, 25 mM *n*-octyl-β-D-glucopyranoside, 5 mM EDTA, and 0.02% sodium azide). Insoluble material was removed by another centrifugation, and the total protein concentration of the supernatants was determined by the BCA method (Pierce Chemical Co.). Each sample was diluted to 0.25 mg/mL in solubilization buffer, and the solubilized FRs were concentrated by passing through Microcon-30 microconcentrators (30K molecular weight cutoff; Millipore Corporation). After a brief acid wash step to release endogenous folates, samples were neutralized and then allowed to bind ^{3}H-folic acid (120 nM ^{3}H-folic acid (Amersham) in 10 mM Na_2PO_4, 1.8 mM KH_2PO_4, pH 7.4, containing 500 mM NaCl, 2.7 mM KCl, and 25 mM *n*-octyl-β-D-glucopyranoside) or ^{3}H-folic acid competed with 120 μM unlabeled folic acid. The concentrators were washed three times with a detergent-based buffer (50 mM *n*-octyl-β-D-glucopyranoside, 0.7 M NaCl in PBS, pH 7.4). After the final wash, the retentates containing the solubilized FRs were recovered with PBS containing 4% Triton-X 100. The samples were then counted in a liquid scintillation counter (Packard Bioscience Co.). CPM values were converted to picomole of FR using the reagent's specific activity, and the final results were normalized with respect to the sample protein content.

Relative Affinity Assay. The relative affinity of various folate derivatives was determined according to the method described by Westerhoff et al. (*17*) with slight modification. Briefly, FR-positive KB cells were suspended into FFRPMI/HIFCS following exposure to 0.25% trypsin in phosphate-buffered saline (PBS) at room temperature for 3 min. Following a 5 min 800*g* spin and one PBS wash, the final cell pellet was suspended in FFRPMI (no serum). Cells were incubated for 15 min on ice with 100 nM of ^{3}H-folic acid in the absence and presence of increasing concentrations of folate-containing test articles. Samples were centrifuged at 10 000*g* for 5 min, cell pellets were suspended in buffer, transferred to individual vials containing 5 mL of scintillation cocktail, and then counted for radioactivity. Negative control tubes contained only the ^{3}H-folic acid in FFRPMI (no competitor). Positive control tubes contained a final concentration of 1 mM folic acid, and CPMs measured in these samples (representing nonspecific binding of label) were subtracted from all samples. Notably, relative

affinities were defined as the inverse molar ratio of compound required to displace 50% of ^{3}H-folic acid bound to FR on KB cells, and the relative affinity of folic acid for the FR was set to 1.

Kinetics and Specificity of EC72 Activity. KB cells were seeded in 12-well Falcon plates and allowed to form adherent monolayers (~50% confluent) overnight in FFRPMI/HIFCS. Thirty minutes prior to the addition of EC72, spent medium was aspirated from all wells and replaced with fresh FFRPMI. Note, designated wells received media containing 100 μM folic acid, and cells within the latter wells were used to determine the targeting specificity, since cytotoxic activity produced in the presence of excess folic acid (enables competition for FR binding) would signify the portion of the total activity that was unrelated to FR-specific delivery. Following a single rinse with 1 mL of media, cells were exposed to 100 nM of EC72 in 1 mL of FFRPMI/HIFCS for only 10 min at 37 °C (pulse). Cells were then washed three times with media and chased for 22, 46, or 70 h. Spent media was aspirated from all wells and replaced with fresh media containing 5 μCi/mL ^{3}H-thymidine. Following a 2 h 37 °C incubation, cells were washed three times with 0.5 mL of PBS, pH 7.4, and then treated with 0.5 mL of ice-cold 5% trichloroacetic acid per well. After 15 min, the trichloroacetic acid was aspirated and the cells solubilized by the addition of 0.5 mL of 0.25 N sodium hydroxide for 15 min. Four hundred and fifty microliters of each solubilized sample were transferred to scintillation vials containing 3 mL of Ecolume scintillation cocktail and then counted in a liquid scintillation counter. Final tabulated results were expressed as the percentage of ^{3}H-thymidine incorporation relative to untreated controls.

Dose-Dependent Activity. Cells were heavily seeded in 12-well Falcon plates and allowed to form nearly confluent monolayers overnight. Following one rinse with 1 mL of fresh FFRPMI/HIFCS, each well received 1 mL of media containing increasing concentrations of EC72 (four wells per sample). Cells were pulsed for 10 min at 37 °C, rinsed four times with 0.5 mL of media, and then chased in 1 mL of fresh media up to 72 h. Cells were incubated with ^{3}H-thymidine and processed as described above. Final tabulated results were expressed as the percentage of ^{3}H-thymidine incorporation relative to untreated controls.

Serum Stability. The stability of EC72 in human serum was determined by an in vitro assay which included a solid-phase extraction procedure for sample cleanup followed by HPLC analysis. EC72 was added to human serum at a 200 μM final concentration, and the sample was incubated in a 37 °C water bath for a total period of 24 h. Two hundred microliters of serum sample ($n = 3$) was removed 1, 2, 4, 8, and 24 h after initiation of incubation, and EC72 was recovered from serum by solid-phase extraction with Oasis HLB cartridges (1 cm^3/30 mg; Waters Corporation). First, 800 μL of 6 M guanidine (pH adjusted to 7.4 with 0.1 M NaOH) was added to each 200 μL serum sample to reduce nonspecific protein binding of the drug. Next, cartridges were conditioned with 1 mL of methanol and equilibrated with 1 mL of 6 M guanidine, pH 7.4. Samples (1 mL) were then loaded onto the cartridges followed by a wash with 5% methanol in water (1 mL). Finally, samples were eluted with 1 mL of methanol, evaporated to dryness, and reconstituted in 200 μL of phosphate-buffered saline, pH 7.4. Ten microliters of the reconstituted sample was injected on an HPLC equipped with a Sunfire C18 3.0 × 100 mm column, a UV detector at 280 nm, 10 mM ammonium acetate, pH 7.0 (mobile phase A), and acetonitrile (mobile phase B). EC72 was eluted with a gradient from 95:5 (A:B) to 60:40 (A:B) in 15 min. Percent recoveries were calculated based on the integrated peak areas assuming that a $t = 0$ serum extracted sample represented 100% recovery. The %RSD for each individual time point was <2%.

In Vivo Studies. Four to seven week-old mice (Balb/c or *nu*/*nu* strains) were purchased from Harlan Sprague Dawley, Inc. (Indianapolis, IN) and were maintained on a folate-free diet (Harlan diet #TD00434) for a total of three weeks prior to and beyond the onset of dosing. Syngeneic, FR-positive M109 tumor cells (0.5×10^6 per Balb/c mouse) or FR-positive KB cells (0.75×10^6 per *nu*/*nu* mouse) were inoculated in the peritoneal cavity and allowed to proliferate for 4 days. Sterile aqueous solutions of test article were dosed ip following a qdx7 or qdx5, 4 wk schedule, as indicated. Doses were 1800 nmol/kg for EC72 and MMC. Animals in the specificity cohort received 1800 nmol/kg EC72 plus 18 000 nmol/kg folic acid. Animal survival and health status were monitored daily, and activity data were reported as the percent survival (in days) of the treated cohorts relative to the untreated cohort.

Blood Clearance. Six week old female Balb/c mice received an 1800 nmol/kg intravenous dose of ^{3}H-methyl-EC72, and blood samples were taken with time. Approximately 100 μL of each blood sample were dissolved in a 1:1 mixture of Soluene-350 (Perkin-Elmer, Boston, MA) and 2-propanol, heated to 60 °C to solubilize, oxidized in 0.6% hydrogen peroxide, heated again to decolorize, mixed with scintillation fluid, and then counted for radioactivity. Data were fitted using a two-phase exponential decay algorithm ($r^2 = 0.999$; GraphPad Prism software, v. 4.02).

Toxicity Assessment. Balb/c mice bearing ip M109 tumors were treated daily with 1800 nmol/kg of test article administered ip. Animals were monitored daily and euthanized upon moribund condition (either from tumor burden or toxicity) using carbon dioxide asphyxiation. Blood samples were collected following the 30th dose and/or at time of euthanasia. Samples were collected via heparinized microhematocrit capillary tubes (Fisher) from the orbital sinus of animals anesthetized with diethyl ether. Blood samples collected at the time of euthanasia were done via cardiac puncture using 1 mL syringes fitted with 25 or 27.5 gauge needles. Blood was allowed to coagulate at room temperature for 30 min and then centrifuged at 6600*g* for 10 min at 4 °C. Sera were collected from these samples and then recentrifuged at the same rate for 6 additional min at 4 °C. Sera were frozen at −20 °C until shipment to Ani-Lytics, Inc. (Gaithersburg, MD) for analysis of AST-SGOT and blood urea nitrogen (BUN) levels. At the time of euthanasia, heart, lung, liver, spleen, kidney, intestine, skeletal muscle, and bone (tibia/fibula) were collected and immediately placed in 10% buffered formalin (Sigma-Aldrich). Preserved organs were sent to Animal Reference Pathology Laboratories (ARUP; Salt Lake City, Utah) for histopathologic tissue evaluation.

RESULTS

Folate-Targeted Chemotherapy. The mechanism of folate-targeted drug delivery is schematically shown in Figure 1. Cells expressing the FR protein bind folate−drug conjugates very tightly and endocytose them inside. Once internalized, the FR changes conformation and releases the conjugate inside the acidic milieu of the

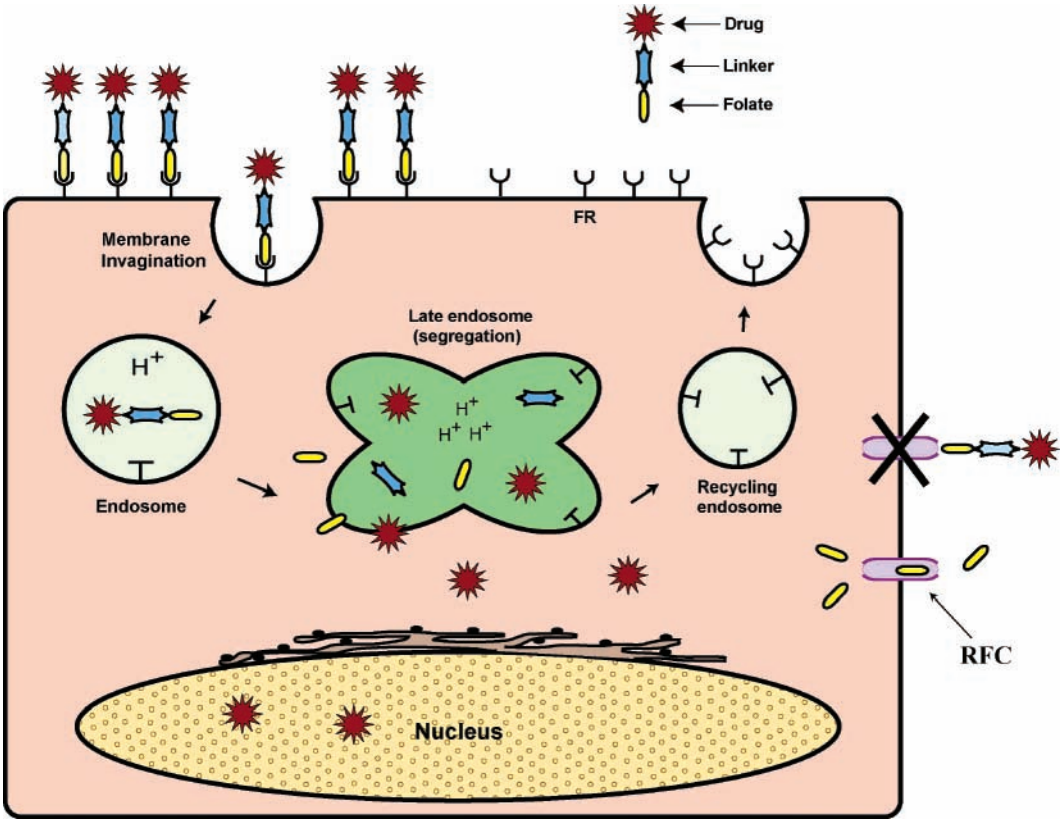

Figure 1. FR-mediated endocytosis of folate−drug conjugates. Exogenously added folate−drug conjugates bind specifically to the FR protein with high affinity. The plasma membrane invaginates around the conjugate:FR complex to form an endosome. As the lumen of the maturing endosome acidifies to ~pH 5, the receptor changes conformation and releases the conjugate. Eventually, the fates of the folate-based ligand, attached drug cargo, and the FR are determined during a sorting process within late endosomal elements. The reduced folate carrier (RFC), which unlike the FR is an anion transporter, can shuttle folate molecules inside the cell. Folate−drug conjugates, however, are not substrates for the RFC.

endocytic elements. Depending on the nature of the chemical linkage between them, separation of the folate and drug moieties can occur within these vesicular structures. Finally, the released drug diffuses across the vesicular membrane to exert its activity. Importantly, unmodified folates can also gain access to the cell cytosol via a membrane-resident anion transporter (reduced folate carrier). However, transport of folate−drug conjugates through this protein has not been experimentally observed (unpublished data).

EC72 Synthesis. The synthesis of EC72 is schematically shown in Figure 2. A thiol containing folate linker, Pte-γGlu-Cys-OH, was coupled in near quantitative yield to pyridyldithioethylmitomycin C to produce EC72 (Pte-γGlu-Cys-SS-MMC). It was purified by preparative reverse-phase HPLC and stored as a lyophilized powder. The structure of EC72 was confirmed by ^{1}H NMR spectroscopy and electrospray ionization mass spectroscopy.

Relative Affinity Assay. EC72 was first evaluated biologically using an in vitro relative affinity assay that measures a ligand's ability to directly compete with folic acid for binding to cell surface FRs. Importantly, a relative affinity value of 1.0 implies that the test article ligand has an affinity equal to that of folic acid for the FR. Likewise, values lower than unity reflect weaker affinity, and values higher than unity reflect stronger affinity.

Cultured KB or M109 cells were incubated with 100 nM ^{3}H-folic acid in the presence of increasing concentrations of nonradioactive folic acid or EC72. Following a 15 min incubation at 4 °C, cells were rinsed free of unbound material and counted for residual cell-associated radioactivity. The quantity of bound radioactivity was plotted against the concentration of unlabeled ligand, and IC_{50} values (concentration of ligand required to block 50% of ^{3}H-folic acid binding) were estimated. As shown in Figure 3, EC72 was experimentally determined to have an affinity of 0.59 relative to that of folic acid for human FRs (KB cells) and an affinity of 0.51 for murine FRs (M109 cells). Thus, chemical modification of folate with the mitomycin C drug motif only slightly altered the vitamin's intrinsic affinity for the FR.

Kinetics of EC72 Activity. Our initial in vitro activity study focused on determining a reasonable endpoint for measuring DNA synthesis inhibition. To accomplish this goal, monolayer KB cells were pulsed for 10 min with 100 nM of EC72 (in the presence and absence of excess folic acid) and then chased for various periods of time thereafter prior to labeling with ^{3}H-thymidine. Although such short pulse incubations are not commonly used when evaluating the in vitro activity of chemotherapeutic drugs (*18*), we felt that this approach was more meaningful for evaluating a targeted agent's activity in vitro since (i) a short incubation pulse should be effective for loading the cell surface receptors with a targeted agent, (ii) folate−drug conjugates are known to rapidly distribute throughout the body and clear from the bloodstream within the first couple of minutes (*19*), and (iii) tumors are not persistently bathed in the presence of drug. As shown in Figure 4, DNA synthesis activity in EC72-pulsed cells had progressively decreased with respect to the amount of chase time. Thus, a ~20% inhibition was measured after 24 h of chase time,

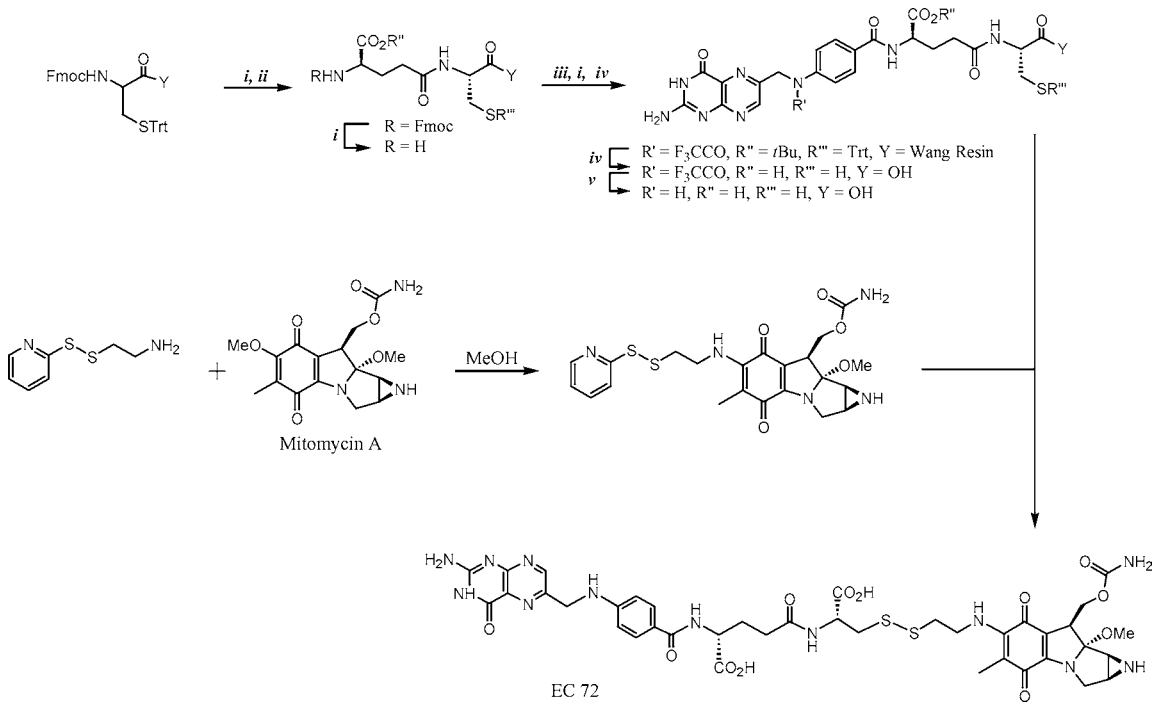

Figure 2. Synthetic route for EC72 (folate−disulfide−MMC). Bulk MMC is first converted into mitomycin A followed by vinylogous amidation to form a thiosulfonyl-ethyl−MMC intermediate. The intermediate is then reacted with Pte-γGlu-Cys to produce EC72. Reagents and conditions: (i) 20% piperidine, DMF; (ii) Fmoc-D-Glu-OtBu, PyBop, DIPEA, DMF; (iii) N^{10}-TFA-Pte-OH, DIPEA, DMSO; (iv) TFAA, $HSCH_2CH_2SH$, $^iPr_3SiH$; (v) H_4NOH, pH = 10.3.

whereas ∼75% inhibition resulted after 72 h. Although it is not shown here, chase times longer than 72 h typically did not produce any greater DNA synthesis inhibition. Importantly, the inhibitory activity manifested by EC72 was completely blocked at all chase times when cells were pulsed in the presence of excess folic acid, thereby confirming EC72's FR targeting specificity.

Dose-Dependent Activity. The activity of EC72 was next evaluated to determine its dose responsive properties. As shown in Figure 5A, EC72's activity was determined to be concentration dependent with an IC_{50} of ∼5 nM when cells were merely pulsed for a 10 min period. Importantly, similar results were obtained if cells were incubated for longer pulse times (2 h; see Figure 5B). Consistent with the data described above, EC72's activity was effectively blocked in the presence of excess free folic acid, indicating that the observed activity was folate-mediated. The latter result is significant, for it suggests that normal tissues that express little to no FR should not be affected by EC72.

A second line of evidence for EC72's specificity was obtained when a series of cell lines were screened in vitro. As shown in Table 1, EC72 was found to be active against only those cell lines that expressed the FR. Thus, DNA synthesis inhibition was measurable in the FR-positive KB, ID8, and M109 cell lines; however, no activity was measurable in the FR-negative 4T1 and A549 cell lines.

Serum Stability and Blood Clearance. Since EC72 contains an intramolecular disulfide bond which could be susceptible to cleavage in a biological matrix, its stability in human serum was investigated at 37 °C. As shown in Figure 6 Panel A, results from an HPLC-based solid-phase extraction method revealed that the percent recovery of intact EC72 decreased with time in the serum matrix with an estimated $t_{1/2}$ of ∼11 h. The relevance of this finding is emphasized by a follow up experiment which assessed the blood clearance of a structurally related analogue of EC72, e.g. a compound that contained a ^{3}H-methyl group on the mitomycin moiety's aziridine nitrogen (^{3}H-methyl-EC72).[1] Thus, an 1800 nmol/kg intravenous dose of ^{3}H-methyl-EC72 was given to Balb/c mice, and blood samples were taken with time to approximately measure the clearance rate. As shown in Figure 6 Panel B, ^{3}H-methyl-EC72 was rapidly removed from systemic circulation. After fitting the data using a two-phase exponential decay algorithm ($r^2 = 0.999$), the approximate half-lives of the alpha and beta phases were estimated to be 1 and 67 min, respectively. Importantly, similar rapid tissue distribution and elimination phenomena have also been observed for other folate−drug conjugates (*19, 20*), and it appears to be representative for this class of targeted small molecules. Taken together, the data in Figure 6 (Panels A and B) suggest that EC72 is likely to reach an FR-positive tumor in an intact form within minutes following an intravenous injection.

In Vivo Activity. (*a) Syngeneic Model.* EC72's activity was next evaluated in vivo. Four days after receiving an ip inoculation of syngeneic, FR-positive M109 tumor cells, animals received daily ip injections of 1800 nmol/kg EC72 or MMC (formulated in saline) following a qdx7, 4 wk schedule. Notably, animals in a specificity cohort received 1800 nmol/kg EC72 plus 18 000 nmol/kg of folic acid. As shown in Figure 7, untreated animals were all moribund by day-24 of the study and had to be euthanized. MMC-treated animals did not statistically live any longer than the controls; importantly, this effect was not due to the lack of antitumor activity, since MMC-treated animals did not present with a significant ip tumor burden upon necropsy. Instead, animals in this cohort apparently died from MMC-related toxicity (vide infra). Using an identical dosing regimen, EC72-treated animals had experienced a significant 185% increase in median survival time relative to the PBS control group ($p = 0.006$), and these

[1] Methyl-EC72 is essentially the porfiromycin analogue of EC72. When tested for activity against KB cells in the same experiment, the IC_{50}s were 5.7 nM and 7.7 nM for EC72 and methyl-EC72, respectively.

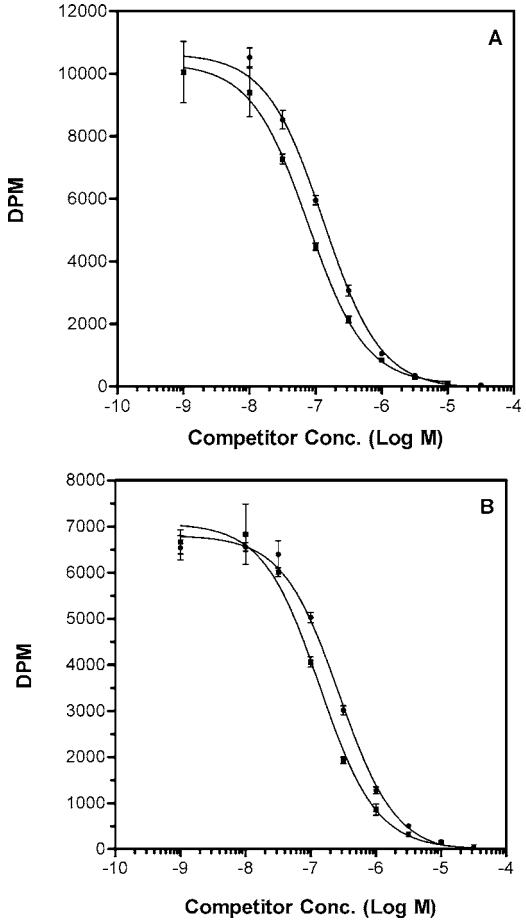

Figure 3. Relative folate receptor binding affinity of EC72. KB cells were incubated for 15 min on ice with 100 nM ^{3}H-folic acid in the presence and absence of increasing competitor concentrations: (■) folic acid; (●) EC72. Error bars represent 1 standard deviation ($n = 3$). A, human KB tumor cells; B, murine M109 tumor cells.

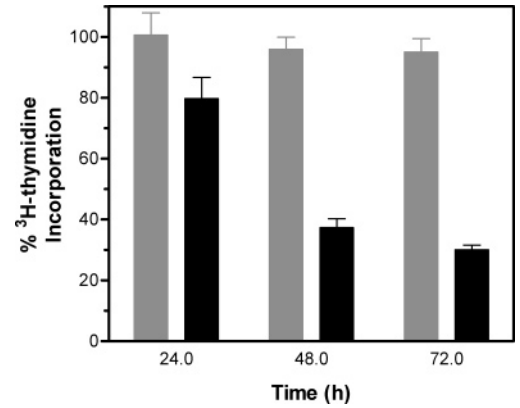

Figure 4. Kinetics of EC72 activity. Adherent KB cells were pulsed for 10 min with 100 nM EC72 in the presence or absence of 0.1 mM folic acid. Following a 22, 46, or 70 h chase in fresh media, cells were incubated with ^{3}H-thymidine for an additional 2 h and then counted for radiolabel incorporation into newly synthesized DNA, as described in Experimental Procedures. Black bars, EC72; grey bars, EC72 plus 0.1 mM folic acid. Data represent the average ± 1 SD ($n = 4$).

animals did not present with any noticeable toxicity (i.e. no weight loss or obvious physical change in behavior) during EC72 therapy. Furthermore, one of four of the EC72-treated animals emerged tumor-free by day-70 postinoculation. The antitumor effect of the EC72 conjugate was also found to be reduced to 112% increase in median survival when the drug was coinjected with a

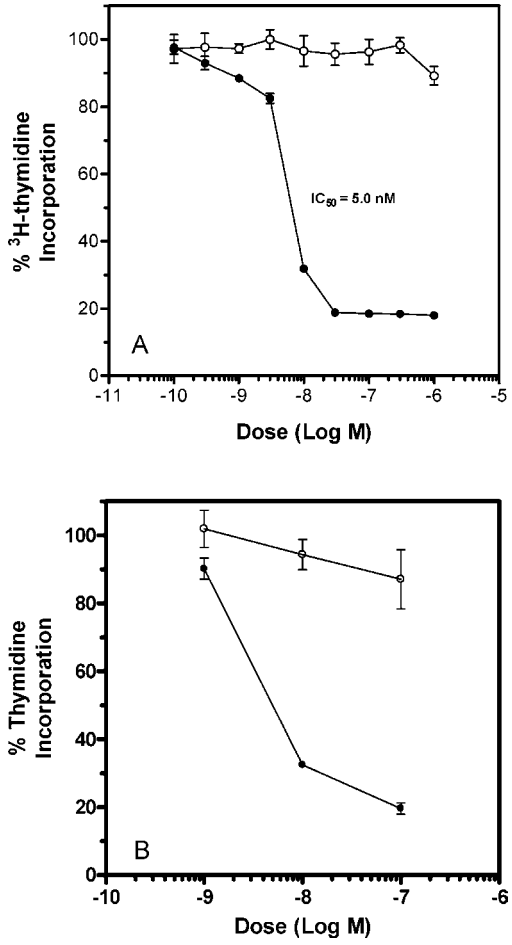

Figure 5. EC72 dose–response. KB cells were treated for 10 min (panel A) or 2 h (panel B) with increasing concentrations of EC72 in the presence or absence of 0.1 mM folic acid (as a competitor). Following a 70 h chase in fresh media, cells were incubated with ^{3}H-thymidine for 2 h and then counted for radiolabel incorporation into newly synthesized DNA, as described in Experimental Procedures. (●), EC72; (○), EC72 plus 0.1 mM folic acid. Data represent the average ± 1 SD ($n = 4$).

Table 1. EC72 Activity on Folate Receptor Positive and Negative Cell Lines[a]

cell line	origin	FR level (pmol/mg cell protein)	EC72 IC_{50} (nM)
KB	human, nasopharyngeal carcinoma	146	5
ID8	murine, ovarian carcinoma	45	100
M109	murine, lung carcinoma	45	100
4T1	murine, breast carcinoma	1.6	>1000
A549	human, lung carcinoma	1.3	>1000

[a] A panel of cell lines with varying levels of FR expression were treated for 10 min with increasing concentrations of EC72. Following a 70 h chase in fresh media, cells were incubated with ^{3}H-thymidine for 2 h and then counted for radiolabel incorporation into newly synthesized DNA, as described in Experimental Procedures. IC_{50} values were calculated from nonlinear fitted dose curves.

moderate, 10-fold excess of folic acid. Although the therapeutic difference between the +/− excess folate cohorts was obvious, the data only support a *p*-value of 0.065. However, different from the highly controllable receptor competition studies that are often performed in vitro (*15*), competition in vivo can be particularly challenging due to (i) nonequilibrium conditions, (ii) dissimilar pharmacokinetics between folic acid and a given folate–drug conjugate, and (iii) the fact that repeated doses of high excess folic acid (e.g. 100-fold over the

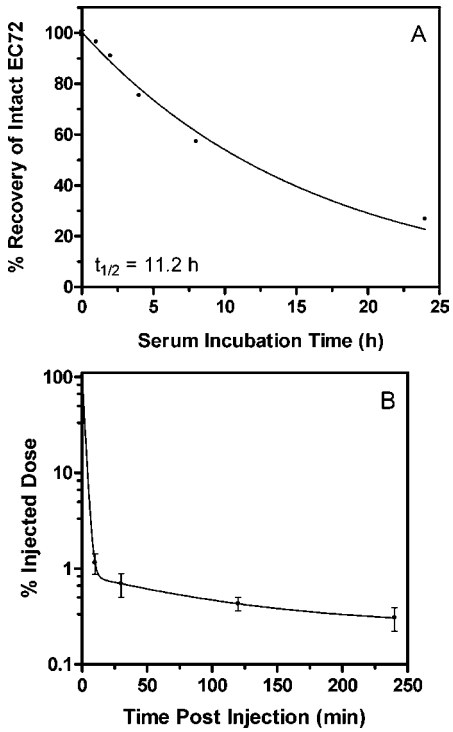

Figure 6. Serum stability and pharmacokinetics. Panel A, stability of EC72 in human serum at 37 °C ($n = 3$ with <2% %RSD). Panel B, blood clearance of ^{3}H-methyl-EC72 following an 1800 nmol/kg intravenous dose to Balb/c mice ($n = 3$).

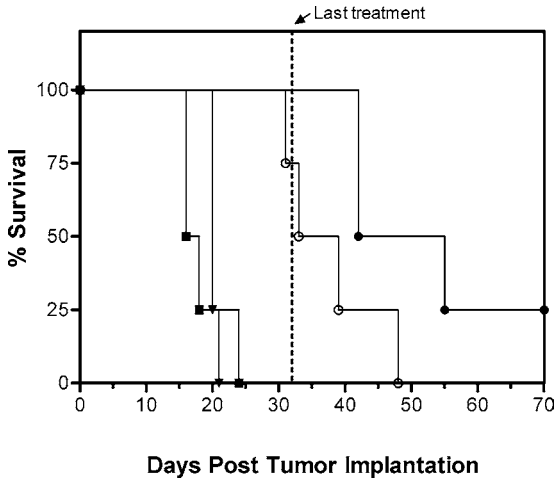

Figure 7. Antitumor activity of EC72 in a syngeneic model. 0.5×10^6 M109 cells were inoculated ip into each *Balb/c* mouse. Four days later, animals were treated intraperitoneally with (●) 1800 nmol/kg of EC72, (○) 1800 nmol/kg EC72 plus 18 000 nmol/kg of folic acid, or (▼) 1800 nmol/kg MMC following a qdx7, 4 wk schedule. A control cohort (■) was not treated. Animal survival was monitored daily ($n = 4$ animals per cohort).

folate−drug) cannot typically be given due to toxicity limitations related to the free vitamin itself (personal observations). Thus, the competition data presented in Figure 7 along with the lack of associated toxicity are believed to be evidence for tumor receptor targeting.

EC72's in vivo activity was also found to be dose responsive. As shown in Figure 8, untreated control animals all died by day 24 PTI. The lowest EC72 dose level of 100 nmol/kg failed to produce meaningful activity (43% ILS), whereas the 400 nmol/kg dose level yielded a 120% ILS. However, animals treated with 1800 nmol/kg responded the best, with one complete responder, and three of four partial responders (240% ILS overall).

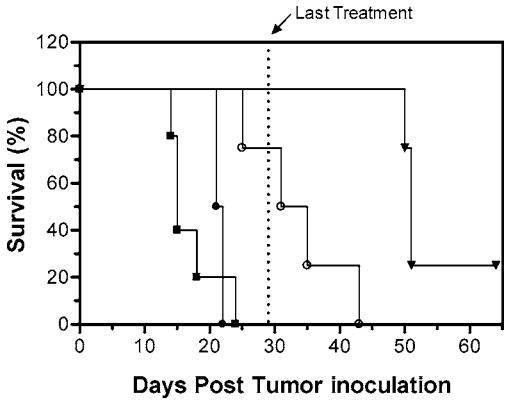

Figure 8. EC72 dose−response. 0.5×10^6 M109 cells were inoculated ip into each *Balb/c* mouse. Four days later, animals were treated intraperitoneally with (●) 100 nmol/kg, (○) 400 nmol/kg, or (▼) 1800 nmol/kg EC72 following a qdx5, 4 wk schedule. A control cohort (■) was not treated. Animal survival was monitored daily ($n = 4$ animals per cohort).

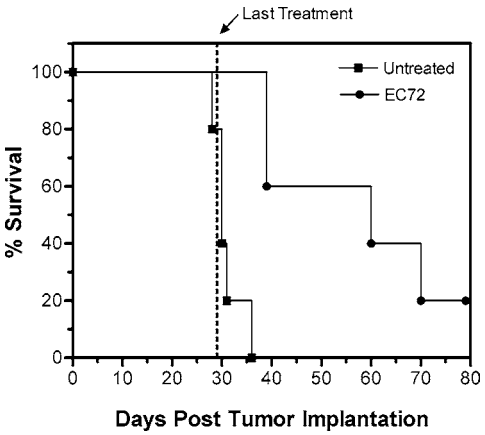

Figure 9. Antitumor activity of EC72 in a human tumor xenograft model. 0.75×10^6 KB cells were inoculated ip into each *nu/nu* mouse. Four days later, animals were treated intravenously with (●) 1800 nmol/kg of EC72 following a qdx5, 4 wk schedule. A control cohort (■) was not treated. Animal survival was monitored daily ($n = 5$ animals per cohort).

(b) Activity in the KB Xenograft Model. EC72 was also evaluated in the KB human tumor xenograft model. Except for using a qdx5, 4 wk regimen, experimental conditions were identical to those described above for the M109-Balb/c model. As shown in Figure 9, EC72-treated mice lived approximately twice as long (200% ILS; similar to the M109 model) compared to the untreated control animals, and one in five treated mice were long-term survivors. Furthermore, no evidence of test article-related gross or pathological toxicity was observed in these animals. Taken together, EC72 has proven to be active in both murine and human FR-positive tumor models.

(c) EC72 Toxicity. In a separate study, M109 tumor-bearing mice (4 days post ip inoculation) received daily ip injections of 1800 nmol/kg EC72 or MMC following a qdx7 schedule for up to 44 consecutive days. Blood samples were collected following the 30th dose and/or at time of euthanasia and then shipped to a contract laboratory for AST-SGOT and BUN quantitation. Major organs were also collected in both the EC72 and MMC mice, formalin fixed, and then shipped to a certified pathologist for examination (see Experimental Procedures). As described in Table 2, MMC-treated animals suffered from extensive myelosuppression, which is a characteristic side effect of MMC therapy (*21*). Although no visible tumors were identified in the peritoneal

Table 2. EC72 Toxicity[a]

test article	dose (nmol/kg)	schedule/ route	duration (days)	liver: AST-SGOT (normal: 72−288)	kidney: BUN (normal: 9−28)	pathological findings
MMC	1800	q1d, ip	21	1043 ± 921	74 ± 32	bone (tibia/fibula) was completely depleted of marrow cells loss of all spleen-derived marrow tissue; significant spleen weight loss heart, lung, liver, intestine, muscle tissue appeared normal
EC72	1800	q1d, ip	44	129 ± 34	31 ± 3.2	bone marrow (tibia/fibula) was normal spleen appeared normal; no tissue degeneration found kidney appeared normal; no tissue degeneration found heart, lung, liver, intestine, muscle tissue appeared normal

[a] Balb/c mice bearing ip M109 tumors were treated daily with 1800 nmol/kg of test article administered ip. All MMC-treated mice were moribund after receiving 21 doses, and they had to be sacrificed; however, major organs (including tibia/fibula and blood samples) were collected at the time of euthanasia. After 30 consecutive daily injections with EC72, blood was collected and AST-SGOT and BUN levels were measured. EC72-treated animals were sacrificed within 7 days following receipt of 44 consecutive daily injections. Major organs were then collected and pathologically evaluated concurrent with the organs from the MMC-treated animals. $N = 4$ animals per cohort.

cavities, all of the animals in this cohort died from apparent drug-related toxicity. In dramatic contrast, animals treated with EC72 displayed no evidence of myelosuppression or renal damage, as the spleen, tibia/fibula bone marrow, and kidneys all appeared microscopically normal to the experienced pathologist. In fact, none of the major organs examined from EC72-treated mice showed signs of tissue damage, and their BUN and AST-SGOT levels following 30 consecutive daily injections with high dose levels of the conjugate (1800 nmol/kg) were found to be within normal limits. Collectively, these results imply that the use of folate−drug conjugates may be an effective form of chemotherapy that does not cause unwanted injury to normal tissues, including the FR-positive kidneys. These data also support the hypothesis that the FR-positive kidney proximal tubules function primarily to shuttle scavenged folates or folate conjugates back into systemic circulation (via kidney-assisted transcellular reabsorption) rather than use them for localized biological consumption (*22*−*24*).

DISCUSSION

The objectives of this investigation were to design and test a folate-MMC conjugate for activity against FR-positive cells and tumors. One drug candidate, named EC72, was created whereby the vitamin folate was coupled to 7-N-modified MMC via a disulfide bond. Notably, due to previous successes with related folate−disulfide−drug constructs (*25*−*27*), the inclusion of the disulfide bond was predicted to be important for efficient release and therapeutic activity of the MMC moiety. EC72 was found to retain high affinity for FR-positive cells, and it produced dose responsive activity in vitro against numerous FR-positive cell lines. This activity was targeted and specific since (i) excess folic acid blocked activity, and (ii) FR-negative cell lines were unresponsive toward EC72.

EC72 proved to be active in both syngeneic and xenograft in vivo models, and this activity occurred in the apparent absence of gross or pathological toxicity. While these preliminary results are encouraging, only ∼25% of the animals in the treated cohorts were tumor free at the end of this study. Admittedly, it is possible that better responses might be obtained if higher dose levels are investigated (vide infra).

The untargeted MMC drug was found to effectively eliminate the ip tumors, but this activity was accompanied by lethal toxicity. Unfortunately, lower dose levels of free MMC were not investigated here, primarily because we wanted to directly compare the therapeutic and toxicological properties of free versus targeted MMC at equivalent dose levels. It is anticipated that lower dose levels of MMC would have provided therapeutic benefit along with lower and perhaps acceptable toxicity. However, given that (i) free MMC is very toxic to humans, (ii) its use is limited to very infrequent dose schedules because of this cumulative toxicity, and (iii) its preclinical activity in rodent models (i.e. high cure rate) was never clinically observed because patients could not withstand the level of toxicity that the rodents experienced, we feel that folate-targeted MMC (EC72) may be the better option for dosing humans with this drug class.

When comparing the in vivo activity of EC72 between our two tested models, similar therapeutic outcomes were observed. While these results are positive, and they do provide evidence for FR targeted activity, EC72 was predicted to have greater activity against the KB tumors since they express higher levels of FR protein per cell compared to the M109 tumors and the fact that the KB cells responded better to EC72 in vitro (see Table 1). Although no formal quantitation of tumor-associated drug was conducted in this investigation, it is possible that EC72's ability to penetrate KB tumors was somewhat compromised relative to the M109 tumors. In fact, such variances are to be expected, especially at the clinical level. But, an alternative explanation for the cause of this result could be that the two models were treated using slightly different schedules. Thus, M109 tumor-bearing mice received EC72 following a qdx7, 4 wk regimen, whereas KB tumor-bearing mice received EC72 following a qdx5, 4 wk regimen. Obviously, more consistent dosing would have favored the M109 tumor-bearing mice, even though the M109 tumors expressed less FR protein. Taken together, it is tempting to speculate that KB tumor-bearing mice might experience greater therapeutic activity if EC72 were dosed following the qdx7, 4 wk schedule.

On the basis of previous biodistribution studies using radiolabeled folate conjugates, we have determined that a dose level of ∼1800 nmol per kg body weight (mouse) is enough to saturate tumor-associated folate receptors following a single iv or ip injection (*28*). For that reason, we elected to use the 1800 nmol/kg dose level for both the M109 and KB in vivo model studies presented within. Notably, since it is very likely that the extent of tumor penetration will vary among different folate−drug conjugates, this parameter must be appropriately studied further. Until then, we pondered the significance of this dose level in the clinical setting. When translated to the human-equivalent dose (based on body surface area conversions), the mouse dose level of 1800 nmol/kg EC72 would be approximately 5.6 μmol/m^2. Interestingly, the

human dose level for MMC is 60 μmol/m^2 given in 6 to 8 week intervals (*29*). From an equivalency standpoint, and not withstanding the fact that EC72 is inherently less toxic than MMC, we estimate that a cancer patient could be safely treated >10 times within a 6 to 8 week cycle with "receptor-saturating" dose levels of EC72. Such a dose density, or metronomic, style of dosing may produce greater therapeutic outcomes. In regards to MMC, this targeted approach may also suddenly revitalize this old drug's clinical utility.

In conclusion, additional animal studies with EC72 are planned to better understand the effects of dose level and dose schedule. We also plan to study the effects of tumor growth rate and FR content on the overall observed antitumor response manifested by EC72 therapy. It is also important to study the effect of alternative dosing routes (ip versus iv or subcutaneous) as well as to vary the location of the tumor (i.e. ip versus subcutaneous). Since EC72 therapy appears to be rather safe, at least at the preclinical level, various combinations of EC72 plus other drugs should also be investigated for possible additive or synergistic responses. This is especially true for those drugs that cannot be dosed in combination with free MMC due to overlapping toxicities.

ACKNOWLEDGMENT

The authors wish to thank Dr. Philip S. Low for his valuable comments, and Dr. Alberto Gabizon for sharing his FR-positive M109 cell line.

LITERATURE CITED

(1) (2003) *National Vital Statistics Report*, p 59, National Center for Health Statistics, Hyattsville, MD.

(2) Kamen, B. A., and Capdevila, A. (1986) Receptor-mediated folate accumulation is regulated by the cellular folate content. *Proc. Natl. Acad. Sci., U.S.A. 83*, 5983−5987.

(3) Leamon, C. P., and Low, P. S. (1991) Delivery of Macromolecules into Living Cells: A Method that Exploits Folate Receptor Endocytosis. *Proc. Natl. Acad. Sci., U.S.A. 88*, 5572−5576.

(4) Boerman, O. C., van Niekerk, C. C., Makkink, K., Hanselaar, T. G., Kenemans, P., and Poels, L. G. (1991) Comparative immunohistochemical study of four monoclonal antibodies directed against ovarian carcinoma-associated antigens. *Int. J. Gynecol. Pathol. 10*, 15−25.

(5) Garin-Chesa, P., Campbell, I., Saigo, P. E., Lewis, J. L., Old, L. J., and Rettig, W. J. (1993) Trophoblast and Ovarian Cancer Antigen LK26. *Am. J. Pathol. 142*, 557−567.

(6) Weitman, S. D., Lark, R. H., Coney, L. R., Fort, D. W., Frasca, V., Zurawski, V. R., and Kamen, B. A. (1992) Distribution of the folate receptor GP38 in Normal and Malignant Cell Lines and Tissues. *Cancer Res. 52*, 3396−3401.

(7) Mattes, M. J., Major, P. P., Goldenberg, D. M., Dion, A. S., Hutter, R. V. P., and Klein, K. M. (1990) Patterns of antigen distribution in human carcinomas. *Cancer Res. Suppl. 50*, 880S.

(8) Coney, L. R., A., T., Carayannopoulos, L., Frasca, V., Kamen, B. A., Colnaghi, M. I., and Zurawski, V. R. J. (1991) Cloning of a Tumor-associated Antigen: MOv18 and MOv19 Antibodies Recognize a Folate-binding Protein. *Cancer Res. 51*, 6125−6132.

(9) Ross, J. F., Chaudhuri, P. K., and Ratnam, M. (1994) Differential regulation of folate receptor isoforms in normal and malignant tissues in vivo and in established cell lines. *Cancer 73*, 2432−2443.

(10) Weitman, S. D., Frazier, K. M., and Kamen, B. A. (1994) The folate receptor in central nervous system malignancies of childhood. *J. Neurol. Oncol. 21*, 107.

(11) Weitman, S. D., Weiberg, A. G., Coney, L. R., Zurawski, V. R., Jennings, D. S., and Kamen, B. A. (1992) Cellular Localization of the Folate Receptor: Potential Role in Drug Toxicity and Folate Homeostasis. *Cancer Res. 52*, 6708−6711.

(12) Toffoli, G., Cernigoi, C., Russo, A., Gallo, A., Bagnoli, M., and Boiocchi, M. (1997) Overexpression of folate binding protein in ovarian cancers. *Int. J. Cancer 74*, 193−198.

(13) Holm, J., Hansen, S. I., Hoier-Madsen, M., and Bostad, L. (1991) High-affinity folate binding in human choroid plexus. *Biochem. J. 280*, 267−271.

(14) Parker, N., Turk, M. J., Westrick, E., Lewis, J. D., Low, P. S., and Leamon, C. P. (2005) Folate receptor expression in carcinomas and normal tissues determined by a quantitative radioligand binding assay. *Anal. Biochem. 338*, 284−293.

(15) Low, P. S., and Antony, A. C. (2004) Folate Receptor-Targeted Drugs for Cancer and Inflammatory Diseases. *Adv. Drug Delivery Rev. 56*, 1055−1238.

(16) Matsui, M., Yamada, Y., Uzu, K., and Hirata, T. (1968) Studies on mitomycins. 3. The synthesis and properties of mitomycin derivatives. *J. Antibiot. (Tokyo) 21*, 189−198.

(17) Westerhof, G. R., Schornagel, J. H., Kathmann, I., Jackman, A. L., Rosowsky, A., Forsch, R. A., Hynes, J. B., Boyle, F. T., Peters, G. J., Pinedo, H. M., and Jansen, G. (1995) Carrier- and receptor-mediated transport of folate antagonists targeting folate-dependent enzymes: Correlates of molecular structure and biological activity. *Mol. Pharm. 48*, 459−471.

(18) Boyd, M. R. (1997) The NCI In Vitro Anticancer Drug Discovery Screen. In *Anticancer Drug Development* Guide: *Preclinical Screening, Clinical trials, and Approval* (Teicher, B., Ed.) pp 23−42, Humana Press Inc., Totowa, NJ.

(19) Leamon, C. P., Parker, M. A., Vlahov, I. R., Xu, L. C., Reddy, J. A., Vetzel, M., and Douglas, N. (2002) Synthesis and Biological Evaluation of EC20: A New Folate-Derived ^{99m}Tc−Based Radiopharmaceutical. *Bioconjugate Chem. 13*, 1200−1210.

(20) Mathias, C. J., Wang, S., Waters, D. J., Turek, J. J., Low, P. S., and Green, M. A. (1998) Indium-111-DTPA-folate as a potential folate-receptor-targeted radiopharmaceutical. *J. Nucl. Med. 39*, 1579−1585.

(21) Baker, L. H., Izbicki, R. M., and Vaitkevicius, V. K. (1976) Phase II study of profiromycin vs mitomycin-C utilizing acute intermittent schedules. *Med Pediatr. Oncol. 2*, 207−213.

(22) Birn, H., Selhub, J., and Christensen, E. I. (1993) Internalization and intracellular transport of folate-binding protein in rat kidney proximal tubule. *Am. J. Physiol. 264*, C302−C310.

(23) Birn, H., Nielsen, S., and Christensen, E. I. (1997) Internalization and apical-to-basolateral transport of folate in rat kidney proximal tubule. *Am. J. Physiol. 272*, F70−8.

(24) Sandoval, R. M., Kennedy, M. D., Low, P. S., and Molitoris, B. A. (2004) Uptake and trafficking of fluorescent conjugates of folic acid in intact kidney determined using intravital two-photon microscopy. *Am. J. Physiol. Cell Physiol. 287*, C517−C526.

(25) Leamon, C. P., Pastan, I., and Low, P. S. (1993) Cytotoxicity of Folate-Pseudomonas Exotoxin Conjugates Toward Tumor Cells. *J. Biol. Chem. 268*, 24847−24854.

(26) Leamon, C. P., DePrince, R. B., and Hendren, R. W. (1999) Folate-mediated drug delivery: Effect of alternative conjugation chemistry. *J. Drug Targeting 7*, 157−169.

(27) Ladino, C. A., Chari, R. V. J., Bourret, L. A., Kedersha, N. L., and Goldmacher, V. S. (1997) Folate-maytansinoids: Target-selective drugs of low molecular weight. *Int. J. Cancer 73*, 859−864.

(28) Paulos, C. M., Reddy, J. A., Leamon, C. P., Turk, M. J., and Low, P. S. (2004) Ligand binding and kinetics of folate receptor recycling in vivo: impact on receptor-mediated drug delivery. *Mol. Pharmacol. 66*, 1406−1414.

(29) Baker, L. H., Opipari, M. I., and Izbicki, R. M. (1976) Phase II study of mitomycin-C, vincristine, and bleomycin in advanced squamous cell carcinoma of the uterine cervix. *Cancer 38*, 2222−2224.

BC049709B

A Peptide Carrier with a Built-In Vaccine Adjuvant: Construction of Immunogenic Conjugates

Dimitrios Krikorian, Eugenia Panou-Pomonis, Chryssa Voitharou, Constantinos Sakarellos, and Maria Sakarellos-Daitsiotis*

Department of Chemistry, Section of Organic Chemistry and Biochemistry, University of Ioannina, 45110 Ioannina, Greece. Received December 13, 2004; Revised Manuscript Received April 18, 2005

A multifunctional carrier combining B/T cell epitopes (i), a built-in vaccine adjuvant (ii), and a universal T cell epitope (iii) for the construction of potent and specific immunogenic conjugates is presented. The IL-1β(163−171) fragment known to reproduce the immunostimulatory and adjuvant effects of the whole IL-1β without possessing any of the pro-inflammatory properties of IL-1β was covalently anchored to the N-terminus of the Sequential Oligopeptide Carrier, SOC_n, formed by the repeating tripeptide unit Lys-Aib-Gly. A promiscuous T cell epitope derived from the tetanus toxin, TT(593−599), was also positioned in the carboxy terminus of SOC_n as a universal immunogen to provide broad immunogenicity. Selected B/T cell epitopes from the Sm and La/SSB autoantigens, against which is directed the humoral autoimmunity in patients with systemic lupus erythematosus and Sjögren's Syndrome, respectively, were coupled to the Lys-$N^{\epsilon}H_2$ groups of the carrier, and the formulated constructs were administered in animals following the conventional immunization protocol of complete/incomplete Freund's adjuvant. The induced immune responses were compared with that produced when the Sm- and La/SSB-reconstituted immunogenic conjugates were injected alone. High titers of specific antibodies recognizing the priming construct, as well as the cognate autoantigen, were obtained when administered alone without the assistance of Freund's adjuvant. It is concluded that our approach provides the conceptual and experimental framework for the development of multifunctional immunogenic conjugates eliciting enhanced, specific, and prolonged humoral response for usage as human vaccine candidates.

INTRODUCTION

Formulation of an effective immunogen that could elicit a potent immune response should incorporate B cell epitopes that mimic the three-dimensional conformation of the antigen and T cell epitopes resulting from the processed protein, both on the same carrier that links the major histocompatibility complex with the T cell receptor (*1, 2*). To achieve enhanced and prolonged humoral and cellular immune response, potent immunogens must be also administered in combination with adjuvants, e.g. incomplete Freund's, CRL1005, QS21, Montanide ISA-51, etc., although the precise mechanism of their action remains unclear, and severe skin toxicities, in some cases, have been reported. The only adjuvants currently approved by the Food and Drug Administration for use with human vaccines are alluminum salts, which, however, have low potency and problems associated with their formulation. To address this problem, adjuvants with low toxicity profiles as for example the granulocyte monocyte colony stimulating factor have been tested (*3, 4*). It has been also proposed that T cells provide "help" to B cells under genetic control. Recently, a number of so-called "promiscuous" T cell epitopes from tetanus toxin (TT), measles virus, or E6 transforming protein have been reported to be universally immunogenic (*5, 6*).

On the basis of the reported issues, an ideal immunogenic conjugate, and consequently an effective human vaccine, should combine specific B and T cell epitopes, adjuvants, and "promiscuous" T cell epitopes. The rational design of such a multivalent conjugate as vaccine candidate requires a synthetic carrier or template on which different peptides with various functionalities could be anchored. Development of synthetic carriers for anchoring immunogenic peptides and producing specific immune responses has been the stimulus of intensive efforts. Among others the lysine core matrix, the Pam_3-Cys-Ser (a palmitoyloxy lipopeptide), and the template-assembled synthetic protein (TASP)[1] deserve to be mentioned (*7−9*).

A new class of Sequential Oligopeptide Carriers, (SOC_n), for anchoring antigenic/immunogenic peptides has been successfully applied in our laboratory. The carrier, formed by the repetitive Lys-Aib-Gly moiety, was designed to display a predetermined 3D structure, so that the attached peptides could obtain a defined spatial

* Corresponding author. Fax: +30-26510-98770, Tel: +30-26510-98386, e-mail: msakarel@cc.uoi.gr.

[1] Abbreviation: Ac_2O, acetic anhydride; Alloc, allyloxycarbonyl; Boc, *tert*-butyloxycarbonyl; Bzl, benzyl; CD, circular dichroism; CFA/IFA, complete/incomplete Freund's adjuvant; CMC, critical micelle concentration; DCM, dichloromethane; DIEA, disopropylethylamine; DMF, dimethylformamide; ESI-MS, electron spray ionization mass spectrometry; Fmoc, 9-fluorenylmethyloxycarbonyl; HF, hydrogen fluoride; HOBt, 1-hydroxybenzotriazole; HPLC, high performance liquid chromatography; IL-1β, interleukin-1β; LC, liquid chromatography; MBHA, 4-methylbenhydrylamine resin; PBS, phosphate-buffered saline; SDS, sodium dodecyl sulfate; SLE, systemic lupus erythematosus; SOC_n, Sequential Oligopeptide Carrier; SPPS, stepwise solid-phase procedure; SS, Sjogren's Syndrome; TASP, template-assembled synthetic protein; TBTU, 2-(1*H*−benzotriazol-1-y1)-1,1,3,3-tetramethyluronium tetrafluoroborate; TFA, trifluoroacetic acid; TFE, trifluoroethanol; TMB, 3,3′,5,5′-tetramethylbenzidine; Tos, tosyl; TT, tetanus toxin.

10.1021/bc049703m CCC: $30.25 © 2005 American Chemical Society
Published on Web 06/10/2005

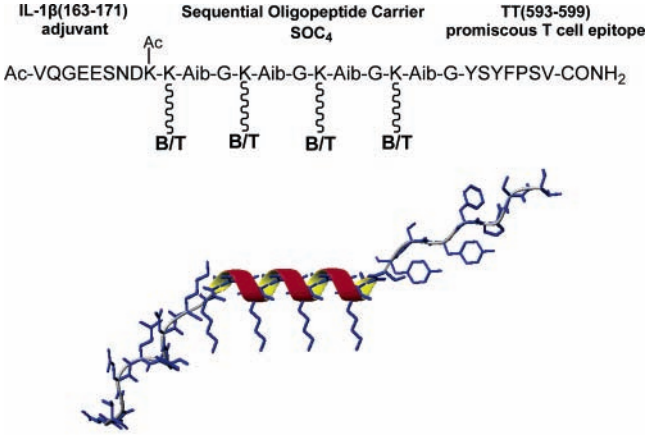

Figure 1. Schematic representation of a multivalent peptide carrier that incorporates an adjuvant, IL-1β(163−171), a promiscous T cell epitope, TT(593−599), and specific B and T cell epitopes anchored to the Lys-N$^{\epsilon}$N$_2$ groups of the sequential oligopeptide carrier (Lys-Aib-Gly)$_4$, SOC$_4$.

orientation. Conformational analysis showed that SOC$_n$ adopt a distorted 3_{10} helicoid structure, while the coupled epitopes preserve their original "active" structure. It has been concluded that the helicoid structure of SOC$_n$ helps the reconstitution and/or mimicking of the native forms of the epitopes, so that potent immunogens could be generated. SOC$_n$-conjugates induced high titers of specific antibodies recognizing the priming peptides, as well as the intact proteins, but not the carrier alone (*10*−*14*).

With the aim of contributing to the development of a carrier that could help to augment and improve the character and the quality of the humoral and cellular immune response, the SOC$_n$ carrier was elongated from the amino-terminus by the IL-1β fragment VQGEESNDK (163−171) as adjuvant. It has been reported that IL-1β-(163−171) is devoid of all pro-inflammatory effects of IL-1β but maintains the immunostimulatory activity of the intact cytokine (*15, 16*). A "promiscuous" T cell epitope deriving from TT, YSYFPSV (593−599), was also covalently attached to the carboxy-terminal group of SOC$_n$, as universal immunogen (*17*). B and T cell epitopes derived (i) from the Sm and (ii) the La/SSB antigens were coupled to the Lys-N$^{\epsilon}$H$_2$ groups of the carrier and the obtained conjugates were administered in animals without adding any adjuvant to test the induction of specific antibodies. The schematic representation of a multivalent peptide vaccine that incorporates an adjuvant IL-1β(163−171), a promiscuous T-cell epitope TT(593−599), and specific B and T cell epitopes is illustrated in Figure 1.

Epitope mapping of the Sm autoantigen revealed that the sequence PPGMRPP, found in three copies in the protein, represents the major B cell epitope of Sm, against which is directed the majority of autoantibodies in SLE patients (*18*). In this regard anti-Sm antibodies are considered as a disease marker for SLE (*19, 20*). Four copies of the PPGMRPP dominant B cell epitope of Sm were covalently anchored to the carrier and the potential of the reconstituted Sm conjugate, Ac-IL-1β-SOC$_4$-Sm$_4$-TT-NH$_2$ (**2**) (Figure 2) to elicit specific immune response without usage of any adjuvant was examined.

La/SSB autoantigen is one of the molecular targets of humoral autoimmunity primarily in SS patients (*21*). In previous studies we have mapped the location of four B cell antigenic determinants of La/SSB (*22*), and we have investigated their ability to induce T cell responses against the La/SSB protein after animal injection (*23*). It was found that the sequence ANNGNLQLRNKEVTWEVLEG corresponding to the region 289−308 of La/SSB is an immunodominant T-cell and a minor B cell epitope. Two copies of the La/SSB (289−308) epitope were covalently linked to the 1st and 4th Lys-N$^{\epsilon}$H$_2$ group of SOC$_4$ to create a mimic of La/SSB. Animal immunization experiments were performed to validate the efficacy of the Ac-IL-1β-SOC$_4$-[Ac$_2$, (La/SSB)$_2$]-TT-NH$_2$ (**3**) conjugate (Figure 2) to induce high titers of specific antibodies without utilizing any adjuvant.

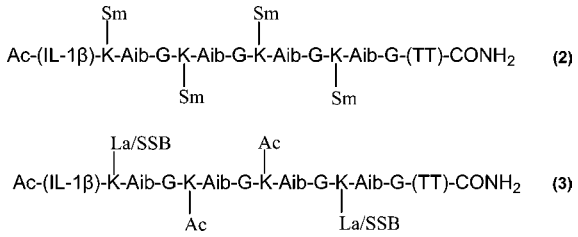

Figure 2. Schematic representation of conjugates Ac-IL-1β-SOC$_4$-Sm$_4$-TT-NH$_2$ (**2**) and Ac-IL-1β-SOC$_4$-[Ac$_2$-(La/SSB)$_2$]-TT-NH$_2$ (**3**), where Sm: PPGMRPP, La/SSB: Ac-ANNGNLQLRNKEVTWEVLEG (289−308), IL-1β: Ac-VQGEESNDK (163−171), and TT: YSYFPSV (593−599).

The produced potent humoral immune response of both conjugates was compared with that obtained when each one of them was injected following the complete/incomplete Freund's adjuvant protocol. Our data suggest that the presented carrier could be employed in engineering potent immunogenic conjugates as human vaccine candidates.

EXPERIMENTAL PROCEDURES

Synthesis of the Ac-IL-1β-SOC$_4$-Ac$_4$-TT-NH$_2$ Carrier (1). The synthesis of **1**, where SOC$_4$ is (K-Aib-G)$_4$, was carried out manually by the SPPS procedure (*24*−*26*) using the MBHA resin (3 g, 0.13 mmol/g capacity). Lysine was introduced as Boc-Lys(Fmoc)-OH, serine as Boc-Ser(Bzl)-OH, tyrosine as Boc-Tyr(2,6-di-Cl−Bzl)-OH, and aspartic acid and glutamic acid as Boc-Asp(Obzl)-OH and Boc-Glu(Obzl)-OH, respectively. Synthetic procedure starts with the step by step couplings, to the resin, of the protected residues (Boc/Bzl) corresponding to the TT(593−599) fragment. The protocol of the synthesis was the following: (i) deprotection with 40% TFA/DCM (1 × 2 min, 1 × 13 min); (ii) washings DCM (3 × 1 min), MeOH (3 × 1 min), DCM (3 × 1 min); (iii) neutralization with 7% DIEA (2 × 2 min); (iv) washings DCM (3 × 1 min), MeOH (3 × 1 min), DCM (3 × 1 min); (v) couplings with three equivalent amino acid derivatives, 2.9 equiv of TBTU, 3 equiv of HOBt, 9 equiv of DIEA in DCM−DMF 4:1 or 1:4 (V/V) mixture depending on the solubility of Boc-amino acid derivatives (2 h); (vi) washings DCM (3 × 1 min), MeOH (3 × 1 min), DCM (3 × 1 min); (vii) ninhydrin assay (*27*). A similar protocol was applied for the sequential propagation of the Boc-K (Fmoc)-Aib-Gly moiety until the formation of the tetrameric SOC$_4$, oligopeptide. The IL-1β(163−171) fragment was inserted step by step following the Boc/Bzl strategy to obtain the protected carrier on the resin.

The N$^{\alpha}$-terminal Boc group (Boc-V) of the carrier was cleaved by 40% TFA in DCM and Val was N$^{\alpha}$-acetylated with Ac$_2$O (30 equiv of Ac$_2$O/pyridine, 20 min). Fmoc-protective groups of Lys-N$^{\epsilon}$H$_2$ were removed by 20% piperidine in DMF (1 × 2 min, 1 × 15 min, washings DCM, MeOH, DCM) followed by N$^{\epsilon}$-acetylation with Ac$_2$O. The peptide was cleaved from the resin support by liquid HF in the presence of phenol and anisole (HF−phenol−anisole = 10 mL:1 g:1 mL) for 30 min at −8 °C and 1.5 h at 0 °C and extracted with 2 M aqueous acetic

acid. The crude peptide (yield 90%) was purified by RP-HPLC using a Supelco Discovery C_{18} semipreparative column (250 mm × 10 mm, 5 μm, 300 Å). The purified peptide (yield 57%) was analyzed by RP-HPLC (t_R = 15.41 min), LC and ESI-MS (M + H^+ calculated/found 3181.5/3181.6).

Synthesis of the Ac−IL-1β-SOC$_4$-Sm$_4$-TT-NH$_2$ Conjugate (2). Initially was synthesized, by the SPPS procedure, on the resin as the protected fragment of the carrier comprising TT and SOC_4, as already described for the synthesis of **1**, except that the fourth lysine was introduced as Alloc-K(Fmoc). After removal of the Fmoc protective groups from the Lys-$N^{\epsilon}H_2$ groups by 20% piperidine in DMF, synthesis of the Sm epitopes was carried out (Boc/Bzl) by the simultaneous attachment of each residue in four copies and afterward the N^{α}-Alloc group of Lys was eliminated under hydrostannolytic cleavage [$PbCl_2(PPh_3)_2$/Bu_3SnH/AcOH in DCM (0.03 equiv of $PbCl_2(PPh_3)_2$, 3 equiv of Bu_3SnH, and 3 equiv of AcOH for 30 min, washings DCM, MeOH, DCM] (*28, 29*), and the N-terminal sequence of IL-1β(163−171) was coupled step by step to the carrier. Arginine was introduced as Boc-Arg(Tos)-OH, while Met was used without side protection as Boc-Met-OH. Dimethyl sulfide was added to each cycle of Boc-removal (TFA/DCM/DMS: 40/59/1) after coupling of Boc-Met-OH to avoid oxidation of Met side chain. The peptide was cleaved from the resin by liquid HF in the presence of *p*-cresol and thiocresol as described for **1**. The crude material (yield 86%) was dialyzed against water (yield 33%) and purified by RP-HPLC using a Supelco Discovery C_{18} semipreparative column as for peptide **1**. The purified peptide (yield 24%) was analyzed by RP-HPLC (t_R = 10.12 min), LC and ESI-MS (M + H^+ calculated/found 5940.95/5940.90).

Synthesis of the Ac-IL-1β-SOC$_4$-[Ac$_2$, (La/SSB)$_2$]-TT-NH$_2$ Conjugate (3). Synthesis of the protected fragment of the carrier, incorporating TT(593−599) and SOC_4, was performed as for **1**, except that lysines at the 1st and 4th position of SOC_4 were introduced as Alloc-K(Fmoc) and Boc-K(Fmoc), respectively, while lysines at the 2th and 3rd position were inserted as Boc-K(Ac)-OH. After cleavage of the Fmoc protective group of lysine side chains, the synthesis of the La/SSB (289−308) epitope was carried out by the simultaneous coupling of each residue in two copies following the Boc methodology, except that lysine within the epitope sequence was introduced as Alloc-Lys(Fmoc)-OH. The $N^{\alpha}H_2$ terminus of the epitopes was acetylated, while after removal of the N^{α}-Alloc protective group of the carrier it was elongated to construct the IL-1β(161−173) N-terminal segment. The peptide was cleaved from the resin by liquid HF in the presence of phenol and anisole as described for **1**. The crude material (yield 91%) was dialyzed against water (yield 70%) and purified by RP-HPLC using a Supelco Discovery C_{18} semipreparative column as for peptide **1**. The purified peptide (yield 18%) was analyzed by RP-HPLC (t_R = 17.10 min), LC and ESI-MS (M + H^+ calculated/found 7619.43/7619.65).

Dialysis. Dialysis tubes, whice are cellulose membranes benzoylated in order to reduce the pore size, with a molecular mass cutoff of ∼1500, were obtained from Sigma (Deisenhofen, Germany). They were supplied in water pack containing 0.002% 1-hydroxypyridine-2-thione as preservative, and they were activated by heating in a solution of 0.1 M $NaHCO_3$ and 0.001 M ethylenediaminetetraacetic acid to just under boiling point.

LC-ESI-MS. LC-ESI-MS of Ac-IL-1β-SOC$_4$-Ac$_4$-TT-NH$_2$ (**1**), Ac-IL-1β-SOC$_4$-Sm$_4$-TT-NH$_2$ (**2**), and Ac-IL-1β-SOC$_4$-[Ac$_2$-(La/SSB)$_2$]-TT-NH$_2$ (**3**) was performed using a Supelco Discovery C_{18} (250 mm × 4.6 mm, 5 μm, 300 Å) reverse phase column with a Waters instrument equipped with a Waters 616 pump and a Waters 2487 Dual λ absorbance detector. Eluent A was 0.1% TFA in water, and eluent B was 0.1% TFA in acetonitrile. A linear gradient for Ac-IL-1β-SOC$_4$-Ac$_4$-TT-NH$_2$ (**1**) and Ac-IL-1β-SOC$_4$-Sm$_4$-TT-NH$_2$ (**2**) was 20% to 50% acetonitrile in 0.1% TFA at a flow rate of 1 mL/min and for Ac-IL-1β-SOC$_4$[Ac$_2$-(La/SSB)$_2$]-TT-NH$_2$ (**3**) was 20% to 40% acetonitrile in 0.1% TFA at a flow rate of 1 mL/min.

RP-HPLC. RP-HPLC purification was carried out on a Waters 4000 semipreparative instrument using a Supelco Discovery C_{18} (250 mm × 10 mm, 5 μm, 300 Å) column with the same linear gradient as LC-ESI-MS at a flow rate of 4.7 mL/min. Detection was carried out at λ = 214 nm.

Mass Spectroscopy. Positive ion electrospray ionization mass spectrometric (ESI-MS) analyses of Ac-IL-1β-SOC$_4$-Ac$_4$-TT-NH$_2$ (**1**), Ac-IL-1β-SOC$_4$-Sm$_4$-TT-NH$_2$ (**2**), and Ac-IL-1β-SOC$_4$-[Ac$_2$-(La/SSB)$_2$]-TT-NH$_2$ (**3**) were performed on a Micromass Platform LC-MS. Capillary and cone voltages were set to 3 kV and 45 V, respectively. Samples were dissolved in water/acetonitrile/trifluoroacetic acid (1/1/0.05 V/V/V).

Circular Dichroism. CD spectra were recorded at 25°C on a Jasco J-710 spectrophotometer using 0.1 cm path-length quartz cell and peptide concentration 10^{-4} M. Experiments were performed in TFE/H_2O mixtures (from 0 to 100%) and in SDS (concentrations ranged from 5 to 15 mM). Spectra were obtained with a 2 nm bandwidth, a scan speed of 4 nm min^{-1} and a time constant of 8 s. The signal-to-noise ratio was improved by accumulating four scans. To eliminate errors from instrumental drift, the baseline in air was recorded and subtracted after each scan. All CD spectra are reported in terms of ellipticity units per mole of peptide residue ($[\Theta]_R$ in deg cm^2 $dmol^{-1}$). The percentage helical content was estimated on the basis of the $[\Theta]_{222}$ nm values, in different environments, as described by Chen et al. (*30*) and using the CD deconvolution (CDNN program) described by Bohn et al. (*31*). Two parameters R1 and R2 described by Rozek et al. (*32*) were also used for analyzing the CD spectra. R1 is the ratio of the intensity of the maximum between 190 and 195 nm and the intensity of the minimum between 200 and 210 nm. R2 is the intensity of the minimum near 222 nm and the intensity of the minimum between 200 and 210 nm.

Rabbit Immunizations. New Zealand white rabbits were immunized, two for each peptide-conjugate, subcutaneously following three different protocols.

Protocol A: 1 mg of each conjugate in 500 μL of H_2O emulsified in 500 μL of CFA was injected on day 1, followed by boostings with 0.5 mg/500 μL H_2O emulsified in 500 μL of IFA with two weeks intervals. Animals were bled after two successive immunizations on day 21, after three injections on day 43, and after five injections on day 86.

Protocol B: 1 mg of each conjugate in 500 μL of H_2O emulsified in 500 μL of IFA was injected following the previous schedule. Animals were also bled after the sixth injection on days 108.

Protocol C: 1 mg of each conjugate in 1 mL of H_2O was injected following the schedule of protocol A adding neither CFA nor IFA. Animals were also bled after the sixth injection on days 108.

Mice Immunization. Mice (Balb/c) were immunized, three for each experiment, subcutaneously following two different protocols.

Protocol A: 50 μg of the conjugate (**3**) in 100 μL of H_2O emulsified in 100 μL of CFA was injected on day 1, followed by boostings with the same quantities of immunogen emulsified in 100 μL of IFA with two weeks intervals. Animals were bled after two successive immunizations.

Protocol B: 50 μg of immunogen in 200 μL of H_2O was injected following the previous schedule without adding CFA/IFA.

ELISA for Antisera. Ninety-six-well polystyrene plates (Nunc Immuno Plates, Denmark) were coated overnight at 4 °C with 10 μg/mL of each peptide-conjugate including the Ac-IL-1β-SOC_4-Ac_4-TT-NH_2 carrier in carbonate buffer, pH 9.6 (100 μL/well). After washings with PBS/pH 7.2, the nonspecific binding sites were blocked with 3% skim milk in PBS and the plates were incubated at room temperature for 2 h. Serum samples from preimmunized and postimmunized animals at dilutions, with blocking buffer, ranging from 1:100 to 1:50.000, were added, and the plates were incubated at 4 °C overnight. After extensive washings with PBS, the wells were incubated with anti rabbit anti-human IgG or goat anti-mouse IgG conjugated to peroxidase (Jackson Immunoresearch) at 37 °C for 1.5 h. Finally the plates were washed, 50 μL of substrate solution of TMB (1 mg/1 mL) and 50 μL of H_2O_2 (1 mL/1 mLH_2O) were added to each well, and the absorbance was measured at 450 nm.

RESULTS

Design and Synthesis of an Innovative Multifunctional Carrier Bearing B and T Cell Epitopes as Potential Immunogenic Conjugates. A new carrier combining (i) the tetrameric repeating unit (Lys-Aib-Gly)$_4$, SOC_4, for anchoring B/T cell epitopes from the Lys-N$^{\epsilon}H_2$ groups to induce specific antibodies, (ii) the IL-1β(163−171) fragment to improve the quality and prolong the immune response, and (iii) the TT(593−599) segment as universal immunogen, was constructed according to the principles of the step by step solid-phase peptide synthesis, following an othogonal system of N-protecting groups (Boc-, Fmoc-, and Alloc-). This approach allowed the formulation of reconstituted potent immunogenic conjugates in good yield and high purity as confirmed by ESI-MS and the corresponding LC. Molecular weights of the reported preparations ranged from 5940 to 7620, approaching the molecular mass of small proteins.

Conformational Study by CD. The CD spectra of the carrier in TFE/H_2O mixtures (10, 30, and 50%) showed a positive band at 192 nm and two negative bands at 208 and 222 nm typical of helical structure, which reaches maximum ellipticity at 100% TFE (Figure 3). It is presumed that trifluoroethanol favors the formation of a more ordered conformation by lowering the dielectric constant of the dissolving medium.

The effect of SDS, a membrane mimetic, on the conformation of the carrier was also studied. In phosphate buffer, pH 6, the CD spectrum exhibits weak helical characteristics. Upon addition of SDS, at concentration 5 mM, below the critical micelle concentration (CMC 8 mM) the typical characteristic bands of helical structure appeared, indicating that upon interaction with SDS even below CMC the helical character of the carrier is enhanced (*33*). The ellipticity remained practically unchanged at 10 and 15 mM SDS, suggesting that the micelle microenvironment at 5 mM is sufficient to induce maximum helical conformation to the carrier.

The percentage helical content of the carrier in phosphate buffers, 5 mM SDS and 100% TFE, calculated on the basis of the $[\Theta]_{222}$ value (*30*) and the CD deconvolution (*31*) was estimated to 6, 20, and 40%, respectively. Moreover, R1 parameter is close to −2 and R2 approximates 1, confirming the helicoid character of the carrier (*32*).

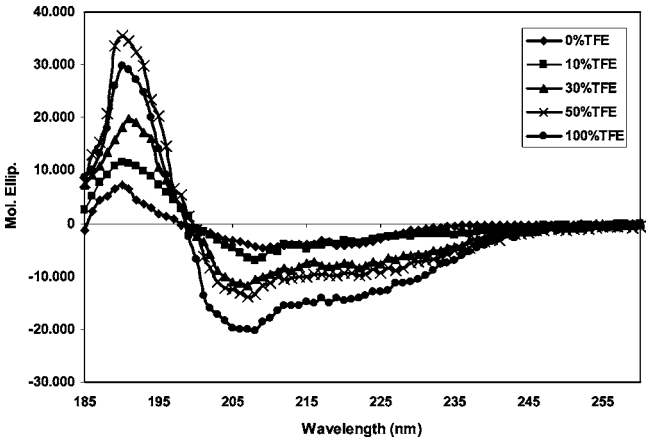

Figure 3. CD spectra of the Ac-IL-1β-SOC_4-Ac_4-TT-NH_2 (**1**) carrier in TFE/H_2O mixtures 10, 30, 50, and 100% TFE.

It seems likely that the helicoid features of SOC_4 (*10*−*14, 34, 35*) are conserved even after its amino and carboxy terminus elongation. One may assume that the persistence of the ordered secondary conformation of the Ac-IL-1β-SOC_4-Ac_4-TT-NH_2 carrier could optimize the B/T cell epitope presentation and help to the formation of functional reconstituted immunogenic conjugates.

Serological Study. Comparison of the Humoral Response in Rabbits Immunized with Three Different Approaches. Sera were collected before the initial immunization, as well as after two subsequent boosts and were tested against the immunizing conjugate. The reactivity of rabbit anti-sera to the Ac-IL-1β-SOC_4-Sm_4-TT-NH_2 conjugate (**2**) following the CFA/IFA procedure increased gradually and remained at high levels after the third immunizatiuon. Dilution curves of sera in anti-Ac-IL-1β-SOC_4-Sm_4-TT-NH_2 ELISA are shown in Figure 4A. Rabbits immunized with the Ac-IL-1β-SOC_4-Sm_4-TT-NH_2 conjugate (**2**) and IFA raised specific antibodies recognizing the priming immunogen after the sixth boosting. Sera samples displayed high reactivity even at 1:50000 dilution (Figure 4B). Antibody specific response in rabbits immunized with Ac-IL-1β-SOC_4-Sm_4-TT-NH_2 (**2**) alone, without administering neither CFA nor IFA was detected after the sixth injection and sera reactivity, as shown in anti-Ac-IL-1β-SOC_4-Sm_4-TT-NH_2 ELISA tests, remained high even at 1:50000 dilution (Figure 4C).

Animals were immunized with Ac-IL-1β-SOC_4-[Ac_2-(La/SSB)$_2$]-TT-NH_2 congugate (**3**) following the previous protocols, and sera were tested for the induction of anti-Ac-IL-1β-SOC_4-[Ac_2-(La/SSB)$_2$]-TT-NH_2 antibodies in ELISA tests. The pattern of the sera reactivity was comparable with that observed when conjugate **2** was injected and the anti-conjugate **3** sera reactivity remained high (1:50000 dilution) even when conjugate **3** was injected alone without the assistance of adjuvant (Figure 5).

Usage of adjuvant is essential to induce strong and prolonged antibody responses although their function is not fully understood. Adjuvants incorporate two components. One is a substance designed to form a deposit protecting the antigen from rapid catabolism, and the other is a substance that stimulates the immune response nonspecifically by activating the antigen-processing cells

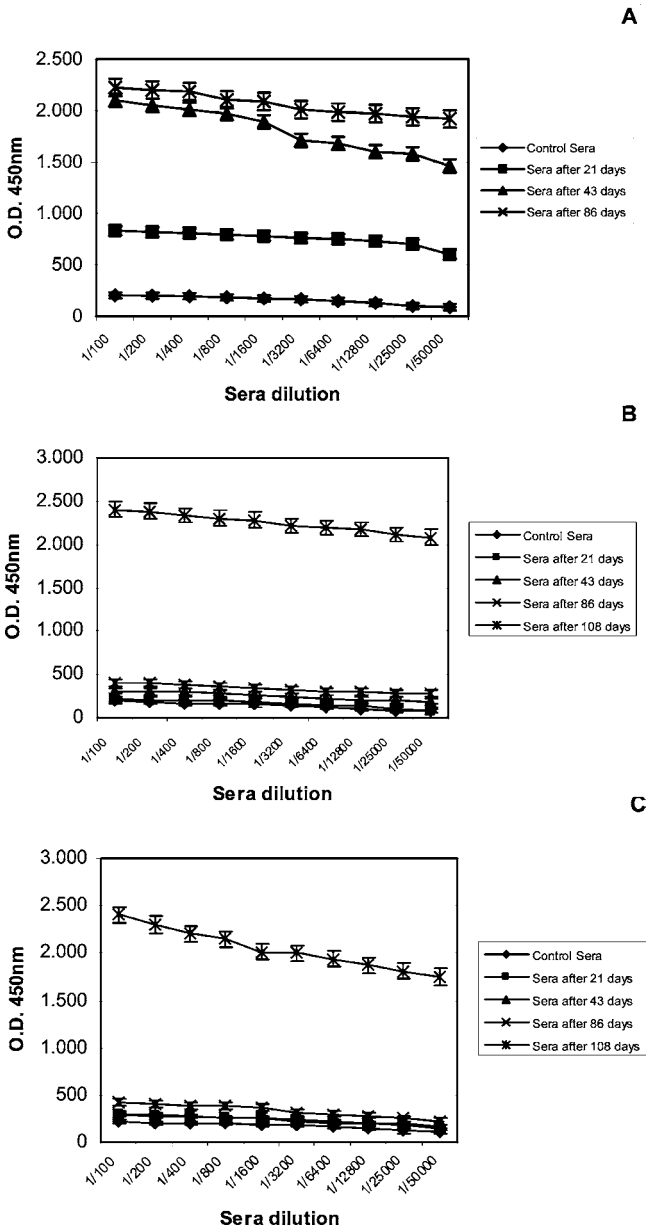

Figure 4. Binding of antisera to the Ac-IL-1β-SOC_4-Sm_4-TT-NH_2 (**2**) conjugate. Antisera raised in rabbits immunized with CFA/IFA (A), IFA (B), and the peptide conjugate alone (C). Data shown as means of three independent experiments carried out in triplicate using a pool of the two rabbit sera that gave similar results when used independently. Control sera: preimmune.

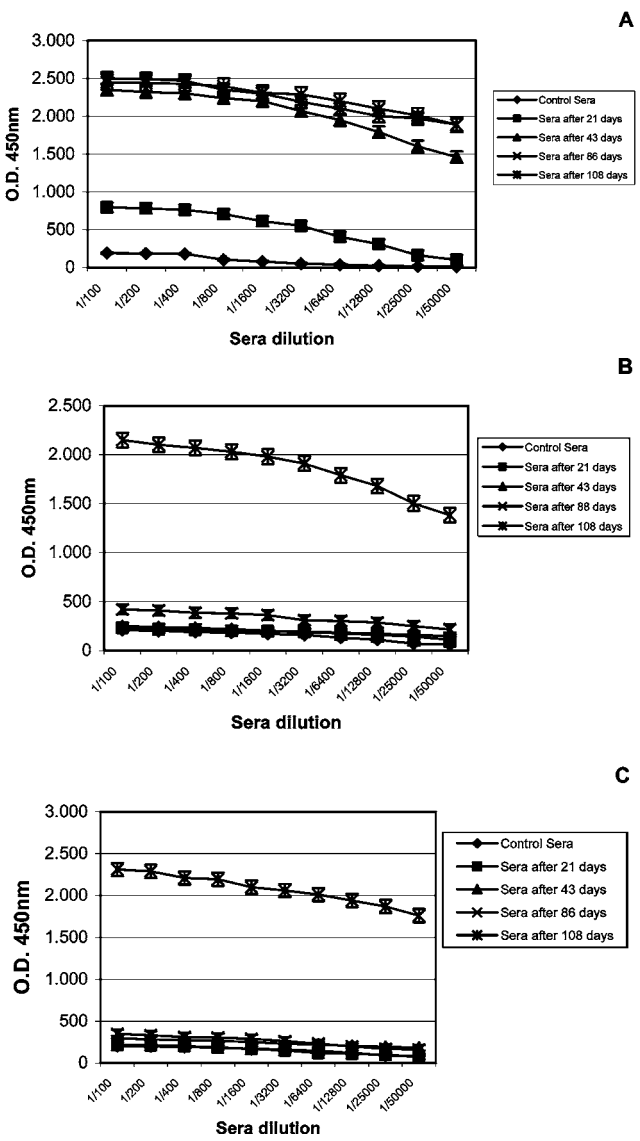

Figure 5. Binding of antisera to the Ac-IL-1β-SOC_4-[Ac_2,(La/$SSB)_2$]-TT-NH_2 conjugate (**3**). Antisera raised in rabbits immunized with CFA/IFA (A), IFA (B), and the peptide conjugate alone (C). Data shown as means of three independent experiments carried out in triplicate using a pool of the two rabbit sera that gave similar results when used independently. Control sera: preimmune

directly. Freund's adjuvant, which is the most commonly used adjuvant for research work, is a water-in-oil emulsion prepared with nometabolizable oils that contains heat-killed tuberculosis mycobacteria. The principal disadvantage of Freund's adjuvant is that it can cause a local inflammatory reaction at the site of injection and invoke very aggressive and persistent granulomas. To avoid these side effects, incomplete Freund's adjuvant, among others, has been proposed although severe skin toxicities have been reported in some cases (*3, 4, 36, 37*).

The profile of the antibody production when immunogens Ac-IL-1β-SOC_4-Sm_4-TT-NH_2 and Ac-IL-1β-SOC_4-[Ac_2-(La/$SSB)_2$]-TT-NH_2 were injected alone leads to the assumption that incorporation of Aib, an enzymatic nondegradable residue, contributes to the slow release of epitopes thus resembling the proposed action of the nometabolizable oily constituents of IFA. On the other hand, the inclusion into the carrier of the IL-1β(163−171) fragment, known to reproduce the immunostimulatory and adjuvant functions of the whole IL-1β but not its numerous side effects (*15, 16*), assisted the generation of an enhanced and sustained immune response, as that of CFA, which is also site specific, as the produced antibodies, so far presented, recognize the priming immunogens.

Specificity of Antibody Recognition. To further assess the specificity of the generated antibodies when the constructed immunogens were injected to animals, the obtained antisera were tested against the carrier Ac-IL-1β-SOC_4-Ac_4-TT-NH_2 (**1**) and SOC_4, Ac-[Lys(Ac)-Aib-Gly]$_4$, without bearing any peptide epitope. Antibodies raised against peptide-conjugate **2** are highly recognized by the priming peptide, but their recognition from the carrier, which incorporates the IL-1β and TT fragments, and SOC_4, when administered without adjuvant is negligible (Figure 6A). Similarly, antibodies raised against peptide-conjugate **3** without adjuvant exhibit negligible reactivity against the carrier compared to their high

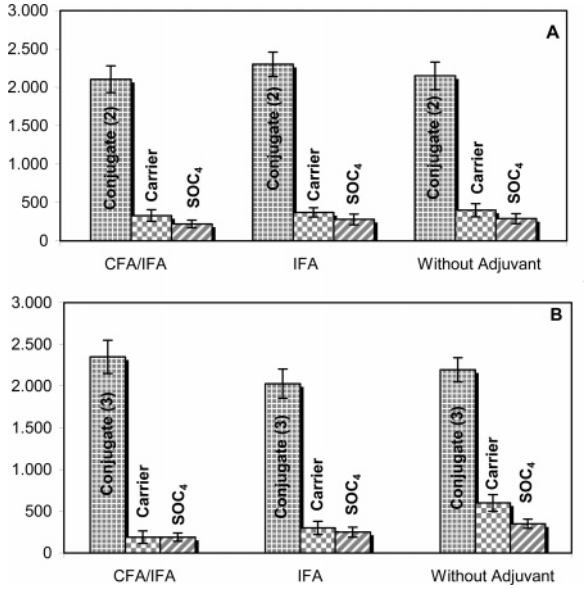

Figure 6. Comparison of the antisera reactivity of rabbits immunized with conjugate Ac-IL-1β-SOC_4-Sm_4-TT-NH_2 (**2**) against **2**, the Ac-IL-1β-SOC_4-Ac_4-TT-NH_2 carrier (**1**), and the SOC_4 carrier (A). Comparison of the antisera reactivity of rabbits immunized with conjugate Ac-IL-1β-SOC_4-[Ac_2-(La/SSB)$_2$]-TT-NH_2 (3) against (3) the Ac-IL-1β-SOC_4-Ac_4-TT-NH_2 carrier (**1**), and the SOC_4 carrier (B). Peptide conjugates **2** and **3** were administered with CFA/IFA, IFA, and without adjuvant as indicated. Sera dilution: 1/800.

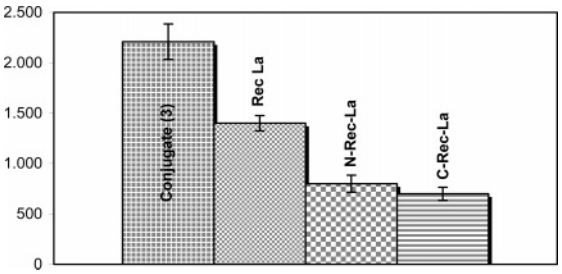

Figure 7. Comparison of the antisera reactivity of rabbits immunized (without adjuvant) with conjugate Ac-IL-1β-SOC_4-[Ac_2-(La/SSB)$_2$]-TT-NH_2 (**3**) alone (without adjuvant) against **3**, recombinant La/SSB (Rec La), N-terminal recombinant La/SSB (N-Rec-La), and C-terminal recombinant La/SSB (C-Rec-La).

recognition by the priming peptide (Figure 6B). These findings indicate that the reported new immunogenic peptide-conjugates induce (without the assistance of adjuvant) a specific enhanced immunostimulatory response without producing nonspecific antibodies recognizing SOC_4 (*23, 38*) or the elongated by IL-1β and TT new carrier.

Rabbit antisera induced after immunization with peptide-conjugate **3** alone, without adjuvant, displayed significant reactivity (~60%) against recombinant La/SSB (*39*) and ~40% reactivity against the C-terminus and N-terminus of the recombinant La/SSB (*39*) compared to the anti-peptide-conjugate **3** antibody recognition (Figure 7). One may assume that immunizations using the conjugates presented in this study, without the addition of an adjuvant, results in polyclonal antibody response against the cognate protein or parts of it, as it was already mentioned when the conventional immunization protocol (CFA/IFA) was followed, suggesting the activation of antigen-specific B cells (*23, 41*).

In an attempt to validate the efficacy of our peptide-conjugates in species other than rabbits, immunizations were performed in mice, applying the peptide-conjugate

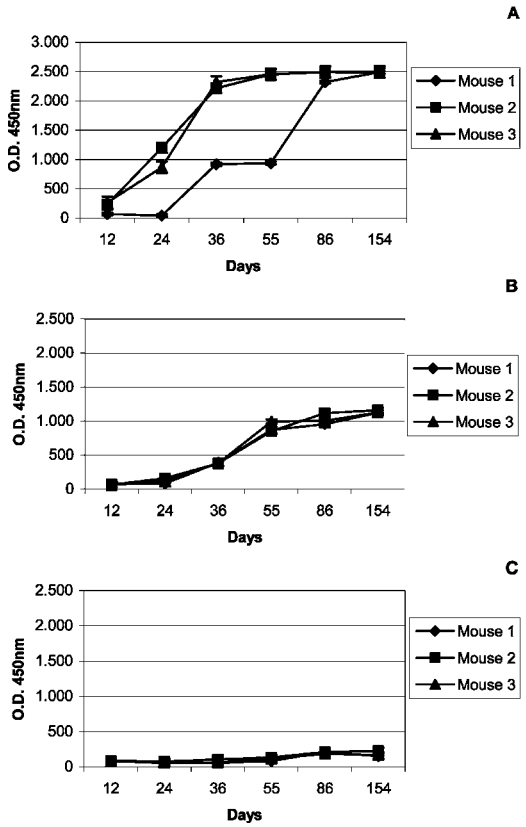

Figure 8. Binding of antisera to the Ac-IL-1β-SOC_4-[Ac_2-(La/SSB)$_2$]-TT-NH_2 (**3**) conjugate at 1/500 dilution. Antisera raised in mice immunized with CFA/IFA (A) and the peptide conjugate alone without adjuvant (B). Data shown as means of three independent experiments carried out in triplicate using a pool of three mice sera that gave similar results when used independently. Control sera: preimmune (C).

3 following the CFA/IFA protocol and without the addition of adjuvant (Figure 8). Although rather lower titers of antibodies were produced when conjugate **3** was administered alone, the immunostimulatory response was specific for the priming peptide-conjugate, indicating the utility of the promiscuous T cell epitope, TT(593−599), in providing a broader spectrum of immunogenicity (*3, 5, 6*).

DISCUSSION

A new multivalent carrier combining B and T cell epitopes, a built-in adjuvant and a "promiscuous" T cell epitope as costimulatory molecules to formulate potential immunogenic conjugates is presented. Following the step-by-step solid-phase peptide synthesis principles and by applying orthogonal side-chain protections, it was feasible to synthesize two peptide-conjugates, as mimics of the Sm and La/SSB proteins, with accurate and unambiguous composition and structure without altering the initial properties of the conjugated epitopes. Moreover, is very probable that the helicoid features of the presented multifunctional carrier, as revealed by CD measurements, contribute to the conformation-dependent recognition of B cell epitopes of Sm and La/SSB proteins to elicit specific antibodies. In particular, the IL-1β(163−171) fragment was covalently linked to the N-terminus of the tetrameric Sequential Oligopeptide Carrier, SOC_4, as immunostimulator, while the TT(593−599) sequence was attached to the carboxy-terminus of SOC_4 as universal immunogen.

The reconstituted Sm and La/SSB immunogenic conjugates **2** and **3** respectively when injected in animals,

without the assistance of CFA/IFA, induced high titers of specific antibodies recognizing the priming peptide-constructs. The antibody reactivity remained high even at high sera dilution (1:50000), indicative of the potency and the good quality of the immune response. It seems likely that the inclusion of IL-1β(163−171) within the synthesized reconstituted immunogenic conjugates may substitute the immunostimulatory activity of Freund's adjuvant, while incorporation of Aib, an enzymatic nondegradable residue, in the repeating tripeptide unit of SOC_4 may replace the function of the nonmetabolizable oily constituents of the incomplete Freund's adjuvant.

Confirmation of the specificity of the generated antibodies, when the constructed immunogens are injected without the assistance of adjuvant, is further assessed from the fact that they do not recognize the Ac-IL-1β-SOC_4-Ac_4-TT-NH_2 carrier, which comprises the IL-1β, and the TT fragments and SOC_4. On the basis of these findings, it is presumed that the immune response is antigen driven, originated from the reported conjugates. It is of particular interest to underline the defined intramolecular spreading of the antibody response when epitope La/SSB(289−308) is injected in the form of Ac-IL-1β-SOC_4-[Ac_2-(La/SSB)$_2$]-TT-NH_2 without the assistance of Freund's adjuvant. The observed immunogenicity of construct **3** when injected in rabbits and mice implies that the inclusion of TT(593−599) in the reported carrier could help to overcome genetic restrictions of the T cell "help" to B cells.

Our study provides the conceptual and experimental framework to formulate multifunctional immunogens as human vaccine candidates without the adverse effects derived from the usage of adjuvants.

ACKNOWLEDGMENT

These studies were supported by grants from the Greek General Secretariat of Research and Technology (GSRT).

Supporting Information Available: Schematic representation of the synthesis of the Ac-IL-1β-SOC_4-Ac_4-TT-NH_2 carrier (**1**) and Ac-IL-1β-SOC_4-[Ac_2-(La/SSB)$_2$]-TT-NH_2 conjugate (**3**). LC and ESI-MS of the Ac-IL-1β-SOC_4-Ac_4-TT-NH_2 carrier (**1**), and Ac-IL-1β-SOC_4-Sm_4-TT-NH_2 (**2**) and Ac-IL-1β-SOC_4-[Ac_2-(La/SSB)$_2$]-TT-NH_2 (**3**) conjugates. This material is available free of charge via the Internet at http://pubs.acs.org.

LITERATURE CITED

(1) Kaumaya, P. T., Berndt, K. D., Heidorn, D. B., Trewhella, J., Kezdy, F. J., and Goldberg, E. (1990) Synthesis and biophysical characterization of engineered topographic immunogenic determinants with alpha alpha topology. *Biochemistry 29*, 13−23.

(2) Kobs-Conrad, S., Lee, H., DiGeorge, A. M., and Kaumaya, P. T. (1993) Engineered topographic determinants with alpha beta, beta alpha beta, and beta alpha beta alpha topologies show high affinity binding to native protein antigen (lactate dehydrogenase-C4). *J. Biol. Chem. 268*, 25285−25295.

(3) Sundaram, R., Dakappagari, N. K., and Kaumaya, P. T. (2002) Synthetic peptides as cancer vaccines. *Biopolymers 66*, 200−216.

(4) Reid, C. D., Stackpoole, A., Meager, A., and Tikerpae, J. (1992) Interactions of tumor necrosis factor with granulocyte-macrophage colony-stimulating factor and other cytokines in the regulation of dendritic cell growth in vitro from early bipotent CD34+ progenitors in human bone marrow. *J. Immunol. 149*, 2681−2688.

(5) Kaumaya, P. T., Kobs-Conrad, S. Seo, Y. H., Lee, H., VanBuskirk, A. M., Feng, N., Sheridan, J., and F. Stevens, V. (1993) Peptide vaccines incorporating a 'promiscuous' T-cell epitope bypass certain haplotype restricted immune responses and provide broad spectrum immunogenicity. *J. Mol. Recognit. 6*, 81−94.

(6) Panina-Bordignon, P., Tan, A., Termijtelen, A., Demotz, S., Corradin, G., and Lanzavecchia, A. (1989) Universally immunogenic T cell epitopes: promiscuous binding to human MHC class II and promiscuous recognition by T cells. *Eur. J. Immunol. 19*, 2237−2242.

(7) Metzger J., Wiesmuller K. H., Schaude, R., Bessler, W. G., and Jung, G. (1991) Synthesis of novel immunologically active tripalmitoyl-S-glycerylcysteinyl lipopeptides as useful intermediates for immunogen preparations. *Int. J. Pept. Protein Res. 37*, 46−57.

(8) Postnett, D. N., McGrath, H., and Tam, J. P. (1988) A novel method for producing anti-peptide antibodies: production of site site-specific antibodies to the T-cell antigen receptor β−chain. *J. Biol. Chem. 263*, 1719−1725.

(9) Mutter, M., Dumy, P., Garrouste, P., Lehmann, C., Mathieu, M., Peggion, C., Peluso, S., Razaname, A., and Tuchscherer, G. (1996) Template assembled synthetic proteins (TASP) as functional mimetics of proteins. *Angew. Chem., Int. Ed. Engl. 35*, 1482−1485.

(10) Tsikaris, V., Sakarellos, C., Cung, M. T., Marraud, M., and Sakarellos-Daitsiotis, M. (1996) Concept and design of a new class of sequential oligopeptides carrier (SOC) for covalent attachment of multiple antigenic peptides. *Biopolymers 38*, 291−293.

(11) Tsikaris, V., Sakarellos, C., Sakarellos-Daitsiotis, M., Orlewski, P., Marraud, M., Cung, M. T., Vatzaki, E., and Tzartos, S. (1996) Construction and application of a new class of sequential oligopeptide carries (SOCn) for multiple anchoring of antigenic peptides-application to the acetylcholine receptor (AChR) main immunogenic region. *Int. J. Biol. Macromol. 19*, 195−205.

(12) Sakarellos-Daitsiotis, M., Tsikaris, V., Sakarellos, C., Vlachoyiannopoulos, P. G., Tzioufas, A. G., and Moutsopoulos, H. M. (2000) A new helicoid-type sequential oligopeptide carrier (SOCn) for developing potent antigens and immunogens. *Vaccine 18*, 302−310.

(13) Sakarellos-Daitsiotis, M., Tsikaris, V., Vlachoyiannopoulos, P. G., Tzioufas, A. G., Moutsopoulos, H. M., and Sakarellos, C. (1999) Peptide Carriers: A helicoid-type sequential oligopeptide carrier (SOCn) for multiple anchoring of antigenic/Immunogenic Peptides. *Methods, A Companion to methods in Enzymology 19*, 133−141.

(14) Keramisanou, D., Tsikaris, V., Sakarellos-Daitsiotis, M., Sakarellos, C., Mikhailova, A. A., and Strelkov, L. A. (2002) Multiple anchoring of myelopeptides on sequential oligopeptide carriers (SOCn): synthesis, conformation and studies in human leukemia cells. *J. Pept. Res. 59*, 1−8.

(15) Tagliabue, A., and Boraschi, D. (1993) Cytokines as vaccine adjuvants: Interleukin 1 and its synthetic peptide 163−171. *Vaccine 11*, 594−595.

(16) Boraschi, D., and Tagliabue, A. (1999) Interleukin-1 and Interleukin-1 fragments as vaccine adjuvants. *Methods 19*, 108−113.

(17) Ho, P. C., Mutch, D. A., Winkel, K. D., Saul, A. J., Jones, G. L., Doran, T. J., and Rzepczyk, C. M. (1990) Identification of two promiscuous T-cell epitopes from tetanus toxin. *Eur. J. Immunol. 20*, 477−483.

(18) James, J. A., and Harley, J. B. (1992) Linear epitope mapping of an Sm B′/B polypeptide. *J. Immunol. 148*, 2074−2079.

(19) Tan, E. M., Cohen, A. S., Fries, J. M., Mashi, A. T., McShane, D. J., Rothfield, N. F., Schallez, J. G., Talal, N., and Winchester, R. J. (1982) The 1982 revised criteria for the classification of systemic lupus erythematosus. *Arthritis Rheum. 25*, 1271−1277.

(20) Petrovas, C. J., Vlachoyiannopoulos, P. G., Tzioufas, A. G., Alexopoulos, C., Tsikaris, V., Sakarellos-Daitsiotis, M., Sakarellos, C., and Moutsopoulos, H. M. (1998) A major Sm epitope anchored to sequential oligopeptide carriers is a suitable antigenic substrate to detect anti-Sm antibodies. *J. Immunol. Methods 220*, 59−68.

(21) Fatenejad, S., Mamula, M., and Craft, J. (1993) Role of intermolecular/intrastructural B- and T- cell determinants

is the diversification of autoantibodies to ribonucleoprotein particles. *Proc. Natl. Acad. Sci. U.S.A. 90*, 12010−12014.
(22) Tzioufas, A. G., Yiannaki, E., Sakarellos-Daitsiotis, M., Routsias, J. G., Sakarellos, C., and Moutsopoulos, H. M. (1997) Fine specificity of autoantibodies to La/SSB. Epitope mapping molecular mimicry and clinical applications. *Clin. Exp. Immunol. 108*, 191−198.
(23) Yiannaki, E., Vlachoyiannopoulos, P. G., Manousakis, M. N., Sakarellos, C., Sakarellos-Daitsiotis, M., Moutsopoulos, H. M., and Tzioufas, A. G. (2000) Study of antibody and T cell responses in rabbits immunized with synthetic human B cell epitope analogues of La/SSB autoantigen. *Clin. Exp. Immunol. 121*, 551−556.
(24) Stewart, J. M., and Young, J. D. Principles of Peptide Synthesis, Second ed. Pierce Chemical Co, Rockford IL, 1984.
(25) Bodansky, M. Principles of Peptide Synthesis, Second ed. Springer: Berlin, 1993.
(26) Bodansky, M., and Bodansky, A. The practice of Peptide Synthesis, Second ed. Springer: Berlin, 1994.
(27) Kaiser, E., Bossinger, C. D., Colescott, R. L., and Olsen, D. B., (1980) Color test for terminal prolyl residues in the solid-phase synthesis of peptides. *Anal. Biochem. 34*, 595−598.
(28) Dangles, O., Guibe, F., Balavoine, G., Lavielle, S., and Marquet, A. (1987) Selective cleavage of the allyl and allyloxycarbonyl groups through palladium-catalyzed hydrostannolysis with tributyltin hydride. Application to the selective protection-deprotection of amino acid derivatives and in peptide synthesis. *J. Org. Chem. 52*, 4984−4993.
(29) Loffet, A., and Zhang, H. X. (1993) Allyl-based groups for side-chain protection of amino acids. *Int. J.* Peptide, Protein Res. *42*, 346−351.
(30) Chen, Y. H., Yang, J. T., and Martinez, H. M. (1972) Determination of the secondary structures of proteins by circular dishroism and optical rotatory dispersion. *Biochemistry 11*, 4120−4131.
(31) Bohm, G., Muhr, R., and Jaenicke, R. (1992) Quantitative analysis of protein far UV circular dichroism spectra by neural networks. *Protein Eng. 5*, 191−195.
(32) Rozek, A., Buchko, G. W., and Cushley, R. J. (1995) Conformation of two peptides corresponding to human apolipoprotein C−I residues 7−24 and 35−53 in the presence of sodium dodecyl sulfate by CD and NMR spectroscopy. *Biochemistry 34*, 7401−7408.
(33) Fasman, G. D. (1996) *Circular Dichroism and the Conformational Analysis of Biomolecules*, Plenum Press, New York.
(34) Alexopoulos, Ch., Tsikaris, V., Rizou, C., Sakarellos-Daitsiotis, M., Sakarellos, C., Cung, M. T., Marraud, M., Vlachoyiannopoulos, P. G., and Moutsopoulos, H. M. (2000) The position of the Lys-$N^{\epsilon}H_2$ grafted antigens along the sequential Oligopeptide carrier, Ac-(Aib-Lys-Aib-Gly)$_n$ (SOC_n-II), influences the antibody recognition: application to the Sm main autoimmune epitope. *Biopolymers 54*, 1−10.
(35) Sakarellos-Daitsiotis, M., Alexopoulos, Ch., and Sakarellos, C. (2004) Sequential oligopeptide carriers, SOC_n, as scaffolds for the reconstitution of antigenic proteins: applications in solid-phase immunoassays. *J. Pharm. Anal. 34*, 761−769.
(36) Gupta, R. K., Relyveld, E. H., Lindblad, E. B., Bizzini, B., Ben-Efraim, S., and Gupta, C. K. (1993) Adjuvants-a balance between toxicity and adjuvanticity. *Vaccine 11*, 293−306.
(37) Gupta, R. K., and Siber, G. R. (1995) Adjuvant for human vaccines-current status problems and future prospects. *Vaccine 13*, 1263−1276.
(38) Vlachoyiannopoulos, P. G., Petrovas, C., Tzioufas, A. G., Alexopoulos, Ch., Tsikaris, V., Guialis, A., Nakopoulos, L., Sakarellos-Daitsiotis, M., Sakarellos, C., Davaris, P., and Moutsopoulos, H. M. (2000) No evidence of epitope spreading after immunization with the magor Sm epitope P−P-G−M-R−P−P anchored to Sequential Oligopeptide Carriers (SOCs). *J. Autoimm. 14*, 53−61.
(39) Yiannaki, E. E., Tzioufas, A. G., Bachmann, M., Hantoumi, J., Tsikaris, V., Sakarellos-Daitsiotis, M., Sakarellos, C., and Moutsopoulos, H. M. (1998) The value of synthetic linear epitope analogues of La/SSB for the detection of autoantibodies to La/SSB.; specificity, sensitivity and comparison of methods. *Clin. Exp. Immunol*. *112*, 152−158.
(40) Mamula, M. J., and Janeway, C. A. Jr. (1993) Do B cells drive the diversification of immune responses? *Immunol. Today 14*, 151−152.
(41) Craft, J., and Fatenejad, S. (1997) Self-antigens and epitope spreading in systemic autoimmunity. *Arthritis Rheum. 10*, 1374−1382.

BC049703M

Complex Formation between a DNA Duplex and Lipid-like Spermine Derivatives: Hydrophobic Protection of DNA from One-Electron Oxidation

Huachuan Cao and Gary B. Schuster*

School of Chemistry and Biochemistry, Georgia Institute of Technology, Atlanta, Georgia 30332. Received January 25, 2005; Revised Manuscript Received June 13, 2005

The one-electron oxidation of DNA leads to formation of a nucleobase radical cation that can migrate to a distant site where it is trapped by H_2O or O_2 to form a "damaged" guanine that is revealed as strand cleavage when the irradiated sample is treated with piperidine. We prepared a series of alkyl-substituted spermine derivatives and assessed their effect on the oxidative reactions of DNA induced by photoexcitation of a covalently linked anthraquinone derivative. The spermine compounds are polycations and bind nonselectively to DNA. When the spermine derivative is substituted with C_8 alkyl chains, it shows lipid-like properties. The reaction of the radical cation at guanine is affected by this lipid-like spermine. The distance dependence of the migration process becomes weaker, and the efficiency of strand cleavage is reduced. These results are attributed to the formation of a hydrophobic layer on the DNA that restricts access of H_2O to the nucleobase radical cation.

INTRODUCTION

The one-electron oxidation of DNA introduces a radical cation ("hole") that can migrate long distances before being consumed in an irreversible reaction that damages a nucleobase and results in strand cleavage upon subsequent treatment with piperidine (*1*). The mechanism of radical cation transport has been extensively studied. It is generally agreed that the hole hops adiabatically over distances greater than two or three base pairs and that it may tunnel from guanine to guanine over shorter distances (*2*−*6*). There has been less examination of the irreversible trapping reactions of these radical cations in DNA.

A pioneering study using isotope tracers showed that sensitized oxidation of 2′-deoxyguanosine in water solution leads to rapid deprotonation of the resulting radical cation and that subsequent reactions of the radical yield little 7,8-dihydro-8-oxo-2′-deoxyguanosine (8-OxoG) (*7*). In contrast, oxidation of guanine-containing duplex DNA in deoxygenated buffer solution was shown to give primarily 8-OxoG by reaction of a base-paired guanine radical cation with H_2O (*7*, *8*). Cullis (*9*) and Burrows (*10*) have shown that piperidine treatment of DNA that contains 8-OxoG does not lead to strand cleavage under the standard conditions. Clearly, formation of 8-OxoG by reaction of guanine radical cations with H_2O is not the only process that occurs in oxidized duplex DNA. In the experiments reported here, we probed the effect of an external hydrophobic "coating" around a DNA duplex on the efficiency of long-distance charge transport and on radical cation trapping by H_2O. We find that the hydrophobic layer increases the efficiency of charge transfer and inhibits trapping.

Our approach to limiting H_2O access to DNA was inspired by the extensive investigation of hydrophobic polycations that enable DNA transfection into cells (*11*−*13*). Microscopy, X-ray analysis, and fluorescence experiments show that these lipid-like materials cover the DNA surface and thereby facilitate migration through the hydrophobic cell membrane (*12*, *14*). We selected a set of derivatives for study that are built on a spermine tetracation core. In this case, the electrostatic interaction of the alkylammonium ions with the phosphate anions of DNA is the major driving force for formation of stable complexes (*15*). The lipid-like tetracations and the anthraquinone (AQ)-DNA duplex oligomer that we studied are shown in Figure 1.

EXPERIMENTAL PROCEDURES

The DNA oligonucleotides were synthesized on an ABI DNA synthesizer using standard solid-phase techniques. Phosphoramidites and 1.0 μM CPG columns were purchased from Glen Research. [γ-^{32}P]ATP was purchased from Amersham Bioscience. T4 polynucleotide kinase (T4PNK) was purchased from New England Biolabs and stored at −20 °C. DNA was deprotected in concentrated ammonium hydroxide and purified using reverse-phase HPLC on a Hitachi system equipped with a Dynamax C18 column. The molecular mass of the DNA was determined by electrospray ionization (ESI) mass spectrometry. The concentrations of the oligomers were determined from their absorbance at 260 nm. Duplex AQ-DNA solutions were prepared by combining equimolar amounts of the single-strand oligomers and annealing them at 90 °C with slow cooling to room temperature. UV melting and cooling curves were recorded on a Cary 1E spectrophotometer equipped with a multicell block, temperature controller, and sample transport accessory. CD spectra were recorded on a JASCO J-720 spectropolarimeter. Fluorescence measurements were recorded on SPEX 1681 Fluorolog spectrometer.

Synthesis of the C_nSp^{+4} "Lipids". The lipid-like compounds shown in Figure 1 all contain a spermine tetracation core and were prepared in seven steps. The synthetic route for these compounds was modeled on that for $C_{18}Sp^{+4}$, which was previously described (*16*). We found that replacement of tetramethylammonium chloride with sodium hydroxide to neutralize L-ornithine hydrochloride gave a better outcome. Details of the synthetic procedures will be reported elsewhere.

10.1021/bc0500185 CCC: $30.25 © 2005 American Chemical Society
Published on Web 06/29/2005

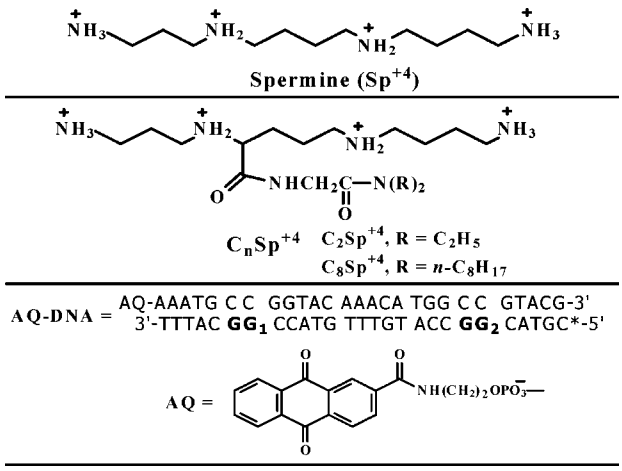

Figure 1. Structures of the spermine derivatives and the DNA oligomers used in this work. The ∗ indicates ^{32}P label.

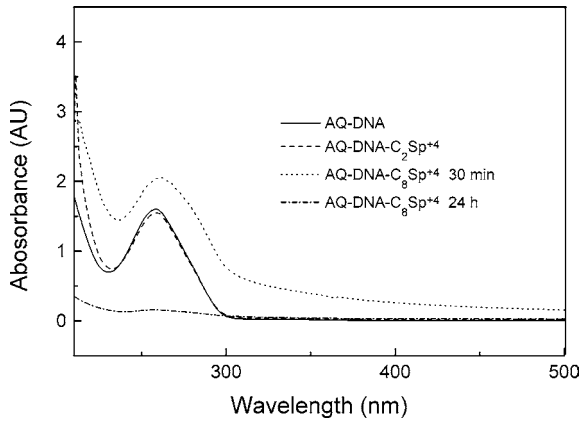

Figure 2. Absorption spectra of AQ-DNA in buffer solution at pH 7.0. The curves are recorded at various conditions as indicated. C_2Sp^{+4} and C_8Sp^{+4} are present at a charge ratio of 4.0.

Melting Temperatures. Melting temperatures were determined in quartz cuvettes sealed with tape. Samples contained duplex AQ-DNA (2.5 μM) in 10 mM sodium phosphate buffer (pH 7.0) and various concentrations of spermine or C_nSp^{+4}. The absorbance of the samples was monitored at 260 nm. The reported T_m values are the peaks in the first-derivative plots of melting profiles obtained by fitting the data with Microcal Origin software.

Fluorescence Spectroscopy. Emission spectra of ethidium bromide (EB, 10 μM) were obtained by exciting at 510 nm and monitoring the integrated emission intensity from 540 to 750 nm. Excitation spectra were obtained by monitoring the emission at 600 nm while scanning the excitation wavelength from 350 to 590 nm. The experiments were performed in a 1 cm path length quartz cuvette containing 1 mL of 2.5 μM AQ-DNA duplex in 10 mM sodium phosphate buffer at pH 7.0. Aliquots of solution containing spermine or C_nSp^{+4} were added to the DNA solution, and the fluorescence emission of the resulting solution was measured after incubation for 15 min.

Circular Dichroism (CD). CD spectra were measured between 200 and 400 nm as aliquots of solutions containing spermine or C_nSp^{+4} were added to an AQ-DNA duplex solution. Each spectrum was accumulated five times and smoothed, and the spectrum of the buffer solution was subtracted.

Cleavage Analysis by Radiolabeling and Polyacrylamide Gel Electrophoresis (PAGE). AQ-DNA was radiolabeled according to standard procedures at the 5′-end of the complementary strand with [γ-^{32}P]ATP and bacterial T4PNK. It was purified by 20% PAGE at 400 V. Samples for irradiation were prepared by hybridizing a mixture of unlabeled (2.5 μM) and radiolabeled (10 000 cpm) oligonucleotides in 10 mM sodium phosphate buffer (pH 7.0). Hybridized samples were incubated with various concentrations of spermine or C_nSp^{+4} as indicated for 30 min (total volume 30 μL) and then irradiated for 3 min at 30 °C in microcentrifuge tubes in a Rayonet photoreactor (Southern New England Ultraviolet Co., Barnsford, CT) equipped with eight 350 nm lamps. After irradiation, the samples were precipitated once with cold ethanol (100 μL) in the presence of glycogen (2 μL, 20 mg/mL), then washed with 80% ethanol (2 × 100 μL), dried (Speedvac, low heat), and treated with piperidine (100 μL of 1 M solution) at 90 °C for 30 min. After evaporation of the piperidine (Speedvac, medium heat), lyophilization twice with water (20 μL), and dissolution in denaturing dye solution (bromophenol blue, 4:1 v/v formamide in water), the samples (3000 cpm) were electrophoresed on a 20% 19:1 acrylamide/bisacrylamide gel containing urea (7 M) at 70 W for 90 min. The gels were dried, and the cleavage sites were visualized by autoradiography. Quantification of cleavage bands was performed on a Fuji phosphorimager.

Reaction of $^1O_2$ with AQ-DNA. A 10 μM solution of AQ-DNA, C_8Sp^{+4} and Rose Bengal (5 mM) was irradiated with light, >450 nm (only the Rose Bengal absorbs). After irradiation, the samples were worked up as described above (the Rose Bengal remains in the ethanol layer) and analyzed by PAGE.

RESULTS

Definition of the Charge Ratio. The experiments reported here were generally carried out in 10 mM sodium phosphate buffer solution at pH 7.0. Under these conditions, spermine (Sp^{+4}) and its derivatives C_nSp^{+4} have four positively charged ammonium groups, and the AQ-DNA duplex has 54 negatively charged phosphate groups. Thus, when the mole ratio of the AQ-DNA to spermine is 1:13.5, there is one positive charge on a spermine or a C_nSp^{+4} derivative for each negative charge on a DNA phosphate. We define this to be a charge ratio equal to 1.0.

Characterization of AQ-DNA Solutions in the Presence of Sp^{+4} and C_nSp^{+4}. DNA duplexes that are much longer than AQ-DNA examined in this work form aggregates and condensates with cationic lipids such as C_nSp^{+4} (*14*, *17*). We carried out experiments to assess the stability of solutions of AQ-DNA in the presence of Sp^{+4} and C_nSp^{+4}. The solutions were evaluated immediately after they were prepared and then monitored over time to determine whether they change during the course of the experiments reported here.

Absorption Spectroscopy. The absorption spectrum of AQ-DNA in solution was monitored in the presence of various concentrations of Sp^{+4} and C_nSp^{+4} (see Figure 2). Spermine and C_2Sp^{+4} do not affect the UV spectrum of AQ-DNA up to a charge ratio of 4.0. Similarly, solutions of AQ-DNA containing C_8Sp^{+4} up to a charge ratio of 2.0 were stable (a small, constant baseline increment is observed, which may indicate the formation of some small aggregates). In contrast, for C_8Sp^{+4} at a charge ratio of 4.0, the absorbance increases significantly (due to scattering) during the first few hours after the sample is prepared, and then there is a sharp decrease in absorbance attributed to precipitation of the AQ-DNA/C_8Sp^{+4}

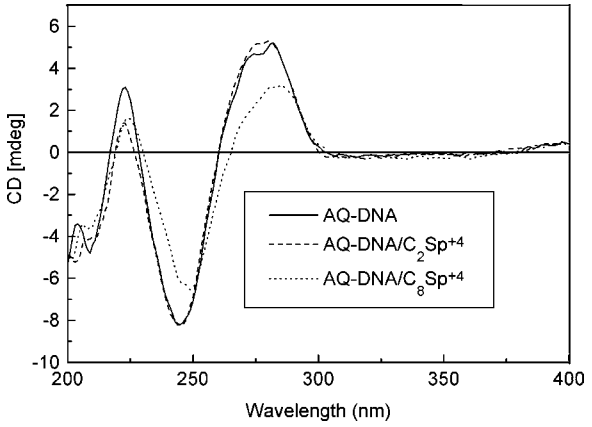

Figure 3. CD spectra of AQ-DNA in buffer solution at pH 7. C_2Sp^{+4} is present at a charge ratio of 2.0; C_8Sp^{+4} is present at a charge ratio of 3.0.

complex from solution. Consequently, we restricted our investigation of the effect of C_8Sp^{+4} on charge transfer in AQ-DNA to a charge ratio of 2.0 or less, where the solutions are stable.

Melting Temperature. We examined the melting behavior of AQ-DNA solutions in the presence of Sp^{+4} and C_nSp^{+4} to assess their interactions with the duplex. The melting temperature (T_m) of AQ-DNA is 58.4 °C. This value increases systematically with the addition of Sp^{+4} or C_nSp^{+4}. Spermine shows the most pronounced effect: an increase of 14 °C in T_m when the charge ratio of Sp^{+4} is 4.0. In contrast, for C_2Sp^{+4}, ΔT_m is 8.4 °C when the charge ratio is 4.0, and for C_8Sp^{+4}, ΔT_m is 4.0 °C at a charge ratio of 2.0.

Circular Dichroism Spectroscopy. As expected, the circular dichroism (CD) spectrum of AQ-DNA is indicative of normal B-form DNA (*18*). We monitored the CD spectra of AQ-DNA solutions containing Sp^{+4}, C_2Sp^{+4}, or C_8Sp^{+4} to assess the effect these additives have on the global structure of the duplex (Figure 3). The addition of Sp^{+4} or C_2Sp^{+4} to solutions of AQ-DNA up to a charge ratio of 4.0 did not significantly affect the CD spectrum. Similarly, there are only minor changes in the CD spectrum when C_8Sp^{+4} is added to AQ-DNA up to a charge ratio of 2.0. However at a charge ratio of 3.0, solutions containing C_8Sp^{+4} show a decrease in intensity and a slight red shift in the peaks with maxima at 220, 240 (negative), and 270 nm. This may indicate a change in the AQ-DNA secondary structure at relatively high concentrations of C_8Sp^{+4}.

Fluorescence Spectroscopy. We evaluated the effect of Sp^{+4} and C_nSp^{+4} on the fluorescence of ethidium bromide (EB) intercalated in AQ-DNA. It is well-known that the quenching of EB fluorescence by water is strongly inhibited when it is intercalated in DNA (*19*). In the absence of DNA, Sp^{+4} and C_nSp^{+4} have no measurable effect on the absorption or fluorescence emission or excitation spectra of EB. Figure 4 shows the normalized fluorescence intensity of the DNA−EB complex with various amounts of Sp^{+4} or C_nSp^{+4}. The addition of Sp^{+4} or C_2Sp^{+4} up to a charge ratio of 2.0 has only a modest effect on the emission intensity of EB. However, addition of C_8Sp^{+4} to the DNA−EB solution results in a nonlinear reduction in EB fluorescence intensity. There is only a moderate effect on EB fluorescence intensity up to a charge ratio of 1.0 for C_8Sp^{+4}, but the intensity decreases ca. 70% when the charge ratio is increased from 1.0 to 2.0. The absorption and emission spectra of the EB shift from those characteristic of intercalation to that of EB in solution when the charge ratio of C_8Sp^{+4} is increased

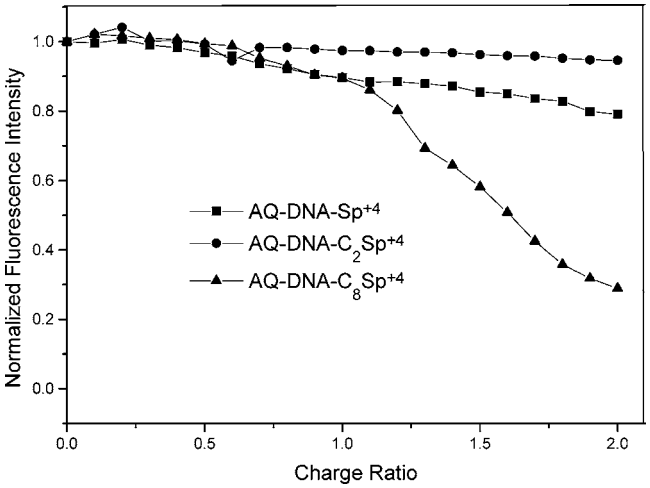

Figure 4. Fluorescence emission intensity of EB in buffer solution containing AQ-DNA and various amounts of spermine, C_2Sp^{+4}, and C_8Sp^{+4} as indicated.

from 1.0 to 2.0. However, the absorption of the AQ-DNA does not change meaningfully under these conditions, which indicates that the DNA/C_8Sp^{+4} complex is still in solution.

The effect of C_8Sp^{+4} on EB fluorescence can be understood as a competition between two equilibrium-controlled processes among DNA, EB, and the C_nSp^{+4} lipids (*20*). First, there is an equilibrium between the DNA−EB intercalated complex and free EB and DNA in solution. This equilibrium greatly favors intercalated EB in the presence of spermine and C_2Sp^{+4} up to a charge ratio of 2.0. The second equilibrium is association of Sp^{4+} and C_nSp^{+4} with AQ-DNA. Below a charge ratio of 1.0, association of C_8Sp^{+4} with AQ-DNA does not affect the intercalation of EB. But above a charge ratio of 1.0, C_8Sp^{+4} blocks the intercalation of EB into DNA, and the first equilibrium moves toward the side of free EB in solution. This is evidence for the formation of a special AQ-DNA complex in the presence of C_8Sp^{+4} above a charge ratio of 1.0. This effect is also detected in the analysis of radical cation transport in AQ-DNA.

Photoinduced Oxidative Damage in DNA−Lipid Complex. Numerous examinations of the one-electron oxidation of DNA have shown that a radical cation introduced at one location migrates through the DNA duplex (*21*, *22*). Some nucleobase sequences in the duplex, such as GG steps, serve as shallow traps where the radical cation reacts irreversibly with H_2O or O_2. Other nucleobase sequences serve as bridges between these traps. The radical cation resides briefly on the bridge but reacts there infrequently. The pattern of reactivity in DNA oligomers that have multiple GG steps has been shown to be controlled by the relative magnitudes of the rates for hopping (k_{hop}) of the radical cation from one GG step to another and that for the trapping reaction of the radical cation (k_{trap}) with H_2O or O_2. Thus k_{hop}/k_{trap} (defined as k_{ratio}) determines the observed pattern of reactivity in DNA oligomers containing multiple GG steps (*5*).

Reaction of a guanine radical cation with H_2O or O_2 forms oxidation products that result in strand cleavage when the sample is treated with piperidine or exposed to the enzyme formamidopyrimidine glycosylase (FPG) (*23*). The amount of strand cleavage is assessed by polyacrylamide gel electrophoresis (PAGE) and autoradiography. At low conversion (single hit conditions), it has been shown that the amount of strand cleavage is

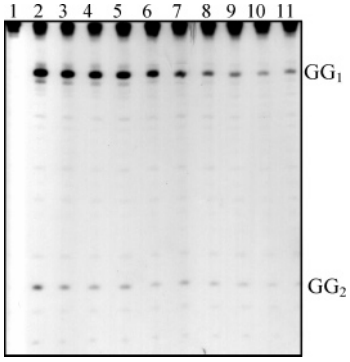

Figure 5. Autoradiogram from the irradiation (350 nm) of AQ-DNA in sodium phosphate buffer solution at pH 7 after treatment with piperidine: lane 1, dark control (no irradiation); lane 2, irradiation for 3 min, no added spermine derivative; lanes 3−11, irradiation (3 min) in the presence of added C_8Sp^{+4} with charge ratio equal to 0.1, 0.2, 0.35, 0.5, 0.75, 1.0, 1.3, 1.7, and 2.0, respectively.

proportional to the probability that the radical cation will occupy a particular GG site (*5*). Thus, this analysis provides a reliable means for assessing the relative magnitudes of k_{hop} and k_{trap}. We employed this method for analysis of the effect of Sp^{+4} and C_nSp^{+4} on radical cation migration and reaction in AQ-DNA.

AQ-DNA has two GG steps on the strand complementary to the one linked to the anthraquinone charge injector. The first step is labeled GG_1 and referred to as proximal because it is closer to the AQ. We refer to GG_2 as the distal step because it is farther from the AQ. Irradiation of the anthraquinone group at 350 nm forms an electronically excited state that is capable of the one-electron oxidation of the DNA. Subsequent reaction of the anthraquinone radical anion with O_2 forms superoxide ($O_2^{-\bullet}$) and leaves a radical cation in the DNA that can migrate until it is consumed in a trapping or annihilation reaction (*24*).

Irradiation of AQ-DNA in sodium phosphate buffer solution and subsequent treatment with piperidine (see Figure 5) or FPG reveals strand cleavage at both the proximal and the distal GG steps. As is typically the case, strand cleavage at the 5′-G of the GG step is greater than that at the 3′-G. And, as expected, there is more strand cleavage at the proximal site than at the distal site. This observation reveals that $k_{ratio} \leq 1$ for the nucleobase sequence of AQ-DNA.

We carried out a series of irradiation experiments in which solutions of AQ-DNA contained various concentrations of Sp^{+4} or C_nSp^{+4} up to a charge ratio of 2.0. Data from the addition of C_8Sp^{+4} are shown in Figure 5 in the form of an autoradiogram, and the results of several experiments are presented graphically in Figure 6. These data show that Sp^{+4} and C_2Sp^{+4} behave similarly up to a charge ratio of 2.0. That is, the relative amount of strand cleavage at the proximal and distal GG steps is unaffected, which indicates that k_{ratio} is unchanged by the addition of Sp^{+4} and C_2Sp^{+4} (*25*). The results are distinctly different for C_8Sp^{+4}. In this case, the relative amount of reaction at the distal GG step increases proportionally to the amount of C_8Sp^{+4} in solution, which at a charge ratio of 2.0 causes a 2-fold decrease in the relative reactivity of the proximal and distal GG steps (Figure 6a). Similarly, the total amount of strand cleavage observed is affected by the addition of Sp^{+4} or C_nSp^{+4}, but again the behavior of C_8Sp^{+4} is unique (Figure 6b). Addition of any of these spermine compounds reduces the sensitivity of the DNA to oxidative damage.

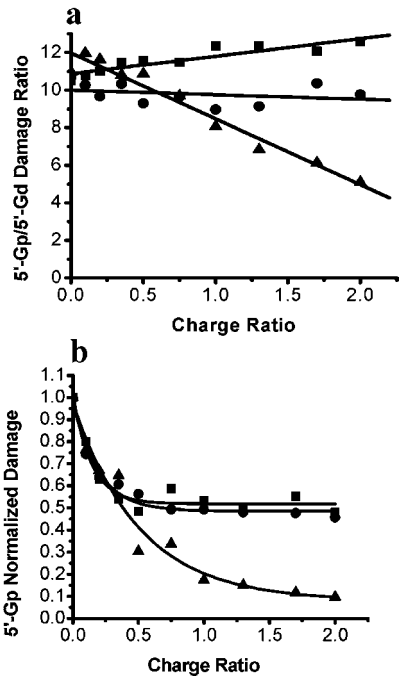

Figure 6. Plots of (a) proximal to distal damage ratio of AQ-DNA as a function of increasing charge ratio and (b) the amount of strand cleavage at the 5′-G of GG_1 as a function of increasing charge ratio: Sp^{+4} (■); C_2Sp^{+4} (●); C_8Sp^{+4} (▲).

However, this effect plateaus for Sp^{+4} or C_2Sp^{+4} at a charge ratio of ca. 0.5, but for C_8Sp^{+4}, this effect continues, and at a charge ratio of 2.0, the sensitivity of the DNA to oxidative damage is only 10% of its value in the absence of a spermine compound. We attribute this effect of C_8Sp^{+4} to a reduction of k_{trap} by the formation of a hydrophobic environment around the DNA duplex.

As noted above, absorption spectroscopy shows that the addition of C_8Sp^{+4} to AQ-DNA at a charge ratio of 2.0 causes a time-dependent change in the baseline that is indicative of aggregate formation. We carried out a control experiment designed to determine whether this affects the photooxidation reactions of AQ-DNA. Buffer solutions of AQ-DNA were incubated with C_8Sp^{+4} at a charge ratio of 2.0 for various periods of time before irradiation. After irradiation, the solutions were treated with piperidine and analyzed by PAGE and autoradiography. These experiments showed that the total amount of reaction at the GG steps of AQ-DNA and the ratio of proximal to distal strand cleavage are not affected by the incubation time with C_8Sp^{+4} up to 24 h (see Figure 7).

A second control experiment was designed to assess the sensitivity of the guanines in AQ-DNA in the presence of C_8Sp^{+4} to reaction with singlet oxygen ($^1O_2$). It is known that $^1O_2$ reacts with guanines in duplex DNA to form oxidation products that are revealed as strand cleavage by treatment with FPG (*26*). The addition of C_8Sp^{+4} up to a charge ratio of 2.0 had no effect on the reaction of AQ-DNA with $^1O_2$ (generated by irradiation of Rose Bengal with visible light greater than 450 nm). This suggests that the effect of C_8Sp^{+4} in the reaction of guanine radical cations that leads to strand cleavage involves a reagent not involved in the $^1O_2$ process, such as water.

DISCUSSION

As expected (*27*), irradiation of AQ-DNA in buffer solution causes reaction leading to strand cleavage at the GG steps. Treatment of the irradiated samples with

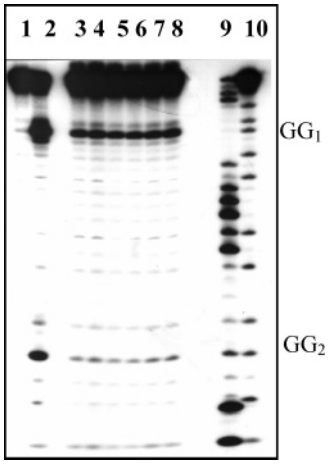

Figure 7. Autoradiogram of the denaturing gel for AQ-DNA incubated with C_8Sp^{+4} lipids (charge ratio of 2.0) for various incubation times. Lane 1 is sample w/o irradiation. Lane 2 is the sample w/o lipid. Lanes 3−8 correspond to sample incubated with C_8Sp^{+4} for 3 min, 30 min, 60 min, 6 h, 12 h, and 24 h, respectively, before 3 min of irradiation. The irradiated samples were treated with 1 M piperidine at 90 °C. Lanes 9 and 10 correspond to Maxam−Gilbert T and A/G sequencing lanes. All samples contain 2.5 μM DNA in 10 mM sodium phosphate buffer at pH 7.0. The minor band migrating slower than intact DNA in irradiated samples may be due to cross-linking.

piperidine leads to strand cleavage at the damaged guanines that is assayed by PAGE and quantified by phosphorimagery. Under the conditions of these experiments, the amount of strand cleavage at the proximal GG_1 step (ca. 20 Å from the AQ-linked terminus) is 11 ± 1 times greater than at the distal GG_2 step (ca. 70 Å from the AQ). These results are shown in Figure 5. The relative amount of reaction at GG_1 and GG_2 is controlled by the magnitude of the rate for radical cation hopping from GG_1 to GG_2 (and vice versa) compared with the rate for irreversible trapping of the radical cation by reaction with H_2O or O_2 (*5*, *28*). When k_{hop} and k_{trap} are of comparable value, $k_{ratio} \approx 1$, the amount of strand cleavage at sequential GG steps falls off approximately exponentially with distance, as is the case for AQ-DNA. Annihilation of the radical cation by back electron transfer (*29*) from superoxide in solution removes the radical cation from the DNA with no net reaction in competition with the trapping reactions that lead eventually to strand cleavage (*30*).

The addition of Sp^{+4} or C_2Sp^{+4} to the AQ-DNA solution before irradiation does not significantly affect the relative amount of proximal to distal strand cleavage detected (see Figure 6a). For example, at a charge ratio of 2.0 for Sp^{+4}, the amount of cleavage at GG_1 is 12 times that at GG_2, and for C_2Sp^{+4} it is 10 times. However, when C_8Sp^{+4} is present at a charge ratio of 2.0, the amount of cleavage at GG_1 is only 4 times greater than it is at GG_2. This finding reveals that in the presence of C_8Sp^{+4} (but not Sp^{+4} or C_2Sp^{+4}) the rate of irreversible trapping of the radical cation that leads to strand cleavage decreases relative to the rate of radical cation hopping; that is k_{ratio} increases, which results in relatively more reaction at the distal GG step (*5*, *28*).

Further evidence for the unique properties of C_8Sp^{+4} is revealed by monitoring the total amount of reaction at the 5′-G of the proximal GG step (see Figures 5 and 6b). Addition of either Sp^{+4}, C_2Sp^{+4}, or C_8Sp^{+4} up to a charge ratio of 0.5 to the AQ-DNA solution causes the amount of cleavage at GG_1 resulting from irradiation to decrease systematically until it reaches ca. 50% of that

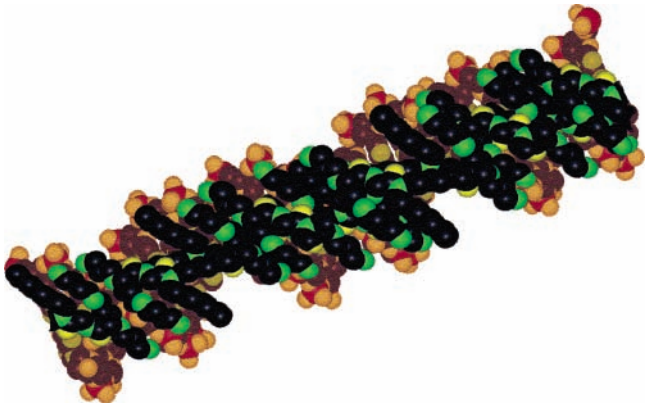

Figure 8. A schematic representation of AQ-DNA covered with 10 molecules of C_8Sp^{+4}. The ammonium groups of the spermine core have been aligned with the phosphates of the DNA. The C_8 chains are shown in black. These structures were minimized separately by molecular mechanics calculation.

observed in the absence of a spermine compound. Further additions of Sp^{+4} or C_2Sp^{+4} up to a charge ratio of 2.0 do not affect the amount of strand cleavage at GG_1. However, the amount of strand cleavage continues to decrease with increasing amounts of C_8Sp^{+4}, and at a charge ratio of 2.0, it is reduced to only 10% of its zero-spermine value. Clearly, radical cation hopping, trapping, or annihilation in DNA are affected when the polycations, Sp^{+4} or C_2Sp^{+4} replace Na^+, but there is an additional effect that protects the DNA oligomers from reaction observed only when the long alkyl chains of C_8Sp^{+4} are incorporated in the polycation.

The mechanism for the special protection of GG steps by C_8Sp^{+4} cannot be described precisely from the experiments reported here because the structures of the bound spermine complexes or soluble aggregates are not known accurately. Numerous experimental and theoretical studies have been directed toward elucidating the nature of spermine binding to DNA. It is generally agreed that a primary interaction is the electrostatic attraction between the negatively charged phosphate backbone of the DNA and the positively charged ammonium groups of spermine (*15*). However, polyamine binding sites in DNA have also been observed within both the minor and major groove of DNA (*31*−*33*), slightly favoring the minor groove in (A·T) rich tracks as shown in an experimental study (*34*). In addition, molecular dynamics simulations suggest that spermine binds in the major groove of GC-rich duplexes (*35*) and to the minor groove of AT-rich duplexes (*36*, *37*). Simulations also indicate that the presence of spermine significantly influences DNA hydration and the interaction of the sodium ions with DNA. These findings indicate that water molecules are expelled from the specific areas of DNA by spermine, which may affect k_{ratio} (*15*).

Both C_2Sp^{+4} and C_8Sp^{+4} have spermine-like polycation structures, and for this reason, we assume that they bind to DNA in the same way that spermine itself binds. In this case, it is possible to construct the model shown in Figure 8 for a complex between AQ-DNA and ten C_8Sp^{+4} molecules. One explanation for the unique properties of C_8Sp^{+4} is that the alkyl chains form a dense hydrophobic layer surrounding the DNA duplex that is absent from either the spermine or C_2Sp^{+4} complexes. This occurs because the hydrocarbon chains of C_8Sp^{+4} minimize adverse hydrophobic interactions by organizing to reduce the surface area they present to the aqueous solution. To accomplish this, the chains must interact with each other. We suggest that they form a compact layer on the

surface of the DNA oligomer. This coating should effectively reduce k_{trap} by impeding the ability of polar reagents such as H_2O to penetrate to the DNA and react with a nucleobase radical cation. The slower reaction at the proximal GG step gives the radical cation a greater probability of hopping to the distal GG steps, and this yields the lower 5′-G_p/5′-G_d ratio observed experimentally. The reduced rate for the reaction with water for the C_8Sp^{+4} complex similarly accounts for the special protective effect observed experimentally. In this case, the reactions that consume a radical cation in DNA without forming a product that leads to strand cleavage, such as reaction with superoxide, become more competitive in the AQ-DNA/C_8Sp^{+4} complex (*29*, *30*).

CONCLUSION

Spermine and the C_nSp^{+4} derivatives prepared and examined in this work form complexes with AQ-DNA. When $n = 2$, these complexes are stable in solution at high charge ratios. When $n = 8$, aggregation and precipitation occurs above a charge ratio of 2.0. Irradiation of the anthraquinone chromophore of AQ-DNA results in one-electron oxidation and the injection of a radical cation in the DNA oligomer. The radical cation migrates through the duplex and initiates reaction at GG steps that is revealed by strand cleavage. This charge hopping and reaction process is affected by the presence of spermine and the C_nSp^{+4} derivatives, but C_8Sp^{+4} is unique. This is attributed to the formation of a hydrophobic coating around DNA complexed with C_8Sp^{+4} that slows the reaction of the radical cation in DNA with water. These findings may have relevance to the protection of genomic DNA from oxidative damage.

ACKNOWLEDGMENT

We are grateful to the NSF and the Vasser−Woolley foundation for the financial support of this work. Dr. Sriram Kanvah prepared the DNA oligomers and assisted with the preparation of this manuscript. Dr. Abraham Joy also assisted in the preparation of this manuscript.

LITERATURE CITED

(1) Schuster, G. B., and Landman, U. (2004) The Mechanism of Long-Distance Radical Cation Transport in Duplex DNA: Ion-Gated Hopping of Polaron-Like Distortions. *Top. Curr. Chem. 236*, 139−162.
(2) Jortner, J., Bixon, M., Voityuk, A. A., and Rosch, N. (2002) Superexchange Mediated Charge Hopping in DNA. *J. Phys. Chem. A 106*, 7599−7606.
(3) Berlin, Y. A., Burin, A. L., and Ratner, M. A. (2002) Elementary steps for charge transport in DNA: thermal activation vs tunneling. *Chem. Phys. 275*, 61−74.
(4) Lewis, F. D., Liu, J., Zuo, X., Hayes, R. T., and Wasielewski, M. R. (2003) Dynamics and Energetics of Single-Step Hole Transport in DNA Hairpins. *J. Am. Chem. Soc. 125*, 4850−4861.
(5) Liu, C.-S., Hernandez, R., and Schuster, G. B. (2004) The Mechanism of Radical Cation Transport in DNA. *J. Am. Chem. Soc. 126*, 2877−2884.
(6) O'Neill, M. A., and Barton, J. K. (2004) DNA Charge Transport: Conformationally Gated Hopping through Stacked Domains. *J. Am. Chem. Soc. 126*, 11471−11483.
(7) Kasai, H., Yamaizumi, Z., Berger, M., and Cadet, J. (1992) Photosensitized Formation of 7,8-Dihydro-8-oxo-2′-deoxyguanosine (8-Hydroxy-2′-deoxyguanosine) in DNA by Riboflavin: A Non Singlet Oxygen Mediated Reaction. *J. Am. Chem. Soc. 114*, 9692−9694.
(8) Ly, D., Kan, Y., Armitage, B., and Schuster, G. B. (1996) Cleavage of DNA by Irradiation of Substituted Anthraquinones: Intercalation Promotes Electron Transfer and Efficient Reaction at GG Steps. *J. Am. Chem. Soc. 118*, 8747−8748.
(9) Cullis, P. M., Malone, M. E., and Merson-Davies, L. A. (1996) Guanine Radical Cations Are Precursors of 7,8-Dihydro-8-oxo-2′-deoxyguanosine But Are Not Precursors of Immediate Strand Breaks in DNA. *J. Am. Chem. Soc. 118*, 2775−2781.
(10) Hickerson, R. P., Prat, F., Muller, J. G., Foote, C. S., and Burrows, C. J. (1999) Sequence and Stacking Dependence of 8-Oxoguanine Oxidation: Comparison of One-Electron vs Singlet Oxygen Mechansms. *J. Am. Chem. Soc. 121*, 9423−9428.
(11) Remy, J. S., Sirlin, C., Vierling, P., and Behr, J. P. (1994) Gene-Transfer with a Series of Lipophilic DNA-Binding Molecules. *Bioconjugate Chem. 5*, 647−654.
(12) Dauty, E., Remy, J.-S., Blessing, T., and Behr, J.-P. (2001) Dimerizable Cationic Detergents with a Low cmc Condense Plasmid DNA into Nanometric Particles and Transfect Cells in Culture. *J. Am. Chem. Soc. 123*, 9227−9234.
(13) Gershon, H., Ghirlando, R., Guttman, S. B., and Minsky, A. (1993) Mode of formation and structural features of DNA-cationic liposome complexes used for transfection. *Biochemistry 32*, 7143−7151.
(14) Radler, J. O., Koltover, I., Salditt, T., and Safinya, C. R. (1997) Structure of DNA-Cationic Liposome Complexes: DNA Intercalation in Multilamellar Membranes in Distinct Interhelical Packing Regimes. *Science 275*, 810−814.
(15) Korolev, N., Lyubartsev, A. P., Laaksonen, A., and Nordenskiold, L. (2002) On the Competition between Water, Sodium Ions, and Spermine in Binding to DNA: A Molecular Dynamics Simulation Study. *Biophys. J. 82*, 2860−2875.
(16) Remy, J.-P., Sirlin, C., Verling, P., and Behr, J.-P. (1994) Gene Transfer with DNA Binding Molecules. *Bioconjugate Chem. 5*, 647−654.
(17) Dias, R. S., Lindman, B., and Miguel, M. G. (2002) DNA interaction with cationic vesicles. *J. Phys. Chem. B 106*, 12600−12607.
(18) Gray, D. M., Hung, S.-H., and Johnson, K. H. (1995) Absorption and Circular Dichroism Spectroscopy of Nucleic Acid Duplexes and Triplexes. *Methods Enzymol. 246*, 19−36.
(19) Olmsted, J., III., and Kearns, D. R. (1977) Mechanism of Ethidium Bromide Fluorescence Enhancement on Binding to Nucleic Acids. *Biochemistry 16*, 3647−3654.
(20) Lepecq, J. B., and Paoletti, C. A (1967) Fluorescent Complex between Ethidium Bromide and Nucleic Acids − Physical-Chemical Characterization. *J. Mol. Biol. 27*, 87.
(21) *Long-Range Charge Transfer in DNA I*; Schuster, G. B., Ed. (2004) Springer: Heidelberg, Germany, Vol. 236.
(22) *Long-Range Charge Transfer in DNA II*; Schuster, G. B., Ed. (2004) Springer: Heidleberg, Germany, Vol. 237.
(23) Bhagwat, M., and Gerlt, J. A. (1996) 3′- and 5′-Strand Cleavage Reactions Catalyzed by the Fpg Protein from *Escherichia coli* Occur via Successive β−and δ-Elimination Mechanisms, Respectively. *Biochemistry 35*, 659−665.
(24) Armitage, B. A., Yu, C., Devadoss, C., and Schuster, G. B. (1994) Cationic Anthraquinone Derivatives as Catalytic DNA Photonucleases: Mechanisms for DNA Damage and Quinone Recycling. *J. Am. Chem. Soc. 116*, 9847−9859.
(25) Hosford, M. E., Muller, J. G., and Burrows, C. J. (2004) Spermine Participates in Oxidative Damage of Guanosine and 8-Oxoguanosine Leading to Deoxyribosoylurea Formation. *J. Am. Chem. Soc. 126*, 9540−9541.
(26) Sies, H. (1993) Singlet oxygen induced DNA damage. *Mutat. Res. 275*, 367−75.
(27) Schuster, G. B. (2000) Long-Range Charge Transfer in DNA: Transient Structural Distortions Control the Distance Dependence. *Acc. Chem. Res. 33*, 253−260.
(28) Liu, C.-S., and Schuster, G. B. (2003) Base Sequence Effects in Radical Cation Migration in Duplex DNA: Support for the Polaron-Like Hopping Model. *J. Am. Chem. Soc. 125*, 6098−6102.
(29) Henderson, P. T., Jones, D., Hampikian, G., Kan, Y., and Schuster, G. B. (1999) Long-Distance Charge Transport in Duplex DNA: The Phonon-Assisted Polaron-Like Hopping Mechanism. *Proc. Natl. Acad. Sci. U.S.A. 96*, 8353−8358.
(30) Misiaszek, M., Crean, C., Joffe, A., Geacintov, N. E., and Shafirovich, V. (2004) Oxidative DNA Damage Associated

with Combination of Guanine and Superoxide Radicals and Repair Mechanisms via Radical Trapping. *J. Biol. Chem. 279*, 32106−32115.
(31) Shui, X. Q., McFail-Isom, L., Hu, G. G., and Williams, L. D. (1998) The B-DNA dodecamer at high resolution reveals a spine of water on sodium. *Biochemistry 37*, 8341−8355.
(32) Tari, L. W., and Secco, A. S. (1995) Base-Pair Opening and Spermine Binding − B-DNA Features Displayed in the Crystal-Structure of a Gal Operon Fragment − Implications for Protein-DNA Recognition. *Nucleic Acids Res. 23*, 2065−2073.
(33) Egli, M., Tereshko, V., Teplova, M., Minasov, G., Joachimiak, A., Sanishvili, R., Weeks, C. M., Miller, R., Maier, M. A., An, H. Y., and Cook, P. D. (1998) Manoharan, M. X-ray crystallographic analysis of the hydration of A- and B-form DNA at atomic resolution. *Biopolymers 48*, 234−252.
(34) Schmid, N., and Behr, J. P. (1991) Location of Spermine and Other Polyamines on DNA as Revealed by Photoaffinity Cleavage with Polyaminobenzenediazonium Salts. *Biochemistry 30*, 4357−4361.
(35) Feuerstein, B. G., Pattabiraman, N., and Marton, L. J. (1990) Molecular Mechanics of the Interactions of Spermine with DNA − DNA Bending as a Result of Ligand-Binding. *Nucleic Acids Res. 18*, 1271−1282.
(36) Feuerstein, B. G., Pattabiraman, N., and Marton, L. J. (1986) Spermine DNA Interactions − a Theoretical-Study. *Proc. Natl Acad. Sci. U.S.A. 83*, 5948−5952.
(37) Zakrzewska, K., and Pullman, B. (1986) Spermine Nucleic-Acid Interactions − a Theoretical-Study. *Biopolymers 25*, 375−392.

BC0500185

Delivery of Antisense Oligonucleotides Using Cholesterol-Modified Sense Dendrimers and Cationic Lipids

Patrick Chaltin,[†] Anca Margineanu,[‡] Damien Marchand,[†] Arthur Van Aerschot,[†] Jef Rozenski,[†] Frans De Schryver,[‡] Andreas Herrmann,[∥] Klaus Müllen,[∥] Rudolph Juliano,[§] Michael H. Fisher,[§] Hyunmin Kang,[§] Steven De Feyter,[‡] and Piet Herdewijn[†,*]

Laboratory for Medicinal Chemistry, Rega Institute, Catholic University of Leuven, Minderbroedersstraat 10, B-3000 Leuven, Belgium, Laboratory of Photochemistry and Spectroscopy, Catholic University of Leuven, Celestijnenlaan 200F, B-3000 Leuven, Belgium, Department of Pharmacology, University of North Carolina School of Medicine, 1106 Mary Ellen Jones Building Campus Box 7365, Chapel Hill, North Carolina 27599-7365, and Max-Planck-Institut für Polymerforschung, Ackermannweg 10, D-55021 Mainz, Germany. Received January 28, 2005; Revised Manuscript Received April 15, 2005

Cholesterol modified mono-, di-, and tetrameric oligonucleotides were synthesized and hybridized with antisense oligonucleotides to study their incorporation in cationic liposomes together with the influence of this dendrimeric delivery system on biological activity. Electrostatic interactions seem to play the most important role during complexation with cationic lipids. This oligonucleotide formulation gives a small but significant increase in the inhibition of P-glycoprotein expression in a cellular system.

INTRODUCTION

Antisense oligonucleotides are very powerful tools for inhibition of gene expression (*1*). The initial hurdles of enzymatic instability and poor hybridization strength of natural antisense oligonucleotides have been largely overcome by introducing chemical modifications. Delivery of oligonucleotides to target cells in vivo, however, is the major bottleneck for the widespread use of antisense oligonucleotides in therapy (*2*).

One of the potential solutions for this delivery problem is the use of liposomes (*3*). The antisense oligonucleotide (negatively charged due to the ionization of the phosphate backbone) interacts electrostatically with the cationic phospholipids forming the vesicles and is delivered to the cell by endocytosis. However, the number of oligonucleotides trapped into one complex is low. The delivery process can be improved by conjugation of the antisense oligonucleotide with cholesterol (*4*) or by the use of cholesterol for liposome formulations (*5*). A disadvantage of the first approach is that the cholesterol moiety is covalently attached to the oligonucleotide which influences the intracellular distribution of the antisense oligonucleotide.

Despite the efforts that have been made to characterize the formation of DNA-cationic liposome complexes (lipoplexes), the process is not yet completely understood. This is because multiple factors can influence their formation, such as the ratio between the number of negative charges in DNA and that of the positive charges in liposomes, the fluidity of the lipid bilayer, and the formation of lipid domains after DNA binding (*6*). Furthermore, the size instability was correlated with high transfection efficiency in vivo (*7*). The current view about the organization of lipoplexes comes from electron microscopy and X-ray diffraction studies (*8*, *9*). According to these, lipoplexes have a multilamellar structure with repeat distances equivalent to the thickness of a lipid bilayer and a single DNA double helix.

Here we investigated the approach of derivatization of an enzymatic labile sense−DNA with cholesterol and delivering the enzymatic stable antisense oligonucleotide as hybrid with this cholesterol−sense−DNA. As well as monomers, dimers and tetramers of sense−DNA were synthesized (Figure 1). Cationic lipids are used for the liposome formulation. This approach has the advantage that the enzymatic stable antisense oligonucleotide itself is not derivatized (i.e. its intracellular distribution and hybridization with its target is not influenced by a reporter group). The cholesterol-modified sense−DNA may stay locked in the endosomes and may be slowly degraded while the enzymatically more stable antisense oligonucleotide can diffuse into the cytoplasm and/or the nucleus (*10*). The synthesis was tested using an 11-mer as well as an 18-mer sense−DNA. For biological activity determination, we selected the 18-mer, as this length seems to be optimal for this purpose (*10*). The antisense oligonucleotide that is used as a model is a phosphorothioate 20 gapmer consisting of 2′-methyloxyethyl (2′-MOE) nucleotides in the flanks and phosphorothioate DNA in the middle (5′-CCAUCCcgacctcgCGCUCC-3′). The phosphorothioate DNA gap of eight nucleotides allows RNaseH to play a role in the mode of action of the antisense oligonucleotide. The phosphorothioate 2′-MOE flanks render the oligonucleotide stable against enzymatic degradation. This sequence has been demonstrated to inhibit P-glycoprotein expression in a cellular system (*11*).

* To whom correspondence should be addressed. Fax: +32 16 337341. Tel.: +32 16 337387. Piet.Herdewijn@rega.kuleuven.ac.be.

[†] Laboratory for Medicinal Chemistry, Rega Institute, Catholic University of Leuven.

[‡] Laboratory of Photochemistry and Spectroscopy, Catholic University of Leuven.

[§] University of North Carolina School of Medicine.

[∥] Max-Planck-Institut für Polymerforschung.

10.1021/bc050022g CCC: $30.25 © 2005 American Chemical Society
Published on Web 06/23/2005

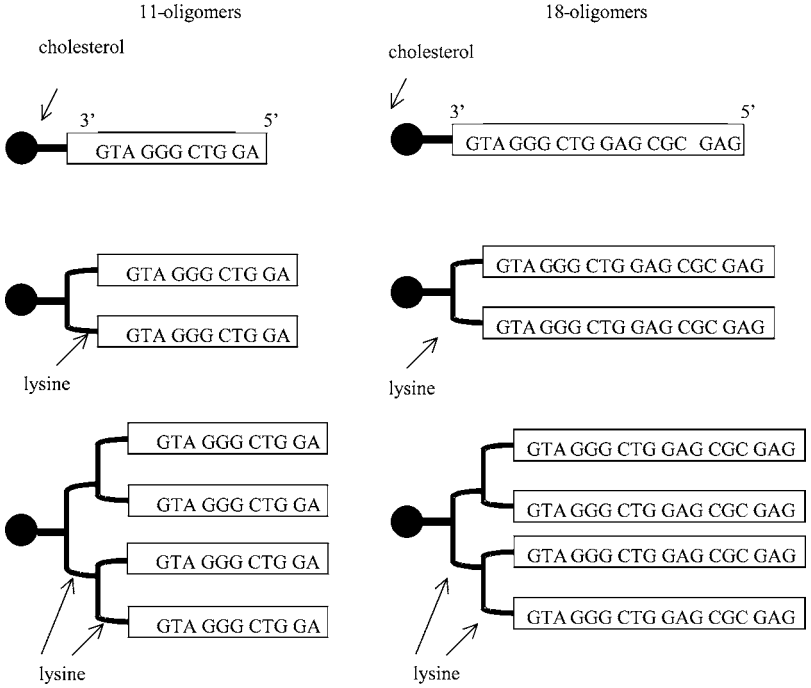

Figure 1. Schematic representation of monomeric and dendrimeric oligonucleotides (DNA) that were used to concentrate antisense oligonucleotides in cationic lipids for cellular delivery (as well, 11-mer as 18-mer oligonucleotides were evaluated as complexing agents for the antisense oligonucleotides).

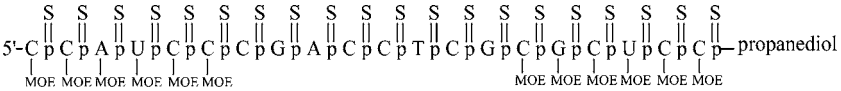

Figure 2. Structure of antisense oligonucleotide directed at mRNA that codes for the P-glycoprotein.

EXPERIMENTAL PROCEDURES

Chemistry. ^{1}H and ^{13}C NMR spectra were recorded at 200 MHz with a Varian Gemini 200 in $CDCl_3$. ^{13}C assignments were based on the usual shift increments and calculus values and where necessary confirmed by APT experiments. Assignments of quaternary carbons of the aromatic rings were based on comparison with other compounds and were mostly tentative. Electron impact mass spectra in positive (EI+) and negative ion mode (EI−) were acquired on a Kratos MS50TC mass spectrometer (Kratos, Manchester, UK), using MASPEC II data acquisition software (Mass Spectrometry Services Ltd., Manchester, UK). Electrospray ionization mass spectra in negative ion mode (ESI−) were recorded on a quadruple orthogonal acceleration/time-of-flight mass spectrometer (Q-TOf-2, Micromass, Manchester, UK). Absorption spectra were recorded with a Perkin-Elmer Lambda 40 spectrophotometer (Wellesley, MA) and fluorescence spectra with a Spex Fluorolog 3−22 fluorimeter (Jobin Yvon-Spex Instruments S. A., Inc., Edison, NJ). Precoated Machery-Nagel Alugram SilG/UV 254 plates were used for TLC, and spots were examined with UV light and a sulfuric acid/anisaldehyde spray. Column chromatography was performed on Acros silica gel (60−200 nm). Anhydrous solvents were obtained as follows: THF was refluxed on $LiAlH_4$ overnight and was distilled; dichloromethane (DCM) was stored on calcium hydride, refluxed, and distilled; pyridine, triethylamine (TEA), and *N*,*N*-diisopropylethylamine (DIEA) were refluxed overnight on potassium hydroxide and distilled. *N*,*N*-Dimethylformamide (DMF) was stored on activated molecular sieves (4 Å) for 3 days and was tested for absence of dimethylamine by the bromophenol test prior to use. DCM, DMF, acetic anhydride (Ac_2O), and pyridine were obtained from BDH (Poole, England). Piperidine, trifluoroacetic acid (TFA), diisopropylcarbodiimide (DIC), 1-hydroxybenzotriazole (HOBt), 1-methylimidazole (NMI), di-*tert*-butyl dicarbonate [$(Boc)_2O$], benzyl chloroformate, 9-fluorenylmethyloxycarbonyl chloride (FmocCl), 1,8-diazabicyclo[5.4.0]undec-7-ene (DBU), and *N*-methylmorpholine were supplied by ACROS (Geel, Belgium). 1-Hydroxy-7-azabenzotriazole (HOAt) and its tetramethyluronium derivative (HATU) were purchased from Perspective Biosystems. [2-(1*H*-bentotriazole-1-yl)-1,1,3,3-tetramethyluronium hexafluorophosphate] (HBTU) from Advanced Chemtech. Benzotriazol-1-yloxytrispyrrolidinophosphonium hexafluorophosphate (PyBOP) was obtained from Advanced Chemtech. Diethyl azodicarboxylate (DEAD) and sodium hydride (NaH) were purchased from Sigma-Aldrich. *p*-[(*R*,*S*)-α-[1-(9*H*-fluoren-9-yl)methoxyformamido]-2,4-dimethoxybenzyl]phenoxyacetic acid (Fmoc-Rink linker) was supplied by Novabiochem. Lipofectamine 2000 was obtained from Invitrogen. PBS buffer (pH7.4) was obtained from Sigma. Oligonucleotide assembly was performed on an Expedite DNA synthesizer (Applied Biosystems) using phosphoramidites from Glen Research.

The 11 and the 18 oligonucleotide sense sequences without cholesterol, as well as the tetramethyl rhodamine (TMR)-labeled oligonucleotide antisense sequence, complementary to the gene encoding the P-glycoprotein (*11*), were obtained from Invitrogen. The phosphorothioate oligonucleotide from Figure 2 is a gift from ISIS.

Cholesterylacetaldehyde Diethylacetal (2). To a solution of cholesterol (5 g, 12.9 mmol, 1 equiv) in a mixture of anhydrous THF/DMF (1:1, 200 mL) were added NaH (3.2 g, 77.6 mmol, 6 equiv) and, after 5 min, bromoacetaldehyde diethylacetal (6.3 mL, 38.8 mmol, 3

equiv) under anhydrous conditions. A nitrogen-flushed reflux condensor was attached, and the mixture was heated at reflux for 18 h. The excess NaH was decomposed using MeOH/CH_2Cl_2 and mild shaking After evaporation to dryness, silica gel-based chromatographic purification was performed with a stepwise gradient of a hexane/EtOAc mixture (98:2 to 95:5) as eluent, yielding 4.3 g (8.56 mmol, 66.3%) of the title compound. ^{13}C NMR: δ = 140.97 (C-3), 121.58 (C-4), 101.46 (β-CH), 79.73 (C-1), 68.77 (α-CH_2), 62.09 (Et, CH_2O), 56.72 (C-7), 56.12 (C-10), 50.11 (C-14), 42.25 (C-11), 39.73; 39.45; 38.97 (C-2; C-12; C-24), 37.15 (C-16), 36.78 (C-15), 36.12 (C-22), 35.72 (C-20), 31.84 (C-5, C-6), 28.26; 28.13; 27.92 (C-17; C-9; C-25), 24.19; 23.73 (C-8; C-23), 22.73; 22.46 (C-26; C-27), 20.97 (C-13), 19.27 (C-18), 18.60 (C-21), 15.27 (Et, CH_3), 11.75 (C-19). Mass calcd for $[M + Cl]^-$ $C_{33}H_{58}O_3Cl_1$: 537.4074, found: (ESI−): 537.4094.

Cholesterylacetaldehyde (3). To a solution of **2** (4.1 g, 8.17 mmol) in CH_2Cl_2 (80 mL) was added 20 mL of TFA/H_2O (1:1), and the reaction mixture was stirred for 4.5 h at room temperature (complete conversion). NaOH (1 N) was used to neutralize the solution, and subsequently an extraction with CH_2Cl_2 was performed. The organic layer was dried over anhydrous $MgSO_4$, filtered, and evaporated in vacuo to dryness, yielding 3.45 g (8.07 mmol, 98%) of the title compound. ^{13}C NMR: δ = 201.70 (β-CH), 140.30 (C-3), 122.22 (C-4), 80.37 (C-1), 73.81 (α-CH_2), 56.69 (C-7), 56.12 (C-10), 50.08 (C-14), 42.25 (C-11), 39.70; 39.42; 38.76 (C-2; C-12; C-24), 36.97 (C-16), 36.72 (C-15), 36.12 (C-22), 35.69 (C-20), 31.81 (C-5, C-6), 28.10; 27.92 (C-17; C-9; C-25), 24.19; 23.73 (C-8; C-23), 22.70; 22.46 (C-26; C-27), 20.97 (C-13), 19.24 (C-18), 18.60 (C-21), 11.75 (C-19). Mass calcd for $[M]^+$ $C_{29}H_{48}O_2$: 428.3654, found (EI+): 428.3647.

Cholesterylacetic Acid (4). Compound **3** (3 g, 7.0 mmol) was dissolved in acetone (105 mL), and 1.5 mL Jones reagent (26.72 g CrO_3/23 mL concentrated H_2SO_4/H_2O to 100 mL) was added dropwise while the reaction mixture was cooled on ice. If necessary (TLC), more Jones reagent was added to completely convert **3** into its carboxylic acid. After 10 min, acetone and MeOH were added, the mixture was filtered, and the remaining filtrate was evaporated to dryness. The residual solid was purified by column chromatography on silica gel by elution with hexane/EtOAc/AcOH (8:2:0.1), yielding 2.1 g (4.76 mmol; 68%) of the title compound. ^{13}C NMR: δ = 173.54 (COOH), 140.00 (C-3), 122.46 (C-4), 80.46 (C-1), 65.16 (α-CH_2), 56.69 (C-7), 56.12 (C-10), 50.05 (C-14), 42.25 (C-11), 39.67; 39.45; 38.61 (C-2; C-12; C-24), 36.90 (C-16), 36.69 (C-15), 36.12 (C-22), 35.69 (C-20), 31.78 (C-5, C-6), 28.13; 28.01; 27.92 (C-17; C-9; C-25), 24.19; 23.73 (C-8; C-23), 22.73; 22.46 (C-26; C-27), 20.97 (C-13), 19.24 (C-18), 18.60 (C-21), 11.75 (C-19). Mass calcd for $[M]^+$ $C_{29}H_{48}O_3$: 444.3603, found (EI−): 444.3606.

Nα-Fmoc-Nϵ-cholesterylacetyl-lysine-O-Me (5). Compound **4** (1.7 g, 3.7 mmol, 1 equiv) and HATU (1.35 g, 4.07 mmol, 1.1 equiv) were suspended in 85 mL of dry DMF. To this suspension was added DIEA (1.3 mL, 7.4 mmol, 2 equiv), and the resulting solution was stirred for 2 h at room temperature. To this mixture was added a solution of Fmoc-Lysine-OMe.HCl (1.7 g, 4.07 mmol, 1.1 equiv) and DIEA (1.3 mL, 7.4 mmol, 2 equiv) in 15 mL of dry DMF, and stirring was continued at room temperature for 18 h. After evaporation, the residue was dissolved in EtOAc, and the organic phase was washed with HCl (1 N), water, saturated Na_2CO_3 solution, brine, and water. The organic layer was dried over sodium sulfate, filtered, and evaporated. The remaining oil was purified by chromatography using a mixture of CH_2Cl_2/MeOH (99:1) as eluent. Evaporation of the pooled fractions yielded 2.5 g (3.1 mmol, 84%) of compound **5**. ^{13}C NMR: δ = 172.66 (Lys, COOMe), 170.41 (CONH); 156.51 (OCONH), 144.04 (Fmoc, C-10/11), 141.73 (Fmoc, C-12/13), 140.12 (Chol, C-3), 127.68 (Fmoc, C-3/6), 127.04 (Fmoc, C-2/7), 125.07 (Fmoc, C-1/8), 122.28 (Chol, C-4), 119.97 (Fmoc, C-4/5), 80.39 (Chol, C-1), 67.47 (Fmoc, CH_2O), 66.52 (Chol, α-CH_2), 56.66 (Chol, C-7), 56.08 (Chol, C-10), 52.38 (Lys, CH_3O), 51.14 (Lys, α-CH) 50.01 (Chol, C-14), 47.22 (Fmoc, C-9), 42.24 (Chol, C-11), 40.61 (Lys, ϵ-CH_2NH), 39.67; 39.45; 38.82 (Chol, C-2; C-12; C-24), 36.93 (Chol, C-16), 36.69 (Chol, C-15), 36.12 (Chol, C-22), 35.69 (Chol, C-20), 32.26 (β-CH_2(Lys)), 31.80 (Chol, C-5, C-6), 29.62 (δ-CH_2(Lys)), 28.13; 28.01; 27.92 (Chol, C-17; C-9; C-25), 24.19; 23.73 (Chol, C-8; C-23), 22.73; 22.46 (Chol, C-26; C-27), 22.34 (γ-CH_2(Lys)) 20.97 (Chol, C-13), 19.27 (Chol, C-18), 18.63 (Chol, C-21), 11.74 (Chol, C-19). Mass calcd for $[M + Cl]^-$ $C_{51}H_{72}N_2O_6Cl_1$: 843.5078, found: (ESI−): 843.5049.

Nα-Fmoc-Nϵ-cholesterylacetyl-lysine (6). The cleavage of the methyl ester was carried as described in the literature (*12*). To compound **5** (1.5 g, 1.8 mmol, 1 equiv) in 20 mL of THF at 0 °C was added 0.2 N LiOH (18 mL, 3.6 mmol, 2 equiv), and the reaction was stirred for 40 min. To the reaction mixture, 50 mL of a biphase of 0.2 N HCl/EtOAc (1:1) was added, aqueous layer was extracted three times with EtOAc, and the combined organic layers were dried over $MgSO_4$, filtered, and evaporated to dryness. The remaining product was purified by column chromatography on silica gel with a CH_2Cl_2/MeOH mixture (95:5) as eluent, yielding 1.1 g (1.4 mmol, 77%) of the title compound. ^{13}C NMR: δ = 174.78 (Lys, COOH), 171.14 (CONH); 156.51 (OCONH), 144.01 (Fmoc, C-10/11), 141.37 (Fmoc, C-12/13), 140.06 (Chol, C-3), 127.71 (Fmoc, C-3/6), 127.07 (Fmoc, C-2/7), 125.10 (Fmoc, C-1/8), 122.31 (Chol, C-4), 120.00 (Fmoc, C-4/5), 80.46 (Chol, C-1), 67.31 (Fmoc, CH_2O), 66.52 (Chol, α-CH_2), 56.63 (Chol, C-7), 56.08 (Chol, C-10), 51.47 (Lys, α-CH) 49.98 (Chol, C-14), 47.19 (Fmoc, C-9), 42.24 (Chol, C-11), 40.58 (Lys, ϵ-CH_2NH), 39.67; 39.45; 38.82 (Chol, C-2; C-12; C-24), 36.90 (Chol, C-16), 36.69 (Chol, C-15), 36.12 (Chol, C-22), 35.72 (Chol, C-20), 32.26 (β-CH_2(Lys)), 31.80 (Chol, C-5, C-6), 29.62, 29.19 (δ-CH_2(Lys)), 28.16; 28.01; 27.92 (Chol, C-17; C-9; C-25), 24.19; 23.76 (Chol, C-8; C-23), 22.73; 22.46 (Chol, C-26; C-27), 22.34 (γ-CH_2-(Lys)), 20.97 (Chol, C-13), 19.24 (Chol, C-18), 18.63 (Chol, C-21), 11.74 (Chol, C-19). Mass calcd for $[M-H]^-$ $C_{50}H_{69}N_2O_6$: 793.5155, found: (ESI−): 793.5143.

Solid-Phase Synthesis. Peptide Synthesis. Synthesis of the conjugates was performed on the LCAA-CPG carrier. For each amino acid or compound to be coupled, different reaction conditions were applied. After every reaction, the solution was filtered and the beads were washed with DMF (two times), CH_2Cl_2 (2 times), and acetonitrile (two times). The beads were dried, and Fmoc- or MMTr- substitution levels were determined. Hereto, an accurately measured quantity of resin was suspended in exactly 25 mL of 20% piperidine in DMF or in a $HClO_4$/EtOH mixture (3:2), respectively. After 15 min the absorbance was measured at 300 nm for fulvene (or adduct) determination and at 475 nm for methoxytrityl cation detection (ϵ_{Fmoc} = 7500, ϵ_{MMTr} = 55000). If the coupling yields were unsatisfactory, a second coupling reaction was performed. Before each new coupling, the remaining amino groups were capped using 1.5 mL of 20% acetic anhydride in THF and 1.5 mL of 20% 1-methylimidazole and 40% 2,4,6-trimethylpyridine in THF for 15 min, and washed with acetonitrile and DMF. Fmoc-deprotection was carried out with a piperidine/

DMF mixture (2:8 v:v, 2 mL) for 5 min and washing for 15 min, while for MMTr-deprotection, 3% TCA in CH_2Cl_2 was used 3 to 4 times for 3 min, until no yellow color was detectable.

Coupling of Fmoc-sarcosine to LCAA-CPG was generally performed as described in the literature (*13*). To a solution of Fmoc-sarcosine (116 mg, 0.37 mmol, 4 equiv), HOBt (31 mg, 2.23 mmol, 2.5 equiv), and HBTU (88 mg, 0.23 mmol, 2.5 equiv) in 2 mL DMF was added DIEA (78 μL, 0.46 mmol, 5 equiv), and the mixture was shaken for 5 min. More DIEA (78 μL, 0.46 mmol, 5 equiv) was added, and the solution was then poured onto LCAA-CPG beads (1 g, 92 μmol, 1 equiv). The reaction mixture was occasionally shaken for 2 h. Coupling of MMTr-butyric acid was obtained by adding a solution of 4-OMMTr-butyric acid (*14*) (220 mg, 0.46 mmol, 5 equiv), HOBT/HBTU (88 mg, 0.23 mmol, 2.5 equiv), and DIEA (158 μL, 0.92 mmol, 10 equiv) in 2 mL of DMF. Following deprotection of MMTr, Fmoc-glycine was coupled to the 4-OH group of 4-OH-butyric acid by occasionally swirling the beads with a reaction mixture of Fmoc-glycine (273 mg, 0.92 mmol, 10 equiv), DIC (72 μL, 0.46 mmol, 5 equiv), and DMAP (17 mg, 13.8 μmol, 0.15 equiv) in DMF (2 mL).

The cholesterylacetamide **6** was attached to glycine by using a solution of **6** (0.29 mg, 0.37 mmol, 4 equiv), HBTU (140 mg, 0.37 mmol, 4 equiv), HOBt (49 mg, 0.37 mmol, 4 equiv), and DIEA (168 μL, 0.92 mmol, 10 equiv) in 1 mL of DMF. The mixture was shaken for 5 min before it was added to the Fmoc-deprotected support (yield: 90%).

For single oligonucleotide loading, 4-O-MMTr-butyric acid was coupled as a linker before starting oligonucleotide synthesis. For the branching-off purposes, Nα-Fmoc-Nϵ-Fmoc-lysine (4 equiv) was used. The protected lysine was attached to the support by adding a solution of HBTU (4 equiv), HOBt (4 equiv), and DIEA (10 equiv) in DMF. Subsequently, 4-O-MMTr-butyric acid was coupled. The amount of 4-O-MMTr-butyric acid used was always 4 times the amount of free NH_2 groups available for coupling.

Oligonucleotide Synthesis. Four different supports were used for assembly of the undeca- and octadecamers. The number of hydroxyl groups per gram of support was determined by detritylation and amounted to 48, 80, and 130 μmol/g for the supports **9**, **11**, **13**, respectively. The assembly of oligonucleotides was done on the Expedite following a standard 1 μmol protocol, using only 0.5 μmol of support and a 4 min coupling time. Following deprotection with AMA (methylamine−ammonia 1:1) for 2 h at 25 °C, the products were purified by gel filtration using 30% aqueous acetonitrile to avoid adsorption of the cholesteryl moieties to the support. Depending whether a single, double, or four chains of oligonucleotides needed to be coupled to the cholesterol moiety, one of the different supports **9**, **11**, **13** were used. The conjugates could be purified by RP-HPLC on PLRP−S (100 Å, 8 μM, 250 × 7 mm, Polymer Laboratories) with a CH_3CN gradient in 0.05 M ammonium acetate, pH 7.0. In general, in ascending order, tetrameric oligo-containing dendrimer eluted before the trimer, dimer, and monomer species. Analysis was accomplished by HPLC/MS on a capillary chromatograph (CapLC, Waters, Milford, CA). Columns of 150 mm × 0.3 mm length (LCPackings, San Francisco, CA) were used. Oligonucleotides were eluted with a triethylammonium-1,1,1,3,3,3-hexafluoro-2-propanol:acetonitrile solvent system, and the flow rate was 5 μL/min. Electrospray spectra were acquired on a quadrupole orthogonal acceleration/time-of-flight mass spectrometer (Q-Tof-2, Micromass, Manchester, U.K.) in negative ion mode. The scan time used was 2 s. The combined spectra from a chromatographic peak were deconvoluted using the MaxEnt algorithm of the software Masslynx 3.4 (Micromass). Theoretical oligonucleotide masses were calculated using the monoisotopic element masses for masses up to 8000 and using the average element masses for masses above 8000. The data are given in Table 1.

Table 1. Results of Mass Spectrometry Analysis of the Monomeric (10), Dimeric (12), and Tetrameric (14) Constructs

	a series		b series	
	calcd	found[c]	calcd	found[c]
monomer	6433.4[a]	6432.8	4226.1[a]	4225.8
dimer	12358.4[b]	12356.4	7937.8[a]	7937.2
tetramer	24202.6[b]	ND[d]	15368.9[b]	15367.0

[a] Monoisotopic mass. [b] Average mass. [c] Mass obtained after deconvolution of the electrospray spectrum. [d] ND: not determined.

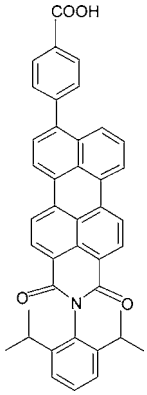

Figure 3. Structure of the perylene monoimide derivative used as a membrane probe.

Fluorescence Resonance Energy Transfer (FRET) Measurements. Lipofectamine 2000 was diluted in PBS (phosphate buffer saline, pH = 7.4) (Sigma) and was labeled with a perylene monoimide derivative (PMI-COOH) (Figure 3) in an approximate ratio of 1 fluorescent molecule for 250 lipid molecules. Hybridization between the antisense oligonucleotide labeled with TMR and the DNA with or without cholesterol was performed by heating appropriate amounts in PBS at 80° for 3 min, followed by cooling at room temperature for 15 min. Hybridized DNA was added in increasing concentrations to the Lipofectamine suspension. The fluorescence energy transfer between PMI-COOH and TMR was monitored by exciting the sample at 450 nm (where the direct excitation of TMR is minimal) and measuring the fluorescence quenching of PMI-COOH at the maximum emission peak (549 nm). The values were corrected for the nonlabeled DNA quenching of PMI-COOH fluorescence and for the TMR emission at 549 nm.

Cells. NIH 3T3 cells stably transfected with a plasmid containing the human *mdr1* gene (pSK1 MDR) were gift from M. M. Gottesman. The MDR-3T3 cells were grown in DMEM (Dulbecco minimal cututred media) medium containing 10% FBS (fetal bovine serum) and 60 mg/mL colchicine.

Treatment of Cells with Antisense Oligonucleotides. The experimental protocols were similar to those previously described (*11*). Briefly, MDR 3T3 cells were grown in 162 mm flasks to 95% confluency and then seeded onto six-well plates at 3×10^5/well in 10% FBS/DMEM and incubated 24 h. The cells were washed twice with PBS. Complexes between dendrimers and antisense

strand were prepared in 10 mM TRIS, 50 mM NaCI, 1 mM EDTA by heating the solutions at 80 °C and cooling to room temperature for 15 min. The complexation of the double stranded dendrimeric form of the antisense was done with Lipofectamine 2000 (Invitrogene) in OptiMEM according to standard procedure. The complexes were added to cells in 10% FBS/DMEM. The cells were incubated with complexes for 4 h. Then the cells were rinsed and further incubated for 68 h in 2% FBS/DMEM. All conditions were performed in triplicate. The P-glycoprotein percent shift is calculated from the lipofectamine 2000 control shift.

Pharmacological Effects of Antisense Treatment. Analysis of the pharmacological effects of dendrimeric delivery was based on a previously described assay (*15*) involving antisense inhibition of P-glycoprotein expression in mouse 3T3 cells stably transfected with the human *MDR1* gene. The cell surface expression of P-glycoprotein was determined by immunostaining and quantitation by flow cytometry, as described (*16*). Briefly, the MRK16 anti-P-glycoprotein antibody (Kamiya Biochemicals), which is directed against an external epitope, was employed as the primary antibody. After the incubation, the cells were washed twice in 10% FBS/PBS. The level of phycoerythrin (PE)-conjugated goat anti-mouse IgG (Sigma, St. Louis, MO was used as the second antibody) in viable cells (viability determined by light scatter) was quantitated using the Summit V3.0 software application (Cytomation Inc.) on a Becton Dickinson flow cytometer.

RESULTS AND DISCUSSION

Synthesis. For the synthesis of the monomeric, dimeric, and tetrameric cholesterol oligonucleotide conjugates, a strategy was used based on lysine chemistry. Lysine has an α- and ϵ-amino group, and binding of one lysine unit via its α carboxyl function to a solid support allows the two functional amino groups to be used for oligonucleotide synthesis.

Cholesterol (**1**) was derivatized at its C-3 hydroxyl group with a functional group that is stable against acid and base and that can be used for the formation of an amide bond (Scheme 1). Reaction of cholesterol with chloroacetic acid in the presence of NaH gives poor yields. Therefore, cholesterol was first reacted with the diethylacetal of bromoacetaldehyde in the presence of NaH in a mixture of THF/DMF for 18 h at 85 °C. In this way cholesterylacetaldehyde diethylacetal (**2**) was obtained in 70% yield. Reaction of **2** with Jones reagent resulted in the formation of the desired cholesterylacetic acid **4**, but the reaction went to completion only after 24 h, and multiple side products were formed. To avoid side reactions, the acetal was first hydrolyzed with trifluoroacetic acid in dichloromethane for 4 h, giving the aldehyde **3**. The oxidation of the aldehyde to the carboxylic acid with Jones reagent was completed after 10 min, giving a clean reaction product. The oxidation using hypochlorite was less effective.

Subsequently, Fmoc-Lysine-OMe was coupled with its free ϵ-NH_2-group to cholesteryl acetic acid using HATU, DIEA, and TEA (Scheme 1). Compound **5** was then deprotected by hydrolyzing the methyl ester with 0.2 N LiOH in THF/H_2O. The carboxylic acid of **6** could then be used to couple **6** to the solid support **7**. This solid support material was obtained by derivatization of LCAA-CPG with sarcosine. Subsequently, MMTr-O-butyric acid was attached to the sarcosine and detritylated

Scheme 1. Synthesis of Cholesterol-Conjugated Lysine on Solid Support[a]

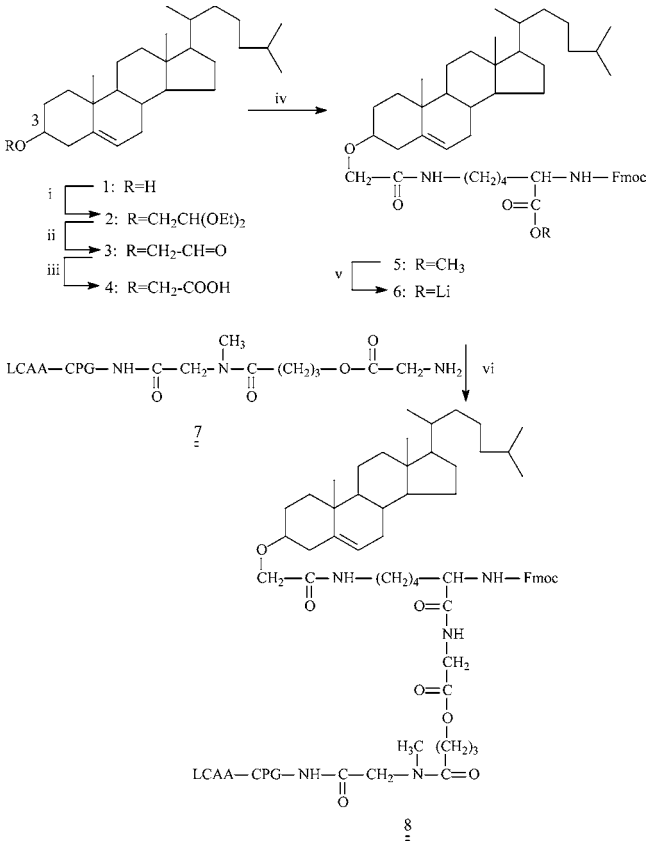

[a] i: $BrCH_2CH(OEt)_2$, NaH, DMF/THF; ii: CF_3COOH aqueous in DCM; iii: CrO_3, H_2SO_4, CH_3COCH_3, H_2O; iv: Fmoc-Lysine-OMe HCL, HATU, DIEA, DMF; v: LiOH, THF, H_2O; vi: HBTU, HOBT, DIEA, DMF.

with trifluoroacetic acid. The free hydroxyl group was used for coupling with Fmoc-glycine with formation of a base-labile ester bond. After Fmoc deprotection, compound **6** was coupled to the solid support **7** using a mixture of HBTU, HOBT, and DIEA (Scheme 1). In this way, a cholesterol-derivatized lysine connected to a solid support via an ester bond was obtained, as general support for the synthesis of the desired oligonucleotide monomers (**10a**,**b**) and dendrimers (**12a**,**b** and **14a**,**b**).

The synthesis of the cholesteryl-lysyl oligonucleotide (monomer **10a**,**b**) is shown in Scheme 2. After Fmoc deprotection of **8**, coupling of MMTr-O-butyric acid, and MMTr deprotection, the solid material **8** was used for oligonucleotide synthesis with the phosphoramidite approach. An 11-mer and 18-mer were assembled with a sequence complementary to the antisense oligonucleotide.

Deprotection using AMA reagent (concentrated aq ammonia−aq methylamine 1:1) yielded **10a**,**b**. The conjugate was concomitantly removed from the solid support by cleavage of the labile ester group with formation of the methylamide (with 5% amide formation according to MS analysis).

Branching of the peptide linker was carried out by coupling of Fmoc-protected lys-OH on deprotected **8** (Scheme 3). After a second deprotection step and binding of hydroxybutyric acid, the solid support can be used for the synthesis of two oligonucleotides on the same cholesteryl derivatized peptide (Scheme 3). Repetition of the protocol of coupling Fmoc-protected lys-OH, Fmoc deprotection, and coupling of hydroxybutyric acid might lead to an exponential branching of the cholesterol-derivatized

Scheme 2. Synthesis of Cholesterol-Modified Oligonucleotide Monomers[a]

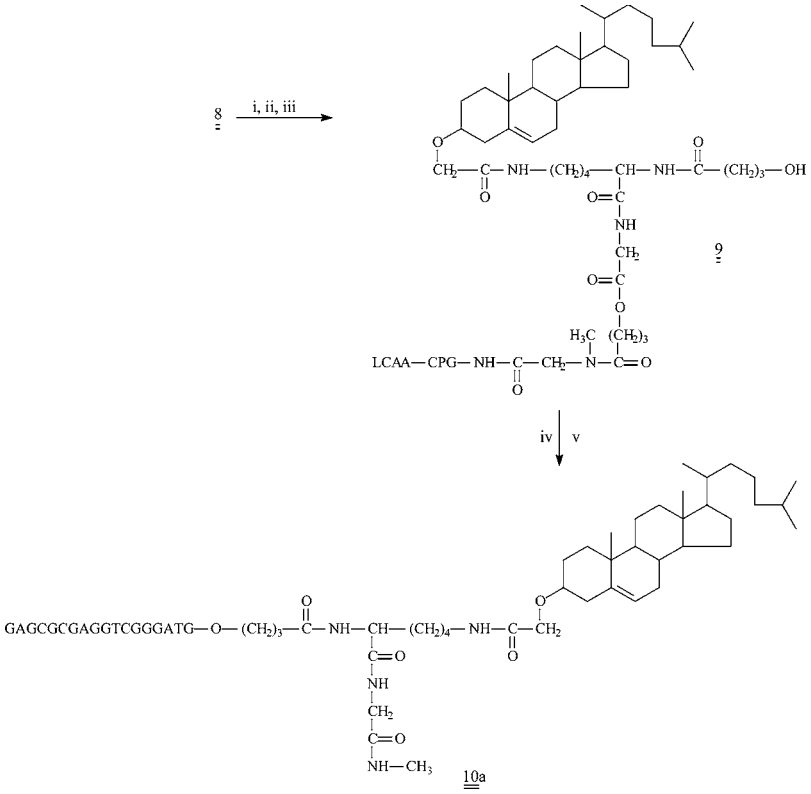

[a] i: piperidine, DMF; ii: $MMTrO(CH_2)_3COOH$, HOBt, HBTU, DIEA, DMF; iii: CCl_3COOH, DCM; iv: oligonucleotide synthesis; v: deprotection (aq. $CH_3NH_2-NH_3$) **10b**: same molecule with oligo sequence: AGGTCGGGATG-.

Scheme 3. Synthesis of Cholesterol-Modified Oligonucleotide Dimers[a]

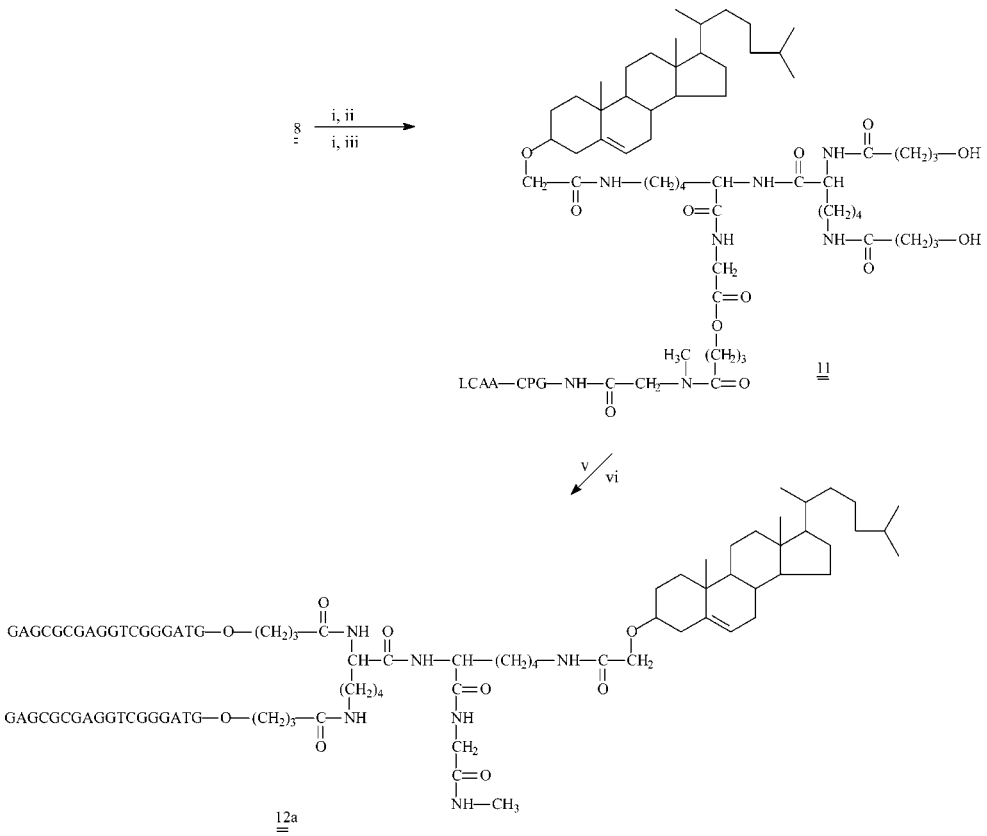

[a] i: piperidine, DMF; ii: $(Fmoc)_2$lys-OH, HBTU, HOBT, DIEA, DMF; iii: $MMTrO(CH_2)_3COOH$, HOBT, HBTU, DIEA, DMF; iv: CCl_3COOH, DCM; v: oligonucleotide synthesis; vi: deprotection (aq. $CH_3NH_2-NH_3$) **12b**: same construct with oligo sequence: AGGTCGGGATG-.

Scheme 4. Synthesis of Cholesterol-Modified Oligonucleotide Tetramers[a]

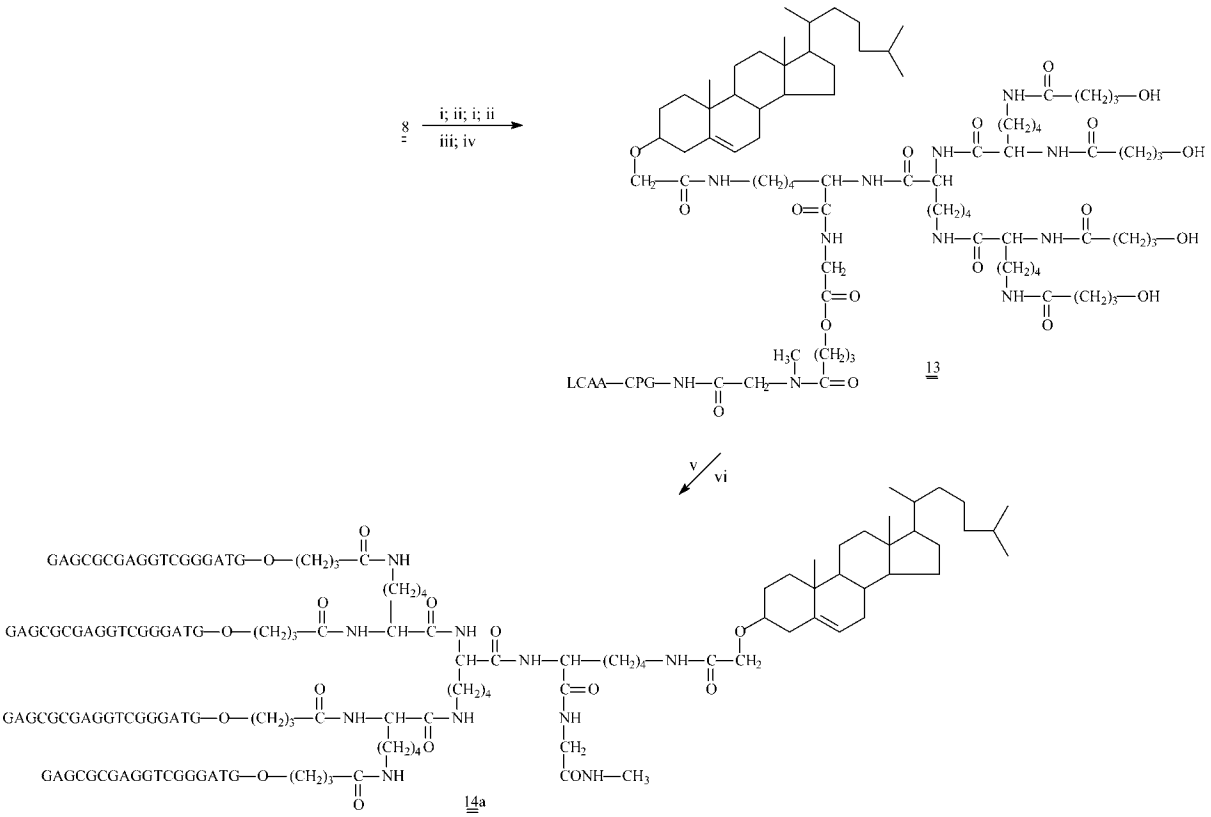

[a] i: piperidine, DMF; ii: $(Fmoc)_2$lys-OH, HBTU, HOBT, DIEA, DMF; iii: $MMTrO(CH_2)_3COOH$, HOBT/HBTU, DIEA, DMF; iv: CCl_3COOH, DCM; v: oligonucleotide synthesis; vi: deprotection procedure (aq. $CH_3NH_2-NH_3$). **14b**: same construct with oligo sequence: AGGTCGGGATG.

solid support, enabling the assembly of multiple oligonucleotides on one cholesterol moiety. This is demonstrated with the branched dendrimer **14a**,**b** in Scheme 4. However, mass spectral analysis of the major fraction shows that only three of the four hydroxybutyryl moieties are used for oligonucleotide synthesis. The HPLC sample of the trimeric compound shows only a small fraction of the four-branched dendrimer. The three-branched molecule has an acetylated lysine moiety (although it is not clear if acetylation has occurred at the α-N or the ϵ-N of lysine). Apparently, steric hindrance or the occurrence of a side reaction hampers the formation of the four-branched construct. We were able, however, to isolate sufficient amounts of the tetrameric construct by chromatographic purification to carry out biological tests.

Using these three different supports, cholesterol oligonucleotide complexes were formed in a ratio of 1:1 (**10a**,**b**), 1:2 (**12a**,**b**), and 1:4 (**14a**,**b**), and the obtained products were used for hybridization with the antisense oligonucleotide followed by cationic liposome complexation. Although it is difficult to analyze the way the antisense oligonucleotides are associated to the sense-dendrimers, the stability of the complex was determined using melting experiments. In all cases, the melting point was above 70 °C, demonstrating that stable complexes are formed.

Lipoplexes Formation Followed by FRET. The dynamics of DNA−liposomes interaction can be monitored in a FRET experiment due to the sixth power dependence of the fluorescence energy transfer efficiency to the distance between donor and acceptor. The process can thus take place on distances of a few nanometers, meaning that only the DNA bound to the surface of liposomes will contribute to the variation of the measured signal. The FRET approach was used to investigate the association between DNA and liposomes with different compositions (*17*), to follow in time the changes in lipid−DNA interaction during lipoplex formation (*18*), or to monitor the oligonucleotide release into living cells (*19*). Theoretical calculations of FRET efficiency particularly applied for the geometry of lipoplexes were also developed (*20*).

In the context of our ongoing study of perylene monoimide derivatives in biological systems, this type of fluorescent molecule has been used in these experiments for several reasons. Due to its hydrophobic rylene core, the molecule is rapidly incorporated into a lipid bilayer, while the hydrophilic carboxylic group most probably anchors the molecule at the phospholipid−water interface. This dye was chosen instead of other fluorescent probes for membranes (e.g. diphenyl hexatriene DPH or its derivatives) because of the very high fluorescence quantum yield (almost 1) and the high photostability in hydrophobic environments of the PMI chromophore (*21*), making possible the detection of fluorescence intensity variations at very low concentrations ($10^{-8}-10^{-7}$ M). The molecule is practically devoid of fluorescence in water, so the dye that was not incorporated into liposomes does not contribute to the total intensity measured (ongoing study). In addition, the carboxylic group is negatively charged at the pH used for these experiments (pH 7.4), which makes the interaction with the positively charged lipids composing the Lipofectamine more efficient when compared to an indocarbocyanine dye with two long alkyl chains (DiI-C18) (data not shown). Third, the high spectral overlap between the PMI-COOH emission and TMR absorption (Figure 4) makes this dye pair very good for FRET measurements.

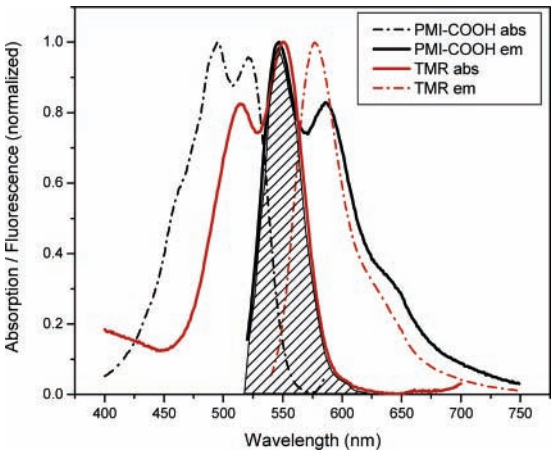

Figure 4. Absorption and emission spectra for PMI-COOH and TMR. The filled area represents the overlap between the emission spectrum of PMI-COOH and the absorption spectrum of TMR. The overlap integral calculated according to the Förster relation (*22*) is $J = 5.2 \times 10^{-13}$ cm^6 mmol^{-1} and the Förster radius is ≈60 Å.

The purpose of our experiments was to observe if cationic liposomes (Lipofectamine) are able to complex more antisense DNA hybridized with the cholesterol-modified sense sequence than the same DNA hybridized with the normal sense oligonucleotide (*10*). Lipofectamine suspension labeled with the donor (PMI-COOH) was kept at constant concentration in all experiments, while increasing acceptor concentrations (hybridized TMR−DNA) were added to the sample. Figure 5a and b show the averages and the standard deviations obtained from three independent experiments for each double strand type [naked DNA (11 DNA and 18 DNA) and cholesterol-modified monomeric (**10a**,**b**), dimeric (**12a**,**b**), and tetrameric (**14a**,**b**) DNA were evaluated]. The intensity of the donor in the presence of the acceptor (I_{DA}) was normalized to the initial intensity of the donor (I_D). Using a logarithmic scale, the first data points in each determination could be linearly fitted, and the values obtained for the slopes are given in Table 2.

As can be observed, hybridizing the 20-mer sequence with the cholesterol-modified sense 11-mer oligonucleotides (**10b**, **12b**, **14b**) shifts the slopes of the linear fitting toward higher values when compared to the unmodified sense sequence. Assuming that each TMR molecule acts as an independent acceptor even when two (**12b**) or four (**14b**) DNA oligonucleotides are linked in the same dendrimer, more donor molecules are quenched for the same DNA amount added to the system when cholesterol-modified sequences are used. Thus, the antisense oligonucleotide quantity bound to the liposomes is slightly higher in the case of cholesterol-modified sense oligonucleotides. The differences between the unmodified and the cholesterol-modified sequence are not very pronounced, but they are statistically significant. On the other hand, it seems that the number of oligonucleotides linked to the same cholesterol molecule does not influence the binding. When the 18-mer sense sequence is used for hybridization, no differences in the uptake in lipoplexes can be observed between the cholesterol-modified (**10a**, **12a**, **14a**) and the unmodified oligonucleotides. Another observation is that the slope values obtained for the 11- and 18-oligonucleotide sequence are not statistically different. Given the small length change from the 11 to the 18 sequences, we can conclude that the electrostatic interaction is the most important factor governing the formation of lipoplexes, while the much weaker hydrophobic interaction due to the presence of cholesterol may have a role in the case of short DNA sequences.

Table 2. Slopes for the Linear Fit of Data in Figure 5

DNA sequence	slope	DNA sequence	slope
11DNA	$(5.14 \pm 0.33) \times 10^6$	18DNA	$(5.68 \pm 0.54) \times 10^6$
10b	$(6.37 \pm 0.35) \times 10^6$	10a	$(5.85 \pm 0.30) \times 10^6$
12b	$(5.70 \pm 0.20) \times 10^6$	12a	$(5.94 \pm 0.42) \times 10^6$
14b	$(6.15 \pm 0.47) \times 10^6$	14a	$(5.82 \pm 0.43) \times 10^6$

The fact that we were not able to find significant differences in the liposome loading does not necessarily mean that a higher transfection efficiency in living cells cannot be obtained with the cholesterol-modified sequences. Previous studies reported a higher transfection efficiency obtained with cholesterol-modified oligonucleotides by themselves due to an increased binding to the cellular membranes (*23*, *24*). It seems thus possible that the uptake and the metabolization pathways, even when using a delivery agent, are different for the cholesterol-modified sequences when compared to the usual ones.

Biological Activity. The biological activity was determined using the 2′-MOE gapmer of phosphorothioate as the antisense strand (Table 3). The concentration was determined spectroscopically. When incubating the antisense oligonucleotide with Lipofectamine 2000, a maximum activity was obtained at 50 nM (giving 42.2% P-gp shift). Therefore, this antisense concentration was used in further experiments. When the cholesterol dendrimers

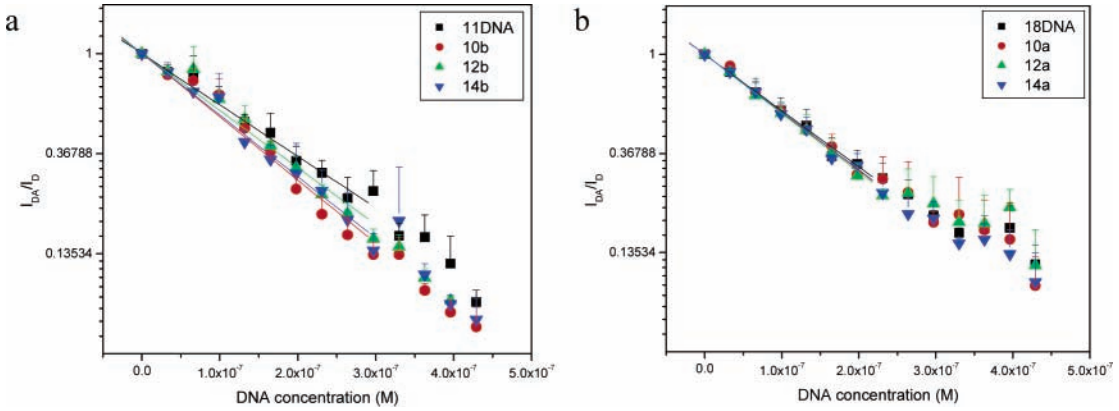

Figure 5. Quenching of PMI-COOH fluorescence (labeling Lipofectamine) using the 11 (a) and the 18 (b) oligonucleotide sequence for hybridization of the TMR-antigene sequence. The intensity of the donor in the presence of the acceptor (I_{DA}) was normalized to the initial intensity of the donor (I_D). Note that logarithmic scale was used. The first data points in each determination could be linearly fitted, and the values obtained for the slopes are given in Table 2.

Table 3. Percent Reduction of P-Glycoprotein Expression Level in Mouse 3T3 Cells by Dendrimer−Antisense Complexes[a]

	antisense alone	dimer 12a + antisense ratio 1:1	tetramer 14a + antisense ratio 1:1	dimer 12a + antisense ratio 1:2	tetramer 14a + antisense ratio 1:4
P-gp	62.8%	68.9%	70.5%	72.4%	74.0%

[a] NIH3T$_3$-MDR cells were transfected with the complexes of **12a** or **14a**, the antisense oligonucleotide, and Lipofectamine 2000. Results were obtained after 48 h incubation in 5% FBS. The ratio between **12a** or **14a** and the antisense oligonucleotide was 1:1, 1:2, and 1:4. The antisense oligonucleotide was always used at 50 nM concentration.

12a and **14a** were tested in complex with the antisense construct but without adding lipofectamine 2000, no significant effect was seen except after very long incubation time (72 h). This means that the dendrimers alone were not effective in delivering the antisense oligonucleotide. Significant effects were obtained when the dendrimers **12a** and **14a** were used in the presence of lipofectamine 2000 (Table 3). After 48 h incubation the antisense oligonucleotide gives 62.8% P-gp shift, while in the presence of the dendrimers and using 1:1, 1:2, or 1:4 molar ratios of dendrimer and antisense oligonucleotides (fixed at 50 nM), the P-gp shift varied from 68.9% to 74.0%. The effect is modest but significant. The biological activity is somewhat increased when the antisense oligonucleotides are more condensed (ratio 1:1 versus ratio 1:2 or 1:4).

CONCLUSION

Using a linker based on lysine chemistry, we were able to synthesize monomeric, dimeric, and tetrameric oligonucleotide constructs covalently linked to a cholesterol moiety. These monomeric and dendrimeric sense DNA were complexed with enzymatic stable antisense oligonucleotides targeting P-glycoprotein expression. Perylene dye was used to monitor uptake of the constructs in cationic lipids. In the case of 11-mer cholesterol-modified sense DNA, a higher amount of antisense oligonucleotide could be incorporated in the cationic liposomes than without cholesterol modification. However, this difference did not exist with the 18-mer cholesterol-modified sense DNA. Also the number of oligonucleotides linked to the same cholesterol moiety does not influence binding to the cationic lipids. In this case, electrostatic interactions seems to play the most important role during complex formations and longer sense DNA gives higher concentration of antisense DNA in the lipoplexes. The previously observed results of the better delivery of duplex oligonucleotide versus single-stranded oligonucleotides (*10*) may be partially explained by this phenomenon. However, dendrimer delivery of the antisense oligonucleotide using cholesterol-modified 18-mer sense DNA and lipofectamine resulted in a small but significant increase in biological activity. This increase in biological activity is, most probably, due to a difference in intracellular metabolism i.e., the kinetics with which the antisense oligonucleotide is delivered to its target mRNA.

ACKNOWLEDGMENT

We thank René De Boer for assistance with the mass spectrometric analysis, and Chantal Biernaux and Tom De Roeck for their excellent editorial help. Steven De Feyter is a postdoctoral fellow of the Fund for Scientific Research − Flanders. The Catholic University of Leuven (IDO/02/014) is acknowledged for financial support. Financial support from the University of North Carolina was provided by the grant P01GM59259 to R. L. Juliano. The authors thank the Federal Science Policy through IUAP-V-03, and the Institute for the promotion of innovation by Science and Technology in Flanders (IWT). Anca Margineanu gratefully acknowledges the Research Foundation of KU Leuven through GOA 2001/2.

LITERATURE CITED

(1) Scherer, L. J., and Rossi, J. J. (2003) Approaches for the sequence-specific knockdown of mRNA. *Nat. Biotechnol. 21*, 1457−1465.
(2) Shoji, Y., and Nakashima, H. (2004) Current status of delivery systems to improve target efficacy of oligonucleotides. *Curr. Pharm. Des. 10*, 785−796.
(3) Boulikas, T. (1996) Liposome DNA delivery and uptake by cells. *Oncol. Rep. 3*, 989−995.
(4) Bijsterbosch, M. K., Manoharan, M., Dorland, R., Waarlo, I. H., Biessen, E. A., and Van Berkel, T.-J. (2001) Delivery of cholesteryl-conjugated phosphorothioate oligodeoxynucleotides to Kupffer cells by lactosylated low-density lipoprotein. *Biochem. Pharmacol. 62*, 627−633.
(5) Girão de Cruz, M. T., Simões, S., Pedroso de Lima, M. C. (2004) Improving lipoplex-mediated gene transfer into C6 glioma cells and primary neurons. *Exp. Neurol. 187*, 65−75.
(6) Zuhorn, I. S., and Hoekstra, D. J. (2002) On the mechanism of cationic amphiphile-mediated transfection. To fuse or not to fuse: is that the question? *J. Membr. Biol. 189*, 167−179.
(7) Barenholz, Y. (2001) Liposome application: problems and prospects. *Curr. Opin. Colloid Interface Sci. 6*, 66−77.
(8) Simberg, D., Danino, D., Talmon, Y., Minsky, A., Ferrari, E., Wheeler, C. J., and Barenholz, Y. (2001) Phase behavior, DNA ordering, and size instability of cationic lipoplexes. Relevance to optimal transfection activity. *J. Biol. Chem. 276*, 47453−47459.
(9) Radler, J. O., Koltover, I., Salditt, T., and Safinya, C. R. (1997) Structure of DNA-cationic liposome complexes: DNA intercalation in multilamellar membranes in distinct interhelical packing regimes. *Science 275*, 810−814.
(10) Astriab-Fisher, A., Fisher, M. H., Juliano, R., and Herdewijn, P. (2004) Increased uptake of antisense oligonucleotides by delivery as double stranded complexes. *Biochem. Pharmacol. 68*, 403−407.
(11) Astriab-Fisher, A., Sergueev, D. S., Fisher, M., Shax, B. R., and Juliano, R. L. (2000) Antisense inhibition of P-glycoprotein expression using peptide−oligonucleotide conjugates. *Biochem. Pharmacol. 60*, 83−90.
(12) Qabar, M. N., Urban, J., and Kahn, M. (1997) A facile solution and solid-phase synthesis of phosphotyrosine mimetic L-4-[diethylphosphono(difluoromethyl)]-phenylalanine (F(2)-Pmp(Eto)(2)) derivatives. *Tetrahedron 53*, 11171−11178.
(13) Stetsenko, D. A., and Gait, M. (2001) A convenient solid-phase method for synthesis of 3′-conjugates of oligonucleotides. *Bioconjugate Chem. 12*, 576−586.
(14) Hovinen, J., Guzaev, A., Azhayev, A., and Lonnberg, H. (1994) Novel solid supports for the preparation of 3′-derivatized oligonucleotides: Introduction of 3′-alkylphosphate tether groups bearing amino, carboxy, carboxamido and mercapto functionalities. *Tetrahedron 50*, 7203−7218.
(15) Alahari, S. K., Dean, N. M., Fisher, M. H., Delong, R., Manoharan, M., Trivel, K. L., and Juliano, R. L. (1996) Inhibition of expression of the multidrug resistance-associated P-glycoprotein of by phosphorothioate and 5′ cholesterol-conjugated phosphorothioate antisense oligonucleotides. *Mol. Pharmacol. 50*, 508−519.
(16) Alahari, S. K., Delong, R., Fisher, M. H., Dean, N. M., Viliet, P., and Juliano, R. L. (1998) Novel chemically modified oligonucleotides provide potent inhibition of P-glycoprotein expression. *J. Pharmacol. Exp. Ther. 286*, 419−428.

(17) Wiethoff, C. M., Gill, M. L., Koe, J. G., and Middaugh, C. R. (2002) The structural organization of cationic lipid-DNA complexes. *J. Biol. Chem. 277*, 44980−44987.

(18) Zhang, Y., Garzon-Rodriguez, W., Manning, M. C., and Anchordoquy, T. J. (2003) The use of fluorescence resonance energy transfer to monitor dynamic changes of lipid-DNA interactions during lipoplex formation. *Biochim. Biophys. Acta 1614*, 182−192.

(19) Zelphati, O., and Szoka, F. C., Jr. (1996) Mechanism of oligonucleotide release from cationic liposomes. *Proc. Natl. Acad. Sci. U.S.A. 93*, 11493−11498.

(20) Madeira, C., Loura, L. M. S., Aires-Barros, M. R., Fedorov, A., and Prieto, M. (2003) Characterization of DNA/lipid complexes by fluorescence resonance energy transfer. *Biophys. J. 85*, 3106−3119.

(21) Vosch, T., Cotlet, M., Hofkens, J., Van Der Biest, K., Lor, M., Weston, K., Tinnefield, P., Sauer, M., Latterini, L., Müllen, K., and De Schrijver, F. C. (2003) Probing Förster type energy pathways in a first generation rigid dendrimer bearing two perylene imide chromophores. *J. Phys. Chem. A 107*, 6920−6931.

(22) Förster, V. T. (1949) Experimentelle und theoretische Untersuchung des zwischenmolekularen Übergangs von Elektronenanregungsenergie. *Z. Naturforsch. 4A*, 321−327.

(23) Ahn, K.-S., Ou, W., and Silver, J. (2004) Inhibition of certain strains of HIV-1 by cell surface polyanions in the form of cholesterol-labeled oligonucleotides. *Virology 330*, 50−61.

(24) Boutorine, A. S., and Kostina, E. V. (1993) Reversible covalent attachment of cholesterol to oligodeoxyribonucleotides for studies of the mechanisms of their penetration into eucaryotic cells. *Biochemie 75*, 35−41.

BC050022G

Synthesis and Bioconjugation of Diene-Modified Oligonucleotides

Rolf Tona and Robert Häner*

Department of Chemistry and Biochemistry, University of Bern, Freiestrasse 3, CH-3012 Bern, Switzerland.
Received February 1, 2005; Revised Manuscript Received June 14, 2005

The preparation of diene-modified oligonucleotides as well as their properties and further derivatization are described. Self-complementary oligonucleotides containing a diene moiety in the loop region form stable, hairpin-like secondary structures. These hairpin mimics can be further derivatized via the Diels–Alder reaction. Diene modification in the stem region leads, in contrast, to a marked destabilization of the hairpin structure. No further reduction in stability is observed, however, upon conjugation of the stem-modified derivatives via the Diels–Alder reaction with an *N*-substituted maleimide dienophile.

INTRODUCTION

The hairpin is one of the most common secondary structural motifs found in nucleic acids (*1*). In RNA, it is an essential element for the assembly of higher order structures (*2*–*5*). By enabling the proper folding, the hairpin contributes to the many functional properties of RNA. Extra stable hairpins containing four bases in the loop (tetraloops) have emerged as a distinct class of hairpins forming highly specific interactions with tetraloop receptor sites (*1*, *6*, *7*). The hairpin motif is also found in DNA, although to a much lesser extent due to the intrinsic double-stranded nature of DNA. The requirements for the formation of DNA hairpins (*8*) and cruciform structures (*9*) in palindromic DNA sequences have been investigated in detail, and the involvement of such structures in the regulation of gene expression has been discussed (*10*, *11*). Furthermore, the hairpin loop also acts as a site of specific metal coordination (*12*–*14*). The central role of the hairpin as a structural and functional element has stimulated the design and synthesis of chemically modified hairpin analogues. Hairpin mimics can serve as tools for the investigation of structure and function of nucleic acids. In addition, they are increasingly gaining importance as building blocks for the construction of defined, nucleic acid-based molecular structures (*15*). Thus, the hairpin loop has been replaced with flexible oligoethylene glycol linkers (*16*–*18*) as well as with more rigid aromatic derivatives (*19*–*23*) and metal complexes (*24*–*26*). Furthermore, the construction of a stilbene-based hairpin mimic forming G-tetrades has been reported very recently (*27*).

The Diels–Alder reaction has been used for the derivatization (*28*–*30*) and immobilization (*31*) of nucleic acids. It was shown that oligonucleotides bearing a 5′-linked diene moiety react site-specifically with dienophiles without interference of the many functional groups present in RNA (*28*) and DNA (*29*, *31*). Despite its established chemoselectivity, however, the Diels–Alder reaction has hitherto not found widespread use for the purpose of DNA modification. Recently, we communicated the successful derivatization of a hairpin mimic with various functional groups (*32*). We showed that a 1,3-butadiene building block can serve as an excellent replacement of the hairpin loop. The so obtained diene-modified hairpin was amenable to derivatization via the Diels–Alder reaction with maleimide dienophiles carrying different pendant groups. We have subsequently extended these studies to the investigation of several aspects, such as the influence of changes in the 1,3-diene building blocks as well as the effect of placement of the 1,3-diene in the stem of the hairpin. Here, we report the synthesis and properties of these modified hairpins as well as their derivatization via the Diels–Alder reaction.

EXPERIMENTAL PROCEDURES

General. Reagents were purchased from Fluka, Sigma-Aldrich, or Acros and were used without further purification. Fluoresceine-derived maleimide **7** was purchased from Vector Laboratories, Inc. Reactions were monitored by thin-layer chromatography (TLC, Machery-Nagel precoated TLC plates SIL G-25 UV_{254}) using mixtures of ethyl acetate/hexane or dichloromethane/methanol. Compounds were visualized with UV light and/or dipping in permanganese- or cerium(IV) reagent followed by heating. Common workup consisted of sequential washing of the organic extract with water and brine, followed by drying over anhydrous sodium sulfate and evaporation under reduced pressure. Column chromatography (CC) was performed on silica gel (sds, SILICE 60 A C.C 40–63 μm). For tritylated compounds, TLC plates and silica gel columns were prepared with solvents containing 0.1% triethylamine. Melting points were recorded using a Büchi 510 apparatus (open capillaries, uncorrected values). ^{1}H (300 MHz), ^{13}C (75 MHz), and ^{31}P (122 MHz) NMR were recorded on a Bruker AC 300 and fitted with 1D WINNMR, and the chemical shifts (δ/ppm) were referenced to chloroform-*d* for ^{1}H and ^{13}C NMR and to phosphoric acid for ^{31}P NMR. Mass spectra were recorded on a VG Platform single quadrupole ESI-MS, Micromass Instruments, Manchester, UK.

Preparation of DNA Oligomers. The DNA oligomers were assembled on cpg solid supports (Transgenomic, Glasgow, UK) using an ABI 392 or an ABI 394 Nucleic Acid synthesizer from Applied Biosystems using the program for a 0.2 μmol synthesis except that the coupling time for modified phosphoramidites was extended to 5 min. Standard reagents and solvents for the phosphotriester method were used. Long chain aminoalkyl controlled pore glass (LCAA-CPG) solid supports with the

* To whom correspondence should be addressed. Fax +41 31 631 8057; e-mail robert.haener@ioc.unibe.ch.

10.1021/bc050025t CCC: $30.25 © 2005 American Chemical Society
Published on Web 06/29/2005

Table 1. Summary of Molecular Weights of Modified Oligonucleotides

oligomer	calcd [g/mol][a]	found [g/mol]	Δ mass [g/mol]
6a	3291	3292	1
6b	3319	3319	0
6c	3347	3348	1
T_4	4243	4243	0
A_4	4279	4279	0
8	3817	3817	0
9	7334	7334	0
10	7916	7913	−3
11	8414	8414	0

[a] For molecular weight $-H^+$.

4,4′-dimethoxytrityl protected 3′-end nucleotide from Transgenomic (Glasgow, UK) were used. Synthesis involved repetitive cycles, each comprising (i) deprotection of the 5′-hydroxyl group by removing the 4,4′-dimethoxytrityl group with trichloroacetic acid, (ii) tetrazole activation and coupling of the following phosphoramidite, (iii) capping of nonprotected 5′-OH with acetic anhydride/1-methylimidazole, and (iv) iodine oxidation to the phosphotriester. The DNA oligomers were cleaved from the solid support using 25% aqueous ammonia hydroxide and then deprotected in the same solution at 55 °C for 15 h. After filtration through a 0.45 μm nylon syringe filter, the crude materials were purified with RP-HPLC using a LiChroCART 250-4 column from Merck (A: 0.1 M triethylammonium acetate in water, B: acetonitrile) at 40 °C. The dried oligonucleotides were desalted with Sep-Pak Cartridges (Waters) and analyzed with ESI-MS and denaturating polyacrylamide gel electrophoresis (PAGE) [Mini-PROTEAN 3 electrophoresis module (Bio-Rad Laboratories), 0.75-mm-thick 12% polyacrylamide, 1× TBE (Tris-borate-EDTA) and 10 M urea, 1× TBE as electrolyte]. Oligonucleotide concentrations were calculated from the absorbance at 260 nm with extinction coefficients calculated according to the program provided at http://paris.chem.yale.edu/extinct.html. For diene-modified and bioconjugated oligonucleotides, extinction coefficients of the respective unmodified sequences were used. Pure oligonucleotides were lyophilized and stored at −30 °C. The molecular weights of the purified oligonucleotides were determined by electrospray mass spectroscopy (see Table 1).

Bioconjugation Reactions. Diene-modified oligodeoxyribonucleotides were incubated in 10 mM sodium acetate buffer (pH 6.5) with 10 equiv of the maleimide derivatives at room temperature for 7 days. The absence of side reactions between maleimide and nucleic acid bases was monitored by MS analysis in control experiments. Fluoresceine-labeled oligodeoxyribonucleotides were purified by RP HPLC purification. The dried fractions were desalted via Sep-Pak Cartridges (Waters) and stored at −30 °C. The molecular weights of the purified conjugates were determined by electrospray mass spectroscopy (see Table 1).

Thermal Denaturation Experiments. UV melting curves were recorded on a Cary 3E UV/VIS spectrophotometer (Varian) equipped with a Cary Temperature Controller, a Sample Transport Accessory and a Multi Cell Block. Aqueous solutions of 2.5 μM oligomer, 10 mM Tris-HCl (pH 7.5), and 100 mM NaCl were used. The strands were allowed to anneal by heating at 85 °C for 1−2 min, followed by slow cooling to room temperature. The samples were heated at a rate of 0.5 °C/min, and the absorbance at 260 nm was plotted every 1 min. The percent hyperchromicity at 260 nm was plotted as a function of temperature. Melting temperatures were determined from the maximum of the first derivative of the melting curve (A_{260} against temperature); each T_m is the average of three independent experiments; exp error: ± 0.5 °C.

Molecular Modeling. The structures shown in Figure 1 were minimized using the amber force field (Hyperchem 7.0, Hypercube, Waterloo, Ontario).

General Methods. (A) Under argon, the diol (10 equiv) in absolute THF (1 mL/mmol) was added dropwise to a suspension of sodium hydride (4 equiv) in absolute THF (1 mL/mmol). After the sample was stirred for 15 h at room temperature, the dibromide, dissolved in absolute THF (1 mL/mmol), was added at room temperature and the reaction mixture was stirred for 1 h at 80 °C. The reaction mixture was then poured onto brine and extracted with EtOAc. After the sample was concentrated under reduced pressure, excess diol was evaporated under high vacuum in a kugelrohr oven (Büchi).

(B) The diol was dissolved in absolute pyridine (20 mL/mmol), and 4,4′-dimethoxytrityl chloride in absolute pyridine (0.8 equiv, 20 mL/mmol) was added dropwise over a period of about 2 h. After the sample was stirred at room temperature for 3 h, the reaction was quenched by the addition of water. The crude product was isolated by extraction with CH_2Cl_2 and concentrated using a rotary evaporator. To avoid decomposition of the product on silica gel, the column was prepared with eluent containing 0.5% triethylamine. Before addition of the crude product, the column was washed with pure eluent to remove surplus triethylamine.

(C) To a suspension of *N*,*N*-diisopropylammonium tetrazolide (2 equiv) and 2-cyanoethyl-bis(*N*,*N*-diisopropyl)amino phosphite (2 equiv) in absolute CH_2Cl_2 (5 mL/mmol), the alcohol (1 equiv) dissolved in absolute CH_2Cl_2 (10 mL/mmol) was added. After the sample was stirred at room temperature for 15 h, the reaction was quenched with saturated aqueous $NaHCO_3$ and extracted with CH_2Cl_2. To avoid decomposition of the product on silica gel, the column was prepared with eluent containing 0.5% triethylamine. Before addition of the crude product, the column was washed with pure eluent to remove surplus triethylamine.

1,6-Dibromo-hexa-2*t*,4*t*-diene (2). A solution of hexa-1,6-diene-3,4-diol (1.50 g, 13.1 mmol) in absolute diethyl ether (5 mL) was added dropwise to phosphorus tribromide (2.24 g, 9.0 mmol) in absolute diethyl ether (5 mL) at 0 °C. After the addition was complete, the mixture was allowed to warm to room temperature. After 3 h the reaction mixture was poured, slowly and under stirring, into ice−water. The mixture was carefully neutralized by the addition of saturated aqueous sodium carbonate solution. The mixture was extracted with diethyl ether and then purified by CC (EtOAc/MeOH, 19:1). The product is a strong lachrymator and should be handled in a fume hood (2.63 g, 11.4 mmol, 87%). ^{1}H NMR ($CDCl_3$) δ: 4.00 (d, 4 H, J = 7.7 Hz), 5.84−5.99 (m, 2 H), 6.21−6.31 (m, 2 H). ^{13}C NMR ($CDCl_3$) δ: 32.50, 130.86, 133.25. mp: (EtOAc) 85−87 °C.

2-[6-(2-Hydroxy-ethoxy)-hexa-2*t*,4*t*-dienyloxy]-ethanol (3a). 3a was synthesized according to general method A from **2** and ethylene glycol. The crude material was purified by CC (EtOAc/MeOH, 19:1). Yield: 24%, as a yellowish oil. ^{1}H NMR ($CDCl_3$) δ: 2.02 (s br, 2 H), 3.52−3.57 (m, 4 H), 3.73 (t, 4 H, J = 4.4 Hz), 4.05 (d, 4 H, J = 5.6 Hz), 5.71−5.80 (m, 2 H), 6.22−6.27 (m, 2 H). ^{13}C NMR ($CDCl_3$) δ: 61.92, 71.26, 77.24, 129.90, 132.03.

3-[6-(3-Hydroxy-propoxy)-hexa-2*t*,4*t*-dienyloxy]-propan-1-ol (3b). 3b was synthesized according to general method A from **2** and 1,3-propandiol. The crude

material was purified by CC (EtOAc/MeOH, 19:1). Yield: 24%, as transparent crystals. ^{1}H NMR ($CDCl_3$) δ: 1.78−1.86 (m, 4 H), 2.34 (s br, 2 H), 3.59 (t, 4 H, J = 56.0 Hz), 3.75 (t, 4 H, 6.0 Hz), 3.99 (d, 4 H, J = 6.0 Hz), 5.69−5.77 (m, 2 H), 6.16−6.26 (m, 2 H). ^{13}C NMR ($CDCl_3$) δ: 32.06, 61.95, 69.41, 71.24, 129.85, 131.88.

4-[6-(4-Hydroxy-butoxy)-hexa-2*t*,4*t*-dienyloxy]-butan-1-ol (3c). 3c was synthesized according to general method A from **2** and 1,4-butanediol. The crude material was purified by CC (EtOAc/MeOH, 19:1). Yield: 17%, as a yellowish oil. ^{1}H NMR ($CDCl_3$) δ: 1.60−1.67 (m, 8 H), 2.26 (s br, 2 H), 3.42 (t, 4 H, J = 5.9 Hz), 3.60 (t, 4 H, 3.0 Hz), 3.97 (d, 4 H, J = 5.6 Hz), 5.67−5.76 (m, 2 H), 6.15−6.25 (m, 2 H). ^{13}C NMR ($CDCl_3$) δ: 26.77, 30.11, 62.52, 70.24, 70.98, 129.83, 131.95.

2-(6-{2-[Bis-(4-methoxy-phenyl)-phenyl-methoxy]-ethoxy}-hexa-2*t*,4*t*-dienyloxy)-ethanol (4a). 4a was synthesized according to general method B from **3a** and 4,4′-dimethoxytrityl chloride. The crude product was purified by CC (EtOAc). Yield: 30%, as a transparent, viscous material. ^{1}H NMR ($CDCl_3$) δ: 1.80−1.87 (m, 4 H), 3.53−3.58 (m, 4 H), 3.76 (s, 6 H), 3.95−4.01 (m, 4 H), 4.07−4.14 (m, 2 H), 5.68−5.75 (m, 2 H), 6.18−6.23 (m, 2 H), 6.77−6.82 (m, 4 H), 7.18−7.31 (m, 7 H), 7.41 (d, 2 H, J = 7.0 Hz). ^{13}C NMR ($CDCl_3$) δ: 52.45, 54.18, 60.80, 68.70, 70.25, 84.96, 112.05, 125.64, 126.73, 127.22, 129.07, 130.25, 131.32, 135.35, 144.08, 157.38.

3-(6-{3-[Bis-(4-methoxy-phenyl)-phenyl-methoxy]-propoxy}-hexa-2*t*,4*t*-dienyloxy)-propan-1-ol (4b). 4b was synthesized according to general method B from **3b** and 4,4′-dimethoxytrityl chloride. The crude material was purified by CC (EtOAc/Hex, 2:3). Yield: 59%, as a transparent oil. ^{1}H NMR ($CDCl_3$) δ: 1.61−1.84 (m, 4 H), 1.97 (s br, 2 H), 3.08 (t, 4 H, J = 6.0 Hz), 3.48−3.56 (m, 4 H), 3.71 (s, 6 H), 3.90−3.95 (m, 4 H), 5.61−5.71 (m, 2 H), 6.10−6.20 (m, 2 H),6.72−6.77 (m, 4 H), 7.10−7.26 (m, 7 H), 7.35 (d, 2 H, J = 12 Hz). ^{13}C NMR ($CDCl_3$) δ: 30.60, 32.26, 55.33, 60.36, 62.07, 67.74, 69.45, 71.05, 71.43, 85.90, 113.12, 126.71, 127.82, 128.33, 129.62, 130.16, 130.62, 131.52, 132.25, 136.74, 145.46, 158.47.

4-(6-{4-[Bis-(4-methoxy-phenyl)-phenyl-methoxy]-butoxy}-hexa-2*t*,4*t*-dienyloxy)-butan-1-ol (4c). 4c was synthesized according to general method B from **3c** and 4,4′-dimethoxytrityl chloride. The crude material was purified by CC (EtOAc). Yield: 37%, as a beige solid. ^{1}H NMR ($CDCl_3$) δ: 1.64 (s, 8 H), 3.04 (t, 2 H, J = 5.8 Hz), 3.37 (t, 2 H, J = 6.0 Hz), 3.45 (t, 2 H, J = 5.7 Hz), 3.60−3.77 (m, 2 H), 3.77 (s, 6 H), 3.98 (dd, 4 H, J = 5.9 and 15.5 Hz), 5.68−5.77 (m, 2 H), 6.15−6.26 (m, 2 H), 6.78−6.82 (m, 4 H), 7.15−7.32 (m, 7 H), 7.41 (d, 2 H, J = 7.1 Hz). ^{13}C NMR ($CDCl_3$) δ: 26.71, 26.80, 30.25, 55.19, 62.78, 63.05, 70.22, 70.29, 70.89, 71.08, 112.95, 126.55, 127.68, 128.20, 129.54, 130.01, 130.45, 131.54, 132.15, 136.67, 145.36, 158.28.

Diisopropyl-phosphoramidous Acid 2-(6-{2-[Bis-(4-methoxy-phenyl)-phenyl-methoxy]-ethoxy}-hexa-2*t*,4*t*-dienyloxy)-ethyl Ester 2-Cyano-ethyl Ester (5a). 5a was synthesized according to general method C from **4a** and 2-cyanoethyl-bis(*N*,*N*-diisopropyl)amino phosphite. The crude material was purified by CC (EtOAc). Yield: 98%, as a transparent oil. ^{1}H NMR ($CDCl_3$) δ: 1.15−1.18 (m, 12 H), 1.54 (s, 2 H), 2.61 (t, 2 H, J = 6.4 Hz), 3.20 (t, 2 H, J = 5.1 Hz), 3.55−3.63 (m, 6 H), 3.77 (s, 6 H), 3.73−3.87 (m, 2 H), 4.06 (t, 4 H, J = 6.0 Hz), 5.71−5.78 (m, 2 H), 6.24−6.28 (m, 2 H), 6.77−6.82 (m, 4 H), 7.17−7.35 (m, 7 H), 7.45 (d, 2 H, J = 7.2 Hz). ^{13}C NMR ($CDCl_3$) δ: 20.27, 24.52, 24.59, 24.62, 24.68, 42.98, 43.14, 55.21, 58.38, 58.63, 62.53, 62.78, 63.24, 69.68, 70.00, 70.09, 71.24, 71.32, 77.44, 113.03, 126.64, 127.74, 128.21, 129.72, 130.07, 130.30, 131.44, 132.03, 136.33, 145.07, 158.37. ^{31}P NMR ($CDCl_3$) δ: 148.78. HRMS (ESI+): $C_{44}H_{60}N_2NaO_7P$: calc.: 727.3488 g/mol, found: 727.3497 g/mol.

Diisopropyl-phosphoramidous Acid 3-(6-{3-[Bis-(4-methoxy-phenyl)-phenyl-methoxy]-propoxy}-hexa-2*t*,4*t*-dienyloxy)-propyl Ester 2-Cyano-ethyl Ester (5b). 5b was synthesized according to general method C from **4b** and 2-cyanoethyl-bis(*N*,*N*-diisopropyl)amino phosphite. The crude material was purified by CC (EtOAc). Yield: 99%, as a transparent, glassy material. ^{1}H NMR ($CDCl_3$) δ: 1.09−1.19 (m, 16 H), 1.81−1.89 (m, 4 H), 2.58−2.63 (m, 2 H), 3.13 (t, 2 H, J = 6.2 Hz), 3.48−3.61 (m, 6 H), 3.71−3.85 (m, 2 H), 3.76 (s, 6 H), 3.97 (t, 2 H, J = 5.5 Hz), 5.67−5.76 (m, 2 H), 6.16−6.26 (m, 2 H), 6.77−6.83 (m, 4 H), 7.14−7.32 (m, 7 H), 7.41 (d, 2 H, J = 7.1 Hz). ^{13}C NMR ($CDCl_3$) δ: 14.06, 20.31, 20.40, 22.99, 24.52, 24.61, 24.70, 30.44, 31.47, 31.57, 42.91, 43.08, 55.19, 58.19, 58.45, 60.22, 60.43, 60.66, 66.88, 67.60, 70.98, 71.05, 85.73, 112.97, 126.58, 127.69, 128.17, 130.01, 130.15, 131.60, 131.75, 136.57, 145.32, 158.31. ^{31}P NMR ($CDCl_3$) δ: 147.72. HRMS (ESI+): $C_{42}H_{58}N_2O_7P$: calc.: 733.3981 g/mol, found: 733.3971 g/mol.

Diisopropyl-phosphoramidous acid 4-(6-{4-[bis-(4-methoxy-phenyl)-phenyl-methoxy]-butoxy}-hexa-2*t*,4*t*-dienyloxy)-butyl ester 2-cyano-ethyl ester (5c). 5c was synthesized according to general method C from **4c** and 2-cyanoethyl-bis(*N*,*N*-diisopropyl)amino phosphite. The crude material was purified by CC (EtOAc/Hex, 1:1). Yield: 97%, as a transparent oil. ^{1}H NMR ($CDCl_3$) δ: 1.14−1.17 (m, 14 H), 1.65 (t, 8 H, J = 3.0 Hz), 2.61 (t, 2 H, J = 6.4 Hz), 3.04 (t, 2 H, J = 5.8 Hz), 3.35−3.44 (m, 4 H), 3.51−3.74 (m, 4 H), 3.77 (s, 6 H), 3.96 (t, 4 H, J = 6.8 Hz), 5.68−5.77 (m, 2 H), 6.15−6.26 (m, 2H), 6.77−6.82 (m, 4 H), 7.15−7.32 (m, 7 H), 7.41 (d, 2 H, J = 12.2 Hz). ^{13}C NMR ($CDCl_3$) δ: 20.32, 20.41, 24.52, 24.60, 24.70, 26.31, 26.72, 28.02, 42.90, 43.07, 55.19, 58.17, 58.42, 63.05, 69.95, 70.26, 70.94, 77.21, 112.95, 126.55, 127.67, 128.19, 130.01, 130.09, 130.15, 131.69, 136.66, 158.29. ^{31}P NMR ($CDCl_3$) δ: 147.45. HRMS (ESI+): $C_{44}H_{62}N_2O_7P$: calc.: 761.4294 g/mol, found: 761.4283 g/mol.

RESULTS AND DISCUSSION

Synthesis of the different conjugated diene building blocks was accomplished as shown in Scheme 1. Thus, diol **1** was converted into the dibromide **2**, according to a literature procedure (*33*). Reaction with the corresponding α,ω-diols afforded the symmetrical diols **3a**−**c**, which were further transformed into the DMT-protected derivatives **4a**−**c**. Standard phosphitylation finally gave the phosphoramidites **5a**−**c**. The different phosphoramidite building blocks were subsequently used for the synthesis of the hairpin mimics **6a**−**c**, shown in Scheme 2, via automated oligonucleotide synthesis. All oligomers were purified by reverse phase HPLC and characterized by electrospray ionization time-of-flight (ESI-TOF) mass spectrometry. For comparison, the two hairpins $\mathbf{T_4}$ and $\mathbf{A_4}$, containing either four thymidine or deoxyadenosine nucleotides in the hairpin loops, were synthesized.

The stabilities of the different hairpin mimics were analyzed by thermal denaturation experiments. The denaturation curves showed a single, cooperative transition for all oligomers (data not shown). Furthermore, melting temperature (T_m) values were independent of the oligomer concentration, which indicates a unimolecular process, i.e., formation and melting of the hairpin structures. The different T_m values are summarized in Table

Scheme 1. Synthesis of Different Diene-Derived Phosphoramidite Building Blocks[a]

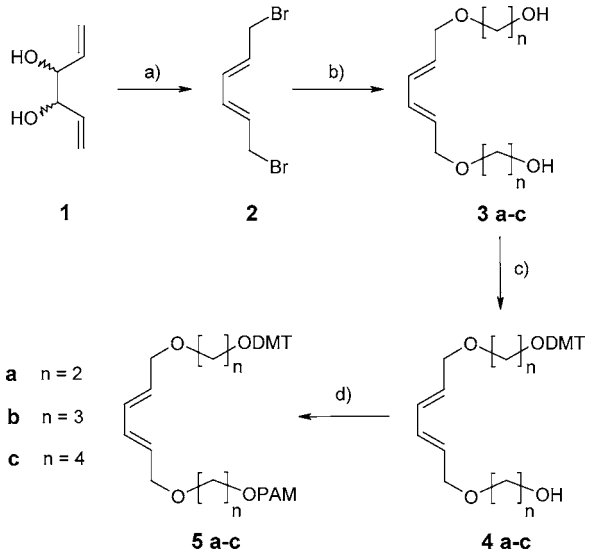

[a] Conditions: (a) PBr_3, rt (87%); (b) $NaO(CH_2)_nOH$, THF, 50 °C (30−43%); (c) 4,4′-dimethoxytrityl chloride, pyridine, rt (46%); (d) bis(*N*,*N*-di-*iso*-propylamino)-2-cyanoethylphosphoramidite, di-*iso*-propylammonium tetrazolide, CH_2Cl_2, rt (98%). PAM: 2-cyanoethyl-di-*iso*-propylaminophosphinoyl; DMT: 4,4′-dimethoxytrityl.

Scheme 2. Different Hairpin Mimics 6a−c Containing Diene Building Blocks as Loop Replacements and Their Comparative Analogues with a T_4 or A_4 Loop

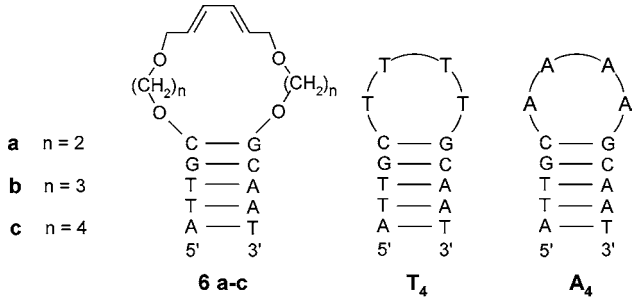

Table 2. T_m Values of Different Hairpins and Hairpin Mimics

hairpin	T_4	A_4	6a	6b	6c	8
T_m [°C][a]	57.8	56.8	63.5	66.5	65.5	67.1[c]
ΔT_m [°C][b]		−1.0	5.7	8.7	7.7	9.3

[a] Conditions: oligomer concentration 2.5 μM, 10 mM Tris-HCl, 100 mM NaCl, pH 7.5; temp gradient: 0.5 °C/min. [b] Difference in T_m relative to T_4. [c] Value taken from ref *32*.

2. All diene-modified oligomers form more stable secondary structures than the control oligonucleotides T_4 or A_4. An increase in the T_m's of 6−9 °C was observed compared to the analogous hairpin containing a T_4 loop. Somewhat surprisingly, the size of the linkers connecting the diene moiety to the hairpin stem had a relatively small influence on the structural stability. The hairpin mimics **6a** and **6c** containing building blocks with two or four methylene units in the linker arms are only 3 and 1 °C less stable than **6b**, which contains three methylene units.

Since the loop region of the hairpin is crucial for intra- and intermolecular interactions, introduction of substituents at this site is desirable. We previously showed (*32*) that introduction of substituents can be readily achieved via the Diels−Alder reaction with maleimide-derived dienophiles, such as **7** (Scheme 3). The obtained conjugate

Scheme 3. Diels−Alder Reaction of 1,3-Butadiene-Based Hairpin Mimic 6b with Maleimide 7

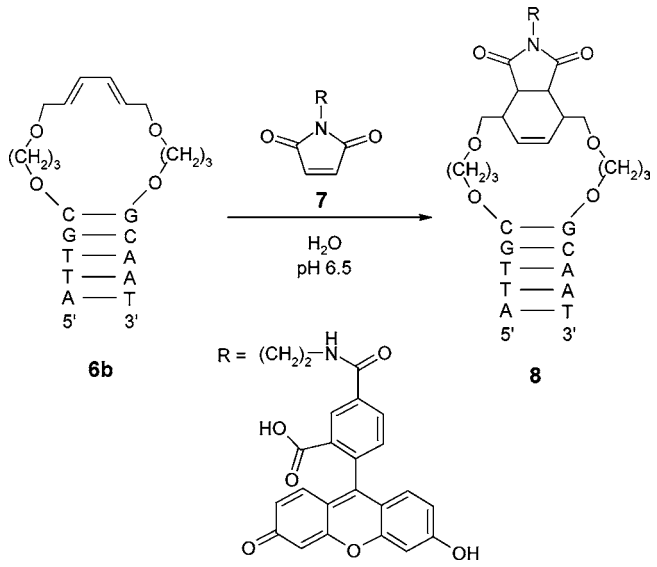

forms a stable secondary structure. Thus, a T_m value of 67.1 °C was obtained for **8** (see Table 2) (*32*). Despite its relative bulkiness, the fluoresceine substituent is well tolerated. The circular dichroism (CD) spectra of **6b** and **8** were consistent with B-form DNA structures (data not shown). On the basis of all the information obtained, we derived models of **6b** and of the fluoresceine bioconjugate **8** (Figure 1). According to amber force field calculations (Hyperchem) (*34*), both possible diene conformations of **6b** (i.e., s-cis and s-trans) form a stable hairpin-like secondary structure. Since the s-cis isomer represents the relevant conformation for the subsequent Diels−Alder reaction, the hairpin mimic is presented in this orientation (Figure 1, middle). The model shows the nonnucleotidic linker on top of the helix, bridging the two nucleic acid strands. The plane of the diene is oriented parallel to the adjacent base pair, providing the proper arrangement for reaction with dienophiles. Thermal Diels−Alder reactions proceed through a concerted syn addition, leading to a cis geometry in the cycloadduct (*35*). Furthermore, the endo pathway is usually favored by far owing to a lowering of its transition state's energy as the result of a secondary π overlap (*35*). We can, thus, assume that the formation of the endo products is preferred in our experiments. Finally, the two faces of the dienophiles used in this study are homotopic. This leaves two unique ways in which the two partners can approach each other. The two faces of the diene are rendered diastereofacial by the chiral nucleic acid. Therefore, the two diastereomeric products shown in Figure 1 can be formed. In one diastereomer, the fluoresceine substituent (green) points into the minor groove (left), and in the other diastereomer, it is oriented toward the major groove. Thus far, we could not find any evidence that one of the diastereomers is formed preferentially. Analysis and purification of the products by HPLC did not result in the resolution or separation of the possible diastereomers. Furthermore, thermal denaturation experiments with the obtained product **8** showed no evidence of two separate transitions as a result of the presence of two diastereomeric hairpins of different structural stability.

The results demonstrate that the hairpin mimics containing diene modifications in the loop region, such as **6b**, are amenable to derivatization through the Diels−Alder reaction with maleimide-derived dienophiles. At-

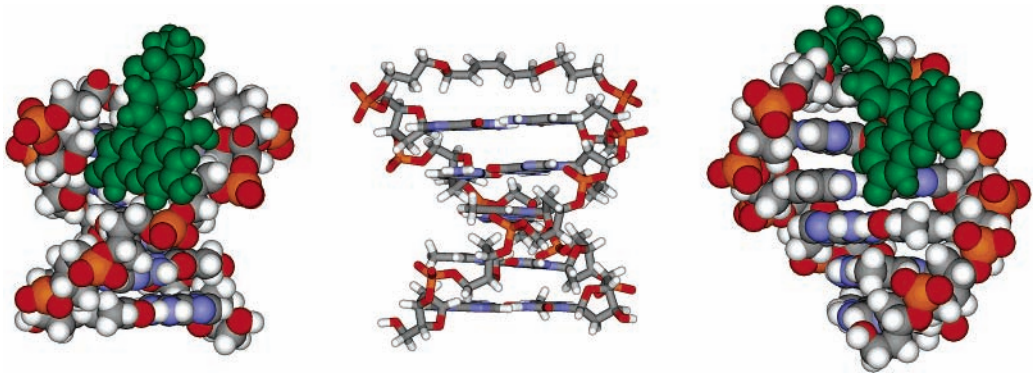

Figure 1. Optimized structures (HyperChem 7.0, amber force field) of the diene-modified hairpin mimic **6b** (middle) and the two possible diastereomeric products **8** arising from an endo Diels–Alder reaction with maleimide **7**. The two diastereomeric products have the fluorescein group (highlighted in green) pointing either into the minor groove (left) or into the major groove (right).

Scheme 4. Hairpins 10 and 11, Containing a Diene Modification or a Diels–Alder Adduct, Respectively, in the Stem[a]

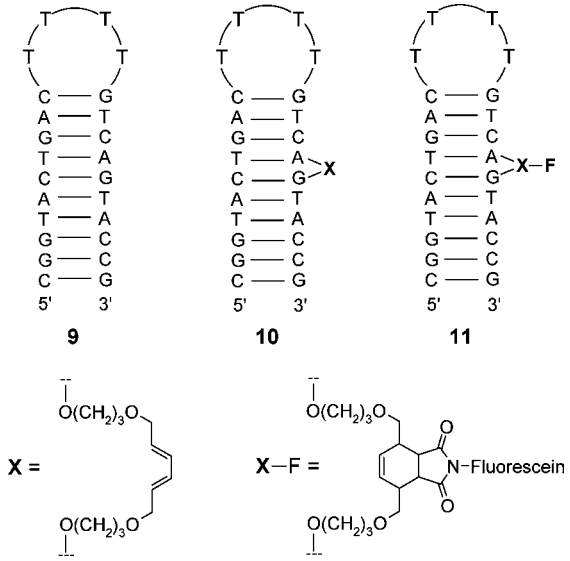

[a] For the detailed structure of the fluorescein derivative see Scheme 3.

tachment of functional or reporter groups might, however, also be desirable in the stem part of a hairpin. Therefore, we investigated whether the approach of bioconjugation via the Diels–Alder reaction might be extended to the stem region of hairpin analogues. For this purpose, a hairpin analogue containing a diene building block in the stem was prepared. Again, the diene modification with three methylene units in the linkers was selected for incorporated into the hairpin oligonucleotide, this time, however, into the stem region. The unmodified hairpin **9** and the diene-containing analogue **10** are shown in Scheme 4. Treatment of **10** with the fluoresceine-substituted maleimide **7** under the same conditions as described above resulted in the formation of the Diels–Alder adduct **11**. The thermal denaturation data are summarized in Table 3. As can be seen, addition of a diene-building block into the stem region causes a strong destabilization of 14 °C. Subsequent Diels–Alder reaction of **11**, however, does not result in a further reduction of stability. In fact, the relatively bulky fluoresceine even reduces the destabilization to some extent (+2.5 °C). Thus, bioconjugation of hairpin analogues containing a diene modification in the stem can also be achieved via the Diels–Alder reaction. The resulting product is markedly destabilized. The destabilization is, however, a consequence of the insertion of an additional, nonnucleosidic building block rather than of the conjugation of the dienophile.

Table 3. T_m Values of Hairpins Modified in the Stem Region

hairpin	**9**	**10**	**11**
T_m [°C][a]	69.0	55.0	57.5
ΔT_m [°C][b]		−14.0	−11.5

[a] Conditions: oligomer concentration 2.5 μM, 10 mM Tris-HCl, 200 mM NaCl, pH 7.5; temp gradient: 0.5 °C/min. [b] Difference in T_m relative to **9**.

In conclusion, hairpin analogues containing diene modifications in the loop or in the stem regions have been synthesized. The hairpin mimics containing the diene modification in the loop region form stable secondary structures, which are relatively insensitive to the length of the synthetic linkers. The diene moiety is amenable to derivatization with an *N*-substituted maleimide, and the resulting conjugate adopts a remarkably stable secondary structure. On the other hand, derivatization with a diene in the stem region leads to a substantial reduction in stability. Subsequent Diels–Alder reaction with an *N*-substituted maleimide, however, occurs smoothly and does not result in any further destabilization.

ACKNOWLEDGMENT

Financial support by the Swiss National Foundation (Grant 31-63380.00) is gratefully acknowledged.

LITERATURE CITED

(1) Batey, R. T., Rambo, R. P., and Doudna, J. A. (1999) Tertiary motifs in RNA structure and folding. *Angew. Chem., Int. Ed. 38*, 2326–2343.
(2) Pley, H. W., Flaherty, K. M., and McKay, D. B. (1994) Model for an RNA tertiary interaction from the structure of an intermolecular complex between a GAAA tetraloop and an RNA helix. *Nature 372*, 111–113.
(3) Gate, J. H., Gooding, A. R., Podell, E., Zhou, K. H., Golden, B. L., Szewczak, A. A., Kundrot, C. E., Cech, T. R., and Doudna, J. A. (1996) RNA tertiary structure mediation by adenosine platforms. *Science 273*, 1696–1699.
(4) Cate, J. H., Gooding, A. R., Podell, E., Zhou, K. H., Golden, B. L., Kundrot, C. E., Cech, T. R., and Doudna, J. A. (1996) Crystal structure of a group I ribozyme domain: Principles of RNA packing. *Science 273*, 1678–1685.
(5) Perbandt, M., Nolte, A., Lorenz, S., Bald, R., Betzel, C., and Erdmann, V. A. (1998) Crystal structure of domain E of Thermus flavus 5S rRNA: a helical RNA structure including a hairpin loop. *FEBS Lett. 429*, 211–215.
(6) Hermann, T., and Patel, D. J. (1999) Stitching together RNA tertiary architectures. *J. Mol. Biol. 294*, 829–849.

(7) Moore, P. B. (1999) Structural motifs in RNA. *Annu. Rev. Biochem. 68*, 287−300.
(8) Hilbers, C. W., Haasnot, C. A. G., Debruin, S. H., Joordens, J. J. M., Vandermarel, G. A., and VanBoom, J. H. (1985) Hairpin formation in synthetic oligonucleotides. *Biochimie 67*, 685−695.
(9) Murchie, A. I. H., and Lilley, D. M. J. (1992) Supercoiled DNA and cruciform structures. *Methods Enzymol. 211*, 158−180.
(10) Weaver, D. T., and Depamphilis, M. L. (1984) The role of palindromic and non-palindromic sequences in arresting DNA-synthesis in vitro and in vivo. *J. Mol. Biol. 180*, 961−986.
(11) Muller, U. R., and Fitch, W. M. (1982) Evolutionary selection for perfect hairpin structures in viral DNAs. *Nature 298*, 582−585.
(12) Mundoma, C., and Greenbaum, N. L. (2002) Sequestering of Eu(III) by a GAAA RNA tetraloop. *J. Am. Chem. Soc. 124*, 3525−3532.
(13) Greenbaum, N. L., Mundoma, C., and Peterman, D. R. (2001) Probing of metal-binding domains of RNA hairpin loops by laser-induced lanthanide(III) luminescence. *Biochemistry 40*, 1124−1134.
(14) Maderia, M., Horton, T. E., and Derose, V. J. (2000) Metal interactions with a GAAA RNA tetraloop characterized by P-31 NMR and phosphorothioate substitutions. *Biochemistry 39*, 8193−8200.
(15) Wengel, J. (2004) Nucleic acid nanotechnology − towards Angstrom-scale engineering. *Org. Biomol. Chem. 2*, 277−280.
(16) Durand, M., Chevrie, K., Chassignol, M., Thuong, N. T., and Maurizot, J. C. (1990) Circular-dichroism studies of an oligodeoxyribonucleotide containing a hairpin loop made of a hexaethylene glycol chain − conformation and stability. *Nucleic Acids Res. 18*, 6353−6359.
(17) Ma, M. Y. X., Reid, L. S., Climie, S. C., Lin, W. C., Kuperman, R., Sumnersmith, M., and Barnett, R. W. (1993) Design and synthesis of RNA miniduplexes via a synthetic linker approach. *Biochemistry 32*, 1751−1758.
(18) Pils, W., and Micura, R. (2000) Flexible nonnucleotide linkers as loop replacements in short double helical RNAs. *Nucleic Acids Res. 28*, 1859−1863.
(19) Salunkhe, M., Wu, T. F., and Letsinger, R. L. (1992) Control of folding and binding of oligonucleotides by use of a nonnucleotide linker. *J. Am. Chem. Soc. 114*, 8768−8772.
(20) Letsinger, R. L., and Wu, T. F. (1995) Use of a stilbenedicarboxamide bridge in stabilizing, monitoring and photochemically altering folded conformations of oligonucleotides. *J. Am. Chem. Soc. 117*, 7323−7328.
(21) Lewis, F. D., Kalgutkar, R. S., Wu, Y. S., Liu, X. Y., Liu, J. Q., Hayes, R. T., Miller, S. E., and Wasielewski, M. R. (2000) Driving force dependence of electron-transfer dynamics in synthetic DNA hairpins. *J. Am. Chem*. Soc. *122*, 12346−12351.
(22) Yamana, K., Yoshikawa, A., and Nakano, H. (1996) Synthesis of a new photo-isomerizable linker for connecting two oligonucleotide segments. *Tetrahedron Lett. 37*, 637−640.
(23) Stutz, A., Langenegger, S. M., and Häner, R. (2003) Phenanthrene-derived DNA hairpin mimics. *Helv. Chim. Acta 86*, 3156−3163.
(24) Lewis, F. D., Helvoigt, S. A., and Letsinger, R. L. (1999) Synthesis and spectroscopy of Ru(II)-bridged DNA hairpins. *Chem. Commun.* 327−328.
(25) Czlapinski, J. L., and Sheppard, T. L. (2004) Template-directed assembly of metallosalen-DNA hairpin conjugates. *ChemBioChem 5*, 127−129.
(26) Bianke, G., and Häner, R. (2004) A metal-coordinating DNA hairpin mimic. *ChemBioChem 5*, 1063−1068.
(27) Lewis, F. D., Wu, Y., and Zhang, L. (2004) Reversible formation of DNA G-quadruplex hairpin dimers from stilbenediether conjugates. *Chem. Commun.* 636−637.
(28) Seelig, B., and Jaschke, A. (1997) Site-specific modification of enzymatically synthesized RNA: Transcription initiation and Diels−Alder reaction. *Tetrahedron Lett. 38*, 7729−7732.
(29) Hill, K. W., Taunton-Rigby, J., Carter, J. D., Kropp, E., Vagle, K., Pieken, W., Mcgee, D. P. C., Husar, G. M., Leuck, M., Anziano, D. J., and Sebesta, D. P. (2001) Diels−Alder bioconjugation of diene-modified oligonucleotides. *J. Org. Chem. 66*, 5352−5358.
(30) Graham, D., Grondin, A., McHugh, C., Fruk, L., and Smith, W. E. (2002) Internal labeling of oligonucleotide probes by Diels−Alder cycloaddition. *Tetrahedron Lett. 43*, 4785−4788.
(31) Husar, G. M., Anziano, D. J., Leuck, M., and Sebesta, D. P. (2001) Covalent modification and surface immobilization of nucleic acids via the Diels−Alder bioconjugation method. *Nucleosides Nucleotides Nucleic Acids 20*, 559−566.
(32) Tona, R., and Häner, R. (2004) Functionalization of a diene-modified hairpin mimic via the Diels−Alder reaction. *Chem. Commun.* 1908−1909.
(33) Spangler, C. W., Mccoy, R. K., Dembek, A. A., Sapochak, L. S., and Gates, B. D. (1989) Preparation of *p*,*p*′-disubstituted-alpha, omega-diphenyl polyenes. *J. Chem. Soc., Perkin Trans. 1* 151−154.
(34) *HyperChem*, Hypercube, Inc., 1115 NW 4th Street, Gainesville, FL 32601, USA.
(35) Fleming, I. (1980) *Frontier Orbitals and Organic Chemical Reactions*, John Wiley & Sons, New York.

BC050025T

Synthesis of 6′-*O*-Lissamine-rhodamine B-Glucosamine as a Novel Probe for Fluorescence Imaging of Lysosomes in Breast Tumors

Kristine Glunde,* Catherine A. Foss, Tomoyo Takagi, Flonne Wildes, and Zaver M. Bhujwalla

JHU ICMIC Program, The Russell H. Morgan Department of Radiology and Radiological Science, Johns Hopkins University School of Medicine, Baltimore, Maryland 21205. Received February 19, 2005; Revised Manuscript Received May 17, 2005

Lysosomes contain multiple proteases, which play a crucial role in breast cancer invasion and metastasis. Noninvasive labeling of lysosomes in breast cancer cells and solid breast tumor models is therefore useful to study lysosomal trafficking and its role in invasion. We have synthesized a novel compound, 6′-*O*-lissamine-rhodamine B-glucosamine, to fluorescently label lysosomes, and evaluated the compound in human breast cancer cells in cell culture or in orthotopic human breast cancer models. We demonstrated that this novel compound biosynthetically labeled lysosomal proteins following addition to cell culture medium or following intravenous injection into mouse models of breast cancer. Fluorescence from 6′-*O*-lissamine-rhodamine B-glucosamine colocalized with several well-established lysosomal markers, such as lysosome-associated proteins 1 and 2 (LAMP-1 and -2) and CD63. We also demonstrated the feasibility of performing in vivo fluorescence imaging of 6′-*O*-lissamine-rhodamine B-glucosamine to image lysosomes in human breast cancer models.

INTRODUCTION

Lysosomes are membranous organelles of ~0.5 μm diameter, which contain several types of hydrolytic enzymes and maintain an acidic lumenal pH of ~5 (*1*). Lysosomes are the terminal degradative compartment of mammalian cells but are also involved in antigen processing (*2*), bone remodeling (*3*), the regulation of growth factors (*4*), and plasma membrane repair (*5*). Tumors with high metastatic potential, such as Lewis lung carcinoma (*6*), melanoma (*7*), and several breast cancers (*8, 9*), exhibit increased lysosomal enzyme expression and activity (*10*). Breast cancer cells can also contain intracellular large acidic vesicles (LAVs,[1] ≥ 5 μM in diameter), carrying endocytosed extracellular matrix (ECM) components (*11, 12*). Breast cancer invasion and metastasis, which is the most life-threatening aspect of malignant breast cancer, requires proteolytic enzymes to degrade ECM proteins (*13*–*15*). Cathepsins D, B, and L, which are sequestered in lysosomal vesicles (*16*), were shown to play a crucial role in cancer invasion and metastasis (*17*–*19*). Lysosomal trafficking may be an important parameter affecting lysosomal enzyme release and endocytosis of ECM proteins. Solid tumors contain hypoxic and acidic regions, which may affect lysosomal trafficking and the release of degradative enzymes by cancer cells (*20, 21*). Extracellular acidosis was shown to alter lysosomal trafficking in human breast cancer cells (*22*), which most likely facilitated lysosomal enzyme release. Effective techniques to fluorescently label lysosomes and optically image lysosomal trafficking in solid tumors are a prerequisite to study the role of lysosomes in breast cancer invasion and metastasis in tumor models.

In fixed tissues or cell specimens, lysosomes can be visualized by immunofluorescence staining using antibodies against a lysosomal protein of choice. Three well-established lysosomal marker proteins are lysosome-associated membrane proteins 1 and 2 (LAMP-1 and -2) (*23, 24*) and CD63 (*25*). LAMPs are highly abundant in lysosomal membranes and have been detected in most human tissues (*26*). Lysosomes in live cell cultures have been fluorescently labeled with substrates for lysosomal hydrolytic enzymes, such as fluorescent casein, which carry a fluorophore that is quenched before but fluoresces after cleavage (*27, 28*). Acidotropic fluorescent probes are a second class of lysosomal markers for live cell imaging, which accumulate in acidic organelles because of their matching pK_a values, e.g. neutral red (*29*), acridine orange (*30*), LysoTracker (*31*), and LysoSensor (*32*). Fluorescent probes such as fluorescent dextrans (*33*), that are endocytosed and accumulate in lysosomes, have been utilized to visualize lysosomes in live cell cultures. These techniques have limited specificity, since they label compartments based on characteristics not unique to lysosomes (*34*). We recently developed a technique to specifically label lysosomes biosynthetically in live breast cancer cell cultures using a dansylated glucosamine (*34*). This labeling technique is based on the fact that most lysosomal proteins, and particularly lysosomal membrane proteins, are highly glycosylated and frequently carry several N-linked glycans (*35*). These glycans consist of mannose, *N*-acetylglucosamine, fucose, galactose, and sialic acid moieties and are thought to protect lysosomal

* Correspondence to Kristine Glunde, Ph.D., Dept. of Radiology, Johns Hopkins University School of Medicine, 212 Traylor Bldg., 720 Rutland Ave., Baltimore, MD 21205. Tel: (410)-614-2705, Fax: (410)-614-1948, E-mail: kglunde@mri.jhu.edu.

[1] Abbreviations: 6-*O*-dansyl-GlcNH_2, 6′-*O*-dansyl-glucosamine; 6-*O*-liss-GlcNH_2, 6′-*O*-lissamine-rhodamine B-glucosamine; Boc, *tert*-butyloxycarbonyl; BODIPY, 4,4-difluoro-4-bora-3a,4a-diaza-s-indacene; d, day(s); DIC, differential interference contrast; DMAP, 4-dimethylaminopyridine; ECM, extracellular matrix; ESI, electrospray ionization; Et_3N, triethylamine; FAB, fast atom bombardment; FOV, field of view; h, hour(s); HMEC, human mammary epithelial cell; LAMP, lysosome-associated membrane protein; LAV, large acidic vesicle; LSM, laser-scanning microscopy; MeOH, methanol; NMR, nuclear magnetic resonance; SCID, severe combined immune deficient; SDS–PAGE, sodium dodecyl sulfate-polyacrylamide gel electrophoresis; TLC, thin-layer chromatography.

10.1021/bc050046n CCC: $30.25 © 2005 American Chemical Society
Published on Web 06/21/2005

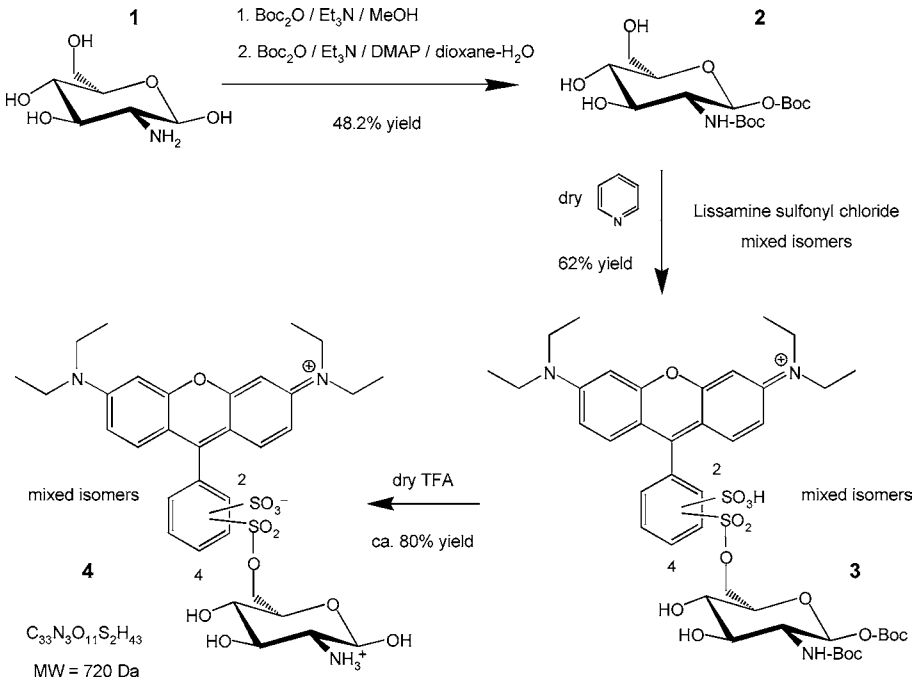

Figure 1. Schematic of the three step chemical synthesis of 6′-*O*-lissamine -rhodamine B-glucosamine (6-*O*-liss-GlcNH$_2$) (**4**).

proteins from degradation by lysosomal proteases (*36*). We previously synthesized and characterized 6-*O*-dansyl-GlcNH$_2$ (*34*), which localized to lysosomes by forming dansylated glycoproteins in live human mammary epithelial cells (HMECs) and live breast cancer cells. We demonstrated that biosynthetic labeling of lysosomes using 6-*O*-dansyl-GlcNH$_2$ is feasible for imaging lysosomes in live HMECs or breast cancer cells by confocal fluorescence microscopy (*34*).

In the present study, we synthesized and biologically characterized a novel fluorescently labeled glucosamine: 6′-*O*-lissamine-rhodamine B-glucosamine (6-*O*-liss-GlcNH$_2$) for in vivo studies in mice. This newly synthesized fluorescent compound is nontoxic and can be administered intravenously in tumor-bearing mice and subsequently localizes to lysosomes in tumors by accumulating in lysosomal proteins. The emission maximum of 6-*O*-liss-GlcNH$_2$ at 570 nm is suitable for in vivo optical imaging, since it lies within the window of low tissue absorption and autofluorescence. We assessed the uptake, relative distribution, and lysosomal localization of 6-*O*-liss-GlcNH$_2$ in MCF-7 and MDA-MB-231 breast cancer cells in cultures and in severe combined immune deficient (SCID) mice bearing MCF-7 and MDA-MB-231 tumors in the mammary fat pad.

MATERIALS AND METHODS

Cell Culture. Three human mammary epithelial cell (HMEC) lines representing different stages of malignancy were used in this study. MCF-12A, a spontaneously immortalized nonmalignant cell line established from MCF-12M mortal cells (*37*), was obtained from American Type Culture Collection (ATCC, Rockville, MD) and cultured in DMEM-Ham's F12 medium (Invitrogen Corporation, Carlsbad, CA) supplemented as described previously (*37*). MCF-7, an estrogen-positive lowly metastatic mammary epithelial cancer cell line, was obtained from ATCC (Rockville, MD) and cultured in EMEM medium (Mediatech, Inc., Herndon, VA) supplemented with 10% fetal bovine serum and antibiotics (*38*). An invasive and metastatic human mammary epithelial cell line, MDA-MB-231 was provided by Dr. R. J. Gillies (Arizona Health Sciences Center, Tuscon, AZ) and maintained in RPMI-1640 medium (Invitrogen Corporation, Carlsbad, CA) supplemented with 10% fetal bovine serum, 100 units/mL penicillin, and 100 μg/mL streptomycin (Invitrogen Corporation, Carlsbad, CA). The human breast cancer cell lines were originally isolated from pleural effusions of patients with breast cancer. All cells were kept at 37 °C in a humidified atmosphere of 5% CO_2 in air.

Tumor Model and Inoculations. MCF-7 or MDA-MB-231 cells were inoculated in the upper left thoracic mammary fat pad of five female severe combined immune deficient (SCID) mice. A quantity of 2×10^6 tumor cells was inoculated in a volume of 0.1 mL of Hanks balanced solution (HBSS, Sigma, St. Louis, MO) at a concentration of 10^6 cells/0.05 mL. An amount of 0.18 mg of 60-day release 17β-Estradiol Pellets (Innovative Research of America, Sarasota, FL) was subcutaneously implanted near the left shoulder of SCID mice inoculated with MCF-7 cells. Mice weighed between 19− 24 g, and tumor sizes ranged between 75 mm^3 and 375 mm^3 when experiments were performed. All experimental animal protocols were approved by the Institutional Animal Care and Use Committee.

Chemical Synthesis of 6′-*O*-Lissamine-rhodamine B-Glucosamine. All chemical reactions are shown in Figure 1. All reagents were purchased from Sigma unless otherwise noted and were of p.a. grade.

1-*O*-Boc, 2-*N*-Boc-β-D-glucosamine (2). Powdered sodium methoxide (500 mg, 9.98 mmol) and 6-(2-amino-2-deoxy-β-D-glucopyranosyl) ether (2.0 g, 9.28 mmol) were added to a baked 25 mL round-bottom flask along with 10 mL of dry methanol. The resulting suspension was stirred for 5 min at room temperature under argon and then filtered over scintered glass. The solid was washed with an additional 10 mL of dry methanol and transferred to a clean 25 mL round-bottom flask. Triethylamine (1.03 g, 10.2 mmol) and di-*tert*-butyl pyrocarbonate (2.23 g, 10.2 mmol) were added to the flask along with 10 mL of dry methanol, and the thick, white suspension was stirred at room temperature under argon for 10 h. Progress was monitored by silica gel thin-layer chroma-

tography (TLC) using 2-propanol/water/ammonium hydroxide (7:2:1 v/v/v) with ninhydrin (Fisher Scientific, Pittsburgh, PA) detection followed by baking. The starting material **1** displayed an R_f of 0.18. The *N*-Boc derivative displayed an R_f of 0.79. The reaction mixture was concentrated under reduced pressure and dissolved in 20 mL of dioxane/water (1:1 v/v). Triethylamine (1.03 g, 10.2 mmol), 4-(dimethylamino)pyridine (50 mg, 0.41 mmol), and di-*tert*-butyl pyrocarbonate (1.1 g, 5.1 mmol) were added, and the clear solution was stirred at room temperature under argon for 24 h. During this time, additional triethylamine (0.51 g, 5.1 mmol) and di-*tert*-butyl pyrocarbonate (1.1 g, 5.1 mmol) were added to the reaction. Progress was monitored by TLC using chloroform/ethyl acetate/methanol (5:2:1 v/v) with ninhydrin detection followed by baking. The *N*-Boc derivative displayed an R_f of 0.14, while the R_f of product **2** was 0.37. The reaction was concentrated under reduced pressure and **2** was purified by silica gel chromatography using chloroform/ethyl acetate/methanol (6:3:1 v/v) and resulted in a 48.2% yield.

6-*O*-Lissamine-rhodamine B-1-*O*-Boc,2-*N*-Boc-glucosamine (3). Dry 1-*O*-Boc,2-*N*-Boc-β-D-glucosamine (500 mg, 1.37 mmol) and Lissamine Rhodamine B sulfonyl chloride, mixed isomers (9-[4-(chlorosulfonyl)-2-sulfophenyl]-3, 6-bis(diethylamino)-xanthylium internal salt) (1 g, 1.78 mmol, Molecular Probes, Eugene, OR), were added to a baked 50 mL round-bottom flask along with dry pyridine (20 mL). The resulting purple suspension was stirred at room temperature under argon for 10 h. The reaction was quenched by addition of a piece of ice followed by removal of the pyridine under reduced pressure. Analysis of this material by TLC using methanol/methylene chloride (1:9 v/v) revealed the presence of product **3**, which exhibits an R_f of 0.6. The product was purified by silica gel chromatography using methanol/methylene chloride (2:8 v/v) to yield pure **3** at 62% yield.

6′-*O*-Lissamine-rhodamine B-glucosamine (4). Dry **3** (500 mg, 0.98 mmol) and dry trifluoroacetic acid (TFA) (10 mL) were stirred in a 50 mL round-bottom flask for 4 h at room temperature. The resulting bright red solution was then concentrated under reduced pressure to give a bright red oil. Analysis by TLC using methanol/methylene chloride (2:8 v/v) revealed the presence of **4**, which exhibits an R_f of 0.5−0.62 (mixed isomers). This oil was purified by silica gel chromatography using methanol/methylene chloride (2:8 v/v) and afforded final product **4** in 60% yield. ^{1}H NMR (500 MHz, CD_3OD): δ 8.68 (d, J = 0.91 Hz, 1H), δ 8.08 (dd, J = 7.94 Hz, 1.53 Hz, 1H), δ 7.38 (d, J = 7.94 Hz, 1H), δ 7.15 (d, J = 9.46 Hz, 2H), δ 7.01 (dd, J = 9.46 Hz, 2.44 Hz, 2H), δ 6.93 (d, J = 2.44 Hz, 2H), δ 3.67 (ddd, J = 7.33 Hz, 7.32 Hz, 7.02 Hz, 2H), δ 3.21 (ddd, J = 7.33 Hz, 7.32 Hz, 7.02 Hz, 5H), δ 1.30 (m, 20H). ^{13}C NMR (100 MHz, CD_3OD): δ 163.31 (q, J_{C-F} = 39.5 Hz), 159.87, 159.14, 157.58, 148.51, 146.48, 134.29, 133.52, 132.12, 129.02, 127.41, 115.91, 115.39, 97.41, 48.32, 47.28, 13.34, 9.71. Mass spectrum (FAB): m/z = 720 Da. Absorbance max (Beckman DU 7500) = 574 nm.

In Vitro Incubation with 6′-*O*-Lissamine-rhodamine B-Glucosamine. In cell cultures, different concentrations of 6-*O*-liss-$GlcNH_2$ (Figure 1, compound **4**) were tested in the range of 250 μM to 2 mM. A concentration of 500 μM 6-*O*-liss-$GlcNH_2$ was found to be sufficient for effective labeling. The time-course of 6-*O*-liss-$GlcNH_2$ uptake and localization to lysosomes was assessed in MCF-12A, MCF-7, and MDA-MB-231 cells grown on chamber slides. Cells were incubated for time periods of 2−96 h in cell culture medium containing 500 μM 6-*O*-liss-$GlcNH_2$. Cells were fixed with 3% paraformaldehyde as described previously (*22, 34*).

In Vivo Treatment with 6′-*O*-Lissamine-rhodamine B-Glucosamine. Female SCID mice bearing MCF-7 or MDA-MB-231 tumors were intravenously injected with 7.8 mg 6-*O*-liss-$GlcNH_2$ (7.8 mg in 0.1 mL saline, sterile filtered). At 2, 24, 48, and 72 h postinjection, tumors were optically imaged in vivo using a home-built small animal fluorescene imaging system, following which mice were sacrificed and tumor, blood, liver, kidney, and muscle tissue were harvested. Freshly cut 1-mm thick tissue sections of harvested organs and blood were placed on microscope slides (Fisher Scientific, Pittsburgh, PA), covered with CoverWell imaging chambers (Grace Bio-Labs, Bend, OR) and optically imaged using fluorescence microscopes. The remaining tumors were immediately frozen using Tissue-Tek O.C.T. Compound (Sakura Finetek U.S.A. Inc, Torrance, CA) and Tissue-Tek cryomolds (Miles Inc., Elkhart, IN) and liquid nitrogen.

In Vivo Optical Imaging of Breast Tumor Models. For in vivo imaging, the tumor region was shaved in anesthetized mice and the animal was lightly taped to minimize motion. A home-built small animal fluorescene imaging system equipped with a Mini Repro Camera Stand (Industria Fototecnica Firenze, Florence, Italy), a 300 W Gemini 300 high-intensity short arc light source with universal adaptor (Chiu Technical Corporation, Kings Park, NY), an optical fiber (Edmunds, Barrington, NJ), a filter cube containing a 510−560 nm band-pass exitation filter and a 575 nm long pass emission filter (Omega Optical, Inc., Brattleboro, VT), and a Nikon Coolpix 990 or Coolpix 5000 digital camera (Nikon, Tokyo, Japan) was used to obtain optical images of mice with tumor xenografts.

Ex Vivo Optical Imaging and Relative Distribution. Fresh tissue sections (1-mm thick) of tumor, liver, kidney, and muscle as well as blood were imaged ex vivo in imaging chambers using bright-field and epi-fluorescence (528−553 nm excitation, 565 nm emission) microscopy using a Nikon eclipse E400 or TS100 attached to a Nikon Coolpix 990 or 5000 digital camera. Exposure times were kept constant for all organ sections and blood. Low power images of whole organ sections were acquired using a 1× lens. High power images were acquired using a 40× or 100× lens. Image analysis was performed using ImageJ (National Institutes of Health, Bethesda, MD). Images were converted to 8-bit gray-scale, the organ section was outlined, fluorescence intensity was measured, and the median fluorescence intensity per pixel was calculated.

Immunofluorescence Staining. Tumors frozen in O.C.T. compound (Sakura Finetek U.S.A. Inc.) were sectioned at 15-μm thickness using a microtome cryostat (Microm Int., Walldorf, Germany) and attached to charged microscope slides (Fisher Scientific, Pittsburgh, PA). The 15-μm tumor sections were fixed using 3% paraformaldehyde. Fixed cells in chamber slides and fixed tumor sections were stained using monoclonal antibodies to LAMP-1 (H4A3), LAMP-2 (H4B4), or CD63 (ab1318, Abcam Inc., Cambridge, MA). hLAMP-1 and hLAMP-2 antibodies (*26*) were kindly provided by Dr. J. Thomas August, Johns Hopkins University, Baltimore, MD. LAMP-1, LAMP-2, and CD63 are three specific marker proteins localized in lysosomal membranes. Tumor sections and cells were incubated with a Cy5-labeled donkey anti-mouse secondary antibody (Jackson ImmunoResearch Laboratories, West Grove, PA), and cell nuclei were counterstained with Hoechst H-33342 (Molecular

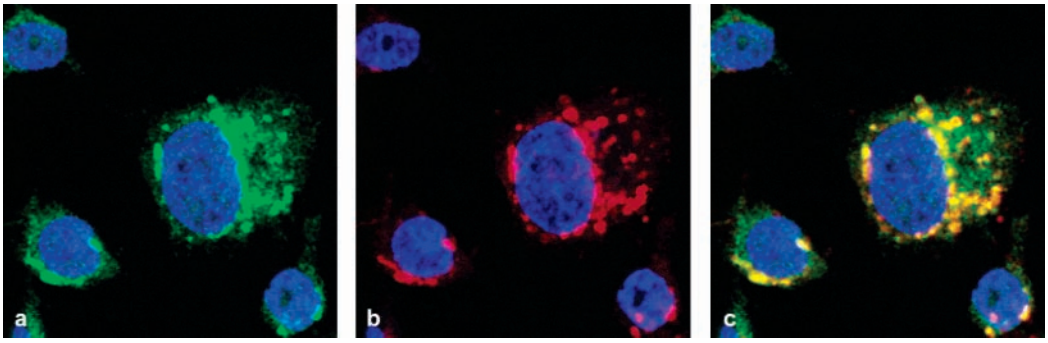

Figure 2. (a) Human MDA-MB-231 breast cancer cells exposed to 500 μM 6-*O*-liss-GlcNH_2 for 24 h. Fluorescence from (a) 6-*O*-liss-GlcNH_2 is displayed in green, and (b) CD63 immunofluorescence is displayed in red. Nuclei are displayed in blue. (c) The overlay of both images demonstrates the colocalization of 6-*O*-liss-GlcNH_2 and CD63, evident by the yellow color. The field of view of all images is 56.2 μm $\times$ 56.2 μm.

Probes, Eugene, OR) and mounted using Faramount aqueous mounting medium (DakoCytomation, Carpinteria, CA).

Confocal Laser-Scanning Fluorescence Microscopy. Fluorescence microscopy of fixed specimen was performed on a Zeiss LSM 510 META confocal laser-scanning microscope (Carl Zeiss, Inc., Thornwood, NY) using a Plan-Apochromat 63x/1.4 oil immersion lens (Zeiss) (The Johns Hopkins University School of Medicine Microscope Facility, Director Dr. Douglas B. Murphy). 6-*O*-liss-GlcNH_2 was excited with a 543 nm laser, and fluorescence emission was detected by a photomultiplier tube using a 565−595 nm band-pass filter. Simultaneously, H-33342 was excited with a 405 nm laser and the fluorescence emission was detected with a second photomultiplier by applying a 490 nm dichroic beam splitter and a 420−480 nm band-pass filter. Cy5 was excited simultaneously with a 633 nm laser and the fluorescence emission was detected with a third photomultiplier by using a 635 nm dichroic beam splitter and a 650 nm long pass filter, to achieve simultaneous detection of all three fluorophores. Confocal Z-sections of 1 μm thickness were imaged. Colocalization coefficients were measured using the LSM Software Release 3.2 (Zeiss).

Western-Blot Analysis. Cells were cultured in 100-mm tissue culture dishes until they reached 60−70% confluence. Following treatment with 500 μM 6-*O*-liss-GlcNH_2 for 2 or 4 days, cells were scraped and homogenized with lysis buffer containing protease inhibitors as previously described (*34*). A 50 μg amount of total protein was loaded in each lane of a 9% sodium dodecyl sulfate (SDS)-polyacrylamide gel, and proteins were resolved by electrophoresis (*34*). Approximate protein molecular weights were determined by comparison with a molecular weight marker (BenchMark, Life Technologies, Rockville, MD). Fluorescence and bright-field images were acquired for the resulting polyacrylamide gels using our home-built small animal fluorescence imaging system.

RESULTS

Chemistry. The novel compound 6′-*O*-lissamine-rhodamine B-glucosamine (6-*O*-liss-GlcNH_2, Figure 1, compound **4**) was synthesized in a three-step procedure analogous to the previously published synthesis of 6-*O*-dansyl-GlcNH_2 (*34*). As summarized in Figure 1, a Lissamine Rhodamine B group (*39*) was regiospecifically introduced to the 6′-hydroxyl group of 6-(2-amino-2-deoxy-β-D-glucopyranosyl)ether hydrochloride while the 2′-amino and 1′-hydroxyl groups were protected with *tert*-butyloxycarbonyl (Boc) groups (*34, 40*). The structure of

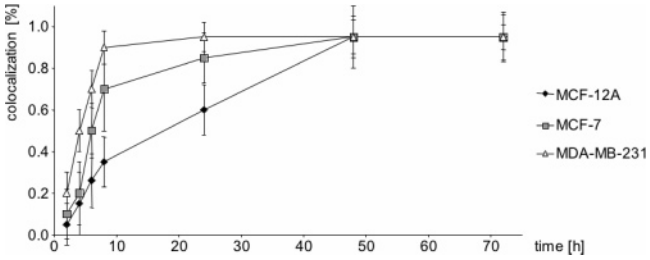

Figure 3. Time course of the colocalization coefficient. The colocalization coefficient (*y*-axis) of 6-*O*-liss-GlcNH_2 fluorescence with CD63 immunofluorescence increased gradually with increasing incubation time (*x*-axis) in MCF-12A HMECs, MCF-7, and MDA-MB-231 breast cancer cells. Colocalization was most rapid in MDA-MB-231 cells, followed by MCF-7 and MCF-12A cells. Values are mean $\pm$ standard error, $n = 15$, for each time point (five fields of view for three independent experiments each).

the final product 6-*O*-liss-GlcNH_2 was verified by ^{1}H and ^{13}C NMR spectroscopy and FAB-mass spectrometry (ppm- and *m/z*-values are given in Materials and Methods).

Uptake and Localization of 6-*O*-Liss-GlcNH_2 in Breast Epithelial and Cancer Cells. 6-*O*-liss-GlcNH_2 was taken up by MCF-12A HMECs and human MCF-7 and MDA-MB-231 breast cancer cells and significantly localized to lysosomes starting from ~8 h of incubation in MDA-MB-231 and MCF-7 breast cancer cells, and from ~24 h of incubation in MCF-12A HMECs. To assess the degree of lysosomal labeling from 6-*O*-dansyl-GlcNH_2, cells were fixed following 6-*O*-liss-GlcNH_2 incubation and costained with lysosomal markers CD63, LAMP-1, or LAMP-2. Representative fluorescence images of MDA-MB-231 breast cancer cells incubated with 6-*O*-liss-GlcNH_2 for 24 h in Figure 2a−c show that labeling from 6-*O*-liss-GlcNH_2 colocalized with the lysosomal marker CD63, as evident from the yellow color in the overlay image in Figure 2c. In Figure 3, the colocalization coefficient from 6-*O*-liss-GlcNH_2 and CD63 fluorescence was quantified from images derived from three independent experiments with each cell line, demonstrating the gradual increase in lysosomal 6-*O*-liss-GlcNH_2 staining. The fastest incorporation of fluorescent 6-*O*-liss-GlcNH_2 label into lysosomes occurred in MDA-MB-231 breast cancer cells, followed by MCF-7 cells and MCF-12A HMECs (Figure 3). Following 2−4 h of incubation, 6-*O*-liss-GlcNH_2 fluorescence was distributed over the cytoplasm of cells and concentrated in some bright nonlysosomal areas close to the nucleus (data not shown). Following 8 h of incubation in MDA-MB-231 cells, or 24−48 h in MCF-7 and MCF-12A cells, lysosomes were labeled up to a colocalization coefficient of 0.8−0.95 with

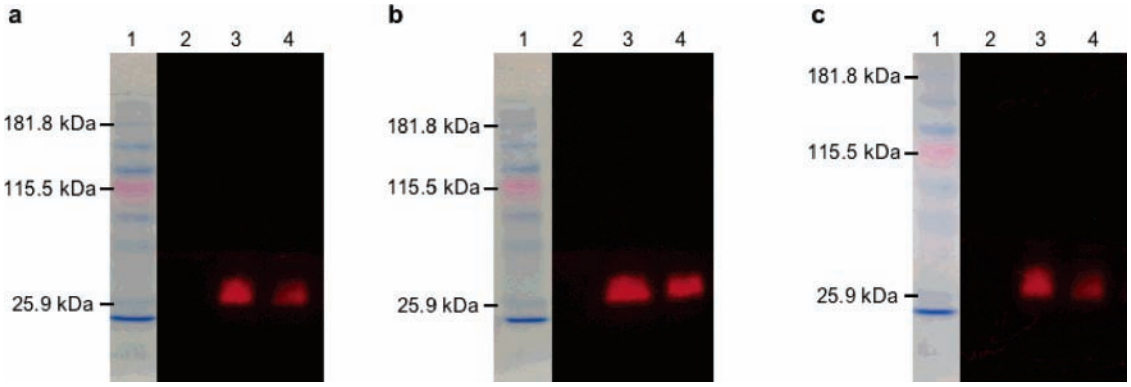

Figure 4. Fluorescence images of SDS−PAGE gels of protein lysates obtained from (a) MCF-12A, (b) MCF-7, and (c) MDA-MB-231 cells incubated with 6-*O*-liss-$GlcNH_2$ for 2 or 4 days. Bright-field images were acquired from the same field of view, and a molecular weight marker lane from bright-field images (lane 1) was copied into the fluorescence image to assign the molecular mass. Lane 1 contains molecular weight marker, lane 2 contains control cell lysate, lane 3 contains cell lysate following 2 days of incubation of cells with 6-*O*-liss-$GlcNH_2$, and lane 4 contains cell lysate following 4 days of incubation of cells with 6-*O*-liss-$GlcNH_2$. 6-*O*-liss-$GlcNH_2$ fluorescence is enriched in protein(s) of an apparent mass of 26−30 kDa following 2−4 days 6-*O*-liss-$GlcNH_2$ incubation.

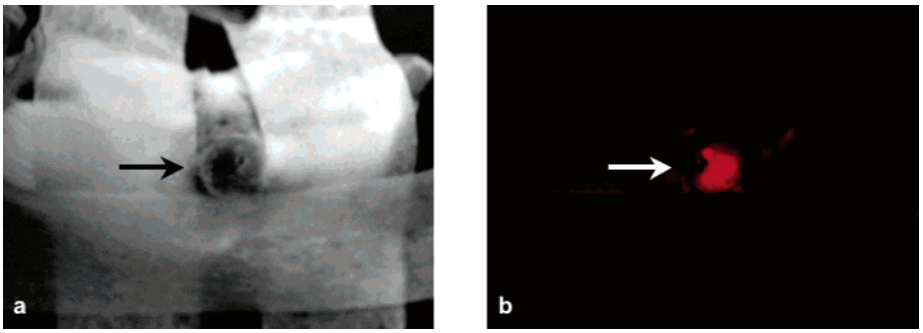

Figure 5. In vivo (a) bright-field and (b) fluorescence images of a representative MCF-7 tumor 2 h following injection of 7.8 mg of 6-*O*-liss-$GlcNH_2$ into the tail vein. Efficient delivery of 6-*O*-liss-$GlcNH_2$ to the tumor (tumor marked by arrow) is evident in these images.

respect to CD63 immunofluorescence (Figure 3), which corresponds to almost complete lysosomal staining. Comparable results were obtained with LAMP-1 and -2 immunofluorescence staining.

Protein Analysis. SDS−PAGE electrophoresis of lysates from 6-*O*-liss-$GlcNH_2$-treated cells was performed, followed by fluorescence imaging of these gels to determine the molecular weight of the protein(s) containing covalently bound 6-*O*-liss-$GlcNH_2$. As displayed in Figure 4, fluorescence imaging of these gels revealed that proteins with an apparent molecular weight of ∼26−30 kDa contained 6-*O*-liss-$GlcNH_2$-fluorescence. This fluorescent protein band was detected in MCF-12A HMECs as well as MCF-7 and MDA-MB-231 breast cancer cells (Figure 4).

Uptake and Localization of 6-*O*-Liss-$GlcNH_2$ in Tumor-Bearing SCID Mice. MCF-7 or MDA-MB-231 tumors in the mammary fat pad of female SCID mice were optically imaged in vivo at 2, 24, and 48 h following intravenous administration of 7.8 mg of 6-*O*-liss-$GlcNH_2$ via the tail vein. Figure 5 demonstrates that fluorescence from 6-*O*-liss-$GlcNH_2$ was detected in MCF-7 tumors at 2 h postinjection but not at 24 or 48 h postinjection. Similar results were obtained with MDA-MB-231 tumors. To assess the relative distribution of 6-*O*-liss-$GlcNH_2$ in selected tissues, bright-field and fluorescence microscopy were performed on freshly cut 1-mm sections from MCF-7 tumors, MDA-MB-231 tumors, liver, kidney, and muscle tissue as well as on blood. Although there was no detectable fluorescence at 24 and 48 h postinjection of 6-*O*-liss-$GlcNH_2$ in vivo, high-resolution fluorescence images of fresh tissue sections revealed that MCF-7 and MDA-MB-231 tumors contained 6-*O*-liss-$GlcNH_2$-fluorescence at 2, 24, and 48 h postinjection, as shown in Figure 6. Fluorescence intensity declined at later time points postinjection (Figures 6, 7). Tumoral 6-*O*-liss-$GlcNH_2$ fluorescence intensity was most pronounced in necrotic tumor areas, but also present in all other tumor regions, as evident from comparison of fluorescence with bright-field images (Figure 6a,b,f,g). High-power fluorescence images revealed that the staining pattern in viable tumor areas changed over time. At 2 h postinjection, 6-*O*-liss-$GlcNH_2$ was detected in the cytoplasm of tumor cells in viable tumor regions (Figure 6c,h). At 24 and 48 h postinjection, a punctate staining pattern from 6-*O*-liss-$GlcNH_2$ fluorescence was observed in viable tumor cells (Figure 6d,i). The liver contained detectable fluorescence intensity from 6-*O*-liss-$GlcNH_2$ only at 2 h postinjection but not at later time points (Figure 6j,k). A small amount of fluorescence intensity was detected in the kidneys at 2 h postinjection. Muscle and blood did not contain any detectable fluorescence from 6-*O*-liss-$GlcNH_2$ at the time points tested (data not shown). Figure 7 displays the time course of 6-*O*-liss-$GlcNH_2$ fluorescence intensity in all tested organs. MCF-7 and MDA-MB-231 tumors retained higher levels of 6-*O*-liss-$GlcNH_2$ fluorescence for a longer time than blood, liver, kidney, and muscle.

Lysosomal Localization of 6-*O*-Liss-$GlcNH_2$ in Tumor-Bearing SCID Mice. The subcellular localization of the tumoral 6-*O*-liss-$GlcNH_2$ staining pattern was assessed by immunofluorescence microscopy of MCF-7 and MDA-MB-231 tumor sections obtained following 6-*O*-liss-$GlcNH_2$ injection. Lysosomal staining with 6-*O*-liss-$GlcNH_2$ was evaluated by colocalization of 6-*O*-liss-$GlcNH_2$ with well-established lysososmal markers, such as CD63, LAMP-1, and LAMP-2. Figure 8 demonstrates

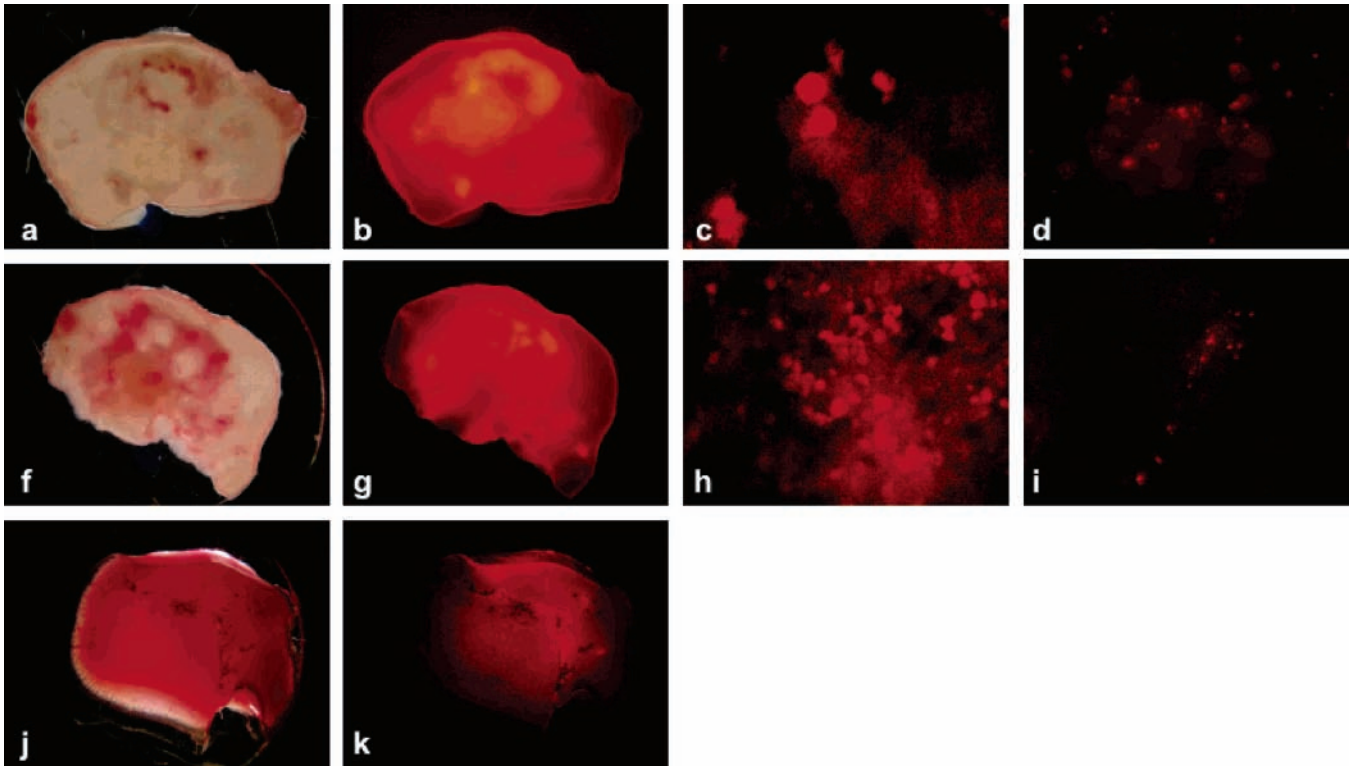

Figure 6. Ex vivo images of freshly cut 1-mm tissue sections (1× lens). Bright-field images of a representative (a) MCF-7 tumor section, (f) MDA-MB-231 tumor section, and (j) liver section and the corresponding 6-*O*-liss-GlcNH_2 fluorescence images of the (b) MCF-7 tumor section, (g) MDA-MB-231 tumor section, and (k) liver section are displayed. High-power (100× lens) fluorescence images of a representative (c) MCF-7 tumor section 2 h postinjection and (d) MCF-7 tumor section 24 h postinjection, as well as a representative (h) MDA-MB-231 tumor section 2 h postinjection and (i) MDA-MB-231 tumor section 24 h postinjection are displayed.

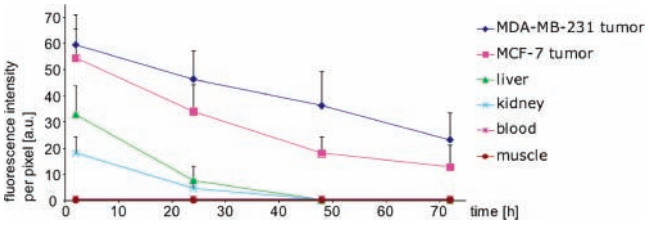

Figure 7. The time course of the mean 6-*O*-liss-GlcNH_2 fluorescence intensity per pixel is shown for MCF-7 tumors, MDA-MB-231 tumors, liver, kidney, muscle, and blood. Values are mean ± standard error, $n = 2-4$ for each time point.

that viable tumor regions from MCF-7 and MDA-MB-231 tumors contained lysosomal 6-*O*-liss-GlcNH_2-fluorescence at 24 h postinjection. This was evident from colocalization of 6-*O*-liss-GlcNH_2 displayed in green (Figure 8a,d) with CD63-staining displayed in red (Figure 8b,e), resulting in the yellow color from the overlay of both images (Figure 8c,f). Nuclei were counterstained and are displayed in blue. The colocalization coefficient for 6-*O*-liss-GlcNH_2 with CD63 fluroescence was 0.92 ± 0.09 ($n = 15$) in viable areas of MCF-7 tumors, as quantified using five sections from three tumors each. In MDA-MB-231 tumors, a colocalization coefficient of 0.96 ± 0.08 ($n = 15$) was observed in viable regions. Comparable results were obtained with the lysosomal markers LAMP-1 and LAMP-2 (data not shown). Necrotic tumor regions displayed abundant 6-*O*-liss-GlcNH_2 staining (Figure 8g) and, as anticipated, very little nuclear staining, since these tumor regions were not viable (Figure 8g–i). In addition, few yellow areas of colocalization were apparent in these necrotic areas (Figure 8i), indicating lack of lysosomal markers in these regions of dying cells (Figure 8g–i).

DISCUSSION

Here we have developed a novel compound, 6′-*O*-lissamine-rhodamine B-glucosamine, to perform noninvasive labeling of lysosomes in vivo and in vitro and to follow lysosomal trafficking in live breast cells and solid breast tumor models. This method will be useful to understand the relationship between lysosomal trafficking and the tumor microenvironment and its role in breast cancer invasion and metastasis.

The synthesis of 6-*O*-liss-GlcNH_2 is a relatively straightforward three-step procedure analogous to the synthesis of 6-*O*-dansyl-glucosamine (*34*). A Lissamine Rhodamine B group was regiospecifically introduced to the 6′-hydroxyl group of 6-(2-amino-2-deoxy-β-D-glucopyranosyl)ether hydrochloride while the 2′-amino and 1′-hydroxyl groups were protected with Boc (*tert*-butyloxycarbonyl) groups (*34, 40*).

Cell culture and animal studies are feasible using 6-*O*-liss-GlcNH_2, since it dissolves well in aqueous solutions. In cell culture studies, a concentration of 500 μM of 6-*O*-liss-GlcNH_2 in the cell culture medium resulted in clearly defined lysosomal fluorescence labeling in HMECs and breast cancer cells. In SCID mice bearing orthotopic breast tumor xenografts, administration of 7.8 mg of 6-*O*-liss-GlcNH_2 into the tail vein resulted in robust lysosomal fluorescence labeling of tumors. Lysosomes in HMECs, breast cancer cell lines, and tumors were specifically labeled by 6-*O*-liss-GlcNH_2 as verified by colocalization of 6-*O*-liss-GlcNH_2 fluorescence with CD63, LAMP-1, and LAMP-2, the latter three of which are well-established marker proteins for lysosomes (*23–26*). Lysosomal labeling of breast cancer cells in culture or solid tumors required relatively long incubation and postinjection uptake times of approximately 24 h. In in vitro cell culture assays, lysosomes in MDA-MB-231 breast cancer

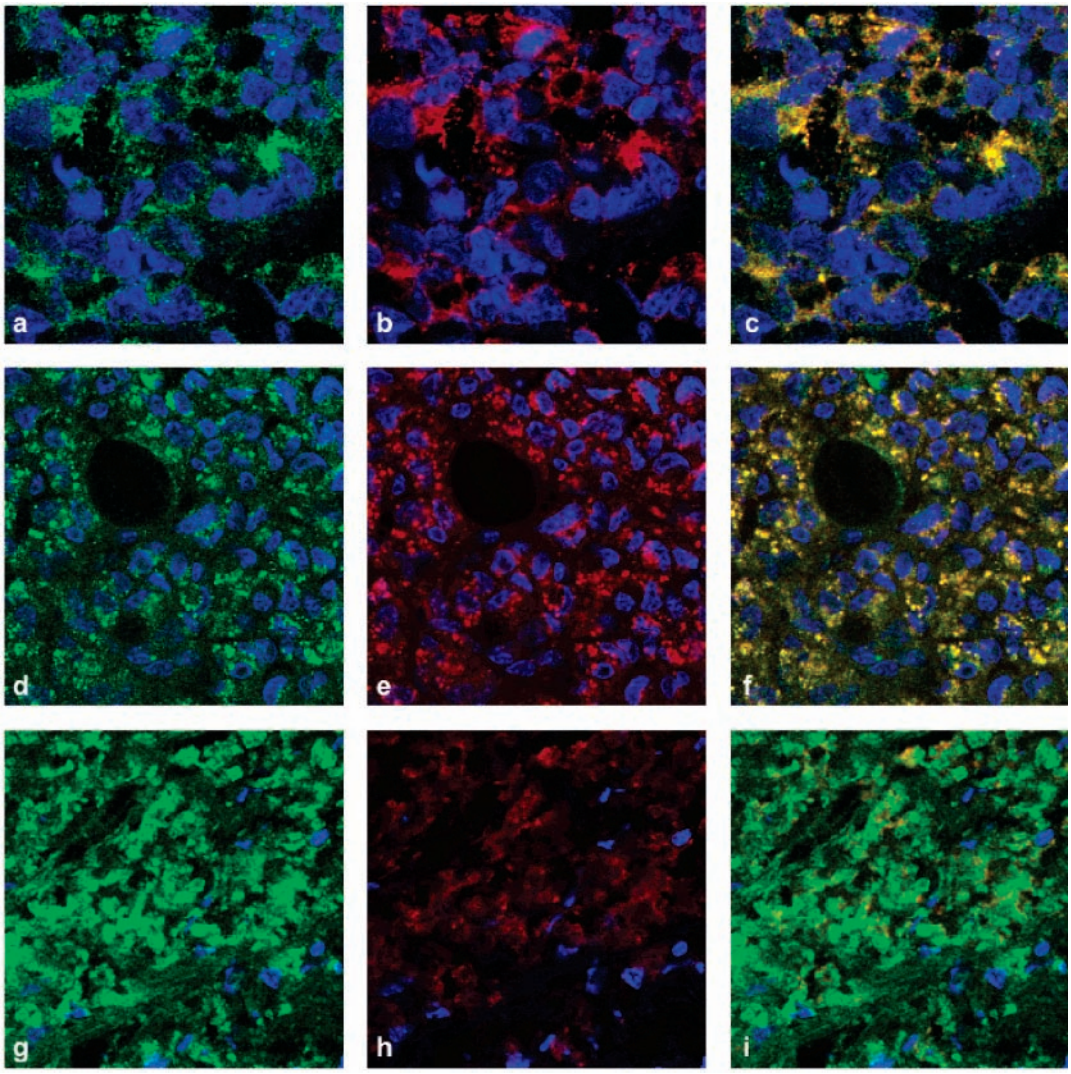

Figure 8. Confocal laser-scanning fluorescence images of (a−c) MCF-7 tumor sections and (d−f) MDA-MB-231 tumor sections. 6-*O*-liss-GlcNH_2 fluorescence images are displayed in green in a representative (a) MCF-7 tumor section and (d) MDA-MB-231 tumor section. The corresponding CD63 immunofluorescence images are displayed in red in the (b) MCF-7 tumor section and (e) MDA-MB-231 tumor section. 6-*O*-liss-GlcNH_2 and CD63 fluorescence images were overlaid for (c) MCF-7 and (f) MDA-MB-231 tumor sections, demonstrating strong colocalization of 6-*O*-liss-GlcNH_2 and CD63 as evident from the yellow color. (g−i) Representative confocal fluorescence images of necrotic regions from a MDA-MB-231 tumor, containing (g) strong 6-*O*-liss-GlcNH_2 fluorescence, and very little fluorescence from (h) lysosomes or (i) nuclei.

cells were labeled faster than lysosomes in MCF-7 and MCF-12A cells. At early incubation or postinjection uptake times, breast cancer cells exhibited a nonvesicular staining pattern. This observation is consistent with our earlier studies with the 6-*O*-dansyl derivative of glucosamine (*34*), where dansyl fluorescence was distributed over the cytoplasm of the cell and concentrated in some bright areas close to the nucleus following 5 h of exposure, and vesicular lysosomal staining appeared following 22 h or longer time periods of exposure (*34*). Similar to the analogous compound 6-*O*-dansyl-GlcNH_2, 6-*O*-liss-GlcNH_2 was most likely biosynthetically incorporated into highly glycosylated lysosomal proteins by passing through cellular sites of protein glycosylation. The lysosomal membrane contains several N-linked glycan-carrying proteins (*35*). N-Linked glycans are added cotranslationally to newly synthesized polypeptides in the endoplasmic reticulum (ER) and are extensively modified, as these glycoproteins mature and move through the ER and Golgi complex to their final destination in the cell (*41,* 42). Protein lysates of cells exposed to 6-*O*-liss-GlcNH_2 exhibited one major band at 26−30 kDa in optically imaged protein SDS−PAGE gels. Apparently, 6-*O*-liss-GlcNH_2 was utilized by breast cells in the biosynthesis of a glycosylated protein highly represented in lysosomes. However, 6-*O*-dansyl-GlcNH_2 was predominantly found in 70 kDa protein(s) (*34*). Although 6-*O*-liss-GlcNH_2 and 6-*O*-dansyl-GlcNH_2 both localized to lysosomes through biosynthetic incorporation into highly glycosylated lysosomal proteins, the difference in apparent molecular weight suggests that two distinct lysosomal proteins were labeled by these compounds. In contrast to commonly used less specific lysosomal probes utilized for live cell imaging, 6-*O*-liss-GlcNH_2 and 6-*O*-dansyl-GlcNH_2 (*34*) confer the advantage of being specifically targeted to lysosomes.

Systemic administration of 6-*O*-liss-GlcNH_2 in SCID mice revealed that this compound is nontoxic in SCID mice. 6-*O*-liss-GlcNH_2 is rapidly cleared from the blood stream within 2 h of intravenous administration, as demonstrated by a lack of 6-*O*-liss-GlcNH_2 fluorescence in the blood at 2 h postinjection. MCF-7 and MDA-MB-231 tumors were intensely fluorescent up to 24−48 h, while the liver and kidney contained moderate 6-*O*-liss-

$GlcNH_2$ fluorescence intensity at similar time points. Thus, 6-*O*-liss-$GlcNH_2$ was efficiently delivered to MCF-7 and MDA-MB-231 breast tumor xenografts in SCID mice. Although 6-*O*-liss-$GlcNH_2$ was detectable in these breast tumor models for more than 3 days, its fluorescence intensity declined over time, indicating elimination of 6-*O*-liss-$GlcNH_2$ from breast tumors. The fluorescence intensity from 6-*O*-liss-$GlcNH_2$ in these tumors was sufficient for tumor in vivo optical imaging at 2 h postinjection. Subcellular localization of 6-*O*-liss-$GlcNH_2$ to lysosomes in tumors required longer time periods. The highest colocalization coefficients of 6-*O*-liss-$GlcNH_2$ fluorescence with lysosomal markers CD63, LAMP-1, and LAMP-2 was detected at 24 h postinjection in viable tumor regions, suggesting that breast cancer cells in these viable tumor regions utilized 6-*O*-liss-$GlcNH_2$ in the biosynthesis of a glycosylated lysosomal protein. The intratumoral distribution of 6-*O*-liss-$GlcNH_2$ appeared to be inhomogeneous, exhibiting higher fluorescence intensity in necrotic areas. Necrotic areas did not contain viable cells, as evident from missing nuclear counterstaining in these areas. Thus, 6-*O*-liss-$GlcNH_2$ accumulation in necrotic tumor regions was nonspecific. While lysosomal localization of fluorescence from 6-*O*-liss-$GlcNH_2$ was most pronounced at 24 h postinjection, in vivo imaging of this fluorescence was not feasible with our system, because the fluorescence intensity was below the detection limit of this system. Images obtained by fluorescence microscopy of fresh tumor slices strongly suggest that intravital fluorescence microscopy or endoscopy of 6-*O*-liss-$GlcNH_2$-labeled lysosomes in solid breast tumor models will have sufficient resolution and sensitivity to detect lysosomal labeling in vivo.

The novel compound 6-*O*-liss-$GlcNH_2$ described here will be valuable not only to understand the role of lysosomes and lysosomal trafficking in breast cancer invasion and metastasis, but also to study cell and animal models of lysosomal diseases. 6-*O*-liss-$GlcNH_2$ itself, or analogous compounds, may, in the future, be utilized for detecting aberrant lysosomal trafficking in clinical settings. 6-*O*-liss-$GlcNH_2$ will prove useful for studying lysosomal storage diseases (*43*) such as Gauchers disease (*44*), as well as neurodegenerative diseases such as Alzheimer's disease (*45, 46*), which exhibit robust activation of the neuronal lysosomal system, namely, endocytosis and autophagy. Although 6-*O*-liss-$GlcNH_2$ may not be able to cross the intact blood−brain barrier (BBB), pathogenesis of increased BBB permeability has been demonstrated in Alzheimer's disease (*47*). 6-*O*-liss-$GlcNH_2$ may also be helpful for assessing host−parasite relationships such as that of *Trypanosoma cruzi* trypomastigotes (*48*), which involve participation of the host's lysosomes, and for following therapeutic targeting of lysosomes.

ACKNOWLEDGMENT

This work was supported by a Career Development Award to Dr. Kristine Glunde through P50 CA103175 (JHU ICMIC Program) and R24 CA92871. We thank Dr. Dmitri Artemov for building the small animal fluorescence imaging system and for technical support with this home-built system. We thank Dr. J. Thomas August for providing us with monoclonal antibodies against hLAMP-1 (H4A3) and hLAMP-2 (H4B4). We thank Dr. Douglas B. Murphy (Director, The Johns Hopkins University School of Medicine Microscope Facility) for technical support. We thank Mr. Gary Cromwell for maintaining the cell lines.

LITERATURE CITED

(1) Holtzmann, E. (1989) *Lysosomes*, 456 pp, Plenum Press, New York, London.
(2) Marks, M. S., Roche, P. A., van Donselaar, E., Woodruff, L., Peters, P. J., and Bonifacino, J. S. (1995) A lysosomal targeting signal in the cytoplasmic tail of the beta chain directs HLA-DM to MHC class II compartments. *J. Cell Biol. 131*, 351−369.
(3) Marks, S. C., Jr. (1989) Osteoclast biology: lessons from mammalian mutations. *Am. J. Med. Genet. 34*, 43−54.
(4) Renfrew, C. A., and Hubbard, A. L. (1991) Degradation of epidermal growth factor receptor in rat liver. Membrane topology through the lysosomal pathway. *J. Biol. Chem. 266*, 21265−21273.
(5) Reddy, A., Caler, E. V., and Andrews, N. W. (2001) Plasma membrane repair is mediated by Ca(2+)-regulated exocytosis of lysosomes. *Cell 106*, 157−169.
(6) Dobrossy, L., Pavelic, Z. P., Vaughan, M., Porter, N., and Bernacki, R. J. (1980) Elevation of lysosomal enzymes in primary Lewis lung tumor correlated with the initiation of metastasis. *Cancer Res. 40*, 3281−3285.
(7) Sloane, B. F., Dunn, J. R., and Honn, K. V. (1981) Lysosomal cathepsin B: correlation with metastatic potential. *Science 212*, 1151−1153.
(8) Krishnan, V., Wang, X., and Safe, S. (1994) Estrogen receptor-Sp1 complexes mediate estrogen-induced cathepsin D gene expression in MCF-7 human breast cancer cells. *J. Biol. Chem. 269*, 15912−15917.
(9) Mathieu, M., Vignon, F., Capony, F., and Rochefort, H. (1991) Estradiol down-regulates the mannose-6-phosphate/insulin-like growth factor-II receptor gene and induces cathepsin-D in breast cancer cells: a receptor saturation mechanism to increase the secretion of lysosomal proenzymes. *Mol. Endocrinol. 5*, 815−822.
(10) Carter, R. L., Birbeck, M. S., and Stock, J. A. (1971) Lysosomal changes and enhanced metastatic growth: an experimental study of the effects of some nonionic surfactants. *Int. J. Cancer 7*, 34−49.
(11) Montcourrier, P., Mangeat, P. H., Valembois, C., et al. (1994) Characterization of very acidic phagosomes in breast cancer cells and their association with invasion. *J. Cell Sci. 107*, 2381−2391.
(12) Montcourrier, P., Mangeat, P. H., Salazar, G., Morisset, M., Sahuquet, A., and Rochefort, H. (1990) Cathepsin D in breast cancer cells can digest extracellular matrix in large acidic vesicles. *Cancer Res.* 50, 6045−6054.
(13) Mignatti, P., and Rifkin, D. B. (1993) Biology and biochemistry of proteinases in tumor invasion. *Physiol. Rev. 73*, 161−195.
(14) Kolkhorst, V., Sturzebecher, J., and Wiederanders, B. (1998) Inhibition of tumour cell invasion by protease inhibitors: correlation with the protease profile. *J. Cancer Res. Clin. Oncol. 124*, 598−606.
(15) Duffy, M. J. (1992) The role of proteolytic enzymes in cancer invasion and metastasis. *Clin. Exp. Metastasis 10*, 145−155.
(16) McGrath, M. E. (1999) The lysosomal cysteine proteases. *Annu. Rev. Biophys. Biomol. Struct. 28*, 181−204.
(17) Rochefort, H., Capony, F., Garcia, M., et al. (1987) Estrogen-induced lysosomal proteases secreted by breast cancer cells: a role in carcinogenesis? *J. Cell. Biochem. 35*, 17−29.
(18) Sloane, B. F., Moin, K., Krepela, E., and Rozhin, J. (1990) Cathepsin B and its endogenous inhibitors: the role in tumor malignancy. *Cancer Metastasis Rev. 9*, 333−352.
(19) Kane, S. E., and Gottesman, M. M. (1990) The role of cathepsin L in malignant transformation. *Semin. Cancer Biol. 1*, 127−136.
(20) Rozhin, J., Sameni, M., Ziegler, G., and Sloane, B. F. (1994) Pericellular pH affects distribution and secretion of cathepsin B in malignant cells. *Cancer Res. 54*, 6517−6525.
(21) Cuvier, C., Jang, A., and Hill, R. P. (1997) Exposure to hypoxia, glucose starvation and acidosis: effect on invasive capacity of murine tumor cells and correlation with cathepsin (L + B) secretion. *Clin. Exp. Metastasis 15*, 19−25.
(22) Glunde, K., Guggino, S. E., Solaiyappan, M., Pathak, A. P., Ichikawa, Y., and Bhujwalla, Z. M. (2003) Extracellular

acidification alters lysosomal trafficking in human breast cancer cells. *Neoplasia 5*, 533−545.
(23) Fukuda, M., Viitala, J., Matteson, J., and Carlsson, S. R. (1988) Cloning of cDNAs encoding human lysosomal membrane glycoproteins, h- lamp-1 and h-lamp-2. Comparison of their deduced amino acid sequences. *J. Biol. Chem. 263*, 18920−18928.
(24) Mane, S. M., Marzella, L., Bainton, D. F., et al. (1989) Purification and characterization of human lysosomal membrane glycoproteins. *Arch. Biochem. Biophys. 268*, 360−378.
(25) Metzelaar, M. J., Wijngaard, P. L., Peters, P. J., Sixma, J. J., Nieuwenhuis, H. K., and Clevers, H. C. (1991) CD63 antigen. A novel lysosomal membrane glycoprotein, cloned by a screening procedure for intracellular antigens in eukaryotic cells. *J. Biol. Chem. 266*, 3239−3245.
(26) Furuta, K., Yang, X. L., Chen, J. S., Hamilton, S. R., and August, J. T. (1999) Differential expression of the lysosome-associated membrane proteins in normal human tissues. *Arch. Biochem. Biophys. 365*, 75−82.
(27) Twining, S. S. (1984) Fluorescein isothiocyanate-labeled casein assay for proteolytic enzymes. *Anal. Biochem. 143*, 30−34.
(28) Jones, L. J., Upson, R. H., Haugland, R. P., Panchuk-Voloshina, N., and Zhou, M. (1997) Quenched BODIPY dye-labeled casein substrates for the assay of protease activity by direct fluorescence measurement. *Anal. Biochem. 251*, 144−152.
(29) Allison, A. C., and Young, M. R. (1969) Vital Staining and Fluorescence Microscopy of Lysosomes. In *Lysosomes in Biology and Pathology* (Dingle, J. T., and Fell, H. B., Eds.) pp 600−628, Vol. 2, North-Holland Pub. Co., Amsterdam-London.
(30) Redai, I., and Halmy, M. (1980) Lysosomal acridine orange uptake in fibroblasts transformed by SV40 or human cytomegalovirus. *Acta Microbiol. Acad. Sci. Hung. 27*, 41−45.
(31) Vult von Steyern, F., Josefsson, J. O., and Tagerud, S. (1996) Rhodamine B, a fluorescent probe for acidic organelles in denervated skeletal muscle. *J Histochem. Cytochem. 44*, 267−274.
(32) Diwu, Z., Chen, C. S., Zhang, C., Klaubert, D. H., and Haugland, R. P. (1999) A novel acidotropic pH indicator and its potential application in labeling acidic organelles of live cells. *Chem. Biol. 6*, 411−418.
(33) Ohkuma, S., and Poole, B. (1978) Fluorescence probe measurement of the intralysosomal pH in living cells and the perturbation of pH by various agents. *Proc. Natl. Acad. Sci. U.S.A. 75*, 3327−3331.
(34) Glunde, K., Guggino, S. E., Ichikawa, Y., and Bhujwalla, Z. M. (2003) A novel method of imaging lysosomes in living human mammary epithelial cells. *Mol. Imaging 2*, 24−36.
(35) Granger, B. L., Green, S. A., Gabel, C. A., Howe, C. L., Mellman, I., and Helenius, A. (1990) Characterization and cloning of lgp110, a lysosomal membrane glycoprotein from mouse and rat cells. *J. Biol. Chem. 265*, 12036−12043.
(36) Kundra, R., and Kornfeld, S. (1999) Asparagine-linked oligosaccharides protect Lamp-1 and Lamp-2 from intracellular proteolysis. *J. Biol. Chem. 274*, 31039−31046.
(37) Paine, T. M., Soule, H. D., Pauley, R. J., and Dawson, P. J. (1992) Characterization of epithelial phenotypes in mortal and immortal human breast cells. *Int. J. Cancer 50*, 463−473.
(38) Soule, H. D., Vazguez, J., Long, A., Albert, S., and Brennan, M. (1973) A human cell line from a pleural effusion derived from a breast carcinoma. *J. Natl. Cancer Inst. 51*, 1409−1416.
(39) Carrano, L., Tavecchia, P., Sponga, F., and Spreafico, F. (1997) Dansyl *N*-acetyl glucosamine as a precursor of fluorescent chitin: a method to detect fungal cell wall inhibitors. *J. Antibiot. (Tokyo) 50*, 177−179.
(40) Schelhaas, M., and Waldmann, H. (1996) Protecting group strategies in organic synthesis. *Angew. Chem., Int. Ed. Engl. 35*, 2056−2083.
(41) Helenius, A., and Aebi, M. (2001) Intracellular functions of N-linked glycans. *Science 291*, 2364−2369.
(42) Verbert, A., and Cacan, R. (1999) Trafficking of oligomannosides released during N-glycosylation: a clearing mechanism of the rough endoplasmic reticulum. *Biochim. Biophys. Acta 1473*, 137−146.
(43) Schiffmann, R., and Brady, R. O. (2002) New prospects for the treatment of lysosomal storage diseases. *Drugs 62*, 733−742.
(44) Zhao, H., and Grabowski, G. A. (2002) Gaucher disease: Perspectives on a prototype lysosomal disease. *Cell Mol. Life Sci 59*, 694−707.
(45) Nixon, R. A., Cataldo, A. M., and Mathews, P. M. (2000) The endosomal-lysosomal system of neurons in Alzheimer's disease pathogenesis: a review. *Neurochem. Res. 25*, 1161−1172.
(46) Glabe, C. (2001) Intracellular mechanisms of amyloid accumulation and pathogenesis in Alzheimer's disease. *J. Mol. Neurosci. 17*, 137−145.
(47) Ballabh, P., Braun, A., and Nedergaard, M. (2004) The blood-brain barrier: an overview: structure, regulation, and clinical implications. *Neurobiol. Dis. 16*, 1−13.
(48) Kima, P. E., Burleigh, B., and Andrews, N. W. (2000) Surface-targeted lysosomal membrane glycoprotein-1 (Lamp-1) enhances lysosome exocytosis and cell invasion by Trypanosoma cruzi. *Cell Microbiol. 2*, 477−486.

BC050046N

Synthesis and Characterization of Positively Charged Porphyrin−Peptide Conjugates

Martha Sibrian-Vazquez, Timothy J. Jensen, Frank R. Fronczek, Robert P. Hammer, and M. Graça H. Vicente*

Department of Chemistry, Louisiana State University, Baton Rouge, Louisiana 70803. Received February 28, 2005; Revised Manuscript Received May 26, 2005

The total syntheses of 14 porphyrin conjugates containing one to four positively charged amino acids and two distinct linkers are described. All conjugates were fully characterized using spectroscopic methods, and the X-ray structure of a porphyrin isothiocyanate precursor was obtained. In vitro studies using HEp2 cells show that these conjugates have low cytotoxicity ($IC_{50} > 250\ \mu M$) and that the extent of their cellular uptake depends significantly on the number, nature, and sequence of amino acids in the peptide, and on the presence of a centrally chelated metal ion. Metal-free conjugates bearing three consecutive arginine residues accumulated the most within cells. On the other hand, the preferential sites of subcellular localization were found to be independent from the number, nature, and sequence of amino acids in the conjugate, the linker, and coordinated metal ion; it is suggested, based on theoretical calculations, that the peptides in these conjugates fold over the porphyrin macrocycle in order to maximize intramolecular hydrophobic interactions.

INTRODUCTION

The biomedical applications of porphyrin-type macrocycles have been the subject of intense research in the past decades because of their unique photophysical and pharmacokinetic properties. In particular porphyrin derivatives have been investigated for use as sensitizers in the photodynamic therapy (PDT) and in the boron neutron capture therapy (BNCT) of tumors (*1*, *2*). PDT and BNCT are binary therapies for cancer treatment that involve the activation of a tumor-localized porphyrin sensitizer with light (in PDT) or low energy neutrons (in BNCT). These therapies have the potential to be highly localized to neoplastic tissue, since the cytotoxic species generated in PDT (mainly $^1O_2$) and BNCT ($^4He^{2+}$ and $^7Li^{3+}$) have short distances of travel through tissue. In fact the preferential subcellular site(s) of localization of porphyrin sensitizers are considered to be an important factor in determining their biological efficacy, as they define the primary site(s) of damage and can thus determine the mechanism(s) of cell death (*3*, *4*). Among the sensitizers, positively charged molecules are particularly interesting because they potentially target the most vulnerable intracellular sites, such as the cell mitochondria and nuclei (*4*−*6*) and have shown to cause effective DNA and RNA damage (*7*−*9*). Furthermore, cationic porphyrins are active in the photoinactivation of bacteria (*10*−*14*) and viruses (*15*, *16*).

With the aim to increase the biological effectiveness of porphyrin sensitizers and to broaden their application as fluorescent bioimaging agents, their conjugation to various proteins (*17*−*20*), peptides (*21*−*23*), oligonucleotides (*24*, *25*), and monoclonal antibodies (*26*, *27*) have been investigated in recent years. Several conjugation techniques have been reported, and the resulting bioconjugates have shown improved cell target ability and enhanced biological efficacy. In our continuing studies of structure−activity relationships in porphyrin macrocycles, we prepared 14 conjugates of a model porphyrin (**1**) to various positively charged amino acids and peptides containing lysine and arginine residues and investigated their cytotoxicity, cellular uptake, and sites of intracellular localization. Arginine (side chain $pK_a \sim 12.5$) and lysine ($pK_a \sim 9.4$) are amphiphilic amino acids that are protonated at physiological pH. Whereas lysine has a localized positive charge on its amino group, the guanidinium group has delocalized charge and is capable of forming multiple hydrogen bonds. Furthermore, the planar geometry and charge distribution of the guanidinium group is ideal for binding negatively charged groups, such as phosphates and carboxylates. Herein we report that porphyrin conjugates containing one to four lysine or arginine amino acid residues have low dark cytotoxicity and localize mainly in cellular vesicles and lysosomes, and that their cellular uptake depends significantly on the nature, number, and sequence of amino acid residues and the presence of a centrally chelated metal ion. Furthermore, we hypothesize that in such conjugates bearing small linkages between the porphyrin and peptide molecules, intramolecular forces favor a fold-over conformation of the conjugates, which might in part explain their similar sites of subcellular localization.

EXPERIMENTAL PROCEDURES

Syntheses. Unless otherwise indicated, all commercially available starting materials were used directly without further purification. Reactions under anhydrous conditions were performed in dried and distilled solvents under an argon atmosphere. All reactions were monitored by TLC using Sorbent Technologies 0.25 mm silica gel plates with or without UV indicator (60F-254). Silica gel Sorbent Technologies 32−63 μm was used for flash column chromatography. ^1H and ^{13}C NMR were obtained on either a DPX-250 or a ARX-300 Bruker spectrometer. Chemical shifts (δ) are given in ppm relative to $CDCl_3$ (7.26 ppm, ^1H; 77.00 ppm, ^{13}C) unless otherwise indi-

* Corresponding author. Phone: (225) 578 7405, Fax: (225) 578 3458, E-mail: vicente@lsu.edu.

10.1021/bc050057g CCC: $30.25 © 2005 American Chemical Society
Published on Web 07/02/2005

cated. Electronic absorption spectra were measured on a Perkin-Elmer Lambda 35 UV−vis spectrophotometer, and fluorescence spectra were measured on a Perkin-Elmer LS55 spectrometer. Mass spectra were obtained on an Applied Biosystems QSTAR XL, a hybrid QqTOF mass spectrometer with a MALDI ionization source using CCA as the matrix. HPLC separation and analysis were carried out on a Dionex system including a P680 pump and a UVD340U detector. Semipreparative HPLC was carried out using a Luna C_{18} 100 Å, 5 μm, 10 × 250 mm (Phenomenex) column and a stepwise gradient; analytical HPLC was carried out using a Delta Pak C_{18} 300 Å, 5 μm, 3.9 × 150 mm (Waters) column and a stepwise gradient (deprotected conjugates) or under isocratic conditions (protected conjugates). The samples were isolated and analyzed using the following solvents: buffer A (5% acetonitrile, 0.1% TFA, H_2O), buffer B (5% H_2O, 0.1% TFA, acetonitrile), and acetonitrile.

The Gasteiger−Huckel computational model and the Tripos Force Field parameters incorporated into the software package SYBYL 7.0 (Tripos, St. Louis, MO) were used for the energy minimization calculations. After initial minimization for each molecule, annealing was performed by heating the molecules to 500 K and then cooled to 0 K over a period of 1000 fs for 10 cycles. Following annealing, minimization was performed using the Powell descent series method. Solvation studies were performed by explicitly including water molecules in the calculation. The solute was solvated with one layer of water (TIP3P model) in a periodic box (46.46 × 46.46 × 46.46 Å), using the appropriate routine within SYBYL, and minimized within that box.

Conjugates 2a and 2b. Boc-L-Lys(Boc)OH (0.030 g, 0.0869 mmol) was dissolved in 0.5 mL of DMF.[1] To this solution were added HOBt (0.0133 g, 0.0869 mmol), DMAP (0.0010 g, 0.0086 mmol), Et_3N (0.0087 g, 0.0869 mmol), porphyrin **1** (0.050 g, 0.079 mmol), and EDCI (0.0166 g, 0.0869 mmol). The reaction mixture was stirred at room temperature for 48 h, after which 10 mL of distilled water and 5 mL of EtOAc were added. The two phases were separated, the organic phase was washed with distilled water (2 × 10 mL), dried over anhydrous Na_2SO_4, filtered, and the solvent was evaporated under vacuum. The protected conjugate was isolated by flash chromatography on silica gel using dichloromethane/methanol in the ratio 99/1. The protected conjugate **2a** was obtained in 96% yield as purple crystals. UV−vis ($CHCl_3$) λ_{max} (ϵ/M^{-1} cm^{-1}) 419 (371,400), 515 (16,400), 551 (7,900), 590 (5,100), 646 (3,700). ^{1}H NMR ($CDCl_3$, 300 MHz): δ 8.79−8.97 (9H, m), 8.13−8.25 (8H, m), 8.00 (2H, d, J = 8.49 Hz), 7.66−7.82 (9H, m), 5.46 (1H, d, J = 6.94 Hz), 4.71−4.73 (1H, m), 4.45 (1H, s), 3.22−3.27 (2H, m), 1.27−1.65 (24H, m), −2.76 (2H, s). ^{13}C NMR ($CDCl_3$, 62.5 MHz): δ 170.99, 156.39, 142.13, 138.05, 137.65, 135.10, 134.52, 131.03, 127.61, 126.65,120.08, 119.56, 118.05, 55.40, 39.59, 31.44, 29.69, 28.49, 28.42, 22.70. LRMS (ESI) m/z 958.40 (M + H^+), calculated for $C_{60}H_{59}N_7O_5$ 958.45. Deprotection was accomplished in quantitative yield using TFA at room temperature for 4 h, following by evaporation of the TFA and washings with Et_2O. Conjugate **2b** was obtained as purple crystals, UV−vis ($CHCl_3$) λ_{max} (ϵ/M^{-1} cm^{-1}) 420 (282,300), 516 (16,300), 552 (7,900), 590 (5,100), 646 (3,800). ^{1}H NMR ($CDCl_3$, 300 MHz): δ 8.83−8.86 (8H, m), 8.80−8.22 (8H, m), 7.93 (2H, d, J = 8.1 Hz), 7.66−7.74 (9H, m), 3.60 (1H, s), 3.21 (4H, s), 2.94 (2H, s), 1.29−1.46 (6H, m), −2.74 (2H, s). HRMS (ESI) m/z 758.3575 (M + H^+), calculated for $C_{50}H_{44}N_9OS$ 758.3607.

5-(4-Isothiocyanatophenyl)-10,15,20-triphenyl-porphyrin (5). To a stirred solution of porphyrin **1** (0.050 g, 0.0793 mmol) in freshly distilled dichloromethane (20 mL) was added 1,1′-thiocarbonyldi-2(1*H*)-pyridone (0.0369 g, 0.1587 mmol). The resulting mixture was stirred at room temperature for 2 h under an argon atmosphere, before being concentrated under vacuum. The residue was dissolved in dichloromethane and the product was isolated by flash chromatography on silica gel using dichloromethane as the eluent. The title product was isolated as purple crystals in 84% yield. HPLC t_R = 13.36 min. UV−vis ($CHCl_3$) λ_{max} (ϵ/M^{-1} cm^{-1}) 414 (336,000), 515 (10,500), 548 (5,600), 589 (3,500), 645 (2,600). ^{1}H NMR ($CDCl_3$, 300 MHz): δ 8.89−8.91 (6H, m), 8.81 (2H, d, J = 4.7 Hz), 8.19−8.26 (8H, m), 7.73−7.84 (9H, m), 7.62 (2H, d, J = 8.3 Hz), −2.74 (2H, s). ^{13}C NMR ($CDCl_3$, 62.5 MHz): δ 142.49, 141.90, 136.89, 135.90, 135.02, 131.56, 128.26, 127.18, 124.53, 121.06, 120.88, 118.65. HRMS (ESI) m/z 672.2238 (M + H^+), calculated for $C_{45}H_{30}N_5S$ 672.2222. The crystal structure of the hemi-CH_2Cl_2 solvate of porphyrin **5** was determined, using data collected at T = 105 K with Mo Kα radiation on a Nonius KappaCCD diffractometer. Crystal data: $C_{45}H_{29}N_5S\cdot 0.5CH_2Cl_2$, triclinic space group P-1, a = 7.020(6), b = 10.789(8), c = 24.120(16) Å, α = 87.55(3), β = 85.04(3), γ = 85.86(7)° V = 1814(2) Å^3, Z = 2, R = 0.086 ($F^2 > 2\sigma$), Rw = 0.245 (all F^2) for 5075 unique data and 487 refined parameters. The solvent molecule is disordered about an inversion center. Crystallographic data (excluding structure factors) for the structure in this paper have been deposited with the Cambridge Crystallographic Data Centre as supplementary publication no. CCDC 263394. Copies of the data can be obtained, free of charge, on application to CCDC, 12 Union Road, Cambridge, CB2 1EZ, UK, (fax: +44- (0)1223−336033 or e-mail: deposit @ccdc.cam.ac.uk).

4-[4-(10,15,20-Triphenyl-porphyrin-5-yl)-phenylcarbamoyl]-butyric Acid (6). Porphyrin **1** (0.1 g, 0.159 mmol) was added to a solution of glutaric anhydride (0.0543 g, 0.4769 mmol) in 2 mL of dry DMF at room temperature, and the final mixture was stirred at room temperature for 48 h. Distilled water (10 mL) was added, followed by 10 mL of EtOAc. The two phases were separated, the organic phase was washed with distilled water (3 × 10 mL), dried over anhydrous Na_2SO_4, and filtered, and the solvent was removed under vacuum. The title compound was purified on a silica gel plug using dichloromethane/methanol (99/1 to 90/10 ratios) for elution, in 100% yield. HPLC t_R = 21.34 min. UV−vis ($CHCl_3$) λ_{max} (ϵ/M^{-1} cm^{-1}) 419 (336,000), 516 (16,900), 551 (7,900), 590 (5,100), 646 (3,800). ^{1}H NMR ($CDCl_3$, 300 MHz): δ 8.8 (7H, s), 8.43 (7H, s); 7.71 (2H, s), 7.60 (10H, s), 2.63 (4H, s), 2.21 (2H, s), −2.79 (2H, s). HRMS (ESI) m/z 744.2865 (M + H^+), calculated for $C_{49}H_{38}N_5O_3$ 744.2896.

Conjugate 10. H-L-Lys(Boc)OtBu·HCl (0.0158 g, 0.0468 mmol) was dissolved in 500 μL of dry DMF under argon. To this solution was added Et_3N (0.0047 g, 0.0468 mmol),

[1] HOBt, 1-hydroxybenzotriazole; DMF, *N,N*-dimethylformamide; DMAP, 4-(dimethylamino)pyridine; Et_3N, triethylamine; CCA, α-cyano-4-hydroxycinnamic acid; EDCI, 1-(3-dimethylaminopropyl)-3-ethylcarbodiimide hydrochloride; DCC, 1,3-dicyclohexylcarbodiimide; TFA, trifluoroactic acid; DIEA, *N,N*-diisopropylethylamine; TBTU, 2-(1*H*-benzotriazole-1-yl)-1,1,3,3-tetramethyluronium tetrafluoroborate; TIS, triisopropylsilane; DMSO, dimethyl sulfoxide; NHS, *N*-hydroxysuccinimide; Boc, *tert*-butoxy carbonyl; Z, benzyloxy carbonyl; Fmoc, fluorenylmethoxy carbonyl; HEPES, 4-(2-hydroxyethyl)-1-piperazineethanesulfonic acid; PBS, phosphate-buffered saline; FBS, fetal bovine serum; MEM, modified eagle medium.

followed by porphyrin **5** (0.031 g, 0.0468 mmol). The reaction mixture was stirred at room temperature for 24 h, and then 10 mL of distilled water and 5 mL of EtOAc were added. The two phases were separated, the organic phase was washed with distilled water (2 × 10 mL), dried over anhydrous Na_2SO_4, and filtered, and the solvent was removed under vacuum. The title compound was purified by flash chromatography on silica gel using dichloromethane/methanol 98/2 for elution, in 93% yield. HPLC t_R = 6.94 min. UV−vis ($CHCl_3$) λ_{max} (ϵ/M^{-1} cm^{-1}) 420 (301,600), 516 (14,000), 552 (7,000), 590 (4,500), 646 (3,400). ^{1}H NMR ($CDCl_3$, 250 MHz): δ 8.83−8.88 (6H, m), 8.20−8.24 (9H, m), 7.71−7.77 (11H, m), 5.19 (1H, s), 4.62 (1H, s), 3.16 (2H, d, J = 6.1 Hz), 1.27−1.63 (24H, m), −2.76 (2H, s). ^{13}C NMR ($CDCl_3$, 62.5 MHz): 180.10, 171.45, 156.07, 142.14, 140.69, 136.04, 134.54, 131.25, 127.75, 126.69, 122.13, 120.42, 120.29, 118.49,117.49, 32.12, 29.74, 28.40, 28.10, 22.30, LRMS (ESI) *m/z* 973.37 (M^+), calculated for $C_{63}H_{57}N_7O_4S$ 973.43.

Conjugate 11. The title compound was synthesized as described above for conjugate **10**, in 45% yield. HPLC t_R = 7.15 min. UV−vis ($CHCl_3$) λ_{max} (ϵ/M^{-1} cm^{-1}) 419 (511,300), 516 (14,600), 552 (7,000), 590 (4,500), 646 (3,400). ^{1}H NMR ($CDCl_3$, 300 MHz): δ 8.85−8.86 (8H, s), 8.23−8.26 (7H, m), 7.73−7.76 (10H, m), 7.25 (1H, s), 5.31 (1H, s), 4.89 (1H, s), 4.61 (1H, s), 3.22 (4H, s), 1.37−2.01 (39H, m), −2.72 (2H, s). ^{13}C NMR ($CDCl_3$, 62.5 MHz): δ 180.30, 172.70, 156.07, 143.63, 137.34, 136.14, 132.77, 129.29, 128.25, 123.82, 121.84, 83.84, 80.76, 59.81, 41.77, 33.26, 31.27, 30.07, 29.67, 24.12. LRMS (ESI) *m/z* 1202.43 (M + H^+), calculated for $C_{71}H_{79}N_9O_7S$ 1202.50.

Conjugate 12. The title compound was synthesized as described above for conjugate **10**, in 35% yield. HPLC t_R = 9.78 min. UV−vis ($CHCl_3$) λ_{max} (ϵ/M^{-1} cm^{-1}) 420 (343,700), 516 (19,600), 552 (9,600), 590 (6,000), 642 (4,700). ^{1}H NMR ($CDCl_3$, 300 MHz): δ 8.86−8.94 (8H, m), 8.22−8.28 (8H, m), 8.06 (1H, d, J = 7.87 Hz), 7.76−7.77 (10H, m), 5.04 (1H, s), 4.66−4.83 (2H, m), 4.16 (1H, s), 3.19 (6H, s), 1.28−1.92 (54H, m), −2.74 (2H, s). ^{13}C NMR ($CDCl_3$, 62.5 MHz): δ 181.21, 174.00, 171.77, 156.77, 142.60, 134.99, 131.56, 128.13, 127.11, 122.58, 121.65, 120.54, 82.17, 40.95, 40.30, 39.44, 31.48, 29.62, 28.52, 28.00, 22.82, 22.42, 21.73. HRMS (ESI) *m/z* 1430.7433 (M + H^+), calculated for $C_{82}H_{100}N_{11}O_{10}S$ 1430.7375.

Conjugate 13. Compound **10** (0.0442 g, 0.043 mmol) was added to a 10 mL round-bottom flask, previously purged with argon for 5 min, followed by 4 mL of TFA. The reaction mixture was stirred at room temperature for 4 h. TFA was evaporated under vacuum, 5 mL of Et_2O was added, and the suspension was transferred to a centrifuge tube. After centrifugation, the residue was washed with Et_2O (6 × 10 mL) to remove residual TFA and dried under vacuum. Yield 100%. HPLC t_R = 22.66 min. UV−vis ($CHCl_3$) λ_{max} (ϵ/M^{-1} cm^{-1}) 419 (384,500), 515 (16,500), 551 (7,800), 590 (5,300), 646 (3,800). ^{1}H NMR ($CDCl_3$, 250 MHz): δ 8.83−8.88 (6H, m), 8.20−8.24 (9H, m), 7.71−7.77 (11H, m), 5.19 (1H, s), 4.62 (1H, s), 3.14−3.19 (2H, m), 1.27−1.63 (6, m), −2.76 (2H, s). ^{13}C NMR ($CDCl_3$, 62.5 MHz): δ 180.10, 172.45, 156.07, 142.14, 140.69, 135.96, 134.96, 130.99, 127.71, 126.66, 122.29, 120.42, 120.29, 30.29, 29.69, 22.30, LRMS (ESI) *m/z* 817.34 (M^+), calculated for $C_{51}H_{43}N_7O_2S$ 817.32.

Conjugate 14. The title compound was deprotected as described above for conjugate **13** in quantitative yield. HPLC t_R = 15.71 min. UV−vis ($CHCl_3$) λ_{max} (ϵ/M^{-1} cm^{-1}) 419 (276,300), 516 (24,100), 551 (11,500), 590 (7,600), 646 (5,600). ^{1}H NMR (CD_3OD, 300 MHz): δ 8.50 (8H, s), 8.20−8.28 (9H, m), 7.76 (12H, s), 3.31−3.5 (4H, m), 1.25−1.96 (12H, m), −2.78 (2H, s). LRMS (ESI) *m/z* 945.48 (M^+), calculated for $C_{57}H_{55}N_9O_8S$ 945.41.

Conjugate 15. The title compound was deprotected as described for conjugate **13** in quantitative yield. HPLC t_R = 10.38 min. UV−vis (2:1 MeOH/$CHCl_3$) λ_{max} (ϵ/M^{-1} cm^{-1}) 414 (280,600), 513 (15,700), 549 (8,700), 589 (5,900), 645 (4,600). ^{1}H NMR (CD_3OD, 300 MHz): δ 8.82−8.95 (7H, m), 8.55−8.57 (7H, m), 8.27−8.38 (2H, m), 8.05 (8H, s), 4.4−4.5 (1H, m), 3.99−4.02 (1H, m), 3.82−3.86 (1H, m), 2.94−3.01 (6H, m), 1.56−1.97 (18H, m). LRMS (ESI) *m/z* 1073.54 (M^+), calculated for $C_{63}H_{67}N_{11}O_4S$ 1073.51.

Conjugate 16. To a solution of porphyrin **6** (0.030 g, 0.043 mmol) in 500 μL of dry DMF were added DIEA (0.032 g, 0.2419 mmol), TBTU (0.0129 g, 0.0403 mmol), and HOBt (0.0062 g, 0.0403 mmol), followed by H-L-Lys-(Boc)OtBu·HCl (0.0136 g, 0.0403 mmol). The reaction mixture was stirred at room temperature for 24 h, diluted with 10 mL of EtOAc, and washed with water (3 × 10 mL). The organic extracts were combined, dried over anhydrous Na_2SO_4, and filtered, and the solvent was evaporated under vacuum. The protected conjugate was purified by flash chromatography on silica gel using 1% methanol/dichloromethane for elution. Yield 71%. HPLC t_R = 7.91 min. UV−vis ($CHCl_3$) λ_{max} (ϵ/M^{-1} cm^{-1}) 417 (359,200), 516 (12,200), 552 (6,900), 590 (4,400), 646 (3,300). ^{1}H NMR ($CDCl_3$, 300 MHz): δ 9.12 (1H, s), 8.86−8.92 (7H, m), 8.16−8.24 (8H, m), 8.02 (2H, d, J = 8.29 Hz), 7.72−7.77 (9H, m), 6.43 (2H, d, J = 7.34 Hz), 4.65 (1H, s), 4.57 (1H, s), 3.15 (2H, t, J = 6.1 Hz), 2.62 (2H, t, J = 4.7, 5.9 Hz), 2.51 (2H, t, J = 5.86, 6.71 Hz), 2.25 (2H, m), 1.37−1.91 (24H, m), −2.74 (2H, s). ^{13}C NMR ($CDCl_3$, 62.5 MHz): δ 172.88, 172.48, 171.66, 156.33, 142.13, 138.30, 137.53, 135.06, 134.53, 131.06, 127.68, 126.66, 120.01, 119.12, 117.76, 82.51, 79.51, 52.78, 39.83, 36.11, 34.74, 31.51, 29.81, 28.43, 28.05, 22.45, 22.01. HRMS (MALDI) *m/z* 1028.5081 (M^+), calculated for $C_{64}H_{66}N_7O_6$ 1028.5074. Deprotection as described above for conjugate **13** gave the title compound in quantitative yield. HPLC t_R = 16.28 min. UV−vis (9:1 MeOH/DMF) λ_{max} (ϵ/M^{-1} cm^{-1}) 414 (284,400), 513 (11,500), 551 (5,900), 587 (3,700), 645 (2,800). ^{1}H NMR (d_6-DMSO, 300 MHz): δ 8.79−8.90 (9H, m), 8.19−8.21 (10H, m), 7.79 (9H, m), 2.72 (2H, s), 2.43 (2H, s), 2.08 (2H, s), 1.3−1.93 (8H, m), −2.91 (2H, s). HRMS (ESI) *m/z* 872.3959 (M + H^+), calculated for $C_{55}H_{50}N_7O_4$ 872.3924.

Conjugate 17. Protected conjugate **17** was synthesized as described above for protected **16** and purified by flash chromatography on silica gel using 1% methanol/dichloromethane for elution. Yield 53%. HPLC t_R = 9.25 min. UV−vis ($CHCl_3$) λ_{max} (ϵ/M^{-1} cm^{-1}) 420 (294,800), 516 (15,700), 552 (8,000), 590 (4,800), 646 (3,700). ^{1}H NMR ($CDCl_3$, 300 MHz): δ 8.77−8.91 (7H, m), 8.04−8.24 (9H, m), 7.68−7.82 (9H, m), 6.84 (1H, d, J = 7.82 Hz), 6.72 (1H, d, J = 5.45 Hz), 5.03 (1H, s), 4.74 (1H, t, J = 6.05 Hz), 4.46−4.55 (2H, m), 3.13 (4H, s), 2.60 (2H, t, J = 6.21 Hz), 2.24 (2H, m), 1.18−1.90 (41H, m), −2.75 (2H, s). ^{13}C NMR ($CDCl_3$, 62.5 MHz): δ 173.48, 172.42, 171.71, 171.29, 156.41, 142.15, 138.55, 137.42, 134.99, 134.51, 131.05, 127.66, 126.65, 120.06, 119.89, 117.82, 82.28, 79.31, 53.77, 52.90, 40.06, 39.39, 35.87, 34.60, 31.73, 31.22, 28.46, 28.43, 22.53, 22.31, 22.08. HRMS (ESI) *m/z* 1278.6389 (M + Na^+), calculated for $C_{75}H_{85}N_9O_9Na$ 1278.6368. Deprotection as described above for **13** afforded the title conjugate in quantitative yield. HPLC t_R = 12.82 min. UV−vis (MeOH) λ_{max} (ϵ/M^{-1} cm^{-1}) 414 (336,000), 515 (10,500), 548 (5,600), 589 (3,500), 645 (2,600).^{1}H NMR (CD_3OD, 300 MHz): δ 8.82 (6H, s), 8.15

(7H, d, J = 6.76 Hz), 8.04 (2H, d, J = 8.20 Hz), 7.78 (8H, d, J = 7.45 Hz), 4.46 (1H, d, J = 6.74 Hz), 4.37−4.39 (1H, m), 3.01 (4H, s), 2.64 (2H, t, J = 7.03 Hz), 2.51 (2H, t, J = 7.01 Hz), 2.16 (2H, t, J = 7.21 Hz), 1.31−1.85 (12H, m). HRMS (MALDI) *m/z* 1000.4878 ($M + H^+$), calculated for $C_{61}H_{61}N_9O_5$ 1000.4796.

Conjugate 18. Protected conjugate **18** was synthesized as described above for protected **16** and obtained in 72% yield. HPLC t_R = 9.34 min. UV−vis ($CHCl_3$) λ_{max} (ϵ/M^{-1} cm^{-1}) 420 (241,600), 516 (15,000), 551 (7,300), 590 (4,600), 647 (3,500). ^{1}H NMR ($CDCl_3$, 300 MHz): δ 8.51−8.90 (7H, m), 8.04−8.23 (8H, m), 7.74−7.76 (9H, m), 7.00 (1H, s), 4.97 (2H, s), 4.51 (2H, s), 3.14 (6H, s), 2.55−2.63 (4H, m), 2.24 (2H, s), 1.21−1.66 (54H, m), −2.75 (2H, s). ^{13}C NMR ($CDCl_3$, 62.5 MHz): δ 173.48, 172.42, 171.71, 171.29, 171.03, 156.27, 142.16, 138.55, 134.98, 134.52, 131.01, 127.67, 126.65, 120.06, 119.90, 117.92, 79.18, 53.75, 52.93, 40.08, 39.7, 31.70, 29.67, 28.44, 27.95, 22.43. HRMS (MALDI) *m/z* 1484.8077 ($M + H^+$), calculated for $C_{85}H_{106}N_{11}O_{12}$ 1484.8022. Deprotection as described above for **13** afforded the title conjugate in quantitative yield. HPLC t_R = 8.70 min. UV−vis (MeOH) λ_{max} (ϵ/M^{-1} cm^{-1}) 415 (225,100), 512 (12,100), 547 (6,200), 589 (3,900), 645 (3,000). ^{1}H NMR (CD_3OD, 300 MHz): 8.88 (7H, s), 8.21 (8H, d, J = 6.44 Hz), 8.06 (2H, d, J = 7.91 Hz), 7.82 (9H, d, J = 6.79 Hz), 4.32−4.37 (2H, m), 2.93−3.01 (6H, m), 2.65 (2H, t, J = 7.22 Hz), 2.51 (2H, t, J = 7.44 Hz), 2.17 (2H, t, J = 7.18 Hz), 1.2−1.83 (20H, m). ^{13}C NMR (CD_3-OD, 62.5 MHz): δ 174.82, 174.25, 156.95, 143.33, 136.16, 135.69, 129.64, 119.61, 40.60, 35.81, 32.38, 28.42, 28.11, 23.72. HRMS (MALDI) *m/z* 1127.5726 (M^+), calculated for $C_{67}H_{73}N_{11}O_6$ 1127.5745.

Zn(II) Conjugate 19. Under an argon atmosphere, conjugate **18** (0.005 g, 0.0044 mmol) and $ZnCl_2$ (0.0024 g, 0.0177 mmol) were dissolved in 2 mL of DMF. To this solution were added 0.1 mL of MeOH and 0.150 mL of pyridine. The final mixture was stirred at room temperature for 18 h, the solvent was removed under vacuum, and the residue was filtered through a silica gel plug. The title compound was obtained in quantitative yield. HPLC t_R = 20.52 min. UV−vis (MeOH) λ_{max} (ϵ/M^{-1} cm^{-1}) 422 (190,000), 557 (5,000), 595 (2,800). ^{1}H NMR (CD_3-OD, 300 MHz): 8.88 (7H, s), 8.21 (8H, d, J = 6.44 Hz), 8.06 (2H, d, J = 7.91 Hz), 7.82 (9H, d, J = 6.79 Hz), 4.32−4.37 (2H, m), 2.93−3.01 (6H, m), 2.65 (2H, t, J = 7.22 Hz), 2.51 (2H, t, J = 7.44 Hz), 2.17 (2H, t, J = 7.18 Hz), 1.20−1.83 (20H, m). LRMS (MALDI) *m/z* 1190.082 (M^+), calculated for $C_{67}H_{71}N_{11}O_6Zn$ 1190.488.

Sn(IV) Conjugate 20. Protected conjugate **18** (0.025 g, 0.0168 mmol) and $SnCl_2$ (0.083 g, 0.0437 mmol) were dissolved in 1 mL of pyridine. The reaction mixture was refluxed for 2 h, cooled to room temperature, and diluted with 10 mL of chloroform. The mixture was washed with water (3 × 20 mL), the organic extracts were combined and dried under anhydrous Na_2SO_4, and the solvent was evaporated under vacuum to give the protected Sn(IV) conjugate in quantitative yield. UV−vis ($CHCl_3$) λ_{max} (ϵ/M^{-1} cm^{-1}) 429 (308,000), 562 (12,700), 603 (9,400). ^{1}H NMR ($CDCl_3$, 300 MHz): δ 9.17−9.27 (7H, m), 8.23−8.33 (7H, m), 8.12 (2H, d, J = 8.20 Hz), 7.81−7.89 (9H, m), 6.98 (1H, s), 5.50 (2H, s), 4.92 (2H, s), 3.12 (6H, s), 2.53 (4H, m), 2.23−2.27 (3H, m), 1.27−1.83 (54H, m). LRMS (ESI) *m/z* 1636.30 (M^+), calculated for $C_{85}H_{103}N_{11}O_{12}SnCl$ 1636.11. Deprotection as described above for conjugate **18** gave the title conjugate in quantitative yield. HPLC t_R = 9.91 min. UV−vis (MeOH) λ_{max} (ϵ/M^{-1} cm^{-1}) 422 (341,600), 557 (9,300), 597 (6,400). ^{1}H NMR (CD_3OD, 300 MHz): δ 9.21−9.43 (7H, m), 8.18−8.22 (8H, m), 8.04−8.08 (2H, m), 7.81 (9H, s), 4.23−4.32 (3H, m), 2.85 (6H, m), 2.52 (2H, t, J = 7.37 Hz), 2.37 (2H, t, J = 7.62 Hz), 2.01−2.07 (2H, m), 1.18−1.62 (18H, m). LRMS (MALDI) *m/z* 1280.84, 1245.27, calculated for $C_{67}H_{71}N_{11}O_6SnCl$ 1280.8988, $C_{67}H_{71}N_{11}O_6Sn$ 1245.46.

Solid-Phase Synthesis of Porphyrin Conjugates. Method A. Peptidyl resin (0.025 mmol) was added to a glass synthesizer, washed with DMF, and left to stand for 1 h, before being filtered. To the resin was added a 500 μL solution containing 0.05 mmol of porphyrin **6**, 0.150 mmol of DIEA, 0.05 mmol of HOBt, and 0.05 mmol of TBTU. The reaction mixture was stirred overnight at room temperature and then filtered to afford a dark purple resin. A fresh solution of porphyrin **6** (0.025 mmol) in DIEA, HOBt, and TBTU was added and the mixture stirred for an additional 12 h. After filtration, the resin was washed repeatedly with DMF until the filtrate was colorless and then with dichloromethane and methanol, before being dried under vacuum. Cleavage and deprotection was accomplished with 3 mL of a mixture of TFA/phenol/TIS/H_2O in 88/5/2/5 ratio, at room temperature for 4 h. The resin was filtered and washed with TFA (3 × 2 mL), and then the filtrates were combined and evaporated under vacuum to give a green residue. Addition of 5 mL of cold Et_2O gave a fine green precipitate which was centrifuged, washed successively with Et_2O, and dried under vacuum. Purification of the conjugates was accomplished by reverse phase HPLC using a Luna C_{18} semipreparative column (10 × 250 mm, 5 μm) and a buffer system of water/acetonitrile, both containing 0.1% TFA with a stepwise gradient from 40 to 75%. The fraction containing the conjugate was collected and lyophilized to yield pure conjugate. The purity of the peptides was >98% as obtained by HPLC on an analytical Delta Pak C_{18} column (3.9 × 150 mm, 5 μm).

Method B. Peptidyl resin (0.050 mmol) was added to a glass synthesizer, washed with DMF, and left to stand for 1 h, before being filtered. To the resin was added a 500 μL solution containing 0.150 mmol of porphyrin **5** and 0.300 mmol of Et_3N. The reaction mixture was stirred overnight at room temperature and filtered, a fresh solution of 0.050 mmol of **5** in Et_3N was added, and the mixture was stirred for another 12 h. After filtration, the resin was washed with DMF, dichloromethane, and methanol as described above and dried under vacuum. Cleavage and deprotection was carried out as described in Method A. The purification of the conjugates was accomplished by reverse phase HPLC using a Luna C_{18} semipreparative column and a water/acetonitrile buffer containing 0.1% TFA with a stepwise gradient from 40 to 95%. The fraction containing the conjugate was collected and lyophilized to yield the pure conjugate. The purity of the peptides was >97% as obtained by HPLC on an analytical Delta Pak C_{18} column.

Conjugate 21 was prepared as described in Method B. Yield 38%. HPLC t_R = 15.25 min. UV−vis (MeOH) λ_{max} (ϵ/M^{-1} cm^{-1}) 414 (205,300), 512 (11,300), 547 (5,000), 590 (3,400), 645 (2,300). ^{1}H NMR (CD_3OH, 250 MHz): δ 8.72−8.77 (8H, m), 8.33 (1H, d, J = 7.42 Hz), 8.19−8.25 (10H, m), 8.03−8.09 (2H, m), 7.77−7.80 (9H, m), 7.42 (2H, s), 7.06−7.09 (3H, m), 3.15−3.19 (6H, m), 3.03−3.08 (2H, m), 1.4−1.6 (18H, m), −0.033 (3H, s). LRMS (MALDI) *m/z* 1284.72 (M^+), calculated for $C_{69}H_{80}N_{20}O_4S$, 1284.63.

Conjugate 22 was prepared as described in Method A. Yield 32%. HPLC t_R = 8.53 min. UV−vis (MeOH) λ_{max} (ϵ/M^{-1} cm^{-1}) 414 (236,400), 515 (6,600), 548 (3,300), 588 (2,300), 645 (2,000). ^{1}H NMR (CD_3OH, 250 MHz): 8.71−8.76 (8H, m), 8.20−8.26 (10H, m), 8.03 (2H, t, J = 8.59 Hz), 7.69−7.80 (16H, m), 2.82−2.85 (6H, m), 2.50 (2H, t,

J = 6.85, 7.36 Hz), 2.35 (2H, t, J = 6.81, 7.95 Hz), 1.91 (2H, t, J = 7.97 Hz), 1.39−1.62 (19H, m), −0.04 (2H, s). HRMS (MALDI) *m/z* 1127.5897, calculated for $C_{67}H_{75}N_{12}O_5$1127.5893.

Conjugate 23 was prepared as described in Method A. Yield 52%. HPLC t_R = 12.56 min. UV−vis (MeOH) λ_{max} (ϵ/M^{-1} cm^{-1}) 414 (227,300), 512 (9,900), 547 (6,600), 590 (3,300), 645 (2,300). ^{1}H NMR (CD_3OH, 250 MHz): δ 8.72−8.76 (8H, m), 8.28−8.32 (2H, m), 8.20 (10H, s), 8.11 (1H, d, J = 7.08 Hz), 8.00 (2H, d, J = 8.07 Hz), 7.68−7.76 (9H, m), 7.56 (1H, s), 7.37−7.43 (3H, m), 2.51 (2H, t, J = 6.84 Hz), 2.37 (2H, t, J = 6.9 Hz), 2.00 (2H, t, J = 7.38, 7.04 Hz), 1.40−1.63 (12H, m), −0.028 (2H, s). HRMS (MALDI) *m/z* 1211.6175 (M + H^+), calculated for $C_{67}H_{75}N_{18}O_5$, 1211.6168.

Conjugate 24 was prepared as described in Method A. Yield 45%. HPLC t_R = 9.13 min. UV−vis (MeOH) λ_{max} (ϵ/M^{-1} cm^{-1}) 414 (235,900), 512 (7,000), 547 (3,500), 588 (2,400), 645 (2,100). ^{1}H NMR (CD_3OH, 250 MHz): δ 8.72−8.77 (8H, m), 8.32−8.34 (1H, d, J = 7.11 Hz), 8.19−8.25 (10H, m), 7.99−8.06 (2H, m), 7.78−7.90 (9H, m), 7.39 (1H, s), 7.06−7.12 (3H, m), 3.09−3.17 (6H, m), 3.06−3.09 (2H, m), 2.51 (2H, t, J = 7.91 Hz), 2.37 (2H, t, J = 7.40 Hz), 1.91 (2H, t, J = 6.45 Hz), 1.4−1.6 (18H, m), −0.03 (2H, s). HRMS (MALDI) *m/z* 1339.7168 (M^+), calculated for $C_{73}H_{86}N_{20}O_6$, 1339.7117.

Conjugate 25 was prepared as described in Method A. Yield 54%. HPLC t_R = 9.65 min. UV−vis (MeOH) λ_{max} (ϵ/M^{-1} cm^{-1}) 414 (263,300), 512 (7,800), 548 (3,800), 588 (2,500), 644 (2,000). ^{1}H NMR (7% D_2O/H_2O, 400 MHz): δ 8.68 (4H, d, J = 8.89 Hz), 8.43−8.56 (5H, m), 8.22 (2H, d, J = 9.31 Hz), 7.67 (2H, s), 7.55 (2H, broad s), 7.14−7.23 (4H, m), 4.28−4.33 (3H, m), 3.19−3.27 (6H, m), 2.98−3.02 (3H, m), 2.70 (2H, t, J = 8.44 Hz), 2.54 (2H, t, J = 9.40 Hz), 2.09−2.17 (2H, m), 1.25−1.87 (18H, m), −0.04 (2H, s). HRMS (MALDI) *m/z* 1340.7141 (M + H^+), calculated for $C_{73}H_{87}N_{20}O_6$ 1340.6264.

Cell Culture. The HEp2 cell line was purchased from ATCC. The cells were maintained in a 50:50 mixture of MEM:Advanced MEM (Gibco) and 5% FBS (Gibco) in a humidified, 5% CO_2 incubator at 37 °C. PBS, FBS, Triton X100, and trypsin were purchased from Gibco. All conjugate solutions were filter sterilized using a 0.22 μm Pal syringe filter.

Cytotoxicity. HEp2 cells were plated at a concentration of 10,000 cells per well on a Costar 96-well plate and allowed to attach overnight. Conjugate stock solutions were prepared in DMSO at a concentration of 50 mM. These stocks were diluted to give a final concentration of 500 μM in medium at 1% DMSO. Serial 2-fold dilutions were then made into medium containing 1% DMSO to give a concentration range of 500 μM down to 7.8 μM and maintaining the 1% DMSO concentration. The cells were then incubated 18 h in the dark. Cytotoxicity was measured using the Promega Cell Titer Blue assay, reading the fluorescent signal using a FluoStar Optima plate reader from BMG at 520 nm excitation and 594 nm emission.

Cellular Uptake. HEp2 cells were seeded as described above and then exposed to 10 μM conjugate in medium for 25, 12, 8, 4, 2, and 1 h time periods. At the end of the loading period, the medium was removed, and the cells were washed three times with PBS and solubilized with 0.25% Triton ×100 in PBS. The intracellular accumulation of conjugate was determined by measuring the porphyrin's fluorescence emission on a BMG FluoStar Optima plate reader using excitation/emission wavelengths of 410 and 650 nm, respectively. Cell numbers were measured using the CyQuant Cell Proliferation Assay (Molecular Probes).

Intracellular Localization. HEp2 cells were seeded onto Lab-Tek II, two-chamber coverglass and incubated for 72 h. Conjugate was then added from a 10 mM stock solution in DMSO to reach a final concentration of 10 μM (the DMSO concentration never exceeded 1%). The cells were incubated overnight (18 h) and then washed with drug-free medium and given medium containing 50 mM HEPES pH 7.2. The coverslips were examined using a Zeiss Axiovert 200M inverted fluorescent microscope fitted with standard FITC and Texas Red filter sets (Chroma Technology Corp.). For colocalization experiments LysoSensor Green DND-189, MitoTracker Green FM and Hoechst 33342 (Molecular Probes) were used. The tracer compounds were diluted into medium to a final concentration of 50 nM (LysoSensor Green), 250 nM (MitoTracker Green) or 1 mg/mL (Hoechst), 10 min before microscopy. The cells were incubated concurrently with conjugate for 30 min (LysoSensor Green and MitoTracker Green) or 10 min (Hoechst) before washing and viewed by microscopy. In addition, three lipid mixtures of conjugates **22** or **23** were added to the cells prior to microscopy. Avanti transfection lipids, Cardiolipin (Avanti Polar Lipids) and Lipofectamine Transfection Reagent (Invitrogen) were used as the delivery vehicles. Since the Avanti lipids were provided in chloroform, the solvent was first removed under nitrogen before resuspension in sterile distilled water at 2 mg/mL. Lipofectamine was supplied in water and used as received. A mixture containing 2.5 μL of the lipid and 25 μL of serum-free medium was incubated for 15 min. Conjugates **22** and **23** (1 μL of 10 mM stock solution) were diluted into 25 μL serum-free medium, mixed with each lipid, and incubated for 45 min. The lipid mixtures were then diluted to 600 μL using serum-free medium, added to cells grown on Lab Tek chamber coverslips, incubated for 2.5 h, before adding 600 μL of medium containing 10% FBS (2×) and the cells incubated overnight. Microscopy was performed as described above.

RESULTS

The coupling of mono-aminoporphyrin **1** with protected amino acids and peptides was performed in either solution- or solid-phase, as described below. Mono-aminoporphyrin **1** was used as the starting material, because of its high solubility in organic solvents and easy synthesis on a multigram scale from *meso*-tetraphenylporphyrin (*28*). Porphyrins bearing *meso*-carboxyphenyl groups have also been used in such conjugation reactions (e.g. *29*) but these molecules are considerably less soluble than the amino derivatives and generally give low yields of the target conjugates. The Boc- and Z-protected peptides were obtained by either solution- or solid-phase syntheses, as previously reported (*30*, *31*). All compounds were completely characterized by spectroscopic methods, as described in the Experimental Section.

Solution-Phase Synthesis of Porphyrin Conjugates. Direct conjugation of **1** to Boc-L-Lys(Boc)OH using DCC/DMAP in dichloromethane (*32*) gave compound **2a** in 65% yield (Scheme 1). Under the same conditions, conjugates **3** and **4** were obtained in 40 and 18% yields, respectively. These yields could be improved to 96, 65, and 45%, respectively, when DMF was used as the solvent and HOBt/EDCI as the coupling agents (*33*, *34*). To further increase the conjugation efficiency, the amino group of **1** was converted into an isothiocyanate (*18*, *35*) by reaction of **1** with 1,1′-thiocarbonyldi-(2*H*)-pyridone,

Scheme 1[a]

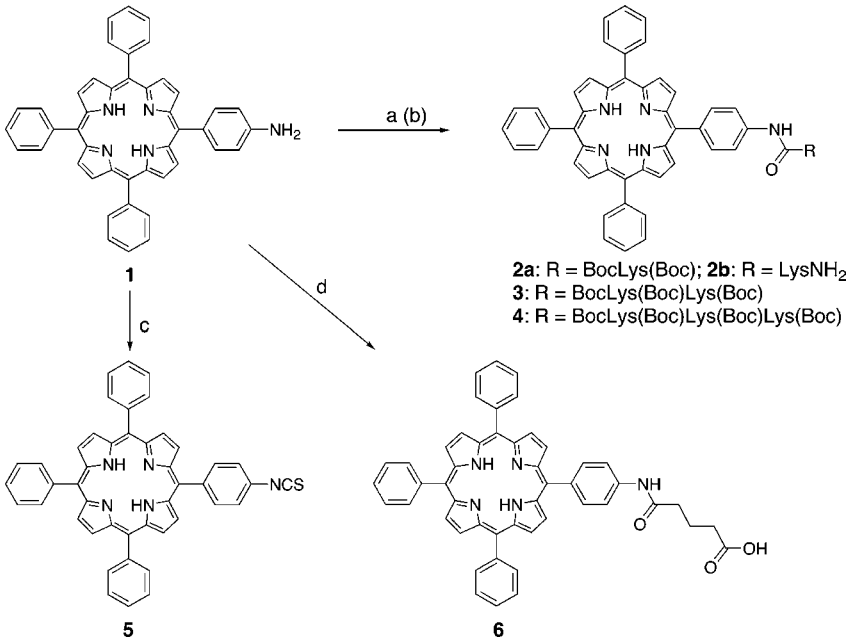

[a] Conditions: (a) Boc-protected amino acid or peptide, DCC, DMAP, CH_2Cl_2, rt, 48 h (18−65%) or HOBt, EDCI, DMAP, Et_3N, DMF, rt, 48 h (45−96%). (b) TFA, rt, 4 h (100%). (c) 1,1′-Thiocarbonyldi-(2*H*)-pyridone, CH_2Cl_2, Ar, rt, 2h (84%). (d) Glutaric anhydride, DMF, rt, 24h (100%).

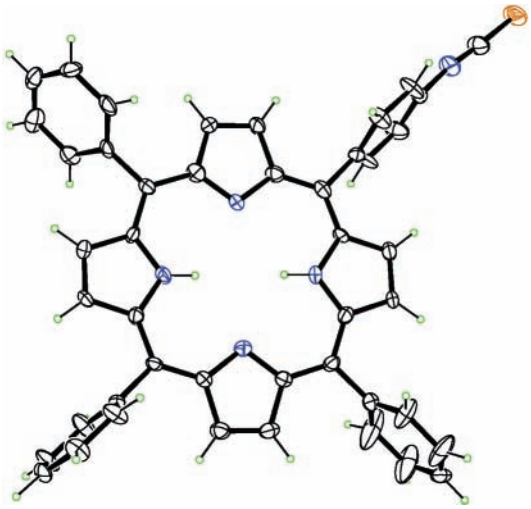

Figure 1. Molecular structure of porphyrin isothiocyanate **5**.

affording **5** in 84% yield (Scheme 1). The molecular structure of porphyrin **5** is shown in Figure 1. The porphyrin core is reasonably planar, having mean deviation of 24 atoms from their best plane only 0.062 Å, and maximum deviation 0.151(7) Å. The phenyl planes form dihedral angles with the porphyrin plane in the range 61.6(1)−82.4(2)° and that involving the ring carrying the isothiocyanate group is in the middle of that range, 76.1-(1)°.

Reaction of porphyrin **1** with glutaric anhydride gave carboxylic acid **6** in quantitative yield (Scheme 1). The use of porphyrin **6** in the conjugation reactions allowed us to study the effect of a five-carbon chain between the porphyrin and the positively charged peptides.

We investigated the conjugation of isothiocyanate **5** with various protected peptides under different reaction conditions and using both free amino terminus Z- and Boc-protected peptides (Table 1). No reaction took place in aqueous solution due to the poor solubility and limited stability of porphyrin **5** in water (Table 1, entry 1).

Table 1. Reaction Conditions for Coupling Porphyrin Isothiocyanate 5 to Protected Peptides

entry	protected peptide	solvent	% yield
1	HLys(Z)OH	DMSO/pH = 9.2, 0.1 M carbonate buffer	no rxn
2	HLys(Z)OBz	THF	90
3	HLys(Z)Lys(Z)OBz	THF	69
4	HLys(Z)Lys(Z)OBz	DMF	67
5	HLys(Z)Lys(Z)Lys (Z)OBz	DMF/$CHCl_3$, 2/1	63
6	HLys(Boc)OtBu	DMF	93
7	HLys(Boc)Lys(Boc)OtBu	DMF	45
8	HLys(Boc)Lys(Boc)Lys(Boc)OtBu	DMF	35

Although high yields of the conjugates were obtained with the Z-protected peptides (Table 1, entries 2−5), the deprotection to the corresponding free peptide conjugates was problematic. Indeed several deprotection methodologies were investigated, including catalytic hydrogenation (*36*), transfer hydrogenation (*37*), and dealkylation using Me_3SiI (*38*), but all were unsuccessful giving mixtures of partially deprotected conjugates. On the other hand, the Boc groups were easily cleaved in quantitative yield using TFA at room temperature (Scheme 2). The thus-obtained deprotected conjugates **13**−**15** were insoluble in water and mainly soluble in polar organic solvents such as $CHCl_3$, DMF, and DMSO.

Conjugates of porphyrin carboxylic acid **6** to Boc-protected peptides were synthesized in good yields using HOBt/TBTU in DMF, as shown in Scheme 3. A similar procedure has been recently reported for the coupling of a carboxy-functionalized porphyrin with the free amino terminus of a cyclic pentapeptide (*39*). Removal of the Boc group as described above produced conjugates **16**−**18** in quantitative yield. In contrast to the porphyrin isothiocyanate conjugates, compounds **16**−**18** are partially soluble in aqueous solutions and their water solubility increases with the number of amino acid residues on the peptide chain. In addition, the metallo-conjugates **19** and **20** were prepared using a similar route in quantitative yields, by either direct insertion of Zn-(II) into conjugate **18** using $ZnCl_2$ in DMF or by reaction

Scheme 2[a]

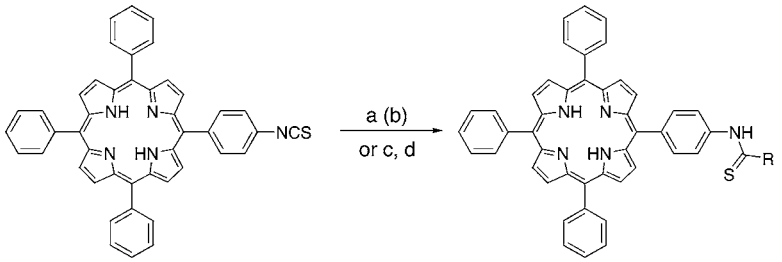

5

7: R = Lys(Z)OBz
8: R = Lys(Z)Lys(Z)OBz
9: R = Lys(Z)Lys(Z)Lys(Z)OBz
10: R = Lys(Boc)OtBu
11: R = Lys(Boc)Lys(Boc)OtBu
12: R = Lys(Boc)Lys(Boc)Lys(Boc)OtBu
13: R = LysOH
14: R = LysLysOH
15: R = LysLysLysOH
21: R = ArgArgLysArgNH$_2$

[a] Conditions: (a) Protected amino acid or peptide, DMF, rt, 48 h (35−93%). (b) TFA, rt, 4 h (100%). (c) Free amino terminus Boc-protected amino acid or peptide, Et_3N, DMF, rt, 24 h. (d) 88:5:2:5 TFA/phenol/TIS/H_2O, rt, 4 h (38% from **5**).

Scheme 3[a]

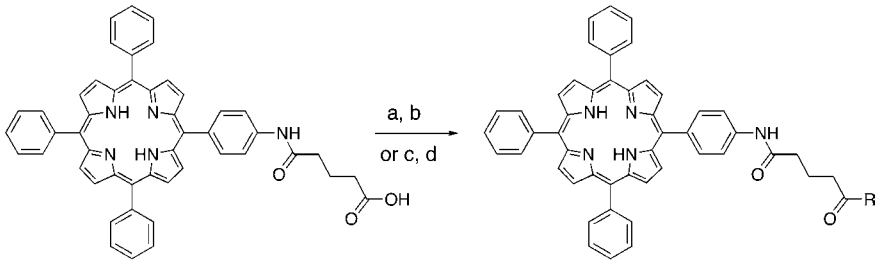

6

16: R = LysOH
17: R = LysLysOH
18: R = LysLysLysOH
22: R = LysLysLysNH$_2$
23: R = ArgArgArgNH$_2$
24: R = LysArgArgArgNH$_2$
25: R = ArgArgLysArgNH$_2$

[a] Conditions: (a) free amino terminus Boc-protected amino acid or peptide, HOBt, TBTU, DIEA, DMF, rt, 48 h (53−72%). (b) TFA, rt, 4 h (100%). (c) free amino terminus Boc-protected peptidyl resin, HOBt, TBTU, DIEA, DMF, rt, 24 h. (d) 88:5:2:5 TFA/phenol/TIS/H_2O, rt, 4h (32−54% from **6**).

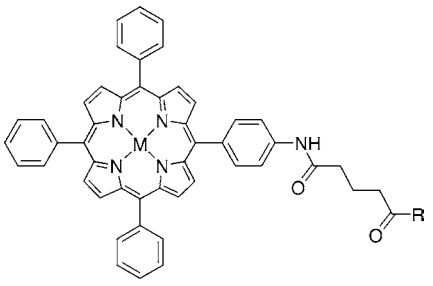

19: R = LysLysLysOH, M = Zn(II)
20: R = LysLysLysOH, M = Sn(IV)

of protected conjugate **18** with $SnCl_2$ in pyridine, followed by deprotection with TFA.

Solid-Phase Synthesis of Porphyrin Conjugates. The peptidyl PAL-PEG-PS resins used in the solid-phase synthesis of conjugates **21**−**25** reacted with porphyrin isothiocyanate **5** or with carboxylic acid **6** in the presence of, respectively, Et_3N or HOBt/TBTU/DIEA, as shown in Schemes 2 and 3 (*40*, *41*). Using this methodology, the deprotection and cleavage of the porphyrin−peptide conjugates from the solid support was achieved in a single step upon treatment with a mixture of TFA, phenol, TIS, and water in the ratio 88:5:2:5. The resulting conjugates **21**−**25** were obtained as the C-terminally amidated peptides, in 32−54% overall yields.

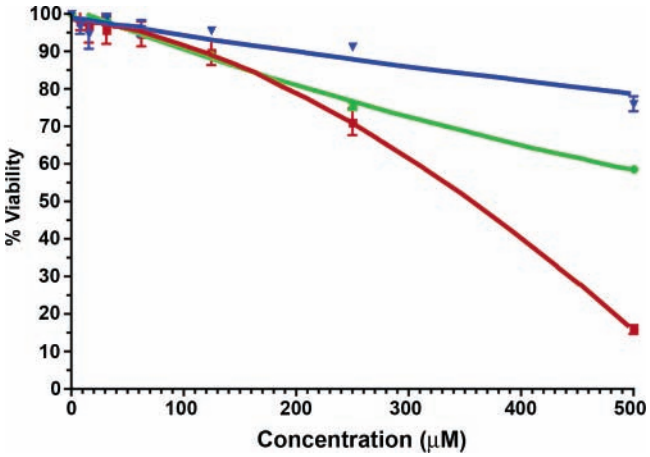

Figure 2. Dark cytotoxicity of conjugates **17** (green), **20** (blue), and **23** (red) toward HEp2 cells using a Cell Titer Blue assay.

Cellular Studies. The dark cytotoxicity and cellular uptake of representative porphyrin conjugates were investigated in human HEp2 cells (Figures 2 and 3). The cytotoxicity was assayed using a Cell Titer Blue assay

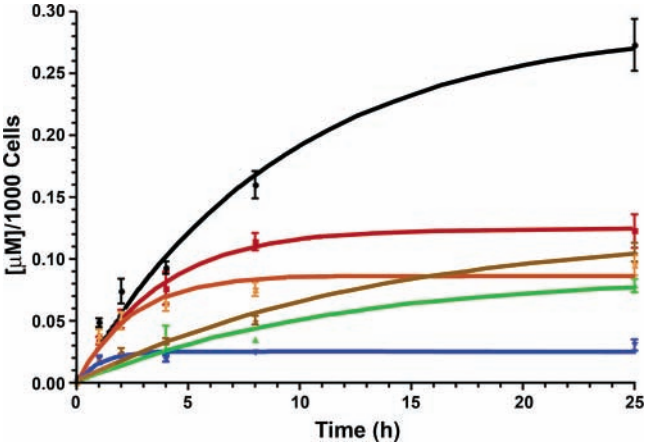

Figure 3. Time-dependent uptake of conjugates **15** (brown), **17** (green), **20** (blue), **23** (red), **24** (black), and **25** (orange) at 10 μM by HEp2 cells.

to evaluate the cytotoxicity of conjugates **17**, **20**, and **23**, at concentrations up to 500 μM, 18 h after exposure (*42*). The conjugates studied were the most water-soluble, and all showed low dark toxicity (IC_{50} > 250 μM) toward HEp2 cells (Figure 2). The time-dependent uptake of conjugates **15**, **17**, **20**, **23**, **24**, and **25** at a concentration of 10 μM in HEp2 cells was investigated. At this concentration all conjugates were nontoxic to the cells, as evaluated using the Cell Titer Blue assay (Supporting Information). Significant differences in the cellular uptake were observed, as seen in Figure 3, indicating that the number, nature, and sequence of amino acids, as well as the presence of a chelated metal ion affect the uptake of the conjugates. The di- and tri-lysine conjugates **17** and **15** show similar uptake kinetics, and at short time points (up to 4 h) there was no significant difference in their uptake by HEp2 cells. However after 25 h, the amount of tri-lysine conjugate **15** accumulated within cells is about 25% higher than that of the di-lysine derivative **17**. The Sn(IV) complex **20** is taken-up faster than **15** and **17**, reaching a plateau after about 2 h exposure time to cells. At longer time points (>4 h), the tri-lysine metal complex **20** is clearly the least accumulated within cells of all conjugates studied. On the other hand, the arginine-containing conjugates (**23**–**25**) were taken-up by HEp2 cells to a much larger amount (>50%) than the lysine derivatives at short time points (up to 4 h). After 25 h, conjugate **24** was clearly the one that accumulated the most within cells, followed by **23**, suggesting that at least three consecutive arginine residues are necessary for high cellular uptake.

The subcellular localization of all conjugates and starting porphyrins was also investigated in HEp2 cells. Figure 4 shows the fluorescent patterns observed for starting porphyrin **1** and conjugates **14**–**16**, **19**, **21**–**24** (supplementary data is available for all conjugates in the Supporting Information). All compounds were found to localize into vesicles, suggesting similar mechanisms of cellular uptake for all conjugates studied. Colocalization experiments were performed for all compounds using the organelle-specific fluorescent probes LysoSensor Green (lysosomes), MitoTracker Green (mitochondria), and Hoechst 33342 (nuclei). As shown in Figure 5 for conjugate **14**, the preferential sites of intracellular localization of **14** were the cell lysosomes. Similar observations were obtained for all other conjugates and for starting por-

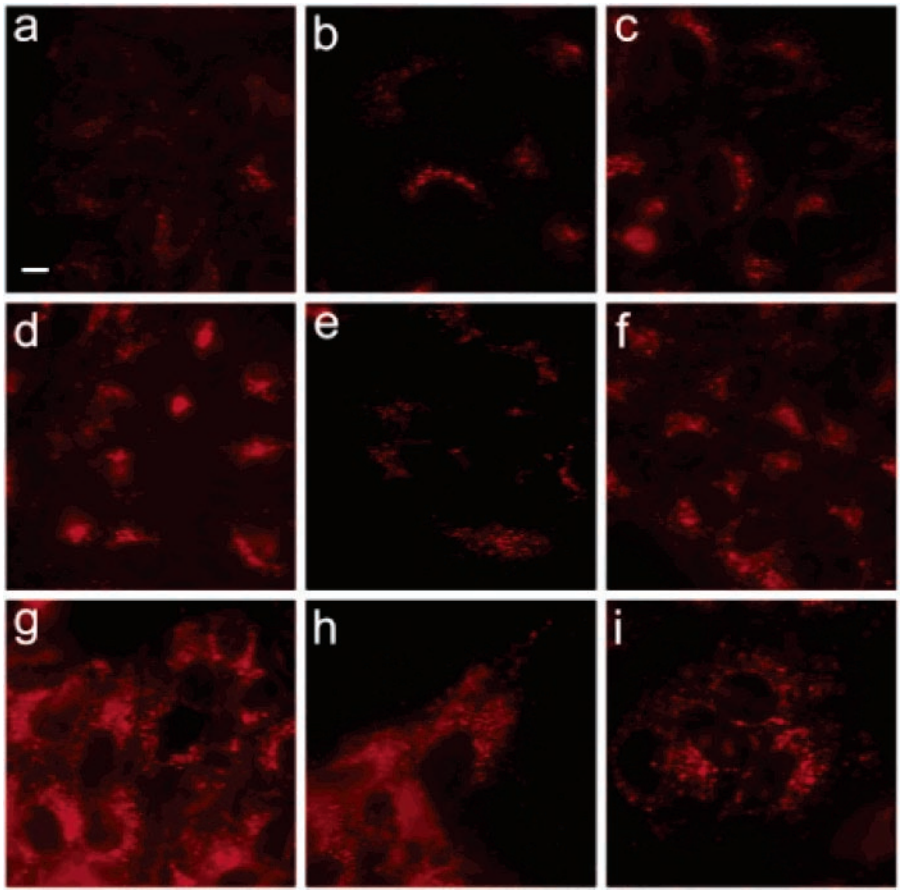

Figure 4. Subcellular fluorescence of (a) porphyrin **1**, and conjugates (b) **14**, (c) **15**, (d) **16**, (e) **19**, (f) **21**, g) **22**, (h) **23**, (i) **24**, in HEp2 cells at 10 μM for 18 h. Scale bar: 10 μm.

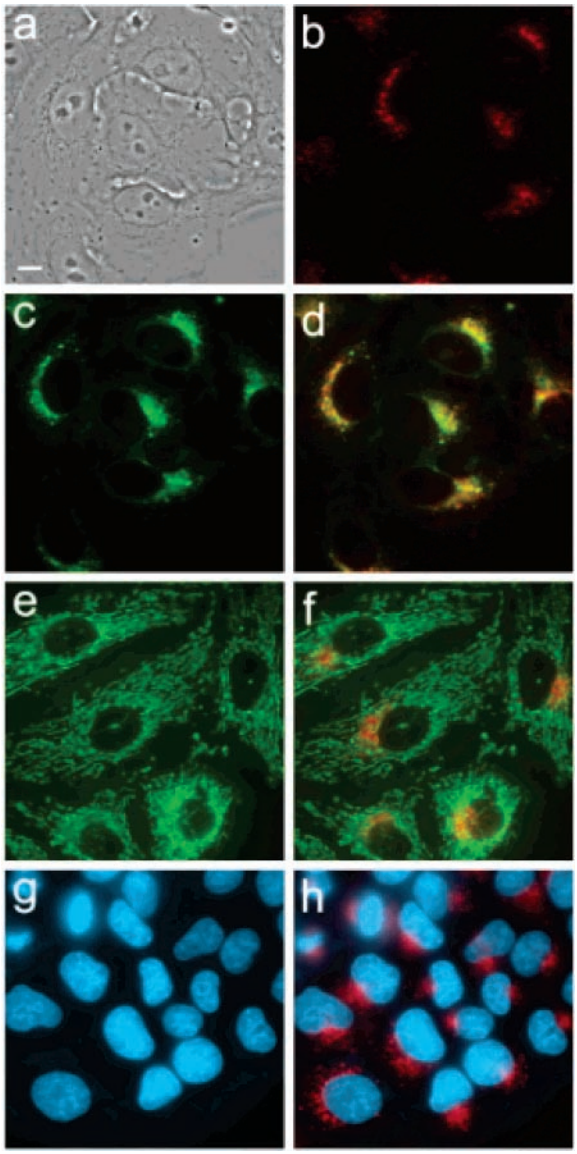

Figure 5. Subcellular localization of conjugate **14** in HEp2 cells at 10 μM for 18 h. (a) Phase contrast, (b) **14** fluorescence, (c) LysoSensor Green fluorescence, (e) MitoTracker Green fluorescence, (g) Hoechst fluorescence, (d, f, h) overlays of organelle tracers with **14** fluorescence. Scale bar: 10 μm.

phyrins **1** and **5** (Supporting Information). To investigate the effect of the route of delivery on cellular localization, three different transfection lipids, Avanti, Cardiolipin, and Lipofectamine, were used as delivery vehicles for conjugates **22** and **23**. Fluorescent microscopy revealed that all lipid mixtures transported the conjugates to the mitochondria of HEp2 cells (Supporting Information). We have previously observed that the use of liposomes as delivery vehicles can have a dramatic effect on the subcellular sites of accumulation of photosensitizers (*42*).

Molecular Modeling. Conformation analysis for conjugates **15**, **18**, **23**, **24**, and **25** was performed in a vacuum and, in the case of conjugate **18**, also in the presence of water. Only the minimum energy conformations were selected and those determined under vacuum are shown in Figure 6. All structures show a bend conformation of the peptides over the porphyrin ring, which is more pronounced in the case of the lysine derivatives bearing the five-carbon linker. In some cases (e.g. Figure 6a) additional stabilization was obtained via formation of an intramolecular bond between the N−H of a lysine residue and the porphyrin inner N−H. Furthermore, additional stabilization via hydrophobic interactions between the aliphatic chain of the lysine residue and the porphyrin aromatic system was observed (e.g. Figure 6b). Our results suggest that hydrogen bonding and hydrophobic interactions of the peptide chain with the porphyrin platform reduce the conformational entropy (by as much as 60 kcal/mol) as compared to the linear conformation. The water effects were evaluated only for conjugate **18**, and the minimum energy conformation found was similar to the vacuum structure shown in Figure 6b, with only a slight change on the position of the amine group of the lysine residues (see Supporting Information). It is, however, likely that in the presence of water, intermolecular forces (such as $\pi-\pi$ stacking of porphyrin macrocycles) predominate over the intramolecular interactions. Although the NMR chemical shifts of the Cα peptidyl protons can also be useful in the assignment of the secondary structure of peptides, we were not able to use this technique because of the overlap of these protons with those of the solvent.

DISCUSSION

The coupling of peptides to aminophenylporphyrin **1** via amide bond formation using traditional coupling reagents (DCC or EDCI) requires several days, due to the weak nucleophilicity of the aromatic amino group in pophyrin **1** and to steric factors, as previously observed (*43*). For example, while the coupling of porphyrin **1** with Boc-glycine produced the corresponding conjugate in 93% yield, the coupling with Boc-lysine under the same conditions resulted in 65% yield, and no conjugate was obtained in the presence of activated Boc-lysine with NHS. The reaction yields decreased with the increasing number of amino acid residues on the protected peptide, even under optimized coupling conditions (HOBt/EDCI/TBTU/DIEA in DMF). Slightly higher yields of the target conjugates were obtained upon conversion of the amino group of porphyrin **1** to a reactive isothiocyanate functionality (*18*, *35*), although steric factors still significantly influenced the reaction yields (Table 1). Using isothiocyanate porphyrin **5**, conjugates **13**−**15** were obtained in solution phase, in 35−93% yields. The free amino terminus Boc-protected peptides resulted in higher yields of the target conjugates, due to the easier cleavage of this protecting group compared with the Z-protected peptides. This result can be due, in the case of catalytic hydrogenation, to the poisoning of the palladium catalyst by the sulfur on the isothiourea group. The solution-phase conjugation of Boc-protected peptides to carboxylic acid porphyrin **6** containing a five-carbon spacer resulted in high yields of the target conjugates **17** and **18** that were independent from the size of the reacting peptide. The Zn(II)− and Sn(IV)−porphyrin conjugates were also prepared to investigate the effect of a centrally chelated diamagnetic metal ion on the cellular uptake and subcellular localization. In complexes **19** and **20** the amino groups on the lysine residues can potentially interact with the metal ion, especially in the case of the Zn(II) complex.

The solid-phase synthesis of C-amidated conjugates **21**−**25** proceeded considerably faster although lower yields were obtained compared with the solution-phase reactions. While the solution-phase conjugations are more time-consuming because they require rigorous isolation, purification, and characterization of the target compounds following each synthetic step, the conjugation to biomolecules built on a solid support allows a stepwise assembly of the conjugates with no isolation of interme-

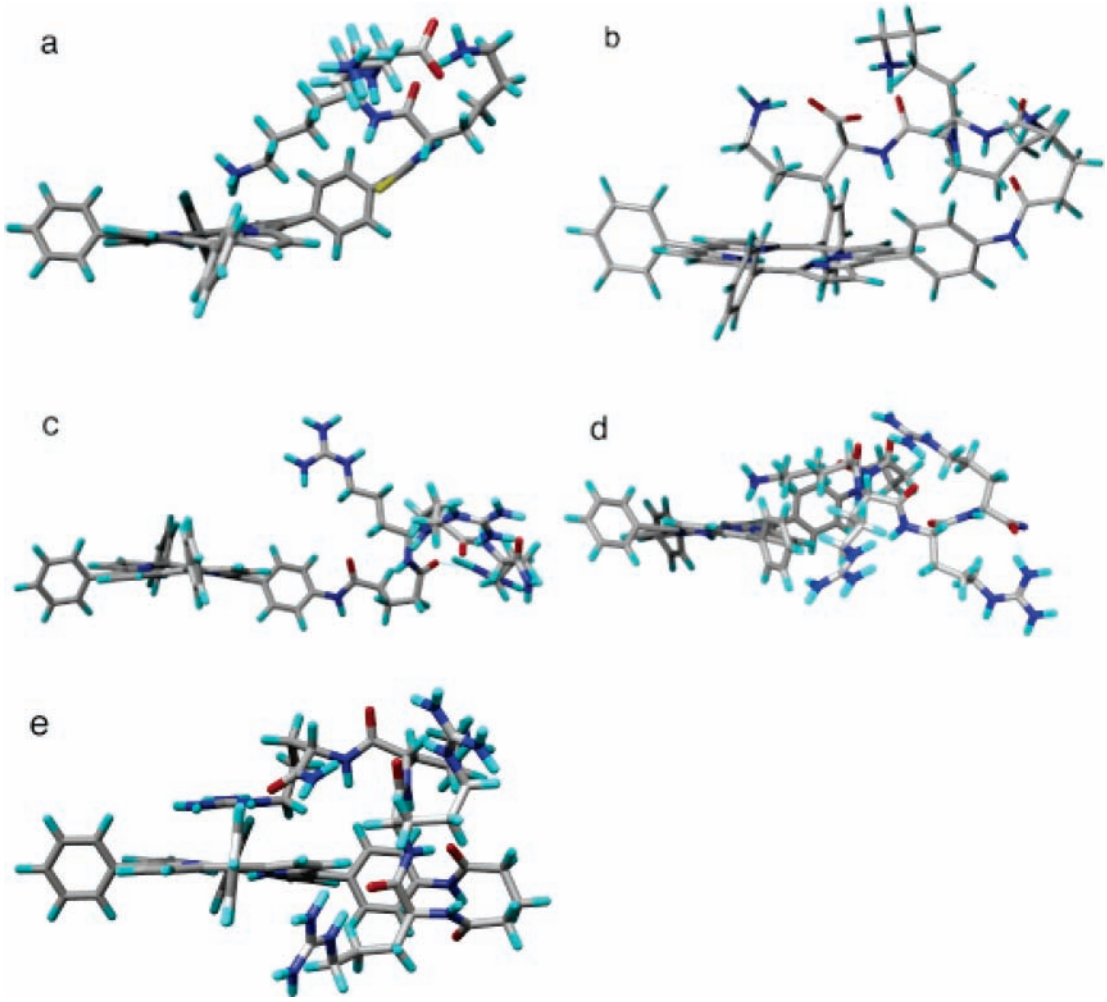

Figure 6. Energy-minimized conformations in a vacuum for conjugates (a) **15**, (b) **18**, (c) **23**, (d) **24**, and (e) **25**.

diates. The yields of the latter route are, however, lower because of poor solvation, increased intra- and intermolecular interactions in the growing peptide chains, and to porphyrin- or peptide-polymer adsorptions. Furthermore, in solid-phase synthesis various byproducts from either incomplete reactions, side reactions, or impure reagents usually accumulate on the resin during chain assembly, contaminating the final product and requiring HPLC purification; lower reactions rates are therefore observed as a result of secondary structures or aggregates formed with other peptide chains or with the polymer support.

The dark cytotoxicity of the most water-soluble porphyrin conjugates bearing two or three lysine or arginine residues was evaluated at concentrations up to 500 μM (Figure 2). All conjugates showed low dark toxicity (IC_{50} > 250 μM), and the least toxic was the Sn(IV) complex **20**, which was also the least accumulated within HEp2 cells at long exposure times (>2 h) (Figure 3). The cellular uptake of the conjugates depended significantly on the number, nature, and sequence of the amino acid residues, the chelated metal ion, and the C-termination (OH vs NH_2), i.e., on the overall molecular charge and its distribution. For all compounds studied, the metal-free conjugates showed similar uptake kinetics, and the amount of conjugate accumulated within cells was higher for those containing three consecutive arginine residues (Figure 3). It has been previously observed that peptides containing cationic amino acids, in particular arginine-rich peptides, have a unique ability to cross cellular membranes (*44*−*47*). This property is attributed to the unique structure of the positively charged guanidinium group and its ability to form bidentate hydrogen bonds with, for example, membrane-containing phosphate groups. Lysine-rich peptides usually show lower uptake compared with arginine peptides, and this uptake is dependent on the number of residues, suggesting that the overall charge is important but certainly not the only factor (*47*). In agreement with these studies our results show that a tri-lysine conjugate (**15**) is taken-up to a higher extent than a di-lysine derivative (**17**), that arginine-containing conjugates (e.g. **23** and **24**) rapidly and most effectively accumulate within cells, and that the amino acid sequence (LysArgArgArg vs ArgArgLysArg, i.e., conjugates **24** and **25**) plays an important role on the cellular uptake of these compounds. Furthermore, the presence of a centrally chelated metal ion (as in **20**) significantly changes the uptake kinetics, promoting higher uptake at low exposure times (<2 h), after which a plateau is reached and, unlike the metal-free conjugates, no significant amount of metalloconjugate is further taken-up by the cells.

The preferential sites of subcellular localization of aminophenylporphyrin **1** and its conjugates are the cell lysosomes (Figure 4), which suggest a similar mode of uptake for all molecules studied, probably involving an endocytic pathway and subsequent localization into the lysosomes. Similar observations have been recently reported for several cationic porphyrins with different degrees of lipophilicity (*48*). The presence of the short

peptide chain and the number, nature, and sequence of amino acids did not change the preferential subcellular sites of the porphyrin macrocycle (Figure 4a). However, in the presence of a lipid delivery vehicle, the main subcellular sites of localization were the mitochondria. Our results suggest that, in the absence of a carrier, these porphyrin−peptide conjugates do not assume distinct extended conformations for the peptidyl chains, either forming aggregates or assuming bend conformations in solution. The preferred conformations of peptides in aqueous media have been previously investigated using molecular dynamics (MD) computer simulations and are known to depend on the number, nature, and sequence of the amino acid residues on the peptide chain (*49*−*51*). For example, conformational studies of a tri-lysine peptide showed that this molecule does not adopt an extended or β-sheet conformation in water; instead it prefers to form an helix-type structure (*50*). Additionally, the electrostatic repulsion observed in MD in a vacuum between two positively charged arginine residues in close proximity was overcome by the presence of bridging water molecules (*52*). Our MD calculation studies of representative conjugates in a vacuum and in water show that the porphyrin ring influences the conformation of the peptide chain by providing extra hydrophobic and hydrogen bonding interactions that favor a bent (over extended) conformation of the peptide chains over the porphyrin ring (Figure 6). The hydrophobic and Coulombic interactions between the porphyrin and the peptides are presumably stronger that those between the short peptide chains, thus favoring a bundle structure for these conjugates. These results do not exclude the possibility of self-assembly of the conjugates in water (*53*) and can in part explain the similar intracellular patterns observed for all conjugates synthesized. Furthermore, our results suggest that a longer linker and longer amino acid sequences will likely favor an extended or β-sheet conformation for the peptide chains conjugated to a porphyrin macrocycle. It is worth noting that although no significant difference was observed in the in vitro subcellular localization of our conjugates, it is possible that their in vivo distribution following systemic administration is quite different, as it depends on multiple factors including the amount and nature of proteins and lipoproteins in the blood. It was recently reported that a porphyrin conjugated to a nuclear localizing sequence peptide has high affinity for low-density lipoproteins (*54*), but no results were reported on the preferential sites of subcellular localization of this conjugate. We anticipate that careful choice of the peptide chain and linker to the porphyrin macrocycle will lead to unique conjugates with ability for crossing cell membranes and localization in specific organelles.

ACKNOWLEDGMENT

The authors thank Martha Juban for peptide synthesis, Tracy McCarley for MS analyses, Guangyu Li for assisting with ^{1}H NMR analyses of porphyrin−tetrapeptide conjugates, and Jorge Escobedo for assisting with MD calculations. This work was supported by the National Science Foundation, grant number CHE-304833.

Supporting Information Available: Additional spectroscopic data including NMR for all compounds synthesized and synthetic routes to protected peptides and conjugates **3**, **4**, **7**−**9**, HPLC separation conditions, additional cytotoxicity data, fluorescence microscopy images, and MD minimized conformation for **18** in water. This material is available free of charge via Internet at http://pubs.acs.org.

LITERATURE CITED

(1) Pandey, R. K., and Zheng, G. (2000). Porphyrins as photosensitizers in photodynamic therapy. *The Porphyrin* Handbook. *Volume 6: Applications: past, present and future* (Kadish, K. M., Smith, K. M., and Guilard, R., Eds.) pp 157−230, Chapter 43, Academic Press, New York.

(2) Vicente, M. G. H. (2001) Porphyrin-based sensitizers in the detection and treatment of cancer: Recent progress. *Curr. Med. Chem. Anti-Cancer Agents 1*, 175−194.

(3) Rosenkranz, A. A., Jans, D. A., and Sobolev, A. S. (2000) Targeted intracellular delivery of photosensitizers to enhance photodynamic efficiency. *Immunol. Cell Biol. 78*, 452−464.

(4) Kessel, D. (2004) Correlation between subcellular localization and photodynamic efficacy. *J. Porphyrins Phthalocyanines 8*, 1009−1014.

(5) Kessel, D., and Luo, Y. (1998) Mitochondrial photodamage and PDT-induced apoptosis. *J. Photochem. Photobiol. B: Biol. 42*, 89−95.

(6) Osterloh, J., and Vicente, M. G. H. (2002) Mechanisms of porphyrinoid localization in tumors. *J. Porphyrins Phthalocyanines 6*, 305−324.

(7) Marzilli, L. G. (1990) Medical aspects of DNA-porphyrin interactions. *New J. Chem. 14*, 409−420.

(8) Mettath, S., Munson, B. R., and Pandey, R. K. (1999) DNA interaction and photocleavage properties of porphyrins containing cationic substituents at the peripheral position. *Bioconjugate Chem. 10*, 94−102.

(9) Bustamante, C., Gurrieri, S., Pasternack, R. F., Purrello, R., and Rizzarelli, E. (1994) Interaction of water-soluble porphyrins with single- and double-stranded polyribonucleotides. *Biopolymers 34*, 1099−1104.

(10) Hamblin, M. R., O'Donnell, D. A., Murthy, N., Contag, C. H., and Hasan. T. (2002) Rapid control of wound infections by targeted photodynamic therapy monitored by in vivo bioluminescence imaging. *Photochem. Photobiol. 75*, 51−57.

(11) Reddi, E., Ceccon, M., Valduga, G., Jori, G., Bommer, J. C., Elisei, F., Latterini, L., and Mazzucato, U. (2002) Photophysical properties and antibacterial activity of meso-substituted cationic porphyrins. *Photochem. Photobiol. 75*, 462−470.

(12) Sol, V., Branland, P., Chaleix, V., Granet, R., Guilloton, M., Lamarche, F., Verneuil, B., and Krausz, P. (2004) Amino porphyrins as photoinhibitors of gram-positive and -negative bacteria. *Bioorg. Med. Chem. Lett. 14*, 4207−4211.

(13) Tome, J. P. C., Neves, M. G. P. M. S., Tome, A. C., Cavaleiro, J. A. S., Soncin, M., Magaraggia, M., Ferro, S., and Jori, G. (2004) Synthesis and antibacterial activity of new poly-S-lysine-porphyrin conjugates. *J. Med. Chem. 47*, 6649−6652.

(14) Lazzeri, D., Rovera, M., Pascual, L., and Durantini, E. N. (2004) Photodynamic studies and photoinactivation of *Escherichia coli* using meso-substituted cationic porphyrin derivatives with asymmetric charge distribution. *Photochem. Photobiol. 80*, 286−293.

(15) Matthews, J. L., Sogandares-Bernal, F., Judy, M., Gulliya, K., Newman, J., Chanh, T., and Marengo-Rowe, A. (1992) Inactivation of viruses with photoactive compounds. *Blood Cells 18*, 75−89.

(16) Casteel, M. J., Jayaraj, K., Gold, A., Ball, L. M., and Sobsey, M. D. (2004) Photoinactivation of hepatitis A virus by synthetic porphyrins. *Photochem. Photobiol. 80*, 294−300.

(17) Cavanaugh, P. G. (2002) Synthesis of chlorin e6-transferrin and demonstration of its light-dependent in vitro breast cancer cell killing ability. *Breast Cancer Res. Treat. 72*, 117−130.

(18) Sutton, J. M., Clarke, O. J., Fernandez, N., and Boyle, R. W. (2002) Porphyrin, chlorin, and bacteriochlorin isothiocyanates: useful reagents for the synthesis of photoactive bioconjugates. *Bioconjugate Chem. 13*, 249−263.

(19) Hamblin, M. R., Miller, J. L., and Ortel B. (2000) Scavenger receptor targeted photodynamic therapy. *Photochem. Photobiol. 72*, 533−540.

(20) Nagae, T., Louie, A. Y., Aizawa, K., Ishimaru, S., and Wilson, S. E. (1998) Selective targeting and photodynamic destruction of intimal hyperplasia by scavenger-receptor mediated protein-chlorin e6 conjugates. *J. Cardiovasc. Surg. (Torino) 39*, 709−715.
(21) Chaloin, L., Bigey, P., Loup, C., Marin, M., Galeotti, N., Piechaczyk, M., Heitz, F., and Meunier, B. (2001) Improvement of porphyrin cellular delivery and activity by conjugation to a carrier peptide. *Bioconjugate Chem. 12*, 691−700.
(22) Rahimipour, S., Ben-Aroya, N., Ziv, K., Chen, A., Fridkin, M., and Koch, Y. (2003) Receptor-mediated targeting of a photosensitizer by its conjugation to gonadotropin-releasing hormone analogues. *J. Med. Chem. 46*, 3965−3974.
(23) De Luca, S., Tesauro, D., Di Lello, P., Fattorusso, R., Saviano, M., Pedone, C., and Morelli, G. (2001) Synthesis and solution characterization of a porphyrin-CCK8 conjugate. *J. Pept. Sci. 7*, 386-394.
(24) Bigey, P., Sonnichsen, S. H., Meunier, B., and Nielsen, P. E. (1997) DNA binding and cleavage by a cationic manganese porphyrin-peptide nucleic acid conjugate. *Bioconjugate Chem. 8*, 267−270.
(25) Mestre, B., Pitie, M., Loup, C., Claparols, C., Pratviel, G., and Meunier, B. (1997) Influence of the nature of the porphyrin ligand on the nuclease activity of metalloporphyrin-oligonucleotide conjugates designed with cationic, hydrophobic or anionic metalloporphyrins. *Nucleic Acid Res. 25*, 1022−1027.
(26) Vrouenraets, M. B., Visser, G. W. M., Loup, C., Meunier, B., Stigter, M., Oppelaar, H., Stewart, F. A., Snow, G. B., and van Dongen, G. A. M. S. (2000) Targeting of a hydrophilic photosensitizer by use of internalizing monoclonal antibodies: A new possibility for use in photodynamic therapy. *Int. J. Cancer 88*, 108−114.
(27) Soukos, N. S., Hamblin, M. R., Keel, S., Fabian, R. L., Deutsch, T. F., and Hasan, T. (2001) Epidermal growth factor receptor-targeted immunophotodiagnosis and photoimmunotherapy of oral precancer in vivo. *Cancer Res. 61*, 4490−4496.
(28) Luguya, R., Jaquinod, L., Fronczek, F. R., Vicente, M. G. H., and Smith, K. M. (2004) Synthesis and reactions of meso-(*p*-nitrophenyl)porphyrins. *Tetrahedron 60*, 2757−2763.
(29) Gradl, S. N., Felix, J. P., Isacoff, E. Y., Garcia, M. L., and Trauner, D. (2003) Protein surface recognition by rational design: nanomolar ligands for potassium channels. *J. Am. Chem. Soc. 125*, 12668−12669.
(30) Xu, H., Kinsel, G. R., Zhang, J., Li, M., and Rudkevich, D. M. (2003) Calixarene amino acids; building blocks for calixarene peptides and peptide-dendrimers. *Tetrahedron 59*, 5837−5848.
(31) Takeoka, S.; Mori, K., Ohkawa, H., Sou, K., and Tsuchida, E. (2000) Synthesis and assembly of poly(ethylene glycol)-lipids with mono-, di- and tetra-acyl chains and a poly(ethylene glycol) chain of various molecular weights. *J. Am. Chem. Soc. 122*, 7927−7935.
(32) Matthews, S. E., Pouton, C. W., and Threadgill, M. D. (1999) Synthesis of porphyrin α,ω-bis(methylamino)peptide constructs. *New J. Chem. 23*, 1087−1096.
(33) Hermanson, G. T. (1996) *Bioconjugate Techniques*. pp 137, 303−307, Academic Press, New York.
(34) Solladie, N., Hamel, A., and Gross, M. (2000) Synthesis of multiporphyrinic α-polypeptides: towards the study of the migration of an excited state for the mimicking of the natural light harvesting device. *Tetrahedron Lett. 41*, 6075−6078.
(35) Hammer, R. P., Owens, C. V., Hwang, S. H., and Soper, S. A. (2002) Asymmetrical water-soluble phthalocyanine dyes for covalent labeling of oligonucleotides. *Bioconjugate Chem. 13*, 1244−1252.
(36) Mazaleyrat, J. P., Xie, J., and Wakselman, M. (1992) Selective hydrogenolysis of the benzyloxycarbonyl protecting group of N^{ϵ}-lysine in cyclopeptides containing a benzylic phenyl ether function. Evidence for N^{ϵ}-methylated lysine side products. *Tetrahedron Lett. 33*, 4301−4302.
(37) Anantharamaiah, G. M., and Sivanandaiah, K. M. (1977) Transfer hydrogenation; a convenient method for removal of some commonly used protecting groups in peptide synthesis. *J. Chem. Soc., Perkin Trans. 1* 490−491.
(38) Lott, R. S., Chauhan, V. S., and Stammer, C. H. (1979) Trimethylsilyl iodide as a peptide deblocking agent. *J. Chem. Soc., Chem. Commun.* 495−496.
(39) Chaleix, V., Sol, V., Guilloton, M., Granet, R., and Krausz, P. (2004) Efficient synthesis of RGD-containing cyclic peptide-porphyrin conjugates by ring closing metathesis on solid support. *Tetrahedron Lett. 45*, 5295−5299.
(40) Knorr, R., Trzeciak, A., Bannwarth, W., and Gillessen, D. (1989) New coupling reagents in peptide chemistry. *Tetrahedron Lett. 30*, 1927−1930.
(41) Reid, G. E., and Simpson, R. J. (1992) Automatized solid-phase peptide synthesis: Use of 2-(1*H*-benzotriazol-1-yl)-1,1,3,3-tetramethyluronium tetrafluoroborate for coupling of *tert*-butyloxycarbonyl amino acids. *Anal. Biochem. 200*, 301−309.
(42) Liu, W., Jensen, T. J., Fronczek, F. R., Hammer, R. P., Smith, K. M., and Vicente, M. G. H. (2005) Synthesis and in vitro Studies of Nonaggregated Water-soluble Phthalocyanines. *J. Med. Chem. 48*, 1033−1041.
(43) (a) Matthews, S. E., Pouton, C. W., and Threadgill, M. D. (1995) Monofunctional electrophilic and nucleophilic derivatives of meso-tetraphenylporphyrin for attachment to peptides.*J. Chem. Soc., Chem. Commun.* 1809−1811. (b) Matthews, S. E., Pouton, C. W., and Threadgill, M. D. (1999) Synthesis of porphyrin α,ω-bis(methylamino)peptide constructs. *New J. Chem. 23*, 1087−1096.
(44) Wender, P. A., Mitchell, D. J., Pattabiraman, K., Pelkey, E. T., Steinman, L., and Rothbard, J. B. (2000) The design, synthesis and evaluation of molecules that enable or enhance cellular uptake: Peptoid molecular transporters. *Proc. Natl. Acad. Sci. 97*, 13003−13008.
(45) Futaki, S., Suzuki, T., Ohashi, W., Yagami, T., Tanaka, S., Ueda, K., and Sugiura, Y. (2001) Arginine-rich peptides. An abundant source of membrane-permeable peptides having potential as carriers for intracellular protein delivery. *J. Biol. Chem. 276*, 5836−5840.
(46) Rothbard, J. B., Jessop, T. C., Lewis, R. S., Murray, B. A., and Wender, P. A. (2004) Role of membrane potential and hydrogen bonding in the mechanism of translocation of guanidinium-rich peptides into cells. *J. Am. Chem. Soc. 126*, 9506−9507.
(47) Mitchell, D. J., Kim, D. T., Steinman, L., Fathman, C. G., and Rothbard, J. B. (2000) Polyarginine enters cells more efficiently than other polycationic homopolymers. *J. Pept. Res. 56*, 318−325.
(48) Ricchelli, F., Franchi, L., Miotto, G., Borsetto, L., Gobbo, S., Nikolov, P., Bommer, J. C., and Reddi, E. (2005) Meso-substituted tetra-cationic porphyrins photosensitize the death of human fibrosarcoma cells via lysosomal targeting. *Int. J. Biochem. Cell Biol. 37*, 306−319.
(49) Pastrana-Rios, B. (2001) Mechanism of unfolding of a model helical peptide. *Biochemistry 40*, 9074−9081.
(50) Eker, F., Cao, X., Nafie, L., and Schweitzer-Stenner, R. (2002) Tripeptides adopt stable structures in water. A combined polarized visible Raman, FTIR, and VCD spectroscopy study. *J. Am. Chem. Soc. 124*, 14330−14341.
(51) Smythe, M. L., Huston, S. E., and Marshall, G. R. (1995) The molten Helix: Effects of salvation on the α- to 3_{10}−Helical transition. *J. Am. Chem. Soc. 117*, 5445−5452.
(52) Sheraga, H. A. (1994) Treatment of Hydration in conformational energy calculations on polypeptides and proteins. In *Structure and Reactivity in Aqueous Solution. Characterization of Chemical and Biological Systems* (Cramer, C. J., and Truhlar, D. G. Eds.) ACS Symposium Series 568*,* pp 360−371, American Chemical Society, Washington, DC.
(53) Arai, T., Inudo, M., Ishimatsu, T., Akamatsu, C., Tokusaki, Y., Sasaki, T., and Nishino, N. (2003) Self-assembling of the porphyrin-linked acyclic penta- and heptapeptides in aqueous trifluoroethanol. *J. Org. Chem. 68*, 5540−5549.
(54) Dozzo, P., Koo, M.-S., Berger, S., Forte, T. M., and Kahl, S. B. (2005) Synthesis, characterization, and plasma lipoprotein association of a nucleus-targeted boronated porphyrin. *J. Med. Chem. 48*, 357−359.

BC050057G

Nucleic Acid Complexing Glycosyl Nucleoside-Based Amphiphile

Jerome Arigon,[†] Carla A. H. Prata,[§] Mark W. Grinstaff,[§] and Philippe Barthélémy*[,†]

Faculté des sciences d'Avignon, 33 rue Louis Pasteur, F-84000 Avignon, France, and Departments of Chemistry and Biomedical Engineering, Metcalf Center for Science and Engineering, Boston University, Boston, Massachusetts 02215. Received February 4, 2005; Revised Manuscript Received April 25, 2005

A neutral amphiphile derived from uridine featuring two oleyl chains and one glucose for DNA binding was prepared using a convenient four-step synthetic route. The nucleic acid binding capabilities of this amphiphile were investigated by UV−vis, quasi-elastic light scattering (QELS), transmission electronic microscopy (TEM), gel electrophoresis, ^{31}P NMR, IR, and circular dichroism (CD). Amphiphile−nucleic acid complex formation is a consequence of the amphiphilic character of the molecule, phosphate−sugar, and nucleobase−nucleobase interactions. This work presents for the first time a glyco-nucleo-amphiphile capable of binding efficiently the nucleic acid double helix structure.

INTRODUCTION

The supramolecular assemblies observed between nucleic acids and different amphiphiles represent elegant examples of the role multiple noncovalent interactions have in governing structure and even function. These assemblies are of fundamental interest, as well as clinical importance, since some of these assemblies are used for the in vitro and in vivo delivery of DNA. The delivery of therapeutic nucleic acid offers the potential to treat diseases by replacing or inhibiting defective genes. The vast majority of DNA supramolecular assemblies are formed with molecular or macromolecular cationic amphiphiles including lipids, linear polymers, and dendritic polymers (*1*−*6*). One caveat with these cationic amphiphiles is that these systems are likely to interact with other biologics, since most proteins are also negatively charged at neutral pH. However, there are a few examples of DNA supramolecular assemblies formed with noncationic amphiphiles (*7*). Recently, neutral sugar- and poly(ethylene glycol)/uridine-based amphiphiles have been reported that complex DNA (*8*−*10*). The neutral glycosyl amphiphiles are particularly interesting since these compounds may provide a means to develop amphiphiles for selective biologic complexation. Such amphiphiles could be of interest for medical and biotechnological applications involving the manipulation or use of DNA or proteins.

With regards to the glycosyl amphiphiles, there are known examples of natural saccharides that bind nucleic acid. For example, S. Shinkai et al. have reported the molecular recognition between adenine, cytosine, and uracil in a single-stranded RNA and schizophyllan, a natural polysaccharide (*12*). It is known that when a given polyol structure, like a saccharide, is added to an aqueous solution containing DNA, the stability of the double helix can be affected. The effects observed depend on the polyol influence on the forces that stabilize the double helix, namely, hydrogen bonding, van der Waals forces, and electrostatic interactions. Consequently, the polyol can either stabilize or destabilize the duplex as evident by a change in the DNA denaturation temperature (T_m). G. Barone and co-workers have studied the effects of different small molecule polyols (i.e., glycerol, arabitol, D-mannitol, D-sorbitol, myo-inositol, etc.) on the thermal denaturation of DNA (*13*). The double helix destabilization was mainly attributed to the polyols interacting with the polynucleotide solvation sites. The polyols displace water molecules and alter the electrostatic interactions between the polynucleotide and its surrounding counterions. Consequently, when the concentration of polyols increases, the Coulombian repulsion between the negative charges of the phosphate groups increases leading to greater destabilization of the DNA double helix. Stabilizing contributions (polyols are less efficient than water in competing with the base−base interstrand hydrogen bonds) are counterbalanced by destabilizing electrostatic repulsions. A stabilization of the DNA double helix has been observed in the presence of a maltoheptaose amphiphile (*14*), where the saccharide promotes stabilization of the double helix versus single strand by the formation of DNA aggregates. This is likely due to the amphiphilic character of the polyols. To further explore the interactions between DNA and a neutral amphiphile, we have designed a noncationic amphiphile possessing both nucleoside and glycosyl moieties (Figure 1). Herein, we report the synthesis and physicochemical properties of this amphiphile as determined by UV−vis, quasi-elastic light scattering (QELS), NMR, IR, circular dichroism (CD), gel electrophoresis, and transmission electronic microscopy (TEM).

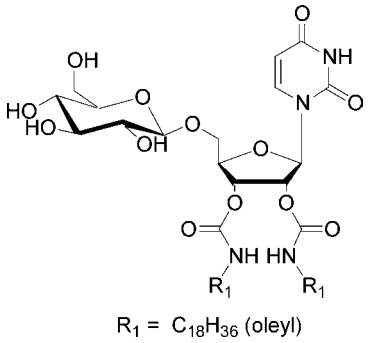

Figure 1. Chemical structures of 1-(2′,3′-dioleylcarbamoyluridine-5′)-β-D-glucopyranoside (DOUGluc).

* To whom correspondence should be addressed. E-mail: philippe.barthelemy@univ-avignon.fr.

[†] Faculté des sciences d'Avignon.

[§] Boston University.

10.1021/bc050029y CCC: $30.25 © 2005 American Chemical Society
Published on Web 06/18/2005

MATERIALS AND METHODS

General Experiments and Analytical Conditions. Unless noted otherwise, all starting materials were obtained from commercial suppliers and were used without further purification; the solvents were redistilled on calcium chloride, calcium hydride, potassium hydroxide, or sodium according to the solvent used. All compounds were characterized using standard analytical and spectroscopic data such as ^{1}H, ^{13}C NMR (apparatus BRUKER Avance DPX-300, ^{1}H at 300.13 MHz, ^{13}C at 75.46 MHz, and ^{31}P at 121.49 MHz) and mass spectrometry (instrument JEOL SX 102, NBA matrix). The NMR chemical shifts are reported in ppm relative to tetramethylsilane using the deuterium signal of the solvent ($CDCl_3$, MeOD) as a heteronuclear reference for ^{1}H and ^{13}C. The ^{1}H NMR coupling constants, J, are reported in hertz. TEM microscopy experiments were performed on a Philips CM 10 (negative staining with ammonium molybdate 1% in water, Cu/Pd carbon-coated grids). Fluorescence spectra were recorded on a Hitachi F2500 using λ_{ex} = 320 nm and λ_{em} = 350−450 nm. The hydrodynamic radii (R_h) were determined at 25 °C using a Wyatt Mini-Dawn quasi-elastic light scattering (QELS) instrument. UV−visible studies were performed on a Perkin-Elmer Lambda 25 Peletier equipped, and circular dichroism was performed on a JASCO J-810 spectropolarimeter. The ^{31}P NMR experiments were performed on a BRUKER AC 250 at 121.49 MHz. The ^{31}P NMR chemical shifts (δP) are reported in ppm relative to phosphoric acid. FTIR spectra were recorded using a NICOLET Fourier transform spectrophotometer. Silica gel 60 (particle size 40−60 μm) was employed for flash chromatography. Thin layer chromatograms were performed with aluminum plates coated with silica gel 60 F_{254} (Merck). Varian silica gel reverse phase C18 MEGA BE-C18, 2GM, 12 mL was used.

Abbreviation. DOUGluc, 1-(2′,3′-dioleylcarbamoyluridine-5′)-β-D-glucopyranoside; HEPES, *N*-(2-hydroxyethyl)piperazine-*N*′-(2-ethanesulfonic acid); M.S., molecular sieves; EtBr, ethidium bromide; DMAP, (dimethylamino)pyridine; DCM, dichloromethane; DMF, dimethylformamide; AcOEt, ethyl acetate; SUV, small unilamellar vesicles; polyA−polyU, polyadenylic acid−polyuridylic acid; polyC−polyG, polycytidylic acid−polyguanylic acid; T_m, melting temperature; RT, room temperature; CDI, carbonyl diimidazole.

Materials. Calf thymus DNA (CAS no. 91080-16-9), pBR322 plasmid DNA (CAS no. 93384-17-9), polyadenylic acid−polyuridylic acid (CAS no. 24936-38-7], and polycytidylic acid−polyguanylic acid (CAS no. 90385-88-9) were obtained from Sigma. Buffer (0.02 M HEPES, 0.01 M NaCl) was prepared with distilled and filtered (0.22 μm) water, and the pH was adjusted to 7.4 with NaOH 0.1 M.

Synthetic Procedures. *2′,3′-Dioleylcarbamoyluridine (**2**).* 5′-Dimethoxytrityluridine **1** (1 g, 1 equiv), carbonyldiimidazole (1.22 g, 2.2 equiv), and a catalytic amount of DMAP were dissolved in 20 mL of anhydrous DMF. After 1 h at room temperature, oleylamine (4 mL, 7 equiv) was added, and then the reaction mixture was stirred for 12 h. DMF was removed under reduced pressure, and 20 mL of DCM was added. To this solution an excess of a 3% trichloroacetic acid solution in DCM was added, and the reaction mixture was stirred for 30 min at room temperature. After addition of methanol (3 mL), the organic layer was washed three times with 10 mL of water and dried over sodium sulfate. Compound **2** (0.54 g) was obtained after chromatography (DCM/MeOH 95/5). Yield: 36%. R_f: 0.32 (DCM/MeOH 95/5). ^{1}H NMR ($CDCl_3$) δ in ppm: 0.96 (s, CH_3), 1.2 (m, CH_2), 2.3 (m, CH_2), 3.2 (m, H5′), 3.92 (m, H4′), 4.2 (m, H3′), 4.95 (m, NH), 5.4 (m, H2′), 5.8 (d, CH, J = 8.1 Hz), 6.1 (d, H1′, J = 3.3 Hz), 7.85 (d, CH, J = 8.0 Hz), 8.6 (s, NH). ^{13}C NMR ($CDCl_3$) δ in ppm: 14 (s, CH_3), 27 (s, $CH_2\beta$), 30 (m, CH_2), 33 (m, $CH_2\alpha$), 42 (s, C−NH), 70 (m, C2,C3), 100 (s, CH), 131 (m, CH═CH), 133 (m, CH), 164 (m, CO carbamates), 170 (m, CO). MS FAB$^+$: [M + Na], m/z = 853.

*1-(2′,3′-Dioleylcarbamoyluridine-5′)-2,3,4,6-tetra-O-acetyl-β-D-glucopyranoside (**3**).* 2,3,4,6-Tetra-*O*-acetyl-α-D-glucopyranosyl trichloroacetimidate (0.2 g, 1.5 equiv) (*15*−*18*), 2′,3′-dioleylcarbamoyluridine **2** (0.2 g, 1 equiv), molecular sieves, and $BF_3{\cdot}Et_2O$ (0.18 g, 1.5 equiv) were dissolved in 10 mL of DCM. The reaction mixture was stirred for 4 h at room temperature. The product was obtained as a white solid (0.15 g) after chromatography (DCM/MeOH 95/5). Yield: 55%. R_f = 0.72 (DCM/MeOH 95/5). ^{1}H NMR ($CDCl_3$) δ in ppm: 0.96 (s, CH_3), 1.2 (m, CH_2), 2.0 (m, CH_3 acetyl), 3.1 (m, $CH_2\alpha$), 3.9 (m, H5′), 4.0 (m, H4′), 4.1 (m, H5), 4.2 (m, H6, H6), 4.7 (m, H3′), 4.85 (m, H2), 5.1 (m, H3), 5.5 (m, H4), 5.6 (d, H1β, J = 8.2 Hz), 5.65 (d, CH, J = 8.2 Hz), 6.1 (d, H1′, J = 3.0 Hz), 7.9 (d, CH, J = 8.1 Hz). ^{13}C NMR ($CDCl_3$) δ in ppm: 14 (s, CH_3), 20 (s, OAc), 27 (s, $CH_2\beta$), 30 (m, CH_2), 33 (m, $CH_2\alpha$), 42 (s, CH_2NH), 61−75 (m, C5,C3,C2,C3′,C4′,C5′), 97 (s, C1), 105 (s, CH), 131 (m, CH═CH), 133 (s, CH), 164 (m, CO carbamates), 170 (m, CO). MS FAB$^+$: [M + H], m/z = 1162.

*1-(2′,3′-Dioleylcarbamoyluridine-5′)-β-D-glucopyranoside (**4**).* 1-(2′,3′-Dioleylcarbamoyluridine-5′)-2,3,4,6-tetra-*O*-acetyl-β-D-glucopyranoside (**3**, 0.15 g) and a catalytic amount of sodium methoxide were dissolved in 10 mL of methanol. The reaction mixture was stirred for 4 h at room temperature. After evaporation of methanol under reduced pressure, the crude was purified by silica gel reverse phase column (DCM/MeOH 3/7) to afford the compound as a white solid (0.12 g). Yield: quantitative. R_f = 0.52 (DCM/MeOH reverse phase). ^{1}H NMR (CD_3OD) δ in ppm: 0.96 (s, CH_3), 1.3 (m, CH_2), 1.5 (m, $CH_2\beta$), 3.1 (m, $CH_2\alpha$), 3.3 (m, H6, H6), 3.7 (m, H3′, H4′), 3.8 (m, H5′, H2′), 4.3 (m, H5), 4.6 (s, H4), 4.8 (s, H3), 5.3 (m, CH═CH), 5.7 (d, H′β, J = 8.2 Hz), 5.8 (d, CH, J = 8.0 Hz), 6.2 (d, H1′, J = 3.0 Hz), 8.0 (d, CH, J = 8.1 Hz). ^{13}C NMR (CD_3OD) δ in ppm: 15 (s, CH_3), 27 (s, $CH_2\beta$), 30 (m, CH_2), 33 (m, $CH_2\alpha$), 42 (s, CH_2NH), 61−75 (m, C5,-C3,C2,C3′,C4′,C5′), 97 (s, C1), 105 (s, CH), 131 (m, CH═CH), 133 (s, CH), 162 (m, CO carbamates), 170 (m, CO). MS FAB$^+$: [M + Na], m/z = 1015. HRMS [M + Na] $m/z_{theoritical}$ = 1015.6551, $m/z_{observed}$ = 1015.6559. $[\alpha]_D^{20}$ = −7.26 (CH_3OH).

Critical Aggregation Concentration. For the measurements of critical micellar concentration, a stock solution of pyrene (0.5 mM) in ethanol was added to test tubes. The ethanol was evaporated by a stream of nitrogen and thereafter under vacuum for 1 h. Varying amounts of amphiphile stock solution in buffer were added to the tubes to give a final volume of 1 mL and a final pyrene concentration of 0.5 μM. The samples were incubated in the dark at 25 °C for 24 h with intermittent vigorous mixing. The fluorescence intensity (I_1, λ = 373 nm) was plotted as a function of the lipid concentration.

Thermal Denaturation and Circular Dichroism Studies. Samples were prepared in the following buffers: (i) 0.02 M HEPES, 0.01 M NaCl, pH = 7.4, and (ii) 0.02 M HEPES, 0.01 M NaCl, 0.01 M $MgCl_2$, pH = 7.4. Solutions at different ratios of polyA−polyU (1 mg/mL) or CT-DNA (1 mg/mL) to **4** were prepared in either sodium (i) or magnesium (ii) buffer and stirred for 10 min.

Scheme 1. Synthetic Route to Glucosyl Dicarbamate Uridine Amphiphile[a]

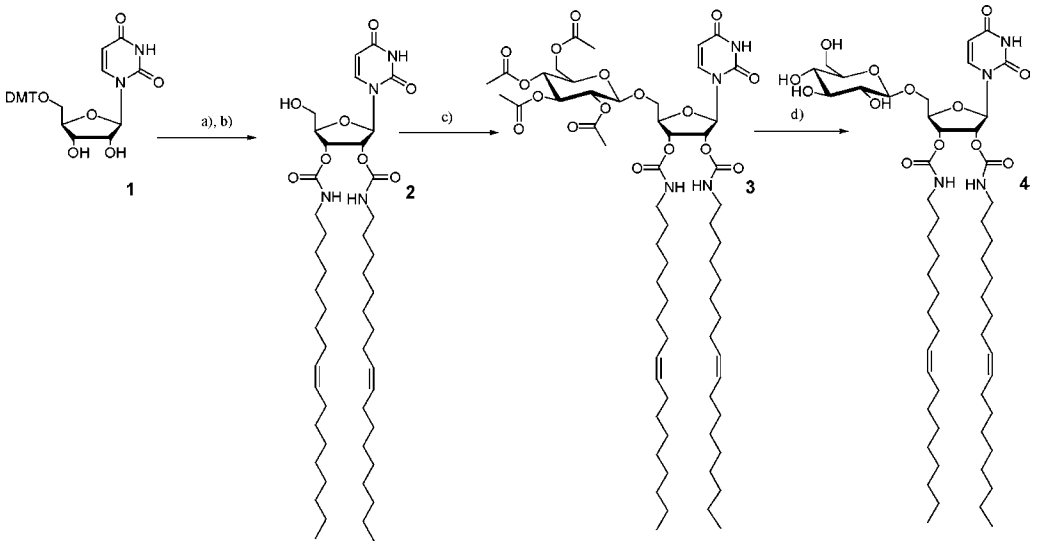

[a] Conditions: (a) CDI/DMAP in DMF 2 h, then oleylamine 12 h; (b) trichloroacetic acid in CH_2Cl_2 (yield$_{a+b}$ = 36%); (c) 2,3,4,6-tetra-*O*-acetyl-α-D-glucopyranosyl trichloroacetimidate, M.S., and BF_3-Et_2O in CH_2Cl_2 (yield = 55%); (d) MeONa in MeOH (yield = quantitative).

The temperature was increased from 15 to 95 °C at 1 °C/min, and the absorbance at 260 nm was measured every 1 °C increments. Hyperchromicity = $A - A_0$, where A is the absorbance measured at $\lambda = 260$ nm and A_0 is the initial absorbance ($\lambda = 260$ nm) at 20 °C. T_m values were determined from first-order derivatives. CD spectra were recorded at 25 °C in rectangular quartz cuvettes of 0.1 cm; each spectrum was averaged from three successive accumulations and was baseline-corrected and smoothed using the software supplied by JASCO.

Quasi-Elastic Light Scattering (QELS). The R_h was measured at a 90° angle and $\lambda = 685$ nm using a flow cell. The solvent was filtered through a 0.02 μm membrane. The lipid and DNA solutions of desired concentrations were prepared and filtered through 0.2 μm pore size filter (Whatman) into the scattering cell. R_h measurements were realized at $t = 0$, 24, and 36 h of **4** (50 equiv per DNA phosphate) in the absence or presence of CT-DNA (1 mg/mL). R_h reported corresponds to the average of three experiments in aqueous HEPES buffer. Astra software (version 4.90.80) was used for data acquisition and analysis.

^{31}P NMR Studies and Job Plot. Na_2HPO_4 (3 mM) solution in D_2O−DMSO-d_6 (8:2) was added with different amounts of **4**, **2,** or D-glucose, and the mixtures were vortexed during 30 s. The chemical shifts (δP) of Na_2HPO_4 were measured by ^{31}P NMR. For the Job plot, the concentration of the mixture was kept constant at 3 mM.

Infrared Spectroscopy. PolyA−polyU (0.5 mg/mL) was mixed with DOUGluc **4** (1.5 mg) in H_2O and vortexed for 30 s; then the solution was freeze-dried. The solid obtained was mixed with KBr, and 64 scans were accumulated. In the case of D_2O experiments, the polyA−polyU/DOUGluc **4** and polyC−polyG/DOUGluc **4** mixtures are prepared in D_2O in the same conditions as for solid FTIR experiments, and the IR spectra are obtained directly from the D_2O solutions.

Agarose Gel Electrophoresis. Plasmid DNA (2 μL, 0.02 g/L in HEPES buffer) was added to various amounts of **4** at RT, and the mixture was vortexed during 30 s and left at RT for 36 h. Then the solutions were loaded into 1% (w/v) agarose gel at 60 V/cm in HEPES buffer. DNA was revealed with EtBr and visualized under UV light.

Transmission Electronic Microscopy (TEM). The samples were prepared with a solution of calf thymus DNA (1 mg/mL in HEPES buffer) and extruded (50 nm filter) HEPES buffer solution containing 50 equiv of DOUGluc **4** (for 1 equiv of phosphate DNA). This solution was vortexed and left for 36 h at RT prior to examination.

RESULTS AND DISCUSSION

The formation of amphiphile−DNA supramolecular assemblies is well-known in the case of cationic lipids; however, only a few examples of neutral amphiphiles that complex with DNA have been reported (*7*, *10*, *14*, *19*). To further increase the known types of DNA-binding neutral amphiphiles, we are designing amphiphiles that are based on a nucleoside and a sugar moiety. In this approach, the nucleoside and sugar derivative can provide sufficient interaction forces with DNA to form nucleic acid−amphiphile supramolecular assemblies. Consequently, we have synthesized the 1-(2′,3′-dioleylcarbamoyluridine-5′)-β-D-glucopyranoside and evaluated the ability of this neutral amphiphile to bind to nucleic acids using UV−vis, QELS, TEM, gel electrophoresis, ^{31}P NMR, FTIR, and CD.

Synthesis. The synthetic strategy is shown in Scheme 1 and involves four steps starting from 5′-dimethoxytrityluridine. The lipophilic intermediate **2** was obtained by coupling oleylamine to the 2′ and 3′ ribose secondary alcohols using CDI to afford carbamate linkages. The dimethoxytrityl protecting group was removed using trichloroacetic acid. Finally, the amphiphilic dioleyl nucleoside derivative **4** was obtained after addition of the glucose moiety via a trichloroacetimidate glycosylation and a deprotection step to remove the acetyl groups. Amphiphile **4** is soluble in water, whereas **2** possesses limited aqueous solubility and is soluble in DMSO.

Physicochemical Studies. The critical aggregation concentration (CAC) of **4** was determined using a fluorescence titration method (*20*, *21*). Thus, to determine the CAC value of our glycosyl nucleoside amphiphile, a stock solution of **4** was added to a pyrene-saturated solution (4×10^{-7} mol/L) at 298.2 K and stirred for 24 h to reach complete equilibrium between amphiphile and pyrene. The fluorescence emission was monitored at 394

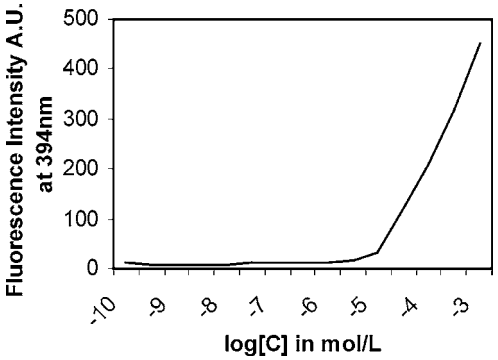

Figure 2. Measurements of pyrene fluorescence at 394 nm (λ_{ext} = 320 nm) versus log(c) in mol/L of compound **4**. CAC obtained was determined to be 1×10^{-5} mol/L.

nm (λ_{ext} was 320 nm). The CAC value for amphiphile **4** is 10^{-5} mol/L (see Figure 2). Note, that this value is similar in magnitude to CACs reported in the literature for mono- and dioleyl amphiphilic polyols or cationic derivatives of **4** suggesting that the nucleoside moiety does not significantly affect the CAC (*22*−*25*).

Nucleic Acid Thermal Denaturation. The nucleic acid binding capability of **4** was next evaluated by studying the thermal denaturation profile of a polyA−polyU double helix in the presence of varying amounts of glycosyl nucleoside amphiphile **4**. The denaturation profiles and corresponding first derivatives obtained in the absence or presence of magnesium are presented in Figure 3. Specifically, panels Ia, IIa, and IIIa of Figure 3 show the thermal denaturation profiles of polyA−polyU at 260 nm in the presence of compound **4**, glucose, and uridine, respectively. The first derivatives of the corresponding absorbances versus temperature are presented in panels Ib, IIb, and IIIb of Figure 3. Likewise, thermal denaturation experiments with polyA−polyU and amphiphile **4** in the presence of a magnesium buffer are shown in Figure 3, panel IVa. The corresponding first derivative is plotted in Figure 3, panel IVb. The DNA thermal denaturation results are summarized in Table 1.

In a HEPES buffer (HEPES 0.02 M, pH 7.4, NaCl 0.01 M), the T_m measured for polyA−polyU is 43.4 °C. A positive shift, ΔT_m [$\Delta T_m = T_m$(**4** + polyA−polyU) − T_m-

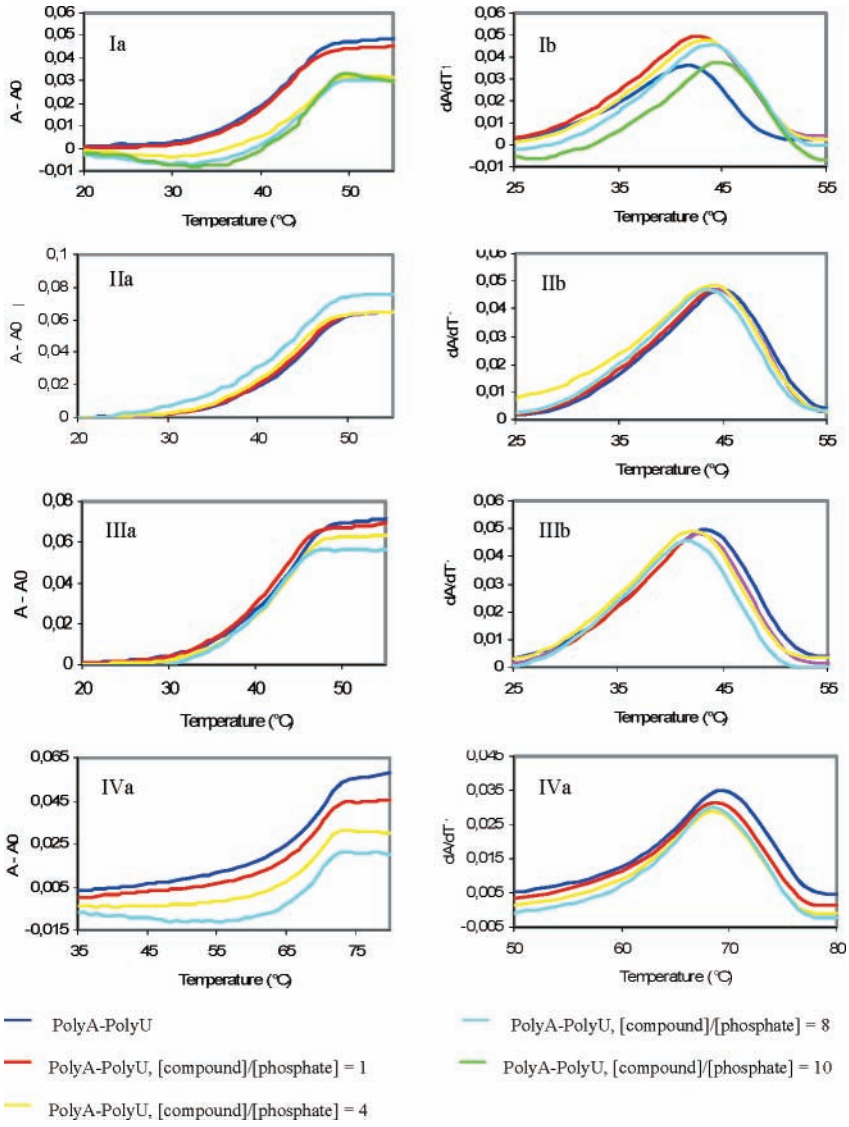

Figure 3. Hyperchromicity at 260 nm versus temperature of polyA−polyU in the presence of compound **4**, glucose, and uridine (respectively, panels Ia, IIa, and IIIa), first derivatives of absorbance versus temperature (respectively, panels Ib, IIb, and IIIb) in aqueous HEPES buffer 0.02 M, pH 7.4, NaCl 0.01 M). Same experiments with polyA−polyU and amphiphile **4** in the presence of magnesium (IVa) and their first derivatives (IVb) are also shown (performed in aqueous HEPES magnesium buffer 0.02 M, pH 7.4, NaCl 0.01 M, $MgCl_2$ 0.01 M).

Table 1. DNA Thermal Denaturation Results

amount of compd (equiv)	ΔT_m[a] (°C) **4** + polyA−polyU[b]	**4** + CT-DNA[c]	**4** + polyA−polyU + Mg[d]	uridine + polyA−polyU[b]	glucose + polyA−polyU[b]
1	1.3	1.5	−0.5	−0.6	−0.5
4	2.2	2.1	−0.7	−0.7	−0.9
8	2.6	2.3	−0.8	−1.7	−1.2
10	3.5	*e*	*e*	*e*	*e*

[a] ΔT_m (°C) = T_m of polyA−polyU + compound mixture − T_m of polyA−polyU (average of three experiments). The error in melting temperature (T_m) does not exceed 0.2 °C. [b] Aqueous HEPES buffer (HEPES 0.02 M, pH 7.4, NaCl 0.01 M). T_m measured for polyA−polyU in this buffer is 43.4 °C. [c] Aqueous HEPES buffer (HEPES 0.02 M, pH 7.4, NaCl 0.01 M). T_m measured for CT-DNA in this buffer is 72.3 °C. [d] Aqueous HEPES magnesium buffer (HEPES 0.02 M, pH 7.4, NaCl 0.01 M, $MgCl_2$ 0.01 M). T_m measured for polyA−polyU in this buffer is 69.6 °C. [e] Not available.

(polyA−polyU)], of the polyA−polyU melting temperature is observed when compound **4** is added to the solution (Figure 3I) indicating a stabilization of the double helix ($\Delta T_m = 2.6$ °C, 8 equiv of **4** for 1 equiv of RNA phosphate). Note that the same phenomenon was observed with a calf thymus (CT) DNA ($\Delta T_m = 2.3$ °C, 8 equiv of **4** for 1 equiv of DNA phosphate). The ΔT_m increases as the number of amphiphile equivalents of **4** is increased suggesting that the stabilization of the double helix is not due to a one to one complex. Since these thermal denaturation experiments were performed with concentrations of amphiphile **4** higher than the CAC (1 equiv of **4** is 1.6×10^{-5} mol/L), the stabilization of the DNA double helix can be attributed to a DNA aggregation resulting from interactions between DNA and amphiphile aggregates.

As expected, in the presence magnesium the T_m-(polyA−polyU) is enhanced with a new value of 69.6 °C. It is well-known that magnesium ions increase T_m by binding to the phosphate backbone and stabilizing the double helix (*26*). When amphiphiles **4** is added to the Mg solution a decrease of the T_m(polyA−polyU) is noted. This small destabilization is consistent with the strong association of diols with the phosphate (*27*). In this case, sugar−phosphate associations compete with the Mg−phosphate complex inducing Mg displacement and consequently a decrease in double helix stability. To estimate the impact of the nucleoside and sugar moieties on the stability of polyA−polyU double helix, the denaturation experiments were performed in the presence of uridine and glucose (without added Mg). A negative ΔT_m was observed for both compounds (Figure 3, panels II and III). These negative values can be rationalized by the polyol interactions with DNA inducing an enhancement of the repulsion between the negative charges of the phosphate groups (*13*). These results underline the importance of the amphiphilic character and the aggregate formation in stabilizing the DNA double helix.

Quasi-Elastic Light Scattering (QELS) Studies. We evaluated the impact of the CT-DNA on amphiphile aggregation. The hydrodynamic radius (R_h) of the aggregates was measured at three time points (t = 0, 24, and 36 h), and Table 2 summarizes the values obtained. Amphiphiles (typical concentration 0.6 mM) were extruded through a 50 nm filter in buffer (HEPES 0.02 M, pH 7.4, NaCl 0.01 M), DNA was then added to the aqueous solutions (DNA phosphate concentration 0.006 mM) containing the amphiphiles. Extruded amphiphile solutions exhibit stable aggregates with hydrodynamic radius of roughly 20 nm even after 36 h ($R_h = 19.8 \pm 0.3$) In the presence of CT-DNA after 36 h, the observed R_h increases to 42.6 ± 1.8 nm. It is reasonable to suggest that this size enhancement is due to the formation of new structures composed of amphiphiles and DNA.

Table 2. Hydrodynamic Radius (R_h, nm) of Amphiphiles and CT-DNA/Amphiphile Aggregates[a]

t (h)	DOUGluc (**4**)	DOUGluc (**4**) + CT-DNA
0	23.1 ± 1.2	22.1 ± 0.4
24	21.2 ± 0.3	22.2 ± 0.8
36	19.8 ± 0.3	42.6 ± 1.8

At t = 0, 24, and 36 h of **4** in the absence or presence of CT-DNA. Average of three experiments realized in aqueous buffer (HEPES 0.02 mM, pH 7.4, NaCl 0.01 mM). Value measured for CT-DNA alone (type XV activated, Sigma) is 3.0 ± 0.5 nm.

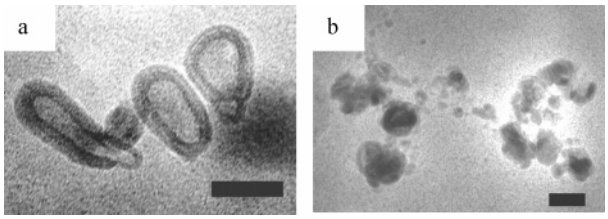

Figure 4. Transmission electronic microscopic (TEM) images of (a) small unilamellar vesicles obtained after extrusion of **4** through a 50 nm filter (bar = 50 nm) and (b) large aggregates (**4** equiv/CT-DNA = 50, bar = 100 nm).

TEM Studies. To confirm the impact of nucleic acids on amphiphile self-assembly, aqueous solutions of **4** were studied either in the absence or in the presence of CT-DNA by transmission electronic microscopy (TEM). As shown in Figure 4a, the extrusion of **4** through a 50 nm filter gives small unilamellar vesicles (SUV). The same solution was also studied after addition of calf thymus DNA. In agreement with the results obtained by QELS experiments, the presence of CT-DNA affects the supramolecular organization. A new population of larger aggregates is present in the solution. TEM images show a decrease in vesicle population and larger aggregates of roughly 100 nm (Figure 4b).

Gel Electrophoresis Studies. Electrophoresis gel shift is a convenient assay of DNA complexation. Thus, in light of the UV−vis, QELS, and TEM studies, agarose gel electrophoresis experiments were conducted by using plasmid pUC18 DNA. Increasing amounts (~0, 5, 10, 15, 25, 50, and 75 equiv based on the amphiphile **4**/phosphate, which correspond to the following concentrations: 0, 0.3, 0.6, 0.8, 1.4, 2.7, and 4.0 mM, respectively) of **4** were mixed with plasmid DNA (plasmid DNA phosphate concentration 0.06 mM) in HEPES buffer (HEPES 0.02 M, pH 7.4, NaCl 0.01 M). After incubation for 36 h at room temperature, the mixtures (20 μL) were loaded into a 1% agarose gel (HEPES 0.02 M, pH = 7.4, NaCl 0.01 M, EtBr 500 ng/mL) using a pipettor. The gel was run at constant power (60 V) and at room temperature for 2.5 h. The DNA−amphiphile complexation is readily monitored under UV. High amphiphile ratios

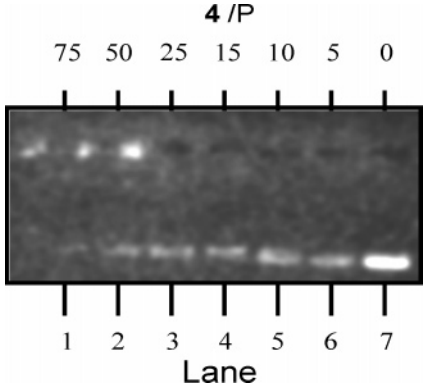

Figure 5. Electrophoretic gel shifts for the complex plasmid−**4**: from lane 1 to lane 7, decreasing amounts of **4** from 75 to 0 equiv.

(50−75 amphiphile/phosphate equiv) behave similarly, and the DNA is immobilized as typically shown in Figure 5. The glycosylated nucleoside amphiphile **4** immobilizes plasmid pUC18 DNA demonstrating the masking of DNA charges by the uncharged amphiphile aggregates.

^{31}P NMR and FTIR Studies. To determine whether the stabilization of the DNA double helix depends on both glucose−phosphate interactions and amphiphile self-organization, the binding of Na_2HPO_4 (guest, $[G]_t$ = total guest concentration) with glucose, **2**, and **4** (hosts, $[H]_t$ = total host concentration) were studied by ^{31}P NMR spectroscopy model systems. NMR titration of phosphate with sugars was performed by keeping the total phosphate concentration constant ($[Na_2HPO_4] = 3.0 \times 10^{-3}$ M) and gradually increasing the sugar derivative concentrations. These studies reveal that the complexation of the phosphate anion is occurring only in the case of the amphiphile. The ^{31}P NMR signal undergoes upfield shifts in the presence of **4** host until saturation is reached at $[H]_t/[G]_t$ ratios higher than 1 (Figure 6a), whereas no significant chemical induced shift is observed for glucose and compound **2**. Such a result indicates that both the glucose moiety and amphiphilic character are needed to induce the formation of a glucose−phosphate complex in aqueous media. Fifty percent complexation occurs for **4** host at $[H]_t/[G]_t = 0.5$ (Figure 6a), that is, at host concentration of $[H]_{50} = 1.5$ mM ($[G]_t = 3$ mM). The implication of $[H]_{50}$ is that $K_{min} = 1/[H]_{50} \approx 6 \times 10^2$ M^{-1} represents the lower limit of the binding constant of H for a molecule of G (where the equilibrium constant $K = [H-G]/[H][G]$, $H + G \rightleftarrows H-G$).[22] The binding affinity, K_{min}, obtained for **4** is slightly lower than those for the oligosaccharide clusters−phosphate complexes (10^3 M^{-1}) in aqueous media (*28*). A Job plot (*29*) for the binding of **4** and phosphate (Figure 6b) showed a maximum between $X = 0.5$ and $X = 0.6$, indicating a preference for 1:1 complexes over 2:1 complexes, which coexist in solution to a minor degree. From the NMR studies, the chemical induced shifts observed are due to phosphate anion coordination incorporated in the aggregate pools via hydrogen bonding. Indeed, in view of its amphiphilic nature, it is not surprising that host **4** forms aggregates, where the hydrogen bond forming anion may link to the sugar moieties. This is because the phosphate ion is associated with the sugar surface of the aggregates and a chemical induced shift is observed. Compound **2** does not possess a glucose moiety and therefore cannot bind phosphate anion. Consequently, the phosphate is not coordinated, and no significant chemical induced shifts are observed.

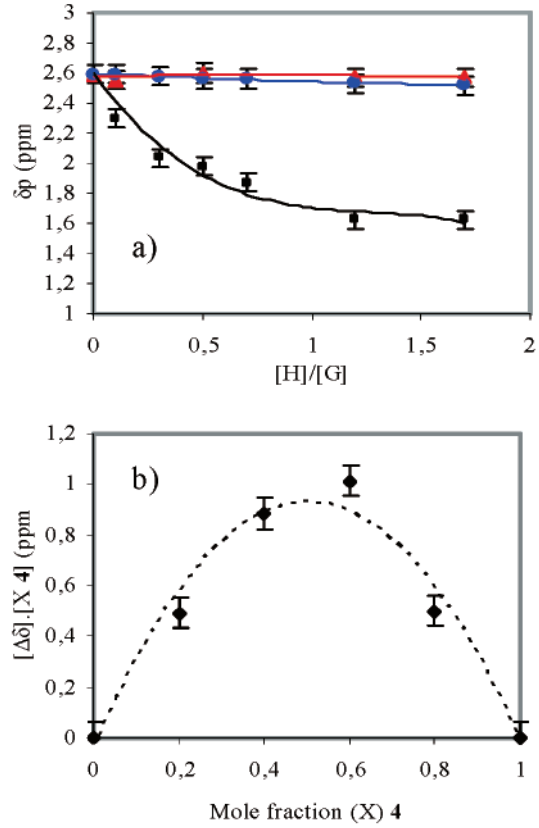

Figure 6. ^{31}P NMR titration (a) of phosphate (guest, [G] = 3 mM) with hosts ([H]) glucose (▲, red), compound **2** (●, blue), and compound **4** (■, black) at 25 °C in D_2O/DMSO-d_6 with δp in reference to external H_3PO_4 in D_2O ($\delta p = 0$) and Job plot (b) for the binding of **4** and phosphate. Concentration of **4** and of phosphate was held constant at 3 mM.

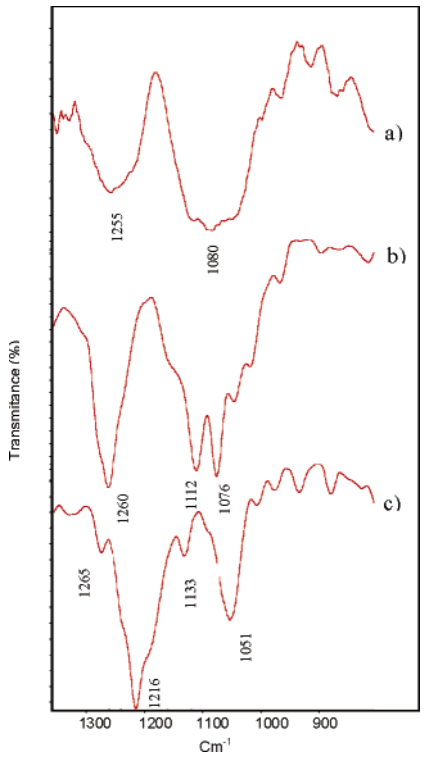

Figure 7. FTIR spectra of (a) polyA−polyU, (b) **4**, and (c) polyA−polyU/**4** 1:1 equiv in the region of 1350−800 cm^{-1}.

The infrared spectra of the polyA−polyU and the polyA−polyU/**4** (1:1 equiv) complexes in the region of

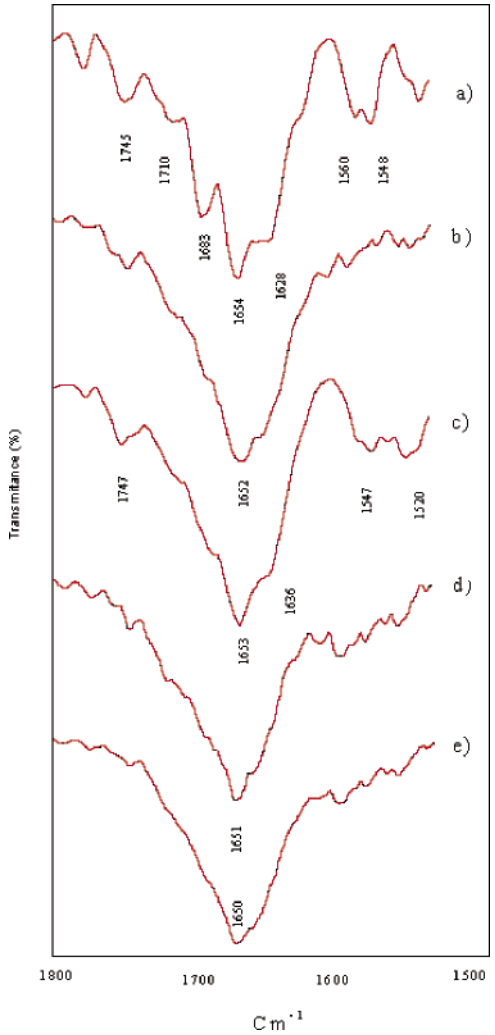

Figure 8. FTIR spectra in solution of (a) **4**/polyA−polyU (1:1), (b) polyA−polyU, (c) **4**, (d) **4**/polyC−polyG (1:1), and (e) polyC−polyG in the region of 1500−1800 cm^{-1}.

1350−800 cm^{-1} are shown in Figure 7. The band around 1080 cm^{-1} in the IR spectrum (Figure 7a) has been assigned to the symmetric PO_2^- stretching mode coupled with the C5′−O5′ vibrations (*30*), whereas the antisymmetric PO_2^- stretching vibrational band is observed around 1255 cm^{-1} (*31*). In the same region, **4** exhibits three bands at 1076 (C−O stretching primary alcohol), 1112 (C−O stretching secondary alcohol), and 1260 cm^{-1} (C−N−C=O vib) (*32*). The phosphate−sugar interactions are characterized by a shift of the antisymmetric PO_2^- stretch at 1216 cm^{-1}, which confirms the amphiphile−RNA complex formation (*33*).

FTIR spectra recorded in D_2O solutions in the region 1500−1800 cm^{-1} are presented in Figure 8. In the case of the mixture **4**/polyA−polyU (1:1) (Figure 8a), two additional bands at 1710 and 1683 cm^{-1} are observed. These absorptions are not observed for polyA−polyU (Figure 8b) and **4** (Figure 8c). According to Dagneaux et al., the absorption at 1712 cm^{-1} is assigned to a reverse Hoogsteen $C_2{=}O_2$ (thymidine, dT*dA-dT) stretching vibration (*34*). The band at 1683 cm^{-1} has been assigned to a $C_2{=}O_2$ stretch of additional base paired uridine (*35*). These results suggest that the base is also involved in the stabilization of the amphiphile/polyA−polyU complex via either Hoogsteen or reverse Hoogsteen nucleobase pairing with the uracil part of the amphiphile. A negative control using a mixture of **4**/polyC−polyG (1:1) is shown in Figure 8d. This FTIR spectrum, which does not show any change compared to polyC−polyG (Figure 8e), confirms the Hoogsteen or reverse Hoogsteen nucleobase pairing observed in the case of the **4**/polyA−polyU (1:1) mixture.

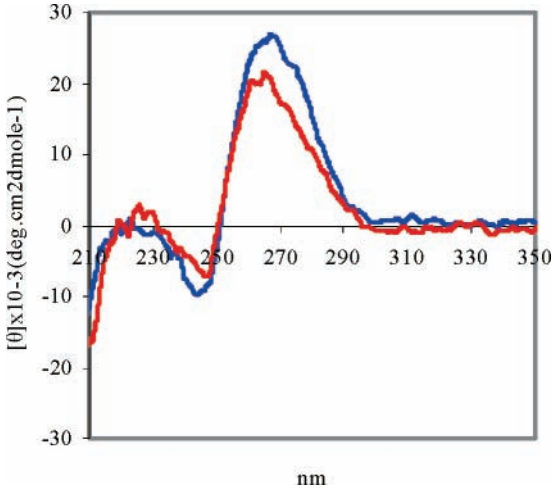

Figure 9. CD spectra of polyA−polyU (blue) and **4**/polyA−polyU (4:1) (red) at 25 °C.

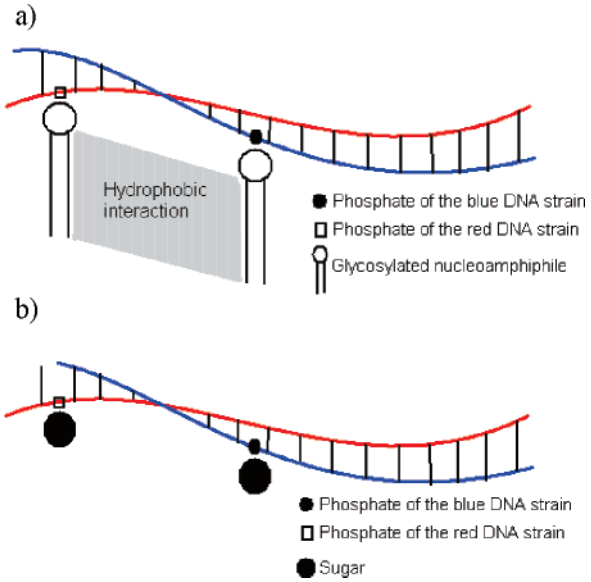

Figure 10. Interaction of (a) DNA−amphiphile, in which the presence of both hydrophobic interactions (amphiphiles−amphiphiles) and hydrogen bonding (sugars−phosphates) lead to a DNA double helix stabilization and (b) DNA−sugar, in which the sugar induces hydrogen bonding only, which gives a double helix destabilization.

Circular Dichroism Studies. The CD spectrum of polyA−polyU was recorded in the presence of **4**. The CD characteristics of the polyA−polyU/**4** complex are different from those of the polyA−polyU duplex. The CD spectrum of the polyA−polyU/**4** complex (red curve) and that of the polyA−polyU duplex (blue curve) are depicted in Figure 9. The RNA−**4** complex is characterized by a positive band at 260 nm and a negative band in the 245 nm region, and both of these bands have lower ellipticity values compared to that of the polyA−polyU duplex, which has a positive band in the 270 nm region, followed by a negative band at 245 nm. These results suggest that the polyA−polyU double helix structure is affected by the complexation with **4**. According to the circular dichroism investigations on U−A duplex and U*A−U triplex reported by Ray et al. (*36*), the lower ellipticity values observed in the case of **4**/polyA−polyU compared to

polyA−polyU duplex could be attributed to amphiphile U*A−U complex.

Proposed 4−DNA Complex. The molecular model for DNA−amphiphile assemblies formed with the glucosyl uridine amphiphile is proposed in Figure 10. In the case of amphiphile **4**, the stabilization of the double helix is due to concomitant phosphate−sugar and hydrophobic interactions (Figure 10a), whereas only phosphate−sugar interactions are responsible for DNA destabilization (*37*) by sugar or uridine (Figure 10b).

CONCLUSION

We describe here a new neutral DNA amphiphile for binding to nucleic acid and subsequent supramolecular assembly formation. The synthetic route to the glucosyl dioleyl uridine amphiphile is reported, which should provide easy access to other nucleoside-based sugar amphiphiles. A critical aggregation concentration of 10^{-5} mol/L for **4** was determined by using fluorescence probing methods. Thermal denaturation experiments of a polyA−polyU double helix in the presence of different amounts of **4** show a positive shift of ΔT_m indicating a double helix stabilization. The formation of amphiphile−nucleic acid complexes was confirmed by QELS, TEM, and gel electrophoresis studies. The ^{31}P NMR investigations reveal that the phosphate anion is associated with the sugar surface of the glucosyl dioleyl uridine amphiphile aggregates. Similarly, the PO_2^- stretch at 1216 cm^{-1} of the polyA−polyU/**4** (1:1 equiv) complex shows the presence of phosphate−sugar interactions. The bands at 1712 and 1683 cm^{-1} observed in aqueous solutions by FTIR and the lower ellipticity values measured by CD suggest that the uridine moiety of **4** is also involved in the stabilization of the amphiphile/polyA−polyU complex. All together, the results strongly support amphiphile−nucleic acid complex formation as a consequence of the amphiphilic character of the molecule, nucleoside, and phosphate−sugar interactions. This glycosyl nucleoside-based amphiphile demonstrates an alternative approach to forming stable nucleic acids supramolecular assemblies. These results expand the current repertoire of DNA complexing amphiphiles and provide further motivation for the design and evaluation of new amphiphiles.

ACKNOWLEDGMENT

This research was supported by the Army Research Office (Grant DAAD 19-02-1-0386). The authors would like to thank Dr. Stephen J. Lee, Estelle Champion, Prof. Catherine Vieillescazes, Michael Hovaneissian, and Prof. Mohamed El Maataoui.

LITERATURE CITED

(1) Felgner, P. L., Gadek, T. R., Holm, M., Roman, R., Chan, H. W., Wenz, M., Northrop, J. P., Ringold, G. M., and Danielsen, M. (1987) Lipofection: a highly efficient, lipid mediated DNA-transfection procedure. *Proc. Natl. Acad. Sci. U.S.A. 84*, 7413−7417.

(2) Leventis, R., and Silvius, J. R. (1990) Interactions of mammalian cells with lipid dispersions containing novel metabolizable cationic amphiphiles. *Biochim. Biophys. Acta 1023*, 124−132.

(3) Gao, X., and Huang, L. (1991) A novel cationic liposome reagent for efficient transfection of mammalian cells. *Biochem. Biophys. Res. Commun. 179*, 280−285.

(4) Lynn, D. M., Anderson, D. G., Putmann, D., and Langer, R. J. (2001) accelerated discovery of synthetic transfection vector: parallel synthesis and screening of a degradable polymer library. *J. Am. Chem. Soc. 123*, 8155−8156.

(5) Tang, M. X., Redmann, C. T., and Szoka, F. C. (1996) In vitro gene delivery by degraded polyamidoamine dendrimers. *Bioconjugate Chem. 7*, 703−714.

(6) Luo, D., Haverstik, K., Belcheva, N., Han, H., and Saltzman, W. M. (2002) Poly(ethylene glycol)-conjugate PAMAM dendrimer for biocompatible, hight-efficency DNA delivery. *Macromolecules 35*, 3456−3462.

(7) Tranchant, I., Mignet, N., Crozat, E., Leblond, J., Girard, C., Scherman, D., and Herscovici, J. (2004) DNA Complexing Lipopolythiourea. *Bioconjugate Chem. 15,* 1342−1348.

(8) Illum, L., Jabbal-Gill, I., Hinchcliffe, M., Fisher, A. N., and Davis, S. S. (2001) Chitosan as a novel nasal delivery system for vaccines. *Adv. Drug Delivery Rev. 51*, 81−96.

(9) Kim, Y. H., Gihm, S. H., Park, C. R., Lee, K. Y., Kim, T. W., Kwon, I. C., Chung, H., and Jeong, S. Y. (2001) Structural Characteristics of Size-Controlled Self-Aggregates of Deoxycholic Acid-Modified Chitosan and Their Application as a DNA Delivery Carrier. *Bioconjugate Chem. 12*, 932−938.

(10) Aoyama, Y., Kanamori, T., Nakai, T., Sasaki, T., Horiuchi, S., Sando, S., and Niidome, T. (2003) Artificial Viruses and Their Application to Gene Delivery. Size-Controlled Gene Coating with Glycocluster Nanoparticles. *J. Am. Chem. Soc. 125*, 3455−3457.

(11) Barthelemy, P., Prata, C. A. H., Filocamos, S. F., Immoos, C. E., Maynor, B. W., Hashmi, S. A. N., Lee, S. J., and Grinstaff, M. W. (2005) Supramolecular assemblies of DNA with neutral nucleoside amphiphiles. *Chem. Commun. 10*, 1261−1263.

(12) Sakurai, K., and Shinkai, S. (2000) Molecular Recognition of Adenine, Cytosine, and Uracil in a Single-Stranded RNA by a Natural Polysaccharide: Schizophyllan. *J. Am. Chem. Soc. 122*, 4520−4521.

(13) Del Vecchio, P., Esposito, D., Ricchi, L., and Barone, G. (1999) The effects of polyols on the thermal stability of calf thymus DNA. *Int. J. Biol. Macromol. 24*, 361−369.

(14) Hayashida, O., Matsuo, A., and Aoyama, Y. (2001) Macrocyclic Saccharide Bundles as a New Type of Firm DNA Binders. *Chem. Lett. 30*, 272.

(15) Wolfrom, M. L., and Thompson, A. (1963) *Methods in Carbohydrate Chemistry*, p 211, Academic Press Inc., New York.

(16) Excoffier, G., Gagnaire, D., and Utile, J. P. (1975) Coupure sélective par l'hydrazine des groupements acétyles anomères de résidus glycosyles acétylés. *Carbohydr. Res. 39*, 368−373.

(17) Schimdt, R. R., and Michel, J. (1980) Facile Synthesis of α- and β-O-Glycosyl Imidates; Preparation of Glycosides and Disaccharides. *Angew. Chem., Int. Ed. Engl. 19*, 731−732.

(18) Schimdt, R. R. (1986) New Methods for the Synthesis of Glycosides and Oligosaccharides − Are There Alternatives to the Koenigs-Knorr Method? *Angew. Chem., Int. Ed. Engl. 25*, 212−235.

(19) Nakai, T., Kanamori, T., Sando, S., and Aoyama, Y. (2003) Remarkably Size-Regulated Cell Invasion by Artificial Viruses. Saccharide-Dependent Self-Aggregation of Glycoviruses and Its Consequences in Glycoviral Gene Delivery. *J. Am. Chem. Soc. 125*, 8465−8475.

(20) Turro, N. J., and Yekta, A. (1978) Luminescent probes for detergent solutions. A simple procedure for determination of the mean aggregation number of micelles. *J. Am. Chem. Soc. 100*, 5951−5952.

(21) Moroi, Y., Humphry-Baker, R., and Gratzel, M. (1987) Determination of micellar aggregation number of alkylsulfonic acids by fluorescence quenching method. *J. Colloid Interface Sci. 119*, 588−591.

(22) Piao, J., Kobayashi, T., Adachi, S., Nakanishi, K., and Matsuno R. (2003) *Biochem. Eng. J. 14*, 79−84.

(23) Zuidam, N. J., and Barenholz, Y. (1998) Electrostatic and structural properties of complexes involving plasmid DNA and cationic lipids commonly used for gene delivery. *Biochim. Biophys. Acta 1368*, 115−128.

(24) Burczyk, B., Wilk, K. A., Sokolowski, A., and Syper, L. (2001) Synthesis and Surface Properties of *N*-Alkyl-*N*-methylgluconamides and *N*-Alkyl-*N*-methyllactobionamides. *J. Colloid Interface Sci. 240*, 552−558.

(25) Johnsson, M., Wagenaar, A., Stuart, M. C. A., and Engberts, J. B. F. N. (2003) Sugar-Based Gemini Surfactants with

pH-Dependent Aggregation Behavior: Vesicle-to-Micelle Transition, Critical Micelle Concentration, and Vesicle Surface Charge Reversal. *Langmuir 19*, 4609−4618.
(26) Eichhorn, G. L., and Shin, Y. A. (1968) Interaction of metal ions with polynucleotides and related compounds. XII. The relative effect of various metal ions on DNA helicity. *J. Am. Chem. Soc. 90*, 7323−7328.
(27) Das G., and Hamilton, A. D. (1997) Carbohydrate recognition: Enantioselective spirobifluorene diphosphonate receptors. *Tetrahedron Lett. 38*, 3675−3678.
(28) Hayashida, O., Kato, M., Akagi, K., and Aoyama, Y. (1999) Interaction of Sugar and Anion in Water via Hydrogen Bonding: Chain-Length Dependent Agglutination of Oligosaccharide Clusters Induced by Multivalent Anion Binding. *J. Am. Chem. Soc. 121*, 11597−11598.
(29) Job, A. (1928) *Ann. Chim. 9* (10th Series), 113−204.
(30) Taillandier, E., Liquier, J., and Taboury, J. A. (1985) In *Advances in Infrared and Raman Spectroscopy* (Clark, R. H., and Hester, R. E., Eds.) Vol. 12, pp 65−114, Wiley-Heyden, New York.
(31) Sarkar, M., Dornberger, U., Rozners, E., Fritzsche, H., Stromberg, R., and Graslund, A. (1997) FTIR Spectroscopic Studies of Oligonucleotides That Model a Triple-Helical Domain in Self-Splicing Group I Introns. *Biochemistry 36*, 15463−15471.
(32) Cross, A. D., and Jones, R. A. (1969) *Pratical infrared spectroscopy*, 3rd ed., Butterworth, London.
(33) Tajmir-Riahi, H. A., Naoui, M., and Diamantoglou, S. (1994) *J. Biomol. Struct. Dyn. 12*, 217−234.
(34) Dagneaux, C., Liquier, J., and Taillandier, E. (1995) FTIR Study of a Nonclassical dT10*dA10−dT10 Intramolecular Triple Helix. *Biochemistry 34*, 14815−14818.
(35) Sarkar, M., Dornberger, U., Rozners, E., Fritzsche, H., Stromberg, R., and Graslund, A. (1997) FTIR Spectroscopic Studies of Oligonucleotides That Model a Triple-Helical Domain in Self-Splicing Group I Introns. *Biochemistry 36*, 15463−15471.
(36) Ray, A., Kumar, G. S., Das, S., and Maiti, M. (1999) Spectroscopic Studies on the Interaction of Aristololactam-β-D-Glucoside with DNA and RNA Double and Triple Helices: A Comparative Study. *Biochemistry 38*, 6239−6247.
(37) Sugars are polyols that displace water molecules and induce a modification of the electrostatic interactions between the polynucleotide and its surrounding counterions. Consequently, when the concentration of polyols increases, the repulsion between the negative charges of the phosphate groups is enhanced, and a gradual destabilization of the DNA double helix occurs.

BC050029Y

Triple Helix-Forming Oligonucleotides Conjugated to New Inhibitors of Topoisomerase II: Synthesis and Binding Properties

Maria Duca,[§] Kahina Oussedik,[§] Alexandre Ceccaldi,[§] Ludovic Halby,[§] Dominique Guianvarc'h,[§,†] Daniel Dauzonne,[‡] Claude Monneret,[‡] Jian-Sheng Sun,[§] and Paola B. Arimondo[§,*]

Muséum National d'Histoire Naturelle, USM0503 MNHN, UMR5153 CNRS, U565 INSERM, 43 rue Cuvier CP26 75231 Paris Cedex 05 France, and UMR176 CNRS-INSTITUT CURIE, Institut Curie Section de Recherche, 26 rue d'Ulm 75248 Paris Cedex 05 France. Received February 7, 2005; Revised Manuscript Received April 14, 2005

Triplex-forming oligonucleotides (TFOs) are among the most specific DNA ligands and represent an important tool for specific regulation of gene expression. TFOs have also been used to target DNA-modifying molecules to obtain irreversible modifications on a specific site of the genome. A number of molecules have been recognized to target topoisomerase II and stabilize double-stranded cleavage mediated by this enzyme thus determining permanent DNA damage. Among these poisons, etoposide (VP16), a 4′-demethylepipodophyllotoxin derivative, is widely used in cancer chemotherapy. In the aim to design DNA site-specific molecules, three analogues of VP16 (**1**, **2**, and **3**), recently described (Duca et al. *J. Med. Chem.* **2005**, *48*, 596−603), were attached to TFOs, together with a fourth one, of which the synthesis is reported here. Two different oligonucleotides, differing by the length (a 16-mer and a 20-mer), and two different linker arms between the oligonucleotide and the drug were used. The coupling reaction between the drug and the TFO was further improved. For the first time, we also report the synthesis of TFO conjugates bearing two molecules of inhibitor linked to the same oligonucleotide end. In total, 16 new conjugates were synthesized and evaluated for their ability to form triple helices. The loss in triplex stability due to the conjugation of the TFO to compounds that do not interact with DNA is compensated by the presence of the ethylene glycol linker arm. This stabilization effect is more pronounced at the 3′ end than at the 5′ end. All conjugates form a stable triplex selectively on the DNA target at 37 °C and pH 7.2.

INTRODUCTION

Synthetic oligonucleotides can recognize short oligopyrimidine·oligopurine regions in double-stranded DNA via hydrogen bond formation with purine bases in the major groove, leading to a local triple helix (*1*−*3*). Triplex-forming oligonucleotides (TFOs[1]) are among the most specific DNA ligands, together with another class of small molecules represented by synthetic hairpin polyamides that bind to DNA in the minor groove (*4*). Triplex-based approaches are an attractive mean to achieve targeted gene regulation, gene manipulation, and directed mutagenesis in vitro and in vivo (*5*−*7*). Therefore, they represent an important tool for specific regulation of gene expression (*1*, *2*, *6*, *8*). In fact, TFOs have been described to modulate transcription in vitro and in cell culture for exogenous and endogenous genes (*9*−*11*), to inhibit DNA replication in cells (*12*), and to direct mutagenesis in vitro and in vivo (*13*). Furthermore, the sequence-specific recognition properties of TFOs can be exploited to direct DNA cleaving and alkylating agents to chosen DNA sequences (*14*). In fact, TFOs linked to the appropriate DNA modifying molecule are able to induce a permanent modification in the proximity of the triplex site (*7*, *15*, *16*). Interestingly, this strategy has been successfully used to target the action of topoisomerase I inhibitors, such as camptothecin (*17*−*19*).

Topoisomerases regulate DNA topology in cells and, therefore, are essential for many vital processes such as replication, transcription and chromosome segregation (*20*, *21*). Topoisomerases I and II represent privileged targets for a number of cytotoxic anticancer drugs, which stimulate strand cleavage by topoisomerases at a variety of sites. These drugs are called topoisomerase poisons or inhibitors (*22*, *23*).

Whereas topoisomerase I is a monomer and, thus, controls DNA topology by a single-strand breaking of DNA, eukaryotic topoisomerase II is an homodimer and acts by passing an intact DNA double helix through a transient double-stranded break (*21*). The DNA/topoisomerase II covalent complex, called the cleavage complex, is the key intermediate of the topoisomerase reaction. In this complex, each monomer of the enzyme is covalently linked, through a phosphotyrosine bond, to one strand of the duplex, to the 5′ phosphate of the 4-bp staggered DNA double-stranded break. This intermediate, which has normally a short lifetime, is stabilized by different molecules, such as etoposide or its derivatives,

* Corresponding author. Tel: +33 1 40 79 38 59. Fax: +33 1 40 79 37 05. E-mail: arimondo@mnhn.fr.

§ Muséum National d'Histoire Naturelle.

‡ Institut Curie Section de Recherche.

† Present address: Laboratoire de Chimie Organique Biologique, Université Paris 6, UMR 7613, 4, place Jussieu, 75005 Paris, France.

[1] Abbreviations: TFO, triplex-forming oligonucleotide; 4′-DMEP, 4′-demethylepipodophyllotoxin; M, 5′-methyl-2′-deoxycytidine; P, 5′-propynyl-2′-deoxyuridine; VP16, etoposide; bp, base pair; PAGE, polyacrylamide gel electrophoresis; DNase I, 2′-deoxyribonuclease I; EDCI, 1-[3-(dimethylamino)propyl]-3-ethylcarbodiimide; HOBt, 1-hydroxybenzotriazole; L_{12}, 8-[(3-aminopropyl)-(7-carboxyheptyl)amino]octanoic acid; L_3, ethylene glycol; L_{18}, hexaethylene glycol; HEPES, *N*-(2-hydroxyethyl)-piperazine-*N*′-(2-ethanesulfonic acid); $(PyS)_2$, dipyridyl disulfide; PPh_3, triphenylphosphine.

10.1021/bc050031p CCC: $30.25 © 2005 American Chemical Society
Published on Web 06/30/2005

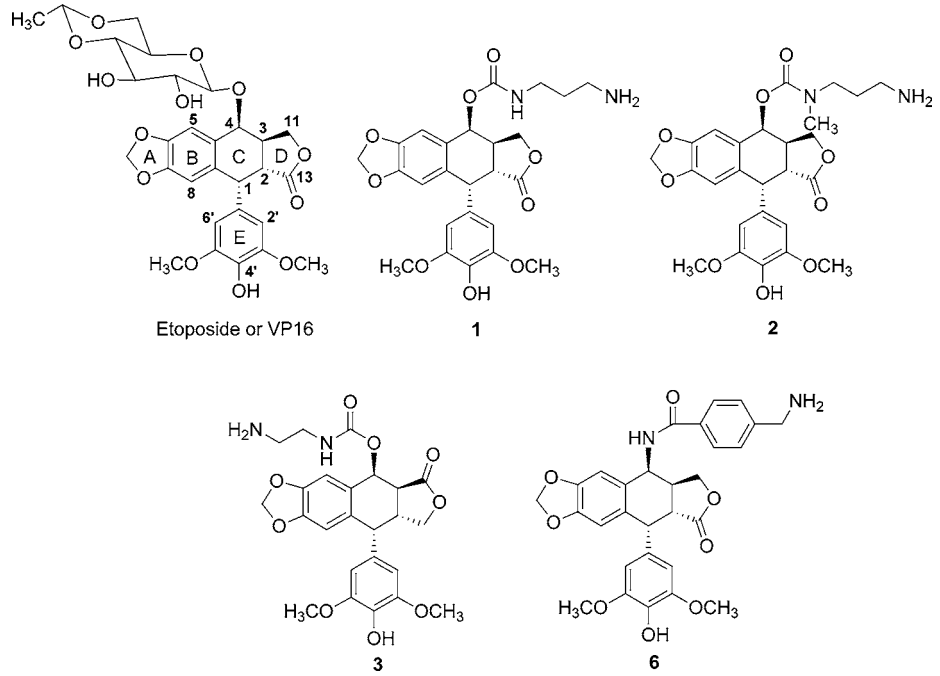

Figure 1. Structure of etoposide and of compounds **1**, **2**, **3**, and **6** used for the coupling to the TFOs.

which are topoisomerase II poisons. These poisons form a stable ternary complex drug/topoisomerase II/DNA and prevent DNA religation. Thereby, they induce breaks in the DNA strands whose accumulation causes cell death (*24*).

So, among the topoisomerase II poisons, some compounds are commonly used as anticancer drugs. Etoposide (VP16, Figure 1), a 4′-demethylepipodophyllotoxin (4′ DMEP) derivative, is one of these drugs and is used as frontline therapy particularly in the treatment of small cell lung cancer, testicular carcinoma, lymphoma and Kaposi's sarcoma (*25*, *26*). Although VP16 is widely used in chemotherapy, the molecular mechanism of action of this compound and, more generally, of this class of topoisomerase II poisons is not yet fully understood. Moreover, etoposide presents several limitations, such as moderate potency, poor water solubility, development of drug resistance, metabolic inactivation and toxic effects. For these reasons, the structure of VP16 has been extensively modified, thus increasing the information about its structure−activity relationships. In this context, it has been shown that the glucopyranose moiety in the 4-position of etoposide is not essential for activity and that other substituents, such as the aminoalkyl or arylamino chains induce a better antitopoisomerase II activity (*27*, *28*). Recently, we reported that some non glycoside 4′-demethylepipodophyllotoxin derivatives bearing a carbamate chain at the 4 position (4′-demethylepipodophyllotoxin-4-aminoalkyl carbamates, such as **1** and **3**, in Figure 1) strongly inhibit topoisomerase II and show antiproliferative effects in vitro and antitumor activity in vivo (*29*). A new 4′-DMEP derivative, bearing an aminobenzoyl group, has also been synthesized, resulting in an active topoisomerase II poison.

To increase the DNA sequence-specificity of these molecules that do not interact with DNA, we covalently attached these derivatives to TFOs, in a way similar to that performed with the topoisomerase I poisons camptothecin and rebeccamycin (*19*, *30*). Sixteen conjugates were synthesized and characterized, using two TFOs (differing by the length) and four VP16 analogues. These derivatives were attached to the 3′ or 5′ end of the TFO with two linker arms of different length (L_{18} and L_3). Conjugates bearing two molecules of poison at the same end of the TFO were also synthesized and characterized. The stability of the triplex formed by the conjugates was evaluated by gel retardation and DNase I footprinting assays.

EXPERIMENTAL PROCEDURES

Methods. ^{1}H NMR and NMR spectra were recorded in chloroform-*d* or methanol-d_4, on a Bruker spectrometer (300 MHz). For all oligonucleotides conjugates, mass determination was accomplished by electrospray ionization on a Q-STAR pulsar I (Appleura) and HPLC purifications were performed upon Agilent 1100 using a Xterra reversed phase C_{18} column (4.6 × 50 mm, 2.5 μm). Absorbance spectrophotometry was performed on a Uvikon 860 (Kontron).

Materials. All chemicals were purchased from Aldrich Chemical Co. All solvents were of analytical grade. 4-(*tert*-Butoxycarbonylaminomethyl)benzoic acid was prepared as previously reported (*31*). Human topoisomerase IIα was purchased from TopoGEN Inc. (Columbus, OH).

Oligonucleotides. All oligonucleotides were purchased from Eurogentec (Belgium). Concentrations were determined spectrophotometrically at 25 °C using molar extinction coefficients at 260 nm calculated from a nearest-neighbor model (*32*). The drug-tethered oligonucleotides were synthesized as described below. The nomenclature of the oligonucleotides and conjugates is as follows. The abbreviation TFO is preceded by a number referring to the length of the oligonucleotide and followed, if attached to the 3′ end, or preceded, if attached through the 5′ end, by the letter L (for linker) and the number of atoms in the linker (L_3 = ethylene glycol; L_{18} = hexaethylene glycol; L_{12} = 8-[(3-aminopropyl)-(7-carboxyheptyl)amino]octanoic acid), and, finally, by the denomination of the 4′-DMEP derivative. For example, 20TFO-L_{18}-**6** stands for the 20-mer TFO linked at its 3′ end through the hexaethylene glycol spacer to compound **6**. The orientation of the triple helix is defined as the orientation of the purine-rich strand of the duplex, the

TFO binding in the major groove in an orientation parallel to the oligopurine strand.

Topoisomerase II Poisons. The synthesis of compounds **1**, **2**, and **3** has been previously described (*29*). Starting material **4** was obtained as reported (*33*).

Synthesis of 4-β-(4-Boc-aminomethylphenyl)amido-4′-*O*-demethyl-4-deoxypodophyllotoxin (5). To a solution of **4** (1 g, 2.5 mmol) in anhydrous CH_2Cl_2 (75 mL), under inert atmosphere, were added 4-(*tert*-butoxycarbonylaminomethyl)benzoic acid (753 mg, 3 mmol), EDCI (575 mg, 3 mmol) and HOBt (405 mg, 3 mmol). The reaction mixture was further stirred at room temperature for 4 h. The medium was then taken up with CH_2Cl_2 (25 mL) and water (50 mL). The organic phase was extracted with H_2O (3 × 50 mL), then dried ($MgSO_4$) and filtered. This product was further purified by silica gel chromatography using CH_2Cl_2/methanol 20:1 as the eluent to give pure compound **5** in 70% yield. $R_f = 0.62$ (CH_2Cl_2/methanol 9:1), mp = 133−135 °C, ^{1}H NMR ($CDCl_3$) ∂: 7.71 (d, 2H, $J = 8.0$ Hz, Ph), 7.32 (d, 2H, $J =$ 7.7 Hz, Ph), 6.80 (s, 1H, 5-H), 6.53 (s, 1H, 8-H), 6.45−6.32 (m, 1H, 4-NH), 6.30 (s, 2H, 2′,6′-H), 5.97 (d, 2H, $J =$ 7.1 Hz, CH_2O_2), 5.50−5.38 (m, 2H, 4-H, 4′-OH), 5.00−4.88 (m, 1H, NH), 4.58 (d, 1H, $J = 3.2$ Hz, 1-H), 4.46 (t, 1H, $J = 8.0$ Hz, 11a−H), 4.30 (s, 2H, *CH*$_2$NH), 3.85 (t, 1H, $J = 9.6$ Hz, 11b−H), 3.77 (s, 6H, 3′,5′-OCH_3), 3.05−2.98 (m, 1H, 3-H), 2.95 (dd, 1H, $J = 4.6$, 14.3 Hz, 2-H); 1.44 (s, 9H, Boc); MS (CI) *m/z*: 650 $[M + NH_4]^+$.

Synthesis of 4-β-(4-Aminomethylphenyl)amido-4′-*O*-demethyl-4-deoxypodophyllotoxin (6). To a solution of **5** (700 mg, 1.1 mmol) in CH_2Cl_2 (10 mL) was added trifluoroacetic acid (TFA, 855 μL, 11.1 mmol). The reaction mixture was stirred for 5 h, and washed with a cold saturated aqueous $NaHCO_3$ solution then with water until pH 6−7. The organic extract was dried over $MgSO_4$ and concentrated in vacuo at 30 °C. The residue was purified by silica gel column chromatography using a CH_2Cl_2/methanol 10:1 mixture as the eluent to afford the pure compound **6** in 76% yield. $R_f = 0.17$ (CH_2Cl_2/methanol 9:1), mp = 178−180 °C, ^{1}H NMR (CD_3OD) ∂: 7.86 (d, 2H, $J = 8.0$ Hz, Ph), 7.46 (d, 2H, $J = 7.7$ Hz, Ph), 6.82 (s, 1H, 5-H), 6.51 (s, 1H, 8-H), 6.36 (s, 2H, 2′,6′-H), 5.93 (d, 2H, $J = 3.5$ Hz, CH_2O_2), 5.52−5.40 (m, 1H, 4-H), 4.58 (d, 1H, $J = 4.8$ Hz, 1-H), 4.42 (t, 1H, $J = 8.1$ Hz, 11a−H), 3.99 (s, 2H, *CH*$_2$NH), 3.83 (t, 1H, $J = 9.8$ Hz, 11b−H), 3.72 (s, 6H, 3′,5′-OCH_3), 3.38−3.22 (m, 1H, 2-H), 3.15−2.98 (m, 1H, 3-H); MS (CI) *m/z*: 550 $[M + NH_4]^+$.

Synthesis of the TFO-(4′-DMEP Derivative) Conjugates. The oligonucleotide conjugates were synthesized and purified according to previously reported procedures with little modifications (*34*). Compounds **1**, **2**, **3**, and **6** have been synthesized with an amino group in order to covalently link them to the phosphorylated poly(ethylene glycol) linker arm at the 3′ end (or the 5′ end) of the oligonucleotides (16TFO and 20TFO). The 3′ or 5′ phosphorylated oligonucleotide (300 μg) was first precipitated as hexadecyltrimethylammonium salt, then dissolved in 50 μL of dry DMSO. Solutions of 4-(*N*,*N*-dimethylamino)-pyridine (5 mg in 50 μL of DMSO, 41 μmol), dipyridyl disulfide (6.6 mg in 25 μL of DMSO, 30 μmol) and triphenylphosphine (7.9 mg in 25 μL of DMSO, 30 μmol) were added. After 15 min incubation at room temperature, the activated oligonucleotide was rapidly precipitated with 2% $LiClO_4$/acetone and resolubilized in water (50 μL). Triethylamine (3 μL) was added, followed by the drug solution (1 mg in 100 μL of a mixture H_2O/DMSO 40:60). After 2 h, the oligonucleotide was precipitated with 2% $LiClO_4$/acetone, rinsed with acetone, then dissolved in 50 μL of water. Reverse phase HPLC was used to separate the product from the initial oligonucleotide (5 → 40% CH_3CN in 0.2 M $(NH_4)OAc$). The product was eluted as a single peak absorbing at 310 nm (oligonucleotide) with retention times between 10 and 12 min. compared to 4−6 min for the initial 16TFO and 20 TFO, respectively. The average yield was 60%. Purity was 100%. 16TFO-L_{18}-**1**, **1**-L_{18}-16TFO MS (ES^+) *m/z*: 5971 $[M + H]^+$ (calculated: 5970), 16TFO-L_{18}-**2**, **2**-L_{18}-16TFO MS (ES^+) *m/z*: 5985 $[M + H]^+$ (calculated: 5984), 16TFO-L_{18}-**3**, **3**-L_{18}-16TFO MS (ES^+) *m/z*: 5957 [M + H] (calculated: 5956), 16TFO-L_{18}-**6**, **6**-L_{18}-16TFO MS (ES^+) *m/z*: 6003 $[M + H]^+$ (calculated: 6002), 16TFO-L_3-**6**, MS (ES^+) *m/z*: 5797 $[M + H]^+$ (calculated: 5796), 20TFO-L_{18}-**1**, **1**-L_{18}-20TFO MS (ES^+) *m/z*: 7234 $[M + H]^+$ (calculated: 7233), 20TFO-L_{18}-**6**, **6**-L_{18}-20TFO MS (ES^+) *m/z*: 7266 $[M + H]^+$ (calculated: 7265).

Synthesis of the TFO-L_{18}-$(6)_2$ Conjugates. Two molecules of compound **6** were attached to the 3′ phosphate of 16TFO-L_{18} and 20TFO-L_{18} using the same procedure as described above but repeating the reaction two times. The products were purified by HPLC (gradient: 0 → 80% CH_3CN in 0.2 M $(NH_4)OAc$). The average yield of the reaction was 45% and 100% purity. All conjugates were analyzed by UV spectroscopy, mass spectrometry and gel electrophoresis under denaturing conditions. 16TFO-L_{18}-$(\mathbf{6})_2$ MS (ES^+) *m/z*: 6545 $[M + H]^+$ (calculated: 6544), 20TFO-L_{18}-$(\mathbf{6})_2$ MS (ES^+) *m/z*: 7780 $[M + H]^+$ (calculated: 7779).

Synthesis of the 20TFO-L_{12}-$(6)_2$ Conjugates. Two molecules of compound **6** were linked to a trifunctional linker containing two carboxylic groups, the 8-[(3-aminopropyl)-(7-carboxyheptyl)amino]octanoic acid, and then coupled to 3′ phoshophorylated 20TFO.

Synthesis of 8-[(3-Boc-aminopropyl)−(7-carboxyheptyl)amino]octanoic Acid (8). 8-Bromooctanoic acid (240 mg, 1.1 mmol) was reacted with N-Boc-1,3-diaminopropane (87 mg, 0.5 mmol, **7**) in anhydrous acetonitrile (10 mL) for 48 h at 50 °C in the presence of K_2CO_3 (210 mg, 1.5 mmol). The solvent was removed under reduced pressure, and the reaction mixture was extracted with methanol/chloroform 9:1 (3 × 5 mL). Organic phases were combined and evaporated in vacuo. The crude product was washed with ether (3 × 5 mL) to afford a white solid in 78% yield. MS (ES^+) *m/z*: 459 $[M + H]^+$ (calculated: 458).

Synthesis of L_{12}-$(6)_2$ (9). To a solution of **6** (7 mg, 13 μmol) in anhydrous DMF were added **8** (2.3 mg, 5 μmol), DCC (3.6 mg, 17 μmol) and HOBt 1 M (17 μL, 17 μmol). The reaction mixture was stirred at room temperature for 12 h and then cooled in ether. This led to the formation of a yellow amorphous solid. The crude product was purified by reversed phase HPLC using an acetonitrile gradient (0 → 90% CH_3CN with 0.1% of TFA), and obtained in 16% yield. MS (ES^+) *m/z*: 1487 $[M + H]^+$ (calculated: 1486).

To a solution of this compound (0.6 mg, 0.4 μmol) in CH_2Cl_2 (50 μL was added TFA (50 μL). The reaction mixture was stirred at room temperature for 4 h. The mixture was concentrated in vacuo, and the crude product was purified by reversed phase HPLC using an acetonitrile gradient (0 → 90% CH_3CN with 0.1% of TFA) to give **9** with a 90% total yield. MS (ES^+) *m/z*: 1387 $[M + H]^+$ (calculated: 1386).

Synthesis of 20TFO-L_{12}-$(6)_2$. 3′-Phosphorylated oligonucleotide 20TFO (210 μg, 33 nmol) was first precipitated as hexadecyltrimethylammonium salt, then dissolved in 50 μL of dry DMF. Solutions of 4-(dimethylamino)pyridine (5 mg in 25 μL of DMF, 41 μmol),

dipyridyl disulfide (6.6 mg in 25 μL of DMF, 30 μmol) and triphenylphospine (7.9 mg in 50 μL of DMF, 30 μmol) were added. After 15 min of incubation at room temperature, **9** (0.6 mg, 430 nmol) was added. The mixture was kept at room temperature for 8 h. The oligonucleotide conjugate was then precipitated with 2% $LiClO_4$ in acetone, rinsed with acetone and purified by reversed phase HPLC using a linear acetonitrile gradient (0 → 80% CH_3CN in 0.2 M $(NH_4)OAc$). The average yield was of 40%. The oligonucleotide conjugate was characterized by UV spectroscopy, denaturing gel electrophoresis and mass spectrometry. 100% purity was obtained. MS (ES^-) *m/z*: 7776 $[M - H]^-$ (calculated: 7776).

Gel Retardation Assay. The oligopyrimidine strand of the 29-bp target duplex was 5′ end-labeled with [γ-^{32}P] ATP (Amersham) by T4 polynucleotide kinase (New England Biolabs) according to the manufacturer instructions.

Increasing concentrations (from 10 nM to 5 μM) of the triplex-forming oligonucleotides were added to 10 nM of the radiolabeled duplex in 10 mM $MgCl_2$, 50 mM NaCl, 50 mM HEPES pH 7.2, 10% sucrose and 0.5 mg/mL tRNA followed by sample incubation at 37 °C during 2 h. Electrophoresis was performed on a nondenaturing 15% polyacrylamide gel containing 10 mM $MgCl_2$ and 50 mM HEPES pH 7.2 at 37 °C. To quantify the formation of the triplex, the gels were dried and scanned with a Typhoon 9410 (Amersham Biosciences). The concentration of conjugate or TFO necessary to obtain 50% of formed triplex (C_{50}) was calculated, and a mean value corresponding to three to five different experiments is reported.

DNase I Protection Assays. The DNA template for DNase I protection assay on the oligopyrimidine-containing strand of the target was obtained by successive digestion of the plasmid described in (*18*) with *Pvu* II and *Eco* RI, yielding a 324-mer fragment suitable for 5′-end labeling by the T4 polynucleotide kinase (Biolabs New England) and γ[^{32}P]-ATP (Amersham) after shrimp alkaline phosphatase treatment, and purified as described. One microliter of DNase I (final concentration 0.03 mg/mL, Sigma) diluted in 1 mM $MgCl_2$, 1 mM $MnCl_2$, and 20 mM NaCl was added to the radiolabeled duplex (20 nM), preincubated previously for 1 h at 30 °C in 50 mM Tris-HCl, pH 7.2, 20 mM NaCl, 1 mM $MgCl_2$, 2 mM $MnCl_2$, in the absence or in the presence of the conjugates (final reaction volume 10 μL). The reaction was performed for 3 min at 20 °C and stopped by ethanol precipitation. The samples were resuspended in 95% formamide and heated at 95 °C for 4 min before being loaded onto a denaturing 8% polyacrylmide gel (19:1 acrylamide: bisacrylamide) containing 7.5 M urea in 1 × TBE buffer (50 mM Tris base, 55 mM boric acid, 1 mM EDTA). To identify DNase I footprinting, the gels were scanned with a Typhoon 9410 (Amersham Biosciences).

Topoisomerase II-Mediated DNA Cleavage Assay. Topoisomerase II poisoning by compound **6** was evaluated as previously described (*29*, *33b*).

The topoisomerase II poisoning by the conjugates was evaluated as the amount of DNA cleavage by topoisomerase II on a 5′-end radiolabeled 96-bp DNA fragment containing the triplex site. The 96-bp DNA fragment was prepared by 5′-[^{32}P]-end labeling of the *Eco*RI or *Not* II/alkaline phosphatase treated plasmid using γ-[^{32}P]-ATP and T4 polynucleotide kinase followed by treatment with *Not*II/*Eco*RI, yielding a fragment radiolabeled on the pyrimidine strand (Y) or on the purine strand (R), respectively. The detailed procedure for isolation and purification have been described previously (*18*). Fifty nanomoles of 96-bp radiolabeled DNA fragment was incubated for 1 h at 30 °C in 50 mM Tris-HCl pH 7.0, 120 mM KCl, 1 mM ATP, 10 mM $MgCl_2$, 0.5 mM DTT, 0.1 mM EDTA, and 30 μg/μL BSA in the presence of the TFO in order to form the triplex or of the drug at 5 μM (total reaction volume 10 μL). Human topo IIα (0.7 units) was added to the duplex preincubated as described above with either the TFO and/or the drugs followed by incubation for 20 min at 30 °C. After ethanol precipitation, all samples were suspended in 6 μL of formamide, heated at 90 °C for 3 min and then chilled on ice for 4 min before being loaded onto a denaturing 8% polyacrylamide gel (19:1 acrylamide:bisacrylamide) containing 7.5 M urea in 1 × TBE buffer (50 mM Tris-base, 55 mM boric acid, 1 mM EDTA) for 120 min at 65 W. To quantitate the extent of cleavage, the gels were scanned with a Typhoon 9410 (Amersham Biosciences). For the determination of cleavage levels, normalization relative to total loading was performed.

Molecular Modeling. Molecular modeling was performed by conformational energy minimization with Jumna program package (version 10.3) (*36*). The coordinates of DNA triple helices, which were derived from the previously published B-like triple helix, were used for the construction of triplex (*37*). The published atomic coordinates of yeast topoisomerase II (*38*) and of gyrase (*39*) were used to build the model.

RESULTS

Oligonucleotides and Topoisomerase II Poisons. The oligonucleotides chosen for this study are a 16-mer (16TFO) and a 20-mer (20TFO) containing 5-methyl-2′-deoxycytidine (M) and 5-propynyl-2′-deoxyuridine (P) (Figure 2A). These base modifications were previously shown to enhance triplex formation (*40*). 16TFO and 20TFO were already shown to form a stable triple helix on a 29-bp target sequence containing a 23-bp oligopyrimidine·oligopurine sequence at 37 °C, pH 7.2, 50 mM KCl, 10 mM $MgCl_2$ (Figure 2A) (*19*, *30*). The TFOs were covalently attached through three types of linker arms (L_3, L_{12}, and L_{18}) to derivatives of 4′-DMEP (Figure 2). Derivatives **1**−**3** have recently been synthesized and characterized (*29*). In these compounds the sugar of VP16 is replaced by an aminoalkyl chain linked to the C-4 of 4′-DMEP by a carbamate group (Figure 1). Compounds **1** and **2** bear a 4-*N*-(3-aminopropyl)carbamate chain or a 4-[*N*-(3-aminopropyl)-*N*-methyl]carbamate substituent, respectively. Compound **3** contains a 4-[*N*-(2-aminoethyl)]-carbamate chain and a supplementary modification on the lactone D ring, called retrolactone modification (*29*, *41*). Furthermore, we chose another 4′-DMEP derivative modified on the 4-position (**6**), containing a secondary aminomethylphenyl side chain with a primary amino group suitable for attachment to the TFO (Figure 1). This compound was designed on the basis of a family of 4′-DMEP derivatives, previously described by Zhou et al. (*42*), bearing aryl chains linked in the 4-position via an amide group. This family of compounds has shown good antitopoisomerase II activity. Compound **6** was synthesized starting from the 4-β-amino-4′-demethylpodophyllotoxin (**4**), prepared, as previously reported (*33*), by reaction with 4-(Boc-aminomethyl)benzoic acid in the presence of 1-(3-dimethylaminopropyl)-3-ethylcarbodiimide (EDCI) and 1-hydroxybenzotriazole (HOBt) (Scheme 1), to provide compound **5**, which, after deprotection, leads to **6** in a 76% yield. Compounds **1** and **3** are good topoisomerase II poisons (38% and 48% of inhibition at 20 μM, respectively, expressed as amount of linearized

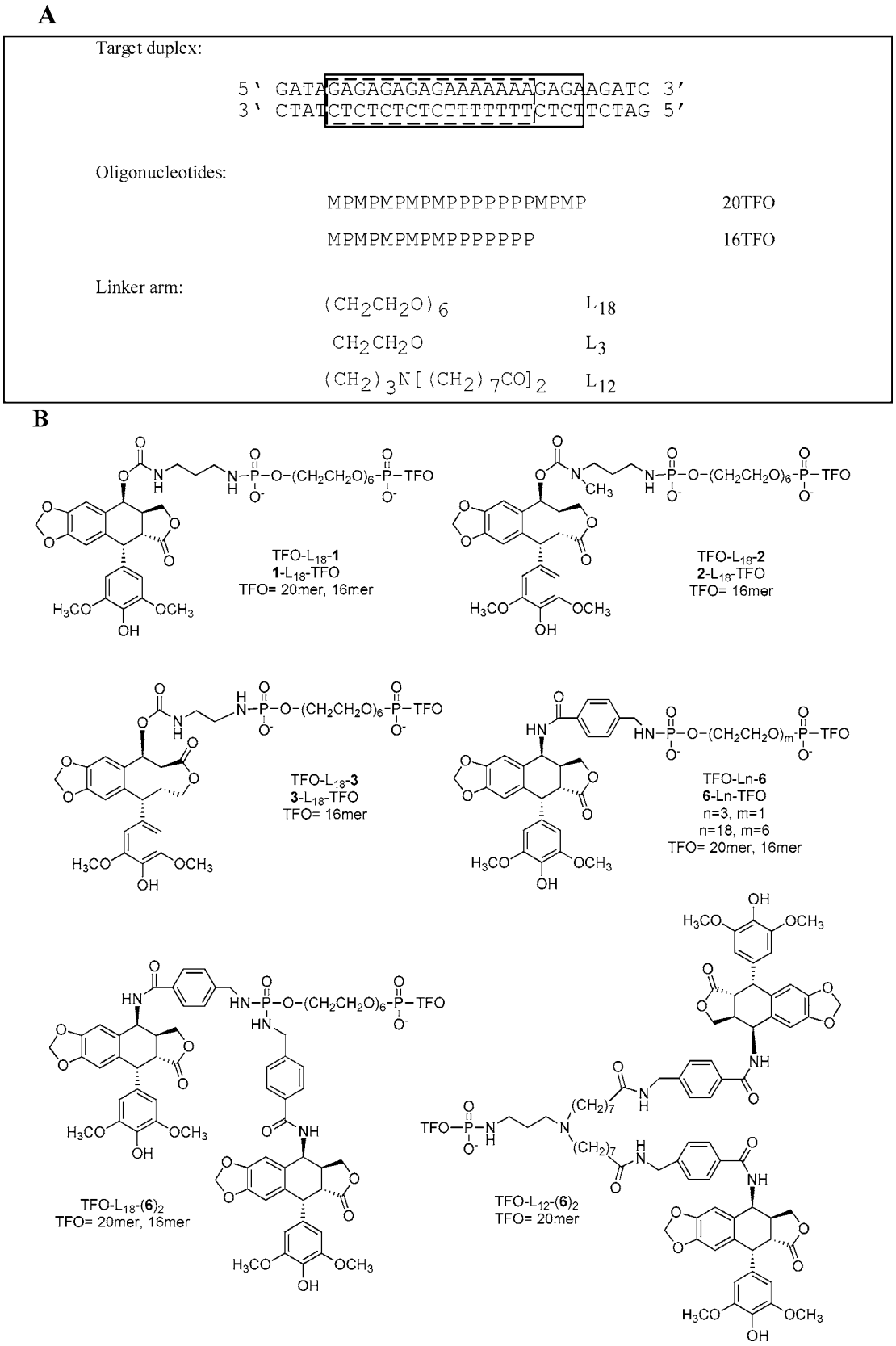

Figure 2. (A) Sequence of the 29-bp target duplex used for gel retardation assay and sequences of the TFOs (M = 5′-methyl-2′-deoxycytosine, P = 5-propynyl-2′-deoxyuracile) and chemical structure of the linker arms. The target sequences of 20TFO and 16TFO are surrounded. (B) Chemical structure of synthesized conjugates. The nomenclature of the oligonucleotides and conjugates is as follows: the abbreviation TFO is preceded by a number referring to the length of the oligonucleotide and followed, if attached to the 3′ end, or is preceded, if attached through the 5′ end, by the letter L (for linker) and the number of atoms in the linker, and finally the designation of the 4′-DMEP derivative.

DNA formed upon reaction of supercoiled DNA with human topoisomerase II and compared to 50% at 20 μM for etoposide used as reference compound), whereas compound **2** is an example of an inactive derivative (8%

Scheme 1. Synthesis of Compound 6[a]

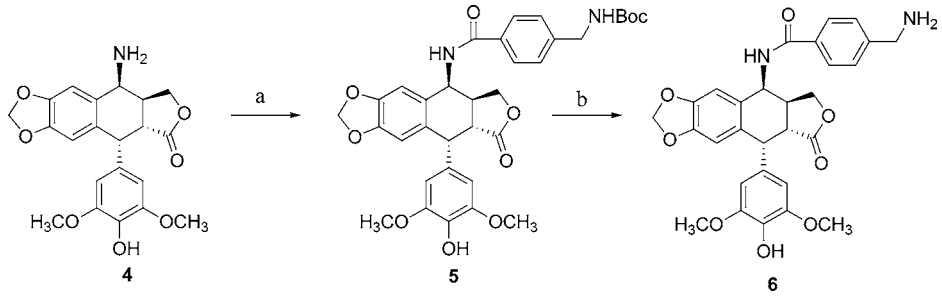

[a] Reagents: (a) 4-(*tert*-butoxycarbonylaminomethyl)benzoic acid, EDCI, HOBt, CH_2Cl_2; (b) TFA, CH_2Cl_2.

of inhibition at 20 μM) (*29*). Compound **6** was tested for its activity against topoisomerase II, showing a 25% of amount of linear DNA measured at 20 μM. All these compounds bear a primary amino group at the end of the secondary chain in order to bind them directly to the phosphate group at the extremity of the TFOs.

Synthesis of TFO−Topoisomerase II Inhibitors Conjugates. We covalently linked derivatives **1**, **2**, **3**, and **6** to the 3′ or 5′ end of the triple-helix forming oligonucleotides 16TFO and 20TFO. The first generation of conjugates bears one poison per TFO.

The chemical structure of these conjugates is depicted in Figure 2B and their synthesis consisted in the activation of the 3′ or 5′ phosphate group of the oligonucleotides in the presence of DMAP, PPh_3 and $(PyS)_2$, followed by the addition of the topoisomerase II inhibitors, as previously reported (*34*). The known procedure used DMSO as solvent for activation of the phosphate group and subsequent reaction with the amino group of the reacting molecule. However, upon use of this protocol, we observed, by HPLC and mass spectrometry, the formation of a secondary product containing both the topoisomerase II poison and a molecule of triphenylphosphine linked to the TFO. To avoid this side-reaction, the TFO activated by DMAP, PPh_3, $(PyS)_2$ in DMSO was rapidly precipitated in $LiClO_4$/acetone and the coupling reaction to the topoisomerase II poison was conducted in water. In this manner, triphenylphosphine was removed from the reaction mixture leading exclusively to the desired product with an average yield of 60%. Compounds **1**, **2**, **3**, and **6** were thus conjugated to 16TFO, and **1** and **6** to 20TFO, using hexaethylene glycol (L_{18}) as the linker arm. For the choice of the linker arm between the TFO and the poison, we were aware, from our study of TFO conjugates of topoisomerase I poisons, of the importance of optimizing its length. Therefore, we built a molecular model, based on the crystal structure and the model of the interaction of topoisomerases II with DNA (*39*, *43*). We docked two triple helices symmetrically on both sides of the topoisomerase II to evaluate whether there is steric clash in such a multicomponent complex. This model allowed us to evaluate the distance between the triplex and the catalytic tyrosines in the active site of topoisomerase II. The results suggested that an 18-atom linker would be the best length, and thus a hexaethylene glycol (L_{18}) was used to couple the VP16 derivatives to the TFOs. A shorter linker, ethylene glycol (L_3), was also used to conjugate compound **6** to the 3′ end of 16TFO, as a control.

In the second generation of conjugates, two VP16 analogues were attached to the same TFO. This is based on the hypothesis of Osheroff's group (*44*), concerning the stoichiometry of the complex formed by etoposide and topoisomerase II. In fact, eukaryotic topoisomerase II is constituted by a homodimer and thus bears two active sites containing two catalytic tyrosines. For this reason, Osheroff proposed that two molecules of etoposide are necessary to generate a double-stranded break and that one molecule of inhibitor leads to a single-stranded break. A conjugate bearing two molecules of topoisomerase II poisons at its end should thus be more efficient than the one bearing just one molecule. Furthermore, the comparison of the two types of conjugates should help to clarify the stoichiometry of the ternary complex formed during the inhibition of the enzyme. Only compound **6** was chosen to apply this strategy, because it gave better yields in the conjugation reaction and, once coupled to the TFO, it resulted more active against topoisomerase II than when compounds **1** and **3** were conjugated (data not shown). Two synthetic pathways were followed (Scheme 2): (1) the introduction of two compounds directly on the same terminal phosphate group of the hexaethylenglycol linker arm (L_{18}) at the 3′ end of the TFO or (2) the attachment of two molecules of **6** to a trifunctional linker arm (L_{12}), containing an amino group for the further coupling to the phosphorylated TFO. In the first pathway, the reaction is conducted as for the synthesis of the mono-conjugates, but it is repeated two times consecutively. We obtained conjugates 16TFO-L_{18}-(**6**)$_2$ and 20TFO-L_{18}-(**6**)$_2$ with 45% of average yield (Schema 2A). Following the second pathway, we prepared the linker starting from 3-*N*-Boc-1,3-propanediamine (**7**) and 8-bromooctanoic acid, which, in the presence of K_2CO_3 and in acetonitrile, gave the 3-*N*-Boc-aminopropane-1-iminodioctanoic acid (**8**) (Scheme 2B). Coupling of two molecules of **6** was achieved on the two activated carboxyl groups leading to product **9**. This latter, after deprotection of the Boc group by TFA in CH_2Cl_2, led to 3-aminopropane-1-aminodioctanoic acid (L_{12}) linked through the carboxyl groups to the amino group of **6**. Finally, the terminal amino group of **9** was reacted with the activated phosphate of the 20TFO to give 20TFO-L_{12}-(**6**)$_2$ as final product.

Triple Helix Formation by the Conjugates and Topoisomerase II Activity. In the second part of our study the capacity of all synthesized conjugates to form a triple-helix was evaluated. Triplex formation involves major groove binding of the oligonucleotidic part of the conjugates via sequence-specific recognition of the oligopurine strand of the duplex. The binding of the conjugated third strand to the duplex was analyzed by PAGE experiments. Increasing concentration of TFOs were incubated with 10 nM of radiolabeled target duplex in 50 mM HEPES pH 7.2, 10 mM $MgCl_2$, 50 mM NaCl at 37 °C for 2 h (Figure 3). The affinity of all conjugates and of the corresponding TFOs for the target 29 mer duplex was measured and expressed by C_{50} values, i.e. the concentration of TFO necessary to obtain 50% of triplex. Results are reported in Table 1.

Scheme 2. Synthesis of Conjugates Bearing Two Molecules of 6 at the Same End of the TFO by Methods A and B[a]

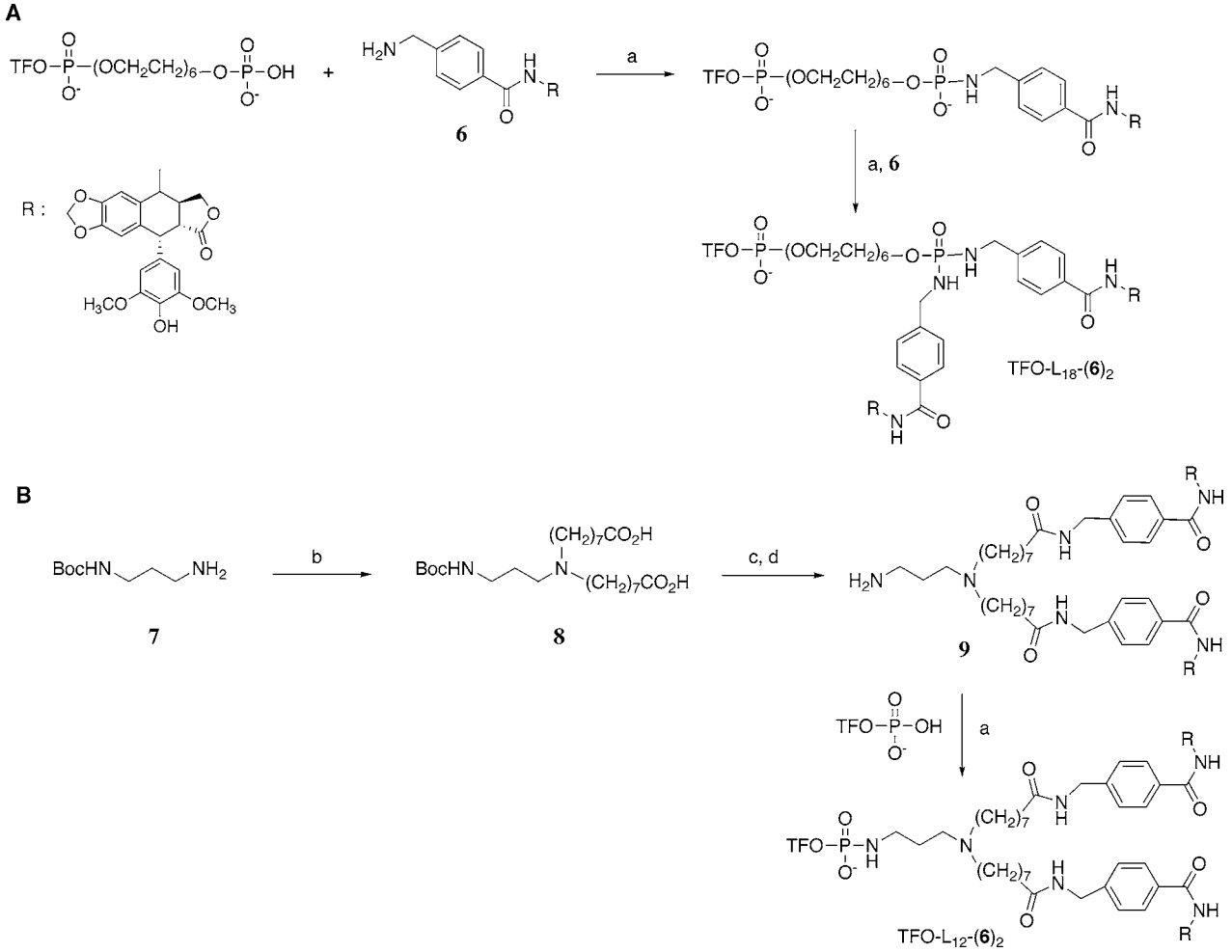

[a] Reagents: (a) DMAP, PPh_3, $(PyS)_2$, DMSO; (b) 8-bromooctanoic acid, K_2CO_3, CH_3CN; (c) **6** (2 equiv), DCC, HOBt, DMF; (d) TFA, CH_2Cl_2.

C_{50} of 16TFO and 20TFO are 0.46 μM and 0.32 μM, respectively. In the case of the 16mer, the introduction of a L_{18} linker arm at the 3′ end increased the affinity for the duplex, diminishing the C_{50} 4-fold. Interestingly, the shorter linker arm L_3 also increased the affinity. The stabilization induced by the linker arm was only 1.4-fold at the 5′ end.

In general, the conjugation of the poisons to the 16TFO caused, at both ends, a decrease in the affinity, with the exception of compound **3**, which bears the retrolactone modification. Furthermore, conjugation at the 3′ end was more destabilizing than at the 5′ end, even if the 3′ conjugates, however, remained 2 times more stable than the 5′ conjugates. The introduction of two molecules of topoisomerase poison **6** at the 3′ end caused an important loss in triplex affinity (about 40-fold less).

The 20 mer TFO, as expected, formed a more stable triple helix. The presence of a linker arm or the conjugation to VP16 analogues had little effect both at the 3′ and 5′ end. The presence of two molecules of **6** at the 3′ end remained, even in this case, very destabilizing with a loss in affinity of 4- and 7-fold for 20TFO-L_{18}-(**6**)$_2$ and 20TFO-L_{12} -(**6**)$_2$, respectively.

Noteworthy, for all conjugates, 100% of formation of the triple helice was always observed above 5 μM.

Evidence for the triplex formation was further confirmed by DNase I footprinting experiments as depicted in Figure 4. The 324-bp duplex fragment radiolabeled at 5′-end of the oligopurine-containing strand was incubated with the TFOs at 5 μM, and subjected to limited DNase I cleavage. DNase I cleavage was strongly inhibited at the target oligopyrimidine·oligopurine sequence and the footprint was clearly extended with the 20 mer TFOs compared to the 16 mer.

As shown in Table 2, all conjugates induce topoisomerase II-mediated DNA cleavage, at the exception of the conjugates of inactive compound **2** that remain inactives. Noteworthy, the experiments were carried out in conditions under which all conjugates form a stable triple helix. TFO conjugates of poison **3** resulted in the less active ones, while the comparison between 16TFO-L_{18}-**6** and 16TFO-L_3-**6** confirmed that the hexaethylene glycol (L_{18}) is the best linker arm. Finally, the double conjugates showed a comparable activity as the corresponding mono-conjugates.

DISCUSSION

Four 4′-demethylepipodophyllotoxin derivatives were chosen to be covalently attached to triplex-forming oligonucleotides (TFO). As in the case of TFO attached to topoisomerase I poison, these conjugates could be used to target topoisomerase II inhibitors to specific sequences on DNA.

Three of them (**1**, **2**, and **3**) were recently reported as part of a 4-substituted 4′-DMEP series bearing ami-

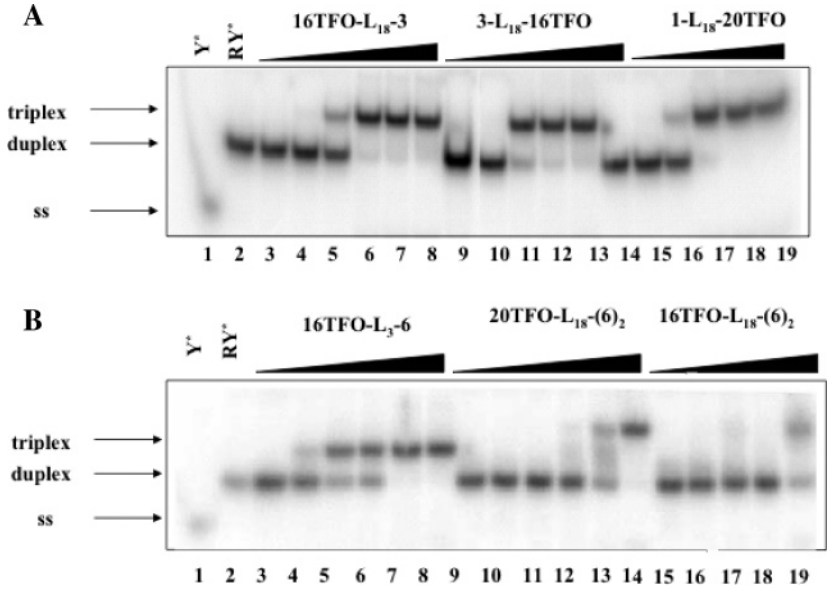

Figure 3. Triplex formation in PAGE experiments. 10 nM of the 29-bp target duplex (RY*, lane 2), 5′-end radiolabeled on the oligopyrimidine-containing strand (Y*, lane 1), was incubated for 2 h at 37 °C in 50 mM HEPES pH 7.2, 10 mM $MgCl_2$ and 50 mM NaCl in the presence of increasing concentrations of (A) 16TFO-L_{18}-**3** (0.01, 0.05, 0.1, 0.5, 1, 5 μM lanes 3−8), **3**-L_{18}-16TFO (0.01, 0.1, 0.5, 1, 5 μM, lanes 9−14), **1**-L_{18}-20TFO (0.01, 0.05, 0.1, 0.5, 1, 5 μM, lanes 15−19); (B) 16TFO-L_3-**6** (0.05, 0.1, 0.5, 1, 2, 5 μM, lanes 3−8), 20TFO-L_{18}-(**6**)$_2$ (0.05, 0.1, 0.5, 1, 2, 5 μM, lanes 9−14) and 16TFO-L_{18}-(**6**)$_2$ (0.05, 0.1, 0.5, 1, 5 μM, lanes 15−19), and then loaded on a 15% nondenaturing polyacrylamide gel. The shifts corresponding to single-stranded DNA (ss), duplex and triplex are indicated by arrows.

Table 1. C_{50} Values for 29R·29Y* TFO Triplexes[a]

TFOs	C_{50} (μM)
16TFO	0.46 ± 0.09
16TFO-L_{18}	0.11 ± 0.09
16TFO-L_{18}-**1**	0.47 ± 0.10
16TFO-L_{18}-**2**	0.30 ± 0.08
16TFO-L_{18}-**3**	0.17 ± 0.02
16TFO-L_{18}-**6**	0.39 ± 0.08
L_{18}-16TFO	0.33 ± 0.04
1-L_{18}-16TFO	0.74 ± 0.10
2-L_{18}-16TFO	0.65 ± 0.05
3-L_{18}-16TFO	0.33 ± 0.02
6-L_{18}-16TFO	0.59 ± 0.05
16TFO-L_3	0.14 ± 0.02
16TFO-L_3-**6**	0.20 ± 0.01
16TFO-L_{18}-(**6**)$_2$	4.1 ± 0.3
20TFO	0.32 ± 0.02
20TFO-L_{18}	0.27 ± 0.01
20TFO-L_{18}-**1**	0.38 ± 0.03
20TFO-L_{18}-**6**	0.32 ± 0.03
L_{18}-20TFO	0.30 ± 0.09
1-L_{18}-20TFO	0.27 ± 0.02
6-L_{18}-20TFO	0.48 ± 0.08
20TFO-L_{18}-(**6**)$_2$	1.3 ± 0.1
20TFO-L_{12}-(**6**)$_2$	2.2± 0.1

[a] The C_{50} values were calculated as the concentrations at which 50% of triplex is formed and an average value corresponding to three different experiments is reported. 29R·29Y (20 nM) was incubated at 37°C for 2 h with increasing concentrations of TFOs in 50 mM HEPES buffer (pH 7.2) containing 50 mM NaCl and 10 mM $MgCl_2$.

noalkyl chains in the 4-position linked by a carbamate group (*29*). In this series, some compounds showed an activity on topoisomerase II comparable to etoposide and even better activity in antitumor assays. The most active compounds contained an *N*,*N*-dimethyl group at the end of the side chain unsuitable for conjugation to TFOs. We thus designed **1**−**3** with a NH_2 group in the aim to conjugate them directly to the phosphate group at the end of the oligonucleotide. Compounds **1** and **3** are still active as topoisomerase II inhibitors, while compound **2** is an example of inactive compound. Interestingly, when **1** and **3** are conjugated to the TFO, they could eventually become more similar to most active compounds of the series because the terminal NH_2 is substituted by the phosphate group of TFO. In addition to these three drugs, we synthesized a new derivative of 4′-DMEP bearing an arylamino side chain linked in the 4-position via an amide group (compound **6**). The choice for such a chain is based on a work devoted to a series of derivatives previously synthesized by Zhou et al. (*42*) that were shown to be active topoisomerase II poisons.

All four VP16 analogues were conjugated to a 16mer TFO through a linker arm, a hexaethylene glycol (L_{18}), attached either at the 3′ end or the 5′ end. Analogues **1** and **6** were also linked, via the L_{18} linker arm, to a 20mer TFO directed against the extended oligopurine·oligopyrimidine duplex sequence. The previously described coupling reaction (*45*) was here further improved and carried out in a water/DMSO mixture in order to eliminate all secondary products and to obtain exclusively the desired product.

We investigate the influence on the triplex stability of: (i) the length of the TFO, a 16-mer vs a 20-mer, (ii) the linker arm, L_3 vs L_{18}, (iii) the modifications of the topoisomerase II poisons (compounds **1**, **2**, **3**, and **6**) and (iv) their position on the TFO, attachment to the 3′ end vs 5′ end. Triplex formation by the conjugates was evaluated by gel retardation assay that allowed us to obtain C_{50} values. The results were further confirmed by DNase I footprinting experiments.

Interestingly, the presence of the phosphorylated linker arm alone has a stabilizing effect in the case of 16TFO. The choice for such a long linker chain was based on reported data suggesting that topoisomerase II protected both strands of DNA over 25-bp region, in which the cleavage site was centrally located (*46*). In addition, Spizner et al. (*47*) have shown that the enzyme might need an accessible 10-bp double-helical region around the cleavage site to efficiently interact and cleave DNA. According to these observations, a relatively long linker, such as the L_{18}, should be the most appropriate in order

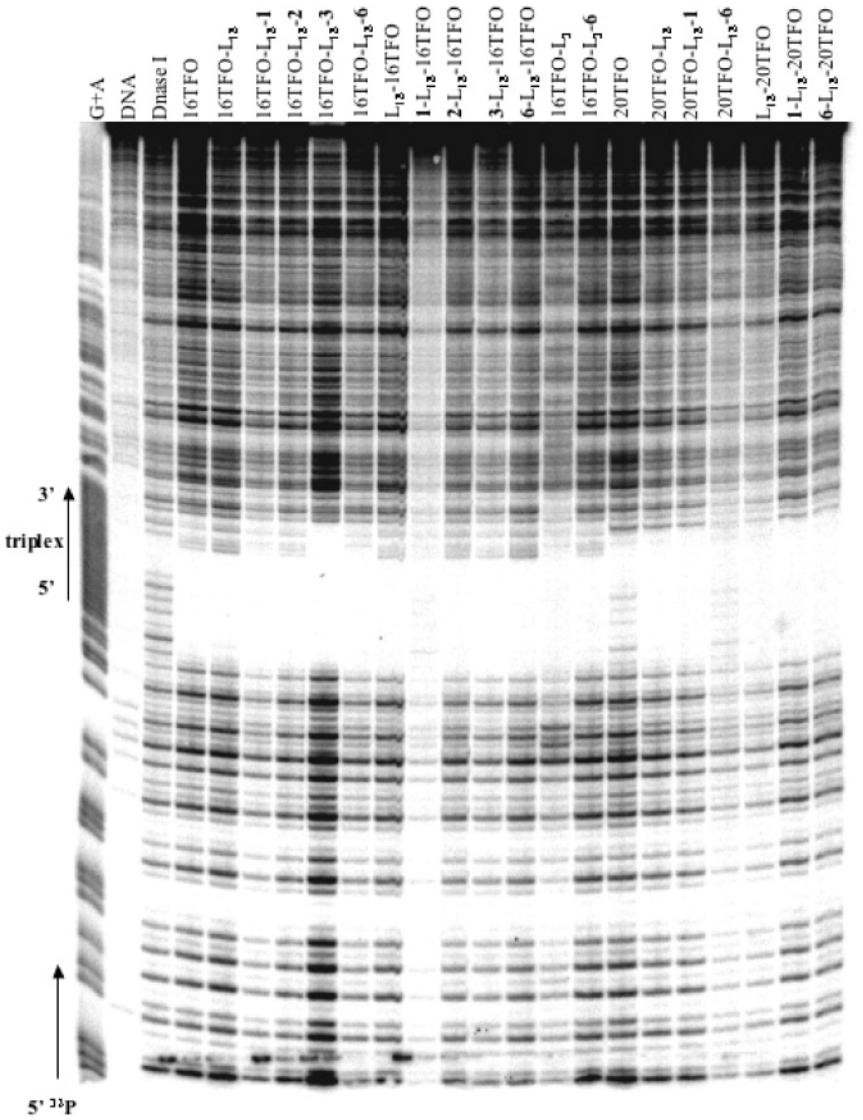

Figure 4. Sequence analysis of the DNase I footprinting experiments on the 324-bp target duplex radiolabeled at the 5′ end of the oligopurine strand in the presence of some TFO conjugates. Control TFOs and conjugates were added at 5 μM. The triplex site and its orientation are indicated by an arrow. Adenine/guanine-specific Maxam−Gilbert chemical cleavage reactions were used as markers.

to access the drug to the catalytic site of topoisomerase II and to prevent steric hindrance between the triple-helical structure and the enzyme.

Noteworthy, the tethered 4′ DMEP derivatives are now able to bind to DNA through the oligonucleotidic part of the conjugate and specifically to the triplex target (as shown by the DNase footprinting experiments). The tethering to the TFOs does not hamper the activity of the 4′ DMEP derivatives against topoisomerase II (Table 2). In the case of compound **2**, an example of inactive topoisomerase II poison, it remains inactive even when conjugated to the TFO. This is different from what is observed with camptothecin, a topoisomerase I poison, for which the conjugation of an inactive derivative to the TFO is able to convert it to an active topoisomerase I poison (*48*). Concerning triplex formation, the conjugation of the poison decreased, as expected, the affinity of the TFOs for the target duplex, the worst cases being the conjugates bearing two molecules of poisons linked to the same TFO end. This destabilization effect is more pronounced at the 3′ end than at the 5′ end, even if 3′ conjugates remain more stable than the respective 5′ conjugates. An exception is compound **3**, bearing the retrolactone, which was comparable in affinity to the 16TFO attached to the linker arm both in the 3′ end or 5′ end. The observed destabilization effect can be explained by the mechanism of action of these poisons. In fact, these molecules do not interact with DNA (*29*), but rather with the enzyme (*49*). The absence of interaction of these latter conjugates with DNA can explain, in part, the absence of stabilization of the triple-helical structure. Other topoisomerase II poisons families, such as amsacrines and antracyclines that intercalate into DNA, induce a stabilization of the triple-helical structure when conjugated to a TFO. In this context, it was shown that daunomycin strongly stabilized triplex formation when conjugated to the 5′ end (*10*, *50*); although no effect was observed at the 3′ end of the triplex (*10*). In the case of amsacrine (mAMSA), an acridine derivative inhibitor of topoisomerase II, a slight stabilization of the triplex structure was obtained when an amsacrine derivative was tethered to the 5′ end of the TFO (*51*). Linkage of the amsacrine derivative to the 3′-end of the TFO decreased triplex stability and the destabilizing effect was less pronounced with the conjugate containing a longer linker side chain (an hexaethylene glycol).

Interestingly, in this study, the 5′ end conjugates were 2-fold less stable than the 3′ end conjugates. This can be

Table 2. Normalized Percentage (%) of Total DNA Cleavage on a Radiolabeled 96-bp DNA Fragment by Topoisomerase II in the Presence of the Free Drugs or Conjugated to the TFOs[a]

drug/TFO[b]	normalized percentage, %
1	42
2	8
3	40
6	45
16TFO-L_{18}-**1**	27
16TFO-L_{18}-**2**	5
16TFO-L_{18}-**3**	20
16TFO-L_{18}-**6**	30
1-L_{18}-16TFO	26
2-L_{18}-16TFO	3
3-L_{18}-16TFO	15
6-L_{18}-16TFO	25
16TFO-L_3-**6**	24
16TFO-L_{18}-(**6**)$_2$	27
20TFO-L_{18}-**1**	30
20TFO-L_{18}-**6**	32
1-L_{18}-20TFO	23
6-L_{18}-20TFO	22
20TFO-L_{18}-(**6**)$_2$	30
20TFO-L_{12}-(**6**)$_2$	26

[a] An average value corresponding to three different experiments is reported. [b] Drugs were evaluated at 50 μM, conjugates at 1 μM at the exception of the double conjugates that were evaluated at 10 μM.

explained, in part, by the fact that triplex formation seems to nucleate at the 5′ end of the triplex (*52*, *53*), and thus the presence of the drug at this end might interfere with the nucleation step and be more destabilizing. In agreement, the above-cited studies, together with previous ones (*54*), have demonstrated that the stabilizing effect of an intercalating drug is more important at the 5′ triplex/duplex junction than on the 3′ side.

Finally, in the case of the more stable 20TFO, very little differences were observed with the exception of the double conjugation that was very destabilizing for triplex formation, even if the effect was less than in the case of 16TFO. The higher affinity of the 20mer compared to the 16mer seems to abolish the differences due to the energetic penalty for the presence of the DNA-noninteracting molecule.

At last, we synthesized TFO conjugates containing two molecules at the same end, either both attached directly to the same phosphate at the end of the linker arm of the TFO (TFO-L_{18}-(**6**)$_2$), or each one attached to a linker arm further conjugated at the same phosphate at the extremity of the TFO (20TFO-L_{12}-(**6**)$_2$). These are the first examples of such a type of conjugates. All three double conjugates showed an important loss in triplex stability, but 100% of formation of triplex was still observed at pH 7.2 and 37 °C at high concentrations (>5 μM). Moreover, the importance of such conjugates resides in the fact that topoisomerase contains two subunits and thus two active sites (two Tyr^{804} for human topoisomerase II). This implies that there may be two sites available for the drug in every cleavage complex (*44*). These double-poison conjugates should represent a priori an important tool for the investigation of such a molecular mechanism. We observed, however, that their ability to stimulate DNA-cleavage on a 96-bp radiolabeled DNA fragment is comparable to that of the mono-conjugate (Table 2).

In conclusion, we synthesized a new poison of topoisomerase II derived from 4′-DMEP. This compound, together with other 4′-DMEP analogues previously reported, was conjugated to triplex-forming oligonucleotides with an average yield of 60%. We then evaluated the stability of the formed triplex and defined the best features for stability. Unexpectedly, the phosphorylated poly(ethylene glycol) linker arm increased the triplex stability and compensated for the presence of the 4′ DMEP derivatives that do not interact with DNA. The 20-mer conjugates form triplexes with comparable stability as the unlinked 20TFO. In the case of the 16mers, conjugation to the 3′ end is preferable to conjugation to the 5′ end. Finally, the conjugates retain the anti-topoisomerase II activity.

ACKNOWLEDGMENT

This work was supported by grants from Ligue Nationale contre le Cancer and Ministère de la Recherche et de l'Industrie (ACI "Molécules et Cibles Thérapeutiques") (to P.B.A.), fellowships from Foundation de France (to D.G.), Association pour la Recherche contre le Cancer (ARC) (to M.D.), and Assocation pour la Recherche sur les Tumeurs de la Prostate (ARTP) (to K.O.).

LITERATURE CITED

(1) Faria, M., and Giovannangeli, C. (2001) Triplex-forming molecules: from concepts to applications. *J. Gene Med. 3*, 299−310.

(2) Praseuth, D., Guieysse, A. L., and Hélène, C. (1999) Triple helix formation and the antigene strategy for sequence-specific control of gene expression. *Biochim. Biophys. Acta 1489*, 181−206.

(3) Giovannangeli, C., and Hélène, C. (2000) Triplex-forming molecules for modulation of DNA information processing. *Curr. Opin. Mol. Ther. 2*, 288−96.

(4) Dervan, P. B., and Edelson, B. S. (2003) Recognition of the DNA minor groove by pyrrole-imidazole polyamides. *Curr. Opin. Struct. Biol. 13*, 284−99.

(5) Faria, M., Wood, C. D., White, M. R., Hélène, C., and Giovannangeli, C. (2001) Transcription inhibition induced by modified triple helix-forming oligonucleotides: a quantitative assay for evaluation in cells. *J. Mol. Biol. 306*, 15−24.

(6) Vasquez, K. M., Narayanan, L., and Glazer, P. M. (2000) Specific mutations induced by triplex-forming oligonucleotides in mice. *Science 290*, 530−3.

(7) Guieysse, A. L., Praseuth, D., Giovannangeli, C., Asseline, U., and Hélène, C. (2000) Psoralen adducts induced by triplex-forming oligonucleotides are refractory to repair in HeLa cells. *J. Mol. Biol. 296*, 373−83.

(8) Giovannangeli, C., and Hélène, C. (2000) Triplex technology takes off. *Nat. Biotechnol. 18*, 1245−6.

(9) Besch, R., Giovannangeli, C., and Degitz, K. (2004) Triplex-forming oligonucleotides—sequence-specific DNA ligands as tools for gene inhibition and for modulation of DNA-associated functions. *Curr. Drug Targets 5*, 691−703.

(10) Carbone, G. M., McGuffie, E., Napoli, S., Flanagan, C. E., Dembech, C., Negri, U., Arcamone, F., Capobianco, M. L., and Catapano, C. V. (2004) DNA binding and antigene activity of a daunomycin-conjugated triplex-forming oligonucleotide targeting the P2 promoter of the human c-myc gene. *Nucleic Acids. Res. 32*, 2396−410.

(11) Carbone, G. M., Napoli, S., Valentini, A., Cavalli, F., Watson, D. K., and Catapano, C. V. (2004) Triplex DNA-mediated downregulation of Ets2 expression results in growth inhibition and apoptosis in human prostate cancer cells. *Nucleic Acids. Res. 32*, 4358−67.

(12) Diviacco, S., Rapozzi, V., Xodo, L., Hélène, C., Quadrifoglio, F., and Giovannangeli, C. (2001) Site-directed inhibition of DNA replication by triple helix formation. *FASEB J. 15*, 2660−8.

(13) Seidman, M. M., and Glazer, P. M. (2003) The potential for gene repair via triple helix formation. *J. Clin. Invest. 112*, 487−94.

(14) Arimondo, P. B., Boutorine, A., and François, J. C. (2002) Oligonucleotide-conjugates targeted to single-stranded and double-stranded nucleic acids. *Recent Res. Dev.. Bioconjugate Chem. 1*, 29−53.

(15) Guillonneau, F., Guieysse, A. L., Nocentini, S., Giovannangeli, C., and Praseuth, D. (2004) Psoralen interstrand cross-link repair is specifically altered by an adjacent triple-stranded structure. *Nucleic Acids. Res. 32*, 1143−53.

(16) Grigoriev, M., Praseuth, D., Guieysse, A. L., Robin, P., Thuong, N. T., Hélène, C., and Harel-Bellan, A. (1993) Inhibition of gene expression by triple helix-directed DNA cross-linking at specific sites. *Proc. Natl. Acad. Sci. U.S.A. 90*, 3501−5.

(17) Arimondo, P. B., Bailly, C., Boutorine, A. S., Ryabinin, V. A., Syniakov, A. N., Sun, J. S., Garestier, T., and Hélène, C. (2001) Directing Topoisomerase I Mediated DNA Cleavage to Specific Sites by Camptothecin Tethered to Minor- and Major-Groove Ligands. *Angew Chem., Int. Ed. 40*, 3045−3048.

(18) Arimondo, P. B., Bailly, C., Boutorine, A. S., Moreau, P., Prudhomme, M., Sun, J. S., Garestier, T., and Hélène, C. (2001) Triple helix-forming oligonucleotides conjugated to indolocarbazole poisons direct topoisomerase I-mediated DNA cleavage to a specific site. *Bioconjugate Chem. 12*, 501−9.

(19) Arimondo, P. B., Boutorine, A., Baldeyrou, B., Bailly, C., Kuwahara, M., Hecht, S. M., Sun, J. S., Garestier, T., and Hélène, C. (2002) Design and optimization of camptothecin conjugates of triple helix-forming oligonucleotides for sequence-specific DNA cleavage by topoisomerase I. *J. Biol. Chem. 277*, 3132−40.

(20) Wang, J. C. (1996) DNA topoisomerases. *Annu. Rev. Biochem. 65*, 635−92.

(21) Champoux, J. J. (2001) DNA topoisomerases: structure, function, and mechanism. *Annu. Rev. Biochem. 70*, 369−413.

(22) Burden, D. A., and Osheroff, N. (1998) Mechanism of action of eukaryotic topoisomerase II and drugs targeted to the enzyme. *Biochim. Biophys. Acta 1400*, 139−54.

(23) Capranico, G., and Binaschi, M. (1998) DNA sequence selectivity of topoisomerases and topoisomerase poisons. *Biochim. Biophys. Acta 1400*, 185−94.

(24) Wilstermann, A. M., and Osheroff, N. (2003) Stabilization of eukaryotic topoisomerase II-DNA cleavage complexes. *Curr. Top Med. Chem. 3*, 321−38.

(25) Hande, K. R. (1998) Etoposide: four decades of development of a topoisomerase II inhibitor. *Eur. J. Cancer 34*, 1514−21.

(26) Hande, K. R. (2003) Topoisomerase II inhibitors. *Cancer Chemother Biol. Response Modif. 21*, 103−25.

(27) Terada, T., Fujimoto, K., Nomura, M., Yamashita, J., Wierzba, K., Yamazaki, R., Shibata, J., Sugimoto, Y., Yamada, Y., Kobunai, T., and et al. (1993) Antitumor agents. 3. Synthesis and biological activity of 4 beta-alkyl derivatives containing hydroxy, amino, and amido groups of 4′−O-demethyl-4-desoxypodophyllotoxin as antitumor agents. *J. Med. Chem. 36*, 1689−99.

(28) Zhu, X. K., Guan, J., Tachibana, Y., Bastow, K. F., Cho, S. J., Cheng, H. H., Cheng, Y. C., Gurwith, M., and Lee, K. H. (1999) Antitumor agents. 194. Synthesis and biological evaluations of 4-beta-mono-, -di-, and -trisubstituted aniline-4′-O-demethyl-podophyllotoxin and related compounds with improved pharmacological profiles. *J. Med. Chem. 42*, 2441−6.

(29) Duca, M., Guianvarc'h, D., Meresse, P., Bertounesque, E., Dauzonne, D., Kraus-Berthier, L., Thirot, S., Léonce, S., Pierré, A., Pfeiffer, B., Renard, P., Arimondo, P. B., and Monneret, C. (2005) Synthesis and biological study of a new series of 4′-demethylepipodophyllotoxin derivatives. *J. Med. Chem. 48*, 593−603.

(30) Arimondo, P. B., Moreau, P., Boutorine, A., Bailly, C., Prudhomme, M., Sun, J. S., Garestier, T., and Hélène, C. (2000) Recognition and cleavage of DNA by rebeccamycin- or benzopyridoquinoxaline conjugated of triple helix-forming oligonucleotides. *Bioorg. Med. Chem. 8*, 777−84.

(31) Gangjee, A., Devraj, R., McGuire, J. J., and Kisliuk, R. L. (1995) Effect of bridge region variation on antifolate and antitumor activity of classical 5-substituted 2,4-diaminofuro-[2,3-*d*]pyrimidines. *J. Med. Chem. 38*, 3798−805.

(32) Cantor, C. R., Warshaw, M. M., and Shapiro, H. (1970) Oligonucleotides interactions. III. Circular dichroism studies of the conformation of deoxyoligonucleotides. *Biopolymers 9*, 1059−1077.

(33) (a) Lee, K. H. *J. Med. Chem.* **1991**, *34*, 3346. (b) Guianvarc'h, D., Duca, M., Boukarim, C., Kraus-Berthier, L., Leonce, S., Pierre, A., Pfeiffer, B., Renard, P., Arimondo, P. B., Monneret, C., and Dauzonne, D. (2004) Synthesis and biological activity of sulfonamide derivatives of epipodophyllotoxin. *J. Med. Chem. 47*, 2365−74.

(34) Grimm, G. N., Boutorine, A. S., and Hélène, C. (2000) Rapid routes of synthesis of oligonucleotide conjugates from nonprotected oligonucleotides and ligands possessing different nucleophilic or electrophilic functional groups. *Nucleosides Nucleotides Nucleic Acids. 19*, 1943−65.

(35) Arimondo, P., Boukarim, C., Bailly, C., Dauzonne, D., and Monneret, C. (2000) Design of two etoposide-amsacrine conjugates: topoisomerase II and tubuline polymerization inhibition and relation to cytotoxicity. *Anticancer Drug Des. 15*, 413−21.

(36) Lavery, R., and Sklenar, H. (1988) The definition of generalized helicoidal parameters and of axis curvature for irregular nucleic acids. *J. Biomol. Struct. Dyn. 6*, 63−91.

(37) Ouali, M., Letellier, R., Adnet, F., Liquier, J., Sun, J. S., Lavery, R., and Taillandier, E. (1993) A possible family of B-like triple helix structures: comparison with the Arnott A-like triple helix. *Biochemistry 32*, 2098−103.

(38) Berger, J. M., Gamblin, S. J., Harrison, S. C., and Wang, J. C. (1996) Structure and mechanism of DNA topoisomerase II. *Nature 379*, 225−32.

(39) Morais Cabral, J. H., Jackson, A. P., Smith, C. V., Shikotra, N., Maxwell, A., and Liddington, R. C. (1997) Crystal structure of the breakage-reunion domain of DNA gyrase. *Nature 388*, 903−6.

(40) Froehler, B. C., Jones, R. J., Cao, X. D., and Terhorst, T. J. (1993) Oligonucleotide derived from 5-(1propynyl)-2-O-allyl-uridine and 5-(1-propynyl)-2-O-allyl-cytidine: Synthesis and RNA duplex formation. *Tetrahedron Lett. 34*, 1003−1006.

(41) Meresse, P., Magiatis, P., Bertounesque, E., and Monneret, C. (2003) Synthesis and antiproliferative activity of retroetoposide. *Bioorg. Med. Chem. Lett. 13*, 4107−9.

(42) Zhou, X. M., Wang, Z. Q., Chen, H. X., Cheng, Y. C., and Lee, K. H. (1993) Antitumor agents. 125. New 4 beta-benzoylamino derivatives of 4′-O-demethyl-4-desoxypodophyllotoxin and 4 beta-benzoyl derivatives of 4′-O-demethylpodophyllotoxin as potent inhibitors of human DNA topoisomerase II. *Pharm. Res. 10*, 214−9.

(43) Fass, D., Bogden, C. E., and Berger, J. M. (1999) Quaternary changes in topoisomerase II may direct orthogonal movement of two DNA strands. *Nat. Struct. Biol. 6*, 322−6.

(44) Bromberg, K. D., Burgin, A. B., and Osheroff, N. (2003) A two-drug model for etoposide action against human topoisomerase IIalpha. *J. Biol. Chem. 278*, 7406−12.

(45) Grimm, G. N., Boutorine, A. S., Lincoln, P., and Hélène, C. (2001) Design and simple routes of synthesis of oligonucleotide conjugates for studies of DNA triple helix formation. *Nucleosides Nucleotides Nucleic Acids. 20*, 909−14.

(46) Lee, M. P.; Sander, M.; Hsieh, T. (1989) Nuclease protection by Drosophila DNA topoisomerase II. Enzyme/DNA contacts at the strong topoisomerase II cleavage sites. *J. Biol. Chem. 264*, 21779−87.

(47) Spitzner, J. R., Chung, I. K., and Muller, M. T. (1995) Determination of 5′ and 3′ DNA triplex interference boundaries reveals the core DNA binding sequence for topoisomerase II. *J. Biol. Chem. 270*, 5932−43.

(48) Arimondo, P. B., Laco, G. S., Thomas, C. J., Halby, L., Pez, D., Schmitt, P., Boutorine, A., Garestier, T., Pommier, Y., Hecht, S. M., Sun, J. S., and Bailly, C. (2005) Activation of Camptothecin Derivatives by Conjugation to Triple Helix-Forming Oligonucleotides. *Biochemistry 44*, 4171−4180.

(49) Kingma, P. S., Burden, D. A., and Osheroff, N. (1999) Binding of etoposide to topoisomerase II in the absence of DNA: decreased affinity as a mechanism of drug resistance. *Biochemistry 38*, 3457−61.

(50) Garbesi, A., Bonazzi, S., Zanella, S., Capobianco, M. L., Giannini, G., and Arcamone, F. (1997) Synthesis and binding

properties of conjugates between oligodeoxynucleotides and daunorubicin derivatives. *Nucleic Acids. Res. 25*, 2121−8.
(51) Arimondo, P., Bailly, C., Boutorine, A., Asseline, U., Sun, J. S., Garestier, T., and Hélène, C. (2000) Linkage of a triple helix-forming oligonucleotide to amsacrine-4-carboxamide derivatives modulates the sequence-selectivity of topoisomerase II-mediated DNA cleavage. *Nucleosides Nucleotides Nucleic Acids*. *19*, 1205−18.
(52) Alberti, P., Arimondo, P. B., Mergny, J. L., Garestier, T., Hélène, C., and Sun, J. S. (2002) A directional nucleation-zipping mechanism for triple helix formation. *Nucleic Acids. Res*. *30*, 5407−15.
(53) Arimondo, P. B., Barcelo, F., Sun, J. S., Maurizot, J. C., Garestier, T., and Hélène, C. (1998) Triple helix formation by (G,A)-containing oligonucleotides: asymmetric sequence effect. *Biochemistry 37*, 16627−35.
(54) Sun, J. S., Francois, J. C., Montenay-Garestier, T., Saison-Behmoaras, T., Roig, V., Thuong, N. T., and Hélène, C. (1989) Sequence-specific intercalating agents: intercalation at specific sequences on duplex DNA via major groove recognition by oligonucleotide-intercalator conjugates. *Proc. Natl. Acad. Sci. U.S.A*. *86*, 9198−202.

BC050031P

N,N-Bis(2-mercaptoethyl)methylamine: A New Coligand for Tc-99m Labeling of Hydrazinonicotinamide Peptides

Sangeeta R. Banerjee,[†] Kevin P. Maresca,[†,‡] Karin A. Stephenson,[||] John F. Valliant,[||] John W. Babich,[‡] Wendy A. Graham,[‡] Marlene Barzana,[§] Qing Dong,[§] Alan J. Fischman,[§] and Jon Zubieta*[,†]

Molecular Insight Pharmaceuticals, 160 Second Street, Cambridge, Massachusetts 02142, Division of Nuclear Medicine of the Department of Radiology, Massachusetts General Hospital, and the Department of Radiology, Harvard Medical School, Boston, Massachusetts 02115, Department of Chemistry, McMaster University, Hamilton, Ontario, Canada L8S 4M1, and Department of Chemistry, Syracuse University, Syracuse, New York 13244. Received February 14, 2005; Revised Manuscript Received April 25, 2005

Hydrazinonicotinamide (HYNIC) forms stable coordination complexes with Tc-99m when reacted with Tc(V)oxo species such as Tc-mannitol or other Tc-polyhydric complexes. However, radio-HPLC of [Tc-For-MLFK-HYNIC] labeled via Tc-polyhydric ligands demonstrated multiple radiochemical species each with unique biodistribution patterns. This is likely due to the fact that Tc can bind to the hydrazino moiety, as well as polyhydric ligands, in a variety of coordination geometries. Tridentate ligands, such as bis(mercaptoethyl)methylamine (NS_2), may constrain the possible coordination geometries and improve overall stability. To investigate this, we synthesized NS_2, converted the [Tc-mannitol-For-MLFK-HYNIC] to the corresponding NS_2-containing complex [Tc-NS_2-For-MLFK-HYNIC], and compared its infection imaging and biodistribution properties with [Tc-mannitol-For-MLFK-HYNIC]. Conversion to the NS_2 complex was confirmed by HPLC which showed a single unique hydrophobic species with retention time greater than the [Tc-mannitol-For-MLFK-HYNIC] complex. Imaging experiments with both preparations were performed in rabbits with *E. coli* infections in the left thigh. Tissue radioactivity measurements demonstrated that compared to Tc-mannitol-peptide, accumulation of Tc-NS_2-peptide was lower in blood, heart, and normal muscle and higher in spleen, infected muscle, and pus ($p < 0.01$). These results indicate that the Tc-NS_2-peptide complex is chemically more homogeneous and exhibits improved infection localization and biodistribution properties. In an effort to model the interactions of the metal-HYNIC core with NS_2 and related ligand types, the reactions of $[ReCl_3(NNC_5H_4NH)(NHNC_5H_4N)]$ and $[^{99}TcCl_3(NNC_5H_4NH)(NHNC_5H_4N)]$, effective structural analogues for the $\{M(NNC_5H_4NH_x)_2\}$ core, with NS_2, C_5H_3N-2,6-$(CH_2SH)_2$, $O(CH_2CH_2SH)_2$, and $S(CH_2CH_2SH)_2$ were investigated and the compounds $[M\{CH_3N(CH_2CH_2S)_2\}(NNC_5H_4N)(NHNC_5H_4N]$ (M = ^{99}Tc (**5a**), Re (**5b**)), $[Re\{C_5H_3N$-2,6-$(CH_2S)_2\}(NNC_5H_4N)(NHNC_5H_4N)]\cdot CH_2Cl_2\cdot 0.5MeOH$ (**7**), $[Re\{SCH_2CH_2)_2O\}(NNC_5H_4N)(NHNC_5H_4N)]$ (**8**), and $[Re\{(SCH_2CH_2)_2S\}(NNC_5H_4NH)(NHNC_5H_4N)]Cl$ (**9**) were isolated. Similarly, the reaction of $[ReCl_3(NNC_5H_4NH)(NHNC_5H_4N)]$ with the bidentate ligands pyridine-2-methanethiol and 3-(trimethlysilyl)pyridine-2-thiol led to the isolation of $[ReCl(C_5H_4N$-2-$CH_2S)(NNC_5H_4N)(NHNC_5H_4N)]$ (**10**) and $[Re(2\text{-}SC_5H_3N\text{-}3\text{-}SiMe_3)_2(NNC_5H_4N)(NHNC_5H_4N)]$ (**11**), respectively, while reaction with *N*-methylimidazole-2-thiol yielded the binuclear complex $[Re(OH)Cl(SC_3H_2N_2CH_3)_2(NNC_5H_4N)_2(NHNC_5H_4N)_2]$ (**12**). The analogous metal-(HYNIC-OH) precursor, $[ReCl_3\{NNC_5H_3NH(CO_2R)\}\{NHNC_5H_3N(CO_2R)\}]$ (R = H, **13a**; R = CH_3, **13b**) has been prepared and coupled to lysine to provide $[RCl_3\{NNC_5H_3NH(CONHCH_2CH_2CH_2CH_2CH(NH_2)CO_2H)\}\{NHNC_5H_3NH(CONHCH_2CH_2CH_2CH_2CH(NH_2)CO_2H)\}]\cdot 2HCl$ (**14**·2HCl), while the reaction of the methyl ester **13b** with 2-mercaptopyridine yields $[Re(2\text{-}SC_5H_4N)_2\{NNC_5H_3N(CO_2Me)\}\{NHNC_5H_3N(CO_2Me)\}]$ (**15**). While the chemical studies confirm the robustness of the M-HYNIC core (M = Tc, Re) and its persistence in ligand substitution reactions at adjacent coordination sites of the metal, the isolation of oligomeric structures and the insolubility of the peptide conjugates of **13**, **14**, and **15** underscore the difficulty of characterizing these materials on the macroscopic scale, an observation relevant to the persistent concerns with reagent purity and identity on the tracer level.

INTRODUCTION

The ability to incorporate readily available radionuclides with optimal decay characteristics into tracer molecules has been the foremost consideration in developing diagnostic radiopharmaceuticals. In this respect, technetium-99m is the ideal choice, and its use in nuclear medicine is well-established (*1*−*14*). This preferential use of ^{99m}Tc radiopharmaceuticals reflects the optimal nuclear properties of the isotope as well as its convenient availability from commercial generator columns. The half-life of ^{99m}Tc of 6 h and the absence of tissue-damaging corpuscular radiation allow the injection of activities of more than 30 mCi with low radiation exposure to the patient (*4*). The half-life is sufficiently long to carry out the labeling syntheses and the scintigraphic measure-

* To whom correspondence should be addressed. Fax: (315) 443-2547; e-mail: jazubiet@syr.edu.
[†] Syracuse University.
[‡] Molecular Insight Pharmaceuticals.
[§] Massachusetts General Hospital.
[||] McMaster University.

10.1021/bc050040y CCC: $30.25 © 2005 American Chemical Society
Published on Web 06/16/2005

ments without significant losses in activity. Furthermore, the energy of the emitted photons of 140 keV is sufficient to study organs lying deep in the body and can be collimated so as to be detected effectively with NaI(T1) scintillation counters. Finally, the relatively stable ^{99m}Tc isotope may be used to develop technetium chemistry and to model technetium radiopharmaceuticals (*15*, *16*).

One approach to radiopharmaceutical design exploits radiolabeled biologically active compounds or drugs. For example, radiolabeled antibodies have been developed to target sites of cancer, cardiovascular, and other diseases (*1*−*3*, *17*). Similarly, the area of small-molecule receptor binding radiopharmaceuticals has witnessed significant development (*2*, *18*). These two strategies are conceptually related, differing only the size of the receptor binding molecule, which may be 1000 kD for antibodies and 2500 kD or less for small molecule receptor binding radiopharmaceuticals.

The use of bifunctional chelates offers one strategy for the linking of radioactive metal cations to macromolecules. The construction of effective radioimmunoconjugates requires selection of an appropriate metal radionuclide and organic chelating agent combination, along with the strategy and conditions for assembling the metal-chelating agent−antibody complex. The bifunctional ligand serves two purposes: to hold the metal radionuclide securely without leakage in vivo and to provide a sidearm for antibody linkage while maintaining maximum antibody integrity.

While numerous examples of labeled conjugates have been investigated, improved bifunctional ligands for efficient and stable incorporation of radiometallic nuclides under mild conditions must be developed to overcome the significant problems often associated with this technology, such as nonspecific binding of the radionuclide, protein denaturation under the conditions required for chelation of the metal, and slow kinetics of radionuclide-labeling. Our original efforts in technetium coordination chemistry (*19*) were directed toward this end and resulted in the development of a series of bifunctional hydrazine ligands which have proved effective and versatile linkers for labeling antibodies and fragments (*20*−*22*). Specifically, when *N*-oxysuccinimidylhydrazinonicotinamide is combined with a macromolecule such as a protein, polypeptide, or glycoprotein in neutral or slightly basic media, the protein-reactive part of the compound reacts with nucleophilic groups in the macromolecule, such as the amine groups of lysine residues, to yield a conjugate containing free hydrazine/hydrazide groups, referred to as HYNIC-protein. In fact, since our initial report of the labeling of polyclonal IgG with ^{99m}Tc-HYNIC (*19*), HYNIC has been employed as a bifunctional chelator for ^{99m}Tc-labeling of proteins (*23*), as well as small biomolecules including somatostatin analogues (*24*), liposomes (*25*), antisense oligonucleotides (*26*), folate receptor ligands (*27*), and polypeptides and other small molecules (*28*, *29*).

The versatility of this HYNIC-linker technology has also been demonstrated recently in the preparation of conjugates of chemotactic peptides, which bind to high affinity receptors on white blood cell membranes and thereby migrate to sites of infection (*30*). The advantages of this type of molecule over antibodies include smaller size and enhanced diffusibility to the extravascular space, faster blood clearance resulting in lower background radiation, the presence of well-defined receptor systems, and the ability to synthesize analogues of these peptides with varying size, charge, and linker properties (*31*).

Scheme 1. For-MLFK−(N$^{\epsilon}$-HYNIC)G

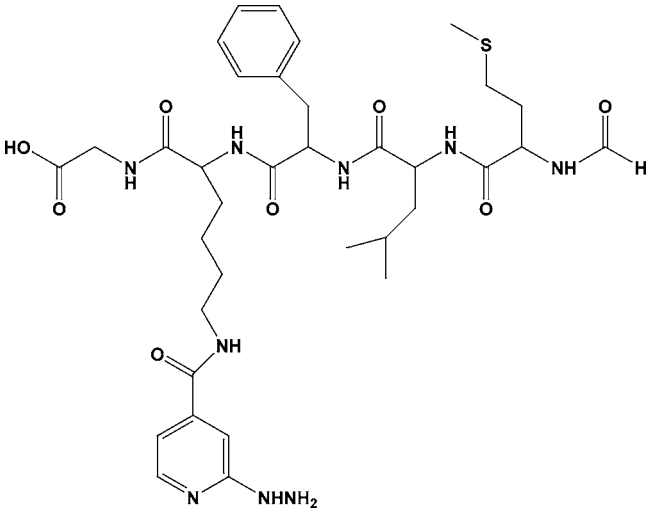

Specifically, For-MLF is a bacterial product that is known to initiate leukocyte chemotaxis by binding to high affinity receptors on the white blood cell membrane (*32*−*34*). These receptors are present on both PMNs and mononuclear phagocytes. As granulocytes respond to the chemoattractant gradient, the affinity of the receptors decreases as additional receptors are expressed, until the granulocyte reaches the site of inflammation, where the concentration of chemoattractant is greatest (*35*−*37*). Previous studies have demonstrated that many synthetic analogues of these small, *N*-formylmethionyl peptides bind to neutrophils and macrophages with equal to or greater affinity compared to the native peptide (*38*−*40*). On the basis of this information, it has been hypothesized that chemoattractant peptide analogues that can be readily radiolabeled with radionuclides suitable for external imaging might be effective agents for the rapid localization of focal sites of inflammation.

We have developed chemotactic peptides which incorporate the ^{99m}Tc binding group HYNIC (hydrazinonicotinamide) (Scheme 1) (*20b*). This complex agent when added to the lysine extended C-terminus of the peptide sequence enabled robust labeling at high specific activity. Separation of the unlabeled peptide from the technetium-labeled peptide was easily achievable on HPLC and facilitated by the nature of the starting technetium complex. Animal studies with high specific activity, technetium-labeled HYNIC chemotactic peptides showed significant improvement over the In-111-DTPA peptides, and comparisons to the clinically accepted imaging agents such as In-111 white blood cells and In-111-IgG demonstrated greater target accumulation and lesion-to-normal tissue ratios exceeding that of the latter two agents (*20a*).

However, radio-HPLC of [^{99}Tc-For-MLFK-HYNIC], labeled using Tc-polyalkoxy ligand complexes, demonstrated multiple radiochemical species with unique biodistribution patterns (*20d*). This observation is likely a consequence of the tendency of Tc to bind to the hydrazino moiety, as well as polyalkoxy ligands, in a variety of coordination geometries (*41*). The recognition that the identity of the polyalkoxy coligand could dramatically influence the biological distribution of the ^{99m}Tc-labeled HYNIC-derivatized chemotactic peptides led to the development of a variety of potential coligands to increase the solution stability and minimize the number of isomers. Coligand development has focused on monodentate water-soluble phosphines (*21c*, *29a*), bidentate nitrogen−sulfur donors (*41*), and a variety of polydentate

alkoxy-based ligands (*20f*, *42*). However, tridentate ligands would ideally constrain the available coordination sites about the $\{M(\mu^2\text{-}NHNC_5H_3NR)(\mu^1\text{-}NNC_5H_3NR)\}^{2+}$ core. Furthermore, the affinity of this metal-bishydrazino core for nitrogen and sulfur donors suggests that tridentate ligands based on the bis(mercaptoethyl)methyamine (NS_2) prototype would effectively constrain the possible coordination geometries and improve overall stability. To investigate this hypothesis, we synthesized NS_2, converted the [^{99}Tc-mannitol-For-MLFK-HYNIC] to the corresponding NS_2-containing complex [Tc-NS_2-For-MLFK-HYNIC], henceforth [Tc-NS_2-HYNIC-peptide], and compared its infection imaging and biodistribution properties with [^{99}Tc-mannitol-For-MLFK-HYNIC]. HPLC, ROI analysis, and tissue radioactivity measurements indicate that the [Tc-NS_2-HYNIC-peptide] complex is chemically homogeneous and exhibits improved infection localization and biodistribution properties.

To provide a structural basis for the interaction of the {Tc-HYNIC} core with NS_2 and related ligand types, the reaction of $[MCl_3(NNC_5H_4NH)(NHNC_5H_4N)]$ (M = Tc, Re) with $CH_3N(CH_2CH_2SH)_2$ (NS_2), C_5H_3N-2,6-$(CH_2SH)_2$, $O(CH_2CH_2SH)_2$, and $S(CH_2CH_2SH)_2$, as well as the bidentate N,S-donor ligands pyridine-2-thiol, 3-(trimethylsilyl)pyridine-2-thiol, and *N*-methyl-imidazole-2-thiol, were investigated. The resulting thiolate derivatized complexes of the {M-HYNIC} core, $[M\{CH_3N(CH_2CH_2S)_2\}(NNC_5H_4N)(NHNC_5H_4N)]$ (M = Tc (**5a**), Re (**5b**)), $[Re\{C_5H_3N\text{-}2,6\text{-}(CH_2S)_2\}(NNC_5H_4N)(NHNC_5H_4N)]\cdot CH_2Cl_2\cdot 0.5MeOH$ (**7**), $[Re\{O(CH_2CH_2S)_2\}(NNC_5H_4N)(NHNC_5H_4N)]$ (**8**), $[Re\{(SCH_2CH_2)_2S\}(NNC_5H_4NH)(NHNC_5H_4N)]Cl$ (**9**), $[ReCl(C_5H_4N\text{-}2\text{-}CH_2S)(NNC_5H_4N)(NHNC_5H_4N)]$ (**10**), $[Re(2\text{-}SC_5H_3N\text{-}3\text{-}SiMe_3)_2(NNC_5H_4N)(NHNC_5H_4N)]$ (**11**), and the unexpected binuclear species $[Re_2(OH)Cl(SC_3H_2N_2CH_3)_2(NNC_5H_4N)_2(NHNC_5H_4N)_2]$ (**12**), were characterized spectroscopically, and in the instances of **5b**, **7**, **9**, **10**, and **12** by X-ray crystallography. In addition, the 6-hydrazinonicotinic acid analogues $[ReCl_3\{NNC_5H_3NH(CO_2R)\}\{NHNC_5H_3N(CO_2R)\}]$ (R = H, **13a**; R = CH_3, **13b**) have been prepared, structurally characterized, and coupled to lysine to give $[ReCl_3\{NNC_5H_3NH(CONHCH_2CH_2CH_2CH(NH_2)CO_2H)\}\{NHNC_5H_3NH(CONHCH_2CH_2CH_2CH(NH_2)CO_2H\}]\cdot 2HCl$ (**14**·2HCl). The reaction of **13** with 2-mercaptopyridine provided the model compound $[Re(2\text{-}SC_5H_4N)_2\{NNC_5H_3NH(CO_2Me)\}\{NHNC_5H_3N(CO_2Me)\}]$ (**15**) whose structure has also been confirmed by X-ray crystallography. Attempts to prepare metalated conjugates of the For-MLFK-HYNIC either by reactions of rhenium precursors with For-MLFK-HYNIC or of **14** with For-MLF under appropriate conditions yielded only insoluble materials which could not be analyzed by NMR or mass spectrometry. These observations emphasize the difficulty of characterizing the metalated conjugates on the macroscopic scale, which has rendered the characterization of materials on the tracer scale problematic.

MATERIALS AND METHODS

Materials. Polystyrene-based *N*-α-9-fluorenylmethoxycarbonyl (Fmoc)-glycine-loaded SASRIN resin (0.69 mmol g^{-1}, 1% divinylbenzene, 200−400 mesh) was obtained from Bachem Inc. Fmoc-protected amino acids were purchased from NovaBiochem Inc., Bachem Inc., and Advanced ChemTech Inc.

N-Formyl-MLFK was prepared on an Advanced ChemTech 348Ω peptide synthesizer using a 40-well reaction vessel. Peptides were analyzed by electrospray mass spectrometry using a Micromass Quattro Ultima instrument in positive ion mode. Samples were dissolved in 50/50 acetonitrile/H_2O prior to analysis. Analytical HPLC was performed using a Varian Pro Star model 330 PDA detector, model 230 solvent delivery system and a C-18 Microsorb column (4.6 × 250 mm, 300 Å-5 μm). Semipreparative HPLC was carried out using a Varian Pro Star HPLC fitted with a model 320 μv-detector, a model 215 solvent delivery system, and a C-18 Microsorb column (10 × 250 mm, 300 Å-5 μm). The elution protocol for both analytical and semipreparative experiments was a linear gradient of 5% acetonitrile containing 0.1% TFA to 100% acetonitrile containing 0.1% TFA over 20 min. The flow rates were 1.0 mL min^{-1} and 4.2 mL min^{-1} for the analytical and semipreparative experiments, respectively. All analytical HPLC experiments were monitored at λ = 254 and 214 nm.

HYNIC acid and succinimidyl-6-tBOC-hydrazinopyridine-3-carboxylic acid were prepared by literature procedures (*20b*). Ammonium perrhenate (Aldrich), 2-mercaptoethyl ether (Aldrich), and triethylamine (Aldrich) were used as received without further purification. The synthetic precursor $[ReCl_3(NNC_5H_4NH)(NHNC_5H_4N)]$ was synthesized by published procedures (*43*) as was the pyridine-2-thiol-3-trimethylsilane (*44*). All the other chemical reagents were purchased from Aldrich and were used without purification.

Technetium-99m-pertechnetate (^{99}Mo/^{99m}Tc generator) and stannous glucoheptonate kits (Glucoscan) were obtained commercially from Dupont radiopharmaceutical division (Bilerica, MA). New Zealand white rabbits (2.5−3 kg) were purchased from Charles River Breeding Laboratories (Boston, MA).

Melting points were determined with a Thomas-Hoover capillary melting point apparatus and are uncorrected. TLC was performed on EM Science 250 μ Silica Gel F254 plates with fluorescent indicator and spots were detected with UV light. Mass spectra were measured on a JEOL JMS-D300 spectrometer.

NMR spectra were recorded on a General Electric QE 300 (^{1}H 300.10 MHz) spectrometer in CD_2Cl_2(δ 5.32) or $(CD_3)_2SO$ (δ 2.50). IR spectra were recorded as KBr pellets with a Perkin-Elmer Series 1600 FTIR. Elemental analysis for carbon, hydrogen, and nitrogen were carried out by Oneida Research Services, Whitesboro, NY.

CAUTION: ^{99}Tc is a weak β-emitter (293 keV). All experiments involving ^{99}Tc were performed in a laboratory designed for and devoted exclusively to the preparation of radioactive materials. Due to strong possibility of contamination, and current licensing regulations for our laboratory, ^{99}Tc-containing species were characterized only by X-ray crystallography and/or elemental analyses.

Preparation of *N*,*N*-Bis(2-mercaptoethyl)methylamine, $CH_3N(CH_2CH_2SH)_2$ (NS_2). All procedures were carried out under an atmosphere of purified dinitrogen. Bis(2-chloroethyl)amine hydrochloride (0.60 g, 0.33 mmol) was dissolved in 25 mL of DMF. Triphenylmethly mercaptan (2.00 g, 7.20 mmol) was added. This was followed by slow addition of 1,8-diazabicyclo[5.4.0]undec-7-ene (1.73 mL, 11.6 mmol) under a nitrogen atmosphere. The reaction was heated at 100 °C for 1 h. The solvent was evaporated, and the residue was dissolved in EtOAc. The solution was first washed with water, then brine, and was dried over sodium sulfate. The solvent was evaporated to give the crude product, which was purified by a short column pretreated with 10 mL of NEt_3 (10% EtOAc/hexane) to give 1.86 g (3.11 mmol, 94%) of bis(2-triphenylmethylsulfidoethyl)amine (**2**) as a yellow solid. IR (KBr, cm^{-1}): 3022 (w), 1596 (m), 1494 (m), 1444 (m), 1262 (w), 1155 (w), 1078 (m), 1031 (m), 919 (w), 804 (w),

758 (m), 734 (s), 700 (s), 658 (m), 620 (w), 605 (m), 493 (w), 468 (w).

Amine **2** (1.86 g, 3.11 mmol) was dissolved in 50 mL of DMF and 10 mL of acetonitrile. Formaldehyde (1.17 mL, 15.6 mmol) was then added. This was followed by the addition of sodium cyanoboron hydride (0.31 g, 4.98 mmol). Ten minutes later, 0.25 mL of acetic acid was added to neutralize the solution. The reaction was stirred at room temperature for 2 h before it was poured into 1 N NaOH (200 mL). The mixture was then extracted with 50% EtOAc/hexane. The organic extracts were combined and washed with brine and dried over sodium sulfate. The mixture was concentrated to give a crude product, which was purified by a short column to give bis(2-triphenylmethylsulfidoethyl)methylamine (**3**) (1.16 g, 1.87 mmol, 61%) as a white solid. IR (KBr, cm^{-1}): 3055 (2), 2345 (w), 1594 (w), 1490 (s), 1444 (s), 1285 (w), 1183 (w), 1034 (w), 742 (s), 700 (s), 622 (m), 565 (w).

Amine **3** (0.10 g, 0.16 mmol) was dissolved in 0.5 mL of methylene chloride. Trifluoroacetic acid (0.5 mL) was then added, and the solution turned yellow. Excess triethylsilane (0.16 mL, 0.98 mmol) was then added dropwise under an out flow of nitrogen, and the reaction turned colorless. The reaction mixture was evaporated to dryness. Hexane (0.5 mL) was added and then decanted. This was repeated three times. The residue was then vacuum-dried to give NS_2 as a white solid (0.04 g) which was used without further purification. IR (KBr, cm^{-1}): 1677 (m), 1596 (m), 1494 (m), 1444 (m), 1199 (s), 1078 (w), 1031 (m), 758 (m), 734 (m), 700 (s), 658 (w), 620 (w), 606 (m), 493 (w), 468 (w).

Chemotactic Peptides. *(a) For-MLFK(N$^{\epsilon}$-HYNIC).* N-For-MLFK was synthesized and purified by standard solid-phase techniques and conjugated with nicotinyl hydrazine to yield N-For-MLFK(N$^{\epsilon}$-HYNIC). The final product was characterized by UV, and mass spectrometry, amino acid analysis, f-MLF receptor binding affinity, and biological activity as previously reported (*20b*).

(b) For-MLFK(N$^{\epsilon}$-HYNIC)G. Fmoc-glycine-loaded SASRIN resin (150 mg/well, 0.69 mmol/g) was added to two wells of the reaction vessel (rv), suspended in DMF (2 mL/well), and shaken at 600 rpm for 1 min. The wells were subsequently filtered, suspended in THF (2 mL/well), shaken at 600 rpm for 1 min, and drained for 90 s. The THF wash was repeated two more times. The DMF wash was then repeated a final two times to complete the general wash cycle. This procedure was used between every deprotection and coupling step.

Fmoc deprotection was accomplished through the addition of a 20% v/v piperidine−DMF solution to the active vessels (2 mL/well) and shaking for 5 min at 600 rpm. Following filtration, the process was repeated, shaking for 10 min. The deprotected resin-bound amino acid was washed using the general wash procedure and subsequently coupled to the next Fmoc-protected amino acid using a standard HBTU coupling technique.

Coupling reactions initially involved adding DMF (200 μL) to the active vessels followed by the addition of a 5-fold excess of the protected amino acid as a 0.5 M solution in DMF. Five equivalents of HBTU as a 0.5 M solution in DMF was then added followed by a 10-fold excess of DIPEA as 2.0 M solution in DMF. The reaction block was subsequently shaken for 80 min at 600 rpm. Following filtration, the resin was washed using the general washing procedure prior to the start of the next cycle. This procedure was repeated to afford the peptide, f-MLFK(N$^{\epsilon}$-Dde)G, while still attached to the resin.

Dde deprotection of f-MLFK(N$^{\epsilon}$-Dde)G was accomplished through the addition of a 2% v/v hydrazine−DMF solution to the active vessels (2 mL/well) and shaking for 5 min at 600 rpm. Following filtration, the process was repeated, shaking for 10 min. The epsilon free amine was then subjected to the general wash cycle and coupled to the HYNIC acid using the HBTU protocol described above, followed with a final wash prior to deprotection.

The peptide was cleaved from the resin support using a TFA cocktail containing EDT (2%), water (2%), and TIS (2%). The cleavage cocktail, cooled to 0° C, was added to the resin and the mixture allowed to warm to room temperature over 60 min. The suspension was filtered into cold diethyl ether and the resulting heterogeneous solution centrifuged at 3000 rpm and −5 °C for 10 min. The resultant pellet was washed with cold ether (3 × 25 mL), dissolved in distilled−deionized water, and lyophilized yielding a white solid. fMLFK(N$^{\epsilon}$-HYNIC)G: ESMS-(+ve) $m/z = 758.4$ (calculated 757.9), HPLC $t_R = 10.2$ min. The final product was characterized by UV and mass spectrometry, amino acid analysis, f-MLF receptor binding affinity, and biological activity as previously reported (*20b*).

Radiolabeling. *^{99m}Tc-Mannitol.* A solution of Sn(II) mannitol was prepared by dissolving 800 mg of mannitol (Aldrich) in dilute HCl followed by the dropwise addition of stannous chloride (1 mg in 0.1 cm^3 6 N HCl). The solutions were purged with nitrogen prior to and during manipulation. The pH of the final Sn(II) mannitol solution was adjusted to between 5 and 6 with NaOH. The final ligand concentration was ca. 80 mg/mL and the Sn(II) concentration [as $Sn(II)Cl_2$] was 100 mg/mL. The solution was filtered using a 0.22 mm Millex GS filter, and 0.5 mL aliquots were transferred to sterile rubber-stoppered glass vials, purged with N_2, and stored at −70 °C until use.

^{99m}Tc-mannitol was prepared by adding 2.0 mL of $\{^{99m}TcO_4\}^-$ in saline to a 0.5 mL aliquot of Sn(II) mannitol solution. The mixture was vortexed briefly and incubated at room temperature for 5 min before radiochemical analysis. The final concentration of radioactivity was 5−10 mCi/mL. Radiochemical analysis was performed by ITLC-sg with acetone and saline as the mobile phases. The R_fs of ^{99m}Tc-mannitol were 0.0 and 1.0 in acetone and saline, respectively. The potential impurities, unreduced TcO_4^- and reduced hydrolyzed TcO_2 have R_fs of 1.0 and 0.0 in these solvent systems.

^{99m}Tc-Labeling of Chemotactic Peptides. The following procedure was used to radiolabel the chemotactic peptide analogues with ^{99m}Tc. Twenty microliters of peptide solution (1 mg/mL in dimethyl sulfoxide) was transferred to a clean glass vial and diluted with 500 μL of 0.1 M acetate buffer (pH 5.2). ^{99m}Tc-mannitol solution (500 μL) was added and vortexed briefly, and the reaction mixture was incubated to room temperature for 1 h.

Peptide labeling was monitored by radio-HPLC using a C_{18}-reverse phase column (300 A, 5 μm, 4.5 mm × 25 cm, Vydac). The elution conditions were as follows: solvent A, 0.1% trifluoroacetic acid in water; solvent B, 0.1% trifluoroacetic acid in acetonitrile; gradient: 0% B to 100% B over 10 min; flow rate 2 mL/min. UV absorption was monitored at 260 and 400 nm with a flow-through spectrophotometer (Dynamax UV-D II, Rainin, Woburn, MA), and radioactivity was monitored using a radioisotope detector (Model 190, Beckman). The outputs of both detectors were recorded and analyzed using a dedicated HPLC controller/integrator (Dynamax HPLC method manager, Rainin, Woburn, MA).

Formyl-MLFK-HYNIC was labeled by incubating equal volumes of Tc-99m-mannitol with peptide [20 μg/mL] in 50 mM acetate buffer pH 5.2 for 1 h. Conversion to the

NS_2-containing complex was accomplished by addition of NS_2 [1 mg/mL DMSO] to the [Tc-mannitol-For-MLFK-HYNIC] solution at room temperature. Alternatively, $^{99m}TcO_4^-$ (1.0 mL) in acetate buffer was added to a solution of NS_2 (1 mg/mL in DMSO) and f-MLFK-HYNIC (10 μg/mL in acetate buffer, pH 5.2) in the presence of excess hydrazine sulfate as reducing agent. HPLC analysis of the purified material exhibited a profile identical to that of [^{99m}Tc-NS_2-HYNIC-peptide] as prepared by addition of NS_2 to [^{99m}Tc-mannitol-HYNIC-peptide].

Injectable solutions of radiolabeled peptide were prepared by isolating ^{99m}Tc-labeled from unlabeled peptide using a modification of the HPLC system described above. A semipreparative C_{18}-reverse phase column (300 A, 5 μm, 10 mm × 250 mm, Vydac, Hesperia, CA) was used, and the elution conditions were as follows: solvent A, 0.1% trifluoroacetic acid in water; solvent B, 0.1% trifluoroacetic acid in acetonitrile; gradient: 0% B from 0 to 2 min, 0% B to 100% B from 2 to 10 min; flow rate 4 mL/min. UV absorption and radioactivity were monitored as described above.

The peptide solutions were heated gently and dried under a stream of N_2 or rotary evaporated under vacuum. The residues were dissolved in 1 mL of absolute ethanol and diluted to an ethanol concentration of 10% with 0.9% NaCl for injection, USP. Sample of injectate were analyzed by HPLC using the analytical HPLC system described above.

Imaging Infected Rabbits. Groups of six male New Zealand white rabbits weighing 2−3 kg were anesthetized with ketamine and xylazine (15.0 and 1.5 mg/kg) and injected in the left posterior thigh muscle with 1.0 mL suspension of approximately 5×110^9 *E. coli*. Twenty-four hours after inoculation, rabbits with gross swelling in the inoculated thigh were injected intravenously through a lateral ear vein with 600−1000 mCi of HPLC purified [^{99m}Tc-mannitol-HYNIC-peptide], [^{99m}Tc-NS_2-HYNIC-peptide] (specific activity > 5000 mCi/μmol, separated from unlabeled peptide by HPLC as described above).

At 3 and 18 h after injection (hpi), the animals were anesthetized with ketamine/xylazine, and anterior images were acquired using a large field of view gamma camera (Technicare Omega 500, Solon, OH) equipped with a high resolution parallel hole collimator and interfaced to a dedicated computer (Technicare 560, Solon, Ohio). Images were recorded for a preset time of 5 min/view with a 15% window centered on the 140 keV photopeak ^{99m}Tc. Regions-of-interest (ROIs) were drawn over the area of infection, and the contralateral normal muscle and T/B ratios were calculated.

Biodistribution. After acquiring the final images, the animals were sacrificed with an overdose of sodium pentobarbital, and biodistribution was determined. Samples of blood, heart, lung, liver, spleen, kidney, adrenal, stomach, GI tract, testes, bone, bone marrow, normal muscle, infected muscle, and pus were weighed, and radioactivity was measured with a well type gamma counter (LKB model # 1282, Wallac Oy, Finland). To correct for radioactive decay and permit calculation of the concentration of radioactivity in each organ as a fraction of the administered dose, aliquots of the injected doses were counted simultaneously. The results were expressed as percent injected dose per gram (%ID/g), infected to normal muscle ratio and pus to normal muscle ratio.

Statistical Methods. The results of the imaging studies were evaluated by two-way analysis of variance (ANOVA) with a linear model in which peptide and time were the classification variable; T/B = Peptide + Time + Peptide × Time. The results of the biodistribution studies were evaluated by two-way analysis of variance (ANOVA) with a linear model in which organ and mannitol were the classification variables; %ID/g or %ID/organ = Organ + Peptide + Organ × Peptide. Post-hoc comparisons of peptide concentrations were performed by Duncan's new multiple range test (*45*). All results are expressed as mean ± SEM.

Syntheses of Model Compounds. *Preparation of [Tc{$CH_3N(CH_2CH_2S)_2$}(NNC_5H_4N)($NHNC_5H_4N$)] (**5a**).* A solution of [$TcCl_3$(NNC_5H_4NH)($NHNC_5H_4N$)] (0.02 g, 0.04 mmol), NS_2 (0.012 g, 0.08 mmol), and NEt_3 (0.016 g, 0.16 mmol) in 2 mL of methanol was stirred for 2 h. After filtration of the solution and evaporation to dryness, red-brown crystals of **5a** were isolated in 10−20% yield. Anal. Calcd for $C_{15}H_{20}N_7S_2Tc$: C, 39.1; H, 4.34; N, 21.3. Found: C, 38.7; H, 4.22; N, 21.2.

*Preparation of [Re{$CH_3N(CH_2CH_2S)_2$}(NNC_5H_4N)($NHNC_5H_4N$)] (**5b**).* A solution of [$ReCl_3$(NNC_5H_4NH)($NHNC_5H_4N$)] (0.025 g, 0.049 mmol) with bis(2,2′-ethanethiol)-*N*-methylamine (0.015 g, 0.098 mmol) and NEt_3 (0.03 g, 0.295 mmol) in 10 mL of methanol was stirred and refluxed for 2 h. The reaction mixture was filtered and evaporated to dryness. Dark brown crystals were grown by slow diffusion of pentane into a solution of **5b** in CH_2Cl_2 (Yield: 5%). Anal. Calcd for $C_{15}H_{20}N_7S_2Re$: C, 32.8; H, 3.64; N, 17.9. Found: C, 32.7; H, 3.81; N, 17.7.

*Preparation of C_5H_3N-2,6-$(CH_2SH)_2$ (**6**).* Compound **6** was prepared according to a modified literature synthesis described in ref 45. In a 100 mL Schlenk flask, a mixture of pyridine-2,6-methanethiol hydrochloride (5.00 g, 0.0285 m), thiourea (5.00 g, 0.0658 m) and 48% aqueous hydrobromic acid (28.80 g, 0.171 mol) was stirred and refluxed under an atmosphere of argon for 20 h. After cooling, a solution of NaOH (8.00 g, 0.200 mol) was slowly added. The mixture was refluxed for an additional 45 min. The resulting yellow solution was allowed to cool before extraction with methylene chloride. The extract was washed with a saturated salt solution (250 mL) and dried over sodium sulfate. Finally the solution was filtered and evaporated to a colorless residue (2.90 g, 59.3%). Due to its instability, compound **6** was made as needed and kept in a solution of CH_2Cl_2. IR (KBr, cm^{-1}); 1568 (s), 1269 (w), 1210 (w), 1064 (m), 995 (w), 814 (m), 751 (m).

*Preparation of [Re{C_5H_3N-2,6-$(CH_2S)_2$}(NNC_5H_4N)($NHNC_5H_4N$)]·CH_2Cl_2·0.5MeOH (**7**).* A solution of [$ReCl_3$(NNC_5H_4NH)($NHNC_5H_4N$)] (0.050 g, 0.098 mmol) with pyridine-2,6-dimethanethiol (0.050 g, 0.295 mmol) and NEt_3 (0.059 g, 0.591 mmol) in 10 mL of methanol was stirred and refluxed overnight whereupon the reaction mixture was filtered and evaporated to dryness. Dark red crystals of **7** were grown by slow diffusion of pentane into CH_2Cl_2 (Yield: 0.012 g, 21%). The material used for elemental analysis was heated at 80 °C under vacuum for 12 h. Anal. Calcd for $C_{17}H_{16}N_7S_2Re$: C, 38.9; H, 2.82; N, 17.2. Found: C, 38.6; H, 2.95; N, 16.9. IR (KBr, cm^{-1}): 1605 (s), 1546 (s), 1500 (m), 1460(m), 1451 (m), 1420 (s), 1300 (m), 1194 (s), 1052 (m), 1007 (w), 773 (m), 669 (w), 509 (w). ^{1}H NMR (MeOH-d_4, ppm): 4.50−4.85 (dd, J = 18 Hz, 4H), 6.55 (t, J = 5.4 Hz, 1H), 6.85 (t, J = 2.4 Hz, 1H), 7.22−7.42 (m, 3H), 7.50−7.80 (m, 3H), 7.90 (m, 2H), 8.50 (d, 1H).

*Preparation of [Re{$(SCH_2CH_2)_2O$}(NNC_5H_4N)($NHNC_5H_4N$)] (**8**).* A solution of [$ReCl_3$(NNC_5H_4NH)($NHNC_5H_4N$)] (0.050 g, 0.098 mmol) with bis(2-mercaptoethyl) ether (0.041 g, 0.295 mmol) and NEt_3 (0.059 g, 0.591 mmol) in 10 mL of methanol was stirred and refluxed overnight.

The reaction mixture was filtered and evaporated to dryness. Dark red crystals were grown by slow diffusion of pentane into a CH_2Cl_2 solution of the reaction residue. Anal. Calcd for $C_{14}H_{17}N_6OS_2Re$: C, 31.4; H, 3.17; N, 15.7. Found: C, 31.6; H, 2.93; N, 15.9, IR (KBr, cm^{-1}) 3446 (w), 1600 (m), 1543 (s), 1456 (m), 1418 (m), 1309 (m), 1192 (s), 1055 (w), 1004 (w), 776 (w). ^1H NMR (CD_2Cl_2): 0.80 (t), 1.45 (s), 2.62 (m), 2.81 (t), 2.94 (m), 3.25 (m), 3.50 (m), 3.67 (m), 4.34 (m), 6.78 (m), 7.10 (d), 7.60 (d), 7.79 (d), 8.26 (d), 8.38 (d).

*Preparation of [Re{$(SCH_2CH_2)_2S$}(NNC_5H_4NH)($NHNC_5H_4N$)]Cl (**9**).* A solution of [$ReCl_3(NNC_5H_4NH)(NHC_5H_4N)$] (0.050 g, 0.098 mmol) with bis(2-mercaptoethyl) sulfide (0.046 g, 0.295 mmol) and NEt_3 (0.059 g, 0.591 mmol) in 10 mL of methanol was stirred and refluxed overnight. After filtration and evaporation to dryness, recrystallization was effected from CH_2Cl_2/pentane. Anal. Calcd for $C_{14}H_{18}N_6S_3ReCl$: C, 29.8; H, 3.19; N, 14.9. Found: C, 29,7; H, 3.12; N, 14.8. IR (KBr, cm^{-1}) 1599 (s), 1540 (s), 1495 (m), 1460 (m), 1415 (s), 1295 (m), 1197(s), 1002 (w), 755 (m), 670 (w), 500 (w). ^1H NMR (CD_2Cl_2): 0.90 (t), 1.40 (s), 2.50 (m), 2.75 (t), 2.94 (m), 3.20 (m), 3.45 (m), 3.60 (m), 4.32 (bs), 4.50 (m), 6.75 (m), 7.15 (d), 7.85 (d), 8.30 (d), 8.38 (d).

*Preparation of [ReCl(C_5H_4N-2-CH_2S)(NNC_5H_4N)($NHNC_5H_4N$)] (**10**).* A solution of [$ReCl_3(NNC_5H_4NH)(NHNC_5H_4N)$] (0.050 g, 0.098 mmol) with pyridine-2-methylenethiol (0.100 g, 0.197 mmol) and NEt_3 (0.040 g, 0.396 mmol) in 10 mL of methanol was stirred and refluxed overnight. The reaction mixture was filtered and evaporated to dryness. Dark red crystals were grown by slow diffusion of pentane into a CH_2Cl_2 solution of the reaction residue. IR (KBr, cm^{-1}): 1654 (m), 1547 (m), 1496 (m), 1458 (s), 1421 (m), 1378 (m), 1294 (w), 1201 (m), 1055 (w), 1009 (w), 779 (w). ^1H NMR [$(CD_3)_2SO$]: 4.54 (d), 6.58 (m), 7.52 (d), 7.67 (d), 7.70 (m), 7.88 (m), 7.97 (m), 8.13 (m), 8.42 (d).

*Preparation of [Re(2-SC_5H_3N-3-$SiMe_3$)$_2$(NNC_5H_4N)($NHNC_5H_4N$)] (**11**).* A solution of [$ReCl_3(NNC_5H_4NH)(NHNC_5H_4N)$] (0.050 g, 0.098 mmol) with pyridine-2-thiol-3-trimethylsilane (0.036 g, 0.197 mmol) and NEt_3 (0.039 g, 0.395 mmol) in 10 mL of methanol was stirred and refluxed overnight. The reaction mixture was filtered and the black precipitate was allowed to air-dry. Dark crystals were grown by slow diffusion of pentane into a CH_2Cl_2 solution of [$Re(C_8H_{12}NSiS)_2(NNC_5H_4NH)(NHNC_5H_4N)$] (0.055 g, 73% yield). Anal. Calcd for $C_{26}H_{33}N_8Si_2S_2Re$ (mol. wt. 763.2): C, 40.8; H, 4.32; N, 14.7. Found C, 40.3; H, 3.90; N, 14.3. IR (KBr, cm^{-1}): 1618 (m), 1565 (s), 1550 (s), 1459 (m), 1438 (w), 1422 (s), 1364 (s), 1299 (m), 1246 (m), 1213 (s), 1138 (m), 1014 (w), 847 (s), 761 (m), 654 (w), 642 (w). ^1H NMR (CD_2Cl_2): 0.42 (s), 1.52 (m), 1.701 (s), 3.17 (d), 6.67 (d), 6.75 (d), 7.08 (m), 7.56 (m), 7.60 (d), 7.75 (m), 7.91 (d), 8.71 (s).

*Preparation of [$Re_2(OH)Cl(SC_3H_2N_2CH_3)_2(NNC_5H_4N)_2$-($NHNC_5H_4N)_2$] (**12**).* *N*-methylimidazole-2-thiol (0.056 g, 0.49 mmol, in 3 mL chloroform) was added to a well stirred solution of [$ReCl_3(NNC_5H_4NH)(NHNC_5H_4N)$] (0.1 g, 0.2 mmol) and triethylamine (60 mg, 0.6 mmol) in 20 mL of chloroform and was heated at reflux for 6 h. After cooling to room temperature, the greenish brown solution was extracted with water (5 × 30 mL), and the organic layer was dried over sodium sulfate. The volume was reduced to 5 mL, and the solution was passed through a silica gel column using 2:98 MeOH:CH_2Cl_2 solution as eluant. Yield: 0.090 g, 42%. ^1H NMR (δ (ppm), $CDCl_3$): 9.21 (d, J = 5.7 Hz, 1H), 9.11 (d, J = 5.7 Hz, 1H), 8.66−8.62 (m, 2H), 7.69−7.48 (m, 6H), 7.04 (d, J = 2.1 Hz, 1H), 6.96−6.88 (m, 3H), 6.81 (d, J = 7.5 Hz, 1H), 6.71−6.55 (m, 2H), 6.54 (d, J = 2.1 Hz, 1H), 6.38 (d, J = 0.8 Hz, 1H), 6.02 (d, J = 1.8 Hz, 1H), 3.50 (s, 3H), 3.23 (s, 3H), ^{13}C ($CDCl_3$): 166.90, 166.58, 166.02, 164.50, 161.07, 159.90, 155.05, 150.58, 150.25, 148.35, 139.43, 139.22, 138.33, 137.96, 128.63, 121.74, 121.44, 120.64, 119.58, 117.77, 117.37, 116.25, 116.06, 36.54, 35.22.

*Preparation of [$ReCl_3${$NNC_5H_3NH(CO_2R)$}{$NHNC_5H_3N$-(CO_2R)}] (R = H, **13a**; R = CH_3, **13b**).* A reaction mixture of [NH_4][ReO_4] (0.10 g, 0.37 mmol), 6-hydrazinonicotinic acid (0.25 g, 1.86 mmol) and 0.24 mL of aqueous 36% HCl (2 mmol) in 15 mL of MeOH was heated at reflux for 2 h. The solution was cooled to room temperature, and the brown precipitate was collected by vacuum filtration and washed with diethyl ether. The crude product was purified by flash chromatography over SiO_2 using MeOH:CH_2Cl_2:AcOH solution as eluant (20:80:1). Crystals were grown by slow evaporation of a solution of the purified product in MeOH:CH_2Cl_2 (1:1) solution. Crystallization afforded the methyl ester **12b**, rather than the free acid form (Yield: 60%). Anal. Calcd for $C_{14}H_{15}Cl_3N_6O_4Re$: C, 27.3; H, 2.53; N, 13.5. Found: C, 27.0; H, 2.42; N, 13.5. IR (KBr, cm^{-1}): 3394 (w), 2929 (w) 1630 (s), 1570 (s), 1544 (s), 1458 (m), 1281 (s), 1215 (s), 1130 (m), 1023 (w), 861 (w), 765 (m), 618 (w), 548 (w). ^1H NMR (δ (ppm), MeOH-d_4): 9.59 (d, 1H), 8.79 (d, 1H), 8.66 (d, 1H), 8.42 (d, 1H), 8.25 (d, 2H), 7.69 (d, 1H). ^{13}C (MeOH-d_4): 164.66, 163.23, 162.5, 152.6, 147.8, 144.01, 1142.94, 140.65, 138.55, 124.11, 121.45, 119.67. ESI-MS: (M^+H) 624.0, (M^+ + Na): 647.0.

*Preparation of [$ReCl_3${$NNC_5H_3NH(CONHCH_2CH_2CH_2$-$CH_2CH(NH_2)CO_2H$}{$NHNC_5H_3N(CONHCH_2CH_2CH_2$-$CH_2CH(NH_2)CO_2H$}]·2HCl (**14**·2HCl).* (a) A solution of [NH_4][ReO_4] (0.10 g, 0.37 mmol) and HYNIC-lysine (0.530 g, 1.49 mmol) in 15 mL of MeOH was heated at reflux for 2 h. The mixture was cooled to room temperature, and the resultant dark brown precipitate was collected by filtration, washed with diethyl ether (3 × 15 mL) and methanol and dried to give the product (Yield: 0.25 g, 78.8%). (b) Alternatively, the compound was prepared by the reaction of **12** (0.11 g, 0.18 mmol) and FMOC-lysine (α-N protected, 0.074 g, 0.20 mmol) in MeOH (15 mL). The insoluble dark brown precipitate was isolated in ca. 75% yield. Anal. Calcd for $C_{24}H_{34}Cl_3N_{10}O_6Re$: C, 30.3; H, 4.03; N, 16.5. Found: C, 30.2; H, 4.20; N, 16.7. IR (KBr, cm^{-1}): 3394 (w), 2929 (w), 1630 (s), 1570 (s), 1544 (s), 1458 (m), 1281 (s), 1215 (s), 1130 (m), 1023 (w), 861 (w), 765 (m), 618 (w), 548 (w). ESI-MS: (M^+ + 1) 851.1. ^1H NMR (δ (ppm), DMSO-d_6): 9.27 (d, 1H), 8.97 (d, 1H), 8.65 (t, 1H), 8.53 (t, 1H), 8.23 (d, 1H), 8.21 (d, 1H) 7.67 (d, 1H), 7.31 (d, 1H), 3.81 (t, 2H), 3.34 (m, 4H), 1.731 (m, 5H), 1.52−1.37 (m, 10H). ^{13}C NMR (DMSO-d_6): 171.38, 163.98, 163.2, 162.46, 160.223, 148.41, 147.24, 137.13, 135.40, 126.67, 122.75, 118.31, 116.91, 53.08, 52.10, 30.04, 28.88, 22.04, 21.85.

*Preparation of [Re($SC_5H_4N)_2$}{$NNC_5H_3N(CO_2Me)$}{$NHNC_5H_3N(CO_2Me)$}] (**15**).* A solution of [NH_4][ReO_4] (0.02 g, 0.08 mmol), 2-mercaptopyridine (0.052 g, 0.42 mmol), and $H_2NNHC_5H_4CO_2Me$ (6-hydrazinonicotinic acid methyl ester, 0.10 g, 0.17 mmol) in 10 mL of MeOH was heated at reflux for 2 h. The reaction mixture was filtered and evaporated to dryness. The crude product was dissolved in a minimum of MeOH and purified by flash chromatography (SiO_2) using MeOH:CH_2Cl_2 (5:95) solution as eluant (Yield:73%). Anal. Calcd for $C_{24}H_{21}H_8O_4ReS_2$: C, 39.1; H, 2.85; N, 15.2; Found: C, 39.0; H, 2.76; N, 15.3. ^1H NMR (δ (ppm), ($CDCl_3$): 9.30 (m, 2H), 8.26 (m, 2H), 7.99 (m, 1H), 7.75 (m, 2H), 7.25 (m, 2H), 6.84 (m, 3H), 3.96 (s, 3H), 3.81 (s, 3H). ^{13}C ($CDCl_3$): 164.66, 163.23, 162.5, 161.90, 153.06, 151.01, 148.96, 148.55, 141.52,

Table 1. Summary of the Crystallographic Data for the Compounds [Re{CH_3-N-($C_2H_4S_2$)$_2$}(NNC_5H_4N)($NHNC_5H_4N$)] (5), [Re(C_5H_3N-2,6-(CH_2S)$_2$}(NNC_5H_4N)($NHNC_5H_4N$)]·CH_2Cl_2·0.5MeOH (7), [Re{(SCH_2CH_2)S}(NNC_5H_4NH)($NHNC_5H_4N$)]Cl (9), [ReCl(C_5H_4N-2-CH_2S)(NNC_5H_4N) ($NHNC_5H_4N$)] (10), [$Re_2OCl(SC_3H_2N_2CH_3)_2(NNC_5H_4N)_2(NHNC_5H_4N)_2$] (12), [$ReCl_3${$NNC_5H_3NH(CO_2H)$}{$NHNC_5H_3N(CO_2H)$}]·0.5$CH_3OH$·0.5$H_2O$·HCl (13a), and [$Re(SC_5H_4N)_2${$NNC_5H_3N(CO_2Me)$}{$NHNC_5H_3N(CO_2Me)$}] (15)

	5	7	9	10	12	13a	15
	$C_{15}H_{20}N_7S_2$-Re	$C_{18.5}H_{20}N_7OS_2$-Cl_2Re	$C_{14}H_{18}N_6S_3$-ReCl	$C_{16}H_{15}N_7SCl$-Re	$C_{28}H_{26}N_{16}ClO$-Re_2S_2	$C_{12.5}H_{14}Cl_4N_6O_5$-Re	$C_{24}H_{21}N_8O_4$-ReS_2
a, Å	8.0008(3)	8.1375(1)	8.1062(2)	14.7905(5)	10.723(1)	14.0240(8)	9.3544(9)
b, Å	20.5058(5)	15.0204(1)	14.6072(2)	14.7131(4)	15.332(1)	13.1938(8)	9.7712(9)
c, Å	11.6366(4)	19.429(1)	17.0107(3)	8.4637(2)	20.686(2)	13.2801(8)	15.181(1)
α, deg	–	–	82.086(1)	–	–	–	104.631(1)
β, deg	90.958(2)	95.290(1)	82.556(1)	91.068(1)	91.622(1)	112.906(1)	100.939(1)
γ, deg	–	–	83.238(1)	–	–	–	99.008(1)
V, Å^3	1908.9(1)	2364.66(3)	1967.96(7)	1841.5(9)	3399.5(5)	2263.4(2)	1287.3(2)
Z	4	4	4	4	4	4	2
fw	548.70	673.1	588.17	559.06	1074.62	656.30	735.81
space group	$P2_1/c$	Pc	$P\bar{1}$	$P2_1/c$	$P2_1/c$	$P2_1/c$	$P\bar{1}$
T, K	150(1)	150(1)	150(1)	293(2)	150(1)	150(1)	150(1)
λ, Å	0.71073	0.71073	0.71073	0.71073	0.71073	0.71073	0.71073
D_{calcd}, g cm^{-1}	1.909	1.891	1.985	2.016	2.100	1.926	1.898
μ, mm^{-1}	6.598	5.567	6.639	6.873	7.369	5.875	4.931
R[a]	0.0768	0.0519	0.0547	0.0596	0.0508	0.0600	0.0473
wR_2[b]	0.1173	0.1163	0.1146	0.1295	0.0916	0.1107	0.1246

[a] $\sum||F_o| - |F_c||/\sum|F_o|$. [b] $[\sum[w(F_o^2 - F_c^2)^2]/\sum[w(F_o^2)^2]]^{1/2}$.

Scheme 2. Synthesis of For-MFLK(N$^\epsilon$-HYNIC)G[a]

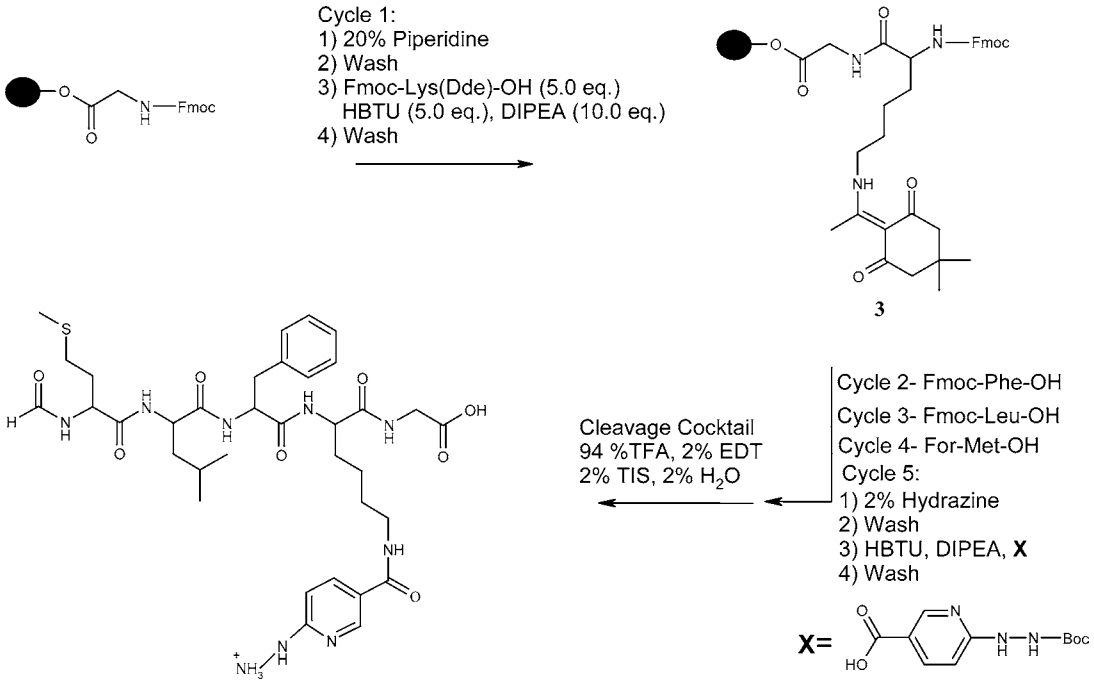

[a] Cycles 2−4 are (i) wash, (ii) deprotection, (iii) wash, (iv) couple.

140.40, 142.94, 140.65, 138.55, 137.03, 129.66, 124.34, 120.70, 119.52, 119.12, 116.64, 53.76.

X-Ray Crystallography. The crystals of **5b**, **7**, **9**, **10**, **12**, **13a**, and **15** were studied using a Bruker SMART diffractometer system using graphite monochromated Mo Kα radiation (λ(Mo Kα) = 0.71073 Å). Data collections for **5b**, **7**, **9**, **12**, **13a**, and **15** were carried out at low temperature while that of **10** was carried out under ambient conditions. The crystal parameters and other experimental details of the data collections are summarized in Table 1. A complete description of the details of the crystallographic methods is given in the Supporting Information. The structures were solved by direct methods (*46*). Neutral atom scattering factors were taken from Cromer and Waber (*47*), and anomalous dispersion corrections were taken from those of Creagh and McAuley (*48*). All calculations were performed using SHELXTL (*49*). Non-hydrogen atoms were refined anisotropically. No anomalies were encountered in refinements of any of the structures. Atomic positional parameters and isotropic temperature factors for the structures are presented in the Supporting Information.

RESULTS

Radiolabeling. The derivatized chemotactic peptide For-MLFK(N$^\epsilon$-HYNIC)G was prepared by solid-phase methods, as outlined in Scheme 2, while For-MLFK-(N$^\epsilon$-HYNIC) was prepared as previously described (*20b*).

After addition of $^{99m}TcO_4^-$ to each Sn(II)-mannitol solution, the desired Tc-mannitol complex was formed as

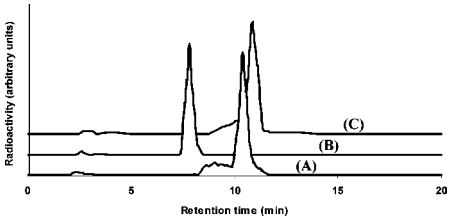

Figure 1. Radio-HPLC chromatograms of (A) [^{99m}Tc-mannitol-f-MLFK-HYNIC], (B) [^{99m}Tc(NS_2)(μ^2-$NHNC_5H_4N$)(μ^1-NNC_5H_4N)], and (C) [^{99m}Tc-NS_2-f-MLFK-HYNIC].

determined by radioanalytical thin-layer chromatography. The R_f values TEEP for the ^{99m}Tc-mannitol complex, determined by instant thin-layer chromatography-silica gel, were 1.0 and 0.0 in 25% NaCl and acetone:water (9:1), respectively. The ^{99m}Tc-mannitol complexes were >95% radiochemically pure. The R_f for the [^{99m}Tc-mannitol-HYNIC-peptide] complex determined by instant thin-layer chromatography silica gel were 0.0 and 1.0 in 25% NaCl and acetone:water (9:1), respectively. After a 1 h incubation of ^{99m}Tc-mannitol with a solution of f-MLFK-HYNIC, the corresponding [^{99m}Tc-mannitol-f-MLFK-HYNIC] was found in >90% radiochemical purity. The addition of NS_2 to the [^{99m}Tc-mannitol-HYNIC-peptide] structure affords the [^{99m}Tc-NS_2-HYNIC-peptide] complex.

Radio-HPLC analysis of the [^{99m}Tc-mannitol-HYNIC-peptide] complex demonstrated a unique chromatographic profile as compared with the [^{99m}Tc-NS_2-HYNIC-peptide] complex. HPLC analysis of the [^{99m}Tc-NS_2-HYNIC-peptide] showed a single unique hydrophobic species with retention time greater than that of the [^{99m}Tc-mannitol-HYNIC-peptide] starting material or of [^{99m}Tc{$CH_3N(CH_2CH_2S)_2$}](μ^2-$NHNC_5H_4N$)(μ^1-NNC_5H_4N)] as shown in Figure 1.

The complex [^{99m}Tc-NS_2-HYNIC-peptide] was also prepared by the reaction of $^{99m}TcO_4^-$ with NS_2, HYNIC-peptide, and excess hydrazine sulfate. After HPLC purification, radio-HPLC analysis revealed a chromatographic profile identical to that of species **C** of Figure 1, confirming that [^{99m}Tc-NS_2-HYNIC-peptide] does not contain mannitol as an additional ancillary ligand.

Imaging Results. At 3−4 h after injection both Tc-peptide preparations displayed similar biodistribution patterns. Both preparations displayed high concentrations of radioactivity in the lung, liver, spleen, and kidney. Concentrations were lower in muscle and gastrointestinal tract.

Region of interest (ROI) analysis of the scintigraphic images are summarized in Figure 2. Representative whole-body anterior images of rabbits at 3 and 18 h after injection of [^{99m}Tc-mannitol-For-MLFK-HYNIC] and [^{99m}Tc-NS_2-HYNIC-peptide] are shown. The data demonstrate that at early imaging times both preparations yield demonstrable accumulation of radioactivity in the injected areas with no significant difference between the two preparations. At later time points both preparations displayed an increased accumulation of activity at the site of injection with the [^{99m}Tc-NS_2-HYNIC-peptide] preparation increasing significantly greater that the [^{99m}Tc-mannitol-HYNIC-peptide]. Normal organ distribution was remarkably similar in samples taken at both 3 and 18 h for both preparations.

Direct Tissue Sampling. The concentrations of radioactivity for both peptide preparations at 18 h are summarized in Figure 3. Overall, the normal organ concentrations are remarkably similar except for heart and normal muscle where the [^{99m}Tc-NS_2-HYNIC-peptide] preparation was lower and in the spleen where it was higher. There was no significant difference in accumulation in GI tract.

Table 2 summarizes the concentrations (%ID/g) of both peptides in normal muscle, infected muscle, and pus. Significantly higher concentrations of [^{99m}Tc-NS_2-HYNIC-peptide] were found in infected muscle and pus ($p < 0.01$).

Infected muscle to normal muscle and pus to normal muscle ratios obtained from direct tissue counting are summarized in Figure 4. In both cases the ratios are significantly greater for [^{99m}Tc-NS_2-HYNIC-peptide] ($p < 0.01$). The average values of the tissue concentrations of [^{99m}Tc-mannitol-HYNIC-peptide] and [^{99m}Tc-NS_2-HYNIC-peptide] in the rabbit at 3 and 18 h after intravenous injection are shown in Table 3.

Model Compounds: Synthesis and Spectroscopic Characterization Compounds. Compounds **5** and **7**−**12** were all obtained in reasonable yields by reacting [$MCl_3(NNC_5H_4NH)(NHNC_5H_4N)$] (M = Tc, Re) with the thiolate ligand, adding base, and allowing the solution to reflux in methanol for 12 h. The syntheses exploit the versatile coordination properties of the hydrazino-2-pyridine ligand which facilitates the replacement of three chlorine atoms with a tridentate ligand of dinegative charge. To balance the charge, the pyridiniumdiazenido ligand is deprotonated so as to transform from the neutral zwitterionic diazene of the parent to a diazenido-(1−) form in the product. The removal of the pyridyl proton allows the rhenium complex to coordinate to the thiolate ligands and remain in the +3 state, which is the favored oxidation state under these conditions (*41*, *43*). By employing the structural versatility of [$ReCl_3(NNC_5H_5NH)(NHNC_5H_4N)$] and the chemical robustness of the {$M(NHNC_5H_4N)(NNC_5H_4N_x)$} ($x = 0, 1$) core, the thiolate complexes have been easily prepared and isolated.

The reaction of [$ReCl_3(NNC_5H_4NH)(NHNC_5H_4N)$] with 3 equiv of bis(2,2′-ethanethiol)-*N*-methylamine in methanol and the presence of NEt_3 yields [Re{$CH_3N(CH_2CH_2S)_2$}(NNC_5H_4N)($NHNC_5H_4N$)] (**5b**) as a brown solid. Dark brown crystals were grown by slow diffusion of pentane into a mixture of **5b** in CH_2Cl_2. The chemistry of the analogous tridentate ligand, pyridine-2,6-dimethanethiol, was also investigated. Under similar reaction conditions employed in the synthesis of **5**, the resulting brown solid was identified as [Re{C_5H_3N-2,6-$(CH_2S)_2$}-(NNC_5H_4N)($NHCN_5H_4N$)]·CH_2Cl_2·0.5MeOH (**7**). The crude product was recrystallized by diffusing pentane into a mixture of **7** in CH_2Cl_2. The infrared spectrum of **7** exhibits strong to medium intensity bands at 1546 and 1500 cm^{-1} which are attributed to ν(N=N), suggesting the presence of multiple bond character. The spectrum also contains a series of bands in the 1600 to 1400 cm^{-1} range assigned to aromatic ring stretching modes ν(C=C) and ν(C=N). The ^{1}H NMR spectrum exhibited multiple ligand peaks between 6.9 and 8.6 ppm, attributed to the aromatic ring protons. In addition, the spectrum displays four sets of multiple peaks between 4.6 and 5.4 ppm attributed to the aliphatic thiolate carbon protons.

Substitution of the nitrogen donor of the thiol ligand $CH_3N(CH_2CH_2SH)_2$ with an oxygen donor provides the analogous (S−O−S) ligand, bis(2-mercaptoethyl) ether. Following an analogous synthetic procedure led to the preparation of [Re{$O(CH_2CH_2S)_2$}(NNC_5H_4N) ($NHNC_5H_4N$)] (**8**). Although dark red crystals of **8** were grown, these proved unsuitable for X-ray analysis due to severe twinning. The infrared spectrum of **8** displays a strong band at 1543 cm^{-1} in the region of ν(N=N), as well as multiple bands between 1400 and 1600 cm^{-1} attributed

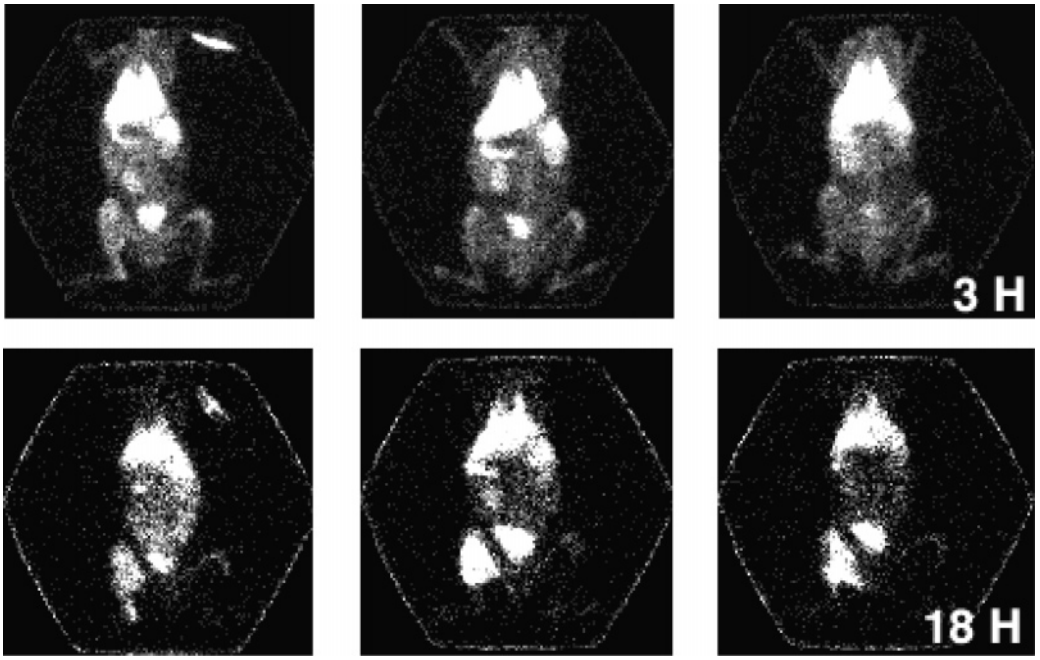

Figure 2. Representative whole-body anterior images of rabbits at 3 and 18 h after injection of [^{99m}Tc-mannitol-For-MLFK-HYNIC] and [^{99m}Tc-NS_2-HYNIC-peptide]. The animals were infected 24 h before radiopharmaceutical administration.

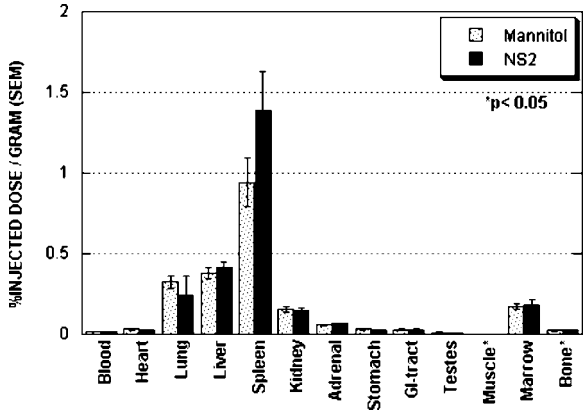

Figure 3. Average values of tissue concentration (% injected dose/g) of [^{99m}Tc-mannitol-HYNIC-peptide] and [^{99m}Tc-NS_2-HYNIC-peptide] in the rabbit at 18 h after intravenous injection (mean ± sem).

to ν(C=C) and ν(C=N). The ^{1}H NMR spectrum displays multiple aromatic protons between 6.7 and 8.4 ppm and peaks in the aliphatic region between 1.4 and 4.4 ppm.

However, substitution of the oxygen donor of $(HSCH_2CH_2)_2O$ with sulfur in the analogous (S−S−S) donor, bis-(2-mercaptoethyl) sulfide, followed by an analogous procedure as that used for the preparation of **8**, provided the cationic complex $[Re\{(SCH_2CH_2)_2S\}(NNC_5H_4NH)(NHNC_5H_4N)]^+$ as the chloride salt, compound **9**. The infrared spectrum of **9** exhibits the characteristic ν(N=N) band at 1539 cm^{-1}, and ν(C=N) and ν(C=C) bands in the 1425−1585 cm^{-1} range. The ^{1}H NMR spectrum exhibits a band at 4.32 ppm, assigned to the exchangeable α-nitrogen proton and the *N*-pyridyl proton which suggests some interconversion or equilibrium in solution.

An analogous bidentate, or "one-armed" derivative of **6**, the ligand pyridine-2-methanethiol was used to prepare $[ReCl(C_5H_4N\text{-}2\text{-}CH_2S)(NNC_5H_4N)(NHNC_5H_4N)]$ (**9**). Despite the use of 2 equiv of pyridine-2-methanethiol and exact reaction conditions employed to produce **5** and **7**−**9**, in the case of **10** the reaction results in the formation of the chloro derivative with retention of the metal-organohydrazine core. The resulting brown solid was recrystallized by diffusing pentane into a mixture of **10** in CH_2Cl_2. The infrared spectrum of **10** displays medium intensity bands at 1547 and 1496 cm^{-1} which are attributed to ν(N=N) of the organohydrazine ligands. The remainder of the spectrum is unexceptional.

The ligand pyridine-2-thiol-3-trimethylsilane was studied in order to evaluate the structural consequences of steric constraints. A solution of $[ReCl_3(\eta^1\text{-}NNC_5H_4NH)(\eta^2\text{-}NHNC_5H_4N)]$ with 2 equiv of pyridine-2-thiol-3-trimethylsilane and triethylamine in methanol was allowed to reflux for 12 h. The resulting black precipitate was obtained in high yields and allowed to air-dry. Dark red crystals of $[Re(2\text{-}SC_5H_3N\text{-}3\text{-}SiMe_3)_2(NNC_5H_4N)(NHNC_5C_5H_4N)]$ (**11**) were grown; however, once again poor crystal quality did not provide useful X-ray data. Elemental analysis confirmed that the rhenium organohydrazine core is preserved and that the rhenium-thiolate ratio is 1:2. This stoichiometry is similar to that previously observed for complexes of the $\{Re(NNR)_2\}^{n+}$ core with potentially bidentate thiolate ligands which form both mono- and bidentate attachments while preserving the {rhenium-bis-organohydrazino} core (eq 1).

$$[ReCl_3(NNC_5H_5NH)(NHNC_5H_4N)] + 2(2\text{-}HSC_5H_3N\text{-}3\text{-}SiMe_3) \Rightarrow [Re(\eta^2\text{-}2\text{-}SC_5H_3N\text{-}3\text{-}SiMe_3) \times (\eta^1\text{-}2\text{-}SC_5H_3N\text{-}3\text{-}SiMe_3) \times (NNC_5H_4N)(NHNC_5H_4N)]\ (\mathbf{11}) + 3\ HCl \quad (1)$$

The infrared spectrum of **11** possesses similar characteristics to the previously described compounds, with ν(N=N) stretches at 1565 and 1550 cm^{-1} and multiple bands between 1600 and 1400 cm^{-1} attributed to ν(C=C) and ν(C=N). It also displays a strong band at 847 cm^{-1} assigned to ν(Si=C). The room temperature ^{1}H NMR spectrum exhibits a broadened resonance for the $SiMe_3$ protons at 0.42 ppm as well as multiple peaks for the aromatic protons between 6.67 and 8.71 ppm.

Table 2. Concentrations of [^{99m}Tc-HYNIC-peptides] in Normal Muscle, Infected Muscle, and Pus Determined by Direct Measurements of Radioactivity, Mean ± SEM, $n = 6$

peptide	infected muscle[a]	pus	normal muscle[b]
[^{99m}Tc-mannitol-For-MLFK-HYNIC]	0.100 ± 0.0076	0.247 ± 0.049	0.0021 ± 0.0002
[^{99m}Tc-NS_2-For-MLFK-HYNIC]	0.180 ± 0.033	0.403 ± 0.098	0.001 ± 0.0001

[a] $p < 0.01$. [b] $p < 0.05$.

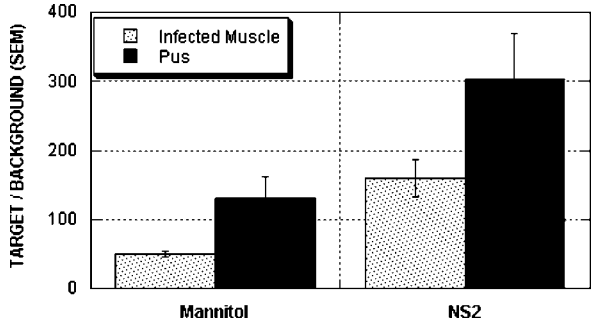

Figure 4. Average values of infected to normal muscle (open bars) and pus to normal muscle (solid bars) ratios at 18 h after injection of [^{99m}Tc-mannitol-For-MLFK-HYNIC and [^{99m}Tc-NS_2-HYNIC-peptide]. The rabbits were infected 24 h before radiopharmaceutical administration. Each value is the mean ± sem for six animals.

Table 3. Infected to Normal Tissue Ratios of [^{99m}Tc-mannitol-HYNIC-peptide] and [^{99m}Tc-NS_2-HYNIC-peptide] Determined by Region of Interest Analysis, Mean ± SEM, $n = 6$

peptide	3 h	18 h[a]
[^{99m}Tc-mannitol-For-MLFK-HYNIC]	3.906 ± 0.3155	11.886 ± 2.2053
[^{99m}Tc-NS_2-For-MLFK-HYNIC]	3.94 ± 0.69	22.40 ± 5.52

[a] $p < 0.01$.

To evaluate the effectiveness of imidazole nitrogen donors in place of pyridine nitrogen, [$ReCl_3(\eta^1$-NNC_5H_4-$NH)(\eta^2$-$NHNC_5H_4N)$] was reacted with 2.5 equiv of *N*-methyl-imidazole-2-thiol in methanol. After isolation and purification, crystals of [$Re_2(OH)Cl(SC_3H_2N_2CH_3)_2$-$(\eta^1$-$NNC_5H_4N)_2(\eta^2$-$NHNC_5H_4N)_2$] (**12**) suitable for X-ray crystallography were obtained as dark green parallels parallelepipeds in moderate yield. The infrared spectrum of **12** displays medium intensity bands at 1549 and 1498 cm^{-1}, attributed to ν(N=N) of the organohydrazine ligands. In addition, a band at 642 cm^{-1} may be associated with the bridging oxo-group ν(Re−O−Re). The ^{1}H NMR spectrum is similar to that of **9** with aromatic and imidazole protons in the 6.00−9.21 ppm range and methyl resonances at 3.23 and 3.50 ppm. The unexceptional NMR spectrum confirms the diamagnetism of **12**, which may be formally considered a Re(III) species.

To confirm that the metal-organohydrazine core can support two peptide chains, the HYNIC derivative [$ReCl_3${$NNC_5H_3NH(CO_2R)$}{$NHNC_5H_3N(CO_2R)$}] (R = H, **13a**; R = CH_3, **13b**) and the lysine-coupled analogue [$ReCl_3${$NNC_5H_3NH(CONHCH_2CH_2CH_2CH_2CH$-$(NH_2)CO_2H$}{$NHNC_5H_3N(CONHCH_2CH_2CH_2CH_2CH$-$(NH_2)CO_2H$}]·2HCl (**13**·2HCl) were prepared. Compounds **13a** and **13b** were isolated from the reaction of [NH_4][ReO_4] with 6-hydrazinonicotinic acid and HCl in MeOH. In the course of the reaction, the hydrazinonicotinic acid was esterified to produce a mixture of **13a** and the methyl ester **13b**. The infrared spectrum of **13a** exhibited medium to strong intensity bands in the 1400−1630 cm^{-1} region, characteristic of ν(N=N) and ν(C=N).

The ^{1}H NMR spectrum of **13a** reveals a characteristic pattern of four aromatic peaks in the range 8.42−9.59 ppm associated with protons of the C5 and C6 ring positions of the pyridyl substituents in two distinct chemical environments of the [$ReCl_3(NNC_5H_3RNH)$-$(NHNC_5H_3RN)$] class of compounds. The detailed analysis of the spectrum will be provided for compound **14**.

The reaction of [NH_4][ReO_4] and HYNIC-lysine, prepared as previously described, in the presence of excess HCl in methanol solution provided **14**·2HCl in good yield. The methyl ester of **14**·2HCl was also found in the reaction mixture, albeit in low yield. The infrared spectrum of **14** is unexceptional with medium to strong bands associated with ν(N=N) and ν(C=N) appearing in the 1450−1630 cm^{-1} range.

The proton and carbon NMR spectra of **14** can be fully assigned on the bases of spin−spin structure, multiplicity, ^{1}H−^{1}H COSY, and ^{1}H−^{13}C HMQC experiments (Figure 5 and Table 4). Two sets of aromatic resonances associated with the two different pyridyl ring environments are observed. A numbering scheme is provided in the inset to Figure **5**. The two doublets at 8.21 ppm (J = 2.4 Hz) and 7.31 ppm (J = 9.0 Hz) are correlated and assigned to H-4 and H-5, respectively, of one pyridyl ring. Similarly, the doublets at 8.23 ppm (J = 2.4 Hz) and 7.68 ppm (J = 9.0 Hz) were assigned to H-4′ and H-5′ of the second pyridyl ring. The H-4/H-4′ peaks are assigned as the most downfield shifted as these protons are ortho to the amide group of the lysine and are also weakly coupled to H-2 or H-2′ at 8.97 (doublet, J = 2.1 Hz) and 9.27 ppm (doublet, J = 1.8 Hz). The corresponding ^{13}C NMR peaks are seen at 116.91 and 135.40 ppm for C-5 and C-4′ and 118.31 ppm and 137.13 pp, for C-6′ and C-5′, respectively. The C-3 and C-3′ resonances appear at 147.24 and 148.41 ppm, respectively.

The ^{1}H−^{1}H COSY experiment (Figure 6) allows assignment of the two triplets at 8.65 and 8.53 ppm as NH protons adjacent to the H-6a protons of the lysine residues. The H-6a/H-6a′ protons are assigned to the intensity four peak at 3.29 ppm. The ^{1}H−^{13}C HMQC data support this assignment, as there is no corresponding carbon resonance observed for these triplets.

The peaks in the aliphatic region were also assigned. Since the lysine residues are remote from the metal coordination site, no significant chemical shift differences were observed in either the ^{1}H and ^{13}C NMR spectra for the lysine substituents on the two HYNIC-lysine moieties. The most deshielded proton H-2a is adjacent to the carboxylic group and appears as a triplet with an integrated intensity of two protons, one from each lysine residue, at 3.81 ppm. Similarly, a single peak is found in the ^{13}C NMR spectrum at 52.34 ppm for the two magnetically equivalent C2 sites.

The proton resonances in the 1.36−1.50 ppm region are assigned to the two pairs of H-4a and H-5a protons, as indicated by their coupling and by the coupling to the H-6a protons at 3.29 ppm. The remaining peak at 1.73 ppm with an integrated intensity of four protons was assigned to the two pairs of H-3a protons. The related ^{13}C NMR peaks appear at 30.04, 28.88, and 22.04 for C-3a, C-5a, and C-4a, respectively. The ^{13}C resonances of the carboxylic acid carbon atoms appear as a single peak at 171.38 ppm with a characteristic doubling of the peak intensity compared to the two unique amide car-

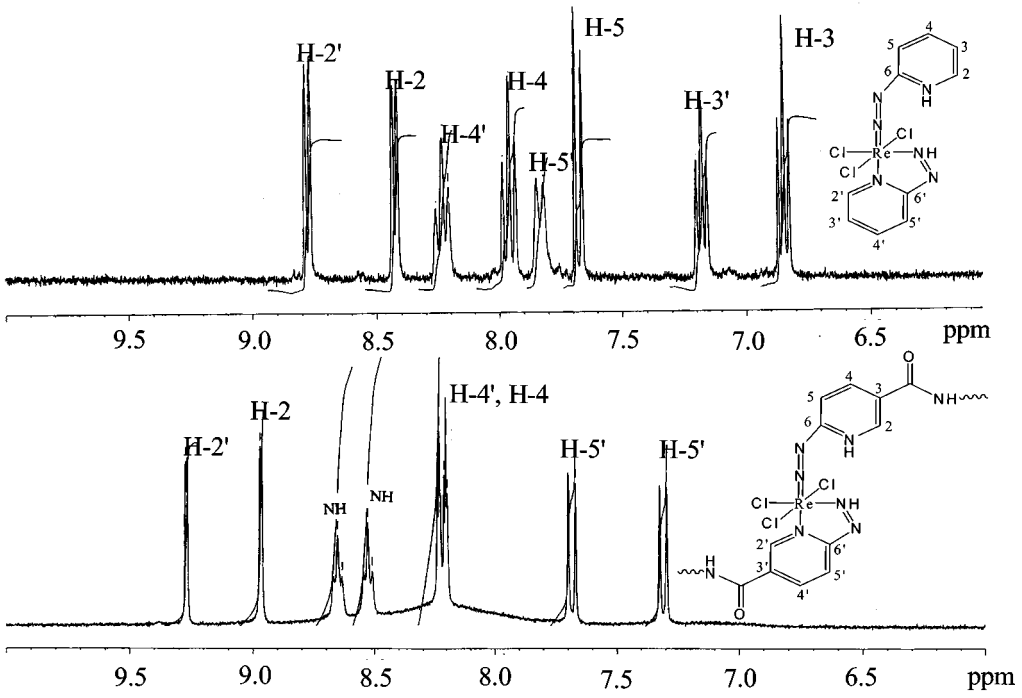

Figure 5. ^{1}H NMR spectra of $[ReCl_3(NNC_5H_4NH)(NHNC_5H_4N)]$ and **14**.

Table 4. ^{1}H NMR Data at Room Temperature for $[ReCl_3(NNC_5H_4NH)(NHNC_5H_4N)]$, 13a, and 14

compound	H-2′	H-2	H-4′	H-4	H-5′	H-5	H-3′	H-3	NH	other aliphatic protons
$[ReCl_3(NNC_5H_4NH)(NHNC_5H_4N)]$[a]	8.77 (d)	8.42 (d)	8.24 (t)	7.96 (t)	7.83 (d)	7.67 (d)	7.18 (t)	6.85 (t)		
14[a]	9.27 (d)	8.97 (d)	8.23 (d)	8.21 (d)	7.67 (d)	7.31 (d)	–	–	8.65, 8.53 (t)	3.81 (t, 2H), 3.34 (m, 2H), 1.731 (m, 4H), 1.52–1.44 (m, 10H)
13a[b]	9.61 (d)	8.80 (d)	8.65 (d)	8.41 (d)	8.26 (d)	7.71 (d)	–	–	–	–

[a] DMSO-d_6. [b] Methanol-d_4.

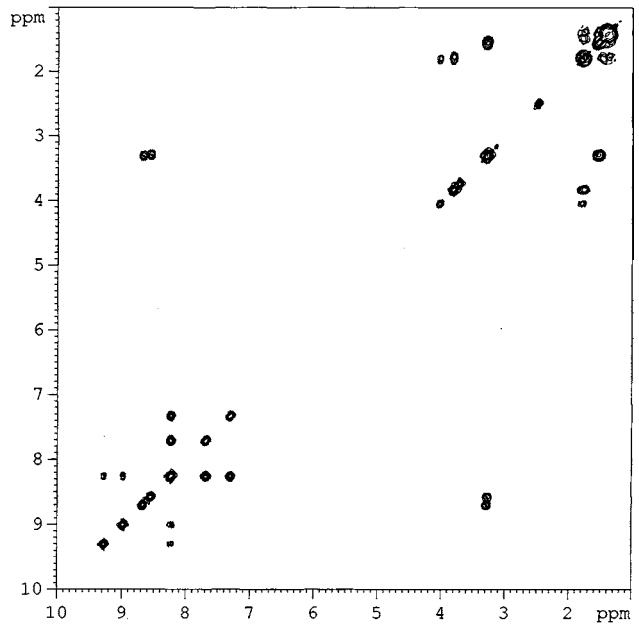

Figure 6. ^{1}H–^{1}H COSY of **14**.

bonyl carbon peaks at 163.98 and 160.23 ppm, which are inequivalent by virtue of their proximity to the chemically inequivalent pyridyl rings.

Model Compounds: X-ray Structures. The structure of $[Re\{CH_3N(CH_2CH_2S)_2\}(NNC_5H_4N)(NHNC_5H_4N)]$ (**5b**) is shown in Figure 7. The geometry about the metal is distorted octahedral, with the rhenium(III) center

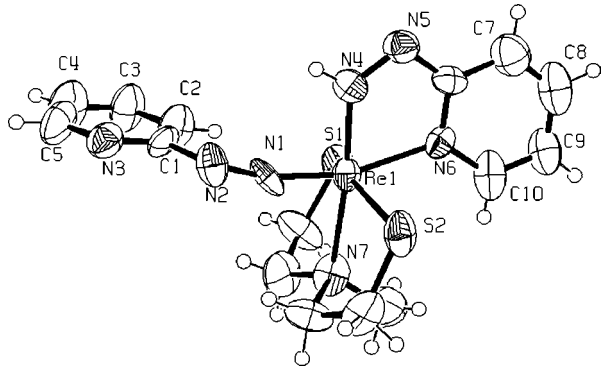

Figure 7. A view of the structure of **5**, showing the atom-labeling scheme and 50% thermal ellipsoids.

surrounded by two hydrazinopyridine ligands and one tridentate aminobisthiolate coordinated through two sulfur and one nitrogen donors. The hydrazino-2-pyridine ligands adopt two distinct binding modes: one binds exclusively through the α-nitrogen and is considered a diazenido(1−) ligand, while the second adopts a bidentate mode using the nitrogen donor of the pyridine ring as well as the α-nitrogen to chelate the metal as a neutral diazene species. The structural differences between these binding modes are quite evident in the internal bond lengths of the ligands. In the case of the diazenido(1−) ligand the Re−N1−N2 unit shows considerable multiple bond character with bond lengths of 1.78(2) Å and 1.26(2) Å for Re−N1 and N1−N2, respectively. The Re−N1−N2 bond angle is 165(2)°. In contrast, the neutral diazene species has Re−N4 and N4−N5 bond lengths of 1.94(2)

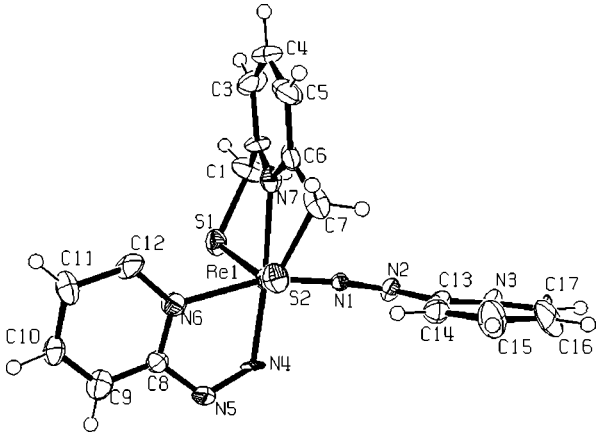

Figure 8. A view of the structure of **7**, showing the atom-labeling scheme and 50% thermal ellipsoids.

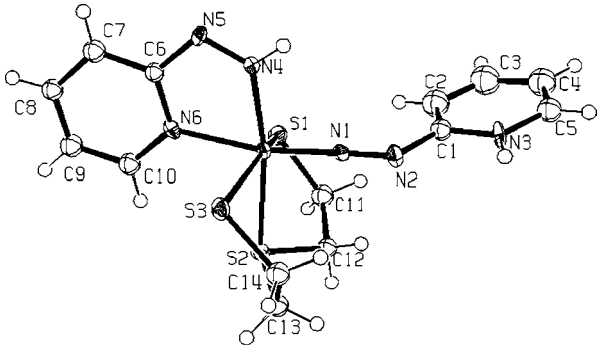

Figure 9. An ORTEP view of the structure of the complex cation of **9**, showing the atom-labeling scheme and 50% thermal ellipsoids.

Å and 1.36(2) Å, respectively. Furthermore, the Re−N6 and Re−N7 bond lengths of 2.16(2) and 2.28(2) Å, respectively, illustrate the range of Re−N single bonds and permit an internal comparison with the Re−N1 and Re−N4 multiple bonds. The average Re−S distance for **5b** is 2.39(1) Å, well within the range of other examples previously reported (*50*−*55*).

The structure of the analogous compound [Re{C_5H_3N-2,6-$(CH_2S)_2$}(NNC_5H_4N) $(NHNC_5H_4N)$] (**7**) consists of a six-coordinate rhenium(III) center with distorted octahedral geometry. The rhenium site is defined by a nitrogen from a monodentate diazenido(−1), two nitrogen donors from a bidentate neutral diazene, and two donor sulfurs and a nitrogen from the S−N−S tridentate thiolate as shown in Figure 8. The Re−N1(α-nitrogen) bond distance of 1.77(1) Å reflects the multiple bond character of the diazenido(1−) ligand and may be directly compared to the Re−N3 (pyridine nitrogen) bond length of 2.15(1) Å. Once again the chelating neutral diazene displays a short Re−N4 distance of 2.00(1) Å. The N1−N2 and N4−N5 bond lengths exhibit multiple bond character consistent with bond lengths of 1.25(2) Å and 1.28(2) Å, respectively (*56*). As anticipated the Re−S distances are similar to those observed in compound **5**, and all other metrical parameters are predictable.

Substitution of the NS_2 donor ligand of [Re{C_5H_3N-2,6-$(CH_2S)_2$}(NNC_5H_4N) $(NHNC_5H_4N)$] (**7**) by the S_3 donor $\{(SCH_2CH_2)_2S\}^{2-}$ provides [Re{$(SCH_2CH_2)_2S$} $(NNC_5H_4NH)(NHNC_5H_4N)$]Cl (**9**). As shown in Figure 9, the structure of the cationic complex consists of a six-coordinate rhenium(III) center with distorted octahedral geometry. In contrast to the structure of **7** which exhibits a monodentate diazenido(1−) ligand, the monodentate organohydrazino ligand of **9** is present as the protonated

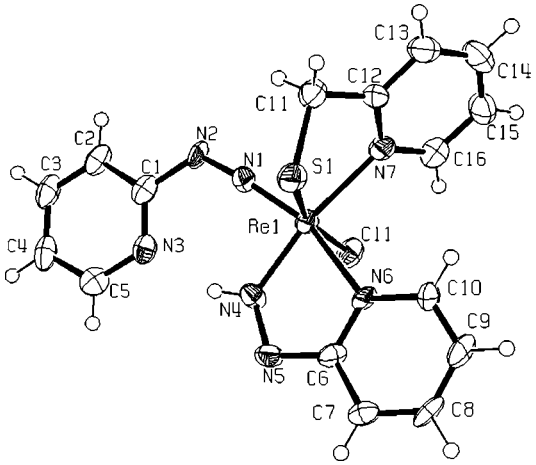

Figure 10. A view of the structure of **10**, showing the atom-labeling scheme and 50% thermal ellipsoids.

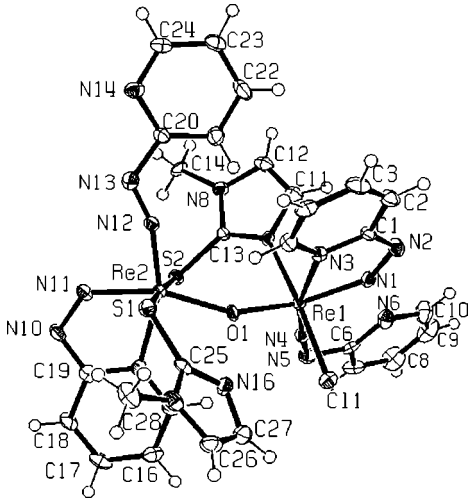

Figure 11. An ORTEP representation of the structure of **12**, showing the atom-labeling scheme and 50% thermal ellipsoids.

and neutral pyridinium-diazenido ligand. The coordination sphere is completed by the two nitrogen donors from the bidentate neutral diazene $(NHNC_5H_4N)$, and the three sulfur donors from the tridentate bis(2-mercaptoethyl)sulfide ligand. Since both organohydrazine ligands are formally neutral, the overall complex charge is +1, with the rhenium center formally in the +3 oxidation state. The Re−N1(α-nitrogen) bond distance of 1.760(9) Å reflects the multiple bond character of the pyridinium-diazenido ligand. The chelating neutral diazene exhibits unexceptional bond lengths of 1.972(8) Å and 2.129(8) Å for the Re−N4 (hydrazino-α-nitrogen) and Re−N6 (pyridine nitrogen) bonds, respectively. The Re-thiolate distances of 2.389(3) Å and 2.398(3) Å are significantly shorter than the Re-sulfide distance of 2.469(2) Å. All other metrical parameters are unexceptional.

The bidentate ligand pyridine-2-methanethiol displaces two chlorine donors of the precursor to form the chloro species [ReCl(C_5H_4N-2-CH_2S)$(NNC_5H_4N)$$(NHNC_5H_4N)$] (**10**), which are illustrated in Figure 10, and consists of a rhenium(III) center with distorted octahedral geometry defined by the sulfur and nitrogen donors of a chelating pyridine-2-methanethiol, the α-nitrogen of a monodentate pyridinediazenido(1-) ligand, the α-nitrogen, the pyridyl nitrogen of the chelating diazene, and a chloride donor.

The structure of the binuclear complex **12** is shown in Figure 11. The compound exhibits two inequivalent six-coordinate Re(III) sites, one with a $\{ReOClN_4\}$ coordina-

Table 5. Selected Bond Distances (Å) for Representative $\{Re(NNC_5H_4NH_x)(NHNC_5H_4N)\}^{n+}$ Core Complexes with Halide and Thiolate Coligands[a]

complex	η^1-M=N	η^2-M=N	η^1-N=N	η^2-N=N	M−N (pyr, amine, or imidazole)	ref
$[ReCl_3(NNC_5H_4NH)(HNNC_5H_4N)]$	1.743(8)	1.934(9)	1.241(1)	1.30(1)	2.165(7)	51
$[HNEt_3][ReCl_3(NNC_5H_4N)(HNNC_5H_4N)]$	1.756(13)	1.956(6)	1.25(2)	1.35(2)	2.170(14)	51
$[Re(C_5H_4NS)_2(NNC_5H_4)(HNNC_5H_4N)]$	1.766(6)	1.956(6)	1.239(9)	1.32(1)	2.127(5)	51
$[Re(C_4H_3N_2S)_2(NNC_5H_4)(HNNC_5H_4N)]$	1.70(3)	1.96(2)	1.27(4)	1.30(4)	2.10(2)	51
$[Re\{CH_3\text{-}N\text{-}(C_2H_4S)_2\}(NNC_5H_4N)(NHNC_5H_4N)]$ (**5b**)	1.78(2)	1.94(2)	1.26(2)	1.36(2)	2.16(2) 2.28(2)	this work
$[Re\{C_7H_3N\text{-}2,6\text{-}(CH_2S)_2\}(NNC_5H_4NH)(NHNC_5H_4N)]$ (**7**)	1.77(2)	2.00(1)	1.25(2)	1.28(2)	2.15(1) 2.21(2)	this work
$[Re\{(S_2CH_2CH_2)S\}(NNC_5H_4NH)(NHNC_5H_4N)]Cl$ (**9**)[b]	1.764(8)	1.974(9)	1.27(1)	1.32(1)	2.139(9)	this work
$[ReCl(C_5H_4N\text{-}2\text{-}CH_2S)(NNC_5H_4N)(NHNC_5H_4N)]$ (**10**)	1.783(9)	1.943(8)	1.24(1)	1.35(1)	2.160(8) 2.226(8)	this work
$[Re_3OCl(SC_3H_2N_2CH_3)_2(NNC_5H_4N)_2(NHNC_5H_4N)_2$ (**12**)	1.762(5) 1.780(5)	1.956(5) 1.966(5)	1.260(8) 1.238(7)	1.324(7) 1.338(7)	2.115(5) 2.144(5) 2.164(5)	this work
$[ReCl_3\{NNC_5H_3NH(CO_2H)\}\{NHNC_5H_3N(CO_2H)\}]$ (**13a**)	1.739(7)	1.921(7)	1.26(1)	1.34(1)	2.179(6)	this work
$[Re(SC_5H_4N)_2\{NNC_5H_3N(CO_2Me)\}\{NHNC_5H_3N(CO_2Me)\}]$ (**15**)	1.766(4)	1.937(4)	1.243(6)	1.354(6)	2.144(4) 2.172(4)	this work

[a] $x = 0$, $n = 2$; $x = 1$, $n = 3$. [b] Values are averages over the two molecular cations of the asymmetric unit.

tion geometry and the second with $\{ReOS_2N_3\}$ coordination. The coordination at the Re1 site is defined by the multiply bonded nitrogen donor of the diazenido(1-) ligand, the α-hydrazine nitrogen donor and pyridyl nitrogen donor of the bidentate and neutral diazene ligand, a nitrogen donor of an N,S-bridging thioimidazole group, a terminal chloride, and a bridging hydroxy group. The Re2 site consists of the analogous diazene nitrogen and diazenido(1-) nitrogen donors, the thiolate sulfur of a terminal, monodentate mercaptoimidazole ligand, the sulfur donor of the bridging mercaptoimidazole and the hydroxide bridge. Consequently, there are two distinct *N*-methyl-2-imidazole-thiolate groups, one monodentate and bonding only through the sulfur, while the second is bidentate and bridging. Both Re sites exhibit the common $\{Re(III)(NNR)(NHNR)\}^{+2}$ core with unexceptional metrical parameters (Table 5).

The structure of $[ReCl_3\{NNC_5H_3NH(CO_2H)\}\{NHNC_5H_3N(CO_2H)\}]$ (**13a**), shown in Figure 12, is analogous to that of the previously reported $[ReCl_3(NNC_5H_4NH)(NHNC_5H_4N)]$ (*41*). The nitrogen donors adopt the conventional meridional geometry with the chloride ligands occupying the remaining coordination sites. The metrical parameters for the $[Re(III)\{\eta^1\text{-}NNC_5H_3NH(CO_2H)\}\{\eta^2\text{-}NHNC_5H_3N(CO_2H)\}]^{2+}$ core of **13a**, listed in Table 5, are unexceptional for compounds of this family.

The structure of the 2-mercaptopyridine derivative **15** of Figure 13 is analogous to that of $[Re(NNC_5H_4N)(NHNC_5H_4N)(SC_5H_4N)_2]$ and exhibits the common distorted six coordinate $\{ReS_2N_4\}$ geometry, with the sulfur donors in a transoid orientation. The metrical parameters for **14** are similar to those previously reported for $[Re(NNC_5H_4N)(NHNC_5H_4N)(SC_5H_4N)_2]$.

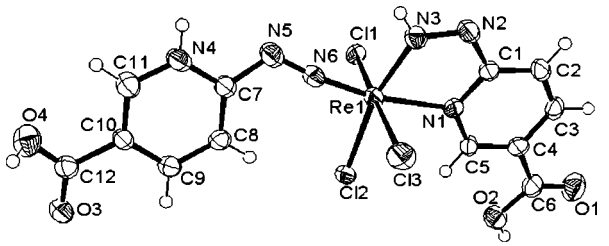

Figure 12. A view of the structure of **13a**, showing the atom-labeling scheme and 50% thermal ellipsoids.

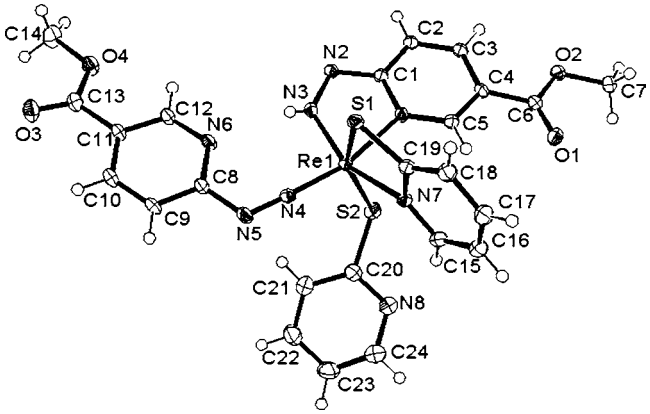

Figure 13. A view of the structure of **15**, showing the atom-labeling scheme and 50% thermal ellipsoids.

DISCUSSION

We have previously developed ^{99m}Tc-labeled HYNIC-chemotactic peptides for imaging focal sites of bacterial infections in a variety of animal models (*20b*). The results of these studies have shown that the radiometal-complexed peptides retain receptor binding affinity and biological activity in vivo, the HYNIC-chemotactic peptides are readily labeled with ^{99m}Tc at very high specific activities and are excellent radiopharmaceuticals for infection imaging. More recently, we demonstrated that the peptides localize at sites of infection predominantly by a specific f-MLF receptor-mediated mechanism (*20a*). These data indicate that ^{99m}Tc-labeled HYNIC-chemotactic peptides satisfy some of the criteria for "ideal" infection imaging agents: rapid localization and retention at the site of infection and concentrations in normal tissues which remain constant or decrease with time and displaying no biological effects.

As previous studies have demonstrated, ^{99m}Tc-mannitol gives superior imaging results when used as the starting species (or coligand) to label formyl-MLFK-HYNIC, as compared with other polyhydric coligands. However, radio-HPLC indicated the presence of several radioactive species. We are interested in producing [^{99m}Tc-HYNIC-peptides] as homogeneous radiochemical species in an effort to generate a well-defined chemical entity and simplify formulation and mechanistic studies.

With the aim of limiting radiochemical speciation of [^{99m}Tc-HYNIC-peptides] radiochemical species with more predictable radiochemical and biological properties, we previously investigated bidentate amino-thiol ligands,

pyrimidinethiols, and pyridinethiols as coligands. The effectiveness of mixed nitrogen/sulfur polydentate ligands in the design of ^{99m}Tc radiopharmaceuticals is well-documented for the N_3S (*57*), N_2S_2 (*58*), and even the NS_2 (*59*) and S_4 (*60*) donor sets. Previous work at the 'carrier' level showed these ligands form stable and reproducible complexes with Tc-hydrazinopyridine. To this end, we investigated the potential of pyrimidinethiols and pyridinethiols as coligands.

These ligands resulted in an improved radiochemical formulation by limiting the number of radiochemical species observed with reverse phase HPLC. However, the use of these ligands resulted in undesirable significant GI tract accumulation.

Tridentate ligands, such as NS_2, may constrain the possible coordination geometries and improved overall stability. To investigate this, we synthesized NS_2, converted the [^{99m}Tc-mannitol-For-MLFK-HYNIC] to the corresponding NS_2-containing complex [^{99m}Tc-NS_2-For-MLFK-HYNIC], and compared its infection imaging and biodistribution properties with [^{99m}Tc-mannitol-For-MLFK-HYNIC]. The biological distribution of the [^{99m}Tc-NS_2-HYNIC-peptide] was remarkably similar to that of the [^{99m}Tc-mannitol-HYNIC-peptide] in most tissues. Slightly greater concentrations were found in spleen and marrow though not significant. Less accumulation was noted in normal muscle ($p < 0.05$).

Perhaps most remarkable was the increase in accumulation in the infected muscle and pus. The [^{99m}Tc-NS_2-HYNIC-peptide] accumulated to almost twice the level of the [^{99m}Tc-mannitol-HYNIC-peptide] in these tissues ($p < 0.01$). This accounted for the much higher target/background ratios observed with gamma camera imaging. Target-to-background ratios are enhanced as well by reduction in normal muscle concentrations.

The improvement in target accumulation and background reduction has resulted in an improved entity for imaging infection. The reasons for this are not completely clear. However, based on the structural studies of the model compounds **5a** and **5b**, several mechanisms may be invoked to account for the superior biological properties.

First, the structures of the model coordination compounds suggest that the peptides (not the α-nitrogens atoms of the HYNIC moieties) adopt a trans orientation. This minimizes steric interface of the two peptides with each other and may allow either peptide access to the formyl-MLF receptor. If the peptides were cis to each other they may interfere with bonding to the receptor by interacting with each other or by sterically blocking the approach of the other to the receptor. This speculation has yet to be proven; however, the fact that the α-nitrogen of HYNIC will not coordinate trans to the α-nitrogen of a second HYNIC would dispose the peptides in a mutually trans arrangement.

Furthermore, the improvement in biological behavior may be derived from the likelihood that in vivo ligand substitution (via glutathione or cysteine) is unfavorable due to the tridentate nature of NS_2. Previous work with the bidentate pyridinethiol and pyrimidinethiol showed two pyridinethiol ligands attached to the metal core: one bidentate and one monodentate through the sulfur. The monodentate pyridinethiol is potentially labile due to the single attachment mode and the trans influence of the sulfur from the bidentate pyridinethiol. On the other hand, the NS_2 ligand may enhance the persistence of the complex by adopting a meridional coordination mode for a tridentate chelate.

Scheme 3. Proposed Structure of [Tc(tricineH_2)-{$P(C_6H_4SO_3Na)_3$}(HYNIC-peptide)]

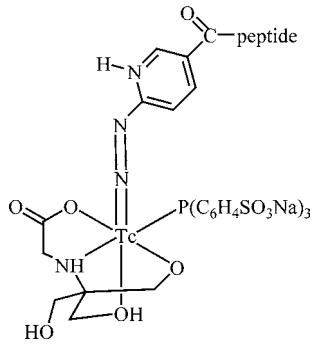

The model studies not only confirm the persistence and chemical robustness of the {$Re(NNC_5H_4NH_x)(NH_yNC_5H_4N)\}^{n+}$ ($x = 0$ or 1; $y = 0$ or 1) core but also illustrate that the flexibility of the core with respect to protonation and overall charge allows the rhenium center to maintain the favorable +3 formal oxidation state in a variety of ligand environments. The chloride coligands of the $[ReCl_3(NNC_5H_4NH)(NHNC_5H_4N)]$ precursor are readily displaced by multidentate thiolate ligands to give chemically robust complexes while maintaining the {$Re(HNNC_5H_4N)(NNC_5H_4NH)\}^{+3}$ core. It is anticipated that the weakly coordinated polyhydric ligands commonly employed in tracer scale chemistry with Tc or Re would also be readily displaced by such effective chelators.

On the other hand, despite the robust nature of the Re- and Tc-HYNIC linkage and the persistence of the {$M(\eta^1\text{-}NNC_5H_3NR)(\eta^2\text{-}NHNC_5H_3NR)\}$ core on the macroscopic scale, definitive characterization of the Re complex with N-For-MLF(N^{ϵ}-HYNIC)K was not achieved as a consequence of the insolubility of the products if the reactions of ReO_4^- with N−For-MLF(N^{ϵ}-HYNIC) K or of **13a** with N-For-MLF. Consequently, unambiguous evidence for the 2:1 HYNIC-peptide:M formulation even on the macroscopic scale remains elusive. Since the alternative formulation with the Tc:HYNIC ratio of 1:1 cannot be totally eliminated, the improvement in target accumulation and background reduction of [^{99m}Tc-NS_2-HYNIC-peptide] may be the consequence of molecular volume and charge considerations, rather than involvement of two peptide pendants on the complex.

Furthermore, it is apparent from the general coordination chemistry of oxometalate species with organohydrazine ligands that the method of synthesis, as well as the nature of the coligands, can profoundly influence the identity of the product (*61*−*63*). For example, in the presence of phosphine ligands, chelating organohydrazine ligands yield monosubstituted complexes, such as $[MCl_2(NNCOC_6H_5)(PPh_3)_2]$ rather than materials with the {$M(\eta^1\text{-}NNC_5H_3NR)(\eta^2\text{-}NHNC_5H_3NR)\}^{2+}$ core (*64*, *65*). Consequently, it is not surprising that under different reaction conditions, the ^{99m}Tc complex [Tc(tricineH_2)-{$P(C_6H_4SO_3Na)_3$}(HYNIC-peptide)], shown in Scheme 3, has been proposed (*66*−*68*). While the mass spectrometry data and other details of the study are quite convincing for the Tc:HYNIC ratio of 1:1 in this case, the details of the structure are more controversial. Hydrazinopyridine is a highly effective chelating ligand, while the tricine amine, carboxylate and alkoxide donors are not particularly suitable for technetium in this oxidation state (*42*). It is more likely that the HYNIC subunit coordinates in a chelating fashion, displacing one of tricine donors. In fact, the mode of tricine coordination remains unresolved, as does the degree of deprotonation under physiological conditions. It is also noteworthy that all attempts to

prepare ^{99}Tc analogues of these phosphine derivatives on a macroscopic scale produced only intractable mixtures. Similarly, reactions of $\{M(\eta^1\text{-}NNC_5H_3NR)(\eta^2\text{-}NHNC_5H_3NR)\}^{2+}$ core model compounds of ^{99}Tc and Re with tricine yield uncharacterizable materials.

A final complication is the tendency of metal-organohydrazine complexes to form oligomers in donor solvents (*69*). This characteristic is reflected in the binuclear structure of **11**, as well as the tetranuclear species $[Re(\eta^1\text{-}NNC_4H_3N_2)(\eta^2\text{-}NHNC_4H_3N_2)(OCH_3)_2]_4$ and $[Re(\eta^1\text{-}NNC_5H_4N)(\eta^2\text{-}NHNC_5H_4N)(OH)_2]_4$ isolated from methanol and water, respectively (*70*).

CONCLUSION

In conclusion we have prepared model [Re(Tc)-NS_2-bis(HYNIC)] complexes and [^{99m}Tc-NS_2-peptides]. The model studies confirm that complexes with the $\{M(\eta_1\text{-}NNR)(\eta_2\text{-}NHNR)\}$ core, such as $[MCl_3(NNC_5H_4NH)(NHNC_5H_6N)]$ (M = Tc, Re), react smoothly with bis(mercaptoethyl)methylamine (NS_2) to yield $[M\{CH_3N(CH_2CH_2S)_2\}(NNC_5H_4N)(NHNC_5H_4N)]$. Complexes of this class are remarkable robust chemical species and, furthermore, demonstrate the persistence of the M-HYNIC core $\{M(\eta^1\text{-}NNR)(\eta^2\text{-}NHNR)\}$ under the conditions of this study. The NS_2 functions as a more effective coligand to this core than the commonly used polyhydroxylic ligands by virtue both of its geometric and steric constraints and of the strong preference of Tc(V) and Re(V) for thiolate coordination rather than alkoxy coordination. The coordination preferences of the thiolate donors dictate a meridional disposition of the NS_2 ligand about a metal site with the $\{M(\eta^1\text{-}NNR)(\eta^2\text{-}NNR)\}$ core. Consequently, substituents such as peptide chains attached to the HYNIC ligands will adopt a *transoid* orientation which may endow the material with enhanced biological properties. Thus, with respect to biological activity, the [Tc-NS_2-HYNIC-peptide] shows superior imaging and target accumulation as compared with less robust coligand systems we have previously studied.

On the other hand, while the HYNIC approach has proved successful in applications to infection imaging and appears to be a versatile technology for the labeling of a variety of biomolecules, it is now evident that, despite years of extensive investigations by a number of groups, HYNIC-based imaging agents are poorly characterized at the tracer level and, in some cases, even the ^{99m}Tc and Re analogues remain structurally elusive. Furthermore, since the synthesis of the HYNIC-peptide conjugate is quite involved and the coordination/coligand chemistry introduces additional synthetic and structural complexities, the commercial viability of the technology remains in question.

ACKNOWLEDGMENT

The work at Syracuse University was supported by a grant from the Department of Energy Office of Health and Environmental Research (DE-FG02-99ER62791).

Supporting Information Available: Tables of experimental conditions, atomic positional parameters and isotropic thermal parameters, bond lengths and angles, anisotropic thermal parameters and hydrogen atom positions for the structural studies of **5**, **7**, **9**, **10**, **11**, **13a**, and **15** in CIF format. This material is available free of charge via the Internet at http://pubs.acs.org.

LITERATURE CITED

(1) Dilworth, J. R., and Parrott, S. J. (1998) The biomedical chemistry of technetium and rhenium. *Chem. Soc. Rev. 27*, 43−55.

(2) Hom, R. K., and Katzenellenbogen, J. A. (1997) Technetium-99m-labeled receptor-specific small-molecule radiopharmaceuticals: recent developments and encouraging results. *Nucl. Med. Biol. 24*, 485−498.

(3) Eckelman, W. C. (1995) Radiolabeling with technetium-99m to study high-capacity and low-capacity biochemical systems. *Eur. J. Nucl. Med. 22*, 249−263 and references therein.

(4) Schwochan, K. (1994) Technetium Radiopharmaceuticals − Fundamentals, Synthesis, Structure, and Development. *Angew. Chem., Int. Ed. Engl. 33*, 2258−2267.

(5) Jurisson, S., Berning, D., Jia, W., and Ma, D. (1993) Coordination compounds in nuclear medicine. *Chem. Rev. 93*, 1137−1156.

(6) (a) Nicolini, M., Bandoli, G., and Mazzi, U., Eds. (1990) *Technetium and Rhenium in Chemistry and Nuclear Medicine*, Raven Press, New York. (b) Deutsch, E., Nicolini, M., and Wagner, H. N., Eds. (1983) *Technetium in Chemistry and Nuclear Medicine*, Cortina International Verona, Italy.

(7) Steigman, J., and Eckelman, W. (1992) *The Chemistry of Technetium in Medicine*, National Academy Press, Washington, D.C.

(8) Pinkerton, T. C., Desilets, C. P., Hoch, D. J., Mikelsons, M. V., and Wilson, G. M. (1985) Bioinorganic activity of technetium radiopharmaceuticals. *J. Chem. Educ. 62*, 965−973.

(9) Deutsch, E., Libson, K., Jurisson, S., and Lindoy, L. F. (1983) Technetium chemistry and technetium radiopharmaceuticals. *Prog. Inorg. Chem. 30*, 75−139.

(10) Special issue on Tc: *Int. J. App. Radiat. Isot.* (1982) *33*.

(11) Deutsch, E. (1979) Inorganic radiopharmaceuticals. *Radiopharmaceuticals II*, pp 129−146, Society of Nuclear Medicine Publishers, New York.

(12) Deutsch, E., and Libson, K. (1984) Recent advances in technetium chemistry: bridging inorganic chemistry and nuclear medicine. *Comments Inorg. Chem. 33*, 83−103.

(13) Liu, S., Edwards, D. S., and Barrett, J. A. (1997) 99mTc Labeling of Highly Potent Small Peptides. *Bioconjugate Chem. 8*, 621−636.

(14) Clark, M. J., and Podlielski, L. (1987) Medical Diagnostic Imaging with Complexes of ^{99m}Tc. *Coord. Chem. Rev. 78*, 253−231.

(15) Pearlstein, R. M., Lock, C. L. J., Faggiani, R., Costello, C. E., Zeng, C. H., Jones, A. G., and Davison, A. (1988) Synthesis and characterization of technetium(V) complexes with amine, alcoholate, and chloride ligands. *Inorg. Chem. 27*, 2409−2413 and references therein.

(16) Konno, T., Kirckhoff, J. R., Hieneman, W. R., and Deutsch, E. (1989) Thiolato-technetium complexes. 2. Synthesis, characterization, electrochemistry, and spectroelectrochemistry of the technetium(III) complexes trans-$[Tc(SR)_2(DMPE)]^+$, where R is an alkyl or benzyl group and DMPE is 1,2-bis(dimethylphosphino)ethane. *Inorg. Chem. 28*, 11745−1179. Konno, T., Heeg, M. J., and Deutsch, E. (1989) Thiolato-technetium complexes. 3. Synthesis and X-ray structural studies on the geometrical isomers cis- and trans-bis(*p*-chlorobenzenethiolato)bis(1,2-bis(dimethylphosphino)ethane) technetium(II). *Inorg. Chem. 28*, 1694−1700 and references therein.

(17) O'Neil, J. P., Carlson, K. E., Anderson, C. J., Welch, M. J., and Katzenellenbogen, J. A. (1994) Progestin radiopharmaceuticals labeled with technetium and rhenium: synthesis, binding affinity, and in vivo distribution of a new progestin N2S2-metal conjugate. *Bioconjugate Chem. 5*, 182−193.

(18) See for example: (a) Welch, M. J., Downer, J. B., and Katzenellenbogen, J. A. (1996) *Current Directions in Radiopharmaceutical Research and Development* (Mather, S. J., Ed.) p 137, Kluwer Academic Press, Netherlands. (b) Spies, H., Glaser, M., Pietzach, H.-J., Hahn, F. E., and Liigger, T. (1995) Synthesis and reactions of trigonal-bipyramidal rhenium and technetium complexes with a tripodal, tetradentate NS_3 ligand. *Inorg. Chim. Acta 240*, 465−478. (c) Kung, H. F., Kim, H.-J., Dung, M. P., Miegalla, S. K., Plössl, K., and Lee, H.-K. (1996) Imaging of dopamine transporters in humans with technetium-99m TRODAT-1. *Eur. J. Nucl. Med. 23*, 1527−1530. (d) Baidoo, K. E., Lin, K.-S., Zhan, Y., Finley, P., Scheffel, U., and Wagner, H. N., Jr. (1995) Design, Synthesis, and Initial Evaluation of High-Affinity Technetium Bombesin Analogs. *J. Nucl. Med. 36*, 28. (e)Vera, D. R., and

Eckelman, W. C. (1984) Receptor 1980 and Receptor 2000: twenty years of progress in receptor-binding radiotracers. *Radiology 151*, 191. (f) Chi, D. Y., O'Neil, J. P. O., Anderson, C. J., Welch, M. J., and Katzenellenbogen, J. A. (1994) Homodimeric and heterodimeric bis(amino thiol) oxometal complexes with rhenium(V) and technetium(V). Control of heterodimeric complex formation and an approach to metal complexes that mimic steroid hormones. *J. Med. Chem. 37*, 928−937. (g) O'Neil, J. P., Wilson, S. R., and Katzenellenbogen, J. A. (1994) Preparation and structural characterization of monoamine-monoamide bis(thiol) oxo complexes of technetium(V) and rhenium(V). *Inorg. Chem. 33*, 319−323. (h) Chi, D. Y., and Katzenellenbogen, J. A. (1993) Selective formation of heterodimeric bis-bidentate aminothiol-oxometal complexes or rhenium(V). *J. Am. Chem. Soc. 115*, 7045−7046.

(19) (a) Schwartz, D. A., Abrams, J. J., Hansen, M. M., Gaul, F. E., Larsen, S. K., Rauh, D., and Zubieta, J. (1991) Preparation of hydrazino-modified proteins and their use for the synthesis of technetium-99m-protein conjugates. *Bioconjugate Chem. 2*, 33−36. (b) Abrams, M. J., Juweid, J., ten Kate, C. I., Schwartz, D. A., Hauser, M. M., Gaul, F. E., Fucello, A. J., Rubin, R. H., Strauss, H. W., Zubieta, J., and Fischman, A. J. (1990) Technetium-99m-human polyclonal IgG radiolabeled via the hydrazino nicotinamide derivative for imaging focal sites of infection in rats. *Nucl. Med. 31*, 2002−2008.

(20) (a) Fischman, A. J., Babich, J. W., and Strauss, H. W. (1993) A ticket to ride: peptide radiopharmaceuticals. *J. Nucl. Med. 34*, 2176−2181. (b) Fischman, A. J., Solomon, H. F., Babich, J. W., Abrams, M. J., Callahan, R. J., Strauss, H. W., and Rubin, R. H. (1994) Imaging of focal sites of inflammation in rhesus monkeys with 99mTc-labeled human polyclonal IgG. *J. Nucl. Med. 34*, 1964−1974. (c) Fischman, A. J., Babich, J. W., and Rubin, R. H. (1994) Infection imaging with technetium-99m-labeled chemotactic peptide analogues. *Semin. Nucl. Med. 24*, 154−168. (d) Babich, J. W., and Fischman, A. J. (1995) Targeted imaging of focal sites of infection. *Handbook of Targeted Delivery of Imaging Agents*, pp 25−30, CRC Press, Boca Raton, FL. (e) Babich, J. W., Graham, W., Barrow, S. A., and Fischman. A. J. (1995) Comparison of the infection imaging properties of a 99mTc labeled chemotactic peptide with 111In IgG. *Nucl. Med. Biol. 22*, 643−648. (f) Babich, J. W., and Fischman, A. J. (1995) Effect of "co-ligand" on the biodistribution of 99mTc-labeled hydrazino nicotinic acid derivatized chemotactic peptides. *Nucl. Med. Biol. 22*, 25−30. (g) Babich, J. W., Graham, W., Barrow, S. A., and Fischman, A. J. (1995) Comparison of the infection imaging properties of a 99mTc labeled chemotactic peptide with 111In IgG. *Nucl. Med. Biol. 22*, 643−648.

(21) (a) Liu, S., Edwards, D. S., Looby, R. J., Harris, A. R., Poirier, M. J., Barrett, J. A., Hemingway, S. J., and Carroll, T. R. (1996) Labeling a Hydrazino Nicotinamide-Modified Cyclic IIb/IIIa Receptor Antagonist with ^{99m}Tc Using Aminocarboxylates as Coligands. *Bioconjugate Chem. 7*, 63−71. (b) Edwards, D. S.; and Li, S. (1998) Literature highlights − 45. 99mTc-labeling of hydrazinonicotinamide (HYNIC) modified highly potent small molecules: problems and solutions. *Trans. Met. Chem. 22*, 425−426. (c) Barrett, J. A., Croher, A. C., Damphouse, D. J., Hemingway, S. J., Liu, S., Edwards, D. S., Harris, A. P., Looby, R. J., Lazewatsky, J. L., Kagan, M., Mazaika, T. J., and Carroll, T. R. (1997) Biological Evaluation of Thrombus Imaging Agents Utilizing Water Soluble Phosphines and Tricine as Coligands When Used To Label a Hydrazinonicotinamide-Modified Cyclic Glycoprotein IIb/IIIa Receptor Antagonist with 99mTc. *Bioconjugate Chem. 8*, 155−160. (d) Liu, S., Edwards, S., Harris, A. P., Hemingway, S. J., and Barrett, J. A. (1999) Technetium Complexes of a Hydrazinonicotinamide-Conjugated Cyclic Peptide and 2-Hydrazinopyridine: Synthesis and Characterization. *Inorg. Chem. 38*, 1326−1335 and references therein.

(22) (a) Hnatowich, D. J., Mardirossian, G., Rusckowski, M., Fogarasi, M., Virzi, F., and Winnard, P. (1993) Directly and indirectly technetium-99m-labeled antibodies—a comparison of in vitro and animal in vivo properties. *J. Nucl. Med. 34*, 109−119. (b) Kolan, H., Li, J., and Thakur, M. L. (1996) Sandostatin labeled with 99mTc: in vitro stability, in vivo validity and comparison with 111In-DTPA-octreotide. *Compd Radiopharm. 9*, 144−150. (c) Classens, R. A., Boerman, O. C., Koenders, E. B., Oyen, W. J., van der Meer, J. W., and Corstens, F. H. (1996) Technetium-99m labelled hydrazinonicotinamido human nonspecific polyclonal immunoglobulin G for detection of infectious foci: a comparison with two other technetium-labelled immunoglobulin preparations. *Eur. J. Nucl. Med. 23*, 414−421. (d) Verbeke, K., Hjelstuen, O., Debrock, E., Cleynhens, B., De Roo, M., and Verbruggen, A. (1995) Comparative evaluation of 99Tcm-HYNIC-HSA and 99Tcm-MAG3-HSA as possible blood pool agents. *Nucl. Med. Commun. 16*, 942−957. (e) Claessens, R. A., Koenders, E. B., Oyen, J. J. G., and Corstens, F. H. (1996) Retention of technetium-99m in infectious foci in rats after release from technetium-99m-labeled human nonspecific polyclonal immunoglobulin G: A dual-label study with hydrazinonicotinamido and iminothiolano immunoglobulin. *Eur. J. Nucl. Med. 23* (11), 1536−1539. (f) Claessens, R. A., Boerman, O. C., Koenders, E. B., Oyen, W. J., van der Meer, J. W., and Corstens, F. H. (1996) Technetium-99m labeled hydrazinonicotinamido human nonspecific polyclonal immunoglobulin G for detection of infectious foci: A comparison with two other technetium-labeled immunoglobulin preparations. *Eur. J. Nucl. Med. 23* (4), 414−421. (g) Hnatowich, D. J., Mardirossian, G., Fogarasi, M., Sano, T., Smith, C. L., Cantor, C. R., Rusckowski, M., and Winnard, P., Jr. (1996) Comparative properties of a technetium-99m-labeled single-stranded natural DNA and a phosphorothioate derivative in vitro and in mice. *J. Pharmacol. Exp. Ther. 276* (1), 326−334. (h) Hnatowich, D. J., Winnard, P., Jr., Virzi, F., Fogarasi, M., Sano, T., Smith, C. L., and Cantor, C. R. (1995) Technetium-99m labeling of DNA oligonucleotides. *J. Nucl. Med. 36* (12), 2306−2314. (i) Lei, K., Rusckowski, M., Chang, F., Qu, T., Mardirossian, G., and Hnatowich, D. J., (1996) Technetium-99m antibodies labeled with MAG3 and SHNH: An in vitro and animal in vivo comparison. *Nucl. Med. Biol. 23* (7), 917−922. (j) Verbeke, K., Hjelstuen, O., Debrock, E., Cleynhens, B., de Roo, M., and Verbruggen, A. (1995) Comparative evaluation of 99Tcm-HYNIC-HSA and 99Tcm-MAG3-HSA as possible blood pool agents. *Nucl. Med. Commun. 16* (11), 942−957. (k) Lister-James, J., Moyer, B. R., and Dean, R. T. (1997) Pharmacokinetic considerations in the development of peptide-based imaging agents. *J. Nucl. Med. 41*, 111−118.

(23) Kemerink, G. J., Liu, X., Kieffer, D., Ceyssens, S., Mortelmans, L., Verbruggen, A. M., Steinmetz, N., Green, A., and Verbeke, K. (2003) Safety, biodistribution, and dosimetry of 99mTc-HYNIC-annexin V, a novel human recombinant annexin V for human application. *J. Nucl. Med. 44*, 947−952 and references therein.

(24) Decristoforo, C., Mather, S. J., Cholewinski, W., Donnemiller, E., Riccabona, G., and Moncayo, R. (2000) 99mTc-EDDA/HYNIC-TOC: A new 99mTc-labeled radiopharmaceutical for imaging somatostatin receptor-positive tumours: First clinical results and intra-patient comparison with 111In-labeled octreotide derivatives. *Eur. J. Nucl. Med. 27*, 1318−1325 and references therein.

(25) Laverman, R., Dams, E. Th. M., Oyen, W. J. O., Storm, G., Koenders, E. B., Prevost, R., van der Meer, J. W. M., Corstens, F. H. M., and Boerman, O. C. (1999) A novel method to label liposomes with 99mTc by the hydrazino nicotinyl derivative. *J. Nucl. Med. 40* 192−197.

(26) Zhang, Y. M., Liu, N., Zhu, Z. H., Rusckowski, M., and Hnatowich, D. (2000) Influence of different chelators (HYNIC, MAG3 and DTPA) on tumor cell accumulation and mouse biodistribution of technetium-99m labeled to antisense DNA. *Eur. J. Nucl. Med. 27*, 1700−1707 and references therein.

(27) Guo, W., Hinkle, G. H., and Lu, R. J. (1999) 99mTc-HYNIC-folate: a novel receptor-based targeted radiopharmaceutical for tumor imaging. *J. Nucl. Med. 40*, 1563−1569.

(28) Ono, M., Arano, Y., Mukai, T., Fujioka, Y., Ogawa, K., Uehara, T., Namba, S., Saga, T., Konishi, J., and Saji, H. (2001) 99mTc-HYNIC-derivatized ternary ligand complexes for 99mTc-labeled polypeptides with low in vivo protein binding. *Nucl. Med. Biol. 28*, 215−224.

(29) (a) Liu, S. (2004) The role of coordination chemistry in the development of target-specific radiopharmaceuticals. *Chem.*

Soc. Rev. 33, 445−461 and references therein. (b) Liu, S., Edwards, D. S., Ziegler, M. C., Harris, A. R., Hemingway, S. J., and Barrett, J. A. (2001) 99mTc-Labeling of a Hydrazinonicotinamide-Conjugated Vitronectin Receptor Antagonist Useful for Imaging Tumors. *Bioconjugate Chem. 12*, 642−629. (c) Liu, S., Harris, A. R., Williams, N. E., and Edwards, D. S. (2002) 99mTc-Labeling of a Hydrazinonicotinamide-Conjugated LTB4 Receptor Antagonist Useful for Imaging Infection and Inflammation. *Bioconjugate Chem. 13*, 902−913.

(30) Hugli, T. E. (1989) Chemotaxis. *Curr. Opin. Immunol. 2*, 19−27.

(31) Fischman, A. J., Pike, M. C., Kroon, D., Fucello, A. J., Rexinger, D., ten Kate, C., Wilkson, R., Rubin, R. H., and Strauss, H. W. (1991) Imaging focal sites of bacterial infection in rats with indium-111-labeled chemotactic peptide analogs. *J. Nucl. Med. 32*, 483−491.

(32) Showell, H. J., Freer, R. J., Zigmond, S. H., Schiffmann, E., Aswanikumar, S., Corcoran, B., and Becker, E. L. (1976) The structure−activity relations of synthetic peptides as chemotactic factors and inducers of lysosomal secretion for neutrophils. *J. Exp. Med. 143*, 1154−1169.

(33) Schiffmann, E., Corcoran, B. A., and Wahl, S. M. (1975) N-formylmethionyl peptides as chemoattractants for leucocytes. *Proc. Natl. Acad. Sci. U.S.A. 72*, 1059−1062.

(34) Williams, L. T., Snyderman, R., Pike, M. C., and Lefkowitz, R. J. (1977) Specific receptor sites for chemotactic peptides on human polymorphonuclear leukocytes. *Proc. Natl. Acad. Sci. U.S.A. 74*, 1204−1208.

(35) Snyderman, R., and Verghese, M. W. (1987) Leukocyte activation by chemoattractant receptors: roles of a guanine nucleotide regulatory protein and polyphosphoinositide metabolism. *Rev. Infect. Dis. 9*, S562−S569.

(36) Fletcher, M. P., Seligman, B. G., and Gallin, J. I. (1988) Correlation of human neutrophil secretion, chemoattractant receptor mobilization, and enhanced functional capacity. *J. Immunol. 128*, 941−948.

(37) Niedel, J., Wilkinson, S., and Cuatrecasas, P. (1979) Receptor-mediated uptake and degradation of 1251-chemotactic peptide by human neutrophils. *J. Biol. Chem. 254*, 10700−10706.

(38) Edwards, D. S., and Liu, S. (2001) Tc-99m-labeled small biomolecules as potential radiopharmaceuticals for infection and inflammation imaging. *Drugs Future 26*, 375−382.

(39) Tzen, K. Y., Oster, Z. H., Wagner, H. N., and Tzan, M. F. (1980) Role of iron-binding proteins and enhanced capillary permeability on the accumulation of gallium-67. *J. Nucl. Med. 21*, 31−35.

(40) Niedel, J., Davis, J., and Cuatrecasas, P. (1980) Covalent affinity labeling of the formyl peptide chemotactic receptor. *J. Biol. Chem. 255*, 7063−7066.

(41) Rose, D. J., Maresca, K. P., Nicholson, T., Davison, A., Jones, A. G., Babich, J., Fischman, A., Graham, W., DeBord, J. R. D., and Zubieta, J. (1998) Synthesis and Characterization of Organohydrazino Complexes of Technetium, Rhenium, and Molybdenum with the $\{M(\mu^1\text{-}H_xNNR)(\mu^2\text{-}H_yNNR)\}$ Core and Their Relationship to Radiolabeled Organohydrazine-Derivatized Chemotactic Peptides with Diagnostic Applications. *Inorg. Chem. 37*, 2701−2716.

(42) Babich, J. W., Coco, W. G., Barrow, S., Fischman, A. J., Femia, F. J., and Zubieta, J. (2000) 99mTc-labeled chemotactic peptides: influence of coligand on distribution of molecular species and infection imaging properties. Synthesis and structural characterization of model complexes with the $\{Re(\mu^2\text{-}HNNC_5H_4N)(\mu^1\text{-}NNC_5H_4N)\}$ core. *Inorg. Chim. Acta 309*, 123−136.

(43) Nicholson, T., Cook, J., Davison, A., Rose, D. J., Maresca, K. P., Zubieta, J., and Jones, A. G. (1996) The synthesis, characterization and X-ray crystal structure of the rhenium organodiazenido, organodiazene complex $[ReCl_2(PPh_3)(N{:}NC_5H_4N)(HN{:}NC_5H_4N)]$. *Inorg. Chim. Acta 252*, 427−430.

(44) Block, E., Gerson, M., Kang, M., and Zubieta, J., (1988) The 3- and 3,6-silylated 2-pyridinethiols. New bulky steric bidentate ligand for unusual silver and copper clusters. *Angew. Chem. 100*, 1389−1391.

(45) Duncan, D. B. (1955) Multiple range tests and multiple F-tests. *Biometrics 11*, 1−41.

(46) *teXan: Texray Structural Analysis Package* (revised), Molecular Structure Corporation: The Woodlands, TX, 1992.

(47) Cromer, D. T., and Waber, J. T. (1974) *International Tables for X-ray Crystallography*, Vol. IV, Kynoch Press, Birmingham, England.

(48) Creagh, D. C., and McAuley, J. W. (1992) *International Tables for X-ray Crystallography*, Vol. C, Table 4, Kluwer Academic, Boston.

(49) SHELXTL PC Siemens Analytical X-ray Instruments, Inc., Madison. WI, 1990.

(50) Femia, F. J., Chan, X., Maresca, K. P., Shoup, T. M., Babich, J. W., and Zubieta, J. (2000) Synthesis and characterization of complexes of the $\{ReO\}^{3+}$ core with SNS and S donor ligands. *Inorg. Chim. Acta 306*, 30−37.

(51) Chen, X., Femia, F. J., Babich, J. W., and Zubieta, J. (2000) Synthesis and characterization of oxorhenium(V)-"3+1" mixed thiolate [SNS]/[S] and [ONS]/[S] complexes. Crystal and molecular structures of $[ReO(\mu^3\text{-}SCH_2C_5H_3NCH_2S)(\mu^1\text{-}C_6H_4\text{-}Br\text{-}4\text{-}S)]$, $[ReO(\mu^3\text{-}SCH_2C_5H_3NCH_2O)(\mu^1\text{-}C_6H_4X\text{-}4\text{-}S)]$ (X = Cl, OMe), $[ReO(\mu^3\text{-}SCH_2C_5H_3NCH_2O)(\mu^1\text{-}C_6H_4OCH_3\text{-}4\text{-}CH_2S)]$ and $[ReO(\mu^3\text{-}SCH_2C_5H_3NCH_2S)(\mu^1\text{-}C_5H_4NH\text{-}2\text{-}S)][Cl]$. *Inorg. Chim. Acta 307*, 88−96.

(52) Chen, X., Femia, F. J., Babich, J. W., and Zubieta, J. (2000) An unexpected '4+2' $[N_3S]/[NS]$ rhenium(IV) complex formed upon cleavage of a Re(V) imido bond. *Inorg. Chim. Acta 310*, 237−241.

(53) Chen, X., Femia, F. J., Babich, J. W., and Zubieta, J. (2000) Schiff base chemistry of the $\{ReO\}^{3+}$ core: structural characterization of the unusual "3+2" complex $[ReO(\mu^3\text{-}OC_6H_4\text{−}CH{=}NC_6H_4\text{-}2\text{-}S)(\mu^2\text{-}OC_6H_4C{=}NC_6H_4\text{-}2\text{-}S)]$. *Inorg. Chim. Acta 307*, 149−153.

(54) Chen, X., Femia, F. J., Babich, J. W., and Zubieta, J. (2000) Investigations of the $\{ReO\}^{3+}$ core: A '2+2' complex from bidentate and potentially trident ligands: $[ReO(\mu^2\text{-}HOC_6H_4\text{-}2\text{-}CH_2NC_6H_4S)(\mu^2\text{-}SC_5H_4N)(Pph_3)]$. *Inorg. Chim. Acta 306*, 38−41.

(55) Maresca, K. P., Femia, F. J., Babich, J. W., and Zubieta, J. (1998) Expansion of the '3+1' concept of oxorhenium-thiolate chemistry to cationic and binuclear complexes. *Inorg. Chem. Commun. 1*, 209−212.

(56) Cowley, A. R., Dilworthy, J. R., and Donnelly, P. S. (2003) Synthesis and characterization of new homoleptic rhenium thiosemicarbazone complexes. *Dalton Trans. 4*, 748−754 and references therein.

(57) Grummon, G., Rajagopalan, R., Palenik, G. J., Koziol, A. E., and Nosco, D. L. (1995) Synthesis, Characterization and Crystal Structures of Technetium(V)-Oxo Complexes Useful in Nuclear Medicine. 1. Complexes of Mercaptoacetylglycylglycylglycine (MAG3) and Its Methyl Ester Derivative (MAG3OMe). *Inorg. Chem. 34*, 1764−1772 and references therein.

(58) See for example, (a) Davison, A., Jones, A. G., Orvig, C., and Sohn, M. (1981) A new class of oxotechnetium(5+) chelate complexes containing a $TcON_2S_2$ core. *Inorg. Chem. 20*, 1629−1632. (b) Fritzberg, A. R., Abrams, P. G., Beaumier, P. L., Kasina, S., Morgan, A. C., Rao, T. N., Reno, J. M., Sanderson, J. A., Srinivasan, A., et al. (1988) Specific and stable labeling of antibodies with technetium-99m with a diamide dithiolate chelating agent. *Proc. Natl. Acad. Sci. U.S.A 85*, 4025−5029. (c) Francesconi, L. C., Graczyk, G., Wehrli, S., Shaikh, S. N., McClinton, D., Liu, S., Zubieta, J., and Kung, H. F. (1993) Synthesis and characterization of neutral $M^{V}O$ (M = technetium, rhenium) amine-thiol complexes containing a pendant phenylpiperidine group. *Inorg. Chem. 32*, 3114−3124. (d) Lever, S. Z., Sun, S.-Y., Scheffel, U. A., Kaltovich, F. A., Baidoo, K. E., Goldfarb, H., and Wagner, H. N., Jr. (1994) Pulmonary Accumulation of Neutral Diamine Dithiol Complexes of Technetium-99m. *J. Pharm. Sci. 83*, 802−809. (e) O'Neil, J. P., Wilson, S. R., and Katzenellenbogen, J. A. (1994) Preparation and structural characterization of monoamine-monoamide bis(thiol) oxo complexes of technetium(V) and rhenium(V). *Inorg. Chem. 33*, 319−323.

(59) (a) Spyriounis, D. M., Pelecanou, M., Stassinopoulou, C. I., Raptopoulou, C. P., Terzis, A., and Chiotellis, E. (1995)

Synthesis and Characterization of Oxotechnetium(V) Complexes with Aza-Substituted 2,6-Dimethyl-4-azaheptane-2,6-dithiol Ligands and Benzyl Mercaptan as Coligand. *Inorg. Chem. 34*, 1077−1082. (b) Mastrostamatis, S. G., Papadopoulos, M. S., Pirmettis, I. C., Paschali, E., Varvarigou, A. D., Stassinopoulou, C. I., Raptopoulou, C. P., Terzis, A., and Chiotellis, E. (1994) Tridentate ligands containing the SNS donor atom set as a novel backbone for the development of technetium brain-imaging agents. *J. Med. Chem. 37*, 3212−3218. (c) Meegalla, S., Plössl, K., King, M.-P., Stevenson, D. A., Liable-Sand, L. M., Rheingold, A. L., and Kung, H. F. (1995) First Example of a 99mTc Complex as a Dopamine Transporter Imaging Agent. *J. Am. Chem. Soc. 117*, 11037−11038. (d) Meegalla, S., Plössl, K., Kung, M.-P., Chumpradit, S., Stevenson, D. A., Frederick, D., and Kung, H. F. (1996) Tc-99m-Labeled Tropanes as Dopamine Transporter Imaging Agents. *Bioconjugate Chem. 7*, 421−429.

(60) Rosen, W., and Busch, D. H. (1969) Nickel(II) complexes of cyclic tetradentate thioethers. *J. Am. Chem. Soc. J. Am. Chem. Soc. 91*, 4691−4694.

(61) Rennen, H. J. J., van Eerd, J. E., Oyen, W. J. G., Corstens, F. H. M., Edwards, D. S., and Boerman, O. C. (2002) Effects of Coligand Variation on the In Vivo Characteristics of Tc-99m-Labeled Interleukin-8 in detection of infection. *Bioconjugate Chem. 13*, 370−377.

(62) Ono, M., Arano, Y., Mukai, T., Saga, T., Fujioka, Y., Ogawa, K., Kawashima, H., Konishi, J., and Saji, H. (2002) Control of Radioactivity Pharmacokinetics of ^{99m}Tc-HYNIC-Labeled Polypeptides Derivatized with Ternary Ligand Complexes. *Bioconjugate Chem. 13*, 491−501.

(63) Decristoforo, C., and Mather, S. J. (2002) The influence of chelator on the pharmacokinetics of 99mTc-labeled peptides. *J. Nucl. Med. 46*, 195−205.

(64) Nicholson, T., and Zubieta, J. (1988) Complexes of rhenium with benzoylazo and related ligands. Crystal and molecular structures of $[ReCl_2(Pph_3)_2(NNCOC_6H_4\text{-}p\text{-}Cl)]$, of the 1-azophthalazine complex $[ReCl_2(Pph_3)_2(NNC_6H_5N_2)]$, and of $[ReCl_2(Pph_3)_2(NNR)L]$ (L = NCMe, NH_3, py). A comparison to the structure of the trans-$[ReCl_2(Pph_3)_2(NNCO_2CH_3)(Me_2NCHO)]$. The structural characterization of $[ReCl_2(Pph_3)_2(NNHR)(NHNHR')]$. *Polyhedron 7*, 171−185.

(65) Although $[ReCl_3(NNC_5H_4N)(NHNC_5H_4N)]$ reacts with bis(o-hydroxyphenyl) phenyl phosphine with retention of the $[Re(\eta^1\text{-}NNC_5H_4N)(\eta^2\text{-}NHNC_5H_4N)]^{2+}$ core: Kovacs, M. S., Hein, P., Sattarzadeh, S., Patrick, B. O., Enge, T. J., and Orvig, C. (2001) Complexes of phosphine-phenolate ligands with the $[Re{:}O]^{3+}$ and $[Re(HNNC_5H_4N)(NNC_5H_4N)]^{2+}$ cores. *Dalton Trans.* 3015.

(66) Edwards, D. S., Liu, S., Barrett, J. A., Harris, A. R., Looby, R. J., Ziegler, M. C., Hemingway, S. J., and Carroll, T. R. (1997) New and Versatile Ternary Ligand System for Technetium Radiopharmaceuticals: Water Soluble Phosphines and Tricine as Coligands in Labeling a Hydrazinonicotinamide-Modified Cyclic Glycoprotein IIb/IIIa Receptor Antagonist with ^{99m}Tc. *Bioconjugate Chem. 8*, 146−154.

(67) Edwards, D. S., and Liu, S. (1999) Tc-99m radiopharmaceuticals based on a ternary ligand system comprised of a water soluble phosphine. *Phosphorus Sulfur 144−146*, 493−496.

(68) Purohit, A., Liu, S., Casebier, D., and Edwards, D. S. (2003) Phosphine-Containing HYNIC Derivatives as Potential Bifunctional Chelators for 99mTc-Labeling of Small Biomolecules. *Bioconjugate Chem. 14*, 720−727.

(69) Hsieh, T.-C., Shaikh, S. N., and Zubieta, J. (1987) Derivatized polyoxomolybdates. Synthesis and characterization of oxomolybdate clusters containing coordinatively bound diazenido units. Crystal and molecular structure of the octanuclear oxomolybdate $(NHEt_3)_2$ $(n\text{-}Bu_4N)_2[Mo_8O_{20}(NNPh)_6]$ and comparison to the structures of the parent oxomolybdate $\alpha\text{-}(n\text{-}Bu_4N)_4[Mo_8O_{26}]$ and the tetranuclear (diazenido)oxomolybdates $(n\text{-}Bu_4N)_2$ $[Mo_4O_{10}(OMe)_2(NNPh)_2]$ and $(n\text{-}Bu_4N)_2[Mo_4O_8(OMe)_2(NNC_6H_4NO_2)_4]$. *Inorg. Chem. 26*, 4079−4089.

(70) Femia, F. J., Chen, X., Maresca, K. P., Babich, J. W., and Zubieta, J. (2000) Syntheses and structural characterization of rhenium-bis-hydrazinopyrimidine core complexes with thiolate and Schiff base coligands. *Inorg. Chim. Acta 310*, 210−216.

BC050040Y

Gene Transfer Efficacies of Novel Cationic Amphiphiles with Alanine, β-Alanine, and Serine Headgroups: A Structure−Activity Investigation†

Joyeeta Sen and Arabinda Chaudhuri*

Division of Lipid Science and Technology, Indian Institute of Chemical Technology, Hyderabad-500 007, India.
Received February 16, 2005; Revised Manuscript Received June 3, 2005

Herein, we report on the relative in vitro efficacies of nine novel nonglycerol based cationic amphiphiles with increasing hydrophobic tails and the amino acids serine, alanine and β-alanine as the headgroup functionalities (lipids **1**−**9**, Scheme 1) in transfecting multiple cultured cells including CHO, COS-1, MCF-7, and HepG2. The gene transfer efficiencies of lipids **1**−**9** were evaluated using the reporter gene assays in all the four cell lines and the whole cell histochemical X-gal staining assays in representative CHO cells. In CHO, HepG2, and MCF-7 cells, cationic lipids with alanine (**4**−**6**) and β-alanine (**7**−**9**) headgroups were found to be remarkably more transfection efficient than their serine headgroup counterparts (**1**−**3**). Most notably, in CHO, HepG2, and MCF-7 cells, in combination with cholesterol as auxiliary lipid, the transfection efficiencies of the cationic lipids with alanine and β-alanine headgroups and myristyl and palmityl tails (lipids **4**, **5**, **7** and **8**) were significantly higher (2−3-fold) than that of LipofectAmine-2000, a widely used commercially available liposomal tranfection vectors. Surprisingly, in COS-1 cells, although cationic lipids with β-alanine headgroups (**7**−**9**) were strikingly transfection efficient (3−4-fold more efficacious than LipofectAmine-2000), the gene transfer properties of both their structural isomers (**4**−**6**) and their serine headgroup counterparts (**1**−**3**) were adversely affected. In summary, the present structure−activity investigation demonstrate that high gene delivery efficacies of cationic amphiphiles containing alanine or β-alanine headgroups can get seriously compromised by substituting the alanine or β-alanine with serine presumably due to the enhanced sensitivity of DNA associated with such serine-head-containing cationic lipids.

INTRODUCTION

Design of safe and efficacious therapeutic gene carriers still remains a critical challenge in gene therapy, the modality to combat myriads of inherited diseases, dreadful viral infections, and cancer. The gene transfer reagents currently in use can be broadly classified into two categories: viral and nonviral. Recombinant viral vectors, although remarkably efficient, suffer from numerous biosafety-related disadvantages (*1*−*3*). Viral vectors are capable of producing potentially replication-competent virus through recombination events with host genome and generating inflammatory and immunogenic responses against their structural components (*4*−*8*). In addition, viral vectors have a low insert-size limit for the therapeutic genes they can pack inside. Consequently, an increasing number of investigations are being reported on the development of safe and efficacious nonviral alternatives including cationic amphiphiles also known as cationic transfection lipids (*9*−*18*), cationic polymers (*19*, *20*), dendrimers (*21*−*23*), etc. Because of their least immunogenic nature, robust manufacture, ability to deliver large pieces of DNA, and ease of handling and preparation techniques, cationic amphiphiles are gaining increasing popularity as the alternative nonviral transfection vectors of choice for delivering genes into our body cells (*9*−*18*, *24*−*52*).

The molecular architectures of cationic amphiphiles consist of a positively charged water-loving (hydrophilic) polar headgroup region and a nonpolar hydrophobic tail region (usually consisting of either two long aliphatic hydrocarbon chains or a cholesterol skeleton) often tethered together via a linker functionality such as ether, ester, amide, amidine group, etc. Systematic structure−activity investigations are being pursued toward understanding how variations in each of these three lipid structural components influence the gene transfer efficacies of cationic amphiphiles continue to be an intensely pursued area of research in nonviral gene delivery (*12*, *16*, *27*, *31*, *34*, *38*, *40*, *41*, *47*−*52*). As part of our ongoing structure−activity program in the area of cationic lipid-mediated gene delivery (*12*, *16*, *17*, *47*−*52*), in the present investigation, we report on the relative in vitro efficacies of nine novel nonglycerol-based cationic amphiphiles with increasing hydrophobic tails and the amino acids serine, alanine and β-alanine as the headgroup functionalities (lipids **1**−**9**, Scheme 1) in transfecting multiple cultured cells including CHO, COS-1, MCF-7, and HepG2. As delineated below, the present structure−activity investigation demonstrates that high gene delivery efficacies of cationic amphiphiles containing alanine or β-alanine headgroups can get seriously compromised by substituting the alanine or β-alanine with serine presumably due to the enhanced sensitivity of DNA associated with such serine-head-containing cationic lipids. The transfection efficacy profiles of the presently described cationic lipids once again reiterate the proposition that gene transfer efficacies of cationic amphiphiles can be significantly modulated by minor structural variations in both the polar headgroup and hydrophobic tail regions of the lipid.

* Corresponding author. Tel: 91-40-27193201. Fax: 91-40-27160757. E-mail: arabinda@iict.res.in.
† IICT Communication No. 041003.

10.1021/bc0500443 CCC: $30.25 © 2005 American Chemical Society
Published on Web 07/01/2005

Scheme 1

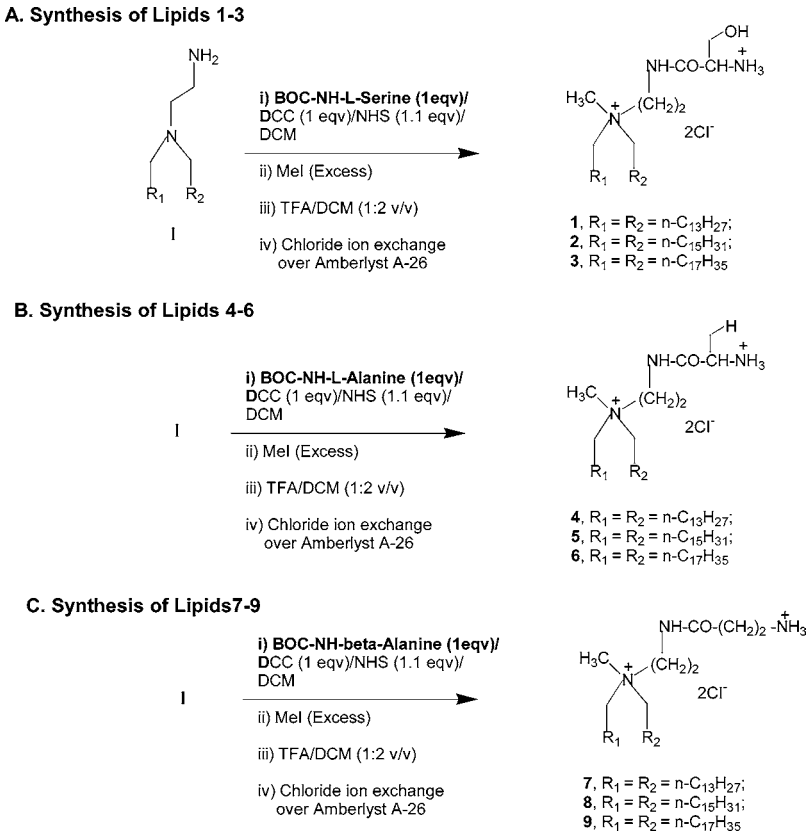

EXPERIMENTAL PROCEDURES

General Procedures and Materials. FABMS data were acquired by the liquid secondary ion mass spectrometry (LSIMS) technique using *m*-nitrobenzyl alcohol as the matrix. LSIMS analysis was performed in the scan range 100−1000 amu at the rate of 3 scans/s. ^{1}H NMR spectra were recorded on a Varian FT 200 MHz, AV 300 MHz, or Varian Unity 400 MHz. 1-Bromotetradecane, 1-bromohexadecane, 1-bromooctadecane, *n*-tetradecylamine, *n*-hexadecylamine, and *n*-octadecylamine were procured from Lancaster (Morecambe, England). The progress of the reactions was monitored by thin-layer chromatography on 0.25 mm silica gel plates. Column chromatography was performed with silica gel (Acme Synthetic Chemicals, India, finer than 200 and 60−120 mesh). p-CMV-SPORT-β-gal plasmid was a generous gift from Dr. Nalam Madhusudhana Rao. Lipofectamine was purchased from Invitrogen life technologies. Cell culture media, fetal bovine serum, 3-(4,5-dimethylthiazol-2-yl)-2,5-diphenyltetrazolium bromide (MTT), poly(ethylene glycol) 8000, *o*-nitrophenyl-β−D-galactopyranoside, and cholesterol were purchased from Sigma, St. Louis, MO. NP-40, antibiotics, and agarose were purchased from Himedia, India. Unless otherwise stated, all the other reagents purchased from local commercial suppliers were of analytical grades and were used without further purification. COS-1 (SV 40 transformed African green monkey kidney cells), CHO (Chinese hamster ovary), HepG2 (human hepatocarcinoma), and MCF-7 (human breast adenocarcinoma) cell lines were procured from the National Centre for Cell Sciences (NCCS), Pune, India. Cells were grown at 37 °C in Dulbecco's modified Eagle's medium (DMEM)[1] with 10% FBS in a humidified atomosphere containing 5% CO_2/95% air. Purity of the final lipids **1**−**9** were determined by Analytical HPLC (Shimadzu Model LC10A) using a PARTISIL 5 ODS-3 WCS analytical column (4.6 × 250 mm, Whatman Inc., Clifton, NJ) in two different mobile phases. One solvent system (A) was methanol:water:trifluoroacetic acid in the ratio 75:25:0.05 (v/v) for 15 min with a flow rate of 0.8 mL/min. The other solvent system (B) was methanol:acetonitrile:water:trifluoroacetic acid in the ratio 65:10:25:0.05 for 15 min with a flow rate of 0.8 mL/min. Peaks were detected by UV absorption at 219 nm. All the target lipids (**1**−**9**) showed more than 95% purity. Typical retention times in mobile phase A were: 3.56 min (lipid **1**); 3.58 mins (lipid **2**); 3.60 min (lipid **3**), 3.59 mins (lipid **4**); 3.63 min (lipid **5**); 3.65 min (lipid **6**); 3.57 min (lipid **7**); 3.61 min (lipid **8**); 3.64 min (lipid **9**).

Synthesis. Lipids **1**−**9** were synthesized essentially applying the same synthetic steps as depicted schematically in Scheme 1. As a representative experimental detail, synthesis of lipid **2** is described below. For all the other lipids, only TLC, ^{1}H NMR, and mass spectral data are provided below. Due to extensive line broadening in ^{1}H NMR spectra of the final deprotected lipids (particularly in the region δ/ppm = 3−5), all the final lipids were characterized by LSIMS. However, ^{1}H NMR spectra of the BOC-protected immediate precursors for all the final

[1] Abbreviations used: BOC, *tert*-butyloxycarbonyl; Chol, cholesterol; DCC, dicyclohexylcarbodiimide; DCM, dichloromethane; DMAP, 4-(*N*,*N*-dimethylamino)pyridine; DMEM, Dulbecco's Modified Eagle's Medium; DMF, *N*,*N*-dimethylformamide; DOPE, 1,2-dioleoyl-*sn*-glycero-3-phosphoethanolamine; FBS, fetal bovine serum; ONPG, *o*-nitrophenyl-β-D-galactopyranoside; PBS, phosphate-buffered saline; TFA, trifluoroacetic acid.

lipids **1**−**9** (provided below) were in complete agreement with their assigned molecular structures.

Synthesis of *N,N*-Di-*n*-hexadecyl-*N*-methyl-*N*-[*N*′-(L-serinyl)aminoethyl]ammonium Chloride (lipid 2). *Step i (Scheme 1, Part A). Synthesis of N,N-Di-n-hexadecyl-N-[N-(Nα-BOC-L-serinyl)aminoethyl]amine.* Solid *N*-hydroxysuccinimide (0.08 g, 0.70 mmol) and DCC (0.16 g, 0.80 mmol) were added sequentially to an ice cold and stirred solution of *N*-*tert*-butyloxycarbonyl-L-serine (0.14 g, 0.70 mmol, prepared from L-serine and di-*tert*-butyl dicarbonate as described previously (*53*)) in dry DCM/dry DMF (9:1, v/v). After five minutes, *N*-(2-aminoethyl)-*N,N*-di-*n*-hexadecylamine (0.35 g, 0.70 mmol, a readily available precursor in our laboratory prepared as described previously (*48*)) and DMAP (catalytic) dissolved in dry DCM were added to the reaction mixture. The resulting solution was stirred at room temperature for 6 h, solid DCU was filtered, and the solvent from the filtrate was evaporated. The residue was taken up in ethyl acetate (100 mL) and washed sequentially with ice-cold 1 N HCl (3 × 100 mL), saturated sodium bicarbonate (3 × 100 mL), and water (3 × 100 mL). The organic layer was dried over anhydrous sodium sulfate and filtered and the solvent from the filtrate removed by rotary evaporation. The residue upon column chromatographic purification with 60−120 mesh silica gel using 3−4% methanol−dichloromethane (v/v) as eluent afforded 0.34 g (yield 71%) of the pure *N,N*-di-*n*-hexadecyl-*N*-[*N*-(*N*α-BOC-L-serinyl)aminoethyl]amine intermediate (R_f = 0.45, 10% methanol−dichloromethane, v/v). ^{1}H NMR (200 MHz, $CDCl_3$): δ/ppm = 0.9 [t, 6H, C*H*$_3$(CH$_2$)$_{14}$]; 1.2−1.4 [m, 56H, (C*H*$_2$)$_{14}$]; 1.4−1.5 [s, 9H, COOC(C*H*$_3$)$_3$]; 2.5 [t, 4H, N(C*H*$_2$-CH$_2$)$_2$]; 2.65 [t, 2H, NC*H*$_2$CH$_2$NHCO]; 3.3 [m, 2H, NCH$_2$C*H*$_2$NHCO]; 3.55 [dd, 1H, CH$_2$NHCOCH(C*H*OH)-NHBOC]; 3.9 [dd, 1H, CH$_2$NHCOCH(CH*H*OH)NHBOC]; 4.05 [m, 1H, CH$_2$NHCOC*H*(CHHOH)NHBOC]; 5.5 (m, 1H, Boc-N*H*); 6.8 [m, 1H, CH$_2$CH$_2$N*H*CO].

Step ii (Scheme 1, Part A). Synthesis of N,N-Di-n-hexadecyl-N-[N(Nα-BOC-L-serinyl)aminoethyl]-N-methylammonium Iodide. The intermediate obtained in step i above was dissolved in 3 mL of dichloromethane/methanol (2:1, v/v), and 3 mL of methyl iodide was added. The solution was stirred at room-temperature overnight. Solvent was removed on a rotary evaporator. The residue upon column chromatographic purification with 60−120 mesh size silica gel and 5−6% methanol in dichloromethane (v/v) as eluent afforded 0.22 g (54% yield) of pure *N,N*-di-*n*-hexadecyl-*N*-[*N*-(*N*α-BOC-L-serinyl)aminoethyl]-*N*-methylammonium iodide intermediate (R_f = 0.3, 10% methanol in dichloromethane, v/v). ^{1}H NMR (200 MHz, $CDCl_3$): δ/ppm = 0.9 [t, 6H, C*H*$_3$(CH$_2$)$_{13}$]; 1.2−1.4 [m, 52H, CH$_3$(C*H*$_2$)$_{13}$]; 1.4−1.5 [s, 9H, COOC(C*H*$_3$)$_3$]; 1.6−1.8 [m, 4H, N$^+$(CH$_2$C*H*$_2$)$_2$]; 3.05 [s, 3H, N$^+$C*H*$_3$]; 3.2−3.3 [m,4H, N$^+$(C*H*$_2$CH$_2$)$_2$]; 3.5 [m,2H, N$^+$C*H*$_2$CH$_2$NHCO]; 3.6−3.75 [m, 3H, N$^+$CH$_2$C*H*$_2$NHCO; dd, 1H, CH$_2$NHCOCH(C*H*OH)NHBOC]; 3.9 [dd, 1H, CH$_2$NHCOCH(CH*H*OH)NHBOC]; 4.15 [m, 1H, CH$_2$NHCOC*H*(CHHOH)NHBOC]; 6.0 [m, 1H, BOCN*H*]; 8.1 [m, 1H, CH$_2$CH$_2$N*H*CO].

Steps iii and iv (Scheme 1, Part A). Synthesis of N,N-Di-n-hexadecyl-N-methyl-N-[N′-(L-serinyl)aminoethyl]-ammonium Chloride (lipid 2). The intermediate obtained above in step ii (0.22 g) was dissolved in dry DCM (2 mL), and TFA (2 mL) was added at 0 °C. The resulting solution was stirred at room-temperature overnight to ensure complete deprotection. Excess TFA was removed by flushing with nitrogen to give the title compound as a trifluoroacetate salt. Column chromatographic purification using 60−120 mesh size silica gel and 12−14% (v/v) methanol−chloroform as eluent followed by chloride ion exchange chromatography (using amberlyst A-26 chloride ion-exchange resin) afforded 102 mg (57% yield) of pure lipid **2** (R_f = 0.3−0.4, 15% methanol in chloroform, v/v). LSIMS (lipid **2**): *m/z*: 611 [M + 1$^+$] (calcd for$C_{38}H_{80}O_2N_3$, 35%).

Lipids **1**, **3**−**9** were synthesized following the same four-step protocols as described above for the synthesis lipid **2** using the appropriate starting mixed amine (**I**, Scheme 1) and *N*-BOC-protected appropriate amino acids shown in Scheme 1. The TLC characteristics, ^{1}H NMR spectral data for the immediate precursor of the remaining final lipids, and the LSIMS data for the remaining final lipids are provided below.

Lipid 1. ^{1}H NMR (200 MHz, $CDCl_3$) of *N,N*-di-*n*-tetradecyl-*N*-[*N*-(*N*α-BOC-L-serinyl)aminoethyl]-*N*-methylammonium iodide (immediate precursor of lipid **1**, R_f = 0.3, 10% methanol in dichloromethane, v/v): δ/ppm = 0.9 [t, 6H, C*H*$_3$(CH$_2$)$_{11}$]; 1.2−1.4 [m, 44H, CH$_3$(C*H*$_2$)$_{11}$]; 1.4−1.5 [s, 9H, COOC(C*H*$_3$)$_3$]; 1.6−1.8 [m, 4H, N$^+$-(CH$_2$C*H*$_2$)$_2$]; 3.05 [s, 3H, N$^+$C*H*$_3$]; 3.2−3.3 [m,4H, N$^+$(C*H*$_2$-CH$_2$)$_2$]; 3.5 [m,2H, N$^+$C*H*$_2$CH$_2$NHCO]; 3.6−3.75 [m, 3H, N$^+$CH$_2$C*H*$_2$NHCO; dd, 1H, CH$_2$NHCOCH(C*H*OH)-NHBOC]; 3.9[dd, 1H, CH$_2$NHCOCH(CH*H*OH)NHBOC]; 4.15 [m, 1H, CH$_2$NHCOC*H*(CHHOH)NHBOC]; 6.0 [m, 1H, BOCN*H*]; 8.1 [m, 1H, CH$_2$CH$_2$N*H*CO]. LSIMS (lipid **1**): *m/z*: 555 [M + 1$^+$] (calcd for$C_{34}H_{72}O_2N_3$, 100%).

Lipid 3. ^{1}H NMR (200 MHz, $CDCl_3$) of *N,N*-di-*n*-octadecyl-*N*-[*N*-(*N*α-BOC-L-serinyl)aminoethyl]-*N*-methylammonium iodide (immediate precursor of lipid **3**, R_f = 0.3, 10% methanol in dichloromethane, v/v). δ/ppm = 0.9 [t, 6H, C*H*$_3$(CH$_2$)$_{15}$]; 1.2−1.4 [m, 60H, CH$_3$(C*H*$_2$)$_{15}$]; 1.4−1.5 [s, 9H, COOC(C*H*$_3$)$_3$]; 1.6−1.8 [m, 4H, N$^+$-(CH$_2$C*H*$_2$)$_2$]; 3.05 [s, 3H, N$^+$C*H*$_3$]; 3.2−3.3 [m,4H, N$^+$(C*H*$_2$-CH$_2$)$_2$]; 3.5 [m,2H, N$^+$C*H*$_2$CH$_2$NHCO]; 3.6−3.75 [m, 3H, N$^+$CH$_2$C*H*$_2$NHCO; dd, 1H, CH$_2$NHCOCH(C*H*OH)-NHBOC]; 3.9[dd, 1H, CH$_2$NHCOCH(CH*H*OH)NHBOC]; 4.15 [m, 1H, CH$_2$NHCOC*H*(CHHOH)NHBOC]; 6.0 [m, 1H, BOCN*H*]; 8.1 [m, 1H, CH$_2$CH$_2$N*H*CO]. LSIMS (lipid **3**): *m/z*: 667 [M + 1$^+$] (calcd for$C_{42}H_{88}O_2N_3$, 100%).

Lipid 4. ^{1}H NMR (200 MHz, $CDCl_3$) of *N*-[*N*-(*N*α-BOC-L-alanyl)aminoethyl]-*N,N*-di-*n*-tetradecyl-*N*-methylammonium iodide (immediate precursor of lipid **4**, R_f = 0.5, 10% methanol in dichloromethane, v/v). δ/ppm = 0.9 [t, 6H, C*H*$_3$(CH$_2$)$_{13}$]; 1.2−1.4 [m, 44H, (C*H*$_2$)$_{11}$; 3H, NHCOCH-(C*H*$_3$)NHBoc]; 1.4−1.5 [s, 9H, COOC(C*H*$_3$)$_3$]; 1.6−1.7 [m, 4H, N$^+$(CH$_2$C*H*$_2$)$_2$]; 3.2 [s, 3H, N$^+$C*H*$_3$]; 3.3 [m,4H, N$^+$(C*H*$_2$-CH$_2$)$_2$]; 3.7−3.9 [bs, 4H, N$^+$C*H*$_2$C*H*$_2$NHCO]; 4.05 [m, 1H, NHCOC*H*(CH$_3$)NHBOC]; 5.2 [m, 1H, BOC N*H*]; 8.2 [m, 1H, CH$_2$CH$_2$N*H*CO]. LSIMS (lipid **4**): *m/z*: 539 [M + 1$^+$] (calcd for$C_{34}H_{72}ON_3$, 100%).

Lipid 5. ^{1}H NMR (200 MHz, $CDCl_3$): *N,N*-di-*n*-hexadecyl-*N*-[*N*-(*N*α-BOC-L-alanyl)aminoethyl]-*N*-methylammonium iodide (immediate precursor of lipid **5**, R_f = 0.5, 10% methanol in dichloromethane, v/v). δ/ppm = 0.9 [t, 6H, C*H*$_3$(CH$_2$)$_{13}$]; 1.2−1.4 [m, 52H, (C*H*$_2$)$_{13}$; 3H, NHCOCH(C*H*$_3$)NHBOC]; 1.4−1.5 [s, 9H, COOC(C*H*$_3$)$_3$]; 1.6−1.7 [m, 4H, N$^+$(CH$_2$C*H*$_2$)$_2$]; 3.2 [s, 3H, N$^+$C*H*$_3$]; 3.3 [m, 4H, N$^+$(C*H*$_2$CH$_2$)$_2$]; 3.7−3.9 [bs, 4H, N$^+$C*H*$_2$C*H*$_2$-NHCO]; 4.05 [m, 1H, NHCOC*H*(CH$_3$)NHBOC]; 5.2 [m, 1H, BOC N*H*]; 8.2 [m, 1H, CH$_2$CH$_2$N*H*CO]. LSIMS (lipid **5**): *m/z*: 595 [M + 1$^+$] (calcd for$C_{38}H_{80}N_3O$, 100%).

Lipid 6. ^{1}H NMR (200 MHz, $CDCl_3$) of *N*-[*N*-(*N*α-BOC-L-alanyl]aminoethyl]-*N,N*-di-*n*-octadecyl-*N*-methylammonium iodide (immediate precursor of lipid **6**, R_f = 0.5, 10% methanol in dichloromethane, v/v). δ/ppm = 0.9 [t, 6H, C*H*$_3$(CH$_2$)$_{13}$]; 1.2−1.4 [m, 60H, (C*H*$_2$)$_{15}$; 3H, NHCOCH-(C*H*$_3$)NHBOC]; 1.4−1.5 [s, 9H, COOC(C*H*$_3$)$_3$]; 1.6−1.7 [m, 4H, N$^+$(CH$_2$C*H*$_2$)$_2$]; 3.2 [s, 3H, N$^+$C*H*$_3$]; 3.3 [m, 4H,

$N^+(CH_2CH_2)_2$]; 3.7−3.9 [bs, 4H, $N^+CH_2CH_2NHCO$]; 4.05 [m, 1H, $NHCOCH(CH_3)NHBOC$]; 5.2 [m, 1H, BOC N*H*]; 8.2 [m, 1H, CH_2CH_2NHCO]. LSIMS (lipid **6**): *m/z*: 651 [M + 1$^+$] (calcd for$C_{42}H_{88}ON_3$, 100%).

Lipid 7. ^{1}H NMR (200 MHz, $CDCl_3$) of *N*-[*N*-(*N*$^\alpha$-BOC-L-*β*-alanyl)]aminoethyl]-*N*,*N*-di-*n*-tetradecyl-*N*-methylammonium iodide (immediate precursor of lipid **7**, R_f = 0.5, 10% methanol in dichloromethane, v/v). *δ*/ppm = 0.9 [t, 6H, $CH_3(CH_2)_{11}$]; 1.2−1.4 [m, 44H, $CH_3(CH_2)_{11}$]; 1.4−1.5 [s, 9H, $COOC(CH_3)_3$]; 1.7 [m, 4H, $N^+(CH_2CH_2)_2$]; 2.45 [t, 2H, $COCH_2CH_2NHBOC$]; 3.3 [s, 3H, N^+CH_3]; 3.4−3.5 [bs, 6H, $N^+(CH_2CH_2)_2$, $N^+CH_2CH_2NH$]; 3.7 [bs, 4H, N^+-$CH_2CH_2NHCOCH_2CH_2NHBOC$]; 5.3 [m, 1H, BOCN*H*]; 8.1 [m, 1H, CH_2CH_2NHCO]. LSIMS (lipid **7**): *m/z*: 539 [M + 1$^+$] (calcd for$C_{34}H_{72}ON_3$, 100%).

Lipid 8. ^{1}H NMR (200 MHz, $CDCl_3$) of *N*-[*N*-(*N*$^\alpha$-BOC-L-*β*-alanyl)]aminoethyl]-*N*,*N*-di-*n*-hexadecyl-*N*-methylammonium iodide (immediate precursor of lipid **8**, R_f = 0.5, 10% methanol in dichloromethane, v/v). *δ*/ppm = 0.9 [t, 6H, $CH_3(CH_2)_{13}$]; 1.2−1.4 [m, 52H, $CH_3(CH_2)_{13}$]; 1.4−1.5 [s, 9H, $COOC(CH_3)_3$]; 1.7 [m, 4H, $N^+(CH_2CH_2)_2$]; 2.45 [t, 2H, $COCH_2CH_2NHBOC$]; 3.3 [s, 3H, N^+CH_3]; 3.4−3.5 [bs, 6H, $N^+(CH_2CH_2)_2$, $N^+CH_2CH_2NH$]; 3.7 [bs, 4H, N^+-$CH_2CH_2NHCOCH_2CH_2NHBOC$]; 5.3 [m, 1H, BOCN*H*]; 8.1 [m, 1H, CH_2CH_2NHCO]. LSIMS (lipid **8**): *m/z*: 595 [M$^+$] (calcd for$C_{38}H_{80}ON_3$, 100%).

Lipid 9. ^{1}H NMR (200 MHz, $CDCl_3$) of *N*-[*N*-(*N*$^\alpha$-BOC-L-*β*-alanyl)]aminoethyl]-*N*,*N*-di-*n*-octadecyl-*N*-methylammonium iodide (immediate precursor of lipid **9**, R_f = 0.5, 10% methanol in dichloromethane, v/v). *δ*/ppm = 0.9 [t, 6H, $CH_3(CH_2)_{15}$]; 1.2−1.4 [m, 60H, $CH_3(CH_2)_{15}$]; 1.4−1.5 [s, 9H, $COOC(CH_3)_3$]; 1.7 [m, 4H, $N^+(CH_2CH_2)_2$]; 2.45 [t, 2H, $COCH_2CH_2NHBOC$]; 3.3 [s, 3H, N^+CH_3]; 3.4−3.5 [bs,6H, $N^+(CH_2CH_2)_2$, $N^+CH_2CH_2NH$]; 3.7 [bs, 4H, N^+-$CH_2CH_2NHCOCH_2CH_2NHBOC$]; 5.3 [m, 1H, BOCN*H*]; 8.1 [m, 1H, CH_2CH_2NHCO]. LSIMS (lipid **9**): *m/z*: 651 [M + 1$^+$] (calcd for$C_{42}H_{88}ON_3$, 100%).

Cell Culture. COS-1 (SV 40 transformed African green monkey kidney cells), CHO (Chinese hamster ovary), HepG2 (human hepatocarcinoma), and MCF-7 (human breast adenocarcinoma cell) cell lines were procured from the National Centre for Cell Sciences (NCCS), Pune, India. Cells were cultured at 37 °C in Dulbecco's modified Eagle's medium (DMEM) with 10% fetal bovine serum, 50 *μ*g/mL penicillin, 50 *μ*g/mL streptomycin, and 20 *μ*g/mL kanamycin in a humidified atmosphere containing 5% CO_2.

Preparation of Liposomes. The cationic lipid and the colipid (Chol) in 1:1 mole ratio were dissolved in a mixture of chloroform and methanol (3:1, v/v) in a glass vial. The solvent was removed with a flow of moisture free nitrogen gas, and the dried lipid film was then kept under high vacuum for 8 h. A 5 mL amount of sterile deionized water was added to the vacuum-dried lipid film, and the mixture was allowed to swell overnight. The vial was then vortexed for 2−3 min at room temperature and occasionally sonicated in a bath sonicator to produce multilamellar vesicles (MLVs). MLVs were then sonicated in an ice bath (usually 45−60 s) until clarity using a Branson 450 sonifier at 100% duty cycle and 25 W output power. The resulting clear aqueous liposomes were used in forming lipoplexes.

Plasmid DNA. pCMV-SPORT-*β*-gal plasmid was a generous gift from Dr. Nalam Madhusudhana Rao (Centre for Cellular and Molecular Biology, Hyderabad, India) and was amplified in DH5α strain of *Escherichia coli*, isolated by alkaline lysis procedure, and finally purified by PEG-8000 precipitation as described previously (*54*). The purity of plasmid was checked by A_{260}/A_{280} ratio (around 1.9) and 1% agarose gel electrophoresis.

Transfection of Cells. Cells were seeded at a density of 15000 (for COS-1) and 20000 cells (for CHO, HepG2, and MCF-7) per well in a 96-well plate 18−24 h before the transfection. A 0.3 *μ*g amount of plasmid DNA was complexed with varying amounts of lipids (0.09−8.1 nmol) in plain DMEM medium (total volume made up to 100 *μ*L) for 30 min. The charge ratios were varied from 0.1:1 to 9:1 (±) over these ranges of the lipids. Immediately prior to transfection, cells plated in the 96-well plate were washed with PBS (2 × 100 *μ*L) followed by the addition of lipoplexes. After 3h of incubation, 100*μ*L of DMEM with 20% FBS was added to the cells. The medium was changed to 10% complete medium after 24 h and the reporter gene activity was estimated after 48 h. The cells were washed twice with PBS (100 *μ*L each) and lysed in 50 *μ*L of lysis buffer [0.25 M Tris-HCl (pH 8.0) and 0.5% NP40]. Care was taken to ensure complete lysis. The *β*-galactosidase activity per well was estimated by adding 50 *μ*L of 2X-substrate solution [1.33 mg/mL of ONPG, 0.2 M sodium phosphate (pH 7.3) and 2 mM magnesium chloride] to the lysate in a 96-well plate. Absorbance of the product *o*-nitrophenol at 405 nm was converted to *β*-galactosidase units by using a calibration curve constructed using pure commercial *β*-galactosidase enzyme. Each transfection experiment was repeated three times on three different days. The transfection values reported were average values from three replicate transfection plates assayed on three different days. The values of *β*-galactosidase units in replicate plates assayed on the same day varied by less than 20%. The day to day variation in transfection efficiency values for identically treated transfection plates was mostly within 2−3-fold and was dependent on the cell density and condition of the cells.

Toxicity Assay. Cytotoxicities of lipids **1**−**9** were assessed by the 3-(4,5-dimethylthiazol-2-yl)-2,5-diphenyltetrazolium bromide (MTT) reduction assay as described earlier (*37*). The cytotoxicity assay was performed in 96-well plates by maintaining the same ratio of number of cells to amount of cationic lipid, as used in the transfection experiments. MTT was added 3 h after addition of cationic lipid to the cells. Results were expressed as percent viability = [A_{540}(treated cells) − background/A_{540}(untreated cells) − background] × 100.

Zeta Potential (*ζ*) and Size Measurements. The sizes and the surface charges (zeta potentials) of liposomes and lipoplexes were measured by photon correlation spectroscopy and electrophoretic mobility on a Zeta sizer 3000HS_A (Malvern, UK). The sizes were measured in deionized water with a sample refractive index of 1.59 and a viscosity of 0.89. The system was calibrated by using the 200 ± 5 nm polystyrene polymer (Duke Scientific Corp., Palo Alto, CA). The diameters of liposomes and lipoplexes were calculated by using the automatic mode. The zeta potential was measured using the following parameters: viscosity, 0.89 cP; dielectric constant, 79; temperature, 25 °C; F(Ka), 1.50 (Smoluchowski); maximum voltage of the current, V. Measurements were done 10 times with the zero field correction. The potentials were calculated by using the Smoluchowski approximation.

DNase 1 Sensitivity Assays. Briefly, in a typical assay, 1.5 nmol of DNA (500 ng) was complexed with lipid using the indicated lipid:DNA charge ratios in 10 mM HEPES buffer (pH 7.4) in a volume of 40 *μ*L and the mixture incubated at room temperature for 30 min on a rotary shaker. Subsequently, the complexes were treated

with DNase I (at a final concentration of 1 ng/1.5 nmol of DNA) in the presence of 10 mM $MgCl_2$ and incubated for 20 min at 37 °C. The reactions were then halted by adding EDTA (to a final concentration of 50 mM) and incubated at 60 °C for 10 min in a water bath. The aqueous layer was washed with 50 μL of phenol:chloroform mixture (1:1, v/v) and centrifuged at 10 000 g for 5 min. The aqueous supernatants were separated, loaded (15 μL) on a 1% agarose gel, and electrophoresed at 100 V for 2 h. The bands were visualized with ethidium bromide staining.

X-Gal Staining. Cells expressing β-galactosidase were histochemically stained with the substrate 5-bromo-4-chloro-3-indolyl-β-D-galactopyranoside (X-gal) as described previously (*47*). Briefly, 48 h after transfection with lipoplexes in 96-well plates, the cells were washed two times (2 × 100 μL) with phosphate-buffered saline (PBS, 137 mM NaCl, 2.7 mM KCl, 10 mM Na_2HPO_4, 2 mM KH_2PO_4, pH 7.4) and fixed with 0.5% glutaraldehyde in PBS (225 μL). After 15 min incubation at room temperature, the cells were washed again with PBS three times (3 × 250 μL) and subsequently were stained with 1.0 mg/mL X-gal in PBS containing 5.0 mM $K_3[Fe(CN)_6]$, and 5.0 mM $K_4[Fe(CN)_6]$ and 1 mM $MgSO_4$ for 2−4 h at 37 °C. Blue colored cells were identified by light microscope (Leica, Germany).

RESULTS

Chemistry. Lipids **1**−**9** were prepared by conventional DCC coupling of the common precursor **I** (a readily available hydrophobic mixed primary-tertiary amine in our laboratory prepared as described previously (*48*)) and the appropriate BOC-protected amino acids (Scheme 1). The resulting intermediates were then subjected to quaternization with excess methyl iodide and BOC-deprotection with trifluoroacetic acid. The BOC-deprotected products afforded pure target lipids upon chloride ion exchange chromatography over Amberlyst-26 (Scheme 1). Minor variation in lipid structures were ensured by designing lipid pairs varying either only in structurally isomeric headgroup functionalities (e.g. lipid pairs **4** and **7**, **5** and **8**, and **6** and **9**) or by designing lipid pairs whose sole structural difference is substitution of a hydrogen atom in the headgroup side chain of one lipid by a hydroxyl functionality in the other (e.g. lipid pairs **1** and **4**, **2** and **5**, and **3** and **6**). Structures of all the synthetic intermediates and the final lipids shown in Scheme 1 were confirmed by ^{1}H NMR and LSIMS.

Transfection Biology. The in vitro gene transfer efficacies of lipids **1**−**9** were first measured by the reporter gene expression assay using equimolar cholesterol as colipid (cholesterol was found to be a more efficacious colipid than the other commonly used colipid dioleoyllphosphatidyl ethanolamine, DOPE, data not shown) and pCMV-SPORT-β-gal plasmid as the reporter gene across the lipid:DNA charge ratios 9:1−0.3:1. Figures 1−4 summarize the relative in vitro gene delivery efficacies of lipids **1**−**9** in transfecting CHO, HepG2, MCF7, and COS-1 cells, respectively. In CHO, HepG2, and MCF-7 cells, cationic lipids with alanine and β-alanine headgroups were, in general, found to be more transfection efficient than LipofectAmine-2000 (by about 2-fold in CHO and MCF-7 cells), a commercially available popular liposomal transfection kit (Figures 1−3, Parts B and C). Except in MCF-7 cells at 1:1 lipid:DNA charge ratio and in COS-1 cells, the sterylated lipids with alanine (lipid **6**) and β-alanine (lipid **9**) headgroups were found to be less efficient than their myristyl and palmityl

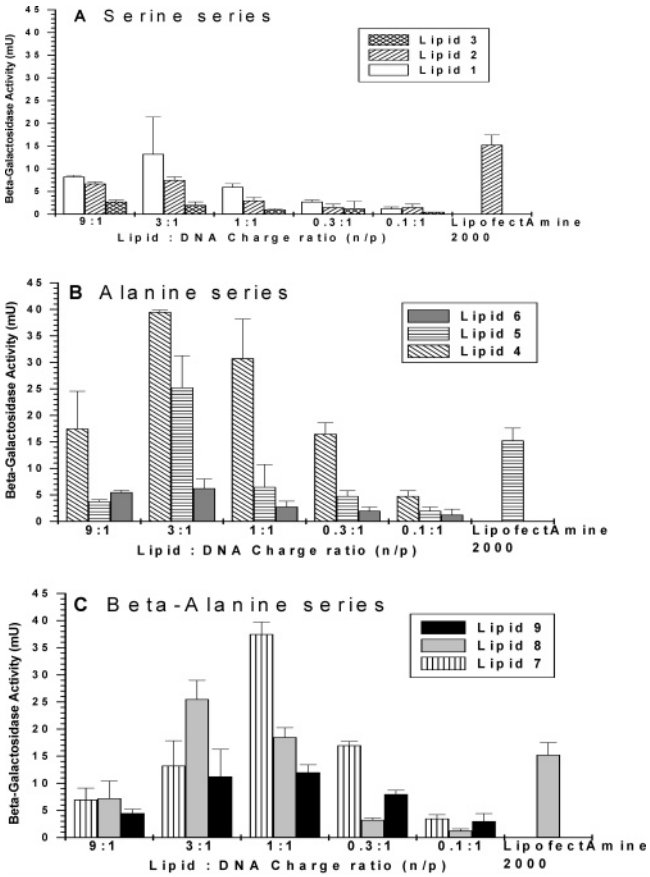

Figure 1. In vitro transfection efficiencies in CHO cells of lipids **1**, **2**, **3** (A); lipids **4**, **5**, **6** (B); and lipids **7**, **8**, **9** (C) using cholesterol as colipid (at lipid:cholesterol mole ratio of 1:1). Units of β-galactosidase activity were plotted against the varying lipid to DNA (±) charge ratios. The transfection efficiencies of the lipids were compared to that of commercially available LipofectAmine 2000. Transfection experiments were performed as described in the text. The transfection values shown are average of duplicate experiments performed on the same day.

analogues (lipids **4** and **5**, and **7** and **8**, respectively, Figures 1−4, parts B and C). However, unlike the previously reported high transfection efficacies of cationic lipids containing hydroxyalkyl headgroups (*31*, *40*, *41*, *49*, *50*, *52*), the cationic lipids with serine headgroups (lipids **1**−**3**) in spite of possessing hydroxymethyl headgroup functionalities were found to be less efficacious than their alanine (lipids **4**−**6**) and β-alanine (lipids **7**−**9**) analogues in transfecting all the four cells (Figures 1−4).

Unlike the comparable gene transfer efficacies of the cationic lipids with structurally isomeric alanine (lipids **4**−**6**) and β-alanine headgroups (lipids **7**−**9**) in CHO, HepG2, and MCF-7 cells (Figures 1−3, parts B and C), lipids **7**−**9** with β-alanine headgroups showed significantly higher transfection properties in COS-1 cells than its alanine analogues (Figure 4, parts B and C). In particular, at 3:1 lipid:DNA charge ratio, lipid **9** was found to be strikingly more efficient (>10-fold) than its alanine counterpart (lipid **6**) in transfecting COS-1 cells (Figure 4, parts B and C). The β-alanine lipid with a palmityl chain (**8**) were 3−4-fold more transfection efficient than LipofectAmine-2000 at lipid:DNA charge ratios of 3:1 (Figure 4, part C). The general transfection profiles for lipids **1**−**9** found in the above-mentioned reporter gene assays (Figures 1−4) were further confirmed by the whole cell histochemical X-gal staining assay. Representative X-gal staining patterns for CHO

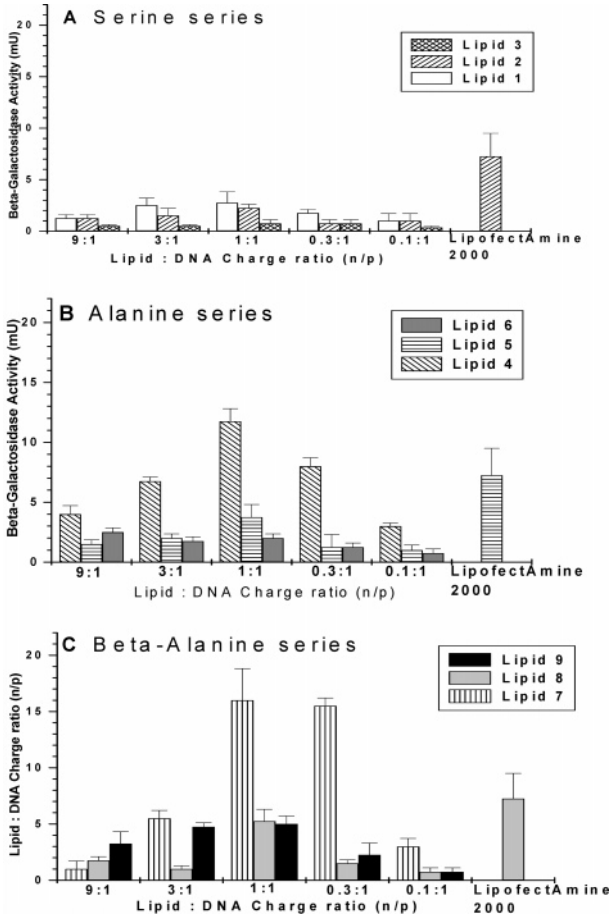

Figure 2. In vitro transfection efficiencies in HepG2 cells of lipids **1**, **2**, **3** (A); lipids **4**, **5**, **6** (B); and lipids **7**, **8**, **9** (C) using cholesterol as colipid (at lipid:cholesterol mole ratio of 1:1). Units of β-galactosidase activity were plotted against the varying lipid to DNA (±) charge ratios. The transfection efficiencies of the lipids were compared to that of commercially available LipofectAmine 2000. Transfection experiments were performed as described in the text. The transfection values shown are average of duplicate experiments performed on the same day.

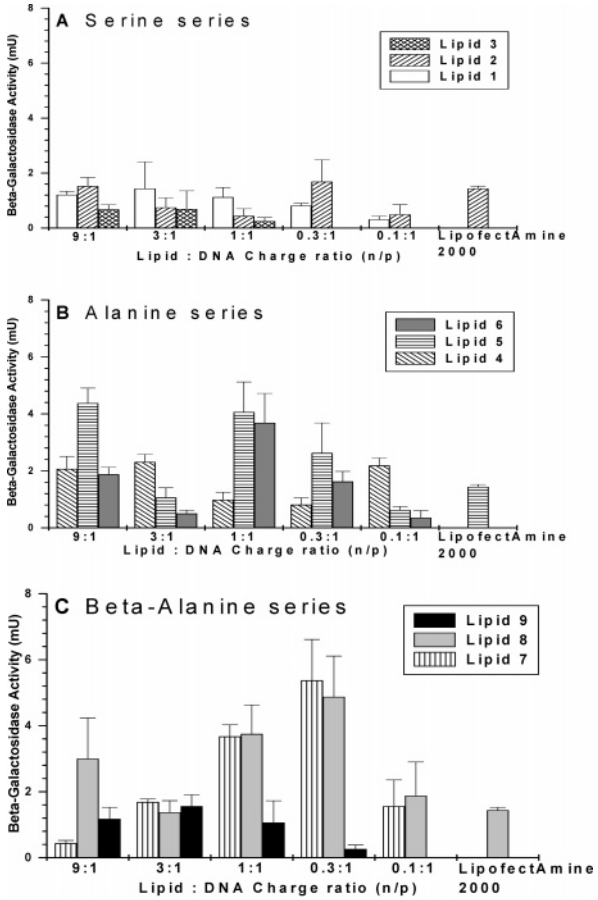

Figure 3. In vitro transfection efficiencies in MCF-7 cells of lipids **1**, **2**, **3** (A); lipids **4**, **5**, **6** (B); and lipids **7**, **8**, **9** (C) using cholesterol as colipid (at lipid:cholesterol mole ratio of 1:1). Units of β-galactosidase activity were plotted against the varying lipid to DNA (±) charge ratios. The transfection efficiencies of the lipids were compared to that of commercially available LipofectAmine 2000. Transfection experiments were performed as described in the text. The transfection values shown are average of duplicate experiments performed on the same day.

cells are shown in Figure 5 for lipids **1**, **3**, **4**, **6**, **7**, and **9** at both lipid:DNA charge ratios of 3:1 and 1:1.

Cell Viabilities. MTT-based cell viability assays were performed in representative CHO cells with lipids **1**−**9** as well as with the commercially available LipofectAmine across the entire range of lipid:DNA charge ratios used in the actual transfection experiments. Percent cell viabilities of lipids **1**−**9** were found to be high (more than 75%), particularly up to the lipid:DNA charge ratios of 3:1 (Figure 6). However, LipofectAmine was found to be less toxic than the present lipids, particularly at lipid:DNA charge ratios 9:1 and 3:1 (Figure 6).

Physicochemical Characterizations of Liposomes and Lipoplexes. Sizes and Zeta Potentials. The nanosizes and the global surface charges of the representative lipoplexes prepared with lipids **1**, **3**, **4**, **6**, **7** and **9** were measured using dynamic laser light scattering instrument equipped with zeta-sizing capacity across the lipid:DNA charge ratios of 0.1:1 to 9:1 in the presence of DMEM. Broadly speaking, the nanosizes of lipoplexes prepared using both transfection efficient (e.g. **4** and **7**) and transfection-incompetent lipids (e.g. **3** and **6**) similarly increased with increasing lipid:DNA charge ratios (up to 3:1) within the range 200−430 nm (data not shown). At the highest lipid:DNA charge ratios of 9:1, all the lipoplexes grew somewhat larger (around 600 nm). Interestingly, in the presence of DMEM, the global surface charges of both the inefficient as well as efficient lipoplexes prepared using lipid:DNA charge ratios of 1:1 or 3:1 were found to be either slightly positive (2−5 mV) or close to electroneutrality (Table 1).

Gel-Mobility Shifts. Toward understanding the role of lipid:DNA electrostatic binding interactions (if any) in modulating the in vitro transfection efficacies of lipids **1**−**9**, gel-mobility shift assays were performed using representative lipoplexes prepared with lipids **1** and **3** (serine head), **4** and **6** (alanine head), and **7** and **9** (β-alanine head) across the lipid:DNA charge ratios of 9:1 to 0.1:1. The band intensities of the free DNA (unassociated or loosely bound with lipoplexes) for all these lipoplexes were found to be remarkably diminished at lipid:DNA charge ratios of 3:1 and 9:1 (Figure 7), indicating that at such high lipid:DNA charge ratios, all the lipids were strongly associated with plasmid DNA. At lower lipid:DNA charge ratios (1:1−0.1:1), the band intensities of free DNA for all the lipoplexes increased significantly, the highest increase being observed with serine-lipids (lipids **1** and **3**, Figure 7, parts A−C).

DNase I Sensitivities. Toward obtaining insights into the relative accessibilities of the lipoplex associated DNA to DNase I, DNase I sensitivity assays were carried out using lipoplexes made with lipids **1**−**9** across the entire range of lipid:DNA charge ratios 0.1:1−9:1. After the free DNA digestion by DNase I, the total DNA (both digested

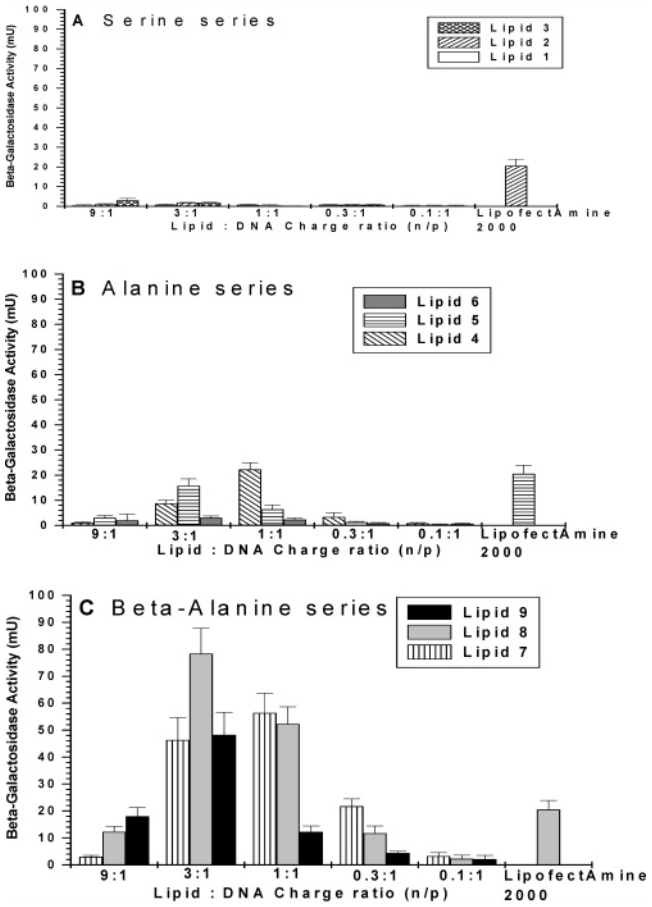

Figure 4. In vitro transfection efficiencies in COS-1 cells of lipids **1**, **2**, **3** (A); lipids **4**, **5**, **6** (B); and lipids **7**, **8**, **9** (C) using cholesterol as colipid (at lipid:cholesterol mole ratio of 1:1). Units of β-galactosidase activity were plotted against the varying lipid to DNA ($\pm$) charge ratios. The transfection efficiencies of the lipids were compared to that of commercially available LipofectAmine 2000. Transfection experiments were performed as described in the text. The transfection values shown are average of duplicate experiments performed on the same day.

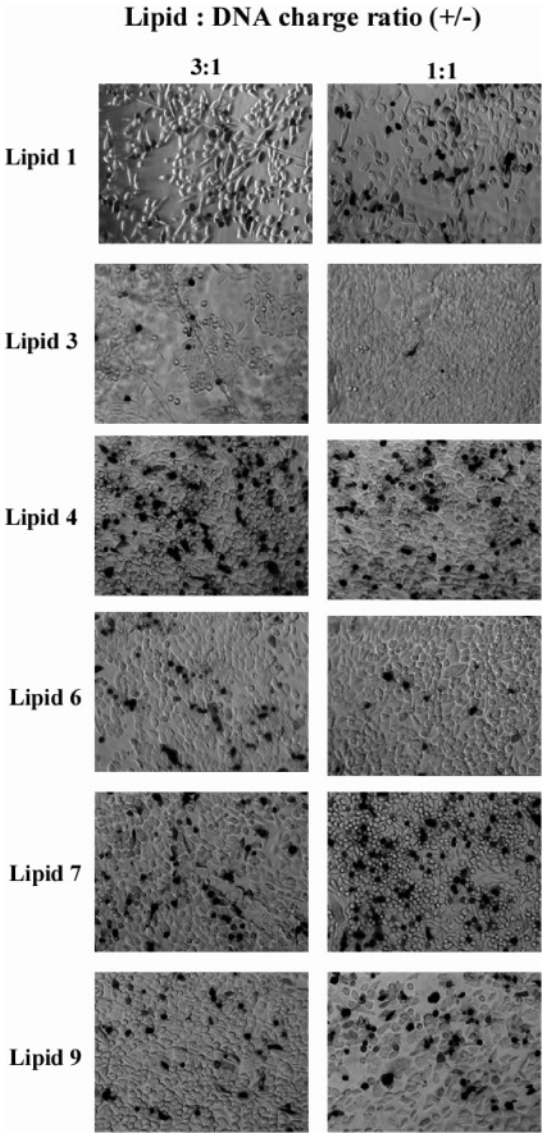

Figure 5. Histochemical whole cell X-gal staining of CHO cells transfected with lipids **1**, **3**, **4**, **6**, **7**, and **9** at lipid:DNA charge ratios of 3:1 and 1:1. Cells expressing β-galactosidase were stained with X-gal as described in the text.

and inaccessible DNA) was separated from the lipid and DNase I (by extracting with organic solvent) and loaded onto a 1% agarose gel. Resulting electrophoretic gel pattens in such DNase I protection experiments for representative lipoplexes prepared with lipids **1** and **3**, **4** and **6**, and **7** and **9** are shown in Parts A–C of Figure 8. In general, the band intensities of inaccessible and therefore undigested DNA associated with transfection incompetent lipids (**1** and **3** in particular) was observed to be significantly less than those associated with transfection efficient lipids (e.g. **4** and **7**, Figure 4, Parts A–C).

DISCUSSION

As a part of our ongoing structure–activity investigations in cationic lipid mediated gene delivery (*12*, *16*, *17*, *47–52*), in the present study, we have studied the influence of minor headgroup modifcations in liposomal gene delivery using nine novel cationic amphiphiles **1**–**9** containing simple aliphatic hydrocarbon chains (myristyl, palmityl, and stearyl) as hydrophobic tails and amino acids alanine, β-alanine and serine as their polar heads. Structurally speaking, lipid series **4**–**6** and **7**–**9** are very similar in nature. Except the headgroups of **4**–**6** being the structural isomers of lipids **7**–**9**, there are no differences between them. The only difference in the headgroup regions of lipids **1**–**3** and lipids **4**–**6** is that one hydrogen atom of the side-chain methyl groups of lipids **4**–**6** is substituted by one hydroxyl group in lipids **1**–**3**. Taking the high transfection efficacies of many previously reported cationic lipids containing a hydroxyalkyl headgroup (*31*, *40*, *41*) including our own (*49*, *50*, *52*) into account, we expected lipids **1**–**3** to be more transfection efficacious than lipids **4**–**6**. Surprisingly, lipids **1**–**3** turned out to be the most inefficient among all the lipids **1**–**9** (Figures 1–5). Findings in MTT-assay-based cell viability assays (Figure 6) ruled out the possibility of varying cell cytotoxicities playing any key role behind the compromised gene transfer efficacies of the serine lipids (**1**–**3**). The compromised transfection efficacies of lipids **1**–**3** in transfecting CHO, HepG2, MCF-7, and COS-1 cells across the entire lipid:DNA charge ratios of 0.1:9:1 (Figures 1–4, parts A) demonstrate that even minor structural substitution in the headgroup region can significantly lower the in vitro gene transfer properties of cationic amphiphiles. Such remarkable influence of minor headgroup modification in cationic lipid-mediated gene delivery is consistent with our recently reported findings on the dramatically superior transfer properties of a cholesterol-based cationic lipid with a β-alanine headgroup to its glycine counterpart (*47*). Findings in the

Table 1. Zeta Potential[a] (mV) of Liposomes and Lipoplexes (in DI water and plain DMEM, respectively)

		lipid:DNA charge ratio (*N*/*P*)					
no.	sample code	1:0	9:1	3:1	1:1	0.3:1	0.1:1
1	Lipid **1**	18.6 ± 1.6	6.4 ± 1.3	3.2 ± 1.6	1.6 ± 2.3	−32.0 ± 1.6	−30.4 ± 1.7
2	Lipid **3**	17.8 ± 1.2	6.6 ± 1.0	0.9 ± 2.1	−0.2 ± 3.4	−29.2 ± 2.4	−33.6 ± 1.8
3	Lipid **4**	27.1 ± 1.6	1.6 ± 2.8	0.4 ± 1.8	−1.9 ± 4.4	−15.5 ± 5.6	−25.6 ± 2.9
4	Lipid **6**	27.7 ± 2.1	2.9 ± 1.9	−4.5 ± 2.1	−8.7 ± 3.2	−22.6 ± 2.8	−30.7 ± 2.4
5	Lipid **7**	20.2 ± 4.7	11.9 ± 6.8	5.9 ± 2.7	0.3 ± 2.5	−33.7 ± 2.0	−28.6 ± 1.9
6	Lipid **9**	28.8 ± 3.2	6.3 ± 1.3	2.3 ± 2.0	1.3 ± 2.4	−30.6 ± 2.4	−27.3 ± 2.2

[a] ξ Potentials were measured by laser light scattering technique using Zetasizer 3000A (Malvern Instruments, UK). Values shown are the averages obtained from 10 (zeta potential) measurements.

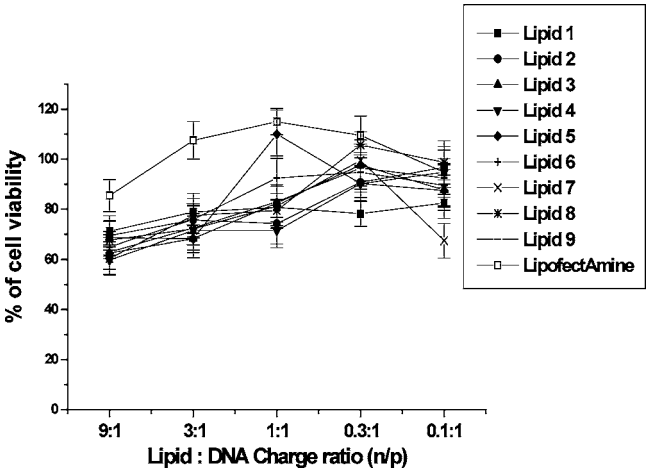

Figure 6. MTT-assay based cellular cytotoxicities of lipids **1**−**9** and commercially available LipofectAmine against representative CHO Cells. The percent cell viability values shown are average of duplicate experiments performed on the same day.

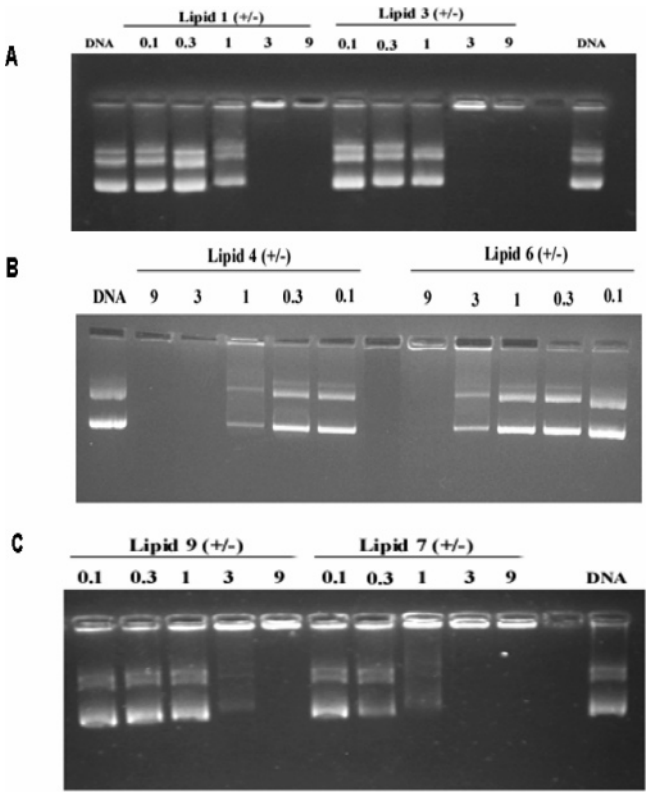

Figure 7. Electrophoretic gel patterns for lipoplex-associated DNA in gel retardation for lipid **1** and **3** (A), for lipid **4** and **6** (B), and for lipid **7** and **9** (C). The lipid:DNA charge ratios are indicated at the top of each lane. The details of treatment are as described in the text.

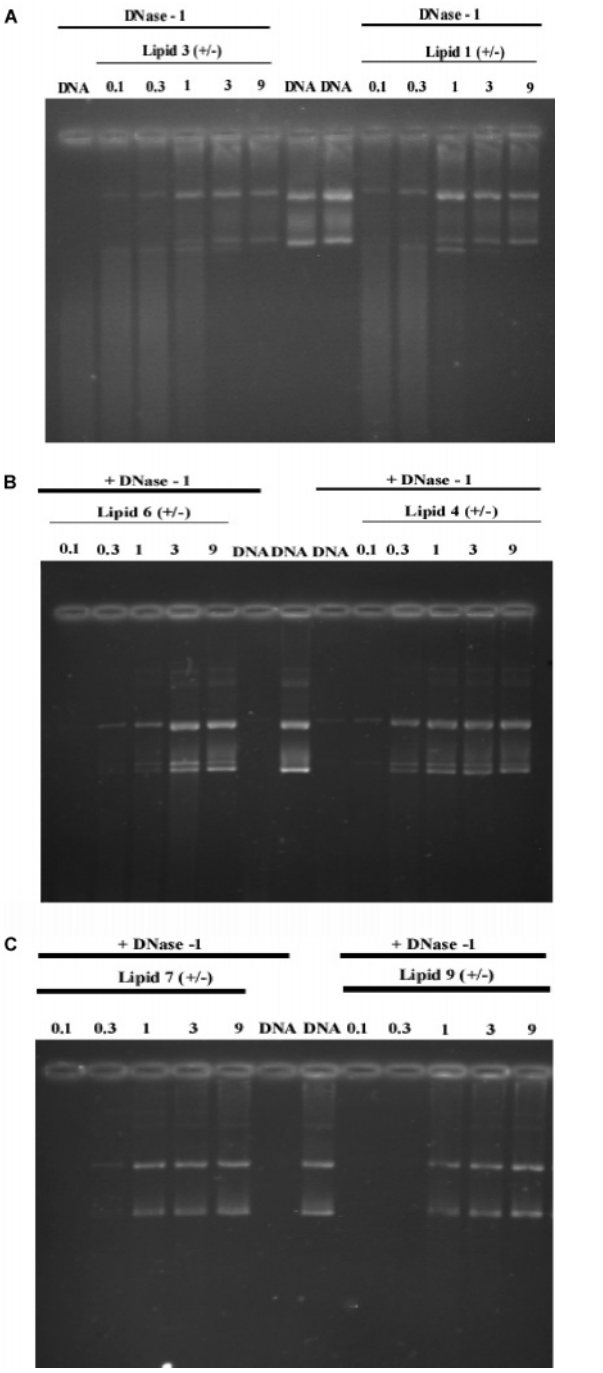

Figure 8. Electrophoretic gel patterns for lipoplex-associated DNA in DNase I sensitivity assay for lipids **1** and **3** (A), for lipids **4** and **6** (B), and for lipids **7** and **9** (C). The lipid:DNA charge ratios are indicated at the top of each lane. The details of treatment are as described in the text.

gel mobility shift assay indicate similar DNA-binding characteristics of lipids **1**−**9** (Figure 7). However, the electrophoretic gel patterns in DNase I sensitivity assays revealed pronounced sensitivities of DNA associated with lipoplexes of lipids **1**−**3** compared to DNA associated with lipids **4**−**9** (Figure 8). Thus, the findings summarized in Figures 7 and 8, taken together, support the notion that enhanced DNase I sensitivity of DNA associated with lipids **1**−**3** might play some important role behind their relatively poor gene transfer properties. However, the origin of such relatively pronounced DNase I sensitivities of the plasmid DNA associated with serine-lipids **1**−**3** across the entire lipid:DNA charge ratios of 9:1 to 0.1:1 remains elusive at this point of investigation.

The transfection profiles in COS-1 cells (Figure 4) provided the most convincing examples of dramatic headgroup influence in cationic lipid-mediated gene delivery. In COS-1 cells, although lipids **7**−**9** with β-alanine headgroups were found to be highly transfection efficient (lipid **8** at lipid:DNA charge ratios of 3:1 were 3−4-fold more transfection efficient than LipofectAmine-2000), gene transfer properties of lipids **4**−**6** containing their structurally isomeric alanine headgroups were observed to be significantly less (Figure 4, parts B and C). The strikingly enhanced gene transfection properties of lipid **9** with a β-alanine headgroup and a stearyl tail compared to lipid **6** with the same stearyl tail but a structurally isomeric alanine headgroup at 3:1 lipid:DNA charge ratio in COS-1 cells (Figure 4, parts B and C) demonstrate that in cationic lipid-mediated gene delivery even lipids with structurally isomeric headgroups can exhibit phenomenally contrasting transfection properties. The compromised transfection efficacies of all the present lipids at 9:1 lipid:DNA charge ratios (Figures 1−5) may partly originate from the big lipoplex sizes (>600 nm, data not shown). The global surface charge data summarized in Table 1 rules out the possibility of varying lipoplex surface potentials playing any key role behind the contrasting transfection profiles of the present lipids.

In conclusion, the present in-depth structure−activity investigation using nine novel cationic lipids with alanine, β-alanine, and serine headgroups demonstrates that high gene delivery efficacies of cationic amphiphiles containing alanine or β-alanine headgroups can get seriously compromised by substituting the alanine or β-alanine with serine, presumably due to the enhanced sensitivity of DNA associated with such serine-head-containing cationic lipids. The transfection efficacy profiles of the presently described cationic lipids once again reiterate the proposition that gene transfer efficacies of cationic amphiphiles can be significantly modulated by minor structural variations in both the polar headgroup and hydrophobic tail regions of the lipid.

ACKNOWLEDGMENT

Financial support received from the Department of Biotechnology, Government of India (to A.C.) is gratefully acknowledged. J.S. sincerely thanks the University Grant Commission (UGC), Government of India, for her doctoral research fellowship.

Supporting Information Available: Reverse phase HPLC chromatograms for the lipids **1**−**9** in two mobile phases with details of used HPLC parameters. This material is available free of charge via the Internet at http://pubs.acs.org.

LITERATURE CITED

(1) Verma, I. M., and Somina, M. (1997) Gene Therapy-Promises, Problems and Prospects. *Nature 389*, 239−242.

(2) Anderson, W. F. (1998) Human Gene Therapy. *Nature 392*, 25−30.

(3) Yla-Herttuala, S., and Martin, J. F. (2000) Cardiovascular Gene Therapy. *Lancet 355*, 213−222.

(4) Yang, Y., Nunes, F. A., Berencsi, K., Furth, E. E., Gonczol, E., and Wilson, J. M. (1994) Cellular Immunity to Viral Antigens Limits E1-Deleted Adenoviruses for Gene Therapy. *Proc. Natl. Acad. Sci. U.S.A. 91*, 4407−4411.

(5) Knowles, M. R., Hohneker, K. W., Zhou, Z., Olsen, J. C., Noah, T. L., Hu, P. C., Leigh, M. W., Engelhardt, J. F., Edwards, L. J., Jones, K. R., and Boucher, R. A. (1995) Controlled Study of Adenoviral-Vector mediated Gene Transfer in the Nasal Epithelium of Patients with Cystic Fibrosis. *New Engl. J. Med. 333*, 823−831.

(6) Crystal, R. G., McElvaney, N. G., Rosenfeld, M. A., Chu, C. S., Mastrangeli, A., Hay, J. G., Brody, S. L., Jaffe, H. A., Eissa, N. T., and Danel, C. (1994) Administration of an Adenovirus containing the Human CFTR cDNA to the Respiratory Tract of Individuals with Cystic Fibrosis. *Nat. Genet. 8*, 42−51.

(7) Yang, Y., Nunes, F. A., Berencsi, K., Gonczol, E., Engelhardt, J. F., and Wilson, J. (1994) Inactivation of E2a in Recombinant Adenoviruses Improves the Prospect for Gene Therapy in Cystic Fibrosis. *Nat. Genet. 7*, 362−369.

(8) Lehrman, S. (1999) Virus Treatment Questioned after Gene Therapy Death. *Nature 401*, 517−518.

(9) McGregor, C., Perrin, C., Monck, M., Camilleri, P., Anthony., and Kirby, J. (2001) Rational Approaches to the Design of Cationic Gemini Surfactants for Gene Delivery. *J. Am. Chem. Soc. 123*, 6215−6220.

(10) Prata, C. A. H., Zhao, Y., Barthelemy, P., Li, Y., Luo, D., McIntosh, T. J., Lee, S. J., and Grinstaff, M. W. (2004) Charge-Reversal Amphiphiles for Gene Delivery. *J. Am. Chem. Soc. 126*, 12196−12197.

(11) Bell, P. C., Bergsma, I. P., Bras, W., Stuart, M. C. A., Rowan, M. C., Feiters, M. C., and Engberts, J. B. F. N. (2003) Transfection mediated by Gemini Surfactants: Engineered Escape from Endosomal Compartment. *J. Am. Chem. Soc. 125*, 1551−1558.

(12) Majeti, B. K., Singh, R. S., Yadav, S. K., Reddy, S. B., Ramkrishna, S., Diwan, P. V., Madhavendra, S. S., and Chaudhuri, A. (2004) Enhanced Intravenous Transgene Expression in Mouse Lung using Cyclic-head Cationic Lipids. *Chem. Biol. 11*, 427−437.

(13) Kumar, V. V., Singh, R. S., and Chaudhuri, A. (2003) Cationic Transfection Lipids in Gene Therapy: Successes, SetBacks, Challenges and Promises. *Curr. Med. Chem. 10*, 1297−1306 and the references therein.

(14) Zhu, J., Munn, R. J., and Nantz, M. H. (2000) Self-cleaving Ortho Ester Lipids: A Class of pH-Vulnerable Ampliphiles. *J. Am. Chem. Soc. 122*, 2645−2646.

(15) Guenin, E., Herve, A. C., Floch, V., Loisel, S., Yaounac, J. J., Clement, J. C., Ferec, C., and des Abbayas, H. (2000) Cationic Phosphonolipids containing Quaternary Phosphonium and Arsonium Groups for DNA Transfection with Good Efficiency and Low Cellular Toxicity. *Angew. Chem., Int. Ed. 39*, 629−631.

(16) Mahidhar, Y. V., Rajesh, M., and Chaudhuri, A. (2004) Strikingly Spacer-Arm Modulated Gene Delivery Efficacies of Novel Cationic Glycolipids: Design, Synthesis and In Vitro Transfection Biology. *J. Med. Chem. 47*, 3938−3948.

(17) Karmali, P. P., Kumar, V. V., and Chaudhuri, A. (2004) Design, Syntheses and InVitro Gene Delivery efficacies of Novel Mono-, Di-, and Tri-lysinated Cationic Lipids: A Structure Activity Investigation. *J. Med. Chem. 47*, 2123−2132.

(18) Miller, A. D. (1998) Cationic Liposomes in Gene Therapy. *Angew. Chem., Int. Ed. 37*, 1768−1785 and the references therein.

(19) Lynn, D. M., Anderson, D. G., Putman, D., and Langer, R. (2001) Accelerated Discovery of Synthetic Transfection Vectors: Parallel Synthesis and Screening of a Degradable Polymer Library. *J. Am. Chem. Soc. 123*, 8155−8156.

(20) Choi, J. S., Joo, D. K., Kim, C. H., Kim, K., and Park, J. S. (2000) Synthesis of a Barbell-like Triblock Copolymer, Poly(L-lysine) Dendrimer-*block*-Poly(ethylene glycol)-*block*-Poly(L-lysine) Dendrimer, and Its Self-Assembly with Plasmid DNA. *J. Am. Chem. Soc. 122*, 474−480.

(21) Tang, M. X., Redemann, C. T., and Szoka, F. C. (1996) In Vitro Gene Delivery by Degraded Polyamidoamine Dendrimers. *Bioconjugate Chem*. *7*, 703−714.

(22) Kukowska-Latallo, J. F., Bielinska, A. U., Johnson, J., Spinder, R., Tomalia, D. A., and Baker, J. R. (1996) Efficient transfer of genetic material into mammalian cells using Starburst polyamidoamine dendrimers. *Proc. Natl. Acad. Sci. U.S.A. 93*, 4897−4902.

(23) Luo, D., Haverstick, K., Belcheva, N., Han, E., and Saltzman, W. M. (2002) Poly(ethylene glycol)-Conjugated PAMAM Dendrimer for Biocompatible, High-Efficiency DNA Delivery. *Macromolecules 35*, 3456−3462.

(24) Ilies, M. A., Seitz, W. A., Ghiviriga, I., Johnson, B. H., Miller, A., Thompson, E. B., and Balaban, A. T. (2004) Pyridinium Cationic Lipids in Gene Delivery: A Structure−Activity Correlation Study. *J. Med. Chem*. *15*, 3744−3754.

(25) Lee, Y., Koo, H., Lim, Y. B., Lee, Y., Mo, H., and Park, J. S. (2004) New Cationic Lipids for Gene Transfer with High Efficiency and Low Toxicity: T-shape Cholesterol Ester Derivatives. *Bioorg. Med. Chem. Lett*. *14*, 2637−2641.

(26) Wang, L., and MacDonald, R. C. (2004) New Strategy for Transfection: Mixtures of Medium-Chain and Long Chain Cationic Lipids Synergistically Enhance Transfection. *Gene Ther*. *11*, 1358−1362.

(27) Niculescu-Duvaz, D., Heyes, J., and Springer, C. J. (2003) Structure−Activity Relationship in Cationic Lipid mediated Gene Transfection. *Curr. Med. Chem. 10*, 1233−1261.

(28) Kirby, A. J., Carmilleri, P., Engberts, J. B. F. N., Feiters, M. C., Nolte, R. J. M., Soderman, O., Bergsma, M., Bell, P. C., Fielden, M. L., Garcia Rodriguez, C. L., Guedat, P., Kremer, A., McGregor, C., Perrin, C., Ronsin, G., and Van Eijik, M. C. P. (2003) Gemini Surfactants: New Synthetic Vectors for Gene Transfection. *Angew. Chem., Int. Ed. 42*, 1448−1457.

(29) Leclercq, F., Cohen-Ohana, M., Mignet, N., Sbarbati, A., Herscovici, J., Scherman, D., and Byk, G. (2003) Design, Synthesis and Evaluation of Gadolinium Cationic Lipids as Tools for Biodistribution Studies of Gene Delivery Complexes. *Bioconjugate Chem*. *14*, 112−119.

(30) Fabio, K., Gaucheron, J., Giorgio, C. D., and Vierling, P. (2003) Novel Galactosylated Polyamine Bolaamphiphiles for Gene Delivery. *Bioconjugate Chem*. *14*, 358−367.

(31) Heyes, J. A., Duvaz, D. N., Cooper, R. G., and Springer, C. J. (2002) Synthesis of Novel Cationic Lipids: Effect of Structural Modification on the Efficiency of Gene Transfer. *J. Med. Chem*. *45*, 99−114.

(32) Ewert, K., Ahmed, A., Evans, H. M., Schmidt, H. W., and Safinya, C. R. (2002) Efficient Synthesis and Cell-transfection Properties of a New Multivalent Cationic Lipid for Non-Viral Gene Delivery. *J. Med. Chem*. *45*, 5023−5029.

(33) Floch, V., Loisel, S., Guenin, E., Herve, A. C., Clement, J. C., Yaouanc, J. J., des Abbayes, H., and Ferec, C. (2000) Cation Substitution in Cationic Phosphono lipids: A New Concept to Improve Transfection Activity and Decrease Cellular Toxicity. *J. Med. Chem*. *43*, 4617−4628.

(34) Fichert, T., Regelin, A., and Massing, U. (2000) Synthesis and Transfection Properties of Novel Nontoxic Monocationic Lipids: Variations of Lipid Anchor, Spacer and Headgroup Structure. *Bioorg. Med. Chem. Lett. 10*, 787−791.

(35) Kawakami, S., Sato, A., Nishikawa, M., Yamashita, F., and Hashida, M. (2000) Mannose Receptor Mediated Gene Tranfer into Macrophases using Novel Mannosylated Cationic Liposomes. *Gene. Ther*. *7*, 292−299.

(36) Choi, J. S., Lee, E. J., Jang, H. S., and Sang, J. P. (2001) New Cationic Liposomes for Gene Transfer into Mammalian Cells with High Efficiency and Low Toxicity. *Bioconjugate Chem. 12*, 108−113.

(37) Byk, G., Wetzer, B., Frederic, M., Dubertret, C., Pitard, B., Jaslin, G., and Scherman, D. (2000) Reduction-Sensitive Lipopolyamines as a Novel Nonviral Gene Delivery System For Modulated Release of DNA with Improved Transgene Expression. *J. Med. Chem*. *43*, 4377−4387.

(38) Byk, G., Dubertret, C., Escriou, V., Frederic, M., Jaslin, G., Rangara, R., Pitard, B., Crouzet, J., Wils, P., Schwartz, B., and Scherman, D. (1998) Synthesis, Activity, and Structure−Activity Relationship Studies of Novel Cationic Lipids for DNA Transfer. *J. Med. Chem*. *41*, 224−235.

(39) Wang, J., Guo, X., Xu, Y., Barron, L., and Szoka, F. C., Jr. (1998) Synthesis and Characterization of Long Chain Alkyl Acyl Carnitine Esters. Potentially Biodegradable Cationic Lipids for Use in Gene Delivery. *J. Med.Chem*. *41*, 2207−2215.

(40) Ghosh, Y. K., Visweswariah, S. S., and Bhattacharya, S. (2000) Nature of linkage between the cationic headgroup and cholesterol skeleton controls gene transfection efficiency. *FEBS. Lett. 473*, 341−344.

(41) Felgner, J. H., Kumar, R., Sridhar, C. N., Wheeler, C. J., Tsai, Y.-J., Border, R., Ramsey, P., Martin, M., and Felgner, P. L. (1994) Enhanced gene delivery and mechanism studies with a novel series of cationic lipid formulations. *J. Biol. Chem*. *269*, 2550−2561.

(42) Zabner, J., Fasbender, Al, J., Moninger, T., Poellinger, K. A., and Welsh, M. J. (1995) Cellular and molecular barriers to gene transfer by a cationic lipid. *J. Biol. Chem. 270*, 18997−19007.

(43) Floch, V., Bolćh, G. L., Gable-Guillaume, C., Bris, N. L., Yaouanc, J−J., Abbayes, H., Ferec, C., and Clement, J.-C. (1998) Phosphonolipids as Non-Viral Vectors for Gene Therapy. *Eur. J. Med. Chem. 33*, 923−934.

(44) Gao, H., and Hui, K. M. (2001) Synthesis of Novel series of Cationic Lipids that can act as Efficient Gene Delivery Vehicles through Systematic Heterocyclic Substitution of Cholesterol Derivatives. *Gene Ther. 8*, 855−863.

(45) Ghosh, Y. K., Visweswariah, S. S., and Bhattacharya, S. (2002) Advantage of the Ether Linkage between the Positive Charge and the Cholesteryl Skeleton in Cholesterol- based Amphiphilkes as vectors for Gene Delivery. *Bioconjugate Chem. 13*, 378−384.

(46) Gaucheron, J., Wong, T., Wong, K. F., Maurer, N., and Cullis, P. R. (2002) Synthesis and Properties of Novel Tetraalkyl Cationic Lipids. *Bioconjugate Chem. 13*, 671−675.

(47) Singh, R. S., and Chaudhuri, A. (2004) Single Additional Methylene Group in the Headgroup Region Imparts High Gene Transfer Efficacy to a Transfection-Incompetent Cationic Lipid. *FEBS Lett. 556*, 86−90.

(48) Kumar, V. V., Pichon, C., Refregiers, M., Guerin, B., Midoux, P., and Chaudhuri, A. (2003) Single Histidine Residue in Headgroup Region is Sufficient to Impart Remarkable Gene Transfection Properties to Cationic Lipids: Evidence for Histidine-mediated Membrane Fusion at Acidic pH. *Gene. Ther. 10*, 1206−1215.

(49) Singh, R. S., Mukherjee, K., Banerjee, R., Chaudhuri, A., Hait, S. K., Moulik, S., Ramadas, Y., Vijayalakshmi, A., and Rao, N. M. (2002) Anchor-dependency for Nonglycerol based Cationic Lipofectins: Mixed Bag of Regular and Anomalous Transfection Profiles. *Chem. Eur. J. 8*, 900−909.

(50) Srilakshmi, G. V., Sen, J., Chaudhuri, A., Ramdas, Y., and Rao, N. M. (2002) Anchor- dependent Lipofection with Nonglycerol based Cytofectins containing Single 2-Hydroxyethyl Head groups. *Biochim. Biophys. Acta 1559*, 87−95.

(51) Banerjee, R., Mahidhar, Y. V., Chaudhuri, A., Gopal, V., and Rao, N. M. (2001) Design, Synthesis and Transfection Biology of Novel Cationic Glycolipids for Use in Liposomal Gene Delivery. *J. Med. Chem. 44*, 4176−4185.

(52) Banerjee, R., Das, P. K., Srilakshmi, G. V., Chaudhuri, A., and Rao, N. M. (1999) A Novel Series of Nonglycerol based Cationic Transfection Lipids for Use in Liposomal Gene Delivery. *J. Med. Chem. 42*, 4292−4299.

(53) Bodanszky, M., and Bodanszky, A. (1984) *The Practice of Peptide Synthesis*, p 20, Springer-Verlag, Berlin, Heidelberg.

(54) Sambrook, J., Fritsch, E. F., and Maniatis, T. (1989) *Molecular Cloning: A Laboratory Manual*, 2nd ed.; Cold Springer Harbor Laboratory Press, Cold Spring Harbor, NY.

BC0500443

Albumin–Insulin Conjugate Releasing Insulin Slowly under Physiological Conditions: A New Concept for Long-Acting Insulin

Yoram Shechter,*,‡ Marina Mironchik,‡ Sara Rubinraut,§ Ayala Saul,‡,§ Haim Tsubery,‡,§ and Mati Fridkin*,§

Departments of Biological Chemistry and Organic Chemistry, Weizmann Institute of Science, Rehovot 76100, Israel. Received February 27, 2005; Revised Manuscript Received April 26, 2005

The covalent linkage of peptides or protein drugs to human serum albumin (HSA) greatly prolongs their lifetime in vivo but is pharmacologically irrelevant when it irreversibly inactivates them. We retain drug bioactivity by synthesizing a heterobifunctional reagent (MAL-Fmoc-OSu, 9-hydroxymethyl-2-(amino-3-maleimidopropionate)-fluorene-*N*-hydroxysuccinimide) that generates HSA–Fmoc–insulin on covalent conjugation to the amino group of insulin and the Cys-34 side chain of HSA. HSA–Fmoc–insulin is water-soluble and, upon incubation in aqueous buffers reflecting normal human serum conditions, slowly, spontaneously, and homogeneously hydrolyzes to release unmodified insulin with a $t_{1/2}$ of 25 ± 2 h. A single subcutaneous or intraperitoneal administration of HSA–Fmoc–insulin to diabetic rodents lowers circulating glucose levels for about 4 times longer than an equipotent dose of Zn^{2+}-free insulin. Following subcutaneous administration, onset of the glucose-lowering effect is delayed 0.5–1 h and persists for 12 h. Thus, we present a prototype insulin formulation possessing three desirable parameters: high aqueous solubility, delayed action following subcutaneous administration, and prolonged therapeutic effect.

INTRODUCTION

Most polypeptide drugs, in particular nonglycosylated proteins of molecular mass less than 50 kDa, are short-lived species in vivo, having circulatory half-lives of 5–20 min (*1*). The short lifetimes of proteins in vivo are attributed to several mechanisms, including glomerular filtration in the kidney and proteolysis at several levels (*2*). Insulin is degraded primarily in the liver through a mechanism defined as receptor-mediated endocytosis (*3*, *4*). This mechanism is an efficient route for terminating the action of the hormone after the levels of glucose and other nutrients have been normalized. Chemically modified insulins with negligible receptor binding affinities are therefore longer-lived species within the circulation; however, they are biologically ineffective (*5*).

IDDM[1] patients receive multiple daily subcutaneous administrations of "rapid" and long-acting insulins (*2*, *6*–*8*). Prolonged long-acting insulin preparations are needed to supply low basal levels of circulating insulin between meals and overnight, this being a physiological requirement for reducing triglyceride breakdown and suppressing hepatic glucose output under "resting" conditions (*9*–*11*).

Most long-acting insulins currently in use are suspensions of crystals, produced either by Zn^{2+} ions or by the addition of basic protamine. Such injected suspensions have decreased rates of absorption from the subcutaneous compartment to the circulatory system. Slow dissolution at the site of injection brings about the protracted effect (*2*, *12*, *13*). The application of subcutaneous infusion pumps was also introduced as a measure for controlled continuous supply of short-acting insulin (reviewed in ref *14*).

In recent years, major efforts have been devoted to prolonging the action of insulins that are soluble in aqueous buffered media. In one such innovative approach, two arginine moieties were covalently linked to insulin to raise the isoelectric point of the hormone. The derivative thus obtained (i.e., insulin-glargine) is formulated in a soluble form in a slightly acidic media and is crystallized and precipitated immediately after injection at the physiological neutral pH of the subcutaneous space (*15*–*17*).

Many versatile polymeric prodrugs have been developed for controlled drug delivery. Thus, conjugates of different drugs with polymeric carriers employing various chemical anchoring modes were developed, for example, hydrazones, esters carbamates, citraconyl, amides and acetals (reviewed in refs *18* and *19*). Noteworthy among the polymeric carriers are derivatives of poly(ethylene glycol) (*20*).

Albumin is long-lived in vivo. Similarly, drugs and endogenous substances that associate tightly with albumin have lower clearance rates than do the unbound substances and exhibit prolonged lifetime profiles in vivo (*21*). Long-chain-free fatty acids bind tightly to albumin ($K_a = 10^8\ M^{-1}$) (*22*), a fact that provided the impetus for

* To whom correspondence should be addressed. YS: Tel 972-8-9344530; fax 972-8-9344118; e-mail y.shechter@weizmann.ac.il. MF: Tel 972-8-9342505; fax 972-8-9344142; e-mail mati.fridkin@weizmann.ac.il.

‡ Department of Biological Chemistry.

§ Department of Organic Chemistry.

[1] Abbreviations used: BSA, bovine serum albumin; DCC, *N*,*N*′-dicyclohexylcarboimide; DCU, *N*,*N*′-dicyclohexylurea; DMF, *N*,*N*′-dimethylformamide; DTNB, 5,5′-dithiobis(2-nitrobenzoic acid); HPLC, high-performance liquid chromatography; HSA, human serum albumin; HSA–Fmoc–insulin, a conjugate of human serum albumin and insulin; IDDM, insulin-dependent diabetes mellitus; MAL-Fmoc-OSu, 9-hydroxymethyl-2-(amino-3-maleimidopropionate)-fluorene-*N*-hydroxysuccinimide; MIB–NHS, *m*-maleimido benzoic acid–*N*-hydroxysuccinimide ester; STZ, streptozocin; TCA, trichloroacetic acid; TFA, trifluoroacetic acid; THF, tetrahydrofurane.

10.1021/bc050055w CCC: $30.25 © 2005 American Chemical Society
Published on Web 07/02/2005

preparation of soluble fatty acid acylated insulins that could bind to serum albumin. However, the affinity of the insulin conjugates for albumin ($K_a \approx 10^5$ M^{-1}) was considerably less than that of the unbound long-chain-free fatty acids, and the conjugates exhibited only moderately prolonged actions in vivo (*23*−*25*).

A series of HSA−peptide conjugates have been recently prepared through formation of a stable covalent bond between maleimido-derivatives of biologically active peptides (e.g., atrial nutriuretic peptide (*26*), dynorphine (*27*), the Kringle 5 region of plasminogen (*28*)) and the mercapto moiety of the Cys-34 of HSA. This was undertaken with the aim of increasing the half-life of the peptide in circulation by reducing elimination through the kidney and concomitantly protecting it from proteolysis by plasma enzymes. The activities of the HSA-bound peptides, though significantly reduced as compared to the parent peptides, were found to be rather substantial. Moreover, the conjugates proved to be long-acting species.

Therapeutically, insulin differs from many other polypeptide drugs in the sense that overdosing may lead to severe hypoglycemia (*29*−*31*). To avoid that, only a limited dosage of insulin can be administered each time. Such a dosage is often insufficient to maintain the basal nighttime insulin level needed to avoid hyperglycemia at dawn (*6*−*8*). This therapeutic drawback can be overcome by engineering an insulin prodrug that is biologically inactive at the time of administration.

In this study, we aim to link insulin to HSA via a covalently stable bond. We expect such a nondissociable molecule to share the longevity of albumin in vivo. Because an extended surface area of the insulin molecule is engaged in receptor binding (*32*, *33*), we initially thought it unlikely that such a conjugate would be biologically (and therapeutically) active. Nevertheless, even an inactive, insulin−HSA chimera could be advantageous if the conjugate is capable of generating the active unmodified parent insulin with a desirable pharmacokinetic pattern. Our efforts in this latter direction are brought here in detail.

METHODS

Materials. Human (Zn^{2+}-free) insulin was donated by Novo Nordisk (Bagsvaerd, Denmark) and by Biotechnology General (Rehovot, Israel) and was used without further purification. D-[U-^{14}C]glucose (4−7 mCi/mol) was obtained from DuPont-NEN (Boston, MA). Collagenase, type I (134 U/mg), was purchased from Worthington (Freehold, NJ). 9-Fluorenylmethoxycarbonyl-*N*-hydroxysuccinimide (Fmoc-OSu) and di-*tert*-butyldicarbonate (t-Boc)$_2$O were obtained from Novabiochem (Laüfelfingen, Switzerland). MIB−NHS was obtained from Sigma-Aldrich (Rehovot, Israel). HSA was acquired from Omrix Biopharmaceutical Ltd. (Weizmann Science Park, Nes-Ziona, Israel). The protein was treated with 1 equiv of dithiothreitol for 20 min at pH 6.0 and then extensively dialyzed. This treatment removes any mixed disulfide form and any other removable protection from cysteine-34 of HSA (*34*). HSA prepared by this procedure contains 0.76 ± 0.03 mol of SH per mol of HSA as determined with DTNB (*35*). All other materials used in this study were of analytical grade.

HPLC analyses were performed using a Spectra-Physics SP-8800 liquid chromatography system with an Applied Biosystems 757 variable wavelength absorbance detector and a Spectra-SYSTEM and P2000 liquid chromatography system with a Spectra-SYSTEM AS100 autosampler and Spectra-SYSTEM UV1000, all controlled by a ThermoQuest chromatography data system (ThermoQuest Inc., San Jose, CA). The column effluents were monitored by UV absorbance at 220 nm. Analytical reverse phase HPLC was performed using a prepacked Chromolith Performance RP-18e column (4.6 mm × 100 mm, Merck KGaA, Darmstadt, Germany). The column was eluted with a binary gradient established between solution A (0.1% TFA in H_2O) and solution B (0.1% TFA in acetonitrile/H_2O; 3:1 v/v). Preparative separations were performed with a prepacked Vydac, RP-18, or RP-4 column (250 mm × 22 mm, Hesperia, CA).

Biological Methods and Procedures. Iodination of insulin and of HSA using [^{125}I] iodine was performed using the chloramine-T method (*36*). Rat adipocytes were prepared from the fat pads of male Wistar rats (100−200 g) by collagenase digestion (*37*). Lipogenesis (during which [U-^{14}C]glucose was incorporated into the lipids) was performed using the procedure of Moody et al. (*38*). Diabetes was induced by a single intravenous injection of freshly prepared streptozocin (STZ) solution (55 mg/kg of body weight) as per the method of Meyerovitch et al. (*39*). Rats were maintained at 24 °C under conditions of controlled lighting and were fed ad libitum. Blood samples for the analysis of blood glucose were taken from the tail veins and measured with a glucose analyzer (Beckman Instruments, Fullerton, CA) by the glucose oxidase method. Groups consisted of five Wistar rats weighing 170 ± 5 g. Data are presented as means ± SE.

Synthesis of 9-Hydroxymethyl-2-(amino-3-maleimidopropionate)-fluorene-*N*-hydroxy-succinimide (2). *9-Hydroxymethyl-2-(amino-3-maleimidopropionate)fluorene (**1**).* 3-Maleimidopropionic acid (1 g, 5.9 mmol) and DCC (0.69 g, 2.95 mmol) were dissolved in 10 mL of DMF and incubated for 4 h. *N*,*N*′-Dicyclohexylurea (DCU) was filtered off, and the anhydride thus formed (2.95 mmol) was dissolved in DMF (12 mL) and added to a suspension of 9-hydroxymethyl-2-amino fluorine (*36*; 0.4 g, 1.9 mmol) and $NaHCO_3$ (0.74 g, 8.85 mmol) in water. The homogeneous reaction mixture was stirred for 40 min, and product formation was monitored by analytical HPLC (Chromolith column, R_t = 4.46 min, 10−100% B over 10 min with a flow rate of 3 mL/min). The crude product was purified using preparative HPLC (RP-18 column, 10−100% B over 60 min with a flow rate of 12 mL/min). Yield, 57%, 1.08 mmol, 0.39 g. ESMS (calcd) 362.38 Da; ESMS (found) 362.42 Da (electrospray MS analyses were carried out with the Micromass Platform LCZ 4000).

*9-Hydroxymethyl-2-(amino-3-maleimidopropionate)-fluorene-N-hydroxysuccinimide (**2**)* was prepared according to the procedure of Albericio et. al. (*40*). Pyridine (0.17 mL, 2 mmol) was added dropwise to a stirred solution of 9-hydroxymethyl-2-(amino-3-maleimidopropionate)fluorene (0.37 g, 1.02 mmol) and triphosgene (0.425 g, 1.43 mmol, 4.2 equiv) in dry THF (10 mL). After 20 min, the precipitated pyridine hydrochloride salt was filtered off, and the THF was removed under vacuum. The oil obtained was dissolved in 10 mL of dry THF containing *N*-hydroxysuccinimide (0.61 g, 5.3 mmol). Pyridine (0.26 mL, 3.2 mmol) was then added, and the solution was stirred for 20 min. The precipitated pyridine hydrochloride salt was filtered off, and the THF was removed by vacuum. The oil obtained was dissolved in chloroform (100 mL) and washed with an aqueous $NaHCO_3$ solution (0.5 N, 3 × 50 mL), HCl (0.1 N, 3 × 50 mL), water (2 × 50 mL), and brine. The organic phase was dried over $MgSO_4$ and evaporated to give the desired product with a yield of 89% (0.9 mmol, 0.45 g). Analytical HPLC (R_t = 5.7 min, 10−100% B over 10 min with a flow rate of 3 mL/min) was used to ascertain the purity of the product.

ESMS (calcd) 503.13 Da; ESMS (found) for $[M + Na]^+$ = 526.38 Da and for $[M + K]^+$ = 542.30 Da.

Preparation of HSA–Fmoc–Insulin. To a stirred solution of Zn^{2+}-free insulin (5.9 mg, 1 μmol in 1.0 mL of 0.1 M phosphate buffer at pH 7.2) was added 505 μg (1 equiv) of MAL-Fmoc-OSu (50.5 μL from a fresh solution of MAL-Fmoc-OSu in DMF, 10 mg/mL). The reaction was carried out for 20 min at 25 °C. HSA (0.37 mL from a solution of 1.6 mM) was then added to a final concentration of 0.42 mM (0.6 mol/mol of insulin). The reaction was carried out for 2 h, and the mixture was then dialyzed overnight against H_2O at 7 °C. HSA–Fmoc–insulin was purified from unreacted insulin and from insulin–Fmoc–MAL that had not reacted with HSA by preparative HPLC (RP-4 column, Hesperia CA. 20–100% B over 60 min with a flow rate of 10 mL/min) The fractions corresponding to HSA–Fmoc–insulin, coeluted with HSA, were collected and lyophilized.

Preparation of HSA–BENZ–Insulin. This (irreversible) HSA–insulin conjugate was prepared under identical conditions to those used for HSA–Fmoc–insulin except that the hetrobifunctional agent used was *m*-maleimido-benzoate–*N*-hydroxysuccinimide ester (MIB–NHS). The reagent (32 μL from a fresh solution of MIB–NHS at 10 mg/mL) was reacted with insulin for 20 min at 25 °C prior to the addition of HSA (see above). HPLC-purified HSA–BENZ–insulin was characterized by MALDI-TOF MS. A mass of 72.432 kDa was found (calculated mass for 1:1 conjugate is 72.570 kDa).

RESULTS

Pharmacological Pattern of Subcutaneously Administered HSA in the Rat. ^{125}I-labeled HSA was administered subcutaneously to rats and the pharmacological pattern as a function of time was constructed by withdrawing blood aliquots at various time points and determining the TCA-precipitable counts for each aliquot. Subcutaneously administered HSA is a long-lived species in the rat circulatory system in vivo. It reached a peak value of 14 ± 1 h after administration and then declined with a $t_{1/2}$ of 41 ± 2 h (see appendix in Supporting Information). For comparison, we subcutaneously administered ^{125}I-insulin under similar experimental conditions. Insulin reached its peak value at 1 ± 0.1 h and then declined with a $t_{1/2}$ of 9.0 ± 1.0 h. Thus, subcutaneously administered HSA exhibits a substantially prolonged lifetime in vivo compared to insulin or any other nonglycosylated peptide or protein of molecular mass lower than 17 kDa (reviewed in ref *41*).

Engineering an HSA–Insulin Conjugate that Releases Insulin under Physiological Conditions. The covalent linking of insulin to HSA with MIB–NHS resulted in a nondissociable HSA–insulin conjugate having negligible biological potencies in vitro (subsequent paragraphs). We therefore designed and synthesized a heterobifunctional agent, consisting of an Fmoc-OSu derivative in which a maleimide group was attached to the flurenyl backbone. The steps involved in the synthesis of MAL-Fmoc-OSu and its structure are illustrated in Figure 1. Using MAL-Fmoc-OSu enabled us to link proteins via their amino side chains to the single cysteinyl residue of HSA. Previously we have found that Fmoc moieties linked to the amino side chains of peptides and proteins undergo slow hydrolysis in aqueous solutions under physiological conditions, generating the unmodified parent peptides and proteins (*41*, *42*).

The procedure described in detail in the Methods section was found optimal for coupling equimolar amounts of insulin to HSA. In brief, MAL-Fmoc-OSu is first reacted stoichiometrically with insulin for 20 min at pH 7.2, this being a pH value at which MAL remains chemically stable for several hours (*43*). Albumin is then added with a stoichiometry of 0.6 mol per mol of derivatized insulin in an attempt to reach a quantitative coupling of insulin–Fmoc–MAL to the cysteinyl-34 of this carrier protein. Unreacted insulin and insulin–Fmoc–MAL are removed by a semipreparative HPLC procedure.

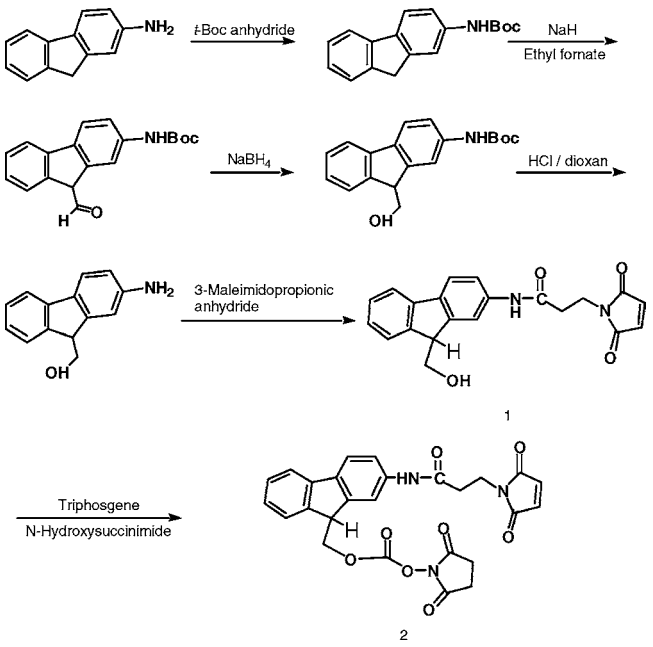

Figure 1. Schematic illustration of the synthesis and the structure of 9-hydroxymethyl-2-(amino-3-maleimido-propionate)-fluorene-*N*-hydroxysuccinimide (MAL-Fmoc-OSu). This heterobifunctional agent was used to conjugate HSA to insulin in the preparation of HSA–Fmoc–insulin.

General Features of HSA–Fmoc–Insulin. Table 1 summarizes several characteristic features of the HPLC-purified HSA–Fmoc–insulin that we prepared. It is a highly water-soluble derivative (>200 mg/mL) in buffered near-neutral solutions (pH 6–7) owing to the extreme solubility of the carrier protein (*44*). MALDI-TOF MS

Table 1. Chemophysical Features of HSA–Fmoc–Insulin

covalently linked insulin[a]		24 ± 3 μg/mg of HSA
solubility in aqueous buffer (pH 7.0)		>200 mg/mL
HPLC analysis retention time[a]		8.6 min
MALDI-TOF mass spectrum analysis[b] (m/z)	calcd	72.650 kDa
	found	73.189 kDa
molar extinction coefficient	calcd[c]	$\epsilon_{280} = 51.328$
		$\epsilon_{280}^{0.1\%} = 0.706$
	found	$\epsilon_{280} = 54.400$
		$\epsilon_{280}^{0.1\%} = 0.744$

[a] Determined by HPLC analysis following incubation of the conjugate in 0.1 M Na_2CO_3 (pH 10.3) for 4 h at 25 °C. Analytical HPLC procedures were carried out under the experimental conditions specified in the legend to Figure 3. Under these conditions, insulin elutes with R_t = 6.91 min and has a surface area of 187 000 ± 9000 mav/μg of insulin, and HSA (either free or linked to insulin) elutes with R_t = 8.1 min and has a surface area of 156 000 ± 7000 mav/μg of HSA. [b] MALDI-TOF MS analyses were carried out with the Bruker-Reflex-Reflection model. The molecular weight of HSA is calculated according to the amino acid composition of this carrier protein (ref *44*). [c] Molar extinction coefficient for HSA–Fmoc–insulin was calculated by combining the ϵ_{280} values of HSA (ϵ_{280} = 35 280, ref *37*), insulin (ϵ_{280} = 5800), and Fmoc (ϵ_{280} = 10 250).

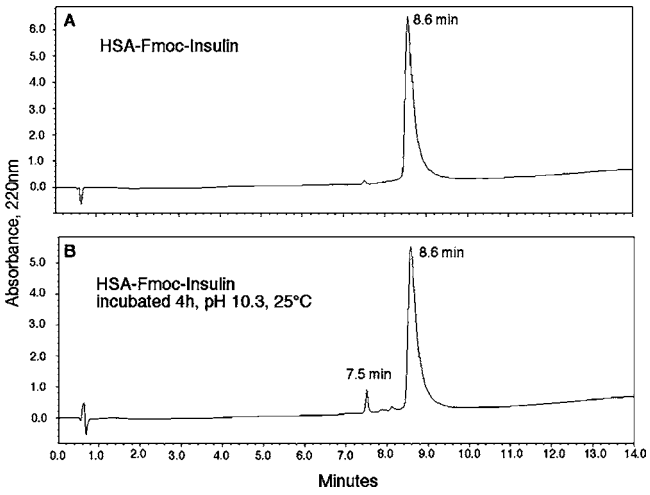

Figure 2. HPLC analysis of purified HSA−Fmoc−insulin before and after the release of insulin by hydrolysis: (A) purified HSA−Fmoc−insulin (100 μg loaded); (B) purified HSA−Fmoc−insulin following 4 h hydrolysis through incubation at pH 10.3, 25 °C. HPLC was conducted with a linear gradient from 0 to 100% of solution A (0.1% TFA) to solution B (acetonitrile−H_2O, 75:25 in 0.1% TFA) over 10 min and then 4 min in solution B, using a Chromolith RP 18e (100 mm × 4 mm) column at a rate of 3 mL/min. The effluent was monitored at 220 nm. Under the same experimental conditions, insulin elutes with $R_t = 6.91$ min and has a surface area of 187 000 ± 9000 mav/μg of insulin.

analysis revealed a molecular mass of 73.189 kDa (calculated mass for the 1:1 conjugate is 72.650 kDa). Analytical HPLC revealed that HSA−Fmoc−insulin coemerges with HSA as a single symmetric peak (Figure 2; retention time 8.6 min). A molar extinction coefficient of ϵ_{280} = 54 400 ($\epsilon_{280}^{0.1\%}$ 0.744) was found (calculated for 1:1 conjugate ϵ_{280} = 51 328). The HSA−Fmoc−insulin thus obtained contains 24 ± 3 μg of covalently linked insulin per mg of HSA as judged by HPLC analysis following the release of the covalently linked insulin from the conjugate by incubation at pH 10.3 for 4 h at 25 °C (Figure 2). In theory, 61 μg of covalently linked insulin per mg of conjugate is expected, based on 0.76 mol of SH per mol of HSA (experimental part). Thus our preparation of HSA−Fmoc−insulin appears to contain also HSA that is not linked to insulin.

Biological Potency of HSA−Fmoc−Insulin. Figure 3 shows the dose−response curve for native insulin and for HSA−Fmoc−insulin in a lipogenic assay in rat adipocytes. Based on the value of 24 ± 3 μg of covalently linked insulin per mg HSA in the conjugate (Table 1), HSA−Fmoc−insulin has 12.5% ± 3% of the biological potency of the native hormone (ED_{50} value = 2.4 ± 0.1 ng/mL versus ED_{50} = 0.3 ± 0.01 ng/mL for insulin, Figure 3). The covalent linking of insulin to HSA using the nonreversible agent MIB−NHS under similar experimental conditions (see Methods) yielded a conjugate having negligible potency (ED_{50} = 130 ± 10 ng/mL, being ~0.2% of the biological potency of insulin).

HSA−Fmoc−Insulin Releases Insulin upon Incubation under Physiological Conditions. Incubation of HSA−Fmoc−insulin at pH 10.3 for 4 h at 25 °C causes the covalently linked insulin to be released quantitatively from the conjugate (Figure 2B). In Figure 4A, HSA−Fmoc−insulin was incubated in 0.1 M phosphate buffer (pH 8.5, 37 °C), and the amount of insulin released from the conjugate as a function of time was quantified by HPLC analysis. At pH 8.5, the rate of Fmoc hydrolysis from Fmoc−protein conjugates is nearly identical to that obtained in normal human serum at 37 °C (*41*, *42*). As shown in the figure, insulin is released from the conjugate in a slow homogeneous fashion, having a half-life of 24 ± 3 h. After 80 and 150 h, the cumulative amount of free insulin reached 71% and 100%, respectively, of the initial HSA−Fmoc−insulin level.

Reactivation of HSA−Fmoc−Insulin upon Incubation. In Figure 4B, aliquots were withdrawn from incubated HSA−Fmoc−insulin (pH 8.5, 37 °C) at different time points and analyzed for their biological potencies in a lipogenic assay in rat adipocytes. As shown in the figure, the conjugate undergoes reactivation upon incubation in a nearly linear fashion. Thus, starting from 12% ± 3% at time 0, lipogenic potency is elevated to 31% ± 3%, 43% ± 4%, and 59% ± 5% following 10, 20, and 40 h of incubation, respectively. Upon 150 h of incubation, HSA−Fmoc−insulin regains its full biological potency (Figure 4B).

A Single Intraperitoneal or Subcutaneous Administration of HSA−Fmoc−Insulin Facilitates a Prolonged Glucose-Lowering Pattern in Mice. In Figure 5, we compare the glucose-lowering pattern of HSA−Fmoc−insulin (0.4 mg/mouse, corresponding to 9.6 μg of covalently linked insulin) to that of Zn^{2+}-free insulin (3 μg/mouse) following a single administration. For Figure 5A, administration was intraperitoneal, while in Figure 5B, it was subcutaneous. As shown in Figure 5A, HSA−Fmoc−insulin facilitates a prolonged and stable glucose-lowering pattern over a period of 14 h, exceeding

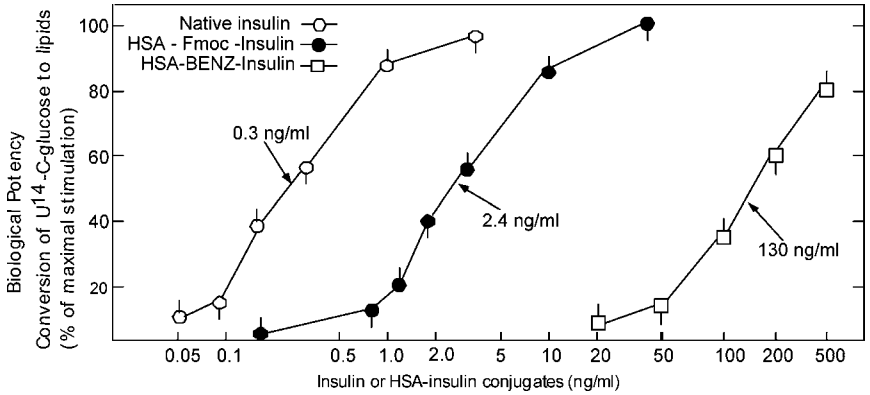

Figure 3. Dosage-dependent stimulation of lipogenesis in rat adipocytes. Lipogenesis was carried out for 2 h at 37 °C in plastic vials containing 0.5 mL of fat cell suspension (1.5 × 10^5 cells) and 0.2 mM [U-^{14}C]glucose in the presence or absence of the indicated concentrations of native insulin or HSA−insulin conjugates. Results are expressed as a percentage of maximal stimulation. Insulin (100 ng/mL) stimulated lipogenesis 4−5-fold above basal levels. HSA−Fmoc−insulin (1 mg/mL) was taken as containing 24 ± 3 μg of insulin per mg of HSA in this assay (see Table 1). The ED_{50} values for native insulin (0.3 ng/mL), for HSA−Fmoc−insulin (2.4 ng/mL), and for HSA−BENZ−insulin (130 ng/mL) are indicated with arrows on the figure.

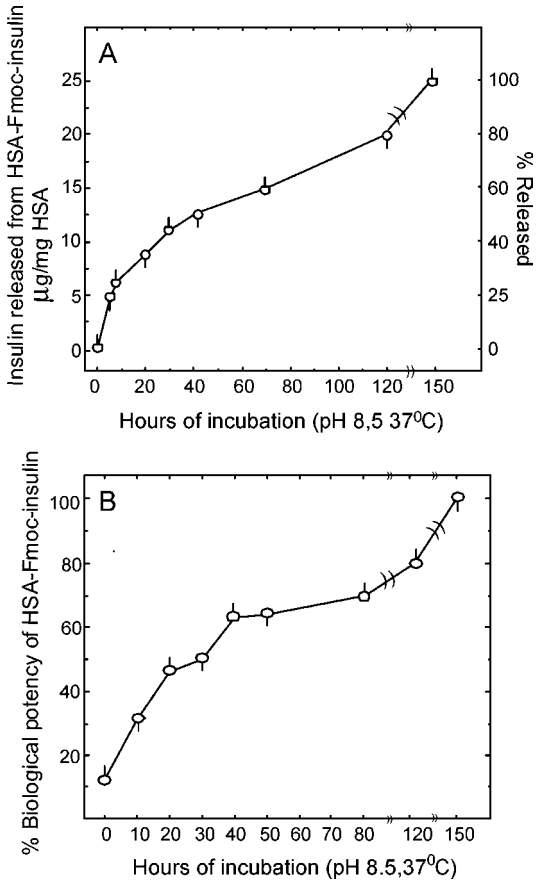

Figure 4. The rate of insulin release from HSA–Fmoc–insulin and reactivation of the conjugate upon incubation at pH 8.5, 37 °C. A solution of HSA–Fmoc–insulin (1 mg/mL) was incubated in 0.1 M phosphate buffer at pH 8.5, 37 °C. At the indicated time points, aliquots (100 μL) were analyzed by HPLC for the amount of released insulin (A) and for biological potency in rat adipocytes (B). Results are expressed as the amount of insulin released per mg of HSA–Fmoc–insulin. An aliquot of HSA–Fmoc–insulin exhibiting ED_{50} value = 3.0 ng/mL in a lipogenic assay was considered to have 10% of the native biological potency.

by about 4 times the duration obtained by the native hormone. Nearly the same glucose-lowering patterns were obtained following subcutaneous administration (Figure 5B). Again, the conjugate produced a prolonged and stable glucose-lowering pattern over many hours. A noticeable difference, however, is a delay of about 0.5 h until the fall in glucose level following subcutaneous administration of the conjugate commences (Figure 5B). This suggests that the rate of conjugate diffusion from the subcutaneous compartment into the circulatory system is considerably slower than that from the peritoneum. Indeed, diffusion and transportation rates of subcutaneously administered proteins across capillary membranes are known to decrease in proportion with increasing size of molecular radius (*21*, *45*).

Glucose-Lowering Pattern of HSA–Fmoc–Insulin in STZ-Rats. Figure 6 shows the glucose-lowering pattern of the conjugate after a single subcutaneous administration in streptozocin-treated hyperglycemic rats. Here we have compared a conjugate dose (7 mg/STZ-rat) that is equipotent to the administered dose of Zn^{2+}-free insulin (20 μg/STZ-rat) at the time of administration. The dosage calculation was based on 24 ± 3 μg of covalently linked insulin per mg of HSA having 12% of the biological potency of the free hormone (Table 1, Figure 3). As shown in Figure 6, the glucose-lowering effect of HSA–Fmoc–insulin is about 2.6 times greater than that of the native hormone. A small decrease is seen shortly after administration (i.e., at 0.5 h). Circulating glucose levels then fall gradually, reaching a maximal decrease at 2–3 h after administration (190 ± 20 mg/dL). Hyperglycemia then reoccurs ($t_{1/2}$ = 4.7 h). The area under the curve of the saline-treated group, following HSA–Fmoc–insulin administration exceeds, by about four times, that obtained with native hormone (integrated from Figure 6). Thus, HSA–Fmoc–insulin is considerably more effective than insulin in lowering circulating glucose levels in insulin-deficient diabetic rats. Figure 6 also shows the glucose-lowering pattern obtained by subcutaneous administration of insulin-glargine. Since the latter insulin derivative was documented to be less potent than the native hormone (*15*), a higher dose (40 μg/STZ-rat) was administered. As shown, this dosage facilitates a glucose-lowering pattern that is nearly similar to that obtained following administration of HSA–Fmoc–insulin (Figure 6).

DISCUSSION

Long fatty-acid acylated insulins that are noncovalently associated with albumin, even with moderate affinity ($K_a = 10^5$ M^{-1}), are long-acting species in vivo (*23–25*). We wondered whether this would be equally valid if an insulin molecule were to be covalently linked to the carrier protein, particularly since HSA–peptide conjugates have been found to retain substantial parent-peptide activity (*26–28*). Since the linkage of insulin to HSA through the nonreversible linker MIB–NHS yielded

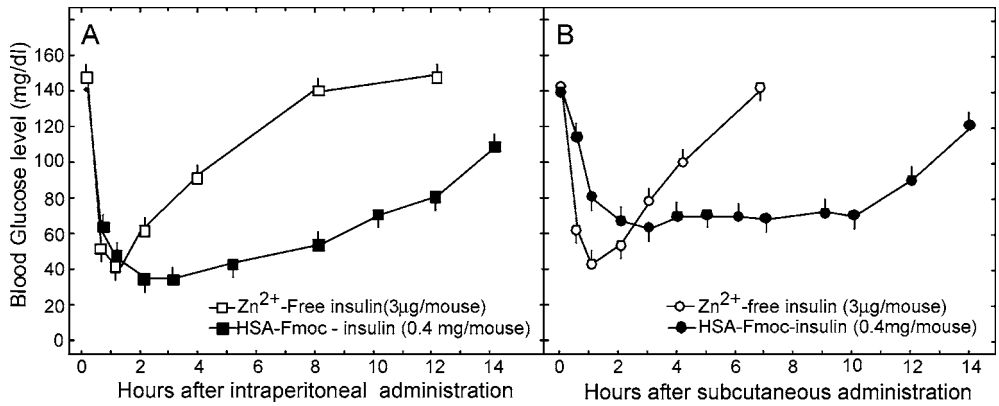

Figure 5. Circulating glucose levels in mice following a single subcutaneous or intraperitoneal administration of HSA–Fmoc–insulin. Mice were injected intraperitoneally (A) or subcutaneously (B) with Zn^{2+}-free insulin (3 μg/mouse in 0.2 mL saline) or HSA–Fmoc–insulin (0.4 mg/mouse). Blood glucose levels were determined at the indicated time points. Food was removed during the experiment. Each point is the arithmetic mean of n = 5 mice ± SE.

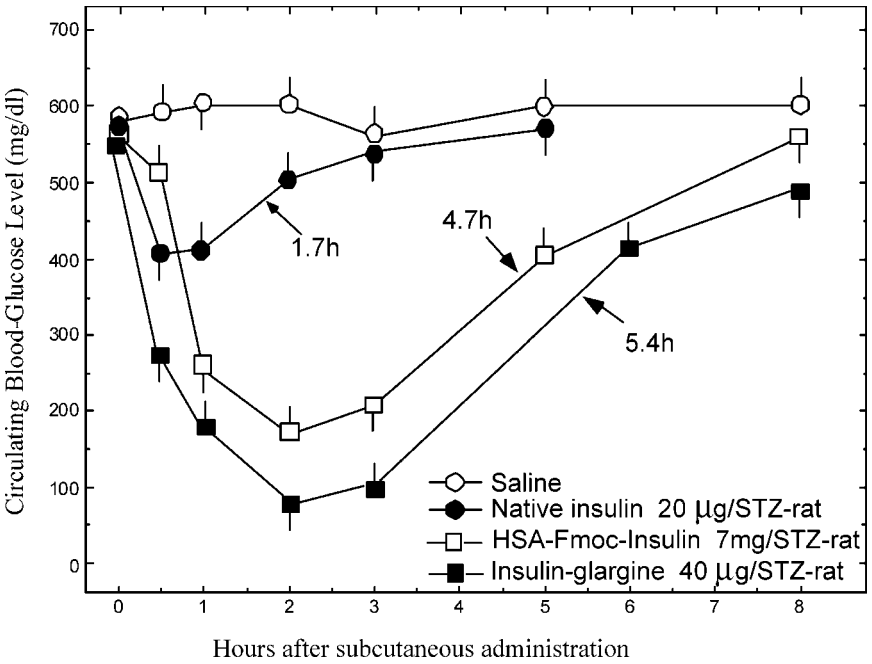

Figure 6. Effect of a single subcutaneous administration of HSA−Fmoc−insulin and of insulin-glargine on blood glucose levels in STZ-rats. STZ-rats received saline solution (control group), Zn^{2+}-free insulin (20 μg/STZ rat), HSA−Fmoc−insulin (7 mg/STZ-rat), and insulin-glargine (40 μg/STZ-rat). Blood glucose levels were determined at the time points indicated in the figure. Each point represents the arithmetic mean of the blood glucose levels of $n = 5$ rats ± SE. Insulin-glargine was diluted to a concentration of 0.2 mg/mL with 1 mM hydrochloric acid prior to injection. Each STZ-rat has received 0.2 mL subcutaneously.

an inactive conjugate (HSA−BENZ−insulin, Figure 3), we designed and synthesized the Fmoc-containing heterobifunctional reagent MAL-Fmoc-OSu (Figure 1). This development enabled us to link insulin (and potentially any other peptide or protein drug) via its amino groups to cysteine-34 of HSA.

HSA is likely to be linked to insulin through the α-amino side chain of Phe^{B1} (under investigation). The latter is considerably more exposed to alkylation, than the α-amino side chain of Gly^{A1} (*32*). At the low pH used for the conjugation (pH 7.2, methods), the ϵ-amino group of Lys^{B29} is fully protonated. Since the linkage between HSA and insulin is fully reversible and the rates of Fmoc-detachment from α- and ϵ-amino groups are similar as found in our previous studies (*41*, *42*), we expect that each new preparation of HSA−Fmoc−insulin would be similar with respect to its pharmacokinetic behavior.

In previous studies, we found that Fmoc moieties linked to proteins are detached in a slow and spontaneous fashion under aqueous physiological conditions generating the unmodified parental proteins (*41*, *42*). The rate of Fmoc hydrolysis is dictated exclusively by the pH, temperature, and protein concentration of the serum, three parameters that are maintained in mammals in strict homeostasis (*46*). We therefore anticipated that HSA−Fmoc−insulin would yield insulin in a rather similar manner.

HSA−Fmoc−insulin is an extremely water-soluble conjugate in which insulin has about 12% of the biological potency of the native hormone (Figure 3) in lipogenesis assay. We had expected it to have negligible activity given that an extended surface area of the insulin molecule is required for receptor binding (*32*, *33*). This activity, however, may stem from release of insulin from its conjugate during the assay, that is, incubation for 2 h at 37 °C in the presence of 20 mg/mL BSA. Indeed, such an explanation would be consistent with the inactivity of the stable covalent conjugate HSA−BENZ−insulin. Yet, upon incubation in aqueous solutions (i.e., pH 8.5, 37 °C), the covalently linked insulin is released from the HSA−Fmoc−insulin conjugate in a nearly homogeneous fashion over a prolonged period ($t_{1/2}$ = 24 ± 3 h) with the concomitant regeneration of insulin possessing full biological potency (Figure 4A,B). HSA−Fmoc−insulin facilitates prolonged glucose-lowering patterns in mice and in STZ-rats following a single subcutaneous or intraperitoneal administration (Figures 5 and 6). Based on administration of equipotent doses of insulin and of the conjugate at time 0, the glucose-lowering potency of HSA−Fmoc−insulin exceeds 3−4 times that facilitated by insulin in terms of longevity as well as efficacy, as judged by the $t_{1/2}$ values and the areas under the curves of the saline-treated rodents.

Lente and ultralente insulins, as well as insulin-glargine, are long-acting formulations following subcutaneous administration, because they are in a crystal form or crystallize in the subcutaneous tissue immediately after injection (*2*, *14*, *15*). Slow dissolution at the site of injection brings about the protracted effect. Our HSA−Fmoc−insulin is a soluble insulin preparation that exerts its prolonged glucose-lowering effect by a different principle, namely, by decreasing the clearance rate of the conjugates through the kidneys as well as by protecting the covalently linked insulin from proteolysis prior to its detachment from the conjugate. Therefore, the comparison to suspended formulations of insulin may be only partially representative. Nevertheless, we have also included in Figure 6 the glucose-lowering pattern of subcutaneously administered insulin-glargine, showing its nearly similar pattern to that obtained with HSA−Fmoc−insulin in STZ-rats (Figure 6). However, it is questionable whether the rat subcutis resembles the human subcutaneous tissue with regard to dissolution and diffusion of insulin-glargine from the subcutaneous compartment to the circulatory system.

The issue of potential immunogenicity of HSA−Fmoc−insulin deserves special consideration. Previously we found that an insulin derivative containing two rigid,

aromatic Fmoc moieties ($Fmoc_2$-insulin) is less immunogenic than the native hormone (*42*). Also, multiple injections of Fmoc-KLH conjugate to rabbits failed to yield antibodies against Fmoc (unpublished observations). It therefore appears that Fmoc is a poor antigen. However, because the HSA–insulin chimera is a new species, albeit combining two endogenous detachable proteins, its antigenicity should be carefully evaluated in future clinical studies.

In summary, taking insulin as a model, we have presented here the first prototype of an HSA–polypeptide/protein conjugate unique in its capability to release the covalently bound peptide/protein drug with a desirable pharmacokinetic pattern. Short-lived protein/peptide drugs can be turned into conjugates of molecular weight higher than 67 kDa and so resist clearance by kidney filtration (*1*). The covalently linked peptide/protein drug is then released by Fmoc hydrolysis, which returns it to its active state at a slow rate determined solely by the stable pH, temperature, and protein levels of the circulatory system. This new development is expected to extend the lifetime, bioavailability, and efficacy of existing peptide drugs and to extend the same in peptide drug candidates that may yet be discovered by genomics and proteomics.

ACKNOWLEDGMENT

Y.S. is the incumbent of the C.H. Hollenberg Chair in Metabolic and Diabetes Research established by the friends and associates of Dr. C. H. Hollenberg of Toronto, Canada. M.F. is the Lester Pearson Professor of Protein Chemistry. We thank Alexandra Singer for editing the manuscript. This research was supported by the Levine Institute of Applied Science and the Howard M. Siegler grant for Diabetes research.

Supporting Information Available: Pharmacokinetic profiles of subcutaneously administered radiolabeled insulin and human serum albumin in rats. This material is available free of charge via the Internet at http://pubs.acs.org.

LITERATURE CITED

(1) Goodman, L., and Gilman, A. G. (1995) *The Pharmacological Basis of Therapeutics*, McGraw-Hill, New York.
(2) Kahn, C. R., and Shechter, Y. (1990) Insulin, oral hypoglycemic agents and the pharmacology of the endocrine pancreas. In *Goodman and Gilman Handbook of Pharmacology* (Goodman, A. G., Ed.) pp 1463–1495, Pergamon Press, New York/Oxford.
(3) Duckworth, W. C. (1988) Insulin-degradation: Mechanisms, products, and significance. *Endocr. Rev. 9*, 319–345.
(4) Benzi, I., Cechetti, P., Ciccarone, A., Pilo, A., Di, C. G., and Navalesi, R. (1994) Insulin degradation in vitro and in vivo: A comparative study in men. Evidence that immunoprecipitable, partially rebindable degradation products are released from cells and circulate in blood. *Diabetes 43*, 297–304.
(5) Chap, Z., Ishida, T., Chou, J., Hartley, C. J., Entman, M. L., and Entman, D. (1987) First-pass hepatic extraction and metabolic effects of insulin and insulin analogues. *Am. J. Physiol. 252*, 209–217.
(6) Albert, K. G. M. M. (1981) Insulin treatment and diabetes; half a century of therapeutic misadventure? *Advanced Medicine*, pp 1–13, Pitman, Bath, United Kingdom.
(7) Thow, J. C., and Johnston, A. B. (1989) Effect of raising injection site temperature on isophane insulin crystal dissociation. *Diabetes Care 12*, 432–434.
(8) Lauritzen, T., Pramming, S., Gale, E., Deckert, T., and Binder, C. (1982) Absorption of isophane (NPH) insulin and its clinical implications. *Br. Med. J. 285*, 159–162.
(9) Shechter, Y. (1982) Evaluation of adenosine and related nucleosides as physiological regulators in adipose tissue. *Endocrinology 110*, 1579–1583.
(10) Shechter, Y., Reitman, P., and Hizi, A. (1982) Evaluation of factors responsible for the inability of insulin to antagonize lipolysis due to high concentrations of catecholamines. *Biochem. Biophys. Res. Commun. 109*, 776–785.
(11) Porte, D. J., and Halter, J. B. (1981) The endocrine pancreas and diabetes mellitus. *Textbook of Endocrinology*, 6th ed. (Williams, R. H., Ed.) pp 716–143, Saunders, Philadelphia, PA.
(12) Hildebrant, P. (1991) Subcutaneous absorption of insulin in insulin-dependent diabetic patients. *Dan. Med. Bull. 38*, 337–346.
(13) Galloway, J. A., and Chance, R. E. (1994) Improving insuling therapy: achievements and challenges. *Horm. Metab. Res. 26*, 591–608.
(14) Davis, S. N., and Granner, D. K. (1996) Insulin, oral hypoglycemic agents and the pharmacology of the endocrine pancreas. In *Goodman and Gilman. The Pharmacological Basis of Therapeutics*, 9th ed. (Handman, J. G., Limbial, L. E., Molinoff, P. B., and Ruddon, R. W., Eds.) pp 1487–1517, Pergamon Press, New York.
(15) Bolli, G. B., DiMarchi, R. D., Park, G. D., Pramming, S., and Koivisto, V. A. (1999) Insulin analogues and their potential in the management of diabetes mellitus. *Diabetologia 42*, 1151–1167.
(16) Kurtzhals, P., Schaffer, L., Sorensen, A., Kristensen, C., Jonassen, I., Schmid, C., and Trub, T. (2000) Correlations of receptor binding and metabolic and mitogenic potencies of insulin analogues designed for clinical use. *Diabetes 49*, 999–1005.
(17) Heinemann, L., Linkeschova, R., Rave, K., Hompesch, B., Sedlak, M., and Heise, T. (2000) Time-action profile of the long-acting insulin analogue insulin glargine (HOE901) in comparison with those of NPH insulin and placebo. *Diabetes Care 23*, 644–649.
(18) Hoste, K., De Winne, K., and Schacht, E. (2004) Polymeric prodrugs. *Int. J. Pharmacol. 277*, 119–131.
(19) Joseph, A., D'souza, M., and Topp, E. M. (2004) Release from polymeric prodrugs: Linkages and their degradation. *J. Pharm. Sci. 93*, 1962–1979.
(20) Greenwald, B., Choe, Y. H., McGuire, J., and Conover, C. D. (2003) Effective drug delivery by PEGylated drug conjugates *Adv. Drug Delivery Rev. 55*, 217–250.
(21) Taylor, A., and Granger, D. N. (1984) Exchange of macromolecules across the microcirculation. *Handbook of Physiology*, pp 467–520, American Physiological Society, Bethesda, MD.
(22) Carter, D. C., and Ho, J. X. (1994) Structure of serum albumin. In *Advances in Protein Chemistry* (Schumaker, V. N., Ed.) pp 153–203, Academic Press, Inc., San Diego, CA.
(23) Kurtzhals, P., Haveland, S., Jonassen, I., Kiehr, B., Larsen, U. D., Ribel, U., and Markussen, J. (1995) Albumin binding of insulins acylated with fatty acids: Characterization of the ligand-protein interaction and correlation between binding affinity and timing of the insulin effect in vivo. *Biochem. J. 312*, 725–731.
(24) Kurtzhals, P., Haveland, S., Jonassen, I., Kiehr, B., Ribel, U., and Markussen, J. (1996) Albumin binding and time action of acylated insulins in various species. *J. Pharm. Sci. 85*, 304–308.
(25) Kurtzhals, P., Havelund, S., Jonassen, I. B., and Markussen, J. (1997) Effect of fatty acids and selected drugs on the albumin binding of a Long-Acting, Acylated Insulin Analogue. *J. Pharm. Sci. 86*, 1365–1368.
(26) Lĕger, R., Robitaille, M., Quraishi, O., Denholm, E., Benquet, C., Carette, J., van Wyk, P., Pellerin, I, Bousquet-Gagnon, N., Castaigne, J. P., and Bridon, D. (2003) Synthesis and in vitro analysis of atrial natriuretic peptide-albumin conjugates. *Bioorg. Med. Chem. Lett. 13*, 3571–3575.
(27) Holmes, D. L., Thibaudeau, K., L'Archevêque, B., Milner, P. G., Ezrin, A. M., and Bridon, D. P. (2000) Site specific 1:1 opioid:albumin conjugate with in vitro activity and long in vivo duration. *Bioconjugate Chem. 11*, 439–444.

(28) Lěger, R., Benquet, C., Huang, X., Quraishi, O., Wyk, P., and Bridon, D. (2004) Kringle 5 peptide-albumin conjugates with anti-migratory activity. *Bioorg. Med. Chem. Lett. 14*, 841−845.
(29) Home, P. D. (1996) Insulin therapy. *The International Textbook of Diabetes*, 2nd ed., pp 899−928, Wiley, Chichester, U.K.
(30) Bolt, V., Berger, M., and Mulhanser, I. (1997) Intensified insulin therapy and the risk of severe hypolglycemia. *Diabetologia 40*, 926−932.
(31) Mulhanser, I., Overmann, H., Bender, R., Bolt, V., and Berger, M. (1998) Risk factors of severe hypoglycaemia in adult patients with type I diabetes—a prospective population based study. *Diabetologia 41*, 1274−1282.
(32) Blundell, T. L., Dodson, G. G., Hodgkin, D. M. C., and Mercola, D. (1972) Insulin, the structure in the crystal and its refleciton in chemistry and biology. *Adv. Protein Chem. 26*, 279−402.
(33) Pullen, R. A., Lindsay, D. G., Wood, S. P., Tickle, I. J., Blundell, T. L., Wolmer, A., Krail, G., Brandenburg, D., Zahn, H., Gilemann, J., and Ganneltoft, S. (1976) Receptor-binding region of insulin. *Nature 259*, 369−373.
(34) Hartley, R. W., Peterson, E. A., and Sober, H. A. (1962) The relation of free sulfhydryl groups to chromatographic heterogeneity and polymerization of bovine plasma albumin. *Biochemistry 1*, 60−68.
(35) Ellman, G. (1958) A colorimetric method for determining low concentrations of mercaptans. *Arch. Biochem. Biophys. 74*, 443−450.
(36) Hunter, W. M., and Greenwood, F. C. (1962) Preparation of iodine-131 labeled human growth hormone of high specific activity. *Nature (London) 194*, 495−496.
(37) Rodbell, M. (1964) Metabolism of isolated fat cells effects of hormones on glucose metabolism and lipolysis. *J. Biol. Chem. 239*, 375−380.
(38) Moody, A. J., Stan, M., and Gliemann, J. (1974) A simple free fat cell bioassay for insulin. *Horm. Metab. Res. 6*, 12−16.
(39) Meyerovitch, J., Farfel, Z., Zack, J., and Shechter, Y. (1987) Oral administration of vanadate ions, normalizes blood glucose level of streptozotocin treated rats, general characterization and mode of action. *J. Biol. Chem. 262*, 6658−6662.
(40) Albericio, F., Cruz, M., Debethune, L., Eritja, R., Giralt, E., Grandas, V., Narchan, J., Pastor, J., Pedroso, E., Rabani, F., and Royo, M. (2001) An improved synthesis of N-[(9-hydroxymethyl)-2-fluorenyl]succinamic acid (HMFS), a versatile handle for the solid-phase synthesis of biomolecules. *Synth. Commun. 31*, 225−232.
(41) Shechter, Y., Goldwaser, I., Lavon, I., Gershonov, E., Mester, B., Mironchik, M., Patt, L. P., and Fridkin, M. (2001) A new approach for prolonging the half-life of peptides, proteins and low-molecular-weight drugs in vivo. *Drugs Future 26*, 669−676.
(42) Gershonov, E., Shechter, Y., and Fridkin, M. (1999) New concept for long-acting insulin, spontaneous conversion of an inactive modified insulin to the active hormone in circulation: 9-fluorenylmethyloxycarbonyl derivative of insulin. *Diabetes 48*, 1437−1442.
(43) Hazum, E., Shisheva, A., and Shechter, Y. (1992) Preparation and application of radioiodinated sulfhydryl reagents for the covalent labeling of SH-proteins present in minute quantities. *J. Biochem. Biophys. Methods 24*, 95−106.
(44) Peters, T. J. (1996) The albumin molecule: Its structure and chemical properties. *All about albumin, Biochemistry, Genetics and medical applications*, pp 24−54, Academic Press, Inc., San Diego, CA.
(45) Eisenberg, D., and Crothers, D. (1979) Physicochemical chemistry with applications to the Life Sciences, pp 700−745, Benjamin/Cummings, Mento Park, CA.
(46) Lentner, C. (1984) *Geigy Scientific Tables*, pp 69−71, CIBA-GEIGY, Basel, Switzerland.

BC050055W

Synthesis, Solution Conformation, and Antibody Recognition of Oligotuftsin-Based Conjugates Containing a β-Amyloid(4−10) Plaque-Specific Epitope

Marilena Manea,[†] Ferenc Hudecz,[‡,§] Michael Przybylski,[†] and Gábor Mezõ[‡,*]

Department of Chemistry, Laboratory of Analytical Chemistry, University of Konstanz, 78457 Konstanz, Germany, Research Group of Peptide Chemistry, Hungarian Academy of Sciences, Eötvös L. University, 1518 Budapest, Hungary, and Department of Organic Chemistry, Eötvös L. University, 1518 Budapest, Hungary.
Received January 10, 2005; Revised Manuscript Received April 13, 2005

One possible therapeutic approach to treat or prevent Alzheimer's disease (AD) is immunotherapy. On the basis of the identification of Aβ(4−10) (FRHDSGY) as the predominant B-cell epitope recognized by therapeutically active antisera from transgenic AD mice, conjugates with defined structures containing the epitope peptide attached to a tetratuftsin derivative as an oligopeptide carrier were synthesized and their structure characterized. To produce immunogenic constructs, the Aβ(4−10) epitope alone or flanked by α- or β-alanine residues was attached through an amide bond to the tetratuftsin derivative (Ac-[TKPKG]$_4$-NH$_2$) or to a carrier peptide elongated by a promiscuous T-helper cell epitope (Ac-FFLLTRILTIPQSLD-[TKPKG]$_4$-NH$_2$). The conformational preferences of the carrier and conjugates were examined by CD spectroscopy in water and in 1:1 and 9:1 TFE:water mixtures (v/v). We found that the presence of flanking dimers in the conjugates had no effects on the generally unordered solution conformation of the conjugates. However, conjugates with an elongated peptide backbone exhibited CD spectra indicative for a partially ordered secondary structure in the presence of TFE. Comparative ELISA binding studies, using monoclonal antibody raised against the β-amyloid (1−17) peptide, showed that conjugates with T-helper cell epitope in the carrier backbone exhibited decreased monoclonal antibody recognition. However, we found that this effect was compensated in conjugates comprising the Aβ(4−10) B-cell epitope with the β-alanine dimer flanking regions at both N- and C-termini. Results suggest that modification of the B-cell epitope peptide from Aβ with rational combination of structural elements (e.g. conjugation to carrier, introduction of flanking dimers) can result in synthetic antigen with preserved antibody recognition.

INTRODUCTION

Alzheimer's disease (AD), a progressive neurodegenerative disorder of the brain, is the most common form of dementia among the elderly. One of the pathological characteristics of AD is the accumulation and invariant deposition of β-amyloid peptide (Aβ) into extracellular toxic plaques in the brain, which is thought to be the cause of cognitive decline (the β-amyloid hypothesis of AD). One possible therapeutic approach of AD is immunotherapy, via active or passive immunization, with the aim of either increasing the clearance of Aβ from the brain or inhibiting its aggregation to amyloid plaques (*1*−*3*). It has been shown that active immunization with Aβ-(1−42) in transgenic mouse models of AD reduces both the accumulation of Aβ plaques in brain and associated cognitive impairment; no adverse effects were observed in these experiments (*4*−*7*). However, a therapeutic trial of immunization with Aβ(1−42) in humans was discontinued because several patients developed significant meningo-encephalitic cellular inflammatory reactions (*8*, *9*). An alternative strategy to the active immunization with the complete Aβ peptide might be the use of peptides that are not fibrillogenic/toxic and not identical to endogeneous Aβ, which should reduce the likelihood of these side effects (*10*).

Using the epitope excision method based on selective proteolytic digestion of the antigen−antibody complex in combination with high-resolution mass spectrometry (*11*), the N-terminal Aβ(4−10) sequence has been identified as the core epitope region recognized by therapeutically active antibodies raised against Aβ(1−42) and/or its oligomeric assemblies (*12*−*15*). Antibodies against the N-terminal regions of Aβ were able to invoke plaque clearance to the same degree as active immunization (*16*, *17*).

It is known that the administration of oligopeptide epitope rarely elicits appropriate immune responses (*18*). One approach to improve the immunogenicity of small peptides is the appropriate replacement of amino acid residues in the epitope core and/or the alteration of the flanking regions connected to the N- and/or C-terminal of the core (*19*, *20*). Another strategy for increasing the sensitivity of the immunogenic or antigen binding properties is the multiplication of copies of the same or defined number of different B- or T-cell epitopes (*19*). It has also been shown that general peptides incorporating helper T-cell determinants and B-cell epitopes in multiple copies in branched architecture (topology) were better immunogens (*18*). To achieve this, epitope peptides can be conjugated to appropriate carrier molecules such as keyhole limpet hemocyanine (KLH), bovine serum albu-

* Corresponding author. Tel: +36-1-2090-555/1426, Fax: +36-1-372−2620, e-mail: mezo@szerves.chem.elte.hu.
[†] University of Konstanz.
[‡] Research Group of Peptide Chemistry, Hungarian Academy of Sciences, Eötvös L. University.
[§] Department of Organic Chemistry, Eötvös L. University.

10.1021/bc0500037 CCC: $30.25 © 2005 American Chemical Society
Published on Web 06/25/2005

min (BSA), tetanus toxoid (TT), and purified protein derivatives (PPD). But these are not applicable in human therapy due to their immunological properties such as immunogenicity, cross-reactivity, and induction of tolerance (*21*−*23*). To overcome these drawbacks, synthetic polymers (*24*), branching lysine core (*25*), and sequential polypeptide (*26*) and carriers with discrete molecular mass and sequence (*27*) were developed and applied with success for preparation of antigens.

The first set of conjugates containing the β-amyloid-(4−10) epitope peptide was prepared in our laboratories using branched chain polymeric polypeptides with serine (SAK) or glutamic acid (EAK) at the branch terminating position (*28*). In these constructs the epitope peptide, elongated by $CysGly_5$ at the N- or Gly_5Cys at the C-terminus was attached to the chloroacetylated carrier via a thioether bond. A third construct contained polymeric carrier (EAK) and an epitope chimera in which a promiscuous T-helper cell epitope and the Aβ(4−10) epitope were joined by a dipeptide (Ahx-Cys) spacer (FFLLTRILTIPQSLD-AhxC-FRHDSGY). Comparative binding studies of the conjugates with a monoclonal antibody raised against amyloid protein beta-(1−17) showed that the chemical nature of the carrier has a significant influence on the antibody recognition. In addition we found that the presence of a T-helper cell epitope peptide in the conjugate resulted in lower antibody binding.

Recently a novel group of sequential oligopeptides based on tuftsin was developed in our laboratory (*29*). The oligotuftsin derivatives consisting of tandem pentapeptide repeat unit $[TKPKG]_n$ ($n = 2, 4, 6, 8$) derived from the canine tuftsin sequence TKPK extended by a C-terminal Gly. These compounds are nontoxic and nonimmunogenic and exhibit tuftsin-like biological properties, e.g. immunostimulatory activity and chemotactic activity on monocytes (*30*, *31*).

Considering the beneficial biological properties of the oligotuftsin derivatives and also their nonpolymeric structure, we prepared a new set of the Aβ(4−10) epitope conjugates to further investigate the effect of chemical structure on the antibody recognition of covalently attached epitope. These constructs are different from those reported earlier (*28*). Conjugates presented in this paper contain (a) sequential oligopeptide carrier instead of polymeric one, (b) amide linkage between the epitope and the carrier, and (c) Aβ(4−10) epitopes flanked by α- or β-alanine residues in contrast to the previously described versions, which possessed pentaglycine additions.

In this paper we report on the synthesis, structural characterization, and antibody binding properties of a new set of peptide-conjugates containing the Aβ(4−10) epitope with or without α- or β-alanine flanks (FRHDSGY, AAFRHDSGYAA, βAβAFRHDSGYβAβA) and a second generation of the tetratuftsin based carrier without (a) or with (b) promiscuous T-helper cell epitope of a hepatitis B surface antigen (Ac-$[TKPKG]_4$-NH_2, Ac-FFLLTRILTIPQSLD-$[TKPKG]_4$-NH_2) (Figure 1). Our results show that conjugates with T-helper cell epitope in the carrier backbone exhibited decreased monoclonal antibody recognition. However, we found that this effect was compensated in conjugates comprising the Aβ(4−10) B-cell epitope with β-alanine dimer flanking regions at both N- and C-termini. Results suggest that modification of the B-cell epitope peptide from Aβ with rational combination of structural elements (e.g. conjugation to carrier, introduction of flanking dimers) can result in synthetic antigen with preserved antibody recognition.

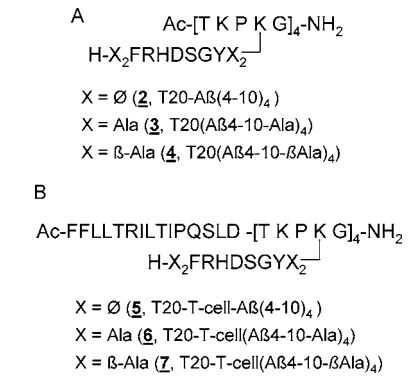

Figure 1. Schematic structure of the Aβ(4−10)−tetratuftsin derivative conjugates (A) and their elongated versions by a helper T-cell epitope (B).

EXPERIMENTAL PROCEDURES

Materials. All amino acid derivatives and MBHA resin were purchased from Reanal (Budapest, Hungary) or NovaBiochem (Laufelfingen, Switzerland). Scavengers, coupling agents, and cleavage reagents (*p*-cresol, dithiothreitol (DTT), *N,N′*-dicyclohexylcarbodiimide (DCC), *N,N′*-diisopropylethylamine (DIEA), 1-hydroxybenzotriazole (HOBt), 1,8-diazabicyclo[5.4.0]undec-7-ene (DBU), piperidine, trifluoroacetic acid (TFA), and hydrogen fluoride (HF)) were Fluka (Buchs, Switzerland) products. Acetic anhydride (Ac_2O) and solvents for synthesis and purification were delivered from Reanal (Budapest, Hungary).

Synthesis of Tetratuftsin Derivative. Ac-$[TKPKG]_4$-NH_2 (Ac-T20, **1**) was synthesized manually on a MBHA resin (1.04 mmol/g capacity) using the Boc/Bzl strategy. The following side-chain protected amino acid derivatives were used: Boc-Lys(ClZ)-OH, Boc-Thr(Bzl)-OH. The protocol was as follows: (i) DCM washing (3 × 0.5 min), (ii) Boc cleavage using 33% TFA in DCM (2+20 min), (iii) DCM washing (5 × 0.5 min), (iv) neutralization with 10% DIEA in DCM (4 × 1 min), (v) DCM washing (4 × 0.5 min), (vi) coupling 3 equiv of Boc amino acid−DCC−HOBt in DCM−DMF (4:1 or 1:4 depends on the solubility of amino acid derivatives) mixture (60 min), (vii) DMF washing (2 × 0.5 min), (viii) DCM washing (2 × 0.5 min), (ix) ninhydrin or isatin assay. After completion of the synthesis, the acetylation of the N-terminus was carried out with acetic anhydride (1 mL) and DIEA (1 mL) in DMF for 1 h. The peptide was cleaved from the resin by the aid of liquid HF in the presence of *p*-cresol and DTT as scavengers (HF−*p*-cresol−DTT=10 mL: 0.5 g: 0.1 g) for 1.5 h at 0 °C. The crude product was precipitated with diethyl ether; the filtrate was washed three times with diethyl ether and solubilized using 10% acetic acid before freeze-drying. The crude material was purified by RP-HPLC on a semipreparative C_{18} column and characterized by RP-HPLC, MALDI-FT-ICR mass spectrometry (Table 1), and amino acid analysis (data not shown).

Tandem Synthesis of Conjugates Composed of Oligotuftsin Derivatives and β-Amyloid(4−10) Epitope Peptides. Conjugates Ac-$[TKPK(H-FRHDSGY)G]_4$-NH_2(T20-A$\beta$$(4-10)_4$, **2**), Ac-$[TKPK(H-AAFRHDSGYAA)G]_4$-$NH_2$(T20-A$\beta$$(4-10\text{-}Ala)_4$, **3**), Ac-$[TKPK(H-\beta A\beta AFRHDSGY-\beta A\beta A)G]_4$-$NH_2$ (T20-A$\beta$$(4-10\text{-}\beta Ala)_4$, **4**), Ac-FFLLTRILTIPQSLD-$[TKPK(H-FRHDSGY)G]_4$-NH_2 (T20-T-cell-A$\beta$$(4-10)_4$, **5**), Ac-FFLLTRILTIPQSLD-$[TKPK(H-AAFRHDSGYAA)G]_4$-NH_2 (T20-T-cell-A$\beta$$(4-10\text{-}Ala)_4$, **6**), Ac-FFLLTRILTIPQSLD-$[TKPK(H-\beta A\beta AFRHDSGY\beta A\beta A)G]_4$-$NH_2$ (T20-T-cell-A$\beta$$(4-10\text{-}\beta Ala)_4$, **7**) containing amide bond between the carrier and the epitope peptide were

Table 1. Characteristics of Tetratuftsin Derivative (Ac-T20) and Epitope Peptide Conjugates

peptide/conjugate	no.	sequence	HPLC t_R (min)[a]	$[M + H]^+$ calcd/found	concn (μmol/L Aβ4−10)[d]
Ac-T20	**1**	Ac-[TKPKG]$_4$-NH$_2$	14.5	2105.2922/2105.2995[b]	-
T20(Aβ4−10)$_4$	**2**	Ac-[TKPK(H-FRHDSGY)G]$_4$-NH$_2$	18.6	5554.7811/5554.7823[c]	0.16 ± 0.052
T20(Aβ4−10-Ala)$_4$	**3**	Ac-[TKPK(H-AAFRHDSGYAA)G]$_4$-NH$_2$	20.7	6691.3747/6691.3538[c]	0.14 ± 0.031
T20(Aβ4−10-βAla)$_4$	**4**	Ac-[TKPK(H-βAβAFRHDSGYβAβA)G]$_4$-NH$_2$	21.1	6691.3747/6691.3455[c]	0.06 ± 0.010
T20-T-cell(Aβ4−10)$_4$	**5**	Ac-FFLLTRILTIPQSLD[TKPK(H-FRHDSGY)G]$_4$-NH$_2$	34.2	7312.7891/7312.8017[c]	0.28 ± 0.058
T20-T-cell(Aβ4−10-Ala)$_4$	**6**	Ac-FFLLTRILTIPQSLDTKPK(H-AAFRHDSGYAA)G]$_4$-NH$_2$	33.5	8449.3827/8449.3996[c]	0.22 ± 0.035
T20-T-cell(Aβ4−10-βAla)$_4$	**7**	Ac-FFLLTRILTIPQSLD[TKPK(H-βAβAFRHDSGYβAβA)G]$_4$-NH$_2$	32.5	8449.3827/8449.4016[c]	0.06 ± 0.015

[a] RP-HPLC column: Phenomenex Synergy C_{12} column (250 × 4.6 mm I.D.) with 4 μm silica (80 Å pore size); eluents: 0.1% TFA/water (A), 0.1% TFA/ACN-water 80:20, V/V (B); flow rate: 1 mL/min; gradient: 0 min 0% B, 5 min 0% B, 50 min 90% B. [b] MALDI and [c]ESI mass spectrometric analyses were performed with a Bruker APEX II FT-ICR instrument equipped with an actively shielded 7T superconducting magnet. [d] The lowest amount of Aβ(4−10) epitope peptide in μmol/L to obtain an OD = 1.0 in direct ELISA experiment.

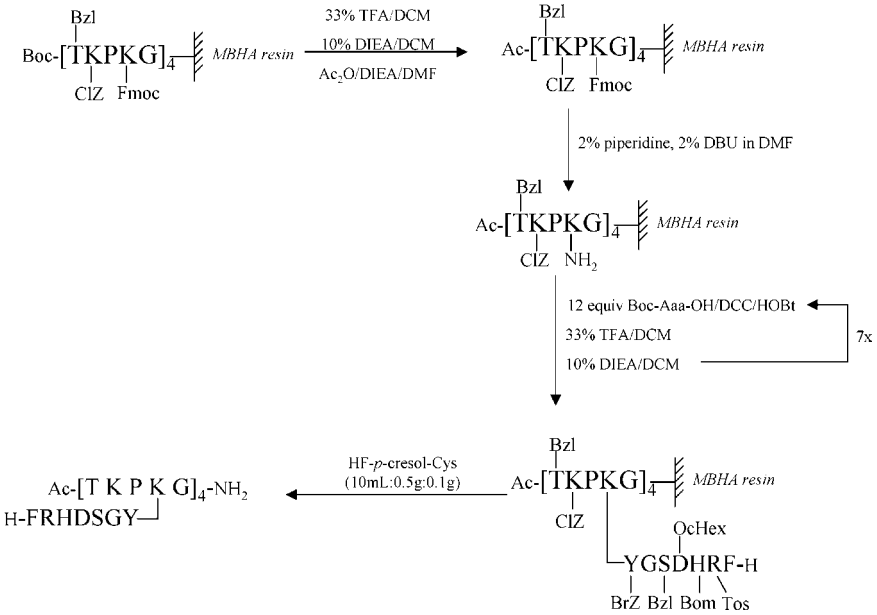

Figure 2. Outline of the synthesis of the Aβ(4−10) epitope peptide−tetratuftsin derivative conjugate (**2**) obtained by total synthesis.

prepared manually by tandem synthesis on a MBHA resin (1.04 mmol/g capacity) using the Boc/Bzl strategy (Figure 2). The following side-chain protected amino acid derivatives were used: Boc-Lys(Fmoc)-OH, Boc-Lys(ClZ)-OH, Boc-Thr(Bzl)-OH, Boc-Asp(OcHex)-OH, Boc-Ser(Bzl)-OH, Boc-Arg(Tos)-OH, Boc-Tyr(BrZ)-OH, Boc-His(Bom)-OH, and the syntheses were performed according to the protocol described above. After completion of the synthesis of the tetratuftsin derivative and its version elongated by T-cell epitope, the acetylation of the N-terminus was carried out with acetic anhydride (1 mL) and DIEA (1 mL) in DMF for 1 h. After removal of the N$^\epsilon$-Fmoc protecting group of Lys by 2% DBU, 2% piperidine in DMF for 2+2+5+15 min, the Aβ(4−10) epitope peptide with/without α- or β-alanine flanking region was built up on the ϵ-amino group of lysine by the Boc/Bzl strategy. A ratio of 12 equiv of Boc-amino acid derivatives and coupling reagents to the four Lys residues were used. The conjugates were cleaved from the resin by the aid of liquid HF in the presence of *p*-cresol and L-Cys (HF-*p*-cresol-Cys=10 mL:0.5 g:0.1 g) for 1.5 h at 0 °C. After their cleavage from the resin, the crude products (**2**, **3**, and **4***)* were purified by RP-HPLC on a semipreparative C_{18} column, while products (**5**, **6**, and **7***)*, on a C_4 column. The purified conjugates were characterized by RP-HPLC, ESI−FT-ICR mass spectrometry (Table 1), and amino acid analysis (data not shown).

Reverse Phase High Performance Liquid Chromatography (RP-HPLC). Analytical RP-HPLC was performed on a Knauer (H. Knauer, Bad Homburg, Germany) HPLC system using a Phenomenex Synergy C_{12}, column (250 × 4.6 mm I.D.) with 4 μm silica (80 Å pore size) (Torrance, CA) or Vydac C_4 column (250 × 4.6 mm I.D.) with 5 μm silica (300 Å pore size) (Hesperia, CA) as stationary phases. Linear gradient elution (0 min 0% B; 5 min 0% B; 50 min 90% B) with eluent A (0.1% TFA in water) and eluent B (0.1% TFA in acetonitrile−water (80:20, V/V)) was used at a flow rate of 1 mL/min at ambient temperature. Peaks were detected at $\lambda = 220$ nm. The samples were dissolved in eluent A or in eluent A and B mixture (in case of compounds **5, 6**, **7**).

The crude products were purified on a semipreparative Phenomenex Jupiter C_{18} column (250 × 10 mm I.D.) with 10 μm silica (300 Å pore size) (Torrance, CA) or Vydac C_4 column (250 × 10 mm I.D.) with 10 μm silica (300 Å pore size) (Hesperia, CA). Flow rate was 4 mL/min. The same eluents as described above with an appropriate linear gradient (0 min 10% B; 5 min 10% B; 50 min 55% B in case of conjugates **2**, **3**, and **4** or 0 min 20% B; 5 min 20% B; 55 min 70% B in case of conjugates **5**, **6**, and **7**) were applied.

Amino Acid Analysis. The amino acid composition of the conjugates was determined by amino acid analysis using a Beckman Model 6300 analyzer (Fullerton, CA). Prior to analysis samples were hydrolyzed in 6 M HCl in N_2 atmosphere at 110 °C for 24 h.

Mass Spectrometry. MALDI−FT-ICR mass spectrometric analysis was performed with a Bruker APEX II

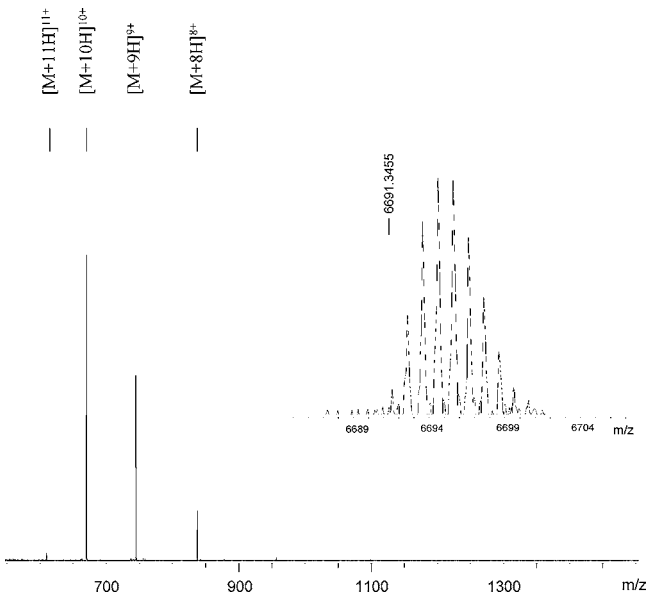

Figure 3. ESI−FT-ICR mass spectrum of T20(Aβ4−10-βAla)$_4$ (**4**). The insert shows the $[M + H]^+$ ion after deconvolution of the ESI−FT-ICR mass spectrum.

FT-ICR instrument equipped with an actively shielded 7T superconducting magnet, a cylindrical infinity ICR analyzer cell, and an external Scout 100 fully automated X−Y target stage MALDI source with pulsed collision gas (Bruker Daltonik, Bremen, Germany). The pulsed nitrogen laser is operated at 337 nm. A 100 mg/mL solution of 2,5-dihydroxybenzoic acid (DHB) (Aldrich, Steinheim, Germany) in acetonitrile:(0.1% trifluoroacetic acid in water) (2:1) was used as a matrix. A 0.5 μL amount of matrix solution and 0.5 μL of sample solution were mixed on the stainless steel MALDI sample target and allowed to dry. Calibration was performed with a standard peptide mixture with an *m/z* range of approximately 5000 (*32*).

ESI−FT-ICR MS were performed with the same Bruker Daltonik Apex II FT-ICR spectrometer (Bremen, Germany) equipped with a 7.0 T actively shielded superconducting magnet (Magnex, Oxford, UK), an APOLLO (Bruker Daltonik) electrospray ionization source, an API1600 ESI control unit, and a UNIX-based Silicon Graphics O2 workstation. Acquisition of spectra was performed with the Bruker Daltonik software XMASS and corresponding programs for mass calculation, data calibration, and processing. The masses of the singly charged ions were calculated by deconvolution of the multiply charged species (Figure 3). For sample preparation, 50% methanol, 2% acetic acid in water was used (*33*).

Circular Dichroism Spectroscopy. Circular dichroism (CD) spectra were recorded on a Jasco spectropolarimeter, model J-720 (Jasco, Espoo, Finland), at room temperature in quartz cells of 0.05 cm path-length, under constant nitrogen flush. The instrument was calibrated with 0.06% (w/v) ammonium-D-camphor-10-sulfonate (Katayama Chemical, Osaka, Japan) in water. Double distilled water and 1:1 and 9:1 mixtures (v/v) of trifluoroethanol (TFE) (Fluka, Buchs, Switzerland) and water were used as solvents. The concentration of the samples was 100 μM (in case of conjugates) and 200 μM (in case of Ac-T20). The spectra were averages of six scans between $\lambda = 190$ and 260 nm. Results are expressed in terms of mean residue ellipticity (deg cm^2 dmol^{-1}) after subtraction of the buffer baseline.

Enzyme-Linked Immunosorbent Assay (ELISA). ELISA studies were performed using the purified type IgG1 monoclonal antibody (mAb) 6E10 (Chemicon, Temecula, CA), raised against Aβ(1−17) as described (*28*). Briefly, a standard dilution of the mAb 6E10 ($c = 1$ mg/mL in PBS) and conjugates as coating antigens was used. Ninety-six-well ELISA plates (BioRad, Hercules, CA) were coated overnight at room temperature with 100 μL/well of conjugates (serial dilutions from 20 μM to 0.0001 μM of Aβ(4−10) epitope concentration). The antigen concentrations were expressed as the Aβ(4−10) epitope concentration, and they were the following: 20 μM, 6.66 μM, 2.22 μM, 0.74 μM, 0.246 μM, 0.082 μM, 0.027 μM, 0.0091 μM, 0.003 μM, 0.001 μM, 0.0003 μM, and 0.0001 μM. After coating, the wells were washed (0.05% Tween-20 v/v in PBS, pH = 7.5), and the nonspecific adsorption sites were blocked (5% BSA w/v in PBS). The mAb 6E10 at $c = 1$ μg/μL was diluted 4000 times in 5% BSA (Sigma-Aldrich, Steinheim, Germany) and added to each well (100 μL). After incubation at room temperature for 2 h and washing steps, 100 μL of peroxidase labeled goat anti-mouse IgG (Jackson Immuno Research, West Grove, PA) diluted 1000 times in 5% BSA was added to each well. After an additional incubation for 2 h and washing three times, 100 μL of *o*-phenylenediamine dihydrochloride (Merck, Darmstadt, Germany) in sodium phosphate-citrate buffer at $c = 1$ mg/mL and 2 μL of 30% hydrogen-peroxide (Merck, Darmstadt, Germany) per 10 mL of substrate buffer was added. After 5 min, the absorbance at $\lambda = 450$ nm was measured on a Wallac 1420 Victor^2 ELISA Plate Counter (PerkinElmer, Boston, MA). The concentration of the antigen, which gave an OD_{450} of 1 was calculated (Table 1).

RESULTS AND DISCUSSION

Synthesis and Structural Characterization of Aβ-(4−10) Epitope Peptide Conjugates. In this work we report on the synthesis and characterization of a new group of synthetic antigens, in which the β-amyloid(4−10) epitope peptide was attached through an amide bond to two sequential carriers, the tetratuftsin derivative consisting of four units of TKPKG pentapeptide and its analogue elongated by a T-helper cell epitope (FFLLTRILTIPQSLD). Both compounds were prepared by solid-phase methodology using Boc-chemistry and orthogonal protecting groups for lysine side-chains: Z(2Cl) in position 2 and Fmoc in position 4 of the pentapeptide unit. The Aβ(4−10) epitope peptide with/without α- or β-alanine flanking regions was connected to the ϵ-amino groups of lysine residues after selective removal of the N$^\epsilon$-Fmoc protecting group under alkaline conditions (Figure 2). After completion of the assembly of the 48−79-mer conjugates (**2**−**7**), the compounds were cleaved from the resin with HF in the presence of *p*-cresol and L-Cys. L-Cys was added to scavenge the formaldehyde derived from the Bom protecting group of His during the cleavage procedure. The compounds were purified by HPLC and characterized by RP-HPLC, high-resolution FT-ICR mass spectrometry (Table 1, Figure 3), and amino acid analysis. In contrast to antigens prepared by the attachment of epitopes with polymeric carrier through thioether bond as published by us earlier (*28*), these new set of conjugates have several advantages: (a) discrete molar mass, (b) structurally identical species, (c) the presence of amide bonds only. In addition these constructs were also different from previous ones since the flanking regions of the Aβ(4−10) epitope were Ala_2 or βAla_2 dimers instead of pentaglycine.

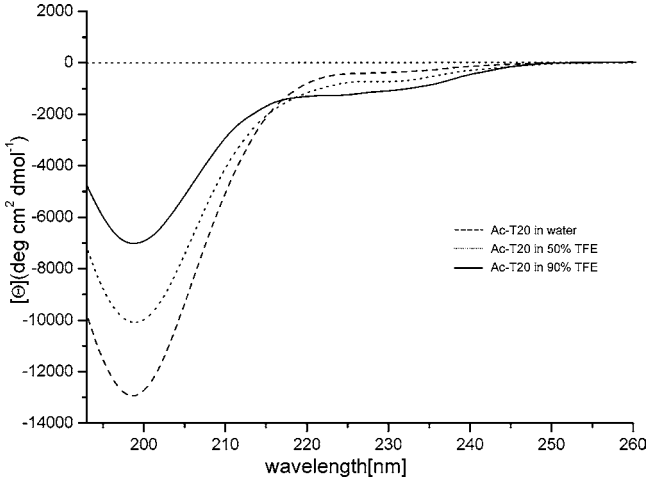

Figure 4. CD spectra of the acetylated tetratuftsin derivative (**1**).

Conformational Analysis by CD Spectroscopy. The conformational preferences of the carrier and epitope peptide conjugates in water and 1:1 and 9:1 TFE:water mixtures (v/v) was analyzed by CD spectroscopy. TFE is known to preferentially stabilize proteins and peptides in a helical conformation (*34*). The CD spectrum of the acetylated tetratuftsin derivative (**1**) recorded in water showed a strong negative $\pi-\pi^*$ band around 198 nm characteristic of unordered structure. The presence of TFE in the solvent mixture did not lead to spectral changes. The CD spectrum measured in 9:1 TFE:water mixture (v/v) reflects the predominance of random coil conformation, characterized by a negative maximum at 198 nm with a small shoulder at approximately 226 nm (Figure 4). Previous studies showed that nonacetylated tetratuftsin is very flexible, adopting a random coil conformation in water, TFE, and 1:1 TFE:water mixture (*29*). These results indicate that the acetylation of the tetratuftsin derivative does not change its conformational properties in solution.

The attachment of β-amyloid(4−10) epitope peptide with/without the α- or β-alanine flanking region to the carrier did not result in significant conformational changes of the carrier (Figure 5). The CD spectra of the Aβ(4−10) epitope peptide−tetratuftsin derivative conjugates recorded in water showed the presence of a negative maximum and an additional positive band around 220 nm which characterized the unordered structure. Compared to pure water as solvent, the CD spectra in 1:1 and 9:1 TFE:water mixture (v/v) showed only a small shift in the $\pi-\pi^*$ electronical transitions toward higher wavelengths and the presence of a small negative shoulder at 222 nm (n−π^* transition). A positive band around 220 nm could be detected only in case of conjugate **2**, and the presence of α- or β-alanine flanking regions in the structure of the conjugates **3** and **4** determined the disappearance of this additional band.

The conjugates **5**−**7** containing in their structure the T-helper cell epitope adopt a random coil conformation in water. Interestingly, in the presence of TFE, they adopt an ordered structure, which is more pronounced by increasing the content of TFE in the solvent mixture (the $\pi-\pi^*$ electronic transitions were shifted toward a higher wavelength, from 198 nm to 204−205 nm, and also the intensity of the n−π^* transition at 225 nm increased) (Figure 6). This indicates that the conformational preferences of the conjugates depend on their primary structure and that TFE enhances existing propensities and does not induce helix formation arbitrarily.

In contrast to the essentially unordered oligotuftsin based carrier, branched chain polymeric polypeptides used for the previous set of antigens (EAK and SAK) have ordered structure (*28*). We found that in both conjugate families the conformation of the carriers has a significant influence on the CD spectra of the respective conjugates. In case of branched polypeptide conjugates we detected high level of ordered structure (*28*). Similarly, conjugates with oligotuftsin derivatives displayed essentially unordered conformation (Figures 5 and 6).

Antigenicity of the Aβ(4−10) Epitope Peptide Conjugates against an Anti-Aβ-(1−17) Monoclonal Antibody. The β-amyloid(4−10) epitope−tetratuftsin derivative conjugates were compared for binding to an anti-Aβ-(1−17) monoclonal antibody by direct ELISA. The conjugates containing the Aβ(4−10) epitope in four copies or the free carrier were coated to ELISA plates. Subsequently mAb, peroxidase-conjugated second Ab, and OPD substrate were added and the absorbance was measured (Table 1, Figures 7A and 7B). The carrier itself did not show any reactivity with mAb (data not shown). On the basis of ELISA data, the influence of the flanking regions neighboring the B-cell epitope and the presence of T-helper cell epitope peptide in the backbone on the antibody binding were compared. The conjugates in which the B-cell epitope was flanked by two β-alanine residues at both N- and C-termini (**4**, **7**) showed the highest binding activity to the mAb (lowest amount of Aβ(4−10) epitope peptide to obtain an OD = 1: 0.06 μmol/L); no differences related to the presence of the T-helper cell epitope in the structure of conjugate **7** could be detected (Table 1). The Aβ(4−10)−tetratuftsin derivative conjugates had similar binding properties, and the presence of α-alanine dimer flanking regions had no significant influence on the antigenicity of B-cell epitope (**2**, **3**). Conjugates **5** and **6**, containing the T-helper cell epitope in the polypeptide backbone, bound to the antibody with similar intensities, but their antigenicity was lower in comparison with that of the constructs **2** and **3** (e.g. 0.28 for **5** vs 0.16 for **2**). We conclude that in the Aβ(4−10) epitope−tetratuftsin construct, the presence of α-alanine adjacent to the B-cell epitope had no marked effect on the antibody binding, whereas the β-alanine flanking region increased significantly the antibody recognition of Aβ(4−10) epitope.

The data presented here suggest that inclusion of appropriate flanks to the B-cell epitope (e.g. β-Ala) may increase the antibody binding of the epitopes attached to the tetratuftsin derivative. Elongation of the carrier backbone by a sequence of amino acids (T-helper cell epitope) only slightly decreased antibody binding to the B-cell epitope (0.16 vs 0.28; 0.14 vs 0.22), but the selection of appropriate flank in the B-cell epitope was able to compensate this effect (0.06 vs 0.06) (Table 1).

The coating ability of different conjugates with oligotuftsin-derived or polymer carriers is probably similar, but the coating itself may reduce the flexibility of the antigenic peptides and affect the binding. However, the data suggest that there is no significant influence on antibody recognition.

CONCLUSION

In this study we report on the preparation and structural and binding characteristics of synthetic antigen conjugates comprising the β-amyloid(4−10) epitope as

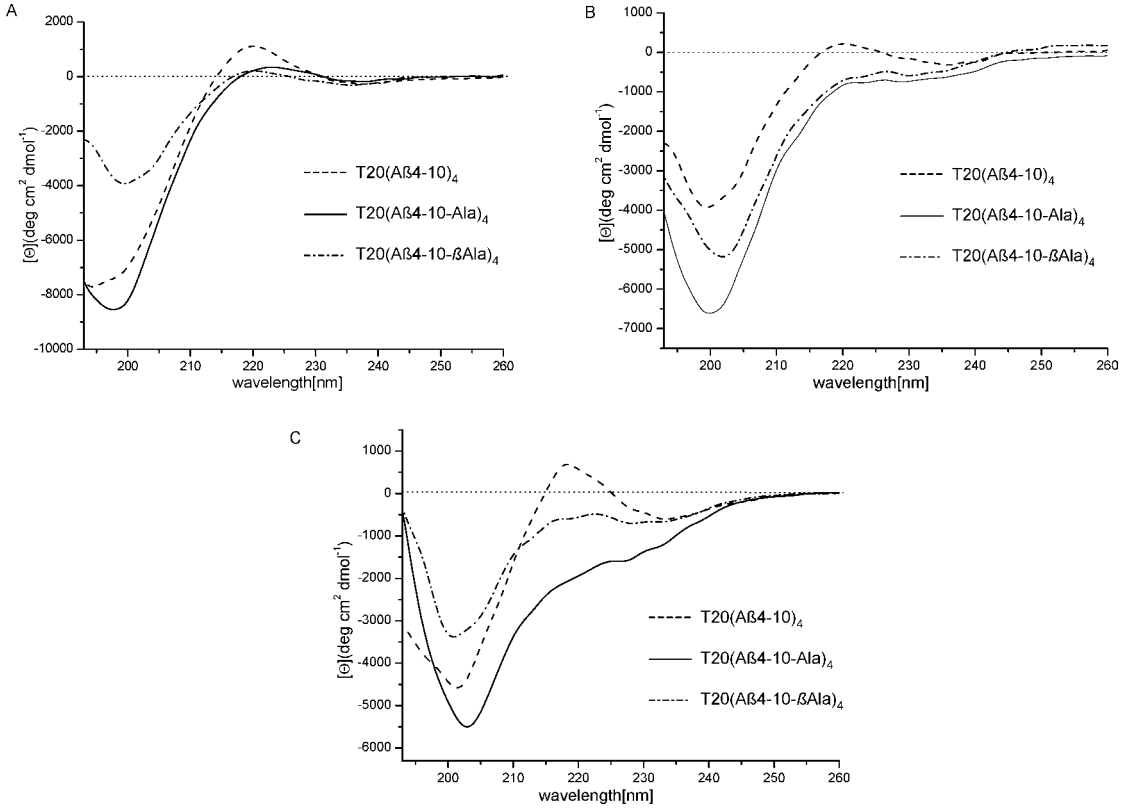

Figure 5. CD spectra of the Aβ(4−10)-tetratuftsin derivative conjugates in water (A) and 1:1 (B) and 9:1 (C) TFE:water mixtures (v/v).

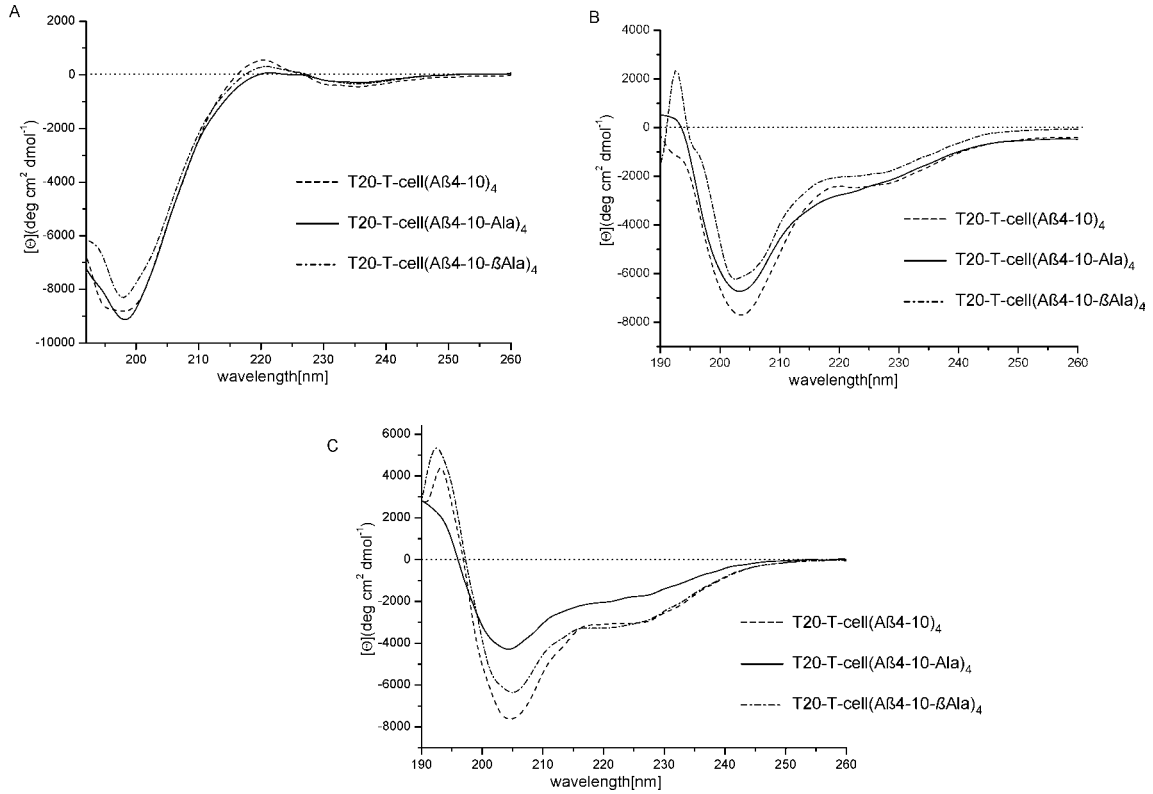

Figure 6. CD spectra of the Aβ(4−10)-tetratuftsin derivative−T-helper-cell epitope conjugates in water (A) and 1:1 (B) and 9:1 (C) TFE:water mixtures (v/v).

lead structures for new type of vaccines against Alzheimer's disease. Constructs with defined structures, in which the Aβ(4−10) epitope was attached through an amide bond to the tetratuftsin derivative as oligopeptide carrier, were successfully prepared by tandem solid-phase methodology. The alteration of the flanking regions connected to the N- and C-terminal ends of the Aβ(4−10)-epitope, e.g. by β-amino acid residues, resulted in increased binding. Comparative ELISA binding studies, using monoclonal antibody raised against the β-amyloid

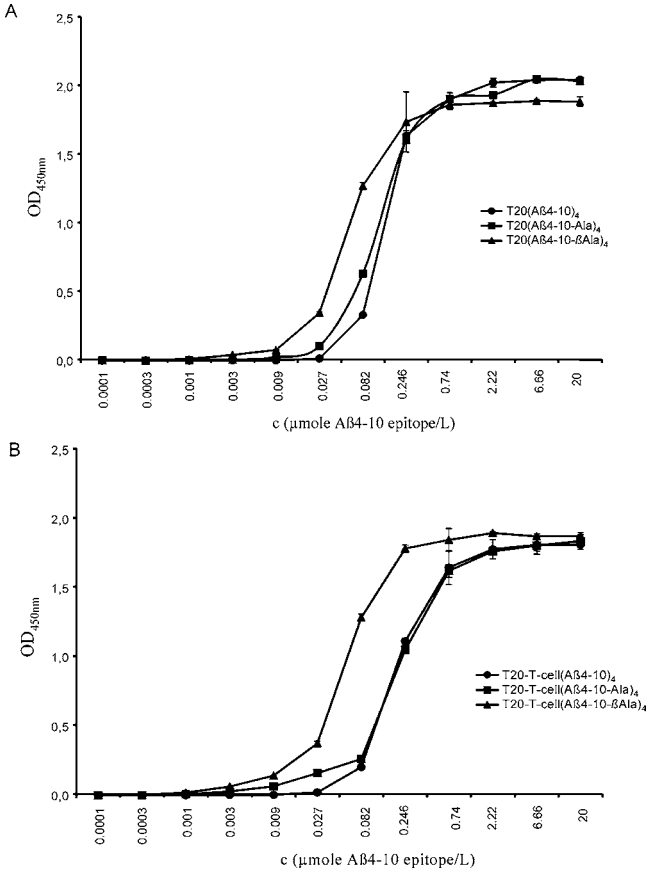

Figure 7. Binding of mouse anti-amyloid protein beta-(1−17) monoclonal antibody to Aβ(4−10) epitope peptide conjugates **2**−**4** (A) and to conjugates **5**−**7** (B), as measured by direct ELISA.

(1−17) peptide, showed that conjugates with a T-helper cell epitope in the carrier backbone exhibited decreased monoclonal antibody recognition. However, we found that this effect was compensated in conjugates comprising the Aβ(4−10) B-cell epitope with β-alanine dimer flanking regions at both N- and C-termini. Taken together, results suggest that modification of the B-cell epitope peptide from Aβ with rational combination of structural elements (e.g. conjugation to carrier, introduction of flanking dimers) can result in a T-cell epitope containing synthetic antigen with preserved, and even improved, antibody recognition. These findings can be utilized for the design of further optimized synthetic antigens. Corresponding immunization studies with Aβ(4−10) epitope conjugates based on these second generation tetratuftsin as well as on branched chain polymeric polypeptide (*28*) carrier are in progress in our laboratories.

ACKNOWLEDGMENT

This work was supported by grants from the Hungarian National Science Fund (OTKA No. T032425, T043576) and the Deutsche Forschungsgemeinschaft (Transregio-SFB Konstanz-Zuerich and Biopolymer-Mass Spectrometry). We thank Dr. Xiaodan Tian for constructive criticism and discussions of this work.

LITERATURE CITED

(1) Shenk, D. (2002) Amyloid-β immunotherapy for Alzheimer's disease: the end of the beginning. *Nature Rev. Neurosci. 3*, 824−828.

(2) Monsonego, A., and Weiner, L. H. (2003) Immunotherapeutic approaches to Alzheimer's disease. *Science 302*, 834−838.

(3) Selkoe, D. J., and Schenk, D. (2003) Alzheimer's disease: Moleular understanding predicts amyloid-based therapeutics. *Annu. Rev. Pharmacol. Toxicol. 43*, 545−584.

(4) Schenk, D., Barbour, R., Dunn, W., Gordon, G., Grajeda, H., Guido, T., Hu, K., Huang, J., Johnson-Wood, K., Khan, K., Kholodenko, D., Lee, M., Zhenmei, L., Lieberburg, I., Motter, R., Mutter, L., Soriano, F., Shopp, G., Vasquez, N., Vandevert, C., Walker, S., Wogulis, M., Yednock, T., Games, D., and Seubert, P. (1999) Immunization with amyloid-β attenuates Alzheimer-disease-like pathology in the PDAPP mouse. *Nature 400*, 173−177.

(5) Janus, C., Pearson, J., McLaurin, J., Mathews, P. M., Jiang, Y., Schmidt, S. D., Chishti, M. A., Horne, P., Heslin, D., French, J., Mount, H. T., Nixon, R. A., Mercken, M., Bergeron, C., Fraser, P. E., St George-Hyslop, P., and Westaway, D. (2000) Aβ peptide immunization reduces behavioral impairment and plaques in a model of Alzheimer's disease. *Nature 408*, 979−982.

(6) Morgan, D., Diamond, D. M., Gottschall, P. E., Ugen, K. E., Dickey, C., Hardy, J., Duff, K., Jantzen, P., DiCarlo, G., Wilcock, D., Connor, K., Hatcher, J., Hope, C., Gordon, M., and Arendash, G. W. (2000) Aβ peptide vaccination prevents memory loss in an animal model of Alzheimer's disease. *Nature 408*, 982−985.

(7) Weiner, H. L., Lemere, C. A., Maron, R., Spooner, E. T., Grenfell, T. J., Mori, C.; Issazadeh, S., Hancock, W. W., and Selkoe, D. J. (2000) Nasal administration of amyloid β-peptide decreases cerebral amyloid burden in a mouse model of Alzheimer's disease. *Ann. Neurol. 48*, 567−579.

(8) Check, E. (2002) Nerve inflammation halts trial for Alzheimer's drug. *Nature 415*, 462.

(9) Nicoll, A. R. J., Wilkinson, D., Holmes, C., Steart, P., Markham H, and Weller, R. O. (2003) Neuropathology of human Alzheimer disease after immunization with amyloid-β peptide: a case report. *Nature Med. 9*, 448−452.

(10) Sigurdsson, E. M., Scholtzova H., Mehta D. P., Frangione B., and Wisniewski T. (2001) Immunization with a nontoxic/nonfibrillar amyloid-β homologous peptide reduces Alzheimer's disease associated pathology in transgenic mice. *Am. J. Pathol. 159*, 439−447.

(11) Macht, M., Fiedler, W., Kurzinger, K., and Przybylski, M. (1996) Mass spectrometric mapping of protein epitope structures of myocardial infarct markers myoglobin and troponin T. *Biochemistry 35*, 15633−15639.

(12) McLaurin, J., Cecal, R., Kierstead, M. E., Tian. X., Phinney, A. L, Manea, M., French, J. E., Lambermon, M. H., Darabie, A. A., Brown, M. E., Janus, C., Chishti, M. A., Horne, P., Westaway, D., Fraser, P. E., Mount, H. T., Przybylski, M., and St George-Hyslop, P. (2002) Therapeutically effective antibodies against amyloid-beta peptide target amyloid-beta residues 4−10 and inhibit cytotoxicity and fibrillogenesis. *Nature Med. 8*, 1263−1269.

(13) Przybylski, M., McLaurin, J., Cecal, R. E., Kierstead, M. E., Tian, X., Janus, C., Manea, M., Horne, P., Westaway, D., Fraser, P. E., and St George-Hyslop, P. (2002) Lead structures for active immunization against Alzheimer's disease (AD) upon elucidation of a plaque-specific epitope recognized by therapeutically active antisera from transgenic AD mice. *Peptides 2002* (Benedetti, E., and Pedone, C., Eds.) pp 862−863, Edizioni Zino, Napoli, Italy.

(14) Cecal, R., McLaurin, J., Tian, X., Manea, M., Janus, C., Westaway, D., Fraser, P., St George-Hyslop, P., and Przybylski, M. (2002) Mass spectrometric elucidation of an amyloid plaque-specific epitope: molecular basis for probing the protheolytic degradation mechanism of Alzheimer's amyloid precursor protein APP. *Peptides 2002* (Benedetti, E., and Pedone, C., Eds.) pp 700−701, Edizioni Zino, Napoli, Italy.

(15) Bard, F., Barbour, R., Cannon, C., Carretto, R., Fox, M., Games, D., Guido, T., Hoenow, K., Hu, K., Johnos-Wood, K., Khan, K., Kholodenko, D., Lee, C., Lee, M., Motter, R., Nguyen, M., Reed, A., Shenk, D., Tang, P., Vasqzez, N., Seubert, P., and Yednock, T. (2003) Epitope and isotype specificities of antibodies to β-amyloid peptide for protection against Alzheimer's disease-like neuropathology. *Proc. Natl. Acad. Sci. U.S.A. 100*, 2023−2028.

(16) Bard, F., Cannon, C., Barbour, R., Burke, R.-L., Games, D., Grajeda, H., Guido, T., Hu, K., Huang, J., Johnson-Wood, K., Khan, K., Kholodenko, D., Lee, M., Lieberburg, I., Motter R., Nguyen, M., Soriano, F., Vasquez, N., Weiss, K., Welch, B., Seubert, P., Schenk, D., and Yednock, T. (2000) Peripherally administered antibodies against amyloid β-peptide enter the central nervous system and reduce pathology in a model of Alzheimer disease. *Nature Med. 6*, 916−920.

(17) DeMattos, R. B., Bales, R. K., Cummins, D. J., Dodart, J. K., Paul, S. M., and Holzman, D. M. (2001) Peripheral anti-Aβ antibody alters CNS and plasma Aβ clearance and decreases brain Aβ burden in a mouse model of Alzheimer's disease. *Proc. Natl. Acad. Sci. U.S.A. 98*, 8850−8855.

(18) Purcell, A. W., Zeng, W., Mifsud, N. A., Ely, L. K., MacDonald, W. A., and Jackson, D. C. (2003) Dissecting the role of peptides in the immune response: theory, practice and the application to vaccine design. *J. Pept. Sci. 9*, 255−281.

(19) Hudecz, F. (2001) Manipulation of epitope function by modification of peptide structure: a minireview. *Biologicals 29*, 197−207.

(20) Wilkinson, K. A., Vordermeier, M. H., Kajtar, J., Jurcevic, S., Wilkinson, R., Ivanyi, J., and Hudecz, F. (1997) Modulation of peptide specific T cell responses by non-native flanking regions. *Mol. Immunol. 34*, 1237−1246.

(21) Schutze, M. P., Leclerc, C., Jolivet, M., Audibert, F., and Chedid, L. (1985) Carrier-induced epitopic suppression, a major issue for future synthetic vaccines. *J. Immunol. 135*, 2319−2322.

(22) Sakata, S., and Atassi, Z. (1981) Immune recognition of serum albumin- -XIII. Autoreactivity with rabbit serum albumin of rabbit antibodies against bovine or human serum albumins and autoimmune recognition of rabbit serum albumin. *Mol. Immunol. 18*, 961−967.

(23) Herzenberg, L. A., Tokuhisa, T., Herzenberg, L. A. (1980) Carrier-priming leads to hapten-specific suppression. *Nature 285*, 664−667.

(24) Hudecz, F., Votavova, H., Gaál, D., Sponar, J., Kajtár, J., Blaha, K., and Szekerke, M. (1985) Branched polypeptides with poly(L-lysine) backbone: synthesis conformation and immunomodulation. *Polymeric Materials in Medication* (Gebelein, Ch. G.; Carraher, Ch. E.) pp 263−289, Plenum Press, New York.

(25) Tam, J. P. (1988) Synthetic peptide vaccine design: synthesis and properties of a high-density multiple antigenic peptide system. *Proc. Natl. Acad. Sci. U.S.A. 85*, 5409−5413.

(26) Trudelle, Y., Bracks, A., Delmas, A., Pedoussant, S., and Rivaille, P. (1987) Synthesis of new carrier for immunization: polytuftsin. *Int. J. Pept. Protein Res. 30*, 54−56.

(27) Tsikaris, V., Sakarellos, C., Cung, M. T., Marraud, M., and Sakarellos-Daitiotis, M. (1996) Concept and design of a new class of sequential oligopeptide carriers (SOC) for covalent attachment of multiple antigenic peptides. *Biopolymers 38*, 291−293.

(28) Manea, M., Mezõ, G., Hudecz, F., and Przybylski, M. (2004) Conjugates containing a b-amyloid plaque specific epitope as lead structure for vaccines against Alzheimer's disease. *Biopolymers 76*, 503−511.

(29) Mezõ, G., Kalászi, A., Reményi, J., Majer, Zs., Hilbert, Á., Láng, O., Kõhidai, L., Barna, K., Gaál, and D., Hudecz, F. (2004) Synthesis, conformation and immunoreactivity of new carrier molecules based on repeated tuftsin-like sequence. *Biopolymers 73*, 645−656.

(30) Fridkin, M., and Najjar, V. A. (1989) Tuftsin: its chemistry, biology, and clinical potential. *Crit. Rev. Biochem. Mol. Biol. 24*, 1−40.

(31) Siemion IZ, and Kluczyk A. (1999) Tuftsin: on the 30-year anniversary of Victor Najjar's discovery. *Peptides 20*, 645−674.

(32) Damoc, E., Youhnovski, N., Crettaz, D., Tissot, J. D., and Przybylski, M. (2003) High-resolution proteome analysis of cryoglobulins using Fourier transform-ion cyclotron resonance mass spectrometry. *Proteomics 3*, 1425−1433.

(33) Rossier, J. S., Youhnovski, N., Lion, N., Damoc, E., Reymond, F., Girault, H. H., and Przybylski, M. (2003) Thin-chip microspray system for high-performance Fourier transform ion-cyclotron resonance mass spectrometry of biopolymers. *Angew. Chem., Int. Ed. 42*, 53−58.

(34) Buck, M. (1998) Trifluoroethanol and colleagues: cosolvents come of age. Recent studies with peptides and proteins. *Q. Rev. Biophys. 31*, 297−355.

BC0500037

Comblike, Monodisperse Polypeptoid Drag-Tags for DNA Separations by End-Labeled Free-Solution Electrophoresis (ELFSE)

Russell D. Haynes,[†] Robert J. Meagher,[‡] Jong-In Won,[‡,§] Felicia M. Bogdan,[‡,⊥] and Annelise E. Barron*[,†,‡]

Departments of Chemistry and Chemical and Biological Engineering, Northwestern University, Evanston, Illinois 60208. Received December 28, 2004; Revised Manuscript Received April 24, 2005

The development of innovative technologies designed to reduce the cost and increase the throughput of DNA separations continues to be important for large-scale sequencing and genotyping efforts. We report research aimed at the further development of a free-solution bioconjugate method of DNA size separation by capillary electrophoresis (CE), in particular, the determination of an optimal molecular architecture for polyamide-based "drag-tags". We synthesized several branched poly(*N*-methoxyethyl glycine)s (poly(NMEG)s, a class of polypeptoids) as novel friction-generating entities for end-on attachment to DNA molecules. A 30-mer poly(NMEG) "backbone," comprising five evenly spaced reactive ϵ-amino groups, was synthesized on solid phase, cleaved, and purified to monodispersity by RP-HPLC. Three different comblike derivatives of this backbone molecule were created by (1) acetylating the ϵ-amino groups or (2) appending small, monodisperse NMEG oligomers (a tetramer and an octamer). Grafting of the oligo(NMEG)s was done using solution-phase amide bond formation chemistry. Once purified to total monodispersity, the three different drag-tags were studied by free-solution electrophoresis to observe the effect of branching on their hydrodynamic drag or "α" and hence their ability to separate DNA. Drag was found to scale linearly with total molecular weight, regardless of branch length. The octamer-branched drag-tag−DNA conjugate was used to separate ssDNA products of 50, 75, 100, and 150 bases in length by free-solution CE in less than 10 min. Hence, the use of branched or comblike drag-tags is both a feasible and an effective way to achieve high frictional drag, allowing the high-resolution separation of relatively large DNA molecules by free-solution CE without the need to synthesize very long polymers.

INTRODUCTION

The development of novel and improved technologies for DNA separation and analysis continues to be driven by a societal need to make sequencing and genotyping more cost-effective. Capillary electrophoresis (CE)[1] and capillary array electrophoresis (CAE) enable high-throughput DNA sequencing and genotyping separations by allowing the use of higher electric fields and greater automation than was possible with the traditional slab gel format. Both CE and CAE require the use of highly viscous polymer solutions (e.g., entangled solutions of linear polyacrylamide) as intracapillary DNA size-separation matrixes. In addition to their expense, these polymer solutions require the application of high pressure to be loaded into narrow capillaries, and generally DNA sequencing read lengths, with even the best polymers and CAE instruments, are limited to about 800 bases at best.

DNA separation cannot normally be achieved by electrophoresis in free solution, that is, in the absence of polymer networks, because the electrophoretic mobility of DNA molecules is independent of their chain length (*1*). It was theorized in 1992 that DNA could be separated by free-solution electrophoresis if one attached a monodisperse perturbing entity or "drag-tag" to DNA fragments of varying size (*2*). That is, it was predicted that the charge-to-friction ratio of DNA can be rendered size-dependent if a monodisperse drag-tag is covalently attached to one end of the DNA molecules to be separated, allowing the DNA chains to be separated by microchannel electrophoresis in a regular, size-dependent fashion. This approach, called end-labeled free-solution electrophoresis (ELFSE), has been under development for the past 10 years as a promising bioconjugate method of DNA sequencing and genotyping that could eliminate the need for viscous polymer solutions in capillary and chip electrophoresis of DNA (*3*−*5*). Experimentally, ELFSE with various types of drag-tags has been used to separate short oligonucleotides with high resolution (*6*, *7*), as well as long double-stranded DNA fragments (*8*). For DNA sequencing applications, ELFSE promises to provide faster separations and longer read lengths than matrix-based electrophoresis and should be particularly well suited for use in microfluidic devices (*5*, *9*, *10*).

The amount of drag created by the drag-tag can be characterized in terms of the parameter "α", which has the units of the hydrodynamic drag of a single base of

* Corresponding author. Mailing address: Northwestern University, Department of Chemical and Biological Engineering, 2145 N. Sheridan Road, Rm. E136, Evanston, IL 60208. Phone: (847) 491-2778. Fax: (847) 491-3728. E-mail: a-barron@northwestern.edu.

[†] Department of Chemistry.

[‡] Department of Chemical and Biological Engineering.

[§] Present address: Department of Chemical Engineering, Hongik University, Seoul, Korea.

[⊥] Present address: Abbott Laboratories, Abbott Park, Illinois.

[1] Abbreviations: ELFSE, end-labeled free-solution electrophoresis; CE, capillary electrophoresis; PEG, poly(ethylene glycol); RP-HPLC, reversed-phase high-performance liquid chromatography; poly(NMEG)s, poly(N-substituted methoxyethyl glycine)s; sulfo-SMCC, sulfosuccinimidyl 4-[*N*-maleimidomethyl] cyclohexane-1-carboxylate.

10.1021/bc0496915 CCC: $30.25 © 2005 American Chemical Society
Published on Web 07/01/2005

ssDNA (*4*). In circumstances and conditions likely to be present in this study, recent theoretical treatments of the electrophoretic mobilities of composite molecules from the Slater group (*11*, *12*) interpret α in terms of hydrodynamic "blobs". The effective friction coefficient α for a drag-tag can be estimated experimentally by measuring (simultaneously) the electrophoretic migration times of unconjugated, "free" DNA and of a drag-tag−DNA conjugate comprising the same DNA. The parameter α can then be calculated with the equation

$$\alpha = N\left(\frac{\mu_0}{\mu} - 1\right) \quad (1)$$

for a conjugate molecule consisting of N bases of DNA and a charge-neutral drag-tag with friction equivalent to α bases of ssDNA, having the electrophoretic mobility μ, where μ_0 is the electrophoretic mobility of unlabeled DNA (about 2.5×10^{-4} cm^2/(V·s) for the conditions herein) (*4*).

High-resolution ELFSE separations of DNA require the ideal drag-tag to be (i) totally monodisperse, (ii) of high enough molecular weight to impart sufficient drag to separate DNA analytes of varying size, (iii) water-soluble and polar but essentially charge-neutral (*13*), and (iv) resistant to nonspecific (band broadening) interactions with microchannel walls. Taken together, the various and in some cases contradictory design criteria make drag-tag design and synthesis a challenging problem in molecular engineering.

Natural proteins and viruses have been proposed as candidate drag-tags (*2*, *4*). This prediction was validated by the successful sequencing of ca. 110 DNA bases in 18 min by free-solution CE with the use of the protein streptavidin as a drag-tag (*14*). This result, although remarkable, highlighted some significant drawbacks of using natural proteins as drag-tags. For instance, the results indicated a problem with obtaining streptavidin in a truly monodisperse preparation and also showed that even a virtually charge-neutral protein can suffer from strong adsorptive interactions with the microchannel wall. These interactions result in band broadening and a decrease in peak resolution. Streptavidin is a tetrameric protein (*15*) (4×13 kDa, totaling 536 amino acid residues) that has numerous biochemical applications (*16*), but despite its relatively large size, it adopts a compact, globular conformation, resulting in a relatively low drag, equal to approximately 30 bases of DNA. This was the primary factor limiting read length in the study by Slater and Drouin (*14*).

Synthetic polymers have also been examined for use as ELFSE drag-tags. Poly(ethylene glycol) (PEG) is water-soluble, relatively nonadsorptive to glass, hydrophilic, and uncharged − all potentially ideal molecular properties for ELFSE. However, even PEGs with a low molecular mass such as 3400 g/mol (*17*) and an ultralow polydispersity index (M_w/M_n) of 1.01 are not sufficiently monodisperse for DNA sequencing or genotyping applications (*18*).

Poly-N-substituted glycines (polypeptoids) are non-natural, sequence-specific polymers based on a polyglycine backbone (*19*). This class of molecules may be synthesized on solid phase in high yield using a "sub-monomer approach," to include a myriad of different side-chain functionalities (*20*, *21*). After cleavage from the solid phase, they can be purified to monodispersity by reversed-phase high-performance liquid chromatography (RP-HPLC).

Table 1. N-Substituted Glycine (Peptoid) Side Chains

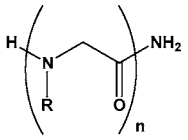

N-substituted glycine oligomer, or *peptoid*

R = Side chain	Designator
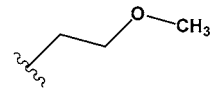	NMEG = *N*-(methoxyethyl) glycine
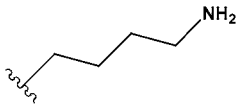	NABG = *N*-(butylamine) glycine

Vreeland et al. successfully employed a family of linear, poly(*N*-methoxyethyl glycine) peptoids (poly(NMEG)s) with PEG-like side chains (Table 1) as drag-tags for the ELFSE separation of short DNA oligonucleotides. Poly-(NMEG) drag-tags ranging in size from 10 to 60 monomers in length were used to separate 20- and 21-base ssDNAs (*6*), as well as single-base extension (SBE) reaction products between 19 and 24 bases in length (*22*). The longest polypeptoids used in these studies were 60 monomers in length, and were obtained in only modest yields by the divergent solid-phase peptide synthesis techniques used.

Aiming to improve upon this work, we hypothesized that the grafting of "branch" molecules onto a "backbone" would be an efficient convergent strategy for the synthesis of monodisperse, high-molecular weight drag-tags that could allow the separation of larger DNA. To test this idea, we designed a 30-mer poly(NMEG) "backbone" (Scheme 1) with five evenly spaced ϵ-amino sites to be grafted via a peptide bond-forming reaction with tetramer (**2**) and octamer (**3**) oligo(NMEG) peptoids possessing a terminal carboxylic acid (Scheme 2). The amino groups arrayed along the backbone of **1** could also be acetylated, yielding a set of three drag-tags with increasing branch length. We anticipated that the testing of these three different molecules as drag-tags for DNA separation by free-solution CE would provide valuable information regarding the relationship between chain architecture, molecular weight, and hydrodynamic drag (α). Grafting reactions could in theory be performed while the backbone molecule (**1**) is still on the solid-phase resin; however, for the coupling methodology to be more widely applicable for various classes of backbone molecules, we chose a solution-phase grafting strategy. In this research article, we describe how unbranched (acetylated), tetramer-branched, and octamer-branched comblike poly-(NMEG) peptoid drag-tags were synthesized, characterized, and evaluated. These drag-tags were attached to both 20- and 30-base DNA primers, and free-solution CE was used to analyze the electrophoretic mobilities of the bioconjugate molecules. We were able to observe and quantify the α values for each of these drag-tags. We also demonstrate the use of one of these drag-tags for the efficient separation of differently sized DNA fragments up to 150 bases long by CE in free solution.

EXPERIMENTAL SECTION

General Methods and Materials. The "sub-monomer" synthesis of the poly-N-substituted glycines or "polypeptoids" used in this work has been described previously (*23*). Scheme 1 depicts the protocol that was used to synthesize the polypeptoid molecules made for

Scheme 1. The Sub-Monomer Solid-Phase Polypeptoid Synthesis Protocol[a]

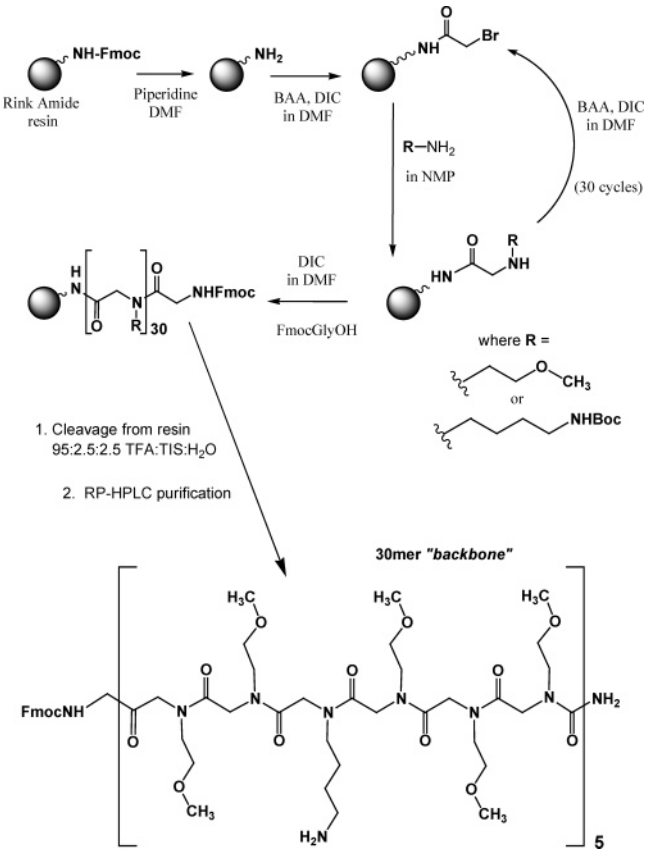

[a] Structure is predominantly poly(*N*-methoxyethyl glycine) (poly(NMEG)) residues with five evenly spaced *N*-butylamine (NABG) monomers included within. The final structure of "backbone" is shown with amino attachment sites deprotected.

Scheme 2. Chemical Structures of the Tetramer (a) and Octamer (b) "Branches"[a]

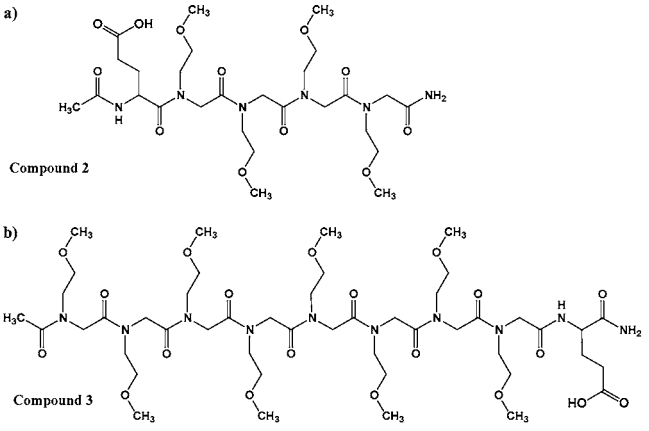

[a] They are oligo(*N*-methoxyethyl glycine) (oligo(NMEG)) peptoids with reactive terminal glutamic acid residues.

this study. All reactions were carried out on an ABI 433A automated peptide synthesizer (Applied Biosystems, Foster City, CA). All reagents used were purchased from Aldrich (Milwaukee, WI), unless stated otherwise. The mass spectra were recorded by MALDI-TOF (Voyager Pro DE, Perseptive Biosystems, Framingham, MA) and ESI (Waters Micromass Quattro II, Milford, MA). For synthesis details, see Supporting Information.

Reversed-Phase High-Performance Liquid Chromatography (RP-HPLC). Analytical RP-HPLC was performed on a column with C18 packing (Vydac, 5 μm, 300 Å, 2.1 mm × 250 mm). The following conditions were employed, unless otherwise stated: a linear gradient of 10−40% B in A was run over 50 min at a flow rate of 0.5 mL/min (solvent A = 0.1% TFA in water; solvent B = 0.1% TFA in acetonitrile) at 58 °C; analytes were detected by UV absorbance at 220 or 260 nm or both. Preparative HPLC was performed on a Vydac C18 column (Vydac, 15 μm, 300 Å, 22 mm × 250 mm) using the same solvent and detection systems; analytes were eluted with a linear gradient of 10−40% B in A over 50 min at 12 mL/min.

Polypeptoid "Backbone" (Compound 1). *Synthesis Details*. Fmoc-Rink amide resin (Nova Biochem, San Diego CA. 0.30 mmol scale) was deprotected by treatment with piperidine in dimethylformamide (DMF) (20% v/v; 2 × 7 mL) in two consecutive 15-min treatments. The oligomer chain was then assembled with alternating cycles of the bromoacetylation step and amine displacement of the alkyl bromide moiety. Bromoacetylation was achieved by mixing the resin with bromoacetic acid (BAA) (1.2 M, 4.3 mL) in DMF and diisopropylcarbodiimide (DIC) (1 mL, 9.9 mmol). The mixture was vortexed for 45 min, the liquid was drained, and the resin was rinsed with DMF (4 × 7 mL). The resin was then mixed and vortexed (45 min) with either methoxyethylamine (1.0 M, 4 mL) or mono-Boc-protected diaminobutane (1.0 M, 4 mL) (*24*) in *N*-methylpyrrolidone (NMP) to introduce the methoxyethyl (NMEG) or butylamine (NABG) side chain moieties (Table 1). The liquid was drained, and the resin was rinsed with DMF (4 × 7 mL). These two reaction cycles were alternated until the polypeptoid was of the desired sequence and length. Finally, an Fmoc protecting group was installed on the amine terminus while the polypeptoid was still on the resin. This was achieved by adding Fmoc-glycine and DIC under the same conditions as used for the bromoacetylation step.

Finally, the polypeptoid was cleaved from the solid support by treatment with 95:2.5:2.5 trifluoroacetic acid (TFA)/triisopropylsilane (TIS)/water for 10 min. The polypeptoid was filtered through a fritted glass vessel to remove the solid support, diluted with water (50 mL), frozen (−80 °C), and then lyophilized. The product of the solid-phase synthesis was evaluated by analytical RP-HPLC. Preparative RP-HPLC was subsequently performed, and appropriate fractions were combined to afford the desired product (**1**) in pure preparation.

Tetramer "Branch" (Compound 2). Using the same methods described above, we synthesized this oligopeptoid using the "sub-monomer" approach (*23*) on a 0.30 mmol scale on Fmoc-Rink amide resin (Scheme 2a). Following procedures outlined above, four additions of the *N*-methoxyethyl glycine monomer were followed by the addition of an *N*-α-Fmoc-L-glutamic acid γ-*tert*-butyl ester (Fmoc-Glu(OtBu)-OH) residue, which involves the coupling of the amino acid to the terminal secondary amine. This coupling was achieved by dissolving the amino acid in NMP (1.0 M; 4 mL) with PyBroP (1.2 M) and DIEA (1.2 M). The Fmoc group at the N-terminus of the glutamic acid residue was subsequently removed using (20% v/v) piperidine in DMF, and the resultant primary amine was capped with acetic anhydride. This was achieved by immersing the resin in fresh acetic anhydride (neat) (Applied Biosystems, Foster City, CA), followed by agitation with occasional venting for 15 min. The resin was filtered and cleaved, as previously described. For the branch molecules, cleavage from the resin also resulted in deprotection of the *t*-butyl-protected glutamic acid side chain functionality, revealing the carboxylic acid group. The oligopeptoid was cleaved from the solid support, frozen, and lyophilized, as previously

Scheme 3. Solution-Phase Coupling Protocol for the Synthesis of Branched and Unbranched Drag-Tags (4−6) via Grafting of Oligopeptoids onto the Backbone Molecule (1)

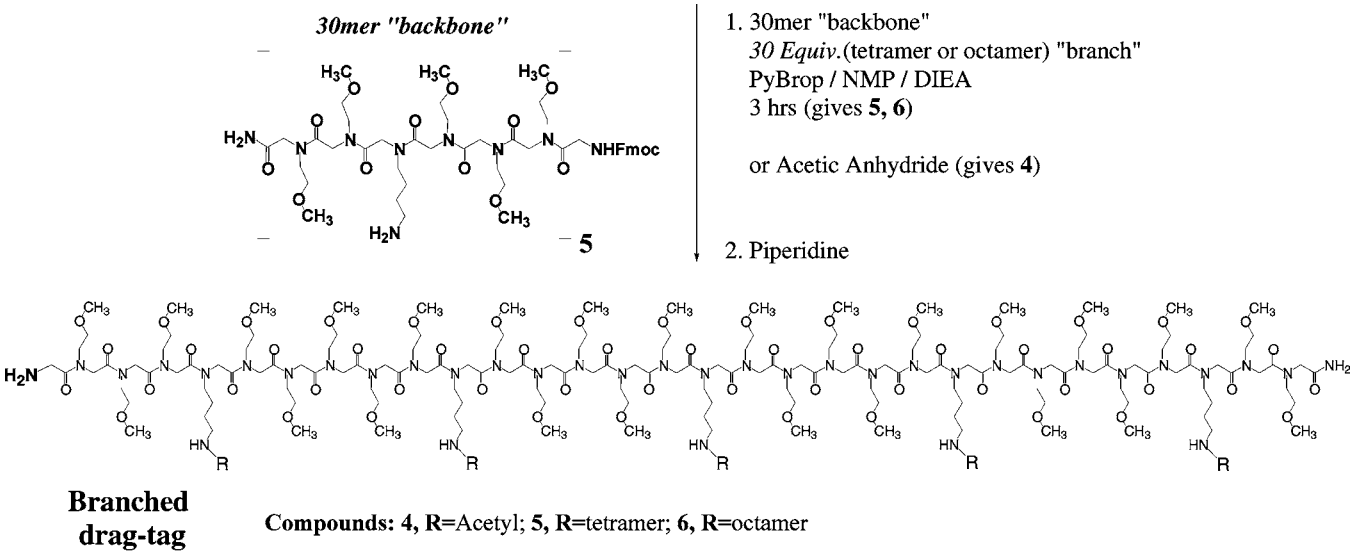

described. The product of the solid-phase synthesis was evaluated by analytical RP-HPLC. Preparative RP-HPLC was performed, and appropriate fractions were combined to afford the desired tetramer (**2**). The product was identified by ESI mass spectrometry and analyzed by RP-HPLC.

Octamer "Branch" (Compound 3). The octamer branch molecule (Scheme 2b) was synthesized by preloading the Rink amide resin with Fmoc-Glu(OtBu)-OH as the first step using standard peptide chemistry. The Fmoc group on the glutamic acid residue was subsequently removed using (20% v/v) piperidine in DMF, followed by the addition of eight monomers of *N*-methoxyethyl glycine. The terminal secondary amine was acetylated, and the oligopeptoid was then cleaved from the solid support, frozen, and lyophilized, as previously described. Preparative RP-HPLC was performed, and appropriate fractions were combined to afford compound **3**. The product was identified by ESI mass spectrometry and was analyzed by RP-HPLC.

Backbone Acetylation (Compound 4). An "unbranched" 30-mer drag-tag was synthesized by the addition of neat acetic anhydride (1 mL) to the purified backbone molecule **1** (5.0 mg, 1.3 μmol) (Scheme 3). Excess acetic anhydride was removed in vacuo, and the reaction mixture was quenched with water (10 mL), frozen (−80 °C), and lyophilized. Preparative RP-HPLC was performed and appropriate fractions were combined to afford **4**. The product was identified by MALDI-TOF mass spectrometry and was analyzed by RP-HPLC.

Backbone Grafting Reactions (Compounds 5 and 6). *Typical synthesis protocol.* Tetramer **2** (25.5 mg, 39 μmol) and PyBroP (24.85 mg, 39 μmol) were added to a cooled solution (0 °C ice-bath) of backbone **1** (5.0 mg, 1.3 μmol) in NMP (1 mL) (Scheme 3). The resultant mixture was stirred under nitrogen for 5 min. The reaction mixture was stirred vigorously and diisopropylethylamine (DIEA) (5 mg, 39 μmol) was added dropwise via cannula under a positive nitrogen atmosphere. The reaction mixture was allowed to warm to room temperature, and the reaction was allowed to proceed for 3 h. NMP was then removed in vacuo, and the solution was diluted with deionized water (12 mL), frozen, and lyophilized. The grafting reaction was monitored by analytical RP-HPLC using a slightly different method than previously stated: A linear gradient of 10−60% B in A was run over 50 min at a flow rate of 0.5 mL/min (solvent A = 0.1% TFA in water, solvent B = 0.1% TFA in acetonitrile) at 58 °C on a C18 packing column (Vydac, 5 μm, 300 Å, 2.1 mm × 250 mm); analytes were detected by UV absorbance at 220 and 260 nm. Preparative HPLC was performed on a Vydac C18 column (Vydac, 15 μm, 300 Å, 22 mm × 250 mm) using the same solvent and detection systems; analytes were eluted with a linear gradient of 10−60% B in A over 50 min at 12 mL/min. Preparative RP-HPLC was performed, and appropriate fractions were combined. Compound **5** was then was treated with 20% (v/v) piperidine in methanol (1 mL) to remove the terminal Fmoc protecting group and stirred for 20 min. The solvent was then removed in vacuo, and the resulting material was repurified by RP-HPLC as previously described. The same conditions were used, and similar results were obtained for the grafting reaction with the octamer branch to produce compound **6**.

Sulfo-SMCC Conjugation. The drag-tags (**4**−**6**), displaying a free amine at the *N*-terminus, were dissolved in 0.1 M sodium phosphate buffer, 0.15 M sodium chloride, pH = 7.18. Sulfo-SMCC (sulfosuccinimidyl 4-[*N*-maleimidomethyl] cyclohexane-1-carboxylate) (Pierce Scientific, Rockford, IL, 10 mg/mL in water) was added to the drag-tag/buffer solution. This reaction mixture was agitated at room temperature for 1 h. The reaction was quenched by the addition of water (2 mL) and then purified by preparative HPLC using the conditions described above. The appropriate fractions were then combined.

Drag-tag−DNA Conjugation. Sulfo-SMCC-activated polypeptoid drag-tags were individually conjugated to 5′-thiolated, fluorescently labeled DNA oligonucleotides of lengths 20 and 30 bases (Integrated DNA Technologies, Coralville, IA). The 20- and 30-base DNA sequences were [5′-$\mathbf{X_1}$GT$\mathbf{X_2}$TTCCCAGTCACGACGTT-3′] and [5′-$\mathbf{X_1}$CC$\mathbf{X_2}$-TTTAGGGTTTTCCCAGTCACGACGTTG-3′], where $\mathbf{X_1}$ was a 5′ thiol modifier (C6 disulfide) and $\mathbf{X_2}$ was an internal fluorescein-labeled dT base. Both sequences are designed to be used as primers for an M13mp18 template; the 30-base sequence includes six nonhybridizing bases at the 5′ end. The thiol linkers were reduced by incubating 125 pmol of thiolated DNA with 5000 pmol of tris-(2-carboxyethylphosphine) hydrochloride (TCEP) (Acros Organics, Morris Plains, NJ) in a total volume of 10 μL

Table 2. Oligonucleotide Sequences Used as Primers for PCR Products of 50, 75, 100, and 150 bp

primer	DNA sequence
	Forward Primer
M13	5′-**X**$_1$CC**X**$_2$TTTAGGGTTTTCCCAGTCACGACGTTG-3′[a]
	Reverse Primers
M13-**50**	5′-TGGCACTGGCCGTCGTTTTA-3′
M13-**75**	5′-GAGTCGACCTGCAGGCATGC-3′
M13-**100**	5′-GAGCTCGGTACCCGGGGATC-3′
M13-**150**	5′-GCGGATAACAATTTCACACA-3′

[a] **X**$_1$ refers to a 5′ thiol linker (C6 disulfide), and **X**$_2$ refers to an internal fluorescein-dT base.

of sodium phosphate buffer (100 mM, pH 7.2) at 40 °C for 110 min.

Reduced DNA was conjugated to sulfo-SMCC-activated polypeptoids by mixing 500 pmol of polypeptoid with 12.5 pmol of the reduced DNA mixture (containing 500 pmol of TCEP) in a volume of 5−7 μL of sodium phosphate buffer (100 mM, pH 7.2). Conjugation reactions proceeded in the dark at room temperature for approximately 6 h before CE analysis.

Preparation of PCR Products. The 30-base thiolated, fluorescently labeled M13 oligonucleotide described above [5′−X$_1$CCX$_2$TTTAGGGTTTTCCCAGTCACGACGTTG-3′] was used as a forward primer. Four different 20-base oligonucleotides (Table 2) were purchased from IDT (Coralville, IA) and served as M13 reverse primers for generating PCR products of 50, 75, 100, and 150 bp in length. M13mp18 ssDNA obtained from Amersham Biosciences (Piscataway, NJ) was used as a template. PCR reactions using *Thermus aquaticus* (*Taq*) DNA polymerase were performed using an MJ Research DNA thermal cycler with 30 cycles of 95 °C for 1 min (denaturing), 55 °C for 1 min (annealing), and 72 °C for 2 min (elongation). The size of each PCR product (dsDNA) was confirmed via 3% agarose gel electrophoresis. The PCR products (with no additional purification) were reduced with Tris(2-carboxyethyl)phosphine (TCEP) and conjugated to drag-tags as described above for the DNA primers.

Free-Solution Capillary Electrophoresis. DNA−polypeptoid conjugates were analyzed by capillary electrophoresis with laser-induced fluorescence detection, using either a BioRad BioFocus 3000 single-capillary instrument (BioRad, Hercules, CA) or an Applied Biosystems Prism 3100 capillary array instrument (Applied Biosystems, Foster City, CA).

Oligonucleotide primers conjugated to polypeptoid drag-tags were analyzed by free-solution electrophoresis using the BioRad BioFocus instrument at 40−55 °C in 25-μm inner-diameter fused silica capillaries (Polymicro Technologies, Phoenix, AZ) cut to a total length of 25 cm (20.4 cm from inlet to detector). The running buffer was 1× TTE with 7 M urea (50 mM Tris, 50 mM TAPS, 2 mM EDTA, 7 M urea, pH = 8.5). Typical DNA sequencing conditions were used to keep the DNA in an unstructured state (7 M urea and a run temperature of 55 °C). The internal surface of the capillary was coated with an adsorbed layer of POP5 polymer (Applied Biosystems, Foster City, CA) using a low-viscosity 3% (v/v) aqueous dilution of the commercially available POP5 solution to reduce electroosmotic flow to negligible levels. Immediately prior to sample injection, the injection end of the capillary was dipped into deionized water to remove any residual buffer salts on the outer surface of the capillary. The samples were introduced into the capillary by pressure injection with pressure−time constants of 5−15 psi·s. Electrophoresis was conducted at 400 V/cm until all peaks had eluted with typical currents of 2.8 μA. Detection of the analytes was accomplished by excitation of the fluorescent label on the DNA using the 488 nm line of an argon-ion laser with emission detected at 520 nm.

Electrophoretic analysis of PCR products conjugated to polypeptoids was carried out in free solution using the Applied Biosystems Prism 3100 genetic analyzer with an array of fused silica capillaries of length 36 cm and inner diameter 50 μM. Analysis conditions were identical to those described above for the BioFocus experiments, except the electric field was 320 V/cm, and samples were introduced by an electrokinetic injection of 22 V/cm for 2 s. The PCR product−polypeptoid conjugates were diluted in deionized formamide (Applied Biosystems, Foster City, CA) and denatured at 95 °C for 5 min prior to electrophoretic analysis to yield single-stranded DNA−drag-tag conjugates.

RESULTS AND DISCUSSION

Branched Drag-Tag Design and Synthesis. Attaching large molecules onto a scaffold containing multiple grafting sites, and achieving full coverage, is a challenging proposition (*25*). For ELFSE applications, the grafting linkages need to be stable enough to withstand further conjugation reactions, purification steps, wide pH ranges, and the high temperatures used in thermal cycling. For this reason, we decided on peptide-bond linkages. We designed the backbone (**1**) to have regularly spaced, pendant ϵ-amino groups as attachment sites for tetramer (**2**) and octamer (**3**) branch molecules with terminal carboxylic acid groups. This is an attractive strategy as it allows for the convergent reaction between large molecules that have been prepurified to monodispersity. Although the resolving power of RP-HPLC could potentially allow for a subsequent removal of the incompletely grafted side-products, complete grafting is a desired outcome, because even slight impurities in the drag-tag are exposed by CE analysis and will limit its usefulness.

Indeed, early attempts in our lab to graft polyamide oligomers onto lysine-containing polypeptides resulted in a ladder of partially grafted products that ultimately proved too difficult to purify to monodispersity (*26*). In the present work, we have used poly(*N*-methoxyethyl glycine)s and their derivatives for both the backbone and branch structures and were able to produce highly monodisperse components in high yield. The structure of poly(NMEG) is consistent with recently proposed rules for creating chemical surfaces that are resistant to adsorption of proteins from solution. Specifically, it was found that surfaces presenting groups that are polar but uncharged and hydrophilic and contain hydrogen-bond acceptors (but not hydrogen-bond donors) are inert to adsorption of proteins from solution (*27*). We hypothesized that poly(NMEG), which has all of these structural features, would be resistant to adsorption from solution onto surfaces. This is a critical feature for capillary electrophoresis, where wall−analyte interactions are a major source of band broadening. Indeed, in previous ELFSE separations using streptavidin as a drag-tag, the interaction between streptavidin and the capillary wall was the primary factor limiting separation efficiency at high electric field strengths (*14*).

We had to design the drag-tag for two stages of conjugation: a grafting reaction that introduced the monodisperse branches and then a conjugation to DNA. To achieve this, the backbone molecule (**1**) was designed

Table 3. Peptoid Structures, Molecular Mass Confirmation, and Crude Purities

compound	peptoid oligomer	monomer sequence (amino-to-carboxy)	molar mass calcd/found	purity,[a] %
1	30-mer backbone	$FmocGly[(NMEG)_3(NABG)(NMEG)_2]_5NH_2$	3818.2/3819.3	77
2	tetramer branch	$AcGlu(OH)(NMEG)_4NH_2$	648.3/648.8	96
3	octamer branch	$Ac(NMEG)_8Glu(OH)NH_2$	1108.6/1109.1	95

[a] As estimated by analytical reversed-phase HPLC of crude product. All compounds were purified to >99% homogeneity before conjugation reactions.

with a glycine group at the N-terminus (Scheme 1), and this resulted in a terminal amine protected with 9-fluorenylmethyloxycarbonyl (Fmoc). The Fmoc protecting group is orthogonal to the *tert*-butyloxycarbonyl (Boc)-protected *N*-butylamine (NABG) ϵ-amino groups along the backbone and, when removed (after grafting), exposes a free N-terminal amine for DNA conjugation. Cleavage from the resin using trifluoroacetic acid (TFA) also conveniently cleaves the Boc groups on the side chains without affecting the Fmoc-protected amino terminus.

The terminal Fmoc-glycine residue also facilitates purification. The increased hydrophobicity afforded by the inclusion of the Fmoc group dramatically increases the HPLC retention time, thus helping separate the desired product from impurities. Also, the UV absorbance of the Fmoc moiety allows for facile identification of the product peak at 260 nm by RP-HPLC. The Fmoc amino group can then be easily deprotected at a later point for conjugation to DNA prior to ELFSE analysis.

Backbone Synthesis. The backbone (**1**) was synthesized (Scheme 1) using commercially available materials and mono-Boc-protected diaminobutane, the latter synthesized and purified in-house according to literature procedures (*24*). RP-HPLC analysis revealed a single major product peak, approximately 77% by area (Table 3) (greater than 99% coupling efficiency per monomer residue). Compound **1** was obtained in pure form by preparative RP-HPLC, and its correct mass was confirmed by ESI mass spectrometry.

Branch Syntheses. The tetramer and octamer branches were both synthesized in excellent yield (Table 3) and purified to monodispersity by RP-HPLC. They were designed as oligo(*N*-methoxyethyl glycine) peptoids with terminal glutamic acid (peptide) functionalities. Previous unsuccessful attempts in our lab to make similar tetramer and octamer branches suitable for high-yield grafting involved using a terminal glycine unit to provide the reactive carboxylic acid group. Specifically, we had synthesized tetramer and octamer oligo(*N*-methoxyethyl glycine) peptoids on preloaded glycine Wang resin that revealed a C-terminal carboxylate upon cleavage. However, the carboxylate groups on these glycine-terminated drag-tags were apparently too sterically hindered for high-yield grafting reactions. In our hands, they failed to react efficiently with the ϵ-amino groups along the backbone. Attempts to graft with these branch molecules resulted in incomplete coverage and hence relatively low yields of the desired fully derivatized drag-tags (<30% crude yield). The tetramer-branched drag-tag obtained using this strategy was successfully isolated in sufficient quantity for conjugating to DNA, but in low overall yield and with a mass that differed for unknown reasons by ~200 g/mol from the correct target molar mass. Hence, the glycine-terminated branch design was abandoned in favor of glutamic acid-terminated branches; as described below, grafting of the backbone with these oligomers yields conjugates with the correct accurate masses.

With the intention of improving the coupling efficiency of the grafting reaction, glutamic acid-terminated oligomer branches were designed with the carboxylic acid functionality at the end of a longer, more flexible side chain. We designed the tetramer (**2**) to have the glutamic acid at the *N*-terminus and the octamer (**3**) with that group at the C-terminus (Scheme 2), since we did not know a priori which strategy was best or whether this would make a difference. Synthetically, the two branch designs differ only slightly but potentially enough to affect the monodispersity, since the acetic anyhdride capping of **1** takes place on a primary amine, while the capping of **2** occurs on a secondary amine. For both branch molecules, however, synthetic yields were high: RP-HPLC analysis revealed a single major product peak; yields were approximately 95% by area for both designs (Table 3). In addition, highly efficient grafting was achieved with both designs as described below (Figure 1).

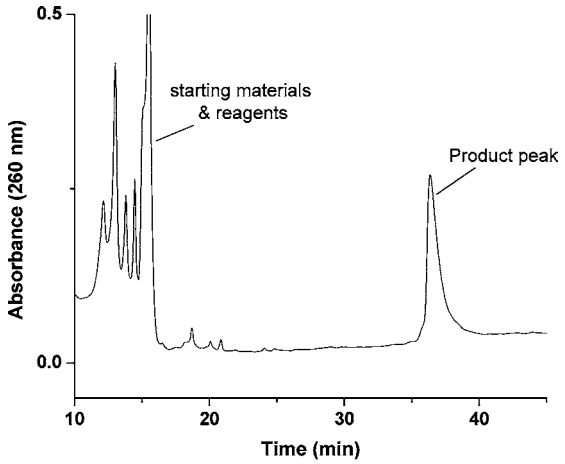

Figure 1. RP-HPLC chromatogram of the crude products of the grafting reaction between the tetramer branches (**2**) and the backbone molecule (**1**). HPLC conditions were C18 250 mm Vydac column, 58 °C, with 10−60% acetonitrile−water (0.1% TFA) over 50 min.

Grafting of Oligomeric Branches to the Polymeric Backbone. The "unbranched" or N-acetylated drag-tag (**4**) was synthesized by the addition of acetic anhydride to a solution of the backbone (**1**) in methanol. Removal of the solvents in vacuo, followed by RP-HPLC purification, afforded a single pure product. The Fmoc protecting group was then removed from the isolated product using piperidine; analysis of the products of this deprotection reaction gave a single peak by RP-HPLC. Compound **4** was collected as a white solid.

One of the most challenging aspects of this synthesis was to achieve complete reaction at all five amino sites on the backbone molecule with the tetramer and octamer branches. To generate a completely monodisperse product, we had to find the best way to couple several large molecules together while forming bonds that are extremely stable. Peptide bond linkages can be formed efficiently and were found to be sufficiently stable to withstand the further manipulations needed to make the drag-tag useable.

Finding the appropriate reagents and conditions to form five simultaneous peptide bonds in one reaction

Table 4. Drag-Tag Structures, Molecular Mass Confirmation, and α Values

compound	drag-tag	molar mass calcd/found	α(20)[a]	α(30)[b]
4	acetylated	4023.2/4023.5	7.9	7.9
5	tetramer-branched	6964.9/6964.6	12.5	13.7
6	octamer-branched	9266.1/9271.4	16.4	17.2

[a] For the 20-base DNA−drag-tag conjugate. [b] For the 30-base DNA−drag-tag conjugate.

initially proved difficult. Solvents including NMP and DMF were examined. Several peptide bond forming coupling reagents including PyBOP, HATU, and PyBroP were examined (*28*−*30*). Optimum results with respect to the efficiency of coupling were obtained utilizing a combination of NMP and PyBroP with DIEA (*26*). The use of freshly lyophilized chemicals and Aldrich "sure-seal" packaging (where available) and the employment of rigorous Schlenk techniques under a positive nitrogen atmosphere were found to be highly important factors in the achievement of complete grafting coverage of the backbone. The backbone molecule was found to be especially sensitive to air, because it possesses five free amines, which may react with carbon dioxide. After optimization of the reaction conditions, the RP-HPLC chromatograms for the analysis of the crude products of the grafting reactions show a single product peak, later identified by mass spectrometry to be the fully grafted comblike polymer. Under the described reaction conditions, the grafting reaction is highly efficient and goes to completion in only a few hours. Using 6 equiv of branch molecule per amino site on the backbone (30 equiv overall) was found to be sufficient to achieve complete grafting of all five sites. Preparative HPLC fractions were collected and lyophilized to afford a white solid. This protocol does expend a large quantity of the branch reagent, but to ensure that the reaction goes to completion (due to the strict monodispersity needs for ELFSE applications), the expense is deemed acceptable.

Isolated yields for the synthesis of these branched drag-tags are difficult to accurately quantitate since on the scale we performed them (5 mg of backbone), the masses of final product are low (ca. 1 mg). The crude yield as determined by RP-HPLC is ∼97% (Figure 1). However, to ensure complete monodispersity, only the product appearing in the central area of the RP-HPLC peak was carried on. The drag-tag conjugate molecules were found to have the correct masses by MALDI-TOF mass spectrometry (Table 4). As described above, the derivatized (branched) molecules were then treated with piperidine and further purified to afford drag-tags with free (and unique) primary amino groups at the N-terminus. These molecules were then ready for sulfo-SMCC activation to enable their conjugation to oligonucleotide primers.

Sulfo-SMCC Activation. The free-amine terminated drag-tags were reacted with the heterobifunctional linker sulfo-SMCC. This reagent consists of two reactive groups: a sulfo-NHS group (reactive toward primary amines) and a maleimide (reactive toward thiols), connected by a cyclohexyl-containing aliphatic linker. The primary amino terminus of the drag-tags reacts with the sulfo-NHS end of the linker. RP-HPLC was then used to remove excess sulfo-SMCC from the reaction mixture, resulting in a high yield (>95%) of drag-tag with a reactive maleimide for subsequent conjugation to thiolated oligonucleotides.

DNA Reduction and Conjugation to Polypeptoids. The 5′-thiolated DNA is obtained as the disulfide dimer, which must be reduced to yield free sulfhydryl groups. Complete reduction of the DNA is essential for obtaining a high yield of the desired conjugate molecule. DNA reduction conditions, involving a 40:1 molar ratio of tris(2-carboxyethyl)phosphine (TCEP) to thiolated DNA incubated at 40 °C for at least 90 min, were found to reliably reduce picomole amounts of disulfide-modified DNA with yields in excess of 80%. Dithiothreitol (DTT) may also be used for reduction at slightly alkaline pH, although in our experience a larger excess of DTT must be used with a significantly longer incubation at 40 °C to achieve a comparable level of reduction with these very small amounts of thiolated DNA. Solid-phase reducing agents (resin-bound DTT or TCEP) have given us inconsistent results.

Literature reports as to the reactivity of TCEP toward maleimides are varied (*31*−*33*). We have found that the presence of excess TCEP does seem to reduce the efficiency of the conjugation of thiolated DNA to maleimide-activated polypeptoids, and addition of maleimide-activated polypeptoid in slight excess relative to TCEP appears to give optimal conjugation yields (data not shown). Since the polypeptoids in this case are available in large quantities relative to the tiny amounts of DNA required for capillary electrophoresis analysis, the removal of excess TCEP by gel filtration or dialysis was not necessary. Conjugation yields were approximately 70% for polypeptoids conjugated to the 20-base DNA and closer to 95% for polypeptoids conjugated to 30-base DNA.

Free-Solution Capillary Electrophoresis Analysis of DNA−Drag-Tag Conjugates and the Determination of α Values. Capillary electrophoresis with laser-induced fluorescence detection is a powerful and sensitive analytical technique in which charged analytes are separated on the basis of differences in their charge-to-friction ratios or electrophoretic mobilities. Separations are carried out in narrow fused silica capillaries, which allow efficient heat removal and thus enable the use of higher electric fields than can be maintained in conventional slab gel electrophoresis. DNA separations are typically carried out in 50- or 75-μm inner diameter capillaries filled with a viscous polymer solution or sieving matrix. In this study, modifying DNA oligonucleotides with the drag-tags allowed the separation of DNA in free solution with no viscous polymer solution. The elimination of the polymer solution simplifies CE operations and allows the use of narrower capillaries (as small as 25 μm in inner diameter), which afford improved resolution.

The highly negatively charged DNA oligomer component of the drag-tag−DNA conjugates endows each of the bioconjugate molecules with a strong electromotive force during electrophoresis. The polypeptoid portion gives each molecule an additional amount of hydrodynamic drag. The analysis of the drag-tag−DNA conjugates by free-solution electrophoresis allows the determination of the frictional parameter α of the drag-tag, as described in the Introduction (eq 1).

The results of the electrophoretic analyses of the drag-tags conjugated to the 20-base oligonucleotide are shown in Figure 2, and α values calculated from the experiments are shown in Table 4. The acetylated 30-mer **4** gives an $\alpha \approx 8$, whereas the addition of tetramer and octamer branches increases α to about 13 and 17, respectively. Note that the 536-residue protein streptavidin gives an α value that is only twice that of the octamer-branched drag-tag (**6**), which comprises only 70 monomers. A high degree of monodispersity is a key property for drag-tags, and these drag-tags display excellent purity (>99% by area). Extremely monodisperse drag-tags are necessary

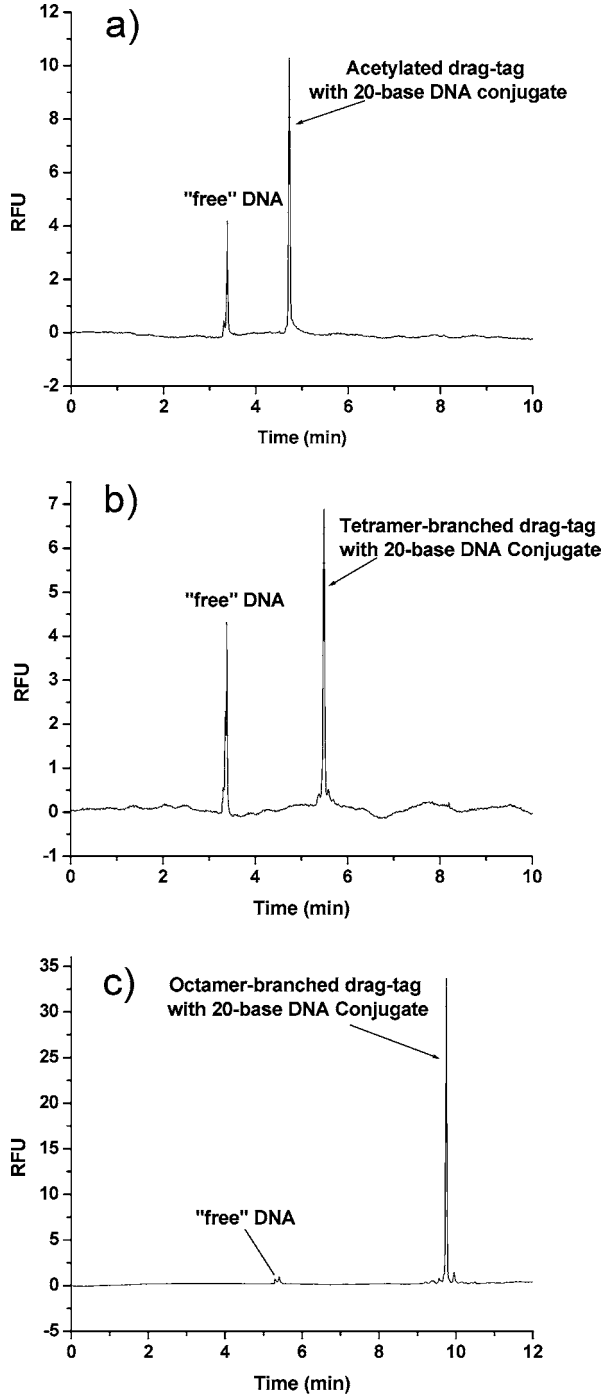

Figure 2. Free-solution capillary electrophoresis analysis of 20-base fluorescently labeled oligonucleotide conjugated to (a) an "unbranched" or acetylated 30-mer drag-tag (**4**), (b) a tetramer-branched drag-tag (**5**), and (c) an octamer-branched drag-tag (**6**). Separations were carried out on a BioRad BioFocus capillary electrophoresis instrument at 40 °C. The running buffer was 50 mM Tris, 50 mM TAPS, 2 mM EDTA, and 7 M urea, pH 8.5, mixed with a 3% (v/v) aqueous dilution of a POP5 solution as a wall coating agent. The fused silica capillary had an inner diameter of 25 μm and a total length of 25 cm (20.6 cm inlet to detector). Samples were introduced by hydrodynamic injection with a pressure−time constant of 5 psi·s. The electric field was 10 kV (400 V/cm) with a typical current of 2.8 μA. The fluorescent label was excited at 488 nm with emission detected at 520 nm.

for ELFSE analysis because impurities lead to multiple peaks for each size of DNA. Such extra peaks would confound the results of sequencing or other ELFSE separations demanding high resolution. These results

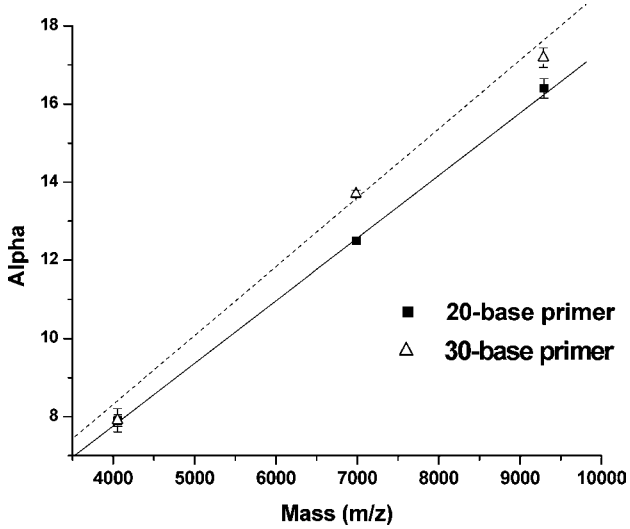

Figure 3. Plot of hydrodynamic drag or "α" against molecular weight for the 20-base and 30-base DNA−drag-tag conjugates (for all three drag-tags, **4**−**6**).

give us good confidence in the viability of making high molar mass peptoids for ELFSE applications.

Interestingly, the relationship between α and the molecular weight of the drag-tag for these poly(*N*-methoxyethyl glycine)-based molecules was found to be essentially linear (Figure 3). Table 4 shows the relative molecular weights and averaged α value for each of these drag-tag conjugates with two DNA primers of different length. This study shows that hydrodynamic drag is not simply a function of the length of the backbone. Rather, drag scales linearly with the total molecular weight or the total number of monomer units. This is in line with previous observations for linear polypeptoids (*6*) and suggests that the polypeptoids, whether branched or linear, adopt an "expanded" conformation in aqueous solution such that all of the monomer units are hydrodynamically exposed to the solvent during electrophoresis.

Separation of PCR Products. The octamer-branched drag-tag (**6**) was utilized in separating thiolated DNA products from a PCR reaction. PCR was used to generate double-stranded DNA fragments of 50, 75, 100, and 150 base pairs in size. The monodisperse, comblike polymer drag-tag **6** was conjugated to each of the fragments following the PCR reaction, and these conjugate products were successfully separated by CE in free solution, as shown in Figure 4a. The PCR products were denatured prior to analysis and analyzed under denaturing conditions, so the analysis represents single-stranded DNA−drag-tag conjugates. The PCR reaction products were not purified prior to analysis; hence there are some shorter products representing partially amplified PCR products shorter than 50 bases. We left these impurities in the mixture to demonstrate the ability of the drag-tag **6** to resolve small DNA with single-base resolution. The peaks for the 50-base and 75-base fragments are actually split into doublets, indicating the presence of two species (perhaps 50 and 51 and 75 and 76 bases). The reason for this could be due to the propensity of *Taq* polymerase to generate "stutter" or "shadow" bands, in this case possibly adding an extra base during the PCR reaction (*34*). Multiple closely spaced peaks are also present for "free" DNA (carrying no drag-tag). There are several different sizes of DNA present in the mixture, including some unreduced disulfide dimers, which may have slightly different mobilities, resulting in the spread of closely

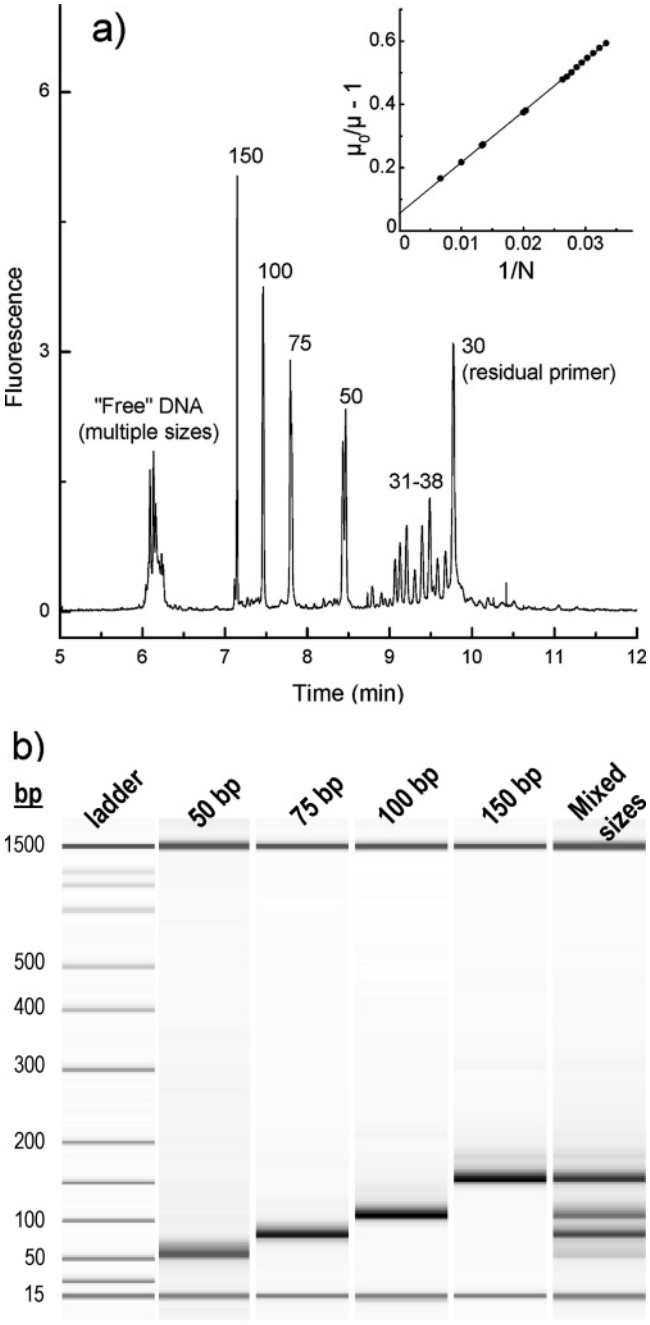

Figure 4. (a) ELFSE separation of 50-, 75-, 100-, and 150-base PCR products (and residual DNA impurities) conjugated to the octamer-branched drag-tag. Samples were denatured in formamide prior to injection. Analysis was performed in free solution on an ABI Prism 3100 instrument with a 36-cm long capillary array (55 μm i.d. capillaries) at 55 °C. The buffer was 50 mM Tris, 50 mM TAPS, 2 mM EDTA, and 7 M urea, pH 8.5, mixed with a 3% (v/v) aqueous dilution of a POP5 solution as a wall coating agent. An electrokinetic injection of ~22 V/cm for 2 s was used. The electric field during the run was ~320 V/cm with a typical current of ~8.5 μA per capillary. The inset is a plot of ($\mu_0/\mu - 1$) for each of the major peaks versus the number of DNA bases N (*4*). (b) Analysis of reduced, thiolated PCR products on Agilent 2100 Bioanalyzer using DNA 1000 sizing kit. Each sample lane includes 15 and 1500 bp markers.

spaced peaks centered around 6.1 min. For comparison, the separation of these PCR products was performed using a chip-based electrophoresis system (the Agilent 2100 Bioanalyzer) with a polymer solution to provide size-based separation of DNA. The correct sizes of the PCR products were confirmed by comparison to DNA size standards (Figure 4b). The DNA polydispersity around 50 bases correlates well with what was found using the ELFSE technique (compare Figure 4, parts a and b).

The inset of Figure 4 shows a plot of the mobility ratio, $\mu_0/\mu - 1$, versus number of bases for each of the major peaks in Figure 4, including the residual primer and impurity peaks. The tallest of the "free" DNA peaks at 6.13 min was chosen as the reference peak for μ_0. As can be observed by a simple rearrangement of eq 1, this plot should yield a straight line with slope equal to α. The resulting plot is highly linear ($R^2 = 0.9997$) with a slope of 16.15, in good agreement with the α values calculated from the separations of the 20-base and 30-base oligonucleotides. The intercept is slightly offset from zero; this may be the result of the fluorescein label, which contains a negative charge and thus slightly affects the electrophoretic mobility of both the conjugates (μ) and the free DNA (μ_0).

This separation of PCR products demonstrates the potential usefulness of branched polypeptoid drag-tags for a wide variety of genotyping or "DNA fingerprinting" applications that require size-based separation of DNA. The mixture shown here was intentionally not purified to demonstrate the resolving power of ELFSE for smaller oligonucleotides (the small impurities are easily separated with single-base resolution). This separation methodology could easily be adapted to analyze double-stranded PCR products as well. The highly monodisperse drag-tag and separation method used here offer excellent resolution and peak shape compared to the previous demonstrations of dsDNA separation by ELFSE using streptavidin (*8*), due to the true monodispersity and favorable chemical properties of these drag-tags. The octamer-branched drag-tag is likely too small for high-resolution separation of much larger PCR products or DNA sequencing fragments, but a similar methodology may be employed to construct much larger branched molecules, for example, using larger branches, a longer backbone, or both.

CONCLUSIONS

In this work, we have developed methodology for creating totally monodisperse, comblike, hydrophilic, and water-soluble copolymers, which were successfully synthesized and characterized. The peptide bonds between the branches and the backbone were formed most efficiently using an excess of glutamic acid-terminated branches and PyBroP as a coupling reagent. By conjugating the drag-tags to monodisperse DNA oligonucleotides 20 and 30 bases in length, we then evaluated these branched molecules by free-solution CE as ELFSE drag-tags in terms of their respective frictional parameters (α). The octamer-branched molecule was also used to successfully separate ssDNA fragments of varying lengths up to 150 bases.

The ELFSE studies of this family of branched drag-tag−DNA bioconjugates reveal a direct linear relationship between molecular weight and hydrodynamic drag. This information will prove useful in the future design of drag-tags for applications in free-solution CE. Achieving significant hydrodynamic drag for poly(NMEG) peptoids may be considered a direct function of molecular weight or the number of monomers, rather than simply the length of the backbone.

We intend to use this structural information about drag-tag design to generate drag-tags with tailored designs that allow the free-solution sequencing of hun-

dreds of bases of DNA. A comblike architecture appears to be an excellent design for drag-tags for the ELFSE technique.

ACKNOWLEDGMENT

We would like to thank Gary W. Slater for many helpful discussions regarding this project. This work was supported by the National Institute of Health and National Human Genome Research Institute (Grant No. 1RO1HG002918-01).

Supporting Information Available: Additional MALDI mass spectral and ELFSE CE data. This material is available free of charge via the Internet at http://pubs.acs.org.

LITERATURE CITED

(1) Olivera, B. M., Baine, P., and Davidson, N. (1964) Electrophoresis of the Nucleic Acids. *Biopolymers 2*, 245−257.

(2) Noolandi, J. (1992) A New Concept for Sequencing DNA by Capillary Electrophoresis. *Electrophoresis 13*, 394−395.

(3) Grossman, P. D. F. S., Menchen, S. M., Woo, S. L., and Winn-Deen, E. S. (1993) Distinguishing different polynucleotide(s) in nonsieving medium − useful in DNA sequencing and target detection in sample. World Patent WO93202-36A1.

(4) Mayer, P., Slater, G. W., and Drouin, G. (1994) Theory of DNA-Sequencing Using Free-Solution Electrophoresis of Protein-DNA Complexes. *Anal. Chem. 66*, 1777−1780.

(5) Meagher, R. J., Won, J. I., McCormick, L. C., Nedelcu, S., Bertrand, M., Bertram, J. L., Drouin, G., Barron, A. E., and Slater, G. W. End-labeled free-solution electrophoresis of DNA. *Electrophoresis 26*, 331−350.

(6) Vreeland, W. N., and Barron, A. E. (2000) Free-solution capillary electrophoresis of polypeptoid-oligonucleotide conjugates. *Abstr. Am. Chem. Soc. 219*, U449−U449.

(7) Volkel, A. R., and Noolandi, J. (1995) Mobilities of Labeled and Unlabeled Single-Stranded-DNA in Free Solution Electrophoresis. *Macromolecules 28*, 8182−8189.

(8) Heller, C., Slater, G. W., Mayer, P., Dovichi, N., Pinto, D., Viovy, J. L., and Drouin, G. (1998) Free-solution electrophoresis of DNA. *J. Chromatogr. A 806*, 113−121.

(9) Sundberg, S., Kopf-Sill, A., Nagle, R., Gallagher, S., Chow, C., Wada, G., Nikiforov, T., and Parce, J. W. (1998) Laboratory on a chip: A new experimentation format. *Am. Lab. 30*, 22.

(10) Kan, C. W., Fredlake, C. P., Doherty, E. A. S., and Barron, A. E. (2004) DNA sequencing and genotyping in miniaturized electrophoresis systems. *Electrophoresis 25*, 3564−3588.

(11) McCormick, L. C., Slater, G. W., Karger, A. E., Vreeland, W. N., Barron, A. E., Desruisseaux, C., and Drouin, G. (2001) Capillary electrophoretic separation of uncharged polymers using polyelectrolyte engines − Theoretical model. *J. Chromatogr. A 924*, 43−52.

(12) Desruisseaux, C., Long, D., Drouin, G., and Slater, G. W. (2001) Electrophoresis of composite molecular objects. 1. Relation between friction, charge, and ionic strength in free solution. *Macromolecules 34*, 44−52.

(13) Won, J. I., Meagher, R. J., and Barron, A. E. (2004) Protein polymer drag-tags for DNA separations by end-labeled free-solution electrophoresis. *Electrophoresis 26*, 2138−2148.

(14) Ren, H., Karger, A. E., Oaks, F., Menchen, S., Slater, G. W., and Drouin, G. (1999) Separating DNA sequencing fragments without a sieving matrix. *Electrophoresis 20*, 2501−2509.

(15) Hendrickson, W. A., Pahler, A., Smith, J. L., Satow, Y., Merritt, E. A., and Phizackerley, R. P. (1989) Crystal-Structure of Core Streptavidin Determined from Multiwavelength Anomalous Diffraction of Synchrotron Radiation. *Proc. Natl. Acad. Sci. U.S.A. 86*, 2190−2194.

(16) Buckland, R. M. (1986) Strong Signals from Streptavidin Biotin. *Nature 320*, 557−558.

(17) Kramer, R. H., and Karpen, J. W. (1998) Spanning binding sites on allosteric proteins with polymer-linked ligand dimers. *Nature 395*, 710−713.

(18) Vreeland, W. N., Desruisseaux, C., Karger, A. E., Drouin, G., Slater, G. W., and Barron, A. E. (2001) Molar mass profiling of synthetic polymers by free-solution capillary electrophoresis of DNA−polymer conjugates. *Anal. Chem. 73*, 1795−1803.

(19) Simon, R. J., Kania, R. S., Zuckermann, R. N., Huebner, V. D., Jewell, D. A., Banville, S., Ng, S., Wang, L., Rosenberg, S., Marlowe, C. K., Spellmeyer, D. C., Tan, R. Y., Frankel, A. D., Santi, D. V., Cohen, F. E., and Bartlett, P. A. (1992) Peptoids − a Modular Approach to Drug Discovery. *Proc. Natl. Acad. Sci. U.S.A. 89*, 9367−9371.

(20) Burkoth, T. S., Fafarman, A. T., Charych, D. H., Connolly, M. D., and Zuckermann, R. N. (2003) Incorporation of unprotected heterocyclic side chains into peptoid oligomers via solid-phase submonomer synthesis. *J. Am. Chem. Soc. 125*, 8841−8845.

(21) Uno, T., Beausoleil, E., Goldsmith, R. A., Levine, B. H., and Zuckermann, R. N. (1999) New submonomers for poly N-substituted glycines (peptoids). *Tetrahedron Lett. 40*, 1475−1478.

(22) Vreeland, W. N., Meagher, R. J., and Barron, A. E. (2002) Multiplexed, high-throughput genotyping by single-base extension and end-labeled free-solution electrophoresis. *Anal. Chem. 74*, 4328−4333.

(23) Zuckermann, R. N., Kerr, J. M., Kent, S. B. H., and Moos, W. H. (1992) Efficient Method for the Preparation of Peptoids Oligo(N-Substituted Glycines) by Submonomer Solid-Phase Synthesis. *J. Am. Chem. Soc. 114*, 10646−10647.

(24) Krapcho, A. P., and Kuell, C. S. (1990) Monoprotected Diamines - N-Tert-Butoxycarbonyl-Alpha,Omega-Alkanediamines from Alpha,Omega-Alkanediamines. *Synth. Commun. 20*, 2559−2564.

(25) Helms, B. M. J. L., Hawker, C. J., and Frechet, M. J. (2004) Dendronized Linear Polymers via "Click Chemistry". *J. Am. Chem. Soc.* **2004**, *126* (46), 15020−15021.

(26) Bogdan, F. M., and Barron, A. E. Unpublished results.

(27) Ostuni, E., Chapman, R. G., Holmlin, R. E., Takayama, S., and Whitesides, G. M. (2001) A survey of structure−property relationships of surfaces that resist the adsorption of protein. *Langmuir 17*, 5605−5620.

(28) Carpino, L. A. (1993) 1-Hydroxy-7-Azabenzotriazole − an Efficient Peptide Coupling Additive. *J. Am. Chem. Soc. 115*, 4397−4398.

(29) Frerot, E., Coste, J., Pantaloni, A., Dufour, M. N., and Jouin, P. (1991) Pybop and Pybrop − 2 Reagents for the Difficult Coupling of the Alpha,Alpha-Dialkyl Amino-Acid, Aib. *Tetrahedron 47*, 259−270.

(30) Dourtoglou, V., Ziegler, J. C., and Gross, B. (1978) Hexafluorophosphate of O-Benzotriazole-N, N-Tetramethyurea - New and Effective Reagent of Coupling Peptide. *Tetrahedron Lett.* 1269−1272.

(31) Tyagarajan, K., Pretzer, E., and Wiktorowicz, J. E. (2003) Thiol-reactive dyes for fluorescence labeling of proteomic samples. *Electrophoresis 24*, 2348−2358.

(32) Shafer, D. E., Inman, J. K., and Lees, A. (2000) Reaction of tris(2-carboxyethyl)phosphine (TCEP) with maleimide and alpha-haloacyl groups: Anomalous elution of TCEP by gel filtration. *Anal. Biochem. 282*, 161−164.

(33) Getz, E. B., Xiao, M., Chakrabarty, T., Cooke, R., and Selvin, P. R. (1999) A comparison between the sulfhydryl reductants tris(2-carboxyethyl)phosphine and dithiothreitol for use in protein biochemistry. *Anal. Biochem. 273*, 73−80.

(34) Shinde, D., Lai, Y. L., Sun, F. Z., and Arnheim, N. (2003) Taq DNA polymerase slippage mutation rates measured by PCR and quasi-likelihood analysis: (CA/GT)(n) and (A/T)(n) microsatellites. *Nucleic Acids Res. 31*, 974−980.

BC0496915

Water-Soluble Phosphines for Direct Labeling of Peptides with Technetium and Rhenium: Insights from Electrospray Mass Spectrometry

William E. P. Greenland[†] and Philip J. Blower*[,†,‡]

Biosciences Department, University of Kent at Canterbury, Canterbury, Kent CT2 7NJ, U.K., and Nuclear Medicine Department, East Kent Hospitals NHS Trust, Kent and Canterbury Hospital, Canterbury CT1 3NG, U.K.. Received March 4, 2005

Direct labeling of salmon calcitonin (sCT) is possible in one step using water-soluble phosphines (sulfonated triphenylphosphines) as the reducing agent both for disulfide and for pertechnetate. Phosphines were the most efficient reducing agent for disulfide bonds among those examined. The phosphines both reduced the pertechnetate to Tc(III), and contributed to the technetium coordination sphere in the labeled product. In contrast, the phosphines did not reduce rhenium below oxidation state V, nor did they participate in the rhenium coordination sphere in the labeled peptide. Instead, the expected oxorhenium(V) moiety was incorporated. Both Tc and Re labeling processes gave rise to dimers with two peptides linked by the metal center, as well as simple monomeric species. Positive mode electrospray mass spectrometry not only revealed the presence of phosphine bound to technetium and oxygen bound to rhenium in the metallopeptides but also revealed the oxidation states of the metals. Electrospray mass spectrometry is proving to be an exceptionally valuable technique for characterizing radiopharmaceuticals. Although the one-step direct labeling method described gives mixed products and poor receptor affinity when applied to the small peptide sCT, it might be readily adapted to monoclonal antibodies.

INTRODUCTION

The radiolabeling of peptides and antibodies with technetium and rhenium isotopes (Tc-99m, Re-186, Re-188) by direct methods (*1*–*5*) is an often-used but rarely understood process for producing diagnostic and therapeutic radiopharmaceuticals. The direct labeling approach exploits the presence of thiolate groups of cysteine side chains, usually generated by reduction of a disulfide bond, as the primary metal-binding groups. Its popular appeal stems from simplicity of execution, requiring no bifunctional chelator that may be costly or may necessitate considerable synthetic expertise. However, in most of the examples in which it has been used to date, it has many disadvantages. The structure of the conjugate is uncontrolled, unpredictable, and often unknown, and the in vivo stability may not be all that is desired. Much effort has therefore been invested in understanding the molecular structures and mechanisms involved (*3*, *6*–*10*). Nevertheless, with some exceptions (*11*), the structures remain poorly understood and unpredictable, and biological and clinical evaluations of several peptide and protein radiopharmaceuticals have been embarked upon without satisfactory understanding of their structure and properties. In the case of Tc and Re, coordination is commonly supposed to involve local nitrogen atoms from amide or amine groups in the peptide backbone or side chains, in addition to cysteine thiolates and a $[M{=}O]^{3+}$ (V) core, although spectroscopic evidence for this is sparse (*7*, *9*). The peptide conformation around the complex may well be heterogeneous. Also, because tetradentate ligands may coordinate in a bis(bidentate) mode due to the relatively low concentration of M compared to the ligand, peptide "dimers" linked by the metal are likely to exist (*12*).

The principal methods used to date to characterize peptide conformation and metal coordination have been ^{1}H NMR (*7*), electronic spectroscopy (*7*), and extended X-ray absorption fine structure (EXAFS) spectroscopy (*9*). A ^{1}H 2D nuclear Overhauser effect spectrometry (NOESY) NMR study of the somatostatin analogue RC160 labeled with Re has been reported. The perrhenate was reduced with stannous citrate, and the disulfide bond was reduced with ascorbate. The authors concluded that the peptide conformation was not grossly modified by labeling and that the Re was six-coordinate with a coordination sphere that, surprisingly, included only one of the two available thiolates but made no comment on the oxidation state of the rhenium (*7*). These conclusions are at variance with expectations from the known coordination chemistry of rhenium (*1*), which suggest that the complex is more likely to be a square pyramid with a $Re{=}O^{3+}$ core (*13*). EXAFS spectroscopy of model Re and Tc complexes with cysteine-containing peptides was more consistent with the latter model, suggesting a range of motifs all based on the $Re{=}O^{3+}$ core, including monomeric peptide$-N_3S[Re{=}O]$ (*13*), "homodimer" (peptide$-NS)_2$-[Re=O], and "heterodimer" (peptide$-N_2S$)(peptide$-$S)-[Re=O] (*4*, *9*). Thus, additional techniques must be brought to bear to improve understanding of these metal–peptide complexes in individual cases. In this paper, using salmon calcitonin (sCT) as a model peptide, we show that mass spectrometry, in particular with electrospray ionization, can offer additional structural insight to complement these methods. We also report a one-step method for simultaneous reduction of pertechnetate and

* To whom correspondence should be addressed. Tel: +44-(0)1227 823475. Fax: +44-(0)1227 763912. E-mail: P.J.Blower@kent.ac.uk.

† University of Kent at Canterbury.

‡ Kent and Canterbury Hospital.

10.1021/bc0500600 CCC: $30.25 © 2005 American Chemical Society
Published on Web 06/18/2005

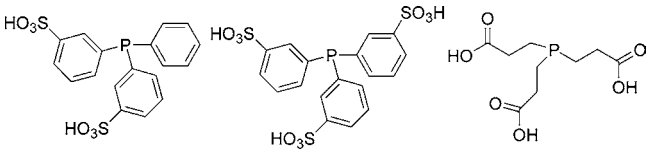

Figure 1. Structures of water-soluble phosphines used in this and related work: left to right, TPPDS (*21*, *22*), TPPTS (*21*, *22*), and $P(CH_2CH_2COOH)_3$ (tris(carboxyethyl) phosphine) (*23*).

peptide disulfide bonds using the water-soluble phosphines triphenylphosphine disulfonate (TPPDS) and triphenylphosphine trisulfonate (TPPTS) (see Figure 1).

Salmon calcitonin is a 32-amino acid neuropeptide with a disulfide loop. It has higher affinity for human calcitonin receptors than human calcitonin and is more stable in vivo. Calcitonin receptors are particularly abundant (ca. 10^6 per cell) in osteoclasts. They have recently been detected in various tumors and tumor-derived cells, including human ovarian small cell carcinoma, breast cancer, prostate cancer, and neuroblastoma, as well as bone tumors (osteoclastoma) and bone cancers and metastases with increased osteoclast activity (*14*, *15*). A suitably labeled calcitonin analogue might therefore have applications in imaging bone diseases and cancer.

MATERIALS AND METHODS

Instant thin layer chromatography (ITLC) was performed using two 1 cm × 8 cm strips (ITLC SG, Gelman Sciences) spotted with ~2 μL of the test solution. Before the spots dried, they were developed in either 1% saline (system I) or 1% saline/acetone/acetonitrile (2:1:1) (system II). The ITLC strips were scanned using a Bioscan Mini-Scan at 0.25 mm s^{-1}. Gamma photons were detected with a Bioscan Flow-Count scanner with a Bioscan B-FC-3200 detector. Data were collected and analyzed using LabLogic Laura GC Ram version 1.3b(104) software. ^{99m}Tc activity was measured using a calibrated CRC-35R ionization chamber and reader from Capintec Inc.

Two HPLC systems were employed in this work. System A comprised an LKB 2152 controller, a 2150 pump, a 2151 variable wavelength monitor, a Bioscan Flow-Count γ detector, a 100 μL injection loop, and LabLogic Laura data collection and analysis software. System B (hyphenated with an electrospray mass spectrometer) was a Hewlett-Packard 1100 system with a G1323A control unit, a 200 μL injection loop, a G1312A pump, a G1314 variable wavelength monitor, and Finnigan Corp Qual Browser software, version 1.2. Electrospray mass spectrometry (ES-MS) was performed on a Finnigan Mat LCQ ion trap mass spectrometer in tandem with HPLC system B described above. Spectra of eluting peaks were acquired in the *m/z* ranges 150−2000 for small organic molecules, 500−4000 for purified peptides, and 150−4000 for reaction mixtures. Calibration was checked with 20 μg of sCT or sCTA (sCTA is an analogue of sCT with arginine in place of lysine-11 (*14*)). The ES-MS system was set up for soft ionization (capillary temperature 220 °C, capillary voltage 19 V), and spectra were analyzed in positive ion mode. Control and data collection were performed using Thermo Quest Corp Tune Plus version 1.2 SP1 software. The analysis was performed using Finnigan Corp Qual Browser version 1.2 software. The *m/z* spectra from selected UV or ion count peaks were summed and interpreted.

Salmon calcitonin (sCT) was synthesized by standard solid-phase peptide synthesis methodology as described previously (*14*, *15*). TPPDS and TPPTS were synthesized as described previously (*16*). Stannous chloride dihydrate was obtained from Aldrich, U.K. Acetic acid and ethanol were obtained from BDH, U.K., and dH_2O (HPLC grade) was obtained from Fisher, U.K. $Na^{99m}TcO_4$ was eluted from a $^{99}Mo/^{99m}Tc$ generator (Mallinckrodt) with 0.9% saline. An acidic saturated stock solution of $HReOCl_4$ in ethanol was prepared as described previously (*17*). $NH_4{}^{99}TcO_4$ (318.2 MBq/g) was obtained from Amersham, U.K., dissolved in water, and filtered to remove traces of black insoluble material prior to use.

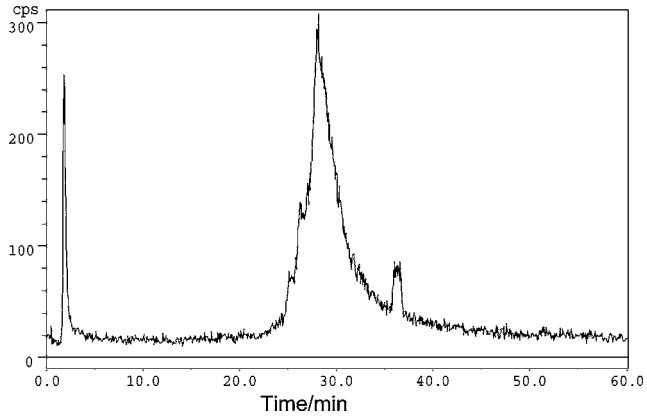

Figure 2. HPLC, with γ detection, of Tc-99m−sCT labeled using the one-step method at low specific activity (20 μg of peptide). Pertechnetate elutes between 1 and 2 min.

One-Step Labeling of sCT with ^{99m}Tc. To a solution of TPPDS (5.0 mg mL^{-1} in 10 mM acetic acid, pH 3.3, 20 μL) in a polypropylene microcentrifuge tube was added 20 μL of $Na^{99m}TcO_4$ eluate (63 MBq) followed by sCT (20 μg or 2 μg; that is, 20 μL of 1.00 or 0.1 mg mL^{-1} solution in 10 mM acetic acid, pH 3.3). A control with 20 μL of 10 mM acetic acid, pH 3.3, in place of the peptide solution was also prepared in an identical manner to test for ^{99m}Tc−TPPDS complexes being misinterpreted as labeled peptide. The reaction mixture was heated at 70−75 °C for 45 min, then removed from the polypropylene reaction tube. The radioactivity of both the reaction mixture and the empty tube was measured. The reaction mixture was analyzed by ITLC as described above and by RP HPLC (system A with a 150 mm × 2.1 mm Hamilton PRP1 10 μm column and a 25 mm × 2.1 mm Hamilton PRP1 10 μm guard column). The binary solvent system comprised solvent A (0.1% trifluoroacetic acid in water) and solvent B (0.085% trifluoroacetic acid in acetonitrile) at a flow rate of 0.5 mL min^{-1} with a linear gradient defined by the following points (min, %B): 0, 5; 2, 5; 5, 20; 45, 50; 55, 100; 56, 5; 60, 5. The UV detector was set at 210 nm. This radiopharmaceutical was used without purification in a qualitative cell binding assay as previously described (*14*, *15*).

Reduction of sCT with TPPDS and Other Reducing Agents. To a solution of TPPDS or TPPTS (0.1 mL of 1.0 mg mL^{-1} in 10 mM acetic acid, pH 3.3) was added a solution of sCT (0.1 mL of 1.0 mg mL^{-1} in 10 mM acetic acid). The solution was incubated at room temperature for 30 min, then analyzed by HPLC and ES-MS (HPLC system B with a Hamilton PRP1 column, 150 mm × 2.1 mm, 5 μm). The binary solvent system comprised solvent A (0.1% trifluoroacetic acid in water) and solvent B (0.085% trifluoroacetic acid in acetonitrile) with a linear gradient defined by the following points (min, %B, mL min^{-1}): 0, 5, 0.5; 2, 5, 0.5; 20, 100, 1.0; 21, 5, 1.0; 25, 5, 0. The UV detector was set at 214 nm. This solution, referred to henceforth as "prereduced-sCT" ($sCTH_2$), was used subsequently to study conjugates with technetium (using Tc-99) and rhenium synthons as described below.

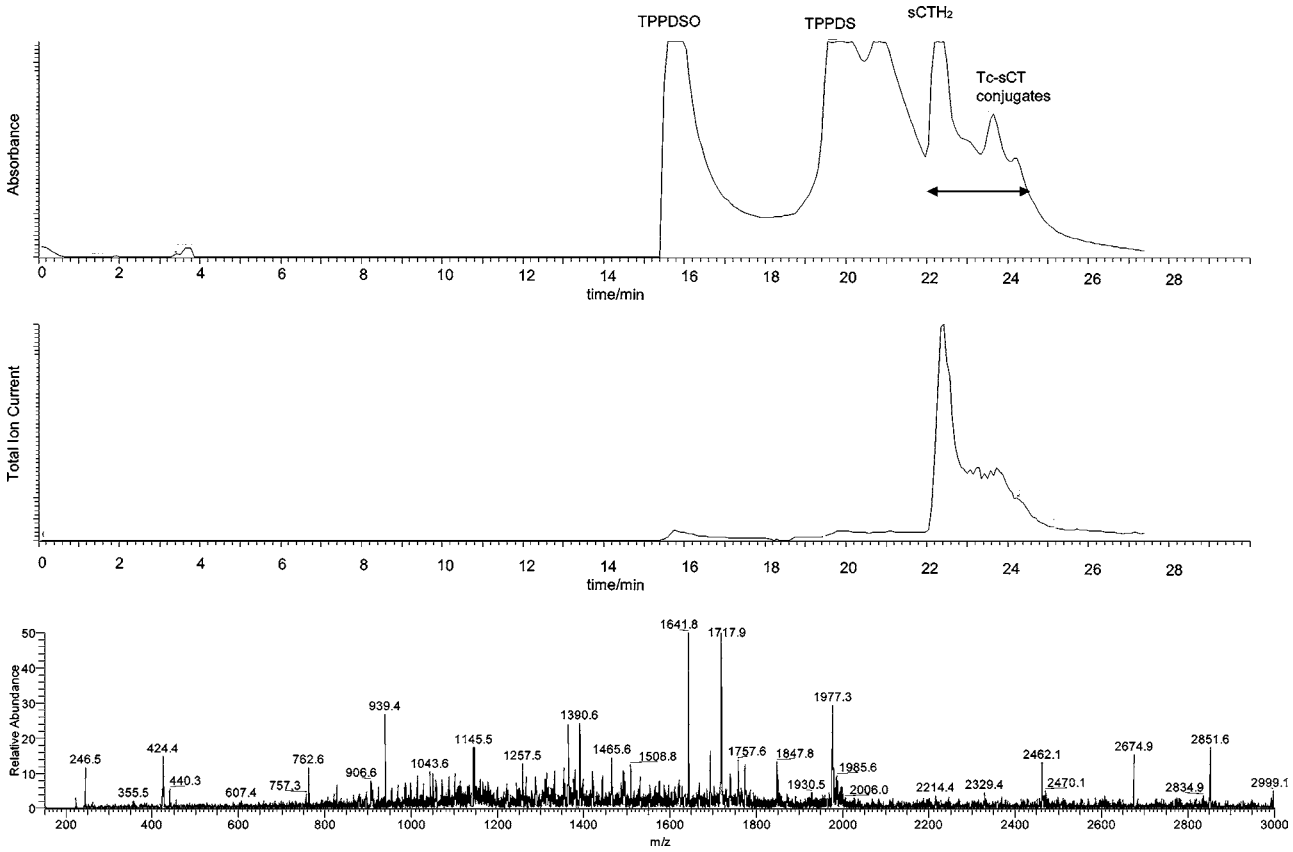

Figure 3. HPLC−ES-MS of sCT treated with TPPDS and $^{99}TcO_4^-$. The top panel shows the HPLC (UV detection) trace. The identity of the principal species in each peak was determined from its ES-MS spectrum. The phosphine TPPDS and its oxide TPPDSO eluted early, followed by unmodified $sCTH_2$ and finally Tc−peptide conjugates. The middle panel shows the total ion count detected in the mass spectrometer during ES-MS of the HPLC effluent. The bottom panel shows the summed ES-MS spectra of all peptide-containing fractions (indicated by the double arrow in the chromatogram, top). See Table 3 for assignments.

Table 1. Binding of ^{99m}Tc−sCT to MCF7 Breast Cancer Cells

labeling method[a]	labeled sCT concn[b] (nM)	MCF7 cells present/absent[c]	nominal cold sCT concn[d] (μM)	bound activity, cpm (SEM)[e]	specific/nonspecific ratio[f]
low sp. ac.	1	present	0	95.8 (4.6)	2.7
low sp. ac.	1	present	1	35.8 (3.4)	
low sp. ac.	1	absent	0	43.8 (4.5)	1.0
low sp. ac.	1	absent	1	44.5 (5.7)	
high sp. ac.	1	present	0	58.2 (16)	3.1
high sp. ac.	1	present	1	18.7 (2.2)	
high sp. ac.	1	absent	0	16.7 (2.5)	1.3
high sp. ac.	1	absent	1	13.2 (2.3)	
sCT-free	0	present	0	22.5 (3.5)	0.9
sCT-free	0	present	1	23.7 (4.3)	
sCT-free	0	absent	0	10.7 (2.1)	0.9
sCT-free	0	absent	0	12.0 (3.8)	

[a] High sp. ac. means 2 μg of sCT; low sp. ac. means 20 μg of sCT. [b] Concentrations of sCT and ^{99m}Tc were adjusted during labeling to ensure that comparable activity was present in 1 nM sample added to cells. [c] Controls with wells containing no cells were employed to check for nonspecific binding to plastic. [d] Unlabeled sCT was added as an inhibitor in some cases to determine nonspecific binding. [e] Bound activity means activity bound to cells, well, or both after removal of supernatant. [f] Counts per minute (cpm) bound in the absence of cold sCT divided by cpm in the presence of 1 μM sCT.

The untreated sCT solution was analyzed similarly and served as a nonreduced control for studies of the reaction with technetium and rhenium synthons. Other reducing agents were examined in a similar manner, replacing the TPPDS solution with the same volume of TPPTS, 2-mercaptoethanol, stannous chloride, or ascorbic acid solution, each at 1 mg mL^{-1} in 10 mM acetic acid.

Reaction of "Prereduced sCT" with Rhenium. "Prereduced sCT" solution (50 μL, prepared using TPPDS as described above) was mixed with a solution of $HReOCl_4$ (saturated solution in ethanol diluted 100-fold with ethanol, 10 μL) and analyzed after 1 h at room temperature by HPLC−ES-MS using the same conditions as described above for "prereduced sCT".

Reaction of "Prereduced sCT" with Technetium. "Prereduced sCT" solution (100 μL, prepared using TPPDS or TPPTS as described above) was mixed with ammonium pertechnetate (20 μL of 1.0 mg mL^{-1} solution in physiological saline) and immediately analyzed by HPLC using the same conditions as described above for "prereduced sCT". In an alternative method, to aid reduction in a sample with a lower concentration of TPPDS, the sample was analyzed on a PRP1 HPLC column that had been pretreated with stannous chloride

Table 2. ES-MS of sCT and Reduced sCT ($sCTH_2$)

ion assignment	formula (uncharged form)	obsd *m/z* (rel. intensity)	calcd *m/z*[a]
Unmodified sCT			
$[sCT + 2H]^{2+}$	$C_{145}H_{240}N_{44}O_{48}S_2$	1716.9 (100)	1717.0
$[sCT + 3H]^{3+}$		1145.1 (49)	1145.0
deconvoluted		3432.3	3431.9
$sCTH_2$ (sCT reduced with TPPDS)			
$[sCTH_2 + 2H]^{2+}$	$C_{145}H_{242}N_{44}O_{48}S_2$	1717.9 (100)	1718.0
$[sCTH_2 + 3H]^{3+}$		1145.5 (60)	1145.6
deconvoluted		3433.7	3433.9

[a] Calculated as the average molecular mass with isotopes at natural abundance, against sCT and sCTA (*14*) as calibrants. Their molecular mass was defined in the same way.

(100 μL of 1 mg mL^{-1} solution in 10 mM acetic acid, loaded onto and washed through the column using solvent A).

RESULTS

Labeling of sCT with ^{99m}Tc using the one-step method with water-soluble triarylphosphines TPPDS and TPPTS (Figure 1) was performed at two different peptide concentrations to evaluate the potential of the method for producing high specific activity labeled peptide. The labeling was investigated by ITLC using two parallel systems (I and II, see Materials and Methods) to determine free pertechnetate and reduced hydrolyzed Tc-99m. In system I, pertechnetate migrated with the solvent front ($R_f = 1$), while "reduced hydrolyzed technetium" and labeled peptide remained at the origin ($R_f = 0$). In system II, pertechnetate migrated with the solvent front ($R_f = 1$), while "reduced hydrolyzed technetium" remained at the origin ($R_f = 0$), and labeled peptide migrated with intermediate R_f values (0.2−0.5). When 2 μg of peptide was labeled, 18% of radioactivity migrated as pertechnetate, and when 20 μg peptide was labeled, 6% migrated as pertechnetate. No significant "reduced hydrolyzed technetium" was detected. Analysis by HPLC (system 1) was qualitatively in agreement with ITLC (see Figure 2). Labeled peptide eluted as a broad multiple peak between 23 and 32 min, indicative of a heterogeneous labeled product. Pertechnetate eluted at 1−2 min, and the radioactivity within this peak increased from 6% for 20 μg to ca. 20% for 2 μg of peptide. When peptide was omitted from the mixture, only pertechnetate eluted from the HPLC column. The heterogeneity of the labeled peptide was in agreement with multiplicity of peaks corresponding to Tc−peptide conjugates seen by HPLC−MS of carrier-level samples (see below and Figure 3).

Receptor affinity of the Tc-99m-labeled peptide was investigated using a semiquantitative MCF7 breast cancer cell binding assay as previously described (*15*) (see Table 1). Tracer concentrations of labeled sCT (1 nM) showed binding to cells that was inhibited by 1 μM unlabeled sCT, indicating some specific receptor binding, but the specific-to-nonspecific ratio (indicated by the ratio of bound counts in the absence and presence of cold sCT) was very modest indeed (ca. 3). This is a consequence of high nonspecific binding to both cells and plastic and low specific binding affinity due to poor radiolabel stability or adverse effects of labeling on peptide structure.

As well as nonspecific binding to the plastic multiwell plates used in the assay, a significant fraction of the radioactive products from the reaction remained bound to the polypropylene reaction tube in which labeling was performed. This behavior may be associated with the presence of a Tc-99m−TPPDS intermediate, since the binding is diminished by increasing the sCT concentration. The binding can be reduced by the addition of 0.01% Triton X100 surfactant, but it has not been determined how this affects the radiolabeled peptide as a whole. Nonspecific binding to these plastics is not observed with calcitonin labeled using the HYNIC method (*15*). A $^{99m}TcO_4^-$ sample exposed to the same reaction conditions but without TPPDS or peptide showed less than 1% binding to the polypropylene reaction tube.

A relatively high concentration of the phosphine was required (5 mg mL^{-1}), as well as heating, for reasonable radiochemical yields to be obtained. Lower concentrations of phosphine were able to reduce the peptide efficiently but led to high pertechnetate levels, while higher phosphine concentration led to formation of a cloudy precipitate on combination with peptide.

The role of the water-soluble phosphine in reduction of the peptide disulfide bond was investigated by HPLC

Table 3. ES-MS of ^{99}Tc-Labeled sCT Products

ion assignment	formula (uncharged form)	obsd *m/z* (rel intensity)	calcd *m/z*[a]
sCT + [^{99}Tc]pertechnetate + TPPDS			
$[sCTH_2 + Tc + TPPDSH_2 + 2H]^{2+}$	$C_{163}H_{254}N_{44}O_{54}S_4PTc$	1976.8 (100)	1977.2
deconvoluted		3952.5	3952.3
sCT + [^{99}Tc]pertechnetate + TPPDS, Stannous Chloride Treated			
$[sCTH_2 + 2H]^{2+}$	$C_{145}H_{242}N_{44}O_{48}S_2$	1718.1 (100)	1718.0
$[sCTH_2 + 3H]^{3+}$		1145.5 (30)	1145.6
deconvoluted		3433.5	3433.9
$[sCTH_2 + (Tc\text{-}3H) + TPPDSH_2 + 2H]^{2+}$	$C_{163}H_{254}N_{44}O_{54}S_4PTc$	1977.3 (61)	1977.2
deconvoluted		3952.5	3952.3
$[2sCTH_2 + (Tc\text{-}3H) + TPPDSH_2 + 3H]^{3+}$	$C_{308}H_{496}N_{88}O_{102}S_6PTc$	2462.0−2462.8 (27)	2463.1
$[2sCTH_2 + (Tc\text{-}3H) + TPPDSH_2 + 4H]^{4+}$		1847.8 (27)	1847.6
deconvoluted		7386.7	7386.3
sCT + [^{99}Tc]pertechnetate + TPPTS, Stannous Chloride Treated			
$[sCTH_2 + 2H]^{2+}$	$C_{145}H_{242}N_{44}O_{48}S_2$	1718.6 (100)	1718.0
$[sCTH_2 + 3H]^{3+}$		1145.8 (52)	1145.6
deconvoluted		3434.5	3433.9
$[sCTH_2 + (Tc\text{-}3H) + TPPTSH_3 + 2H]^{2+}$	$C_{163}H_{254}N_{44}O_{57}S_5PTc$	2017.3 (34)	2017.2
deconvoluted		4032.5	4032.4
$[2sCTH_2 + (Tc\text{-}3H) + TPPTSH_3 + 3H]^{3+}$	$C_{308}H_{496}N_{88}O_{105}S_7PTc$	2489.3 (52)	2489.8
$[2sCTH_2 + Tc + TPPTSH_3 + 4H]^{4+}$		1867.8 (82)	1867.6
deconvoluted		7464.7	7466.3

[a] Calculated as the average molecular mass with isotopes at natural abundance, against standard calibrant sCT and sCTA, the molecular mass of which was defined in the same way.

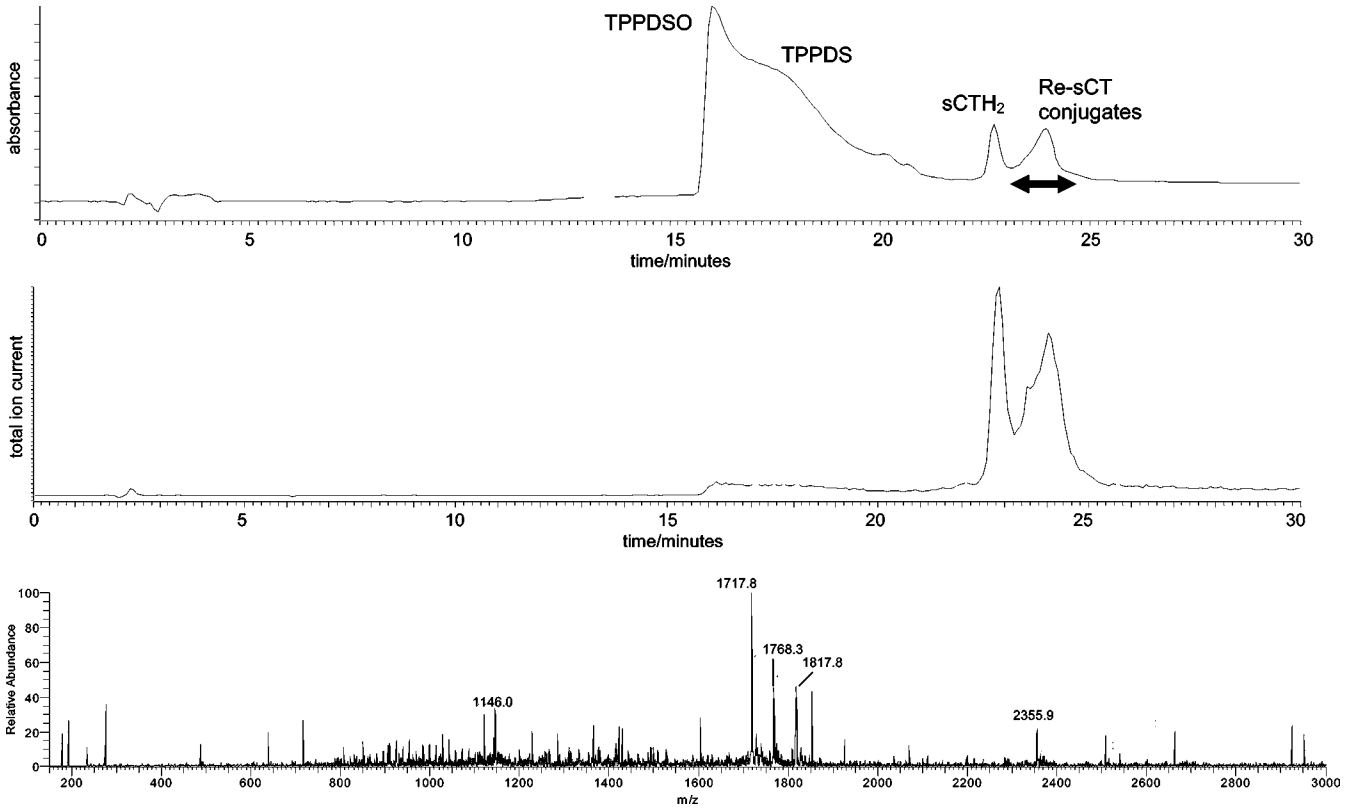

Figure 4. HPLC−ES-MS of sCT treated with TPPDS and $ReOCl_4^-$. The top panel shows the HPLC (UV detection) trace. The identity of the principal species in each peak was determined from its ES-MS spectrum. The phosphine TPPDS and its oxide TPPDSO eluted early, followed by unmodified $sCTH_2$ and finally Re−peptide conjugates. The middle panel shows the total ion count detected in the mass spectometer during ES-MS of the HPLC effluent. The bottom panel shows the summed ES-MS spectra of all peptide-containing fractions eluting after unmodified $sCTH_2$ (indicated by the double arrow in the chromatogram, top). See Table 4 for assignments.

Table 4. ES-MS of Re-Labeled sCT Products

ion assignment	formula (uncharged form)	obsd *m/z* (rel. intensity)	calcd *m/z*[a]
	sCT + TPPDS + $ReOCl_4^-$		
$[sCTH_2 + 2H]^{2+}$	$C_{145}H_{242}N_{44}O_{48}S_2$	1717.8 (100)	1718.0
$[sCTH_2 + 3H]^{3+}$		1146.0 (25)	1145.6
deconvoluted		3434.0	3433.9
$[sCTH_2 + (ReO\text{-}3H) + 2H]^{2+}$	$C_{145}H_{239}N_{44}O_{49}S_2Re$	1817.8 (56)	1818.0[b]
deconvoluted		3633.5	3633.9[b]
$[2sCTH_2 + ReO + 3H]^{3+}$	$C_{290}H_{481}N_{88}O_{97}S_4Re$	2355.9 (26)	2356.9[b]
$[2sCTH_2 + (ReO\text{-}3H) + 4H]^{4+}$		1768.3 (56)	1768.0[b]
deconvoluted		7066.2−7069.2	7067.8[b]

[a] Calculated as the average molecular mass with isotopes at natural abundance, against standard calibrant sCT and sCTA (*14*), the molecular mass of which was defined in the same way. [b] Based on the more abundant ^{187}Re isotope, not the average. The ^{185}Re peak is detected within the envelope but not reported separately.

and ES-MS, in comparison with other conventional disulfide bond reducing agents including 2-mercaptoethanol, stannous chloride, and ascorbic acid. The phosphine and phosphine oxide eluted as broad peaks at 15−22 min and were detected in the ES-MS at *m/z* 424 and 440. Untreated (unreduced) calcitonin eluted as a single sharp peak at 23.4 min using the HPLC conditions described above. ES-MS of this peak showed only the expected molecular ions (see Table 2) and a peak at 3432 in the deconvoluted spectrum. After treatment with TPPDS for 30 min at room temperature, the peptide eluted as a sharp peak slightly earlier (22.5 min) than the untreated peptide with *m/z* peaks corresponding to a peptide 2 Da heavier than untreated peptide (Table 2) and only a peak at 3434 in the corresponding deconvoluted mass spectrum. No other species were detected (e.g., no phosphine adducts, see Discussion section). This HPLC and ES-MS analysis is consistent with efficient and quantitative reduction of the disulfide bond. By contrast, treatment of sCT with stannous chloride under these conditions gave HPLC−ES-MS results corresponding to only unreduced peptide; heating to 90 °C for 30 min produced only a small shoulder in the HPLC profile corresponding to the reduced peptide. Traces of reduced peptide were detected in the ES-MS. None of the eluted fractions gave ES-MS peaks assignable to tin adducts of the peptide. This was true also if the peptide was prereduced with TPPDS before treatment with stannous chloride. Treatment of sCT with 2-mercaptoethanol gave a modest yield (ca. 20%) of reduced peptide, while the majority of peptide eluted within the 23.4 min peak. Ascorbic acid similarly gave variable but incomplete reduction under these conditions (20−90%).

The species formed on reductive labeling of sCT with pertechnetate using TPPDS was investigated using macroscopic amounts of ammonium [^{99}Tc]pertechnetate.

Scheme 1. Probable Mechanism of Oxidation of Disulfide by Tertiary Phosphine

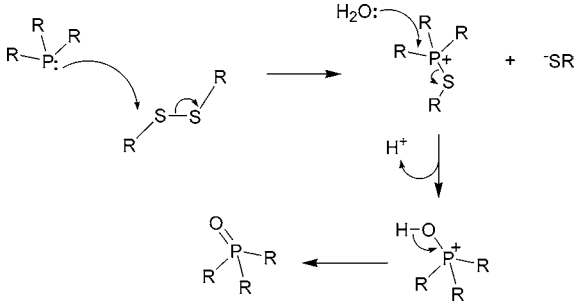

The increased levels of TPPDS required to reduce the larger quantity of pertechnetate compared to the no-carrier-added reaction caused precipitation from solution. Nevertheless, modified peptide conjugates (see Table 3) were detected in the HPLC eluate by UV absorbance and ES-MS. Ions with the same *m/z* but with improved signal-to-noise ratios were obtained by using a smaller concentration of phosphine with pertechnetate reduction supplemented by passing through a $SnCl_2$-treated column.

The peaks eluting at 22−25 min (Figure 3) gave ES-MS results (Figure 3) in which several peptide species were detected (Table 3), including reduced peptide (3434), an adduct of one sCT with one Tc and one TPPDS (3952), and an adduct comprising two sCT molecules with one Tc and one TPPDS (7387). The *m/z* values contributing to these deconvoluted peaks are given in Table 3. No ions with *m/z* corresponding to Tc−peptide conjugates without phosphine or with tin were observed. Analogous results were obtained with TPPTS in place of TPPDS (Table 3). The multiplicity of the Tc-containing HPLC peaks, coupled with the observation of only two different molecular mass conjugates in the ES-MS, indicates that in addition to monomers and dimers, isomeric forms of one or both of these species must be present.

Labeling of the "prereduced sCT" with Re(V) was achieved for ES-MS analysis by treating "prereduced sCT" with $ReOCl_4^-$ with TPPDS still present. HPLC−ES-MS analysis (Figure 4) revealed peaks eluting between 22.7 min (reduced peptide) and 24.0 min (Table 4). ES-MS revealed several species including reduced peptide (3434), an adduct comprising one sCT, one Re, and one O (3634), and an adduct comprising two sCT molecules, one Re, and one O (7066−7069). The *m/z* peaks contributing to these values are listed in Table 4, and the spectra are shown in Figure 4. No adducts containing TPPDS were detected in the ES-MS. Unreduced sCT mixed with $ReOCl_4^-$ showed only peaks corresponding to unmodified peptide both in the HPLC and ES-MS.

Scheme 2. Simultaneous Reduction of Disulfide and Pertechnetate by Water-Soluble Phosphine (PR_3 = TPPDS or TPPTS)[a]

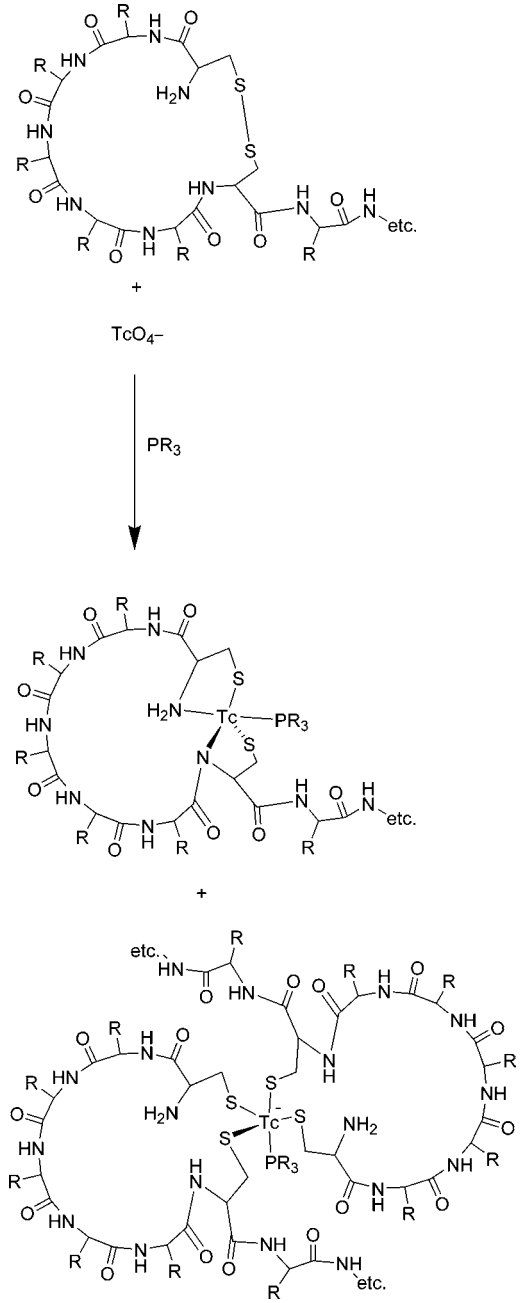

[a] The reaction shows possible monomeric and dimeric topologies for coordination of Tc(III) by reduced peptide that among others may account for the observed ES-MS (the multiplicity of HPLC peaks indicates that more than one isomer is present).

DISCUSSION

Use of the water-soluble phosphines TPPDS and TPPTS provides a convenient, single-step direct labeling method for incorporating Tc-99m into disulfide-containing peptides. Water-soluble phosphines have been used successfully on previous occasions both for disulfide bond reduction (*18*−*20*) and as an ancillary ligand for HYNIC-linked technetium (*21*, *22*). For example, $P(CH_2CH_2COOH)_3$ (see Figure 1) was successfully used to generate thiol groups in a monoclonal antibody prior to Re-188 labeling (*23*). However, the labeled sCT conjugate produced by the single-step method has poor calcitonin receptor affinity and high nonspecfic binding or "stickiness" and does not have a homogeneous structure. Rather, it consists of isomeric forms of both monomeric and dimeric species. This behavior contrasts with the sCT conjugate labeled via a HYNIC bifunctional chelator, which gave a single sharp HPLC peak under similar conditions and retained excellent receptor affinity and stability (*15*). These water-soluble phosphines, however, emerge from this study as highly efficient reducing agents for the disulfide bond in peptides. In this respect, they are preferable to stannous chloride, ascorbic acid, and 2-mercaptoethanol, all of which have been used to reduce protein and antibody disulfide bonds previously (with conflicting conclusions about their efficacy (*24*−*32*)) but all of which failed to reduce the disulfide bond of sCT fully under similar conditions. The phosphines are less efficient, however, in the reduction and temporary coor-

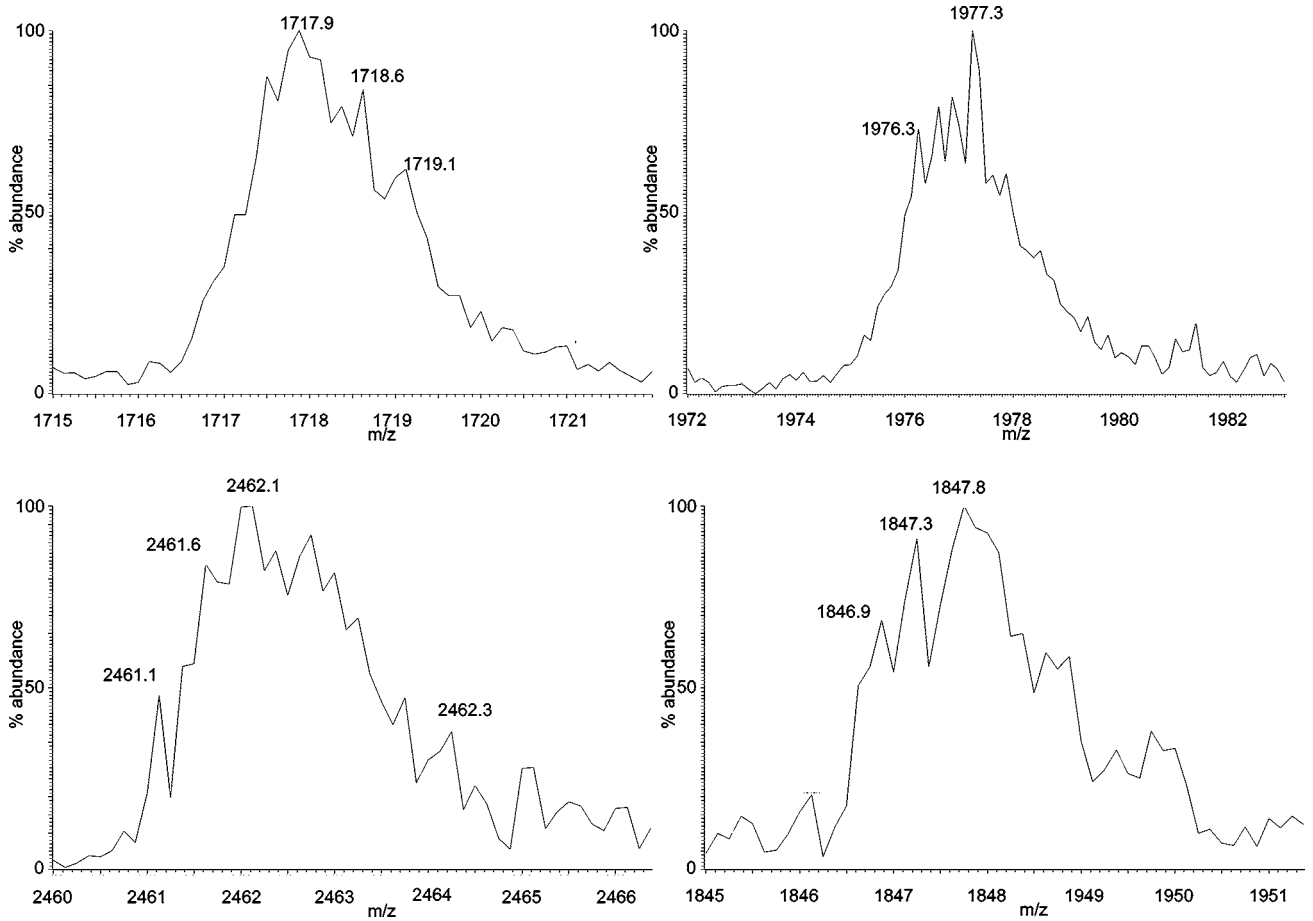

Figure 5. Expansion of peaks in the ES-MS of ^{99}Tc-labeled sCT: *m/z* = 1717.9 (top left, assigned as $sCTH_2$), 1977.3 (top right, assigned as $[sCTH_2 + (Tc\text{-}3H) + TPPDSH_2 + 2H]^{2+}$), 2462.1 and 1847.8 (bottom left and right, assigned as $[2sCTH_2 + (Tc\text{-}3H) + TPPDSH_2 + 3H]^{3+}$ and $[2sCTH_2 + (Tc\text{-}3H) + TPPDSH_2 + 4H]^{4+}$, respectively). The best fit to these peak values indicates that the technetium is in oxidation state III.

dination of the technetium, although TPPTS has been used previously in this capacity (*33*). This role requires higher concentration of phosphine, which in some instances resulted in precipitation of insoluble intermediates.

The application of electrospray mass spectroscopy illuminates several aspects of the labeling chemistry. First, it can address the question of the presence of stable intermediates in the reduction of the peptide bonds. For example, phosphine−thiolate adducts $[PR_3SR]^+$ are known to be formed during reduction of the disulfide bond (presumably as a result of the initial nucleophilic attack by phosphine on the disulfide, see Scheme 1). This intermediate is presumed to hydrolyze rapidly to the phosphine oxide under the aqueous reaction conditions but is otherwise sufficiently stable to be structurally characterized by crystallography (*34*). ES-MS revealed no evidence for such a species among the products of the reduction reaction. There is evidence in the literature that thiolate groups, generated by reduction of peptide in the presence of stannous ion, are able to chelate Sn(II) or Sn(IV) to a significant degree (*6*, *31*). However, no evidence for such chelates was detected in the ES-MS of the stannous reduction products.

Because of the prevalence of the Tc(V) and Re(V) oxo cores in chelates based on tetradentate ligand designs with SN3 or S2N2 donor sets (*1*), it is commonly supposed that this core is present when cysteine-containing peptides bind to technetium. This is possibly justified (although supported by very little direct evidence) when transfer ligands, such as glucoheptonate, that favor the Tc(V) oxidation state are employed (*9*). However, it is clear that great care must be exercised in making such assumptions generally: in the present case, there is no evidence for the presence of the Tc(V)oxo core. Instead, a Tc−phosphine core is shown by ES-MS to bind to the peptide, as shown in Scheme 2. The presence of such a large, hydrophobic group attached to the cysteine-containing domain (which is known to be critical for receptor binding (*35*, *36*)) of the peptide may be a major contributor to the loss of receptor affinity. Moreover, the ES-MS reveals the presence of dimeric species (containing two sCT peptides linked by a Tc−phosphine core, indicated by the peak in the deconvoluted spectrum at 7386), accounting for at least one of the several possible species suggested by the broad HPLC peak. This behavior is also observed in the TPPTS analogue, which shows the corresponding peak at 7465.

Careful inspection of the shift in *m/z* values of the various peaks in the ESMS upon Tc-labeling permits conclusions to be drawn about the oxidation state of the metal, by virtue of the number of protons it displaces from the peptide. The relative molecular mass of the $TcTPPDSH_2$ fragment (containing fully protonated sulfonic acid groups) is 521. The reduced peptide shows a *m/z* peak at 1718.1 ($[sCTH_2 + 2H]^{2+}$) and 1145.5 ($[sCTH_2 + 3H]^{3+}$). After incorporation of Tc the corresponding peaks shift to 1977.3, a shift of 259.2 (corresponding to a change in mass of 518.4, see Figure 5). This mass change is best accounted for as the result of replacement of $3H^+$ by $TcTPPDSH_2^{3+}$, that is, the Tc complex is probably in oxidation state III, and certainly between II

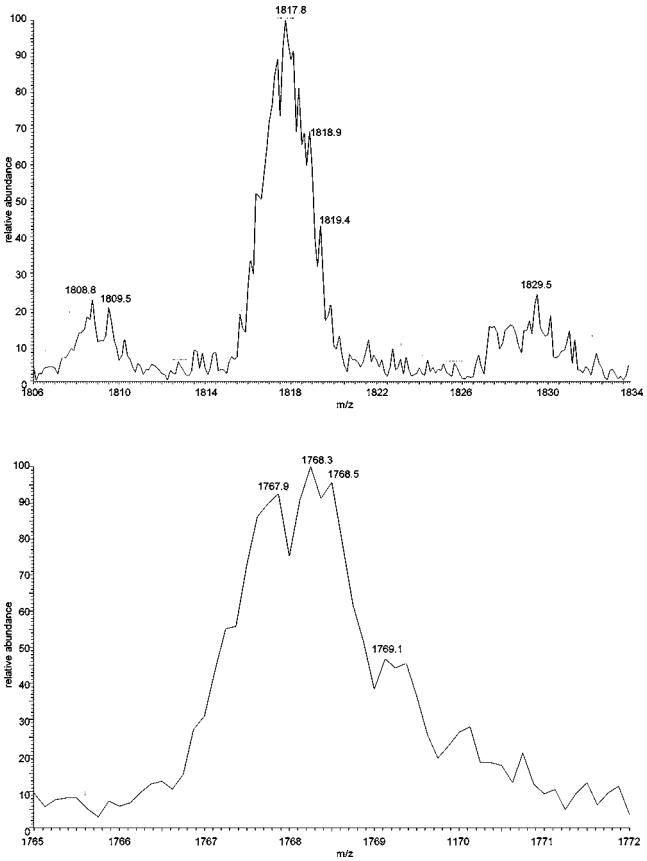

Figure 6. Expansion of peaks in the ES-MS of Re-labeled $sCTH_2$: $m/z = 1817.8$ (top, assigned as $[sCTH_2 + (ReO\text{-}3H) + 2H]^{2+}$) and 1768.3 (assigned as $[2sCTH_2 + (ReO\text{-}3H) + 4H]^{4+}$). The best fit to these peak values indicates that the rhenium is in oxidation state V.

and IV. This estimate of the oxidation state is supported by similar analysis of the dimeric $[(sCTH_2)_2(TcDPPDSH_2) + 3H]^{3+}$ and $[(sCTH_2)_2(TcDPPDSH_2) + 4H]^{4+}$ peaks in the spectrum and of the ES-MS of the products of the analogous reaction with TPPTS (Table 4). Because of the width of the isotope distribution envelope and statistical noise in the spectra, this type of analysis requires very precise determination of the *m/z* for the peaks (see Figure 5), which was obtained by combining the results of several analyses involving different samples. Errors due to approximation of the isotope distribution, using the average molecular weight as the predictor of the highest peak in the envelope, are canceled both by the measurement of *m/z relative* to a standard of similar molecular weight and by the measurement of *m/z* shifts from the unmodified peptide, rather than relying on absolute *m/z* values. Full mathematical modeling of mass spectra (*14*, *37*, *38*) was therefore not necessary.

It is well-known that electron-transfer processes may occur during the electrospray ionization process, especially with redox-active analytes such as transition metals; therefore it is not possible to be completely certain that the observed oxidation states are those that exist in solution. However, the conclusions are consistent with the known coordination chemistry of technetium. Phosphines readily reduce technetium below Tc(V), to give oxidation states from Tc(I) to Tc(IV) (*39*, *40*), most often Tc(III) (*41*). Tc(III) complexes with phosphine and thiolate ligands in the coordination sphere are well-known (*42*−*44*). A common structure for both rhenium(III) (*45*, *46*) and technetium(III) (*42*−*44*) is the trigonal bipyramidal pentacoordinate complex with three anionic

Scheme 3. Reaction of $ReOCl_4^-$ with Reduced Peptide in the Presence of Water-Soluble Phosphine (PR_3 = TPPDS)[a]

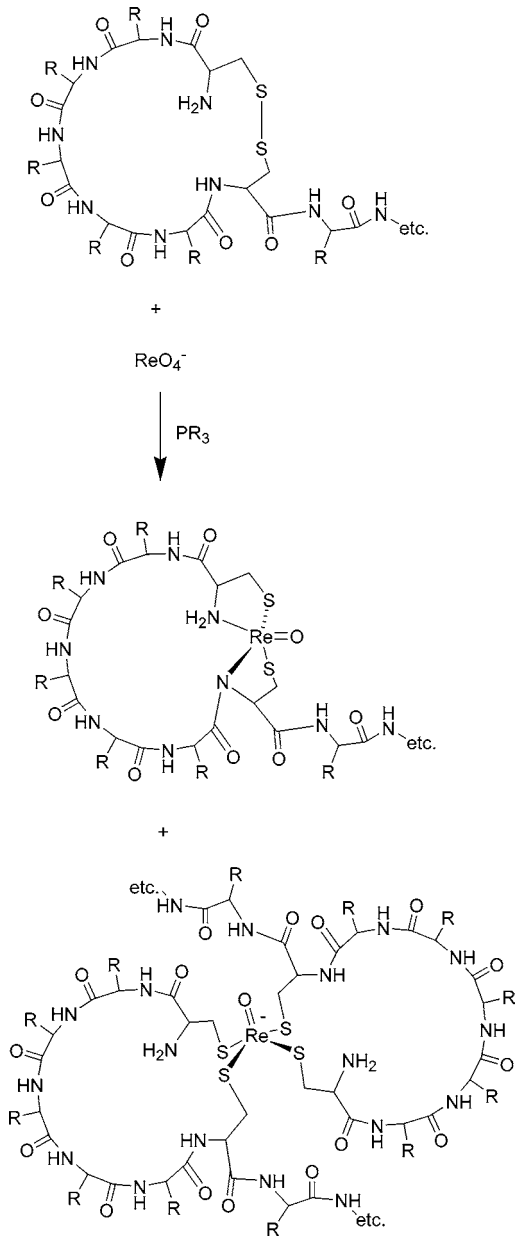

[a] The reaction shows possible monomeric and dimeric topologies for coordination of Re(V) by reduced peptide that among others may account for the observed ES-MS (the multiplicity of HPLC peaks indicates that more than one isomer is present).

ligands in the equatorial positions and a phosphine or other ligand in one or both of the axial positions. Some possibilities are shown in Scheme 2, although without other forms of spectroscopic evidence (e.g., EXAFS, NMR) no conclusions can be drawn about which is the most likely product.

The direct labeling method was also investigated with rhenium, but because harsher conditions are generally required to reduce rhenium than technetium, the metal was presented in prereduced form ($HReOCl_4$). This species is known to undergo hydrolysis in the presence of water but neverless proved suitable for the formation of rhenium−peptide conjugates analyzable by ES-MS. Analysis of the rhenium−sCT conjugate by HPLC−ES-MS revealed HPLC peaks eluting at 22.7 min (reduced sCT) and a broad peak at 24 min. Despite the pres-

ence of excess phosphine in the reaction mixture, the latter gave ES-MS showing no sign of phosphine incorporation into the conjugate. Rather, it was consistent with the presence of the expected oxorhenium(V) core bound to $sCTH_2$ (3634). In addition, ions at *m/z* 2355.9 and 1768.3, assignable to dimers with two sCT molecules linked by the ReO^{3+} core, were detected. Again, the precise shifts in the *m/z* values resulting from labeling can be used to identify the rhenium oxidation state. The $[sCTH_2 + 2H]^{2+}$ peak at 1717.8 is shifted to 1817.8 (Figure 6), corresponding to an increase in molecular mass of 200. This in turn corresponds to replacement of $3H^+$ by ReO^{3+} (calculated on the basis of the most abundant isotope Re-187). Thus, with the minor reservations mentioned above for the Tc-labeled species, we conclude that the spectrum is consistent with rhenium having oxidation state V. Thus, in contrast to the technetium reaction, the presence of TPPDS neither reduces the rhenium below oxidation state V, nor contributes to the rhenium coordination sphere. Although it is not possible to define with certainty which residues within the peptide are bound directly to the rhenium, it seems certain that at least one of the cysteine thiolates is involved, since no adducts are observed unless the peptide is prereduced. It is possible that a number of isomeric forms exist, perhaps including those shown in Scheme 3. Other spectroscopic techniques such as EXAFS and high-field NMR may help to distinguish these possibilities, although such analysis would be hampered by the presence of mixtures of isomeric species.

SUMMARY

Phosphine is the most efficient reducing agent for disulfide bonds among those examined. Direct labeling of sCT is possible using water-soluble phosphine as the reducing agent both for disulfide and for pertechnetate, but the method gives mixed products and poor receptor affinity. This raises serious doubts about the acceptability of direct labeling of peptides in general, unless it can be shown by detailed spectroscopic methods that the product is structurally homogeneous and stable. Although this direct labeling method is unsuitable for sCT and probably other small disulfide-containing peptides, it may prove to be readily adaptable for application to larger vehicles such as monoclonal antibodies. The phosphine both reduces the pertechnetate and contributes to the technetium coordination sphere. In contrast, the phosphine does not reduce rhenium below oxidation state V, nor does it participate in the rhenium coordination sphere in the labeled peptide. Instead, the expected oxorhenium(V) moiety is incorporated. Both Tc and Re labeling processes give rise to dimers linked by the metal center, as well as simple monomeric species. Positive mode ES-MS of the metallopeptides not only revealed the presence of phosphine bound to technetium and oxygen bound to rhenium but also revealed the oxidation state of the metal in each case. ES-MS is proving to be an exceptionally valuable technique for characterizing radiopharmaceuticals, and when combined with other techniques (NMR and EXAFS, in particular), it can contribute to detailed structural characterization of metallopeptides, especially as recent technology offers sensitivity approaching carrier-free concentrations (*21*). Indeed, it may be argued that HPLC−ES-MS characterization should now be regarded as essential before it is permissible to embark on in vivo evaluation of small labeled peptides either in animals or in humans.

ACKNOWLEDGMENT

We thank Zeina Nasif, Elaine Cheung, K. Howland, and J. Hardy for technical assistance, Dr. Mathias Glaser for $HReOCl_4$ and Dr. Sushumna Prakash for TPPDS and TPPTS. We thank BBSRC for a studentship to W.E.P.G.

LITERATURE CITED

(1) Blower, P. J., and Prakash, S. D. (1999) The chemistry of rhenium in nuclear medicine. In *Perspectives on Bioinorganic Chemistry* (Hay, R. W., Dilworth, J. R., and Nolan, K. B., Eds.) pp 91−144, JAI Press, Stamford, CT.

(2) Okarvi, S. M. (1999) Recent developments in $^{99}Tc^{m}$-labeled peptide-based radiopharmaceuticals: An overview. *Nucl. Med. Commun. 20*, 1093−1112.

(3) Jurisson, S. S. (2002) Tc and Re peptide chemistry: direct labeling. In *Technetium, Rhenium and Other Metals in Chemistry and Nuclear Medicine* (Nicolini, M., and Mazzi, U., Eds.) pp 15−21, SGEditoriali, Padova, Italy.

(4) Iznaga-Escobar, N. (2001) Direct radiolabeling of monoclonal antibodies with rhenium-188 for radioimmunotherapy of solid tumors − a review of radiolabeling characteristics, quality control and in vitro stability studies. *Appl. Radiat. Isot. 54*, 399−406.

(5) Fichna, J., and Janecka, A. (2003) Synthesis of target-specific radiolabeled peptides for diagnostic imaging. *Bioconjugate Chem. 14*, 3−17.

(6) Dadachova, E., and Mirzadeh, S. (1997) The role of tin in the direct labeling of proteins with rhenium-188. *Nucl. Med. Biol. 24*, 605−608.

(7) Varnum, J. M., Thakur, M. L., Schally, A. V., Jansen, S., and Mayo, K. H. (1994) Rhenium-labeled somatostatin analogue RC-160 − H-1-nmr and computer modeling conformational-analysis. *J. Biol. Chem. 269*, 12583−12588.

(8) John, E., Wilder, S., and Thakur, M. L. (1994) Structural perturbations of monoclonal-antibodies following radiolabeling − in-vitro evaluation of different techniques. *Nucl. Med. Commun. 15*, 24−28.

(9) Jankowsky, R., Kirsch, S., Spies, H., and Johannsen, B. (1999) Solution structures of technetium(V) and rhenium(V) peptide complexes as studied by EXAFS spectroscopy and capillary electrophoresis (CE). In *Technetium, Rhenium and Other Metals in Chemistry and Nuclear Medicine* (Nicolini, M., and Mazzi, U., Eds.) pp 229−234, SGEditoriali, Padova, Italy.

(10) Pimm, M. V., Rajput, R. S., Frier, M., and Gribben, S. J. (1991) Anomalies in reduction-mediated Tc-99m labeling of monoclonal antibodies. *Eur. J. Nucl. Med. 18*, 973−976.

(11) Giblin, M. F., Jurisson, S. S., and Quinn, T. P. (1997) Synthesis and characterization of rhenium-complexed α-melanotropin analogues. *Bioconjugate Chem. 8*, 347−353.

(12) Glaser, M., Howard, M. J., Howland, K., Powell, A. K., Rae, M. T., Wocadlo, S., Williamson, R. A., and Blower, P. J. (1998) Structural characterisation and bioconjugation of an active ester containing oxorhenium(V) complex incorporating a thioether donor. *J. Chem. Soc., Dalton Trans.*, 3087−3092.

(13) Santimaria, M., Mazzi, U., Gatto, S., Dolmella, A., Bandoli, G., and Nicolini, M. (1997) Rhenium complexes with phosphine-containing peptides. Synthesis and characterization of oxorhenium(V) complexes with *N*-{*N*-[3-(diphenylphosphino)-propionyl]glycyl}-l-*S*-benzylcysteine and its methyl ester. *J. Chem. Soc., Dalton Trans.* 1765−1771.

(14) Greenland, W. E. P. (2002) Ph.D. Thesis, University of Kent, Canterbury, U.K.

(15) Greenland, W. E. P., Howland, K., Hardy, J., and Blower, P. J. (2003) Solid-phase synthesis of peptide radiopharmaceuticals using Fmoc-*N*-ϵ-(hynic-Boc)-lysine, a technetium-binding amino acid. Application to Tc-99m-labeled salmon calcitonin. *J. Med. Chem. 46*, 1751−1757.

(16) Prakash, S. D. (1996) Ph.D. Thesis, University of Kent, Canterbury, U.K.

(17) Lis, T., and Jezowska-Trzebiatowska, B. (1977) Preparation of oxopentachlororhenate(VI) and oxotetrachlororhenate(V). The crystal and molecular structure of $AsPh_4ReOCl_4$. *Acta Crystallogr. B33*, 1248−1250.

(18) DeMurphy, C. A., MelendezAlafort, L., MartinezRivero, O., Gomez, E., and FerroFlores, G. (1997) Phosphine reduced IgG: a new method for Tc-99m labeling immunoglobulins. *J. Radioanal. Nucl. Chem. 220*, 41−45.

(19) Blauenstein, P., Locher, J. T., Seybold, K., Koprivova, H., Janoki, G. A., Mäcke, H. R., Hasler, P., Ammann, A., NovakHofer, I., Smith, A., and Schubiger, P. A. (1995) Experience with the I-123 and Tc-99m labeled antigranulocyte antibody Mab47 − a comparison of labeling methods. *Eur. J. Nucl. Med. 22*, 690−698.

(20) Hermanson, G. T. (1996) *Bioconjugation Techniques*, Academic Press, San Diego.

(21) Liu, S., Edwards, D. S., Ziegler, M. C., and Glajch, J. L. (1999) Charaterization of technetium complexes using FAB-MS and LC-MS. In *Technetium, Rhenium and Other Metals in Chemistry and Nuclear Medicine* (Nicolini, M., and Mazzi, U., Eds.) pp 121−127, SGE Editoriali, Padova, Italy.

(22) Bartis, J., Liu, S., Ziegler, M. C., and Edwards, D. S. (1999) Hynic technology for therapeutic rhenium radiopharmaceuticals. In *Technetium, Rhenium and Other Metals in Chemistry and Nuclear Medicine* (Nicolini, M., and Mazzi, U., Eds.) pp 409−417, SGE Editoriali, Padova, Italy.

(23) Seitz, U., Neumaier, B., Glatting, G., Kotzerke, T., Bunjes, D., and Reske, S. N. (1999) Preparation and evaluation of the rhenium-188-labeled anti-nca antigen monoclonal antibody BW 250/183 for radioimmunotherapy of leukaemia. *Eur. J. Nucl. Med. 26*, 1265−1273.

(24) Gandomkar, M., Najafi, R., Ebrahimi, S. E. S., Shafiee, A., Babaei, M. H., Rabbani, M., and Shabani, G. A. (2003) Direct labeling of octreotide with Tc-99m: effect of different concentration of reducing agents and amount of sodium pertechnetate on radiolabelling efficiency. *Appl. Radiat. Isot. 58*, 361−364.

(25) Hnatowich, D. J., Virzi, F., Winnard, P., Fogarasi, M., and Rusckowski, M. (1994) Investigations of ascorbate for direct labeling of antibodies with technetium-99m. *J. Nucl. Med. 35*, 127−134.

(26) Ferro-Flores, G., Pimentel-Gonzalez, G., Gozalez-Zabala, M. A., Arteaga De Murphy, C., Melendez-Alafort, L., Tendilla, J. I., and Croft, B. Y. (1998) Preparation, biodistribution and dosimetry of ^{188}Re-labeled MAb for CEA1 and its $F(ab')_2$ fragments by avidin biotin strategy. *Nucl. Med. Biol. 25*, 57−62.

(27) Griffiths, G. L., Goldenberg, D. M., Knapp, F. F., Callahan, A. P., Chang, C. H., and Hansen, H. J. (1991) Direct radiolabeling of monoclonal-antibodies with generator-produced Re-188 for radioimmunotherapy − labeling and animal biodistribution studies. *Cancer Res. 51*, 4594−4602.

(28) Mushtaq, A., Pervez, S., and Haider, I. (2000) Preparation of Re-188-lanreotide peptide and its quality control. *Radiochim. Acta 88*, 495−498.

(29) Pervez, S., Mushtaq, A., and Arif, M. (2001) Technetium-99m direct radiolabeling of lanreotide: a somatostatin analog. *Appl. Radiat. Isot. 55*, 647−651.

(30) Qi, P., Muddukrishna, S. N., Torokboth, R., Rahn, J., and Chen, A. (1996) Direct $^{(99)m}$Tc-labeling of antibodies by sodium dithionite reduction, and role of ascorbate as a stabilizer in cysteine challenge. *Nucl. Med. Biol. 23*, 827−835.

(31) Rhodes, B. A. (1991) Direct labeling of proteins with Tc-99m. *Nucl. Med. Biol. 18*, 667−676.

(32) Thakur, M. L. (1994) Ascorbate plays a major role in labeling proteins with Tc-99m. *J. Nucl. Med. 35*, 1566−1567.

(33) Pasqualini, R., Duatti, A., Bellande, V., Comazzi, V., Brucato, V., Hoffschir, D., Fagret, D., and Comet, M. (1994) Bis(dithiocarbamato) nitrido technetium-99m radiopharmaceuticals: a class of neutral myocardial imaging agents. *J. Nucl. Med. 35*, 334−341.

(34) Blower, P. J., Dilworth, J. R., Hutchinson, J. P., Nicholson, T., and Zubieta, J. A. (1984) Rhenium complexes with sterically hindered thiolate ligands. Structures of $[ReO(SC_6H_3Pr^i_2)]^-$ and a complex with an unexpected cation, $[Ph_3PSC_6H_3Pr^i_2]$-$[ReO(SC_6H_2Me_3)_4]1.5CH_3CH_2OH$. *Inorg. Chim. Acta 90*, L27−30.

(35) Zaidi, M., Moonga, B. S., Bevis, P. J. R., Bsacal, Z. A., and Breimer, L. H. (1990) The calcitonin gene peptides: biology and clinical relevance. *Crit. Rev. Clin. Lab. Sci. 28*, 109−174.

(36) Sexton, P. M., Findlay, D. M., and T. J., M. (1999) Calcitonin. *Curr. Med. Chem. 6*, 1067−1093.

(37) Wehofsky, M., Hoffmann, R., Hubert, M., and Spengler, B. (2001) Isotopic deconvolution of matrix-assisted laser desorption/ionization mass spectra for substance-class specific analysis of complex samples. *Eur. J. Mass Spectrom. 7*, 39−46.

(38) Yergey, J., Heller, D., Hansen, G., Cotter, R. J., and Fenselau, C. (1983) Isotopic distributions in mass spectra of large molecules. *Anal. Chem. 55*, 353−356.

(39) Freiberg, E., Davis, W. M., Nicholson, T., Davison, A., and Jones, A. G. (2002) Reduction of the pertechnetate anion with bidentate phosphine ligands. *Inorg. Chem. 41*, 5667−5674.

(40) Rochon, F. D., Melanson, R., and Kong, P. C. (2000) Synthesis of new mixed-ligands tc complexes containing monodentate phosphine and isothiocyanato ligands: Crystal structures of complexes $Tc(P(C_3H_7)_3)_2(NCS)_4$, $Tc(P(CH_3)_2Ph)_4$-$(NCS)_2$ and $Tc(P(OCH_3)Ph_2)_4(NCS)_2.1/2CH_2Cl_2$. *Inorg. Chim. Acta 300*, 43−48.

(41) Rochon, F. D., and Kong, P. C. (2000) Syntheses of new ionic technetium(III) complexes containing four monodentate phosphine ligands. Crystal structures of *trans*-$Tc(PMe_2Ph)_4Cl_2$ PF_6, *trans*-$Tc(PMe_3)_4Cl_2$ BPh_4, and *trans*-$Tc(PMe_3)_4Cl_2$ PF_6. *Inorg. Chem. 39*, 5757−5762.

(42) Pietzsch, H. J., Tisato, F., Refosco, F., Leibnitz, P., Drews, A., Seifert, S., and Spies, H. (2001) Synthesis and characterization of novel trigonal bipyramidal technetium(III) mixed-ligand complexes with SES/S/P coordination (E = O, $N(CH_3)$, S). *Inorg. Chem. 40*, 59−64.

(43) Spies, H., Glaser, M., Pietzsch, H. J., Hahn, F. E., and Lugger, T. (1995) Synthesis and reactions of trigonal-bipyramidal rhenium and technetium complexes with a tripodal, tetradentate NS_3 ligand. *Inorg. Chim. Acta 240*, 465−478.

(44) Tisato, F., Refosco, F., Bandoli, G., Bolzati, C., and Moresco, A. (1994) Synthesis and characterization of neutral technetium(III) complexes with mixed S,P-bidentate phosphine thiolate ligands − crystal-structure of $Tc(SCH_2CH_2PPh_2)_2$-$(SCH_2CH_2PPh_2O)$. *J. Chem. Soc., Dalton Trans.*, 1453−1461.

(45) Blower, P. J., and Dilworth, J. R. (1985) Rhenium nitrido, arylimido, nitrile and carbonyl complexes with sterically hindered thiolate ligands. *J. Chem. Soc., Dalton Trans.*, 2305−2309.

(46) Dilworth, J. R., Neaves, B. D., Hutchinson, J. P., and Zubieta, J. A. (1982) 5-co-ordinate rhenium thiolato-complexes − the preparations and structures of $[ReO(SPh)_4]^-$, $[Re(SPh)_3(MeCN)(PPh_3)]$ and $[Re(NPPh_3)(SPh)_4]$. *Inorg. Chim. Acta Lett. 65*, L223-L224.

BC0500600

Oxoazabenzo[*de*]anthracenes Conjugated to Amino Acids: Synthesis and Evaluation as DNA-Binding Antitumor Agents

Nathalie Dias,[†] Jean-François Goossens,[‡] Brigitte Baldeyrou,[†] Amélie Lansiaux,[†] Pierre Colson,[§] Alberto Di Salvo,[∥] Jeanne Bernal,[∥] Agnes Turnbull,[∥] David J. Mincher,[∥] and Christian Bailly*[,†,⊥]

INSERM U-524 et Laboratoire de Pharmacologie Antitumorale du Centre Oscar Lambret, IRCL, 59045 Lille, France, Laboratoire de Chimie Analytique, Faculté des Sciences Pharmaceutiques et Biologiques, Université de Lille 2, 59006 Lille, France, Biospectroscopy and Physical Chemistry Unit, Department of Chemistry and Natural and Synthetic Drugs Research Center, University of Liege, Sart-Tilman, 4000 Liege, Belgium, and Napier University, School of Life Sciences, 10 Colinton Road, Edinburgh EH10 5DT, UK .
Received March 7, 2005; Revised Manuscript Received May 6, 2005

We report the synthesis of an original series of oxoazabenzo[*de*]anthracenes conjugated to an amino acid: Ala, Phe, Pro, Lys, or Gly (**4a**−**e**, respectively). The compounds, derived from 1,8-dihydroxyanthracene-9,10-dione, were studied for DNA binding and cytotoxicity. Melting temperature, fluorescence quenching, and surface plasmon resonance methods all indicated that the lysine derivative **4d** binds to DNA much more strongly that the Pro, Ala, and Gly conjugates whereas the Phe analogue showed the lowest DNA binding capacity. These compounds form intercalation complexes with DNA, as judged from electric linear dichroism and topoisomerase I-based DNA unwinding experiments. Preferential binding of **4d** to defined sequences such as 5′-CTAAAGG and 5′-ATGC was evidenced by DNase I footprinting. This Lys conjugate was found to be over 20 times more cytotoxic to CEM human leukemia cells than the other conjugates, with an IC_{50} in the submicromolar range. A high antiproliferative activity, likely attributable to the enhanced DNA binding capacity, is maintained despite the incapacity of the compound to stabilize topoisomerase−DNA covalent complexes. The cell cycle effects of **4d** consisted in an S phase accumulation of cells coupled with a pro-apoptotic action (appearance of hypodiploid sub-G1 cells) which were confirmed by measuring the inhibition of BrdU incorporation into DNA and labeling of phosphatidylserine residues with annexin V-FITC by means of flow cytometry. Altogether, the work provides interesting structure−activity relationships in the oxoazabenzo[*de*]anthracene−amino acid conjugate series and identifies the lysine derivative **4d** as a promising candidate for further in vivo evaluation and drug design.

INTRODUCTION

DNA topoisomerase enzymes are the targets of many clinically important anticancer drugs. Topoisomerase II was recognized as an important therapeutic target during the development of a number of drugs including doxorubicin, mitoxantrone, and etoposide, while camptothecin analogues were shown to inhibit topoisomerase I (*1*). Inherent structural lability problems associated with the camptothecins have stimulated the growth in developing new topoisomerase I inhibitors with diverse structures (*2*). Research efforts to overcome the clinical limitations of topoisomerase inhibitors remain intense (*3*).

The majority of these agents (topoisomerase 'poisons') are cytotoxic via stabilization of the normally transient, covalently bound cleavable complex formed between DNA and enzyme. Drug-stabilized DNA−enzyme complexes (ternary complexes) are believed to be lethal upon DNA replication when irreversible double-stranded DNA breaks are formed, causing various chromosomal aberrations culminating in cell death (*4*, *5*). The development of resistance to topoisomerase-targeting drugs, however, presents a major clinical problem; resistance commonly is manifested as classical multidrug resistance, caused by overexpression of the *mdr1* and *MRP* gene products, leading to increased efflux of drug from the cell, thereby reducing cytotoxic efficacy (*6*). Furthermore, acquired drug resistance characterized by alterations in individual topoisomerase expression resulting from antitopoisomerase drug therapy additionally limits clinical applications (*7*).

For the majority of topoisomerase inhibitors, DNA binding properties are crucial determinants of the pattern of topoisomerase enzyme inhibition in addition to their cytotoxic properties. We have previously noted (*8*) that key examples of spacer-linked anthraquinone−amino acid conjugates, capable of binding to DNA by intercalation of the planar aminoanthraquinone ring system, interact with topoisomerase I and topoisomerase II with selectable isoform specificity and have in vivo activity against experimental colon cancer (*9*). The foregoing anthraquinones have been shown to favor inhibition of topoisomerase II, in common with many compounds that bind strongly to DNA by intercalation, and, not unlike the dual topoisomerase I and II inhibitor, DACA, type I and II enzyme preference is influenced by the nature of the cationic side chain and nuclear substitution pattern (*10*).

In the present study, we postulated that the grafting of an additional ring onto the anthraquinone skeleton

* Corresponding author: E-mail: christian.bailly@lille.inserm.fr; christian.bailly@pierre-fabre.com.

[†] INSERM U-524 et Laboratoire de Pharmacologie Antitumorale du Centre Oscar Lambret.

[‡] Université de Lille 2.

[§] University of Liege.

[∥] Napier University.

[⊥] Present address: Centre de Recherche en Oncologie Expérimentale, Institut de Recherche Pierre Fabre, 3 rue des satellites, 31140 Toulouse, France.

10.1021/bc050065x CCC: $30.25 © 2005 American Chemical Society
Published on Web 06/24/2005

Scheme 1

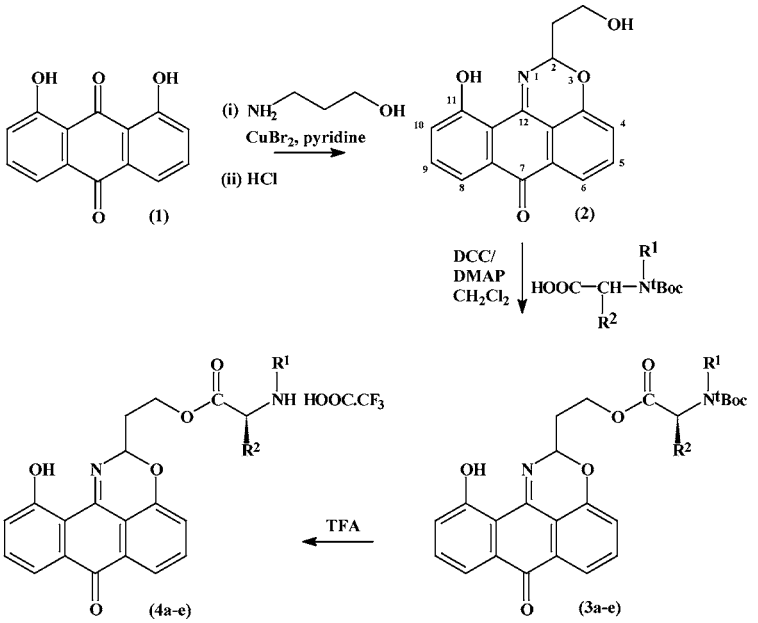

Cpd #	R1	R2	Amino Acid Motif
4a	H	CH_3	Ala
4b	H	CH_2Ph	Phe
4c		$-CH_2-CH_2-CH_2-$	Pro
4d	H	$(CH_2)_4NH_2\,HOOC.CF_3$	Lys
4e	H	H	Gly

could modulate the DNA-binding properties and consequently the pattern of topoisomerase enzyme inhibition. To this end, a 1,3-oxazine ring was annealed onto the anthraquinone nucleus (Scheme 1) to afford the tetracyclic, oxa-aza-benzo[*de*]anthracene fused template ring system (**2**). This intermediate spacer compound was esterified to afford a series of amino acid conjugates (**4a**−**e**). It was anticipated that the angular disposition of the spacer-linked, cationic amino acid conjugate side chains would not be precluded from functioning as DNA minor groove-directed components. Additionally, it was recognized that the oxa-aza-benzo[*de*]anthracene formation would effectively mask one of the quinone carbonyl groups, potentially eliminating deleterious effects of quinone bioreduction, and that the conjugates might share common transport mechanisms with structurally related DNA-binding benzo[*e*]pyrimidines, some of which have been observed to overcome multidrug resistance protein-mediated drug efflux (*11*, *12*). In this paper, we report the synthesis and complete characterization of the DNA-binding properties of five oxa-aza-benzo[*de*]anthracene−amino acid conjugates (**4a**−**e**), together with a first evaluation of their biological activities. This work identifies the lysine derivative **4d** as a sequence-selective DNA-intercalating agent endowed with potent cytotoxic and pro-apoptotic activities. The structure−activity relationships are discussed.

EXPERIMENTAL SECTION

Synthetic Chemistry. Metal-promoted direct nuclear alkylamination of 1-hydroxyanthracene-9,10-dione (*13*) and 1,4-dihydroxyanthracene-9,10-dione (*14*) have been reported for which the metal ion was proposed to function as an effective oxidizing agent via formation of a metal chelate complex between the quinone carbonyl and an α-hydroxy group.

The key intermediate oxa-aza-benzanthracene (**2**) was synthesized in good yield via the amination at the C-9 carbonyl group of 1,8-dihydroxyanthracene-9,10-dione (**1**) with 3-amino-1 propanol followed by a copper(II) ion-promoted oxidative cyclization to form the 1,3-oxazine ring (Scheme 1).

Ester-linked amino acid conjugates of **2** were prepared by dicyclohexylcarbodiimide (DCC) coupling of N-^{t}Boc-protected amino acids, in the presence of 4-(dimethylamino)pyridine (DMAP), to afford the intermediate adducts **3a**−**e**. Standard removal of the ^{t}Boc-protecting groups with trifluoroacetic acid (TFA) gave the trifluoroacetate salts of the alanine (**4a**), phenylalanine (**4b**), proline (**4c**), lysine (**4d**), and glycine (**4e**) conjugates (Scheme 1).

Materials and Methods. N-^{t}Boc-protected amino acids and coupling reagents were commercially available from Novabiochem (Nottingham, UK), and 1,8-dihydroxyanthracene-9,10-dione (**1**) was from Aldrich (Poole,

UK). ^{1}H NMR spectra were recorded at 200 MHz [Bruker] in DMSO-d_6 or $CDCl_3$ as appropriate. Mass spectra were recorded using a Bruker Esquire 3000 spectrometer with electrospray ionization in positive or negative mode [ES (+) or ES (−)] or by fast atom bombardment [FAB (+)]. Chromatography was performed on silica gel 60 [Merck] with dichloromethane−ethyl acetate (4:1).

2-(2-Hydroxyethyl)-11-hydroxy-2*H*-3-oxa-1-aza-benzo[*de*]anthracen-7-one (2). To a solution of 1,8-dihydroxyanthracene-9,10-dione (**1**) (2.0 g; 8.2 mmol) in pyridine (80 mL) was added copper(II) bromide (3.7 g; 16 mmol). 3-Aminobutan-1-ol (50 mL) was then added dropwise, and the mixture was stirred at room temperature for 3 h. The reaction mixture was concentrated under reduced pressure and treated with water (200 mL) and concentrated hydrochloric acid to pH 2 (for 30 min) to decompose the copper chelate complexes of the product. The solution was neutralized with saturated sodium bicarbonate, and the resulting solid was removed by filtration. The solid was extracted with dichloromethane, dried ($MgSO_4$), concentrated under reduced pressure, and applied to a silica gel flash chromatography column. Elution with dichloromethane−ethyl acetate (4:1) gave the title compound (**2**) as a chromatographically homogeneous orange-yellow solid in 60% yield, mp 114 °C. ^{1}H NMR (DMSO-d_6) δ: 2.2 (2H, q, CH_2); 3.8 (2H, t, CH_2O); 4.8 (1H, s, OH); 6.2 (1H, t, H-2); 7.25−7.4 (2H, m, H-4, −10); 7.65−7.8 (4H, m, H-5, -6, -8, -9); 13.3 (1H, s, 11-OH). FAB(+) MS: *m/z* 296 $[M + H]^+$.

2-(*N*-*tert*-butoxycarbonylamino)propionic Acid 2-(11-Hydroxy-7-oxo-2,7-dihydro-3-oxa-1-aza-benzo-[*de*]anthracene-2-yl)ethyl Ester (3). N-^{t}Boc-Ala-OH (0.4 g; 2.2 mmol) and DCC (0.4 g; 2 mmol) were added to a solution of **2** (0.6 g; 2 mmol) in dichloromethane (50 mL) containing DMAP (20 mg), and the mixture was stirred at room temperature for 12 h. Precipitated dicyclohexylurea was removed by filtration, and the solution was washed with saturated sodium bicarbonate, dried ($MgSO_4$), and evaporated, in vacuo to afford a solid residue. The latter was redissolved in dichloromethane−ethyl acetate (4:1; 20 mL) and chromatographed on silica gel in the same solvent mixture. Fractions containing the major product were combined, filtered, and evaporated to a solid residue that afforded the yellow crystalline title compound (**3**) from ethanol in 57% yield, mp 105−107 °C. ^{1}H NMR (DMSO-d_6) δ: 1.35−1.45 (12H, m, unresolved ^{t}Boc + CH_3); 2.35 (2H, q, CH_2); 4.3 (1H, q, α-CH); 4.5 (2H, m, CH_2O); 5.05 (1H, br s, N*H*CO); 6.1 (1H, t, H-2); FAB (+) MS *m/z* 467 $(M + H)^+$; 489 $(M + Na)^+$.

2-Aminopropionic Acid 2-(11-Hydroxy-7-oxo-2,7-dihydro-3-oxa-1-aza-benzo[*de*]anthracene-2-yl)ethyl Ester Trifluoroacetate (4a). The N-protected alanine conjugate **3** (0.25 g; 0.5 mmol) was dissolved in dry trifluoroacetic acid (20 mL) and left at room temperature for 25 min. The solution was evaporated and re-evaporated from ethanol to afford a viscous residue that crystallized from ethanol−diethyl ether to afford the alanine conjugate trifluoroacetate salt (**4a**) (quantitative). ^{1}H NMR (DMSO-d_6) δ: 1.4 (3H, d, CH_3); 2.4 (2H, q, CH_2); 4.0 (1H, q, α-CH); 4.5 (2H, m, CH_2O); 6.2 (1H, t, H-2); 7.25−7.4 (2H, m, H-4, −10); 7.6−7.8 (4H, m, H-5,-6, -8, -9); 8.5 (3H, br s, NH_3^+); 13.2 (1H, s,11-OH). ES(+) MS *m/z* 367 $[RNH_3]^+$, 389 $[RNH_2 + Na]^+$; ES(−) *m/z* 113 $(CF_3{\cdot}COO^-)$.

2-Amino-3-phenylpropionic Acid 2-(11-Hydroxy-7-oxo-2,7-dihydro-3-oxa-1-aza-benzo[*De*]anthracene-2-yl)ethyl Ester Trifluoroacetate (4b). The phenylalanine conjugate (**4b**) was prepared by an identical sequence to that described for (**4a**) except that N-^{t}Boc-phe-OH replaced N-^{t}Boc-Ala. ^{1}H NMR (DMSO-d_6) δ: 2.3 (2H, q, CH_2); 3.2 (2H, m, CH_2Ph); 4.3- (1H, m, α-CH); 4.55 (2H, m, CH_2O); 5.9 (1H, t, H-2); 7.2−7.4 (7H, m, H-4, −10 + Ph); 7.6−7.8 (4H, m, H-5, -6, -8, -9); 8.6 (3H, br s, NH_3^+); 13.2 (1H, s, 11-OH). ES(+) MS *m/z* 443 $[RNH_3]^+$, ES(−) *m/z* 113 $(CF_3{\cdot}COO^-)$.

Pyrrolidine-2-carboxylic Acid 2-(11-Hydroxy-7-oxo-2,7-dihydro-3-oxa-1-aza-benzo[*de*]anthracene-2-yl)ethyl Ester Trifluoroacetate (4c). The proline conjugate (**4c**) was prepared by an identical sequence to that described for (**4a**) except that N-^{t}Boc-pro-OH replaced N-^{t}Boc-Ala. ^{1}H NMR (DMSO-d_6) δ: 1.8−2.1 (3H, m, γ-CH_2 + β-CH); 2.3 (1H, m, β-CH); 2.5 (2H, q, CH_2); 3.2 (2H, m, δ-CH_2); 4.3−4.55 (3H, m, CH_2O + α-CH) 6.25 (1H, t, H-2); 7.25−7.4 (2H, m, H-4, −10); 7.6−7.8 (4H, m, H-5, -6, -8, -9); 9.2 (2H, br s, NH_2^+); 13.2 (1H, s, 11-OH). ES(+) MS *m/z* 392 $[RR'NH_2^+]$; ES(−) MS *m/z* 113 $(CF_3{\cdot}COO^-)$.

2,6-Diaminohexanoic Acid 2-(11-Hydroxy-7-oxo-2,7-dihydro-3-oxa-1-aza-benzo[*de*]anthracene-2-yl)-ethyl Ester Bis-α,ϵ-trifluoroacetate (4d). The lysine conjugate (**4d**) was prepared by an identical sequence to that described for **4a** except that N-^{t}Boc-lys(N-^{t}Boc)-OH replaced N-^{t}Boc-Ala. ^{1}H NMR (DMSO-d_6) δ: 1.3−1.7 (4H, m, δ-CH_2, γ-CH_2,); 1.8 (2H, m, β-CH_2); 2.4 (2H, m, CH_2); 2.75 (2H, t, ϵ-CH_2); 4.0 (1H, t, α-CH); 4.5 (2H, m, CH_2O); 6.3 (1H, t, H-2); 7.3−7.4 (2H, m, H-4, −10); 7.65−7.8 (4H, m, H-5, -6, -8, -9); 8.15 (6H, br s, α,ϵ-NH_3^+); 13.25 (1H, s,11-OH). ES(+) MS *m/z* 425 $[R(NH_2)NH_3^+]$; ES(−) *m/z* 113 $(CF_3{\cdot}COO^-)$.

2-Aminoethanoic Acid 2-(11-Hydroxy-7-oxo-2,7-dihydro-3-oxa-1-aza-benzo[*de*]anthracene-2-yl)ethyl Ester Trifluoroacetate (4e). The glycine conjugate (**4e**) was prepared by an identical sequence to that described for (**4a**) except that N-^{t}Boc-gly-OH replaced N-^{t}Boc-Ala. ^{1}H NMR (DMSO-d_6) δ: 2.4 (2H, q, CH_2); 3.9 (2H, s, α-CH_2N); 4.5 (2H, m, CH_2O); 6.2 (1H, t, H-2); 7.25−7.4 (2H, m, H-4, −10); 7.6−7.8 (4H, m, H-5,-6, -8, -9); 8.25 (3H, br s, NH_3^+); 13.2 (1H, s,11-OH). ES(+) MS *m/z* 353 $[RNH_2^+]$; ES(−) *m/z* 113 $(CF_3{\cdot}COO^-)$.

Absorption Spectroscopy and Melting Temperature Studies. Absorption spectra and melting curves were measured using an Uvikon 943 spectrophotometer coupled to a Neslab RTE111 cryostat. Titrations of the drug with DNA, covering a large range of DNA-phosphate/drug ratios (P/D), were performed by adding aliquots of a concentrated DNA to a ligand solution at constant concentration (20 μM). The T_m measurements were performed in BPE buffer pH 7.1 (6 mM Na_2HPO_4, 2 mM NaH_2PO_4, 1 mM EDTA). The temperature inside the cuvette (10 mm path length) was increased over the range 30−100 °C with a heating rate of 1 °C/min. The "melting" temperature T_m was taken as the midpoint of the hyperchromic transition.

Fluorescence Measurements. A competitive displacement fluorometric assay with DNA-bound ethidium was carried out to evaluate the binding properties of the tested drugs (*15*, *16*). Fluorescence data were recorded at room temperature with a SPEX Fluorolog fluorometer. Excitation was set at 515 nm, and fluorescence emission was monitored over the range of 550 to 700 nm. Experiments were performed with an [ethidium]:[DNA] molar ratio of 12.6:10 and a drug concentration range of 0.01 to 100 μM in a BPE buffer pH 7.1. C_{50} values for ethidium displacement were calculated using a fitting function incorporated into Prism 3.0, and the apparent equilibrium binding constants (K_{app}) were calculated as follows:

$K_{app} = (1.26\ \mu M/C_{50}) \times K_{ethidium}$, with $K_{ethidium} = 10^7\ M^{-1}$

Surface Plasmon Resonance. The experimental procedure has been recently described in details (*17*, *18*). Measurements were performed in HBS-EP buffer sterile filtered and degassed, which was obtained from Biacore (0.01 M HEPES pH 7.4, 0.15 M NaCl, 3 mM EDTA, 0.0005% Surfactant P20). The hairpin oligonucleotide d(biotin- CGAATTCGTCTCCGAATTCG) (hairpin loop underlined) was purchased (PAGE purified) from Eurogentec (Belgium).

Electric Linear Dichroism (ELD). Calf thymus DNA (Pharmacia) was deproteinized with sodium dodecyl sulfate (protein content <0.2%) and extensively dialyzed against 1 mM sodium cacodylate-buffered solution pH 7.0. ELD measurements were performed with a computerized optical measurement system using the procedures previously outlined (*19*). All experiments were conducted with a 10 mm path length Kerr cell having 1.5 mm electrode separation. The samples were oriented under an electric field strength varying from 1 to 14 kV/cm. Unless specified, 10 μM of the tested drug was incubated with 200 μM of DNA. This electrooptical method senses only the orientation of the polymer-bound ligand: free ligand is isotropic and does not contribute to the signal (*19*).

Topoisomerase I Inhibition. The experimental procedure has been previously detailed (*20*). Supercoiled pKMp27 DNA (0.2 μg) was incubated with 4 units of human topoisomerase I (TopoGen Inc.) at 37 °C for 1 h in relaxation buffer (10 mM Tris-HCl pH 7.9, 100 mM NaCl, 1 mM EDTA, 0.1% BSA, 0.1 mM Spermidine, 5% Glycerol) in the presence of varying concentrations of the drug under study. Reactions were terminated by adding SDS to 0.25% and proteinase K to 250 μg/mL. DNA samples were then added to the electrophoresis dye mixture (5 μL) and electrophoresed in a 1% agarose gel at room temperature for 2 h at 120 V. Gels were stained with ethidium bromide (1 μg/mL), washed, and photographed under UV light.

DNase I Footprinting. The complete procedure has been recently detailed (*21*). Briefly, the 117 and 265 bp DNA fragments were prepared by 3′-[^{32}P]-end labeling of the *Eco*RI-*Pvu*II double digest of the pBS plasmid (Stratagene) using α-[^{32}P]-dATP (Amersham, 3000 Ci/mmol) and AMV reverse transcriptase (Roche). The labeled digestion products were separated on a 6% polyacrylamide gel under nondenaturing conditions in TBE buffer (89 mM Tris-Borate pH 8.3, 1 mM EDTA), and the requisite band of DNA was excised and crushed in water. Then, the labeled DNA was precipitated with ethanol and resuspended in a solution containing 10 mM Tris pH 7.0 and 10 mM NaCl. Samples (2 μL) of the labeled DNA fragments were incubated with 6 μL of the buffered solution containing the ligand at the appropriate concentration. After 10 min incubation at room temperature to ensure equilibration of the binding reaction, the digestion was initiated by the addition of 2 μL of a DNase I solution whose concentration was adjusted to yield a final enzyme concentration of about 0.03 unit/mL in the reaction mixture. After 3 min, the reaction was stopped by freeze-drying. Samples were lyophilized and resuspended in 5 μL of a 80% formamide solution containing the tracking dyes. The DNA samples were then heated at 90 °C for 4 min and chilled in ice for 4 min prior loading.

DNA cleavage products were resolved by gel electrophoresis under denaturating conditions (8% acrylamide containing 7 M urea). After electrophoresis, gels were soaked in 10% acetic acid for 10 min, transferred to a Whatman 3MM paper, and dried under vacuum at 80 °C. Molecular Dynamics 425E PhosphorImager was used for data analysis. Each resolved band was assigned to a particular bond within the DNA fragments by comparison of its position relative to sequencing standards generated by treatment of the DNA with dimethyl sulfate followed by piperidine-induced cleavage at the modified guanine bases in DNA (G-track).

Cell Culture and Survival Assay. Human CEM leukemia cells were obtained from the American Tissue Culture Collection. Cells were grown at 37 °C in a humidified atmosphere containing 5% CO_2 in RPMI 1640 medium, supplemented with 10% fetal bovine serum, 4.5 g/L glucose, 10 mM HEPES, 1 mM sodium pyruvate, penicillin (100 IU/mL), and streptomycin (100 μg/mL). The cytotoxicity of the tested compounds was assessed using a cell proliferation assay developed by Promega (CellTiter 96 AQueous one solution cell proliferation assay). Briefly, 2×10^4 exponentially growing cells were seeded in 96-well microculture plates with various drug concentrations in a volume of 100 μL. After 72 h incubation at 37 °C, 20 μL of the tetrazolium dye was added to each well, and the samples were incubated for a further 1.5 h at 37 °C. Plates were analyzed on a Labsystems Multiskan MS (type 352) reader at 492 nm.

Cell Cycle Analysis. For flow cytometric analysis of DNA content, 0.7×10^6 cells in exponential growth were treated with graded concentrations of the tested drug for 24 h and then washed with 1 mL of PBS. After centrifugation, the cell pellet was resuspended in 1 mL of cold ethanol for 1 h at 4 °C. The ethanol was removed, and the pellet was washed with 1 mL PBS and then incubated for 30 min in a solution containing 50 μg/mL PI and 100 μg/mL RNase. Samples were analyzed on a Becton Dickinson FACScan flow cytometer using the CellQuest software, which was also used to determine the percentage of cells in the different phases of the cell cycle. PI was excited at 488 nm, and fluorescence analyzed at 620 nm on channel Fl-2.

Externalization of Phosphatidyl Serines. Surface exposure of phosphatidyl serine (PS) by CEM cells was measured by cytometry by adding Annexin V-FITC to 0.7×10^6 cells per sample according to the manufacturer's specifications (Becton Dickinson, San Jose, CA). Simultaneously, the cells were stained with propidium iodide (50 μg/mL). Excitation was set at 488 nm, and the emission filters used were 515−545 (green, FITC) and 600 (red, PI). Data analysis was performed with the CellQuest software.

Bromodeoxyuridine (BrdU) Incorporation. Cells (0.7×10^6) were cultured in complete RPMI 1640 medium with the tested drug at different concentrations for 24 h prior to harvesting and then pulse labeled with 10 μM BrdU for 60 min in complete medium. Cells were pelleted, washed twice with PBS containing 0.1% sodium azide, and then fixed in ethanol 70% for 1 h at 4 °C. Cells were washed once again with PBS and then denatured in 2 N HCl for 15 min at 37 °C (or 30 min at room temperature) under gentle stirring. pH was adjusted by short incubation (5 min) in 3 mL 0.1 M $Na_2B_4O_7$, pH 8.5 before centrifugation (5 min, 500 g, 4 °C). The cell pellet was then washed with 5 mL of buffer containing PBS, 0.05% Tween, and 0.1% BSA (bovine serum albumin fraction V), resuspended in 100 μL of this buffer, and then incubated with the fluorescein isothiocyanate (FITC)-conjugated anti-BrdU monoclonal antibody (Becton Dickinson, San Jose, CA) for 30 min at room temperature in

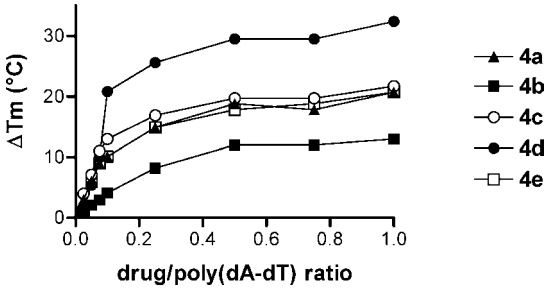

Figure 1. Melting temperature variation ΔT_m ($T_m^{\text{drug–DNA complex}} - T_m^{\text{DNA alone}}$, in °C) of the poly(dAT)$_2$ DNA after incubation with various compounds. The T_m measurements were performed at different drug/DNA-phosphate ratios. The poly(dAT)$_2$ concentration was fixed at 20 μM while the drug concentration varied from 0.5 to 20 μM. T_m measurements were performed in BPE buffer pH 7.1 (6 mM Na_2HPO_4, 2 mM NaH_2PO_4, 1 mM EDTA), in 1 cm quartz cuvettes at 260 nm with a heating rate of 1 °C/min. The T_m values were obtained from first-derivative plots.

Table 1. Binding to DNA and Cytotoxicity

compd	ΔT_m (°C)[a]	K_{app} (10^7 M^{-1})[b]	IC_{50} (μM)[c]
4a	5.9	0.38 ±0.04	5.56 ±0.78
4b	4	<0.01	5.61 ±2.35
4c	4.9	0.54 ±0.09	3.52 ±0.44
4d	15.5	5.06 ±0.67	0.13 ±0.06
4e	6.8	0.75 ±0.04	2.97 ±0.05

[a] T_m measurements were performed in BPE buffer pH 7.1 (6 mM Na_2HPO_4, 2 mM NaH_2PO_4, 1 mM EDTA) using 20 μM drug and 20 μM calf thymus DNA (nucleotide concentration) with a heating rate of 1 °C/min. [b] Apparent binding constant measured by fluorescence ($n = 3$). [c] Drug concentration (μM) that inhibits CEM leukemia cell growth by 50% after incubation in liquid medium for 72 h.

the dark. Cells were counterstained with 10 μg/mL of propidium iodide and treated with RNase (1 μg/mL). For the negative controls, the pellet was incubated with the antibody but not with BrdU. Samples were analyzed on a Becton Dickinson FACScan flow cytometer using the CellQuest software.

RESULTS

Affinity for DNA. Two complementary approaches were used to compare the affinity of the drugs for DNA. First, we measured the capacity of the compounds to protect the polynucleotide poly(dAT)$_2$ against heat denaturation. Under our experimental conditions, the AT polymer melted at 42 °C and this T_m value was increased in the presence of the different compounds. Figure 1 shows the concentration dependence on the ΔT_m ($T_m^{\text{complex}} - T_m^{\text{DNA}}$) values for the different poly(dAT)$_2$-drug complexes. It is already clear at this point that the nature of the amino acid substituent on the oxoazabenzo[*de*]anthracene chromophore strongly modulates the capacity of the drug to interact with DNA. The Phe derivative **4b** is considerably less efficient than the Lys derivative **4d** at stabilizing the duplex structure of DNA and the three other compounds bearing an uncharged Pro, Ala, or Gly residue showed similar behavior, intermediate between those of the charged Lys compound and the aromatic Phe conjugate. The extent of stabilization was very high with the Lys compound, reaching 30 °C at a drug/nucleotide-DNA ratio of 0.5 which represents a considerable stabilization of the double helical structure. Similar experiments were also performed with calf thymus DNA at a single drug/nucleotide ratio of 1 and the ΔT_m values are collated in Table 1. Here again, the Lys derivative **4d** proved to be the most potent compound in the series to protect DNA from heat-induced melting.

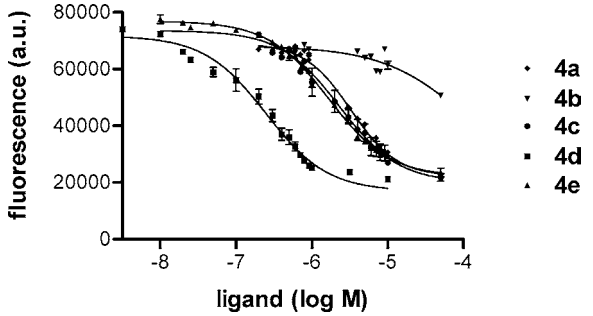

Figure 2. Dose-dependent quenching of the fluorescence of ethidium bromide bound to DNA in the presence of increasing concentrations (0.01 to 100 μM) of the tested compounds. Measurements were performed in BPE buffer, with an excitation wavelength of 515 nm and an [ethidium]:[DNA] molar ratio of 1.26. These ethidium displacement curves were used to calculate the apparent equilibrium binding constants (K_{app}) given in Table 1.

In a second phase, binding affinities for all five compounds were quantitated by means of fluorescence, using a well-established quenching assay based on the displacement of the intercalating drug ethidium bromide (EB) from calf thymus DNA. In this competition assay, binding of the tested compound to DNA leads to the removal of EB molecules inserted between the base pairs, and the resulting EB molecules not bound to DNA become much less fluorescent than the bound EB molecules because of the surrounding water molecules which quench the fluorescence. This conventional displacement assay is useful to calculate the concentration of the competing drug molecule required to reduce the EB fluorescence by 50%, and this value was then used to calculate the binding constant K_a for each conjugate (Table 1). The measured K_a values agree very well with the ΔT_m values. Compound **4b** poorly competed with EB for binding to DNA whereas **4d** was considerably more efficient than the other conjugates at displacing EB molecules from their intercalation sites. The quenching plots shown in Figure 2 indicate than **4d** is at least 200 times more efficient than **4b** and roughly 10-fold more potent than the Gly, Pro, and Ala conjugates. These three latter compounds exhibit comparable effects on the binding of EB to DNA, and this is in complete agreement with the ΔT_m data. The quantitative analysis of the binding plots gave a K_a value of 5×10^7 M^{-1} for UB368, 10 times higher than that calculated for the Pro derivative **4c**. In terms of DNA binding affinity the compounds rank in the order **4d** ≫ **4e** > **4c**, **4a** ≫ **4b**. As one would have expected, the linkage of a cationic Lys residue is thus highly favorable compared to an uncharged amino acid. On the opposite, the attachment of an aromatic phenyl ring is detrimental to the DNA interaction of the oxoazabenzo[*de*]anthracene moiety.

The binding of the compound showing the highest affinity for DNA, **4d**, was investigated further by absorption spectroscopy and surface plasmon resonance (SPR). The UV–visible titration spectra of **4d** with calf thymus DNA show both strong hypochromic and bathochromic effects (Figure 3a). The drug absorption bands centered at 282 and 393 nm are both strongly decreased upon addition of DNA, and a significant red shift (17 nm) occurs in the 400 nm band corresponding to the tetracyclic oxoazabenzoanthracene ring. SPR measurements were performed with a 20-mer hairpin oligonucleotide presenting the duplex sequence CGAATTCG. This oligonucleotide equipped with a biotin group at the 5′-end was immobilized on the sensor surface through streptavidin–biotin coupling. To provide a signal directly pro-

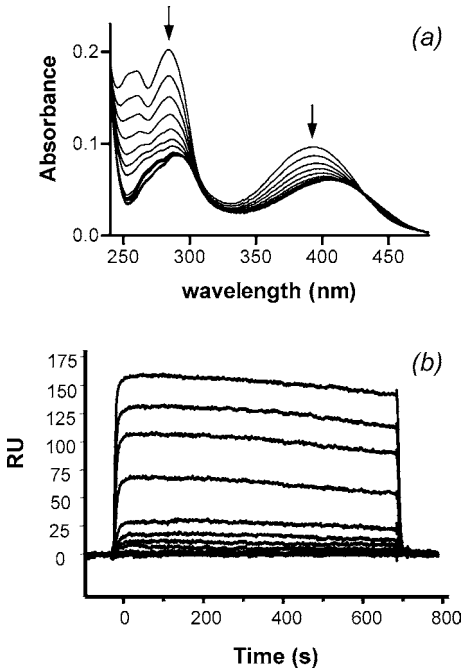

Figure 3. (a) DNA titration of **4d**. To 1 mL of drug solution at 20 μM were added aliquots of a concentrated calf thymus DNA solution. The phosphate-DNA/drug ratio increased from 0 to 20 (top to bottom curves, at 280 nm). Measurements were performed in BPE buffer pH 7.1 (6 mM Na_2HPO_4, 2 mM NaH_2PO_4, 1 mM Na_2EDTA). Spectra are referenced against DNA solutions of exactly the same DNA concentration and were adjusted to a common baseline. (b) SPR sensorgrams representing the binding of **4d** to the AATT hairpin oligonucleotide in HBS-EP buffer (BIA Certified from BIACORE, containing 0.01 M HEPES, 0.15 M NaCl, 3 mM EDTA, 0.005% polysorbate 20 (v/v), pH 7.4), at 25 °C. The concentration of the unbound ligand in the flow solution varies from 1 nM in the lowest curve to 10 μM in the top curve.

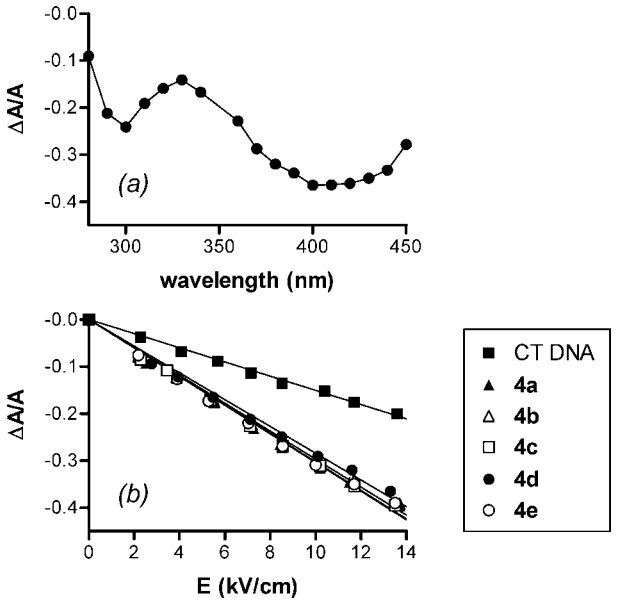

Figure 4. (a) Electric linear dichroism spectrum of the DNA-bound **4d**. $\Delta A/A$ was measured at 13.6 kV/cm, with a nucleotide/drug ratio of 25 (250 μM DNA, 10 μM drug). (b) Dependence of the reduced dichroism $\Delta A/A$ on the electric field strength for the different compounds bound to calf thymus DNA. Measurements were performed at 400 nm for the drug−DNA complexes and at 260 nm for the DNA alone. All measurements were performed at room temperature (20 °C) in 1 mM sodium cacodylate buffer, pH 7.0.

portional to the amount of bound compound, the reference response of an oligonucleotide-free blank cell was subtracted from the response in the channel with the target oligonucleotide. A set of SPR sensorgrams at different concentrations of **4d** binding to the CGAATTCG sequence is shown in Figure 3b. A concentration-dependent interaction was detected but the binding is very fast, and as a result, the kinetic parameters could not be measured. The association of the compound with the duplex oligonucleotide reaches a steady-state plateau in a few seconds. The dissociation of this cationic intercalating agent from DNA is also rapid and easily obtained just by injection of buffer solution. The binding affinity was measured from the steady-state SPR binding data. The plot or RU versus **4d** concentration (not shown) and the fitting of the binding results with a one site model gave a macroscopic binding constant of 1.56×10^6 M^{-1}. The difference with the binding constant determined by the fluorescence assay accounts for the higher ionic strength buffer used in the SPR experiments (HBS-EP buffer which contains 150 mM NaCl) compared to the fluorescence method (BPE buffer containing 16 mM NaCl).

Mode of Binding to DNA. Electric linear dichroism (ELD) experiments were performed to define the orientation of the compounds with respect to the DNA helix. In these experiments, the DNA is oriented in an electric field and the respective orientation of the molecules bound to DNA is probed using a linearly polarized light. The ELD spectrum of **4d** bound to calf thymus DNA is presented in Figure 4a. The reduced dichroism $\Delta A/A$ is negative in the drug absorption band. The 350−450 nm negative band reflects the orientation of the drug chromophore along the electric field. For each compound, we measured the reduced dichroism as a function of the electric field strength because the intensity of the ELD signal is a function of the degree of alignment of the DNA molecules in the electric field (Figure 4b). These measurements were performed in a low ionic strength buffer (1 mM Na cacodylate, as required for the ELD experiments due to the high electric field applied to the solution) at a high DNA−drug ratio (P/D = 25) to ensure that all drug molecules are bound to DNA. Strongly negative and equally intense signals were obtained with all compounds. There was no difference between the amino acid substitutions. The identical negative reduced dichroism values measured with the different compounds at 400 nm in the absorption band of the oxoazabenzoanthracene chromophore reflect a common orientation of the planar ring system perpendicular to the helix axis (or electric field direction), as expected for an intercalative binding. The higher $\Delta A/A$ values measured with the drug−DNA complexes compared to naked DNA most likely reflects drug-induced stiffening effects which would favor the orientation of the DNA molecules in the electric field. This phenomenon is commonly seen with intercalating agents (*22*, *23*).

We also used a DNA unwinding assay based on the relaxation of supercoiled plasmid DNA in the presence of topoisomerase I to compare the DNA binding properties of the amino acid conjugates. Supercoiled DNA was treated with topoisomerase I in the presence of increasing concentrations of the tested drugs. The DNA relaxation products were then resolved by agarose gel electrophoresis (Figure 5). Compound **4b** shows relatively small effect on the relaxation of DNA by topoisomerase I whereas the other compounds totally inhibit the relaxation of the DNA. Here again, the effect is more pronounced with **4d** compared to the other compounds (compare the 5 μM lanes in Figure 5). These results, showing that the compounds unwind closed circular duplex DNA, are

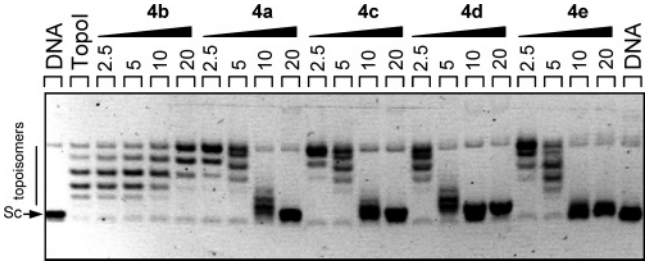

Figure 5. Effect of the compounds on the relaxation of plasmid DNA by human topoisomerase I. Native supercoiled DNA (0.2 μg) (lane DNA) was incubated with 3 units topoisomerase I in the absence (lane Topo I) or presence of the tested compounds at the indicated concentration (μM). Reactions were stopped with sodium dodecyl sulfate and treatment with proteinase K. DNA samples were separated by electrophoresis. The agarose gel was subsequently stained with ethidium bromide (1 μg/mL) and photographed under UV light. Sc, supercoiled DNA.

consistent with the intercalative binding mode. It is useful to mention at this point that the compounds affect topoisomerase I activity via DNA intercalation but they do not inhibit the catalytic activity of the enzyme. In parallel experiments (not shown), we observed that the drugs do not promote DNA cleavage by topoisomerases I or II. The intensity of the band corresponding to nicked DNA (for topoisomerase I) and linear DNA (for topoisomerase II) was not amplified in the presence of these oxoazabenzoanthracene derivatives.

Sequence Selectivity. The DNase I footprinting methodology was employed to compare the sequence selectivity of the compounds. Two DNA restriction fragments of 117- and 265-bp, both derived from the plasmid pBS, were prepared by 3′-end radiolabeling with ^{32}P. With each fragment, the products of digestion by DNase I in the absence and presence of the test drugs were resolved by polyacrylamide gel electrophoresis. Typical DNase I digestion patterns observed in the absence and presence of the tested compounds are illustrated in Figure 6. Significant differences between the control lanes and the drug-containing lanes can easily be seen. Well-resolved footprints are detected with **4d** and to a lower extent with the other compounds. The extent of DNase I protection is directly dependent to the affinity of the drug for DNA. The Phe derivative **4b** practically does alter the DNase I cleavage profiles. The Pro, Ala, and Gly derivatives appear to bind to the same type of sequences as the Lys analogue but with a reduced affinity. A typical example can be seen with the 117-bp

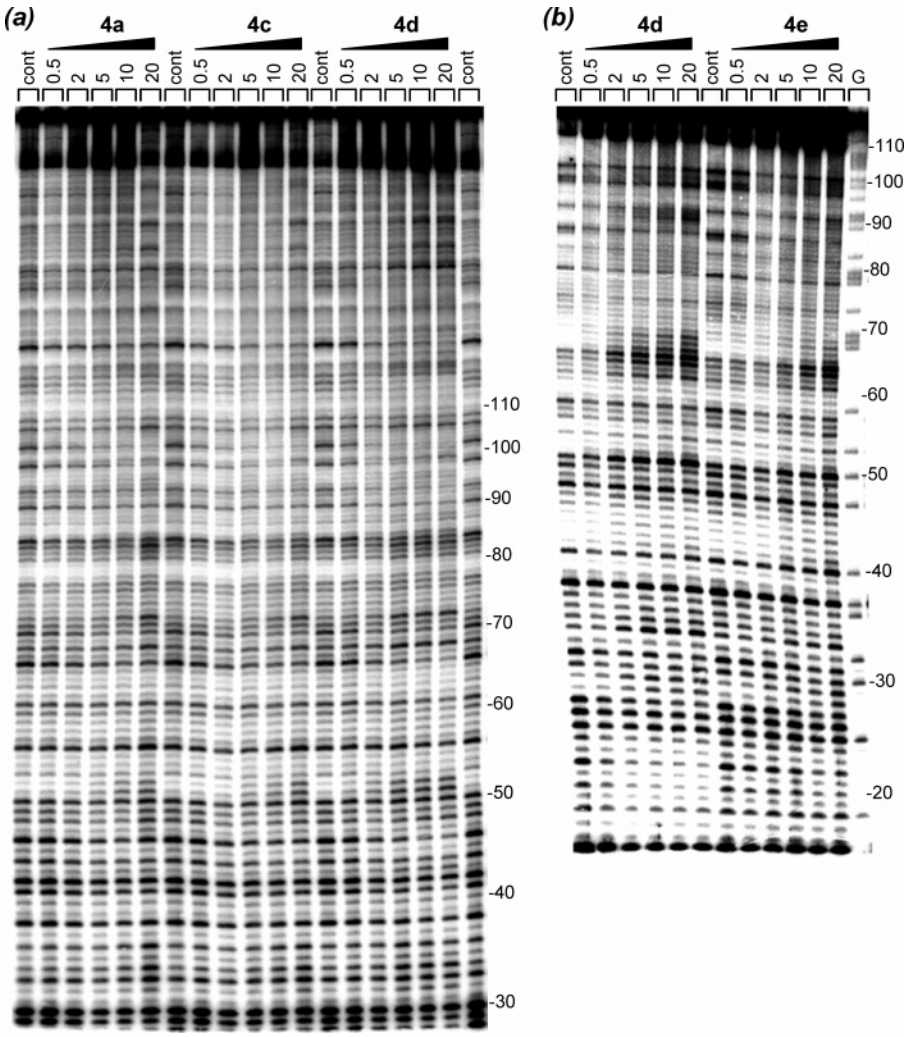

Figure 6. DNase I footprinting of the tested compounds on (a) the 265-bp and (b) the 117-bp *Eco*RI-*Pvu*II DNA restriction fragments from plasmid pBS. In both cases, the DNA was 3′-end labeled with [α-^{32}P]dATP in the presence of AMV reverse transcriptase. The products of nuclease digestion were resolved on 8% polyacrylamide gels containing 7 M urea. Control tracks (cont) contained no drug. The concentrations (μM) of the tested drug are shown at the top of the appropriate gel lanes. Tracks labeled "G" represent dimethyl sulfate−piperidine markers specific for guanines. Numbers on the right side of the gels refer to the standard numbering scheme for the nucleotide sequence of the DNA fragment.

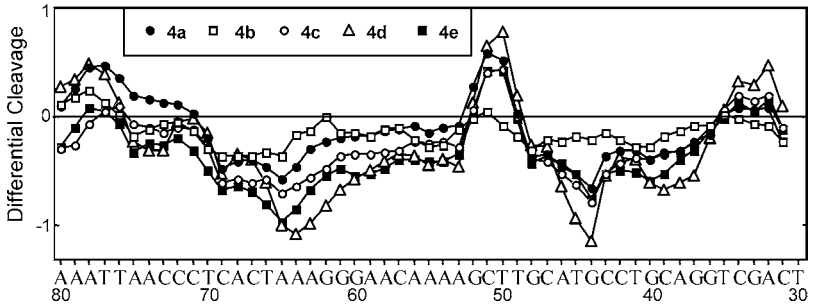

Figure 7. Differential cleavage plots showing the susceptibility of the 265bp fragment to DNase I cutting in the presence of the tested compound (10 μM each). Negative values correspond to a ligand-protected site and positive values represent enhanced cleavage. Vertical scales are in units of $\ln(f_a) - \ln(f_c)$, where f_a is the fractional cleavage at any bond in the presence of the drug and f_c is the fractional cleavage of the same bond in the control, given closely similar extents of overall digestion. Only the region of the restriction fragment analyzed by densitometry is shown.

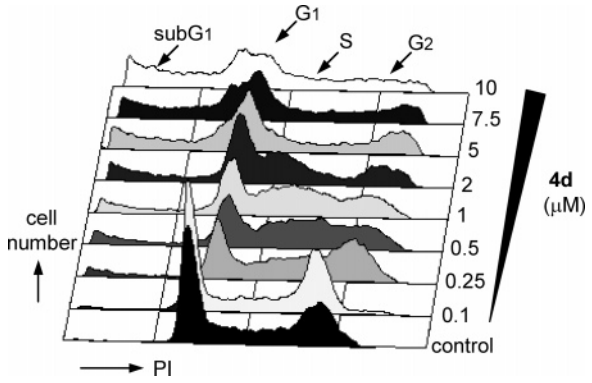

Figure 8. Cell cycle distribution determined by flow cytometry in CEM cells treated for 24 h with graded concentrations of **4d**. Cells were analyzed with the FACScan flow cytometer. Results show a typical experiment that has been repeated at least three times.

fragment where a solid footprint develops around nucleotide position 20 with **4d**, but there is almost nothing with **4e**. The difference between the two drugs is also clearly visible in terms of drug-induced enhanced DNase I cleavage, such as around position 64 where **4d** strongly promotes the activity of the enzyme, most likely as a result of intercalation-induced perturbation of the double helix structure (*24*). A densitometric analysis of the different patterns was performed to estimate the location and relative strength of binding at particular DNA sites. Figure 7 shows the differential cleavage plots for the 265-bp DNA fragment in the presence of the five compounds. The dips in these plots (negative values) indicate sites of protection from DNase I cleavage, whereas peaks (positive values) indicate regions of drug-induced enhancement of nuclease cleavage. The binding sites are broad and contain mixed sequences of AT and GC bp. Compound **4d** protects the sequences 5′-CTAAAGG and 5′-ATGC from DNase I cleavage. The recognized sequences are neither GC-rich nor do they contain exclusively AT bp. No clear preferential binding sequence could be deduced.

Cytotoxicity and Cell Cycle Effects. A tetrazolium-based assay was applied to determine the drug concentration required to inhibit the growth of CEM human

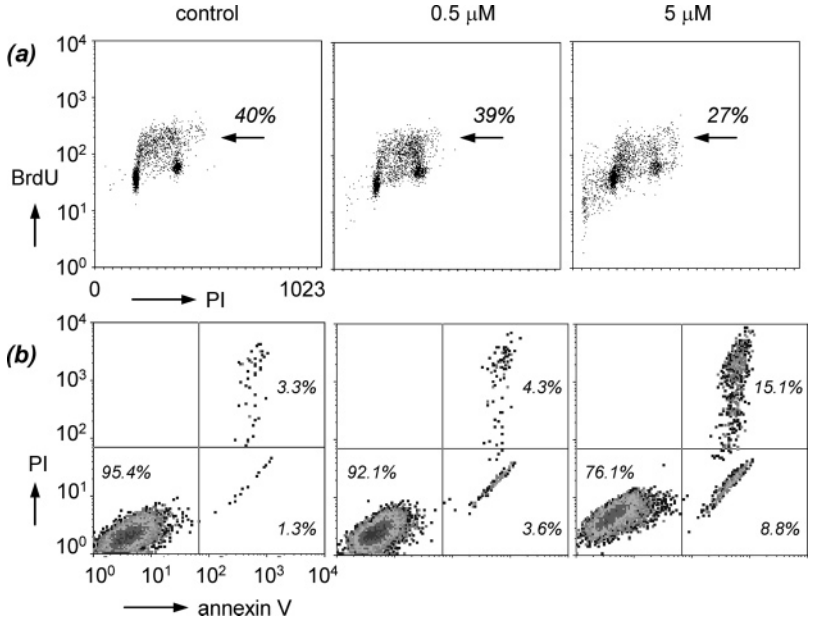

Figure 9. (a) Contour plots showing the reduction of bromodeoxyuridine incorporation in CEM cells treated with **4d**. Cells were treated for 24 h with the drug (0.5 or 5 μM) prior to labeling with the BrdU−FITC conjugate for 30 min and counterstained with propidium iodide (PI). In each case, the percentage of $BrdU^+$ cells is indicated. Drug-induced externalization of phosphatidylserine residues. CEM cells were treated with 0.5 or 5 μM **4d** for 24 h and then stained with propidium iodide (PI) and an annexin V-FITC conjugate specifically detecting the exposure of phosphatidylserine (PS) residues at the cell surface. Fluorescence intensities are shown as log scales. In each case, the percentage of annexin-V^+/IP^- cells (lower right square) and annexin-V^+/IP^+ cells (upper right square) is given (± 3%). Results show typical experiments that have been repeated twice.

leukemia cells by 50% (IC_{50}) after incubation in the culture medium for 72 h. Interestingly, the Lys derivative **4d** proved to be considerably, 20 to 40-times, more cytotoxic than the other amino acid derivatives (Table 1). This may be an indication that its superior affinity for DNA contributes to its enhanced cytotoxicity. Flow cytometric analysis of propidium iodide-labeled CEM cells revealed that **4d** induces a slight accumulation of cells in the G2/M phase at low concentrations and then in the S phase at higher concentrations, concomitant to a decrease of the G0/G1 cell population (Figure 7). The percentage of cells in the S phase increases from 22 to more than 40% upon treatment of the CEM cells with 1 μM **4d** for 24 h. The Phe derivative showed absolutely no effect on the cell cycle progression (not shown). To get a more precise view of the effect of **4d** at the S phase level, cells were labeled with bromodeoxyuridine (BrdU), a thymidine analogue which is incorporated into newly synthesized strands of DNA. As shown in Figure 9a, much fewer $BrdU^+$ cells, labeled in S-phase at the time of treatment, were detected after 24 h incubation with **4d** compared to the control cell population. The Lys derivative was the most potent compound in the series at inhibiting the incorporation of BrdU into DNA. The enhanced DNA binding capacity of **4d** likely accounts for the potent inhibition of DNA synthesis which is probably at the origin of the increased cytotoxicity of this Lys derivative.

Drug-Induced Apoptosis. During the cell cycle measurements, in parallel to the S block, a characteristic hypo-diploid DNA content peak (sub-G_1) was detected with **4d**. The effect is dose-dependent (Figure 8). The progressive generation of cells having a hypodiploid DNA content is usually characteristic of apoptosis and reflects fragmented DNA. These cell cycle analysis suggested that CEM leukemia cells accomplish apoptosis under treatment with **4d**. Therefore, to investigate further this question, we performed a biparametric cytofluorimetric analysis using propidium iodide and annexin V-FITC which stain DNA and phosphatidylserine (PS) residues, respectively. Annexin V is a Ca^{2+}-dependent phospholipid binding protein with high affinity for PS. After the drug treatment, CEM cells were labeled with these two dyes and washed, and the resulting red (PI) and green (FITC) fluorescence was monitored by flow cytometry. As indicated in Figure 9b, the percentage of annexin V positive cells slightly increased upon treatment with **4d**. At 5 μM, about 9% of the cells stained positively with annexin V, and this cell population characteristic of an early stage of apoptosis always remained <12% even with a higher drug concentration (data not shown). Rapidly, we detected the accumulation of cells doubly stained in green with annexin V and in red by PI corresponding to late stages of apoptosis and/or dead or necrotic cells. The loss of membrane asymmetry and the ensuing increased accessibility of PS residues to annexin V-FITC is a good criteria indicating that **4d** induces apoptosis but the effect is relatively modest and this compound can probably also cause cell death via a nonapoptotic pathway.

DISCUSSION

The oxoazabenzo[*de*]anthracene-amino acid conjugates reported here derive from a previous series of anthraquinone-amino acid conjugates endowed with potent cytotoxic activities and topoisomerase inhibitory properties. In an effort to enhance the cytotoxic activity of the molecules, it was hypothesized that the expansion of the planar chromophore could favor DNA binding and recognition and possibly promote the biological activity. This hypothesis was only partially validated. Indeed, it appears that the conversion of the anthraquinone nucleus into a tetracyclic oxa-aza-benzo[*de*]anthracene-fused ring system abolishes the capacity of the compounds to function as topoisomerase poisons. None of the compounds reported here efficiently stabilize topoisomerase−DNA covalent complexes, be it with topoisomerase I or topoisomerase II. However, the DNA binding properties and cytotoxic potential are preserved. The amino acid conjugates maintain DNA intercalation properties, and one compound in the series, the lysine derivative **4d**, appears to be a potent DNA binder and displays marked cytotoxic and pro-apoptotic activities. This cationic compound strongly binds to DNA, as evidenced by several spectroscopic techniques, forms intercalation complexes and preferentially recognized certain sequences. Nevertheless, the sequence selectivity is relatively modest, as it is generally the case with intercalating drugs. At the cellular level, **4d** inhibits DNA synthesis during the S phase of the cell cycle. This is potentially linked to its DNA binding properties. The compound shows submicromolar activity against the leukemia cell line. Although apoptotic cells have been identified upon treatment with **4d**, it seems that this compound can provoke cell death by different processes, not restricted to apoptosis. Compound **4d** is certainly a valid candidate for further pharmacological studies, with complementary tumor cell lines and in vivo tumor models.

The structure−activity relationships are relatively straightforward. The incorporation of a Lys amino acid with a cationic side chain strongly promotes DNA binding whereas the addition of a neutral amino acid results in a much weaker DNA interaction. The introduction of a hydrophobic amino acid appears to be detrimental to DNA interaction. Although this is not always the case (Phe derivative could favor DNA intercalation as well), it is common to observe that this type of relationship between compound hydrophobicity or charge and the DNA binding strength. More surprising is the positive relationship between DNA affinity and cytotoxicity. Compound **4d** has turned out to be a very cytotoxic compound, and the cell data (S phase arrest, inhibition of BrdU incorporation) suggest that the enhanced cytotoxicity is linked to the DNA binding activity. This is not so common. Apparently the cationic nature of the compound is not an obstacle for its cellular penetration. **4d** is over 20 times more cytotoxic than the other amino acid conjugates. It will therefore be interesting to pursue the synthesis of other cationic oxoazabenzo[*de*]anthracene conjugates equipped with other basic amino acids (e.g. arginine) or polyamine side chains, to exploit the polyamine transport system that is frequently overexpressed in tumor cells (*25*−*29*). The design of drugs linked to Lys-containing di- and tripeptides is also considered. In the past, we also successfully elaborated peptide−intercalator conjugates encompassing one or two Ser-Pro-Lys-Lys (SPKK) motifs (*30*−*32*). The same motif could also be adequate to optimize the activity of the oxoazabenzo[*de*]anthracene ring system. The molecule **4d** provides interesting opportunities to develop novel DNA-targeted anticancer agents.

ACKNOWLEDGMENT

This work was supported by grants (to C.B.) from the Ligue Nationale Contre le Cancer (Comité du Nord) and the Institut de Recherches sur le Cancer de Lille (IRCL). N.D. is the recipient of a fellowship from the Ligue Nationale Contre le Cancer. Support by the "Ac-

tions intégrées Franco-Belge, Program Tournesol" is acknowledged.

LITERATURE CITED

(1) Pommier, Y. (1998) Diversity of DNA topoisomerase I and inhibitors. *Biochimie 80*, 255−270.
(2) Bailly, C. (2000) Topoisomerase I poisons and suppressors as anticancer drugs. *Curr. Med. Chem. 7*, 39−58.
(3) Denny, W. A. (2004) Emerging DNA topoisomerase inhibitors as anticancer drugs. *Expert Opin. Emerg. Drugs 9*, 105−133.
(4) Pommier, Y., Pourquier, P., Fan, Y., and Strumberg, D. (1998) Mechanism of action of eukaryotic DNA topoisomerase I and drugs targeted to the enzyme. *Biochim. Biophys. Acta 1400*, 83−106.
(5) Burden, D. A., and Osheroff, N. (1988) Mechanism of action of eukaryotic topoisomerase II and drugs targeted to the enzyme. *Biochim. Biophys. Acta 1400*, 139−154.
(6) Larsen, A. K., and Skladonowski, A. (1998) Cellular resistance to topoisomerase-targeted drugs: from drug uptake to cell death. *Biochim. Biophys. Acta 1400*, 257−274.
(7) Willmore, E., Frank, A. J., Padget, K., Tilbey, M. J., and Austin, C. A. (1998) Etoposide targets topoisomerase II alpha and II beta in leukemic cells: isoform-specific cleavable complexes visualized and quantified in situ by a novel immunofluorescence technique. *Mol. Pharmacol. 53*, 78−85.
(8) Gilmour, P. S., Austin, C. A., Lowe, G., Turnbull, A., and Mincher, D. J. (1998) Biochemistry of topoisomerase II-alpha and II-beta inhibition by novel anthraquinone-peptide conjugates: Design of isoform-specific agents. *Ann. Oncol. 9*, 236.
(9) Mincher, D. J., and Turnbull, A. (2004) European Patent Specification EP1087935B1 [WO1999/065866]. Anthracene derivatives as anti-cancer agents.
(10) Bridewell, D. J., Finlay, G. J., and Baguley, B. C. (2001) Topoisomerase I/II selectivity among derivatives of N-[2-(dimethylamino)ethyl]acridine-4-carboxamide (DACA). *Anti-Cancer Drug Des. 16*, 317−324.
(11) Bu, X., Deady, L. W., Finlay, G. J., Baguley, B. C., and Denny, W. A. (2001) Synthesis and cytotoxic activity of 7-oxo-7H-dibenz[f,ij]isoquinoline and 7-oxo-7*H*-benzo[*e*]perimidine derivatives. *J. Med. Chem. 44*, 2004−2014.
(12) Tkaczyk-Gobis, K., Tarasiuk, J., Seksek, O., Stefanska, B., Borowski, E., and Garnier-Suillerot, A. (2001) Transport of new non-cross-resistant antitumor compounds of the benzoperimidine family in multidrug resistant cells. *Eur. J. Pharmacol. 413*, 131−141.
(13) Matsuoka, M., Makino, Y., Yoshida, K., and Kitao, T. (1980) A novel 2-amination of quinizarin promoted by copper ions. *Dyes Pigments 1*, 27−37.
(14) Matsuoka, M., Takei, T., Nakamura, I., Yoshida, K., and Kitao, T. (1981) A novel ring-closure reaction between 1,4-dihydroxyanthraquinone and diamines promoted by copper ions. *Bull. Soc. Chem. Jpn. 54*, 2735−2738.
(15) Baguley, B. C., Denny, W. A., Atwell, G. J., and Cain, B. F. (1981) Potential antitumor agent. 34. Quantitative relationships between DNA binding and molecular structure for 9-anilino-acridines substituted in the anilino ring. *J. Med. Chem. 24*, 170−177.
(16) Pavlov, V., Kong Thoo Lin, P., and Rodilla, V. (2001) Cytotoxicity, DNA binding and localisation of novel bis-naphthalimidopropyl polyamine derivatives. *Chem. Biol. Interact. 137*, 15−24.
(17) Carrasco, C., Facompré, M., Chisholm, J. D., Van Vranken, D. L., Wilson, W. D., and Bailly, C. (2002) DNA sequence recognition by the indolocarbazole antitumor antibiotic AT2433-B1 and its diastereoisomer. *Nucleic Acids Res. 30*, 1774−1781.
(18) Carrasco, C., Vezin, H., Wilson, W. D., Ren, J., Chaires, J. B., and Bailly, C. (2002) DNA binding properties of the indolocarbazole antitumor drug NB-506. *Anti-Cancer Drug Des. 16*, 99−107.
(19) Colson, P., Bailly, C., and Houssier, C. (1996) Electric linear dichroism as a new tool to study sequence preference in drug binding to DNA. *Biophys. Chem. 58*, 125−140.
(20) Bailly, C. (2001) DNA relaxation and cleavage assays to study topoisomerase I inhibitors. *Methods Enzymol. 340*, 610−623.
(21) Bailly, C., Kluza, J., Martin, C., Ellis, T., and Waring, M. J. (2004) DNase I footprinting of small molecule binding sites on DNA. In *Methods in Molecular Biology*, *vol. 288 Oligonucleotide Synthesis: Methods and Applications* (Herdewijn, P., Ed.) pp 319−342, Humana Press Inc., Totowa, NJ.
(22) Bonjean, K., De Pauw-Gillet, M.-C., Defresne, M.-P., Colson, P., Houssier, C., Dassonneville, L., Bailly, C., Greimers, R., Wright, C., Quetin-Leclercq, J., Tits, M., and Angenot, L. (1998) The DNA intercalating alkaloid cryptolepine interferes with topoisomerase II and inhibits primarily DNA synthesis in B16 melanoma cells. *Biochemistry 37*, 5136−5146.
(23) Bailly, C., Laine, W., Baldeyrou, B., De Pauw-Gillet, M.-C., Colson, P., Houssier, C., Cimanga, K., Van Miert, S., Vlietinck, A. J., and Pieters, L. (2000) DNA intercalation, topoisomerase II inhibition and cytotoxic activity of the plant alkaloid neocryptolepine. *Anti-Cancer Drug Des. 15*, 191−201.
(24) Fox, K. R., and Waring, M. J. (2001) High-resolution footprinting studies of drug−DNA complexes using chemical and enzymic probes. *Methods Enzymol. 340*, 412−430.
(25) Gardner, R. A., Delcros, J. G., Konate, F., Breitbeil, F., 3rd, Martin, B., Sigman, M., Huang, M., and Phanstiel, O., IV (2004) N1-substituent effects in the selective delivery of polyamine conjugates into cells containing active polyamine transporters. *J. Med. Chem. 47*, 6055−6069.
(26) Wang, L., Price, H. L., Juusola, J., Kline, M., and Phanstiel, O., IV (2001) Influence of polyamine architecture on the transport and topoisomerase II inhibitory properties of polyamine DNA−intercalator conjugates. *J. Med. Chem. 44*, 3682−3691.
(27) Wang, C., Delcros, J. G., Biggerstaff, J., and Phanstiel, O., IV (2003) Molecular requirements for targeting the polyamine transport system. Synthesis and biological evaluation of polyamine−anthracene conjugates. *J. Med. Chem. 46*, 2672−2682.
(28) Wang, C., Delcros, J. G., Biggerstaff, J., and Phanstiel, O., IV (2003) Synthesis and biological evaluation of N1-(anthracen-9-ylmethyl)triamines as molecular recognition elements for the polyamine transporter. *J. Med. Chem. 46*, 2663−2671.
(29) Phanstiel, O., IV, Price, H. L., Wang, L., Juusola, J., Kline, M., and Shah, S. M. (2000) The effect of polyamine homologation on the transport and cytotoxicity properties of polyamine−(DNA−intercalator) conjugates. *J. Org. Chem. 65*, 5590−5599.
(30) Bailly, F., Bailly, C., Waring, M. J., and Henichart, J. P. (1992) Selective binding to AT sequences in DNA by an acridine-linked peptide containing the SPKK motif. *Biochem. Biophys. Res. Commun. 184*, 930−937.
(31) Bailly, F., Bailly, C., Nehbecque, N., Pommery, N., Colson, P., Houssier, C., and Henichart, J. P. (1992) Relationship between DNA-binding and biological activity of anilinoacridine derivatives containing the nucleic acid-binding unit SPKK. *Anti-Cancer Drug Des. 7*, 83−100.
(32) Flock, S., Bailly, F., Bailly, C., Waring, M. J., Hénichart, J. P., Colson, P., and Houssier, C. (1994) Interaction of two peptide-acridine conjugates containing the SPKK peptide motif with DNA and chromatin. *J. Biomol. Struct. Dyn. 11*, 881−900.

BC050065X

Arginine-Rich Peptide Conjugation to Morpholino Oligomers: Effects on Antisense Activity and Specificity

Michelle H. Nelson, David A. Stein, Andrew D. Kroeker, Susie A. Hatlevig, Patrick L. Iversen, and Hong M. Moulton*

AVI BioPharma, Inc., Corvallis, Oregon 97333. Received April 3, 2005; Revised Manuscript Received June 9, 2005

Noncharged antisense compounds, such as phosphorodiamidate morpholino oligomers (PMOs), do not readily enter mammalian cells in culture. A simple and effective means for cellular delivery of PMOs is through their conjugation to arginine-rich peptides. Understanding the effect of peptide conjugation on the efficacy, toxicity, and specificity of PMOs is important to the successful application of this antisense delivery method. We investigated the effects of conjugation of arginine-rich peptides to PMO on the thermal stability, efficacy and specificity for targeted RNA of the resulting compound. In vitro translation assays showed that (1) R9F2−PMO generated antisense activity 3−25-fold higher than corresponding nonconjugated PMO, (2) the level of antisense activity enhancement by R9F2−PMO over a corresponding nonconjugated PMO is related to the GC content of the PMO sequence, (3) R9F2 conjugation reduced the minimum length of a PMO required to inactivate a target RNA from 20 bases to 14 bases, and (4) nonspecific effects of R9F2−PMO occur at lower concentrations than corresponding PMO alone. Thermal stability of heteroduplexes of PMO and complementary RNA were increased by conjugation of PMO to R9F2 peptide, likely accounting for the increased specific antisense activity of conjugated over nonconjugated PMO. A cell-culture based assay demonstrated that while conjugation to unnatural peptides increased PMO efficacy without causing nonspecificity at concentrations ≤10 μM, only L-peptide conjugation retained high specificity at higher concentrations. This study demonstrates that conjugation of PMO to an arginine-rich peptide generally increases the binding affinity of the PMO to complementary RNA and increases its antisense potency. Additionally, it is shown that the enzymatic stability of an L- or unnatural peptide used for PMO conjugation affects the antisense properties of the resulting compound.

INTRODUCTION

Antisense compounds can be powerful reagents for the exploration of gene function and have potential for therapeutic applications. The efficacy of an antisense compound depends on its biological stability, delivery to intracellular targets, binding affinity with target nucleic acids, and sequence specificity. Phosphorodiamidate morpholino oligomers (PMOs) (*1*, *2*) are a modified structural type, an oligonucleotide mimic with morpholine rings replacing the deoxyribose of DNA coupled by nonionic intersubunit linkages (Figure 1). This noncharged backbone structure is resistant to enzymatic degradation (*3*, *4*) and has higher RNA binding affinity than DNA (*5*). In eukaryotic cells, PMO can work as a translational or RNA splicing blocker or both by base-pairing to complementary target RNA and sterically blocking access of other biomolecules to a target sequence (*2*, *6*).

We have previously reported the successful delivery of PMOs by short arginine-rich peptides (ARPs) such as HIV Tat and R9F2, resulting in the correction of the pre-mRNA missplicing of mutant human β-globin (*7*, *8*) and inhibition of the replication of coronaviruses (*9*, *10*) and several flaviviruses (*11*, *12*) in cell culture. Successful ARP-mediated intracellular delivery of a PMO requires covalent conjugation, rather than merely the simultaneous presence of PMO and ARP in the cell culture media

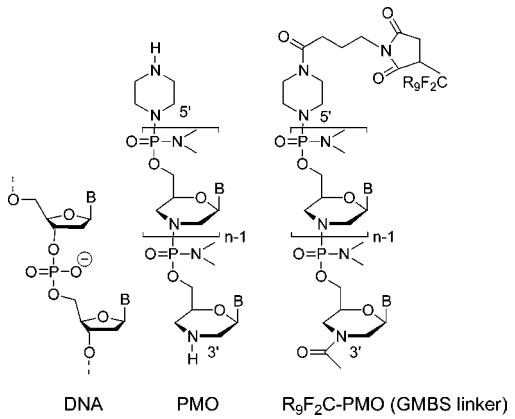

Figure 1. Structure of DNA, PMO, and R9F2C−PMO (PPMO) conjugate.

(*8*). Important issues in the development of this PMO delivery system, for both research and therapeutic applications, include understanding the influences that ARP conjugation has on the antisense efficacy, cytotoxicity and target specificity of the PMO. This will facilitate the design of peptide sequences, selection of amino acids, and conjugation chemistry, as well as interpretation of "gene-knockdown" experimental data. In this study, we investigated the following: (1) the effect of conjugation of PMO to an ARP, R9F2 on antisense activity and specificity in both in vitro translation and cell culture assays, (2) the effect of enzymatic stability of a conjugated ARP on antisense efficacy and specificity of a PMO, and

* Corresponding author. Mailing address: AVI BioPharma, Inc., 4575 SW Research Way, Suite 200, Corvallis, OR 97333. Phone: (541) 753-3635. Fax: (541) 754-3545. E-mail: moulton@avibio.com.

10.1021/bc0501045 CCC: $30.25 © 2005 American Chemical Society
Published on Web 07/02/2005

Table 1. Nomenclature and Sequences of Peptides and PMOs

Peptides[a]

name	sequence
R9F2	NH_2-RRRRRRRRRFFC-$CONH_2$
RXR	NH_2-$(RXR)_4$C-$CONH_2$[b]
D-R9F2	NH_2-RRRRRRRRRFFC-$CONH_2$ (D-isomer)

Morpholino Oligomers[c]

name	sequence	% GC
PMO_{CMYC}	ACG TTG AGG GGC ATC GTC GC	65
$PMO_{CMYC(I)}$	ACG TTG AII IGC ATC GTC GC	50
PMO_{WNV}	CTT AGA CAT CGA GAT CTT CGT G	45
PMO_{3A2}	AGC TGA AAG CAG GTC CAT CC	55
PMO_{HCV}	GGC CTT TCG CGA CCC AAC AC	65
$PMO_{705(20mer)}$	CCT CTT ACC TCA GTT ACA AT	40
PMO_{705}	CCT CTT ACC TCA GTT ACA	44
$PMO_{705-2MM}$	CCT CTT A**A**C TC**C** GTT ACA	44
$PMO_{705-4MM}$	CCT **A**TT A**A**C TC**C** GTT **C**CA	44
$PMO_{705-SCR}$	CTC TCT CAC CAT TGA CAT	44
PMO_{Ran1}	TCA GTA GTC TAC TGA CGT C	47
PMO_{Ran2}	AGT CTC GAC TTG CTA CCT CA	50
PMO_{IHNVL}	GGA GTC CCA TCT TTC TGT GAT G	50

[a] The sequences of peptides are written using the standard one letter amino acid symbols from N to C terminus. [b] X = 6-aminohexanoic acid. [c] PMO sequences are written in standard orientation from 5′- to 3′-end. Mismatched bases are boldface.

(3) the effect of the R9F2 peptide conjugation on the thermal stability of PMO/RNA heteroduplexes.

EXPERIMENTAL PROCEDURES

Peptides, PMOs, and Peptide−PMO Conjugates. The nomenclature and sequences of ARPs and PMOs are listed in Table 1. PMOs or fluorescein-tagged PMOs were synthesized at AVI BioPharma as described elsewhere (*1*, *7*, *13*). R9F2 and RXR peptides were synthesized at AVI BioPharma and the D-R9F2 peptide was synthesized by Global Peptide Services (Ft. Collins, CO). The purity of all peptides was >90%. The conjugation, purification and analysis of peptide−PMO conjugates were carried out as described previously (*7*, *8*). Each peptide was conjugated to the 5′-end of a PMO through the GMBS (*N*-[γ-maleimidobutyryloxy]succinimide ester) linker (Pierce, Rockford, IL) unless otherwise specified. The specific gene target of a PMO is written as a subscript. For example, PMO targeted to the human c-*myc* gene is designated as PMO_{CMYC}. The R9F2, RXR, or D-R9F2 peptide conjugated PMOs are designated as PPMO, (RXR)PMO, or D-PPMO, respectively. The chemical structures of PMOs and PPMOs are shown in Figure 1.

In Vitro Translation Assays. The coding sequence for firefly luciferase was subcloned into the multiple cloning site of plasmid pCiNeo (Promega, Madison, WI) at the *Sal*I and *Not*I sites. Subsequently, complementary oligonucleotides of sequences identical to those in West Nile virus (WNV), the cytochrome P450 3A2, a three-nucleotide mutant P450 3A2, human c-*myc*, or a segment of IRES sequence from hepatitis C virus (HCV) were duplexed and subcloned into the *Nhe*I and *Sal*I sites. The WNV leader sequence replaces the start codon of the luciferase gene with sequence encoding bases −29 to +16 relative to the A of the AUG translation initiation codon of the WNV polyprotein gene (bases 68−113, Genbank accession no. AF196835), including the complete −13 to +9 target site for the WNV PMO. The CYP3A2 leader sequence replaces the start codon of the luciferase gene with sequence encoding bases −31 to +16 relative to the A of the AUG translation initiation codon of the rat CYP3A2 gene (bases 43−90, Genbank accession no. U09724), including the complete −2 to +18 target site for the CYP3A2 PMO. The CYP3A2/3MP leader sequence is identical to the CYP3A2 leader except three guanine bases are replaced with three thymine bases. Relative to the A of the ATG, these thymine bases are −2, +4, and +9. The c-*myc* leader sequence replaces the start codon of the luciferase gene with sequence encoding bases −14 to +14 relative to the A of the AUG translation initiation codon of the c-*myc* gene (bases 4053−4081, Genbank accession no. AY214166), including the complete −6 to +14 target site for the c-*myc* PMO. The HCV IRES leader sequence includes bases 249−287 (Genbank accession no. NC_004102) of the HCV genome. The translational start site of luciferase is functional in this construct, and the sequence includes the complete target site of the HCV IRES PMO.

RNA was produced from these plasmids (pCN(WNV)-luc, pCN(3A2)luc, pCN(3A2/3MP)luc, pCN(myc)luc, and pCN(HCV−IRES)luc) after linearization with *Not*I, using the T7 polymerase-based MEGAscript kit and protocol (Ambion, Austin, TX). In vitro translations were carried out using transcribed RNA at a final concentration of 1 nM in each reaction with 12 μL of nuclease-treated rabbit reticulocyte lysate (Promega) and either PMO or water. After 1 h of incubation at 37 °C followed by 15 min at room temperature, 10 μL of the translation reaction mixture was combined with 50 μL of luciferase assay reagent (Promega) according to the manufacturer's instructions. Light emission was read on an FLx800 microplate luminometer (Bio-tek, Winooski, VT). Reactions were assayed for relative light units with the KC Junior program (Bio-tek) by using the luminescence function with a sensitivity setting of 125. Twelve reactions were assayed at one time, including water control reactions in the first and last wells of each row. The relative light units produced by each reaction were normalized to the mean of all control reactions and expressed as percent inhibition of luciferase translation. IC_{50}'s, the concentrations resulting in 50% inhibition, were derived from inhibition curves using GraphPad Prism 4.0 software (San Diego, CA).

Cell Culture Assay. The HeLa pLuc 705 (*8*, *14*) cell line (Gene Tools, Philomath, OR) was cultured in RPMI 1640 supplemented with 2 mM L-glutamine, 100 μg/mL streptomycin, 100 U/ml penicillin, and 10% fetal bovine serum (FBS) (Hyclone, Ogden, UT). The correction of pre-mRNA missplicing was carried out as described previously (*8*).

Thermal Stability. Thermal stability of a PMO hybridized to its complementary RNA target sequence was determined as described previously (*15*) with the following modifications. The PMO and the RNA were each present at a concentration of 2.5 μM. The solution was heated to 95 °C (with the exception of 100 °C for the PMO_{CMYC}/RNA and $PPMO_{CMYC}$/RNA samples) and cooled to 25 °C at a rate of 0.2 °C/min in a Cary 1 UV−vis spectrometer with a temperature controller (Varian, Mulgrave, Victoria, Australia). The absorbance was recorded at 260 nm. The T_m value was taken as the maximum of the first derivative of the absorbance vs temperature plot using Cary WinUV software (Varian).

Enzymatic Stability of Conjugates. PMO_{705} conjugated to R9F2, (RXR)R9F2, or D-R9F2 (each at 61 μM) and 10 units of proteinase K (Sigma, St. Louis, MO) were incubated in 100 μL of reaction buffer (50mM Tris-HCl, 5mM CaCl, pH 7.4) for 5 min at 37 °C. The reaction was stopped by placing the tube in crushed dry ice and then storing at −80 °C until analysis by matrix-assisted laser desorption ionization time-of-flight mass spectrometry

(MALDI TOF MS). Intracellular stability of a conjugate was determined as described below. The culture media was removed from about 50% confluent HeLa pLuc 705 cells in a T-175 flask and replaced with 20 mL of fresh medium containing 10 μM of a conjugate. Cells were treated for 24 h. The treatment medium was removed, and the cells were washed with 20 mL of PBS, trypsinized with 7 mL of trypsin for 7 min at 37 °C, and neutralized with 18 mL of FBS-containing medium. The suspension was pelleted, washed with 500 μL of PBS, then pelleted and resuspended in 200 μL of ice-cold water containing protease inhibitor cocktail (Roche Diagnostics). Each sample was then subjected to three freeze−thaw cycles with a crushed dry ice/ethanol bath and a room-temperature water bath. Ice-cold acetonitrile (600 μL) was then added to precipitate cellular proteins and debris. Samples were placed on ice for 15 min and then centrifuged for 5 min at 5000*g*. The supernatant was lyophilized. Each sample was brought up in 25 μL of water and analyzed by MALDI TOF MS.

Data Process and Statistical Analysis. Data were plotted and analyzed using GraphPad Prism 4.0 software (GraphPad Software, San Diego, CA).

RESULTS

R9F2 Conjugated PMO Is More Potent Than Corresponding PMO in an In Vitro Translation Assay. Inhibition of targeted gene expression by PMO and PPMO was determined by cell-free in vitro translation assays using rabbit reticulocyte lysates. In each case the PMO was complementary to targeted RNA produced by in vitro transcription from chimeric plasmids containing the luciferase reporter gene fused downstream from sequence of human c-*myc* (c-*myc*), the rat cytochrome P450 3A2 (3A2), hepatitis C virus (HCV), or West Nile virus (WNV). Figure 2A−D represents the antisense activity of five PMO and six PPMO against their respective RNA targets at various concentrations. The five PMO used were PMO_{CMYC}, $PMO_{CMYC(I)}$, PMO_{HCV}, PMO_{3A2}, and PMO_{WNV}. The six PPMO used in this study included the five PMO described above conjugated to R9F2 at their 5′-ends and $PMO_{CMYC(I)}$ with R9F2 conjugated at its 3′-end (3′-$PPMO_{CMYC(I)}$). The antisense activity of PMO or PPMO is represented as the percent inhibition of luciferase reporter relative to a vehicle control versus concentrations. In each graph of Figure 2, a log dose versus response curve of PMO was compared to that of the corresponding PPMO in inhibition of target RNA c-*myc* (Figure 2A), HCV (Figure 2B), 3A2 (Figure 2C), and WNV (Figure 2D).

Concentration-dependent inhibition was observed for all PMO and PPMO against complementary targets. The concentration required to achieve 50% inhibition of target/reporter expression (IC_{50}) was used to quantitatively compare the effectiveness of PPMO to PMO. In each case (except c-*myc*), the PPMO was more efficacious than its corresponding PMO, as reflected by a lower IC_{50} value (Figure 2E). However, the magnitude of difference in inhibitory activity between a PMO and its corresponding PPMO varied among PMO sequences. The efficacies were essentially the same for $PPMO_{CMYC}$ and PMO_{CMYC} (IC_{50} at 46 and 50 nM, respectively), 3-fold higher for $PPMO_{HCV}$ compared to PMO_{HCV} (IC_{50} at 38 and 106 nM, respectively), 7-fold higher for $PPMO_{3A2}$ than PMO_{3A2} (IC_{50} at 21 and 140 nM, respectively), and 25-fold higher for $PPMO_{WNV}$ than PMO_{WNV} (IC_{50} at 40 and 1011 nM, respectively) (Figure 2E).

We hypothesized that ARP conjugation would provide a greater activity enhancement for a PMO with lower

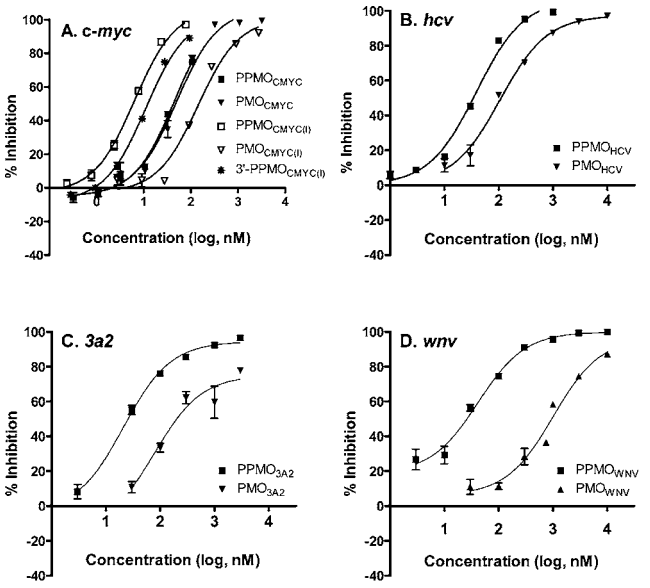

E. IC_{50}(nM)

RNA Target	PPMO	PMO	PPMO(I)	PMO(I)	3′-PPMO(I)
c-*myc*	46	50	7	143	10
hcv	38	106	ND	ND	ND
3a2	21	140	ND	ND	ND
wnv	40	1011	ND	ND	ND

Figure 2. In vitro translation assays show that an R9F2-conjugated PMO is more potent than the corresponding PMO. Chimeric RNAs containing the coding sequence of luciferase fused downstream from the sequence from c-*myc* (A), HCV (B), 3A2 (C), or WNV (D) were used to program rabbit reticulocyte lysate in vitro translation reactions. Each graph shows the relationship between the log concentrations of PPMO or PMO and antisense activity, represented as % inhibition of the reporter luciferase compared to a vehicle-only control. Each data point was an average ± the range of means of two independent experiments each consisting of triplicate samples. The data were also represented as IC_{50} (E), the compound concentration required for 50% inhibition. $PMO_{CMYC(I)}$ contained three inosines, replacing three guanines in the PMO_{CMYC} sequence. 3′-$PPMO_{CMYC(I)}$ is a $PMO_{CYMC(I)}$ with the R9F2 peptide conjugated to its 3′-end. All other PPMOs had R9F2 peptide conjugated to the 5′-end.

RNA binding affinity. To specifically test this, the RNA binding affinity of PMO_{CMYC} was purposely reduced by replacing the three guanine (G) bases at positions 8, 9, and 10 with three inosines (I) bases. The inosine-substituted PMO_{CMYC}, either without ($PMO_{CMYC(I)}$) or with the peptide conjugation ($PPMO_{CMYC(I)}$), was compared to nonsubstituted PMO_{CMYC} in inhibition of c-*myc*−luciferase expression (Figure 2A). The replacement of G with I increased the IC_{50} of PMO_{CMYC} from 50 to 143 nM (Figure 2E). Conjugation of the R9F2 peptide to the 5′- or 3′-end of $PMO_{CMYC(I)}$ lowered the IC_{50} value of $PMO_{CMYC(I)}$ from 143 nM to 7 or 10 nM, respectively (Figure 2E).

Conjugation to the R9F2 Peptide Reduces the Minimum Inactivating Length of PMO. Having shown that a PPMO generally has greater antisense activity than the corresponding PMO, we investigated whether R9F2 peptide conjugation would allow a decrease in the length of the PMO necessary to attain a given IC_{50}. Several truncated PMO_{3A2} (Table 2B) and the corresponding PPMO were tested against the 3A2 leader−luciferase RNA in the in vitro translation assay. These PMO/PPMO had 18, 16, 14, and 12 bases, derived by removing one, two, three, and four bases, respectively, from each end of the 20 base starting PMO_{3A2}/$PPMO_{3A2}$

Table 2. Conjugation of R9F2 Peptide Reduces the Minimum Inactivating Length of PMO:[a] (A) Data Are Represented as IC_{50};[b] (B) Sequence Alignment of PMO_{3A2} with 20, 18, 16, 14, and 12 Bases

A

	perfectly matched RNA IC_{50} (nM)		three-mismatched RNA[c] IC_{50} (nM)	
PMO length	PMO_{3A2}	$PPMO_{3A2}$	PMO_{3A2}	$PPMO_{3A2}$
20	140	21	>3000	630
18	430	61	>3000	1000
16	3000	83	>3000	550
14	3000	97	>3000	510
12	>3000	280	>3000	1000

B

AGCTGAAAGCAGGTCCATCC	20mer
GCTGAAAGCAGGTCCATC	18mer
CTGAAAGCAGGTCCAT	16mer
TGAAAGCAGGTCCA	14mer
GAAAGCAGGTCC	12mer

[a] PMO or PPMO of different lengths targeted to 3A2 RNA were assayed for inhibition of luciferase reporter expression in two in vitro translation assays. The chimeric RNA contained the luciferase gene fused downstream from either the targeted sequence of CYP3A2 or the targeted sequence of CYP3A2 with three mutations. [b] Each IC_{50} was obtained from a dose/response curve constructed using the data from two independent experiments each consisting of triplicate samples. [c] Sequences of perfectly matched RNA (GGATGGACCTGCTTTCAGCT) and 3-mismatched RNA with mismatched bases boldface (**T**GATG**T**ACCT**T**CTTTCAGCT).

(Table 2B). As the IC_{50} values show in Table 2A, PMO became markedly less inhibitory as its length decreased. The IC_{50} value for the 14mer PMO_{3A2} was ≥15-fold greater than the 20mer PMO_{3A2} (3000 and 140 nM, respectively). However, shortening the PMO length had less effect on PPMO with IC_{50} values increasing by only 5-fold for the 14mer $PPMO_{3A2}$ compared to the 20mer $PPMO_{3A2}$ (97 and 21 nM, respectively). The 14mer $PPMO_{3A2}$ had an inhibition curve nearly identical to the 20mer PMO_{3A2} (data not shown), indicating that conjugation to the R9F2 peptide shortened the PMO_{3A2} length requirement by six bases to attain the IC_{50} of the nonconjugated PMO.

Shortening PMO Length Does Not Increase Nonspecificity of PPMO. The panel of various lengths of 3A2 PMO and corresponding PPMO was assayed against the $3A2_{3MM}$−luciferase RNA to determine the effect of the R9F2 peptide on the specificity of each of these PMO sequences. $3A2_{3MM}$ RNA had three mismatched bases in relation to the PMO_{3A2} sequence (Table 2). None of the nonconjugated PMO_{3A2}, at concentrations up to 3000 nM, inhibited the expression of three-mismatched RNA, while the corresponding PPMO generated IC_{50} values between 500 and 1000 nM (Table 2). However, unlike the results from the perfectly matched 3A2 RNA, which generated increasing IC_{50} values with decreasing PMO length, the IC_{50} of PPMO tested against mismatched RNA did not depend on PMO length. PPMO caused a similar degree of nonspecificity regardless of the length of the PMO component, suggesting that the observed nonspecific inhibition was entirely dependent on the molar concentration of R9F2 present.

PPMOs Have Greater Off-Target Effects Than PMOs. The target specificity of a PMO compared to its corresponding PPMO was assessed by comparing inhibitions of nontarget RNAs in three in vitro translation assays. The HCV−, 3A2−, and WNV−luciferase plasmid-derived RNAs were challenged with some or all of the following PMOs or PPMOs: (1) two random sequences (PMO_{Ran1} and PMO_{Ran2}), (2) a sequence targeted to a mutated site of human β-globin intron 2 (PMO_{705}), and (3) PMO_{CMYC}, PMO_{3A2}, and PMO_{WNV}. None of the PMOs or PPMOs had sequences containing significant identity with any of the RNAs used. None of the unrelated PMOs, at concentrations up to 10 μM, inhibited luciferase expression of any of the three plasmid generated RNAs (Figure 3). The unrelated PPMO caused little or no inhibition at concentrations <1 μM but did cause various degrees of inhibition at ≥1 μM (Figure 3). The concentration that caused inhibition and the level of those inhibitions varied among both the PPMOs and target RNAs. $PPMO_{Ran2}$ at 3 μM caused 91%, 83%, and 70% inhibition of WNV, 3A2, and HCV reporter expression, respectively. $PPMO_{705}$ had little inhibition of WNV expression at 3 μM, but the same concentration caused 50% inhibition of 3A2 expression. $PPMO_{3A2}$ at 1 μM had no inhibition of WNV expression, but conversely $PPMO_{WNV}$ inhibited 3A2 expression by 60%. Free R9F2 peptide alone had no inhibition against 3A2 RNA up to 3 μM.

Enzymatic Stability of PPMOs. RXR and D-R9F2 peptides were designed to be more resistant to enzymatic degradation than R9F2 peptide. RXR peptide was made of L-arginine and the unnatural amino acid, 6-aminohexanoic acid, and D-R9F2 peptide consisted of D-amino acids (Table 1). The enzymatic stability of the fluorescein-tagged PMO_{705} (PMO_{705}−Fl) conjugated to each of the three peptides was determined by treating a conjugated compound with proteinase K and by applying a conjugate onto cells and then retrieving cellular contents for analysis. Mass spectrometry analysis (Figure 4) showed that the R9F2 portion of the $PPMO_{705}$−Fl was mostly degraded by proteinase K after 5 min of treatment, as indicated by the change in mass-to-charge ratio (*m/z*) from 8333 to 6633, corresponding to the loss of 1700 Da, that is, the mass of nine arginines and two phenylalanines. Neither (RXR)PMO_{705}−Fl nor D-$PPMO_{705}$−Fl was degraded by this enzyme after 5 min of treatment. However, the $(RXR)_4$ portion of (RXR)PMO_{705}−Fl was partially degraded after a 2-h treatment, while D-$PPMO_{705}$−Fl remained completely stable (data not shown). The major component retrieved from the cells treated with $PPMO_{705}$−Fl or (RXR)PMO_{705}−Fl had a *m/z* of 6632, which corresponds to mass of the cysteine−GMBS−PMO_{705}−Fl portion of each conjugate, indicating that the R9F2 or $(RXR)_4$ portion of each conjugate has been removed by cellular enzymes (Figure 4).

Effect of an ARP on Antisense Activity and Specificity of PPMO in a Cell-Based Assay. Effects of conjugation to an ARP on the antisense activity and specificity of PMO was further characterized in cell culture using the previously described "positive read-out" splice-correction assay (*8*, *14*). This was addressed by examining a series of compounds consisting of one of several ARPs with differing enzymatic stabilities conjugated to one or all PMOs that were exactly, partially, or noncomplementary to their RNA targets. PMO_{705} is complementary to a region of human β-globin pre-mRNA intron 2 that contains a mutation at position 705. $PMO_{705-2MM}$ and $PMO_{705-4MM}$ are partially complementary to the PMO_{705} target with two or four mismatched bases (Table 1), respectively. $PMO_{705-SCR}$ is a noncomplementary scrambled sequence of PMO_{705}. Five additional noncomplementary PMOs unrelated to the RNA target were used in this experiment: PMO_{IHNV}, PMO_{HCV}, $PPMO_{3A2}$, PMO_{WNV}, and PMO_{CMYC}. Three different ARPs, R9F2, RXR, and D-R9F2, were conjugated to some or all of the above PMOs.

Activity of a PPMO in the splice-correction assay was evidenced by increased luciferase reporter signal over

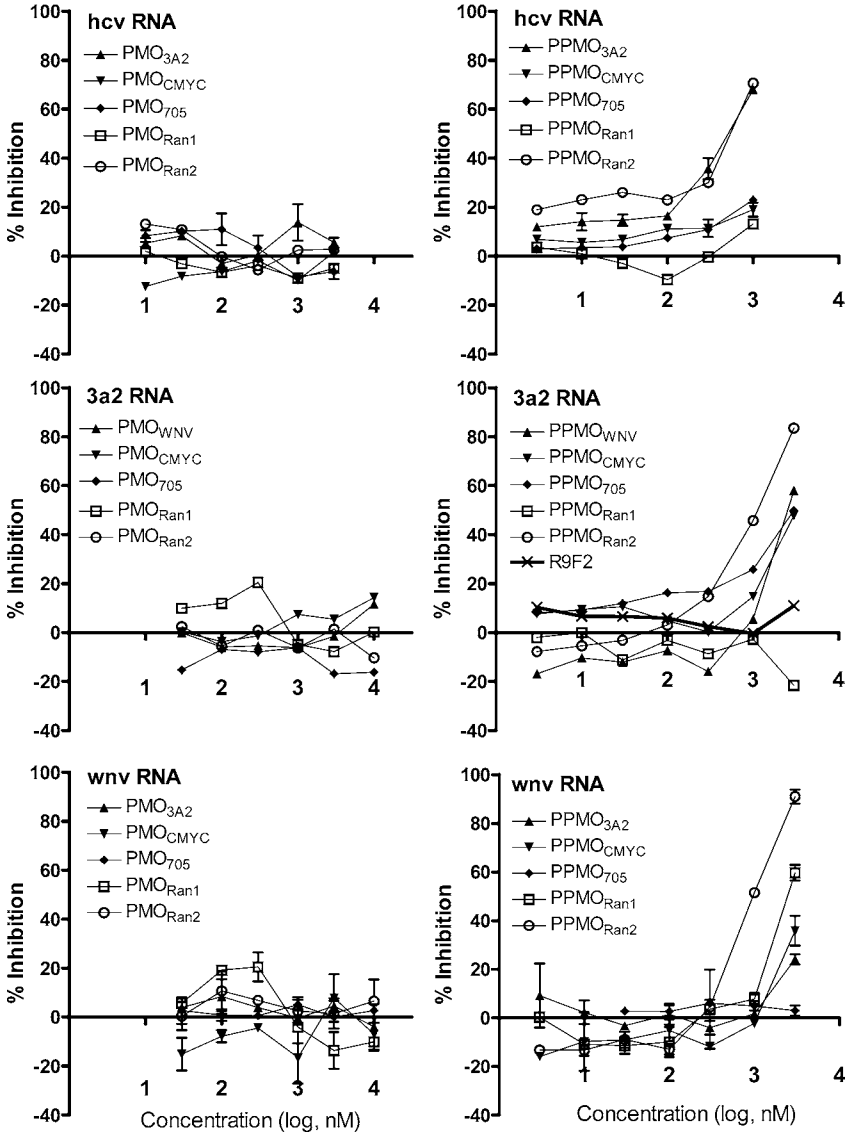

Figure 3. In vitro translation assays show that PPMOs have greater off-target effects than PMOs at concentrations >1 μM. PMOs (left panels) their corresponding PPMOs (right panels) or peptide alone (R9F2, right middle panel) were assayed for inhibition of luciferase reporter expression of HCV (top), 3A2 (middle), or WNV (bottom) RNA. Each PMO has a noncomplementary sequence to the challenge-RNA. Each graph shows the relationship between the log concentrations of PPMO or PMO and nonspecific activity, represented as % inhibition of the reporter luciferase compared to a vehicle-only control. Each data point was an average ± the range of means of two independent experiments each consisting of triplicate samples.

background. $PPMO_{705}$ corrected splicing and up-regulated luciferase reporter expression over background (Figure 5A,B). At treatment concentrations up to 10 μM, none of the five unrelated PPMOs resulted in an increased luciferase level (Figure 5A). Neither the partially complementary PPMOs ($PPMO_{705-2MM}$ or $PPMO_{705-4MM}$) nor the noncomplementary scrambled PPMO ($PPMO_{705-SCR}$) generated luciferase activity at concentrations up to 20 μM. (Figure 5B).

We hypothesized that cellular proteases might rapidly degrade the R9F2 portion of a PPMO after cell entry. The degradation of the peptide component could eliminate the peptide-associated nonspecificity documented in the results from the in vitro translation assays (Figure 3). To test this, the exactly-, partially-, or noncomplementary scrambled PMO was conjugated to the RXR or D-R9F2 peptide. Both (RXR)PMO_{705} and D-$PPMO_{705}$ had 2-fold higher specific antisense activity than $PPMO_{705}$ (Figure 5). (RXR)PMO_{705} or D-$PPMO_{705}$ at 5 μM caused cells to produce the same amount of luciferase as $PPMO_{705}$ at 10 μM. Nonspecific effects were not observed with RXR and D-R9F2 conjugated PMOs at concentrations <10 μM but were observed at higher concentrations. Specifically, cells treated with RXR-conjugated four-mismatched PMO and scrambled PMO at concentrations up to 20 μM did not produce luciferase activity above the background levels, whereas the cells treated with RXR-conjugated two-mismatched PMO at ≥10 μM did (Figure 5C). At concentrations ≤10 μM, neither of the mismatched or noncomplementary scrambled PMOs conjugated to D-R9F2 produced significant luciferase activity. However, the mismatched or scrambled D-PPMO did generate some nonspecificity at 20 μM, as indicated by the inappropriate production of luciferase (Figure 5D).

PPMO/RNA Heteroduplexes Have Higher Thermal Stability Than the Corresponding PMO/RNA Heteroduplexes. Having observed that ARP conjugation to a PMO increased antisense activity as well as caused nonspecificity at high concentrations, we hypothesized that the binding of PPMO and RNA is strengthened by interactions between peptide and RNA. The melting temperature (T_m) of a PMO/RNA heteroduplex

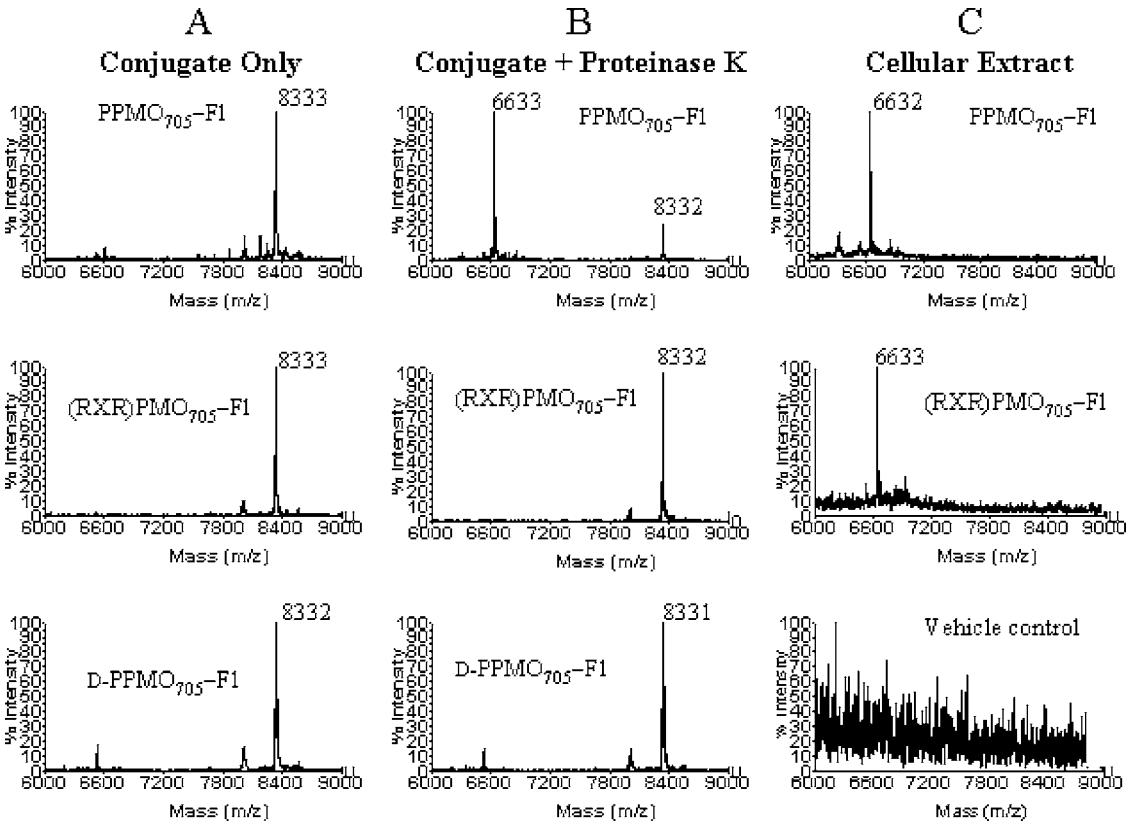

Figure 4. Enzymatic stability of peptide−PMO conjugates. The mass spectra of the fluorescein-tagged $PPMO_{705}$, $(RXR)PMO_{705}$, or D-$PPMO_{705}$ are shown: (A) no treatment performed on the conjugates; (B) the conjugate treated with proteinase K; (C) cellular extract of HeLa cells treated with $PPMO_{705}$ (upper), $(RXR)PMO_{705}$ (middle), or vehicle control (lower).

reflects the strength of the interaction between the two molecules of the duplex. T_m of a heteroduplex of PMO/RNA was compared to that of the corresponding PPMO/RNA. As shown in Table 3, T_m of the heteroduplexes of PMO_{CMYC}, PMO_{WNV}, or PMO_{705} with each of their complementary RNAs was 88.7, 74.8, or 74.1 °C, respectively. All corresponding PPMOs exhibited higher T_m's than the PMOs with values of 90.1, 78.8, and 80.1 °C, respectively. The differences in T_m between PMO/RNA and PPMO/RNA heteroduplexes were statistically significant ($p < 0.001$) as analyzed by the *t*-tests of GraphPad Prism software.

DISCUSSION

Throughout this study, we found that the antisense potency of PMO can be increased by conjugation to an ARP. This was demonstrated by the lower IC_{50} values of PPMOs than corresponding PMOs at inhibiting targeted RNA translation (Figure 2) and by a decrease of the inactivating length of PMOs (Table 2) in in vitro translation assays. These results were complemented by the demonstration in cultured cells that PMOs conjugated to less-degradable ARPs exhibited an increase in sequence-specific antisense activity compared to PMOs conjugated to a degradable ARP (Figure 5C,D). At higher concentrations, ARP conjugation to PMO caused greater nonspecific activity than the corresponding PMO alone. This conclusion was based on two specific observations: first inhibition of the translation of unrelated RNA in the in vitro translation assays by PPMO (Figure 3) and second inappropriately corrected pre-mRNA splicing in cultured cells when less degradable peptides were conjugated to partially complementary or noncomplementary scrambled PMO_{705} at concentrations ≥ 10 μM (Figure 5C,D). This nonspecificity was not observed in cell culture with PMO conjugated to the degradable peptide R9F2 at concentrations up to 20 μM.

We hypothesize that the increased antisense activity and nonspecificity of PPMOs compared to PMOs could be due to the following: the interactions between peptide and RNA strengthen the binding of peptide-conjugated PMOs to the targeted RNA, the peptide portion of the PPMO may provide additional steric blocking of the RNA, thus further hindering access of the RNA target to other biomolecules and thereby causing a higher degree of translation inhibition, or both. The thermal stability of the PPMO/RNA heteroduplexes was greater than that of PMO/RNA (Table 3), indicating that the binding strength between a PMO and its target RNA is enhanced by the presence of a conjugated ARP. An ARP conjugation accelerates the rate of association of a DNA oligo to its complementary DNA by 164-fold (*16*). The guanidine headgroups of an ARP have favorable binding with phosphate groups through bidentate hydrogen-bonding and electrostatic interactions (*17*, *18*). An ARP likely increases the association rate and decreases the dissociation rate of a PMO for its RNA, which accounts for the enhanced potency and off-target effects.

We investigated whether the peptide portion of PPMO provides additional interference with mRNA-binding translational components by comparing the activity of two PPMOs with the R9F2 peptide conjugated to either the 3′-end or the 5′-end of $PMO_{CMYC(I)}$ in an in vitro translation assay. The IC_{50} values of 3′-end and 5′-end conjugated $PMO_{CMYC(I)}$ were not much different from each other (Figure 2E). The data suggests that the peptide portion of PPMO does not increase potency of a PMO by interfering with a specific translational component.

The degree to which conjugation to an ARP increased PMO potency varies with the PMO sequence. This

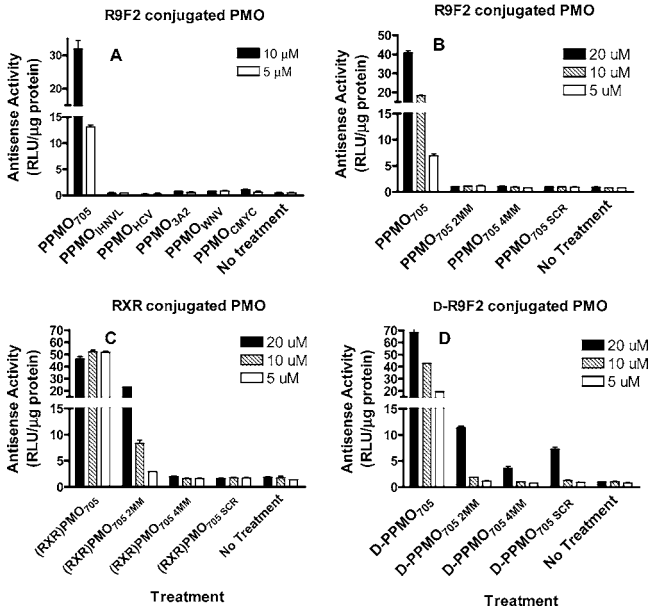

Figure 5. Antisense activity and specificity of PPMO in a cell-based splice-correction assay. R9F2-, RXR-, or D-R9F2-conjugated PMOs that were exactly (PMO_{705}), partially ($PMO_{705-2MM}$, $PMO_{705-4MM}$), or noncomplementary to the RNA target were tested in the splice-correction assay with HeLa pLuc 705 cells. Noncomplementary PMOs included PMO_{705} with scrambled bases ($PMO_{705-SCR}$) and PMOs that were unrelated to the RNA target (PMO_{IHNVL}, PMO_{HCV}, PMO_{WNV}, PMO_{CYP3A2}, and PMO_{C-MYC}): (A) $PPMO_{705}$ and unrelated PPMOs; (B) $PPMO_{705}$, $PPMO_{705-2MM}$, $PPMO_{705-4MM}$, and $PPMO_{705-SCR}$; (C) (RXR)-PMO_{705}, (RXR)$PMO_{705-2MM}$, and (RXR)$PMO_{705-SCR}$; (D) D-PP-MO_{705}, D-$PPMO_{705-2MM}$, D-$PPMO_{705-4MM}$, and D-$PPMO_{705-SCR}$. Cells were treated with a conjugate for 24 h in culture medium and then assayed for luciferase activity. Activity of a peptide−PMO conjugate in the splice-correction assay is indicated by increased production of the luciferase reporter over background level (no treatment). Data are represented as relative light units normalized to micrograms of total protein (RLU/μg of protein). Each data point was an average ± the range of means of two independent experiments each consisting of triplicate samples.

Table 3. PMO Conjugation to the R9F2 Peptide Increases the Thermal Stability of PMO/RNA Heteroduplex as Indicated by the Melting Temperatures of PMO or the Corresponding PPMO Heteroduplexed with Complementary RNA[a]

	PMO		PPMO		
	mean (SD), °C	n	mean (SD), °C	n	ΔT_m, °C
c-*myc* RNA	88.7 (0.1)	6	90.1 (0.5)	6	1.4
WNV RNA	74.8 (0.1)	6	78.8 (0.4)	6	4.0
705 RNA	74.1 (0.5)	5	80.1 (0.4)	5	6.0

[a] The data are reported as an average of the T_m, the standard derivation (SD), number of determinations (n), and the difference in T_m (ΔT_m) between the PPMO and PMO.

appears to correlate with the GC content and length of the PMO. PMOs with lower GC content had greater increases in T_m and greater decreases in IC_{50} after peptide conjugation. $PMO_{705(20mer)}$, PMO_{WNV}, and PMO_{CMYC} have GC contents of 40%, 45%, and 65%, respectively. Conjugation to the R9F2 peptide caused 6.0, 4.0, and 1.4 °C increase in T_m, respectively. PMO_{CMYC} and PMO_{HCV}, both with a high GC content of 65%, were least affected by peptide conjugation. PMO_{WNV}, with a GC content of 45%, the lowest among all PMO tested in the in vitro translation assays, was much affected by peptide conjugation, with a resultant 25-fold decrease in IC_{50} (Figure 2E).

To further verify the correlation between the GC content of PMO and the increase in efficacy generated by peptide conjugation, the inosine-substituted PMO_{CMYC} ($PMO_{CMYC(I)}$) and $PPMO_{CMYC(I)}$ were compared with the unsubstituted PMO_{CMYC} and $PPMO_{CMYC}$ in an in vitro translation assay. Unlike Watson−Crick pairing with perfect pairing geometry and triple hydrogen bonds between a G and a C, interaction between an I and a C form a wobble base pair with double hydrogen bonds. The inosine substitutions reduced the GC content of PMO_{CMYC} from 65% to 50% and decreased efficacy as shown by the increased IC_{50} value from 50 to 143 nM. $PMO_{CMYC(I)}$ had lower target binding affinity than PMO_{CMYC} as indicated by an 11 °C reduction in T_m (data not shown). Peptide conjugation had little effect on the IC_{50} of PMO_{CMYC} but caused significant change for $PMO_{CMYC(I)}$ with a 23-fold increase in efficacy compared to the corresponding PMO. This is consistent with the observed trend that PMOs with lower GC content have a larger IC_{50} shift upon conjugation.

ARP conjugation caused a greater increase in antisense activity for shorter-length than for longer-length PMOs. Reduction of the PMO_{3A2} length from 20 bases to 14 bases decreased its potency by 15-fold (Table 2). Conjugation to R9F2 peptide caused a larger increase in antisense potency for PMO_{3A2} 14mer than for PMO_{3A2} 20mer, evidenced by a 31- or 10-fold decrease in IC_{50} values, respectively (Table 2). Taken together, we conclude that the increase in antisense activity afforded by peptide conjugation depends, at least in part, on the intrinsic potency of the PMO to which it is conjugated, with a greater antisense enhancement effect when conjugated to a less potent PMO.

All PMOs tested in these studies exhibited a high degree of specificity (Figure 3); however, at higher concentrations, the ARP-conjugated PMOs exhibited considerable nonspecificity (Figures 3 and 5C,D). The electrostatic and hydrogen-bonding interactions between an ARP and RNA are not sequence-specific. When a high concentration of the PPMO was used, this nonspecific binding likely became more prominent and resulted in increased off-target effects. The degree of peptide-caused nonspecificity differed among various PPMOs against the same noncomplementary RNA target and also among a single PPMO against various RNA targets. There appears to be little correlation between the potency of a nonconjugated PMO and the degree of nonspecificity observed.

The nonspecificity observed in cell culture with (RXR)-PMO_{705} and D-$PPMO_{705}$, but not with $PPMO_{705}$ (Figure 5), is likely due to their relative stability toward proteases. Although cellular proteases degraded the R9F2 or $(RXR)_4$ portion of $PPMO_{705}$ or (RXR)PMO_{705} (Figure 4), the degradation rate for D-R9F2 and RXR peptide is likely significantly slower than that for L-R9F2. This conclusion is supported by the data of proteinase K or trypsin treatment. Treatment of $PPMO_{705}$ with proteinase K (Figure 4) or trypsin (data not shown) rapidly degraded L-R9F2, while the same treatment had slower effect on the (RXR)−PMO conjugate and had no effect on the D-R9F2−PMO conjugate. The intracellular rates of degradation of these conjugates are currently under investigation.

When an ARP is conjugated to a PMO for applications in cell culture or in vivo, several factors should be considered: (1) the intrinsic toxicity of the peptide, (2) the type of amino acids (e.g., D vs L) used in peptide synthesis, (3) the linker chemistry employed between peptide and PMO, and (4) experimental treatment conditions (e.g., concentrations of compound, duration of treatment, tissue culture conditions). ARPs have concen-

tration- and cell type-dependent cellular toxicity (*7*, *8*). Conjugating PMOs to a less degradable peptide made of unnatural amino acids through a noncleavable linker enhances specific antisense activity at lower concentrations but causes some nonspecificity at higher concentrations. The degree of nonspecificity caused by ARP conjugation depends on PMO sequences and RNA targets. To avoid the misinterpretation of cellular toxicity and nonspecific effects as an antisense effect, it seems advisable to use more than one irrelevant sequence control oligomer (preferably of roughly the same GC content and length) conjugated to the same peptide as the specific antisense compounds.

ACKNOWLEDGMENT

We thank Drs. Jon D. Moulton and Dan Mourich for critical reading of the manuscript. We are grateful to the chemistry team at AVI BioPharma for synthesis, purification, and analysis of peptides and PMOs.

LITERATURE CITED

(1) Summerton, J., and Weller, D. (1997) Morpholino antisense oligomers: design, preparation, and properties. *Antisense Nucleic Acid Drug Dev. 7*, 187−195.
(2) Summerton, J. (1999) Morpholino antisense oligomers: the case for an RNase H-independent structural type. *Biochim. Biophys. Acta 1489*, 141−158.
(3) Hudziak, R. M., Barofsky, E., Barofsky, D. F., Weller, D. L., Huang, S. B., and Weller, D. D. (1996) Resistance of morpholino phosphorodiamidate oligomers to enzymatic degradation. *Antisense Nucleic Acid Drug Dev. 6*, 267−272.
(4) Arora, V., Knapp, D. C., Reddy, M. T., Weller, D. D., and Iversen, P. L. (2002) Bioavailability and efficacy of antisense morpholino oligomers targeted to c-myc and cytochrome P-450 3A2 following oral administration in rats. *J. Pharm. Sci. 91*, 1009−1018.
(5) Summerton, J. E. (2003) Morpholinos and PNAs Compared. In *Peptide Nucleic Acids, Morpholinos and Related Antisense Biomolecules* (Janson, C. G., and During, M. J., Eds.) Kluwer/Plenum Publishers.
(6) Ghosh, C., Stein, D., Weller, D., and Iversen, P. (2000) Evaluation of antisense mechanisms of action. *Methods Enzymol. 313*, 135−143.
(7) Moulton, H. M., Hase, M. C., Smith, K. M., and Iversen, P. L. (2003) HIV Tat peptide enhances cellular delivery of antisense morpholino oligomers. *Antisense Nucleic Acid Drug Dev. 13*, 31−43.
(8) Moulton, H. M., Nelson, M. H., Hatlevig, S. A., Reddy, M. T., and Iversen, P. L. (2004) Cellular uptake of antisense morpholino oligomers conjugated to arginine-rich peptides. *Bioconjugate Chem. 15*, 290−299.
(9) Neuman, B. W., Stein, D. A., Kroeker, A. D., Paulino, A. D., Moulton, H. M., Iversen, P. L., and Buchmeier, M. J. (2004) Antisense morpholino-oligomers directed against the 5′ end of the genome inhibit coronavirus proliferation and growth. *J. Virol. 78*, 5891−5899.
(10) Neuman, B. W., Stein, D. A., Kroeker, A. D., Churchill, M. J., Kim, A. M., Kuhn, P., Dawson, P., Moulton, H. M., Bestwick, R. K., Iversen, P. L., and Buchmeier, M. J. (2005) Inhibition, escape, and attenenuated growth of severe acute respiratory syndrome coronavirus treated with antisense morpholino oligomers. *J. Virol.*, in press.
(11) Deas, T. S., Binduga-Gajewska, I., Tilgner, M., Ren, P., Stein, D. A., Moulton, H. M., Iversen, P. L., Kauffman, E. B., Kramer, L. D., and Shi, P. Y. (2005) Inhibition of flavivirus infections by antisense oligomers specifically suppressing viral translation and RNA replication. *J. Virol. 79*, 4599−4609.
(12) Kinney, R. M., Huang, C. Y., Rose, B. C., Kroeker, A. D., Dreher, T. W., Iversen, P. L., and Stein, D. A. (2005) Inhibition of dengue virus serotypes 1 to 4 in Vero cell cultures with morpholino oligomers. *J. Virol. 79*, 5116−5128.
(13) Summerton, J., and Weller, D. (1991) Uncharged morpholino-based polymers having phosphorus containing chiral intersubunit linkages. U.S. Patent 5185444.
(14) Kang, S. H., Cho, M. J., and Kole, R. (1998) Up-regulation of luciferase gene expression with antisense oligonucleotides: implications and applications in functional assay development. *Biochemistry 37*, 6235−6239.
(15) Stein, D., Foster, E., Huang, S. B., Weller, D., and Summerton, J. (1997) A specificity comparison of four antisense types: morpholino, 2′-O-methyl RNA, DNA, and phosphorothioate DNA. *Antisense Nucleic Acid Drug Dev. 7*, 151−157.
(16) Corey, D. R. (1995) 48000-fold acceleration of hybridization by chemically modified oligonucleotides. *J. Am. Chem. Soc. 117*, 9373−9374.
(17) Rothbard, J. B., Kreider, E., VanDeusen, C. L., Wright, L., Wylie, B. L., and Wender, P. A. (2002) Arginine-rich molecular transporters for drug delivery: role of backbone spacing in cellular uptake. *J. Med. Chem. 45*, 3612−3618.
(18) Rothbard, J. B., Jessop, T. C., and Wender, P. A. (2005) Adaptive translocation: the role of hydrogen bonding and membrane potential in the uptake of guanidinium-rich transporters into cells. *Adv. Drug Deliv. Rev. 57*, 495−504.

BC0501045

Polyaspartamide Gadolinium Complexes Containing Sulfadiazine Groups as Potential Macromolecular MRI Contrast Agents

Guo-Ping Yan,*,† Mai-Li Liu,‡ and Li-Yun Li‡

School of Materials Science and Engineering, Wuhan Institute of Technology, Wuhan 430073, P. R. China, and State Key Laboratory of Magnetic Resonance and Atomic and Molecular Physics, Wuhan Institute of Physics and Mathematics, The Chinese Academy of Sciences, Wuhan 430071, P. R. China. Received February 1, 2005; Revised Manuscript Received May 16, 2005

Both diethylenetriaminepentaacetic acid (DTPA) and sulfadiazine (SD) were incorporated into polyaspartamides with different side chains, including poly-α,β-[*N*-(2-hydroxyethyl)-L-aspartamide] (PHEA), poly-α,β-[*N*- (3-hydroxypropyl)-L-aspartamide] (PHPA), poly-α,β-[*N*-(2-aminoethy1)-L-aspartamide] (PAEA), poly-α,β-[*N*-(4-aminobuty1)-L-aspartamide] (PABA), and poly-α,β-[*N*-(6-aminohexyl)-L-aspartamide] (PAHA). The polyaspartamide ligands containing DTPA and SD groups were further reacted with gadolinium chloride to give the corresponding macromolecular gadolinium complexes. Experimental data of ^{1}H NMR, IR, UV, and elemental analysis exhibited the formation of the polyaspartamide ligands and gadolinium complexes. Relaxivity studies indicated that the macromolecular chelates possess higher relaxivities than that of the clinically used Gd-DTPA. MR imaging showed that the macromolecular chelate PAEA-Gd-DTPA-SD greatly enhanced the contrast of MR images of hepatoma in the lower limb of mice and provided prolonged intravascular duration. Thus the polyaspartamide gadolinium complex containing SD groups is expected to be used as the potential macromolecular MRI contrast agents for hepatoma in mice.

INTRODUCTION

Magnetic resonance imaging (MRI) is a noninvasive clinical imaging modality, which relies on the detection of NMR signals emitted by hydrogen protons in the body placed in a magnetic field. MRI contrast agent is a unique class of pharmaceutical that enhances the image contrast between normal and diseased tissue and indicates the status of organ function or blood flow after administration by increasing the relaxation rates of water protons in tissue in which the agent accumulates (*1*−*3*).

The clinically used MRI contrast agents, for example, gadolinium diethylenetriaminepentaacetic acid (Gd-DTPA), are small ionic molecules that can diffuse freely through the extracellular space and are excreted rapidly by the kidney. Their biodistribution is nonspecific although Gd-DTPA works well in the brain and spinal cord (*4*, *5*). The binding of small gadolinium complex to a macromolecule has been shown to provide a mechanism of proton relaxation enhancement through longer rotational correlation times. The macromolecular MRI contrast agent thus obtained may show prolonged intravascular retention due to the bulky molecular volume, resulting in the clinical use as a blood pool contrast agent. In addition, when a tumor-targeting group is attached to this macromolecular metal chelate, it can be endowed with tumor-specific property (*3*, *6*).

Polyaspartamide is a water-soluble, biologically well-tolerated synthetic polymer with a protein-like structure that was used as a plasma extender and a drug carrier because it is nontoxic, nonantigenic, and degradable in living systems and modified readily by the reaction with the side chain (*7*, *8*). As reported, antiviral drugs and antiinflammatory agents were covalently linked to poly-α,β-[*N*-(2-hydroxyethyl)-D,L-aspartamide] (PHEA) forming drug−polymer conjugates capable of increasing drug stability and bioavailility. Therefore polyaspartamide can be used as polymer carriers for MRI contrast agents (*9*−*12*).

Sulfadiazine derivatives were reported to be concentrated into Walker carcinoma or Yoshida sarcoma by a factor of about 2−3 compared with the uptake in the liver (*13*−*14*). Previously we have used sulfadiazine (SD) as a tumor-selective group and evaluated Gd-DTPA derivatives containing SD groups as the potential tumor-specific contrast agents. The biodistribution and MRI studies indicated that the incorporation of SD into Gd-DTPA increased their uptake by hepatoma and Ehrlich ascites carcinoma in mice, and the gadolinium complexes exhibited tumor-selective properties (*15*).

In this work, the polyaspartamide ligands were synthesized by the incorporation of both DTPA and SD into polyaspartamides with different side chains. The ligands were further reacted with gadolinium chloride to give the corresponding polyaspartamide gadolinium complexes (Scheme 1). The polyaspartamide ligands and gadolinium complexes were characterized by ^{1}H NMR, IR, UV, and elemental analysis. Relaxivity and magnetic resonance imaging of hepatoma (H_{22}) in mice were evaluated.

EXPERIMENTAL PROCEDURES

Instrumentation and Materials. The compounds prepared were characterized using a Spectrum One infrared spectrophotometer, a Lambda Bio40 UV/Vis spectrophotometer, a Varian Mercury-VX300 NMR spectrometer, and a Carlo Erba 1106 analyzer. The molecular weight and polydispersity of polyaspartamide were measured by GPC [software version millemmium 32, Waters

* To whom correspondence should be addressed. E-mail: guopyan@hotmail.com.
† Wuhan Institute of Technology.
‡ The Chinese Academy of Sciences.

10.1021/bc050026l CCC: $30.25 © 2005 American Chemical Society
Published on Web 07/06/2005

Scheme 1. Synthetic Route to Polyaspartamide MRI Contrast Agents

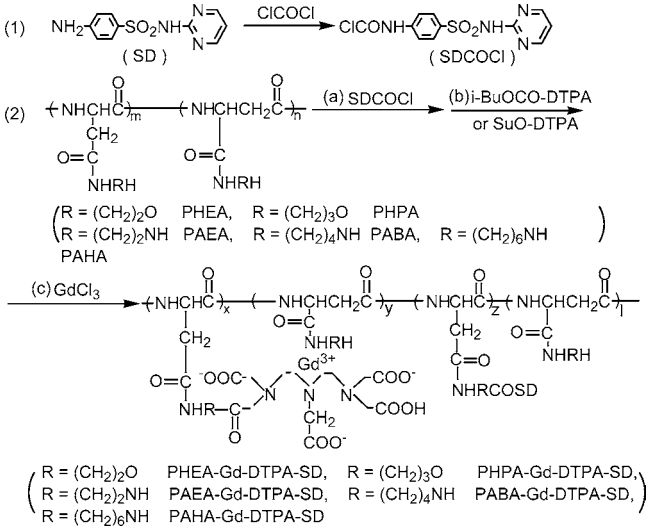

2960D separation module, Ultrahydrogel 2000 column, poly(Ethylene Glycol) standard, 0.1 M KH_2PO_4 solvent, 0.5 mL·min^{-1} flow, 35 °C column temperature and 30 °C detector temperature]. The concentration of the paramagnetic species [Gd^{3+}] was measured by an ICP Atomscan-2000 spectrometer. The solvent longitudinal relaxation time (T_1) for gadolinium complexes in distilled water was determined by a Varian Mercury-VX300 NMR spectrometer. MR image was performed on a 4.7 T BIOSPEC 47/30 MR Scanner (Bruker Medical, Ettlingen, Germany). KunMing mice bearing with hepatoma (H_{22}) in the right lower limb (weight: 30 ± 2 g) were provided by the Department of Pharmacy (School of Medicine, Huazhong University of Science and Technology, China) and were cultured according to the method described in the literature (*16*). Hepatoma (H_{22}) cells were provided by the China Center for Type Culture Collection of Wuhan University, China.

All the chemicals and solvents were of analytical grade. The solution of phosgene in toluene (2.0 M) (*17*), DTPA active ester including DTPA mono(carbonyloxyisobutyl ester) (i-BuOCO-DTPA) and DTPA mono(hydroxysuccinimidyl ester) (SuO-DTPA) (*18*), poly-α,*β*-[*N*-(2-hydroxyethyl)-L-aspartamide] (PHEA), poly-α,*β*-[*N*-(2-aminoethyl)-L-aspartamide] (PAEA), poly-α,*β*-[*N*-(3-hydroxypropyl)-L-aspartamide] (PHPA), poly-α,*β*-[*N*-(4-aminobutyl)-L-aspartamide] (PABA), and poly-α,*β*-[*N*-(6-aminohexyl)-L-aspartamide] (PAHA) (*19*) were prepared according to the literature.

Synthesis of Polyaspartamide Ligands. *Synthesis of PHEA-DTPA-SD and PHPA-DTPA-SD.* Sulfadiazine (SD, 1.0 g, 4 mmol) was dissolved in 20 mL of *N*,*N*-dimethylformamide (DMF) and 5 mL of pyridine. The mixture was added slowly to a solution of phosgene in toluene (10 mL) with rapid stirring at −10 °C to −5 °C. The reaction was stirred for 2 h at this temperature and a further 2 h at 0 °C under an argon atmosphere. After filtration, a brown solution of SDCOCl in DMF was obtained.

The solution of SDCOCl (4 mmol) in DMF obtained above was added slowly to a solution of PHEA (1.58 g, 10 mmol) in 40 mL of DMF and 8 mL of triethylamine with rapid stirring at 0 °C. The reaction was stirred for 4 h at 0 °C and a further 24 h at room temperature. After filtration, the filtrate was collected and cooled to −5 °C. The solution of DTPA mono(carbonyloxyisobutyl ester) (i-BuOCO-DTPA, 3.82 g, 8 mmol) in DMF (20 mL) was added dropwise to the filtrate at −5 °C. The reaction was continued stirring for 4 h at −5 °C and a further 48 h at room temperature. The resultant mixture was filtered and precipitated with ethanol and ethyl ether. The precipitate was reprecipitated from DMF using ethanol and ethyl ether, filtered, and dried under vacuum to yield a white polyaspartamide ligands containing DTPA and SD groups PHEA-DTPA-SD (M_1) (2.0 g, 30.1%). ^{1}H NMR (D_2O, δ, ppm): 8.1−7.7 (C_6H_4, $C_4N_2H_2$), 4.5, 4.2, 4.0 (CH, CH_2), 3.7(CH_2CO), 3.4−3.3(NCH_2CH_2N), 3.2, 3.0, 2.8, 2.6−2.4 ($NHCH_2$, CH_2); IR(KBr, cm^{-1}): 3426.6 (OH), 2975.7−2492.1 (C−H), 1711(COO), 1634.7(CONH), 1397.2, 1172.5(S=O), 1154.6(C−N), 1094.2 (C−O), 907.2, 840.3, 803.8(C_6H_4, $C_4N_2H_2$); UV(H_2O, nm): 272.9.

The polyaspartamide ligands containing differing amounts of DTPA linked to polymeric repeat units were synthesized by the same method to give the following results PHEA-DTPA-SD (M_2, 28%) and PHPA-DTPA-SD (32%).

PHEA-DTPA-SD (M_2): ^{1}H NMR (D_2O, δ, ppm): 8.1−7.7 (C_6H_4, $C_4N_2H_2$), 4.5, 4.2, 4.0 (CH, CH_2), 3.7(CH_2CO), 3.4−3.3(NCH_2CH_2N), 3.2, 3.0, 2.8, 2.6−2.4 ($NHCH_2$, CH_2); IR(KBr, cm^{-1}): 3436.1(OH), 2975.4−2492(C−H), 1710(COO), 1637.4(CONH), 1474.2, 1433.9(C_6H_4, $C_4N_2H_2$), 1397.9, 1171.5(S=O), 1229.1(C−N), 1036.2 (C−O), 910.7, 849.1, 804.4(C_6H_4, $C_4N_2H_2$); UV(H_2O, nm): 272.9.

PHPA-DTPA-SD: ^{1}H NMR (D_2O, δ, ppm): 8.2−7.7-(C_6H_4, $C_4N_2H_2$), 4.5, 4.2, 4.0 (CH, CH_2), 3.7(CH_2CO), 3.4−3.2(NCH_2CH_2N), 3.0, 2.8, 2.6−2.4 ($NHCH_2$, CH_2); IR(KBr, cm^{-1}): 3434.4(OH), 2975.3−2491.9(C−H), 1713(COO), 1636.0(CONH), 1474.5, 1434.1(C_6H_4, $C_4N_2H_2$), 1397.9, 1171.3(S=O), 1229.4(C−N), 1036.2 (C−O), 909.8, 849.1, 804.4(C_6H_4, $C_4N_2H_2$); UV(H_2O, nm): 268.

Synthesis of PAEA-DTPA-SD, PABA-DTPA-SD and PAHA-DTPA-SD. The solution of SDCOCl (4 mmol) in DMF obtained above was added slowly to a solution of PAEA (1.57 g, 10 mmol) in 100 mL of distilled water and 8 mL of triethylamine with rapid stirring at −5 °C. The reaction was stirred for 4 h at −5 °C and a further 24 h at room temperature. After filtration, the filtrate was collected and cooled to −5 °C. The solution of DTPA mono(hydroxysuccinimidyl) ester (SuO-DTPA, 3.92 g, 8 mmol) in DMF (20 mL) was added dropwise to the filtrate at −5 °C. The reaction was continued stirring for 4 h at −5 °C and a further 48 h at room temperature. The resultant mixture was filtered and precipitated with ethanol and ethyl ether. The precipitate was reprecipitated from distilled water using ethanol and ethyl ether, filtered, and dried under vacuum to yield a white polyaspartamide ligands containing DTPA and SD groups PAEA-DTPA-SD (M_1) (2.1 g, 31.2%). ^{1}H NMR (D_2O, δ, ppm): 8.0−7.6 (C_6H_4, $C_4N_2H_2$), 4.5, 4.2, 4.0 (CH, CH_2), 3.7(CH_2CO), 3.4−3.1(NCH_2CH_2N), 3.0−2.8, 2.8−2.4, 2.4−2.2($NHCH_2CH_2NH$); IR(KBr, cm^{-1}): 3433.4(NH_2), 3071.2−2932.3(C−H), 1711(COO), 1644.4, 1545.4(CONH), 1435.3-(C_6H_4, $C_4N_2H_2$), 1398.7, 1171.7(S=O), 1321.5(C−N), 1090.3(C−O), 912.4, 849.1, 800.4(C_6H_4, $C_4N_2H_2$); UV-(H_2O, nm): 301.8.

The polyaspartamide ligands containing differing amounts of DTPA linked to polymeric repeat units were synthesized by the same method to give the following results PAEA-DTPA-SD (M_2, 29.2%), PABA-DTPA-SD (33%) and PAHA-DTPA-SD (33.5%).

PAEA-DTPA-SD (M_2): ^{1}H NMR (D_2O, δ, ppm): 8.0−7.6 (C_6H_4, $C_4N_2H_2$), 4.5, 4.2, 4.0 (CH, CH_2), 3.8(CH_2CO), 3.6−3.2(NCH_2CH_2N), 3.2−3.0, 2.8, 2.6−2.4 ($NHCH_2CH_2$-NH); IR(KBr, cm^{-1}): 3398.2(NH_2), 3057.3−2927.6(C−H), 1709(COO), 1648.1, 1535.3(CONH), 1432(C_6H_4, $C_4N_2H_2$),

1394.8, 1174.0(S=O), 1236.9(C−N), 1088.1(C−O), 909.1, 848.1, 800.4(C_6H_4, $C_4N_2H_2$); UV(H_2O, nm): 301.8.

PABA-DTPA-SD: ^{1}H NMR (D_2O, δ, ppm): 8.1−7.6 (C_6H_4, $C_4N_2H_2$), 4.5, 4.1, 4.0 (CH, CH_2), 3.7(CH_2CO), 3.4−3.3(NCH_2CH_2N), 3.0, 2.8, 2.6−2.4 ($NHCH_2$, CH_2); IR(KBr, cm^{-1}): 3445.2(NH_2), 2975.6−2491.8(C−H), 1708.6(COO), 1634.8, 1535.3(CONH), 1473.9, 1434.0(C_6H_4, $C_4N_2H_2$), 1397.9, 1171.1(S=O), 1226.8(C−N), 1036.1(C−O), 909.1, 849.6, 805.0(C_6H_4, $C_4N_2H_2$); UV(H_2O, nm): 268.5.

PAHA-DTPA-SD: ^{1}H NMR (D_2O, δ, ppm): 7.9−7.7 (C_6H_4, $C_4N_2H_2$), 4.5, 4.1, 4.0 (CH, CH_2), 3.8(CH_2CO), 3.5−3.3(NCH_2CH_2N), 3.0, 2.8, 2.6−2.4, 2.2 ($NHCH_2$, CH_2); IR-(KBr, cm^{-1}): 3436.2(NH_2), 3063.9−2934.2(C−H), 1714-(COO), 1641.7, 1541.5(CONH), 1435.3(C_6H_4, $C_4N_2H_2$), 1395.5, 1177(S=O), 1229.1(C−N), 1047.9(C−O), 907.8, 850, 804(C_6H_4, $C_4N_2H_2$); UV(H_2O, nm): 291.

Preparation of Polyaspartamide Gadolinium Chelates. The polyaspartamide gadolinium complexes with differing amounts of Gd-DTPA linked to polymeric repeat units and differing polymers were synthesized according to the following standard procedure. PHEA-DTPA-SD (M_1, 1.08 g, 5 mmol) was dissolved in 20 mL of distilled water and gadolinium chloride ($GdCl_3$, 1.98 g, 7.5 mmol) was added. The mixture was stirred for 1 h, adjusted with 2 M NaOH solution to pH 5, and continued to stir for 12 h at room temperature. After dialysis, the dialyzed solution was evaporated and the solid residue was dried under vacuum to yield polyaspartamide gadolinium complex PHEA-Gd-DTPA-SD (M_1, 1.18 g, 73.5%). PHEA-Gd-DTPA-SD (M_2, 65%), PHPA-Gd-DTPA-SD (74%), PAEA-Gd-DTPA-SD (M_1, 77%), PAEA-Gd− DTPA-SD (M_2, 71%), PABA-Gd-DTPA-SD (72%) and PAHA-Gd-DTPA-SD (68%) were similarly synthesized.

PHEA-Gd-DTPA-SD (M_1): IR(KBr, cm^{-1}): 3445.2(OH), 2932.2(C−H), 1659.0, 1642.0 (COO, CONH), 1542.1(C_6H_4, $C_4N_2H_2$), 1411, 1155(S=O), 1261.8(C−N), 1059.8(C−O), 930.8, 868.2, 801.0(C_6H_4, $C_4N_2H_2$). Elem. Anal.(%) found (calcd): C 42.40(42.70), N 15.59(15.70), H 5.73(5.69). The average mole ratio of attached Gd-DTPA and SD to all polymeric repeat units (mol %): Gd-DTPA 7.93 (as determined by an ICP Atomscan-2000 spectrometer), SD 0.57 (as determined by ^{1}H NMR); UV(H_2O, nm): 272.9.

PHEA-Gd-DTPA-SD (M_2): IR(KBr, cm^{-1}): 3431.3(OH), 2927.7(C−H), 1646.9, 1658.3, 1555.6(COO, CONH), 1542.1, 1435.5(C_6H_4, $C_4N_2H_2$), 1409.4, 1091.8(S=O), 1265.6(C−N), 1057.2(C−O), 931.8, 867, 801(C_6H_4, $C_4N_2H_2$). Elem. Anal.(%) found (calcd): C 40.50(40.96), N 14.33(14.49), H 5.32(5.26). The average mole ratio of attached Gd-DTPA and SD to all polymeric repeat units (mol %): Gd-DTPA 15.75 (as determined by an ICP Atomscan-2000 spectrometer), SD 0.23 (as determined by ^{1}H NMR); UV-(H_2O, nm): 272.9.

PHPA-Gd-DTPA-SD: IR(KBr, cm^{-1}): 3422.3(OH), 2931, 2882.1(C−H), 1658.4, 1641.3, 1542.1(COO, CONH), 1473.2, 1433.5(C_6H_4, $C_4N_2H_2$), 1411.1, 1198.4(S=O), 1322.7(C−N), 1053.9(C−O), 930.6, 868, 847.7(C_6H_4, $C_4N_2H_2$). Elem. Anal.(%) found (calcd): C 45.13(45.43), N 14.58(14.67), H 6.25(6.22). The average mole ratio of attached Gd-DTPA and SD to all polymeric repeat units (mol %): Gd-DTPA 8.17 (as determined by an ICP Atomscan-2000 spectrometer), SD 0.97 (as determined by ^{1}H NMR); UV-(H_2O, nm): 268.

PAEA-Gd-DTPA-SD (M_1): IR(KBr, cm^{-1}): 3383.8-(NH_2), 3069.8, 2977.5, 2932(C−H), 1655.3, 1596.3(COO, CONH), 1437.2(C_6H_4, $C_4N_2H_2$), 1405.3, 1177.7(S=O), 1324.1(C−N), 1092.6(C−O), 929.9, 868.3, 800.1(C_6H_4, $C_4N_2H_2$). Elem. Anal.(%) found (calcd): C 41.00(41.44), N 20.27(20.49), H 5.74(5.69). The average mole ratio of attached Gd-DTPA and SD to all polymeric repeat units (mol %): Gd-DTPA 14.75 (as determined by an ICP Atomscan-2000 spectrometer), SD 3.75 (as determined by ^{1}H NMR); UV(H_2O, nm): 301.8.

PAEA-Gd-DTPA-SD (M_2): IR(KBr, cm^{-1}): 3422.1-(NH_2), 3068.3, 2927.6(C−H), 1658.0, 1595.2(COO, CONH), 1438.1(C_6H_4, $C_4N_2H_2$), 1407.4, 1176.6(S=O), 1326(C−N), 1093.3(C−O), 931.2, 867, 800.7(C_6H_4, $C_4N_2H_2$). Elem. Anal.(%) found (calcd): C 37.13(37.86), N 15.35(15.65), H 4.86(4.73). The average mole ratio of attached Gd-DTPA and SD to all polymeric repeat units (mol %): Gd-DTPA 45.04 (as determined by an ICP Atomscan-2000 spectrometer), SD 7.54 (as determined by ^{1}H NMR); UV-(H_2O, nm): 301.8.

PABA-Gd-DTPA-SD: IR(KBr, cm^{-1}): 3444.1(NH_2), 3079.8, 2932.4(C−H), 1641.5, 1597.8(COO, CONH), 1438.2(C_6H_4, $C_4N_2H_2$), 1403.6, 1169(S=O), 1322(C−N), 1092(C−O), 929.9, 866.4, 801.7(C_6H_4, $C_4N_2H_2$). Elem. Anal.(%) found (calcd): C 43.69(44.25), N 16.90(17.11), H 6.30(6.24). The average mole ratio of attached Gd-DTPA and SD to all polymeric repeat units (mol %): Gd-DTPA 21.67(as determined by an ICP Atomscan-2000 spectrometer), SD 2.21 (as determined by ^{1}H NMR); UV-(H_2O, nm): 268.5.

PAHA-Gd-DTPA-SD: IR(KBr, cm^{-1}): 3434.2(NH_2), 3078.9, 2933.7, 2860.8(C−H), 1658.3, 1647.0, 1601, 1542.3-(COO, CONH), 1473.2, 1437.3(C_6H_4, $C_4N_2H_2$), 1399.3, 1121.4(S=O), 1322.4, 1270.9(C−N), 1092.8(C−O), 930.5, 866.5, 800.8(C_6H_4, $C_4N_2H_2$). Elem. Anal.(%) found (calcd): C 51.48(51.78), N 17.56(17.66), H 7.81(7.79). The average mole ratio of attached Gd-DTPA and SD to all polymeric repeat units (mol %): Gd-DTPA 8.86 (as determined by an ICP Atomscan-2000 spectrometer), SD 2.59 (as determined by ^{1}H NMR); UV(H_2O, nm): 291.

Relaxivity. In the absence of solute−solute interactions, the solvent relaxation rates are linearly dependent on the concentration of the paramagnetic species ([M]); Relaxivity, r_1, is defined as the slope of this dependence (*2*):

$$(1/T_1)_{obsd} = (1/T_1)_d + r_1[M]$$

where $(1/T_1)_{obsd}$ is the observed solvent relaxation rate in the presence of a paramagnetic species, $(1/T_1)_d$ is the solvent relaxation rate in the absence of a paramagnatic species. In this experiment, the concentrations of the paramagnetic species [Gd^{3+}] were measured by an ICP Atomscan-2000 spectrometer. The solvent longitudinal relaxation time (T_1) for gadolinium complexes were carried out on a 10^{-3} M solution of gadolinium complexes in distilled water. Thus r_1 for gadolinium complexes in distilled water could be calculated.

MR Imaging. KunMing mice bearing hepatoma (H_{22}) in the right lower limb (weight: 30 ± 2 g) were anesthetized with 10% urethane solution (10 mL/kg), positioned prone and fixed to a polystyrene cradle with adhesive tape to minimize the motion. After performing nonenhanced MR imaging, a solution of PAEA-Gd-DTPA-SD (M_1, 0.1 mmol/kg) in 0.9% sodium chloride was injected via the tail vein. Coronal images of the right lower limb were obtained with a T_1-weighted spin−echo sequence [Repetition time (TR) 500 ms, echo time (TE) 15 ms, the field of view is 40 mm, with an image matrix of 128×128. Six slices were taken and slice thickness was 2 mm, with a 1 mm interslice gap.].

Statistical Analysis. Six T_1-weighted image slices were taken for the hepatoma in the right lower limb of each mouse. The top and bottom slices were not included in the data analysis to prevent confounding partial volume effects at the edges of the tumors. The average

Table 1. M_n, M_w, and Polydispersity of Polyaspartamide

polymer carriers	M_n ($\times 10^4$)	M_w ($\times 10^4$)	polydispersity
PHEA	2.6	3.8	1.46
PAEA	1.2	1.9	1.58
PHPA	1.5	2.4	1.60
PABA	2.0	3.4	1.70
PAHA	1.8	2.2	1.22

Table 2. Relaxivity of Gadolinium Complexes[a]

gadolinium complex	r_1 [1/(mmol/L)/s]
Gd-DTPA	7.0 ± 0.4
PHEA-Gd-DTPA-SD (M_1)	24.7 ± 1.2
PHEA-Gd-DTPA-SD (M_2)	12.0 ± 0.7
PHPA-Gd-DTPA-SD	14.8 ± 0.5
PAEA-Gd-DTPA-SD (M_1)	14.3 ± 0.7
PAEA-Gd-DTPA-SD (M_2)	8.1 ± 0.6
PABA-Gd-DTPA-SD	9.9 ± 0.3
PAHA-Gd-DTPA-SD	9.2 ± 0.2

[a] Temp: 17 °C NMR, frequency: 300 MHz, $T_{1d} = 2.579 \pm 0.017$ s.

relative signal intensities (pre-injection and postinjection at different times) within the region of interest were normalized to the water label background ($RI_{background}$) at each of the imaging conditions. The percentage of contrast enhancement in the signal from the tumors was calculated according to the following

$$\text{enhancement (\%)} = 100\%\ (RI_{post} - RI_{pre})/(RI_{pre} - RI_{background})$$

RESULTS AND DISCUSSION

A series of water-soluble polyaspartamide ligands PHEA-DTPA-SD, PHPA-DTPA-SD, PAEA-DTPA-SD, PABA-DTPA-SD, and PAHA-DTPA-SD were synthesized and their gadolinium complexes were also prepared. The ^{1}H NMR and UV spectra showed the characteristic peaks of benzene group, indicating that sulfadiazine was covalently bound to polyaspartamide (Table 1). The IR spectra of the free polyaspartamide ligands showed characteristic absorption peaks of carboxyl with 1715−1630 cm^{-1}, while these peaks disappeared and strong absorption peaks with 1660−1540 cm^{-1} were present in IR spectra of their gadolinium complexes. Thus the results exhibited the formation of gadolinium complexes. Moreover, the average mole ratio of attached DTPA to polymeric repeat units increased and the amount of gadolinium ion in the polyaspartamide complexes became larger as the mole ratio of DTPA active ester/(polymeric repeat units) in feed in the reaction process increased.

Macromolecular MRI contrast agents usually exhibit more effective relaxation rates than that of the low molecular weight metal complexes alone and improve the relaxivity per gadolinium atom due to a slowly tumbling systems and an increase in rotational correlation time. Table 2 illustrated that polyaspartamide gadolinium chelates containing SD groups possessed higher relaxivities than that of Gd-DTPA.

The T_1-weight images of hepatoma at various points in time are shown in Figure 1. Compared to those mice receiving no injection of MRI contrast agent, the signal intensities (SI) of the tumors in mice injected with PAEA-Gd-DTPA-SD (M_1, 0.1 mmol/kg) were obviously enhanced, the irradiated portion of the tumors was brighter and the demarcation became clearer during the detection time, while those of the surrounding tissues, such as the muscle in the lower limb, showed a little change.

Two hours after injection with PAEA-Gd-DTPA-SD (M_1), the signal in hepatoma in mice were still enhanced

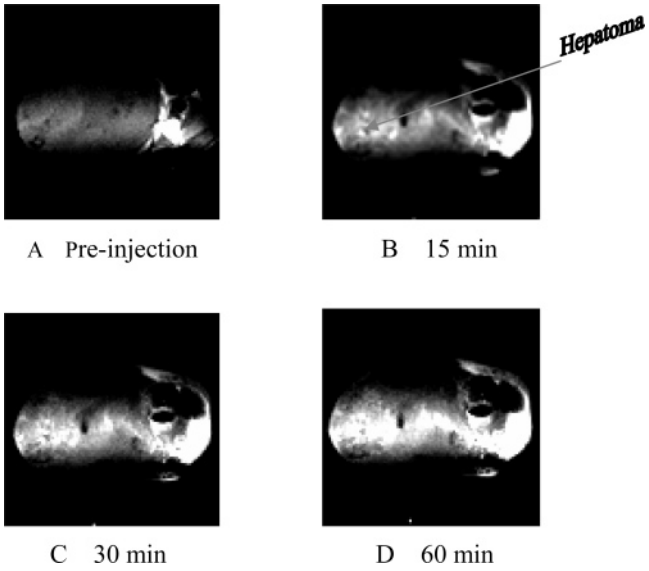

Figure 1. A is the T_1-weighted image of the right lower limb of mice with H_{22} receiving no MRI contrast agent; B, C, and D are the T_1-weighted images of the right lower limb of mice with H_{22} which received injection with PAEA-Gd-DTPA-SD (0.1 mmol/kg) after 15 min, 30 min, and 60 min, respectively.

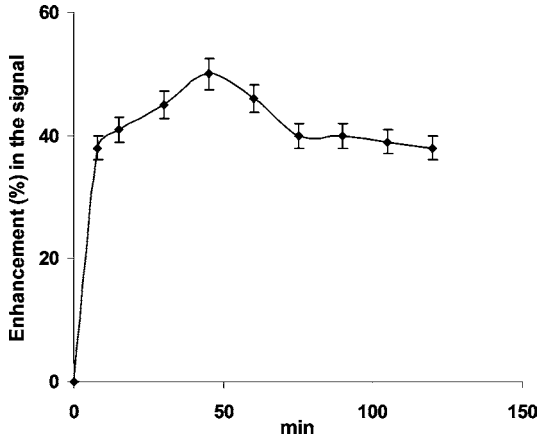

Figure 2. Signal enhancement (%) of the tumors in mice at different times after injection with PAEA-Gd-DTPA-SD (M_1, 0.1 mmol/kg).

by 138%, indicating it had a prolonged intravascular duration time in tumors of approximately 2 h (Figure 2). Thus the polyaspartamide gadolinium chelates containing SD groups could provide the prolonged enhancement of the tumors (Figure 2).

In summary, polyaspartamide gadolinium complexes containing sulfadiazine groups possess higher relaxation effectiveness than Gd-DTPA. MR imaging showed that PAEA-Gd-DTPA-SD (M_1) greatly enhanced the contrast of MR images of hepatoma in the lower limb of mice and provided prolonged intravascular duration. Thus the polyaspartamide gadolinium chelate is expected to be used as the potential macromolecular MRI contrast agents for hepatoma in mice.

ACKNOWLEDGMENT

We thank the QUT's Postdoctoral Research Fellowship Scheme and the Chinese National Natural Science Foundation (No. 29874028) for their financial support.

LITERATURE CITED

(1) Lauterbur, P. C. (1973) Image formation by induced local interactions: examples employing nuclear magnetic resonance. *Nature 242*, 190−191.

(2) Lauffer, R. B. (1987) Paramagnetic metal complexes as water proton relaxation agents for NMR imaging: theory and design. *Chem. Rev. 87*, 901−927.
(3) Caravan, P., Ellison, J. J., Mcmurry, T. J., and Lauffer, R. B. (1999) Gadolinium (III) chelates as MRI contrast agents: structure, dynamics, and applications. *Chem. Rev. 99*, 2293−2352.
(4) Wen, J., Zhuo, R. X., and Wang, L. (1998) Aromatic DTPA-Bis(amide) gadolinium complexes as hepatobiliary contrast agents for magnetic resonance imaging. *Chin. J. Magn. Reson. 15* (3), 217−221.
(5) Van Beer, B. E., Gallez, B., and Pringot, J. (1997) Contrast-enhanced MR imaging of the liver. *Radiology 203*, 297−306.
(6) Yan, G. P., and Zhuo, R. X. (2001) Research progress of magnetic resonance imaging contrast agents. *Chin. Sci. Bull. 46* (7), 531−538.
(7) Giammona, G., Carlisi, B., and Palazzo, S. (1987) Reaction of α,β-poly (N-hydroxyethyl)-D,L-aspartamide with derivatives of carboxylic acids. *J. Polym. Sci. Polym. Chem. 25*, 2813−2818.
(8) Giammona, G., Carlisi, B., Cavallaro, G., Donato, I., Pinio, F., and Turco Liveri V. (1990) Calorimetric investigation of the interaction betweenα,β-Poly (N-hydroxy-ethyl)-D,L-aspartamide and surfactants. *Int. J. Pharm. 64*, 239−242.
(9) Giammona, G., Carlisi, B., Pitarresi, G., and Fontana, G. (1991) Hydrophilic and hydropholic polymeric derivatives of antiinflammatory agents such as Alclofenac, Ketoprofen and Ibuprofen. *J. Bioact. Compat. Polym. 6*, 129−141.
(10) Giammona, G., Carlisi, B., Pitarresi, G., Cavallaro, G., and Turco Liveri, V. (1992) Water-soluble copolymers of an antiviral agent: synthesis and their interaction with a biomembrane model. *J. Controlled Release 22*, 197−204.
(11) Giammona, G., Fontana, G., Pitarresi, G., and Carlisi, B. (1998) Coupling of the antiviral agent zidovudine to polyaspartamide and in vitro drug release studies. *J. Controlled Release 54*, 321−331.
(12) Yan, G. P., Zhuo, R. X., Xu, M. Y., Li, L. Y., and Tang, Y. F. (2001) Liver-targeting macromolecular MRI contrast agents. *Sci. China, Ser. B 44* (4), 344−352.
(13) Bartulin, J., Przybylski, M., Ringsdorf, H., and Ritter, H. (1994) Pharmacologically active polymers, 6: sulfadiazine and boron derivatives as potential carriers for polymers into cancer tissue. *Macromol. Chem. 175*, 1007−1010.
(14) Huang, J. L., Wang, H. Y., and Zhou, C. L. (1995) Ring-opening polymerization of ethylene oxide by anion initiation using sulfadiazine as parents compound. *J. Appl. Polym. Sci. 58*, 11−8.
(15) Yan, G. P., Zheng, C. Y., Cao, W., Li, W., Li, L. Y., Liu, M. L., Zhang, Y. X., and Zhou, R. X. (2003) Synthesis and preliminary evaluation of gadolinium complexes containing sulfonamide groups as potential MRI contrast agents. *Radiography 9*, 35−41.
(16) Shi, F. Q. (1990) How to copy the disease model of animals. *YiXue DongWu ShiYan FangFa*, pp 226−232, Chapter 4, RenMing WeiSheng Press, Bejing, China.
(17) Yan, G. P., Zhuo, R. X., and Zheng C. Y. (2001) Study on the anticancer drug 5-fluorouracil-conjugated polyaspartamides containing hepatocyte-targeting group. *J. Bioact. Compat. Polym. 16* (4), 277−293.
(18) Yan, G. P., Zhuo, R. X., Zhang, X., Zhang, X., Li, L. Y., and Liu, M. L. (2002) Tumor-selective macromolecular MRI contrast agents. *J. Bioact. Compat. Polym. 17* (2), 139−151.
(19) Neuse, E. M., Perlwitz, A. G., and Schmitt, S. (1991) Water-soluble polyamides as potential drug carriers. *Angew. Makromol. Chem. 192*, 35−50.

BC050026L

A Thermoresponsive Chitosan–NIPAAm/Vinyl Laurate Copolymer Vector for Gene Transfection

Shujun Sun,[†] Wenguang Liu,*[,†] Nan Cheng,[†] Bingqi Zhang,[†] Zhiqiang Cao,[†] Kangde Yao,[†] Dongchun Liang,[‡] Aijun Zuo,[‡] Gang Guo,[‡] and Jingyu Zhang[‡]

Research Institute of Polymeric Materials, Tianjin University, Tianjin 300072, P. R. China, and Institute of Endocrinology, Tianjin Medical University, Tianjin 300070, P. R. China

Received March 9, 2005; Revised Manuscript Received June 13, 2005

A carboxyl-terminated *N*-isopropylacrylamide/vinyl laurate (VL) copolymer was prepared and coupled with chitosan (molecular weight = 2000) to produce a chitosan–NIPAAm/VL copolymer (PNVLCS) vector. The aqueous solution of PNVLCS displayed an obvious thermoresponsive behavior with a lower critical solution temperature (LCST) about 26 °C. The transmission electron microscopy (TEM) showed that the size of PNVLCS/DNA complexes varied with charge ratios (+/−), and the smaller nanoparticles were formed at higher charge ratios. DLS revealed that the size of complex particles was dependent on temperature. The results of temperature-variable circular dichroism (CD), UV, and electrophoresis retardation indicated that at lower charge ratios, DNA in the complexes assume a B conformation, whereas increasing charge ratios caused B → C type conformation transformation; the dissociation–formation of PNVLCS/DNA complexes could be tuned by varying temperature: at 37 °C, the collapse of PNIPAAm in PNVLCS was favorable for the formation of compact complexes, shielding more DNA from exposure; at 20 °C, the hydrated and extended PNIPAAm chains facilitated the unpacking of DNA from PNVLCS, increasing the exposure of DNA. PNVLCS was used to transfer plasmid-encoding β-galactosidase into C_2C_{12} cells. The level of gene expression could be controlled by varying incubation temperature. The transfection efficiency of PNVLCS was well improved by temporarily reducing culture temperature to 20 °C, whereas naked DNA and Lipofectamine 2000 did not demonstrate the characteristics of thermoresponsive gene transfection.

INTRODUCTION

In the past decade, much progress has been made in the study of chitosan (CS)-based nonviral vectors for gene transfection, and many encouraging results have been acquired (*1*–*4*). To further improve gene transfection level, a variety of strategies were reportedly employed recently, such as coupling deoxycholic acid (*5*), galactose (*6*), poly(vinyl pyrrolidone) (*7*), and urocanic acid (*8*) to chitosan. Although there were reports supporting that the modification of chitosan could really increase the transfection efficiency of chitosan–DNA complexes, and there was even in vivo study on using chitosan as a vector for gene therapy (*9*, *10*), the transfection efficiency of chitosan is relatively lower compared with that of liposome (*11*, *12*).

Like conventional polycationic vectors, chitosan forms polyelectrolyte complex (PEC) with DNA through electrostatic interaction between primary amino and phosphate groups. The strong electrostatic interaction is favorable for the formation of PEC, but on the other hand, it prevents gene dissociation from its carrier in nucleus, impeding the access of RNA polymerase to DNA so that gene expression level is decreased (*13*).

To weaken the electrostatic attraction of chitosan with DNA, long hydrophobic alkyl side chains were incorporated into chitosan, and transfection efficiency was increased with elongating the length of side chains. It was considered that the hydrophobic chains promoted the cell entry and the unpacking of genes from alkylated chitosan vector (*14*), but the alkylated chitosans were insensitive to environment, so gene expression could not be controlled by varying external stimuli. To fulfill this objective, Hennink's team explored the feasibility of thermosensitive poly(*N*-isopropylacrylamide)(PNIPAAm) copolymer as a smart gene delivery vector (*15*). They merely investigated the influence of temperature on the stability of the complexes, but not on temperature-dependent gene transfection. Recently, Kurisawa et al. reported a thermoreversible terpolymer vector, poly(*N*-isopropylacrylamide (NIPAAm)-*co*-2-(dimethylamino)-ethyl methacrylate DMAEMA)-*co*-butyl methacrylate (BMA)) (*16*). It was found that at a temperature above LCST of this copolymer, a tight copolymer/pCMV-lacZ plasmid DNA complex was formed, which was beneficial for the cellular uptake and protection of DNA from DNase attack. While lowering incubation temperature below LCST, the gene dissociated from its carrier, improving gene transfection even with small doses of DNA. Both branched and linear polyethyleneimines (PEI) have been extensively used to transfect a variety of cells in vitro and in vivo (*17*, *18*). But its significant toxicity has been a bottleneck for its clinical application (*19*, *20*). Türk et al. prepared temperature-sensitive PNIPAAm-*b*-PEI copolymers (*21*). The copolymerization with PNIPAAm reduced the cytotoxicity of branched PEIs with higher molecular weights, and PNIPAAm/PEI25L (linear PEI with molecular weight of 25 kDa) did not show any

* To whom correspondence should be addressed: E-mail: wgliu@tju.edu.cn.

[†] Research Institute of Polymeric Materials, Tianjin University.

[‡] Institute of Endocrinology, Tianjin Medical University.

10.1021/bc0500701 CCC: $30.25 © 2005 American Chemical Society
Published on Web 06/28/2005

significant toxicity. At body temperature, this copolymer vector could ferry more DNA into Hela cells. In particular, PEI25L obtained the most successful gene expression with low toxicity. Novel smart gene vectors of poly(L-lysine)-*graft*-poly(*N*-isopropylacrylamide) were also designed by Oupický et al. (*22*). It was demonstrated that the structural density and surface charge of the copolymer/DNA complexes could be adjusted by temperature. Moreover, it increased as the PNIPAM grafts collapsed above their phase transition temperature. In addition, more DNA tended to be released from polyelectrolyte complexes in the presence of PNIPAAm with addition of heparin.

To our best knowledge, research work on controllable gene expression of chitosan-based vectors has not been reported yet in the literature to date. In this study, we synthesized carboxyl-terminated NIPAAm/vinyl laurate (VL) random copolymer and coupled PNIPAAm/PVL to chitosan to generate a thermoresponsive CS−NIPAAm/VL (PNVLCS) copolymer vector. The PNVLCS was investigated as temperature-sensitive transgene vector for the first time. The temperature-dependent physicochemical properties of PNVLCS−DNA complexes were elucidated in detail. This copolymer vector was applied to the mediation of plasmid DNA transfection into C_2C_{12} cells, and the control of gene expression was examined at varied temperatures.

EXPERIMENTAL SECTION

Materials. *N*-Isopropylacrylamide (NIPAAm, Aldrich Chemical. Co.) was purified by recrystallization in hexane and dried in vacuo at 25 °C. Vinyl laurate (VL) was purchased from Fluka. The chain transfer agent, thioglycolic acid (TGA) (Sigma) was utilized to include carboxylic acid ends to the copolymer chains. The initiator, 2,2′-azoisobutyronitrile (AIBN) was recrystallized from methanol. Chitosan (degree of deacetylation = 80.3%, molecular weight = 2 kDa) was supplied by Qingdao Haihui Bioengineering Ltd. China. The water-soluble activating agent, 1-ethyl-3-(3-dimethylaminopropyl)carbodiimide hydrochloride (EDAC) was obtained from Sigma. Plasmid pTracer-CMV/Bsd/*lacZ* and Lipofectamine 2000 reagent were provided by Invitrogen. Ethidium bromide (EB) and *N*,*N*,*N*′,*N*′-tetramethylethylenediamine (TEMED) were provided by Fluka. All other reagents used were analytical grade and used as received.

C_2C_{12} cells were maintained in Dulbecco's Modified Eagles Medium (DMEM, Sigma) supplemented with L-glutamine, penicillin/streptomycin, and 10% fetal bovine serum. Cells were incubated at 37 °C in a humidified atmosphere containing 5% CO_2 and used at appropriate degrees of confluence.

Synthesis of Copolymers. First, the carboxylic acid-terminated copolymer of NIPAAm and vinyl laurate (PNVLCOOH) was synthesized by a free radical polymerization in THF. *N*-Isopropylacrylamide(2.0 g), vinyl laurate(0.98 g), TGA (50 μL), and AIBN (20 mg) were dissolved in THF (25 mL). Polymerization was conducted under nitrogen-atmosphere, in a sealed reactor placed into a thermostated oil bath at 65 °C for 8 h. Once cooled to room temperature, the solution was added to excess amount of diethyl ether to precipitate PNVLCOOH. To remove the impurities in precipitated copolymer, dissolution−precipitation procedure was repeated three times, and the resultant precipitate was dried in a vacuum overnight.

Second, PNVLCOOH was coupled to chitosan (CS) by the reaction of the carboxylic acid groups activated with EDAC with the amine groups of chitosan. Chitosan (2.2 g) was dissolved in TEMED/HCl buffer (pH4.8, 25 mL) at 10 °C, and PNVLCOOH(1.5 g) was added to the solution. After 0.21 g of EDAC was added, the solution was stirred at 10 °C for 10 h. For purification, the solution of copolymer was raised to 28 °C, and the precipitate was collected by centrifugation (15000 rpm for 5 min) at 28 °C. Other water-soluble impurities in precipitate were removed by dialysis (MWCO 3500) against deionized water for 5 days at 4 °C. The final copolymer (PNVLCS) was recovered by lyophilization of the dialyzed solution.

PNVLCS/DNA Complexes Formation. To ensure that chitosan in PNVLCS was positively charged, PNVLCS was dissolved in 0.1 M sodium acetate/0.1 M acetic acid buffer (pH 5.4) to form a solution of 1.0 mg/mL, and 0.1 mg/mL of DNA solution was prepared in the same way. A series of PNVLCS/DNA complexes at various charge ratios were prepared by mixing PNVLCS solutions with a DNA solution, vortexing for 15 s, and incubating for 30 min at 37 °C prior to characterization use. It was noted that during complex preparation, the volume of DNA was constant and the volume of PNVLCS solution was varied to adjust the theoretical charge ratio (+/−) (molar ratio of amine to phosphate groups). All complexes for the characterization below were prepared in terms of this method unless otherwise statement.

FTIR Analysis. The solutions of chitosan, PNVLCOOH, and PNVLCS were poured into freshly cleaned plastic dishes and maintained in a vacuum overnight at 50 °C for film formation. FTIR spectra of the samples were measured over 4000−800 cm^{-1} on a Bio-Rad FTS 135 spectrophotometer.

^{1}H NMR Spectroscopy. To estimate the composition ratios of copolymers, ^{1}H NMR spectra of PNVLCOOH and PNVLCS were measured at ambient temperature with a Varian UNITY plus-400 NMR spectrometer using D_2O as a solvent.

Gel Permeation Chromatography (GPC). The molecular weights and molecular weight distributions of PNVLCOOH and PNVLCS were determined by gel permeation chromatography(GPC Waters 510/M32) using water as a mobile phase. Monodisperse polystyrene (Polymer Laboratories Inc., MA) was used for calibration. GPC analysis showed $\overline{M}_n$ = 3079, PDI = 1.66 (PNVLCOOH) and $\overline{M}_n$ = 4715, PDI = 1.37 (PNVLCS). Noted that the measured molecular weight is lower than theoretical value, 5079. This discrepancy is probably from polystyrene calibration standard and aggregation of NIPAAm−VI chains.

Determination of LCST of Polymer Solution. The variation in the turbidity of 1.0 wt % aqueous copolymer solutions was monitored as a function of temperatures at a fixed wavelength of 500 nm on a UV PC2501 UV−vis spectrophotometer equipped with a circulating water bath. The LCSTs were taken at the inflection point in the curves of optical density versus temperature.

Transmission Electron Microscopy(TEM). The morphology and size of PNVLCS/plasmid DNA complexes at different charge ratios (+/−) were observed using a JEOL JEM-100CXII TEM. First, one drop of the complexes was deposited on carbon-coated grids. After 5 min on the grids, 1.5% phosphotungstic acid (PTA) was added immediately to negatively stain the complexes for additional 5 min, and then the complexes were recorded on films with TEM.

Dynamic Light Scattering (DLS). Particle size of PNVLCS/DNA complexes was measured by dynamic

light scatting (DLS). DLS measurement was carried out with an argon ion laser system tuned at 514 nm. The complex solutions were filtered through a 0.45 μm filter (Millipore) directly into a freshly cleaned 10 mm-diameter cylindrical cell. The intensity of autocorrelation was measured at a scattering angle (θ) of 90° with a Brookhaven BI-9000AT digital autocorrelator at room temperature. When the difference between the measured and the calculated baselines was less than 0.1%, the correlation function was accepted. The mean diameter was evaluated by the Stokes−Einstein relationship. In this experiment, particle size of complexes was determined at 20 and 37 °C, respectively.

Circular Dichroism (CD). Samples were prepared at various PNVLCS/DNA charge ratios with DNA concentration of 40 μg/mL. Then the solutions were diluted with 0.1 M sodium acetate/0.1 M acetic acid buffer to a final DNA concentration of 1.1×10^{-4} M. CD spectra were collected in a 1 cm path length cuvette using a J-7150 spectropolarimeter in a range of wavelengths of 320−180 nm at 20 and 37 °C, respectively. Measurements were performed with a speed of 20 nm/min and a resolution of 0.5 nm. The spectra were corrected by subtracting the background of sodium acetate/acetic acid buffer, and three spectra were accumulated and averaged for each sample. The CD signal was converted to molar ellipticity [θ], deg·cm^2/dmol.

Temperaure-Variable UV. Temperaure-variable UV spectrophotometer was used to analyze the formation and dissociation of PNVLCS/DNA complex. The complexes at various charge ratios (+/−) were prepared by mixing different amount of PNVLCS solution with 3 μL of plasmid DNA solution. The total volume of the complexes was adjusted to 1 mL before incubation. The absorbance of the complexes at 20 °C and 37 °C was separately recorded at 260 nm on UV-2501PC spectrophotometer. The solvent was used as blank reference.

Gel Retardation Assay. PNVLCS/DNA complexes with varied charge ratios were prepared as mentioned above. The complex formation was carried out for 30 min at 20 and 37 °C, respectively. Aliquots of the complex solutions were loaded onto 0.6 wt % agarose gel (100V), and DNA bands were visualized by ethidium bromide staining. These gel assays were performed at temperature below and above LCST of PNVLCS solution for 20 min.

In Vitro Gene Expression. Preparation and Purification of Plasmid. Plasmid pTracer-CMV/Bsd/*lacZ* was amplified in *E. coli* and then prepared and purified using Wizard Purification Plasmid DNA Purification System (Promega). DNA concentration and purity were assessed via UV optical intensity at 260 nm and 280 nm. The plasmid DNA was stored at −20 °C until transfection experiments.

Cell Transfection. C_2C_{12} cells, a mouse myoblast cell line derived from mouse skeletal muscle, were used in this experiment considering that (1) this cell line has been shown to be a suitable host for stable transfection of exogenes (*14*); (2) C_2C_{12} myoblast has proved to be capable of synthesizing some osteogenesis factors (*23*) and secreting the hormone or growth factors (*24*). Thus for our future gene therapeutic application, a target gene will be delivered into muscle cells within the cavum articulare by PNVLCS vector to treat cartilage injury.

C_2C_{12} cells were seeded at a concentration of 6×10^4/mL, 0.5 mL/well, in 24-well plate. These wells were then incubated at 37 °C in 5% CO_2 for 24 h in DMEM supplemented with fetal bovine serum (FBS) and antibiotics. Before transfection the medium in each well was removed, and rinsed with fresh DMEM (without FBS and antibiotics). Then the transfection solutions (containing PNVLCS/DNA complexes described above) were placed in each well and left in the CO_2 incubator. Three hours later, the medium containing complex solution was removed and then incubated in fresh DMEM medium supplemented with FBS and antibiotics at different temperatures and times: (1) 45 h at 37 °C, and (2) 18 h at 37 °C + 3 h at 20 °C + 24 h at 37 °C.

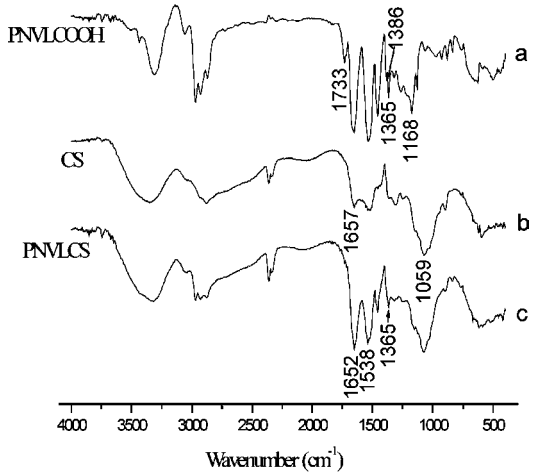

Figure 1. FTIR spectra of PNVLCOOH (a), chitosan (b), and PNVLCS (c).

After the incubation was finished, the activity of β-galactosidase in transfected cells was determined using β-Galactosidase Enzyme Assay System with Reporter Lysis Buffer (Promega, Madison, WI). The cells were washed twice with PBS and harvested with reporter lysis buffer. The β-galactosidase activity in transfected cells was measured at wavelength 450 nm by plate-reader of Labsystem using *o*-nitrophenyl-β-D-galactopyranoside (ONPG) as substrate. Cell lysates and a series of protein standard solutions prepared with bovine serum albumin (BSA) were subjected to BCA Protein Assay (Pierce, Rockford, IL) to quantify the total amount of protein in the transfected cells. The transfection efficiency was evaluated as the β-galactosidase expression level per microgram of cellular protein harvested (milliunit/mg protein). For comparison, the naked DNA and Lipofectamine 2000 were used as controls. The ratio of Lipofectamine 2000 to DNA was 2 μL/1 μg according to the recommended protocol. Each transfection experiment was carried out in triplicate.

Statistical Analysis. Both Student's t-test and one-way ANOVA with post hoc tests were used to evaluate the thermoresponsive transfection efficiency with $P < 0.05$. The transfection efficiency at constant 37 °C was treated as a control.

RESULTS AND DISCUSSION

Characteristics of PNVLCS Copolymer. The FTIR spectra of the PNVLCOOH, chitosan, and PNVLCS are given in Figure 1. As shown in Figures 1a and 1c, the amide peaks of NIPAAm units appear at 1650−1660 cm^{-1} (C=O stretching, amide I), 1530−1540 cm^{-1} (N−H bending, amide II), and 3420−3550 cm^{-1} (N−H stretching). A C=O stretching peak (related to carboxylic acid unit and ester unit of vinyl laurate) appears at 1730−1740 cm^{-1} in Figure 1a. This peak decreases when the copolymerization between PNVLCOOH and CS occurred (in Figure 1c). The bands at 1365 and 1386 cm^{-1} are attributed to the deformation of the two methyl groups in isopropyl groups (*25*). In the chitosan spectrum (Figure

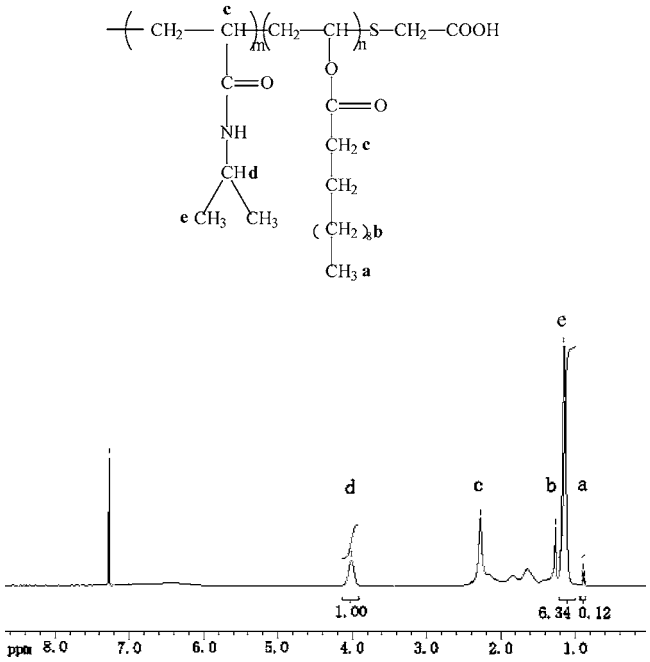

Figure 2. ^{1}H NMR spectrum of PNVLCOOH (in D_2O). The composition ratio(NIPAAm/VL, mol/mol) of PNVLCOOH is determined by comparing the peak areas of d and a in the spectrum.

1b), the characteristic absorbance of amide I is around 1657 cm^{-1}, and C−O stretching peak of pyranose ring is at 1029−1071 cm^{-1} (*26*), whose appearance in Figure 1c indicates the introduction of the chitosan unit into the copolymer chain.

The ^{1}H NMR spectrum of PNVLCOOH is depicted in Figure 2. It is evident that the peaks of NIPAAm and VL are well resolved (*27*, *28*), so the composition ratio (NIPAAm/VL, mol/mol) of PNVLCOOH is determined by comparing the peak areas of d and a in ^{1}H NMR spectrum, which represent the proton of the isopropyl CH in NIPAAm and the CH_3 of laurate (*28*), respectively. The calculated NIPAAm/VL composition ratio is 25:1, suggesting that only partial VL monomer reacted with NIPAAm supposedly due to its low reactivity caused by its steric hindrance of long alkyl chain (the actual feed ratio is 4:1). Noted that in Figure 2, the structure of PNVLCOOH does not necessarily reflect the single case of chain transfer; statistically, thioglycolic acid is likely to attach to the NIPAAm end. Herein, only one case is presented.

In our study, hydrophobic vinyl laurate was used to lower the LCST of the copolymer so that the formation and dissociation of PNVLCS/DNA complexes can be easily modulated by controlling temperature. It was also expected that incorporation of a small quantity of laurate vinyl could increase the cellular entry of PNVLCS vector. In addition, we will focus on the effect of charge ratios of vector to DNA on the properties of the complexes.

In ^{1}H NMR spectrum of PNVLCS (Figure 3), there still appear some feature peaks of NIPAAm (*29*), but the signal peaks of VL cannot be differentiated. The peaks at 2.702, 3.449, and 4.434 ppm are assigned to the H-2, H-3, and H-1 of chitosan (*30*). The signals of H-4, H-5, H-6 of chitosan cannot be resolved due to overlapping with those of NIPAAm. Combining the results of FTIR and NMR, it is reasonable to consider that chitosan has been coupled to PNVLCOOH.

In designing chitosan−NIPAAm/vinyl laurate, we first considered the LCST of the resultant copolymer solution.

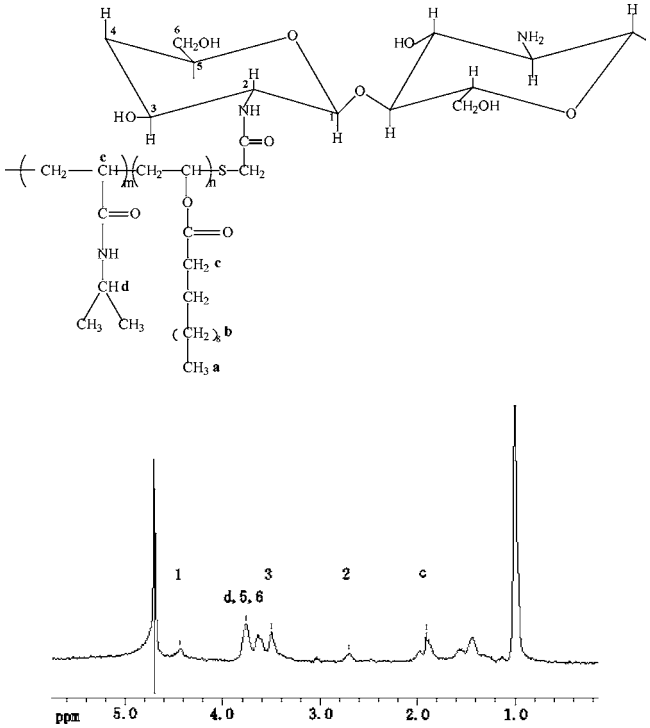

Figure 3. ^{1}H NMR spectrum of PNVLCS (in D_2O).

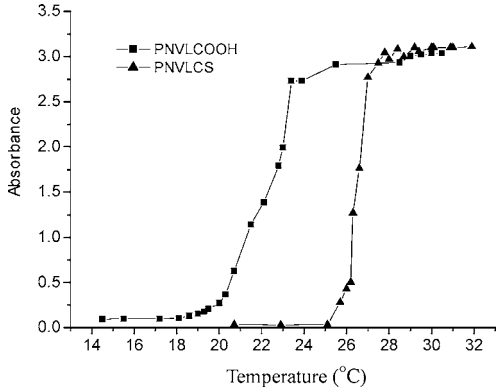

Figure 4. Absorbance versus temperature plots obtained for 1.0 wt % aqueous solutions of PNVLCOOH and PNVLCS. The LCSTs were taken at the inflection point in the curves of optical density versus temperature.

Figure 4 presents the variation in the turbidity of PVLCOOH and PNVLCS solutions as a function of temperature. From the figure, it is seen that there exist sharp changes of absorbance in both cases of PNVLCOOH and PNVLCS solutions. Obviously, introducing hydrophobic laurate moieties to the PNIPAAm chains causes a significant decrease in LCST from 32 °C to 20 °C. While the influence of hydrophilic carboxyl-capping on LCST can be neglected. In comparison, the LCST of PNVLCS solution is increased to 26 °C when PNVLCOOH is coupled with hydrophilic chitosan chains.

Physicochemical Properties of PNVLCS/DNA Complexes. The representative TEM images of PNVLCS vector and PNVLCS/DNA complexes with varied charge ratios are exhibited in Figure 5. The complexes at the selected charge ratios display globular shape, and the average sizes of globules in TEM images are summarized in Table 1. Somewhat surprisingly, PNVLCS also appears micelle-like morphology, and its average diameter is as high as 118 nm. In our previous work on thermoresponsive transition behavior of vinyl laurate-

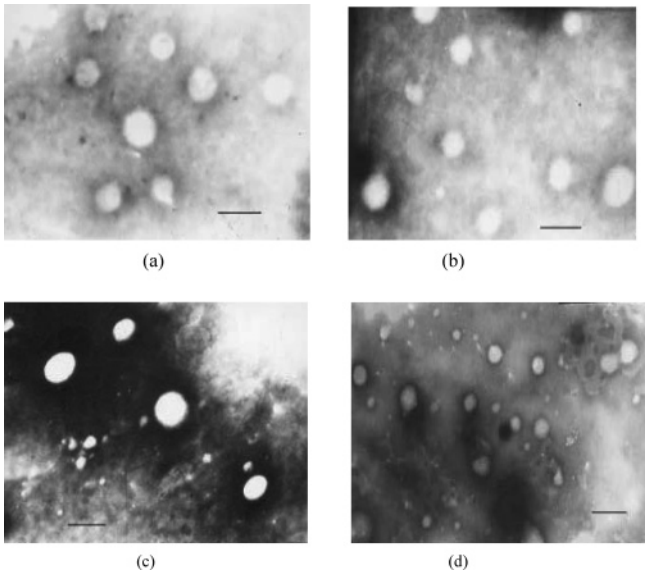

Figure 5. TEM images of PNVLCS (a) and PNVLCS/DNA complexes at charge ratios of 1:2 (b), 1:1 (c), and 5:1 (d). The scale bars = 200 nm. 1.5% phosphotungstic acid (PTA) was used as a negative staining agent.

Table 1. Particle Size Obtained from TEM Images

complex charge ratio (+/−)	diameter (nm)
PNVLCS	118 ± 10
1:8	100 ± 9
1:2	121 ± 15
1:1	148 ± 29
2:1	87 ± 23
5:1	83 ± 13
15:1	67 ± 14

Table 2. Mean Diameters of PNVLCS/DNA Complexes at 20 and 37 °C[a]

	mean diameter (nm)	
complex charge ratio (+/−)	at 20 °C	at 37 °C
1:8	87 ± 11	92 ± 15
1:2	158 ± 24	202 ± 23
1:1	146 ± 22	141 ± 17

[a] Values are the results of three measurements and are denoted as mean ± SD.

modified PNIPAAm copolymer solution (*28*), we found that incorporation of VL moieties could facilitate hydrophobic aggregation of chains far below the LCST. Therefore, NIPAAm/VL-coupled hydrophilic chitosan copolymer is inclined to form a larger micelle-like structure even at room temperature.

With the increment of charge ratio, the size of complexes increases and reaches a maximum at 1:1. Interestingly, with a further increasing charge ratio up to 15:1, the size of complex shows a decreasing trend. The size of complex is dependent on the interplay of hydrophobic and electrostatic interactions between DNA and PNVLCS. At lower charge ratio, the self-aggregation from hydrophobic alkyl chains of VL in PNVLCS causes a slight increase in the size of complex. Whereas at higher charge ratio, more compact complexes may be resulted from the strong electrostatic attraction.

To study the effects of temperature on the size of PNVLCS/DNA complexes, DLS experiment was performed at 20 °C (lower than LCST) and 37 °C (higher than LCST). In our experiment, we only selected three charge ratios, 1:8, 1:2, and 1:1 (Table 2). In the cases of 1:8 and 1:2, the mean diameter of complexes is increased

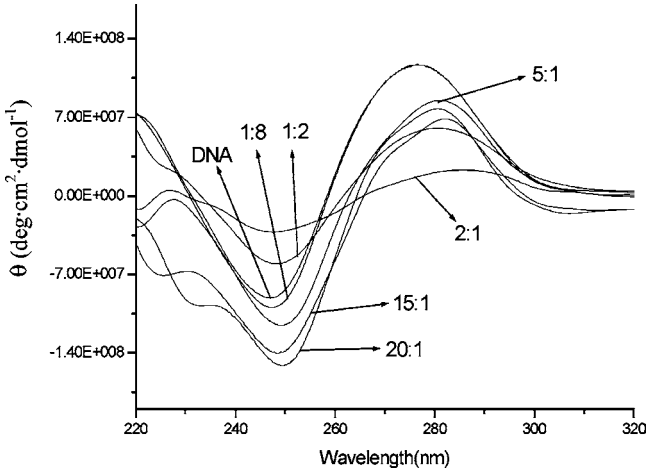

Figure 6. CD spectra of DNA and PNVLCS/DNA complexes at different charge ratios (at 20 °C). In each complex solution, the concentration of DNA is 1.1×10^{-4} M. The spectra were corrected by subtracting the background of sodium acetate/acetic acid buffer (pH 5.4), and three spectra were accumulated and averaged for each sample.

while temperature is raised from 20 to 37 °C. For charge ratio of 1:1, the diameter is diminished to a measurable extent while temperature is increased. The temperature-dependent change in the size of complex could be ascribed to two opposite factors. On one hand, at temperature above LCST, PNIPAAm chains collapse to form highly compacted structure, but meanwhile the hydrophobic chains are prone to self-aggregate. In some range of charge ratios, the aggregation plays a dominant role, rendering the size of complexes larger; at other charge ratios, the role of aggregation is marginal, and instead the collapse of PNIPAAm chains in combination with electrostatic attraction facilitates the formation of dense complexes, that is, a smaller size of particles.

The CD spectra of PNVLCS/DNA complexes with various charge ratios determined at 20 °C are illustrated in Figure 6. The positive and negative ellipticities centered around 275 and 245 nm arise from the DNA itself, revealing a type of double-stranded structure of DNA. The free DNA shows a typical CD spectrum for B-type DNA conformation.

At 1:8 charge ratio, the peak intensity remains nearly unchanged compared to that of free DNA; with the increase of charge ratio, the molar ellipticities of the DNA are suppressed, and the positive band at 275 nm is red-shifted. Interestingly, one can see two distinct variation trends of DNA conformation in the selected range of charge ratios. From 1:8 to 2:1, DNA in these complexes assumes a B conformation. A similar result was reported in our previous work on chitosan/DNA complexes (*31*), but the Cotton patterns observed with charge ratios from 5:1 to 15:1 demonstrate that the DNA changes from B to C conformation. The B−C type transformation was also reported in PLL-*g*-dextran/DNA complex system (*32*). We also recorded the CD spectra for the above series of PNVLCS/DNA complexes at 37 °C. The variation trend of CD pattern is identical to that at 20 °C. Though at the temperature above LCST, a heavy syneresis of PNIPAAm occurs, we see no B−A type transformation.

Figure 7a displays the CD spectra of complexes with varied charge ratios at 20 and 37 °C. It should be pointed out that at 37 °C, the intensity of free DNA is slightly decreased. To isolate the thermoresponsive phase transition, the difference in the CD intensity caused by temperature has been subtracted in the data treatment. It

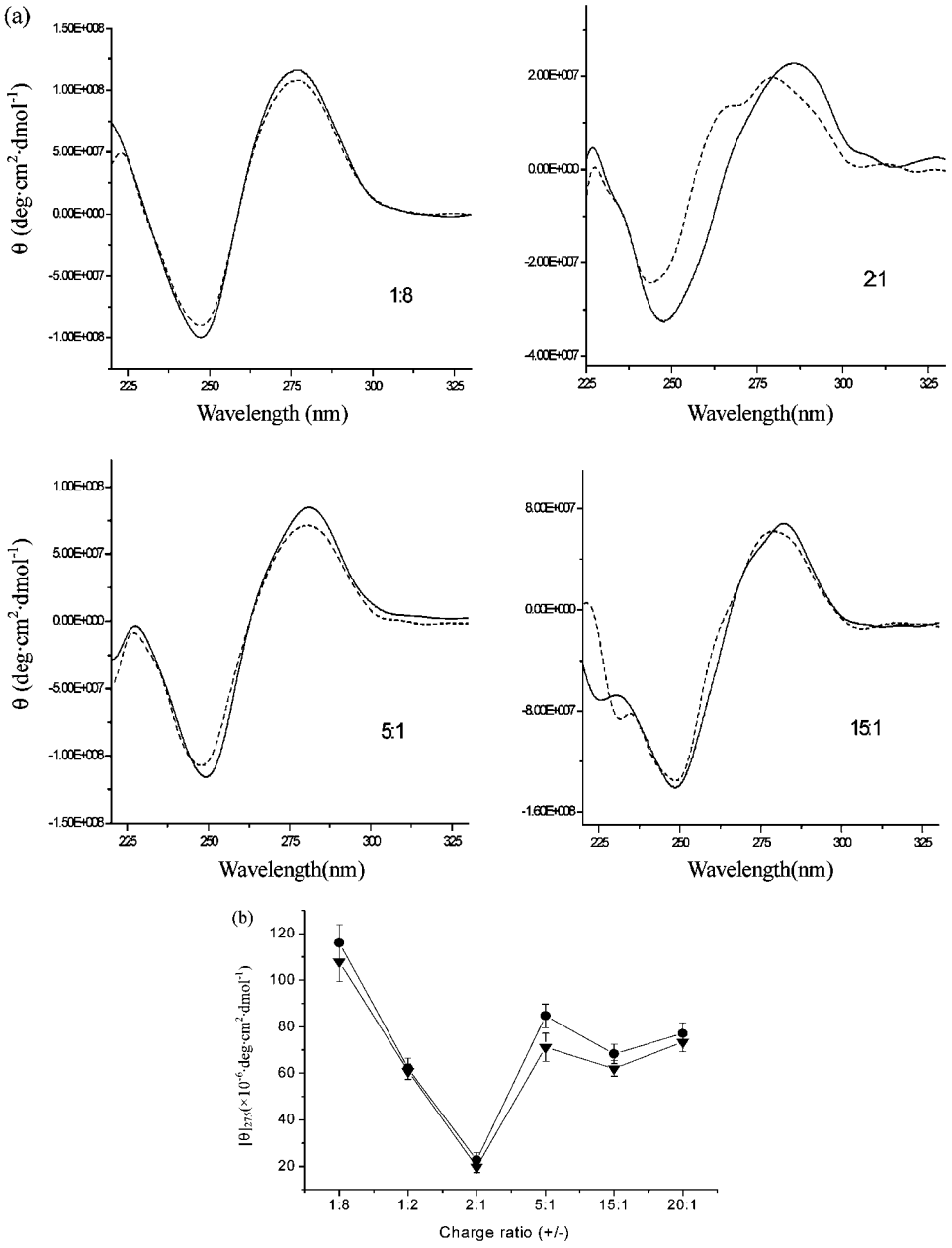

Figure 7. Effect of temperature-induced phase transition of PNVLCS on CD spectra of complexes. (a) Representative CD spectra of complexes at various charge ratios. (Solid line: 20 °C; dash line: 37 °C). The difference in the intensity of CD caused by temperature has been subtracted to eliminate the influence of the decrease in the intensity of free DNA at 37 °C. (b) Dependence of $[\theta]_{275}$ on charge ratios determined at 20 and 37 °C. (●): 20 °C; (▼): 37 °C.

is clearly seen from the figures that the CD intensity decreases to a certain degree when the temperature is increased from 20 °C to 37 °C. To give a clear observation of the effect of temperature-induced hydrophobicity on the CD signal, we plotted $[\theta]$ values of the CD signal at 275 nm determined at 20 and 37 °C versus charge ratios (Figure 7b). Obviously, the values of $[\theta]_{275}$ at 20 °C are greater than at 37 °C. It has been confirmed that at temperatures below LCST, PNIPAAm chains are hydrated; thus a loose structure of PNVLCS/DNA complex is formed in this case, rendering more DNA exposure, while at 37 °C, the PNIPAAm chains in PNVLCS collapse due to heavy dehydration. The collapsed chains tightly cover the surface of complex, protecting DNA from exposure. Therefore, the CD signals are suppressed at an elevated temperature.

To further verify the influence of thermoresponsive phase transition of PNVLCS on the packing−unpacking of DNA in the complexes, temperature-variable UV was performed. Figure 8 shows the change in OD_{260} of free DNA and the complex solutions at 20 and 37 °C versus charge ratios. As shown in the figure, OD_{260} of free DNA is constant at these two temperatures. At the selected temperature, DNA is not denatured, so the direct influence of temperature on the variation in the absorbance of naked DNA can be rationally neglected. We can see that after complexing with PNVLCS vectors, the OD_{260} values decrease relative to that of free DNA. It is not hard to figure out that with the addition of PNVLCS, DNA is condensed in polyelectrolyte complexes, which reduces the exposure of base-pairs; hence the OD_{260} decreases. Figure 8 also provides other useful information that all the OD_{260} values at 37 °C are lower than those at 20 °C. As aforementioned, while the temperature is raised to 37 °C, the PNIPAAm chains in PNVLCS collapse to tightly bind to the surface of complexes, resulting in more

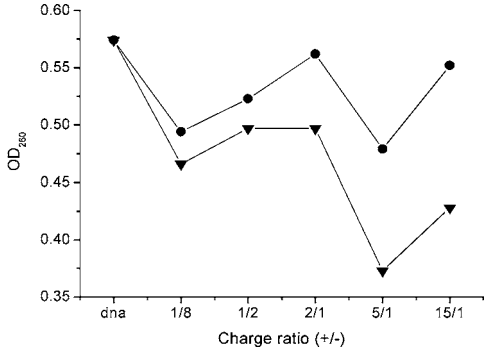

Figure 8. Change in OD_{260} of free DNA and PNVLCS/DNA complex solutions at 20 and 37 °C versus charge ratios. (●): 20 °C; (▼): 37 °C.

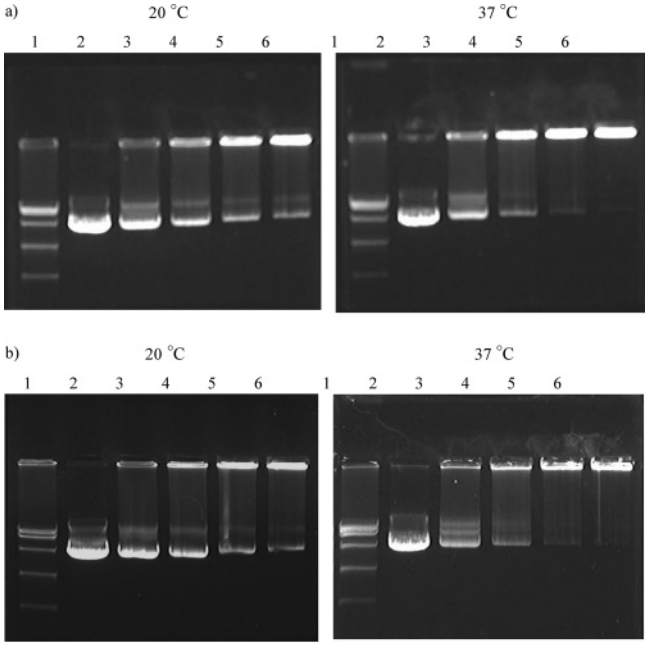

Figure 9. Electrophoresis of PNVLCS/DNA on agarose gels. (a) PNVLCS/DNA complexes were formed at 20 °C or 37 °C, and run at about 15 °C. (b) PNVLCS/DNA complexes were formed at 20 °C or 37 °C, and run at about 37 °C. Lane 1: DNA marker; lane 2: plasmid DNA; lane 3: +/− = 1/2; lane 4: 1/1; lane 5: 2/3; lane 6: 2:1.

compact structure of complexes, and consequently protecting DNA from exposure. This result is in good agreement with that of CD above. It is noted that the variation in OD_{260} is reversible upon increasing or decreasing temperature. It is safe to say that at temperature above LCST, more DNA molecules are trapped in PNVLCS/DNA complex compartments owing to the combined electrostatic and hydrophobic interactions. This is important for the cellular entry of complexes as well as hindrance for the attack of nuclease. Additionally, the temperature reversibility of PNVLCS can be used to adjust the packing and unpacking of gene in its vector, by which a controllable gene expression could be realized by simply varying temperature.

To examine the dependence of PNVLCS/DNA complexes on temperature, a temperature-variable electrophoresis was carried out. In experiment, we prepared the complexes at 20 and 37 °C, and the electrophoresis assay was performed at 15 and 37 °C, respectively (Figure 9). One can see that the migration of PNVLCS/DNA complexes is reduced with increasing charge ratio from 1:2 to 2:1 and much more DNA is restricted into gel slots. A

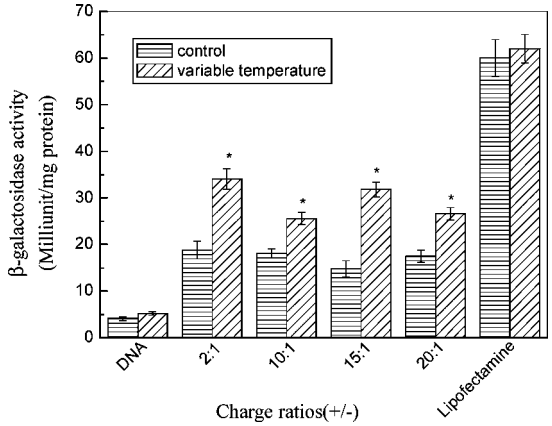

Figure 10. Thermoresponsive transfection efficiency of PNVLCS/DNA complexes at different charge ratios. The transfection level at constant 37 °C was used as a control. Data are shown as mean ± SD ($n = 3$). $P^* < 0.05$ (compared to the control).

complete retardation of DNA occurs at charge ratio of 2:1 (complex formed at 37 °C). These retardations are indicative of neutralization of negatively charged plasmid DNA as well as large size complex formation. A close inspection of temperature influence discloses that in the case of PNVLCS/DNA complexes formed at 20 °C, DNA cannot be retarded completely. Even at 2:3 and 2:1 charge ratios, a small quantity of DNA complex can still migrate out of slots. But the complexes of the same charge ratios formed at 37 °C can impede the DNA migration significantly; all DNA is retained in gel slot at 2:1 charge ratio. It is further confirmed that not only electrostatic interaction but also temperature change exerts an effect on the formation of PNVLCS/DNA complexes. For complexes formed above LCST (at 37 °C), greater retardation is achieved, implying the formation of more stable complexes at higher temperature.

In addition, in gel retardation assay run at varied temperatures, an interesting phenomenon is shown. The bands of complexes with charge ratios of 2/3 and 2/1 run on a agarose gel in liquid of 15 °C is brighter, while they become dimmer at the same charge ratios when liquid temperature is 37 °C. This fact suggests that the complexes formed at initial stage are just metastable. When the complexes are immersed in electrophoresis liquid of 37 °C, the PNIPAAm chains continue to collapse, causing more compact structure of the complexes in which DNA is shielded to a maximum extent.

Thermoresponsive Gene Transfection of C_2C_{12} Cells. The transfection efficiency was evaluated in C_2C_{12} cell lines using pTracer-CMV/Bsd/*lacZ* plasmid encoding β-galactosidase(β-gal). We adopted two routes to examine the thermal regulation of transfected gene expression; one is the constant temperature approach: the culture temperature was kept at 37 °C; the other is the variable temperature approach: the transfected cells were incubated for 18 h at 37 °C, 3 h at 20 °C, and an additional 24 h at 37 °C. Figure 10 displays the dependence of transfection efficiency achieved with naked DNA, PNVLCS and Lipofectamine 2000. As shown in the figure, the β-gal activities of PNVLCS obtained with variable temperature approach are 1.42−2.27 times that of constant 37 °C case. t-test analysis demonstrates a significant difference between variable temperature route and the control (constant 37 °C). In comparison, although the transfecion efficiencies of naked DNA and Lipofectamine 2000 are marginally enhanced, no significant difference is observed. In addition, with the variable temperature method, the β-gal activities of PNVLCS are

raised 5−8-fold to that of naked DNA. Note that the level of gene transfection mediated by PNVLCS is only up to 50% that of Lipofectamine 2000, but the order of magnitude is the same.

The thermoresponsive transfection efficiency should be attributed to the change of affinity between PNVLCS vector and DNA. From the analysis above, the phase transition of PNVLCS plays an important role in the formation and dissociation of the complexes responding to the change of temperature. At body temperature (37 °C), the PNIPAAm chains in PNVLCS become dehydrated and exist in a collapsed form, leading to compacted complexes. This tight form could be internalized easily via endocytosis and protects DNA from degradation by DNase during transportation into cells. After 18 h incubation at 37 °C, the transfected cells were lowered to 20 °C and incubated for 3 h. Below LCST, the PNIPAAm moieties in PNVLCS copolymer are hydrated and become loose and extended, which could promote dissociation of complexes or gene exposure, aiding in the accessibility of RNA polymerase, and consequently gene expression is increased.

It is necessary to point out that the timing for post-transfection at 37 °C and lowering the incubation temperature is critical for realizing the objective of gene expression control. An improper choice of timing might deteriorate transfection efficiency due to declined cell vitality in low-temperature surroundings and/or premature dissociation of genes in the endosome. In our experiment, although the timing cannot be guaranteed optimum, at least it is effective for improving gene expression.

CONCLUSIONS

A thermoresponsive chitosan−NIPAAm/VL copolymer (PNVLCS) vector was synthesized by coupling chitosan to carboxyl-capped NIPAAm/VL copolymer. The LCST of PNVLCS aqueous solution was ca. 26 °C. At lower charge ratios (+/−), DNA in the complexes remained in B conformation; while B → C type conformation transformation occurred at higher charge ratios. The affinity between DNA and PNVLCS could be tuned by varying surrounding temperature. At temperatures above LCST, tight and stable complexes were formed due to the collapse of PNIPAAm chains in PNVLCS. Reducing temperature below LCST facilitated the dissociation of PNVLCS/DNA complexes, resulting in the exposure of more DNA molecules. The level of gene expression could be thermally controlled and increased by lowering incubation temperature to 20 °C when PNVLCS/DNA complexes were applied to C_2C_{12} cells, which was attributed to the effective unpacking gene from PNVLCS at temperature below LCST. In contrast, the naked DNA and LipofectamineTM 2000 did not show temperature-sensitive behavior in mediating gene transfection, but the transfection level of PNVLCS was still inferior to that of Lipofectamine 2000, leaving much to be desired.

ACKNOWLEDGMENT

The authors are indebted to the financial support from National Natural Science Foundation of China (Grant 30300086).

LITERATURE CITED

(1) Sato, T., Ishii, T., and Okahata, Y. (2001) In vitro gene delivery mediated by chitosan. Effect of pH, serum, and molecular mass of chitosan on the transfection efficiency. *Biomaterials 22*, 2075−2080.

(2) Corsi, K., Chellat, F., Yahia, L., and Fernandes, J. C. (2003) Mesenchymal stem cells, MG63 and HEK293 transfection using chitosan-DNA nanoparticles. *Biomaterials 24*, 1255−1264.

(3) Lee, M. K., Chun, S. K., Choi, W. J., Kim, J. K., Choi, S. H., Kim, A., Oungbho, K., Park, J. S., Ahn, W. S., and Kim, C. K. (2005) The use of chitosan as a condensing agent to enhance emulsion-mediated gene transfer. *Biomaterials 26*, 2147−2156.

(4) Köping-Höggård, M., Tubulekas, I., Guan, H., Edwards, K., Nilsson, M., Vårum, K. M., and Artursson, P. (2001) Chitosan as a nonviral gene delivery system. Structure−property relationships and characteristics compared with polyethyleneimine in vitro and after lung administration in vivo. *Gene Ther. 8*, 1108−1121.

(5) Kim, Y. H., Gihm, S. H., and Park, C. R. (2001) Structural characteristics of size-controlled self-aggregates of deoxycholic acid-modified chitosan and their application as a DNA delivery carrier. *Bioconjugate Chem. 12*, 932−938.

(6) Kim, T. H., Park, I. Y., Nah, J. W., Choi, Y. J., and Cho, C. S. (2004) Galactosylated chitosan/DNA nanoparticles prepared using water-soluble chitosan as a gene carrier. *Biomaterials 25*, 3783−3792.

(7) Park, I. K., Ihm, J. E., Park, Y. H., Choi, Y. J., Kim, S. I., Kim, W. J., Akaike, T., and Cho, C. S. (2003) Galactosylated chitosan (GC)-graft-poly(vinyl pyrrolidone) (PVP) as hepatocyte-targeting DNA carrier: Preparation and physicochemical characterization of GC-graft-PVP/DNA complex (1). *J. Controlled Release 86*, 349−359.

(8) Kim, T. H., Ihm, J. E., Choi, Y. J., Nah, J. W., and Cho, C. S. (2003) Efficient gene delivery by urocanic acid-modified chitosan. *J. Controlled Release 93*, 389−402.

(9) Chen, J., Yang, W. L., Li, G., Qian, J., Xue, J. L., Fu, S. K., and Lu, D. R.(2004) Transfection of mEpo gene to intestinal epithelium in vivo mediated by oral delivery of chitosan-DNA nanoparticles. *World J. Gastroenterol. 10*, 112−116.

(10) Roy, K., Mao, H. Q., Huang, S. K., and Leong, K. W. (1999) Oral gene delivery with chitosan-DNA nanoparticles generates immunologic protection in a murine model of peanut allergy. *Nat. Med. 5*, 387−391.

(11) Aral, C., and Akbuga, J. (2003) Preparation and in vitro transfection efficiency of chitosan microspheres containing plasmid DNA: poly(L-lysine) complexes. *J. Pharm. Pharm. Sci. 6*, 321−326.

(12) Romoren, K., Pedersen, S., Smistad, G., Evensen, O., and Thu, B. J. (2003) The influence of formulation variables on in vitro transfection efficiency and physicochemical properties of chitosan-based polyplexes. *Int. J. Pharm. 261*, 115−127.

(13) Kawamura, K., Oishi, J., Kang, J. H., Kodama, K., Sonoda, T., Murata, M., Niidome, T., and Katayama, Y. (2005) Intracellular signal-responsive gene carrier for cell-specific gene expression. *Biomacromolecules 6* (2), 908−913.

(14) Liu, W. G., Zhang, X., Sun, S. J., Sun, G. J., Yao, K. D., Liang, D. C., Guo, G., and Zhang, J. Y. (2003) N-alkylated chitosan as a potential nonviral vector for gene transfection. *Bioconjugate Chem. 14*, 782−789.

(15) Hinrichs, W. L. J., Schuurmans-Nieuwenbroek, N. M. E., van de Wetering, P., and Hennink, W. E. (1999) Thermosensitive polymers as carriers for DNA delivery. *J. Controlled Release 60*, 249−259.

(16) Kurisawa, M., Yokoyama, M., and Okano, T. (2000) Gene expression control by temperature with thermo-responsive polymeric gene carriers. *J. Controlled Release 69*, 127−137.

(17) Tseng, W. C., and Jong, C. M. (2003) Improved stability of polycationic vector by dextran-grafted branched polyethylenimine. *Biomacromolecules 4*, 1277−1284.

(18) Kichler, A., Leborgne, C., Coeytaux, E., and Danos, O. (2001) Polyethylenimine-mediated gene delivery: a mechanistic study. *J. Gene Med. 3*, 135−144.

(19) Petersen, H., Fechner, P. M., Fischer, D., and Kissel, T. (2002) Synthesis, characterization, and biocompatibility of polyethylenimine-*graft*-poly(ethylene glycol) block copolymers. *Macromolecules 35*, 6867−6874.

(20) Forrest, M. L., Koerber, J. T., and Pack, D. W. (2003) A degradable polyethylenimine derivative with low toxicity for highly efficient gene delivery. *Bioconjugate Chem. 14*, 934−940.

(21) Türk, M., Dinçer, S., Yuluğ, I. G., and Pişkin, E. (2004) In vitro transfection of HeLa cells with temperature sensitive polycationic copolymers. *J. Controlled Release 96*, 325−340.

(22) Oupický, D., Reschel, T., Koňák, Č., and Oupická, L. (2003) Temperature-controlled behavior of self-assembly gene delivery vectors based on complexes of DNA with poly(L-lysine)-*graft*-poly(*N*-isopropylacrylamide). *Macromolecules 36*, 6863−6872.

(23) Zhu, W., Rawlins, B. A., Boachie-Adjei, O., Myers, E. R., Arimizu, J., Choi, E., Lieberman, J. R., Crystal, R. G., and Hidaka, C. (2004) Combined bone morphogenetic protein-2 and −7 gene transfer enhances osteoblastic differentiation and spine fusion in a rodent model. *J. Bone Miner. Res. 19*, 2021−2032.

(24) Wilson, M. O., Scougall, K. T., Ratanamart, J., McIntyre, E. A., and Shaw, J. A. (2005) Tetracycline-regulated secretion of human (pro)insulin following plasmid-mediated transfection of human muscle. *J. Mol. Endocrinol. 34*, 391−403.

(25) Gupta, K. C., and Khandekar, K. (2003) Temperature-responsive cellulose by ceric(IV) ion-initiated graft copolymerization of *N*-isopropylacrylamide. *Biomacromolecules 4*, 758−765.

(26) Banerjee, T., Mitra, S., Kumar, S. A., Kumar, S. R., and Maitra, A. (2002) Preparation, characterization and biodistribution of ultrafine chitosan nanoparticles. *Int. J. Pharm. 243*, 93−105.

(27) Koňák, Č., Reschel, T., Oupický, D., and Ulbrich, K. (2002) Thermally controlled association in aqueous solutions of pPoly(L-lysine) grafted with poly(*N*-isopropylacrylamide). *Langmuir 18*, 8217−8222.

(28) Cao, Z. Q., Liu, W. G., Gao, P., Yao, K. D., Li, H. X., and Wang, G. C. (2005) Toward an understanding of thermo-responsive transition behavior of hydrophobically modified N-isopropylacrylamide copolymer solution. *Polymer 46*, 5268−5277.

(29) Deshmukha, M. V., Vaidyab, A. A., Kulkarnib, M. G., Rajamohanana, P. R., and Ganapathy, S. (2000) LCST in poly(*N*-isopropylacrylamide) copolymers: high-resolution proton NMR investigations. *Polymer 41*, 7951−7960.

(30) Ramos, V. M., Rodríguez, N. M., Rodríguez, M. S., Herasc, A., and Agulló, E. (2003) Modified chitosan carrying phosphonic and alkyl groups. *Carbohyd. Polym. 51*, 425−429.

(31) Liu, W. G., Sun, S. J., Cao, Z. Q., Zhang, X., Yao, K. D., Lu, W. W., and Luk, K. D. K. (2005) An investigation on the physicochemical properties of chitosan/DNA polyelectrolyte complexes. *Biomaterials* 26, 2705−2711.

(32) Sato, Y. I., Kobayashi, Y., Kamiya, T., Watanabe, H., Akaike, T., Yoshikawa, K., and Maruyama, A. (2005) The effect of backbone structure on polycation comb-type copolymer/DNA interactions and the molecular assembly of DNA. *Biomaterials 26*, 703−711.

BC0500701

DNA-Directed Coupling of Organic Modules by Multiple Parallel Reductive Aminations and Subsequent Cleavage of Selected DNA Sequences

Morten Nielsen,[§] Vita Dauksaite,[†] Jørgen Kjems,[†] and Kurt V. Gothelf*[,§]

Department of Chemistry, Langelandsgade 140, and Department of Molecular Biology, C. F. Møllers Allé, Building 130, Aarhus University, 8000 Århus C, Denmark. Received March 15, 2005; Revised Manuscript Received April 29, 2005

A new method for DNA-directed assembly of organic modules by multiple parallel reductive aminations is presented. Linear oligonucleotide-functionalized modules (LOMs) consist of a rigid oligo(phenylene ethynylene) backbone with two salicylaldehyde termini, and each terminus is conjugated with an oligonucleotide sequence. The stability of the tetrahydrosalen-linked modules toward elevated temperature, low pH, nucleophiles, and metal chelators is studied and compared to the analogous metal−salen-linked modules. A linear oligonucleotide-functionalized disulfide-linked module (LOSM) containing cleavable linkers between the organic module and the two DNA sequences is coupled by DNA-directed reductive aminations to nonmodified LOM modules. This enables selective cleavage of the DNA strands of a central module in a structure consisting of three modules, and the reactions are analyzed by electrophoresis and ^{32}P-labeling of one of the DNA sequences of the central LOSM.

INTRODUCTION

DNA-directed synthesis has in just a few years evolved from chemical ligation to being an advanced tool for controlling chemical reactivity. This is obtained by the encoding of organic compounds with DNA sequences to react only with other compounds connected to complementary sequences (*1*−*3*). Liu and co-workers have demonstrated this principle to be applicable to a series of organic reactions ranging from acylation reactions to palladium-catalyzed cross-couplings (*4*, *5*). Several fascinating applications of DNA-directed chemistry have already been reported such as new DNA sequence detection methods (*6*−*8*), PNA-templated drug release (*9*−*11*), combinatorial synthesis and selection of libraries of potential drug candidates (*12*), and discovery of new organic reactions (*13*).

We have applied DNA-directed reactions for the assembly and coupling of multiple organic modules in parallel to form macromolecular nanostructures with predetermined connectivity (*14, 15*). The applied building blocks were rigid linear oligonucleotide-functionalized modules (LOM) and tripoidal oligonucleotide-functionalized modules (TOM) (*14, 16*). The LOM module shown in Figure 1A consists of an oligo(phenylene ethynylene) backbone and contains salicylaldehyde-derived termini to which two 15-nucleotide DNA sequences are attached (*16*). In former studies by us (*2, 14, 15*), and by others (*17, 18*), DNA-directed couplings of salicylaldehydes have been performed by metal salen formation using manganese acetate and ethylenediamine (EDA) (Figure 1B). DNA-directed formation of Ni−salen (*17, 18*) and Al−salen (*15*) have also been reported, and we have found that a variety of metal salts of Co, Fe, Cu, and U form metal−salen products in DNA-directed couplings.

EXPERIMENTAL PROCEDURES

Synthesis of LOMs and LOSMs. The linear oligonucleotide-functionalized modules (LOMs) and disulfide-modified modules (LOSMs) were prepared by incorporation of linear module (LM) phosphoramidites into oligonucleotides by standard automated oligonucleotide synthesis (DNA Technology, Aarhus, Denmark) according to previously published procedures (*14*−*16, 19*). The DNA sequences are given in Table 1.

Dimerization and Trimerization. A solution (10 μL) of the two or three LOM modules (5 μM each) in 100 mM KCl, 50 mM EPPS (pH 8.0 or pH 5.0) were heated to 60 °C for 5 min and cooled slowly to room temperature in a water bath. The coupling reactions were performed by addition of either 0.25 mM ethylenediamine, 1 mM $Mn(OAc)_2$ (for the salen formation at pH 8.0), or 0.25 mM ethylenediamine and 10 mM $NaCNBH_3$ (for the reductive amination at pH 5.0) and incubation for 2 h at 30 °C. Analysis of the reaction products was performed by electrophoresis at 90 V in 7.5% polyacrylamide gels (30:1.6) in 50 mM Tricine (pH 8.1) and 8 M urea. Samples were loaded in 8 M urea without heating and addition of dyes. Gels were fixed in 50% (v/v) ethanol, stained with ethidium bromide, and photographed in UV light.

Stability Testing. Dimers of LOMs coupled via a Mn−salen bond or via a tetrahydrosalen bond was prepared as described above. Stability tests were performed by subjecting the prepared complexes to heat (75 °C for 1 h), acid (acetate buffer, pH 3.8, 200 mM, 5 μL, 75 °C for 1 h)), amine ($MeNH_2$, 40% aq solution, 2 μL, 75 °C for 1 h), and EDTA (EDTA, pH 7.0, 100 mM, 5 μL, 75 °C for 1 h). Analysis of the reaction products by electro-

* To whom correspondence should be addressed. Tel: (+45) 8942 3907; fax (+45) 8619 6199; e-mail: kvg@chem.au.dk.
[§] Department of Chemistry.
[†] Department of Molecular Biology.

10.1021/bc0500793 CCC: $30.25 © 2005 American Chemical Society
Published on Web 07/01/2005

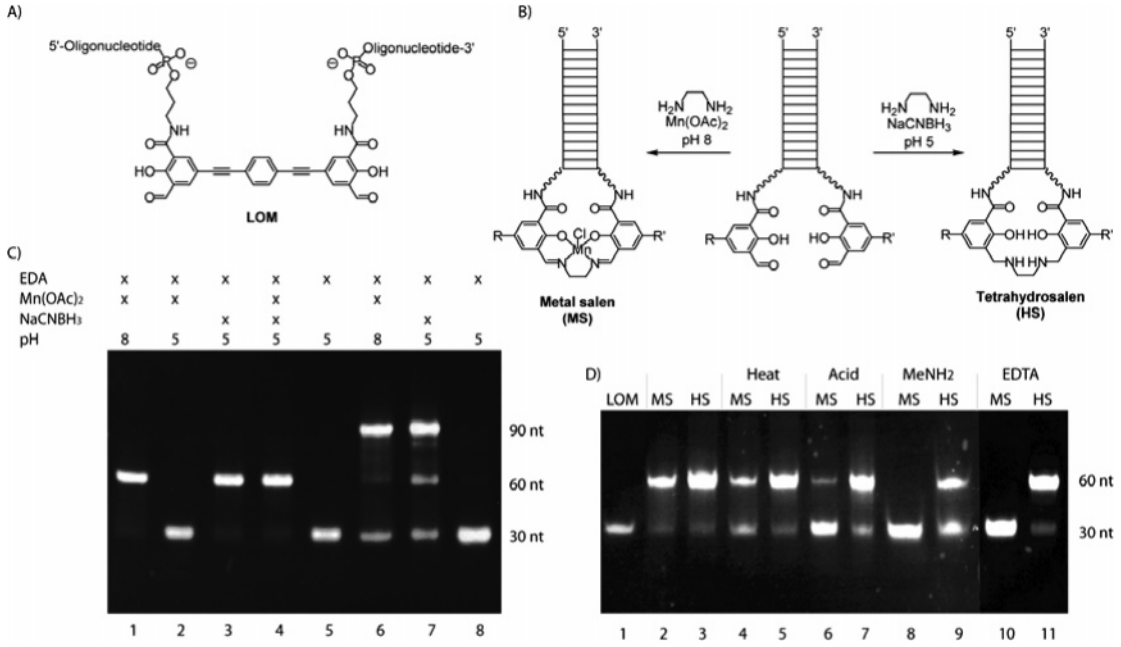

Figure 1. Comparison of DNA-directed dimerization and trimerization of LOMs by metal−salen formation and by reductive amination. (A) Structure of the linear oligonucleotide-functionalized module (LOM). (B) DNA-directed metal−salen formation and tetrahydrosalen formation from the same salicylaldehyde precursors. (C) Analysis of the prerequisites for salen formation and reductive amination on a 7.5% denaturing polyacrylamide gel. Top: Reagents and pH values in the different reaction vessels. Gel: Denaturing PAGE in 8 M urea of **LOM-1**−**LOM-2** dimerizations (lanes 1−5) and **LOM-1**−**LOM-2**−**LOM-3** trimerizations (lanes 6−8). (D) Stability of **LOM-1**−**LOM-2** dimers linked via a metal−salen complex (MS) and by a tetrahydrosalen moiety (HS) toward heat, acidic condition, amines, and metals; lane 1: **LOM-1** monomer; lane 2: LOM−MS dimer; lane 3: LOM−HS dimer; lanes 4 and 5: 75 °C for 1 h; lanes 6 and 7: pH 3.8 at 75 °C for 1 h; lanes 8 and 9: 10 mM methylamine at 75 °C for 1 h; lanes 10 and 11: 10 mM EDTA at 75 °C for 1 h.

Table 1. DNA Sequences for the LOM and LOSM Structures

module[a]	DNA sequence
LOM-1	5′-AGCGCCTTGTTAGAG-LM-TTAGGTCCTAGTTGT-3′
LOM-2	5′-AGGAGTAAGCGTGGA-LM-CTCTAACAAGGCGCT-3′
LOM-3	5′-ACTATTTCCGGCAAC-LM-TCCACGCTTACTCCT-3′
LOM-4	5′-ATTGATCTAGTTGAT-LM-TGTACATCTACACTT-3′
LOSM-5	5′-AAGTGTAGATGTACA-ss-LM-ss-ACTTCAGTTGGTCGT-3′
LOM-6	5′-ACGACCAACTGAAGT-LM-CTGTAGACATATGTT-3′

[a] LM: linear module; LOM: linear oligonucleotide-functionalized module; LOSM: linear oligonucleotide-functionalized diulfide-linked module; ss: disulfide spacer.

phoresis at 90 V in 7.5% polyacrylamide gels (30:1.6) in 50 mM Tricine (pH 8.1), 8 M urea. Samples were loaded in 8 M urea without heating and addition of dyes. Gels were fixed in 50% (v/v) ethanol, stained with ethidium bromide, and visualized by fluorography.

Radioactive Labeling. LOSM-5 (5 μM) was labeled with 24.2 pmol of gama-^{32}P-ATP (Amersham, 7000 Ci/mmol) in 50 μL of T4 polynucleotide kinase buffer using 2 μL of T4 PNK (10 U/μL) for 1h at 37 °C. The labeled oligonucleotide was purified on MicroSpin G-50 columns (Amersham Biosciences).

Disulfide Cleavage. Couplings of **LOM-4**, **LOSM-5**, and **LOM-6** to the desired dimers or trimers were performed as described previously. The disulfide cleavage was performed by addition of tricine buffer (pH 8.1, 2 μL, 500 mM) and tris(2-carboxyethyl)phosphine (TCEP) (pH 7.0, 5 μL, 50 mM) and incubation at 35 °C for 2 h. Traditional analysis of the reaction products was performed by electrophoresis at 90 V in 7.5% polyacrylamide gels (30:1.6) in 50 mM Tricine (pH 8.1), 8 M urea. Samples were loaded in 8 M urea without heating and addition of dyes. Gels were fixed in 50% (v/v) ethanol and stained with ethidium bromide. The wet gel was visualized by fluorography or autoradiography for 15 min and analyzed using Imagequant Software (Biorad).

RESULTS AND DISCUSSION

The metal−salen coupled macromolecular structures obtained in this manner are susceptible to hydrolysis at pH < 6 and other conditions. Consequently, we have investigated the DNA-directed double reductive amination of salicylaldehydes in the presence of EDA to form tetrahydrosalen (Figure 1B). This amine-linked structure is expected to be much more stable than the corresponding imine-linked metal−salens. The tetrahydrosalen is also an excellent ligand for various metals, which will ensure the ordered structure of the linkage between the modules (*20*). Incorporation of metals in the tetrahydrosalen will also maintain the potential conductivity of the macromolecules (*15*).

The results from the coupling experiments between two LOMs or three LOMs under various conditions for Mn−salen formation and reductive amination are shown in the PAGE gel in Figure 1C. Dimerization reactions of **LOM-1** and **LOM-2** are shown in lanes 1−5. Mn−salen formation proceeds quantitatively at pH 8, whereas no conversion is observed at pH 5. Importantly, reductive amination also proceeds almost quantitatively and in the presence of $Mn(OAc)_2$. In the absence of reductant and metal, but in the presence of EDA, the expected imine intermediate does not have the stability to withstand the

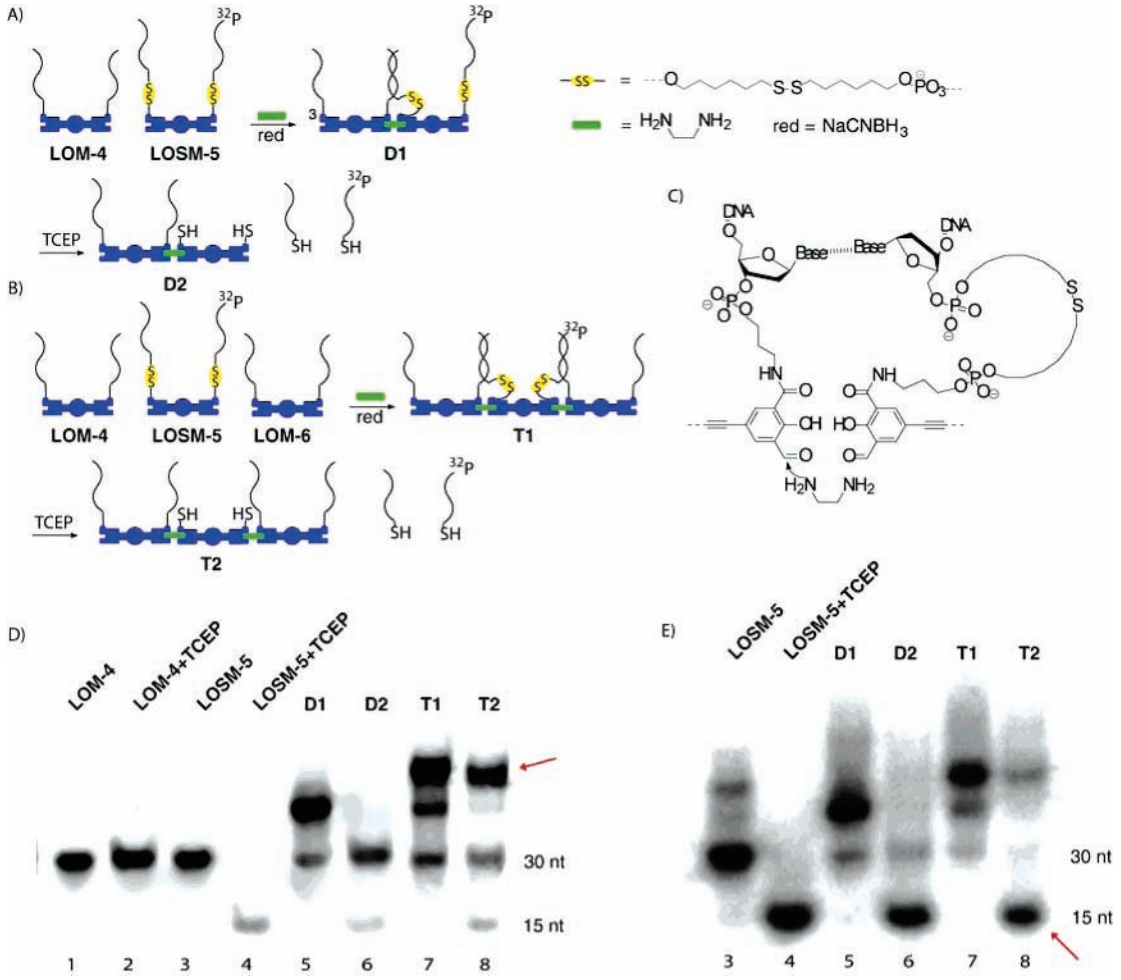

Figure 2. DNA-directed couplings and subsequent selective cleavage of DNA sequences. (A and B) Coupling of modules by reductive amination at pH 5 and subsequent cleavage of disulfide-linked DNA sequences by TCEP (color code: blue = organic module, green: ethylenediamine, curved black lines = 15-nucleotide DNA sequences). (C) Conformation required for the first steps of the DNA-directed reductive amination. (D) Electrophoresis was performed in 8 M urea, followed by ethidium bromide staining and fluorography. (E) Same gel developed by autoradiography.

reaction conditions or the conditions for denaturing electrophoresis since only starting material is observed at pH 5 (lane 5). The same observation has been made at pH 8 (*14*). Trimerization of **LOM-1**, **LOM-2**, and **LOM-3** showed a similar trend (lanes 6−8). To probe the expected increase in stability of the tetrahydrosalen (HS)-linked **LOM-1**−**LOM-2** dimer compared to the corresponding Mn−salen (MS), we have submitted the products to various harsh conditions. The MS dimer is relatively stable toward heating at 75 °C for 1 h although some hydrolysis is observed (Figure 1D, lane 4). The HS dimer is inert to these conditions (lane 5). Treatment with acid (pH 3.8) for 1 h at 75 °C completely hydrolyzes the MS dimer whereas the HS dimer remain inert (lanes 6 and 7). Methylamine (10 mM, 75 °C for 1 h) also cleaves the MS dimer, but only partly decomposition of the HS dimer is observed (lanes 8−9). We have observed that the presence of EDTA in buffers leads to decomposition of the MS dimer (lane 10). Probably EDTA is capable of capturing the metal from MS−salen, and the resulting salen decomposes in situ or during gel electrophoresis. This is supported by the observed inertness of the HS dimer toward EDTA (lane 11).

The increased stability of the linkages between organic modules in the nanostructures described above encouraged us to investigate the selective cleavage of DNA sequences from macromolecular DNA organic hybrid assemblies. In a previous report we have described the synthesis and cleavage of disulfide-linked oligonucleotides in the LOSM module (*15*). The LOSM module contains two $(CH_2)_6$−S−S−$(CH_2)_6$ spacers between the organic module (LM) and the two 15-nucleotide DNA sequences. It was observed that the Mn−salen linkage in LOM dimers was labile to the reagent used for disulfide cleavage: tricarboxyethylphosphine (TCEP). Al−salen-linked dimers were stable toward TCEP, and we demonstrated that the 15-nucleotide DNA sequences were cleaved off a LOSM Al−salen dimer, but we were unable to identify the organic residue (*15*).

In contrast, tetrahydrosalen-linked LOM dimers were completely stable toward TCEP. We have therefore applied the reductive amination for couplings between LOMs and LOSM to induce a partial cleavage of DNA strands from the products (Figure 2A−E). Since the LOSM module contains a chain of 17 additional atoms between the organic module and the oligonucleotides, the reacting salicylaldehydes are not optimally positioned to form the annealed LOM−LOM couple. This is illustrated in Figure 2C. However, the coupling between **LOM-4** and **LOSM-5** to give the dimer **D1** proceeded in high yield, as it appears from denaturing gel electrophoresis (Figure 2A and 2D, lane 5). The release of two of the four DNA sequences in **D1** was performed by cleavage of the disulfides with TCEP. Analysis of this reaction by PAGE

using ethidium bromide staining and fluorography did not give a clear picture of the outcome of the reaction (Figure 2D, lane 6). We observed a strong band at around 30 nucleotides whereas the band at 15 nucleotides is weak, indicating cleavage of the dimer in LOM and LOSM monomers rather than cleavage of disulfides. It is, however, well-known that short ssDNA sequences bind ethidium bromide poorly and give rise to weak bands (*21*). The conjugated organic backbone in monomeric LOMs and in structures such as **D1** is highly fluorescent, which will contribute to the stronger signal at 30 nucleotides. To obtain a clearer picture of this reaction we have radiolabeled the LOSM module at the 5′-end of the oligonucleotide with ^{32}P and analyzed the reaction by autoradiography (2E, lanes 5 and 6) (*21*). It is clear from this gel that the radiolabeled 15-nucleotide sequence is released in high yield (2E, lane 6). The mobility of the organic residue strongly indicates that the nonlabeled disulfide-linked DNA sequence has also been released (2D, lane 6). In the second reaction sequence (Figure 2B), **LOM-4**, **LOSM-5**, and **LOM-6** undergo DNA-directed coupling to form trimer **T1** in high yield, and the major product has a mobility in PAGE which corresponds well with a trimer (2D, lane 7). The weaker bands result from slight discrepancies in the stoichiometry between the three species involved. Incubation of **T1** with TCEP for 2 h in tricine buffer leads to the major product observed in Figure 2D, lane 8. The low mobility of this product initially led us to believe that the disulfide cleavage had failed. From the autoradiography (2E, lane 8) it is clear, however, that the radiolabeled 15-nucleotide DNA sequence had been cleaved and, as shown in the previous experiment, the nonlabeled disulfide-linked DNA sequence was also cleaved by TCEP. The mobility of the 60-nucleotide product **T2** in PAGE was unusual low compared to the other 60-nucleotide product **D1** (2D, lane 5). This can, however, be explained by the different environment of the DNA. In product **D1** the two central DNA sequences are complementary and, due to the covalent bond between the modules, forms in principle a 30-nucleotides hairpin structure (*18*), which may only be partly denatured in 8 M urea. Product **T2** contains four noncomplementary sequences, and this reduces the mobility in PAGE. It is well-known that, for example, a 30-nucleotide hairpin structure has a much higher mobility in denaturing PAGE than a 30-nucleotide ssDNA sequence. We believe that this is also the reason for the low mobility of **T2** compared to **D1**. Cleaving the DNA sequences of the central module in a trimer and conserving the rest of the DNA sequences is ultimately proving that these structures are indeed held together by covalent bonds.

The modular approach using encoded LOMs, LOSMs, and TOMs as shown here and in previous publications (*2, 14*−*16*) provides a novel method for assembly of molecular nanostructures. By application of the reductive amination demonstrated here for the coupling between modules, we have been able to construct assemblies that have superior stability compared to the metal−salen-linked structures. If metals are incorporated into the tetrahydrosalen linkage, it will give structures with a rigidity comparable to metal−salens will be formed. The incorporation of metals will also give these macromolecular assemblies properties as potential conductors. The selective cleavage of disulfide groups to release the LOSM DNA sequences is an important new feature of these macromolecules, and the generated thiol groups can be used for further functionalization of the structures or for immobilization on gold surfaces. In particular, the free thiols in the terminal positions of this type of macromolecular nanostructure would enable the attachment to electrodes.

ACKNOWLEDGMENT

This study was funded in part by the Danish Technical Research Council, the Danish National Research Foundation, and the Carlsberg Foundation.

LITERATURE CITED

(1) Li, X., and Liu, D. R. (2004) DNA-Templated Organic Synthesis: Nature's Strategy for Controlling Chemical Reactivity Applied to Synthetic Molecules. *Angew. Chem., Int. Ed. 43*, 4848−4870.

(2) Gothelf, K. V., and Brown, R. S. (2005) A Modular Approach to DNA-Programmed Self-assembly of Macromolecular Nanostructures. *Chem. Eur. J. 11*, 1062−1069.

(3) Summerer, D., and Marx A. (2002) DNA-templated synthesis: More versatile than expected. *Angew. Chem., Int. Ed. 41*, 89−90.

(4) Gartner, Z. J., and Liu, D. R. (2001) The Generality of DNA-Templated Synthesis as a Basis for Evolving Non-Natural Small Molecules. *J. Am. Chem. Soc. 123*, 6961−6963.

(5) Gartner, Z. J., Kanan, M. W., and Liu, D. R. (2002) Expanding the Reaction Scope of DNA-Templated Synthesis. *Angew. Chem., Int Ed. 41*, 1796−1800.

(6) Ma, Z., and Taylor, J.-S. (2001) Nucleic Acid Triggered Catalytic Drug and Probe Release: A New Concept for the Design of Chemotherapeutic and Diagnostic Agents. *Bioorg. Med. Chem. 9*, 2501−2510.

(7) Cai, J., Li, X., Yue, X., and Taylor, J.-S. (2004) Nucleic Acid-Triggered Fluorescent Probe Activation by the Staudinger Reaction. *J. Am. Chem. Soc. 126*, 16324−16325.

(8) Xiao, Y., Pavlov, V., Naizov, T., Dishon, A. Kotler, M., and Willner, I. (2004) Catalytic beacons for the Detection of DNA and Telomerase Activity. *J. Am. Chem. Soc. 126*, 7430−7431.

(9) Ma, Z., and Taylor, J.-S. (2000) Nucleic Acid Triggered Catalytic Drug Release. *Proc. Natl. Acad. Sci. 97*, 11159−11163.

(10) Brunner, J., Mokhir, A., and Krämer, R. (2003) DNA-templated metal catalysis. *J. Am. Chem. Soc. 125*, 12410−12411.

(11) Zelder, F. H., Brunner, J., and Krämer, R. (2004) DNA-templated catalysis using a metal-cleavable linker. *Chem. Commun.*, 902−903.

(12) Gartner, Z. J., Tse, B. N., Grubina, R., Doyon, J. B., Snyder, T. M., and Liu, D. R. (2004) DNA-Templated Organic Synthesis and Selection of a Library of Macrocycles. *Science 305*, 1601−1605.

(13) Kanan, M. W., Rozenman, M. M., Sakurai, K., Snyder, T. M., and Liu, D. R. (2004) Reaction Discovery Enabled by DNA-Templated Synthesis and In Vitro Selection. *Nature 431*, 545−549.

(14) Gothelf, K. V., Thomsen, A. H., Nielsen, M., Cló, E., and Brown, R. S. (2004) Modular DNA-Programmed Assembly of Linear and Branched Conjugated Nanostructures. *J. Am. Chem. Soc. 126*, 1044−1046.

(15) Brown, R. S., Nielsen, M., and Gothelf, K. V. (2004) Self-assembly of aluminium-salen coupled nanostructures from encoded modules with cleavable disulfide DNA-linkers. *Chem. Commun.*, 1464−1465.

(16) Nielsen, M., Thomsen, A. H., Cló, E., Kirpekar, F., and Gothelf, K. V. (2004) Synthesis of Linear and Tripoidal Phenylacetylene-Based Organic Modules for Application in DNA-programmed Assembly. *J. Org. Chem. 69*, 2240−2250.

(17) Czlapinski, J. L., and Sheppard, T. L. (2001) Nucleic Acid Template-Directed Assembly of Metallosalen-DNA Conjugates. *J. Am. Chem. Soc. 123*, 8618−8619.

(18) Czlapinski, J. L., and Sheppard, T. L. (2004) Template-directed assembly of metallosalen-DNA hairpin conjugates. *ChemBioChem. 5*, 127−129.

(19) Waybright, S. M., Singleton, C. P., Wachter, K., Murphy, C. J., and Bunz, U. H. (2001) Oligonucleotide directed assembly of materials: defined oligomers. *J. Am. Chem. Soc. 123*, 1828−1833.

(20) Böttcher, A., Elias, E., Jäger, E.-G., Langfelderova, H., Mazur, M., Müller, L., Paulus, H., Pelikan, P., Rudolph, M., and Valko, M. (1993) Comparative study on the coordination chemistry of cobalt(II), nickel(II), and copper(II) with derivatives of salen and tetrahydrosalen: metal-catalyzed oxidative dehydrogenation of the carbon−nitrogen bond in coordinated tetrahydrosalen. *Inorg. Chem. 32*, 4131−4138.

(21) Sambrook, J., Fritsch, E. F., Maniatis, T. (1989) *Molecular Cloning. A Laboratory Manual*, Cold Spring Harbor Laboratory Press, New York.

BC0500793

Single Cell Kinetics of Intracellular, Nonviral, Nucleic Acid Delivery Vehicle Acidification and Trafficking

Rajan P. Kulkarni,[†,‡] Swaroop Mishra,[§] Scott E. Fraser,[‡] and Mark E. Davis*[,§]

Option in Biochemistry and Molecular Biophysics, Division of Biology, and Chemical Engineering, California Institute of Technology, Pasadena, California 91125. Received March 16, 2005; Revised Manuscript Received May 10, 2005

Mechanistic understanding of the intracellular trafficking of nonviral nucleic acid delivery vehicles remains elusive. A live, single cell-based assay is described here that is used to investigate and quantitate the spatiotemporal, intracellular pH microenvironment of polymeric-based nucleic acid delivery vehicles. Polycations such as polyethylenimine (PEI), poly-L-lysine (PLL), β-cyclodextrin-containing polymers lacking or possessing imidazole termini (CDP or CDP-imid), and cyclodextrin-grafted PEI (CD-PEI) are used to deliver an oligonucleotide containing a single fluorophore with two emission lines that can be employed to measure the pH. Delivery vehicles were also sterically stabilized by addition of poly(ethylene glycol) (PEG) and investigated. The intracellular trafficking data obtained via this new methodology show that vectors such as PEI and CDP-imid can buffer the endocytic vesicles while PLL and CDP do not. Additionally, the PEGylated vectors reveal the same buffering capacity as their unstabilized variants. Here, the live cell, spatiotemporal mapping of these behaviors is demonstrated and, when combined with cell uptake and luciferase expression data, shows that there is not a correlation between buffering capacity and gene expression.

INTRODUCTION

There is renewed interest in replacing viral vectors with biocompatible, polymeric vectors for gene delivery and potential gene therapy in humans because of recent difficulties and costs with viral delivery vectors (*1*, *2*). Although viruses can be useful for ex vivo gene delivery, they present many problems for systemic, in vivo use, including stimulation of immune responses, potential pathogenicity, lack of designable targeting to specific tissues and cell types, and cost of manufacturing. By comparison, the polymeric vectors can be prepared so that they do not elicit an immune response and are capable of carrying nucleic acids of virtually any size. Additionally, the synthetic delivery vehicles can be targeted to specific cells using appropriate ligands (*3*−*6*).

The delivery efficiency of nonviral vectors is much lower than with viral vectors. Increasing the intracellular delivery efficiency of nonviral vectors remains one of the major challenges in nonviral nucleic acid delivery. For effective delivery, the vector must first reach the cell of interest. Once internalized by receptor-mediated endocytosis, the delivery system should actively transport the nucleic acid out of the endocytic pathway and allow for movement into the nucleus. At some point during the delivery process, the nonviral vector must release the nucleic acid payload, although it is unclear where unpackaging should occur to enable the most effective delivery. Thus, the synthetic vector must perform multiple functions for effective intracellular trafficking (*7*−*9*).

An important process of the intracellular trafficking of nonviral delivery vehicles is their behavior in the endocytic pathway. The vehicles enter into this pathway by endocytosis and must escape in order to avoid degradation by the lysosomal system (*10*−*12*). Little is known about the spatiotemporial pH changes that the vectors face as they travel intracellularly or how these changes affect delivery and expression (*13*, *14*). Certain polymers, such as polyethyleneimine (PEI), are said to exhibit a 'proton sponge' effect since they have titratable amine groups (pK_a values in the range of 4−7) and have the ability to buffer pH changes as endocytic vesicles acidify (*15*). Other polymers, such as poly-L-lysine (PLL) or β-cyclodextrin-containing polymers (CDP), do not possess this ability (*16*). Thus, it is important to understand how the delivery vectors respond to pH changes in the endocytic pathway and how those responses affect export to the cytoplasm to allow the cytoplasmic transport and nuclear delivery of the nucleic acid.

Prior studies examining endosomal pH changes utilized flow cytometry to look at averages of hundreds of cells simultaneously for different types of polyplexes (PLL and PEI) (*10*, *17*), or employed an indirect approach that depended on colocalization of dextrans (*18*). Here, we develop a new methodology to monitor the spatiotemporial pH experienced by nucleic acids in single cells using polymeric delivery vehicles. Our work differs from previous nucleic acid delivery studies in that we employ a single pH-sensitive fluorophore, SNARF-4F, directly conjugated to the nucleic acid of interest. This method avoids concerns about relative labeling density or interactions between multiple fluorophores, makes no assumptions regarding colocalization, and directly evaluates the pH microenvironment of the nucleic acid of interest. While valuable, previous studies involving average values from numerous cells do not offer the specificity of the single cell approach described below. Also, the

* To whom correspondence should be addressed. E-mail: mdavis@cheme.caltech.edu.
[†] Option in Biochemistry and Molecular Biophysics.
[‡] Division of Biology.
[§] Chemical Engineering.

10.1021/bc050081u CCC: $30.25 © 2005 American Chemical Society
Published on Web 06/28/2005

delivery particles that are in different locations in the cell, or endocytosed at different times, cannot be distinguished by cell averaging methods. In contrast, the single cell analysis method we present here using confocal laser scanning microscopy allows for direct examination of uptake of delivery particles in single cells in real time. Particles at different locations in the cell can easily be identified, and pH differences quantified, as nuclear transport of all types of particles is rather slow, and it can take on the order of tens of minutes for them to travel from the periphery of the cell to the nucleus.

Identifying pH differences as a function of delivery particle chemical composition and location within the cell will be important for better understanding of how trafficking occurs and may assist in the design process and search for more efficient delivery vectors. Here, we show that the pH microenvironment can be correlated to transfection progression and particle location through direct visualization. This method allows for monitoring of the entire pathway, from early internalization onward, and can be directly visualized in real time to measure individual differences among the cells.

MATERIALS AND METHODS

Labeled Oligonucleotide. A 21-base RNA phosphorothioate oligonucleotide was synthesized (Caltech Biological Synthesis Facility, Pasadena, CA) with sequence 5′-GACGUAAACGGCCACAAGUUC-3′. The 5′ end of the oligonucleotide was capped with the 5′-amino modifier 5 (Glen Research, Sterling, VA), supplying a 5′ terminal primary amine to which an NHS-ester of the SNARF-4F fluorophore could be reacted. To carry out this reaction, the dry oligonucleotide was resuspended in phosphate-buffered saline (pH 7.4). The pH-sensitive fluorescent molecule SNARF-4F-carboxylic acid (Molecular Probes, Eugene, OR) was converted to an NHS-ester by reaction with 1-ethyl-3-(3-dimethylaminopropyl)carbodiimide hydrochloride (EDC) (1:1 molar equiv) and *N*-hydroxysulfosuccinimide (sulfo-NHS) (5:1 molar equiv) in MES buffer (pH 6.0) for 15 min. Subsequently, the oligonucleotide was added to the reaction mixture (10:1 molar equiv, SNARF-4F:oligonucleotide) and reacted for 2 h at room temperature in the dark. The SNARF-4F-labeled oligonucleotide was purified from unreacted SNARF-4F with CentriSep 20 columns (Princeton Separations, Adelphia, NJ). In multiple reactions, yield of labeled oligonucleotide was 50−60%.

Delivery Vectors. The β-cyclodextrin-containing polycation (CDP) and imidazole-terminated β-cyclodextrin-containing polycation (CDP-imid) were synthesized as described previously (*19*). Solutions of these cyclodextrin-containing polycations were prepared at 2.06 mg/mL in dH_2O. Branched polyethylenimine (bPEI) (25 kDa) (Aldrich, Milwaukee, WI) solution was formulated at 0.067 mg/mL in 20 mM HEPES buffer with 5% glucose. Poly-L-lysine (Sigma) solution was prepared at 0.06 mg/mL in 0.3 M NaCl. Cyclodextrin-grafted linear polyethylenimine (CD-PEI) was synthesized as described previously (*20*) and a solution formulated at 10 mg/mL in dH_2O. Lipofectamine (Invitrogen) was diluted to 0.025 mg/mL in Opti-MEM serum-free medium (Gibco/Invitrogen).

Formulation of Labeled Complexes. The SNARF-4F-labeled oligonucleotide was diluted in dH_2O to a concentration of 0.1 mg/mL. Polycation−oligonucleotide complexes were prepared by adding a polycation solution (as described above) to an equal volume of SNARF-4F-oligonucleotide. Complexes were then incubated at room temperature for 30 min. These conditions produce complexes at an *N*/*P* ratio of 10/1 for CDP and CDP-imid, 5/1 for bPEI, and 3/1 for poly-L-lysine. Lipoplexes were prepared by adding lipofectamine at a concentration of 25 μg/mL in Opti-MEM to the nucleic acid at a concentration of 10 μg/mL in Opti-MEM.

PEGylation of Complexes. An adamantane−poly(ethylene glycol)5000 conjugate (AD-PEG) was prepared as previously described (*19*). CDP complexes and CDP-imid complexes were salt-stabilized by the addition of 35 μg of AD-PEG (100 mg/mL in dH_2O) per microgram of oligonucleotide. bPEI complexes were salt-stabilized by addition of 4 μg of methoxy-PEG5000-succinimidyl propionate (Nektar, San Carlos, CA; 20 mg/mL in dH_2O) per microgram of oligonucleotide. Solutions were incubated at room temperature for an additional 30 min after PEGylation. For examples of these types of PEGylation methods and results of stabilization within cells, see ref 21.

Cells. HeLa cells were grown in 10-cm culture dishes (Becton-Dickinson) at 37 °C in a humid 5% CO_2 atmosphere. Each dish held 10 mL of growth media, which consisted of DMEM with 10% fetal bovine serum, 100 units/mL penicillin, 100 units/mL streptomycin, 10 mM HEPES, 0.1 mM nonessential amino acids, and 2 mM L-glutamine (Irvine Scientific). The cells were passaged once a week and plated onto glass-bottom tissue culture plates (Labtek) for each imaging experiment. The total medium volume per well was 0.7 mL after seeding, and the cells were incubated for 24 h before transfection.

Fluorescence Microscopy. An inverted Zeiss LSM 510 META confocal microscope was used for all fluorescence and brightfield measurements. A 63× oil objective (NA 1.4) was employed for all measurements. Excitation of the SNARF fluorophore was achieved with the 543 nm line of the He−Ne laser line supplied with the microscope. The fluorescence signal was detected by the PMTs within the META detector after passing through a variable confocal pinhole set to 2 Airy units (chosen to maximize the S/N ratio while minimizing out-of-plane light). The META detector allows for the emitted wavelengths to be separated into ∼10 nm bins of light. For the SNARF fluorophore, the collected emission light was separated into three distinct bins: 569−601 nm, 601−633 nm, and 633−687 nm.

pH Calibration Assay. Buffers with pH = 4.2, 5.0, 6.0, 7.0, and 8.0 were prepared as follows. The pH 4.2 and pH 5 buffers were made by adjusting the pH of a 0.2 M potassium acetate solution to the appropriate pH with glacial acetic acid. The pH 6.0 buffer was prepared by mixing 1.2 mL of 1 M Na_2HPO_4 and 8.8 mL of 1 M NaH_2PO_4. The pH 7.0 buffer was formulated by mixing 5.8 mL of 1 M Na_2HPO_4 and 4.2 mL of 1 M NaH_2PO_4. The pH 8.0 buffer was prepared by mixing 9.3 mL of 1 M Na_2HPO_4 and 0.7 mL of 1 M NaH_2PO_4. The pH of these latter three buffers was adjusted with 6 M NaOH. To determine the pH calibration curve, PLL, CDP, and CDP−PEG particles were incubated as follows. Aliquots (2 μL) of each polyplex solution (prepared as described above) were added to 100 μL of each buffer and allowed to equilibrate for at least 3 h. Each sample was then imaged under the microscope, as described, and the intensity measurements for each of the three bins were collected. The intensity values were normalized with respect to the middle bin (601−633 nm emission light) to generate calibration curves for the different pH values. The ratios of the intensity values of the 633−687 emission bin divided by those of the 569−601 emission bin do not differ significantly for all three types of particles

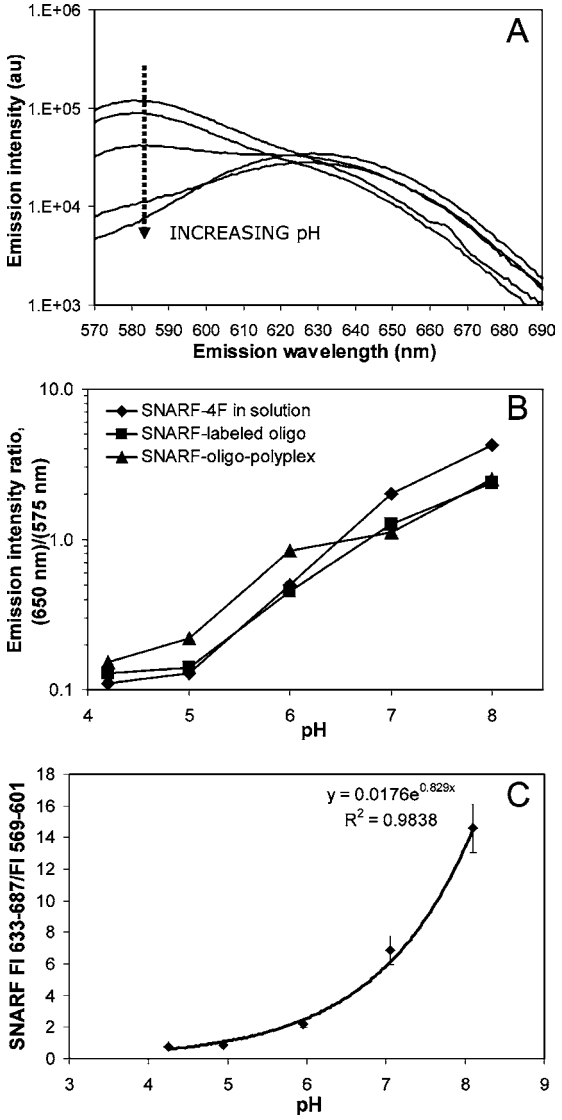

Figure 1. a: Fluorescence emission spectra of SNARF-4F as a function of pH. At low pH values, the peak at 575 nm is prominent, while the peak at 650 nm is low. As the pH rises, the 575 nm peak decreases in intensity, while the 650 nm peak rises to a maximum. pH measurements were taken in buffers with pH of 4.2, 5, 6, 7, and 8. b: Ratio of emission intensities for SNARF-4F dye. Attaching the dye to oligonucleotides or complexing the labeled oligonucleotides into particles does not appreciably change the emission spectrum of the dye, compared to free dye in solution. c: Mean fluorescence signal from 633 to 687 nm divided by signal from 569 to 601 nm for SNARF-4F as a function of pH for different particles in buffered solutions (see text).

at the same pH values; hence, we are able to use these ratios to determine intracellular pH.

In Vitro Transfection Imaging. After 24 h, the growth medium in each well was removed and replaced with an equal amount of Opti-MEM medium. A 2 μL amount of delivery particle-containing solution was then added to each well and placed in a 37 °C incubator for 2 h to allow for sufficient uptake. The cells were then imaged at 37 °C, with the fluorescence emission collected into three channels as previously described. Cells with delivery particles at different locations and stages of transport were imaged to generate a 'pH map' of the cell. Fluorescence intensity ratios were then calculated and compared to the calibrated pH values to determine the intracellular pH environment for each of the individual signals.

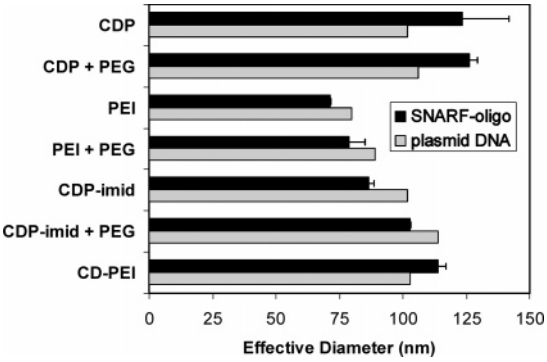

Figure 2. Average diameters of the various particles used in this study. Dynamic light scattering was employed to measure the effective diameters of the particles formulated. Most of these particles were formulated with an average effective diameter between 75 and 125 nm. Complexation of the polycation to either the SNARF-oligonucleotides or plasmid DNA resulted in particles of similar size.

Plasmid Uptake and Expression. The firefly luciferase-expressing DNA plasmid pGL3-Control Vector (5256 bp) was obtained from Promega (Madison, WI) and amplified using the Ultramobius 1000 kit (Novagen). One day prior to transfection, HeLa cells were plated at a density of 5×10^4 cells/mL in 24-well plates (1 mL/well). For transfection, polyplex solutions were diluted 10× in prewarmed Opti-MEM serum-free medium (Invitrogen), while lipoplex solutions were applied as formulated (in Opti-MEM). Uptake was assessed 4 h after transfection as described previously (*21*). Briefly, cells were transfected in duplicate with YOYO-1-labeled plasmid DNA, and the YOYO-1 fluorescence of viable cells was measured 4 h after transfection using a FACScalibur instrument (Becton Dickinson, Franklin Lakes, NJ). Expression of firefly luciferase was assayed as previously described (*22*). Briefly, the polyplex-containing medium was aspirated 4 h after transfection and replaced with regular growth medium equal to the original volume, and luciferase assays were conducted in triplicate 48 h after transfection.

RESULTS

Fluorescence pH Assay. The emission spectrum of SNARF-4F varies as a function of pH and has two peaks, one at 575 nm that increases in intensity as the pH declines, and one at 650 nm that increases in intensity as the pH increases; the crossover occurs at ~620 nm (Figure 1a). Thus, SNARF-4F can be used alone to monitor the pH in the range of 4−8, precisely the region useful for following the intracellular trafficking involving the endocytic pathway. SNARF-4F was conjugated to the 5′ end of an RNA phosphorothioate oligonucleotide and the pH sensitivity of the conjugate observed whether the labeled oligonucleotide was free in solution or was bound by a cationic polymer and condensed into delivery particles. SNARF-4F signals are approximately the same pH value independent of whether it is free in solution, conjugated to the nucleic acid or bound in a delivery vehicle (Figure 1b). The labeled oligonucleotide was used to prepare particles with a variety of nonviral gene delivery vectors; for most systems examined, the resulting particles were ~100 ± 25 nm in size (Figure 2), and the oligonucleotide exhibited stability against serum when packaged in delivery particles (data not shown). The intracellular trafficking of these fluorescently labeled particles was monitored in cultured cells as shown below.

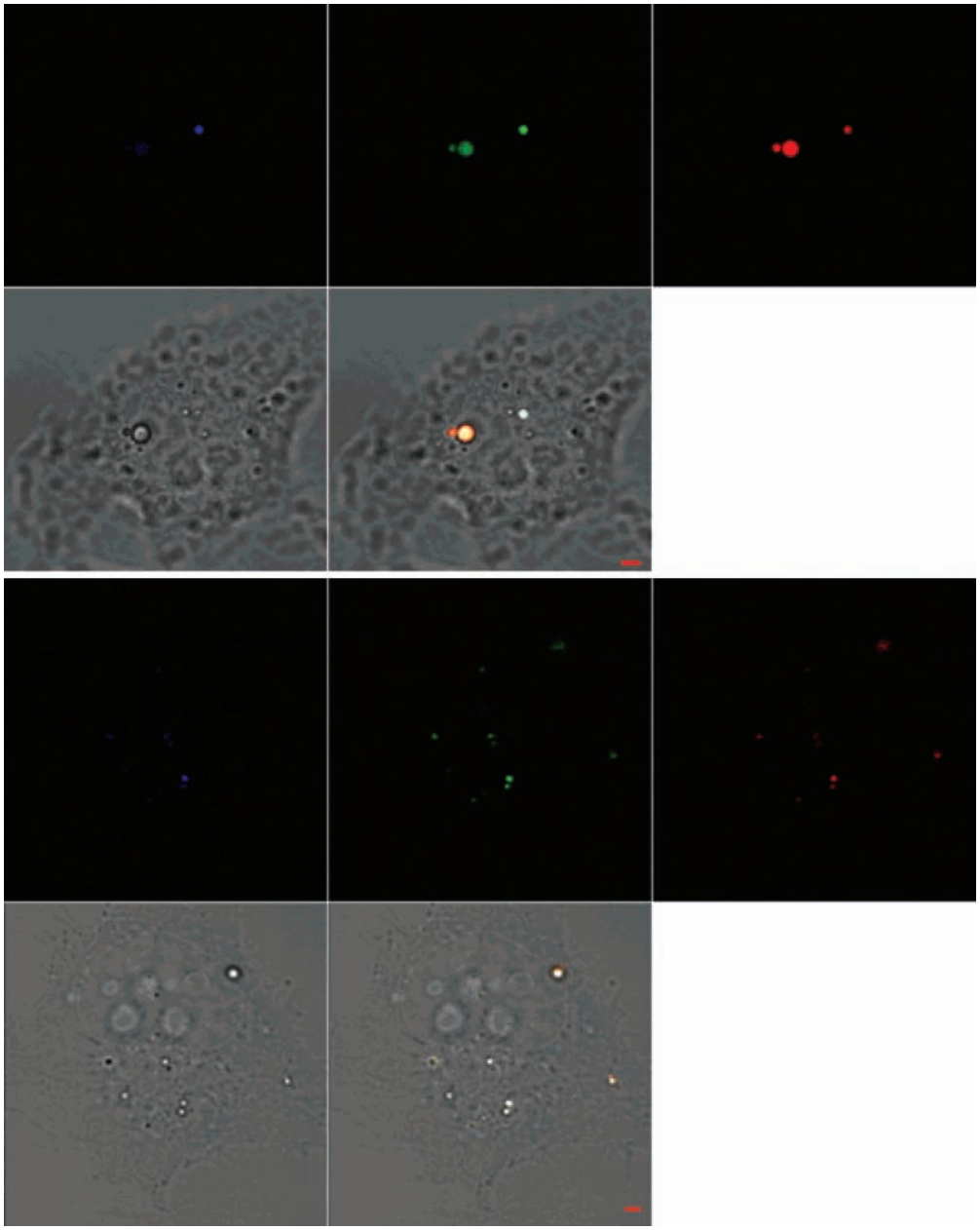

Figure 3. (Top) Image of PLL particles within cells after 2 h incubation. Blue represents the 569−601 nm channel, green the 601−633 nm channel, and red the 633−687 nm channel. In this case, the large spot has not acidified, while the smaller one to the right has acidified to pH 4.5. This image illustrates the inherent cell−cell variability of the uptake process, indicating that acidification does not occur uniformly or in a set time window. (Bottom) Image of PEI particles in a cell after 24 h incubation. The spots below the nucleus are at ~ pH 6, while the large one in the upper right corner is still at pH 7.5, suggesting that the particles in the upper right may have entered much later than the others. Scale bars = 1 μm.

To measure pH changes in cells via confocal microscopy, a META attachment was employed to separate the fluorescence emission into three wavelength bins (569−601, 601−633, and 633−687 nm). To generate a pH calibration curve, PLL and PEGylated CDP particles were prepared with the SNARF-4F RNA conjugate and were incubated in buffers with pH ranging from 4.2 to 8.1 and directly visualized under the microscope. The pH of the environment was quantitated by measuring the SNARF-4F emission in all three bins and sequentially calculating the ratios of all three bins compared to each other. The ratios did not differ significantly for PLL and PEGylated CDP particles in solution, and the data were combined to generate a single calibration curve. It was determined that the 633−687/569−601 nm ratio was the most sensitive to pH changes. An exponential curve was fit to these data points to determine an equation for calculating pH from the fluorescence intensity ratios, which was then used to determine intracellular endosomal pH values (Figure 1c).

By labeling the nucleic acids, and not the delivery vectors, the assay determines the pH environment of the delivered nucleic acids whether bound to the delivery vector or free in solution. It is relatively straightforward to directly visualize the SNARF-4F fluorescence when it is in a particle (Mishra et al. show high-resolution TEM and fluorescent confocal microscopy results that confirm vesicle containment of intact particles using some of the vector systems employed here (*21*)) as the signal appears as a round cluster. Figure 3 shows an example of intact PLL polyplexes after 4 h incubation and PEI polyplexes after 24 h incubation imaged within different regions of the cell. The pH is depicted colorimetrically in this image; those polyplexes experiencing a lower pH environment

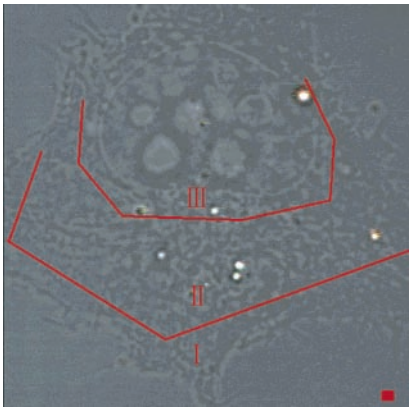

Figure 4. A schematic of a cell depicting the three regions (I, II, III) described in the text. Region I is the area of the cell within 2 μm of the cell membrane, region III is the region within 2 μm of the nucleus, and region II depicts the area in between. Scale bar = 1 μm.

appear more strongly blue colored whereas those experiencing a higher pH appear more strongly red colored. Diffuse staining indicative of unpackaged SNARF-oligonucleotide was not observed in these experiments, suggesting that unpackaged conjugate is diluted below the detection limit.

Intracellular pH Measurements. HeLa cells were exposed to the delivery particles for 2 h to allow for uptake and trafficking. While this time may seem long for endocytic processes, numerous reports have indicated that particle uptake and trafficking is notably slower (*6*, *10*). The media was then replaced to remove most of the free particles in solution, and the cells were incubated for up to 24 h before imaging. Because of the direct nature of our assay, it is not necessary to completely remove the free particles; in fact, particles that have entered more recently can be visualized and the endosomal pH values individually quantitated.

A major advantage of direct visualization is that different regions of an individual cell can be quantitated separately and not averaged into a bulk measurement. We have found that, early in the transfection process (less than 4 h), there appear to be regional differences in pH values within the cell (Figures 3 and 4). Specifically, the cytoplasm can be divided into three regions: region I, within 2 μm of the cell membrane; region II, the cytoplasmic region between the other regions; region III, within 2 μm of the nuclear membrane. We did not observe intact particles or labeled nucleic acids within the nucleus for any imaging condition. This is not unexpected for the CDP delivery systems, as Mishra et al. have shown that intact particles do not enter the nucleus (only released nucleic acids can be visualized in the nuclear compartment) (*21*).

As the particles are first internalized, their pH is uniformly high in region I for all examined classes of delivery vectors; however, the pH drops for PLL, CDP, and lipofectamine particles as they travel toward the nucleus (Figures 5 and 6). The reduction in pH for PLL is rather rapid and is complete by 2 h after initial incubation for those particles that reach region II. For the CDP vector, particles in region I are still at neutral pH after 4 h, those in region II are at an average pH of 6.1 with significant variability in pH, while those close to the nucleus have acidified by 4 h to an average pH of 5.2. Lipofectamine particles also display such an acidification, reaching an average pH of 4.6 by 16 h. Again, the average value does not tell a complete story; certain

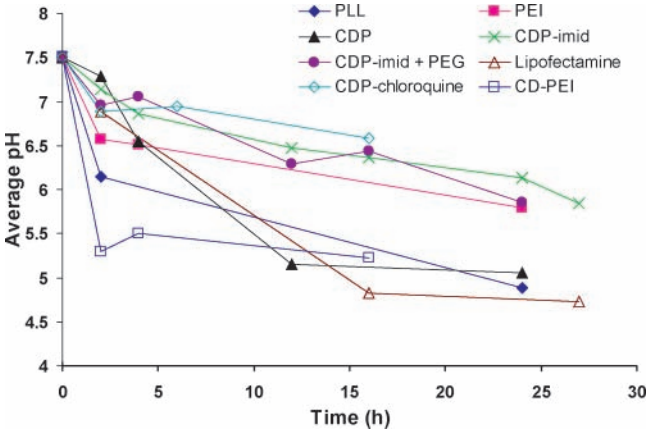

Figure 5. Plots of average pH of all cells and regions as a function of time.

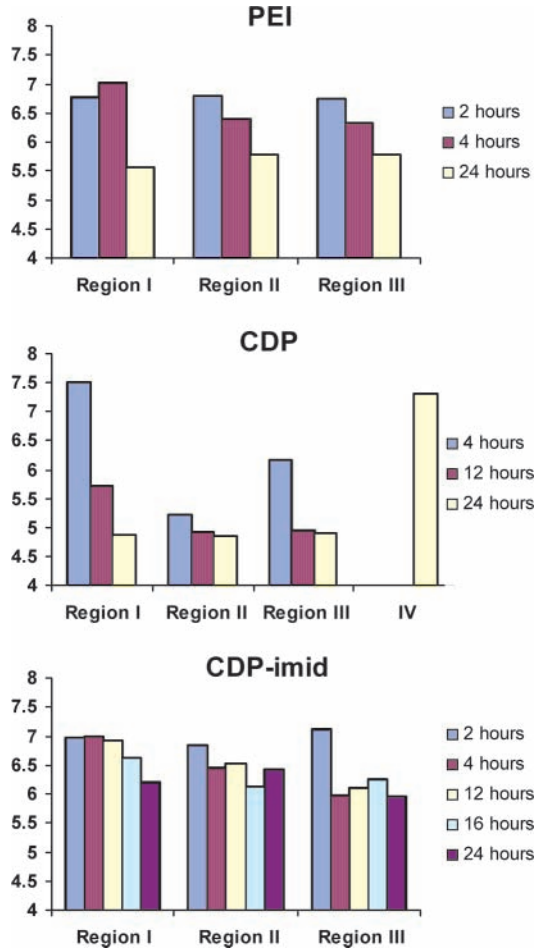

Figure 6. Regional pH values for PEI, CDP, and CDP-imidazole particles as a function of time and region within the cell. Greater variability can be seen for particles at earlier times and by region, highlighting the cell-to-cell variability inherent in these measurements.

particles in region II have fully acidified, while others are slower to do so.

In contrast, PEI particles display relatively consistent pH values for each time point, independent of region. Over time, the PEI particles do acidify from pH ~6.6 to ~5.8; however, the decrease is not as prominent as for PLL or CDP, which have acidified in all three regions by 24 h. Even at this time point, however, there are still a few cells (~1−4%) that show particles that are not acidified, possibly because they have entered the cells

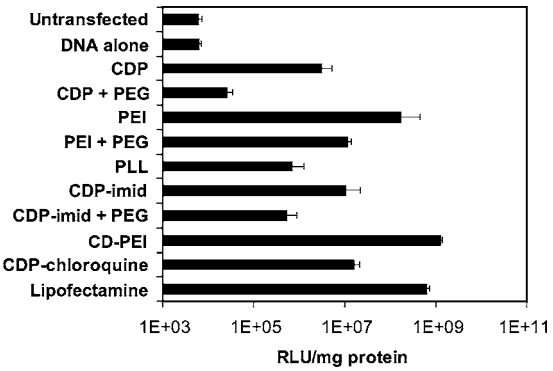

Figure 7. Gene delivery efficiency for each of the particles used in this study. The delivery vectors were complexed with plasmid DNA encoding luciferase, and used to transfect HeLa cells. The relative luciferase expression varies markedly for each type of particle. In general, stabilizing particles through PEGylation resulted in lower luciferase expression.

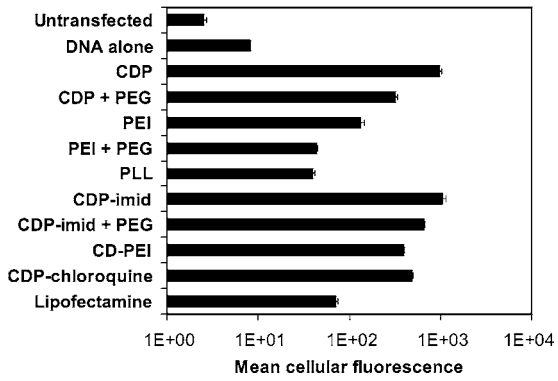

Figure 8. Measure of DNA uptake for each type of particle. Fluorescently labeled plasmid DNA was complexed with each type of delivery vector, and administered to HeLa cells. After 4 h, the cells were collected and analyzed by flow cytometry. The mean cellular fluorescence was used as a measure of DNA uptake.

only recently; these particles are indicated as being in region IV (see Figure 6). CD-PEI exhibits acidification to pH ~5.5 rather quickly, even in region I. However, it does not fully acidify below this pH, even after 16 h.

Although CDP particles do not buffer pH, modifications can be introduced to allow for buffering capacity. Conjugation of an imidazole group to the polymer termini produces CDP-imid, a vector that displays a limited buffering of pH. The acidification of CDP-imid particles occurs gradually, and even after 16 h, the average endosomal pH was ~6.3. Further acidification was observed to occur, with the average pH reaching ~6 by 24 h. Administration of chloroquine in conjunction with CDP particles resulted in a comparable buffering effect, with the pH remaining at ~6.6 even after 16 h.

Three types of particles (CDP, CDP-imid, PEI) permitted facile comparison between PEGylated and unPEGylated variants. Interestingly, differences between PEGylated and unPEGylated variants of the same polyplex type were minor. For instance, at 16 h after transfection, the average pH for PEGylated CDP-imid was ~6.4, while it was ~6.3 for the unPEGylated CDP-imid (Figure 4). Similar results were obtained for the other types of particles at each time point (data not shown).

Transfection Data. To explore the implications of the buffering behavior on the gene delivery efficiency of the examined delivery vectors, the delivery of luciferase plasmid DNA was employed. The examined delivery vectors generate similarly sized particles regardless of whether they are used to condense the SNARF-labeled oligonucleotide or plasmid DNA (Figure 2). The gene delivery activity of the various delivery vectors was assessed by transfecting cells with firefly luciferase-expressing plasmid DNA and assaying for luciferase expression (Figure 7). DNA uptake by cells was quantified using fluorescently labeled plasmid DNA and analysis by flow cytometry (Figure 8). The cellular fluorescence intensity can be correlated with relative uptake of plasmid DNA because the fluorescent label used (YOYO-1) was shown on a fluorimeter to be pH-insensitive (data not shown).

DISCUSSION

The fluorescence-based pH assay described herein provides the ability to follow and track individual particles within cells over time and thus gives insight into the nature of their trafficking within the cell. The development of this methodology was enabled by the facile labeling of the oligonucleotide and by the preservation of the label's pH sensitivity even when the conjugated oligonucleotides were condensed into delivery particles. Here, only a single fluorophore is used per nucleic acid molecule, thus avoiding the issue of uneven labeling (of nucleic acids or within particles) that can be present with two-fluorophore experiments.

Individual cells are examined in this assay, and particles residing in different zones within a given cell can be visualized and their local pH environment examined. Specifically, a 'pH map' of the delivery vectors can be determined as a function of the time-dependent spatial locations (i.e., close to the cell membrane, near the nucleus, or between) of the vectors as they traverse the cell. The relevance of this approach is demonstrated, for example, by the small percentage of cells showing PEI particles in region IV (those that are not acidified even after 24 h). In a bulk assay, this information would be lost, with such individual differences combined into a statistical average. Here, we directly access spatiotemporal information and use it to refine models of intracellular trafficking of delivery particles.

The current model of delivery vehicle transport through the cell suggests that the particles are first internalized within endosomal compartments, after which the compartments mature from early endosomes to late endosomes and finally to lysosomes; the pH of these compartments progressively declines until reaching pH ~4.5 (*10*, *17*, 23). Our results support this model of trafficking through the endocytic pathway by demonstrating and quantifying the reduction in pH experienced by delivered nucleic acids as they move through the cell. The ability of the delivery vehicles to circumvent or alter the steps of the endocytic pathway is of interest for understanding how efficiencies and transport rates are affected. Specifically, those particles that contain titratable amines at pH values between approximately 4 and 7 (such as PEI) are thought to buffer the endosomal compartments and prevent maturation into lysosomes. The buffering thus affects delivery. It is believed that those polymers that can buffer act as 'proton sponges' and promote osmotic swelling and lysis of endosomes. This lysis is speculated to allow endocytic pathway release that thus improves delivery efficiency (*11*, *15*).

In general, these models have been developed without an assessment of the spatial and temporal localization of the relevant pH changes. Each endosome is an individual entity and acidifies at a different rate that is

dependent upon cell type and other factors. Here, we specifically examine acidification within HeLa cells and find that spatial differences are prominent for CDP and PLL particles at early times (before 4 h). When these particles have trafficked for more than 12 h, they reach a pH of roughly 4.8−5.0 and show little difference regardless of position within the cell. These low pH values suggest that the endosomes have fully acidified and are at the lysosomal stage. For PEI, the spatial localization is less important than temporal differences, and the pH values are relatively constant throughout the cell for a given time point. After 24 h, the pH is ∼5.8, indicating that full acidification does not occur. For CDP-imid particles, the pH values are also relatively constant throughout the cell for a particular time point; the imidazole group acts to buffer the pH (relative to CDP particles), and the pH remains above 6 for almost 24 h (similar to PEI).

The uptake, intracellular trafficking, and gene delivery efficiency of PEGylated gene delivery particles differs from that of their unPEGylated variants (*21*). Comparing PEGylated CDP, PEGylated CDP-imid, and PEGylated PEI particles to their unPEGylated variants, we observe no significant differences in the extent or kinetics of acidification. This result indicates the PEG coating does not affect acidification or progression through the endocytic pathway. Retention of buffering capacity with the PEGylated particles is significant because systemic, in vivo administraton of nonviral gene delivery particles will require PEGylation or other means of salt-stabilization.

The relatively high delivery efficiency of PEI has been linked to its ability to act as a 'proton sponge', and there is evidence to support this hypothesis (*11*, *15*, *24*, *25*). Improvements in nonviral transfection efficiency in the presence of chloroquine have also provided credence to the 'proton sponge' hypothesis. It is shown here that chloroquine confers significant buffering activity to a vector system that otherwise readily acidifies. However, by comparing vectors with and without pH buffering capacity, it is clear that buffering capacity alone does not necessarily correlate with gene delivery efficiency. Despite similar pH buffering capacity, the three types of PEGylated particles generate reduced expression relative to their unPEGylated variants. The terminal imidazole group confers significant pH buffering capacity to CDP-imid that is not present for CDP; at the charge ratio examined here, the buffering activity does not correlate with significant improvements in transfection efficiency. Conversely, the significant buffering capacity of PEI is not seen in CD-PEI, but both vectors give strong expression, consistent with published results (*20*). The lack of correlation between buffering and gene expression has been observed by others (*13*, *26*). Forrest et al. revealed that acetylated PEI gave both reduced buffering capacity and improved transfection efficiency relative to unmodified PEI (*26*). (The buffering capacity of both CD-PEI and this acetylated PEI is reduced because some amine groups of PEI have been converted to other functionalities (*20*, *26*).) Also, recent reports have shown that new polymeric vectors designed with buffering capacity do not necessarily perform well as gene delivery vectors (*13*, *27*).

The data gathered here by a single-cell approach can be analyzed in aggregate for comparison with prior studies that have utilized flow cytometry to compile aggregate data. Our results in HeLa cells and those of Akinc and Langer in NIH 3T3 cells (*17*) both indicate that PEI shows a strong buffering capacity relative to PLL. This is consistent with a simple model where the titratable amines of PEI that are not present on PLL confer buffering capacity. In contrast, Forrest and Pack observed almost the opposite behavior, with PEI showing little to no buffering capacity as a function of cell line and PLL particles showing sharp variability as a function of cell line (*10*), including almost no reduction in pH in HepG2 cells even 15 h after transfection. Of note, fluorescently labeled nucleic acids were utilized in our study and that of Akinc and Langer, while Forrest and Pack conducted their experiments by fluorescently labeling the delivery vectors.

It has been widely observed that chloroquine treatment produces increases in transfection efficiency for many types of nonviral gene delivery particles (*16*, *28*), as seen in this study with CDP particles. The mechanism of this improvement is unclear. One possibility is that high intracellular or intravesicular concentrations of chloroquine induce the unpackaging of delivered nucleic acids from delivery vectors (*28*, *29*). Chloroquine is also known to buffer the vesicles of the endocytic pathway (*30*), and this buffering may inhibit the transfer of endocytosed gene delivery particles to lysosomes. Our results do not resolve the questions surrounding this mechanism, but they do show that chloroquine treatment inhibits acidification of intracellular CDP particles in HeLa cells. In the bulk assay of Akinc and Langer, chloroquine buffered the average pH of PLL particles in NIH 3T3 cells. In contrast to our results, their data included a sharp fluctuation where the average pH of the intracellular PLL particles dropped sharply to pH ∼4 in the first 2 h before rising upward in the next 2 h (*17*). The kinetics of chloroquine uptake may differ for the two cell lines. Although Forrest and Pack did not observe buffering by PEI, their bulk assay showed significant buffering when PEI transfection was accompanied by chloroquine (*10*).

When acidification of endocytic vesicles is buffered by gene delivery particles, the vesicles still progress through the endocytic pathway. PEI, for example, is shown here to demonstrate strong buffering capacity in a gene delivery particle. Lecocq et al. used centrifugation methods to show that intracellular PEI eventually colocalizes with the lysosomal marker cathepsin C (*31*). Kichler et al. observed that in vitro reporter gene expression was impaired when endosome acidification was inhibited with bafilomycin A1, indicating that, despite its buffering activity, PEI relies on the acidification process for transfection (*32*). Similarly, Singh et al. histidylated two cationic lipids to confer pH buffering and found that gene delivery with these lipids was less efficient in the presence of bafilomycin A1 (*33*).

Single-cell methods can supply new information on intracellular trafficking that will be useful in the design of improved gene delivery vectors. For example, various researchers have sought to enhance intracellular vector unpackaging by preparing acid-labile polycation−DNA particles (*14*, *34*). A detailed description of the spatial and temporal pH changes experienced by these particles in cells would indicate the probable intracellular location(s), timing, and extent of the particle degradation, thus facilitating refinement of the pH-sensitive vectors.

The compact, intense clusters of SNARF-4F fluorescence observed within cells are assumed to represent nucleic acids contained within vesicles. The small size of the SNARF-oligonucleotide suggests that the fluorescent signal from unpackaged intracellular oligonucleotides would appear diffuse. The absence of such diffuse staining could indicate that the majority of delivered nucleic acids remained within the delivery particles (*21*). Alternatively, the unpackaged oligonucleotide may present

a signal so diffuse that it is below the detection limit, or it may be rapidly degraded and/or expelled from cells.

One question that arises is why there might be any particles still remaining in region I (near the cell membrane) at 12 or even 24 h after transfection. One plausible explanation is that these particles have entered only a few hours earlier and have not had time to acidify. Particles in this category might have been stuck on the outer surface for hours before being endocytosed. However, this does not fully explain the existence of very low pH endosomes near the cell membrane. A second possibility is that such endosomes are trafficking very slowly toward the nucleus, or are traveling in a random trajectory and have fully acidified but happen to be close to the membrane when imaged. The particles must be transported along microtubules within endosomes in order to navigate the cytoplasm; the trajectories of these endosomes are often stochastic (*35*, *36*).

The advantages of the method presented here include the ability to directly visualize each cell and follow the internalization and endosome trafficking of delivery vehicles over time. This approach avoids or minimizes some of the problems of bulk imaging by flow cytometry that include quantitation of dead cells, presence of particles on the surface of the cell, and suppression of variability by intracellular region. The dynamics of the uptake and acidification process can be quantitated in both time and space, and any escape or other behavior monitored. By analyzing single cells, any variability in the process can be revealed and not buried in the overall average. This variability is especially evident at early times, as particles in certain spatial regions exhibit a broad range of pH values. We can also measure and segregate small subpopulations that would otherwise be combined into the statistical mean. Through the use of this assay, individual cells can be tracked for hours, and the spatial and temporal pH profile analyzed to better understand intracellular trafficking of nonviral gene delivery vectors. In summary, this new methodology has yielded data from which we have carried out further analyses of prior experiments performed in aggregate, quantified the differences in buffering capacity among a variety of delivery vectors, revealed that PEGylation does not significantly affect buffering capacity, and verified that chloroquine can confer buffering to gene delivery particles. The results presented here raise further questions about the role of pH buffering in the endocytic pathway and its importance to gene delivery efficiency.

ACKNOWLEDGMENT

We thank Dr. John Murphy for helpful discussions. R.P. Kulkarni acknowledges support from an NDSEG fellowship. We thank Insert Therapeutics, Inc., for partial support of this work. M. E. Davis is a consultant to and has financial interest in Insert Therapeutics, Inc.

LITERATURE CITED

(1) Davis, M. E. (2002) Nonviral gene delivery systems. *Curr. Opin. Biotechnol. 13*, 128−131.

(2) Godbey, W. T., and Mikos, A. G. (2001) Recent progress in gene delivery using nonviral transfer complexes. *J. Controlled Release 72*, 115−125.

(3) Boussif, O., Lezoualc'h, F., Zanta, M. A., Mergny, M. D., Scherman, D., Demeneix, B., and Behr, J. P. (1995) A versatile vector for gene and oligonucleotide transfer into cells in culture and in vivo: polyethylenimine. *Proc. Natl. Acad. Sci. U.S.A. 92*, 7297−7301.

(4) Luo, D., and Saltzman, W. M. (2000) Synthetic DNA delivery systems. *Nat. Biotechnol. 18*, 33−37.

(5) Stayton, P. S., Hoffman, A. S., Murthy, N., Lackey, C., Cheung, C., Tan, P., Klumb, L. A., Chilkoti, A., Wilbur, F. S., and Press, O. W. (2000) Molecular engineering of proteins and polymers for targeting and intracellular delivery of therapeutics. *J. Controlled Release 65*, 203−220.

(6) Godbey, W. T., Wu, K. K., and Mikos, A. G. (1999) Tracking the intracellular path of poly(ethylenimine)/DNA complexes for gene delivery. *Proc. Natl. Acad. Sci. U.S.A. 96*, 5177−81.

(7) Bieber, T., Meissner, W., Kostin, S., Niemann, A., and Elsasser, H. P. (2002) Intracellular route and transcriptional competence of polyethylenimine-DNA complexes. *J. Controlled Release 82*, 441−454.

(8) Remy-Kristensen, A., Clamme, J. P., Vuilleumier, C., Kuhry, J. G., and Mely, Y. (2001) Role of endocytosis in the transfection of L929 fibroblasts by polyethylenimine/DNA complexes. *Biochim. Biophys. Acta 1514*, 21−32.

(9) Hwang, S. J., and Davis, M. E. (2001) Cationic polymers for gene delivery: designs for overcoming barriers to systemic administration. *Curr. Opin. Mol. Ther. 3*, 183−191.

(10) Forrest, M. L., and Pack, D. W. (2002) On the kinetics of polyplex endocytic trafficking: implications for gene delivery vector design. *Mol. Ther. 6*, 57−66.

(11) Sonawane, N. D., Szoka, F. C., Jr., and Verkman, A. S. (2003) Chloride accumulation and swelling in endosomes enhances DNA transfer by polyamine-DNA polyplexes. *J. Biol. Chem. 278*, 44826−44831.

(12) Akinc, A., Lynn, D. M, Anderson, D. G., and Langer, R. (2003) Parallel synthesis and biophysical characterization of a degradable polymer library for gene delivery. *J. Am. Chem. Soc. 125*, 5316−5323.

(13) Funhoff, A. M., van Nostrum, C. F., Koning, G. A., Schuurmans-Nieuwenbroek, N. M., Crommelin, D. J., and Hennink, W. E. (2004) Endosomal escape of polymeric gene delivery complexes is not always enhanced by polymers buffering at low pH. *Biomacromolecules 5*, 32−39.

(14) Choi, J. S., MacKay, J. A., and Szoka, F. C., Jr. (2003) Low-pH-sensitive PEG-stabilized plasmid-lipid nanoparticles: preparation and characterization. *Bioconjugate Chem. 14*, 420−429.

(15) Behr, J. P. (1997) The proton sponge: A trick to enter cells the viruses did not exploit. *Chimia 51*, 34−36.

(16) Gonzalez, H., Hwang, S. J., and Davis, M. E. (1999) New class of polymers for the delivery of macromolecular therapeutics. *Bioconjugate Chem. 10*, 1068−1074.

(17) Akinc, A., and Langer, R. (2002) Measuring the pH environment of DNA delivered using nonviral vectors: implications for lysosomal trafficking. *Biotechnol. Bioeng. 78*, 503−508.

(18) Chen, Q. R., Zhang, L., Luther, P. W., and Mixson, A. J. (2002) Optimal transfection with the HK polymer depends on its degree of branching and the pH of endocytic vesicles. *Nucleic Acids Res. 30*, 1338−1345.

(19) Davis, M. E., Pun, S. H., Bellocq, N. C., Reineke, T. M., Popielarski, S. R., Mishra, S., and Heidel, J. D. (2004) Self-assembling nucleic acid delivery vehicles via linear, water-soluble, cyclodextrin-containing polymers. *Curr. Med. Chem. 11*, 179−197.

(20) Pun, S. H., Bellocq, N. C., Liu, A., Jensen, G., Machemer, T., Quijano, E., Schluep, T., Wen, S., Engler, H., Heidel, J., and Davis, M. E. (2004) Cyclodextrin-modified polyethylenimine polymers for gene delivery. *Bioconjugate Chem. 15*, 831−840.

(21) Mishra, S., Webster, P., and Davis, M. E. (2004) PEGylation significantly affects cellular uptake and intracellular trafficking of nonviral gene delivery particles. *Eur. J. Cell. Biol. 83*, 97−111.

(22) Popielarski, S. R., Mishra, S., and Davis, M. E. (2003) Structural effects of carbohydrate-containing polycations on gene delivery. 3. Cyclodextrin type and functionalization. *Bioconjugate Chem. 14*, 672−678.

(23) Sonawane, N. D., Thiagarajah, J. R., and Verkman, A. S. (2002) Chloride concentration in endosomes measured using a ratioable fluorescent Cl− indicator: evidence for chloride accumulation during acidification. *J. Biol. Chem. 277*, 5506−5513.

(24) Akinc, A., Thomas, M., Klibanov, A. M., and Langer, R. (2005) Exploring polyethyleneimine-mediated DNA transfection and the proton sponge hypothesis. *J. Gene Med. 7*, 657−663.

(25) Fukushima, S., Miyata, K., Nishiyama, N., Kanayama, N., Yamasaki, Y., and Kataoka K. (2005) PEGylated polyplex micelles from triblock catiomers with spatially ordered layering of condensed pDNA and buffering units for enhanced intracellular gene delivery. *J. Am. Chem. Soc. 127*, 2810−2811.

(26) Forrest, M. L., Meister, G. E., Koerber, J. T., and Pack, D. W. (2004) Partial acetylation of polyethylenimine enhances in vitro gene delivery. *Pharm. Res. 21*, 365−371.

(27) Dubruel, P., Christiaens, B., Rosseneu, M., Vandekerckhove, J., Grooten, J., Goossens, V., and Schacht, E. (2004) Buffering properties of cationic polymethacrylates are not the only key to successful gene delivery. *Biomacromolecules 5*, 379−388.

(28) Erbacher, P., Roche, A. C., Monsigny, M., and Midoux, P. (1996) Putative role of chloroquine in gene transfer into a human hepatoma cell line by DNA/lactosylated polylysine complexes. *Exp. Cell. Res. 225*, 186−194.

(29) Allison, J. L., O'Brien, R. L., and Hahn, F. E. (1965) DNA: reaction with chloroquine. *Science 149*, 1111−1113.

(30) Maxfield, F. R. (1982) Weak bases and ionophores rapidly and reversibly raise the pH of endocytic vesicles in cultured mouse fibroblasts. *J. Cell. Biol. 95*, 676−681.

(31) Lecocq, M., Wattiaux-De Coninck, S., Laurent, N., Wattiaux, R., and Jadot, M. (2000) Uptake and intracellular fate of polyethylenimine in vivo. *Biochem. Biophys. Res. Commun. 278*, 414−418.

(32) Kichler, A., Leborgne, C., Coeytaux, E., and Danos, O. (2001) Polyethylenimine-mediated gene delivery: a mechanistic study. *J. Gene. Med. 3*, 135−144.

(33) Singh, R. S., Goncalves, C., Sandrin, P., Pichon, C., Midoux, P., Chaudhuri, A. (2004) On the gene delivery efficacies of pH-sensitive cationic lipids via endosomal protonation: a chemical biology investigation. *Chem. Biol. 11*, 713−723.

(34) Walker, G. F., Fella, C., Pelisek, J., Fahrmeir, J., Boeckle, S., Ogris, M., and Wagner, E. (2005) Toward Synthetic Viruses: Endosomal pH-Triggered Deshielding of Targeted Polyplexes Greatly Enhances Gene Transfer in vitro and in vivo. *Mol. Ther. 11*, 418−425.

(35) Kulkarni, R. P., Wu, D. D., Davis, M. E., and Fraser, S. E. (2005) Quantitating intracellular transport of polyplexes by spatio-temporal image correlation spectroscopy. *Proc. Natl. Acad. Sci. U.S.A. 102*, 7523−7528.

(36) Suh, J., Wirtz, D., and Hanes, J. (2003) Efficient active transport of gene nanocarriers to the cell nucleus. *Proc. Natl. Acad. Sci. U.S.A. 100*, 3878−3882.

BC050081U

Gadolinium-Rhodamine Nanoparticles for Cell Labeling and Tracking via Magnetic Resonance and Optical Imaging

Kien Vuu,[†,‡] Jianwu Xie,[‡] Michael A. McDonald,[‡] Marcelino Bernardo,[§] Finie Hunter,[‡] Yantian Zhang,[∥] King Li,[‡] Mark Bednarski,[⊥] and Samira Guccione,*[,⊥]

Howard Hughes Medical Institute−National Institutes of Health Research Scholars Program, 4000 Jones Bridge Road, Chevy Chase, Maryland, 20815-6789, Molecular Imaging Laboratory, Department of Diagnostic Radiology, Clinical Center, National Institutes of Health, Bethesda, Maryland, 20892, National Cancer Institute, National Institutes of Health, 6116 Executive Boulevard, Room 3036A, Bethesda, Maryland, 20892-5477, National Institute of Biomedical Imaging and Bioengineering, National Institutes of Health, 6707 Democracy Boulevard, Suite 202, Bethesda, Maryland, 20892-5477, and Department of Radiology, Lucas Center for MR Spectroscopy and Imaging, Stanford, California 94305-5488. Received March 19, 2005

A novel dual-labeled nanoparticle for use in labeling and tracking cells in vivo is described. We report the construction and characterization of these gadolinium−rhodamine nanoparticles. These particles are constructed from lipid monomers with diacetylene bonds that are sonicated and photolyzed to form polymerized nanoparticles. Cells are efficiently labeled with these nanoparticles. We have inoculated labeled tumor cells subcutaneouosly into the flanks of C3H mice and have been able to image these labeled tumor cells via MRI and optical imaging. Furthermore, the labeled tumor cells can be visualized via fluorescent microscopy after tissue biopsy. Our results suggest that these nanoparticles could be used to track cells in vivo. This basic platform can be modified with different fluorophores and targeting agents for studying metastisic cell, stem cell, and immune cell trafficking among other applications.

INTRODUCTION

The ability to localize transplanted cells in vivo and monitor their tissue biodistribution is prerequisite to an understanding of cellular migration after transplantation. Analysis of pathophysiological processes as diverse as the homing of T cells in response to pathogens or tumors, cancer cell metastasis, and tracking stem cells or transplanted cells require a fundamental understanding of the biology of cellular trafficking. One of the most promising areas of investigation that will benefit from the ability to noninvasively monitor cell migration and function over time is stem cell research. Stem cells have the capacity to differentiate into virtually any cell type in the body and therefore carry the potential to replace injured or diseased endogenous cell populations (*1*).

Among the most important issues related to the fate of transplanted cells are biodistribution, viability, and differentiation after reaching the target site. There is a great need to develop improved means of monitoring cell migration in vivo. Histological techniques, often utilized to determine the fate and migration of cells, lack the ability to serially track the full body distribution of the transplanted cells (*2*−*4*). A more recent methodology involves the use of polycationic transfection agents and superparamagnetic iron oxide particles for intracellular magnetic labeling of cells. While this technique may allow in vivo tracking of implanted cells via MRI, resolution limitations prevent the ability to characterize the transplanted cells at the cellular level (*5*−*7*). By using a modifiable nanoparticle platform, adapted in previous studies for targeted gene delivery and targeted radiotherapy (*8*), we tested the ability of similarly constructed nanoparticles to label and track cells in vivo. Gadolinium−rhodamine nanoparticles (Gd−Rd-NPs), a dual modality contrast agent, can potentially be used for serial monitoring of cell trafficking in vivo via MRI and/or in vivo optical imaging, MR/optical-guided tissue procurement, and fluorescence-enabled cellular characterization and isolation.

MATERIALS AND METHODS

Preparation of Monomers. *N*,*N*-Bis[[[[(13,15-pentacosadiynamido-3,6,9-trioxaundecyl)carbamoyl]methyl]-ethyl](carboxymethyl)amino]ethyl]glycine−gadolinium complex (Gd-lipid) was synthesized as previously described (*9*). All other lipids used for Gd−Rd-NP synthesis were obtained from Avanti polar lipids. 1,2-Dioleoyl-3-trimethylammonium-propane (DOTAP) and 1-palmitoyl-2,10,12-tricosadiynoyl-sn-glycero-3-phosphocholine (PC) were dissolved in chloroform (Sigma) to make 20 mg/mL stock solutions. Stock solutions of 1,2-dioleoyl-sn-glycero-3-phosphoethanolamine-*N*-(Lissamine Rhodamine B Sulfonyl) (Liss-Rd) were prepared by dissolving 5 mg of the solid per milliliter of chloroform. All lipids were stored at −80 °C and thawed at room temperature prior to use.

Synthesis of Gadolinium−Rhodamine-Nanoparticles (Gd−Rd-NPs). Lipid monomer components (50% PC, 29% Gd-lipid, 1% Liss-Rd, 20% DOTAP) were mixed extensively and dried in vacuo while being shielded from

* Address correspondence to Samira Guccione, Lucas MRS/I Center, Room P284, 1201 Welch Road, MC 5488. Stanford, CA 94305-5488. Phone: 650-725-4936. Fax: 650-723-5795. Samira.guccione@stanford.edu.

† Howard Hughes Medical Institute−National Institutes of Health Research Scholars Program.

‡ Department of Diagnostic Radiology, National Institutes of Health.

§ National Cancer Institute, National Institutes of Health.

∥ National Institute of Biomedical Imaging and Bioengineering, National Institutes of Health.

⊥ Department of Radiology, Lucas Center for MR Spectroscopy and Imaging.

10.1021/bc050085z CCC: $30.25 © 2005 American Chemical Society
Published on Web 07/02/2005

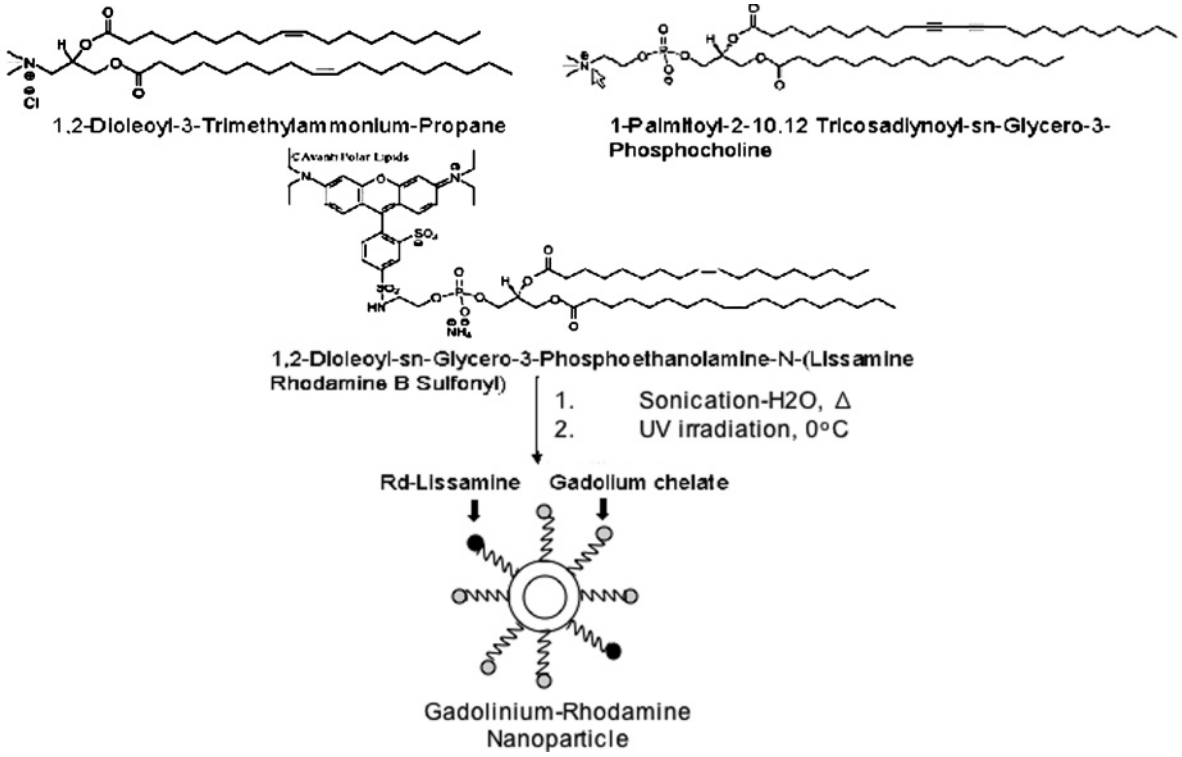

Figure 1. Diagram outlining key steps in the synthesis of the gadolinium−rhodamine nanoparticle.

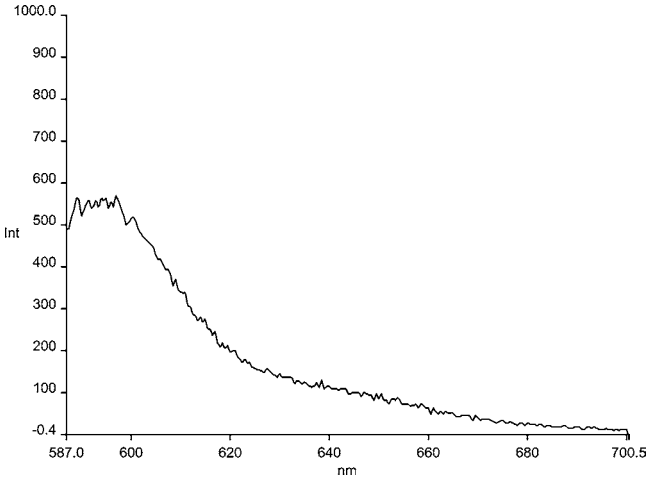

Figure 2. Fluorescence emission spectra of gadolinium−rhodamine nanoparticle in water. Plot of intensity (arbitrary units) vs wavelength (nm) depicting Gd−Rd-NP fluorescence after excitation at 570 nm.

light. The solid residue was resuspended with double-distilled water to a final lipid concentration of 15 mM and subsequently sonicated at 20 kHz (Branson 450 sonicator) while maintaining temperature above the gel-liquid crystal phase transition point. Polymerization of Gd−Rd-NPs was conducted at 0 °C under UV light (254 nm). The nanoparticles were then filtered through a 0.2 μm filter (Millipore) (Figure 1).

Physical Properties of Nanoparticles. Nanoparticle size was determined by dynamic laser light scattering using the Brookhaven particle size analyzer. Zeta potential was measured using a Zeta Potential analyzer (ZetaPALS, Brookhaven Instruments, NY).

Fluorescence Spectra. The fluorescence emission spectrum of the rhodamine-labeled nanoparticle was obtained using a LS 55 Luminescence spectrometer (PerkinElmer, Shelton, CT).

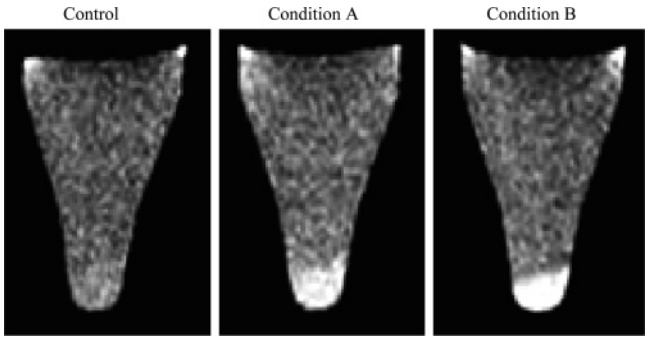

Figure 3. T1-weighted MR image of unlabeled, pelleted T47D breast cancer cells (~1.5×10^6) and pelleted cells labeled with gadolinium−rhodamine nanoparticle under conditions A or B. The average relative pixel intensity of the labeled versus unlabeled (control) cell pellets increases with labeling concentration of Gd−Rd-NPs.

Relaxivity Measurements. Relaxivity measurements were performed on a 4.7 T Bruker MR Scanner (Bruker, Houston, TX) at ambient temperature. The nanoparticle samples were diluted to concentrations of 2.17, 1.08, 0.54, 0.27, and 0.135 mM Gd with deionized water and transferred to a 200 μL-well plastic microtiter plate. T1 values were obtained from saturation recovery experiments performed with a standard spin−echo sequence and single slice acquisition (TR: 100, 200, 400, 600, 800, 1000, 1400, 2000 ms, TE: 15 ms). T2 values were obtained from spin−echo experiments with multislice acquisition (TR: 5 s, TE: 30 ms, number of echo images: 64). T1 and T2 were calculated using the ParaVision ISA tool to fit T1 recovery or T2 decay curve in circular region of interests for each sample. The resulting T1 and T2 values were averaged over the region of interest and plotted as 1/T1 or 1/T2 vs mM Gd^{3+}. The slope of these lines provides the molar relaxivity, R1 and R2, respectively.

Cell Labeling and in Vitro Imaging. Cell labeling was performed by incubating 60% confluent human T47D

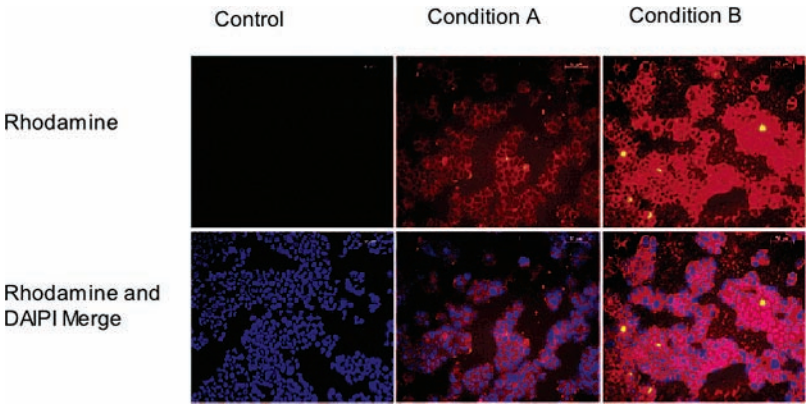

Figure 4. Fluorescence micrographs showing T47D breast cancer cell uptake of gadolinium−rhodamine nanoparticle in vitro. After 4 h of NP incubation, T47D cells demonstrate significant rhodamine fluorescence (RED). The amount of NP uptake into cells is proportional to the labeling concentration of the Gd−Rd-NP starting material (see Materials and Methods). Positive DAPI counterstaining (BLUE) indicates the viability of both Gd−Rd-NP-labeled and -unlabeled (control) cells.

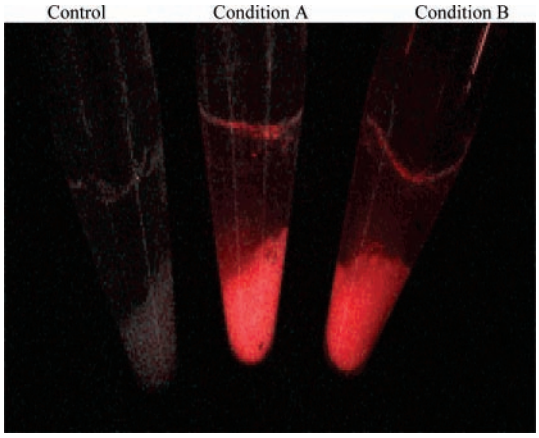

Figure 5. In vivo optical Imaging (Maestro *In Vivo* Multispectral Imaging System; Woburn, MA) of unlabeled cell pellet (left) and gadolinium−rhodamine nanoparticle-labeled cell pellets prepared under Conditions A (middle) and B (right).

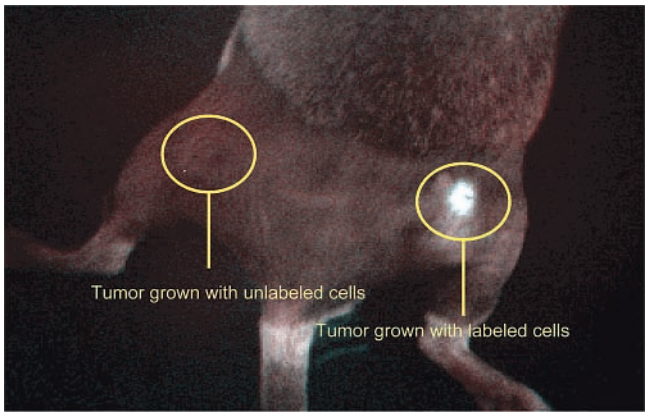

Figure 6. In vivo optical imaging (Maestro *In Vivo* Multispectral Imaging System; Woburn, MA) of mouse hind limb after inoculation with unlabeled tumor cells or gadolinium−rhodamine nanoparticle-labeled tumor cells. A female C3H mouse bearing unlabeled tumor (left flank) and Gd−Rd-NP-labeled tumor (right flank) imaged 7 days post subcutaneous inoculation (1×10^6 cells in each flank). Note that the fluorescent signal is localized only to the labeled tumor site and that no signal was received from the unlabeled (control) tumor.

breast cancer cells with Gd−Rd-NPs in 100 mm diameter culture dishes containing 5 mL of RPMI1640 culture medium supplemented with 10% fetal calf serum. Two different preparations of Gd−Rd-NPs were used for cell labeling studies: Condition A used a concentration of nanoparticles yielding 0.348 mM Gd3+ and 0.012 mM Rd; Condition B used a nanoparticle concentration yielding of 1.4 mM Gd3+ and 0.048 mM Rd. Labeling was carried out for 2 h in a cell culture incubator. Unlabeled (control) T47D cells were prepared under the same conditions excluding labeling with the nanoparticle. Prior to harvesting, cells were washed three times in PBS, trypsinized, and washed. Cells were then counted, transferred to 1.5 mL Eppendorf tubes at a concentration of $\sim 1.5 \times 10^6$ cells/tube, and pelleted. Each test tube was last topped with 0.5 mL of 4% gelatin. MRI of the cell pellets was conducted at 7 T using a T1-weighted SE sequence (as described above). In vivo optical imaging of the pellets was completed using the Maestro *In Vivo* Multispectral Imaging System (CRI, Woburn, MA). Cell labeling was also visualized using fluorescent microscopy. Labeled T47D breast cancer cells (under Conditions A and B described above) and unlabeled cells were prepared for fluorescence microscopy by plating in cultured chambers, washing the cells in PBS, and fixation in neutral 4% paraformaldehyde-PBS at room temperature. Prior to imaging, nuclei were counterstained with DAPI for ease of identification and demonstration of cell viability.

Tumor Inoculation and in Vivo Imaging. Approximately 1×10^6 Gd−Rd-NP-labeled tumor cells (Condition A) or an equivalent concentration of unlabeled (control) tumor cells were inoculated subcutaneously on opposite flanks of the hind legs of C3H mice. Seven days post inoculation the mice were imaged via MRI and in vivo optical imaging for anatomical visualization and localization of signal enhancement from labeled tumor cells.

RESULTS

Physical Properties of Nanoparticles: Gd−Rd-NPs are approximately 85 nm in diameter, and the polydispersity is 0.255. The zeta potential was determined to be 63 mV. Gd−Rd-NPs have an excitation maxima at 570 nm and peak fluorescence emission at ~595 nm in water (Figure 2). The R1 and R2 relaxivities for Gd−Rd-NP measured at 4.7T are 3.9 and 6.5, respectively.

Magnetic Resonance Imaging of Gd−Rd-NP-Labeled and -Unlabeled T47D Breast Cancer Cells. A T1-weighted MR image of pelleted, unlabeled. and Gd−Rd-NP-labeled T47D cells shows concentration dependent signal intensity enhancement secondary to cellular uptake of Gd−Rd-NPs (Figure 3). There is a 139% increase

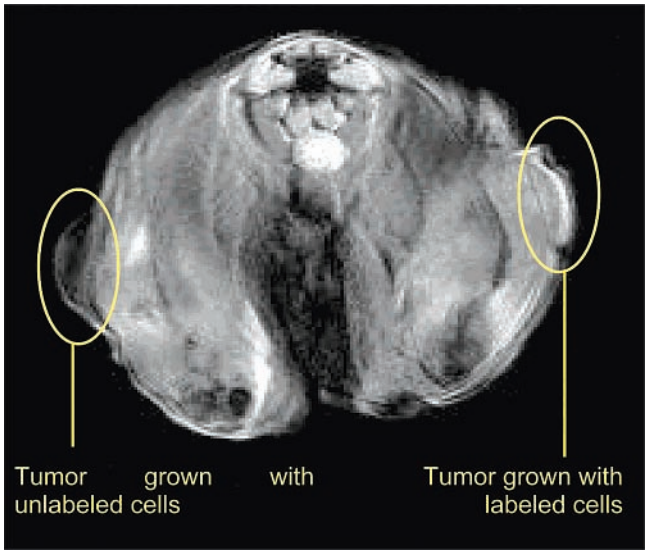

Figure 7. Axial MRI section of mouse 7 days after inoculation with unlabeled tumor cells and gadolinium−rhodamine nanoparticle-labeled tumor cells. Using the same mouse from Figure 4, a standard T1-weighted GEFI pulse sequence (TR = 30 ms, TE = 3 ms, matrix size = 256 × 256, 2 mm slice thickness) was used to acquire axial images over the entire body of the animal. Marked contrast enhancement can be visualized in the Gd−Rd-NP-labeled tumor vs unlabeled (control) tumor.

in average relative pixel intensity for T47D breast cancer cells labeled with Gd−Rd-NP under Condition A versus unlabeled (control), and a 146% increase for T47D cells labeled under Condition B.

Fluorescent Microscopy Gd−Rd-NPs-Labeled and -Unlabeled T47D Cells. Fluorescent microscopy reveals that the Gd−Rd-NPs accumulate in tumor cells after less than 2 h of incubation. Similar to MR images (Figure 3), Figure 4 demonstrates that the intensity of rhodamine fluorescence in breast cancer cells due to NP uptake is directly proportional to the fluorophore concentration in the Gd−Rd-NP starting material (Condition A vs B). Gd−Rd-NPs are endocytosed quickly by T47D cells and are evenly distributed in the cytoplasm. Morphologically identical DAPI staining of breast cancer cell nuclei is demonstrated in both labeled and unlabeled cells, further indicating cell viability after Gd−Rd-NP labeling

Optical Imaging of Cell Pellets. Gd−Rd-NP-labeled cell pellets visualized via the Maestro *In Vivo* Multispectral Imaging System demonstrate concentration dependent uptake of the NPs (Figure 5).

Whole Animal Optical Imaging. Similar subcutaneous tumor growth rates are observed on mouse flanks inoculated with either labeled or unlabeled T47D breast cancer cells (Figure 6). In vivo optical imaging of the whole mouse reveals fluorescent signal enhancement localized to the labeled tumor cells. In contrast, no signal is generated in tumors grown from unlabeled cells on the opposite flank.

Whole Animal Magnetic Resonance Imaging. Axial 2.0 mm slices across the mouse's body allow both the labeled and unlabeled tumors to be visualized in the same MR image (Figure 7). A representative image shows symmetrical contrast for anatomical structures about the long axis of the animal. However, using a T1-weighted pulse sequence, tumors grown from cells labeled with Gd−Rd NPs demonstrate marked signal enhancement compared to the unlabeled (control) tumor.

Histological Analysis. Histological sections of labeled and unlabeled tumor were prepared after in vivo imaging. Gd−Rd-NP-labeled tumor cells retain their optical properties as demonstrated by fluorescence microscopy (Fig-

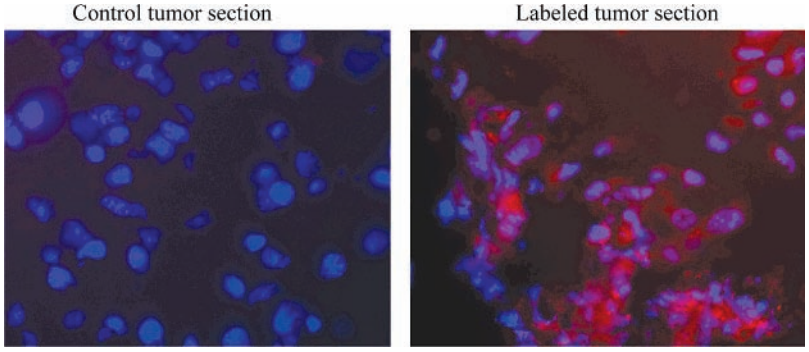

Figure 8. Fluorescence microscopy images of tumor cells from unlabeled and gadolinium−rhodamine nanoparticle-labeled tumor sections. Although the fluorescent signal is predominately localized to labeled tumor cells, some nonspecific labeling was noted upon sectioning.

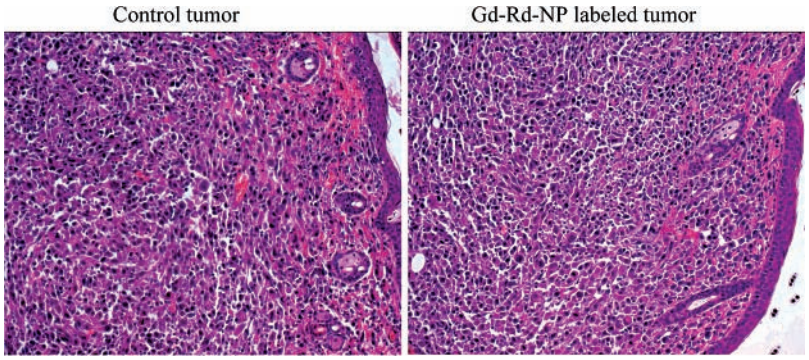

Figure 9. Light micrograph showing stained histological sections from mouse tumors grown from unlabeled tumor cells and gadolinium−rhodamine nanoparticle-labeled tumor cells. H&E stain demonstrates no change in cellular or tissue morphology between Gd−Rd-NP-labeled tumor sections and unlabeled (control) tumor sections.

ure 8). H&E staining of both the labeled and unlabeled tumor sections is indistinguishable: the labeled tumor cells showed no change in morphology and growth pattern as compared to unlabeled (control) cells (Figure 9).

DISCUSSION

In our experiments a novel fluorescent and paramagnetically labeled polymerized nanoparticle contrast agent, Gd−Rd-NPs, have been used to efficiently and quickly label tumor cells permitting detection by MRI, in-vivo optical imaging, and fluorescent microscopy. Gd−Rd-NPs offer the advantage of facilitating in vivo T1-weighted cellular imaging by MRI as well as detailed histological analysis through fluorescent microscopy. Cells labeled with Gd−Rd-NPs are viable and demonstrate little to no sign of altered cellular morphology. In addition, fluorescent labeling using Gd−Rd-NPs may also be used for isolation of cells via flow cytometry or laser capture microdissection. The ease of modification and complete control over synthesis conditions provided by our nanoparticle platform allows the construction of a myriad other nanoparticles with multiple labels and targeting moieties. Gd−Rd-NPs represent a new contrast material that provides facile cell labeling for noninvasive monitoring of cell migration and function using in vivo imaging techniques and histological analysis.

ACKNOWLEDGMENT

K.V. is pleased to acknowledge the Howard Hughes Medical Institute−National Institutes of Health Research Scholars Program for their support of his work. The authors also thank Martin Lizak and the staff at the Mouse Imaging Facility, NINDS, NIH, for expert assistance during animal experiments.

LITERATURE CITED

(1) Cowan C. A., Klimanskaya I., McMahon J., Atenza J., Witmyer J., Zucker J., Wang S., Morton C. C., McMahon A. P., Powers D., and Melton D. A. (2004) Derivation of embryonic stem-cell lines from human blastocyts. *N. Engl. J. Med*. *350* (13), 1353−1356.

(2) Jackson K. A., Majka S. M., Wang H., Pocius J., Hartley C. J., Majesky M. W., Entman M. L., Michael L. H., Hirschi K. K., and Goodell M. A. (2001) Regeneration of ischemic cardiac muscle and vascular endothelium by adult stem cells. *J. Clin. Invest. 107* (11), 1395−1402.

(3) Orlic D., Kajstura J., Chimenti S., Jakoniuk I., Anderson S. M., Li B., Pickel J., McKay R., Nadal-Ginard B., Bodine D. M., Leri A., and Anversa P. (2001) Bone marrow cells regenerate infarcted myocardium. *Nature 410* (6829), 701−705.

(4) Toma C., Pittenger M. F., Cahill K. S., Byrne B. J., and Kessler P. D. (2002) Human mesenchymal stem cells differentitate to a cardiomyocyte phenotype in the adult murine heart. *Circulation 105* (1), 93−98.

(5) Frank J. A., Zywicke H., Jordan E. K., Mitchell J., Lewis B. K., Miller B., Bryant L. H., Jr., and Bulte J. W. (2002) Magnetic intracellular labeling of mammalian cells by combining (FDA-approved) superparamagnetic iron oxide MR contrast agents and commonly used transfection agents. *Acad. Radiol. 9* (2), 484−487.

(6) Kraitchman D. L., Heldman A. W., Atalar E., Amado L. C., Martin B. J., Pittenger M. F., Hare J. M., and Bulte J. W. (2003) In vivo magnetic resonance imaging of mesenchymal stem cells in myocardial infarction. *Circulation 107* (18), 2290−2293.

(7) Bulte J. W., Douglas T., Witwer B., Zhang S. C., Strable E., Lewis B. K., Zywicke H., Miller B., van Gelderen P., Moskowitz B. M., Duncan I. D., and Frank J. A. (2001) Magnetodendrimers allow endosomal magnetic labeling and in vivo tracking of stem cells. *Nat. Biotechnol. 19* (12), 1141−1147.

(8) Storrs R. W., Tropper F. D., Li H. Y., Song C. K., Sipkins D. A., Kuniyoshi J. K., Bednarski M. D., Strauss H. W., and Li K. C. (1995) Paramagnetic polymerized liposomes as new recirculating MR contrast agents. *J. Magn. Reson. Imaging. 5* (6), 719−724.

(9) Storrs R. W., Tropper F. D., Li H. Y., Song C. D,. Sipkins D. A., Kuniyoshi J. K., Dorothy A., Li K. C., and Bednarski M. D. (1995) Paramagnetic polymerized liposomes for magnetic resonance imaging: synthesis and characterization. *J. Am. Chem. Soc. 117* (28), 7301−7306.

BC050085Z

Synthesis and Evaluation of Insulin–Human Serum Albumin Conjugates

Karen Thibaudeau, Roger Léger,* Xicai Huang, Martin Robitaille, Omar Quraishi, Chantal Soucy, Nathalie Bousquet-Gagnon, Pieter van Wyk, Véronique Paradis, Jean-Paul Castaigne, and Dominique Bridon

ConjuChem Inc., 225 President-Kennedy Avenue, Montreal, QC, H2X 3Y8 Canada. Received April 1, 2005; Revised Manuscript Received May 18, 2005

A series of human insulin maleimido derivatives with short and long linkers was synthesized by exploiting the variations in the pK_a values and environment of the three amino groups present in the protein. The syntheses were accomplished in organic solvent because of maleimide's instability in basic aqueous media. The derivatives thus obtained were conjugated to the free thiol on Cys34 of human serum albumin (HSA) and purified. A structure–activity relationship based on in vitro receptor binding and activation results for this series of insulin–HSA conjugates showed that the best compounds were attached at the B1 position of insulin with either short or long linkers. Two conjugates were administered subcutaneously to streptozotocin-induced diabetic rats and found to possess blood glucose normalizing activity up to 8 h postadministration. The return to diabetic plasma glucose levels was not observed within the time frame of the experiment (48 h). In comparison, the insulin-treated group's normalization activity lasted 2 h and returned to a diabetic level at 8 h. The onset of the conjugate activities were delayed by 1 h when compared to the activity of human insulin. The study results led to the identification of CJC-1575 as a potent and long lasting human insulin analogue.

INTRODUCTION

Insulin is a vital endocrine hormone that binds to its cellular surface receptor, setting off a cascade of events culminating in glucose absorption from the blood. Low plasma levels of insulin lead to severe disorders such as types I and II diabetes. Type I diabetes is a life threatening disease where the patient must self-administer quick acting insulin for survival. In Type II diabetes, the therapeutic objective is glycemic control to reduce the onset of long-term pathological consequences. The treatment with insulin becomes necessary after the failure of lifestyle changes or glucose lowering drugs. A long lasting form of insulin will lead to better glycemic control and reduce the amount of injections, resulting in increased patient appreciation and compliance (*1*–*3*).

There are several known "long lasting" insulin drugs in various stages of development or available on the market. Some examples include slow release from the injection site (*4*), noncovalent binding to blood proteins through lipophilic interactions (*5*–*12*), PEGylation (*13*–*14*), or conjugation to a polymeric support (*15*). Alternatively, the conjugation of a maleimido derivative of a peptide to Cys34 human serum albumin (HSA) can prolong the presence of the bioactive species in plasma by protecting it against elimination through metabolic or excretion pathways (*16*–*21*). We became interested in the application of this methodology to human insulin, **1** (Figure 1), to demonstrate how a small protein can be coupled regioselectively to human serum albumin (HSA) and evaluate the new conjugate's properties.

An insulin–HSA fusion protein prepared through genetic engineering has recently been reported (*22*). The fusion protein has the insulin linked to the *N*-terminus of HSA and the two A and B chains tethered together by a peptidic chain. Edman degradation analysis identified the B chain amino acids sequence, indicating that the attachment of the insulin to HSA was at the C-terminus of the A chain. Although the resulting protein was bioactive, there was no further discussion of a structure–activity relationship (SAR) in the study. The product of conjugation of insulin to transferrin was also reported (*23*). In that study, the insulin was linked to transferrin by a disulfide-containing linking group attached to exposed lysine residues on both molecules. This nonregioselective technique can potentially cause important variations in biological responses due to a possible lack of batch-to-batch reproducibility.

Insulin contains two peptide chains with three disulfide bonds and three free amines. Hence, the challenge was to use insulin as a starting material and selectively attach a single maleimido group to each of the available amine sites. We report herein the synthesis of maleimido derivatives of human insulin, their conjugation to HSA, and the in vitro and in vivo biological evaluation of the conjugates.

EXPERIMENTAL PROCEDURES

Recombinant human insulin was obtained from ICN Chemicals as a 0.4% zinc salt. Flash column chromatography was carried out by using Biotage "40*i* flash chromatography" modular system. Unless otherwise specified, semipreparative HPLC purifications were done on a Waters "Breeze" system 1500 series using a Phenomenex luna (RP-18, 10 μ phenyl-hexyl 250 × 21.2 mm) column. The flow rate was 9.5 mL/min, and 9.5 mL fractions were collected. A gradient of acetonitrile (0.1%TFA) in water (0.1%TFA) was used with further details indicated within each compound's synthetic pro-

* To whom correspondence should be addressed. ConjuChem Inc, Research Department, 225 President-Kennedy Ave, Suite 3950, Montreal QC, H2X 3Y8 Canada. Phone: 514-844-5558. FAX: 514-844-1119. E-mail: leger@conjuchem.com.

10.1021/bc050102k CCC: $30.25 © 2005 American Chemical Society
Published on Web 06/25/2005

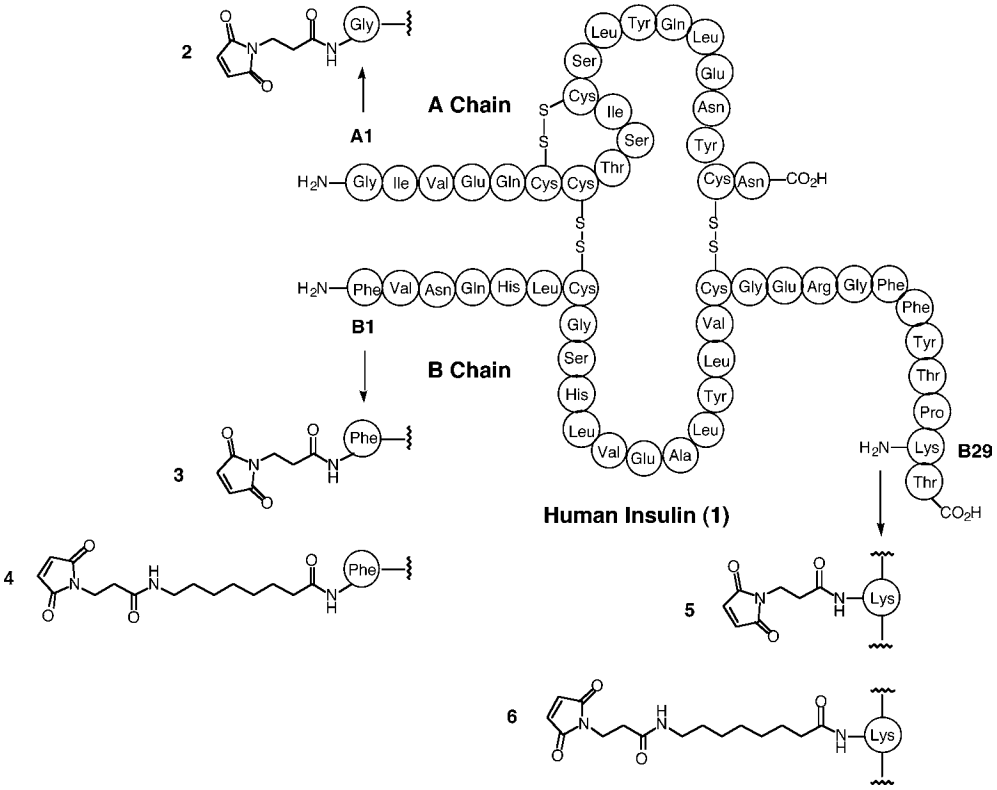

Figure 1. Maleimide derivatives of human insulin (**1**).

cedure. Outflow was monitored by UV absorbance at 214 and 254 nm. Fractions containing the desired product profile were identified by mass spectrometry. Preparative scale purification was done on a Gilson 690 system using a Phenomenex luna column (RP-18, 10 μ phenyl-hexyl 250 × 50.0 mm) using an acetonitrile (0.1% TFA)/water (0.1% TFA) as above. The flow rate was 50 mL/min, and 50 mL fractions were collected. Outflow was monitored by UV absorbance at 214 and 254 nm. Fractions containing the desired product profile were identified by mass spectrometry. LC/MS was performed using an Agilent 1100 series LC-MSD with a single quadrupole and an ESI electrospray source. The liquid chromatography part was done using a Vydac C18 (4.6 × 250 mm) column with a gradient of acetonitrile (0.1%TFA) in water (0.1%TFA) of 20−80% over 20 min. Automated Edman degradation (Applied Biosystems Procise 492 protein sequencer) and high-resolution mass spectroscopy analyses were done at the Sheldon Institute (Genome Quebec) of McGill University (Montreal, QC, Canada). Proton nuclear magnetic resonance spectra were gathered on a Varian 300 MHz Gemini instrument. SDS-PAGE electrophoresis was done on a SE 250 Mighty Small II (Pharmacia/Hoefer) using low range SDS−PAGE Molecular weight standards from BioRad (cat. # 161-0304).

***N*-Succinimidyl 3-Maleimidopropanoate, MPA-OSu, 8.** To 3-maleimidopropionic acid, **7** (20.5 g), *N*-hydroxysuccinimide (30.7 g), and *N*-(3-dimethylaminopropyl)-*N*′-ethylcarbodiimide (EDC, 51.1 g) in dichloromethane (300 mL) was added *N*-methylmorpholine (133 mL), and the mixture was stirred for 16 h at ambient temperature. The solvent was evaporated and the residue redissolved in dichloromethane (2 L). The organic layer was washed with 0.1 N HCl and brine and dried (Na_2SO_4). The solution was passed through a glass funnel filled with silica gel (1 kg). The silica gel was rinsed with dichloromethane (2 L) followed by a 1:1 dichloromethane/ethyl acetate mixture (4 L). The fractions containing product were combined, and the solvent was removed to give a white powder (23.7 g, 73%) (*24*). MS (*m/z*) 267 (M + 1). ^{1}H NMR (300 MHz, $CDCl_3$) δ 2.78 (s, 4H), 2.98 (t, J = 7 Hz, 2H), 3.89 (t, J = 7 Hz, 3H), 6.70 (s, 2H).

8-(3-Maleimidopropionamido)octanoic Acid, MPA-OA, 9. **8** (6.02 g) was added to a solution of 8-aminooctanoic acid hydrochloride salt (3.95 g) in *N*,*N*-dimethylformamide (50 mL) in the presence of *N*-methylmorpholine (24 mL). The reaction mixture was stirred at ambient temperature for 16 h. The solvent was removed under vacuum. The residue was acidified by addition of 1 N HCl and the product extracted with ethyl acetate (2 × 500 mL). The combined extracts were washed with water and brine and dried (Na_2SO_4). The solvent was removed under reduced pressure, and the crude product (7.14 g) was used in the next step.

4-Nitrophenyl 8-(3-Maleimidopropionamido)octanoate, MPA-OA-OPNP, 10. Crude **9** (4.56 g) was dissolved in dichloromethane (100 mL). *N*-Methylmorpholine (3.2 mL) and *p*-nitrophenyl chloroformate (2.96 g) were added successively, and the reaction was stirred for 45 min at ambient temperature. The solvent was evaporated under reduced pressure, and the residue was taken up into dicholoromethane and divided into three portions. Each portion was injected into a Biotage flash column (40M) eluting with dichloromethane. The fractions containing product were combined and concentrated to give the desired product (4.2 g) as a white solid. Further purification was accomplished by recrystallization from ethyl acetate/hexane to give the desired product (3.14 g, 50%) as a white solid. MS (*m/z*) 432 (M + 1). Mp 149−150 °C. Thin-layer chromatography R_f = 0.31 (CH_2Cl_2/EtOAc 1:1). ^{1}H NMR (300 MHz, $CDCl_3$) δ 1.2−1.5 (m, 8H), 1.64−1.8 (m, 2H), 2.48 (t, J = 7 Hz, 2H), 2.57 (t, J = 7 Hz, 2H), 3.18 (m, 2H), 3.81 (t, J = 7 Hz, 2H), 5.50 (bs, 1H), 6.67 (s, 2H), 7.23 (m, 2H), 8.23 (m, 2H).

(A1)-MPA-insulin, 2. **1** (100 mg) was dissolved in *N*,*N*-dimethylformamide (2 mL) with trifluoroacetic acid

(100 μL). *N*-Methylmorpholine (200 μL) and **8** (9.2 mg, 2.5 equiv) were added, and the reaction was stirred for 2 h. The reaction was quenched by addition of water and adjusted to pH 4 with acetic acid. The precipitate was dissolved with water/acetonitrile (3:1, total volume 20 mL). The resulting solution was injected into semipreparative HPLC using a 27 to 31% acetonitrile gradient over 120 min. The fractions at t_R = 36−46 min were combined and lyophilized to give **2** as a white powder (40 mg) along with recovered **1** (23 mg). LC/MS t_R = 15.1 min. (*m/z*) 5958.0 (M + 4), UV (214 nm) purity >99%. HRMS calculated for $C_{264}H_{388}N_{66}O_{80}S_6$ + $4H^+$ 5958.696, found 5958.697.

(A1B29)-Bis-Boc-insulin, 11. 1 (1.0 g) was dissolved in anhydrous dimethyl sulfoxide (10 mL) and triethylamine (1.0 mL) under sonication. Boc_2O (84 mg, 2.2 equivalents) in dimethyl sulfoxide (0.5 mL) was added to the solution, and the reaction was stirred at ambient temperature for 30 min. The reaction was quenched by addition of acetic acid (14 mL) and water (100 mL). The resulting solution was injected into preparative HPLC using a 27 to 40% acetonitrile gradient over 60 min. The fractions at t_R = 38−47 min. were combined and lyophilized to give **11** as a white powder (674 mg, 65%). MS (*m/z*) 6007.8 (M + 4). HRMS calcd for $C_{267}H_{399}N_{65}O_{81}S_6$ + $3H^+$ 6006.766, found 6006.804.

(B1)-MPA-insulin, 3. 11 (51 mg) in *N*,*N*-dimethylformamide (3 mL) was treated with **8** (36 mg) in the presence of triethylamine (30 μL). The reaction was stirred for 2 h at ambient temperature. The solvent was removed under vacuum, and TFA (2 mL) added to the residue and stirred for 10 min. The TFA was evaporated, and the crude product was dissolved in water/acetonitrile (3:1). The resulting solution was injected into semipreparative HPLC using a 27 to 32% acetonitrile gradient over 120 min. The fractions at t_R = 58−59 min were combined and lyophilized to give **3** as a white powder (29 mg, 57%). LC/MS t_R = 15.7 min. (M/z) 5958.4 (M + 4), UV (214 nm) purity >99%. HRMS calcd for $C_{264}H_{388}N_{66}O_{80}S_6$ + $4H^+$ 5958.696, found 5958.671.

(B1)-MPA-OA-insulin, 4. 11 (1.0 g) was dissolved in *N*,*N*-dimethylformamide (20 mL) in the presence of *N*-methylmorpholine (300 μL). **10** (1.0 g) was then added, and the reaction was stirred at ambient temperature for 4 h in the dark. The reaction was quenched by precipitation with Et_2O (120 mL) and the precipitate isolated by centrifuge. The residue was treated with TFA (2 mL) for 10 min. The TFA was evaporated, and the crude product was dissolved in acetic acid (20 mL) and water (100 mL). The resulting solution was injected into preparative HPLC using a 27 to 40% acetonitrile gradient over 60 min. The fractions at t_R = 28−37 min were combined and lyophilized to give **4** as a white powder (654 mg, 63%). LC/MS t_R = 16.1 min. (*m/z*) 6099.6 (M + 4), UV (214 nm) purity >99%. HRMS calcd for $C_{272}H_{403}N_{67}O_{81}S_6$ + $3H^+$ 6098.803, found 6098.783.

(A1B1)-Bis-Boc-insulin, 12. 1 (74 mg) was dissolved in anhydrous dimethyl sulfoxide (2 mL) and acetic acid (46 μL). Boc_2O (6.9 mg, 2.5 equiv) was added to the solution, and the reaction was stirred for 5 h at ambient temperature. Water (15 mL) and acetonitrile (5 mL) were added to the reaction mixture, and the resulting solution was injected into semipreparative HPLC using a 27 to 40% acetonitrile gradient over 120 min. The fractions at t_R = 64−71 min were combined and lyophilized to give **12** (30 mg, 40%) as a white powder. MS (*m/z*) found 6006.8 (M + 4). HRMS calcd for $C_{267}H_{399}N_{65}O_{81}S_6$ + $3H^+$ 6006.766, found 6006.759.

(B29)-MPA-insulin, 5. 12 (30 mg) in *N*,*N*-dimethylformamide (2 mL) and *N*-methylmorpholine (100 μL) was reacted with **8** (10 mg) for 60 min. The solvent was removed under vacuum and the residue treated with TFA for 10 min. The TFA was removed under reduced pressure, the residue was dissolved in water/acetonitrile (3:1) and the solution injected into semipreparative HPLC using a 27 to 32% acetonitrile gradient over 120 min. The fractions at t_R = 39−49 min were combined and lyophilized to give **5** as a white powder (22.2 mg, 75%). LC/MS t_R = 13.1 min. (*m/z*) 5958.0 (M + 4), UV (214 nm) purity >99%. HRMS calcd for $C_{264}H_{388}N_{66}O_{80}S_6$ + $4H^+$ 5958.696, found 5958.690.

(B29)-MPA-OA-insulin, 6. 12 (20 mg) in *N*,*N*-dimethylformamide (1 mL) and *N*-methylmorpholine (100 μL) was reacted with **10** (20 mg) for 5 h at ambient temperature in the dark. The solvent was removed under vacuum and the residue treated with TFA for 10 min. The TFA was removed under reduced pressure, the residue was dissolved in water and the solution injected into semipreparative HPLC using a 27 to 31% acetonitrile gradient over 120 min. The fractions at t_R = 55−63 min. were combined and lyophilized to give **6** as a white powder (11 mg, 53%). LC/MS t_R = 15.6 min. (*m/z*) 6099.5 (M + 4), UV (214 nm) purity 97.8%. HRMS calcd for $C_{272}H_{403}N_{67}O_{81}S_6$ + $4H^+$ 6098.803, found 6098.858.

General Procedure for the Hydrolysis of Maleimide. The appropriate MPA-insulin (or MPA-OA-insulin) (20 mg) was dissolved in 10 mL of aqueous sodium hydroxide (0.1 N) and stirred at ambient temperature for 10 min. The reaction mixture was brought to pH 4 by addition of acetic acid. The resulting solution was injected into semipreparative HPLC using a 27 to 32% acetonitrile gradient over 120 min. The fractions at t_R = 45−54 min were combined and lyophilized to give the desired hydrolyzed material. The yields, purity, and mass analysis are described in Supporting Information.

Preparation of Conjugates. Each maleimido insulin derivative was solubilized in Nanopure water at a concentration of 10 mM then diluted to 1 mM into a solution of HSA (25%, Cortex-Biochem, San Leandro, CA). The samples were then incubated at 37 °C for 30 min. Prior to their purification, each conjugate solution was diluted to 5% HSA in 20 mM sodium phosphate buffer (pH 7) composed of 5 mM sodium octanoate and 750 mM $(NH_4)_2SO_4$.

Purification of Conjugates. Using an ÄKTA purifier (Amersham Biosciences, Uppsala, Sweden), each conjugate was loaded at a flow rate of 2.5 mL/min onto a 50 mL column of butyl sepharose 4 fast flow resin (Amersham Biosciences, Uppsala, Sweden) equilibrated in 20 mM sodium phosphate buffer (pH 7) composed of 5 mM sodium octanoate and 750 mM $(NH_4)_2SO_4$. When all flow through waste material was removed, a linear gradient of decreasing $(NH_4)_2SO_4$ concentration (750 to 0 mM) was applied over four column volumes. The fractions containing the conjugate were combined, desalted and concentrated using Amicon ultra centrifugal (30 kDa) filter devices (Millipore Corporation, Bedford, MA). The resulting solution containing purified conjugate was immersed into liquid nitrogen, lyophilized, and stored at −80 °C. The analytical results of the individual conjugates are displayed in Table 2 in the text.

SDS−PAGE of Conjugates. A sample (5 μg of protein/well) of the conjugates was subjected to nonreducing SDS−PAGE using a 10% (w/v) gel. A constant current 20 mA/gel for 1.5 h in separating gel was applied (*25*). The gels were then stained with 0.1% Coomassie Brilliant Blue R-250 for 30 min at room temperature, followed by

Scheme 1. Synthesis of Activated Maleimides with Different Chain Lengths

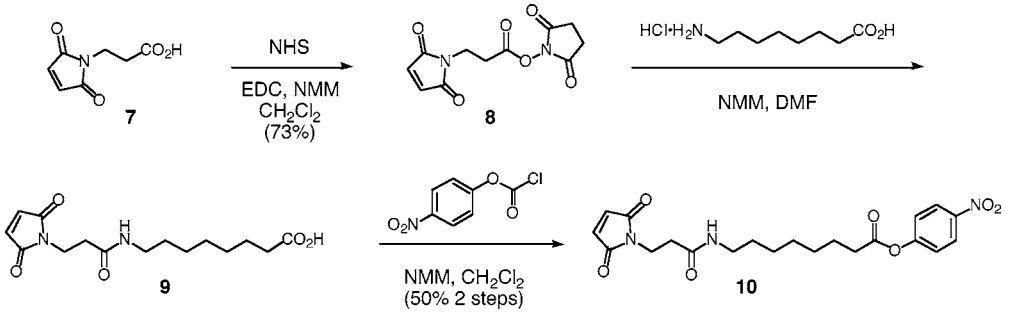

destaining in 10% (v/v) acetic acid and 30% (v/v) methanol in water.

Insulin Receptor Binding. Liver membranes from male Wistar rats (175 ± 25 g) were prepared in modified Na−K phosphate pH 7.4 buffer using standard techniques. Three milligram aliquots of membrane were incubated with 30 pM ^{125}I-insulin and the various other compounds for 16 h at 4 °C. Nonspecific binding was estimated in the presence of 1 μM insulin. Each compound was tested at 10^{-9}, 10^{-8}, 3.0×10^{-8}, 10^{-7}, 10^{-6}, and 10^{-5} M, and the insulin control had an extra concentration of 10^{-10} M. The membranes were filtered and washed three times with PBS buffer, and the filters were counted to determine the ^{125}I-insulin specifically bound.

Glucose Uptake Assay. Epidimymal fat tissue (0.03 g/mL) obtained from Wistar rats (175 ± 25 g) was degraded by collagenase in modified HEPES solution pH 7.4 at 37 °C. The test compounds at 10^{-9}, 10^{-8}, 10^{-7}, 10^{-6}, and 10^{-5} M and control (with an extra concentration of 10^{-10} M) were incubated with 500 μL aliquots of tissue in modified HEPES buffer pH 7.4 in the presence of D-[3-^{3}H]glucose (2.5 μCi/mL) at 37 °C for 2 h. The cells were harvested using GF/B filtermats, washed with PBS buffer, and dried, and the filtermats were counted to determine the cellular uptake of radioactive glucose.

Evaluation of Conjugates in Streptozotocin-Induced Diabetic Rats. Eight-week old male Sprague−Dawley rats (Charles River, St-Constant, QC, Canada) were administered a single intravenous injection of streptozotocin (60 mg/kg in 25 mM citrate/0.9% saline, pH4.5) to induce type I diabetes. Diabetic animals had mean blood glucose levels of 25.9 to 29.2 mM while glycemia ranged from 6.0 to 6.4 mM in normal rats. The test compounds (saline control, insulin 0.14 mg/kg, **3**−HSA and **4**−HSA 8.7 and 21.7 mg/kg) in 0.9% saline were administered as a single subcutaneous bolus injection in the dorsal area 2 days after streptozotocin treatment. Blood sampling was done via the tail tip, and glucose levels were measured using a hand-held glucometer (On Touch Ultra, Lifescan, Canada). The animals were supplied water and standard rat chow (Charles River Diet #5075) ad libitum and monitored throughout the experiment. Blood glucose levels were measured 30 min predose, 1, 2, 3, 4, 6, 8, 10, 11, 24, 30, and 48 h postdose.

Pharmacokinetics of 1 and 4−HSA. Subcutaneous pharmacokinetic profiles were done in 7−8 week old male Sprague−Dawley rats with body weights ranging 322−347 g. Each treatment group consisted of four rats. **4**−HSA was reconstituted in 0.9% saline while **1** was first dissolved in acidified water and further diluted to the required concentration with 0.9% saline. Blood samples were drawn at the following time points: −2, 10, 15, 20, 30, 40 min, 1, −2, 3 h and 2, 30 min, 1, 2, 4, 8, 24, 48, 72 h postadministration for **1** and **4**−HSA, respectively. Serum levels of **1** and **4**−HSA were determined using a human insulin ELISA kit (Linco Research, cat# EZHI-14K). The reference curves were generated with reference standards of known concentrations of **1** and **4**−HSA diluted in rat serum.

Ethics and Statistical Analyses. The experimental protocols were performed according to the Canadian Council on Animal Protection following approval by the Université du Québec à Montréal Institutional Committee on Animal Protection. All results are expressed as mean ± SEM or ± SD performed using GraphPad Prism software.

RESULTS AND DISCUSSION

Chemistry. The overall objective was to obtain the insulin−HSA conjugate with the best activity profile. In the case of the fatty acid and PEG derivatives, the focus was on the B1 or the B29 positions of **1** as points of attachment. This approach is in agreement with the proposed insulin receptor interaction (*26*). If direct acylation was to be used as a strategy, in most cases, the A1 position arose as the most abundant product from the mixture except when the C-terminal B30 was removed, which then favored acylation at B29 (*27*). In our approach, the exploitation of the pK_as (approximated as 11.1 for *N*ϵ-Lys B29, 8.4 for *N*α-Gly A1, and 7.1 for *N*α-Phe B1 in water) (*28*) and steric environments of the three amines was proposed as a means to selectively attach a single maleimidopropionamide (MPA) to each of the three individual positions of **1** as illustrated in Figure 1, more specifically A1 (**2**), B1 (**3** and **4**), and B29 (**5** and **6**).

Before initiating the synthesis of the insulin derivatives, two activated maleimide containing acylation reagents were prepared as described in Scheme 1. **8** was prepared from **7** using *N*-hydroxysuccinimide (NHS) and EDC (*24*). **8** was then used to prepare the longer linker maleimide by direct coupling to 8-aminooctanoic acid to give the intermediate **9** which was used crude in the next step. Attempts to make the succinimidyl ester of **9** led to purification difficulties and a tendency to decompose in aqueous media. **10** was ultimately made under mild conditions using *p*-nitrophenyl chloroformate (*29*−*30*) and was found to be easily purified and had a much improved stability profile.

Acylation using aqueous buffers could not be used in this strategy because of the tendency of the maleimido group to hydrolyze leading to a product that loses all ability to conjugate to HSA. This led to the development of buffer like conditions in *N*,*N*-dimethylformamide (DMF) with a mixture of trifluoroacetic acid (TFA) and *N*-methylmorpholine (NMM). These conditions were found to be convenient to solubilize the starting insulin and as a buffering medium. NMM has a lower pK_a than the ϵ amine on the B29 lysine. The latter will therefore, remain

Scheme 2. Synthesis of *N*α-A1-insulin MPA Derivative 2 Using Bufferlike Conditions in Organic Solvent

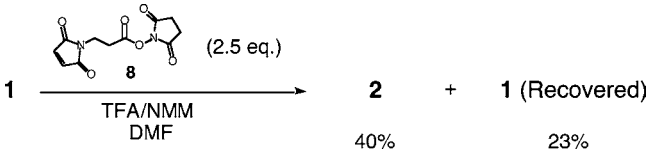

protonated while the α amine of the A1 glycine of insulin will have a larger portion of free amine at equilibrium resulting in more acylation product. The B1 phenylalanine is too sterically hindered to react and will require a different strategy.

As shown on Scheme 2, the A1 position remained the predominant product from the direct acylation of **1**. Compound **2** was obtained in 40% yield in a single step, along with 23% recovered starting insulin after purification. The remainder was a mixture of other positional isomers and bis-acylation products.

To obtain the other two B1 and B29 acylation products, a selective protection strategy was required. The bis *tert*-butyloxycarbamate (bis-Boc) A1 and B29 protection of **1** gave the best improvement in yield of the B1 derivatives. As shown in Scheme 3, intermediate **11** was prepared in 65% yield using a mixture of triethylamine and dimethyl sulfoxide as solvent and 2.5 equiv of di-*tert*-butyl dicarbonate (Boc_2O) (*31*−*34*).

Compound **11** was then converted to **3** and **4** using either **8** or **10**, respectively, under identical coupling conditions. The intermediate product from the acylation reaction was not isolated. Instead, the crude product was treated with TFA and purified. The final compounds **3** and **4** were obtained in similar yields of 57 and 63%, respectively.

Obtaining selective A1, B1 bis-Boc insulin **12** involved the addition of acetic acid to the reaction mixture (Scheme 4). In this case, the ammonium/free amine equilibrium in DMSO was such that only the lysine remained protonated throughout the process. **12** was obtained in low yield but enough material could be made to carry on. The completion of the syntheses of **5** and **6** was accomplished as described in Scheme 4. The yield of **5** was similar to the B1 acylation products but the conversion to **6** gave a slightly lower yield. Each synthesis was repeated to give multiple batches of **3**, **4**, **5**, and **6**, which were combined after examination of the purity profiles.

The demonstration of the position of attachment was done by Edman degradation. The amide bonds on maleimide were labile under high pH aqueous conditions used in routine automated Edman degradation. The study was therefore undertaken on the prehydrolyzed material to minimize any possible ambiguous results. The corresponding structures and compound numbers of the hydrolysis products are shown in Scheme 5, and the Edman degradation results are shown in Table 1.

The sequences read during the Edman degradation showed that in the case of **1** both chain amino acids were identified, indicating that no N-terminal amine was acylated. In the case of **13**, only the sequence associated with chain B was read, indicating that chain A was acylated. When this logic was applied to compounds **14** through **17**, it became possible to confirm that the initial maleimido derivative structures were correctly assigned.

Preparation of Insulin−HSA Conjugates. The conjugation of maleimido derivatives to Cys34 of HSA and subsequent purification using hydrophobic chromatography (*17*), where a purified conjugate is defined as free of starting HSA (mercaptalbumin and cystinylated albumin also termed "capped" HSA) and free of residual maleimido derivative of insulin, has recently become an efficient process. The conjugation step involved mixing the individual derivatives with 25% HSA and incubating for 30 min at 37 °C. The conjugation reactions were found to be very rapid, and there was no maleimide hydrolysis observed. Thereafter, the resulting mixtures were loaded directly onto a column packed with butyl sepharose 4 fast flow resin. The insulin−HSA conjugates adsorbed onto the hydrophobic resin whereas essentially all nonconju-

Scheme 3. Synthesis of the *N*α-B1 Insulin MPA Derivatives 3 and 4

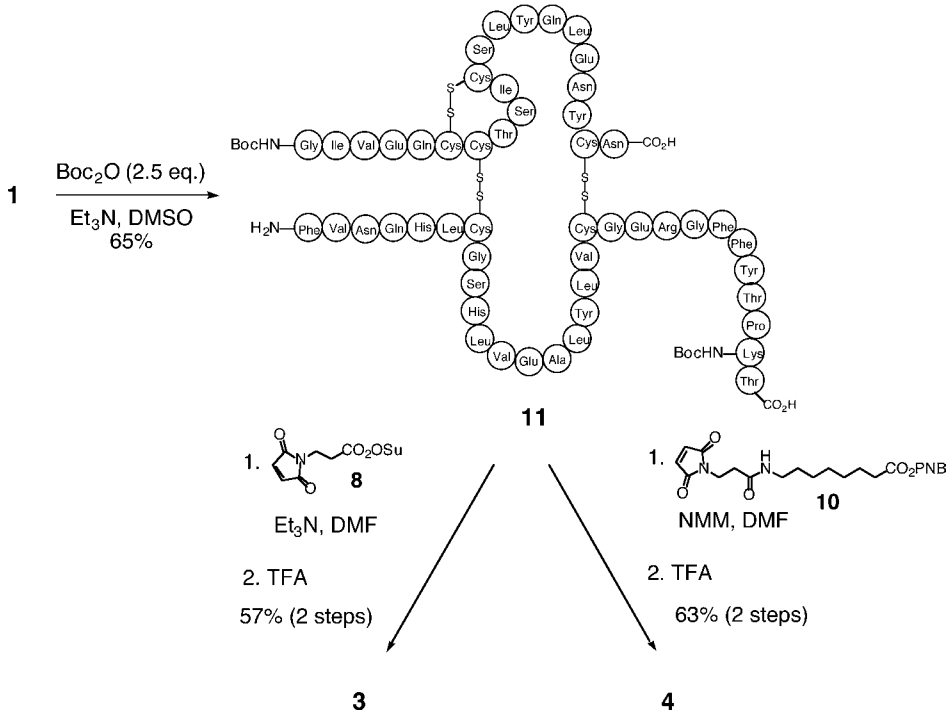

Scheme 4. Synthesis of *N*ϵ-B29 Insulin MPA Derivative 5 and 6

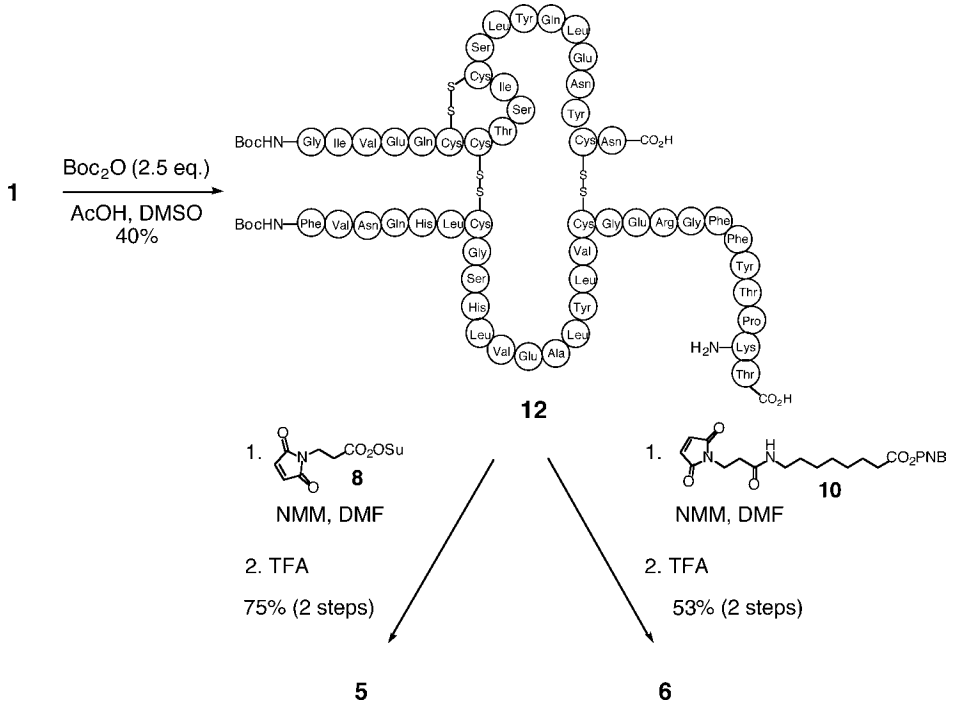

Scheme 5. Hydrolysis of Maleimide Derivatives of Insulin

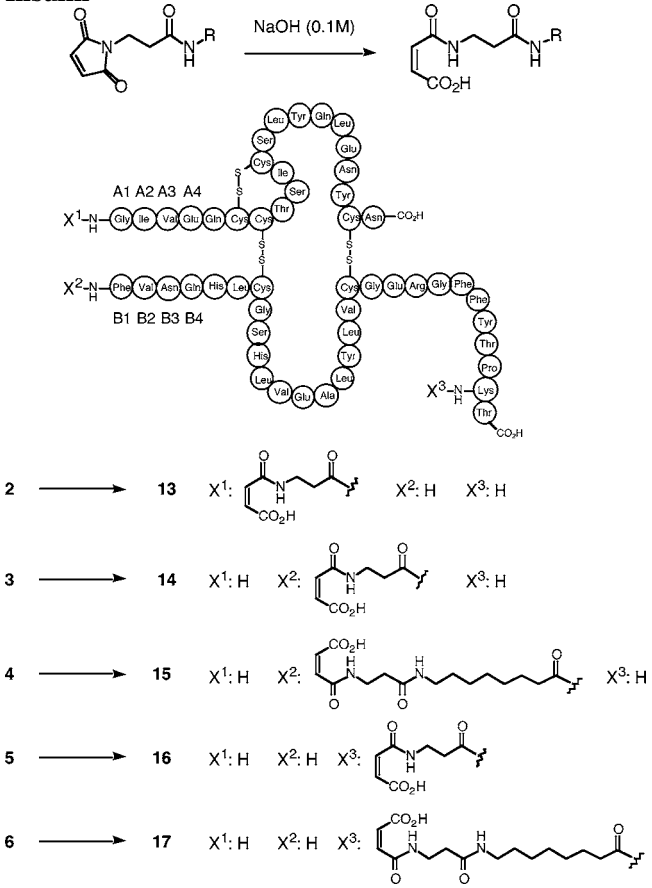

gated HSA eluted within the void volume of the column. Each conjugate was further purified from any free (unreacted) maleimido insulin derivatives by applying a linear gradient of decreasing ionic strength. The synthetic results are shown in Table 2.

The mass spectral analysis of starting HSA indicated that the MS peaks corresponding to the mercaptalbumin and capped albumin species were in a ratio of approximately 2:1, respectively. In the unpurified conjugate, the peaks corresponding to mercapatalbumin diminished while the conjugate peak appeared. Once purified, no residual unreacted HSA in either the mercaptalbumin or capped forms were found. The final products were stored as lyophilized powders.

Table 1. Edman Degradation of Hydrolyzed Insulin MPA Derivatives

		Edman degradation results (positions)			
compound	chain	1	2	3	4
1	**A**	Gly	Ile	Val	Glu
	B	Phe	Val	Asn	Gln
13	**A**	- -	- -	- -	- -
	B	Phe	Val	Asn	Gln
14	**A**	Gly	Ile	Val	Glu
	B	- -	- -	- -	- -
15	**A**	Gly	Ile	Val	Glu
	B	- -	- -	- -	- -
16	**A**	Gly	Ile	Val	Glu
	B	Phe	Val	Asn	Gln
17	**A**	Gly	Ile	Val	Glu
	B	Phe	Val	Asn	Gln

SDS−PAGE analysis of the HSA conjugates was done, and the results are shown in Figure 2. As illustrated, all the insulin−HSA conjugates had adequate purity profiles and migrated in the general area corresponding to proteins of molecular weights similar to albumin. A very faint band was observed above each conjugate as well as HSA. This band corresponds to HSA dimer and is often observed when analyzing HSA with gel electrophoresis.

In Vitro Evaluation. Insulin is produced in pancreatic Langerhans and acts by binding to the insulin receptor found on the surface of a variety of cell types. The insulin receptor is composed of two extracellular α units and two transmembrane β units. Insulin binds to the extracellular component causing the stimulation of tyrosine kinase activity of the β unit, leading to a cascade of phosphorylations that cause the activation of glycogen synthase as well as the translocation of glucose transporter 4 (GLUT4) to the cell membrane, thus initiating

Table 2. Results from Conjugate Synthesis

starting material	M_r theoretical	M_r measured	conjugated product	yield, %[a]
2 (22.8 mg)	72403.8	72393.0	**2**−HSA (173.8 mg)	71
3 (29.0 mg)	72403.8	72391.8	**3**−HSA (246.4 mg)	75
4 (164.6 mg)	72543.2	72543.8	**4**−HSA (1382.6 mg)	77
5 (26.1 mg)	72403.8	72396.5	**5**−HSA (212.9 mg)	72
6 (15.5 mg)	72543.2	72536.2	**6**−HSA (107.9 mg)	63

[a] Yield based on the amount of maleimido starting material.

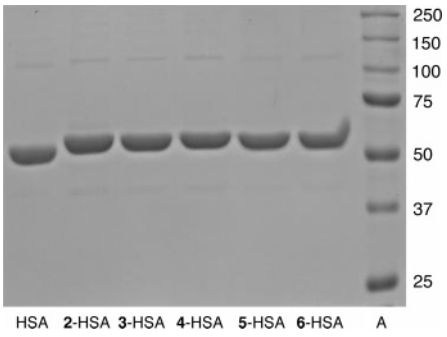

Figure 2. SDS PAGE 10% gel (5 μg/well) analysis under nonreducing conditions, Coomassie Blue staining. Lane A contains reduced molecular weight standards, and the values are expressed in kDa.

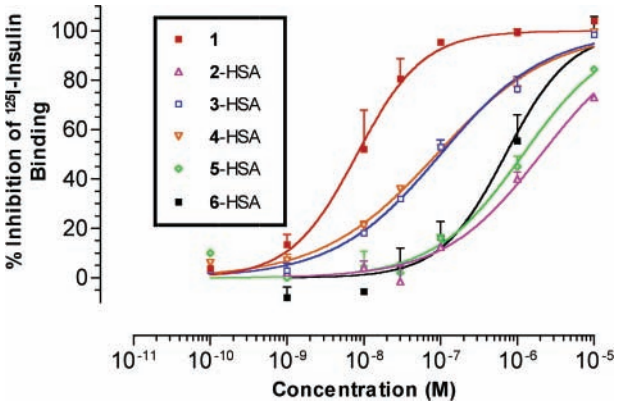

Figure 3. Binding response curves for insulin−HSA conjugates on insulin receptor expressing rat hepatocytes (n = 2−4).

the uptake of glucose into the cell (*35*). The optimum insulin derivative will be able to bind and activate the insulin receptor on the exterior of the cell at the lowest possible concentration, and the response will be the uptake of glucose from the surrounding medium in vitro or the lowering of plasma glucose in vivo.

The primary evaluation of conjugated insulin derivatives was done in vitro. The binding to the insulin receptor was accomplished using a homogenized rat hepatocyte membrane assay (*36*) as shown in Figure 3. The insulin receptor activation was measured in a glucose uptake assay on rat epididymal fat cells (*37*) as shown in Figure 4. The individual IC_{50} and EC_{50} values for receptor binding and glucose uptake, respectively, are shown in Table 3.

The structure−activity results from the in vitro evaluation of the five insulin−HSA conjugates indicate that B1 is the best position of attachment on insulin. The short linker on the A1 and B29 positions and the long linker on the B29 position caused large losses in binding affinity as demonstrated in the responses of **2**−HSA, **5**−HSA, and **6**−HSA, respectively. The short and long linker derivatives **3**−HSA and **4**−HSA, respectively, were essentially equipotent in the binding and glucose uptake assays. An approximately 10-fold loss versus **1** in glucose

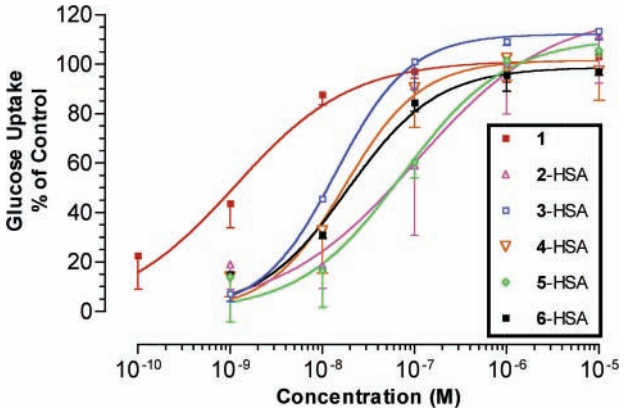

Figure 4. Glucose uptake−response curves on rat epididymal fat cells in the presence of insulin−HSA conjugates (n = 2−4).

Table 3. In Vitro Insulin Receptor Binding and Activation Results

compound	binding,[a] IC_{50} (nM)	glucose uptake,[b] EC_{50} (nM)
1	9.1 ± 3.6	1.3 ± 0.8
2−HSA	2059 ± 226	117 ± 78
3−HSA	100 ± 19	14 ± 2
4−HSA	89 ± 14	18 ± 11
5−HSA	1191 ± 267	78 ± 15
6−HSA	747 ± 376	18.9 ± 0.4

[a] Rat hepatocytes. [b] Rat epididymal fat cells.

uptake EC_{50} was observed for the two derivatives in this particular assay. Both conjugates were therefore chosen for in vivo evaluation.

In Vivo Evaluation. Type I diabetes was induced with STZ in free feeding Sprague−Dawley rats to an average basal blood glucose titer of >25 mmol/L. The blood glucose level was at an average of 5−6 mmol/L in normal nondiabetic rats. Each diabetic rat was administered a single bolus subcutaneous injection of **1**, **3**−HSA conjugate, **4**−HSA conjugate, or saline and were allowed to feed ad libidum. The blood glucose levels for all groups were monitored over a 2-day period. The dose of **1** was limited to 24 nmol/kg per animal to avoid more severe hypoglycemic events observed at higher doses. The experimental results are shown in Figure 5.

The glucose lowering effect of **1** was observed at the first time point (1 h). The glucose level proceeded to rise steadily after 2 h and returned to the STZ control group level by 8 h. It should be noted that in another experiment, **1** was injected at 120 nmol/kg and the glycemia returned to a diabetic level after 6−8 h as well (data not shown). **3**−HSA and **4**−HSA showed dose-dependent decreases in plasma glucose level where the effects reached their maximum between 4 and 6 h postadministration. At the highest doses, both conjugates were able to control the glucose level beyond 48 h.

Other parameters such as water and food intake as well as weight gain were monitored over the study period. The results showed that for both **3**−HSA and **4**−HSA, the three parameters resembled those from the normal rat group for the whole 48-hour data-gathering period.

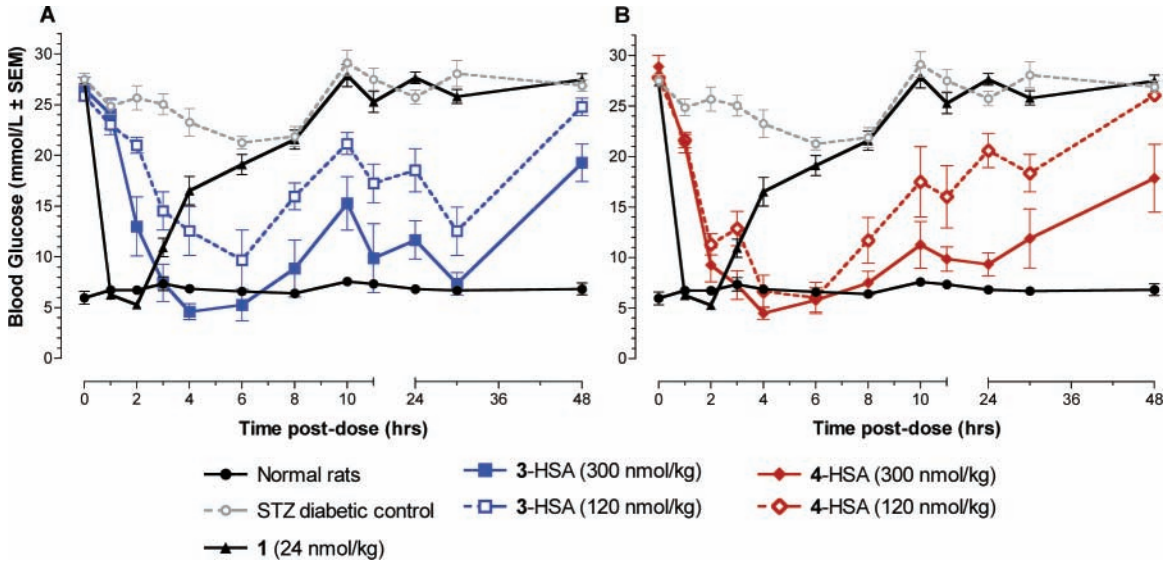

Figure 5. Glycemic control by insulin–HSA conjugates in streptozotocin (STZ)-induced type I diabetes in Sprague–Dawley rats. The results of plasma glucose measurements for **3**–HSA (A) and **4**–HSA (B). The insulin, STZ diabetic, and normal controls are the same in A and B.

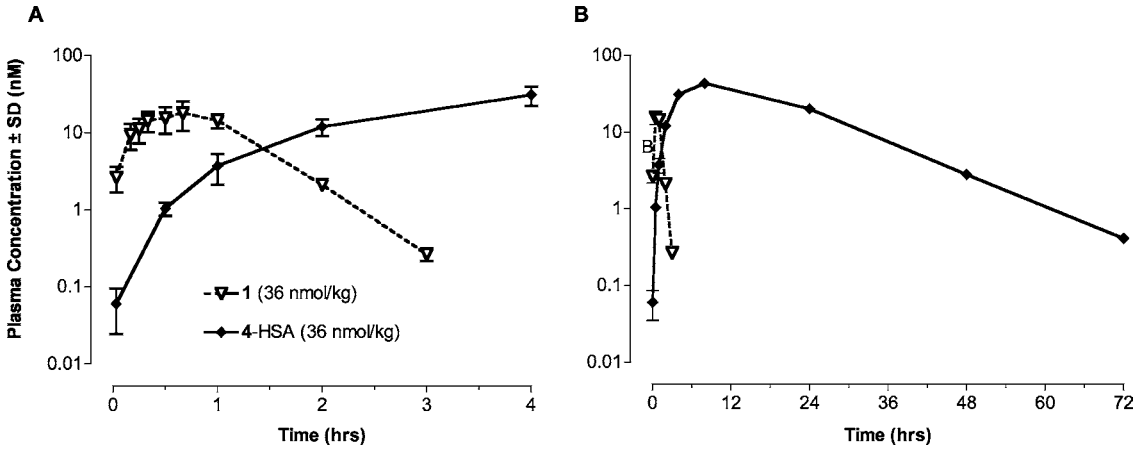

Figure 6. Pharmacokinetic profiles of **1** and **4**–HSA in normal Sprague–Dawley rats. The test compounds were administered subcutaneously, and plasma levels were monitored using a human insulin ELISA kit. Part A shows the first 4 h and part B the full 72 h.

Alternately, the diabetic control group as well as the one receiving insulin drank more water, ate less, and lost weight. It can be generalized that the STZ-induced diabetic animals returned to a normal feeding and weight gain pattern when administered insulin–HSA conjugates while the animals treated with **1** did not.

4–HSA was chosen for pharmacokinetic evaluation in normal rats using **1** for comparison. The plasma concentration as a function of time is shown in Figure 6.

When **1** was injected subcutaneously to rats, its peak plasma concentration was observed at 50 min and was no longer detectable after 3 h. On the other hand, the **4**–HSA plasma concentration peaked at 8 h and was still detectable at 72 h postadministration. These results correlate well with the glycemic control experiment where the peak glucose lowering activity was between 1 and 2 h for **1** and 4 and 6 h for **4**–HSA.

In summary, the three possible direct acylation positional maleimido derivatives of human insulin with either short or long linkers were synthesized. These derivatives were conjugated to HSA in good yield and purified using hydrophobic chromatography. In vitro analysis of the conjugates demonstrated that the B1 linking position of insulin led to the best overall binding and glucose uptake. Further in vivo evaluation identified **4**–HSA, also known as CJC-1575, as a delayed action and long lasting human insulin analogue. CJC-1575 is currently in preclinical development as a potential therapeutic agent.

Supporting Information Available: The mass spectral and purity data from the maleimide hydrolysis and Edman degradation results. This material is available free of charge via the Internet at http://pubs.acs.org.

ACKNOWLEDGMENT

The authors thank Pierre Pepin from the Sheldon Institute for performing the Edman degradations and Patricia Liscourt for skilled technical assistance in the pharmacokinetic experiment.

LITERATURE CITED

(1) Hirsch, I. B. (2005) Insulin analogues. *N. Engl. J. Med. 352*, 174–183.

(2) Lindholm, A. (2002) New insulins in the treatment of diabetes mellitus. *Best Pract. Res. Clin. Gastroenterol. 16*, 475–492.

(3) Gerich, J. E. (2002) Novel insulins: expanding options in diabetes management. *Am. J. Med. 113*, 308–316.

(4) Gerich, J. E. (2004) Insulin glargine: long-acting basal insulin analogue for improved metabolic control. *Curr. Med. Res. Opin. 20*, 31−37.
(5) Barlocco, D. (2003) Insulin detemir. Novo Nordisk. *Curr. Opin. Investig. Drugs 4*, 449−454.
(6) Kurtzhals, P., Havelund, S., Jonassen, I., Kiehr, B., Ribel, U., and Markussen, J. (1996) Albumin binding and time action of acylated insulins in various species. *J. Pharm. Sci. 85*, 304−308.
(7) Kurtzhals, P., Havelund, S., Jonassen, I., Kiehr, B., Larsen, U. D., Ribel, U., and Markussen, J. (1995) Albumin binding of insulins acylated with fatty acids: characterization of the ligand-protein interaction and correlation between binding affinity and timing of the insulin effect in vivo. *Biochem. J. 312*, 725−731.
(8) Dea, M. K., Hamilton-Wessler, M., Ader, M., Moore, D., Schäffer, L., Loftager, M., Vølund, A., and Bergman, R. N. (2002) Albumin binding of acylated insulin (NN304) does not deter action to stimulate glucose uptake. *Diabetes 51*, 762−769.
(9) Hamilton-Wessler, M., Ader, M., Dea, M. K., Moore, D., Loftager, M., Markussen, J., and Bergman, R. N. (2002) Mode of transcapillary transport of insulin and insulin analog NN304 in dog hind limb: evidence for passive diffusion. *Diabetes 51*, 574−582.
(10) Tsai, Y. J., Rottero, A., Chow, D. D., Hwang, K. J., Lee, V. H. L., Zhu, G., and Chan, K. K. (1997) Synthesis and purification of NB1-palmitoyl insulin. *J. Pharm. Sci. 86*, 1264−1268.
(11) Hashimoto, M., Takada, K., Kiso, Y., and Muranishi, S. (1989) Synthesis of palmitoyl derivatives of insulin and their biological activities. *Pharm. Res. 6*, 171−176.
(12) Nakashima, K., Miyagi, M., Goto, K., Matsumoto, Y., and Ueoka, R. (2004) Enzymatic and hyperglycemia stability of chemically modified insulins with hydrophobic acyl groups. *Bioorg. Med. Chem. Lett. 14*, 481−483.
(13) Hinds, K. D., and Kim, S. W. (2002) Effects of PEG conjugation on insulin properties. *Adv. Drug Delivery Rev. 54*, 505−530.
(14) Hinds, K., Koh, J. J., Joss, L., Liu, F., Baudyš, M., and Kim, S. W. (2000) Synthesis and characterization of poly(ethylene glycol)-insulin conjugates. *Bioconjugate Chem. 11*, 195−201.
(15) Baudyš, M., Letourneur, D., Liu, F., Mix, D., Jozefonvicz, J., and Kim, S. W. (1998) Extending insulin action in vivo by conjugation to carboxymethyl dextran. *Bioconjugate Chem. 9*, 176−183.
(16) Chuang, V. T. G., Kragh-Hansen, U., and Otagiri, M. (2002) Pharmaceutical strategies utilizing recombinant human serum albumin. *Pharm. Res. 19*, 569−577.
(17) Léger, R., Thibaudeau, K., Robitaille, M., Quraishi, O., van Wyk, P., Bousquet-Gagnon, N., Carette, J., Castaigne, J.-P., and Bridon, D. P. (2004) Identification of CJC-1131-albumin bioconjugate as a stable and bioactive GLP-1(7−36) analog. *Bioorg. Med. Chem. Lett. 14*, 4395−4398.
(18) Léger, R., Benquet, C., Huang, X., Quraishi, O., van Wyk, P., and Bridon, D. (2004) Kringle 5 peptide-albumin conjugates with anti-migratory activity. *Bioorg. Med. Chem. Lett. 14*, 841−845.
(19) Léger, R., Robitaille, M., Quraishi, O., Denholm, E., Benquet, C., Carette, J., van Wyk, P., Pellerin, I., Bousquet-Gagnon, N., Castaigne, J.-P., and Bridon, D. P. (2003) Synthesis and in vitro analysis of atrial natriuretic peptide-albumin conjugates. *Bioorg. Med. Chem. Lett. 13*, 3571−3575.
(20) Kratz, F., Warnecke, A., Scheuermann, K., Stockmar, C., Schwab, J., Lazar, P., Drückes, P., Esser, N., Drevs, J., Rognan, D., Bissantz, C., Hinderling, C., Folkers, G., Fichtner, I., and Unger, C. (2002) Probing the cysteine-34 position of endogenous serum albumin with thiol-binding doxorubicin derivatives. Improved efficacy of an acid-sensitive doxorubicin derivative with specific albumin-binding properties compared to that of the parent compound. *J. Med. Chem. 45*, 5523−5533.
(21) Holmes, D. L., Thibaudeau, K., L'Archeveque, B., Milner, P. G., Ezrin, A. M., and Bridon, D. P. (2000) Site specific 1:1 opioid:albumin conjugate with in vitro activity and long in vivo duration. *Bioconjugate Chem. 11*, 439−444.
(22) Duttaroy, A., Kanakaraj, P., Osborn, B. L., Schneider, H., Pickeral, O. K., Chen, C., Zhang, G., Kaithamana, S., Singh, M., Schulingkamp, R., Crossan, D., Bock, J., Kaufman, T. E., Reavey, P., Carey-Barber, M., Krishnan, S. R., Garcia, A., Murphy, K., Siskind, J. K., McLean, M. A., Cheng, S., Ruben, S., Birse, C. E., and Blondel, O. (2005) Development of a long-acting insulin analog using albumin fusion technology. *Diabetes 54*, 251−258.
(23) Xia, C. Q., Wang, J., and Shen, W. C. (2000) Hypoglycemic effect of insulin-transferrin conjugate in streptozotocin-induced diabetic rats. *J. Pharmacol. Exp. Ther. 295*, 594−600.
(24) Keller, O., and Rudinger, J. (1975) Preparation and some properties of maleimido acids and maleoyl derivatives of peptides. *Helv. Chim. Acta. 58*, 531−541.
(25) Laemmli, U.K. (1970) Cleavage of structural proteins during the assembly of the head of bacteriophage T4. *Nature 227*, 680−685.
(26) Huang, K., Xu, B., Hu, S. Q., Chu, Y. C., Hua, Q. X., Qu, Y., Li, B., Wang, S., Wang, R. Y., Nakagawa, S. H., Theede, A. M., Whittaker, J., De Meyts, P., Katsoyannis, P. G., and Weiss, M. A. (2004) How insulin binds: the B-chain alpha-helix contacts the L1 beta-helix of the insulin receptor. *J. Mol. Biol. 341*, 529−550.
(27) Hansen, L. B. Selective Acylation Method. US 5,905,140 (May 18, 1999).
(28) Gao, J., Mrksich, M., Gomez, F. A., and Whitesides, G. M. (1995) Using capillary electrophoresis to follow the acetylation of the amino groups of insulin and to estimate their basicities. *Anal. Chem. 67*, 3093−3100.
(29) Glattahard, R., and Matter, M. (1963) Neues, mildes verfahren zur herstellung von aktiven carbonsäure-estern und deren verwendung als acylierungsmittel. *Helv. Chim. Acta 46*, 795−804.
(30) Kim, S., Lee, J. I., and Kim, Y. C. (1985) A simple and mild esterification method for carboxylic acids using mixed carboxylic-carbonic anhydrides. *J. Org. Chem. 50*, 560−565.
(31) Liu, F., Song, S. C., Mix, D., Baudys, M., and Kim, S. W. (1997) Glucose-induced release of glycosylpoly(ethylene glycol) insulin bound to a soluble conjugate of concanavalin A. *Bioconjugate Chem. 8*, 664−672.
(32) Markussen, J., Halstrom, J., Wiberg, F. C., and Schaffer, L. (1991) Immobilized insulin for high capacity affinity chromatography of insulin receptors. *J. Biol. Chem. 266*, 18814−18818.
(33) Losse, G., Naumann, W., and Raddatz, H. (1983) Untersuchungen zur *tert*-butyloxycarbonylferung von insulin. *Z. Chem. 23*, 22−23.
(34) Losse, G., and Richler, B. (1981) Darstellung von B1−Boc- und B29−Boc-insulin-B−Ketten-di-S-sulfonat. *Z. Chem. 21*, 70−71.
(35) De Meyts, P., and Whittaker, J. (2002) Structural biology of insulin and IGF1 receptors: implications for drug design. *Nat. Rev. Drug Discovery 1*, 769−783.
(36) Koch, R., and Weber, U. (1981) Partial purification of the solubilized insulin receptor from rat liver membranes by precipitation with concanavalin A. *Hoppe Seylers Z. Physiol. Chem. 362*, 347−351.
(37) Moody, A. J., Stan, M. A., Stan, M., and Gliemann, J. (1974) A simple free fat cell bioassay for insulin. *Horm. Metab. Res. 6*, 12−16.

BC050102K

Ligand-Directed Labeling of a Single Lysine Residue in hGST A1-1 Mutants

Sofia Hederos, Beatrice Karlsson, Lotta Tegler, and Kerstin S. Broo*

IFM Chemistry, Division of Organic Chemistry, Linköping University S-581 83 Linköping, Sweden .
Received April 12, 2005; Revised Manuscript Received June 7, 2005

Previously, we discovered that human glutathione transferase (hGST) A1-1 could be site-specifically acylated on a tyrosine residue (Y9) to form ester products using thiolesters of glutathione (GS-thiolesters) as acylating reagents. Out of a total of 20 GS-thiolester reagents tested, 15 (75%) are accepted by hGST A1-1 and thus this is a very versatile reaction. The present investigation was aimed at obtaining a more stable product, an amide bond, between the acyl group and the protein, in order to further increase the value of the reaction. Three lysine mutants (Y9K, A216K, and Y9F/A216K) were therefore prepared and screened against a panel of 18 GS-thiolesters. The Y9K mutant did not react with any of the reagents. The double mutant Y9F/A216K reacted with only one reagent, but in contrast, the A216K mutant could be acylated at the introduced lysine 216 with eight (44%) of the GS-thiolesters. The reaction can take place in the presence of glutathione and even in a crude cell lysate for five (28%) of the reagents. Through the screening process we obtained some basic rules relating to reagent requirements. We have thus produced a mutant (A216K) that can be rapidly and site-specifically modified at a lysine residue to form a stable amide linkage with a range of acyl groups. One of the successful reagents is a fluorophore that potentially can be used in downstream protein purification and protein fusion applications.

INTRODUCTION

Redesigning a protein scaffold to obtain a novel function is still a challenging task, even though progress has been made through rational design and combinatorial approaches (*1*−*5*). We have, along with some other groups (*6*−*12*), chosen to try to create new function by chemical modification of a protein scaffold to introduce an artificial group. We use the glutathione transferases (GSTs, EC 2.5.1.18)[1,2] as scaffolds in our reengineering experiments. They are detoxication enzymes (phase II) that catalyze the nucleophilic addition of glutathione (GSH, Scheme 1) to a wide range of hydrophobic electrophilic molecules (*13*−*16*). The proteins form homo- or heterodimers (*15*, *17*), and the mode of binding of GSH is basically conserved throughout the classes (*13*, *18*). The differences between the isoenzymes are primarily located in the promiscuous hydrophobic binding sites (H-sites) to provide a broad and overlapping substrate specificity (*19*). In the alpha class, the catalytic function is dependent on a conserved tyrosine residue (Y9) in the glutathione-binding site (G-site) that aids in the ionization of GSH to form the more reactive thiolate ion (*13*). The GSTs are close to ideal from a redesign aspect since they have modular features with specific binding of GSH in the G-site and an adjacent, promiscuous H-site. This, in combination with their high stability, ease of purification (*20*) and the extensive knowledge of structure−activity relationships (*21*) single out the GSTs as excellent candidates for chemical reengineering experiments.

Scheme 1

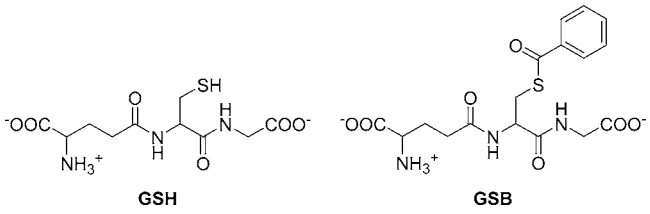

We have previously reported that a synthetic thiolester of glutathione (GS-thiolester) termed GSB (Scheme 1) is able to rapidly modify Y9 of human GST A1-1 (hGST A1-1, Figure 1) (*22*). The reaction is very precise and targets 1 out of 51 nucleophiles in the protein. Through a combinatorial screening process, we then expanded the number of GS-thiolesters that can modify Y9 of hGST A1-1 to a total of 15 reagents (*23*). The reagents include fluorescent probes and a unique aldehyde handle that can be used in further chemical derivatization experiments. This reaction was thus found to be very versatile, fast, and site-directed toward one residue in the protein with minimal side reactions. This is due to the glutathione-based backbone of the reagents that orients the suitably reactive thiolester functionality in close proximity to the reactive Y9 residue (*22*) while the adjacent, promiscuous H-site accepts a large variety of acyl groups. We can thus reengineer folded protein scaffolds with the goal of obtaining new function through the design and synthesis of appropriate GS-thiolesters.

* To whom correspondence should be addressed. Phone: +46-13-28 66 71, Fax: +46-13-12 25 87, E-mail: kerbr@ifm.liu.se.

[1] Abbreviations: ACN, acetonitrile; C18, octadecyl; CDNB, 1-chloro-2,4-dinitrobenzene; GSH, glutathione, γ-Glu-Cys-Gly; GST, glutathione transferase; hGST A1-1, GST A1-1 isoform from human; G-site, glutathione-binding site; GS-thiolester, thiolester of glutathione; HPLC, high performance liquid chromatography; H-site, hydrophobic electrophile binding site; MALDI-MS, matrix assisted laser desorption mass spectrometry; NaP_i, sodium phosphate; TFA, trifluoroacetic acid; TOF, time-of-flight; UV, ultraviolet; wt, wild-type.

[2] This nomenclature is derived from that recommended by Mannervik, B. et al. (1992) *Biochem. J. 282* (Pt 1), 305−306.

10.1021/bc050111t CCC: $30.25 © 2005 American Chemical Society
Published on Web 07/02/2005

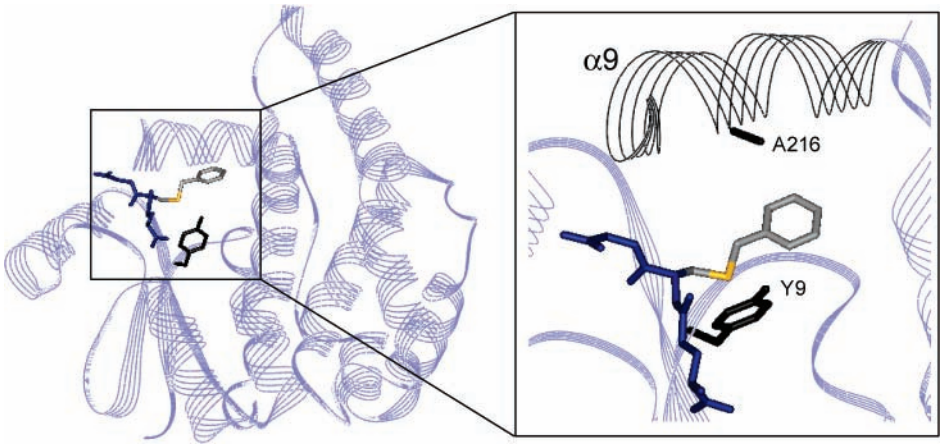

Figure 1. A close-up of the crystal structure (1GUH) of hGST A1-1 in a complex with *S*-benzylglutathione (*18*). The amino acids (Y9 and A216) subjected to mutation are shown in "stick" representation and helix 9 (α9) is also indicated in the figure. The protein is dimeric but shown here as a monomer for reasons of clarity of presentation.

Scheme 2

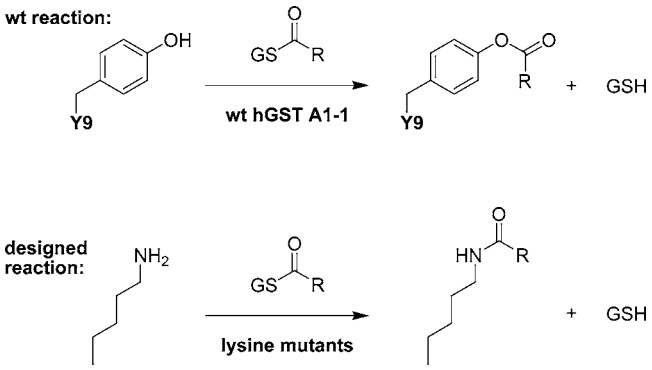

However, the reaction suffers some drawbacks mainly because the product is an ester formed from Y9 and the acyl group (Scheme 2). The product is unstable toward GSH (*22*), and addition of a fresh batch of another GS-thiolester to premodified protein results in scrambling of the acyl groups (*23*). Even though the benzoic acid-derived Y9-ester is stable, for other Y9-esters this bond is slowly hydrolyzed (*23*), and with this in mind we designed and prepared two lysine mutants of hGST A1-1, Y9K and A216K, that we hoped would form stable amide bonds with the acyl groups of the reagents (Scheme 2). The Y9K mutant is a straightforward change to see whether the targeted tyrosine could be directly substituted by a lysine. Position 216 was chosen because we have in another line of investigation found that a A216H mutant can, through a Y9-intermediate, function as a novel hydrolytic enzyme for GSB (*24*). We therefore knew that position 216 interacts with a Y9-ester and hoped that a potential intermediate could perhaps be transferred to a lysine residue. We also prepared a double mutant Y9F/A216K mainly for mechanistic reasons since we were interested in the role of the critical Y9 residue. We then screened these three mutants against a panel of 18 GS-thiolesters (Scheme 3 plus GSB) and used proteolytic digestion and MALDI-MS to investigate the outcome of the experiments. The reagents represents a broad range of sizes and physical properties (*23*) in order to increase the chances of finding reagents that are compatible with the lysine mutants, and also to not miss any potential information regarding reagent requirements.

MATERIALS AND METHODS

All chemicals and reagents used were of the highest purity available. All solid-phase syntheses were carried out in a VacMaster (International Sorbent Technology). The HPLC experiments were carried out using a Kromasil C_8-column (4.6 mm × 250 mm, Supelco Inc., Bellefonte, PA) attached to a Varian system with a ProStar 230 Delivery System, a ProStar 330 Photodiode Array Detector, controlled by the Varian LC Software. All masspectra were recorded using a MALDI-TOF MS (Voyager System 4212, Applied Biosystems) with detection in the positive mode. The UV measurements were performed using a Varian Cary 100 Scan UV−Visible spectrophotometer and analyzed with the CaryWin UV software. The syntheses of the reagents have been described before, and we used the stock solutions described in the previous report (*23*). The synthesis of the substrate GSB has also been described previously (*22*). All tripeptide reagents were analyzed with reversed-phase HPLC using a C_8 column and a shallow H_2O:ACN (both 0.1% TFA) gradient. The identities of the products were confirmed with MALDI-TOF MS using an α-cyano-4-hydroxycinnamic acid matrix with detection in the positive mode. The measured masses of the GS-thiolesters were in good agreement with the calculated masses.

Site-Directed Mutagenesis, Protein Expression, and Purification. The hGST A1-1 mutants were prepared by site-directed mutagenesis using the QuikChange kit (Stratagene). The vector pET-21a(+) with the hGST A1-1 gene inserted between the *Nde1* and *Sal1* restriction sites was used as template DNA, and mismatch oligonucleotide primers were purchased from DNA Technology A/S (Aarhus, Denmark). Mutants were identified by sequence analysis and the verified mutants were electroporated into *Escherichia coli* BL21(DE3) (Novagen, San Diego, CA). Protein expression of the mutants were performed in 1 L of 2 x YT medium with 100 μg/mL of ampicillin, and the expression was induced by 1 mM isopropyl β-thiogalactopyranoside followed by incubation at 37 °C for 3 h. The cells were harvested by centrifugation and lysed in an X-press (Biox), and the cell debris was then removed by centrifugation. The supernatant was desalted using PD-10 columns (Amersham Biosciences), and the proteins were purified by cation exchange chromatography as described previously (*25*) using a HiTrap SP column and an ÄKTA system (Amersham Biosciences, Piscataway, NJ). Purities were

Scheme 3

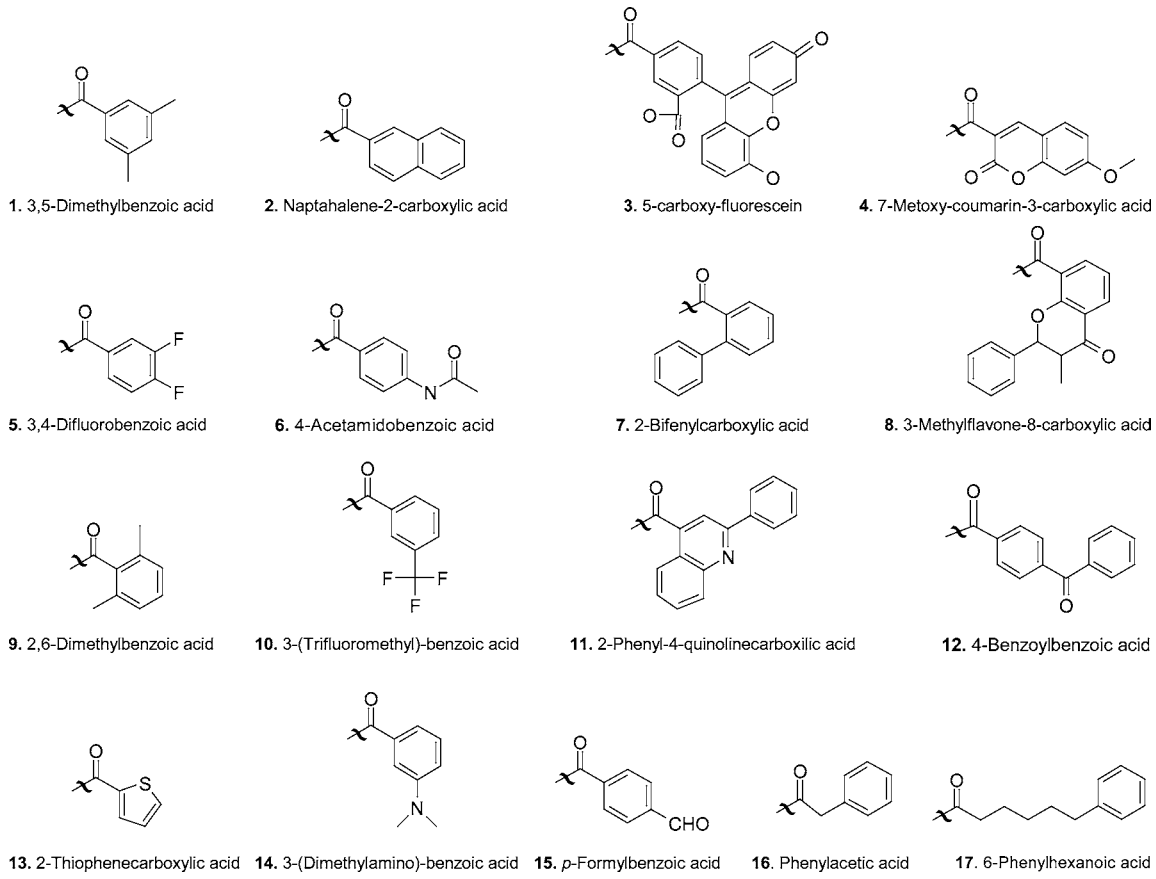

confirmed by SDS−PAGE, and the protein concentrations were determined spectrophotometrically using ϵ_{280} = 24 700 $M^{-1}\cdot cm^{-1}$ (*25*). The activities of the GSTs were tested with a standard assay (*26*) containing 1 mM each of 1-chloro-2,4-dinitrobenzene and GSH (pH 6.5 in 0.1 M NaP_i at 30 °C). The K_M measurements were performed in the same fashion using increasing concentrations (0.5 mM to 3.5 mM) of CDNB. The proteins were stored in NaP_i-buffered solutions containing NaCl and 10% glycerol at −80 °C or −20 °C until used in the experiments.

Fluorescence Measurements. Fluorescence measurements were performed on a Hitachi f-4500 fluorescence spectrophotometer, with excitation at 280 nm and emission scanning between 310 and 380 nm. The proteins were diluted to 1 μM in 100 mM NaP_i, pH 7.0, and the fluorescence spectrum of wt hGST A1-1 was also collected for comparison purposes (Supporting Information).

Modification Reactions. The modification reactions were performed with 100 μM GS-thiolester and 10 μM GST in buffer (0.1 M NaP_i, pH 7). The wt protein was also incubated with the reagents as a positive control. The reaction was allowed to proceed at 25 °C for 5 h. To control the temperature, the incubation was performed in an Eppendorf Master cycler gradient.

In the case of A216K, further investigations were made with respect to the stability toward GSH. Premodified protein was incubated with 1 mM GSH for up to 26 h at 25 °C. Samples were withdrawn at five and 26 h and the mixtures were digested before MALDI-MS analysis. In a separate experiment GSH (1 mM) was added to the buffer (0.1 M NaP_i, pH 7.0) prior to adding A216K (10 μM) and GS-thiolester (100 μM). The mixtures were then incubated for 5 h at 25 °C before being subjected to MALDI-MS analyses.

Modification Reactions in *E. coli* Lysate. A lysate were prepared from *Escherichia coli* BL21(DE3) cells (Novagen) in 50 mL of 2 x YT medium grown at 37 °C for 12 h. The cells were harvested by centrifugation and resuspended in 0.1 M NaP_i, pH 7, containing Complete Mini EDTA-free protease inhibitor cocktail (Roche Diagnostics) and lysed by sonication. The modification reactions were carried out by adding A216K (25 μM) and GS-thiolester (250 μM) to the cell lysate, and the mixtures were then incubated for 5 h at 25°C. The lysate itself was also analyzed by MALDI-MS to identify lysate-specific peaks (Supporting Information).

Proteolytic Digestion of Modified GSTs. The digestions were performed in the following way: 5 μL of modification mixture was diluted with 13 μL buffer (50 mM NH_4CO_3, pH 7.8), 2 μL *Staphylococcus Aureus* V-8 Protease from Pierce Biotechnology, Inc., Rockford, IL (stock solution 1 $\mu g/\mu l$) was added, and the sample was incubated at 25 °C for up to 2 h. A control reaction was also performed for each protein, containing unmodified protein, buffer, and protease. The fragment that contains K216 has the sequence K_{216}RKIFRF and the Y9 fragment has the sequence AEKPKLHY_9FNARGRME with one missed cleavage. Following incubation, 0.5 μL of the reaction mixture was mixed with 0.5 μL of saturated α-cyano-4-hydroxycinnamic acid matrix and analyzed by MALDI-TOF MS (Voyager 4212, Applied Biosystems) with detection in the positive mode. In the lysate experiments, all mixtures were acidified using 0.1% TFA and desalted with C_{18} Zip Tips before being subjected to MALDI-MS analyses.

Mechanistic Studies. A216K (10 μM) and Y9F/A216K were each incubated with GSB (100 μM), and samples were withdrawn at various time points starting at t = 0 min and the last ones after 24 h incubation at

Table 1. Specific Activities toward CDNB (μmol·min^{-1}·mg^{-1})

hGST A1 mutant	specific activity
wt[a]	75
Y9F[b]	1.9
Y9K[c]	n.d
A216K	24
A216H	20
Y9F/A216K	0.07

[a] From reference (*32*). [b] From reference (*31*). [c] Present investigation. Not detectable over the background rate.

25 °C. In a separate experiment, A216K was also incubated with GS-4 in a similar fashion. The samples were immediately quenched with TFA and stored at −20 °C until digestion and analysis using MALDI-MS. The samples were digested both at pH 7.8 as described above and at pH 4 using 50 mM NH_4OAc as buffer. In this semiquantitative experiment we avoided using C_{18} Zip Tips since that would have artificially increased the amount of modified, i.e., more hydrophobic, fragment relative to unmodified fragment. The data were analyzed by dividing the area of the *m/z* peak resulting from the modified fragment containing either Y9 or K216 by that of the respective (unmodified + modified) fragment.

RESULTS

Fluorescence and Activity Measurements of the Lysine Mutants. The lysine mutants were prepared and purified according to previously published protocols. Only the A216K mutant showed substantial activity toward the standard substrate CDNB, about 32% of wt hGST A1-1 activity (Table 1). We tried to measure the K_M for CDNB but the substrate precipitated (at 3.5 mM) before the enzyme showed signs of saturation (Supporting Information). Fluorescence measurements indicate that the proteins are folded, even though the Y9K mutant displays a spectrum with a slightly red-shifted maximum (Supporting Information).

Addition of the GS-Thiolesters to the Lysine Mutants. The outcome of adding the GS-thiolesters to the lysine mutants of hGST A1-1 was investigated by MALDI-MS. Each reagent (100 μM) was incubated with each mutant (10 μM) at 25 °C for 5 h. The samples were then analyzed by MALDI-MS following proteolytic digestion. To simplify subsequent analyses we used *S. aureus* V-8 protease since it cleaves after glutamic acid residues (and aspartic acid depending on reaction conditions) and is thus unaffected by any covalent modification of a lysine residue. In general, if a residue becomes covalently modified, the mass of the fragment containing this residue will increase with the mass of the corresponding acid minus the mass of water (Scheme 2). For control purposes, all three mutants were also digested after incubation in buffer without addition of any GS-thiolester. The Y9K mutant was unaffected by the addition of the reagents (Table 2). The A216K mutant on the other hand reacted with eight (44%) of the reagents to form a new amide bond between the corresponding acyl group and K216 (Table 2, Figure 2). The Y9 residue of A216K was not modified at the end of the 5-h incubation (Supporting Information). The double mutant Y9F/A216K did react with one substrate, GSB, to form K216-modified protein (Table 2, Figure 2). A positive classification in Table 2 corresponds to more than 10% modified lysine-containing fragment relative to the parent fragment (unmodified fragment). This relatively low threshold was set because MALDI-MS is not a quantitative technique and also because we use the same screening conditions for all GS-thiolesters, and the reaction conditions are therefore not optimized for each individual reagent and protein combination. This threshold was discussed at length in our previous paper (*23*).

Table 2. Modification Reactions of the GSTs

	hGST			
reagent	wt A1-1[a]	A216K[b]	A216K/Y9F[b]	Y9K[c]
GSB	+	+	+	−
GS-4	+	+	−	−
GS-5	+	+	−	−
GS-6	+	+	−	−
GS-8	+	+	−	−
GS-13	+	+	−	−
GS-14	+	+	−	−
GS-16	−	+	−	−

[a] + and − corresponds to modified or not modified Y9 fragment (*23*). [b] + and − corresponds to modified or not modified K216 fragment. [c] + and − corresponds to modified or not modified K9 fragment.

Stability of the K216 Modification Reaction toward GSH. The stability of premodified A216K with respect to added GSH was also investigated using the panel of GS-thiolesters. For each one of the eight successful reagents, 10 μM A216K was preincubated with a GS-thiolester (100 μM) for 5 h at 25 °C. After incubation, GSH was added to a final concentration of 1 mM, 10 times the concentration that has been shown to quantitatively remove the Y9-ester of wt hGST A1-1 within 10 min (*22*). The mixtures were then incubated for 26 h at 25 °C, and MALDI-MS experiments following digestion showed as expected that none of the acyl groups were removed by GSH (Table 3, Figure 3C). A more challenging experiment was then performed where GSH (1 mM) was added to A216K (10 μM) in buffer prior to addition of GS-thiolester reagent (100 μM). The mixtures were then incubated for 5 h at 25 °C before being analyzed with MALDI-MS. Out of the eight GS-thiolester reagents that could modify K216 in buffer; five were successful in the presence of GSH (Table 3, Figure 3D).

Modification Reactions in a Cell Lysate. In the case of wt hGST A1-1 we were able to label Y9 in an *E. coli* lysate (*22*). This reaction is, however, not so practical since the ester can be removed by addition of GSH. In light of the stability of the K216 modification toward GSH, we investigated the possibility of modifying A216K in a cell lysate. The protein (25 μM A216K) and the GS-thiolesters (250 μM) were added to lysed BL-21 (DE3) cells, and the mixtures were incubated at 25 °C for 5 h. To obtain reasonable signals, the mixtures had to be desalted using C_{18} Zip Tips before being subjected to MALDI-MS analyses. We found (Table 3, Figure 4) that five of the GS-thiolesters were able to modify K216 in lysed *E. coli* cells.

Mechanistic Studies Concerning A216K Modification. To investigate the mechanism of the reaction more closely, A216K (10 μM in 100 mM NaP_i, pH 7) was incubated with GSB and GS-4 (100 μM, respectively) at 25 °C. Samples were withdrawn at a number of time points, digested, and analyzed with MALDI-MS to obtain semiquantitative data regarding the amount of modification of each side-chain, Y9 and K216, respectively (Figure 5). The samples were digested both at pH 7.8 as usual and also at pH 4 in order to ensure the preservation of any unstable intermediates. The reaction with the double mutant Y9F/A216K was also analyzed in this fashion using GSB, the only substrate that modifies its K216 side-chain (Figure 6). Only in the reaction between GS-4 and A216K and only in the sample digested at pH 4,

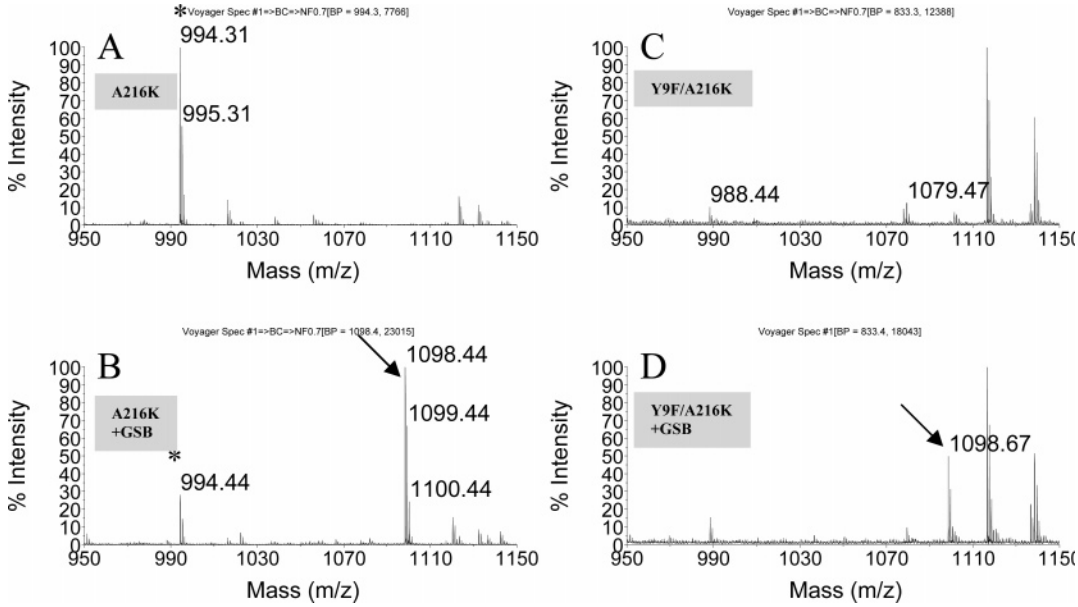

Figure 2. MALDI-MS spectra of proteolytic (*S. aureus* V-8) peptide fragments from (A) A216K; (B) A216K (10 μM) incubated with GSB (100 μM) for 5 h; (C) Y9F/A216K; and (D) Y9F/A216K (10 μM) incubated with GSB (100 μM) for 5 h. The *m/z* interval containing the K216 fragment (K_{216}RKIFRF) is shown in the figure. Parent fragments are indicated with asterisks, and modified fragments are highlighted with arrows. The parental fragment could not be detected for the Y9/A216K mutant.

Table 3. Modification Reactions of A216K[a]

	A216K			
reagent	in buffer	26 h GSH[b]	with GSH[c]	in lysate
GSB	+	+	+	+
GS-4	+	+	+	+
GS-5	+	+	+	+
GS-6	+	+	−	−
GS-8	+	+	−	−
GS-13	+	+	−	−
GS-14	+	+	+	+
GS-16	+	+	+	+

[a] + and − corresponds to modified or not modified K216 fragment. [b] Premodified protein incubated in 1 mM GSH for 26 h. [c] GSH was added before incubation of A216K and GS-thiolester.

could we observe a modified Y9 fragment. The modified Y9 fragment appeared to reach a maximum concentration around 30 min of incubation (Figure 7). We were not able to detect a Y9-intermediate in the reaction between GSB and A216K (Figure 5B).

DISCUSSION

The versatility, speed, and site-selectivity of the covalent modification reaction between Y9 of the hGSTs from the alpha class and numerous GS-thiolesters encouraged us to try to refine this reaction with respect to the stability of the end-product. We therefore prepared three lysine mutants of hGST A1-1 in the hope that at least one would be amenable to ligand-directed labeling in the folded state at the introduced lysine thus forming a stable amide bond. Since it is impossible to know beforehand what reagent (if any) would work, we chose to go about this in a combinatorial fashion and studied the outcome of adding a panel of 18 GS-thiolesters to these three mutants. As discussed previously, the GS-thiolesters vary widely in size, shape, hydrophobicity, and also reactivity (pK_a of the corresponding acid) (*23*).

A216K Shows GST Activity. Of the three mutants, only A216K shows any measurable GST activity toward the standard substrate CDNB (Table 1). The activity is only 32% of that of wt hGST A1-1, probably because helix 9 (α9) has to be folded over the H-site (Figure 1) during the catalytic cycle (*27*−*29*). The introduced K216 residue thus becomes positioned in the H-site, and this presumably lowers the hydrophobicity substantially and thus interferes with the binding of CDNB. In fact, the K_M for CDNB is too high to measure since CDNB precipitates at 3.5 mM, before the enzyme shows signs of saturation. This is in contrast to the wt protein that displays a K_M of 0.56 mM^{-1} for CDNB (*30*). It is not surprising that the enzymatic activity is demolished for Y9K and Y9F/A216K since this has previously been demonstrated when Y9 is mutated (*31*) (Table 1).

Lysine 216 Can Be Covalently Modified. Ideally, the covalent modification reaction should be as versatile as possible when it comes to accommodating different types of acyl groups since our goal is to chemically reengineer protein scaffolds toward novel functions. We were thus pleased to observe that the A216K mutant can be modified at the introduced K216 with as many as eight of the 18 GS-thiolesters in the panel (Table 2). The wt hGST A1-1 can be labeled at Y9 with 14 out of 18 reagents, and more than half of the GS-thiolesters work for both the wt protein and the A216K mutant even though different positions as well as different types of amino acid side-chains are targeted. The final target (K216) for this reaction is 1 out of 52 nucleophiles in the protein, and it is thus a very selective reaction. The extent of modification varies presumably at least in part due to the standardized conditions we used for all reactions. This is plainly visible when comparing the modification reactions between A216K and GSB and GS-4, respectively (Figure 6). After the standard 5 h of incubation, the yield is quantitative in the GS-4 reaction but the GSB reaction has only reached about 70% completion. The yield can thus most likely be fine-tuned since this was possible in the case of GSB and hGST A1-1 where the degree of modification was a function of both time and concentration of reagent (*22*).

The reason behind the high number of accepted acyl groups is of course the relaxed hydrophobic substrate specificity of the GSTs that originates from their biological function as detoxication enzymes. The combination

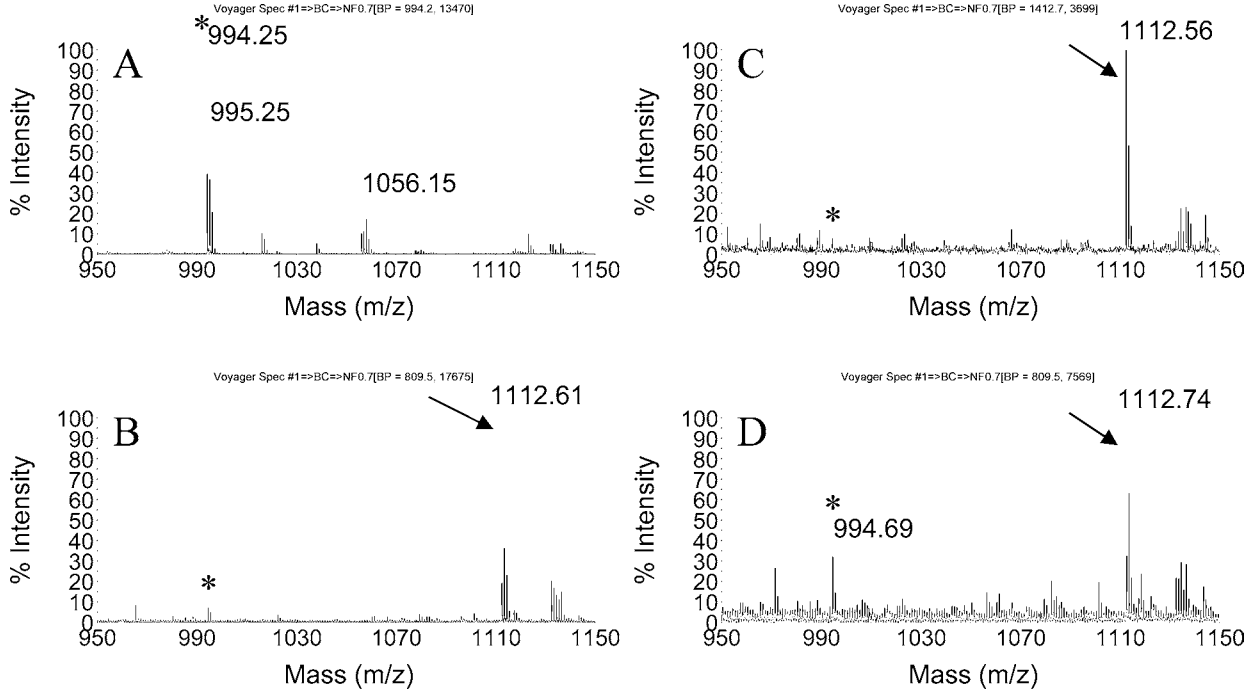

Figure 3. MALDI-MS spectra of proteolytic (*S. aureus* V-8) peptide fragments from (A) A216K after 4 h in 1 mM GSH; (B) A216K (10 μM) incubated with GS-16 (100 μM) in buffer for 5 h; (C) A216K (10 μM) preincubated with GS-16 (100 μM) in buffer for 5 h and then subjected to 1 mM GSH for 26 h; and (D) A216K (10 μM) incubated in 1 mM GSH with GS-16 (100 μM) for 5 h. The *m/z* interval containing the K216 fragment (K_{216}RKIFRF) is shown in the figure. Parent fragments are indicated with asterisks, and modified fragments are highlighted with arrows.

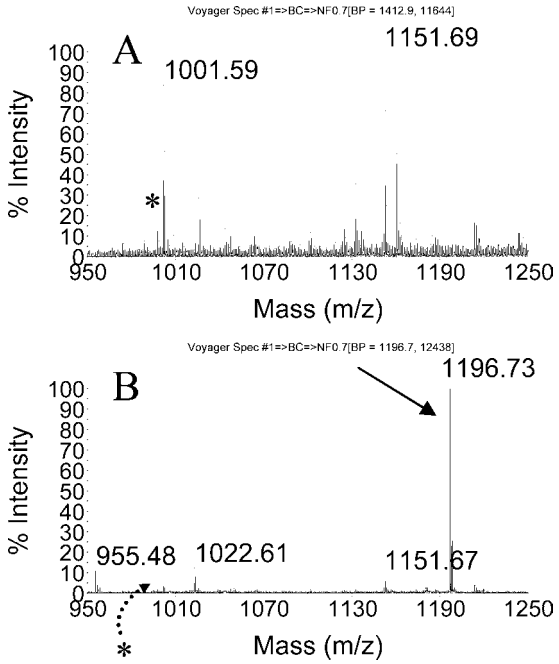

Figure 4. MALDI-MS spectra of proteolytic (*S. aureus* V-8) peptide fragments from (A) A216K incubated in an *E. coli* lysate for 5 h; (B) A216K (25 μM) incubated with GS-4 (250 μM) in an *E. coli* lysate for 5 h. The *m/z* interval containing the K216 fragment (K_{216}RKIFRF) is shown in the figure. Parent fragments are indicated with asterisks and the modified fragment is highlighted with an arrow.

of a stringent G-site guiding the reagent and the adjoining promiscuous H-site undeniably makes the GSTs ideally suited as protein scaffolds in reprogramming experiments. It is interesting to note that a minor change at a carefully chosen position in the amino acid sequence of a protein (1 out of 222 residues) can lead to not just deterioration of the natural activity, something that is commonly found, but to a whole new function. We also observed this when we introduced a histidine residue at position 216, thus turning hGST A1-1 into a novel thiolester hydrolase (*24*).

Interestingly, only one reagent GS-16 (phenyl acetic acid, Figure 3) modifies K216 but not Y9 in the wt protein. This reagent was, however, found to be hydrolyzed to some extent in the presence of hGST A1-1, and it is quite probable that Y9 is acylated as an intermediate in this reaction (*23, 24*) and that the introduced lysine residue now quenches the reaction forming an amide bond instead.

We now have targeted a new position (216) thus leaving Y9 intact (Supporting Information and Figure 5), and this enhances our chances of developing new sensors and catalysts by the use of appropriate GS-thiolesters, since we can now choose to place the new functional group at either position Y9 (using the wt protein) or K216 (using A216K).

A Correlation between logP of the Acyl Group and the Activity of the GS-Thiolester. In our previous study we could not detect a systematic reason (size, reactivity, hydrophobicity, etc.) predicting the ability of a GS-thiolester to modify hGST A1-1. The reaction seemed pretty general, and we found only one reagent (GS-9) that was not able to modify any of the four alpha class hGSTs that we investigated. This acyl group (2,6-dimethylbenzoic acid) is di-ortho-substituted, and we concluded that GS-9 is too sterically hindered to function, especially since the di-meta-substituted analogue GS-1 (3,5-dimethylbenzoic acid) is an excellent derivatization reagent for all four proteins.

Unlike Y9 modification of wt hGST A1-1, there does, however, seem to be a correlation between the hydrophobicity of the acyl group and the ability to modify residue K216. The hydrophobicities of the acyl groups can be estimated using logP values (the partitition coefficient between water and *n*-octanol), the lower the logP value,

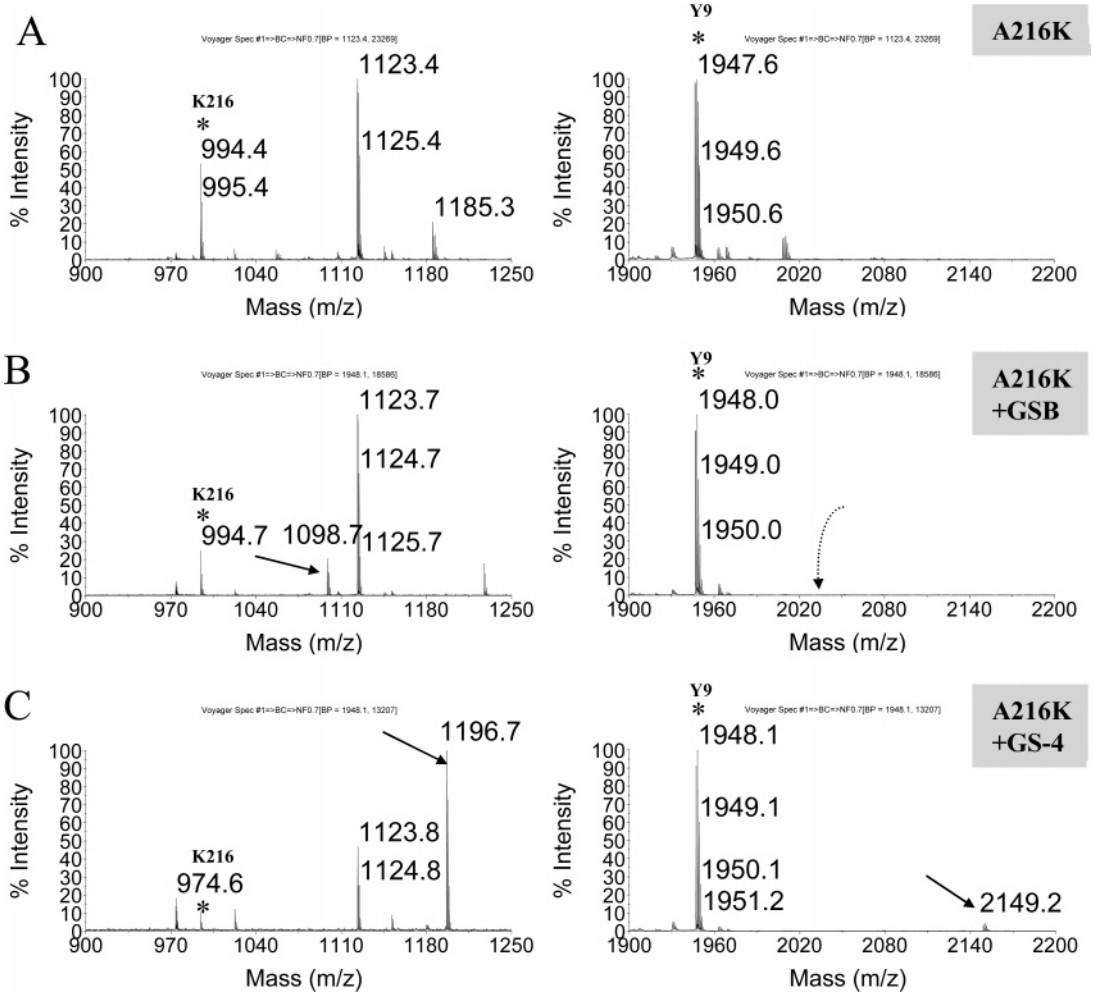

Figure 5. MALDI-MS spectra showing the reaction between A216K (10 μM) and GSB (100 μM) and GS-4 (100 μM), respectively. Time points were withdrawn, quenched with TFA and treated with protease (*S. aureus* V-8) at pH 4. The spectra show (A) A216K prior to the reaction; (B) A216K + GSB after 30 min of incubation and (C) A216K + GS-4 after 30 min of incubation. The *m/z* intervals that contain the K216 (K_{216}RKIFRF) and the Y9 fragments (AEKPKLHY$_9$FNARGRME, one missed cleavage) are shown for each reaction at $t = 30$ min. Parent fragments are indicated with asterisks, and modified fragments are highlighted with arrows. The mass (2051.1) that a modified Y9 fragment would have in the reaction between GSB and A216K is illustrated with a dotted arrow.

the more hydrophilic the acyl group. The logP values span a range from 1.3 (4-acetamidobenzoic acid) to 3.8 (2-phenyl-4-quinolinecarboxylic acid) and only the acids with a logP value below 2.3 are able to label K216 (Table 4). The exception is GS-9 even though it has a logP of 2.2, but this is not surprising as discussed above (*23*). This means that K216 cannot be modified with di-ortho-substituted or very hydrophobic GS-thiolesters, presumably due to the hydrophilic character of the lysine side-chain.

The size of the acyl group could perhaps also be of importance since most of the accepted acyl groups are among the smallest ones. However, the large 3-methylflavone-8-carboxylic acid (GS-8) is also able to modify K216, so this is not a very strict criterion, something that is not so surprising since the natural substrates of GSTs range widely in size and shape (*19*).

We now have some a priori knowledge that can guide us in the design of appropriate GS-thiolesters targeted for A216K derivatization. The acyl group should preferably have a logP below 2.3, and it should probably not be too large.

The K216 Modification Reaction is Resilient to GSH. One of the main drawbacks of the Y9 modification reaction using wt hGST A1-1 is that the product is an ester (Scheme 2) in equilibrium with added GSH. For example, addition of 100 μM GSH to 5 μM benzoic acid-modified hGST A1-1 quantitatively removes the acyl group within 10 min and thus shifts the equilibrium to the left (GSB and unmodified protein) (*22*). Hydrolysis of the Y9-ester is presumably also a problem for some of the reagents (*23*). Since an amide should be immune to addition of GSH if the reverse reaction is not catalyzed somehow, we added GSH to premodified A216K and were pleased to observe that the newly formed amide bond is completely stable toward added GSH. For five of the eight GS-thiolesters, the reaction could even take place in the presence of 1 mM GSH. This substantially increases the value of the reaction since we now have a stable end product that can be exposed to a variety of conditions and still survive.

The K216 Modification Reaction Can Be Carried Out in a Cell Lysate. It would be ideal if the labeling reaction could be carried out in crude bacterial lysate to avoid having to first purify the protein, modify it, and then purify the conjugate. Indeed, we were able to get the reaction to work in a lysate for some of the GS-thiolesters involved in Y9-modification of hGST A1-1 (*22*). We used an *E. coli* lysate and added A216K in order to know the protein concentration. The amount of protein

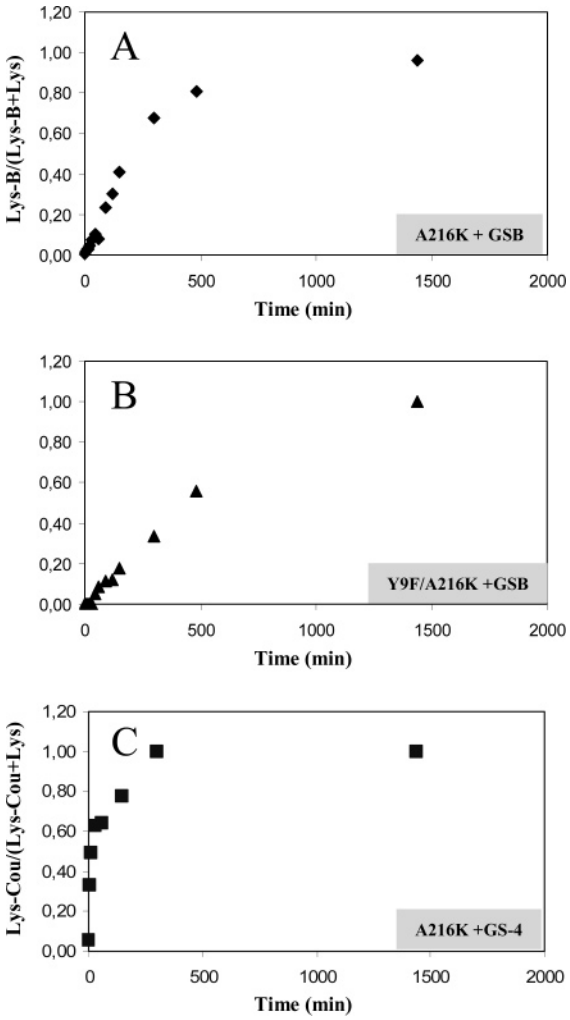

Figure 6. Semiquantitative analysis of the reactions between (A) A216K (10 μM) + GSB (100 μM); (B) Y9F/A216K (10 μM) + GSB (100 μM); and (C) A216K (10 μM) + GS-4 (100 μM) obtained from MALDI-MS experiments. Samples were withdrawn at the indicated time points, quenched with TFA and treated with protease (*S. aureus* V-8) at pH 7.8. The ratio of modified K216 fragment divided by the total amount of fragment (K216 + modified K216 fragment) is plotted vs time.

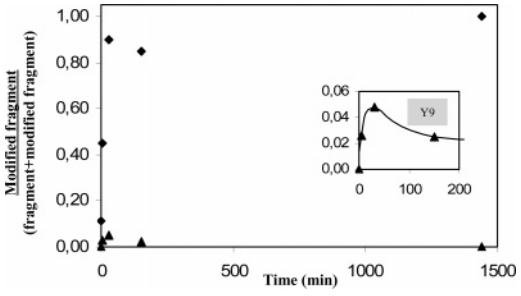

Figure 7. Semiquantitative analysis of the reaction between A216K (10 μM) + GS-4 (100 μM) obtained from MALDI-MS experiments. Samples were withdrawn at the indicated time points, quenched with TFA, and treated with protease (*S. aureus* V-8) at pH 4. The ratio of modified K216 fragment (◆) or Y9 fragment (▲) divided by the total amount of fragment (K216 + modified K216 fragment) or (Y9 + modified Y9 fragment) is plotted vs time. The inset is an expansion of the early time points showing the Y9-intermediate.

used (25 μM) is lower than what is achieved during normal expression of wt hGST A1-1 where the yield frequently is >100 mg of pure protein from 1 L of cell culture concentrated in 10 mL of buffer after harvesting

Table 4. Acids Ranked According to logP Values[a]

acid	logP	A216K[b]	A1-1[c]
4-acetamidobenzoic acid	1.31	+	+
phenylacetic acid	1.41	+	−
2-thiophenecarboxylic acid	1.57	+	+
benzoic acid	1.87	+	+
3-(dimethylamino)benzoic acid	2.05[b]	+	+
2,6-dimethylbenzoic acid	2.21	−	−
3,4-difluorobenzoic acid	2.28[b]	+	+

[a] http://chemfinder.cambridgesoft.com/result.asp and CompuDrug, I., Inc., Sedona, AZ. [b] Estimated logP values (*23*). [c] + and − corresponds to modified or not modified K216 fragment. [d] + and − corresponds to modified or not modified Y9 fragment.

Scheme 4

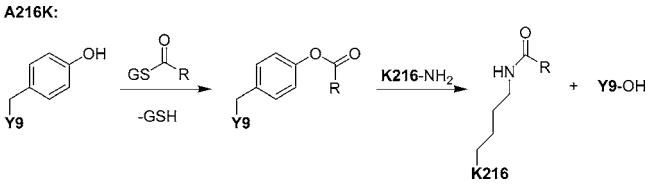

the cells. Gratifyingly, five of the GS-thiolester reagents were able to modify K216 in protein-doped *E. coli* lysate. One of the reagents is a fluorophore (GS-4) that could potentially be used in downstream protein purification and protein fusion applications. Interestingly, the five successful reagents are the same ones as those that were able to modify K216 in the presence of GSH, indicating that the binding interactions are stronger for this subset compared to the three that only work in buffer alone (Table 3). We now have a robust reaction that can take place directly in a cell lysate and that is unaffected by the presence of GSH.

A Y9-Intermediate in the Reaction between A216K and GS-4. By collecting proteolytic data from early time points in the reaction between GS-4 and A216K, we could show that the reaction actually passes through an Y9-ester intermediate (Figures 5 and 7, Scheme 4). The amount of Y9-intermediate reaches a maximum at around 30 min (Figure 7). At any given time point, the amount of Y9-modified fragment is tiny, and we can therefore not report a separate rate constant for this step of the reaction.

Even though numerous time points were analyzed using proteolytic digestion both at pH 4 and 7.8, we were not able to detect any Y9-intermediate in the reaction between GSB and A216K. On the basis of the findings with GS-4, this could be due to a very fast intramolecular transfer from such a hypothetical intermediate to the lysine residue. However, we cannot exclude the possibility of a direct reaction between GSB and K216 since this is the only reagent that was able to modify the double mutant Y9F/A216K, albeit at a much slower rate (Figure 6). In any case, the hydroxyl group of Y9 speeds up the reaction between GSB and K216.

The Rate of the Modification Reaction of A216K Differs Greatly between Reagents. The reaction between A216K and GSB is much slower than the rate of modification of Y9 in wt hGST A1-1 (*22*). On the basis of semiquantitative MALDI-MS analyses, it takes roughly 200 min to reach 50% completion for K216-modification compared to about 20 min under similar reaction conditions in the wt reaction between GSB and Y9. In the case of GSB, we have thus increased the stability of the protein conjugate at the expense of the speed of the reaction. However, the rate is highly reagent-dependent

since the reaction between GS-4 and A216K is actually faster than the wt reaction with GSB. With GS-4 it takes approximately 10 min to reach 50% completion (Figure 6). This is even faster than the wt reaction with GSB, thus further adding to the value of the reaction. In any case, we have not decreased the yield of the reaction since it virtually goes to completion (Figure 6).

Why Does GSB React with Y9F/A216K? We do not know why Y9F/A216K reacts with GSB and no other reagent. It could be due to a more or less perfect fit that only in the case of GSB does the thiolester orient ideally with respect to K216. There might be unique binding properties in the case of GSB since other investigations by us (unpublished results) have also indicated that GSB is ideally suited as a substrate for the catalytic hGST A1-1 mutant A216H. This would be an effect similar to that of the mutant Y9F that displays some residual activity in the case of the natural GST activity (Table 1), even though the crucial hydroxyl group that aids in the ionization of GSH is removed (*31*).

CONCLUSIONS

We have introduced a single lysine at position 216 that can be site-specifically labeled by adding GS-thiolesters to the folded hGST A1-1 mutant. The resulting amide bond is stable, and the chemical labeling reaction can be carried out in the presence of GSH and even in a crude cell lysate. The set of reagents includes a fluorescent probe that could be utilized in future protein purification or fusion experiments. A more spectacular use would be to introduce a chemically reactive functional group that could take part in novel catalytic reactions.

ACKNOWLEDGMENT

Kerstin S. Broo thanks the Wenner-Gren Foundation for a postdoctoral fellowship. This work was financially supported by The Wenner-Gren Foundation, The Carl-Trygger Foundation, the Knut and Alice Wallenberg Foundation, and the Swedish Research Council.

Supporting Information Available: Fluorescence spectra showing wt hGST A1-1, Y9K, A216K, and Y9F/A216K at pH 7 and 298 K. MALDI-MS spectra of A216K showing the *m/z* range for would-be modified Y9 at the end of a 5 h incubation with GSB. MALDI-MS spectra of the cell (*E. coli*) lysate as well as the A216K-doped lysate. Attempted K_M measurements toward CDNB. This material is available free of charge via the Internet at http://pubs.acs.org/BC.

LITERATURE CITED

(1) Farinas, E. T., Bulter, T., and Arnold, F. H. (2001) Directed enzyme evolution. *Curr. Opin. Biotechnol. 12*, 545−551.

(2) Bolon, D. N., Voigt, C. A., and Mayo, S. L. (2002) Enzyme-like proteins by computational design. *Curr. Opin. Chem. Biol. 6*, 125−129.

(3) Dwyer, M. A., Looger, L. L., and Hellinga, H. W. (2004) Computational design of a biologically active enzyme. *Science 304*, 1967−1971.

(4) Kaplan, J., and DeGrado, W. F. (2004) De novo design of catalytic proteins. *Proc. Natl. Acad. Sci. U.S.A. 101*, 11566−11570.

(5) Wei, Y., and Hecht, M. H. (2004) Enzyme-like proteins from an unselected library of designed amino acid sequences. *Protein Eng., Des. Sel. 17*, 67−75.

(6) Qi, D., Tann, C. M., Haring, D., and Distefano, M. D. (2001) Generation of new enzymes via covalent modification of existing proteins. *Chem. Rev. 101*, 3081−3111.

(7) Ren, X., Jemth, P., Board, P. G., Luo, G., Mannervik, B., Liu, J., Zhang, K., and Shen, J. (2002) A semisynthetic glutathione peroxidase with high catalytic efficiency. *Chem. Biol. 9*, 789−794.

(8) DeSantis, G., and Jones, J. B. (1999) Chemical modification of enzymes for enhanced functionality. *Curr. Opin. Biotechnol. 10*, 324−330.

(9) Hamachi, I., Nagase, T., Tajiri, Y., and Shinkai, S. (1997) Incorporation of an artificial receptor into a native protein: new strategy for the design of semisynthetic enzymes with allosteric properties. *Bioconjugate Chem. 8*, 862−868.

(10) Hamachi, I., Nagase, T., and Shinkai, S. (2000) A General Semisynthetic Method for Fluorescent Saccharide-Biosensors Based on a Lectin. *J. Am. Chem. Soc. 122*, 12065−12066.

(11) Nagase, T., Nakata, E., Shinkai, S., and Hamachi, I. (2003) Construction of Artificial Signal Transducers on a Lectin Surface by Post-Photoaffinity-Labeling Modification for Fluorescent Saccharide Biosensors. *Chem. Eur. J. 9*, 3660−3669.

(12) Nakata, E., Nagase, T., Shinkai, S., and Hamachi, I. (2004) Coupling a Natural Receptor Protein with an Artificial Receptor to Afford a Semisynthetic Fluorescent Biosensor. *J. Am. Chem. Soc. 126*, 490−495.

(13) Sheehan, D., Meade, G., Foley, V. M., and Dowd, C. A. (2001) Structure, function and evolution of glutathione transferases: implications for classification of nonmammalian members of an ancient enzyme superfamily. *Biochem. J. 360*, 1-16.

(14) Strange, R. C., Spiteri, M. A., Ramachandran, S., and Fryer, A. A. (2001) Glutathione-S-transferase family of enzymes. *Mutat. Res. 482*, 21−26.

(15) Armstrong, R. N. (1997) Structure, catalytic mechanism, and evolution of the glutathione transferases. *Chem. Res. Toxicol. 10*, 2−18.

(16) Mannervik, B. (1996) Evolution of glutathione transferases and related enzymes for the protection of cells against electrophiles. *Biochem. Soc. Trans. 24*, 878−880.

(17) Pettigrew, N. E., and Colman, R. F. (2001) Heterodimers of glutathione S-transferase can form between isoenzyme classes pi and mu. *Arch. Biochem. Biophys. 396*, 225−230.

(18) Sinning, I., Kleywegt, G. J., Cowan, S. W., Reinemer, P., Dirr, H. W., Huber, R., Gilliland, G. L., Armstrong, R. N., Ji, X., Board, P. G., and et al. (1993) Structure determination and refinement of human alpha class glutathione transferase A1-1, and a comparison with the Mu and Pi class enzymes. *J. Mol. Biol. 232*, 192−212.

(19) Hayes, J. D., and Pulford, D. J. (1995) The glutathione S-transferase supergene family: regulation of GST and the contribution of the isoenzymes to cancer chemoprotection and drug resistance. *Crit. Rev. Biochem. Mol. Biol. 30*, 445−600.

(20) Lim, K., Ho, J. X., Keeling, K., Gilliland, G. L., Ji, X., Ruker, F., and Carter, D. C. (1994) Three-dimensional structure of *Schistosoma japonicum* glutathione S-transferase fused with a six-amino acid conserved neutralizing epitope of gp41 from HIV. *Protein Sci. 3*, 2233−2244.

(21) Ketterer, B. (2001) A bird's eye view of the glutathione transferase field. *Chem. Biol. Interact 138*, 27−42.

(22) Håkansson, S., Viljanen, J., Broo, K. S. (2003) Programmed delivery of novel functional groups to the alpha class glutathione transferases. *Biochemistry 42*, 10260−10268.

(23) Viljanen, J., Tegler, L., and Broo, K. S. (2004) Combinatorial Chemical Reengineering of the Alpha Class Glutathione Transferases. *Bioconjugate Chem. 15*, 718−727.

(24) Hederos, S., Broo, K. S., Jakobsson, E., Kleywegt, G. J., Mannervik, B., and Baltzer, L. (2004) Incorporation of a single His residue by rational design enables thiol-ester hydrolysis by human glutathione transferase A1-1. *Proc. Natl. Acad. Sci. U.S.A. 101*, 13163−13167.

(25) Gustafsson, A., and Mannervik, B. (1999) Benzoic acid derivatives induce recovery of catalytic activity in the partially inactive Met208Lys mutant of human glutathione transferase A1-1. *J. Mol. Biol. 288*, 787−800.

(26) Habig, W. H., and Jakoby, W. B. (1981) Assays for differentiation of glutathione S-transferases. *Methods Enzymol 77*, 398−405.

(27) Dirr, H. W., and Wallace, L. A. (1999) Role of the C-terminal helix 9 in the stability and ligandin function of class alpha glutathione transferase A1-1. *Biochemistry 38*, 15631-15640.

(28) Nieslanik, B. S., Ibarra, C., and Atkins, W. M. (2001) The C-terminus of glutathione S-transferase A1-1 is required for entropically driven ligand binding. *Biochemistry 40*, 3536−3543.

(29) Gustafsson, A., Etahadieh, M., Jemth, P., and Mannervik, B. (1999) The C-terminal region of human glutathione transferase A1-1 affects the rate of glutathione binding and the ionization of the active-site Tyr9. *Biochemistry 38*, 16268−16275.

(30) Widersten, M., Bjornestedt, R., and Mannervik, B. (1996) Involvement of the carboxyl groups of glutathione in the catalytic mechanism of human glutathione transferase A1-1. *Biochemistry 35*, 7731−7742.

(31) Stenberg, G., Board, P. G., and Mannervik, B. (1991) Mutation of an evolutionarily conserved tyrosine residue in the active site of a human class Alpha glutathione transferase. *FEBS Lett. 293*, 153−155.

(32) Bjornestedt, R., Stenberg, G., Widersten, M., Board, P. G., Sinning, I., Jones, T. A., and Mannervik, B. (1995) Functional significance of arginine 15 in the active site of human class alpha glutathione transferase A1-1. *J. Mol. Biol. 247*, 765−773.

BC050111T

A Glutathione-Based Hydrogel and Its Site-Selective Interactions with Water

Sumit S. Mahajan,[†,§] Rajan Paranji,[‡,§] Ranjana Mehta,[†] Robert P. Lyon,[†] and William M. Atkins*[,†]

Department of Medicinal Chemistry, Box 357610, and Department of Chemistry, Box 351700, University of Washington, Seattle, Washington 98195-7610. Received April 27, 2005; Revised Manuscript Received June 9, 2005

Glutathione (γ-glutamyl-cysteinyl-glycine; GSH) is ubiquitous biological tripeptide with multiple functions and possible therapeutic uses. The oxidized disulfide form (GSSG) self-assembles into fibrillar aggregates and gels in organic solvents, but not in solvent mixtures with high water content. Here, the disulfide bond has been replaced with a pyrenyl moiety in order to test the ability of GSH to direct noncovalent self-assembly in H_2O, when combined with a hydrophobic driving force for aggregation. The resulting GSH-pyrene forms gels in 95% H_2O:5% DMSO. The γ-glutamyl group is critical for gelation, as it is with GSSG organo-gels, inasmuch as neither *S*-(pyrenyl)-cysteinyl-glycine nor the iodo-acetamido-pyrene precursor gels under any conditions studied. Circular dichroism and fluorescence spectroscopy indicate that the pyrene moieties cluster within the gels. Scanning and transmission electron microscopy reveal fibrous networks with individual strands of ~50−100 nm diameter. Saturation transfer difference (STD) NMR studies demonstrate that water interacts strongly with GSH-borne protons in both solution and gel states, but only the gels include water−pyrenyl interactions with significant residence times.

INTRODUCTION

Self-assembling gels have potential use in numerous bio-nanotechnologies including tissue engineering, biosensors, bioadhesives, and drug delivery (*1*−*13*). For several applications, bioactive peptide hydrogels with tunable sol−gel behavior are the desired endpoint. Recent examples of 'responsive' gels include vancomycin-sensitive Fmoc-D-ala-D-ala gels (*14*), and peptide gels triggered by enzymatic activity (*15*) or IR radiation (*16*). A significant challenge has been the design of low molecular weight (< ~1000 kDa) peptide-based systems that self-assemble in water, although a few examples based on amino acids or short peptides have been described (*16*−*20*). A design strategy that has yielded elegant self-assembled mesoscopic structures involves grafting orthogonal self-recognition elements into single molecules (*6*, *8*, *14*). Here, we report the utility of this strategy with the highly polar peptide of biological interest, glutathione (γ-glutamyl-cysteinyl-glycine, GSH), grafted onto pyrene. This expands the pool of low molecular weight hydrogelators to include a ubiquitous biomolecule with extremely diverse functions. We previously characterized organo-gels derived from GSSG (**1**, Figure 1, *19*). Upon gelation in DMF, DMSO, or MeOH, a specific local conformation of the −S−S− dihedral angle is favored, as suggested also for aroyl-cysteine derivatives (*21*). Furthermore, inter- and intramolecular hydrogen bonds at the γ-glutamyl group drive self-assembly of 75 nm wide nanofibers, which coincides with gelation. Therefore, we hypothesized that the highly polar γ-glutamyl group could be exploited as a self-recognition element, and, when combined with a sufficient hydrophobic driving force, GSH could provide a scaffold for low molecular weight peptide hydrogels. GSH is a major determinant of cellular thiol redox status, and it is a well-established antioxidant (*22*). GSH also has potential utility in cystic fibrosis therapy (*23*, *24*), and it is exploited widely as an affinity ligand for immobilizing fusion proteins on surfaces (*25*, *26*). Thus, GSH could provide a scaffold for hydrogels with novel therapeutic value or material applications.

Although there are an increasing number of examples of hydrogels incorporating biomolecules, very few mechanistic details of the self-assembly process have been elucidated, and kinetically relevant intermediates en route to gel formation have not been documented in any cases, to our knowledge. In particular it is unclear how solvent water is affected by the gelation agents and whether specific functional groups within the gelators are responsible. To address this aspect of gelation, we have utilized saturation-transfer NMR methods to monitor the site-specific interactions between water and gelator within the hydrogels. This method may be generally useful for understanding sol−gel behavior.

EXPERIMENTAL PROCEDURES

Materials and Chemicals. GSH, *S*-hexyl-GSH (**5**) and β-mercaptoethanol were purchased from Sigma (St. Louis, MO) and used without further purification. *N*-(1-Pyrene)iodoacetamide (**6**) was purchased from Molecular Probes (Eugene, OR).

The synthesis of **2** was achieved as follows: *N*-(1-pyrene)iodoacetamide (10 mgs, 0.025 mmol) was dissolved in DMSO (400 μL). To this solution was added GSH (2-fold molar excess), and the reaction mixture was stirred overnight protected from light. Excess water (10−15 mL) was added followed by centrifugation to isolate the GSH−pyrene conjugate as a solid pellet. The above procedure was repeated at least two times to ensure complete removal of excess GSH. The pellet

* To whom correspondence should be addressed. Tel: (206) 685-0379. Fax: (206) 685-3252. E-mail: winky@u.washington.edu.
† Department of Medicinal Chemistry.
‡ Department of Chemistry.
§ These authors contributed equally to this work.

10.1021/bc0501294 CCC: $30.25 © 2005 American Chemical Society
Published on Web 06/30/2005

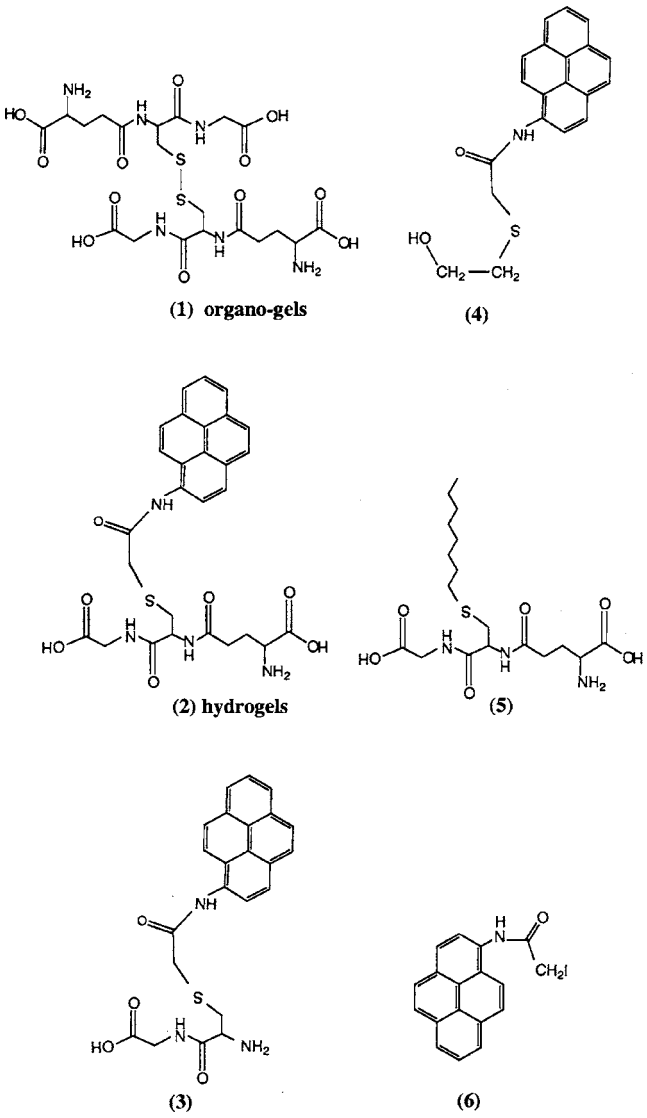

Figure 1. Structures of compounds compared in this work. **1** has been previously shown to form organo-gels.[19] **2** is a hydrogelator, as described within. Compounds **3**–**6** do not induce gelation under the conditions studied here.

obtained was then washed successively with acetonitrile and diethyl ether to obtain a gray solid. The solid was further dried to remove traces of water and ether (12 mgs, 82% yield). MS: calcd $M^+ = 564$, obsvd. $(M + 1)^+ = 565.2$. Compounds **3** and **4** were synthesized by an identical procedure, substituting either L-cysteine or β-mercaptoethanol for GSH.

Circular Dichroism. CD was performed with a Jasco J-720 spectropolarimeter with a scan rate of 50 nm/min and a path length of 2 mm, at 25 C. Samples were 1 mL containing 0.75 mM **2** in solvents described in the Figure 2 legend.

Fluorescence Spectroscopy. Fluorescence emission spectra were obtained with an SLM-Aminco 8100 fluorimeter, with slit widths of 4 nm, and excitation at 340 nm. Temperature was controlled with a circulating water bath.

Electron Microscopy. TEM was performed with a JEOL electron microscope at 80 keV. Gel samples were 'smeared' on a Formvar-coated copper grid (200 mesh, Fullam, Inc. Latham, N.Y.). The surface was washed briefly with EtOH and then stained for 1 min with 2% uranyl acetate in 95% EtOH. For SEM, gel samples were dried, sputter-coated, and placed on a polylysine-coated cover slip. Images were obtained at 15 keV on a JEOL 6300F scanning microscope.

^{1}H NMR. Saturation transfer difference experiments were performed on a Bruker AV500 system equipped with a H, C, F triple resonance probe, at 301 or 320 K at six saturation times (250 ms, 500 ms, 1 s, 2 s, 3 s, 4 s). Selective saturation of the water resonance was obtained by using a Gaussian cascade for the necessary saturation duration, followed by excitation sculpting for water suppression (*29*–*31*). Control spectra were obtained by placing the saturation frequency to −1.0 ppm followed by shifting the saturation frequency to the water resonance. Each experiment was conducted in an interleaved manner by collecting the control and saturated spectra in alternate scans and storing them in separate memory blocks, to average the effects of instrument instability over the period of the data collection. The STD amplification factor is defined here to be

$$\% \text{ amplification factor} = [I_0 - I_{sat}]/I_0 \times 100$$

where I_0 and I_{sat} are the spectral intensities of any single proton without and with water saturation, respectively.

Also, T1 relaxation measurements at 301 K were performed on a Bruker AV300 system. An inversion recovery sequence was employed to collect T1 data with a recycle delay of 10 s to ensure the complete recovery of magnetization at the end of each scan. The magnetization recovery curve given by

$$M_z = M_0\,[1 - 2 \times \exp(-t/\mathrm{T1})]$$

where M_z and M_0 are the magnetization vectors along the 'z' axis at time t and M_0 is in the initial net magnetization, respectively, was fitted to the data and T1 values were extracted. Care was taken to fit this single exponential recovery curve only in the initial rate regime to avoid the contamination of exchange rates on the measured T1 values (*27*–*29*). The NMR samples were prepared by using 30 mM solution of GSH pyrene in DMSO-d_6 followed by addition of water to get a 50:50 mixture. The samples were mixed well to get a homogeneous solution and then transferred immediately to a NMR tube.

The pulse sequence for the STD NMR experiment was adopted from 1D NOE difference pulse sequence developed by Meyer and co-workers (*27*). The on-resonance irradiation of water was performed at a chemical shift of 4.45 ppm. To minimize the error due to magnet instability, a reference spectrum was also collected simultaneously with off-resonance irradiation applied at −1 ppm, as no signals of GSH pyrene were observed in that region. The total numbers of scans was 256 with 16 'dummy' scans.

RESULTS

On the basis of the apparent selectivity of the γ-glutamyl group of GSSG in directing supramolecular self-assembly of organogels (*19*), we hypothesized that a hydrophobic moiety attached to GSH could provide a thermodynamic driving force for gelation in water. Analogues containing the γ-glutamyl group could provide a versatile range of gelators, in a manner analogous to the organo-gels derived from GSSG. Therefore, **2** was synthesized and its hydrogelation properties were **c**ompared to the des-γ-glutamyl analogue **3**, and to **4**, **5**, and **6** (Figure 1). Addition of H_2O to stock solutions of **2** in DMSO immediately yielded transparent, fluorescent gels. In solvents ranging from 95:5–40:60 (vol/vol) H_2O:DMSO, at

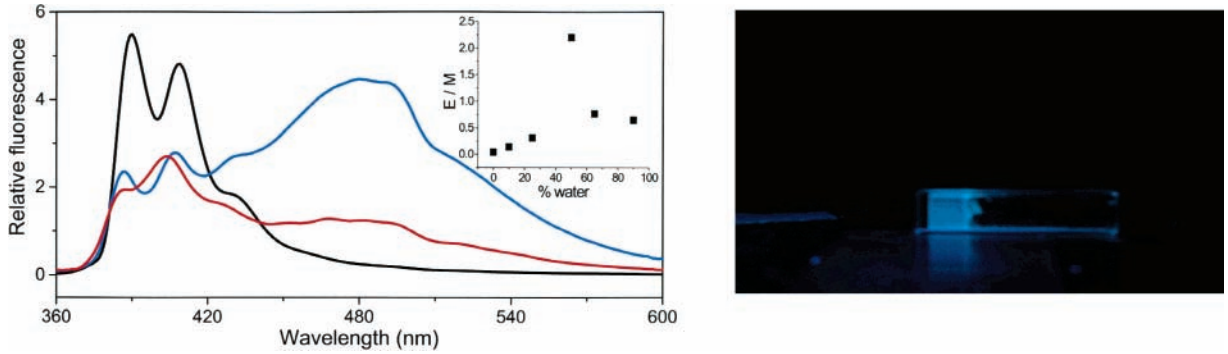

Figure 2. Left Panel: Fluorescence emission of **2** (0.75 mM) in different sol−gel states. The emission from excimers (485 nm) correlates with formation of gels. Black, 100% DMSO; red, 90:10 H_2O:DMSO; blue, 50:50 H_2O:DMSO. Inset: The maximal E/M ratio, 50:50 H_2O:DMSO yields the stiffest gels, but gels are formed even at 95:5 H_2O:DMSO. E/M = intensity at 485 nm/intensity at 390 nm. Excitation = 340 nm. Right Panel: Photograph of a fluorescent hydrogel (95:5 H_2O:DMSO) formed from 1 mM **2** in a cuvette lying on its side.

final concentrations of 1 mM to 10 mM, only **2** yielded transparent, fluorescent gels; in contrast, **1**, **3**, **4**, **5**, and **6** yielded clear solutions or precipitates, and no gels under any conditions studied. The uniqueness of **2** as a hydrogelator among the other analogues is interesting and reminiscent of the specificity observed for GSSG as an organogelator among structural congeners. The γ-glutamyl linkage may be useful in driving gelation in a wide variety of systems.

Fluorescence Characterization. Other pyrene-containing gelators have yielded excimer emission upon gelation, and this provides a convenient low resolution probe of pyrene-pyrene interactions (*7*, *30*). Gelation of **2** coincided with formation of a pyrene excimer fluorescence spectrum (485 nm) in contrast to monomer emission at 370−390 nm for the solution state (Figure 2). Although the absolute fluorescence intensity changed with solvent composition, the excimer:monomer ratio (E/M) clearly increased at higher ratios of H_2O:DMSO, with a maximum at 50:50 (Figure 2, inset). The E/M ratio corresponded well with the apparent stiffness of the gels, which was also maximal in this range. At 1 mM **2**, the gels were sufficiently stiff to remain in an inverted vessel even at 95:5 H_2O:DMSO.

Circular Dichroism. Ground-state chromophore interactions were monitored by circular dichroism (CD). Pyrene CD excitation bands at 290−400 nm were observed in the gel state, but not the solution state. The CD bands are characteristic of chiral pyrene complexes and indicate direct ground-state chromophore interaction (Figure 3). Although the rheological properties of these gels remain to be studied in detail, the temperature-dependent CD spectrum (Figure 3, inset) yields a T_m for gelation of 46 °C for 1 mM **2** in 90:10 H_2O:DMSO. Interestingly, there was a modest increase in ellipticity at 366 nm with increasing temperature, until the gel melted at ∼46 °C. Perhaps, the hydrophobic effect resulted in stronger, or more complete, pyrene−pyrene interactions with increasing temperature, until the gels melt at 46 °C.

In the previous work with GSSG gels a negative CD band at 240−250 nm was observed only in the gel state. In the sol state, a positive band was observed at this wavelength. On the basis of this, and comparison to CD spectra of cysteine-containing peptides (*31*), we assigned the negative CD band to the γ-Glu-Cys bond, which apparently is conformationally restricted in the gels. Due to the intense CD band of the pyrene groups, we were unable to observe this spectroscopic signature in the hydrogels from **2**.

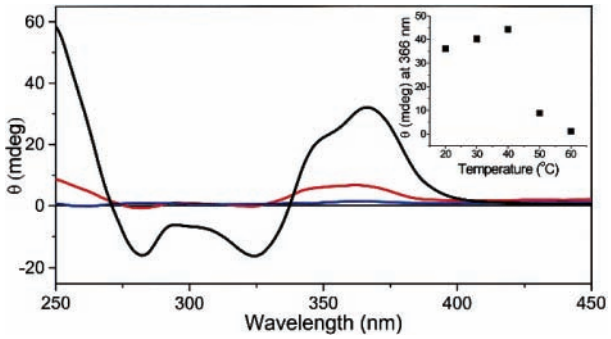

Figure 3. Sol-gel transition of **2** (0.75 mM) monitored by circular dichroism. The spectra are color coded as follows: Black, 20 °C, 90:10 H_2O:DMSO; red, 20 °C, 50:50 H_2O:DMSO; blue, 20 °C 100% DMSO. Inset: The CD bands at 260−400 nm are observed only in the gel state, and are lost at a T_m of 46 °C (90:10 H_2O:DMSO). The molar ellipticity at 366 nm represents the *y*-axis.

The temperature-dependent sol−gel conversion was reversible, although with a pronounced hysteresis requiring up to a few hours for gelation. At identical concentrations, neither **3**, **4**, **5**, or **6** in any H_2O/DMSO combination yielded fluorescent excimers or CD bands, further indicating the specificity of the γ-glutamyl-cys linkage in directing the self-assembly of pyrene complexes. As with the previously observed organo-gels (*19*), the γ-glutamyl-cys linkage is critical for the aqueous sol−gel transition of **2** among the pyrene derivatives studied.

Electron Microscopy. The mesoscale morphology of the gel state was monitored by transmission electron microscopy (TEM) and scanning electron microscopy of gel slices, which revealed highly branched fibrous networks, as observed for the GSSG organo-gels (Figure 4). Based on TEM and SEM, the width of individual strands is 50−100 nm, as also observed with the GSSG organo-gels. Possibly, the organo-gels and hydrogels share a similar supramolecular structure. Also evident in EM images were spherical masses of ∼50 nm diameter decorating the filamentous structures. Under all conditions studied, both morphologies were observed, suggesting multiple possible high order structures. We found no clear correlation between the relative fiber vs sphere morphology upon changing solvent composition or temperature. Both morphologies were observed also with the GSSG organo-gels, but with a significantly greater preference for fibers. The fiber morphology is clearly preferred in the hydrogels as well. The relative homogeneity of the fiber diameter suggests a highly specific self-assembly process, rather than a nonspecific aggrega-

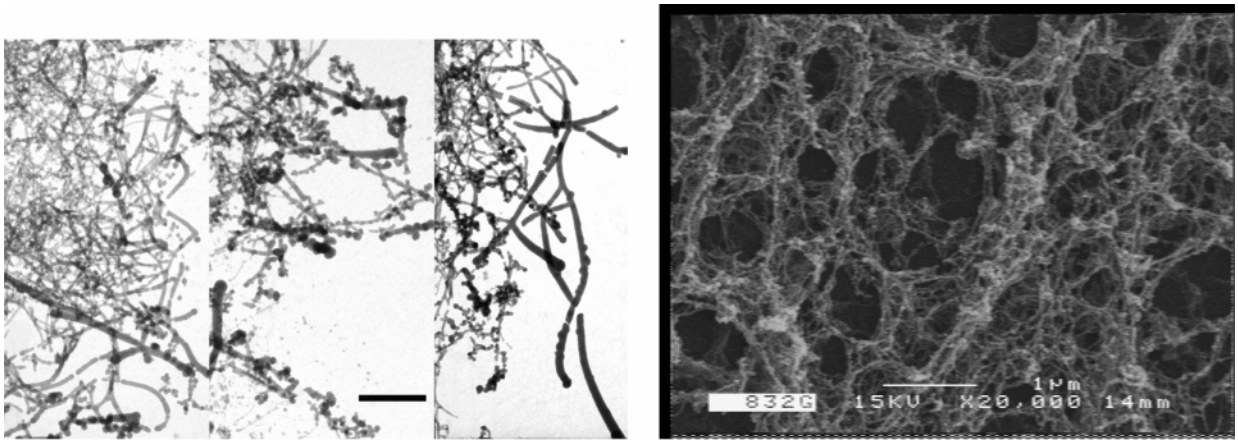

Figure 4. Electron microscopy of gels formed from **2**. Left three panels: TEM at increasing magnification. The branched fibrous network consists of strands approximately 50−100 nm in diameter. The bar in the center panel of the TEM micrographs is 1 μm. Right Panel: Scanning EM of a gel formed from 10 mM **2**.

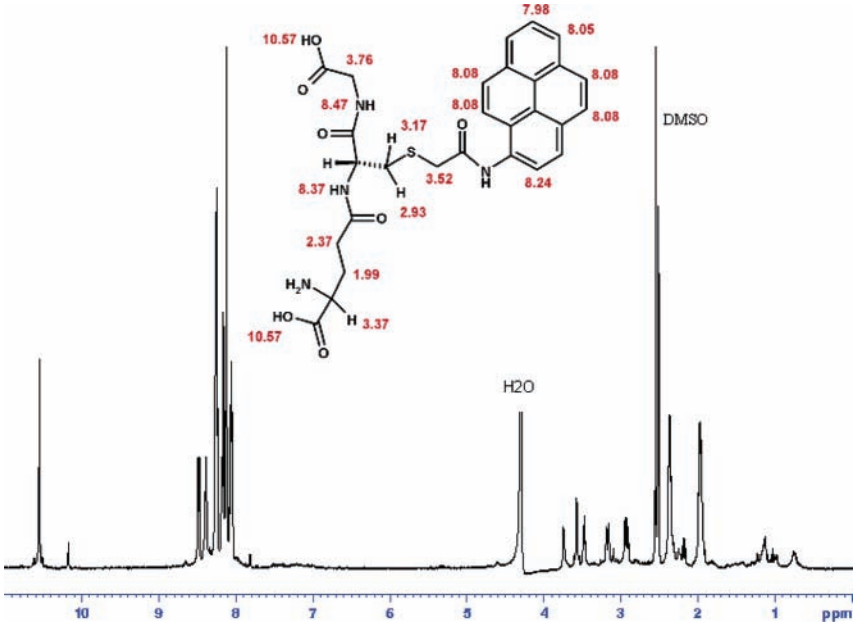

Figure 5. ^{1}H NMR spectrum of **2** in 50:50 H_2O:DMSO after gelation has started. The chemical shifts of the assignable protons are annotated on the chemical structure.

tion. Also, a high degree of branching is evident, which suggests the possibility of obtaining thermostable gels, by manipulation of the gelation kinetics. Although the EM images do not directly address the structure of gels in the hydrated state, the fact that no such fibers are observed in samples generated from **3**, **4**, **5**, or **6** suggests that fibril formation correlates with gelation.

^{1}H NMR. The properties of water within hydrogels remain uncharacterized. Because it is ultimately desirable to 'tune' these properties, additional methods are required to monitor solvent dynamics and solvent−gelator interactions (*32*). To identify specific water−gelator interactions with **2**, we performed saturation transfer difference (STD) ^{1}H NMR experiments, wherein the solvent water was irradiated with a saturating pulse, and the subsequent transfer of magnetization to GSH-pyrene protons was monitored. An analogous technique has been used to monitor the dynamics of protein−ligand interactions, with saturation transfer from the protein to the bound ligand (*27*−*29*). Because H_2O is absolutely required for the hydrogel formation from **2**, we have adapted the strategy to saturate water in the gels, and to look for differential saturation transfer or magnetization to the protons on **2**. In this strategy, water is the large reservoir of magnetization, which can be transferred to GSH-pyrene. With this strategy we were able to compare STD spectra in the gel state, in a sample that was just beginning to gel, and of the solution state, using the same sample after raising the temperature to 46 °C, just above the transition temperature. The former case represents a sample *in the process of gelling*, rather than a fully gelled sample. Therefore, the comparison between the spectra is only a qualitative indication of which protons are effected upon gelation and not a quantitative measure of changes in solvent interaction. To our knowledge, the dynamics of water in hydrogels have not been studied previously by this method.

The ^{1}H NMR spectrum of **2** in viscous fluid 'gels' is shown in Figure 5. It was not possible to record well-resolved NMR spectra in stiff gels in 95:5 H_2O:DMSO, so the NMR experiments were conducted at higher DMSO content. Under these conditions, gels begin to form but they are not sufficiently rigid to afford complete line broadening. To generate the STD spectrum, first the water signal was preirradiated for a sufficiently long time to achieve saturation, and a 1D spectrum was recorded. Next, a control spectrum was recorded without any presaturation on the water signal. The difference in

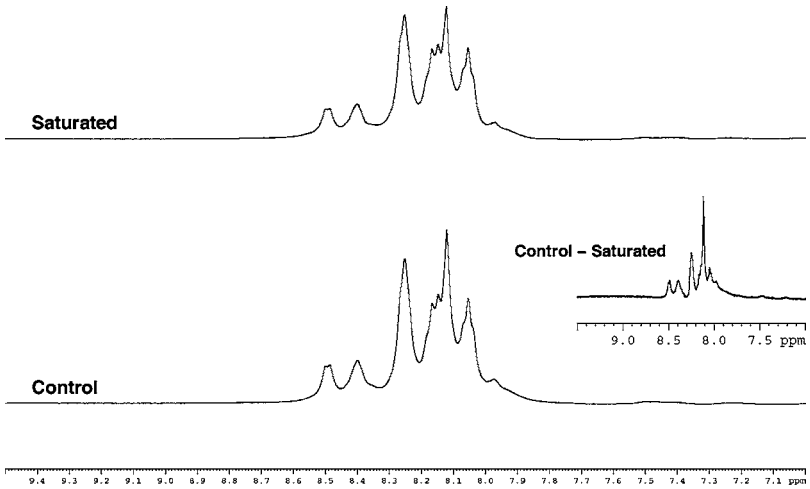

Figure 6. Aromatic region of the ^{1}H NMR spectrum of **2** in 50:50 H_2O:DMSO with off-resonance saturation (control) and on-resonance saturation of water (saturated) in 'fluid' gels. The inset is the STD spectrum for this spectral region.

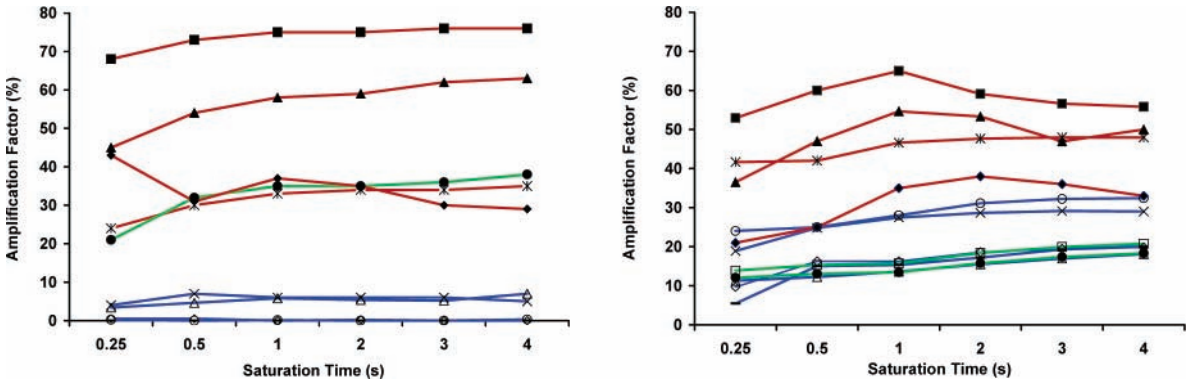

Figure 7. STD amplification factors vs t_{sat} in solution (left panel) and in gels (right panel). The red curves correspond to aliphatic protons on the GSH group, the blue curves are the aromatic protons on the pyrenyl group, and the green curves are the exchangeable amide protons. The specific protons are 8.24 ppm, open circles; 8.16 ppm, open triangles; 8.08 ppm, X's; 8.05 ppm, open diamonds; 8.01 ppm, crosses; 7.98 ppm, dashes; 3.17 ppm, closed squares; 2.93 ppm, closed triangles; 8.47 ppm, open squares; 8.37 ppm, closed circles.

intensity of resonances for the native spectrum of **2**, with off-resonance saturation minus the intensity of the spectrum with on-resonance water saturation yields an STD spectrum as also shown in Figure 6. The largest differences were observed for the protons on the GSH moiety, but they were readily apparent also for the aromatic pyrenyl protons in the gels, as shown in Figure 6.

The intensity of any individual proton resonance in the difference STD spectrum depends on the off-rate of the water from that site, the saturation time, and the concentration of the proton in the gel.

Water molecules tightly bound to specific protons, on the appropriate NMR time scale, can transfer magnetization. However, if the gelator protons interact too strongly with the water, then the magnetization will be transferred only from the small subset of water that is bound to it. More efficient saturation transfer is obtained for the entire population if the off-rate of water from the proton of interest is fast relative to the saturation time (t_{sat}), so that many water protons can interact with gelator, *but also slow enough to allow transfer of* magnetization. The STD amplification factor was calculated, as described in Experimental Procedures, for most of the protons in the 1D spectrum. We recorded the results for a range of presaturation times i.e., 250 ms to 4 s, and the STD amplification factors as a function of saturation times are plotted in Figure 7 for all the resolvable peaks from the GSH group, pyrenyl protons, and the observed amide protons of the GSH-pyrene gel. A few of the aliphatic peaks were not selected because they were too close to the water peak, thus hampering accurate determination of the peak intensity after saturation. Also, a few of the protons were not unambiguously assigned. For all protons, we observed that the maximum saturation transfer is already reached for a saturation time of 2 s.

In the solution state, all of the pyrenyl aromatic protons have very low STD amplification factors; some are 4-8% and others are essentially zero. For the GSH-borne aliphatic protons ($\delta = 2-3$ ppm), the amplification factors range from 30% to 70%, with the greatest magnetization transfer occurring with the protons on the β-carbon of the cysteinyl group. It is clear from these results that water only very transiently interacts with the aromatic protons (blue), if at all, but water does have significant residence times on the aliphatic protons in the GSH-moiety (red). The residence times of solvent water on aliphatic groups in peptides has been shown to increase when nearby groups are polar, as with the GSH peptide. In solution, only one amide proton is observed (8.37 ppm, cysteinyl amide). The other amides presumably are severely broadened due to chemical exchange.

Upon gelation, there is a dramatic redistribution of STD amplification factors. The maximum STD amplification factor ranges from 45% to 65% for the aliphatic peaks of interest in the GSH group (Figure 7, red). For the pyrenyl protons (Figure 7, blue) this range increases even more, to 15% − 30%. In the case of the amide protons,

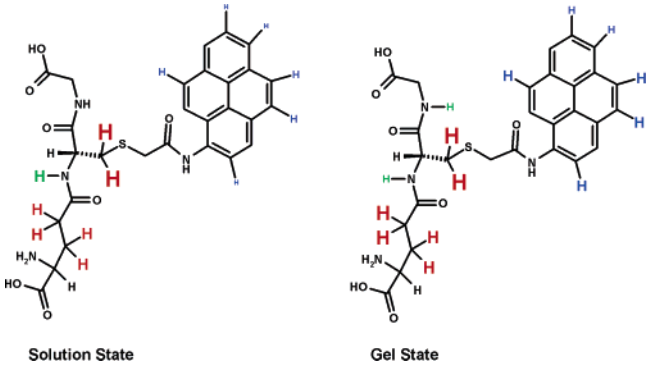

Figure 8. Schematic of changes in STD amplification factors upon gelation. The protons are color-coded as in Figure 7. The relative size reflects the relative amplification factors. The aromatic protons are strongly affected by gelation.

Table 1. Representative T1 Relaxation Times and STD Amplification Factors

peak position (ppm)	T1 (s)	STD amplification factor
2.37 (GSH)	0.26	48%
8.16 (pyrene)	0.97	18%
8.47 (NH)	0.44	21%

the maximum STD amplification factors are 18% for the peak at 8.37 ppm and 20% for the peak at 8.47 ppm, which is now observed. Presumably, the amide proton at 8.47 ppm in the gel, which is not observed in solution, reflects a decrease in the chemical exchange rate of this proton. Regardless of the complexity for amide protons, as discussed further below, there is a clear and significant difference in saturation transfer from water to different protons of GSH-pyrene upon gelation with a marked increase in the amplification factors for the aromatic pyrenyl protons (Figure 7). It is striking that the data cluster into groups defined by the 'type' of proton. The aliphatic GSH protons (red) have the highest amplification factors in both solution and gel states. The aromatic pyrenyl protons (blue) have near zero amplification factors in solution but become spread over a wide range including some with factors as high as 30%, in the gels. For the single amide proton observed in both states, the amplification factor actually decreases upon gelation. These data are presented schematically in Figure 8, where the structure of **2** includes protons with sizes scaled according to their STD amplification factors, in the solution vs gel state.

The recovered STD amplification factors must be considered in the context of T1 relaxation processes. The slower on/off rate of H_2O from the atoms it interacts with can lead to larger transfer of saturation from H_2O, whereas efficient T1 relaxation process counteracts the saturation transfer process. Therefore, we measured T1 relaxation times. Table 1 summarizes the results, with exemplary values, and demonstrates that GSH aliphatic protons relax most efficiently and in contrast the pyrenyl protons relax slowly. The NH proton's relaxation time is intermediate between them. Despite the efficient relaxation of GSH-associated protons, their maximum achievable STD amplification factor for the gels is about 2- to 2.5-fold larger than for pyrenyl protons or the NH protons. On the basis of the relative T1 and STD amplification factors of GSH and pyrene, it must be true that H_2O has higher affinity for GSH backbone than for pyrene group, and the residence time of H_2O interacting with the GSH group is longer. This leads to increased saturation transfer efficiency for the GSH group protons (48%) when compared with the pyrenyl group (18%), despite the faster T1 relaxation processes. A similar conclusion is true for all other aliphatic, nonexchangeable, GSH-associated protons as seen from Figure 7. Figure 7 clearly shows that the STD amplification factors are distinctly different for GSH-borne protons, when compared with pyrenyl protons. Apparently, solvent water does not interact with the pyrenyl protons, or it does only extremely transiently in solution. Most importantly, gelation correlates specifically with stronger water interactions with the pyrenyl group, without much effect on the GSH−water interactions.

Considering the NH protons, their chemical exchange with a large reservoir of 'saturated' protons should lead to larger saturation transfer and large amplification factors. This situation is in stark contrast to the scenario, where the faster on/off rate of water leads to less efficient saturation transfer efficiency in the case of protons of GSH or pyrene. Given the fact that distinct NH resonances are observed in the case of the GSH-pyrene gel system, the chemical exchange of the NH protons falls in the 'infrequent' or the so-called 'slow' exchange regime (*33*−*35*). In fact, with identical solvent conditions, but in the sol state, the amide resonances are not observed and they appear only when the sample begins to gel. Clearly, the amide−solvent chemical exchange reactions are much slower in the gel state than in the sol state, as expected. This may indicate the participation of the amides in intermolecular hydrogen bonds that are formed uniquely in the gel state. Thus, the gelation process itself would be expected to decrease the amplification factors from a theoretical maximum at which chemical exchange was sufficiently slow to allow for transfer, but sufficiently fast to allow transfer to a large population of GSH amide protons. In short, the magnetization transfer from solvent to amide protons is more complex than the other protons on the gelator, and the interpretation is ambiguous. Table 1 suggests that the efficiency of the exchange process of NH with water seems to lie between the saturation transfer efficiency of GSH and pyrene.

For a gel system like the GSH-pyrene, the average viscosity is clearly higher than that of a solution. This also means that the time scale of random fluctuations in such gels is larger than that of solutions, and therefore spin lattice relaxation times for gel systems around room-temperature lie close to the T1 minimum on the T1 vs correlation time graph (*33*). From this perspective, when the T1 values for two groups such as GSH and pyrene within the same molecule differ substantially, it generally translates into a significant difference in their time scales of motion. Apparently, the GSH portion of the molecule is more mobile than the pyrenyl group in the gels.

DISCUSSION

A common design strategy exploited for the preparation of self-assembling hydrogels includes the combination within a single amphiphilic molecule of hydrophobic groups and water-soluble components. Here, we have applied the term 'hydrogel' to our system which includes 5% organic solvent as a lower limit, but which has an absolute requirement for the addition of water to initiate gelation. Numerous examples of hydrogelators include short peptides or sugars as the hydrophilic component (*1*). We have extended this strategy by incorporation of the polycyclic aromatic hydrocarbon pyrene to the 'unusual' peptide GSH. The gels described here are interesting for several reasons.

Of primary interest is the use of GSH derivatives. GSH has numerous biological functions including antioxidant

roles, detoxification, and enzyme regulation. Of course, many of these functions require the free thiol group contained in GSH, and the hydrogelator described here (**2**) has lost this group. However, these results provide proof-of-principle that GSH conjugates can be hydrogelators, and is it reasonable to expect that the thiol group of other hydrogelating GSH-conjugates could be recovered by simple changes in pH or temperature, or enzymatically. Several types of chemical linkage to the GSH thiol are known to be reversible (*36*). Thus, although we have initiated the exploration of GSH-based hydrogels with **2**, other GSH-conjugates are easily imagined that could be 'cycled' through the hydrogel state and the biologically functional state with a free thiol. Speculatively, in fact, GSH-conjugates with nontoxic, or even therapeutically useful, hydrophobic removable groups could be used as slow release formulations for delivery of GSH itself, which has been widely used as an antioxidant and potential therapeutic for cystic fibrosis (*23*, *24*). Furthermore, GSH-conjugates may be directly useful as therapeutic anticancer adjuvants, without the need for a free thiol group (*37*, *38*), and it is conceivable that hydrogel formulations could have utility. In such applications, the GSH released from the 'conjugate gels' would not reform gels, but would simply mix with the endogenous pools of GSH. Furthermore, immobilized GSH analogues are widely used in protein purification protocols that exploit glutathione S-transferase (GST)-fusion technology (*25*, *26*). For these purposes, a free thiol group on GSH is not a strict requirement, and it is possible that hydrogels bearing pendant S-linked GSH peptides could immobilize GST-fusion proteins, thus providing a strategy for delivery of engineered proteins to hydrogel surfaces. Although the current work does not achieve such putative 'applications', it does suggest their feasibility.

A second important aspect of this work is the extension of the previously reported specificity of the γ-glutamyl group as a self-assembly unit to hydrogels. As we observed previously with GSSG in organic solvent, the γ-glutamyl group is uniquely able to drive hydrogelation within the series of analogues studied here that contain the same hydrophobic moiety. Although the molecular basis for this apparent specificity remains unknown, it could, in principle, be exploited in non-GSH γ-glutamyl-containing hydrogelators, once it is adequately understood. We are careful to note that, although the previously described organo-gels and the gelation of **2** in water both exhibit an apparent specificity for the γ-glutamyl group and both exhibit similar gross structures, the specific molecular interactions in the two type of gel may be different.

A critical, and general, aspect of hydrogels that has not been experimentally addressed in sufficient detail is the structure and dynamics of water sequestered in them (*32*). It is likely that a complete understanding of solvent dynamics in hydrogels would facilitate control over their sol−gel properties. Although it is generally accepted that hydrogels 'entrap' large amounts of water on a molar basis, there are few experimental data that provide details of the behavior of solvent at the molecular level. The STD NMR spectra represent initial steps toward such an understanding, and a potential general method to probe local solvent dynamics in other hydrogel systems.

In the case of covalently bonded ^{1}H atoms, which are part of either the GSH or the pyrene group, the two important factors that affect the efficiency of magnetization transfer from the H_2O are the on/off rate of water to/from these atoms and the spin−lattice relaxation time (T1) experienced by these atoms. While the on/off rates determine the affinity with which water is binding to the group of atoms under consideration and the residence time of their complex, the T1 value is dependent on the dynamic state of the same. As a matter of fact, these two processes counteract each other so that, while the resonances from the atoms that have strong affinity to the saturated water get saturated themselves, the spin−lattice relaxation process restores the magnetization of these atoms to their equilibrium values. While similar processes exist also for the exchangeable NH protons, it is necessary to recognize a subtle difference between the mechanism of saturation transfer from H_2O to the amide protons and the covalent-bonded protons in GSH or pyrene. In the case of NH protons the 'chemical exchange' process includes detachment of the proton from the NH group and replacement by a solvent proton. If the spin of this exchanged ^{1}H were to be in a 'saturated' state, the resulting NH group inherits this state of saturation. Thus, for the amide protons the STD amplification factor is also a function of the chemical exchange rates.

Although the spectroscopic methods used here do not provide a high-resolution structural model for the arrangement of **2** within gels, taken together they do suggest a general picture in which pyrenyl groups are aggregated within a central core of fibers that are coated on the periphery with the GSH moieties. Obviously, the dimensions of fibers observed by SEM are too large to correspond to individual molecule of **2** arranged in a linear array, and many molecules of **2** must self-assemble laterally as well as along the major axis of the fibers. The 'close-packed' pyrenes, apparently, do not interact with solvent as effectively, and they are relatively rigid compared to the more mobile GSH moieties, which lie on the outside of the fibers and have access to solvent. However, although the interaction of water with the pyrenyl groups is 'less strong' the formation of gels coincides with a significant increase in the pyrenyl−water interactions, which are essentially absent in the solution state. It is likely that solvent networks are stabilized in the gels, and these networks span the hydrogen bonding groups on GSH and the aromatic pyrenyl groups. Further structural characterization is required to understand how this 'low resolution' model accommodates the apparent essentiality of the γ-glutamyl groups and their presumed participation in intermolecular hydrogen bonds. A critical demonstration of the STD results is that the hydrophobic moieties are not excluded from interactions with solvent water in the gels. Rather, the pyrene groups specifically participate in 'new' solvent interactions in the gel state, presumably through cooperative interactions with the GSH groups. Furthermore, the STD experiments here suggest parallels between hydrogelation and protein solvation (*39*), wherein hydrophobic aromatic groups can interact strongly with water when nearby polar residues can also participate, and this is likely to be the critical feature of gelators.

LITERATURE CITED

(1) *Supramolecular Self-assembly for Biological Applications* (Yui, N., Ed.) CRC Press, Boca Raton, FL.

(2) Kobayashi, H., Friggeri, A., Kuomoto, K., Amaike, M., Shinkai, S. and Reinhoudt, D. N. (2002) Molecular design of "super" hydrogelators: understanding the gelation process of azobenzene-based sugar derivatives in water. *Org. Lett. 4*, 1423−1426.

(3) Schneider, J. P., Pochan, D. J., Ozbas, B., Rajagopal, K., Pakstis, L., and, Kretsinger, J. (2002) Responsive hydrogels from the intramolecular folding and self-assembly of a designed peptide. *J. Am. Chem. Soc. 124*, 15030−15037.

(4) Wang, G., and Hamilton, A. D. (2003) Low molecular weight organogelators for water. *Chem. Commun. 3*, 310−311.
(5) Wang, G., and Hamilton, A. D. (2002) Synthesis and self-assembling properties of polymerizable organogelators. *Chemistry 8*, 1954−1961.
(6) Hartgerink, J. D., Beniash, E., and Stupp, S. I. (2002) Peptide-amphiphile nanofibers: a versatile scaffold for the preparation of self-assembling materials. *Proc. Natl. Acad. Sci. U.S.A. 99*, 5133−5138.
(7) Hartgerink, J. D., Beniash, E., and Stupp, S. I. (2001) Self-assembly and mineralization of peptide-amphiphile nanofibers. *Science 294*, 1684−1688.
(8) Xing, B., Yu, C.-W., Chow, K.-H., Ho, P.-L., Fu, D., and Xu, B. (2002) Hydrophobic interaction and hydrogen bonding cooperatively confer a vancomycin hydrogel: a potential candidate for biomaterials. *J. Am. Chem. Soc. 124*, 14846−14847.
(9) Lutolf, M. P., Lauer-Fields, J. L., Schmoekel, H. G., Metters, A. T., Weber, F. E., Fields, G. B., and Hubbell, J. A. (2003) Synthetic matrix metalloproteinase-sensitive hydrogels for the conduction of tissue regeneration: engineering cell-invasion characteristics *Proc. Natl. Acad. Sci. U.S.A. 100*, 5413−5418.
(10) Collier, J. H., Hu, B. H., Ruberti, J. W., Zhang, J., Shum, P., Thompson, D. H., and Messersmith, P. B. (2001) Thermally and photochemically triggered self-assembly of peptide hydrogels. *J. Am. Chem. Soc. 123*, 9463−9464.
(11) Estroff, L. A., and Hamilton, A. D. (2004) Water gelation by small organic molecules. *Chem. Rev. 104*, 1201−1217.
(12) Hoffman, A. S. (2002) Hydrogels for biomedical applications. *Adv. Drug Delivery Rev. 43*, 3−12.
(13) Zhang, Y., Yang, Z., Yuan, F., Gu, H., Gao, P., and Xu, B. *J*. (2004) Molecular recognition remolds the self-assembly of hydrogelators and increases the elasticity of the hydrogel by 10(6)-fold. *J. Am. Chem. Soc. 126*, 15028−15029.
(14) Zhang, Y., Gu, H., Yang, Z., and Xu, B. (2003) Supramolecular hydrogels respond to ligand -receptor interaction. *J. Am. Chem. Soc. 125*, 13680−13681.
(15) Hu, B. H., and Messersmith, P. B. (2003) Rational design of transglutaminase substrate peptides for rapid enzymatic formation of hydrogels. *J. Am. Chem. Soc. 125*, 14298−14299.
(16) Collier, J. H., Hu, B. H., Ruberti, J. W., Zhang, J., Shum, P., Thompson, D. H., and Messersmith, P. B. (2001) Thermally and photochemically triggered self-assembly of peptide hydrogels. *J. Am. Chem. Soc. 123*, 9463−9464.
(17) Nowak, A. P., Breedveld, V., Pakstis, L., Ozbas, B., Pine, D. J., Pochan, D., and Deming, T.J. (2002) Rapidly recovering hydrogel scaffolds from self-assembling diblock copolypeptide amphiphiles. *Nature 417*, 424−428.
(18) Suzuki, M., Yumoto, M., Kimura, M., Shirai, H., and Hanabusa, K. A. (2003) A family of low-molecular-weight hydrogelators based on L-lysine derivatives with a positively charged terminal group. *Chemistry 9*, 348−354.
(19) Lyon, R. P., and Atkins, W. M. J. (2001) Self-assembly and gelation of oxidized glutathione in organic solvents. *J. Am. Chem. Soc. 123*, 4408−4413.
(20) Menger, F. M., and Caran, K. L. (2000) Anatomy of a Gel. Amino Acid Derivatives that Rigidify Water at Submillimolar Concentrations. *J. Am. Chem. Soc. 122*, 11679−11691.
(21) Dickinson, D. A., and Forman, H. J. (2002) Glutathione in defense and signaling: lessons from a small thiol. *Ann. N. Y. Acad. Sci. 973*, 488−504.
(22) Meister, A. (1994) Glutathione, Ascorbate and Cellular Protection. *Cancer Res. 54*, 1969s−1975s.
(23) Hudson, V. M. (2004) New insights into the pathogenesis of cystic fibrosis: pivotal role of glutathione system dysfunction and implications for therapy. *Treat. Respir. Med. 3*, 353−363.
(24) Weng, T. X., Godley, B. F., Jin, G. F., Mangini, N. J., Kennedy, B. G., Yu, A. S., and Wills, N. K. (2002) Oxidant and antioxidant modulation of chloride channels expressed in human retinal pigment epithelium. *Am. J. Physiol. Cell Physiol. 283*, C839−849.
(25) Rodal, A. A., Duncan, M., and Drubin, D. (2002) Purification of glutathione S-transferase fusion proteins from yeast. *Methods Enzymol. 351*, 168−172.
(26) Murray, A. M., Kelly, C. D., Nussey, S. S., and Johnstone, A. P. (1998) Production of glutathione-coated microtitre plates for capturing recombinant glutathione S-transferase fusion proteins as antigens in immunoassays. *J. Immunol. Methods. 218*, 133−139.
(27) Mayer, M., and Meyer, B. (2001) Group epitope mapping by saturation transfer difference NMR to identify segments of a ligand in direct contact with a protein receptor. *J. Am. Chem. Soc. 123*, 6108−6117.
(28) Mayer, M., and James, T. L. (2002) Detecting ligand binding to a small RNA target via saturation transfer difference NMR experiments in D(2)O and H(2)O. *J. Am. Chem. Soc. 124*, 13376−13377.
(29) Meyer, B., and Peters, T. (2003) NMR spectroscopy techniques for screening and identifying ligand binding to protein receptors. *Angew. Chem. 42*, 864−890.
(30) Rangarajan, B., Coons, L. S., and Scranton, A. B. (1996) Characterization of hydrogels using luminescence spectroscopy. *Biomaterials 17*, 649−661.
(31) Coleman, P. L., and Blout, E. R. (1968) The optical activity of the disulfide bond in L-cysteine and some derivatives of L-cysteine. *J. Am. Chem. Soc. 90*, 2405−2415.
(32) Mukhopadhyay, S., Maitra, U., Ira; Krishnamoorthy, G., Schmidt, J., and Talmon, Y. (2004) Structure and dynamics of a molecular hydrogel derived from a tripodal cholamide. *J. Am. Chem. Soc. 126*, 15905−15914.
(33) Levitt, M. H. (2002) *Spin Dynamics*, p 524, John Wiley, New York.
(34) Hwang, T.-L., and Shaka, J. (1995) Water suppression that works. Excitation sculpting using arbitrary waveforms and pulsed field gradients, *J. Magn. Reson. A112*, 275−279.
(35) Cavanagh, J., Fairbrother, W. J., Palmer, A. G., and Skelton, N. J. (1996) *Protein NMR Spectroscopy: Principles and Practice*, Academic Press, New York.
(36) Ibarra, C., Grillo, M. P., Lo Bello, M., Nucettelli, M., Bammler, T. K., and Atkins, W. M. (2003) Exploration of in vitro pro-drug activation and futile cycling by glutathione S-transferases: thiol ester hydrolysis and inhibitor maturation. *Arch. Biochem. Biophys. 414*, 303−311.
(37) van Bladeren, P. J., and van Ommen, B. (1991)The inhibition of glutathione S-transferases: mechanisms, toxic consequences and therapeutic benefits. *Pharmacol. Ther. 51*, 35−46.
(38) Kauver, L. M., Morgan, A. S., Sanderson. P. E., and Henner, W. D. (1998) Glutathione based approaches to improving cancer treatment. *Chem. Biol. Interact. 111−112*, 225−238.
(39) Beck, D. A. C., Alonso, D. O. V., and Daggett, V. (2003) A microscopic view of peptide and protein solvation. *Biophys. Chem. 100*, 221−237.

BC0501294

TECHNICAL NOTES

Thiol-Functionalized Polymeric Micelles: From Molecular Recognition to Improved Mucoadhesion

Marie-Hélène Dufresne,[†] Marc A. Gauthier,[‡] and Jean-Christophe Leroux*[,†]

Canada Research Chair in Drug Delivery, Faculty of Pharmacy, University of Montreal, P.O. Box 6128, Downtown Station, Montreal (QC), Canada, H3C 3J7, and Department of Chemistry, University of Montreal, P.O. Box 6128, Downtown Station, Montreal (QC), Canada, H3C 3J7. Received January 12, 2005; Revised Manuscript Received April 20, 2005

Surface-modified colloids which can selectively interact with biological species or surfaces show promise as drug delivery systems. However, the preparation of such targeted devices remains challenging, especially when considering polyion complex micelles for which side reactions with the ionic core components (typically carboxylic acid or amino groups) can occur. To solve this issue, an innovative synthetic strategy is proposed and used to prepare an asymmetric poly(ethylene glycol)-*block*-poly-(2-(*N*,*N*-dimethylamino)ethyl methacrylate) copolymer presenting a thiol group at the end of the poly-(ethylene glycol) chain. Thiol groups are highly appealing given that they react almost exclusively and quantitatively with maleimides under physiological conditions, thereby facilitating the chemical functionalization of the copolymer. The simplicity of the derivatization procedure is illustrated by preparing model biotin-capped copolymers. The biotinylated copolymers are shown to self-assemble with an oligonucleotide in aqueous media to form polyion complex micelles with biotin groups at their outer surface. These micelles are capable of molecular recognition toward streptavidin. Alternatively, thiol-decorated (nonderivatized) micelles are prepared and show improved mucoadhesion through the formation of disulfide bonds with mucin. Finally, intermicellar disulfide bonds are generated under oxidative conditions to promote the formation of stimuli-responsive micellar networks.

INTRODUCTION

Colloids which can selectively interact with biological species or surfaces show promise as nanoscopic biosensors, diagnostic tools, and therapeutic devices. For instance, liposomes decorated with monoclonal antibodies are currently being investigated as immunosensors (*1*) and targeted drug carriers (*2*). Other examples include folate-decorated lipid nanoparticles which have been studied for their greater antitumor activity (*3*), and polyester nanoparticles which achieve specific cellular interaction through ligands attached to their surface via avidin−biotin coupling (*4*, *5*). Polymeric micelles (10−100 nm) are yet other examples of colloids which would greatly benefit from surface modification. Polymeric micelles typically result from the self-assembly of amphiphilic copolymers in a selective solvent above a threshold concentration (*6*). Micellization can also proceed through the complexation, neutralization, and self-association of oppositely charged polyions (*7*), these structures being referred to as polyion complex micelles (PICM). Both polymeric micelles and PICM possess core−shell architectures with sequestering capabilities which account for their use as solubilizers (*8*, *9*), DNA delivery vectors (*10*), and bionanoreactors (*11*). If nanocarriers such as micelles have the ability to passively accumulate in specific pathological areas, their therapeutic efficiency can be further enhanced by attaching targeting devices on their surface (*12*, *13*). However, the surface modification of micelles can be very challenging, especially for PICM given that their ionic core components (typically amino or carboxylic acid groups) can interfere with conventional coupling reactions.

Surface-functionalization of colloids with recognition molecules is typically achieved using bifunctional spacers which obey standard acid/amine coupling chemistry. Drawbacks of such procedures include poor labeling efficiency, defects in the tethered structure, and formation of side products which are often difficult to eliminate. An alternative (and preferred) strategy is to synthesize heterotelechelic polymers directly from functionalized initiators. For instance, Bes et al. have used glucose and galactose derivatives to initiate the polymerization poly-(ethylene glycol) (PEG) methyl ether methacrylate and benzyl methacrylate (*14*). The resulting block copolymers were shown to form tethered micelles in the presence of water and were capable of selective affinity for a lectin column. Alternatively, Kataoka's group has devoted significant effort into designing heterobifunctional PEG macroinitiators which can be discriminately modified at one chain end. Among such macroinitiators, α-acetal-ω-methanesulfonate PEG and α-acetal-ω-hydroxyl PEG were successfully used to prepare cationic block copolymers which self-assembled with DNA into acetal- and

* Corresponding author. Tel: (+514) 343-6455. Fax: (+514) 343-6871. E-mail: jean-christophe.leroux@umontreal.ca.
[†] Faculty of Pharmacy, University of Montreal.
[‡] Department of Chemistry, University of Montreal.

10.1021/bc050007b CCC: $30.25 © 2005 American Chemical Society
Published on Web 07/02/2005

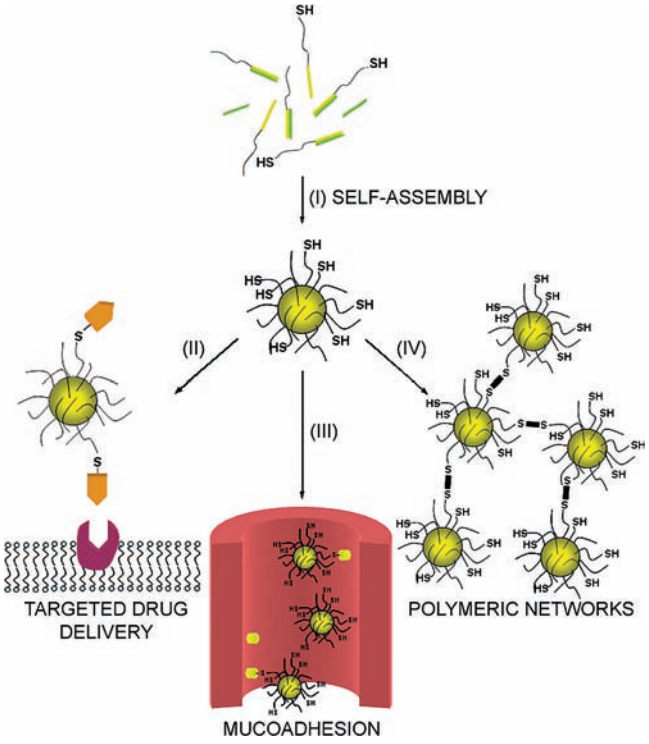

Figure 1. Preparation and uses of thiolated PICM. Oppositively charged copolymers (cationic copolymer shown in yellow and anionic biomacromolecule shown in green) self-assemble in aqueous media into surface-modified polymeric micelles (I). These micelles can be reacted with proteins or antibodies for targeted drug delivery applications (II) or used as such for improved mucoadhesion (through the formation of disulfide bonds with mucus) (III) and formation of redox-sensitive polymeric networks (IV).

aldehyde-decorated PICM (*15*, *16*). In light of this, we propose an alternate synthetic scheme for the preparation of a heterotelechelic macroinitiator possessing a thiol group at one extremity and a hydroxyl group at the other (namely α-*tert*-butanethio-ω-hydroxyl PEG, *t*Bu-S-PEG-OH). This work further illustrates how *t*Bu-S-PEG-*block*-poly((*N,N*-dimethylamino)ethyl methacrylate) (*t*Bu-S-PEG-*b*-PDMAEMA) copolymers can be used to prepare targeted micelles, mucoadhesive assemblies, and redox-sensitive polymeric networks (Figure 1). The synthetic approach proposed herein judiciously takes advantage of thiols for biorelated applications. Terminal thiol groups are very interesting given their ability to react selectively and quantitatively with maleimides or thiols under physiological conditions, thereby facilitating the functionalization of the polymer (*17*, *18*). Thiols have also been used in the biomedical field in order to increase the mucoadhesion of drug delivery systems (*19*) and to stabilize nanoassemblies through the formation of disulfide bridges (*20*).

EXPERIMENTAL PROCEDURES

Materials. A 20-mer antisense phosphorothioate oligodeoxirobonucleotide (ODN; 5′-GTTCTCGCTGGTGAGTTTCA-3′) and its fluorescein-labeled derivative (labeled at the 5′ end via a phosphorothioate bond) were prepared by Medicorp Inc. (Montreal, QC, Canada). Streptavidin-coated plates (binding capacity of ≥12 pmol biotin per well) were obtained from Thermo Electron Corporation (Vantaa, Finland). Porcine stomach mucin immobilized on a polygalactose gel was purchased from EY Laboratories Inc. (San Mateo, CA) and transferred to Bio-Spin chromatography columns (Bio-Rad Laboratories Ltd, Mississauga, ON, Canada). The 4-hydroxyazobenzene-2-carboxylic acid reagent (HABA; used for the spectrometric determination of biotin levels) was bought as a ready-to-use HABA/avidin lyophilized powder (Sigma-Aldrich Canada Ltd, Oakville, ON, Canada). All other chemicals were purchased from Sigma-Aldrich and used as received, except for the following: tetrahydrofuran (THF) was dried over sodium with benzophenone as indicator; *tert*-butyl mercaptan was dried over calcium oxide, distilled under argon, and stored over molecular sieves; ethylene oxide (EO) was passed through a sodium hydroxide column, dried over CaH_2, and cryodistilled prior to use; triethylamine was dried over potassium hydroxide and purified by distillation; 2-(*N,N*-dimethylamino)ethyl methacrylate (DMAEMA) was vacuum-distilled prior to polymerization.

Techniques. ^{1}H NMR spectra were recorded on a Bruker NMR spectrometer operating at 300 MHz. Solutions were either prepared in deuterated chloroform ($CDCl_3$) or water (D_2O). Gel permeation chromatography (GPC) measurements were performed in THF using an Alliance GPCV 2000 system (Waters, Milford, MA) equipped with a differential refractive index detector. Adequate molecular weight separation was achieved using three Waters Styragel columns (HR1, HR3, and HR4) in series at a flow rate of 1.0 mL/min and a temperature of 40 °C. A calibration curve was obtained with near-monodisperse PEG standards. The mean hydrodynamic diameter, size distribution, and scattering intensity of the micelles were determined using a Malvern Autosizer 4800 equipped with a 488-nm uniphase argon-ion laser (Malvern Instruments, Worcestershire, U.K.). Measurements were performed in triplicate at a scattering angle of 90° and a temperature of 25 °C. The CONTIN program was used to extract size distributions from the autocorrelation functions.

Synthesis of Asymmetric *t*Bu-S-PEG-OH. *tert*-Butyl mercaptan was used to initiate the anionic polymerization of EO in the presence of various molar ratios of potassium naphthalene. Anhydrous THF, potassium naphthalene (0.3 M solution in THF), and *tert*-butyl mercaptan were loaded into a sealed 100-mL round-bottom flask. The components were allowed to react for at least 10 min to ensure the formation of thiolates (evidenced as white precipitates), at which point liquid EO was added using a two-head needle. The polymerization reaction was carried out for 48 h, and the product was recovered by precipitation in diethyl ether. ^{1}H NMR ($CDCl_3$) δ (ppm): 3.68 (250H, m, $(CH_2CH_2O)_n$), 2.75 (2H, t, $CH_2SC(CH_3)_3$), 1.89 (s, CH_2CH_2OH), 1.33 (9H, s, $CH_2SC(CH_3)_3$). Trifluoroacetic anhydride was added to the NMR tube in order to shift the signal of the methylene group adjacent to the terminal hydroxyl group and allow for the determination of the thiol functionalization degree. ^{1}H NMR ($CDCl_3$ with 7.5% (v/v) trifluoroacetic anhydride) δ (ppm): 4.50 (2H, t, CH_2OCOCF_3), 3.68 (250H, m, $(CH_2CH_2O)_n$), 2.75 (2H, t, $CH_2SC(CH_3)_3$), 1.33 (9H, s, $CH_2SC(CH_3)_3$).

Synthesis of Block Ionomers. PEG ($M_n = 2000$, $M_w/M_n = 1.08$) and *t*Bu-S-PEG-OH ($M_n = 2900$, $M_w/M_n = 1.03$) were converted to atom transfer radical polymerization (ATRP) macroinitiators by reaction with 2-bromoisobutyryl bromide *(21)*. Basically, PEG was dissolved in anhydrous THF and stirred for 15 min in the presence of triethylamine (10 equiv). 2-Bromoisobutyryl bromide (4 equiv) was then added dropwise and the reaction carried out for 48 h at room temperature. The crude product was solubilized in dichloromethane and purified by successive washings with 10% HCl, 1 N NaOH, and brine.

The organic phase was dried over magnesium sulfate and the ATRP macroinitiator precipitated in diethyl ether. The polymerization reactions were then carried out as follows: the macroinitiator (1 equiv), DMAEMA (15 equiv), *N*,*N*,*N*′,*N*′,*N*″-pentamethyldiethylenetriamine (1.4 equiv), and Cu(I)Br (0.7 equiv) were solubilized in THF and degassed for 20 min with argon. The polymerization reaction was initiated by bringing the reaction medium to 60 °C for 16 h, after which the copper catalyst was removed by filtration through a silica gel column. Polymers were purified by dialysis (molecular weight cutoff of 3500) and recovered by freeze-drying. MeO-PEG_{45}-*b*-$PDMAEMA_{17}$: $M_n = 4800$, $M_w/M_n = 1.23$. ^{1}H NMR (D_2O) δ (ppm): 4.14 (34H, broad s, $COOCH_2CH_2N(CH_3)_2$), 3.67 (180H, m, $(CH_2CH_2O)_n$), 3.35 (3H, s, $CH_3O(CH_2CH_2O)_n$), 2.71 (34H, broad s, $COOCH_2CH_2N(CH_3)_2$), 2.30 (102H, broad s, $COOCH_2CH_2N(CH_3)_2$), 2.10−1.70 (34H, m, $(CH_2C(CH_3))_n$), 1.20−0.78 (6H, s, $C(CH_3)_2(CH_2C(CH_3))_n$) + 51H, m, $(CH_2C(CH_3))_n$)). *t*Bu-PEG_{66}-*b*-$PDMAEMA_{15}$: M_n = 5300, $M_w/M_n = 1.11$. ^{1}H NMR (D_2O) δ (ppm): 4.14 (30H, broad s, $COOCH_2CH_2N(CH_3)_2$), 3.67 (264H, m, $(CH_2CH_2O)_n$), 2.70 (30H, broad s, $COOCH_2CH_2N(CH_3)_2$), 2.30 (90H, broad s, $COOCH_2CH_2N(CH_3)_2$), 2.10−1.70 (30H, m, $(CH_2C(CH_3))_n$), 1.30 (9H, s, $(CH_3)_3S(CH_2CH_2O)_n$), 1.20−0.78 (6H, s, $C(CH_3)_2(CH_2C(CH_3))_n$) + 45H, m, $(CH_2C(CH_3))_n$)).

Synthesis of Thiol-Terminated Block Ionomer. The terminal thiol group was recovered by successive cleavage of the *t*Bu unit in DMSO/trifluoroacetic acid (TFA) (*22*) and reduction of the disulfide bond obtained thereafter. The polymer was first dissolved in a 10/90 (v/v) mixture of DMSO/TFA to a final polymer concentration of 20 mg/mL. The deprotection reaction was conducted for 3 h, after which the TFA was removed by rotary evaporation. The crude polymer extract was then purified by dialysis (to remove all traces of DMSO) and the product recovered by freeze-drying. This procedure allowed for the conversion of the *t*Bu-PEG_{66}-*b*-$PDMAEMA_{15}$ to its disulfide analogue. Free thiol groups were generated by reacting the oxidized polymer with an excess of sodium borohydride in ethanol for 16 h. The reaction was stopped by the addition of a 10% HCl/ethanol solution and the solvent removed under reduced pressure. The thiolated polymer was purified by passage through a Sephadex G25 column and recovered by freeze-drying. The thiol loading was determined to be 82 μmol/g of polymer using Ellman's reagent (the loading was calculated against a cysteine calibration curve).

Synthesis of Biotin-Terminated Block Ionomers. The thiolated polymer was dissolved in degassed phosphate-buffered saline pH 7.4 to a final polymer concentration of 5 mg/mL. Biotin-maleimide (4-fold excess) was then added, and the coupling reaction was carried out overnight. The excess biotin was removed by passage through a Sephadex G25 column and the polymer recovered by freeze-drying. The amount of biotin in the copolymers was determined by monitoring the change in absorbance accompanying the displacement of HABA by biotin from the HABA/avidin complex. The coupling efficiency was calculated to be 97%.

Preparation of PICM. The copolymers (PEG_{45}-*b*-$PDMAEMA_{17}$, HS-PEG_{66}-*b*-$PDMAEMA_{15}$, or biotin-PEG_{66}-*b*-$PDMAEMA_{15}$) and the ODN were separately dissolved in 10 mM Tris HCl pH 7.4. PICM were obtained by addition of the copolymer solution to the ODN solution to a final N/P ratio of 1.5.

Molecular Recognition Experiments. Biotinylated (with 5 mol % biotin-PEG_{66}-*b*-$PDMAEMA_{15}$) and nonbiotinylated PICM were prepared using the fluorescently labeled ODN. The complexes were loaded into streptavidin-coated wells in the presence or absence of free biotin (6-fold excess) and allowed to react for 1 h at 37 °C. Unbound micelles were removed by three washings with a 50 mM phosphate buffer at pH 6.8. The proportion of bound micelles was evaluated by dosing the fluorescence of the ODN using a Safire plate reader (Tecan, Medford, MA; $\lambda_{ex} = 494$ nm, $\lambda_{em} = 518$ nm). Significant differences between the binding of the groups were evaluated by analysis of variance followed by Dunnett's multiple comparison test. Data were considered to differ significantly when $p < 0.05$.

Mucoadhesion Experiments. Immobilized porcine stomach mucin was treated with 25 mM dithiothreitol and extensively washed to generate free thiol groups. Thiolated (with 25 mol % HS-PEG_{66}-*b*-$PDMAEMA_{15}$) and nonthiolated PICM were immediately applied to the resin in the presence or absence of exogenous thiols (100-fold excess cystein) and allowed to react for 1 h at 37 °C. Unbound micelles were eluted by successive washings with 10 mM Tris HCl pH 7.4. The fluorescent ODN was dosed in each elution fraction to evaluate the proportion of bound micelles. At the end of the experiment, the ODN was massively eluted using a 0.1 M carbonate solution at pH 10 (condition known to disrupt micelles (*23*)) to recover 100% of the applied material.

Aggregation of Thiolated Micelles. The sensitivity of thiolated (with 50 mol % HS-PEG_{66}-*b*-$PDMAEMA_{15}$) PICM toward oxidative (air) conditions was monitored by measuring time-dependent changes in their mean hydrodynamic diameter by dynamic light scattering (DLS). Nonthiolated PICM served as a reference. The effect of exogeneous thiols and an antioxidant on micelle aggregation was evaluated by preparing thiolated micelles in the presence of 5 mM mercaptoethanol and 2.8 mM ascorbic acid, respectively.

RESULTS AND DISCUSSION

Polymer Synthesis. The proposed synthetic route allows for the preparation of a thiol-terminated PEG-*b*-PDMAEMA copolymer from a *t*Bu-S-PEG-OH macroinitiator (Scheme 1). *t*Bu-S-PEG-OH was synthesized by initiating the anionic polymerization of EO with *tert*-butyl mercapatan. Potassium naphthalene was used to activate the sulfhydryl and was found to have an effect not only on the reaction kinetics but also on the degree of end functionalization. It is seen in Figure 2 that a potassium naphthalene/*tert*-butyl mercaptan molar ratio of 1/1 yields complete monomer conversion but is very sensitive to water contaminants (with only 23% of the chains possessing a terminal thiol group). By reducing the proportion of potassium naphthalene, it is possible to gain control over the selectivity of the initiation reaction. However, this is achieved at the expense of the monomer conversion which only reaches 57% (when the potassium naphthalene/*tert*-butyl mercaptan ratio is 0.4/1). Subsequent reactions were therefore conducted using 50 mol % potassium naphthalene, as this metalation level gave nearly quantitative degrees of thiol functionalization (>95%) while maintaining a reasonable rate of polymerization. Polymers with molecular weight distributions lower than 1.05 were typically obtained. The molecular weight of the *t*Bu-S-PEG-OH polymer was controlled by varying the monomer to initiator molar ratio. A typical ^{1}H NMR spectrum of *t*Bu-S-PEG-OH in $CDCl_3$ is presented in Figure 3A. The peak of the *tert*-butyl protons is seen at 1.32 ppm while that of the methylene protons

Scheme 1. Synthetic Route to the Preparation of Thiol-Terminated and Biotin-Terminated Block Ionomers

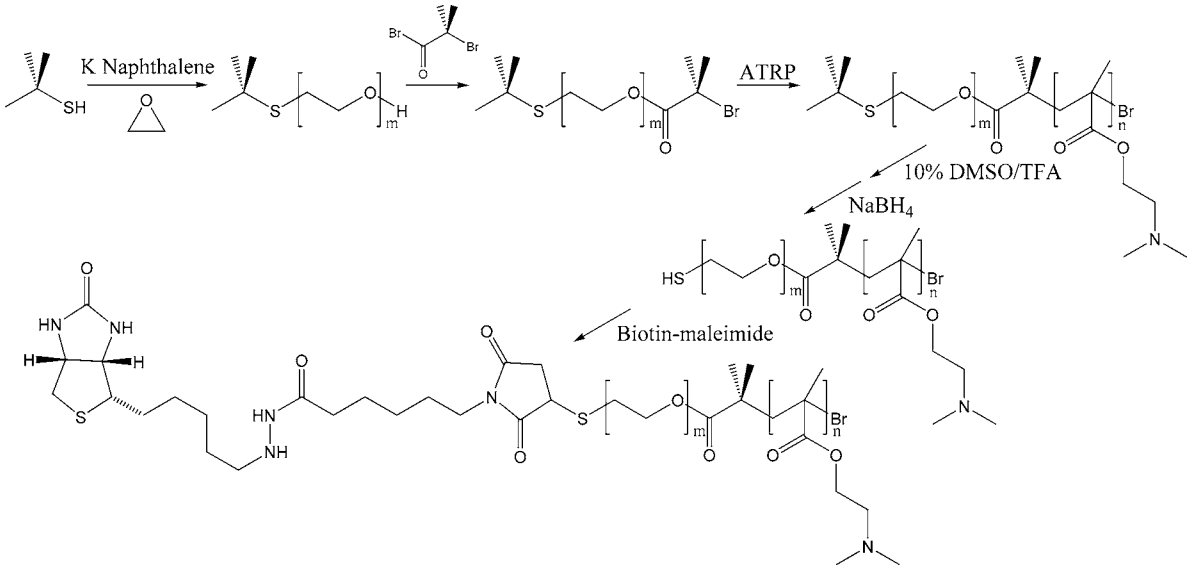

adjacent to the thioether appears at 2.74 ppm. The degree of end functionalization was estimated by derivatizing the hydroxyl group of *t*Bu-S-PEG-OH to a trifluoroacetate using trifluoroacetic anhydride (*24*). The formation of the trifluoroacetate shifted the peak of the adjacent methylene group downfield, thus separating it from the other methylene protons of PEG and allowing its quantification relative to the *tert*-butyl group.

PEG monomethoxyether and *t*Bu-S-PEG-OH were then converted to ATRP macroinitiators and used to prepare copolymers with varying PEG/DMAEMA molar ratios (*25*). More specifically, the copolymers selected for this study were composed of MeO-PEG_{45}-*b*-$PDMAEMA_{17}$ ($M_w/M_n = 1.23$) and *t*Bu-S-PEG_{66}-*b*-$PDMAEMA_{15}$ ($M_w/M_n = 1.11$). The *t*Bu-S-PEG-OH segment ($M_n = 2900$) was designed to be longer than the PEG monomethoxyether ($M_n = 2000$) so that the thiol groups or ligands would protrude from the micelle surface and be readily available for interaction. Indeed, studies conducted on PEGylated liposomes modified with a transduction protein revealed that the ligand needed to be accessible and nonshielded for efficient cellular interaction (*26*). In turn, the number of DMAEMA units was kept below 20. PICM prepared from polymers with longer DMAEMA chain lengths yielded aggregated micelles with broader size distributions (data not shown). Figure 3B presents the ^{1}H NMR spectrum of *t*Bu-S-PEG_{66}-*b*-$PDMAEMA_{15}$ in D_2O, where the terminal *tert*-butyl protons are clearly seen at 1.30 ppm. The terminal thiol group was recovered by cleavage of the *tert*-butyl group in oxidative conditions (DMSO/TFA) followed by reduction of the disulfide bond thereby obtained.

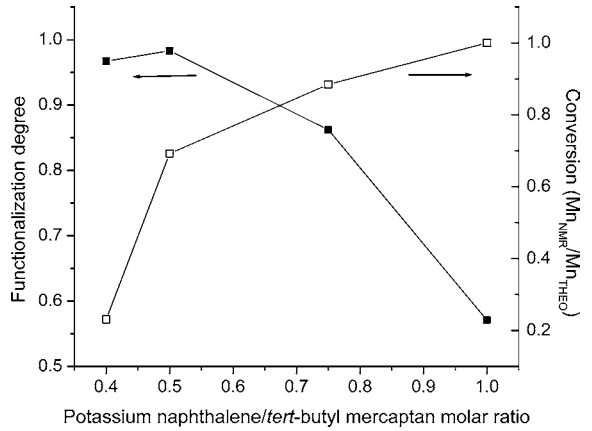

Figure 2. Effect of the potassium naphthalene/*tert*-butyl mercaptan molar ratio on the chain end functionalization and monomer conversion.

Molecular Recognition. A copolymer capped with biotin was prepared to demonstrate the ease with which targeted micelles can be generated. The functionalized copolymer was obtained through the direct coupling of HS-PEG_{66}-*b*-$PDMAEMA_{15}$ with a maleimide derivative of biotin. PICM composed of 5 mol % biotin-PEG_{66}-*b*-$PDMAEMA_{15}$, PEG_{45}-*b*-$PDMAEMA_{17}$, and the fluorescein-labeled ODN were prepared and found to have diameters of ~50 nm. Similar micelles made of PEG_{45}-*b*-$PDMAEMA_{17}$ and heparin (as the polyanion) have been previously prepared and shown to self-assemble into spherical entities, as determined by atomic force microscopy (*23*). The ability of the biotinylated PICM to molecularly recognize streptavidin was studied by loading the micelles into streptavidin-coated wells. The proportion of

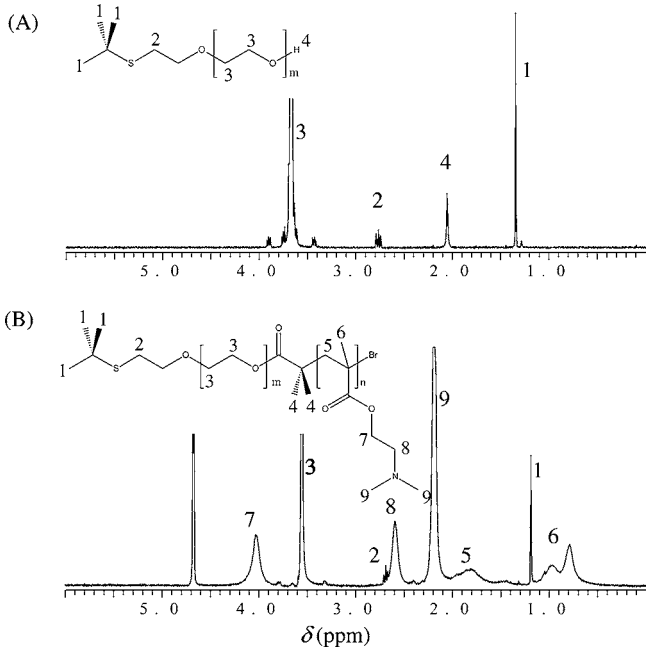

Figure 3. ^{1}H NMR spectra of *t*Bu-S-PEG-OH in $CDCl_3$ (A) and *t*Bu-S-PEG-*b*-PDMAEMA in D_2O (B).

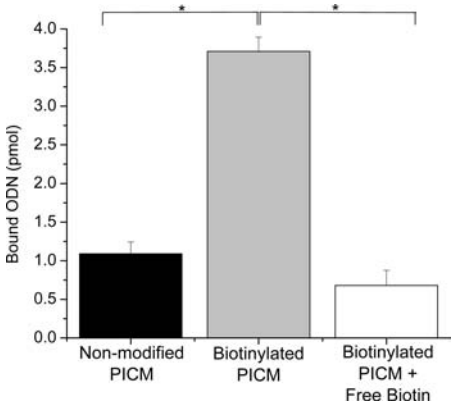

Figure 4. Affinity experiment showing the ability of biotinylated PICM to molecularly recognize streptavidin. Biotinylated micelles bound preferentially to streptavidin relative to nonmodified micelles. Binding of the biotinylated micelles was hindered in the presence of a 6-fold excess free biotin. Mean ± SD ($n = 4$), * $p < 0.05$, Dunnett test.

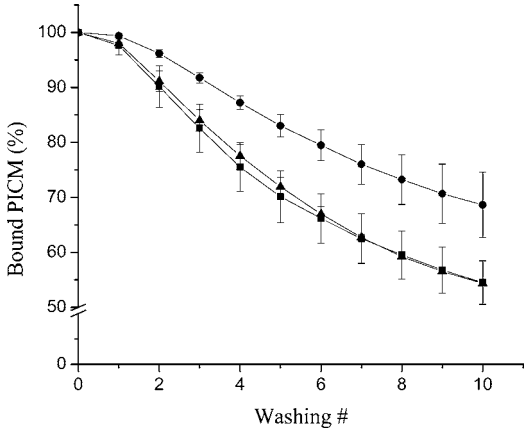

Figure 5. Retention of nonthiolated PICM (square) and thiolated PICM (circle) on an immobilized mucin matrix as a function of the number of washings. Thiolated PICM were also loaded on the resin in the presence of exogenous thiols (triangle) to evidence the role of the formation of disulfide bonds in the mucoadhesion. The quantity of bound micelles is expressed relative to the amount loaded. Mean ± SD ($n = 3$).

bound micelles was evaluated by dosing the fluorescence of the ODN. The latter is representative of the amount of adhered PICM, given that it is a structural component of the micelles. Figure 4 reveals that the adhesion of PICM bearing 5 mol % biotin to streptavidin increased by a factor of 4 relative to biotin-free micelles. This result suggests that, as expected, the biotin molecules are located at the surface of the micelles and are available for interaction. The nonspecific binding observed for the nontargeted micelles probably results from electrostatic interactions between streptavidin and the micelle core components. As shown in Figure 4, the binding of the biotinylated PICM was greatly reduced in the presence of free biotin, confirming the specificity of the interaction. Such a protocol could be applied for the straightforward attachment of other homing devices including monoclonal antibodies and peptides via thioether linkages.

Mucoadhesion. Another application stemming from the presence of surface sulfhydryl groups is the preparation of mucoadhesive particles for peroral drug delivery. Work by Bernkop-Schnürch and co-workers (*19*) suggests that it is possible to increase the residence time of a drug delivery system in the gastrointestinal tract by modifying it with thiol groups. Surface-exposed thiols are thought to form disulfide bonds with cysteine-rich subdomains of mucus glycoproteins (*27*). We have therefore evaluated the ability of thiolated PICM to covalently bind mucin. Figure 5 presents the elution profile of thiolated and nonthiolated micelles applied on a mucin matrix. While 70% of the thiolated micelles were still found to adhere to the matrix after 10 washings, half of the nonthiolated micelles were released by that time. The improved mucoadhesion of the thiolated micelles can be ascribed to their increased interaction with mucin. Although seemingly marginal, this difference in mucoadhesion is in fact appreciable, considering that PEG itself is oftentimes used as an adhesion promoter. For instance, De Ascentiis et al. found that incorporation of PEG chains in poly(2-hydroxyethyl methacrylate) microspheres significantly improved their mucoadhesion due to the penetration of the PEG chains across the mucosa−polymer interface (*28*). Likewise, Shojaei et al. were able to enhance the mucoadhesion of poly(acrylic acid) films by adding PEG chains to the formulation (*29*). In light of this, it is not surprising that the nonthiolated micelles themselves displayed mucoadhesion. Another consideration is the fact that the thiolated micelles examined in this study possessed a lower thiol density (30 μmol thiol/g of micelles) than other thiolated systems studied in the literature (400−780 μmol thiol/g of polymer) (*27*). Figure 5 also reveals that the adhesion of the functionalized PICM was impaired in the presence of a large excess of cysteine, with the thiolated micelles displaying an elution profile equivalent to that of the nonthiolated micelles. This observation reinforces the concept of mucoadhesion being promoted by the formation of disulfide bonds between the mucin and particle. Indeed, free cysteine molecules act as disulfide bond breaking agents which could cleave or prevent the formation of disulfide bonds between the mucin and micelles. However, the thiolated micelles maintained their ability to bind to mucin in the presence of a small excess of cysteine (data not shown), suggesting that in vivo mucoadhesion may not be affected by the presence of protein digests.

Aggregation of Thiolated Micelles. If covalent bonds were formed between thiol-decorated micelles and the mucus, it is likely that they will also form between micelles. This was confirmed by studying the time-dependent stability of thiolated and nonthiolated micelles. The initial hydrodynamic diameter of the nonthiolated micelles was 60 nm while that of the thiolated micelles was 45 nm. The difference in size can be attributed to the different EO to DMAEMA molar ratios of the copolymers. A representation of the size distribution of the thiolated micelles prior to oxidation is given in Figure 6A. A marked association of the thiolated micelles occurred after 6 h in oxidative (air) conditions, as observed by an increase of their mean diameter (Figure 6B). This aggregation was delayed in the presence of 2-mercaptoethanol and hindered in the presence of ascorbic acid (an antioxidant), clearly demonstrating that it is driven by the formation of intermicellar disulfide bonds. Furthermore, treatment with 15 mM dithiothreitol promoted the dissociation of the aggregates. The size of the micellar assemblies went from 100 to 65 nm within minutes of treatment with dithiothreitol, demonstrating the redox sensitivity of the system. Concomitantly, the reduction in size was associated with a marked decrease of the polydispersity index of the micelles (0.17 vs. 0.07). The aggregation of the chains achieved through disulfide bridges is potentially interesting for the design of depot formulations and eventually hydrogels. It can be hypothesized that covalently bridged micelles administered subcutaneously could be individually released in a sus-

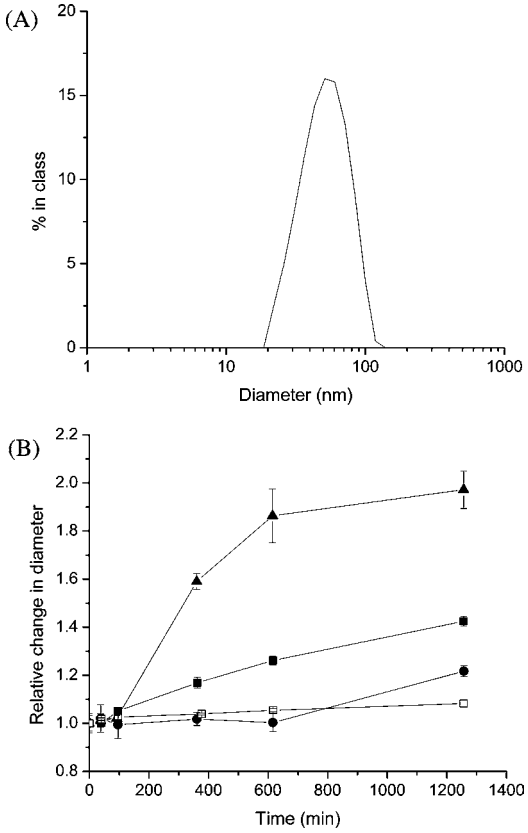

Figure 6. (A) Representation of the size distribution of thiolated micelles prior to oxidation. (B) Variations in the hydrodynamic diameters of nonthiolated PICM (open square) and thiolated PICM (triangle) as a function of time as determined by DLS. The presence of 5 mM 2-mercaptoethanol (square) and 2.8 mM ascorbic acid (circle) hindered the formation of disulfides between micelles. Changes in the hydrodynamic diameter of the micelles are normalized to their initial values for ease of comparison. Mean ± SD ($n = 3$).

tained fashion upon cleavage of the disulfide bonds in the reducing extracellular environment. These results further indicate that, when oral applications are sought, the thiolated micelles could be stored in the presence of an antioxidant to preserve their integrity and mucoadhesive activity.

CONCLUSION

This work demonstrates the ease with which thiol-bearing PICM can be prepared and tailored for specific applications. The thiol groups were reacted with a maleimide derivative of biotin to produce targeted nanoparticles capable of molecular recognition. Alternatively, the thiol-decorated micelles were used as such to improve the mucoadhesion of the system or to form stimuli-responsive micellar networks fitted as a depot formulation. This synthetic approach could be easily adapted to the preparation of thiolated anionic or amphiphilic block copolymers and will undoubtedly facilitate the preparation of various surface-modified nanoparticles.

ACKNOWLEDGMENT

This work was financially supported by the Natural Sciences and Engineering Research Council of Canada, and the Canada Research Chair Program. M.H.D. and M.A.G. further acknowledge graduate research scholarships from Fonds Québécois de la Recherche sur la Nature et les Technologies.

LITERATURE CITED

(1) Hianik, T., Snejdarkova, M., Sokolikova, L., Meszar, E., Krivanek, R., Tvarozek, V., Novotny, I., and Wang, J. (1999) Immunosensors based on supported lipid membranes, protein films and liposomes modified by antibodies. *Sens. Actuators, B. 57*, 201−212.

(2) Lukyanov, A. N., Elbayoumi, T. A., Chakilam, A. R., and Torchilin, V. P. (2004) Tumor-targeted liposomes: doxorubicin-loaded long-circulating liposomes modified with anticancer antibody. *J. Controlled* Release *100*, 135−144.

(3) Stevens, P. J., Sekido, M., and Lee, R. J. (2004) A folate receptor-targeted lipid nanoparticle formulation for a lipophilic paclitaxel prodrug. *Pharm. Res. 21*, 2153−2157.

(4) Gref, R., Couvreur, P., Barratt, G., and Mysiakine, E. (2003) Surface-engineered nanoparticles for multiple ligand coupling. *Biomaterials 24*, 4529−4537.

(5) Nobs, L., Buchegger, F., Gurny, R., and Allémann, E. (2004) Poly(lactic acid) nanoparticles slabeled with biologically active Neutravidin for active targeting. *Eur. J. Pharm. Biopharm. 58*, 483−490.

(6) Allen, C., Maysinger, D., and Eisenberg, A. (1999) Nano-engineering block copolymer aggregates for drug delivery. *Colloids Surf. B: Biointerfaces 16*, 3−27.

(7) Harada, A., and Kataoka, K. (1999) Chain length recognition: core−shell supramolecular assembly from oppositely charged block copolymers. *Science 283*, 65−67.

(8) Le Garrec, D., Ranger, M., and Leroux, J. C. (2004) Micelles in anticancer delivery. *Am. J. Drug Delivery 2*, 15−42.

(9) Kwon, G. S. (2003) Polymeric micelles for drug delivery of poorly water-soluble compounds. *Crit. Rev. Ther. Drug Carrier Syst. 20*, 357−403.

(10) van de Wetering, P., Cherng, J.-Y., Talsma, H., Crommelin, D. J. A., and Hennink, W. E. (1998) 2-(Dimethylamino)ethyl methacrylate based (co)polymers as gene transfer agents. *J. Controlled Release 53*, 145−153.

(11) Jaturanpinyo, M., Harada, A., Yuan, X., and Kataoka, K. (2004) Preparation of bionanoreactor based on core−shell structured polyion complex micelles entrapping trypsin in the core cross-linked with glutaraldehyde. *Bioconjugate Chem. 15*, 344−348.

(12) Torchilin, V. P., Lukyanov, A. N., Gao, Z., and Papahadjopoulos-Sternberg, B. (2003) Immunomicelles: targeted pharmaceutical carriers for poorly soluble drugs. *Proc. Natl. Acad. Sci. U.S.A. 100*, 6039−6044.

(13) Merdan, T., Callahan, J., Petersen, H., Kunath, K., Bakowsky, U., Kopecková, P., Kissel, T., and Kopecek, J. (2003) Pegylated polyethylenimine-Fab′ antibody fragment conjugates for targeted gene delivery to human ovarian carcinoma cells. *Bioconjugate Chem. 14*, 989−996.

(14) Bes, L., Angot, S., Limer, A., and Haddleton, D. M. (2003) Sugar-coated amphiphilic block copolymer micelles from living radical polymerization: recognition by immobilized lectins. *Macromolecules 36*, 2493−2499.

(15) Kataoka, K., Harada, A., Wakebayashi, D., and Nagasaki, Y. (1999) Polyion complex micelles with reactive aldehyde groups on their surface from plasmid DNA and end-functionalized charged block copolymers. *Macromolecules 32*, 6892−6894.

(16) Wakebayashi, D., Nishiyama, N., Itaka, K., Miyata, K., Yamasaki, Y., Harada, A., Koyama, H., Nagasaki, Y., and Kataoka, K. (2004) Polyion complex micelles of pDNA with acetal-poly(ethylene glycol)-poly(2-(dimethylamino)ethyl methacrylate) block copolymer as the gene carrier system: physicochemical properties of micelles relevant to gene transfection efficacy. *Biomacromolecules 5*, 2128−2136.

(17) van Dijk-Wolthuis, W. N. E., van de Wetering, P., Hinrichs, W. L. J., Hofmeyer, L. J. F., Liskamp, R. M. J., Crommelin, D. J. A., and Hennink, W. E. (1999) A versatile method for the conjugation of proteins and peptides to poly[2-(dimethylamino)ethyl methacrylate]. *Bioconjugate Chem. 10*, 687−692.

(18) Nobs, L., Buchegger, F., Gurny, R., and Allémann, E. (2003) Surface modification of poly(lactic acid) nanoparticles by covalent attachment of thiol groups by means of three methods. *Int. J. Pharm. 250*, 327−337.

(19) Bernkop-Schnürch, A., Krauland, A. H., Leitner, V. M., and Palmberger, T. (2004) Thiomers: potential excipients for non-invasive peptide delivery systems. *Eur. J. Pharm. Biopharm. 58*, 253−263.

(20) Kakizawa, Y., Harada, A., and Kataoka, K. (2001) Glutathione-sensitive stabilization of block copolymer micelles composed of antisense DNA and thiolated poly(ethylene glycol)-*block*-poly(L-lysine): a potential carrier for systemic delivery of antisense DNA. *Biomacromolecules 2*, 491−497.

(21) Ranger, M., Jones, M. C., Yessine, M. A., and Leroux, J. C. (2001) From well-defined diblock copolymers prepared by a versatile atom transfer radical polymerization method to supramolecular assemblies. *J. Polym. Sci., Part A: Polym. Chem. 39*, 3861−3874.

(22) Cuthbertson, A., and Indrevoll, B. (2003) Regioselective formation, using orthogonal cysteine protection, of an α-conotoxin dimer peptide containing four disulfide bonds. *Org. Lett. 5*, 2955−2957.

(23) Dufresne, M. H., and Leroux, J. C. (2004) Study of the micellization behavior of different order amino block copolymers with heparin. *Pharm. Res. 21*, 160−169.

(24) Jo, S., Shin, H., Shung, A. K., Fisher, J. P., and Mikos, A. G. (2001) Synthesis and characterization of oligo(poly(ethylene glycol) fumarate) macromer. *Macromolecules 34*, 2839−2844.

(25) Coessens, V., Pintauer, T., and Matyjaszewski, K. (2001) Functional polymers by atom transfer radical polymerization. *Prog. Polym. Sci. 26*, 337−377.

(26) Torchilin, V. P., Rammohan, R., Weissig, V., and Levchenko, T. S. (2001) TAT peptide on the surface of liposomes affords their efficient intracellular delivery even at low temperature and in the presence of metabolic inhibitors. *Proc. Natl. Acad. Sci. U.S.A. 98*, 8786−8791.

(27) Leitner, V. M., Walker, G. F., and Bernkop-Schnürch, A. (2003) Thiolated polymers: evidence for the formation of disulphide bonds with mucus proteins. *Eur. J. Pharm. Biopharm. 56*, 207−214.

(28) De Ascentiis, A., deGrazia, J. L., Bowman, C. N., Colombo, P., and Peppas, N. A. (1995) Mucoadhesion of poly(2-hydroxyethyl methacrylate) is improved when linear poly(ethylene oxide) chains are added to the polymer network. *J. Controlled Release 33*, 197−201.

(29) Shojaei, A. H., and Li, X. (1997) Mechanisms of buccal mucoadhesion of novel copolymers of acrylic acid and polyethyleneglycol monomethylether monomethacrylate. *J. Controlled Release 47*, 151−161.

BC050007B

Polyelectrolyte Complex Micelles Composed of *c-raf* Antisense Oligodeoxynucleotide−Poly(ethylene glycol) Conjugate and Poly(ethylenimine): Effect of Systemic Administration on Tumor Growth

Ji Hoon Jeong,[†] Sun Hwa Kim,[†] Sung Wan Kim,[‡] and Tae Gwan Park*,[†]

Department of Biological Sciences, Korea Advanced Institute of Science and Technology, Daejeon 305-701, Korea (South), and Center for Controlled Chemical Delivery (CCCD)/Department of Pharmaceutics and Pharmaceutical Chemistry, University of Utah, Salt Lake City, Utah 84112. Received November 9, 2004; Revised Manuscript Received May 5, 2005

An antisense oligodeoxynucleotide (ODN) delivery system based on polyelectrolyte complex (PEC) micelles composed of an ODN−poly(ethylene glycol) (PEG) conjugate and polyethylenimine (PEI) was demonstrated. The PEC micelles having a core/shell structure were spontaneously formed in an aqueous solution by ionic interactions between ODN part in the conjugate and PEI. The ODN/PEI polyelectrolyte complex formed an inner core while PEG chains surrounded it as a shell. The morphology of the micelles was visualized as a separate sphere by atomic force microscopy (AFM). When the micelles containing a *c-raf* antisense ODN were intravenously administered into tumor-bearing nude mice, significant antitumor activities against human lung cancer were observed. The intravenously injected micelles also showed significantly higher accumulation level in the solid tumor region compared to that of naked ODN.

INTRODUCTION

Novel drug delivery systems based on self-assembled polymeric micelles have drawn much attention due to their unique properties in therapeutic applications (*1*−*6*). Polymeric micelles, mostly prepared from various hydrophobic and hydrophilic A−B type di-block copolymers, are generally composed of a hydrophobic core and a surrounding hydrophilic shell (*7*, *8*). Alternatively, polyelectrolyte complex micelles were prepared by using a di-block copolymer composed of a charged polymer segment and a hydrophilic PEG segment. Macromolecules having counterions were interacted to form a polyelectrolyte complex core with generating a PEG shell. The small size (usually less than 100 nm) and surrounding hydrophilic corona structure provide the micelles with a possibility to escape from opsonization and the clearance by reticuloendothelial system (RES) (*9*, *10*). These properties also permit the micellar carriers to have enhanced permeability through loosened interendothelial junctions in the vicinity of solid tumors (*11*).

Antisense ODN has been thought to be a promising therapeutic agent for treatment of various diseases including cancer. However, the therapeutic effect of antisense ODN in vivo has not been as efficient as expected due to several inherent properties of ODN, which are susceptibility to enzymatic degradation and limited uptake into target tissue (*12*−*14*). To improve the cellular uptake, various kinds of cationic carriers were utilized to produce nanosized complex particulates that can be more readily endocytosed into cells than naked ODN. The formation of polyelectrolyte complexes between ODN and cationic lipids or polymers was a prerequisite step for enhancing the cellular uptake. Among the cationic polymers, PEG-*b*-poly(L-lysine) di-block copolymer (*15*) and PEG-grafted PEI (*16*) were used to form polyelectrolyte complex (PEC) micelles by interacting with ODN. These systems could provide ODN with an improved stability against nuclease attacks (*17*). Nevertheless, the stability of the polyelectrolyte complex micelles in the bloodstream has been issued as a major obstacle for in vivo applications (*18*).

Previously, we have shown efficient *c-myb* and *c-raf* antisense ODN delivery systems based on PEC micelles, which were formed by combining ODN−PEG conjugate and cationic fusogenic peptide (*19*) or polycations (PEI, poly(L-lysine), and protamine) (*19*, *20*). The PEC micelles having a spherical shape with about 70 nm in diameter could be efficiently transported within cells and could significantly inhibit the growth of smooth muscle cells and tumor cells in a dose-dependent manner. Moreover, when the PEC micelles containing *c-raf* ODN were administered intratumorally, they exhibited superior tumor suppression effect compared to naked ODN. In this study, *c-raf* antisense ODN PEC micelles were administered intravenously using an animal tumor model to explore their antitumor activities and tissue distribution behaviors.

EXPERIMENTAL PROCEDURES

Materials. Twenty-base oligonucleotides (ODN) with 5′-terminal amine group (antisense *c-raf* ODN, TCCCGCCTGTGACATGCATT; random ODN, TCACATTGGCGCTTAGC-CGT) and fluorescence-labeled *c-raf* ODN (AATGCATGTCACAGGCGGGA) with a complementary sequence to antisense *c-raf* ODN were purchased from Bioneer (Daejeon, Korea). *N*-Hydroxylsuccinimide-derivatized methoxy-poly(ethylene glycol) (mPEG-NHS,

* To whom correspondence should be addressed. Tel: +82-42-869-2621, Fax: +82-42-869-2610, E-mail: tgpark@kaist.ac.kr.
[†] Korea Advanced Institute of Science and Technology.
[‡] University of Utah.

10.1021/bc0497315 CCC: $30.25 © 2005 American Chemical Society
Published on Web 06/18/2005

Scheme 1. A Synthetic Scheme of ODN−PEG Conjugate

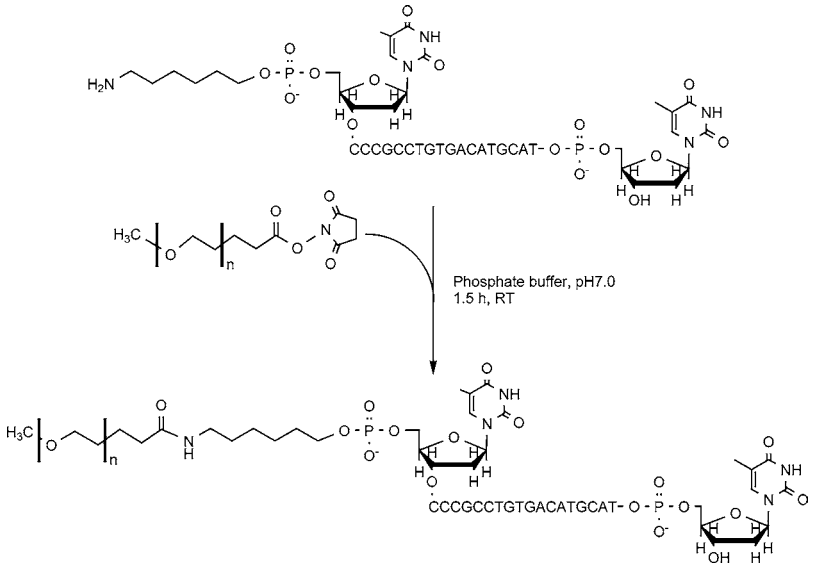

MW 2000) was obtained from Nektar (Huntsville, AL). Polyethylenimine (branched PEI, MW 25 000) was purchased from Aldrich (Milwaukee, WI). Cell culture materials, Roswell Park Memorial Institute 1640 medium (RPMI 1640), and fetal bovine serum (FBS) were purchased from Invitrogen (Carlsbad, CA). All other chemicals were of analytical grade and used without further purification.

Synthesis of ODN−PEG Conjugate. To synthesize ODN−PEG conjugate, 5′-amine-derivatized ODN (1 mg, 180 nmol) was mixed with mPEG-NHS (M_w 2000, 1 mg, 540 nmol) in sodium phosphate buffer (10 mM NaH_2PO_4/Na_2HPO_4, 100 mM NaCl, pH 7.0). After 1.5 h incubation at room temperature, the resulting product was dialyzed against deionized water (MWCO 5000). The synthesis of ODN−PEG conjugate was analyzed by reversed-phase chromatography, which was carried out on C18 column (200 × 4.6 mm, Waters, Milford, MA) with detection at 260 nm using a gradient from 5% acetonitrile in 0.1 M triethylammonium acetate to 50% acetonitrile in 0.1 M triethylammonium acetate with a flow rate of 1.0 mL/min at 56 °C. The conjugate fraction of the ODN−PEG was about 65%. The fractionated conjugate was analyzed by using a matrix-assisted laser desorption ionization time-of-flight (MALDI-TOF) mass spectrometry (Voyager DE-STR, Perkin-Elmer Biosystems, Boston, MA). The matrix for the ODN−PEG conjugate was α-cyano-4-hydroxycinnamic acid.

Formation and Characterization of Polyelectrolyte Complex Micelles. Polyelectrolyte complex (PEC) micelles between ODN−PEG conjugate and polyethylenimine were formed as previously described (*20*). Briefly, the ODN−PEG conjugate diluted in PBS was filtered through 0.2 μm filter (Millipore, Bedford, MA) and mixed with PEI solution at a nitrogen/phosphate (N/P) ratio of 2.5:1. The micelles were incubated for 30 min to stabilize the complexes. The PEC micelles were visualized by using atomic force microscopy (AFM). The micelle solution was dropped on a clean mica surface and air-dried at room temperature. AFM analysis was carried out in a constant tapping mode by using Nanoscope II (Digital Instruments, Woodbury, NY). A standard Nanoprobe silicon single-crystal lever was used as a cantilever, and a constant force mode was used with a scan speed at 0.5 Hz. The scanning image was collected in 0.5 × 0.5 μm area.

Cell Culture. Human lung carcinoma cells (A549 cells) were purchased from the Korean Cell Line Bank (Seoul, Korea). A549 cells were maintained in RPMI 1640 medium, supplemented with 100 units/mL penicillin, 100 μg/mL streptomycin, and 10% fetal bovine serum. The cells were cultured as a monolayer in a humidified atmosphere containing 5% CO_2 at 37 °C. For mice injection, A549 cells were grown until confluence, detached with trypsin/EDTA, washed three times with PBS, and resuspended in PBS.

Tumor Growth Regression Studies. To generate an animal tumor model, A549 cells (1×10^6 cells) were injected subcutaneously into rear flanks of seven-week old female nude mice (*nu/nu*, Charles River Laboratories, Wilmington, MA). When a minimum tumor volume reached about 30 mm^3, various ODN formulations (naked antisense ODN, antisense ODN polyelectrolyte complex micelles, or mismatched ODN polyelectrolyte complex micelles) were intravenously administered via a tail vein at 2.5 mg kg^{-1} $injection^{-1}$ at predetermined time intervals. Tumor growth was monitored by measuring perpendicular diameters three times a week. The tumor volumes were determined as previously described (*21*). Statistical significance was evaluated by using a Student's *t*-test and defined as $P < 0.05$.

Assay of ODN Accumulated in Tumor. Fluorescein-labeled ODN was prepared as previously described (*20*). Fluorescein-labeled ODN−PEG/PEI polyelectrolyte complex micelles (0.1 mg) were administered to tumor-bearing nude mice via a tail vein. A group of mice were sacrificed at 3, 12, and 24 h after the injection. The tumor tissues were ground in a hypotonic solution by using a tissue homogenizer, centrifuged, and filtered through 0.45 μm filter membrane (Millipore, Bedford, MA). In vivo deposition of ODN in tumor was determined by measuring fluorescence intensity monitored from the tissue extract using spectrofluorometry (SLM-AMINCO 8100, SLM Instruments Inc., Urbana, IL) and expressed as a percent initial dosage per gram tissue.

RESULTS AND DISCUSSION

A synthetic scheme of ODN−PEG conjugate is shown in Scheme 1. *c-raf* antisense ODN derivatized with an amine group at a 5′ terminal end was conjugated with a mPEG-NHS derivative to form an ODN−PEG conjugate.

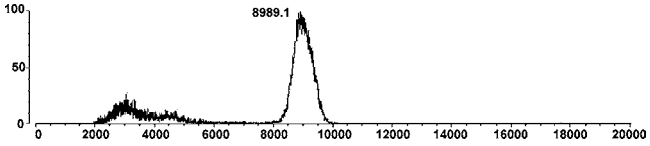

Figure 1. MALDI-TOF analysis of ODN−PEG conjugate purified by reversed-phase chromatography.

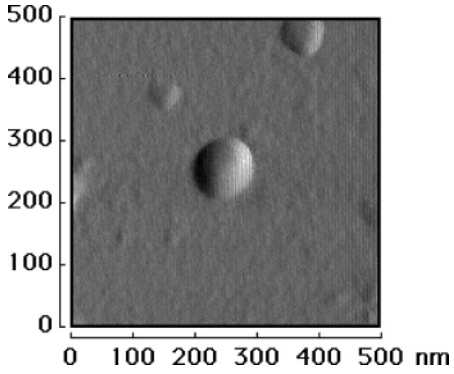

Figure 2. Atomic force microscopy (AFM) image of the polyelectrolyte complex micelles formed by the interaction between ODN−PEG and PEI.

The conjugation efficiency was ca. 65% as determined by reversed-phase HPLC. An average molecular weight of the purified conjugate analyzed by MALDI-TOF MS was 8989.1, which corresponds to the molecular weight sum of ODN and PEG (Figure 1).

Polyelectrolyte complex micelles (PEC micelles) could be formed by ionic interactions between the ODN−PEG conjugate and polyethylenimine (PEI). The ODN part of the conjugate interacted with PEI to form a charge-neutralized ODN/PEI complex core, while the hydrophilic PEG segment of the conjugate surrounded it. The formation and characterization of the PEC micelles were previously reported (*19*, *20*). The hydrodynamic diameter of the PEC micelles determined by dynamic light scattering (DLS) was ca. 70 nm with a narrow size distribution as described previously (*20*). The morphology of the PEC micelles was a round shaped structure as visualized on mica surface by using AFM (Figure 2). The size of PEC micelles observed by AFM was very consistent with that determined by DLS.

We previously showed that the antisense ODN−PEG conjugate containing a noncleavable linkage between ODN and PEG could hybridize with its corresponding complementary sense ODN sequence like naked antisense ODN (*20*). The thermal melting behavior of antisense ODN−PEG/sense ODN duplex was the same as that of antisense ODN/sense ODN duplex, indicating that the presence of a PEG chain adjacent to ODN segment did not perturb the antisense/sense ODN hybridization process. When the antisense *c-raf* ODN−PEG/PEI conjugate PEC micelles were treated with human ovarian cancer A2780 cells, they exhibited a dose-dependent antiproliferative activity. Furthermore, they showed significant retardation of tumor growth after intratumoral administration. In this study, the antitumor activity of systemically administered PEC micelles containing *c-raf* antisense ODN was investigated using nude mice having subcutaneously implanted human lung carcinoma cells (A549). Compared to control groups (mice treated with a saline solution, naked antisense ODN, and PEC micelles containing mismatched ODN with a random sequence), antisense ODN PEC micelles suppressed tumor growth significantly. The PEC micelles containing *c-raf* antisense ODN noticeably retarded the tumor growth after 10 days (Figure 3). This could be attributed to passive targeting effect of the nanosized PEC micelles by an enhanced permeation and retention (EPR) effect. The leaky vascular structure in solid tumor causes facilitated penetration and accumulation of nano-particulates. Polymer conjugates, liposomes, and polymeric micelles containing various anticancer agents showed increased accumulation in solid tumors (*22*−*24*). Likewise, the PEC micelles with ca. 70 nm in diameter were expected to penetrate into the interstitial space between loosened endothelial cell junctions and to accumulate in the tumor site that has insufficient lymphatic drainage. Figure 4 shows significant amount of the PEC micelles containing *c-raf* ODN accumulated in the tumor compared to naked ODN. After 12 h, the PEC micellar formulation showed about 3-fold higher local deposition amount of ODN in the tumor compared to that of naked ODN. Highly flexible PEG layers surrounding the PEC micelles could also play an important role in prolonging their circulation time in blood stream by suppressing nonspecific adsorption of opsonins and other serum proteins and by avoiding the recognition of reticuloen-

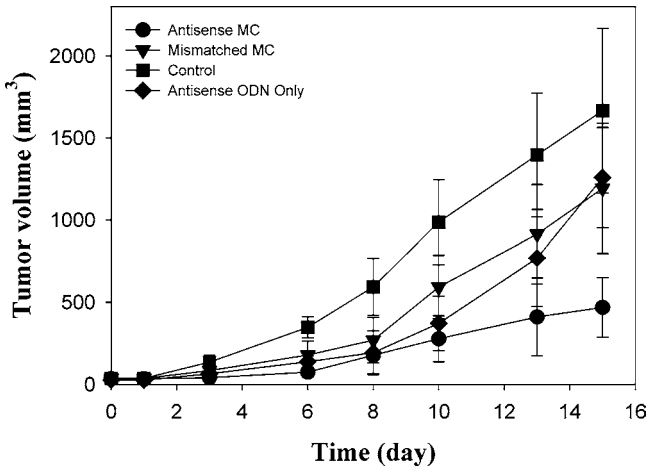

Figure 3. Effect of ODN−PEG/PEI polyelectrolyte complex micelles containing antisense *c-raf* ODN on the growth of A549 tumors in nude mice ($n = 4$−6). Tumors were allowed to grow until a mean volume of tumor reached 0.1 cm^3 before treatment. Each ODN formulation was administered through tail vein at 2.5 mg kg^{-1} $injection^{-1}$. The ODN formulations were injected at day 1, 3, 6, 8, 10, 13, and 15.

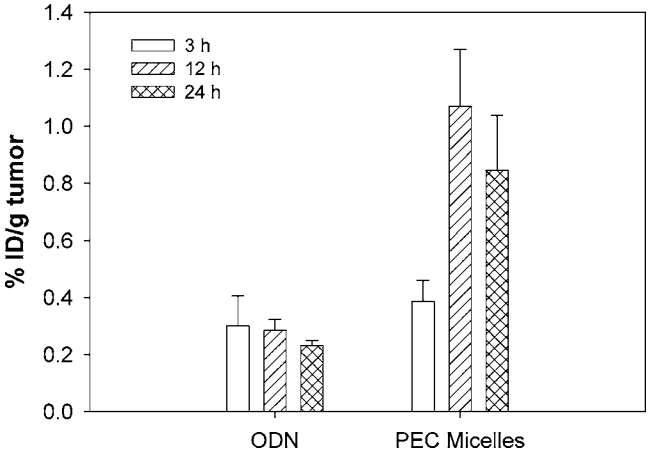

Figure 4. Accumulation of ODN−PEG/PEI PEC micelles in solid tumor after intravenous administration. Each ODN formulation containing 0.1 mg ODN was administered through mouse tail vein. The amount of ODN in each organ was measured by spectrofluorometric analysis and was shown as percent initial dose per gram of tumor.

dothelial systems (RES). The PEC micelles formed from the interaction between an ODN−PEG conjugate and linear-type PEI were reported to be stable against nuclease attack and showed minimal adsorption of serum proteins (*25*).

This study demonstrated that the PEC micelles containing a *c-raf* antisense ODN, which were spontaneously formed by the interaction between ODN−PEG conjugate and PEI in an aqueous milieu, could significantly reduce the growth of tumor after systemic administration. The PEC micelle also showed enhanced accumulation in the tumor. This suggests that the ODN delivery system based on PEC micelles could be successfully used for systemic antisense ODN delivery for treatment of cancer.

ACKNOWLEDGMENT

This work was supported by the grant from the Ministry of Science and Technology, Republic of Korea.

LITERATURE CITED

(1) Kataoka, K., Kwon, G., Yokoyama, T., Okano, T., and Sakurai, Y. (1993) Block copolymer micelles as vehicles for drug delivery. *J. Controlled Release 24*, 119−132.
(2) Kwon, G., Naito, M., Yokoyama, M., Okano, T., Sakurai, Y., and Kataoka, K. (1995) Physical entrapment of adriamycin in AB block copolymer micelles. *Pharm. Res. 12*, 192−195.
(3) Yoo, H. S., and Park, T. G. (2001) Biodegradable polymeric micelles composed of doxorubicin conjugated PLGA-PEG block copolymer. *J. Controlled Release 70*, 63−70.
(4) Yu, B. G., Okano, T., Kataoka, K., and Kwon, G. (1998) Polymeric micelles for drug delivery: solubilization and haemolytic activity of amphotericin B. *J. Controlled Release 53*, 131−136.
(5) La, S. B., Okano, T., and Kataoka, K. (1996) Preparation and characterization of the micelle-forming polymeric drug indomethacin-incorporated poly(ethylene oxide)-poly(beta-benzyl L-aspartate) block copolymer micelles. *J. Pharm. Sci. 85*, 85−90.
(6) Yoo, H. S., Lee, E. A., and Park, T. G. (2002) Doxorubicin-conjugated biodegradable polymeric micelles having acid-cleavable linkages. *J. Controlled Release 82*, 17−27.
(7) Malmsten, M., and Lindman, B. (1992) Self-assembly in aqueous block copolymer solution. *Macromolecules 25*, 5440−5445.
(8) Kwon, G., Naito, M., Yokoyama, M., Okano, T., Sakurai, Y., and Kataoka, K. (1993) Micelles based on AB block copolymers of poly(ethylene oxide) and poly(beta-benzyl L-aspartate). *Langmuir 9*, 945−949.
(9) Bader, H., Ringsdorf, B., and Schmidt, B. (1984) Water soluble polymers in medicine. *Angew. Makromol. Chem. 124,* 457−485.
(10) Klibanov, A. L., Maruyama, K., Torchilin, V. P., and Huang, L. (1990) Amphipathic poly(ethylene glycol)s effectively prolong the circulation time of liposomes. *FEBS Lett. 268*, 235−237.
(11) Kwon, G., and Okano, T. (1996) Polymeric micelle as new drug carriers. *Adv. Drug Delivery Rev. 16*, 107−116.
(12) Stein, C. A., and Cheng, Y. C. (1993) Anti-sense oligonucleotides as therapeutic agents -is the bullet really magical? *Science 261*, 1004−1012.
(13) Wagner, R. W. (1994) Gene inhibition using anti-sense oligodeoxynucleotides. *Nature 372*, 333−335.
(14) Jeong, J. H., and Park, T. G. (2001) Novel polymer-DNA hybrid polymeric micelles composed of hydrophobic poly(D,L-lactic-*co*-glycolic acid) and hydrophilic oligonucleotides. *Bioconjugate Chem. 12*, 917−923.
(15) Kataoka, K., Togawa, H., Harada, A., Yasugi, K., Matsumoto, T., and Katoyose, S. (1996) Spontaneous formation of polyion complex micelles with narrow distribution from antisense oligonucleotide and cationic block copolymer in physiological saline. *Macromolecules 29*, 8556−8557.
(16) Vinogradof, S., Batrakova, E., Li, S., and Kabanov, A. (1999) Polyion complex micelles with protein-modified corona for receptor-mediated delivery of oligonucleotides into cells. *Bioconjugate Chem. 10*, 851−860.
(17) Katayose, S., and Kataoka, K. (1998) Remarkable increase in nuclease resistance of plasmid DNA through supramolecular assembly with poly(ethyeneglycol)-poly(L-lysine) block copolymer. *J. Pharm. Sci. 87*, 160−163.
(18) Kakizawa, Y., Harada, A., and Kataoka, K. (2001) Glutathione-sensitive stabilization of block copolymer micelles composed of antisense DNA and thiolated poly(ethyleneglycol)-*block*-poly(L-lysine): A potential carrier for systemic delivery of antisense DNA. *Biomacromolecules 2*, 491−497.
(19) Jeong, J. H., Kim S. W., and Park, T. G. (2003) Novel intracellular delivery system of anti-sense oligonucleotide by self-assembled hybrid micelles composed of DNA/PEG conjugate and cationic fusogenic peptide. *Bioconjugate Chem. 14*, 473−479.
(20) Jeong, J. H., Kim, S. W., and Park, T. G. (2003) A new anti-sense oligonucleotide delivery system based on self-assembled ODN/PEG hybrid conjugate micelles. *J. Controlled Release 93*, 183−191.
(21) McPhillips, F., Mullen, P., Monia, B. P., Ritchie, A. A., Dorr, F. A., Smyth, J. F., and Langdon, S. P. (2001) Association of *c-Raf* expression with survival and its targeting with antisense oligonucleotides in ovarian cancer. *Br. J. Cancer 85*, 1753−1758.
(22) Shiah, J.-G., Sun, Y., Peterson, C. M., and Kopecek, J. (1999) Biodistribution of free and N-(2-hydroxypropyl)-methacrylamide copolymer-bound mesochlorin e_6 and adriamycin in nude mice bearing human ovarian calcinoma OVCAR-3 xenografts. *J. Controlled Release 61*, 145−157.
(23) Weissig, V., Whiteman, K. R., and Torchilin, V. P. (1998) Accumulation of protein-loaded long-circulating micelles and liposomes in subcutaneous Lewis lung carcinoma in mice. *Pharm. Res. 15*, 1552−1556.
(24) Yoo, H. S., and Park, T. G. (2004) Folate receptor targeted biodegradable polymeric doxorubicin micelles. *J. Controlled Release 96*, 273−283.
(25) Oishi, M., Sasaki, S., Nagasaki, Y., and Kataoka, K. (2003) pH-responsive oligonucleotide (ODN)-poly(ethyleneglycol) conjugate through acid-labile β-thiopropionate linkage: preparation and polyion complex micelle formation. *Biomacromolecules 4*, 1426−1432.

BC0497315

Oligonucleotides Conjugated to Short Lysine Chains

Johannes Winkler, Ernst Urban, and Christian R. Noe*

Department of Medicinal Chemistry, Universität Wien, Althanstrasse 14, 1090 Wien, Austria.
Received November 10, 2004; Revised Manuscript Received April 15, 2005

A new method for synthesizing oligonucleotide peptide conjugates by an in-line approach is presented. A phosphorothioate oligonucleotide with the sequence of bcl-2 targeted Oblimersen by employing a modified 2′-amino-2′-desoxy-uridine nucleotide bearing a succinyl linker at the 2′ position was prepared. The carboxyl group was protected for solid-phase synthesis as the benzyl ester. Ester cleavage was afforded by a phase transfer reaction using palladium nanoparticles as catalyst and cyclohexadiene as hydrogen donor. Short tails of up to three lysyl residues were conjugated to the oligonucleotide by an inverse stepwise peptide synthesis. The conjugates were characterized by HPLC, mass spectrometry, and circular dichroism. Influence of lysyl tails on CD spectra were minimal. Melting profiles revealed only minimal destabilizing effects on duplexes by conjugation of peptides.

INTRODUCTION

The aim of the antisense strategy (*1*) is the sequence specific inhibition of a gene by hybridization of a single-stranded oligonucleotide to the complementary mRNA in order to prevent the expression of the corresponding protein product. Besides the inhibition of translation by binding to the mRNA to give double-stranded nucleic acid, activation of the RNA degrading RNAse H is a key effect of antisense substances (*2*, *3*). In addition to this pharmacodynamic effect, which is determined by the nucleotide sequence of the antisense oligonucleotide, sufficient pharmacokinetic properties of these substances are essential for achieving the desired effect.

Unmodified phosphodiester oligonucleotides lack sufficient stability against degradation by mainly exo- but also endonucleases and are therefore not suited for therapy. Numerous modifications have been introduced and tested for their binding affinity and biological properties (*4*, *5*). Initially, modifications of the phosphodiester backbone were the main field of activity. Phosphorothioate oligonucleotides, often called antisense molecules of the first generation, possess better stability against enzymatic degradation. Although their hybridization properties are poorer than that of natural oligonucleotides, their advantageous pharmacokinetic characteristics and the ability to activate RNAse H made them a promising new class of antisense molecules (*6*). The first approved antisense drug, fomivirsene (*7*), and most of the substances currently in various phases of clinical trials (*8*) are phosphorothioate oligonucleotides.

Oblimersen sodium is one of the most progressed antisense drugs in clinical trials (*9*). A large multicenter phase III study against malignant melanoma, in which Oblimersen was administered in combination with the standard dacarbazine treatment, was recently concluded. Despite an increase in progression-free survival (PFS), Genta withdrew its appeal for approval after a review by the FDA advisory committee, because median survival, the primary end-point, was not prolonged statistically significantly (*10*). Still other phase III trials against several cancer types are ongoing.

Oblimersen is a phosphorothioate oligonucleotide targeted to the first six codons of the open reading frame of Bcl-2 (*11*). Bcl-2 is an important inhibitor of apoptosis (*12*) and has been shown to be overexpressed in a large numbers of tumors. Because of its phosphorothioate backbone, a 5′-TC dinucleotide, and two distinct CpG motifs, some non-antisense effects may contribute to the antiproliferative action of Oblimersen. A sequence-specific true antisense effect has been shown in some in vitro and in vivo experiments (*13*−*15*), while others reported that the cytostatic properties are independent from the antisense effect (*16*, *17*).

The second generation of antisense oligonucleotides bears modifications at the 2′-position (*18*−*20*). Oligonucleotides with an alkoxy substituent in position 2′ proved to be stable against DNA or RNA cleaving enzymes. This increased stability has been explained by the steric hindrance, which inhibits the attack of nucleases at the phosphate groups. Base pairing properties decrease with increasing length of alkyl substituent. 2′-Ethylene glycol-modified oligonucleotides showed better base pairing properties (*6*, *21*), and the 2′-methoxy ethyl group is particularly suited. As a drawback, 2′-O-substitued oligonucleotides proved to be unable to catalyze enzymatic degradation of the complementary RNA by activation of RNAse H (*22*). Hence, so-called gapmere oligonucleotides, bearing modified nucleotides at both the 3′ and 5′ end, but with an unmodified region of at least five nucleotides between, were introduced. They provide good stability against exonucleases while the unmodified region is sufficient to activate RNAse H (*23*).

Zwitterionic antisense oligonucleotides are seen as the third generation. Introduction of a 6-aminohexyl group at the 2′ position not only increases stability against enzymatic degradation, but also minimizes the electrostatic repulsion of the sense and antisense strands leading to improved hybridization affinity (*24*).

Other more rigorous modifications include substitution of the polyanionic phosphate backbone by peptides (PNA), change of the ribose moiety to morpholino groups (MNA) (*25*), and introducing a methylene bridge between oxygen

* To whom correspondence should be addressed. Phone: +431 4277 55103, Fax: +431 4277 9551, E-mail: christian.noe@univie.ac.at.

10.1021/bc049729d CCC: $30.25 © 2005 American Chemical Society
Published on Web 07/02/2005

2′ and carbon 4′ of the carbohydrate to increase rigidity of the backbone (locked nucleic acids, LNA) (*26*, *27*).

Lately, the focus in improving oligonucleotide properties has been shifted toward conjugation of ligands (*28*). This approach allows a directed change of molecule characteristics enhancing binding affinity or pharmacokinetic parameters such as hydrophobicity and improvements in biodistribution or cellular uptake. A large number of ligands has successfully been ligated to oligonucleotides, among them lipophilic molecules such as cholesterol (*29*) and lipids (*30*), vitamin B_6 (*31*), a synthetic ligand to the asialoglycoprotein receptor for tissue and cell-specific targeting to parenchymal liver cells (*32*), and various proteins (*28*). Conjugates of oligonucleotides with penetratins (*33*) or signal peptides acquire increased uptake rates due to the membrane dislocation properties of these peptides. Conjugation of a PNA to a monoclonal antibody of the rat transferrin receptor via the biotin streptavidin complex enabled the transport through the blood−brain barrier (*34*). Attachment of arginine rich SV40 nuclear localization signal efficiently transported DNA as well as PNA (*35*, *36*). Conjugates with either a 35 amino acid basic sequence of the HIV Tat protein or a 16 amino acid basic sequence from the *Drosophila antennapedia* protein improved cellular uptake of antisense phosphorothioate oligonucleotides without loss of specificity to target RNA (*37*, *38*). It has been firmly established that an increase in cellular uptake of oligonucleotides can be achieved by conjugation or complexation of the oligonucleotide to poly-L-lysine (*39*−*42*). A tail of one, two, or four lysine moieties at the 5′-end of a PNA oligonucleotide improved cellular uptake (*43*). The extent of uptake was dependent on the number of conjugated lysine monomers. The affinity to the target sequence was not increased nor was the nuclear translocation process influenced. It was concluded that the lysine chain improved the transport through the cell membrane or enhanced the release from endosomes.

Herein, we report the conjugation of oligonucleotides with short lysyl chains. The majority of oligonucleotide peptide conjugates have been prepared by linkage at either the 3′ or the 5′ end of the oligonucleotide (*28*). The two components were either synthesized independently by distinct solid-phase syntheses and ligated afterward or on the same solid phase by sequential stepwise synthesis. Commonly used linkers are disulfides (*44*−*46*), maleimides, thioethers, and amides (*28*). In an in-line synthesis, first described by Haralambidis (*47*), the peptide and oligonucleotide are synthesized sequentially on automatic synthesizers. Using an acid labile amino protection group, a possibility for stepwise peptide synthesis at the 5′-end of an oligonucleotides prepared on the same solid support was described (*48*).

Conjugation at the 2′ position of the carbohydrate moiety of the oligonucleotide has previously been achieved by use of the 6-aminohexyl (*49*, *50*) and 4-aminopropyl linkers (*51*). Ligands have been coupled to the primary amino group by amide bonds or the use of a chloroformate or carbonate to give a carbamate or by an active ester to give an amide (*49*). Recently, a procedure for the attachment of amines to an allyl-protected carboxyl linker attached at the 2′-position of uridine has been published (*52*). The allyl ester was removed by treatment with Pd(0) and morpholine. Subsequently, several small peptides were coupled to the free carboxyl group.

Our approach relies closely on the previously published procedure for a fluoresceine oligonucleotide conjugate *(53)*. We derivatized 2′-amino-2′-desoxy-uridine with succinic anhydride to give the hemisuccinate. Protection of the carboxyl group for the solid-phase synthesis was achieved by preparing the corresponding benzyl ester. This nucleotide building block was incorporated in an oligonucleotide at the 3′ terminus. Conjugation of fluorescein was done after deprotection of the carboxyl group by a catalytic phase transfer reaction with palladium nanoparticles and 1,4-cyclohexadiene as the hydrogen donor. After establishing this simple and convenient procedure for conjugating ligands at the 2′ position of a 3′-terminal uridine nucleoside of an oligonucleotide, we decided to expand this method into the field of oligonucleotide peptide conjugates. For the preparation of oligonucleotide peptide conjugates, protein synthesis had to be achieved in N to C, the inverse direction. We designed a suitably protected lysine synthon to build up short peptide strands at the hemisuccinate. In addition to the synthesis, we present data of circular dichroism spectroscopy and binding affinity to the sense strand.

EXPERIMENTAL PROCEDURES

Reagents were used in standard quality for synthesis. Acetonitrile was heated over potassium carbonate and distilled, followed by heating over calcium hydride and distillation. Dichloromethane was dried over phosphorus pentoxide and distilled. Melting points were measured on a Kofler melting point apparatus and are uncorrected. NMR spectra were recorded on a Bruker Avance 200 MHz or a Varian Unity 300 MHz machine. Shifts are reported relative to the solvent peak ($CHCl_3$ in $CDCl_3$: δ 7.26 and 77.00), coupling constants are in Hz. Spin multiplicities are given with the following abbreviations: s singlet, d doublet, t triplet, q quartet, m multiplet. Thin-layer chromatography (TLC) was performed using silica gel 60-F_{254} precoated aluminum plates by Merck. Spots were visualized by UV.

***N*(ϵ)-Trifluoracetyl-L-lysine Benzyl Ester 2.** *N*(ϵ)-Trifluoracetyl-L-lysine (**1**, 300 mg, 1.24 mmol) was triturated with *p*-toluenesulfonic acid monohydrate (480 mg, 2.52 mmol) and 7 mL of benzyl alcohol. The resulting paste was dissolved in 18 mL of benzene and heated to reflux for 18 h. The arising water was removed from the reaction by a Soxhlet apparatus filled with molecular sieve (4 Å). After cooling, the solvent was removed in vacuo. The reaction product was crystallized by adding 10 mL of diethyl ether. After cooling at 4 °C overnight, the precipitate was collected by filtration and dried in vacuo to give the *p*-toluenesulfonic acid salt of *N*(ϵ)-trifluoracetyl-L-lysine benzyl ester (**2**, 570 mg, 91%). The free base was gained by extraction with saturated sodium bicarbonate solution.

Tosylate: ^{1}H NMR ($CDCl_3$, 200 MHz): δ = 7.70 (d, J = 7.8, 2H, Ar-H (tos)), 7.37 (s, 5H, Ar-H (bzl)), 7.21 (d, J = 7.8, 2H, Ar-H (tos)), 5.29 (d, J = 12.1, 1H, CH_2−Ph (1)), 5.22 (d, J = 12.6, 1H, CH_2−Ph (2)), 4.06 (t, J_{32} = 5.8, 1H, H-2), 3.20 (t, J_{56} = 6.6, 1H, H-6), 2.35 (s, 3H, CH_3), 1.88 (m, 2H, H-3), 1.56−1.29 (m, 4H, H-4, H-5). ^{13}C NMR ($CDCl_3$, 50 MHz): δ = 170.35 (C-1), 143.42 (C-4 (tos)), 141.76 (ArC-1 (tos)), 136.41 (ArC-1 (bzl)), 129.84, 129.80 and 129.70 (ArC-2,6, ArC-3,5, ArC-4 (bzl), ArC-3,5 (tos)), 126.92 (ArC-2,6 (tos)), 117.53 (q, J = 286, CF_3), 69.08 (CH_2-bzl), 53.85 (C-2), 40.12 (C-6), 31.03 (C-3), 29.24 (C-5), 23.03 (C-4), 21.30 (CH_3). Fp: 144−145 °C. $C_{22}H_{27}F_3N_2O_6S$: calcd C 52.37 H 5.39 N 5.55 S 6.36 found C 52.22 H 5.53 N 5.52 S 6.39.

2: ^{1}H NMR ($CDCl_3$, 200 MHz): δ = 7.27 (s, 5H, Ar-H), 5.07 (s, 2H, CH_2−Ph), 3.38 (m, 2H, H-2), 3.25 (d, $J_{6'6}$ = 6.4, 1H), 3.19 (d, $J_{66'}$ = 6.4, 1H), H-6′), 1.91 (bs, 2H, NH2), 1.75−1.13 (m, 6H, H-3, H-4, H-5). ^{13}C NMR

($CDCl_3$, 50 MHz): $\delta = 175.52$ (COObzl), 135.47 (ArC-1), 128.55, 128.39 and 128.26 (ArC-3,5, ArC-2,6, ArC-4), 115.87 (q, $J = 286$, CF_3), 66.73 (CH_2−Ph), 53.96 (C-2), 39.45 (C-6), 33.64 (C-3), 28.04 (C-5), 22.45 (C-4).

Loading of Solid Support. TentaGel-NH_2 (230 mg, 60 μmol free NH_2-groups), purchased from Fluka, was loaded with succinyl modified uridine **3** and *N*,*N*′-diisopropylcarbodiimide, 1-hydroxy-1*H*-benzotriazole, and 4-(dimethylamino)pyridine as described earlier (*53*). Degree of loading was around 190 μmol/g.

Oligonucleotide Synthesis. Standard phosphoroamidites and tetrazole solution were obtained from Carl Roth GmbH & Co. KG. Oligonucleotide syntheses were carried out on a ABI 392 Applied Biosystems DNA/RNA-Synthesizer in standard 1 μmol scale in DMT[1]-on mode. Coupling of the first nucleotide to solid-supported modified nucleoside was prolonged to 2 min. Sulfurization was done with tetraethyldiuram disulfide, which was purchased from Sigma and recrystallized (*54*). For the synthesis of phosphorothioates, the sulfurization step was performed before capping. 1*H*-Tetrazol was used as activation reagent. Other reagents used for DNA synthesis were obtained in analytical quality and purified before use.

Preparation of Oligonucleotide−Lysine Conjugates. The synthesis column was removed from the synthesizer and opened. The resin-bound oligonucleotide was transferred to an 5 mL reaction tube of a Quest 210 manual synthesizer. Cleavage of the benzyl protecting group was achieved by phase-transfer hydrogenation with PVP-stabilized palladium nanoparticles (0.7 mL) (*53*) and 1,4-cyclohexadiene (0.05 mL) as hydrogen donor. Cyclohexadiene was added to the PVP-stabilized suspension of palladium, and the resulting solution was microfiltrated (0.22 μm) to ensure no precipitated palladium was applied to the resin. The reaction mixture was stirred at room temperature for 3 h.

The resin was washed three times with methanol and three times with DMF. Prior to coupling, the carboxyl group was activated by a solution of 1-hydroxy-1*H*-benzotriazole (0.4 mg, 3.0 μmol) and *N*,*N*′-diisopropylcarbodiimide (1.1 mg, 8.7 μmol) in 1 mL of DMF. The mixture was stirred for 3 h, and the solution was again filtered off. Coupling was done by adding a solution of 1-hydroxy-1*H*-benzotriazole (0.4 mg, 3.0 μmol), *N*,*N*′-diisopropylcarbodiimide (0.4 mg, 8.7 μmol), and lysine building block **2** (2.0 mg, 6.0 μmol) in 1 mL of DMF and stirring for 18 h. The resin was washed three times with DMF and three times with water. For the preparation of conjugates with two and three lysines, the deprotection and coupling procedures were repeated. For cleavage and deprotection of oligonucleotides, 2 mL of concentrated ammonia was added and the mixture was heated to 55 °C for 18 h. The solution was filtered, and the solvent was evaporated in vacuo.

Purification and Analyses of Oligonucleotides. Oligonucleotide concentrations were determined by measuring OD_{260} in a Hitachi U3000 spectrophotometer. Molar extinction coefficents were calculated as the sum of nucleotides (A: 15400, G: 11700, C: 7300, T: 8800, U: 9950).

Initial purifications of DMT-on oligonucleotides were done with Poly-Pak columns obtained from Carl Roth GmbH & Co. KG according to manufacturer except for elution, which was done with 20% acetonitrile. Analytical HPLC was performed on a Nucleosil CC 250/4 100−5 C18 column with the following gradient system: A: 0.1 M triethylammonium acetate in water, B: 0.1 M triethylammonium acetate in 80% acetonitrile, linear gradient 10−40% B in 0−30 min, flow rate 1 mL/min. If the purity after Poly-Pak-purification was deemed insufficient, preparative HPLC was performed on a LiChrosphere 100 RP-18 using the same gradient as for analytical HPLC.

Scheme 1. Synthesis and Structure of Solid-Phase-Bound Starter Nucleotide 4[a]

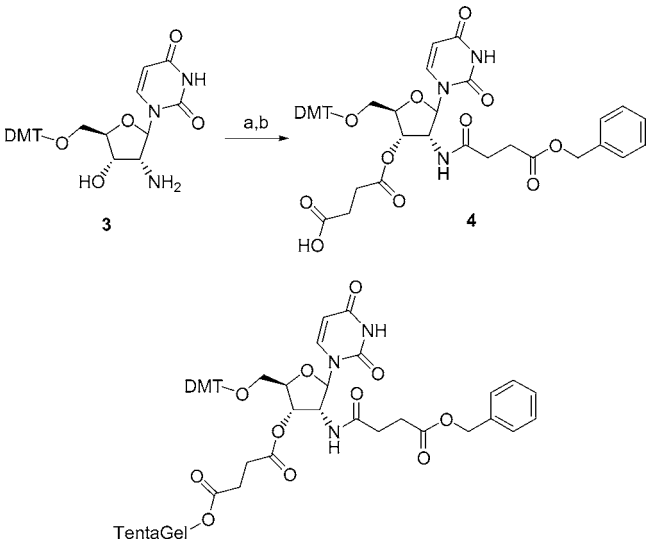

[a] Reagents and conditions: (a) benzyl succinyl ester, DIC, HOBt, THF, rt; (b) succinic anhydride, pyr, 30 °C.

Mass spectrometric analysis was done on a Kratos seq MALDI mass spectrometer. Sample preparation was done following the method described by Pieles et al. (*55*). One microliter of sample (100 pmol/μL in water) was briefly vortexed with 10 μL of a 0.5 M solution of 2,4,6-trihydroxyacetophenone in ethanol and 5 μL of a 0.1 M solution of di-ammonium hydrogen citrate. One microliter of this mixture was spotted on the target and allowed to air-dry. The mass spectrometer was run in the negative ion and reflectron mode, and spectra were usually obtained by summing up 100 single laser pulses.

Circular dichroism spectrometry was performed on a Jasco J-810 spectropolarimeter equipped with a Neslab RTE 7 thermostatic unit. Oligonucleotides were diluted to a 9 μM solution in 0.15 M NaCl and 0.01 M Tris-HCl (pH 7.0) buffer. CD spectra were collected from 320 to 210 nm using a quartz cuvette (Hellma 100-QS) with a path length of 1 mm. Duplexes were measured after heating the equimolar mixture of complementary strands to 50° for 10 min and subsequent slow cooling to room temperature.

Melting temperatures (T_m) of the duplexes were determined in the Jasco J-810 by slowly heating from 30 to 90 degrees (50 °C/h) and recording CD at 248 nm or OD at 260 nm as a function of temperature. Melting curves showed cooperative form and T_m were obtained from the maxima of the first derivative plots. Temperatures given are that of the cuvette holder.

RESULTS

Conjugation of cationic peptides has been shown to improve properties of antisense oligonucleotides and enhance their efficacy. The synthesis of nucleoside building block **4** was described earlier (Scheme 1). It proceeds straightforward from 2′-amino-2′-desoxy-uridine by reac-

[1]Abbreviations: DMT, dimethoxytriphenylmethyl; PVP, poly(vinylpyrrolidone); CD, circular dichroism; DIC, *N*,*N*′-diisopropylcarbodiimide; HOBt, 1-hydroxy-1*H*-benzotriazole.

Scheme 2. Lysine Building Block[a]

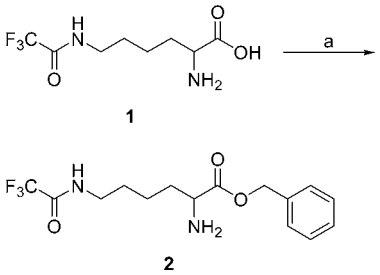

[a] Reagents and conditions: (a) benzyl alcohol, *p*-toluenesulfonic acid, benzene, reflux.

Scheme 3. Structure of Oligonucleotide Conjugates 5 ($n = 1$), 6 ($n = 2$), and 7 ($n = 3$)

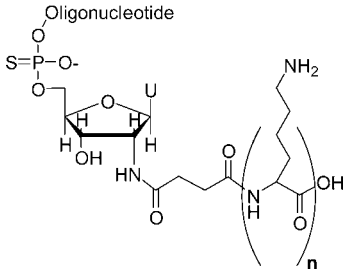

Table 1. HPLC Retention Times and Melting Temperatures of Oligonucleotide Duplexes with the Complementary DNA Strands

	HPLC retention time (min)	T_m (°C)
antisense-DNA		78.7 ± 0.1
Oblimersen	19.13	69.5 ± 1.3
4	17.95	65.5 ± 0.8
4	18.06	67.4 ± 0.1
5	18.37	67.6 ± 1.0
6	18.56	68.2 ± 0.4

tion with succinic acid mono benzyl ester with an excellent selectivity for the amino group (*53*).

For peptide synthesis, a suitable lysine derivative had to be protected at the carboxyl group and the ϵ-amino function. We decided that the trifluoracetyl group was well suited for masking the terminal amino group, because it can be cleaved in the same step as the nucleic base protecting groups (*56*). Because attachment is conducted after complete assembly of the oligonucleotide, the reported replacement of the trifluoracetyl group by the acetyl capping reagent (*57*) is of no importance. Additionally, no cleavage of peptide bonds was reported to occur using concentrated ammonia for deprotection (*58, 59*).

Easily available *N*(ϵ)-trifluoracetyl-L-lysine (**1**) was reacted with benzyl alcohol under catalysis of *p*-toluenesulfonic acid to give benzyl ester **2** (Scheme 2).

A fluorescent dye was successfully coupled to the succinic linker by using a 3-fold excess of DIC and HOBt as catalysts (*53*). Coupling of **2** to solid bound deprotected modified nucleoside monomer using the same conditions gave only poor yields of 30−40% as judged by HPLC analysis. Thus, we used an optimized protocol for inverse solid-phase peptide synthesis (*60*). After a prior activation step with an 8-fold excess of DIC and a 3-fold excess of HOBt, coupling was achieved with 3-fold excesses each of DIC, HOBt, and **2**. This procedure resulted in good yields when tried with solid bound nucleoside monomer.

Consequently, it was employed for conjugating short lysine tails to an 18mer all-phosphorothioate oligonucleotide (**4**) with a sequence according to that of

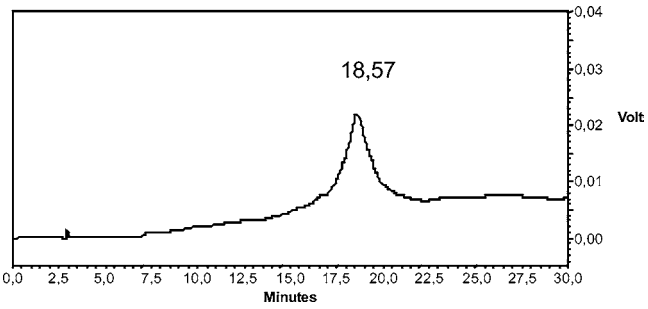

Figure 1. HPLC of oligonucleotide trilysine conjugate **7**.

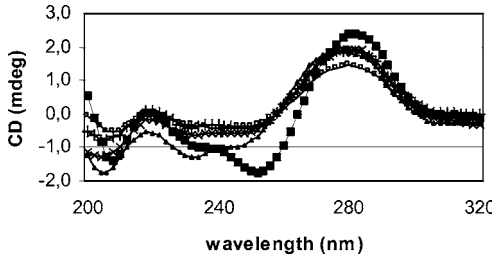

Figure 2. CD spectra of single strands of **4** (+), **5** (▲), **6** (○), **7** (×), and Oblimersen (■).

Oblimersen (5′-TCTCCCAGCGTGCGCCA*U*-3′). Conjugates containing one (**5**), two (**6**), and three (**7**) lysyl residues were prepared (Scheme 3). Purification was achieved using Poly-Pak-cartridges and the standard protocol. HPLC analysis with a reversed phase column showed clear differences in retention times of the three products and unconjugated oligonucleotide. With increasing number of lysyl residues, the retention times were prolonged as can be seen in Table 1. Due to the broad peaks of phosphorothioate oligonucleotides, no reliable measurement of coupling yields could be determined. For example, Figure 1 shows the HPLC chromatogram of trilysyl oligonucleotide **7**. Structures were verified by MALDI mass spectrometry.

CD spectra of the conjugation products were recorded and compared to that of Oblimersen and unconjugated succinyl modified oligonucleotide **4**. All single stranded oligomers gave relatively weak CD curves (Figure 2) with only a well-defined positive band around 280 nm that showed small variability for all substances. In the far UV region of 200−250 nm, a small positive band could be observed at 220 nm, while generally negative CD values were recorded in that area. No straightforward relation of spectra with lysyl substitution could be detected.

Duplexes with complementary unmodified phosphodiester DNA were prepared by mixing of single strands in equimolar amounts in 0.01 M Tris buffer (pH 7.0) with 0.15 M concentration of NaCl. To ensure completion of duplex binding, the mixture was heated to 50 °C for 10 min and subsequently cooled. The formation of duplexes was verified by comparing the spectra of single strands and duplexes recorded at 10 °C (*53*). All oligonucleotides gave nearly identical CD curves (Figure 3). Comparison of the CD values at 200 nm shows smaller results for lysine substituted oligonucleotides, although there is no simple correlation with the number of substitutions.

To determine hybridization affinity and duplex stability, melting profiles were recorded either using CD value at 248 nm or UV absorption at 260 nm. Both methods gave cooperative curves with identical melting temperature. A minimum of four distinct profiles were recorded for each oligonucleotide. Melting temperature of modified oligonucleotides were generally lower than that of control

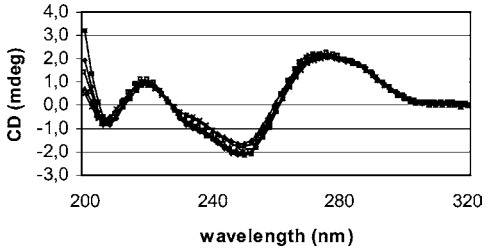

Figure 3. CD spectra of duplexes of **4** (+), **5** (▲), **6** (○), **7** (×), and Oblimersen (■) with sense-DNA.

Oblimersen. Lysyl-substituted substances gave higher melting points than unconjugated oligonucleotide **4**.

DISCUSSION

Our method for preparing oligonucleotide conjugates proved to be easy and convenient for the synthesis of a fluoresceine conjugate (*53*). Herein, we show that it is also a versatile method and can be employed for conjugation of at least short peptides in an in-line approach. Sequential solid-phase synthesis of first the oligonucleotide and then a peptide chain of up to three lysyl residues has been achieved. Preparation of lysyl building block was straightforward. Protection of Lys gamma amino function was accomplished as trifluoracetyl amide. This group is cleaved in the same deprotection step as nucleic base masking groups with concentrated ammonia. Because the trifluoracetyl-protected amine is introduced after complete oligonucleotide synthesis, no side products due to transamination caused by the capping reagent are generated (*57*). The carboxyl function was protected as a benzyl ester, because a cleavage protocol by phase transfer-catalyzed reaction has been established for succinyl linker modified oligonucleotide (*53*). The deprotection reaction was completed after 3 h at room temperature.

Initially, we tried coupling the lysyl building block to solid-bound monomer by direct reaction with DIC and HOBt, but the yields of around 40% were disappointing. Therefore, we decided to use a protocol published for the inverse N to C peptide synthesis (*60*), which resulted in nearly quantitative yields. Prior to coupling, free carboxyl group was activated with a large excess of DIC (8-fold) for 3 h. Coupling was performed with a 3-fold excess of DIC, HOBt, and lysine building block **2** with a reaction time of 18 h. No further optimization attempts were made, although switching to other reagents such as HATU/TMP may result in shorter coupling times (*61*, *62*). Peptide synthesis in the so-called inverse direction usually results in poorer yields than synthesis in established C to N direction. Additionally, a certain extent of racemization is often imminent. Therefore, for preparing conjugates of **4** with larger peptides, distinct syntheses of the components followed by ligation seems to be the favorable option. But for peptides consisting of up to three amino acids, the danger of racemization can be neglected. Even very short cationic peptides have an enhancing influence on the properties of antisense oligonucleotides, especially on cell uptake (*43*).

Conjugates of modified oligonucleotide **4**, bearing the sequence of Oblimersen, targeted to apoptosis inhibitor bcl-2 with one, two, and three lysyl residues were prepared by this procedure. HPLC analyses gave broad peaks because of the diastereomeric attributes of phosphorothioate oligonucleotides. Although exact quantification of coupling yields was therefore impossible, successful conjugation with good yields was proved by changes in retention times. No shoulders on the peaks could be detected. Coinjection of unsubstituted conjugate **4** with lysyl modified conjugates **5**−**7** revealed the presence of two different substances. MALDI analyses confirmed the successful conjugation, as the expected masses were found. The mass of mono- or dilysyl substituted oligonucleotide could not be found in the MALDI mass spectrum of **7**.

CD spectra of single strands were quite similar in their shape showing a B-DNA type curve. Phosphorothioate oligonucleotides generally give lower intensities in CD than phosphodiester DNA (*53, 63*). Positive cotton effect at 280 nm, an indicator of base stacking, was practically identical in all substances. No characteristic curve was observed in the far UV region (200−250 nm) indicating no pronounced secondary structure. No clear influence of lysine substitution could be detected. At neutral pH, poly-L-lysine gives a typical random coil CD spectrum with low intensities in the wavelength region over 210 nm, whereas at lower wavelength, an intense negative band centered at 195 nm is observed (*64*). Although CD values of lysyl-substituted oligonucleotides at 200 nm are lower than that of Oblimersen, there is no correlation with the number of lysyl residues. Measurement at this wavelength was considerably noisy due to the increasing absorption of sodium chloride. No substantial influence on the CD curve is caused by the introduction of short lysyl chains, because the concentration of conjugates **5**−**7** is too low for a reliable measurement of peptide secondary structure. With regard to the short peptide strand, the concentration of conjugate **7** is around 3 μg/mL. A typical concentration for recording peptide CD spectra is 500 μg/mL (*60*).

CD spectra of duplexes with sense DNA exhibited less differences between **5**−**7** and Oblimersen. A well defined helical structure with characteristics of B-DNA is obviously caused by the DNA strand. Differences between conjugates and Oblimersen are minimized. Again, lysyl substitution does not seem to influence CD values. The 18 mer oligonucleotide presumably is extremely dominant concerning CD spectroscopy over the short lysine tail with a maximum of three amino acids.

Melting point determination was done by temperature-dependent measurement of either CD value or UV absorption. Oblimersen gives a melting temperature of 69.5 °C, 9.2 °C lower compared to phosphodiester oligonucleotide (*53*). Unconjugated oligonucleotide **4** shows a decrease of 4 °C. Substitution of the free carboxyl group with lysine increases the duplex stability. Melting point of **7** is only 1.3 °C lower than that of Oblimersen and very similiar to that of a fluoresceine conjugated oligonucleotide (*53*). Differences between **5**, **6**, and **7** are small and partly within standard deviation, but a tendency toward duplex stabilization by an increasing number of lysine monomers can be observed. This effect can be explained by partial neutralization of the negatively charged phosphate backbone by cationic terminal amino groups of lysine. The electrostatic repulsion of the two strands is thus decreased. This stabilizing effect evidently overcomes the destabilizing effect of the increasing steric bulk in the minor groove. On the other hand, the increasing steric hindrance seems to be responsible for the somewhat lower increase in melting temperature than expected.

In conclusion, our previously reported procedure for preparing oligonucleotide conjugates has been shown to be suitable for preparing conjugates with short peptide tails in an in-line approach. Increasing length of the oligolysyl chain resulted in both better base pairing ability, reflecting the high potential of conjugated basic

peptides to improve the therapeutical properties of nucleic acid analogues. The conjugation of oligolysyl chains to the 3′-terminal 2′-position altered physical and biological properties only to a minimal extent and is therefore a technique to specifically enhance oligonucleotides characteristics by ligating functional or cationic peptides or proteins.

LITERATURE CITED

(1) Zamecnik, P. C., and Stephenson, M. L. (1978) Inhibition of Rous sarcoma virus replication and cell transformation by a specific oligodeoxynucleotide. *Proc. Natl. Acad. Sci. U.S.A. 75*, 280−284.

(2) Crooke, S. T. (2000) Potential roles of antisense technology in cancer chemotherapy. *Oncogene 19*, 6651−6659.

(3) Crooke, S. T. (1999) Molecular mechanisms of action of antisense drugs. *Biochim. Biophys. Acta 1489*, 31−44.

(4) Urban, E., and Noe, C. R. (2003) Structural modifications of antisense oligonucleotides. *Farmaco. 58*, 243−258.

(5) Freier, S. M., and Altmann, K. H. (1997) The ups and downs of nucleic acid duplex stability: structure−stability studies on chemically modified DNA: RNA duplexes. *Nucleic Acids Res. 25*, 4429−4443.

(6) Levin, A. A. (1999) A review of the issues in the pharmacokinetics and toxicology of phosphorothioate antisense oligonucleotides. *Biochim. Biophys. Acta 1489*, 69−84.

(7) Orr, R. M. (2001) Technology evaluation: fomivirsen, Isis Pharmaceuticals Inc/CIBA vision. *Curr. Opin. Mol. Ther. 3*, 288−294.

(8) Tamm, I., Dorken, B., and Hartmann, G. (2001) Antisense therapy in oncology: new hope for an old idea? *Lancet 358*, 489−497.

(9) Bayes, M., Rabasseda, X., and Prous, J. R. (2004) Gateways to clinical trials. *Methods Find Exp Clin Pharmacol. 26*, 473−503.

(10) Frantz, S. (2004) Lessons learnt from Genasense's failure. *Nat Rev Drug Discovery 3*, 542−543.

(11) Klasa, R. J., Gillum, A. M., Klem, R. E., and Frankel, S. R. (2002) Oblimersen Bcl-2 antisense: facilitating apoptosis in anticancer treatment. *Antisense Nucleic Acid Drug Dev. 12*, 193-213.

(12) Adams, J. M., and Cory, S. (1998) The Bcl-2 protein family: arbiters of cell survival. *Science. 281*, 1322−1326.

(13) Jansen, B., Wacheck, V., Heere-Ress, E., Schlagbauer-Wadl, H., Hoeller, C., Lucas, T., Hoermann, M., Hollenstein, U., Wolff, K., and Pehamberger, H. (2000) Chemosensitisation of malignant melanoma by BCL2 antisense therapy. *Lancet 356*, 1728−1733.

(14) Wacheck, V., Krepler, C., Strommer, S., Heere-Ress, E., Klem, R., Pehamberger, H., Eichler, H. G., and Jansen, B. (2002) Antitumor effect of G3139 Bcl-2 antisense oligonucleotide is independent of its immune stimulation by CpG motifs in SCID mice. *Antisense Nucleic Acid Drug Dev. 12*, 359−367.

(15) Dias, N., and Stein, C. A. (2002) Potential roles of antisense oligonucleotides in cancer therapy. The example of Bcl-2 antisense oligonucleotides. *Eur. J. Pharm. Biopharm. 54*, 263−269.

(16) Raffo, A., Lai, J. C., Stein, C. A., Miller, P., Scaringe, S., Khvorova, A., and Benimetskaya, L. (2004) Antisense RNA down-regulation of bcl-2 expression in DU145 prostate cancer cells does not diminish the cytostatic effects of G3139 (Oblimersen). *Clin Cancer Res. 10*, 3195−3206.

(17) Lai, J. C., Benimetskaya, L., Santella, R. M., Wang, Q., Miller, P. S., and Stein, C. A. (2003) G3139 (oblimersen) may inhibit prostate cancer cell growth in a partially bis-CpG-dependent non-antisense manner. *Mol Cancer Ther. 2*, 1031−1043.

(18) Manoharan, M. (1999) 2′-carbohydrate modifications in antisense oligonucleotide therapy: importance of conformation, configuration and conjugation. *Biochim. Biophys. Acta 1489*, 117−130.

(19) Wagner, E., Oberhauser, B., Holzner, A., Brunar, H., Issakides, G., Schaffner, G., Cotten, M., Knollmueller, M., and Noe, C. R. (1991) A simple procedure for the preparation of protected 2′-O-methyl- or 2′-O-ethylribonucleoside 3′-O-phosphoramidites. *Nucleic Acids Res. 19*, 5965−5971.

(20) Cotten, M., Oberhauser, B., Brunar, H., Holzner, A., Issakides, G., Noe, C. R., Schaffner, G., Wagner, E., and Birnstiel, M. L. (1991) 2′−O-methyl, 2′-O-ethyl oligoribonucleotides and phosphorothioate oligodeoxyribonucleotides as inhibitors of the in vitro U7 snRNP-dependent mRNA processing event. *Nucleic Acids Res. 19*, 2629−2635.

(21) Werner, D., Brunar, H., and Noe, C. R. (1998) Investigations on the influence of 2′−O-alkyl modifications on the base pairing properties of oligonucleotides. *Pharm. Acta Helv. 73*, 3−10.

(22) Lima, W. F., and Crooke, S. T. (1997) Binding affinity and specificity of *Escherichia coli* RNase H1: impact on the kinetics of catalysis of antisense oligonucleotide-RNA hybrids. *Biochemistry. 36*, 390−398.

(23) Monia, B. P., Lesnik, E. A., Gonzalez, C., Lima, W. F., McGee, D., Guinosso, C. J., Kawasaki, A. M., Cook, P. D., and Freier, S. M. (1993) Evaluation of 2′-modified oligonucleotides containing 2′-deoxy gaps as antisense inhibitors of gene expression. *J. Biol. Chem. 268*, 14514−14522.

(24) Manoharan, M., Prakash, T. P., Barber-Peoc′h, I., Bhat, B., Vasquez, G., Ross, B. S., and Cook, P. D. (1999) *N*-(2-Cyanoethoxycarbonyloxy)succinimide: A New Reagent for Protection of Amino Groups in Oligonucleotides. *J. Org. Chem. 64*, 6468−6472.

(25) Summerton, J. (1999) Morpholino antisense oligomers: the case for an RNase H-independent structural type. *Biochim. Biophys. Acta 1489*, 141−158.

(26) Braasch, D. A., and Corey, D. R. (2001) Locked nucleic acid (LNA): fine-tuning the recognition of DNA and RNA. *Chem. Biol. 8*, 1−7.

(27) Braasch, D. A., Liu, Y., and Corey, D. R. (2002) Antisense inhibition of gene expression in cells by oligonucleotides incorporating locked nucleic acids: effect of mRNA target sequence and chimera design. *Nucleic Acids Res. 30*, 5160−5167.

(28) Tung, C.-H., and Stein, S. (2000) Preparation and Applications of Peptide−Oligonucleotide Conjugates. *Bioconjugate Chem. 11*, 605−618.

(29) Letsinger, R. L., and Chaturvedi, S. (1998) Tailored hydrophobic cavities in oligonucleotide-steroid conjugates. *Bioconjugate Chem. 9*, 826−830.

(30) Shea, R. G., Marsters, J. C., and Bischofberger, N. (1990) Synthesis, hybridization properties and antiviral activity of lipid-oligodeoxynucleotide conjugates. *Nucleic Acids Res. 18*, 3777−3783.

(31) Stein, S., and Zhu, T. (1997) Preparation of vitamin B6-peptide and vitamin B6-peptide−oligonucleotide conjugates. *Methods Enzymol. 280*, 51−58.

(32) Maier, M. A., Yannopoulos, C. G., Mohamed, N., Roland, A., Fritz, H., Mohan, V., Just, G., and Manoharan, M. (2003) Synthesis of antisense oligonucleotides conjugated to a multivalent carbohydrate cluster for cellular targeting. *Bioconjugate Chem. 14*, 18−29.

(33) Derossi, D., Chassaing, G., and Prochiantz, A. (1998) Trojan peptides: the penetratin system for intracellular delivery. *Trends Cell Biol. 8*, 84−87.

(34) Pardridge, W. M., Boado, R. J., and Kang, Y.-S. (1995) Vector-mediated delivery of a polyamide (\"peptide\") nucleic acid analog through the blood-brain barrier in vivo. *Proc. Natl. Acad. Sci. U S A. 92*, 5592−5596.

(35) Branden, L. J., Mohamed, A. J., and Smith, C. I. E. (1999) A peptide nucleic acid-nuclear localization signal fusion that mediates nuclear transport of DNA. *Nat. Biotechnol. 17*, 784−787.

(36) Benimetskaya, L., Guzzo-Pernell, N., Liu, S. T., Lai, J. C., Miller, P., and Stein, C. A. (2002) Protamine-fragment peptides fused to an SV40 nuclear localization signal deliver oligonucleotides that produce antisense effects in prostate and bladder carcinoma cells. *Bioconjugate Chem. 13*, 177−187.

(37) Astriab-Fisher, A., Sergueev, D., Fisher, M., Shaw, B. R., and Juliano, R. L. (2002) Conjugates of Antisense Oligonucleo-

tides with the Tat and Antennapedia Cell-Penetrating Peptides: Effects on Cellular Uptake, Binding to Target Sequences, and Biologic Actions. *Pharm. Res. 19*, 744−754.
(38) Fisher, A. A., Ye, D., Sergueev, D. S., Fisher, M. H., Shaw, B. R., and Juliano, R. L. (2002) Evaluating the specificity of antisense oligonucleotide conjugates. A DNA array analysis. *J. Biol. Chem. 277*, 22980−22984.
(39) Leonetti, J. P., Degols, G., and Lebleu, B. (1990) Biological activity of oligonucleotide-poly(L-lysine) conjugates: mechanism of cell uptake. *Bioconjugate Chem. 1*, 149−153.
(40) Degols, G., Leonetti, J. P., Benkirane, M., Devaux, C., and Lebleu, B. (1992) Poly(L-lysine)-conjugated oligonucleotides promote sequence-specific inhibition of acute HIV-1 infection. *Antisense Res. Dev. 2*, 293−301.
(41) Clarenc, J. P., Degols, G., Leonetti, J. P., Milhaud, P., and Lebleu, B. (1993) Delivery of antisense oligonucleotides by poly(L-lysine) conjugation and liposome encapsulation. *Anti-Cancer Drug Des. 8*, 81−94.
(42) Ginobbi, P., Geiser, T. A., Ombres, D., and Citro, G. (1997) Folic acid−polylysine carrier improves efficacy of c-myc antisense oligodeoxynucleotides on human melanoma (M14) cells. *Anticancer Res. 17*, 29−35.
(43) Sazani, P., Kang, S. H., Maier, M. A., Wei, C., Dillman, J., Summerton, J., Manoharan, M., and Kole, R. (2001) Nuclear antisense effects of neutral, anionic and cationic oligonucleotide analogs. *Nucleic Acids Res. 29*, 3965−3974.
(44) Eritja, R., Pons, A., Escarceller, M., Giralt, E., and Albericio, F. (1991) Synthesis of defined peptide−oligonucleotide hybrids containing a nuclear transport signal sequence. *Tetrahedron 47*, 4113−4120.
(45) Bongartz, J. P., Aubertin, A. M., Milhaud, P. G., and Lebleu, B. (1994) Improved biological activity of antisense oligonucleotides conjugated to a fusogenic peptide. *Nucleic Acids Res. 22*, 4681−4688.
(46) Corey, D. R., Munoz-Medellin, D., and Huang, A. (1995) Strand invasion by oligonucleotide−nuclease conjugates. *Bioconjugate Chem. 6*, 93−100.
(47) Haralambidis, J., Chai, M., and Tregear, G. W. (1987) Preparation of base-modified nucleosides suitable for non-radioactive label attachment and their incorporation into synthetic oligodeoxyribonucleotides. *Nucleic Acids Res. 15*, 4857−4876.
(48) Zaramella, S., Yeheskiely, E., and Stromberg, R. (2004) A method for solid-phase synthesis of oligonucleotide 5′-peptide-conjugates using acid-labile alpha-amino protections. *J. Am. Chem. Soc. 126*, 14029−14035.
(49) Manoharan, M., Tivel, K. L., and Cook, P. D. (1995) Lipidic nucleic acids. *Tetrahedron Lett. 36*, 3651−3654.
(50) Manoharan, M., Inamati, G., Tivel, K. L., Conklin, B., Ross, B. S., and Cook, P. D. (1997) 2′- and 3′- cholesterol-conjugated adenosine and cytosine nucleoside building blocks: synthesis of lipidic nucleic acids. *Nucleosides Nucleotides 16*, 1141−1143.
(51) Hwang, J.-T., and Greenberg, M. M. (2001) Synthesis of 2′-Modified Oligodeoxynucleotides via On-Column Conjugation. *J. Org. Chem. 66*, 363−369.
(52) Kachalova, A., Zubin, E., Stetsenko, D., Gait, M., and Oretskaya, T. (2004) Oligonucleotides with 2′−O-carboxymethyl group: synthesis and 2′-conjugation via amide bond formation on solid phase. *Org. Biomol. Chem. 2*, 2793−2797.
(53) Winkler, J., Urban, E., Losert, D., Wacheck, V., Pehamberger, H., and Noe, C. R. (2004) A novel concept for ligand attachment to oligonucleotides via a 2′-succinyl linker. *Nucleic Acids Res. 32*, 710−718.
(54) Vu, H., and Hirschbein, B. L. (1991) Internucleotide phosphite sulfurization with tetraethylthiuram disulfide. Phosphorothioate oligonucleotide synthesis via phosphoramidite chemistry. *Tetrahedron Lett. 32*, 3005−3008.
(55) Pieles, U., Zurcher, W., Schar, M., and Moser, H. E. (1993) Matrix-assisted laser desorption ionization time-of-flight mass spectrometry: a powerful tool for the mass and sequence analysis of natural and modified oligonucleotides. *Nucleic Acids Res. 21*, 3191−3196.
(56) Gilbert, M. (1999) *Optimierung von Antisense-Oligonukleotiden − zwitterionische Nukleinsäuren und Trägersystemvariationen*, Shaker Verlag, Aachen, Germany.
(57) Griffey, R. H., Monia, B. P., Cummins, L. L., Freier, S., Greig, M. J., Guinosso, C. J., Lesnik, E., Manalili, S. M., Mohan, V., Owens, S., Ross, B. R., Sasmor, H., Wancewicz, E., Weiler, K., Wheeler, P. D., and Cook, P. D. (1996) 2′-O-aminopropyl ribonucleotides: a zwitterionic modification that enhances the exonuclease resistance and biological activity of antisense oligonucleotides. *J. Med. Chem. 39*, 5100−5109.
(58) Soukchareun, S., Tregear, G. W., and Haralambidis, J. (1995) Preparation and characterization of antisense oligonucleotide−peptide hybrids containing viral fusion peptides. *Bioconjugate Chem. 6*, 43−53.
(59) de La Torre, B. G., Albericio, F., Saison-Behmoaras, E., Bachi, A., and Eritja, R. (1999) Synthesis and binding properties of oligonucleotides carrying nuclear localization sequences. *Bioconjugate Chem. 10*, 1005−1012.
(60) Henkel, B., Zhang, L., and Bayer, E. (1997) Investigations on solid-phase peptide synthesis in N-to-C direction (inverse synthesis). *Liebigs Annalen/Recueil.* 2161−2168.
(61) Gutheil, W. G., and Xu, Q. (2002) N-to-C solid-phase peptide and peptide trifluoromethylketone synthesis using amino acid tert-butyl esters. *Chem. Pharm. Bull. 50*, 688−691.
(62) Zaramella, S., Yeheskiely, E., and Stromberg, R. (2004) A method for solid-phase synthesis of oligonucleotide 5′-peptide-conjugates using acid-labile alpha-amino protections. *J. Am. Chem. Soc. 126*, 14029−14035.
(63) Clark, C. L., Cecil, P. K., Singh, D., and Gray, D. M. (1997) CD, absorption and thermodynamic analysis of repeating dinucleotide DNA, RNA and hybrid duplexes [d/r(AC)]12.[d/r(GT/U)]12 and the influence of phosphorothioate substitution. *Nucleic Acids Res. 25*, 4098−4105.
(64) Greenfield, N. J., and Fasman, G. D. (1969) Computed circular dichroism spectra for the evaluation of protein conformation. *Biochemistry. 8*, 4108−4116.

BC049729D

The First Total Synthesis of α-D-Glucopyranosyl-(1→2)-β-D-galactopyranosyl-*O*-pyridinoline, an Important Hallmark of Human Joint Diseases†

Pietro Allevi,* Riccardo Cribiù, Elios Giannini, and Mario Anastasia

Dipartimento di Chimica, Biochimica e Biotecnologie per la Medicina, Università di Milano, via Saldini 50, I-20133 Milano, Italy. Received April 5, 2005; Revised Manuscript Received June 16, 2005

The first total synthesis of α-D-glucopyranosyl-(1→2)-β-D-galactopyranosyl-*O*-pyridinoline using a short "one-pot" assembly of its 1,4,5-trisubstituted 3-hydroxypyridinium ring is reported.

INTRODUCTION

This paper describes the first total synthesis of the optically pure α-D-glucopyranosyl-(1→2)-β-D-galactopyranosyl-*O*-pyridinoline (Glc-Gal-PYD, **1**; Figure 1), a natural glycosylated analogue of the collagen cross-linked pyridinoline **2a**, recently found in human synovium by Gineyts et al. (*1*). Glc-Gal-PYD, **1**, appears to be specific of human synovium, and its levels are considered strongly predictive markers of joint destruction progression in various diseases, including rheumatoid arthritis (*1*−*4*). Moreover, Glc-Gal-PYD, **1**, with its attractive and challenging structure, rich in stereogenic centers in both the amino acidic and the glycosidic portions, represents an attractive goal for organic chemists.

Although several different strategies for the synthesis of pyridinoline **2a**, the aglycone portion of Glc-Gal-PYD (**1**), and of its congener deoxypyridinoline **2b** have been published (*5*, *6*), starting from simple amino acids, no attempt was reported until now to synthesize the important glycoconjugate **1**, which, in principle, could be obtained by glycosylation of an appropriate aglycone such as **3** (*6*, *7*) with a glucosyl-galactosyl donor or, in a longer route, with a galactosyl donor having a participating and orthogonally cleavable protective group at position 2, which should allow a successive extension of the glycosylation in the 2 direction of galactose.

Moreover, herein we report a completely different procedure for the synthesis of Glc-Gal-PYD, **1,** adopting, as a key step, the "one-pot protocol" for the assembly of its 1, 4, 5-trisubstituted 3-hydroxypyridinium ring, originally reported by us (*5*, *8*, *9*).

EXPERIMENTAL PROCEDURES

General Methods. Nuclear magnetic resonance spectra were recorded at 303 K on Bruker AM-500 spectrometer operating at 500.13 MHz for ^{1}H and 125.76 MHz for ^{13}C. Chemical shifts are reported in parts per million (ppm, δ units) and are referenced to residual $CHCl_3$ (δ_H = 7.24 ppm) and to $CDCl_3$ (δ_C = 77.0 ppm) for solutions in $CDCl_3$ or to internal CH_3OD (δ_H = 3.30 ppm and δ_C = 49.0 ppm) for solutions in D_2O. ^{1}H NMR data are tabulated in the following order: number of protons, multiplicity (s, singlet; d, doublet; bs, broad singlet; m, multiplet), coupling constant(s) in hertz, assignment of proton(s). The ^{1}H and ^{13}C resonances were assigned by ^{1}H decoupling, ^{1}H−^{1}H COSY, and ^{1}H−^{13}C correlation experiments.

Optical rotations were taken on a Perkin-Elmer 241 polarimeter, and $[\alpha]_D$ values are given in 10^{-1} deg cm^2 g^{-1}.

Mass spectra were obtained using a Finnigan LCQdeca (ThermoQuest) ion trap mass spectrometer fitted with an electrospray source (ESI). The spectra were collected in continuous flow mode by connecting the infusion pump directly to the ESI source. Solutions of compounds were infused at a flow rate of 5 mL/min. The spray voltage was set at 5.0 kV in the positive and at 4.5 kV in the negative ion mode with a capillary temperature of 220 °C. Full-scan mass spectra were recorded by scanning a *m/z* range of 100−2000.

All reactions were monitored by thin-layer chromatography (TLC) carried out on 0.25 mm E. Merck silica gel plates (60 F_{254}) using UV light, 50% sulfuric acid or 0.2% ninhydrin in ethanol, and heat as developing agents. E. Merck 230−400 mesh silica gel was used for flash column chromatography (*10*).

Preparation of *tert*-Butyl (2*S*,5*R*)-6-Amino-2-benzyloxycarbonylamino-5-[(2,3,4,6-tetra-*O*-benzyl-α-D-glucopyranosyl)-(1→2)-(3,4,6-tri-*O*-benzyl-β-D-galactopyranosyl)]hexanoate, 5. To a stirred solution of anhydrous $SnCl_2$ (240 mg, 1.27 mmol) in anhydrous tetrahydrofuran (8 mL), PhSH (496 μL, 4.84 mmol) and Et_3N (4.96 μL, 3.56 mmol) were added. Then, *tert*-butyl (2*S*,5*R*)-6-azido-2-benzyloxycarbonylamino-5-[(2,3,4,6-tetra-*O*-benzyl-α-D-glucopyranosyl)-(1→2)-(3,4,6-tri-*O*-benzyl-β-D-galactopyranosyl)]hexanoate, **4** (1.00 g, 0.75 mmol), was added. After the reaction was stirred at 25 °C for 1 h, the solvent was evaporated, and the crude residue was purified by rapid chromatography with elution of the byproducts with dichloromethane−methanol (100:8, v/v) and the glycosylated amine **5** (834 mg; *Y* = 85%) with dichloromethane−methanol (100:10, v/v). The amine **5**, an oil, showed the following: $[\alpha]^{20}_D$ +30.5 ($CHCl_3$, *c* 1). ^{1}H NMR δ_H (500 MHz, $CDCl_3$): 5.60 (1H, d, *J* 3.3 Hz, H_{glu}-1), 4.56 (1H, d, *J* 7.7 Hz, H_{gal}-1), 4.16 (1H, dd, *J* 10.2 and 3.3 Hz, H_{gal}-2), 4.09 (1H, m, H_{lys}-2), 2.84 (1H, dd, *J* 13.3 and 2.1 Hz, H_{lys}-6a), 2.59 (1H, dd, *J* 13.3 and 6.1 Hz, H_{lys}-6b). ^{13}C NMR δ_C ($CDCl_3$): 171.1 ($CO_2{}^t$Bu), 155.9 ($NHCO_2{}^t$Bu), 101.7 (C_{gal}-1), 95.7 (C_{glu}-1), 53.9(C_{lys}-2), 44.9 (C_{lys}-6). ESI-MS (positive) *m/z*: 1331.6

† This paper is dedicated to Prof. Guido Tettamanti on the occasion of his 70th birthday.

* To whom correspondence should be addressed. Fax: +039 02503 16040. E-mail: pietro.allevi@unimi.it.

10.1021/bc050107h CCC: $30.25 © 2005 American Chemical Society
Published on Web 06/25/2005

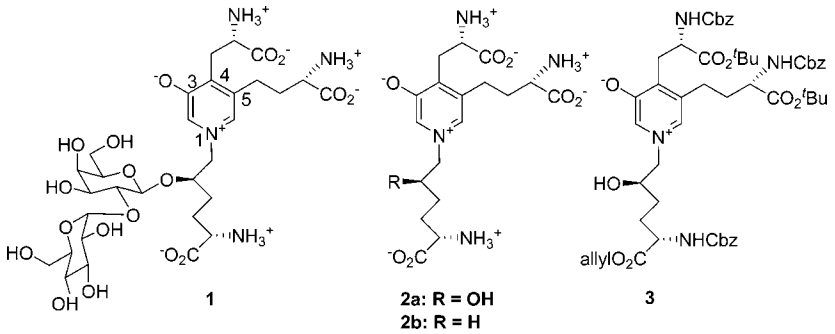

Figure 1. Chemical structures of glycosylated and free collagen cross-links.

(37%), 1330.6 (82%), 1329.6 (100%; M + Na^+), 1307.6 (23%; M + H^+).

Preparation of Completely Protected α-D-Glucopyranosyl-(1→2)-β-D-galactopyranosyl-*O*-pyridinoline, 7. To a solution of the *tert*-butyl (2*S*,5*R*)-6-amino-2-benzyloxycarbonylamino-5-[(2,3,4,6-tetra-*O*-benzyl-α-D-glucopyranosyl)-(1→2)-(3,4,6-tri-*O*-benzyl-β-D-galactopyranosyl)]hexanoate, **5** (600 mg, 0.46 mmol), in CH_3CN (30 mL) containing Na_2CO_3 (900 mg, 8.5 mmol), the protected bromoketone **6** (436 mg, 1.15 mmol) was added, and the mixture was stirred under nitrogen for 6 h. At this time, the disappearance of both the starting glycosylated amine **5** and the initially formed monoalkylated product was observed (TLC, CH_2Cl_2/MeOH 100/5 v/v; R_f = 0.28 and 0.72, respectively). Then, the solvent was evaporated under vacuum, and the crude residue was recovered with MeOH (30 mL) and was vigorously shaken under a slight pressure of oxygen (1.3 atm) at room temperature for 60 h. At this time, the mixture was diluted with dichloromethane (50 mL) and filtered on a pad of Celite. Evaporation of the solvent afforded a crude residue, which was purified by rapid chromatography on silica. Elution with dichloromethane−methanol (100:4, v/v) afforded the protected glycosylated pyridinoline **7** (537 mg; $Y = 62\%$) as a resinous material: $[\alpha]^{20}_D$ +28.2 ($CHCl_3$, *c* 1). UV λ_{max}(EtOH)/nm (ϵ/dm^3 mol^{-1} cm^{-1}): 258.5 (5175), 340 (5962). ^{1}H NMR δ_H (500 MHz, $CDCl_3$): 5.41 (1H, d, *J* 3.5 Hz, H_{glu}-1), 4.54 (1H, d, *J* 7.4 Hz, H_{gal}-1), 4.12−4.06 (4H, overlapping, H_{1chain}-1a, H_{1chain}-1b, H_{4chain}-2, H_{5chain}-3), 3.26 (1H, dd, *J* 11.7 and 11.7 Hz, H_{4chain}-1a), 2.85 (1H, dd, *J* 11.7 and 2.5 Hz, H_{4chain}-1b). ^{13}C NMR δ_C ($CDCl_3$): 171.2, 171.2, 170.5 (3 × $CO_2{}^t$Bu), 156.0 (C-3), 143.6, 140.7, 136.3, 130.2 (pyridinium ring carbons), 103.3 (C_{gal}-1), 96.0 (C_{glu}-1), 56.6, 53.7, 53.6 (3 × amino acidic α-carbons). ESI-MS (positive) *m/z*: 1911.0 (24%), 1910.0, (55%), 1909.2 (100%), 1908.5 (91%; M + Na^+), 1888.5 (13%), 1887.5 (21%), 1886.5 (17%; M + H^+).

Preparation of α-D-Glucopyranosyl-(1→2)-β-D-galactopyranosyl-*O*-pyridinoline, 1, by Successive Regeneration of the Protected Functionalities. *i. Preparation of the Partially Protected Glc-Gal-PYD **8**.* The completely protected Glc-Gal-PYD **7** (400 mg; 0.212 mmol) was dissolved in triflouroacetic acid−water (8 mL, 95:5, v/v), and the resulting solution was stirred at 25 °C for 1.5 h. Evaporation of the mixture afforded the partially protected Glc-Gal-PYD **8** as its tetrafluoroacetate salt (389 mg; $Y = 93\%$) as a glass: $[\alpha]^{20}_D$ +33.4 ($CHCl_3$, *c* 1). ^{1}H NMR δ_H (500 MHz, CD_3OD): 8.25, 8.21 (2H, 2 × bs, pyridinium ring protons), 5.43 (1H, d, *J* 2.9 Hz, H_{glu}-1), 4.46 (1H, d, *J* 8.0 Hz, H_{glu}-1), 4.12 (1H, m, H_{1chain}-2), 4.02 (1H, dd, *J* 8.8 and 8.8 Hz, H_{1chain}-5), 3.78−3.74 (2H, overlapping, H_{gal}-1 and H_{5chain}-3). ^{13}C NMR δ_C (CD_3OD): 175.2, 171.2, 170.5 (3 × $CO_2{}^t$Bu), 161.3 (q, *J* 37.5 Hz, CF_3COO), 157.0 (C-3), 141.8, 141.4, 138.2, 130.0 (pyridinium ring carbons), 117.4 (q, *J* 298 Hz, CF_3COO), 103.2 (C_{gal}-1), 97.4 (C_{glu}-1), 54.5, 53.3, 52.2 (3 × amino acidic α-carbons). ESI-MS (positive) *m/z*: 1519.8 (41%), 1518.8 (90%), 1517.8 (100%; M + H^+), 1540.7 (16%), 1539.6 (16%; M + Na^+).

*ii. Preparation of the α-D-Glucopyranosyl-(1→2)-β-D-galactopyranosyl-O-pyridinoline, **1**.* The partially protected Glc-Gal-PYD **8** (390 mg, 0.20 mmol) dissolved in aqueous HCl (100 mL, 10^{-3} M) was hydrogenated in the presence of $PdCl_2$ (100 mg) at 25 °C and atmospheric pressure. When the absorption of hydrogen was completed, the mixture was filtered over a pad of Celite, and the solution was lyophilized to afford the expected α-D-glucopyranosyl-(1→2)-β-D-galactopyranosyl-*O*-pyridinoline, **1** (170 mg; $Y = 92\%$), as its tetrahydrochloride salt dihydrate ($C_{29}H_{46}N_4O_{18}$·4HCl·2H_2O), an amorphous solid: $[\alpha]^{20}_D$ +47.6.0 (H_2O, *c* 1). ^{1}H NMR δ_H (500 MHz, D_2O): 8.31, 8.29 (2H, 2 × bs, pyridinium ring protons), 5.32 (1H, d, *J* 3.8 Hz, H_{glu}-1), 4.51 (1H, d, *J* 7.7 Hz, H_{gal}-1), 4.33 (1H, m, H_{1chain}-2), 4.15 (1H, dd, *J* 6.3 and 6.3 Hz, H_{5chain}-3), 4.08 (1H, dd, *J* 6.3 and 6.2 Hz, H_{1chain}-5), 3.81 (1H, d, *J* 3.5 and <1 Hz, H_{gal}-4), 3.54 (1H, dd, *J* 9.8 and 7.7 Hz, H_{gal}-2), 3.48 (1H, dd, *J* 9.5 and 3.8 Hz, H_{glu}-2), 3.37 (1H, dd, *J* 9.5 and 9.5 Hz, H_{glu}-4), 3.08 (1H, ddd, *J* 14.7, 11.9, and 5.4 Hz, H_{5chain}-1a), 2.93 (1H, ddd, *J* 14.7, 11.5, and 5.6 Hz, H_{5chain}-1b). ^{13}C NMR δ_C (CD_3OD): 172.7, 172.4, 171.8 ((3 × CO_2H), 155.8 (C-3), 141.3, 141.1 (C-4 and C-5), 137.9, 131.1 (C-2 and C-6), 102.8 (C_{gal}-1), 98.5 (C_{glu}-1), 76.7 (C_{1chain}-2), 75.5 ((C_{gal}-5), 75.4 (C_{gal}-2), 73.8 (C_{glu}-3), 72.6, 72.5 (C_{glu}-2 and C_{glu}-5), 72.1 (C_{gal}-3), 70.4 (C_{glu}-4), 69.7 (C_{gal}-4), 65.1 (C_{1chain}-1), 61.7 (C_{gal}-6), 61.4 (C_{glu}-6), 53.6 (C_{1chain}-5), 53.4 (C_{5chain}-3), 52.3 (C_{4chain}-2), 30.8 (C_{5chain}-2), 28.4 (C_{1chain}-3), 28.1 (C_{4chain}-1), 26.5 (C_{5chain}-1), 26.4 (C_{1chain}-4). ESI-MS (positive) *m/z*: 777.4 (3%), 776.5 (7%), 775.5 (26%; M + Na^+), 755.6 (7%), 754.6 (32%), 753.6 (100%; M + H^+).

RESULTS AND DISCUSSION

For the total synthesis of α-D-glucopyranosyl-(1→2)-β-D-galactopyranosyl-*O*-pyridinoline (Glc-Gal-PYD), we first performed some unsuccessful explorative experiments in which the direct glycosylation of the protected aglycone **3**, previously prepared in our laboratory (*6, 7*), was studied. However, after some efforts, we observed that this strategy presents some objective difficulties. First of all, an obvious competitive glycosylation of the phenolic group and of the lysine hydroxy group of the aglycone **3** occurs. Moreover, other problems arose from the fact that the formation of the *O*-galactoside bond of **1** requires an exclusive β-stereoselection, which appeared difficult to reach in the absence of a suitable participating group at the 2-position of the galactose. Fortunately, as shown in Scheme 1, we subsequently have found a successful and concise synthesis, which involves, as a key step, the "one-pot assembly" of the 1,4,5-trisubstituted 3-hydroxypyri-

Scheme 1. Synthesis of Glucogalactopyridinoline[a]

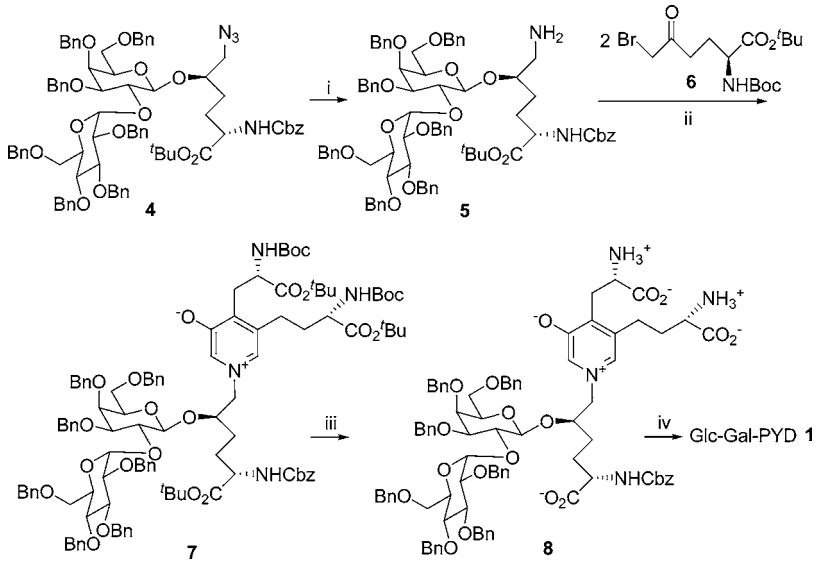

[a] Reagents and conditions: (i) $SnCl_2$, PhSH, Et_3N, THF, 25 °C, 1 h, 85%; (ii) Na_2CO_3, MeCN, 25 °C, 6 h, then Na_2CO_3, O_2, MeOH, 25 °C, 60 h, 62%; (iii) TFA, 25 °C, 1.5 h, 93%; (iv) H_2, $PdCl_2$, aq. HCl 10^{-3} M, 25 °C, 92%.

dinium ring of **1** using as starting building blocks the protected (*11, 12*) glycosylated hydroxylysine **4** and the bromoketone derivative **6** (*8*).

At the beginning, while we were confident about the general scope of our "one-pot" protocol, we were quite uncertain about its successful application to our synthesis. In fact, the "one-pot" formation of the pyridinium ring of the target compound **1** should carry the amino group of the glycosylated hydroxylysine **5** into a series of cascade reactions leading to the formation of the aromatic ring. In particular, the prolonged basic conditions required for the final formation of the pyridinium ring by oxidative aromatization could be critical for the stability of the carbohydrate portion of **5**. In fact, the susceptibility of benzylated sugars and of *O*-glycopeptides to the base-catalyzed β-elimination of a glycan has been widely documented by us (*13*) and by others (*14*). Moreover, our protocol (Scheme 1) works as planned, and we successfully obtained the desired compound Glc-Gal-PYD, **1**, in amounts and purity suitable for its use in biological experiments.

The glycosylated hydroxyazide **4**, prepared by elaboration of L-glutamic acid (*11*, *12*), followed by a stereoselective introduction of the disaccaridic portion in two steps, was reduced to the glycosylated hydroxylysine **5** in quantitative yields and in a short time (1 h), using a tin(II) complex prepared by treatment of $SnCl_2$ with appropriate amounts of thiophenol and triethylamine in acetonitrile (*15*). These conditions were selected as the more favorable in terms of reaction time and yield, after some less satisfactory attempts performed using inter alia triphenylphosphine or polystyrene-linked triphenylphosphine (*16*) or a thiolytic reduction catalyzed by diisopropylethylamine (*17*).

The glycoside **5** was successively reacted with an excess (1:2.5 molar ratio) of the bromoketone derivative **6** (*8*) in CH_3CN containing solid Na_2CO_3 to obtain in "one pot" the glycoconjugate **7**, containing a 3-hydroxypyridinium ring. The reaction was continued until the disappearance of both the starting glycosylated amine and the initially formed monoalkylated product (TLC). Successively, the CH_3CN was replaced by MeOH, and the resulting mixture was vigorously shaken under a slight pressure of oxygen (1.3 atm) at room temperature for 60 h. These conditions, which are different from those described in the general protocol for the synthesis of 3-hydroxy-4,5-disubstituted pyridines from a cyclic compounds (*5*, *8*), afforded the best yields of the final compound **7**. In fact, when the previously reported bases (K_2CO_3) or air in place of oxygen for the alkylation, followed by self-condensation of the initially formed diketo amine, were used, less satisfactory yield were obtained and the reaction times were noticeably longer (4 days). This appeared to be due to the final step including the formation of the intermediate cyclic α,β-unsaturated ketone (*8*) and its aromatization to the final fluorescent compound **7**. In fact, comparable yields were obtained when the reaction was initially performed in CH_3CN and in the presence of K_2CO_3 and then this salt was substituted by Na_2CO_3 before changing the solvent with MeOH. Most probably, the solubility in methanol of Na_2CO_3, relatively higher than that of K_2CO_3, and the increased solubility of the pure oxygen, due to its higher partial pressure (with respect to the air oxygen), accelerate the reaction and avoid the formation of byproducts (evident in TLC as nonfluorescent compounds) formed by side reaction. Standard work-up and chromatographic purification on silica afforded then the 3-hydroxypyridinium derivative **7** (in 62% yields, as a resinous material). This showed the correct elemental analysis and molecular ion, together with appropriate UV and NMR evidence, which support the presence of the 3,4-hydroxypyridinium ring (λ_{max} 340.0 and 258.5 nm in EtOH; ^{13}C signals at 156.0, 143.6, 140.7, 136.3 and 130.2 ppm). On the other hand, the presence of the intact β-galactosidic and α-glucosidic bonds was confirmed by the expected resonances and coupling constants of the anomeric protons in the ^1H NMR spectra (two doublets at 4.54 ppm with $J = 7.4$ Hz and at 5.41 ppm with $J = 3.5$ Hz), attributed to the anomeric protons of the galactosyl and glucosyl portions, respectively.

The presence in compound **7** of the three amino acidic functionalities was supported by the ^{13}C resonances of the carboxylic groups and of the α-carbons (signals at 56.6, 53.7, and 53.6 ppm).

Treatment of compound **7** with trifluoracetic acid regenerates all the carboxylic groups and the amino groups at the amino acid chains at position 4 and 5, thus

affording the benzylated derivative **8**. Finally hydrogenolysis of the surviving benzyloxy and *N*-carbobenzyloxy groups afforded the title compound **1** in high yield (total *Y* from **4** = 45%).

It is worth pointing out that the hydrogenolysis of the benzyloxy groups of the benzyl derivative **8** with palladium on carbon (10%) under several sets of conditions (also acidic) was unexpectedly unsuccessful, although palladium on carbon works well in the deprotection of benzyl derivatives of pyridinolines (*5*−*9*) and glycosylated hydroxylysines (*11*, *12*). In contrast, when the reaction was performed in acidic water under the catalysis of $PdCl_2$, the desired compound **1** was obtained without evident inhibition of the catalyst by the pyridine group present in the starting compound or by the amine group initially formed by the hydrogenolysis. On the other hand, all attempts where the hydrogenolytic cleavage of all benzyloxy groups was performed before the acidic hydrolysis of the *tert*-butyl esters were unsatisfactory.

The obtained glycoconjugate **1** shows the expected physicochemical properties and behavior in HPLC and mass-spectrometry analyses, under the conditions described by Gyneyts et al. (*1*), superimposable to that of Glc-Gal-PYD present in the urine of a patient with rheumatoid arthritis.

In conclusion, herein we report the first synthesis and complete characterization of Glc-Gal-PYD, **1**, an important hallmark of human joint diseases. The synthesis of this collagen cross-link represents a confirmation of the structure assigned to the native Glc-Gal-PYD and allows us to generate the compound in amounts suitable for biological studies.

ACKNOWLEDGMENT

This work was financially supported by Italian Ministero dell'Istruzione e della Ricerca Scientifica (MIUR).

Supporting Information Available: ^1H and ^{13}C spectra and 2D experiments ($^1H-^1H$ COSY and $^1H-^{13}C$ CHCORR) for compounds **5**, **7**, **8**, and **1.** This material is available free of charge via the Internet at http://pubs.acs.org.

LITERATURE CITED

(1) Gineyts, E., Garnero, P., and Delmas, P. (2001) Urinary excretion of glucosyl-galactosyl pyridinoline: a specific biochemical marker of synovium degradation. *Rheumatology 40*, 315−323.

(2) Garnero, P., and Delmas, P. D. (2003) Biomarkers in osteoarthritis. *Curr. Opin. Rheumatol. 15*, 641−646.

(3) Garnero, P., Gineyts, E., Christgau, S., Finck, B., and Delmas, P. D. (2002) Association of baseline levels of urinary glucosyl-galactosyl-pyridinoline and type II collagen C-telopeptide with progression of joint destruction in patients with early rheumatoid arthritis. *Arthritis Rheum. 46*, 21−30.

(4) Roth, M., and Uebelhart, D. (2003) Search for new urinary biochemical markers of collagen degradation in man. *Clin. Chim. Acta 327*, 81−86.

(5) For a description of the published protocols for the syntheses of pyridinolines, see: Anastasia, L., Anastasia, M., and Allevi, P. (2001) A practical protocol for the synthesis of 3-hydroxy-4,5-disubstituted pyridine derivatives from acyclic compounds. *J. Chem. Soc., Perkin Trans. 1* 2404−2408 and references therein.

(6) Allevi, P., and Anastasia, M. (2003) A simple modular synthesis of pyridinoline, a collagen cross-link of biochemical interest. *Tetrahedron: Asymmetry 14*, 2005−2012.

(7) Allevi, P., Galligani, M., and Anastasia, M. (2002) A simple and convenient transformation of L-lysine into pyridinoline and deoxypyridinoline, two collagen cross-links of biochemical interest. *Tetrahedron: Asymmetry 13*, 1901−1910.

(8) Allevi, P., Longo, A., and Anastasia, M. (1999) Total synthesis of deoxypyridinoline, a biochemical marker of collagen turnover. *J. Chem. Soc., Chem. Commun*. 559−560. Our protocol was successively adopted by other authors: Adamczyk, M., Johnson, D. D., and Reddy, R. E. (1999) An efficient one-pot synthesis of (+)-deoxypyridinoline. *Tetrahedron Lett. 40*, 8993−8994 and Corrigendum (2001) *Tetrahedron Lett. 42*, 767. Adamczyk, M., Johnson, D. D., and Reddy, R. E. (2000) Bone collagen cross-links: an efficient one-pot synthesis of (+)-pyridinoline and (+)-deoxypyridinoline. *Tetrahedron: Asymmetry 11*, 2289−2298 and Corrigendum (2000) *Tetrahedron: Asymmetry*, *11*, 5017.

(9) Allevi, P., Longo, A., and Anastasia, M. (1999) A new modular synthesis of deoxypyridinoline a primary reference material for monitoring the bone metabolism. *J. Chem. Soc., Perkin Trans. 1*, 2867−2868.

(10) Still, W. C., Kahn, M., and Mitra, A. (1978) Rapid Chromatographic Technique for Preparative Separations with Moderate Resolution. *J. Org. Chem. 43*, 2923−2925.

(11) Allevi, P., Anastasia, M., Paroni, P., and Ragusa, A. (2004) The first synthesis of glucosylgalactosyl hydroxylysine (glu-gal-hyl) an important biological indicator of collagen turnover. *Bioorg. Med. Chem. Lett. 14*, 3319−3321.

(12) Allevi, P., Anastasia, M., Paroni, P., and Ragusa, A. (2004) Hydroxylysine containing glycoconjugate: an efficient synthesis of natural galactosylhydroxylysine (Gal-Hyl) and glucosylgalactosylhydroxylysine (Glu-Gal-Hyl) and of their 5-(*S*)-epimers. *Tetrahedron: Asymmetry 15*, 3139−3148.

(13) Anastasia, M., Allevi, P., Ciuffreda, P., Fiecchi, A. and Scala, A. (1991) Action of Alkali on O−Benzylated Aldoses: A Simple Rationalization of Some Reactions Occurring in Alkaline Media. *J. Org. Chem. 56*, 3054−3058.

(14) Wakabayashi, K., and Pigman, W. (1974) Synthesis of some glycodipeptides containing hydroxyamino acids, and their stabilities to acids and bases. *Carbohydr. Res. 35*, 3−14.

(15) Bartra, M., Romea, P., Urpì, F., and Vilarrasa, J. (1990) A fast procedure for the reduction of azides and nitro-compounds based on the reducing ability of $Sn(SR)_3$-species. *Tetrahedron 46*, 587−594.

(16) Gololobov, Y., and Kasukhin, L. F. (1992) Recent advances in the Staudinger reaction *Tetrahedron 48*, 1353−1406.

(17) Meinjohanns, E., Meldal, M., Jensen, T., Werdelin, O., Galli-Stampino, L., Mouritsen, S., and Bock, K. (1997) Versatile solid-phase thiolytic reduction of azido and N-Dts groups in the synthesis of haemoglobin (67−76) O-glycopeptides and photoaffinity labeled analogues to study glycan T-cell specificity. *J. Chem. Soc., Perkin Trans. 1*, 871−884.

BC050107H

CORRECTIONS

Volume 15, Number 3, May/June, 2004.

Audrey Roth, Socorro Espuelas, Christine Thumann, Benoît Frisch, and Francis Schuber*

SYNTHESIS OF THIOL-REACTIVE LIPOPEPTIDE ADJUVANTS. INCORPORATION INTO LIPOSOMES AND STUDY OF THEIR MITOGENIC EFFECT ON MOUSE SPLENOCYTES

Pages 541−553. The synthesis of Pam_2GAG (**19**) and Pam_2GAG-Mal (**21**) was based on the publication by J. W. Metzger et al. (1991) *Int. J. Pept. Protein Res. 38,* 545−554. Unfortunately we have discovered since that it contains errors in configuration assignments. For example, on page 552 of their publication the authors state that "Reaction with *S*-(−)-glycidol yields the respective *R*-configurated *S*-glycerylcyteinyl derivative". This is incorrect, and for this particular compound *R*-(−)-glycidol should be used as starting material. This error invalidates the configuration attributed to the stereochemically pure lipopeptides synthesized according to Metzger et al. The consequences for our own work are that compounds **19** and **21** are (*S*)-configured instead of (*R*) as published and thus are expected to be less biologically active than anticipated.

BC050105X

10.1021/bc050105x
Published on Web 06/30/2005

Volume 16, Number 2, March/April, 2005.

Jayant Khandare, Parag Kolhe, Omathanu Pillai, Sujatha Kannan, Mary Lieh-Lai, and Rangaramanujam M. Kannan*

SYNTHESIS, CELLULAR TRANSPORT, AND ACTIVITY OF POLYAMIDOAMINE DENDRIMER−METHYLPREDNISOLONE CONJUGATES

Page 336. Reference 11: The first author should be Abu-Rmaileh, R.

Page 337: Reference 25: The last author should be D'Emanuele, A.

BC058064S

10.1021/bc058064s
Published on Web 06/02/2005

SEPTEMBER/OCTOBER 2005
Volume 16, Number 5

© Copyright 2005 by the American Chemical Society

Bioconjugate Chemistry

COMMUNICATIONS

Cationic Lipophosphoramidates and Lipophosphoguanidines Are Very Efficient for in Vivo DNA Delivery

Erwann Picquet,[†] Karine Le Ny,[†] Pascal Delépine,[‡] Tristan Montier,[‡] Jean-Jacques Yaouanc,[†] Dominique Cartier,[†] Hervé des Abbayes,[†] Claude Férec,[‡] and Jean-Claude Clément*,[†]

UMR CNRS 6521, UFR Sciences et Techniques, Université de Bretagne Occidentale, 6, Av. Le Gorgeu, C.S. 93837, F-29238 Brest Cedex 3, France, and INSERM, U 613, Université de Bretagne Occidentale, C.S. 2653, F-29275 Brest Cedex, France. Received March 29, 2005; Revised Manuscript Received August 5, 2005

Two new families of cationic lipids were designed and synthesized for gene delivery, namely "lipophosphoramidates" and "lipophosphoguanidines", whose efficiency was noteworthy. The most efficient have an arsonium cation as the polar head, and the unsaturated lipidic tails (e.g. oleyl) gave the better in vivo results (mice lungs).

INTRODUCTION

Although currently less efficient than viral vectors, synthetic vectors can encapsulate and, theoretically, carry out large genetic material (>100 kb) and do not lead to immunogenic response, hence a growing investment in the search for nonviral vectors with increased efficiency and lower toxicity. Among those, cationic lipids hold, together with polymers, the most important place (*1*). In these lipids, one must note that, with a few exceptions, the cationic or polycationic charge is always carried by nitrogen atoms. As an exception, precisely, we showed that in the case of cationic phosphonolipids, the replacement of an ammonium by a phosphonium or an arsonium polar head led to an increased efficiency (up to 7 times according to the cell lines tested) and decreased cytotoxicity (*2*).

Going on with our search for even more efficient vectors, we looked into the possibility of using the intrinsic properties of cells for designing synthetic vectors possessing a weak linker between the lipidic part and the polar cationic head, to split off the lipidic part after cell internalization. Indeed, the pH decrease, from more than 7 extracellular to 5−6 in endosomes and about 4 in some late lysosomes, is well established. Such a principle was recently described in novel cationic lipids incorporating an acid-sensitive acylhydrazone linker (*3*). Another example was the incorporation of an acid-labile vinyl ether linkage in the lipidic part of the cationic lipid (*4*). Something similar was recently described in the case of polymers: linear polyethyleneimine (PEI) reticulated with a linker including two ester bonds susceptible to hydrolysis at physiological conditions was more efficient and less toxic than reticular PEI (*5*).

In the field of phosphorylated compounds, the hydrolysis of the P(O)−N bond is well documented (*6*), and the

* To whom correspondence should be addressed. E-mail: jean-claude.clement@univ-brest.fr.
[†] UMR CNRS 6521, UFR Sciences et Techniques, Université de Bretagne Occidentale.
[‡] INSERM, U 613,Université de Bretagne Occidentale, C.S. 2653.

10.1021/bc050097k CCC: $30.25 © 2005 American Chemical Society
Published on Web 08/27/2005

Scheme 1. Synthesis of Cationic Lipophosphoramidates[a]

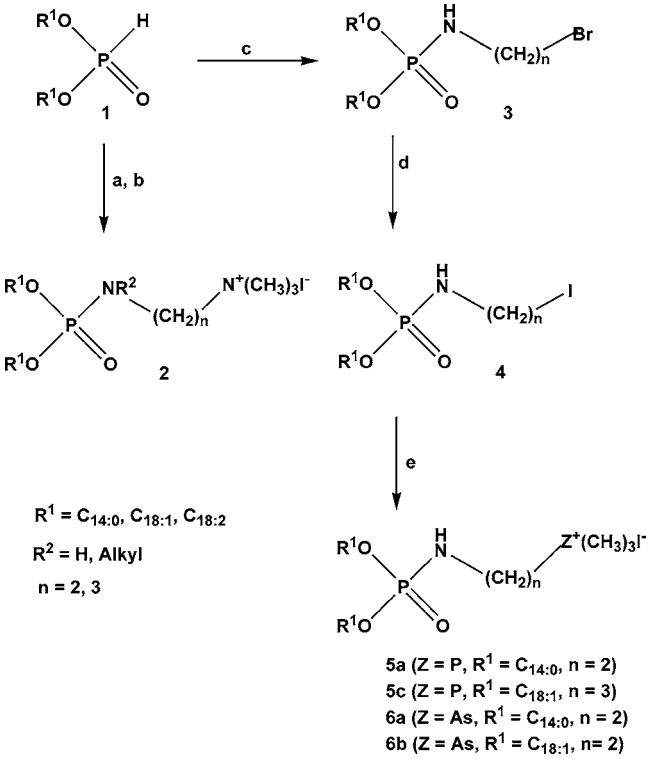

[a] (a) $R^2HN(CH_2)_n$-$N(CH_3)_2/CCl_4$; (b) CH_3I, RT, 12 h; (c) $H_2N(CH_2)_nBr$,HBr/CCl_4; (d) NaI/acetone; (e) for Z = P: $(CH_3)_3P$/THF, 40 °C, 2 days; for Z = As: $(CH_3)_3As$, neat, 45 °C, 1 week.

dialkyl phosphite group is sometimes used as a protecting group for amines (*7*) and polyamines (*8*). Deprotection generally occurs easily in dilute mineral acids, but the P−N bond shows a relative stability in organic and Lewis acids (*7a*). Moreover and more significant, the enzymatic hydrolysis of the P−N bond of phosphoramidates by phosphoramidases active at pH 3.5−7.5 is well established (*9*).

Taking these facts into account, we designed and synthesized two novel families of DNA monocationic carriers, namely "lipophosphoramidates" and "lipophosphoguanidines".

RESULTS

The main route leading to phosphoramidates is the reaction of a hydrogen phosphite with an amine, in the presence of CCl_4, under phase-transfer catalysis conditions (*10*) or not (*11*). We adapted these two procedures for reacting lipidic phosphites **1** with various diamines to get, after quaternisation with methyl iodide, a set of "lipophosphoramidates" **2** with an ammonium cation. Replacement of diamines by bromoalkylamines led to bromoalkylphosphoramidates **3**. After metathesis Br → I for increased reactivity, compounds **4** were reacted with trimethylphosphine or trimethylarsine, thus leading to lipophosphoramidates with trimethylphosphonium **5** or trimethylarsonium **6** cations, respectively (Scheme 1).

Hydrolysis of phosphoguanidines has been known for a long time because of many studies about conversion of phosphocreatine to creatinine and inorganic phosphate (*12*). With the same purpose as for lipophosphoramidates, we designed and synthesized cationic "lipophosphoguanidines". The first step of their synthesis was adapted for lipidic phosphites **1** from those of simple phosphoguanidines, i.e., the phosphorylation of 2-ethyl-2-thiopseudourea (*13*). Subsequent reaction with unsymmetrical diamines followed by quaternization of the terminal amine led to lipophosphoguanidines **8** with an ammonium cation (Scheme 2).

Scheme 2. Synthesis of Cationic Lipophosphoguanidines[a]

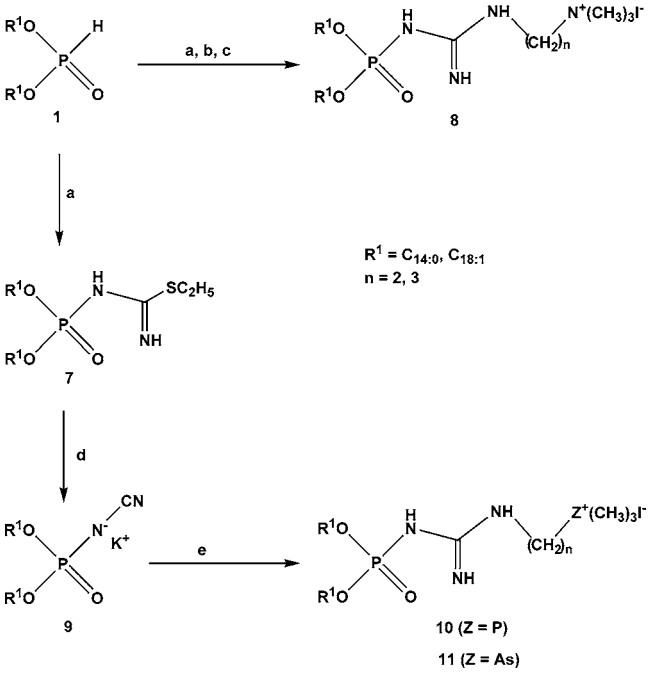

[a] (a) 2-Ethyl-2-pseudothiourea; (b) $H_2N(CH_2)_nN(CH_3)_2$; (c) CH_3I; (d) K_2CO_3/HgO; (e) $H_3N^+(CH_2)_nZ^+(CH_3)_3I^-$.

Dibenzyl (or diphenyl) phosphoryl isothioureas undergo ethanethiol elimination when reacted with sufficiently basic amines in the presence of HgO (*14*). In the case of lipophilic phosphoryl isothioureas **7**, replacement of amines by K_2CO_3 led to isolable potassium salts **9** which, upon reaction with aminoalkylphosphonium or arsonium hydrobromides led directly to "cationic lipophosphoguanidines" with a trimethyl phosphonium (**10**) or arsonium (**11**) cation, respectively (*15*).

Several examples of cationic lipids **2**, **5**, and **6** were submitted to transfection activity assays (*16*): in vitro (HeLa, CHO cell lines or CF nasal polyps primary cultures) and in vivo (mice lung). For in vitro experiments with HeLa cell line and CF primary culture, the luciferase activity was measured 2 days after transfection, using a chemiluminescent assay. For CHO, the percentage of GFP^+ cells was measured by Facs flow analysis. Whatever cell or technique used (*17*), the activity with lipid **6b** ($R^1 = C_{18:1}$, $n = 2$) or **8a** ($R^1 = C_{14:0}$, $n = 3$), for instance, was systematically 20−25% greater than DOTAP or Lipofectine, two commercial references, and corresponded to 25−30% of GFP^+ viable cells. More significant were the results of in vivo assays on mice lung (Figure 1) (the lipid-to-DNA charge ratio used was 4, as this ratio had been previously shown to be the optimal (*18*)). Lipids **5a** ($R^1 = C_{14:0}$, $n = 2$), **5c** ($R^1 = C_{18:1}$, $n = 3$), **6a** ($R^1 = C_{14:0}$, $n = 2$), and **6b** exhibit a luciferase expression up to 3600 times higher than DOTAP (*19*).

As checked on a model compound (**2**, $R^1 = C_2H_5$, $R^2 = CH_3$, $n = 3$, for solubility reasons) the acid-catalyzed hydrolysis of the P−N bond is not very fast (4 days for 100% P−N hydrolysis at pH = 2). So, the total hydrolysis of the P−N bond seems unnecessary to get the high levels of in vivo observed efficiency, since the highest expression levels were reached within 24 h (in vivo) or 48 h (in vitro).

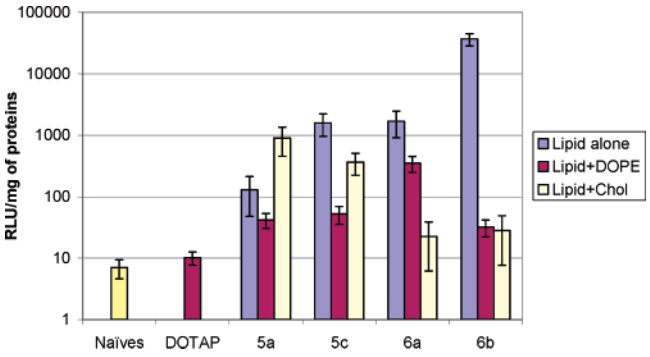

Figure 1.

But it may also be presumed that these noteworthy in vivo results are due to an enzymatic activity (which remains to be proved), accelerating the rate of the P−N bond hydrolysis, which does not work in vitro. Since this relevant efficiency seems accompanied by a weak cytotoxicity, a more complete biological evaluation is currently under investigation from our group.

ACKNOWLEDGMENT

The "Conseil Régional de Bretagne" and "Brest Métropole Océane" are gratefully acknowledged for financial support (grants to E.P. and K.L.N.).

LITERATURE CITED

(1) For reviews, see (a) Miller, A. D. (1998) Cationic liposomes for gene therapy. *Angew. Chem., Int. Ed. 37*, 1768−1785. (b) Martin, B., Sainlos, M., Aissaoui, A., Oudrhiri, N., Hauchecorne, M., Vigneron, J. P., Lehn, J. M., and Lehn, P. (2005) The design of cationic lipids for gene delivery. *Curr. Pharm. Des. 11*, 375−394.

(2) (a) Guénin, E., Hervé, A. C., Floch, V., Loisel, S., Yaouanc, J. J., Clément, J. C., Férec, C., and Des Abbayes, H. (2000) Cationic phosphonolipids containing quaternary phosphonium and arsonium groups for DNA transfection with good efficiency and low cellular toxicity *Angew. Chem., Int. Ed. 39*, 629. (b) Floch, V., Loisel, S., Guénin, E., Hervé, A. C., Yaouanc, J. J., Clément, J. C., Férec, C., and Des Abbayes, H. (2000) Cation substitution in cationic phosphonolipids: A new concept to improve transfection activity and decrease cellular toxicity. *J. Med. Chem. 43*, 4617−4628.

(3) Aissaoui, A., Martin, B., Kan, E., Oudrhiri, N., Hauchecorne, M., Vigneron, J. P., Lehn, J. M., and Lehn, P. (2004) Novel cationic lipids incorporating an acid-sensitive acylhydrazone linker: synthesis and transfection properties. *J. Med. Chem. 47*, 5210−5223.

(4) Boomer, J. A., Thompson, D. H., and Sullivan, S. M. (2002) Formation of plasmid-based transfection complexes with an acid-labile cationic lipid: Characterization of in vitro and in vivo gene transfert. *Pharm. Res. 19*, 1292−1301.

(5) Laird Forrest, M., Koerber, J. T., and Pack, D. W. (2003) A degradable polyethyleneimine derivative with low toxicity for highly efficient gene delivery. *Bioconjugate Chem. 14*, 934−940.

(6) Garrison, A. W., and Boozer, C. E. (1968) The acid-catalyzed hydrolysis of a series of phosphoramidates. *J. Am. Chem. Soc. 90*, 3486−3494.

(7) (a) Zhao, Y.-F., Ji, G.-J., Xi, S.-K., Tang, H.-G., Song, A.-T., and Wei, S.-Z. (1983) The application of dialkyl phosphite as the amino protection reagent in organic synthesis. *Phosphorus Sulfur 18*, 155−158. (b) Savignac, P., Dreux, M., and Plé, G. (1973) Phosphoramides ω-aminés.I. Synthèse de diaminométhanes et diaminopropanes. *J. Organomet. Chem. 60*, 103−113, and refs quoted therein.

(8) (a) Burguete, M. I., Lopez-Diago, L., Garcia-España, E., Galindo, F., Luis, S. V., Miravet, J., and Sroczynski, D. (2003) New efficient procedure for the use of diethoxyphosphoryl as a protecting group in the synthesis of polyazamacrocycles. *J. Org. Chem. 68*, 10169−10171. (b) Qian, L., Sun, Z., Mertes, M. P., and Bowman Mertes, K. (1991) Synthesis of selectively protected polyaza macrocycles. *J. Org. Chem. 56*, 4904−4907.

(9) Holzer, M. E., Burrow, D. J., and Smith, R. A. (1962) Metabolism of phosphoramidates. I. Enzymic hydrolysis and transfer reactions. *Biochim. Biophys. Acta 56*, 491−501, and ref quoted therein.

(10) Zwierzak, A. (1975) Phase-Transfert-Catalysed Phosphorylation of amines in an aqueous system. *Synthesis* 507−509.

(11) Atherton, F. R., Openshaw, H. T., and Todd, A. R. (1945) Studies on phosphorylation. Part II. The reaction of dialkyl phosphates with polyhalogen compounds in the presence of bases. A new method for the phosphorylation of amines. *J. Chem. Soc.* 660.

(12) (a) Allen, G. W., and Haake, P. (1973) Hydrolysis of phosphoroguanidines. A model system for phosphorylation by phosphorocreatine. *J. Am. Chem. Soc. 95*, 8080−8087. (b) Lillocci, C., and Vernon, C. A. (1981) The mechanism of hydrolysis of phosphorocreatine to creatinine. *Gazz. Chim. Ital. 111*, 23−25.

(13) Xi, S.-K., Zhao, Y. F., Lin, W. O., and Costa de Souza, M. (1990) Synthesis of bidentate organophosphorous compounds with urea substituents. *Synth. Commun. 20*, 3295−3301.

(14) Cramer, F., and Vollmar, A. (1958) Darstellung von isothioureido-phosphaten und phosphoguanidinen. *Chem. Ber. 91*, 919−923.

(15) Both lipophosphoramidates and lipophosphoguanidines gave satisfactory ^{1}H, ^{31}P, and ^{13}C NMR spectra.

(16) Cationic lipids were dissolved in chloroform in glass vials. Chloroform was then evaporated by vacuum, resulting in a dry lipid film. Sterile pyrogen-free distilled water was added in appropriate amounts to the lipid. The vials were then sealed and stored overnight at 4 °C. The resulting solution was sonicated for 10 min in a bath sonicator. The plasmid and lipid were then combined and incubated for 30 min at room temperature to form the lipoplexes.

(17) For a preliminary in vitro and ex vivo biological evaluation of lipophosphoramidates, see Montier, T., Delépine, P., Marianowski, R., Le Ny, K., Le Bris, M., Gillet, D., Potard, G., Mondine, P., Frachon, I., Yaouanc, J. J., Clément, J. C., Des Abbayes, H., and Férec, C. (2004) CFTR transgene expression in primary ΔF 508 epithelial cell cultures from human nasal polyps following gene transfer with cationic phosphonolipids. *Mol. Biotechnol. 26,* 193−205.

(18) Floch, V., Delepine, P., Guillaume, C., Loisel, S., Chasse, S., Le Bolc'h, G., Gobin, E., Leroy, J.-P., and Ferec, C. (2000) Systemic administration of cationic phosphonolipids/DNA complexes and the relationship between formulation and lung transfection efficiency. *Biochim. Biophys. Acta 1464* (1), 95−103.

(19) For in vivo mice lung assays, the following protocol was implemented: Five-week-old female Swiss mice were used. Once anesthetized by ether inhalation, each mouse received 200 μL of the lipoplex solution containing 50 μg of plasmid encoding luciferase as an intravenous bolus in the tail vein. Lungs were harvested 24 h after injection. Each tissue was crushed in a mortar cooled by liquid nitrogen and incubated with lysis buffer (Promega) for 30 min. A centrifugation at 10 000*g* was performed, and supernatant luciferase activity was assayed in a 'MLX microtiter plate luminometer' (Dynex technologies) using a 'luciferase assay system' (Promega). Five mice were used for each time point. The total protein concentration of these supernatants was measured with the 'Coomassie Plus Protein Assay Kit' (Pierce). Results are expressed in RLU per mg of total proteins.

BC050097K

A Novel Fluorescent Probe: Europium Complex Hybridized T7 Phage

Chin-Mei Liu, Qiaoling Jin, April Sutton, and Liaohai Chen*

Biosciences Division, Argonne National Laboratory, 9700 South Cass Avenue, Argonne, Illinois 60439.
Received April 6, 2005; Revised Manuscript Received August 8, 2005

We report on the creation of a novel fluorescent probe of europium-complex hybridized T7 phage. It was made by filling a ligand-displayed T7 ghost phage with a fluorescent europium complex particle. The structure of the hybridized phage, which contains a fluorescent inorganic core surrounded by a ligand-displayed capsid shell, was confirmed by electron microscope, energy-dispersive X-ray analysis (EDX), bioassays, and fluorescence spectrometer. More importantly, as a benefit of the phage display technology, the hybridized phage has the capability to integrate an affinity reagent against virtually any target molecules. The approach provides an original method to fluorescently "tag" a bioligand and/or to "biofunctionalize" a fluorophore particle. By using other types of materials such as radioactive or magnetic particles to fill the ghost phage, we envision that the hybridized phages represent a new class of fluorescent, magnetic, or radioprobes for imaging and bioassays and could be used both in vitro and in vivo.

Fluorescent probes play important roles in biology, medicine, and biotechnology (*1*, *2*). Conventionally, a fluorescent probe is made by chemically conjugating a fluorophore molecule or a quantum dot to a biomolecule (such as an affinity reagent). Recently, a few unconventional probes have been developed. For instance, researchers at a number of laboratories have explored the use of aequorea-derived fluorescent proteins (AFP) (*3*, *4*). As an alternative to AFP, tetracysteine-biarsenical labeling also has been demonstrated as a very useful probing tool (*5*). In both cases, the "fluorophores" (fluorescent proteins, such as AFP and tetracysteine-biarsenical complex) are fused to the affinity regents by molecular biology methods instead of chemical conjugation.

The concept for a hybridized phage probe is based on the fact that certain tailed phages build their protein shells first and subsequently condense the nucleic acid within them (*6*). As a result, an empty capsid ("ghost phage" or "pseudo phage") from the tailed phage is stable without interior DNA. The architecture of a ghost phage can function as a unique nanocontainer for uniform fabrication of a nanosized functional (fluorescent, magnetic, or radioactive, etc.) particle inside. Consequently, such a hybridized system contains a functional core and a capsid protein shell.

We chose to use a tailed icosahedral T7 bacteriophage for fabricating a hybridized phage. Structurally, T7 phage consists of a capsid shell, a head−tail connector, tail, and tail fibers. The morphogenesis of T7 and its DNA package have been well documented in the literature, thanks to the major contributions by Dr. William Studier (*7*, *8*). It was demonstrated that empty capsid shells of T7 were assembled prior to the DNA packaging and can be isolated at the early stage of the lytic infection. Given the diameter of T7 phage (approximately 55 nm); a ghost T7 phage provides a cavity of ∼40 nm, which can be used to accommodate fluorescent materials, thus leading to a fluorescent material hybridized T7 phage.

An intrinsic advantage of using fluorescent material hybridized T7 phage as a fluorescence probe is that it has the capability to carry a specific affinity reagent against virtually any target molecules via phage display technology (*9*−*11*). In phage display, ligands (such as recombinant antibody fragments, cDNA-encoded segments, or combinatorial peptides chains) are expressed as fusions to a capsid protein present on the surface of viral particles. Libraries of millions to billions of phage particles, each displaying a different fusion protein, are screened (usually by affinity selection) for members displaying the desired properties or binding affinities. Normally, three rounds of screening (biopanning) processes will yield the isolation of a specific binding phage against the target molecule. Subsequently, one can make the corresponding ghost phage and use the ghost as the container to host the fluorescence material inside the ghost to form a hybridized phage. The approach of constructing a fluorescent core and ligand displayed capsid shell structure provides a revolutionary way to "tag" a fluorescence material with affinity reagents or to "functionalize" a bioligand with fluorescence. Thus, the hybridized phage represents a novel class of fluorescent probe.

Among the fluorophores used in the fluorescent probes, the lanthanide complex (such as europium or terbium complex) exhibits unique spectral characteristics (*12*). Lanthanide complexes are superior to conventional organic fluorophores because they have very sharp emission spectra with more than a 300-nm Stoke shift, plus an extremely long fluorescence lifetime (∼1 ms), which can be easily detected by time-resolved fluorescence spectroscopy. Thus, lanthanide complexes are the ideal fluorophores to overcome the problems associated with background fluorescence in a biological sample. However, making a lanthanide probe, like making other fluorescence probes, involves chemically conjugating a ligand

* Address correspondence to this author. phone 630-252-3975, fax: 630-252-3387, e-mail: lhchen@anl.gov.

10.1021/bc050108+ CCC: $30.25 © 2005 American Chemical Society
Published on Web 08/18/2005

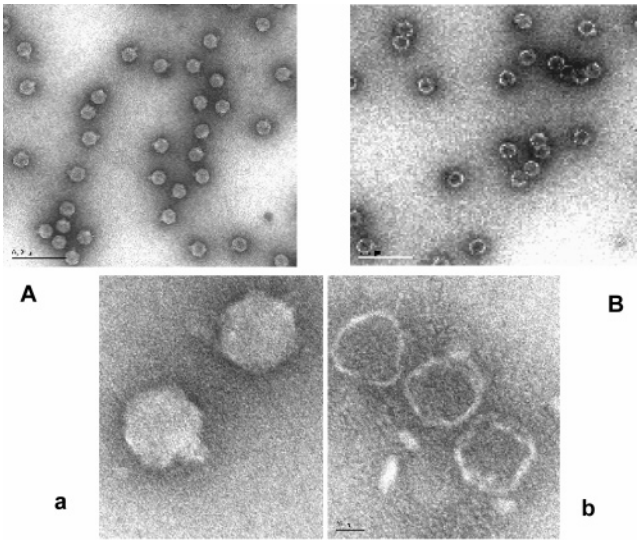

Figure 1. TEM images of uranyl acetate negatively stained T7 phage particles. Left: normal phage particles. Right: ghost phage particles obtained by osmotic shock. Scale bars: 200 nm (a,b: 20 nm).

molecule (affinity reagent) to the chelator molecule, which requires cumbersome synthetic efforts.

In this study, we used a special T7 phage, on which 415 copies of a 15-mer peptide (termed as S-tag) were displayed on its capsid (Novagen). The interaction of S-tag with a 104 amino acid (aa) S-protein derived from pancreatic ribonuclease A has well been characterized in the literature (*13*). After producing the corresponding T7 ghost phage, we were able to synthesize a europium-complex particle inside the ghost phage. Given the unique photophysical properties of europium complex, the hybridized phage can be followed by using both conventional and time-resolved fluorescence spectrometers. Most importantly, the fluorescence hybridized phage retains the binding affinity to the target protein.

T7 ghost was made by osmotic shocking the normal T7 phage. Since the density of encapsulated T7 DNA (~450 mg/mL) is at least 5-fold higher than that in metaphase chromatin (*14*), the DNA of T7 will burst to the outside after the T7 capsid is disrupted by the osmotic shock. By rapidly diluting pure T7 phages (10^{12} pfu/mL) with a sodium sulfate solution (3 M) in the presence of DNAase, it was found that the osmotic shock caused the escape of DNA debris (as a result of DNAase activity) from the capsid shell. However, the integrity of capsid shell remained after removing the osmotic shocking conditions. The shocked phage particles were collected by ultracentrifuging (60 000 rpm for 1 h at 4 °C). The ghost phages were then separated from the normal virus particles by banding in a cesium chloride density gradient (42% CsCl banding position for normal phage and 20.8% CsCl band position for the ghost phage), followed by dialyzing against the PBS buffer solution to remove cesium chloride. Capillary zone electrophoresis also confirmed the generation of T7 ghost phage. On the basis of the peak areas of the ghost particle and survived phage, it was estimated the yield of ghost phages generated by osmotic shock was 55%.

To visualize the ghost particles, phage samples prepared from the above methods were negatively stained with uranyl acetate (1%) and examined by transmission electron microscope (TEM, Philips CM-120). As shown in Figure 1 (A and a), the packing of DNA inside a normal T7 phage is very tight, thus preventing uranyl acetate presented at the virus core of intact viruses, as shown by the brighter contrast on the image. On the contrary, the ghost T7 particles are slightly shrunk, with an average diameter of 48 nm. Since uranyl acetate can diffuse inside the capsid, ghost particles have darker contrast in the middle (Figure 1, B and b). Most of the ghost particles observed did not possess any tails; thus, we assumed that the tails became detached from the particles during the osmotic shock.

Europium-complex hybridized phage particles were synthesized by the reaction of europium ions with either naphthoyltrifluoroacetone (NTA) or dicarboxylic anthraquinone (DCAQ) in the presence of ghost T7 phage (*15*). In brief, ghost T7 particles (0.4 mg/mL) were incubated with 4 mM of europium ions in an acetate acid buffer solution (pH = 8.0) for 1 h. 4 mM of NTA or DCAQ in the same in acetate acid buffer solution was then introduced, and the resulting solution was incubated for 3 h. During the incubation, insoluble europium−NTA or europium−DCAQ complex particles were formed. As the size of the particles increased, the diffusion of europium-complex particles inside the ghost phage were limited by the permeable size of capsid shell; thus, larger europium-complex particles were stuck inside the ghost phage and continued to grow until the particles occupied the entire interior space of the ghost. The formed hybridized phage was purified by using magnetic beads coated with S-protein. Because of the specific interaction between the S-tag displayed T7 ghost and S-protein, the hybridized phages were immobilized on the surface of the beads. Europium-complex particles formed outside the phage were washed away with the acetate acid buffer solution containing 4 mM of NTA or DCAQ solution using a magnetic separator. Finally the hybridized phage was released from the beads using a competing assay by introducing T7 tag elution buffer (T7 Tag affinity purification Kit, Novagen).

The formed europium complex hybridized phage particles have the typical Eu(III) complex luminescence feature. The emission peak is centered at 617 nm when excited at 370 nm, which can be attributed to the $^5D_0 \rightarrow {}^7F_2$ transition (Figure 2A). Thus, the specific binding function of the hybridized phage against S-protein can be verified by a time-resolved fluorescence immunosorbent assay. An intact T7 phage, which went through the same procedures as making a europium complex hybridized phage, was used as a control. Both types of phages (hybridized and intact) were added to the microtiter plate wells coated with the S-protein and incubated at room temperature for 2 h. After the wells were washed three times with TBS, the fluorescence signals of the plate were recorded by a plate reader (Wallac 1420 Victor multiabel counter) equipped with a time-resolved fluorescence detector. As shown in Figure 2B, we observed a strong time-resolved fluorescence signal in the sample of hybridized phage, indicating the strong binding between the S-protein and the hybridized phage (blue line). On the other hand, intact T7 phage only showed very weak signal because of the lack of europium complex (red line). At the same time, a conventional ELISA, using 50 μL of S-protein labeled with horseradish peroxidase (HRP) and ABTS solution for visualization, was also conduced, and the ELISA confirmed the binding of both samples to the S-protein (data not shown here).

To visualize the hybridized phage particles, the samples were loaded onto a freshly glow discharged TEM grid and imaged directly without negatively staining. As demonstrated in Figure 3A, hybridized T7 phages with uniform europium particles inside were dominated on the TEM

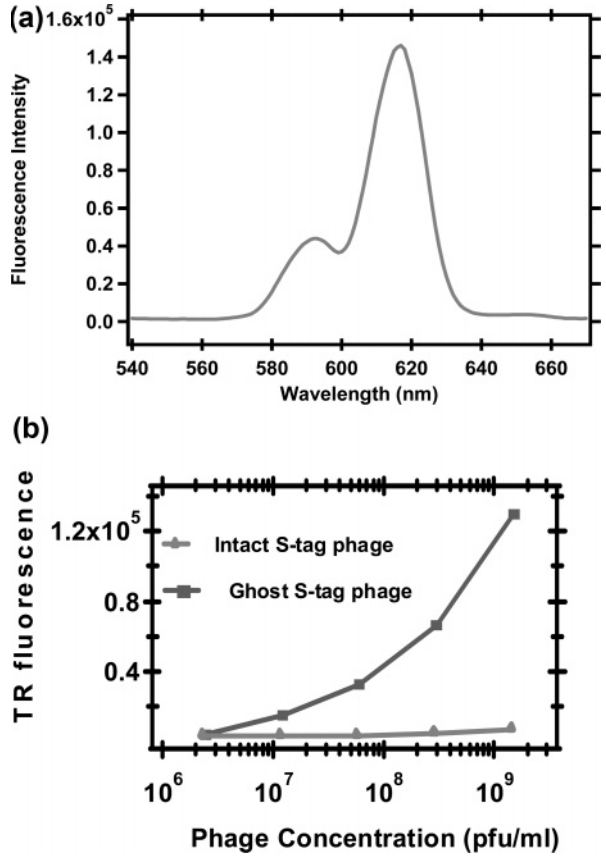

Figure 2. (A) Fluorescence spectrum of europium complex hybridized T7 phage particles. (B) Time-resolved fluorescence immunosorbent assay.

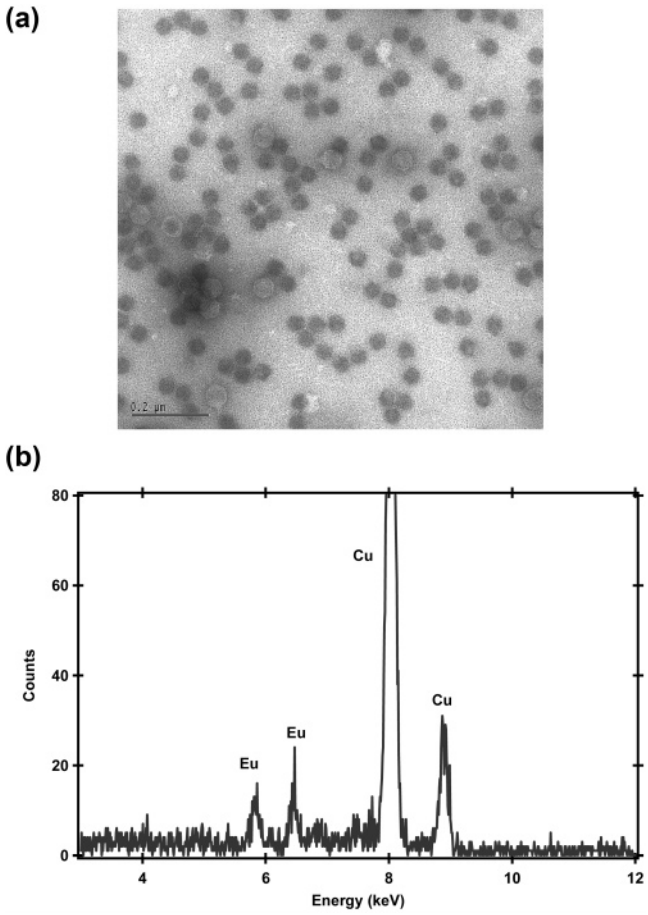

Figure 3. (A) TEM image of europium-complex hybridized T7 phages (scale bar = 200 nm). (B) EDX spectrum indicating the dominated europium element inside T7 ghosts.

images. The size of europium-complex particles inside the ghost T7 is about ~35 nm in diameter with excellent monodispersed size distribution. EDX analysis confirmed the presence of europium (Figure 3B) as the major element inside the ghost T7.

Since the fabrication of europium-complex hybridized T7 involves loading the cavity of T7 ghost with europium ions, a negatively charged phage capsid will help to attract Eu^{3+} ions, thus facilitate the synthesis of europium-complex particles inside the T7 ghost. Although it is hard to describe the exact interior charge nature of the T7 ghost, we estimated that T7 capsid is negatively charged when it is in the solution of neutral pH (~7) or above. This is supported by the fact that the capsid of T7 is made of many (up to eight) capsid proteins. The isoelectric point (pI) of major capsid protein (P10) is 6.0, and the pIs of dominated internal protein (P15 and P16) of T7 capsid are 5.4 and 6.6, respectively (*16*). The negatively charged nature of the T7 ghost phage at neutral or base conditions benefits the loading of cationic europium ions, and so europium complex particles can be efficiently synthesized inside the T7 ghost.

It should be noted that the observed time-resolved fluorescence signal is almost 3 orders of magnitude higher than the background noise and nonspecific signals in the time-resolved fluorescence immunosorbent assay experiments. Compared to a conventional ELISA assay, the europium-complex hybridized phage provides a superior signal-to-noise ratio as a fluorescent probe.

In summary, we have demonstrated the generation of a europium-complex hybridized T7 phage. As a new class of fluorescent probe, hybridized phages have monodispersed europium-complex particle core inside and uniform affinity reagent displayed capsid shell outside. Currently, we are expanding the scope of hybridized phage and have been successful in synthesizing cobalt metal and rhenium oxide (an analogue to ^{99}technetium oxide due to similar chemical properties of these two elements) hybridized phages. Since the inorganic cores in the hybridized phages are fully surrounded by the capsid proteins, in principle, the hybridized phage should be biocompatible in vivo. We envision that the hybridized phage will be the next generation of probing reagents for bioassay, biosensor, targeted reagent delivery, and medical imaging.

ACKNOWLEDGMENT

This work is supported by DARPA (8C67400-110). We thank Ms. Yimei Chen and Dr. Xiaozhou Liao in the Department of Molecular Genetics and Cell Biology, University of Chicago, for the help with TEM imaging EDX analysis, as well as Dr. Fred Stevens's group (Argonne) for the help with time-resolved fluorescence measurement. We also thank Dr. William Studier and Dr. Brian Kay for reviewing the manuscript and providing insightful comments.

LITERATURE CITED

(1) Zhang, J., Campbell, R. E., Ting, A. Y., and Tsien. R. Y. (2002) Creating new fluorescent probes for cell biology. *Mol. Cell Biol. 3*, 906−918.

(2) Bartlett, J. M. (2004) Fluorescence in situ hybridization: technical overview. *Methods Mol. Med. 97*, 77−87.

(3) Ormö, M., Cubitt, A. B., Kallio, K., Gross, L. A., Tsien, R. Y., and Remington, S. J. (1996) Crystal structure of the *Aequorea victoria* green fluorescent protein. *Science 273*, 1392−1395.
(4) Nagai, T., Ibata, K., Park, E. S., Kubota, M., Mikoshiba, K., and Miyawaki, A. (2002) A variant of yellow fluorescence protein with fast and efficient maturation for cell-biological applications. *Nature Biotechnol. 20*, 87−90.
(5) Adams, S. R., Campbell, R. E., Gross, L. A., Martin, B. R., Walkup, G. K., Yao, Y., Llopis, J., Tsien, R. Y. (2002) New biarsenical ligands and tetracysteine motifs for protein labeling in vitro and *in vivo*: synthesis and biological applications. *J. Am. Chem. Soc. 124*, 6063−6076.
(6) Casjens, S., (1985) Nucleic acid packaging by viruses. *Virus Structure and Assembly* (Casjens, S., Ed.), pp 75−147, Jones and Bartlett, Boston.
(7) Studier, W. (1972) Bacteriophage T7. *Science 176*, 367−376.
(8) Studier, W. (1969) The genetics and physiology of bacteriophage T7. *Virology 39*, 562−574.
(9) Rodi, D. J., and Makowski, L. (1999) Phage-display technology − finding a needle in a vast molecular haystack. *Curr. Opin. Biotechnol 10*, 87−93.
(10) Kasanov, J., Pirozzi, G., Uveges, A. J., and Kay, B. K. (2001) Defining the ligand specificity of WW domains using phage-displayed combinatorial peptides. *Chem. Biol. 8*, 231−241.
(11) Kay, B. K., Kasanov, J., and Yamabhai, M. (2001) Screening phage-displayed combinatorial peptide libraries. *Methods 24*, 240−246.
(12) Selvin, P. R. (2002) Principles and biophysical applications of lanthanide-based probes. *Annu. Rev. Biophys. Biomol. Struct. 31*, 275−302.
(13) Raines, R. T., Mccormick, M., VanOosbree, T. R., and Mierendorf, R. C. (2000) The S·tag fusion system for protein purification. *Methods Enzymol. 326*, 362−376.
(14) Cerritelli, M. E., Cheng, N., Rosenberg, A. H., McPherson, C. E., Booy F. P., and Steven, A. C. (1997) Encapsidated conformation of bacteriophage T7 DNA. *Cell 91*, 271−280.
(15) Diamandis, E. P. (1992) Europium and terium chelators as candidate substrates for enzyme-labeled time-resolved fluorimetric immunoassays. *Analyst 117*, 1879−1884.
(16) Roeder, S., and Sadowski, P. (1977) Bacteriphage T7 Morphogenesis: phage-related particles in cells infected with wild-Type and mutant T7 phage. *Virology 76*, 263−285.

BC050108+

ARTICLES

Formation and Characterization of Stable Human Serum Albumin−Tris-malonic Acid [C_{60}]Fullerene Complex

Bogdan Belgorodsky,[§] Ludmila Fadeev,[§] Varda Ittah,[†] Hadar Benyamini,[‡] Stanislav Zelner,[§] Dan Huppert,[§] Alexander B. Kotlyar,[⊥] and Michael Gozin*[,§]

School of Chemistry, Faculty of Exact Sciences, and Department of Biochemistry and Bioinformatics Unit, Faculty of Life Sciences, Tel Aviv University, Tel Aviv, 69978, Israel, and School of Chemistry, Faculty of Exact Sciences, Bar Ilan University, Ramat Gan, 52900, Israel. Received April 3, 2005; Revised Manuscript Received June 2, 2005

The preparation and characterization of the stable human serum albumin (HSA)-C_3 isomer of tris-malonic acid [C_{60}]fullerene complex is reported. Other than the anti-fullerene antibody, a stable protein−fullerene complex with a native protein has never been observed. This study may provide valuable answers to the growing concern regarding the effects of carbonaceous nanomaterials on human health on one hand and, on the other, may lead to the development of novel antioxidant therapeutic agents, radiopharmaceuticals, and components for bioelectronic devices.

INTRODUCTION

Since the discovery of fullerenes (*1, 2*), a broad range of bioactivity was found for various fullerene-derived materials. This includes antiviral and antibacterial properties, antioxidant and neuroprotective activities, cell signaling and apoptosis, and compounds with the potential to be developed as anticancer drugs and diagnostic agents (*3*−*6*). A number of fullerene derivatives were reported to interact with proteins (*7*−*11*) and even function as enzyme inhibitors (*3*−*6, 12*). However, other than the anti-fullerene antibody (*13*), a stable and well-defined protein−fullerene complex with a native protein has never been observed. Here we report the preparation and structural and functional characterization of a complex formed between human serum albumin (HSA) and the *eee*-isomer of tris-malonic acid [C_{60}]fullerene (CF) (*14*). The study of such complexes may provide valuable answers to the growing concern regarding the effects of carbonaceous nanomaterials on human health (*15*−*16*) on one hand and, on the other, may lead to the development of novel functional biomaterials.

EXPERIMENTAL PROCEDURES

Complex Preparation. CF was synthesized according to the previously reported methods (*17*−*19*). Fatty acid and globulin free HSA, fine chemicals and solvents were purchased from Sigma-Aldrich. A solution of 100.0 mg of HSA and 3.1 mg of CF (3.0 μmole) in 1.5 mL of tris-acetate buffer (100 mM, pH 7.2) was incubated for 12 h at RT. Then, the complexation solution was loaded on a Sephadex G-25 gel-permeation column (Pharmacia Biotech) or on HPLC TSK-GEL column (as described below) and noncomplexed CF was removed by elution with a tris-acetate buffer (1.0 M, pH 7.2). The buffer concentration was reduced by reloading the complex-containing fraction on the second Sephadex G-25 column and eluting the complex with a tris-acetate buffer (1.0 mM, pH 7.2). The resulting solution of the complex was lyophilized for storage and further experiments. After reconstitution in water, the complex concentration in solution was determined by UV−vis spectroscopy and a BioRad protein assay (Bio-Rad Lab). All UV−vis spectra were recorded at RT on a S-3150 diode array spectrophotometer (Scinco).

Size-Exclusion Chromatography. Size-exclusion high performance liquid chromatography of a monomeric HSA, CF and HSA−CF complex was performed on a 300 × 7.8 mm G3000SW_{XL} TSK-GEL column (Tosoh Biosep) using a tris-acetate buffer (100 mM, pH 7.2) as the isocratic eluent. All HPLC analyses and separations were performed on the SpectraSYSTEM equipped with a UV6000-LP diode array detector (ThermoFinnigan).

Time-Resolved FRET Spectroscopy. Time-resolved fluorescence was measured using the time-correlated single-photon counting (TCSPC) technique. As an excitation source, we used a CW mode-locked Nd:YAG-pumped dye laser (Coherent Nd:YAG Antares and a 702 dye laser), providing a high repetition rate (>1 MHz) of short pulses (2 ps at full width half-maximum, fwhm). The (TCSPC) detection system is based on a Hamamatsu 3809U, photomultiplier, Tennelec 864 TAC, Tennelec 454 discriminator and a computer-based multichannel analyzer (nucleus PCA-II). The overall instrumental response was about 50 ps (fwhm). Measurements were taken at 10 nm spectral width.

* To whom correspondence should be addressed. Tel: (+972) 3-640-5878, Fax: (+972) 3-640-5879, E-mail: cogozin@mgchem.tau.ac.il.

[§] School of Chemistry, Faculty of Exact Sciences, Tel Aviv University.

[‡] Bioinformatics Unit, Faculty of Life Sciences, Tel Aviv University.

[†] School of Chemistry, Faculty of Exact Sciences, Bar Ilan University.

[⊥] Department of Biochemistry, Faculty of Life Sciences, Tel Aviv University.

10.1021/bc050103c CCC: $30.25 © 2005 American Chemical Society
Published on Web 07/21/2005

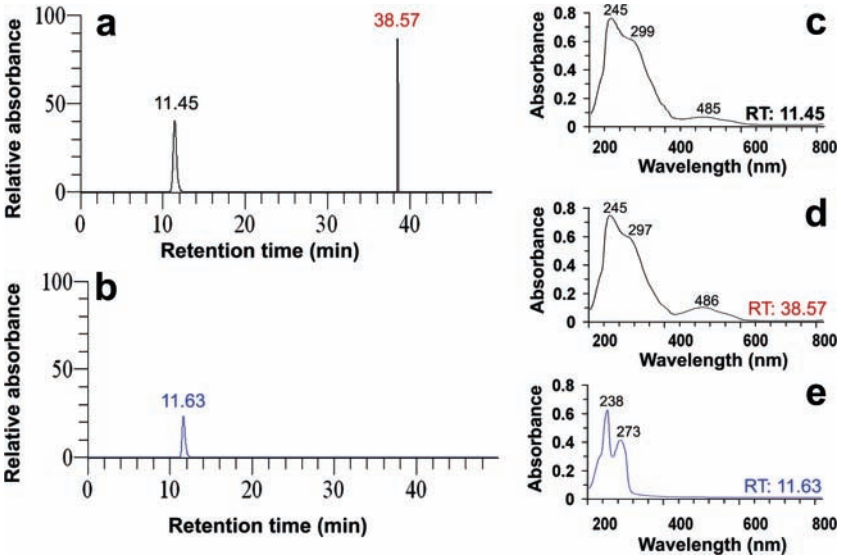

Figure 1. (a) Size-exclusion chromatogram of a sample containing HSA–CF complex (t_R = 11.45 min) and an unbound CF ligand (t_R = 38.57 min). (b) Size-exclusion chromatogram of a monomeric HSA reference standard. Both chromatograms a and b were monitored by diode array detector (200–800 nm) and reported here at 240 nm. (c) UV–vis spectrum obtained for an HSA–CF complex peak in chromatogram a. (d) UV–vis spectra obtained for a CF's peak in chromatogram a. (e) UV–vis spectrum obtained for an HSA reference standard in chromatogram b.

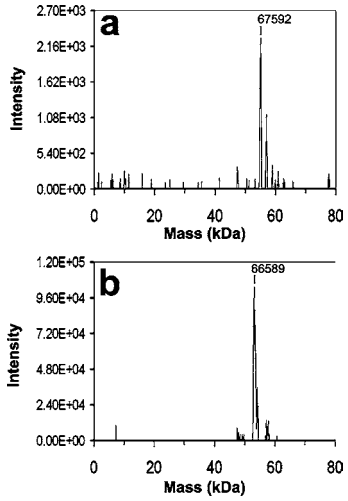

Figure 2. Deconvoluted ESI-mass spectra of (a) HSA–CF complex and (b) monomeric HSA.

RESULT AND DISCUSSION

Complex Formation. The HSA–CF complex formation was obtanied at physiological pH, by incubation of the fatty acid free native HSA solution with a 2-fold excess of CF. The resulting HSA–CF complex was found to be stable enough to be purified by size-exclusion liquid chromatography, and sustained variations in pH, lyophylization, and reconstitution. The size-exclusion chromatorgaphic conditions, suitable for separation of HSA protein monomers and dimers, were used for analysis and purification of the complex from an excess of an unbound CF ligand. Under these conditions the retention time (RT) of the HSA–CF complex elution (Figure 1a) closely resembled the RT of a ligand-free monomeric HSA (Figure 1b), while the complex's UV–vis spectrum clearly indicated incorporation of fullerene chromophore (Figure 1c). The excess of the noncomplexed CF was eluted much later, with the RT and UV–vis spectrum (Figure 1d) matching a separately analyzed CF reference standard.

UV–vis analysis and standard BioRad assay of the purified HSA–CF complex revealed that only a single CF molecule is bound by a monomeric HSA host. These findings were confirmed by electrospray mass spectroscopy analysis, unambiguously showing that the molecular mass of the complex (Figure 2a) corresponds to a sum of masses of monomeric HSA (Figure 2b) and one CF ligand (see Supporting Information, Figure S1).

Binding Constant by Fluorescence Titration Studies. To quantitatively determine the stability of the

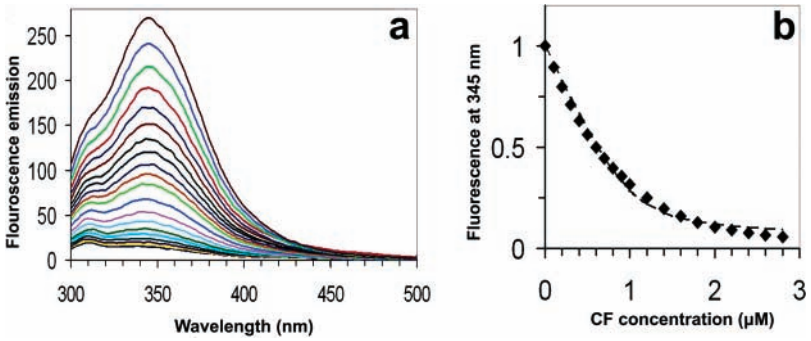

Figure 3. (a) Reduction in HSA's Trp_{214} fluorescence during a titration with CF. To 1 μM of HSA solution in 10 mM tris acetate buffer (pH 7.2) were added (solution concentration of CF was increased from 0 to 2.8 μM) aliquots of CF until no substantial changes in the emission intensity were detected. The excitation was performed at λ = 280 nm, and emission was measured at λ_{max} = 345 nm. (b) Graph describing the intensity of the HSA's fluorescence emission (at 345 nm) as a function of CF concentration (◆) and calculated binding isotherm (intermittent line).

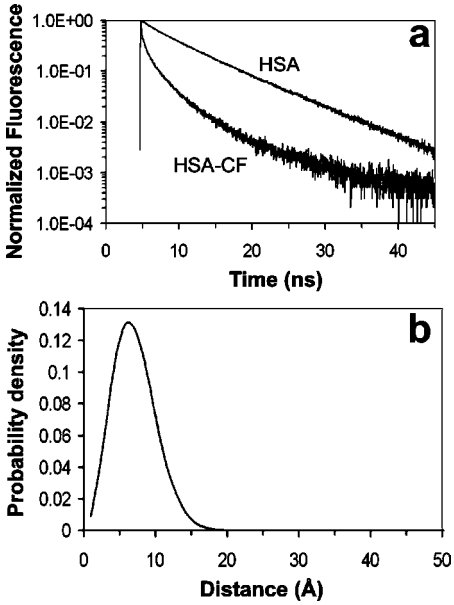

Figure 4. (a) Experimental fluorescence decay curves of monomeric HSA (blue) and HSA−CF complex (black). The excitation was performed at $\lambda = 280$ nm and emission was measured at $\lambda_{max} = 345$ nm. (b) The distance distribution between the HSA's Trp_{214} and the CF.

complex, a binding study was performed by gradual addition of CF to HSA. The HSA−CF complex formation was measured by monitoring the HSA's Trp_{214} fluorescence quenching in solution, upon addition of the CF aliquots (Figure 3a). Fitting the titration results to a theoretical rectangular hyperbola curve (binding isotherm), calculated by nonlinear least-mean-square algorithm (*20*), produced a binding constant for CF of 1.2×10^7 M^{-1} (Figure 3b).

tr-FRET Experiments and CF Location Assessment. To assess the intramolecular distance between HSA's Trp_{214} donor and the CF acceptor in the complex, time-resolved fluorescence decay (tr-FRET) experiments of ligand-free HSA protein and HSA−CF complex were performed (Figure 4a). Theoretical decay curves were calculated by numerical solution of the second-order differential equation for each tr-FRET experiment and fitted to the corresponding experimental curves (*21, 22*). The distance distribution function was obtained from simultaneous global analysis of two experimental fluorescence decay curves, using the Marquardt nonlinear least-squares method (Figure 4b, for calculation details see Supporting Information) (*22,23*). It was found that in HSA−CF complex the mean distance between the Trp_{214} donor and CF acceptor is 7.1 Å (with fluctuations of ±3.4 Å).

Calculations and Docking Studies. An additional attempt to estimate the location of CF in HSA's three-dimensional structure was based on the molecular docking program. Coordinates of the known structure of the HSA protein (*24*) and a Hartree−Fock energy-minimized structure of the CF ligand (see Supporting Information) were used for building plausible docking models of the complex. The PatchDock program was applied without using any a priori data indicating a CF putative binding site (*25*). An examination of generated docking models revealed that the eight highest ranked solutions posi-

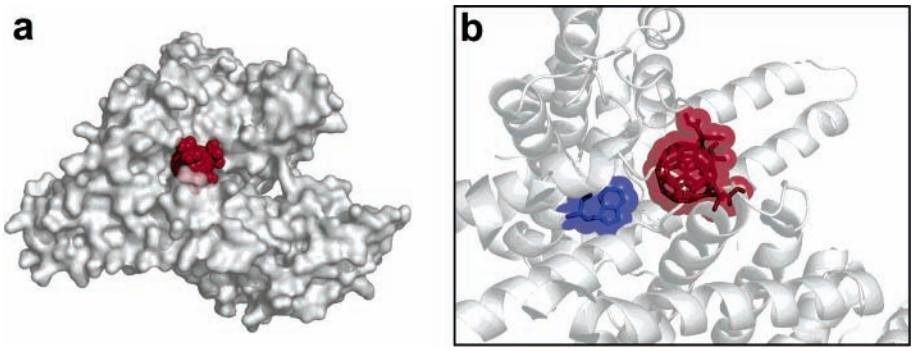

Figure 5. (a) The overall view of the highest score docking model of the HSA−CF complex, in which the HSA is presented by its van der Waals surface and a space-filling model of CF (in red) is located in its binding pocket. (b) Close-up view of the CF-binding pocket in HSA's subdomain IIA, showing close proximity between the HSA's Trp_{214} (in blue) and the CF ligand (in red).

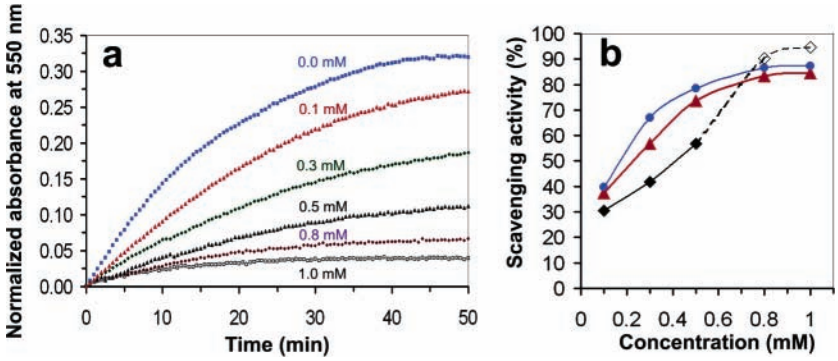

Figure 6. (a) Graph presenting changes in concentrations of Cytochrome *c* (Fe^{II}) at pH 7.4 (monitored at 550 nm), due to superoxide scavenging activity of HSA−CF complex added at various concentrations (0−1.0 mM of the complex). (b) Graph comparing the scavenging activity of the free HSA (●), the HSA−CF complex (red ▲), and the noncomplexed CF (◆) at various concentrations. Scavenging activity is defined as $([V - b] \times 100/V)$, where V is the rate of cytochrome *c* (Fe^{II}) formation during the linear phase (0−7 min) of a control experiment (without antioxidants); and b is the rate of cytochrome *c* (Fe^{II}) formation during the linear phase in the presence of tested antioxidants in various concentrations. Scavenging activity of the noncomplexed CF, at concentrations above 0.6 mM (◇), was found to be unusually high, possibly due to assay readings interference by CF's absorbance or CF clusters formation.

tioned CF in the same cavity, with differences mostly in the ligand's orientation. In all these models, the CF was found located at a distance of approximately 5 Å from the Trp_{214} residue (Figure 5), which is in excellent agreement with our tr-FRET experiments' global analysis.

Determination of SOD-like Activity for Complex by in Vitro Xanthineoxidase/Cytochrome C Assay. CF was extensively investigated as a free radical scavenger in vitro (*17*−*19*) and in vivo (*26*) and was recently described as a superoxide dismutase mimetic (*27*). Free HSA protein has also been reported to have antioxidant activity (*28*). To examine the antioxidant properties of the new HSA−CF complex, a standard xanthine oxidase/cytochrome *c* assay was utilized (Figure 6a) (*29, 30*). It was found that the ability of HSA−CF complex to quench superoxide radicals was slightly lower than that of the free HSA protein and was measurably higher than of the free CF ligand (Figure 6b). Although no additive antioxidant activity was observed for the HSA−CF complex, the free radical scavenging capabilities of the HSA protein were almost unaffected.

Our experimental data and docking calculations lead to the conclusion that an amphiphilic, negatively charged CF ligand is bound in the HSA's subdomain IIA (a binding site formed by hydrophobic side chains with the entrance to the pocket surrounded by positively charged residues) (*31, 32*). The binding constant of the CF was found to be comparable with published values for other organic molecules that strongly bind to same site of HSA, such as bilirubin (9.5×10^7 M^{-1}), iodipamide (9.9×10^6 M^{-1}), and 3-carboxy-4-methyl-5-propyl-2-furanpropanoate (1.3×10^7 M^{-1}) (*32*). We believe that, in addition to improved water solubility and biocompatibility, stable protein−fullerene derivative complexes have the potential to be developed as antioxidant therapeutic agents, target-specific radiopharmaceuticals, or components for future bioelectronic devices.

ACKNOWLEDGMENT

This work was supported by the Israel Science Foundation and the Multiple Sclerosis Center Foundation of Brigham & Women's Hospital (Massachusetts General Hospital).

Supporting Information Available: Materials, characterization of HSA−CF complex by mass spectroscopy, determination of CF binding constant by fluorescence spectroscopy, and determination of distance between HSA's Trp_{214} and CF in HSA−CF complex by global analysis of time-resolved FRET spectroscopy. This material is available free of charge via the Internet at http://pubs.acs.org.

LITERATURE CITED

(1) Kroto, H. W., Heath, J. R., O'Brien, S. C., Curl, R. F., and Smalley, R. E. (1985) C_{60}: buckminsterfullerene. *Nature 318*, 162−163.

(2) Kraetschmer, W., Lamb, L. D., Fostiropoulos, K., and Huffman, D. R. (1990) Solid C60: a new form of carbon. *Nature 347*, 354−358.

(3) Bosi, S., Da Ros, T., Spalluto, G., and Prato, M. (2003) Fullerene derivatives: an attractive tool for biological applications. *Eur. J. Med. Chem. 38*, 913−923.

(4) Pantarotto, D., Tagmatarchis, N., Bianco, A., and Prato, M. (2004) Synthesis and biological properties of fullerene-containing amino acids and peptides. *Mini-Rev. Med. Chem. 4*, 805−814.

(5) Nakamura, E., and Isobe, H. (2003) Functionalized Fullerenes in Water. The First 10 Years of Their Chemistry, Biology, and Nanoscience. *Acc. Chem. Res*. *36*, 807−815.

(6) Wilson, S. R. (1997) The potential of fullerene compounds in biology and medicine. *Proc. Electrochem. Soc. 97*−*42* (Recent Advances in the Chemistry and Physics of Fullerenes and Related Materials, Vol. 5), 322−331.

(7) Braun, M., Atalick, S., Guldi, D. M., Lanig, H., Brettreich, M., Burghardt, S., Hatzimarinaki, M., Ravanelli, E., Prato, M., van Eldik, R., and Hirsch, A. (2003) Electrostatic complexation and photoinduced electron transfer between Zn-cytochrome c and polyanionic fullerene dendrimers. *Chem. Eur. J. 9*, 3867−3875.

(8) Prabha, C. R., Patel, R., and Murthy, C. N. (2004) Studies on Protein-[60]Fullerene Interactions: The Lysozyme-[60]-Fullerene Model System. *Fullerenes, Nanotubes, Carbon Nanostruct. 12*, 405−412.

(9) Kotelnikova, R. A., Bogdanov, G. N., Frog, E. C., Kotelnikov, A. I., Shtolko, V. N., Romanova, V. S., Andreev, S. M., Kushch, A. A., Fedorova, N. E., Medzhidova, A. A., and Miller, G. G. (2003) Nanobionics of pharmacologically active derivatives of fullerene C_{60}. *J. Nanopart. Res. 5*, 561−566.

(10) Nednoor, P., Capaccio, M., Gavalas, V. G., Meier, M. S., Anthony, J. E., and Bachas, L. G. (2004) Hybrid nanoparticles based on organized protein immobilization on fullerenes. *Bioconjugate Chem. 15*, 12−15.

(11) Capaccio, M., Gavalas, V. G., Meier, M. S., Anthony, J. E., and Bachas, L. G., (2005) Coupling Biomolecules to Fullerenes through a Molecular Adapter. *Bioconjugate Chem. 16*, 241−244.

(12) Wolff, D. J., Papoiu, A. D. P., Mialkowski, K., Richardson, C. F., Schuster, D. I., and Wilson, S. R. (2000) Inhibition of Nitric Oxide Synthase Isoforms by Tris-Malonyl-C_{60}−Fullerene Adducts. *Arch. Biochem. Biophys. 378*, 216−223.

(13) Braden, B. C., Goldbaum, F. A., Chen, B.-X., Kirschner, A. N., Wilson, S. R., and Erlanger, B. F. (2000) X-ray crystal structure of an anti-Buckminsterfullerene antibody Fab fragment: biomolecular recognition of C60. *Proc. Nat. Acad. Sci. U.S.A. 97*, 12193−12197.

(14) Hirsch, A., Lamparth, I., and Karfunkel, H. R. (1994) Fullerene chemistry in three dimensions: isolation of seven regioisomeric bisadducts and chiral trisadducts from C_{60} and bis(ethoxycarbonyl)methylene. *Angew. Chem., Int. Ed. Engl. 33*, 437−438.

(15) Service R. F. (2004) Nanotoxicology. Nanotechnology grows up. *Science 304*, 1732−1734.

(16) Oberdorster, E. (2004) Manufactured nanomaterials (fullerenes, C_{60}) induce oxidative stress in the brain of juvenile largemouth bass. *Environ. Health Persp. 112*, 1058−1062.

(17) Dugan, L. L., Turetsky, D. M., Du, C., Lobner, D., Wheeler, M., Almli, C. R., Shen, C. K.-F., Luh, T.-Y., Choi, D. W., and Lin, T.-S. (1997) Carboxyfullerenes as neuroprotective agents. *Proc. Nat. Acad. Sci. U.S.A. 94*, 9434−9439.

(18) Foley, S., Curtis, A. D. M., Hirsch, A., Brettreich, M., Pelegrin, A., Seta, P., and Larroque, C. (2002) Interaction of a water soluble fullerene derivative with reactive oxygen species and model enzymatic systems. *Fullerenes, Nanotubes, Carbon Nanostruct. 10*, 49−67.

(19) Tsao, N., Luh, T.-Y., Chou, C.-K., Chang, T.-Y., Wu, J.-J., Liu, C.-C., and Lei, H.-Y. (2002) In vitro action of carboxyfullerene. *J. Antimicrob. Chemother*. *49*, 641−649.

(20) Wilcox C. S. (2001) *Frontiers in Supramolecular Organic Chemistry and Photochemistry* (Schneider H.-J., Durr H., Eds.), VCH, New York.

(21) Haas, E. (1996) The problem of protein folding and dynamics: time-resolved dynamic nonradiative excitation energy transfer measurements. *I.E.E.E. J. Sel. Top. Quantum Electron. 2*, 1088−1106.

(22) Beechem J. M., and Haas E. (1989) Simultaneous determination of intramolecular distance distributions and conformational dynamics by global analysis of energy transfer measurements. *Biophys. J. 55*, 1225−36.

(23) Grinvald, A., and Steinberg, I. Z. (1974) Analysis of fluorescence decay kinetics by the method of least-squares. *Anal. Biochem. 59*, 583−98.

(24) He, X. M., and Carter, D. C. (1992) Atomic structure and chemistry of human serum albumin. *Nature 358,* 209−215.

(25) Schneidman-Duhovny, D., Inbar, Y., Polak, V., Shatsky, M., Halperin, I., Benyamini, H., Barzilai, A., Dror, O., Haspel, N., Nussinov, R., and Wolfson, H. J. (2003) Taking geometry to its edge: fast unbound rigid (and hinge-bent) docking. *Proteins 52*, 107−112.

(26) Lin, A. M.-Y., Fang, S.-F., Lin, S.-Z., Chou, C,-K., Luh, T.-Y., and Ho, L.-T. (2002) Local carboxyfullerene protects cortical infarction in rat brain. *Neuroscience Res. 43*, 317−321.

(27) Ali, S. S., Hardt, J. I., Quick, K. L., Kim-Han, J. S., Erlanger, Bernard, F., Huang, T.-T., Epstein, C. J., and Dugan, L. L. (2004) A biologically effective fullerene (C_{60}) derivative with superoxide dismutase mimetic properties. *Free Rad. Biol. Med. 37*, 1191−202.

(28) Nicholson, J. P., Wolmarans, M. R., and Park, G. R. (2000) The role of albumin in critical illness. *Br. J. Anaesth. 85*, 599−610.

(29) Quick, K. L., Hardt, J. I., and Dugan, L. L. (2000) Rapid microplate assay for superoxide scavenging efficiency. *J. Neurosci. Methods 97*, 139−144.

(30) McCord, J. M., and Fridovich, I. (1969) Superoxide dismutase. Enzymic function for erythrocuprein (hemocuprein). *J. Biol. Chem. 244*, 6049−6055.

(31) Peters T. J. (1996) *All about Albumin: Biochemistry, Genetics, and Medical Applications,* Academic Press, San Diego, CA.

(32) Kragh-Hansen, U., Chuang, Vi. T. G., and Otagiri, M. (2002) Practical aspects of the ligand-binding and enzymatic properties of human serum albumin. *Bio. Pharm. Bull. 25*, 695−704.

BC050103C

A Nanoparticle-Based Model Delivery System To Guide the Rational Design of Gene Delivery to the Liver. 1. Synthesis and Characterization

Stephen R. Popielarski, Suzie H. Pun,† and Mark E. Davis*

Chemical Engineering, California Institute of Technology, Pasadena, California 91125. Received April 14, 2005

Nonviral gene delivery systems are amenable to forming colloidal particles with a wide range of physicochemical properties that include size, surface charge, and density and type of ligand presented. However, it is not known how to best design these particles without having a set of physicochemical design constraints that have been optimized for the intended gene delivery application. Here, a nanoparticle-based model delivery system is developed that can mimic the surface properties of nonviral gene delivery particles, and this model system is used to define design constraints that should be applied to next generation gene delivery particles. As a test case, a well-defined nanoparticle-based system is developed to guide the rational design of gene delivery to hepatocytes in the liver. The synthetic scheme utilizes monodisperse polystyrene particles and provides for variation of mean particle size and particle size distribution through variation in reaction conditions. The nanoparticles are PEGylated to provide stability in serum and also incorporate targeting ligands, e.g., galactose, at tunable densities. Four nanoparticles are synthesized from uniformly sized polystyrene beads specifically for the purpose of identifying design constraints to guide next generation gene delivery to the liver. These four nanoparticles are Gal-50 and Gal-140, that are galactosylated 50 and 140 nm nanoparticles, and MeO-50 and MeO-140, that are methoxy-terminated 50 and 140 nm nanoparticles. All four particles have the same surface charge, and Gal-50 and Gal-140 have the same surface galactose density. The availability of galactose ligands to receptor binding is demonstrated here by agglutination with RCA_{120}.

INTRODUCTION

Gene therapy promises to revolutionize the clinical treatment of countless genetic disorders (*1*), including many diseases of the liver (*2*). Though human gene therapy of liver diseases is still in its infancy, preclinical studies in animal models of disease have demonstrated proof of concept results in nearly all varieties of liver diseases that are conceptually amenable to gene therapy treatment (*3*−*6*).

However, numerous investigators have identified the importance of carefully designing and controlling the properties of gene delivery systems for selectively targeting the liver. A prerequisite to selective targeting is particle stability in vivo and the minimization of nonspecific uptake. We and others have previously demonstrated the importance of PEGylation (PEG: poly(ethylene glycol)) to stabilize polyplexes and to reduce their nonspecific uptake (*7*). Nonspecific uptake of particles is commonly due to rapid clearance by cells of the mononuclear phagocytic system (*8*) and adhesion to the endothelial lining of the vascular system (*9*). Such undesirable uptake is minimized by surfaces with little or no protein adsorption. In particular, certain proteins called opsonins interact with phagocyte receptors and promote recognition by scavenger cells of the reticuloendothelial organs. Phagocytosis is frequently initiated by adsorption of opsonins onto the surface of particles followed by complement activation or other recognition, leading to internalization by macrophages and intracellular processing. Dunn et al. (*10*) have demonstrated that interaction of PEGylated polystyrene nanoparticles with nonparenchymal liver cells in vitro decreased with higher surface densities of PEG and also resulted in longer circulation times following intravenous injection into rats.

By formulating PEGylated cyclodextrin-based gene-delivery particles under different conditions, the size, surface charge, and ligand density of the final gene delivery particle can all readily be adjusted (*11*). However, the power of this flexibility cannot be maximized without a set of physicochemical design constraints that have been optimized for the intended gene-delivery application. In particular, we are interested in generating a set of design requirements to guide gene delivery to the liver. In this pursuit, we describe herein the development of a nanoparticle-based model system that will facilitate the systematic identification of relevant physicochemical properties that alter the hepatic distribution of nanoparticles. Further, this nanoparticle-based model is intended to mimic the surface properties achievable with nonviral delivery systems but specifically with the linear, cyclodextrin-based gene delivery system developed in our laboratory (*12*−*15*). As such, the model system will be PEGylated and must facilitate variation of parameters such as particle size, surface charge, and ligand type and density.

In the present work, we detail the synthesis and characterization of PEGylated nanoparticles with tunable physicochemical properties. The synthesized nanoparticles are slightly anionic to minimize nonspecific uptake in vivo, and galactose will be used as a targeting ligand since galactose receptors in vivo are almost exclusively

* To whom correspondence should be addressed. E-mail: mdavis@cheme.caltech.edu.

† Current address: Department of Bioengineering, University of Washington, Box 352255, Seattle, WA 98195.

10.1021/bc050113d CCC: $30.25 © 2005 American Chemical Society
Published on Web 08/31/2005

Scheme 1. Synthesis of Galactose-PEG$_{5000}$-NH$_2$ (1)

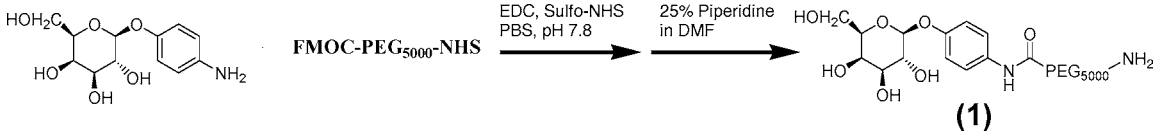

Scheme 2. Synthesis of PEGylated Nanoparticles (2)

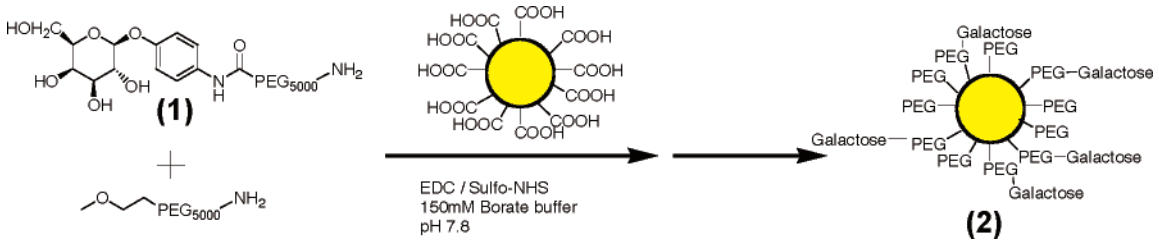

found in the liver. In particular, four nanoparticles will be described that are appropriate for uptake experiments: Gal-50 and Gal-140 are galactosylated nanoparticles with diameters of 50 and 140 nm, while MeO-50 and MeO-140 are methoxy-terminated 50 and 140 nm nanoparticles. Through the use of these nanoparticles, the effects of nanoparticle size and surface presentation of galactose on hepatic distribution in mice can be explored, and the results of in vitro and in vivo uptake experiments are presented in Part 2 of our work (*16*).

MATERIALS AND METHODS

Fmoc-PEG$_{5000}$-NHS was purchased from Nektar (San Carlos, CA) and used as received. All other reagents and solvents were obtained from commercial suppliers and were used as received, unless specifically noted. Matrix-assisted, laser desorption/ionization time-of-flight mass spectroscopy (MALDI-TOF) was performed on a PerSeptive Biosystems Voyager DE PRO BioSpectrometry Workstation (PerSeptive Biosystems; Framingham, MA) in the positive ion mode using a 2,5-dihydroxy benzoic acid matrix. HPLC was performed on an Agilent 1100 Series HPLC (Agilent Technologies; Palo Alto, CA) with a Prevail C18 5μm column (Alltech; Deerfield, IL) and a SEDEX Model 75 Evaporative Light Scattering (ELS) detector (Richard Scientific; Novato, CA).

Synthesis of Galactose-PEG$_{5000}$-amine. (**1**, Scheme 1). 4-Aminophenyl β-D-galactopyranoside (1.79 g, 6.38 mmol) and Fmoc-PEG$_{5000}$-NHS (2.17 g, 0.43 mmol) were dissolved in about 16 mL of phosphate-buffered saline (PBS, pH 7.4, 137 mM sodium chloride, 10 mM phosphate, 2.7 mM potassium chloride). Sulfo-NHS (97 mg, 0.44 mmol) was added, the pH was adjusted to pH 7.8, and the reaction was stirred at ambient temperature. After 6 h, EDC was added (435 mg, 2.27 mmol), and the reaction was stirred for an additional 48 h. The crude reaction mixture was dialyzed in 500 molecular-weight cutoff (MWCO) Float-A-Lyzers (Pierce; Rockford, IL) against water for 2 days with twice daily dialysate changes. The solution was dried on a rotary evaporator at temperatures not exceeding 35 °C. Deprotection of the amine was accomplished by stirring the off-white product in 50 mL of 25% piperidine in DMF for 4 h at room temperature. The solution was then concentrated under reduced pressure at temperatures not exceeding 40 °C. The viscous liquid was transferred to polypropylene centrifuge tubes and water was added. Centrifugation and filtration through a 0.2 μm HT Tuffryn Membrane filter (VWR; West Chester, PA) resulted in complete Fmoc removal from the crude reaction mixture. The solution was subjected to extensive dialysis in 500 MWCO Float-A-Lyzers before being lyophilized to dryness. Purity was confirmed by HPLC-ELS and MALDI-TOF mass spectroscopy. Final yield: 1.25 g, 59%.

Synthesis of PEGylated-polystyrene Nanoparticles. (**2**, Scheme 2). Fluorescein-embedded PEGylated-polystyrene nanoparticles were synthesized by reaction of Fluospheres (Molecular Probes; Eugene, OR) with MeO-PEG$_{5000}$-NH$_2$ or Galactose-PEG$_{5000}$-NH$_2$ (**1**). Two sizes of Fluospheres were used as starting materials in this work. Fluospheres (28 nm) were used to synthesize PEGylated nanoparticles with final diameters up to 60 nm, while nanoparticles up to 160 nm were synthesized by PEGylation of 105 nm Fluospheres. Fluospheres (28 nm) were sonicated then centrifuged at 14 000*g* for 20 min prior to use. All Fluospheres were sonicated immediately before being added to reaction vials. Typically, 500 μL of a 2% Fluosphere suspension (3.21 μmol COOH for 105 nm Fluospheres) is added to 32 mg of MeO-PEG$_{5000}$-NH$_2$ (6.42 μmol) in a 1.5 mL Eppendorf tube and mixed to dissolve the PEG. Sulfo-NHS (6.3 mg) (Pierce) is added to each tube, and 200 mM borate buffer, pH 8.2, is added up to 1 mL total volume per tube. The pH of each reaction tube is adjusted to pH 7.80, and then 1.0 mg of EDC (5.13 mmol) is added to each tube and vortex mixed for 6 h. Purification of 50 nm nanoparticles was accomplished by dialysis in 100k MWCO DispoDialyzers (Pierce) against a variety of salt solutions starting with 3 M NaCl and ending with PBS. A minimum of seven dialysate changes were performed until no free PEG was detected by HPLC-ELS. Workup of 140 nm nanoparticles was accomplished by cold centrifugation and repeated washes in salt solutions ranging from 4 M NaCl to final resuspension in PBS. Bead concentrations were determined by comparison to fluorescence of known concentrations of as-received Fluospheres on a SpectraFluor Plus fluorescence plate reader (Tecan; Research Triangle Park, NC) with FITC filters (ex: 485 nm; em: 530 nm). Yields: 50 nm nanoparticles, typically 40%; 140 nm nanoparticles, typically 70%.

Particle Size and ζ-Potential Measurements. Colloidal particle size was determined by photon correlation spectroscopy in 150 mM NaCl at a wavelength of 532 nm, scattering angle of 90°, and refractive index of 1.59 using a ZetaPALS instrument (Brookhaven Instruments; Holtsville, NY). Ten measurements on each diluted nanoparticle sample were taken, and the mean hydrodynamic diameter was reported. Nanoparticles (50 nm) were typically measured at 1×10^{13} particles/mL while 140 nm nanoparticles were typically measured at 1.5×10^{10} particles/mL. ζ-Potential measurements were calculated from electrophoretic mobilities using the Smoluchowski

equation. Nanoparticle electrophoretic mobilities were measured in 150 mM NaCl using a ZetaPALS instrument with the following conditions: fluid refractive index 1.334, electric field 5.41 V/cm and adjusted to a conductance of 15.0 mS. Three samples were each measured seven times, and the mean ± standard deviation of each was reported.

Determination of Galactose Surface Density. Concentration of galactose on the surface of nanoparticles was determined with the Amplex Red Galactose/Galactose Oxidase Assay Kit (Molecular Probes; Eugene, OR) by comparison to standard curves of galactose in solution with unmodified polystyrene beads. The reaction was allowed to proceed for a minimum of 120 min before final absorbance readings were taken due to the different rates of reaction of galactose oxidase with galactose in solution versus with surface-immobilized galactose.

RCA_{120} Lectin Agglutination. A suspension of 5.4×10^{12} nanoparticles in 500 μL of PBS was added to 4.7×10^{14} molecules of RCA_{120} lectin (Sigma-Aldrich; St. Louis, MO) in 500 μL of PBS. Each lectin has two identical binding sites, for a total of 9.5×10^{14} galactose binding sites per experiment. Agglutination was monitored by measurement of absorbance at 560 nm. After 30 min, 8×10^{18} molecules of galactose were added in 100 μL of PBS to disaggregate the system.

TEM of Nanoparticles. Nanoparticles in water were applied to 400-mesh, freshly glow-discharged, carbon-coated copper grids for 45 s. After this time, excess water was removed by blotting with filter paper, and the sample was negatively stained with 2% uranyl acetate for 45 s before blotting. A Philips 201 electron microscope, operated at 80 kV, was used to record images.

Serum-Induced Nanoparticle Aggregation. Mouse serum (Sigma) was incubated in 96-well plates at 37 °C and 5% CO_2 for a minimum of 2 h before use. Nanoparticles (5×10^{10}) were added to each 90 μL of equilibrated sera, and aggregation was monitored by measurement of absorbance at 560 nm at 37 °C.

RESULTS AND DISCUSSION

Gal-PEG_{5000}-NH_2 Synthesis and Characterization. Fmoc-PEG_{5000}-NHS was converted to high-purity Gal-PEG_{5000}-NH_2. The reaction was driven to completion by a large excess of 4-aminophenyl β-D-galactopyranoside and an additional dosing of carbodiimide coupling agent, EDC. Optimum reaction pH in NHS-mediated peptide coupling reactions is a tradeoff between the amide formation rate and the rate of hydrolysis of the activated NHS-ester. PEG_{5000}-NH_2 has a pK_a of about 9.2 (*17*) and NHS-esters on the PEG chains deactivate quickly, especially above a pH of about 8. An optimal pH of about 7.8 was determined for this reaction. While the concentration of Fmoc-PEG_{5000}-NHS did not significantly influence reaction yield, supplementation with additional Sulfo-NHS and EDC was necessary to reactivate any carboxylic esters on the PEG that had hydrolyzed.

The purity of the final purified compound was determined by HPLC-ELS, as shown in Figure 1. Peaks representing starting materials (Figure 1a) and intermediates were resolved relative to the Gal-PEG_{5000}-NH_2 peak (Figure 1b). Purity was typically greater than 98%, as determined by HPLC.

MALDI-TOF mass spectroscopy also confirmed that the reaction went to completion. Primary peaks in the MALDI-TOF spectra (Figure 2) line up well with predicted molecular weights (Table 1) of Fmoc-PEG_{5000}-NHS

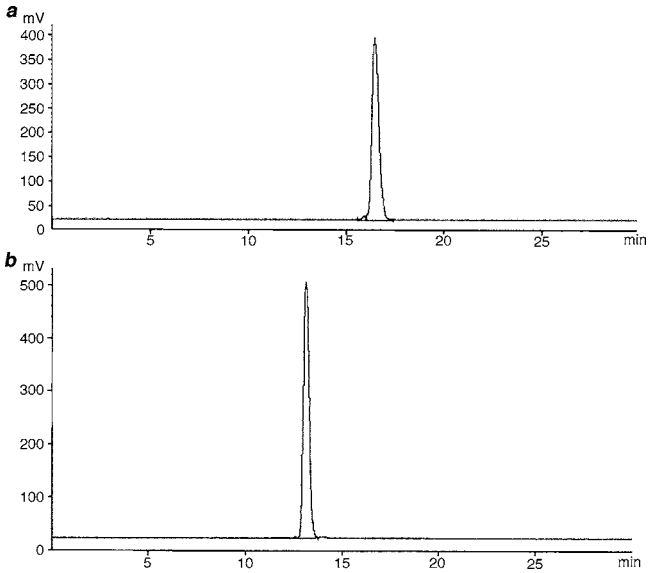

Figure 1. HPLC spectra of (a) Fmoc-PEG_{5000}-COOH and (b) Gal-PEG_{5000}-NH_2.

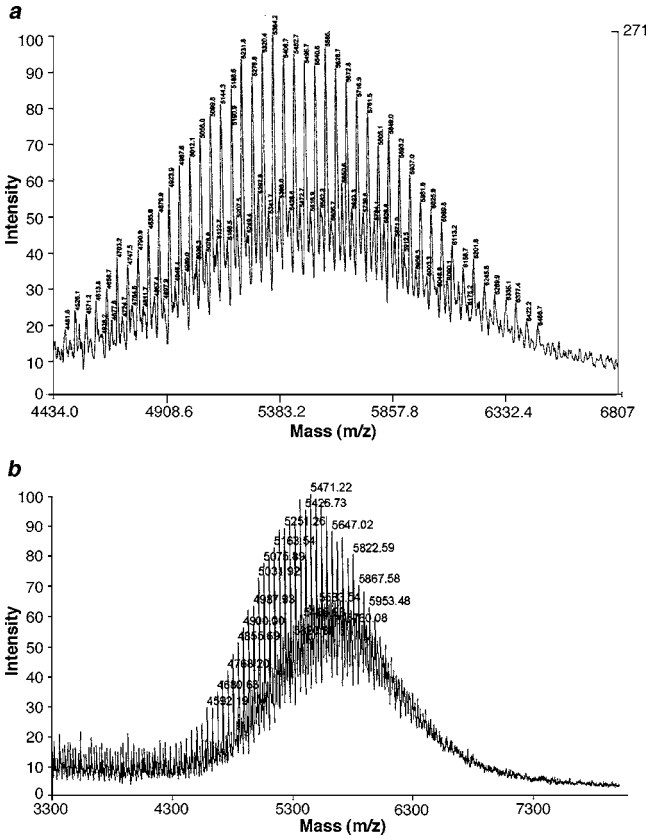

Figure 2. MALDI-TOF mass spectra of (a) Fmoc-PEG_{5000}-NHS and (b) Gal-PEG_{5000}-NH_2.

(Figure 2a) and Gal-PEG_{5000}-NH_2 (Figure 2b), according to the following formulas:

$$MW_{Fmoc-PEG-NHS} = \underset{[EO\ repeat]}{44.026n} + \underset{[(CH_2)_2C(O)\text{-}NHS]}{170.042} + \underset{[NH\text{-}Fmoc]}{238.082}$$

$$MW_{Gal-PEG-NH2} = \underset{[EO\ repeat]}{44.026n} + \underset{[(CH_2)_2C(O)\text{-}Gal]}{326.354} + \underset{[NH_2]}{16.023}$$

Table 1. Molecular Weights of Fmoc-PEG$_{5000}$-NHS and Gal-PEG$_{5000}$-NH$_2$ for Incremental Numbers of Ethylene Oxide Repeat Units, with Sodium Counterion for Comparison to Peaks of MALDI-TOF Spectra

n	predicted $MW_{Fmoc-PEG-NH} + Na^+$	observed $MW_{Fmoc-PEG-NHS} + Na^+$	predicted $MW_{Gal-PEG-NH2} + Na^+$	observed $MW_{Gal-PEG-NH2} + Na^+$
111	5318.1	5320.4	5251.3	5250.8
112	5362.0	5364.2	5296.3	5294.3
113	5406.1	5408.7	5340.3	5337.9
114	5450.1	5452.7	5384.3	5382.2
115	5494.1	5496.7	5428.4	5426.6
116	5538.1	5540.6	5472.4	5470.7
117	5582.2	5585.1	5516.4	5514.7
118	5626.2	5628.7	5560.4	5558.4
119	5670.2	5672.8	5604.5	5602.1
120	5714.2	5716.9	5648.5	5646.0
121	5758.3	5761.5	5692.5	5691.0
122	5802.3	5805.1	5736.5	5733.1

The primary population of peaks in Figure 2 is from $[M + Na]^+$, while the subpopulation comes from $[M + H]^+$. In addition to MALDI-TOF, the average molecular weight per galactose of the final product was determined to be about 5500 with the Amplex Red Galactose Assay Kit, as expected for nearly complete galactosylation of the PEG. Thus, the molecular weight determined from this technique compares well with the results of MALDI-TOF analysis.

PEGylated Nanoparticle Synthesis and Characterization. Most previous reports of PEGylating carboxy-polystyrene nanoparticles used 1 μm beads or larger (*17*−*20*). These large particles are relatively insensitive to reaction conditions, and broadening of particle size distribution was not reported. Ploehn and Goodwin (*21*) PEGylated smaller carboxy-polystyrene beads (115 and 347 nm diameter), but no indication was given that polydispersity was monitored during that reaction. For the current purpose of determining physicochemical design parameters for next generation gene delivery vectors, polydispersity of the final PEGylated nanoparticles should be low, monomodal, and well-defined. We were interested in working with nanoparticles with hydrodynamic diameters in the range of about 45−150 nm. These relatively small polystyrene beads were found to be much more sensitive to reaction conditions than larger 200 nm beads, thus requiring careful study to identify reaction and purification conditions that resulted in pure nanoparticles with desired mean diameter, particle size distribution, and extent of surface PEGylation.

The extent of PEGylation, and hence the final nanoparticle hydrodynamic diameter, was controlled by varying the concentrations of PEG and EDC during nanoparticle synthesis, as shown by the results given in Figure 3. While varying the concentration of PEG in the reaction simply shifted the final mean particle size without affecting the distribution, EDC concentrations above about 15 mM resulted in significant broadening of the particle size distribution.

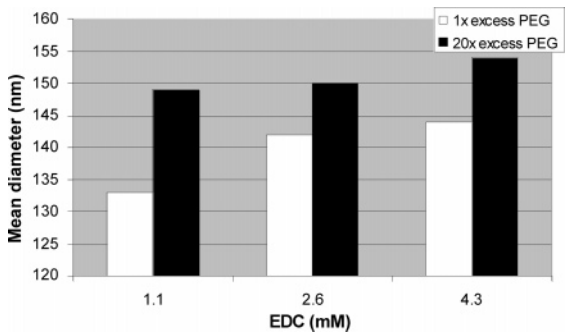

Figure 3. Mean hydrodynamic diameters following PEGylation of 105 nm Fluospheres with different reagent concentrations.

By carefully controlling reaction conditions, nanoparticles could be synthesized with size distributions (Figure 4b) that closely match those of the cyclodextrin-based gene delivery particles (Figure 4a) they intend to mimic. PEGylated nanoparticles larger than 105 nm can be synthesized with very tight monodisperse distributions under appropriate reaction conditions (Figure 4c). The polydispersity of the 50 nm nanoparticles and polyplexes is about 0.06, while that of the 140 nm nanoparticles is about 0.005. Low polydispersities such as these allow the effect of nanoparticle size on biodistribution to be clearly determined.

TEM imaging of unmodified nanoparticles validated the particle sizes measured by photon correlation spectroscopy (PCS). Particle size of unmodified polystyrene nanoparticles was found to be in good agreement between TEM and PCS measurements. This was expected, given the spherical shape of the particles and hence the appropriateness of the Stokes−Einstein expression to relate the diffusion coefficient, which is measured by PCS, to the particle size. Further, PCS measurements of particle size were performed at various concentrations

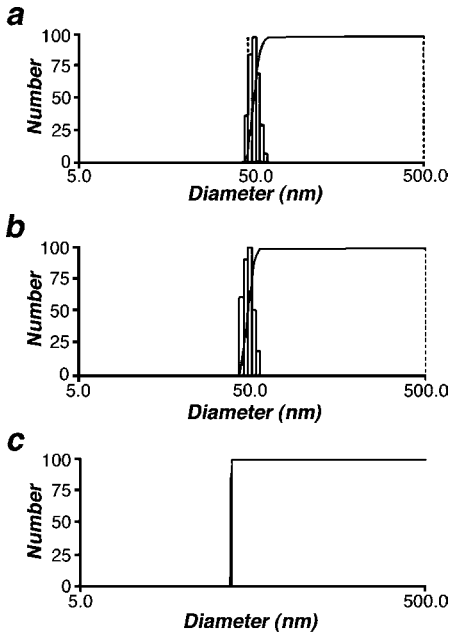

Figure 4. Histograms of nanoparticle hydrodynamic diameter distributions, as measured by PCS in 150 mM NaCl, for (a) 50 nm PEGylated polyplexes, (b) 50 nm PEGylated nanoparticles, and (c) 140 nm PEGylated nanoparticles.

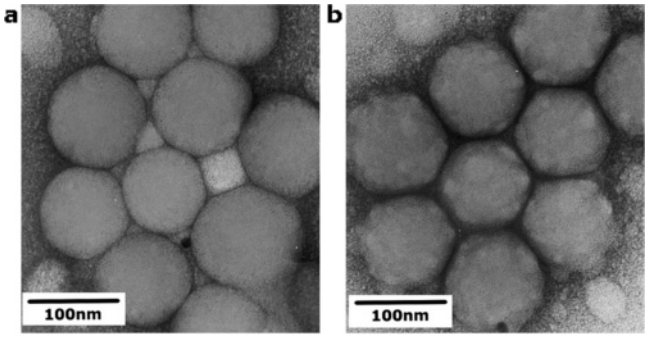

Figure 5. TEM images of (a) unmodified 105 nm Fluosphere nanoparticles and (b) PEGylated 105 nm polystyrene nanoparticles.

to ensure the accuracy of the reported result (*22*), and insignificant difference was found between these measurements.

As seen in the TEM images in Figure 5a, unmodified polystyrene Fluospheres adopt a close-packed arrangement with direct polystyrene-polystyrene contact between beads, while PEGylated nanoparticles (Figure 5b) are separated by darkly stained PEG coronas and avoid polystyrene−polystyrene contact. Because the nanoparticles must be dried for TEM analysis, the PEG layer is dehydrated and the diameter of PEGylated nanoparticles as determined by TEM is significantly smaller than their hydrodynamic diameter. Further evidence of consistent surface PEGylation was provided by our inability to separate PEGylated polystyrene nanoparticles into multiple populations by hydrophobic interaction chromatography, as described by Gbadamosi et al. (*23*). Moghimi demonstrated (*24*) that it is critical for the entire nanoparticle surface to be PEGylated to minimize nonspecific uptake of nanoparticles by the reticuloendothelial system. It is also important that the PEGylated nanospheres be well-shielded to avoid aggregation in serum. Additionally, the monodispersity of the 105 nm Fluospheres is evident from this image.

The stability of aqueous suspensions of 220 nm PEGylated polystyrene nanoparticles has been shown to increase dramatically for particles with hydrodynamic layer thicknesses of between 10 and 15 nm (*25*). The impact of PEGylated surfaces is even more critical in salt solution, where the Debye screening length will be much shorter than the hydrodynamic layer thickness. In 150 mM NaCl, for example, the Debye screening length is about 0.8 nm. As such, any charge−charge repulsion that originated from the particle surface in pure water will no longer be influential, and the PEG layer is entirely responsible for sterically shielding the particles. In the present work, 140 nm PEGylated nanoparticles were synthesized by grafting PEG onto 105 nm polystyrene nanoparticles, resulting in hydrodynamic layer thickness of slightly more than 15 nm. As such, this PEG corona is expected to provide near maximum protection against nanoparticle flocculation. Similarly, 50 nm PEGylated nanoparticles synthesized from 28 nm polystyrene have approximate hydrodynamic layer thicknesses of 11 nm. The decreased hydrodynamic thickness of PEG with the same molar mass on the smaller beads can be explained by the increased available angular segment volume with increased surface curvature (*26*). PEG_{5300} has a radius of gyration of 3.2 nm and an interfacial overlap concentration, $\sigma_{ol} = (\pi R_g^2)^{-1} = 0.031$ chains/nm^2 (*27*). The nanoparticles used in this study have a PEG surface density of about 0.14 chains/nm^2, that is much higher than σ_{ol} so it is expected that significant interactions are occurring between polymer chains on the nanoparticle surface. This interaction manifests itself as a PEG layer that is considerably thicker than $2R_g$, the expected PEG thickness in the absence of polymer chain interaction.

Table 2. Fifty-Nanometer PEGylated Nanoparticles with Different Surface Densities of Galactose for Use in RCA120 Agglutination Assay

no. of beads per experiment	no. of galactose per bead	pmol galactose per cm^2	total no. of galactose per experiment	total no. of RCA_{120} binding sites per experiment
5.4×10^{12}	1142	81.3	6.2×10^{15}	9.5×10^{14}
5.4×10^{12}	556	39.6	3.0×10^{15}	9.5×10^{14}
5.4×10^{12}	357	25.4	1.9×10^{15}	9.5×10^{14}
5.4×10^{12}	183	13.0	9.9×10^{14}	9.5×10^{14}
5.4×10^{12}	0	0	0	9.5×10^{14}

Availability of Galactose for Receptor Binding. As discussed earlier, galactose was used as a targeting ligand on some of the PEGylated nanoparticles. The surface density of galactose on the nanoparticles can be controlled by varying the ratio of Gal-PEG_{5000}-NH_2 to MeO-PEG_{5000}-NH_2 in the reaction. Further, the overall ratio of PEG-NH_2 to carboxylate groups enabled nanoparticles with different galactose moieties to be presented on the surface of nanoparticles through attachment via a 5000 Da PEG chain. To test whether the galactose moieties are accessible to bind large proteins, the particles were exposed to RCA_{120}. RCA_{120} is a 120 000 Da lectin with two identical and independent galactose binding sites per molecule (*28*). Five 50 nm PEGylated nanoparticles were synthesized for this study with different surface densities of galactose, as shown in Table 2. When RCA_{120} lectin is mixed with an appropriate number of galactosylated nanoparticles, agglutination is expected to occur. This effect is schematically illustrated in Figure 6, where lectins can be seen cross-linking galactosylated nanoparticles. This cross-linked network scatters light, and progress of agglutination can be monitored by measuring absorbance at 560 nm. Agglutination should be rapidly reversible by the addition of free galactose.

By fixing the numbers of lectin molecules and nanoparticles in all experiments, the effect of galactose surface density on agglutination can be seen (Figure 7). Turbidity, expressed as absorbance at 560 nm, is found to increase more quickly and to a greater extent for nanoparticles with a higher surface density of galactose than for comparable nanoparticles with lower surface densities of galactose. For nanoparticles with less than about 13 pmol galactose/cm^2, there are comparable numbers of galactose binding sites available on the RCA_{120} lectin and galactose available on the surface of nanoparticles, and no agglutination is observed. While this result may indicate that all galactose molecules are not accessible to binding, the general availability of nanoparticle-bound galactose for protein binding is confirmed for the higher values.

As compared to the rapid network disruption associated with galactose addition to the agglutinated solution (Figure 7), addition of an equal volume and concentration of glucose does not disrupt the cross-linked network (Figure 8). The only effect caused by addition of 100 μL of a glucose solution to the cuvette is related to dilution and is identical to the effect of adding 100 μL of water. It is thus confirmed that agglutination is due to interaction between nanoparticle-bound galactose and RCA_{120} lectin molecules.

Description of Nanoparticles for Uptake Studies. It has thus far been demonstrated that nanoparticles can

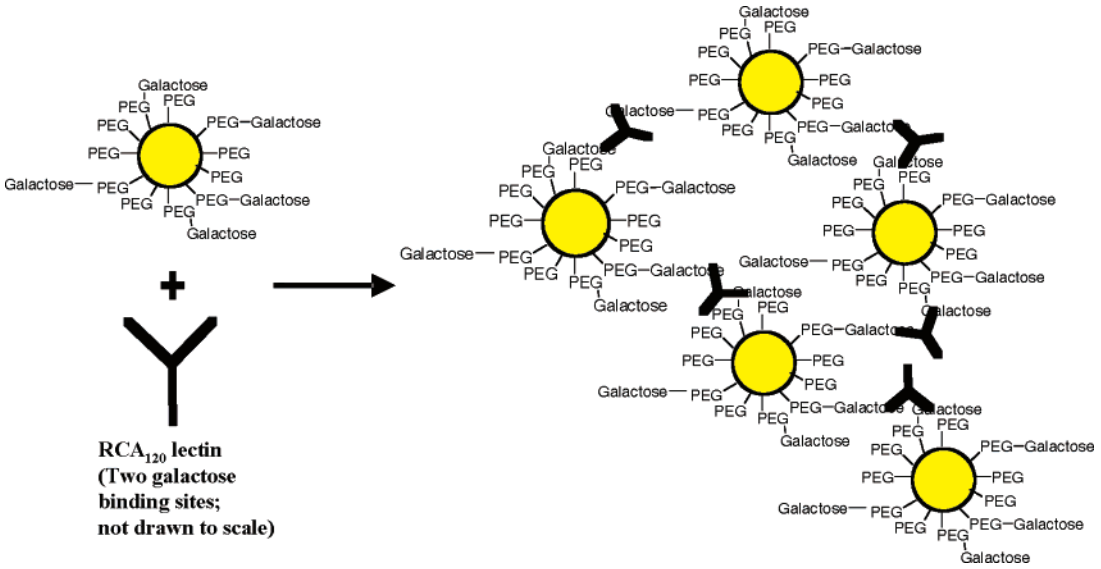

Figure 6. Schematic illustration of nanoparticle agglutination as a result of RCA_{120} lectin binding galactosylated nanoparticles.

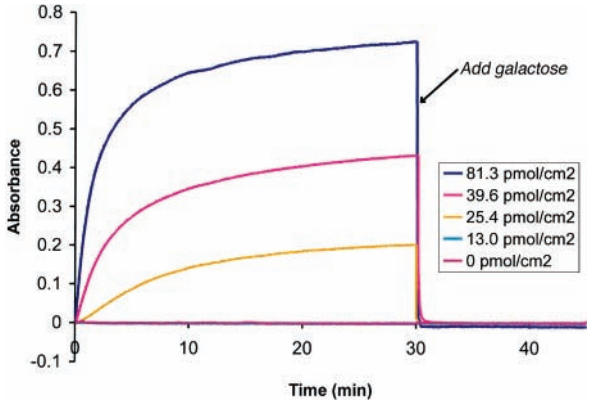

Figure 7. Turbidity increase due to agglutination of galactosylated 50 nm nanoparticles with RCA_{120} lectin. Galactose (100 μL of 140 mM solution) in PBS is added at 30 min.

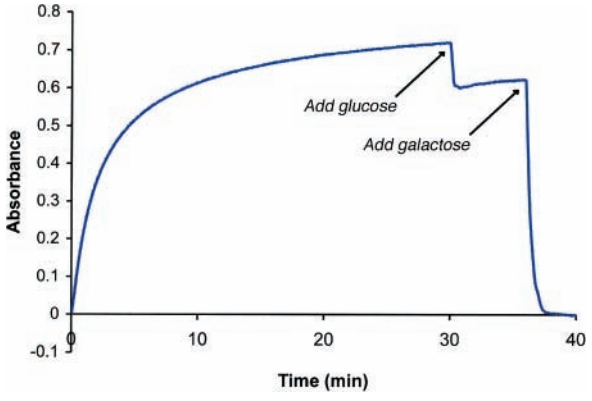

Figure 8. Turbidity increase of 50 nm nanoparticle with 81.3 pmol/cm^2 surface galactose density due to agglutination with RCA_{120} lectin. Glucose (100 μL of 140 mM solution) in PBS is added at 30 min, and then 100 μL of 140 mM galactose in PBS is added at 35 min.

be synthesized with a wide range of physicochemical properties. However, a select few must be chosen for in vitro and in vivo uptake experiments. Four nanoparticles were selected for this role, and their properties are detailed in Table 3.

Nanoparticles with mean diameters of 50 and 140 nm were selected for use because (1) cyclodextrin-based gene delivery particles can be conveniently synthesized in the range of about 45 nm to about 150 nm, so the nanoparticles selected for use in the present study approximate the bounds of that range, (2) access to hepatocytes through the hepatic sinusoidal wall requires passage through endothelial-cell pores that are estimated at 150−200 nm (*29*), and (3) 50 nm is below the 70 nm cutoff that has been proposed for neutral liposome uptake via ASGPr (*30*). The effect of galactose presentation on the surface of the nanoparticles were investigated for 50 and 140 nm nanoparticles with galactose surface densities of 25−30 pmol/cm^2. Galactosylated 50 and 140 nm nanoparticles are referred to as Gal-50 and Gal-140. The equivalent nontargeted nanoparticles have methoxy terminated PEG chains and are referred to as MeO-50 and MeO-140.

Table 3. Summary of Physicochemical Properties of the Four Nanoparticles To Be Used in Uptake Experiments

bead name	mean diameter (nm)	ζ-potential (mV)	galactose surface density (pmol/cm^2)
Gal-50	51.5	-2.7 ± 1.8	25.4
MeO-50	53.5	-2.7 ± 2.8	0
Gal-140	138.1	-2.6 ± 2.1	30.6
MeO-140	138.7	-3.2 ± 2.3	0

All nanoparticles in Table 3 have slightly anionic surface potentials (at the plane of hydrodynamic shear) to minimize nonspecific uptake. Cationic particles are internalized nonspecifically through proteoglycan receptors and may stick to anionic cell surface membranes, while highly anionic polystyrene nanoparticles have increased nonspecific uptake by scavenger receptors following complement activation (*31*, *32*). Unmodified, carboxylated, polystyrene beads (as-received starting material) have ζ-potentials of approximately −45 mV. The PEGylated nanoparticles have mean ζ-potentials of about −3 mV. These surfaces are nearly neutral due to the combined effect of carboxylate group conversion to amides on the nanoparticle surfaces and PEG shielding of the surface charge.

Serum Aggregation of PEGylated Nanoparticles. To investigate the effect of particle size on specific uptake phenomena, the nanoparticles must remain dispersed in the presence of serum. They also must not bind serum opsonins with great affinity, as such binding has been shown to increase the hepatic uptake of 50 and 500 nm polystyrene nanoparticles (*33*).

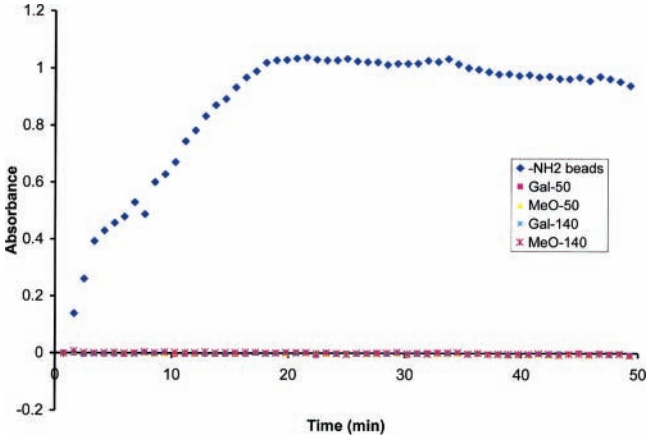

Figure 9. Nanoparticle aggregation in the presence of active mouse serum.

If serum proteins bind the surface of nanoparticles, cross-linking between nanoparticles would be expected to occur. Since many serum proteins are anionic, cross-linking should be more significant for cationic nanoparticles. For this reason, amino-modified polystyrene nanoparticles were used as a positive control in serum stability studies. As shown by the data in Figure 9, amine-functionalized nanoparticles cross-linked quickly and extensively in active mouse serum, while the PEGylated nanoparticles did not. The role of serum proteins in inducing aggregation of the amine-functionalized nanoparticles is supported by the lack of aggregation of any of the nanoparticles in PBS. Despite considerable effort, aggregation of the PEGylated nanoparticles could not be induced under any conditions.

CONCLUSIONS

Here, we report the synthesis and characterization of PEGylated polystyrene nanoparticles. These nanoparticles have slightly anionic surface potentials to minimize nonspecific interactions with cells and tissues in vivo. The synthetic scheme allows for the variation of mean particle size and particle size distribution through changes in reaction conditions. The nanoparticle synthesis is also amenable to incorporation of various ligand types with variable surface densities. The synthesized nanoparticles are shown to have PEGylated surfaces that resist aggregation in serum. Finally, the availability of galactose to receptor binding is demonstrated by agglutination with RCA_{120}.

Nanoparticles were synthesized here specifically for the purpose of identifying design constraints to guide next generation gene delivery to the liver. In preparation for in vitro and in vivo uptake experiments, four nanoparticles were prepared: Gal-50 and Gal-140 that are galactosylated 50 and 140 nm nanoparticles, and MeO-50 and MeO-140 that are methoxy-terminated 50 and 140 nm nanoparticles. Through the use of these nanoparticles, the effects of nanoparticle size and presence of galactose on the nanoparticle surface on the biodistribution in liver are explored in Part 2 of this work (*16*).

LITERATURE CITED

(1) Verma, I. M., and Somia, N. (1997) Gene therapy − promises, problems and prospects. *Nature 389*, 239−242.
(2) Prieto, J., Qian, C., Hernandez-Alcoceba, R., Gonzalez-Aseguinolaza, G., Mazzolini, G., Sangro, B., and Kramer, M. G. (2004) Gene therapy of liver diseases. *Expert Opin. Biol. Ther. 4*, 1073−1091.
(3) Kren, B. T., Chowdhury, N. R., Chowdhury, J. R., and Steer, C. J. (2002) Gene therapy as an alternative to liver transplantation. *Liver Transplant. 8*, 1089−1108.
(4) Walsh, C. E. (2003) Gene therapy Progress and Prospects: Gene therapy for the hemophilias. *Gene Ther. 10*, 999−1003.
(5) Shlomai, A., and Shaul, Y. (2004) RNA interference − small RNAs effectively fight viral hepatitis. *Liver Int. 24*, 526−531.
(6) Germain, D. P. (2004) Gaucher's disease: a paradigm for interventional genetics. *Clin. Genet. 65*, 77−86.
(7) Mishra, S., Webster, P., and Davis, M. E. (2004) PEGylation significantly affects cellular uptake and intracellular trafficking of nonviral gene delivery particles. *Eur. J. Cell Biol. 83*, 97−111.
(8) Moghimi, S. M., and Patel, H. M. (1998) Serum-mediated recognition of liposomes by phagocytic cells of the reticuloendothelial system − The concept of tissue specificity. *Adv. Drug Delivery Rev. 32*, 45−60.
(9) Dan, C., and Wake, K. (1985) Modes Of Endocytosis Of Latex-Particles In Sinusoidal Endothelial And Kupffer Cells Of Normal And Perfused Rat-Liver. *Exp. Cell Res. 158*, 75−85.
(10) Dunn, S. E., Brindley, A., Davis, S. S., Davies, M. C., and Illum, L. (1994) Polystyrene-Poly(Ethylene Glycol) (Ps-Peg2000) Particles As Model Systems For Site-Specific Drug-Delivery. 2. The Effect Of Peg Surface-Density On The In−Vitro Cell-Interaction And In−Vivo Biodistribution. *Pharm. Res. 11*, 1016−1022.
(11) Davis, M. E., Pun, S. H., Bellocq, N. C., Reineke, T. M., Popielarski, S. R., Mishra, S., and Heidel, J. D. (2004) Self-assembling nucleic acid delivery vehicles via linear, water-soluble, cyclodextrin-containing polymers. *Curr. Med. Chem. 11*, 179−197.
(12) Pun, S. H., and Davis, M. E. (2002) Development of a nonviral gene delivery vehicle for systemic application. *Bioconjugate Chem. 13*, 630−639.
(13) Reineke, T. M., and Davis, M. E. (2003) Structural effects of carbohydrate-containing polycations on gene delivery. 1. Carbohydrate size and its distance from charge centers. *Bioconjugate Chem. 14*, 247−254.
(14) Reineke, T. M., and Davis, M. E. (2003) Structural effects of carbohydrate-containing polycations on gene delivery. 2. Charge center type. *Bioconjugate Chem. 14*, 255−261.
(15) Popielarski, S. R., Mishra, S., and Davis, M. E. (2003) Structural effects of carbohydrate-containing polycations on gene delivery. 3. Cyclodextrin type and functionalization. *Bioconjugate Chem. 14*, 672−678.
(16) Popielarski, S. R., Hu-Lieskovan, S., French, S. W., Triche, T. J., and Davis, M. E. (2005) A Nanoparticle-Based Model Delivery system to Guide the Rational Design of Gene Delivery to the Liver. 2. In Vitro and In Vivo Uptake Results. *Bioconjugate Chem. 16*, 1071−1080.
(17) VanDelden, C. J., Bezemer, J. M., Engbers, G. H. M., and Feijen, J. (1996) Poly(ethylene oxide)-modified carboxylated polystyrene latices − Immobilization chemistry and protein adsorption. *J. Biomat. Sci.-Polym. E. 8*, 251−268.
(18) Meng, F. H., Engbers, G. H. M., and Feijen, J. (2004) Polyethylene glycol-grafted polystyrene particles. *J. Biomed. Mater. Res.-A 70A*, 49−58.
(19) Meng, F. H., Engbers, G. H. M., Gessner, A., Muller, R. H., and Feijen, J.(2004) Pegylated polystyrene particles as a model system for artificial cells. *J. Biomed. Mater. Res.-A 70A*, 97−106.
(20) Valentine, M. T., Perlman, Z. E., Gardel, M. L., Shin, J. H., Matsudaira, P., Mitchison, T. J., and Weitz, D. A. (2004) Colloid surface chemistry critically affects multiple particle tracking measurements of biomaterials. *Biophys. J. 86*, 4004−4014.
(21) Ploehn, H. J., and Goodwin, J. W. (1990) Rheology Of Aqueous Suspensions Of Polystyrene Latex Stabilized By Grafted Poly(Ethylene Oxide). *Faraday Discuss. 90*, 77−90.
(22) Dejaeger, N., Demeyere, H., Finsy, R., Sneyers, R., Vanderdeelen, J., Vandermeeren, P., and Vanlaethem, M. (1991) Particle Sizing By Photon-Correlation Spectroscopy. 1. Monodisperse Lattices − Influence Of Scattering Angle And Concentration Of Dispersed Material. *Part. Part. Syst. Charact. 8*, 179−186.

(23) Gbadamosi, J. K., Hunter, A. C., and Moghimi, S. M. (2002) PEGylation of microspheres generates a heterogeneous population of particles with differential surface characteristics and biological performance. *FEBS Lett. 532*, 338−344.
(24) Moghimi, S. M. (2002) Chemical camouflage of nanospheres with a poorly reactive surface: towards development of stealth and target-specific nanocarriers. *Biochim. Biophys. Acta (Mol. Cell Res.) 1590*, 131−139.
(25) Wind, B., and Killmann, E. (1998) Adsorption of poly-(ethylene oxide) on surface modified silica stability of bare and covered particles in suspension. *Colloid Polym. Sci. 276*, 903−912.
(26) Killmann, E., and Sapuntzjis, P.(1994) Dynamic Light-Scattering Of Polystyrene Latex And Silica With Adsorbed Poly(Ethylene Oxide) Layers − Influence Of Ionic-Strength And Coverage. *Colloids Surface. A 86*, 229−238.
(27) Devanand, K., and Selser, J. C. (1991) Asymptotic-Behavior And Long-Range Interactions In Aqueous-Solutions Of Poly-(Ethylene Oxide). *Macromolecules 24,* 5943−5947.
(28) Van Wauwe, J. P., Loontiens, F. G., and Debruyne, C. K. (1973) Interaction Of Ricinus-Communis Hemagglutinin With Polysaccharides And Low-Molecular Weight Carbohydrates. *Biochim. Biophys. Acta 313,* 99−105.
(29) Wisse, E., Dezanger, R. B., Charels, K., Vandersmissen, P., and McCuskey, R. S. (1985) The Liver Sieve − Considerations Concerning The Structure And Function Of Endothelial Fenestrae, The Sinusoidal Wall And The Space Of Disse. *Hepatology 5*, 683−692.
(30) Rensen, P. C. N., Sliedregt, L., Ferns, A., Kieviet, E., van Rossenberg, S. M. W., van Leeuwen, S. H., van Berkel, T. J. C., and Biessen, E. A. L.(2001) Determination of the upper size limit for uptake and processing of ligands by the asialoglycoprotein receptor on hepatocytes in vitro and in vivo. *J. Biol. Chem. 276*, 37577−37584.
(31) Gref, R., Miralles, G., and Dellacherie, E. (1999) Polyoxyethylene-coated nanospheres: effect of coating on zeta potential and phagocytosis. *Polym. Int. 48*, 251−256.
(32) Ogawara, K., Yoshida, M., Higaki, K., Kimura, T., Shiraishi, K., Nishikawa, M., Takakura, Y., and Hashida, M. (1999) Hepatic uptake of polystyrene microspheres in rats: Effect of particle size on intrahepatic distribution. *J. Controlled Release 59*, 15−22.
(33) Ogawara, K., Yoshida, M., Takakura, Y., Hashida, M., Higaki, K., and Kimura, T. (1999) Interaction of polystyrene microspheres with liver cells: roles of membrane receptors and serum proteins. *Biochim. Biophys. Acta (Gen. Subjects) 1472*, 165−172.

BC050113D

A Nanoparticle-Based Model Delivery System To Guide the Rational Design of Gene Delivery to the Liver. 2. In Vitro and In Vivo Uptake Results

Stephen R. Popielarski,[†] Siwen Hu-Lieskovan,[‡] Samuel W. French,[§] Timothy J. Triche,[‡] and Mark E. Davis[†,*]

Chemical Engineering, California Institute of Technology, Pasadena, California 91125, Department of Pathology, Childrens Hospital Los Angeles, 4650 Sunset Bl., Los Angeles, California 90027, and Department of Pathology, Harbor-UCLA Medical Center, Torrance, California 90509. Received April 14, 2005; Revised Manuscript Received August 3, 2005

In Part 1 of our work (*1*), four nanoparticles were synthesized specifically for the purpose of identifying design constraints to guide next generation gene delivery to the liver. The four nanoparticles are Gal-50 and Gal-140 (galactosylated 50 and 140 nm nanoparticles) and MeO-50 and MeO-140 (methoxy-terminated 50 and 140 nm nanoparticles). All four particles have the same surface charge, and Gal-50 and Gal-140 have the same surface galactose density (ca. 25−30 pmol/cm^2). Here, the hepatocyte uptake in vitro and hepatic distribution in vivo of these four nanoparticles is investigated. With freshly isolated hepatocytes, Gal-50 nanoparticles are taken up to a greater extent than are MeO-50, and both 50 nm beads are taken up to a much greater extent than either of the 140 nm nanoparticles. In mice, about 90% of the in vivo dose of Gal-140 nanoparticles is found within the liver 20 min after tail-vein injection. TEM and immunohistochemistry images confirm that Gal-140 nanoparticles are primarily internalized by Kupffer cells, though isolated examples of a few Gal-140 in hepatocytes are also observed. Gal-50 nanoparticles are overwhelmingly found in vesicles throughout the cytoplasm of hepatocytes, with only isolated examples of Kupffer cell uptake 20 min after tail vein injections in mice. Despite similar surface charge and ligand density, 50 nm nanoparticles are primarily found in hepatocytes while 140 nm nanoparticles are primarily observed in Kupffer cells. These results clearly show that slightly anionic, galactose-PEGylated nanoparticles with 25−30 pmol/cm^2 galactose should be about 50 nm in diameter to preferentially target hepatocytes while they should be about 140 nm in diameter to selectively target Kupffer cells.

INTRODUCTION

Gene therapy has the potential for treating numerous liver diseases (*2*). To prepare effective gene therapeutics for liver diseases, the therapeutics must target cells in the liver. Investigators have identified the importance of carefully designing and controlling the properties of nonviral gene delivery systems for targeting the liver. In Part 1 of our work, the synthesis and characterization of galactose-containing, slightly anionic PEGylated polystyrene nanoparticles are described, and these well-defined particles are appropriate for in vitro and in vivo biodistribution experiments to target liver (*1*). In particular, four nanoparticles were selected for in vivo experiments, and their properties are shown in Table 1.

Here, the in vitro hepatocyte uptake and in vivo hepatic distribution of the four nanoparticles described in Table 1 are determined. Comparable 50 nm nanoparticles and 140 nm nanoparticles that differ only in the presence of galactose on their surfaces allow the effect of galactose on biodistribution to be identified. Galactose is utilized as the targeting ligand in this work because galactose receptors are almost exclusively found in the liver, though both hepatocytes and Kupffer cells display galactose receptors. Hepatocytes abundantly express an asialoglycoprotein receptor (ASGPr) that selectively recognizes galactose and *N*-acetylgalactosamine (GalNAc) residues on small molecules, proteins, and particles. Kupffer cells abundantly express a galactose-particle receptor (GPr) that primarily recognizes galactose residues bound to solid surfaces without recognizing small galactosylated molecules (*3*). While both ASGPr and GPr recognize galactosylated particles, uptake via these receptors is differentially affected by particle size. While an upper size limit of about 70 nm has been proposed for ASGPr-mediated uptake of particles (*4*), Kupffer cells preferentially internalize 500 nm particles over 80 nm particles (*5*). Gal-50 is below the proposed cutoff in size for ASGPr-mediated uptake, while Gal-140 is above this critical size and may also be recognized more readily by the Kupffer cell GPr.

Table 1. Summary of Physicochemical Properties of the Four Nanoparticles To Be Used in Uptake Experiments

bead name	mean diameter (nm)	ζ-potential (mV)	galactose surface density (pmol/cm^2)
Gal-50	51.5	−2.7 ± 1.8	25.4
MeO-50	53.5	−2.7 ± 2.8	0
Gal-140	138.1	−2.6 ± 2.1	30.6
MeO-140	138.7	−3.2 ± 2.3	0

In vitro uptake experiments used here are with freshly isolated hepatocytes as compared to hepatocellular carcinoma cell lines to provide results that more closely

* To whom correspondence should be addressed. E-mail: mdavis@cheme.caltech.edu.
[†] California Institute of Technology.
[‡] Childrens Hospital Los Angeles.
[§] Harbor-UCLA Medical Center.

10.1021/bc0501146 CCC: $30.25 © 2005 American Chemical Society
Published on Web 08/31/2005

represent hepatocyte uptake in vivo. By their nature, carcinoma cells divide much more rapidly than nononcogenic hepatocytes, and their uptake mechanisms are altered accordingly. Since we are interested in studying nanoparticle uptake and distribution in hepatic tissue, use of primary hepatocytes will more closely approximate the uptake response of hepatocytes in vivo than would immortalized cell lines. Furthermore, many cultured cell lines have been cultured for extended periods of time, resulting in heterogeneous populations of cells. Microarray comparison of mRNA expression levels of whole rat liver, several rat liver cell lines, and primary cultured hepatocytes indicated that the cell lines were most dissimilar from whole liver, and that they also differed significantly from primary hepatocytes (*6*). In addition, the duration of culture had a profound effect on mRNA levels. Significant differences in ethanol toxicity (*7*), transferrin internalization rate (*8*), and ASGPr receptor levels have also been reported between hepatocellular carcinoma cell lines and normal hepatocytes. For example, HepG2 cells, a human malignant hepatic cell line, have only about 225 000 ASGPr per cell. Rat hepatocytes have approximately 550 000 ASGPr total per cell. Although HepG2 cells present 87% of the total cellular ASGPr on the cell surface (*9*), only about 250 000 (*10*) of the hepatocyte ASGPr are expressed on the cell surface while the additional 300 000 constitute an intracellular pool. This intracellular pool of ASGPr has been implicated in intracellular trafficking and processing of receptor and ligand, including a role in transport in the secretory pathway following ligand internalization (*11*). Therefore, immortalized cell lines such as HepG2 do not provide an ideal in vitro system to guide in vivo hepatic biodistribution studies, and freshly isolated hepatocytes will be used in this work.

In vitro uptake into hepatocytes is assayed both as adherent cells, to compare the dose fraction internalized by the cells, and as suspended cells to study the kinetics of nanoparticle association with hepatocytes. In vivo hepatic distribution is determined by collection of liver tissue and analysis by transmission electron microscopy (TEM) and immunohistochemistry, that allow for the visualization of liver sections from mice that received tail-vein injections of the different nanoparticles described in Table 1.

MATERIALS AND METHODS

Animals. Female Balb/c mice were obtained from Charles River Laboratories (Wilmington, MA) and were approximately 10−15 weeks old at the time of the study. The animals were fed autoclaved LabDiet 5010 (Purina Mills; St. Louis, MO) and drank reverse osmosis, 1 ppm chlorine, autoclaved water from bottles. The mice were housed on ventilated racks with autoclaved nestlets and Aspen Chip bedding (Nepco; Warrensburg, NY) on a 13-h light cycle at 72−76 °F and 30−70% humidity. Caltech specifically complies with the recommendations of the *Guide for Care and Use of Laboratory Animals* with respect to restraint, husbandry, surgical procedures, feed and fluid regulation, and veterinary care. The animal program at Caltech is AAALAC accredited.

Hepatocyte Isolation. Mouse hepatocytes were isolated from female Balb/c mice (18−25 g, 10−15 weeks old) by the standard two-step perfusion with collagenase by the Cell Culture Core of the USC Research Center for Liver Diseases, as previously described (*12*). Briefly, mice were anesthetized with pentobarbital sodium (60 mg/kg), and the liver was perfused via the portal vein at 3 mL/min first with Ca^{2+} and Mg^{2+}-free perfusion buffer (10 mM *N*-2-hydroxyethylpiperazine-*N*′-2-ethanesulfonic acid (HEPES), 137 mM NaCl, 5 mM KCl, 0.5 mM NaH_2PO_4, and 0.4 mM Na_2HPO_4, pH 7.2) for 3 min and then with perfusion buffer supplemented with 5 mM $CaCl_2$ and 0.05% (w/v) collagenase (type IV; pH 7.5) for 3 min. The liver was then carefully removed, and its capsular membrane was gently peeled off. The dispersed cells, in cold Hank's−HEPES buffer containing 0.1% BSA, were filtered through cotton mesh and allowed to settle. Dead parenchymal hepatocytes were removed by density gradient centrifugation on Percoll (Amersham Biosciences; Piscataway, NJ) to give parenchymal cells of >90% purity and >90% viability, as determined by trypan blue exclusion. Appropriate numbers of hepatocytes, as described in the following sections, were transferred to collagen-coated dishes that were maintained at 37 °C with 95% humidity and 5% CO_2. After 1 h, the unattached cells were removed by aspiration, and culture medium changes were performed daily thereafter. Complete hepatocyte media consisted of Dulbecco's Modified Eagle's Medium/F12 without phenol red (Invitrogen; Carlsbad, CA), supplemented with L-methionine, 100 U/mL penicillin, 0.1 mg/mL streptomycin, 0.25 mg/mL amphotericin B (Invitrogen), and 9% fetal bovine serum.

Nanoparticle Uptake by Adherent Hepatocytes. Following hepatocyte isolation, 100 000 hepatocytes were transferred to each well of collagen-coated 24-well plates. After a minimum of 24 h of incubation in complete medium, hepatocytes were incubated in OptiMem (Invitrogen) that does not contain any Cu^{2+} or Zn^{2+} ions for 2 h prior to experimentation, to allow the hepatic asialoglycoprotein receptor (ASGPr) to adopt an accessible conformation and to achieve maximum uptake potential (*13*). The medium in each well was then replaced with the appropriate nanoparticle-containing medium, or PBS-containing medium for wells to be used in the preparation of standard curves. Hepatocytes were incubated in 200 μL of Optimem containing 7.5×10^9 nanoparticles/mL for 40 min. After this time, the medium was removed, and cells were washed with cold HEPES buffer then lysed with 1X Cell Culture Lysis Reagent (Promega; Madison, WI). Fluorescence of the soluble portion of the cell lysates was measured and compared to standard curves prepared by adding known numbers of beads to hepatocyte cell lysates.

Preparation of Suspended Hepatocytes. Following hepatocyte isolation, about 7×10^6 hepatocytes were transferred to a collagen-coated 10 cm^2 dish and incubated for a minimum of 24 h in complete medium. Hepatocytes were detached with trypsin−EDTA (Invitrogen), spun down at 400*g* for 5 min, and resuspended at 2×10^6 cells/mL in complete hepatocyte media in 50 mL polypropylene tubes, 10 mL total per tube, with 40 μm polypropylene Falcon Cell Strainers (Fisher; Hampton, NH) to minimize contamination while permitting gas exchange. After incubating at 37 °C and 5% CO_2 overnight, hepatocytes were spun down, washed with HEPES buffer, and resuspended in Optimem with 3% fetal bovine serum in polypropylene tubes. Following 2 h incubation in media lacking Cu^{2+} or Zn^{2+} ions, hepatocytes were spun down, resuspended in Optimem, and aliquoted for experimentation. Experimental details concerning data collection are described in the following section.

Flow Cytometry Analysis of Nanoparticle Uptake Kinetics. Single cell suspensions of 2×10^6 hepatocytes per mL were prepared as described above and kept on ice prior to analysis. Immediately before use, cell suspensions were warmed to 37 °C, nanoparticles were added

to the FACS tube, and analysis was started within 10 s. Flow cytometry analyses were performed using a BD Bioscience FACSCalibur (San Jose, CA) equipped with a 488 nm argon laser and a 635 diode laser and Cellquest software. Dead cells, aggregates, and Kupffer cells were removed from the analyses by live gating on forward and side scatter. Green fluorescence emitted by the beads was measured with a 530/30 nm band-pass filter. Autofluorescent cells were removed by using a red channel measured by a 585/42 nm band-pass filter to gate out bright cells. Flow rates were kept constant at 35 μL per minute. Per cell mean fluorescence from gated cells was analyzed by downloading the Cellquest list mode data file to FlowJo (Tree Star Inc.; Ashland, OR), gating the cells, and then exporting the gated data to Microsoft Excel. Mean fluorescence signals were averaged over all cells analyzed in 5 s intervals. The percentage of FITC-positive cells was calculated based on the ratio of the number of FITC-positive cells in each 5 s interval to the total number of cells counted in that interval. FITC mean values are normalized by the number of fluorescein equivalents per bead.

Bulk Liver Uptake of Nanoparticles. Twenty minutes after tail-vein injection of 100 μL of saline containing 8×10^{11} nanoparticles per 20 g mouse, mice were sacrificed and their livers were immediately excised, weighed, and split into two comparable pieces. Each piece was then transferred to individual Lysing Matrix D tubes (Qbiogene; Irvine, CA) and subjected to three cycles of mechanical agitation in a FastPrep FP120 instrument (Qbiogene). Cellular membranes were disrupted by three freeze−thaw cycles, and an additional cycle of mechanical agitation resulted in homogeneous liver samples that were lyophilized to dryness. FITC was subsequently extracted into chloroform for comparison to a standard curve. Standard curves were created by adding a known number of nanoparticles to liver pieces from untreated mice, followed by identical homogenization and extraction processing to the samples described above. Data as shown represent tissue uptake of nanoparticles, that has been determined by subtracting the approximate fluorescence due to nanoparticles in liver blood vessels from the fluorescence of the wet liver tissue. All experiments were repeated in triplicate.

TEM Imaging of Liver Tissue. For electron microscopy, excised liver tissue was cut into 1 mm^3 cubes and fixed in 2% glutaraldehyde in 100 mM sodium cacodylate buffer (pH 7.4). After being washed in a sodium cacodylate buffer, the tissue was postfixed in 1% osmium tetroxide in sodium cacodylate buffer for 1 h. After being rinsed, the tissue was embedded in Epon-Spurr resin. Thin sections were prepared, contrasted with uranyl acetate and lead citrate, and observed on a Hitachi 600 electron microscope (Hitachi Ltd.; Tokyo, Japan).

Overlay of Fluorescence and TEM Images. Mouse parenchymal liver cells were isolated as described above. Cells were seeded at a density of 3×10^5 cells per collagen-coated glass cover slip in six-well culture plates. After a minimum of 24 h incubation in complete medium, hepatocytes were incubated in OptiMem (Invitrogen) for 2 h prior to experimentation. Medium in each well was then replaced with 200 μL Optimem containing 7.5×10^9 nanoparticles/mL and incubated for 40 min. Cells were then washed with HEPES buffer and fixed in 2.5% glutaraldehyde for 2 h at room temperature. Glass cover slips were mounted with Vectashield mounting media (Vector Laboratories; Burlingame, CA). To identify the same cell for light microscopy and TEM, spots were made with an ultrafine tipped pen on the cell-containing cover slip.

Immunohistochemical Staining. Mice received a 100 μL tail-vein injection containing 8×10^{11} nanoparticles per 20 g mouse weight. The injection was performed over less than 5 s using a 26-gauge needle in all cases. Twenty minutes after the injection of nanoparticles, mice were sacrificed and their livers were immediately excised, embedded in Tissue-Tek OCT embedding compound (Sakura Finetek USA; Torrance, CA), and stored in 2-methylbutanol on dry ice. Frozen liver sections were cut 12 μm thick, and two sections were placed on each slide for imaging. Remaining blocks were stored at −80 °C. The slides were washed with PBS to remove OCT, and a perimeter was drawn around each pair of sections with an ImmEdge pen (Vector Laboratories). Each section was then fixed with 4% paraformaldehyde and rinsed with TBS (100 mM Tris and 150 mM NaCl, adjusted to pH 7.4). Slides were incubated with blocking buffer, and then any biotin or streptavidin in the sections was blocked with the Streptavidin/Biotin Blocking Kit (Vector Laboratories) and rinsed with TBS. Continuing with TBS washes between each step, slides were sequentially incubated with donkey blocking buffer, goat anti-ASPGR1 antibody (Santa Cruz Biotechnology; Santa Cruz, CA), donkey anti-goat IgG-biotin (Santa Cruz Biotechnology), and finally QDot655 streptavidin conjugate (Quantum Dot Corp.; Hayward, CA). Following a final set of TBS washes, slides were mounted with Vectashield Mounting Medium with DAPI (Santa Cruz Biotechnology) nuclear stain.

Immunohistochemistry Imaging. Images were acquired at the CHLARI Congressman Julian Dixon Cellular Image Core with a Leica DM RXA microscope using a HC Plan 20x/0.70NA Ph2 DIC C objective lens, 1.25× optovar, and Koehler illumination (Leica Microsystems Inc.; Bannockburn, IL). A SKY/CD-300/VDS-1300 spectral imager with EasyFISH software (Applied Spectral Imaging, Inc.; Carlsbad, CA) was used. The 640 × 480 pixel images were acquired with 2 × 2 binning (1.039 μm/pixel). All images acquired during a single session for each size nanoparticle were captured with identical exposure times and saved as 16-bit/channel EasyFISH files. Images were also saved as 24-bit RGB color images using constant slope contrast settings for each channel. Phase contrast and GFP images were acquired using a Chroma 41004 filter set (HQ480/40x, Q505LP dichroic, HQ535/50m), DAPI images were acquired using a Chroma 41001 filter set (HQ480/40x, Q505LP, HQ535/50m) (Chroma Technology Corp.; Brattleboro, VT), and QD655 images were acquired with a Leica N2.1 filter set 513832 (BP515-560, 580, LP590).

RESULTS AND DISCUSSION

In Vitro Uptake Results. Hepatocytes have access to high concentrations of amino acids and other nutrients from the digestive tract and endogenous protein catabolism, as well as a rich network of endoplasmic reticulum that enables their efficient secretory processes (*14*). As such, hepatocytes are the primary site of secretory protein synthesis in the body and are accordingly involved in many disease states. Hepatocytes are therefore a highly desirable target for gene therapy.

Nanoparticle uptake into cultured hepatocytes can provide an initial indication of the effect of size and galactose targeting on hepatic uptake. Besides the complex microenvironment in the liver surrounding each

Table 2. In Vitro Uptake of Nanoparticles by Freshly Isolated Hepatocytes, as Quantified by the Overall Fluorescence of Cell Lysates by Comparison to a Standard Curve Also Using Hepatocyte Lysates

nanoparticle type	% dose in hepatocyte lysate
Gal-50	21.9
MeO-50	9.0
Gal-140	1.6
MeO-140	1.5

hepatocyte, as compared to the loosely packed monolayer of hepatocytes in culture, freshly isolated hepatocytes were found to have only 17% of their ASGPr on the cell surface (*15*) as compared to between 40% and 60% ASGPr presentation for hepatocytes in the liver. After incubation at 37 °C, the receptor distribution in isolated hepatocytes has been reported to approach 50% on the cell surface with the remainder associated with intracellular Golgi, microsomal, and lysosomal membranes (*16*). To minimize the transient nature of these effects, hepatocytes were incubated in complete hepatocyte medium, as described in Materials and Methods, for a minimum of 24 h prior to use.

Nanoparticle uptake by plated hepatocytes was assayed by measuring the fluorescence of whole cell lysates after incubating freshly isolated hepatocytes with nanoparticles and washing with chilled HEPES buffer. In all in vitro uptake experiments, hepatocytes were incubated for 2 h in media that does not contain any Cu^{2+} or Zn^{2+} ions. McAbee and Jiang (*13*) have demonstrated that these ions result in the reversible accumulation of inactive ASGPr both intracellularly and on the cell surface, so hepatocytes were incubated at 37 °C and washed in the absence of Cu^{2+} or Zn^{2+} before experiments were initiated.

The results of nanoparticle uptake into plated hepatocytes are shown in Table 2. It is apparent that nanoparticles with 50 nm diameters are taken up to a much greater extent than are those with 140 nm diameter. The presence of galactose on 140 nm beads has no apparent effect, with about 1.5% of each MeO-140 and Gal-140 dose being internalized by hepatocytes. Galactose presentation does, however, significantly affect the uptake of 50 nm beads. While about 9% of MeO-50 nanoparticles were internalized during the course of the experiment, greater than 20% of Gal-50 nanoparticles were internalized. These results presented in Table 2 are consistent with the findings of Rensen et al. (*4*) that hepatocytes preferentially internalize targeted liposomes with diameters less than about 70 nm. In place of glycolipid-containing liposomes, the present work makes use of slightly anionic PEGylated nanoparticles that closely mimic the surface properties of stabilized gene delivery polyplexes. Since PEGylation is commonly required to achieve long circulation times of nanoparticles in vivo, the results obtained with this system are expected to directly translate to a wide variety of gene and drug delivery systems.

When formation of endocytic vesicles is accompanied by uptake of extracellular fluid along with any macromolecules or particles present, uptake is said to occur by fluid-phase endocytosis, or pinocytosis. Vesicles resulting from pinocytosis are generally less than 100 nm in diameter, so it can be speculated that the fairly high uptake of nontargeted 50 nm nanoparticles by hepatocytes in vitro may at least partially be due to pinocytosis.

To help guide in vivo experiments and to better understand in vitro uptake, nanoparticle uptake kinetics were monitored with suspended, freshly isolated hepatocytes, and the results are shown in Figure 1. This experiment confirms the results obtained with plated hepatocytes. Gal-140 and MeO-140 are taken up only minimally compared to the 50 nm nanoparticles (Figure 1a), and no difference in uptake was seen in 140 nm beads (Figure 1b) displaying galactose or methoxy on their surfaces. Once again, uptake of the nontargeted MeO-50 nanoparticles does occur, but Gal-50 are taken up to a greater extent. At least 10 nanoparticles were associated with each hepatocyte within 30 s of their addition to the hepatocyte suspension (data not shown). This result is not unreasonable considering that ASGPr clustering has been observed within 15 s of ligand introduction (*17*), approximately 50% of ASGPr-ligand complexes are internalized within 3 min (*15*, *18*) and that at saturation, each hepatocyte can take up 5×10^6 ligands by ASGPr per hour (*10*).

Following pinocytic uptake by hepatocytes in vivo, vesicles follow one of three distinct paths (*19*). About 80% of pinocytosis material is rapidly exchanged with extracellular fluid, about 18% is processed deeper into the cell, and about 2% is secreted into bile. The fraction of internalized fluid that is regurgitated back into plasma does so with $t_{1/2}$ about 1−2 min in hepatocytes. This $t_{1/2}$ is considerably shorter than is seen in macrophages, fibroblasts or adipocytes. Based on these uptake results, it is estimated that hepatocytes pinocytose the equivalent of 20% or more of their volume and at least 5 times their plasma membrane surface area each hour (*19*). This high recycle rate of pinocytosed materials has also been confirmed with suspended rate hepatocytes (*20*), and the shape of the MeO-50 uptake curve in Figure 1a can be explained by this mechanism (*21*). For the first 30−60 s of hepatocyte exposure to MeO-50 nanoparticles, uptake is proceeding quickly without significant nanoparticle release back into the extracellular fluid. However, an average pinosome recycling time of about 1−2 min means that increasing amounts of pinocytosed material is released after about 60 s until steady-state conditions are reached after about 200 s. Under steady-state conditions, 80% of all pinocytosed material is rapidly recycled while 20% is retained within the cell and contribute to ongoing increases in cell fluorescence. As such, an initial region of linearly increasing uptake is expected to occur until about 30−60 s, at which time a transition to another linear uptake region with a shallower slope is observed after about 200 s. The MeO-50 kinetic uptake curve shown in Figure 1a matches this description.

The shape of the Gal-50 uptake curve is similar to that of MeO-50 (Figure 1a). This can be understood if the primary mechanism of uptake of Gal-50 in vitro is also pinocytosis, but with additional ASGPr-mediated uptake as well. Suspended rat hepatocytes have been shown (*20*) to uptake transferrin primarily by pinocytosis, despite the presence of a transferrin receptor on their cell surface. Nearly 80% of transferrin uptake was attributed to pinocytosis, with the remainder coming through receptor-mediated endocytosis. The half-time for internalization via the ASGPr is about 180 s (*22*), with an average time to recycle to the cell surface of about 4 min (*9*). Because of the similarity of these two uptake processes and the suggested dominant role of pinocytosis on uptake, it is expected that Gal-50 is internalized to a greater extent than MeO-50, but that the shape of the two kinetic uptake curves is similar. In the presence of Cu^{2+} and Zn^{2+} ions, uptake of Gal-50 and MeO-50 is indistinguishable (data not shown), suggesting that the difference in uptake between the two nanoparticles is ASGPr-mediated.

Optimization of Experimental Conditions for In Vivo Experiments. To allow direct comparison between

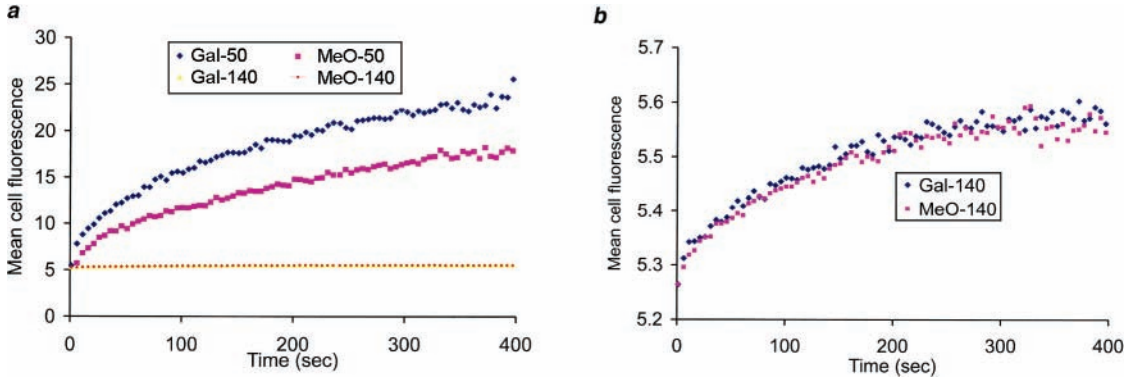

Figure 1. Kinetics of nanoparticle uptake by suspended hepatocytes, as analyzed by flow cytometry. (a) Uptake of 50 and 140 nm nanoparticles are shown on the same scale. (b) Uptake of 140 nm nanoparticles are shown on an expanded scale.

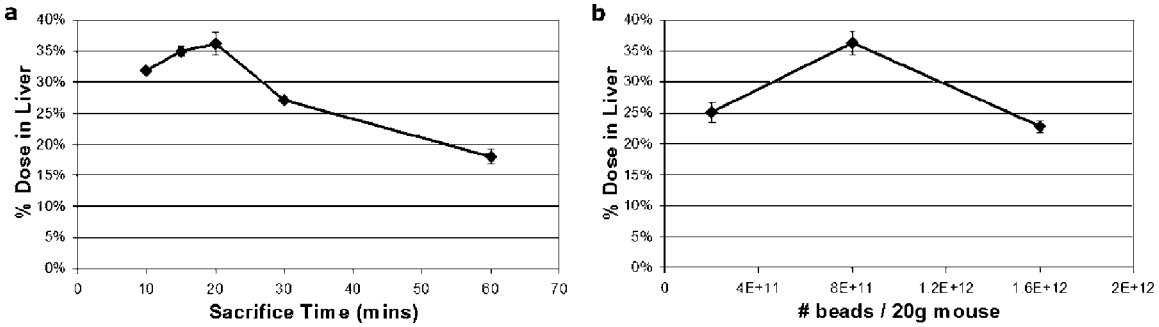

Figure 2. Optimization of experimental conditions for in vivo experiments by assaying total fluorescence of mouse liver following homogenization of liver and extraction of fluorophore. (a) Determination of optimal time between tail-vein injection of nanoparticles and liver removal. 8×10^{11} Gal-50 nanoparticles were injected via tail-vein per 20 g mouse, two mice per group, and sacrificed at the time shown. (b) Determination of optimal bead dose. Mice received tail-vein injections of Gal-50 nanoparticles and were sacrificed 20 min postinjection.

all in vivo experiments, a set of experimental conditions was identified that maximizes hepatic uptake following injection of nanoparticles. For this purpose, Gal-50 nanoparticles were utilized. The percentage of the injected dose in the liver was determined by homogenizing the livers of two mice per set of experimental conditions and extracting the fluorescent dye in chloroform.

Nanoparticles can be administered in a variety of ways to mice. Since hepatic uptake is desired, direct injection into the liver can be accomplished via portal vein or inferior vena cava. While portal vein injections are possible in humans, unnecessary surgical procedures are preferentially avoided. Therefore, the nanoparticles are introduced into systemic circulation and pass through the liver with the general blood flow. Tail-vein injection in mice is the most convenient method of introducing materials into the mouse circulation and is used in all in vivo experiments. Injection of large volumes relative to the circulating blood volume of the mouse have been found to result in transiently increased cell membrane permeability (*23*) that could obscure the effects of nanoparticle-size galactose presence. Therefore, low-pressure tail-vein injections of nanoparticles (100 μL per 20 g mouse) are employed here for all in vivo experiments.

As shown in Figure 2, Gal-50 accumulates in the liver up to about 20 min, after which time its amount decreases. The effect of the Gal-50 dose on liver uptake was also investigated, over a dose range that is reasonable for nonviral gene delivery particles. On the basis of the results of these liver uptake experiments, it was determined that 8×10^{11} beads in 100 μL of saline per 20 g mouse would be administered via tail-vein injection, with liver removal 20 min postinjection.

Bulk Liver Uptake of Nanoparticles. As in the previous experiment, the uptake of nanoparticles into liver tissue can be determined by homogenizing the liver and extracting the fluorescent dye. The comparison of bulk liver uptake of each nanoparticle is shown in Figure 3. It is apparent that galactosylated nanoparticles are taken up to a much greater extent than are nongalactosylated nanoparticles, which is as expected given the unique presence of galactose receptors in the liver on hepatocytes and Kupffer cells. In particular, nearly the entire dose of Gal-140 is found in the liver, as compared to about one-third of the Gal-50 dose. Concentrations of both MeO-50 and MeO-140 in the liver are quite low. In vitro, neither of the two types of 140 nm beads were internalized to a significant extent by hepatocytes, but it is clear that Gal-140 nanoparticles are taken up by the liver in vivo. As shown in the following sections, Kupffer cells are primarily responsible for Gal-140 uptake in vivo.

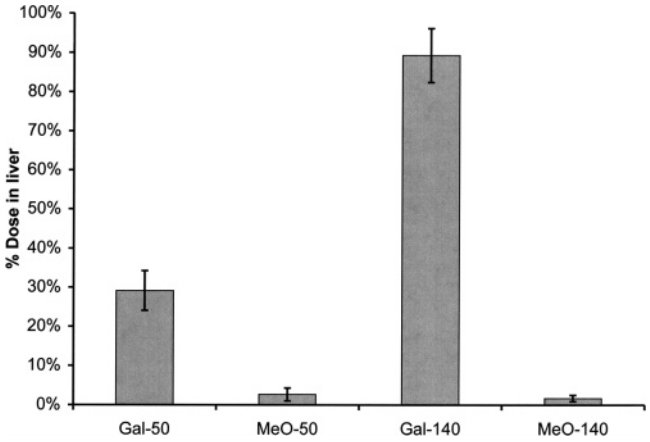

Figure 3. Overall uptake of nanoparticles into hepatic tissue. Results are shown as mean ± standard deviation of three mice per group.

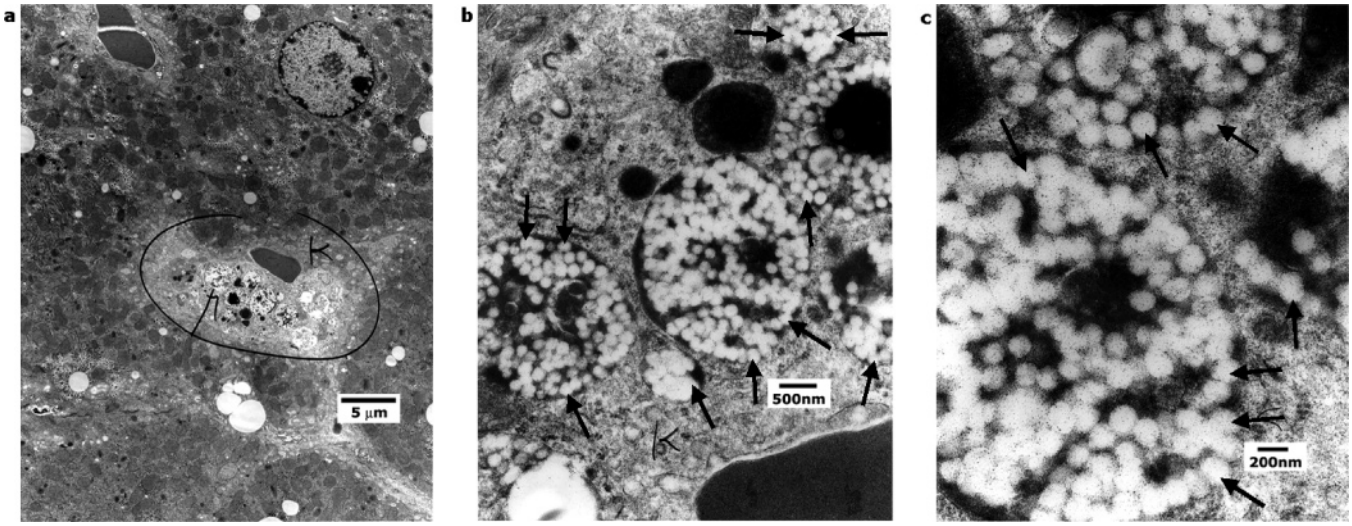

Figure 4. TEM images taken of the same 20 nm thick liver section following tail-vein injection of 8×10^{11} Gal-140 nanoparticles per 20 g mouse at scope magnifications of (a) 2000×, (b) 15 000×, and (c) 30 000×. Examples of individual nanoparticles are labeled with arrows in parts b and c.

TEM Imaging Following Tail-Vein Injection of Nanoparticles. Bulk liver uptake experiments indicated significant differences in the uptake of targeted and nontargeted nanoparticles, but gave no indication of the hepatic distributions. TEM analysis of liver cross-sections following tail-vein injection of nanoparticles provided information on hepatic distribution and intracellular trafficking of the nanoparticles. All images are representative of the overall hepatic distribution for each type of nanoparticle.

Hepatic Distribution of 140 nm Nanoparticles. Figure 4 shows TEM images of a 20 nm thick section of liver tissue that had been exposed to Gal-140 by tail-vein injection of these nanoparticles. The image in Figure 4a shows six hepatocytes surrounding a single Kupffer cell (marked 'K'). Hepatocytes are polyhedral cells with eight or more surfaces and regular, round nuclei that represent about 60% of the cells in the liver but almost 80% of hepatic volume since they are the largest of the cells. Kupffer cells are hepatic macrophages that have irregular nuclei and generally are located in the lumen of hepatic sinusoids adjacent to hepatocytes. Kupffer cells are in direct contact with the bloodstream and represent about 10% of the cells in the liver.

Though isolated examples of Gal-140 in hepatocytes could be found (images not shown), only a few beads are found per cell in those cases, while nearly all Kupffer cells contain a large number of internalized beads as shown in Figure 4b. This image clearly demonstrates Kupffer cell uptake of Gal-140, with hundreds of nanoparticles in each of the large phagocytic compartments (Figure 4c). At 8×10^{11} nanoparticles injected per 20 g mouse, approximately 50 000 nanoparticles are being injected per Kupffer cell in the liver. Since the Kupffer cell galactose-particle receptor has been documented to endocytose as many as 4200 galactosylated particles per cell per minute (*24*), the large number of nanoparticles observed per cell is reasonable.

Nanoparticle aggregation is not observed in Figure 4c, despite extremely concentrated conditions in the confines of phagocytic compartments. This provides additional evidence that the nanoparticles are stable and do not aggregate or fall apart either in serum or intracellularly, confirming the results of in vitro stability assays. The size stability in vivo allows the direct correlation of nanoparticle size with uptake results.

Unlike Gal-140, MeO-140 nanoparticles are not taken up to a great extent by any hepatic cells. In fact, most cells did not contain any MeO-140 beads, and few examples could be found of aggregates of MeO-140. However, of the cells that contained nanoparticles, MeO-140 were primarily internalized by Kupffer cells (images not shown).

Hepatic Distribution of 50 nm Nanoparticles. TEM images of liver sections following exposure to 50 nm nanoaparticles were quite different than those exposed to Gal-140. Neither MeO-50 or Gal-50 were found concentrated in Kupffer cells, though liver that was exposed to Gal-50 had an unusually large number of 100−200 nm vesicles throughout the cytoplasm of most hepatocytes, as shown in Figure 5b. As compared to hepatocytes from mice that received tail-vein injection of MeO-50 (Figure 5a), which contain occasional vesicles in the cytosol, hepatocytes exposed to Gal-50 contain many hundreds of clearly defined vesicles.

The result that Gal-140 are much more concentrated in Kupffer cells than are Gal-50 is consistent with literature reports that Kupffer cells tend to uptake 80 nm particles much more slowly than they internalize 500 nm particles (*5*). However, identification of individual nanoparticles in the hepatocyte vesicles is not as clear in the case of Gal-50 as it was for Gal-140. It is therefore critical to demonstrate that vesicles as shown in Figure 5b do in fact contain nanoparticles.

To confirm that the vesicles shown in Figure 5b contain nanoparticles, the same cell was imaged by both fluorescence microscopy and by TEM. By carefully marking and photographically documenting the cell of interest, the same cell could be identified following workup for TEM. In Figure 6, the capability of the technique is demonstrated by imaging the same cell with light microscopy and TEM. The nuclei and overall cell membrane shape, as well as relation to adjacent cells (not visible in Figure 6), confirm that the same cell may be identified and imaged on separate microscopes on separate days. Any slight differences in cell morphology may be attributed to the fact that the entire thickness of the cell is photographed with the light microscope, while only a thin section is imaged by TEM.

By comparing green regions seen by fluorescence microscopy of a plated hepatocyte in vitro with vesicle-containing regions seen by TEM, it was confirmed that

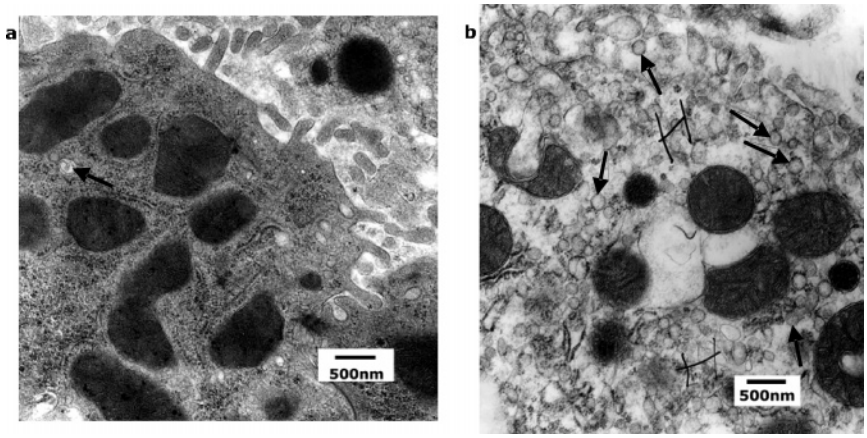

Figure 5. TEM images of hepatocytes following tail-vein injection of (a) MeO-50 and (b) Gal-50 nanoparticles, 8×10^{11} per 20 g mouse. Examples of individual vesicles are labeled with arrows.

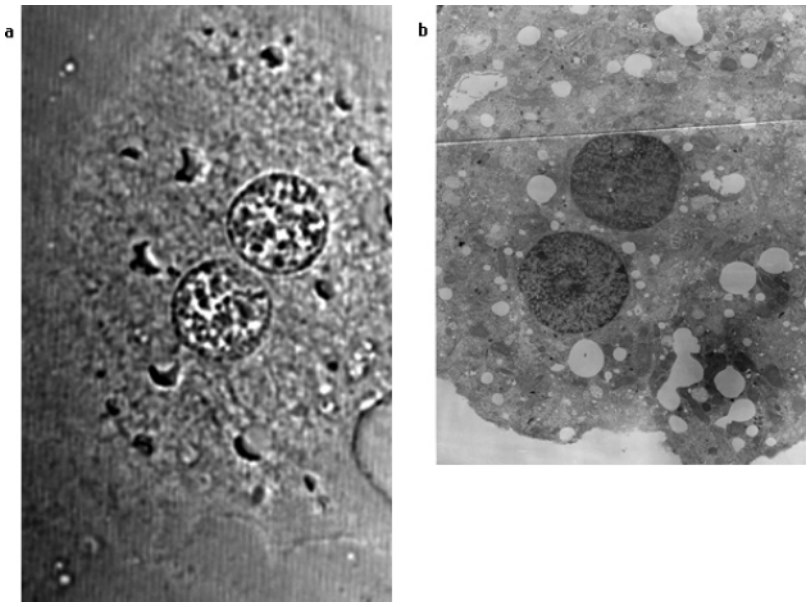

Figure 6. Comparison of images of the same cell, obtained by (a) confocal microscopy and (b) TEM.

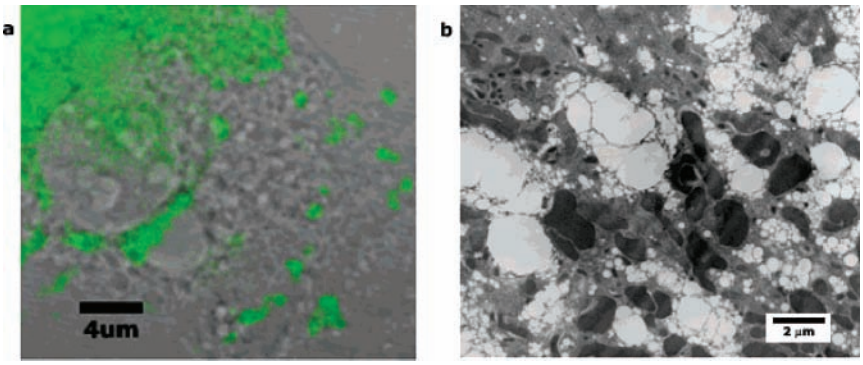

Figure 7. Imaging of a hepatocyte, 24-h postisolation that had been exposed to Gal-50 nanoparticles. Comparison of (a) light and fluorescence images and (b) TEM image of the green perinuclear region on the top left side of part a.

the vesicles in hepatocytes exposed to Gal-50 in vivo contain nanoparticles. In Figure 7a, the majority of a hepatocyte is seen by fluorescence and light microscopy. This plated hepatocyte was exposed to Gal-50 in vitro before being fixed with glutaraldehyde and imaged by confocal microscopy. Heavy-metal staining of the cell and embedding in Epon resin allowed TEM to be taken of the same cell. Since all nanoparticles used in these experiments have FITC embedded in their polystyrene core, they show up as green in the fluorescence image (Figure 7a). From this image it is apparent that the majority of Gal-50 beads are in the perinuclear region of the cell. When perinuclear regions of the cell are magnified by TEM (Figure 7b), an unnaturally large number of vesicles are seen. There are few vesicles in regions of the hepatocyte that do not show up green by fluorescence, so it is apparent that the green fluorescence originates from the large number of intracellular vesicles. Isolated clusters of vesicles on TEM show up as bright spots by fluorescence, while clusters in close proximity, as shown

in Figure 7b, show up as diffuse green regions by fluorescence. Analogous to the situation seen in vivo following injection of Gal-50, individual nanoparticles cannot be easily identified inside vesicles, but green fluorescence is clearly originating from these vesicles. We therefore conclude that Gal-50 nanoparticles are trapped within the vesicles observed by TEM.

Hepatocytes and Kuppfer cells are not the only hepatic cells capable of internalizing nanoparticles. Under the appropriate conditions, both hepatic stellate cells (HSC) and liver sinusoidal endothelial cells (LSEC) display phagocytic behavior. Following hepatic injury, hepatic stellate cells (HSC) differentiate into an activated phenotype that is capable of taking up 1 μm carboxylate-modified latex particles (*25*). Despite liver enzyme assays indicating no toxicity associated with the nanoparticles used in this study (data not shown), and hence no reason for HSC activation, HSC uptake of nanoparticles was considered and excluded based on TEM and FACS results (data not shown). LSEC have been shown to nonspecifically internalize a number nanoparticles, including lecithin-coated 240 nm polystyrene beads (*26*), uncoated 240 nm and 330−800 nm polystyrene beads (*27*), and 12 nm iron oxide nanoparticles (*28*). Furthermore, LSEC are indicated in the efficient ingestion and rapid degradation of naked pDNA in vivo and in vitro (*29*). Despite intense scrutiny, no evidence could be found of LSEC association or internalization of the PEGylated nanoparticles employed in this study.

By TEM, a significant difference in hepatic distribution and uptake of 50 and 140 nm nanoparticles that present either galactose or methoxy moieties on their surface was confirmed. Although TEM provides a very detailed view of intracellular trafficking, it is limited by the small area that can be examined at a time and by lack of scalability, thus preventing conclusions to be drawn concerning distribution of the nanoparticles across the cross-sectional area of the liver.

Immunohistochemistry Following Tail-Vein Injection of Nanoparticles. To provide a more general view of the liver, an immunohistochemical staining (IHC) procedure was developed. This technique is scalable in that processing may be done to multiple slides simultaneously. Twenty minutes after nanoparticles were injected via tail-vein into mice, the liver was embedded in OCT blocks and stored in 2-methylbutanol on dry ice. Liver sections (12 μm thick) were cut from the OCT blocks, excess OCT was dissolved away, and endogenous biotin activity was blocked. ASGPr was then stained red through a three-component antibody system. Goat anti-ASGPr1 was used as the primary antibody to provide a target for attachment of a donkey anti-goat IgG-biotin antibody. Since exogenous biotin was already blocked, incubation with QDot655-streptavidin and subsequent washes permitted specific visualization of the ASGPr receptor in the red fluorescence channel. Blocking of exogenous biotin was critical to minimize nonspecific binding of QDot655-streptavidin to liver tissue. Finally, slides were stained with DAPI-containing VectaShield mounting media, providing blue staining to nucleic acids in cell nuclei.

In Figure 8, an example of the ASGPr staining pattern is placed on a TEM image of normal mouse liver. ASGPr is expressed primarily on the hepatocytic basal and lateral membranes, which are directed toward the perisinusoidal and pericellular spaces and make up about 75% of the hepatocyte circumference. The density of ASGPr on these surfaces is 7- to 14-fold higher than on the apical surfaces (*30*, *31*). Staining is therefore expected around

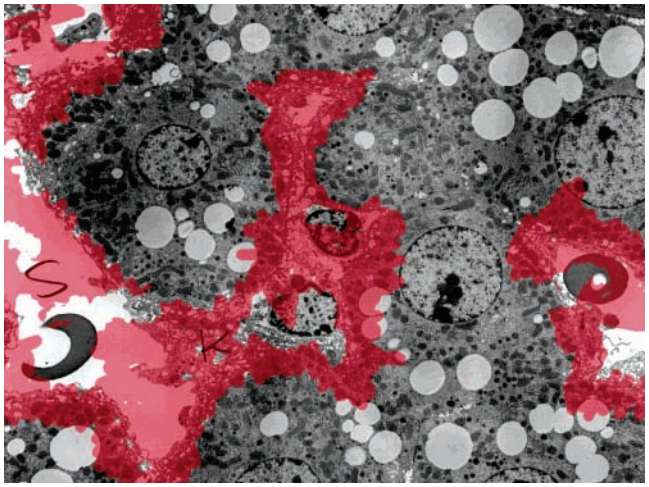

Figure 8. Illustration of the staining that results from the immunohistochemical staining of the hepatic asialoglycoprotein receptor (ASGPr).

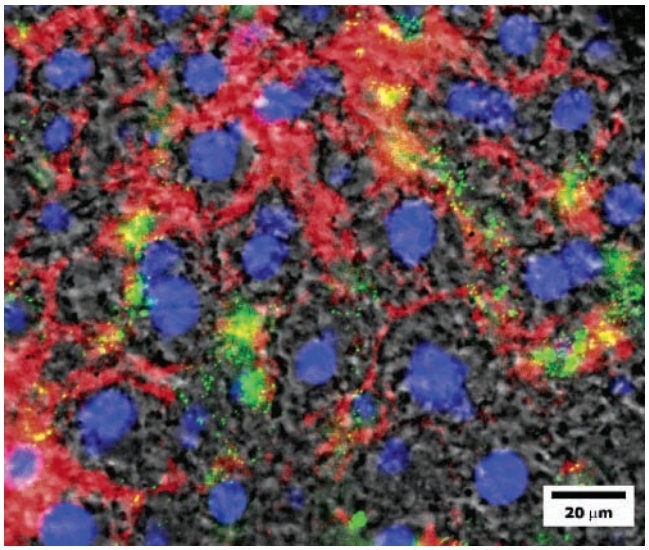

Figure 9. Immunohistochemistry image of 12 μm-thick section of mouse liver following tail-vein injection of 8×10^{11} MeO-140 nanoparticles. ASGPr is stained red, nuclei are blue, and nanoparticles are green/yellow.

the perimeter of sinusoids and around Kupffer cells, but hepatocyte−hepatocyte junctions should remain largely unstained. Additionally, sections used for IHC are 12 μm thick, so the three-dimensionality of the sinusoids must also be considered. Liver sinusoids have an average diameter of about 7.3 μm (*32*); thus, it is likely that hepatocyte membranes located just above or below sinusoids are partially included in the 12 μm thick IHC section. It is therefore probable that sinusoidal endothelial cells are included in the red-stained regions. Similarly, since Kupffer cells tend to border sinusoids and sinusoid-facing perimeters of hepatocytes, it is to be expected that many Kupffer cells will also be stained red.

A representative immunohistochemistry image obtained after tail-vein injection of MeO-140 nanoparticles into mice is shown in Figure 9. In this image, a sinusoid is seen running from the top center of the image toward the bottom right corner before wrapping around a pair of hepatocyte nuclei and returning toward the top-center. Along the length of this sinusoid, a large number of individual MeO-140 beads can be seen. The situation just described is similar to that seen in sinusoids running vertically down the left side and center of the image, in

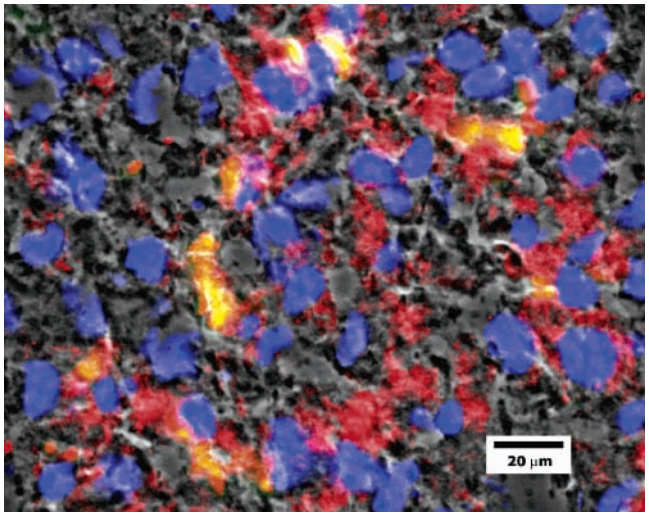

Figure 10. Immunohistochemistry image of 12 μm-thick section of mouse liver following tail-vein injection of 8×10^{11} Gal-140 nanoparticles. ASGPr is stained red, nuclei are blue, and nanoparticles are green/yellow.

which the nanoparticles do not appear to be aggregated. Few examples of MeO-140 aggregation could be found, indicating that these beads are largely present in hepatic sinusoids and are not internalized to any great extent in hepatic cells. This situation is similar to that observed for MeO-50 beads (not shown). No difference in nanoparticle distribution or density was observed between regions near the portal vein inlet to the liver and regions near the hepatic vein outlet.

The immunohistochemistry image obtained following Gal-140 injection is much different. In the image shown in Figure 10, large aggregates of nanoparticles are observed. These aggregates show up as yellow due to bright green overlaying red. While both MeO-140 and Gal-140 are shown to primarily overlay sinusoidal or Kupffer cell regions of the liver, the massively aggregated state of Gal-140 point to uptake by either Kupffer or sinusoidal endothelial cells since no mechanism exists for particle aggregation in the sinusoids. By TEM, no evidence of nanoparticle uptake into endothelial cells could be found, so the massive aggregates of Gal-140 nanoparticles are concluded to be resident in Kupffer cells. This result supports the conclusion drawn from TEM studies. Immunohistochemistry provides the ability to image a 1−2 cm cross-section of liver, permitting the distribution of beads to be seen across the liver from portal-vein inlet to hepatic-vein outlet. While both sized methoxy-beads are seen in sinusoids in similar concentrations across the liver, a somewhat higher concentration of Gal-140 beads are observed near the portal-vein inlet to the liver. This observation is consistent with the observation that Gal-140 are taken up into cells while MeO-50 and MeO-140 remain largely in the sinusoids.

In agreement with the TEM observations presented, immunohistochemistry on liver tissue from mice that received tail-vein injections of Gal-50 nanoparticles shows that Gal-50 are primarily internalized by hepatocytes (Figure 11). In this image, a pair of sinusoids is seen running from the bottom right corner of the image diagonally toward the upper left corner. Unlike the images taken following injection of any of the other beads, few Gal-50 beads are seen to overlap red-stained regions of liver. The majority of nanoparticles in this image have been internalized by hepatocytes, including all nanoparticles surrounded by red circles. A few Gal-50 nanoparticles may be in sinusoidal spaces or in Kupffer cells, located near the center of the image and toward the bottom right, where the green fluorescence overlays the red ASPGr staining, but the majority of Gal-50 are internalized by hepatocytes.

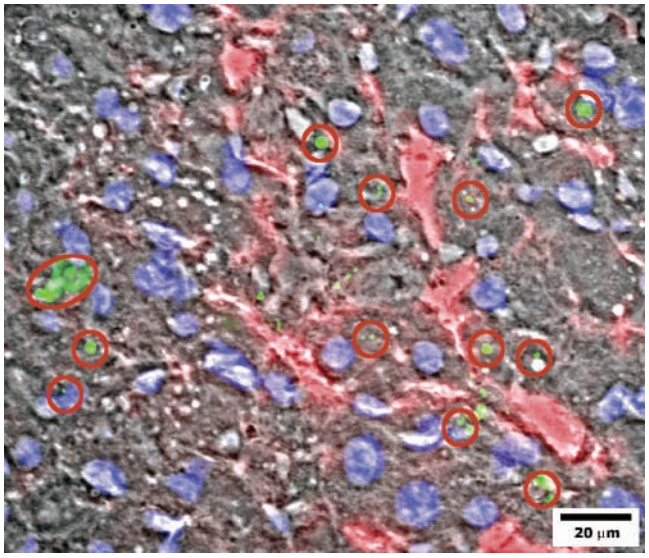

Figure 11. Immunohistochemistry image of 12 μm-thick section of mouse liver following tail-vein injection of 8×10^{11} Gal-50 nanoparticles. ASGPr is stained red, nuclei are blue, and nanoparticles are green/yellow.

CONCLUSIONS

Here, hepatocyte uptake in vitro and hepatic distribution in vivo of four slightly anionic, PEGylated-polystyrene nanoparticles were investigated. Slightly anionic surface charge is utilized to minimize nonspecific proteoglycan-mediated uptake or interaction with anionic cell surface membranes. In freshly isolated hepatocytes, Gal-50 nanoparticles are taken up to a greater extent than are MeO-50, but both 50 nm beads are taken up to a much greater extent than 140 nm nanoparticles, whether they contain galactose or not. About 90% of the in vivo dose of Gal-140 nanoparticles is found within the liver 20 min after tail-vein injection. TEM and immunohistochemistry images confirm that Gal-140 are primarily internalized by Kupffer cells, though isolated examples of a few Gal-140 in hepatocytes can also be found. Gal-50 nanoparticles are overwhelmingly found in vesicles throughout the cytoplasm of hepatocytes, with only isolated examples of Kupffer cell uptake. Despite similar surface charge and ligand density, 50 nm nanoparticles are primarily found in hepatocytes while 140 nm nanoparticles are primarily seen in Kupffer cells. It is therefore clear that slightly anionic, galactose-PEGylated nanoparticles should be about 50 nm in diameter to preferentially target hepatocytes while they should be about 140 nm in diameter to selectively target Kupffer cells.

ACKNOWLEDGMENT

We are grateful to Dr. Hide Tsukamoto for generously offering the services of his lab to isolate nonparenchymal liver cells and for helpful discussions. Dr. Rochelle Diamond went out of her way to assist with in vitro FACS experiments, and we thank George McNamara of the CHLARI Image Core for advice and assistance in acquiring images following immunhistochemical staining.

LITERATURE CITED

(1) Popielarski, S. R., Pun, S. H., and Davis, M. E. (2005) A Nanoparticle-Based Model Delivery System to Guide the Rational Design of Gene Delivery to the Liver. 1. Synthesis and Characterization. *Bioconjugate Chem. 16*, 1063−1070.
(2) Prieto, J., Qian, C., Hernandez-Alcoceba, R., Gonzalez-Aseguinolaza, G., Mazzolini, G., Sangro, B., and Kramer, M. G. (2004) Gene therapy of liver diseases. *Exp. Opin. Biol. Ther. 4*, 1073−1091.
(3) Kawasaki, T., Ii, M., Kozutsumi, Y., and Yamashina, I. (1986) Isolation And Characterization Of A Receptor Lectin Specific For Galactose/N−Acetylgalactosamine From Macrophages. *Carbohyd. Res. 151*, 197−206.
(4) Rensen, P. C. N., Sliedregt, L., Ferns, A., Kieviet, E., van Rossenberg, S. M. W., van Leeuwen, S. H., van Berkel, T. J. C., and Biessen, E. A. L. (2001) Determination of the upper size limit for uptake and processing of ligands by the asialoglycoprotein receptor on hepatocytes in vitro and in vivo. *J. Biol. Chem. 276*, 37577−37584.
(5) Rahman, Y. E., Cerny, E. A., Patel, K. R., Lau, E. H., and Wright, B. J. (1982) Differential Uptake Of Liposomes Varying In Size And Lipid-Composition By Parenchymal And Kupffer Cells Of Mouse-Liver. *Life Sci. 31*, 2061−2071.
(6) Boess, F., Kamber, M., Romer, S., Gasser, R., Muller, D., Albertini, S., and Suter, L. (2003) Gene expression in two hepatic cell lines, cultured primary hepatocytes, and liver slices compared to the in vivo liver gene expression in rats: Possible implications for toxicogenomics use of in vitro systems. *Toxicol. Sci. 73*, 386-402.
(7) Castaneda, F., and Kinne, R. K. H. (2000) Cytotoxicity of millimolar concentrations of ethanol on HepG2 human tumor cell line compared to normal rat hepatocytes in vitro. *J. Cancer Res. Clin. 126*, 503−510.
(8) Tanaka, T., Fujishima, Y., and Kaneo, Y. (2001) Receptor mediated endocytosis and cytotoxicity of transferrin-mitomycin c conjugate in the HepG2 cell and primary cultured rat hepatocyte. *Biol. Pharm. Bull. 24*, 268−273.
(9) Schwartz, A. L., Fridovich, S. E., and Lodish, H. F. (1982) Kinetics Of Internalization And Recycling Of The Asialoglycoprotein Receptor In A Hepatoma-Cell Line. *J. Biol. Chem. 257*, 4230−4237.
(10) Warren, R., and Doyle, D. (1981) Turnover Of The Surface-Proteins And The Receptor For Serum Asialoglycoproteins In Primary Cultures Of Rat Hepatocytes. *J. Biol. Chem. 256*, 1346−1355.
(11) Stoorvogel, W., Schwartz, A. L., Strous, G. J., and Fallon, R. J. (1991) A Pool Of Intracellular Phosphorylated Asialoglycoprotein Receptors Which Is Not Involved In Endocytosis. *J. Biol. Chem. 266*, 5438−5444.
(12) Lu, S. C., Ge, J. L., Huang, H. Y., Kuhlenkamp, J., and Kaplowitz, N. (1993) Thiol-Disulfide Effects On Hepatic Glutathione Transport − Studies In Cultured Rat Hepatocytes And Perfused Livers. *J. Clin. Invest. 92*, 1188−1197.
(13) McAbee, D. D., and Jiang, X. (1999) Copper and zinc ions differentially block asialoglycoprotein receptor-mediated endocytosis in isolated rat hepatocytes. *J. Biol. Chem. 274*, 14750−14758.
(14) Siekevitz, P., and Palade, G. E. (1960) A Cytochemical Study On The Pancreas Of The Guinea Pig.5. Invivo Incorporation Of Leucine-C-14 Into The Chymotrypsinogen Of Various Cell Fractions. *J. Biophys. Biochem. Cytol. 7*, 619−630.
(15) Weigel, P. H., and Oka, J. A. (1983) The Large Intracellular Pool Of Asialoglycoprotein Receptors Functions During The Endocytosis Of Asialoglycoproteins By Isolated Rat Hepatocytes. *J. Biol. Chem. 258*, 5095−5102.
(16) Pricer, W. E., and Ashwell, G. (1976) Subcellular-Distribution Of A Mammalian Hepatic Binding-Protein Specific For Asialoglycoproteins. *J. Biol. Chem. 251*, 7539−7544.
(17) Wall, D. A., Wilson, G., and Hubbard, A. L. (1980) The Galactose-Specific Recognition System Of Mammalian Liver − The Route Of Ligand Internalization In Rat Hepatocytes. *Cell 21*, 79−93.
(18) Wolkoff, A. W., Klausner, R. D., Ashwell, G., and Harford, J. (1984) Intracellular Segregation Of Asialoglycoproteins And Their Receptor − A Prelysosomal Event Subsequent To Dissociation Of The Ligand−Receptor Complex. *J. Cell Biol. 98*, 375−381.
(19) Scharschmidt, B. F., Lake, J. R., Renner, E. L., Licko, V., and Vandyke, R. W. (1986) Fluid Phase Endocytosis By Cultured Rat Hepatocytes And Perfused-Rat-Liver − Implications For Plasma-Membrane Turnover And Vesicular Trafficking Of Fluid Phase Markers. *Proc. Nat. Acad.* Sci. *U.S.A. 83*, 9488−9492.
(20) Rudolph, J. R., and Regoeczi, E. (1991) Relationship Between Pinocytic Rate And Uptake Of Transferrin By Suspended Rat Hepatocytes. *Biol. Met. 4*, 166−172.
(21) Kjeken, R., Mousavi, S. A., Brech, A., Gjoen, T., and Berg, T. (2001) Fluid phase endocytosis of [I-125]iodixanol in rat liver parenchymal, endothelial and Kupffer cells. *Cell Tissue Res. 304*, 221−230.
(22) Tolleshaug, H., Berg, T., Nilsson, M., and Norum, K. R. (1977) Uptake And Degradation Of I-125-Labeled Asialo-Fetuin By Isolated Rat Hepatocytes. *Biochim. Biophys. Acta 499*, 73−84.
(23) Kobayashi, N., Nishikawa, M., Hirata, K., and Takakura, Y. (2004) Hydrodynamics-based procedure involves transient hyperpermeability in the hepatic cellular membrane: implication of a nonspecific process in efficient intracellular gene delivery. *J. Gene Med. 6*, 584−592.
(24) Teradaira, R., Kolbbachofen, V., Schlepperschafer, J., and Kolb, H. (1983) Galactose-Particle Receptor On Liver Macrophages − Quantitation Of Particle Uptake. *Biochim. Biophys. Acta 759*, 306−310.
(25) Vinas, O., Bataller, R., Sancho-Bru, P., Gines, P., Berenguer, C., Enrich, C., Nicolas, J. M., Ercilla, G., Gallart, T., Vives, J., Arroyo, V., and Rodes, J. (2003) Human hepatic stellate cells show features of antigen-presenting cells and stimulate lymphocyte proliferation. *Hepatology 38*, 919−929.
(26) Kanai, M., Murata, Y., Mabuchi, Y., Kawahashi, N., Tanaka, M., Ogawa, T., Doi, M., Soji, T., and Herbert, D. C. (1996) In vivo uptake of lecithin-coated polystyrene beads by rat hepatocytes and sinusoidal endothelial cells. *Anat. Rec. 244*, 175−181.
(27) Dan, C., and Wake, K. (1985) Modes Of Endocytosis Of Latex-Particles In Sinusoidal Endothelial And Kupffer Cells Of Normal And Perfused Rat-Liver. *Exp. Cell Res. 158*, 75−85.
(28) Briley-Saebo, K., Bjornerud, A., Grant, D., Ahlstrom, H., Berg, T., and Kindberg, G. M. (2004) Hepatic cellular distribution and degradation of iron oxide nanoparticles following single intravenous injection in rats: implications for magnetic resonance imaging. *Cell Tissue Res. 316*, 315−323.
(29) Hisazumi, J., Kobayashi, N., Nishikawa, M., and Takakura, Y. (2004) Significant role of liver sinusoidal endothelial cells in hepatic uptake and degradation of naked plasmid DNA after intravenous injection. *Pharm. Res. 21*, 1223−1228.
(30) Hubbard, A. L., Wall, D. A., and Ma, A. (1983) Isolation Of Rat Hepatocyte Plasma-Membranes. 1. Presence Of The 3 Major Domains. *J. Cell Biol. 96*, 217−229.
(31) Matsuura, S., Nakada, H., Sawamura, T., and Tashiro, Y. (1982) Distribution Of An Asialoglycoprotein Receptor On Rat Hepatocyte Cell-Surface. *J. Cell Biol. 95*, 864−875.
(32) Hess, F. A., Weibel, E. R., and Preisig, R. (1973) Morphometry Of Dog Liver − Normal Base-Line Data. *Virchows Arch. B 12*, 303−317.

BC0501146

Properties of Isonucleotide-Incorporated Oligodeoxynucleotides and Inhibition of the Expression of Spike Protein of SARS-CoV

Zhanli Wang, Jifeng Shi, Hongwei Jin, Liangren Zhang,* Jingfeng Lu, and Lihe Zhang

National Research Laboratory of Natural and Biomimetic Drugs, School of Pharmaceutical Sciences, Peking University, Beijing 100083, China. Received September 21, 2004; Revised Manuscript Received April 11, 2005

Antisense oligonucleotides are recognized to be very efficient tools for the inhibition of gene expression in a sequence specific way. For the discovery of a novel efficient way to modify oligonucleotides, a series of single isonucleotide-incorporated antisense oligodeoxynucleotides have been synthesized, in which an isonucleotide was introduced at different positions of the sequences. The binding behaviors of modified oligodeoxynucleotides to the complementary sequence were studied by UV, CD, and molecular dynamics simulation. The results showed that although the incorporated isonucleotides at certain positions of the sequence interfere with the binding ability to a different extent, B-form duplexes were maintained and the binding abilities of the 3′-end-modified duplexes were better than the corresponding mismatched duplexes. The digestion of modified oligodeoxynucleotides by snake venom phosphodiesterase showed that an isonucleotide strongly antagonizes hydrolysis. The DNA/RNA hybrid formed by a modified oligodeoxynucleotide and its target RNA could activate RNase H. The 3′-end-modified antisense oligodeoxynucelotides inhibited S-glycoprotein expression of SARS-CoV at the mRNA levels in insect Sf9 cells. This study indicated the possibility of designing a novel and effective antisense oligodeoxynucleotide by incorporating an isonucleotide at the 3′-end of the sequence.

INTRODUCTION

Since the first report of the inhibition of Rous sarcoma viral replication by an antisense oligonucleotide in a cell culture in 1978 (*1*), antisense technology has been rapidly developed either in studying gene function or in developing genetic therapy. As a class of potential therapeutic agents, antisense oligonucleotides have been developed for the treatment of diseases such as cancer, inflammation, and virus infection (*2*, *3*). The first antisense drug (Vitravene/formivirsen) was approved by FDA for the treatment of CMV retinitis in patients with AIDS in 1998, and there are also dozens of antisense therapeutics in clinical trials (*4*). As antisense technology progressed to become a therapeutic option, several drawbacks have emerged that negatively affect its therapeutic efficacy. For example, natural oligodeoxynucleotides are readily degraded in the serum or in vivo and show poor uptake by the cell membrane. To improve the biostability of oligonucleotides, chemical modification is widely used. Among the modifications, the phosphorothioate oligodeoxynucleotide is most frequently used, which is resistant to nuclease digestion, is recognized by RNase H, and is easyily mass-produced. Though phosphorothioate oligodeoxynucleotides are currently used as the standard choice of chemically modified oligodeoxynucleotides, its non-sequence-specific protein binding leads to significant side effects, including complement activation, thrombocytopenia, inhibition of cell−matrix interaction, or reduction of cell proliferation (*5*). To overcome these limitations, intensive efforts were focused on the development of other kinds of chemically modified oligonucleotides, which were named as a second generation of oligonucleotides. For example, modifications of the 2′ position of riboses with electronegative substituents such as the 2′-*O*-(2-methoxy)ethyl (MOE) group (*6*) or a 2′-*O*,4′-*C*-methylene bridge (locked nucleic acid; LNA) were performed (*7*). Since such ribose modifications confer an RNA-like conformation to the oligonucleotide, they increase the target RNA binding affinity and cellular uptake. But on the other hand, the RNA-like conformation leads to the disappearance of the oligonucleotide's ability to activate RNase H which is considered to be an important pathway of antisense action. Therefore, the 2′-ribose-modified oligonucleotide has been successfully introduced only in the format of mixed-backbone analogues, in which the modified nucleotides are placed at the ends to leave an RNase H-compatible DNA gap (*8*).

Isonucleosides represent a novel class of nucleoside analogues in which the nucleobase is linked to various positions of ribose other than C-1′. Because of the shift of N-glycosidic bond, the chemical and enzymatic stabilities of the nucleoside are increased. Previous studies showed that homo-oligoisonucleotides antagonized the hydrolysis of snake venom phosphodiesterase. Furthermore, some kinds of homo-oligoisonucleotides also showed strong binding abilities to their complementary sequences though they were a little weaker than the native counterpart (Figure 1**a**, **b**, **c**) (*9*−*12*). The results suggested that antisense oligonucleotide constructed from isonucleotide could antagonize the hydrolysis of nuclease and give acceptable binding ability. A practical way is to build a mixed backbone, in which the isonucleotide is placed at the critical position of the sequence. 3′-Exonuclease is the most common nuclease in vivo. The isonucleotide-modified oligodeoxynucleotide at the 3′-end will provide a model for studying the effects of isonucleotide-modified antisense oligonucleotide. In this study, an 18-mer antisense sequence 5′- AAC ATC TCC TGA GGG AAC −3′, which was complementary to the mRNA region encoding spike (S) glycoprotein of the SARS-CoV (22398−22415bp) (*13*, *14*), was designed based on the reported strategy (*15*, *16*). An isonucleotide was incorporated at the 3′-end or

* To whom correspondence should be addressed. Tel: +86-10-82802567, Fax: +86-10-82802724. E-mail: liangren@bjmu.edu.cn.

10.1021/bc049769h CCC: $30.25 © 2005 American Chemical Society
Published on Web 08/30/2005

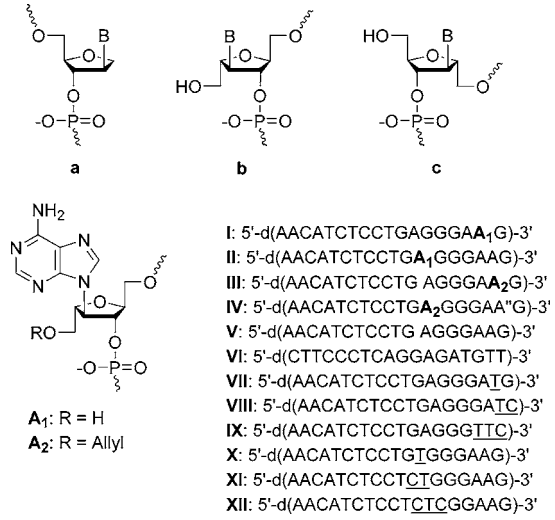

Figure 1. Structures of isonucleotides and the sequences of isonucleotide-incorporated oligodeoxynucleotides (**I**−**V**), complementary sequence (**VI**), and mismatched sequences (**VII**−**XII**, the mismatched bases are underlined).

center of the sequence (Figure 1). The effects of the isonucleotide-modified antisense oligonucleotides on the binding ability, nuclease degradation, and RNase H activity were investigated. Molecular dynamics simulation was used to evaluate the effects of incorporation of isonucleotide on the regularity of duplex formation. Meanwhile, the oligodeoxynucleotide with an isonucleotide incorporated at the center of the sequence and mismatched oligonucleotides were also used as controls. It was reported that the existence of hydroxymethyl group on the isonucleotide could affect the binding ability of duplex formation very obviously (*11*), the allyl group-protected isonucleotide was also used for studying the effect of a hydroxyl group on the duplex formation of modified oligonucleotides.

EXPERIMENTAL SECTION

General. Chemical reagents were purchased from Acros or Sigma Co. Column chromatography was performed on silica gel (200−300 mesh; Qingdao Chemical Co.). UV spectra were recorded with a Varian Cary 300 Bio UV-visible spectrophotometer. NMR spectra were recorded on a Varian VXR-300 or Varian Inova-500 with TMS as internal standard. FAB-MS was determined with a VG-ZAB−HS.

Synthesis. *6′-O-Benzoyl-1′-dimethoxytrityl-4′-deoxy-3′-O-(2-cyanoethyl-N,N-diisopropyl)phosphoramidite-4-(N⁶-benzoyladenin-9-yl) -2′,5′-anhydro-*L*-mannitol (**3**).* All reagents were deoxygenated before use. 6′-*O*-Benzoyl-1′-dimethoxytrityl-4′-deoxy-4-(*N*⁶-benzoyladenin-9-yl)-2′,5′-anhydro-L-mannitol (**2**) (460 mg, 0.58 mmol) was dissolved in dry THF (8 mL) under an atmosphere of argon. Diisopropylethylamine (DIPEA) (0.41 mL, 2.5 mmol) was added at 0 °C, followed by adding dropwise 2-cyanoethyl *N,N,N′,N′*-tetraisopropylphosphordiamidite (0.28 mL, 0.88 mmol). Ten minutes later, a white precipitate appeared. After the mixture was kept at room temperature for 30 min, methanol (1 mL) was added and white precipitate disappeared in 10 min. The solution was diluted with EtOAc (25 mL) and extracted with 5% $NaHCO_3$ (10 mL × 2), saturated aqueous NaCl (10 mL × 1), and deionized H_2O (10 mL × 1) in turn. The aqueous phase was extracted with EtOAc (15 mL), and the combined organic layer was dried with anhydrous Na_2SO_4. After filtration and concentration, the residue was applied to flash silica gel chromatography eluting with cyclohexane/ dichloromethane/acetic acetate (10:1:1−4:1:1, 0.5% Et_3N) to give compound **3** (485 mg, white foam, 84%).

*6′-O-Allyl-1′-O-dimethoxytrityl-4′-deoxy-3′-O-(2-cyanoethyl-N,N-diisopropyl)phosphoramidite-4′-(N⁶-benzoyladenin-9-yl)-2′,5′-anhydro-*L*-mannitol (**6**).* Compound **6** was prepared from 6′-*O*-allyl-1′-*O*-dimethoxytrityl-4′-deoxy-4′-(*N*⁶-benzoyladenin-9-yl)-2′,5′-anhydro-L-mannitol (**5**) in a similar approach to the preparation of compound **3** from **2** in 84.0% yield as white foam.

Solid-Phase Synthesis of Oligodeoxynucleotides. Oligodeoxynucleotide synthesis was carried out in 1 μmoL scale with a DNA synthesizer model 392 (Applied Biosystem) applying regular phosphoramidite chemistry. The isonucleotide monomer (compound **3** or **6**) was incorporated into the proper position based on the requirement of the oligodeoxynucleotide sequence. Cleavage and deprotection of the oligomers were performed in concentrated ammonium at 50 °C for 24 h. The crude product was purified by 15% PAGE (7 moL·L^{-1} urea) and desalted by C18 column. The pure oligonucleoties were lyophilized and stored at −20 °C.

Thermal Denaturation and Circular Dichroism Studies. Oligodeoxynucleotide and its complementary sequence at an equivalent concentration (6 μmoL·L^{-1}) were heated to 80 °C in the buffer solution (0.14 M NaCl, 0.01 M Na_2HPO_4, pH 7.2, 1.0 M EDTA) and then cooled to room-temperature slowly. The hyperchromicity curves of the hybridized duplex were recorded on a Varian Cary 300 Bio UV-visible spectrophotometer. CD spectra were recorded by a JASCO J-715 spectropolarimeter at 15 °C in a thermostatically controlled 1 cm cuvette.

Molecular Modeling. All calculations were performed on an SGI OCTANE 2 workstation. The initial structures of DNA duplexes were built from the canonical B-form structure using Insight II simulation program. The AMBER 7.0 suite of molecular simulation programs and ff99 force field were used in the computations (*17*). The molecular mechanical parameters of isonucleotides were obtained using Gaussian 98 program under HF/6-31G** level of theory. The constructed oligodeoxynucleotide duplex was immersed in a periodic TIP3P water box, which extended 10 Å away from any solute atom. This yielded about 4400 water molecules used for solvation. To neutralize the negative charges of simulated molecules, Na^+ counterions were placed next to each phosphate group.

Molecular dynamics (MD) simulations were carried out by using the SANDER module of AMBER 7.0 with SHAKE algorithm applied to hydrogen atoms. Each simulation began with 1000 steps of minimization followed by 25 ps of equilibration dynamics at 300 K with full constraints on duplex and a 9-Å nonbonded Lennard−Jones cutoff. The duplex then was gradually allowed to relax by sequentially lowering restraints. The final production simulations of 1.5 ns for duplexes **I/VI**, **II/VI**, **III/VI**, or **IV/VI** and 1.0 ns for duplex **V/VI** were performed at constant pressure (1 atm) and temperature (300 K). The final structure of each duplex was obtained from the averaged structure of the last 800 ps of molecular dynamics calculation followed by 1000 steps of minimization. All duplexes were analyzed with CURVES 5.3 program.

Nuclease Resistance Analysis. The modified and unmodified oligodeoxynucleotides were 5′-^{32}p labeled with [γ-^{32}p]ATP using T_4 polynucleotide kinase. Labeled material was purified by gel electrophoresis on 20% 7M urea polyacrylamide gels. ^{32}p-labeled DNA was incubated with 100 ng of snake venom phosphodiesterase I in buffer,

Scheme 1. Synthesis of Isonucleotide-Incorporated Oligodeoxynucleotides[a]

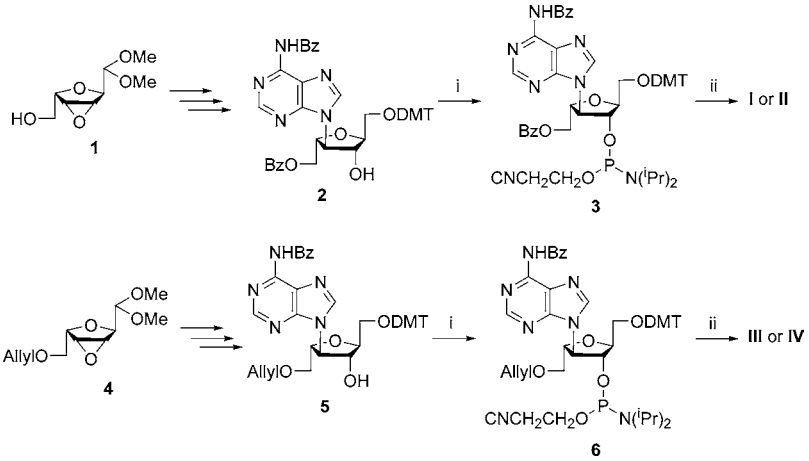

[a] Reagents and conditions: (i) DIPEA, 2-cyanoethyl *N*,*N*,*N*′,*N*′-tetraisopropylphosphorodiamidite, THF, rt; (ii) solid-phase DNA synthesis.

which contained 50 mM Tris-HCl (pH 8), 5 mM $MgCl_2$ at 21 °C. Total reaction volume was 50 μL. After 10 min, aliquots were mixed with 100 μL of stop solution which contained 0.05% (w/v) bromophenol blue and 0.05% (w/v) xylene cyanol in 95% formamide. Aliquots were subjected to 20% polyacrylamide gel electrophoresis and visualized by autoradiography.

In Vitro Transcript of SARS Fragment. The 75 nt of SARS-CoV DNA fragment corresponding to nucleotides 22380 to 22455 was generated by PCR amplification using the DNA template (gift from Beijing Institute of Genomics) and primers 5′-ATT TAG GTG ACA CTA TAG AAC CTC TAA TTT CAG GG-3′ (sense primer) or 5′-CTC CAA AAG GAC ACA AGT TTG TAA-3′(antisense primer). Sp6 promotor sequence was introduced at the 5′-end by the use of primers. All PCR products were sequenced prior to in vitro transcription. Transcription was performed directly from PCR-amplifying DNA fragments using sp6 RNA polymerase. RNAs were purified by gel electrophoresis on 20% 7 M urea polyacrylamide gels.

RNase H Cleavage. The in vitro transripted RNAs of SARS fragment were 5′-^{32}p labeled with [γ-^{32}p]ATP as described above. ^{32}p-labeled RNA and the modified or unmodified oligonucleotides were incubated with 0.5 units of RNase H and 50 units of RNase inhibitor in buffer for 30 min at 21 °C. The buffer contained 50 mM Tris-HCl (pH 8), 10 mM $MgCl_2$, and 5 mM DTT. Loading buffer (30% glycerol with 0.14 nM bromophenol blue, and 0.19 nM xylene cyanol FF) was added, and samples were loaded on a 20% polyacrylamide gel and run at room temperature and recorded by autoradiography.

Infection of Sf9 Cells with Viruses and Antisense Oligonucleotides Treatment. Sf9 cells (fall armyworm ovary, *S. frugiperda*) were cultured in Sf-900 II SFM medium (Sigma) supplemented with 10% heat-inactivated fetal bovine serum (FBS) at 27 °C. The recombinant baculoviruses routinely propagated and titrated by plaque assay in Sf9 cells and working virus stocks were stored frozen in the dark at −80 °C.

Sf9 cells were subcultured prior to antisense oligodeoxynucleotide treatment and maintained in logarithmic growth phase with viability of 98%. The oligodeoxynucleotide was added to Sf9 cells after the recombinant baculoviruses inoculated for 24 h. Each monolayer of Sf9 cells at 7×10^4 cells/well in six-well plates were transfected with oligodeoxynucleotide by liposome-mediated transfection with lipofectamine (Invitrogen). After 4 h, the medium was replaced with SFM medium supplemented with 10% heat-inactivated fetal bovine serum, and culture was continued with fresh medium containing the oligodeoxynucleotide. Plates of each transfected group were treated with recombinant baculoviruses. The same amounts of viruses were inoculated at 27 °C as control.

RT-PCR Analysis. Total RNA was extracted from control and antisense oligonucleotide-treated cells using Trizol (Invitrogen). RNA concentrations were determined spectrophotometrically from the absorbencies of samples at 260 nm. RT-PCR was performed using the SuperScript One Step RT-PCR System (Invitrogen) following the instructions of the manufacturer. Forward and reverse primers for SARS gene were 5′-CCA CCT CTG CTC ACT GAT GAT AT-3′ and 5′-CCT TGT TAA ATT GGT TGG CGA TTT GTT-3′, respectively, which amplified a fragment of 205 bp. GAPDH mRNA was used as an internal control, and the primers were 5′-CGG GAA ACT GTG GCG TGA TGG-3′ (forward) and GTC GCT GTT GAA GTC AGA GGA GA-3′ (reverse). The expected product was 292 bp. RT-PCR was performed using 100 ng of total RNA. Each reaction contained 0.2 μM forward and reverse gene-specific primers in addition to reagents present in the SuperScript PCR buffer. RNA was reverse-transcribed for 50 min at 42 °C and then subjected to 30 cycles of PCR (94 °C, 30 s; 55 °C, 40 s; 72 °C, 50 s). Samples were analyzed on 2% agarose gels.

Western Blot Analysis. Protein samples were subjected to sodium dodecyl sulfate-polyacrylamide gel electrophoresis (SDS−PAGE) and transferred to nitrocellulose membrane (Amersham Pharmacia Biotech). The membrane was blocked with 5% skim milk in TBST (20 mM Tris-HCl [pH 7.4], 150 mM NaCl, 0.1% Tween 20), reacted with anti-His antibody (Qiagen) at a 1:1000 dilution. Proteins were detected using horseradish peroxidase-conjugated anti-mouse immunoglobulin G (Sigma) and an enhanced chemiluminescence detection system (ECL; Amersham Pharmacia Biotech).

RESULTS AND DISSCUSSIONS

Synthesis. The phosphoramidite **3** and **6** were synthesized from the corresponding epoxides **1** and **4**, respectively (Scheme 1) (*18*). Compound **3**. ^{1}H NMR (500 MHz, DMSO-d_6) δ 0.58 (d, J = 7.0 Hz, 3H, CH_3), 0.74 (d, J = 6.5 Hz, 3H, CH_3), 0.92 (d, J = 7.0 Hz, 6H, CH_3), 1.18 (t, J = 7.0 Hz, 2H, CH_2CN), 2.41 (m, 2H, CH), 3.27 (m, 2H, H-1′), 3.45 (m, 2H, $-POCH_2$), 3.70 (s, 6H, OCH_3), 4.30 (m, 1H, H-2′), 4.53 (m, 2H, 6′-CH_2), 5.01 (m, 1H,

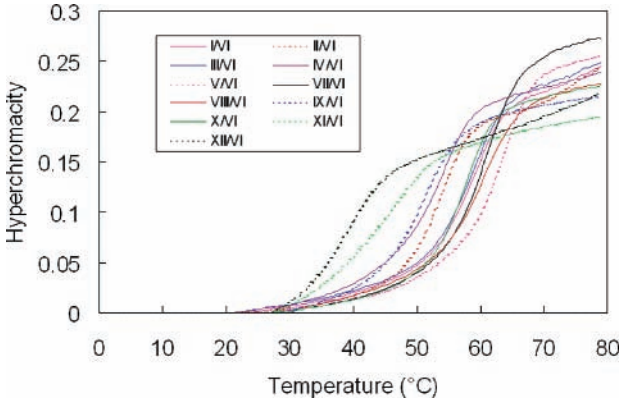

Figure 2. The melting behaviors of duplexes formed by isonucleotide-modified or mismatched oligodeoxynucleotides with their complementary sequence.

Table 1. T_m Values of the Duplexes of Modified and Unmodified Oligonucleotides with the Complementary DNA Sequence

duplexes	T_m (°C)	ΔT_m (°C)
I/VI	59.3	−2.2
II/VI	54.2	−7.7
III/VI	58.6	−2.9
IV/VI	54.1	−7.4
V/VI	61.5	-
VII/VI	58.0	−3.5
VIII/VI	58.0	−3.5
IX/VI	49.1	−12.4
X/VI	56.2	−5.3
XI/VI	44.3	17.2
XII/VI	37.1	24.4

H-5′), 5.20 (m, 1H, 4′-H) 5.32 (m, 1H, 3′-H), 6.89 (d, J = 8.5 Hz, 4H, Ph-H), 7.21−7.40 (m, 8H, Ph-H), 7.55−7.65 (m, 7H, Ph-H), 7.78 (m, 2H, Ph-H), 8.05 (m, 2H, Ph-H), 8.67 (s, 1H, H-2), 8.69 (s, 1H, H-8), 11.20 (s, 1H, 6-NH). ^{31}P NMR: 151.7, 152.5. Compound **6:** ^{1}H NMR (500 MHz, DMSO-d_6): δ 0.56 (d, 3H, CH_3), 0.74 (d, J = 7.0 Hz, 3H, CH_3), 0.92 (d, J = 6.5 Hz, 6H, CH_3), 1.18 (t, J = 7.0 Hz, 2H, CH_2CN), 2.41 (m, 2H, 2CH), 3.20−3.38 (m, 4H, $POCH_2$, H-1′), 3.60 (m, 2H, H-6′), 3.75 (s, 6H, OCH_3), 3.99 (m, 2H, OCH_2 (allyl)), 4.21 (m, 1H, H-2′), 4.77 (m, 1H, H-5′), 5.02−5.20 (m, 2H, H-3′, H-4′), 5.22 (m, 2H, CH_2=), 5.85 (m, 1H, =CH), 6.90 (m, 5H, Ph-H), 7.20−7.34 (m, 7H, Ph-H), 7.48−7.65 (m, 9H, Ph-H), 8.05 (t, J = 5 Hz, 2H, Ph-H), 8.63 (s, 1H, H-2), 8.71 (s, 1H, H-8), 11.19 (s, 1H, 6-NH). ^{31}P NMR: 150.5, 150.1.

The isonucleotide-incorporated oligodeoxynucleotides were synthesized by using phosphoramidite solid-phase strategy. The syntheses were performed in an automated DNA/RNA synthesizer on a 1 μmol scale according to the regular phosphoramidite protocol except for a prolonged coupling time to ensure an adequate coupling yield when using phosphoramidite **3** or **6**. For convenience, the synthesis was started with commercially available cytosine-loaded controlled pore glass (CPG). The coupling efficiency was determined by the release of DMT, and the yield was over 92% for coupling isonucleotide phosphoramidite. After cleavage from the solid support and removal of the protecting groups with concentrated aqueous ammonia, the oligodeoxynucleotides were purified by PAGE and desalted by a C18 column. Four kinds of isonucleotide-incorporated oligonucleotides were synthesized, in which the isonucleotide was at the 3′-end or in the center of the sequence, and the 6′-OH of isonucleotide was free or protected by an allyl group. All oligonucleotides were confirmed by MALDI-TOF mass spectroscopy, and the masses were in good agreement with the calculated values. MALDI-TOF MS: **I**, 5590.2 (M + Na, calcd 5590.4); **II**, 5589.7 (M + Na, calcd 5590.4); **III**, 5548.5 (M + Na, calcd 5549.8,); **IV**, 5549.1 (M + Na, calcd 5549.8).

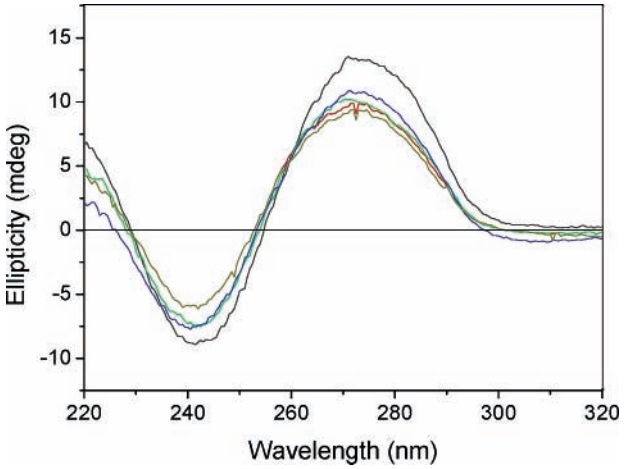

Figure 3. CD spectra of duplexes formed by the isonucleotide-modified oligodeoxynucleotides and their complementary sequence. Red, **I/VI**; green, **II/VI**; dark yellow, **III/VI**; blue: **IV/VI**; black, **V/VI**.

Binding Behaviors with Oligodeoxynucleotide. Thermal denaturation study was used to evaluate the duplex stability formed by isonucleotide-incorporated oligodeoxynucleotide and its complementary sequence (Figure 2). The result showed that the single isonucleotide incorporation interfered with the stability of the formed duplex, which depends on the position of incorporation. When isonucleotide was at the 3′-end of the sequence (**I**, **III**), the T_m value decreased about 3 °C compared with its natural counterpart (Table 1). When isonucleotide was in the center of the sequence (**II**, **IV**), the T_m value decreased about 7 °C. The different stabilities of the hybrid duplex might result from the different neighbor influence. When isonucleotide was at the end of the sequence, the effect would mainly involve one side of base pair, whereas when isonucleotide was in the central position of the sequence, the effects involve the base pairs of two sides. Comparing to the consecutive isonucleotide-incorporated oligonucleotide, which leads to a decrease of T_m of about 0.4 °C (*11*), single isonucleotide incorporation resulted in a more intensive decrease of duplex stability. The previous finding showed that the 6′-OH of the isonucleotide could stabilize the duplex formed by the homo-oligoisonucleotide and its complementary sequence. In this study no obvious difference was observed when the 6′-OH of the isonucleotide was free or protected, which indicated herein that the single 6′-OH did not affect the stability of duplex significantly. For comparison, one to three nucleoside-mismatched sequences (**VII**−**XII**) were also investigated. The results showed that when the isonucleotide was located at 3′-end, the duplex was more stable than the corresponding mismatched sequences, whereas when isonucleotide was located at the center of the sequence, the duplex was less stable than the corresponding single-nucleoside-mismatched sequence but was more stable than multi-nucleoside-mismatched sequence.

Circular dichroism (CD) spectra showed that the hybrid duplex formed by modified oligodeoxynucleotides and their complementary sequence possessed very similar conformations (Figure 3). Different from the consecutive isonucleotide-incorporated oligonucleotide, which formed a distorted B-form duplex when hybridized with

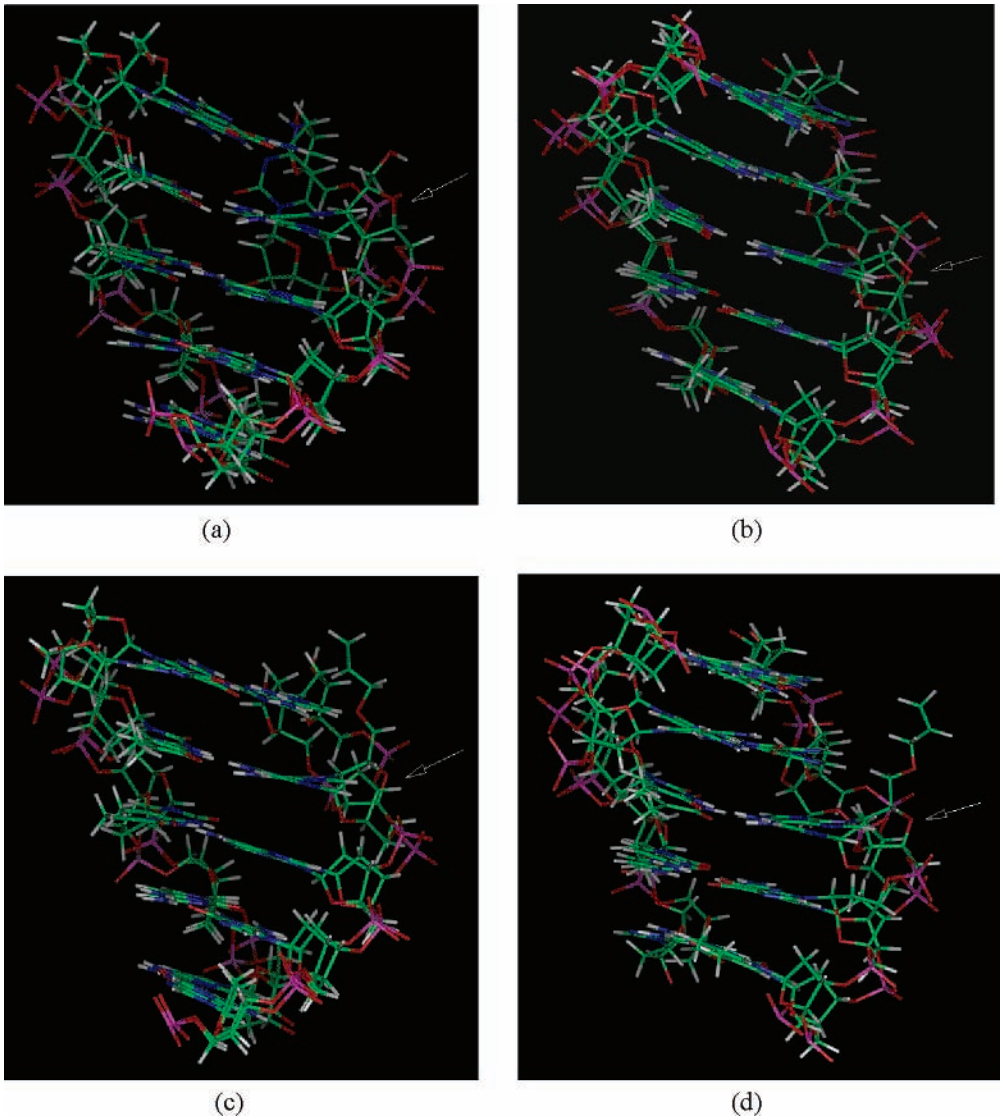

Figure 4. Overlap of simulated structures of isonucleotide-modified oligodeoxynucleotide-formed duplex with the native DNA duplex. The structures are from the part of the averaged structure of the last 800 ps molecular dynamics simulation. White arrows point to the position of the isonucleotide. (a) **I/VI**, (b) **II/VI**, (c) **III/VI**, (d) **IV/VI**.

its complementary sequence, the single isonucleotide-modified oligodeoxynucleotides formed typical B-form duplexes such as natural oligodeoxynucleotides. The computer simulation results also showed that B-form duplexes were maintained during the entire course of simulation. The result indicated that the incorporation of isonucleotide into the oligodeoxynucleotide might only lead to the local conformational change of the duplex. The averaged structure of the native DNA duplex was overlapped with the isonucleotide-modified duplexes, respectively. It clearly indicated that the helical parameters for the modified oligonucleotide duplexes were very similar to the native DNA duplex. The presence of the isonucleotides A_1 or A_2 mainly affected the local conformation of phosphorodiester backbone (Figure 4).

Strand−strand interactions of the five simulated DNA duplexes (**I/VI, II/VI, III/VI, IV/VI, and /V/VI**) were investigated (Table 2). The interaction energy (E_{inter}) was obtained from the total energy of the duplex (E_{duplex}) subtracted by the sum of two individual strands ($E_{strand1}$, $E_{strand2}$), i.e., $E_{inter} = E_{duplex} - (E_{strand1} + E_{strand2})$, and here the energy is composed of nonbonded van der Waals interaction and electrostatic interaction. The amount of interaction energy reflected the binding ability of oligodeoxynucleotide with its complementary sequence. The results indicated that the native DNA duplex **V/VI** possessed the strongest nonbonded interaction, and the duplexes **I/VI** and **III/VI** possessed stronger nonbonded interaction than duplexes **II/VI** or **IV/VI**. The calculated results were in good agreement with the thermal denaturation results.

Table 2. The Interaction Energy (kcal/mol) of the DNA Duplexes from the MD Trajectories[a]

duplex	E_{duplex}	$E_{strand1}$[b]	$E_{strand2}$[c]	E_{inter}
I/VI	−1156.1	−441.0	−386.4	−328.7
II/VI	−973.6	−325.7	−323.9	−324.0
III/VI	−1084.1	−418.2	−337.7	−328.2
IV/VI	−1121.2	−394.9	−404.0	−322.3
V/VI	−1190.2	−452.5	−393.1	−344.6

[a] Energy being from the averaged structure over the last 800 ps of the molecular dynamics simulation. [b] Energy of isonucleotide incorporated strand. [c] Energy of native complementary sequence.

Nuclease Hydrolysis and RNase H Cleavage. The hydrolysis behaviors of 5′-^{32}P-labeled isonucleotide-incorporated oligodeoxynucleotides by snake venom phosphodiesterase (SVPDE) were observed by gel electrophoresis (Figure 5). The results showed that the controlled

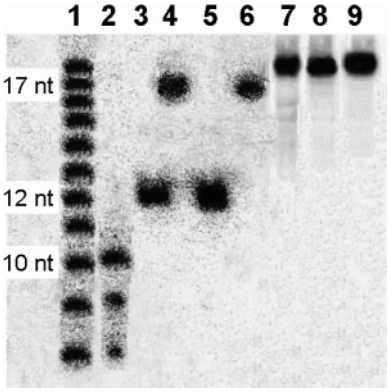

Figure 5. Autoradiogram of SVPDE digestion profiles of oligodeoxynucleotides. Lanes 1−6: marker, **V**, **II**, **I**, **IV**, **III**, respectively. Lanes 7−9: undigested oligonucleotide **V**, **I**, **III**, respectively.

natural oligodeoxynucleotide was completely hydrolyzed to small fragments after 10 min digestion, whereas the isonucleotide-incorporated oligodeoxynucleotide **I** or **III** was hydrolyzed to the 17-mer residues, and **II** or **IV** was hydrolyzed to 12-mer residue under the same conditions. The size of the hydrolyzed residues of the modified oligodeoxynucleotides was in accordance with the incorporation position of isonucleotide, i.e., the hydrolysis was inhibited at the point of isonucleotide substitution. The hydroxyl free or protected isonucleotides (**I** or **III**) have similar properties. Compared with some modified oligodeoxynucleotide, such as 2′-*O*-[2-(guanidium)ethyl]-modified oligonucleotide, which needs to have at least two consecutive modified nucleotides at the 3′-terminus for maintaining acceptable stability against exonuclease digestion (*19*), isonucleotide modification showed a much better antagonistic property. The result indicated that either hydroxymethyl free or protected isonucleotide could antagonize the activity of phosphodiesterase. It implied that an enzymatic stable oligonucleotide could be constructed by incorporating isonucleotide to the ends of oligodeoxynucleotide.

RNA cleavage by RNase H in the DNA/RNA hybrid was investigated (Figure 6). After the hybrid duplexes were digested by RNase H for 30 min, DNA/RNA hydrids showed different digestion patterns. Though the digested RNA fragments have not been investigated in this study, the efficiency of RNase H digestion in the presence of different oligodeoxynucleotides could be determined by measuring the intact RNA band in each lane. In general, the extent of the target RNA cleavage by RNase H in the hybrids formed by isonucleotide-modified DNA/RNA duplexes is higher than in the natural DNA/RNA. Both kinds of isonucleotide-modified oligodeoxynucleotides yielded similar RNA cleavage patterns. The results showed that the efficiency of RNase H cleavage in the presence of free or allyl-protected hydroxymethy isonucleotide-modified or unmodified oligodeoxynucleotides were in the order of allyl (**III**, **IV**) > free (**I**, **II**) > normal (**V**). It was reported that the efficiency of RNase H digestion was dependent on the feasibility of the formation of the DNA/RNA/RNase H complex, which was associated with many factors, such as the necessity of an A-form duplex, the width of the minor groove, and the duplex stability (*20*). Our result implied that the modified oligodeoxynucleotide sequences **III** and **IV** were more suitable for the formation of the DNA/RNA/RNase H complex. It was in inverse accordance with their binding abilities to the complementary sequences. The

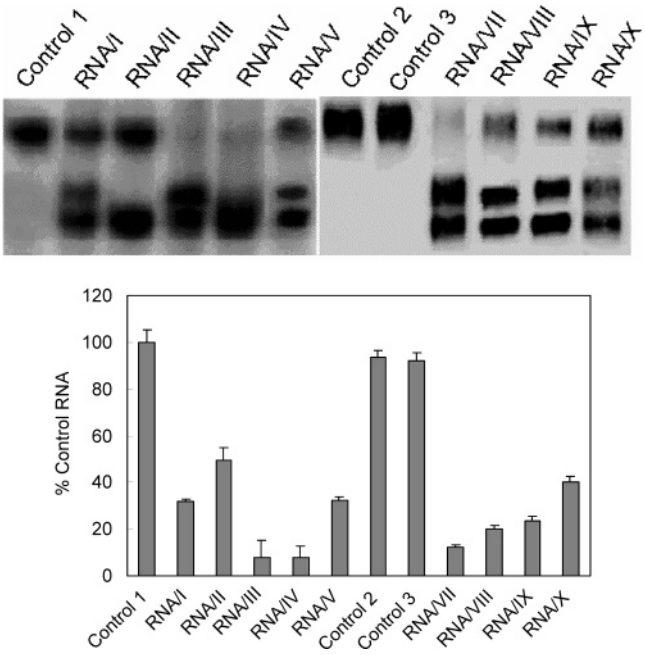

Figure 6. Autoradiogram of 5′-end-[γ-^{32}P]-labeled RNA treated with RNase H in the presence of isonucleotide-incorporated antisense oligodeoxynucleotide or mismatched antisense oligonucleotide. Control 1: RNA, control 2: RNA + RNase H, control 3: RNA + **V**.

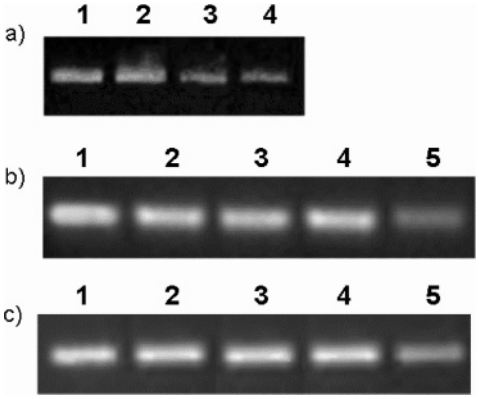

Figure 7. Effects of modified or mismatched antisense oligodeoxynucleotides on SARS coronavirus spike protein gene mRNA expression upon treatment at 50 μmol/L for 36 h. (a). Lanes 1−4: negative control, **V**, **I**, **III,** respectively; (b and c) Lanes 1−4: negative control, **VII**, **VIII**, **IX,** respectively; Lane 5: **I** (b), **III** (c).

sequences with nucleotides mismatched at the 3′-end (**VII**, **VIII**, **IX**, and **X**) also showed some efficient digestions.

Antisense-Induced Down-Regulation of S Protein. To determine the effect of 3′-isonucleotide-modified antisense oligodeoxynucleotides on gene expression of SARS coronavirus spike protein, Sf9 cells were transfected with 50 μM of oligodeoxynucleotides **I**, **III**, and **V** or mismatched controls **VII**−**IX**, and total RNA was isolated after 36 h. The level of SARS RNA was determined by RT-PCR. A remarkable decrease in gene expression of spike protein was observed in the cells treated by modified oligodeoxynucleotide **I** or **III**, whereas no obvious change was observed after the cell was treated by controlled native or mismatched antisense oligonucleotide (Figure 7).

The concentration dependence of gene expression in samples incubated with various concentrations of oligodeoxynucleotide **I** or **III** was investigated (Figure 8).

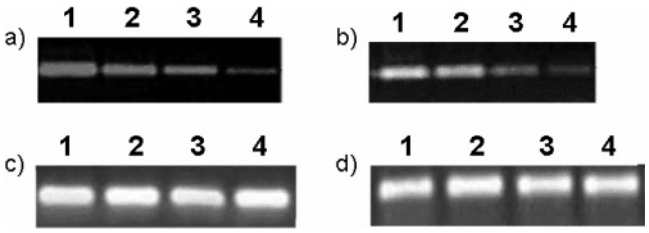

Figure 8. Effects of various concentrations of isonucleotide-incorporated antisense oligodeoxynucleotide on SARS coronavirus spike protein gene mRNA or on GAPDH mRNA after 36 h of treatment. Lanes 1−4: 0, 1, 10, 100 μmol/L, respectively. (a) (SARS-CoV, **I**), (b) (SARS-CoV, **III**), (c) (GAPDH, **I**), (d) (GADPH, **III**).

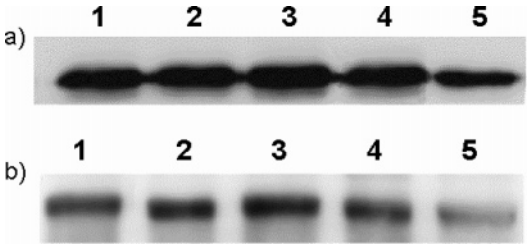

Figure 9. Effects of oligonucleotide on SARS coronavirus spike protein gene protein levels upon treated at 50 μmol/L for 36 h. Lane 1: negative control, lane 2−4: **VII**−**IX**, lane 5: **I** (a), **III** (b).

These data indicated that the modified oligodeoxynucleotide was able to inhibit transcription of the endogenous spike protein gene and was more effective than the native counterpart. We also measured the levels of glyceraldehyde-3-phosphate dehydrogenase (GAPDH). As expected, the expression of the GAPDH was not affected in these treated samples (Figure 8c,d). Western blot showed that modified oligodeoxynucleotides **I** and **III** decreased the protein expression remarkably and that **III** was stronger than **I**, whereas one to three mismatch controls (**VII**, **VIII**, **IX**) had almost no effect on the gene expression protein levels (Figure 9).

In conclusion, isonucleotide-modified oligodeoxynucleotides strongly antagonized the hydrolysis of snake venom phosphodiesterase. Furthermore, the modified antisense oligodeoxynucleotide also activated the RNase H though the incorporation of an isonucleotide into the oligodeoxynucleotide which led to a change of local conformation of the duplex. It was found that the 3′-isonucleotide-modified antisense oligodeoxynucelotides inhibited S glycoprotein expression of SARS-CoV at the mRNA levels in the insect Sf9 cells. The inhibition was dependent upon the concentration of the antisense oligomer. Therefore, this study provided a new strategy of designing a novel and effective antisense oligodeoxynucleotide by incorporating an isonucleotide at the 3′-end of the sequence.

ACKNOWLEDGMENT

This work was supported by the National Natural Science Foundation of China (20132030, SFCBIC 20320130046). Insect cell Sf9 and the recombinant baculoviruses used in this study were kindly provided by Professor Jianguo Chen (Peking University, Beijing, China).

LITERATURE CITED

(1) Zamecnik, P. C., and Stephensen, M. L. (1978) Inhibition of Rous sarcoma virus replication and cell transformation by a specific oligodeoxynucleotide. *Proc. Natl. Acad. Sci. U.S.A. 75*, 280−284.

(2) Wagner, R. W., and Flanagan, W. M. (1997) Antisense technology and prospects for therapy of viral infections and cancer. *Mol. Med. Today 3*, 31−38.

(3) Holmlund, J. T., Monia, B. P. Kwoh, T. J., and Dorr, F. A. (1999) Toward antisense oligonucleotide therapy for cancer: ISIS compounds in clinical development. *Curr. Opin. Mol. Ther. 1*, 372−385.

(4) Opalinska, J. B., and Gewirtz, A. M. (2002) Nucleic-acid therapeutics: basic principles and recent applications. *Nat. Rev. Drug. Discovery 1*, 1503−1514.

(5) Lebedeva, I. V., and Stein, C. A. (2000) Antisense oligonucleotides in cancer: recent advances. *Biodrugs 13*, 195−216.

(6) Baker, B. F., Lot, S. S., Condon, T. P., Cheng-Flournoy, S., Lesnik, E. A., Sasmor, H. M., and Bennett, C. F. (1997) 2′-O-(2-Methoxy)ethyl-modified anti-intercellular adhesion molecule 1 (ICAM-1) oligonucleotides selectively increase the ICAM-1 mRNA level and inhibit formation of the ICAM-1 translation initiation complex in human umbilical vein endothelial cells. *J. Biol. Chem. 272*, 11994−12000.

(7) Wahlestedt, C., Salmi, P., Good, L., Kela, J., Johnsson, T., Hokfelt, T., Broberger, C., Porreca, F., Lai, J., Ren, K., Ossipov, M., Koshkin, A., Jakobsen, N., Skouv, J., Oerum, H., Jacobsen, M. H., and Wengel, J. (2000) Potent and nontoxic antisense oligonucleotides containing locked nucleic acids. *Proc. Natl. Acad. Sci. U.S.A. 97*, 5633−5638.

(8) Stahel, R. A., and Zangemeister-Wittke, U. (2003) Antisense oligonucleotides for cancer therapy- an overview. *Lung Cancer 41*, S81−85.

(9) Yang, Z.-J., Zhang, H.-Y., Min, J.-M., Ma, L.-T., and Zhang, L.-H. (1999) Synthesis and enzymatic stability of oligonucleotides consisting of isonucleotides. *Pure Appl. Chem. 71*, 1143−1146.

(10) Yang, Z.-J., Zhang, H.-Y., Min, J.-M., Ma, L.-T., and Zhang, L.-H. (1999) Synthesis and duplex stabilization of oligonucleotides consisting of isonucleotides. *Helv. Chim. Acta 82*, 2037−2043.

(11) Lei, Z., Zhang, L., Zhang, L.-R., Chen, J., Min, J.-M., and Zhang, L.-H. (2001) Hybrid characteristics of oligonucleotides consisting of isonucleotide 2′,5′-anhydro-3′- deoxy-3′-(thymin-1-yl)-D-mannitol with different linkage modes. *Nucleic Acids Res. 29*, 1470−1475.

(12) Chen, J., Zhang, L.-R., Min, J.-M., and Zhang, L.-H. (2002) Studies on the synthesis of a G-rich octaoligoisoncleotide $(isoT)_2(isoG)_4(isoT)_2$ by the phosphotriester approach and iths formation of G-quartet structure. *Nucleic Acids Res. 30*, 3005−3014.

(13) Holmes K. V., and Enjuanes, L. (2003) Virology. The SARS coronavirus: a postgenomic Era. *Science 300*, 1377−1378.

(14) Gallagher, T. M., and Buchmeier, M. J. (2001) Coronavirus spike proteins in viral entry and pathogenesis. *Virology 279*, 371−374.

(15) Jayaraman, A., Walton, S. P., Yarmush, M. L., and Roth, C. M. (2001) Rational selection and quantitative evaluation of antisense oligonucleotides. *Biochim. Biophys. Acta 1520*, 105−114.

(16) Sugimoto, N., Nakano, S., Katoh, M., Matsumura, A., Nakamuta, H., Ohmichi, T., Yoneyama, M., and Sasaki, M. (1995) Thermodynamic parameters to predict stability of RNA/DNA hybrid duplexes. *Biochemistry 34*, 11211−11216.

(17) AMBER 7 users' manual. (2002) University of California, San Francisco.

(18) Shi, J.-F., Wang, Z.-L., Zhang, L.-R., and Zhang, L.-H. (2004) Synthesis of isonucleotide incorporated oligonucleotides and their binding abilities with complementary sequences. *J. Chin. Pharm. Sci. 13*, 4−9.

(19) Prakash, T. P., Puschl, A., Lesnik, E., Mohan, V., Tereshko, V., Egli, M., and Manoharan, M. (2004) 2′-O-[2-(Guanidinium)ethyl]-modified oligonucleotides: stabilizing effect on duplex and triplex structures. *Org. Lett. 6*, 1971−1974.

(20) Zamaratski, E., Pradeepkumar, P. I., and Chattopadhyaya, J. (2001) A critical survey of the structure−function of the antisense oligo/RNA heteroduplex as substrate for RNase H. *J. Biochem. Biophys. Methods 48*, 189−208.

BC049769H

Micropattern Printing of Adhesion, Spreading, and Migration Peptides on Poly(tetrafluoroethylene) Films To Promote Endothelialization

Virginie Gauvreau[†] and Gaétan Laroche*[,†,‡]

Unité de Biotechnologie et de Bioingénierie, Centre de Recherche de l'Hôpital Saint-François d'Assise, C.H.U.Q., 10 rue de l'Espinay, Québec, Québec, Canada, G1L 3L5, and Département de Génie des Mines, de la Métallurgie et des Matériaux, Centre de Recherche en Science et en Ingénierie des Macromolécules, Faculté des sciences et génie, Université Laval, Québec, Québec, Canada, G1K 7P4. Received November 26, 2004; Revised Manuscript Received May 6, 2005

We report here the development of an original multistep micropatterning technique for printing peptides on surfaces, based on the ink-jet printer technology. Contrary to most micropatterning methods used nowadays, this technique is advantageous because it allows displaying 2D-arrays of multiple biomolecules. Moreover, this low cost procedure allies the advantages of computer-aided design with high flexibility and reproducibility. A Hewlett-Packard printer was modified to print peptide solutions, and Adobe Illustrator was used as the graphic-editing software to design high-resolution checkerboard-like micropatterns. In a first step, PTFE films were treated with ammonia plasma to introduce amino groups on the surface. These chemical functionalities were reacted with heterobifunctional cross-linker sulfo-succinimidyl 4-(*N*-maleimidomethyl)cycloexane-1-carboxylate (S-SMCC) to allow the subsequent surface covalent conjugation of various cysteine-modified peptides to the polymer substrate. These peptidic molecules containing RGD and WQPPRARI sequences were selected for their adhesive, spreading, and migrational properties toward endothelial cells. On one hand, our data demonstrated that the initial cell adhesion does not depend on the chemical structure and combination of the peptides covalently bonded either through conventional conjugation or micropatterning. On the other hand, spreading and migration of endothelial cells is clearly enhanced while coconjugating the GRGDS peptide in conjunction with WQPPRARI. This behavior is further improved by micropatterning these peptides on specific areas of the polymer surface.

INTRODUCTION

The surface of cells displays a complex combination of receptors and ligands to mediate cell adhesion, spreading, migration, proliferation, and communication. These receptors and ligands are protein molecules that clasp one another like a lock and a key. Typically, receptors are proteins integrated in the cell membrane with domains extending beyond the membrane either or both inside and outside the cell. Ligands are proteins integrated in a neighboring cell membrane, part of the extracellular matrix or freely diffusing in the cell environment. Via receptor and ligand links, cells attach to each other and to the matrix to form tissue structure. Ligands from the milieu may code for a cell to adhere, to migrate, to grow and proliferate, or even to die. A well-known example of this is the $\alpha_5\beta_1$ integrin receptor that attaches with fibronectin proteins of the extracellular matrix, more specifically at the RGD binding site (*1*). A multitude of different receptors are present on the surface of a single cell at any given moment. Likewise, an impressive diversity of ligands are present on the extracellular matrix.

For over a decade, various proteins have been immobilized on polymer surfaces to enhance endothelial cells adhesion (*2*−*5*). Multiple strategies have been employed to that end, the most common being adsorption or grafting of fibronectin (*6*−*8*) and RGD peptides (*9, 10*). The common point between these strategies is that they all aim to mimic the extracellular matrix normally supporting and interacting with cells, hence possibly leading to a better integration and a more natural host response to the biomaterial.

It is known that vascular grafts that could support a layer of endothelial cells would have better resistance to thrombosis and graft stenosis in long-term applications (*11, 12*). In this study, RGD type peptides were grafted on the PTFE surface because this sequence is widely acknowledged as a cell-binding signal (*13, 14*), the goal being to promote in vivo endothelialization of ePTFE arterial prosthesis. RGD was originally identified as the fibronectin receptor sequence of the integrin $\alpha_5\beta_1$, but nowadays it has been identified as a recognition motif for various ligands of several different integrins (*15*). It is found in numerous plasma and extracellular matrix proteins such as fibronectin, vitronectin, and type I collagen (*1*). Massia et al. in the 1990s have investigated human umbilical vein endothelial cells (HUVECs) attachment, spreading, and cytoskeletal organization on substrates covalently grafted with RGD peptides (*4*). They observed that this strategy enhanced cell adhesion on substrates such as glycophase glass, poly(ethylene terephthalate) (PET), and poly(tetrafluoroethylene) (PTFE) that were otherwise repellent to cells.

Fundamental to the development of biologically integrated biomaterials is the ability to display a micropat-

* Corresponding author. Phone: (418) 656-2131 ext. 7983, Fax: (418) 656-5343, E-mail: gaetan.laroche@gmn.ulaval.ca.
[†] Centre de Recherche de l'Hôpital Saint-François d'Assise.
[‡] Université Laval.

10.1021/bc049717s CCC: $30.25 © 2005 American Chemical Society
Published on Web 09/02/2005

terned array of several specifically targeted ligands to mimic the extracellular matrix on the polymer surfaces. Since 1978, with MacAlear and Wehrung, who applied the photoresist technology from the semiconductor industry to create patterns on an underlying compressed proteinaceous layer (*16, 17*), several other techniques have been examined in the fields of micro- and nanopatterning to create two-dimensional arrays of proteins or other biologically active molecules on surfaces. These techniques include photoresist lithography, photochemistry, and self-assembled monolayers (*18*).

While each of these micropatterning techniques may be useful for some applications, each also has inherent limitations, for the most part concerning multiple protein binding, nonspecific binding, and immobilization of proteins while retaining their maximum biological activity (*18*).

In most cases, protein micropatterning is simply about immobilization through physical adsorption of proteins to a surface (*19, 20*). Entropy drives protein adsorption which always results from attractive forces such as ionic, hydrophobic, or van der Waals interactions (*21*). A more stable means to immobilize proteins to surfaces is to covalently bind the proteins to the surfaces via the use of heterobifunctional cross-linkers such as silanes (*22*), which bind at one end to a glass surface via a silanol group and to a protein at the other end via a variable pendant group. Finally, another way to provide a stable immobilization of proteins to surfaces is through the use of high-affinity ligand pairs such as avidin−biotin (*23*).

The central hypothesis of this study was that adhesion, spreading, and migration signals should be simultaneously present on the surface of arterial grafts to promote complete integration and endothelialization. Thus, in addition to RGD adhesion peptides, spreading and migration peptides should be present on the surface. The amino acid sequence WQPPRARI originating from the 33kDa fragment of the A chain of fibronectin was recognized in the literature (*24, 25*) for enhancing adhesion, spreading and migration of endothelial cells. It was therefore selected as the second signal to be grafted on the PTFE surface for the purpose of this study.

In this work, surface modifications were performed on Teflon (PTFE) films since small diameter arterial grafts are in general made of ePTFE, i.e., microporous or expanded PTFE. The first step of our approach consisted in an ammonia plasma treatment allowing the incorporation of amino groups on the PTFE surface. These highly reactive functionalities were conjugated, in a second step, with the heterobifunctional cross-linker Sulfo-SMCC, thus introducing maleimide functionalities on the PTFE surface. To exploit the very straightforward reaction between these maleimido groups and thiolic groups, the various peptides were synthesized with a cysteine at their terminal end. This study was thus performed with the peptide sequences CRGD, CGRGDS, and CWQPPRARI. Next, to graft this variety of specifically targeted peptides simultaneously on the polymer surface, we chose to develop a novel multistep micropatterning technique based on the ink-jet printing technology. This very advantageous ink-jet microprinting technique is an ultralow cost procedure that allows the flexibility of computer-aided design. The color cartridge of a commercial Hewlett-Packard printer (HP DeskJet 5500) was simply modified to print the biological peptide solutions according to a defined micropattern designed using Adobe Illustrator as the graphic-editing software. This micropatterning technique enabled rapid and precise deposition of both adhesion and migration peptides on PTFE films.

EXPERIMENTAL SECTION

Materials. Poly(tetrafluoroethylene) (Teflon or PTFE) films 0.05 mm thick were purchased from Goodfellow (Huntingdon, England). Vapor-phase chemical derivatization was performed with 5-bromosalicylaldehyde purchased from Sigma, St Louis, MO. The cross-linker sulfosuccinimidyl-4-(*N*-maleidomethyl)cyclohexane-1-carboxylate (S-SMCC) to be grafted on the PTFE surface was also obtained from Sigma. The various peptide sequences (CRGD, CGRGDS, CRGE, CRGDY, and CWQPPRARI) grafted on the polymer surface were synthesized by Service de synthèse de peptides de l′est du Québec, CHUQ, Québec, QC, Canada. Peptide solutions were prepared in phosphate-buffered saline (PBS) and glycerol that were purchased from VWR Canlab, Ville Mont-Royal, QC, Canada and Laboratoire MAT, Montréal, QC, Canada, respectively. The buffer solutions were prepared in filtered, deionized water (Nanopure system) while fine adjustments of the pH were made by adding either 0.1 M of HCl or NaOH to reach the desired value. CRGDY peptides were iodated using Iodo-Beads Iodination Reagent from Pierce, Brockville, ON, Canada, and sodium iodide from Sigma. All chemicals were of commercial grades of highest purity and were used without further purification.

The cell culture experiments were performed with human umbilical vein endothelial cells (HUVECs) recolted and cultured at our lab. The culture medium M199 supplemented with 0.09 g/L of heparin sodium salt and the porcine gelatin were purchased from Sigma. This medium was also supplemented with fetal bovine serum (FBS) provided by Wiscent, St-Bruno, Qc, Canada, and endothelial cell growth supplement (ECGS) provided by VWR Canlab. Cells were cultured in 25 cm^2 tissue culture-treated polystyrene flasks or plated in 48-well culture plates from BD Falcon. Trypsin-EDTA used to detach the cells from the culture surfaces was purchased at Invitrogen Canada inc., Burlington, ON, Canada. Rezasurine purchased from Sigma was used for fluorescence emission. Products required for HUVECs fixation and staining procedures including formaldehyde, bovine serum albumin (BSA), Saponine, 4′,6-diamidino-2-phenylindole (DAPI), Rhodamine−Phalloidine, and Tween 20 were also acquired from Sigma.

Methods. *Ammonia Plasma Treatment.* The ammonia radiofrequency (rf) plasma treatment and system apparatus were previously described elsewhere (*26, 27*). Briefly, the treatments were performed at a rf power of 20 W and a pressure of 300 mTorr for 100 s using high purity ammonia gas. The 3 cm × 3 cm PTFE films were held by a Teflon-made circular sample holder and treated in a cylindrical plasma chamber. Using such a plasma configuration and geometry allows to modify only the internal side of the film.

Surface Functionalization. The cross-linker S-SMCC was reacted with the ammonia plasma-treated film in 3 mg/mL of reagent in PBS 0.2 M at pH 7.4. The reaction was then allowed to proceed for 2 h in a nitrogen environment and under low light intensity to protect the reagents against UV-induced degradation. The characterization of this reaction has been presented elsewhere (*28*). Briefly, this reaction is complete and allows the introduction of maleimido groups on the PTFE surface. These functions were used to subsequently conjugate the

peptides through a sulfhydryl containing N-terminal Cystein residue.

Peptide Solutions. The peptide sequences CRGD, CGRGDS, CRGE, CRGDY, and CWQPPRARI were synthesized and solutions of 10 μg peptide/μL of PBS 0.2M at pH 7.4 containing 7.5% glycerol were prepared. Glycerol was added to prevent rapid evaporation of the solution when the peptides were printed and to adjust the peptide solution viscosity to a value similar to that of the ink normally used by the printer. These solutions were used either to print the peptides or homogeneously conjugate them on the polymer surface. The occurrence of the peptide graftings on the SMCC-conjugated surfaces was ascertained by iodating a tyrosine-containing peptide (CRGDY) using Iodo-Beads and sodium iodide (*29*) using one bead to iodinate 0.2 mg of peptides. CRGDY peptides were first iodated and then grafted to the PTFE surface. The I3d XPS signal was used to confirm the peptide conjugation.

Ink-Jet Printer. A commercial HP 5500 Deskjet printer was modified to print the peptide solutions. We carefully chose this printer because it offered an optimized resolution up to 4800 dots per inch (dpi) according to the manufacturer and most importantly because the cartridges were not monocoque, as are most of the new generation cartridges. Therefore, these cartridges could be refilled easily. First, the top of the tricolor cartridge HP#57 was cut so as to leave the contour in place, since it was essential to click the cartridge back in the cradle; the internal sponges made of polyurethane foam were then removed as well as the little grids and filter-papers covering the wells. The cartridges were then extensively washed with deionized water and ethanol. The peptide solutions were then deposited with micropipets directly into the wells situated very next to the printhead.

Calibration of the Printer. The ink-jet printer drivers interpret the colors drawn on the computer screen that intrinsically work in RGB (red, green, blue) color-space, or additive light, to print them with a CMYK (cyan, magenta, yellow, black) color cartridge, or subtractive light. Therefore, it is essential to carefully calibrate the printer so that it prints pure color, or in this case, pure peptide and not a mixture of the peptide solutions. It is recommended to work in RGB color space if the artwork will only be displayed on-screen in the case of a web-site for example, and in CMYK if the work will be printed with a commercial printer (*30*), as the HP DeskJet 5500 used in this study. However, we tried both modes, looking at every printed surface with an optical microscope, and surprisingly it appeared that pure colors could be achieved more easily by working in RGB. Since the HP Deskjet printer used is targeted at the mass market, its drivers are probably not as trustwothy, in regard to color-space translation, as those of a real four-color-process commercial CMYK laser printer. Adobe Illustrator graphic-editing software was used to design the desired patterns and define the pure colors. In the RGB mode, fine color adjustments are obtained by adjusting the intensity of each color, or wavelength, on a scale from 0 to 255 (8 bits). The full spectrum of colors is then achieved by combination of the three scales. Since we are in the additive color space, 0, 0, 0 of red, green, blue would give black, and 255, 255, 255 would give white. On the basis of this knowledge, and verifying the printed surfaces with an optical microscope, we obtained pure cyan with 0, 255, 255, pure magenta with 255, 0, 255, and pure yellow with 255, 255, 0. However, printing 255, 255, 0 for example, meaning 100% yellow, deposited too much ink on the surface, and independent droplets combined together. For that reason, we reduced the quantity of ink for each droplet by incrementing the third factor to 100 (ex.: 255, 255, 100), therefore obtaining a lighter color.

Grafting Peptides in Solution and Printing Peptides. The same peptide solutions were use for control, i.e., peptides homogeneously conjugated on the polymer surface, and for printing. Conventional in-solution grafting was performed using 1 mL of the peptide solutions for each 1 cm^2 of plasma-treated SMCC-grafted PTFE films. The reaction was performed for 120 min at room temperature under mechanical agitation. To graft the peptides through the micropatterning technique, 30 μL of the solution of the individual peptide were micropipetted directly into the adjacent wells of the printer cartridge. The peptides were then printed on the ammonia plasma-treated SMCC-grafted PTFE films according to the micropattern designed using Adobe Illustrator software. Squares of 300 μm width of both adhesion peptides and spreading and migration peptides were printed next to the other just like a checkerboard. Concerns about the viscosity and the wetting properties of the peptide solutions affecting the quality of the arrays were considered. Moreover, to ensure the covalent grafting of the peptides to SMCC-grafted PTFE, the individual peptide spots had to remain in the aqueous form and not evaporate too rapidly. The viscosity of the solution was therefore adjusted with 7.5% glycerol (*31*). Printed surfaces were maintained in a humidification chamber for 120 min at room temperature.

X-ray Photoelectron Spectroscopy (XPS) Characterization. Immediately following the ammonia plasma treatment, samples of the aminated PTFE film were cut in a glovebox purged with dry nitrogen. These samples were analyzed by XPS without delay to assess the exact atomic composition of the surface following the plasma treatment. SMCC grafted surfaces, as well as all the peptide-grafted surfaces, were also analyzed by XPS after having been vacuum-dried overnight at ambient temperature. The XPS spectra were recorded using a PHI 5600-ci spectrometer (Physical Electronics, Eden Prairie, MN). A monochromatic aluminum X-ray source (1486.6 eV) at 400 W with neutralizer was used to record the survey spectra while high-resolution spectra were obtained using the monochromatic magnesium X-ray source (1253.6 eV) at 400 W without charge neutralization. The detection was performed at 45° with respect to the surface normal.

Amine Quantification. Samples of ammonia plasma-treated films were used to quantify the amine surface concentration through vapor-phase chemical derivatization using 5-bromosalicylaldehyde as described elsewhere (*26*). Briefly, the reaction was performed at 85 °C for 2 h in a sealed glass tube in which a 1 cm-thick bed of soda-lime glass beads was used to separate the reagent from the reactive surface. The surfaces were then vacuum-dried overnight at 40 °C and analyzed by XPS.

Endothelial Cell Culture. HUVECs were cultured in a 25 cm^2 tissue culture-treated polystyrene flasks covered with porcine gelatin. The culture medium M199 with heparin was supplemented with FBS and ECGS, and the cells were grown in a 37 °C incubator with a humidified atmosphere of 5% CO_2 and 95% air. For cell culture experiments, modified PTFE films of 27 mm^2 (5.86 mm of diameter) were deposited in a 48-well microplate and HUVECs were seeded at 50 000 cells/well for adhesion tests and 25 000 cells/well for proliferation tests. Adhesion measurements were performed for 2 h in a serum-free M199 medium to ensure that RGD peptides grafted to the surface, and not the serum protein contained in the medium, favored HUVEC adhesion to PTFE. For

spreading and migration measurements, the serum-free medium was removed from the wells after 2 h of adhesion and replaced by a fresh culture medium supplemented with serum and growth factor. Spreading and migration tests were performed for 72 h.

Counting the Number of HUVECs Adhered to Surfaces. After 2 h of adhesion, HUVECs seeded on different surfaces were detached in order to evaluate the number of cells capable of adhesion on the various peptide-grafted PTFE surfaces. The culture medium and nonadhered cells were first aspirated from the wells. The surfaces were then rinsed twice with PBS and the rinse transferred to new wells to prevent detachment and counting of cells adhered to the well walls. Cells were then detached from the surface using 90 μL of trypsin-EDTA per well and incubated at 37 °C for 3 min. Trypsin activity was then inhibited with 10 μL of FBS per well. Aliquots were withdrawn from each well, and cells were counted the usual way using a hemacytometer.

In a different way, the number of HUVECs adhered to the various surfaces were also estimated by monitoring fluorescence emission of cells incubated with resazurine. The cell dehydrogenase enzyme converts resazurine into resorufine, the concentration of which was monitored by measuring the intensity of fluorescence for each surface and comparing with a blank. First, the culture medium and the cells in suspension were aspirateded from the wells, and the surfaces were rinsed with PBS. A solution of 1/10 of resazurine 250μg/mL and 9/10 of culture medium M199 supplemented with heparin and FBS was prepared and maintained at 37 °C. Aliquots of 100 μL were added to each wells, and the surfaces were stored in the incubator. Fluorescence measurements were made on a Bio-Tek FL600 luminescence spectrometer with settings of excitation and emission wavelengths at 485 nm and 590 nm, respectively. All experiments were performed in triplicate.

HUVEC Fixation and Staining. After the 2 h of adhesion or the 72 h of spreading and migration, the culture medium was aspired from the wells and HUVECs were fixed for 30 min at room temperature with 3.7% formaldehyde in PBS. The formaldehyde solution was then removed from the wells, and cells were washed three times with PBS. Cell permeability was increased with a solution of PBS with 3% BSA and 0.1% saponine for 1 h 30 min at room temperature. This solution was removed, and cells were stained using 1:3000 DAPI and 1:400 Rhodamine−Phalloidin in PBS and maintained in the 37 °C incubator for 1 h. Cells were then washed six times with PBS and 0.05% Tween 20 before the surfaces were fixed between blade and lamella to be observed under the microscope.

Microscopy and Image Analysis. Microscopic pictures of every HUVECs seeded surfaces were taken using a Nikon E800 confocal microscope equipped with a Hamamatsu Orca ER digital camera (Nikon Canada, Mississauga ON). Pictures taken in microscopy were analyzed using Adobe Photoshop histogram and color selection pixels count functions. Image color selection allowed to distinguish between background and cellular bodies. A ratio between the number of pixels corresponding to cellular bodies and the total number of pixels provided a percentage of cellular coverage of the surface. The total number of pixels was of course similar for all images (all microscope images compared in this study being the same size).

RESULTS AND DISCUSSION

The various peptides were grafted on the surface through simple chemical reactions. First, an ammonia plasma treatment allowed the introduction of about 13% of nitrogen-containing species, one-third of which were amino groups according to vapor-phase chemical derivatization using 5-bromosalicylaldehyde (*26,* 28). S-SMCC was then allowed to react with the highly reactive amino groups to provide maleimido groups on the polymer surface. According to previous results (*28*), this reaction is complete. The maleimide functionalities were useful to covalently conjugate peptides through terminal end thio-containing cysteine residues. A schematic example of these chemical reactions and the XPS spectra monitored after each step of the conjugation procedure are shown in Figure 1.

As can be seen in Figure 1, the peptide graftings on the SMCC-conjugated surfaces did not bring important changes from a XPS point of view. Therefore, to ascertain the covalent conjugation of these peptides on the PTFE surface, a CRGDY peptide was iodinated using the simple chemical reaction between the tyrosine residue and Iodobeads (Figure 2). Iodine has a high XPS sensitivity index, and therefore its detection on the PTFE surface confirmed the covalent binding of the peptides on the polymer surface (Figure 3) through the reaction between the thiolic group of the terminal cysteine and the maleimido group previously introduced on the polymer surface.

All peptide-grafted surfaces, both in solution and homogeneously printed (meaning that the peptide solution was printed everywhere on the PTFE surface), were analyzed by XPS. Similar results were obtained for each grafting procedure (Table 1), indicating that the printing technique did not alter the capacity of the peptides to react with the maleimide functionalities previously grafted on the PTFE surface.

The two most common ink jet dispensing technologies are thermal and piezoelectric. Both modes have been tested in the literature, and the thermal dispensing technology appears to be more reliable for printing biological solutions (*32*). This technology is based on the expulsion of picoliter-sized droplets from the capillary nozzles of the printhead which is assembled directly on the cartridge and consists of a nozzle plate with multiple capillaries or ink-ejection orifices surrounded by resistive heater elements. When a current pulse is received by an individual heater element, the rapid transfer of heat to a small portion of the sample solution located in a capillary causes its vaporization, creating a vapor bubble. The vapor bubble creates a volume displacement that leads to the expulsion of a droplet. Therefore, it was important that the conductivity of the original ink and our peptide solutions be identical (0.08 μS/cm or a resistance of 12 Mohm-cm). The local temperature applied to a small sample volume by the heater elements can reach 200 °C. Concerns about the integrity of the peptides have been addressed, and no degradation has been observed, as relative surface concentrations obtained through XPS analyses were similar for printed peptides as compared to conventional in-solution grafted peptides. This result is in agreement with various studies who have addressed this question concerning other biomolecules such as DNA, enzymes, and proteins (*31, 33*). Furthermore, we did not observed clogging problems caused by heat-aggregation of peptides in the printhead. Therefore, the commercial tricolor cartridge can be successfully washed and refilled with peptide solutions for

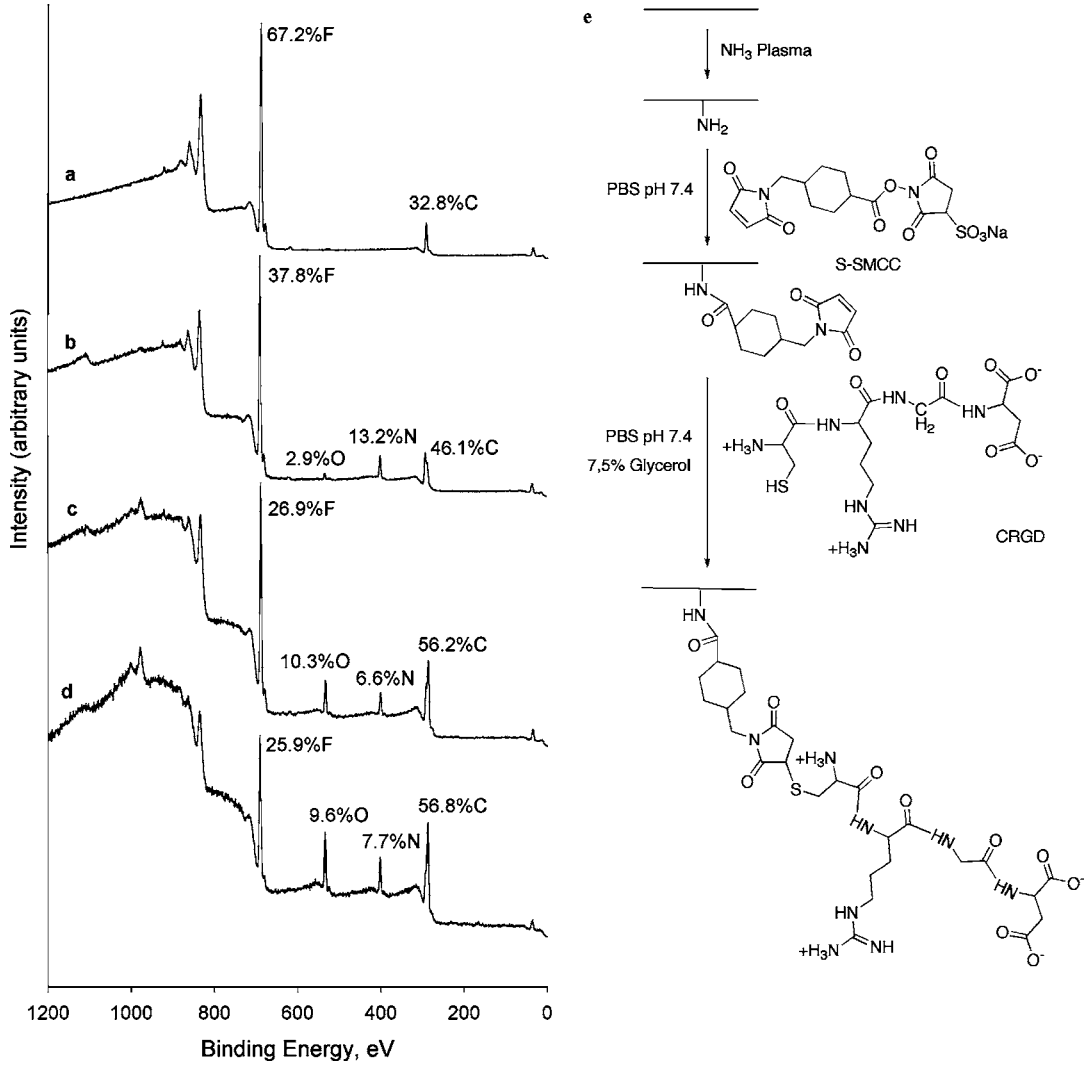

Figure 1. XPS spectra monitoring each reaction step of the CRGD grafting procedure: a**.** Virgin PTFE. b**.** Ammonia plasma-treated PTFE. c**.** SMCC-grafted PTFE. d**.** CRGD conjugated to plasma-treated SMCC-grafted PTFE. e**.** Synthetic scheme of CRGD peptide grafting on a PTFE film.

precise microdeposition of the surfaces. This procedure did not compromise the performance of the printer nor did it damage the printhead or alter the integrity of the various peptides. The use of the tricolor cartridge instead of the black one allowed the deposition of arrays containing up to three different peptides at the time.

The quantity of peptides deposited in each printed spot was calculated by weighing the cartridge before and after printing a large known number of spots (*33*). In the present study, it was found that each 300 μm wide spot printed on the polymer contained 0.18 nL of the peptide solutions (0.18 nL/spots of 90 000 μm^2 or 2.0 fL/μm^2). Roda et al. (*33*), using a HP DeskJet 600 and printing horseradish peroxidase (HRP) on cellulose paper, found that 17 nL/spots of 1 mm in diameter (21.6 fL/μm^2) were deposited on the surface of their substrate. This large difference is mainly attributed to the properties of the surface to be printed on. Cellulose paper is absorbent, and the authors used the highest quality printer settings to deposit the HRP, whereas PTFE is impermeable and printing with the highest quality printer mode deposited a volume of solution too large to maintain independent spots and retain the micropatterned design. Okamoto and al. (*31*) have printed DNA on glass surfaces using Bubble Jet printers from Canon (BJC-600 and BJC-700J). The resolution of their printer was 360 $\times$ 720 dpi, and they printed 24 pL of their solution per droplet (9.6 fL/μm^2) onto a glass surface. Again, the quantity of solution deposited is higher than the quantity we deposited on PTFE, and this can probably be explained by the more hydrophilic property of the glass substrate compared to ammonia plasma-treated PTFE.

To determine whether it was easier to print pure color in RGB color-space mode or in CMYK mode, we printed individual colors on premium picture paper and observed the prints with an optical microscope. The pure-color prints were obtained in the RGB color-scale mode with codes 0, 255, 255 for pure cyan, 255, 0, 255 for pure magenta, and 255, 255, 0 for pure yellow. Droplets on clean PTFE film presented a diameter of 10 μm or a surface area of 80 μm^2 (Figure 4a). Unsurprisingly, because plasma-treated PTFE is hydrophilic and still maintains its nonabsorbance property, droplets of this size could not be obtained on this surface. With this printer, the smallest micropatterned spots obtained were squares of 300 μm of width since smaller independent droplets combined together (Figure 4b).

To evaluate the peptides' capacity to promote adhesion, PTFE surfaces conjugated in solution with each individual peptide and with combination of CRGD/CWQPPRARI and CGRGDS/CWQPPRARI were seeded with HUVECs. After 2 h of HUVECs adhesion, the surfaces

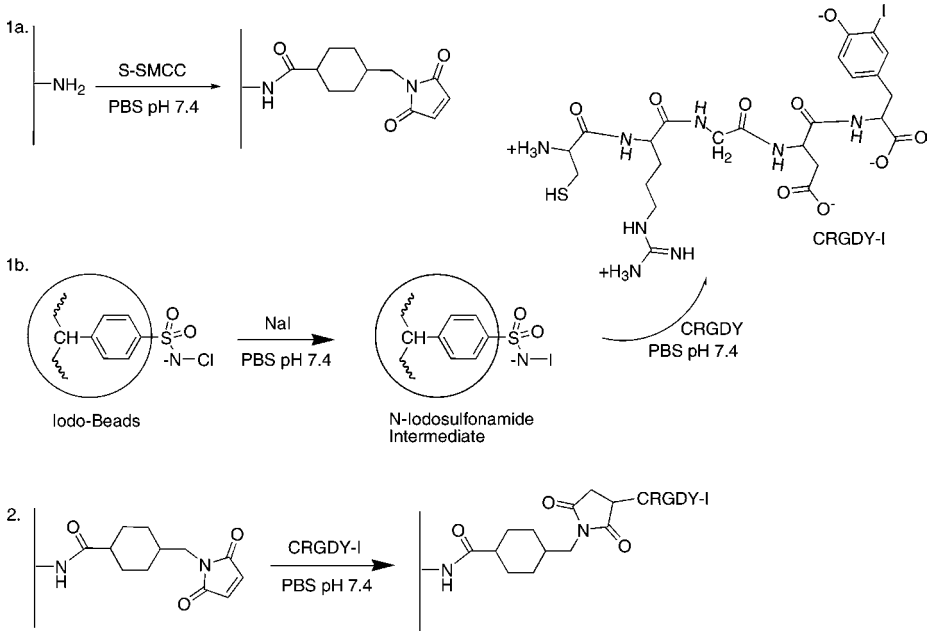

Figure 2. Synthetic scheme of iodination of CRGDY peptide and subsequent conjugation to plasma-treated SMCC-grafted PTFE film.

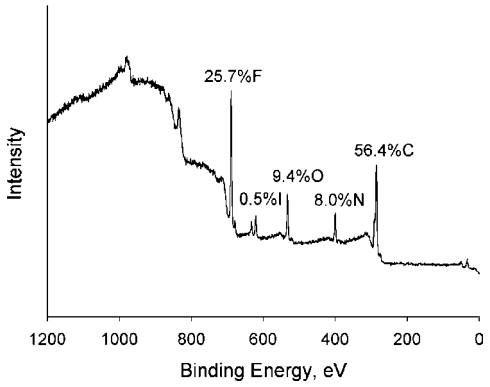

Figure 3. XPS spectrum of PTFE film conjugated with CRGDY-I.

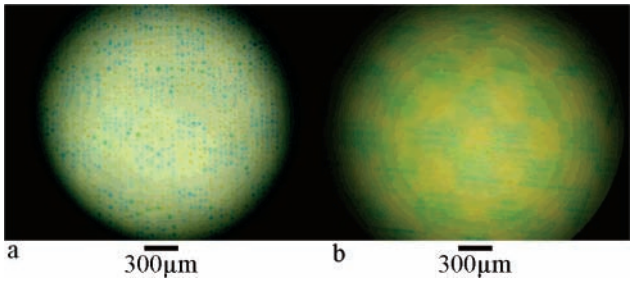

Figure 4. a**.** Ink spots of 10 μm on virgin PTFE. b**.** Spots of 300 μm on plasma-treated PTFE.

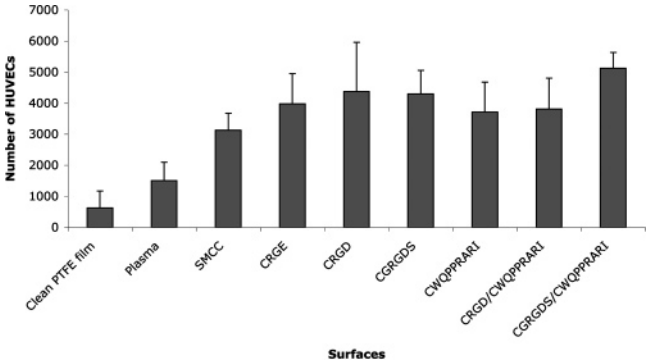

Figure 5. The number of HUVECs harvested with trypsin-EDTA on PTFE surfaces after 2 h of adhesion; aliquots were withdrawn from each well for the cells to be counted with a hemacytometer.

were rinsed with sterile PBS, and cells were harvested using trypsin-EDTA and counted (Figure 5). From these results, some important trends need to be pointed out. First, there is a significant difference in the capacity of the peptide-grafted surfaces to favor adhesion compared to the control surfaces. Surfaces grafted with peptides were more attractive to cells than control surfaces. Another important point to notice is that, although CRGE peptide is stated in the literature (*34*) as a negative control of CRGD, in the sense that it does not support adhesion of cells, in this part of the study the short adhesion period of 2 h was insufficient at demonstrating a difference between these two peptides. Probably for the same reason, CGRGDS, which is known to better enhance adhesion of cells on surfaces (*35*), did not stand out from CRGD. Finally, the peptide CWQPPRARI, which was shown (*24, 25*) to favor adhesion, spreading and migration of endothelial cells, did favor adhesion of HUVECs to PTFE in a comparable way to CRGD. Similar trends were noticed while the cells attached to the surfaces were counted after incubating the cells with resazurine (Figure 6); that is to say that no individual peptide appeared more adhesive than one other, but peptide-grafted surface were more favorable to adhesion of HUVECs than control surfaces. Therefore, the initial HUVEC adhesion does not depend on the chemical structure of the peptides nor does it depend on the combination of peptides covalently bonded to the PTFE surface.

Adhesion, spreading, and migration of HUVECs on surfaces either grafted with individual peptides in solution, peptide mixtures in solution, or combination of peptides micropatterned was also examined in microscopy (Table 2). These images confirmed the results presented in Figures 5 and 6, as they also demonstrated that the initial cellular adhesion did not depend on the

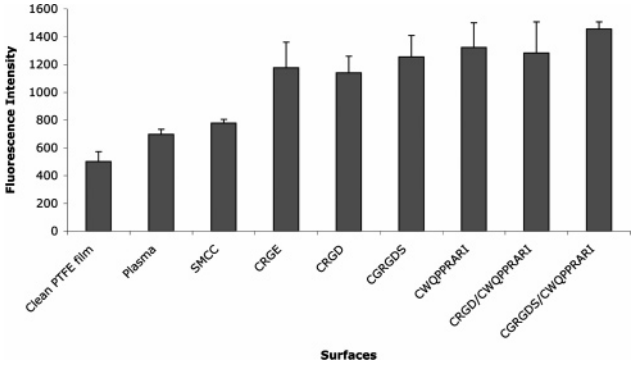

Figure 6. The number of HUVECs adhered to the different surfaces was estimated by monitoring fluorescence emission of cells incubated with resazurine after 2 h of adhesion on various PTFE surfaces.

chemical structure of the peptides conjugated to the surface. In addition, they also revealed that similar cellular adhesion was observed for combination of peptides either coconjugated in solution or micropatterned on the PTFE surface, in accordance with our previous statement that the printing technique did not alter neither the peptides integrity nor their capacity to promote adhesion of cells. Typical examples of these images are presented in Table 2. From these images, qualitative conclusions can be drawn. First, clean PTFE film does not support adhesion of endothelial cells, although some cells were observed on the surface. These cells were very small in size, and the actin cytoskeleton was disrupting. This cytoskeletal disruption alone presets apoptosis (*36*), and therefore no cells were observed on the virgin PTFE surface after 72 h. Microscopic images of CRGE- and CRGD-grafted surfaces in adhesion tests were very similar with small round cells, indicating poor adhesion and spreading, and other larger spreading cells. Besides these early adhesion results, there was a major difference between these two types of modified surfaces after 72 h. Cells on the CRGE-conjugated surfaces were deprived of any attachment signal, and most of them did not survive over a three-day period of time. Hence, almost no cells were observed on the CRGE surfaces in the spreading and migration tests, and the ones that were present looked abnormal with fragmented nuclei and distorted cytoskeletons. On the contrary, cells on the CRGD surfaces were larger, some were still round-shaped, but many were spreading and their nuclei were intact. These observations are in accordance with what we know from the literature; cellular functions are regulated both by the adhesion of cells to the surface via the integrin receptors (*1*) and by their subsequent spreading (*37, 38*). Whitesides and colleagues have also demonstrated that reduction of cell spreading is associated with a decrease in cell survival, as the more retracted and round the cells, the greater the apoptotic rate (*39*). PTFE surfaces conjugated with CGRGDS did not exhibit many more adhered cells than CRGD surfaces after 2 h of adhesion, but the cells on the CGRGDS surfaces were wider and their cytoskeleton was more developed. Again in the 72-h spreading and migration tests, there were not more cells on the CGRGDS surfaces compared to the CRGD surface, but cell spreading was obvious. Some cells on the CWQPPRARI surface, after 2

Table 1. XPS Analysis of Plasma-Treated SMCC-Grafted PTFE Surfaces Conjugated with Various Peptides Either in Solution or Printed

	CRGE		CRGD		CGRGDS		CWQPPRARI	
	solution	printed	solution	printed	solution	printed	solution	printed
%C	56.8	56.5	56.8	56.2	56.5	55.2	61.2	59.6
%F	25.6	24.6	25.9	26.5	27.6	28.7	18.4	19.8
%N	7.5	8.5	7.7	7.6	8.2	8.5	10.3	10.2
%O	10.1	10.4	9.6	9.7	7.7	7.6	10.1	10.4

Table 2: Typical Microscopic Images (100×) of the Various Surfaces without Distinction between the Grafting Technique for Individual Peptides and with Distinction between the Grafting Procedure Performed Either in Solution or via the Microprinting Technique for the Surfaces Conjugated with a Combination of Peptides[a]

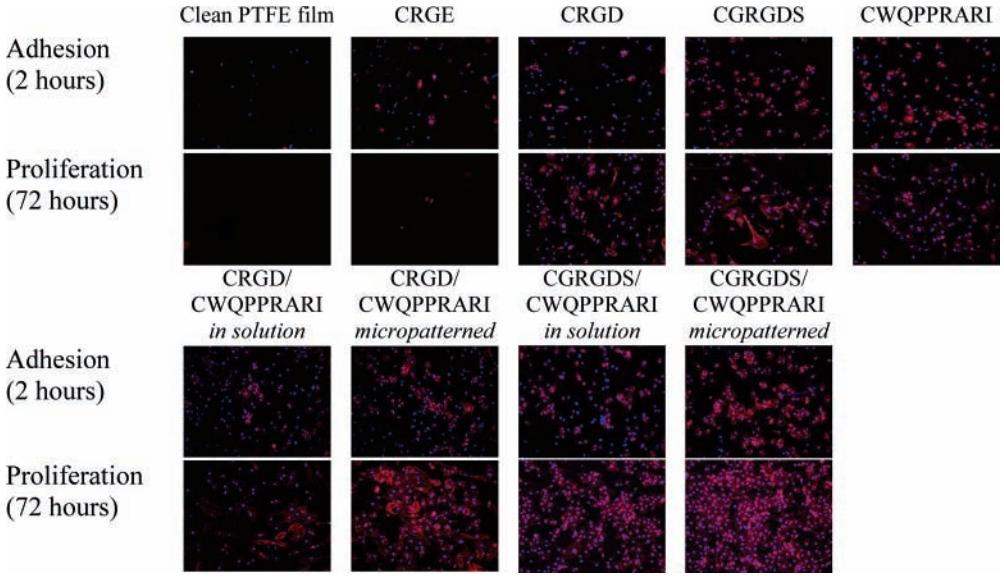

[a] Cells were fixed and colored with DAPI and Rhodamine−Phalloidin after 2 h in the adhesion experiments and after 72 h in the proliferation experiments.

h of adhesion, were round-shaped and did not present much of a cytoskeleton, but in general they seemed well-adhered to the surface and undergoing spreading. After 72 h of spreading and migration on these surfaces, the cells were fully spread and some appeared to be in motion with projections in similar directions. This is in agreement with results in the literature presenting this amino acid sequence as an adhesion signal (*40*) and spreading and migration signal (*24, 25*).

Microscopic images captured for the surfaces conjugated with a combination of peptides, either CRGD or CGRGDS and CWQPPRARI, did not present noteworthy differences between the substrates conjugated with the peptides in solution or via the micropatterning technique after 2 h of adhesion. On the other hand, there was a significant difference between the two combinations of peptides. The simultaneous conjugation of adhesion signal CRGD and spreading and migration signal CWQPPRARI did seem to define a more adhesive surface than CWQPPRARI peptide alone but not to a great extent. Concurrently, the conjugation of CGRGDS and CWQPPRARI did definitely define a more adhesive surface than individual peptides alone. Quantitatively, there were not a greater number of cells adhered to the surface, but from the glimpse of an eye, it was obvious that the cells were larger and spreading out.

After 72 h of spreading and migration, there was a major difference between the peptide-combined surfaces grafted in solution and via the printing technique. On the CRGD/CWQPPRARI surfaces, cells were spreading and the cytoskeleton was effusive. There were more cells on the micropatterned surface than on the surface with the combination of peptides conjugated in solution. Moreover, there seems to be a certain directional organization in the spreading of these cells, indicating that cells might be communicating with one another. Surfaces conjugated with both CGRGDS and CWQPPRARI fully supported endothelial cell attachment and spreading. The microscopic images captured for these surfaces indicated that this combination of adhesion and proliferation signal was the key combination in this study to promote endothelialization of PTFE surfaces, the ultimate goal being to develop ePTFE vascular grafts able to promote and support an endothelial cell layer at the luminal face. CGRGDS and CWQPPRARI peptides grafted in solution did enhance attachment and spreading of HUVECs to a great extent. Nevertheless, the micropatterning printing technique seems to be advantageous in promoting endothelialization since the surfaces were nearly fully covered with cells. These results are in agreement with Whitesides and colleagues who have demonstrated the influence of micropatterned surfaces on the control of cell shape, position, and function (*41*).

To draw some quantitative conclusions from these microscopic images, they were processed through Adobe Photoshop histogram function. Values corresponding to the percentage of cell coverage of the surfaces were calculated from ratios between the number of pixels corresponding to cell bodies and the total number of pixels. Results for the adhesion and the spreading and migration experiments are presented in Figures 7 and 8.

Unsurprisingly, from these results it can be concluded that virgin PTFE is not suitable at promoting and supporting adhesion of endothelial cells over a period of 72 h. Thus, even though some cells were present on this surface after 2 h of adhesion, none were capable of surviving over a 3-day period of time. In the same way, CRGE did not support adhesion, spreading, and migration of HUVECs over the same period of time. The ability of CRGD surfaces to promote adhesion of endothelial cells and the inability of CRGE to do so is in agreement with previous studies in the literature (*42*−*44*). Again, there was only a slight difference between CRGD and CGRGDS in their capacity of promoting and supporting adhesion of HUVECs. Although CWQPPRARI alone did no better than RGD-type peptides at promoting adhesion, spreading, and migration of HUVECs, the combination of CRGD/CWQPPRARI and most appreciably the combination of CGRGDS/CWQPPRARI did enhance adhesion, spreading, and migration of endothelial cells significantly.

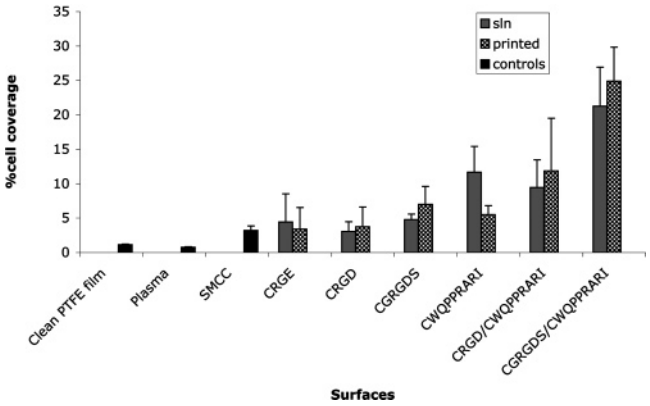

Figure 7. Percentage of cellular coverage of PTFE surfaces after 2 h of adhesion calculated from a ratio between the number of pixels corresponding to cellular bodies/total number of pixels for microscopic pictures. PTFE surfaces were grafted with various peptides and combinations of peptides, either in solution or printed in micropatterns of 300 μm.

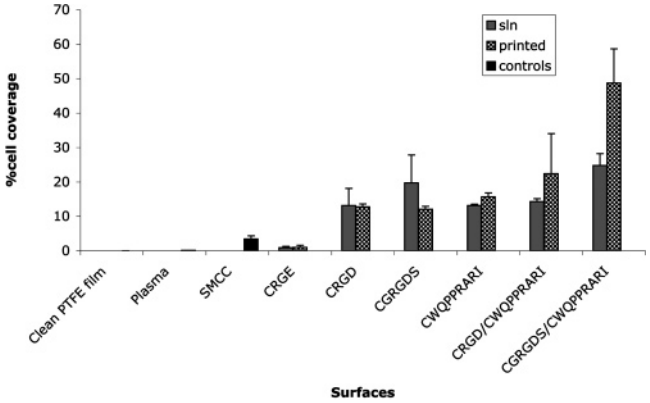

Figure 8. Percentage of cellular coverage of PTFE surfaces after 72 h of spreading and migration calculated from a ratio between the number of pixels corresponding to cellular bodies/total number of pixels for microscopic pictures. PTFE surfaces were grafted with various peptides and combinations of peptides, either in solution or printed in micropatterns of 300 μm.

Therefore, it appeared that a combination of both adhesion and, spreading, and migration peptides is better than individual peptide at promoting and supporting endothelialization of PTFE films. Although CGRGDS was not markedly better than CRGD at enhancing HUVECs adhesion, in the presence of CWQPPRARI, CGRGDS was more effective than CRGD for endothelialization of PTFE. In addition, our data clearly demonstrated that micropatterning CWQPPRARI and CGRGDS side by side on the polymer surface rather than coconjugating them led to an improvement of the HUVEC migration and spreading after 72 h.

CONCLUSIONS

In this study, PTFE surfaces were covalently conjugated with various peptides containing RGD and WQPPRARI sequences which were selected for their adhesive, spreading, and migration properties toward endothelial cells. Our data indicate that the initial cell adhesion does not depend on the chemical structure and combination of the peptides covalently bonded to the PTFE surface either through conventional in-solution conjugation or through the micropatterning printing technique. Despite these initial adhesion results, our data clearly indicate that spreading and migration of endothelial cells are enhanced while coconjugating RGD-type peptide and WQPPRARI peptides. Outstanding results for adhesion, spreading, and migration of endothelial cells on the modified PTFE surface were obtained with the combination of GRGDS and WQPPRARI. This behavior was further improved by micropatterning these peptides on specific areas of the polymer surface.

ACKNOWLEDGMENT

Special thanks to Dr. Pascale Chevallier for XPS analyses, Richard Janvier for technical assistance with HUVEC culture, Dr. Stephane Turgeon for multidisciplinary technical assistance, and Louis Gagné for undergraduate work. We would also like to extend our gratitude to Dr. Madeleine Carreau for providing the microscope facilities and Dr. René C.-Gaudreault for advice and providing the HUVECs. We kindly acknowledge Gilles Brassard from ARC/PreciJet for excellent advice concerning printers and cartridges, as well as providing some cartridges. Finally, special thanks to Nicolas Dubé for computer engineering support and numerous advice. We acknowledge grants from the National Science and Engineering Research Council (NSERC) of Canada and the Fonds pour la Recherche en Santé du Québec (FRSQ) (G.L). V. Gauvreau acknowledges a graduate scholarship from NSERC.

LITERATURE CITED

(1) Hynes, R. O. (1992). Integrins: versatility, modulation, and signaling in cell adhesion. *Cell*. *69*, 11−25.

(2) Sipehia, R. (1993). Enhanced attachment and growth of human endothelial cells derived from umbilical veins on ammonia plasma modified surfaces on PTFE and ePTFE synthetic vascular graft biomaterials. *Biomater. Artif. Cells Immobilization Biotechnol. 21*, 455−468.

(3) Dekker, A., Reitsma, K., Beugeling, T., Bantjes, A., Feijen, J., and van Aken, W. G. (1991). Adhesion of endothelial cells and adsorption of serum proteins on gas plasma-treated polytetrafluoroethylene. *Biomaterials 12*, 130−138.

(4) Massia, S. P., and Hubbell, J. A. (1991). Human endothelial cell interactions with surface-coupled adhesion peptides on a nonadhesive glass substrate and two polymeric biomaterials. *J. Biomed. Mater. Res. 25*, 223−42.

(5) Ramires, P. A., Mirenghi, L., Romano, A. R., Palumbo, F., and Nicolardi, G. (2000). Plasma-treated PET surfaces improve the biocompatibility of human endothelial cells. *J. Biomed. Mater. Res. 51*, 535−539.

(6) Koenig, A. L., Gambillara, V., and Grainger, D. W. (2003). Correlating fibronectin adsorption with endothelial cell adhesion and signaling on polymer substrates. *J. Biomed. Mater. Res*. *64A*, 20−37.

(7) Klueh, U., Goralnick, S., Bryers, J. D., and Kreutzer, D. L. (2001). Binding and orientation of fibronectin on surfaces with collagen-related peptides. *J. Biomed. Mater. Res. 56*, 307−323.

(8) Kowalczynska, H. M., Nowak-Wyrzykowska, M., Dobkowski, J., Kolos, R., Kaminski, J., Makowska-Cynka, A., and Marciniak, E. (2002). Adsorption characteristics of human plasma fibronectin in relationship to cell adhesion. *J. Biomed. Mater. Res. 61*, 260−269.

(9) Reinhart-King, C. A., Dembo, M., and Hammer, D. A. (2003). Endothelial cell traction forces on RGD-derivatized polyacrylamide substrata. *Langmuir 19*, 1573−1579.

(10) Maheshwari, G., Brown, G., Lauffenburger, D. A., Wells, A., and Griffith, L. G. (2000). Cell adhesion and motility depend on nanoscale RGD clustering. *J. Cell Sci. 113*, 1677−1686.

(11) Salacinski, H. J., Punshon, G., Krijgsman, B., Hamilton, G., and Seifalian, A. M. (2001). A Hybrid Compliant Vascular Graft Seeded with Microvascular Endothelial Cells Extracted from Human Omentum. *Artif. Organs 25*, p 974−982.

(12) Tiwari A, Punshon, S. H., Hamilton G., and Seifalian A. M. (2002). Development of a hybrid cardiovascular graft using a tissue engineering approach. *FASEB J. 16,* 791−796.

(13) Massia, S. P., and Stark, J. Immobilized RGD peptides on surface-grafted dextran promote biospecific cell attachment. (2001). *J. Biomed. Mater. Res. 56*, 390−399.

(14) Porte-Durrieu, M. C., Labrugere, C., Villars, F., Lefebvre, F., Dutoya, S., Guette, A., Bordenave, L., and Baquey, C. (1999). Development of RGD peptides grafted onto silica surfaces: XPS characterization and human endothelial cell interactions. *J. Biomed. Mater. Res. 46*, 368−375.

(15) Plow, E. F., Haas, T. A., Zhang, L., Loftus, J., and Smith, J. W. Ligand binding to integrins. (2000). *J. Biol. Chem. 275,* 21785−21788.

(16) MacAlear, J., and Wehrung, J. (1978). Microsubstrate and method for making micropattern devices. US Patent 4,103,-073.

(17) MacAlear, J., and Wehrung, J. (1978). Microdevice substrate and method for making micropattern devices. US Patent 4,103,064.

(18) Blawas, A. S., and Reichert, W. M. Protein patterning. (1998). *Biomaterials 19*, 595−609.

(19) Lin, J. N., Andrade, J. D., and Chang, I. N. (1989). The influence of adsorption of native and modified antibodies on their activity. *J. Immunol. Methods 125*, 67−77.

(20) Soderquist, M. E., and Walton, A. G. (1980). Structural changes in proteins adsorbed on polymer surfaces. *J. Colloid Interface Sci. 75*, 386-397.

(21) Norde, W., and Lyklema, J. (1991). Why proteins prefer interfaces. *J. Biomater. Sci. Polym. Ed. 2*, 183−202.

(22) Weetall, H. H. (1993). Preparation of immobilized proteins covalently coupled through silane coupling agents to inorganic supports. *Appl. Biochem. Biotechnol. 41*, 158−188.

(23) Park, J. P., Lee, S. J., Park, T. J., Lee, K.-B., Choi, I. S., Lee, S. Y., Kim, M.-G., and Chung, B. H. (2004). Microcontact printing of biotin for selective immobilization of streptavidin-fused proteins and SPR analysis. *Biotechnol. Bioprocess Eng. 9*, 137−142.

(24) Mooradian, D. L., McCarthy, J. B., Skubitz, A. P., Cameron, J. D., and Furcht, L. T. (1993). Characterization of FN−C/H−V, a novel synthetic peptide from fibronectin that promotes rabbit corneal epithelial cell adhesion, spreading, and motility. *Investig. Ophthalmol. Vis. Sci. 34*, 153−164.

(25) Huebsch, J. C., McCarthy, J. B., Diglio, C. A., and Mooradian, D. L. (1995). Endothelial cell interactions with synthetic peptides from the carboxyl-terminal heparin-binding domains of fibronectin. *Circ. Res. 77,* 43−53.

(26) Chevallier, P., Castonguay, M., Turgeon, S., Dubrulle, N., Mantovani, D., McBreen, P. H., Wittmann, J. C., and Laroche, G. (2001). Ammonia RF−Plasma on PTFE Surfaces: Chemical Characterization of the Species Created on the Surface by Vapor-Phase Chemical Derivatization. *J. Phys. Chem. B 105*, 12490−12497.

(27) Mantovani, D., Castonguay, M., Pageau, J. F., Fiset, M., and Laroche, G. (1999). Ammonia RF-plasma treatment of tubular ePTFE vascular prostheses. *Plasmas Polym. 4*, 207−228.

(28) Gauvreau, V., Chevallier, P., Vallières, K., Petitclerc, É., C.-Gaudreault, R., and Laroche, G. (2004). Engineering Surfaces for Bioconjugation: Developing Strategies and Quantifying the Extent of the Reactions. *Bioconjugate Chem. 15*, 1146−1156.

(29) Hermanson, G. T., *Bioconjugate Techniques*. (1996), San Diego: Academic Press. 785.
(30) Stever, S. (2002). *The Illustrator 10 Wow! Book*, p 407, Peachpit Press, Berkeley.
(31) Okamoto, T., Suzuki, T., and Yamamoto, N. (2000). Microarray fabrication with covalent attachment of DNA using bubble jet technology. *Nature Biotechnol. 18,* 438−441.
(32) Allain, L. R., Askari, M., Stokes, D. L., and Vo-Dinh, T. (2001). Microarray sampling-platform fabrication using bubble-jet technology for a biochip system. *Fresenius J. Anal. Chem. 371,* 146−150.
(33) Roda, A., Guardigli, M., Russo, C., Pasini, P., and Baraldini, M. (2000). Protein microdeposition using a conventional ink-jet printer. *BioTechniques 28,* 492−496.
(34) Fussell, G. W., and Cooper, S. L. (2004). Endothelial cell adhesion on RGD-containing methacrylate terpolymers. *J. Biomed. Mater. Res. 70A,* 265−273.
(35) Pfaff, M., McLane, M., Beviglia, L., Niewiarowski, S., and Timpl, R. (1994). Comparison of disintegrins with limited variation in the RGD loop in their binding to purified integrins alpha IIb beta 3, alpha V beta 3 and alpha 5 beta 1 and in cell adhesion inhibition. *Cell Adhes. Commun. 2,* 491−501.
(36) Flusberg, D. A., Numaguchi, Y., and Ingber, D. E. (2001). Cooperative control of Akt phosphorylation, bcl-2 expression, and apoptosis by cytoskeletal microfilaments and microtubules in capillary endothelial cells. *Mol. Biol. Cell 12,* 3087−3094.
(37) Ingber, D. E. (2002). Mechanical Signaling and the Cellular Response to Extracellular Matrix in Angiogenesis and Cardiovascular Physiology. *Circ. Res. 91*, 877−887.
(38) Ingber, D. E. (2003). Tensegrity II. How structural networks influence cellular information processing networks. *J. Cell Sci. 116*, 1397−1408.
(39) Chen, C. S., Mrksich, M., Huang, S., Whitesides, G. M., and Ingber, D. E. (1997). Geometric control of cell life and death. *Science 276*, 1425−1428.
(40) Woods, A., McCarthy, J. B., Furcht, L. T., and Couchman, J. R. (1993). A synthetic peptide from the COOH-terminal heparin-binding domain of fibronectin promotes focal adhesion formation. *Mol. Biol. Cell. 4*, 605−613.
(41) Chen, C. S., Mrksich, M., Huang, S., Whitesides, G. M., and Ingber, D. E. (1998). Micropatterned surfaces for control of cell shape, position, and function. *Biotechnol. Prog. 14*, 356−363.
(42) Irvine, D. J., Mayes, A. M., and Griffith, L. G. (2001). Nanoscale clustering of RGD peptides at surfaces using Comb polymers. 1. Synthesis and characterization of Comb thin films. *Biomacromolecules 2,* 85−94.
(43) Lin, H. B., Sun, W., Mosher, D. F., Garcia-Echeverria, C., Schaufelberger, K., Lelkes, P. I., and Cooper, S. L. (1994). Synthesis, surface, and cell-adhesion properties of polyurethanes containing covalently grafted RGD-peptides. *J. Biomed. Mater. Res. 28*, 329−342.
(44) Harrison, D., Johnson, R., Tucci, M., Puckett, A., Tsao, A., Hughes, J., and Benghuzzi, H. (1997). Interaction of cells with UHMWPE impregnated with the bioactive peptides RGD, RGE or Poly-L-lysine. *Biomed. Sci. Instrum. 34*, 41−46.

BC049717S

Affinity Enhancement Bivalent Morpholinos for Pretargeting: Surface Plasmon Resonance Studies of Molecular Dimensions

Jiang He,* Xinrong Liu, Surong Zhang, Guozheng Liu, and Donald J. Hnatowich

Division of Nuclear Medicine, Department of Radiology, University of Massachusetts Medical School, 55 Lake Avenue North, Worcester, Massachusetts 01655. Received March 4, 2005; Revised Manuscript Received July 18, 2005

Bivalent effectors have been reported to provide superior pretargeting by affinity enhancement. We recently reported that one bivalent MORF (phosphorodiamidate morpholino, a DNA analogue oligomer) exhibited affinity enhancement (ratio of bivalent to monovalent equilibrium constants for binding) to immobilized complementary DNA (cDNA) by surface plasmon resonance (SPR). Because bivalent effectors using oligomers are easily synthesized with molecular spacing between binding sites, an important determinant of binding, adjustable simply by selecting linkers of different dimensions and/or lengthening or shortening the oligomer chain length, they may have advantages over existing bivalent effectors. We synthesized four bivalent MORFs with different dimensions between binding sites and measured binding affinities and affinity enhancement by SPR. An 18 mer (MORF18) was made bivalent by dimerizing both with disuccinimidyl suberate (DSS) and disuccinimidyl glutarate (DSG) linkers. By again using DSS but adding seven nonbinding adenine bases and by eliminating six binding bases, a total of four bivalent effectors, DSS-MORF12, DSG-MORF18, DSS-MORF18, and DSS-MORF25, were prepared with two different hybridization affinities (i.e. MORF12 and MORF18/25) and three different spacings (i.e. 20, 25, and 100 Å) between binding sites. The biotinylated cDNA was immobilized on a sensor chip at 500 and 100 RU coating densities providing an average cDNA separation of 25 and 80 Å. As expected, bimolecular binding dominated monomolecular binding in all cases, especially at lower MORF effector concentrations and at higher coating densities. All bivalent MORFs showed equilibrium constants superior to their monovalent form and therefore affinity enhancement. DSS-MORF25 showed the highest equilibrium constant for bimolecular binding presumably because of its larger separation between binding sites. Nevertheless, DSS-MORF12 showed the largest affinity enhancement of almost 3 orders of magnitude presumably because the shorter chain lowered the equilibrium constant for monomolecular binding. We have shown that bivalent effectors may be easily synthesized using MORF. The results provide further evidence that the use of bivalent effectors can greatly improve MORF pretargeting and, finally, that bivalent MORFs with reduced equilibrium constants may actually exhibit higher affinity enhancement.

INTRODUCTION

Pretargeting has been intensively studied for tumor imaging and therapy (*1*–*4*). Two pretargeting methods have entered clinical trials using either bispecific antibodies with specificity for both tumor antigens and a radiolabeled effector or several avidin/streptavidin–biotin recognition systems (*5*–*8*). The success claimed for the former approach has been attributed in large part to affinity enhancement resulting from the bridging of two antibodies on the tumor surface by the radiolabeled bivalent effector (i.e. "affinity enhancement system" or AES). The bivalent effectors used successfully include Ac-Lys(In-DTPA)-Tyr-Lys(In-DTPA)-Lys(TscG-Cys-)-NH_2 (*7*, *9*), Janus bivalent hapten (*10*), pGlu-Leu-Tyr-Glu-Asn-Lys(DTPA)-Pro-Arg-Arg-Pro-Tyr-Ile-Leu and DTPA-Gly-Glu-Leu-Tyr-Glu-Asn-Lys(Ac)-Pro-Arg-Arg-Pro-Tyr-Ile-Leu (DTPA-Gly-NT) (*11*), and Ac-Phe-Lys(-DTPA)-Tyr-Lys(DTPA)-NH_2 (*12*) and have been variously radiolabeled with ^{99m}Tc, ^{188}Re, ^{125}I, ^{131}I, ^{111}In, and most recently ^{68}Ga for radioimmunodetection and radiotherapy in tumor animal models (*7*, *13*–*16*). One observation from these investigations has been the importance of molecular spacing between binding sites. It may be estimated that about 25 Å between the binding sites has been successfully used previously (*12*). Furthermore, a recent publication has shown that a bivalent receptor binding agent showed a 200-fold increase in affinity as the spacer between binding sites varied from 4 to 20 carbon atoms (i.e. 5–25 Å) (*17*). This laboratory has previously reported encouraging results in tumored mice with pretargeting but using DNA and its analogues (collectively: oligomers) in which an antitumor antibody conjugated with an oligomer, currently a phosphorodiamidate morpholino (MORF), serves as the first injection while the radiolabel is administered later on the complementary oligomer, currently a complementary MORF (i.e. cMORF), as effector (*18*–*21*).

One advantage of using oligomers for pretargeting is the ease with which bivalent effectors for affinity enhancement pretargeting may be constructed and the ease with which the molecular dimension separating the binding sites may be shortened or elongated. In a previous paper (*22*), we reported initial observations of affinity enhancement. We now describe further evaluations by surface plasmon resonance (SPR) of the influence of spacing, effector concentration, coating density, and oligomer chain length on affinity enhancement. Bivalent MORFs were synthesized with molecular dimension varied either by attaching linkers of different dimension or by elongating or shortening the oligomer chain.

* To whom correspondence should be addressed. Phone: 508-856-2187. Fax: 508-856-4572. E-mail: jiang.he@umassmed.edu.

10.1021/bc050061s CCC: $30.25 © 2005 American Chemical Society
Published on Web 09/01/2005

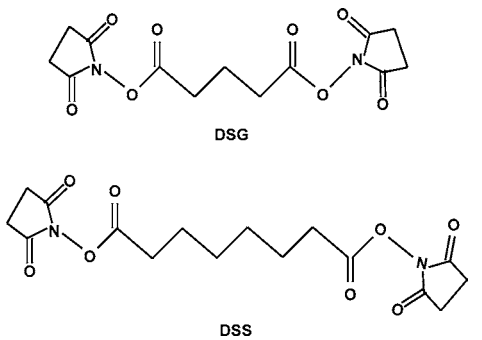

Figure 1. Molecular structures of DSS and DSG.

Specifically, an 18 mer amino-derivitized MORF (i.e. MORF18) was made bivalent by dimerizing both with disuccinimidyl suberate (DSS) and disuccinimidyl glutarate (DSG) linkers. Again using DSS as linker, the bivalent MORF was further elongated by adding seven bases (all adenines and therefore not participating in hybridization). Thus DSG-MORF18, DSS-MORF18, and DSS-MORF25 were prepared with 20, 25, and 100 Å between binding sites. Investigations of these three bivalent MORFs suggested that further improvements might result from reducing the number of hybridizing bases by subtracting six bases. Therefore, by again using DSS as linker, DSS-MORF12 was synthesized with 25 Å between binding sites but with a lower binding affinity by virtue of fewer bases. SPR was used to measure the affinity (i.e. equilibrium constant) for bivalent and monovalent binding of each of the four MORFs and affinity enhancement defined as the ratio of equilibrium constants of the bivalent over the corresponding monovalent MORF. To measure these properties, a biotinylated cDNA was immobilized on a sensor chip at two densities and the hybridization properties of bivalent and monovalent MORFs were measured.

MATERIALS AND METHODS

All MORFs and cMORFs [collectively: (c)MORF] were purchased prepurified with amine modification on the 3′ equivalent end (Gene-Tools, Corvallis, OR) and were used as received. The MORF linker of this investigation was $C(O)OCH_2C_6H_4CH_2NH_2$ except in the case of MORF25 in which only the $C(O)CH_2CH_2NH_2$ linker was supplied by the manufacturer. Because of the longer dimensions of the bivalent MORF25s, the 7−8 Å difference in linker dimensions is immaterial. Biotinylated (c)DNA having the same sequences as the (c)MORF were purchased from Qiagen Inc. (Valencia, CA) and were also used as received. Biotinylated (c)DNAs were obtained with a flexible tetra(ethylene glycol) (TEG) linker of about 26 Å in length. Disuccinimidyl suberate (DSS) and disuccinimidyl glutarate (DSG) were purchased from Pierce (Rockford, IL) while anhydrous dimethylformamide (DMF), *N*-methyl-2-pyrrodinone (NMP), and diisopropylethylamine (DIEA) were from Sigma-Aldrich (St Louis, MO). All other chemicals were reagent grade and were used without purification. The DSS-MORF18 used in this investigation is identical to the bivalent MORF used previously by this laboratory (*22*).

Synthesis of Bivalent MORF. The structures of DSS and DSG linkers are shown in Figure 1. When the bivalent MORF is prepared by the attachment of one MORF to each end of the linker, the DSG linker adds about 20 Å to the overall length of the bivalent MORF while the DSS linker adds about 25 Å. The preparation of bivalent MORFs was as previously described (*22*). Typically, about 1.5 mg (0.25 μmol) of amine-derivitized MORF was dissolved in 1.0 mL of 1-methyl-2-pyrrolidinone (NMP). A 0.125 μmol amount of DSS or DSG in NMP solution at 2 mg/mL was added, followed by 0.66 μmol of *N*,*N*-diisopropylethylamine (DIEA). This mixture was incubated at room temperature for 2 d. The bivalent MORF was purified by Q Sepharose ion exchange (IE) HPLC. The collected fractions of bivalent MORFs were passed through a PD-10 column in 50 mM phosphate buffer. The molecular weight of the product was confirmed by MALDI-TOF before storage at freezer temperatures for future use. The spacings between the two binding regions are about 20, 25, and 100 Å for DSG-MORF18, DSS-MORF18, and DSS-MOR25, respectively.

The average distance between binding sites of the immobilized cDNA on the sensor chip may be estimated using the manufacturer's value of 10000 pg streptavidin/mm^2 on the SA chip (i.e. 1.66×10^{-13} mol streptavidin/mm^2). Since the sensorgram response is directly related to the concentration bound, it may be estimated that saturating the streptavidin coating with cDNA would provide a response of about 4000 RU (response units). From this a density of about 99×10^{-12} mm^2/DNA and 19.8×10^{-12} mm^2/DNA can be estimated for a coating density of 100 RU and 500 RU. Therefore, the distance between the attachment of two neighboring cDNAs would be 80 Å and 25 Å for 100 RU and 500 RU, respectively. However, since the nonbinding regions of each immobilized cDNA is estimated to be about 26 Å and the immobilized cDNAs are capable of free rotation about their tether, with the exception of the shortest bivalent (DSG-MORF18) at the lowest cDNA density, all bivalent MORFs of this investigations were capable of bridging cDNAs at both densities.

Chromatography. Ion exchange chromatography was used to purify the bivalent from unreacted monovalent MORFs as previously described (*22*), taking advantage of the fact that tyrosine bases will be negatively charged at pH 12. Ion exchange (IE) HPLC was performed using a HiTrap Q HP column (Amersham Biosciences, Uppsala, Sweden) with 0.01 N NaOH (solvent A) and 0.01 N NaOH in 2 N NaCl (solvent B) at a flow rate of 1.0 mL/min, going from 100% A to 70% A over 30 min. Before each analysis, the column was stabilized with 0.01 N NaOH and after each analysis the column was cleaned with solvent B. For small scale preparative purification, samples were loaded on the column by several injections in running solvent A but without exceeding the column's maximum binding capability. The bivalent MORF was collected in fractions during the gradient elution.

Surface Plasmon Resonance Measurements. SPR was performed on a BIAcore 2000 (BIAcore, Piscataway, NJ) instrument operating at room temperature as previously described (*22*). As before, (c)DNAs rather than (c)-MORFs were immobilized because of earlier difficulties in immobilizing biotinylated (c)MORFs. Biotinylated (c)-DNA at 20 nM was added in 5−10 μL aliquots to a new streptavidin−dextran-coated sensor chip (SA) at a flow rate of 20 μL/min only until a response of about 100 (±10) or 500 (±30) RU was reached. The absence of mass transfer effects was confirmed by running separately one concentration of free MORF at three different flow rates (10, 30, and 75 μL/min) and demonstrating identical response and curve shape for all three sensorgrams. When the identical measurement was performed on a sensor chip to which cDNA was added to a response of 750 RU, evidence of mass transfer effects was observed and accordingly this chip was not used in subsequent studies. Solutions of free monovalent and bivalent MORFs

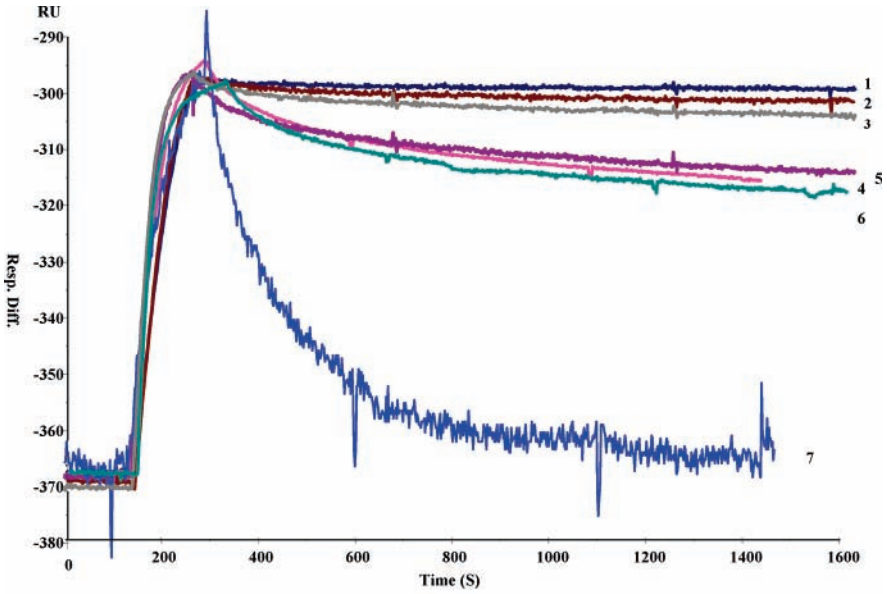

1. DSS-MORF25; 2.DSS-MORF18; 3.DSG-MORF18; 4. DSS-MORF12; 5.MORF18; 6.MORF25; 7.MORF12

Figure 2. Normalized sensorgrams showing similar association kinetics but strikingly different dissociation kinetics for DSS-MORF25 (trace 1), DSS-MORF18 (trace 2), DSG-MORF18 (trace 3), DSS-MORF12 (trace 4), MORF18 (trace 5), MORF25 (trace 6), and MORF12 (trace 7). Obtained at 10 nM concentration and at 100 RU coating density.

Table 1. Properties of Bivalent MORFs (base sequences of native MORFs, MW calculated, MW found)

bivalent MORF	MORF sequence	MW expected (found ± SD), Da
DSG-MORF18	TCTTCTACTTCACAACTA	12424 (12397± 27)
DSS-MORF18	TCTTCTACTTCACAACTA	12466 (12474± 8)
DSS-MORF25	TCTTCTACTTCACAACTA-AAAAAAA	17034 (16998± 36)
DSS-MORF12	TCTTCTACTTCA	8508 (8498± 10)

were prepared at six concentrations of MORF from 0.0 to 40 nM in the same running buffer (10 mM HEPES, 150 mM NaCl, 3.4 mM Na_2EDTA, 0.005% P20, pH 7.4) and injected separately onto the active (cDNA) or control (DNA) surface at a flow rate of 30 μL/min to minimize the mass transfer effect. The chip surface was regenerated by injection of 100 mM HCl. To correct for nonspecific binding and refractive index changes, the control responses were subtracted from those obtained from the active surface. A minor baseline drift resulting from a slow dissociation of the complex on the active and control surfaces was eliminated by also subtracting sensorgrams obtained following the injection of running buffer (*23*).

In the first series of experiments, samples of monovalent MORFs (MORF18 and MORF25) and bivalent MORFs (DSS-MORF18, DSG-MORF18, DSS-MORF25) were run at six concentrations on both the 100 and 500 RU chips and with a dissociation time of only 25 min. In the second series of experiments, all six concentrations were again run but with dissociation time of 1 h to obtain more accurate values for the dissociation rate constants. In the third series of experiments, the monovalent MORF12 and bivalent DSS-MORF12 were run at the six concentrations on both 100RU and 500RU chips for 25 min. In every case, the measurement was repeated four times and, as mentioned above, each sample was run on both the cDNA and DNA chips at the same surface density so that results with the latter could be used to correct for bulk refractive index changes (*23*).

Sensorgram Kinetic Analysis. Sensorgram curves were evaluated using numerical integration algorithms (BIAevaluation 3.0, BIAcore, Piscataway, NJ). The algorithm may be programmed for simple monomolecular 1:1 Langmuir interactions of a monovalent effector (A) or for a bivalent effector (AA) binding monomolecularly (i.e. A+L→AL where A is the effector, in this case MORF, and L is immobilized ligand, in this case cDNA) or binding bimolecularly (i.e. AA+L→AAL and AAL+L→LAAL). In addition, the algorithm may be programmed to analyze globally (i.e. all effector concentrations considered together to provide one value for each of the two rate constants, association and dissociation) or locally (i.e. each effector concentration considered separately to provide one value for each of the two rate constants for each effector concentration). An added complication in the case of bivalent effector binding is the possibility that the binding may be both monomolecular and bimolecular and thus cannot be accurately modeled. To emphasis this fact, the rate constants in this report for bivalent MORFs are referred to as "apparent". While different model and fitting methods were used by us previously, in this study, the simple monomolecular 1:1 Langmuir interaction model was used to compare the four bivalent MORFs with their corresponding monovalent form. It should be noted that in each comparison, the concentrations were adjusted to the same molarity of effector and therefore the MORF molarity of the bivalent effector was twice that of the monovalent effector. Finally, the program provides for each analysis a Chi2 (χ^2) value that is a statistical measure of how closely the model fits the experimental data. In general, χ^2 values lower than about 10 signify a good fit.

RESULTS

Synthesis of Bivalent MORF. The amine derivatized MORFs were dimerized with DSS or DSG for 2 days in the presence of NMP and DIEA followed by purification by ion exchange chromatography. Changing from alkaline solution to phosphate buffer or water was performed on a PD-10 column. The correct structure of all four bivalent MORFs was confirmed by MALDI-TOF MS as shown in Table 1.

Surface Plasmon Resonance Measurements. The SPR measurements were performed at both cDNA surface densities of 100 and 500 RUs and at six concentrations of the monovalent and bivalent MORFs in the concentration range from 0 to 40 nM. Figure 2 presents

Table 2. Kinetics Rate Constants and Equilibrium Constants for Monovalent MORF12, MORF18, and MORF25 and the Apparent Kinetic Rate Constants and Equilibrium Constants for the Corresponding Bivalent MORFs Obtained at Both CDNA Surface Densities[a]

density	cDNA effectors	k_a (1/Ms) × 10^5	kd (1/s) × 10^{-5}	K_{equ} (1/M) × 10^{10}	χ^2	affinity enhancement
100RU	DSG-MORF18	1.15 (0.2)	6.25 (0.29)	0.18 (0.03)	6.7	1.6
	DSS-MORF18	8.10 (2.1)	4.85 (0.57)	1.67 (0.29)	5.1	15
	DSS-MORF25	6.25 (3.6)	2.97 (0.31)	2.10 (0.13)	3.6	22
	DSS-MORF12	3.31 (1.32)	13.5 (0.69)	0.246 (0.16)	7.9	502
	MORF12	0.206 (0.02)	419 (38.7)	0.00049	0.93	
	MORF18	2.62 (0.19)	24 (3.4)	0.11 (0.02)	6.1	
	MORF25	1.89 (0.13)	20 (2.6)	0.095 (0.02)	7.8	
500RU	DSG-MORF18	2.78 (0.41)	1.18 (0.38)	2.36 (0.35)	14	24
	DSS-MORF18	13.7 (3.56)	3.55 (0.47)	3.87 (0.61)	25	39
	DSS-MORF25	5.54 (1.74)	0.98 (0.16)	5.68 (0.72)	9.5	52
	DSS-MORF12	12.86 (4.6)	26.2 (0.43)	0.477 (0.13)	1.7	1036
	MORF12	0.38 (0.04)	826 (77)	0.00046	1.2	
	MORF18	4.80 (0.23)	48 (5.1)	0.10 (0.02)	2.01	
	MORF25	3.31 (0.21)	31 (4.2)	0.11 (0.01)	4.9	

[a] Analysis by global fitting using the 1:1 Langmuir interaction model. k_a: association rate constant; k_d: dissociation rate constant; K_{equ}: equilibrium constant; X^2: index for goodness of fit. Standard deviations in parentheses.

normalized sensograms of the four bivalent and the three monovalent MORFs at 10 nM concentration and at 100 RU cDNA coating density. The sensorgram of all seven MORFs have been overlayed to illustrate the striking differences in dissociation rate. Among the bivalent MORFs, the order of increased stability to dissociation is DSSMORF25 > DSSMORF18 > DSGMORF18 > DSSMORF12. Among the monovalent MORFs, this order is MORF25 ~ MORF18 ≫ MORF12 (there should be no significant difference between MORF25 and MORF18 since they have the same binding region in this study). Furthermore the bivalent MORF12 exhibited stability comparable to that of the larger monovalent MORF25. Finally, except for this similarity, all bivalent MORFs showed increased stability over all monovalent MORFs. The kinetic rate constants and equilibrium constants for monovalent MORF12, MORF18, and MORF25 and the apparent kinetic rate constants and equilibrium constants for the corresponding bivalent DSG-MORF18, DSS-MORF18, DSS-MORF25, and DSS-MORF12 obtained at both cDNA surface densities are presented in Table 2. Analysis was by global fitting using the simpler 1:1 Langmuir interaction algorithm. Included in the table are the ratios of affinity constants for bivalent over corresponding monovalent binding at both cDNA densities. As shown, the equilibrium constants for the three monovalent MORFs binding are little changed between cDNA densities. Figure 3 presented sensorgrams obtained at 5 nM for the bivalent and monovalent MORF12s only. At both surface densities, the bivalent MORF12 shows a profoundly higher association and lower dissociation phase and therefore a significantly improved equilibrium constant due to bimolecular binding.

Considering first only DSG-MORF18, DSS-MORF18, and DSS-MORF25, although these three bivalent MORFs possess the same binding region, they show statistically significantly ($p < 0.04$) different affinity enhancement presumably as a result of the different molecular dimension. As shown in the table, at low cDNA coating density of 100 RU, both DSS-linked MORFs show affinity enhancements of about 20-fold compared to about 2 for the shorter DSG-MORF18. This result could be predicted on the basis of molecular dimensions. At the lowest 100 RU coating density, the separation between attached cDNAs is estimated to be about 80 Å. The maximum radius of each cDNA when fully extended is about 26 Å, leaving a gap of about 28 Å. Because of its longer 25 Å length, bivalent MORFs attached with the DSS linker are capable of bridging this gap. By contrast, bivalent MORFs attached via the 20 Å DSG linker are too short and therefore are capable only of monovalent binding with the result that affinity enhancement is prevented. However, at high coating density, all three sets of bivalent MORFs showed superior K_{equ} with the highest improvement of 40−50-fold for DSS-MORF18 and DSS-MORF25. These results are reasonable since high coating densities should favor bivalent binding of the bivalent MORFs. Only in the case of low coating density and the bivalent MORF with the shortest linker, DSG-MORF18, was the enhancement minimal over the monovalent MORF.

Furthermore, the bivalent MORF12 showed much higher association rate constants along with lower dissociation rate constant both at 100 RU or 500 RU cDNA coating density compared with monovalent MORF12 to provide equilibrium constants 500 to1000-fold higher (i.e. 500 to1000 higher affinity enhancement) at both cDNA densities. The striking affinity enhancement due to bimolecular binding in the case of bivalent MORF is clearly seen in Figure 3 by comparison of sensorgrams with the monovalent MORF12 at both coating densities. Sensorgrams of DSS-MORF12 show greater response in association phase at each concentration (data not presented). Furthermore, the dissociation of monovalent MORF12 is essentially completed by about 1500 s while at this time DSS-MORF12 is still about 55% and 87% intact at 100 RU and 500 RU, respectively.

DISCUSSION

Earlier this laboratory reported that binding of one bivalent MORF to immobilized cDNA was bimolecular under the conditions of that study and, presumably as a result, exhibited a faster association rate and a slower dissociation rate and therefore a higher affinity constant and affinity enhancement. Since the probability of monomolecular binding (AAL) compared to bimolecular binding (LAAL) will depend on the molecular dimensions of the bivalent effector (in this case MORF) and the concentration (spacing) and flexibility of the ligand molecules (in this case cDNA) on the immobilized surface (*24*), in this present investigation, SPR was used to compare the behavior of four bivalent MORFs differing in the spacing between binding sites with their corresponding monovalent form during hybridization to immobilized cDNA at two densities

In general, low cDNA densities and higher MORF effector concentrations will favor monomolecular binding,

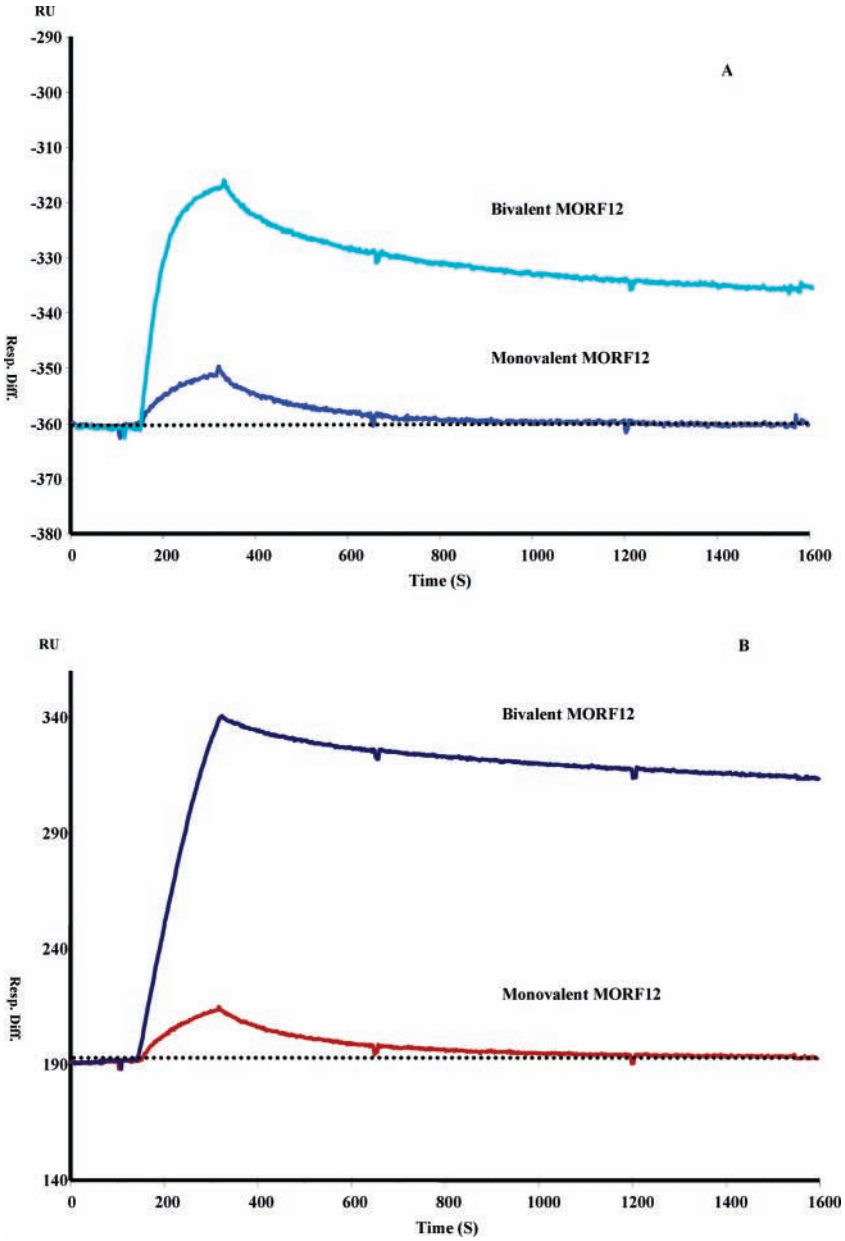

Figure 3. Sensorgrams obtained at 5 nM for the bivalent and monovalent MORF12 at 100RU (panel A) and 500RU (panel B) surface densities showing the significantly improved association and dissociation constant of the bivalent MORF12 due to bimolecular binding. The MORF concentrations of the bivalent MORF are twice the effector concentrations.

in the first instance because of the greater spacing between cDNAs (thus making more difficult bridging by the effector) and in the latter instance because the cDNAs are more likely to be saturated with MORF bound monomolecularly (since bimolecular binding is a two-step process initially requiring monomolecular binding). Therefore, six concentrations not exceeding 40 nM (to avoid monomolecular binding saturation) of all effectors and two coating densities of 100 RU and 500 RU were used in this investigation. As shown in Table 2, presumably because of its shorter spacing between binding sites, the bivalent DSG-MORF18 showed affinity enhancement at the 500 RU cDNA density but not at the lower 100 RU density. By contrast, the bivalent MORFs DSS-MORF18 and DSS-MORF25 with their longer spacing between binding sites showed comparably higher affinity enhancement compared to their corresponding monovalent MORF18 and MORF25 respectively at both densities.

It is important to point out that in the sensorgram analysis, quantitative evaluation was made difficult by the high cDNA densities required to achieve bimolecular binding. These high densities can result in mass transport effects and, furthermore, can complicate the analysis by permitting rebinding during dissociation. In this investigation it was possible to prevent mass transport complications by adjusting the flow rate to be in a range where the response was shown to be flow-rate-independent. However, it was not possible to eliminate rebinding effects especially in case of effectors with very high intrinsic affinities. Thus rebinding contributed partially to the resulting kinetic analysis. This was the case for monovalent MORF18, monovalent MORF25, and all bivalents due to their high affinity. Rebinding effects may be suspected when the dissociation rates are slower at lower effector concentrations compared to higher concentrations. Normally all concentrations should give the same affinity constants. At very low concentration as used in this investigation, the cDNA is not saturated at the high coating density and thus rebinding is possible. Under these conditions, the dissociation rates are slower

at low effector concentrations compared to higher concentrations. That the dissociation rate of monovalent 12 mer MORF at all six concentrations was identical even at the highest 500 RU density (data not presented) may imply little rebinding in the case of this effector. This result is presumably due to an intrinsic low affinity resulting from the shorter chain length. Therefore the "rebinding" (lower dissociation rate at lower concentration) for the bivalent 12 mer MORF (DSS-MORF12) must be due to the enhanced affinity from bimolecular binding. However, while rebinding will complicate accurate analysis of SPR results, it may favorably contribute to a longer retention of the effector in tumor.

The importance of selecting the proper molecular dimensions in oligomer effectors intended for affinity enhancement pretargeting rests in the promise of greatly improved target/nontarget ratios. A higher equilibrium constant for bimolecular binding over monomolecular binding (i.e. affinity enhancement) would favor dissociation and minimal binding in blood and other nontarget tissues because of the lower cMORF densities in these sites at the time of effector administration. One result of this investigation is the observation that higher affinity of binding (i.e. higher equilibrium constants) of effector does not necessarily translate into higher affinity enhancement. Since affinity enhancement is the ratio of equilibrium constants for bimolecular over monomolecular binding, a high equilibrium constant for monomolecular binding may reduce the ratio to insignificance. This is apparently the case for DSS-MORF18 and DSS-MORF25, both of which show higher equilibrium constants than DSS-MORF12 yet both show lower affinity enhancements.

CONCLUSION

As shown herein, the distance between binding sites in MORF effectors may be adjusted simply by changing the linker length and/or by elongating or shortening the base chain. These results also show that bimolecular binding was occurring in the case of the bivalent MORF by the higher equilibrium constants for the bivalent MORF compared to their corresponding monovalent form. Furthermore, these results also provide further evidence that bivalency may be superior to monovalency in MORF pretargeting applications in the affinity enhancement observed in all cases of bivalent MORF and cDNA densities. However, since affinity enhancement is the ratio of equilibrium constants for bimolecular over monomolecular binding, that the bivalent MORF derivatized from shorter chain effector (i.e., DSS-MORF12) showed the greatest affinity enhancement suggests that higher equilibrium constant and higher affinity enhancement may not be synonymous.

ACKNOWLEDGMENT

Financial support for this investigation was provided, in part, by the National Institutes of Health (CA 94994).

LITERATURE CITED

(1) Goodwin, D. A., Meares, C. F., McTigue, M., Mccall, M. J., and David, G. S. (1986) Rapid localization of haptens in sites containing previously administered antibody for immunoscintigraphy with short half-life tracers [abstract]. *J. Nucl. Med. 27*, 959.

(2) Chang, C., Sharkey, R. M., Rossi, E. A., Karacay, H., McBride, W., Hansen, H. J., Chatal, J., Barbet, J., and Goldenberg, D. M. (2002) Molecular advances in pretargeting radioimmunotherapy with bispecific antibodies. *Mol. Cancer Ther. 1*, 553−563.

(3) Hnatowich, D. J., Virzi, F., and Rusckowski, M. (1987) Investigations of avidin and biotin for imaging applications. *J. Nucl. Med. 28*, 1294−302.

(4) Kuijpers, W. H., Bos, E. S., Kaspersen, F. M., Veeneman, G. H., and van Boeckel, C. A. (1993) Specific recognition of antibody-oligonucleotide conjugates by radiolabeled antisense nucleotides: a novel approach for two-step radioimmunotherapy of cancer. *Bioconjugate Chem. 4*, 94−102.

(5) Hamblett, K. J., Kegley, B. B., Hamlin, D. K., Chyan, M. K., Hyre, D. E., Press, O. W., Wilbur, D. S., and Stayton, P. S. (2002) A streptavidin−biotin binding system that minimizes blocking by endogenous biotin. *Bioconjugate Chem. 13*, 588−598.

(6) Wilbur, D., Pathare, P. M., Hamlin, D. K., and Weerawarna, S. A. (1997) Biotin Reagents for Antibody Pretargeting. 2. Synthesis and in Vitro Evaluation of Biotin Dimers and Trimers for Cross-Linking of Streptavidin. *Bioconjugate Chem. 8*, 819−832.

(7) Karacay, H., McBride, W. J., Griffiths, G. L., Sharkey, R. M., Barbet, J., Hansen, H. J., and Goldenberg D. M. (2000) Experimental pretargeting studies of cancer with a humanized anti-CEA x murine anti-[In-DTPA] bispecific antibody construct and a 99mTc-/188Re-labeled peptide. *Bioconjugate Chem. 11*, 842−854.

(8) Gruaz-Guyon, A., Janevik-Ivanovska, E., Raguin, O., De Labriolle-Vaylet, C., and Barbet, J. (2001) Radiolabeled bivalent haptens for tumor immunodetection and radioimmunotherapy. *Q. J. Nucl. Med. 45*, 201−6.

(9) Cardillo, T. M., Karacay, H., Goldenberg, D. M., Yeldell, D., Chang, C. H., Modrak, D. E., Sharkey, R. M., and Gold D. V. (2004) Improved targeting of pancreatic cancer: experimental studies of a new bispecific antibody, pretargeting enhancement system for immunoscintigraphy. *Clin. Cancer Res. 10*, 3552−3561.

(10) Goodwin, D. A., Meares, C. F., McTigue, M., Chaovapong, W., Diamanti, C. I., Ransone, C. H., and McCall M. J. (1992) Pretargeted immunoscintigraphy: Effect of hapten valency on murine tumor uptake. *J. Nucl. Med. 33*, 2006−2013.

(11) Hillairet De Boisferon, M., Raguin, O., Thiercelin, C., Dussaillant, M., Rostene, W., Barbet, J., Pelegrin, A., and Gruaz-Guyon, A. (2002) Improved tumor selectivity of radiolabeled peptides by receptor and antigen dual targeting in the neurotensin receptor model. *Bioconjugate Chem. 13*, 654−662.

(12) Boerman, O. C., van Eerd, J., Oyen, W. J. G., and Corstens, F. H. M. (2001) A 3-Step Pretargeting Strategy to Image Infection. *J. Nucl. Med. 42*, 1405−1411.

(13) Barbet, J., Peltier, P., Bardet, S., Vuillez, J. P., Bachelot, I., Denet, S., Olivier, P., Leccia, F., Corcuff, B., Huglo, D., Proye, C., Rouvier, E., Meyer, P., and Chatal, J. F. (1998) Radioimmunodetection of medullary thyroid carcinoma using indium-111 bivalent hapten and anti-CEA x anti-DTPA-indium bispecific antibody. *J. Nucl. Med. 39*, 1172−1178.

(14) Gautherot, E., Rouvier, E., Daniel, L., Loucif, E., Bouhou, J., Manetti, C., Martin, M., Le Doussal, J. M., and Barbet, J. (2000) Pretargeted radioimmunotherapy of human colorectal xenografts with bispecific antibody and 131I-labeled bivalent hapten. *J. Nucl. Med. 41*, 480−487.

(15) Griffiths, G. L., Chang, C. H., McBride, W. J., Rossi, E. A., Sheerin, A., Tejada, G. R., Karacay, H., Sharkey, R. M., Horak, I. D., Hansen, H. J., Goldenberg, D. M. (2004) Reagents and methods for PET using bispecific antibody pretargeting and 68Ga-radiolabeled bivalent hapten-peptide-chelate conjugates. *J. Nucl. Med. 45*, 30−39.

(16) Hosono, M., Hosono, M. N., Kraeber-Bodere, F., Devys, A., Thedrez, P., Fiche, M., Gautherot, E., Barbet, J., and Chatal, J. F. (1998) Biodistribution and dosimolecular study in medullary thyroid cancer xenograft using bispecific antibody and iodine-125-labeled bivalent hapten. *J. Nucl. Med. 39*, 1608−1613.

(17) Sridhar, J., Wei, Z., Nowak, I., Lewin, N. E., Ayers, J. A., Pearce, L. V., Blumberg, P. M., and Kozilowski, A. P. (2003) New bivalent PKC ligands linked by a carbon spacer: Enhancement in binding affinity. *J. Med. Chem. 46*, 4196−4204.

(18) Mang'era, K. O., Liu, G., Wang, Y., Zhang, Y., Liu, N., Gupta, S., Rusckowski, M., and Hnatowich, D. J. (2001)

Initial investigations of 99mTc-labeled morpholinos for radiopharmaceutical applications. *Eur. J. Nucl. Med. 28*, 1682−1689.

(19) Liu, G., Mang'era, K., Liu, N., Gupta, S., Rusckowski, M., and Hnatowich, D. J. (2002) Tumor pretargeting in mice using 99mTc-labeled morpholino, a DNA analog. *J. Nucl. Med. 43*, 384−391.

(20) Liu, G., Liu, C., Zhang, S., He, J., Liu, N., Gupta, S., Rusckowski, M., and Hnatowich, D. J. (2003) Investigations of technetium-99m morpholino pretargeting in mice. *Nucl. Med. Commun. 24*, 697−705.

(21) He, J., Liu, G., Gupta, S., Zhang, Y., Rusckowski, M., and Hnatowich, D. J. (2004) Amplification targeting: a modified pretargeting approach with potential for signal amplification-proof of a concept. *J. Nucl. Med. 45*, 1087−1095.

(22) He, J., Liu, G., Vanderheyden, J.-L., Dou, S., Rusckowski, M., and Hnatowich, D. J. (2005) Affinity Enhancement Bivalent Morpholino for Pretargeting: Initial Evidence by Surface Plasmon Resonance. *Bioconjugate Chem. 16*, 338−345.

(23) He, J., Liu, G., Zhang, S., Vanderheyden, J.-L., Liu, N., Liu, C., Zhang, Y., Gupta, S., Rusckowski, M., and Hnatowich, D. J. (2003) A comparison of in vitro and in vivo stability in mice of two morpholino duplexes differing in chain length. *Bioconjugate Chem. 14*, 1018−1023.

(24) Muller, K. M., Arndt, K. M., and Pluckthun, A. (1998) Model and simulation of multivalent binding to fixed ligands. *Anal. Biochem. 261*, 149−158.

BC050061S

A Dielectric-Sensitive Fluorescent DNA Probe for Monitoring Polarities on the Interior of a DNA-Binding Protein

Akimitsu Okamoto,*,† Kazuki Tainaka,† and Isao Saito*,‡

Department of Synthetic Chemistry and Biological Chemistry, Faculty of Engineering, Kyoto University, Kyoto 615-8510, Japan, and NEWCAT Institute, School of Engineering, Nihon University, and SORST, Japan Science and Technology Agency, Tamura, Koriyama 963-8642, Japan. Received March 15, 2005; Revised Manuscript Received July 8, 2005

We report a novel fluorescent nucleobase, ^{DNC}U, for the mapping of the local dielectric properties around DNA. Fluorescence spectra of the nucleoside d^{DNC}U showed a significant shift depending on the solvent polarity. This property was used to determine the dielectric constants of the interior of DNA-binding proteins, such as DNA polymerases. We were able to demonstrate that the DNA-binding region of the Klenow fragment is a lower polarity site, as shown by the blue shift of the fluorescence peak originating from ^{DNC}U.

INTRODUCTION

Local variations in the structure and dynamics of biomolecules play important roles in mediating the interaction events between biomolecules, such as DNA-protein recognition. In particular, monitoring of the local dielectric property change in DNA is very important because the structures of DNA−protein complexes and their interactions are influenced by their local dielectric effects (*1*−*3*). For such a purpose, a fluorescent probe, which is incorporated site specifically into the DNA sequence of interest and is sensitive to the change of its local microenvironment, is highly desirable. The well-known fluorophore 6-(dimethylamino)-2-acylnaphthalene (DAN) and its derivatives are among the most promising candidates for such a dielectric-sensitive fluorescent probe, because they show a sensitive solvatofluorochromic behavior (*4*−*8*). In addition, DAN is free from the contribution of ionic interactions because it has no permanent charge. Recently, an alanine derivative of DAN, Aladan, was developed and incorporated site-selectively into buried and exposed sites using a nonsense suppression method (*9*). It was sensitive to the polarity of its surroundings. Thus, such DAN derivatives would also be useful as dielectric-sensitive fluorescence probes for examining the change in the polarity of the microenvironments of DNA surroundings and the DNA−protein interaction site. In particular, when the fluorophore is tethered to a nucleobase in oligodeoxynucleotide (ODN) probes via a rigid linker, the change in the dielectric properties at a specific site on the target sequences would be easily monitored.

Herein, we report a mapping of the dielectric nature of the microenvironment around DNA using a novel DAN family, 6-(dimethylamino)-2-naphthalenecarboxamide (DNC)-tethered 2′-deoxyuridine (^{DNC}U), which can be easily prepared via a short synthetic process. This fluorescent nucleoside offers high sensitivity toward the solvent polarity. A series of fluorescence spectra for ^{DNC}U-containing ODN showed a large shift, indicating a significant change in the dielectric constants of the microenvironment around ^{DNC}U. We also monitored the local dielectric properties of the DNA-binding region of DNA polymerase using the fluorescence change of ^{DNC}U-containing ODN.

EXPERIMENTAL PROCEDURES

General. ^{1}H NMR and ^{13}C NMR spectra were measured with Varian Mercury 400 spectrometer. Coupling constants (J value) are reported in hertz. The chemical shifts are shown in ppm downfield from tetramethylsilane, using residual chloroform (δ = 7.24 in ^{1}H NMR, δ = 77.0 in ^{13}C NMR), dimethyl sulfoxide (δ = 2.48 in ^{1}H NMR, δ = 39.5 in ^{13}C NMR), and methanol (δ = 3.30 in ^{1}H NMR) as an internal standard. Fast-atom bombardment (FAB) masses were recorded on a JEOL JMS HX-110A spectrometer.

The reagents for DNA synthesis were purchased from Glen Research. Masses of oligodeoxynucleotides were determined with a matrix-assisted laser desorption-ionization time-of-flight mass spectrometry (MALDI-TOF MS) (Perseptive Voyager Elite, acceleration voltage 21 kV, negative mode) with 2′,3′,4′-trihydroxyacetophenone as a matrix, using T_8 ([M − H]$^-$ 2370.61) and T_{17} ([M − H]$^-$ 5108.37) as internal standards for oligodeoxynucleotides. The Klenow fragment was purchased from Takara. Calf intestinal alkaline phosphatase (Promega), *Crotalus adamanteus* venom phosphodiesterase I (USB), and *Penicillium citrinum* nuclease P1 (Roche) were used for the enzymatic digestion of ODNs. All aqueous solutions utilized purified water (Millipore, Milli-Q sp UF). Reversed-phase high-performance liquid chromatography (HPLC) was performed on CHEMCOBOND 5-ODS−H columns (10 × 150 mm, 4.6 × 150 mm) with a Gilson Chromatograph, Model 305, using a UV detector, Model 118, at 254 nm.

6-Dimethyl-2-naphthoylpropargylamide (2). To a solution of 6-amino-2-naphthoic acid (**1**) (500 mg, 2.67 mmol) in methanol (20 mL) was added cyanoborohydride

* To whom correspondence may be addressed. Phone: (+81) 75-383-2755 (A.O.); (+81) 24-956-8911 (I.S.). Fax: (+81) 75-383-2759 (A.O.); (+81) 24-956-8924 (I.S.). E-mail: okamoto@sbchem.kyoto-u.ac.jp (A.O.); saito@mech.ce.nihon-u.ac.jp (I.S.).
† Kyoto University.
‡ Nihon University and Japan Science and Technology Agency.

10.1021/bc050077i CCC: $30.25 © 2005 American Chemical Society
Published on Web 09/01/2005

Scheme 1. Synthesis of ^{DNC}U-containing ODN[a]

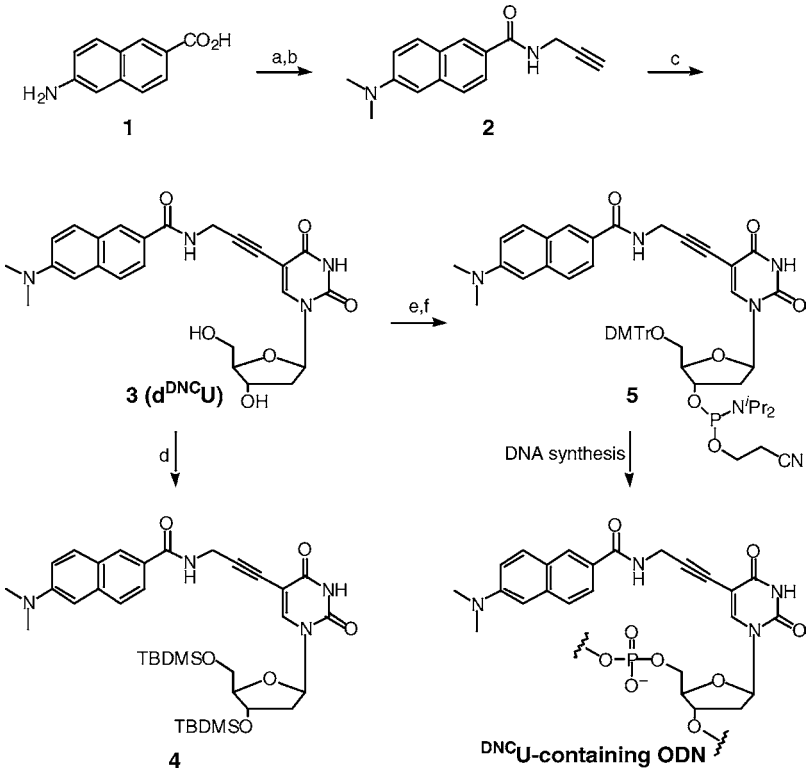

[a] (a) Formaldehyde, sodium cyanoborohydride, methanol, room temperature, 2 h, 99%; (b) propargylamine, PyBOP, DMF, room temperature, 1 h, 84%; (c) 5-iodo-2′-deoxyuridine, CuI, $Pd(PPh_3)_4$, triethylamine, DMF, room temperature, 6 h, 94%; (d) *tert*-butyldimethylsilyl chloride, imidazole, DMF, room temperature, 5 h, 54%; (e) 4,4′-dimethoxytrityl chloride, pyridine, room temperature, 6 h, 61%; (f) 2-cyanoethyl tetraisopropylphosphorodiamidite, tetrazole, acetonitrile, room temperature, 2 h, quant.

(600 mg, 9.55 mmol) and formaldehyde (37% in water, 4 mL). The mixture was stirred at room temperature for 2 h, and the solvent was dried in vacuo. The crude product was dissolved in water (100 mL) and washed with ethyl acetate (100 mL). Concentrated HCl was added to adjust the pH of the solution (pH 1.0), and the suspension was extracted with ethyl acetate to yield a pale-yellow solid (570 mg, 99%): ^{1}H NMR (CD_3OD, 400 MHz) δ = 8.39 (s, 1H), 7.85 (dd, 1H, J = 8.4, 1.6 Hz), 7.79 (d, 1H, J = 9.2 Hz), 7.64 (d, 1H, J = 8.4 Hz), 7.13 (dd, 1H, J = 9.2, 2.8 Hz), 6.95 (d, 1H, J = 2.8 Hz), 3.08 (s, 6H); MS (EI$^+$) *m/z* (%) 215 [M$^+$]; HRMS (FAB) calcd for $C_{13}H_{13}O_2N$ [M$^+$] 215.0946, found 215.0946.

To a solution of the product (570 mg, 2.65 mmol) in dry DMF (20 mL) was added PyBOP (1.39 g, 2.67 mmol). The mixture was stirred at room temperature, and propargylamine (746 μL, 10.68 mmol) was added to the solution. The reaction mixture was stirred for 1 h, concentrated in vacuo, and diluted with ethyl acetate (40 mL). This solution was washed with aqueous $NaHCO_3$ (20 mL) and brine (20 mL), dried over Na_2SO_4, filtered, and evaporated. The crude product was purified by silica gel column chromatography (ethyl acetate:hexane = 1:2) to yield **2** (559 mg, 84%) as a pale-yellow solid: ^{1}H NMR ($CDCl_3$, 400 MHz) δ = 8.18 (d, 1H, J = 1.6 Hz), 7.76−7.73 (m, 2H), 7.61 (d, 1H, J = 8.4 Hz), 7.13 (dd, 1H, J = 8.8, 2.4 Hz), 6.85 (d, 1H, J = 2.4 Hz), 4.27 (dd, 2H, J = 5.2, 2.4 Hz), 3.06 (s, 6H), 2.26 (t, 1H, J = 2.4 Hz); ^{13}C NMR (DMSO-d_6, 100 MHz) δ = 166.4, 149.7, 136.4, 130.0, 127.7, 126.8, 125.9, 125.0, 124.5, 116.8, 105.1, 81.8, 72.9, 40.2, 28.7; MS (FAB, NBA/$CHCl_3$) *m/z* (%) 252 [M$^+$]; HRMS (FAB) calcd for $C_{16}H_{16}N_2O$ [M$^+$] 252.1266, found 252.1263.

5-[3-(6-Dimethylaminonaphthalenecarboxamido)-propynyl]-2′-deoxyuridine (3, d^{DNC}U). To a solution of **2** (907 mg, 3.6 mmol), 2′-deoxy-5-iodouridine (850 mg, 2.4 mmol), and triethylamine (270 μL) in 1 mL of anhydrous DMF were added tetrakis(triphenylphosphine)palladium(0) (555 mg, 0.48 mmol) and copper(I) iodide (183 mg, 0.96 mmol) under nitrogen. The mixture was stirred at room temperature for 6 h. The resulting mixture was concentrated in vacuo and diluted with ethyl acetate (30 mL). This solution was washed with 5% EDTA solution (30 mL) and 5% sodium bisulfite solution (30 mL), dried over Na_2SO_4, filtered, and evaporated. The crude product was purified by silica gel column chromatography (chloroform:methanol = 20:1) to yield **3** (1.08 mg, 94%) as a pale-yellow solid: ^{1}H NMR (DMSO-d_6, 400 MHz) δ = 11.61 (s, 1H), 8.93 (t, 1H, J = 5.5 Hz), 8.28 (d, 1H, J = 1.6 Hz), 8.15 (s, 1H), 7.80−7.77 (m, 2H), 7.66 (d, 1H, J = 8.8 Hz), 7.25 (dd, 1H, J = 9.2, 2.6 Hz), 6.93 (d, 1H, J = 2.6 Hz), 6.09 (t, 1H, J = 6.7 Hz), 5.21 (d, 1H, J = 4.2 Hz), 5.07 (t, 1H, J = 5.0 Hz), 4.30 (d, 2H, J = 5.5 Hz), 4.22−4.18 (m, 1H), 3.77 (dd, 1H, J = 6.5, 3.4 Hz), 3.61−3.51 (m, 2H), 3.02 (s, 6H), 2.11−2.08 (m, 2H); ^{13}C NMR (DMSO-d_6, 100 MHz) δ = 166.3, 161.9, 149.8, 149.7, 143.8, 136.4, 130.0, 127.8, 126.7, 125.9, 125.0, 124.5, 116.8, 105.1, 98.5, 90.3, 87.8, 84.9, 74.3, 70.5, 61.2, 40.3, 29.5; MS (FAB, NBA/DMSO) *m/z* (%) 479 [(M + H)$^+$]; HRMS (FAB) calcd for $C_{25}H_{26}N_4O_6$ [M$^+$] 478.1850, found 478.1852.

3′,5′-Bis-*O*-(*tert*-butyldimethylsilyl)-5-[3-(6-dimethylaminonaphthalenecarboxamido)propynyl]-2′-deoxyuridine (4). To a solution of **3** (74 mg, 0.16 mmol) in dry DMF (1 mL) was added *tert*-butyldimethylchlorosilane (70 mg, 0.46 mmol) and imidazole (32 g, 0.46 mmol). The mixture was stirred at room temperature for 5 h. The mixture was concentrated in vacuo and diluted with chloroform (30 mL). This solution was washed with aqueous $NaHCO_3$ (30 mL) and brine (30 mL), dried over

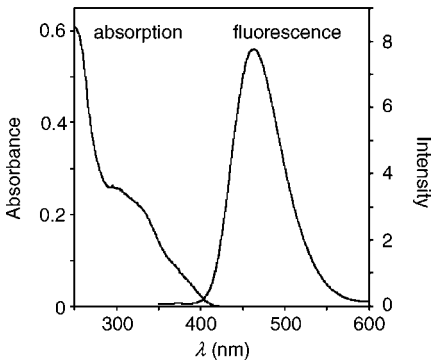

Figure 1. Absorption and fluorescence spectra of 2.5 μM d^{DNC}U in 50 mM sodium phosphate and 0.1 M sodium chloride (pH = 7.0). λ_{exc} = 332 nm, λ_{fl} = 463 nm.

Na_2SO_4, filtered, and evaporated. The crude product was purified by silica gel column chromatography (chloroform:methanol = 50:1) to yield **4** (58.7 mg, 54%) as a pale-yellow solid: ^{1}H NMR ($CDCl_3$, 400 MHz) δ = 8.83 (s, 1H), 8.20 (s, 1H), 8.04 (s, 1H), 7.79−7.74 (m, 2H), 7.65 (d, 1H, J = 8.6 Hz), 7.21 (d, 1H, J = 8.2 Hz), 6.87 (s, 1H), 6.66 (s, 1H), 6.28 (dd, 1H, J = 7.3, 6.0 Hz), 4.47 (d, 2H, J = 4.9 Hz), 4.39 (dt, 1H, J = 5.7, 2.6 Hz), 3.97 (dd, 1H, J = 4.6, 2.2 Hz), 3.89 (dd, 1H, J = 11.5, 2.6 Hz), 3.75 (dd, 1H, J = 11.5, 2.2 Hz), 3.08 (s, 6H), 2.31 (ddd, 1H, J = 13.2, 5.9, 2.7 Hz), 2.02 (ddd, 1H, J = 13.2, 7.3, 5.9 Hz); ^{13}C NMR ($CDCl_3$, 100 MHz) δ = 167.1, 161.6, 149.0, 143.2, 136.7, 130.1, 129.1, 127.8, 127.6, 126.4, 124.1, 116.6, 113.2, 99.4, 89.9, 88.4, 85.9, 74.8, 72.3, 62.9, 42.1, 30.6, 26.0, 25.7, 18.4, 18.0, −4.7, −4.9, −5.4, −5.6; MS (FAB, NBA) *m/z* (%) 706 [M$^+$]; HRMS (FAB) calcd for $C_{37}H_{54}N_4O_6Si_2$ [M$^+$] 706.3582, found 706.3597.

5-[3-(6-Dimethylaminonaphthalenecarboxamido)-propynyl]-5′-*O*-(4,4′-dimet hoxytrityl)-2′-deoxyuridine 3′-*O*-cyanoethyl-*N*,*N*′-diisopropylphosphoramidite (5). To a solution of **3** (1.08 g, 2.51 mmol) in dry pyridine (20 mL) was added 4,4′-dimethoxytrithyl chloride (1.27 g, 3.76 mmol). The mixture was stirred at room temperature for 6 h. The mixture was concentrated in vacuo and diluted with ethyl acetate (200 mL). This solution was washed with aqueous $NaHCO_3$ (150 mL) and brine (150 mL), dried over Na_2SO_4, filtered, and evaporated. The crude product was purified by silica gel column chromatography (chloroform:methanol = 100:1 containing 5% triethylamine) to yield a pale-yellow solid (1.20 g, 61%): ^{1}H NMR (DMSO-d_6, 400 MHz) δ = 11.65 (s, 1H), 8.82 (t, 1H, J = 5.3 Hz), 8.27 (d, 1H, J = 1.3 Hz), 7.89 (s, 1H), 7.79−7.76 (m, 2H), 7.66 (d, 1H, J = 8.8 Hz), 7.39−7.37 (m, 2H), 7.30−7.16 (m, 7H), 6.94 (d, 1H, J = 2.4 Hz), 6.88 (dd, 4H, J = 9.1, 2.7 Hz), 6.09 (t, 1H, J = 6.7 Hz), 5.30 (d, 1H, J = 4.6 Hz), 4.26−4.22 (m, 2H), 4.16 (d, 2H, J = 5.3 Hz), 3.91−3.88 (m, 1H), 3.70 (d, 6H, J = 2.2 Hz), 3.26−3.22 (m, 1H), 3.07−3.04 (m, 1H), 3.02 (s, 6H), 2.26 (dt, 1H, J = 13.7, 6.8 Hz), 2.15 (ddd, 1H, J = 13.5, 6.3, 3.6 Hz); ^{13}C NMR (DMSO-d_6, 100 MHz) δ = 166.2, 161.8, 158.3, 158.2, 149.7, 149.5, 145.0, 143.4, 136.4, 135.9, 135.4, 130.0, 129.9, 129.8, 128.1, 127.8, 127.7, 125.8, 124.9, 124.5, 116.8, 113.44, 113.40, 105.1, 98.6, 90.2, 86.0, 85.2, 70.7, 64.0, 55.2, 40.2, 29.4; MS (FAB, NBA/$CHCl_3$) *m/z* (%) 780 [(M + H)$^+$]; HRMS (FAB) calcd for $C_{46}H_{44}N_4O_8$ [(M + H)$^+$] 780.3159, found 780.3163.

To a solution of the product (45 mg, 0.058 mmol) in dry acetonitrile (2 mL) was added 2-cyanoethyl tetraisopropyldiphosphoramidite (19 μL, 0.058 mmol) and tetrazole (4.9 mg, 0.070 mmol). The mixture was stirred at room temperature for 2 h. The solvent was evaporated, and the residue was directly used in an automated DNA synthesizer without further purification.

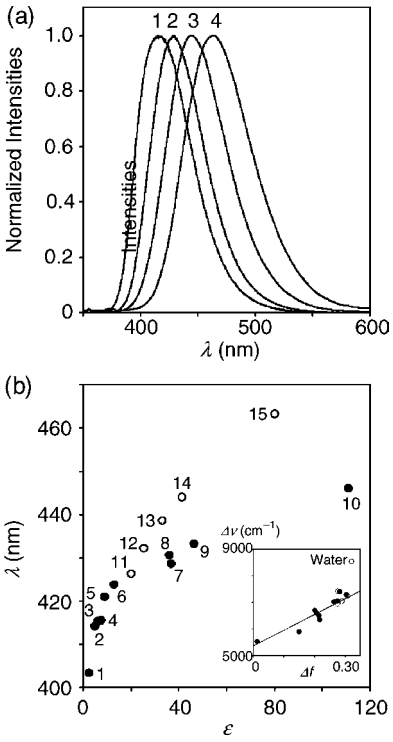

Figure 2. Shift of fluorescence maxima of d^{DNC}U in different solvents. (a) Fluorescence emission spectra of d^{DNC}U (2.5 μM) in different solvents. Spectra are normalized with respect to peak intensities. 1, Ethyl acetate; 2, *N*,*N*-dimethylformamide; 3, glycol; 4, water. (b) Shift of the fluorescence emission maximum of d^{DNC}U in different dielectric environments. Emission maxima (λ_{fl}) of d^{DNC}U (2.5 μM) were plotted against dielectric constants (ϵ) of aprotic (filled circles) and protic solvents (open circles). 1, Toluene; 2, chloroform; 3, ethyl acetate; 4, tetrahydrofuran; 5, dichloromethane; 6, pyridine; 7, *N*,*N*-dimethylformamide; 8, acetonitrile; 9, dimethyl sulfoxide; 10, formamide; 11, 2-propanol; 12, ethanol; 13, methanol; 14, glycol; 15, water. (Inset) Lippert plot of corrected Stokes shift in wavenumbers ($\Delta\nu$) against the orientational polarizability of the solvents (Δf).

Oligodeoxynucleotide (ODN) Synthesis and Characterization. ODNs were synthesized by a conventional phosphoramidite method by using an Applied Biosystems 392 DNA/RNA synthesizer. ODNs were purified by reverse-phase HPLC on a 5-ODS−H column (10 × 150 mm, elution with 0.1 M triethylamine acetate (TEAA), pH 7.0, linear gradient over 50 min from 0 to 50% acetonitrile at a flow rate 3.0 mL/min). ODNs containing modified nucleotides were fully digested with calf intestine alkaline phosphatase (50 U/mL), snake venom phosphodiesterase (0.15 U/mL), and P1 nuclease (50 U/mL) at 37 °C for 3 h. Digested solutions were analyzed by HPLC on a CHEMCOBOND 5-ODS−H column (4.6 × 150 mm), elution with a solvent mixture of 0.1 M triethylamine acetate (TEAA), pH 7.0, flow rate 1.0 mL/min). Concentration of each ODN was determined by comparing peak areas with standard solution containing dA, dC, dG, and dT at a concentration of 0.1 mM. 5′-d(TTGCTCATCTTGTT^{DNC}UTGCCGACGCTACATT-GCCAAGG)-3′: MALDI-TOF [(M − H)$^-$] calcd 10930.13, found 10930.36.

UV Absorption Measurements. Absorption spectra were obtained using an Ultraspec 3000pro UV−vis spectrophotometer (Amarsham Pharmacia Biotech) at room temperature using a 1-cm path length cell.

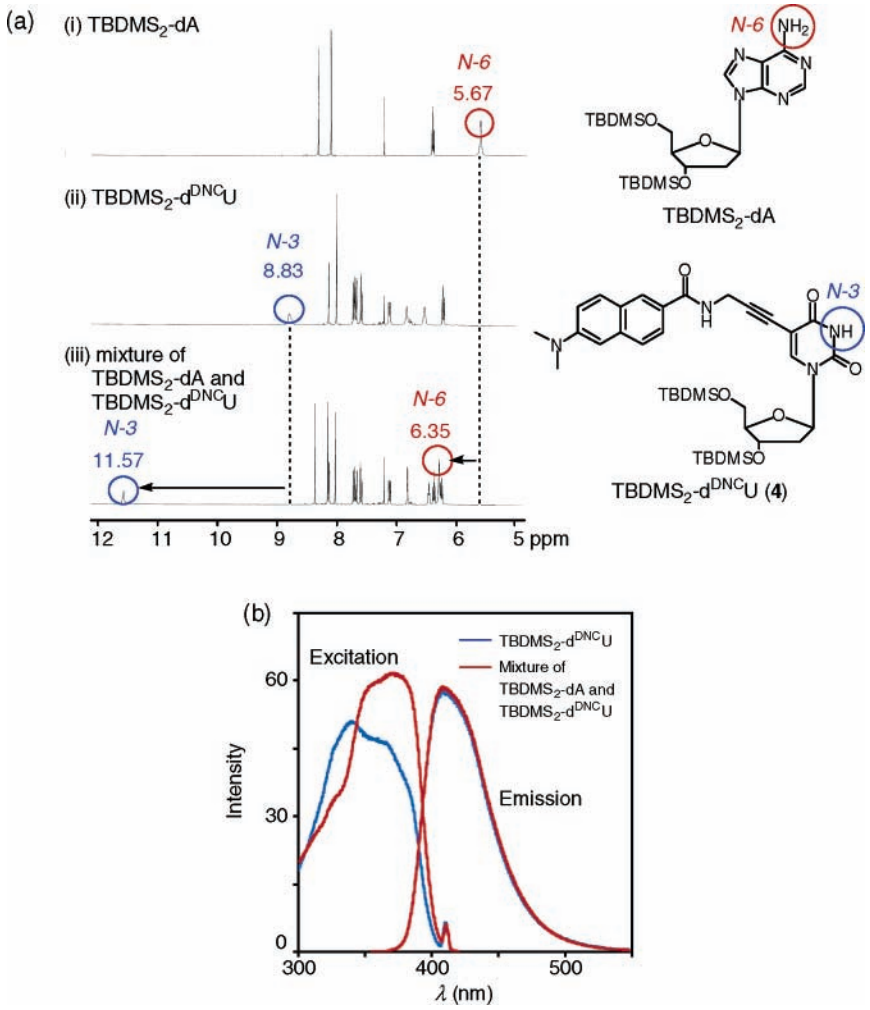

Figure 3. Effect of hydrogen bonds between a ^{DNC}U−A base pair on fluorescence wavelength. (a) ^{1}H NMR spectra of (i) 0.1 M TBDMS$_2$-dA, (ii) 0.1 M TBDMS$_2$-d^{DNC}U, and (iii) 1:1 mixture of 0.1 M TBDMS$_2$-dA and 0.1 M TBDMS$_2$-d^{DNC}U in $CDCl_3$ at 25 °C. (b) Fluorescence excitation and emission spectra of 1 mM TBDMS$_2$-d^{DNC}U in the presence and absence of 1 mM TBDMS$_2$-dA in $CDCl_3$ at 25 °C. $\lambda_{exc} = 350$ nm, $\lambda_{fl} = 414$ nm.

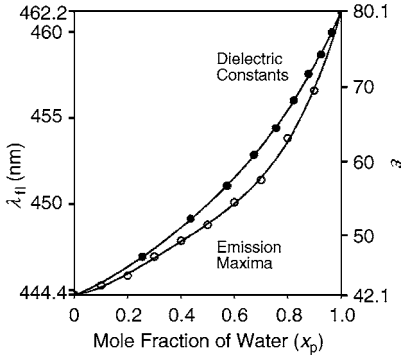

Figure 4. Variation of the fluorescence emission maxima (λ_{fl}, open circles) and dielectric constants (ϵ, filled circles) for water−glycol binary mixtures at 20 °C. For the dielectric constants in the figure, the data described in ref 13 are used.

Fluorescence Experiments. Fluorescence spectra were obtained using a Shimadzu RF-5300PC spectrofluorophotometer at 25 °C using 1-cm path length cell. The excitation bandwidth was 1.5 nm. The emission bandwidth was 1.5 nm.

The fluorescence quantum yields (Φ_F) were determined using 9,10-diphenylanthracene as a reference with a known Φ_F of 0.95 in ethanol. The area of the emission spectrum was integrated using the software available in the instrument, and the quantum yield is calculated according to the following equation

$$\Phi_{F(S)}/\Phi_{F(R)} = [A_{(S)}/A_{(R)}] \times [(\mathrm{Abs})_{(R)}/(\mathrm{Abs})_{(S)}] \times [n_{(S)}^2/n_{(R)}^2] \quad (1)$$

Here, $\Phi_{F(S)}$ and $\Phi_{F(R)}$ are the fluorescence quantum yield of the sample and the reference, respectively. $A_{(S)}$ and $A_{(R)}$ are the area under the fluorescence spectra of the sample and the reference, respectively, $(\mathrm{Abs})_{(S)}$ and $(\mathrm{Abs})_{(R)}$ are the respective optical densities of the sample and the reference solution at the wavelength of excitation, and $n_{(S)}$ and $n_{(R)}$ are the values of refractive index for the respective solvents used for the sample (1.333) and the reference (1.383).

RESULTS AND DISCUSSION

Synthesis of the novel deoxyuridine-based fluorophore, d^{DNC}U (**3**), is outlined in Scheme 1. Commercially available 6-amino-2-naphthoic acid (**1**) was methylated through the reduction of the imine and then condensed with propargylamine to yield **2**. Sonogashira coupling of **2** with 5-iodo-2′-deoxyuridine afforded the fluorescence-labeled nucleoside **3**.

The DNC fluorophore in ^{DNC}U possesses an amide group, unlike conventional DAN fluorophores. The amide group facilitated the incorporation of the fluorophore to a substrate (i.e., uracil base), but it may show a different

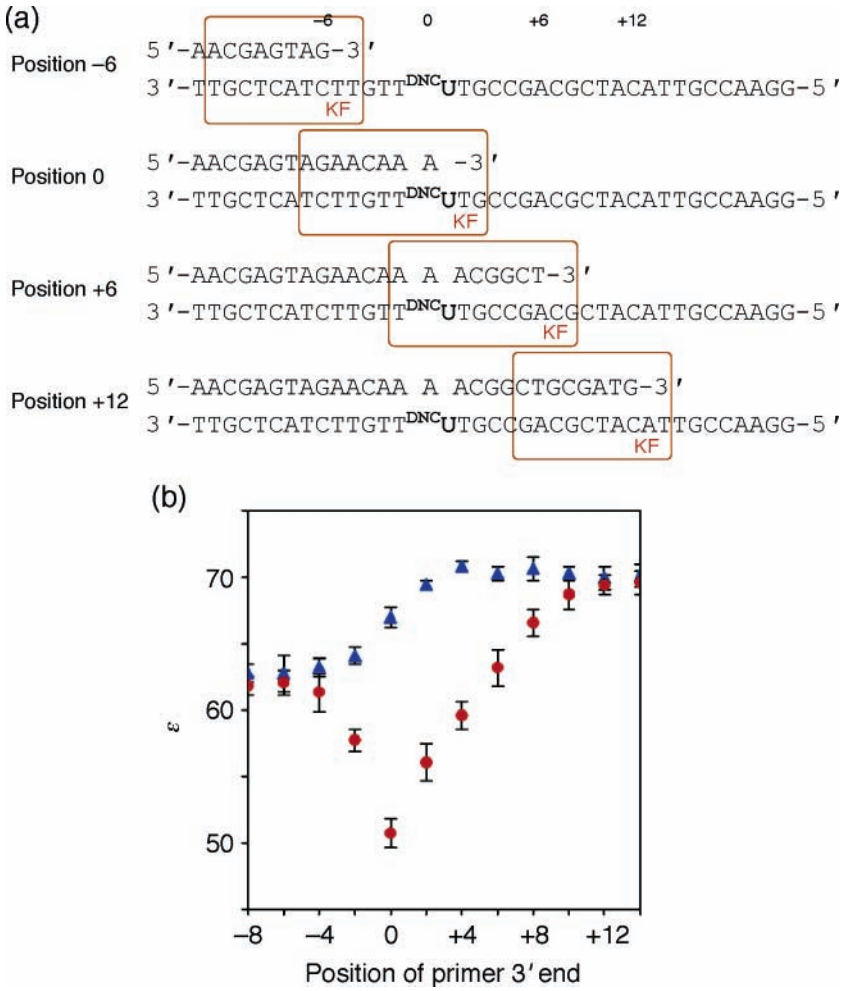

Figure 5. Monitoring the dielectric environments near ^{DNC}U in ODN duplexes containing primers of different length. (a) The examples of primer−template duplexes used in this study. The numbering system used for duplexes defines the position of ^{DNC}U as 0. The region of duplex binding with the KF is depicted by orange frames. (b) Variation of the dielectric constants around ^{DNC}U in the primer−template duplex for different primer length. According to Figure 4, each of the dielectric constants was calculated from the emission wavelength obtained by measurement of the fluorescence emission spectra of 2.5 μM of primer−template duplexes in the presence of KF (1.0 equiv) in 100 mM Tris−HCl (pH 7.5), 70 mM magnesium chloride, and 1 mM dithiothreitol on 326-nm excitation. The change of the dielectric constants observed for primer−template duplexes is depicted with blue triangles, and the data for duplexes bound by KF are plotted with red circles.

dielectric sensitivity from DAN fluorophores. Therefore, we initially measured absorption and fluorescence spectra of a nucleoside d^{DNC}U. The UV absorption of d^{DNC}U had a shoulder from 290 to 410 nm in sodium phosphate buffer (pH 7.0), and the fluorescence was observed at 463 nm on excitation at 332 nm ($\Phi_F = 0.019$) (Figure 1). The fluorescence of d^{DNC}U was dependent on the solvent, e.g., $\lambda_{fl} = 444$ nm, $\Phi_F = 0.140$ in glycol, and $\lambda_{fl} = 415$ nm, $\Phi_F = 0.208$, in ethyl acetate (Figure 2a). The fluorescence emission maxima of d^{DNC}U observed in different solvents were plotted against the dielectric constant for each solvent (*10*) (Figure 2b). A series of fluorescence spectra showed significant shifts of the fluorescence emission with solvent polarity, and the fluorescence emission maxima were shifted from 403 nm (toluene) to 463 nm (water). The shift by solvent polarity can be explained in terms of the dipole interaction theory of Lippert and Mataga (*11*, *12*). An inset in Figure 2b shows a plot of the Stokes shifts ($\Delta\nu$) against the orientational polarizability (Δf) of the solvent. Solvents that can form hydrogen bonds as a proton donor produce larger $\Delta\nu$ than do aprotic solvents. In particular, the $\Delta\nu$ of water clearly deviated from a straight line in the plot. Large solvatofluorochromic shifts of d^{DNC}U in protic solvents were attributed to specific solute−solvent interactions, such as hydrogen bonding.

This solvatofluorochromic shift is due to DNC chromophore−solvent interactions. Hydrogen bonding to the uracil region of d^{DNC}U may also alter the fluorescence properties of d^{DNC}U. To investigate the effect of uracil−solvent interaction on the fluorescence shift, we prepared a chloroform-soluble nucleoside **4**, which was synthesized by protection of the hydroxy groups of **3** with *tert*-butyldimethylsilyl (TBDMS) groups (Scheme 1). The fluorescence spectra of **4** did not show a significant shift on the addition of *O*,*O*′-bis(TBDMS)-protected dA in deuterated chloroform, although the change of the chemical shift of the N3 imino proton of **4** by hydrogen bonding with adenine was observed in ^{1}H NMR spectra (Figure 3). Therefore, the solvatofluorochromic shift of d^{DNC}U fluorescence was predominantly due to the DNC chromophore−solvent interaction not to the hydrogen bonding at the uracil base of ^{DNC}U.

We next examined the change in the fluorescence emission of ^{DNC}U in binary mixtures of water (dielectric constant, $\epsilon = 80.1$) and glycol ($\epsilon = 42.1$) to correlate the fluorescence emission with dielectric constants (Figure 4). The emission wavelength increases monotonically

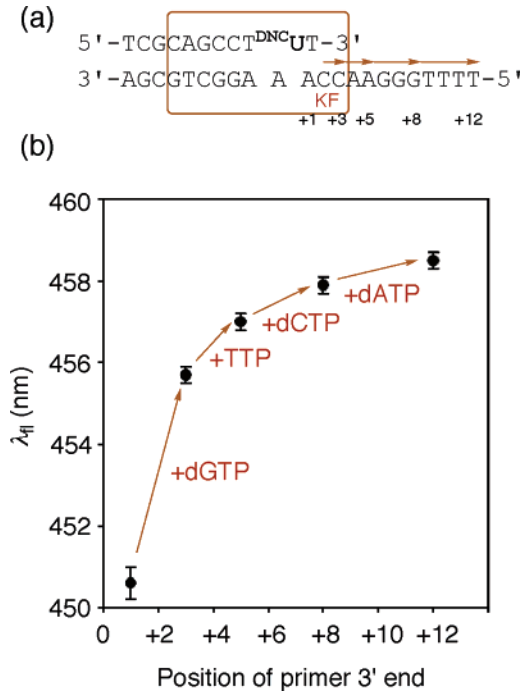

Figure 6. (a) Sequence of a ^{DNC}U-labeled primer−template duplex used for a primer extension assay. (b) Variation of the fluorescence emission maxima (λ_{fl}) of a duplex-KF complex on the addition of dNTP. A sample solution contained 2.5 μM of primer−template duplexes and KF (1.0 equiv) in 100 mM Tris−HCl (pH 7.5), 70 mM magnesium chloride, and 1 mM dithiothreitol. The emission wavelength was obtained by measuring fluorescence emission spectra of the sample where each dNTP (250 μM) was successively added (λ_{exc} = 326 nm).

with increasing water/glycol ratio. The curvature of the fluorescence emission maxima of d^{DNC}U in binary mixtures roughly corresponded to that for the dielectric constants (*13*), although a small gap caused by a preferential solvation process was observed (*14*, *15*). These data facilitate the direct conversion of the given fluorescence emission wavelength to dielectric constants.

Having established the variation of fluorescence wavelength of d^{DNC}U with solvent dielectric constant, we next examined the incorporation of ^{DNC}U into ODNs and measured their fluorescence spectra. Nucleoside **3** was converted to cyanoethyl phosphoramidite **5** for the DNA synthesizer (Scheme 1). After ODN synthesis, deprotection was conducted with aqueous ammonia at 55 °C for 16 h to give ^{DNC}U-containing ODN. By use of a ^{DNC}U-containing 37-mer ODN (template ODN) prepared according to the above procedure (MALDI-TOF [(M − H)$^-$] calcd 10930.13, found 10930.36), we examined the hybridization with short ODNs with different nucleotide lengths (primer ODNs) (Figure 5a). By variation of the length of the hybridized primer ODNs, the local dielectric constants of single-stranded sites, duplex regions, and single strand−duplex junction sites were examined. The numbering system used for duplexes defines the position of ^{DNC}U as 0. The fluorescence maxima observed for each duplex were converted to the local dielectric constants according to Figure 4, and the result is shown in Figure 5b (blue triangles). When ^{DNC}U was located at a single-strand site (the 3′ end of the primer ODN was at positions −8 to −4), the wavelength of the emission maximum was 452 nm on excitation at 326 nm, and the dielectric constant of the ^{DNC}U site corresponded to 63. On the other hand, when ^{DNC}U was located in a duplex region (the 3′ end of the primer ODN was at positions +4 to +14), the maximum of the fluorescence emission was observed at 456 nm. The dielectric constant of the duplex was estimated to be 70. At the single strand−duplex junction, the emission maximum of ^{DNC}U gradually shifted from 452 to 456 nm as the primer ODN was extended. The fluorescence shift induced by site-specific incorporation of ^{DNC}U reflects the difference in dielectric constants between the outside of the duplex major groove and the inside of a folded single strand. In the duplex, the DNC fluorophore attached to the uracil C-5 position via a rigid propargyl linker extruded to the outside of the major groove, a water-accessible site, due to base pairing with an adenine base, whereas ^{DNC}U in the coiled single strand would be shielded from the aqueous phase. ^{DNC}U incorporated into DNA effectively acted as a dielectric-sensitive probe.

We monitored the dielectric nature of the binding site of DNA-binding proteins using the fluorescence of ^{DNC}U-containing ODN. We investigated the dielectric constants of the DNA-binding site in the Klenow fragment (KF) of DNA polymerase I from *Escherichia coli*, which contains the polymerase and 3′−5′ proofreading exonuclease activities and has long been used as a good model system for studying the molecular mechanism of template-directed DNA synthesis (*16*−*19*). The change in the emission maxima of the 1:1 complexes formed by KF and ^{DNC}U-containing duplex was monitored. The local dielectric constants, which were calculated from the emission wavelength of the ^{DNC}U-containing template ODN hybridized with primer ODNs of different length, were plotted as shown in Figure 5b (red circles). When the 3′ end of the primer was at position −6, the dielectric constant of the KF−duplex complex was almost the same as that observed for the KF-free sample. Also, for the duplexes where the end of the primer exceeded position +10, the dielectric constant was nearly equal to that for the polymerase-free sample. On the other hand, when the 3′ end of the primer was located between positions −2 and +6, the emission maximum showed a characteristic blue shift on binding to KF, suggesting that the dielectric constants of the microenvironments around ^{DNC}U drastically decreased. The decrease in the dielectric constants observed for the complex of ^{DNC}U-containing ODN and KF was in good agreement with the fact that about 8 base pairs of the duplex region upstream of the primer end were covered with KF, as demonstrated by DNA footprinting experiments (*16*, *20*). In particular, when the 3′ end of the primer was at position 0, a minimum dielectric constant was observed (λ_{fl} = 448 nm, ϵ = 51). In this case, ^{DNC}U was located in the vicinity of the incorporation site of triphosphate in KF. The duplex in the incorporation site of triphosphates is known to be tightly captured by the side chains of the palm and thumb subdomains (*21*, *22*). We were able to confirm easily the lower hydrophilicity of the microenvironment around the incorporation site of triphosphates in KF.

We next examined a primer extension assay in the presence of dNTPs using KF. The ^{DNC}U-labeled primer−template duplex used for this assay is shown in Figure 6a. In this assay, dGTP was initially added to a sample containing the duplex and KF, and then TTP, dCTP, and dATP were added successively. The fluorescence observed after the addition of each dNTP gradually shifted to longer wavelength (Figure 6b). This result shows that the location of a ^{DNC}U base on the primer shifted from less polar enzyme interior to more polar exterior, in tandem with KF migration through the DNA polymerization process. We were able to monitor the change of microenvironmental polarities of the enzyme from inside

to outside using a ^{DNC}U-containing probe. These results suggest that the ^{DNC}U-containing probe can be used to investigate polarities on the inside of DNA-binding protein.

In conclusion, we prepared a novel fluorescent nucleoside ^{DNC}U via a few synthetic steps. This nucleoside offers high fluorescence sensitivity to the solvent polarity and was able to directly sense local dielectric properties by the fluorescence change. A series of fluorescence spectra showed a remarkable shift depending on the polarity of the microenvironment around ^{DNC}U. In addition, the change of fluorescence emission of ^{DNC}U by the close contact with KF enabled us to determine dielectric constants of each DNA-binding site of KF. Therefore, ^{DNC}U-containing ODN serves as an effective dielectric-sensitive fluorescence probe for monitoring the change of local dielectric properties on the interior of a DNA-protein complex.

LITERATURE CITED

(1) Honig, B., and Nicholls, A. (1995) Classical electrostatics in biology and chemistry. *Science 268*, 1144−1149.

(2) Pitera, J. W., Falta, M., and van Gunsteren, W. F. (2001) Dielectric properties of proteins from simulation: the effects of solvent, ligands, pH, and temperature. *Biophys. J. 80*, 2546−2555.

(3) Schutz, C. N., and Warshel, A. (2001) What are the dielectric "constants" of proteins and how to validate electrostatic models? *Proteins 44*, 400−417.

(4) Weber, G., and Farris, F. J. (1979) Synthesis and spectral properties of a hydrophobic fluorescent probe: 6-propionyl-2-(dimethylamino)naphthalene. *Biochemistry 18*, 3075−3078.

(5) Macgregor, R. B., and Weber, G. (1986) Estimation of the polarity of the protein interior by optical spectroscopy. *Nature 319*, 70−73.

(6) Balter, A., Nowak, W., Pawelkiewicz, W., and Kowalczyk, A. (1988) Some remarks on the interpretation of the spectral properties of PRODAN. *Chem. Phys. Lett. 143*, 565−570.

(7) Pierce, D. W., and Boxer, S. G. (1992) Dielectric-relaxation in a protein matrix. *J. Phys. Chem. 96*, 5560−5566.

(8) Samanta, A., and Fessenden, R. W. (2000) Excited-state dipole moment of PRODAN as determined from transient dielectric loss measurements. *J. Phys. Chem. A 104*, 8972−8975.

(9) Cohen, B. E., McAnaney, T. B., Park, E. S., Jan, Y. N., Boxer, S. G., and Jan, L. Y. (2002) Probing protein electrostatics with a synthetic fluorescent amino acid. *Science 296*, 1700−1703.

(10) Mulov, S. L., Carmichael, I., and Hug, G. L. (1993) *Handbook of Photochemistry*, Marcel Dekker, Inc., New York.

(11) Lippert, E. (1957) Spectroscopic determination of the dipole moment of aromatic compounds in the first excited singlet state. *Z. Electrochem. 61*, 962−975.

(12) Mataga, N., Kaifu, Y., and Koizumi, M. (1956) Solvent effects upon fluorescence spectra and the dipole moments of excited molecules. *Bull. Chem. Soc. Jpn. 29*, 465−470.

(13) Corradini, F., Marcheselli, L., Tassi, L., and Tosi, G. (1993) Ethane-1,2-diol water solvent system-relative permittivity as a function of temperature and binary composition. *J. Chem. Soc., Faraday Trans. 89*, 123−127.

(14) Suppan, P. (1987) Local polarity of solvent mixtures in the field of electronically excited molecules and exciplexes. *J. Chem. Soc., Faraday Trans. 1 83*, 495−509.

(15) Rachofsky, E. L., Osman, R., and Ross, J. B. A. (2001) Probing structure and dynamics of DNA with 2-aminopurine: effects of local environment on fluorescence. *Biochemistry 40*, 946−956.

(16) Yadav, P. N. S., Yadav, J. S., and Modak, M. J. (1992) A molecular model of the complete three-dimensional structure of the Klenow fragment of *Escherichia coli* DNA polymerase I: binding of the dNTP substrate and template-primer. *Biochemistry 31*, 2879−2886.

(17) Beese, L. S., Derbyshire, V., and Steitz, T. A. (1993) Structure of DNA polymerase I Klenow fragment bound to duplex DNA. *Science 260*, 352−355.

(18) Joyce, C. M., and Steitz, T. A. (1994) Function and structure relationships in DNA polymerises. *Annu. Rev. Biochem. 63*, 777−822.

(19) Brautigam, C. A., and Steitz, T. A. (1998) Structural and functional insights provided by crystal structures of DNA polymerises and their substrate complexes. *Curr. Opin. Struct. Biol. 8*, 54−63.

(20) Joyce, C. M., Ollis, D. L., Rush, J., Steitz, T. A., Konigsberg, W. H., and Grindley, N. D. F. (1986) *Protein Structure, Folding and Design, UCLA Symposia on Molecular and Cellular Biology*, Liss, New York, U.S.A., pp 197−205.

(21) Turner, R. M., Jr., Grindley, N. D. F., and Joyce, C. M. (2003) Interaction of DNA polymerase I (Klenow fragment) with the single-stranded template beyond the site of synthesis. *Biochemistry 42*, 2373−2385.

(22) Purohit, V., Grindley, N. D. F., and Joyce, C. M. (2003) Use of 2-aminopurine fluorescence to examine conformational changes during nucleotide incorporation by DNA polymerase I (Klenow fragment). *Biochemistry 42*, 10200−10211.

BC050077I

Targeted Delivery of Plasmid DNA into the Nucleus of Cells via Nuclear Localization Signal Peptide Conjugated to DNA Intercalating Bis- and Trisacridines

Takehiko Shiraishi, Ramin Hamzavi,† and Peter E. Nielsen*

Department of Medical Biochemistry and Genetics, The Panum Institute, University of Copenhagen, Blegdamsvej 3c, 2200 Copenhagen N, Denmark. Received March 23, 2005; Revised Manuscript Received July 15, 2005

Efficient nuclear targeting via nonviral delivery of DNA is still an unmet challenge in gene therapy. We have synthesized a novel 9-aminoacridine amino acid monomer that conveniently allows multiple acridines to be incorporated into peptide conjugates. In particular we have prepared bis- and trisacridine conjugates of nuclear localization signal peptide (NLS) ($(Acr)_2$−NLS and $(Acr)_3$−NLS) and studied these as functional transporters for the nuclear delivery of DNA. We show that these conjugates can enhance transfection efficacy as well as nuclear localization of plasmid DNA by more than 50-fold when combined with polyethylenimine at an N:P ratio of 2−3. These conjugates have high reversible affinity for double stranded DNA by intercalation and the technique provides a simple means of associating NLS with DNA of any sequence and at any ratio.

INTRODUCTION

Low efficiency of gene transfer is a major barrier for the development of nonviral gene therapy. Compared with adenovirus vectors (*1*), which provide nearly 100% transduction of endothelial cells *in* vivo and in vitro, the efficiency of nonviral gene transfer methods are far inferior (*2*−*4*). Transfection of DNA by nonviral systems is limited by cellular uptake, endosomal escape, as well as translocation of the DNA from the cytoplasm into the nucleus. Especially, transfer of plasmid DNA to the nucleus remains a critically limiting step (*5*, *6*). It has been shown that expression of a gene from plasmid DNA injected directly into the nucleus is much higher than from plasmid injected into the cytoplasm (*7*), for which less than 1% is typically internalized in the nucleus. In contrast, the efficiency of adenovirus transduction is attributed to the efficiency of receptor recognition, endosome escape, and nuclear pore recognition. However, adding replication-deficient adenovirus to lipid−DNA complexes during transfection provides an only modest increase in transfection efficiency (*8*). These results indicate that even with endosome escape facilitated by adenovirus, translocation of cytoplasmic plasmid DNAs to the nucleus remains a significant limiting step in nonviral gene transfer.

Molecules, larger than 30−60 kDa, require active transport system via nuclear localization signals to be transported into the nucleus from the cytoplasm (*9*). To achieve an effective nuclear translocation of target molecules, the SV40 basic nuclear localization signal (NLS) peptide has been used extensively as a carrier for large proteins (*9*), as well as for DNA (*3*). Recently, Sebestyen et al. (*10*) demonstrated a significant increase of nuclear uptake of plasmid DNA upon covalent conjugation to the NLS peptide. However, as a consequence of this modification, the DNA significantly lost biological activity. Branden et al. (*3*) exploited a peptide nucleic acid (PNA) for noncovalent conjugation of NLS to plasmid DNA via sequence-specific binding of PNA to the DNA, thereby improving the nuclear translocation of DNA without decreasing gene expression activity. However, their method requires introduction and/or selection of a PNA-binding sequence that does not interfere with the proliferation and transcriptional activities of the vector. In addition, specific PNA/NLS conjugates must be synthesized for each target DNA. Therefore, more simple methods for noncovalent conjugation of DNA to a NLS peptide could be advantageous.

We decided to take advantage of the high affinity of bis- and tris-intercalating compounds (*11*) in order to achieve strong reversible binding of nuclear localization signal peptide (NLS) to dsDNA. We now report the synthesis of a novel 9-aminoacridine amino acid monomer that allows multiple acridines to be incorporated into peptide conjugates. In particular we have prepared bis- and trisacridine conjugates of NLS ($(Acr)_2$−NLS and $(Acr)_3$−NLS) and studied these as functional transporters for the nuclear delivery of DNA.

EXPERIMENTAL PROCEDURES

Synthesis of 9-Aminoacridine NLS Conjugate (Acr−NLS). The sequences and nomenclature of the Acr−NLS conjugates and NLS are listed in Figure 1. Peptide conjugate and PNA syntheses were carried out by standard solid support methodology as reported elsewhere (*12*). The peptides were high-performance liquid chromatography purified and characterized by matrix-assisted laser desorption-ionization time-of-flight (MALDI-TOF) mass spectrometry (Figure 1B). Purified peptides were lyophilized and stored at 4 °C until use.

Synthesis of Acr^{aeg} Monomer (Scheme 1). Reagents and solvents were obtained from commercial sources and used without further purification unless indicated. NMR spectra were recorded in DMSO-*d6* on a 500-MHz Bruker

* To whom correspondence may be addressed. Tel: +45-35327762. Fax: +45-35396042. E-mail: pen@imbg.ku.dk.

† Present address: Institut fur Pharmazie und Molekulare Biotechnologie Universitat Heidelberg Im Neuenheimer Feld 364, 69120 Heidelberg, Germany.

10.1021/bc050093f CCC: $30.25 © 2005 American Chemical Society
Published on Web 09/01/2005

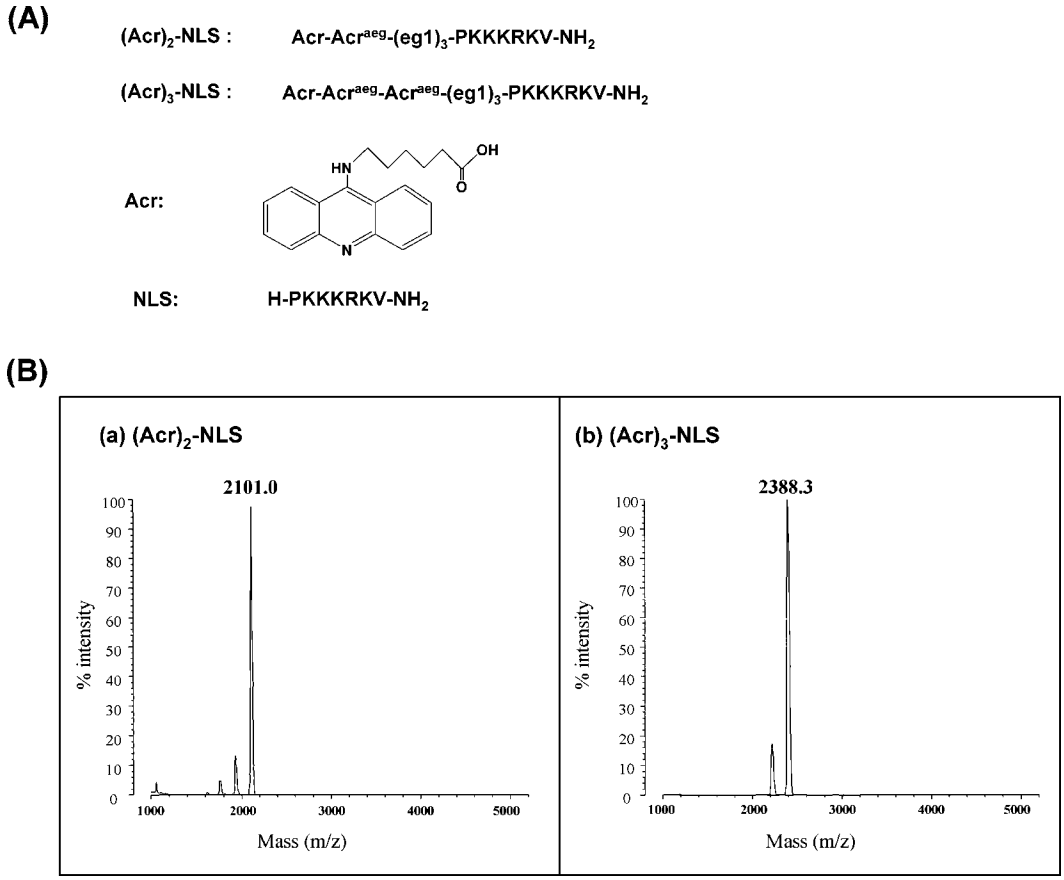

Figure 1. (A) Chemical structures of the compounds used in this study. (B) MALDI-TOF mass spectra of $(Acr)_2$−NLS (a) and $(Acr)_3$−NLS (b). Calculated masses = 2097.6 (a) and 2389.0 (b), respectively.

Scheme 1

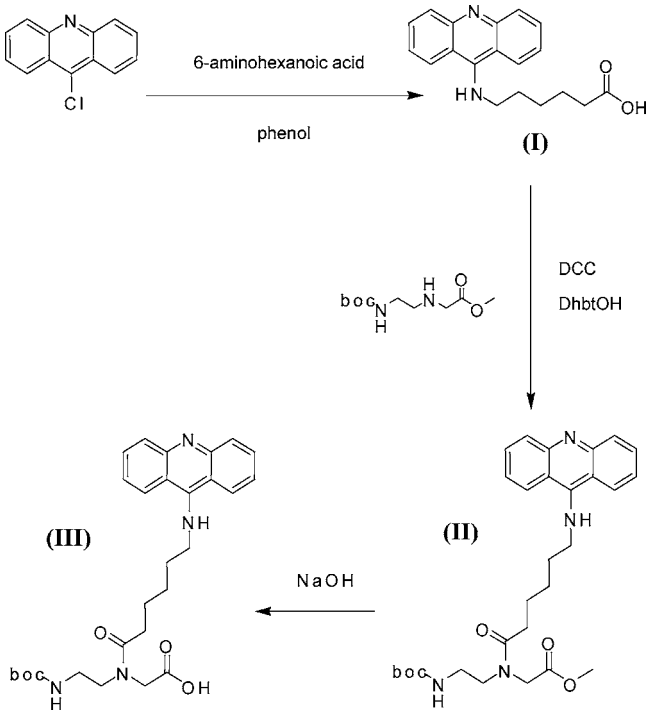

spectrometer and fast-atom bombardment (FAB) mass spectra on a JEOL HX 110/110 mass spectrometer.

N-(Acridine-9-yl)-6-aminohexanoic acid (**I**) was prepared essentially as described (13): 9-chloroacridine (2.1 g, 10 mmol), 6-aminohexanoic acid (1.1 g, 8.4 mmol), and phenol (9.4 g, 0.1 mol) were mixed and stirred at 85 °C overnight. The reaction mixture was cooled to room temperature, and ethyl acetate (200 mL) was added and extracted with saturated aqueous $NaHCO_3$. The organic phase was dried over $MgSO_4$ and evaporated to dryness. The title compound (2.2 g, 85%) was obtained as a yellow powder. Mp: 160−162 °C; MS (FAB) *m/z* 309 (M + H); ^{1}H NMR (DMSO-*d6*): δ 8.6−7.4 (m, 8H, acridine aromatics), 4.03 (t, 2H, J = 7.0 Hz), 2.22 (t, 2H, J = 7.0 Hz), 1.90 (m, 2H), 1.55 (m, 2H), 1.40 (m, 2H); ^{13}C NMR (DMSO-*d6*): δ 174.22, 156.36, 134.03, 129.07, 125.67, 122.75, 118.76, 115.02, 112.25, 48.37, 33.36, 28.54, 25.58, 23.91; HRMS $(M + H)^+$, calcd (found) for $C_{19}H_{20}N_2O_2$: 309.1603 (309.1610).

Methyl-N-(2-bocaminoethyl)-N-[N-(acridine-9-yl)-6-aminohexanoyl]]glycinate (**II**). Compound **I** (3.1 g, 10 mmol), DhbtOH (1.8 g, 11 mmol), and DCC (3.1 g, 15 mmol) were dissolved in DMF (50 mL) and stirred for 30 min under nitrogen. A solution of *N*-(2-bocaminoethyl)glycine methyl ester (14) (2.1 g, 9 mmol) in DMF (10 mL) was added, and the reaction mixture was stirred overnight. Volatiles were removed under vacuum, and the residue was dissolved in ethyl acetate. Insoluble DCU was filtered off, and the filtrate was extracted with saturated aqueous $NaHCO_3$. The organic phase was dried over $MgSO_4$ and evaporated to dryness under vacuum. The residue was purified on a silica gel column eluting with ethyl acetate/methanol (7:1 v/v) to provide **2** (3.3 g, 63.5%) as yellow crystals. Mp: 65−67 °C; MS (FAB) *m/z* 523 (M + H); ^{1}H NMR (DMSO-*d6*) (major rotamer): δ 8.3−7.2 (m, 8H, acridine aromatics), 6.85 (t, 1H, J = 7.0 Hz), 3.95 (s, 2H), 3.80 (t, 2H, J = 7.0 Hz), 3.60 (s, 3H), 3.4−3.2 (m, 3H), 3.1−3.0 (m, 3H), 2.25 (t, 2H, J = 7 Hz), 1.8−1.7 (m, 2H), 1.5 (m, 2H), 1.3 (S, 9H); ^{13}C NMR (DMSO-*d6*): δ 205.08, 204,91, 202.77, 202.47, 187.96, 184.18, 162.51, 162.37,

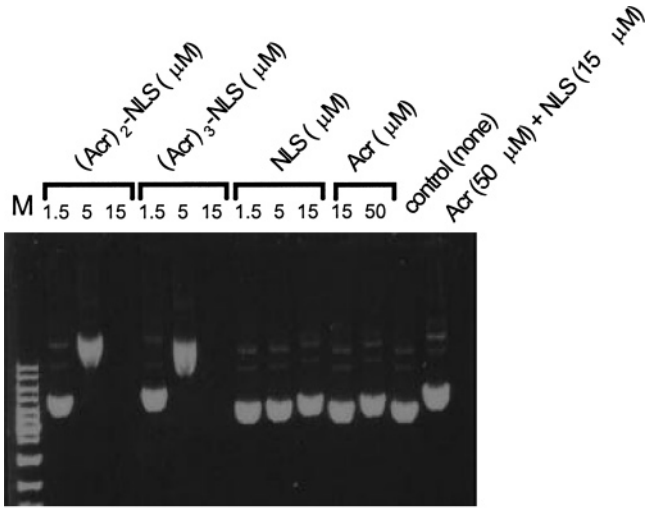

Figure 2. Gel-shift assay of Acr−NLSs binding to plasmid DNA. Plasmid pRL-CMV (2 μg) was incubated with test compounds for 30 min at room temperature. After incubation, the samples were analyzed by electrophoresis in 0.75% agarose gel using ethidium bromide staining for DNA detection. Lane M is a GeneRuler DNA Ladder Mix (MBI Fermentas).

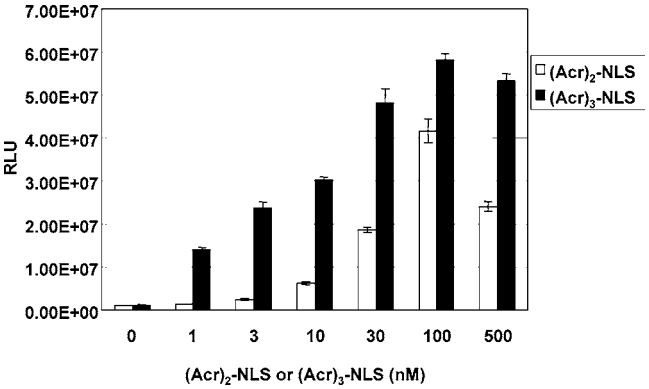

Figure 3. Effect of $(Acr)_2$−NLS or $(Acr)_3$−NLS concentrations on the transfection of JAR cells. A luciferase DNA vector (1 μg/mL of pGL3-control vector, Promega) in complex with polyethylenimine (PEI) (at the N:P ratio 3) was complexed with $(Acr)_2$−NLS or $(Acr)_3$−NLS at the different concentrations. The cells were transfected with the complex of DNA/$(Acr)_3$−NLS/PEI or DNA/$(Acr)_2$−NLS/PEI for 24 h and subsequently assayed for luciferase activity. Luciferase values are mean ± SD of at least three experiments and are presented as RLUs (relative light units) after normalization for protein concentrations.

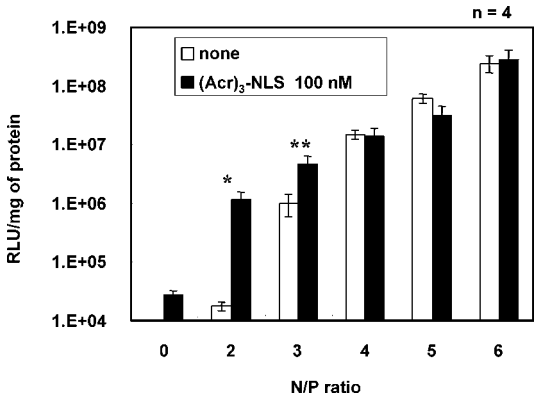

Figure 4. Effect of N:P ratio on the transfection of JAR cells by the luciferase vector DNA. pGL3-control vector (1 μg/mL, Promega) in complex with $(Acr)_3$−NLS and PEI at the different N:P ratios was used. The cells were transfected with the DNA/$(Acr)_3$−NLS/PEI or DNA/PEI complex for 24 h and subsequently assayed for luciferase activity. Luciferase values are mean ± standard deviation (SD) of at least four experiments and have been normalized for protein concentrations. An asterisk indicates significant difference between DNA/PEI and Acr−NLS/DNA/PEI ($P < 0.01$). Two asterisks indicate a significant difference between DNA/PEI and Acr−NLS/DNA/ PEI ($P < 0.05$).

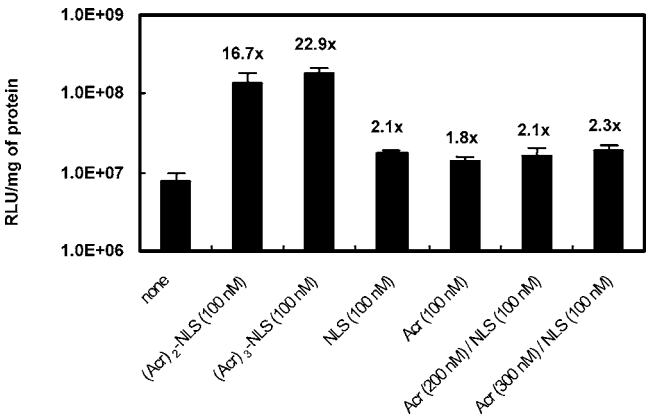

Figure 5. Transfection of JAR cells by complexes of luciferase vector DNA. pGL3 control vector (1 μg/mL, Promega) and test compounds at the indicated concentrations in complex with PEI (N:P ratios = 3) was used. The cells were transfected with the complex for 24 h and subsequently assayed for luciferase activity. Luciferase values are mean ± SD of at least three experiments and have been normalized for protein concentrations. The numbers on each bar indicate the fold of activation compare to the value from the control (DNA/PEI, no test compounds).

157.25, 153.82, 110.15, 109.95, 92.10, 84.41, 83.96, 81.91, 79.86, 79.50, 78.54, 70.55, 64.25, 63.84, 63.18, 60.52, 60.46, 58.55, 56.85, 56.58, 53.10, 46.42; HRMS $(M + H)^+$, calcd (found) for $C_{29}H_{39}N_4O_5$: 523.2920 (523.2913).

*N-(2-Bocaminoethyl)-N-[N-(acridine-9-yl)-6-aminohexanoyl]]glycine (***III***).* Compound **II** (2.6 g, 5 mmol) was dissolved in tetrahydrofuran (10 mL). NaOH (20 mL, 2M) was added, and the reaction mixture was stirred for 15 min. The pH adjusted to 4 by addition of HCl (2 M). The precipitate was filtered off and washed with water. The title compound (2.1 g, 84%) was obtained as a yellow powder. MS (FAB) *m/z* 509 (M + H); ^{1}H NMR (DMSO-*d6*) (major rotamer): δ 8.6−7.4 (m, 8H), 6.85 (br. s, 1H), 4.1−3.9 (m, 4H), 3.4−3.3 (m, 2H), 3.1−3.0 (m, 2H), 2.32 (t, 2H, $J = 7$ Hz), 2.0−1.8 (m, 2H), 1.6−1.5 (m, 2H), 1.4 (m, 2H), 1.3 (S, 9H); ^{13}C NMR (DMSO-*d6*): δ 210.19, 205.05, 204.10, 187.94, 185.00, 162.97, 157.43, 153.96, 149.88, 139.32, 129.50, 110.01, 109.72, 98.04, 92.83, 82.35, 70.37, 65.49, 64.38, 64.20, 62.95, 60.70, 60.46, 59.75, 57.46, 56.59, 54.08; HRMS $(M + H)^+$, calcd (found) for $C_{28}H_{37}N_4O_5$: 509.2764 (509.2763).

Cell Culture. JAR cells were used for transfections and were cultivated in RPMI-1640 (Sigma) supplemented with 10% fetal bovine serum, 1% Glutamax (Gibco), 100 IU/mL penicillin, and 100 μg/mL streptomycin. All cultures were incubated at 37 °C in humidified air with 5% CO_2.

Gel Mobility Shift Assay of Acr−NLSs for the DNA Binding. The plasmid DNA (100 μg/mL of pRL-CMV, Promega) was incubated at room temperature for 30 min with Acr−NLSs or other test compounds at the desired concentrations. Then the complexes were analyzed on a 0.75% agarose gel (*15*) with 1 × TBE buffer. After separation, gels were stained by ethidiumbromide (EtBr) and subjected to image analysis.

Formation and Transfection of Acr−NLS/DNA/PEI Complex. Cells were reseeded and incubated for

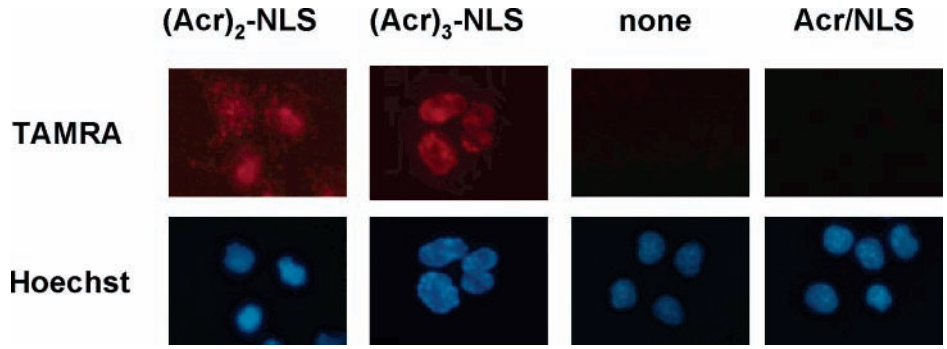

Figure 6. Increase of nuclear localization of the transfected DNA by $(Acr)_2$−NLS and $(Acr)_3$−NLS. JAR cells were transfected with the complex of TAMRA−PNA-labeled DNA (1 μg/mL, see Materials and Methods for detail) and auxiliary compounds in combination with PEI (N:P ratio at 3). After 24 h incubation, the cells were incubated with 2 μg/mL Hoechst33342 for 10 min at 37 °C and subjected to fluorescence microscopy analysis without fixation. TAMRA and Hoechst indicate the fluorescence images from TAMRA and Hoechst3342, respectively. $(Acr)_2$−NLS, 100 nM; $(Acr)_3$−NLS, 100 nM; Acr/NLS, Acr (300 nM)/NLS (100 nM).

16−24 h at 37 °C in 5% CO_2 to give 40−60% cell confluency at the time of transfection. For transfection of the plasmid DNA, cells were seeded in 24-well plates (Nunc) or 4-well chamber slides (Nunc), respectively. Before transfections, cell culture medium were replaced with 0.2 mL of OPTI-MEM (Gibco) supplemented with 1% FBS. To prepare the complexes of Acr−NLS, DNA, and polyethylenimine (PEI), 250 ng of DNA was incubated for 30 min at room temperature with Acr−NLS or other compounds in 25 μL of 150 mM NaCl. Then this solution was mixed with 25 μL of PEI solution in 150 mM NaCl. After 15 min of incubation at room temperature, 50 μL of Acr−NLS/DNA/PEI solution was added to the cells in the 0.2 mL of OPTI-MEM (1% FBS).

Luciferase Assay. Twenty-four hours after transfection, cells were subjected to the luciferase assay (Promega kit) according to the manufacturers instruction. Luciferase activities were normalized by protein concentrations and are presented as relative light unit (RLU). Protein concentrations were determined by BCA protein assay kit (Pierce) according to the manufacturers instruction.

Fluorescence Microscopic Analysis. For the nuclear localization studies of DNA, plasmid DNA (pRL-CMV, Promega) labeled with a TAMRA−bis-PNA conjugate was used (*16*, *17*). (The sequence of bis-PNA is TAMRA-(eg1)2-$T_{lys}TT_{lys}CT_{lys}$CTT-(eg1)3-TTJTJTTT-NH2, where TAMRA is 5(6)-carboxy-tetramethylrhodamine, J is pseudo-isocytosine (*16*) (placed in the Hoogsteen strand), T_{lys} is a lysine backbone PNA T-monomer (*18*), and eg1 is an 8-amino-3,6-dioxaoctanoic acid linker). For the labeling, 100 μg/mL of plasmid DNA was incubated with the 4 μM bis-PNA in water overnight at 37 °C. The complex of the DNA/bis-PNA was purified prior to transfection by using a PCR Cleaning Kit (BIO-RAD). Complexation and transfection of the complex (DNA/Acr−NLS/PEI) was performed as described above. Twenty-four hours after transfection, cells were incubated with 2 μg/mL of Hoechst33342 for 10 min at 37 °C, rinsed twice with phosphate-buffered saline, and subjected to fluorescence microscopic analysis using a LEITZ WETZLAR fluorescent microscope (DIALUX 22EB(Germany)) at 400× magnification.

RESULTS AND DISCUSSION

Bis- and tris-intercalating agents bind to double-stranded DNA with extremely high affinity ($K_d < 10^{-9}$ M), with slow off-rate kinetics, and without pronounced sequence selectivity (*11*, *15*). We therefore decided to investigate whether such ligands might be exploited to strongly and reversibly attach multiple copies of nuclear localization peptide (NLS) to plasmid DNA in order to facilitate nuclear delivery in gene-therapy approaches. To this end we designed a Boc-protected 9-aminoacridine amino acid monomer based on the peptide nucleic acid aminoethylglycine backbone (*18*) (Scheme 1). This monomer (eventually in combination with *N*-(acridine-9-yl)-6-aminohexanoic acid) allowed us to construct NLS oligoacridine conjugates by conventional continuous solid-phase peptide synthesis (Figure 1).

Gel Shift Assay for DNA Binding of the 9-Aminoacridine−NLS Conjugates (Acr−NLS). To study the association of Acr−NLS with plasmid DNA, an agarose gel-shift assay was carried out (*15*). Plasmid DNA (pRL-CMV) was mixed with increasing amounts of $(Acr)_2$−NLS or $(Acr)_3$−NLS and analyzed by electrophoresis in a 0.75% agarose gel. As shown in Figure 2, both $(Acr)_2$−NLS and $(Acr)_3$−NLS retarded the migration of the plasmid DNA at a concentration of 5 μM, while at 15 μM of $(Acr)_2$−NLS or $(Acr)_3$−NLS the DNA was retained in the wells. In contrast, NLS peptide or Acr monomer (Acr) (or a combination of the two) did not retard the DNA migration even at the highest concentrations tested (15 μM and 50 μM respectively). Therefore, as expected, only the bis- and trisacridine derivatives have sufficient DNA affinity to remain bound to the DNA during electrophoresis and cause band shifts (*15*).

Enhancement of Plasmid DNA Transfection Efficiency and Nuclear Localization of the Plasmid DNA by Acr−NLSs. For the transfection study with the luciferase-coding plasmid DNA, the polycationic transfection reagent PEI was used in complex with Acr−NLS/DNA. PEI is required for neutralization and condensation of the DNA to obtain spontaneous cellular uptake. We first determined the dose effect of the Acr−NLS conjugates (Figure 3). These results revealed first of all that the trisacridine conjugate is more potent than the bisacridine conjugate and second that both reagents show optimal effects around 100 nM at the conditions used. To establish the maximal DNA transfection efficiency by the Acr−NLS conjugates, the N:P ratio between nitrogen residues (of PEI) and phosphate residues (of DNA) was optimized. Luciferase plasmid DNA or the plasmid DNA/Acr−NLS complex was mixed with different concentration of PEI (at N:P ratio of 0, 2, 3, 4, 5, and 6) and used for transfection. Without PEI addition, DNA and $(Acr)_3$−NLS/DNA complex did not accomplish significant transfection (Figure 4), whereas using a combined $(Acr)_3$−NLS/DNA/PEI complex resulted in higher transfection efficiency compared to the control DNA/PEI complex alone (no Acr−

NLS addition) at an N:P ratio of 2 and 3. However, the effect of the $(Acr)_3$−PNA disappeared at N:P ratio 4, 5, and 6. $(Acr)_2$−NLS gave results similar to those of $(Acr)_3$−NLS at the N/P ratio 2 and 3 (data not shown).

Control experiments (Figure 5) showed that neither NLS or acridine alone or in combination yielded transfection efficiencies comparable to those obtained with either of the conjugates. Similar results were obtained from the experiments with GFP plasmid and also with HeLa cells (data not shown). These results suggest that this method can be used for double stranded DNA regardless of sequence.

Finally, the effects of Acr−NLS on the localization of the fluorescence-labeled DNA were investigated. JAR cells were transfected with rhodamine-labeled plasmid DNA with or without addition of 100 nM of Acr−NLSs in combination with PEI at the N:P ratio of 3. The accumulation of fluorescence in the nucleus was observed in the cells transfected by DNA/$(Acr)_2$−NLS/PEI and DNA/$(Acr)_3$−NLS/PEI complexes, whereas no accumulation of fluorescence was seen in the nucleus of the cells treated with Acr/NLS/DNA/PEI complexes (Figure 6). In addition, neither Acr nor NLS peptide itself induced a significant accumulation of fluorescent DNA in the nucleus (data not shown). Thus the observed increase of the DNA nuclear localization would explain the increment of transfection efficiency of luciferase plasmid DNA by Acr−NLSs.

CONCLUSIONS

The present results demonstrate that bis- and trisacridine NLS conjugates, due to their high affinty for double-stranded DNA, can be used as auxiliary agents for promoting nuclear localization of cellularly transfected DNA vectors, thereby enhancing their expression. We also observe that in our experiments the enhancing effect is limited to a narrow N:P ratio of transfection agent to DNA. However, it may well be possible to optimize the effect using other transfection reagents and by further optimization of the NLS conjugates. Finally, we note that the new acridine monomer may have a multitude of applications in constructing other peptides and ligands that bind strongly to dsDNA by intercalation.

ACKNOWLEDGMENT

This work was supported by the Lundbeck Foundation and the Danish Medical Research Council.

LITERATURE CITED

(1) Acsadi, G., Jani, A., Massie, B., Simoneau, M., Holland, P., Blaschuk, K., and Karpati, G. (1994) A differential efficiency of adenovirus-mediated in vivo gene transfer into skeletal muscle cells of different maturity. *Hum. Mol. Genet. 3*, 579−584.

(2) Tseng, W. C., Haselton, F. R., and Giorgio, T. D. (1997) Transfection by cationic liposomes using simultaneous single cell measurements of plasmid delivery and transgene expression. *J. Biol. Chem. 272*, 25641−25647.

(3) Branden, L. J., Mohamed, A. J., and Smith, C. I. (1999) A peptide nucleic acid-nuclear localization signal fusion that mediates nuclear transport of DNA. *Nat. Biotechnol. 17*, 784−787.

(4) Godbey, W. T., Wu, K. K., and Mikos, A. G. (1999) Tracking the intracellular path of poly(ethylenimine)/DNA complexes for gene delivery. *Proc. Natl. Acad. Sci. U.S.A. 96*, 5177−5181.

(5) Felgner, P. L., Gadek, T. R., Holm, M., Roman, R., Chan, H. W., Wenz, M., Northrop, J. P., Ringold, G. M., and Danielsen, M. (1987) Lipofection: a highly efficient, lipid-mediated DNA-transfection procedure. *Proc. Natl. Acad. Sci. U.S.A. 84*, 7413−7417.

(6) Zabner, J., Fasbender, A. J., Moninger, T., Poellinger, K. A., and Welsh, M. J. (1995) Cellular and molecular barriers to gene transfer by a cationic lipid. *J. Biol. Chem. 270*, 18997−19007.

(7) Capecchi, M. R. (1980) High efficiency transformation by direct microinjection of DNA into cultured mammalian cells. *Cell 22*, 479−488.

(8) Edgell, C. S., Curiel, D. T., Hu, P., and Marr, H. (1998) Efficient gene transfer to human endothelial cells using DNA-complexed to adenovirus particles. *Biotechniques 25*, 264−268.

(9) Gorlich, D., and Mattaj, I. W. (1996) Nucleocytoplasmic transport. *Science 271*, 1513−1518.

(10) Sebestyen, M. G., Ludtke, J. J., Bassik, M. C., Zhang, G., Budker, V., Lukhtanov, E. A., Hagstrom, J. E., and Wolff, J. A. (1998) DNA vector chemistry: the covalent attachment of signal peptides to plasmid DNA. *Nat. Biotechnol. 16*, 80−85.

(11) Wirth, M., Buchardt, O., Koch, T., Nielsen, P. E., and Norden, B. (1988) Interactions between DNA and mono-, bis-, tris-, tetrakis-, and hexakis(aminoacridines). A linear and circular dichroism, electric orientation relaxation, viscometry, and equilibrium study. *J. Am. Chem. Soc. 110*, 932−939.

(12) Christensen, L., Fitzpatrick, R., Gildea, B., Petersen, K. H., Hansen, H. F., Koch, T., Egholm, M., Buchardt, O., Nielsen, P. E., and Coull, J. (1995) Solid-phase synthesis of peptide nucleic acids. *J. Pept. Sci. 1*, 175−183.

(13) Karup, G., Meldal, M., Nielsen, P. E., and Buchardt, O. (1988) 9-Acridinylpeptides and 9-acridinyl-4-nitrophenylsulfonylpeptides. Synthesis, binding to DNA, and photoinduced DNA cleavage. *Int. J. Pept. Protein. Res. 32*, 331−343.

(14) Dueholm, K. L., Egholm, M., and Buchardt, O. (1993) An efficient synthesis of Boc-aminoacetaldehyde and its application to the synthesis of N−(2-Boc-aminoethyl) glycine esters. *Org. Prep. Proced. Int. 25*, 457−461.

(15) Nielsen, P. E., Zhen, W. P., Henriksen, U., and Buchardt, O. (1988) Sequence-influenced interactions of oligoacridines with DNA detected by retarded gel electrophoretic migrations. *Biochemistry 27*, 67−73.

(16) Egholm, M., Christensen, L., Dueholm, K. L., Buchardt, O., Coull, J., and Nielsen, P. E. (1995) Efficient pH-independent sequence-specific DNA binding by pseudoisocytosine-containing bis-PNA. *Nucleic Acids Res. 23*, 217−222.

(17) Mearini, G., Nielsen, P. E., and Fackelmayer F. O. (2004) Localization and dynamics of small circular DNA in live mammalian nuclei. *Nucleic Acids Res. 32*, 2642−51.

(18) Haaima, G., Lohse, A., Buchardt, O., and Nielsen, P. E. (1996) Peptide nucleic acids (PNAs) containing thymine monomers derived from chiral amino acids: hybridization and solubility properties of d-lysine PNA. *Angew. Chem., Int. Ed. Engl. 35*, 1939−1941.

BC050093F

Combined Radioimmunotherapy and Chemotherapy of Breast Tumors with Y-90-Labeled Anti-Her2 and Anti-CEA Antibodies with Taxol

Desiree M. Crow,[†] Lawrence Williams,[‡] David Colcher,[†] Jeffrey Y. C. Wong,[†] Andrew Raubitschek,[†] and John E. Shively*[,§]

Department of Radioimmunotherapy, Division of Radiation Oncology, City of Hope National Medical Center, Duarte, California 91010, Division of Radiology, City of Hope National Medical Center, Duarte, California 91010, and Division of Immunology, Beckman Research Institute of the City of Hope, Duarte, California 91010. Received March 23, 2005; Revised Manuscript Received July 20, 2005

Because breast cancer cells often express either Her2/neu or carcinoembryonic antigen (CEA) or both, these tumor markers are good targets for radioimmunotherapy using Y-90-labeled antibodies. We performed studies on nude mice bearing xenografts from MCF7, a cell line that has low Her2 and CEA expression, to more accurately reflect the more usual situation in breast cancer. Although uptake of In-111 anti-CEA into tumors was lower than that for In-111-labeled anti-Her2, radioimmunotherapy (RIT) with Y-90 anti-CEA was equivalent to that of Y-90 anti-Her2. When either Y-90 antibody was combined with a split-dose treatment with Taxol, the antitumor effect was greater than with either agent alone. When Y-90 anti-CEA was combined with a single dose of Taxol, the results were equivalent to the split-dose regimen. RIT plus cold Herceptin had no additional effects on tumor size reduction over RIT alone. When animals were first treated with Y-90 anti-Her2 and imaged 1−2 weeks later with In-111 anti-CEA or anti-Her2, tumor uptake was higher for anti-CEA and improved over tumor uptake with no prior RIT. These results suggest that a split dose of RIT with anti-Her2 antibody followed by anti-CEA antibody would be more effective than a single dose of either. This prediction was partially confirmed in a controlled study comparing single- vs split-dose anti-Her2 RIT followed by either anti-Her2 or anti-CEA RIT. These studies suggest that combined RIT and Taxol therapy are suitable in breast cancers expressing either low amounts of Her2 or CEA, thus expanding the number of eligible patients for combined therapies. They further suggest that split-dose RIT using different combinations of Y-90-labeled antibodies is effective in antitumor therapy.

INTRODUCTION

Despite the use of combination chemotherapy, metastatic breast cancer is invariably a fatal disease (*1*). The advent of monoclonal antibodies as therapeutic approaches has made it possible to directly target cell surface receptors that are required for tumor cell growth. One of the most studied antibodies in this approach is Herceptin (trastuzumab) that targets Her2, a member of the EGFR family (*2*, *3*). Unfortunately, anti-Her2 therapy is limited to tumors that overexpress Her2, limiting this therapy to a small subset (15−20%) of breast cancer patients (*4*). A further problem is that Herceptin as a single agent is cytostatic (*5*) and must be used in combination with chemotherapeutic agents to achieve maximum therapeutic benefit (*6*). Among the combination therapies, it has been used with doxorubicin/cyclophosphamide (AC), Taxol (*7*), and more recently, docetaxel plus platinum salts (*8*). Although response rates of up to 79% have been reported (*8*), the median time to progression of 9.9−15.5 months suggests that further improvement is warranted. In addition, prolonged use of Herceptin with some drugs, especially doxorubicin, have led to cardiac toxicity in as many as 27% of treated patients (*9*).

In view of these problems, we have been exploring the use of Y-90 radioimmunotherapy (RIT) as an alternative to cold antibody therapy. Y-90 is a high-energy beta emitter with a half-life of 2.7 days and a maximum path length of 11 mm in tissue. Antibodies conjugated to chelates such as DTPA (*10*) and DOTA (*11*) readily bind Y-90 just prior to injection, thus making this approach attractive in the clinic. A major advantage of RIT is that the once the antibody is targeted to the tumor, it exerts a direct cytotoxic effect. Disadvantages of this approach are the logistical production of radiolabeled antibodies with associated waste disposal and the time required for effective targeting to the tumor because while the radiolabeled antibody is in circulation there is accumulated bone marrow toxicity (*12*, *13*). While many researchers have tried to decrease blood circulation time by engineering small-sized antibody fragments, the net effect is usually faster renal excretion reducing tumor uptake accordingly (*14*). As a result most RIT approaches have relied on whole antibodies engineered as chimeric (*15*−*17*) or humanized (*18*−*21*) versions to maximize tumor uptake while reducing immunogenicity.

The excellent targeting properties of radiolabeled anti-Her2 antibodies has long been appreciated and shown to be effective in reducing tumor size in animal models (*11*, *22*). However, these studies, like therapy with cold Herceptin, have been focused on tumors that overexpress

* To whom correspondence should be addressed.
[†] Department of Radioimmunotherapy, Division of Radiation Oncology, City of Hope National Medical Center.
[‡] Division of Radiology, City of Hope National Medical Center.
[§] Division of Immunology, Beckman Research Institute of the City of Hope.

10.1021/bc0500948 CCC: $30.25 © 2005 American Chemical Society
Published on Web 08/26/2005

Her2. Similarly, we have focused our efforts on the use of radiolabeled anti-carcinoembryonic antigen (anti-CEA) antibodies on tumors that overexpress CEA (*23*). In clinical trials in which Y-90 anti-CEA Mab cT8.66 was administered as a single agent to patients with colorectal cancer, only modest effects on tumors were seen, while in CEA-positive breast cancer patients the effects were more impressive (*16*, *24*). The conclusion from these studies is that combination therapies of RIT plus chemotherapy will be required to produce more lasting results. CEA is an attractive cell surface target in that it is expressed in about 50% of breast cancers (*25*) and is a reliable marker for breast cancer recurrence (*26*−*28*). Since most breast cancers express Her2 at some level, the combined expression of Her2 and CEA in breast cancers is about 50%. In this study, we now ask the question, can RIT, especially RIT combined with chemotherapy, be effective against breast tumors that have low to moderate amounts of target antigens such as Her2 and CEA? To answer this question in a preclinical setting, we have grown dual Her2 and CEA positive MCF7 cells as xenografts in nude mice and treated the animals with either Y-90-labeled Herceptin or cT84.66 in the presence or absence of Taxol. This cell line has low amounts of cell surface Her2 (*29*) that fall below the amount required for successful cold Herceptin therapy and has moderate to low amounts of cell surface CEA (*30*). The results suggest that in combination with Taxol, the amount of RIT to produce sustained tumor reductions can be reduced 50% or more over that required producing equivalent results as a single agent. Quite surprising, while In-111-labeled cT84.66 tumor targeting was low (tumor-to-blood ratio of 1.0), RIT with Y-90-labeled cT84.66 was as effective as Y-90-labeled Herceptin in this animal model. The results are encouraging in that the use of RIT with these antibodies may be effective even in tumors with low amounts of cell surface antigen, thus opening up this therapy to a larger group of patients compared to the current scenario with cold Herceptin. A second intriguing result from this study was that animals treated with Y-90 Herceptin exhibited an increased uptake of In-111 cT84.66 compared to In-111 Herceptin, suggesting that sequential RIT first with Y-90 Herceptin and then with Y-90 cT84.66 may be possible in tumors that express both Her2 and CEA. This approach would be especially attractive in treating tumors that downregulate a target antigen after initial therapy.

MATERIALS AND METHODS

Materials. MCF-7 cells were obtained from ATCC and maintained in sterile growth media consisted of Eagle's Minimal Essential media 1× (EMEM) (Cellgro, Herndon, VA) supplemented with 10% heat-inactivated fetal bovine serum (FBS) (Omega Scientific, Tarzana, CA), and 1% L-glutamine, 10 mM sodium pyruvate, 0.1 mM nonessential AA. Media was sterile filtered through a 0.2 μm vacuum filter. Herceptin was obtained from the City of Hope Pharmacy and dialyzed vs PBS prior to conjugation. 1B4M chelate was a generous gift from Dr. Martin Brechbiel (NCI) and was conjugated to Herceptin according to established methods (*10*). DOTA-conjugated chimeric anti-CEA antibody cT84.66 has been previously described by us (*31*, *32*). The number of chelates per antibody which were determined using In-111 isotope dilution in $InCl_3$ essentially according to Lewis et al. (*32*) was 3 and 2.4 for 1B4M-Herceptin and DOTA-cT84.66, respectively. Chelate conjugated antibodies were radiolabled with In-111 (Amersham, 1−2 mCi per 0.1 mg of protein) as previously described (*32*).

MCF-7 Xenograft Model. Female, athymic nu/nu mice (Charles River), 10−12 weeks old, were exposed to 200 RADS external beam Co-60 irradiation 3 days prior to MCF-7 implantation and given sulfatrim antibiotic water for two weeks. Two days prior to MCF-7 implantation mice were administered 0.8 mg of Delestrogen IM injection in the thigh. MCF-7 cells (5×10^6) in EMEM and Matrigel were implanted into each mouse subcutaneous in the flank. Tumors were established within 10−14 days postinjection. Before therapy studies began, tumor-bearing animals were separated into treatment groups based on tumor size (100−200 mg), so all groups average tumor volumes were similar at the onset of the therapy studies. Tumor volumes were estimated twice weekly using the formula length × width^2/2. Relative tumor volume was calculated as the ratio of the current measurement to the initial value. Weights of the animals, measured in grams, were recorded once a week; no animal had more than a 2% weight loss during the course of the experiment.

Radioimaging and Biodistribution Studies. Athymic mice bearing MCF-7 xenografts were injected with 200 μL (2.8 μg of 0.9 μCi/μg) of In-111-labeled 1B4M-Herceptin via tail vein. Five mice per time point were sacrificed at 0, 2, 24, 48, 72, and 96 h postinjection and biodistributions performed (blood, liver, spleen, kidneys, lungs, tumor, and carcass). Alternatively, mice were tail injected with 200 μL (3.2 μg of 1.25 μCi/μg) of In-111-DOTA-cT84.66. Results were calculated as percent injected dose per gram (%ID/g) vs time. For radioimaging, mice were injected with 15 μCi In-111-1B4M-Herceptin (6 μg) and imaged using a BIOSPACE γ imager instrument with settings of 154−188 keV and 220−270 keV.

RIT and Combined Therapy Studies. *RIT and Cold Herceptin*. Four Y-90-DOTA cT84.66 RIT treatment groups (eight Athymic mice per group bearing MCF-7 xenografts) were as follows: 50 μCi RIT, 100 μCi RIT, 50 μCi RIT with cold Herceptin, and 100 μCi RIT with cold Herceptin. A fifth group of mice received only cold Herceptin, which was used as a non-RIT control. The three groups that received the cold Herceptin were administered two IP injection doses (200 μg each), 9 days apart. The sixth group of mice received a single IP injection of sterile saline (no treatment control). The six groups of mice were monitored daily for 5 weeks.

RIT and Single Dose Taxol. Four Y-90-DOTA-cT84.66 RIT treatment groups (eight athymic mice per group bearing MCF-7 xenografts) were as follows: 20 μCi RIT, 40 μCi RIT, 20 μCi RIT with Taxol, and 40 μCi RIT with Taxol. The fifth group received Taxol only. The three groups that received Taxol were administered a single bolus IP of 600 μg Taxol admininistered 24 h post RIT. The sixth group received a single IP injection of sterile saline (no treatment control). The six groups of mice were monitored daily for 5 weeks.

RIT and Two Doses of Taxol. Four Y-90-DOTA-cT84.66 RIT treatment groups (eight athymic mice per group bearing MCF-7 xenografts) were as follows: 40 μCi RIT, 80 μCi RIT, 40 μCi RIT with Taxol, or 80 μCi RIT with Taxol. The fifth group received Taxol only. The three groups that received Taxol were administered two IP injections of 300 μg Taxol 48 and 72 h after RIT. The sixth group received a single IP injection of sterile saline (no treatment control). The six groups of mice were monitored daily for 5 weeks. An identical study was performed with Y-90-1B4M-Herceptin.

RIT Followed by In-111 Antibody Biodistribution. Eight treatment groups (8 athymic nude mice bearing MCF-7 xenografts per group) were as follows: four

groups received 60 μCi Y-90-1B4M-Herceptin, two of which received 200 μL either In-111-labeled cT84.66 (1.7 μg of 2.4 μCi/μg) or Herceptin (1.7 μg of 2.4 μCi/μg) 7 days after initial therapy and two groups of which received either In-111-labeled DOTA-cT84.66 (2.5 μg of 2.4 μCi/μg) or In-111 1B4M-Herceptin (2 μg of 2.35 μCi/μg) 14 days after initial therapy. The other four groups were as follows: no RIT, two groups on day 7 received either In-111-labeled DOTA-cT84.66 or In-111-labeled 1B4M-Herceptin. The final two groups received either In-111-labeled DOTA-cT84.66 or 1B4M-Herceptin on day 14. The In-111-labeled anibody was injected via tail vein, and animals were sacrificed 72 h postinjection and biodistributions were performed (blood, liver, spleen, kidneys, lungs, tumor, and carcass).

RIT Followed by Second-Dose RIT. Six treatment groups (10 athymic nude mice bearing MCF-7 xenografts per group) were as follows: three groups received 60 μCi (8 μg) of Y-90-1B4M-Herceptin of which one group received no second therapy, one received a second therapy with 40 μCi (5.6 μg) of Y-90-1B4M-Herceptin and the final group received a second therapy with 40 μCi (6 μg) of Y-90-DOTA-cT84.66 administered 14 days after the first RIT. Two other groups received no initial RIT but on day 14 received either 40 μCi (5.6 μg) of Y-90-1B4M-Herceptin or 40 μCi (6 μg) of Y-90-DOTA-cT84.66. The final group received only saline via tail vein and served as the no-treatment therapy control. All RIT was administered via tail vein in 200 μL total volume injected.

Data Analysis. For biodistribution studies, the results were reported as %ID/g of tissue vs time. Comparisons were made by t-test and p values were calculated. For RIT or combined RIT and Taxol studies, average relative tumor volumes vs time were reported and the curves were analyzed by ANOVA (two-factor without replication).

Table 1. Biodistributions for Nude Mice Bearing MCF7 Xenografts with In-111 Anti-Her2 or In-111 Anti-CEA Antibodies[a]

In-111 Anti-Her2 Antibodies						
	0 h	2 h	24 h	48 h	72 h	96 h
blood	31.84 ±1.48	25.15 ±2.40	12.26 ±1.23	10.81 ±0.95	11.42 ±1.24	8.25 ±2.35
liver	6.98 ±1.63	5.85 ±0.87	4.60 ±1.49	4.48 ±1.56	3.96 ±0.18	4.83 ±1.08
spleen	6.31 ±1.97	5.50 ±1.33	3.62 ±0.86	3.20 ±0.32	4.71 ±1.18	3.22 ±1.34
kidney	4.95 ±0.52	5.65 ±0.83	3.36 ±0.40	3.60 ±0.69	3.04 ±0.29	3.16 ±0.39
lung	8.31 ±1.00	8.41 ±1.04	5.05 ±0.56	5.03 ±0.92	4.66 ±0.43	3.81 ±0.44
tumor	0.51 ±0.11	2.25 ±0.24	16.41 ±5.40	20.47 ±2.67	25.01 ±5.64	23.08 ±4.44
carcass	2.11 ±0.32	3.02 ±0.09	3.32 ±0.31	3.43 ±0.23	3.37 ±0.21	3.19 ±0.10

In-111 Anti-CEA Antibodies				
	0 h	24 h	48 h	72 h
blood	33.15 ±2.30	10.49 ±2.46	11.24 ±1.64	7.88 ±3.36
liver	6.39 ±0.50	3.99 ±1.19	3.78 ±0.59	3.96 ±1.42
spleen	5.09 ±1.41	2.65 ±1.21	2.71 ±0.46	4.42 ±1.84
kidney	6.42 ±0.67	3.11 ±0.40	3.39 ±0.83	3.49 ±1.12
lung	9.59 ±1.60	4.06 ±0.98	4.05 ±1.41	3.94 ±1.18
tumor	0.75 ±0.11	7.02 ±1.31	11.58 ±2.30	10.78 ±2.27
carcass	1.76 ±0.15	3.12 ±0.35	3.45 ±0.43	3.36 ±0.11

[a] Five animals per each time point were analyzed for the indicated tissues. Results are reported as %ID/g with the standard deviation given below.

RESULTS

Biodistributions of In-111-Labeled Anti-CEA and Anti-Her2 Antibodies in MCF-7 Xenografts. CEA and Her2 are expressed in breast cancer in variable amounts (*2*, *25*). The overall positivity for CEA is about 50%, but the expression level is usually much less than in colon cancer. Her2 is overexpressed in 15−20% of breast cancers but is moderately expressed in higher numbers, perhaps up to 30−40% (*33*). However, Herceptin therapy is only appropriate in the tumors that overexpress Her2. We were therefore interested in testing the possibility of using RIT or combined RIT and Taxol therapy to treat tumors that had low to moderate amounts of either antigen. For these reasons, we chose MCF-7 cells which express both Her2 and CEA in low to moderate amounts. To determine the potential for RIT, we first compared the uptake of In-111-labeled anti-CEA (cT84.66) and anti-Her2 (Herceptin) in nude mice bearing MCF-7 xenografts. As shown in Table 1 tumor uptake reached a maximum in 48−72 h with values of 11.6 (±2.3) and 25.0 (±5.6) %ID/g for anti-CEA and anti-Her2, respectively. The tumor-to-blood ratios at maximum uptake were 1.0 and 2.0 for anti-CEA and anti-Her2, respectively. The low tumor-to-blood ratio for the anti-CEA study was especially worrisome, since bone marrow toxicity is the major side effect in high dose RIT. In general, tumor-to-blood ratios of at least 2:1 are preferred to minimize this toxicity. Thus, from the results of the biodistribution data, we predicted that anti-Her2 would be the superior antibody for RIT in this tumor model. Nonetheless, we proceeded to compare both antibodies in RIT since the tumor model provided a unique opportunity to see if the biodistribution results would correctly predict the RIT results.

RIT and Taxol Therapy with Y-90-Labeled Anti-CEA and Anti-Her2 Antibodies in MCF-7 Xenografts. Since previous studies have shown that only high-dose RIT with or without autologous blood or marrow transplant (BMT) gave superior responses for single agent therapy (*34*), we considered from the outset to perform combined RIT plus chemotherapy in the tumor model system. Taxol was chosen as the agent of choice because of its prevalent use in breast cancer therapy especially when used with Herceptin cold antibody therapy. On the basis of the results of DeNardo and co-workers in which RIT with various taxol combinations were explored (*35*), we chose to administer single-dose RIT followed by two doses of taxol IP (300 μg). Since previous experience established that 100−120 μCi/mouse of Y-90-cT84.66 therapy was sufficient to cause >50% tumor growth inhibition (*11*), we explored the use of lower-dose RIT (40 and 80 μCi) so that the effect of Taxol (if any) would not be obscured by the RIT. As shown in Figure 1A, the relative tumor volume of the control animals increased by 2−2.5-fold over 35 days, while Taxol-only treated animals showed a brief period of tumor growth inhibition but ultimately reached the same size as control animals. Animals treated with 40 μCi of Y-90-cT84.66 exhibited a similar reduction in tumor growth compared to Taxol alone (p = 0.29), but by the end of 35 days tumor regrowth was apparent. When the RIT dose was increased to 80 μCi/animal a substantial tumor growth inhibition was seen, even at the end of 35 days (p =

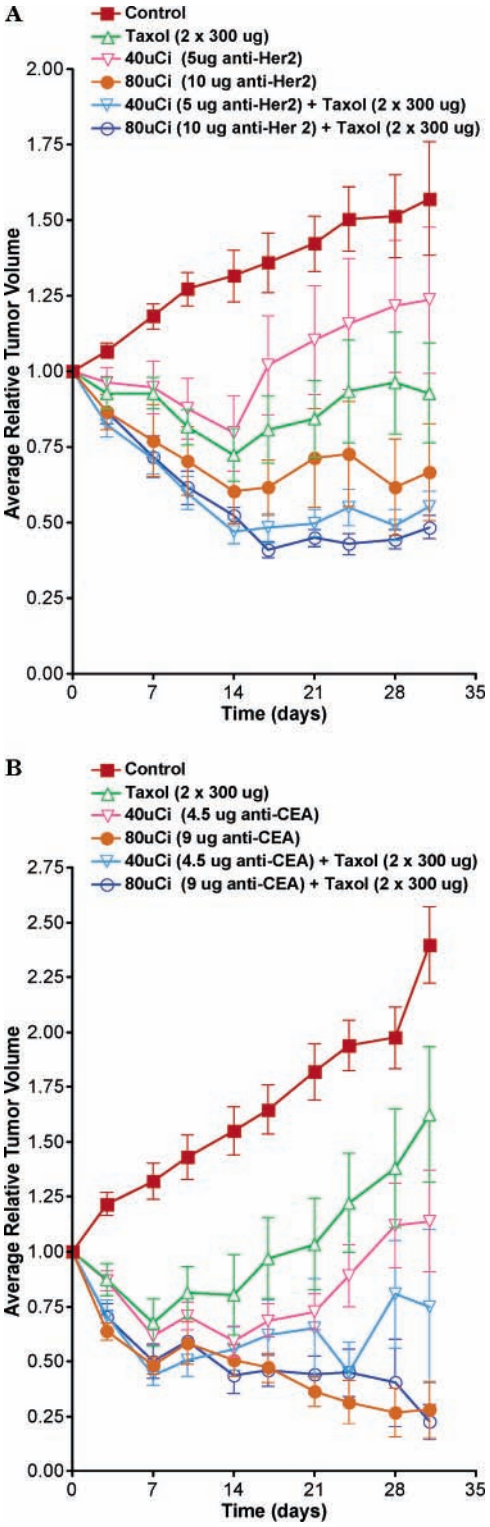

Figure 1. Radioimmunotherapy of established MCF-7 tumors in nude mice with Y-90-labeled anti-Her2 or anti-CEA antibodies in combination with a split dose dose of Taxol. Groups of eight mice were injected IV with either (A) Y-90-labeled anti-Her2 antibody or (B) Y-90-labeled anti-CEA antibody. Taxol (300 μg) was administered IP 48 and 72 h post RIT. The tumor volume for each mouse at the time indicated was normalized to the tumor volume at the start of treatment (average relative tumor volume) and was plotted versus days after the start of treatment.

0.0006). The addition of Taxol to the 40 μCi RIT and 80 μCi RIT further improved the tumor effect ($p = 0.003$ for both). Essentially similar results were obtained for

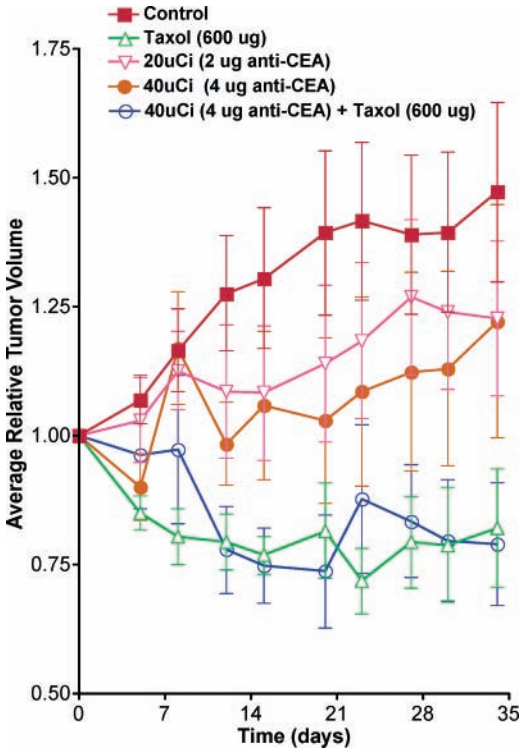

Figure 2. Radioimmunotherapy of established MCF-7 tumors in nude mice with Y-90-labeled anti-CEA antibody in combination with a single dose of Taxol. Groups of eight mice were injected IV with Y-90-labeled anti-CEA antibody. Taxol (600 μg) was administered IP 48 h post RIT. The tumor volume for each mouse at the time indicated was normalized to the tumor volume at the start of treatment (average relative tumor volume) and was plotted versus days after the start of treatment.

Y-90-labeled anti-Her2 RIT at two dose levels with or without Taxol (Figure 1B).

At first inspection, the results surprised us because based on the biodistribution results shown in Table 1 we expected superior results with anti-Her2 RIT vs anti-CEA RIT. Since the tumor cell line and animal model are identical, we tentatively conclude that there is an inherent advantage to anti-CEA RIT over anti-Her2 RIT. We therefore decided to explore this phenomenon more thoroughly by performing other RIT studies with Y-90 anti-CEA, one using RIT plus a single dose of Taxol and another using RIT plus cold Herceptin.

RIT with Y-90-Labeled Anti-CEA and Taxol or Cold Herceptin in MCF-7 Xenografts. Since DeNardo and co-workers (*35*) had shown that a single dose of 600 μg of Taxol IP 24 h after RIT was equivalent to a split dose of 300 μg of Taxol at 48 and 72 h post RIT, we chose the single-dose regimen to repeat the study and chose the 40 μCi dose of RIT with Taxol to determine if the single dose was equivalent to the split-dose regimen. The results shown in Figure 2 demonstrate a more prolonged tumor suppression with the single dose of Taxol compared to the split-dose regimen (compare Figure 1 to Figure 2, taxol only, $p = 0.01$) while the 40 μCi RIT only demonstrated tumor reduction followed by regrowth, similar to the results shown in Figure 1. Single-dose Taxol plus 40 μCi of RIT resulted in prolonged tumor suppression, greater than that observed for either Taxol or RIT alone ($p = 0.00007$ and 0.0003, respectively). In this case, the results were essentially equivalent to the higher-dose RIT combined therapy results shown in Figure 1 ($p = 0.56$). Thus, it is likely either single or split doses of Taxol plus single-dose RIT are promising therapies for CEA-positive breast cancers.

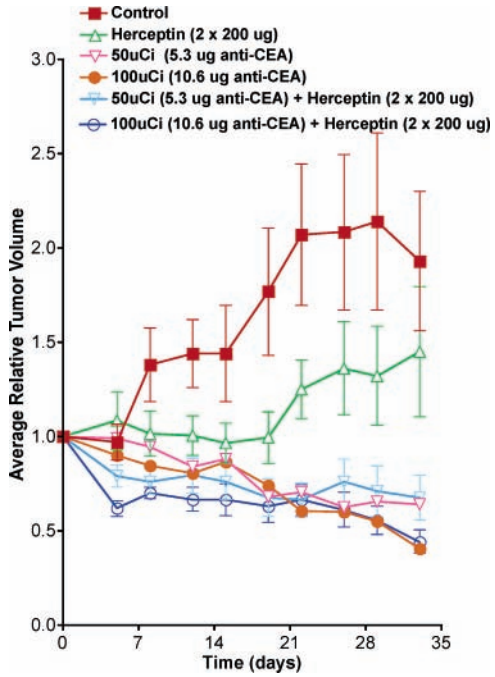

Figure 3. Radioimmunotherapy of established MCF-7 tumors in nude mice with Y-90-labeled anti-CEA antibody in combination with a split dose of cold anti-Her2 antibody. Groups of eight mice were injected IV with Y-90-labeled anti-CEA antibody. Anti-Her2 antibody (200 μg) was administered IP at day 0 and day 9 post RIT. The tumor volume for each mouse at the time indicated was normalized to the tumor volume at the start of treatment (average relative tumor volume) and was plotted versus days after the start of treatment.

It has been previously shown that cold Herceptin has a minimal effect on tumors with a low expression level of Her2 (*36*). Since the expression level of Her2 is low and the gene is not amplified in MCF-7 cells (*29*), we expected that treatment of the animals with cold Herceptin would have no effect on tumor growth. Nonetheless, it is evident that many patients with low levels of Her2 expression are still treated with Herceptin, and we felt it prudent to determine if RIT plus cold Herceptin had an additive tumor effect. Therefore, MCF-7 xenograft-bearing animals were treated with Herceptin alone (200 μg IP at days 0 and 9), RIT alone (50 or 100 μCi), and Herceptin plus RIT (Figure 3). Tumor growths curves for untreated, day 0−33, or Herceptin-treated, day 19−50, animals after initial tumor suppression were essential identical ($p = 0.28$), while either 50 or 100 μCi of RIT with Y-90 anti-CEA produced substantial tumor growth inhibition ($p = 0.000004$ for both) with a good separation between the two doses of RIT. The addition of cold Herceptin had no additive effect on either dose of RIT ($p = 0.57$, $p = 0.14$, respectively).

Effect of Y-90 Anti-Her2 RIT on Anti-CEA and Anti-Her2 Uptake. The above results suggest that either anti-Her2 or anti-CEA RIT would have antitumor effects even in tumors expressing low levels of one or the other antigen. However, we were also interested in the possibility of treating tumors expressing both antigens by sequential RIT first with one then the other Y-90-labeled antibody. The rationale for this approach is that single agent RIT against a tumor antigen may cause selective outgrowth of tumors that downregulate the antigen even further, thus rendering the complete ablation of the tumor unfeasible even with subsequent doses. If the tumor were treated first with one RIT agent and then a second, one would predict that the sequential dual therapy would be more efficacious than repeated administration of the single agent. As a first step in testing this approach, we treated MCF-7 xenograft-bearing animals with Y-90 anti-Her2 (60 μCi) for 7 or 14 days at which point the tumor growth reduction had reached its maximal effect and then administered In-111-labeled anti-Her2 or anti-CEA to determine if either or both antibodies have altered tumor uptake. Because the number of animals required to perform this experiment, we limited the biodistribution data to 72 h after administration of the In-111-labeled antibody in which the maximum tumor uptake is know to occur (see Table 1). We also performed whole animal imaging at various times to verify that tumor uptake of In-111 antibody was uniform over the time course of RIT. The results shown in Table 2 demonstrate that the tumor and blood values are statistically similar for In-111 anti-Her2 with or without Y-90 anti-Her2 RIT ($p = 0.06$); however, for In-111 anti-CEA, there is a substantial increase in tumor uptake after Y-90 anti-Her2 therapy ($p = 0.0005$). The results are even more striking because the In-111 anti-Her2 results serve as a control for the In-111 anti-CEA results.

Whole body images of the mice after 7 days of RIT and 74 h after administration of In-111 anti-CEA revealed about a 2-fold increase in tumor uptake, comparing animals imaged with In-111 anti-Her2 or those receiving

Table 2. Biodistributions of In-111-Labeled Anti-Her2 or In-111-Labeled Anti-CEA Antibodies in Nude Mice Bearing MCF7 Xenografts 7 or 14 Days after Treatment with Y-90-Labeled Anti-Her2 Antibody[a]

7 Days				
	In-111 anti-Her2, 72 h		In-111 anti-CEA, 72 h	
	no RIT	RIT	no RIT	RIT
blood	11.96	11.89	11.29	15.83
	2.87	*2.76*	*1.74*	*2.02*
liver	5.52	5.87	5.07	5.48
	1.56	*2.52*	*1.96*	*1.25*
spleen	4.35	5.46	3.25	5.35
	0.72	*1.08*	*0.91*	*1.52*
kidney	6.79	6.24	3.62	4.83
	0.69	*0.58*	*0.60*	*0.64*
lung	5.14	5.64	4.35	6.95
	0.87	*0.96*	*1.01*	*0.60*
tumor	21.14	19.84	29.72	39.31
	3.45	*1.89*	*8.05*	*7.87*
carcass	3.08	3.17	2.47	2.98
	0.37	*0.26*	*0.31*	*0.31*

14 Days				
	In-111 anti-Her2, 72 h		In-111 anti-CEA, 72 h	
	no RIT	RIT	no RIT	RIT
blood	13.06	13.71	13.77	16.35
	2.20	*1.11*	*2.37*	*1.68*
liver	6.07	3.73	7.00	4.09
	1.80	*0.75*	*1.67*	*1.25*
spleen	3.43	3.85	3.22	3.74
	0.73	*0.47*	*0.69*	*0.37*
kidney	4.27	4.54	4.46	4.70
	0.44	*0.45*	*0.42*	*0.58*
lung	5.21	5.32	5.59	6.43
	1.11	*0.33*	*1.14*	*0.96*
tumor	22.33	21.77	27.63	38.95
	2.35	*4.53*	*7.34*	*8.60*
carcass	2.62	2.65	2.56	2.74
	0.25	*0.18*	*0.34*	*0.22*

[a] Five animals were analyzed for the indicated tissues at the 72 h time point. Results are reported as %ID/g with the standard deviation given below.

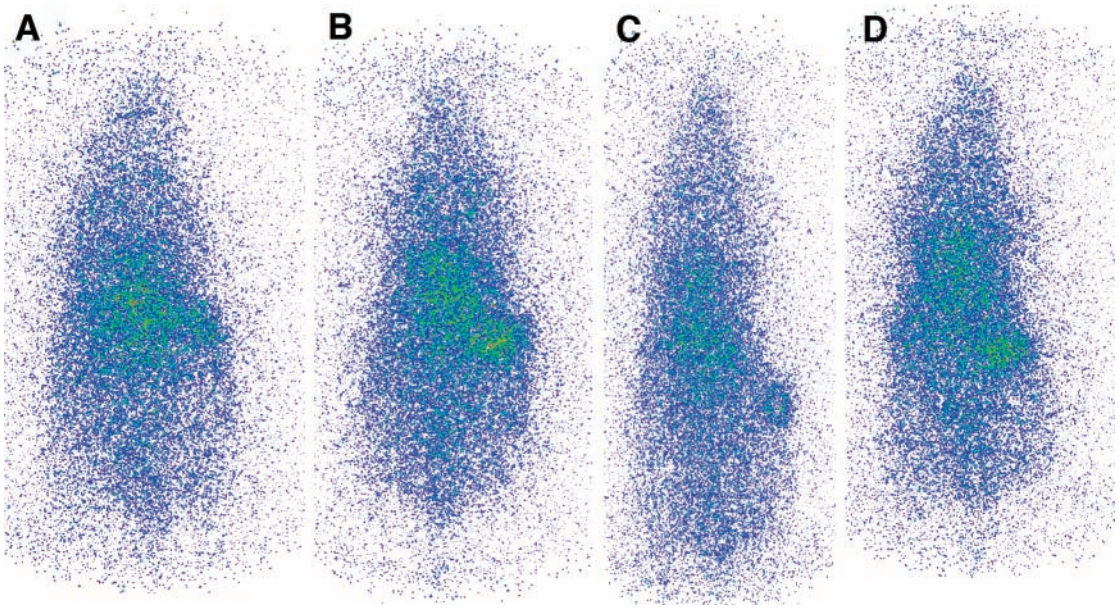

Figure 4. Radioimmunoimaging of established MCF-7 tumors in nude mice with In-111-labeled anti-Her2 or anti-CEA antibody, pretreated with Y-90-labeled anti-Her2 antibody. Groups of eight mice were treated IV with 60 μCi (6 μg) of Y-90-labeled anti-Her2 antibody followed by either 15 μCi (6 μg) of In-111-labeled anti-Her2 or 15 μCi (12 μg) of In-111-labeled anti-CEA antibody 7 days after the start of RIT. Images were acquired 74 h after injection of In-111-labeled antibodies. The central organ is liver and SC tumors are on located on the right side. A and C: In-111-labeled anti-Her2 antibody. B and D: In-111-labeled anti-CEA. A and B: images taken 10 days after start of RIT. C and D: images taken 10 days after injection of saline (no treatment controls).

no therapy (Figure 4). Similar results were obtained for animals treated for 14 days and then imaged with either In-111-labeled antibody. These images agree with the results of the animal biodistributions and demonstrate that prior RIT did not affect the time course of In-111 antibody uptake in tumor or normal tissues.

Split-Dose RIT with Y-90-Labeled Anti-Her2 Followed by Y-90-Labeled Anti-CEA or Anti-Her2 Antibodies. Since In-111-labeled anti-CEA uptake increased after Y-90-labeled anti-Her2 RIT, we proceeded to test the effect of split-dose RIT, first with anti-Her2 and second with anti-Her2 or anti-CEA RIT. The first dose of RIT was administered at 60 μCi as suggested by the optimal anti-CEA uptake seen in Figure 4. The second dose of RIT was reduced to 40 μCi and administered 7 days after the first dose to minimize bone marrow toxicity. As seen in Figure 5, the single dose of Y-90-labeled anti-Her2 RIT resulted in significant tumor reduction compared to controls, but the tumors continued to grow at a reduced rate. In animals that received no first dose of RIT but received the "second" dose of either Y-90-labeled antibody, tumor growth followed the controls until the "second" dose was administered at which point tumor growth was retarded but remained above 1.25 in relative tumor volume units. In animals that received the first dose of RIT followed by the second dose of either Y-90-labeled antibody, tumor volume showed a substantial reduction below 1.00 relative tumor volume units out to 60 days. It also appears that second RIT treatment with Y-90-labeled anti-CEA is more effective than that with Y-90-labeled anti-Her2 antibody. The curves are significantly different when analyzed by ANOVA ($p < 0.05$) but not significantly different when analyzed by the t-test ($p = 0.05$). Thus, we conclude that a split dose of RIT with either antibody is effective and that the increased uptake of In-111-labeled anti-CEA observed in Figure 4 (Table 2) may predict a more effective split-dose RIT for anti-Her2/anti-CEA vs anti-Her2/anti-Her2. To confirm this prediction additional experiments would be necessary with different doses of RIT for each antibody. We believe that experiments of this nature are beyond the useful limits of this animal model.

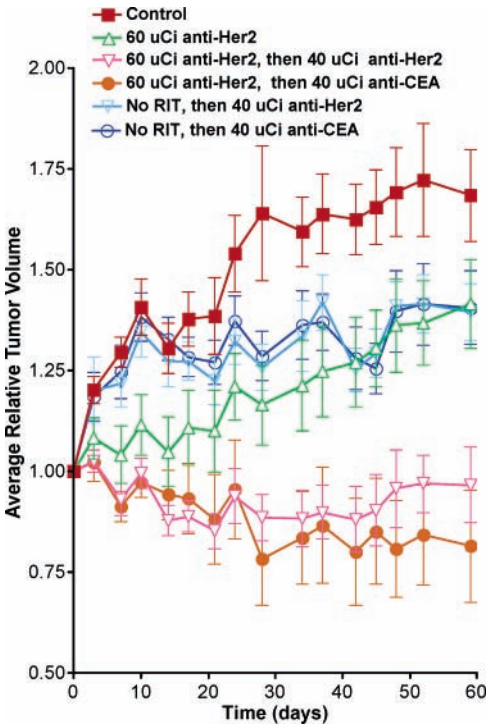

Figure 5. Radioimmunotherapy of established MCF-7 tumors in nude mice with Y-90-labeled anti-Her2 antibody followed by either Y-90-labeled anti-Her2 or anti-CEA antibody. Groups of 10 mice were injected IV with 60 μCi (8 μg) of Y-90-labeled anti-Her2 antibody followed by either 40 μCi (5.6 μg) of Y-90-labeled anti-Her2 or 40 μCi (6 μg) of Y-90-labeled anti-CEA 14 days later. The tumor volume for each mouse at the time indicated was normalized to the tumor volume at the start of treatment (average relative tumor volume) and was plotted versus days after the start of treatment.

DISCUSSION

Since it is unlikely that single agent therapies will be effective against metastatic breast cancer, new approaches to combined therapies need to be explored. In this regard, the combination of RIT and chemotherapy is relatively untried, and as previously mentioned, may allow the treatment of a greater number of patients than is possible for cold antibody/chemotherapy combinations. Our initial hypothesis that RIT would be more effective than cold antibody even against a tumor with relatively low to moderate amounts of target antigen was verified in the case of Her2 expression on MCF-7 cells. Surprisingly, in the case of CEA expression, which is also low on MCF-7 cells and led to disappointing tumor targeting as judged by a tumor-to-blood ratio of 1.0, RIT was equally effective for anti-CEA as for anti-HER2. Furthermore, we were able to reduce the amount of RIT required to produce an effective reduction in tumor size by the addition of Taxol as a chemotherapeutic agent. In our study, we were guided by the previous work of DeNardo and co-workers [35] who showed that the optimal combination of Taxol with RIT was either a single IP dose 24 h post RIT or a split IP dose at 48 and 72 h post RIT. Since in their study administration of Taxol prior to RIT was equivalent to single agent therapy, we tested only the single or split-dose regimen. Likewise, since the blood levels of Taxol were previously studied by DeNardo and co-workers (*35*) and shown to be within the effective range for 3−4 days, we did not measure blood levels. Our results closely mimic those obtained by DeNardo and co-workers (*35*) who performed their studies in a different tumor model (HBT 3477) with a different Y-90-labeled antibody (ChL6). Thus, it appears that the increased efficacy of RIT plus Taxol can be generalized, especially in the case of breast tumors. In our study, we had roughly equivalent results between the single or split-dose Taxol plus RIT regimens, suggesting that the largest antitumor effect occurred within the first few days of treatment, with tumor reductions of greater than 50% lasting up to 35 days. Since tumor growth was not monitored beyond 35 days, it is possible that some of the tumors would eventually regrow, requiring a second round of treatment. However, in one of the groups (80 μCi 90Y-cT84.66 ± Taxol), no detectable tumors were seen in 6/15 animals out to 35 days.

Although it is generally recognized that only tumors that overexpress Her2 respond to cold Herceptin therapy, we felt compelled to determine if cold Herceptin therapy plus RIT was effective in this animal model. In this study, a split IP dose of cold Herceptin (200 μg) was administered at day 0 and day 9 after RIT. This regimen was adopted from our previous study in which we administered either 50 or 200 μg of cold 4D5, the parent monoclonal antibody for Herceptin, to nude mice bearing MCF-7/Her2 xenografts [11]. In that study, there was a 50% reduction in tumor growth at the end of 28 days. However, in our current study no long-term antitumor effect was observed for cold Herceptin only, as expected for a low Her2 expressing tumor (compared to the Her2 transfected MCF-7 cells used in the previous study). Furthermore, cold Herceptin therapy did not increase the antitumor effect of RIT, demonstrating the complete lack of an antitumor effect for Herceptin even in the presence of other cytotoxic agents. The findings of this study as a control for the next study (Herceptin RIT followed by antibody uptake at later times) are relevant in that even high-dose Herceptin has no antitumor tumor effect on MCF-7 xenografts. Thus, the antitumor effect is due to RIT alone.

When animals bearing MCF-7 xenografts were treated with Y-90 anti-Her2 and followed by In-111 anti-Her2 or anti-CEA 7−14 days later, a substantial increase in anti-CEA but not anti-Her2 uptake was observed compared to untreated controls. These results suggest that sequential treatment of tumors positive for both Her2 and CEA is feasible and may have an advantage over repeated RIT with the same agent. The mechanism for the increase in anti-CEA uptake was not studied. Possibilities include that anti-Her2 RIT induced expression of CEA or that prior therapy made CEA produced by the tumor more accessible. In consideration, of the latter possibility, antibody uptake is limited by tumor perfusion, which is known to be inhibited by high local intratumoral pressure (*37*−*39*). It is likely that some of this barrier is disrupted by tumor and vascular necrosis caused by RIT. Furthermore, in the untreated tumors (no RIT), tumor size has increased by 20% (Table 2), while tumor size has been reduced by 15% in the RIT-treated animals. Since uptake is measured as %ID/g, and we have observed that smaller tumors have an apparent advantage in uptake over larger tumors (*23*, *40*), the increase in uptake is not surprising. However, the same effect is not observed for anti-Her2 uptake. Again, the mechanism was not studied. Thus, in this case the above arguments are unlikely to apply. In fact, one possibility is that antigen expression actually decreased in treated animals and was offset by the expected increase in uptake for a smaller tumor size. While further studies are warranted to unravel the underlying mechanisms, we conclude that sequential RIT therapy using different antibodies, especially combined with Taxoids such as paclitaxel and docetaxel are worth exploring.

ACKNOWLEDGMENT

This research was supported by NCI Grant CA43904 and the Army Medical Research and Materiel Command DAMD 17-98-1-8031.

LITERATURE CITED

(1) O'Shaughnessy, J., Miles, D., Vukelja, S., Moiseyenko, V., Ayoub, J. P., Cervantes, G., Fumoleau, P., Jones, S., Lui, W. Y., Mauriac, L., Twelves, C., Van Hazel, G., Verma, S., and Leonard, R. (2002) Superior survival with capecitabine plus docetaxel combination therapy in anthracycline-pretreated patients with advanced breast cancer: phase III trial results. *J. Clin. Oncol. 20*, 2812−2823.

(2) Albanell, J., and Baselga, J. (1999) The ErbB receptors as targets for breast cancer therapy. *J. Mammary Gland Biol. Neoplasia 4*, 337−351.

(3) Baselga, J., Norton, L., Albanell, J., Kim, Y. M., and Mendelsohn, J. (1998) Recombinant humanized anti-HER2 antibody (Herceptin) enhances the antitumor activity of paclitaxel and doxorubicin against HER2/neu overexpressing human breast cancer xenografts. *Cancer Res. 58*, 2825−2831.

(4) Baselga, J., Seidman, A. D., Rosen, P. P., and Norton, L. (1997) HER2 overexpression and paclitaxel sensitivity in breast cancer: therapeutic implications. *Oncology 11*, 43−48.

(5) Baselga, J. (2000) Clinical trials of single-agent trastuzumab (Herceptin). *Semin. Oncol. 27*, 20−26.

(6) Baselga, J. (2001) Herceptin((R)) Alone or in Combination with Chemotherapy in the Treatment of HER2−Positive Metastatic Breast Cancer: Pivotal Trials. *Oncology 61*, 14−21.

(7) Slamon, D. J., Leyland-Jones, B., Shak, S., Fuchs, H., Paton, V., Bajamonde, A., Fleming, T., Eiermann, W., Wolter, J., Pegram, M., Baselga, J., and Norton, L. (2001) Use of chemotherapy plus a monoclonal antibody against HER2 for metastatic breast cancer that overexpresses HER2. *N. Engl. J. Med. 344*, 783−792.

(8) Pegram, M. D., Pienkowski, T., Northfelt, D. W., Eiermann, W., Patel, R., Fumoleau, P., Quan, E., Crown, J., Toppmeyer, D., Smylie, M., Riva, A., Blitz, S., Press, M. F., Reese, D., Lindsay, M. A., and Slamon, D. J. (2004) Results of two open-label, multicenter phase II studies of docetaxel, platinum salts, and trastuzumab in HER2-positive advanced breast cancer. *J. Natl. Cancer Inst. 96*, 759−769.

(9) Theodoulou, M., and Seidman, A. D. (2003) Cardiac effects of adjuvant therapy for early breast cancer. *Semin. Oncol. 30*, 730−739.

(10) Blend, M. J., Stastny, J. J., Swanson, S. M., and Brechbiel, M. W. (2003) Labeling anti-HER2/neu monoclonal antibodies with 111In and 90Y using a bifunctional DTPA chelating agent. *Cancer Biother. Radiopharm. 18*, 355−363.

(11) Tsai, S. W., Sun, Y. Y., Williams, L. E., Raubitschek, A. A., Wu, A. M., and Shively, J. E. (2000) Biodistribution and radioimmunotherapy of human breast cancer xenografts with radiometal-labeled DOTA conjugated anti-her2/neu antibody 4D5. *Bioconjugate Chem. 11*, 327−334.

(12) O'Donoghue, J. A., Baidoo, N., Deland, D., Welt, S., Divgi, C. R., and Sgouros, G. (2002) Hematologic toxicity in radioimmunotherapy: dose−response relationships for I-131 labeled antibody therapy. *Cancer Biother. Radiopharm. 17*, 435−443.

(13) DeNardo, S. J., Williams, L. E., Leigh, B. R., and Wahl, R. L. (2002) Choosing an optimal radioimmunotherapy dose for clinical response. *Cancer 94*, 1275−1286.

(14) Williams, L. E., Liu, A., Wu, A. M., Odom-Maryon, T., Chai, A., Raubitschek, A. A., and Wong, J. Y. (1995) Figures of merit (FOMs) for imaging and therapy using monoclonal antibodies. *Med. Phys. 22*, 2025−2027.

(15) Behr, T. M., Griesinger, F., Riggert, J., Gratz, S., Behe, M., Kaufmann, C. C., Wormann, B., Brittinger, G., and Becker, W. (2002) High-dose myeloablative radioimmunotherapy of mantle cell non-Hodgkin lymphoma with the iodine-131-labeled chimeric anti-CD20 antibody C2B8 and autologous stem cell support. Results of a pilot study. *Cancer 94*, 1363−1372.

(16) Wong, J. Y. C., Chu, D. Z., Yamauchi, D. M., Williams, L. E., Liu, A., Wilczynski, S., Wu, A. M., Shively, J. E., Doroshow, J. H., and Raubitschek, A. A. (2000) A phase I radioimmunotherapy trial evaluating 90yttrium-labeled anti-carcinoembryonic antigen (CEA) chimeric T84.66 in patients with metastatic CEA-producing malignancies. *Clin. Cancer Res. 6*, 3855−3863.

(17) O'Donnell, R. T., DeNardo, S. J., DeNardo, G. L., Miers, L., Lamborn, K. R., Kukis, D. L., and Meyers, F. J. (2000) Efficacy and toxicity of radioimmunotherapy with (90)Y-DOTA-peptide-ChL6 for PC3-tumored mice. *Prostate 44*, 187−192.

(18) Colnot, D. R., Roos, J. C., de Bree, R., Wilhelm, A. J., Kummer, J. A., Hanft, G., Heider, K. H., Stehle, G., Snow, G. B., and van Dongen, G. A. (2003) Safety, biodistribution, pharmacokinetics, and immunogenicity of 99mTc-labeled humanized monoclonal antibody BIWA 4 (bivatuzumab) in patients with squamous cell carcinoma of the head and neck. *Cancer Immunol. Immunother. 52*, 576−582.

(19) Milenic, D., Garmestani, K., Dadachova, E., Chappell, L., Albert, P., Hill, D., Schlom, J., and Brechbiel, M. (2004) Radioimmunotherapy of human colon carcinoma xenografts using a 213Bi-labeled domain-deleted humanized monoclonal antibody. *Cancer Biother. Radiopharm. 19*, 135−147.

(20) Postema, E. J., Frielink, C., Oyen, W. J., Raemaekers, J. M., Goldenberg, D. M., Corstens, F. H., and Boerman, O. C. (2003) Biodistribution of 131I-, 186Re-, 177Lu-, and 88Y-labeled hLL2 (Epratuzumab) in nude mice with CD22-positive lymphoma. *Cancer Biother. Radiopharm. 18*, 525−533.

(21) Richman, C. M., and DeNardo, S. J. (2001) Systemic radiotherapy in metastatic breast cancer using 90Y-linked monoclonal MUC-1 antibodies. *Crit. Rev. Oncol. Hematol. 38*, 25−35.

(22) De Santes, K., Slamon, D., Anderson, S. K., Shepard, M., Fendly, B., Maneval, D., and Press, O. (1992) Radiolabeled Antibody Targeting of the HER-2/*neu* Oncoprotein. *Cancer Res. 52*, 1916−1923.

(23) Williams, L. E., Beatty, B. G., Shively, J. E., and Beatty, J. D. (2001) Accumulation of radiolabeled anti-CEA antibody (mT84.66) in the case of multiple LS174T tumors in a nude mouse model. *Cancer Biother. Radiopharm. 16*, 147−157.

(24) Wong, J. Y., Shibata, S., Williams, L. E., Kwok, C. S., Liu, A., Chu, D. Z., Yamauchi, D. M., Wilczynski, S., Ikle, D. N., Wu, A. M., Yazaki, P. J., Shively, J. E., Doroshow, J. H., and Raubitschek, A. A. (2003) A Phase I trial of 90Y-anti-carcinoembryonic antigen chimeric T84.66 radioimmunotherapy with 5-fluorouracil in patients with metastatic colorectal cancer. *Clin. Cancer Res. 9*, 5842−5852.

(25) Esteban, J. M., Felder, B., Ahn, C., Simpson, J. F., Battifora, H., and Shively, J. E. (1994) Prognostic relevance of carcinoembryonic antigen and estrogen receptor in breast cancer patients. *Cancer 74*, 1575−1583.

(26) Soletormos, G., Nielsen, D., Schioler, V., Mouridsen, H., and Dombernowsky, P. (2004) Monitoring different stages of breast cancer using tumour markers CA 15−3, CEA and TPA. *Eur. J. Cancer 40*, 481−486.

(27) Given, M., Scott, M., McGrath, J. P., and Given, H. F. (2000) The predictive of tumour markers CA 15−3, TPS and CEA in breast cancer recurrence. *Breast 9*, 277−280.

(28) Lumachi, F., Ermani, M., Brandes, A. A., Basso, S., Basso, U., and Boccagni, P. (2001) Predictive value of different prognostic factors in breast cancer recurrences: multivariate analysis using a logistic regression model. *Anticancer Res 21*, 4105−4108.

(29) Ballangrud, A. M., Yang, W. H., Palm, S., Enmon, R., Borchardt, P. E., Pellegrini, V. A., McDevitt, M. R., Scheinberg, D. A., and Sgouros, G. (2004) Alpha-particle emitting atomic generator (Actinium-225)-labeled trastuzumab (Herceptin) targeting of breast cancer spheroids: efficacy versus HER2/neu expression. *Clin. Cancer Res. 10*, 4489−4497.

(30) Meyer, D. L., Law, K. L., Payne, J. K., Mikolajczyk, S. D., Zarrinmayeh, H., Jungheim, L. N., Kling, J. K., Shepherd, T. A., and Starling, J. J. (1995) Site-specific prodrug activation by antibody-beta-lactamase conjugates: preclinical investigation of the efficacy and toxicity of doxorubicin delivered by antibody directed catalysis. *Bioconjugate Chem. 6*, 440−446.

(31) Lewis, M. R., Raubitschek, A., and Shively, J. E. (1994) A facile, water-soluble method for modification of proteins with DOTA. Use of elevated temperature and optimized pH to achieve high specific activity and high chelate stability in radiolabeled immunoconjugates. *Bioconjugate Chem. 5*, 565−576.

(32) Lewis, M. R., Kao, J. Y., Anderson, A. L., Shively, J. E., and Raubitschek, A. (2001) An improved method for conjugating monoclonal antibodies with N-hydroxysulfosuccinimidyl DOTA. *Bioconjugate Chem. 12*, 320−324.

(33) Bacus, S. S., Chin, D. M., Stern, R. K., Ortiz, R., Ruby, S. G., and Weinberg, D. S. (1992) HER-2/neu oncogene expression, DNA ploidy and proliferation index in breast cancer. *Anal. Quant. Cytol. Histol. 14*, 433−445.

(34) Mayer, A., Tsiompanou, E., Flynn, A. A., Pedley, R. B., Dearling, J., Boden, R., and Begent, R. H. (2003) Higher dose and dose-rate in smaller tumors result in improved tumor control. *Cancer Invest. 21*, 382−388.

(35) Denardo, S. J., Richman, C. M., Kukis, D. L., Shen, S., Lamborn, K. R., Miers, L. A., Kroger, L. A., Perez, E. A., and Denardo, G. L. (1998) Synergistic therapy of breast cancer with Y-90-chimeric L6 and paclitaxel in the xenografted mouse model: development of a clinical protocol. *Anticancer Res. 18*, 4011−4018.

(36) Lewis, G. D., Figari, I., Fendly, B., Wong, W. L., Carter, P., Gorman, C., and Shepard, H. M. (1993) Differential responses of human tumor cell lines to anti-p185HER2 monoclonal antibodies. *Cancer Immunol. Immunother. 37*, 255−263.

(37) Hori, K., and Saito, S. (2003) Microvascular mechanisms by which the combretastatin A-4 derivative AC7700 (AVE8062) induces tumour blood flow stasis. *Br. J. Cancer 89*, 1334−1344.

(38) Brekken, C., Bruland, O. S., and de Lange Davies, C. (2000) Interstitial fluid pressure in human osteosarcoma xeno-

grafts: significance of implantation site and the response to intratumoral injection of hyaluronidase. *Anticancer Res*. *20*, 3503−3512.
(39) Rohde, D., Wiesner, C., Graf, D., Wolff, J., Fuzesi, L., and Jakse, G. (2000) Interstitial fluid pressure is increased in renal cell carcinoma xenografts. *Urol. Res. 28*, 1−5.
(40) Williams, L. E., Duda, R. B., Proffitt, R. T., Beatty, B. G., Beatty, J. D., Wong, J. Y., Shively, J. E., and Paxton, R. J. (1988) Tumor uptake as a function of tumor mass: a mathematic model. *J. Nucl Med*. *29*, 103−109.

BC0500948

Synthesis and Biological Evaluation of Diethylenetriamine Pentaacetic acid−Polyethylene Glycol−Folate: A New Folate-Derived, ^{99m}Tc-Based Radiopharmaceutical

Min Liu,[†] Wen Xu,[†] Ling-jie Xu,[†] Gao-ren Zhong,[†] Shao-liang Chen,[‡] and Wei-yue Lu*[,†]

Fudan-Pharmco Targeting Drug Research Center, Department of Pharmaceutics, School of Pharmacy, University of Fudan, Shanghai, 200032, China, and Department of Nuclear Medicine, Zhongshan Hospital, Shanghai, China. Received April 21, 2005; Revised Manuscript Received August 2, 2005

^{99m}Technetium-labeled diethylenetriamine pentaacetic acid−polyethylene glycol−folate (DTPA−PEG−folate) was synthesized and tested as a radiopharmaceutical agent, which targeted the lymphatic system with metastatic tumor. Folic acid was reacted with $H_2N-PEG-NH_2$ to yield $H_2N-PEG-$folate. After purification by anion-exchange chromatography, the product was reacted with cyclic DTPA. By removal of unreacted DTPA by size-exclusion chromatography, DTPA−PEG−Folate was obtained. Fluorescein-5-isothiocyanate (FITC)-labeled DTPA−PEG−folate and DTPA−PEG−OCH_3 were prepared via a dicyclohexylcarbodiimide-mediated coupling. In vitro competitive binding test showed that the uptake of [^{125}I] folic acid was inhibited by DTPA−PEG−folate and the 50% inhibitory concentration was 4.37 pmol/L ($R^2 = 0.9922$). The relative affinity of DTPA−PEG−FITC was 0.18 for human folate receptor comparing with folic acid. In cultured tumor cells, uptake of fluorescence-labeled DTPA−PEG−folate was found to increase significantly in folate-deficient medium compared with that of untargeted DTPA−PEG−OCH_3 and FITC−ethylenediamine. The competition with free folic acid blocked the cell uptake of DTPA−PEG−folate. These results confirmed the DTPA−PEG−folate entered into KB cells through the folate receptor endocytosis pathway in vitro. The radiolabeled yield of [^{99m}Tc] DTPA−PEG−folate was in excess of 98%, and specific activities of 7.4 kBq (0.2μCi/μg) were achieved. After subcutaneous injection, [^{99m}Tc] DTPA−PEG−folate exhibited an initial increase and successive decline of accumulation in popliteal nodes in normal Wistar rats. Expect for the kidney, uptake by other tissues was rather low. In a normal rabbit imagine study, the lymphatic vessels were readily visualized by single-photon-emmission computed tomography following subcutaneous injection of [^{99m}Tc] DTPA−PEG−folate. In conclusion, the [^{99m}Tc] DTPA−PEG−folate conjugate may have a potential as a lymphatic tumor-targeted radiopharmaceutical.

INTRODUCTION

The lymphatic system comprises a network of lymphatic vessels and lymph nodes throughout the body. It often serves as a primary route for dissemination of many solid tumors, including carcinomas of colon, lung, breast, renal, cervix, and prostate (*1*−*4*). Furthermore, lymph nodes could provide ideal tumor-cell "incubators" with long residence time. Assessment of lymph node status could determine the stage of numerous malignancies. Therefore, it would be great interest to develop reliable techniques for evaluating the lymph nodes stage in cancer patients.

The direct lymphography (such as lymphoangiogram) and other modern indirect techniques (such as compounded tomography and magnetic resonance) are commonly used for detecting nodal metastases. However, these methods could only detect the lymph node's abnormality by nodal enlargement, but that does not always imply malignant involvement at the initial stage (many nodes have been infiltrated or replaced by tumor without change in size) (*5*). Since Sherman first reported lymph node accumulation of interstitially injected radioactive colloidal gold in 1953, many studies have exploited radiolabeled colloidal particles (liposomes, emulsions, or micelles) and macromolecules (dextran, polylysine, human serum albumin, monoclonal antibody and their fragments, polyethylene glycol, and other synthetic polymers) for better detection of lymph nodes (*5*−*14*). Among these radiological agents, only monoclonal antibodies could actively bind and target to tumor cells in the lymph nodes and detect occult metastases of tumor (*10*, *11*). On the contrary, labeling with monoclonal antibodies has been rather disappointed because of its concomitant clearance by lymph node macrophages as well as the lack of a uniform expression of surface antigen specific for a designed monoclonal antibody.

Folate receptor is a glycosyl-phosphatidylinositol-linked membrane glycoprotein with an apparent molecular weight of ~38−40 kDa. It preferentially expresses with enhanced binding affinity for folic acid in many types of tumors, including ovarian, lung, colorectal, renal, breast cell cancers, and non-Hodgkin's lymphomas (*15*). Radioactive tracers and drug carriers utilizing folate conjugates for tumor targeting have been studied (*15*−*21*). Additionally, folate receptor was associated with parameters of biological aggressiveness in cancers. With high histological grade, advanced stage, and serious histology in ovarian neoplasmas, folate receptor was overexpressed to a higher degree. A multiple comparison

* Corresponding author. School of Pharmacy, University of Fudan, 138 Yixueyuan load, 190 BOX, Shanghai, 200032, People's Republic of China. Fax: (86 21) 64178790. E-mail: wylu@shmu.edu.cn.

[†] University of Fudan.

[‡] Zhongshan Hospital.

10.1021/bc050122m CCC: $30.25 © 2005 American Chemical Society
Published on Web 09/02/2005

analysis showed that folate receptor expression of stage IV and omental metastases was significantly higher that that in stage I (*22*). Moreover, it had been reported that folate–fluorescein could be easily distinguished the tumor loci of submillimeter size, which spread through the vascular system, from adjacent normal tissues (*23*). Thus, folic acid owned a potential value as a targeting ligand for metastatic tumor through lymphatic system. To our knowledge, few were reported in the literatures concerning folate conjugates for lymphatic targeting.

As a first step toward the design of a radiological agent for imaging the tumor metastatic lymph node, we adopted a macromolecular receptor-binding radiotracer, [^{99m}Tc] diethylenetriamine pentaacetic acid–polyethylene glycol–folate (DTPA–PEG–folate). The only study where PEG was adopted for targeting lymphatic system after subcutaneous injection was reported by Desser et al. (*9*). In their work, PEG conjugate provided excellent popliteal nodal enhancement. However, further study on delivering H_2N–PEG–folate conjugates to tumor metastatic lymph nodes via receptor-mediated pathways has not yet been reported. In this paper, we described the synthesis of DTPA–PEG–folate conjugates, which displayed good targeting activities for tumor cells via the folate receptor in vitro, as well as lymphatic system in the normal animal.

EXPERIMENTAL PROCEDURES

Materials. H_2N–PEG–NH_2 (MW 2000) and H_2N–PEG–OCH_3 (MW 2000) were prepared as described previously (*24*). Cyclic DTPA dianhydride, folic acid, *N*,*N*′-dicyclohexylcarbodiimide, and ethylenediamine (EDA) were purchased from Sigma (St. Louise, Mo, USA). Fluorescein-5-isothiocyanate (FITC) was obtained from Molecular Probes, Co. (Eugene, Oregon, USA). [^{125}I] folic acid came from Naval radioimmunity center (Beijing, China, the radioactivity was 7.69 TBq/mmol). Other chemicals reagents used in the study were certified analytical reagent grade (Shanghai Chemical Reagent Company, Shanghai, China). Solvents for high-performance liqui chromatography (HPLC) were HPLC grade accordingly. KB cell, a human oral epidermoid carcinoma cell line that overexpresses folate receptor, was provided by Shanghai Institutes for Biological Sciences (Chinese Academic of Sciences).

Synthesis of H_2N–PEG–Folate. Two grams (1 mmol) of H_2N–PEG–NH_2 was dissolved in 15 mL of dry dimethyl sulfoxide containing an equimolar folic acid. Dicyclohexylcarbodiimide (0.2 g) and 40μL of pyridine were added. The mixture was stirred overnight in the dark at 25 °C. Deionized water (30 mL) was added, ss and the insoluble byproduct, dicyclohexylurea, was removed by centrifugation. The supernate was dialyzed against deionized water to remove dimethyl sulfoxide in the reaction mixture and lyophilized. A yellow powder (0.35 g) was obtained. The H_2N–PEG–folate was separated from folate–PEG–folate and unreacted folic acid and H_2N–PEG–NH_2 by using a DEAE–sepharose anion-exchange column (26 mm × 10 cm, Biosciences, Uppsala, Sweden) on a ÄKTA explorer 100 system (Amersham Biosciences, Uppsala, Sweden) consisting of Pump P-900, Pump P-950, Monitor UV-900, and Frac-900 at room temperature. The column was loaded with 10 mg of H_2N–PEG–folate crude sample per mL bed volume. The column was then washed with a gradient (eluent A, 100 mM ammonium acetate buffer, pH 10.0; eluent B, water; gradient, 90% B for 3 column volumes, 90–75% B at 3 column volumes, keeping 75% B and 50% B at 1 column volume, respectively, in the end washing the column with 0.5 M NaCl, at a flow rate of 5 mL/min). The result was seen in Figure 1. Fractions were collected, desalted, and lyophilized.

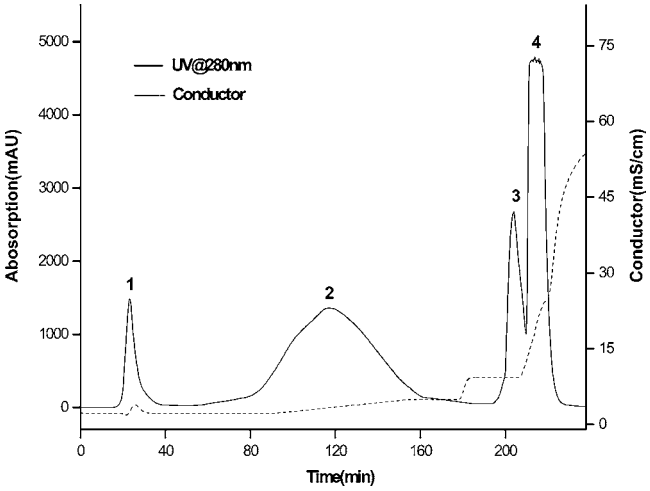

Figure 1. Purified H_2N–PEG–folate on a DEAE–Sepharose anion-exchange column by gradient elution. Peak 1, uncharged impurities including H_2N–PEG–NH_2 and some small molecules; peak 2, H_2N–PEG–folate; peak 3, folate–PEG–folate; peak 4, folic acid.

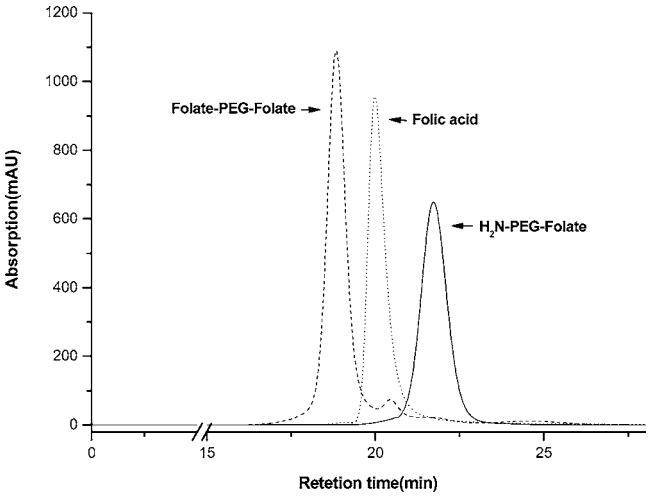

Figure 2. Analysis for H_2N–PEG–folate and impurities on a TSK GEL G4000PW$_{XL}$ column 4.6 mm × 30 cm. Elution, 5 mM NaCl; flow rate, 0.5 mL/min; temperature, 25 °C; detection, UV@280 nm).

Analytical chromatography was performed on an Agilent 1100 series quaternary HPLC system (Palo Alto, California, USA) equipped with a vacuum degasser, an autosampler, a thermostetted column, and a UV and refractive index detector. The chemical purity of H_2N–PEG–folate was examined by analytical HPLC on a 300 × 7.8 mm inside diameter TSK-GEL G4000PW$_{XL}$ (10 μm particle size, 300 Å pore size, Tosoh Corporation, Minato-ku, Tokyo, Japan) with a TSK-GUARDCOLUMN at 25 °C [H_2N–PEG–folate, t_R = 21.76 min; folic acid, t_R = 19.97 min; folate–PEG–folate, t_R = 18.89 min; H_2N–PEG–NH_2, t_R = 31.84 min; eluent, 5 mM NaCl]. The results were shown in Figure 2. ^{1}H NMR (500 MHz, D_2O) δ (ppm) for H_2N–PEG–folate: 8.67 (s, C7–H, 1H), 7.66 (d, 2′,6′-H, 2H), 6.63 (d, 3′,5′-H, 2H), 4.34 (minor and major αCH_2 of Glu, 1H), and ~2.0–2.4 (m, β, γ-CH_2 of GLu, 4H) for folate; ~3.1–4.0 (m, $-OCH_2CH_2$) for PEG.

Synthesis of DTPA–PEG–Folate. DTPA–PEG–folate was obtained by reacting 200 mg H_2N–PEG–folate

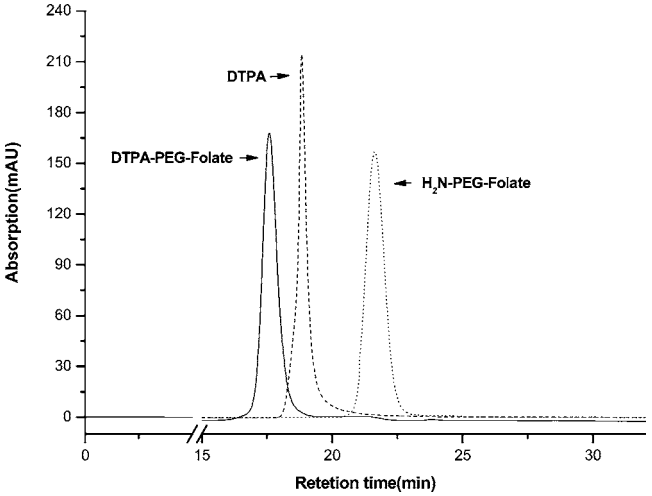

Figure 3. Analysis for DTPA−PEG−folate and impurities on a TSK GEL G4000PW_{XL} column 4.6 mm × 30 cm. Elution, 5 mM NaCl; flow rate, 0.5 mL/min; temperature, 25 °C; detection, UV@280 nm for both DTPA−PEG−folate and H_2N−PEG−folate, UV@200 nm for DTPA).

with 1.25 times molar quantity of DTPA dianhydride in 10 mL of dimethyl sulfoxide at 25 °C. When analytical HPLC showed the absence of the H_2N−PEG−folate, 10 mL of deionized water was added to the mixture. The mixture was dialyzed against deionized water to remove dimethyl sulfoxide in the reaction solution and lyophilized. The DTPA−PEG−folate was separated using the ÄKTA explorer 100 system equipped with a Sephadex G-15 column to remove unreacted DTPA. The eluent was 50 mM acetate buffer (pH 3.2) containing 50% alcohol with 1 mL/min flow rate. The sample was collected, desalted, and lyophilized. Analytical HPLC on the TSK GEL G4000PWXL column revealed a single peak with a retention time of 17.59 min (eluent, 5 mM NaCl). The starting material DTPA and H_2N−PEG−folate was individually eluted at 18.84 min and 21.76 min. Figure 3 revealed the results. ^{1}H NMR (500 MHz, D_2O) δ (ppm) for DTPA−PEG−folate: 3.29 (t, C5, C7−2H) and 3.42 (t, C4, C8−2H) for DTPA; 8.67 (s, C7−H, 1H), 7.66 (d, 2′,6′-H, 2H), 6.63 (d, 3′,5′-H, 2H), 4.34 (minor and major αCH_2 of Glu, 1H), and ∼2.0−2.4 (m, β,γ-CH_2 of GLu, 4H) for folate; ∼3.6−3.8 (bs, $-OCH_2CH_2$) for PEG.

Similarly, we used the above method to obtain the conjugate of DTPA−PEG−OCH_3. ^{1}H NMR (500 MHz, D_2O) δ (ppm): 3.29 (t, C5, C7−2H) and 3.42 (t, C4, C8−2H) for DTPA; ∼3.6−3.8 (bs, $-OCH_2CH_2$) for PEG.

Synthesis and Purification of the FITC−EDA. FITC (62 mg, 0.16 mmol) dispersed in 0.2 mL of *N*,*N*′-dimethylformamide was reacted with 50 molar equiv of EDA at 25 °C for 30 min. The resulting EDA−FITC was mixed with the same volume of deionized water and separated from unreacted FITC and EDA by HPLC on SymmetryPrep C-18 reversed column (300 mm × 19 mm, Waters Co.) using a stepped gradient (eluent A, 10 mM CH_3COONH_4; eluent B, 15% acetonitrile in 10 mM CH_3COONH_4; gradient, 2 column volume for eluent A, and then 2 column volume for eluent B at a flow rate 10 mL/min). The eluent time for EDA, EDA−FITC, and FITC were 8.2, 30, and 39 min, respectively.

Analytical chromatography was performed on an SHIMADZA HPLC equipped with a liquid chromatography, a vacuum degasser, an autosampler, and a fluorescence detector (Japan). The chemical purity and identity of EDA−FITC was examined by analytical HPLC on a Diamonsil C-18 reversed-phase column (200 mm × 4.6 mm, Dikma Technologies) [EDA−FITC, T_R = 8.5 min; FITC, T_R = 13.2 min; the eluent, 15% acetonitrile in 10 mM CH_3COONH_4 at a flow rate of 0.8 mL/min; Fluorescence detection, E_x = 490 nm, E_m = 518 nm]. High-resolution mass spectroscopy (MS) (Agilent, California, USA): EDA−FITC, $C_{23}H_{19}O_5N_3S$ $[M + H]^+$ 450.5, found 450.0.

Fluorescent Labeling of PEG Derivatives. DTPA−PEG−folate (5.6 mg, 2 mmol) and dicyclohexylcarbodiimide (1.5 mg, 7.3 mmol) were dissolved in 0.25 mL of dimethyl sulfoxide containing 10 μL of pyridine. The reaction mixture was stirred for 1 h before FITC−EDA (0.9 mg, 2 mmol) was added. The free FITC−EDA was monitored of by analytical HPLC on a TSK GEL G4000PWXL column (300 mm × 7.8 mm,) [FITC-labeled DTPA−PEG−folate, T_R = 26.1 min; FITC−EDA, T_R = 35.9 min; the eluent, 20% acetonitrile in 100 mM NaCl at a flow rate of 0.5 mL/min; fluorescence detection, E_x = 490 nm, E_m = 518 nm]. As soon as the free FITC−EDA disappeared, the same amount of deionized water was added to the reaction mixture and the unsolved material was filtered. Other small molecules were removed by G-15 sephadex column. The chemical purity assay of FITC-labeled DTPA−PEG−folate was conducted as described above.

As a nontargeted agent, FITC-labeled DTPA−PEG−OCH_3 was prepared similarly.

In Vitro Competitive Binding Assay. All biological experiments were carried out with KB cell line, enriched with folate receptors. The competitive binding-assay was conducted as described previously (*18*, *25*, *26*) with slight modification. Briefly, 24 h prior to experiment, KB cell were cultured in folate-deficient RPMI medium (RPMI-1640, Gibcol Co., USA) supplemented with 10%v/v heat-inactivated fetal calf serum (Gibcol Co., USA), and temperature was maintained at 37 °C in an atmosphere containing 5% carbon dioxide/95% air humidified atmosphere. A total of 5 × 10^5 KB cells in 0.5 mL of serum-supplemented folate-deficient RPMI medium was added to the plastic test tube containing 0.1 mL [^{125}I] folic acid. Nonradiolabeled folic acid, DTPA−PEG−OCH_3, and DTPA−PEG−folate with different concentrations were added to the cell suspension, respectively. After incubation for 1 h at 4 °C, the KB cells were centrifuged to remove the unbinding [^{125}I] folic acid and washed 3 times with phosphated-buffered saline and placed in a γ counter (SN-682 Radioimmunity γ-Counter, Shanghai Institutes for Nuclear Sciences, China) to determine the amount of cell-associated [^{125}I] folic acid. The total binding and nonspecific binding were determined at the same time. All data were recounted depending on [^{125}I] decay, and the result was shown in Figure 4.

Fluorescent Microscopy Studies. KB cells were transferred to 33-mm culture dishes at 2 × 10^5 cells per dish 24 h prior to the assay adopting folate-deficient RPMI-1640 medium supplemented with 10%v/v heat-inactivated fetal calf serum. The cells were incubated for 24 h at 37 °C with 0.5 μM solution of FITC-labeled DTPA−PEG−folate, DTPA−PEG−OCH_3, and FITC−EDA diluted in folate-deficient culture medium, respectively. In free folate competition studies, 1 mM folic acid was added to incubation medium. After washing three times with PBS, the cell-associated fluorescence was determined by FITC fluorescence on an Olympus Image-Pro Plus fluorescence microscope (Japan).

Radiolabeling of DTPA−PEG−Folate. To label DTPA−PEG−folate with ^{99m}Tc as described previously (*13*, *18*), first a solution of DTPA−PEG−folate (10 mg/mL) in 10 mmol/L phosphate buffer (pH 7.2, 0.9%NaCl)

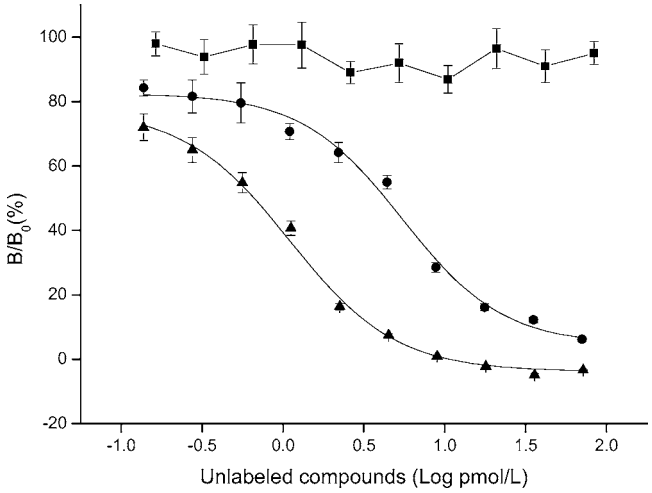

Figure 4. Competition study of binding to cellular folate receptor with free folic acid (--▲--), DTPA−PEG−OCH_3 (--■--), and DTPA−PEG−folate (--●--). Radiolabeled folic acid was added to KB cell monolayers, which were incubated at 4 °C for 1 h with or without the competitions at the concentrations shown ($n = 3$).

was mixed with 0.02 mL solution of tin chloride (10 mg $SnCl_2-2H_2O$ in 1 mL of 1 mol/L HCl followed by 8.8 mL of distilled water). Second, the mixture was incubated with freshly eluted 0.1 mL (approximately 74 MBq) of sodium pertechnetate ($NaTcO_4$). The reaction was allowed to stand for 15 min at room temperature. The purity of radiolabeled compound was analyzed by paper chromatography (*27*−*29*) and by electrophoresis (*30*). The paper chromatography was used for distinguishing [^{99m}Tc] DTPA−PEG−folate from unbounded $Na^{99m}TcO_4$, and the electrophoresis was performed for determining the [^{99m}Tc] colloid.

Biodistribution and Imaging of [^{99m}Tc]DTPA−PEG−Folate. The biodistribution of Wistar rats was obtained following subcutaneous injection of [^{99m}Tc] DTPA−PEG−folate. During the test, Wistar rats (three weeks old) were fed on normal folate-rich diet. [^{99m}Tc] DTPA−PEG−folate (0.1 mL, 10 mg/ml) was injected into foodpad of Wistar rats. Three rats were studied at each time point. At different times after injection, the animals were euthanized and popliteal lymph nodes and other tissues were excised and assayed for radioactivity. The biodistribution of the tracer in each animal was calculated as a percentage of injected dose per gram of tissue wet weight (%ID/g), using reference counts from an accurately diluted sample of the original injection.

In addition, [^{99m}Tc] DTPA−PEG−folate (0.1 mL, 10 mg/mL) was injected into the web space between the second and third in both hind feed of the rabbits. Then the continuous imaging was performed in whole body and the radioactivity change of [^{99m}Tc] DTPA−PEG−folate was measured by single-photon-emmission computed tomography (SPECT) at 5, 15, and 120 min, respectively. The experiment results were given in Figure 7.

RESULTS

Synthesis. The general strategy of the synthesis is shown in Figure 8. $H_2N-PEG-$folate was synthesized as previously described (*14*). The conjugation of folic acid to the unprotected primary amine of PEG was a complicated process. Because of no selectivity of two end functional groups of $H_2N-PEG-NH_2$, the byproduct folate−PEG−folate was synthesized as soon as the yield ratio of $H_2N-PEG-$folate was over 25% (determined by HPLC). Additionally, unreacted folic acid and $H_2N-PEG-NH_2$ interfered with the purity of $H_2N-PEG-$folate. Because of the ionic difference of these molecules, we decided to adopt ion-exchange chromatography for separation. Figure 1 showed the optimized gradient purification of crude $H_2N-PEG-$folate performed on a DEAE−Sepharose anion-exchange column. As expected, the uncharged $H_2N-PEG-NH_2$ was eluted first, followed by $H_2N-PEG-$folate, folate−PEG−folate, and folic acid successively. The purity was confirmed by analytical HPLC (Figure 2). The liquid exclusion−adsorption chromatography (LEAC), which we reported previously (*17*), was an important method for a qualifying HPLC analysis of PEG derivatives. On the basis of LEAC, $H_2N-PEG-$folate could be efficiently identified from other impurities. Since $H_2N-PEG-NH_2$ could not be detected by UV spectroscope, we had adopted refractive index detection (data not shown).

The DTPA−PEG−folate conjugate was obtained by reaction of DTPA dianhydride with the purified H_2N-

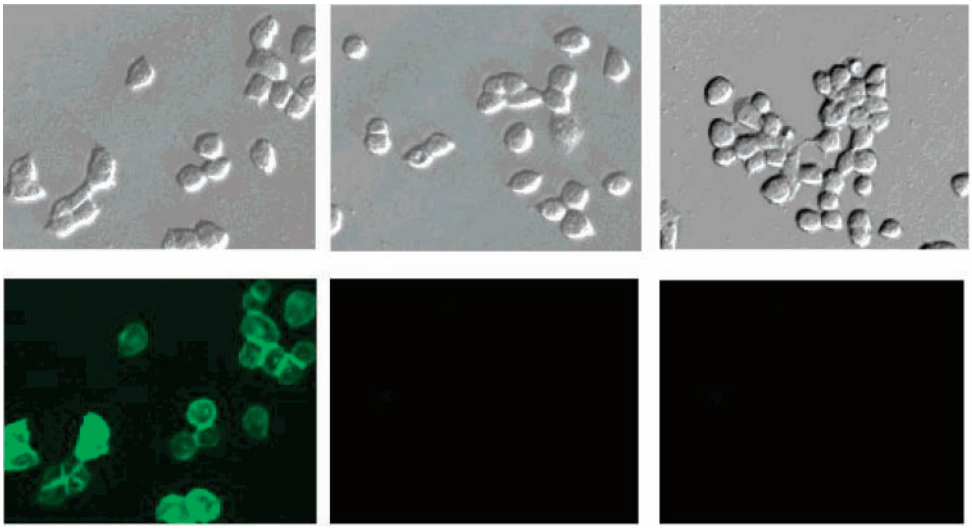

Figure 5. Cellular accumulation of fluorescein-labeled PEG conjugates in KB cells. Cells were incubated with 0.5 μM substrates for 24 h at 37 °C and photographed in both the phase-contrast and fluorescence mode on microscope as described in methods. Left, KB cells treated with FITC-labeled DTPA−PEG−folate; middle, cells treated with DTPA−PEG−OCH_3; right, cells treated with FITC-labeled DTPA−PEG−folate containing 1 mM of free folic acid. Upper panels, micrographs taken in the phase-contrast mode; lower panels, the same field viewed in the fluorescence mode.

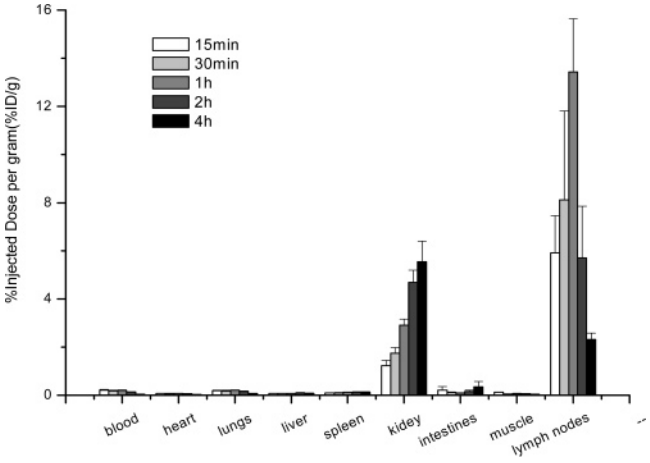

Figure 6. Percent injected dose vs time of lymphotrophic imaging agent [^{99m}Tc] DTPA−PEG−Folate using the Wistar rats. Data were acquired following subcutaneous administration of the radiotracers ($n = 3$; DTPA−PEG−folate dose = 1 mg per rat).

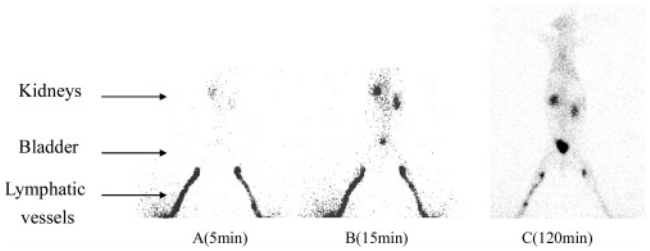

Figure 7. SPECT imagines of rabbits injected subcutaneously in the hind feet with [^{99m}Tc] DTPA−PEG−folate. ($n = 2$; DTPA−PEG−folate dose = 1 mg/per rabbit).

PEG−folate. Because of higher reactive activity of cyclic DTPA, the synthesis was completed within 10 min. To control the process more easily, the amount of DTPA was a little more than that of H_2N−PEG−folate. The major side product DTPA−bis-PEG−folate did not emerge when the H_2N−PEG−folate had run out. Therefore, the excess of unreacted DTPA became the only impurity in the reaction mixture and was easily removed by size-exclusion chromatography. Figure 3 showed the purity of DTPA−PEG−folate.

EDA was conjugated to FITC to serve as a linker between the fluorescein and DTPA−PEG−Folate. The mass spectroscope analysis showed the FITC-EDA $[M + H]^+$ parent ion peak at $m/e = 450.5$ (calculated 450.0), indicating the desired 1/1conjugation ratio. The chemical purity was confirmed by analytical HPLC. FITC-labeled PEG conjugates were synthesized in order to evaluate, by fluorescence-sensitive techniques, whether the conjugated folate altered the PEG compounds accumulation in KB cells. FITC-labeled DTPA−PEG−folate and DTPA−PEG−OCH_3 were prepared via a dicyclohexylcarbodiimide-mediated coupling. The chemical purity was also confirmed by analytical HPLC. In fact, the FITC labeling in the DTPA−PEG compounds was randomly placed. It is possible that the FITC−EDA moiety reacted with not the carboxylates of DTPA but also the lone remaining carboxylate group of folic acid.

Competition Binding Study in Vitro. To determine whether DTPA−PEG−folate could compete as the folate receptor against [^{125}I] folic acid, the in vitro binding tests on KB cell line were carried out. As shown in Figure 4, with the increasing concentration of the unlabeled folic acid and DTPA−PEG−folate, the uptake of [^{125}I] folic acid by KB cell gradually decreased. As a control group,

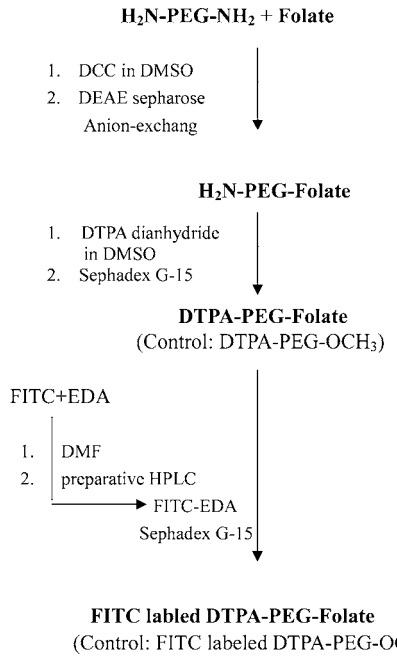

Figure 8. Synthesis of DTPA−PEG−folate and FITC-labeled PEG conjugates.

unlabeled DTPA−PEG−OCH_3 had no effect on the uptake of [^{125}I] folic acid. Therefore, DTPA−PEG−folate, as well as folic acid, could combine with folate-receptor enriched on KB cell membrane. The data were analyzed adopting Graphpad Prim 4.0 software. Compared with free folic acid, DTPA−PEG−folate had higher IC_{50} values (folic acid, $IC_{50} = 0.7726$ pmon/L; DTPA−PEG−folate, $IC_{50} = 4.37$ pmol/L ($R^2 = 0.9922$).

The relative affinity was adopted to evaluate a ligand's ability of folate derivatives to directly compete with folic acid for binding to cell surface receptors. Simply, the relative affinity was defined as the inverse molar ratio of compound required to displace 50% of [^{125}I] folic acid bound to folate receptor on KB cells, and the relative affinity of folic acid for the folate receptor was set to 1. Therefore, we calculated that DTPA−PEG−folate had an affinity of 0.18 relative to that of folic acid for human folate receptors. Thus, DTPA−PEG modification of folate lowered the vitamin's intrinsic affinity for folate receptors. The possible reason may be the interference by PEG lineal molecule.

Cell Uptake Studies of Fluorescence-Labeled PEG Derivatives. All biological experiments were carried out with the KB cell line, enriched with folate receptors. The cell uptake of FITC-labeled compounds was evaluated by the fluorescent microscopy. The results clearly indicated that the uptake of DTPA−PEG−folate increased significantly in folate-deficient medium compared with the uptake of untargeted DTPA−PEG−OCH_3 and FITC−EDA. The competition with free folic acid blocked the cell uptake of DTPA−PEG−folate (shown in Figure 5). These results confirmed the DTPA−PEG−folate entered into KB cells through the folate receptor endocytosis pathway.

Radiolabeling. The paper chromatography demonstrated an absence of unbounded $Na^{99m}TcO_4$ that would be detected by the radioactivity profile at the front (data not shown). [^{99m}Tc] Colloid was detected in the product by electrophoresis, which would be existed by radioactivity profile at the end (data not shown). The radiolabeled yield was in excess of 98%. The specific activity was 7.4 kBq (0.2μCi/μg).

Biodistribution. Figure 6 showed the %ID/g for the popliteal nodes and other tissues at 15 min, 30 min, 1 h, 2 h, and 4 h postadministration of [^{99m}Tc] DTPA−PEG−folate. In this test, a fast accumulation and clearance was obtained throughout popliteal nodes. The amount of radioactivity in the lymph nodes was 5.913 ± 1.549 %ID/g at 15 min postinjection, increased to the maximum (13.432 ± 2.207 %ID/g) at 1 h postinjection and then decreased to 2.314 ± 0.278 %ID/g at 4 h. In addition, this radiotracer kept a high accumulation in the kidney during the whole test.

Figure 7 showed continuous images obtained 2 h after subcutaneous injection of [^{99m}Tc] DTPA−PEG−folate at web space between second and third toes in both hind feet of rabbits. The lymphatic vessels were prominent as early as 5 min after injection. The lymph images continued to develop at 15 min as well as the early development of a body pool. Kidneys and bladders began to be prominent at this time. At the end of 2 h, node images faded.

DISCUSSION

The lymphatic route is known to be one of the primary pathways for tumor metastasis. Tumor cells that have detached from the tissue or have invaded a lymphatic vessel became trapped in the meshwork of a lymph node. Some metastatic cancers appear to spread via lymphatics, particularly those of epithelial origin including breast, colon, lung, ovary, and prostate (*1*−*4*). The previous studies have shown that the folate receptor is overexpressed in many types of tumors derived from epithelial cancers (*15*). Furthermore, high dedifferentiated metastatic cancers express considerably more folate receptor than their localized, low-grade counterparts (*22*). Therefore, with respect to folic acid with high affinity for folate receptors ($K_d = 10^{-9}$−10^{-10} M) (*31*, *32*), the vitamin was worthy of attention as a targeting ligand for metastatic tumor thought lymphatic system. To our knowledge, most studies about tumor located the lymphatic system focused on monoclonal antibodies, which could actively bind and target to tumor cells in the lymph nodes (*10*, *11*). Compared with monoclonal antibody, folic acid has lower imunogenicity and relatively simpler chemistry. Thus, folate conjugate was made for targeting lymphatic tumor in this study. Otherwise, the widely used macromolecules targeting the lymphatic system include dextran, polylysine, human serum albumin, monoclonal antibodies, and other synthetic polymers. Our choice of PEG as a molecular backbone was based on the following reason: PEG is hydrophilic and structurally flexible, potentially evading the recognization and phagocytosis by macrophage cells in the lymphatic system. This enables folate-modified PEG to selectively bind with a metastatic tumor-cell leading to receptor-mediated endocytosis. As a first step, in this paper, we prepared the folate conjugates, determined the folate receptors mediated endocytosis in vitro, and lymphatic targeting in normal animals. Our following study was the demonstration of the tumor model with lymphatic metastases to better verify folate conjugate targeting.

Our results from competition binding study and cell uptake studies in vitro demonstrated the receptor-mediated endocytosis properties of the folate conjugate with a PEG backbone. The biodistribution and imaging measurement in a normal animal revealed a lymph targeting effect of DTPA−PEG−folate. These properties are highly desirable for a targeted radiopharmaceutical for imaging neoplastic cells overpressing folate receptors in lymphatic system.

In the biological test, the DTPA−PEG−folate showed a high uptake in the kidneys in normal rabbits, consistent with the known presence of folate receptors in the proximal tubules of the kidneys (*33*−*36*). In fact, the amount of the radiopharmaceutical in the kidneys was affected by two factors: first, the kidneys behaving as a clearance organ; second, as a tissue capable of receptor-specific trace accumulation. We once determinated the biodistribution of [^{99m}] DTPA−PEG−folate in the athymic mice. Dates showed that the kidneys' uptake of the agent was 3.872 ± 0.294, 5.844 ± 0.442, and 0.130 ± 0.009 %ID/g (n = 4) at 1 h, 4 h, and 24 h, respectively, at a dose of 1 mg per rat. The agent was absolutely cleared by the kidney at 24 h. At present, the folate receptor positive tumor model in the lymphatic system is being set up. The suitable time point would be identified for not only adequate clearance of the DTPA−PEG−folate in the kidneys but keeping folate receptor mediated bound in tumor.

According to previous studies (*14*), compounds with MW > 16 000 Da are mainly absorbed by the lymphatic vessels, hardly gaining access to blood capillaries. In our paper, the molecular weight of DTPA−PEG−folate is about 2 800 Da. We considered whether the micelles appear during subcutaneous administration of DTPA−PEG−folate. To test the hypothesis, we tried to determine the hydrodynamic diameter of DTPA−PEG−folate by dynamic light scattering (Zeta Potential/Particle Sizer NICOMP 380ZLS (PSS·NICOMP, USA). The conjugate was assayed for 20 min at a concentration of 10 mg/mL in phosphate buffer (pH 7.2, 0.9% NaCl). However, there were no nanoparticles to be detected. Additionally, we investigated the biodistribution of DTPA−PEG−folate at different concentrations (from 0.1 to 10 mg/mL) after subcutaneous injection; the data still revealed the popliteal node targeting. In addition, DTPA−PEG−OCH_3 also showed lymph nodes targeting after subcutaneous injection (13.243 ± 2.345 and 23.730 ± 5.473 %ID/g at 1 and 4 h, respectively, in athymic mice after subcutaneous injection at dose of 1 mg per rat). Therefore, we supposed the possible reasons resulting in the phenomenon, which might be due to its linear structure and negatively charged free carboxyl groups in the DTPA−PEG−folate conjugate. It was reported that negatively charged particles showed a faster lymph delivery than cationic charged or neutral ones (*14*). Certainly, this hypothesis still needs further verification.

ACKNOWLEDGMENT

This work was supported by the National Science Foundation of China (No. 39670859) and by the Research Fund for the Doctoral Program of Higher Education (No. 20030246050).

LITERATURE CITED

(1) Swartz, M. A. (2001) The physiology of lymphatic system. *Adv. Drug Deliv. Rev. 50*, 3−20.

(2) Ayhan, A., Glutekin, M., Taskiran, C., Celik, N. Y., Usubutun, A., Kucukali, T., and Yuce, K. (2005) Lymphatic metastasis in epithelial ovarian carcinoma with respect to clinicopathological variables. *Gynecol. Oncol. 97*, 400−404.

(3) Gajdos, C., Tartter, P. I., and Bleiweiss, I. J. (1999) Lymphatic invasion, tumor size, and age are independent predictors of axillary lymph node metastases in women with Ti breast cancers. *Ann. Surg. 230*, 692−896.

(4) Gunther, K., Leier, J., Henning, G., Dimmler, A., Weissbach, R., Hohenberger, W., and Forster, R. (2005) Prediction of lymph node metastasis in coloretal carcinoma by expression of chemokine receptor CCR7. *Int. J. Cancer 116*, 726−733.

(5) Moghimi, S. M., and Bonnemain, B. (1999) Subcutaneous and intravenous delivery of diagnostic agent to the lymphatic system: applications in lymphoscintigraphy and indirect lymphography. *Adv. Drug Deliv. Rev. 37*, 295−312.
(6) Oussoren, C., and Storm, G. (2001) Liposomes to target the lymphatics by subcutaneous administration. *Adv. Drug Delivery Rev. 50*, 143−156.
(7) Torchilin, V. P. (2002) PEG-based micelles as carrier of contrast agent for different imaging modalities. *Adv. Drug Delivery Rev. 54*, 235−252.
(8) Nishioka, Y., and Yoshino, H. (2001) Lymphatic targeting with nanoparticulate system. *Adv. Drug Delivery Rev. 47*, 55−64.
(9) Desser, T. S., Rubin, D. L., Muller, H., Melntire G. L., Bacon, E. R., and Hollister, K. R. (1999) Interstitial MR and CT lymphography with Gd-dTPA- co-alpha, omega-diamino PEG (1450) and Gd-dTPA-*co*-1,6-diaminohexane polymers: preliminary experience. *Acad. Radiol. 6*, 112−118.
(10) Weinstein, J. N., Steller, M. A., Keenan, A. M., Covell, D. G., Sieber, S. M., Oldham, R. K., Hwang, K. M., and Parker, R. J. (1983) Monoclonal antibody in the lymphatics: selective delivery to lymph node metastases of a solid tumor. *Science 222*, 423−426.
(11) Weinstein, J. N., Steller, M. A., Covell, D. G., Holton, O. D., Keenan, A. M., Sieber, S. M., and Parker, R. J. (1984) Monoclonal antitumor antibodies in the lymphatics. *Cancer Treat. Rep. 68*, 257−264.
(12) Vera, D. R., Wisner, R., and Stadalnik, R. C. (1997) Sentinel node imagine via a nanoparticulate receptor-binding radiotracer. *J. Nucl. Med. 38*, 530−535.
(13) Vera, D. R., Wallace, A. M., Hoh, C. K., and Mattrey, R. F. (2001) A synthetic macromolecule for sentinel node detection: ^{99m}Tc-DTPA-Mannosyl-Dextran. *J. Nucl. Med. 42*, 951−959.
(14) Hawley, A. E., David, S. S., and Illum, L. (1995) Targeting of colloids to lymph nodes: influence of lymphatic physiology and colloidal characteristics. *Adv. Drug Delivery Rev. 17*, 129−148.
(15) Sudimach, B. A. J., and Lee, R. J. (2000) Targeted drug delivery via the folate receptor. *Adv. Drug Delivery Rev. 41*, 147−162.
(16) Trump, D. P., Mathias, C. J., Yang, Z. F., Low, P. S., Marmion, M., and Green, M. A. (2002) Synthesis and evaluation of ^{99m}Tc(CO_3)-DTPA-foalte as a folate receptor-targeted radiopharmaceutical. *Nucl. Med. Biol. 29*, 569−573.
(17) Mathias, C. J., Wang, S., Low, P. S., Waters, D. J., and Green, M. A. (1999) Receptor-mediated targeting of 47Ga-defeoxamine-folate to folate-receptor -positive human KB tumor xenografts. *Nucl. Med. Biol. 26*, 23−25.
(18) Leamon, C. P., Parker, M. A., Vlahov, I. R., Xu, L. C., Reddy, J. A., Vetzel, M. V., and Douglas, N. (2002) Synthesis and biological evaluation of EC20: a new folate-derived, ^{99m}TC-based radiopharmaceutical. *Bioconjugate Chem. 13*, 1200−1210.
(19) Lee, R. J., and Low, P. S. (1995) Folate-mediated tumor cell targeting of liposome-entrapped doxorubicin in vitro. *Biochim. Biophys. Acta 1223*, 134−144.
(20) Aronov, O., Horowitz, A. T., Gabizon, A., and Gibson, D. (2003) Folate- Targeted PEG as a potential carrier for carboplatin analogues. Synthesis and in vitro studies. *Bioconjugate Chem. 14*, 563−574.
(21) Leamon, C. P., Weigl, D., and Hendren, R. H. (1999) Folate copolymer-mediated transfection of cultured cells. *Bioconjugate Chem. 10*, 947−957.
(22) Toffoli, G., Claudia C., Russo, A., Gallo, A., Bagnoli, M., and Boiocchi, M. (1997) Overexpression of folate binding protein in ovarian cancers. *Int. J. Cancer 74*, 193−197.
(23) Kennedy, M. D., Jallad, K. N., Thompson, D. H., Amotz, D. B., and Low, P. S. (2003) Optical imagining of metastatic tumors using a folate-targeted fluorescent probe. *J. Biomed. Opt. 8*, 636−641.
(24) Liu, M., Xie, C., Xu, W., Lu, W. Y. (2004) Separation of poly(ethylene glycol)s and their amino substituted derivatives by high-performance gel filtrations chromatography at low ionic strength with refractive index detection. *J. Chromatogr., A 1046*, 121−126.
(25) Gabizon, A., Horowitz, A. T., Goren, D., Tzemach, D., Shavit, F. M., Qazen, M. M., and Zalipsky, S. (1999) Targeting folate receptor with folate linked to extremities of poly(ethylene glycol)-grafted liposomes: In Vitro studies. *Bioconjugate Chem. 10*, 289−298.
(26) Leamon, C. P. and Reddy, J. A. (1987) Folate-targeted chemotheraphy. *Adv. Drug Delivery Rev. 56*, 1127−1141.
(27) Waldman, D. L., Weber, D. A., Oberdorster, G., Drago, S. R., Utell, M. J., Hyde, R. W., and Morrow, P. E. (1987) Chemical breakdown of technetium ^{99m}DTPA during nebulization. (1987) *J. Nucl. Med. 28*, 378−382.
(28) Carla, J. M., David, H., Philip, S. L., and Mark, A. G. (2000) Synthesis of [99mTc]DTPA-Folate and its evaluation as a folate-receptor-targeted radiopharmaceutical. *Bioconjugate Chem. 11*, 253−257.
(29) Castiglia, S. G., Suarez, A. F., and Mitta, A. E. A. (1982) Control decalidad en radiofamacos usados usados en meducian nuclear. *Acta Bioquim. Clin. Latinoam. 16*, 307−310.
(30) Vera, D. R., Wallace, A. M., and Hoh, C. K. (2001) [^{99m}Tc]Mag_3-mannosyl- dextran: a receptor-binding radiopharmaceutical for sentinal node detection. *Nucl. Med. Biol. 28*, 493−498.
(31) Wang, X., Shen, F., Freisheim, L. H., Gentry, L. E., and Ratnam, M. (1992) Differential stereospepecificities and affinities of folate receptor isoforms for folate compounds and antifolates. *Biochem. Pharmacol. 44*, 1898−1901.
(32) Maziarz, K. M., Monaco, H. L., Shen, F., and Ratnam, M. (1999) Complete mapping of divergent amino acids responsible for differential ligand binding of folate receptors alpha and beta. *J. Biol. Chem. 274*, 11086−11091.
(33) Selhub, J. and Franklin, W. A. (1984) The folate binding protein of rat kidney. *J. Biol. Chem. 259*, 6601−6606.
(34) Selhub, J., Emmanouel, D., Stavropoulos, T., and Arnold, R. (1987) Renal folate adsorption and the kidney folate binding protein. I. Urinary clearance studies. *Am. J. Physiol. 252*, F750−756.
(35) Selhub, J., Nakamura, S., and Carone, F. A. (1982) Renal folate adsorption and the kidney binding protein. II. *Am. J. Physiol. 252*, F757−760.
(36) Williams, W. M. and Huang, K. C. (1982) Renal tubular transport of folic acid and methotrexate in the monkey. *Am. J. Physiol. 272*, F757−760.

BC050122M

Matrix Metalloprotease Triggered Delivery of Cancer Chemotherapeutics from Hydrogel Matrixes

Jovita R. Tauro[†] and Richard A. Gemeinhart*[,†,‡]

Departments of Biopharmaceutical Sciences and Bioengineering, The University of Illinois, Chicago, Illinois 60612-7231. Received April 28, 2005; Revised Manuscript Received July 19, 2005

Glioblastoma multiforme (GBM) is a highly advanced and invasive brain tumor due to which current treatments cannot completely treat GBM or prevent recurrence. Therefore, adjunctive treatments are required. As part of the invasive and angiogenic nature of GBM, it has been well established that matrix metalloprotease-2 (MMP-2) and MMP-9 are overactive. To better treat GBM using chemotherapy, we have designed a hydrogel-based delivery system that can control the release of drugs based on the activity of MMPs. A model chemotherapeutic agent, cisplatin (CDDP), complexed to an MMP substrate (peptide-linker) was incorporated into poly(ethylene glycol) diacrylate hydrogel wafers having different poly(ethylene glycol) chain lengths ($M_n \approx 574$ and 4000). Hydrogel wafers were studied for physical characteristics and drug release in the presence and absence of MMPs. There was a substantial increase in CDDP release for the poly(ethylene glycol) 4000 hydrogel indicating that this chain length provides a mesh size that is sufficient to permit MMP activity within the hydrogel. CDDP bioactivity increased when the cell media was spiked with MMPs (0% cell survival) in case of the longer chain length as compared to in the absence of MMPs (approximately 50% cell survival). The results suggest that this system can be used for selective, local delivery of drugs where higher amounts of the drug are released in response to metastasis, angiogenesis, and invasion-promoting proteases. This strategy may prove to be a novel and effective method to overcome inadequacies in current controlled drug release systems.

INTRODUCTION

Brain tumors are especially difficult to treat due to the lack of chemotherapeutic agent blood-brain barrier (BBB) transport. Of all brain tumors, the most advanced stage of astrocytic brain tumor, glioblastoma multiforme (GBM) or World Health Organization Grade IV glioma, is highly proliferative and shows wide areas of necrosis surrounded by invasive tumor tissue and extensive neovascularization (*1*, *2*). The mean survival time for patients with GBM is one year due to the highly invasive nature of the disease (*1*) leading to recurrence even after treatment (*3*). Currently available chemotherapeutic agents, including cisplatin (CDDP), can only slightly prolong the mean survival time of patients (*4*). Therefore, better treatment strategies are necessary to effectively treat GBM and other forms of brain tumor. In an attempt to better treat brain tumors, local delivery of chemotherapeutics has been utilized (*5*). These local drug delivery systems release drugs at a constant rate that is dictated by hydrolysis of a polymeric carrier; drug delivery is not correlated with any biologic response. Over the last several decades, it has been recognized that the current paradigm of arbitrary and nonspecific delivery of chemotherapeutics can be improved by targeting the activation or release of the chemotherapeutic at a desired site via specific active mechanisms (*6*, *7*). With this in mind, systems that utilize tumor biology have been proposed and utilized to improve the outcome for brain tumor and other cancer patients (*8*).

Several aspects of tumor biology can be exploited to utilize tumor biology for delivery of chemotherapeutics, including tissue invasion, angiogenesis, and metastasis, all of which require the degradation of extracellular matrix (ECM) proteins. Many proteases are implicated in ECM degradation and matrix metalloproteases (MMPs) have been shown to actively participate in degradation of ECM and activation of invasion promoting growth factors (*9*). MMPs play an important and beneficial role in tissue remodeling, wound healing, and angiogenesis along with negative roles in tumor invasion and neovascularization (*10*, *11*). Unequivocal data confirms that the levels of MMP-2 and MMP-9 are observed to increase in correlation with tumor progression in human gliomas (*12*, *13*). Initial attempts to exploit MMPs as a chemotherapeutic target using synthetic MMP inhibitors (MMPis) prevented glioma invasion by inhibiting MMP activity. MMPis reduced glioma growth and invasion in vitro and in animal models (*14*, *15*) but have achieved disappointing results in Phase I, II, and III clinical trials for many reasons (*16*). Despite these disappointing clinical results with MMPis, MMPs may still be an excellent target for chemotherapeutic delivery if an alternate approach is taken: a prodruglike approach.

To achieve a prodruglike approach, an understanding of MMPs proteolytic character is needed. Each MMP has different specificities for the constituents of the ECM; however, MMP-2 and MMP-9 show a great amount of overlap in their substrate specificities. Substrates common to both gelatinases include gelatins, collagens IV and V, elastin, and aggrecans (*17*). By use of these overlapping specificities, it is possible to design peptide sub-

* To whom correspondence should be addressed. Mailing address: 833 South Wood Street (MC 865), Departments of Biopharmaceutical Sciences and Bioengineering, The University of Illinois, Chicago, IL 60612-7231. Tel: (312) 996-2253. Fax: (312) 996-2784. E-mail: rag@uic.edu.

[†] Department of Biopharmaceutical Sciences.

[‡] Department of Bioengineering.

10.1021/bc0501303 CCC: $30.25 © 2005 American Chemical Society
Published on Web 08/30/2005

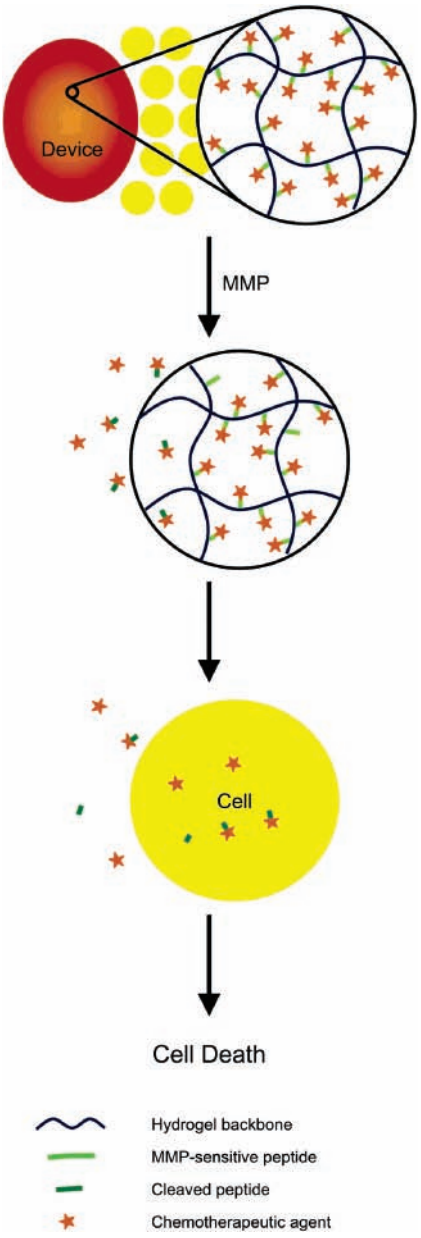

Figure 1. Schematic representation of the drug activation mechanism proposed. In this, CDDP (orange star) is complexed to peptides (light-green lines) pendant on the backbone of a hydrogel matrix (blue lines) of a hydrogel device (red circle) placed near tumor cells (yellow circles). As matrix metalloproteases diffuse through the matrix, the peptides are cleaved releasing CDDP−peptide (dark-green lines) complexes. These complexes may dissociate or enter cells as a complex. CDDP is then able to have the therapeutic effect only when released from the hydrogel matrix. Once released by MMP cleavage (or nonspecific means), the chemotherapeutic agent can enter a cell and have the therapeutic effect (cell death).

strates for releasing drug when MMPs are active similar to a traditional prodrug. In this hydrogel-based prodrug system, peptide substrates act as MMP degradable spacers binding the chemotherapeutic agent to a hydrogel matrix; therefore, the prodrug is retained at the site of implantation by the hydrogel matrix. Our rationale for this design was to use a peptide−drug complex that will release an active form of the drug from the matrix when the peptide is cleaved by MMPs (Figure 1).

Hydrogels were chosen as matrixes due to the inherent biocompatibility of the cross-linked polymeric network (*18*). Hydrogel biocompatibility can be attributed to their hydrophilicity and ability to imbibe large amounts of biological fluids (*19*, *20*). Also, hydrogels closely resemble natural living ECM (*21*) creating a perfect environment for a matrix to mimic MMPs natural activity. In addition, poly(ethylene glycol) diacrylate (PEGDA) hydrogels of different PEG chain lengths are known to allow protein diffusion through the matrix if appropriate mesh size is attained (*22*). Hydrogels of this type have even been produced to allow degradation via MMPs thereby releasing PEG chains and natural products and allowing for aid in regeneration (*23*).

The described study utilizes a PEGDA-based hydrogel to locally target one of the major characteristics of GBM and utilizes this characteristic to selectively deliver a model chemotherapeutic agent, CDDP. Physical properties and in vitro activity of the system have been studied to confirm that MMPs can be used to activate a chemotherapeutic agent from a synthetic hydrogel matrix. With the application of this technology, the problems of recurrence and invasion are expected to be mitigated as the drug will be activated as a tumor attempts to metastasize or recur locally. Localized delivery minimizes systemic toxicity and targets activation of the drug to the site of malignancy. The ability of a delivery system to release the drug when activated by MMPs may help in the development of a successful strategy for treatment of GBM and should be explored further in relation to GBM and other solid tumors.

EXPERIMENTAL PROCEDURES

The MMP-sensitive peptide substrate, CGLDD, and the expected cleaved fragment, LDD (*24*), were synthesized by the University of Illinois at Chicago Research Resources Center with the N-terminal amine blocked by acylation. Peptide structures were confirmed by liquid chromatography mass spectrometry. MMP-2 and MMP-9 were purchased from Calbiochem and activated as suggested by the manufactured using 4-(hydroxymercury)-benzoic acid (Acros Organics, NJ). Short-chain PEGDA ($M_n = 700$, PEG(574)DA) macromer was purchased from Sigma Aldrich Chemical company (Milwaukee, WI). Long-chain PEGDA ($M_n = 4126$, PEG(4000)DA) macromer was purchased from Polysciences, Inc. (Warrington, PA). All remaining chemicals were purchased from Fisher Scientific (Fairlawn, NJ) and used without further purification unless specified.

Preparation and Characterization of Hydrogels. MMP-sensitive peptide substrate (2 mM) was dissolved in water and mixed with PEG(574)DA (100 mM) or PEG-(4000)DA (15.9 mM) and stirred overnight. Michael addition of the acrylate group to the sulfhydryl group on cysteine (*25*) was confirmed using Ellman's reagent (Pierce, Milwaukee, WI), thereby quantifying reduction in free sulfhydryl groups (*26*). PEGDA−peptide solutions (or peptide-free PEGDA at the concentrations listed above) were polymerized without further purification between glass slides to form sheets of hydrogels using ammonium persulfate (20 mM) and N,N,N,N-tetramethylethylenediamine (51.6 mM) as the initiator pair. Hydrogels were cut into 6 mm diameter wafers using a biopsy punch, washed repeatedly in deionized water to remove unpolymerized monomers, and finally allowed to dry in a vacuum oven. CDDP was aquated at pH 7.4 using silver nitrate (*27*) and reacted overnight with hydrogels. Hydrogels containing the peptide were washed to remove excess CDDP. CDDP was entrapped in hydrogels without peptide by using the same procedure as described without washing. CDDP entrapment and complexation in hydrogels was determined by spectropho-

tometeric *o*-phenylenediamine (OPDA) assay (*28*). The mesh size (ξ) of hydrogels was determined to compare with MMP penetration (*29*).

Cell Culture and MMP Activity. A malignant glioma cell line (U-87 MG, ATTC #HTB-14) was grown and maintained in Eagles minimum essential media with 10% fetal bovine serum, 1% penicillin/streptomycin, sodium pyruvate (110 mg/L), L-glutamine (292 mg/L), and nonessential amino acids. Cells were cultured at 37 °C in 5% CO_2. To confirm MMP expression and activity in U-87 MG cells, cells were subcultured under standard conditions for 24 h, then supplemented media was replaced with serum-free media and cultured for an additional 24 or 48 h. The serum-free media was removed and analyzed for presence for MMPs by gelatin zymography (*30*). Cell-treated media (10 μL) was loaded on Ready Gel zymography gels (Bio-Rad Laboratories, Hercules, Ca) and electrophoresed at 100 V. The gels were then washed, incubated, stained, and analyzed for presence of MMPs.

CDDP Release. CDDP release from the hydrogels was determined at 37 °C in a buffer containing Tris−HCl (50 mM), NaCl (0.2 M), $CaCl_2 \cdot 2H_2O$ (10 mM), Brij-35 (0.05%), and $ZnSO_4 \cdot 7H_2O$ (50 μM) in the presence and absence of MMPs (at a final concentration of 10 nM). Released CDDP was determined using the spectrophotometeric OPDA assay (*28*). CDDP release profiles were compared to CDDP release profiles for hydrogels with entrapped CDDP; no peptide was present in the hydrogel for entrapped CDDP studies, which act as a diffusional release control.

Peptide Toxicity and CDDP Activity. To determine the activity of released CDDP, the cleaved peptide fragment LDD was complexed with CDDP using the same procedure as described earlier for hydrogels. Cytotoxicity of the MMP cleaved fragment, LDD, and LDD−CDDP complex was determined by incubating U-87 MG cells with varying concentrations of these peptides in supplemented serum free media for 24 h.

To determine the activity of the hydrogel−CDDP complex devices, hydrogels were incubated with cells in supplemented serum-free media for 24 h. For specific samples, MMP (10 nM) was added to media to supplement the MMPs expressed by U-87 MG cells (*31*) and thus accentuate the MMP effect on CDDP release. Activity of the hydrogel−CDDP complex devices was also studied in the absence of added MMPs. Cell viability with respect to the untreated control was calculated using a modified MTT assay (Cell Titer 96 Aqueous One Solution Cell Proliferation Assay; Promega; Madison, WI) (*32*).

RESULTS

Preparation of Hydrogels. Peptide−PEGDA conjugation was nearly complete after overnight incubation at room temperature as determined by quantitative analysis of free sulfhydryl groups. There was 74.1 ± 3.2% efficiency for conjugation with the PEG(574)DA and 76.1 ± 1% efficiency for conjugation with the PEG(4000)-DA, and the reaction did not proceed further following extended incubation under these conditions. Since this reaction mixture was not further purified prior to polymerization, further incorporation of the peptide is expected by further Michael reaction or chain-transfer reactions with the peptide (*33*). In similar studies with fluorescent-labeled peptide, no peptide was released from the hydrogel without addition of MMPs (data not shown).

PEGDA and PEGDA−peptide hydrogels reached the critical gelation point within 5 min of initiation, but the reaction was continued at 37 °C for a minimum of 1 h to increase the extent of polymerization. PEG(574)DA hydrogels had a mesh size (21±4 nm) that was smaller than PEG(4000)DA hydrogels (79±7 nm). This was expected since PEG(4000)DA hydrogels have significantly longer PEG chains; this increased mesh size allows for substantially higher water content. This larger mesh size was expected to allow MMP-2 and MMP-9 to more freely diffuse in the PEG(4000)DA hydrogel than the PEG(574)-DA hydrogel.

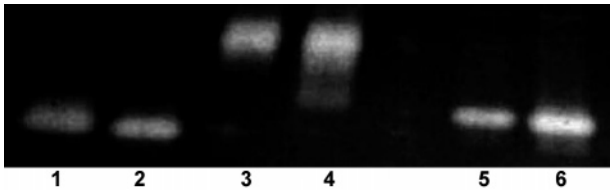

Figure 2. Detection of MMPs by gelatin zymography. Lane 1, Pro-MMP-2; Lane 2, active MMP-2; Lane 3, Pro-MMP-9; Lane 4, active MMP-9; Lane 5, 24 h U-87 MG expression; Lane 6, 48 h U-87 MG expression.

As expected, entrapped CDDP content was found to be much higher than complexed CDDP content since washing removed CDDP that was not complexed to the hydrogel. PEG(574)DA entrapped 22.1 ± 0.9 μg (0.317 μg/mm^3), and 8.6 ± 0.1 μg (0.122 μg/mm^3) was retained as CDDP−hydrogel complexes. Also, the CDDP content was found to be higher in the PEG(4000)DA hydrogels than in the PEG(574)DA hydrogels. PEG(4000)DA hydrogels entrapped 55.7 ± 6.1 μg (0.43 μg/mm^3) while 20.5 ± 1.4 μg (0.157 μg/mm^3) was retained as peptide−CDDP complexes.

MMP Activity. U-87 MG cells express MMP-2 when cultured in media for 24 and 48 h (Figure 2). Pro-MMP-2 increased as cells are incubated for extended periods. Active MMP-2 was detected at 48 h. MMP-9 was not expressed at detectable levels in the cells for up to 48 h. However, this cell line may be used as an in vitro model since the expression and functions of MMP-2 and MMP-9 are known to be heterogeneous in clinical GBM presentation (*9*, *12*) and MMP-2 and MMP-9 have overlapping substrate specificities.

CDDP Release. CDDP was complexed with the carboxyl groups of aspartic acids in the substrate peptide (Figure 3) (*27*). We have previously shown that CDDP complexation delays the release of CDDP from hydrogel particles (*34*). This was confirmed for peptide complexation in this study. CDDP entrapped in PEGDA hydrogels with no carboxylic content was released nearly instantaneously in a burst profile (Figure 4). Peptide complexed CDDP exhibited a slowed release over time even without MMPs present indicating that the complexation was taking place but was not sufficient for complete retention of the drug. However, with the addition of MMPs, there was a marked increase in the amount of CDDP released from the PEG(4000)DA hydrogels but not the PEG(574)DA hydrogels. This suggests that the peptide CGLDD was cleaved from the PEG-(4000)DA hydrogels in a manner dependent upon MMPs if the MMPs are able to enter the hydrogel matrix.

Peptide Toxicity and CDDP Activity. As anticipated, the expected cleaved fragment, LDD, showed no toxicity when incubated with U-87 MG cells. However, the complex, LDD−CDDP, had activity (EC_{50} = 234.7 μM) approximately an order of magnitude below CDDP (EC_{50} = 41.5 μM) (Figure 5). Complexed CDDP retained activity with some loss due to complexation. PEGDA hydrogels and PEGDA−peptide hydrogels without CDDP

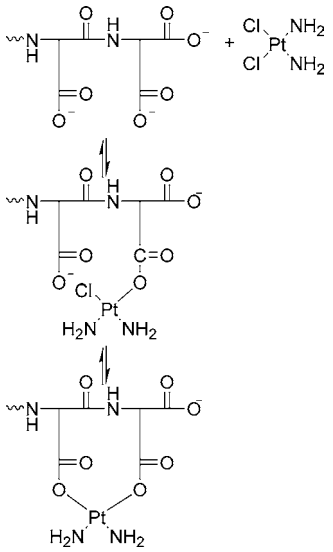

Figure 3. Generalized complexation chemistry of CDDP with carboxylic acid groups, which was utilized in this study. Platinum can interact with aspartic acid side groups as shown or with the carboxyl-terminal group in the peptide. The complexation is dynamic, so both interactions are expected.

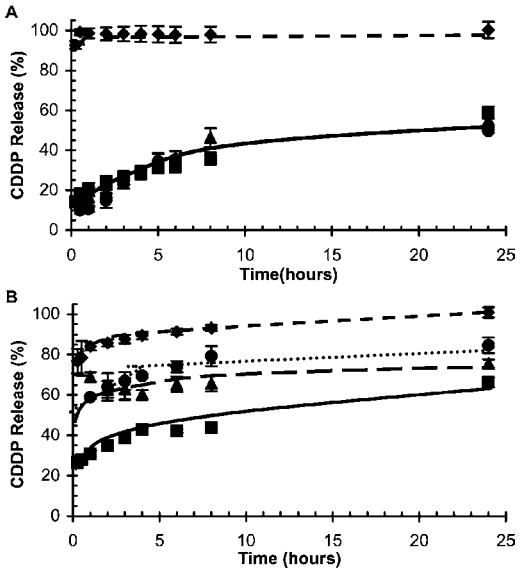

Figure 4. (a). CDDP release from PEG(574)DA hydrogels where (◆) CDDP was entrapped with no complexation, (■) CDDP was complexed to the hydrogel, (●) CDDP was complexed to the hydrogel with MMP-9 added to the release media (10 nM), and (▲) CDDP was complexed to the hydrogel with MMP-2 added to the release media (10 nM). (b) CDDP release from PEG(4000)DA hydrogels where (◆) CDDP was entrapped with no complexation, (■) CDDP was complexed to the hydrogel, (●) CDDP was complexed to the hydrogel with MMP-9 added to the release media (10 nM), and (▲) CDDP was complexed to the hydrogel with MMP-2 added to the release media (10 nM).

were not cytotoxic in the presence or absence of MMP-2 or MMP-9 (Figure 6). CDDP entrapped in PEGDA hydrogels exhibited similar activity to the amount of CDDP that was loaded into the hydrogel. Upon complexation, PEGDA−peptide−CDDP hydrogels exhibited activity at a level well below the amount of CDDP loaded. Activity of CDDP released from PEG(574)DA peptide−CDDP complex hydrogels was not influenced by MMP addition. CDDP released from PEG(4000)DA peptide−CDDP complex hydrogels showed higher activity than CDDP released from PEG(574)DA hydrogels with and without the addition of MMPs. Also, with the addition

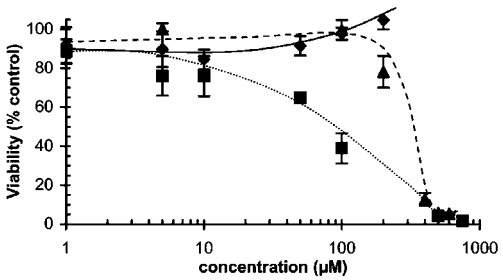

Figure 5. Cytotoxic activity of the (◆) cleaved fragment, LDD, the (▲) expected released peptide−CDDP complex, LDD−CDDP, and (■) CDDP as determined by modified MTT assay using U-87 MG malignant glioma cells.

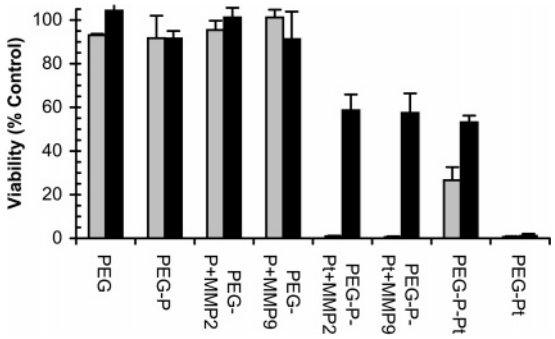

Figure 6. Activity of CDDP released from (dark bars) PEG(574)DA and (light bars) PEG(4000)DA hydrogels. Hydrogels without CDDP or peptides (PEG), hydrogels with peptide incorporated but with CDDP in the absence (PEG-P), and presence of MMP-2 (PEG-P + MMP2) or MMP-9 (PEG-P + MMP9), hydrogels with entrapped CDDP but without peptide for complexation (PEG-Pt), and hydrogels with peptide−CDDP complex in the absence (PEG-P−Pt) and presence of MMP-2 (PEG-P−Pt + MMP2) or MMP-9 (PEG-P−Pt + MMP9).

of MMP-2 or MMP-9 to PEG(4000)DA peptide−CDDP complex hydrogels, higher CDDP activity was observed than in the absence of MMPs. This was not seen with the PEG(574)DA hydrogels. The increase in CDDP activity supports and reinforces the data obtained by CDDP release suggesting that more CDDP was released in the presence of MMPs.

DISCUSSION

PEGDA hydrogels have been widely accepted in many biomedical applications over the last several years (*35*). Hydrogels prepared using PEG(574)DA and PEG(4000)-DA have adequate physical characteristics for implantation and manipulation prior to placement. The current formulations are biodegradable, but the time course for biodegradation is quite slow. This would cause accumulation of PEGDA hydrogel at the site of implantation. To overcome this problem, PEGDA hydrogels could be made to biodegrade at a faster rate by several modifications (*36*). PEGDA hydrogels can be made biodegradable by incorporating a biodegradable cross linker or by utilizing biodegradable copolymers (*37*−*40*). The extent and rate or degradation would be controlled by the specific degradation mechanism used. Future generations of this type of system should integrate such biodegradable nature. However, it was necessary to confirm the possibility of drug activation prior to adding a potentially confounding variable such as biodegradation. Once proteolytic release of anticancer agents is understood, appropriate degradation mechanisms can be incorporated into the system that allow full control of release while limiting accumulation of the hydrogel at the site of implantation. It should be noted, however, that PEGDA

hydrogels are well tolerated in the body even when left for significant periods.

PEGDA hydrogels are hydrophilic, biocompatible, nontoxic, and exhibit variable mesh size depending upon PEG macromer length. Large PEG chain lengths allow proteins to diffuse throughout the matrix while smaller PEG chain lengths can be used to control the accessibility of the matrix to specific proteins (*22*). This work has shown that adequate PEGDA chain length can be attained to allow diffusion of MMPs throughout the matrix, thus releasing a chemotherapeutic agent from the matrix via MMP cleavage of peptide substrates. Hydrogels containing peptide−CDDP complex provided a level of control for the release of CDDP to the tumor cells. We did not show complete control over delivery of CDDP; the CDDP−peptide complex allows nonspecific release of approximately 50% of bound CDDP in the first day regardless of chain length. Increasing CDDP binding efficiency with a hydrogel by increasing the carboxylic acid content has been shown to slow the nonspecific CDDP release from hydrogel particles (*34*). Alternate platinum chemistries are also possible if platinum-based drugs are desired to be delivered. Our group has successfully bound platinum to amine groups of hydrogel and showed limited release over a week or longer (*41*). Utilization of covalent coupling of alternate drugs could also alleviate the problem of nonspecific release (*8*). Alternate chemistries should allow a more specific release of chemotherapeutics from the device. A perfectly designed system would allow release of the chemotherapeutic agent in a MMP dose-dependent manner. Most importantly, when no MMP is present, no chemotherapeutic should be released. As the concentration of MMP increases, the amount of chemotherapeutic should increase. This would ensure minimal toxicity due to the chemotherapeutic and maximum release with protease activity. Despite the setback of nonspecific release, we were able to confirm that MMP-specific release of CDDP is possible from a hydrogel matrix.

When glioma cells attempt to grow and invade the surrounding tissue or even in culture, MMPs are expressed (Figure 2). This led to increased CDDP release when MMPs were present (Figure 4). The fact that PEG(574)DA hydrogels do not allow increased release of CDDP upon MMP addition while PEG(4000)DA hydrogels do allow accelerated release of CDDP confirms our hypothesis that adequate mesh size can be obtained. Thus, this system will deliver a higher dose of the drug selectively to the most invasive portion of the tumor. This was also confirmed by examining the activity of the devices (Figure 6). Cells are not influenced by any hydrogels that do not possess CDDP, and when no CDDP complexation exists, cells are not able to survive. Upon peptide−CDDP complexation within PEG(574)DA hydrogels, intermediate CDDP activity was observed after 24 h with no increase upon MMP addition. When peptide−CDDP is complexed within PEG(4000)DA hydrogels, CDDP was substantially more active. Without MMPs, fewer cells survive when treated with PEG(4000)DA hydrogels than when treated with equivalent PEG(574)DA hydrogels. This is due to MMP diffusion into the PEG(4000)DA hydrogels and subsequent increased release of CDDP. CDDP activity was increased by addition of MMPs as expected for a Michaelis−Menten-type kinetics ($V_{max} = k_{cat} \cdot [E]_{tot}$). Further studies are needed to better characterize the exact kinetics of release under these circumstances, and we hope to report these results in the future. The end result is not in question, increased CDDP was released when MMPs are added to the system. This type of delivery should greatly increase the efficacy of drug delivery systems.

Local delivery and controlled activation of the drug reduces unnecessary exposure to other organs. Since the drug was released in high doses at the tumor site it may have better efficacy. Problems with currently utilized routes of chemotherapeutic agent delivery, such as inability to cross the BBB and systemic toxicity, would be averted. Since the conjugation of the peptide within PEGDA has a high yield, loading of the drug can be maximized by increasing the concentration of the peptide. The peptide used for the study is a substrate for MMP-2 and MMP-9 with efforts underway to design substrates specific for these and other enzymes. Having an array of substrates would allow for tailoring a device to a specific patient or for a particular tumor type. Not only is peptide choice important for specificity and kinetic control of cleavage but activity of the released drug is also influenced by peptide modification.

Minimization of loss of activity of the drug due to complexation has to be considered in designing peptides; our current example indicated a reduction in activity from CDDP (Figure 5). By selective control over peptides, more active CDDP (or other drug) analogue can be released from the hydrogel matrix. Our data showed that peptide substrates for MMP-2 and MMP-9 can be cleaved by these enzymes within hydrogels thus releasing an active form of CDDP.

Other groups have shown activity of drugs when covalently attached to MMP substrates (*42*) or released from MMP-sensitive micelles (*31*). We have focused on localized delivery due to questions that exists concerning the heterogeneity of tumor vascular permeability in different tumor types and proteases present within the blood. In our system, the activity of the complexed drug toward the glioma cell line was retained (although slightly attenuated) after cleavage. We have not overlooked the fact that transport of materials away from the device may hinder the area of effectiveness, but we also believe that polymer therapeutics that rely on vascular permeability have potential liabilities that can be addressed using local device placement. We hope to report in vivo results with this system soon. From these studies, hydrogel-based matrixes may prove to be excellent carriers for chemotherapeutics when local delivery is desired particularly when a prodruglike approach is used.

CONCLUSION

Current treatments have not improved the poor prognosis of GBM to a significant degree. It is necessary to develop drug delivery systems that reduce the problems of toxicity, recurrence, and invasion in this disease. By utilization of the biology of GBM, we have proposed a novel method of utilizing the overactivity of MMP-2 and MMP-9 in GBM to activate a prodrug from a hydrogel matrix. When CDDP is entrapped within PEGDA hydrogels, CDDP is released within a short period (greater than 95% within an hour). CDDP can be retained in PEGDA hydrogels by complexation with aspartate-containing peptides (approximately 50% release in 24 h). When MMPs are present, CDDP is released at an accelerated rate when adequate mesh size of the hydrogel matrix is present. PEG(4000)DA hydrogels have sufficient mesh size for MMP diffusion but not PEG(574)DA hydrogels. Thus, PEG(4000)DA hydrogels containing drug−peptide prodrugs have shown great promise for locally controlling the release of chemotherapeutics. Active drug was cleaved from the hydrogel in the pres-

ence of MMPs and the cleaved drug retained activity toward glioma cells. This system warrants future research with MMP substrates and drugs and should be further explored.

ACKNOWLEDGMENT

The authors thank Dr. Hayat Onyuksel for use of equipment, Bob Lee for peptide production, Avni Shah for technical assistance, Xiaoliang Yan for helpful discussion, and Ernest J. Gemeinhart for technical assistance, helpful discussion, and review of this manuscript. This study was supported in part by the National Eye Institute (R03 EY014357) and the American Brain Tumor Association, Kathy Murphy Translational Research Grant. This investigation was conducted in a facility constructed with support from Research Facilities Improvement Program Grant Number C06 RR15482 from the National Center for Research Resources, NIH.

LITERATURE CITED

(1) Holland, E. C. (2001) Gliomagenesis: Genetic Alterations and Mouse Models. *Nat. Rev. Gen. 2*, 120−129.
(2) Rao, J. S. (2003) Molecular Mechanisms of Glioma Invasiveness: The Role of Proteases. *Nat. Rev. Cancer*. *3*, 489−501.
(3) Chintala, S. K., Tonn, J. C., and Rao, J. S. (1999) Matrix Metalloproteases and Their Biological Function in Human Gliomas. *Int. J. Dev. Neurosci. 17*, 495−502.
(4) Avgeropoulos, N. G., and Batchelor, T. T. (1999) New Treatment Strategies for Malignant Gliomas. *Oncologist 4*, 209−224.
(5) Brem, H., and Gabikian, P. (2001) Biodegradable Polymer Implants to Treat Brain Tumors. *J. Controlled Release 74*, 63−67.
(6) Moses, M. A., Brem, H., and Langer, R. (2003) Advancing the Field of Drug Delivery: Taking Aim at Cancer. *Cancer Cell 4*, 337−341.
(7) Kost, J., and Langer, R. (2001) Responsive Polymeric Delivery Systems. *Adv. Drug Delivery Rev. 46*, 125−148.
(8) Duncan, R. (2003) The Dawning Era of Polymer Therapeutics. *Nat. Rev. Drug Discovery 2*, 347−360.
(9) Rao, J. S., Yamamoto, M., Mohaman, S., Gokaslan, Z. L., Fuller, G. N., Stetler-Stevenson, W. G., Rao, V. H., Liotta, L. A., Nicolson, G. L., and Sawaya, R. E. (1996) Expression and Localization of 92 Kda Type Iv Collagenase/Gelatinase B (Mmp-9) in Human Gliomas. *Clin. Exp. Metas. 14*, 12−18.
(10) Woessner, J. F. (1991) Matrix Metalloproteases and Their Inhibitors in Connective Tissue Remodelling. *FASEB J. 5*, 2145−2154.
(11) Mignatti, P., and Rifkin, D. B. (1993) Biology and Chemistry of Proteinases in Tumor Invasion. *Phys. Rev. 73*, 161−185.
(12) Sawaya, R. E., Yamamoto, M., Gokaslan, Z. L., Wang, S. W., Mohaman, S., Fuller, G. N., McCutcheon, I. E., Stetler-Stevenson, W. G., Nicolson, G. L., and Rao, J. S. (1996) Expression and Localization of 72 Kda Type Iv Collagenase (Mmp-2) in Human Malignant Gliomas in Vivo. *Clin. Exp. Metas. 14*, 35−42.
(13) Forsyth, P. A., Wong, H., Laing, T. D., Rewcastle, N. B., Morris, D. G., Muzik, H., Leco, K. J., Johnston, R. N., Brasher, P. M. A., Sutherland, G., and Edwards, D. R. (1999) Gelatinase-a (Mmp-2), Gelatinase-B (Mmp-9) and Membrane Type Matrix Metalloproteinase-1 (Mt1-Mmp) Are Involved in Different Aspects of the Pathophysiology of Malignant Gliomas. *Br. J. Cancer 79*, 1828−1835.
(14) Tonn, J. C., Kerkau, S., Hanke, A., Bouterfa, H., Mueller, J. G., Wagner, S., Vince, G. H., and Roosen, K. (1999) Effect of Synthetic Matrix-Metalloproteinase Inhibitors on Invasive Capacity and Proliferation of Human Malignant Gliomas in Vitro. *Int. J. Cancer 80*, 764−772.
(15) Price, A., Shi, Q. A., Morris, D., Wilcox, M. E., Brasher, P. M. A., Rewcastle, N. B., Shalinsky, D., Zou, H., Appelt, K., Johnston, R. N., Yong, V. W., Edwards, D., and Forsyth, P. (1999) Marked Inhibition of Tumor Growth in a Malignant Glioma Tumor Model by a Novel Synthetic Matrix Metalloproteinase Inhibitor Ag3340. *Clin. Cancer Res. 5*, 845−854.
(16) Coussens, L. M., Fingleton, B., and Matrisian, L. M. (2002) Matrix Metalloproteinase Inhibitors and Cancer: Trials and Tribulations. *Science 295*, 2387−2392.
(17) Nagase, H., and Fields, G. B. (1996) Human Matrix Metalloprotease Specificity Studies Using Collagen Sequence-Based Synthetic Peptides. *Biopolymers 40*, 399−416.
(18) Hill-West, J. L., Chowdhury, S. M., Slepian, M. J., and Hubbell, J. A. (1994) Inhibition of Thrombosis and Intimal Thickening by *in Situ* Photopolymerization of Thin Hydrogel Barriers. *Proc. Natl. Acad. Sci. U.S.A. 91*, 5967−5971.
(19) Brannon-Peppas, L. *Preparation and Characterization of Cross-linked Hydrophilic Networks in Absorbent Polymer Technology*, Brannon-Peppas, L. and Harland, R. S., Eds. 1990, Elsevier: Amsterdam; pp 45−66.
(20) Peppas, N. A., and Mikos, A. G. *Preparation Methods and Structure of Hydrogels in Hydrogels in Medicine and Pharmacy*, Peppas, N. A., Ed. 1986, CRC Press: Boca Raton, FL; pp 1−27.
(21) Ratner, B. D., and Hoffman, A. S. *Synthetic Hydrogels for Biomedical Applications in Hydrogels for Medical and Related Applications*, Andrade, J. D., Ed. 1976, American Chemical Society: Washington, DC; pp 1−36.
(22) Elbert, D. L., Pratt, A. B., Lutolf, M. P., Halstenberg, S., and Hubbell, J. A. (2001) Protein Delivery from Materials Formed by Self-Selective Conjugate Addition Reactions. *J. Controlled Release 76*, 11−25.
(23) Lutolf, M. P., Lauer-Fields, J. L., Schmoekel, H. G., Metters, A. T., Weber, F. E., Fields, G. B., and Hubbell, J. A. (2003) Synthetic Matrix Metalloproteinase-Sensitive Hydrogels for the Conduction of Tissue Regeneration: Engineering Cell-Invasion Characteristics. *Proc. Natl. Acad. Sci. U.S.A. 100*, 5413−5418.
(24) Tauro, J. R., and Gemeinhart, R. A. (2004) Peptide-Based Targeted Activation of Platinates by Matrix Metalloproteases. *Neuro-Oncology 6*, 335−336.
(25) Heggli, M., Tirelli, N., Zisch, A., and Hubbell, J. A. (2003) Michael-Type Addition as a Tool for Surface Functionalization. *Bioconjugate Chem. 14*, 967−973.
(26) Ellman, G. L. (1959) Tissue Sulfhydryl Groups. *Arch. Biochem. Biophys. 82*, 70−77.
(27) Gianasi, E., Buckley, R. G., Latigo, J., Wasil, M., and Duncan, R. (2002) Hpma Copolymers Platinates Containing Dicarboxylato Ligands. Preparation, Characterisation and in Vitro and in Vivo Evaluation. *J. Drug Target 10*, 549−556.
(28) Golla, E. D., and Ayres, G. H. (1973) Spectrophotometric Determination of Platinum with O−Phenylenediamine. *Talanta 20*, 199−210.
(29) Peppas, N. A. *Characterization of the Cross-Linked Structure of Hydrogels. in Hydrogels in Medicine and Pharmacy*, Peppas, N. A., Ed. 1987, CRC Press, Inc.: Boca Raton, FL; pp 27−56.
(30) Munaut, C., Noel, A., Hougrand, O., Foidart, J.-M., Boniver, J., and Deprez, M. (2003) Vascular Endothelial Growth Factor Expression Correlates with Matrix Metalloproteases Mt1-Mmp, Mmp-2 and Mmp-9 in Human Glioblastomas. *Int. J. Cancer 106*, 848−855.
(31) Bae, M., Cho, S., Song, J., Lee, G. Y., Kim, K., Yang, J., Cho, K., Kim, S. Y., and Byun, Y. (2003) Metalloprotease-Specific Poly(Ethylene Glycol) Methyl Ether-Peptide-Doxorubicin Conjugate for Targeting Anticancer Drug Delivery Based on Angiogenesis. *Drug Exp. Clin. Res. 29*, 15−23.
(32) Paull, K. D., Shoemaker, R. H., Boyd, M. R., Parsons, J. H., Risbood, P. A., Barbera, W. A., Sharma, M. N., Baker, D. C., Hand, E., Scudiero, D. A., Monks, A., Alley, M. C., and Grote, M. (1988) The Synthesis of Xtt- a New Tetrazolium Reagent That Is Bioreducible to a Water Soluble Formazan. *J. Heterocycl. Chem. 25*, 911−914.
(33) Fussell, G. W., and Cooper, S. L. (2004) Endothelial Cell Adhesion on Rgd-Containing Methacrylate Terpolymers. *J. Biomed. Mater. Res. Part A. 70A*, 265−273.
(34) Yan, X., and Gemeinhart, R. A. Cisplatin Delivery from Poly(Acrylic Acid-Co-Methyl Methacrylate) Microparticles. *J. Controlled Release. 106*, 198−208.

(35) Peppas, N. A., Keys, K. B., Torres-Lugo, M., and Lowman, A. M. (1999) Poly(Ethylene Glycol)-Containing Hydrogels in Drug Delivery. *J. Controlled Release 62*, 81−87.
(36) Sawhney, A. S., Pathak, C. P., van Rensburg, J. J., Dunn, R. C., and Hubbell, J. A. (1994) Optimization of Photopolymerized Bioerodible Hydrogel Properties for Adhesion Prevention. *J. Biomed. Mater. Res. 28*, 831−838.
(37) Sawhney, A. S., Pathak, C. P., and Hubbell, J. A. (1993) Bioerodible Hydrogels Based on Photopolymerized Poly-(Ethylene Glycol)-Co−Poly(Alpha-Hydroxy Acid) Diacrylate Macromers. *Macromolecules 26*, 581−587.
(38) Park, K., Shalaby, W. S. W., and Park, H. *Biodegradable Hydrogels for Drug Delivery*. 1993, Lancaster, PA: Technomic Pub. ix, 252.
(39) Watanabe, J., Ooya, T., Nitta, K. H., Park, K. D., Kim, Y. H., and Yui, N. (2002) Fibroblast Adhesion and Proliferation on Poly(Ethylene Glycol) Hydrogels Cross-linked by Hydrolyzable Polyrotaxane. *Biomaterials 23*, 4041−4048.
(40) Yamini, C., Shantha, K. L., and Rao, K. P. (1997) Synthesis and Characterization of Poly[N-Vinyl-2-Pyrrolidone-Polyethylene Glycol Diacrylate] Copolymeric Hydrogels for Drug Delivery. *J. Macromol. Sci. A34*, 2461−2470.
(41) Tauro, J. R., and Gemeinhart, R. A. (2005) Development of Amine-Containing Polymeric Particles. *J. Biomater. Sci. Polym. Ed. 16*, 1233−1244.
(42) Kline, T., Torgov, M. Y., Mendelsohn, B. S., Cerveny, C. G., and Senter, P. D. (2004) Novel Antitumor Prodrugs Designed for Activation by Matrix Metalloproteinases-2 and -9. *Mol. Pharm. 1*, 9−22.

BC0501303

Synthesis of Biodegradable Cross-Linked Poly(*β*-amino ester) for Gene Delivery and Its Modification, Inducing Enhanced Transfection Efficiency and Stepwise Degradation

Tae-il Kim,[†] Hyo Jung Seo,[†] Joon Sig Choi,[‡] Jae Keun Yoon,[†] Jung-un Baek,[†] Kwan Kim,[†] and Jong-Sang Park[†,*]

School of Chemistry & Molecular Engineering, Seoul National University, San 56-1, Shillim-dong, Kwanak-gu, Seoul 151-742, Korea and Department of Biochemistry, Chungnam National University, 220 Gung-dong, Yuseong-gu, Daejeon 305-764, Korea. Received December 15, 2004

Biodegradable cross-linked poly(*β*-amino ester) (CLPAE) was synthesized by Michael addition of pentaerythritol triacrylate and *N*,*N*-dimethylethylenediamine and modified with aminohexanoic acid and lysine to CLPAE-Ahx and CLPAE-Lys, respectively, for a gene delivery system. They could self-assemble with plasmid DNA, forming nanosized polyplexes, and CLPAE-Ahx polyplex released plasmid DNA slowly during a week through stepwise degradation. The polymers showed minimal cytotoxicity on 293 cells due to their biodegradability and biocompatibility. Transfection efficiencies of CLPAE-Ahx and CLPAE-Lys were comparable to that of PEI in 293 cells and C2C12 cells. Additionally, high transfection of CLPAE-Ahx on primary rat aorta vascular smooth muscle cells (SMC) and primary mouse embryonic fibroblast cells (MEF) shows a potential for a gene delivery system on primary cells, restenosis treatment of human SMC, and MEF cell function research. In conclusion, CLPAE-Ahx could be used as a nontoxic and highly efficient gene delivery system.

INTRODUCTION

During the past decade, intensive research and development in multidisciplinary fields have been directed toward developing safer and more efficient methods for transferring therapeutic genes into cells and for eventual use in human gene therapy (*1*).

Several successful clinical trials reported so far involved viral vector systems (retroviruses, adenoviruses) that provide efficient transduction and high levels of gene expression. However, their severe immunogenicity and toxicity are still major obstacles for viral vector-mediated gene therapy (*2*). For these reasons, as alternative tools to such risky viral vectors, nonviral vectors have been introduced and studied for their potential to provide safer, more desirable methods for gene delivery and clinical gene therapy (*3*−*6*).

Studies have been performed to improve gene delivery efficiency of polymeric gene carriers and to reduce their cytotoxicity in many labs. Among them, the introduction of biodegradability such as ester, phosphoester, or disulfide bonds to the polymeric carriers was proved to be very successful for lowering cytotoxicity (*7*−*10*). However, the results from these approaches were dependent on specific conditions, so structure−activity relationships could not be obtained easily. Recently, Langer et al. constructed structurally manifold polymer libraries by using combinatorial reactions of amine derivatives and diacrylate monomers and screened them by high-throughput cell-based screening assay (*11*−*13*). Through this strategy, they discovered a few candidates showing very high gene delivery efficiency.

In general, linear cationic polyester polymers are reported to be degraded very fast in aqueous solution and to release DNA from polyplexes within a few hours (*14*). This means that the application of linear polyester polymers could be limited in the long term because of its fast degradation rate. So, we designed a novel cross-linked poly(*β*-amino ester) polymer (CLPAE) to control its degradation rate and deliver DNA for a longer period.

In this report, we present the synthesis, characterization of CLPAE, and further modification of the polymer for application to gene delivery. Also, self-assembly of polymers with plasmid DNA, in vitro DNA release, and cell-based experiments investigating cytotoxicity and transfection efficiency are performed and presented.

EXPERIMENTAL PROCEDURES

Materials. Poly(ethylenimine) (25 kDa), pentaerythritol triacrylate, *N*,*N*-dimethylethylenediamine (95%), *N*,*N*-diisopropylethylamine (DIPEA), piperidine, and 3-[4,5-dimethylthiazol-2-yl]-2,5-diphenyltetrazolium bromide (MTT) were purchased from Sigma-Aldrich (St. Louis, MO). *N*-Hydroxybenzotriazole (HOBt) and 2-(1*H*-benzotriazol-1-yl)-1,1,3,3-tetramethyluronium hexafluorophosphate (HBTU) were purchased from Anaspec, Inc. (San Jose, CA). Fmoc-6-aminohexanoic acid (Fmoc-*ϵ*-Ahx-OH) and Fmoc-Lys(Fmoc)-OH were purchased from Novabiochem (Laufelfingen, Switzerland). pGL3-control vector, Luciferase 1000 Assay System, and Reporter Lysis Buffer were purchased from Promega (Madison, WI). The luciferase expression plasmid (pCN-Luci) was a kind gift from Hyung-suk Jang in Samsung Medical Center (Seoul, Korea). pCN-Luci was constructed by subcloning cDNA of *Photinus pyralis* luciferase with a 21-amino acid nuclear localization signal from SV40 large T antigen to pCN (*15*). PicoGreen was purchased from Molecular Probes (Eugene, OR). Fetal bovine serum (FBS), Minimal Essential Medium (MEM), and Dulbecco's modified Eagle's medium (DMEM) were purchased from GIBCO (Gaithersburg, MD). Micro BCA protein assay kit was purchased from Pierce (Rockford, IL). All other chemicals were purchased and used without any further purification.

* To whom correspondence should be addressed. Phone: 82-2-880-6660, Fax: 82-2-877-5110, E-mail: pfjspark@plaza.snu.ac.kr.
[†] Seoul National University.
[‡] Chungnam National University.

10.1021/bc0497012 CCC: $30.25 © 2005 American Chemical Society
Published on Web 09/01/2005

Polymer Synthesis. *N*,*N*-Dimethylethylenediamine (0.481 mL, 4.16 mmol) and pentaerythritol triacrylate (0.526 mL, 2.08 mmol) were dissolved in methylene chloride (3 mL), respectively. Then, diamine solution was added to triacrylate solution dropwise, keeping it at 50 °C. After 2 days when a yellow precipitate was found in the reaction mixture, it was cooled to room temperature and evaporated under vacuum. The remnant was precipitated into diethyl ether two times to remove residual amine, leaving a light yellow solid, CLPAE.

Also, CLPAE was further modified to acquire the enhanced properties of gene delivery by the introduction of aminohexanoic acid (Ahx) or lysine (Lys) residues. These conjugation reactions were conducted by coupling the carboxylic group of the acid to the hydroxyl group of the triacrylate with HOBt/HBTU. Fmoc-protected Ahx and Lys were used to prevent side reactions.

(1) Aminohexanoic Acid-Conjugated CLPAE (CLPAE-Ahx). First, 100 mg of CLPAE was mixed in DMF with a large excess of Fmoc-ϵ-Ahx-OH (248 mg, 0.702 mmol), HOBt (94.8 mg, 0.702 mmol), and HBTU (266 mg, 0.702 mmol). At this time, a large excess of coupling reagents was used to complete the conjugation because we did not know the exact amount of hydroxyl groups in CLPAE. Then, DIPEA (245 μL, 1.40 mmol) was added to the reaction mixture. The reaction was allowed to proceed at room temperature for 2 days to complete the reaction. After the coupling reaction was completed, the product was precipitated with an excess of diethyl ether three times to remove the excess of coupling reagents and DMF. Dried under a vacuum, the product was dissolved in DMF and mixed with an equal volume of piperidine (30% in DMF) at room temperature for 20 min to remove the Fmoc group of aminohexanoic acid. The reaction mixture was precipitated again with diethyl ether to remove the piperidine and reaction remnants and dried under vacuum, leaving a sticky yellow solid, CLPAE-Ahx. Each coupling reaction and Fmoc-deprotection reaction was confirmed by ^{1}H NMR.

(2) Lysine-Conjugated CLPAE (CLPAE-Lys). CLPAE (100 mg) was mixed in DMF. Then an equimolar amount of Fmoc-Lys-(Fmoc)-OH (415 mg, 0.702 mmol), HOBt, HBTU, and DIPEA in accordance with the above procedure was dissolved in DMF and added to the CLPAE solution. Afterward, following the coupling reaction, the Fmoc-deprotection and diethyl ether precipitation steps were carried out in the same way as in the above-mentioned CLPAE-Ahx synthesis.

^{1}H NMR Spectroscopy. ^{1}H NMR spectra of the polymers were obtained using a Bruker DPX-300 NMR spectrometer (300 MHz). For analysis, the polymer samples were dissolved in D_2O or MeOD containing 0.05% 3-(trimethylsilyl)propionic-2,2,3,3-d_4 acid sodium salt as an internal reference (0 ppm). A known molar quantitiy of benzoic acid was added to sample solutions as a NMR standard to quantify the degree of modification with Ahx and Lys for further experiments.

Molecular Weight Analysis. The average molecular weight of polymers was determined by multiangle laser light scattering (MALLS) in combination with size exclusion chromatography (SEC). The SEC system included a P680 HPLC pump from Dionex Corp. (Sunnyvale, CA). Polymer samples were detected by a three-angle laser light scattering detector (miniDAWN Tristar, 30 mW GaAs laser, 690 nm, K5 cell) and an interferometric refractometer (Optilab DSP, P10 cell) from Wyatt Technologies (Santa Barbara, CA). The MALLS system was operated by Astra software version 4.90. DMF (HPLC grade, Mallinckrodt) was used as an eluent after being filtered through a 0.22 μm filter and degassed before use. A Styragel HR 3 column from Waters (Milford, MA) was used. All sample solutions were filtered through a 0.45 μm filter again. The solution was delivered to a flow cell inlet at a constant flow rate of 0.5 mL/min.

Quantitative Analysis of Primary Amine Numbers of CLPAE-Ahx and CLPAE-Lys. A series of ethanol amine solutions of various concentrations was mixed with 50 mM borate buffer to 800 μL of the total volume to construct the standard calibration curve. Fluorescamine solution (1 mg/mL in DMF) (200 μL) was mixed with the amine solution. After 12 min incubation, 1.5 mL of stop solution (DMF/water, 50% v/v) was added to quench the reaction. Fluorescence measurements were carried out with a FP-750 spectrofluorometer (Jasco) at room temperature. Excitation and emission wavelengths were 360 and 465 nm. In the case of polymer samples, fluorescence was measured in the same way. A standard curve prepared in this way was used to analyze the amount of primary amines/μg polymer quantitatively.

Gel Retardation Assays. Polymer/plasmid complexes (polyplexes) at various weight ratios ranging from 0.5 to 7 were prepared in HEPES-buffered saline (HBS, 20 mM HEPES, 150 mM NaCl, pH 7.4). After 30 min incubation at room temperature for complex formation, the samples were electrophoresed on a 0.7% (w/v) agarose gel and then stained in a 1% (w/v) ethidium bromide solution. After 40 min staining, the gel was analyzed on a UV illuminator to show the location of the DNA.

Polymer/DNA Self-Assembly Analysis by PicoGreen Assay. PicoGreen assay was carried out to analyze the self-assembly of polymer/plasmid DNA quantitatively as reported recently (*16*). Briefly, PicoGreen reagent (200X) was diluted to 200-fold in TE buffer before the experiment. The diluted PicoGreen stock solution (200 μL) was mixed with the same volume of blank solution or polyplex solution (1 μg DNA, 1X HBS) prepared at various weight ratios ranging from 0 to 10. After 2 min incubation, each solution was added to 1.6 mL of TE buffer in a test tube. Fluorescence was measured with a FP-750 spectrofluorometer (Jasco) at room temperature. Excitation and emission wavelength were set at 480 and 520 nm, respectively.

Polyplex Size Measurements. The hydrodynamic diameters of the polymer/plasmid DNA complexes were determined by light scattering. Polyplex solutions (500 μL) containing 10 μg of DNA were prepared at various weight ratios ranging from 0.5 to 40. After 30 min incubation, polyplex solutions were diluted to a final volume of 2 mL prior to measurements. Polyplex sizes were measured using a Zetasizer 3000HS (Malvern Instruments, UK). The laser used is a nominal 5 mW HeNe laser having a 633 nm wavelength. Scattered light was detected at a 90° angle. The refractive index (1.33) and the viscosity (0.89) of ultrapure water were used at 25 °C for measurements. Zetasizer 3000 (Advanced) Size mode v1.61 software was used for data acquisition. Data analysis was performed in automatic mode. Measured sizes were presented as the average values of 10 runs.

Atomic Force Microscopy (AFM). The particle shapes and sizes of the polymer/plasmid DNA complexes were analyzed using atomic force microscopy (Nanoscope IIIa system, Digital Instruments, Inc., Santa Barbara. CA). The samples were prepared by mixing 0.1 μg of plasmid DNA with aqueous polymer solution at various weight ratios to obtain a final DNA concentration of 10 ng/μL. After 30 min incubation, 1 μL aliquots of the complex solutions were placed on freshly cleaved mica surface and allowed to stick for 1−2 min. Excess solution was removed by careful absorption onto filter paper, and the mica surface was further dried at room temperature for 24 h. The image mode was set to tapping mode, and the scanning speed was 1−5 Hz.

Zeta-Potential Measurements. One hundred microliter quantities of polyplex solutions containing 2 μg of DNA were prepared at various weight ratios ranging from 0.5 to 10. After 30 min incubation, 25 μL quantities of polyplex solutions were diluted to 10 mL of the final volume prior to measurements. Zeta-potential measurements were carried out using a Zetasizer 3000HS (Malvern Instruments, UK) at 25 °C. Zetasizer 3000 (Advanced) Zeta mode v1.61 software was used for data acquisition. The sampling time was set to automatic. Potential values were presented as the average value of 5 runs.

In Vitro DNA Release Measurements. In vitro DNA release from polyplex according to the degradation of polymer in aqueous solution was analyzed by PicoGreen assay. Each procedure was identical to that in the experiments described above except that the weight ratio of polyplex used was 20 where polymers formed stable complexes with plasmid DNA. The polyplexes formed in HBS (pH 7.4) were incubated at 37 °C and collected for assay at various times ranging from the first to the 10th day. Results were expressed in % fluorescence relative to control plasmid DNA.

Cell Lines. HepG2 human hepatocellular carcinoma cells were maintained in MEM, and 293 human kidney transformed

cells and C2C12 mouse myoblast cells were maintained in DMEM medium with 10% fetal bovine serum (FBS) at 37 °C in 5% CO_2. The primary rat aorta vascular smooth muscle cells (SMC) were a kind gift from Hyung-suk Jang in Samsung Medical Center (Seoul, Korea) and maintained in DMEM/F12 medium with 10% fetal bovine serum (FBS) at 37 °C in 5% CO_2. The primary mouse embryonic fibroblast cells (MEF) were a kind gift from Prof. Han-Woong Lee in Sungkyunkwan University, School of Medicine. MEFs were prepared from 13.5 day postcoitus mouse (FVB/NJ strain) embryos and maintained in DMEM medium with 10% fetal bovine serum (FBS) at 37 °C in 5% CO_2. All media contained 1% antibiotic agent.

Cytotoxicity Assay. The cytotoxicity of the polymers was measured by MTT assay. 293 cells were seeded in a 96-well tissue culture plate at 10^4 cells per well in 90 μL of DMEM medium containing 10% FBS. Cells achieving 70−80% confluence after 24 h were exposed to 10 μL of the polymer solutions having various concentrations for 24 h. Then, 25 μL of stock solution of MTT (2 mg/mL in DPBS) were added to each well. After 4 h of incubation at 37 °C, each medium was removed and 150 μL of DMSO was added to each well to dissolve the formazan crystal formed by proliferating cells. Absorbance was measured at 570 nm using a microplate reader (Molecular Devices Co., Menlo Park, CA) and recorded as a percentage relative to untreated control cells.

In Vitro Transfection. HepG2 and 293 cells were seeded at a density of 1.5×10^5 cells/well in a 24-well plate in medium containing 10% FBS and grown to reach 70−80% confluence prior to transfection. C2C12 (7×10^4 cells/well) cells, SMC (4×10^4 cells/well) cells, and MEF (6×10^4 cells/well) cells were seeded in the same way. Before transfection, the cells were rinsed with DPBS, and serum-free or serum-containing medium was added to each well. The cells were treated with polyplex solutions containing 2 μg of plasmid DNA at different weight ratios for 4 h at 37 °C. All the cells were tested with the control pGL3 plasmid except MEF cells for which pCN-Luci plasmid was used. In the presence of serum, the cells were incubated for 24 h after transfection. After exchange of medium, cells were further incubated for 2 days after transfection. Then the growth medium was removed, and the cells were rinsed with DPBS and shaken for 30 min at room temperature in 120 μL of Reporter Lysis Buffer. Luciferase activity was measured by a luminescence assay, and a protein assay was performed using a Micro BCA Protein Assay Reagent Kit. Ten microliters of the lysate was dispensed into a luminometer tube, and luciferase activity was integrated over 10 s with a 2 s measurement delay in a Lumat LB 9507 luminometer (Berthold, Germany) with an automatic injection of 50 μL of Luciferase Assay Reagent. The final results were reported in terms of RLU/mg cellular protein.

RESULTS AND DISCUSSION

Synthesis of CLPAE, CLPAE-Ahx, and CLPAE-Lys. It was reported by Ferruti et al. in 1970 (*17*) that linear poly(amido amine) was synthesized by simple Michael addition of bifunctional amines and bisacrylamides. Poly(amido amine)s of both linear and dendritic structure have been investigated and applied in various fields including gene delivery (*18*−*20*).

Recently, Langer et al. reported a series of achievements in relation to synthesis of poly(amino ester) polymers, their identification, and application to gene transfer by a high-throughput cell-based screening assay (*11*−*13*). They possessed several advantages for gene transfer such as a simple and inexpensive polymerization step and low cytotoxicity due to the biodegradability of the polymer. However, considerable screening is required to find nontoxic efficient gene delivery carriers among the library of randomly synthesized candidate polymers. Moreover, it is well-known that linear polyester polymers tend to be degraded within several hours in aqueous solution (*7*, *14*). The instability and fast degradation of polyplexes formed from these linear polymers limit their potential for long-term application including in vivo gene delivery.

So, we designed cross-linked poly(amino ester) polymers to improve stability and to reduce the fast degradation rate of the polymer. It was reported that cross-linked ester polymer was degraded more slowly under physiological conditions than linear polymer and possessed the endosome buffering effect due to its three-dimensional structure and internal tertiary amines, yielding high transfection efficiency (TE) in mammalian cells (*21*). To synthesize cross-linked polymers, triacrylate was used as a trivalent linker. Pentaerythritol triacrylate was chosen because it has the shortest carbon backbone length among analogous acrylate monomers for high charge density, which is known to generally lead to high TE in cells. Moreover, it has a hydroxyl group, which would enhance water solubility of the polymer and enable further modification of the polymer with other functional groups after polymerization. In the case of the amine monomer, we used *N*,*N*-dimethylethylenediamine that has only one primary amine which could react with acrylates, thus avoiding the formation of excessively complex polymer networks insoluble in aqueous solution.

Scheme 1 shows the synthesis of CLPAE and its modification procedures to prepare CLPAE-Ahx and CLPAE-Lys. CLPAE was synthesized from the nucleophilic Michael addition of *N*,*N*-dimethylethylenediamine with pentaerythritol triacrylate in MC at 50 °C for 2 days. Attempts to synthesize CLPAE under other solvent conditions (DMF, THF etc.) resulted in polymers that could not condense DNA efficiently and showed a very low TE in 293 cells through preliminary experiments (data not shown) So, MC was selected as the optimal solvent for the preparation of CLPAE.

In the case of linear poly(amino ester) polymers, the molar reaction ratio between amine and diacrylate must be equal for a complete stoichiometric reaction yielding the highest molecular weight of the polymer. However, for cross-linked polymers, investigation of the optimal mole ratio was required because triacrylate has three functional groups and diamine has two. CLPAE was synthesized at 1, 2, and 3 mole ratios (amine/acrylate). To determine the optimal ratio, they were analyzed by ^{1}H NMR. From the ^{1}H NMR spectra, we found that CLPAE showed residual unreacted acrylate groups at a mole ratio of 1, and the peaks of acrylate groups had vanished completely at a mole ratio of 2 (data not shown). Therefore, the reaction mole ratio was set to 2 throughout the experiments.

After 2 days of polymerization, a weak yellow precipitate was observed in the reaction mixture. The product was precipitated in an excess volume of diethyl ether two times, leaving a yellow solid. CLPAE was soluble in water and methanol but not in DMF.

Then, CLPAE was further modified by conjugating with aminohexanoic acid (Ahx) and lysine (Lys). Ahx and Lys residues were introduced in order to enhance the DNA-condensing ability of the polymers. The conjugation reaction was performed by coupling the hydroxyl groups of the triacrylate backbone in CLPAE with carboxylic acid using HOBt and HBTU as coupling agents. Because it was complicated work to quantify the amount of hydroxyl groups in CLPAE, we used excessive molar quantities of Fmoc-protected acids and coupling agents for complete conjugation. Also, the reaction time was prolonged to 2 days for the same reason.

After 2 days of coupling in DMF at room temperature, DMF-insoluble CLPAE was dissolved in the reaction mixture in DMF, suggesting that Fmoc-Ahx or Fmoc-Lys was coupled to CLPAE, increasing its solubility in DMF. The reaction solution was evaporated and then precipi-

Scheme 1. The Synthetic Scheme of CLPAE, CLPAE-Ahx, and CLPAE-Lys

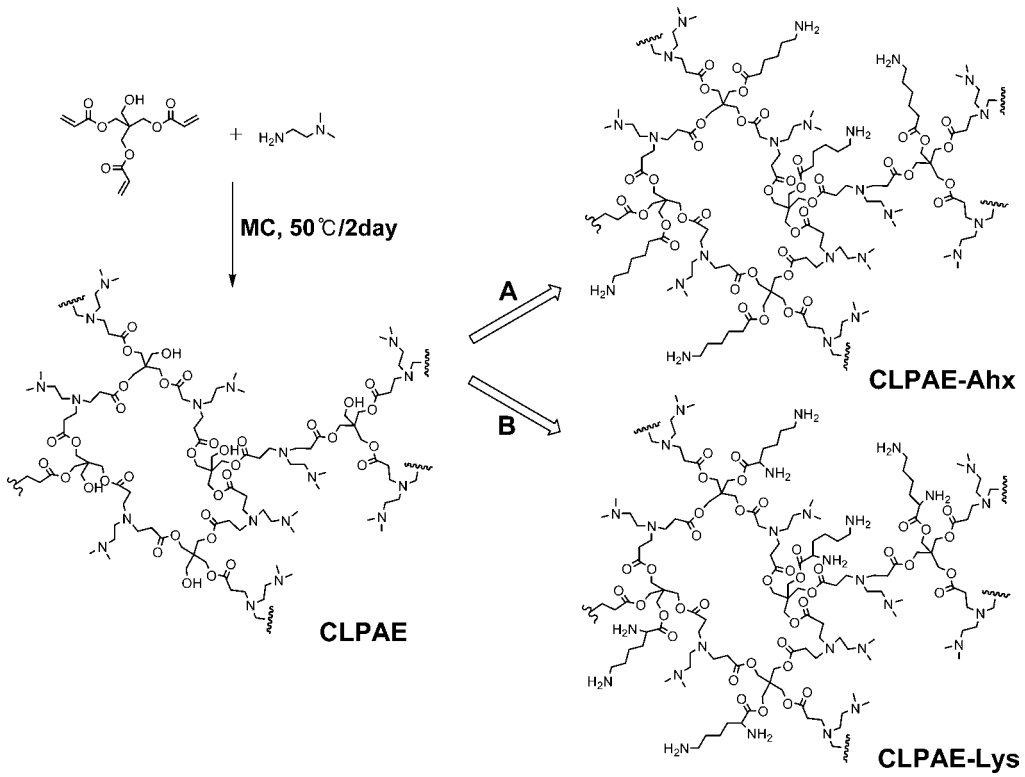

tated in diethyl ether three times to remove the excess of residual coupling agents and starting materials (Ahx or Lys). Then, Fmoc groups of aminohexanoic acid or lysine were removed by 15% piperidine solution at room temperature for 20 min to expose primary amines.

Characterization of CLPAE, CLPAE-Ahx, and CLPAE-Lys. The molecular weights (MWs) of the polymers were determined by multiangle laser light scattering (MALLS) combined with size exclusion chromatography. This method is known to be able to determine the absolute MWs of polymers without the need for reference standard polymers (*22*). Molecular weights were calculated by Astra software version 4.90. The eluent solvent was DMF.

The molecular weights of the polymers were as follows. CLPAE-Ahx: $M_n = 2.54 \times 10^4$ g/mol, $M_w = 3.40 \times 10^4$ g/mol (PDI = 1.34), dn/dc = 0.0498; CLPAE-Lys: $M_n = 2.18 \times 10^4$ g/mol, $M_w = 3.28 \times 10^4$ g/mol (PDI = 1.50), dn/dc = 0.0548. The MW of CLPAE could not be obtained by MALLS because it was not soluble in DMF. The increased MW of CLPAE-Ahx is thought to be due to the number of the coupled Ahx being greater than for Lys, a view that corresponds with the following ^{1}H NMR spectra and primary amine quantification results.

We obtained ^{1}H NMR spectra of CLPAE-Ahx and CLPAE-Lys to examine the average degree of modification of aminohexanoic acid or lysine, and the molecular weight of only CLPAE based on the NMR results. A known molar quantity of benzoic acid was added as an internal standard because its proton peaks do not overlap with those of CLPAE and it does not react with CLPAE. We could obtain the number of conjugated aminohexanoic acid or lysine molecules per polymer by calculating the ratio between the number of moles of benzoic acid protons and the NMR peak intensities.

Table 1 shows the average degree of Ahx or Lys modification and the molecular weights of the polymers. We found that an average of 77 molecules of Ahx were conjugated to CLPAE-Ahx and 66 molecules of Lys to CLPAE-Lys. The molecular weight of only CLPAE can be inversely calculated because the value after subtraction of the total MW of conjugated Ahx or Lys from the MW of modified CLPAEs equals the MW of unmodified CLPAE. The molecular weight of only CLPAE was determined to be 2.52×10^4 g/mol and 2.43×10^4 g/mol based on calculations from CLPAE-Ahx and CLPAE-Lys, respectively. The lower degree of modification of Lys compared to Ahx is thought to be due to steric hindrance of di-Fmoc-lysine and this result agrees well with primary amine quantification assay as follows.

Table 1. Molecular Weights of the Polymers and the Degree of Modification with Ahx or Lys[a]

	M_n from MALLS (g/mol)	M_w from MALLS (g/mol)	degree of modification from NMR	M_w of CLPAE from calculation (g/mol)
CLPAE-Ahx	2.54×10^4	3.40×10^4	77	2.52×10^4
CLPAE-Lys	2.18×10^4	3.28×10^4	66	2.43×10^4

[a] Molecular weights of CLPAE-Ahx and CLPAE-Lys were obtained from MALLS.

Quantification of primary amine amount by fluorescamine assay showed that CLPAE-Ahx had 2.0 nmol primary amines/μg of polymer and CLPAE-Lys had 1.5 nmol/μg. Only CLPAE showed a negligible value, confirming that CLPAE itself had no effect on amine quantification.

Formation of Polymer/DNA Polyplexes. The self-assemblies of each polymer and plasmid DNA were observed by using agarose gel electrophoresis and PicoGreen assay, respectively. Figure 1 shows the gel retardation results of each polymer with plasmid DNA. CLPAE was found not to retard plasmid DNA until the weight ratio reached 3. In contrast to CLPAE, the polyplexes of CLPAE-Ahx and CLPAE-Lys with DNA showed complete retardation even at a weight ratio of 1.

These results were compared with PicoGreen exclusion

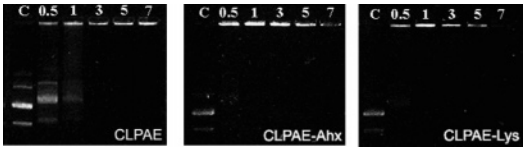

Figure 1. Gel retardation assay. C: DNA only. Numbers represent the weight ratio of the polyplexes.

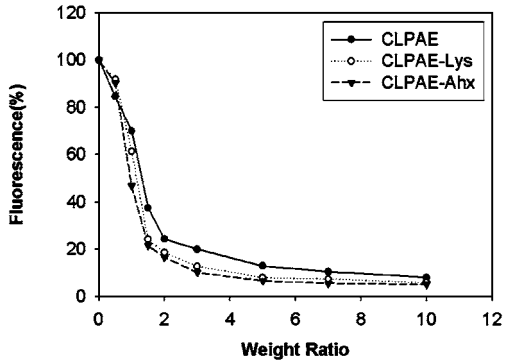

Figure 2. DNA complexation assay using PicoGreen reagent. Excitation and emission wavelength were set at 480 and 520 nm, respectively.

assay results (Figure 2). PicoGreen reagent is a DNA intercalating dye like ethidium bromide (*23*). So, the fluorescence of PicoGreen reagent is inhibited when the DNA is condensed into particles by self-assembly with cationic polymers. CLPAE/DNA polyplex showed an 85% relative fluorescence at a weight ratio of 0.5, which decreased sharply to 8% at a weight ratio of 10. CLPAE-Ahx and CLPAE-Lys were observed to show a greater DNA condensing ability than CLPAE. CLPAE-Ahx polyplex showed a 90% fluorescence value at a weight ratio of 0.5 and this decreased abruptly to 5% at a weight ratio of 10. Although the fluorescence of CLPAE-Lys polyplex was slightly higher than that of CLPAE-Ahx for all the weight ratios examined, the profile was similar to that of CLPAE-Ahx polyplex. These results correspond with gel retardation results and mean that a series of newly synthesized polymers could condense plasmid DNA efficiently with differences of a degree. Polymers condensed DNA compactly in order of CLPAE-Ahx > CLPAE-Lys > CLPAE. This may be due to the differences in the amount of primary amine or amine density, according to amine quantification results. However, at a weight ratio of 1 each polymer showed no less than 47, 61, 70% fluorescence in order of CLPAE-Ahx, CLPAE-Lys, CLPAE, respectively. This is thought to be due to the high sensitivity of the PicoGreen reagent.

Average Size Measurements of Polyplexes. The polyplex sizes and their distributions were determined by a Zetasizer. Each polyplex was prepared at various weight ratios ranging from 0.5 to 40 at room temperature. As shown in Figure 3, the polymers were found to have a similar tendency for average sizes of polyplexes to be about 120−180 nm over a weight ratio of 2, which were thought to be appropriate sizes for gene transfer. Abrupt size increments of polyplexes due to hydrophobic interaction between polyplexes arising from charge neutralization were observed at a low weight ratio. Interestingly, although CLPAE and CLPAE-Lys polyplexes showed maximum sizes (370, 352 nm respectively) at a weight ratio of 1, CLPAE-Ahx was observed to have a maximum size (334 nm) at a lower weight ratio of 0.7, not 1. This means CLPAE-Ahx possessed a higher amine density and was able to condense DNA more compactly than the other

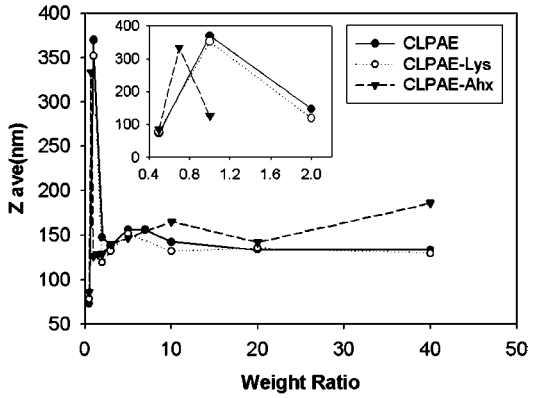

Figure 3. Average size measurements of polyplexes by Zetasizer. The inside box shows values at subdivided weight ratios ranging from 0.5 to 2.0.

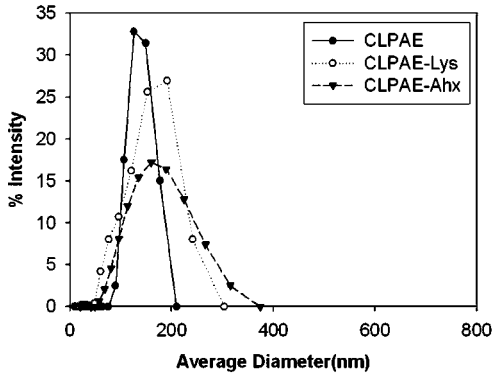

Figure 4. Average size distributions of the polyplexes at weight ratio of 20.

polymers synthesized, agreeing well with the amine quantification results.

Figure 4 shows the size distribution of each polyplex at a weight ratio of 20. CLPAE polyplexes were found to have a 97% population for a size range from 106 to 177 nm. Aggregates larger than 1 μm were not observed in any complexes. However, CLPAE-Lys and CLPAE-Ahx polyplexes were observed to have broader size distributions. It is considered that the irregularly modified polymer structure could lead to the formation of less homogeneous complexes with plasmid DNA. DLS results show that the polymers could form nanosized complexes with plasmid DNA having narrow size distributions.

Morphology of Polyplexes. The morphologies of polyplexes of the polymers were observed by AFM. Figure 5 shows AFM images of CLPAE polyplexes at various weight ratios ranging from 1 to 20. At a weight ratio of 1, CLPAE could not condense DNA completely (Figure 5A). Aggregates of 388−424 nm diameter and partially condensed DNA of irregular form were found. However, as the weight ratio of polymer increased to 10, they disappeared and compact sphere polyplexes of 125−190 nm size were observed (Figure 5B). Like CLPAE, CLPAE-Lys and CLPAE-Ahx showed compact spherical polyplex particles of about 80−200 nm size at a weight ratio of 20 (Figure 5C, 5D). These results agreed well with DLS data. The height of each polyplex was also determined to be 7−15 nm. As the weight ratio of polymer increased, the heights of polyplexes decreased. In general, a convolution of the imaging-tip's shape with the object's actual shape is known to affect the width of the object, while in such convolutions the height of the object is affected only by the compressibility of the object (*24*). So, it was

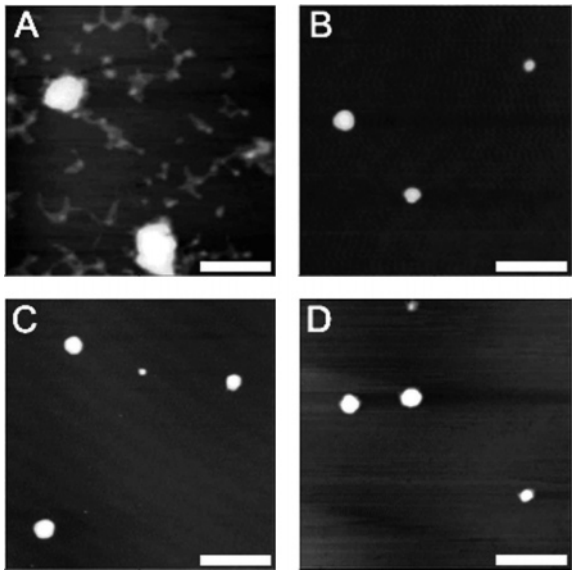

Figure 5. AFM images of the polyplexes. CLPAE: (A) weight ratio of 1, (B) 10, CLPAE-Lys: (C) 20, CLPAE-Ahx: (D) 20. The scale bars represent 1 μm.

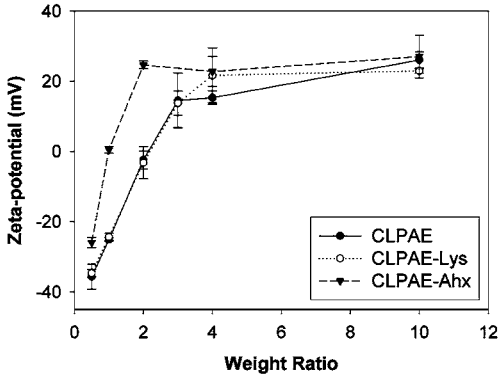

Figure 6. Zeta-potential measurements. Potential values are presented as the average value of 5 runs at 25 °C.

revealed that the polyplexes formed smaller and more compact particles as the weight ratio of polymer to DNA increased.

Zeta-Potential Measurements. Zeta-potentials of each polyplex were determined at various weight ratios. As shown in Figure 6, CLPAE and CLPAE-Lys polyplexes were found to have similar zeta-potential values at all weight ratios examined. They did not show positive values until the weight ratio was increased up to 2. However, the zeta-potential value of CLPAE-Ahx polyplex rose to almost the zero point even at a weight ratio of 1, and it showed a value of 24.6 ± 1.1 mV at 2. Because negative zeta-potential values of polyplexes were induced by phosphate anions of DNA of complex surfaces at low weight ratios where cationic polymers could not condense DNA completely, positive values of complexes mean the formation of stably compact complexes. Positively charged polyplexes are known to bind cellular membranes well, inducing endocytosis of the polyplexes (*25*). This result agreed well with our expectation and previous reports that a large number of CLPAE-Ahx-conjugated primary amines would lead to polyplex formation earlier than for tertiary amines of CLPAE.

In Vitro DNA Release Study. Linear types of biodegradable ester backbone polymers (PHPE, PAGA, etc.) were found to be decomposed in pH 7.4 solution within a few hours (*7*, *14*). This means biodegradable linear

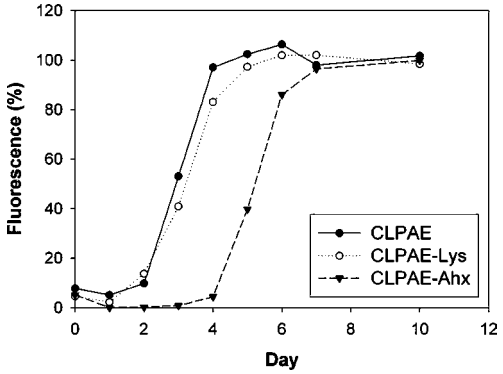

Figure 7. In vitro release profile of DNA from polyplexes by Picogreen reagent assay. Results are expressed in % fluorescence relative to control plasmid DNA.

polymeric gene carriers would not be suitable for in vivo gene delivery for long-term applications. On the other hand, a cross-linked polyester polymer (n-PAE, etc.) showed a slower degradation rate and a prolonged DNA release profile in vitro, due to its structural property that one bond break could not cause a whole split of a polymer molecule directly (*21*). So, we designed a cross-linked poly(amino ester) polymer for gene delivery and examined the DNA release from polyplexes to confirm its merit.

In vitro DNA release was observed by PicoGreen assay, measuring the fluorescence quenching of DNA from polyplexes (Figure 7). We could not observe any significant increase in the fluorescence values of all polyplexes during the first 2 days. After 2 days, CLPAE and CLPAE-Lys/plasmid complexes showed gradual increases in DNA release values (53% and 41%, respectively, on day 3). CLPAE polyplex released almost 100% of the DNA by day 4, while, on the other hand DNA release reached 97% on day 5 in the case of CLPAE-Lys polyplex. However, CLPAE-Ahx polyplex was found to show a negligible value for DNA release until even day 4. On day 5, DNA release of CLPAE-Ahx polyplex increased to only 40% and reached 100% by day 7.

We confirm that these new cross-linked polymers are degraded more slowly than linear-type ester polymers and could release DNA outward polyplex in a more retained pattern, so, for long-term in vivo application, this type of polymer would have therapeutic merits. It may be due to the primary amines of the polymer binding with plasmid DNA more effectively that CLPAE-Ahx polyplex showed the most retained release profile among them.

Moreover, this result shows that DNA release due to the degradation of the polymers possibly would follow a stepwise mechanism (Scheme 2). During the time from day 2 to day 4 when the amount of DNA release rose to 100%, CLPAE backbone and tertiary amine moieties might be degraded and so CLPAE could not condense DNA anymore (first degradation step). Also, CLPAE-Ahx polyplex is thought to be under the same 'first degradation step' during this time. However, CLPAE-Ahx could condense plasmid DNA due to the primary amines of aminohexanoic acids after degradation, in contrast to CLPAE. Then, aminohexanoic acids of the polymer would be gradually degraded and cleaved from the polymer, inducing plasmid DNA release from day 4 to day 7 (second degradation step). We think that this stepwise degradation mechanism might result from the differences in the susceptibility to hydrolysis between the ester bonds of the CLPAE backbone and the ester linkages of

Scheme 2. The Degradation Mechanism of CLPAE and CLPAE-Ahx Polyplexes with Plasmid DNA

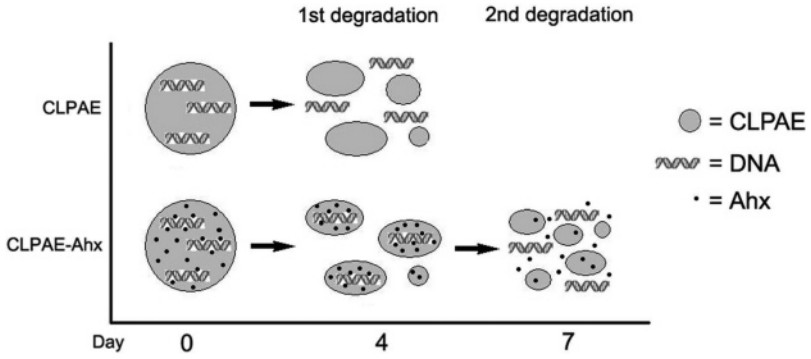

aminohexanoic acid to CLPAE. In the case of CLPAE-Lys, this effect was slight due to the polymer having fewer primary amines. Because primary amines of these 'self-destroying polymers' are thought to bind to DNA phosphates, not to attack ester bonds after forming polyplexes, the degradation rate of CLPAE-Ahx polyplex would be slower than that of CLPAE polyplex (*7*).

Cytotoxicity. Nontoxicity is one of the most important features for gene delivery carriers. In general, cytotoxicity is known to arise from the accumulation of nondegraded and nondischarged polymers in cells. So, many trials have been performed to reduce the toxicity of the gene carrier until now, which included the introduction of biodegradability to the polymer through such functionalities as ester, phosphoester, or disulfide bonds. Lim et al. reported that cationic polymers composed of ester backbone were barely toxic to mammalian cells (*8*, *21*).

We investigated the cytotoxicity of CLPAE, CLPAE-Ahx, and CLPAE-Lys by using MTT assay in 293 cells (Figure 8). The viability of 293 cells decreased abruptly according to an increase in the concentration of PEI, which shows the well-known cytotoxicity of PEI. CLPAE, CLPAE-Ahx and CLPAE-Lys provided favorable results. They showed about 80% cell viability even at a high concentration (50 μg/mL polymer concentration). This low toxicity may be due to the nontoxic building blocks and degradation products of polymers arising from a backbone of ester bonds. CLPAE-Ahx was found to show the lowest cell viability across the whole concentration range. It is thought that large numbers of primary amines of CLPAE-Ahx damage cells.

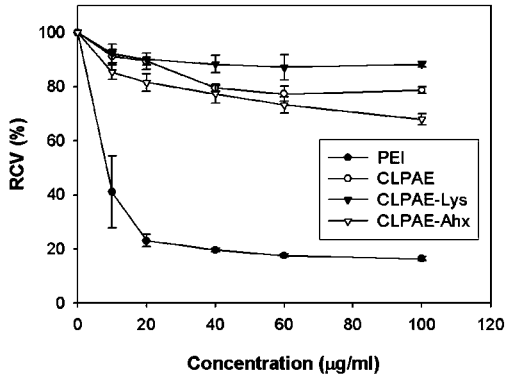

Figure 8. Cytotoxicity in 293 cells by MTT assay. Each data point represents the mean ± standard deviation ($n = 5$).

Transfection Efficiency (TE). The transfection abilities of CLPAEs were evaluated on three kinds of cell lines (293 human kidney transformed cells, C2C12 mouse myoblast cells, HepG2 human hepatocellular carcinoma cells), primary rat aorta vascular smooth muscle cells, and primary mouse embryonic fibroblast cells. PEI was used as the control for the standard gene carrier (*26*). As shown in Figure 9A, CLPAE showed very low TE but CLPAE-Ahx and CLPAE-Lys showed considerably enhanced TE compared with CLPAE on 293 cells. At the optimized weight ratio, TE of CLPAE-Ahx increased to 22 and 306 times over that of CLPAE in the absence and presence of serum, respectively. CLPAE-Lys also showed

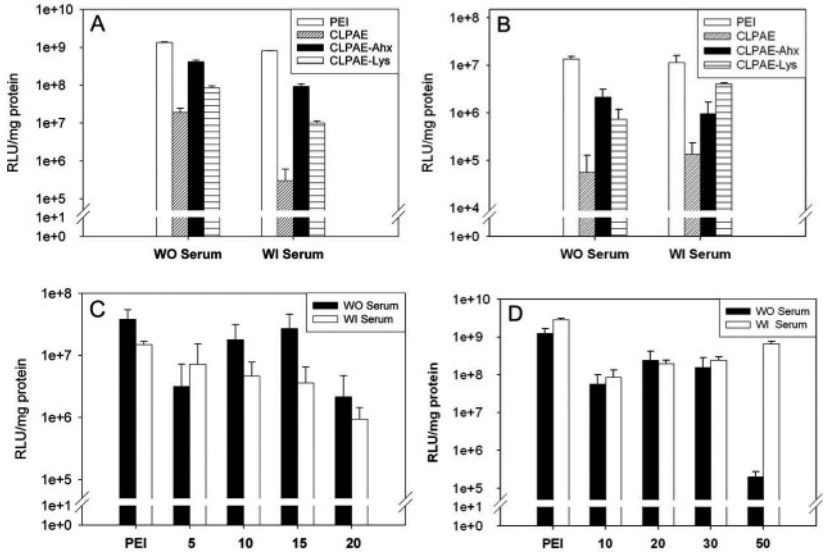

Figure 9. Transfection efficiencies of the polymers on 293 cells (A), C2C12 cells (B). (C and D) Transfection efficiency of CLPAE-Ahx on SMC and MEF cells, respectively. Numbers represent weight ratios.

enhanced TE (4−33 times that of CLPAE) although not by as much as for CLPAE-Ahx. We found similar enhancement effects on TE of CLPAE-Ahx and CLPAE-Lys as for CLPAE against C2C12 cells (Figure 9B). Fibroblast cells such as C2C12 are known to be hardly transfected, so the TE of PEI on C2C12 decreased to about 1% of TE on 293 cells. The TE of CLPAE-Ahx was enhanced 38 times more than that of CLPAE in the absence of serum. Although, interestingly, CLPAE-Lys showed an increase in its TE 30 times greater than CLPAE in the presence of serum, the existence of serum was found to reduce the TE of the polymers generally because cationic gene carriers possessing many positive charges are known to interact with negatively charged serum proteins (*27*, *28*).

The transfection efficiency of CLPAE was found to be much enhanced after coupling with aminohexanoic acid and lysine. Although CLPAE formed nanosized polyplexes having physicochemical properties very similar to those of CLPAE-Ahx and CLPAE-Lys with the exception of their having a slightly lower condensing ability, the TE of CLPAE was very low in the cell lines tested. This result suggests that a self-assembling ability with DNA to the compact nanoparticles simply could not lead to high transfection efficiency on cells. Therefore, primary amine residues such as aminohexanoic acid or lysine residue of CLPAE-Ahx and CLPAE-Lys are thought to certainly participate in the cellular uptake of polyplexes because CLPAE does not have primary amines but rather tertiary amines.

To examine applications on primary cells of CLPAE-Ahx showing generally the highest TE, transfection was carried out on the primary rat aorta vascular smooth muscle cells (SMC) and primary mouse embryonic fibroblast (MEF) cells. The accelerated proliferation of SMCs was reported to be a characteristic feature of atherosclerosis, or renarrowing of the artery (restenosis) after insertion of a stent within the artery wall for coronary artery disease (*29*, *30*). The mechanism of those two syndromes was partially understood but thought to be induced by the manifestation of genetic products such as platelet-derived growth factor (PDGF) (*31*). So, it could probably be a powerful tool for treating these diseases with gene therapy to deliver therapeutic genes with CLPAE-Ahx to vascular smooth muscle cells.

MEF cells are usually used as feeder cells to establish pluripotent embryonic stem (ES) cells. It is important to analyze the real functions of MEF cells and the secreted factors to influence ES cells within the culture system for establishment of a feeder-free culture environment (*32*). To study these through in vitro and ex vivo research, efficient delivery of various functional genes to MEF cells with CLPAE-Ahx could provide a useful tool.

As shown in Figure 9C and 9D, CLPAE-Ahx showed TE comparable to that of PEI on primary SMCs and MEF cells. It is due to higher expression level of pCN-Luci vector than pGL3 vector that TEs of polymers on MEF cells are much enhanced in contrast to those on SMCs. MEF cells showed sensitivity to cytotoxicity of PEI, so the TE of PEI was lower in the absence of serum than in the presence of serum contrary to transfection on other cells. Therefore, CLPAE-Ahx could be used for coronary artery diseases by in vivo gene delivery systems or research of primary MEF cell functions due to its high TE comparable to that of PEI on SMC and MEF cells and its low toxicity would ensure safe gene delivery.

CONCLUSION

We designed and synthesized a cross-linked poly(β-amino ester) for gene delivery to control its degradation rate and conjugated it with aminohexanoic acid or lysine to improve its transfection efficiency on mammalian cells. These CLPAE, CLPAE-Ahx, and CLPAE-Lys polymers showed great ability to form nanosized spherical polyplexes with DNA having narrow size distributions. Fulfilling our expectations, polyplexes of CLPAE-Ahx could release DNA even for a week through stepwise degradation. The polymers had low cytotoxicity in 293 cells. CLPAE-Ahx and CLPAE-Lys showed greatly enhanced transfection efficiencies in comparison to CLPAE on various cell lines, and the TE of CLPAE-Ahx is comparable to that of PEI on primary SMCs and MEF cells. It is evident that we could control the in vitro release rate of DNA by using cross-linked ester polymers, and the TE of polymeric gene carrier could be enhanced by conjugation with aminohexanoic acid or lysine. Therefore, CLPAE-Ahx has much potential as a nontoxic and efficient gene carrier.

ACKNOWLEDGMENT

We thank Hyung-suk Jang in Samsung Medical Center for providing pCN-Luci vector and SMCs and Prof. Han-Woong Lee and Young Hoon Sung in Sungkyunkwan University, School of Medicine, for providing MEF cells and helpful discussion. This study was supported by the National R & D Program Grant of The Ministry of Science and Technology (M10422010006-04N2201-00610), the SRC-Molecular Therapy Research Center at Sungkyunkwan University (R11-2000-080-10003-0)(2004), the Korea Health 21 R&D Project of The Ministry of Health & Welfare (0405-BO02-0205-0001), and the Gene Therapy Project of The Ministry of Science and Technology (M1053403004-05N3403-00410).

LITERATURE CITED

(1) Crystal, R. G. (1995) Transfer of genes to humans: early lessons and obstacles to success. *Science 270*, 404−410.
(2) Kay, M. A., Liu, D., and Hoogerbrugge, P. M. (1997) Gene therapy. *Proc. Natl. Acad. Sci. U.S.A. 94*, 12744−12746.
(3) Wolfert, M. A., Schacht, E. T., Toncheva, V., Ulbrich, K., Nazarova, O., and Seymour, L. (1996) Characterization of vectors for gene therapy formed by self-assembly of DNA with synthetic block co-polymers. *Human Gene Ther. 7*, 2123−2133.
(4) Luo, D., and Saltzman, W. M. (2000) Synthetic DNA delivery systems. *Nat. Biotechnol. 18*, 33−37.
(5) Zauner, W., Ogris, M., and Wagner, E. (1998) Polylysine-based transfection systems utilizing receptor-mediated delivery. *Adv. Drug Delivery Rev. 30*, 97−113.
(6) Veena, V., Thomas, T., and Thomas, T. J. (2002) DNA nanoparticles and development of DNA delivery vehicles for gene therapy. *Biochemistry 41*, 14085−14094.
(7) Lim, Y., Kim, C., Kim, K., Kim, S. W., and Park, J. (2002) Development of a safe gene delivery system using biodegradable polymer, poly[α-(4-aminobutyl)-L-glycolic acid]. *J. Am. Chem. Soc. 122*, 6524−6525.
(8) Lim, Y., Kim, S., Lee, Y., Lee, W., Yang, T., Lee, M., Suh, H., and Park, J. (2001) Cationic hyperbranched poly(amino ester): a novel class of DNA condensing molecule with cationic surface, biodegradable three-dimensional structure, and tertiary amine groups in theinterior. *J. Am. Chem. Soc. 123*, 2460−2461.
(9) Wang, J., Mao, H., and Leong, K. W. (2001) A novel biodegradable gene carrier based on polyphosphoester. *J. Am. Chem. Soc. 123*, 9480−9481.
(10) Gosselin, M. A., Guo, W., and Lee, R. J. (2001) Efficient gene transfer using reversibly cross-linked low molecular weight polyethylenimine. *Bioconjugate Chem. 12*, 989−994.

(11) Lynn, D. M., and Langer, R. (2000) Degradable poly(β-amino esters): synthesis, characterization, and self-assembly with plasmid DNA. *J. Am. Chem. Soc. 122*, 10761−10768.
(12) Lynn, D. M., Anderson, D. G., Putnam, D., and Langer, R. (2001) Accelerated discovery of synthetic transfection vectors: parallel synthesis and screening of a degradable polymer library. *J. Am. Chem. Soc. 123*, 8155−8156.
(13) Anderson, D. G., Lynn, D. M., and Langer, R. (2003) Semi-automated synthesis and screening of a large library of degradable cationic polymers for gene delivery. *Angew. Chem., Int. Ed. 42*, 3153−3158.
(14) Lim, Y., Choi, Y. H., and Park, J. (1999) A self-destroying polycationic polymer: biodegradable poly(4-hydroxy-L-proline ester). *J. Am. Chem. Soc. 121*, 5633−5639.
(15) Lee, M. J., Cho, S. S., You, J. R., Lee, Y., Kang, B. D., Choi, J. S., Park, J. W., Suh, Y. L., Kim, J. A., Kim, D. K., and Park, J. S. (2002) Intraperitoneal gene delivery mediated by a novel cationic liposome in a peritoneal disseminated ovarian cancer model. *Gene Ther. 9*, 859−866.
(16) Choi, J. S., Nam, K., Park, J.-y., Kim, J., Lee, J., and Park, J.-S. (2004) Enhanced transfection efficiency of PAMAM dendrimer by surface modification with L-arginine. *J. Controlled Release 99*, 445−456.
(17) Danusso, F., and Ferruti, P. (1970) Synthesis of tertiary amine polymers. *Polymer 11*, 88−113.
(18) Ferruti, P., Ranucci, E., Sartore, L., Bignotti, F., Marchisio, M. A., Bianciardi, P., and Veronese, F. M. (1994) Recent results on functional polymers and macromonomers of interest as biomaterials or for biomaterial modification. *Biomaterials 15*, 1235−1241.
(19) Kukowska-Latallo, J. F., Bielinska, A. U., Johnson, J., Spindler, R., Tomalia, D. A., and Baker, J. R., Jr (1996) Efficient transfer of genetic material into mammalian cells using starburst polyamidoamine dendrimers. *Proc. Natl. Acad. Sci. U.S.A. 93*, 4897−4902.
(20) Tang, M. X., Redemann, C. T., and Szoka, F. C., Jr. (1996) In vitro gene delivery by degraded polyamidoamine dendrimers. *Bioconjugate Chem. 7*, 703−714.
(21) Lim, Y., Kim, S., Suh, H., and Park, J. (2002) Biodegradable, endosome disruptive, and cationic network-type polymer as a highly efficient and nontoxic gene delivery carrier. *Bioconjugate Chem. 13*, 952−957.
(22) Wyatt, P. J. (1993) Light scattering and the absolute characterization of macromolecules. *Anal. Chim. Acta 272*, 1−40.
(23) Singer, V. L., Jones, L. J., Yue, S. T., and Haugland, R. P. (1997) Characterization of PicoGreen reagent and development of a fluorescence-based solution assay for double-stranded DNA quantitation. *Anal. Biochem. 249*, 228−238.
(24) Allen, M. J., Hud, M. V., Balooch, M., Tench, R. J., Siekhaus, W. J., and Balhorn, R. (1992) Tip-radius-induced artifacts in AFM images of protamine-complexed DNA fibers. *Ultramicroscopy 42−44*, 1095−1100.
(25) Kopatz, I., Remy, J.-S., and Behr, J.-P. (2004) A model for non-viral gene delivery: through syndecan adhesion molecules and powered by actin. *J. Gene Med. 6*, 769−776.
(26) Boussif, O., Lezoualc'h, F., Zanta, M. A., Mergny, M. D., Scherman, D., Demeneix, B., and Behr, J.-P. (1995) A versatile vector for gene and oligonucleotide transfer into cells in culture and in vivo: polyethylenimine. *Proc. Natl. Acad. Sci. U.S.A. 92*, 7297−7301.
(27) Dodds, E., Dunckley, M. G., Naujoks, K., Michaelis, U., and Dickson, G. (1998) Lipofection of cultured mouse muscle cells: a direct comparison of Lipofectamine and DOSPER. *Gene Ther. 5*, 542−551.
(28) Ghosh, Y. K., Visweswariah, S. S., and Bhattacharya, S. (2000) Nature of linkage between the cationic headgroup and cholesteryl skeleton controls gene transfection efficiency. *FEBS Lett. 473*, 341−344.
(29) Schwartz, S. M., deBlois, D., and O'Brien, E. R. M. (1995) The intima. Soil for atherosclerosis and restenosis. *Circ. Res. 77*, 445−465.
(30) Schwartz, S. M. (1997) Smooth muscle migration in atherosclerosis and restenosis. *J. Clin. Invest. 100*, S87−89.
(31) Lymn, J. S., Gallagher, K. L., Clunn, G. F., Fexby, S. E., Patel, M. K., and Hughes, A. D. (2003) PDGF stimulates DNA synthesis in human vascular smooth muscle cells via a novel wortmannin-insensitive phosphatidylinositol 3-kinase. *FEBS Lett. 555*, 591−596.
(32) Pedersen, R. A. (2002) Feeding hungry stem cells. *Nat. Biotechnol. 20*, 882−883.

BC0497012

Chemoselective Assembly and Immunological Evaluation of Multiepitopic Glycoconjugates Bearing Clustered Tn Antigen as Synthetic Anticancer Vaccines

Saulius Grigalevicius,[†,§] Sabine Chierici,[†] Olivier Renaudet,[†] Richard Lo-Man,[‡] Edith Dériaud,[‡] Claude Leclerc,[‡] and Pascal Dumy*[,†]

LEDSS UMR 5616 and ICMG-FR2607, Université Joseph Fourier, BP 53, 38041 Grenoble Cedex 9, France, Unité de Biologie des Régulations Immunitaires, INSERM E352, Institut Pasteur, 75724 Paris Cedex 15, France, and Department of Organic Technology, Kaunas University of Technology, Radvilenu plentas 19, LT 50254, Kaunas, Lithuania. Received January 19, 2005; Revised Manuscript Received July 1, 2005

In this paper we investigated the use of regioselectively addressable functionalized templates (RAFTs) as new scaffolds for the design of anticancer vaccine candidates. We report the synthesis of well-defined multiepitopic RAFT scaffolds and their immunological evaluation. These conjugates exhibit clustered Tn analogue as tumor-associated carbohydrate antigen (TACA, B-cell epitope) and the $CD4^+$ helper T-cell peptide from the type 1 poliovirus. The saccharidic and peptidic epitopes were both synthesized separately and combined regioselectively to the RAFT core using a sequential oxime bond formation strategy. B- and T-antigenicity and immunogenicity of the vaccine candidates were investigated in vitro and in vivo. These studies clearly demonstrate that the saccharidic part of the conjugates is recognized by Tn-specific monoclonal antibodies. Moreover, the antibodies elicited by immunization of mice with our vaccine candidates recognize the native form of Tn epitope expressed on human tumor cells. Together with oxime ligation technique, these results suggest that the RAFT scaffold provides a promising and suitable tool for engineering potent synthetic anticancer vaccine.

INTRODUCTION

Tumor-associated carbohydrate antigens (TACAs) such as Tn, TF, and sTn are overexpressed in clusters at the malignant cell surface in breast, prostate, lung, and pancreatic cancers (*1*−*5*). While these carbohydrate-based cancer antigens represent attractive targets for epithelial cancer immunotherapy (*6*−*10*), their weak immunogenicity remains critical for the design of efficient synthetic anticancer vaccines. A first generation of vaccines in which the TACAs are conjugated to an immunogenic carrier protein such as KLH (*6*, *11*−*17*), BSA, or OSA (*16*, *18*, *19*) has been developed few years ago. Particularly, a mucin-derived glycopeptide−KLH conjugate containing three Tn antigens designed by S. Danishefsky has been used in clinical trials as putative synthetic vaccine against prostate cancer (*16*). This approach has proved to induce an immune response specifically directed against the targeted tumors. However, in most cases the low level of the desired antibodies, due to the low molecular ratio of the TACA over the carrier protein, the resulting irrelevant response against the carrier, and the undefined composition of the molecule, represent major limitations for their use in cancer therapy.

An alternative class of fully synthetic vaccines based on peptide or lipopeptide cores (*20*−*23*) has been designed to circumvent some of these drawbacks. Especially, branched templates of accurate chemical definition such as dendrimeric lysine scaffolds, namely multiple antigen peptide (MAP) (*24*−*29*) or multiple antigen glycopeptide (MAG) (*25*, *30*), have been used as a nonimmunogenic carrier in which the B-cell antigens are radiated from the core to immunogenic T-cell helper peptides. This alternative has emerged considerable interests by presenting a high density of clustered antigens at the surface of a small peptidic scaffold as found for Tn antigen on tumors and eliciting also a strong specific antibody response (*31*, *32*). Indeed, MAG molecule exhibiting four copies of a $CD4^+$ T-cell epitope together with the tri-Tn glycotope presented high immunogenicity in mice (*32*) and in nonhuman primates (*33*) and afforded good protection in prophylactic and therapeutic vaccinations against the development of Tn-expressing tumor cells in mice. The humoral response was dominated by IgG antibodies supporting the notion that a T-cell dependent response was induced.

Following a similar approach, we investigated in this study the use of regioselectively addressable functionalized templates (RAFTs) (*34*), as new scaffolds for the design of anticancer vaccines. RAFTs are topological templates which are commonly composed of a backbone-cyclized decapeptide containing two proline-glycine as β-turns inducers (*35*) that stabilize their conformation in solution. They have found useful applications in the past as protein mimics (*36*−*39*) and more recently as vectors for neo-vasculature targeting in tumor therapy (*40*) or as cell surface mimics for multivalent presentation of carbohydrates (*41*, *42*). These cyclic templates should also provide a suitable tool for the multimeric presentation of B- and T-epitopes. Indeed they offer the advantages via lysinyl side chains of displaying two independent functional faces, one dedicated to the attachment of the TACA moieties in a multivalent manner and the

* To whom correspondence should be addressed. Phone: 33 (0) 4 76 63 55 45. Fax: 33 (0) 4 76 51 43 82. E-mail: pascal.dumy@ujf-grenoble.fr.

[†] Université Joseph Fourier.

[‡] Institut Pasteur.

[§] Kaunas University of Technology.

10.1021/bc050010v CCC: $30.25 © 2005 American Chemical Society
Published on Web 09/02/2005

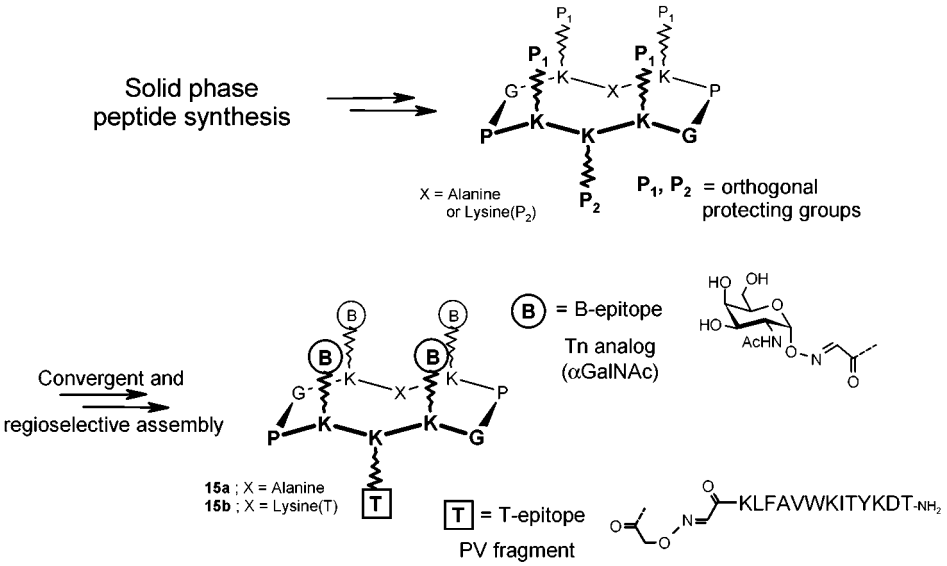

Figure 1. Strategy for the convergent assembly of the synthetic vaccine candidates **15a** and **15b** via an oxime-based methodology.

other to the T-cell peptide epitopes. We thus synthesized new multiepitopic neoglycoconjugates combining clustered Tn antigen analogue as TACA and T-cell epitope from the type 1 poliovirus as a $CD4^+$ T-cell epitope (Figure 1).

B- and T-antigenicity of our vaccine candidates RAFT-(4GalNAc,1PV)[1] **15a** and RAFT(4GalNAc,2PV) **15b** were finally investigated in vitro by ELISA and T-cell stimulation assays. Their immunogenicity was also studied in vivo by immunization of mice. Synthetic and biological results are reported in details in this paper.

EXPERIMENTAL PROCEDURES

Syntheses. Protected amino acids and Rink amide MBHA resin were purchased from France Biochem S.A. or Advanced ChemTech Europe. All chemical reagents and solvents were purchased from Sigma Aldrich, Fluka, Acros, or Carlo-Erba and were used without further purification. Analytical TLCs were performed on 0.2 mm silica 60 coated aluminum foils with F-254 indicator (Merck). Preparative column chromatographies were done using silica gel (Merck 60, 200−63 μm). Melting points were measured on an Electrothermal Series IA9100 apparatus. ^{1}H and ^{13}C NMR spectra were recorded on Bruker AC300 spectrometers and chemical shift (δ) are reported in parts per million (ppm). Spectra were referenced to the residual proton solvent peaks. The cyclic templates **12a**,**b** (*34*, *40*) and biotin sulfone (*43*) were prepared as previously described. Reverse phase HPLC analyses were performed on Waters equipment using C_{18} columns. The analytical (Nucleosil 120 Å 3 μm C_{18} particles, 30 × 4.6 mm^2) was operated at 1.3 mL/min and the preparative column (Delta-Pak 300 Å 15 μm C_{18} particles, 200 × 25 mm^2) at 22 mL/min with UV monitoring at 214 and 250 nm using a linear A−B gradient (buffer A: 0.09% TFA in water; buffer B: 0.09% TFA in 90% acetonitrile). Mass spectra were obtained by electron spray ionization (ES-MS) on a VG Platform II or by chemical ionization (CI-MS) on a Thermofinnigan Polaris Q in the positive mode.

[1] To facilitate the reading of this manuscript, we used a simplified nomenclature for the RAFT conjugates. For instance, RAFT(4GalNAc,1PV) **15a** denotes the RAFT presenting four GalNAc moieties on the upper face and one PV fragment on the other face.

3,4,6-Tri-*O*-acetyl-2-azido-2-deoxy-D-galactopyranosyl Fluoride (4). The glycosylfluoride **4** was prepared from **3** after azidonitration of the commercial 3,4,6-tri-*O*-acetyl galactal **1** (*44*) then denitration reaction (*45*) using the following procedure. Under inert gas, the compound **3** (4.36 g, 13.2 mmol) was dissolved in dry THF (116 mL) and the solution was cooled at −30 °C. Diethylaminosulfur trifluoride (2.08 mL, 15.8 mmol) was then added, and the solution was stirred at room temperature during 30 min. After addition of methanol (10 mL) at −30 °C, the solution was concentrated and taken up with dichloromethane. The organic layer was washed successively with saturated solution of $NaHCO_3$ then water, dried over sodium sulfate, and evaporated to get the compound **4** (4.30 g, 97%) as a colorless oil; ^{1}H NMR (300 MHz, $CDCl_3$) δ 5.71 (dd, $J_{1\alpha,2\alpha}$ = 2.6 Hz, $J_{1\alpha,F}$ = 52.2 Hz, H-1$_\alpha$), 5.48 (dd, $J_{4\alpha,5\alpha}$ = 1.2 Hz, $J_{3\alpha,4\alpha}$ = 3.2 Hz, H-4$_\alpha$), 5.36−5.34 (m, H-3$_\alpha$), 5.32 (td, $J_{4\beta,5\beta}$ = 1.1 Hz, $J_{3\beta,4\beta}$ = 3.3 Hz, H-4$_\beta$), 5.09 (dd, $J_{1\beta,2\beta}$ = 7.5 Hz, $J_{1\beta,F}$ = 51.8 Hz, H-1$_\beta$), 4.83 (ddd, $J_{3\beta,F}$ = 0.8 Hz, $J_{3\beta,4\beta}$ = 3.3 Hz, $J_{2\beta,3\beta}$ = 10.9 Hz, H-3$_\beta$), 4.36 (td, $J_{4\alpha,5\alpha}$ = 1.2 Hz, $J_{5\alpha,6\alpha}$ = 6.4 Hz, H-5$_\alpha$), 4.17−4.06 (m, H-6$_{\alpha,\beta}$), 3.96 (bt, $J_{5\beta,6\beta}$ = 6.3 Hz, H-5$_\beta$), 3.78 (ddd, $J_{1\beta,2\beta}$ = 7.5 Hz, $J_{2\beta,3\beta}$ = 10.9 Hz, $J_{2\beta,F}$ = 12.7 Hz, H-2$_\beta$), 3.78−3.68 (m, H-2$_\alpha$), 2.13−2.01 (6s, 6OCOCH$_3$); ^{13}C NMR (75 MHz, $CDCl_3$) δ 170.7 (C=O), 170.3 (C=O), 170.2 (C=O), 170.0 (C=O), 169.6 (C=O), 108.3 (d, $J_{C-1\beta,F}$ = 217 Hz, C-1$_\beta$), 106.2 (d, $J_{C-1\alpha,F}$ = 224 Hz, C-1$_\alpha$), 71.6 (C-5$_\beta$), 71.0 (d, $J_{C-3\beta,F}$ = 11 Hz, C-3$_\beta$), 69.5 (C-5$_\alpha$), 68.5 (C-3$_\alpha$), 67.2 (C-4$_\alpha$), 66.3 (C-4$_\beta$), 61.8 (C-6$_\alpha$), 61.5 (C-6$_\beta$), 61.2 (d, $J_{C-2\beta,F}$ = 22 Hz, C-2$_\beta$), 57.8 (d, $J_{C-2\alpha,F}$ = 24 Hz, C-2$_\alpha$), 21.0 (OCOCH$_3$), 20.9 (OCOCH$_3$), 20.8 (OCOCH$_3$). This product was used without further purification.

***O*-(3,4,6-Tri-*O*-acetyl-2-azido-2-deoxy-D-galactopyranosyl)-*N*-oxyphthalimide (5).** To a stirring solution in dichloromethane (200 mL) containing compound **4** (4.30 g, 13.0 mmol), *N*-hydroxyphthalimide (2.12 g, 13.0 mmol), and triethylamine (1.81 mL, 13.0 mmol) was added $BF_3{\cdot}Et_2O$ (3.52 mL, 65.0 mmol). The reaction was stirred at room temperature until completion (reaction monitored by thin-layer chromatography). After addition of dichloromethane (200 mL), the organic layer was washed several times with 10% aqueous sodium hydrogenocarbonate, dried under sodium sulfate, and evaporated. The alpha and beta anomers were finally separated by silica gel chromatography (dichloromethane/ethyl

acetate, 9/1) to give pure compound **5** (2.35 g, 38%) after crystallization from diethyl ether/pentane; mp 105−107 °C; ^{1}H NMR (300 MHz, $CDCl_3$) δ 7.85−7.75 (m, 4 H, $H_{ar.}$), 5.57 (bd, 2 H, $J_{1,2} = J_{3,4} = 3.4$ Hz, H-1, H-4), 5.47 (dd, 1 H, $J_{1,2} = 3.4$ Hz, $J_{2,3} = 11.3$ Hz, H-3), 5.17 (bt, 1 H, $J_{5,6a} = 6.4$ Hz, H-5), 4.23 (dd, 1 H, $J_{5,6a} = 6.4$ Hz, $J_{6a,6b} = 11.3$ Hz, H-6a), 3.97−3.92 (m, 2 H, H-2, H-6b), 2.14, 2.06, 2.02 (3s, 9 H, $3OCOCH_3$); ^{13}C NMR (75 MHz, $CDCl_3$) δ 170.8 ($C{=}O_{Ac}$), 170.3 ($C{=}O_{Ac}$), 169.9 ($C{=}O_{Ac}$), 163.3 ($C{=}O_{Pht}$), 135.2 ($CH_{ar.}$), 129.1 ($C_{ar.}$), 124.2 ($CH_{ar.}$), 103.5 (C-1),69.2 (C-5), 68.2 (C-4), 67.7 (C-3), 61.6 (C-6), 57.0 (C-2), 21.1 ($OCOCH_3$); MS-ES (positive mode): calcd for $C_{20}H_{19}N_4O_{10}$-Na: 498.09 $[M + Na]^+$, found: 497.96. The corresponding beta anomer (3.09 g; 50%) was also obtained; mp 78−80 °C; ^{1}H NMR (300 MHz, $CDCl_3$) δ = 7.92−7.78 (m, 4 H, $H_{ar.}$), 5.37 (dd, 1 H, $J_{4,5} = 1.1$ Hz, $J_{3,4} = 3.3$ Hz, H-4), 5.03 (d, 1 H, $J_{1,2} = 8.4$ Hz, H-1), 4.89 (dd, 1 H, $J_{3,4} = 3.3$ Hz, $J_{2,3} = 10.7$ Hz, H-3), 4.20−4.13 (m, 2 H, H-6), 4.00 (dd, 1 H, $J_{1,2} = 8.4$ Hz, $J_{2,3} = 10.7$ Hz, H-2), 3.91 (td, 1 H, $J_{4,5} = 1.1$ Hz, $J_{5,6} = 6.9$ Hz, H-5), 2.18, 2.09, 1.97 (3s, 9 H, $3OCOCH_3$); ^{13}C NMR (75 MHz, $CDCl_3$) δ = 170.6 ($C{=}O_{Ac}$), 170.4 ($C{=}O_{Ac}$), 170.0 ($C{=}O_{Ac}$), 163.0 ($C{=}O_{Pht}$), 135.2 ($CH_{ar.}$), 129.1 ($C_{ar.}$), 124.3 ($CH_{ar.}$), 106.2 (C-1), 71.8 (C-5), 71.4 (C-3), 66.1 (C-4), 61.1 (C-6), 59.5 (C-2), 21.0 ($OCOCH_3$), 20.9 ($OCOCH_3$), 20.9 ($OCOCH_3$).

***O*-(2-Acetamido-3,4,6-tri-*O*-acetyl-2-deoxy-α-D-galactopyranosyl)-*N*-oxyphthalimide (6).** To compound **5** (1.68 g, 3.5 mmol) dissolved in a solution of methanol/acetic anhydride (9/1, 40 mL) was added Pd/C 10% (0.38 g, 0.3 mmol). The mixture was stirred at room temperature under an atmosphere of hydrogen for 1 h. The catalyst was then removed by filtration under Celite and washed with methanol. After evaporation of the solvent under reduced pressure, the residue was finally purified by silica gel chromatography (dichloromethane/ethyl acetate, 4/1 then pure ethyl acetate) to afford *N*-acetylated derivative **6** (0.92 g, 53%) as a white powder after precipitation from dichloromethane/diethyl ether; mp 148−150 °C; ^{1}H NMR (300 MHz, $CDCl_3$) δ 7.86−7.77 (m, 4 H, $H_{ar.}$), 6.07 (d, 1 H, $J_{2,NH} = 9.6$ Hz, NH), 5.54 (d, 1 H, $J_{3,4} = 3.0$ Hz, H-4), 5.38 (d, 1 H, $J_{1,2} = 3.4$ Hz, H-1), 5.34 (dd, 1 H, $J_{3,4} = 3.0$ Hz, $J_{2,3} = 11.3$ Hz, H-3), 5.08 (bt, 1 H, $J_{5,6} = 6.4$ Hz, H-5), 4.80 (ddd, 1 H, $J_{1,2} = 3.4$ Hz, $J_{2,NH} = 9.6$ Hz, $J_{2,3} = 11.3$ Hz, H-2), 4.30 (dd, 1 H, $J_{5,6} = 6.4$ Hz, $J_{6a,6b} = 11.3$ Hz, H-6a), 4.00 (dd, 1 H, $J_{5,6} = 6.4$ Hz, $J_{6a,6b} = 11.3$ Hz, H-6b), 2.18, 2.12, 2.09, 2.04 (4s, 12 H, $3OCOCH_3$, $NHCOCH_3$); ^{13}C NMR (75 MHz, $CDCl_3$) δ 171.2 (C=O), 135.2 ($CH_{ar.}$), 129.1 ($C_{ar.}$), 124.2 ($CH_{ar.}$), 105.4 (C-1), 71.5, 69.5, 67.7, 61.9 (C-3, C-4, C-5, C-6), 47.7 (C-2), 21.1 ($OCOCH_3$).

***O*-α-D-Galactopyranosyloxyamine (7).** The compound **6** (0.86 g, 1.7 mmol) was dissolved in a solution of ethanol/methylhydrazine (1/1, 10 mL) and stirred at room-temperature overnight. After evaporation of the mixture, the residue was purified by flash silica gel chromatography (dichloromethane/ethanol, 7/3 then pure ethanol) to obtain the pure aminooxylated product **7** (0.37 g, 90%) as a white powder; ^{1}H NMR (300 MHz, D_2O) δ 4.99 (d, 1 H, $J_{1,2} = 4.1$ Hz, H-1), 4.24 (dd, 1 H, $J_{1,2} = 4.1$ Hz, $J_{2,3} = 11.3$ Hz, H-2), 4.03−3.99 (m, 2 H, H-4, H-5), 3.89−3.76 (m, 3 H, H-3, H-6), 2.08 (s, 3 H, $HNCOCH_3$); ^{13}C NMR (75 MHz, D_2O) δ 175.0 ($HNCOCH_3$), 101.0 (C-1), 71.4, 68.8 (C-4, C-5), 68.0 (C-3), 61.5 (C-6), 49.6 (C-2), 22.3 ($HNCOCH_3$); MS-CI (positive mode): calcd for $C_8H_{17}N_2O_6$ 237.10 $[M + H]^+$, found: 237.1.

OHCOC-KLFAVWKITYKDT-NH_2 (11). The protected peptide sequence, precursor of peptide **10**, H-S(*t*Bu)K-(Boc)LFAVW(Boc)K(Boc)IT(*t*Bu)Y(*t*Bu)K(Boc)D(*t*Bu)T-(*t*Bu)-NH_2, was built up by Fmoc/*t*Bu strategy from 200 mg of Rink amide MBHA resin (substituted at ca. 0.61 mmol/g). Coupling steps were performed using 2 equiv of Nα-Fmoc-protected amino acid activated in situ with 2 equiv of PyBOP and 4 equiv of DIPEA in DMF (5 mL) for 40 min. Removal steps of Nα-Fmoc protecting groups were achieved by treatment with a piperidine/DMF solution (1/4, 5 mL) three times during 10 min. Finally, the peptide was recovered upon acid cleavage by a solution of TFA/TIS/H_2O/*p*-cresol 89/1/5/5 (5 mL x 30 min, three times). The cleavage solutions were concentrated under vacuum and the peptide H-SKLFAVWKITYKDT-NH_2 **10** was obtained as TFA salt (114 mg, 41%) after precipitation from ether and RP-HPLC purification (0 to 50% B in 30 min); $t_R = 8.3$ min (5 to 100% B in 15 min, 214 and 250 nm); ES-MS calcd for $C_{82}H_{127}N_{19}O_{20}$ (1699.0): *m/z* 850.3 $(M + 2H)^{2+}$, 567.3 $(M + 3H)^{3+}$. The serine oxidation of the peptide **10** (40 mg, 17.6 μmol) was carried out in a phosphate buffer 0.01 M pH 7.3 (2×10^{-3} M solution) using 1.5 equiv of $NaIO_4$ (5.6 mg) for 40 min. The solution was purified by RP-HPLC (5 to 100% B in 30 min) to afford the aldehyde **11** (31 mg, 83%) as a white salt; $t_R = 8.6$ min (5 to 100% B in 15 min, 214 and 250 nm); ES-MS calcd for $C_{81}H_{122}N_{18}O_{20}$ (1667.9): *m/z* 834.6 $(M + 2H)^{2+}$, 556.8 $(M + 3H)^{3+}$.

RAFT(4Ser,1$COCH_2ONH_2$)[1] (13a). Removal of Boc moieties from RAFT(4Boc,1Alloc) **12a** (360 mg, 0.240 mmol) was carried out in a solution containing 50% TFA in DCM (15 mL) for 1h at room temperature. The crude was concentrated, triturated and washed with diethyl ether to yield RAFT(4NH_2,1Alloc) as a white TFA salt (305 mg, 82%). This compound (295 mg, 0.19 mmol) was dissolved in 20 mL of DMF, BocSer(*t*Bu)OH (198 mg, 0.76 mmol), and PyBOP (394 mg, 0.76 mmol) were added and the pH was adjusted to 8−9 by adding DIPEA (198 μL, 1.14 mmol). The solution was stirred 2 h at room temperature, the solvent was removed, and diethyl ether was added to precipitate the RAFT(4BocSer(*t*Bu),1Alloc)-used without further purification (275 mg, 70%); $t_R = 14.8$ min (5 to 100% B in 15 min, 214 nm); ES-MS calcd for $C_{99}H_{173}N_{19}O_{28}$ (2077.6): *m/z* 1039.7 $(M + 2H)^{2+}$, 693.3 $(M + 3H)^{3+}$. Alloc group was removed from the crude (0.13 mmol) dissolved in 20 mL of dry DCM/THF (10/1) under argon by adding $PhSiH_3$ (583 μL, 3.25 mmol) and then $Pd(PPh_3)_4$ (55 mg, 0.03 mmol) for 1 h. The solution was filtrated on C_{18} silica gel, the filtrate was evaporated and precipitated in ether to get after purification (5 to 100% B in 30 min) the RAFT(4BocSer(*t*Bu),1NH_2) (231 mg, 84%); $t_R = 13.4$ min (5 to 100% B in 15 min, 214 nm); ES-MS calcd for $C_{95}H_{169}N_{19}O_{26}$ (1993.5): *m/z* 1993.9 $(M + H)^+$, 997.5 $(M + 2H)^{2+}$. To a solution of RAFT(4BocSer-(*t*Bu),1NH_2) (60 mg, 28 μmol) in 10 mL of DMF, $BocNHOCH_2CO_2Su$ (10 mg, 34 μmol) was added and DIPEA (12 μL, 68 μmol) to adjust the pH at 8−9. The reaction was stirred for 45 min at room temperature and then concentrated under reduce pressure. The crude RAFT(4BocSer(*t*Bu),1$COCH_2ONHBoc$) was obtained (49 mg, 81%) as a white powder after precipitation and washing with diethyl ether; $t_R = 14.6$ min (5 to 100% B in 15 min, 214 nm). Removal of Boc and *t*Bu moieties were achieved by treatment with 10 mL of a solution of TFA/TIS/H_2O 95/2.5/2.5 for 2 h. Evaporation of solvent and precipitation in diethyl ether afforded the template RAFT(4Ser,1$COCH_2ONH_2$) **13a** (40 mg, 87%); $t_R = 5.6$ min (5 to 100% B in 15 min, 214 nm); ES-MS calcd for $C_{61}H_{108}N_{20}O_{20}$ (1441.6): *m/z* 721.3 $(M + 2H)^{2+}$, 481.2 $(M + 3H)^{3+}$, 361.2 $(M + 4H)^{4+}$.

RAFT(4Ser,2$COCH_2ONH_2$) (13b). The same procedure applied from **12b** (100 mg, 0.06 mmol) allowed to get the intermediate RAFT(4BocSer(*t*Bu),2NH_2) (60 mg,

0.03 mmol) in 43% overall yield. t_R = 12.5 min (5 to 100% B in 15 min, 214 nm). The RAFT(4BocSer(*t*Bu),2NH_2) gave, after coupling of Boc$NHOCH_2CO_2Su$ and Boc and *t*Bu removals, the peptide **13b** (40 mg, 0.018 mmol) in 68% yield. t_R = 5.5 min (5 to 100% B in 15 min, 214 nm); ES-MS calcd for $C_{66}H_{118}N_{22}O_{22}$ (1571.8): *m/z* 786.4 $(M + 2H)^{2+}$, 524.7 $(M + 3H)^{3+}$, 393.2 $(M + 4H)^{4+}$.

RAFT(4Ser,1PV) (14a). RAFT(4Ser,1$COCH_2ONH_2$) **13a** (16 mg, 7.9 μmol) and PV aldehyde **11** (16.8 mg, 7.9 μmol) were ligated in 5 mL of sodium acetate buffer 0.1 M pH 4. After 24 h under stirring the mixture was purified by RP-HPLC (5 to 40% B in 30 min) and the RAFT(4Ser,1PV) **14a** was obtained as a white powder (25 mg, 78%); t_R = 10.9 min (5 to 60% B in 15 min); ES-MS calcd for $C_{142}H_{228}N_{38}O_{39}$ (3091.6): *m/z* 1546.5 $(M + 2H)^{2+}$, 1031.3 $(M + 3H)^{3+}$, 773.8 $(M + 4H)^{4+}$, 619.3 $(M + 5H)^{5+}$.

RAFT(4Ser,2PV) (14b). The same procedure was applied from RAFT(4Ser,2$COCH_2ONH_2$) **13b** (12 mg, 5.3 μmol) and an excess of PV aldehyde **11** (34 mg, 16 μmol). The excess of **11** was trapped by adding benzyloxyamine and the mixture was purified by RP-HPLC (0 to 50% B in 40 min) to yield **14b** (24 mg, 72%); t_R = 14.4 min (0 to 50% B in 15 min, 214 and 250 nm). ES-MS calcd for $C_{228}H_{358}N_{58}O_{60}$ (4871.7): *m/z* 1624.4 $(M + 3H)^{3+}$, 1218.8 $(M + 4H)^{4+}$, 975.3 $(M + 5H)^{5+}$, 812.9 $(M + 6H)^{6+}$, 696.9 $(M + 7H)^{7+}$, 609.9 $(M + 8H)^{8+}$, 542.3 $(M + 9H)^{8+}$.

RAFT(4GalNAc,1PV) (15a). The RAFT(4Ser,1PV) **14a** (10.5 mg, 3.4 μmol) was oxidized using a polymer supported periodate (2.5 μmol/mg, 19.75 μmol) in phosphate buffer (0.01 M, pH 7.3) for 5 h. The mixture was filtered to remove the polymer-resin and purified to yield RAFT(4COCHO,1PV) (8.7 mg, 86%) (5 to 40% B in 30 min). t_R = 11.4 min (5 to 60% B in 15 min, 214 and 250 nm). RAFT(4COCHO,1PV) (8.7 mg, 2.9 μmol) and αGalNAc-ONH_2 sugar **7** (6.4 mg, 27 μmol) were stirred in sodium acetate buffer (0.1 M, pH 4) for 36 h and the solution was purified by RP-HPLC (15 to 45% B in 45 min) to afford the RAFT(4GalNAc,1PV) **15a** (7.4 mg, 66%); t_R = 11.3 min (15 to 45% B in 15 min, 214 and 250 nm); ES-MS calcd for $C_{170}H_{264}N_{42}O_{59}$ (3840.2): *m/z* 1920.6 $(M + 2H)^{2+}$, 1280.7 $(M + 3H)^{3+}$, 970.3 $(M + K+3H)^{4+}$, 776.5 $(M + K + 4H)^{5+}$.

RAFT(4GalNAc,2PV) (15b). The RAFT(4Ser,2PV) **14b** (15 mg, 2.4 μmol) was oxidized using the same procedure to afford after purification (5 to 100% B in 30 min) RAFT(4COCHO,2PV) (11.8 mg, 87%); t_R = 9.1 min (5 to 100% B, 15 min, 214 and 250 nm). RAFT(4COCHO,2PV) (10 mg, 1.76 μmol) and 8 equiv of αGalNAc-ONH_2 **7** (3.3 mg, 14 μmol) were stirred in 1 mL of sodium acetate buffer (0.1 M, pH 4) for 40 days. The mixture was purified by RP-HPLC (15 to 45% B in 30 min) and **15b** (7.2 mg, 63%) was obtained as a white lyophilisat; t_R = 13.7 min (15 to 45% B in 15 min, 214 and 250 nm); ES-MS calcd for $C_{256}H_{394}N_{62}O_{80}$ (5620.4): *m/z* 1405.4 $(M + 4H)^{4+}$, 1124.7 $(M + 5H)^{5+}$, 937.5 $(M + 6H)^{6+}$.

RAFT(4Ser,1Biotin) (16). The biotin sulfone (10.6 mg, 38 μmol) was coupled on the template RAFT-(4BocSer(*t*Bu),1NH_2) (40 mg, 19 μmol) using PyBOP as activating agent (20 mg, 38 μmol), and DIPEA (20 μL, 114 μmol) in 6 mL of DMF. After 3 h under stirring, the solvent was concentrated and the crude product precipitated from diethyl ether. It was triturated and washed several times in ether to afford the intermediate RAFT-(4BocSer(*t*Bu),1Biotin) (30 mg, 70%) after purification (5 to 100% B in 30 min); t_R = 13.3 min (5 to 100% B in 15 min, 214 nm); ES-MS calcd for $C_{105}H_{183}N_{21}O_{30}S$ (2251.8): *m/z* 1126.9 $(M + 2H)^{2+}$, 751.3 $(M + 3H)^{3+}$. Removal of Boc and *t*Bu protecting groups were achieved by treatment with 10 mL of TFA for 2 h. Evaporation of solvent and precipitation with diethyl ether allowed to get the RAFT(4Ser,1Biotin) **16** (24 mg, 86%) after purification (5 to 40% B in 40 min); t_R = 6.1 min (5 to 100% B in 15 min, 214 nm); ES-MS calcd for $C_{69}H_{119}N_{21}O_{22}S$ (1626.9): *m/z* 814.0 $(M + 2H)^{2+}$, 543.2 $(M + 3H)^{3+}$.

RAFT(4Glc,1Biotin) (17) and RAFT(4GalNAc,1-Biotin) (18). The serine oxidation of **16** (20 mg, 9.6 μmol) was carried out in 1 h using 4.8 equiv of $NaIO_4$ (10 mg) in 5 mL of water. The solution was directly purified by RP-HPLC (0 to 50% B in 30 min) to afford the RAFT-(4COCHO,1Biotin) (12 mg, 83%); t_R = 8.9 min (0 to 50% B in 15 min, 214 nm). To a solution containing the intermediate RAFT(4COCHO,1Biotin) (6 mg, 4 μmol) in 2 mL of sodium acetate buffer (0.1 mM, pH 4) was added the βGlc-ONH_2 derivative **9** (6.3 mg, 32 μmol) or the αGalNAc-ONH_2 **7** (7.5 mg, 32 μmol). The reactions followed by RP-HPLC were placed under stirring at room temperature for 24 h. Conjugates RAFT(4Glc,1Biotin) **17** (5.3 mg, 66%) and RAFT(4GalNAc,1Biotin) **18** (6.3 mg, 60%) were isolated after RP-HPLC purification (0 to 50% B in 30 min) as white powders; **17**: t_R = 9.2 min (0 to 50% B in 15 min, 214 and 250 nm); ES-MS calcd for $C_{89}H_{143}N_{21}O_{42}S$ (2211.3): *m/z* 1106.5 $(M + 2H)^{2+}$; **18**: t_R = 9.1 min (0 to 50% B in 15 min, 214 and 250 nm); ES-MS calcd for $C_{97}H_{155}N_{25}O_{42}S$ (2375.5): *m/z* 1188.8 $(M + 2H)^{2+}$, 792.4 $(M + 3H)^{3+}$.

ELISA and Flow Cytometry. The antigenicity of the RAFT(4GalNAc,1Biotin) **18** was assessed by ELISA using two monoclonal antibodies specific for the Tn antigen, the 83D4 (IgM; kindly given by Dr. E. Osinaga, Facultad de Medicina, Montevideo, Uruguay) and the 6E11 (IgG3; produced in our lab (unpublished data)). RAFT-(4Ser,1Biotin) **16** and RAFT(4Glc,1Biotin) **18** were used as control for specificity. The immunogenicity of the RAFT compounds was assessed in BALB/c mice (CER Janvier, Le Genest St Ile, France). For this purpose, mice were ip immunized with the different RAFTs containing one and two PV sequences **15a**,**b** and **14a**,**b** in alum. Various times after immunization sera were collected and tested for IgG antibodies by ELISA using RAFT-(4GalNAc,1Biotin) **18** or RAFT(4Ser,1Biotin) **16**. Serial dilutions of sera were performed and bound antibodies were revealed using goat anti-mouse IgG peroxidase conjugate (Sigma, St. Louis, MO) and *O*-phenyldiamine/H_2O_2 substrate. Plates were read photometrically at 492 nm in an ELISA auto-reader (Dynatech, Marnes la Coquette, France). The negative control consisted of naive mouse sera diluted 100-fold. ELISA antibody titers were determined by linear regression analysis, plotting dilution versus absorbance at 492 nm. The titers were calculated to be the Log_{10} highest dilution which gave twice the absorbance of normal mouse sera diluted 1/100. Titers are given as the arithmetic mean ± SD of the Log_{10} titers. Sera were also tested at 1/50 dilution by flow cytometry for recognition of Tn-expressing human Jurkat tumor cell line. Cells were first incubated for 30 min with serial dilutions of sera at 4 °C in PBS containing 5% fetal calf serum and 0.05% sodium azide. Then, cells were incubated for 30 min with an anti-mouse IgG conjugated to phycoerythrin (Caltag, Burlingame, CA). Cells were analyzed using a FACScan flow cytometer (Becton Dickinson, Mountain View, CA), and data analysis was performed with CellQuest software (Becton Dickinson). The data are shown as histograms corresponding to the fluorescence of cells incubated with the secondary reagent alone or together with sera.

T-Cell Assays. The recognition by specific T-cells of the poliovirus T-cell epitope contained in the RAFT-

Scheme 1. Synthesis of Aminooxylated Tn Antigen 7 (A) and Glucose 9 (B)[a]

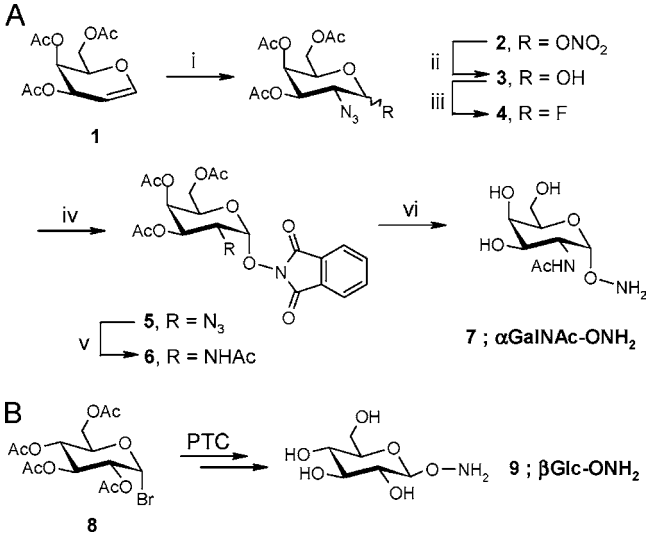

[a] Reagents and conditions: (A) (i) NaN_3, CAN, CH_3CN, −15 °C; (ii) $NaNO_2$, dioxane/H_2O (1/1), 80 °C; (iii) DAST, THF; (iv) PhtOH, TEA, CH_2Cl_2, $BF_3{\cdot}Et_2O$; (v) H_2, Pd/C, CH_3OH/Ac_2O (9/1); (vi) $MeHNNH_2$; (B) phase-transfer catalysis (PTC) (*70*).

(4Ser,1PV) **13a** and the RAFT(4GalNAc,1PV) **15a** was analyzed using a specific T-cell hybridoma and bone marrow-derived dendritic cells as antigen-presenting cells. T-cell hybridomas (10^5) were cultured with dendritic cells (10^5) in the presence of the RAFT at several concentrations for 24 h in RPMI 1640 supplemented with 10% FCS, antibiotics, L-glutamine, and mercaptoethanol. Interleukin 2 production by hybridoma T-cells was assessed by the measure of the proliferative response of the interleukin 2-dependent CTLL cell line using [^{3}H]-thymidine.

RESULTS AND DISCUSSION

Design of the Vaccine Candidates. Taking advantages of the synthetic versatility of the RAFT platform, we designed our vaccine candidates **15a** and **15b** so that to mimic through one domain of the template the clustering of the mucin-associated Tn antigen (Figure 1) which characterizes the surface of epithelial tumors (*4*, *5*). We assembled regioselectively on the other domain a peptide fragment from poliovirus in order to stimulate $CD4^+$ T-cells and activate the production of specific antibodies for the TACA by B-cells (Figure 1). We chose the peptide fragment KLFAVWKITYKDT from the type I-poliovirus protein since it previously proved to provide efficient T-cell help for the induction of antibody responses in BALB/c mice (*31*).

One critical aspect of our approach focuses on controlling the molecular assembly processes which are essential to warrant the structure of the target molecule. While many chemical methodologies including solution and solid-phase synthesis protocols have been reported so far, the assembly of carbohydrate-based bioconjugates remains fastidious due to numerous manipulations of orthogonal protecting groups (*46*−*49*). As an attractive synthetic alternative, we and other have demonstrated recently that chemoselective ligation via oxime or polyoxime bond formation offers a convenient strategy for the convergent assembly of bioconjugates (*40*−*42*, *50*−*59*). Indeed, this ligation technique is highly efficient, compatible with a wide range of chemical functions and allows the ligation between unprotected fragments in minimal chemical transformations without any coupling reagent. Moreover, the oxime linkage has been shown to be stable under physiological conditions (*51*, *60*), and its use for ligation of peptide epitopes in vaccines has been found advantageous (*61*−*63*).

Such oxime-based strategy requires the synthesis of the RAFT molecule, bearing serine residues as masked glyoxylyl aldehyde functions on the upper domain and protected aminooxy groups on the other domain, and of the B/T-epitopes displaying the suitable complementary functions. For this purpose, we prepared the aminooxylated αGalNAc moiety **7** as a carbohydrate analogue of the native Tn form (αGalNAcSer/Thr) in mucin glycoproteins (*1*−*3*). Since it was previously attested that other carbohydrate-based Tn analogues present similar antigenicity as the native antigen (*21*, *64*−*66*), we expected that this modification should not affect the immunological properties of our constructions. Especially, a vaccine bearing an *O*-aliphatic aglycone instead of natural amino acid carrier has proved to be more antigenic than the natural Tn-based conjugate (*67*). In the case of the PV fragment moiety, this one was functionalized by an *N*-terminal aldehyde spacer prior to its grafting to the RAFT template.

Synthesis of the Aminooxylated Tn Analogue 7 and Glucose 9. The Tn analogue (αGalNAc-ONH_2) **7** containing an aminoxy group at its anomeric position has been synthesized according to the previously published procedure (Scheme 1A) (*68*). Starting from the commercial triacetylated galactal **1**, the azidonitration reaction described by R. U. Lemieux and R. M. Ratcliffe (*44*) followed by the anomeric denitration of compound **2** with sodium nitrite in aqueous dioxane at 80 °C (*45*) gave **3**. Treatment of **3** with DAST in THF (*69*) provided glycosyl fluoride **4** which was glycosylated in CH_2Cl_2 with *N*-hydroxyphthalimide as precursor of the aminooxy function using $BF_3{\cdot}Et_2O$ as a promoter in the presence of triethylamine. The alpha and beta anomers were easily separated by silica gel chromatography to obtain **5** in 50% yield (38% for the beta anomer). The azido group was then converted into the NHAc function by a catalytic hydrogenation in CH_3OH/Ac_2O to get **6**. After complete acetate deprotection and aminooxy formation with methylhydrazine, we obtained the alpha aminooxylated Tn antigen **7** in 90% yield. The aminooxylated β-glucose **9** was obtained following the phase-transfer catalysis pro-

Scheme 2. Synthesis of T-Epitope Peptide 11[a]

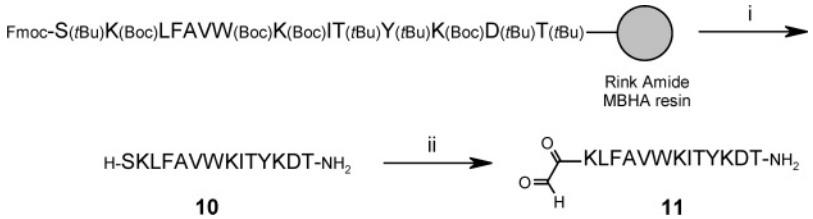

[a] Reagents and conditions: (i) TFA/TIS/H_2O/*p*-cresol (89/1/5/5); (ii) $NaIO_4$, phosphate buffer 0.01 M, pH 7.3.

Scheme 3. Synthesis of Vaccine Candidates 15a,b[a]

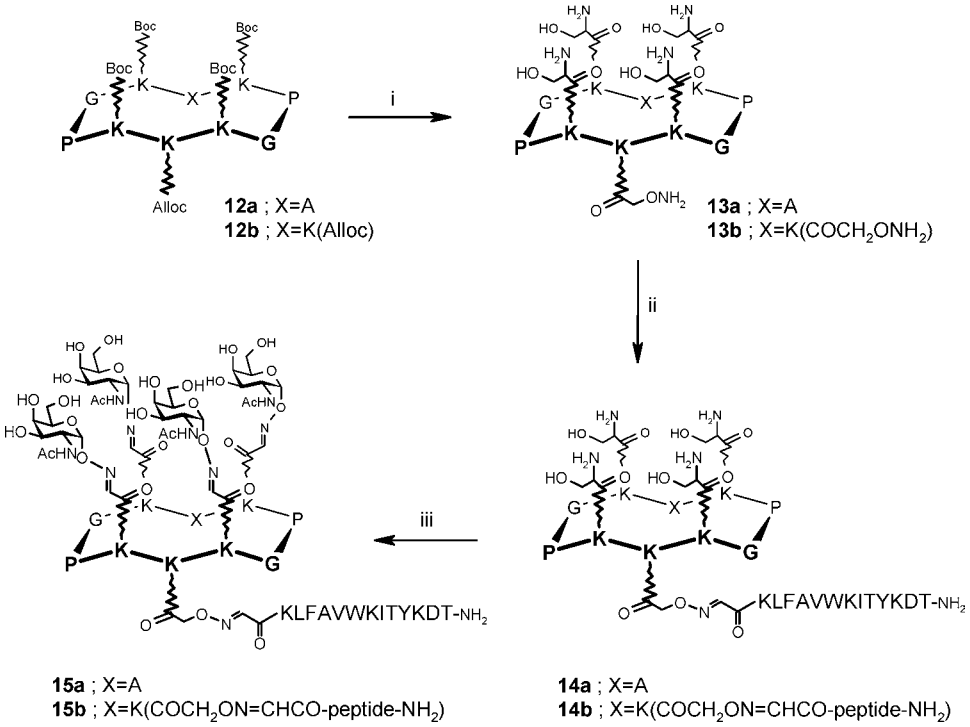

[a] Reagents and conditions: (i) a) 50% TFA/CH_2Cl_2; b) BocSer(*t*Bu)OH, PyBOP, DIPEA, DMF; c) $Pd(PPh_3)_4$/$PhSiH_3$, CH_2Cl_2; d) $BocNHOCH_2CO_2Su$, DIPEA, DMF; e) TFA/TIS/H_2O (95/2.5/2.5); (ii) **11**, AcONa buffer 0.1 M pH 4; (iii) a) $NaIO_4$, phosphate buffer 0.01 M, pH 7.3; b) **7**, AcONa buffer 0.1 M pH 4.

cedure described by R. Roy from the activated derivative **8** (Scheme 1B) (*70*).

Synthesis of the T-Cell PV Epitope Aldehyde 11. The minimal $CD4^+$ T-cell epitope sequence from the poliovirus type 1, KLFAVWKITYKDT, corresponds to the 103−115 amino acid sequence that is immunogenic in BALB/c mice. We have introduced a serine residue at the N-terminal position to access to the aldehyde function after oxidation. The targeted sequence H-SKLFAVWKI-TYKDT-NH_2 **7** was built up by standard Fmoc/*t*Bu strategy from the Rink amide MBHA resin using PyBOP as coupling reagent and diisopropylethylamine (DIPEA) as base. We obtained the fully unprotected peptide **10** in 41% overall yield after removal from the resin and reverse phase HPLC purification (Scheme 2). An adapted oxidation procedure was used for the sodium periodate oxidation of the serine residue due to the presence of tryptophane. We carried out the reaction in phosphate buffer at pH 7.3, and the peptide aldehyde **11** was obtained in 83% yield.

Synthesis of the RAFT Scaffolds 13a,b. The chemoselective oxime-based strategy requires the appropriate RAFT cores **13a** or **13b** to combine the PV aldehyde **11** and the aminooxy sugars **7** and **9**. These key intermediates **13a**,**b** present two distinct domains, one bearing aminooxy acetyl sites to ligate the PV sequence and the other bearing four serine residues allowing the combination with the sugar moieties after an oxidation step. They have been prepared (Scheme 3) from the corresponding cyclic scaffolds **12a** and **12b** (*34*, *40*) presenting Alloc and Boc orthogonal protecting groups at the lysinyl side chains. The removal of Boc groups from the four lysine residues was first achieved in acidic conditions (50% of TFA in CH_2Cl_2) and followed by the coupling of protected serine BocSer(*t*Bu)OH residues using standard coupling conditions. The aminooxyacetyl moieties were incorporated on the other face as *N*-Boc-*O*-(carboxymethyl)hydroxylamine succinimide ester (*71*)

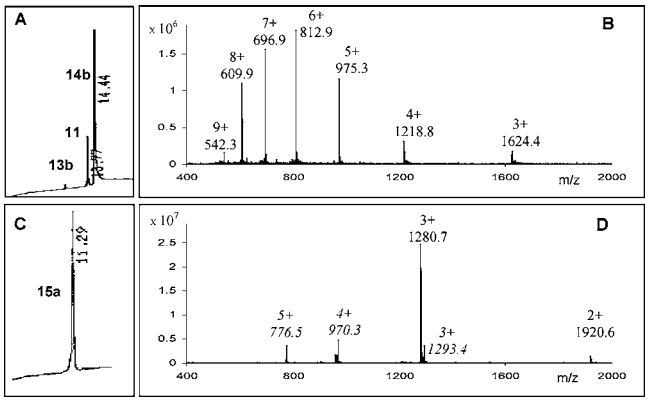

Figure 2. (A) HPLC profile (Nucleosil 100 Å 5 μm C_{18} particles, 250 × 4.6 mm; solvent B: 0.09% TFA in 90% acetonitrile and solvent A: 0.09% TFA; 1.3 mL/min; linear gradient 100:0 A:B to 50:50 in 15 min; detection $\lambda = 214$ and 250 nm) of the reaction mixture **14b** after 20 h (the RAFT core **13b** is completely consumed after 24 h); (B) ES-MS (positive mode) of **14b** after purification; (C) HPLC profile (linear gradient 85:15 A:B to 55:45 A:B in 15 min; detection $\lambda = 214$ and 250 nm) of the reaction mixture **15a** after 36 h; (D) ES-MS (positive mode) of **15a** after purification: numbers in italics correspond to the potassium adducts.

after the removal of the Alloc groups using $Pd(PPh_3)_4$/$PhSiH_3$ procedure (*72*). Further removal of the Boc and *t*Bu from the serine and aminooxyacetyl residues gave the appropriate templates **13a** and **13b** in 72% and 68% yields, respectively.

Regio/chemoselective Assembly of the Vaccine Candidates 15a and 15b. We prepared vaccine candidates bearing four copies of the Tn analogues and one or two copies of the T-cell epitope sequence to determine whether we could further increase the immunogenicity of our vaccines. The ligation of the T-cell peptide fragment **11** and αGalNAc-ONH_2 **7** were carried out by consecutive oxime bond formation (Scheme 3). PV alde-

Scheme 4. Synthesis of Biotinylated Compounds 16−18[a]

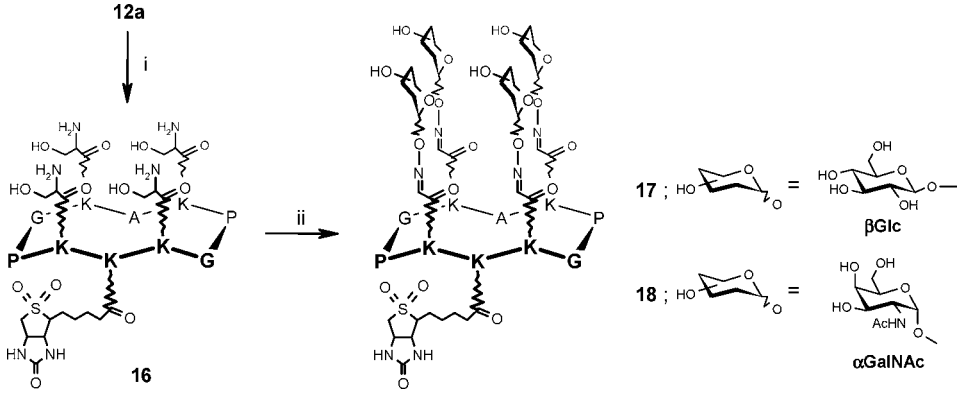

[a] Reagents and conditions: (i) (a) 50% TFA/CH_2Cl_2; (b) BocSer(*t*Bu)OH, PyBOP, DIPEA, DMF; (c) $Pd(PPh_3)_4/PhSiH_3$, CH_2Cl_2; (d) Biotin sulfone, PyBOP, DIPEA, DMF; (e) TFA; (ii) (a) $NaIO_4$, water; (b) **7** or **9**, AcONa buffer 0.1 M pH 4.

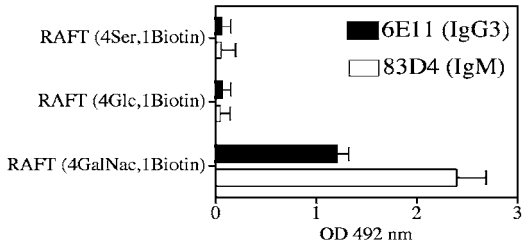

Figure 3. Antigenicity of the RAFT bearing the Tn antigen analogue. 6E11 (IgG3) and 83D4 (IgM) monoclonal antibodies specific for the tumor-associated Tn carbohydrate antigen were tested by ELISA for the recognition of RAFT(4GalNAc,1Biotin) **18**, RAFT(4Glc,1Biotin) **17** or RAFT(4Ser,1Biotin) **16** directly coated on microtiter plates. Error bars refer to the standard error to the mean of triplicate measures.

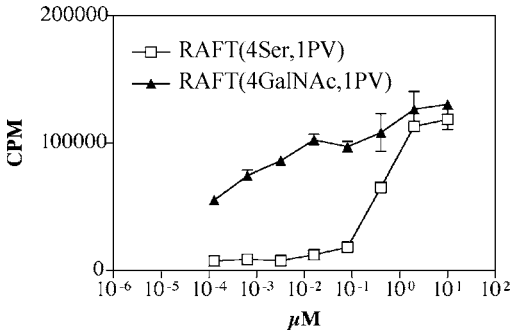

Figure 4. Activation of a PV-specific T-cell hybridoma by the PV-containing RAFTs **14a** and **15a** in the presence of antigen-presenting cells. T-cell hybridoma were cultured with dendritic cells in the presence of the indicated RAFTs at different doses. Interleukin-2 secretion following T-cell hybridoma stimulation was assessed by the proliferation of the interleukin 2-dependent CTLL cell line using [^{3}H]-thymidine. Error bars refer to the standard error to the mean titer of 5 individual sera.

hyde **11** was first assembled to the cores **13a** and **13b** in sodium acetate buffer following the typical chemoselective ligation procedure we previously described (*40*−*42*). The progress of the reactions was monitored by RP-HPLC, and no significant difference of reactivity was noticed between the templates **13a** and **13b**. The completeness of the coupling reaction required up to 24 h to give cleanly mono- and bivalent compounds **14a** and **14b** which have been fully characterized by ES-MS (Figure 2A,B). These conjugates **14a**,**b** bearing serine residues have been used as reference compounds in immunological assays. After liberation of the four aldehyde functions by sodium periodate oxidation of serine moieties, the aminooxylated Tn antigen **7** was incorporated through the same chemoselective coupling conditions. As we expected, the crude reaction mixtures were clean confirming the high efficiency of the chemoselective ligation method (Figure 2C,D). The conjugates **15a**,**b** were finally isolated in almost 65% yield after semipreparative HPLC purification.

Synthesis of Biotinylated Glycoconjugates. Several compounds presenting a biotin moiety instead of the PV fragment on the lower face of the core have also been synthesized for the ELISA tests. The conjugates **16**, **17**, and **18** (Scheme 4) bearing serine, β-Glc, or α-GalNAc residues, respectively, have been used as reference compounds to assess the specificity of the immune response. They were prepared from the intermediate displaying four protected serine residues and one unprotected lysine site for biotin attachment. While preliminary experiments have shown that biotins are partially oxidized during the oxidative cleavage of serines, we decided to incorporate biotin sulfone (*43*) to get well-defined conjugates. The biotin was directly coupled using amide linkage to get **16** after removal of Boc and *t*Bu protecting groups of serine. Oxidation of **16** and further ligation of aminooxy sugars α-GalNAc-ONH_2 **7** and β-Glc-ONH_2 **9** afforded the glycoconjugates **18** and **17** in 60 and 66% yield, respectively.

B-Cell Antigenicity. We first investigated by ELISA the ability of the GalNAc moiety incorporated into the RAFT platform to be recognized by monoclonal antibodies (mAbs) specific for the Tn antigen. The two anti-Tn mAbs, an IgG3 (6E11) and an IgM (83D4), were both able to interact with the RAFT(4GalNAc,1Biotin) **18**, but not with the RAFT(4Ser,1Biotin) **16** or the RAFT(4Glc,1Biotin) **17** (Figure 3). This clearly demonstrates that the recognition is directed specifically toward the carbohydrate moiety of compound **18**.

These results also give an accurate view of the display of TACA at the RAFT surface for antibody recognition. The recognition of RAFT(4GalNAc,1Biotin) by these antibodies indicates that the multimeric presentation in the RAFT system is able to mimic the carbohydrate part of the repeated glycosylated serine/threonine unit found on natural tumor-associated mucins. Therefore, our unnatural Tn analogues represent suitable models for humoral stimulation as other reported analogues (*64*−*67*).

T-Cell Antigenicity. To elicit an IgG humoral response, an efficient presentation of the T-cell epitope by MHC II molecules on the antigen-presenting cells (APC) surface is required for T-cell stimulation. Therefore, we analyzed in vitro by a T-cell stimulation assay the recognition of the PV epitope when incorporated into the

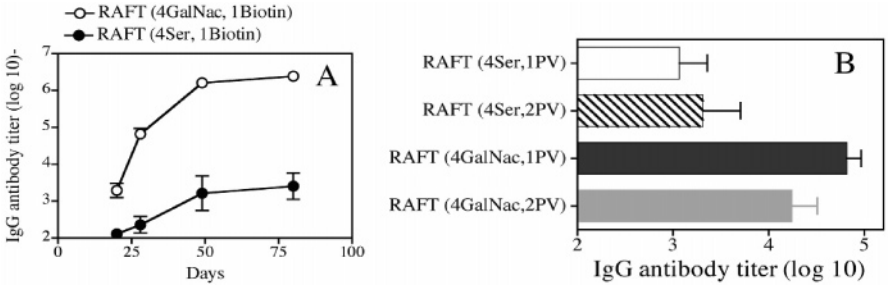

Figure 5. Immunogenicity of the RAFT displaying the Tn analogue. (A) BALB/c mice ($n = 5$) were immunized on days 0, 21 and 42 with 10 μg of RAFT(4GalNAc,1PV) **15a** in alum. Mice were then bled at various times after immunization. Sera from these mice were analyzed by ELISA for antibody titers against RAFT(4GalNAc,1Biotin) **18** or RAFT(4Ser,1Biotin) **16** as indicated. (B) Mice were immunized on days 0 and 21 with 10 μg of RAFT(4GalNAc,1PV) **15a**, RAFT(4GalNAc,2PV) **15b**, RAFT(4Ser,1PV) **14a** or RAFT-(4Ser,2PV) **14b**. Sera collected at day 28 were analyzed for antibody titers against RAFT(4GalNAc,1Biotin) **18**. Results are expressed as mean of log10 IgG antibody titers.

RAFT core. Dendritic cells were incubated with the RAFT(4GalNAc,1PV) **15a** or the RAFT(4Ser,1PV) **14a** in the presence of a PV-specific T-cell hybridoma. Secreted interleukin-2 (IL-2) was determined in a radioactive proliferation assay by measuring the incorporation of [^{3}H]-thymidine by the IL-2 dependent CTLL cell line (Figure 4). IL-2 secretion by activated T-cell hybridoma following the recognition of peptide-MHC II complexes on the dendritic cell surface by T-cell receptors (TCR) correlates with the incorporation of [^{3}H]-thymidine by CTLL cells.

As shown in Figure 4, both the unglycosylated **14a** and the glycosylated **15a** conjugates stimulate the PV-specific T-cell hybridoma. This indicates that despite being ligated in an unnatural way the T-cell determinant is efficiently presented by APC to CD4$^+$ T-cells. The response (IL-2 production) induced by the RAFT **15a** was dramatically enhanced at significantly lower doses compared to the response obtained with the unglycosylated RAFT **14a**. Indeed, T-cell stimulation was obtained with about 10 000-fold less RAFT **15a** dose compared to the RAFT **14a**, suggesting that the presence of the Tn antigen increases the presentation of the PV peptide by MHC class II molecules. This result further confirms previous observations on the enhanced T-cell stimulation induced by peptides bearing the Tn antigen (*31*, *64*). Although the mechanism underlying this phenomenon is unclear, it may strongly benefit to the glycosylated RAFT **15a** for stimulating immune responses.

Immunogenicity. We next evaluated the immunogenicity of our RAFT constructs exhibiting one or two copies of PV peptide in BALB/c mice. The RAFT(4GalNAc,1PV) **15a** was first used to immunize mice and to elicit Tn-specific IgG antibodies. Indeed, sera from immunized mice and tested by enzyme-linked immunosorbent assay against biotinylated conjugates were able to strongly recognize the RAFT(4GalNAc,1Biotin) **18** (Figure 5A).

Only 0.1−1% of the antibodies raised by the RAFT-(4GalNAc,1PV) **15a** recognized the RAFT devoid of the GalNAc moiety (i.e. RAFT(4Ser,1Biotin) **16**) demonstrating a limited reactivity against the RAFT platform. These results confirm the ability of the cyclic template as nonimmunogenic carrier for vaccine constructs which is in good agreement with a previous study (*39*).

To determine whether we could further increase the immunogenicity of our conjugates, the antibody response induced by the RAFT(4GalNAc,2PV) **15b** carrying two copies of the T-helper PV peptide was also investigated. However, the incorporation of a second copy of the T-cell epitope did not result in an increase of immunogenicity since we observed a similar antibody response when compared with **15a** (Figure 5B). In addition, the immune

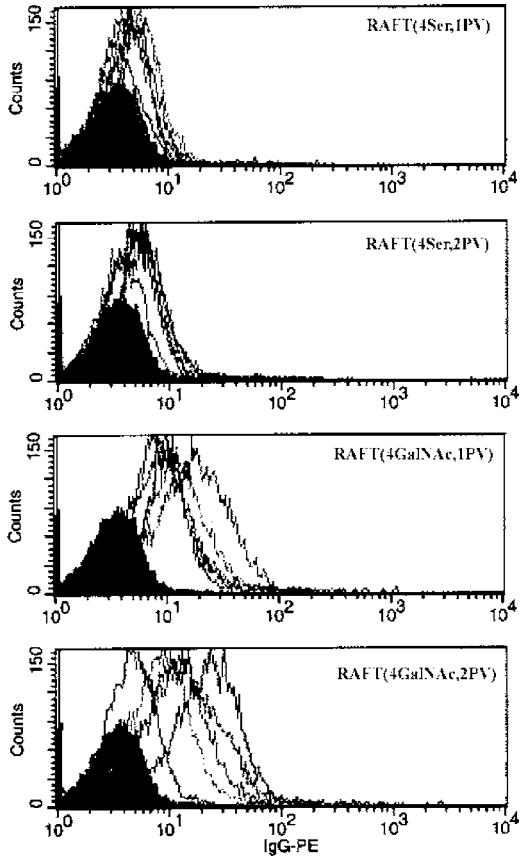

Figure 6. Antibodies induced following immunization with **15a** or **15b** recognize the native form of Tn on human Jurkat cells. Sera obtained from mice (n=5) immunized with RAFT-(4GalNAc,1PV) **15a**, RAFT(4GalNAc,2PV) **15b**, RAFT(4Ser,1PV) **14a** or RAFT(4Ser,2PV) **14b** were analyzed by flow cytometry for the recognition of native Tn on Jurkat cells. FACS data are shown as histograms corresponding to the mean fluorescence intensity of Jurkat cells stained with sera or in the absence of serum and revealed PE-conjugated anti-mouse IgG antibodies. For each group, staining obtained with five individual mouse sera (empty histogram) is shown as compared to the fluorescence obtained with PE-conjugated anti-mouse IgG antibodies in the absence of serum (plain histogram).

response induced by our RAFT-based vaccine candidates results probably from the convenient presentation of multiple copies of the B-cell epitope on the RAFT surface. Indeed, a previous study using dimeric or trimeric molecules based onto a lysine core bearing both T-cell and B-cell determinants has shown that the presentation of the determinants to T-cells may be different for linear compared to branched immunogens bearing the same determinants (*27*). Particularly, the number of the B-cell

epitopes into a branched construct could facilitate its uptake by specific B-cells in vivo and the subsequent presentation to helper T-cells.

RAFT(4GalNAc,1PV) 15a Induces Abs That Recognize Tumor Cells. To clearly determine whether the antibodies elicited by the RAFT are able to recognize the native form of Tn, we tested by flow cytometry their binding to the human Jurkat tumor cell line expressing the Tn antigen. As shown in Figure 6, sera from mice immunized with RAFT(4GalNAc,1PV) **15a** or RAFT-(4GalNAc,2PV) **15b** were able to recognize the Jurkat cells, whereas control RAFT(4Ser,1PV) **14a** and RAFT-(4Ser,2PV) **14b** devoid of TACA did not.

These results show the ability of the RAFT constructs bearing Tn- and PV-epitopes to elicit an immune response specifically directed against the native form of Tn displayed by cancer cells.

CONCLUSION

In conclusion, we investigated here the use of the RAFT platforms for the preparation of potential anticancer vaccine candidates. On the basis of previous studies, we designed RAFT molecules displaying clustered Tn antigen analogue to mimic the epithelial tumor surface and immunogenic $CD4^+$ T-cell epitope. The synthesis of such well-defined multiepitopic glycoconjugates is based on a sequential oxime bond ligation between the carrier and the B/T-cell epitopes. The immunological evaluation of our RAFT glycoconjugates clearly demonstrate a promising potential of such scaffold as a nonimmunogenic build-in vaccine carrier. Indeed, the antibodies elicited by immunization of mice with our molecules recognize the native form of Tn epitope expressed on human tumor cells, suggesting that the RAFT display Tn antigen analogues in a convenient clustered manner. Altogether, this preliminary study opens interesting perspectives to employ the RAFT scaffold in engineering potent immunogenic conjugates as vaccine candidates. Indeed, the modularity and versatility of the molecular assembly as well as the efficiency of oxime-based strategy might be further exploited to improve the immune response by combining TACAs with other immunogenic peptides and/or immunoadjuvants and to develop multicomponent therapeutic vaccines.

ACKNOWLEDGMENT

We thank the Association pour la Recherche contre le Cancer (ARC), the Centre National pour la Recherche Scientifique (CNRS), the Ministère de la Recherche (MENRT), the Institut National de la Santé et de la Recherche Médicale (INSERM), and the Institut Universitaire de France (IUF) for supporting this work.

LITERATURE CITED

(1) Springer, G. F. (1984) T and Tn, general carcinoma autoantigens. *Science 224*, 1198−1206.
(2) Itzkowitz, S. H., Yuan, M., Montgomery, C. K., Kjeldsen, T., Takahashi, H. K., Bigbee, W. L., and Kim, Y. S. (1989) Expression of Tn, sialosyl-Tn, and T antigens in human colon cancer. *Cancer Res. 49*, 197−204.
(3) Kim, Y. S., Gum, J., and Brockhausen, I. (1996) Mucin glycoproteins in neoplasia. *Glyconjugate J. 13*, 693−707.
(4) Springer, G. F. (1997) Immunoreactive T and Tn epitopes in cancer diagnosis, prognosis, and immunotherapy. *J. Mol. Med. 75*, 594−602.
(5) Springer, G. F. (1995) T and Tn pancarcinoma markers: autoantigenic adhesion molecules in pathogenesis, prebiopsy carcinoma-detection, and long-term breast carcinoma immunotherapy. *Crit. Rev. Oncogenesis 6*, 57−85.
(6) Danishefsky, S. J., and Allen, R. J. (2000) From the laboratory to the clinic: a retrospective on fully synthetic carbohydrate-based anticancer vaccines. *Angew. Chem., Int. Ed. 39*, 836−863.
(7) Livingston, O. P., and Zhang, S. (1997) Carbohydrate vaccines that induce antibodies against cancer as targets for active specific immunotherapy. 1. Rationale. *Cancer Immunol. Immunother. 45*, 1−9.
(8) Livingston, O. P., and Ragupathi, G. (1997) Carbohydrate vaccines that induce antibodies against cancer as targets for active specific immunotherapy. 2. Previous experience and future plans. *Cancer Immunol. Immunother*. 45, 10−19.
(9) Toyokuni, T., and Singhal, A. K. (1995) Synthetic carbohydrate vaccines based on tumour-associated antigens. *Chem. Soc. Rev.* 231−242.
(10) Hakomori, S. I. (2001) Tumor-associated carbohydrate antigens defining tumor malignancy: basis for development of anti-cancer vaccines. *Advances in Exp. Med. Biol. 491*, 369−402.
(11) Ragupathi, G. (1996) Carbohydrate antigens as targets for active specific immunotherapy. *Cancer Immunol. Immunother. 43*, 152−157.
(12) Ragupathi, G., Koganty, R. R., Qiu, D., Lloyd, K. O., and Livingston, P. O. (1998) A novel and efficient method for synthetic carbohydrate conjugate vaccine preparation: synthesis of sialyl Tn-KLH conjugate using a 4-(4-N-maleimidomethyl) cyclohexane-1-carboxyl hydrazide (MMCCH) linker arm. *Glycoconjugate J. 15*, 217−221.
(13) Deshpande, P. P., Kim, H. M., Zatorski, A., Park, T.-K., Ragupathi, G., Livingston, P. O., Live, D., and Danishefsky, S. J. (1998) Strategy in oligosaccharide synthesis: an application to a concise total synthesis of the KH-1(adenocarcinoma) antigen. *J. Am. Chem. Soc. 120*, 1600−1614.
(14) Allen, J. R., Allen, J. G., Zhang, X.-F., Williams, L. J., Zatorski, A., Ragupathi, G., Livingston, P. O., and Danishefsky, S. J. (2000) A second generation synthesis of the MBr1 (Globo-H) breast tumor antigen: new application of the *n*-pentenyl glycoside method for achieving complex carbohydrate protein linkages. *Chem. Eur. J. 6*, 1366−1375.
(15) Ragupathi, G., Howard, L., Cappello, S., Koganty, R. R., Qiu, D., Longenecker, B. M., Reddish, M. A., Lloyd, K. O., and Livingston, P. O. (1999) Vaccines prepared with sialyl-Tn and sialyl-Tn trimers using the 4-(4-maleimidomethyl)-cyclohexane-1-carboxyl hydrazide linker group result in optimal antibody titers against ovine submaxillary mucin and sialyl-Tn-positive tumor cells. *Cancer Immunol. Immunother. 48*, 1−8.
(16) Kuduk, S. D., Schwartz, J. B., Chen, X.-T., Glunz, P. W., Sames, D., Raupathi, G., Levingston, P. O., and Danishefsky, S. (1998) Synthetic and immunological studies on clustered modes of mucin-related Tn and TF *O*-linked antigens: the preparation of a glycopeptide-based vaccine for clinical trials against prostate cancer. *J. Am. Chem. Soc. 120*, 12474−12485.
(17) Reddish, M. A., Jackson, L., Koganty, R. R., Qiu, D., Hong, W., and Longenecker, B. M. (1997) Specificities of anti-sialyl-Tn and anti-Tn monoclonal antibodies generated using novel clustered synthetic glycopeptide epitopes. *Glycoconjugate J. 14,* 549−560.
(18) Kunz, H., and Birnbach, S. (1986) Synthesis of tumor associated Tn- and T-antigen type O-glycopeptides and their conjugation to bovine serum albumin. *Angew. Chem., Int. Ed. Engl. 98*, 354−355.
(19) Toyokuni, T., Hakomori, S., and Singhal, A. K. (1994) Synthetic carbohydrate vaccines: synthesis and immunogenicity of Tn antigen conjugates. *Bioorg. Med. Chem. 2*, 1119−1132.
(20) Kunz, H. (2003) Synthetic glycopeptides for the development of tumor-selective vaccines. *J. Pept. Sci. 9*, 563−573.
(21) Bousquet, E., Spadaro, A., Pappalardo, M. S., Bernardini, R., Romeo, R., Panza, L., and Ronsisvalle, G. (2000) Synthesis and immunostimulating activity of a thioglycolipopeptide glycomimetic as a potential anti-cancer vaccine derived from Tn antigen. *J. Carbohydr. Chem. 19*, 527−541.
(22) Miyajima, K., Nekado, T., Ikeda, K., and Achiwa, K. (1998) Synthesis of Tn, sialyl Tn and HIV-1-derived peptide antigen

conjugates having a lipid A analog as an immunoadjuvant for synthetic vaccines. *Chem. Pharm. Bull. 46*, 1676−1682.
(23) Toyokuni, T., Dean, B., Cai, S., Boivin, D., Hakomori, S., and Singhal, A. K. (1994) Synthetic vaccines: synthesis of a dimeric Tn antigen-lipopeptide conjugate that elicits immune responses against Tn-expressing glycoproteins. *J. Am. Chem. Soc. 116*, 395−396.
(24) Veprek, P., and Jezek, J. (1999) Peptide and glycopeptide dendrimers. Part I. *J. Pept. Sci. 5*, 5−23.
(25) Veprek, P., and Jezek, J. (1999) Peptide and glycopeptide dendrimers. Part II. *J. Pept. Sci. 5*, 203−220.
(26) Jezek, J., Velek, J., Veprek, P., Velkova, V., Trnka, T., Pecka, J., Ledvina, M., Vondrasek, J., and Pisacka, M. (1999) Solid-phase synthesis of glycopeptide dendrimers with Tn antigenic structure and their biological activities. Part I. *J. Pept. Sci. 5*, 46−55.
(27) Fitzmaurice, C. J., Brown, L. E., McInerney, T. L., and Jackson, D. C. (1996) The assembly and immunological properties of nonlinear synthetic immunogens containing T-cell and B-cell determinants. *Vaccine 14*, 553−560.
(28) Grandjean, C., Rommens, C., Gras-Masse, H., and Melnyk, O. (2000) One-pot synthesis of antigen-bearing lysine-based cluster mannosides using two orthogonal chemoselective ligation reactions. *Angew. Chem., Int. Ed. 39*, 1068−1072.
(29) Tam, J. P., and Lu, Y. A. (1989) Vaccine engineering: enhancement of immunogenicity of synthetic peptide vaccines related to hepatitis in chemically defined models consisting of T- and B-cell epitopes. *Proc. Natl. Acad. Sci. U.S.A. 86*, 3879−3883.
(30) Bay, S., Lo-Man, R., Osiniga, E., Nakada, H., Leclerc, C., and Cantacuzéne, D. (1997) Preparation of a multiple antigen glycopeptide (MAG) carrying the Tn antigen. *J. Pept. Res. 49*, 620−625.
(31) Lo-Man, R., Bay, S., Vichier-Guerre, S., Dériaud, E., Cantacuzéne, D., and Leclerc, C. (1999) A fully synthetic immunogen carrying a carcinoma-associated carbohydrate for active specific immunotherapy. *Cancer Res. 59*, 1520−1524.
(32) Lo-Man, R., Vichier-Guerre, S., Bay, S., Dériaud, E., Cantacuzéne, D., and Leclerc, C. (2001) Anti-tumor immunity provided by a synthetic multiple antigenic glycopeptide displaying a tri Tn glycotope. *J. Immunol. 166*, 2849−2854.
(33) Lo-Man, R., Vichier-Guerre, S., Perraut, R., Dériaud, E., Huteau, V., BenMohamed, L., Diop, O., Livingstone, P., Bay, S., and Leclerc, C. (2004) A fully synthetic therapeutic vaccine candidate targeting carcinoma-associated Tn carbohydrate antigen induces tumor specific antibodies in non-human primates. *Cancer Res. 64*, 4987−4994.
(34) Dumy, P., Eggleston, I. M., Cervigni, S., Sila, U., Sun, X., and Mutter, M. (1995) A convenient synthesis of cyclic peptides as regioselectively addressable functionalized templates (RAFT). *Tetrahedron Lett. 36*, 1255−1258.
(35) Peluso, S., Rückle, T., Lehmann, C., Mutter, M., Peggion, C., and Crisma, M. (2001) Crystal structure of a synthetic cyclodecapeptide for template-assembled synthetic protein design. *ChemBioChem 2*, 432−437.
(36) Mutter, M., Dumy, P., Garrouste, P., Mathieu, M., Peggion, C., Peluso, S., Razaname, A., and Tuchscherer, G. (1996) Template assembled synthetic proteins (TASP) as functional mimetics of proteins. *Angew. Chem., Int. Ed. Engl. 35*, 1481−1485.
(37) Tuchscherer, G., Lehmann, C., and Mathieu, M. (1998) New protein mimetics: the zinc finger motif as a locked-in tertiary fold. *Angew. Chem., Int. Ed. 37*, 2990−2993.
(38) Peluso, S., Dumy, P., Nkubana, C., Yokokawa, Y., and Mutter, M. (1999) Solid-phase strategies for the assembly of template-based protein mimetics. *J. Org. Chem. 64*, 7114−7120 and references herein.
(39) Tuchscherer, G., Servis, C., Corradin, G., Blum, U., Rivier, J., and Mutter, M. (1992) Total chemical synthesis, characterization, and immunological properties of an MHC class I model using the TASP concept for protein de novo design. *Protein Sci. 1*, 1377−1386.
(40) Boturyn, D., Coll, J.-L., Garanger, E., Favrot, M.-C., and Dumy, P. (2004) Template assembled cyclopeptides as multimeric system for integrin targeting and endocytosis. *J. Am. Chem. Soc. 126*, 5730−5739.
(41) Renaudet, O., and Dumy, P. (2003) Chemoselectively template-assembled glycoconjugates as mimics for multivalent presentation of carbohydrates. *Org. Lett. 5*, 243−246.
(42) Singh, Y., Renaudet, O., Defrancq, E., and Dumy, P. (2005) Preparation of a Multitopic Glycopeptide−Oligonucleotide Conjugate. *Org. Lett. 7*, 1359−1362.
(43) Lett, R., and Marquet, A. (1974) Conformational analysis of thiophane derivatives, sulfoxides, and corresponding sulfones. *Tetrahedron 30*, 3365−3377.
(44) Lemieux, R. U., and Ratcliffe, R. M. (1979) The azidonitration of tri-*O*-acetyl-D-galactal. *Can. J. Chem. 57*, 1244−1251.
(45) Grundler, G., and Schmidt, R. R. (1984) Anwendung des Trichloracetimidatverfahrens auf 2-Azidoglucose- und 2-Azidogalactose-Derivate. *Justus Liebigs Ann. Chem.* 1826−1847.
(46) Herzner, H., Reipen, T., Schultz, M., and Kunz, H. (2000) Synthesis of glycopeptides containing carbohydrate and peptide recognition motifs. *Chem. Rev. 100*, 4495−4537.
(47) Seitz, O. (2000) Glycopeptide synthesis and the effects of glycosylation on protein structure and activity. *ChemBioChem 1*, 214−246.
(48) Seitz, O., Heinemann, I., Mattes, A., and Waldmann, H. (2001) Synthetic peptide conjugates-tailor-made probes for the biology of protein modification and protein processing. *Tetrahedron 57*, 2247−2277.
(49) Davis, B. G. (2002) Synthesis of glycoproteins. *Chem. Rev. 102*, 579−601.
(50) Rose, K. (1994) Facile synthesis of homogeneous artificial proteins, *J. Am. Chem. Soc. 116*, 30−33.
(51) Shao, J., and Tam, P. (1995) Unprotected peptides as building blocks for the synthesis of peptide dendrimers with oxime, hydrazone, and thiazolidine linkages. *J. Am. Chem. Soc. 117*, 3893−3899.
(52) Canne, L. E., Botti, P., Simon, R. J., Chen, Y., Dennis, E. A., and Kent, S. B. H. (1999) Chemical protein synthesis by solid-phase ligation of unprotected peptide segments. *J. Am. Chem. Soc. 121*, 8720−8727.
(53) Katajisto, J., Virta, P., and Loennberg, H. (2004) Solid-phase synthesis of multiantennary oligonucleotide glycoconjugates utilizing on-support oximation. *Bioconjugate Chem. 15*, 890−896.
(54) Neuner, P., Gallo, P., Orsatti, L., Fontana, L., and Monaci, P. (2003) An efficient and versatile synthesis of bis PNA-peptide conjugates based on chemoselective oxime formation. *Bioconjugate Chem. 14*, 276−281.
(55) Rodriguez, E. C., Winans, K. A., King, D. S., and Bertozzi. C. R. (1997) A strategy for chemoselective synthesis of *O*-linked glycopeptides with native sugar-peptide linkages. *J. Am. Chem. Soc. 119*, 9905−9906.
(56) Cervigni, S. E., Dumy, P., and Mutter, M. (1996) Synthesis of glycopeptides and lipopeptides by chemoselective ligation. *Angew. Chem., Int. Ed. Engl. 35*, 1230−1232.
(57) Forget D., Boturyn, D., Defrancq, E., Lhomme, J. and Dumy, P. (2001) Highly efficient synthesis of peptide−oligonucleotide conjugates: chemoselective oxime and thiazolidine formation. *Chem. Eur. J. 7*, 3976−3984.
(58) Chen, J., Zeng, W., Offord, R., and Rose, K. (2003) A novel method for the rational construction of well-defined immunogens: the use of oximation to conjugate Cholera Toxin B subunit to a peptide-polyoxime complex. *Bioconjugate Chem. 14*, 614−618.
(59) Cremer, G.-A., Bureaud, N., Lelievre, D., Piller, V., Piller, F., and Delmas, A. (2004) Synthesis of branched oxime-linked peptide mimetics of the MUC1 containing a universal T-helper. *Chem. Eur. J. 10*, 6353−6360.
(60) Nardin, E. H., Calvo-Calle, J. M., Oliveira, G. A., Clavijo, P., Nussenzweig, R., Simon, R., Zeng, W., and Rose, K. (1998) *Plasmodium falciparum* polyoximes: highly immunogenic synthetic vaccines constructed by chemoselective ligation of repeat B-cell epitopes and a universal T-cell epitope of CS protein. *Vaccine 16*, 590−600.
(61) Zeng, W., Jackson, D. C., Murray, J., Rose, K., and Brown, L. E. (2000) Totally synthetic lipid-containing polyoxime peptide constructs are potent immunogens. *Vaccine 18*, 1031−1039.

(62) Rose K., Zeng W., Brown, L. E., and Jackson, D. C. (1995) A synthetic peptide-based polyoxime vaccine construct of high purity and activity. *Mol. Immunol. 32*, 1031−1037.
(63) Zeng, W., Ghosh, S., Macris, M., Pagnon, J., and Jackson, D. C. (2001) Assembly of synthetic peptide vaccines by chemoselective ligation of epitopes: influence of different chemical linkages and epitope orientations on biological activity. *Vaccine 19*, 3843−3852.
(64) Cipolla, L., Rescigno, M., Leone, A., La Ferla, B., and Nicotra, F. (2002) Novel Tn antigen-containing neoglycolipides: synthesis and evaluation as anti-tumor vaccines. *Biorg. Med. Chem. 10*, 1639−1646.
(65) Vichier-Guerre, S., Lo-Man, R., Huteau, V., Dériaud, E., Leclerc, C., and Bay, S. (2004) Synthesis and immunological evaluation of an antitumor neoglycopeptide vaccine bearing a novel homoserine Tn antigen. *Biorg. Med. Chem. Lett. 14*, 3567−3570.
(66) Keding, S. J., Endo, A., and Danishefsky, S. J. (2003) Synthesis of non-natural glycosylamino acids containing tumor-associated carbohydrate antigens. *Tetrahedron 59*, 7023−7031.
(67) Ragupathi, G., Coltart, D. M., Williams, L. J., Koide, F., Kagan, E., Allen, J., Harris, C., Glunz, P. W., Livongston, P. O., and Danishefsky, S. J. (2002) On the power of chemical synthesis: immunological evaluation of models for multiantigenic carbohydrate-based cancer vaccines. *Proc. Natl. Acad. Sci. U.S.A. 99*, 13699−13704.
(68) Renaudet, O., and Dumy, P. (2001) Expedient synthesis of aminooxylated-carbohydrates for chemoselective access of glycoconjugates. *Tetrahedron Lett. 42*, 7575−7578.
(69) Posner, G. J., and Haines, S. R. (1985) A convenient, one-step, high-yield replacement of an anomeric hydroxyl group by a fluorine atom using DAST. Preparation of glycosyl fluorides. *Tetrahedron Lett. 26*, 5−8.
(70) Cao, S., Tropper, F. D., and Roy, R. (1995)Stereoselective phase transfer catalysed syntheses of glycosyloxysuccinimides and their transformations into glycoprobes. *Tetrahedron 51*, 6679−6686.
(71) Ide, H., Akamatsu, K., Kimura, Y., Michiue, K., Makino, K., Asaeda, A., Takamori, Y., and Kubo, K. (1993) Synthesis and damage specificity of a novel probe for the detection of abasic sites in DNA. *Biochemistry 32*, 8276−8283.
(72) Thieriet, N., Alsina, J., Giralt, E., Guibé, F., and Albericio, F. (1997) Use of Alloc-amino acids in solid-phase peptide synthesis. Tandem deprotection-coupling reactions using neutral conditions. *Tetrahedron Lett. 38*, 7275−7278.

BC050010V

Preparation of Efficient Gene Carriers Using a Polyamidoamine Dendron-Bearing Lipid: Improvement of Serum Resistance

Toshinari Takahashi,[†] Atsushi Harada,[†] Nobuhiko Emi,[‡] and Kenji Kono*,[†]

Department of Applied Chemistry, Graduate School of Engineering, Osaka Prefecture University, 1-1 Gakuen-cho, Sakai, Osaka 599-8531, Japan, and Department of Hematology, Nagoya University Graduate School of Medicine, Nagoya, Aichi 466−8550, Aichi, Japan. Received January 20, 2005; Revised Manuscript Received July 4, 2005

In a previous study, we developed a novel cationic lipid consisting of polyamidoamine dendron of third generation and two dodecyl chains, designated as DL-G3, which in combination with a fusogenic lipid dioleoylphosphatidylethanolamine (DOPE) achieves efficient transfection of CV1 cells by synergetic action of the proton sponge effect and membrane fusion. This study examines the effect of serum on the transfection activity of the DL-G3−DOPE−plasmid DNA lipoplexes. The transfection activity of a lipoplex with a composition optimized in the absence of serum decreased markedly in the presence of serum. However, the lipoplexes that induce efficient transfection in the presence of serum were obtainable by controlling the charge ratio of the primary amine of the DL-G3 to the phosphate group (N/P ratio) and DOPE content. The complex, which exhibited the highest transfection activity in the presence of serum, has a lower N/P ratio and higher DOPE content than that optimized in the absence of serum. Whereas disintegration of these complexes was induced by addition of heparin, which is a polysaccharide with negatively charged groups, the complex that retained transfection activity in the presence of serum required more negative charges of heparin for complex disintegration. That result implies its higher stability against negatively charged serum proteins. Comparison of the serum-resistant complex with some commercially available transfection reagents, such as Lipofectamine and SuperFect, indicates that the DL-G3 complex achieved more efficient transfection of these cells in the presence of serum.

INTRODUCTION

Development of nonviral systems that introduce therapeutic genes efficiently into a target cell has been highly desired for the establishment of gene therapy. Synthetic systems based on lipids or polymers with positive charges have been studied actively for this purpose, but their activity still requires improvement. These systems can form complexes with plasmid DNA, which are termed lipoplexes (lipid-based complexes) and polyplexes (polymer-based complexes) through electrostatic interactions (*1*, *2*). These complexes can interact strongly with cells through electrostatic interactions. They are taken up by the cells through the endocytic pathway. Avoidance of plasmid DNA degradation in the lysosome and its transfer into cytosol are considered to be a key process for efficient transfection. Cationic lipid-based systems are considered to promote this process by fusing with and destabilizing the endosomal membrane with the help of fusogenic lipids such as dioleoylphosphatidylethanolamine (DOPE). Some synthetic cationic polymers such as poly(ethylenimine) (*3*, *4*) and polyamidoamine dendrimers (*5*) also induce efficient transfection of cells by enhancing the transfer of plasmid DNA into cytosol through the so-called proton sponge effect (*6*).

In a previous study (*7*), we developed a novel type of cationic lipids that consist of two dodecyl groups and a polyamidoamine dendron as a headgroup because these dendron-bearing lipids can form lipoplexes with DOPE and plasmid DNA, which achieve efficient transfection of cells by the synergetic action of membrane fusion and the proton sponge effect. In fact, in combination with DOPE, the lipid with the third generation dendron, DL-G3 (Figure 1), achieved more efficient transfection of CV1 cells, a green monkey kidney cell line, than widely used nonviral vectors.

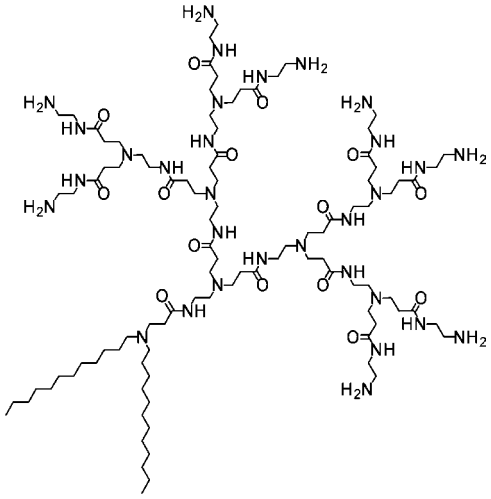

Figure 1. Structure of DL-G3.

A major problem for the cationic lipid/polymer-based gene carriers is their sensitivity to serum proteins: their transfection activity is lowered dramatically in the presence of serum proteins (*8*−*14*). Their complexes with plasmid DNA interact with serum components and cause

* Corresponding author. E-mail: kono@chem.osakafu-u.ac.jp. Tel: +81-722549330. Fax: +81-722549913.
[†] Osaka Prefecture University.
[‡] Nagoya University Graduate School of Medicine.

10.1021/bc050012f CCC: $30.25 © 2005 American Chemical Society
Published on Web 08/27/2005

their disintegration, resulting in plasmid DNA release and its degradation (*12*−*15*). Therefore, optimal transfection with these systems must be performed in the absence of serum. Such a serum-sensitive property of the cationic lipid/polymer-based gene carriers apparently restricts their in vivo application and reduces their usefulness as a vector for gene therapy.

To overcome the inhibitory effect of serum on transfection mediated by these gene carriers, many efforts have been made by various approaches. Among them are enhancement of cellular uptake of the complexes through endocytosis by increasing positive charges of the complexes (*12*, *16*) or by attaching target cell specific ligands to the complexes (*17*, *18*), and promotion of transfer of endocytosed genes into cytosol by conjugation of membrane disruptive molecules with the complexes (*17*, *19*, *20*, *21*).

In a previous study, we examined transfection activity of the lipoplexes containing dendron-bearing lipids in the absence of serum. However, considering the strong ability of these dendron-bearing lipid-based lipoplexes to enhance transfer of the gene into cytosol and controllability of their charge density by changing their composition, it is expected that these lipoplexes could achieve efficient transfection in the presence of serum proteins. Therefore, this study is particularly intended to produce lipoplexes that can achieve efficient transfection using DL-G3 and DOPE. Their lipoplex with an optimized composition was found to possess a much higher activity than some commercially available transfection reagents, such as Lipofectamine and SuperFect. We describe the importance of both the ratio of the primary amines of the DL-G3 to the phosphate groups of plasmid DNA and the content of DOPE of lipoplexes for the production of lipoplexes with serum resistance.

EXPERIMENTAL PROCEDURES

General Methods. DOPE was kindly donated by Nippon Oil and Fats Co. (Tokyo, Japan). Fetal calf serum (FCS) was obtained from JRH Biosciences (Tokyo, Japan). Dulbecco's modified Eagle's medium (DMEM) was from Nissui Pharmaceutical (Tokyo, Japan). Tris(hydroxymethyl)aminomethane (Tris) was obtained from Kishida Chemical (Osaka, Japan). Heparin sodium salt was purchased from Sigma (St. Louis, MO). Agarose was purchased from nacalai tesque (Kyoto, Japan). Ethidium bromide was purchased from Wako Pure Chemical Industries (Osaka, Japan). Lipofectamine and SuperFect were purchased from Invitrogen (Carlsbad, CA) and Qiagen (Hilden, Germany), respectively. DL-G3 was synthesized by the procedure previously described (*7*).

Preparation of Lipoplexes. To a dry thin membrane of a mixture of the DL-G3 and a given amount of DOPE was added phosphate-buffered saline (PBS), and the mixture was sonicated for 2 min using a bath-type sonicator to afford a lipid suspension. Plasmid DNA p10, which contains a firefly luciferase coding sequence derived from pGL3-basic (Promega, Madison, WI) between Rous sarcoma virus LTR and polyadenylation signal, (1 μg), was dissolved in 20 mM Tris-HCl buffer (pH 7.4, 50 μL), was mixed with the lipid suspension (50 μL), and incubated for 30 min at room temperature to afford a lipoplex with a given ratio of primary amino group of DL-G3 to DNA phosphate (N/P ratios).

Transfection. Transfection of CV1 cells was done according to the following procedures unless otherwise noted in the text. The cells were seeded in 0.5 mL of DMEM supplemented with 10% FCS in 24-well culture plates at 5.0×10^4 cells per well the day before transfection. The cells were washed with PBS containing 0.36 mM $CaCl_2$ and 0.42 mM $MgCl_2$ [PBS(+)] and then covered with DMEM supplemented with a given amount of FCS (1 mL). The lipoplex-containing plasmid DNA (1 μg) was added gently to the cells and incubated at 37 °C for 4 h. Then, the cells were rinsed with PBS(+), covered with DMEM containing 10% FCS, and incubated at 37 °C. After 40 h, the cells were lysed by adding 50 μL of Luc-PGC-50 detergent (Toyo Ink, Tokyo, Japan). A 20 μL aliquot from each dish was used for one luciferase assay using a kit (Toyo Ink) and a Lumat LB9507 luminometer (Berthold, Bad Wildbad, Germany). The protein content of the lysate was measured by Coomassie Protein Assay Reagent (Pierce, IL) using bovine serum albumin as the standard. Transfection by Lipofectamine and SuperFect was performed according to their protocols recommended by the manufacturers. Transfection of HepG2 cells was performed according to the above procedure except that the cells were seeded 2 days before the transfection.

Interaction of the Lipoplexes with Heparin. The DL-G3−DOPE lipoplexes with varying N/P ratios and DOPE contents were prepared by mixing plasmid DNA (1 μg) dissolved in 20 mM Tris-HCl buffer (2.5 μl) and lipid suspension (2.5 μL). After 30 min-incubation at room temperature, the DL-G3−DOPE lipoplexes were added to a given amount (0−2 μg) of heparin dissolved in PBS (5 μL) and incubated for 30 min at room temperature. The samples (10 μL) were electrophoresed on 0.6 wt % agarose gel in 40 mM Tris, 20 mM sodium acetate, and 2 mM EDTA buffer (pH 8.0) containing 1 μg/mL ethidium bromide at 100 V for 30 min. The ethidium bromide-stained bands were visualized using a LAS-1000UVmini (FUJIFILM, Japan) and analyzed with Science Lab 2003 Multi Gauge software (FUJIFILM, Japan).

RESULTS AND DISCUSSION

Effects of Lipoplex Composition on Transfection Activity in the Presence of Serum. Our previous study developed cationic lipids that comprise two dodecyl groups and polyamidoamine dendron of varying generations because we expected that these lipids can form lipoplexes, which achieve an efficient transfection of cells through the synergy of membrane fusion and the proton sponge effect, with DOPE (*7*). When mixed with DOPE, one dendron-bearing lipid, DL-G3, induced transfection of CV1 cells more efficiently than a widely used lipoplex consisting of DC-chol and DOPE in a medium without serum.

We have already established the composition of a lipoplex composed of DL-G3, DOPE, and plasmid DNA with high transfection activity. Specifically, we described lipoplexes with an N/P ratio of 5 and DL-G3/DOPE ratio of 1/5 (*7*). Thereby, we first examined the effect of serum concentration on transfection activity of DL-G3−DOPE lipoplexes with that composition. Figure 2 depicts luciferase activity of CV 1 cells treated with the lipoplex in a medium with varying serum contents. As Figure 2 shows, the presence of even 10% of serum abolished the transfection activity of the DL-G3−DOPE lipoplex. Many studies have revealed that the transfection activity of lipoplexes is reduced dramatically in the presence of serum by interaction between lipoplexes and serum proteins (*12*−*15*). This result indicates that the DL-G3−DOPE lipoplex with this composition is as highly serum-sensitive as other types of cationic lipid-based vectors.

As mentioned previously, the optimum composition of the DL-G3−DOPE lipoplex was established under condi-

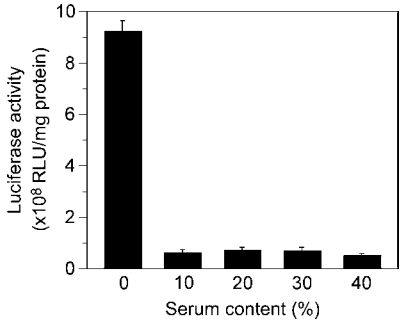

Figure 2. Effect of serum on transfection of CV1 cells mediated by the DL-G3−DOPE lipoplex with N/P ratio of 5 and DOPE/DL-G3 ratio of 5. The cells (5×10^4) were treated with the lipoplexes containing 1 μg of DNA in the medium with varying contents of FCS. Each bar represents the mean ± SD ($n = 3$).

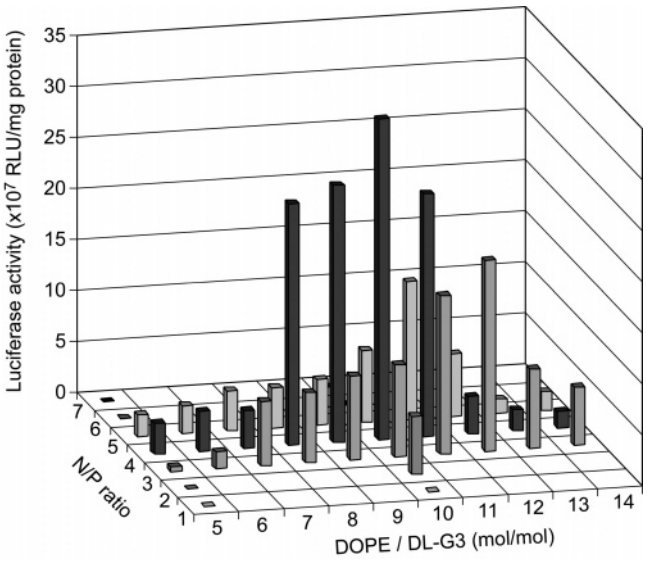

Figure 3. Influences of N/P and DOPE/DL-G3 ratios of lipoplexes on their transfection activity. The cells (5×10^4) were treated with the lipoplexes containing 1μg DNA in the presence of 9.1% FCS. Each bar represents the mean ($n = 4$).

tions without serum. Therefore, the optimum composition of the lipoplex for transfection in the presence of serum might differ from the composition optimized in the absence of serum. For that reason, we next attempted the optimization of the composition of the DL-G3−DOPE lipoplex in the presence of serum (Figure 3).

Inclusion of DOPE in the lipoplex is important because this lipid provides fusion ability to the lipoplex (*22*, *23*). We prepared dispersions of mixtures of DL-G3 and DOPE with varying molar ratios and incubated them with plasmid DNA to obtain lipoplexes with varying DOPE contents at varying N/P ratios. Expression of luciferase in the CV 1 cells treated with these lipoplexes is shown in Figure 3. As that figure shows, the cellular expression of luciferase is dependent on the lipoplex's DOPE content. For example, when the lipoplexes with an N/P ratio of 4 were used, the cellular luciferase activity increased 10-fold as the DOPE content of the lipoplex increased from 5 to 10. However, higher DOPE content of the lipoplexes eliminated their activity. Because DOPE is an electronically neutral lipid, the charge density of the lipoplexes decreases with increasing DOPE content, thereby reducing their affinity to the cellular surface. A similar tendency was shown by lipoplexes with N/P ratios of 3 and 5, but their maximum activities were apparent at DOPE/DL-G3 ratios of 12 and 11 for lipoplexes with the N/P ratios of 3 and 5, respectively. These results indicate that inclusion of DOPE is crucial to obtain potent lipoplexes for use in the presence of serum.

On the other hand, the N/P ratio is another important factor which affects lipoplex activity. As Figure 3 shows, transfection activity of the DL-G3−DOPE lipoplexes changed remarkably depending on the N/P ratio. For lipoplexes with the DOPE/DL-G3 ratio of 10, the activity increases concomitant with an increasing N/P ratio and becomes greatest at the ratio of 4. The transfection activity of the DL-G3−DOPE lipoplexes was affected markedly by both the DOPE/DL-G3 and N/P ratios. However, Figure 3 illustrates that a lipoplex with a DOPE/DL-G3 ratio of 10 and the N/P ratio of 4 exhibited the highest activity in the presence of serum.

As mentioned previously, the lipoplex optimized in the absence of serum has an N/P ratio of 5 and a DOPE/DL-G3 ratio of 5. Compared with this, the lipoplex optimized in the presence of serum has a slightly lower N/P ratio and a two-times-higher DOPE/DL-G3 ratio. Both the lower N/P ratio and the higher DOPE content mean that the lipoplex obtained in this study has a lower charge density than the lipoplex optimized in the absence of serum. The electrostatic force is likely to play an important role in interaction of the lipoplex with serum proteins. Therefore, the lower charge density of the lipoplex may contribute to its weaker interaction with serum proteins and prevent the loss of transfection activity induced by interaction with serum proteins. Indeed, the interaction of the lipoplex with the cellular membrane is based on their electrostatic interaction. For that reason, the low charge density of the lipoplex may also cause a weak interaction with the cell that could result in a lower transfection activity. However, the higher DOPE content of the lipoplex might increase fusion ability of the lipoplex, which could compensate the reduced affinity. As a result, the lipoplex obtained in this study exhibited the high transfection activity.

Figure 4 illustrates the influence of serum concentration on transfection activity of the DL-G3−DOPE lipoplexes optimized in the presence of serum and absence of serum. When serum was absent, both lipoplexes exhibited similar and high transfection activities (Figure 4A), though the activity of the lipoplex optimized in the presence of serum was somewhat higher than that of the lipoplex optimized in the absence of serum. This may be due to the difference of the procedures for optimization of these lipoplexes (*7*). When the serum was present, both lipoplexes reduced the transfection activity. However, the extent of reduction of that activity differed between these lipoplexes. As Figure 4B shows, the lipoplex optimized in the absence of serum retained only 7% of the original activity when 10−40% of serum was contained in the medium of transfection. In contrast, the lipoplex prepared in this study exhibited 20−30% of the original activity under the same conditions. Consequently, we infer that the DL-G3−DOPE lipoplex with the low N/P ratio and the high DOPE content are more resistant to serum.

Interaction of Lipoplexes with Heparin. As mentioned above, the serum-resistance of DL-G3−DOPE lipoplexes was affected significantly by the N/P ratio and the DOPE content. Transfection activity of the lipoplex with the N/P ratio of 5 and the DOPE/DL-G3 ratio of 5 was diminished strongly by serum, whereas the lipoplex with a slightly lower N/P ratio and a higher DOPE content can retain its activity in the presence of serum.

Inactivation of the DL-G3−DOPE lipoplex in the presence of serum is considered to be induced mainly by electrostatic interaction between the lipoplexes with negatively charged serum proteins. In fact, disintegration

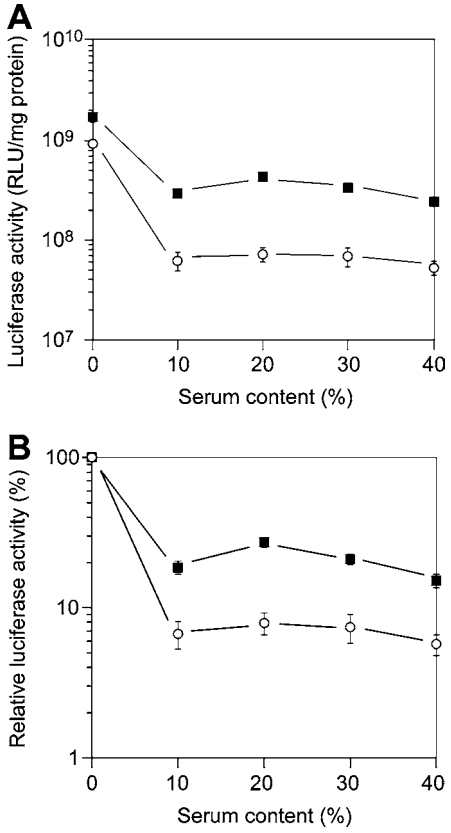

Figure 4. Serum-induced reduction of transfection activity for DL-G3−DOPE lipoplex with N/P ratio of 5 and DOPE/DL-G3 ratio of 5 (○) and DL-G3−DOPE lipoplex with N/P ratio of 4 and DOPE/DL-G3 ratio of 10 (■). Cellular luciferase activity (A) and percentage of cellular luciferase activity in the absence of serum (B) were shown as a function of serum content of the transfection medium. The cells (5×10^4) were treated with DL-G3−DOPE lipoplexes containing 1μg DNA. Each point represents the mean ± SD ($n = 3$).

of lipoplexes associated with the release of plasmid DNA has often been observed in the presence of serum because the plasmid DNA bound to the cationic lipid molecules is replaced by the negatively charged serum proteins (*12*−*15*).

Some polyanions, such as heparin and dextran sulfate, are also known to dissociate DNA from lipoplexes (*24*, *25*). They have been used to estimate the stability of the lipoplexes. Therefore, we examined the effect of addition of heparin on dissociation of plasmid DNA from the DL-G3−DOPE lipoplexes to evaluate their stability using agarose gel retardation assay (Figure 5). In this experiment, lipoplexes with varying N/P ratios and DOPE/DL-G3 ratios were incubated with varying amounts of heparin for 30 min, then electrophoresed on an agarose gel. As Figs. 5A−C show, a band corresponding to free plasmid DNA appeared as the amount of heparin added to the lipoplexes was increased, indicating that these lipoplexes were disintegrated by interaction with heparin.

Liberation of plasmid DNA was caused mainly by their electrostatic interaction. Therefore, we investigated the correlation between the amount of released plasmid DNA and the charge balance of the mixture of the lipoplex and heparin. Heparin is known to be a highly sulfated glycosaminoglycan consisting of (1 → 4)-*O*-(α-L-idopyranosyluronic acid 2-sulfate)−(1→ 4)-(2-deoxyl-2-sulfamino-α-D-glucopyranosyl 6-sulfate) as a major repeating unit (*26*, *27*). Thus, we calculated the amount of negative charge of heparin by assuming the structure of heparin as repeats of this disaccharide unit. Figure 5D depicts

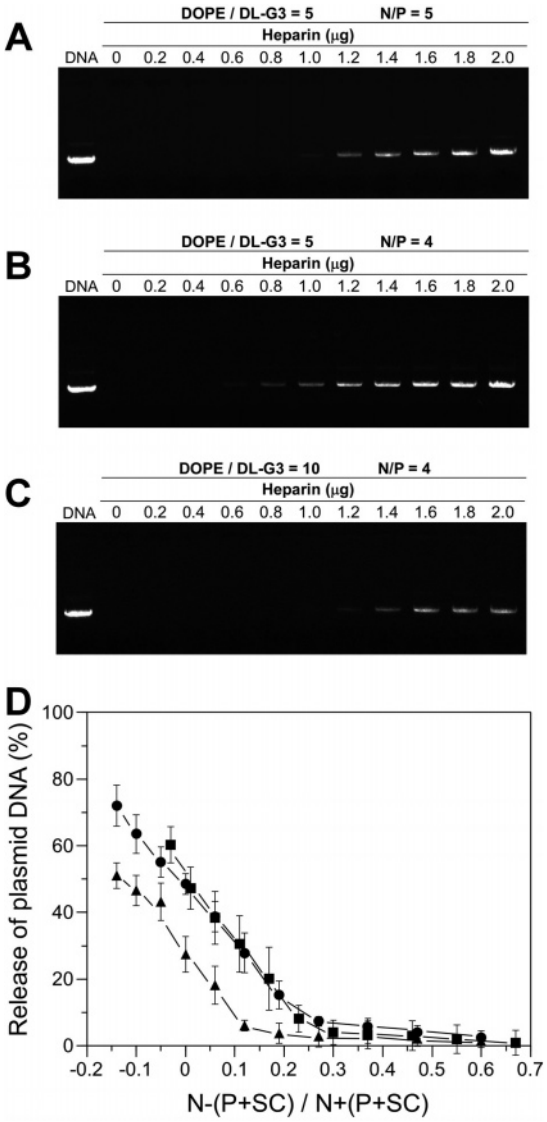

Figure 5. Agarose gel electrophoresis of DL-G3−DOPE lipoplexes with N/P ratio of 5 and DOPE/DL-G3 ratio of 5 (A), with N/P ratio of 4 and DOPE/DL-G3 ratio of 5 (B) and with N/P ratio of 4 and DOPE/DL-G3 ratio of 10 (C) in the presence of varying amounts of heparin. (D) Percent release of plasmid DNA from DL-G3−DOPE lipoplexes with varying compositions as a function of difference between negative and positive charges of lipoplexes normalized by their total charge: ■, lipoplex with N/P ratio of 5 and DOPE/DL-G3 ratio of 5; ●, lipoplex with N/P ratio of 4 and DOPE/DL-G3 ratio of 5; ▲, lipoplex with N/P ratio of 4 and DOPE/DL-G3 ratio of 10. Each point represents the mean ± SD ($n = 3$). N, P, and SC represent amounts of charge of the primary amine of the DL-G3, phosphate group of DNA, and total of sulfonate and carboxyl groups of heparin, respectively.

the percentage of released plasmid DNA as a function of the difference between positive and negative charges of the lipoplex−heparin mixture normalized by its total amount of charge. Figure 5D shows the curve for a lipoplex with an N/P ratio of 5 and with a DOPE/DL-G3 ratio of 5 (■). It also depicts the curve for a lipoplex with an N/P ratio of 4 and a DOPE/DL-G3 ratio of 5 (●). They are approximately identical. This result indicates that the liberation of plasmid DNA from these lipoplexes is controlled simply by their charge balance when the DOPE content of the lipoplexes was the same. However, comparison between the lipoplex with the N/P ratio of 4 and the DOPE/DL-G3 ratio of 5 and the lipoplex with the same N/P ratio and with the DOPE/DL-G3 ratio of

10 (▲) indicates that the latter requires more negative charge than the former for liberation of plasmid DNA, suggesting that inclusion of DOPE contributes to lipoplex stability. Probably, DOPE molecules inserted in the complex could stabilize the electrostatic binding between DNA and the DL-G3 by hydrophobic interaction and cover the DNA efficiently, isolating it from the outer environment and suppressing interaction with negatively charged molecules. Therefore, it is likely that the high content of DOPE in the lipoplex with the N/P ratio of 4 and the DOPE/DL-G3 ratio of 10 can enhance stability of the lipoplex and provide a high serum-resistant property to the lipoplex.

In addition, particle size of the complexes can be another factor that affects interaction of the lipoplexes with serum protein and their serum-sensitivity. Thus, we measured size of the lipoplexes by DLS. The sizes of serum-resistant and serum-sensitive lipoplexes were shown to be 767 ± 183 nm and 616 ± 193 nm, respectively. The slightly smaller size of the latter may enhance its serum sensitivity to some extent, because it would interact more actively with serum proteins due to their larger surface area.

To know whether the optimized DL-G3-based lipoplex can be used for another type of cells, we further examined transfection of HepG2 cells, which are frequently used for the evaluation of transfection activity for various types of gene vectors. We found that the cells after treatment with this lipoplex in the absence and in the presence of serum exhibited the luciferase activity of 3.2 ± 0.4 × 10^8 RLU/mg protein and 2.2 ± 0.4 × 10^8 RLU/mg protein ($n = 6$), respectively. Since CV1 cells treated with this lipoplex in the absence and in the presence of serum showed luciferase activity of about 20 × 10^8 RLU/mg protein and about 3.5 × 10^8 RLU/mg protein, respectively (Figure 4A), this lipoplex seems to be somewhat less effective for HepG2 than CV1 cells. However, the cellular luciferase activity induced by the treatment in the presence of serum was 70% of the luciferase activity induced by the treatment in the absence of serum. This result indicates that this optimized lipoplex could be useful for the transfection of various types of cells in the presence of serum.

Comparison with Various Vectors. To estimate the potential of the DL-G3−DOPE lipoplex as a gene vector, we compared its transfection activity with those of Lipofectamine and SuperFect: both are widely used and commercially available vectors. CV1 cells were treated with the DL-G3−DOPE lipoplexes, the Lipofectamine-plasmid DNA complex, and the SuperFect-plasmid DNA complex in the absence of serum or in the presence of 10% FCS. Figure 6 represents the expression of luciferase in the cells treated with these lipoplexes or complexes. In the absence of serum, DL-G3−DOPE lipoplex induced roughly a two-times-higher level and a six-times-higher level of luciferase expression than Lipofectamine complex and SuperFect complex, respectively. As expected, a decrease in transfection efficiency was shown for all vectors in the presence of serum. Especially, the influence of serum was significant for the Lipofectamine complex. In this case, luciferase expression was reduced to 1/180th of that in the absence of serum. A remarkable decrease in transfection efficiency induced by serum was again evident in transfection with the SuperFect complex, in which the cellular luciferase expression was reduced to 1/50th of that in the absence of serum. A 1/6th-fold reduction was apparent in the case of the DL-G3−DOPE lipoplex-mediated transfection in the presence of serum. However, this lipoplex displayed a reduction with much less extent of magnitude than other complexes. As a result, this lipoplex achieved 48−64-times higher expression of the introduced gene in CV1 cells than these widely used vectors under experimental conditions, suggesting its usefulness as a vector for use in the presence of serum.

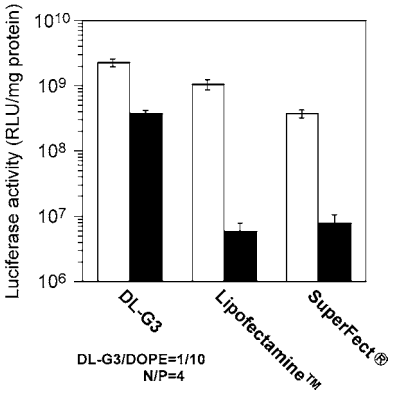

Figure 6. Comparison of transfection activity of DL-G3−DOPE lipoplex with Lipofectamine and SuperFect reagents. The cells (5×10^4) were treated with vectors containing 1μg DNA in the absence (open bars) and presence of 10% FCS (closed bars). The DL-G3−DOPE lipoplex with N/P ratio of 4 and DOPE/DL-G3 ratio of 10 was used. Each bar represents the mean ± SD ($n = 3$).

CONCLUSION

This work was intended to prepare an efficient vector that can achieve gene transfection of cells in the presence of serum using polyamidoamine dendron-bearing lipid DL-G3 and fusogenic lipid DOPE, by the synergetic action of membrane fusion and the proton sponge effect. Results show that transfection activity of the DL-G3−DOPE lipoplexes was highly dependent on their composition, such as the N/P and DOPE/DL-G3 ratios. However, by adjusting the N/P and DOPE/DL-G3 ratios to 4 and 10, respectively, we obtained a lipoplex that exhibited high transfection activity in the presence and absence of serum. Although the obtained lipoplex showed some extent of reduction of transfection activity in the presence of serum, the lipoplex retained much higher activity than some widely used and commercially available transfection reagents. These results strongly suggest that the DL-G3−DOPE lipoplex is a promising nonviral vector for gene therapy.

ACKNOWLEDGMENT

This work was partly supported by the Grant-in-Aid from Japanese Ministry of Education, Culture, Sports, Science, and Technology (16300159). T. Takahashi thanks the Research Fellowships of the Japan Society for the Promotion of Science for Young Scientists.

LITERATURE CITED

(1) Brown, M. D., Schätzlein, A. G., and Uchegbu, I. F. (2001) Gene delivery with synthetic (non viral) carriers. *Int. J. Pharm. 229*, 1−21.
(2) Behr, J. P. (1993) Synthetic gene-transfer vectors. *Acc. Chem. Res. 26*, 274−278.
(3) Zou, S. M., Behr, J. P., Goula, D., and Demeneix, B. (2000) Gene delivery with polyethylenimine. *Gene Therapy: Therapeutic mechanisms and strategies* (Templeton, N. S., Lasic, D. D., Eds.) pp 131−139, Marcel Dekker, New York.
(4) Godbey, W. T., Wu, K. K., and Mikos, A. G. (1999) Poly(ethylenimine) and its role in gene delivery. *J. Controlled Release 60*, 149−160.
(5) Kubasiak, L. A., and Tomalia, D. A. (2004) Cationic dendrimers as gene transfection vectors: dendri- poly(amidoam-

ines) and dendri- poly(propyleneimines). *Polymeric Gene Delivery: Principles and Applications* (Amiji, M. M., Ed.) pp 133−157, Chapter 9, CRC Press, Boca Raton.
(6) Boussif, O., Lezoualc′h, F., Zanta, M. A., Mergny, M. D., Scherman, D., Demeneix, B., and Behr, J. P. (1995) A versatile vector for gene and oligonucleotide transfer into cells in culture and in vivo: Polyethylenimine. *Proc. Natl. Acad. Sci. U.S.A. 92*, 7297−7301.
(7) Takahashi, T., Kono, K., Itoh, T., Emi, N., and Takagishi, T. (2003) Synthesis of novel cationic lipids having polyamidoamine dendrons and their transfection activity. *Bioconjugate Chem. 14*, 764−773.
(8) Farhood, H., Bottega, R., Epand, R. M., and Huang, L. (1992) Effect of cationic cholesterol derivatives on gene-transfer and protein-kinase-C activity. *Biochim. Biophys. Acta 1111*, 239−246.
(9) Wilke, M., Bijma, A., Timmers-Reker, A. J., Scholte, B. J., and Sinaasapp, A. (1997) Complementation of the genetic defect in Gunn rat hepatocytes in vitro by highly efficient gene transfer with cationic liposomes. *Gene Ther. 4*, 1305−1312.
(10) Escriou, V., Ciolina, C., Lacroix, F., Byk, G., Scherman, D., and Wils, P. (1998) Cationic lipid-mediated gene transfer: effect of serum on cellular uptake and intracellular fate of lipopolyamine/DNA complexes. *Biochim. Biophys. Acta 1368*, 276−288.
(11) Turek, J., Dubertret, C., Jaslin, G., Antonakis, K., Scherman, D., and Pitard, B. (2000) Formulations which increase the size of lipoplexes prevent serum-associated inhibition of transfection. *J. Gene Med. 2*, 32−40.
(12) Yang, J. P., and Huang, L. (1997) Overcoming the inhibitory effect of serum on lipofection by increasing the charge ratio of cationic liposome to DNA. *Gene Ther. 4*, 950−960.
(13) Yang, J. P., and Huang, L. (1998) Time-dependent maturation of cationic liposome-DNA complex for serum resistance. *Gene Ther. 5*, 380−387.
(14) Li, S., Tseng, W. C., Stolz, D. B., Wu, S. P., Watkins, S. C., and Huang, L. (1999) Dynamic changes in the characteristics of cationic lipidic vectors after exposure to mouse serum: implications for intravenous lipofection. *Gene Ther. 6*, 585−594.
(15) Crook, K., Stevenson, B. J., Dubouchet, M., and Porteous, D. J. (1998) Inclusion of cholesterol in DOTAP transfection complexes increases the delivery of DNA to cells in vitro in the presence of serum. *Gene. Ther. 5*, 137−143.
(16) Tranchant, I., Thompson, B., Nicolazzi, C., Mignet, N., and Scherman, D. (2004) Physicochemical optimisation of plasmid delivery by cationic lipids. *J. Gene Med. 6*, S24−S35.
(17) Kono, K., Torikoshi, Y., Mitsutomi, M., Itoh, T., Emi, N., Yanagie, H., and Takagishi, T. (2001) Novel gene delivery systems: complexes of fusogenic polymer-modified liposomes and lipoplexes. *Gene. Ther. 8*, 5−12.
(18) Kursa, M., Walker, G. F., Roessler, V., Ogris, M., Roedl, W., Kircheis, R., and Wagner, E. (2003) Novel shielded transferrin-polyethylene glycol-polyethylenimine/DNA complexes for systemic tumor-targeted gene transfer. *Bioconjugate Chem. 14*, 222−231.
(19) Kyriakides, T. R., Cheung, C. Y., Murthy, N., Bornstein, P., Stayton, P. S., and Hoffman, A. S. (2002) pH-Sensitive polymers that enhance intracellular drug delivery in vivo. *J. Controlled Release 78*, 295−303.
(20) Kichler, A., Mechtler, K., Behr, J. P., and Wagner, E. (1997) Influence of membrane-active peptides on lipospermine/DNA complex mediated gene transfer. *Bioconjugate Chem. 8*, 213−221.
(21) Finsinger, D., Remy, J. S., Erbacher, P., Koch, C., and Plank, C. (2000) Protective copolymers for nonviral gene vectors: synthesis, vector characterization and application in gene delivery. *Gene Ther. 7*, 1183−1192.
(22) Farhood, H., Serbina, N., and Huang, L. (1995) The role of dioleoyl phosphatidylethanolamine in cationic liposome mediated gene transfer. *Biochim. Biophys. Acta 1235*, 289−295.
(23) Hui, S. W., Langner, M., Zhao, Y. L., Ross, P., Hurley, E., and Chan, K. (1996) The role of helper lipids in cationic liposome-mediated gene transfer. *Biophys. J. 71*, 590−599.
(24) Zelphati, O., and Szoka, F. C. (1996) Mechanism of oligonucleotide release from cationic liposomes. *Proc. Natl. Acad. Sci. U.S.A. 93*, 11493−11498.
(25) Moret, I., Peris, J. E., Guillem, V. M., Benet, M., Revert, F., Dasi, F., Crespo, A., and Alino, S. F. (2001) Stability of PEI-DNA and DOTAP-DNA complexes: effect of alkaline pH, heparin and serum. *J. Controlled Release 76*, 169−181.
(26) Casu, B. (1985) Structure and biological activity of heparin. *Adv. Carbohydr. Chem. Biochem. 43*, 51−134.
(27) Rabenstein, D. L. (2002) Heparin and heparan sulfate: structure and function. *Nat. Prod. Rep. 19*, 312−331.

BC050012F

Synthesis and Photodynamic Activity of Novel Asymmetrically Substituted Fluorinated Phthalocyanines

Wesley M. Sharman and Johan E. van Lier*

Department of Nuclear Medicine and Radiobiology, Faculty of Medicine, Université de Sherbrooke, Sherbrooke, Québec, Canada J1H 5N4. Received January 31, 2005; Revised Manuscript Received June 9, 2005

A series of asymmetrically substituted dodecafluorinated phthalocyanines has been synthesized via the Kobayashi ring expansion reaction of the corresponding dodecafluorinated boron subphthalocyanine with differently substituted 1,3-diiminoisoindolines. The mild reaction conditions employed during this ring expansion reaction gave rise exclusively to 3:1 asymmetrically substituted dodecafluorinated phthalocyanines. Metal insertion into the metal-free phthalocyanines was accomplished by heating at 40 °C in *N*,*N*-dimethylformamide in the presence of zinc bromide. The resulting zinc dodecafluorophthalocyanines were formulated as Cremophor EL oil−water emulsions and evaluated as photosensitizers in vitro against EMT-6 mouse mammary tumor cells. As compared to the previously studied zinc hexadecafluorophthalocyanine, these new asymmetrical zinc dodecafluorophthalocyanines exhibited improved photodynamic activity.

INTRODUCTION

Tetrapyrrolic macrocycles such as porphyrins represent one of the most important and more interesting ligand systems, not only due to their ubiquitous presence in nature but also because of their unique physical, chemical, biological, and spectral properties. Phthalocyanines (Pc)[1] are azoporphyrin derivatives and have been extensively studied to examine structure−activity relationships and to improve upon some of the unique characteristics of the tetrapyrrolic chromophore (*2*−*4*). Since their serendipitous discovery and identification (*2*, *3*), phthalocyanines have been used extensively as dyes and pigments in the paint, printing, textile, and paper industries due to their intense blue-green color, high dyeing power, photostability, insolubility in most solvents, and chemical inertness (*4*). In addition, phthalocyanines have found industrial applicability as photoconducting agents in photocopying devices and as catalysts for important industry reactions (*1*, *5*). In fact, cobalt phthalocyanine derivatives are used in the Merox process for the oxidation of sulfur compounds in gasoline fractions (*6*). More recently, phthalocyanines have found high-technology applications in electrophotography (*7*), ink jet printing (*8*), and data storage (*9*, *10*). Even with these important industrial and high-technology applications, the potential of phthalocyanines remains relatively untapped. Due to their unique chemical and physical properties, the importance of phthalocyanines is rapidly growing in a number of other fields. These fields include chemical sensors (*11*), electrochromism (*12*), molecular metals (*13*), liquid crystals (*14*), Langmuir−Blodgett films (*15*), functional polymers (*16*), semiconductors (*17*), nonlinear optical (NLO) applications (*18*), and photosensitizers for photodynamic therapy (PDT) (*19*, *20*).

Diverse applications such as those proposed for Pcs require compounds with distinct and well-defined physical, chemical, and electronic properties. These necessitate synthetic approaches for the preparation of single isomers or well-defined isomeric mixtures of substituted Pcs and for the preparation of Pcs bearing novel substituents. In addition, for a number of these applications, the physical and chemical properties of Pcs are enhanced when the Pcs are asymmetrically substituted. For instance, whereas symmetrically substituted Pcs exhibit large optical nonlinearities and third-order harmonic generation due to their extensively delocalized 18-π electron system, second-order nonlinear optical effects are present in only noncentrosymmetric molecules and are enhanced by electron-donating, electron-withdrawing push−pull systems (*18*). In light of this, the synthesis of unsymmetrically substituted Pcs bearing both electron-donating and electron-withdrawing functional groups has been investigated (*21*, *22*). In addition to the potential utility in NLO applications, it has been established that asymmetrically substituted phthalocyanines often exhibit increased potential as photosensitizers for photodynamic therapy (*23*, *24*).

A number of different strategies have been investigated to prepare asymmetrically substituted noncentrosymmetric Pcs. The most commonly used synthetic approach is the statistical mixed condensation of differently substituted phthalocyanine precursors (*25*). Although the yield of the desired substitution pattern has been enhanced by carefully selecting the substituents on the phthalocyanine precursors, the molecular proportions of the individual precursors, and the reaction conditions used, the statistical mixed condensation method involving

* Author to whom correspondence should be addressed [telephone (819) 564-5409; fax (819) 546-5442; e-mail johan.e.vanlier@USherbrooke.ca].

[1] Abbreviations: $AlPcS_4$, aluminum tetrasulfonated phthalocyanine; CRM, Cremophor EL; DDQ, 2,3-dichloro-5,6-dicyano-1,4-benzoquinone; DMF, *N*,*N*-dimethylformamide; DMSO, dimethyl sulfoxide; FBS, fetal bovine serum; HPLC, high-performance liquid chromatography; HPPI, 3α-hydroperoxy-1,2,3,3α,8,8α-hexahydropyrrolo[2,3β]indole-2-carboxylic acid; LD_{50}, light dose required for 50% cell inactivation; LD_{90}, light dose required for 90% cell inactivation; LDL, low-density lipoproteins; MgPc, magnesium phthalocyanine; MTT, 3-(4,5-dimethylthiazol-2-yl)-2,5-(diphenyltetrazolium bromide); NLO, nonlinear optics; NMP, 1-methyl-2-pyrrolidinone; PBS, phosphate-buffered saline; PEG, polyethylene glycol; Pc, phthalocyanines; PS, photosensitizers; subPc, subphthalocyanines; THF, tetrahydrofuran.

10.1021/bc0500241 CCC: $30.25 © 2005 American Chemical Society
Published on Web 09/02/2005

two differently substituted phthalocyanine precursors does lead to a mixture of six differently substituted phthalocyanine products that must be separated, usually by chromatography. If the two Pc precursors used differ significantly in their solubility in a given solvent, separation of the differently substituted Pcs may be relatively simple due to the different solubilities of the resulting Pcs. However, in most cases, this separation has proven to be troublesome.

Another method investigated is a polymer-support route in which one of the phthalocyanine precursors is covalently attached to a polymer support prior to the synthesis of the Pc (*26*). Following the synthesis of the macrocycle, the polymer-bound Pc is obtained by filtration and the bond to the polymer is cleaved to yield pure 3:1 unsymmetrically substituted Pc. Although this method has been used successfully to prepare pure unsymmetrically substituted Pcs, it is limited by the number of functional groups that can be covalently bonded to the polymer support. Furthermore, yields are less than satisfactory due to the low bonding capacity of the polymer support.

The Kobayashi ring expansion reaction of boron subphthalocyanines provides an efficient method for preparing 3:1 unsymmetrically substituted Pcs (*27*). Boron subPc are the lower homologues of phthalocyanines, consisting of a tripyrrolic macrocycle (*28*). The loss of an isoindoline unit causes a hypsochromic shift in the Q-band of the electronic spectra to around 560−580 nm, lending a reddish purple color to solutions of these subPcs. Whereas Pcs are extremely stable molecules exhibiting a high degree of planarity in their central aromatic core, subPcs have a cone-shaped structure, with the boron coordinated in a tetrahedral geometry with a single axial ligand. Their extensively delocalized 14-π electron system and their cone-shaped structure have led to investigations in the utility of subPcs in NLO applications (*29*). In light of this, a number of substituted subPcs have been prepared (*29*−*34*). In addition, attempts have been made to alter the properties of subPcs by varying the axial ligand coordinated to the boron (*32*, *35*, *36*). It has been demonstrated that the less stable subPcs readily react with 1,3-diiminoisoindolines in a ring enlargement reaction to yield 3:1 unsymmetrically substituted Pcs (*27*, *37*). First disclosed by Kobayashi in 1990, this ring enlargement reaction unfortunately may lead to a mixture of differently substituted Pcs, and it has been proposed that the ring enlargement reaction of subPcs is a nonselective multistep reaction which depends greatly on the nature of the substituents on the subPcs, the reactivity of the 1,3-diiminoisodoline, the solvent, and the reaction conditions used (*21*, *38*, *39*). Although this greatly limits the general synthetic utility of this reaction, this reaction protocol has been shown to be useful in a number of examples, giving the desired 3:1 unsymmetrically substituted Pc in good yields and as a pure single phthalocyanine product (*27*, *37*, *40*−*43*).

To further investigations carried out by our group using zinc hexadecafluorophthalocyanine and zinc dodecafluorophthalo-4-sulfophthalocyanine, the Kobayashi ring expansion reaction of boron dodecafluorosubphthalocyanine (**2**) has been examined. We have found that subPc **2** readily reacts with 1,3-diiminoisoindolines under extremely mild conditions to give the corresponding 3:1 unsymmetrically substituted phthalocyanine in good yields and without contamination with phthalocyanines with differing substitution patterns. Furthermore, we have found that the starting boron subPc **2** can be prepared under much milder conditions than those described in the literature (*34*). The photodynamic activity, in terms of both singlet oxygen generation and in vitro photocytotoxicity, of some of the resulting unsymmetrically substituted dodecafluorinated Pcs has been determined and has indicated that asymmetry, even in lipophilic photosensitizers, improves the photodynamic efficacy of these compounds.

EXPERINEMTAL PROCEDURES

All solvents were of HPLC grade and were used without further purification unless otherwise stated. Tetrafluorophthalonitrile, 3-nitrophthalonitrile, and 4-*tert*-butylphthalonitrile were purchased from TCI America (Portland, OR). 1-Dodecyne, 1,2-dicyanobenzene, 1,2,4,5-tetracyanobenzene, 4-nitrophthalonitrile, 1,3-diiminoisoindoline, dichlorobis(triphenyl-phosphine)palladium(II), 10% palladium on carbon, 1 M boron tribromide in dichloromethane, and zinc bromide were purchased from Aldrich (Oakville, ON, Canada). 4-Iodophthalonitrile (*44*), 3-iodophthalonitrile (*45*), 4,5-diiodophthalonitrile (*46*), 5-*tert*-butyl-1,3-diiminoisoindoline, 5-nitro-1,3-diiminoisoindoline, 5-iodo-1,3-diiminoisoindoline, 4-iodo-1,3-diiminoisoindoline, 5,6-diiodo-1,3-diiminoisoindoline, 5,6-dicyano-1,3-diiminoisoindoline, 2,3-dihydro-1,3-diimino-1*H*-benz[*f*]isoindole (*47*−*50*), $ZnPcF_{16}$ (*51*), $ZnPcF_{12}S_1$ (*52*), and $AlPcS_4$ (*53*, *54*) were prepared by using modified literature procedures. UV−vis spectra were recorded with a Hitachi U-2000 spectrophotometer. ^1H and ^{19}F NMR spectra were obtained on a Brucker AC-300 spectrometer. FAB-MS were obtained on an LG Autospec Q mass spectrometer.

4,5-(1-Dodecynl)phthalonitrile. 4,5-Diiodophthalonitrile (2.61 g; 6.87×10^{-3} mol) was dissolved in 50 mL of triethylamine and 5 mL of DMF. To this was added 300 mg of dichlorobis(triphenylphosphine)palladium(II). The reaction mixture was stirred at 100 °C under an inert atmosphere and 6.4 mL of 1-dodecyne (2.99×10^{-2} mol; 4.35 equiv). The reaction was monitored by thin-layer chromatography (TLC) (10% diethyl ether in hexanes). After 2 h, the reaction was cooled and filtered, and the filtrate was evaporated to dryness under reduced pressure. The resulting solid was purified by column chromatography on silica using 10% diethyl ether in hexanes as eluant. The desired product was obtained in a yield of 2.66 g (84.7%): $C_{32}H_{44}N_2$, MS (EI), *m/e* 456 (M^+), 385 [$M^+ - CH_3(CH_2)_4$], 371 [$M^+ - CH_3(CH_2)_5$]; HR MS (EI), *m/z* calcd for $C_{32}H_{44}N_2$, 456.3504, found, 456.3522.

4,5-(Dodecyl)phthalonitrile. 4,5-(1-Dodecynl)phthalonitrile (2.5 g; 5.47×10^{-3} mol) was dissolved in 200 mL of tetrahydrofuran (THF). To this solution was added 500 mg of 10% palladium on carbon. The suspension was stirred at room temperature, and hydrogen gas was bubbled through the reaction mixture. The reaction was monitored by TLC (10% diethyl ether in hexanes). After 6 h, the reaction mixture was filtered to remove the catalyst, and the filtrate was evaporated to dryness under reduced pressure. The resulting solid was purified by column chromatography on silica using 10% diethyl ether in hexanes as eluant. The desired product was obtained in a yield of 2.42 g (95.2%): $C_{32}H_{52}N_2$ MS (EI), *m/e* 464 (M^+), 449 ($M^+ - CH_3$), 435 ($M^+ - 2CH_3$), 421 ($M^+ - CH_3$, CH_3CH_2); HR MS (EI), *m/z* calcd for $C_{32}H_{52}N_2$, 464.4130, found, 464.4122.

5,6-Didodecyl-1,3-diiminoisoindoline (3g). Sodium metal (68.5 mg; 2.98×10^{-3} mol) was dissolved in 30 mL of methanol. Ammonia gas was bubbled through the reaction mixture for 5 min prior to the addition of 4,5-(dodecyl)phthalonitrile (919 mg; 1.98×10^{-3} mol). The

mixture was stirred at 60 °C with periodic bubbling of ammonia. The reaction was monitored by TLC (20% methanol in toluene). After 10 h, the mixture was cooled to 0 °C, saturated with ammonia gas, sealed, and stirred at 4 °C overnight. The reaction mixture was then warmed to room temperature, and the solvent was removed under reduced pressure. The resulting solid was washed with concentrated NH_4Cl, water, and ice-cold methanol and dried. The desired product was obtained in a yield of 938 mg (98.5%): $C_{32}H_{55}N_3$ MS (EI), *m/e* 482 ($M^+ + H$); HR MS (EI), *m/z* calcd for $C_{32}H_{55}N_3$, 481.4396, found, 481.4401.

Dodecafluorosubphthalocyanato Boron(III) Bromide (SubPcF$_{12}$) (2). Tetrafluorophthalonitrile (**1**) (518 mg; 2.59×10^{-3} mol) was dissolved in a minimum amount of chlorobenzene (1.8 mL). The resulting solution was stirred at room temperature, and 1.8 mL of 1 M BBr_3 in dichloromethane (1.80×10^{-3} mol of BBr_3; 0.7 equiv) was added. After 5 min, the reaction mixture was heated to 60 °C and after 1 h cooled to room temperature. The solvent was removed by rotary evaporation at reduced pressure, and the resulting solid was dissolved in 30% THF in hexanes. This solution was filtered and purified by column chromatography over neutral alumina using 30% THF in hexanes as eluant. The desired product was obtained in a yield of 402 mg (67.4%): $C_{24}N_6BBrF_{12}$ MS (FAB), *m/e* 692 ($M^+ + H$), 612 ($M^+ - Br$); ^{19}F NMR (dichloromethane) δ −59.76, −59.81, −70.18, −70.23 [$\delta = 0$ for trifluoroacetic acid (TFA)]; UV−vis, λ (dichloromethane) (log ϵ) 577 nm (4.93), 532 nm (2.01).

Synthesis of Dodecafluorinated Phthalocyanines. *1,2,3,4,8,9,10,11,15,16,17,18-Dodecafluorophthalocyaninate (H$_2$PcF$_{12}$) (**4a**).* To a stirred solution of (dodecafluorosubphthalocyanato)boron(III) bromide (**2**) (400 mg; 5.78×10^{-4} mol) in 4 mL of DMSO was added a solution of 1,3-diiminoisoindoline (**3a**) (451 mg; 3.11×10^{-3} mol; 5.4 equiv) in 6 mL of DMSO at room temperature. The reaction mixture instantly lost its intense purple color and gradually became blue. After 2−4 h, the reaction mixture was added to a large excess of methanol (50 mL). The suspension was left at 4 °C overnight, and then the green solid was collected by centrifuging. The desired product was obtained in a yield of 244 mg (59.5%): MS (FAB), *m/e* 731 ($M^+ + H$); HR MS (FAB), *m/z* calcd for $C_{32}H_6N_8F_{12}$, 730.0524, found, 730.0572; UV−vis, λ (DMF) 671, 601 nm.

The following dodecafluorinated phthalocyanine derivatives were prepared using the same synthetic procedure described above. Note that for 5,6-didodecyl-1,3-diiminoisoindoline (**3g**), the reaction was accomplished using a 1:1 solvent mixture of DMSO and chlorobenzene.

*1,2,3,4,8,9,10,11,15,16,17,18-Dodecafluoro-23-tert-butylphthalocyaninate (**4b**).* Yield, 40.5%; MS (FAB), *m/e* 786 ($M^+ + H$); UV−vis, λ (DMF) 673, 606 nm.

*1,2,3,4,8,9,10,11,15,16,17,18-Dodecafluoro-23-nitrophthalocyaninate (**4c**).* Yield, 20.7%; MS (FAB), *m/e* 776 ($M^+ + H$); UV−vis, λ (DMF) 684, 667, 635 nm.

*1,2,3,4,8,9,10,11,15,16,17,18-Dodecafluoro-23-iodophthalocyaninate (**4d**).* Yield, 25.9%; MS (FAB), *m/e* 857 ($M^+ + H$); UV−vis, λ (DMF) 671, 607 nm.

*1,2,3,4,8,9,10,11,15,16,17,18-Dodecafluoro-22-iodophthalocyaninate (**4e**).* Yield, 18.7%; MS (FAB), *m/e* 857 ($M^+ + H$); UV−vis, λ (DMF) 680, 612 nm.

*1,2,3,4,8,9,10,11,15,16,17,18-Dodecafluoro-23,24-diiodophthalocyaninate (**4f**).* Yield, 30.3%; MS (FAB), *m/e* 983 ($M^+ + H$); UV−vis, λ (DMF) 669, 612 nm.

*1,2,3,4,8,9,10,11,15,16,17,18-Dodecafluoro-23,24-didodecylphthalocyaninate (**4g**).* Yield, 11.7%; MS (FAB), *m/e* 1067 ($M^+ + H$); UV−vis, λ (DMF) 676, 613 nm.

*1,2,3,4,8,9,10,11,15,16,17,18-Dodecafluoro-23,24-dicyanophthalocyaninate (**4h**).* Yield, 28.8%; MS (FAB), *m/e* 780 (M^+); UV−vis, λ (DMF) 689, 661, 636 nm.

*(1,2,3,4,8,9,10,11,15,16,17,18-Dodecafluoro)tribenzo[b,g,l]naphthalo[2,3-q]-porphyrazine (**4i**).* Yield, 51.8%; MS (FAB), *m/e* 780 (M^+); UV−vis, λ (DMF) 700, 675, 620, 604 nm.

Synthesis of Dodecafluorinated Zinc Phthalocyanines. *1,2,3,4,8,9,10,11,15,16,17,18-Dodecafluorophthalocyaninato Zinc (**5a**).* 1,2,3,4,8,9,10,11,15,16,17,18-Dodecafluorophthalocyaninate (**4a**) (100 mg; 1.37×10^{-4} mol) was suspended in 5 mL of DMF. To this was added zinc bromide (72 mg; 3.20×10^{-4}; 2.3 equiv). The reaction mixture was heated to 40 °C for 2 h and was then cooled to room temperature. The solvent was removed by rotary evaporation under reduced pressure, and the resulting solid was washed twice with 1.2 M hydrochloric acid (25 mL each) and twice with 95% ethanol (25 mL each). The solid was dried and then dissolved in tetrahydrofuran and purified by column chromatography on silica gel (40% THF in hexanes). The desired product was obtained in a yield of 105 mg (96%): MS (FAB), *m/e* 793 ($M^+ + H$); HR MS (FAB), *m/z* calcd for $C_{32}H_4N_8F_{12}Zn$, 791.9659, found, 791.9648; UV−vis, λ (THF) (log ϵ) 674 (5.13), 604 (4.38), 356 nm (4.57).

The following dodecafluorinated zinc phthalocyanine derivatives were prepared using the same synthetic procedure described above.

*1,2,3,4,8,9,10,11,15,16,17,18-Dodecafluoro-23-tert-butylphthalocyaninato Zinc [ZnPcF$_{12}$(tert-butyl)] (**5b**).* Yield, 98%; MS (FAB), *m/e* 849 ($M^+ + H$); UV−vis, λ (THF) (log ϵ) 663 (5.16), 629 (4.91), 355 nm (4.89).

*1,2,3,4,8,9,10,11,15,16,17,18-Dodecafluoro-23-nitrophthalocyaninato Zinc [ZnPcF$_{12}$(NO$_2$)] (**5c**).* Yield, 91%; $C_{32}H_3N_9O_2F_{12}Zn$ MS (FAB), *m/e* 838 ($M^+ + H$); UV−vis, λ (THF) (log ϵ) 678 (4.92), 667 (4.88), 620 (4.55), 601 (4.53), 340 nm (4.89).

*1,2,3,4,8,9,10,11,15,16,17,18-Dodecafluoro-23-iodophthalocyaninato Zinc [ZnPcF$_{12}$(4-I)] (**5d**).* Yield, 95%; $C_{32}H_3N_8F_{12}IZn$ MS (FAB), *m/e* 919 ($M^+ + H$); UV−vis, λ (THF) (log ϵ) 671 (5.10), 640 (4.66), 608 (4.48) 357 nm (4.66).

*1,2,3,4,8,9,10,11,15,16,17,18-Dodecafluoro-22-iodophthalocyaninato Zinc [ZnPcF$_{12}$(3-I)] (**5e**).* Yield, 92%; $C_{32}H_3N_8F_{12}IZn$ MS (FAB), *m/e* 919 ($M^+ + H$); UV−vis, λ (THF) (log ϵ) 680 (5.19), 612 (4.54), 344 nm (4.66).

*1,2,3,4,8,9,10,11,15,16,17,18-Dodecafluoro-23,24-diiodophthalocyaninato Zinc [ZnPcF$_{12}$(I$_2$)] (**5f**).* Yield, 97%; $C_{32}H_2N_8F_{12}I_2Zn$ MS (FAB), *m/e* 1045 ($M^+ + H$); UV−vis, λ (THF) (log ϵ) 676 (5.21), 643 (4.69), 355 nm (4.91).

*1,2,3,4,8,9,10,11,15,16,17,18-Dodecafluoro-23,24-didodecylphthalocyaninato zinc (ZnPcF$_{12}$(C$_{12}$)$_2$) (**5g**).* Yield, 88%; $C_{56}H_{52}N_8F_{12}Zn$ MS (FAB), *m/e* 1129 ($M^+ + H$); UV−vis, λ (THF) (log ϵ) 683 (4.90), 664 (4.86), 359 nm (4.61).

*1,2,3,4,8,9,10,11,15,16,17,18-Dodecafluoro-23,24-dicyanophthalocyaninato Zinc [ZnPcF$_{12}$(CN)$_2$] (**5h**).* Yield, 90%; $C_{34}H_2N_{10}F_{12}Zn$ MS (FAB), *m/e* 843 ($M^+ + H$); UV−vis, λ (THF) (log ϵ) 675 (5.11), 620 (4.75), 359 nm (4.88).

*(1,2,3,4,8,9,10,11,15,16,17,18-Dodecafluoro)tribenzo[b,g,l]naphthalo[2,3-q]-porphyrazine Zinc (ZnPcF$_{12}$nap) (**5i**).* Yield, 98%; $C_{36}H_6N_8F_{12}Zn$ MS (FAB), *m/e* 843 ($M^+ + H$); UV−vis, λ (THF) (log ϵ) 710 (4.96), 679 (4.92), 352 (4.55), 337 nm (4.39).

Drug Formulation. To impart water solubility, phthalocyanines **5a**−**5i** were formulated as Cremophor EL emulsions as previously published (*55*). Briefly, the Pcs were dissolved in THF, and 1 mL of Cremophor EL and 0.3 mL of 1,2-propanediol were added to the solutions. The solutions were then sonicated for 30 min,

followed by removal of the THF solvent by rotary evaporation under reduced pressure. Phosphate-buffered saline (PBS) (8.7 mL) was added to the viscous liquid, and the mixture was sonicated for 30 min. The resulting emulsion was filtered (0.45 μm, Millipore). Concentrations were determined by serial dilution of the stock preparation with THF.

l-Tryptophan Photooxidation (*56*). A solution of 5 μM Pc and 5 mM L-tryptophan in PBS (1 mL total volume) was irradiated using a high-intensity xenon light source (model IL 302) equipped with a CermaxR xenon short-arc 300 W lamp (model LX300F) (ILC Technology, Sunnydayle, CA). A liquid guide fiber-optic (model 77556, Oriel Corp., Stratford, CT) was used to deliver the light. Two filters, an LS-700 and an LL-600 (Corion, Holliston, MA), were used to allow transmission of light in the 600−700 nm range. [Note that the LS-700 filter was removed when (1,2,3,4,8,9,10,11,15,16,17,18-dodecafluoro)tribenzo[*b*,*g*,*l*]naphthalo[2,3-*q*]porphyrazine zinc was used.] The fluence rate was 150 mW cm^{-2}. After 2 and 4 min of irradiation, 80 μL samples were removed from the photooxidation reaction and were analyzed by HPLC to quantify the characteristic hydroperoxide products of singlet oxygen tryptophan peroxidation (3a-hydroperoxy-1,2,3,3a,8,8a-hexahydropyrrolo[2,3-*b*]indole-2-carboxylic acid; HPPI isomers) (t_R = 5.8 and 8.6 min, t_R for tryptophan = 15.7 min). The relative HPPI yield was measured from the HPPI chromatogram peak areas using a Shimadzu HPLC system (Kyoto, Japan) composed of an LC-600 pump, an SP-6AV UV−visible detector, a DGV-4A degasser, an LPM-600 low-pressure mixing system, a rheodyne injector, and the EZChrom chromatography data acquisition and analysis system. During this analysis, a C18 Radial Pak cartridge (10 × 0.8 cm) filled with 4 μm Nova Pak C18 reversed phase packing was eluted at 1.5 mL min^{-1} with 0.1% TFA in water and a linear gradient over 25 min from 1 to 30% methanol (0.1% TFA). The wavelength of a UV−vis detector was set at 280 nm. The relative HPPI yield was evaluated by comparing the peak areas corresponding to the HPPI isomers to the total tryptophan peak area and then arbitrarily comparing this ratio to the ratio obtained using $AlPcS_4$ in PBS.

In Vitro Photocytotoxicity. A suspension of ~1.5 × 10^4 EMT-6 cells per well in 100 μL of Waymouth 15% FBS was incubated overnight at 37 °C with 5% CO_2 in 96-well microtitration plates (Falcon). The FBS solution was supplemented with 1% L-glutamine and 1% penicillin−streptomycin. The first column (eight wells) served as a blank control (no cells), wheres the second and third columns (16 wells) served as a control (no phthalocyanine added, 100% cell survival). The cells were rinsed twice with PBS, and then 50 μL of Pcs **5a**, **5b**, and **5g** was added at concentrations of 1 and 5 μM in Waymouth 1% FBS. The plates were incubated at 37 °C with 5% CO_2 for 1 or 24 h. Before irradiation, the cells were rinsed twice with PBS and then refed with 100 μL of Waymouth 15% FBS. Irradiation consisted of illuminating the microtitration plates with red light (660−700 nm) at graded fluences of 0−54 J cm^{-2} at a fluence rate of 100 mW cm^{-2}. The light source consisted of two 500 W tungsten/halogen lamps (GTE Sylvania, Drummondville, PQ, Canada) fitted with a circulating refrigerated filter containing aqueous rhodamine B (Sigma, ON, Canada) (OD_{580} = 1.25). Cell survival was then assessed by means of the colorimetric MTT assay (*23*).

A MTT (Aldrich Canada Ltd., Oakville, ON, Canada) stock solution of 5 mg mL^{-1} was prepared and kept at 4 °C in the dark. Upon a 5-fold dilution in Waymouth 15% FBS, 50 μL of the MTT solution was added to all of the wells of the microtitration plate, and the cells were incubated for 4 h at 37 °C with 5% CO_2. Acidic sodium dodecyl sulfate (SDS) solution (10% SDS in 0.01 N HCl) (100 μL) was then added to each well, and the cells were incubated for 24 h at 37 °C with 5% CO_2. Following this incubation, the microtitration plates were agitated at room temperature for 10 s, and the absorbance at 595 nm was read on a microplate reader (Bio-Rad, ON, Canada). The percent cell survival was determined as follows. The average absorbance of the blank cells containing only MTT solution was subtracted from the average absorbance obtained from the wells of identical treatment as well as subtracted from the average absorbance measured from the control wells containing untreated cells (which represent 100% cell viability). The percent cell survival was calculated by dividing the absorbance of the treated cells by the absorbance of the nontreated cells and multiplying by 100. Eight replicates were run, and experiments were repeated three times.

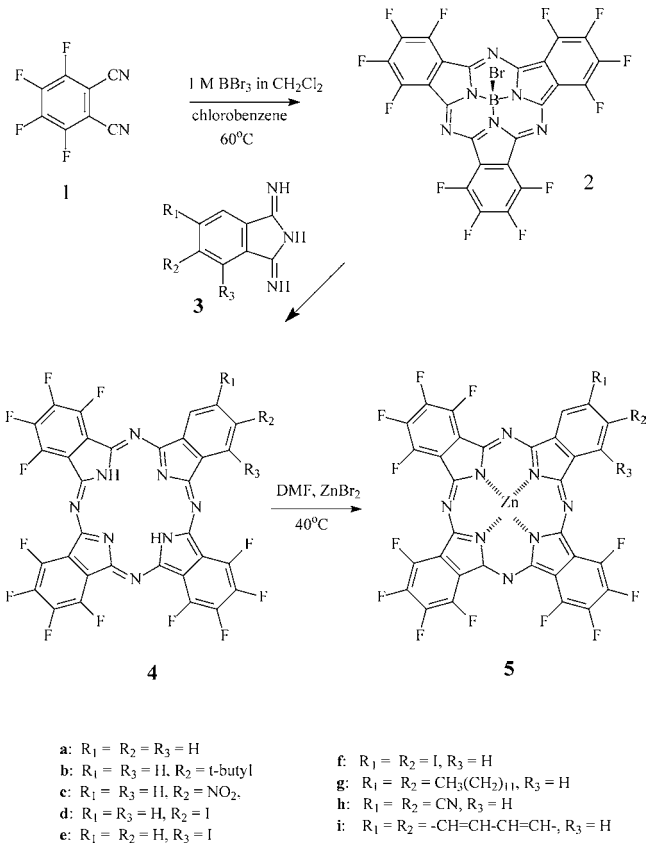

Figure 1. Synthesis of dodecafluorinated phthalocyanines **4a**−**i** via the Kobayashi ring expansion reaction of dodecafluorosubphthalocyanato boron(III) bromide (**2**).

RESULTS

Synthesis of Boron Dodecafluorinated Subphthalocyanine (2). The tetrafluorophthalonitrile readily reacts with the stronger Lewis acid boron tribromide in chlorobenzene at temperatures of 40−60 °C, with the reaction mixture rapidly adopting the characteristic intense purple color of the corresponding subPc (Figure 1). In fact, the reaction proceeded relatively smoothly in dichloromethane at room temperature, although yields of the desired tripyrrolic macrocycle were significantly lower and reaction times were longer. The use of chlorobenzene instead of the higher boiling 1-chloronaphthalene greatly eased the purification of the dodecafluoro-

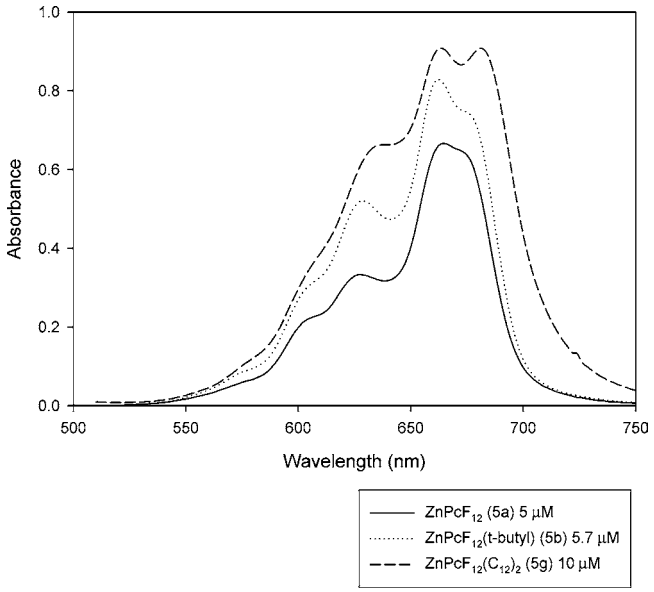

Figure 2. UV−vis spectra of **5a**, **5b**, and **5g** in THF.

subphthalocyanine **2**. The latter product was purified by column chromatography on neutral alumina in the dark (70% yield).

At lower reaction temperatures (0 °C) in either dichloromethane or chlorobenzene a transient blue intermediate, which absorbed around 660 nn, was obtained instead of the desired intensely purple subPc **2**.

Kobayashi Ring Expansion Reaction of the Boron Dodecafluorinated Subphthalocyanine (2). SubPc 2 readily reacted with various 1,3-diiminoisoindolines (**3a**−**3i**) in DMSO to give the corresponding 3:1 unsymmetrically substituted dodecafluorinated phthalocyanines (**4a**−**4i**) (Figure 1). The reaction proceeded exceptionally rapidly, being complete after 1 h, with an immediate loss of the intense purple color of the subPc solution. In the case of 5,6-didodecyl-1,3-diiminoisoindoline (**3g**), the 1,3-diiminoisoindoline was only marginally soluble in DMSO, necessitating the use of a 1:1 mixture of DMSO and chlorobenzene as reaction solvent. The metal-free Pcs **4a**−**4i** prepared by this reaction were typically insoluble in the reaction solvent and precipitated from solution in yields ranging from 10 to 60%. In cases where the Pc product was slightly soluble in the reaction solvent, the product could readily be isolated by adding the reaction mixture to a large excess of methanol. The resulting green precipitate could be isolated by centrifugation or filtration. Mass spectra of all final Pc products exhibited intense peaks corresponding to the molecular ion (M^+) or $M^+ + 1$. The metal-free dodecafluorinated phthalocyanines **4a**−**4i** were practically insoluble in most common organic solvents but slightly soluble in DMF. Electronic absorption spectra in DMF displayed characteristic Q-band absorptions around 670−680 nm with a weaker satellite in the range of 600−620 nm (Figure 2). The extended conjugation of (1,2,3,4,8,9,10,11,15,16,17,-18-dodecafluoro)tribenzo[*b*,*g*,*l*]naphthalo[2,3-*q*]porphyrazine (**4i**) shifted the absorption to a longer wavelength (700, 675 nm) as would be expected. Metal ion insertion was accomplished in nearly quantitative yield by suspending the metal-free dodecafluorinated Pcs **4a**−**i** in DMF at 40−60 °C in the presence of the metal ion (Figure 1). Other reaction solvents such as NMP failed to give the corresponding ZnPc and led to important macrocycle degradation. Attempts were undertaken to prepare the corresponding dodecafluorinated ZnPc directly by adding zinc ions to the Kobayashi ring expansion reaction. However, although the reaction appeared to give the desired 3:1 unsymmetrically substituted Pc, yields were greatly decreased. In addition, the ZnPcs exhibited higher solubility in the reaction solvent, leading to significant difficulties in isolating and purifying the final phthalocyanine product.

Table 1. Relative Hydroperoxide Yields as a Result of L-Tryptophan Photooxidation

photosensitizer[a]	λ_{max} (nm)	relative peroxide yield
$AlPcS_4$ (in PBS)[b]	680	1
$AlPcS_4$	678	1.15
$ZnPcF_{16}$	678	1.40
$ZnPcF_{12}S$	674	1.82
$ZnPcF_{12}$ (**5a**)	674	1.38
$ZnPcF_{12}$(*tert*-butyl) (**5b**)	663	1.49
$ZnPcF_{12}(NO_2)$ (**5c**)	678, 667	2.30
$ZnPcF_{12}$(4-I) (**5d**)	671	2.43
$ZnPcF_{12}$(3-I) (**5e**)	680	2.31
$ZnPcF_{12}(I_2)$ (**5f**)	676	2.00
$ZnPcF_{12}(C_{12})_2$ (**5g**)	683, 664	1.17
$ZnPcF_{12}(CN)_2$ (**5h**)	675	1.64
$ZnPcF_{12}$nap (**5i**)	710, 679	1.85

[a] Formulated as 0.5% Cremophor EL emulsions unless otherwise noted. [b] The singlet oxygen yield for $AlPcS_4$ in phosphate buffer (1% Triton X) has been reported to be 0.43 (*72*).

Tryptophan Photooxidation. The asymmetrically substituted dodecafluorinated ZnPcs **5a**−**5i** formulated as Cremophor/PBS emulsions were exposed to red light in the presence of L-tryptophan. The relative yield of HPPI isomers was then determined by HPLC and compared to that of $AlPcS_4$ in PBS, the yield of which was arbitrarily set at 1 (Table 1). The CRM emulsions of **5a**−**5i** exhibited improved yields of the HPPI isomers as compared to $AlPcS_4$ in PBS. Formulation of $AlPcS_4$ in CRM also led to slightly improve L-tryptophan photooxidation, most likely as a result of decreased aggregation of the chromophore. The most significant photooxidation of L-tryptophan was obtained using the iodinated Pc derivatives, with relative HPPI yields of 2.43, 2.31, and 2.00 obtained for Pcs **5d**, **5e**, and **5f**, respectively. The nitro-substituted derivative **5c** also provided L-tryptophan photooxidation that was >2 times higher than that observed for $AlPcS_4$ in PBS. On the other hand, the dodecafluorinated ZnPc substituted with two long alkyl chains (**5g**) gave HPPI yields comparable to $AlPcS_4$ in 1% CRM.

In Vitro Photodynamic Activity. Using a constant dye concentration of 1 or 5 μM, the photocytotoxicity of dodecafluorinated zinc phthalocyanines **5a**, **5b**, and **5g** on EMT-6 murine mammary tumor cells was measured after illumination for various amounts of time at a fluence rate of 100 mW/cm^2 as calculated over the range of the Q-band of phthalocyanines (660−700 nm). The light doses required to induce 50 and 90% cell death (LD_{50} and LD_{90}) were extrapolated from the resulting cell survival curves. No significant dark toxicity was observed for any of the photosensitizers examined at either concentration. Figure 3 shows histograms reporting the LD_{50} and LD_{90} after 1 and 24 h of incubation with photosensitizers **5a**, **5b**, and **5g** and for hexadecafluorinated ZnPc ($ZnPcF_{16}$), a photosensitizer that has already been extensively studied (*55*, *57*−*59*). The asymmetrically substituted photosensitizers **5a**, **5b**, and **5g** were more phototoxic than the symmetrically substituted $ZnPcF_{16}$ at both dye concentrations. The improved photocytotoxicity was more pronounced for the photosensitizers substituted with a *tert*-butyl group (**5b**) and was even more prominent for the dodecafluorinated phthalocyanine

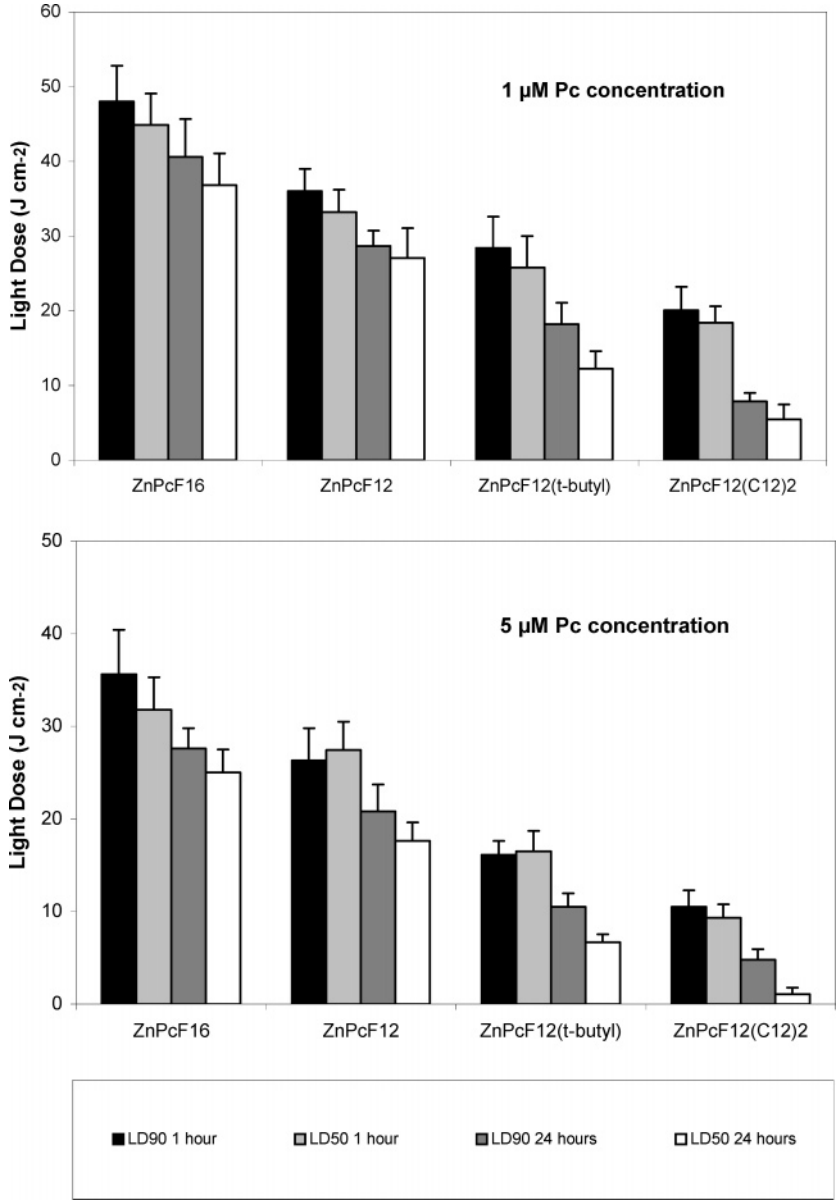

Figure 3. Photocytotoxicity of asymmetrically substituted fluorinated phthalocyanines: phototoxic activity of a 1 μM (top) or 5 μM (bottom) solution of zinc dodecafluorinated phthalocyanines **5a**, **5b**, and **5g** toward EMT-6 murine mammary tumor cells.

substituted with two dodecyl groups (**5g**). The difference in photocytotoxicity between these two photosensitizers and $ZnPcF_{16}$ is appreciably more important after incubation for 24 h.

DISCUSSION

Dodecafluorosubphthalocyanato boron(III) bromide (**2**) was successfully synthesized by the cyclotrimerization reaction of tetrafluorophthalonitrile with BBr_3 in chlorobenzene at 40−60 °C. Yields as high as 70% were obtained, which compare to 26% yield previously reported for the reaction of boron trichloride and tetrafluorophthalonitrile in benzene or 1-chloronaphthalene at elevated temperatures (*34*). It has been established that the reactivity of trisubstituted boron compounds toward the cyclotrimerization reaction is $B(alkyl)_3 < BPh_3 < BF_3 < BCl_3 < BBr_3$, an order that is closely related to the Lewis acidity of the boron compounds (*29*). In addition, the presence of four strongly electron-withdrawing fluorine atoms on the tetrafluorophthalonitrile starting material will activate the nitrile groups toward the cyclotrimerization reaction. A combination of the increased reactivity of the boron source and the activation of the nitrile groups of tetrafluorophthalonitrile toward the cyclotrimerization reaction results in the possibility of the reaction being carried out under milder reaction conditions, thus ensuring a higher yield of the desired boron dodecafluoro subPc. No exchange of fluorine for bromine was observed. This is despite the strong Lewis acidity of the boron tribromide and the known reactivity of tetrafluorophthalonitrile toward exchange reactions (*60*).

The resulting dodecafluorinated tripyrrolic macrocycle was purified by flash column chromatography on neutral alumina in the dark. It has been reported that subPcs bearing bromine axial ligands are fairly unstable with respect to axial ligand exchange and that purification of bromosubPcs via column chromatography resulted in an appreciable amount of replacement of the bromine axial ligand by OH (*29*). To overcome this, it has been suggested that these labile subPcs can be purified by precipitation or Soxhlet extraction with an appropriate solvent (*33*). However, in the current study, it was observed that addition of the chlorobenzene reaction mixture to excess hexanes led to degradation of the

macrocycle. This is despite reports that subPcs are stable in apolar solvents (*61*). On the other hand, it has been reported that dodecafluorosubphthalocyanato boron(III) chloride undergoes thermal decomposition in hexanes (*62*). Soxhlet extraction with dry dichloromethane of the solid obtained either by precipitation from excess hexanes or by evaporation of the dichlorobenzene from the reaction mixture also led to degradation of the subPc, significantly decreasing the yield of the desired product. Purification by flash column chromatography using 30% THF in hexanes or using dichloromethane proved to be the most efficient method of purifying dodecafluorosubphthalocyanato boron(III) bromide (**2**).

When attempts were made to prepare **2** at 0 °C, a labile blue product was obtained. Interestingly, we observed similar labile blue products when the cyclotrimerization of other phthalonitriles substituted with electron-withdrawing groups (such as 4-nitrophthalonitrile, 4-iodophthalonitrile, and 4,5-dicyanophthalonitrile) was carried out at 0 °C (results not presented). Although the identity of this labile species has not been fully elucidated, identification of this species may help determine the mechanism of the cyclotrimerization reaction, which in turn may help investigators in improving the synthesis and the utility of subPcs. The literature describes that dodecafluorosubphthalocyanato boron(III) chloride undergoes thermal decomposition in hexanes to yield a light blue product, the structure of which was not determined (*62*). We attempted to prepare Pc by reacting the transient blue complex with various 1,3-diiminoisoindolines. However, no green/blue product corresponding to phthalocyanines was obtained.

There are a number of possible identities for this transient blue species. It is well-known that boron trihalides readily form charge-transfer complexes with nitrile functional groups (*63*), and one would expect that some type of charge-transfer complex with the dinitrile functionality of phthalonitriles would form at some point during the synthesis of subPcs. However, it was observed that this transient blue intermediate transformed into the desired $subPcF_{12}$ upon heating of the reaction mixture. Furthermore, treatment of $subPcF_{12}$ with $NaBH_4$ resulted in a loss of the characteristic Q-band at 577 nm and the formation of a broad absorption around 660 nm, whereas treatment of the blue intermediate with DDQ led to a broad transient absorption centered near 580 nm. Because the bromide **2** absorbs at 577 nm and the transient blue species exhibits a broad absorption centered approximately at 660 nm, these results imply that the transient blue species requires oxidation in order to form the subPc. A bathochromic shift of the absorption from the subPc to the incompletely oxidized blue intermediate would not be unexpected. A loss of conjugation in tetrapyrrolic macrocycles is known to lead to red shifts in the λ_{max}. For instance, although the completely conjugated protoporphyrin IX absorbs at 630 nm, the incompletely conjugated verteporfin absorbs at 690 nm (*64*). It has been reported that the singlet excited state of dodecafluorosubphthalocyanato boron(III) chloride is a strong oxidant (*62*) with a one-electron reduction potential estimated to be approximately 1.7 V, suggesting that the relationship between the subPc and the blue species may pass via a photoexcited state of the subPc.

In the current study, the Kobayashi ring expansion reaction of the subPc **2** with various 1,3-diiminoisoindolines (**3a**−**3i**) selectively yielded the desired 3:1 asymmetrically substituted dodecafluorinated Pcs (**4a**−**4i**). Yields for the dodecafluorinated Pcs ranged from 18% to as high as 60%, although lower yields were obtained using 4-iodo-1,3-diiminoisoindoline (**3e**), probably a result of steric effects. Lower yields of Pc were also obtained using 5,6-didodecyl-1,3-diiminoisoindoline (**3g**). Both the steric effect and solubility of **3g** may have played a part in the lower yields obtained for 2,3,4,8,9,10,11,15,16,17,-18-dodecafluoro-23,24-didodecylphthalocyaninate (**4g**). Whereas the other 1,3-diiminoisoindoline derivatives employed could be solubilized in DMSO upon sonication, **3g** required the use of a 1:1 mixture of DMSO and chlorobenzene to obtain a solution. Conversely, when 5-*tert*-butyl-1,3-diiminoisoindoline was used instead of its unsubstituted derivative, the reaction did proceed to give some tetra-*tert*-butylphthalocyanine in pure DMSO, although yields were low (*37*).

Due to the known tendency of tetrafluorophthalonitrile to undergo an exchange reaction with DMF (*60*), attempts to insert metal ions such as Zn^{2+} into the metal-free dodecafluorinated phthalocyanines using solvents such as NMP were undertaken. Unfortunately, these metal ion insertion reactions were sluggish and gave unacceptable yields. To avoid any possible reaction between DMF and the perfluorinated macrocycle, reaction temperatures between 30 and 50 °C were employed and led to the corresponding zinc dodecafluorinated phthalocyanines in nearly quantitative yields.

Singlet oxygen is believed to be the most important reactive species generated during PDT and is capable of inducing important characteristic oxidative damage to a number of biologically important molecules including amino acids (*65*). L-Tryptophan photooxidation was used to evaluate the photodynamic potential of the asymmetrically substituted zinc dodecafluorinated phthalocyanines by comparing the relative HPPI yields obtained using these Pcs to the yield obtained using $AlPcS_4$ in PBS (which was arbitrarily set as 1) (*56*). In light of the heavy atom effect, it is not unexpected that these dodecafluorinated photosensitizers exhibit improved HPPI yields as compared to $AlPcS_4$, with the iodinated derivatives giving the highest singlet oxygen yields. The heavy atom effect dictates that the exchange of hydrogen atoms with heavier atoms (such as fluorine atoms) on a chromophore increases intersystem crossing from the singlet to the triplet state by increasing spin−orbital coupling, thus allowing otherwise forbidden changes in the spin state ($S_1 \rightarrow T_1$) (*66*). Accordingly, the exchange of hydrogen atoms for fluorine atoms of the periphery of phthalocyanine photosensitizers improves the photodynamic potential of the photosensitizer by improving triplet state yields.

Interestingly, for a series of zinc tetrahalogenated Pcs ($ZnPcX_4$, where X is Cl, Br, or I), it was observed that increases in triplet state formation and decreases in triplet-state lifetimes increased in the order Cl < Br < I, as would be expected in terms of spin−orbital coupling theory (*67*). However, the production of singlet oxygen was only slightly increased by the nature of the halogen atom. Although these results were not fully explained, it was noted that the tendency of these macrocycles to aggregate was in the order Br > I > Cl > H. As such, the improved photodynamic potential that results from the heavy atom effect may be somewhat counteracted by the tendency of Pcs to aggregate in solution. It has been shown that amphiphilic unsymmetrically substituted phthalocyanines bearing long alkyl chains exhibit decreased HPPI yields in the L-tryptophan photooxidation assay (*24*), even as CRM emulsion, due to important aggregation of the macrocycle, with the long alkyl chains increasing the lipophilicity of the Pcs. Whereas the zinc dodecafluorinated phthalocyanines are all lipophilic pho-

tosensitizers, it is believed that the longer alkyl chains promote aggregation of the phthalocyanine **5g**, even in CRM emulsions, resulting in decreased HPPI yields under these experimental conditions.

Most lipophilic Pcs, including unsubstituted ZnPc and AlOHPc, are highly insoluble in most common solvents. Thus, despite important photodynamic activity, the utility of such lipophilic Pcs is rather limited. Fluorine is very similar in atomic radius to hydrogen and can mimic hydrogen in biological environments. In addition, exchange of hydrogen atoms for fluorine atoms increases lipid solubility and thus may lead to enhanced interactions with biological membranes. A number of water-soluble amphiphilic fluorinated zinc phthalocyanines have also been synthesized and shown to have enhanced properties for photodynamic therapy (*68*, *69*). Additionally, a novel three-dimensional zinc perfluorinated phthalocyanine comprising 64 fluorine atoms has been synthesized from a novel nonplanar perfluorinated phthalonitrile and has been shown to have improved PDT efficiency as compared to $ZnPcF_{16}$ (*70*).

Preliminary in vitro PDT against EMT-6 tumor cells indicates that asymmetrically substituted dodecafluorinated phthalocyanines **5a**, **5b**, and **5g** are more photodynamically active than the symmetrically substituted $ZnPcF_{16}$ in CRM emulsions after incubations of 1 or 24 h (see Figure 3). Intriguingly, despite lower HPPI yields in the L-tryptophan photooxidation assay, **5g** was the most photodynamically active Pc examined. Whereas it was proposed that the lack of an appreciable activity of $ZnPcF_{16}$ and $ZnPcCl_{16}$ against M6 melanoma cells was due to aggregation of the PS even in the complicated environment of cells (*71*), the current study indicates that aggregation becomes less important in such biological systems, possibly due to interaction of proteins and lipoproteins with the planar Pc reducing the extent of aggregation.

CONCLUSION

DodecafluorosubPc boron(III) bromide (**2**) was prepared under milder conditions and shown to react readily with numerous 1,3-diiminoisoindolines in DMSO (Kobayashi ring expansion reaction), leading to the selective preparation of 3:1 unsymmetrically substituted dodecafluorinated phthalocyanines. Upon chelation to Zn^{2+} the resulting asymmetrically substituted dodecafluorinated ZnPcs were shown to be effective photosensitizers for the production of singlet oxygen. Preliminary in vitro photodynamic therapy against EMT-6 murine mammary tumor cells indicates that these compounds have potential as photosensitizers for PDT.

ACKNOWLEDGMENT

The Canadian Institute of Health Research is gratefully acknowledged for their financial support (CIHR Grant MOP-37768). We thank C. La Madeleine, Dr. H. Ali, and Dr. C. M. Allen for technical assistance and helpful discussion.

LITERATURE CITED

(1) Leznoff, C. C., and Lever, A. B. P., Eds. (1989−1996) *Phthalocyanines: Properties and Applications*, Vol. 1−04, VCH: Weinheim, Germany.
(2) Braun, A., and Tscherniac, J. (1907) Products of the action of acetic anhydride on phthalamide. *Ber. Dtsch. Chem. Ges. 40*, 2583−2584.
(3) Robertson, J. M. (1935) An X-ray study of the structure of the phthalocyanines. Part I. The metal-free, nickel, copper and platinum compounds. *J. Chem. Soc.* 615−621.
(4) Gregory, P. (2000) Industrial applications of phthalocyanines. *J. Porphyrins Phthalocyanines 4*, 432−437.
(5) McKeown, N. B. (1999) Out of the blue. *Chem. Ind.* 92−98.
(6) Douglas, W. M. (1978) Mercaptan oxidations in a liquid hydrocarbon with a metal phthalocyanine catalyst. U.S. Patent 4,088,569, May 9.
(7) Murakami, M., Tsuchiya, S., and Omote A. (1992) Phthalocyanine photosensitive material for electrophotography and process for making the same. U.S. Patent 5,087,540, Feb 11.
(8) Shawcross, A. P., and Wright, G. (2003) Phthalocyanine compounds used in inks for ink jet printing. U.S. Patent 6,-508,873, Jan 21.
(9) Stawitz, J.-W., Berneth, H., Bieringer, T., Bruder, F.-K., Hagen, R., Hassenruck, K., Kostromine, S., and Oser, R. (2004) Optical data stores containing a Co−phthalocyanine complex in the information layer recordable using light. U.S. Patent 6,713,146, March 30.
(10) Berneth, H., Bruder, F.-K., Haese, W., Hagen, R., Hassenruck, K., Kostromine, S., Landenberger, P., Oser, R., Sommermann, T., Stawitz, J.-W., and Bieringer, T. (2004) Optical data store comprising an axially substituted cobalt phthalocyanine in the light-writeable information layer. U.S. Patent 6,737,142, May 18.
(11) Snow, A. W., and Barger, W. R. (1989) Phthalocyanine films in chemical sensors. In *Phthalocyanines: Properties and Applications* (Leznoff, C. C., and Lever, A. B. P., Eds.) Vol. 1, pp 341−392, VCH Publishers: New York.
(12) Bardin, M., Bertounesque, E., Plinchon, V., Simon, J., Ahsen, V., and Bekaroglu, O. (1989) Electrochemistry of lutetium crowned ether diphthalocyanine films. *J. Electroanal. Chem. 271*, 173−180.
(13) Achar, B. N., and Jayasree, P. K. (1999) New "molecular metals" based on symmetrically tetrasubstituted copper phthalocyanine complexes. *Can. J. Chem. 77*, 1690−1696.
(14) van Nostrum, C. F., Picken, S. J., Schouten, A.-J., and Nolte, R. J. M. (1995) Synthesis and supramolecular chemistry of novel liqud crystalline crown-ether-substituted phthalocyanines: toward molecular wires and molecular ionoelectronics. *J. Am Chem. Soc. 117*, 9957−9965.
(15) Burghard, M., Schmelzer, M., Roth, S., Haisch, P., and Hanack, M. (1994) Langmuir−Blodgett film formation of a series of peripherally octasubstituted metallophthalocyanines. *Langmuir 10*, 4265−4269.
(16) Wöhrle, D. (2001) Phthalocyanine in macromolecular phases−methods of synthesis and properties of the materials. *Macromol. Rapid Commun. 22*, 68−97.
(17) Bao, Z. (1999) Organic thin film transistor having a phthalocyanine semiconductor layer. U.S. Patent 5,969,376, Oct 19.
(18) de la Torre, G., Vázquez, P., Agulló-López, F., and Torres, T. (1998) Phthalocyanines and related compounds: organic targets for nonlinear optical applications. *J. Mater. Chem. 8*, 1671−1683.
(19) Ali, H., and van Lier, J. E. (1999) Metal complexes as photo- and radiosensitizers. *Chem. Rev. 99*, 2379−2450.
(20) Allen, C. M., Sharman, W. M., and van Lier, J. E. (2001) Current status of phthalocyanines in the photodynamic therapy of cancer. *J. Porphyrins Phthalocyanines 5*, 161−169.
(21) Sastre, Á., del Rey, B., and Torres, T. (1996) Synthesis of novel unsymmetrically substituted push−pull phthalocyanines. *J. Org. Chem. 61*, 8591−8597.
(22) Maya, E. M., Garciá, C., Garciá-Frutos, E. M., Vázquez, P., and Torres, T. (2000) Synthesis of novel push−pull unsymmetrically substituted alkynyl phthalocyanines. *J. Org. Chem. 65*, 2733−2739.
(23) Margaron, P., Grégoire, M.-J., Åasnár, V., Ali, H., and van Lier, J. E. (1996) Structure−photodynamic activity relationships of a series of 4-substituted zinc phthalocyanines. *Photochem. Photobiol. 63*, 217−223.
(24) Allen, C. M., Langlois, R., Sharman, W. M., La Madeleine, C., and van Lier, J. E. (2002) Photodynamic properties of amphiphilic derivatives of aluminum tetrasulfophthalocyanine. *Photochem. Photobiol. 76*, 208−216.
(25) Schmid, G., Sommerauer, M., Geyer, M., and Hanack, M. (1996) Synthesis and chromatographic separation of tetrasubstituted and unsymmetrically substituted phthalocya-

nines. In *Phthalocyanines: Properties and Applications* (Leznoff, C. C., and Lever, A. B. P., Eds.) Vol. 4, pp 1−18, VCH Publishers: New York.
(26) Leznoff, C. C., Svirskaya, P. I., Khouw, B., Cerny, R. L., Seymour, P., and Lever, A. B. P. (1991) Syntheses of monometalated and unsymmetrically substituted binuclear phthalocyanines and a pentanuclear phthalocyanine by solution and polymer support methods. *J. Org. Chem. 56*, 82−90.
(27) Kobayashi, N., Kondo, R., Nakajima, S., and Osa, T. (1990) New route to unsymmetrical phthalocyanine analogues by the use of structurally distorted subphthalocyanines. *J. Am. Chem. Soc. 112*, 9640−9641.
(28) Meller, A., and Ossko, A. (1972) Phthalocyaninartige Kor-Komplexe. *Monatsch. Chem. 103*, 150−155.
(29) Claessens, C. G., González-Rodríguez, D., and Torres, T. (2002) Subphthalocyanines: singular nonplanar aromatic compounds—synthesis, reactivity and physical properties. *Chem. Rev. 102*, 835−853.
(30) Stork, J. R., Potucek, R. J., Durfee, W. S., and Noll, B. C. (1999) The synthesis and structure of mixed subphthalocyanine/subnaphthalocyanine complexes. *Tetrahedron Lett. 40*, 8055−8058.
(31) Ali, H., Sim, S. K., and van Lier, J. E. (1999) Synthesis of highly unsymmetrical phthalocyanines. *J. Chem Res. (S)* 496−497.
(32) Claessens, C. G., and Torres, T. (2000) A new substitution pattern in subphthalocyanines: regioselective synthesis and separation of "ortho" derivatives. *Eur. J. Chem.* 1603−1607.
(33) Cao, W.-F., Tu, H.-Y., Wang, J., Tian, H., Wang, Y., Gu, D., and Gan, F. (2002) Synthesis and optical properties of axially bromo-substituted subphthalocyanines. *Dyes Pigments 54*, 213−219.
(34) Ohno-Okumura, E., Sakamoto, K., Kato, T., Hatano, T., Fukui, K., Karatsu, T., Kitamura, A., and Urano, T. (2002) Synthesis of subphthalocyanine derivatives and their characterization. *Dyes Pigments 53*, 57−65.
(35) Rauschnabel, J., and Hanack, M. (1995) New derivatives and homologues of subphthalocyanines. *Tetrahedron Lett. 36*, 1629−1632.
(36) del Rey, B., Martínez-Díaz, M. V., Barberá, J., and Torres, T. (2000) Synthesis and thermotropic properties of hydroxyl and silyloxy axially substituted phthalocyanines. *J. Porphyrins Phthalocyanines 4*, 569−573.
(37) Kobayashi, N., Ishizaki, T., Ishii, K., and Konami, H. (1999) Synthesis, spectroscopy and molecular orbital calucations of subazaporphyrins, subphthalocyanines, subnaphthalocyanines and compounds derived thereform by ring expansion. *J. Am Chem. Soc. 121*, 9096−9110.
(38) Weitemeyer, A., Kliesch, K., and Wöhrle, D. (1995) Unsymmetrically substituted phthalocyanine derivatives via a modified ring enlargement reaction of unsubstituted subphthalocyanine. *J. Org. Chem. 60*, 4900−4904.
(39) Sastre, A., Torres, T., and Hanack, M. (1995) Synthesis of novel unsymmetrical monoaminated phthalocyanines. *Tetrahedron Lett. 36*, 8501−8504.
(40) Kasuga, K., Idehara, T., Handa, M., and Isa, K. (1992) Preparation of unsymmetrical phthalocyanine by means of a ring expansion of subphthalocyanine. *Inorg. Chim. Acta 196*, 127−128.
(41) Dabak, S., Gül, A., and Bekaroglu, Ö. (1994) Hexakis-(alkylthio)-substituted unsymmetrical phthalocyanines. *Chem. Ber. 127*, 2009−2012.
(42) Kudrevich, S. V., Gilbert, S., and van Lier, J. E. (1996) Syntheses of trisulfonated phthalocyanines and their derivatives using boron(III) subphthalocyanines as intermediates. *J. Org. Chem. 61*, 5706−5707.
(43) Kudrevich, S. V., Brasseur, N., La Madeleine, C., Gilbert, S., and van Lier, J. E. (1997) Syntheses and photodynamic activities of novel trisulfonated zinc phthalocyanine derivatives. *J. Med. Chem. 40*, 3897−3904.
(44) Marcuccio, S. M., Svirskaya, P. L., Greenberg, S., Lever, A. B. P., Leznoff, C. C., and Tomer, K. B. (1985) Binuclear phthalocyanines convalently linked through two- and four-atom bridges. *Can. J. Chem. 63*, 3057−3069.
(45) Leznoff, C. C., Terekhov, D. S., McArthur, C. R., Vigh, S., and Li, J. (1995) Multisubstituted phthalonitriles, naphthalenedicarbonitriles and phenanthrenetetracarbonitriles as precursors for phthalocyanine syntheses. *Can. J. Chem. 73*, 435−443.
(46) Terekhov, D. S., Nolan, K. J. M., McArthur, C. R., and Leznoff, C. C. (1996) Synthesis of 2,3,9,10,16,17,23,24-octaalkynlphthalocyanines and the effects of concentration and temperature on their ^{1}H NMR spectra. *J. Org. Chem. 61*, 3034−3040.
(47) Liu, Y., Zhu, D., Wada, T., Yamada, A., and Sasabe, H. (1994) Synthesis and characterization of a novel unsymmetrical metal-free phthalocyanine with donor−acceptor substituents. *J. Heterocycl. Chem. 31*, 1017−1020.
(48) Maya, E. M., Haisch, P., Vázquez, P., and Torres, T. (1998) Synthesis and characterization of tetraethynylphthalocyanines. *Tetrahedron 54*, 4397−4404.
(49) Wheeler, B. L., Nagasubramanian, G., Bard, A. J., Schechtman, L. A., Dininny, D. R., and Kenney, M. E. (1984) A silicon phthalocyanine and a silicon naphthalocyanine: synthesis, electrochemistry and electrogenerated chemiluminescence. *J. Am. Chem. Soc. 106*, 7404−7410.
(50) Ouyang, J., Shigehara, K., Yamada, A., and Anson, F. C. (1991) Hexafluoro- and octacyano phthalocyanines as electrocatalysts for the reduction of dioxygen. *J. Electroanal. Chem. 297*, 489−498.
(51) Birchall, J. M., Hazeldine, R. N., and Morley, J. O. (1970) Polyfluoroarenes. Part XIV. Synthesis of halogenophthalocyanines. *J. Chem. Soc. (C)* 2667−2672.
(52) Kudrevich, S. V., Ali, H., and van Lier, J. E. (1994) Syntheses of monsulfonated phthalocyanines, benzonaphthoporphyrazines and porphyrins via the Meerwein reaction. *J. Chem. Soc., Perkin Trans. 1* 2767−2774.
(53) Weber, J. H., and Busch, D. H. (1965) Complexes derived from strong field ligands. XIX. Magnetic properties of transition metal derivatives of 4,4′,4″,4‴-tetrasulfophthalocyanine. *Inorg. Chem. 4*, 469−471.
(54) Ali, H., Langlois, R., Wagner, J. R., Brasseur, N., Paquette, B., and van Lier, J. E. (1988) Biological activities of phthalocyanines. X. Syntheses and analyses of sulfonated phthalocyanines. *Photochem. Photobiol. 47*, 713−717.
(55) Boyle, R. W., Rousseau, J., Kudrevich, S. V., Obochi, M. O. K., and van Lier, J. E. (1996) Hexadecafluorinated zinc phthalocyanine: Photodynamic properties against the EMT-6 tumour in mice and pharmacokinetics using ^{65}Zn as a radiotracer. *Br. J. Cancer 73*, 49−53.
(56) Langlois, R., Ali, H., Brasseur, N., Wagner, J. R., and van Lier, J. E. (1986) Biological activities of phthalocyanines IV. Type II sensitized photooxidation of L-tryptophan and cholesterol by sulfonated metallo phthalocyanines. *Photochem. Photobiol. 44*, 117−123.
(57) Allémann, E., Brasseur, N., Benrezzak, O., Rousseau, J., Kudrevich, S. V., Boyle, R. W., Leroux, J.-C., Gurny, R., and van Lier, J. E. (1995) PEG-coated poly(lactic acid) nanoparticles for the delivery of hexadecafluoro zinc phthalocyanine to EMT-6 mouse mammary tumours. *J. Pharm. Pharmacol. 47*, 382−387.
(58) Allémann, E., Rousseau, J., Brasseur, N., Kudrevich, S. V., Lewis, K., and van Lier, J. E. (1996) Photodynamic therapy of tumours with hexadecafluoro zinc phthalocyanine formulated in PEG-coated poly(lactic acid) nanoparticles. *Int. J. Cancer 66*, 821−824.
(59) Allémann, E., Brasseur, N., Kudrevich, S. V., La Madeleine, C., and van Lier, J. E. (1997) Photodynamic activity and biodistribution of fluorinated zinc phthalocyanine derivatives in the murine EMT-6 tumour model. *Int. J. Cancer 72*, 289−294.
(60) Birchall, J. M., Haszeldine, R. N., and Morley, J. O. (1970) Polyfluoroarenes. Part XI. Reactions of tetrafluorophthalonitrile with nucleophilic reagents. *J. Chem. Soc. (C)* 456−462.
(61) del Rey, B., Keller, U., Torres, T., Rojo, G., Agulló-López, F., Nonell, S., Marti, C., Brasselet, S., Ledoux, I., and Zyss, J. (1998) Synthesis and nonlinear optical, photophysical and electrochemical properties of subsphthalocyanines. *J. Am. Chem. Soc. 120*, 12808−12817.
(62) Kipp, R. A., Simon, J. A., Beggs, M., Ensley, H. E., and Schmehl, R. H. (1998) Photophysical and photochemical

investigation of dodecafluorosubphthalocyanine derivative. *J. Phys. Chem. 102*, 5659−5664.
(63) Gerrard, W., and Lappert, M. F. (1958) Reactions of boron trichloride with organic compounds. *Chem. Rev. 58*, 1081−1111.
(64) Mody, T. D. (2000) Pharmaceutical development and medical applications of porphyrins-type macrocycles. *J. Porphyrin. Phthalocyanines 4*, 362−367.
(65) Sharman, W. M., Allen, C. M., and van Lier, J. E. (2000) Role of activated oxygen species in photodynamic therapy. *Methods Enzymol. 319*, 376−400.
(66) Wainwright, M. (1996) Non-porphyrin photosensitizers in biomedicine. *Chem. Soc. Rev.* 351−359.
(67) Zhang, X.-F., and Xu, H.-J. (1993) Influence of halogenation and aggregation on photosensitizing properties of zinc phthalocyanine (ZnPc). *J. Chem. Soc., Faraday Trans. 89*, 3347−3351.
(68) Fukushima, K., Tabata, K., and Okura, I. (1998) Photochemical properties of water-soluble fluorinated zinc phthalocyanines and their photocytotoxicity against HeLa cells. *J. Porphyrins Phthalocyanines 2*, 219−222.
(69) Oda, K., Ogura, S., and Okura, I. (2000) Preparation of water-soluble fluorinated zinc phthalocyanines and its effect for photodynamic therapy. *J. Photochem. Photobiol. B: Biol. 59*, 20−25.
(70) Bench, B. A., Beveridge, A., Sharman, W. M., Diebold, G. J., van Lier, J. E., and Gorun, S. M. (2002) Introduction of bulky perfluoroalkyl groups at the periphery of zinc perfluorophthalocyanine: chemical, structural, electronic, and preliminary photophysical and biological effects. *Angew. Chem., Int. Ed. Engl. 41*, 747−50.
(71) Decreau, R., Richard, M.-J., and Juillard, M. (2001) Photodynamic therapy against achromic M6 melanocytes: phototoxicity of lipophilic axially substituted aluminum phthalocyanines and hexadecahalogenated zinc phthalocyanines. *J. Porphyrins Phthalocyanines 5*, 390−396.
(72) Redmond, R. W., and Gamlin, J. N. (1999) A compilation of singlet oxygen yields form biologically relevant molecules. *Photochem. Photobiol. 70*, 391−475.

BC0500241

Tat Peptide as an Efficient Molecule To Translocate Gold Nanoparticles into the Cell Nucleus

Jesus M. de la Fuente*,§ and Catherine C. Berry

Centre for Cell Engineering, Institute of Biomedical and Life Science, Joseph Black Building, University of Glasgow, Glasgow G12 8QQ, U.K Received February 9, 2005; Revised Manuscript Received June 10, 2005

The labeling of targeting molecules with nanoparticles has revolutionized the visualization of cellular or tissue components by electron microscopy. A particularly desirable target is the nucleus, because the genetic information is there. To date, utilizing nanoparticles for nuclear targeting has not proved very successful due to the impermeable nature of the plasma and nuclear membranes; thus nanoparticle design and synthesis is a critical factor. We report in this article the synthesis of water-soluble gold nanoparticles functionalized with a Tat protein-derived peptide sequence by a straightforward and economical methodology. The particles were subsequently tested in vitro with a human fibroblast cell line by optical and transmission electron microscopy to determine the biocompatibility of these nanoparticles and whether the functionalization with the translocation peptide allowed particles to transfer across the cell membrane and locate in the nucleus.

INTRODUCTION

During the last 20 years, there has been a great deal of interest in the self-assembly fabrication of hybrid materials from inorganic nanoparticles and biomolecules (*1*). Nanoparticles are similar in size range to many common biomolecules and thus appear to be natural companions in hybrid systems. At present, it is straightforward to control and modify the properties of nanostructures to better suit their integration with biological systems, for example, controlling their size and modifying their surface layer for enhanced aqueous solubility, biocompatibility, or biorecognition (*2*, *3*).

This proposal of merging biological and nonbiological application systems at the nanoscale level has been used for research in cell and molecular biology for biosensing, bioimaging, masking of immunogenic moieties to targeted drug delivery, and interaction studies (*4*−*6*). For example, gold nanoparticles were initially used in biological applications in 1971, when Faulk and Taylor devised the immunogold staining procedure. More recently, the labeling of targeting molecules with nanoparticles has revolutionized the visualization of cellular or tissue components by electron microscopy (*7*). In fact, metal, semiconductor, polymer, and magnetic particles have been previously used to target cells (*8*−*14*). Most of these studies exclusively concerned particle entry into the cell cytoplasm. However, the nucleus is a particularly desirable target, because the genetic information of the cell and transcription machinery resides there. The diagnoses of disease phenotype, the identification of potential drug candidates, and the treatment of disease by novel methods such as antisense therapy could be enhanced greatly by the efficient transport of materials to living cell nuclei (*15*). However, one of the impediments in the use of nanoparticles for this purpose is their particularly low translocation efficiency into the cell nucleus.

Our research group is developing biocompatible fluorescence quantum dots and gold nanoparticles functionalized with different peptides to specifically label different receptors on the cell. Recently, we have reported the synthesis of CdS nanoparticles functionalized with a Tat protein-derived peptide sequence (*16*). This peptide sequence has previously been used as an efficient way of internalizing a number of marker proteins in cells (*17*, *18*).

In this study, gold nanoparticles protected with the non-amino-acid tiopronin and functionalized with a Tat protein-derived peptide were synthesized using a straightforward method. These nanoparticles are biocompatible and have been able to cross the cell and the nuclear membranes and accumulate in the cell nucleus.

EXPERIMENTAL PROCEDURES

Chemicals. Hydrogen tetrachloroaureate(III) trihydrate (99.9+%), (*N*-(3-dimethylaminopropyl)-*N*′-ethylcarbodiimide hydrochloride, and 2-[*N*-morpholino]ethanesulfonic acid (99.5%) were purchase from Sigma-Aldrich, *N*-(2-mercaptopropionyl)glycine (>98%) and *N*-hydroxysuccinimide (>97%) from Fluka, $NaBH_4$ (98%) from Lancaster, and Tat protein-derived peptide sequence (GRKKRRQRRR) from Southampton Polypeptides Ltd. House distilled water was further purified using a Milli-Q reagent grade water system (Millipore). Buffers were prepared according to standard laboratory procedure. Other chemicals were reagent grade and used as received.

General Procedures. ^{1}H NMR[1] spectra were acquired on Bruker DRX-400 spectrometers, and chemical shifts are given in ppm (δ) relative to the residual signal

* To whom correspondence should be addressed. Tel: +34-954489568. Fax: +34-95440565. E-mail: lafuente@iiq.csic.es.

§ Current address: Laboratory of Glyconanotechnology, Grupo de Carbohidratos, Instituto de Investigaciones Quimicas, CSIC, Isla de La Cartuja, Americo Vespucio 49, 41092 Sevilla, Spain.

[1] Abbreviations: UV/vis, ultraviolet−visible; NMR, nuclear magnetic resonance; FT-IR, Fourier transfer infrared; TEM, transmission electron microscopy; EDC, *N*-(3-dimethylaminopropyl)-*N*′-ethylcarbodiimide hydrochloride; NHS, *N*-hydroxysuccinimide; MES, 2-[*N*-morpholino]ethanesulfonic acid; MTT, 3-(4,5-dimethylthiazol-2-yl)-2,5-diphenyltetrazolium bromide; DMSO, dimethylsulphoxide; FCS, fetal calf serum; SP, surface plasmon; HIV, human immunodeficiency virus.

10.1021/bc050033+ CCC: $30.25 © 2005 American Chemical Society
Published on Web 08/26/2005

of the solvent used. UV spectra were carried out with a UV/vis Shimadzu UV-3101PC spectrometer in Milli-Q water. Infrared spectra of solid samples pressed into a KBr plate were recorded from 4000 to 750 cm^{-1} with a JASCO FT/IR 410 model spectrometer.

For TEM examinations, a single drop (10 μL) of the aqueous solution (0.1 mg mL^{-1}) of the gold nanoparticles was placed onto a copper grid coated with a carbon film. The grid was left to dry in air for several hours at room temperature. TEM analysis was carried out in a JEM-1200EX electron microscope working at 80 kV. Particle size distribution of the Au clusters was evaluated from several micrographs using an automatic image analyzer. The number of particles selected for consideration was around 400, which resulted in a stable size-distribution statistic.

Au@tiopronin. Hydrogen tetrachloroaureate(III) trihydrate (0.15 g, 0.4 mmol, 1 equiv) and *N*-(2-mercaptopropionyl)glycine (tiopronin; 0.19 g, 1.2 mmol, 3 equiv) were codissolved in 20 mL of 6:1 methanol/acetic acid, giving a ruby red solution. $NaBH_4$ (0.30 g, 8.0 mmol, 20 equiv) in 7.5 mL of H_2O was added with rapid stirring. The black suspension that was formed was stirred for an additional 30 min after cooling, and the solvent was then removed under vacuum at 40 °C. The crude **Au@tiopronin** was completely insoluble in methanol but quite soluble in water. It was purified by dialysis, in which the pH of 130 mg of crude product dissolved in 20 mL of water was adjusted to 1 by dropwise addition of concentrated HCl. This solution was loaded into 15 cm segments of seamless cellulose ester dialysis membrane (Sigma, MWCO = 10.000), placed in 4 L beakers of water, and stirred slowly, recharging with fresh water approximately every 10 h over the course of 72 h. The dark blue **Au@tiopronin** solutions were collected from the dialysis tubes and were lyophilized. The product materials were found to be spectroscopically clean (NMR, absence of signals due to unreacted thiol or disulfide byproducts). Yield: 96 mg. Average diameter: 2.8 nm. ^{1}H NMR (400 MHz, D_2O): δ = 4.40−3.75 (m), 3.70 (bs), 2.20−1.30 (m). UV/vis (H_2O): υ = 450, 560 nm (surface plasmon band). FT-IR (KBr): υ = 3436, 2920, 2855, 1624, 1385, 1297, 1260, 1019, 804 cm^{-1}.

Au@Tat. (*N*-(3-Dimethylaminopropyl)-*N*′-ethylcarbodiimide hydrochloride (EDC; 2 mg, 0.01 mmol) and *N*-hydroxysuccinimide (NHS; 3 mg, 0.025 mmol) were added to 4 mL of **Au@tiopronin** (2 mg) in 2-[*N*-morpholino]ethanesulfonic acid (MES) (50 mM, pH 6.5). The reaction proceeded for 30 min. After that, Tat peptide (112 μg, 0.000 08 mmol) was added, and the mixture was stirred for 24 h more. This solution was loaded into 6 cm segments of seamless cellulose ester dialysis membrane (Sigma, MWCO = 10.000), placed in 4 L beakers of water, and stirred slowly, recharging with fresh water approximately every 10 h over the course of 24 h. The dark blue **Au@Tat** solutions were collected from the dialysis tubes and were lyophilized. Yield: 1 mg. ^{1}H NMR (400 MHz, D_2O): δ = 4.65−4.80 (m), 4.25−3.75 (m), 3.66 (bs), 3.30−3.60 (m), 2.00−1.30 (m). UV/vis (H_2O): υ = 450, 560 nm (surface plasmon band). FT-IR (KBr): υ = 3419, 2917, 2842, 2357, 2330, 1647, 1635, 1452, 1418, 1385, 1310, 1283, 1111, 1024, 901, 799, 772 cm^{-1}.

Biocompatibility Assay. HTERT-BJ1 cells (10 000 cells) were cultivated in a 96 well plate at 37 °C in 5% CO_2. After 24 h, the medium was replaced with fresh medium containing the gold nanoparticles in varying concentrations. After cultivation again for 24 h, 20 μL of MTT dye solution (5 mg/mL in PBS) was added to each well. After 3 h of incubation at 37 °C and 5% CO_2, the medium was removed, the cells were washed with PBS, and formazan crystals were dissolved in 100 μL of DMSO. The absorbance of each well was read on a microplate reader (Dynatech MR7000 instruments) at 550 nm. The spectrophotometer was calibrated to zero absorbance using culture medium without cells. The relative cell viability (%) related to control wells containing cell culture medium without gold nanoparticles was calculated by $[A]_{test}/[A]_{control} \times 100$.

Scheme 1. Preparation of Au@Tat Nanoparticles

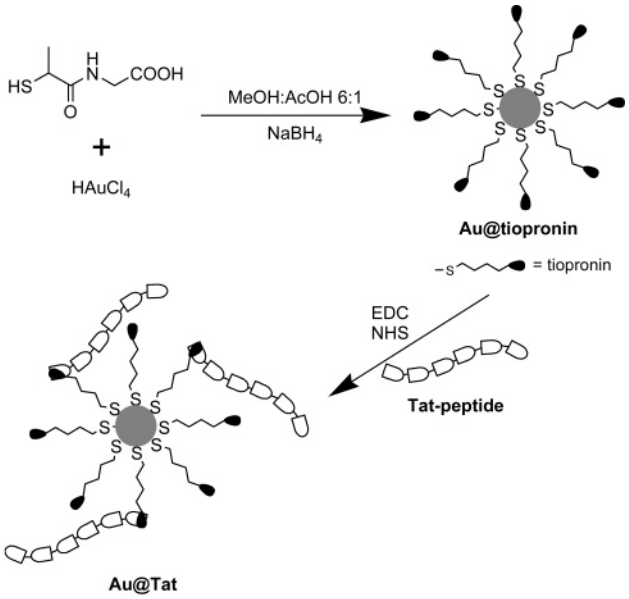

Cell Culture. Infinity telomerase-immortalized primary human fibroblasts (hTERT-BJ1, Clontech Laboratories, Inc., Palo Alto, CA) were seeded onto glass coverslips (13 mm diameter) at a density of 1×10^4 cells per disk in 1 mL of complete medium. The medium used was 71% Dulbecco's Modified Eagles Medium (DMEM) (Sigma, U.K.), 17.5% Medium 199, 9% fetal calf serum (FCS), 1.6% 200 mM L-glutamine, and 0.9% 100 mM sodium pyruvate. The cells were incubated at 37 °C with a 5% CO_2 atmosphere for 24 h. At this time point, the cells were incubated in complete medium supplemented with 0.05 mg mL^{-1} (≈1 μM) gold nanoparticles for 1 h more.

TEM. On removal of excess nanoparticles, cell samples were fixed in 1.5% gluteraldehyde (Sigma, Dorset, U.K.) in 0.1 M sodium cacodylate buffer (Agar, Essex, U.K.). Samples were subsequently post-fixed and stained with 1% osmium tetraoxide in buffer and were dehydrated through a series of alcohol concentrations (30%, 40%, 50%, 60%, 70%, 90%, 96%, 100%), prior to being resin-embedded. Sections were further enhanced with lead nitrate and viewed under a Zeiss 902 electron microscope at 80 kV.

RESULTS

Au@tiopronin nanoparticles were prepared using the procedure of Murray et al. (*19*). The reaction was executed in a methanolic/acetic acid mixture. Codissolution of $HAuCl_4$ and tiopronin gave a stable ruby-red solution. The addition of $NaBH_4$ reductant provided a dark brown solution (Scheme 1). The suspension was shaken for about 30 min, and then the solvent was removed. The nanoparticles were purified by dialysis and characterized by ^{1}H NMR, FT-IR, UV/vis and TEM. Figure 1 shows the TEM image and core size distribution histogram for **Au@tiopronin**. A mean diameter of 2.8 nm was found for the gold core of the nanoparticles. The

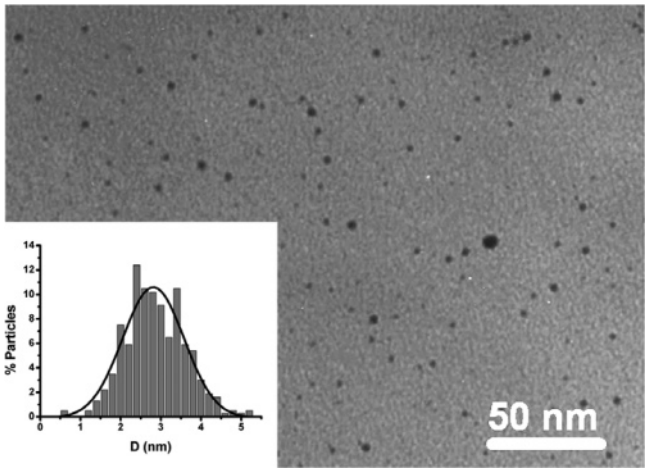

Figure 1. Transmission electron micrographs and core size-distribution histograms (inset) of **Au@tiopronin** nanoparticles.

UV/vis absorption spectrum showed a nondetectable surface plasmon band (SP band) (data not shown) as consequence of the small size of the clusters. ^{1}H NMR and FT-IR spectra confirmed the presence of tiopronin in the nanoparticles and the absence of other impurities.

The functionalization of **Au@tiopronin** with the Tat protein-derived sequence (GRKKRRQRRR) was carried out using the reactivity of the free carboxyl group of the tiopronin (Scheme 1). The reaction utilizes the water-soluble carbodiimide EDC to catalyze reactions between the nanoparticle acid groups and any of the amine groups of the peptide (*20*). We included NHS in the reaction mixture to improve the efficiency of the carbodiimide-mediated amide-forming reaction by producing hydrolysis-resistant active ester reaction intermediates (*21*). The resultant nanoparticles were analyzed by UV/vis, FT-IR, ^{1}H NMR, and TEM; nonagglutination was observed after Tat peptide coupling.

Biocompatibility studies of the **Au@tiopronin** and **Au@Tat** nanoparticles were undertaken by evaluating the cell viability of hTERT-BJ1 human fibroblasts by the MTT assay (*22*) (Figure 2). The metabolic activity and proliferation of fibroblasts was thus measured after 24 h culture and revealed no appreciable cytotoxic effects to cells at concentration as high as 5 μM, and the values reached 80% compared to untreated controls at concentrations higher than 10 μM.

TEM images taken after 1 h incubation with the particles (Figure 3) show that **Au@tiopronin** and **Au@Tat** were both taken up into the cell body. While **Au@Tat** particles were mainly located in the nucleus, only a few **Au@tiopronin** particles appeared to be taken into the cell through membrane invaginations and accumulate in the mitochondrial surroundings. **Au@tiopronin** nanoparticles were not detected in the nucleus in any case.

DISCUSSION

Based on our previous experience of sulfide-protected glyconanoparticles (*3*, *23*), we now report the simple synthesis of water-soluble and stable gold nanoparticles functionalized with a Tat protein-derived peptide sequence as a vehicle for ferrying nanoparticles into the cell nucleus.

The **Au@tiopronin** particles have been previously used in material science studies due their small size and their water-solubility, although their use in cell biology has not been extensively explored. These nanoparticles

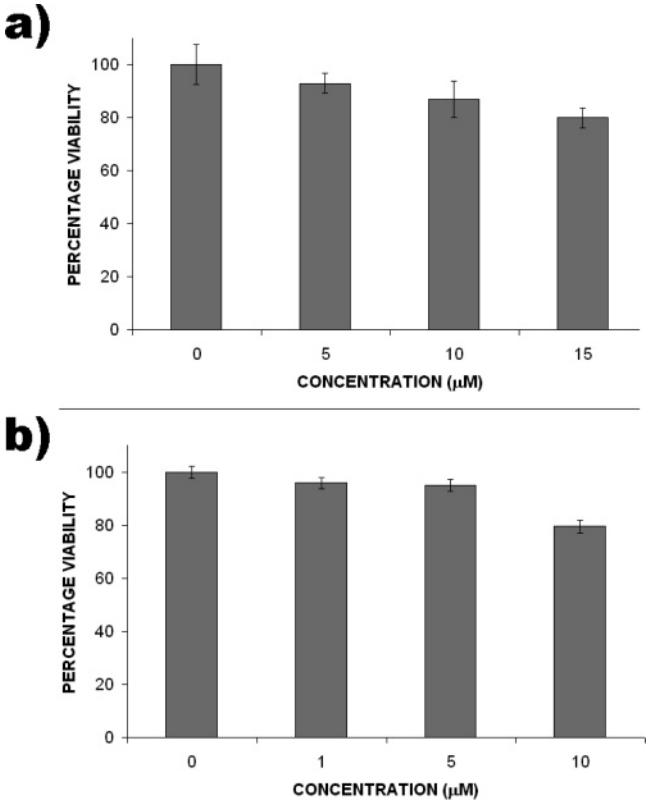

Figure 2. Cytotoxicity profiles of **Au@tiopronin** (a) and **Au@Tat** (b) nanoparticles when incubated with human fibroblasts as determined by MTT assay. Percentage of viability of fibroblasts was expressed relative to control cells ($n = 5$). Results are represented as mean ± standard deviations.

are useful tools for immunolabeling or as drug carriers due the absence of agglutination in physiological conditions and their easy functionalization. As previously stated, the free carboxyl group of the tiopronin is available for covalent coupling to various biomolecules by cross-linking to reactive amino groups. In this study, a peptide sequence derived from the HIV-1 Tat peptide has been coupled to the nanoparticle surface with a view to transfer gold nanoparticles into the cell nucleus.

The biocompatibility of **Au@tiopronin** and **Au@Tat** particles was studied using the MTT assay (*22*). This assay relies on the mitochondrial activity of fibroblasts and represents a parameter for their metabolic activity. Furthermore, it is a simple nonradiactive colorimetric assay allowing simple measurements of cell cytotoxicity, proliferation, or viability. Briefly, MTT is a yellow, water-soluble tetrazolium salt that metabolically active cells are able to convert into a water-insoluble dark-blue formazan by reductive cleavage of the tetrazolium ring. Formazan crystals can be dissolved in dimethylsulfoxide and quantified. Only 20% cytotoxicity was detected in both types of nanoparticles at concentrations up to 10 μM. Below this concentration, cellular metabolic activity did not change much in comparison with control cells (Figure 2). This low cytotoxicity allows us to use concentrations of these nanoparticles up to 10 μM for our cell nuclear labeling purposes.

The absence of impurities in the nanoparticles has been confirmed by ^{1}H NMR and FT-IR. Tat specific signals were not found in ^{1}H NMR due the low Tat/tiopronin ratio (≈1:50) (*19*) and the typical broadening of the ^{1}H NMR signals for this type of gold nanoparticles (*3*). The TEM images (Figure 1) and the almost nondetectable

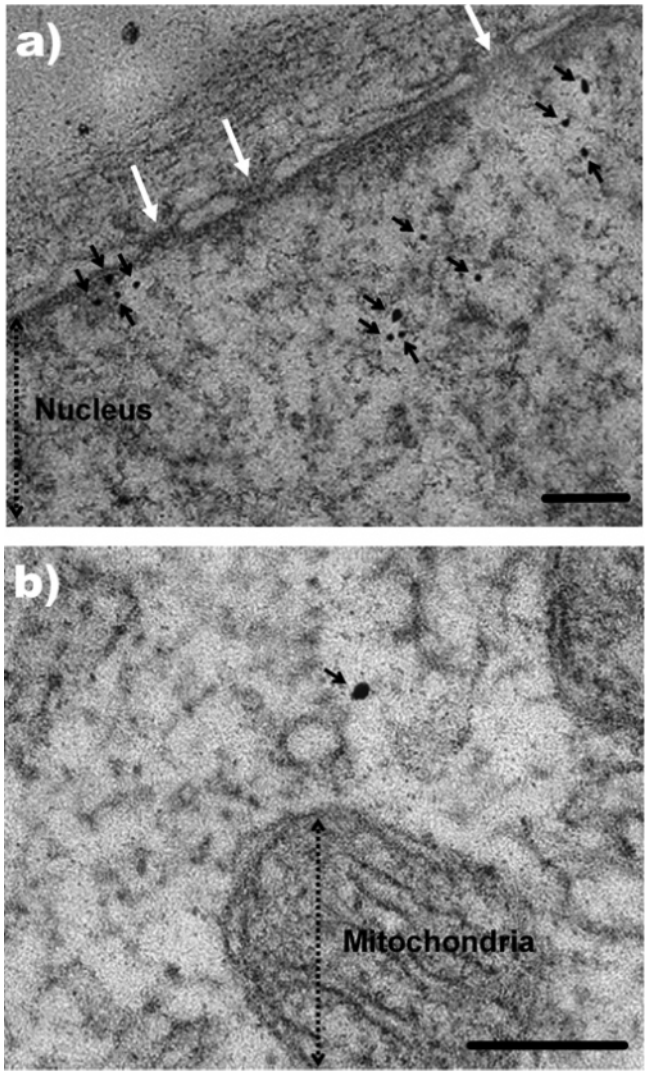

Figure 3. Transmission electron micrographs of human fibroblasts incubated with **Au@Tat** (a) and **Au@tiopronin** (b) nanoparticles. The black dots indicated with arrows are nanoparticles, and white arrows show nuclear membrane pores. (scale bars = 50 nm).

surface plasmon band confirm the small size of the clusters and the absence of aggregates.

In the present study, **Au@Tat** nanoparticles were explored to achieve nuclear targeting of human fibroblasts cells. Targeted nuclear delivery is a challenging task, because the **Au@Tat** nanoparticles must enter the cell, escape endosomal/lysosomal pathways, possess a nuclear localization sequence, and be small enough (<30 nm) to cross the nuclear membrane via nuclear pores. TEM studies have been developed to study cell and nuclear uptake.

It should be noted that the synthetic methodology reported here does not allow us to control the amino group of the Tat peptide that reacts with the nanoparticle. However, the different cell responses to **Au@Tat** in comparison with **Au@tiopronin** particles confirm the correct coupling of the Tat peptide sequence and its activity after the coupling.

The nucleus was clearly visible via TEM, and despite dense background nuclear staining, only **Au@Tat** particles were observed in the nucleus (Figure 3a). Nuclear membrane pores, the only known route of direct nucleocytoplasmic exchange of matter, were evident at the 30 nm size range and are thought to be the method of particle entry into the nucleus. **Au@tiopronin** particles were only detected in the cytoplasm in vacuoles or surrounding the mitochondria (Figure 3b), thus demonstrating the specificity of **Au@Tat** particles to be translocated and accumulate in the cell nucleus.

In conclusion, we have prepared and designed stable and water-soluble gold nanoparticles functionalized with a Tat protein-derived peptide sequence with an adequate size range to pass through nucleus pores. This functionalization has allowed the nanoparticles to penetrate the cell membrane and target the nucleus. This research has many potential applications in cell imaging, but also extends to wider biomedical applications, such as gene therapy and drug delivery.

ACKNOWLEDGMENT

This work was supported by EC, MEC, and University of Glasgow. J.M.F. thanks the MEC for a postdoctoral fellowship. We thank Mr. Jim Gallagher for help with TEM and Dr L. Cronin, Prof. A. S. G. Curtis, and Dr. M. Riehle for fruitful discussions.

LITERATURE CITED

(1) Niemeyer, C. M. (2001) Nanoparticles, proteins, and nucleic acids: Biotechnology meets materials science. *Angew. Chem., Int. Ed. 40*, 4128−4158.
(2) Katz, E., and Willner, I. (2004) Integrated nanoparticle-biomolecule hybrid systems: Synthesis, properties, and applications. *Angew. Chem., Int. Ed. 43*, 6042−6108.
(3) Barrientos, A. G., de la Fuente, J. M., Rojas, T. C., Fernandez, A., and Penades, S. (2003) Gold glyconanoparticles: Synthetic polyvalent ligands mimicking glycocalyx-like surfaces as tools for glycobiological studies. *Chem.—Eur. J. 9*, 1909−1921
(4) Daniel, M. C., and Astruc, D. (2004) Gold nanoparticles: Assembly, supramolecular chemistry, quantum-size-related properties, and applications towards biology, catalysis, and nanotechnology. *Chem. Rev. 104*, 293−346.
(5) Berry, C. C., and Curtis, A. S. G. (2003) Functionalisation of magnetic nanoparticles for applications in biomedicine. *J. Phys. D: Appl Phys. 36*, R198−R206.
(6) de la Fuente, J. M., and Penades, S. (2004) Understanding carbohydrate-carbohydrate interactions by means of glyconanotechnology. *Glycoconjugate J. 21*, 149−163.
(7) Kerr, M. A., and Thorpe, R., Eds. (1994) All about immunogold staining. *Immunochemistry Labfax*, BIOS Scientific Publishers: Oxford, U.K.
(8) West, J., and Halas, N. (2000) Applications of nanotechnology to biotechnology: Commentary. *Curr. Opin. Biotechnol. 11*, 215−217.
(9) Hogemann, D., Ntziachristos, V., Josephson, L., and Weissleder, R. (2002) High throughput magnetic resonance imaging for evaluating targeted nanoparticles probes. *Bioconjugate Chem. 13*, 116−121.
(10) Bruchez, M., Moronne, M., Gin, P., Weiss, S., and Alivisatos, A. (1998) Semiconductor nanocrystals as fluorescent biological labels. *Science 281*, 2013−2016.
(11) Liu, J., Zhang, Q., Remsen, E., and Wooley, K. (2001) Nanostructured materials designed for cell binding and transduction. *Biomacromolecules 2*, 362−368.
(12) Marikanos, S. M., Anderson, M. F., Ryan, J., Martin, L. D., and Feldheim, D. L. (2001) Encapsulation, permeability, and cellular uptake characteristics of hollow nanometer-sized conductive polymer capsules. *J. Phys. Chem. B 105*, 8872−8876.
(13) Feldherr, C., Lanford, R., and Akin, D. (1992) Signal-mediated nuclear transport in simian virus 40-transformed cells is regulated by large tumor antigen. *Proc. Natl. Acad. Sci. U.S.A. 89*, 11002−11005.
(14) Tkachenko, A. G., Xie, H., Coleman, D., Glomm, W., Ryan, J., Anderson, M. F., Frazen, S., and Feldheim, D. L. (2003) Multifunctional gold nanoparticle-peptide complexes for nuclear targeting. *J. Am. Chem. Soc. 125*, 4700−4701.

(15) Kole, R., and Sazani, P. (2001) Antisense effects in the cell nucleus: Modification of splicing. *Curr. Opin. Mol. Ther. 3*, 229−234.
(16) De la Fuente, J. M., Fandel, M., Berry, C. C., Riehle, M., Cronin, L., Aitchison, G., and Curtis, A. S. G. (2005) Quantum dots protected with tiopronin: A new fluorescence system for cell biology studies. *ChemBioChem 6*, 989−991.
(17) Ford, K. G., Souberbielle, B. E., Darling, D., and Farzanech, F. (2001) Protein transduction: An alternative to genetic intervention? *Gene Ther. 8*, 1−4.
(18) Lewin, M., Carlesso, N., Tung, C.-H., Tang, X. W., Cory, D., Scadden, D. T., and Weissleder, R. (2000) Tat peptide-derivatized magnetic nanoparticles allow in vivo tracking and recovery of progenitor cells. *Nat. Biotechnol. 18*, 410−414.
(19) Templeton, A. C., Chen, S., Gross, S. M., and Murray, R. W. (1999) Water-soluble, isolable gold clusters protected by tiopronin and coenzyme A monolayers. *Langmuir 15*, 66−76.
(20) Detar, D. F., and Silverstein, R. (1996) Reactions of carbodiimides. I. The mechanisms of the reactions of acetic acid with dicyclohexylcarbodiimide. *J. Am. Chem. Soc. 88*, 1013−1019.
(21) Templeton, A. C., Cliffel, D. E., and Murray, R. W. (1999) Redox and fluorophore functionalization of water-soluble, tiopronin-protected gold clusters. *J. Am. Chem. Soc. 121*, 7081−7089.
(22) Mosmann, T. J. (1983) Rapid colorimetric assay for cellular growth and survival-application to proliferation and cytotoxicity assays. *Immunol. Methods 65*, 55−63.
(23) de la Fuente, J. M., Barrientos, A. G., Rojas, T. C., Rojo, J., Canada, A., Fernandez, A., and Penades, S. (2001) Gold glyconanoparticles as water-soluble polyvalent models to study carbohydrate interactions. *Angew. Chem., Int. Ed. 40*, 2257−2261.

BC050033+

Folate-Conjugated Iron Oxide Nanoparticles for Solid Tumor Targeting as Potential Specific Magnetic Hyperthermia Mediators: Synthesis, Physicochemical Characterization, and in Vitro Experiments

Fabio Sonvico,[†,‡,||] Stéphane Mornet,[§] Sébastien Vasseur,[§] Catherine Dubernet,[†] Danielle Jaillard,[⊥] Jeril Degrouard,[⊥] Johan Hoebeke,[+] Etienne Duguet,[§] Paolo Colombo,[‡] and Patrick Couvreur*[,†]

UMR CNRS 8612 Physico-chimie, Pharmacotechnie, Biopharmacie - Université de Paris-Sud, Châtenay-Malabry, France, Dipartimento Farmaceutico - Università degli Studi di Parma, Parma, Italy, UPR CNRS 9048 Institut de Chimie de la Matière Condensée de Bordeaux, Université Bordeaux-1, France, National Institute for the Physics of the Matter, Parma, Italy, UMR CNRS 8080 Développement et Evolution - Centre Commun de Microscopie Electronique, Université de Paris Sud, Orsay, France, and UPR CNRS 9021 Immunologie et Chimie Thérapeutiques, Université de Strasbourg, Strasbourg, France. Received February 24, 2005; Revised Manuscript Received July 28, 2005

New folate-conjugated superparamagnetic maghemite nanoparticles have been synthesized for the intracellular hyperthermia treatment of solid tumors. These ultradispersed nanosystems have been characterized for their physicochemical properties and tumor cell targeting ability, facilitated by surface modification with folic acid. Preliminary experiments of nanoparticles heating under the influence of an alternating magnetic field at 108 kHz have been also performed. The nanoparticle size, surface charge, and colloidal stability have been assessed in various conditions of ionic strength and pH. The ability of these folate "decorated" maghemite nanoparticles to recognize the folate receptor has been investigated both by surface plasmon resonance and in folate receptor expressing cell lines, using radiolabeled folic acid in competitive binding experiments. The specificity of nanoparticle cellular uptake has been further investigated by transmission electron microscopy after incubation of these nanoparticles in the presence of three cell lines with differing folate receptor expression levels. Qualitative and quantitative determinations of both folate nanoparticles and nontargeted control nanoparticles demonstrated a specific cell internalization of the folate superparamagnetic nanoparticles.

INTRODUCTION

In recent years, colloidal carriers have elicited many hopes for their potential as vectors for therapeutics and diagnostics in cancer therapy (*1*, *2*). As reviewed recently, metal-based colloids have many interesting applications in the biomedical field, too (*3*, *4*). For example, iron oxide nanoparticles, prospected in diagnostic clinical practice as magnetic resonance imaging enhancers in the mid 80s and currently in clinical phase IV, are nowadays among the most successful application of nanotechnologies in medicine (*5*, *6*). Nevertheless, some decades ago, such particles were already suggested as a tool to manage hyperthermia in solid tumors by heating them with alternating magnetic fields (*7*). Hyperthermia treatment of tumor and metastasis has, indeed, been demonstrated to be effective, either alone, the neoplastic cells being more thermosensitive than the normal ones, or in association with classical chemo- or radiotherapies (*8*−*10*). Despite some preliminary interesting results in preclinical tumor animal models (*11*), hyperthermia using superparamagnetic iron oxide particles has, however, been overlooked for almost a decade. Thanks to a new wave of interest for this technique, since the early 90s, a lot of progress has been made, especially in the field of superparamagnetic materials, so that finally the time seems to be ripe for the start of clinical studies (*12*, *13*). The hyperthermia is obtained by applying an alternating magnetic field of suitable frequency that produces heat dissipation through the oscillation of the internal magnetic moment of the superparamagnetic particles (*14*). Among the developments that have been considered for nanoparticle-mediated hyperthermia, we have focused our attention on the opportunity to achieve an intracellular hyperthermia treatment (*15*). The interest lies in the specific delivery of heat to target cells causing selective damage to their cytoplasm structures. Recently, a very similar approach, in which laser-absorbing gold nanoparticles were used, has been successfully applied to obtain specific targeting and killing of cancer cells (*16*). In the present study, we describe a new type of dextran-coated maghemite superparamagnetic nanoparticles targeted toward solid tumors through folate, covalently bound to the nanoparticle surface using a poly(ethylene)-

* To whom correspondence should be addressed. Université de Paris XI - Centre d'études pharmaceutiques, 5, rue J.B Clément, 92296 Châtenay-Malabry, France. Phone: +33-(0)1-46835396. Fax: +33-(0)1-46619334. E-mail: Patrick.couvreur@cep.u-psud.fr.

† UMR CNRS 8612 Physico-chimie, Pharmacotechnie, Biopharmacie - Université de Paris-Sud.

‡ Università degli Studi di Parma.

§ Université Bordeaux-1.

|| National Institute for the Physics of the Matter.

⊥ UMR CNRS 8080 Développement et Evolution - Centre Commun de Microscopie Electronique, Université de Paris Sud.

+ Université de Strasbourg.

10.1021/bc050050z CCC: $30.25 © 2005 American Chemical Society
Published on Web 09/02/2005

glycol (PEG) spacer. Folic acid (FA) has been chosen as the targeting moiety, since it has been observed that many solid tumors, such as ovarian and breast cancers, overexpress the specific receptor for this vitamin. In this paper, these FA-conjugated superparamagnetic nanoparticles have been characterized for their physicochemical properties, their heating capacity, and their efficacy in targeting cancer cells overexpressing the folate receptor.

MATERIALS AND METHODS

All chemicals and reagents, except where indicated, were provided by SIGMA-Aldrich (St.Quentin Fallavier, France). Cell culture media and reagents were obtained from Invitrogen-Lifetechnologies (Cergy Pontoise, France).

Superparamagnetic Nanoparticles Preparation. *Dextran-Coated Maghemite Nanocrystals Production.* Dextran-coated superparamagnetic maghemite (γ-Fe_2O_3) nanocrystals have been produced through a procedure already described (*14*, *15*). Briefly, the cores were produced by the coprecipitation of Fe(III) and Fe(II) ions in alkaline conditions, oxidation, and peptization to obtain a maghemite (γ-Fe_2O_3) cationic ferrofluid as previously reported (*16*). Subsequently, the surface modification of crystals was carried out by adding an amino silane coupling agent, γ-(aminopropyl)triethoxysilane, in methanol/water medium (1:1), followed by thermal treatment at 100−110 °C in glycerol for 2 h under vacuum. The flocculated particles were then washed with acetone and water and peptized with nitric acid until pH = 3. Such a ferrofluid was stable in a pH range of 1 to 8. The magnetic nanoparticles were sterically stabilized by activated dextran (70 kD). The activation was performed by partial oxidization of dextran vicinal diols into aldehyde groups with sodium metaperiodate. The oxidized dextran was allowed to react with the amino groups of maghemite in order to be anchored through covalent imine bonds (Shiff's bases). The colloidal suspension was washed by tangential ultrafiltration against 3 L of ultrapure water with a poly(ethersulfone) membrane (cutoff 100 000 g/mol) and stored at room temperature. Such dextran-coated maghemite nanoparticles may be described as a new covalent platform useful for MRI contrast enhancement as well as hyperthermia mediators. They were called VUSPIO for versatile ultrasmall superparamagnetic iron oxide (*14*, *15*).

Folate Conjugation. N-Hydroxysuccinimide ester of FA (NHS-folate) was prepared according to a method previously described (*17*). Briefly, 5 g of FA, dissolved in 100 mL of dry dimethyl sulfoxide containing 2.5 mL of triethylamine, was reacted with 2.6 g of *N*-hydroxysuccinimide in the presence of 4.7 g of dicyclohexylcarbodiimide overnight at room temperature. After removing the byproduct (dicyclohexylurea) by filtration, the yellow solid NHS-folate was then extracted by precipitation in diethyl ether, washed several times with anhydrous ether, and dried under vacuum. Amino−PEG−folate was prepared as follows: 1.351 g of NHS-folate was dissolved in 50 mL of DMSO and slowly added to 250 mL of carbonate/bicarbonate buffer (1 M, pH 11 adjusted with HCl 37%) containing 5 g of diaminotelechelic−PEG (Jeffamine ED-2003 from Huntsman, Salt Lake City). Two hours later, the solution was dialyzed against 5 L of water (MwCo 1000 g/mol). The dialysis procedure was repeated every 24 h for a total of 5 times. Amino−PEG−folate was characterized by ^{1}H NMR (300 MHz, DMSO-d_6): δ 8.61 (s, 7-H of FA, 1H), 7.65 (d, 13,15-H of FA, 2H), 6.64 (d, 12,16-H of FA, 2H), 4.25−4.15 (m, 19-H of FA, 1H), 3.75−3.45 (m, CH_2CH_2 of PEG, ∼170H), 1.07−0.87 (m, propylene CH_3 Jeffamine ED-2003, ∼15H). UV analysis allowed the determination of the folate content in the final product: 26.3 mg of amino−PEG−FA were dissolved in 2 mL of 10 mM phosphate buffer, 0.15 M NaCl, pH 7.5, diluted 50 times in phosphate buffer and analyzed by UV. The folate content was estimated on the basis of the FA extinction coefficient $\epsilon_M = 6197\ M^{-1}\cdot cm^{-1}$ at 363 nm and found equal to the average value of 1.02 folate group per amino−PEG−FA macromolecule.

Maghemite nanoparticles coated with activated dextran were then reacted with 75 mol % of monoamino−PEG and 25% of amino−PEG−FA in a 0.1 M borate buffer pH 9 in the presence of sodium borohydride 0.206 M. The pH was maintained at pH 9 by adding dropplets of NaOH 0.1 M. When the pH value was stabilized, the solution was left to react for 4 h at room temperature. In such conditions, the generated Schiff's bases were stabilized by reductive amination (VUSPIO−PEG−FA). The excess of unreacted materials and borate salts were removed through tangential ultrafiltration. The control nanoparticles were prepared according to the same procedure with 100% of monoamino−PEG (VUSPIO−PEG).

Physicochemical Characterization of Nanoparticles. *Nanoparticles Size and Surface Charge.* The mean particle size was determined by dynamic light scattering (DLS, N4Plus, Beckman-Coulter, USA). Hydrodynamic diameter measurements were performed at 20 °C and 90° angle, after dilution of the sample to 150 μg/mL iron oxide concentration either in NaCl solutions of increasing concentrations (up to 1 M), or in 0.01 M phosphate buffers at various pH (ranging from 4 to 10). Each sample was analyzed six times for a total period of analysis of 20 min. The surface charge of the nanoparticles was investigated through ζ potential measurements (Zetasizer 4, Malvern Instruments, UK) after dilution of the samples in 0.01 M phosphate buffers at pH between 4 and 10. Smoluchowsky approximation was applied in the calculation of ζ potential.

Nanoparticle Density. The density of the nanoparticles in suspension was measured at 20 °C using a high-precision digital densitometer (Analyzer Beer 2, Anton Paar, Austria). The densitometer was standardized using air (0.001238 g/cm^3) and water (0.998314 g/cm^3) at the same temperature. The nanoparticle density was calculated, as previously described (*21*), by successive approximation from the nanoparticles concentration and the density values obtained for the suspension and for the suspending medium (MilliQ water adjusted at pH 7.4 with NaOH), assuming that no interaction occurred between the nanoparticles and the suspending fluid.

Nanoparticle Structure and Morphology. The morphology of the nanoparticles was investigated by transmission electron microscopy (TEM, EM208 Philips, The Netherlands, operating at 80 keV) and high-resolution TEM (JEOL 2010, JEOL, Japan, operating at 200 keV) observations. Colloid suspensions were deposited on UV-ionized copper grids coated with Formvar film (200 mesh). After 5 min, the excess suspension was removed and the samples were observed. Electron diffraction experiments on samples prepared in the same way, but with nickel grids, have been performed in order to confirm the presence of the iron oxide crystals in the nanoparticles (CM 12, Philips, Netherlands).

Nanoparticle Heating. Magnetic heating of aqueous suspensions of nanoparticles (in the concentration range 2.5−3 $g_{maghemite}$/L) were performed under an alternating field of H_{max} = 88 mT and ν = 108 kHz, produced by a

Celes inductor C97104. Temperature was monitored by alcohol thermometer to avoid any inductive or capacitive heating of the temperature probe. The specific absorption rate was calculated using the simplified relation

$$SAR = \frac{C_{\text{water}}}{x_{\text{Fe}}} \frac{\Delta T}{\Delta t}$$

where C_{water} is the specific heat capacity of water, x_{Fe} is the mass fraction of iron, and $\Delta T/\Delta t$ is the slope of the temperature vs time dependence.

Targeting Properties of the Folate-Conjugated Nanoparticles. *Surface Plasmon Resonance Measurements.* Surface plasmon resonance was used to investigate the efficacy of the interaction between the FA binding protein (FBP) and the folate-functionalized nanoparticles. Measurements were carried out using a BIAcore 3000 (Pharmacia Biosensor AB, Sweden). Cows milk FBP was immobilized onto the surface of a carboximethyldextran-coated gold film (Sensor chip CM-5, BIAcore, Sweden) by amine coupling performed according to the general procedure recommended by the BIAcore supplier (*22*). Briefly, the flow channel of BIAcore was equilibrated with Hepes buffered saline (HBS = 10 mM Hepes pH 7.4, 150 mM NaCl, 3 mM EDTA, 0.005% surfactant P20), and then the following samples were successively injected into the system: (a) *N*-hydroxysuccinimmide solution + *N*′-(3-dimethyl-amino-propyl)-*N*-ethylcarbodiimide solution (1/1, v/v) to activate the carboxylated-dextran surface; (b) 1 mg/mL of FBP in 100 mM phosphate buffer pH 7.0, 4 mM mercaptoethanol, 10% v/v glycerol, and (c) 1 M ethanolamine pH 8.5, to quench residual *N*-hydroxysuccinimidyl esters on the sensor chip. FBP immobilization was then carried out afterward using a flow rate of 5 μL/min. Nanoparticle suspensions in HBS (1.07 mg/mL of Fe) were injected into the BIAcore flow channel at a flow rate of 5 μL/min and allowed to interact with the immobilized receptor for 10 min. The specific interaction with the protein shifted the wavelength at which the surface plasmon resonance occurred. This shift was registered as response units (RU). In a subsequent experiment of binding, a competitive inhibition was performed, nanoparticles being injected under the above operative conditions in the presence of 4 mM free FA.

In Vitro Cell Culture Experiments. *Cell Culture.* The cells cultivated for in vitro experiments were human epithelial mouth carcinoma, KB 3-1 (gift of Dr. S. Chevillard, Fontenay-aux-Roses, France), human breast adenocarcinoma, MCF7 (ATCC, USA), and human cervix adenocarcinoma, HeLa cell line (gift of Prof. C. Malvy, Institut Gustave Roussy, Paris, France). All cell lines were grown in folate-free Dulbecco Modified Eagle's Medium (FFDMEM) with 10% fetal calf serum, 100 units/mL penicillin and 100 μg/mL streptomycin, 4 mM L-glutamine at 37 °C in a 5% CO_2/95% air humidified atmosphere. The concentration of FA was 5−6 nM in folate-free medium containing serum, therefore close to the natural physiologic conditions (5−30 nM) (*23*, *24*). Cells were grown in the above-mentioned conditions at least 1 week prior the experiments to reach the maximal expression level of the folate receptor (FR) for KB and HeLa cells as described in a previous study (*25*). MCF7 cells, which do not express the FR, were used as control.

Cytotoxicity. Nanoparticle cytotoxicity was assessed by the 3-(4,5-dimethylthiazol)-2-diphenyltertrazolium bromide (MTT) test (*26*). Cells were seeded in 96-well tissue culture plates at a density of 5×10^4 cells/well. After 24 h, the culture medium was replaced with 200 μL of FFDMEM containing increasing concentrations of nanoparticles. After 3 h incubation, 20 μL of a solution of MTT (5 mg/mL in NaCl 0.9%) was added to each well and a further 3 h incubation at 37 °C was allowed. At the end of this time the supernatant was carefully removed from each well, without taking off the blue formazan crystals produced by viable cells. Then to completely dissolve the crystals, 200 μL of solvent (1:1, dimethylformamide/sodium dodecylsulfate 20% aqueous solution) were added to each well followed by 3 h incubation at 37 °C. Colorimetric measurements were performed at 570 nm with a scanning multiwell spectrometer (Multiskan MS, Labsystems, Finland). Absorbance values for untreated wells were taken as control reference (100% survival).

Inhibition of the Uptake of Radiolabeled FA into Cells by Nanoparticles. The interaction of nanoparticles with cells expressing the folate receptors was assessed through the measurement of the inhibition of the free tritium-labeled FA uptake ([^{3}H]-FA), as has been shown previously (*27*). Briefly, KB 3-1 cells were allowed to grow in folate-free medium for 1 week. Thereafter, 5×10^5 cells were seeded in 6-well plates. Wells containing medium but without cells were used as control for the unspecific adsorption of the radiolabeled FA on plastic surfaces. Twenty-four hours later, after careful washing with phosphate-buffered saline (PBS), cells were incubated for 30 min at 37 °C with 1 mL of FFDMEM containing 0.1 μM radiolabeled FA and increasing amounts of FA-functionalized iron oxide particles. Afterward, the plates were rinsed twice with PBS, pH 7.4 at 4 °C. Cells were then treated overnight at ambient temperature with 1 mL of 0.1% v/v Triton ×100, and the amount of radioactivity present in the cell lysate was determined by liquid scintillation counting (LS6000 TA, Beckman-Coulter, USA). The results were expressed as percentage of cell-associated radioactivity, the amount found in the absence of nanoparticles being taken as the 100% uptake value. Experiments were repeated in the same conditions but using control nanoparticles (VUSPIO−PEG). All experiments were replicated at least three times.

Folate-Targeted Nanoparticles Cell Uptake Experiments. The cell uptake of γ-Fe_2O_3 nanoparticles was investigated using TEM. Samples were prepared by the following procedure (*28*): cells grown for 1 week in FFDMEM were incubated for 3 h with nanoparticles (150 μg/mL of γ-Fe_2O_3 in FFDMEM). Then, after repeated washing with PBS, pH 7.4, cells were fixed with 2.5% glutaraldehyde in 0.1 M cacodylate buffer (5 mM $CaCl_2$, 5 mM $MgCl_2$, 0.1 M sucrose, pH 7.2) for 1 h at 4 °C. Samples were postfixed in 1% osmium tetroxide in the same buffer for 1 h at room temperature and washed. Cells were scraped and concentrated in 2.5% agar in 0.05 M cacodylate buffer. The specimens were then treated with 2% uranyl acetate solution for 1 h. The material was subsequently dehydrated by means of ethanol/water solutions, with increasing ethanol content and embedded in a epoxy resin (Epikote 812, Fluka, Switzerland). The samples were cut at 70 nm (ultrathin sections) with an ultramicrotome (Ultracut UCT, Leica, Austria). Ultrathin sections of the preparation were stained with 5% uranyl acetate and Reynolds reagent (0.2% lead citrate) and observed on a transmission electron microscope at 80 kV (EM 208, Philips, Netherlands)

Ultrathin sections (70 nm) of the preparation were obtained and rapidly double stained with 5% uranyl acetate, followed by Reynolds reagent (0.2% lead citrate). The presence of iron oxide nanocrystals within the cells

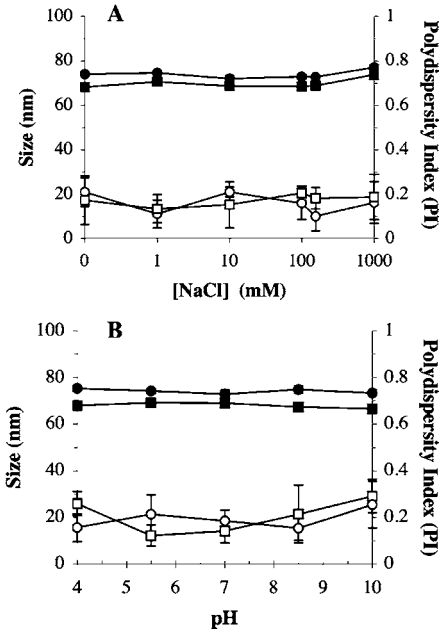

Figure 1. Influence of NaCl concentration (A) and pH (B) of dispersion medium on the hydrodynamic diameter (solid symbols) and polydispersity index (empty symbols) of iron oxide nanoparticles functionalized with PEG (●, ○) and with PEG−FA (■, □). $n = 6 \pm$ standard deviation (SD).

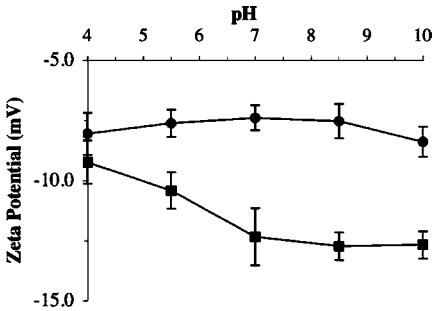

Figure 2. ζ potential values of iron oxide nanoparticles (●, VUSPIO−PEG; ■, VUSPIO−PEG−FA) dispersed in 0.01 M phosphate buffer with pH values between 4 and 10. $n = 10 \pm$ SD.

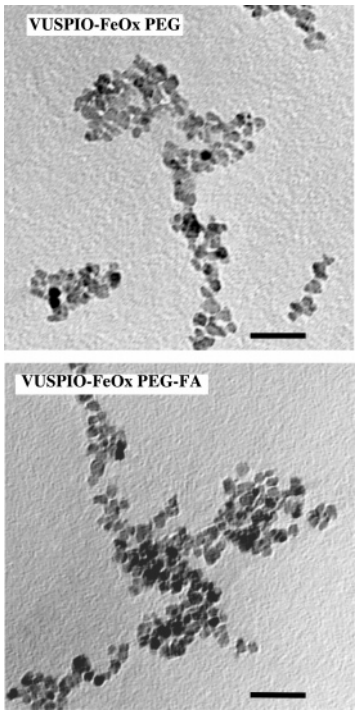

Figure 3. TEM images of PEG−FA and PEG-modified dextran-coated iron oxide nanoparticles (Bar = 50 nm).

has been confirmed by energy-dispersive X-ray (EDX) spectroscopy and by dark-field observations in TEM (CM12, Philips, The Netherlands, equipped with an EDAX−EDX analyzer). Qualitative and quantitative determination of nanoparticle uptake were obtained by visual localization and counting of the nanoparticles on 10 cell sections for each sample. For each of the three different cell lines a specific uptake index (SUI) was determined and calculated as the ratio between the number of folate-targeted nanoparticles taken up by the cells and the number of nontargeted particles taken up in the same conditions (i.e., nonspecific uptake).

To approximately evaluate the iron oxide concentration achievable within lysosomes, where targeted cells appear to be gathered, an image analysis has been performed using the software ImageJ 1.32j (Wayne Rasband, National Institute of Health, USA). The area of the entire lysosome presented in Figure 9 and the number of particles enclosed have been evaluated. The minimum and maximum values used for detecting particles were 10 and 100 pixels. With the knowledge that the slice observed is 70 nm thick and making the limiting approximation that we see only iron oxide nanocrystals of 5 nm diameter and of known density (4.87 g/cm^3 as calculated for maghemite crystals), we can calculate the iron oxide concentration.

RESULTS

Nanoparticle Size and Surface Charge. As shown in Figure 1, iron oxide nanoparticles, functionalized with PEG or with PEG−FA had a mean diameter between 60 and 80 nm and polydispersity indexes lower than 0.3. pH and ionic strength did not influence significantly either the mean size or the polydispersity index of the nanoparticles. ζ potential measurements showed slight negative values for dextran-coated iron oxide nanoparticles before pegylation (Figure 2). When these nanoparticles were functionalized with PEG, their ζ potential was not affected by the pH of the dispersing medium. On the contrary, when coated with folate-derivatized PEG, the nanoparticle charge got increasingly negative with rising pH which is probably due to the progressive deprotonation of the FA carboxylic groups.

Nanoparticle Morphology and Density. As observed by TEM, iron oxide nanoparticles were roughly round shaped with narrow size distribution (Figure 3). Furthermore, it was possible to identify more electron-dense structures nonhomogeneously distributed in their bodies. Their crystalline nature was showed by high-resolution microscopy, while their electron diffraction pattern identified them as maghemite (γ-Fe_2O_3) nanocrystals (Figure 4). The overall particle diameter was between 10 and 20 nm, while the embedded nanocrystals were between 5 and 10 nm. The observed "grapelike" organization of the particles in TEM micrographs is a consequence of the removal of the dispersing phase during sample preparation and is not representative of the real state of nanoparticles in suspension. The difference in the mean sizes obtained by PCS measurements, and electron microscopy has already been observed with other materials (*29*), possibly due to the hydrophilic polymer coating of the particles which increases significantly the hydrodynamic diameter, especially with very

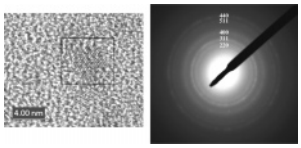

Figure 4. High-resolution TEM image of dextran-coated iron oxide nanoparticle (left). Electron diffraction pattern obtained with the particles, which matches with the one expected for γ-Fe_2O_3 crystals (right).

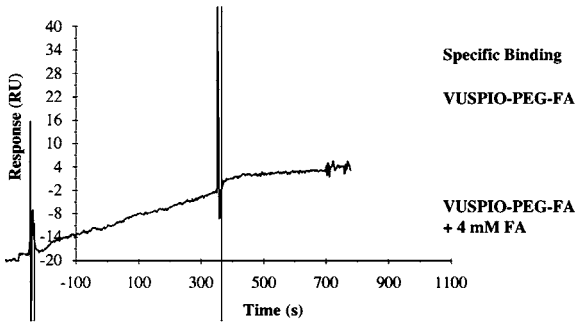

Figure 5. Surface plasmon resonance sensorgram of iron oxide nanoparticles functionalized with PEG−FA (VUSPIO−PEG−FA) and of the same nanoparticles in the presence of 4 mM free FA (VUSPIO−PEG−FA + 4 mM FA). Subtraction of the sensogram in the presence of folate from that in absence of folate gives the specific binding of the nanoparticles to FBP.

small colloids. However, a slight aggregation of nanoparticles in suspension could not be excluded.

The nanoparticle density was found to be 2.76 g/cm^3 due to the presence of high-density nanocrystals (4.87 g/cm^3, as calculated for maghemite crystals). Thus, the number of nanocrystals embedded in individual nanoparticles could be calculated, from the concentration and the density for both of them. The values obtained for different sized nanoparticles varied from 1 to 8 crystals for nanoparticles with diameters between 10 and 20 nm, which is comparable with the TEM observations.

Nanoparticle Heating. Experiments performed on pegylated and folate-conjugated nanoparticles dispersed in water led to quite similar results, with a heating ramp of 7 ± 1 °C per 20 min period. The specific absorption rate, defined as the heating power of the magnetic material per gram, was calculated: SAR = 13 ± 3 W/g_{Fe}. These results are coherent with the ones obtained for the maghemite nanocrystals alone (SAR = 13.8 W/g_{Fe}).

Nanoparticle Cytotoxicity. Both pegylated and folate-linked nanoparticles were tested for their cytotoxicity on three cell lines (HeLa, KB, MCF7) at various concentrations up to 200 μg/mL of Fe_2O_3 (see Supporting Information). After 3 h of incubation only slight cytotoxicity was observed, survival rates being higher than 75% even at the higher nanoparticles concentrations (*30*). Furthermore, no significant difference was shown between the cytotoxicities of the targeted and nontargeted particles (unpaired two-tailed t-test, $p > 0.20$).

Folate Targeting Efficiency. The interaction of the folate-conjugated nanoparticles with the FBP was observed by surface plasmon resonance. In Figure 5, it can be observed that, at the time of sample injection, the addition of a solution having a different refractive index compared to the eluent induced a spike in the signal (RU). The subsequent and progressive increase of the response signal for the folate-conjugated nanoparticles was a sign of the progressive binding of these nanoparticles to the protein linked onto the chip surface. During the washing procedure following the interaction

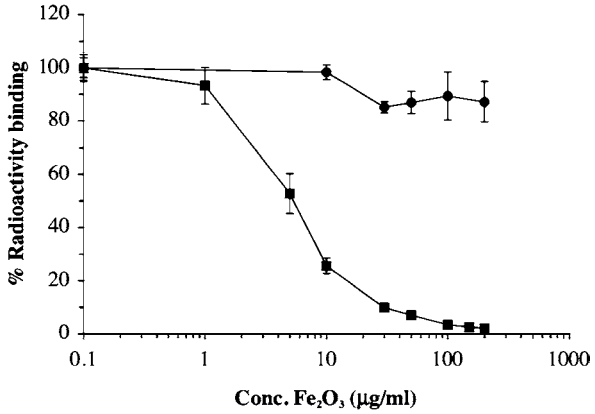

Figure 6. Commpetitive inhibition of the uptake of tritium labeled FA in the presence of increasing concentrations of iron oxide nanoparticles functionalized with PEG−FA (■, VUSPIO−PEG−FA) or PEG alone (●, VUSPIO−PEG). $n = 3 \pm$ SD.

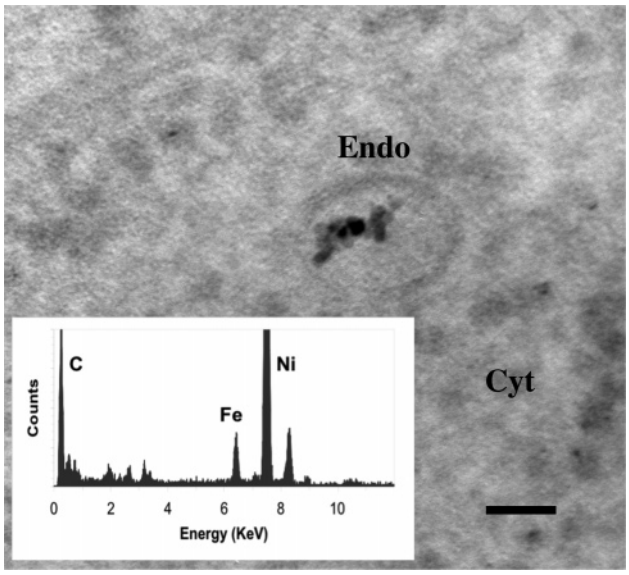

Figure 7. TEM image of an of an agglomerate of few nanoparticles in an endosome in KB cells. The EDX analysis of the object is reported superimposed. (C = carbon; Fe = iron; Ni = nickel; Cyt = cytoplasm; E = endosome; bar = 50 nm).

phase, only a very slight decrease in the signal could be observed, demonstrating a strong specific interaction between the nanoparticles and the FBP. When the experiment was carried out in the presence of free FA (4 mM), no positive signal could be recorded, indicating that the interaction between the folate-functionalized nanoparticles and the chip surface was competitively inhibited by FA free in solution. In control experiments performed with dextran-coated iron oxide nanoparticles functionalized with PEG, no signal was elicited.

To ascertain whether specific interactions between folate-functionalized maghemite nanoparticles and the folate receptor also occurred in vitro, in cell culture conditions, further experiments with tritium-labeled FA were carried out with the KB cell line, which expresses the folate receptor at a dramatically high level (Figure 6). When incubated with radiolabeled FA alone, KB cells avidly captured the radioactive compound. Conversely, FA uptake progressively decreased along with the addition of increasing amounts of folate-targeted nanoparticles (VUSPIO−PEG−FA). It is noteworthy that, for the higher nanoparticle concentrations, almost no cell-associated radioactivity could be detected. Finally, if control nanoparticles (VUSPIO−PEG) were incubated in

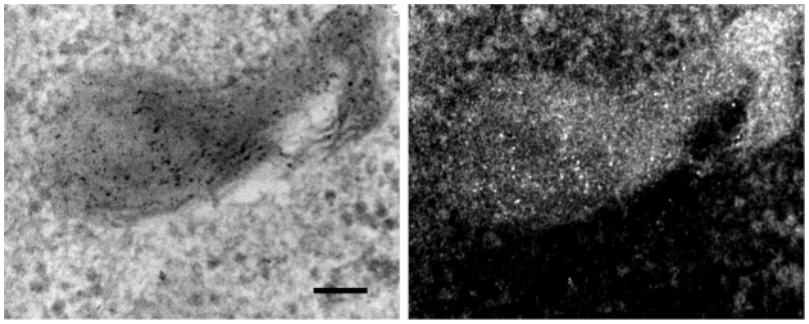

Figure 8. A classic (left) and a dark-field TEM image (right) of a lysosome in KB cells. The electron-diffracting maghemite crystals appear as bright spot in the right image.

Table 1. Uptake of Iron Oxide Nanoparticles by Cells

	nanoparticles taken up per cell[a]		
cell line	VUSPIO−PEG	VUSPIO−PEG-FA	t-test probability
HeLa	15.4 ± 6.9	46.3 ± 18.6	<0.05
KB 3-1	45.2 ± 8.5	307.5 ± 69.7	<0.01
MCF7	58.4 ± 38.3	65.7 ± 60.0	>0.2

[a] Data are presented as mean ± SD (n = 10).

the same conditions, almost no inhibition of the radioactivity cell uptake was observed.

Cell Uptake of Nanoparticles. The uptake of nanoparticles by the different cell lines was investigated by TEM. The presence of iron particles in the intracellular compartment could clearly be identified by EDX spectroscopy, as shown in Figure 7. Maghemite nanocrystals were also recognized by dark-field TEM observations. In these experiments the orientation of the sample was set in order to collect electrons predominantly diffracted by maghemite nanocrystals. Images of KB cell lysosomes containing several nanocrystals are shown in Figure 8.

As predicted from the cytotoxicity experiments, TEM observations showed that cellular structures were well preserved with no visible abnormalities, following incubation with the nanoparticles. In the case of HeLa and KB cells, folate-conjugated nanoparticles were found intracellularly, mainly in endosomes and, especially, in several large multivesicular structures, identified as late endolysosomes, also called residual bodies (see Figure 8). In MCF7 cells, which do not express the folate receptor, we found some nanoparticles near the cell plasmatic membranes and a small number of them were found in lysosomal structures too. Incubation of the three cell lines with control iron oxide nanoparticles without FA bound onto their surface (VUSPIO−PEG) was performed under the same conditions to evaluate the nonspecific cell uptake. The mean number of particles found per cell was calculated for targeted and nontargeted superparamagnetic nanoparticles for each cell line. These results along with a statistical evaluation of their differences (unpaired two-tailed t-test) are presented in Table 1. The targeting efficacy of the folate nanoparticles has been expressed using the SUI, calculated as the ratio between the number of folate-targeted nanoparticles taken up by the cells and the number of nontargeted particles taken up in the same conditions (i.e., unspecific uptake) (Figure 9). In the case of the folate receptor expressing KB and HeLa cells, nanoparticle uptake was greater for targeted nanoparticles (VUSPIO−PEG−FA); the SUI value was approximately 7 (for KB cells) and 3 (for HeLa cells). Conversely, MCF7 cell uptake level of targeted and control particles was quite similar, the SUI being nearly equal to 1. Folate-targeted nanoparticles appeared to be gathered into numerous lysosomes. To determine if the quantity of nanocrystals taken up by cells would be

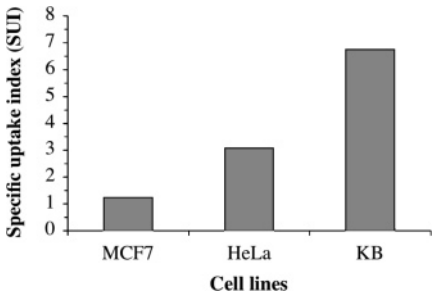

Figure 9. Specific uptake index for the three cell lines. The index is calculated as the ratio between the number of folate-targeted particles (VUSPIO−PEG−FA) internalized by cells and the number of control particles (VUSPIO−PEG) captured by cells in the same conditions.

sufficient for an efficient and rapid heating, we evaluated their concentration in those cellular structures. We calculated that the concentration of iron oxide attained in the endolysosome presented in Figure 8 was in the order of 3 mg/mL.

DISCUSSION

The design of superparamagnetic iron oxide nanoparticles interacting with tumors has received increasing interest in the past few years, as indicated by the number of papers recently published on this subject (*31*−*33*). In particular, the challenge has been to obtain nanoparticles stable in physiological conditions, able to selectively target tumor cells. We produced here iron oxide nanocrystals coated with dextran and successively modified at their surface with PEG and FA. Despite the relatively low surface charge of these nanoparticles, a good colloidal stability has been obtained at both acid and alkaline pH, as well as in the presence of high salt concentrations. This suggests that stabilization of maghemite nanoparticles was primarily dependent on steric repulsion due to their coating with hydrophilic polymers. Thus, dextran and PEG covalently bound to the particle surface are efficient in avoiding their aggregation in the tested conditions, which opens the way for their use in still more complex biological media. These characteristics of stability and steric repulsion should allow these small particles to circulate for a prolonged time in the blood compartment, avoiding the scavenging of the macrophages of the reticulo-endothelial system (*34*, *35*) and allowing the diffusion toward the tumor site, by virtue of the known enhanced permeability and retention effect (*36*, *37*). Furthermore, their superparamagnetic properties were shown not to be modified by the surface functionalization, and particles were able to increase the temperature of an aqueous suspension at a constant rate under an appropriate oscillating magnetic field. With regard to the targeting efficacy, the set of experiments performed in

this study, with plasmon resonance, cell culture competitive assays, and cell nanoparticle capture have clearly demonstrated the capacity of these folate functionalized nanoparticles to specifically target cancer cells with membrane expression of the FA receptor. In fact, as shown in Table 1, the MCF7 cells, deprived of FA receptors, did not uptake more folate-functionalized nanoparticles than the control nanoparticles (no significant difference between the two uptake). In the same conditions, in HeLa and KB cells the folate nanoparticles were taken up in much greater number than the control nanoparticles (significant difference, $p < 0.05$ and $p < 0.01$ respectively). The receptor-mediated endocytotic process ended in the accumulation of the nanoparticles in one of the common metabolic degradation pathways of foreign materials taken up by cells. In fact, the accumulation of folate-targeted molecular conjugates in lysosomes has already been observed with antifolate drugs and folate-targeted carriers such as polyplexes and cyclodextrines (*27*, *38*, *39*). Interestingly, the increase of nanoparticle uptake appeared to be proportional to the folate receptor expression level in HeLa and KB cells. Indeed, as reported before, the folate receptor was 3−4 times more expressed in KB cells compared to HeLa cells (*25*). In addition, the iron concentration attained in cellular structure as lysosomes (3 g/L) appeared to be well suited to obtain a local intracellular heating. Temperature increase to values above 43 °C for a sufficient period of time should be able to cause selective damage and death of cells containing high amounts of iron oxide nanoparticles (*9*).

CONCLUSIONS

In a scientific panorama in which folate-mediated solid tumor targeting seems to become one of the major breakthrough in tumor diagnosis and treatment, the new targeted maghemite nanoparticles presented here are very promising nanosystems for performing a targeted intracellular hyperthermic treatment of tumors overexpressing the folate receptor. Our current research efforts consist in building a hyperthermia apparatus equipped with a large solenoid in which magnetic alternating current field will be homogeneous at the Petri dish scale. Then, in vitro heating experiments will be envisaged and their therapeutic effect will be evaluated.

ACKNOWLEDGMENT

The excellent assistance of Mme. Odile Kaitasov in electron microscopy experiments and of M. Richard Harvey in text reviewing are gratefully acknowledged. Authors would like to thank the Association pour la Recherche sur le Cancer for the financial support to the work of F.S.

Supporting Information Available: Graphs reporting the cytotoxicity of toward HeLa, KB 3-1, and MCF7 cells. This material is available free of charge via the Internet at http://pubs.acs.org/BC.

LITERATURE CITED

(1) Davis, S. S. (1997) Biomedical applications of nanotechnology—implications for drug targeting and gene therapy. *Trends Biotechnol. 15*, 217−224.

(2) Brigger, I., Dubernet, C., and Couvreur, P. (2002) Nanoparticles in cancer therapy and diagnosis. *Adv. Drug Del. Rev. 54*, 631−651.

(3) Sonvico, F., Dubernet, C., Colombo, P., and Couvreur, P. Metallic based nanotechnology, applications in diagnosis and therapeutics. *Curr. Pharm. Des. 11*, 2091−2105.

(4) Mornet, S., Vasseur, S., Grasset, F., and Duguet, E. (2004) Magnetic nanoparticles for medical diagnosis and therapy. *J. Mater. Chem. 14*, 2161−2175.

(5) Weissleder, R., and Papisov, M. (1992) Pharmaceutical iron oxides for MR imaging. *Rev. Magn. Reson. Med. 4*, 1−20.

(6) Weissleder, R., Bogdanov, A., Neuwelt, E. A., and Papisov, M. (1995) Long circulating iron oxides for MR imaging. *Adv. Drug Del. Rev. 16*, 321−334.

(7) Gilchrist, R. K., Medal, R., Shorey, W. D., Hanselman, R. C., Parott, J. C., and Taylor, C. B. (1957) Selective inductive heating of lymph nodes. *Ann. Surg. 146*, 596−606.

(8) van der Zee, J. (2002) Heating the patient: a promising approach? *Ann. Oncol. 13*, 1173−1184.

(9) Hildebrandt, B., Wust, P., Ahlers, O., Dieing, A., Sreenivasa, G., Kerner, T., Felix, R., and Riess, H. (2002) The cellular and molecular basis of hyperthermia. *Crit. Rev. Oncol. Hematol. 43*, 33−56.

(10) Engin, K. (1996) Biological rationale and clinical experience with hyperthermia. *Control. Clin. Trials 17*, 316−342.

(11) Gordon, R. T., Hines, J. R., and Gordon, D. (1979) Intracellular Hyperthermia - A biophysical approach to cancer treatment via intracellular temperature and biphysical alteration. *Med. Hypotheses 5*, 83−102.

(12) Moroz, P., Jones, S. K., and Gray, B. N. (2002) Magnetically mediated hyperthermia: current status and future directions. *Int. J. Hyperthermia 18*, 267−284.

(13) Jordan, A., Scholz, R., Maier-Hauff, K., Johannsen, M., Wust, P., Nadobny, J., Schirra, H., Schmidt, H., Deger, S., Loening, S., Lanksch, W., and Felix, R. (2001) Presentation of a new magnetic field therapy system for the treatment of human solid tumors with magnetic fluid hyperthermia. *J. Magn. Magn. Mater. 225*, 118−126.

(14) Bacri, J. C., Da Silva, M. F., Perzynski, R., Pons, J. N., Roger, J., Sabolovic, D., and Halbreich, A. (1997) *Use of magnetic nanoparticles for thermolysis of cells in a ferrofluid. Scientific and clinical applications of magnetic carriers*. Häfeli, U., Schutt, W., Teller, J., and Zborowski, M., Eds. pp 597−606, Plenum Press, New York.

(15) Jordan, A., Scholz, R., Wust, P., Schirra, H., Schiestel, T., Schmidt, H., and Felix, R. (1999) Endocytosis of dextran and silan-coated magnetite nanoparticles and the effect of intracellular hyperthermia on human mammary carcinoma cells in vitro. *J. Magn. Magn. Mater. 194*, 185−196.

(16) Pitsillides, C. M., Joe, E. K., Wei, X., Anderson, R. R., and Lin, C. P. (2003) Selective cell targeting with light-absorbing microparticles and nanoparticles. *Biophys. J. 84*, 4023−4032.

(17) Mornet, S., Portier, J., and Duguet, E. (2003) Ferrofluides stables en milieu neutre et ferrofluides modifiés obtenus par modification de la surface des particules de ces ferrofluides. French Patent 0306279.

(18) Mornet, S., Portier, J., and Duguet, E. (2005) A method for synthesis and functionalization of ultrasmall superparamagnetic covalent carriers based on maghemite and dextran. *J. Magn. Magn. Mater. 293*, 127−134.

(19) Massart, R. (1982) Magnetic fluids and process for obtaining them. U.S. Patent 4,329,241.

(20) Lee, R. J., and Low, P. S. (1994) Delivery of liposomes into cultured KB cells via folate receptor-mediated endocytosis. *J. Biol. Chem. 295*, 3198−3204.

(21) Lemarchand, C., Couvreur, P., Besnard, M., Costantini, D., and Gref, R. (2003) Novel polyester-polysaccharide nanoparticles. *Pharm. Res. 20*, 1284−1292.

(22) Johnsson, B., Lofas, S., and Lindquist, G. (1991) Immobilization of proteins to a carboxymethyldextran-modified gold surface for biospecific interaction analysis in surface plasmon resonance sensors. *Anal. Biochem. 198*, 268−277.

(23) Antony, A. C. (1992) The biological chemistry of folate receptors. *Blood 79*, 2807−2820.

(24) Gabizon, A., Horowitz, A. T., Goren, D., Tzemach, D., Mandelbaum-Shavit, F., Qazen, M. M., and Zalipsky, S. (1999) Targeting folate receptor with folate linked to extremities of poly(ethylene glycol)-grafted liposomes: in vitro studies. *Bioconjug. Chem. 10*, 289−298.

(25) Sonvico, F., Stella, B., Appel, M., Chacun, H., Marsaud, V., Renoir, M., Colombo, P., and Couvreur, P. Setup of an in

vitro model expressing the folate receptor for the investigation of targeted delivery systems. *J. Drug Delivery Sci. Technol.*, in press.
(26) Carmichael, J., DeGraff, W. G., Gazdar, A. F., Minna, J. D., and Mitchell, J. B. (1987) Evaluation of a tetrazolium-based semiautomated colorimetric assay: assessment of chemosensitivity testing. *Cancer Res. 47*, 936−942.
(27) Salmaso, S., Semenzato, A., Caliceti, P., Hoebeke, J., Sonvico, F., Dubernet, C., and Couvreur, P. (2004) Specific antitumor targetable beta-cyclodextrin-poly(ethylene glycol)-folic acid drug delivery bioconjugate. *Bioconjug. Chem. 15*, 997−1004.
(28) Pinto-Alphandary, H., Balland, O., and Couvreur, P. (1995) A new method to isolate polyalkylcyanoacrylate nanoparticle preparations. *J. Drug Target. 3*, 167−169.
(29) Bootz, A., Vogel, V., Schubert, D., and Kreuter, J. (2004) Comparison of scanning electron microscopy, dynamic light scattering and analytical ultracentrifugation for the sizing of poly(butyl cyanoacrylate) nanoparticles. *Eur. J. Pharm. Biopharm. 57*, 369−375.
(30) Csaba, N., Caamano, P., Sanchez, A., Dominguez, F., and Alonso, M. J. (2005) PLGA: poloxamer and PLGA: poloxamine blend nanoparticles: new carriers for gene delivery. *Biomacromolecules 6*, 271−278.
(31) Petri-Fink, A., Chastellain, M., Juillerat-Jeanneret, L., Ferrari, A., and Hofmann, H. (2005) Development of functionalized superparamagnetic iron oxide nanoparticles for interaction with human cancer cells. *Biomaterials 26*, 2685−2694.
(32) Zhang, Y., Sun, C., Kohler, N., and Zhang, M. (2004) Self-assembled coatings on individual monodisperse magnetite nanoparticles for efficient intracellular uptake. *Biomed. Microdevices 6*, 33−40.
(33) Zhang, Y., Kohler, N., and Zhang, M. (2002) Surface modification of superparamagnetic magnetite nanoparticles and their intracellular uptake. *Biomater. 23*, 1553−1561.
(34) Lemarchand, C., Gref, R., and Couvreur, P. (2004) Polysaccharide-decorated nanoparticles. *Eur. J. Pharm. Biopharm. 58*, 327−341.
(35) Moghimi, S. M., Hunter, A. C., and Murray, J. C. (2001) Long-circulating and target-specific nanoparticles: theory to practice. *Pharmacol. Rev. 53*, 283−318.
(36) Hobbs, S. K., Monsky, W. L., Yuan, F., Roberts, W. G., Griffith, L., Torchilin, V. P., and Jain, R. K. (1998) Regulation of transport pathways in tumor vessels: role of tumor type and microenvironment. *Proc. Natl. Acad. Sci. U.S.A. 95*, 4607−4612.
(37) Gabizon, A. A. (2001) Stealth liposomes and tumor targeting: one step further in the quest for the magic bullet. *Clin. Cancer Res. 7*, 223−225.
(38) Mislick, K. A., Baldeschwieler, J. D., Kayyem, J. F., and Meade, T. J. (1995) Transfection of folate-polylysine DNA complexes: evidence for lysosomal delivery. *Bioconjugate Chem. 6*, 512−515.
(39) Jansen, G., Barr, H., Kathmann, I., Bunni, M. A., Priest, D. G., Noordhuis, P., Peters, G. J., and Assaraf, Y. G. (1999) Multiple mechanisms of resistance to polyglutamatable and lipophilic antifolates in mammalian cells: role of increased folylpolyglutamylation, expanded folate pools, and intralysosomal drug sequestration. *Mol. Pharmacol. 55*, 761−769.

BC050050Z

A New Strategy for the Preparation of Peptide-Targeted Technetium and Rhenium Radiopharmaceuticals. The Automated Solid-Phase Synthesis, Characterization, Labeling, and Screening of a Peptide-Ligand Library Targeted at the Formyl Peptide Receptor

Karin A. Stephenson,[†] Sangeeta Ray Banerjee,[‡] Oyebola O. Sogbein, Murali K. Levadala,[‡] Nicole McFarlane,[†] Douglas R. Boreham,[†] Kevin P. Maresca,[§] John W. Babich,[§] Jon Zubieta,[‡] and John F. Valliant*,[†]

Department of Chemistry, McMaster University, Hamilton, ON, Canada L8S 4M1, The Medical Physics and Applied Radiation Sciences Unit, McMaster University, Hamilton, ON, Canada, L8S 4M1, Department of Chemistry, Syracuse University, Syracuse, New York 13244-4100, and Molecular Insight Pharmaceuticals Inc., Cambridge, Massachusetts 02142. Received March 3, 2005; Revised Manuscript Received June 16, 2005

A new solid-phase synthetic methodology was developed that enables libraries of peptide-based Tc(I)/Re(I) radiopharmaceuticals to be prepared using a conventional automated peptide synthesizer. Through the use of a tridentate ligand derived from N-α-Fmoc-L-lysine, which we refer to as a single amino acid chelate (SAAC), a series of 12 novel bioconjugates [R-NH(CO)ZLF(SAAC)G, R = ethyl, isopropyl, *n*-propyl, *tert*-butyl, *n*-butyl, benzyl; Z = Met, Nle] that are designed to target the formyl peptide receptor (FPR) were prepared. Construction of the library was carried out in a multiwell format on an Advanced ChemTech 348 peptide synthesizer where multi-milligram quantities of each peptide were isolated in high purity without HPLC purification. After characterization, the library components were screened for their affinity for the FPR receptor using flow cytometry where the K_d values were found to be in the low micromolar range (0.5−3.0 μM). Compound **5j** was subsequently labeled with ^{99m}Tc(I) and the product isolated in high radiochemical yield using a simple Sep-Pak purification procedure. The retention time of the labeled compound matched that of the fully characterized Re-analogue which was prepared through the use of the same solid-phase synthesis methodology that was used to construct the library. The work reported here is a rare example of a method by which libraries of peptide-ligand conjugates and their rhenium complexes can be prepared.

INTRODUCTION

Short peptide sequences are one of the most effective vectors for targeting radionuclides to specific receptor systems (*1*). As a result, there are a number of peptide-based imaging agents that are currently used clinically or that are undergoing clinical trials (*2*). The archetypal example is ^{111}In-labeled Octreotide, which is a somatostatin analogue used to image neuroendocrine tumors (*3*).

One of the attractive features of peptides is that they can be easily modified to optimize receptor binding affinity, pharmacokinetics, and clearance rates and pathways. The sequence of the amino acids, the addition of prosthetic groups, and, in the case of metalloradionuclides, the nature of the chelating group can all be changed to obtain the desired biodistribution profile. Because of this flexibility, the opportunity presents itself to prepare libraries of peptide-ligand conjugates in parallel or in combination as a means of rapidly identifying the ideal choice of factors. Despite recent reports on the development of new solid-phase synthetic procedures (*4*−*7*), the majority of radiopharmaceuticals continue to be prepared using linear discovery strategies which are significantly less efficient than contemporary drug discovery methodologies.

Recently we described a novel solid-phase synthetic strategy for incorporating a Tc(I)/Re(I) binding ligand, which we refer to as a single amino acid chelate (SAAC) (**1a**, Figure 1), into peptides (*8*, *9*). The SAAC, which is derived from lysine, can be introduced into a peptide as if it were a natural amino acid making the chelate a convenient and versatile synthon for preparing peptide-targeted radiopharmaceuticals. The current objective was to develop the means to use the SAAC system to prepare libraries of chelate-derived peptides as a new strategy for discovering novel radiopharmaceuticals.

As a model system, we selected the fMLF peptide which has been used to direct ^{99m}Tc to sites of infection and inflammation by targeting the formal peptide receptor (FPR) on leukocytes (*10*−*24*). Unfortunately, fMLF is an agonist which causes unwanted side effects (neutropenia) even when the apparent specific activity of the tracer is very high (*23*). One approach to overcoming this issue is to develop an analogue of fMLF which behaves as an antagonist rather than an agonist (*16*).

By changing the nature of the formyl group in fMLF to substituted ureas, a series of antagonists for the FPR that have reasonably high binding affinities were discovered (*25*). A ^{99m}Tc-labeled SAAC analogue of the urea-derived peptides could therefore be used to image sites of infection and inflammation without causing neutro-

* To whom correspondence should be addressed. Tel: 905-525-9140 ext. 22840; FAX: 905-522-2509; E-mail: valliant@mcmaster.ca.
[†] McMaster University.
[‡] Syracuse University.
[§] Molecular Insight Pharmaceuticals Inc.

10.1021/bc0500591 CCC: $30.25 © 2005 American Chemical Society
Published on Web 08/26/2005

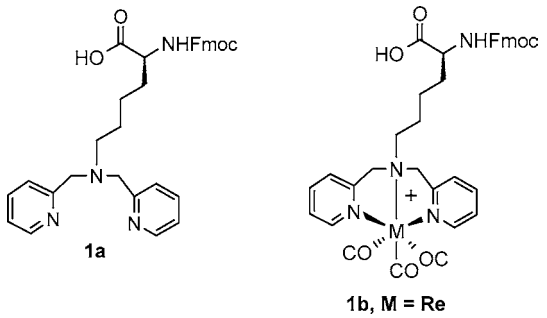

Figure 1. A Single Amino Acid Chelate (SAAC) and its complex with the $[Re(CO)_3]^+$ core.

penia. To obtain a viable agent, the peptide-SAAC derivative must maintain reasonable affinity for the FPR while also possessing the appropriate distribution kinetics and clearance mechanism (*16*, *23*). As a means of identifying compounds that meet these criteria, a parallel array of RNHC(O)ZLF(SAAC)G derivatives were prepared in which factors that can change receptor binding affinity and/or the distribution/mode of clearance (i.e. the substituents off the urea (R) and the nature of the first amino acid (Z)) were varied.

EXPERIMENTAL PROCEDURES

Materials. Unless otherwise stated, all reagents and solvents were ACS grade or higher and used without further purification from commercial suppliers. Polystyrene-based *N*-α-9-fluorenylmethoxycarbonyl (Fmoc)-glycine loaded SASRIN resin (0.69 mmol g^{-1}, 1% divinylbenzene, 200−400 mesh) was obtained from Bachem Inc. Fmoc-protected amino acids were purchased from Nova-Biochem Inc., Bachem Inc., and Advanced ChemTech Inc. Fluorescein-labeled fNLFNTK was purchased from Molecular Probes Inc. (product # F-1314). The isocyanates were purchased shortly before use from Sigma-Aldrich Co.

Instrumentation. All peptides were prepared on an Advanced ChemTech 348 Ω Peptide Synthesizer using a 40-well reaction block. Peptides were analyzed by positive ion electrospray mass spectrometry on a Micromass Quattro Ultima instrument. Samples were dissolved in 50/50 CH_3CN/H_2O prior to analysis. FTIR spectra were acquired on a Bio-Rad FTS-40 FTIR spectrometer. NMR experiments were performed using a Bruker AV 600 NMR spectrometer. In terms of signals, s refers to a singlet, d refers to doublet, dd refers to doublet of doublets, and m refers to multiplet.

Analytical HPLC was performed using a Varian Pro Star model 330 PDA detector and model 230 solvent delivery system and a C-18 Microsorb column (4.6 × 250 mm, 300 Å/5 μm). For the peptides and the analysis of the Re complex, the elution protocol was a linear gradient of 100% water containing 0.1% TFA to 100% acetonitrile containing 0.1% TFA over 20 min. The flow rate was 1.0 mL min^{-1}, and all runs were monitored at $\lambda = 254$ and 214 nm. For the reactions involving ^{99m}Tc, HPLC experiments were performed on a Varian Prostar Model 230 HPLC (high performance liquid chromatography) instrument coupled to a Bio-Rad IN/US γ-detector using a Nucleosil (L x ID = 250 × 4.6 mm), analytical column (300 Å/5 μm, RP-C18). The mobile phase consisted of Solvent A = triethylammonium phosphate buffer (pH = 2−2.5), Solvent B = CH_3OH. Gradient: 0−3 min, 100% A; 3−6 min, 100% A to 75% A; 6−9 min, 75% A to 67% A; 9−20 min, 67% A to 0% A; 20−22 min, 0% A; 22−25 min, 0% A to 100% A; 25−30 min, 100% A.

Solid-Phase Peptide Synthesis. Fmoc-glycine-loaded SASRIN resin (150 mg, 0.69 mmol/g) was added to 12 wells of the reaction block, suspended in DMF (2 mL/well), and shaken at 900 rpm for 1 min. The wells were subsequently filtered, suspended in THF (2 mL/well), shaken at 900 rpm for 1 min, and drained for 90 s. The THF wash was repeated two more times. The DMF wash was then repeated a final two times to complete the general wash cycle. This procedure was used between every deprotection and coupling step. Fmoc deprotection was brought about through the addition of 25% v/v piperidine−DMF solution to the active vessels (2 mL/well) and shaking for 5 min at 900 rpm. Following filtration, the process was repeated, shaking for 10 min. The deprotected resin-bound amino acid was washed using the general wash procedure and subsequently coupled to the next Fmoc-protected amino acid using a standard HBTU coupling technique. Coupling reactions initially involved adding DMF (200 μL) to the active vessels followed by the addition of a 4-fold excess of the protected amino acid as a 0.5 M solution in DMF. Four equivalents of HBTU as a 0.5 M solution in DMF was then added followed by a 8-fold excess of DIPEA as 2.0 M solution in DMF. The reaction block was subsequently shaken for 80 min at 900 rpm. Following filtration, the resin was washed using the general washing procedure prior to the start of the next cycle.

Once the final amino acid had been added and the Fmoc group removed, a pause was introduced into the peptide program so that 10 equiv of the isocyanates in DMF (0.5 M solution) could be added. The reaction block was then shaken at 900 rpm under nitrogen for 12 h. The reaction vessels were emptied and the resins washed using the general wash cycle. Peptides were cleaved from the resin support using a TFA cocktail containing EDT (2%), water (2%), and TIS (2%). The cleavage cocktail, cooled to 0 °C, was added to the resin and the mixture allowed to warm to room temperature over 60 min. The suspension was filtered into cold diethyl ether and the resulting heterogeneous solution centrifuged at 3000 rpm and −5 °C for 10 min. The resulting pellet was washed with cold diethyl ether (3 × 25 mL), dissolved in distilled−deionized water, and lyophilized, yielding a white solid for all compounds.

Preparation of $[^{99m}Tc(CO)_3(OH_2)_3]^+$. A 10 mL penicillin vial containing $K_2[BH_3{\cdot}CO_2]$, (8.5 mg, 63 μmol), $Na_2B_4O_7{\cdot}10H_2O$ (2.9 mg, 8.0 μmol), Na/K-tartrate (15.0 mg, 53 μmol), and Na_2CO_3 (4.0 mg, 38 μmol) was fitted with a rubber septum and the vial flushed with N_2(g) for 15 min. ^{99m}Tc-generator eluate (370 MBq, 10 mCi) in 500 μL of saline was added by a syringe, and the solution was heated to 95 °C for 30 min. After cooling on an ice-bath, the alkaline solution was neutralized by the addition of 28 μL of HCl (12 M HCl in 100 μL of H_2O). Quality control was performed by gradient HPLC (yields ≥ 95%).

Radiolabeling 5j. An aliquot (250 μL) of **5j** (0.5 mg, 0.58 μmol) dissolved in 200 μL of 100 mM phosphate buffer (pH = 7.2) and 300 μL of CH_3CN was added to the solution containing $[^{99m}Tc(CO)_3(OH_2)_3]^+$ by syringe and the mixture heated to 70 °C for 45 min. The reaction mixture was cooled in an ice bath and the product isolated using a Sep-Pak (Waters, C_{18}). The Sep-Pak was conditioned prior to use with absolute ethanol (10 mL), acetonitrile (10 mL), 1:1 acetonitrile/10 mM HCl (10 mL), and 10 mM HCl (10 mL). After loading the reaction solution onto the conditioned Sep-Pak, the column was washed with 10 mM HCl (7 × 1 mL), 1:4 acetonitrile/10 mM HCl (2 × 1 mL), 1:1 acetonitrile/10 mM HCl (2 × 1 mL), 4:1 acetonitrile/10 mM HCl (2 × 1 mL), and finally

Scheme 1

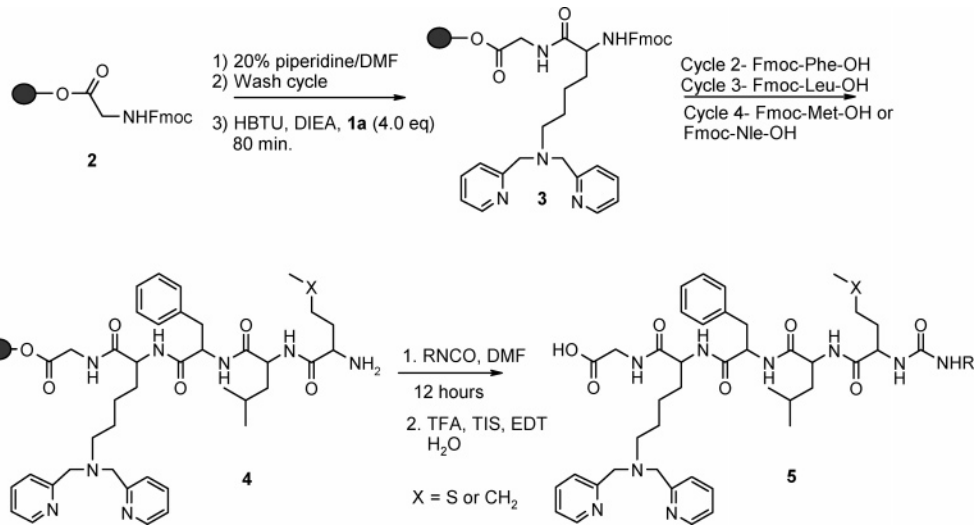

acetonitrile (5 × 1 mL). Compound **6b** eluted in fractions 12−17 (radiochemical yield = 90%, radiochemical purity ≥ 98%).

Ligand Challenge Experiments. Cysteine (0.13 μmol in 5 mL of ddH_2O) and histidine (0.13 μmol in 5 mL of ddH_2O) were added to two separate vials each containing 11.1 MBq to 18.5 MBq (300−500 μCi) of purified **6b** in 250 μL of 100 mM phosphate buffer. Both vials were incubated at 37 °C for 24 h. Aliquots were taken periodically and analyzed by HPLC.

Leukocyte Preparation. Whole human blood (10−15 mL) was collected in vacutainer tubes (Becton Dickinson) containing sodium heparin. The red blood cells were lysed using a modified ammonium chloride method (1 part whole blood to 23 parts 0.145 M ammonium chloride solution containing 1.5 mM potassium bicarbonate and 0.1 mM EDTA). Tubes were incubated at room temperature for 15 min and then centrifuged in a Beckman Coulter Allegra 6R centrifuge at 900 rpm (400 g) for 7 min at 5 °C. The supernatant was removed and the pellet of leukocytes subsequently resuspended in HBSS containing 0.1% BSA, 10 mM HEPES, and 1.5 mM $CaCl_2$ (HBSS+). The cells were spun for 7 min at 400 g at 5 °C, the supernatant was removed, and the pellet was resuspended in HBSS+. Cell counts were performed using a hemacytometer and a Beckman Coulter Z2 Coulter Particle Count and Size Analyzer. Cell concentrations were adjusted to 2×10^6 mL^{-1}.

Flow Cytometry. Samples were run on a Beckman Coulter EPICS XL, equipped with an argon laser (488 nm excitation wavelength). Fluorescence was measured using a 525 ± 15 nm band-pass filter. The flow cytometer was calibrated with fluorescein isothiocyanate (FITC) labeled beads (Quantum 26 Beads, Bangs Laboratories, Inc, Fishers, IN) prior to sample analysis. The fluorescence intensity of the standard was provided by the manufacturer in units of Molecules of Equivalent Soluble Fluorochrome (MESF) and ranged from 5300 to 468 800. A linear fit of MESF versus mean channel number of the beads was used to convert all subsequent mean channel values to MESF values.

Equilibrium Binding Assay. The equilibrium-binding assay was used to determine the number of formyl peptide receptors (FPRs) on the surface of the neutrophils and the dissociation constant (K_d) of the fluorescein-labeled fNLFNTK (Molecular Probes) (1.0 nM) by preparing a saturated binding curve of peptide concentrations verses fluorescence intensity. Peptide stock solutions were made by dissolving the peptide derivatives in DMSO and then diluting with HBSS+ to the desired concentrations, ensuring the concentration of DMSO was less than 0.1%. Cells at 1×10^6 mL^{-1} were equilibrated with 0.25, 0.50. 1.0, 3.0, 5.0, 10.0, and 20.0 nM solutions of the peptide derivatives (U) in duplicate. The samples were incubated for 2 h at 0 °C in the dark and then run on the flow cytometer. Neutrophils were gated on the basis of forward and side scatter parameters using Expo 32 ADC software (Beckman Coulter). All samples were repeated in the presence of 30 μM fMLF to account for nonspecific binding. The number of receptor−ligand complexes per cell (B) was determined using the following equation, where Q is a normalization factor used by Waller et al. (*28*) and F is the total fluorescence per cell:

$$\mathrm{B(in\ ligand\ bound\ per\ cell)} = F\left(\frac{\mathrm{MESF}}{\mathrm{cell}}\right) \times Q$$

The level of nonspecific binding did not vary significantly with the concentration of labeled peptide; thus, an average value of nonspecific binding was subtracted from the total fluorescence per cell, F, when determining the number of receptor−ligand complexes. The total number of N-formyl peptide receptors, R_{tot}, and the equilibrium dissociation constant, K_d, were evaluated by minimizing the squared residual of the equilibrium solution using a one-site binding model (see the following equation). The values of R_{tot} and K_d for each donor were solved simultaneously.

$$[\mathrm{LR}] = \frac{R_{\mathrm{tot}}[\mathrm{L}]}{[\mathrm{L}] + K_d}$$

RESULTS

Peptide Synthesis. Solid-phase synthesis (Scheme 1) was carried out on an advanced Advanced ChemTech 348 Ω synthesizer using all L-amino acids. For each peptide, the synthesis began by coupling Fmoc protected SAAC to SASRIN resin bound glycine using a standard HBTU coupling protocol. After deprotection with 20% piperidine in DMF, the phenylalanine and leucine residues were added. Following removal of the Fmoc group on leucine, Fmoc-methionine or Fmoc-norleucine were added and subsequently deprotected.

Conversion of **4** to the corresponding ureas (see Table 4) was carried out by adding different isocyanates to the

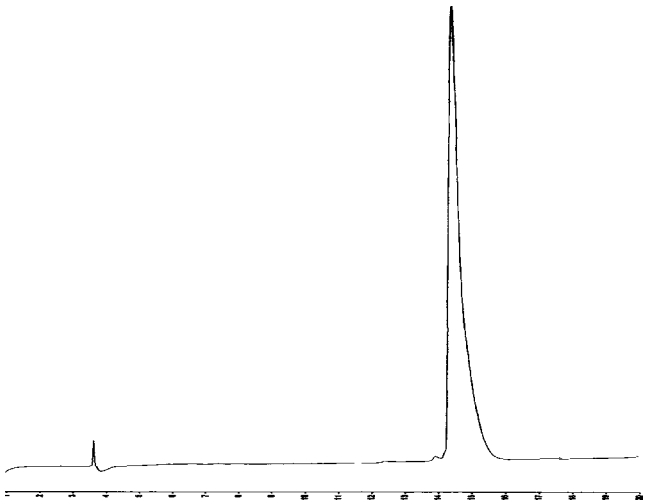

Figure 2. HPLC chromatogram (UV-detection, $\lambda = 254$ nm) of **5j**.

Table 1. HPLC Elution Times, Electrospray MS, and Select IR Data

compd	elution time (min)	found *m/z*	calcd *m/z*	[urea C(O)] (cm^{-1})	N[M(CO)] (cm^{-1})
5a	12.9	848	847	1545	-
5b	13.5	862	861	1549	-
5c	13.6	862	861	1547	-
5d	13.8	876	875	1543	-
5e	14.6	910	909	1553	-
5f	14.7	876	875	1549	-
5g	13.2	830	829	1551	-
5h	13.7	844	843	1544	-
5i	13.8	844	843	1549	-
5j	14.4	858	857	1543	-
5k	14.2	858	857	1547	-
5l	14.0	892	891	1546	-
6a	16.9	1128	1127	1535	1916, 2031

reaction wells. The duration of the reaction needed to achieve complete conversion to the urea (12 h) was determined in advance of preparing the library by carrying out a model reaction using the least reactive isocyanate (*tert*-butyl isocyanate). During these experiments, samples of resin were periodically extracted from the reaction well and exposed to ninhydrin (*26*) until complete conversion to the urea was indicated.

Peptides were cleaved from the support under argon or nitrogen using a cocktail consisting of 94% TFA, 2% EDT, 2% TIS, and 2% water (*27*). It was important to exclude moisture and oxygen during the cleavage reaction to avoid oxidation of the methionine containing peptides. Following precipitation using cold diethyl ether and centrifugation, the peptide conjugates were dissolved in water, lyophilized, and analyzed for purity. The HPLC chromatograms of the peptides, including the *tert*-butyl derivative **5j** (Figure 2), showed that the products had been prepared in very high purity in all cases and that no further purification was needed. The Re complex of **5j** was prepared using an identical solid-phase synthetic procedure except that compound **1b** was substituted for **1a**.

Characterization. Peptides were analyzed by electrospray mass spectrometry, and in each case the observed molecular ions were consistent with the mass of the desired compounds (Table 1). IR analysis confirmed the presence of the urea group, in which the C=O stretch appeared between 1535 cm^{-1} and 1553 cm^{-1} (Table 1). In the case of the Re complex of **5j**, the metal CO stretches appeared at 1916 cm^{-1} and 2031 cm^{-1}.

Table 2. ^{1}H NMR Assignments and Coupling Constant for 5j

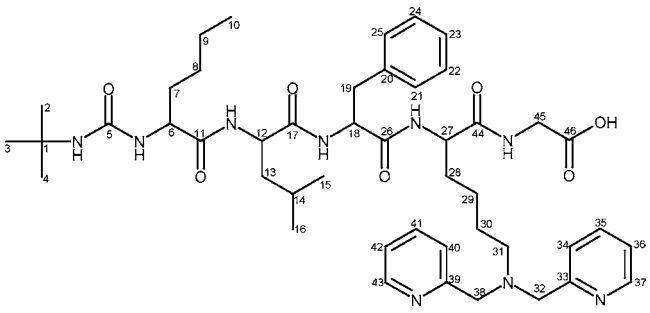

^{1}H	chemical shift (ppm)	coupling constant (Hz)
2−4	1.292 (s)	
6	4.042 (m)	
7 (2H)	1.704 (m)	
8 (2H)	1.280 (m)	
9 (2H)	1.280 (m)	
10 (3H)	0.840 (m)	
12	4.419 (m)	
13 (2H)	1.279 (m)	
14	1.562 (m)	$^3J(14, 15) = 6.6$ $^3J(14, 16) = 6.6$
15 (3H)	0.804 (d)	
16 (3H)	0.840 (d)	
18	4.695 (m)	
19′	3.112 (m)	
19″	2.971 (m)	
21, 25 (2H)	7.221 (m)	
22−24 (3H)	7.172 (m)	
27	4.419 (m)	
28′	1.562 (m)	
28″	1.704 (m)	
29 (2H)	1.279 (m)	
30 (2H)	1.562 (m)	
31 (2H)	2.647 (m)	
32/38 (4H)	4.270 (s)	
34/40 (2H)	8.009 (d)	$^3J(34, 35) = 7.8$
35/41 (2H)	8.515 (dd)	$^3J(35, 36) = 7.2$
36/42 (2H)	7.948 (dd)	$^3J(36, 37) = 6.0$
37/43 (2H)	8.724 (d)	
45 (2H)	3.939 (d)	

Table 3. ^{13}C NMR Assignments for 5j

^{13}C	chemical shift (ppm)	^{13}C	chemical shift (ppm)
1	54.5	21, 25	130.3
2−4	29.5	22−24	128.6, 130.9
5	177.6	26	174.5
6	57.7	27	54.2
7	32.7	28	32.7
8	24.1	29	23.4
9	29.2	30	26.5
10	14.4	31	56.2
11	175.2	32/38	56.8
12	55.4	33/39	153.4
13	41.4	34/40	129.5
14	26.0	35/41	149.6
15	21.9	36/42	128.9
16	23.3	37/43	143.5
17	175.4	44	175.3
18	56.9	45	42.6
19	38.9	46	173.6
20	137.2		

The *tert*-butyl urea **5j** was further characterized using ^{1}H and ^{13}C NMR spectroscopy (Tables 2 and 3). The ^{1}H NMR of **5j** (Figure 3) shows a number of multiplets in the aromatic region which were assigned to the pyridine rings of the SAAC and the aromatic group of phenylalanine. The alpha protons of the amino acids appear between 4 and 5 ppm, which along with the side chain residues, were readily assigned using standard two-dimensional experiments (COSY, HSQC, and HMBC). A

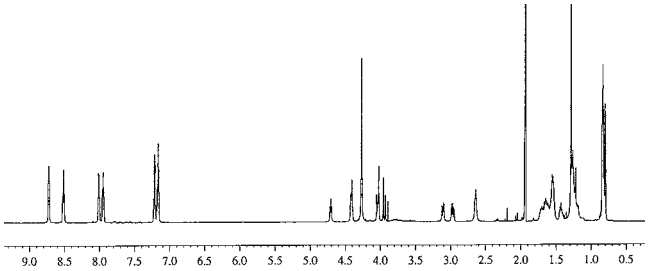

Figure 3. ^{1}H NMR of **5j** (600 MHz, 1:1 CD_3CN/TFA-*d*).

Table 4. Peptides and Binding Affinities (K_d)

compd	peptide	K_d (μM)
5a	ethyl-NH(CO)-Met-Leu-Phe-SAAC-Gly	2.9 ± 0.8
5b	isopropyl-NH(CO)Met-Leu-Phe-SAAC-Gly	3.0 ± 0.3
5c	*n*-Propyl-NH(CO)-Met-Leu-Phe-SAAC-Gly	1.3 ± 0.2
5d	*tert*-Butyl-NH(CO)-Met-Leu-Phe-SAAC-Gly	2.3 ± 0.4
5e	benzyl-NH(CO)-Met-Leu-Phe-SAAC-Gly	1.7 ± 0.2
5f	*n*-Butyl-NH(CO)-Met-Leu-Phe-SAAC-Gly	0.5 ± 0.1
5g	ethyl-NH(CO)-Nle-Leu-Phe-SAAC-Gly	1.2 ± 0.2
5h	isopropyl-NH(CO)-Nle-Leu-Phe-SAAC-Gly	1.2 ± 0.3
5i	*n*-Propyl-NH(CO)-Nle-Leu-Phe-SAAC-Gly	1.1 ± 0.6
5j	*tert*-Butyl-NH(CO)-Nle-Leu-phe-SAAC-Gly	2.6 ± 0.7
5k	*n*-Butyl-NH(CO)-Nle-Leu-Phe-SAAC-Gly	0.7 ± 0.2
5l	benzyl-NH(CO)-Nle-Leu-Phe-SAAC-Gly	0.8 ± 0.1
5m	fMLF	0.032 ± 0.003

singlet corresponding to the tBu group appeared at 1.29 ppm in the ^{1}H NMR while the signal arising from the alpha proton of norleucine was present at 4.04 ppm, which showed a correlation to the urea carbonyl carbon (177.6 ppm) in the HMBC spectrum. The resonances remaining in the carbonyl region of the ^{13}C NMR spectrum were consistent with the number of amide/acid groups in the peptide backbone. The carbonyl groups were assigned using a TOCSY experiment, which in turn confirmed the proposed connectivity of the peptide.

In Vitro Screening Studies using Flow Cytometry. Peptides were screened on a flow cytometer using a competitive binding assay where the concentration of the competitor was allowed to vary while maintaining the concentration of the fluorescent peptide (*28*−*30*). Competitive binding data was obtained on the same day using the same human donor as for the equilibrium binding data, to minimize variability in the number of receptors. Cells (10^6 mL^{-1}) were incubated with 1.0 nM fluorescein-labeled fNLFNTK and 0, 1, 15, 100, 300, 700, 1000, and 1400 nM competitor in duplicate for 3 h at 0 °C in the dark. The equilibrium dissociation constant for the competing unlabeled ligand, K_d, was determined following literature procedures by fitting the specific ligand bound data to the same one-site binding model. The peptide, fMLF was used as a reference standard. Its K_d value was in good agreement with the value reported in the literature (*21*, *28*). The K_d values for a reference standard (fMLF) and library constituents are given in Table 4.

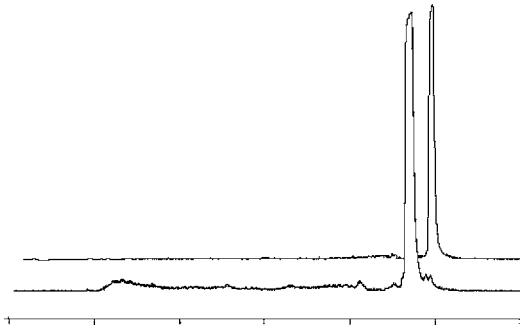

Figure 4. γ-Radiochromatograms of $[^{99m}Tc(CO)_3(OH_2)_3]^+$ and **5j** after 45 min at 70 °C (bottom) and purified **6b** (top).

Radiochemistry. The peptide **5j** (250 μg) was combined with 307 MBq (8.3 mCi) of $[^{99m}Tc(CO)_3(OH_2)]^+$ in a mixture of PBS buffer and acetonitrile (Scheme 2). After heating the reaction to 70°C for 45 min, the desired product, **6b**, was isolated, free from any unlabeled peptide, using a simple Sep-Pak purification method. The radiochemical yield of the isolated product was 90% with a radiochemical purity of greater than 98%. The γ-HPLC trace of the crude reaction mixture and the purified product are shown in Figure 4.

Compound **6b** was subsequently incubated with a large excess of cysteine and histidine as a preliminary means of evaluating the complexes tendency to undergo transchelation in the presence of a large excess of competing donors. After 24 h, the labeled peptide showed no signs of degradation which is consistent with the low spin d^6 electronic configuration of the octahedral metal complex.

DISCUSSION

The single amino acid chelate (SAAC) is a lysine derivative where the Fmoc protected form can be readily incorporated into a growing peptide using conventional peptide synthesis protocols. The chelate, which is soluble in water (when completely deprotected) and organic solvents (when protected), was prepared in very high yield on the multigram scale using a one-pot procedure involving relatively inexpensive starting materials. In the work reported here, a convenient solid-phase synthesis strategy was developed for preparing a small 12-member library of N-terminal urea derivatives of MLF(SAAC)G and NleLF(SAAC)G peptides where the nature of the urea substituent was varied. The peptides **5a**−**l** were prepared using a standard coupling/deblocking procedure in very high purities without having to employ preparative HPLC. The fact that the products were produced in such high purity contrasts the synthesis of the *N*-formyl analogue where it was necessary to purify fMLF(SAAC)G by HPLC because the methionine group rapidly epimerized during synthesis to give two diastereomers. With the approach reported here, there was no evidence of epimerization in the HPLC or the NMR data.

Scheme 2

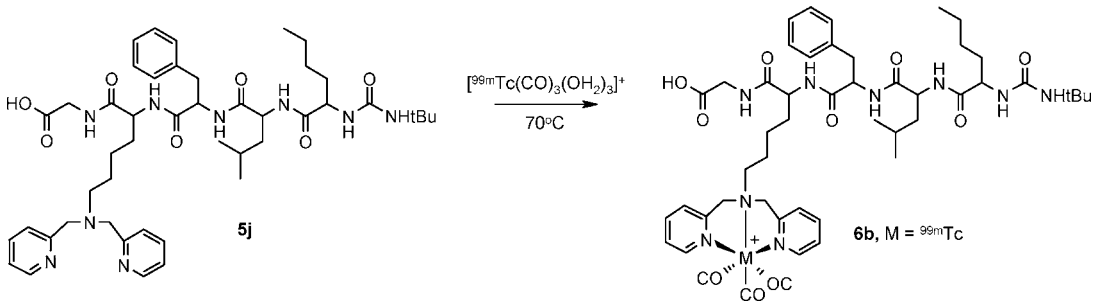

The reported methodology was capable of producing sufficient quantities of each peptide to allow for both detailed characterization of the desired products and in vitro screening studies (vide infra). The electrospray mass spectrometry data agreed in all cases with the calculated spectra, and, as mentioned previously, HPLC confirmed the purity of each sample. Additional characterization of the library constituents can be obtained through ^{1}H and ^{13}C NMR experiments. The spectra, including the data presented for compound **5j**, were consistent with the proposed structures of the peptides.

In terms of binding to the FPR receptor, all compounds had K_d values in the low micromolar range which is in agreement with the data reported by Higgins et al. (*25*). These results indicate that the addition of the SAAC group does not have a detrimental influence on the behavior of the peptide in terms of binding to the FPR receptor. This observation in turn is consistent with the data reported by Cavicchioni et al. which suggests that C-terminal variants of fMLF type peptides do not significantly influence the peptides receptor binding affinity (*31*). The structure of the urea appeared to have a small affect on the K_d values where bulky groups (tBu, ^{i}Pr) generally reduced the K_d values whereas the peptides containing linear alkyl substituents, particularly the ^{n}Bu groups, showed somewhat higher affinity. In addition to considering K_d values, it is important to note that changing the nature of the urea and first amino acid will have a significant impact on the distribution and mode of clearance of the agents. Consequently, the ^{99m}Tc complexes of the library components will be screened in vivo in the appropriate animal model and the derivative showing the optimal distribution profile evaluated further.

We have previously established that the single amino acid chelates form stable complexes with Re(I). To demonstrate that the SAAC-peptide derivatives can also be labeled efficiently with ^{99m}Tc, compound **5j** was reacted with $[^{99m}Tc(CO)_3(OH_2)]^+$, which was prepared using a formulation that is employed in commercially available carbonyl labeling kits. The labeled peptide, **6b**, was isolated in excellent yield using a small amount of ligand (250 μg). To verify the nature of the ^{99m}Tc complex, the corresponding Re complex **6a** was prepared via the same solid-phase synthetic procedure used to prepare **5j** except that compound **1b** was employed in place of **1a**. The HPLC retention time of a sample of compound **6a**, which had been previously characterized by LCMS, matched that for **6b**.

The ability to verify the nature of a ^{99m}Tc complex using a well characterized Re standard is an attractive feature of the SAAC system. With a number of traditional ligand systems (*32*−*36*) it is often difficult to prepare the corresponding Re or ^{99}Tc complexes (let alone to use them for solid-phase synthesis) which in turn complicates the process of identifying compounds produced at the tracer level. With the SAAC system, the Re complexes can be prepared after hits from the library are identified or they can be synthesized in concert with the free ligands without having to significantly modify the original solid-phase synthetic methodology.

CONCLUSIONS

The reported methodology demonstrates the ease with which a library of peptide-ligand derivatives can be developed using the SAAC system. Increasing the size and structural diversity of the library is readily achievable by not only varying the end terminal groups and the nature of the natural amino acids, but also the position of the SAAC. Furthermore, because the ligand is based on a natural amino acid, either enantiomer of the SAAC can be readily incorporated at any position in a peptide. As such, the SAAC chelating system can be used to prepare libraries of a wide range of peptide-based radiopharmaceuticals using a conventional automated peptide synthesizer. In the case reported here, the library constituents show similar K_d values and will therefore be screened in vivo to determine the impact of the various substitutions on biodistribution profiles.

ACKNOWLEDGMENT

We would like to acknowledge the Ontario Research and Development Challenge Fund (ORDCF) and The National Sciences and Engineering Research Council (NSERC) of Canada for funding and for providing a Scholarship for K.A.S.

Supporting Information Available: HPLC, ESMS, ^{1}H and ^{13}C NMR, FT-IR, and select competitive binding data. This material is available free of charge via the Internet at http://pubs.acs.org.

LITERATURE CITED

(1) Liu, S., and Edwards, D. S. (1999) ^{99m}Tc-Labeled Small Peptides as Diagnostic Radiopharmaceuticals. *Chem. Rev. 99*, 2235−2268.

(2) Welch, M. J., and Redvanly, C. S. (2002) *Handbook of Radiopharmaceuticals: Radiochemistry and Applications,* John Wiley and Sons, New York.

(3) Kwekkeboom, D., Krenning, E. P., and de Jong, M. (2000) Peptide Receptor Imaging and Therapy. *J. Nucl. Med. 41*, 1704−1713.

(4) Gershell, L. J., and Atkins, J. H. (2003) A Brief History of Novel Drug Discovery Technologies. *Nat. Rev. Drug Discovery 2*, 321−327.

(5) Smith, C. J., Gali, H., Sieckman, G. L., Higginbotham, C., Volkert, W. A., and Hoffman, T. J. (2003) Radiochemical Investigations of ^{99m}Tc-N(3)S-X-BBN[7−14]NH_2: An in Vitro/in Vivo Structure−Activity Relationship Study Where X = 0-, 3-, 5-, 8-, and 11-Carbon Tethering Moieties. *Bioconjugate Chem. 14*, 93−102.

(6) Gariépy, J., Rémy, S., Zhang, X., Ballinger, J. R., Bolewska-Pedyczak, E., Rauth, M., and Bisland, S. K. (2002) A Simple Two-Step Approach for Introducing a Protected Diamine-dithiol Chelator during Solid-Phase Assembly of Peptides. *Bioconjugate Chem. 13*, 679−684.

(7) Greenland, W. E. P., Howland, K., Hardy, J., Fogelman, I., and Blower, P. J. (2003) Solid-Phase Synthesis of Peptide Radiopharmaceuticals Using Fmoc-N-ϵ-(Hynic-Boc)-Lysine, a Technetium-Binding Amino Acid: Application to Tc-99m-Labeled Salmon Calcitonin. *J. Med. Chem. 46*, 1751−1757.

(8) Stephenson, K. A., Zubieta, J., Banerjee, S. R., Levadala, M. K., Taggart, L., Ryan, L.; McFarlane, N., Boreham, D. R.; Maresca, K. P., Babich, J. W., and Valliant, J. F. (2004) A New Strategy For The Preparation of Peptide-Targeted Radiopharmaceuticals Based on an Fmoc-Lysine-Derived Single Amino Acid Chelate (SAAC). Automated Solid-Phase Synthesis, NMR Characterization, and in Vitro Screening of fMLF(SAAC)G and fMLF[(SAAC)-$Re(CO)_3)^+$]G. *Bioconjugate Chem. 15*, 128−136.

(9) Banerjee, S. R., Levadala, M. K., Lazarova, N., Wei, L.; Valliant, J. F., Stephenson, K. A., Babich, J. W., Maresca, K. P., and Zubieta, J. (2002) Bifunctional Single Amino Acid Chelates (SAAC) for Labeling of Biomolecules with $\{Tc(CO)_3\}^{+1}$ and $\{Re(CO)_3\}^{+1}$ cores. The crystal and molecular structures of $[ReBr(CO)_3(H_2NCH_2C_5H_4N)]$, $[Re(CO)_3\{X(Y)NCH_2CO_2CH_2CH_3\}]Br$, (X = Y = 2-pyridylmethyl; X = 2-pyridylmethyl, Y = 2-(1-methylimidazolyl)methyl; X = Y= 2-(1-methylimidazolyl)methyl, $[ReBr(CO)_3\{(C_5H_4NCH_2)NH(CH_2C_4H_3S)\}]$ and $[Re(CO)_3\{(C_5H_4NCH_2)N(CH_2C_4H_3S)CH_2CO_2)\}]$. *Inorg. Chem. 41*, 6417−6425.

(10) Babich, J. W., Coco, W. G., Barrow, S., Fischman, A. J., Femia, F. L., and Zubieta, J. (2000) ^{99m}Tc-Labeled Chemotactic Peptides: Influence of Coligand on Distribution of Molecular Species and Infection Imaging Properties. Synthesis and Structural Characterization of Model Complexes with the {Re(η^2-HNNC$_5$H$_4$N)(η^1-NNC$_5$H$_4$N)}core. *Inorg. Chim. Acta 309*, 123−136.

(11) Babich, J. W., Graham, W., Barrow, S. A., Dragotakes, S. C., Tompkins, R. G., Rubin, R. H., and Fischman, A. J. (1993) Technetium-99m-Labeled Chemotactic Peptides: Comparison with Indium-111-Labeled White Blood Cells for Localizing Acute Bacterial Infection in the Rabbit. *J. Nucl. Med. 34*, 2176−2181.

(12) Babich, J. W., Graham, W., Barrow, S. A., and Fischman, A. J. (1995) Comparison of the Infection Imaging Properties of a ^{99m}Tc Labeled Chemotactic Peptide with ^{111}In IgG. *Nucl. Med. Biol. 22*, 643−648.

(13) Babich, J. W., Solomon, H., Pike, M. C., Kroon, D., Graham, W., Abrams, M. J., Tompkins, R. G., Rubin, R. H., and Fischman, A. J. (1993) Technetium-99m-Labeled Hydrazino Nicotinamide Derivatized Chemotactic Peptide Analogues for Imaging Focal Sites of Bacterial Infection. *J. Nucl. Med. 34*, 1964−1974.

(14) Baidoo, K. E., Scheffel, U., Stathis, M., Finley, P., Lever, S. Z., Zhan, Y., and Wagner, H. N., Jr. (1998) High-Affinity No−Carrier-Added ^{99m}Tc-Labeled Chemotactic Peptides for Studies of Inflammation In Vivo. *Bioconjugate Chem. 9*, 208−217.

(15) Edwards, D. S., Liu, S., Ziegler, M. C., Harris, A. R., Crocker, A. C., Heminway, S. J., Barrett, J. A., Bridger, G. J., Abrams, M. J., and Higgins, J. D., III (1999) RP463: A Stabilized Technetium-99m Complex of a Hydrazino Nicotinamide Derivatized Chemotactic Peptide for Infection Imaging. *Bioconjugate Chem. 10*, 884−891.

(16) Pollak, A.; Goodbody, A. E.; Ballinger, J. R.; Duncan, G. S.; Tran, L. L.; Dunn-Dufault, R.; Meghji, K.; Lau, F.; Andrey, T. W.; Boxen, I.; and Sumner-Smith, M. Imaging Inflammation with ^{99m}Tc-Labelled Chemotactic Peptides: Analogues with Reduced Neutropenia. *Nucl. Med. Commun.* **1996**, *17*, 132−139.

(17) Van Der Laken, C. J.; Boerman, O. C.; Oyen, W. J. G.; Van De Ven, M. T. P.; Edwards, D. S.; Barrett, J. A.; Van Der Meer, J. W. M.; and Corstens, F. H. M. Technetium-99m-Labeled Chemotactic Peptides in Acute Infection and Sterile Inflammation. *J. Nucl. Med.* **1997**, *38*, 1310−1315.

(18) Verbeke, K., Verbeke, A., Vanbilloen, H.; and Verbruggen, A. (2002) Preparation and Preliminary Evaluation of ^{99m}Tc-EC-For-MLFK. *Nucl. Med. Biol. 29*, 585−592.

(19) Verbeke, K., Snauwaert, K., Cleynhens, B., Scheers, W., and Verbruggen, A. (2000) Influence of the Bifunctional Chelate on the Biological Behavior of ^{99m}Tc-Labeled Chemotactic Peptide Conjugates. *Nucl. Med. Biol. 27*, 769−779.

(20) Rennen, H. J., Boerman, O. C., Oyen, W. J., and Corstens, F. H. (2001) Imaging Infection/Inflammation in the New Millenium. *Eur. J. Nucl. Med. 28*, 241−252.

(21) Rennen, H. J., Boerman, O. C., Oyen, W. J. G., and Corstens, F. H. M. (2002) Scintigraphic Imaging of Inflammatory Processes. *Curr. Med. Chem.: Antiinflammatory & Anti-Allergy Agents 1*, 63−75.

(22) Rennen, H. J., Corstens, F. H., Oyen, W. J., and Boerman, O. C. (2001) New Concepts in Infection/Inflammation Imaging. *Quart. J. Nucl. Med. 45*, 167−173.

(23) Fischman, A. J., Rauh, D., Solomon, H., Babich, J. W., Tompkins, R. G., Kroon, D., Strauss, H. W., and Rubin, R. H. (1993) In Vivo Bioactivity and Biodistribution of Chemotactic Peptide Analogues in Nonhuman Primates. *J. Nucl. Med. 34*, 2130−2134.

(24) Edwards, D. S., and Liu, S. (2001) Tc-99m-Labeled Small Biomolecules as Potential Radiopharmaceuticals for Infection and Inflammation Imaging. *Drugs Future 26*, 375−382.

(25) Higgins, J. D., III, Bridger, G. J., Derian, C. K., Beblavy, M. J., Hernandez, P. E., Gaul, F. E., Abrams, M. J., Pike, M. C., and Soloman, H. F. (1996) N-terminus Urea-Substituted Chemotactic Peptides: New Potent Agonists and Antagonists Toward the Neutrophil fMLF Receptor. *J. Med. Chem. 39*, 1013−1015.

(26) Sarin, V. K., Kent, S. B., Tam, J. P., and Merrifield, R. B. (1981) Quantitative Monitoring of Solid-Phase Peptide Synthesis by the Ninhydrin Reaction. *Anal. Biochem. 117*, 147−157.

(27) Chan, W. C., and White, P. D. (2000) *FMOC Solid-Phase Peptide Synthesis, A Practical Approach,* Oxford University Press, New York.

(28) Waller, A., Pipkorn, D., Sutton, K. L., Linderman, J. J., and Omann, G. M. (2001) Validation of Flow Cytometric Competitive Binding Protocols and Characterization of Fluorescently Labeled Ligands. *Cytometry 45*, 102−114.

(29) Fay, S. P., Posner, R. G., Swann, W. N., and Sklar, L. A. (1991) Real-Time Analysis of the Assembly of Ligand, Receptor, and G Protein by Quantitative Fluorescence Flow Cytometry. *Biochemistry 30*, 5066−5075.

(30) Hoffman, J. F., Keil, M. L., Riccobene, T. A., Omann, G. M., and Linderman, J. J. (1996) Interconverting Receptor States at 4 °C for the Neutrophil N-formyl Peptide Receptor. *Biochemistry 35*, 13047−13055.

(31) Cavicchioni, G., Varani, K., Niccoli, S., Rizzuti, O., and Spisani, S. (1999) An Evaluation of fMLF Pocket Dimensions and Features using formyltetrapeptides. *J. Pept. Res. 54*, 336−343.

(32) Su, Z. i.-F., He, J., Rusckowski, M., and Hnatowich, D. J. (2003) In Vitro Cell Studies of Technetium-99m Labeled RGD-HYNIC Peptide, A Comparison of Tricine and EDDA as Coligands. *Nucl. Med. Biol. 30*, 141−149.

(33) Ono, M., Arano, Y., Mukai, T., Saga, T., Fujioka, Y., Ogawa, K., Kawashima, H., Konishi, J., and Saji, H. (2002) Control of Radioactivity Pharmacokinetics of ^{99m}Tc−HYNIC-Labeled Polypeptides Derivatized with Ternary Ligand Complexes. *Bioconjugate Chem. 13*, 491−501.

(34) Qu, T., Wang, Y., Zhu, Z., Rusckowski, M., and Hnatowich, D. J. (2001) Different Chelators and Different Peptides Together Influence the In Vitro and Mouse In Vivo Properties of ^{99m}Tc. *Nucl. Med. Commun. 22*, 203−215.

(35) Rennen, H. J., Oyen, W. J., Cain, S. A., Monk, P. N., Corstens, F. H., and Boerman, O. C. (2003) Tc-99m-Labeled C5a and C5a des Arg74 for Infection Imaging. *Nucl. Med. Biol. 30*, 267−272.

(36) Francesconi, L., Zheng, Y., Bartis, J., Blumenstein, M., Costello, C., and De Rosch, M. A. (2004) Preparation and Characterization of [^{99}TcO] Apcitide: A Technetium Labeled Peptide. *Inorg. Chem. 43*, 2867−2875.

BC0500591

Quaternary Ammonium Polysaccharides for Gene Delivery

Ira Yudovin-Farber,[†] Chava Yanay,[‡] Tony Azzam,[†] Michal Linial,[‡] and Abraham J. Domb*[,†,§]

Department of Medicinal Chemistry and Natural Products, School of Pharmacy, Faculty of Medicine, The Hebrew University of Jerusalem, P.O.B. 12065 Jerusalem 91120, Israel, Department of Biological Chemistry−Life Science, The Hebrew University of Jerusalem, Jerusalem 91905, Israel, and Alex Grass Center for Drug Design and Synthesis, The Hebrew University of Jerusalem. Received March 8, 2005; Revised Manuscript Received July 27, 2005

Cationic polysaccharides were synthesized by conjugation of various monoquaternary (MQ) ammonium oligoamines to oxidized dextran by reductive amination and tested for gene transfection. Polycations of dextran grafted with MQ ammonium oligoamines of two to four amino groups were investigated for their ability to cause pCMV-GFP encoding for green fluorescence protein and β-Gal encoding for β-galactosidase protein transfection on EPC and HEK-293 cell lines. These polycations were expected to strongly complex DNA due to increased surface cationic charge of the carrier, which may result in a higher transfection yield. However, the transfection yields were much lower compared to the parent vector, dextran-spermine conjugate, which was highly effective both in vitro and in vivo.

INTRODUCTION

The basic concept of gene therapy is that disease can be treated by transfer of genetic material into specific cells of a patient to supplement defective genes responsible for disease development (*1*). The main problem of gene therapy is gene delivery to gain high expression with maximal safety to the patient. A number of techniques have been developed for DNA delivery: direct introduction of transgene using cell electroporation, microinjection of DNA, and incorporation of the gene by viruses (*2*) and synthetic vectors (*3*). Viral vectors including retroviruses, adenoviruses, and adeno-associated viruses impress by their high efficiency in introducing their genetic material into host cells (*4*), although immunogenicity, inflammatory effects, and safety concerns restrict their usefulness. The advantages of nonviral vectors are that they do not integrate into chromosome, can introduce DNA into nondividing cells, do not possess infective risk, and are significantly less expensive and easy to handle than viral vectors (*5*). The major disadvantage of nonviral systems is their low transfection efficiency. The nonviral delivery vectors should overcome intracellular barriers, such as endosomes and nuclear membranes (*6*).

Polycations are a leading class of nonviral gene delivery systems due to their versatility in molecular weight, polymer type, polymer-DNA ratio, molecular architecture, and the ability to introduce target-specific moieties. Polycations and negatively charged nucleic acids can spontaneously form nanocomplexes by electrostatic interaction.

Polycation reduces the electrostatic repulsion between DNA and the cell membrane by neutralizing the DNA negative charge and also protects it from enzymatic digestion by nucleases in serum and extracellular fluids. Cationic materials that are commonly used in gene delivery include poly(L-lysine) (*7*), cationic liposomes (*8*), polyethyleneimine (*9*), dendrimers (*9*), poly(L-histidine) (*10*), polyvinylpyridine, and cationic polysaccharides (*11*, *12*). Polycations that are used as gene delivery systems are polyamines that contain primary, secondary, or tertiary amines (*11*). Under physiological conditions, polyamines become cationic and condense DNA into compact structures.

In our previous publications, we reported on a new type of biodegradable polycation based on grafted oligoamine residues on natural polysaccharides (*13*). From a large number of oligoamine conjugates, the dextran−spermine conjugate was found to be the most active in transfecting a wide range of cell lines and plasmids in vitro and in vivo (*14*). This high transfection of dextran−spermine may be attributed to the spermine residues and architecture of the polysaccharide, which apparently play a significant role in cell transfection (*14*, *15*).

The effectiveness of the carrier is related to the ability of the polycation to condense DNA that is dependent on the structure of the polymer, the distance of cationic charge from the backbone, charge spacing along the polymer backbone, order of charged amine, and molecular weight. One way to achieve improved uptake into cells is by increasing the surface charge of complexes (*16*). This modification is expected to result in higher affinity to negatively charged cell membrane constituents and therefore to a higher rate of uptake. The charge of the carrier can also influence the size of the polymer−DNA complex (polyplex) that plays a significant role in the endosomal uptake (*17*), the cytoplasmatic transport and the migration through the nucleoporecomplexes which mediate the bidirectional transport between cytoplasm and nucleus.

This report focuses on the synthesis of various oligoamines bearing a quaternary ammonium group conjugated to dextrans (Scheme 2) and investigates their transfection capacity in vitro. Monoquaternary (MQ) ammonium oligoamine−dextran conjugates were prepared and tested for their gene transfection efficiency on EPC and HEK-293 cell lines. These agents showed

* To whom correspondence should be addressed. Phone: 972-2-6757573. Fax: 972-2-6758959. E-mail: adomb@md.huji.ac.il.
[†] Department of Medicinal Chemistry and Natural Products.
[‡] Department of Biological Chemistry−Life Science.
[§] Alex Grass Center for Drug Design and Synthesis.

10.1021/bc050066p CCC: $30.25 © 2005 American Chemical Society
Published on Web 08/27/2005

Scheme 1. Synthesis of MQ Ammonium Spermine

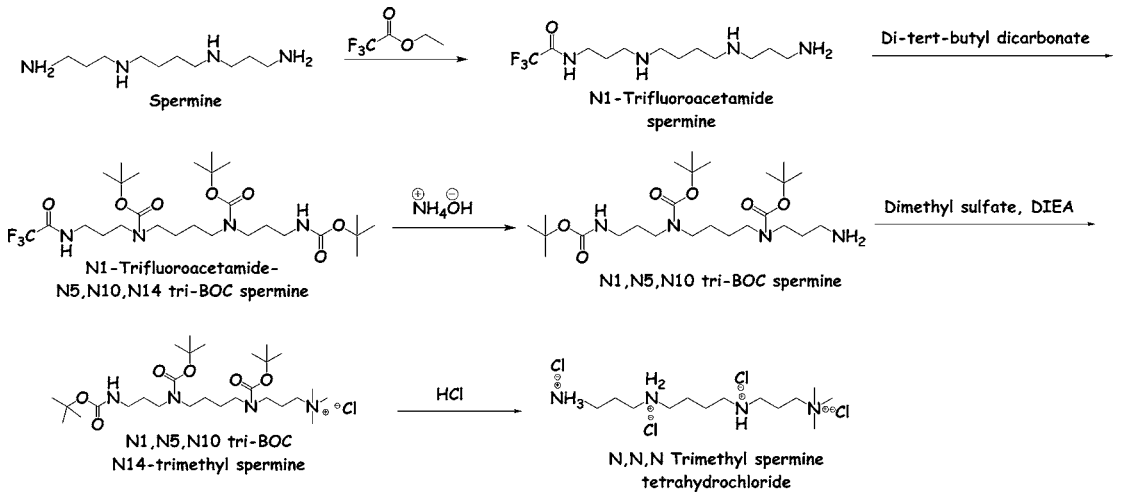

Scheme 2. Grafting of Spermine Residues on Oxidized Dextran

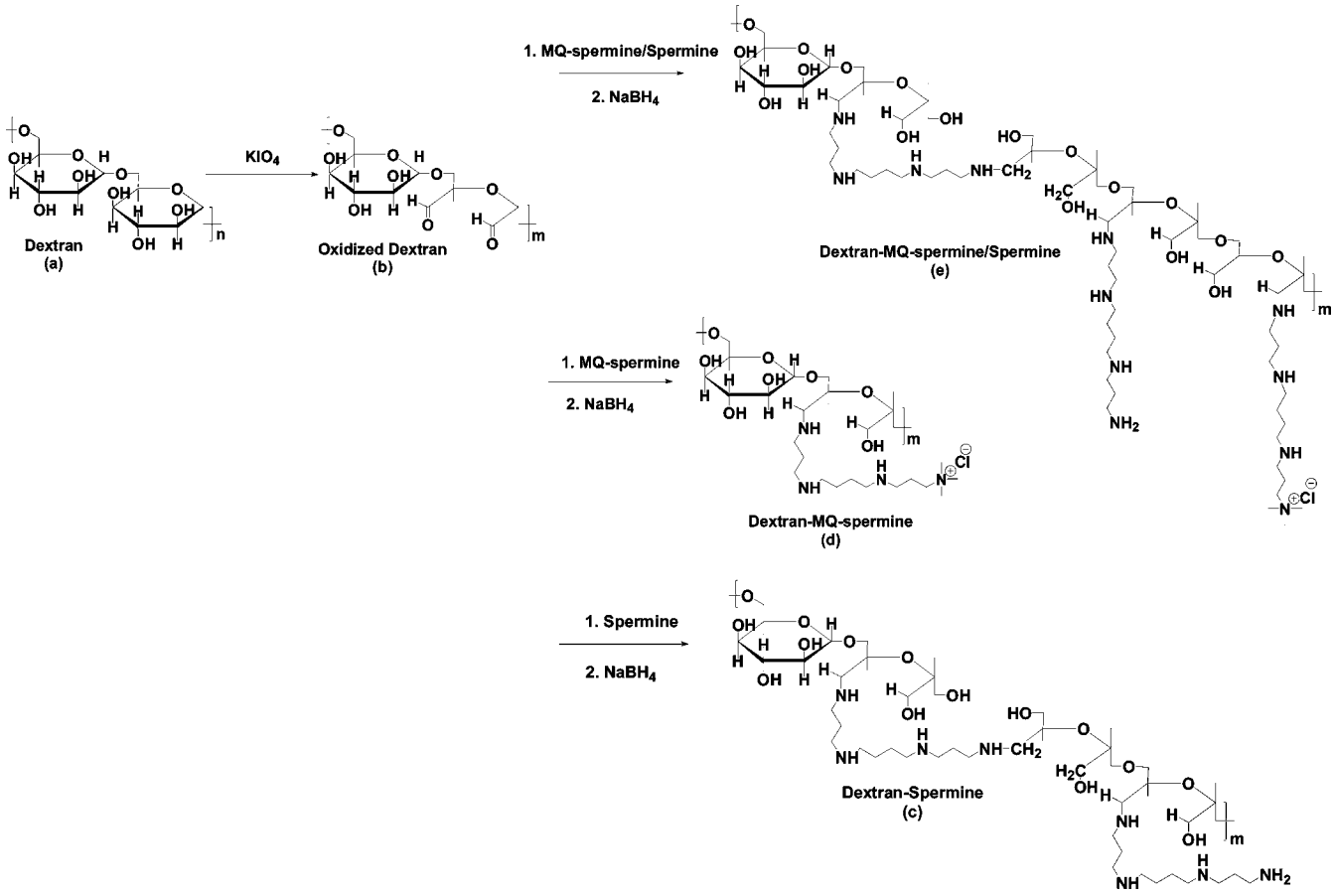

moderate toxicity when tested on human embryonal kidney HEK-293 cells.

MATERIALS AND METHODS

Materials. Dextran of an average molecular weight of 40 kDa, 1,4-butane diamine and 1,2-ethylenediamine, potassium periodate (KIO_4), sodium borohydride ($NaBH_4$), di-*tert*-butyl dicarbonate, and diisopropylethylamine (DIEA) were obtained from Sigma-Aldrich Israel, Rehovot. Spermine and ethyl trifluoroacetate were obtained from Fluka Chemie (Buchs, Switzerland). All solvents and reagents were of analytical grade and were used as received. Tetrahydrofuran (THF) was dried by distillation over sodium/benzophenone.

A sage-metering pump model-365 (Orion, NJ) was used for slow and reproducible addition of reactants. Average molecular weights of polycations were estimated by a GPC-Spectra Physics instrument (Darmstadt, Germany) consisting of a pump, column (Shodex KB-803), and refractive index (RI) detector using pullulan standards (PSS, Mainz, Germany) with molecular weights between 5 800 and 212 000. Eluents used were 0.05 M $NaNO_3$ for the uncharged polymers and 5% (w/v) NaH_2PO_4 in 3% (v/v) acetonitrile (pH 4) for the cationic conjugates (*18*). The degree of conjugation was estimated by elemental microanalysis of nitrogen (%N) using a Perkin-Elmer 2400/II CHN analyzer. ^1H NMR spectra (D_2O, $CDCl_3$ or DMSO-d_6) were obtained on a Varian 300-MHz spec-

trometer in 5-mm outside diameter tubes. D_2O/$CDCl_3$/DMSO-d_6 containing tetramethylsilane served as solvent and shift reference. Fourier transform (FT) IR spectra were recorded on a Perkin-Elmer, 2000 FTIR. Purified plasmid (pCMV-GFP and pCMV-β-Gal) were from Qiagen kit, Germany. Fetal calf serum (FCS), 4 mM glutamine, penicillin, streptomycin, and amphotericin B were from Beit Haemek, Israel. Alamarblue reagent was from Biosorce, Israel. Cell transfection with pCMV-GFP was analyzed by fluorescence microscope instrument using model Axiovert 35, Zeiss, Jena, Germany.

Methods. *Synthesis of tri-tert-Butyl Carbonyl Spermine (tri-BOC Spermine).* Spermine was selectively protected on one of the primary amino functional groups by reaction with ethyl trifluoroacetate. Spermine (21.96 mmol, 4.4 g) was dissolved in 250 mL of absolute methanol, and the solution was cooled to −78 °C, then an equimolar (21.96 mmol, 3.1 g) amount of ethyl trifluoroacetate was added during 1 h at −78 °C under nitrogen atmosphere. Stirring was continued for 1 h at 0 °C to complete the reaction. The remaining three amino functional groups were BOC protected with di-*tert*-butyl dicarbonate (4.0 equiv, 87.84 mmol, 19.1 g) that was added, and the mixture was stirred at 0 °C for 1 h under nitrogen atmosphere and then overnight at room temperature. The trifluoroacetamide protecting group was then cleaved by adding 30 mL of 25% ammonia solution (pH of the mixtrure was 11), and stirring was continued for 16 h at room temperature under nitrogen atmosphere. The resulting tri-BOC spermine was purified from di-BOC spermine by chromatography over silica gel (dichloromethane (DCM):MeOH:NH_4OH 70:10:1 to 50:10:1 v/v/v). Average yield: 50%.

^{1}H NMR (DMSO, ppm): 1.4 (s, 27H, BOC hydrogens), 1.6 (m, 4H, NH(BOC)$(CH_2)_3$N(BOC)CH_2*CH_2*CH_2N-(BOC)$(CH_2)_3NH_2$), 1.72 (m, 4H, NH(BOC)CH_2*CH_2*CH_2N-(BOC)$(CH_2)_4$ N(BOC)CH_2*CH_2*CH_2NH_2), 2.6 (m, 2H, NH-(BOC)$(CH_2)_3$N(BOC)$(CH_2)_4$N(BOC)CH_2CH_2*CH_2NH_2), 3.1 (m, 10H, NH(BOC)*CH_2*CH_2*CH_2*N(BOC) *$CH_2CH_2CH_2$*-*CH_2*N(BOC)*$CH_2CH_2CH_2NH_2$*).

Synthesis of MQ Ammonium Spermine (MQ−Spermine). Tri-BOC spermine (2.0 mmol, 1.0 g) was dissolved in 25 mL of anhydrous THF. The solution was cooled to 0 °C, then diisopropylethylamine (5.0 equiv, 10.0 mmol, 1.75 mL) and dimethyl sulfate (4.0 equiv, 8.0 mmol, 0.75 mL) dissolved in minimum amount of THF were added to the flask. The mixture was stirred for 24 h at room temperature under nitrogen atmosphere. Diisopropylethylammonium salt was discarded by filtration. The filtrate was evaporated under reduced pressure. The crude was dissolved in a mixture of trifluoroacetic acid (TFA) and DCM (TFA:DCM 10:90 v/v) for 2 h at room temperature to deprotect three amino functional groups. DCM and TFA were evaporated under reduced pressure, and the residue was redissolved in double deionized water (DDW) and purified from sulfate by Dowex-1 anion-exchange resin (chloride form). The fractions were picked and freeze dried. Average yield: 90%.

^{1}H NMR (D_2O, ppm, tetrahydrochloride form): 1.62 (m, 4H, $H_3N(CH_2)_3NH_2CH_2$*CH_2*$CH_2CH_2NH_2(CH_2)_3$N-$(CH_3)_3$), 1.9 (m, 2H, H_3NCH_2*$CH_2CH_2NH_2(CH_2)_4$ NH_2-$(CH_2)_3N(CH_3)_3$), 2.08 (m, 2H, $H_3N(CH_2)_3NH_2(CH_2)_4$- NH_2-CH_2*$CH_2CH_2N(CH_3)_3$), 3.0 (m, 12H, $H_3NCH_2CH_2$*CH_2*-NH_2*$CH_2CH_2CH_2$*CH_2NH_2-*CH_2CH_2*$CH_2N(CH_3)_3$), 3.28 (m, 9H, $H_3N(CH_2)_3NH_2(CH_2)_4NH_2CH_2CH_2CH_2N$*$(CH_3)_3$*). Elemental Analysis: %N = 13.36, %Cl = 34.

Synthesis of Dextran−MQ−Spermine Conjugate. Oxidized polysaccharide (1.0 g, 6.25 mmol of aldehyde groups) (*19*) was dissolved in 100 mL of DDW, and the solution was slowly added over several hours to a solution containing 6.25 mmol MQ−spermine dissolved in 50 mL of borate buffer (0.1 M, pH 11). The mixture was stirred at room temperature for 24 h. $NaBH_4$ (1.0 g, 4.0 equimolar) was added to reduce the formed imine bonds and stirring was continued for 48 h at room temperature. The reduction was repeated with an additional portion of $NaBH_4$ (1 g), and stirring was continued for additional 24 h. The resulting solution was poured into a dialysis membrane (3 500 cutoff, Membrane Filtration Products, Inc., San Antonio, TX) and dialyzed against DDW at 4 °C for 3 days. The dialysate was lyophilized to dryness. Average yield: 50% (w/w).

^{1}H NMR (D_2O, ppm): 1.45 (m, 4H, MQ−spermine hydrogens), 1.63 (m, 4H, MQ−spermine hydrogens), 2.64 (m, 10H, MQ−spermine hydrogens), 3.0 (m, 9H, methyl hydrogens of MQ−spermine), 3.0 (m, 2H, MQ−spermine hydrogens), 3.30−4.45 (m, glucose hydrogens), and 5.01 (m, 1H, anomeric hydrogen).

Synthesis of BOC-1,2-ethylenediamine. Solution of di-*tert*-butyl dicarbonate (2.45 g, 0.011 mol) in dioxane (30 mL) was added over a period of 3 h to a solution of 1,2-ethylenediamine (5.25 g, 0.087 mol) in 30 mL of dioxane. The mixture was allowed to stir for 24 h at room temperature, and the solvent was removed under reduced pressure. The residue was dissolved in 50 mL of DDW, and the insoluble bis-substituted product was collected by filtration. The white filtrate that contained monoprotected 1,2-ethylenediamine was extracted with DCM (3 × 50 mL), dried over anhydrous $MgSO_4$, filtered, and evaporated to dryness. The crude yellow oil was further dried under vacuum over solid NaOH pellets. Average yield: 90%.

^{1}H NMR ($CDCl_3$, ppm): 1.4 (s, 9H, COOC*$(CH_3)_3$*), 2.8 (t, 2H, -*CH_2*−NH_2), 3.15 (m, 2H, BOC−NH-*CH_2*-) and 5.02 (br, 1H, *NH*-BOC).

Synthesis of MQ Ammonium 1,2-Ethylenediamine (MQ−1,2-Ethylenediamine). BOC-1,2-ethylenediamine (1.0 g, 6.25 mmol) was dissolved in 5 mL of anhydrous dimethylformamide (DMF), then 3.7 mL of anhydrous tributylamine (TBA) was added to the flask. The mixture was cooled to 0 °C, and 3.3 g of methyl iodide (3.5 equimolar) was added. Stirring was continued overnight at room temperature under nitrogen atmosphere. Solvent and excess TBA were removed under reduced pressure and the resulting product was incubated for 2 h in 5 mL of TFA:DCM (10:90 v/v) at room temperature to deprotect the amino groups. The product was precipitated in 100 mL of diethyl ether, and the yellow precipitate was further dried under vacuum over solid NaOH pellets. The yellow precipitate was dissolved in DDW (5 mL) and purified from iodide by Dowex-1 anion-exchange resin (chloride form). The fractions were picked and freeze dried. Average yield: 80%.

^{1}H NMR (DMSO, ppm, dichloride form): 3.140 (s, 9H, −N(*CH_3*)$_3$), 3.282 (t, 2H, −*CH_2*−NH_3), 3.481 (t, 2H, −*CH_2*−$N(CH_3)_3$), and 7.942 (br, 3H, −CH_2*NH_3*).

Synthesis of Dextran−MQ−1,2-Ethylenediamine Conjugate. Oxidized dextran (100.0 mg, 0.625 mmol) was dissolved in 10 mL of DDW, and the solution was slowly added over several hours to a solution containing 0.625 mmol of MQ ammonium−1,2-ethylenediamine (1.0 equimolar) dissolved in 5 mL of borate buffer (0.1 M, pH 11). The mixture was stirred at room temperature for 24 h. $NaBH_4$ powder (100.0 mg, 4 equimolar) was added to reduce the imine bonds to amines, and the mixture was further stirred for 48 h under the same conditions. The reduction was repeated with an additional portion of $NaBH_4$ (100.0 mg), and stirring was continued for ad-

ditional 24 h under the same conditions. Then, the reaction mixture was dialyzed (3500 cutoff, Membrane Filtration Products, Inc., San Antonio, TX) against DDW at 4 °C for 3 days. The dialysate was lyophilized to dryness. Average yield: 35% w/w.

^{1}H NMR (D_2O, ppm): 2.9 (m, 2H, methylene hydrogens), 3.3 (s, 9H, methyl hydrogens), 3.3 (m, 2H, methylene hydrogens), 3.3−4.45 (m, glucose hydrogens) and 5.01 (m, 1H, anomeric hydrogen).

Synthesis of BOC−1,4-Butane Diamine. Solution of di-*tert*-butyl dicarbonate (2.45 g, 0.011 mol) in dioxane (30 mL) was added over a period of 3 h to a solution of 1,4-butane diamine (7.67 g, 0.087 mol) in 30 mL of dioxane. The mixture was stirred for 24 h at room temperature, and the solvent was evaporated. The residue was dissolved in 50 mL of DDW, and the insoluble bis-substituted product was collected by filtration. Contained monoprotected 1,4-butane diamine filtrate was extracted with DCM (3 × 50 mL), dried over anhydrous $MgSO_4$, filtered, and evaporated to dryness. The crude was dried under vacuum over solid NaOH pellets. Average yield: 90%.

^{1}H NMR ($CDCl_3$, ppm): 1.4 (m, 9H, COOC*(CH_3)$_3$*), 1.45 (m, 4H, BOC−NH−CH_2−*(CH_2)$_2$*−CH_2−NH_2), 2.6 (t, 2H, −*CH_2*−NH_2), 3.07 (m, 2H, BOC−NH−*CH_2*−), and 4.8 (br, 1H, *NH*-BOC).

Synthesis of MQ Ammonium−1,4-Butane Diamine (MQ−1,4-Butane Diamine). BOC−1,4-butane diamine (1.0 g, 5.31 mmol) was dissolved in 5 mL of anhydrous dimethylformamide (DMF), then 3.2 mL of anhydrous tributylamine (TBA) was added to the flask. The mixture was cooled to 0 °C, and 2.8 g of methyl iodide (3.5 equimolar) was added. Solution was stirred overnight at room temperature under nitrogen atmosphere. Solvent and excess TBA were removed under reduced pressure, and the resulting product was incubated for 2 h in 5 mL of TFA:DCM (10:90 v/v) at room temperature. The product was precipitated in 100 mL of diethyl ether, and the precipitate was further dried under vacuum over solid NaOH pellets. Average yield: 80%.

^{1}H NMR (D_2O, ppm, dichloride form): 1.8 (m, 2H, −*CH_2*−CH_2−NH_3), 1.9 (m, 2H, −*CH_2*−CH_2−$N(CH_3)_3$), 3.09 (m, 2H, −*CH_2*−NH_3), 3.15 (s, 9H, −$N(CH_3)_3$), and 3.4 (t, 2H, −*CH_2*−$N(CH_3)_3$).

Synthesis of Dextran−MQ−1,4-Butane Diamine Conjugate. Oxidized dextran (100.0 mg, 0.625 mmol) was dissolved in 10 mL of DDW, and the solution was slowly added over several hours to a solution containing 0.625 mmol of MQ ammonium 1,4-butane diamine (1.0 equimolar) dissolved in 5 mL of borate buffer (0.1 M, pH 11). The mixture was stirred at room temperature for 24 h. $NaBH_4$ (100.0 mg, 4 equimolar) was added to reduce the imine bonds to amines, and the mixture was further stirred for 48 h under the same conditions. The reduction was repeated with an additional portion of $NaBH_4$ (100.0 mg), and stirring was continued for additional 24 h under the same conditions. Then, the reaction mixture was dialyzed (3500 cutoff, Membrane Filtration Products, Inc., San Antonio, TX) against DDW at 4 °C for 3 days. The dialysate was lyophilized to dryness. Average yield: 35% w/w.

^{1}H NMR (D_2O, ppm): 1.41 (m, 2H, −*CH_2*−CH_2−NH−glucose unit), 1.7 (m, 2H, −*CH_2*−CH_2−$N(CH_3)_3$), 2.5 (m, 2H, −*CH_2*−NH−glucose unit), 3.25 (m, 2H, −*CH_2*−$N(CH_3)_3$), 3.3 (m, 9H, −N*(CH_3)$_3$*), 3.3−4.45 (m, glucose hydrogens), and 5.01 (m, 1H, anomeric hydrogen).

Preparation of Plasmid DNAs. Plasmid DNAs used in the transfection experiments were pCMV-GFP encoding for green fluorescence protein and pCMV-β-Gal encoding β-Galactosidase. Plasmid DNAs were separately amplified in a XL-blue *Escherichia coli* and isolated using Qiagen Maxi kit-25 (Qiagen kit, Germany). Briefly, the grown bacteria were harvested and lysed in a 1% aqueous solution of sodium dodecyl sulfate (SDS) and 0.1% RNase A solution in NaOH (pH 8.0). The lysate was neutralized by the addition of 3 M potassium acetate (pH 5.5). After separation of the insoluble portion by centrifuging at 14 000 *g* for 30 min, the lysate was applied to an anion-exchange resin (Qiagentip, Germany), followed by high salt washing (buffer containing 1 M NaCl) to remove traces of RNAs and denatured proteins. The plasmid DNA was eluted with an elution buffer containing 1.25 M NaCl at pH 8.5, desalted, and precipitated by 2-propanol. The precipitated plasmid DNA was centrifuged at 14 000 rpm for 10 min at 4 °C, and washed twice with 70% ethanol−water. After centrifugation (14 000 rpm, 2 min, 4 °C), the resulting plasmid DNA was air dried and dissolved in a small volume of 10 mM Tris−Cl pH 7.5. The purity of plasmid DNA was checked routinely, and the absorbance ratio of 260 nm to 280 nm ranged from 1.8 to 2.0.

In vitro Transfection. In vitro transfection procedure was based on the previous publications (*20*). Human embryonal kidney (HEK-293) cells were used in the transfection experiments. Purified plasmid per well of transfected cells (0.5 μg) was mixed with the polycation at various weight-mixing ratios ranging from 3 to 9 w/w (polycation/ DNA). The polycation/DNA complex mixtures were diluted to a final volume of 200 μL with Dulbecco's modified Eagle's Medium (DMEM) and allowed to stand at room temperature for 40 min. Twenty-four-well plates coated with polyethyleneimine were seeded 24 h before transfection at 7 × 10^4 cells per well. Cultures were washed with preheated (37 °C) phosphate-buffered saline (PBS), and the solution of the complexes was added to the wells and cultured at 37 °C in 95% air/5% CO_2. Four hours after transfection, cell medium was replaced with DMEM containing 10% fetal calf serum (FCS), 4 mM glutamine, penicillin, streptomycin, and amphotericin B. Cells were further cultured for 48−72 h. At this time, transfection efficiency and toxicity were assayed.

For determination of the transfection efficiency, cultures were washed gently with warm PBS and then subjected to lysis and colorimetric β-galactosidase quantitative determination, measuring the amount of 2-nitrophenol formed in situ from cleavage of 2-nitrophenyl-B-D-galactopyranoside (ONPG) by β-galactosidase. Briefly: 300 μL of the reaction solution consisting of 1 mM $MgCl_2$, 45 mM β-mercaptoEtOH, 73 mM Na_2HPO_4, 16 mM NaH_2PO_4, 0.1% SDS, and 0.88 mg/mL ONPG were applied onto each well, and the cells were then incubated at 37 °C for 30 min until a yellow color developed. Reaction was stopped with 500 μL of 1 M solution Na_2CO_3. The amount of 2-nitrophenol formed was determined by measuring optical density at 420 nm.

Cells transfected with pCMV-GFP were analyzed for gene expression using fluorescence microscope instrument.

For the assessment of the number of vital cells in each well, Alamarblue method was used, in which the reduction of Alamarblue from the oxidized indigo blue, non-fluorescing state to the reduced fluorescent pink state is indicative of the proportion of living cells in each well. Alamarblue reagent was diluted to 5% in growing media and applied to the culture for 4 h, after which the OD at 570 nm was measured.

Percent toxicity was calculated as 100 − OD_{570}SAMPLE/OD_{570}CTRL × 100, where the control group was not

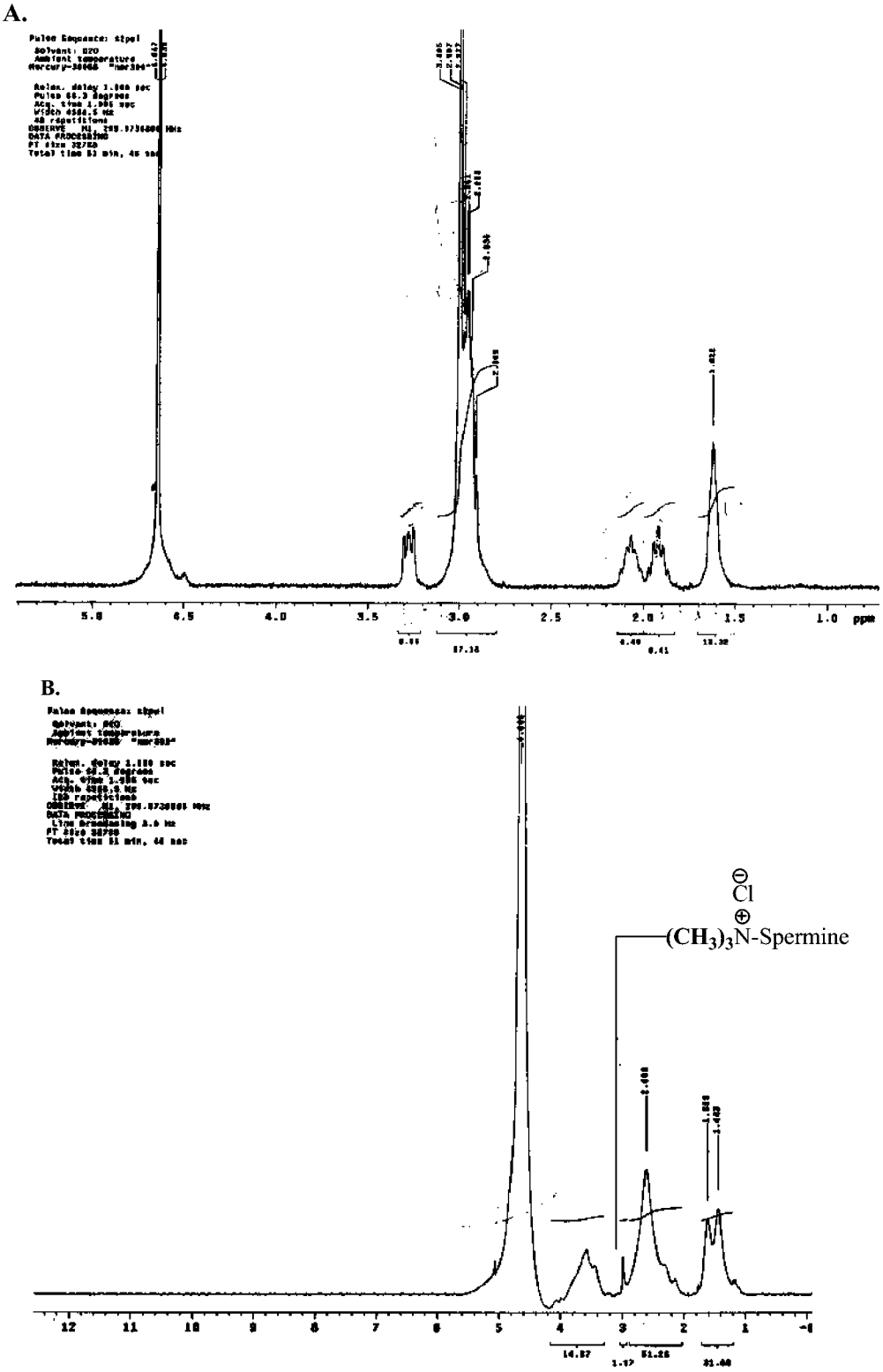

Figure 1. (A) ^{1}H NMR spectrum of the MQ−spermine. (B) ^{1}H NMR spectrum of the compound #C.

subjected to any treatment but underwent the identical culturing and washing procedure.

RESULTS AND DISCUSSION

Chemistry. In the present study, we have prepared quaternorized conjugates and investigated their transfection efficiency and cytotoxicity. Oligoamine derivatives having a quaternary ammonium salt in one end and a primary amine group in the other end were synthesized as illustrated in Scheme 1. Tri-BOC spermine derivative was prepared in several steps using TFA and BOC orthogonal protecting groups. Ethyl trifluoroacetate was added at −78 °C to obtain the predominantly monotrifluoroacetamide derivative, followed by reaction with excess of di-*tert*-butyl dicarbonate to obtain the fully mixed protected derivative. The trifluoroacetamide protecting groups were removed by concentrated ammonia, yielding the tri-BOC spermine derivative. The tri-BOC spermine was then treated with dimethyl sulfate or methyl iodide to obtain the tri-BOC monoquaternary

Table 1. Structures of Oligoamines Used in the Preparation of Dextran−Oligoamine Polycations

Oligoamine used for conjugation	Oligoamine structure	^{1}H-NMR (ppm)
Spermine	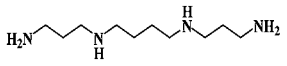	(D_2O):1.645 (m), 1.804 (m) and 2.185 (m)
MQ-spermine	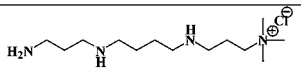	(D_2O):1.62 (m), 1.9 (m), 2.08 (m), 3 (m) and 3.28 (m)
MQ-1,2- ethylene diamine	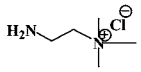	(DMSO):3.1 (s), 3.28 (t) and 3.48 (m)
MQ-1,4-butane diamine	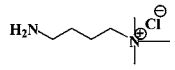	(D_2O):1.8 (m), 1.9 (m), 3.09 (m), 3.15 (s) and 3.4 (t)

Table 2. Chemical Characterization of Dextran−Oligoamine Conjuagates[a]

code	oligoamine	%N[b]	primary amine[c]	Mn[d]	P	relative transfection yield[e]
A	MQ−spermine:spermine 5:95 mole ratio	9.08	0.56	14.400	3.3	0.2
B	MQ−spermine:spermine 10:90 mole ratio	9.05	0.64	13.300	2.7	0.16
C	MQ−spermine:spermine 20:80 mole ratio	9.01	0.58	15.600	3.1	0.13
D	MQ−spermine:spermine 5:95 mole ratio	9.78	0.822	1800	1.7	0.17
E	MQ−spermine:spermine 10:90 mole ratio	9.96	0.66	1100	2.5	0.09
F	spermine	10.73	1.7	13.600	1.6	1.46
G	100% MQ−spermine	4.13	0.05	7.900	1.17	0
H	100% MQ−1,2-ethylenediamine	5.57	0.02	5.700	1.35	0
I	100% MQ−1,4-butane diamine	4.13	0.05	4.500	1.75	0

[a] Oligoamine was reacted with oxidized dextran (~50% dialdehyde) at a 1:1 aldehyde/oligoamine mole ratio. [b] Found nitrogen content (elemental analysis). [c] Amount of primary amine (mmol/g) in conjugates determined by the TNBS method. [d] Average molecular weight (Mn) and polydispersity (P = Mw/Mn) were determined by GPC. The remarkable difference in molecular weight of the #A and #B and #D and #E conjugates is explained by the use of dextran of 40 and 10 kDa as starting material. [e] β-Galactosidase quantitative determination (OD). Trasfection yield of the polycations, prepared at 3:1 weight ratio (polymer/DNA), were compared to calcium phosphate used as a positive reference (OD = 1.307).

ammonium spermine derivative as a sulfate or iodide salt. Deprotection of BOC groups was achieved by treating with trifluoroacetic acid to obtain the MQ−spermine derivative. Figure 1A shows the ^{1}H NMR spectrum obtained from this derivative. The remaining MQ ammonium alkane diamine derivatives were similarly prepared.

Oxidized dextrans having similar molecular weight and aldehyde content were reacted under the same conditions with MQ ammonium tetramine and diamine (Table 1) followed by treating with sodium borohydride to obtain the amine conjugate (Scheme 2). MQ−oligoamine derivatives were chemically characterized (Table 2). The degree of substitution with MQ−oligoamine moieties was estimated by microanalysis (%N), primary amine content (TNBS) (*13*), and ^{1}H NMR spectroscopy. Negligible primary amino group content was obtained for conjugates that were fully grafted with MQ ammonium oligoamines. This was expected by the fact that these oligoamine derivatives are being all grafted and terminated with quaternary ammonium functionalities.

Transfection Results. Transfection experiments of grafted oxidized dextran with MQ−spermine, MQ ammonium−1,4-butane diamine, and MQ ammonium−1,2-ethylenediamine were performed using EPC cell line in serum-free medium (SFM). Plasmid used for these studies was pCMV-luciferase encoding for luciferase protein. Luciferase was quantitatively assayed using commercial enzyme-linked immunosorbent assay kits according to standart protocols. Dextran−spermine based polycations were found to be highly effective in transfecting cells in vitro (*21*) and in vivo (*14*, *22*), therefore dextran−spermine was used as a positive reference.

Since spermine is clearly the active moiety in the transfection (*21*), it was plausible that increasing the charge level of the carrier by MQ−spermine conjugation onto dextran (Scheme 2, product #d) would result in enhanced transfection efficiency. However, in comparison with leading derivative dextran−spermine, all quaternary ammonium derivatives resulted in negligible transfection in all tests (Table 2). Possible explanation for this behavior is probably a result of the high cationic nature of the quaternary ammonium moieties, which form a too strong complex with DNA. In other words, quaternary ammonium groups seem to form too strong and stable complexes with DNA to be released, which led to a dramatic decrease in the transfection efficiencies. These results strengthen Margreet hypothesis about quaternary ammonium groups that form complexes efficiently with DNA, reflecting a stronger bond than with primary amino groups (*23*). We hypothesize that an additional explanation for the reduced transfection yield is the difference in the branching of the polymer. It was shown that dextran−spermine is a branched polymer with some

spermine residues serve as branching agents (*13*, *23*). The degree of branching can be determined according to the following equation

$$\%\text{branching} = [(\text{spermine (total)} - \text{spermine (graft)})/\text{spermine (total)}] \times 100$$

where spermine (total) is determined by %N (microanalysis) and spermine (graft) can be determined by primary amine content (TNBS). In our case, 11% branching spermine moieties were obtained in the compound #F. On the other hand, use of the MQ−spermine reduces the degree of branching and thus a less branched polycation is obtained which affects the transfection yield. More studies will be needed to confirm this hypothesis. The structures of dextran−spermine and dextran−MQ−spermine are given in Scheme 2 (products #c and #d, respectively).

Grafting of the oligoamines mixtures to oxidized dextran was the further step of our study. Dextran conjugates of mixtures of intact spermine and MQ−spermine were prepared by reacting oxidized dextran starting from different molecular weights with mixtures of spermine: MQ−spermine at 95:5 to 80:20 mole ratios followed by reduction with $NaBH_4$ (Scheme 2, product #e). Chemical characteristic of these compounds and ^1H NMR spectrum of one of them is given in Table 2 (compounds #A−E) and Figure 1B, respectively. The purpose of this step was to evaluate transfection efficiencies of these polymers as a function of MQ ammonium spermine percentages to the total grafted oligoamine.

The transfection with these derivatives was performed in SFM applying HEK-293 cells. Plasmids used for these studies were pCMV-GFP encoding for green fluorescence protein as a marker gene and β-Gal encoding for β-galactosidase protein. Stock solutions of DNA and polycations were mixed at various weight ratios, diluted with DMEM, and left at room temperature. After 40 min, complex solutions were added separately to each cell well. After 4 h, SFM was replaced with a fresh medium. Incubation was continued for 48−72 h to complete transfection. Transfection yield was defined by colorimetric β-galactosidase quantitative determination, measuring the amount of 2-nitrophenol formed in situ from cleavage of 2-nitrophenyl-B-D-galactopyranoside by β-galactosidase. In the case of GFP protein, the transfection yield was quantified by visual counting of fluorescent cells in a certain field using a fluorescent microscope (data not shown). Calcium phosphate precipitating technique and dextran−spermine were used as positive reference. MQ ammonium conjugates were prepared and tested for their transfectivity. Each single polymer was tested over a range of polymer/DNA ratios from 3 to 9. Figure 2 demonstrates a series of transfection results, applying HEK-293 cells and β-Gal transfection systems. These conjugates showed low transfection yield even at 5% MQ−spermine content at both low and high molecular weight conjugates (compounds #A and #D). Further increase of weight ratio (polymer/DNA) resulted only in a slight improvement of the transfection yield (Figure 2). These results indicate that conjugation of MQ−spermine and probably other quaternary ammonium derivatives have negative effect on the transfection yield and that spermine remains the most effective as oligoamine graft.

Evaluation of the Cytotoxicity. One of the requirements of the polymeric vectors for use in gene therapy is the absence of cytotoxicity. Cytotoxicity evaluation of the tested conjugates was performed by the Alamarblue method (*24*). Polycation solutions and plasmid DNA were mixed at 3:1, 6:1, and 9:1 weight ratios (polymer/DNA). Toxicity of the polyplexes was presented by the number of vital cells in each well. Several conjugates showed a dose−response correlation between the polymer concentration and cell-growth inhibition (compounds #F and #A). Majority of the compounds demonstrated moderate effect on the cell viability or no toxicity at all at 3:1 weight ratio (dextran−spermine/DNA). However, an additional increase in the weight ratio resulted in a raise of cytotoxic properties of the majority of the samples (Figure 3).

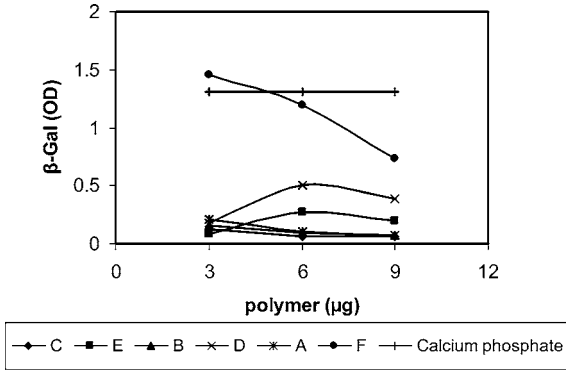

Figure 2. Transfection efficiencies of β-Gal system in HEK-293 cells applying on mixed MQ−spermine/spermine grafted derivatives as vectors (Table 2). Calcium phosphate and dextran−spermine were used as positive reference.

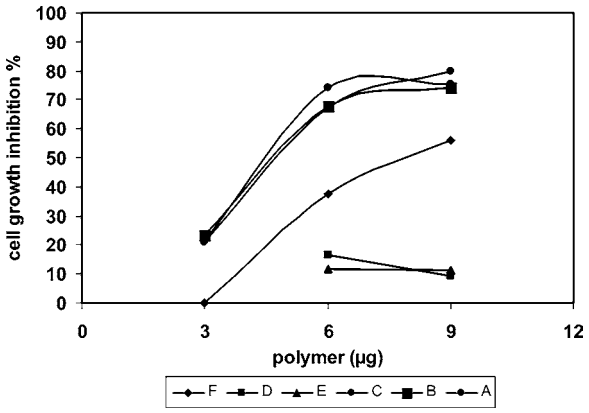

Figure 3. Average cytotoxicity of the tested compounds. Cytotoxicity test was performed using Alamarblue method (*24*) on HEK-293 cells applying dextran−spermine and mixed MQ−spermine/spermine derivatives (see Table 2).

CONCLUSION

On the basis of the assumption that quaternorization may enhance the DNA-condensing ability of the cationic polysaccharides, various polycations were prepared by reductive amination between MQ ammonium oligoamines and oxidized dextran. The cationic polysaccharides demonstrated low transfection efficiency in EPC and HEK-293 cells. Mixed grafted MQ−spermine/spermine caused loss of transfection yield. This study proves again that the dextran−spermine conjugate, a biodegradable cationic polysaccharide, remains to be a promising gene carrier. Further attempts to improve its performance by quaternorization of the spermine residue resulted in the loss of activity and increased toxicity.

ACKNOWLEDGMENT

This study was supported in part by the US−Israel Binational Fund and by the AFIRST, France−Israel initiative.

LITERATURE CITED

(1) Anderson, W. F. (1992) Human Gene-Therapy. *Science 256*, 808−813.
(2) Saleh, M., Wiegmans, A., Malone, Q., Stylli, S. S., and Kaye, A. H. (1999) Effect of in situ retroviral interleukin-4 transfer on established intracranial tumors. *J. Natl. Cancer Inst. 91*, 438−445.
(3) Aoki, K., Yoshida, T., Sugimura, T., and Terada, M. (1995) Liposome-Mediated in Vivo Gene-Transfer of Antisense K−Ras Construct Inhibits Pancreatic Tumor Dissemination in the Murine Peritoneal-Cavity. *Cancer Res. 55*, 3810−3816.
(4) Crystal, R. G. (1995) Transfer of Genes to Humans − Early Lessons and Obstacles to Success. *Science 270*, 404−410.
(5) Ledley, F. D. (1995) Nonviral Gene-Therapy - the Promise of Genes as Pharmaceutical Products. *Hum. Gene Ther. 6*, 1129−1144.
(6) Ferrari, S., Geddes, D. M., and Alton, E. (2002) Barriers to and new approaches for gene therapy and gene delivery in cystic fibrosis. *Adv. Drug Delivery Rev. 54*, 1373−1393.
(7) Kabanov, A. V. (1999) Taking polycation gene delivery systems from in vitro to in vivo. *Pharmaceutical Sci. Technol. Today 2*, 365−372.
(8) Zuidam, N. J., Hirsch-Lerner, D., Margulies, S., and Barenholz, Y. (1999) Lamellarity of cationic liposomes and mode of preparation of lipoplexes affect transfection efficiency. *Biochim. Biophys. Acta 1419*, 207−220.
(9) Merdan, T., Kopecek, J., and Kissel, T. (2002) Prospects for cationic polymers in gene and oligonucleotide therapy against cancer. *Adv. Drug Delivery Rev. 54*, 715−758.
(10) Cho, Y. W., Kim, J. D., and Park, K. (2003) Polycation gene delivery systems: escape from endosomes to cytosol. *J. Pharm. Pharmacol. 55*, 721−734.
(11) De Smedt, S. C., Demeester, J., and Hennink, W. E. (2000) Cationic polymer based gene delivery systems. *Pharmaceutical Res. 17*, 113−126.
(12) Yamaoka, T., Hamada, N., Iwata, H., Murakami, A., and Kimura, Y. (1998) Effect of cation content of polycation-type gene carriers on in vitro gene transfer. *Chem. Lett.* 1171−1172.
(13) Azzam, T., Eliyahu, H., Shapira, L., Linial, M., and Barenholz, Y. et al. (2002) Polysaccharide-oligoamine based conjugates for gene delivery. *J. Med. Chem. 45*, 1817−1824.
(14) Hosseinkhani, H., Azzam, T., Tabata, Y., and Domb, A. J. (2004) Dextran-spermine polycation: an efficient nonviral vector for in vitro and in vivo gene transfection. *Gene Ther. 11*, 194−203.
(15) Eliyahu, H., Azzam, T., Domb, A. J., and Barenholz, Y. Unpublished results.
(16) Thanou, M., Florea, B. I., Geldof, M., Junginger, H. E., and Borchard, G. (2002) Quaternized chitosan oligomers as novel gene delivery vectors in epithelial cell lines. *Biomaterials 23*, 153−159.
(17) Prabha, S., Zhou, W. Z., Panyam, J., and Labhasetwar, V. (2002) Size-dependency of nanoparticle-mediated gene transfection: studies with fractionated nanoparticles. *Int. J. Pharmaceutics 244*, 105−115.
(18) Kumar, N., Azzam, T., and Domb, A. J. (2002) Molecular mass distribution of polycations and dextrans by high-performance size exclusion chromatography. *Polym. Adv. Technol. 13*, 1071−1077.
(19) Azzam, T., Raskin, A., Makovitzki, A., Brem, H., and Vierling, P. et al. (2002) Cationic polysaccharides for gene delivery. *Macromolecules 35*, 9947−9953.
(20) Azzam, T., Eliyahu, H., Makovitzki, A., Linial, M., and Domb, A. J. (2004) Hydrophobized dextran-spermine conjugate as potential vector for in vitro gene transfection. *J. Controlled Release 96*, 309−323.
(21) Azzam, T., Eliyahu, H., Makovitzki, A., and Domb, A. J. (2003) Dextran-spermine conjugate: An efficient vector for gene delivery. *Macromol. Symp.* 195, 247−261.
(22) Eliyahu, H., Makovitzki, A., Azzam, T., Zlotkin, A., and Joseph, A. (2005) Novel dextran-spermine conjugates as transfecting agents: comparing water-soluble and micellar polymers. *Gene Ther. 12*, 494−503.
(23) Wolfert, M. A., Dash, P. R., Nazarova, O., Oupicky, D., and Seymour, L. W. (1999) Polyelectrolyte vectors for gene delivery: Influence of cationic polymer on biophysical properties of complexes formed with DNA. *Bioconjugate Chem. 10*, 993−1004.
(24) Grant, E. R., Dubin, A. E., Zhang, S. P., Zivin, R. A., and Zhong, Z. (2002) Simultaneous intracellular calcium and sodium flux imaging in human vanilloid receptor 1 (VR1)-transfected human embryonic kidney cells: A method to resolve ionic dependence of VR1-mediated cell death. *J. Pharmacol. Exp. Therapeutics 300*, 9−17.

BC050066P

Membrane Activity and Transfection Ability of Amphipathic Polycations as a Function of Alkyl Group Size

Darren H. Wakefield,[†] Jason J. Klein,[†] Jon A. Wolff,[‡] and David B. Rozema*[,†]

Mirus Bio Corporation, 505 S. Rosa Road, Madison, Wisconsin 53711, and Waisman Center, Department of Pediatrics and Medical Genetics, University of Wisconsin—Madison, Madison, Wisconsin 53705.
Received March 8, 2005; Revised Manuscript Received July 15, 2005

Cationic membrane disruptive peptides such as melittin would appear to have attributes necessary for DNA delivery: DNA binding via electrostatic interactions and membrane lysis to enable cytoplasmic delivery. However, the relatively small overall charge of membrane disruptive peptides results in weak interactions with DNA. As a model of cationic membrane disruptive peptides, amphiphilic polyvinyl ethers were synthesized. The number of positively charged groups incorporated into these polymers is substantially greater than membrane-active peptides, which enables these polymers to form stable complexes with DNA. By varying the length of the hydrophobic groups incorporated into the polymer from one to four carbons, the dependence of membrane activity on side chain length was established. The ability of these polymers to transfect DNA in tissue culture was tested, and it was found that transfection efficiency is dependent upon the membrane disruptive activity of the polymer. Comparison of melittin and synthetic polymers suggests that transfection and toxicity appear to be dependent upon their affinity for DNA. This demonstration of relationships among membrane lysis, transfection, DNA binding, and polymer side-chain composition establishes a new class of transfection reagents and may guide in the design of polymers and formulations that will enable efficient in vivo transfection.

INTRODUCTION

To protect DNA from nucleases and facilitate gene delivery, DNA is complexed with a cationic agent, either a cationic lipid, lipoplexes, or a cationic polymer, polyplexes (*1*). Either "plex" enters the cell via endocytosis and is contained in intracellular vesicles that mature into degradative lysosomes. To escape to the cytoplasm and ultimately gain entry to the nucleus, some form of endosomolytic activity must be incorporated into the delivery system. We report in this communication the creation of polymers that simultaneously possess DNA complexation and membrane-disruptive properties. Use of these polymers greatly simplifies formulation of polyplexes and improves biologically relevant delivery of DNA to cells.

Membrane-disruptive polycations in polyplexes is a relatively uncommon strategy to promote endosomolysis. All membrane-lytic peptides and polymers are amphipathic in character, i.e., they contain both hydrophilic and hydrophobic functional groups. The most studied membrane-disruptive polymers are negatively charged peptides that form amphiphilic helices capable of membrane insertion. Formation of the helices is pH-dependent and occurs in the acidic environment of the mature endosome or lysosome. Examples of these types of peptides are those derived from viral coat proteins, such as the influenza hemagglutinin-like peptide GALA (*2*, *3*). Synthetic polymers polyethyl and polypropyl acrylic acids also have pH-dependent membrane disruptive (*4*, *5*) and transfection (*6*) activities.

In addition to membrane-active anionic peptides, there are also membrane disruptive cationic peptides, such as melittin (GIGAILKVLATGLPTLISWIKNKRKQ) and the lysine analogue of GALA (*7*) (KALA: WEAKLAKALAKALAKHLAKALAKALKACEA) that have been studied for their ability to transfect DNA. However, the interaction between DNA and small polycations such as melittin and KALA (both with +5 net charge) are relatively weak compared to larger polycations, resulting in the formation of particles that dissociate in the presence of physiological salt (*8*, *9*). Therefore, it is not surprising that recent studies using cationic membrane-disruptive peptides as transfection reagents covalently attach the peptides to larger polycations such as poly-L-lysine and polyethyleneimine (*10*–*12*).

To combine DNA binding ability and membrane disruptive activity into the same polymer, we synthesized polycations that mimic the amphipathic nature of membrane-active peptides, but with charge sufficient for the formation of stable DNA complexes. Since the hydrophobic/hydrophilic ratio required to attain membrane lysis has, in contrast to polyanions (*4*, *5*), not been considered for polycations, we systematically varied the size of the hydrophobic groups.

EXPERIMENTAL SECTION

Materials. 2-Vinyloxyethylphthalimide was synthesized according to literature procedure from phthalimide and 2-chloroethyl vinyl ether (*13*). 2-Chloroethyl vinyl ether, phthalimide, ethyl vinyl ether, propyl vinyl ether, butyl vinyl ether, and boron trifluoride diethyl etherate ($BF_3{\cdot}OEt_2$) were purchased from Aldrich. Methyl vinyl ether was purchased from Matheson. Melittin was synthesized by an Applied Biosystems 433A peptide synthesizer using standard peptide synthesis methods.

Synthesis of Polyvinyl Ethers. 2-Vinyloxyethylphthalimide (1 g, 4.6 mmol) and methyl vinyl ether (0.267 g, 4.6 mmol), ethyl vinyl ether (0.332 g, 4.6 mmol), propyl vinyl ether (0.396 g, 4.6 mmol), or butyl vinyl ether

* Corresponding author e-mail: dave.rozema@mirusbio.com.
[†] Mirus Bio Corporation.
[‡] University of Wisconsin—Madison.

10.1021/bc050067h CCC: $30.25 © 2005 American Chemical Society
Published on Web 08/31/2005

(0.460 g, 4.6 mmol) were dissolved in 25 mL of anhydrous dichloromethane. These solutions were then brought to −78 °C, $BF_3{\cdot}OEt_2$ (0.065 g, 0.46 mmol) was added, and the reaction was allowed to proceed for 3 h at −78 °C. The polymerization was then stopped by the addition of 50/50 mixture of ammonium hydroxide in methanol. The solvents were then removed by rotary evaporation. The polymer was then dissolved in 30 mL of 1,4-dioxane/methanol (2/1). To this solution was added hydrazine (0.147 g, 46 mmol), and the mixture was heated to reflux for 3 h. The solvents were then removed by rotary evaporation, and the resulting solid was then brought up in 20 mL of 0.5M HCl and refluxed for 15 min, diluted with 20 mL distilled water, and refluxed for additional 1 h. This solution was then neutralized with NaOH, cooled to room temperature, transferred to 3500 molecular weight cutoff cellulose tubing, and dialyzed for 24 h (2 × 20L) against distilled water and lyophilized.

Separation of Polymers by Size Exclusion Chromatography. Lyophilized polymer was dissolved in water. A 5 mL aliquot was placed onto a 2.5 × 20 cm column packed with Sephacryl S-200. The column was eluted with 25 mM $(NH_4)_2CO_3$ 5% ethanol, pH 9. Ten microliter fractions were collected after the dead volume (25 mL). Fractions were then assayed by trinitrobenzenesulfonic acid for amine content. The eluted polymer was pooled into four equal fractions and lyophilized. Fractions were submitted for carbon, nitrogen, and hydrogen elemental analysis at Galbraith Laboratories (Knoxville, TN). Due the hydroscopic nature of the polymers, only the carbon and nitrogen data were used to determine monomer incorporation ratios. The fourth fractions showed the most consistent incorporation ratios and were therefore used in subsequent assays.

DNA Labeling. Covalent labeling of plasmid DNA with fluorophores was performed using tetramethylrhodamine (TMR) LabelIT reagent (Mirus Corp., Madison, WI) as previously described (*14*). LabelIT reagents are nitrogen mustard alkylating reagents that react primarily with guanine bases (*15*). Briefly, plasmid DNA and a solution of LabelIT reagent in methyl sulfoxide (100 mg/mL) were mixed in 1 mL of 10 mM HEPES, pH 7.5, at a LabelIT/DNA ratio of 5:1 (w/w). The reaction mixture was incubated for 1 h at 37 °C. Labeled DNA was then precipitated three times in 70% ethanol with 0.2 MNaCl.

DNA Condensation Assay. The collapse of TMR-labeled DNA was assessed using a quantitative assay based on condensation-induced quenching of a fluorophore covalently attached to DNA (*14*). Briefly, TMR-DNA (10 μg) was mixed with various quantities of polyvinyl ethers or melittin in 0.5 mL of 10 mM HEPES, pH 7.5. Rhodamine fluorescence of the samples was measured using a Varian spectrofluorometer (excitation wavelength (λ_{ex}) of 546 nm; emission wavelength (λ_{em}) of 576 nm) at room temperature. A graph of fluorescence as a function of added polymer was composed of two regions: a condensation phase where each addition of polymer resulted in a linear decrease in fluorescence, and the condensed phase where the labeled DNA was fully condensed. The concentration of polymer required for condensation was calculated by fitting of the steepest portion of the condensation phase and condensed phase to linear equations and determining the intercept of the two lines. A summary of data is presented in Table 2. Titration curves are presented as supplementary data.

Determination of Polymer Size. The molecular weights of the polymers were then determined by GPC using Eprogen Inc. CATSEC100, CATSEC300, and CATSEC1000 columns in series. The running buffer was 200 mM NaCl and 10% MeOH. Polyvinylpyridine standards (1.5, 6.5 12, 21, 47, 65, 78, 115, 287, and 1,260 kD) were used as the calibration curve. To detect the polyvinyl ethers, they were labeled with Cy3 with Cy3-*N*-hydroxysuccinimide (Amersham), which was detected at 555 nm.

The log of the molecular weight of the polyvinylpyridine standards were linear with respect to retention time, and from this relationship we were able to estimate the molecular at any retention time. From this relationship, we calculated the molecular weight M_w of the polymers according to the equation $M_w = \sum_t A_t M_t / \sum_t M_t$ where A_t is the absorbance measured at time t and M_t is the molecular weight based upon standards that elutes at that time.

Table 1. Composition and Size of Amphipathic Polyvinyl Ethers

polymer	formula from EA	mw per charge by EA[a]	mw per charge by DNA (ratio of two charge density determinations)
methyl	C_5N	147	154 (1.0)
ethyl	C_7N	165	147 (0.9)
propyl	C_6N	153	153 (1.0)
butyl	C_7N	164	166 (0.8)
mellitin		680	891 (0.8)

[a] Molecular weight of polyvinyl ethers per charge is calculated as amine free base. Melittin's molecular weight is calculated using a trifluoroacetate counterion.

Table 2. Characterization of Amphipathic Polyvinyl Ethers

polymer	molecular weight of polymer[a] (charge)	[NaCl]* (M)[b]
methyl	8500 (57)	0.6
ethyl	2500 (15)	0.4
propyl	4200 (27)	0.5
butyl	5000 (30)	0.5
melittin	3275 (5)	0.1

[a] Molecular weight based on free bases, number of charges per polymer in parentheses. [b] [NaCl]*,the concentration of NaCl required to displace polycation from plasmid DNA.

Polycation-pDNA Stability Assay. To determine the relative strength of the interactions between the peptides and polycations, the concentration of salt required to displace a polycation from TMR-labeled DNA was determined. TMR-DNA (10 μg) was condensed at N:P ratio of 2:1, as determined by condensation assays, in 10 mM HEPES, pH 7.5. To this solution were added increasing concentrations of NaCl from a 5 M stock. The fluorescence of the samples was then measured (λ_{ex}= 546 nm λ_{em}= 576 nm). A graph of fluorescence as a function of [NaCl] was a composed of two regions: a lag phase where increasing salt resulted in little or no increase in fluorescence and a decondensation phase where each addition of salt resulted in a linear increase in fluorescence. The concentration of NaCl required for decondensation was calculated by fitting of the lag phase and decondensed phase to a linear equation and determining the intercept of the two lines.

Particle Sizing. To a solution of 5 mM HEPES pH 7.5, 150 mM NaCl, and 10 μg/mL plasmid pCIluc was added polyvinyl ether to 20 μg/mL or polyethyleneimine to 10 μg/mL. After 30 min, the size of the particles was measured by light scattering at 532 nm using a Brookhaven Instruments Corporation, ZetaPlus Particle Sizer, I90.

Liposome Lysis. Egg phosphatidylcholine (10 mg) was hydrated with 1 mL of buffer containing 100 mM carboxyfluorescein (CF) and 10 mM HEPES pH 7.5.

Scheme 1. Synthesis of Amphipathic Polyvinyl Ethers

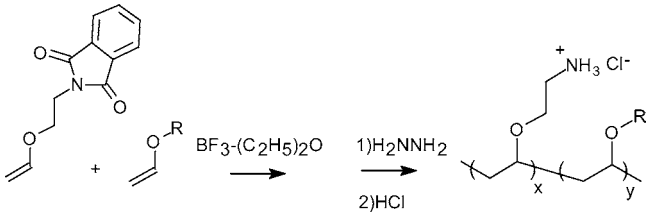

Liposomes were then extruded through 100-nm pore polycarbonate filters (Nucleopore, Pleasanton, CA). Unentrapped CF was removed by size exclusion chromatography using Sepharose 4B-200 eluting with 10 mM HEPES, pH 8, 0.1 M NaCl. A 200 μL aliquot of the CF-loaded liposomes was added to 1.8 mL of isotonic buffer. Fluorescence ($\lambda_{ex} = 488$, $\lambda_{em} = 540$) was measured 30 min after addition of 0.25 μg of polymers or melittin to vesicle suspensions. At the end of each experiment, vesicles were disrupted by the addition of 40 μL of a 1% Triton X-100 solution to determine maximal lysis.

Transfection. Hepa-1clc7 cells (mouse hepatoma) were cultured in 1 mL of Dubelco's modified Eagle Media containing 10% fetal bovine serum. Amphipathic polyvinyl ethers, melittin, or PEI was added to plasmid DNA at a 2:1 wt:wt ratio, which corresponds to approximately a 4:1 N:P ratio (10 μg/mL, pCIluc; prepared according to published procedure (*16*)) in 0.5 mL of 150 mM NaCl and 5 mM HEPES, pH 7.5. Formulated DNA (1 μg) was added to the cells, and 48 h later the confluency of the cells was estimated. All samples, except melittin, had levels of confluency comparable to cells grown in the absence of polymer. The cells were harvested and assayed for luciferase expression as previously reported (*17*). The amount of transfection is average transfection for two separate wells of cells.

Cell Toxicity Assay. After 48 h of incubation with DNA−polycation complexes according to transfection protocol, 500 μg of MTT in PBS solution (5 mg/mL) was added to the culture for 1 h. The media were then aspirated, and the cells were washed with 1 mL of PBS. The cells were then dissolved by addition of 1 mL of 10% SDS in 10 mM HCl. After rocking the samples overnight at room temperature, 300 μL of solution was transferred into 96-well plates and the absorbance of the solution at 410 nm was measured using a Molecular Devices SpectraMax Plus (Sunnyvale, CA). Absorbances were normalized to cells grown in the absence of transfection complexes. Each experiment was average of six experiments.

RESULTS AND DISCUSSION

Amphiphilic polyvinyl ethers were synthesized from amino and hydrophobic vinyl ether monomers. Amino groups were incorporated into polyvinyl ethers using an amine-protected phthalimido vinyl ether (*13*). Alkyl groups were incorporated using methyl, ethyl, propyl, or butyl alkyl vinyl ethers (R = CH_3, CH_2CH_3, $CH_2CH_2CH_3$, or CH_2 CH_2CH_3 in Scheme 1). After removal of the phthalimido groups, the polymers were dialyzed to remove salts, monomers, and oligomers. The polymers were further purified using size exclusion chromatography to remove unreacted monomers and oligomers.

The incorporation of monomers into the polymers was measured by elemental analysis, which determines the ratio of carbon to nitrogen and thereby the ratio of amine to alkyl groups in the polymer (Table 1). By elemental analysis and DNA condensation (vide infra), we determined that the smaller size exclusion fractions had amine to alkyl group incorporation ratios that were more consistent with each other in the series and with the feed ratios. For this reason, only comparisons between these fractions are presented in this report.

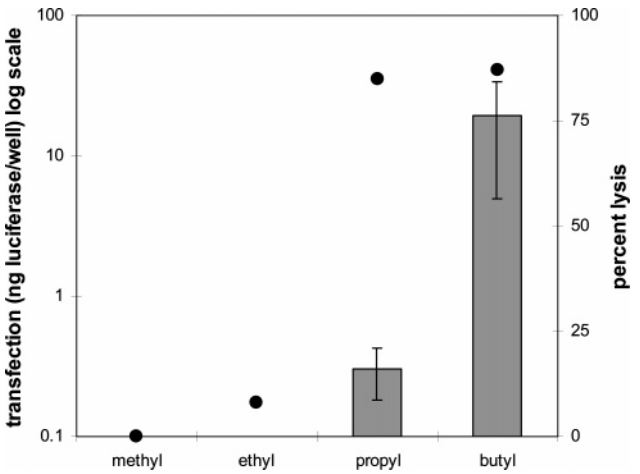

Figure 1. Transfection and lysis as function of side chain composition. Transfection ability (bars, see Table 3) and liposome lysis activity of polymers as a function of polymer side chain length.

In addition to measuring amine incorporation ratios by elemental analysis, the charge density, and consequently the amine content, of the polymer was measured by determining the amount of polymer required to condense fluorophore-labeled DNA (Table 1) (*14*). As one would expect, the DNA condensing ability of a polycation correlates with the number of positively charged functional groups. For comparison, the charge density of the amphipathic peptide melittin was also measured. Note that, in low salt, melittin's charge density as measured by its ability to condense DNA does correlate with its charge.

The molecular weights, and thereby the number of amines, of the polymers were measured using size exclusion columns. The smallest polymer, the ethyl vinyl ether-derived polymer, had an average charge of +15, which is well above melittin and KALA. More importantly for transfection is that these polymers bind DNA in the presence of physiological concentrations of salt, which roughly corresponds to 150 mM NaCl. To establish the relative stabilities of the complexes between the polycations and DNA, we determined the amount of salt required to induce release of DNA from the complex ([NaCl]* in Table 2). Using fluorophore-labeled DNA condensed at a 2:1 amine-to-phosphate ratio, we measured the amount of NaCl to induce DNA release. For the oligocation melittin, the DNA complex completely dissociates below physiological salt concentrations, ca. 70 mM NaCl. In contrast, the amphiphilic polyvinyl ethers are displaced at much higher concentrations of salt (>400 mM).

The membrane-lytic abilities of the amphipathic polyvinyl ethers were measured by analyzing their ability to lyse carboxyfluorescein-loaded liposomes. Similar to data obtained by others studying membrane-lytic polyanions (*4*, *5*), the abilities of the polyvinyl ethers to lyse liposomes are indeed dependent on the size of the hydrophobic chain. The polymer containing butyl groups is the most lytic followed by the propyl and ethyl in order of lytic ability (Figure 1, circles). The butyl-containing polymer possesses lytic activity comparable to melittin (80% lysis with 0.25 μg of melittin). The methyl-derived polymer was completely inactive for lysis.

Table 3. Transfection and Toxicity of Amphipathic Polycations in Hepa Cells

polycation	ng luciferase per well	% MTT[a]
methyl vinyl ether	0.068 ± 0.029	94 ± 11
ethyl vinyl ether	0.054 ± 0.028	100 ± 3
propyl vinyl ether	0.30 ± 0.12	90 ± 4
butyl vinyl ether	19 ± 14	94 ± 9
polyethyleneimine	1.1 ± 0.4	105 ± 5
melittin	0.015 ± 0.003	67 ± 12

[a] Percent of metabolized MTT relative to cells grown in absence of DNA complexes.

The ability of the amphiphilic polyvinyl ethers to transfect DNA was tested at various (N/P) ratios using a mouse hepatoma cell line. Optimal transfections are observed for the polyvinyl ethers at a 4/1 N/P ratio (Figure 1: bars and Table 3: column 1). Branched PEI, a standard polyplex-based transfection reagent, and melittin were also tested in the assay at a 8:1 and 4:1 N:P ratios, respectively. The ability of the polyvinyl ethers to transfect DNA positively correlated with their membrane lytic activity; the highest levels of transfection were obtained with the polymers containing butyl groups, whereas transfection levels obtained using polymers containing shorter alkyl side chains were progressively lower. These data suggest that transfection activity of the polymers is derived at least in part from membrane activity. Similar results were obtained using the HEK (human epithelial kidney) 293 cell line (see Supporting Information).

The sizes of the complexes are important for transfection. Complexes were formulated at physiologically relevant ionic strength (150 mM NaCl), which results in particles that are roughly 900 ± 200 nm in size. Formulation at low salt conditions does result in smaller particles (ca 100 nm); however, these particles are roughly 100 times less effective transfection reagents. This dependence upon size is seen for other transfection reagents (*18*, *19*). The reason for the dependence of transfection upon complex size is a matter of debate; however, the dependence appears to be common to all transfection reagents and is an impediment that needs to be removed for most in vivo delivery applications.

One would expect membrane active polymers to have inherent cell toxicity. Cell confluencies, a qualitative measure of cell viability based upon cell coverage on the well surface as judged by microscopy, indicated little or no toxicity at the levels used for transfection. We do observe decreased levels of cell confluency if higher concentrations of butyl-containing polymer were used. To get a more quantitative measure of cell viability, we assayed cell metabolism using methylthiazolyldiphenyltetrazolium bromide (MTT). MTT is reduced by mitochondrial dehydrogenases of metabolically active cells into a water insoluble blue formazan, which may be quantified by absorbance spectroscopy. Testing the transfection complexes we found that there appears to be slight, although only the propyl-containing polymer is statistically significant, toxicity (Table 3). In general, more toxicity was observed for 293 cells (see Supporting Information), which, as expected, correlates with membrane lytic activity.

The polycation PEI is, to date, the most effective and studied polyplex-based transfection reagent. However, under the conditions reported in Table 3, the butyl-based polyvinyl ether is 10-fold more effective at DNA delivery. Transfection levels comparable to the butyl polyvinyl ether can be achieved with PEI at higher N:P ratios and if the transfection is performed in serum free conditions. These requirements are achievable in vitro but put severe limitations on the use of PEI in vivo.

As might be predicted given its weak interaction with DNA, melittin performed extremely poorly as a transfection reagent. Poor transfection efficiency was observed for melittin at all N:P ratios with greater toxicity at increased levels of melittin. DNA−melittin complexes dissociate under physiological conditions (Table 3), which we believe is the cause of poor transfection and toxicity. In contrast, the relatively strong interaction between the butyl-containing polyvinyl ether and DNA attenuates its membrane lytic activity and, presumably, its cell toxicity. The butyl-containing polymer with DNA has slight toxicity (Table 3), but polymer alone without DNA causes observable toxicity (75 ± 5% MTT metabolized relative to untreated cells). The inhibition of polymer membrane activity by DNA is also demonstrated in the observation that toxicity is observed for the butyl-containing polymer at higher N:P ratios. For amphiphilic polycation-based transfections, membrane lytic activity may be masked until endocytosis forces the membrane surface to come in close contact with the polymer. Contact with the membrane causes displacement of the polymer from DNA, membrane lysis, and, ultimately, transfection. A similar displacement of cation and DNA is hypothesized to occur in cationic lipid-based transfections (*20*). The transfection activity of the butyl-containing polyvinyl ether may then be a result of a fine balance between DNA and membrane binding, which implies that modifications of either interaction would greatly affect transfection efficiency. We believe this is the first study to demonstrate a correlation among transfection activity, membrane lytic ability, and polymer side-chain composition for polycations, which creates a new class of transfection reagents and will aid in the design of polymers and formulations that will enable efficient in vivo transfection.

ACKNOWLEDGMENT

The authors thank Sean Monahan for synthesis of melittin, Stephanie Bertin for tissue culture work, and So Wong and Vladimir Budker for helpful discussions.

Supporting Information Available: Charge density titrations, salt displacement titrations, and 293 cell transfection data. This material is available free of charge via the Internet at http://pubs.acs.org.

LITERATURE CITED

(1) Felgner, P., et al. (1997) Nomenclature for synthetic gene delivery systems. *Hum Gene Ther. 8*, 511−2.

(2) Li, W., Nicol, F., and Szoka, F. C., Jr. (2004) GALA: a designed synthetic pH-responsive amphipathic peptide with applications in drug and gene delivery. *Adv. Drug Delivery Rev. 56,* 967−85.

(3) Plank, C., Oberhauser, K., Mechtler, K., and Koch, C. (1994) The influence of endosome-disruptive peptides on gene transfer using synthetic virus-like gene transfer systems. *J. Biol. Chem. 269*, 12918−12924.

(4) Tirrell, D. A., Takigawa, D. Y., and Seki, K. (1985) pH sensitization of phospholipid vesicles via complexation with synthetic poly(carboxylic acid)s. *Ann. N.Y. Acad. Sci. 446*, 237−48.

(5) Murthy, N., Robichaud, J. R., Tirrell, D. A., Stayton, P. S., and Hoffman, A. S. (1999) The design and synthesis of polymers for eukaryotic membrane disruption. *J. Controlled Release 61*, 137−43.

(6) Cheung, C. Y., Murthy, N., Stayton, P. S., and Hoffman, A. S. (2001) A pH-sensitive polymer that enhances cationic lipid-mediated gene transfer. *Bioconjugate Chem. 12*, 906−10.

(7) Wyman, T. B., Nicol, F., Zelphati, O., Scaria, P. V., Plank, C., and Szoka, F. C., Jr., (1997) Design, synthesis, and characterization of a cationic peptide that binds to nucleic acids and permeabilizes bilayers. *Biochemistry 36*, 3008−17.

(8) Trubetskoy, V. S., Wolff, J. A., and Budker, V. G. (2003) The role of a microscopic colloidally stabilized phase in solubilizing oligoamine-condensed DNA complexes. *Biophys. J. 84*, 1124−30.

(9) Record, M. T., Jr., Mazur, S. J., Melancon, P., Roe, J. H., Shaner, S. L., and Unger, L. (1981) Double helical DNA: conformations, physical properties, and interactions with ligands. *Annu. Rev. Biochem. 50*, 997−1024.

(10) Lee, H., Jeong, J. H., and Park, T. G. (2001) A new gene delivery formulation of polyethylenimine/DNA complexes coated with PEG conjugated fusogenic peptide. *J. Controlled Release 76*, 183−92.

(11) Lee, H., Jeong, J. H., and Park, T. G. (2002) PEG grafted polylysine with fusogenic peptide for gene delivery: high transfection efficiency with low cytotoxicity. *J Controlled Release 79*, 283−91.

(12) Ogris, M., Carlisle, R. C., Bettinger, T., and Seymour, L. W. (2001) Melittin enables efficient vesicular escape and enhanced nuclear access of nonviral gene delivery vectors. *J. Biol. Chem. 276*, 47550−5.

(13) Hashimoto, T., Ibuki, H., Sawamoto, M., and Higashimura, T. (1988) Living Cationic Polymerization of 2-Vinyloxyethyl Phthalimide: Synthesis of Poly(vinyl ether) with Pendant Amino Functions. *J. Polym. Sci.: Part A: Polym. Chem. 26*, 3361−3374.

(14) Trubetskoy, V. S., Slattum, P. M., Hagstrom, J. E., Wolff, J. A., and Budker, V. G. (1999) Quantitative assessment of DNA condensation. *Anal. Biochem. 267*, 309−13.

(15) Slattum, P. S., Loomis, A. G., Machnik, K. J., Watt, M. A., Duzeski, J. L., Budker, V. G., Wolff, J. A., and Hagstrom, J. E. (2003) Efficient in vitro and in vivo expression of covalently modified plasmid DNA. *Mol. Ther. 8*, 255−63.

(16) Danko, I., Williams, P., Herweijer, H., Zhang, G., Latendresse, J. S., Bock, I., and Wolff, J. A. (1997) High expression of naked plasmid DNA in muscles of young rodents. *Hum Mol Genet. 6*, 1435−43.

(17) Wolff, J. A., Malone, R. W., Williams, P., Chong, W., Acsadi, G., Jani, A., and Felgner, P. L. (1990) Direct gene transfer into mouse muscle in vivo. *Science 247*, 1465−8.

(18) Ross, P. C., and Hui, S. W. (1999) Lipoplex size is a major determinant of in vitro lipofection efficiency. *Gene Ther. 6*, 651−9.

(19) Ogris, M., Steinlein, P., Kursa, M., Mechtler, K., Kircheis, R., and Wagner, E. (1998) The size of DNA/transferrin-PEI complexes is an important factor for gene expression in cultured cells. *Gene Ther. 5*, 1425−33.

(20) Xu, Y.; and Szoka, F. C., Jr., (1996) Mechanism of DNA release from cationic liposome/DNA complexes used in cell transfection. *Biochemistry 35*, 5616−23.

BC050067H

Tools To Analyze Protein Farnesylation in Cells

Jerry M. Troutman,[†] Michael J. Roberts,[†] Douglas A. Andres,[†] and H. Peter Spielmann[†,‡,§,*]

Department of Molecular and Cellular Biochemistry, Department of Chemistry, and Kentucky Center for Structural Biology, University of Kentucky, Lexington, Kentucky 40536-0084. Received March 8, 2005; Revised Manuscript Received June 20, 2005

Farnesylation of proteins is catalyzed by protein farnesyl transferase (FTase) and is obligatory for the function of the oncoprotein Ras and a variety of other physiologically important proteins. The rapid and selective detection of cellular protein farnesylation status is crucial to understanding both the function of farnesylated proteins and FTase inhibitors. The unnatural FPP analogue 8-anilinogeranyl diphosphate (AGPP, **3b**) is an effective alternative substrate for mammalian FTase. Using antibodies specific for the anilinogeranyl moiety, we show that the alcohol precursor (AGOH, **5b**) of AGPP is incorporated into cellular proteins in an FTase dependent manner competitive with endogenous pools of FPP. Continuous treatment of HEK-293 cells with 100 μM AGOH for up to 3 days is neither cytotoxic or cytostatic. Antibodies to detect the unnatural anilinogeranyl group were raised against bovine serum albumin (BSA) and keyhole limpet hemocyanin (KLH) bioconjugates of the activated hapten *N*-hydroxyphthalimido-succinyl-(*S*-anilinogeranyl)-L-cysteine methyl ester **9a**. Polyclonal antisera containing anti-anilinogeranyl antibodies were generated by immunization of rabbits and a monoclonal anti-anilinogeranyl antibody was raised in mice. ELISA and western blotting of anilinogeranyl modified proteins were used to show the selectivity and measure the titer of the antibodies. The unnatural FPP analogue and corresponding antibodies provide a simple and rapid method for monitoring FTase activity in cells and detection of cellular proteins modified by AGOH **5a**.

INTRODUCTION

A wide variety of proteins, including Ras, require posttranslational prenylation for their proper membrane localization and activity (*1*–*5*). Protein farnesyl transferase (FTase) catalyzes the transfer of a farnesyl group from farnesyl diphosphate (FPP, **1b** Figure 1) to proteins with a cysteine residue located in a C-terminal Ca_1a_2X motif where C is the modified cysteine, a_1 and a_2 are often an aliphatic residue, and X is Ser, Met, Ala, or Gln (*6*–*8*). Specifically, prenylation is obligatory for the oncogenic effects of mutant Ras (*9*). Mutated forms of Ras genes are among the most common genetic abnormality in human cancer, occurring in 10 to 30% of all neoplasms (*10*–*13*). These observations have lead to the development of a number of FTase inhibitors (FTIs) which block Ras farnesylation and appropriate subcellular localization and activity, in addition to inhibiting growth of Ras transformed cells. Various FTIs are currently in phase I, II, and III clinical trials as antineoplastic agents (*14*–*16*). Farnesylation is the first and obligatory step in an ordered series of posttranslational modifications which mediate membrane localization and possibly protein–protein interactions for a variety of proteins involved in cellular regulatory events (*17*–*19*). After farnesylation, the a_1a_2X peptide is cleaved by the endopeptidase RCE1 (*20*) followed by methylation of the carboxyl of the now terminal farnesylated cysteine residue by the protein-S-isoprenylcysteine O-methyltransferase (*21*). Similar posttranslational modifications occur on the relatively small set of farnesylated cellular proteins, not all of which have

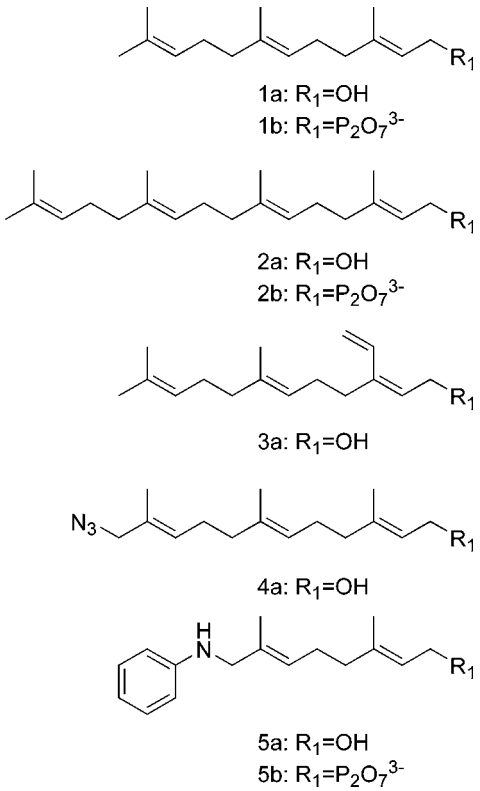

Figure 1. Analogues of FPP.

* To whom correspondence should be addressed. E-mail: hps@uky.edu.

† Department of Molecular and Cellular Biochemistry.

‡ Department of Chemistry.

§ Kentucky Center for Structural Biology.

[1] Abbreviations: FTase, farnesyl transferase; FPP, farnesyl diphosphate; GGPP, geranylgeranyl diphosphate; FTI, farnesyl transferase inhibitor; GGTI, geranylgeranyl transferase inhibitors; AG, anilinogeranyl; polyAG-Ab, polyclonal anilinogeranyl antibody.

10.1021/bc050068+ CCC: $30.25 © 2005 American Chemical Society
Published on Web 09/07/2005

been identified or characterized. Interestingly, various lines of evidence suggest that one or more of these other proteins, other than Ras, are the actual functional target of FTIs (*22*−*25*). Therefore, the rapid and selective detection of cellular protein farnesylation status and easy isolation of farnesylated proteins is crucial to understanding both the function of farnesylated proteins and of FTase inhibitors.

Monitoring the prenylation state of proteins in cells is a challenging undertaking. Initially, prenylation of proteins was discovered by metabolic labeling with [^{3}H]mevalonolactone (*26*). In these experiments, some of the tritium label was incorporated into both farnesylated and geranylgeranylated proteins. Subsequently, a salvage pathway was discovered where radiolabeled farnesol **1a** (FOH) and geranylgeraniol **2a** (GGOH), precursors of FPP **1b** and GGPP **2b**, were selectively incorporated into their respective farrnesylated or geranylgeranylated proteins (*27*). A significant drawback of these approaches is the inherently low sensitivity of autoraidographic detection of the weak tritium β-emission. In fact, it can take up to four weeks to visualize proteins extracted from cells labeled with tritiated mevalonate or farnesol by autoradiography (*28*). Also, the incorporation of tritiated prenyl groups does not provide a convenient method for isolation of these modified proteins.

The facile detection, isolation and purification of farnesylated proteins based solely on their posttranslational modification status is essential to understanding the mechanism of cellular growth inhibition by FTIs. Antibodies are useful both in the routine detection and immunoprecipitation of proteins with other posttranslational modifications, such as phosphorylation (*29*). However, reports of previous attempts to produce antibodies to detect farnesylated proteins have had mixed results. Two of these reports described nonspecific antibodies that could not differentiate between proteins modified by farnesylation, geranylgeranylation, or other lipids (*30*, *31*). The other report from Baron et al. does describe the production of anti-farnesyl antibodies specific for farnesylation, but the analysis for specificity was limited (*32*). These antibodies are apparently not available commercially, and all of the commercially available sources for anti-farnesyl antibodies cross-react with geranylgeranylated proteins.

An attractive alternative to targeting the natural farnesyl moiety is to detect proteins modified with unnatural farnesyl analogues. Several unnatural analogues of FPP appear to be utilized by cells and incorporated into the proteins by FTase, including the unnatural FPP analogue 3-vinyl-farnesol **3a**, a prodrug of the FTase transferable 3-vinyl-farnesyl diphosphate (3vFPP) **3b**, and 8-azido-farnesol **4** (*28*). A tagging-via-substrate (TAS) approach to the detection and isolation of farnesylated proteins involving the incorporation of **4** into cellular proteins has been developed by Kho et al. (*33*). Modified proteins were isolated from cell lysates using a biotinylated phosphine capture reagent and subsequently identified by mass spectrometry. However, the sensitivity is relatively low, and the technique does not lend itself to the routine detection of modified proteins. A more convenient method to simplify the detection of such proteins would be to use antibodies specific for the unnatural modification.

A variety of FPP analogues that may be useful in implementing this strategy have been prepared by our group and others (*34*−*37*). Anilinogeranyl diphosphate (AGPP) **5b** is transferred by FTase to protein substrates with kinetics similar to that of FPP and does not resemble any known natural protein modification (*38*, *39*). Antibodies against an anilinogeranyl (AG) epitope may circumvent the problems associated with tritium labeling, and the preparation of anti-farnesyl antibodies and provide a facile way to detect and isolate prenylated proteins.

We report the preparation of anti-anilinogeranyl antibodies (polyAG-Ab) raised against hapten **9a** that detect proteins modified with an anilinogeranyl moiety derived from AGPP **5b**. Activated ester hapten **9a** was synthesized and coupled to immunogenic carrier proteins and used to raise antibodies directed to the anilinogeranyl modification. The primary antibodies were able to bind proteins with an intact analogue modified C-terminal Ca_1a_2X motif. We demonstrate that anilinogeraniol **5a**, a prodrug form of AGPP **5b**, is incorporated into cellular proteins in an FTase dependent manner, and that endogenous protein labeling was competitive with endogenous FPP **1b**. Combining the unnatural FPP analogue AGPP with anti-anilinogeranyl antibodies provides a useful reagent system to monitor the prenylation status and effects of FTIs in cells.

EXPERIMENTAL PROCEDURES

General. All reactions were conducted under dry argon and stirred magnetically, except as noted. Reaction temperatures refer to the external bath temperatures. Analytical TLC was performed on precoated (0.25 mm) silica gel 60F-245 (Merck) plates and developed with given solvent conditions. Visualization was achieved by UV irradiation, iodine, or by subjecting the plates to a 15% sulfuric acid, 1% ceric ammonium sulfate, 2% molybdic anhydride solution followed by heating. Flash chromatography was performed on Merck silica gel 60 (230−400 mesh ASTM). All chromatography solvents were purchased from VWR (EM Science-Omnisolv high purity) and used as received. All reagents were purchased from Aldrich or Alfa Aesar. NMR Spectra were obtained in $CDCl_3$ (unless otherwise noted) at 200 or 400 MHz. Chemical shifts for the following deuterated solvents are reported in ppm downfield using the indicated reference peaks: $CDCl_3$ ($CDCl_3$ internal peak 7.27 ppm for ^{1}H, 77.4 ppm for ^{13}C). ESI-MS was performed at the University of Kentucky Mass Spectra Facility.

Anilinogeranyl Cysteine Methyl Ester. 2-Amino-3-(3,7-dimethyl-8-phenylamino-octa-2,6-dienylsulfanyl)-propionic Acid Methyl Ester (7a). Chloride **6a** was prepared from the corresponding alcohol (734 mg, 3.0 mmol) in 10 mL of acetonitrile as previously described (*38*). A solution of L-cysteine methyl ester hydrochloride (1.13 g, 6.50 mmol) in 20 mL of 7 M NH_3/MeOH was added to the cooled solution (−20 °C) of chloride **6a**. The reaction initially formed a white precipitate which quickly disappeared. After 3 h, the reaction mixture was allowed to warm to room temperature over 1 h. The reaction mixture was partitioned between ether and water and extracted with ether (3×). The combined organic extracts were then dried over $MgSO_4$, and solvent was evaporated. Purification by flash chromatography (1:2:8) i-PrOH:EtOAc:hexane yielded 625 mg (60%) of a yellow oil. R_f = 0.32 in 1:2:5 i-PrOH:EtOAc:hexane ^{1}H NMR ($CDCl_3$, 200 MHz) 7.10 (t, 2H, J = 8.0 Hz), 6.63 (t, 1H, J = 7.2 Hz), 6.55 (d, 2H, J = 8.0 Hz) 5.39 (t, 1H, J = 8.0 Hz), 5.23 (t, 1H, J = 8 Hz), 3.75 (s, 3H), 3.59 (m, 3H), 3.13 (m, 2H), 2.86−2.95 (2d, 1H), 2.65−2.76 (2d, 1H), 2.06−2.19 (m, 4H), 1.63 (s, 3H), 1.62 (s, 3H) ^{13}C NMR ($CDCl_3$, 50 MHz) 174.58, 148.77, 139.42, 132.96, 129.38, 125.75, 120.53, 117.39, 113.08, 54.51, 52.49, 51.96, 39.50, 36.61, 30.14, 26.30, 16.33, 14.98; MS: (ESI, +) ($M - H^+$) 363

Farnesyl Cysteine Methyl Ester. 2-Amino-3-(3,7,-11-trimethyl-dodeca-2,6,10-trienylsulfanyl)-propionic Acid Methyl Ester (7b). Into a 100 mL round-bottomed flask at 0 °C was added L-cysteine methyl ester (1.38 g, 10.2 mmol) in 60 mL of 7 M NH_3/MeOH. Neat farnesyl bromide (**6b**) (1.00 g 3.52 mmol) was then added, and the solution was stirred at 0 °C for 4 h. The reaction mixture was partitioned between ether and water and extracted 3× with ether, and extracts were combined, dried over $MgSO_4$, filtered, and evaporated. Purification by flash chromatography (1% MeOH:$CHCl_3$) yielded 881 mg (74%) of a clear oil. $R_f = 0.22$ in 5% MeOH in $CHCl_3$. ^{1}H NMR ($CDCl_3$, 400 MHz): 5.24 (t, 1H, $J = 8$ Hz), 5.10 (m, 2H), 3.75 (s, 3H), 3.64 (q, 1H), 3.10−3.25 (m, 2H), 2.86−2.91 (2d, 1H), 2.65−2.71 (2d, 1H), 2.04−2.10 (m, 6H), 2.04(m, 6H) 2.0 (t, 2H), 1.69 (s, 3H), 1.68 (s. 3H), 1.60 (s, 6H); ^{13}C NMR ($CDCl_3$, 50 MHz) 174.93, 139.91, 135.71, 131.62, 124.69, 124.11, 120.35, 54.64, 52.35, 39.93, 36.77, 30.15, 26.98, 26.67, 25.86, 17.86, 16.33, 16.21 MS: (ESI, +) ($M - H^+$) 340.

General Conditions for Succinylation (8a,b). Cysteine methyl ester **7b** (881 mg, 2.6 mmol) was diluted in 20 mL of 1:1 THF:CH_2Cl_2 in a 100 mL round-bottomed flask. Succinic anhydride (280 mg, 2.8 mmol) was then added and the mixture stirred for 4 h, followed by evaporation of solvent. The residue was diluted in ether, washed sequentially with water and brine, and then dried over sodium sulfate and concentrated in vacuo.

Anilinogeranyl Cysteine Succinate. *N*-[2-(3,7-Dimethyl-8-phenylamino-octa-2,6-dienylsulfanyl)-1-methoxycarbonyl-ethyl]-succinamic Acid (8a). Cysteine methyl ester **7a** (302 mg, 0.83 mmol) provided 250 mg (65%) of succinate **8a** as a white solid. Purification by flash chromatography (1:4:5: 0.1 i-PrOH:EtOAc: hexane:acetic acid) $R_f = 0.32$ (1:4:5 i-PrOH:EtOAc: hexane.) ^{1}H NMR ($CDCl_3$, 400 MHz) 7.12 (t, 2H, $J = 8.0$ Hz), 6.65 (t, 2H, $J = 8.0$ Hz), 6.58 (t, 2H), 5.34 (t, 1H, $J = 8.0$ Hz) 5.14 (t, 1H, $J = 8.0$ Hz), 4.75 (m, 1H), 3.72 (s, 3H), 3.60 (s, 2H), 3.11 (m, 2H), 2.79−2.93 (m, 2H), 2.65 (t, 2H, $J = 8.0$ Hz), 2.52 (t, 2H, $J = 8$ Hz), 2.11 (t, 2H, $J = 8$ Hz) 2.02 (t, 2H, $J = 8$ Hz), 1.63 (s, 3H), 1.62 (s, 3H); ^{13}C NMR ($CDCl_3$, 50 MHz) 176.95, 171.84, 171.55, 148.48, 139.80, 132.79, 129.34, 125.86, 120.06, 117.68, 113.36, 52.91, 52.13, 39.42, 33.55, 30.69, 30.19, 29.53, 28.92, 26.22, 16.25, 14.96 MS: (ESI, +) ($M - H^+$) 463.

Farnesyl Cysteine Succinate. *N*-[1-Methoxycarbonyl-2-(3,7,11-trimethyl-dodeca-2,6,10-trienylsulfanyl)-ethyl]-succinamic Acid (8b). Cysteine methyl ester **7b** (881 mg, 2.6 mmol) provided 937 mg (82%) of succinate **8b** as a white solid. Puification by flash chromatography (1:2:7 i-PrOH:EtOAc:hexane) ^{1}H NMR ($CDCl_3$, 400 MHz) 10.55 (bs, 1H), 6.72 (d, 1H, $J = 8$ Hz), 5.17 (t, 1H, $J = 8$ Hz), 5.07 (m, 2H), 4.75−4.80 (q, 1H), 3.73−3.73 (s, 3H), 3.13 (m, 2H), 2.90−2.94 (m, 1H), 2.80−2.85 (m, 1H), 2.69 (t, 2H), 2.57 (t, 2H), 1.92−2.08 (m, 8H), 1.65 (s, 3H), 1.64 (s, 3H), 1.57 (s, 6H); ^{13}C NMR ($CDCl_3$, 100 MHz) 177.40, 171.90, 171.64, 140.17, 135.44, 131.38, 124.44, 124.38, n123.85, 123.78, 119.60, 119.55, 52.80, 52.75, 52.01, 51.97, 39.79, 39.72, 33.28, 31.67, 30.55, 29.96, 29.39, 26.80, 26.51, 25.79, 22.74, 17.78, 16.19, 16.10; MS: (ESI, +) ($M - H^+$) 438.

General Conditions for Activated Ester Formation (9a,b). Succinamic acid **8c** (59.6 mg, 0.126 mmol) was dissolved in 10 mL of dry acetonitrile in a 100 mL round-bottomed flask. Carbonyldiimidazole (26.4 mg 0.163 mmol) was then added, and the mixture was allowed to stir for 5 min. *N*-Hydroxypthalimide (26.4 mg, 0.163 mmol) was added, and the solution was stirred for 1.5 h. The solvent was then evaporated.

Anilinogeranyl Cysteine Succinyl Phthalimide. *N*-[2-(3,7-Dimethyl-8-phenylamino-octa-2,6-diensulfanyl)-1-methoxycarbonyl-ethyl]-succinamic Acid 1,3-Dioxo-1,2-;dihydro-isoindol-2-yl Ester (9a). Succinate **8a** (30 mg, 0.07 mmol) provided 25 mg (63%) of phthalimide **9a** as a yellow/brown oil. Purified by column chromatography ($CHCl_3$). $R_f = 0.28$ (1:1) hexane:EtOAc ^{1}H NMR ($CDCl_3$, 400 MHz): 7.88 (q, 2H), 7.78 (q, 2H), 7.16 (t, 2H), 6.68 (t, 1H), 6.60 (d, 2H), 6.37 (d, 1H), 5.37 (t, 1H), 5.17 (t, 1H), 4.83 (m, 1H), 3.76 (s, 3H), 3.63 (s, 2H), 3.15 (m, 2H), 3.06 (t, 2H), 2.92 (m, 2H), 2.71 (t, 2H), 2.03−2.18 (m, 4H), 1.67 (s, 3H), 1.65 (s, 3H); ^{13}C NMR ($CDCl_3$, 50 MHz): 171.43, 169.94, 169.12, 161.93, 148.70, 139.79, 134.06, 132.89, 129.34, 125.72, 124.19, 120.08, 117.38, 113.07, 52.86, 52.10, 51.97, 39.43, 33.64, 30.63, 30.21, 26.78, 26.25, 16.26, 14.94 MS: (ESI, +) ($M - H^+$) 608.

Farnesyl Cysteine Succinyl Phthalimide. *N*-[1-Methoxycarbonyl-2-(3,7,11-trimethyl-dodeca-2,6,10-trienylsulfanyl)-ethyl]-succinamic Acid 1,3-Dioxo-1,2-dihydro-isoindol-2-yl Ester (9b). Succinate **9b** (60 mg, 0.14 mmol) provided 80 mg (58%) of phthalimide **10b** as a brown oil. Purified by column chromatography ($CHCl_3$). $R_f = 0.3$ (1:1) hexane:EtOAc. ^{1}H NMR ($CDCl_3$, 400 MHz) 7.88 (q, 2H), 7.79 (q, 2H), 6.38 (d, 1H), 5.20(t, 1H), 5.09 (t, 2H), 4.82 (m, 1H), 3.76 (s, 3H), 3.74 (s, 2H), 3.11−3.22 (m, 2H), 3.07 (t, 2H), 2.86−3.00 (m, 2H), 2.74 (t, 2H), 1.95−2.10 (m, 8H), 1.68 (s, 3H), 1.66 (s, 3H), 1.60 (s, 6H); ^{13}C NMR ($CDCl_3$, 100 MHz) 171.44, 169.90, 169.93, 161.91, 140.29, 135.57, 134.96, 131.53, 129.06, 124.50, 124.19, 123.90, 119.64, 52.85, 52.00, 39.88, 39.81, 33.54, 30.62, 30.14, 29.03, 28.23, 26.90, 26.75, 26.59, 25.90, 17.89, 16.31, 16.21.

General Conditions for Benzylamine Coupling (10a,b). Phthaimide **9b** (47.2 mg, 0.08 mmol) was dissolved in 1 mL of acetonitrile and 5 mL of 5% $NaHCO_3$ buffer pH = 9 in a 25 mL round-bottom flask. Benzylamine (17.3 mg, 0.16 mmol) was then added, and the reaction was allowed to stir for 1.5 h at room temperature. Water (10 mL) was added, the aqueous phase was extracted with ether (3×) and dried over $MgSO_4$, and the organic solvent was evaporated.

Anilinogeranyl Benzylamine. 2-(3-Benzylcarbamoyl-propionylamino)-3-(3,7-dimethyl-8-phenylamino-octa-2,6-dienylsulfanyl)-propionic Acid Methyl Ester (10a). Phthalimide **9a** (133 mg, 0.22 mmol) provided 59 mg (48%) of amide **10a** as a white solid. Purification by column chromatography (3:7) hexane:EtOAc. ^{1}H NMR ($CDCl_3$, 400 MHz) 7.21−7.31 (m, 5H), 7.12 (t, 2H), 6.55−6.66 (m, 4H), 6.23 (bt, 1H), 5.34 (t, 1H), 5.14 (t, 1H), 4.71 (q, 1H), 4.38 (d, 2H, $J = 6$ Hz), 3.70 (s, 3H), 3.59 (bs, 2H), 3.10 (m, 2H), 2.76−2.91 (m, 2H), 2.50−2.61 (m, 4H), 1.99−2.13 (m, 4H), 1.63 (s, 3H), 1.62 (s, 3H) ^{13}C NMR ($CDCl_3$, 50 MHz): 172.23, 171.94, 171.46, 148.63, 139.77, 138.41, 132.84, 129.42, 129.34, 129.19, 128.94, 128.87, 128.08, 127.93, 127.73, 125.74, 120.08, 117.411, 113.10, 52.82, 52.09, 51.963, 43.85, 39.45, 33.50, 31.71, 31.66, 30.12, 26.25, 16.28, 14.95 MS: (ESI, +) ($M - H^+$) 552.

Farnesyl Benzylamine. 2-(3-Benzylcarbamoyl-propionylamino)-3-(3,7,11-trimethyl-dodeca-2,6,10-trienylsulfanyl)propionic Acid Methyl Ester (10b). Phthalimide **10b** (47 mg, 0.08 mmol) provided 42 mg (67%) of amide **11b** as a white solid. Purification by column chromatography (4:6) hexane:EtOAc. ^{1}H NMR ($CDCl_3$, 400 MHz) 7.25−7.34 (m, 5H), 6.623 (d, 1H), 6.28 (t, 1H), 5.20 (t, 1H), 5.09 (t, 2H), 4.75 (q, 1H), 4.44 (d, 2H), 3.75 (s, 3H), 3.09−3.22 (m, 2H), 2.81−2.96 (m, 2H), 2.55−2.67 (m, 4H), 1.96−2.13 (m, 8H), 1.68 (s, 3H), 1.67 (s, 3H), 1.60 (s, 6H); ^{13}C NMR ($CDCl_3$, 50 MHz): 172.21,

171.94, 171.47, 140.29, 138.44, 135.60, 131.54, 128.87, 127.94, 127.64, 124.53, 123.93, 119.72, 52.79, 52.07, 43.89, 39.92, 39.84, 33.47, 31.77, 31.73, 30.12, 26.95, 26.66, 25.91, 17.90, 16.36, 16.23; MS: (ESI, +) ($M - H^+$) 529.

General Conditions for Protein Coupling (11a,b and 12a,b). Phthalimido esters (**9a**,**b**) were dissolved in 6 mL of 1:5 acetonitrile and 5% $NaHCO_3$ in a 100 mL pear-shaped flask. BSA (**12**) (0.1 mL of 10 mg/mL solution in phosphate buffered saline (PBS) pH 7.2) or KLH protein (**11**) (3 mL of 10 mg/mL solution in PBS pH 7.2) was added and stirred vigorously for 2 h or until analysis by TLC in 1:1 hexane:EtOAc showed no residual activated phthalimide ester spot. The solution was dialyzed overnight in 20% DMSO, PBS pH 7.5 then PBS (3 × 1L, 6 h each).

Antibody Generation. Hapten protein conjugates **11a** and **11b** were used to immunize rabbits subcutaneously by emulsifying 1.5 mg of each conjugate with Freund's complete adjuvant. This was followed by six secondary boosters of the same dose with incomplete Freund adjuvant at intervals of 14 days. The rabbits were bled 10 days after each boost. Blood was allowed to coagulate overnight in 50 mL centrifuge tubes, and sera was collected and stored at 0 °C.

ELISA Screening. ELISA plates (96-well polystyrene) were coated with 100 μL per well of BSA conjugates or BSA (1 μg/mL) in PBS (pH = 7.6) and incubated for 1 h at 37 °C. The plates were then washed thoroughly with 10% Tween in PBS buffer (PT) (pH = 7.4). One hundred fifty microliters of serum diluted 1:100 in PT buffer containing casein (PCT) was added and diluted 1:3 down the plate, then incubated 1 h at 37 °C. The plates were washed with PT buffer, and 100 μL of secondary antibody (1:10 000) was added to each well. The plates were incubated 1 h at 37 °C and again washed. One hundred microliters of *p*-nitrophenyl phosphate was added to each well (2 pills in 10 mL of Tris buffer pH = 9.5). After 20 min, color began to develop and absorbance was read at 405 nm.

FTase Protein Substrate Modification. Two micrograms of recombinant bacterially expressed RDJ2 (*40*) was incubated with 20 μM AGPP **5b** or FPP **1b** and 5 μg of FTase in 50 μL of Tris-HCl buffer (pH = 7.4) The reactions were incubated for 30 min at 37 °C and then boiled with SDS, and PAGE was performed using the protein concentrations indicated on the blots.

Cell Culture and Transient Transfection of GST-Tagged Q61LH-Ras. HEK-293 cells were routinely subcultured twice weekly at a split ratio of 1:4 in DMEM containing 5% FBS to maintain exponential growth. Cells used for experiments were of passage number 0−20. HEK cells were seeded 24 h prior to transfection at 60−70% confluency onto poly-L-lysine-coated plates. Monolayers of HEK cells were transiently transfected with 2 μg of pEBG-H-Ras-Q61L or pEBG alone (*41*) in a 35 mm dish using the calcium phosphate precipitation method as previously described (*42*) The cells were harvested at 48 h, washed with 2 × 10 mL of PBS, lysed by sonication, and frozen at −70 °C.

AGOH Labeling and FTI Inhibition of Label in HEK-293 Cells. Plates were coated with poly-L-lysine and seeded with HEK cells in Dulbecco's modified Eagle's medium with 5% fetal bovine serum. Cells were incubated in medium containing 30 μM lovostatin and 10 μM GGOH for 24 h. The media were poured off then replenished with media without lovostatin and GGOH and were treated with 3 μM FTI-277 (calbiochem), 20 μM GGTI-2147 (calbiochem), or no inhibitor and incubated at 37 °C for 1 h. DMSO as a vehicle, or 100 μM AGOH **5a** was then added and incubated at 37 °C for 2 h. Medium was then removed, and cells were extracted into 300 μL of PBS-containing protease inhibitor cocktail set 1 (Calbiochem). The samples were sonicated and centrifuged for 5 min. The supernatant was removed and used for western blotting.

AGOH Incorporation into Unblocked Cells. Plates were coated with poly-L-lysine and seeded with HEK cells in Dulbecco's modified Eagle's medium with 5% fetal bovine serum. The cells were then treated with DMSO as a vehicle, or 30 μM AGOH **5a** was then added and incubated at 37 °C for the indicated time points. Medium was then removed, and cells were extracted into 300 μL of PBS-containing protease inhibitor cocktail set 1 (Calbiochem). The samples were sonicated and centrifuged for 5 min. The supernatant was removed and used for western blotting.

Western Blot Analysis. Cells were harvested by scraping into 300 μL of phosphate-buffered saline containing protease inhibitor cocktail set 1 (Calbiochem), followed by sonication on ice. Protein concentration was determined using a Bradford reagent kit (Pierce). The proteins from the FTase reaction mixtures or cell lysates were then separated using 12% SDS-polyacrylamide gels followed by transfer to nitrocellulose membranes. The membranes were incubated in blocking buffer PCT (see ELISA) for 1 h at room temperature, after which the following sequential steps were used: incubation with polyAG-Ab 1:1000 to 1:10 000 in PCT for 1 h; 3 × 15 min washes with vigorous shaking in PT buffer (see ELISA); incubation at room-temperature 1 h with goat anti-rabbit horseradish peroxidase-conjugated secondary antibody (Zymed) at a dilution of 1:20 000 in PCT buffer; four 15 min washes with PT buffer. The membranes were then subjected to enhanced chemiluminescence detection by incubation in 20 mL of detection buffer (Pierce Super Signal) for 1 min.

RESULTS

Synthesis of Analogue-Modified Antigen. The preparation of the prenyl analogue carrier protein conjugates **11a**,**b** and **12a**,**b** is outlined in Scheme 1. The haptens were designed to mimic the C-terminal peptide of a fully processed prenylated protein that had undergone both endoproteolysis and C-terminal methylation. Thioether **7a** was obtained in 60−74% yield by addition of a solution of L-cysteine methyl ester HCl in NH_3/MeOH to the previously described chloride **6a** (*39*) The farnesyl thioether **6b** was prepared by addition of farnesyl bromide **6b** to L-cysteine methyl ester HCl in NH_3/MeOH. Condensation of amines **7a**,**b** with succinic anhydride in THF:CH_2Cl_2 afforded succinates **8a**,**b** in 57%-85% yield after chromatography (*43*) Activated esters **9a**,**b** were prepared from carboxylates **8a**,**b** in 58%-85% yield by reaction with CDI followed by condensation with *N*-OH phthalimide (*44*) The *N*-hysdroxysuccimidyl (NHS) ester of a similar farnesyl hapten is reported to undergo an undesired intramolecular cyclization to an unreactive succinimide (*30*). In contrast to the NHS ester, phthalimdies **9a**,**b** were stable and showed no evidence of intramolecular cyclization. The suitability of phthalimdies **9a**,**b** to form conjugates with carrier protein was modeled under conditions typical for coupling activated esters to lysine residues. Condensation of benzylamine with phthalimdies **9a**,**b** in 1:5 acetonitrile:5% $NaHCO_3$ gave model amides **10a**,**b** in 51%-76% yield.

With activated haptens in hand, we proceeded to generate anilinogeranyl and farnesyl immunoconjugates.

Scheme 1. Synthesis of Analogue-Modified Haptens[a]

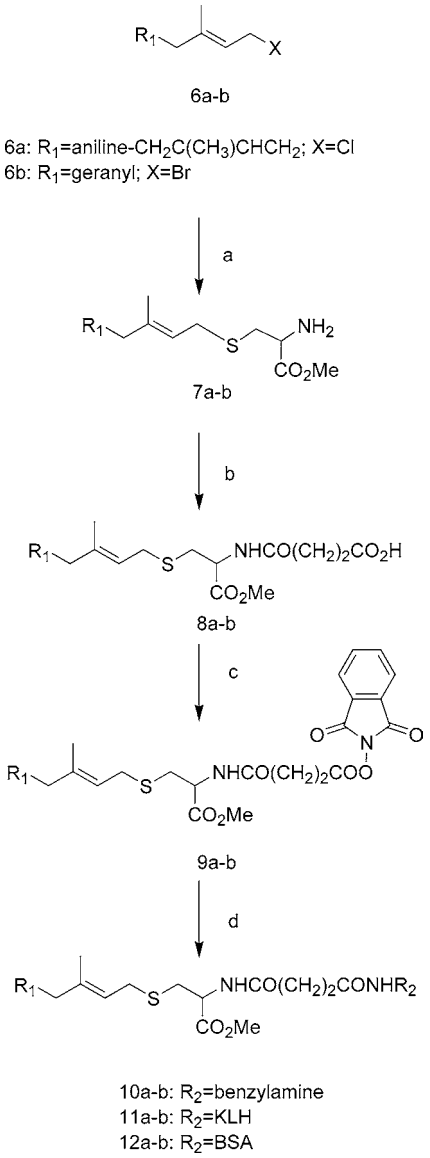

[a] Reagents: (a) Cysteine methyl ester HCl, NH_3/MeOH, 0 °C. (b) Succinic anhydride, THF/CH_2Cl_2. (c) *N*-Hydroxyphthalimide, CDI, MeCN. (d) R^2, $NaHCO_3$(aq)/MeCN.

Phthalimides **9a**,**b** were reacted with carrier proteins KLH and BSA to provide hapten conjugated proteins **11a**,**b** (AG-KLH and F-KLH) and **12a**,**b** (AG-BSA and F-BSA). BSA has approximately 32 reactive lysine residues and the extent of covalent modification of immunoconjugates **12a**,**b** was quantified by measuring the remaining free amino groups relative to unmodified BSA. BSA, and each of the BSA conjugates **12a**,**b** was reacted with trinitrobenzene sulfonate, and the ratio of free amines in unmodified BSA to modified BSA was determined by UV absorbance at 335 nm (*45*). We found that 50% of the lysine residues in immunoconjugates **12a**,**b** were modified by the activated esters **9a**,**b**. As KLH is a heterogeneous protein, similar assays to quantify the coupling efficiency were not performed. By analogy with the BSA results, we assumed a similar coupling efficiency for the KLH bioconjugates.

Generation of Anti-anilinogeranyl Antibodies. Polyclonal antibodies to the anilinogeranyl modification were prepared by immunizing rabbits with AG-KLH (**11a**). In our hands, F-KLH (**11b)** elicited no immunogenic response. This is in agreement with previous reports in which attempts to prepare anti-farnesyl antibodies have resulted in weakly binding reagents that recognize both farnesyl and geranylgeranyl isoprenoid lipids (*30*−*32*). Due to the poor immune response to the F-KLH protein (**11b**), we abandoned attempts to prepare an anti-farnesyl antibody. Polyclonal immune sera collected from the rabbits were screened using an enzyme linked immunosorbent assay (ELISA). No ELISA response was detected to unmodified BSA or AG-BSA (**12a)** in preimmune sera. Gratifyingly, sera antibodies raised against AG-KLH **11a** (polyAG-Ab) were able to bind to AG-BSA (**12a)** (Figure 2).

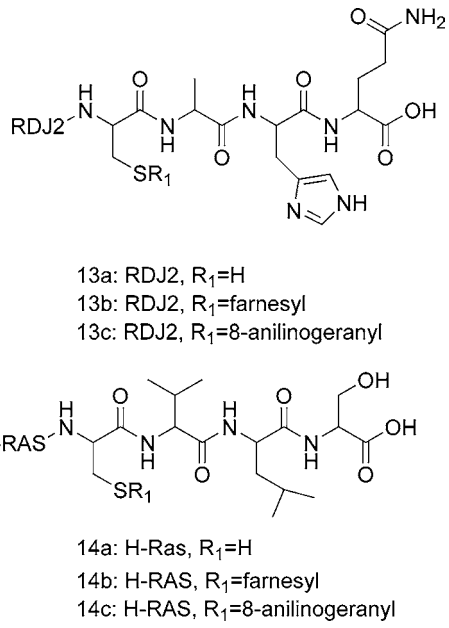

Figure 2. Ca_1a_2X modification.

Specificity and Analysis of Anti-anilinogeranyl Antibodies. The antibodies generated in this study were directed to proteins modified with cysteine methyl ester analogues of FPP. However, the actual antigen that is presented to the immune system is unknown, as the ester may be hydrolyzed by enzymes in the whole animal. Additionally, it is possible that in vivo incorporation of unnatural analogues into proteins will alter the normal Ca_1a_2X endoproteolysis and C-terminal methylation steps. The utility of the polyclonal anilinogeranyl antibodies might well be limited if they only recognized the cysteine methyl ester form of modified proteins. Therefore, it was essential to test the ability of these antibodies to recognize proteins modified by FTase with the anilinogeranyl moiety without subsequent endoproteolysis and C-terminal methylation. Bacterially expressed DNAJ-like RDJ2 (*40*) and Q61L oncogenic H-Ras proteins contain the unfarnesylated and unprocessed CAHQ and CVLS Ca_1a_2X motifs, respectively. FTase catalyzed in vitro modification of these proteins with FPP **1b** and AGPP **5b** provided lipid thioether linked proteins with intact Ca_1a_2X motifs **13a**−**c** and **14a**−**c** (Figure 2). These reaction mixtures were then analyzed by western blot with polyAG-Ab sera. Figure 3 shows that the polyAG-Ab was able to bind to AG-BSA **12a** derivatized by the methyl ester hapten as well as the AG-RDJ2 **13c** but showed no reactivity to the unmodified RDJ2 **13a**. Identical results were found when AG-Ras **14c** was examined (data not shown). Additionally, the antibodies were also unreactive toward farnesylated F-RDJ2 (**13b**) and F-Ras (**14b**) (data not shown).

FTase Dependent Anilinogeraniol Incorporation into Cellular Proteins. Farnesol **1a**, geranylgeraniol

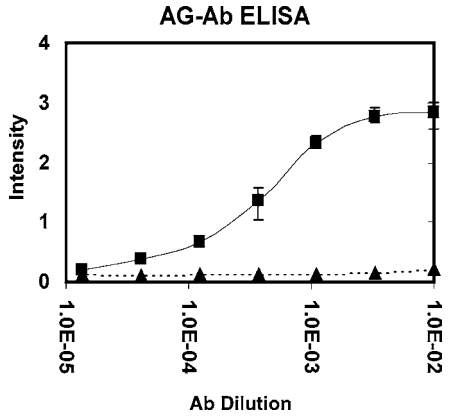

Figure 3. polyAG-Ab ELISA response to AG-BSA **11a** (squares), and unmodified BSA (triangles) (0.1 μg/well).

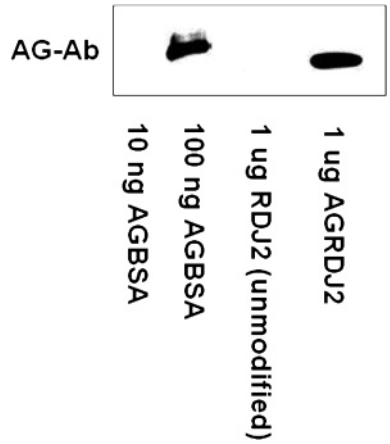

Figure 4. Western Blot analysis of anilinogeranyl modified RDJ2 and BSA proteins. RDJ2 proteins were modified in vitro with AGPP **5b** (AGRDJ2; lane 4). Standard chemically modified BSA proteins (AG-BSA **11a**; lanes 1 and 2) and unmodified RDJ2 proteins (AGPP lane 3 analyzed as negative control.)

2a, and a number of farnesol analogues become incorporated into cellular proteins when added to the culture media of growing cells (*27*, *28*, *46*, *47*). These compounds are thought to traverse the plasma membrane and act as a substrate for sequential kinase reactions to give FPP **1b**, GGPP **2b**, or the diphosphate analogue which can then be utilized by FTase or GGTaseI to appropriately modify cellular proteins (*46*, *48*). The kinases involved in the phosphorylation reactions have been characterized in plants but not in mammalian cells. In vitro, both FPP **1b** and AGPP **5b** are transferable by FTase to a CVLS substrate with similar k_{cat} and K_m values (*49*). Therefore, we speculated that anilinogeraniol might also cross the plasma membrane of cells, be converted to the diphosphate **5b**, and become incorporated into proteins by FTase. However, it was also possible that anilinogeraniol **5a** might be toxic to mammalian cells. Accordingly, the acute cytoxicity of anilinogeraniol **5a** was examined by incubating human embryonic kidney (HEK-293) cells with up to 100 μM anilinogeraniol **5a** for 3 days. Somewhat surprisingly, we found that cells treated with anilinogeraniol showed no morphological changes and no decrease in cell growth relative to controls at any of the concentrations tested (data not shown).

The polyAG-Ab's were used to probe extracts of HEK-293 cells incubated in the presence of AGOH **5a** to determine if the anilinogeranyl group was incorporated into cellular proteins. These cells were initially blocked with lovostatin an upstream inhibitor of endogenous FPP and GGPP formation and treated with GGOH for the geranylgeranylation of proteins critical to cell survival (*50*). Figure 5a shows that there are numerous anilinogeranyl modified proteins in cells treated with AGOH **5a**, while no proteins were detected in the absence of the unnatural FPP analogue. To determine whether the protein modification was FTase dependent, cells were incubated in the presence of AGOH **5a** and either the farnesyl transferase inhibitor FTI-277 (*51*) or the geranylgeranyl transferase I inhibitor GGTI-2147 (*52*). Lane 3 of Figure 4 shows that no anilinogeranyl modified proteins were detected in the presence of the FTI. However, in the presence of the geranylgeranyl transferase I inhibitor, the pattern of proteins modified with anilinogeranyl moiety was very similar to that without any inhibitor present. Interestingly, some additional, lower molecular weight polyAG-Ab reactive bands appear when GGTaseI is inhibited. FTase-catalyzed transfer of the anilinogeranyl lipid to protein is the most consistent explanation for these observations. These results also suggest that FTase may be able to utilize AGPP to modify some normally geranylgeranylated proteins when GGTaseI is inhibited. This is not unreasonable, as the normally farnesylated K-Ras4B becomes geranylgeranylated in the presence FTIs (*53*, *54*).

The AGOH analogue must undergo diphosphorylation to be incorporated into cellular proteins. This diphosphorylation may not be on a time-scale that allows competitive modification of proteins in the presence of FPP. Cells were incubated without a lovastatin blockade on endogenous FPP formation with 30 μM AGOH and sampled every few hours. Figure 5b shows that anilinogeranyl incorporation into proteins begins within 2 h of incubation with AGOH and is therefore competitive with the endogenous pools of FPP. Importantly, these experiments demonstrate that intracellular concentrations of AGPP **5b** can be achieved that are high enough to compete with the endogenous pool of FPP **1b** for FTase dependent transfer to proteins.

Figure 4 shows that a number of proteins with molecular weights ranging from 30 to 70 kDa are modified with the anilinogeranyl moiety. However, protein bands for Ras and other normally farnesylated small molecular weight GTPases in the 19−27 kDa range are conspicuously absent. Previous reports have shown that the majority of small molecular weight GTPases are normally geranylgeranylated and that the farnesylated small molecular weight GTPases are present in relatively low abundance (*27*). Consequently, the farnesylated small molecular weight GTPases are difficult to detect, and only faint bands corresponding to these molecules are found when tritium labeled farnesol **1a** is incubated with glioma cells (C6) or green monkey kidney cells (CV-1) (*46*). Determination of Ras prenylation status is an important assay in the evaluation of FTI efficacy and is most often carried out by metabolic labeling with ^{3}H-mevalonate (*25*). We probed extracts of cells overexpressing a GST-Ras fusion protein grown in the presence of AGOH with the polyAG-Ab to overcome the low natural levels of endogenous Ras. HEK-293 cells were transiently transfected with a vector expressing glutathione S-transferase (GST) tagged wild-type H-Ras. The cells were then incubated with AGOH **5a**, lysed, analyzed by SDS−PAGE, and probed with primary antibodies to the GST-tag and to the polyAG-Ab modification. Figure 6 shows a representative blot in which anilinogeranyl group is incorporated into the GST-tagged Ras protein and other higher molecular weight proteins. These results suggest that anilinogeranyl modified Ras is present in cells not

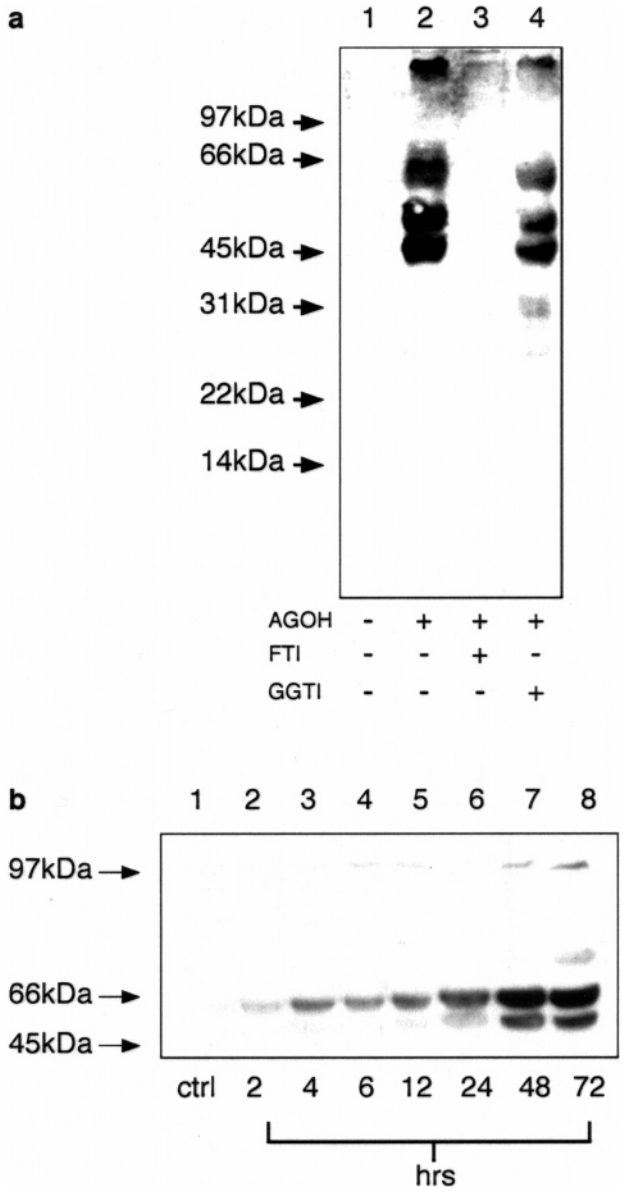

Figure 5. (a) Incorporation and detection of anilinogeranyl modified endogenous proteins. HEK-293 cells were incubated with 30 μM lovostatin and 10 μM GGOH for 1 day, and then media was poured off and the cells were incubated with or without 100 μM AGOH **3a** (lanes 1 and 2), in the presence and absence of an FTI or a GGTI (lanes 2−4). The cells were then analyzed by western blot with the AG-Ab sera. (b) Cells with no lovostatin blockade were incubated with 30 μM AGOH for the given time points then were harvested and lysed. Fifty micrograms of total protein was loaded onto an SDS−PAGE gel, transferred to nitrocellulose, and immunodetected using the polyAG-Ab.

overexpressing GST-Ras at concentrations below the level of detection possible with this antibody.

DISCUSSION

This report outlines a general strategy for detecting prenylated proteins using antibodies directed toward unnatural analogues of FPP **1b** bearing unique epitopes that can be transferred to proteins by FTase. We have found that the farnesol **1a** analogue AGOH **5a** can be utilized by a cell to modify proteins in an FTase dependent manner and is not particularly toxic. The structure of the anilinogeranyl moiety is also dissimilar to any other known cellular components or protein modifications making it an excellent epitope for selective antibody recognition. In this report we show that the AGPP prodrug anilinogeraniol is incorporated into cellular protein in the presence of the endogenous FPP pool. Previous reports of FPP analogue incorporation into cellular proteins have required lovastatin to block endogenous FPP formation in order to detect modified proteins. These reagents may be useful for the analysis of FTase-mediated protein modification and cellular events further downstream. The lack of acute cellular toxicity of AGOH **5a** may allow for long-term analysis of proteins modified by FTase by immunohistochemical methods. These antibodies could be especially useful for screening the activity and protein targeting of farnesyl transferase inhibitors helping to identify the targets of these reagents to better understand the role of farnesylated proteins in cancer biology.

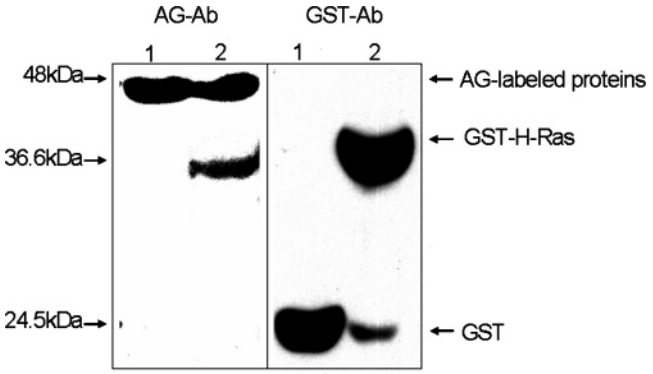

Figure 6. Incorporation into cells overexpresssing Ras. HEK-293 cells overexpressing GST-labeled Ras were incubated in medium containing 30 μM lovostatin and 10 μM GGOH overnight and then were treated with 100 μM AGOH **3a** in medium without the lovostatin blockade. The cells were lysed, run on an SDS−PAGE gel, and analyzed by western blot. Blots were probed with an anti-GST antibody (GST-Ab) or AG-Ab sera (AG-Ab). Lane 1 contains control cells without Ras overexpression, and lane 2 contains cells overexpressing GST-Ras. All cells were labeled with AGOH.

ACKNOWLEDGMENT

This work was supported in part by the Kentucky Lung Cancer Research Program (to H.P.S. and D.A.A.) and the National Institutes of Health (GM66152-01 to H.P.S.), and the NMR instruments used in this work were obtained with support from NSF CRIF Grant No. CHE-9974810. We thank Dr. Sidney W. Whiteheart, Todd Schraw, and Garland Crawford for help with rabbit immunization and bleeding. We thank Gamma One Laboratories, Inc., for monoclonal antibody preparations. We thank Dr. Carol Fierke, Heather Hartman, Katherine Hicks, and Jennifer Pickett for the gift of mammalian protein farnesyl transferase.

Supporting Information Available: ^{1}H and ^{13}C NMR and MS spectra of all new small molecules synthesized. This material is available free of charge via the Internet at http://pubs.acs.org/BC

LITERATURE CITED

(1) Adjei, A. A. (2003) An overview of farnesyltransferase inhibitors and their role in lung cancer therapy. *Lung Cancer*, *41 Suppl 1*, S55−62.
(2) Rowinsky, E. K., Windle, J. J., and Von Hoff, D. D. (1999) Ras protein farnesyltransferase: A strategic target for anticancer therapeutic development. *J. Clin. Oncol. 17*, 3631−52.
(3) Zhu, K., Hamilton, A. D., and Sebti, S. M. (2003) Farnesyltransferase inhibitors as anticancer agents: current status. *Curr. Opin. Investig. Drugs 4*, 1428−35.

(4) Zhang, F. L., and Casey, P. J. (1996) Protein prenylation: molecular mechanisms and functional consequences. *Annu. Rev. Biochem. 65*, 241−69.
(5) Vergnes, L., Peterfy, M., Bergo, M. O., Young, S. G., and Reue, K. (2004) Lamin B1 is required for mouse development and nuclear integrity. *Proc. Natl. Acad. Sci. U.S.A. 101*, 10428−33.
(6) Roskoski, R., Jr. (2003) Protein prenylation: a pivotal posttranslational process. *Biochem. Biophys. Res. Commun. 303*, 1−7.
(7) Dunten, P., Kammlott, U., Crowther, R., Weber, D., Palermo, R., and Birktoft, J. (1998) Protein Farnesyltransferase: Structure and Implications for Substrate Binding. *Biochemistry 37*, 7907−7912.
(8) Caplin, B. E., Ohya, Y., and Marshall, M. S. (1998) Amino acid residues that define both the isoprenoid and CAAX preferences of the Saccharomyces cerevisiae protein farnesyltransferase. Creating the perfect farnesyltransferase. *J. Biol. Chem. 273*, 9472−9.
(9) Adjei, A. A. (2001) Blocking oncogenic Ras signaling for cancer therapy. *J. Natl. Cancer Inst. 93*, 1062−74.
(10) Anwar, K., Nakakuki, K., Shiraishi, T., Naiki, H., Yatani, R., and Inuzuka, M. (1992) Presence of ras oncogene mutations and human papillomavirus DNA in human prostate carcinomas. C*ancer Res. 52*, 5991−6.
(11) Watanabe, M., Shiraishi, T., Yatani, R., Nomura, A. M., and Stemmermann, G. N. (1994) International comparison on ras gene mutations in latent prostate carcinoma. *Int. J. Cancer 58*, 174−8.
(12) Konishi, N., Hiasa, Y., Matsuda, H., Tao, M., Tsuzuki, T., Hayashi, I., Kitahori, Y., Shiraishi, T., Yatani, R., Shimazaki, J., and et al. (1995) Intratumor cellular heterogeneity and alterations in ras oncogene and p53 tumor suppressor gene in human prostate carcinoma. *Am. J. Pathol. 147*, 1112−22.
(13) Konishi, N., Hiasa, Y., Tsuzuki, T., Tao, M., Enomoto, T., and Miller, G. J. (1997) Comparison of ras activation in prostate carcinoma in Japanese and American men. *Prostate 30*, 53−7.
(14) Santucci, R., Mackley, P. A., Sebti, S., and Alsina, M. (2003) Farnesyltransferase inhibitors and their role in the treatment of multiple myeloma. *Cancer Control 10*, 384−7.
(15) Sebti, S. M., and Hamilton, A. D. (2000) Farnesyltransferase and geranylgeranyltransferase I inhibitors and cancer therapy: lessons from mechanism and bench-to-bedside translational studies. *Oncogene 19*, 6584−93.
(16) Reid, T. S., and Beese, L. S. (2004) Crystal structures of the anticancer clinical candidates R115777 (Tipifarnib) and BMS-214662 complexed with protein farnesyltransferase suggest a mechanism of FTI selectivity. *Biochemistry 43*, 6877−84.
(17) Ramamurthy, V., Roberts, M., van den Akker, F., Niemi, G., Reh, T. A., and Hurley, J. B. (2003) AIPL1, a protein implicated in Leber's congenital amaurosis, interacts with and aids in processing of farnesylated proteins. *Proc. Natl. Acad. Sci. U.S.A. 100*, 12630−5.
(18) Scheffzek, K., Stephan, I., Ole N. Jensen5, Illenberger, D., and Gierschik, P. (2000) The Rac-RhoGDI complex and the structural basis for the regulation of Rho proteins by RhoGDI. *Nat. Struct. Biol. 7*, 122−126.
(19) Chen, X., Yano, Y., Hasuma, T., Yoshimata, T., Yinna, W., and Otani, S. (1999) Inhibition of farnesyl protein transferase and P21ras memebrane association by d-limonene in human pancreas tumor cells in vitro. *Chin. Med. Sci. J. 14*, 138−44.
(20) Bergo, M. O., Ambroziak, P., Gregory, C., George, A., Otto, J. C., Kim, E., Nagase, H., Casey, P. J., Balmain, A., and Young, S. G. (2002) Absence of the CAAX endoprotease Rce1: effects on cell growth and transformation. *Mol. Cell Biol. 22*, 171−81.
(21) Michaelson, D., Ali, W., Chiu, V. K., Bergo, M., Silletti, J., Wright, L., Young, S. G., and Philips, M. (2005) Postprenylation CAAX Processing Is Required for Proper Localization of Ras but Not Rho GTPases. *Mol. Biol. Cell 4*, 1606−16.
(22) Cox, A. D. (2001) Farnesyltransferase inhibitors: potential role in the treatment of cancer. *Drugs 61*, 723−32.
(23) Fiordalisi, J. J., Johnson, R. L., 2nd, Weinbaum, C. A., Sakabe, K., Chen, Z., Casey, P. J., and Cox, A. D. (2003) High affinity for farnesyltransferase and alternative prenylation contribute individually to K-Ras4B resistance to farnesyltransferase inhibitors. *J. Biol. Chem. 278*, 41718−27.
(24) Crespo, N. C., Ohkanda, J., Yen, T. J., Hamilton, A. D., and Sebti, S. M. (2001) The farnesyltransferase inhibitor, FTI-2153, blocks bipolar spindle formation and chromosome alignment and causes prometaphase accumulation during mitosis of human lung cancer cells. *J. Biol. Chem. 276*, 16161−7.
(25) Ashar, H. R., Armstrong, L., James, L. J., Carr, D. M., Gray, K., Taveras, A., Doll, R. J., Bishop, W. R., and Kirschmeier, P. T. (2000) Biological effects and mechanism of action of farnesyl transferase inhibitors. *Chem. Res. Toxicol. 13*, 949−52.
(26) Maltese, W. A. (1990) Posttranslational modification of proteins by isoprenoids in mammalian cells. *FASEB J. 4*, 3319−28.
(27) Andres, D. A., Crick, D. C., Finlin, B. S., and Waechter, C. J. (1999) Rapid identification of cysteine-linked isoprenyl groups by metabolic labeling with [3H]farnesol and [3H]-geranylgeraniol. *Methods Mol. Biol. 116*, 107−23.
(28) Gibbs, B. S., Zahn, T. J., Mu, Y., Sebolt-Leopold, J. S., and Gibbs, R. A. (1999) Novel Farnesol and Geranylgeraniol Analogues: A Potential New Class of Anticancer Agents Directed against Protein Prenylation. *J. Med. Chem. 42*, 3800−3808.
(29) Gronborg, M., Kristiansen, T. Z., Stensballe, A., Andersen, J. S., Ohara, O., Mann, M., Jensen, O. N., and Pandey, A. (2002) A mass spectrometry-based proteomic approach for identification of serine/threonine-phosphorylated proteins by enrichment with phospho-specific antibodies: identification of a novel protein, Frigg, as a protein kinase A substrate. *Mol. Cell Proteomics 1*, 517−27.
(30) Liu, X. H., Suh, D. Y., Call, J., and Prestwich, G. D. (2004) Antigenic prenylated peptide conjugates and polyclonal antibodies to detect protein prenylation. *Bioconjugate Chem. 15*, 270−7.
(31) Lin, H. P., Hsu, S. C., Wu, J. C., Sheen, I. J., Yan, B. S., and Syu, W. J. (1999) Localization of isoprenylated antigen of hepatitis delta virus by anti-farnesyl antibodies. *J. Gen. Virol. 80 (Pt 1)*, 91−6.
(32) Baron, R., Fourcade, E., Lajoie-Mazenc, I., Allal, C., Couderc, B., Barbaras, R., Favre, G., Faye, J. C., and Pradines, A. (2000) RhoB prenylation is driven by the three carboxyl-terminal amino acids of the protein: evidenced in vivo by an anti-farnesyl cysteine antibody. *Proc. Natl. Acad. Sci. U.S.A. 97*, 11626−31.
(33) Kho, Y., Kim, S. C., Jiang, C., Barma, D., Kwon, S. W., Cheng, J., Jaunbergs, J., Weinbaum, C., Tamanoi, F., Falck, J., and Zhao, Y. (2004) A tagging-via-substrate technology for detection and proteomics of farnesylated proteins. *Proc. Natl. Acad. Sci. U.S.A. 101*, 12479−84.
(34) Turek-Etienne, T. C., Strickland, C. L., and Distefano, M. D. (2003) Biochemical and Structural Studies with Prenyl Diphosphate Analogues Provide Insights into Isoprenoid Recognition by Protein Farnesyl Transferase. *Biochemistry 42*, 3716−3724.
(35) Rawat, D. S., and Gibbs, R. A. (2002) Synthesis of 7-Substituted Farnesyl Diphosphate Analogues. *Org. Lett. 4*, 3027−3030.
(36) Davisson, V. J., Woodside, A. B., Neal, T. R., Stremler, K. E., Muehlbacher, M., and Poulter, C. D. (1986) Phosphorylation of Isoprenoid Alcohols. *J. Org. Chem. 51*, 4768−4779.
(37) Holstein, S. A., Wohlford-Lenane, C. L., Wiemer, D. F., and Hohl, R. J. (2003) Isoprenoid Pyrophosphate Analogues Regulate Expression of Ras-Related Proteins. *Biochemistry 42*, 4384−4391.
(38) Chehade, K. A., Andres, D. A., Morimoto, H., and Spielmann, H. P. (2000) Design and synthesis of a transferable farnesyl pyrophosphate analogue to Ras by protein farnesyltransferase. *J. Org. Chem. 65*, 3027−33.
(39) Chehade, K. A., Kiegiel, K., Isaacs, R. J., Pickett, J. S., Bowers, K. E., Fierke, C. A., Andres, D. A., and Spielmann, H. P. (2002) Photoaffinity analogues of farnesyl pyrophosphate transferable by protein farnesyl transferase. *J. Am. Chem. Soc. 124*, 8206−19.

(40) Andres, D. A., Shao, H., Crick, D. C., and Finlin, B. S. (1997) Expression cloning of a novel farnesylated protein, RDJ2, encoding a DnaJ protein homologue. *Arch. Biochem. Biophys. 346*, 113−24.
(41) Shi, G. X., and Andres, D. A. (2005) Rit contributes to nerve growth factor-induced neuronal differentiation via activation of B−Raf-extracellular signal-regulated kinase and p38 mitogen-activated protein kinase cascades. *Mol. Cell Biol. 25*, 830−46.
(42) Berger, T. S., Parandoosh, Z., Perry, B. W., and Stein, R. B. (1992) Interaction of glucocorticoid analogues with the human glucocorticoid receptor. *J. Steroid Biochem. Mol. Biol. 41*, 733−8.
(43) Berndt, P., Fields, G. B., and Tirrell, M. (1995) Synthetic Lipidation of Peptides and Amino Acids: Monolayer Structure and Properties. *J. Am. Chem. Soc. 117*, 9515−9522.
(44) G. Yang, J. C., Arakawa-Uramoto, H., Wang, X., M. A. Gawinowicz, Zhao, K., and Landry, D. W. (1996) Anti-Cocaine Catalytic Antibodies: A Synthetic Approach to Improved Antibody Diversity. *J. Am. Chem. Soc. 118*, 5881−5890.
(45) Habeeb, A. F. S. A. (1966) Determination of free amino groups in protien by trinitrobenzene sulfonic acid. *Anal. Biochem. 14*, 328.
(46) Crick, D. C., Andres, D. A., and Waechter, C. J. (1995) Farnesol is utilized for protein isoprenylation and the biosynthesis of cholesterol in mammalian cells. *Biochem. Biophys. Res. Commun. 211*, 590−9.
(47) Crick, D. C., Andres, D. A., and Waechter, C. J. (1997) Novel salvage pathway utilizing farnesol and geranylgeraniol for protein isoprenylation. *Biochem. Biophys. Res. Commun. 237*, 483−7.
(48) Thai, L., Rush, J. S., Maul, J. E., Devarenne, T., Rodgers, D. L., Chappell, J., and Waechter, C. J. (1999) Farnesol is utilized for isoprenoid biosynthesis in plant cells via farnesyl pyrophosphate formed by successive monophosphorylation reactions. *Proc. Natl. Acad. Sci. U.S.A. 96*, 13080−5.
(49) Chehade, K. A. H., Andres, D. A., Morimoto, H., and Spielmann, H. P. (2000) Design and Synthesis of a Transferable Farnesyl Pyrophosphate. *J. Org. Chem. 65*, 3207−3033.
(50) McGuire, T. F., and Sebti, S. M. (1997) Geranylgeraniol potentiates lovastatin inhibition of oncogenic H-Ras processing and signaling while preventing cytotoxicity. *Oncogene 14*, 305−12.
(51) Shi, Y., Wu, J., Mick, R., Cerniglia, G. J., Cohen-Jonathan, E., Rhim, J. S., Koch, C. J., and Bernhard, E. J. (2005) Farnesyltransferase inhibitor effects on prostate tumor microenvironment and radiation survival. *Prostate 62*, 69−82.
(52) Lesh, R. E., Emala, C. W., Lee, H. T., Zhu, D., Panettieri, R. A., and Hirshman, C. A. (2001) Inhibition of geranylgeranylation blocks agonist-induced actin reorganization in human airway smooth muscle cells. *Am. J. Physiol. Lung Cell Mol. Physiol. 281*, L824−31.
(53) Rowell, C. A., Kowalczyk, J. J., Lewis, M. D., and Garcia, A. M. (1997) Direct demonstration of geranylgeranylation and farnesylation of Ki-Ras in vivo. *J. Biol. Chem. 272*, 14093−7.
(54) Whyte, D. B., Kirschmeier, P., Hockenberry, T. N., Nunez-Oliva, I., James, L., Catino, J. J., Bishop, W. R., and Pai, J. K. (1997) K- and N-Ras are geranylgeranylated in cells treated with farnesyl protein transferase inhibitors. *J. Biol. Chem. 272*, 14459−64.

BC050068+

Sulfhydryl-Selective, Covalent Labeling of Biomolecules with Transition Metallocarbonyl Complexes. Synthesis of (η^5-C_5H_5)M(CO)$_3$(η^1-*N*-Maleimidato) (M = Mo, W), X-ray Structure, and Reactivity Studies

Bogna Rudolf,[†] Marcin Palusiak,[‡] Janusz Zakrzewski,*[,†] Michèle Salmain,*[,§] and Gérard Jaouen[§]

Department of Organic Chemistry, University of Lodz, 90-136 Lodz, Narutowicza 68, Poland, Department of Crystallography, University of Lodz, 90−236 Lodz, Pomorska 149/153, Poland, and Ecole Nationale Supérieure de Chimie de Paris, Laboratoire de Chimie et Biochimie des Complexes Moléculaires (UMR CNRS 7576), 11 rue Pierre et Marie Curie 75231 Paris Cedex 05, France. Received March 11, 2005;
Revised Manuscript Received July 25, 2005

The photochemical reaction of (η^5-C_5H_5)Mo(CO)$_3$I with maleimide in the presence of diisopropylamine yielded complex (η^5-C_5H_5)Mo(CO)$_3$(η^1-*N*-maleimidato) **4** in 52% yield. The single-crystal X-ray structure of this complex was determined and shows unusual interactions between oxygen atoms of the maleimidato ligand and carbon atoms of the *cis*-C≡O ligands. The tungsten analogue of **4**, (η^5-C_5H_5)W(CO)$_3$(η^1-*N*-maleimidato) **5**, was synthesized in 37% yield by the reaction of (η^5-C_5H_5)W(CO)$_3$I with the thallium(I) salt of maleimide. Complexes **4** and **5** reacted with cysteine ethyl ester and glutathione to afford products of the addition of the sulfhydryl group to the ethylenic bond of the maleimidato ligand. The reaction of **4** and **5** with glutathione proceeded faster than the reaction of the analogous complex (η^5-C_5H_5)Fe(CO)$_2$(η^1-*N*-maleimidato) (**3**). However, all these complexes react with glutathione more slowly than *N*-ethylmaleimide. Complexes **4** and **5** were used for labeling of bovine serum albumin (BSA), enriched in thiol groups by reaction with Traut's reagent. Reaction of thiolated BSA containing 7.4 SH groups with **4** and **5** gave bioconjugates bearing 6.9 and 6.4 metallocarbonyl moieties, respectively. Under the same conditions, reaction with **3** afforded a BSA conjugate containing 7.6 metallocarbonyl moieties. Labeling was presumed to be site-specific, as the number of metallocarbonyl entities matched very well with the initial number of SH groups measured for the thiolated BSA sample. IR spectra of BSA labeled with **4** and **5** show intense $\nu_{(C\equiv O)}$ bands (2042 and 1948 cm^{-1} in the latter case), enabling sensitive detection of the bioconjugates in biological samples. Complexes **4** and **5** (especially the latter) should be of interest as heavy atom phasing reagents for protein X-ray crystallography.

INTRODUCTION

Side-chain selective, covalent labeling of biomolecules such as proteins with transition organometallic complexes endows the resulting bioconjugates with unusual redox properties (*1*), IR absorption (*2*) or luminescence features (*3*) enabling their sensitive detection in biological samples. In the particular case where the transition metal belongs to the second or third row, thus exhibiting high electron density, such a labeling may also be helpful in overcoming "the phase problem", one of the bottlenecks of X-ray protein crystallography (*4*).

The thiol group of free cysteine residues side-chain is the most reactive protein function because of its high nucleophilicity and as such an interesting target to introduce transition organometallic complexes into proteins. Maleimido compounds are often used to selectively alkylate thiols (*5*) but are seldom encountered in the transition organometallic series. For instance, a tetrairidium cluster carrying a single maleimido group was synthesized (*6*) and used to introduce heavy atoms into ribososomal particles for X-ray crystallographic studies (*7*). A related tetrairidium cluster was used for cryoelectron microscopy studies of the hepatitis B virus capsid (*8*). The ferrocenyl maleimides **1a** and **1b** were prepared and successfully used to attach a redox active ferrocenyl entity to genetically engineered cytochrome P_{450cam} (*9*) and β-lactamase (*10*). The cationic rhenium(I) polypyridine tricarbonyl maleimide complex **2** was used to attach strongly luminescent groups to several polypeptides and oligonucleotides (*2c*).

A few years ago we described the synthesis of the iron(II) dicarbonyl maleimide complex **3** (*11*). This compound was initially designed to introduce IR-detectable (η^5-C_5H_5)Fe(CO)$_2$ (Fp) moieties into thiol-containing biomolecules, such as the protein bovine serum albumin (BSA) (*12*) and the tripeptide glutathione (*13*) More recently, we were also able to label PAMAM generation 4 dendrimer by alkylation of its terminal free amino groups by complex **3** (*14*). The Fp moiety, as all the metallocarbonyl complexes, gives rise to very strong IR absorption bands, $\nu_{C\equiv O}$, appearing in the 1850−2100 cm^{-1} spectral

* To whom correspondence should be addressed. J.Z.: Telephone: +4842 635 5750. fax:+ 4842 678 e-mail: janzak@uni.lodz.pl. M.S.: Telephone: +33 1 44 27 67 32. fax: +33 1 43 26 00 61. e-mail: michele-salmain@enscp.fr.
[†] Department of Organic Chemistry, University of Lodz.
[‡] Department of Crystallography, University of Lodz.
[§] Ecole Nationale Supérieure de Chimie de Paris.

10.1021/bc050073d CCC: $30.25 © 2005 American Chemical Society
Published on Web 09/01/2005

region which is devoid of any absorption due to proteins or biological matrixes.

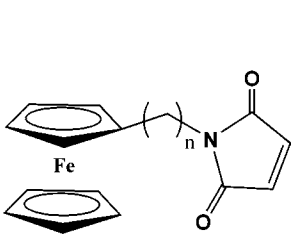

1 (n = 0, 2)

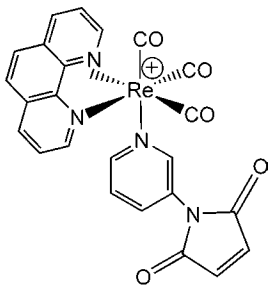

2

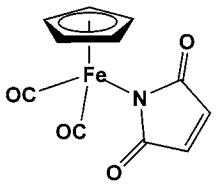

3

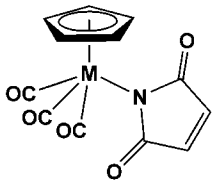

4 M = Mo
5 M = W

Herein we describe the synthesis of the molybdenum(II) and tungsten(II) cyclopentadienyl tricarbonyl complexes **4** and **5**, respectively, both containing the η^1-*N*-maleimidato ligand, along with reactivity studies toward cysteine ethyl ester, the cysteine-containing tripeptide glutathione, and a model protein, thiolated BSA. These two new metallocarbonyl maleimides are of interest as protein labeling reagents since they combine two features: an easy and sensitive IR detection of the organometallic probe with a possibility of application in protein X-ray crystallography (especially complex **5**).

EXPERIMENTAL SECTION

All syntheses were carried out under argon. Solvents were dried by using standard procedures. Compounds (η^5-C_5H_5)M(CO)$_3$I (M = Mo, W) were prepared by reaction of [(η^5-C_5H_5) M(CO)$_3$]$_2$ with iodine (*15*). Compound **3** was prepared according to an earlier published procedure (*11*). All other reagents are commercially available and were used as received. Chromatographic separations were carried out on silica gel 60 (Merck, 230−400 mesh ASTM). Phosphate-buffered saline (PBS) pH 7.4 was prepared by dissolving 8 g NaCl, 0.2 g KCl, 1.42 g $Na_2HPO_4 \cdot 2H_2O$, and 0.34 g KH_2PO_4 in 1 L of double-distilled grade water. Borate buffer pH 8.0 was prepared by dissolving 0.87 g B(OH)$_3$ and 0.57 g $Na_2B_4O_7 \cdot 10\ H_2O$ in 0.1 L of double-distilled grade water. ^{1}H NMR spectra were recorded on a Varian Gemini 200 BB (200 MHz) and a Bruker DRX 500 (500 MHz) spectrometers and were referenced to internal TMS. Reverse-phase HPLC analysis of glutathione conjugates was performed on a System Gold (Beckman Coulter) equipped with a 4.6 × 250 mm, 5 μm Si-C8 column (Kromasil, Eka Nobel). Compounds were eluted by applying 5 min after the injection a linear gradient from 10 to 100% of MeCN-0.1% TFA in water − 0.1% TFA in 20 min.

(η^5-C_5H_5)Mo(CO)$_3$ (η^1-*N*-Maleimidato) (4). A stirred, water-ice cooled, and argon-saturated solution of (η^5-C_5H_5)Mo(CO)$_3$I (244 mg, 0.67 mmol) and maleimide (58 mg, 0.6 mmol) in toluene (20 mL) containing diisopropylamine (1 mL) was illuminated with visible light (4 × 100 W tungsten lamps) for 2 h. The initial dark red color of the solution turned orange-yellow upon illumination. The grayish solid formed was filtered off, and the filtrate was evaporated to dryness under reduced pressure. The residue was dissolved in chloroform and purified by column chromatography. A deep red band containing a small amount of the starting molybdenum complex was eluted with chloroform, followed by an orange band of **4** eluted with chloroform−methanol 3:1. The product was crystallized from chloroform−heptane. X-ray grade crystals were obtained from layered dichloromethane−hexane. Yield 106 mg (52%). ^{1}H NMR (δ, ppm): 6.70 (s, 2H, olefinic H's), 5.53 (s, 5H, Cp). IR (cm^{-1}): 2054, 1977 (C≡O), 1659 (CO imide). Anal. ($C_{12}H_7MoNO_5$) C, H, N.

(η^5-C_5H_5)W(CO)$_3$ (η^1-*N*-Maleimidato) (5). The thallium(I) salt of maleimide was prepared by treatment of a solution of maleimide (152 mg, 1.56 mmol) in ethanol (3.5 mL) with thallium(I) ethoxide (120 μL, 1.56 mmol). After 20 min stirring, the yellow solid formed was filtered off, washed with ethanol, and dried under vacuum. Then it was dissolved in DMF (6 mL), (η^5-C_5H_5)W(CO)$_3$I (162 mg, 0.35 mmol) was added, and the resulting solution was heated, with stirring, to 50 °C for 2 h. The solid formed was filtered off and the filtrate evaporated to dryness. The residue was dissolved in chloroform, washed five times with water, and dried (Na_2SO_4). Evaporation to dryness and flash chromatography recovered a small amount of (η^5-C_5H_5)W(CO)$_3$I (red band eluted with dichloromethane), followed by **5** (orange band eluted with dichloromethane−methanol 3:1). An analytical sample of **5** was prepared by recrystallization from dichloromethane−hexane. Yield 55 mg (37%). ^{1}H NMR (δ, ppm): 6.72 (s, 2H, olefinic H's), 5.64 (s, 5H, Cp). IR (cm^{-1}): 2046, 1957 (C≡O), 1664 (CO imide). Anal. ($C_{12}H_7NO_5W$) C, H, N.

Reaction of 4 and 5 with L-Cysteine Ethyl Ester. A solution of L-cysteine ethyl ester hydrochloride (28 mg, 0.15 mmol) and **4** or **5** (0.13 mmol) in methanol (5 mL) containing triethylamine (0.3 mL) was stirred at. r.t. for 2 h and evaporated to dryness. The residue, dissolved in chloroform, was chromatographed on SiO_2. First, small amounts of unreacted **4** or **5** were eluted with chloroform and then the products **6** or **7** were eluted with chloroform−methanol (95:5).

6: (orange oil). Yield 55 mg (87%). ^{1}H NMR (δ, ppm): 5.52 (s, 5H), 4.20 (q, J = 7.2 Hz, 2H), 3.80 (m, 2H), 2.8−3.4 (m, 3H), 2.47 (dd, J = 18.1 Hz, 3.8 Hz, 1H), 1.81 (bs, 2H) 1.288 and 1.284 (two triplets, J = 7.2 Hz, 3H). IR: (cm^{-1}) 2054, 1977, 1728, 1649. Anal. ($C_{17}H_{18}\ MoN_2O_7S$) C, H, N.

7: (orange oil). Yield 68 mg (91%). ^{1}H NMR (δ, ppm): 5.63 (s, 5H), 4.20 (q, J = 7.2 Hz, 2H), 3.65 (m, 2H), 2.8−3.4 (m, 3H), 2.49 (dd, J = 18.0 Hz, 3.8 Hz, 1H), 1.81 (bs, 2H) 1.29 (t, J = 7.2 Hz, 3H). IR: (cm^{-1}) 2046, 1959, 1732, 1655. Anal. ($C_{17}H_{18}\ N_2O_7SW$) C, H, N.

Kinetics Studies. Solutions (1 mL) containing compounds **4** or **5** (1×10^{-4} M) and glutathione (1×10^{-4} M) were prepared in PBS, and the reactions were monitored at 285 nm at room temperature. Second-order rate constants k and half-lives were calculated from the equation $(A_\infty - A_0)/(A_\infty - A) = kct + 1$ where A_0 is the absorbance at t = 0, A_∞ is the final absorbance, and c the initial concentration of reagents (i.e. 1×10^{-4} M).

Thiolation of BSA with Traut's Reagent. A mixture of BSA (5×10^{-5} M) and Traut's reagent (1×10^{-3} M) in borate buffer containing 10 mM EDTA was incubated for 1 h at 26 °C (sample volume = 3 mL). The solution was applied to a prepacked 10 mL gel desalting column

(Pierce Chemicals), and species were eluted with PBS containing 1 mM EDTA. The fractions containing the protein were pooled and the concentration of sulfhydryl groups was immediately determined by the Ellman's assay (*16*) whereas the BSA concentration was determined by optical density measurement at 280 nm taking an extinction coefficient ϵ of 43 600 M^{-1} cm^{-1} (*17*).

Labeling of Thiolated BSA with 3, 4, or 5. Mixtures of freshly prepared thiolated BSA (2.1×10^{-5} M) and **3**, **4**, or **5** (2.86×10^{-4} M) were incubated in PBS containing 1 mM EDTA for 24 h at 26 °C (sample volume = 1 mL). Solutions were applied to a 5 mL prepacked gel desalting column (Pierce Chemicals) and species eluted with PBS. Fifteen 0.5 mL fractions were collected, and those containing the protein were pooled and submitted to UV-visible analysis. The concentration of molybdenum and tungsten tricarbonyl succinimidato moieties was calculated from the optical density of the corresponding sample at 438 nm, taking ϵ equal to 460 M^{-1}·cm^{-1} for Mo or 710 M^{-1}·cm^{-1} for W. The concentration of iron dicarbonyl succinimidato moieties was calculated from the optical density of the corresponding sample at 365 nm, taking ϵ equal to 600 M^{-1}·cm^{-1}. The concentration of BSA was calculated from the optical density of the solutions at 280 nm after subtraction of the contribution of the metallocarbonyl succinimidato entities at this wavelength (ϵ(Mo-succinimidato) = 2960 M^{-1}·cm^{-1}; ϵ(W-succinimidato) = 3500 M^{-1}·cm^{-1}; ϵ(Fe-succinimidato) = 2400 M^{-1}·cm^{-1}).

RESULTS AND DISCUSSION

Synthesis of 4 and 5. The iron complex **3** had been prepared by the photochemical reaction of (η^5-C_5H_5) Fe($CO)_2$I with maleimide in the presence of diisopropylamine (dipa) (*11*). Considering the close analogy in the photochemical behavior of (η^5-C_5H_5) Fe($CO)_2$I and (η^5-C_5H_5)M($CO)_3$I (M = Mo, W) (*18*), we thought at first that it would be possible to apply the same approach for the synthesis of **4** and **5**.

We found unexpectedly that only (η^5-C_5H_5)Mo($CO)_3$I underwent photochemical substitution of iodide by the anion of maleimide upon illumination with visible light with maleimide and dipa in benzene (eq 1). Product **4** was isolated in 52% yield and characterized by spectroscopic methods, elemental analysis, and X-ray diffraction (vide infra).

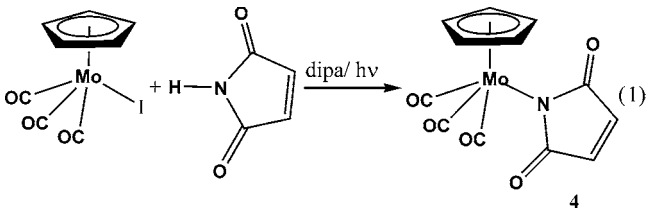

(1)

4

Attempts to prepare **5** in the same way starting from (η^5-C_5H_5)W($CO)_3$I failed. This complex proved completely inert when irradiated with visible light in benzene containing maleimide and dipa. A significantly lower photochemical reactivity of (η^5-C_5H_5)W($CO)_3$I in comparison to its molybdenum analogue had been previously reported and attributed to shorter lifetimes of the chemically reactive excited states, due to enhanced spin−orbit coupling facilitating physical deactivation pathways (*18c*).

We thus prepared **5** by reaction of (η^5-C_5H_5)W($CO)_3$I with the thallium salt of maleimide (eq 2). (A similar method was used earlier to prepare the $Mn(CO)_5$ complex of the succinimide anion (*19*)).

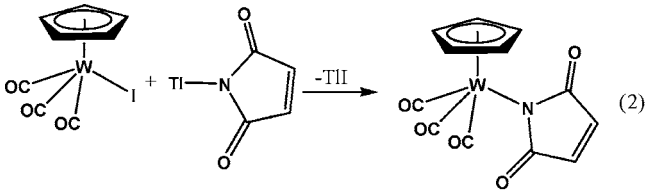

(2)

5

The thallium(I) salt of maleimide was prepared by reaction of maleimide with thallium(I) ethoxide in anhydrous ethanol. The product precipitating from the reaction mixture (assumed to be the expected thallium salt) was filtered off, dried, and used immediately in the reaction with (η^5-C_5H_5)W($CO)_3$I. The reaction proceeded smoothly in DMF at 50 °C and was accompanied by precipitation of TlI. Complex **5** was isolated in 37% yield and characterized by spectral methods and elemental analysis.

The IR and ^{1}H NMR spectral data of complexes **3**−**5** are collected in Table 1. Similarly as in **3**, the η^1-*N*-maleimidato ligand in **4** and **5** displays its $\nu_{(C=O)}$ imide band shifted toward lower wavenumbers in comparison to that of maleimide (1713 cm^{-1}). The NMR signals of the olefinic protons in **3**−**5** were slightly shifted upfield relative to the signal of the olefinic protons in maleimide (6.74 ppm). The above data are consistent with a significant increase of the electron density at the η^1-*N*-maleimidato ligand in **3**−**5** in comparison to maleimide, due to a high polarity of the metal−nitrogen bond and a d_π-p_π repulsion. Therefore, a reduced reactivity of **3**−**5** toward thiols can be expected, which was confirmed earlier for **3**. Hopefully, this complex still proved sufficiently reactive to enable the labeling of BSA (*12*). Complexes **4** and **5** are also characterized by the presence of two $\nu_{(C\equiv O)}$ bands in agreement with the local C_{3v} symmetry of the metallocarbonyl units.

Solid-State Structure of 4. The structure of **4** in the solid state, as determined by X-ray diffraction, is shown in Figure 1. Crystal and refinement data are collected in Table 2, and selected bond distances and angles in Table 3. Compound **4** crystallizes in the monoclinic $P2_1/c$ space group with one molecule in the asymmetric unit cell. The molybdenum atom is five-coordinated, with the *Cg* of the cyclopentadienyl ring at the apex and three carbonyls and the nitrogen atom of the η^1-N-coordinated maleimidato ligand in the basal positions of the square pyramid (a "four-legged piano stool structure"). Such a structure is typical for $CpM(CO)_3X$ molecules, where X denotes a 2e anionic ligand (*20*). The distance between the molybdenum atom and a *Cg* of the cyclopentadienyl ring is 2.001(2) Å. The Mo−C bond for the *trans*-C≡O ligand (1.991(3) Å) is substantially shorter than those for for the *cis*-C≡O ligands (2.029(3) Å and 2.028(3) Å). This means that the *trans*-C≡O ligand is stronger back-bonded than its cis-counterparts, presumably because of σ-donor and π-donor properties of the imidato ligand (*19*). An interesting feature observed in the crystal structure of **4** are short contacts between oxygen atoms of the maleimidato ligand and carbon atoms of the *cis*-C≡O ligands (the distances O(14)···C(20) and O(11)···C(40) are

Table 1. IR and ^{1}H NMR Data of Complexes 3−5 (in $CHCl_3$ or $CDCl_3$)

complex	$\nu_{(C\equiv O)}$, cm^{-1}	$\nu_{(C=O)}$, cm^{-1}	δ(Cp), ppm	δ (maleimide), ppm
3	2056, 2008	1651	5.06	6.62
4	2054, 1977	1659	5.53	6.70
5	2046, 1957	1664	5.64	6.72

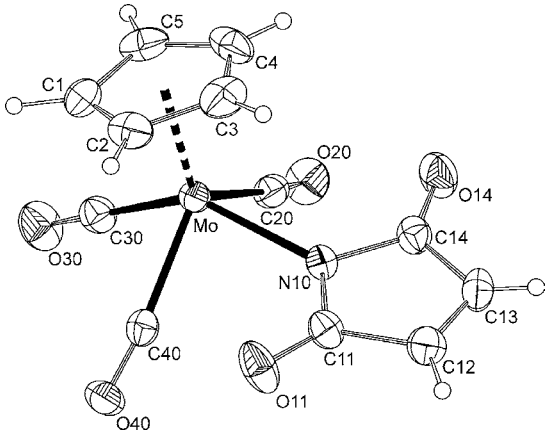

Figure 1. Molecular view of compound **4** with atom labeling scheme. Ellipsoids are drawn at 30% probability.

Table 2. Crystal and Refinement Data for 4

Crystal Data	
empiric formula	C_{12} H_7 Mo N O_5
formula weight	341.13
crystal description	Orange plate
crystal size (mm^3)	0.4 × 0.4 × 0.05
space group	P 2_1/c
unit cell dimensions	
a (Å)	9.8718(10)
b (Å)	8.740(3)
c (Å)	15.8384(14)
β (deg)	116.062(6)
V (Å^3)	1227.6(5)
d_x (g cm^{-3})	1.846
Data Collection	
diffractometer	Rigaku AFC5S
radiation type λ (Å)	Mo K$_\alpha$ 0.71069
μ (mm^{-1})	1.083
temperature (K)	293(2)
data collected (h, k, l)	$-12 \le h \le 12$
	$-10 \le k \le 10$
	$-19 \le l \le 19$
numbers of reflections measured	9286
numbers of independent reflections	2405
R_{int}	0.0547
numbers of reflections with $I > 2\sigma(I)$	1621
Solution and Refinement	
solution	Patterson method
refinement method	full-matrix least-squares on F^2
number of parameters	172
$R(F)^a$ (all data)	0.0537
$wR(F^2)^b$ (all data)	0.0479[c]
$R(F)^a$	0.0231 for 1622 reflections
$wR(F^2)^b$	0.0459[c] for 1622 reflections
$(\Delta/\sigma)_{max}$	0.000
different peak/hole (eÅ^{-3})	0.487/−0.389

[a] $R(F) = \Sigma(|F_o - F_c|)/|F_o|$. [b] $wR(F^2) = [\Sigma w(|F_o - F_c|)^2/\Sigma|F_o|^2]^{1/2}$. [c] $w = 1/[\sigma^2 (F_o^2) + (0.0182P)^2]$ where $P = (F_o^2 + 2F_c^2)/3$.

2.673(4)Å and 2.796(4)Å, respectively). These interactions, which may have electrostatic nature, bring about tilting of C(20) and C(40) toward O(14) and O (11), respectively, and change angles O20−C20−Mo and O40−C40−Mo (172.7(3)° and 173.3(2)°, respectively, to compare with the angle O30−C30−Mo that equals 178.3(3)°). Similar interactions between organic carbonyl groups are frequently observed in X-ray structures (*21*). Since these interactions are intramolecular, they may exist not only in the crystal state, but also in solution, and may influence the reactivity of the maleimidato ligand.

Reaction of 4 and 5 with L-Cysteine Ethyl Ester and Glutathione. Having complexes **4** and **5** in hand, we first checked their reactivity toward the thiol group of L-cysteine ethyl ester. We found that this compound (generated in situ by reaction of L-cysteine ethyl ester hydrochloride with triethylamine) was readily S-alkylated by either **4** or **5** in methanol to afford the η^1-*N*-succinimidato complexes **6** and **7** in high yields (Scheme 1).

Table 3. Structure of 4[a]

Mo−N10	2.180(2)
Mo−C20	2.029(3)
Mo−C30	1.991(3)
Mo−C40	2.028(3)
Mo−C1	2.288(4)
Mo−C2	2.354(3)
Mo−C3	2.376(4)
Mo−C4	2.325(4)
Mo−C5	2.289(4)
N10−C11	1.389(4)
N10−C14	1.394(4)
C12−C13	1.315(5)
O11−C11	1.217(4)
O14−C14	1.213(5)
Mo−C20−O20	172.7(3)
Mo−C30−O30	178.3(3)
Mo−C40−O40	173.3(2)
C11−N10−C14	106.3(2)
Mo−N10−C11−C12	−172.4(2)
C11−C12−C13−C14	−0.2(4)
C12−C13−C14−O14	178.1(3)
O11−C11−C12−C13	−177.0(3)

[a] Selected bond lengths (Å) and angles (deg).

The addition of the sulfhydryl group of L-cysteine ethyl ester to the C=C bond of the maleimidato ligand was confirmed by the lack of the characteristic $\nu_{(S-H)}$ absorption in the IR spectra of **6** and **7** (this absorption appears at 2474 cm^{-1} in the IR spectrum of L-cysteine ethyl ester). The complexity of the ^{1}H NMR spectra of **6** and **7** suggests the formation of two diastereomers as a result of the creation of the stereogenic center at the succinimide ring.

To compare the reactivity of **4** and **5** with that of **3**, the rate of reaction of these complexes with the cysteine-containing tripeptide glutathione was monitored from the change of absorbance at 285 nm in the UV−vis spectra accompanying the addition of glutathione to the maleimide C=C bond. Formation of the S-alkylation adducts was also monitored by reverse phase HPLC. In all cases, the reaction rate followed a second-order kinetics. Measured rate constants and reaction half-lives are gathered in Table 4.

As seen from Table 4, the addition of glutathione to **4** and **5** is faster than its addition to **3**. This difference may arise from a weaker d_π-p_π repulsion between the formally anionic maleimidato ligand and the d^4 metal (Mo(II) or W(II)) in **4** and **5** than the d^6 Fe(II) center in **3**. This repulsion is expected to increase the electron density at the C=C bond, making it less reactive toward nucleophilic attack. Similarly, a decrease of d_π-p_π repulsion is expected on going from Mo to W (the latter participates more in the back-bonding toward CO ligands), which may explain the slightly larger reaction rate of **5** in comparison with **4**. The aforementioned trends in back-bonding toward maleimidato ligand are reflected in the IR spectra of **3**−**5** (Table 1). The $\nu_{(C=O)}$ of imide carbonyls increases in the order **3** < **4** < **5**. Consequently, the extent of the back-bonding to the maleimidato ligand should follow the order **3** > **4** > **5**. Note finally that the rate of S-alkylation of glutathione with **4** or **5** was still slower than that of *N*-ethylmaleimide.

Both glutathione conjugates, analyzed by reverse phase HPLC under conditions reported in Experimental Sec-

Scheme 1. S-Alkylation of l-Cysteine Ethyl Ester by 4 or 5

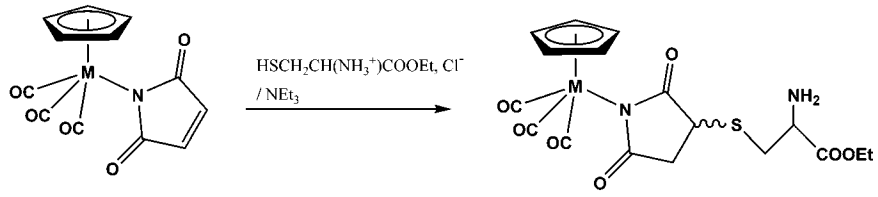

6 M = Mo
7 M = W

Table 4. Rate Constants and Half-Lives of Reaction of 3–5 and *N*-Ethylmaleimide with Glutathione in Water–Methanol (9:1) at pH = 7.4 and 24 °C

complex	k [$M^{-1}\cdot min^{-1}$]	$t_{1/2}$ [min]	reference
3	382	26.0	12
4	1111	9.0	this work
5	1732	5.8	this work
N-ethylmaleimide	9532	1.0	*12*

Scheme 2

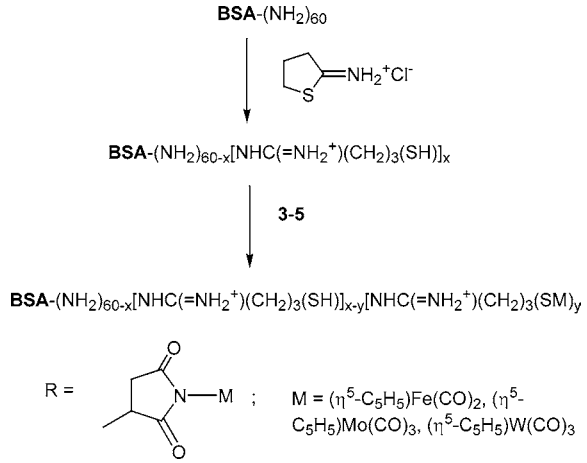

tion, were eluted in the form of two very close peaks at retention time of 15.7 min, in agreement with the formation of two diastereoisomers. The almost equal intensity of both peaks suggests that addition of glutathione to **4** or **5** is not stereoselective.

Reactivity of 4 and 5 toward Thiolated BSA. Having demonstrated the reactivity of **4** and **5** toward the sulfhydryl group in two cysteine derivatives, we became interested in their reactivity toward a protein containing this group. Bovine serum albumin (BSA) is a well-characterized, low cost protein, which is widely used in labeling experiments. Unfortunately, BSA contains only one free cysteine (cysteine 34), and in the commercially available BSA samples, this residue is partially blocked by conjugation with other sulfhydryl compounds such as glutathione (*17*). Therefore, spectroscopic evidence of BSA labeling with **4** or **5** could be difficult to determine because of the expected very low small number of organometallic units bound to the protein. To overcome this problem, we decided to introduce onto BSA additional sulfhydryl groups before reaction with **4** or **5**. This was achieved by treatment of BSA with Traut's reagent, which enables conversion of some of the protein free amino groups (BSA possesses 60 such groups) into sulfhydryl groups (*5*) (Scheme 2).

Under the conditions described in Experimental section, we obtained a thiolated BSA sample containing an average of 7.4 SH groups per protein (including the existing free cysteine residue). This modified protein was then incubated with a 2-fold molar excess of **4** or **5** over the starting concentration of SH groups at pH 7.4 and 26 °C for 24 h. For comparison, an experiment using **3** in place of **4** or **5** was also run under the same conditions. These reaction conditions had been previously shown to enable selective labeling of BSA's thiol (*12*). The metalloconjugates were purified by gel filtration chromatography. The numbers n of metallocarbonyl entities introduced to thiolated BSA, as determined from UV-visible measurements, are reported in Table 5.

Table 5. Labeling of Thiolated BSA (containing 7.4 SH groups) with 3–5 (1.8 molar equiv per SH group) at pH 7.4 and 26 °C for 24 h

labeling complex	n (yield)
4	6.9 (93%)
5	6.4 (86%)
3	7.6 (103%)

It appears from Table 5 that complexes **4** and **5** (as well as complex **3**) were very efficient labeling agents of the protein thiols, with labeling yields all above 85%. The

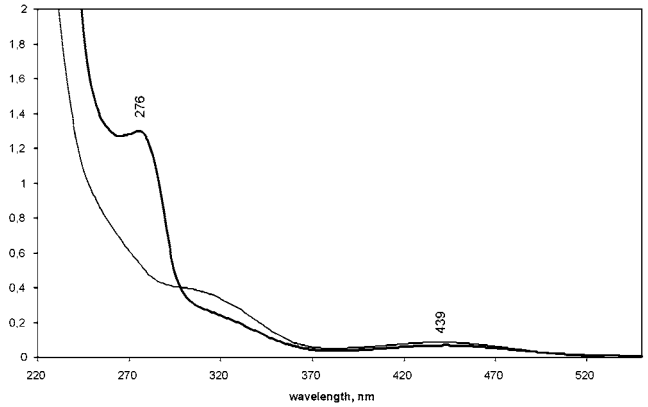

Figure 2. UV-visible spectra of complex **4** (2×10^{-4} M in MeOH, thin line) and its thiolated BSA conjugate (1.97×10^{-5} M in PBS, thick line).

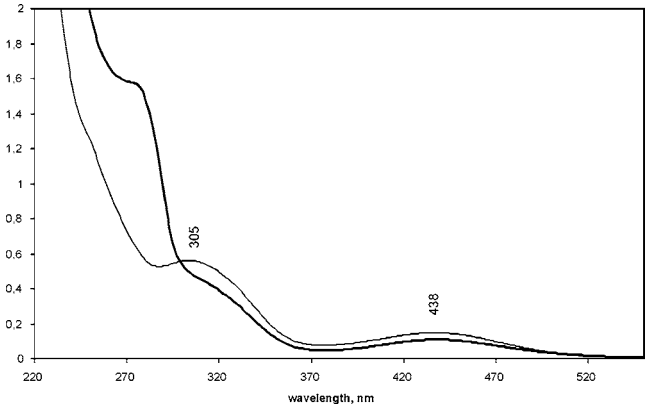

Figure 3. UV-visible spectra of complex **5** (2×10^{-4} M in MeOH, thin line) and its thiolated BSA conjugate (2.07×10^{-5} M in PBS, thick line).

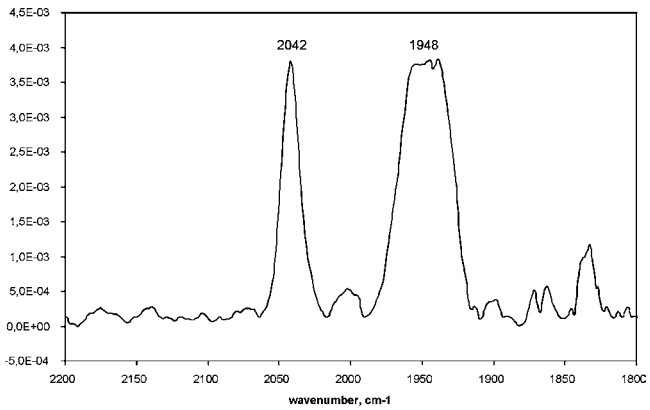

Figure 4. IR spectrum of the conjugate resulting from the reaction of **5** with thiolated BSA (10 μL of a 2.07 $\times$ 10^{-5} M deposited on a 6 mm diameter nitrocellulose membrane).

reaction also appeared to be site-specific in the chosen conditions of reaction, as the number of metallocarbonyl entities matched very well with the initial number of SH groups measured for the thiolated BSA sample. The UV-visible and IR spectra of the metalloconjugates depicted in Figures 2−4 confirmed the covalent binding of both metallocarbonyl complexes to BSA.

CONCLUSION

We have synthesized metallocarbonyl complexes of Mo and W containing the (η^1-*N*-maleimidato) ligand, (η^5-C_5H_5)M(CO)$_3$(η^1-*N*-maleimidato). These complexes react with sulfhydryl groups of cysteine in cysteine ethyl ester and glutathione as well as with sulfhydryl groups introduced to BSA in reaction with Traut's reagent to afford the corresponding S-alkylated IR-detectable bioconjugates. The potential advantage of the synthesized complexes is the presence of heavy metal atoms, which may be helpful for solving proteins structure by X-ray crystallography.

ACKNOWLEDGMENT

The Centre National de la Recherche Scientifique is gratefully acknowledged for financial support of B.R.'s stay in Paris.

Supporting Information Available: Tables of crystallographic data. This material is available free of charge via the Internet at http://pubs.acs.org.

LITERATURE CITED

(1) Van Staveren, D. R., and Metzler-Nolte, N. (2004) Bioorganometallic chemistry of ferrocene. *Chem. Rev. 104*, 5931−5985.

(2) Salmain, M., and Jaouen, G. (2003) Side-chain selective and covalent labelling of proteins with transition organometallic complexes. *C. R. Chimie 6*, 249−258.

(3) (a) Guo, X. Q., Castellano, F. N., Li, L., and Lakowicz, J. R. (1998) Use of a long-lifetime Re(I)complex in fluorescence polarization immunoassays of high-molecular-weight analytes. *Anal. Chem. 70*, 632−637.(b) Dattelbaum, J. D., Abugo, O. O., and Lakowicz, J. R. (2000) Synthesis and characterization of a sulfhydryl-reactive rhenium metal−ligand complex. *Bioconjugate Chem. 11*, 533−536. (c) Lo, K. K., Hui, W. K., Ng, D. C., and Cheung, K. K.(2002) Synthesis, characterization, photophysical properties, and biological labeling studies of a series of luminescent rhenium(I) polypyridine maleimide complexes. *Inorg. Chem. 41*, 40−46.

(4) Blundell, T. L., and Johnson, L. N. (1976) *Protein Crystallography*, Academic Press, London.

(5) Hermanson, G. T. (1996) *Bioconjugate Techniques*, Academic Press, San Diego CA.

(6) Jahn, W. (1989) Synthesis of water soluble tetrairidium clusteres suitable for heavy atom labelling of proteins. *Z. Naturforsch. 44b*, 79−82.

(7) Weinstein, S., Jahn, W., Hansen, H., Wittmann, H. G. and Yonath, A. (1989) Novel procedures for derivatization of ribosomes for crystallographic studies. *J. Biol. Chem. 264*, 19138−19142.

(8) Cheng, N. Conway, J. F., Watts, N. R., Hainfeld, J. F., Joshi, V., Powell, R. D., Stahl, S. J., Wingfield, P. E., and Steven, A. C. (1999) Tetrairidium, a four-atom cluster as a density label in three-dimensional cryo-EM maps of proteins at 10−25 Å resolution. *J. Struct. Biol. 127*, 169−176.

(9) (a) Lo, K. K.-W, Wong, L.-L., and Hill, H. A. O. (1999) Surface-modified mutants of cytochrome $P450_{cam}$: enzymatic properties and electrochemistry. *FEBS Lett. 451*, 342−346. (b) Di Gleria, K., Nickerson, D. P., Hill, H. A. O., Wong, L.-L., and Fülöp, V. (1998) Covalent attachment of an electroactive sulfhydryl reagent in the active site of cytochrome $P450_{cam}$ as revealed by the crystal structure of the modified protein. *J. Am. Chem. Soc. 120*, 46−52. (c) Di Gleria, K., Hill, H. A. O., and Wong, L.-L. (1996) *N*-(2-Ferrocene-ethyl)-maleimide: a new electroactive sulfhydryl-specific reagent for cysteine-containing peptides and proteins. *FEBS Lett. 390*, 142−144.

(10) Di Gleria, K., Halliwell, C. M., Jacob, C., and Hill, H. A. (1997) Site-specific introduction of an electroactive label into a non-electroactive enzyme (β-lactamase I). *FEBS Lett. 400*, 155−157.

(11) Rudolf, B., and Zakrzewski,J. (1994) (η^5−Cyclopentadienyl) $Fe(CO)_2$-complex of maleimide anion: An organometallic carbonyl probe for biomolecules containing HS groups. *Tetrahedron Lett. 35*, 9611−9612.

(12) Rudolf, B., Zakrzewski, J., Salmain, M., and Jaouen, G. (1998) Metallo-carbonyl complexes based on the CpFe$(CO)_2$-(η^1-N− imidato) system as protein labelling reagents: reactivity and selectivity studies using bovine serum albumin as a model protein. *New J. Chem.* 813−818.

(13) Salmain, M., Jaouen G., Rudolf, B., and Zakrzewski, J. (1999) Inhibition and photo-deinhibition of glutathione *S*-transferase activity by an organometallic complex: *S*-[3-CpFe$(CO)_2$(η^1-*N*-succinimidato]glutathione. *J. Organomet. Chem. 589*, 98−102.

(14) (a) Salmain, M., Fischer-Durand, N., Cavalier, L., Rudolf, B., Zakrzewski, J., and Jaouen, G. (2002) Transition metal−carbonyl labeling of biotin and avidin for use in solid-phase Carbonyl Metallo Immunoassay (CMIA). *Bioconjugate Chem. 18*, 693−698. (b) Rudolf, B., Zakrzewski, J., Celichowski, G., Salmain, M., Vessières, A., and Jaouen, G. (2004) (b) Specific binding of a biotinylated, metallocarbonyl-labelled dendrimer to immobilised avidin detected by Diffuse Reflectance Infrared Fourier Transform (DRIFT) spectroscopy. *Appl. Organomet. Chem. 18*, 105−110. (c) Fischer-Durand, N., Salmain, M., Rudolf, B., Vessières, A., Zakrzewski, J., and Jaouen. G. (2004) Synthesis of metal carbonyl-dendrimer-antibody immunoconjugates: towards a new format for Carbonyl Metallo ImmunoAssay (CMIA). *ChemBioChem. 5*, 519−525.

(15) (a) Abel, A. E., Singh, W., and Wilkinson, G. (1960) Some π-cyclopentadienyl- molybdenum and -tungsten halides. *J. Chem. Soc.* 1321−1324. (b) Burckett- St. Laurent, J. C. T. R., Field, J. S., Haines, R. J., and McMahon, M. (1978) Halogenation of bis (η-cyclopentadienyltricarbonylmolybdenum and -tungsten) via bridged intermediates- formation of some monocyclopentadienyl derivatives of molybdenum (IV). *J. Organomet. Chem. 153,* C19−C22.

(16) Ellman, G. L. (1958) A colorimetric method for determining low concentrations of mercaptans. *Arch. Biochem. Biophys. 74*, 443−450.

(17) Peters, P. J. (1985) Serum albumin. *Adv. Protein Chem. 37*, 161−245.

(18) (a) Alway, D. G., and Barnett, K. W. (1978) Photochemical processes in cyclopentadienylmetal carbonyl complexes. *Adv. Chem. Ser. 168*, 115−131. (b) Alway, D. G., Barnett, K. W. (1975) Photochemical isomerization of cyclopentadienylmetal complexes. *J. Organomet. Chem. 99*, C52−C54. (c) Alway, D.

G., and Barnett, K. W. (1980) Photochemistry of cyclopentadienylmolybdenum and cyclopentadienyltungsten carbonyl halide complexes. *Inorg. Chem. 19*, 1533−1543. (d) Pan, X., Philbin, C. E., Castellani, M. P., and Tyler, D. R. (1988) Photochemistry of organometallic halide complexes. Mechanism for the formation of ionic products. *Inorg. Chem. 27*, 671−676.

(19) Adams, H., Bailey, N. A., Briggs, T. N., McCleverty, J. A., Colquhoun, H. M., and Williams, D. J. (1986) Transition-metal complexes with terminal and bridging imidato (1−) ligands. X-ray crystal structures of *trans*-[Ir(CO)($NCOC_2F_4$-CO)(PPh_3)$_2$] and [{Pd(o-C_5H_4CHNPh)(m-$NCOC_2H_4CO$)}$_2$]·CH_2Cl_2, spectroscopic studies on [$Mn(CO)_5(NCOC_2H_4CO)$] and the nature of the metal-nitrogen bond. *J. Chem. Soc., Dalton Trans*. 813−821.

(20) Bueno, C., and Churchill, M. R. (1981) Structural studies on some (η^5-C_5H_5)M$(CO)_3$X molecules: (η^5-C_5H_5)W$(CO)_3$Cl, (η^5-C_5H_5)Mo$(CO)_3$Cl and (η^5-C_5H_5)Mo$(CO)_3$HgCl. *Inorg. Chem. 20*, 2197−2202.

(21) Allen, F. H., Baalham, C. A., Lommerse, J. P. M., and Raithby, P. R. (1998) Carbonyl-carbonyl interaction can be competitive with hydrogen bond. *Acta Crystallogr. B54*, 320−329.

BC050073D

Monoclonal Antibody-Based Quantitation of Poly(ethylene glycol)-Derivatized Proteins, Liposomes, and Nanoparticles

Tian-Lu Cheng,[†,#,*] Chiu-Min Cheng,[‡,#] Bing-Mae Chen,[§] Der-An Tsao,[⊥] Kuo-Hsiang Chuang,[†] Sheng-Wen Hsiao,[‡] Yi-Hung Lin,[∥] and Steve R. Roffler[§,*]

Faculty of Biomedical Science and Environmental Biology, MedicoGenomic Research Center, Kaohsiung Medical University, Kaohsiung, Taiwan; Institute of Medicine, Kaohsiung Medical University, Kaohsiung, Taiwan; Institute of Biomedical Sciences, Academia Sinica, Taipei, Taiwan; Department of Medical Technology, Fooyin University, Kaohsiung, Taiwan; and R&D Planning Division Office of Strategy and R&D Planning, Industrial Technology Research Institute, Hsin Chu, Taiwan. Received May 4, 2005; Revised Manuscript Received June 16, 2005

Covalent attachment of poly(ethylene glycol) (PEG) molecules to drugs, proteins, and liposomes is a proven technology for improving their bioavailability, safety, and efficacy. Qualitative and quantitative analysis of PEG-derivatized molecules is important for both drug development and clinical applications. We previously reported the development of a monoclonal IgM antibody (AGP3) to PEG. We now describe a new IgG_1 monoclonal antibody (E11) to PEG and show that it can be used in combination with AGP3 to detect and quantify PEG-derivatized molecules. Both antibodies bound the repeating subunits of the PEG backbone and could detect free PEG and PEG-modified proteins by ELISA, immunoblotting, and flow cytometry. Detection sensitivity increased with the length and the number of PEG chains on pegylated molecules. Both antibodies also efficiently accelerated the clearance of a PEG-modified enzyme in vivo. A sandwich ELISA in which E11/AGP3 were employed as the capture/detection antibodies was developed to detect PEG-modified proteins at concentrations as low as 1.2 ng/mL. In addition, the ELISA could also quantify, in the presence of 10% fetal bovine serum, free methoxy-$PEG_{20,000}$, $PEG_{2,000}$-quantum dots, and $PEG_{2,000}$-liposomes at concentrations as low as 20 ng/mL (1.0 nM), 1.4 ng/mL (3.1 pM), and 2.4 ng/mL (3.13 nM phospholipids), respectively. Finally, we show that the sandwich ELISA could accurately measured the in vivo half-life of a PEG-modified enzyme. These antibodies should be generally applicable to the qualitative and quantitative analysis of all PEG-derivatized molecules.

INTRODUCTION

PEG[1] is a water-soluble, nontoxic, nonantigenic, biocompatible polymer that has been approved by the Food and Drug Administration (FDA) for human intravenous, oral, and dermal applications (*1*). Attachment of PEG chains to proteins can reduce their immunogenicity (*2*, *3*), minimize proteolytic cleavage (*4*, *5*), and increase their serum half-life (*6*, *7*). PEG-interferon α (*8*, *9*), PEG-filgrastim (*10*, *11*), and PEG-visomant (*12*) have been approved for clinical use by the FDA. PEG-modified liposomes are being developed for controlled-release and selective-delivery of drugs (*13*) and genes (*14*). PEG has also been attached to small molecules such as camptothecin (CPT) to produce greater tumor accumulation as compared to unmodified CPT (*15*). PEG-derivatization of superparamagnetic iron oxide (*16*) and quantum dots (*17*, *18*) can improve their biocompatibility and reduce receptor-mediated uptake by the reticuloendothelial system. It is anticipated that PEG will be increasingly employed to improve the properties of therapeutic agents as more proteins, macromolecular drugs, and imaging agents enter clinical trials.

Clinical development of PEG-modified molecules requires measurement of pharmacokinetic parameters in animals and patients. Ideally, the concentration of intact PEG-modified molecules should be measured in vivo. Until recently, however, simple and sensitive methods to measure intact PEG−protein conjugates were unavailable. We helped alleviate this problem by developing a monoclonal IgM antibody (AGP3) with specificity for PEG (*19*). AGP3 can be employed to measure PEG-modified protein by ELISA (*20*). We now report the development of a new monoclonal IgG antibody (E11) that specifically binds to PEG. We compare AGP3 and E11 for the detection of free PEG and PEG-modified proteins in immunoblots, ELISA, and flow cytometry. Because the specificity of two-step targeting strategies depends on the efficient clearance of the first-step targeting agent from the circulation (*21*), we also investigated the effectiveness of AGP3 and E11 for the in vivo clearance of PEG−enzyme conjugates. Finally, a sandwich ELISA using E11

* Corresponding authors: Dr. Steve R. Roffler, telephone +886-2-2652-3079; fax +886-2-2782-9142; e-mail: sroff@ibms.sinica.edu.tw; Dr. Tian-Lu Cheng, telephone +886-7-3121101-2697, fax +886-7-3227508, e-mail: tlcheng@kmu.edu.tw.

† MedicoGenomic Research Center, Kaohsiung Medical University.

‡ Institute of Medicine, Kaohsiung Medical University.

§ Academia Sinica.

⊥ Fooyin University.

∥ Industrial Technology Research Institute.

# Equal contribution.

[1] Abbreviations: PEG, poly(ethylene glycol); ELISA, enzyme-linked immunosorbent assay; FBS, fetal bovine serum; βG, *Escherichia coli* β-glucuronidase; DNS, dansyl (5-(dimethylamino)-1-naphthalenesulfononic acid), DNS scFv, anti-dansyl single chain antibody; DNS−PEG, PEG modified with a dansyl moiety; PBS-T, phosphate-buffered saline containing 0.05% Tween-20; HRP, horseradish peroxidase.

10.1021/bc050133f CCC: $30.25 © 2005 American Chemical Society
Published on Web 08/20/2005

as the capture antibody and AGP3 as the detection antibody was examined for the quantitation of free methoxy PEG, PEG−enzymes, PEG−quantum dots, and PEG−liposomes.

EXPERIMENTAL PROCEDURES

Reagents. Recombinant *E. coli*-derived β-glucuronidase (βG) was produced as described (*6*). Methoxy-PEG_{750}-NH_2 (750 Da) was obtained from Fluka Chemie (Buchs, Switzerland). PEG_{3400}-disuccinimidyl succinamide (3400 Da) and methoxy-PEG succinimidyl propionate (2000, 5000, and 20 000 Da) were purchased from Nektar Therapeutics (Birmingham, AL). Methoxy-PEG_{5000}-NH_2 (5000 Da), NH_2-PEG_{3400}-NH_2 (3400 kDa), methoxy-PEG_{2000}-OH (2000 Da), NH_2-PEG_{1500}-NH_2 (1500 Da), dansyl choride, dansylcadaverine, fluorescamine, and *p*-nitrophenyl-β-D-glucuronide were purchased from Sigma-Aldrich Chemical Co. (St. Louis, MO). Amino-PEG_{2000}-qdot nanoparticles (10∼20 nm, 440 kDa) were purchased from Quantum Dot Corporation (Hayward, CA). $PEG_{2,000}$-liposomes were composed of hydrogenated soy phosphatidylcholine, cholesterol, and poly(ethylene glycol)-distearoylphosphatidylethanolamine with a mean size of 107 nm (polydispersity = 0.097) as described (*22*). Sephacryl S-200 HR gel was from Amersham Pharmacia Biotech Asia Pacific Ltd. (Taiwan). Specific pathogen-free BALB/c mice were obtained from the National Laboratory Animal Center, Taipei, Taiwan.

Antibodies and Cells. 1E8 (IgG_1 mAb against βG) and AGP3 (IgM mAb against PEG) have been described (*19*). Horseradish peroxidase (HRP)-conjugated goat anti-mouse IgM μ-chain antibody and HRP-conjugated goat anti-mouse IgG Fc were from Jackson ImmunoResearch Laboratories (Westgrove, PA). B16/DNS melanoma cells that stably express a functional anti-dansyl single-chain antibody (DNS scFv) on their surface have been described (*23*). To generate mAb E11 (IgG_1 mAb against PEG), female BALB/c mice were first iv injected with 200 μg of RH1−βG−PEG, a conjugate formed between a murine antibody and PEG-derivatized βG (*19*). The mice were ip injected with 100 μg RH1−βG−PEG one week later and then sc injected at weekly intervals with 50 μg of βG−PEG in complete Freund's adjuvant, 30 μg of βG−PEG in incomplete adjuvant, 30 μg of BSA−PEG in incomplete adjuvant, and 10 μg of BSA−PEG in incomplete adjuvant. Three days before fusion with FO myeloma cells, the mice were ip injected with 30 μg of BSA−PEG in PBS. Subsequent steps were the same as employed to generate AGP3 (*19*).

Synthesis of DNS−PEG Derivatives. NH_2-PEG_{1500}-NH_2 and NH_2-PEG_{3400}-NH_2 were reacted with dansyl chloride at a molar ratio of 5:1 in dichloromethane containing 0.1% triethylamine at room temperature for 1 h. The reaction mixture was separated on silica gel with dichloromethane-methanol (8:2 vol:vol) to produce DNS−PEG_{1500}-NH_2 and DNS−PEG_{3400}-NH_2. The presence of the dansyl group was verified by UV detection whereas primary amine groups were detected by reaction with nihydrin/2% solution (Sigma). PEG_{3400}-disuccinimidyl succinamide was reacted with dansylcadaverine at a molar ratio of 2:1 in dry dichloromethane containing 0.1% triethylamine at room temperature for 1 h. The resulting DNS−PEG_{3400}-succinimidyl succinamide (DNS−PEG_{3400}−SSA) was detected under UV illumination, eluted from silica gel with dichloromethane-methanol (9:1 vol:vol) and then immediately reacted with βG.

PEG Modification of βG. βG was passed through a Sephadex G-25 column equilibrated with 0.1 M $NaHCO_3$, pH 8.0, and then concentrated by ultrafiltration to 2 mg/mL. DNS−PEG_{3400}−SSA (4 mg per mg βG) was added for 2 h at room temperature. One-tenth volume of a saturated solution of glycine (pH 8.0) was added to stop the reaction. Unreacted PEG was removed by gel filtration on a Sephacryl S-200 HR column. Protein concentrations were determined by the bicinchoninic acid assay (Pierce, Rockford, IL) with bovine serum albumin used as the reference protein. The number of PEG molecules introduced in βG was estimated by measuring amine groups before and after PEG modification with fluorescamine (*23*). An average of 3.5 DNS_{3400}−PEG chains was attached to each 70-kDa subunit of the βG tetramer to form a 3.5DNS−PEG_{3400}−βG conjugate. Methoxypoly(ethylene glycol) succinimidyl propionate with MW of 20,000, 5000, and 2000 Da was reacted with βG (20 mg per mg βG) as previously described (*20*). An average of 5.1, 7.1, and 11.4 PEG chains were introduced per subunit of the βG tetramer to form 5.1$PEG_{20,000}$−βG, 7.1PEG_{5000}−βG, 11.4PEG_{2000}−βG with retention of 70%, 50%, and 43% of original βG enzymatic activity, respectively.

Immunoblotting of Free PEG and PEG−βG. Samples of βG (5 μg), 3.5DNS−PEG_{3400}−βG (5 μg), NH_2-PEG_{1500}-NH_2 (30 μg), and CH_3-PEG_{2000}-OH (30 μg) were electrophoresed in an 8% sodium-dodecyl sulfate polyacrylamide gel under reducing conditions before overnight transfer to nitrocellulose paper by capillary transfer in blotting buffer (50 mM NaCl, 2 mM EDTA, 0.5 mM 2-mercaptoethanol, 10 mM Tris-HCl, pH 7.5). Blots were blocked for 2 h with 5% skim milk and incubated for 1 h at 37 °C with 1 μg/mL 1E8, AGP3 or E11 in PBS containing 0.05% BSA. The blots were washed 3 times with PBS-T (0.05% Tween 20 in PBS) and twice with PBS before incubation with goat anti-mouse Ig-HRP for 40 min at 37°C. The blots were then washed three times with PBS-T and twice with PBS before specific bands were visualized by ECL detection according to the manufacturer's instructions (Pierce, Rockford, IL).

Antibody ELISA. Maxisorp 96-well microplates (Nalge Nunc International, Roskilde, Denmark) were coated with 10 μg/well CH_3-PEG_{750}-NH_2, NH_2-PEG_{1500}-NH_2, NH_2-PEG_{3400}-NH_2, or 3.5DNS−PEG_{3400}−βG in 0.1 M $NaHCO_3$, pH 8.0, for 3 h at 37 °C and then blocked with 2% skim milk. Graded concentrations of AGP3 and E11 were added to the plates at 37 °C for 1 h. The plates were washed three times with PBS-T and two times with PBS and then stained with HRP-labeled goat anti-mouse IgM μ chain (2 μg/mL) or HRP-labeled goat anti-mouse IgG Fc (2 μg/mL) for 1 h at 37 °C, respectively. The plates were washed and bound peroxidase activity was measured by adding 100 μL/well ABTS solution (0.4 mg/mL 2,2′-azino-di(3-ethylbenzthiazoline-6-sulfonic acid), 0.003% H_2O_2, 100 mM phosphate-citrate, pH 4.0) for 30 min at room temperature. Absorbance (405 nm) of wells was measured in a microplate reader (Molecular Device, Menlo Park, CA). Binding of CH_3-PEG_{750}-NH_2, NH_2-PEG_{1500}-NH_2, NH_2-PEG_{3400}-NH_2, and 3.5DNS−PEG_{3400}−βG to the microtiter plates was determined by assaying for the presence of amine groups with fluorescamine (*24*).

Flow Cytometer Analysis. B16/DNS cells (5×10^5) were incubated with 200 μL of DNS−PEG_{1500}-NH_2 (10 μg/mL), DNS−PEG_{3400}-NH_2 (10 μg/mL), 3.5DNS−PEG_{3400}−βG (10 μg/mL), or PBS at 4 °C for 1 h. The cells were washed twice with cold PBS and sequentially stained with AGP3 (5 μg/mL) and FITC-labeled goat anti-mouse IgM μ chain (5 μg/mL) or E11 (5 μg/mL) and FITC-labeled goat anti-mouse IgG Fc (5 μg/mL). The surface immun-

ofluorescence of 10 000 viable cells was measured with a flow cytometry (Beckman-Coulter, Miami, FL).

Clearance of PEG−*β*G Conjugates. Groups of 3 BALB/c mice were iv injected with100 μg of 5.1PEG$_{20,000}$−βG, 7.1PEG$_{5000}$−βG, or 11.4PEG$_{2000}$−βG at time zero. Blood samples (30 μL) were taken at 0.5, 3.5, and 9 h before iv injection of PBS, 150 μg of E11, or 180 μg of AGP3 at 9 h. Additional blood samples were taken at subsequent times (11, 14, and 28 h), and the serum concentration of βG−PEG was measured by a βG enzyme microassay as described (*19*). Sample concentrations were calculated by comparison of absorbance values with a standard curve constructed from known concentrations of 5.1PEG$_{20000}$−βG, 7.1PEG$_{5000}$−βG, and 11.4PEG$_{2000}$−βG. For meaningful comparison of clearance results, the measured concentrations of PEG−βG conjugates in mice injected with clearing antibodies were normalized to the mean concentration of PEG−βG conjugates in control (uncleared) mice just before clearance as previously described (*19*).

Sandwich ELISA. Maxisorp 96-well microplates were coated with 50 μL/well of E11 (20 μg/mL) or AGP3 (20 μg/mL) in 0.1 M $NaHCO_3$, pH 8.0, for 3 h at 37 °C. The plates were blocked with 2% skim milk in PBS overnight and then washed twice with PBS before graded concentrations of 3.5DNS−PEG$_{3400}$−βG, methoxy-PEG$_{20000}$ succinimidyl propionate (inactivated with 0.1 M Tris, pH 8.0), and PEG$_{2000}$-quantum dots or PEG$_{2000}$-liposomes in PBS containing 10% FBS were added for 1 h at 37 °C. The plates were washed three times with PBS-T and twice with PBS and were then sequentially stained with 50 μL/well AGP3 (20 μg/mL) and HRP-labeled goat anti-mouse IgM μ chain (5 μg/mL) or E11 (20 μg/mL) and HRP-labeled goat anti-mouse IgG Fc (5 μg/mL). The plates were washed and 100 μL/well ABTS substrate was added for 30 min at room temperature. The absorbance (405 nm) of the wells was measured in a microplate reader.

Determination of 3.5DNS−PEG$_{3400}$−*β*G Pharmacokinetics. BALB/c mice were iv injected with 150 μg of 3.5DNS−PEG$_{3400}$−βG and serum was isolated from blood samples (30 μL) that were periodically removed from the tail vein of the mice (0.17, 1.5, 4, 7, 11, 24, and 48 h). The concentration of 3.5DNS−PEG$_{3400}$−βG was measured by the new sandwich ELISA and by a βG enzyme microassay (*19*). βG concentrations were calculated by comparison of absorbance values with a standard curve constructed from known concentrations of 3.5DNS−PEG$_{3400}$−βG.

Data Analysis. Statistical significance of differences between mean values was estimated with Excel (Microsoft, Redmond, WA) using the independent *t*-test for unequal variances.

RESULTS

Detection of Free PEG and PEG-Modified Molecules. The specificity of the anti-PEG antibodies AGP3 and E11 was first examined in immunoblots. Figure 1a shows that the anti-βG antibody 1E8 detected βG and 3.5DNS−PEG$_{3400}$−βG, but not free NH_2-PEG$_{1500}$-NH_2 or CH_3-PEG$_{2000}$-OH. AGP3 and E11, in contrast, did not bind βG but detected 3.5DNS−PEG$_{3400}$−βG as well as free NH_2-PEG$_{1500}$-NH_2 and CH_3-PEG$_{2000}$-OH (Figures 1b and 1c). The ability of AGP3 and E11 to bind both NH_2-PEG$_{1500}$-NH_2 and CH_3-PEG$_{2000}$-OH demonstrates that these antibodies bind to the repeating OCH_2CH_2 backbone of PEG rather than to terminal CH_3, NH_2, or OH groups.

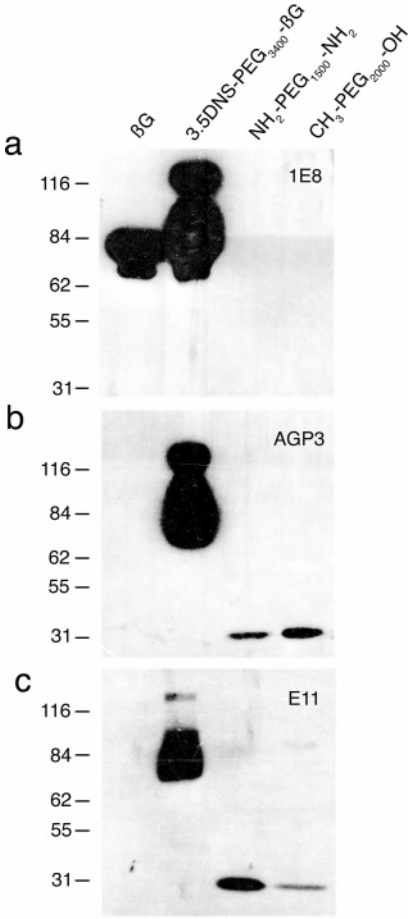

Figure 1. Immunoblot of free PEG and a PEG-modified enzyme. Samples were electrophoresed on a 8% reduced SDS polyacrylamide gel, transferred to nitrocellulose paper, and probed with mAb 1E8 (a), AGP3 (b) or E11 (c) as described in Experimental Procedures. Lane 1, βG; lane 2, 3.5DNS−PEG$_{3400}$−βG; lane 3, NH_2-PEG$_{1500}$-NH_2; lane 4, CH_3-PEG$_{2000}$-OH. kDa, molecular mass in thousands.

The binding of AGP3 and E11 to different lengths of free PEG (MW 750, 1500, 3400, and 5000 Da) was examined by first coating NH_2-PEG in the wells of microtiter plates and then performing ELISA. Coating of NH_2-PEG in the wells was verified by detecting the presence of the amine groups of NH_2-PEG with fluorescamine. Figure 2a shows that NH_2-PEG and 3.5DNS−PEG$_{3400}$−βG were successfully coated in the wells as demonstrated by increased fluorescence as compared with uncoated wells. Measurement of AGP3 (Figure 2b) and E11 (Figure 2c) binding to NH_2-PEG revealed that both antibodies bound NH_2-PEG$_{1500}$-NH_2, NH_2-PEG$_{3400}$-NH_2, and CH_3-PEG$_{5000}$-NH_2 but not CH_3-PEG$_{750}$-NH_2. Furthermore, the assay sensitivity was proportional to the length of the PEG chains, especially for E11. These results suggest that the binding epitope of both antibodies consists of at least 16 OCH_2CH_2 subunits (the number of subunits in PEG$_{750}$).

Adsorption of PEG chains to the plastic surface of microtiter plates could affect antibody binding. We therefore employed flow cytometry to measure AGP3 and E11 binding to PEG attached to the surface of mammalian cells. This was accomplished by introducing a dansyl moiety to the terminus of PEG to create DNS−PEG$_{1500}$-NH_2, DNS−PEG$_{3400}$-NH_2, and 3.5DNS−PEG$_{3400}$−βG. These conjugates were allowed to specifically bind to DNS scFv present on the surface B16/DNS cells. The cells were then sequentially stained with AGP3 and

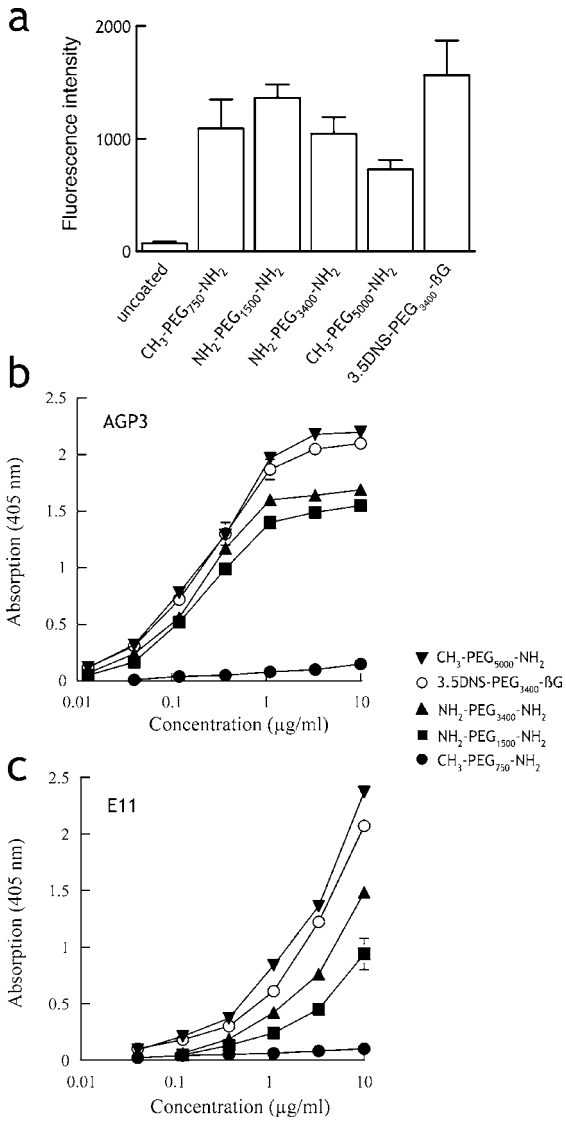

Figure 2. Qualitative analysis of PEG-derivatized molecules. (a) Coating of PEG and PEG-modified βG in microplates was confirmed by measuring the fluorescence intensity ($n = 3$) after reaction of amine groups with fluorescamine. Bars, SD. The binding of AGP3 (b) and E11 (c) to PEG and PEG-modified βG coated in microplates was detected by ELISA as described in the Experimental Procedures. The mean absorbance values (405 nm) of triplicate determinations are shown. Bars, SD.

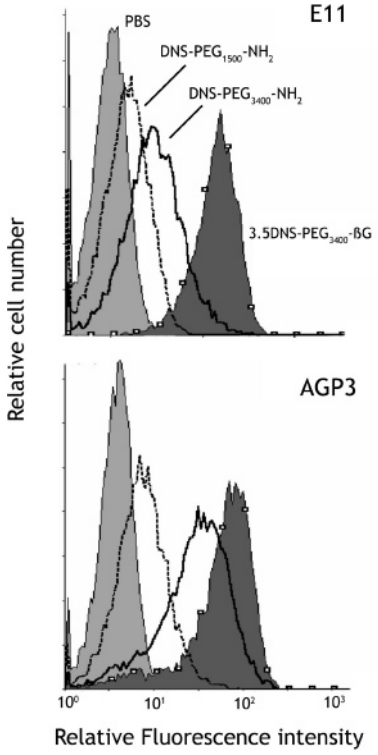

Figure 3. Flow cytometry analysis of PEG-derivatized molecules. B16/DNS cells were treated with PBS, DNS−PEG_{1500}-NH_2, DNS−PEG_{3400}-NH_2 or 3.5DNS−PEG_{3400}−βG at 4 °C for 1 h. The cells were washed and sequentially stained with E11 and FITC-labeled goat anti-mouse IgG Fc (upper panel) or AGP3 and FITC-labeled goat anti-mouse IgM μ chain (lower panel). The surface immunofluorescence of 10,000 viable cells was measured with a FACScaliber flow cytometer.

FITC-labeled goat anti-mouse IgM μ chain or E11 and FITC-labeled goat anti-mouse IgG Fc. Figure 3 shows that AGP3 and E11 could detect DNS−PEG_{1500}-NH_2, DNS−PEG_{3400}-NH_2, and 3.5DNS−PEG_{3400}−βG on B16/DNS cells. Consistent with the ELISA results, longer PEG chains resulted in increased sensitivity of the assay.

In Vivo Clearance of PEG−βG. To investigate the ability of AGP3 and E11 to clear PEG-modified proteins from the circulation, BALB/c mice were iv injected with 100 μg of 11.4PEG_{2000}−βG, 7.1PEG_{5000}−βG, or 5.1PEG_{20000}−βG, followed 9 h later by iv injection of AGP3 or E11 (2 nmoles of antigen-binding sites). Figure 4 shows that both AGP3 and E11 accelerated the clearance of PEG−βG conjugates from the circulation. E11 cleared significantly more PEG−βG conjugate than did AGP3. E11 was particularly effective at clearing βG modified with long-chained PEG; the serum concentration of 5.1$PEG_{20,000}$−βG was reduced by 200-fold in 2 h and 580-fold within 19 h after E11 administration as compared to control mice. These results suggest that AGP3 and E11 may be useful for accelerating the clearance of PEG-modified proteins in vivo.

Quantitative Sandwich ELISA. A sandwich ELISA was developed in which E11/AGP3 or AGP3/E11 was used for the capture/detection antibodies to measure free PEG and PEG-modified substances. Figure 5a shows that the assay sensitivity was about 4-fold greater when using E11 for capture and AGP3 for detection of 3.5DNS−PEG_{3400}−βG as compared with the opposite format. This assay could detect 3.5DNS−PEG_{3400}−βG at concentrations as low as 1.2 ng/mL (14.5 pM). In addition, the sandwich ELISA assay could also detect free methoxy-PEG_{20000}, PEG_{2000}-quantum dots, and PEG_{2000}-liposomes at concentrations as low as 20 ng/mL (1.0 nM), 1.4 ng/mL (3.1 pM) and 2.4 ng/mL (3.13 nM phospholipids), respectively (Figure 5b). The presence of 10% bovine serum in the samples did not affect assay sensitivity. To determine whether the sandwich ELISA assay could detect PEG-modified proteins in vivo, BALB/c mice were iv injected with 150 μg of 3.5DNS−PEG_{3400}−βG, and serum samples were periodically assayed for the concentration of the conjugate by the new sandwich ELISA or by measuring βG enzyme activity. Figure 5c shows that the measurement of 3.5DNS−PEG_{3400}−βG concentration by the sandwich ELISA and βG enzyme microassay gave similar results with estimated terminal half-lives of 6.3 and 5.5 h, respectively.

DISCUSSION

An increasing number of PEG conjugates are in late stage clinical trials or already approved for human use by the FDA including PEG-Intron for hepatitis C (*25*, *26*), PEG-Neupogen for neutropenia associated with cancer

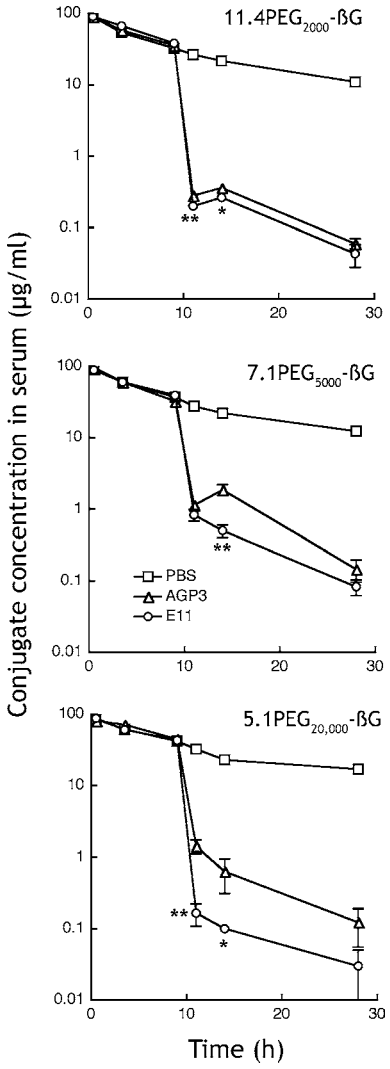

Figure 4. In vivo clearance of PEG−βG conjugates. Groups of 3 BALB/c mice were iv injected with 100 μm 11.4PEG$_{2000}$−βG (upper panel), 7.1PEG$_{5000}$−βG (middle panel) or 5.1PEG$_{20,000}$−βG (lower panel) at time zero. The mice received an iv injection of PBS (□), AGP3 (△) or E11 (○) at 9 h. The concentrations of the βG−PEG conjugates in serum at the indicated times were determined by assaying βG enzymatic activity. Bars, SD. Significant differences between βG−PEG concentrations after E11 and AGP3 treatment are indicated: *, $p \leq 0.05$; **, $p \leq 0.005$.

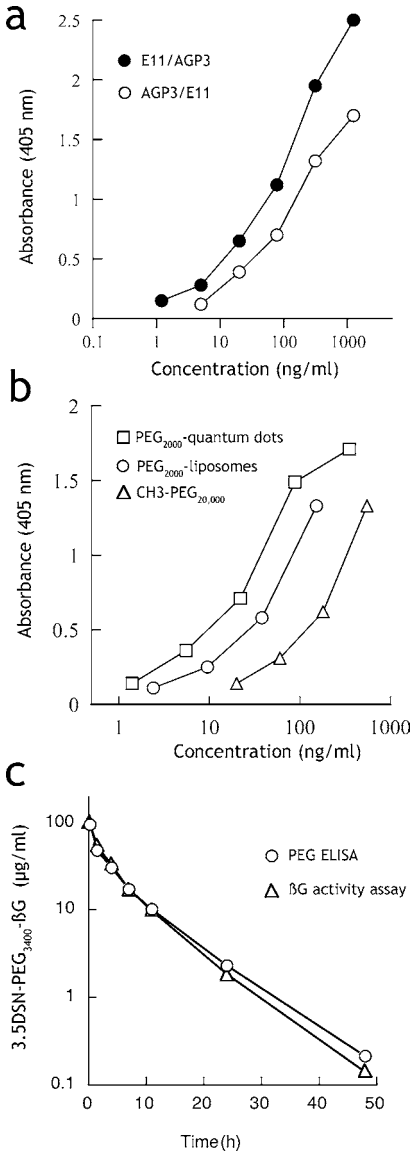

Figure 5. Quantitative analysis of PEG-derivatized molecules by ELISA. (a) Graded concentrations of 3.5DNS−PEG$_{3400}$−βG were assayed with a sandwich ELISA in which E11/AGP3 (●) or AGP3/E11 (○) were used for the capture/detection antibodies, respectively. The mean absorbance values of triplicate determinations are shown. Bars, SE. (b) A sandwich ELISA with E11 and AGP3 employed as the capture and detection antibodies, respectively, was used to measured the concentrations of PEG$_{2000}$-quantum dots (□), PEG$_{2000}$-liposomes (○) or free methoxy-PEG$_{20,000}$ (△) in PBS containing 10% serum. (c) Groups of three mice were iv injected with 3.5DNS−PEG$_{3400}$−βG at time zero. The concentration of 3.5DNS−PEG$_{3400}$−βG is serum was measured by the E11/AGP3 sandwich ELISA (O) or by the βG enzyme microassay (△). Bars, SD.

chemotherapy (*27*), PEG-Visomant for acromegaly (*28*), and PEG-coated liposomal doxorubicin (Caelyx) for cancer therapy (*29*). The ability to effectively control these diseases and minimize the injection frequency can result in better compliance and improved patient quality of life. For noninvasive imaging, PEG−quantum dots and PEG−superparamagnetic iron oxide have been extensively used in cell and animal biology for cell trafficking studies (*30*, *31*), tumor targeting (*18*, *32*), and diagnostics (*33*, *34*). Qualitative and quantitative analysis of poly(ethylene glycol)-derivatized molecules is important to determine their pharmacodynamic and pharmacokinetic parameters in animals and patients. In this report, we found that AGP3 and E11 recognize the repeating (OCH_2CH_2) subunits of the PEG backbone and could effectively clear PEG−βG from the circulation of mice. Furthermore, we developed a sandwich ELISA for the sensitive quantitation of PEG-modified molecules.

PEG can be linked to biological molecules by terminal group derivatization (*35*). First generation, low molecular weight PEG chains were found to poorly cover the surface of macromolecules and often drastically decreased the biological or pharmacological potency of proteins (*36*−*38*). To solve these problems, high molecular weight PEG can be used to maximize protection with better preservation of the bioactivity of pegylated molecules, allowing improved and prolonged performance (*39*). We found that AGP3 and E11 bind to the PEG backbone so that antibody binding did not depend on the identity of the pegylated molecule. These antibodies could therefore detect pegylated proteins, liposomes, and nanoparticles. The detection sensitivity increased with the length of the PEG chains on pegylated molecules. These results indicate that multiple AGP3 and E11 antibodies can bind to a single PEG chain, allowing amplification of the signal

as PEG chain length increases. These antibodies are therefore particularly suitable for the qualitative and quantitative analysis of high molecular weight PEG-modified molecules.

Given the well-known ability of PEG to decrease the immunogenicity of proteins (*2*, *3*), it is interesting that we have successfully generated two monoclonal antibodies against PEG. Antibodies can theoretically be generated against any molecule if it is first attached to a carrier protein to allow activation of cognate T helper cells. Indeed, antibodies have been generated against polymers such as dextran (*40*) and double-stranded synthetic polyribonucleotide complexes (*41*). PEG-modified proteins have been known to induce anti-PEG antibodies in rabbits (*42*) and repeated injections of rabbits with liposomes containing a PEG derivative of phosphatidyl ethanolamine induced anti-PEG antibodies (*43*). It should be appreciated, however, that we generated a reasonable anti-PEG antibody response in mice only after repeated immunizations with PEG−protein conjugates, indicating the difficulty in inducing a robust immune response against this polymer.

We have previously shown that AGP3 can accelerate the clearance of PEG_{5000}-modified proteins and improve the tumor/blood ratios of antibody−βG−PEG_{5000} conjugates for glucuronide prodrug therapy of cancer (*21*). In the present study, we found that both AGP3 and E11 reduced the serum concentration of $7.1PEG_{5000}$−βG as well as $11.4PEG_{2000}$−βG and $5.1PEG_{20,000}$−βG from the blood. Thus, effective clearance could be achieved for conjugates containing different lengths of PEG chains. AGP3 induced rapid uptake of radiolabeled antibody−βG−PEG conjugates in the liver of mice (*21*). Although in the present study we did not follow the distribution of the conjugates in tissues after clearance with E11, the liver is a likely route of elimination. These results indicate that AGP3 and E11 can be used to clear PEG-modified conjugates from the circulation and control the serum half-life to regulate the bioactivity of PEG-modified molecules in vivo.

Measurement of PEG-modified molecules by ELISA and flow cytometry revealed that AGP3 allowed greater assay sensitivity as compared to E11 (Figures 2 and 3). This is likely due to the higher avidity of AGP3 (10 antigen-binding sites versus 2 for E11) as well as the presence of 5 μ chain domains in AGP3, providing more binding sites for secondary detection antibodies. Increased binding of secondary detection antibodies may also explain why the combination of E11/AGP3 was more sensitive than AGP3/E11 as the capture/detection antibodies in the sandwich ELISA.

The newly developed sandwich ELISA can measure the concentrations of PEG-modified proteins, liposomes, quantum dots, and free PEG. The assay sensitivity ranged from the low nM to low pM level, several orders of magnitude more sensitive than previous methods (*24*, *44*). Assay sensitivity can likely be further increased by employing more sensitive colorimetric or fluorometric substrates (*45*, *46*). The sandwich ELISA did not require prior separation of conjugates from complex mixtures and allowed the detection of PEG−βG in serum samples. These characteristics should simplify measurement of PEG-modified molecules in serum samples for pharmacological and pharmacokinetic studies in vivo.

In summary, AGP3 and E11 bind to the repeating ethylene oxide subunits of PEG and therefore can detect PEG independently of the identity of the pegylated compound or chemistry of the linker. The sensitivity of detection depends on the length of the PEG chains; longer PEG chains result in increased sensitivity. These two antibodies should be generally applicable to quantify a wide-range of PEG-derivatized molecules. The newly developed sandwich ELISA may also be useful to measure PEG-modified molecules in patients for preclinical and clinical studies.

ACKNOWLEDGMENT

We thank the Biomedical Engineering Center, Industrial Technology Research Institute, Hsin Chu, Taiwan for providing $PEG_{2,000}$-liposomes. This work was supported by Academia Sinica, the National Research Program for Genomic Medicine (NRPGM), National Science Council, Taipei, Taiwan (NSC92-3112-B-037-002), and the National Health Research Institutes (NHRI-EX94-9420BI).

LITERATURE CITED

(1) Fu, J., Fiegel, J., Krauland, E., and Hanes, J. (2002) New polymeric carriers for controlled drug delivery following inhalation or injection. *Biomaterials 23*, 4425−33.

(2) Chaffee, S., Mary, A., Stiehm, E. R., Girault, D., Fischer, A., and Hershfield, M. S. (1992) IgG antibody response to polyethylene glycol-modified adenosine deaminase in patients with adenosine deaminase deficiency. *J. Clin. Invest 89*, 1643−51.

(3) Yang, Z., Wang, J., Lu, Q., Xu, J., Kobayashi, Y., Takakura, T., Takimoto, A., Yoshioka, T., Lian, C., Chen, C., Zhang, D., Zhang, Y., Li, S., Sun, X., Tan, Y., Yagi, S., Frenkel, E. P., and Hoffman, R. M. (2004) PEGylation confers greatly extended half-life and attenuated immunogenicity to recombinant methioninase in primates. *Cancer Res. 64*, 6673−8.

(4) Brinckerhoff, L. H., Kalashnikov, V. V., Thompson, L. W., Yamshchikov, G. V., Pierce, R. A., Galavotti, H. S., Engelhard, V. H., and Slingluff, C. L., Jr. (1999) Terminal modifications inhibit proteolytic degradation of an immunogenic MART-1(27−35) peptide: implications for peptide vaccines. *Int. J. Cancer 83*, 326−34.

(5) Roseng, L., Tolleshaug, H., and Berg, T. (1992) Uptake, intracellular transport, and degradation of polyethylene glycol-modified asialofetuin in hepatocytes. *J. Biol. Chem. 267*, 22987−93.

(6) Cheng, T. L., Chen, B. M., Chan, L. Y., Wu, P. Y., Chern, J. W., and Roffler, S. R. (1997) Poly(ethylene glycol) modification of beta-glucuronidase-antibody conjugates for solid-tumor therapy by targeted activation of glucuronide prodrugs. *Cancer Immunol. Immunother. 44*, 305−15.

(7) Cantin, A. M., Woods, D. E., Cloutier, D., Dufour, E. K., and Leduc, R. (2002) Polyethylene glycol conjugation at Cys232 prolongs the half-life of alpha1 proteinase inhibitor. *Am. J. Respir. Cell Mol. Biol. 27*, 659−65.

(8) Heathcote, E. J., Shiffman, M. L., Cooksley, W. G., Dusheiko, G. M., Lee, S. S., Balart, L., Reindollar, R., Reddy, R. K., Wright, T. L., Lin, A., Hoffman, J., and De Pamphilis, J. (2000) Peginterferon alfa-2a in patients with chronic hepatitis C and cirrhosis. *N. Engl. J. Med. 343*, 1673−80.

(9) Reddy, K. R., Wright, T. L., Pockros, P. J., Shiffman, M., Everson, G., Reindollar, R., Fried, M. W., Purdum, P. P., 3rd, Jensen, D., Smith, C., Lee, W. M., Boyer, T. D., Lin, A., Pedder, S., and DePamphilis, J. (2001) Efficacy and safety of pegylated (40-kd) interferon alpha-2a compared with interferon alpha-2a in noncirrhotic patients with chronic hepatitis C. *Hepatology 33*, 433−8.

(10) van Der Auwera, P., Platzer, E., Xu, Z. X., Schulz, R., Feugeas, O., Capdeville, R., and Edwards, D. J. (2001) Pharmacodynamics and pharmacokinetics of single doses of subcutaneous pegylated human G-CSF mutant (Ro 25−8315) in healthy volunteers: comparison with single and multiple daily doses of filgrastim. *Am. J. Hematol. 66*, 245−51.

(11) Morstyn, G., Foote, M. A., Walker, T., and Molineux, G. (2001) Filgrastim (r-metHuG-CSF) in the 21st century: SD/01. *Acta Haematol 105*, 151−5.

(12) Goffin, V., and Touraine, P. (2002) Pegvisomant. Pharmacia. *Curr Opin Investig Drugs 3*, 752−7.
(13) Sharpe, M., Easthope, S. E., Keating, G. M., and Lamb, H. M. (2002) Polyethylene glycol-liposomal doxorubicin: a review of its use in the management of solid and haematological malignancies and AIDS-related Kaposi's sarcoma. *Drugs 62*, 2089−126.
(14) Kim, J. K., Choi, S. H., Kim, C. O., Park, J. S., Ahn, W. S., and Kim, C. K. (2003) Enhancement of polyethylene glycol (PEG)-modified cationic liposome-mediated gene deliveries: effects on serum stability and transfection efficiency. *J. Pharm Pharmacol. 55*, 453−60.
(15) Conover, C. D., Greenwald, R. B., Pendri, A., Gilbert, C. W., and Shum, K. L. (1998) Camptothecin delivery systems: enhanced efficacy and tumor accumulation of camptothecin following its conjugation to polyethylene glycol via a glycine linker. *Cancer Chemother Pharmacol. 42*, 407−14.
(16) Zhang, Y., Sun, C., Kohler, N., and Zhang, M. (2004) Self-assembled coatings on individual monodisperse magnetite nanoparticles for efficient intracellular uptake. *Biomed Microdevices 6*, 33−40.
(17) Ballou, B., Lagerholm, B. C., Ernst, L. A., Bruchez, M. P., and Waggoner, A. S. (2004) Noninvasive imaging of quantum dots in mice. *Bioconjug Chem. 15*, 79−86.
(18) Kim, S., Lim, Y. T., Soltesz, E. G., De Grand, A. M., Lee, J., Nakayama, A., Parker, J. A., Mihaljevic, T., Laurence, R. G., Dor, D. M., Cohn, L. H., Bawendi, M. G., and Frangioni, J. V. (2004) Near-infrared fluorescent type II quantum dots for sentinel lymph node mapping. *Nat. Biotechnol. 22*, 93−7.
(19) Cheng, T. L., Wu, P. Y., Wu, M. F., Chern, J. W., and Roffler, S. R. (1999) Accelerated clearance of poly(ethylene glycol)-modified proteins by anti-poly(ethylene glycol) IgM. *Bioconjugate Chem. 10*, 520−8.
(20) Tsai, N. M., Cheng, T. L., and Roffler, S. R. (2001) Sensitive measurement of polyethylene glycol-modified proteins. *Biotechniques 30*, 396−402.
(21) Cheng, T. L., Chen, B. M., Chern, J. W., Wu, M. F., and Roffler, S. R. (2000) Efficient clearance of poly(ethylene glycol)-modified immunoenzyme with anti-PEG monoclonal antibody for prodrug cancer therapy. *Bioconjug Chem 11*, 258−66.
(22) Vaage, J., Mayhew, E., Lasic, D., and Martin, F. (1992) Therapy of primary and metastatic mouse mammary carcinomas with doxorubicin encapsulated in long circulating liposomes. *Int. J. Cancer 51*, 942−8.
(23) Cheng, T. L., Liao, K. W., Tzou, S. C., Cheng, C. M., Chen, B. M., and Roffler, S. R. (2004) Hapten-directed targeting to single-chain antibody receptors. *Cancer Gene Ther. 11*, 380−8.
(24) Stocks, S. J., Jones, A. J., Ramey, C. W., and Brooks, D. E. (1986) A fluorometric assay of the degree of modification of protein primary amines with polyethylene glycol. *Anal. Biochem 154*, 232−4.
(25) Keating, G. M., and Plosker, G. L. (2005) Peginterferon alpha-2a (40KD) Plus Ribavirin: A Review of its Use in the Management of Patients with Chronic Hepatitis C and Persistently 'Normal' ALT Levels. *Drugs 65*, 521−36.
(26) Siebert, U., and Sroczynski, G. (2005) Effectiveness and cost-effectiveness of initial combination therapy with interferon/peginterferon plus ribavirin in patients with chronic hepatitis C in Germany: a health technology assessment commissioned by the German Federal Ministry of Health and Social Security. *Int J Technol Assess Health Care 21*, 55−65.
(27) Yang, B. B., Lum, P. K., Hayashi, M. M., and Roskos, L. K. (2004) Polyethylene glycol modification of filgrastim results in decreased renal clearance of the protein in rats. *J. Pharm Sci. 93*, 1367−73.
(28) Ross, R. J., Leung, K. C., Maamra, M., Bennett, W., Doyle, N., Waters, M. J., and Ho, K. K. (2001) Binding and functional studies with the growth hormone receptor antagonist, B2036−PEG (pegvisomant), reveal effects of pegylation and evidence that it binds to a receptor dimer. *J. Clin. Endocrinol. Metab. 86*, 1716−23.
(29) Hong, R. L., and Tseng, Y. L. (2001) Phase I and pharmacokinetic study of a stable, polyethylene-glycolated liposomal doxorubicin in patients with solid tumors: the relation between pharmacokinetic property and toxicity. *Cancer 91*, 1826−33.
(30) Tkachenko, A. G., Xie, H., Liu, Y., Coleman, D., Ryan, J., Glomm, W. R., Shipton, M. K., Franzen, S., and Feldheim, D. L. (2004) Cellular trajectories of peptide-modified gold particle complexes: comparison of nuclear localization signals and peptide transduction domains. *Bioconjugate Chem 15*, 482−90.
(31) Kircher, M. F., Allport, J. R., Graves, E. E., Love, V., Josephson, L., Lichtman, A. H., and Weissleder, R. (2003) In vivo high-resolution three-dimensional imaging of antigen-specific cytotoxic T-lymphocyte trafficking to tumors. *Cancer Res. 63*, 6838−46.
(32) Gao, X., Cui, Y., Levenson, R. M., Chung, L. W., and Nie, S. (2004) In vivo cancer targeting and imaging with semiconductor quantum dots. *Nat. Biotechnol. 22*, 969−76.
(33) Denis, M. C., Mahmood, U., Benoist, C., Mathis, D., and Weissleder, R. (2004) Imaging inflammation of the pancreatic islets in type 1 diabetes. *Proc. Natl. Acad. Sci. U.S.A. 101*, 12634−9.
(34) Kloepfer, J. A., Mielke, R. E., Wong, M. S., Nealson, K. H., Stucky, G., and Nadeau, J. L. (2003) Quantum dots as strain- and metabolism-specific microbiological labels. *Appl. Environ. Microbiol. 69*, 4205−13.
(35) Li, J., and Kao, W. J. (2003) Synthesis of poly(ethylene glycol) (PEG) derivatives and PEGylated-peptide biopolymer conjugates. *Biomacromolecules 4*, 1055−67.
(36) Veronese, F. M. (2001) Peptide and protein PEGylation: a review of problems and solutions. *Biomaterials 22*, 405−17.
(37) Photos, P. J., Bacakova, L., Discher, B., Bates, F. S., and Discher, D. E. (2003) Polymer vesicles in vivo: correlations with PEG molecular weight. *J Controlled Release 90*, 323−34.
(38) Gref, R., Luck, M., Quellec, P., Marchand, M., Dellacherie, E., Harnisch, S., Blunk, T., and Muller, R. H. (2000) 'Stealth' corona-core nanoparticles surface modified by polyethylene glycol (PEG): influences of the corona (PEG chain length and surface density) and of the core composition on phagocytic uptake and plasma protein adsorption. *Colloids Surf. B Biointerfaces 18*, 301−313.
(39) Roberts, M. J., Bentley, M. D., and Harris, J. M. (2002) Chemistry for peptide and protein PEGylation. *Adv. Drug Delivery Rev. 54*, 459−76.
(40) Newman, B. A., and Kabat, E. A. (1985) An immunochemical study of the combining site specificities of C57BL/6J monoclonal antibodies to alpha (1- - - -6)-linked dextran B512. *J. Immunol. 135*, 1220−31.
(41) Nahon-Merlin, E., Michelson, A. M., Lacour, F., and Camus, G. (1980) Immunological recognition of three polynucleotide structures associating adenylic and uridylic acids. *Ann Immunol. (Paris) 131C*, 279−87.
(42) Richter, A. W., and Akerblom, E. (1983) Antibodies against polyethylene glycol produced in animals by immunization with monomethoxy polyethylene glycol modified proteins. *Int. Arch. Allergy Appl. Immunol. 70*, 124−31.
(43) Srroda, K., Rydlewski, J., Langner, M., Kozubek, A., Grzybek, M., and Sikorski, A. F. (2005) Repeated injections of PEG-PE liposomes generate anti-PEG antibodies. *Cell Mol. Biol. Lett. 10*, 37−47.
(44) Habeeb, A. F. (1966) Determination of free amino groups in proteins by trinitrobenzenesulfonic acid. *Anal. Biochem 14*, 328−36.
(45) Porstmann, T., and Kiessig, S. T. (1992) Enzyme immunoassay techniques. An overview. *J. Immunol. Methods 150*, 5−21.
(46) Huang, Z., Olson, N. A., You, W., and Haugland, R. P. (1992) A sensitive competitive ELISA for 2,4-dinitrophenol using 3,6-fluorescein diphosphate as a fluorogenic substrate. *J. Immunol. Methods 149*, 261−6.

BC050133F

Monomolecular Multimodal Fluorescence-Radioisotope Imaging Agents

Zongren Zhang, Kexian Liang, Sharon Bloch, Mikhail Berezin, and Samuel Achilefu*

Department of Radiology, Washington University, St. Louis, Missouri 63110. Received May 5, 2005; Revised Manuscript Received August 8, 2005

Diagnosis of diseases by different imaging methods can provide complementary information about the functional status of diseased tissues or organs. To overcome the current difficulties in coregistering images from different imaging modalities with a high degree of accuracy, we prepared near-infrared (NIR) monomolecular multimodal imaging agents (MOMIAs) consisting of a heptamethine carbocyanine and ^{111}In−DOTA chelate that served as antennae for optical and scintigraphic imaging, respectively. Their spectral properties clearly show that coordination of indium to MOMIA increased the fluorescence intensity of the compounds. The MOMIAs are exceptionally stable in biological media and serum up to 24 h at 37 °C. Biodistribution of the compounds in mice obtained by fluorescence photon and γ-counts demonstrated a similar distribution trend of the molecular probe in different tissues, suggesting that the detected fluorescence and γ-emissions emanated from the same source (MOMIA). At 24 h postinjection, the MOMIAs were excreted by the renal and hepatobiliary systems and the blood level of a representative MOMIA was very low, thereby reducing background noise caused by circulating molecular probes. These findings demonstrate the feasibility of preparing single molecules with the capacity to emit discernible and diagnostic fluorescent and γ-radiations for optical and nuclear imaging of living organisms.

INTRODUCTION

Coregistration of tissue with different imaging modalities can furnish unique and complementary information that improves the accuracy of disease diagnosis and enhances patient management (*1*, *2*). For example, coregistration of tumors with magnetic resonance imaging (MRI) and positron emission tomography provides anatomical and functional information, which can be used to visualize metastatic foci and localize its exact position (*3*). These possibilities have led to the development of multimodal imaging instruments for clinical and preclinical applications.

Optical imaging is an emerging method that can benefit from a multimodal imaging strategy. The method is highly sensitive, with the capability of detecting minute amounts of light emitting materials in heterogeneous mediums (*4*, *5*). In addition, optical imaging also uses low energy radiation in the visible and infrared regions of the electromagnetic spectrum of light to assess biological processes in tissues. The distribution of chromophores within a few micrometers from the light source and detector systems can be localized with high resolution, thereby permitting the differentiation of normal from pathologic tissues (*6*−*8*). However, the ability to detect diagnostic chromophores and the image resolution obtained by optical methods degrade rapidly as the distance between source−detector pair and the target tissue volume progressively increases beyond several centimeters. This poor resolution is caused by the intrinsic absorption and scattering of light by tissue. Therefore, for noninvasive deep tissue imaging, optical methods would benefit from a multimodal strategy that can complement this weakness. Additionally, a multimodal approach that combines optical with one of the established imaging methods could accelerate its acceptance in clinical settings.

Recently, Ntziachristos et al. (*9*) coregistered indocyanine green (ICG)-enhanced optical images of breast cancer patients with DTPA−Gd-enhanced MRI. The results demonstrate that diffuse optical tomography can adequately localize and quantify exogenous optical contrast agents in breast cancers. Typical of most current multimodal imaging procedures, the investigators administered two different contrast agents to patients: a paramagnetic gadolinium DTPA chelate for MRI and ICG for optical imaging. Expectedly, the pharmacokinetics of both probes were very different and the potential toxic effects of each component can be additive. Understandably, a major problem with developing a single molecular entity that can produce detectable signals for each imaging method derives from differences in the sensitivities of each modality. For example, the design of a monomolecular Gd-based MRI−optical monomolecular multimodal imaging agent (MOMIA) must incorporate multiple Gd chelates per dye moiety to compensate for the relatively low sensitivity of the MRI method. Some common strategies employed to compensate for the large differences in local tissue sensitivities of different imaging systems require the use of large biomolecules, polymeric materials, liposomes, micelles, or nanoparticles (*10*−*13*). However, the inherent problems with large molecules, including low diffusion rate into diseased tissue, rapid uptake by the liver, and the potential to elicit adverse immune reactions, limit their utility as contrast agents for in vivo imaging studies (*14*). Recent approaches include the use of smaller molecular constructs to obtain multimodal agents for MRI and optical imaging studies (*15*).

The sensitivities of fluorescence and radionuclear

* To whom correspondence should be addressed. Tel: 314-362-8599. Fax: 314-747-5191. E-mail: achilefus@mir.wustl.edu.

10.1021/bc050136s CCC: $30.25 © 2005 American Chemical Society
Published on Web 08/25/2005

methods are comparable, which enable the incorporation of antennae for both methods into a relatively small molecular mass (<6 kDa) single molecule in a 1:1 signaling ratio. This optical−radionuclear molecular construct would allow the use of a short-lived radioisotope component of the MOMIA to localize diseases in deep tissue without the depth limitation of optical methods. After mapping the region of interest, longitudinal monitoring of the diseased tissue can be conducted by optical methods outside radioactivity restricted areas. Optical imaging in the near-infrared (NIR) region minimizes light attenuation by endogenous chromophores and facilitates deep tissue imaging. Accordingly, we report the synthesis of NIR light emitting dye−DOTA conjugates linked by alkyl or peptidyl units. We further assessed their spectral properties and biodistribution in mice. The fluorescence and γ-counts of the MOMIAs in different tissues were similar and demonstrate the feasibility of developing these molecular constructs for multimodal imaging by tandem optical and radionuclear methods.

MATERIALS AND METHODS

General. All solvents and chemicals were reagent grade and used without further purification. *N,N*-Diisopropylcarbodiimide (DIC) and glutaconaldehyde dianilide monohydrochloride were purchased from Lancaster Synthesis (Windham, NH). Dichloromethane (DCM), *N*,*N*-dimethylformamide (DMF), MeOH, and MeCN were from purchased from Fisher Scientific (Pittsburgh, PA). Fluorenylmethyl amino acids (Fmoc) and trifluoroacetic acid (TFA) were purchased from, respectively, AnaSpec Inc. (San Jose, CA) and Advanced ChemTech (Louisville, KY). Other commercial chemicals were purchased from Sigma-Aldrich (St. Louis, MO). Mass spectral analyses were performed on a Waters ZQ 4000 positive electrospray at a cone voltage of 67 V. All of the compounds including the intermediates and final products were fully identified by mass spectrometry/electrospray ionization high-performance liquid chromatography (MS/ESI HPLC) analyses performed on a Vydac C-18 polymeric reverse phase column (218TP, 5 μm, 300 Å, 4.6 mm × 250 mm) at a flow rate of 1.0 mL/min. Semipreparative HPLC was performed on a Vydac C-18 polymeric reverse phase column (218TP, 10 μm, 300 Å, 22 mm × 250 mm) at 9.5 mL/min. HPLC solvents consist of water containing 0.1% TFA (solvent A) and MeCN containing 0.1% TFA (solvent B). The elution protocol for analytical HPLC started with 90% A for 1 min, followed by a linear gradient to 30% A over 20 min, held at 30% A for 5 min, continued to 10% A for 5 min, and finally returned to 90% A over 2 min. The elution profiles of MOMIAs were monitored by UV absorbance at 254 and 214 nm. Absorbance spectra were measured on a Beckman Coulter DU 640 UV−visible spectrophotometer. Fluorescence spectra were recorded on a Fluorolog-3 spectrofluorometer (Horiba Jobin Yvon, Inc., Edison, NJ). Stock solutions (1.0 mM) of the dye and its conjugates were prepared by dissolving each sample in DMSO. UV−vis and fluorescence measurements were carried out by sequentially adding 0.5−2.0 μL aliquots of the stock solutions via a micropipet into 3 mL of 20% aqueous DMSO solution or other solvents in a quartz cuvette. The mixtures were stirred briefly for equilibration prior to data acquisition.

Synthesis of Cypate (1). Ac_2O (226 μL, 2.4 mmol) in DCM (1 mL) was added slowly to a stirred solution of glutaconic aldehyde dianilide hydrochloride (0.6 g, 2 mmol) and diisopropyl ethylamine (DIEA, 700 μL, 4 mmol) in DCM (4 mL). The solution was added to a warm (50 °C), stirred MeCN (10 mL) solution of NaOAc (0.8 g, 9.5 mmol) and 1-hydroxycarbonylethyl-2,3,3-trimethylbenzoindoleninium bromide (2.0 g, 5.5 mmol), which was prepared as described previously (*16*). The mixture was stirred for 30 min at 50 °C to give noticeable precipitates. Additional precipitates were obtained by adding ether to the reaction mixture. The solid was filtered and washed sequentially with ether, MeCN, ether, and water (1% TFA) to give 1.06 g (85%) of **1** as a red glistening solid. MS/ESI: 625 [M^+].

Synthesis of Tri-*t*-butyl DOTA (2). Benzyl bromoacetate (4.0 g, 17 mmol) in MeCN (80 mL) was added dropwise (3.5 h) to an ice-cooled mixture of K_2CO_3 (6.5 g, 47 mmol) and 1,4,7,10-tetraazacyclododecane tetrahydrochloride (5.0 g, 15.7 mmol) in MeCN (50 mL). The mixture was stirred for 30 min at 0 °C. K_2CO_3 (3.5 g, 25 mmol) was added as a solid, followed by dropwise (1 h) addition of *tert*-butyl bromoacetate (12.3 g, 62.8 mmol) in MeCN (80 mL). The resulting mixture was stirred at 0 °C overnight, and the solid was filtered. After the solid was further washed with MeCN/MeOH, the collected filtrates were combined and acidified with TFA to pH 5. The precipitate obtained after acidification was filtered and concentrated on a rotary evaporator. The solid residue was washed with ether and dried to give 9.3 g of a white powder. HPLC and MS studies indicated that powder consisted of 60% benzyl tri-*tert*-butyl DOTA and 40% tetra-*tert*-butyl DOTA. Because the tetra-*tert*-butyl byproduct is not reactive, the product mixture can be used in subsequent reactions without prior purification. MS/ESI: 663 [$M + H^+$], 701 [$M + K^+$].

Hydrogen was bubbled through a mixture of the solid (3 g) and Pd/C (10 wt %, 300 mg) in THF (180 mL)/MeOH (180 mL) at atmospheric pressure for 15 h. The Pd/C catalyst was removed by filtration, and the solvent was removed on a rotary evaporator to give crude solid product. The solid was further purified by recrystallization in acetone/*t*-BuOMe/hexanes system to give **2** (1.8 g) as a white solid. MS/ESI: 573 [$M + H^+$].

Synthesis of Tri-*t*-butyl DOTA−Hexanediamine−Cypate (4a). A mixture of tri-*tert*-butyl DOTA (349.2 μmol, 200 mg), 2-(1*H*-benzotriazol-1-yl)-1,1,3,3-tetramethyluronium hexafluorophosphate (HBTU, 134 mg, 358 μmol), and *N*-hydroxybenzotriazole (HOBt, 50 mg, 326 μmol) in DMF/DCM (50:50 vol %, 7 mL) was shaken for 5 min. DIEA (92 μL, 523.8 μmol) was then added, and the mixture was shaken again for 10 min. 1,6-Hexanediamine (419.04 μmol, 49 mg) was added as a solid, and the mixture was shaken for 2 h before cypate (327 mg, 523.8 μmol), activated similarly, was added. The resulting mixture was shaken for 4 h. It was neutralized with dilute HCl (0.1 M). DCM was removed on a rotary evaporator, and the concentrated solution was treated with ether to precipitate the product, which was further washed sequentially with water, ether, and ethyl acetate. Pure product was isolated by semipreparative HPLC to give 40 mg of **4a**. MS/ESI: 1277 [M^+].

Synthesis of DOTA−Hexanediamine−Cypate (4). Tri-*tert*-butyl DOTA−hexanediamine−cypate (**4a**, 10.5 mg, 8.2 μmol) in TFA (2 mL) was stirred for 2 h at room temperature. TFA was removed, and the resulting green solid was washed with ether and separated by semipreparative HPLC to give 1.3 mg (1.17 μmol, 15% yield) of **4** as a green solid. MS/ESI: 1109 [M^+].

Synthesis of α−DOTA−Lys(ϵ-Cypate)−OH (5). Fmoc−Lys(Dde)−OH (655 mg, 1.23 mmol) in DCM (5 mL) and DMF (0.2 mL) was cooled by ice bath, and DIC (615 μmol, 96 μL) was added. The mixture was stirred at 0 °C for 20 min. DCM was removed on a rotary evaporator, and the residue was dissolved in DMF (5 mL).

The solution was transferred to a mixture of 4-(dimethylamino)pyridine (2.5 mg, 20.5 μmol) and Wang resin (100−200 mesh, 0.82 mmol/g, 250 mg, 205 μmol) preswelled in DMF. The mixture was shaken for 3 h, followed by filtration and sequential washing with DMF−MeOH−DMF−DCM−DMF. Fmoc was removed with 20% piperidine in DMSO and tri-*tert*-butyl DOTA (352 mg, 615 μmol), activated with HOBt (94 mg, 615 μmol)/HBTU (233 mg, 615 μmol)/DIEA (1.23 mmol. 214 μL), was conjugated to the α-amino group of lysine for 20 h. The Dde group was removed with 2% hydrazine in DMF and cypate (307 mg, 492 μmol) in DMF (2 mL)/DCM (2 mL), preactivated with HBTU (187 mg, 492 μmol) and HOBt (75 mg, 492 μmol), and DIEA (656 μmol, 114 μL) was added to the resin. The mixture was shaken for 5 h, filtered, and washed sequentially with DMF−DCM−DMF−DCM−DMF solvent system. The crude product was cleaved from the resin by shaking in TFA (5 mL) for 3 h. The product was purified by semipreparative HPLC to give 40 mg of the compound as a green solid. MS/ESI: 1139 $[M^+]$.

Synthesis of DOTA−Gly−Ser−Gly−Lys(ε-Cypate)−Ahx[1]−NH_2 (6). The peptides were prepared with ACT APEX 396 peptide synthesizer by standard Fmoc protocol (*17*), as described previously (*18*, *19*). Briefly, starting with a Rink amide resin, the Fmoc−Ahx−OH (75 μmol) was activated with a mixture of the coupling reagents HOBt (75 μmol) and HBTU (75 μmol) in the presence of DIEA (150 μmol). Deprotection of the Fmoc protecting group was accomplished with 20% piperidine in DMF. The tri-*tert*-butyl DOTA (75 μmol) was automatically coupled to the N-terminal amino group. The orthogonal protecting lysine group 2-(4,4-dimethyl-2.6-dioxycyclohexylidene)ethyl (Dde) was selectively removed with 2% hydrazine in DMF before adding the NIR probe, cypate. Simultaneous removal of side chain protecting groups and cleavage of the product from solid support were accomplished with a cleavage mixture of 95% TFA and 5% water. After lyophilization, the crude product was obtained as a green powder and purified by semipreparative HPLC to give **6** (6.5 mg, 18% yield). MS/ESI: 1453 $[MH]^+$, 727 $[M + 2H]^{2+}$.

Synthesis of Nonradioactive ^{115}In−MOMIAs (7 and 8). The labeling of compound **6** to give **8** is typical of the procedure used to successfully label MOMIAs with indium. Two drops of absolute ethanol were added to 2.3 mg (1.5 μmol) of compound **6** to form slurry. To this slurry was added 1 mL of a NaOAc−sodium ascorbate buffer (50 mM of NaOAc and 25 mM of sodium ascorbate). A solution of $InCl_3$ in 0.1 M HCl (1 mL, 1.1 mg, 4.74 μmol) was added to the reaction mixture to obtain a solution of pH 4.9. The solution was heated at 80 °C for 1 h, and the mixture was allowed to cool to room temperature. The solution retained its green color, and the product was purified by semipreparative HPLC using MeCN/H_2O gradient elution protocol (see General section above) to give 1.2 mg (0.77 μmol, 49% yield) of **6**. MS/ESI: 1564 $[M]^+$.

Similarly, compound **7** was prepared by adding $InCl_3$ (18.5 mg, 16 μmol) to a MeCN/water solution of **4** (15 mg, 13 μmol). The mixture was purified by semipreparative HPLC to obtain 2 mg (13%) of **7**. MS/ESI: 1221 $[M]^+$.

Radiolabeling of MOMIAs with ^{111}In (9). $^{111}InCl_3$ was purchased from Mallinckrodt, Inc. Compound **6** was radiolabeled by incubating 5.0 μg of it with 50 μCi of ^{111}In in a 25 mM NaOAc and 12.5 mM sodium ascorbate buffer. The pH was adjusted to 4.9 with 0.1 M HCl to give a total volume of 55 μL. The mixture was heated at 80 °C for 30 min. An equal volume of PBS containing 5% EtOH was added, and the solution was allowed to cool to room temperature. Visual inspection shows that it retained its green coloration after 24 h. Radio-TLC showed that the labeling was successful. An aliquot was placed in a tube and imaged with a Kodak Multistation Imager.

Stability of ^{115}In−DOTA−Gly−Ser−Gly−Lys(ε-Cypate)−Ahx−NH_2 (8). The stability of the representative compound was conducted using HPLC (Waters, Co.) by monitoring the signal intensity at 700 nm from a dual UV-vis absorbance detector. The 700 nm wavelength was chosen to avoid otherwise strong overlapping of signals between the serum and the compound **8** at lower wavelengths. HPLC analyses were conducted using Vydac C-18 polymeric reverse phase column (218TP, 5 μm, 300 Å, 4.6 mm × 100 mm) with water/MeCN−0.1% TFA mobile phase with a gradient from 10 to 95% MeCN in water in 14 min.

Approximately 0.2 mg of the lyophilized complex was dissolved first in 20 μL of DMSO and diluted with 80 μL of water. The solution was split into two vials: 60 μL was added into 940 μL of human serum in a 2 mL vial, and 30 μL was diluted with 470 μL of water (MQ). The vial with serum was capped and placed in an incubator at 37 °C. Aliquots of 60 μL were analyzed without dilution at different time points. The vial without serum was used as a reference standard. In addition, a standard serum solution was prepared by mixing 12 μL of DMSO, 48 μL of water (MQ), and 940 μL of human serum.

Biodistribution of MOMIAs by Fluorescence Method. All in vivo studies were performed in compliance with the Washington University Animal Study Committee's requirements for the care and use of laboratory animals in research. Nude mice were anesthetized with xylazine/ketamine cocktail via intraperitoneal injection. The samples were dissolved in 20% aqueous DMSO, and animals were injected via the lateral tail vein with doses of 0.3 μmol/kg body weight in a volume of 100 μL for each mouse. We used a noninvasive in vivo continuous wave fluorescence imaging apparatus to visualize the distribution and preferential tissue uptake of the MOMIAs.

Light from two laser diodes of nominal wavelength 780 nm and nominal power of 50 mW was launched into a fiber optic bundle. We used two laser diodes to produce as much uniform illumination of the whole animal or organ parts as possible. A defocusing lens in position after the bundle expanded the beam such that the whole mouse was illuminated. A Photometrics CCD camera (16 bit, 1024 × 1024 pixels, back illuminated, thermoelectric Peltier cooled with forced air) was used to capture the emitted photons. An interference filter (830 nm) was mounted in front of the CCD camera input lens such that only emitted fluorescent light from the contrast agent was imaged. Real-time acquisition, display, and data processing software (WinView/32) were used to obtain the optical imaging data.

At 24 h postinjection of the probe, the mice were euthanized and some organ parts were excised and rinsed with water. The tissues were placed under the CCD camera and the fluorescence emission from each organ was measured after excitation with the 780 nm laser sources. Tissue parts, instead of whole organs, were used to minimize problems associated with depth-dependent nonlinear fluorescence emission. A statistical program in the WinView package was used to estimate the mean fluorescence intensity per organ part.

[1] 6-Amino hexanoic acid.

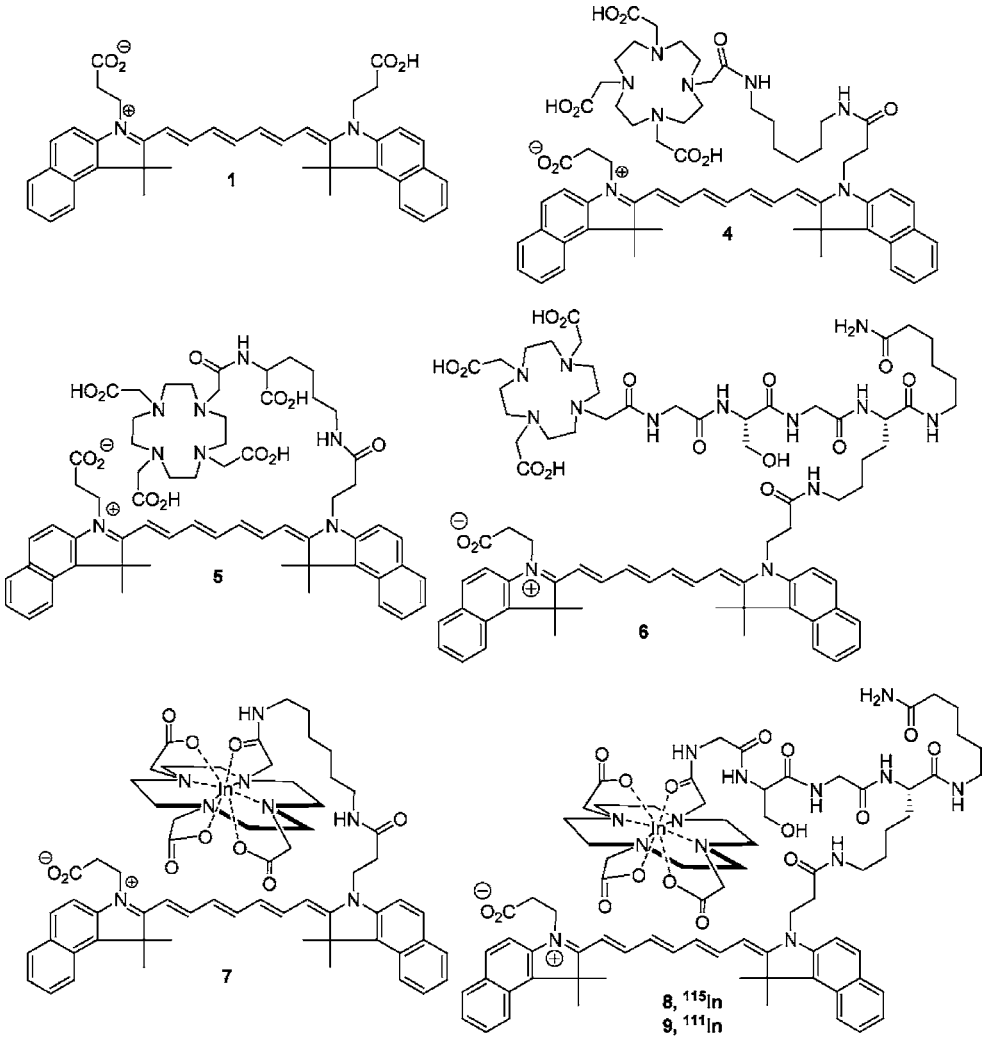

Figure 1. Structures of cypate, DOTA−cypate, and In−DOTA−cypate derivatives.

Scheme 1. Synthesis of DOTA−Ahx−Cypate MOMIA by Solution Method

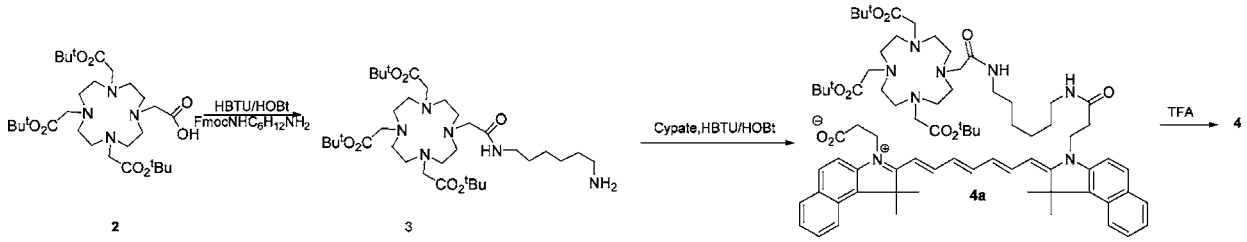

Biodistribution of MOMIAs by γ-Counts Method. The mice were anesthetized as described above and injected with 10 μCi (100 μL) of ^{111}In labeled **9** via the lateral tail vein. Mice were imaged 1, 4, and 24 h postinjection with a Kodak Multistation Imager. At 24 h postinjection, we sacrificed the animals and weighed the organ parts and the activity/g organ was determined with a Packard Cobra II γ-counter.

RESULTS AND DISCUSSION

The primary focus of this study was to develop novel optical−radionuclear MOMIAs that could provide complementary diagnostic information, minimize patient's exposure to ionizing radiation, simplify image reconstruction for optical diffusion tomography, and provide a means to monitor continuously the status of pathologic conditions by optical methods after the decay of a short-lived radioactive component. The use of NIR fluorescent dye for the optical signal allows for deep tissue imaging because absorption of light by tissue in this region is low, thereby allowing NIR light to penetrate several centimeters (*20*, *21*). We used ^{115}In isotope for nonradionuclear related studies to avoid contaminating routine laboratory instruments with radioactivity.

Synthesis. The MOMIAs (Figure 1) were synthesized by either solid phase or solution methods, based on the target compounds prepared.

Synthesis of MOMIAs by Solution Method. The procedure for the synthesis of **4** is summarized in Scheme 1. Both DOTA and cypate possess multiple carboxylic acid groups, and linkage of the two components via amide bonds with a diamino group would result in an intractable mixture of products. To improve reaction selectivity, we first reacted an orthogonally protected tri-*tert*-butyl DOTA (**2**) with a mono-Fmoc−1,6-hexyldiamine, followed by purification of the crude product on a silica gel column.

Scheme 2. Solid Phase Approach to the Synthesis of MOMIAs

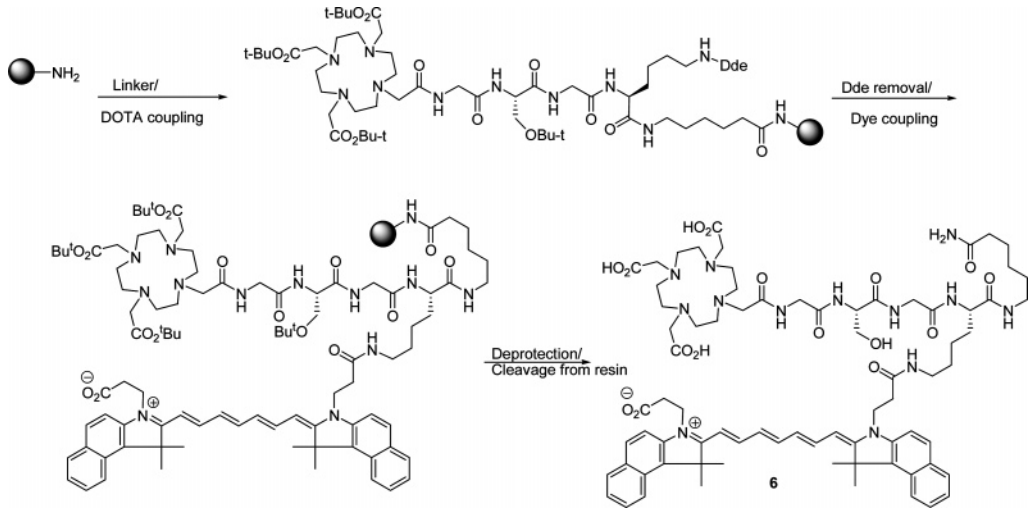

It turned out that the Fmoc derivative was unstable during column purification, and compound **3** was isolated as the major product. This protocol, therefore, results in the direct synthesis of monoamino derivative of tri-*tert*-butyl DOTA. Through a careful control of the reaction conditions, compound **3** reacted with only one of the two carboxylic acid groups of cypate to afford **4a**. Subsequent treatment of **4a** with TFA gave the desired compound **4** in good yield. However, the intermediate Fmoc-protected DOTA−amine was unstable under ambient conditions and its purification was tedious. Consequently, we evaluated the preparation of MOMIAs by solid phase method (*17*, *18*).

Synthesis of MOMIAs by Solid Phase Method. Syntheses of MOMIAs **5** and **6** were conducted on solid support as summarized in Scheme 2 for the synthesis of **6**. The use of orthogonally protected amino acid strategy enabled us to selectively couple DOTA and cypate without interference from each other. Cleavage of the product from resin using TFA and subsequent workup afforded the desired compounds.

Labeling MOMIAs with Indium. The stability of the metal complexes of MOMIAs is a critical criterion for the use of DOTA−cypate conjugates for multimodal imaging. For this reason, we labeled the MOMIAs with both radioactive (^{111}In) and nonradioactive (^{115}In) isotopes. The radiolabeled analogues were used to evaluate the stability of the chelates in buffers and to perform the in vivo imaging studies. We used the nonradioactive chelate to monitor the HPLC stability of MOMIAs in serum by fluorescence assay and the effects of the metal complex on the fluorescence intensity relative to the unlabeled MOMIAs. The compounds were stable under HPLC purification conditions. Interestingly, the chelated and nonchelated MOMIAs had similar retention times when they were coinjected in the column. This suggests that the chelation of MOMIAs with indium has little effect on the hydrophilicity of the compounds. Mass spectral analysis of the purified MOMIA showed that the metal chelation was successful.

Spectral Properties of MOMIAs. An important consideration in designing MOMIAs is to ensure that the fluorescence emission of the compounds is not quenched after metal chelation. Consequently, we compared the spectral properties of the labeled and nonlabeled MOMIAs. The spectra of **6** and its In−DOTA complex **8** are typical of the indium-labeled MOMIAs. Both compounds are soluble in water, making it possible to prepare metal

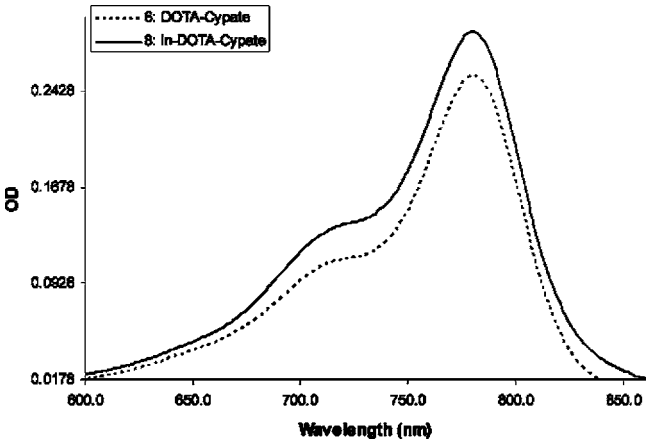

Figure 2. Absorption spectral properties of compounds **6** and **8** in water. The optical density and molar absorptivity of In chelate **8** are higher than those of the nonchelate analogue **6** at 1.8 μM.

complexes and study their spectral properties in aqueous medium. Equimolar concentrations (1.8 μM) of pure (>99% HPLC/MS purity) chelated and nonchelated compounds were prepared in deionized water. The absorption spectra of the compounds are shown in Figure 2. Interestingly, coordination of the metal increased the absorbance of **8** as compared with the nonchelated **6**. This spectral observation was confirmed by analysis of the molar absorptivity of both compounds, which showed a 16% increase in the molar absorptivity of **8** (ϵ 1.67 $\times$ 10^5 M^{-1} cm^{-1}) relative to the nonchelated **6** (ϵ 1.43 $\times$ 10^5 M^{-1} cm^{-1}).

Similarly, we evaluated the fluorescence emission of the compounds at an equimolar concentration of 1.8 μM at 760 and 780 nm excitation wavelengths. The full emission spectra at 760 nm excitation are shown in Figure 3, and the changes in their relative fluorescence intensity at 805 nm emission wavelength are shown in Table 1. This observation is consistent with the established effects of metals on the fluorescence properties of dyes (*22*, *23*). Particularly, this study suggests that radioisotopes of trivalent metals such as indium could play a dual role of providing γ-emissions for radionuclear imaging and augmenting the fluorescent intensity of molecular probes that would increase the sensitivity of detecting their distribution in tissues. Another interesting implication of the observed increase in fluorescence intensity after chelation of indium is that the changes

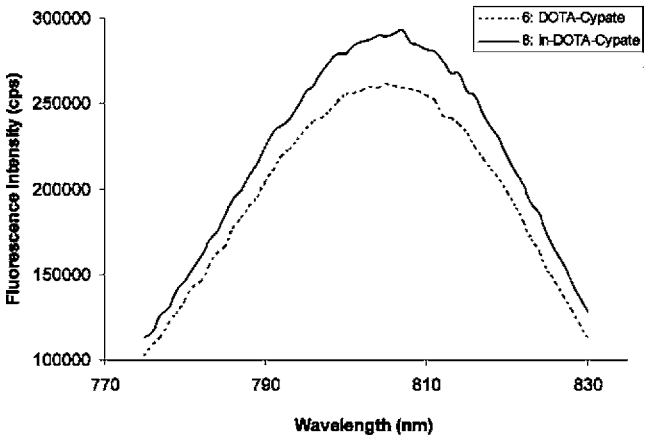

Figure 3. Fluorescence spectra of **6** (DOTA−cypate) and **8** (In−DOTA−cypate complex) in water at 760 nm excitation.

Table 1. Fluorescence Intensities of 6 and 8 at 760 and 780 nm Excitation Monitored at 805 nm Emission

excitation wavelength (nm)	fluorescence intensity of **6** at 805 nm/10^5 (cps)[a]	fluorescence intensity of **8** at 805 nm/10^5 (cps)	increase in fluorescence intensity (%)
760	2.60	2.93	13
780	2.29	2.42	6

[a] cps, photon counts per second.

are wavelength-dependent (Table 1). Conceptually, such wavelength dependency could be used for ratiometric imaging at two or more different wavelengths to increase the specificity of optical imaging methods.

Stability in Biological Media. The stability study of **8** was conducted by monitoring the signals from a dual UV absorbance detector at 254 and 700 nm on an HPLC system. At 254 nm, the signals from serum and **8** (retention time 8.4 min) strongly overlapped with prevailing signals from serum proteins. At 700 nm, the overlap was much weaker and the absorbance from **8** was dominant. Figure 4a,b shows the HPLC spectra of **8** and serum, which were also used as reference standards. Degradation was typically manifested by a gradual increase of one or more peaks as a function of time.

The indium complex showed remarkable hydrolytic stability in human serum. Taken within the first 2.5 h, the chromatograms were practically indistinguishable (Figure 5). Even after 48 h, no significant variations were observed in indium complex signal intensity (Figure 6), although some changes are noticeable between 1 and 6 min of the retention time.

Radio-TLC analyses (for radioactive indium MOMIA) showed that the compounds are stable in buffers up to 4 h postpreparation of the materials. The biodistribution studies did not show uptake of the MOMIAs in bone tissues, which is a useful index of chelate stability in vivo. Therefore, the MOMIAs are stable in serum and biological buffers.

The ability to monitor stability profile of the probes at 700 nm is advantageous because only the NIR probes absorb significantly in this spectral region, thereby eliminating the need to isolate the compounds before analysis. The data are reproducible with high precision because specific volumes from the same sample can be injected and the sample absorbance at the onset of the experiment acts as reference throughout the study.

Biodistribution of MOMIAs in Mice. *Optical Method.* Injection of MOMIAs into the lateral veins of mice and monitoring the distribution of the probe as a function of time showed that at 24 h postinjection, the molecular

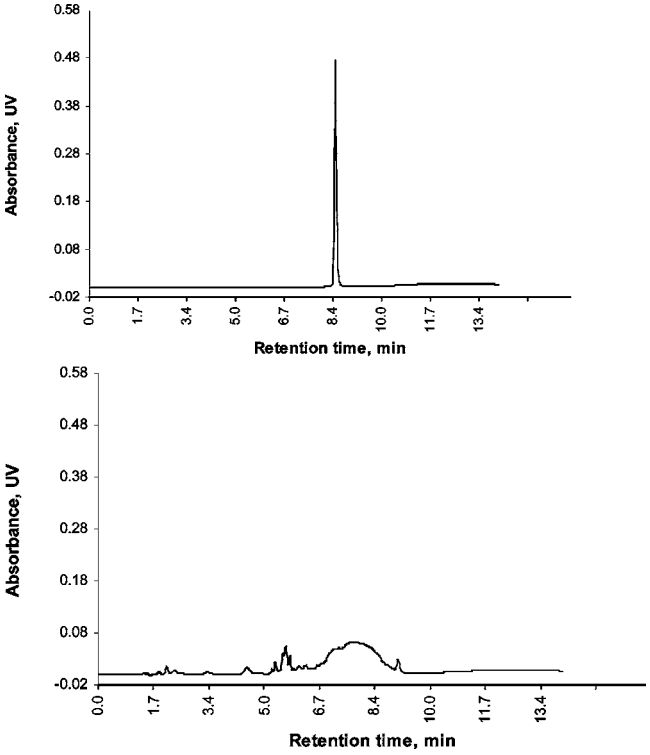

Figure 4. (a) HPLC spectrum of a standard:indium complex in DMSO/water; (b) HPLC spectrum of a standard:human serum with DMSO/water.

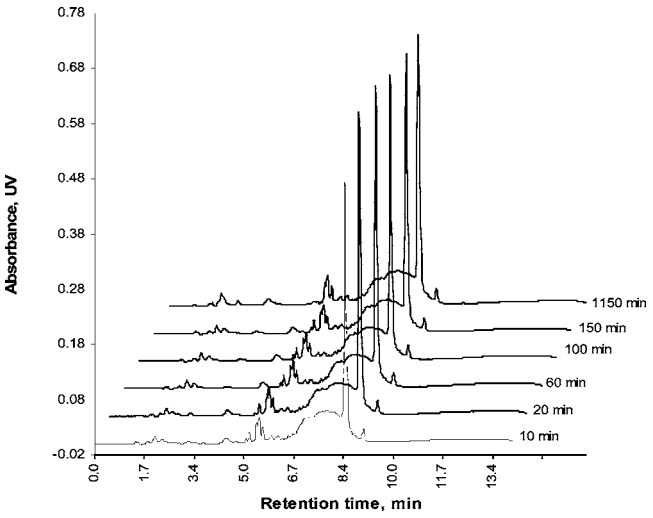

Figure 5. HPLC spectra of indium complex **8** incubating in human serum at 37 °C at different time intervals shows outstanding hydrolytic stability of the complex. Chromatograms were shifted in both *x*- and *y*-axes for clarity.

probe was retained primarily in the liver and kidneys (Figure 7). The relative fluorescence intensity was obtained as the average intensity in the organs of interest. Expectedly, the more hydrophobic **4** was retained in many normal tissues as compared with **6**, which cleared from all organs at 24 h postinjection, except the liver and kidneys. For practical purposes, rapid clearance of molecular probes from nontarget tissues is highly desirable during imaging studies to minimize background signals from these probes. As a result, detection of high fluorescence in nonexcretory organs would provide important diagnostic information within a short period postinjection of the probe. This result suggests that compound **6** is suitable for designing target specific molecular probes for multimodal imaging.

Table 2. Fluorescence Intensity[a] Distribution of Compounds 4 and 6 in Mice at 24 h Postinjection

	organ/blood ratios (of relative fluorescence) at 24 h postinjection							
compd	liver	kidney	spleen	pancreas	muscle	adrenal	heart	brain
4	11.2 ±1.2	6.6 ±1.1	3.4 ±1.1	2.6 ±1.1	1.5 ±1.0	3.0 ±1.1	NA	NA
6	78.8 ±10.3	38.1 ±4.0	1.9 ±0.9	3.8 ±1.1	2.4 ±1.1	4.5 ±1.3	3.3 ±1.1	1.7 ±1.0

[a] Fluorescence intensity was initially normalized relative to blood.

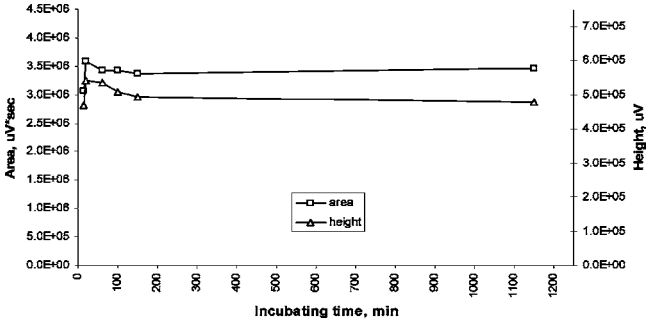

Figure 6. Quantitative results obtained by integration of area and height measurements at 8.3 min retention time shows the stability of indium complex **8**. The trace was obtained from a single test sample.

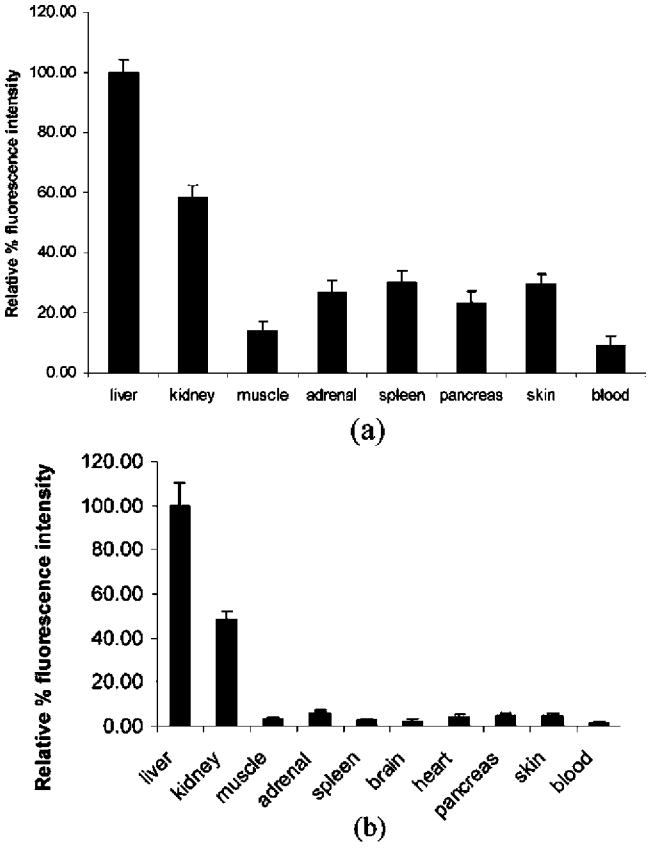

Figure 7. Distribution of (a) **4** and (b) **6** in nude mice at 24 h postinjection. Fluorescence intensity normalized to blood.

The ratio of the fluorescence intensity at 24 h relative to blood is shown in Table 2, indicating that most of the probe cleared from the body via urine (injected dose is 0.3 μmol/kg body weight of mouse; collected urine samples fluoresced). Interestingly, the fluorescence intensity of compound **6** in the brain was nearly twice relative to blood. Although this intensity is low as compared with the liver, it raises the possibility of optimizing compound **6** for brain imaging. Designing compounds that can cross the blood−brain barrier remains a challenge for imaging the brain with nonradionuclide imaging agents because

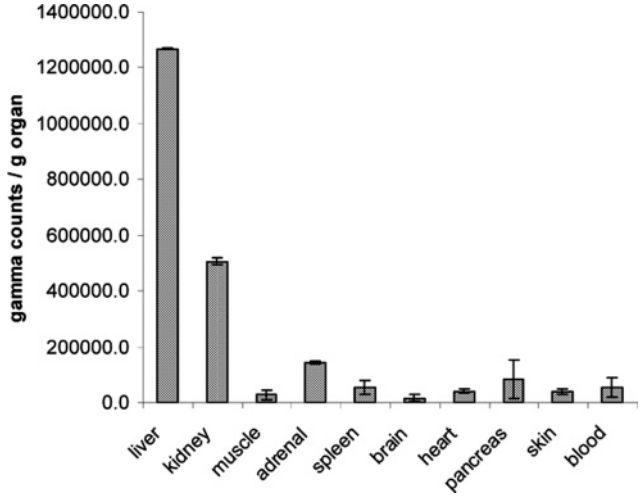

Figure 8. Biodistribution of **9** obtained by γ-counting method at 24 h postinjection.

Table 3. Distribution of 9 in Mice at 24 h Postinjection

	organ/blood ratios of γ-counts/ g organ at 24 h postinjection							
compd	liver	kidney	spleen	pancreas	muscle	adrenal	heart	brain
9	40.3	15.8	2.3	1.2	1.3	4.6	1.5	0.8

of the typical low molecular weight and nonionic molecule requirements. However, a closer look at the structure of **6** shows that the molecule can adopt a neutral configuration where all of the four carboxylic acid groups are neutralized by the tertiary amino groups. Subsequent transport across the blood−brain barrier could be mediated by phosphorylation of the serine hydroxyl group. Further studies will be needed to explore this possibility.

Radionuclear Method. γ-Emitters are routinely used for radionuclear imaging by planar or 3D SPECT techniques (*24*, *25*). Our interest in γ-scintigraphy is due to its simplicity and high sensitivity. Unlike MR and CT imaging methods that require local tissue concentration of 10^{-4} (gadolinium or manganese) and 10^{-2} M (iodine or barium) of contrast agents for diagnostic imaging, γ-scintigraphy detects about 10^{-10} M of radiopharmaceuticals (^{111}In or ^{99m}Tc) in tissues (*1*, *10*). This sensitivity is improved in SPECT, which also has a higher anatomical resolution. The detection sensitivity of optical methods falls with the range of γ-scintigraphy, depending on the optical technique employed.

The radioactive indium was prepared as described in the Materials and Methods section. We injected 10 μCi of the ^{111}In−MOMIA (**9**) and conducted the scintigraphy on a Kodak multistation imager at 1, 4, and 24 h postinjection. At 24 h postinjection, we sacrificed the animals and weighed the organ parts and the activity was determined with a γ-counter. Figure 8 shows the biodistribution of the γ-counts normalized per gram organ, and Table 3 depicts the ratios of the γ-counts normalized to 1 g of blood. The biodistribution trend observed is similar to that obtained by the fluorescence intensity method, as summarized in Figure 9. The reason for the observed slight differences in the signal intensities

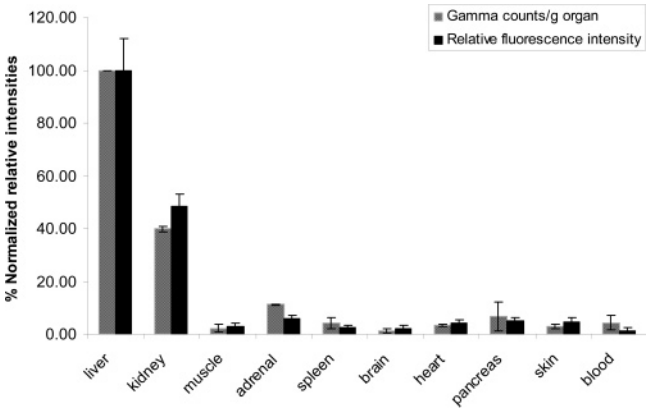

Figure 9. Comparative distribution of **8** and **9** obtained by γ- and fluorescence emission methods, respectively, at 24 postinjection of the molecular probes.

by both methods in some organs such as the kigneys and adrenal glands is probably due to interanimal biological variations.

CONCLUSION

We successfully prepared MOMIAs in good yields and successfully labeled them with radioactive and nonradioactive indium. As shown above, indium chelates of MOMIAs either retained or increased their fluorescence emission relative to the nonchelated MOMIAs. We also showed that the chelated and nonchelated MOMIAs are exceptionally stable in serum up to 48 h postincubation at 37 °C. The biodistribution studies by optical and radionuclear methods showed similar trends, indicating that both fluorescence and γ-emissions emanated from the same source. These findings demonstrate the feasibility of using MOMIA strategy to image tissues by combined optical and nuclear methods.

ACKNOWLEDGMENT

This study was supported by the National Institutes of Health (R33 CA100972).

LITERATURE CITED

(1) Allport, J. R., and Weissleder, R. (2001) In vivo imaging of gene and cell therapies. *Exp. Hematol. 29*, 1237−1246.
(2) Sabbah, P., Foehrenbach, H., Dutertre, G., Nioche, C., and DeDreuille, O., et al. (2002) Multimodal anatomic, functional, and metabolic brain imaging for tumor resection. *Clin. Imaging 26*, 6−12.
(3) Rubello, D., Casara, D., Fiore, D., Muzzio, P., and Zonzin, G., et al. (2002) An ectopic mediastinal parathyroid adenoma accurately located by a single-day imaging protocol of tc-99m pertechnetate-mibi subtraction scintigraphy and mibi-spect-computed tomographic image fusion. *Clin. Nucl. Med. 27*, 186−190.
(4) Chance, B., Kang, K., He, L., Weng, J., and Sevick, E. (1993) Highly sensitive object location in tissue models with linear in-phase and antiphase multielement optical arrays in one and 2 dimensions. *Proc. Natl. Acad. Sci. U.S.A. 90*, 3423−3427.
(5) Ntziachristos, V., and Weissleder, R. (2001) Experimental three-dimensional fluorescence reconstruction of diffuse media by use of a normalized born approximation. *Opt. Lett. 26*, 893−895.
(6) Graves, E. E., Ripoll, J., Weissleder, R., and Ntziachristos, V. (2003) A submillimeter resolution fluorescence molecular imaging system for small animal imaging. *Med. Phys. 30*, 901−911.
(7) Patwardhan, S. V., Bloch, S. R., Achilefu, S., and Culver, J. P. (2005) Time-dependent whole-body fluorescence tomography of probe bio-distributions in mice. *Opt. Express 13*, 2564−2577.
(8) Ntziachristos, V., Ripoll, J., Wang, L. H. V., and Weissleder, R. (2005) Looking and listening to light: The evolution of whole-body photonic imaging. *Nat. Biotechnol. 23*, 313−320.
(9) Ntziachristos, V., Yodh, A. G., Schnall, M., and Chance, B. (2000) Concurrent mri and diffuse optical tomography of breast after indocyanine green enhancement. *Proc. Natl. Acad. Sci. U.S.A. 97*, 2767−2772.
(10) Torchilin, V. P. (2002) Peg-based micelles as carriers of contrast agents for different imaging modalities. *Adv. Drug Delivery Rev. 54*, 235−252.
(11) Trubetskoy, V. S. (1999) Polymeric micelles as carriers of diagnostic agents. *Adv. Drug Delivery Rev. 37*, 81−88.
(12) Josephson, L., Kircher, M. F., Mahmood, U., Tang, Y., and Weissleder, R. (2002) Near-infrared fluorescent nanoparticles as combined mr/optical imaging probes. *Bioconjugate Chem. 13*, 554−560.
(13) Modo, M., Cash, D., Williams, S. C. R., Mellodew, K., and Price, J., et al. (2004) Mapping transplanted stem cell migration after a stroke: A serial, in vivo magnetic resonance imaging study. *Neuroimage 21*, 311−317.
(14) Ballou, B., Fisher, G. W., Hakala, T. R., and Farkas, D. L. (1997) Tumor detection and visualization using cyanine fluorochrome- labeled antibodies. *Biotechnol. Prog. 13*, 649−658.
(15) Manning, H. C., Bornhop, D. J., Goebel, T., Thompson, R. C., and Price, R. R., et al. (2004) Targeted molecular imaging agents for cellular-scale bimodal imaging. *Bioconjugate Chem. 15*, 1488−1495.
(16) Zhang, Z., and Achilefu, S. (2004) Synthesis and evaluation of polyhydroxylated near-infrared carbocyanine molecular probes. *Org. Lett. 6*, 2067−2070.
(17) Atherton, E., and Sheppard, R. C. (1989) Solid-phase peptide synthesis: A practical approach. In *Practical Approach Series* (Rickwood, D., and Hames, B. D., Eds.) Oxford University Press, Oxford, England.
(18) Achilefu, S., Jimenez, H. N., Dorshow, R. B., Bugaj, J. E., and Webb, E. G., et al. (2002) Synthesis, in vitro receptor binding, and in vivo evaluation of fluorescein and carbocyanine peptide-based optical contrast agents. *J. Med. Chem. 45*, 2003−2015.
(19) Achilefu, S., Dorshow, R. B., Bugaj, J. E., and Rajagopalan, R. (2000) Novel receptor-targeted fluorescent contrast agents for in vivo tumor imaging. *Invest. Radiol. 35*, 479−485.
(20) Hawrysz, D. J., and Sevick-Muraca, E. M. (2000) Developments toward diagnostic breast cancer imaging using near-infrared optical measurements and fluorescent contrast agents. *Neoplasia 2*, 388−417.
(21) Achilefu, S. (2004) Lighting up tumors with receptor-specific optical molecular probes. *Technol. Cancer Res. Treat. 3*, 393−409.
(22) Geddes, C. D., Cao, H., Gryczynski, I., Gryczynski, Z., and Fang, J. Y., et al. (2003) Metal-enhanced fluorescence (mef) due to silver colloids on a planar surface: Potential applications of indocyanine green to in vivo imaging. *J. Phys. Chem. A 107*, 3443−3449.
(23) Tarazi, L., George, A., Patonay, G., and Strekowski, L. (1998) Spectral characterization of a novel near-infrared cyanine dye: A study of its complexation with metal ions. *Talanta 46*, 1413−1424.
(24) Higuchi, T., Yang, D. J., Ilgan, S., Tansey, L. W., and Zareneyrizi, F., et al. (1999) Biodistribution and scintigraphy of in-111 dtpa-adriamycin in mammary tumor-bearing rats. *Anti-Cancer Drugs 10*, 89−95.
(25) Swailem, F. M., and Shah, J. (1998) In-vivo tissue uptake and retention of sn-117m(4+)dtpa in a human subject with metastatic bone pain and in normal mice (vol 25, pg 279, 1998). *Nucl. Med. Biol. 25*, 515−515.

BC050136S

Protamine as an Efficient Membrane-Translocating Peptide

Fred Reynolds, Ralph Weissleder, and Lee Josephson*

Center for Molecular Imaging Research, Massachusetts General Hospital/Harvard Medical School, Boston, Massachusetts 02129. Received May 19, 2005; Revised Manuscript Received August 11, 2005

Protamine, a mixture of positively charged proteins from salmon roe used in diverse pharmaceutical applications, was reacted with the *N*-hydroxysuccinimide ester of tetramethylrhodamine to yield tetramethylrhodamine-labeled protamines (Pro(Rh)) containing one mole of fluorochrome per mole of protein. The internalization of tetramethylrhodamine-labeled protamine (Pro(Rh)) and the fluorescein-labeled tat peptide (Tat(Fl)) showed a similar dependence on time and concentration. Pro(Rh) and Tat(Fl) showed strong nuclear localizations, evident with both live cells and fixed cells costained with DAPI, a nuclear stain. The loss of fluorescence when cells were loaded with Pro(Rh) or Tat(Fl) was similar, further supporting a strong similarity between these two materials. Finally, when Pro(Ph) was covalently attached to the amino-CLIO nanoparticle, the cellular uptake of the nanoparticle was greatly enhanced. All experiments were performed with HeLa and CaCo-2 cells with similar results. These observations imply that protamine, a protein in regular clinical use, might be used for the design of novel membrane translocating/nuclear localizing pharmaceuticals whose development was initiated with other membrane-translocating peptides. In addition, the fluorescent protamines developed here might be used to further our understanding of this important pharmaceutical.

INTRODUCTION

Protamine, a mixture of proteins extracted from salmon roe, is in regular clinical use as an excipient in insulin formulations (*1*, *2*) and to reverse the anticoagulant properties of heparin (*3*). The biological role of protamine is to bind DNA and to provide a highly compact configuration of chromatin in the nucleus of the sperm (*4*, *5*). Protamine is arginine rich, a feature it shares with some viral proteins which utilize arginine rich sequences of amino acids to provide membrane-translocating and/or nuclear-localizing activities (*6*), see Table 1. We noted that protamine was not only arginine rich, but in common with viral translocation sequences had short sequences consisting of seven or more arginine residues (6). In addition, protamine has a single reactive amine at the N-terminus and a single carboxyl group at the C-terminus, a situation that might facilitate site-specific modification and the design of protamine-based probes.

We therefore investigated the membrane-translocating activity of protamine to add to the understanding of this important pharmaceutical and because protamine might be superior to other membrane-translocating peptides for drug delivery applications due to its ease of modification, low cost, availability, sterility, and GMP manufacture. Synthetic polyarginyl peptides have been exploited to provide improved forms of cyclosporine (*7*), improved radiotherapeutic agents (*8*), and improved methods of intracellular delivery of DNA and enzymes (*9*−*11*). Using fluorescent protamines, we show that protamine has a membrane-translocating activity comparable to that of the HIV[1] tat peptide and therefore might be an ideal carrier for drug delivery applications. Studies following the intracellular disposition of fluorescent protamines in vivo may prove helpful in understanding the fate of this widely used pharmaceutical after injection.

MATERIALS AND METHODS

The *N*-hydroxysuccinimide esters of 5-carboxytetramethylrhodamine and 5-carboxyfluorescein were from Molecular Probes (Eugene, OR). Protamine sulfate was from American Pharmaceutical Partners (Schaumburg, IL). Carbodiimide (1-ethyl-3(3′dimethylaminopropyl)carbodiimide) was from Novabicohem (LaJolla, CA). The Tat(Fl) peptide, see Table 1, was synthesized on an Advanced Chemtech Apex 396 peptide synthesizer (Advanced Chemtech, Louisville, KY) as described (*12*), except that an *N*-hydroxysuccinimide ester of fluorescein rather than fluorescein isothiocyanate was used. Tat(Fl)-CLIO was prepared as described (*13*).

To synthesize fluorescent protamines, 0.5 mg of the *N*-hydroxysuccinimide ester of either tetramethylrhodamine or fluorescein in 100 μL of DMSO was added to 5 mg of protamine (in 500 μL of 0.85 M NaCl as supplied) and 100 μL of PBS, and allowed to react overnight at 4°C. Peptides were purified using a reverse phase C18 column with acetonitrile/water gradients, and products were characterized by MALDI-MS. The molecular weights (M + 1) of the fluorescent protamines we synthesized were within 1 Da of the expected values (Table 1). Fluorescein-labeled protamine is denoted Pro(Fl), and tetramethylrhodamine-labeled protamine is denoted Pro(Rh).

To synthesize protamine-derivatized nanoparticles, amino-CLIO (*14*) was first reacted with Cy5.5 to yield CLIO(Cy5.5) as described (*15*). Unreacted Cy5.5 was removed by Sephadex G-25 gel filtration and Cy5.5 concentration determined spectrophotometrically (absorption at 675 nm, extinction coefficient of 250 000 L/mol-cm). Since there are 200−240 amines per 8000 Fe with the CLIO nanoparticle (*16*, *17*), and 8.0 were

* To whom correspondence should be addressed. Tel. 617-726-6478; Fax. 617-726-5708; e-mail: ljosephson@partners.org.

[1] Abbreviations: CLIO, cross-linked iron oxide; Pro, protamine; Rh, 5-carboxytetramethylrhodamine; Fl, 5-carboxyfluorescein; HIV, human immunodeficiency virus; HTLV-II, human T-cell lymphotrophic virus type-II; BMV, brome mosaic virus; FHV, flock house virus.

10.1021/bc0501451 CCC: $30.25 © 2005 American Chemical Society
Published on Web 09/02/2005

Table 1. Protamine and Fluorescent Protamines[a]

name	sequence	mass (M + 1) exp
protamine 1	PRRRR SSSRP VRRRR RPRVS RRRRR RGGRR RR (22R's of 32)	4252.1
protamine 2	PRRRR SSSRP IRRRR PRRAS RRRRR RGGRR RR (22R's of 32)	4237.5
protamine 3		4321.5
protamine 4		4065.5
protamine 1-tetramethylrhodamine	P(Rh)PRRRR SSSRP VRRRR RPRVS RRRRRRRGGR RRR (22R's of 32)	4664.6
protamine 1-fluorescein	P(Fl)RRRR SSSRP VRRRR RPRVS RRRRR RRGGR RRR (22R's of 32)	4610.8
HIV-1 Tat (48−60)	GRKKR RQRRR RGP (7R's of 13)	NA
HIV Rev (34−50)	TRQAR RNRRR RWRER QR (10R's of 17)	NA
FHV coat (35−49)	RRRRN RTRRN RRRVR (11R's of 15)	NA
BMV Gag (7−25)	KMTRA QRRAA ARRNR WTAR (7R's of 19)	NA
HTLV-II Rex (4−16)	TRRQR TRRAR RNR (8R's of 13)	NA

[a] Protamine is a mixture of four peptides, protamines 1, 2, 3, and 4. Also shown are the arginyl rich sequences of peptides derived from viral genes that show a strong nuclear localizing activity (*6*). Numbers in parentheses are the numbers of arginines and total amino acids.

consumed by reaction with Cy5.5, the remaining amines were available to react with the C-terminal carboxyl group of Pro(Rh). The CLIO(Cy5.5) nanoparticle (1 mg Fe, 5.73 mg Fe/mL) was added to 200 μL of Pro(Ph) (2.65 mM). Eight milligrams of 1-ethyl-3(3′dimethyl-aminopropyl)carbodiimide in 1 mL of MES buffer (0.1 M, pH 4.9) were added, the mixture allowed to sit overnight, and unreacted Pro(Rh) was removed by gel filtration on Sephadex G50. There were 28 Pro(Rh) attached per 8000 Fe atoms determined from tetramethylrhodamine absorption (565 nm, extinction coefficient of 91 000 L/mol-cm). The nanoparticle is denoted Pro(Rh)-CLIO(Cy5.5).

CaCo-2 and HeLa cells were from ATCC (Manassas, VA) and grown according to ATCC specifications, except for the addition of penicillin/streptomycin. Cell culture reagents were from CellGrow (Herndon, VA).

Cell uptake of peptides or nanoparticles was determined using 24-well plates (250 μL media/well). Cells were incubated with peptide or nanoparticle for the indicated times and concentrations. Cells were washed three times with PBS and lysed (0.1% Triton X-100 μL in PBS), and fluorescence was determined on a plate reader (Molecular Devices, Sunnyvale, CA) (Figure 3). Cells were trypsinized for FACS measurements (FACS Caliber, Becton Dickinson, San Jose, CA) (Figure 1C). Cell counts were made with a Beckman Coulter Z1 cell counter (San Jose, CA). Amounts of cell associated peptide were determined by use of standards of fluorescent peptides.

To obtain the time course of fluorescence loss (Figure 4), cells were allowed to internalize peptide, washed, and incubated with media for varying times. Cell-associated fluorescence was determined after trypsinization and FACS. To demonstrate the uptake of nanoparticles (Figure 5), cells were trypsinized and cell-associated fluorescence determined by FACS. A portion of cells was spun down and lysed, and the iron uptake was obtained by calibration with fluorescent standards of each nanoparticle.

For microscopy, cells were grown on glass slides (Fisher Scientific, Pittsburgh, PA), exposed to 5 μM peptide for 4 h, and washed three times with PBS. Unfixed cells (Figure 1) were examined using a Nikon Eclipse TE2000-S epifluorescence microscope with long focal length optics (Torrance, CA). Cells were also fixed with 70% ethanol at 4 C for 90 min, washed with PBS, mounted using Vector Shield with DAPI (Vector Laboratories, Burlingame, CA), and examined by epifluorescence (Figure 2). Fluorescence microscopy used a Nikon Eclipse 80i epifluorescence microscope (Torrance, CA).

RESULTS

Protamine is a mixture of four proteins listed in the order of their peak height determined by mass spectrometry in Table 1. The mass of protamine 1 is that of the protamine denoted AI, gene accession number P02327 (NCBI-protein database). The mass of protamine 2 is that of the protamine denoted AII, gene accession number B02669 (NCBI-protein database). The composition of protamine 3 and protamine 4 is not known. Also shown are the arginyl rich sequences derived from viral genes that show a strong nuclear localizing activity (*6*) and membrane-translocating sequence of the tat peptide (*18*). Numbers in parentheses are the number of arginines and total number of amino acids for the peptide. Both protamine and viral-translocating sequences share an overall arginine rich character that consists of seven or more arginines.

Fluorescent protamines were synthesized by reacting the *N*-hydroxysuccinimidyl esters of 5-carboxytetramethylrhodamine and 5-carboxyfluorescein with protamine, to produce proteins containing a single fluoro-

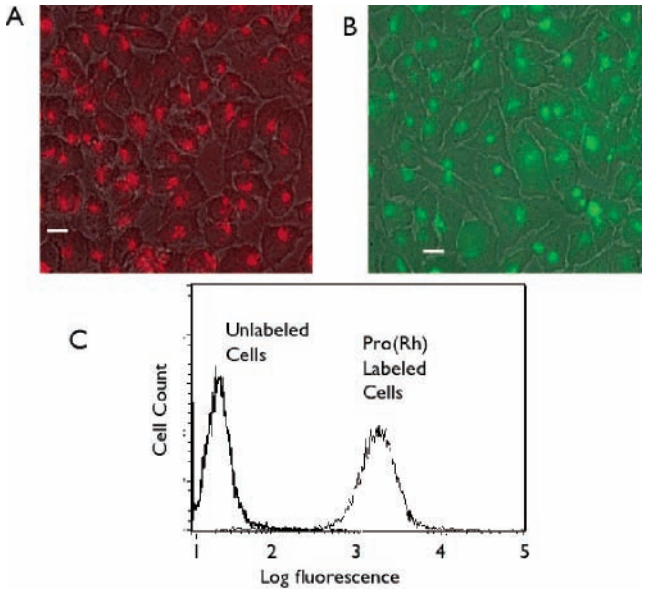

Figure 1. Internalization of rhodamine-labeled protamine and fluorescein-labeled tat peptide. HeLa cells were incubated (2 μM, 4 h) with either Pro(Rh) (A) or Tat(Fl) (B). Phase contrast images on unfixed cells were taken, and images from rhodamine channel (A) or fluorescein channel (B) were superimposed. Scale marker is 10 μm. (C) HeLa cells labeled with Pro(Ph) as above were trypsinized and analyzed by FACS.

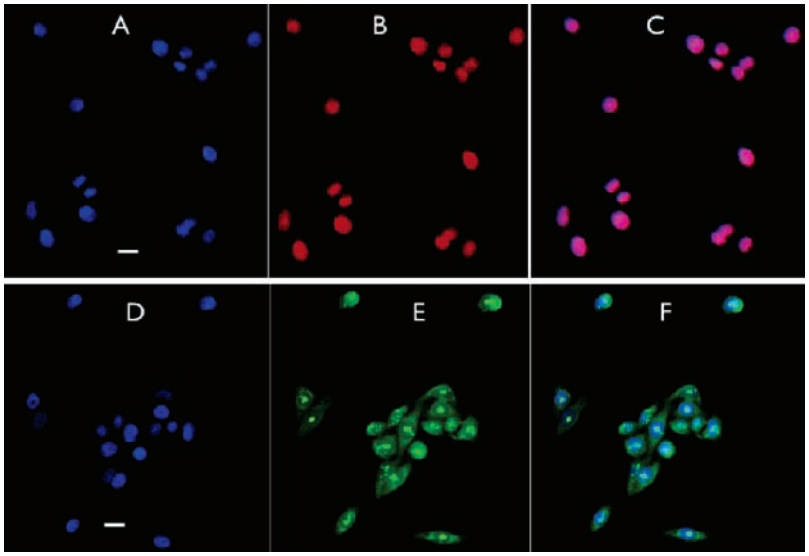

Figure 2. Nuclear localization of protamine or tat peptide. Cells were incubated with Pro(Rh) (A, B, C) or Tat(Fl) (D, E, F) at 2 μM fluorochrome for 4 h. Cells were washed, fixed, and stained with DAPI, a nuclear stain. (A and D) Cell nuclei shown by the DAPI (ultraviolet) channel. (B) Pro(Rh) visualized in rhodamine channel. (C) Overlay of parts A and B. (E) Tat(Fl) visualized in the fluorescein channel. (F) Overlay of parts D and E. Scale marker is 10 μm.

chrome as shown in Table 1. The site of attachment is presumed to be N-terminal proline residue, since none of the other amino acids have a reactive primary amine. The amines of the guanidinium group of arginine are not chemically reactive (*19*). After reaction with 5-carboxytetramethylrhodamine, the four protamines exhibited an increase in molecular weight consistent with the addition of a residue weight of tetramethylrhodamine ($C_{25}H_{20}O_4$, 412.45 Da). Similarly, after reaction with 5-carboxyfluorescein, four proteins were identified with an increase in molecular weight consistent with the addition of a residue of 5-carboxyfluorescein ($C_{21}H_{10}O_6$, 358.3 Da). The molecular weights obtained by reaction of protamine 1 with tetramethylrhodamine or fluorescein are given in Table 1. Protamine labeled with tetramethylrhodamine is denoted Pro(Rh), fluorescein-labeled protamine is denoted Pro(Fl), and fluorescein-labeled tat peptide is denoted Tat(Fl).

The uptake of Pro(Rh) and Tat(Fl) by HeLa cells is shown in Figure 1A and B, respectively after 4 h of incubation with each peptide and after cells were washed with PBS (three times) to remove any loosely adsorbed peptide. Phase contrast images and fluorescence micrographs in the rhodamine channel were obtained for cells exposed to Pro(Rh) and the images superimposed as shown in part A. Under these conditions, an intense fluorescence was seen in the center of the cell, which appeared to represent a nuclear accumulation as is discussed further below. Fluorescence was not associated with the cell membrane or in a punctate pattern in the cytoplasm typical of endosomal accumulation. A similar pattern was seen when HeLa cells were incubated with the Tat(Fl) peptide and the fluorescence from the fluorescein channel superimposed on phase contrast images (B). Pro(Rh)-treated HeLa cells were then trypsinized and the distribution of fluorescence obtained by FACS, as shown in Figure 1C. Pro(Rh) uniformly labeled cells in a manner to that seen with Tat(Fl) labeling; see for example Figure 2 of ref 15. All experiments in this report were performed on HeLa cells and CaCo-2 cells, with similar results, an example of which is shown in Figure 3.

To confirm that fluorescence was nuclear, the nuclei of cells incubated with Pro(Rh) or Tat(Fl) were stained with the nuclear stain DAPI. Figures 2A and 2D show the well-defined nuclei visualized as the fluorescence from DAPI nuclear stain. Figure 2B shows the tetramethylrhodamine fluorescence from cells incubated with Pro(Ph), which, based on the overlay, appeared to be nuclear (Figure 2C). Figure 2D shows the result obtained when cells were incubated with Tat(Fl) (fluorescein channel), which, based on the overlay with the DAPI stain, again appeared to be nuclear (Figure 2E). Thus, Rh(Pro) was internalized by cells and showed a nuclear accumulation in a manner similar to Tat(Fl).

We next examined the time course of internalization of the fluorescent protamines (Pro(Rh) and Pro(Fl)) and compared it with tat peptide (Tat(Fl)) as a function of time (Figure 3A) and concentration (Figure 3B). The internalization of Pro(Rh) was complete within 1 h and did not show saturation behavior with respect to concentration.

Previous studies with arginine rich peptides have shown internalization within 1 h and either a linear dependence of uptake on peptide concentration or some evidence of saturation at high peptide concentrations (*6*, *20*, *21*). The internalization of protamine was strongly dependent on the attached fluorochrome, with the uptake of Pro(Rh) being far greater than Pro(Fl), which may reflect an interaction between the negative charge on fluorescein and the positive charges on protamine. Data comparing the uptake of Pro(Ph) with HeLa cells and CaCo-2 cells is shown as example of the data we obtained showing the similar behavior of all proteins and peptides with these two cell types in all experiments. Data shown in Figure 3 is the cell-associated fluorescence measured after lysis and determination of fluorescence with a microtiter plate reader and standards, a procedure which permits expression of results in moles per cell. Trypsinization and FACS yielded similar relationships about the time course and amounts of uptake for the three peptides examined (data not shown). Thus, the kinetics of uptake and relative amounts of cell-associated Tat(Fl) and Pro(Ph) were similar when fluorescence was determined by lysis of adherent cells or with trypsinization and FACS (data not shown).

We next examined the loss of cell-associated fluorescence after HeLa cells were loaded with fluorescent

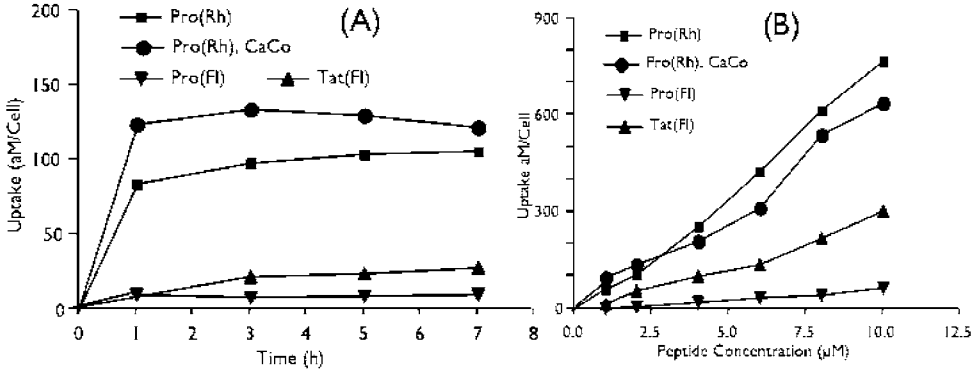

Figure 3. Uptake of protamine and tat peptide by HeLa cells. (A) Uptake of rhodamine protamine (Pro(Rh)) or fluorescein protamine (Pro(Fl)) and tat peptide (Tat(Fl)) as a function of time at 2 μM fluorochrome. (B) Uptake of Pro(Rh), Pro(Fl)), and Tat(Fl) as a function of peptide concentration at 4 h. Experiments were with HeLa cells except where indicated. Total cell-associated fluorescence was obtained after lysis.

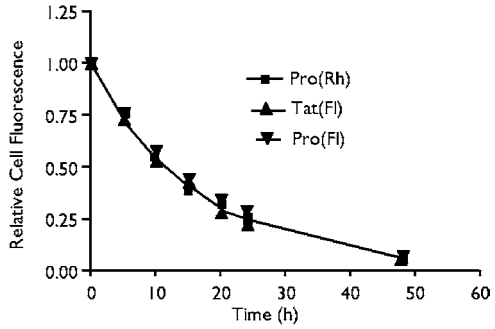

Figure 4. Loss of fluorescence after loading with protamine and tat peptide. HeLa cells were loaded with fluorescent protamines or tat peptide (2 μM, 4 h), washed, and incubated in peptide and protein free media for the indicated time. Cells were trypsinized, and fluorescence was determined by FACS.

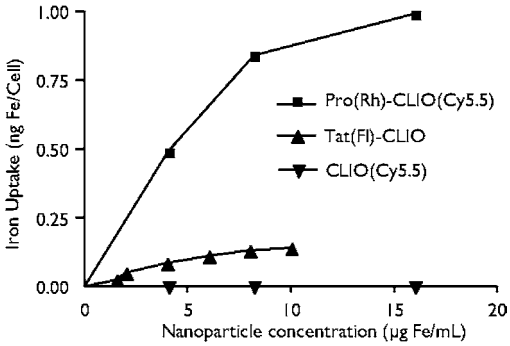

Figure 5. Uptake of protamine nanoparticles by HeLa Cells. Pro(Rh) was conjugated to the amino-CLIO nanoparticle to obtain Pro(Rh)CLIO(Cy5.5). Incubation was for 4 h. Cells were trypsinized, and fluorescence was determined by FACS.

protamines or Tat(Fl) as shown in Figure 4. The loss of fluorescence for Pro(Rh) was fit to single-exponential decay model and yielded half-lives of 12.2 h (Pro(Rh), 10.8 h (Tat(Fl)), and 13.0 h (Pro(Fl). All fits had values of r^2 greater than 0.99. Thus, the loss of cell-associated fluorescence was similar regardless of whether cells were loaded with either fluorescent protamine or the tat peptide.

A feature of the tat peptide is that when it is conjugated to enzymes, nanoparticles, or liposomes, it induces internalization and/or nuclear localization of these macromolecular or supramolecular materials (*22*−*24*). To examine whether protamine could act similarly, we attached Pro(Rh) to an amino-CLIO nanoparticle labeled with Cy5.5, by using a carbodiimide to react the C-terminal carboxyl group (Table 1) with the primary amine of the nanoparticle. The resulting nanoparticles are denoted Pro(Rh)-CLIO(Cy5.5) and CLIO(Cy5.5). As shown in Figure 5, polymer-coated nanoparticles such as CLIO(Cy5.5) are not significantly internalized by nonphagocytic cells such as HeLa cells. Conjugation of the Tat(Fl) peptide greatly increases nanoparticle internalization, an effect noted earlier (*13*, *22*). The attachment of protamine yielded a nanoparticle, Pro(Rh)-CLIO-(Cy5.5), that was internalized at 4−5 times higher levels than that of the nanoparticle with the tat peptide attached, Tat(Fl)-CLIO. Although the cellular uptake of CLIO(Cy5.5) was too low to quantitate in these fluorescence-based experiments, experiments with radiolabeled nanoparticles have demonstrated that the attachment of the tat peptide induces a 100-fold increase in nanoparticle internalization (*22*). Protamine, like tat peptide, can be conjugated to nanoparticles, and the resulting peptide−nanoparticle conjugate is readily internalized by cells.

DISCUSSION

Our goal was to demonstrate that protamine is an efficient membrane-translocating peptide, a previously unrecognized activity of this protein, by comparing its behavior with that of the tat peptide, a peptide with a well-recognized membrane-translocating activity. When HeLa cells where incubated with either peptide for 4 h, a time chosen to allow intracellular processing of peptides to proceed, both Pro(Rh) and Tat(Fl) showed a clear nuclear localization in living, unfixed cells (Figure 1). Nuclear localization with both peptides was also seen with fixed cells (Figure 2). Both peptides reached a nearly constant level of internalization by the initial time point of 1 h (Figure 3); the rapid kinetics of tat peptide internalization at shorter time points been described in detail elsewhere *(20*, *26)*. The similar disposition of Pro-(Ph) and Tat(Fl) by microscopy and their similar rates of efflux (Figure 4) indicate that both peptides are processed in a similar fashion by HeLa cells. Finally, when Pro(Rh) was attached to the magnetic nanoparticles, the cellular uptake of the nanoparticle was enhanced more than that obtained by conjugation of the tat peptide (Figure 5). The ability of the tat peptide to enhance the internalization of enzymes, liposomes, and other materials when conjugated to them is a characteristic of this peptide (*23*−*25*). Though in early studies the nuclear localization of tat peptide was not dependent on fixation (*18*), more recent studies have reported the tat peptide in cytoplasmic endocytic vesicles after membrane translocation and attributed the earlier nuclear localiza-

tion to the use of fixation procedures (*26*, *27*). In our hands, protamine and tat peptide gave similar images of nuclear localization with fixed and unfixed cells. Regardless of the final resolution of the intracellular fate of internalized tat peptide, the tat peptide is widely accepted as having a membrane-translocating activity (*28*−*31*). Since our data indicate that protamine and tat peptide behaved similarly, we therefore conclude that protamine, like other high arginine-containing peptides, is a membrane-translocating peptide.

Our results indicate that protamine has a membrane-translocating activity and nuclear localizing activity in vitro and suggest that protamine could have these activities in vivo, including after its intramuscular administration in insulin formulations. The development of fluorescent protamines may lead to an improved understanding of a material long used in pharmaceutical applications.

Our results also suggest the possible use of protamine for the design of new membrane-translocating peptide-based diagnostic or therapeutic pharmaceuticals, including some whose development has been initiated with other membrane-translocating peptides. The use of protamine in this fashion would have several advantages. First, the cost of the natural product protamine is currently substantially less than synthetic peptides. Protamine is available as a sterile solution (10 mg/mL, 5 mL) at less than $50/ampule compared to a price of at least $500 for 50 mg of 10 amino acid peptide made by solid-phase synthesis. This decreased cost could stimulate research or the clinical development of protamine-based conjugates. Second, protamine has a long history of use establishing its biological effects and general safety in humans. Finally protamine has only one reactive amine, the N-terminal proline, and, one carboxyl group, the C-terminus, facilitating the single point attachment of fluorochromes or drugs to protein. Our observations suggest that a protamine, a protein in regular parenteral use, might be a convenient raw material for use in the design of novel membrane-translocating/nuclear-localizing pharmaceuticals.

ACKNOWLEDGMENT

This work was supported by NIH grants RO1-EB00662 and R01 EB004626.

LITERATURE CITED

(1) Brange, J., and Langkjaer, L. (1992) Chemical stability of insulin. 3. Influence of excipients, formulation, and pH. *Acta Pharm. Nord. 4*, 149−58.

(2) Brange, J., and Langkjaer, L. (1997) Insulin formulation and delivery. *Pharm. Biotechnol. 10*, 343−409.

(3) Carr, J. A., and Silverman, N. (1999) The heparin-protamine interaction. A review. *J. Cardiovasc. Surg. (Torino) 40*, 659−66.

(4) Fuentes-Mascorro, G., Serrano, H., and Rosado, A. (2000) Sperm chromatin. *Arch. Androl. 45*, 215−25.

(5) Meistrich, M. L., Mohapatra, B., Shirley, C. R., and Zhao, M. (2003) Roles of transition nuclear proteins in spermiogenesis. *Chromosoma 111*, 483−8.

(6) Futaki, S., Suzuki, T., Ohashi, W., Yagami, T., Tanaka, S., Ueda, K., and Sugiura, Y. (2001) Arginine-rich peptides. An abundant source of membrane-permeable peptides having potential as carriers for intracellular protein delivery. *J. Biol. Chem. 276*, 5836−40.

(7) Rothbard, J. B., Garlington, S., Lin, Q., Kirschberg, T., Kreider, E., McGrane, P. L., Wender, P. A., and Khavari, P. A. (2000) Conjugation of arginine oligomers to cyclosporin A facilitates topical delivery and inhibition of inflammation. *Nat. Med. 6*, 1253−7.

(8) Polyakov, V., Sharma, V., Dahlheimer, J. L., Pica, C. M., Luker, G. D., and Piwnica-Worms, D. (2000) Novel Tat-peptide chelates for direct transduction of technetium-99m and rhenium into human cells for imaging and radiotherapy. *Bioconjugate Chem. 11*, 762−71.

(9) Eguchi, A., Akuta, T., Okuyama, H., Senda, T., Yokoi, H., Inokuchi, H., Fujita, S., Hayakawa, T., Takeda, K., Hasegawa, M., and Nakanishi, M. (2001) Protein transduction domain of HIV-1 Tat protein promotes efficient delivery of DNA into mammalian cells. *J. Biol. Chem. 276*, 26204−10.

(10) Ford, K. G., Souberbielle, B. E., Darling, D., and Farzaneh, F. (2001) Protein transduction: an alternative to genetic intervention? *Gene Ther. 8*, 1−4.

(11) Snyder, E. L., and Dowdy, S. F. (2001) Protein/peptide transduction domains: potential to deliver large DNA molecules into cells. *Curr. Opin. Mol. Ther. 3*, 147−52.

(12) Wunderbaldinger, P., Josephson, L., and Weissleder, R. (2002) Tat peptide directs enhanced clearance and hepatic permeability of magnetic nanoparticles. *Bioconjugate Chem. 13*, 264−8.

(13) Zhao, M., Kircher, M. F., Josephson, L., and Weissleder, R. (2002) Differential conjugation of tat Peptide to superparamagnetic nanoparticles and its effect on cellular uptake. *Bioconjugate Chem. 13*, 840−4.

(14) Josephson, L., Perez, J. M., and Weissleder, R. (2001) Magnetic nanosensors for the detection of oligonucleotide sequences. *Agnew Chem. Int. Ed. 40*, 3204−3206.

(15) Koch, A. M., Reynolds, F., Kircher, M. F., Merkle, H. P., Weissleder, R., and Josephson, L. (2003) Uptake and metabolism of a dual fluorochrome Tat-nanoparticle in HeLa cells. *Bioconjugate Chem. 14*, 1115−21.

(16) Reynolds, F., O'Loughlin, T., Weissleder, R., and Josephson, L. (2005) Method of determining nanoparticle core weight. *Anal. Chem. 77*, 814−7.

(17) Koch, A. M., Reynolds, F., Merkle, H. P., Weissleder, R., and Josephson, L. (2005) Transport Of Surface-Modified Nanoparticles Through Cell Monolayers. *Chembiochem 6*, 337−345.

(18) Vives, E., Brodin, P., and Lebleu, B. (1997) A truncated HIV-1 Tat protein basic domain rapidly translocates through the plasma membrane and accumulates in the cell nucleus. *J. Biol. Chem. 272*, 16010−7.

(19) Hermanson, G. T. (1996) *Bioconjugate Techniques*, Academic Press, San Diego CA.

(20) Suzuki, T., Futaki, S., Niwa, M., Tanaka, S., Ueda, K., and Sugiura, Y. (2002) Possible existence of common internalization mechanisms among arginine-rich peptides. *J. Biol. Chem. 277*, 2437−43.

(21) Mann, D. A., and Frankel, A. D. (1991) Endocytosis and targeting of exogenous HIV-1 Tat protein. *EMBO J 10*, 1733−9.

(22) Josephson, L., Tung, C. H., Moore, A., and Weissleder, R. (1999) High-efficiency intracellular magnetic labeling with novel superparamagnetic-Tat peptide conjugates. *Bioconjugate Chem. 10*, 186−91.

(23) Fawell, S., Seery, J., Daikh, Y., Moore, C., Chen, L. L., Pepinsky, B., and Barsoum, J. (1994) Tat-mediated delivery of heterologous proteins into cells. *Proc. Natl. Acad. Sci. U. S. A. 91*, 664−8.

(24) Schwarze, S. R., and Dowdy, S. F. (2000) In vivo protein transduction: intracellular delivery of biologically active proteins, compounds and DNA. *Trends Pharmacol. Sci. 21*, 45−8.

(25) Torchilin, V. P., Rammohan, R., Weissig, V., and Levchenko, T. S. (2001) TAT peptide on the surface of liposomes affords their efficient intracellular delivery even at low temperature and in the presence of metabolic inhibitors. *Proc Natl. Acad. Sci. U. S. A. 98*, 8786−91.

(26) Richard, J. P., Melikov, K., Vives, E., Ramos, C., Verbeure, B., Gait, M. J., Chernomordik, L. V., and Lebleu, B. (2003) Cell-penetrating peptides. A reevaluation of the mechanism of cellular uptake. *J. Biol. Chem. 278*, 585−90.

(27) Lundberg, M., Wikstrom, S., and Johansson, M. (2003) Cell surface adherence and endocytosis of protein transduction domains. *Mol. Ther. 8*, 143−50.
(28) Lindgren, M., Hallbrink, M., Prochiantz, A., and Langel, U. (2000) Cell-penetrating peptides. *Trends Pharmacol. Sci. 21*, 99−103.
(29) Vives, E., Richard, J. P., Rispal, C., and Lebleu, B. (2003) TAT peptide internalization: seeking the mechanism of entry. *Curr. Protein Pept. Sci. 4*, 125−32.
(30) Futaki, S. (2005) Membrane-permeable arginine-rich peptides and the translocation mechanisms. *Adv. Drug Delivery Rev. 57*, 547−58.
(31) Wadia, J. S., and Dowdy, S. F. (2005) Transmembrane delivery of protein and peptide drugs by TAT-mediated transduction in the treatment of cancer. *Adv. Drug Delivery Rev. 57*, 579−96.

BC0501451

Antigen-Decorated Shell Cross-Linked Nanoparticles: Synthesis, Characterization, and Antibody Interactions

Maisie J. Joralemon,[†] Norah L. Smith,[‡] David Holowka,[‡] Barbara Baird,[‡] and Karen L. Wooley[†,*]

Center for Materials Innovation and Department of Chemistry, Washington University in Saint Louis, One Brookings Drive, Saint Louis, Missouri 63130-4899, and Department of Chemistry and Chemical Biology, Cornell University, Ithaca, New York 14853-1301. Received May 26, 2005

Antigen-decorated shell cross-linked knedel-like nanoparticles (SCKs) were synthesized and studied as multivalent nanoscale surfaces from which antibody-binding units were presented in a manner that was designed to approach virus particle surfaces. The SCK nanostructures were fabricated with control over the number of antigenic groups, from mixed micellization of amphiphilic diblock copolymer building blocks that contained either an antigen (2,4-dinitrophenyl) or an ethylpropionate group at the hydrophilic α-chain terminus. Amphiphilic diblock copolymers were synthesized by atom transfer radical polymerization of *tert*-butyl acrylate and methyl acrylate sequentially from either a 2,4-dinitrophenyl-functionalized initiator or ethyl 2-bromopropionate, followed by selective removal of the *tert*-butyl groups to afford 2,4-dinitrophenyl-poly(acrylic acid)$_{60}$-*b*-poly(methyl acrylate)$_{60}$ (DNP-PAA$_{60}$-*b*-PMA$_{60}$) and poly(acrylic acid)$_{70}$-*b*-poly(methyl acrylate) (PAA$_{70}$-*b*-PMA$_{70}$). Micelles were assembled via addition of water to THF solutions of the polymers in 0:1, 1:1, and 1:0 molar ratios of DNP-PAA$_{60}$-*b*-PMA$_{60}$ to PAA$_{70}$-*b*-PMA$_{70}$, followed by dialysis against water. The acrylic acid groups of the micelle coronas were partially cross-linked (nominally 50%) with 2,2′-(ethylenedioxy)bis-(ethylamine), in the presence of 1-(3′-dimethylaminopropyl)-3-ethylcarbodiimide methiodide. Following extensive dialysis against water, the 0%, 50%, and 100% dinitrophenylated shell cross-linked nanoparticles (DNP-SCKs) were characterized with dynamic light scattering (DLS), transmission electron microscopy (TEM), atomic force microscopy (AFM), differential scanning calorimetry (DSC), thermogravimetric analysis (TGA), infrared and UV−vis spectroscopies, and analytical ultracentrifugation (AU). The surface accessibility and bioavailability of the DNP units upon the DNP-SCKs were investigated by performing quenching titrations of fluorescein-labeled IgE antibody in solution and degranulation of IgE sensitized RBL-2H3 cells. The DNP antigens proved to be surface-available and able to form multivalent bonds with IgE antibodies, causing degranulation.

INTRODUCTION

Since Edward Jenner's successful protection of humans from small pox was achieved by vaccination with cowpox in 1796, many resources have been devoted to devising formulations that train the human body to defend itself against attacks from diseases (*1*). These heroic efforts have grown into the diverse field of immunology, encompassing not only attacks from pathogens, but also allergic responses and autoimmune diseases. Traditionally, synthetic vaccines employ weakened strains of a pathogen to protect humans from disease and often consist of an antigen and a carrier or adjuvant. In some cases, the carrier acts as an adjuvant and has a marked role in the performance of the vaccine, lending improved properties that the antigen alone is unable to achieve. Examples of improved characteristics provided by the carrier include immunostimulation (*2*, *3*), enhanced solubility and circulation (*4*), and the display of multiple copies of the haptenic groups that identify the antigen (*5*).

Nanoparticle platforms that have been employed as antigenic carriers include liposomes and virosomes (*6*−*8*), immune stimulating complexes (ISCOMs) (*9*), chitosan (*10*−*12*), inorganic (*13*−*16*), polymer micelles (*17*, *18*), dendrimers (*19*−*21*), and other types of nanoparticles (*22*−*24*). These nanosized scaffolds hold the ability to impart the advantages of traditional antigen carriers, as well as unique characteristics such as the presentation of targeting ligands (*25*−*30*) and the sequestration and release of guest molecules (i.e. imaging agents and therapeutics) (*31*−*37*). SCKs (*38*−*40*) have demonstrated the ability to display multiple copies of biologically active ligands (*41*−*48*) and sequester guests (*49*−*54*) and could potentially improve the solubility and circulation of small guest molecules in vivo. The employment of SCKs as antigen carriers was, therefore, self-evident and as a fundamental investigation, a well-known antigenic group, 2,4-dinitrophenyl (DNP), was displayed multivalently from shell cross-linked nanoparticles.

This type of multivalent antigen presentation is important for participation in triggering an immune response (*55*−*57*). For example, the allergic response requires cross-linking of IgE that are bound to a receptor on a cell surface (*1*). Specifically upon cross-linking by multivalently displayed DNP, anti-DNP IgE antibodies bound to the high affinity receptor, FcεRI, on the surface of RBL-2H3 mast cells trigger release of histamine and other immune effectors, thus eliciting an immune response (*58*). The 2,4-dinitrophenylated shell cross-linked nanoparticles were designed to display the hapten both multivalently and at a sufficient surface density, based on the fundamental work of Baird et al. (*59*), to cross-

* Corresponding author. E-mail: klwooley@artsci.wustl.edu Tel: (314) 935-7136 Fax: (314) 935-9844
[†] Washington University in Saint Louis.
[‡] Cornell University.

10.1021/bc0501505 CCC: $30.25 © 2005 American Chemical Society
Published on Web 09/02/2005

link the IgE antibodies bound to RBLs. In their study it was discovered that a third generation dendrimer was able to elicit an allergic immune response, while earlier generations were not. The density of the antigenic termini on SCKs were, therefore, varied to allow for comparisons of the multivalent binding interactions as a function of surface density for antigen presentation.

EXPERIMENTAL SECTION

Materials. Polymerizations were performed on a double manifold (0.1 mmHg vacuum, 99.99% N_2), with glassware and syringes that were dried in an oven (100 °C) for at least 1 h, and with syringes that were washed with N_2 (3 ×), prior to use. Tetrahydrofuran (99%), methyl acrylate (99%), and *tert*-butyl acrylate (99%) were received from Sigma-Aldrich Company (St. Louis, MO) and distilled from sodium/benzophenone and calcium hydride, respectively, under N_2 prior to use. Sodium bicarbonate (certified ACS) and magnesium sulfate (certified anhydrous) were obtained and used directly from Fisher Scientific (Pittsburgh, PA). All other materials were used as received from Sigma-Aldrich Company. Flash column chromatography was performed using 32−63 D 60 Å silica gel from ICN SiliTech (ICN Biomedicals GmbH, Eschwege, Germany). Spectra/Por membranes (Spectrum Medical Industries, Inc., Laguna Hills, CA) used for dialysis were obtained from Fisher Scientific (Pittsburgh, PA).

Anti-DNP IgE antibodies were purified (*60*) and labeled with FITC as described previously (*61*). RBL-2H3 cells were maintained as described previously (*60*, *62*) and used 3 to 5 days after passage. Dinitrophenylated bovine serum albumin (DNP-BSA) with an average of 16 DNP groups per protein was prepared as previously reported (*63*). All cell media and tissue culture additives were obtained from Gibco (Grand Island, NY).

Instrumentation. Infrared spectra were obtained on a Perkin-Elmer Spectrum BX FT-IR system using diffuse reflectance sampling accessories. ^{1}H NMR (300 MHz) and ^{13}C NMR (75 MHz) spectra were recorded in solution on a Varian Mercury 300 spectrometer with the solvent signal as reference. Glass-transition temperatures (T_g) were measured on a Mettler Toledo (Columbus, OH) DSC822^e differential scanning calorimeter. Data were acquired and analyzed with Thermal Analysis PC software (version 7.01; Mettler Toledo). Heating rates were 10 °C/min, and the T_g was taken as the midpoint of the inflection tangent, upon the third heating scan. Thermogravimetric analysis was performed on a Mettler Toledo SDTA851 TGA module with Thermal Analysis PC software (version 7.01; Mettler Toledo). Heating rates were 10 °C/min, and the onset temperature for weight loss was the point at which two tangential lines in the TGA curves intersected.

Gel permeation chromatography injections were made on a Waters Chromatography, Inc. (Milford, MA) 1515 isocratic HPLC pump, equipped with a Waters Chromatography, Inc. inline degasser AF, Breeze (version 3.30, Waters Chromatography, Inc.) software, a Model 2414 differential refractometer (Waters Inc.), a Precision Detectors, Inc. (Bellingham, MA) Model PD2020 dual-angle (15° and 90°) light scattering detector, and four PLgel polystyrene-*co*-divinylbenzene gel columns supplied by Polymer Laboratories, Inc. (Amherst, MA) connected in the following series: 5 μm Guard (50 × 7.5 mm), 5 μm Mixed-C (300 × 7.5 mm), 5 μm 10^4 Å (300 × 7.5 mm), and 5 μm 500 Å (300 × 7.5 mm). Data collection was performed with Precision Detectors, Inc. Precision Acquire 32 Acquisition Program. Data analysis was performed with Precision Detectors, Inc. Discovery 32 (version 1.027.000) software. Interdetector delay volume and the light scattering detector calibration constant were determined from a nearly monodisperse polystyrene calibrant (Pressure Chemical Co., $M_n = 90\,000$ g/mol, $M_w/M_n < 1.04$). The dn/dc values of the analyzed polymers were then determined from the differential refractometer response.

Hydrodynamic diameters (D_n) and size distributions for the SCKs in aqueous solutions were determined by dynamic light scattering (DLS). The DLS instrumentation consisted of a Brookhaven Instruments Limited (Worcestershire, U.K.) system, including a model BI-200SM goniometer, a model BI-9000AT digital correlator, a model EMI-9865 photomultiplier, and a model 95-2 Ar ion laser (Lexel, Corp.; Farmindale, NY) operated at 514.5 nm. Measurements were made at 20 ± 1 °C. Prior to analysis, solutions were centrifuged in a model 5414 microfuge (Brinkman Instruments, Inc.; Westbury, NY) for 4 min to remove dust particles. Scattered light was collected at a fixed angle of 90 °C. The digital correlator was operated with 522 ratio spaced channels and initial delay of 0.1 μs, a final delay of 5.0 μs, and a duration of 15 min. A photomulitplier aperture of 200 μm was used, and the incident laser intensity was adjusted to obtain a photon counting of 200 kcps. Only measurements in which the measured and calculated baselines of the intensity autocorrelation function agreed to within 0.1% were used to calculate particle size. Particle size distributions were performed with the ISDA software package (Brookhaven Instruments Company), which employed single-exponential fitting, cumulants analysis, and non-negatively constrained least-squares particle size distribution analysis routines. Transmission electron microscopy samples were diluted in water (9:1) and further diluted with a 1% phosphotungstic acid (PTA) stain (1:1). Carbon grids were prepared by a plasma treatment to increase the surface hydrophilicity. Micrographs were collected at 100 000× magnification and calibrated using a 41 nm polyacrylamide bead from NIST. Averages of particle diameters were generated from the analysis of a minimum of 150 particles from at least three different micrographs.

The height measurements and distributions for the SCKs were determined by tapping-mode AFM under ambient conditions in air. The AFM instrumentation consisted of a Nanoscope III BioScope system (Digital Instruments, Veeco Metrology Group; Santa Barbara, CA) and standard silicon tips (type, OTESPA-70; L, 160 μm; normal spring constant, 50 N/m; resonance frequency, 246−282 kHz). The sample solutions were drop (2 μL) deposited onto freshly cleaved mica and allowed to dry freely in air.

Analytical ultracentrifugation experiments were conducted on a Beckman Instruments, Inc. (Fullerton, CA) model Optima XL-I analytical ultracentrifuge fitted with a model An60-Ti four-hole rotor, and Epon charcoal-filled, six-channel centerpiece sample cells with matched sapphire windows. All data were recorded using the instrument's Rayleigh interferometric (refractive index) detection optics at 20 °C and 5000, 4000, and 3000 rpm, respectively, with a centrifugation time of 3−5 days to reach sedimentation equilibrium. The solution volume was 110 μL, and the optical path length was 12 mm. A Mettler-Parr model DMA 602 high-precision digital density meter was employed to determine the density at 20.0 °C for all solutions. All densities were an average of five runs, with measurements of 100 periods per run. The

weight-average degree of aggregation, N_{agg}, was computed as previously reported (*47*).

Synthesis of *N*-(2,4-Dinitrophenyl)ethanolamine (1). The previously described synthesis was followed (*64*). Into a 50 mL two-neck round-bottom flask fitted with a stopper and an inlet stopper was charged 1-iodo-2,4-dinitrobenzene (3.94 g, 13.4 mmol) and DMSO (15 mL). Upon stirring for 5 min at RT, all of the starting material had dissolved and ethanolamine (2.40 mL, 40.2 mmol) was added, followed by potassium hydroxide pellets (3.36 g, 60.3 mmol). The reaction was allowed to stir at RT for 2 h and was monitored by TLC (10% MeOH in CH_2Cl_2, $R_{f(product)} = 0.49$). The reaction mixture was poured over ice, and the bright yellow solid was isolated by vacuum filtration and recrystallized in ethanol. Isolated yield 1.58 g (52%). IR: 3571−3000, 3354, 3000−2750, 1616, 1580, 1330, 1301, 920 cm^{-1}. ^1H NMR (CD_2Cl_2): δ 1.96 (t, J = 5 Hz, 1H, $NHCH_2CH_2OH$), 3.58 (overlapping dt, J = 5 Hz, 2H, $NHCH_2CH_2OH$), 3.97 (overlapping dt, J = 5 Hz, 2H, $NHCH_2CH_2OH$), 7.00 (d, J = 10 Hz, 1H, ortho to $NHCH_2CH_2OH$), 8.26 (dd, J = 10 and 2 Hz, 1H, meta to $NHCH_2CH_2OH$), 8.80 (br s, 1H, $NHCH_2CH_2OH$), 9.09 (d, J = 2 Hz, 1H, meta to $NHCH_2CH_2OH$ and ortho to each NO_2) ppm. ^{13}C NMR (CD_2Cl_2): δ 45.9, 61.0, 114.9, 124.7, 130.8, 149.3 ppm. HRMS (ESI): calcd for ($C_8H_9N_3O_5$+H): 227.0542, found 227.0540 ± 1.0 ppm (MH^+).

Synthesis of 2-Bromopropionic Acid 2-(2,4-Dinitrophenylamino)ethyl Ester (2). A 50 mL two-neck round-bottom flask that was fitted with a N_2 inlet was flame-dried under vacuum and allowed to cool to RT under a flow of N_2. A solution of **1** (0.50 g, 2.2 mmol) in THF (6 mL) was added to the reaction flask via syringe, followed by addition of triethylamine (0.30 mL, 2.2 mmol) via syringe. The reaction mixture was allowed to stir under N_2 at 0 °C for 30 min. Prior to use, the 2-bromopropionyl bromide reagent bottle was allowed to stand in an ice bath for 30 min. 2-Bromopriopionyl bromide (0.50 mL, 4.8 mmol) was added to the reaction via syringe, and the reaction mixture was allowed to stir under N_2 at 0 °C for 2 h. The reaction progress was monitored by TLC (CH_2Cl_2, $R_{f(product)} = 0.86$). The reaction mixture was dissolved in CH_2Cl_2 and extracted three times with a saturated aq. solution of $NaHCO_3$, followed by three extractions with H_2O. The organic layer was dried with $MgSO_4$ and filtered, and the filtrate was concentrated by rotary evaporation to yield a yellow oil. The oil was dissolved in CH_2Cl_2 and eluted on a silica gel column with CH_2Cl_2 and then further purified by recrystallization in ether. Isolated yield 0.68 g (86%). IR: 3350, 3100−2700, 1818, 1740, 1617, 1589, 1440, 744, 557 cm^{-1}. ^1H NMR ($CDCl_3$): δ 1.84 (overlapping doublets, J = 6 Hz, 3H, CH_3CHBr), 3.78 (overlapping dt, J = 6 Hz, 2H, $NHCH_2CH_2$), 4.41 (m, J = 7 Hz, 2H, $NHCH_2CH_2$), 4.50 (m, J = 6 Hz, 1H, CH_3CHBr), 7.02 (d, J = 9 Hz, 1H, ortho to $NHCH_2CH_2O$), 8.33 (d of d, J = 9 Hz, 2 Hz, 1H, meta to $NHCH_2CH_2O$), 8.75 (br t, J = 6 Hz, 1H, $NHCH_2CH_2O$), 9.17 (d, J = 2 Hz, 1H, meta to $NHCH_2CH_2O$ and ortho to each NO_2) ppm. ^{13}C NMR ($CDCl_3$): δ 21.6, 39.4, 42.1, 63.2, 114.0, 124.5, 130.7, 148.3, 170.4 ppm. HRMS (FAB): calcd for ($C_{11}H_{12}N_3O_6Br$+Li): 368.0069, found 368.0057 ± 3.4 ppm (MH^+).

Synthesis of 2,4-Dinitrophenylateded Poly(*tert*-butyl acrylate)$_{60}$ (3). A 100 mL two-neck round-bottom flask that was fitted with a gas inlet adapter and a stopcock was flame-dried under vacuum and allowed to cool to ambient temperature under N_2. The flask was charged with CuBr (0.368 g, 2.48 mmol), and a septum was placed over the stem of the stopcock. Under positive pressure of N_2, a solution of **2** (0.447 g, 1.24 mmol) dissolved in *tert*-butyl acrylate (36.3 mL, 0.25 mol) was added via syringe, followed by addition of pentamethyldiethylenetriamine (PMDETA) (0.52 mL, 2.5 mmol), via syringe. Following three freeze−pump−thaw degassing cycles, the reaction was allowed to stir for 3.5 h at 50 °C. After quenching of the polymerization by submerging the flask in liquid nitrogen, the mixture was allowed to warm to ambient temperature. The reaction mixture was diluted with tetrahydrofuran and filtered through an alumina plug. The filtrate was precipitated three times from tetrahydrofuran into a 70% methanol, deionized water solution: Isolated yield 18.69 g (88%). M_n = 8400 g/mol, M_w/M_n = 1.5 from SEC. DSC: $T_{g(DNP-PtBA)}$ = 45 °C, TGA: 210−242 °C = 43% mass loss, 242−294 °C = 10% mass loss, 294−500 °C = 33% mass loss, 500 °C = 14% mass remaining. IR: 3429, 3100−2600, 1734, 1717, 1617, 1474, 1253, 1166, 845 cm^{-1}. ^1H NMR($CDCl_3$): δ 1.42, (s, $C(CH_3)_3$), 1.70−2.00 (br, m, C*H* polymer backbone), 2.21 (br s, CH_2 polymer backbone), 3.73 (br m, $NHCH_2CH_2$), 4.36 (br m, $NHCH_2CH_2$), 7.02 (br m, 1H, ortho to $NHCH_2CH_2O$), 8.31 (br m, 1H, meta to $NHCH_2CH_2O$), 8.75 (br s, 1H, $NHCH_2CH_2O$), 9.14 (s, 1H, meta to $NHCH_2CH_2O$ and ortho to each NO_2) ppm. ^{13}C NMR ($CDCl_3$): δ 28.2, 37.5, 42.5, 80.5, 174.4 ppm. Elem. Anal. Theoretical C 64.27% H 9.17% N 0.52%, Br 0.99 Found C 64.49% H 9.17% N 0.36% Br 1.10%.

Synthesis of 2,4-Dinitrophenylateded Poly(*tert*-butyl acrylate)$_{60}$-*b*-poly(methyl acrylate)$_{60}$ (4). A 50 mL two-neck round-bottom flask that was fitted with a gas inlet adapter and a stopcock was flame-dried under vacuum and allowed to cool to ambient temperature under N_2. A septum was placed over the stem of the stopcock and under a positive pressure of N_2, and CuBr (0.0502 g, 0.350 mmol) was added followed by a solution of **3** (2.87 g, 0.34 mmol) dissolved in methyl acrylate (5.0 mL, 55 mmol). After three freeze−pump−thaw degassing cycles, PMDETA (0.07 mL, 0.3 mmol) was added via syringe under a positive pressure of N_2. Following a freeze−pump−thaw degassing cycle, the reaction mixture was allowed to stir for 4 h at 50 °C. After quenching the polymerization, by submersion of the flask in liquid nitrogen, and allowing the mixture to warm to ambient temperature, the reaction mixture was diluted with tetrahydrofuran and filtered through an alumina plug. The filtrate was precipitated three times from tetrahydrofuran into a 70% methanol, deionized water solution: Isolated yield 3.13 g (64%). M_n = 14280 g/mol, M_w/M_n = 1.1 from SEC. DSC: $T_{g(DNP-PtBA)}$ = 40 °C, $T_{g(PMA)}$ = 18 °C, TGA: 225−245 °C = 35% mass loss, 245−300 °C = 10% mass loss, 300−350 °C = 10% mass loss, 350−500 °C = 35% mass loss, 500 °C = 10% mass remaining. IR: 3434, 3100−2800, 1737, 1717, 1617, 1589, 1477, 1262, 1169, 845 cm^{-1}. ^1H NMR($CDCl_3$): δ 1.44 (br s, $C(CH_3)_3$), 1.20 − 2.00 (br m, CH_2 polymer backbone), 2.10−2.41 (br m, C*H* polymer backbone), 3.67 (br s, $COOCH_3$), 4.38 (br m, 3H, $CH_2COOCHCH_3$), 7.04 (br m, ortho to $NH_2CH_2CH_2$), 8.32 (br m, meta to $NH_2CH_2CH_2$), 8.75 (br m, $NHCH_2CH_2$), 9.16 (br m, meta to $NH_2CH_2CH_2$ and ortho to each NO_2) ppm. ^{13}C NMR ($CDCl_3$): δ 28.2, 35.4, 41.5, 51.9, 80.5, 174.4, 175.1 ppm. Elem. Anal. Theoretical C 60.95% H 8.33%, N 0.32%, Found C 63.01% H 9.06%, N 0.31%.

Synthesis of 2,4-Dinitrophenylateded Poly(acrylic acid)$_{60}$-*b*-poly(methyl acrylate)$_{60}$ (5). A 250 mL round-bottom flask, fitted with a gas inlet, was charged with **6** (2.00 g, 0.14 mmol) and a solution of trifluoroacetic acid (6.00 mL, 77.9 mmol) in dichloromethane (20.0 mL). The reaction was allowed to stir at ambient temperature overnight. The solvent was removed under vacuum, and

the resulting solid was taken up in tetrahydrofuran. The solution was transferred to a dialysis bag (MWCO 6−8 kDa), and the solution was dialyzed against a continuous flow of deionized water for 24 h. The final amphiphilic diblock copolymer was isolated by lyophilization: Isolated yield 1.46 g, (89%). DSC: $T_{g(DNP-PAA)}$ = 86 °C, $T_{g(PMA)}$ = 14 °C, TGA: 30−90 °C = 4% mass loss, 170−270 °C = 24% mass loss, 270−500 °C = 34% mass loss, 500 °C = 38% mass remaining. IR: 3670−3069, 3069−2729, 1730, 1712, 1694, 1557, 1446, 1210, 802 cm^{-1}. ^1H NMR (D_2O): δ 1.20−1.90 (br m, CH_2 polymer backbone), 2.10−2.40 (br s, CH polymer backbone), 3.70 (s, COOCH_3), 7.29 (br m, ortho to $NH_2CH_2CH_2$), 8.35 (br m d, meta *to* NH_2CH_2-CH_2), 9.11 (br s, meta to $NH_2CH_2CH_2$ and ortho to each NO_2) ppm. ^{13}C NMR (DMSO-d_6): δ 39.0, 40.1, 51.6, 174.5, 175.9 ppm.

Synthesis of Poly(*tert*-butyl acrylate)$_{70}$ (6). A 100 mL two-neck round-bottom flask that was fitted with a gas inlet adapter and a stopcock was flame-dried under vacuum and allowed to cool to ambient temperature under N_2. The flask was charged with CuBr (0.57 g, 3.97 mmol). A septum was placed over the stem of the stopcock, and under positive pressure of N_2, *tert*-butyl acrylate (22.0 mL, 150 mmol) was added via syringe, followed by addition of PMDETA (0.83 mL, 3.97 mmol), via syringe. After three freeze−pump−thaw degassing cycles, ethyl 2-bromopropionate (0.19 mL, 1.50 mmol) was added via syringe under a positive pressure of N_2. Following a freeze−pump−thaw degassing cycle, the reaction was allowed to stir for 1.5 h at 50 °C. The polymerization was quenched by submerging the flask in liquid nitrogen, and the mixture was allowed to warm to ambient temperature. The reaction mixture was diluted with tetrahydrofuran and filtered through an alumina plug. The filtrate was precipitated three times from tetrahydrofuran into a 70% methanol, deionized water solution: Isolated yield 13.0 g, (92%). M_n = 9420 g/mol, M_w/M_n = 1.1 from SEC. DSC: $T_{g(PtBA)}$ = 41 °C, TGA: 197−230 °C = 44% mass loss, 230−500 °C = 46% mass loss, 500 °C = 10% mass remaining. IR: 3100−2800, 1722, 1365, 1142, 844 cm^{-1}. ^1H NMR ($CDCl_3$): δ 1.15 (t, J = 5 Hz, 3H, CH_2CH_3 end group), 1.21 (d, J = 5 Hz, 3H, CH_3CH end group), 1.43, (br s, C(CH_3)$_3$), 1.20−1.70 (br m, CH polymer backbone), 2.0−2.4, (br m, CH_2 polymer backbone), 4.11 (q, J = 5 Hz, 2H, CH_2CH_3 end group) ppm. ^{13}C NMR ($CDCl_3$): δ 28.2, 37.6, 42.5, 80.5, 174.4 ppm. Elem. Anal. Theoretical C 64.96% H 9.35%, Br 0.87%, Found C 65.17% H 9.43%.

Synthesis of Poly(*tert*-butyl acrylate)$_{70}$-*b*-poly(methyl acrylate)$_{70}$ (7). A 100 mL two-neck round-bottom flask that was fitted with a gas inlet adapter and a stopcock was flame-dried under vacuum and allowed to cool to ambient temperature under N_2. The flask was charged with CuBr (0.29 g, 2.0 mmol). A septum was placed over the stem of the stopcock, and under positive pressure of N_2, **1** (9.51 g, 1.01 mmol) dissolved in methyl acrylate (9.1 mL, 0.1 mol) was added via syringe. After three freeze−pump−thaw degassing cycles, PMDETA (0.42 mL, 2.0 mmol) was added via syringe under a positive pressure of N_2. Following a freeze−pump−thaw degassing cycle, the reaction was allowed to stir for 2 h at 50 °C. The polymerization was quenched by submerging the flask in liquid nitrogen, and the mixture was allowed to warm to ambient temperature. The reaction mixture was diluted with tetrahydrofuran and filtered through an alumina plug. The filtrate was precipitated three times from tetrahydrofuran into a 70% methanol, deionized water solution: Isolated yield 13.0 g, (72%). M_n = 16820 g/mol, M_w/M_n = 1.1 from SEC. DSC: $T_{g(PtBA)}$ = 39 °C, $T_{g(PMA)}$ = 19 °C, TGA: 236−250 °C = 25% mass loss, 250−374 °C = 16% mass loss, 374−500 °C = 50% mass loss, 500 °C = 9% mass remaining. IR: 3670−3300, 3100−2800, 1748, 1714, 1454, 1372, 849 cm^{-1}. ^1H NMR-($CDCl_3$): δ 1.42 (br s, C(CH_3)$_3$), 1.20−1.90 (br m, CH_2 polymer backbone), 2.10−2.40 (br m, CH polymer backbone), 3.65 (br s, COOCH_3), 4.11 (q, J = 5 Hz, 2H, CH_2-CH_3 end group) ppm. ^{13}C NMR($CDCl_3$): δ 28.2, 35.2, 41.5, 51.9, 80.6, 174.4, 175.1 ppm. Elem. Anal. Theoretical C 61.30% H 8.43%, Found C 61.36% H 8.32%.

Synthesis of Poly(acrylic acid)$_{70}$-*b*-poly(methyl acrylate)$_{70}$ (8). A 250 mL round-bottom flask, fitted with a gas inlet adapter, was charged with **2** (10.1 g, 0.56 mmol) and a solution of trifluoroacetic acid (30.0 mL, 0.39 mol) in dichloromethane (100.0 mL). The reaction was allowed to stir at ambient temperature for 9 h. The solvent was removed under vacuum, and the resulting solid was taken up in tetrahydrofuran. The solution was transferred to a dialysis bag (MWCO 6−8 kDa), and the solution was dialyzed against a continuous flow of deionized water for 24 h. The final amphiphilic diblock copolymer was isolated by lyophilization: Isolated yield 4.8 g, (77%). DSC: $T_{g(PAA)}$ = 116 °C, $T_{g(PMA)}$ = 14 °C, TGA: 253−329 °C = 20% mass loss, 329−500 °C = 70% mass loss, 500 °C = 10% mass remaining. IR: 3670−2276, 1748, 1717, 1453, 1267, 1174, 828 cm^{-1}. ^1H NMR (DMSO-d_6): δ 1.16 (t, J = 5 Hz, 3H, CH_2CH_3 end group), 1.20−1.90 (br m, CH_2 polymer backbone), 2.10−2.40 (br s, CH polymer backbone), 3.60 (br s, COOCH_3), 4.03 (q, J = 5 Hz, 2H, CH_2CH_3 end group) ppm. ^{13}C NMR (DMSO-d_6): δ 34.6, 40.9, 51.6, 174.5, 175.9, 176.0 ppm. Elem. Anal. Theoretical C 52.82% H 6.35%, Found C 53.02% H 6.44%.

Assembly of 0% DNP Micelle (9). Nanopure water (1.00 L, 18 MΩ-cm) was added dropwise via a syringe pump at a rate of 15.0 mL/h to a THF solution of **8** (1.2 g in 1.0 L). The solution was dialyzed (MWCO 6−8 kDa) against Nanopure water for 3 days. DLS: D_{av} = 12 ± 1 nm. ζ = −39 ± 1 mV.

Assembly of 50% DNP Micelle (10). Nanopure water (500 mL, 18 MΩ-cm) was added dropwise via a syringe pump at a rate of 15.0 mL/h to a THF solution of **8** (250 mL, 1.00 mg/mL) and **5** (250 mL, 1.00 mg/mL). The solution was dialyzed (MWCO 6−8 kDa) against Nanopure water for 3 days. DLS: NA, no correlation function due to the low concentration of the sample. ζ = −52 ± 1 mV.

Assembly of 100% DNP Micelle (11). Nanopure water (500 mL, 18 MΩ-cm) was added dropwise via a syringe pump at a rate of 15.0 mL/h to a THF solution of **5** (500 mL, 1.00 mg/L). The solution was dialyzed (MWCO 6−8 kDa) against Nanopure water for 3 days. DLS: D_{av} = 41 ± 10 nm. ζ = −35 ± 1 mV.

Synthesis of 0% DNP SCK (12). A solution of 2,2′-(ethylenedioxy)bis(ethylamine) in Nanopure water (1.82 mL, 1.23 mmol, 100 mg/mL) was added dropwise to the micelle solution (3.10 L, 4.92 mmol acrylic acid). The mixture was allowed to stir at RT for 1 h, and a solution of 1-(3′-dimethylaminopropyl)-3-ethylcarbodiimide methiodide in Nanopure water (7.31 mL, 2.46 mmol, 100 mg/mL) was then added dropwise to the reaction flask. The reaction was allowed to stir at RT for 12 h and was then dialyzed against Nanopure water (MWCO 12−14 kDa) for 4 days. DSC: T_g = 8 °C, TGA: 190−335 °C = 15% mass loss, 335−500 °C = 64% mass loss, 500 °C = 21% mass remaining. IR: 3685−3000, 3000−2670, 1737, 1651, 1639, 1440, 1265, 1166, 827 cm^{-1}. DLS: D_{av} = 24 ± 3 nm, AFM: H_{av} = 1.2 ± 0.3 nm, D_{av} = 47 ± 12 nm, TEM: D_{av} = 13 ± 2 nm. ζ = −25 ± 1 mV.

Synthesis of 50% DNP SCK (13). A solution of 2,2′-(ethylenedioxy)bis(ethylamine) in Nanopure water (1.15 mL, 0.78 mmol, 100 mg/mL) was added dropwise to the micelle solution (1.72 L, 3.11 mmol acrylic acid). The mixture was allowed to stir at RT for 1 h, and a solution of 1-(3′-dimethylaminopropyl)-3-ethylcarbodiimide methiodide in Nanopure water (4.64 mL, 1.56 mmol, 100 mg/mL) was then added dropwise to the reaction flask. The reaction was allowed to stir at RT for 12 h and was then dialyzed against Nanopure water (MWCO 12−14 kDa) for 4 days. DSC: T_g = 14 °C, TGA: 40−185 °C = 4% mass loss, 185−350 °C = 18% mass loss, 350−500 °C = 60% mass loss, 500 °C = 18% mass remaining. IR: 3685−3100, 3100−2660, 1734, 1631, 1639, 1445, 1260, 1164, 825 cm^{-1}. DLS: $D_{av} = 23 \pm 3$ nm, AFM: $H_{av} = 1.1 \pm 0.2$ nm, $D_{av} = 96 \pm 21$ nm, TEM: $D_{av} = 24 \pm 3$ nm. $\zeta = -31 \pm 1$ mV.

Synthesis of 100% DNP SCK (14). A solution of 2,2′-(ethylenedioxy)bis(ethylamine) in Nanopure water (1.10 mL, 0.75 mmol, 100 mg/mL) was added dropwise to the micelle solution (1.56 L, 3.01 mmol acrylic acid). The mixture was allowed to stir at RT for 1 h, and a solution of 1-(3′-dimethylaminopropyl)-3-ethylcarbodiimide methiodide in Nanopure water (4.50 mL, 1.51 mmol, 100 mg/mL) was then added dropwise to the reaction flask. The reaction was allowed to stir at RT for 12 h and was then dialyzed against Nanopure water (MWCO 12−14 kDa) for 4 days. DSC: T_g = 11 °C, TGA: 45−75 °C = 4% mass loss, 200−335 °C = 13% mass loss, 335−500 °C = 59%, 500 °C = 24% mass remaining. IR: 3600−3100, 3100−2665, 1735, 1661, 1647, 1450, 1265, 1167, 821 cm^{-1}. DLS: $D_{av} = 22 \pm 5$ nm, AFM: $H_{av} = 1.1 \pm 0.2$ nm, $D_{av} = 77 \pm 16$ nm, TEM: $D_{av} = 12 \pm 2$ nm. $\zeta = -27 \pm 1$ mV.

Titration of FITC-IgE Quenching by SCK Particles. Experiments were performed as previously reported (*59*, *61*). Briefly, aliquots of the SCKs in Nanopure water were added to a thermostatically controlled (37 °C), continuously stirred, acrylic cuvette containing a solution of fluorescein−isothiocyanate (FITC)-modified anti-DNP IgE (2 μg/mL) in buffered saline solution (BSS: 135 mM NaCl, 5 mM KCl, 1 mM $MgCl_2$, 5.6 mM glucose, 20 mM HEPES, pH 7.4) containing gelatin (1 mg/mL). Fluorescence was monitored with a SLM 8000C spectrofluorometer(λ_{ex} = 490 nm, λ_{em} = 520 nm) over time, allowing the signal to reach equilibrium before the addition of another aliquot. Aliquots were added until the maximal quenching occurred, and the signal did not change significantly; this value was taken as saturation of the IgE. The fraction of bound IgE sites was calculated as:

$$\text{fraction of bound sites} = (I_o - I)/(I_o - I_f) \qquad (1)$$

where I_o is the average intensity of the IgE solution before the addition of aliquots, I_f is the average intensity of solution after maximal quenching, and I is the average of the last six data points of each addition, representing the intensity after addition of each aliquot of particles.

Degranulation Assays. Experiments were performed as previously reported (*65*, *66*). Briefly, a 96-well plate containing RBL-2H3 cells (10^6 cells/well) that had been sensitized with anti-DNP IgE at a 2−5 molar excess overnight (*62*) were stimulated with solutions of SCKs in Nanopure water (10^3−10^8 SCKs/cell), DNP-BSA (0.1 μg/mL), or TX-100 (0.1%) and allowed to incubate at 37 °C for 1 h. The release of β-hexosaminidase was monitored as previously described (*65*), using a fluorescence microplate reader (Tecan, Inc.). The percent degranulation was calculated based on the amount of β-hexosaminidase released upon treatment with 0.1% Triton-X 100 and corrected for spontaneous release in unstimulated cells. Experiments were performed in triplicate for each condition.

RESULTS AND DISCUSSION

Antigen-decorated SCKs were constructed from a combination of nonfunctionalized and chain-end functionalized amphiphilic diblock copolymers, which were assembled into micelles and cross-linked throughout the shell. The block lengths were intentionally maintained as relatively short segments in order to form small micelles, and amounts of DNP attached to the SCKs were controlled by the stoichiometric ratio of chain-end functionalized and nonfunctionalized polymers. The nanoparticles were designed to be flexible, shape-adaptable structures (*40*, *67*) having sizes of tens of nanometers in diameter to mimic the typical dimensions of virus particles. These allowed an appropriate density of surface-available antigens to bind multiple cell surface receptors per particle, since according to the immunon hypothesis, a minimum of 10 receptors must be clustered to induce a response (*56*). The physicochemical properties of the nanoparticles were fully characterized by IR and UV−vis spectroscopies, DLS, AFM, TEM, AU sedimentation equilibrium, DSC, TGA, and zeta potential measurements. The surface availability of the 2,4-dinitrophenylated chain-ends was evaluated by monitoring quenching caused upon binding of fluorescently labeled anti-DNP IgE antibodies with the SCKs and by measuring the degranulation caused by the binding of SCKs with anti-DNP IgE sensitized RBL cells.

To grow the chain-end functionalized amphiphilic diblock copolymer, from which the nanoparticles were constructed, a 2,4-dinitrophenylated atom transfer radical polymerization (ATRP) initiator was synthesized in two steps, shown in Scheme 1. Ethanolamine was added to the commercially available 1-iodo-2,4-dinitrobenzene starting material in the presence of KOH as previously reported (*64*), to afford the 2,4-dinitrophenylated alcohol **1**. The antigen-functionalized alkyl bromide initiator was then synthesized upon addition of 2-bromopropionyl bromide to **1** at 0 °C in the presence of triethylamine (TEA). Poly(*tert*-butyl acrylate)$_{60}$, **3**, was grown from the antigen-functionalized initiator under ATRP conditions. A poly(methyl acrlayte)$_{60}$ segment was then synthesized from the antigen-functionalized macroinitiator **3**, again under ATRP conditions, to yield 2,4-dinitrophenyl-poly(*tert*-butyl acrylate)$_{60}$-*b*-poly(methyl acrylate)$_{60}$ **4**. This diblock copolymer was transformed into an amphiphilic diblock copolymer through cleavage of the *tert*-butyl groups with a 30% solution of trifluoroacetic acid (TFA) in dichloromethane. Following dialysis of the reaction mixture into water, the amphiphilic diblock copolymer, 1,2-dinitrophenyl-poly(acrylic acid)$_{60}$-*b*-poly(methyl acrylate)$_{60}$ **5**, was formed, where the poly(acrylic acid) block was hydrophilic and the poly(methyl acrylate) block was hydrophobic. This amphiphilic character allowed assembly of the polymer chains into multimolecular micellar structures.

Selective cleavage of the tertiary ester side chain groups and retainment of the primary ester-linked antigenic chain-end group upon TFA treatment was confirmed via ^{1}H NMR spectroscopy. As shown in Figure 1, resonances characteristic of the 2,4-DNP aromatic region (protons a, b, and c) were observed from 7.2 to 9.2 ppm. Unfortunately, since the antigen is a chain-end moiety, the intensities of these proton signals were very weak

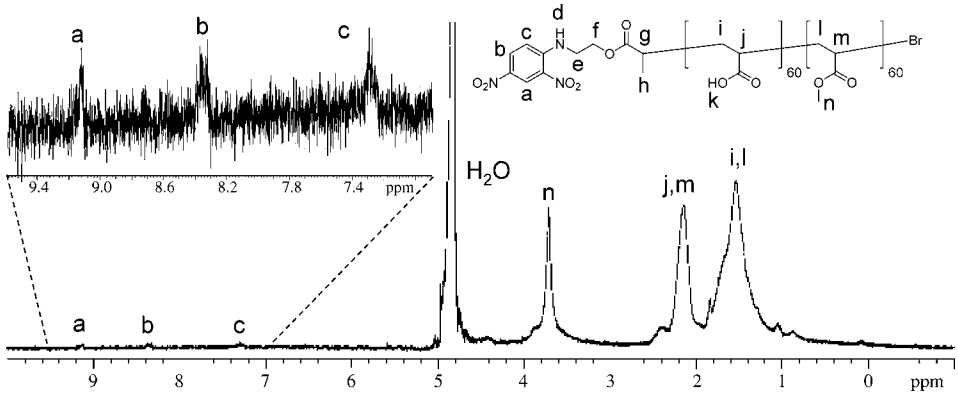

Figure 1. ^{1}H NMR (300 MHz, D_2O) spectrum of DNP-PAA_{60}-*b*-PMA_{60}, revealing resonances unique to the antigenic chain-end.

Scheme 1. Synthesis of 2,4-Dinitrophenylated Amphiphilic Diblock Copolymer, 5, via ATRP

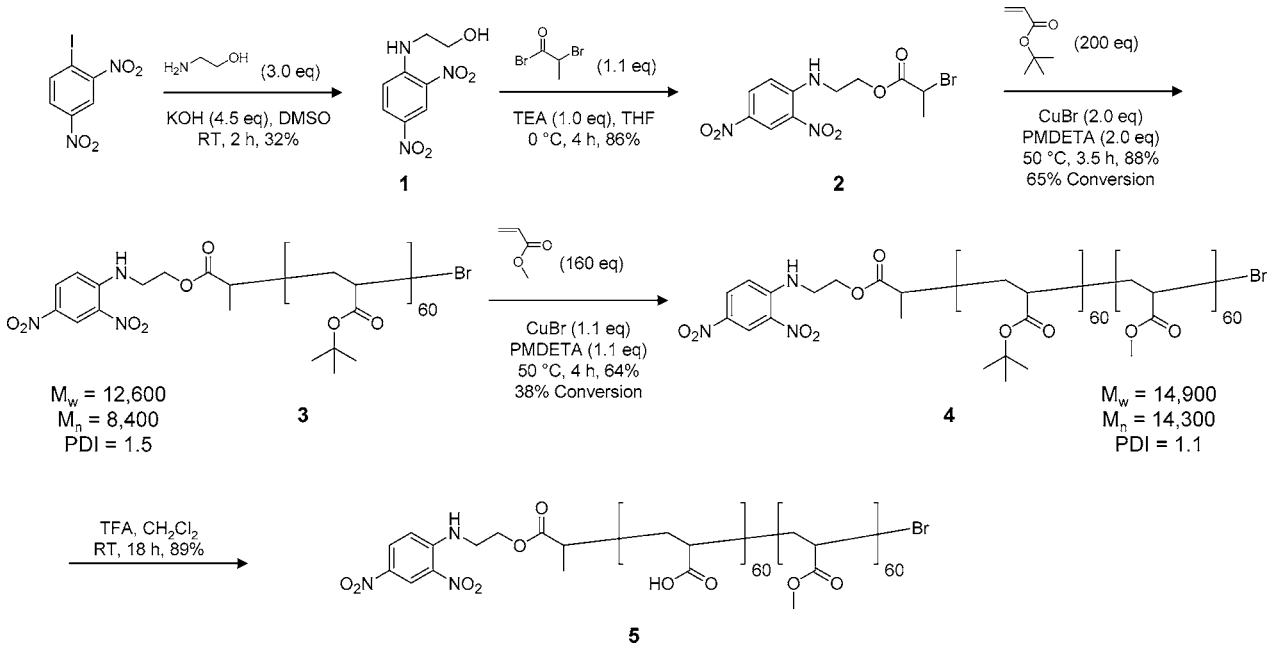

Scheme 2. Synthesis of the Nonfunctionalized Amphiphilic Diblock Copolymer, 8, via ATRP

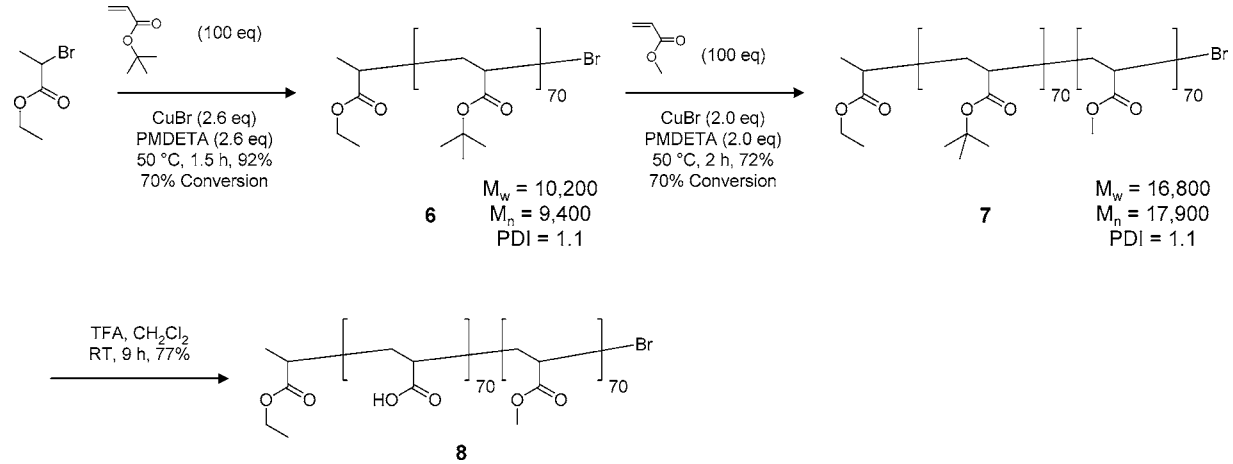

compared to the resonances of the polymer chain repeat unit protons; thus, integration of the unique 2,4-DNP signals was not quantitatively valid.

A nonfunctionalized amphiphilic diblock copolymer, similar in block length and composition, was synthesized in the same fashion as was performed for **5**, but with initiation from 2-ethyl bromopropionate, an alkyl bromide initiator for ATRP, as illustrated in Scheme 2. Again, under ATRP conditions, poly(*tert*-butyl acrylate) was grown to serve as a macroinitiator for the polymerization of methyl acrylate, which yielded poly(*tert*-butyl acrylate)$_{70}$-*b*-poly(methyl acrylate)$_{70}$. The *tert*-butyl groups were cleaved in the presence of TFA, to afford the amphiphilic diblock copolymer **8**. Each block was an average of 70 repeat units, giving the nonfunctionalized polymer both similar length and composition as the 2,4-

Scheme 3. Construction of 0%, 50%, and 100% Dinitrophenylated Shell Cross-Linked Nanoparticles

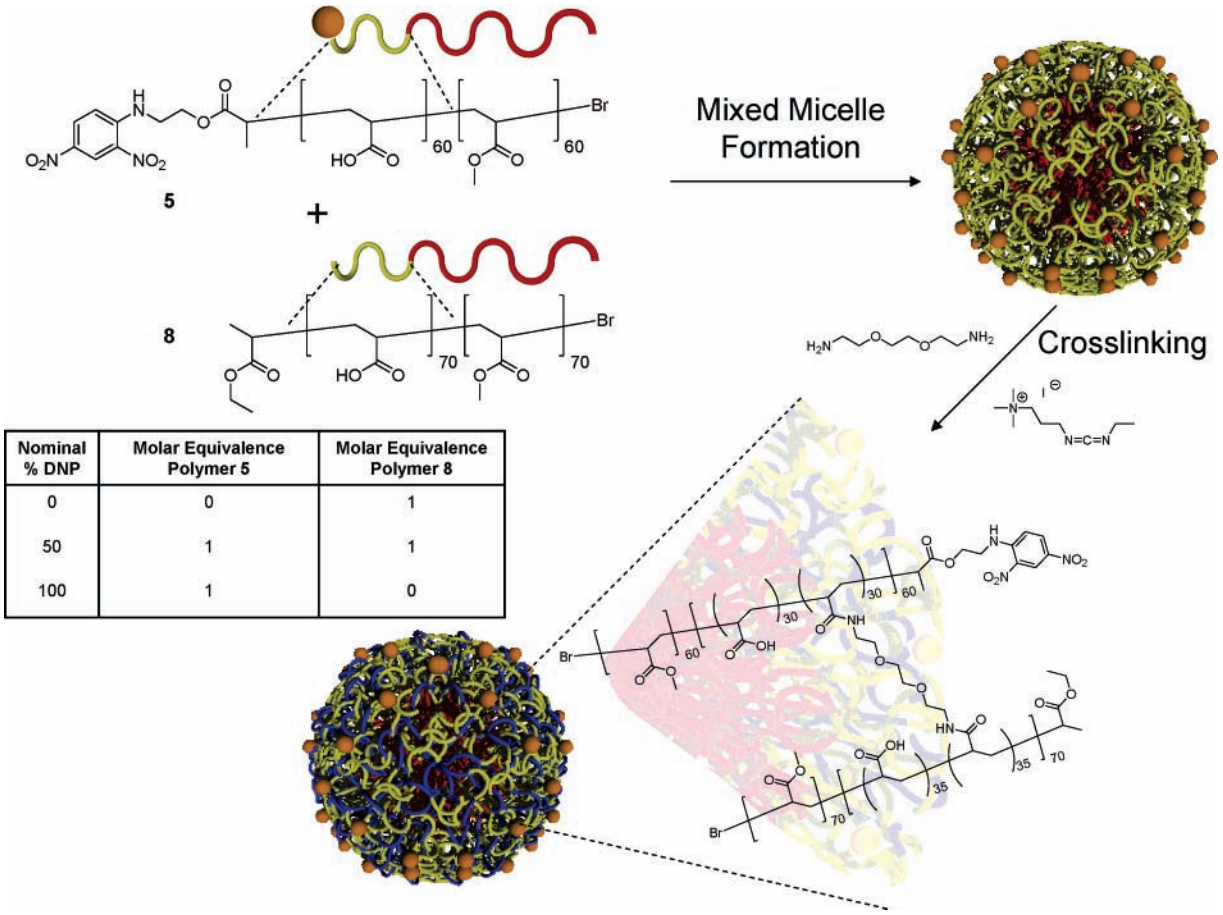

Table 1. Characterization of 0%, 50%, and 100% DNP-Functionalized SCKs

		AFM					
nominal % DNP	DLS D_{av} (nm)	H_{av} (nm)	D_{av} (nm)	TEM D_{av} (nm)	M_{app} (g/mol)	N_{agg} (chains/SCK)	ζ (mV)
0	24 ± 3	1.3 ± 0.3	47 ± 12	13 ± 2	142,700 ± 33,300	10 ± 2	−25 ± 0.8
50	23 ± 3	1.1 ± 0.2	96 ± 21	24 ± 3	1,367,700 ± 232,900	120 ± 20	−31.1 ± 0.7
100	22 ± 5	1.1 ± 0.2	77 ± 16	12 ± 2	368,000 ± 112,100	40 ± 11	−27.4 ± 1.1

dinitrophenyl-terminated polymer. The similarities in both block length and composition were desired in order to promote the assembly of uniform micelles from a mixture of polymers **8** and **5**.

Micelles of nominally 0%, 50%, and 100% 2,4-dinitrophenyl-terminated polymer chains were assembled from the nonfunctionalized polymer **8**, a 1:1 stoichiometric mixture of the nonfunctionalized polymer **8** and the functionalized polymer **5**, and the functionalized polymer **5**, respectively. Each type of micelle was formed in the same general fashion involving slow addition of water (15 mL/h) to a solution of the polymer, or mixture of polymers, in tetrahydrofuran (THF). The micelle assemblies were then trapped by exchange of the THF with water via dialysis and further stabilized upon cross-linking of a portion of acrylic acid groups throughout the shell. Nominally, the nanoparticles were cross-linked to 50% upon addition of a bifunctional amine, 2,2′-(ethylenedioxy)bis(ethylamine), and a water soluble carbodiimide activator, 1-(3′-dimethylaminopropyl)-3-ethylcarbodiimide methiodide, as shown in Scheme 3, to yield 0%, 50%, and 100% 2,4-dinitrophenylated SCKs, **12**, **13**, and **14**, respectively.

The nanoparticles were characterized extensively by DLS, AFM, TEM, and AU sedimentation equilibrium, which allowed determination of the size and apparent molecular weight of the SCKs (Table 1). As expected from designing nonfunctionalized and functionalized amphiphilic diblock copolymers of similar length and composition, each type of nanoparticle exhibited similar diameters and heights, by DLS, and AFM techniques. However, TEM and AU sedimentation equilibrium experiments revealed differences between the 50% DNP-SCK and the other nanoparticles, which appeared to be of greater heterogeneity, possibly resulting from the mixed micellization conducted for this sample. Dynamic light scattering measurements of the nanoparticles in aqueous solution produced similar hydrodynamic diameters, ca. 23 nm (Table 1). Each type of SCK exhibited a low height value as measured by AFM, which is in agreement with their expected flexible, shape-adaptable character imparted by the poly(methyl acrylate) core material. The poly(methyl acrylate) chain segments exhibited T_g values below room temperature, and thus were fluidlike at room temperature and allowed the nanoparticles to flatten under the AFM tip on the mica substrate that was utilized for the AFM measurements (*40*, *67*). The flattening of the SCKs on the mica substrate

is further supported by the large diameters measured by AFM, although these diameters are qualitative, due to the inherent error caused by the width of the AFM tip.

The TEM measurements produced similar diameters (Table 1) for the 0% and 100% DNP nanoparticles of about 13 nm, whereas the 50% DNP-SCK had a larger diameter of 24 nm. This difference is especially interesting because the 50% DNP nanoparticle was the only particle derived from a mixed micelle system, and because both AFM and DLS measurements produced similar results for the 50% DNP-SCK in comparison to the 0% and 100% DNP-SCKs. Analytical ultracentrifugation sedimentation equilibrium measurements provided more insight into this intriguing difference.

AU sedimentation equilibrium measurements of three different concentrations of SCKs in both phosphate buffer and deuterated phosphate buffer, at three different speeds, along with acoustical density measurements of each solution, were employed to calculate the apparent molecular weight (M_{app}) of each type of nanoparticle (*47*). The M_{app} values and molecular weights of the amphiphilic diblock copolymers were then utilized (along with the molar fraction of each diblock for the 50% DNP-SCK) to calculate the number of chains per particle, or aggregation number (N_{agg}). From these measurements and calculations, it was determined that the 50% DNP-SCK was formed from a larger number of chains per particle (120 ± 20 chains/SCK) than were the 0% and 100% DNP-SCKs (10 ± 2 chains/SCK and 38 ± 11 chains/SCK), thus supporting the TEM finding that the 50% DNP nanoparticle was larger than the 0% and 100% DNP nanoparticles. Even though when measured in solution (DLS) and on a mica surface (AFM) each of the particles was of similar size, TEM and AU sedimentation equilibrium measurements were able to detect the difference between the 50% DNP SCK and the 0% and 100% DNP SCKs. The nanoparticles are of similar size, shape, and composition and thus differ mainly in the amount of chain-ends that are labeled with DNP. An increased propensity for aggregation, promoted by the heterogeneous surface composition, could provide an alternative explanation for the apparent differences with the 50% DNP SCK, relative to the homogeneous 0% and 100% DNP SCKs.

The surface availability of the DNP chain-ends on SCKs was evaluated by their capacity to quench fluorescent IgE in solution. Quenching titrations were achieved by making serial additions of SCK solutions to FITC modified IgE in solution. As antibodies bound to the DNP hapten attached to the nanoparticles, the fluorescence from the fluorecein derivatives near the binding pockets of the antibody was quenched; thus, the degree of fluorescence quenching can be related to the fraction of sites bound. Because the FITC modified IgE has fluorecein molecules both at the binding pocket and away from it, even when all the binding sites are occupied, there is still residual fluorescence. For this reason, the saturation point of the IgE is taken to be the point where addition of more antigen causes no additional quenching (Figure 2).

Interestingly, the 50% DNP-SCKs quenched approximately 25% more fluorescence at saturation than the 100% DNP-SCKs (data not shown), indicating that the 50% DNP particles may interact differently with the IgE in solution. As the SCKs are malleable, perhaps the spacing of DNP groups on the 50% particles is such that the particle can quench FITC fluorescence farther away from the site to which it is bound. The 100% DNP-SCK had a larger initial slope, indicating a higher apparent affinity (*58*). The 0% DNP SCKs caused limited quenching, consistent with little to no nonspecific binding interactions. It is evident from the titrations that the DNP antigens were presented from the SCKs as surface-available ligands that promoted the expected specific interactions with anti-DNP IgE in solution.

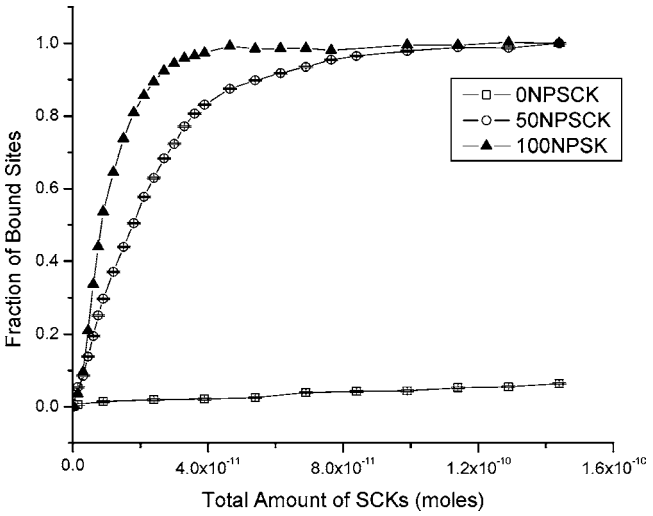

Figure 2. Fluorescence quenching of FITC−IgE by titration with 0%, 50%, and 100% DNP-SCKs. Data were normalized such that when $I = I_f$, the fraction of bound sites equaled 1.

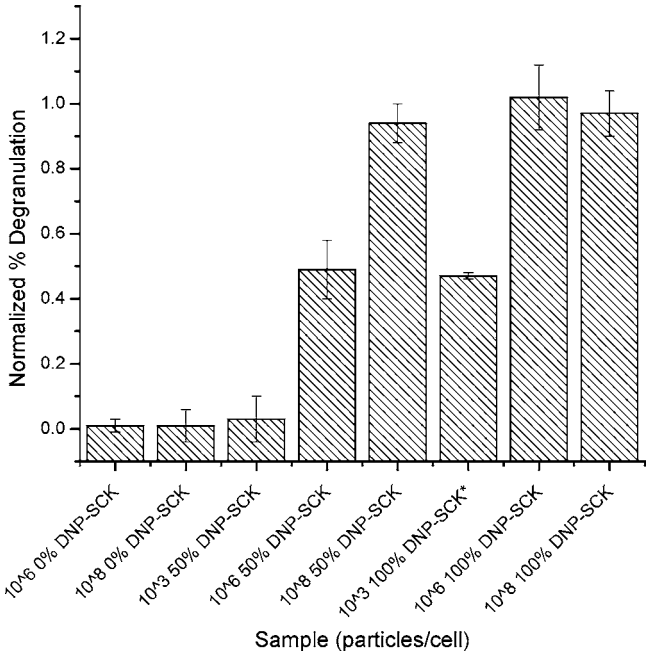

Figure 3. Percent degranulation observed from IgE sensitized cells. Degranulation Values were normalized to β-hexosaminidase release caused by DNP-BSA, which was 50% of maximal release by cells.

The capacity of the nanoparticle-bound antigen to be recognized by antibodies bound to cells, as well as their functional capacity to elicit an immune response, were evaluated through degranulation assays.

As expected from the bioavailiblity study with IgE in solution, the DNP groups on the SCK surface were able to bind IgE-FcϵRI on the surface of RBL-2H3 cells. At a concentration of 10^8 particles/cell the 50% and 100% DNP-SCKs stimulated degranulation comparable to standard DNP-BSA antigen (Figure 3). The 0% DNP-SCKs caused little to no degranulation at all concentrations examined. At lower concentrations, the 100% DNP-BSA SCKs stimulated maximal degranulation, relative to the

50% DNP-SCKs, yet modest degranulation was observed at the lower concentrations, 10^6 and 10^3 particles/cell, respectively. This may be a reflection of their higher apparent affinity for IgE or their capacity to cause more cross-linking of receptor complexes on the surface of the cell. One of the initial events in IgE-FcϵRI mediated signaling is the phosphorylation of specific motifs on the cytoplasmic domains of the receptor (*58*, *59*). Therefore, the tyrosine phosphorylation upon stimulation was examined by western blotting (*59*). Both the 50% and 100% DNP-SCKs were capable of causing an amount of stimulated tyrosine phosphorylation roughly similar to DNP-BSA, whereas the non-DNP-decorated SCKs were not. Taken together with the degranulation response, these results show that the DNP groups are both available for binding and, when presented polyvalently, are capable of causing a specific immune response.

CONCLUSIONS

Antigen-decorated SCKs with varying amounts of haptenic groups (0%, 50%, and 100% DNP) were constructed from self-assembled block copolymer micelles, followed by cross-linking throughout the shell, to achieve stabilization. The nanoparticles were characterized extensively and shown to be of similar size and composition to one another. However, the 50% DNP-SCK was of larger size and size distribution, as observed by TEM and AU sedimentation equilibrium experiments. These differences were attributed to the mixed micelle methodology employed for the assembly of the 50% DNP micelle, which resulted in two different polymers incorporated into the nanoparticle, giving a heterogeneous surface composition as well.

The DNP chain-ends were shown to be surface available while attached to the nanoparticles, by both fluorescence quenching titrations and degranulation assays. The 100% DNP-SCK displayed the highest apparent affinity for binding with anti-DNP IgE antibodies in solution. The 0% DNP-SCK demonstrated very little nonspecific interaction with the anti-DNP IgE in both the florescent quenching titrations and degranulation assays. Both the 50% and 100% DNP nanoparticles cross-linked the IgE antibodies bound to RBL cells and stimulated degranulation. The percentage of degranulation varied with nanoparticle dosage, as well as the amount DNP chain-ends in the nanoparticle. Both the 50% and 100% DNP-SCKs caused degranulation to similar degrees as the hapten bound to a traditional carrier (DNP-BSA positive control), thus behaving as effectors of an immune response, similar to the third generation dendrimer reported by Baird et al., rather than an inhibitor of the immune response.

The nanoparticle provides a good substrate from which antigens are displayed since the antigen is surface-available and multiple copies of the antigen are displayed from each SCK, allowing participation in multivalent binding events. These promising results indicate that shell cross-linked nanoparticles hold the potential to serve as multifunctional platforms for surface presentation of antigens, which in combination with efforts to define the structure and composition of the interior cavity of these nanoscale objects (*51*, *68*) is leading to their development as synthetic viruslike particles and eventually to their application as synthetic vaccines.

ACKNOWLEDGMENT

This material is based upon work supported by the National Science Foundation under Grant numbers 0210247 and 0451490 and by the National Institutes of Health grant AI22449 (B.B.). Acknowledgment is also made to the donors of the Petroleum Research Fund, administered by the American Chemical Society, for partial support of this research. M.J.J. was supported by a Chemistry-Biology Interface Program fellowship under an NIH Training Grant No NIHNRSA T32 GM08785-05.

LITERATURE CITED

(1) Janeway, C. A. J., Travers, P., Walport, M., and Shlomchik, M. J. (2005) Immunobiology: the immune system in health and disease. *Immunobiology: the immune system in health and disease*, *6th ed.*, pp 1−3, 527−541, Garland Science Publishing, New York.

(2) Cui, Z., Han, S.-J., Vangasseri, D. P., and Huang, L. (2005) Immunostimulation mechanism of LPD nanoparticles as a vaccine carrier. *Mol. Pharm. 2*, 22−28.

(3) Huang, H.-I., Wu, P.-Y., Teo, C.-Y., Chen, M.-N., Chen, Y.-C., Silin, D., and Tao, M.-H. (2004) Improved immunogenicity of a self-tumor antigen. by covalent linkage to CD40 ligand *Int. J. Cancer 108*, 696−703.

(4) Sedlik, C., Saron, M.-F., Sarraseca, J., Casal, I., and Leclerc, C. (1997) Recombinant parvovirus-like particles as an antigen carrier: A novel nonreplicative exogenous antigen to elicit protective antiviral cytotoxic T cells. *Proc. Natl. Acad. Sci. U.S.A. 94*, 7503−7508.

(5) Saksena, R., Ma, X., and Ková, P. (2003) One-pot preparation of a series of glycoconjugates with predetermined antigen-carrier ratio from oligosaccharides that mimic the O-PS of *Vibrio cholerae* O:1, serotype Ogawa. *Carbohydr. Res. 338*, 2591−2603.

(6) Glück, R., and Metcalfe, I. C. (2003) Novel approaches in the development of immunopotentiating reconstituted influenza virosomes as efficient antigen carrier systems. *Vaccine 21*, 611−615.

(7) Li, L., Wartchow, C. A., Danthi, S. N., Shen, Z., Dechene, N., Pease, J., Choi, S., Doede, T., Chu, P., Ning, S., Lee, D. Y., Bednarski, M. D., and Knox, S. J. (2004) A novel antiangiogenesis therapy using an integrin antagonist or anti-FLK-1 antibody coated ^{90}Y-labeled nanoparticles. *Int. J. Radiat. Oncol. 58*, 1215−1227.

(8) Zurbiriggen, R., Novak-Hofer, I., Seelig, A., and Glück, R. (2000) IRIV-adjuvanted hepatitis A vaccine: in vivo absorption and biophysical characterization. *Prog. Lipid Res. 39*, 3−18.

(9) Morein, B., Hu, K.-F., and Abusugra, I. (2004) Current status and potential applications of ISCOMs in veterinary medicine. *Adv. Drug Delivery Rev. 56*, 1367−1382.

(10) Bivas-Benita, M., Laloup, M., Versteyhe, S., Dewit, J., De Braekeleer, J., Jongert, E., and Borchard, G. (2003) Generation of *Toxoplasma gondii* GRA1 protein and DNA vaccine loaded chitosan particles: preparation, characterization, and preliminary in vivo studies. *Int. J. Pharm. 266*, 17−27.

(11) Chew, J. L., Wolfowicz, C. B., Mao, H.-Q., Leong, K. W., and Chua, K. Y. (2003) Chitosan nanoparticles containing plasmid DNA encoding house dust mite allergen, Der p 1 for oral vaccination in mice. *Vaccine 21*, 2720−2729.

(12) Sun, C.-J., Pan, S.-P., Xie, Q.-X., and Xiao, L.-J. (2004) Preparation of chitosan-plamid DNA nanoparticles encoding zona pellucida glycoprotein-3α and its expresstion in mouse. *Mol. Reprod. Dev. 68*, 182−188.

(13) Yuan, R., Zhang, L., Li, Q., Chai, Y., and Cao, S. (2005) A label-free amperometric immunosensor based on multi-layer assembly of polymerized *o*-phenylenediamine and gold nanoparticles for determination of Japanese B encephalitis vaccine. *Anal. Chim. Acta 531*, 1−5.

(14) Wu, Z.-S., Li, J.-S., Luo, M.-H., Shen, G.-L., and Yu, R.-Q. (2005) A novel capacitive immunosensor based on gold colloid monolayers associated with a sol−gel matrix. *Anal. Chim. Acta 528*, 235−242.

(15) Huhtinen, P., Soukka, T., Lövgren, T., and Härmä, H. (2004) Immunoassay of total prostate-specific antigen using europium(III) nanoparticle labels and strptavidin−biotin technology. *J. Immunol. Methods 294*, 111−122.

(16) Svarovsky, S. A., Szekely, Z., Barchi, J. J. J. (2005) Synthesis of gold nanoparticle bearing the Thomsen-Friedenreich disacchardie: a new multivalent presentation of an important tumor antigen. *Tetrahedron: Asymmetry 16*, 587−598.
(17) Prokop, A., Kozlov, E., Newman, G. W., and Newman, M. J. (2002) Water-based nanoparticulate polymeric system for protein delivery: Permeability control and vaccine application. *Biotechnol. Bioeng. 78*, 459−466.
(18) Schöll, I., Weissenböck, A., Förster-Waldl, E., Untersmayr, E., Walter, F., Willheim, M., Boltz-Nitulescu, G., Scheiner, O., Gabor, F., and Jensen-Jarolim, E. (2004) Allergen-loaded biodegradable poly(D, L-lactic-*co*-glycolic) acid nanoparticles down-regulate an ongoing Th2 response in the BALB/c mouse model. *Clin. Exp. Allergy 34*, 315−321.
(19) Sadler, K., and Tam, J. P. (2002) Peptide dendrimers: Applications and synthesis *Reviews in Molecular Biotechnology 90*, 195−229.
(20) Roy, R., and Kim, J. M. (2003) Cu(II)-self-assembling bipyridyl-glycoclusters and dendrimers bearing the Tn-antigen cancer marker: Syntheses and lectin binding properties. *Tetrahedron 59*, 3881−3893.
(21) Gillies, E. R., and Fréchet, J. M. J. (2005) Dendrimers and dendritic polymers in drug delivery. *Drug Discovery Today 10*, 35−43.
(22) Cui, Z., Patel, J., Tuzova, M., Ray, P., Phillips, R., Woodward, J. G., Nath, A., Mumper, R. J. (2004) Strong T cell type-1 immune responses to HIV-1 Tat (1−72) protein-coated nanoparticles. *Vaccine 22*, 2631−2640.
(23) Stevenson, A., and Roberts, M. (2004) Intranasal immunisation against tetanus with an attenuated *Bordetella bronchiseptica* vector expressing FrgC: improved immunogenicity using a Bvg-regulated promoter to express FrgC. *Vaccine 22*, 4300−4305.
(24) Georgantas, R. W. I., Leong, K. W., and August, J. T. (2000) Antigen-specific induction of peripheral T cell tollerance in vivo by codelivery of DNA vectors encoding antigen and Fas ligand. *Hum. Gene Ther. 11*, 851−858.
(25) Kelly, K. A., Allport, J. R., Tsourkas, A., Shinde-Patil, V. R., Josephson, L., and Weissleder, R. (2005) Detection of vascular adhesion molecule-1 expression using a novel multimodal nanoparticle. *Circ Res. 96*, 327−336.
(26) Farokhazad, O. C., Jon, S., Khademhosseini, A., Tran, T.-N. T., LaVan, D. A., Langer, R. (2004) Nanoparticle-aptamer bioconjugates: A new approach for targeting prostate cancer cells. *Cancer Res. 64*, 7668−7672.
(27) Felnerova, D., Viret, J.-F., Glück, R., Moser, C. (2004) Liposomes and virosomes as delivery systems for antigens, nucleic acids and drugs. *Curr. Opin. Biotechnol. 15*, 518−529.
(28) Schiffelers, R. M., Ansari, A., Xu, J., Zhou, Q., Tang, Q., Storm, G., Molema, G., Lu, P. Y.; S. P. V., and Woodle, M. C. (2004) Cancer siRNA therapy by tumor selective delivery with ligand-targeted sterically stabilized nanoparticle. *Nucleic Acids Res. 32*, e149/1-e149/10.
(29) Zhang, L., Hou, S., Mao, S., Wei, D., Song, X., and Lu, Y. (2004) Uptake of folate-conjugated albumin nanoparticles to the SKOV3 cells. *Int. J. Pharm. 287*, 155−162.
(30) Calvo, P., Gouritin, B., Brigger, I., Lasmezas, C., Deslys, J.-P., Williams, A., Andreux, J. P., Dormont, D., and Couvreur, P. (2001) PEGylated polycyanoacrylate nanoparticles as vector for drug delivery in prion diseases. *J. Neurosci. Methods 111*, 151−155.
(31) Irache, J. M., Merodio, M., Arnedo, A., Camapanero, M. A., Mirshahi, M., and Espuelas, S. (2005) Albumin nanoparticles for the intravitreal delivery of anticytomegaloviral drugs. *Mini-Rev. Med. Chem. 5*, 293−305.
(32) Cui, Z., Han, S.-J., and Huang, L. (2004) Coating of mannan on LPD particles containg HPV E7 peptide significantly enhances immunity agains HPV-positive tumor. *Pharmaceut. Res. 21*, 1018−1025.
(33) Prabha, S., and Labhasetwar, V. (2004) Nanoparticle-mediated wild-type p53 gene delivery results in sustained antiproliferative activity in breast cancer cells. *Mol. Pharm. 1*, 211−219.
(34) Williams, J., Lansdown, R., Sweitzer, R., Romanowski, M., LaBell, R., Ramaswami, R., and Unger, E. (2003) Nanoparticle drug delivery system for intravenous delivery of topoisomerase inhibitors. *J. Controlled Release 91*, 167−172.
(35) Kreuter, J., Ramge, P., Petrov, V., Hamm, S., Gelperina, S. E., Engelhardt, B., Alyautdin, R., von Briesen, H., and Begley, D. J. (2003) Direct evidence that polysorbate-80-coated poly(butylcyanoacrylate) nanoparticles deliver drugs to the CNS via specific mechanisms requiring prior binding of drug to the nanoparticles. *Pharmaceut. Res. 20*, 409−416.
(36) Yu, S., and Chow, G. M. (2004) Carboxyl group ($-CO_2H$) functionalized ferrimagnetic iron oxide nanoparticles for potential bio applications. *J. Mater. Chem. 14*, 2781−2786.
(37) Labhasetwar, V., Song, C., and Levy, R. J. (1997) Nanoparticle drug delivery system for restenosis. *Adv. Drug Delivery Rev. 24*, 63−85.
(38) Thurmond, K. B., II, Kowalewski, T., and Wooley, K. L. (1996) Water-soluble knedel-like structures: The preparation of shell-*cross*-linked small particles. *J. Am. Chem. Soc. 118*, 7239−7240.
(39) Wooley, K. L. (2000) Shell cross-linked polymer assemblies: Nanoscale constructs inspired from biological systems. *J. Polym. Sci. Part A: Polym. Chem. 38*, 1397−1407.
(40) Huang, H., Kowalewski, T., and Wooley, K. L. (2003) Nanodroplets of polyisoprene fluid contained within poly(acrylic acid-*co*-acrylamide) shells. *J. Polym. Sci.*, *Part A: Polym. Chem. 41*, 1659−1668.
(41) Pan, D. J., Turner, L., and Wooley, K. L. (2004) Shell cross-linked nanoparticles designed to target angiogenic blood vessels via $\alpha_V\beta_3$ receptor−ligand interactions. *Macromolecules 37*, 7109−7115.
(42) Pan, D. J., Turner, L., and Wooley, K. L. (2003) Foilic acid-conjugated nanostructured materials designed for cancer cell targeting. *Chem. Commun.* 2400−2401.
(43) Becker, M. L., Remsen, E. E., Pan, D., and Wooley, K. L. (2004) Peptide-derivatized shell-*cross*-linked nanoparticles. 1. Synthesis and characterization. *Bioconjugate Chem. 15*, 699−709.
(44) Becker, M. L., Bailey, L. O., and Wooley, K. L. (2004) Peptide-derivatized shell-*cross*-linked nanoparticles. 2. Biocompatibility evaluation. *Bioconjugate Chem. 15*, 710−717.
(45) Liu, J., Zhang, Q., Remsen, E. E., and Wooley, K. L. (2001) Nanostructured materials designed for cell binding and transduction *Biomacromolecules 2*, 362−368.
(46) Qi, K., Ma, Q., Remsen, E. E., Clark, C. G. J., and Wooley, K. L. (2004) Determination of the bioavailability of biotin conjugated onto shell cross-linked (SCK) nanoparticles. *J. Am. Chem. Soc. 126*, 6599−6607.
(47) Joralemon, M. J., Murthy, K. S., Remsen, E. E., Becker, M. L., and Wooley, K. L. (2004) Synthesis, characterization, and bioavailability of mannosylated shell cross-linked nanoparticles. *Biomacromolecules 5*, 903−913.
(48) Becker, M. L., Liu, J., and Wooley, K. L. (2005) Functionalized Micellar Assemblies Prepared via Block Copolymers Synthesized by Living Free Radical Polymerization upon Peptide-loaded Resins. *Biomacromolecules 6*, 220−228.
(49) Thurmond, K. B. I., Remsen, E. E., Kowalewski, T., and Wooley, K. L. (1999) Packaging of DNA by shell cross-linked nanoparticles. *Nucleic Acids Res. 27*, 2966−2971.
(50) Sanji, T., Nakatsuka, Y., Ohnishi, S., and Sakurai, H. (2000) Preparation of nanometer-sized hollow particles by photochemical degradation of polysilane shell cross-linked micelles and reversible encapsulation of guest molecules. *Macromolecules 33*, 8524−8526.
(51) Turner, J. L., and Wooley, K. L. (2004) Nanoscale cage-like structures derived from polyisoprene-containing shell cross-linked nanoparticle templates. *Nano Lett. 4*, 683−688.
(52) Murthy, K. S., Ma, Q., Clark, C. G. J., Remsen, E. E., and Wooley, K. L. (2001) Fundamental design aspects of amphiphilic shell-cross-linked nanoparticles for controlled release applications. *Chem. Commun.* 773−774.
(53) Huang, H., Wooley, K. L., and Schaefer, J. (2001) REDOR determination of the composition of shell cross-linked amphiphilic core−shell nanoparticles and the partitioning of sequestered fluorinated guests. *Macromolecules 34*, 547−551.

(54) Kao, H.-M., O'Connor, R. D., Mehta, A. K., Huang, H., Poliks, B., Wooley, K. L., and Schaefer, J. (2001) Location of cholic acid sequestered by core−shell nanoparticles using REDOR NMR. *Macromolecules 34*, 544−546.

(55) Yang, Z.-Q., Puffer, E. B., Pontrello, J. K., and Kiessling, L. L. (2002) Synthesis of a mulitvalent display of a CD22-binding trisaccharide. *Carbohydr. Res. 337*, 1605−1613.

(56) Sulzer, B., and Perelson, A. S. (1997) Immunons revisted: Binding of multivalent antigens to B cells. *Mol. Immunol. 34*, 63−74.

(57) Dower, S. K., DeLisi, C., Titus, J. A., and Segal, D. (1981) Mechanism of binding of multivalent immune complexes to Fc receptors. 1. Equilibrium binding. *Biochemistry 20*, 6326−6334.

(58) Holowka, D., and Baird, B. (1996) Antigen-mediated IgE receptor aggregation and signaling: A window on cell surface structure and dynamics. *Annu. Rev. Biophys. Biomol. Struct. 25*, 79−112.

(59) Baird, E., Holowka, D., Coates, G. W., and Baird, B. (2003) Highly effective poly(ethylene glycol) architectures for specific inhibition of immune receptor activation. *Biochemistry 42*, 12739−12748.

(60) Barsumian, E. L., Isersky, C., Petrino, M. G., and Siraganian, R. P. (1981) IgE-induced histamine release from rat basophilic leukemia cell lines: isolation of releasing and nonreleasing clones. *Eur. J. Immunol. 11*, 317−323.

(61) Erickson, J., Kane, P., Goldstein, B., Holowka, D., and Baird, B. (1986) Cross-linking of IgE-receptor complexes at the cell surface: A fluorescence method for studying the binding of monovalent and bivalent haptens to IgE. *Mol. Immunol. 23*, 769−781.

(62) Weetall, M., Holowka, D., and Baird, B. (1993) Heterologous desensitization of high affinity receptor for IgE (FcϵR1) on RBL cells. *J. Immunol. 150*, 4072−4083.

(63) Eisen, H. N., Kern, M., Newton, W. T., and Helmreich, E. (1959) Distribution of 2,4-dinitrobenzene sensitizers between isolated lymphnode cells and extracellular medium in relation to induction of contact skin sensitivity. *J. Exp. Med. 110*, 187−206.

(64) Zorina, L. N., Safiev, O. G., Rakhmankulov, D. L., and Paushkin, Y. M. (1989) *Doklady akademii Nauk SSSR 308*, 1150−1154.

(65) Harris, N. T., Goldstein, B., Holowka, D., and Baird, B. (1997) Altered patterns of tyrosine phosphorylation and Syk activation for sterically restricted cyclic dimers of IfE-FcϵRI. *Biochemistry 36*, 2237−2242.

(66) Naal, R. M. Z. G., Tabb, J., Holowka, D., and Baird, B. (2004) In situ measurement of degranulation as a biosensor based on RBL-2H3 mast cells. *Biosensors Bioelectronics 20*, 791−796.

(67) Murthy, K. S., Ma, Q., Remsen, E. E., Kowalewski, T., and Wooley, K. L. (2003) Thermal Shaping of Shell-crosslinked (SCK) Nanoparticles, Facilitated by Nanoconfinement of Fluid-like Cores *J. Mater. Chem. 13*, 2785−2795.

(68) Turner, J., Chen, L. Z., and Wooley, K. L. (2005) Regiochemical Functionalization of a Nanoscale Cage-like Structure: Robust core−shell nanostructures crafted as vessels for selective uptake and release of small and large guests *J. Controlled Release*, in press.

BC0501505

Competitive Binding Assay Using Fluorescence Resonance Energy Transfer for the Identification of Calmodulin Antagonists

Bethel Sharma,[†] Sapna K. Deo,[‡] Leonidas G. Bachas,[‡] and Sylvia Daunert*[,†,‡]

Department of Pharmaceutical Sciences, University of Kentucky, Lexington, Kentucky 40536-0082, and Department of Chemistry, University of Kentucky, Lexington, Kentucky 40506-0055. Received June 6, 2005; Revised Manuscript Received August 12, 2005

The ubiquitous calcium regulating protein calmodulin (CaM) has been utilized as a model drug target in the design of a competitive binding fluorescence resonance energy transfer assay for pharmacological screening. The protein was labeled by covalently attaching the thiol-reactive fluorophore, *N*-[2-(1-maleimidyl)ethyl]-7-(diethylamino)coumarin-3-carboxamide (MDCC) to an engineered C-terminal cysteine residue. Binding of the environmentally sensitive hydrophobic probe 2,6-anilinonaphthalene sulfonate (2,6-ANS) to CaM could be monitored by an increase in the fluorescence emission intensity of the 2,6-ANS. Evidence of fluorescence resonance energy transfer (FRET) from 2,6-ANS (acting as a donor) to MDCC (the acceptor in this system) was also observed; fluorescence emission representative of MDCC could be seen after samples were excited at a wavelength specific for 2,6-ANS. The FRET signal was monitored as a function of the concentration of calmodulin antagonists in solution. Calibration curves for both a selection of small molecules and a series of peptides based upon known CaM-binding domains were obtained using this system. The assay demonstrated dose-dependent antagonism by analytes known to hinder the biological activity of CaM. These data indicate that the presence of molecules known to bind CaM interfere with the ability of FRET to occur, thus leading to a concentration-dependent decrease of the ratio of acceptor:donor fluorescence emission. This assay can serve as a general model for the development of other protein binding assays intended to screen for molecules with preferred binding activity.

INTRODUCTION

Fluorescence-based technologies are of great importance in pharmacological screening assays as they are amenable to miniaturization, and provide high sensitivity and signal-to-noise ratio. Fluorescence resonance energy transfer (FRET) is a valuable tool for characterizing proximity relationships within and between biomolecules (*1*−*11*). Many FRET assays make use of variants of the green fluorescent protein (GFP), in both in vitro and in vivo applications. In particular, fusion proteins between a target protein and two spectrally overlapping GFP's have been used in these types of assays (*12*). One limitation of GFP-based FRET assays is that fusion of one (or two) GFP molecules to a protein could affect the folding of the hybrid protein. Additionally, the bulkiness of GFP could place constraints on any associated ligand-induced conformational changes, thus hindering the use of this fluorescent protein as a signal generator for bioanalysis. Consequently, development of FRET labeling strategies that minimize interference in the target protein's normal folding and binding activities is advantageous. To that end, this manuscript describes the use of a FRET donor−acceptor pair that requires only a single residue modification that is distant from the binding site of the target protein for site-specific covalent attachment of the acceptor.

The efficiency of energy transfer in FRET is inversely related to the distance between the donor and acceptor fluorophores. Proximity (less than 100 Å) is important in achieving nonradiative transfer between the two fluorophores, even if there is a significant overlap of the donor emission and acceptor excitation wavelengths. Thus, FRET assays are useful as a type of "molecular gauge" of proximity relationships. This allows for great sensitivity in the detection of structural transitions or alterations (*13*).

As the human proteome becomes elucidated, new therapeutic targets are progressively identified. To evaluate libraries of drug candidates against these targets, initial screening assays for potency, selectivity, and activity are necessary. Accordingly, new screening assays that are fast, simple, with no complex separation steps, inexpensive, and easily amenable to miniaturization are critical tools in the drug discovery process. In that regard, we have used calmodulin (CaM) as a model drug target to demonstrate the feasibility of a newly designed method for rapid assessment of binding affinities of drug candidates in a homogeneous format. CaM is a small calcium-modulated protein found in all eukaryotes that binds to and activates its numerous target proteins (*14*−*18*).

Herein, we report the development of a screening assay to evaluate protein-binding activity employing FRET between a fluorescent molecule in the assay solution and CaM site-specifically labeled with *N*-[2-(1-maleimidyl)-ethyl]-7-(diethylamino)coumarin-3-carboxamide (MDCC). This assay is used to assess binding of a selection of antagonists including both drug molecules and peptides representative of CaM-binding domains, in the presence of the hydrophobic fluorescent probe, 2,6-anilinonaphthalene sulfonate (2,6-ANS). Upon binding of 2,6-ANS to CaM, energy transfer occurs between 2,6-ANS, which binds to CaM but can be displaced by the analyte, and

* To whom correspondence should be addressed: 217 Chemistry-Physics Building, University of Kentucky, Lexington, KY 40506. Phone: 859-257-7060, Fax: 859-323-1069, E-mail: daunert@uky.edu.

[†] Department of Pharmaceutical Sciences.

[‡] Department of Chemistry.

10.1021/bc050161y CCC: $30.25 © 2005 American Chemical Society
Published on Web 09/02/2005

the covalently attached MDCC at the C-terminus of the protein. When there is drug or peptide present in the sample, the binding event displaces the noncovalently bound 2,6-ANS in a competitive manner. This consequently increases the distance between the two fluorophores, leading to a decrease in the observed emission signal from the FRET acceptor, MDCC. A change in the concentration of analyte present in the sample thereby alters the ratio of FRET acceptor to FRET donor fluorescence emission. We have constructed calibration curves to evaluate the response of a series of drugs and peptides with known affinity for calmodulin as well as selected control compounds.

MATERIALS AND METHODS

Reagents. All test compounds, buffers, salts, the myosin light chain kinase inhibitor peptide, and CaM-dependent protein kinase II-delta fragment peptide were purchased from Sigma (St. Louis, MO). All other CaM binding peptides were obtained from Calbiochem (San Diego, CA). Dithiothreitol (DTT) was acquired from Gold Biotech (St. Louis, MO). Isopropyl-β-D-thiogalactopyranoside (IPTG) and ampicillin were obtained from U.S. Biochemical (Cleveland, OH). Synthetic oligonucleotides used as primer sequences for PCR were prepared by Operon (Alameda, CA). Taq DNA polymerase, the protein expression kit, and any necessary restriction enzymes were purchased from New England Biolabs (Beverly, MA). The fluorescent probes MDCC and 2,6-ANS were obtained from Molecular Probes (Eugene, OR). The Bio-Rad protein assay reagent was purchased from Bio-Rad Laboratories (Hercules, CA).

Apparatus. Starter cell cultures were grown in an orbital shaker from Forma Scientific (Marietta, OH). Fermentation of bacterial cultures was performed using a bioreactor from New Brunswick Scientific (New Brunswick, NJ). Optical density of cell cultures was measured on a Spectronic 21-D spectrophotometer from Milton Roy (Rochester, NY). Protein samples were concentrated using a Christ lyophilizer (Osterode, Germany). Protein purity was verified by sodium dodecyl sulfate-polyacrylamide gel electrophoresis (SDS−PAGE) on a PhastSystem from Pharmacia Biotech (Uppsala, Sweden). Fluorescence studies were carried out on either a Fluorolog-2 spectrofluorometer from Spex-JY Horiba (Edison, NJ) or a Cary Eclipse spectrofluorometer equipped with a multiwell plate reader from Varian (Palo Alto, CA).

Protein Expression, Purification, and Labeling. *Cloning.* The New England Biolabs IMPACT-TWIN system was used to create a C-terminal fusion between a cleavable intein (solely for affinity purification on a chitin bead column) and a mutant CaM-containing a C-terminal cysteine residue. To generate the C-terminal cysteine CaM, a single round of PCR was performed with *Taq* DNA polymerase using the plasmid pVUC-1 (*19*) as a template. To add *Nde*I and *Sap*I sites at the 5′- and 3′-termini, respectively, and include an insertion of a single cysteine at the C-terminus, the forward primer (CaMNdeI-F) 5′-GGTGGTGGTGGTGGCATATGATGGCTGATCAGCTGACT-3′ and the reverse primer (CaMSapI-R) 5′-GGTGGTGGTGGTTGCTCTTCCGCAACATGATCCT-CCTCCGGACTTAGCCATCATAACCTG-3′ were designed. Gene amplification was carried out for 30 cycles using a Perkin-Elmer Gene Amp thermal cycler (Norwalk, CT). The PCR denaturation was at 94 °C for 0.5 min, the annealing at 55 °C for 1 min, and the elongation at 72 °C for 1 min. The *Sap*I and *Nde*I restriction sites were used to insert the PCR-amplified synthetic calmodulin gene into the pTWIN1 vector. The plasmid containing the inserted gene was transformed into *E. coli* strain ER2566. Transformants were grown on selective media, and positive transformants were sequenced to verify the presence of the plasmid pTWIN1−CaM, containing the C-terminal cysteine CaM gene.

Expression and Purification. The IMPACT-TWIN system was also used to express and purify the recombinant calmodulin. *E. coli* ER2566 cells harboring the pTWIN1−CaM plasmid were grown at 37 °C in Luria Bertani medium containing 100 μg/mL ampicillin for approximately 16 h, until the OD_{600} reached 0.6. Protein expression was induced with a final concentration of 1 mM IPTG for 4 h followed by centrifugation for 20 min at 3800*g* to harvest the cells. The pellet was resuspended in a pH 7.0 buffer containing 20 mM Tris-HCl, 500 mM NaCl, and 1 mM EGTA.

Following sonication to lyse the cells, and centrifugation to clarify the crude cell extract, the supernatant was loaded onto a 5-mL column of chitin beads equilibrated in the same 20 mM Tris-HCl buffer in order to selectively purify the CaM−chitin binding domain fusion protein from the cellular milieu. Two washes were performed to remove any remaining unbound protein. The first was with the same buffer used to resuspend the cells, and a second wash used the same buffer, but with the NaCl concentration increased to 1 M. Then, three column volumes of 20 mM Tris-HCl, pH 8.5, containing 500 mM NaCl and 40 mM DTT were passed through the column, the column flow was stopped, and the column was stored at 4 °C for 16 h while the on-column cleavage reaction occurred. The next day, three more column volumes of the DTT-containing buffer were used to elute the bound protein, releasing the CaM from the bound chitin-binding domain at the intein cleavage site. The mutant CaM was isolated at greater than 90% purity based on SDS−PAGE. Protein concentrations were measured using the Bio-Rad protein reagent, a modified Bradford assay reagent. Further purification occurred after the labeling reaction.

Labeling. The protein was labeled by covalently attaching the thiol-reactive fluorophore, MDCC to the engineered C-terminal cysteine residue on CaM. The concentration of the unlabeled protein fraction varied from batch to batch, but the molar ratio of fluorophore to protein in the reaction mixture was always approximately 10:1. The labeling reaction and subsequent separation of labeled protein from unbound fluorophore using size-exclusion chromatography was performed as in ref 29. The extent of MDCC labeling was assessed using the following equation:

$$\frac{\text{moles dye}}{\text{moles protein}} = \frac{A_x}{\epsilon \times b} \times \frac{\text{MW}_{\text{protein}}}{\text{mg}_{\text{protein}}/\text{mL}}$$

where A_x is the absorbance at 420 nm (MDCC maximum), ϵ is the extinction coefficient for MDCC = 50 200 cm^{-1} M^{-1}, and b is the path length in cm. Labeling efficiencies were typically around 70%.

Fluorescence Studies of Interaction between Calmodulin and 2,6-ANS. *Energy Transfer Studies*. 2,6-ANS binding to unlabeled CaM could be monitored by the increase in fluorescence emission intensity of the 2,6-ANS when samples were excited at 360 nm and emission was measured at 420 nm. To observe energy transfer from 2,6-ANS to a 0.5 μM concentration of MDCC-labeled CaM, the donor excitation wavelength used was 360 nm, and the acceptor emission was measured at 460 nm using

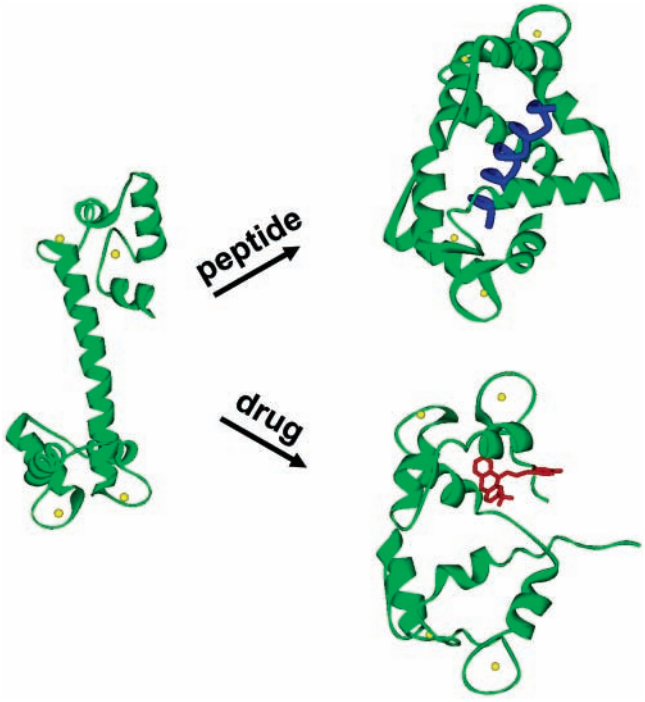

Figure 1. Crystal structure of Ca^{2+}−CaM (1EXR) bound to the myosin light chain kinase CaM-binding domain peptide, shown in blue (1CDL), and to the antipsychotic drug trifluoperazine, shown in red (1CTR). Calcium ions are shown in yellow. Protein databank (PDB) (*46*) files are indicated in parentheses.

a conventional benchtop fluorometer and poly(methyl methacrylate) cuvettes. Both studies were performed in a buffer containing 20 mM Tris-HCl, pH 8.0, with calcium-saturated CaM−MDCC.

Competitive Binding Experiments. CaM−MDCC was diluted to a final concentration of 0.5 μM in an assay volume of either 1.5 mL or 250 μL depending upon the assay platform used (conventional fluorometer or microtiter plate reader, respectively). The CaM solution was prepared in 20 mM Tris-HCl, pH 7.5, containing 100 mM KCl, 10 mM $CaCl_2$, and 0.5 μM 2,6-ANS. Each test sample was diluted to the final concentration with either buffer alone or varying concentrations of drug prepared in the buffer solution. The fluorescence was measured directly after a brief mixing step. Samples were excited at the donor excitation wavelength of 360 nm (2,6-ANS), and donor and acceptor emissions were measured at 410 nm (2,6-ANS) and 460 nm (MDCC). The ratio of acceptor to donor fluorescence was plotted versus analyte concentration to construct calibration curves.

RESULTS AND DISCUSSION

The crystal structures of three different conformations of calmodulin (Ca^{2+}−CaM, Ca^{2+}-peptide−CaM, and Ca^{2+}-TFP−CaM) are displayed in Figure 1. On the right, trifluoperazine (TFP) is shown bound to the C-terminal domain of the globular protein. While it is commonly acknowledged that the CaM−trifluoperazine complex has a 1:1 stoichiometry, evidence has been offered (including crystallographic data) that CaM can bind up to four molecules of trifluoperazine (TFP) in solution and form a compact globular structure (*20*−*23*). Assays have been developed to measure interactions of CaM with drugs and biomolecules previously. Calmodulin has been employed since the early 1990s as a calcium sensor (*24*, *25*). These biosensing systems utilized CaM labeled with fluorescent probes, either randomly or site selectively. In addition, other systems have been employed in ex vivo or in vivo Ca^{2+} detection utilizing the fusion of CaM to two flanking GFPs (*5*, *15*, *16*, *26*−*28*). Also, two different systems for the detection of phenothiazine-type drugs for high-throughput screening applications using calmodulin have been presented (*29*, *30*). Moreover, in another study a doubly labeled, agarose immobilized, CaM−maltose binding protein fusion protein was constructed for use in a FRET assay for single molecule detection of a CaM-binding peptide (*31*).

It is well established that solvent-exposed hydrophobic surfaces are formed upon Ca^{2+} binding to CaM (*14*−*16*). Anilinonaphthalene sulfonates (ANS) can serve as fluorescent probes of hydrophobicity as their quantum yield and emission maxima are dependent upon their environment. In water, ANS is virtually nonfluorescent, but in nonpolar environments it emits a bright blue fluorescence with a quantum yield ~0.70 (*32*). ANS has been used previously to measure the surface hydrophobic character of proteins and membranes, particularly during the folding/unfolding of proteins (*33*−*36*).

LaPorte et al. demonstrated through differential binding in the presence and absence of calcium that there are 2.1 ANS binding sites in CaM (*37*). Tsurata and Sano later argued that under LaPorte's experimental conditions, CaM could not be saturated with calcium, and that there were likely two to four ANS binding sites with binding constants ranging from 2.91 to 3.86 $\times$ 10^{-4} M^{-1} (*38*). Some investigators propose that the mode of ANS binding occurs through ion-pair formation between the sulfonate moiety and cationic groups on the protein (*39*−*41*). In fact, it has been suggested that ANS may be a conformational tightening agent, and that ANS fluorescence may not be entirely due to interactions with hydrophobic sites on the protein, but instead to less interaction with water (*40*). Taking into consideration the discussion over the true character of ANS binding, we have developed a system that operates at a constant ANS concentration to overcome any possible discrepancies due to the number of ANS molecules bound at any given time to CaM. We have also set the ANS concentration at a level below that at which the inner filter effect causes the ANS fluorescence to decrease.

In the presence of ANS and MDCC-labeled CaM, fluorescence was observed at the wavelength corresponding to the emission maximum of MDCC, with no direct excitation of the latter. This provided evidence that FRET could be monitored using our system. We achieved this by selectively exciting the ANS molecules, which exhibit weak fluorescence in aqueous solution and become noticeably fluorescent when CaM is present. We hypothesized that if ANS binds to CaM in its C-terminal hydrophobic region, it will be in close enough proximity to the C-terminal MDCC on the protein for fluorescence resonance energy transfer to occur, provided that the two molecules have sufficient spectral overlap. In fact, these two molecules were chosen because the emission of ANS and the excitation of MDCC are both close to 420 nm. Figure 2 depicts the principle of the FRET application described herein. On the right, a molecule of 2,6-ANS is shown near the hydrophobic binding pocket of the C-terminal domain of CaM, a potential binding site for ANS. In this instance, the bound MDCC at the C-terminus is in close enough proximity to the molecule of bound 2,6-ANS for energy transfer to occur. In the presence of phenothiazine-type compounds or CaM-binding peptides, a competitive binding interaction is introduced as the analyte (TFP in this case) replaces 2,6-ANS in the hydrophobic pocket of CaM. By removing the

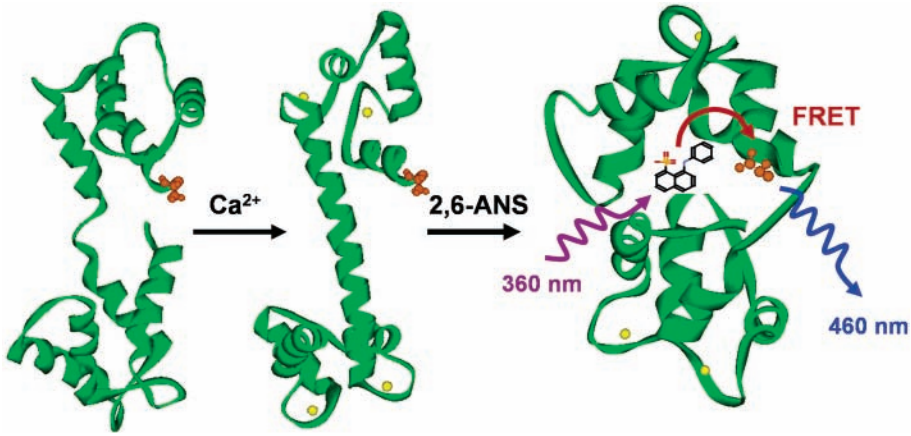

Figure 2. Proposed scenario demonstrating the predicted energy transfer from the bound 2,6-ANS to the C-terminal attached MDCC. It is hypothesized that energy transfer is inhibited when the protein binds to drugs or model peptide molecules. The C-terminal residue, where MDCC is attached, is highlighted in orange and 2,6-ANS is black.

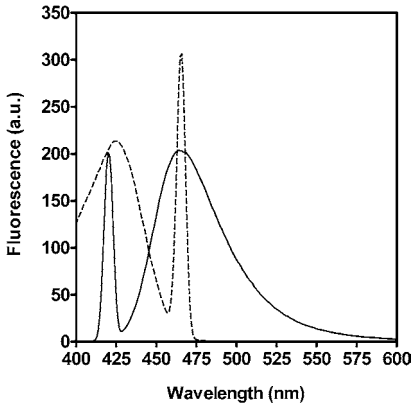

Figure 3. Excitation (- - -) and emission (—) spectra of 1 μM CaM−MDCC. The emission wavelength for the excitation trace was 460 nm. The excitation wavelength was set at 420 nm for the emission spectrum.

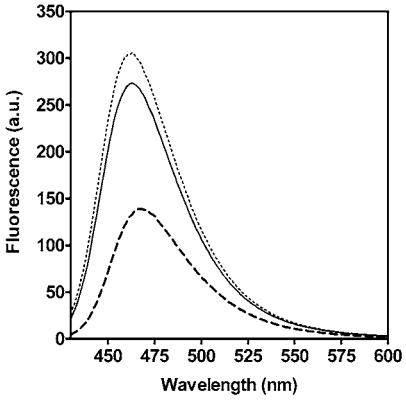

Figure 4. Effect of changing calcium concentrations on 1 μM CaM−MDCC fluorescence. 10 mM Ca^{2+} (- - -), 1 mM Ca^{2+} (—), and 1 mM EDTA (− − −) are shown. Excitation was at 420 nm.

bound 2,6-ANS from CaM, FRET is limited as the 2,6-ANS is too far away for any significant radiationless energy transfer to the bound MDCC molecule to occur.

The excitation and emission spectra of 1 μM CaM−MDCC in the presence of saturating calcium are shown in Figure 3. The effect of changing calcium concentrations on CaM−MDCC fluorescence was also assessed. In the presence of the metal complexing agent EDTA, the fluorescence of CaM−MDCC was lower than when Ca^{2+} was present (Figure 4). A concentration of 10 mM Ca^{2+} was

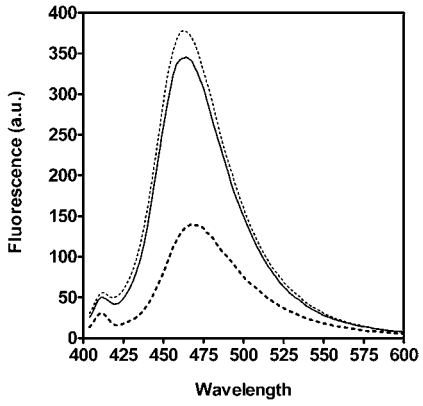

Figure 5. Effect of calcium concentration on energy transfer from 1 μM 2,6-ANS to 1 μM CaM−MDCC. 10 mM Ca^{2+} (- - -), 1 mM Ca^{2+} (—), and 1 mM EDTA (− − −) are shown. Excitation was at 360 nm.

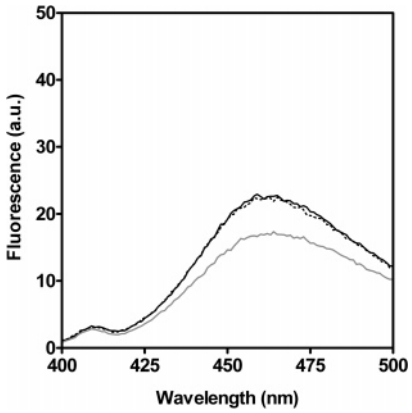

Figure 6. Effect of changing calcium concentrations on 0.25 μM CaM−MDCC with 1 μM 2,6-ANS. 10 mM Ca^{2+} (- - -), 1 mM Ca^{2+} (—), and 1 mM EDTA (—) are shown. The excitation was at 360 nm.

required to obtain maximum fluorescence emission at 460 nm. Thus, all assay buffers contained 10 mM calcium.

We also considered the effect of calcium on the efficiency of the FRET interaction. The calcium dependence of FRET between the two chromophores using 1 μM 2,6-ANS and 1 μM CaM−MDCC was studied, and the results are shown in Figure 5. The emission intensity at 460 nm was slightly higher when 10 mM calcium was present. Notice also that the ANS emission peak is shifted to 410 nm. The FRET ratios were thus calculated using 460/410 nm for the subsequent calibrations.

Table 1. Description of Peptides Used in This Study

synthetic peptide	amino acids	sequence	mw	description
CaM inhibitory peptide	17	Ac-RRKWQKTGHAVRAIGRL-NH_2	2074.5	based upon CaM binding domain of MLCK
CaM inhibitory peptide (control)	17	Ac-RRKEQKTGHAVRAIGRE-NH_2	2034.3	control for CaM inhibitory peptide
CaM binding domain	20	LKKFNARRKLKGAILTTMLA	2274.3	CaM kinase II residues 290−309
CaM kinase II inhibitor	29	MHRQETVDCLKKFNARRKLKGAILTTMLA	3374.1	CaM kinase II residues 281−309
myosin light chain kinase inhibitor	11	KRRWKKNFIAV-NH_2	1445	chicken smMLCK CaM binding domain
CaM dependent PK II-δ fragment(residues 345−358)	14	KSDGGVKKRKSSS	1450.6	substrate for brain Ca^{2+}/CaM-dependent PK IV

CaM−MDCC could be detected at concentrations above 10 nM (shown in Supporting Information). We selected 0.25 μM as the final concentration for the assay to minimize the amount of protein used that could give a signal at least 100-fold higher than the blank when using the Varian Cary Eclipse microtiter plate reader. The appropriate concentration of 2,6-ANS to use in the assay was determined by monitoring the change in ANS fluorescence in the presence of the previously selected 0.25 μM CaM−MDCC concentration. The fluorescence of ANS quickly diminishes as the concentration of the molecule in solution increases due to the inner filter effect. Therefore, an assay concentration of 1 μM was determined to be appropriate for our system. We then combined all of these conditions and measured the emission in smaller volume (250 μL) microtiter plate samples with 0.25 μM CaM−MDCC and 1 μM 2,6-ANS and evaluated the effect of calcium on the energy transfer under the final assay conditions. A calcium concentration of 1 mM resulted in a higher emission signal than when EDTA was present. Figure 6 demonstrates that in this case, changes in calcium concentration from 1 mM to 10 mM did not visibly alter the acceptor (MDCC) fluorescence emission at 460 nm.

Using the previously described conditions, energy transfer from 2,6-ANS to MDCC was observed and the ratio of acceptor to donor fluorescence intensity was related to the amount of drug or peptide present in each sample. Calibration curves for a series of peptides and drug compounds were obtained using this system. Table 1 and Figure 7 show the structures of all of the compounds that were tested using this assay, including negative controls that were used for selectivity testing (aspirin, propranolol, serotonin, and warfarin). The data indicate that the presence of known CaM antagonists interferes with the FRET activity, thus leading to a concentration-dependent decrease in the resultant fluorescence emission ratio. The observed changes could be a combination of dual effects, including the proposed displacement of 2,6-ANS, but also alteration of the local environment of the MDCC molecule upon drug or peptide binding. The graph in Figure 8 shows dose−response curves for changing concentrations of several peptides in the presence of CaM−MDCC and 2,6-ANS. Similar

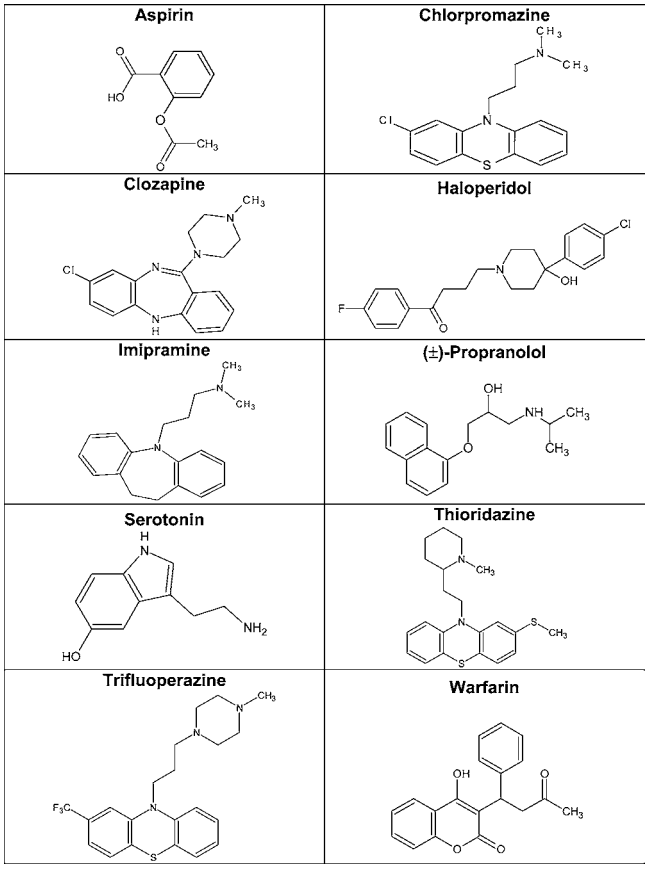

Figure 7. Structures of test compounds. Compounds listed are known CaM antagonists and are classified as phenothiazine (chlorpromazine, thioridazine, and trifluoperazine), dibenzazepine (clozapine, haloperidol), or tricyclic antidepressant (imipramine) drugs. The other compounds listed are controls.

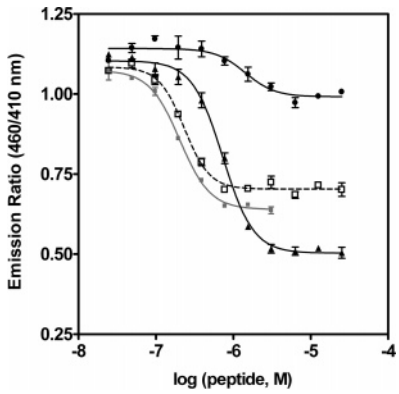

Figure 8. Calibration plots for MLCK inhibitor peptide (●), CaM inhibitory peptide (▲), CaM binding domain peptide (△), and CaM kinase II inhibitor peptide (■), are all described in Table 1.

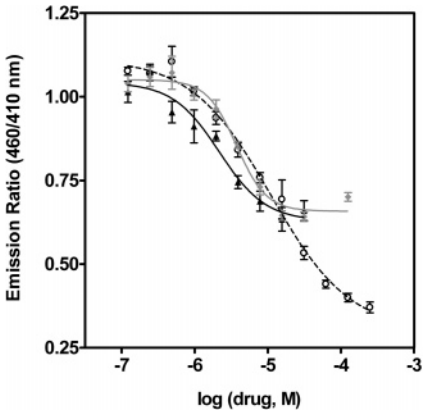

Figure 9. Calibration plots for the phenothiazine drugs chlorpromazine (◆), thioridazine (▲), and clozapine (○).

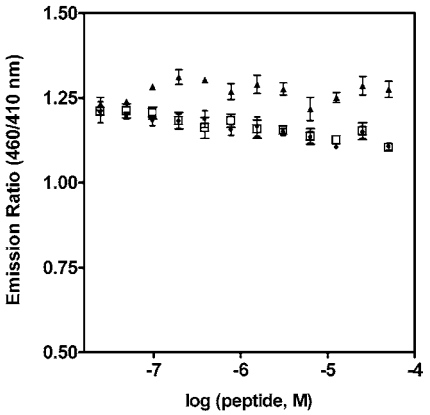

Figure 10. Calibration plots for CaM inhibitory peptide (control) (▲), and CaM dependent PK II-δ fragment (□) demonstrate results similar to when no peptide is present (●).

Table 2. Calculated IC_{50} Values Based upon Curve Fitting of Sigmoidal Dose−Response Curves Such as Those in Figures 8 and 9

peptide	IC_{50} (μM)	% FRET inhibition
CaM inhibitory peptide	0.731	100
CaM kinase II inhibitor	0.204	57
CaM binding domain	0.232	45
MLCK inhibitor	1.424	12

drug	IC_{50} (μM)	known K_i (μM)[a]
imipramine	12.5	14
thioridazine	2.16	-
clozapine	8.83	-
chlorpromazine	4.31	1.5
trifluoperazine	1.14	1.1
haloperidol	14.8	-

[a] Data from Reynolds and Claxton (1982).

results with a few representative drug compounds can be seen in Figure 9. Results from all peptides and drugs tested that affected the FRET have been compiled and presented in Table 2. The IC_{50} values represent the effective concentration corresponding to 50% of the maximum acceptor:donor FRET ratio.

It should be noted that no significant change in the FRET emission ratio was observed in the presence of compounds not known to affect the physiological behavior of CaM, such as aspirin and propranolol, which were used as negative controls (data not shown). Reynolds and Claxton have determined apparent K_i values for CaM with trifluoperazine, chlorpromazine, and imipramine, which are also listed in Table 2 (*42*). Their experiments measured the inhibition of CaM-activated guinea-pig heart phosphodiesterase by these compounds. IC_{50} values relate to the affinity of the interaction between ligands and receptors and have been shown by theoretical modeling to correlate with the K_D values (*43*). The present study and that of Reynolds and Claxton are in agreement with respect to the order of affinity of calmodulin for certain drugs, namely, trifluoperazine > chlorpromazine > imipramine.

The results from the peptides are indicative of their relative potencies. The CaM inhibitory peptide differs from the CaM inhibitory peptide (control) by only two residues selected to disrupt the interaction with calmodulin (*44*, *45*). The control peptide showed no change in the FRET emission ratio at any concentration tested, and similar results were obtained with the Ca^{2+}/CaM dependent protein kinase II-δ fragment as seen in Figure 10. The latter is actually a substrate for Ca^{2+}/CaM dependent protein kinase IV and was not expected to bind to CaM. For the peptides in Figure 8, we ranked the percent inhibition of FRET relative to the FRET inhibition obtained with the CaM inhibitory peptide (Table 2). The Ca^{2+}/CaM kinase II inhibitor peptide and CaM binding domain peptide, both derived from the CaM Kinase II CaM binding site, were found to be moderate FRET inhibitors, but had lower IC_{50} values than the CaM inhibitory peptide. A possible explanation for this difference in percent inhibition may relate to displacement of more than one molecule of 2,6-ANS per CaM. The myosin light chain kinase inhibitor peptide is a truncated version of the chicken smooth muscle myosin light chain kinase CaM binding domain. Thus, it was not surprising that is was the poorest inhibitor of FRET in our assay.

CONCLUSION

In summary, we have demonstrated the use of a competitive binding assay using FRET for the detection of drug and peptide antagonists of CaM. ANS has been shown to bind to hydrophobic binding sites and monitor binding events in a variety of proteins (*34*, *35*}. ANS has also been used as a monitor of conformation and an indicator of protein folding (*36*, *37*). Therefore, it is reasonable to conclude that ANS could be employed for applications in monitoring ligand-induced conformational changes in a wide range of binding proteins. Although ANS and the antagonists presumably bind at the same site in CaM, this is not a requirement for the type of FRET assay described herein. The only criterion is that the binding of a ligand to a protein binding site alters the binding constant of ANS to the protein. The two sites where ANS and the ligand bind need not be identical, and allosteric interaction would be sufficient. Thus, this FRET assay could be a model for other protein binding assays intended for use in pharmacological screening to detect compounds with desired properties. The assay has been proven to be rapid, simple, and economical, as it requires single rather than dual labeling for FRET. These are characteristics key to designing assays for drug candidate selection. The assay protocol developed also renders itself to automation, as it does not require complex separation steps. Finally, the sensitivity for both drug molecules and peptides has been demonstrated and compared among structurally related and unrelated compounds.

ACKNOWLEDGMENT

This work was funded by the National Aeronautics and Space Administration and the National Science Foundation. B.S. gratefully recognizes support from an Integrated Graduate Education and Research Traineeship predoctoral fellowship.

Supporting Information Available: CaM−MDCC calibration plot. This material is available free of charge via the Internet at http://pubs.acs.org.

LITERATURE CITED

(1) Szollosi, J., Nagy, P., Sebestyen, Z., Damjanovicha, S., Park, J. W., and Matyus, L. (2002) Applications of fluorescence resonance energy transfer for mapping biological membranes. *J. Biotechnol. 82*, 251−266.

(2) Boute, N., Jockers, R., and Issad, T. (2002) The use of resonance energy transfer in high-throughput screening: BRET versus FRET. *Trends Pharmacol. Sci. 23*, 351−354.

(3) Heyduk, T. (2002) Measuring protein conformational changes by FRET/LRET. *Curr. Opin. Biotechnol. 13*, 292−296.

(4) Kohl, T., Heinze, K. G., Kuhlemann, R., Koltermann A., and Schwille, P. (2002) A protease assay for two-photon crosscorrelation and FRET analysis based solely on fluorescent proteins. *Proc. Natl. Acad. Sci. U.S.A. 99*, 12161−12166.

(5) Miyawaki, A., Llopis, J., Heim, R., McCaffery, J. M., Adams, J. A., Ikura M., and Tsien, R. Y. (1997) Fluorescent indicators

for Ca^{2+} based on green fluorescent proteins and calmodulin. *Nature* 388, 882−887.
(6) Pollok, B. A., and Heim, R. (1999) Using GFP in FRET-based applications. *Trends Cell Biol.* 9, 57−60.
(7) Sills, M. A., Weiss, D., Pham, Q., Schweitzer, R., Wu, X., and Wu, J. J. (2002) Comparison of assay technologies for a tyrosine kinase assay generates different results in high throughput screening. *J. Biomol. Screen. 7*, 191−214.
(8) Takakusa, H., Kikuchi, K., Urano, Y., Higuchi, T., and Nagano, T. (2001) Intramolecular fluorescence resonance energy transfer system with coumarin donor included in beta-cyclodextrin. *Anal. Chem. 73*, 939−942.
(9) Truong, K., Sawano, Mizuno, A. H., Hama, H., Tong, K. I., Mal, T. K., Miyawaki, A., and Ikura, M. (2001) FRET-based in vivo Ca^{2+} imaging by a new calmodulin-GFP fusion molecule. *Nat. Struct. Biol. 8*, 1069−1073.
(10) Truong, K., and Ikura, M. (2001) The use of FRET imaging microscopy to detect protein−protein interactions and protein conformational changes in vivo. *Curr. Opin. Struct. Biol. 11*, 573−578.
(11) Sittampalam, G. S., Kahl, S. D., and Janzen, W. P. (1997) High-throughput screening: advances in assay technologies. *Curr. Opin. Chem. Biol. 1*, 384−391.
(12) Umezawa, Y. (2005) Genetically encoded optical probes for imaging cellular signaling pathways. *Biosens. Bioelectron. 20*, 2504−2511.
(13) Cheung, H. C. (1991) Resonance Energy Transfer. *Topics in Fluorescence Spectroscopy, Vol. 2: Principles,* pp 127−176, Plenum, New York.
(14) Ikura, M. (1996) Calcium binding and conformational response in EF-hand proteins. *Trends Biochem. Sci. 21*, 14−17.
(15) Chin, D., and Means, A. R. (2000) Calmodulin: a prototypical calcium sensor. *Trends Cell Biol. 10*, 322−328.
(16) Hinrichsen, R. D. (1993) Calcium and calmodulin in the control of cellular behavior and motility. *Biochim. Biophys. Acta 1155*, 277−293.
(17) Weinstein, H., and Mehler, E. L. (1994) Ca^{2+} -binding and structural dynamics in the functions of calmodulin. *Annu. Rev. Physiol. 56*, 213−236.
(18) Williams, R. J. (1992) Calcium and calmodulin. *Cell Calcium 13*, 355−362.
(19) Roberts, D. M., Crea, R., Malecha, M., Alvarado-Urbina, G., Chiarello, R. H., and Watterson, D. M. (1985) Chemical synthesis and expression of a calmodulin gene designed for site-specific mutagenesis. *Biochemistry 24*, 5090−5098.
(20) Cook, W. J., Walter, L. J., and Walter, M. R. (1994) Drug binding by calmodulin: crystal structure of a calmodulin-trifluoperazine complex. *Biochemistry 33*, 15259−15265.
(21) Matsushima, N., Hayashi, N., Jinbo, Y., and Izumi, Y. (2000) Ca^{2+}-bound calmodulin forms a compact globular structure on binding four trifluoperazine molecules in solution. *Biochem. J. 347*, 211−215.
(22) Vandonselaar, M., Hickie, R. A., Quail, J. W. and Delbaere, L. T. (1994) Trifluoperazine-induced conformational change in Ca^{2+}-calmodulin. *Nat. Struct. Biol. 1*, 795−801.
(23) Vertessy, B. G., Harmat, V., Bocskei, Z., Naray-Szabo, G., Orosz, F., and Ovadi, J. (1998) Simultaneous binding of drugs with different chemical structures to Ca^{2+}-calmodulin: crystallographic and spectroscopic studies. *Biochemistry 37*, 15300−15310.
(24) Blair, T. L., Yang, S. T., Smith-Palmer, T., and Bachas, L. G. (1994) Fiber optic sensor for Ca^{2+} based on an induced change in the conformation of the protein calmodulin. *Anal. Chem. 66*, 300−302.
(25) Schauer-Vukasinovic, V., Cullen, L., and Daunert, S. (1997) Rational Design of a Calcium Sensing System Based on Induced Conformational Changes of Calmodulin. *J. Am. Chem. Soc. 119*, 11102−11103.
(26) Griffin, B. A., Adams, S. R., and Tsien R. Y. (1998) Specific covalent labeling of recombinant protein molecules inside live cells. *Science 281*, 269−272.
(27) Kasturi, R., Vasulka C., and Johnson, J. D. (1993) Ca $^{2+}$, caldesmon, and myosin light chain kinase exchange with calmodulin. *J. Biol. Chem. 268*, 7958−7964.
(28) Persechini, A., and Cronk, B. (1999) The relationship between the free concentrations of Ca^{2+} and Ca^{2+}-calmodulin in intact cells. *J. Biol. Chem. 274*, 6827−6830.
(29) Douglass, P. M., Salins, L. L., Dikici, E., and Daunert S. (2002) Class-selective drug detection: fluorescently labeled calmodulin as the biorecognition element for phenothiazines and tricyclic antidepressants. *Bioconjugate Chem. 13*, 1186−1192.
(30) Dikici, E., Deo, S. K., and Daunert, S. (2003) Drug detection based on the conformational changes of calmodulin and the fluorescence of its enhanced green fluorescent protein fusion partner. *Anal. Chim. Acta 500*, 237−245.
(31) Allen, M. W., Urbauer R. J. B., and Johnson C. K. (2004) Single-molecule assays of calmodulin target binding detected with a calmodulin energy-transfer construct. *Anal. Chem. 76*, 3630−3637.
(32) Stryer, L. (1965) The interaction of a naphthalene dye with apomyoglobin and apohemoglobin: a fluorescent probe of nonpolar binding sites. *J. Mol. Biol. 13*, 482−495.
(33) Schonbrunn, E., Eschenburg, S., Luger, K., Kabsch, W., and Amrhein, N. (2000) Structural basis for the interaction of the fluorescence probe 8-anilino-1-naphthalene sulfonate (ANS) with the antibiotic target MurA. *Proc. Natl. Acad. Sci. U.S.A. 97*, 6345−6349.
(34) Haskard, C. A., and Li-Chan, E. C. Y. (1998) Hydrophobicity of bovine serum albumin and ovalbumin determined using uncharged (PRODAN) and anionic (ANS) fluorescence probes. *J. Agric. Food Chem. 46*, 2671−2677.
(35) Parul, D. A., Bokut, S. B., Milyutin, A. A., Petrov, E. P., Nemkovich, N. A. Sobchuk, A. N., and Dzhagarov, B. M. (2000) Time-resolved fluorescence reveals two binding sites of 1,8-ANS in intact human oxyhemoglobin. *J. Photochem. Photobiol. B. 58*, 156−162.
(36) Ayed, A., and Duckworth, H. W. (1999) A stable intermediate in the equilibrium unfolding of *Escherichia coli* citrate synthase. *Prot. Sci. 8*, 1116−1126.
(37) LaPorte, D. C., Wierman, B. M., and Storm, D. R. (1980) Calcium-induced exposure of a hydrophobic surface on calmodulin. *Biochemistry 19*, 3814−3819.
(38) Tsuruta, H., and Sano, T. (1990) A fluorescence temperature-jump study on Ca^{2+}-induced conformational changes in calmodulin. *Biophys. Chem. 35*, 75−84.
(39) Matulis, D., and Lovrien, R. (1998) 1-Anilino-8-naphthalene sulfonate anion-protein binding depends primarily on ion pair formation. *Biophys. J. 74*, 422−429.
(40) Matulis, D., Baumann, C. G., Bloomfield, V. A., and Lovrien, R. A. (1999) 1-anilino-8-naphthalene sulfonate as a protein conformational tightening agent. *Biopolymers 49*, 451−458.
(41) Ali, V., Prakash, K., Kulkarni, S., Ahmad, A., Madhusudan, K. P., and Bhakuni, V. (1999) 8-anilino-1-naphthalene sulfonic acid (ANS) induces folding of acid unfolded cytochrome *c* to molten globule state as a result of electrostatic interactions. *Biochemistry 38*, 13635−13642.
(42) Reynolds, C. H., and Claxton, P. T. (1982) Inhibition of calmodulin-activated cyclic nucleotide phosphodiesterase: multiple binding-sites for tricyclic drugs on calmodulin. *Biochem. Pharmacol. 31*, 419−421.
(43) Bachas, L. G., and Meyerhoff, M. E. (1986) Theoretical models for predicting the effect of bridging group recognition and conjugate substitution on hapten enzyme immunoassay dose−response curves. *Anal. Biochem. 156*, 223−238.
(44) Torok, K., and Trentham, D. R. (1994) Mechanism of 2-chloro-(epsilon-amino-Lys75)-[6-[4-(*N*,*N*-diethylamino)phenyl]-1,3,5-triazin-4-yl]calmodulin interactions with smooth muscle myosin light chain kinase and derived peptides. *Biochemistry 33*, 12807−12820.
(45) Bayley, P. M., Findlay, W. A., and Martin S. R. (1996) Target recognition by calmodulin: dissecting the kinetics and affinity of interaction using short peptide sequences. *Protein Sci. 5*, 1215−1228.
(46) Berman, H. M., Westbrook, J., Feng, Z., Gilliland, G., Bhat, T. N., Weissig, H., Shindyalov, I. N., and Bourne, P. E. (2000) The Protein Data Bank. *Nucleic Acids Res. 28*, 235−242.

BC050161Y

A Novel Approach to a Bifunctional Photosensitizer for Tumor Imaging and Phototherapy

Yihui Chen,[†] Amy Gryshuk,[†,‡] Samuel Achilefu,[§] Tymish Ohulchansky,[∥] William Potter,[†] Tuoxiu Zhong,[⊥] Janet Morgan,[†] Britton Chance,[⊥] Paras N. Prasad,[∥] Barbara W. Henderson,[†] Allan Oseroff,[‡] and Ravindra K. Pandey*[,†,§]

PDT Center, Cell Stress Biology, Roswell Park Cancer Institute, Buffalo, New York 14263, Department of Dermatology, Roswell Park Cancer Institute, Buffalo, New York 14263, Department of Radiology, Washington University School of Medicine, St. Louis, Missouri 63110, Department of Chemistry, State University of New York, Buffalo, New York 14221, and Department of Biophysics, Anatomy Chemistry Building, University of Pennsylvania, Philadelphia, Pennsylvania. Received June 20, 2005; Revised Manuscript Received July 20, 2005

Optical imaging has attracted a great attention for studying molecular recognitions because minute fluorescent tracers can be detected in homogeneous and heterogeneous media with existing laboratory instruments. In our preliminary study, a clinically relevant photosensitizer (HPPH, a chlorophyll-a analog) was linked with a cyanine dye (with required photophysical characteristics but limited tumor selectivity), and the resulting conjugate was found to be an efficient tumor imaging (fluorescence imaging) and photosensitizing agent. Compared to HPPH, the presence of the cyanine dye moiety in the conjugate produced a significantly higher uptake in tumor than skin. At a therapeutic/imaging dose, the conjugate did not show any significant skin phototoxicity, a major drawback associated with most of the porphyrin-based photosensitizers. These results suggest that tumor-avid porphyrin-based compounds can be used as "vehicles" to deliver the desired fluorescent agent(s) to tumor. The development of tumor imaging or improved photodynamic therapy agent(s) by itself represents an important step, but a dual function agent (fluorescence imaging and photodynamic therapy) provides the potential for tumor detection and targeted photodynamic therapy, combining two modalities into a single cost-effective "see and treat" approach.

INTRODUCTION

As photosensitizing agents, porphyrin-based compounds have played a central role in photodynamic therapy (PDT), the sensitization of tumor tissue to destruction by light (*1*−*3*). Photofrin, which was developed in the Roswell Park Cancer Institute (RPCI), is being used worldwide for the treatment of a wide variety of solid tumors. In the US, Photofrin PDT is approved for the treatment of obstructive esophageal cancer, early- and late-state lung cancer, and high-grade dysplasia associated with Barretts esophagus (*4*). The demonstrated clinical usefulness of PDT has spawned the development of a large number of new photosensitizers, and numerous tetrapyrrole-based compounds have been synthesized in various laboratories (*5*, *6*). Since the introduction of first PDT drug Photofrin, there have been continuous efforts in various laboratories to improve photosensitizer's tumor selectivity and specificity (*7*). Tumor cells in general have nonspecific affinity for porphyrins, the mechanism of porphyrin retention in tumors is not well understood, although the balance between hydrophilicity and hydrophobicity is recognized as an important factor. Some attempts have been made to direct photosensitizers to a known cellular target by creating a photosensitizer conjugates, where the other molecule is a ligand specific to the target (*8*, *9*). Some other examples of such photosensitizers are: conjugates with cell-membrane cholesterol (*10*) antibody (*11*−*13*), chemotherapeutic agents (*14*), etc. Certain proteins and microspheres were also made to improve the pharmacology of the compounds (*15*, *16*). These strategies seldom work well because the pharmacological properties of both compounds are drastically altered.

At RPCI, we have identified highly promising photosensitizing agents among a series of alkyl ether analogues of pyropheophorbide-a, (665 nm) (*17*, *18*), purpurinimides (705 nm) (*19*−*22*), and bacteriopurpurinimides (796 nm) (*23*−*25*) on the basis of quantitative structure−activity relationship (SAR) and/or SAR studies. One of the compounds in a pyropheophorbide-a series [3-devinyl-3-(1-hexyloxy)ethyl analogue (HPPH)] is currently in Phase I/II clinical trials at RPCI for the treatment of esophageal, lung, and cutaneous tumors (*26*−*27*).

Porphyrins and related compounds have also been investigated for use in optical diagnostic technologies based on their fluorescent properties, e.g., fluorescence being exploited as a possible technique for guidance of surgical intervention (*28*). In such surgical-assist applications, the ability to provide real-time information about surgical margins would be highly useful. Unfortunately, despite the attractiveness of the porphyrin-based compounds as photosensitizers for PDT, most of these compounds do not possess the excitation and emission spectra favorable for fluorescent contrast agents for imaging deep tissues. First, to maximize penetration depth into tissues, excitation between 750 and 800 nm

* To whom correspondence should be addressed. E-mail: ravindra.pandey@roswellpark.org. Phone: 716-845-3203. Fax: 716-845-8920.

[†] PDT Center, Cell Stress Biology, Roswell Park Cancer Institute.

[‡] Department of Dermatology, Roswell Park Cancer Institute.

[§] Washington University School of Medicine.

[∥] SUNY Buffalo.

[⊥] University of Pennsylvania.

10.1021/bc050177o CCC: $30.25 © 2005 American Chemical Society
Published on Web 09/03/2005

is preferred and the Stokes shift must be large to enable discrimination of the small fluorescent component from the overwhelming large component of excitation light. An insufficient Stokes shift of 10−15 nm complicates the process of rejecting multiply scattered light, as the efficiency of the filters cannot be guaranteed. For these reasons, the usefulness of PDT agents for contrast is largely limited to superficial epithelial linings of accessible tissues.

In recent years, a number of optical imaging approaches have been reported (*29*). These techniques rely on fluorescence, reflectance, absorption, or bioluminescence as the source of contrast, while imaging systems can be based on diffuse optical tomography, surface-weighted imaging, phase-array detection, confocal imaging, multiphoton imaging, or microscopic imaging with intravital microscopy. However, with the exception of near-infrared (NIR) fluorescence imaging (*30*) and superficial confocal and two-photon imaging, these techniques currently are limited to experimental imaging to small animals. Unlike fluorescence microscopy of cells or thin-tissue samples, in vivo imaging is preferably performed in the NIR region (700−900 nm) because of more efficient tissue penetration of photons and minimal auto fluorescence in this region (*31*). Recently, this technology has been extended to in vivo imaging of biological targets and disease. It has been shown that frequency−domain photon migration (FDPM) with an image-intensified charge-coupled device (CCD) can be used for the detection of diseased tissues in vivo using fluorescent contrast agents (*32*). A number of different NIR fluorochromes such as cyanine dyes have been described with variable stabilities, quantum efficiencies, and ease of synthesis (*33*, *34*). Despite their excellent photophysical properties, except a few folic acid (*35*) or certain peptide-linked (*36*) cyanine dyes, most of them (e.g., indocyanine green) are not tumor specific and are eliminated rapidly from the organism. By realization of the importance of porphyrin-based compounds in tumor avidity and photosensitizing efficacy and the advantages of cyanine dyes for tumor imaging due to their inherent characteristic of NIR absorbance and emission, we were interested in designing "bifunctional agents" consisting of these two chromophores, which could produce the desired photophysical properties suitable for both tumor detection by optical imaging as well as therapy (PDT). Such image-guided PDT would represent a new paradigm for tumor treatment. To provide a proof of principle concept, we have prepared and preliminarily evaluated a conjugate comprised of the photosensitizer HPPH and cyanine dye IR820.

EXPERIMENTAL PROCEDURES

For ^{1}H NMR data, chemical shifts are expressed in ppm with reference to trimethylsilane (0.00 ppm). Column chromatographic separations were performed over silica gel 60 (70−230 mesh) or neutral alumina (Grade III (6% water), ∼150 mesh). Preparative thin-layer chromatography (TLC) was performed on silica 20 × 20 cm^2 TLC plates. The cyanine dye 1 was purchased from Aldrich Chemicals.

Cyanine Dye 3. Compound **1** (60 mg) and 4-aminothiophenol (60 mg) were dissolved in dry DMF and stirred overnight. DMF was removed by high vacuum, the residue was purified by chromatography using MeOH/CH_2Cl_2 (1:3) as the eluting solvent system, and **3** was obtained in ∼80% yield. NMR [MeOH (d4)], δ (ppm) 9.0 (d, 2H, H−a), 8.2 (d, 2H, H−b), 8.0 (t, 4H, H−c), 7.62 (d, 4H, H−d), 7.48 (2d overlapped to be triplet, 2H, H−e), 7.12 (d, 2H, H−f), 6.70 (d, 2H, H−g), 6.35 (d, 2H, H−h), 4.30 (t, 4H, H−i), 2.95 (t, 4H, H−j), 2.80 (m, 4H, H−k), 2.00 (m, 10H, 4H for H−l, 6H for m, n, o), 1.90 (s, 12H, H−p), 1.30 (s, H−q). MS for **3**: calcd $C_{52}H_{56}N_3NaO_6S_3$, 937; found, 937. High resolution (HR) MS for **3**: calcd $C_{52}H56N_3NaO_6S_3$, 937.3229; found, MH^+, $C_{52}H_{57}N_3NaO_6S_3$, 938.3320.

HPPH−Cyanine Dye Conjugate 5. HPPH **4** (100 mg) and DCC (110 mg) were dissolved in 1 mL of dry DMF and stirred for 10 min, and the solution of **3** (145 mg) in DMF (2 mL) and 10 mg DMAP were added. Twenty-four hours later, the reaction mixture was worked up. The residue was purified by chromatography using MeOH/CH_2Cl_2 (1:3) as the eluting solvent system, and **5** was obtained in ∼65% yield. UV−vis in H_2O: 848 nm (ϵ = 97547), 664 nm (ϵ = 53800), 413 nm (ϵ = 101456). UV−vis in MeOH: 833 nm (ϵ = 207455), 660 nm (ϵ = 53856), 408 nm (ϵ = 95222). NMR ($CHCl_3$) δ (ppm) for compound **5**: 9.47 (s, 1H, meso-H in HPPH part), 8.46 (s, 1H, meso-H in HPPH part), 8.35 (br-s, 3H, 1H for meso-H in HPPH part, 2H for H−a), 7.50 (m, 5H, 1H for H−b, 4H for H−c), 7.30 (m, 3H, 1H for H−b, 2H for H−e), 7.20 (s, 2H, H−f), 7.05 (s, 4H, H−d), 6.85 (s, 2H, H−g), 6.61 (s, 2H, H−h), 5.70 (br, 3H, 1H for H-3^1, 1H for H-17, 1H for H-18), 4.54 (br-doublet, 1H, H-13^2), 4.22 (br, 2H, H−i), 3.66 (br, 2H, H−i), 3.20 (br, 9H, 5H for HPPH part: 3H for 7-CH_3, 2H for 3^1-OC*H*$_2$(CH$_2$)$_4$CH$_3$, 4H for H−j), 3.03 (m, 4H, H−k), 2.90 (s, 1H, −CON*H*), 2.72 (br, 7H, 2H for 8-C*H*$_2$CH$_3$, 2H for 17-CH_2CH_2CO-, 3H for 2-CH_3), 2.55 (br, 5H, 2H for 17-CH_2CH_2CO-, 3H for 12-CH_3), 1.88 (br, 3H, 3-$CHCH_3$), 1.72−0.72 (many multiples, 36 protons, 22 H for dye part: 12H for H−p, 4H for H−l, 6H for H−m, n, o; 14 H for HPPH part, 3H for 18-CH_3, 3 H for 8-CH_2C*H*$_3$, 8H for 3^1-OCH$_2$(C*H*$_2$)$_4$CH$_3$), 0.62 (m, 3H, 3^1-OCH$_2$(CH$_2$)$_4$C*H*$_3$. MS for **5**: calcd $C_{91}H_{102}N_7NaO_9S_3$, 1555.6; found, 1555.7. HRMS for **5**: calcd $C_{91}H_{102}N_7NaO_9S_3$, 1555.6798; found MH^+ $C_{91}H_{103}N_7NaO_9S_3$, 1555.6920.

Formulation of the Conjugates. HPPH and the corresponding cyanine dye conjugate were insoluble in water. Therefore, these compounds were formulated in 1% Tween-80/5% dextrose solution. The concentration of the final formulation was determined by following the Beer−Lambert's law. The stability and purity of the conjugates in formulation was ascertained by high-performance liquid chromatography analysis.

Photophysical Characterization. Photophysical properties of the synthesized conjugates were examined in different solvents (water, methanol, chloroform, etc., depending on solubility). Methods of electronic absorption and steady-state and time-resolved luminescence spectroscopy were used (*37*). Steady-state measurements were performed using a Shimadzu UV-3101PC spectrophotometer (absorption spectra) and Fluorolog-3 spectrofluorometer (Jobin Yvon) (fluorescence spectra). A SPEX 270M spectrometer (Jobin Yvon) equipped with an InGaAs photodetector (Electrooptical Systems Inc., USA) was used for acquisition of singlet oxygen emission spectra and dye emission in the NIR spectral range. A diode-pumped solid-state laser (Verdi, Coherent) at 532 nm was the excitation source in this case.

For the measurement of fluorescence decays, a Becker & Hickl Photon counting module (SPC-830), equipped with a fast PMT (Hamamatsu H7422) having a system response of about a 300-ps full width at half maximum, was used. A Ti:Sapphire laser (Tsunami from Spectra Physics) tunable in the range of 740−880 nm (∼100-fs pulses at 82 MHz) using BBO crystal and the obtained

light were used to excite the sample solution in a cuvette. A PHD-400-X high-speed photodiode module was used to provide a synchronization signal from the Ti:Sapphire laser.

Cell Line. For HPPH and the corresponding cyanine dye conjugate, RIF (radiation induced fibrosarcoma) cells were cultured in αMEM medium. Semiconfluent culture was used for in vitro studies of photosensitivity (survival studies) and drug localization as well as propagation of tumors in vivo by following the methodology routinely used in our laboratory.

Intracellular Localization of Conjugates. To determine subcellular localization, HPPH and the conjugate were co-incubated with organelle-specific fluorescent probes. RIF cells were seeded at 2×10^5 on poly-L-lysine-coated cover slips in six-well plates and cultured for 24 h to allow attachment and spreading. HPPH or conjugates at appropriate concentrations (typically 0.5−2 μM) were added to cells in culture medium, and the cells incubated for 3 or 24 h at 37 °C, 5% CO_2 in the dark. To determine subcellular localization, cells were co-incubated with fluorescent probes (Molecular Probes, Invitrogen Carlsbad, CA) known to target mitochondria (Rhodamine 123, 1 μM or Mitotracker Green, 200 nM) or lysosomes (yellow-green Fluospheres 0.1 μm diameter, 1:10 000 dilution). Mitotracker Green and Fluospheres were added 24 h prior to microscopy, the latter with gently rocking and the R-123 was added during the final 30 min of incubation. The cells were then rinsed briefly with phosphate-buffered saline (PBS) and examined immediately by fluorescence microscopy (Zeiss Axiovert 35, Carl Zeiss, Inc., Germany) with a 200-W mercury arc lamp light source.

Fluorescence was imaged with a CCD camera and intensifier as previously described (*38*) and processed with Metamorphose 4.5 (Universal Imaging Corp., Downington, PA). Images of photosensitizers and co-localizing dyes in the same field were taken in rapid succession. Photosensitizers were detected using a combination of 530−580-nm excitation and 600-nm dichroic/615-nm long-pass emission filters. R-123, Mitotracker Green, and Fluospheres were detected using 445−490-nm excitation and 510-dichroic/520−560-nm long pass/emission filters.

In vitro Photosensitizing Efficacy. RIF tumor cells (*18*) were cultured in αMEM (Invitrogen, Carlsbad, CA) supplemented with 10% fetal calf serum (Herndon,VA) in 100% humidity with 5% CO_2. Cells were harvested and used for in vitro assays in the log phase of growth. In a typical experiment, cells will be seeded in replicates at 5×10^4 cells/well in 96-well plates. Cells were incubated overnight before adding the desired conjugate at variable concentrations (0.125, to 4.0 μM). After 3 or 24 h incubation with the drug in the dark, cells were exposed to laser light at the longest wavelength absorption peak of the conjugate to deliver doses of 0.5−4 J/cm^2. After light treatment, fresh medium was added and the cells were incubated for 48 h. Phototoxicity for each photosensitizer was assessed after 48 h by comparing growth of treated cells to control cells (no drug, no light) as measured by formazan production using the 3-[4,5-dimethylthiazol-2-yl]-2,5-diphenylyetrazolium bromide (MTT) assay (*39*). Ten microliters of MTT (Sigma, St. Louis, MO) at 4 mg mL^{-1} in PBS was added, and the cells were incubated for 4 h. The medium was removed and the formazan crystals were dissolved in dimethyl sulfoxide (DMSO, FisherBiotech, Fair Lawn, NJ) at 100 μL per well. Formazan absorbance was read on a 96-well plate reader (Titertek Multiskan Plus MK II Miles Inc.) at 560 nm.

Tumor Uptake by in vivo Reflectance Spectroscopy. Tumor-bearing mice were anesthetized using ketamine/xylazine (2.2 mg/20 g mouse). The optical density as a function of wavelength was recorded before the intravenous (iv) injection of the conjugate (*40*). The monochromator was set to the expected longest wavelength of the experimental drug's in vitro absorption spectrum. The drugs were then administered by tail vein injection, and the light signal was recorded. The second spectrum was altered by the presence of drug in the tumor. This in vivo drug absorption spectrum was best displayed by taking the ratio of the post-injection spectrum to the pre-injection spectrum. This ratio offered the same advantages as a double beam absorption spectrophotometer. Data obtained before drug administration represented the reference spectrum. The ratio of these two spectra was not influenced by the wavelength dependence of the instrument. As a safeguard against day-to-day or hour-to-hour drift in the total light output of the lamp, both spectra (before and after administration) were normalized by dividing the signal strength at a wavelength where the drug absorption is negligible. To determine the uptake/clearance of tumor vs skin, another probe was used to record the in vivo absorption spectrum of the compound present in skin.

In vivo Antitumor Effect. Photosensitizers were injected intravenously (tail vein) in approximately 0.2-mL volumes. Mice bearing transplantable tumors were restrained without anesthesia in Plexiglas holders designed to expose only the tumor and a 2−4-mm angular margin of skin to light. For mice bearing spontaneous tumors at unpredictable sites, light exposure was flexibly adjusted to accommodate exposure of these sites. The tumors were exposed with a laser light source at appropriate absorption wavelength (Spectra Physics coherent argon-pumping tunable dye lasers, ranging from 630 to 800 nm, and ILX Light wave laser diode controller containing diodes of desired wavelength). The drug and light dosimetry followed the experimental design outlined previously (*18*). A typical experiment was as follows: Day 0: implant tumor. Staging day: select mice with tumor measuring 4.5−5.5 mm (longest axis), prepare photosensitizers, record body weight, and inject test photosensitizer (iv). Treatment day (chosen based on prior tumor uptake data determined by in vivo reflectance spectroscopy): expose tumors to light, measure tumor dimensions (orthogonal diameters) by caliper every other day for tumor growth/regrowth assays. The tumor volume, V, is calculated with the formula $V = (lw^2/2)$, where l is the longest axis of the tumor and w is the axis perpendicular to l. Observe treatment field, i.e., record observations of edema, erythema, and escar formation. Record time to regrowth of tumors to 400 mm^3 (those mice in which there was no tumor regrowth for 90 days, accounted as cured mice). Mice were sacrificed for ethical consideration when tumors reach that volume (400 mm^3).

Normal Tissue Responses. Foot response was judged using a 0−3 scale. 0 = no apparent difference from normal, 0.1 = very slight edema, 0.3 = slight edema, 0.5 = moderate edema, 0.75 = large edema and/or slight erythema, 1.0 = large edema and/or erythema with exudate, 1.2 = moderate erythema, with slight scaly or crusty appearance, 1.5 = definite erythema with definite scaly or crusty appearance, 1.65 = slight damage and or slight fusion of toes, *2.0 = most toes fused but general shape unchanged, 2.5 = foot shapeless with no toes, 3.0 = only stub of foot remaining (*41*).

Assessment of Vascular Perfusion. Fluorescein was used as a marker for vascular perfusion or changes

thereof (*42*). At various time points after PDT exposures of normal skin, each mouse was given intravenous injection of 0.2 mg of fluorescein dye (10 mg of sodium fluorescein per milliliter of HBSS; Baker Chemical, Phillipsberg, NJ). Immediately thereafter, the animal's back was illuminated with UV light (Black-Ray longwave lamp, Ultra-Violet products, Inc., San Gabriel, CA), and the fluorescein distribution between the treatment area and surrounding skin was visualized and recorded. To quantify the vascular photosensitivity, the PDT light doses were adjusted by increments of 5−25 J cm^{-2} (λ_{ex}, 490 nm; λ_{em}, 520 nm) from a base dose where no dye exclusion was observed until a minimum light dose to give complete exclusion of fluorescein from the treatment area, i.e., occlusion of the skin vasculature was established (*43*).

High-Resolution Tumor Imaging. Frozen tumor tissue was embedded in an ethanol−glycerol−water mixture (freezing point: −30 °C) and mounted in a redox machine: a 3D, high-resolution cryofluorometer scan system for 3D surface fluorometric scanning (*28*). The frozen tumor sample was ground flat for imaging before it was further ground down to obtain images usually every 100 μm. A bifurcated optical fiber bundle (7 quartz fibers, 70 μm core diameter for each, 1 fiber for emission in center, 6 fibers for excitation around the emission fiber) stepped across the tissue surface at a fixed distance from the tissue surface (70 μm). The filters for each substance's fluorescence excitation and emission were chosen based on the absorption and emission spectra of each fluorophores. By use of a mercury arc lamp as the excitation light source, the fluorescent signals of conjugate **5** (filters: ex, 405DF40; em, 670DF20), cyanine dye (filters: ex, 780; em, 856) were imaged for each depth of the tumor. The scanning was performed at 128 × 128 steps that covered 1.024 × 1.024 cm^2 area (80 μm per step). The fluorescence signals were recorded digitally on a PC and reconstructed later with MATLAB.

Whole-Body Imaging and Biodistribution Assays. Animal studies were performed in accordance with the Guide for the Use of Laboratory Animals. A noninvasive in vivo continuous wave fluorescence imaging apparatus was used to assess the localization and distribution of the conjugates, as described previously (*44*, *45*). Briefly, light from two laser diodes of nominal wavelength 780 or 808 nm and nominal power of 50 mW was launched into fiber optic bundles. The nominal 50 mW of incident power was reduced to about 20 mW at the output of the fiber optic bundle. A defocusing lens in position after the bundle was used to expand the beam such that nearly the whole mouse was illuminated. Digital images were recorded with a Photometrics CoolSNAP HQ CCD camera (12 bit, 1024 × 1024 pixels, back illuminated, thermoelectric Peltier cooled with forced air) equipped with an 830−870-nm interference filter. Images were acquired and processed using WinView software from Princeton Instruments. Data analysis consists of subtracting (pixel by pixel) the pre-injection or background image from the post-injection images and displaying the false color results. Integration of the relative fluorescence intensities of tumor vs surrounding tissues indicated qualitatively the extent of selective uptake of the molecular probe. Typically, the probes were administered via the lateral tail vein at dosages of 0.3 and 3.5 μmol/kg body weight of the mouse (depending on optimal therapeutic dose). Images were taken at 24, 48, and 72 h post-injection of the probe. The tumor-bearing mice (3 mice/group) were anesthetized with ketamine/xylazine via intraperitonial injection, and the conjugate was administered intravenously at a therapeutic dose. At the best imaging time (24 or 48 h), the animal was euthanized and selected organs were removed, washed, and placed on a dark background for fluorescence imaging. Tissue parts, instead of whole organs, were used to determine the relative fluorescence intensity in each organ to minimize problems associated with depth-dependent nonlinear fluorescence emission. A statistical program in the WinView package was used to estimate the mean fluorescence intensity per organ part.

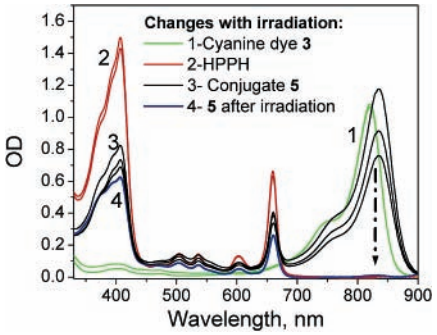

Figure 1. The absorption spectra of compounds **3**−**5** in dichloromethane. In conjugate **5**, irradiation of the HPPH absorption at 660 nm caused a significant decrease in the absorption of the cyanine dye at 831 nm (broad peak) and finally its complete photodestruction with a simultaneous increase in the intensity of HPPH absorption.

RESULTS AND DISCUSSION

Chemistry. As proof-of-principle of our approach to develop compounds with both imaging and therapeutic capabilities, we synthesized a conjugate **5** consisting of a highly effective photosensitizer, HPPH, and a cyanine dye exhibiting long wavelength absorption at 660 and 836 nm, respectively, with a strong emission at 865 m. In our preliminary study, the conjugate, designated as our lead compound, was evaluated for its photophysical characteristics, intracellular localization, in vivo tumor vs skin uptake, in vitro/in vivo photosensitizing efficacy, whole body imaging, biodistribution characteristics, and in vivo mechanistic and skin phototoxicity. These studies support the validity of our approach. The results are summarized as follows.

Synthesis of HPPH−Cyanine Dye Conjugate. The cyanine dye, namely, 2-[2-[2-chloro-3-[{1,3-dihydro-1,1-dimethyl-3-(4-sulfobutyl)-2H-benzo-(e)-indol-2-ylidene]-ethyl-indene]-1-cyclohexen-1-yl}ethenyl]-1,1-dimethyl-3-(4-sulfobutyl)-1H-benzo[e] indolium hydroxide, inner salt, sodium salt] **1** was first reacted with 4-aminophenylthiol and the corresponding 2-(4-aminophenylthioether) analogue **3** was isolated in 80% yield. Reaction of **3** with HPPH **4** (HPPH was prepared from chlorophyll-a by following the methodology developed in our laboratory) in the presence of DCC, and the desired HPPH−cyanine dye conjugate **5** was isolated in good yield (65%) (Scheme 1). UV, NMR, and mass spectrometry analyses confirmed the structure of the desired conjugate. The photophysical characteristic of the conjugate was first investigated before comparing its in vitro and in vivo photosensitizing efficacies and tumor-imaging capability with cyanine dye **3** and HPPH **4**.

Photophysical Studies. The electronic absorption spectrum of the conjugate **5** contains the characteristic absorption bands for two chromophores, i.e., HPPH **4** and the modified cyanine dye **3** (see Figure 1). The absorption characteristics of the HPPH moiety in the conjugate **5** remains practically unchanged in respect to the free HPPH.

Scheme 1. Synthesis of Conjugate 5

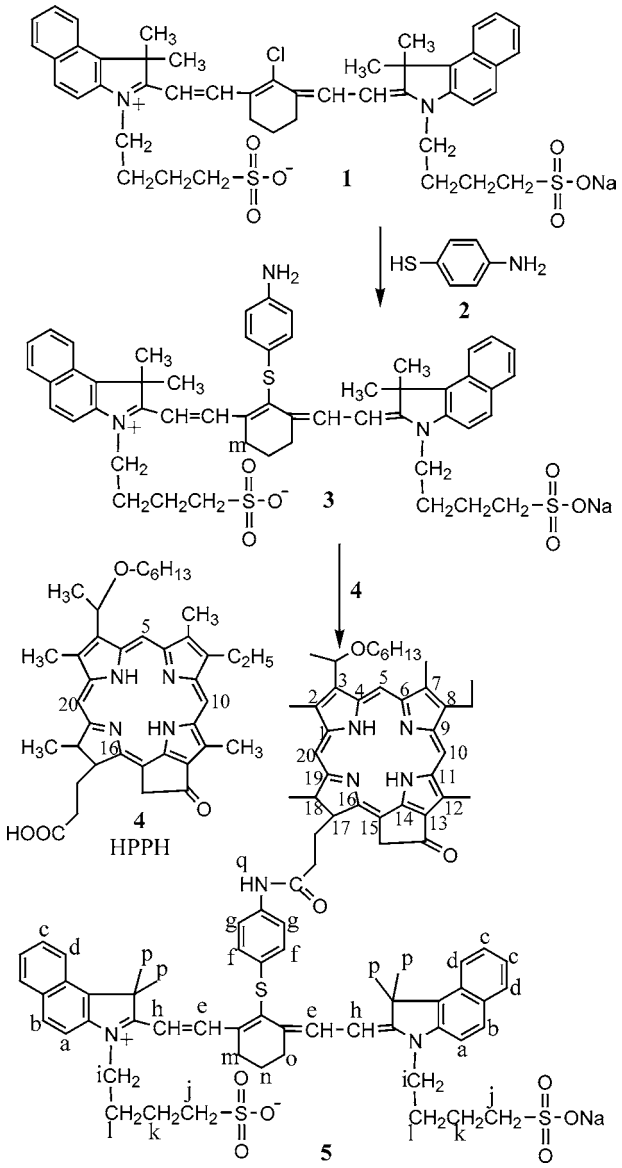

Compared to the free cyanine dye, in conjugate **5**, the absorption band for the cyanine dye moiety was found to be red shifted by 15 nm (820−835 in methanol), which is apparently associated with a change in environmental polarity caused by the presence of the HPPH moiety. Because of the similarity of the absorption spectra of HPPH and cyanine dye in conjugate **5** with respect to individual chromophores (without formation of any new absorption bands), it appears that the HPPH and cyanine dye π-electron systems in conjugate **5** absorb light practically independently. At the same absorption at the wavelength of excitation, the fluorescence intensity from the HPPH moiety in **5** was found to be significantly lower than observed for free HPPH. The electronic excitation energy transfer most probably occurs in **5** from the HPPH (donor) to the cyanine dye (acceptor). In methanol solution, irradiation of conjugate **5** at 532 nm (i.e., activation of HPPH) caused photolysis of cyanine dye moiety, and significant changes were observed in both absorption and fluorescence spectra. With increasing time of irradiation, absorption and fluorescence from the cyanine dye moiety at 835 and 875 nm, respectively, decreased, with a simultaneous increase in the intensity of fluorescence/absorption of the HPPH moiety. This is certainly due to the destruction of the π-electron system of the acceptor with subsequent discontinuation of a channel for the electronic excitation energy transfer. Comparison of the absorbance intensity ratios between nonirradiated vs irradiated −HPPH conjugate **5** (Figure 1) shows that the absorbance intensity of HPPH was increased by approximately 3-fold as a result of irradiation at 665 nm.

It was observed that, during irradiation (at 660 nm), the destruction of the cyanine dye moiety in conjugate **5** takes place continuously with a simultaneous increase in $^1O_2$ production (not shown). What is interesting to note is that the noticeable destruction of the cyanine dye moiety was observed only by excitation of the HPPH moiety and that the compound was found to be quite stable on exciting at the wavelengths that correspond to the cyanine dye moiety. Therefore, conjugate **5** shows an interesting characteristic for a suitable "bifunctional agent" that could be used for tumor imaging and therapy. Further detailed in vitro and in vivo photophysical investigations including the electrochemical studies with conjugate **5** are currently in progress and will be published elsewhere.

In vitro Photosensitizing Efficacy. The in vitro efficacy of the conjugate was determined in RIF cells, and the conjugate **5** was evaluated by performing two sets of experiments. After incubating the cells in the dark at 37 °C with 5 at various drug concentrations for 24 h, the medium was replaced with drug-free complete medium and cells were exposed to light either at 665 or 810 nm and the in vitro photosensitizing efficacy was determined by MTT assay (*39*).

In the first set of experiments, the photosensitizing activity of conjugate **5** was compared with HPPH. The cells were exposed to 665-nm laser light. As can be seen from Figure 2A, compared to HPPH the conjugate **5** was found to be equally effective. Interestingly, in a second set of experiments, on exposing cells to 810-nm diode light there was not any significant cell kill for either the cyanine dye **3** or conjugate **5** (Figure 2B). These results further confirm that the cyanine dye part of the moiety in conjugate **5** does not produce any significant singlet oxygen, which is a key cytotoxic agent for the destruction of tumor cells by PDT.

Comparative Intracellular Localization. Mitochondria have been identified as the most sensitive intracellular targets for PDT (*43*, *44*), and HPPH has been found to localize to the mitochondria (*46*). We therefore determined whether the conjugation of HPPH to cyanine dye affected the subcellular distribution of the photosensitizer. The localization of HPPH **4** and the corresponding cyanine dye conjugate **5** was investigated by co-incubating photosensitized RIF cells with Mitotracker Green (Molecular Probes, Eugene, OR) or Fluospheres (0.1 μm diameter latex heads labeled withfluorescein isothiocyanate 1/10 000 dilution by Molecular Probes, Eugene, OR), which target mitochondria and lysosomes, respectively. Fluorescence was imaged with a CCD camera and intensifier, and the images of photosensitizers and Mitotracker Green or Fluosphere localization were taken in rapid succession by following the literature procedure (*44*, *45*). From the results summarized in Figure 3, the imaging data clearly indicate that the HPPH and the conjugate localize in the same subcellular region as the mitochondrial marker, suggesting their affinity to mitochondria. The results obtained by using Fluospheres as a counterstain did not show any lysosomal colocalization (data not shown).

In vivo Photosensitizing Activity. The in vivo photosensitizing efficacy was determined in C3H mice transplanted with RIF tumors. Once the tumors reached

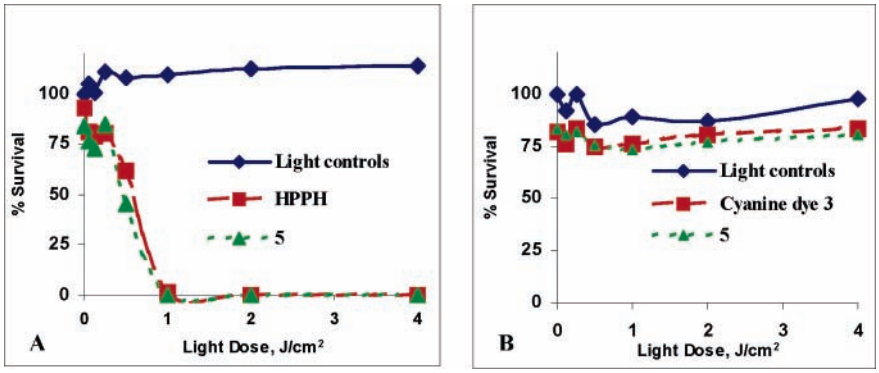

Figure 2. Comparative in vitro photosensitizing efficacy of the cyanine dye **3**, HPPH, and the corresponding cyanine dye conjugate **5** at equimolar concentration (0.6 μM) in RIF tumor cells: (A) the cells incunated with HPPH and the conjugate **5** were exposed to light at 665 nm and (B) the cyanine dye **3** and the conjugate **5** were exposed to light at 810 nm at variable light doses.

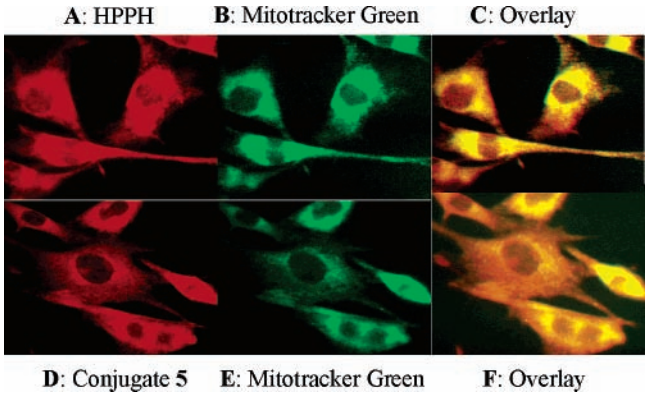

Figure 3. Comparative localization (false images) of HPPH **4** and conjugate **5** with Mitotracker Green (mitochondrial probe) in RIF cells after incubating for 24 h (for details, see the text).

4−5 mm^3, they were exposed to light (135 J/cm^2) at 24 h after injection of the conjugate at variable drug doses. The tumor growth (to reach >400 mm^3) was monitored daily for 30−90 days. As can be seen from Figure 4, clear dose−response relationships were observed, with a dose of 3.5 μmol/kg of the conjugate being highly effective in controlling the tumor regrowth (8/10 mice were tumor free at day 90). This therapeutic dose was subsequently chosen for tumor imaging.

High-Resolution Tumor Image. We have assessed the three-dimensional distribution of conjugate **5** in frozen sections of the RIF tumor, by means of fluorescence spectrophotometric imaging of successive slices through the frozen tissue block (*47*). Figure 5 illustrates a diffuse, heterogeneous distribution of **5** with maximal levels at the growing edge of the tumor, particularly indicated in the 300- and 900-μm sections, with little in the necrotic center. The histogram (D) for the distribution of conjugate **5** is broad Sand bimodal, ranging from 50 to >250 intensity values representing the low accumulation in the center compared to the viable periphery. The median tissue fluorescence in the absence of **5** was ~30 (C and F). The localized distribution of cyanine dye **3** is indicated in the same range. The dye is localized mainly in the tumor, both in the necrotic portion of the tumor and in the actively growing edge (see the 600-μm slice 3).

In vivo Imaging. Results of whole body fluorescence imaging (*48*) in the RIF tumor-bearing mouse, with excitation of the fluorescent cyanine dye moiety of conjugate **5** 24 h after administration, are shown in Figure 5. It was exciting to note that even at a dose of 0.3 μmol/kg, which was later found to be 8−10-fold less than the therapeutic dose, the conjugate showed significant tumor-imaging capability. Once the optimum therapeutic dose of 3.5 μmol/kg was determined, further imaging experiments were carried out to determine the time course of the tumor and the organ distribution of conjugate **5** in intact mice (Figure 5G) and in the isolated organs (Figure 6).

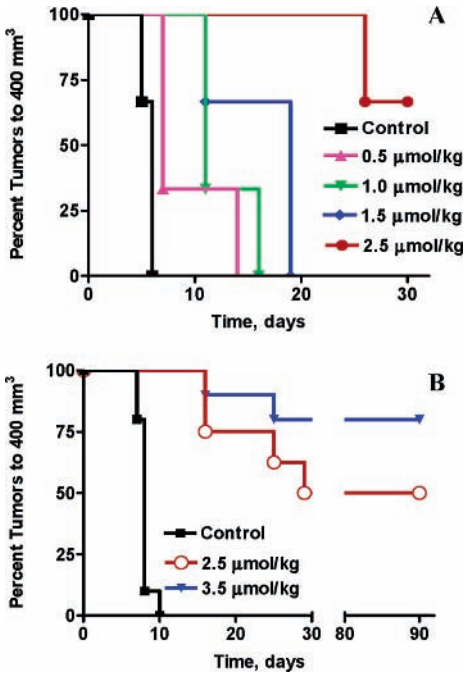

Figure 4. In vivo photosensitizing efficacy of conjugate **5** in C3H mice (10 mice/group) bearing RIF tumors and variable concentrations. The tumors were exposed to a laser light (665 nm, 135 J/cm^2) at 24 h after injection. (A) Drug concentrations = 0.5−2.5 μmol/kg. (B): Drug concentrations = 2.5 and 3.5 μmol/kg.

The organ distribution shown in Figure 6 confirms the whole mouse images. To quantitate the relative fluorescence intensity in each organ, we determined the mean fluorescent counts per organ, represented in a histogram format in Figure 6 (24, 48, and 72 h after injection). At 24 h, the probe is distributed in several organs, which confounds localization of the tumor by fluorescence imaging. However, 48 and 72 h after injection, the probe content in tumor is very high relative to the blood and to the different organs. The data demonstrate the high selectivity of the conjugate and clearly indicate the feasibility of identifying a tumor by optical imaging using a bifunctional cyanine photosensitizer probe.

Determination of Tumor/Skin Uptake Ratios and Skin Photosensitization. Persistence of photosensitizer

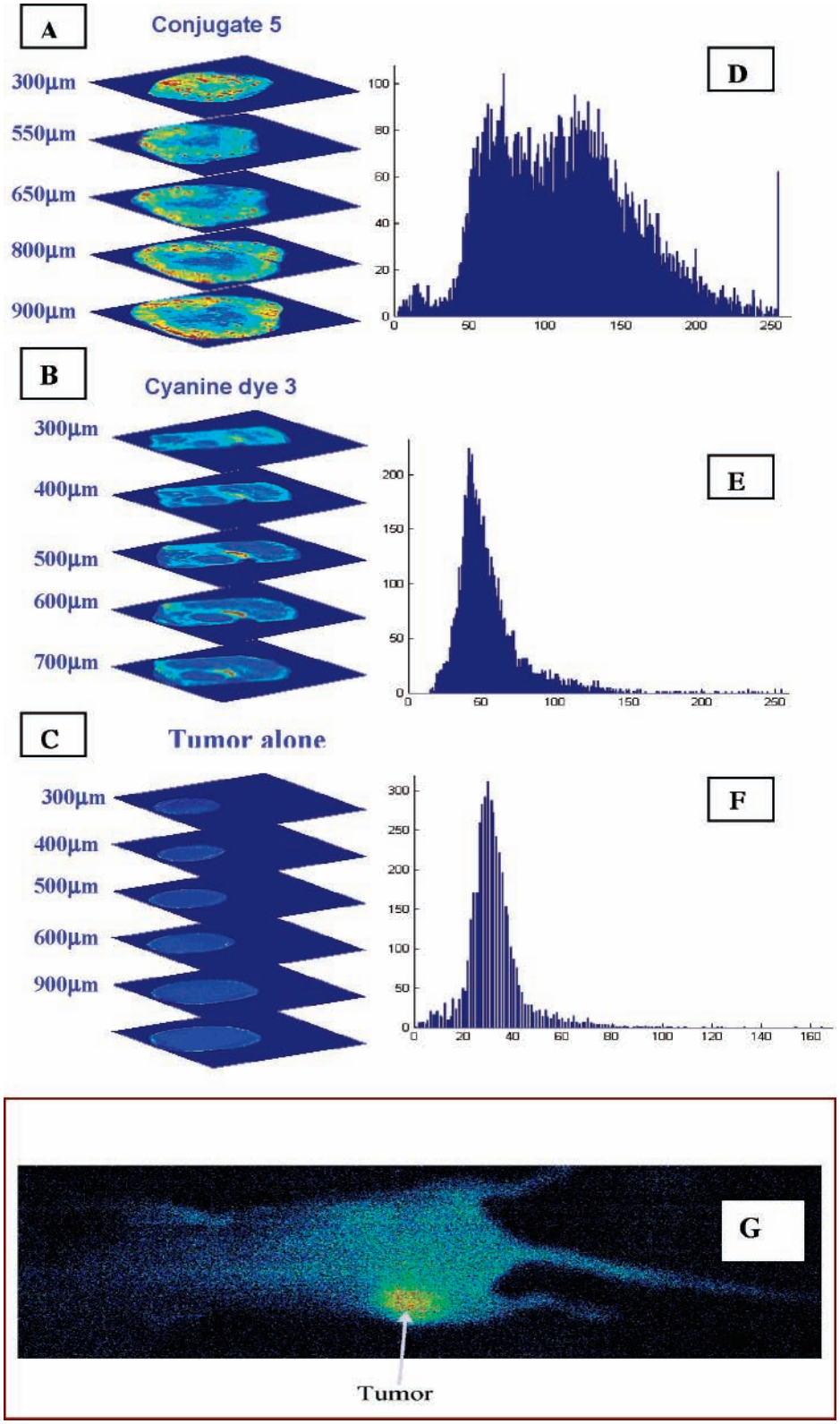

Figure 5. High-resolution tumor images at 24 h after injection: (A) conjugate **5** (3.5 μmole/kg), (B) cyanine dye **3** (3.5 μmole/kg), and (C) control (tumor alone). D, E, and F are their respective histograms (λ_{ex}, 780 nm; λ_{em}, 865 nm). (G) Localization of the conjugate **5** in a live mouse 24 h after injection (drug dose = 0.3 μmol/kg).

in the skin and resultant prolonged cutaneous photosensitivityhave been a major drawback for clinical PDT with porphyrin-based compounds (*49*). A high tumor:skin ratio of photosensitizer uptake therefore is critical for both tumor imaging and treatment.

The uptake of conjugate **5** (in tumor and skin) was determined by in vivo reflectance spectroscopy. In brief, conjugate **5** (3.5 μmol/kg) was injected into a C3H mouse bearing RIF tumors, and the in vivo absorption spectra of the conjugate present in tumor and skin were recorded at various time intervals by following the methodology routinely used in our laboratory. As can be seen from Figure 7A, the conjugate **5** produced a significantly higher uptake in tumor than skin at 24 h after injection.

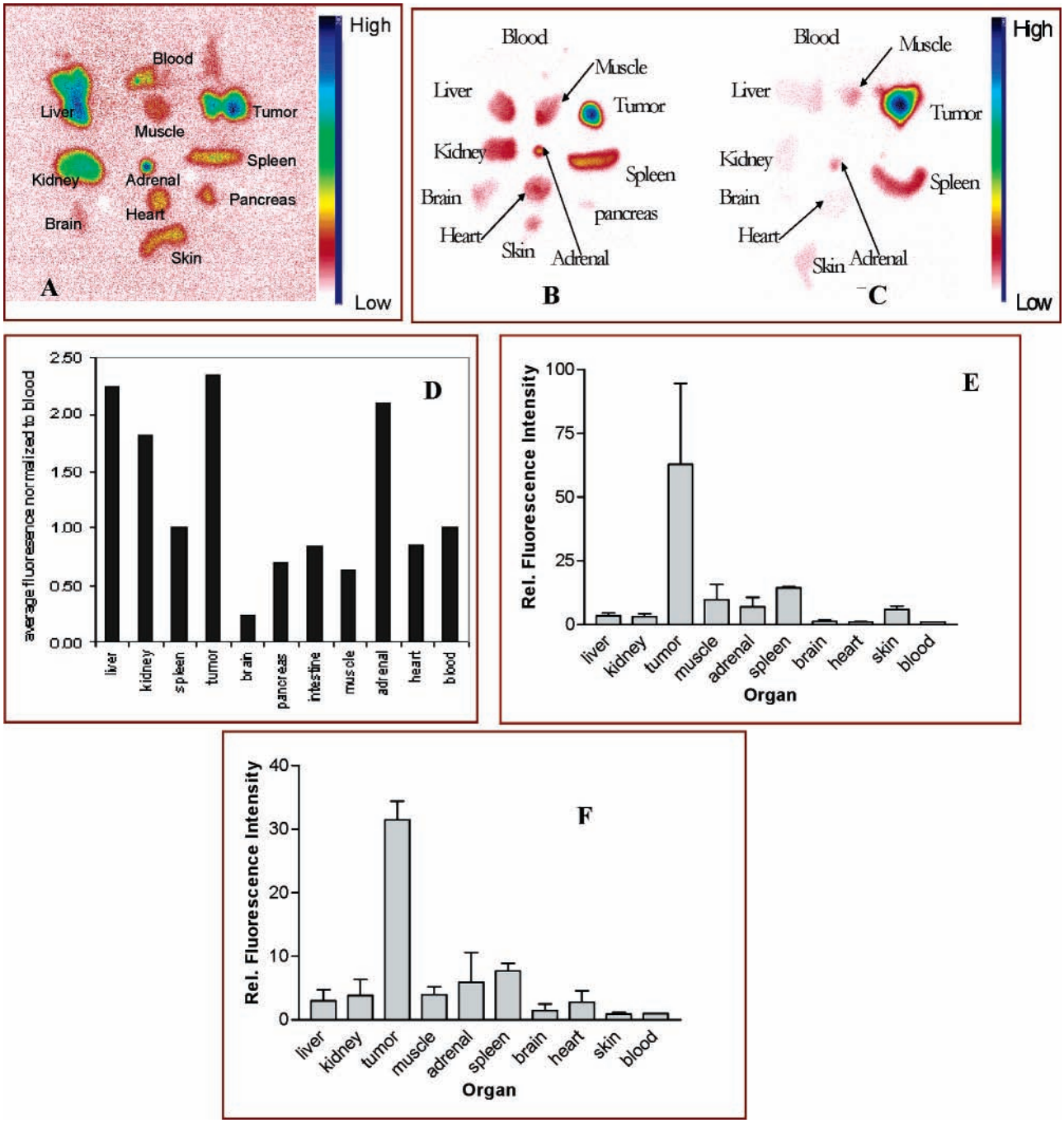

Figure 6. A, B, C: Images of the distribution of **5** in various organ parts at 24, 48, and 72 h after injection, respectively (drug dose = 3.5 μmol/kg). D, E, F: Relative fluorescence of conjugate **5** in selected organs at 24, 48, and 72 h after injection (2 mice/group). All intensities are relative to blood.

In a tumor, a substantial increase in drug uptake was observed from 24 to 48 h without a concomitant change in skin uptake. After 48 h, the drug concentration in tumor and skin began to decline, reaching negligible levels in the skin by 72 h while still maintaining relatively high tumor levels (Figure 7A). In contrast, as shown in Figure 7B, the cyanine dye **3** did not show any tumor selectivity and it cleared rapidly from tumor and skin, suggesting a remarkable difference in pharamacokinetic characteristics of the two compounds.

To validate the finding of low skin drug levels, general skin phototoxicity was assessed. The HPPH−cyanine dye conjugate **5** at a dose of 3.5 μmol/kg (therapeutic dose) was compared with HPPH and Photofrin at approximately equi-effective therapeutic doses. In each experiment, the mice (3 mice/group) were restrained without anesthesia in holders designed to allow the exposure of one hind foot. The foot was exposed to solar-simulated light for 30 min, either 24, 48, 72, and 96 h after injection. Foot response was judged using a 0−3 scale. As can be seen from Figure 7C, conjugate **5** had a minimal, transient response (score 0.1 24 h after injection) with no photosensitizing activity 48 h after injection, whereas HPPH at a 7.4-fold lower dose had greater skin phototoxicity 72 h after administration (Figure 7D). In contrast, Photofrin caused very significant phototoxicity, with scores of 1.5 (24 h), 1.5 (48 h), 1.4 (72 h), and 1.25 (96 h) (data not shown). These functional data confirm the imaging and absorption findings.

Effects on the Vasculature. In PDT-mediated therapy, it has been shown that vascular destruction in the tumor and immediate tumor-surrounding tissue can

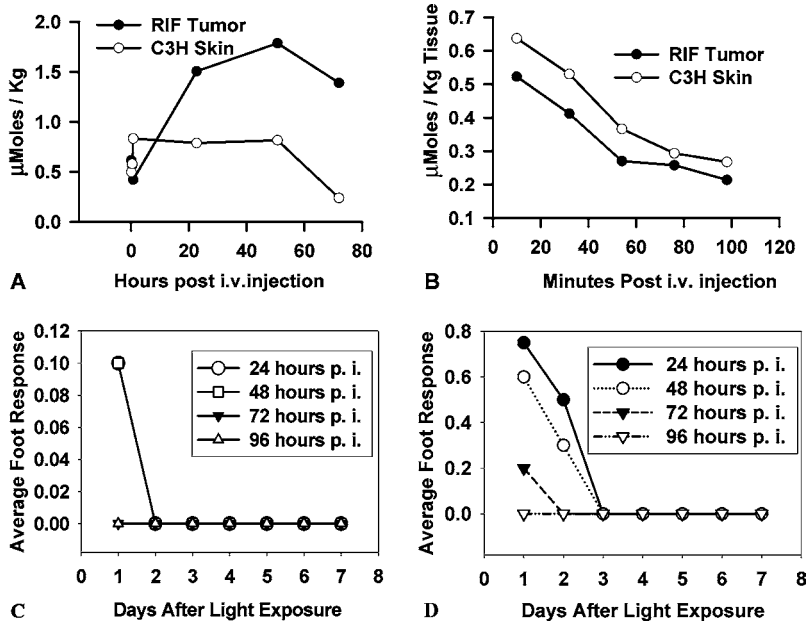

Figure 7. A and B: Tumor vs skin uptake of conjugate **5** and cyanine dye **3**, respectively, in C3H mice bearing RIF tumors at variable time points. C and D: Foot response in Swiss mice as a function of time after light and time interval between injection and light: (C) effect of conjugate **5** vs (D) HPPH on foot response at respective therapeutic doses (**5**, 3.5μmole/kg; HPPH, 0.47 μmol/kg) at various time intervals (for details see the text).

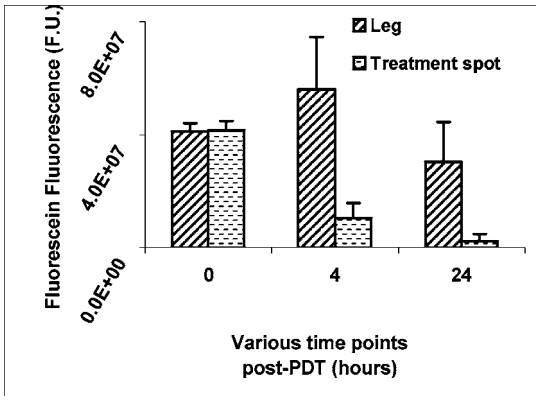

Figure 8. Vascular shutdown results obtained by fluorescein exclusion assay at 4 and 24 h after PDT.

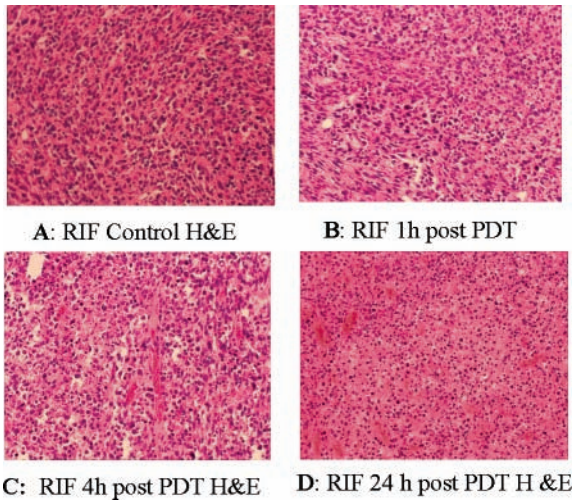

Figure 9. Histological analyses of conjugate **5** (after PDT). The dilated vessels at 4 h and necrosis at 24 h are evident.

contribute significantly to tumor control (*50*, *51*). Therefore, we determined the effects of the conjugate on the cutaneous vasculature. Conjugate **5** was injected intravenously, and 24 h later the mice in groups of three were treated with laser light at 665 nm for a total light dose of 135 J/cm^2 at a fluence rate of 75 mW/cm^2 (1 cm^2 diameter spot). The mice were evaluated for PDT-induced changes in vascular perfusion at various time points after PDT (0, 4, and 24 h) by injecting 0.20 cm^3 fluorescein (ex, 490 nm; em, 520 nm) intravenously as a perfusion marker. An in vivo fluorescence probe was then utilized to quantitate fluorescein fluorescence in the treatment site as compared to a nonlight treatment site. Each column represents the mean from three mice at each time point in comparison to the nontreated site.

As can be seen by Figure 8, immediately after PDT there is no difference in fluorescein fluorescence when comparing the drug/light treatment site to an unirradiated site of the leg.

However, at 4 and 24 h after PDT, there is a significant difference, with minimal to nearly no fluorescein fluorescence in the treated site, indicating that fluorescein was unable to penetrate due to vascular destruction. Histologic analysis confirmed this conclusion showing dilated and obstructed vessels, progressing toward hemorrhagic necrosis (Figure 9).

CONCLUSION

Our results indicate that (a) tumor-avid porphyrin-based compounds can be used as vehicles to deliver the optical imaging agent to tumor, (b) the inherent characteristics of two chromophores complement each other and their individual characteristics can be used for tumor detection and therapy, and (c) the presence of the cyanine dye appears to further improve the pharmacokinetics of the molecule, resulting in even faster clearance from the skin and elimination of prolonged skin phototoxicity, a major drawback associated with most porphyrin-based photosensitizers.

Our approach provides a unique opportunity for developing more tumor-specific, bifunctional agents for tumor detection and therapy by targeting those receptors known for high expression in tumors. Currently, the syntheses and biological studies of such target-specific

bifunctional agents containing more tumor-avid photosensitizers than HPPH and exhibit long-wavelength absorptions in the range of 700−800 nm are in progress.

ACKNOWLEDGMENT

The financial support from the NIH (CA55792), Roswell Park Alliance Foundation, and shared resources of the RPCI Support Grant (P30CA16056) is appreciated. One of the authors (A.G.) thanks the National Science Foundation under the Integrative Graduate Education and Research Traineeship (Grant DGE0114330) for the graduate fellowship.

LITERATURE CITED

(1) Henderson, B. W., and Dougherty, T. J. (1992) How does photodynamic therapy work. *Photochem. Photobiol. 55* (1), 145−157.

(2) Dougherty, T. J., Gomer, C., Henderson, B. W., Jori, G., Kessel, D., Korbelik, M., Moan, J., and Peng, Q. (1998) Photodynamic Therapy. *J. Natl. Cancer Inst*. *90*, 889.

(3) Dolmans, D. E. J. G. J., Fukumura, D., and Jain, R. K. (2003) Photodynamic Therapy for Cancer. *Nat. Rev., Cancer 3* (5), 380.

(4) Dougherty, T. J., and Levy, J. G. (2002) Photodynamic Therapy (PDT) and clinical applications. *Biomedical Photonics Handbook* (Vo-Dinh, T., Ed.), CRC Press, Boca Raton.

(5) Chen, Y., Li, G., and Pandey, R. K. (2004) Synthesis of bacteriochlorins and their potential utility in photodynamic therapy (PDT). *Curr. Org. Chem. 8* (12), 1105−1134.

(6) Ali, H., and van Lier, J. E. (1999) Metal complexes as photo- and radiosensitizers. *Chem. Rev*. *99*, 2379−2450.

(7) Pandey, R. K. (2002) Synthetic strategies in designing porphyrin-based photoensitizers for photodynamic therapy. In *Biomedical Photonics Handbook* (Vo-Dinh, T., Ed.), CRC Press, Boca Raton.

(8) Schmidt-Erfurth, U., Diddens, H., Birngruber, R., and Hasan, T. (1997) Photodynamic targeting of human retinoblastoma cells using covalent low-density lipoprotein conjugates. *Br. J. Cancer 75*, 54−61.

(9) Finger, V. H., Guo, H. H., Lu, Z. H., and Peiper, S. C. (1997) Expression of chemokine receptor by endothelial cells: detection bu intravital microscopy using chemokine-located fluorescent microspheres. *Methods Enzymol. 18*, 148−158.

(10) Hombrecher, H. K., Schell, C., and Thiem, J. (1999) Synthesis and investigation of galactopyranosyl-cholesterloxy substituted porphyrins. *Bioorg. Med. Chem. Lett. 6*, 1199−1202.

(11) Donald, P. J., Cardiff, R. D., He, D., and Kendell, K. (1991) Monoclonal antibody-porphyrin conjugate for head and neck cancer, the possible magic bullet. *Otolaryng. Head Neck 105* (6), 781−787.

(12) Hamming, A. W., Davis, N. L., Dubois, B. Quenville N. F., and Finley R. J. (1993) Photodynamic therapy of squamous cell carcinoma. An evaluation of a new photosensitization agent, benzoporphyrin derivatives and a new photoimmunoconjugate. *Surg. Oncol., 2* (3), 187−196.

(13) Vrouenraets, M. B., Visser, G. W. M., Stewart, F. A., Stigter, M., Oppelaar, H., Postmus, P. E., Snow, G. B., and van Dongen, G. A. M. S. (1999) Development of meso-tetrahydroxyphenyl-chlorin-monoclonal antibody conjugate for photoimmunotherapy. *Cancer Res*. *59*, 1505−1513.

(14) Karagianis, G., Reiss, J. A. Marchesini, R., DeCesare, M., Zunino, F., and Philips, D. R. (1996) Biophysical and biological evaluation of porphyrin-bisacridine conjugates. *Anti Cancer Drug Des. 11*, 205−220.

(15) Bachor, B. S., Shea, C. R., Gillis, R., and Hasan, T. (1991) Photosensitized destruction of human bladder carcinoma cells treated with chlorine6-conjugated microspheres. *Proc. Natl. Acad. Sci. U.S.A. 88*, 1580−1584.

(16) Li, G., Pandey, S. K., Graham, A., Dobhal, M. P., Mehta, R., Chen, Y., Gryshuk, A., Olson, K., Oseroff, A., and Pandey, R. K. (2004) Functionalization of OEP-based benzochlorins to develop carbohydrate-conjugated photosensitizers. Attempt to target β-galactoside-recognized proteins. *J. Org. Chem. 69*, 158−172.

(17) Pandey, R. K, Sumlin, A. B, Potter, W. R, Bellnier, D. A, Henderson, B. W, Constantine, S., Aoudia, M., Rodgers, M. A. J, Smith, K. M., and Dougherty, T. J. (1996) Structure and photodynamic efficacy among alkyl ether analogues of chlorophyll-a derivatives. *Photochem. Photobiol. 63*, 194−205.

(18) Henderson, B. W., Bellnier, D. A., Graco, W. R., Sharma, A., Pandey, R. K., Vaughan, L., Weishaupt, K. R., and Dougherty, T. J. (1997) A quantitative structure−activity relationship for a congeneric series of pyropheophorbide derivatives as photosensitizers for photodynamic therapy. *Cancer Res*. *57*, 4000−4007.

(19) Zheng, G., Potter, W. R., Sumlin, A., Dougherty, T. J., and Pandey, R. K. (2000) Photosensitizers related to purpurin-18-N-alkylimides: A comparative in vivo tumoricidal ability of ester versus amide functionalities. *Bioorg. Med. Chem. Lett. 10*, 123−127.

(20) Rungta, A., Zheng, G., Missert, J. R., Potter, W. R., Dougherty, T. J., and Pandey, R. K. (2000). Purpurinimides as photosensitizers: Effect of the presence and position of the substituents in in vivo photodynamic efficacy. *Bioorg. Med. Chem. Lett. 10*, 1463−1466.

(21) Zheng, G., Potter, W. R., Camacho, S. H., Missert, J. R., Wang, G., Bellnier, D. A., Henderson, B. W., Rodgers, M. A. J., Dougherty, T. J., and Pandey, R. K. (2001) Synthesis, photophysical properties, tumor uptake and preliminary in vivo photosensitizing efficacy of a homologous series of 3-(1′-alkyloxy)ethyl-3-devinylpurpurin-18-N-alkylimides with variable lipophilicity. *J. Med. Chem*. *44*, 1540−1559.

(22) Gryshuk, A. L., Graham, A., Pandey, S. K., Potter, W. R., Missert, J. R., Oseroff, A., Dougherty, T. J., and Pandey, R. K. (2002) A first comparative study of purpurinimide-based fluorinated vs nonfluorinated photosensitizers for photodynamic therapy. *Photochem. Photobiol. 76* (5), 555−559.

(23) Chen, Y., Graham, A., Potter, W., Morgan, J., Vaughan, L., Bellnier, D. A., Henderson, B. W., Oseroff, A., Dougherty, T. J., and Pandey, R. K. (2002) Highly stable and potent photosensitizers for photodynamic therapy. *J. Med. Chem. 45* (2), 255−258.

(24) Li, G., Graham, A., Chen, Y., Dobhal, M. P., Morgan, J., Zheng, G., Kozyrev, A., Oseroff, A., Dougherty, T. J., and Pandey, R. K. (2003) Synthesis, comparative photosensitizing efficacy, human serum albumin (site II) binding ability and intracellular localization characteristics of novel benzobacteriochlorins derived from vic-dihydroxybacteriochlorins. *J. Med. Chem. 46*, 5349−5359.

(25) Chen, Y., Sumlin, A., Morgan, J., Gryshuk, A., oseroff, A., Henderson, B. W., Dougherty, T. J., and Pandey, R. K. (2004) Synthesis and photosensitizing efficacy of isomerically pure bacteriopurpurinimides. *J. Med. Chem. 47*, 4814−4817.

(26) Dougherty, T. J., Pandey, R. K., Nava, H. R., Smith, J. A., Douglass, H. O., Edge, S. B., Bellnier, D. A., O'Malley, L., Cooper, M. (2000) Preliminary clinical data on a new photodynamic therapy photosensitizers HPPH for treatment of obstructive esophageal cancer. *Proc. SPIE 3009*, 25−27.

(27) Bellnier, D. A., Greco, W. R., Loewen, G. M., Nava, V., Oseroff, A. Pandey, R. K., Tsuchida, T., and Dougherty, T. J. (2003) Population pharmacokinetics of the photodynamic therapy agent HPPH in cancer patients. *Cancer Res. 63*, 1806−1813.

(28) Zhang, Z., Blesington, D., Hui, L., Busch, T. M., Glickson, J., Juo, Q., Chance, B., and Zheng, G. (2004) Redox ratio of mitochondria as an indicator for the response of photodynamic therapy. *J. Biomed. Opt. 9* (4), 772−778 and references therein.

(29) Harisingham, M. G., Willenberg, J., and Weissleder, R. (2003) *Primer of Diagnostic Imaging*, 3rd ed.; Elsevier.

(30) Sevick-Muraca, E. M., Kuwana, E., Godavarty, A., Houston, J. P., Thompson, A. B., and Roy, R. (2002) Near-infrared fluorescence imaging and spectroscopy in random media and tissues. Chapter 33 in *Biomedical Photonics Handbook* (Vo-Dinh, T., Ed.), CRC Press, Boca Raton.

(31) Lobel, J., MacDonald, I. Ciesielski, M. J., Barone, T., Potter, W. R., Pollina, J., Plunkett, R. J., Fenstermaker, R. A., and

Dougherty, T. J. (2001) 2-(1-hydroxyethyl)-2-devinylpyropheophorbide-a (HPPH) in a nude rat glioma model: implications for photodynamic therapy. *Laser Surg. Med*. *29* (5), 397−405.

(32) Garfinkel, M., Thomson, A. B., Ralston, W., Troy, T. L., Moore, T. A., Gust, J. D., Tatman, D., Reynolds, J. S., Muggenburg, B., Nikula, K., Mayer, R. H., Hawrysz, D. J., and Sevick-Muraca, E. (2000) Pharmacokinetics of indocyanine green and carotene-HPPH conjugate for detection of normal and tumor tissue using fluorescence, near-infrared continuous wave imaging. *Photochem. Photobiol. 72*, 94−102 and references therein.

(33) Majumdar, S. R., Majumdar, R. B., Grant, C. M., and Waggoner, A. S. (1996) Cyanine-labeling reagents: sulfobenzindocyanine succinimidyl esters *Bioconjugate Chem*. *7*, 356−362.

(34) Strekowski, L., Mason, C. J., Lee, H., Gupta, R., Sowell, J., and Patonay, G. (2003) Synthesis of water-soluble near-infrared cyanine dyes functionalized with 9succiniimdioxyl)-carbonyl group. *J. Heterocycl. Chem. 40*, 913−916.

(35) Tung, C. H., Lin, Y., Moon, W. K., and Weissleder R. A. (2002) A receptor-targeted near-infrared fluorescence probe in in vivo tumor imaging. *Chembiochem. 8*, 784−786.

(36) Becker, A., Hessenius, C., Licha, K, Ebert, B., Sukowski, U., Semmler, W., Wiedenmann, B., and Grotzinger, C. (2001) Receptor-targeted optical imaging of tumors with near-infrared fluorescent ligands. *Nature Biotechnol. 19*, 327−331.

(37) Ohulchanskyy T. Y., Donnelly D. J., Detty M. R., and Prasad P. N. (2004*)* Heteroatom substitution induced changes in excited-state photophysics and singlet oxygen generation in chalcogenoxanthylium dyes: effect of sulfur and selenium substitutions. *J. Phys. Chem. B 108*, 8668−8672.

(38) Kessel, D., Luo, Y., Deng, Y., and Chang, C. K. (1997) The role of subcellular localization in inhibition of apoptosis by photodynamic therapy. *Photochem. Photobiol. 65* (3), 422−426.

(39) Kawada, K., Yonei, T., Ueoka, H., Kiura, K., Tabata, M., Takigawa, N., Harada, M., and Tanimoto, M. (2002) Comparison of chemosensitivity tests. Clonogenic assay versus MTT assay. *Acta Med. Okayama 56* (3), 129−134.

(40) Patterson, M. S., Hayward, J. E., Farrell, T. J., and Wilson, B. C. A general purpose instrument for PDT dosimetry. *SPIE* 2371, 477−481.

(41) Bellnier, D. A. (1991) Potentiation of photodynamic therapy in mice with recombinant human tumor necrosis factor-a. *J. Photochem. Photobiol. 8*, 203−210.

(42) Bellnier, D. A., Potter, W. A., Vaughan L. A., Sitnik T. M., Parsons, J. C., Greco, W. R., Whitaker J., Johnson, P., and Henderson, B. W. (1995) The validation of a new vascular damage assay for photodynamic therapy agents. *Photochem. Photobiol. 62* (5), 596−905.

(43) Henderson, B. W., Vaughan, L., Bellnier, D. A., and Oseroff, A. R. (1995) photosensitization of murine tumor, vasulature and skin by 5-aminolevulinic acid induced porphyrin. *Photochem. Photobiol*. *62*, 780−789.

(44) Kessel, D., and Luo, Y. (1998) Mitochondrial photodamage and PDT-induced apoptosis. *J. Photochem. Photobiol. B 42* (2), 89−95.

(45) Morgan, J., and Oseroff A. R. (2001) Mitochondria-based anti-cancer photodynamic therapy. *Advanced Drug Delivery Reviews-Drug and DNA delivery to mitochondria* (Eds. Weissig and Torchilin, V. P.), *49*, 71−86.

(46) MacDonald, I., and Dougherty, T. J. (2001) Basic principles of photodynamic therapy. *J. Porphyrin Phthalocyanines 5* (2), 105−129.

(47) Chance, B., Schoener, B., Oshino, R., Itshak, F., and Nakase, Y. (1979) Oxidation−reduction ratio studies of mitochondria in freeze-trapped samples and flavoprotein fluorescence signals. *J. Biol. Chem. 254* (11), 4764−4771.

(48) Achilefu, S., Jimenez, H. N., Dorshow, R. B., Bugaj, J. E., and Webb, E. G. (2002) Synthesis, in vitro receptor binding and in vivo evaluation of fluorescein and carbocyanine peptide-based optical contrast agents. *J. Med. Chem. 45*, 2003−2015.

(49) Belliner, D. A., Greco, W. R., Parsons, J. C., Oseroff, A., Kuebler, A., and Dougherty, T. J. (1997) An assay for the quantitation of Photofrin in tissues and fluids. *Photochem. Photobiol. 66*, 237−244.

(50) Fingar, V. H., Siegel, K. A., Wieman, T. J., and Doak, K. W. (1993) The effect of thromboxane inhibitors on the microvascular and tumor response to photodynamic therapy. *Photochem. Photobiol. 58*, 393−399.

(51) Dolman, D. E. J. G., Kadambi, A., Hill, J. S., Flores, K. R., Gerber, J. N., Walker, J. P., Borel Rinkes, I. H. M., Jain, R. K., and Fukumura, D. (2002) Targeting Tumor Vasculature and Cancer Cells in Orthotopic Breast Tumor by Fractionated Photosensitizer Dosing Photodynamic Therapy. *Cancer Res. 62*, 4289−4294.

BC050177O

Monofunctional Near-Infrared Fluorochromes for Imaging Applications

Scott A. Hilderbrand, Kimberley A. Kelly, Ralph Weissleder, and Ching-Hsuan Tung*

Center for Molecular Imaging Research, Massachusetts General Hospital, Harvard Medical School, Room 5406, 149 13th Street, Charlestown, Massachusetts 02129. Received June 21, 2005;
Revised Manuscript Received August 9, 2005

In this report, the development of a new class of monocarboxylate functionalized cyanine derivatives using improved synthetic procedures is detailed. The employed synthetic strategy relies on efficient nucleophilic attack of alkyl-thiols on cyanine dyes bearing chloro-substituted polymethinic linkers. Monocarboxylate derivatized fluorochromes (CyTE dyes) can be prepared in one step in greater than 90% yield without the need for additional purification. Several of the fluorochromes synthesized by this route show no tendency to aggregate in aqueous solution and have excitation and emission maxima greater than 800 nm. The potential utility of the CyTE fluorochromes was demonstrated through direct labeling of phage displaying a vascular cellular adhesion molecule-1 (VCAM-1) targeting peptide. Endothelial cell internalization of the VCAM-1 targeted phage was monitored via near-infrared fluorescence microscopy.

INTRODUCTION

In recent years, there has been significant interest in the development of monofunctional, water-soluble near-infrared fluorochromes for use in a myriad of imaging applications. The development of new bright, water-soluble near-infrared (NIR) fluorochromes that are synthesized readily and are suitable for bioconjugation is necessary for the preparation of improved NIR probes for in vivo imaging. Fluorochromes with absorption and emission maxima between 650 and 900 nm are ideally suited for imaging in tissue due to the minimal absorption coefficients from hemoglobin, water, and lipids over this range (*1*). A variety of carboxylic acid derivatized cyanine dyes emitting in the NIR have been prepared (*2*−*11*). Many commonly used monofunctional dyes are asymmetric with a single carboxylic acid group attached to one of the indoleninium or benzindoleninium moieties (*3*, *4*, *6*, *9*). The condensation reactions to prepare these fluorochromes proceed in a stepwise fashion resulting in formation of the undesired symmetric dye as a byproduct with overall yields typically less than 10%. Although these dyes are components of a variety of receptor targeted (*9*, *12*−*15*) and fluorogenic (*16*−*18*) probes for optical imaging in vivo, the difficulty in preparation of large quantities of the purified fluorochromes may limit their widespread utility.

New high-yield routes for the synthesis of NIR fluorochromes suitable for imaging applications are needed. One strategy that provides access in 90% or greater yields to fluorochromes that can be conjugated is via nucleophilic attack on chloro-substituted cyanine dyes (*19*). A variety of water-soluble dyes containing aryl-ether, aryl-thioether, and alkyl-ether linkages have been prepared using this route (*2*, *7*, *10*, *11*, *20*). However, none of these dyes are optimal for imaging applications. Although they are water-soluble, cyanine fluorochromes containing an additional aryl group, such as an aryl-ether-modified cyanine dye, show an increased tendency to aggregate in aqueous solution (*2*), and the aryl-ether linkage in some of these fluorochromes is susceptible to cleavage (*21*). Several aryl-ether-, aryl-thioether-, and alkyl-ether-functionalized fluorochromes have been reported but there are only a few reports of their alkyl-thioether congeners (*22*, *23*). In this report, we detail general procedures for the synthesis of a variety of alkyl-thioether-containing cyanine fluorochrome derivatives (CyTE dyes). Some of these fluorochromes may be prepared in one step with excellent yields starting from commercially available dyes, show no tendency to aggregate in aqueous solution, and display absorption and emission maxima above 800 nm. To assess the utility of the CyTE fluorochromes, phage displaying the vascular cellular adhesion molecule-1 (VCAM-1) targeting peptide (VHSPNKK) (*24*) on the pIII coat protein of the phage were labeled with fluorochrome and imaged in live cells. Cell uptake experiments with the fluorochrome-labeled phage demonstrate the potential of the synthetically accessible CyTE dyes for use in NIR fluorescence imaging.

MATERIALS AND METHODS

General Considerations. All chemicals were purchased from Aldrich (Milwaukee, WI) or TCI America (Portland, OR) except PEG_7 thiol propionic acid, which was purchased from Polypure AS (Oslo, Norway), and were used as received. The dyes IR-783, IR-806, and IR-820 were purchased from Aldrich. All solvents including anhydrous dimethylformamide (DMF) and anhydrous dimethyl sulfoxide (DMSO) were obtained from Aldrich. High-performance liquid chromatography (HPLC) was performed on a Hitachi D-7000 instrument equipped with a L-7455 diode array detector. Nuclear magnetic resonance (NMR) data were collected on a Bruker DPX-400 spectrometer at ambient temperature and referenced to tetramethylsilane (TMS) or 2,2-dimethyl-2-silapentane-5-sulfonate sodium salt (DSS) internal standards. Absorption spectra were obtained on a Varian Cary 50-Bio UV/visible spectrophotometer (Palo Alto, CA). All extinc-

* Corresponding author. Tel: (617) 726-5779. Fax: (617) 726-5708.

10.1021/bc0501799 CCC: $30.25 © 2005 American Chemical Society
Published on Web 08/26/2005

tion coefficient measurements in phosphate-buffered saline (PBS), pH 7.4, 10 mM phosphate, 2.7 mM potassium chloride, and 137 mM NaCl were performed in triplicate. For determination of the extinction coefficients, fresh stock solutions of HPLC-purified dye were prepared for each trial by dissolution of 2−3 mg portions of the dye, weighed on a Mettler AT201 analytical balance with an error of ±0.01 mg, in PBS using a 10 mL volumetric flask. The typical standard deviation for the extinction coefficient measurements is less than 5%. Fluorescence data were collected on a Horiba Jobin Yvon Fluorolog-3 spectrofluorometer (Edison, NJ) and were corrected for the detector sensitivity. Quantum yield measurements, performed in triplicate following published procedures (*25*), were collected using samples with absorbance values under 0.10 OD in PBS using indocyanine green (ICG) in DMSO ($\Phi_F = 0.106$) (*26*) as a standard. All samples used for the quantum yield determinations were excited at 775 nm. High-resolution electrospray ionization (ESI) mass spectra were collected on a Bruker Daltonics APEXII 3 T Fourier transform mass spectrometer in the Department of Chemistry Instrumentation Facility (DCIF) at the Massachusetts Institute of Technology.

CyTE-777 (1). To a solution of IR-783 (225 mg, 0.30 mmol) in 4 mL of anhydrous DMF was added 3-mercaptopropionic acid (30.5 μL, 0.35 mmol) and triethylamine (TEA) (49 μL, 0.35 mmol). The green solution was allowed to stir in the dark. After 15 h, the reaction was complete as monitored by HPLC. Crude **1**, which has sufficient purity for routine work, was isolated in 93% yield as a green solid by precipitation with *tert*-butyl methyl ether (TBME) and was washed with TBME (3 × 10 mL). Compound **1** was further purified by reverse-phase C-18 chromatography (Waters Sep-Pak C18 cartridge) with a mixture of 25% CH_3CN, 75% H_2O, and 0.1% TFA followed by 30% CH_3CN, 70% H_2O, and 0.1% TFA to yield pure **1** (204 mg, 83%). ^{1}H NMR (400 MHz, CD_3OD): δ 8.89 (d, 2H, J = 14.2 Hz), 7.49 (d, 2H, J = 7.4 Hz), 7.41 (t, 2H, J = 7.6 Hz), 7.34 (d, 2H, J = 7.8 Hz), 7.25 (t, 2H, J = 7.5 Hz), 6.32 (d, 2H, J = 14.3 Hz), 4.19 (t, 4H, J = 6.7 Hz), 3.06 (t, 2H, J = 7.0 Hz), 2.90−2.87 (m, 4H), 2.70 (t, 4H, J = 5.9 Hz), 2.56 (t, 2H, J = 6.9 Hz) 2.00−1.92 (m, 10H), 1.76 (s, 12H). λ_{max} (PBS, pH 7.4): 777 nm (ϵ = 130 000 M^{-1} cm^{-1}). Φ_F (PBS, pH 7.4): 0.02. HRMS-ESI $[M]^+$ *m/z* calcd for $C_{41}H_{53}N_2O_8S_3$ 797.2959, found 797.2976.

Intermediate (2). 1-(4-Sulfonatobutyl)-2,3,3-trimethylindoleninium-5-sulfonate (5) (1.25 g, 3.0 mmol), *N*-[(3-(anilinomethylene)-2-chloro-1-cyclohexen-1-yl)methylene]-aniline monohydrochloride (540 mg, 1.5 mmol), and potassium acetate (295 mg, 3.0 mmol) were dissolved in 20 mL of a 2:1:1 solution of MeOH, acetic anhydride, and pyridine. The solution was sealed in a thick-walled glass pressure reactor and heated at 140 °C for 25 min giving a dark blue solution containing a dark blue precipitate. After the mixture cooled to room temperature, the blue solid was isolated by filtration. Purification of the crude material by reverse-phase C-18 chromatography (Waters Sep-Pak C18 cartridge) with a mixture of 15% CH_3CN, 85% H_2O, and 0.1% TFA yields pure **2** (450 mg, 30%) as a green solid. ^{1}H NMR (400 MHz, D_2O): δ 8.16 (d, 2H, J = 13.8 Hz), 7.85 (s, 2H), 7.74 (d, 2H, J = 8.3 Hz), 7.27 (d, 2H, J = 8.4 Hz), 6.13 (d, 2H, J = 13.9 Hz), 4.10 (broad singlet, 4H), 2.96 (t, 4H, J = 6.6 Hz), 2.41 (broad singlet, 4H), 1.89−1.79 (m, 10H), 1.63 (s, 12H). λ_{max} (PBS, pH 7.4): 781 nm (ϵ = 248 000 M^{-1} cm^{-1}). Φ_F (PBS, pH 7.4): 0.02. HRMS-ESI $[M - 2H]^-$ *m/z* calcd for $C_{38}H_{46}ClN_2O_{12}S_4$ 885.1628, found 885.1567; $[M - 3H]^{2-}$ *m/z* calcd for $C_{38}H_{45}ClN_2O_{12}S_4$ 442.0777, found 442.0760.

CyTE-783 (3). To a solution of **2** (100 mg, 0.10 mmol) in 5 mL of anhydrous DMSO was added 3-mercaptopropionic acid (17.5 μL, 0.20 mmol) and TEA (28 μL, 0.20 mmol). The reaction was completed in 15 h as determined by HPLC. The crude product was precipitated by addition of 25 mL of toluene. This blue-green solid was collected by centrifugation and was washed with toluene (2 × 25 mL) followed by diethyl ether (2 × 25 mL) to give crude **3** (92 mg, 86%), which is sufficiently pure for routine work. The product was further purified by reverse-phase C-18 chromatography (Waters Sep-Pak C18 cartridge) with a mixture of 10% CH_3CN, 90% H_2O, and 0.1% TFA followed by 15% CH_3CN, 85% H_2O, and 0.1% TFA to yield pure **3** (76 mg, 71%) as a green solid. ^{1}H NMR (400 MHz, DMSO-d_6): δ 8.70 (d, 2H, J = 14.1 Hz), 7.75 (d, 2H, J = 1.5 Hz), 7.63 (dd, 2H, J = 8.2 Hz, J = 1.5 Hz), 7.37 (d, 2H, J = 8.3 Hz), 6.36 (d, 2H, J = 14.2 Hz), 4.17 (broad singlet, 4H), 2.98 (t, 2H, J = 6.9 Hz), 2.67 (t, 4H, J = 5.7 Hz), 2.49−2.44 (m, 6H), 1.84−1.63 (m, 22H). λ_{max} (PBS, pH 7.4): 783 nm (ϵ = 174 000 M^{-1} cm^{-1}). Φ_F (PBS, pH 7.4): 0.02. HRMS-ESI $[M]^+$ *m/z* calcd for $C_{41}H_{53}N_2O_{14}S_5$ 957.2095, found 957.2125.

CyTE-822 (4). To a solution of IR-820 (255 mg, 0.30 mmol) in 4 mL of anhydrous DMF was added 3-mercaptopropionic acid (30.5 5 μL, 0.35 mmol) and TEA (30.5 μL, 0.35 mmol). The green solution was allowed to stir in the dark. After 15 h, the reaction was complete as monitored by HPLC. Crude **4** (246 mg, 89%) was isolated by precipitation from the reaction by addition of 10 mL of TBME and was washed with TBME (3 × 10 mL). Reverse-phase C-18 column chromatography (Waters Sep-Pak C18 cartridge) of the crude material eluting with 35% CH_3CN, 65% H_2O, and 0.1% TFA afforded **4** (143 mg, 52%) as a green solid. ^{1}H NMR (400 MHz, DMSO-d_6): δ 8.83 (d, 2H, J = 14.0 Hz), 8.30 (d, 2H, J = 8.4 Hz), 8.09−8.02 (m, 4H), 7.80 (d, 2H, J = 8.9 Hz), 7.65 (t, 2H, J = 7.4 Hz), 7.51 (t, 2H, J = 7.4 Hz), 6.40 (d, 2H, J = 13.7 Hz), 4.33 (br s, 4H), 3.06 (t, 2H, J = 6.6 Hz), 2.72 (br s, 4H), 2.65−2.55 (m, 6H), 1.97 (s, 12H), 1.89−1.78 (m, 10H). λ_{max} (PBS/20% DMSO, pH 7.4): 822 nm (ϵ = 128 000 M^{-1} cm^{-1}). HRMS-ESI $[M]^+$ *m/z* calcd for $C_{49}H_{57}N_2O_8S_3$ 897.3272, found 897.3259.

CyTE-823 PEG (5). To a solution of IR-820 (255 mg, 0.30 mmol) in 4 mL of anhydrous DMF was added PEG_7 thiol propionic acid (183 mg, 0.40 mmol) and TEA (56 μL, 0.40 mmol). The green solution was allowed to stir in the dark for 15 h. A green solid was isolated by precipitation with 10 mL of TBME and was washed with 35 mL of TBME. The crude material was purified by reverse-phase C-18 chromatography (Waters Sep-Pak C18 cartridge) with a mixture of 25% CH_3CN, 75% H_2O, and 0.1% TFA, followed by 30% CH_3CN, 70% H_2O, and 0.1% TFA, and finally 35% CH_3CN, 65% H_2O, and 0.1% TFA to yield pure **5** (212 mg, 56%) as a green solid. ^{1}H NMR (400 MHz, DMSO-d_6): δ 8.89 (d, 2H, J = 14.1 Hz), 8.30 (d, 2H, J = 8.6 Hz), 8.10−8.02 (m, 4H), 7.81 (d, 2H, J = 9.0 Hz), 7.65 (t, 2H, J = 7.3 Hz), 7.51 (t, 2H, J = 7.6 Hz), 6.41 (d, 2H, J = 14.3 Hz), 4.34 (br s, 4H), 3.64 (t, 2H, J = 6.4 Hz), 3.58 (t, 2H, J = 6.4 Hz), 3.53−3.41 (m, 28H), 3.04 (t, 2H, J = 6.5 Hz), 2.72 (br s, 4H), 2.64 (t, 4H, J = 7.3 Hz), 2.43 (t, 2H, J = 6.3 Hz), 1.99 (s, 12H), 1.88−1.78 (m, 10H). λ_{max} (PBS/20% DMSO, pH 7.4): 823 nm (ϵ = 116 000 M^{-1} cm^{-1}). HRMS-ESI $[M]^+$ *m/z* calcd for $C_{65}H_{89}N_2O_{16}S_3$ 1249.5369, found 1249.5345.

CyTE-807 (6). To a solution of IR-806 (221 mg, 0.30 mmol) in 4 mL of anhydrous DMF was added 3-mercaptopropionic acid (30.5 μL, 0.35 mmol) and TEA (49 μL, 0.35 mmol). After being stirred for 15 h, the reaction was complete as monitored by HPLC. Crude **6** (223 mg, 93%)

was isolated by precipitation from the reaction by addition of 10 mL TBME and was washed with TBME (3 × 10 mL). The crude material, which is sufficiently pure for routine work, was further purified by reverse-phase C-18 chromatography (Waters Sep-Pak C18 cartridge) with a mixture of 25% CH_3CN, 75% H_2O, and 0.1% TFA, followed by 30% CH_3CN, 70% H_2O, and 0.1% TFA to yield pure **6** (194 mg, 80%) as a green solid. ^{1}H NMR (400 MHz, DMSO-d_6): δ 8.03 (d, 2H, J = 14.0 Hz), 7.60 (d, 2H, J = 7.3 Hz), 7.46−7.39 (m, 4 H), 7.25 (d, 2H, J = 7.4 Hz), 6.21 (d, 2H, J = 14.1 Hz), 4.18 (t, 4H, J = 6.7 Hz), 3.10 (t, 2H, J = 6.7 Hz), 2.94 (s, 4H), 2.60−2.52 (m, 6H), 1.83−1.73 (m, 8H), 1.66 (s, 12H). λ_{max} (PBS, pH 7.4): 807 nm (ϵ = 120 000 M^{-1} cm^{-1}). Φ_F (PBS, pH 7.4): 0.02. HRMS-ESI $[M]^+$ *m/z* calcd for $C_{40}H_{51}N_2O_8S_3$ 783.2802, found 783.2821.

CyTE-777 Succinimide Ester (7). To a solution of **1** (100 mg, 0.122 mmol) in 6 mL of anhydrous DMF was added *N*-hydroxysuccinimide (NHS) (1.40 g, 12.2 mmol), *N*,*N*′-diisopropylcarbodiimide (DIC) (1.91 mL, 12.2 mmol), and *N*-methylmorpholine (268 μL, 2.44 mmol). The resulting suspension was stirred at room temperature for 45 min. HPLC analysis of the crude reaction indicated over 90% conversion to the succinimide ester. The reaction was filtered to remove excess solid NHS and 20 mL of Et_2O was added to give a green oil. The ether layer was decanted, and the green oil was redissolved in 1 mL of DMF. This solution was precipitated by addition of 20 mL of Et_2O to yield a dark green paste. After this step was repeated one additional time, a free flowing green solid was isolated. The crude solid was subjected to preparative HPLC chromatography using a gradient of 22.5% CH_3CN to 90% CH_3CN in H_2O with 0.1% TFA to yield analytically pure **7** (47 mg, 42%). ^{1}H NMR (400 MHz, DMSO-d_6): δ 8.67 (d, 2H, J = 14.0 Hz), 7.59 (d, 2H, J = 7.3 Hz), 7.47−7.39 (m, 4H), 7.26 (t, 2H, J = 7.3 Hz), 6.37 (d, 2H, J = 14.2 Hz), 4.20 (t, 4H, J = 6.7 Hz), 3.12 (t, 2H, J = 7.1 Hz), 3.01 (t, 2H, J = 6.3 Hz), 2.79 (s, 4H), 2.68 (br , 4H), 2.53 (t, partially overlapping the solvent peak, 4H, J = 7.3 Hz), 1.82−1.71 (m, 10H), 1.68 (s, 12H). HRMS-ESI $[M]^+$ *m/z* calcd for $C_{45}H_{56}N_3O_{10}S_3$ 894.3122, found 894.3155.

Phage Preparation and Labeling. Phage containing the VCAM-1 targeting sequence VHSPNKK (VHS-peptide) were isolated and amplified in *Escherichia coli*, and their titer was determined as described previously (*24*). Following isolation and titer determination, the phage were labeled directly with the activated ester of **CyTE-777** using a modified literature procedure (*27*). **CyTE-777** succinimidyl ester (5 μL at 5 μg/μL in DMSO) was added to 1 × 10^{12} plaque forming units (pfu) of VHS-peptide-displaying phage (VHS−phage) in 50 μL of Dulbecco's phosphate-buffered saline (DPBS) supplemented with 1 mM Ca^{2+} and 10 mM Mg^{2+}. The volume was increased to 100 μL with 0.1 M $NaHCO_3$ buffer, pH 8.3, and allowed to incubate for 1 h in the dark at room temperature while shaking. After incubation, the phage was precipitated by addition of 20 μL of a PEG 8000/2.5 M NaCl solution (40% w/v) and allowed to stand on ice for 1 h. The fluorochrome-labeled phage was pelleted by centrifugation at 10 000 rpm for 15 min, and the supernatant was discarded. The light green pellet was resuspended in 400 μL of the supplemented DPBS and subjected to an additional round of PEG precipitation to minimize residual free fluorochrome and to remove bacterial protein contaminants. The degree of labeling was determined by using the extinction coefficient of **CyTE-777** in PBS.

NIR Fluorescence Cellular Imaging. Murine cardiac endothelial cells (MCECs) constitutively expressing VCAM-1 were isolated and prepared as described previously (*28*, *29*). The cells were incubated with 1 × 10^{12} pfu of the **CyTE-777**-labeled VHS−phage in 400 μL of supplemented DPBS for 1 h at 37 °C, 5% CO_2. Following incubation, the cells were washed twice with DPBS/0.01% Tween 20, fixed with 2% paraformaldehyde supplemented with 10 mM Mg^{2+} and 1 mM Ca^{2+}, and then mounted to preserve fluorescence using VectaShield (Vector Laboratories, Burlingame, CA) containing the nuclear stain 4′,6-diamidino-2-phenylindole (DAPI). The cells were imaged on a Nikon Eclipse 80i fluorescence microscope with a 40× objective equipped with a Photometrics Cascade 512B CCD camera using excitation and emission filters from Chroma Technology. The nuclear stain DAPI was imaged using a 365 ± 5 nm band-pass filter for excitation and a 400 ± 5 nm cutoff filter for emission. The NIR fluorochrome **CyTE-777** was imaged using a 775 ± 25 nm band-pass filter for excitation and a 845 ± 28 nm band-pass filter for emission. Images with **CyTE-777** were acquired using a 2 s exposure time.

RESULTS AND DISCUSSION

Synthesis. In an effort to develop improved methods for the synthesis of cyanine NIR fluorochromes suitable for bioconjugation, new paths to generate symmetric monocarboxylic acid derivatives were explored. The ability to prepare a symmetric monofunctional dye streamlines the synthetic methodology by removing the need for the stepwise synthesis used to prepare asymmetric cyanine fluorochromes. One route to these symmetric fluorochromes, first reported in 1992, relies on the reaction of nucleophiles with cyanine dyes containing an activated chloro-substituent on the polymethinic linker (*19*). With this approach, it is possible to prepare a variety of symmetric cyanine dyes with several different nucleophiles. However, when ethylthiolate, prepared by deprotonation of mercaptoethane with sodium hydride, was used as the nucleophile, only the dehalogenated cyanine dye was obtained. We have developed a modified procedure using anhydrous DMF and triethylamine as a base that allows for the facile synthesis of symmetric alkylthioether derivatives. Conversion of the commercially available dye IR-783, which contains two alkyl sulfonate moieties, under these conditions with a slight excess of 3-mercaptopropionic acid gives the symmetric carboxylic acid functionalized **CyTE-777** in nearly quantitative yield (Scheme 1). The crude product from this reaction is sufficiently pure for subsequent transformation to the activated succinimide ester or for direct activation and use in solid-phase synthesis (unpublished results). Pure **CyTE-777** may be obtained by reverse-phase C-18 column chromatography in 83% yield.

To evaluate the effects of the degree of sulfonation on the properties of the fluorochromes, the tetrasulfonate analogue of **CyTE-777** was prepared. The synthesis of this derivative, **CyTE-783**, begins with the preparation of the tetrasulfonate intermediate **2**. This chloro-containing intermediate was prepared by the condensation of 2 equiv of 1-(4-sulfonatobutyl)-2,3,3-trimethylindoleninium-5-sulfonate with *N*-[(3-(anilinomethylene)-2-chloro-1-cyclohexen-1-yl)methylene]aniline monohydrochloride in the presence of methanol, TEA, and acetic anhydride. The methanol improves the solubility of the highly polar indoleninium precursor in the reaction mixture, thus enabling a shorter reaction time. The reaction was performed with heating to 140 °C for 25 min in a sealed pressure reactor. After the reaction mix cooled, column

Scheme 1

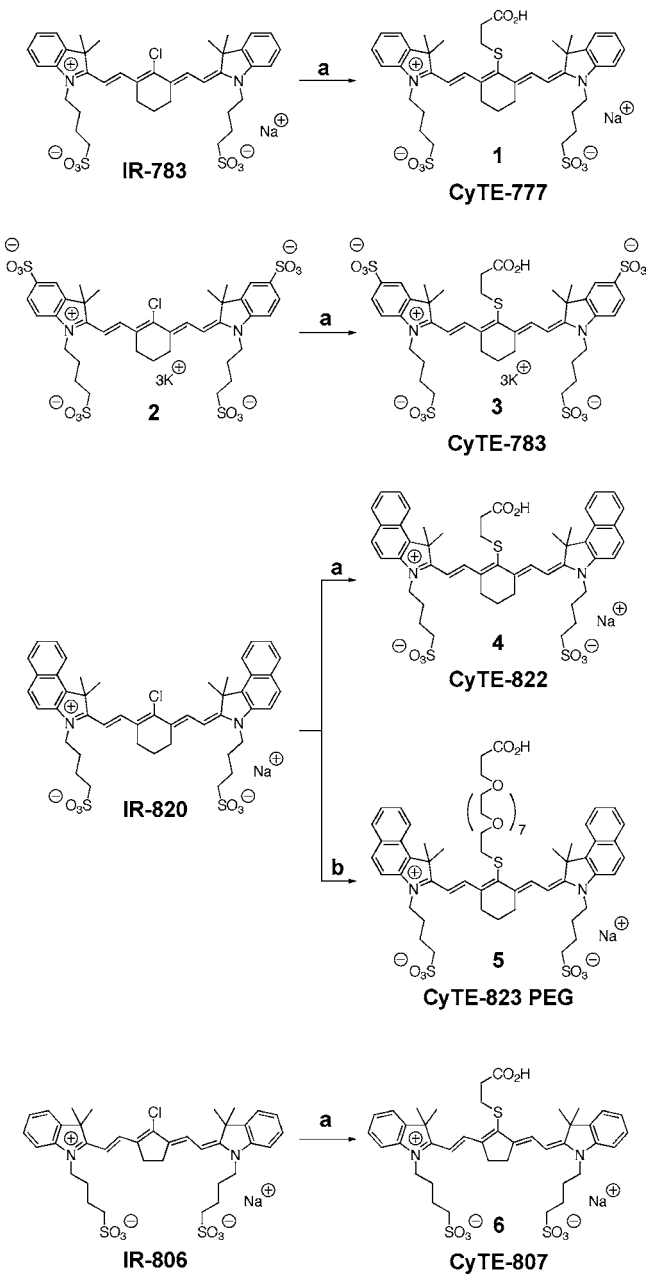

chromatography of the dark blue solid obtained from the reaction gives pure **2** in moderate yield. Due to the high degree of sulfonation on **2**, it is only moderately soluble in DMF; thus for the nucleophilic displacement with 3-mercaptopropionic acid, anhydrous DMSO was used as the solvent. As with the synthesis of **CyTE-777**, the reaction to generate **CyTE-783** (Scheme 1) is complete in less than 15 h as indicated by complete consumption of the starting chloro-functionalized dye. The purity of **CyTE-783** from the crude reaction is adequate for further work, and it can be purified rigorously by reverse-phase C-18 chromatography in 71% yield.

In an effort to prepare fluorochromes with absorption and emission greater than 800 nm, commercially available IR-820 was investigated as a precursor. The conditions used for generation of **CyTE-822** are similar to those used for **CyTE-777** (Scheme 1) and give a dark green solid in 52% yield after purification. In an effort

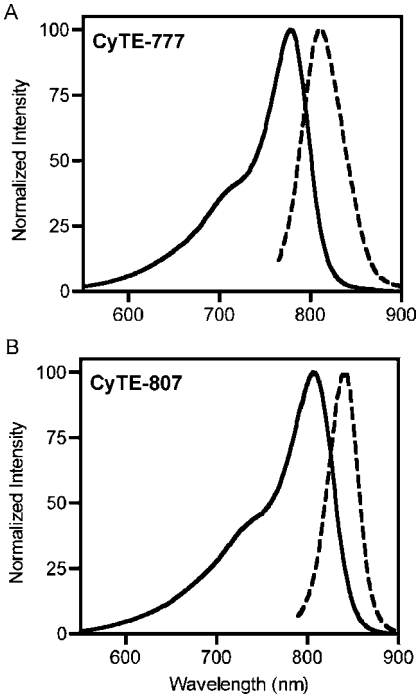

Figure 1. Normalized absorption (solid line) and emission (dashed line) spectra of 10 μM solutions of (A) **CyTE-777** and (B) **CyTE-807** in PBS.

Table 1. Optical Properties of the CyTE Dyes in PBS, pH 7.4

	$\lambda_{max,abs}$ (nm)	$\lambda_{max,em}$ (nm)	ϵ (M^{-1} cm^{-1})
CyTE-777	777	812	130 000
CyTE-783	783	814	174 000
CyTE-822[a]	822	845	128 000
CyTE-823 PEG[a]	823	847	116 000
CyTE-807	807	839	120 000

[a] In PBS, pH 7.4, with 20% DMSO.

to devise derivatives that are less likely to aggregate in aqueous solution than **CyTE-822**, which is structurally similar to indocyanine green, a dye known to aggregate in aqueous media, functionalization of IR-820 with monodisperse PEG_7 thiol propionic acid was probed. Nucleophilic attack of the polyethylene glcyol (PEG) thiol on the chloro-substituted polymethinic linker of IR-820 gives **CyTE-823 PEG** (Scheme 1). Despite incorporation of the large PEG acid, purification of the fluorochrome is straightforward giving high-purity product in 56% yield. A final long wavelength fluorochrome, **CyTE-807**, was prepared through use of IR-806 in 80% yield following purification (Scheme 1). With this dye, the cyclic six-membered ring containing linker present in the previous CyTE fluorochrome derivatives is replaced by a more constrained five-membered ring. The removal of one methylene carbon from the cyclic ring results in significantly altered optical properties in comparison to the related **CyTE-777**.

Optical Properties. All of the alkyl-thioether-functionalized fluorochromes display long wavelength absorption and emission bands. The optical properties of these dyes are summarized in Table 1. **CyTE-777** and **CyTE-783** have absorption and emission bands that match closely those of ICG in water, which has an absorption maximum of 780 nm. Therefore these two dyes are well suited for imaging using currently available filter sets optimized for ICG. The absorption and emission spectra of **CyTE-777** are shown in Figure 1a. With **CyTE-777**, there is no indication for aggregation in PBS, which

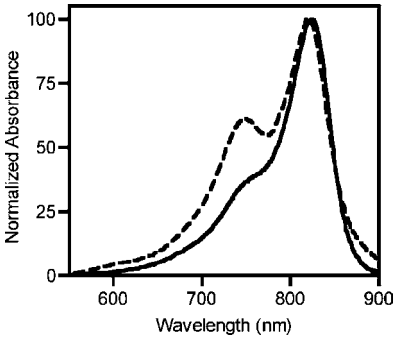

Figure 2. Absorption spectra of 1 μM solutions of **CyTE-823 PEG** in PBS (dashed line) showing the dimer at 750 nm, while in PBS with 20% DMSO (solid line), only the monomer is observed.

would manifest itself as a second absorption band approximately 70 nm to shorter wavelength (*30*). The short wavelength shoulder visible in the absorption spectrum of **CyTE-777** is a common feature of virtually all cyanine-based fluorochromes and is observed in less polar solvents such as DMSO and MeOH where there is no tendency for aggregation. The formation of dimers and other aggregates is undesirable because they frequently result in intermolecular quenching of fluorescence emission (*30*). The only significant difference in the optical properties between the disulfonate **CyTE-777** and the tetrasulfonate **CyTE-783** is their extinction coefficients, where a 25% increase is observed in PBS with the tetrasulfonate **CyTE-783**. In contrast to the increased extinction coefficient of **CyTE-783** when compared to **CyTE-777**, there are only minor differences in the absorption and emission maxima and quantum yields of the two dyes.

The long wavelength dye **CyTE-822** with benzindoleninium end groups is structurally similar to ICG; however, the alkyl-thioether moiety in the polymethinic linker results in a significant bathochromic shift of the absorption and emission maxima in comparison to ICG. As with ICG, **CyTE-822** shows a tendency to aggregate in aqueous solution. This aggregation is evident even at concentrations as low as 1 μM in PBS. The free monomer is only obtained in PBS with 20% DMSO. Aggregation of this derivative limits its potential utility for use as a fluorescent label for imaging applications.

To reduce the tendency for aggregation in aqueous solution, **CyTE-822** was modified with a hydrophilic poly(ethylene glycol) chain. This modified dye, **CyTE-823 PEG**, retains the long wavelength excitation and emission properties of **CyTE-822**; however, as with **CyTE-822**, it shows a tendency to aggregate in PBS (Figure 2). This indicates that the short PEG_7 chain is not sufficiently long to increase the solvent−dye affinity, which would result in diminished dye−dye aggregate formation.

Scheme 2

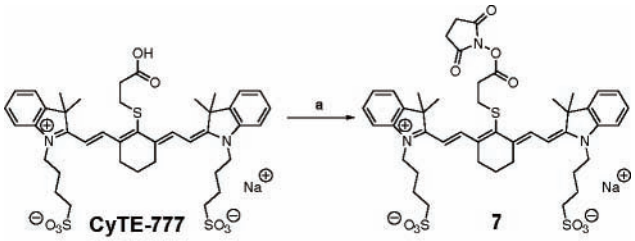

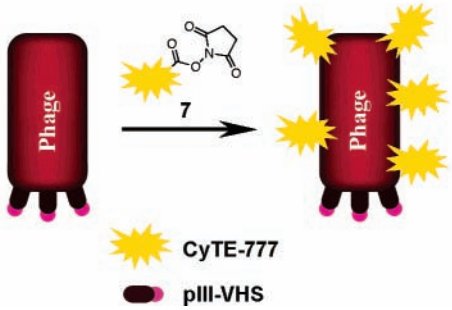

As an alternative for the preparation of a monocarboxylic acid derivatized fluorochrome with long wavelength absorption and emission, IR-806 was investigated as a building block. The alkyl-thioether containing **CyTE-807** has an absorption maximum of 807 nm in PBS and an emission maximum of 839 nm (Figure 1b). It also behaves like **CyTE-777** in PBS with no observable dye−dye aggregation. When compared to the structurally related **CyTE-777**, the absorption and emission bands shift 30 and 27 nm to longer wavelength, respectively. In addition to the wavelength shifts induced by the steric strain imposed by the cyclopentyl-containing polymethinic linker of **CyTE-807**, a slight decrease in the extinction coefficient from 130 000 M^{-1} cm^{-1} for **CyTE-777** to 120 000 M^{-1} cm^{-1} is observed. **CyTE-807** as well as other potential dyes containing a cyclopentyl-based polymethinic linker hold promise for use in imaging applications. Coupled with the proper filter sets, it may be possible to add an 800+ nm NIR fluorescence imaging channel to the currently used shorter wavelength channels.

Phage Labeling. To demonstrate the general applicability of the CyTE fluorochromes, **CyTE-777** was activated for use in phage labeling. Activation was

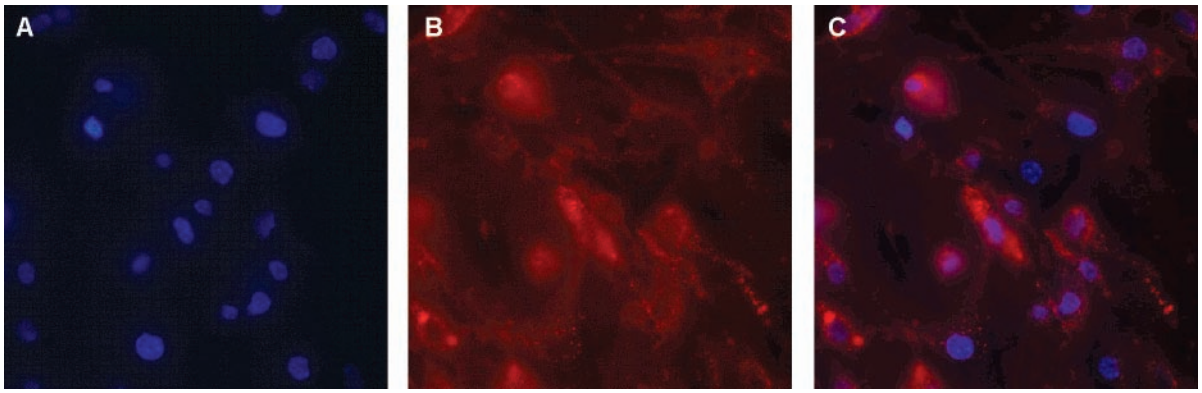

Figure 3. Fluorescence microscopy of MCECs incubated with **CyTE-777**-labeled VHS−phage for 1 h: (A) nuclear staining with DAPI; (B) staining of the **CyTE-777** conjugated phage; (C) the merged image indicating internalization of the labeled phage.

accomplished by treatment of **CyTE-777** with NHS in the presence of DIC and *N*-methylmorpholine (Scheme 2). Greater than 90% conversion to the activated ester was observed by HPLC. To label the VHS−phage, a modified literature procedure (*27*) was used where 1×10^{12} pfu of phage were treated with 25 μg of the activated fluorochrome for 1 h under slightly basic conditions (Scheme 2). By monitoring the fluorochrome absorbance, we determined the degree of labeling to be 1700 dye molecules per phage. The efficient labeling will facilitate imaging applications by enabling delivery of a large quantity of fluorochrome to the phage target. Conjugation of the dye to the phage was supported by observation of a shift in the absorption band of the conjugated **CyTE-777** from 777 to 798 nm in DPBS buffer. Bathochromic shifts in the absorption maxima of cyanine dyes are observed frequently in conjunction with a decrease in polarity of the fluorochrome local environment, such as provided by conjugation to the phage. In a similar system, the absorption maximum of ICG was reported to shift from 780 nm in water to 800 nm when bound to albumin (*30*).

Fluorescence Microscopy. To assess the performance of the fluorochrome-labeled VHS−phage for imaging, the probe was incubated with MCECs expressing VCAM-1. Following incubation for 1 h, the cells were monitored by fluorescence microscopy to visualize the distribution of the VCAM-1-specific phage. Dual channel fluorescence microscopy of stained nuclei and phage particles clearly shows phage internalization (Figure 3). The strong fluorescence signal observed is the result of multiple factors. Due to the high degree of fluorochrome labeling, the phage is capable of delivering a large fluorochrome payload, resulting in increased signal. In addition, binding and recognition of the phage by the surface receptors (VCAM-1) is a highly selective event. The VHS−phage have a high affinity for VCAM-1 since the peptides are present in 4−5 copies on the phage pIII coat proteins (*31*) resulting in multivalency, which increases the affinity through avidity effects (*32*). Finally, the VHS−phage is internalized by VCAM-1-expressing endothelial cells resulting in increased signal-to-noise ratios by biological amplification.

The alkyl-thioether-derivatized NIR fluorochromes hold promise for use in a wide variety of imaging applications. They are easily prepared from commercially available starting materials and require no additional purification prior to bioconjugation. One derivative, **CyTE-807**, displays absorption and emission maxima greater than 800 nm and does not aggregate in aqueous solution. By conjugation of **CyTE-777** to VHS−phage, imaging of VCAM-1-mediated internalization of the phage is possible. The fluorochrome-labeled phage constructs demonstrate a new potential imaging strategy that allows for highly selective, efficient delivery of large fluorochrome payloads.

ACKNOWLEDGMENT

This research was supported in part by NIH Grants P50-CA86355, R21-CA114149, and RO1-CA99385. S.A.H. was supported by Grant T32-CA79443.

LITERATURE CITED

(1) Weissleder, R., and Ntziachristos, V. (2003) Shedding light onto live molecular targets. *Nat. Med. 9*, 123−128.

(2) Flanagan, J. H., Jr., Khan, S. H., Menchen, S., Soper, S. A., and Hammer, R. P. (1997) Functionalized tricarbocyanine dyes as near-infrared fluorescent probes for biomolecules. *Bioconjugate Chem. 8*, 751−756.

(3) Lin, Y., Weissleder, R., and Tung, C. H. (2002) Novel near-infrared cyanine fluorochromes: synthesis, properties, and bioconjugation. *Bioconjugate Chem. 13*, 605−610.

(4) Mader, O., Reiner, K., Egelhaaf, H. J., Fischer, R., and Brock, R. (2004) Structure property analysis of pentamethine indocyanine dyes: identification of a new dye for life science applications. *Bioconjugate Chem. 15*, 70−78.

(5) Mujumdar, R. B., Ernst, L. A., Mujumdar, S. R., Lewis, C. J., and Waggoner, A. S. (1993) Cyanine dye labeling reagents: sulfoindocyanine succinimidyl esters. *Bioconjugate Chem. 4*, 105−111.

(6) Mujumdar, S. R., Mujumdar, R. B., Grant, C. M., and Waggoner, A. S. (1996) Cyanine-labeling reagents: sulfobenzindocyanine succinimidyl esters. *Bioconjugate Chem. 7*, 356−362.

(7) Narayanan, N., and Patonay, G. (1995) A new method for the synthesis of heptamethine cyanine dyes: synthesis of new near-infrared fluorescent labels. *J. Org. Chem. 60*, 2391−2395.

(8) Pham, W., Lai, W. F., Weissleder, R., and Tung, C. H. (2003) High efficiency synthesis of a bioconjugatable near-infrared fluorochrome. *Bioconjugate Chem. 14*, 1048−1051.

(9) Pham, W., Medarova, Z., and Moore, A. (2005) Synthesis and application of a water-soluble near-infrared dye for cancer detection using optical imaging. *Bioconjugate Chem. 16*, 735−740.

(10) Strekowski, L., Mason, C. J., Lee, H., Gupta, R., Sowell, J., and Patonay, G. (2003) Synthesis of water-soluble near-infrared cyanine dyes functionalized with [(succinimido)oxy]-carbonyl group. *J. Heterocyclic Chem. 40*, 913−916.

(11) Zhang, Z., and Achilefu, S. (2004) Synthesis and evaluation of polyhydroxylated near-infrared carbocyanine molecular probes. *Org. Lett. 6*, 2067−2070.

(12) Tung, C. H., Lin, Y., Moon, W. K., and Weissleder, R. (2002) A receptor-targeted near-infrared fluorescence probe for in vivo tumor imaging. *ChemBioChem 3*, 784−786.

(13) Tung, C. H., Quinti, L., Jaffer, F. A., and Weissleder, R. (2005) A branched fluorescent peptide probe for imaging of activated platelets. *Mol. Pharm. 2*, 92−95.

(14) Chen, X., Conti, P. S., and Moats, R. A. (2004) In vivo near-infrared fluorescence imaging of integrin alphavbeta3 in brain tumor xenografts. *Cancer. Res. 64*, 8009−8014.

(15) Zaheer, A., Lenkinski, R. E., Mahmood, A., Jones, A. G., Cantley, L. C., and Frangioni, J. V. (2001) In vivo near-infrared fluorescence imaging of osteoblastic activity. *Nat. Biotechnol. 19*, 1148−1154.

(16) Law, B., Curino, A., Bugge, T. H., Weissleder, R., and Tung, C. H. (2004) Design, synthesis, and characterization of urokinase plasminogen-activator-sensitive near-infrared reporter. *Chem. Biol. 11*, 99−106.

(17) Weissleder, R., Tung, C. H., Mahmood, U., and Bogdanov, A., Jr. (1999) In vivo imaging of tumors with protease-activated near-infrared fluorescent probes. *Nat. Biotechnol. 17*, 375−378.

(18) Xing, B., Khanamiryan, A., and Rao, J. (2005) Cell-permeable near-infrared fluorogenic substrates for imaging beta-lactamase activity. *J. Am. Chem. Soc. 127*, 4158−4159.

(19) Strekowski, L., Lipowska, M., and Patonay, G. (1992) Substitution reactions of a nucleofugal group in heptamethine cyanine dyes. Synthesis of an isothiocyanato derivative for labeling proteins with a near-infrared chromophore. *J. Org. Chem. 57*, 4578−4580.

(20) Flanagan, J. H., Jr., Owens, C. V., Romero, S. E., Waddell, E., Kahn, S. H., Hammer, R. P., and Soper, S. A. (1998) Near-infrared heavy-atom-modified fluorescent dyes for base-calling in DNA-sequencing applications using temporal discrimination. *Anal. Chem. 70*, 2676−2684.

(21) Zaheer, A., Wheat, T. E., and Frangioni, J. V. (2002) IRDye78 conjugates for near-infrared fluorescence imaging. *Mol. Imaging 1*, 354−364.

(22) Matsui, M., Hashimoto, Y., Funabiki, K., Jin, J.-Y., Yoshida, T., and Minoura, H. (2005) Application of near-infrared absorbing heptamethine cyanine dyes as sensitizers for zinc oxide solar cell. *Synth. Met. 148*, 147−153.

(23) Song, F., Peng, X., Lu, E., Zhang, R., Chen, X., and Song, B. (2004) Synthesis, spectral properties and photostabilities of novel water-soluble near-infrared cyanine dyes. *J. Photochem. Photobiol. A 168*, 53−57.
(24) Kelly, K. A., Allport, J. R., Tsourkas, A., Shinde-Patil, V. R., Josephson, L., and Weissleder, R. (2005) Detection of vascular adhesion molecule-1 expression using a novel multimodal nanoparticle. *Circ. Res. 96*, 327−36.
(25) Demas, J. N., and Crosby, G. A. (1971) The measurement of photoluminescence quantum yields. A review. *J. Phys. Chem. 75*, 991−1024.
(26) Reindl, S., Penzkofer, A., Gong, S.-H., Landthaler, M., Szeimies, R. M., Abels, C., and Bäumler, W. (1997) Quantum yield of triplet formation for indocyanine green. *J. Photochem. Photobiol. A 105*, 65−68.
(27) Jaye, D. L., Geigerman, C. M., Fuller, R. E., Akyildiz, A., and Parkos, C. A. (2004) Direct fluorochrome labeling of phage display library clones for studying binding specificities: applications in flow cytometry and fluorescence microscopy. *J. Immunol. Methods 295*, 119−127.
(28) Allport, J. R., Lim, Y. C., Shipley, J. M., Senior, R. M., Shapiro, S. D., Matsuyoshi, N., Vestweber, D., and Luscinskas, F. W. (2002) Neutrophils from MMP-9- or neutrophil elastase-deficient mice show no defect in transendothelial migration under flow in vitro. *J. Leukocyte Biol. 71*, 821−828.
(29) Tsourkas, A., Shinde-Patil, V. R., Kelly, K. A., Patel, P., Wolley, A., Allport, J. R., and Weissleder, R. (2005) In vivo imaging of activated endothelium using an anti-VCAM-1 magnetooptical probe. *Bioconjugate Chem. 16*, 576−581.
(30) Philip, R., Penzkofer, A., Bäumler, W., Szeimies, R. M., and Abels, C. (1996) Absorption and fluorescence spectroscopic investigation of indocyanine green. *J. Photochem. Photobiol. A 96*, 137−148.
(31) Smith, G. P., and Petrenko, V. A. (1997) Phage display. *Chem. Rev. 97*, 391−410.
(32) Lees, W. J., Spaltenstein, A., Kingery-Wood, J. E., and Whitesides, G. M. (1994) Polyacrylamides bearing pendant α-sialoside groups strongly inhibit agglutination of erythrocytes by influenza A virus: multivalency and steric stabilization of particulate biological systems. *J. Med. Chem. 37*, 3419−3433.

BC0501799

Reduction–Alkylation Strategies for the Modification of Specific Monoclonal Antibody Disulfides

Michael M. C. Sun, Kevin S. Beam, Charles G. Cerveny, Kevin J. Hamblett, Richard S. Blackmore, Michael Y. Torgov, Felicia G. M. Handley, Nathan C. Ihle, Peter D. Senter, and Stephen C. Alley*

Seattle Genetics, Inc., 21823 30th Drive SE, Bothell, Washington 98021. Received July 8, 2005; Revised Manuscript Received August 17, 2005

Site-specific conjugation of small molecules and enzymes to monoclonal antibodies has broad utility in the formation of conjugates for therapeutic, diagnostic, or structural applications. Precise control over the location of conjugation would yield highly homogeneous materials that could have improved biological properties. We describe for the first time chemical reduction and oxidation methods that lead to preferential cleavage of particular monoclonal antibody interchain disulfides using the anti-CD30 IgG1 monoclonal antibody cAC10. Alkylation of the resulting cAC10 cysteine thiols with the potent antimitotic agent monomethyl auristatin E (MMAE) enabled the assignment of drug conjugation location by purification with hydrophobic interaction chromatography followed by analysis using reversed-phase HPLC and capillary electrophoresis. These analytical methods demonstrated that treating cAC10 with reducing agents such as DTT caused preferential reduction of heavy-light chain disulfides, while reoxidation of fully reduced cAC10 interchain disulfides caused preferential reformation of heavy-light chain disulfides. Following MMAE conjugation, the resulting conjugates had isomeric homogeneity as high as 60–90%, allowing for control of the distribution of molecular species. The resulting conjugates are highly active both in vitro and in vivo and are well tolerated at efficacious doses.

Monoclonal antibodies (mAbs) have been used extensively as carriers of fluorophores, radionuclides, cytotoxic agents, and enzymes, yielding conjugates that find utility in therapeutic (*1*–*3*) and imaging applications (*4*, *5*), ELISA-based assays (*6*), and for the investigation of protein structure and dynamics (*7*). The methods employed for making mAb-based conjugates can be classified in two general categories: those that involve the random modification of mAb amino acid residues, and those that are highly regioselective. Examples of random modification procedures include the acylation of lysine ϵ-amino groups (*8*), alkylation of tyrosines (*9*), and amidation of carboxylates (*10*). The biological and functional properties of these conjugates are often acceptable; however, random modification of mAbs may impair antigen binding and leads to conjugate heterogeneity.

In the past several years, a number of selective methods have been described to introduce molecules of interest onto mAbs. The ability to control the location and stoichiometry of conjugation can significantly improve the properties of mAb conjugates in some applications. The greatest selectivities are obtained using recombinant technologies for the production of fusion proteins (*11*–*14*). Selective modification has also been reported for such chemically based methods as reductive amination of oxidized mAb carbohydrates (*15*), photoaffinity labeling of unconventional mAb binding sites (*16*), and reduction–alkylation of antibody interchain disulfides (*17*, *18*).

We have previously described the preparation of mAb–drug conjugates for use as antitumor agents (*17*, *19*). The potent antimitotic agent monomethyl auristatin E (MMAE)[1] was conjugated to the chimeric anti-CD30 mAb cAC10, an IgG1 mAb with four interchain disulfides (Figure 1). Conjugates were formed through full reduction of all interchain disulfides, followed by alkylation with the drug–linker complex. The resulting mAb–drug conjugates were homogeneous in composition, with about eight drugs/mAb. Since mAb interchain disulfides are distant from the antigen binding site and are generally not required to maintain mAb integrity (*20*), this site-specific conjugation strategy yielded conjugates that were potent and selective for CD30-positive hematologic malignancies (*17*, *19*).

We recently demonstrated that drug-load stoichiometry significantly influenced conjugate pharmacokinetics, and that conjugates with fewer drugs/mAb had larger therapeutic windows (*21*). Specifically, conjugates with four drugs/mAb were highly active and significantly less toxic than their counterparts with eight drugs/mAb. However, such partially loaded conjugates are not homogeneous, and the number of drugs on each mAb vary from 0 to 8, with several isomers at each drug substitution level. To minimize the heterogeneity of these partially loaded conjugates with four drugs/mAb, we explored various reduction–alkylation strategies and evaluated the distribution of species formed. We recognized that the

* To whom correspondence should be addressed: Tel: 425-527-4752; Fax: 425-527-4001; e-mail: SAlley@seagen.com.

[1] Abbreviations: ADC, mAb drug conjugate; DTNB, 5,5′-dithiobis(2-nitrobenzoic acid); DTPA, diethyeletriaminepentaacetic acid; DTT, dithiothreitol; E0, E2, E4, E6, E8, cAC10 with 0, 2, 4, 6, 8 MMAE per mAb, respectively; H0, H1, H2, H3, heavy chain with 0, 1, 2, 3 MMAE, respectively; HIC, hydrophobic interaction chromatography; L0, L1 light chain with 0, 1 MMAE, respectively; mAb, monoclonal antibody; MMAE, monomethyl auristatin E; MTD, maximum tolerated dose; TCEP, tris(2-carboxyethyl)phosphine; vcMMAE, maleimidocaproyl-valine-citruline-PABA-MMAE.

10.1021/bc050201y CCC: $30.25 © 2005 American Chemical Society
Published on Web 09/07/2005

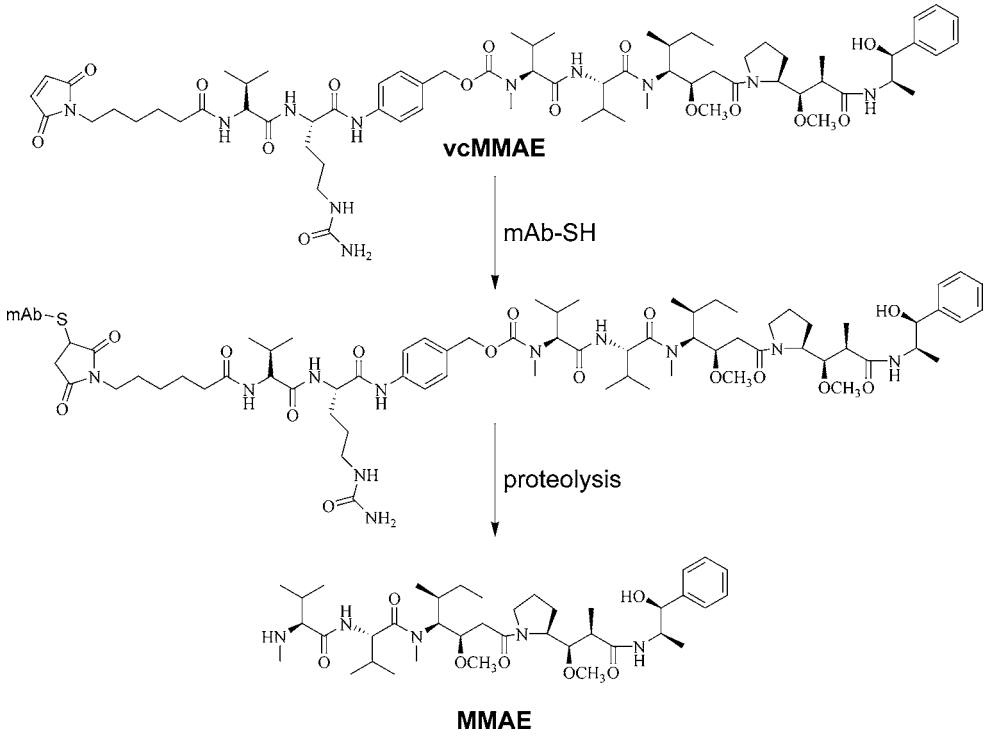

Figure 1. Conjugation strategy. The drug-linker vcMMAE reacts with a mAb cysteine to form the ADC. The potent antimitotic agent MMAE is released from the ADC following proteolysis. As many as eight molecules of vcMMAE can react with each mAb following reduction of the four interchain disulfides present in cAC10.

absolute drug loading and the isomeric distribution could play a role in efficacy and toxicity. However, the literature does not describe how to chemically control the isomeric distribution of drug loading, nor does it illustrate how to determine which of the various mAb thiols are drug substituted. To address these issues, analytical technologies were established to determine the sites of drug substitution, and conjugation methods were developed that allowed for isomeric homogeneities as high as 60−90%. The in vitro and in vivo properties of these conjugates are also described.

MATERIALS AND METHODS

Materials. cAC10, vcMMAE, and cAC10 with eight MMAE/mAb (E8) were prepared as previously described (*17*, *22*). DTT, DTPA, and 4,4′-dithiodipyridine were obtained from Sigma-Aldrich (St. Louis, MO). EDTA and sodium chloride were obtained from Cambrex (Rockland, ME). Sodium borate, sodium phosphate, and citric acid were obtained from Mallinckrodt (Phillipsburg, NJ). DTNB was obtained from Pierce (Rockford, IL). TCEP and aminoethanethiol were obtained from Acros (Morris Plains, NJ). Cysteine was obtained from Alfa Aesar (Ward Hill, MA).

Preparation of ADCs. cAC10-vcMMAE with an average of four MMAE/mAb, referred to as E4 mixture, was prepared as follows. Methods A and D were used to make cAC10-vcMMAE with 2 MMAE/mAb, referred to as E2 mixture, with the indicated substitutions.

Method A: Limited DTT Reduction. cAC10 was treated with 3.25 molar equiv of DTT (2.25 molar equiv for E2 mixture) in 0.025 M sodium borate pH 8, 0.025 M NaCl, 1 mM DTPA for 2 h at 37 °C. The excess DTT was purified away from the partially reduced cAC10 in the following manner. The mixture was first diluted 5-fold with water and applied to a hydroxyapatite column (Macroprep ceramic type I 40 μm, BioRad, Hercules, CA) at a flow rate of 10 mL/min. The column size was 1 mL per 10 mg of cAC10. The column was previously equilibrated with five column volumes of 0.5 M sodium phosphate pH 7, 10 mM NaCl and five column volumes of 10 mM sodium phosphate pH 7, 10 mM NaCl. Following application, the column was washed with five column volumes of 10 mM sodium phosphate pH 7, 10 mM NaCl and then eluted with 100 mM sodium phosphate pH 7, 10 mM NaCl. DTPA was added to 1 mM following elution. The protein concentration was quantified using an absorbance value of 1.58 at 280 nm for a 1.0 mg/mL solution, and the molar concentration was determined using a molecular weight of 148 449 g/mol. The concentration of mAb−cysteine thiols produced was determined by titrating with DTNB, typically resulting in 4.0 to 4.5 thiols/mAb when 3.25 molar equiv of DTT were used.

Partially reduced cAC10 was alkylated with 1.1 molar equiv of vcMMAE/mAb-cysteine thiol. The alkylation reaction was performed at 0 °C for 30 min. Cysteine (1 mM final) was used to quench any unreacted, excess vcMMAE. cAC10-vcMMAE was purified by hydroxyapatite chromatography as described above. Following elution, the buffer was changed to phosphate buffered saline (Invitrogen, Carlsbad, CA) using Amicon (Millipore, Bedford, MA) Ultrafree 30K cutoff spin concentration devices. The protein concentration was quantified using an absorbance value of 1.62 at 280 nm for a 1.0 mg/mL solution.

Method B: Limited TCEP Reduction. cAC10 was treated with 2.75 molar equiv of TCEP in 0.025 M sodium borate pH 8, 0.025 M NaCl, 1 mM DTPA for 2 h at 37 °C. Without purification, the mixture was then cooled to 0 °C and partially reduced cAC10 alkylated with vcMMAE as described above. cAC10-vcMMAE was purified using PD-10 columns (Amersham Biosciences, Piscataway, NJ) equilibrated with phosphate buffered saline.

Method C: Reduction of cAC10 with Aminoethanethiol. cAC10 was reduced with aminoethanethiol as previously

described for gamma globulin (*23*). The reduced mAb was alkylated with vcMMAE as described above.

Method D: DTNB Reoxidation of Fully Reduced cAC10. cAC10 was treated with a large excess (10 mM) of DTT in 0.025 M sodium borate pH 8, 0.025 M NaCl, 1 mM DTPA for 1 h at 37 °C and purified by hydroxyapatite chromatography as described above. The fully reduced cAC10 was cooled to 0 °C and then treated with 2.0 equiv of DTNB (3.0 for E2 mixture) or 4,4′-dipyridyldithiol (from 10 mM stock solutions) with rapid mixing. This mixture was incubated at 0 °C for 20 min. Without further purification, partially reoxidized cAC10 was alkylated with vcMMAE as previously described and the resulting conjugate was purified by hydroxyapatite chromatography as described above.

cAC10 Reduction Time Course. cAC10 was reduced with 3.0 equiv of DTT in 50 mM sodium phosphate pH 7.5 and 5 mM EDTA at 37 °C. At various times, samples were removed, quenched with an equal volume of ice-cold 200 mM sodium citrate pH 5, and purified using PD-10 columns equilibrated with phosphate buffered saline containing 5 mM EDTA. Reduced cAC10 was treated with vcMMAE as previously described and purified using PD-10 columns equilibrated with phosphate buffered saline.

Purification of E2, E4, and E6 by HIC. cAC10-vcMMAE was purified by HIC as previously described to yield ADCs with exactly two, four, or six MMAE/mAb (referred to as E2, E4, and E6, respectively) (*21*). Briefly, NaCl was added to cAC10-vcMMAE to give a final concentration of 2.0 M and this mixture applied to a phenyl HIC column. E2, E4, and E6 were eluted using step gradients of decreasing NaCl concentration. These purified fractions were analyzed by HIC−HPLC to determine drug loading purity as previously described (*21*, *24*). HIC peaks corresponding to E2, E4, or E6 were identified as previously described: cAC10 and vcMMAE have distinct absorbance maxima ($\lambda_{max} = 280$ and 248 nm, respectively) and overlaying the UV spectra of these peaks yields A248/280 ratios that increase with drug loading (*21*, 24). The HIC−HPLC method was also used to isolate small amounts of E2, E4, and E6.

Characterization of ADCs. The drug loading was estimated using the molar extinction coefficients at 248 and 280 nm of the mAb (9.413×10^4 and 2.3415×10^5 M^{-1} cm^{-1}, respectively) and drug (1.5×10^3 and 1.59×10^4 M^{-1} cm^{-1}, respectively) as previously described (*21*, *24*). Size-exclusion HPLC and C_{12} reversed-phase HPLC were used as previously described (*17*) to determine the amount of aggregate and free vcMMAE, respectively, present in the ADCs.

Analysis of ADCs by Capillary Electrophoresis. The ADCs were analyzed under denaturing but nonreducing conditions using an Agilent Bioanalyzer (Palo Alto, CA). A protein 200 chip was used under denaturing but nonreducing conditions as described by the manufacturer. Briefly, 4 μL of 1 mg/mL cAC10-vcMMAE was mixed with 2 μL of nonreducing loading buffer and heated to 100 °C for 5 min. Water (84 μL) was added and 6 μL of this mixture was loaded into each well of the chip. The molecular weights of peaks were determined using the molecular weight ladder provided and run concurrently, allowing assignment of L, H, HL, HH, HHL, and LHHL. Unconjugated cAC10 confirmed the assignment of LHHL, while E8 confirmed the assignment of L and H.

Analysis of ADCs by Reversed-Phase HPLC. ADCs were analyzed under denaturing and reducing conditions using a 2.1 × 150 mm, 8 μ, 1000 Å PLRP-S column (Polymer Laboratories, Amherst, MA). The flow rate was 1 mL/min, and the column temperature was 80 °C. Solvent A was 0.05% trifluoroacetic acid in water and solvent B was 0.04% trifluoroacetic acid in acetonitrile. The method consisted of the following: Isocratic 25% B for 3 min, a 25-min linear gradient to 50% B, a 2-min linear gradient to 95% B, a 1-min linear gradient to 25% B, and isocratic 25% B for 2 min. Injections were 10−20 μL of 1 mg/mL cAC10-vcMMAE previously reduced with 20 mM DTT at 37 °C for 15 min to cleave the remaining interchain disulfides. The number of moles and mole fraction of each chain was determined using the following molar extinction coefficients: 30 160 M^{-1} cm^{-1} (L0); 31 660 M^{-1} cm^{-1} (L1); 86 915 M^{-1} cm^{-1} (H0); 88 415 M^{-1} cm^{-1} (H1); 89 915 M^{-1} cm^{-1} (H2); 91 415 M^{-1} cm^{-1} (H3). Peak assignments were made with unconjugated cAC10 (L0 and H0) and E8 (L1 and H3). H1 and H2 were assigned by their elution time (eluting between H0 and H3) and UV spectra (the A248/280 ratio increases with drug loading).

Determination of Isomeric Distribution. The isomeric distribution for E2 and E6 was determined using solely reversed-phase HPLC data from the mole fractions determined above. For E2 isomer A, the mole fraction of L0 and H1 are equal, while for E2 isomer B, the mole fraction of L0, L1, H0, and H1 are equal. With the sum of the mole percent of L0, L1, H0, and H1 set to 100%, the percent isomer B can be determined as follows:

$$\%\,B = 2(\%\ \mathrm{L1}) + 2(\%\ \mathrm{H0}) \qquad (1)$$

where %L1 = mole fraction of L1 and %H0 = mole fraction H0. The percent of isomer A is assumed to be 100 − %B.

Similarly, for E6 isomer A, the mole fraction of L1 and H2 are equal, while for E6 isomer B, the mole fractions of L0, L1, H2, and H3 are equal. With the sum of the mole percent of L0, L1, H2, and H3 set to 100%, the percent isomer B can be determined as follows:

$$\%\,B = 2(\%\ \mathrm{L0}) + 2(\%\ \mathrm{H3}) \qquad (2)$$

where%L0 = mole fraction of L0 and %H3 = mole fraction H3. The percent of isomer A is assumed to be 100 − %B.

Due to more possible isomers, the percentages of the E4 isomers cannot be obtained solely from the reversed-phase HPLC data because no isomer gives a unique light and heavy chain pattern. The amount of E4 isomer A was first determined from capillary electrophoresis data using the HHL, HH, and HL peak areas as follows:

$$\%\,A = \frac{\dfrac{\mathrm{HHL}}{124720.8}}{\dfrac{\mathrm{HHL}}{124720.8} + \dfrac{\mathrm{HH}}{100992.6} + \dfrac{\mathrm{HL}}{2 \times 74224.5}} \qquad (3)$$

With the sum of the mole percent of L0, L1, H1, and H2 set to 100%, reversed-phase HPLC data was then used to solve for the remaining contribution of E4 isomers B and C using the following formulas:

$$\%\,B = \%\ \mathrm{H1} + \%\ \mathrm{L1} - 0.5(\%\,A) \qquad (4)$$

$$\%\,C = \%\ \mathrm{H2} + \%\ \mathrm{L0} - 0.5(\%\,A) \qquad (5)$$

where %H1 = mole fraction of H1, %L1 = mole fraction L1, %H2 = mole fraction H2, and %L0 = mole fraction L0.

Simulations. The simulated partial reduction of cAC10 was carried out using a series of coupled ordinary

differential equations (*25*) with an integration algorithm (fourth order Runge−Kutta) implemented as a VBA function in Excel (Microsoft Corp., Redmond, WA). The rate constants for reduction of heavy-light and heavy-heavy disulfides were equal. The simulation assumes 2 equivalent heavy-light and 2 equivalent heavy-heavy disulfides per mAb, with the relative rate constants for the reduction of the first and second of these equivalent disulfides being 2:1 due to the 2:1 stoichiometry (for example, when the first heavy-light disulfide is reduced, there are two heavy-light disulfides present, whereas when the second heavy-light disulfide is reduced, there is only one heavy-light disulfide present). The simulation used a concentration of reductant sufficient to reduce an average of two disulfides per mAb. Figures S1 and S2 show the mechanism and the differential equations used in the simulation.

Binding Studies. ADCs were labeled with 36 molar equiv of europium N1-isothiocyanate (Perkin-Elmer Biosciences, Wellesley MA) overnight at 4 °C in 50 mM Na_2CO_3, pH 9.0. Small molecular weight agents were removed by gel filtration on PD-10 columns equilibrated with Tris buffered saline (TBS, 50 mM Tris HCl, pH 8.0, 150 mM NaCl) followed by dialysis overnight in TBS at 4 °C. Conjugate concentration was determined by UV absorbance. Analysis of the europium content (by release into DELFIA enhancement solution, Perkin-Elmer) indicated that there were 5−7 europium labels/mAb. Karpas 299 ALCL cells (100 μL/well at 1×10^6/mL in TBS + 0.5% FBS, 10 μM EDTA) were incubated with increasing dilutions of labeled ADC or parental cAC10 for 1 h at 4 °C on a plate rocker. Following incubation, the cells were washed three times in TBS, resuspended in 200 μL of enhancement solution, transferred to DELFIA yellow sided plates, and incubated on an orbital shaker for 5 min at room temperature. Fluorescence was monitored using a Fusion HTS microplate reader (Perkin-Elmer) using the time-resolved fluorescence mode using an excitation wavelength of 335 nm and emission wavelength set at 620 nm. The time delay between excitation and emission was 400 μs. After reading, data were reduced and binding analyzed using the one-site binding model in GraphPad Prism version 4.01 for Windows (GraphPad Software, San Diego CA). Binding curves experiments were performed a minimum of three times to ensure accuracy.

Cytotoxicity Assays. The experiments were performed as previously described (*17*). Briefly, Karpas 299 cells were treated with ADCs for 92 h before adding resazurin and incubating an additional 4 h. Dye reduction was measured using a fluorescent plate reader.

In Vivo Studies. In vivo efficacy of ADCs in xenograft models of human $CD30^+$ tumors in SCID mice and the maximum tolerated dose of ADCs in BALB/c mice were performed as previously described (21). Briefly, subcutaneous Karpas-299 tumors were grown in C.B.-17 SCID mice, with the test articles administered when tumors reached approximately 100 mm^3 (length $\times$ width^2)/2. Animals (7−10/group) were injected iv with the ADCs at the doses indicated. Animals were considered cured if they were tumor free 101 days post tumor implant. Groups were compared for statistical significance by pair wise treatment of Kaplan−Meier analysis using GraphPad Prism version 4.01. To evaluate the MTD, BALB/c mice (parent strain of the C.B.-17 SCID) were administered with ADCs. Animal weights were measured and clinical observations were recorded over a 14 day period. The MTD was assigned as the highest single dose administered to an animal that did not result in weight loss ≥20% or lead to any signs of distress.

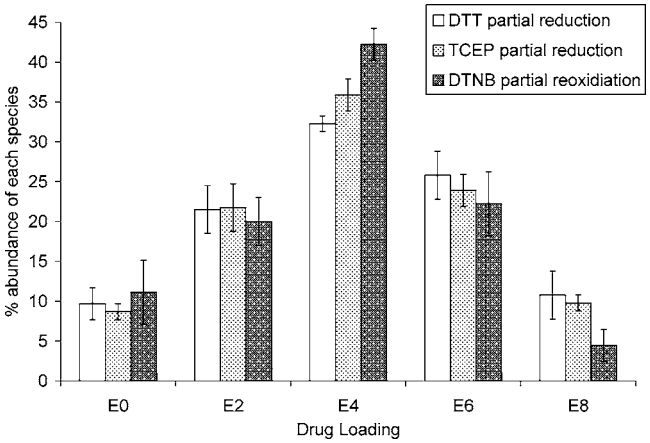

Figure 2. Composition of E4 mixture as a function of conjugation methodology. HIC−HPLC chromatograms were integrated to determine the abundance of E0, E2, E4, E6, and E8 in the mixtures. Values are ± standard deviation for four (DTT partial reduction), three (TCEP partial reduction), or six (DTNB partial reoxidation) separate experiments. The contributions from odd-loaded species, typically less than 10%, are not shown. The sum of E0, E2, E4, E6, and E8 was normalized to 100%.

RESULTS

Reduction Methods. Two general strategies were used to prepare ADCs with an average of four MMAE/mAb (referred to as E4 mixture). The first involved limited reduction of the interchain disulfides of the chimeric mAb cAC10, an IgG1, followed by alkylation with maleimidocaproyl-val-cit-PABA-MMAE (vcMMAE). This two-step process led to the formation of cAC10-vcMMAE. About 3.25 and 2.75 molar equiv of the strong reducing agents DTT and TCEP, respectively, were sufficient to cleave two interchain disulfide bonds, yielding an average of four cAC10 cysteines/mAb. Partial reduction of cAC10 could also be accomplished using the weaker reducing agent aminoethanethiol, which at pH 5 requires about 500 molar equiv to yield 4 cAC10 cysteines/mAb. Unlike the thiol-based reducing agents, phosphines such as TCEP react poorly with maleimides, and the excess reducing agent does not have to be removed before adding vcMMAE.

A second general strategy for controlled drug substitution involves fully reducing cAC10 with DTT and then partially reoxidizing the resulting thiol groups with DTNB. This reoxidation process is very efficient, requiring 2.0 equiv of DTNB to reoxidize eight mAb cysteines back to four. Treatment of this reoxidized mAb with a thiol such as cysteine does not liberate any bound thionitrobenzoic (TNB) acid, suggesting that the reoxidized cysteines are in the form of mAb disulfides rather than mixed TNB−cysteine disulfides. The remaining mAb cysteines can then be conjugated to vcMMAE.

Quantification of Drug Loading Levels. Figure 2 shows the normalized percentages of the even drug-loaded species prepared by DTT partial reduction, TCEP partial reduction, and partial DTNB reoxidation as determined by HIC−HPLC. The DTNB partial reoxidation method yields a slightly higher percentage of E4 (42%) than the partial reduction methods (32% for DTT and 36% for TCEP). This comes at the expense of mainly E6 and E8, which total about 37% for DTT partial reduction and 34% for TCEP partial reduction, while only 27% for DTNB partial reoxidation.

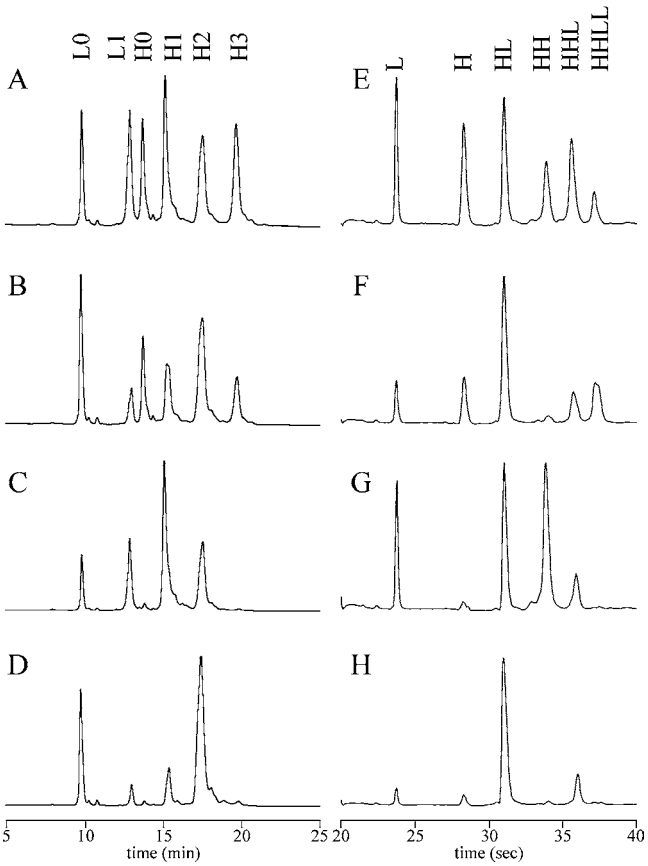

Figure 3. Analytical characterization of ADCs. (A−D) Reversed-phase HPLC and (E−H) capillary electrophoresis were used to analyze (A, E) E4 mixture made by partial DTT reduction followed by MMAE conjugation; (B, F) E4 mixture made by DTNB partial reoxidation followed by MMAE conjugation; (C, G) E4 made by partial DTT reduction followed by MMAE conjugation and purified by preparative HIC; and (D, H) E4 made by partial DTNB reoxidation followed by MMAE conjugation and purified by preparative HIC. HPLC injections were 20 μL of 1 mg/mL cAC10-vcMMAE treated with 20 mM DTT for 15 min at 37 °C. Separations were performed at 80 °C. Capillary electrophoresis was performed under nonreducing conditions.

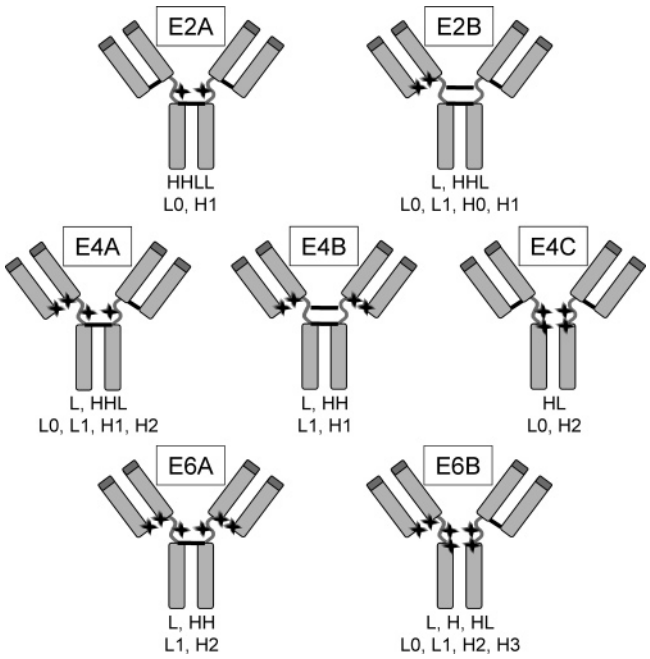

Figure 4. Potential isomers for E2, E4, and E6. Isomers with one heavy-heavy disulfide (2A, 4A, and 6A) can be further subdivided into isomers with either the first or the second disulfide intact, but because the analytical methods described herein cannot distinguish these subgroups, only one isomer is shown. Below the isomer are the chain compositions under denaturing conditions (first line, nonreducing; second line, reducing). For denaturing and nonreducing conditions, the possible species formed are L, H, HL, HH, HHL, and LHHL, where the remaining interchain disulfides link the indicated chains. For denaturing and reducing, the possible species formed are L0, L1, H0, H1, H2, and H3, in which the numbers indicate how many drug molecules are attached to the light or heavy chain. The locations of MMAE conjugation are indicated by stars. Unconjugated cAC10 (E0) and fully conjugated cAC10 (E8) are not shown.

Isomeric Populations. To determine the isomeric population of each of the drug loaded species, cAC10-vcMMAE prepared with various methods was first separated by preparative HIC, yielding E2, E4, and E6. The purities of these materials, with respect to their drug loading levels, was at least 95% as determined by analytical HIC−HPLC (*21*). The HIC-purified materials were then subjected a combination of reducing and nonreducing methods to assign the distribution of the drugs on the mAb. Reducing and denaturing reversed-phase HPLC was used to separate and quantify various light and heavy chain species. In this method, pretreatment of the ADC with an excess of DTT breaks the remaining interchain disulfides and allows separation of light chain with 0 or 1 drugs (L0 and L1) from heavy chain with 0, 1, 2, or 3 drugs (H0, H1, H2, and H3) (Figure 3, A−D). A second form of analysis involved nonreducing and denaturing capillary electrophoresis, allowing for the separation of 6 potential mAb species: L, H, HL, HH, HHL, and LHHL (Figure 3, E−H). Figure 4 shows the possible isomers of E2, E4, and E6 and the expected distribution of mAb fragments under denaturing conditions in both reducing and nonreducing environments. The isomeric populations of E2 and E6 were readily determined by reversed-phase HPLC since each isomer yields a unique fragment pattern. For example, isomer E2B yields L1 and H0 under denaturing and reducing conditions, while E2A yields L0 and H1. Under denaturing and nonreducing conditions, isomer E2A yields LHHL, while E2B yields L and HHL. For E4, the three potential isomers do not yield unique fragment patterns on reversed-phase HPLC or capillary electrophoresis alone, requiring that the combined results must be used to assign the isomeric population.

Figure 5 shows the percent composition for each of these isomers. Both partial reduction methods gave similar isomer populations. However, for E2, DTT partial reduction and DTNB partial reoxidation gave contrasting isomeric populations: the former method yielded 92% E2B, while the latter method yielded 77% E2A. Similarly, E4B is the predominant isomer for DTT partial reduction (59%), while E4C is the predominant isomer for DTNB partial reoxidation (75%). The chemistry used to prepare the reduced antibody plays a significant role in the location of the drugs in the resulting conjugate. Interestingly, both methods yield E6B as the predominant E6 isomer in very high yields (96−98%). There are also smaller differences in the distribution of isomers observed from the DTT and TCEP partial reduction methods, the largest of which can be seen in isomers E4B and E4C. DTT partial reduction yields about 2:1 E4B to E4C, while TCEP partial reduction yields about 1:1.

Simulated Partial Reduction. The observed drug loading levels and isomeric populations are significantly different for the partial reduction and partial reoxidation methods, which may indicate that there is some degree

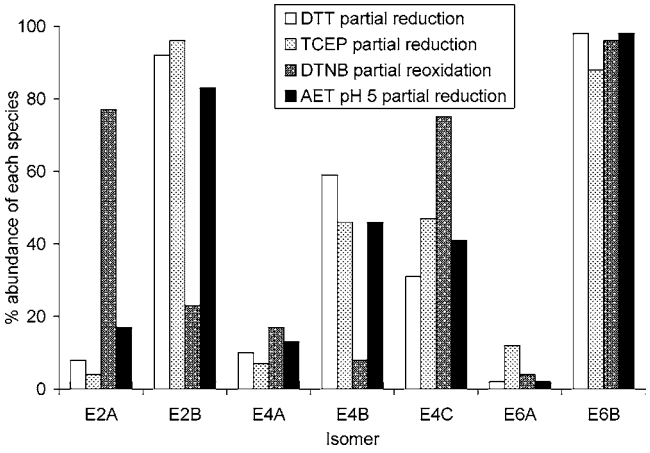

Figure 5. Composition of isomeric population of purified E2, E4, and E6. The percent of the E2 and E6 isomers were determined from reversed-phase HPLC data using eqs 1 and 2, respectively. The percent of E4A was determined from capillary electrophoresis data using eq 3 and then the percent of E4B and E4C were determined from reversed-phase HPLC data using eqs 4 and 5. For each drug loading level, the sum of the isomers is equal to 100%.

of selectivity in reducing and oxidizing mAb heavy-light and heavy-heavy disulfides. A simulation of cAC10 partial reduction was performed in which disulfides were allowed to be randomly reduced under conditions where the rate constants for the reduction of heavy-light and heavy-heavy disulfides were equal. Figure 6a shows the simulated drug loading levels for E0, E2, E4, E6, and E8 and the percent difference between these simulated values and the HIC−HPLC data for DTT and TCEP partial reduction. The percent difference varies systematically, in that the experimentally determined amounts of E0 and E8 were significantly larger than the simulated values, while the amounts of E2, E4, and E6 were slightly less than the simulated values. Figure 6b shows the simulated isomer populations and the percent difference between the simulation and the values determined from reversed-phase HPLC and capillary electrophoresis. The experimentally determined isomer abundances were as much as 250% more and up to nearly 100% less than the simulated values. No experimentally determined isomer abundance was within 75% of the simulated values. These results strongly suggest that the reduction is not a random process, and the rate constants for reduction of individual cAC10 disulfides are widely different.

DTT Reduction Time Course. Because of the long reduction time necessary to form partially reduced cAC10 with DTT, the isomeric population could change during the reduction reaction and using the end point of the reaction would not be representative of the overall reduction process. To address this, the isomeric compositions of the product ADCs were determined at various time intervals after the addition of the reducing agent. Reduction times of 10 to 120 min yielded drug loadings of 1.3 to 3.9 drugs/mAb. Table 1 shows that the isomeric composition does not change over the course of the reduction reaction. Thus, the reduction process is under kinetic rather than thermodynamic control, and using the end point of the reaction is appropriate.

Binding to CD30 Positive Cells. cAC10-vcMMAE conjugates were tested for their abilities to bind to CD30 positive Karpas 299 Anaplastic Large Cell Lymphoma cells. Table 2 shows that unmodified cAC10 and ADCs with two drugs/mAb bound with similar affinities, 2.0 to 3.6 nM. ADCs with four and eight drugs/mAb bound slightly weaker, 6.5 to 7.8 nM. The chemistry used to

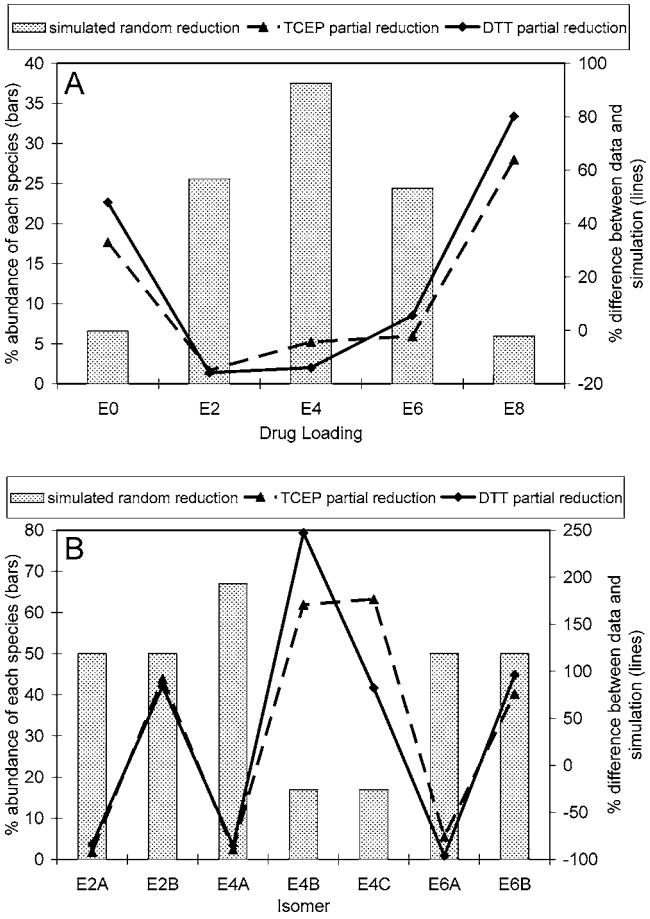

Figure 6. Simulation of random reduction reaction. cAC10 reduction was simulated with equal rate constants for reduction of heavy-heavy and heavy-light disulfides. (A) The simulated drug loading abundance is shown with bars for the reduction of an average of two disulfides to yield an average of four antibody cysteines. The percent differences between the experimentally determined drug loading abundance from HIC−HPLC data for DTT and TCEP partial reduction shown in Figure 2 and the simulated values are shown in lines. (B) The simulated isomer distribution is shown in bars. The percent differences between the experimentally determined isomer abundances shown in Figure 5 and the simulated values are shown in lines. In both panels, a positive number indicates that the experimental data is greater than the simulated value, while a negative number indicates that the experimental data is lower than the simulated value.

prepare the ADCs did not significantly influence the ability of the ADCs to bind to the cells.

In Vitro Cytotoxicity. Mixtures with an average of two and four drugs/mAb as well as HIC purified E2 and E4 were investigated for their in vitro activities on Karpas 299 cells. Table 2 shows the ADCs with two and four drugs/mAb have IC_{50} values from 11.4 to 13.8 ng/mL and 3.4 to 5.0 ng/mL, respectively. E8 gave the lowest value of 2.7 ng/mL and unconjugated cAC10 showed no effect. Thus, cytotoxic activity increases with increased drug substitution, but is not dependent on ADC isomeric composition.

In Vivo Toxicity and Therapeutic Efficacy. MTD values in immunocompetent BALB/c mice were determined by iv ADC injections. As previously described, the MTD of E8 was 50 mg/kg (*21*). Significantly more of the ADCs could be administered with lower drug loading. The best tolerated ADC was E2 made by DTT partial reduction, which was devoid of toxicity at 250 mg/kg, the highest dose tested. The MTD of E4 prepared by the DTNB partial reoxidation method was 120 mg/kg, which

Table 1. Time Course of Isomer Distribution for DTT Partial Reduction[a]

time (min)[b]	drugs/ mAb[c]	E2A[d]	E2B[e]	E4A[e]	E4B[f]	E4C[f]	E6A[g]	E6B[g]
10	1.3	12	88	9	63	28	N/D	N/D
20	2.1	9	91	7	65	29	7	93
35	2.7	9	91	7	63	31	6	94
55	3.3	9	91	7	63	30	8	92
80	3.6	9	92	7	61	32	6	94
120	3.9	11	90	8	61	31	7	93

[a] Numbers given are in mole fraction. For each drug loading level, the sum of the isomers is equal to 100%. [b] Reduction time. Once reduced, all antibodies were treated with vcMMAE for identical times. [c] Determined by HIC−HPLC. [d] Determined from reversed-phase HPLC data using eq 1. [e] Determined from capillary electrophoresis data using eq 3. [f] Determined from reversed-phase HPLC data using eqs 4 and 5. [g] Determined from reversed-phase HPLC data using eq 2. N/D, not determined. At this time point, very little E6 was produced, and this material was not sufficient for determining the isomer population.

Table 2. In Vitro Binding and Cytotoxicity of CAC10-vcMMAE

ADC	binding K_d (nM)[a]	Karpas 299 IC_{50} (ng/mL)[b]
E0 (cAC10)	2.70 ± 1.91	N/D
E2 mixture DTT	N/D	11.4 ± 2.4
E2 DTT	3.57 ± 2.41	13.8 ± 3.6
E2 mixture DTNB	N/D	11.7 ± 4.5
E2 DTNB	2.02 ± 1.22	13.2 ± 2.7
E4 mixture DTT	N/D	3.4 ± 1.2
E4 DTT	7.76 ± 3.93	4.8 ± 0.7
E4 mixture DTNB	N/D	5.0 ± 0.0
E4 DTNB	7.69 ± 4.42	4.3 ± 0.9
E8	6.53 ± 3.09	2.7 ± 0.2

[a] Binding to Karpas 299, determined from four to seven independent measurement ± standard deviation. N/D, not determined. [b] In vitro cytotoxicity, in ng cAC10/mL, determined from three independent measurements ± standard deviation. N/D, not determined. cAC10 alone displays poor activity against Karpas 299.

was slightly less toxic than the corresponding E4 ADC prepared by DTT partial reduction (MTD of 100 mg/kg). Consistent with in vitro cytotoxicity, the number of drugs/mAb had a much more pronounced influence on toxicity than the placement of the drug on the mAb.

Therapeutic efficacy experiments were performed in SCID mice with subcutaneous Karpas 299 tumors. Single doses of the ADCs were given 11 (E4) or 14 (E2) days after tumor implant, when the tumors had reached approximately 100 mm^3. Figure 7a shows that for E2 made by DTT partial reduction and DTNB partial reoxidation methods, 1.0 mg/kg of ADC both gave delays in tumor growth. Although E2 made by DTT partial reduction gave five cures out of seven while E2 made by DTNB partial reoxidation provided one cure out of seven, Kaplan−Meier analysis for survival showed that there was not a statistical difference between these two chemistries ($P = 0.08$). However, since the P value is trending toward significance ($0.05 < P < 0.1$), further studies are required with larger group sizes to determine if these chemistries yield differences in efficacy. The E4 ADCs which were made by DTT partial reduction, TCEP partial reduction, and DTNB partial reoxidation gave delays in tumor growth at both 0.5 and 1.0 mg/kg (Figure 7b). Nearly identical cure rates were obtained at 1 mg/kg for all three production methods (eight to ten cures out of ten), suggesting that the production methods yielded ADCs with similar efficacies ($P = 0.15$ for E4 made by TCEP partial reduction compared to E4 made by either DTT partial reduction or DTNB partial reoxidation).

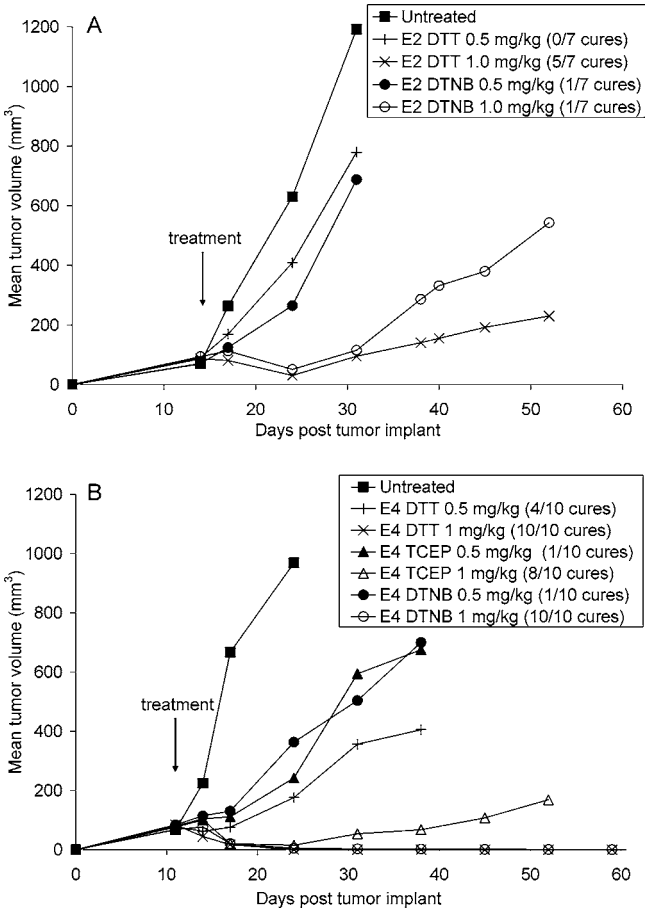

Figure 7. Single dose efficacy of E2 and E4. SCID mice with Karpas 299 tumors were treated with single doses of (A) E2 made by DTT partial reduction and DTNB partial reoxidation and (B) E4 made by DTT partial reduction, TCEP partial reduction, and DTNB partial reoxidation. Animals were considered cured if they were tumor free 101 days post tumor implant.

DISCUSSION

We have demonstrated for the first time that IgG1 interchain disulfide bonds can be distinguished by chemical reduction and oxidization methods. This was made possible using the drug MMAE to fix the disulfide bonding pattern by alkylating free cysteines, allowing separation of the drug loading levels by HIC, and facilitating the analysis of the isomeric populations.

As shown in Figure 3, the production method significantly affects the location of the drugs, suggesting that the mAb disulfides can be selectively reduced. Partial DTT reduction yields predominantly isomer E2B, which results from reduction of one of the heavy-light chain disulfides. Conjugates consisting of E4 were comprised mainly of isomer E4B, which results from the reduction of both heavy-light chain disulfides. The main E6 species detected was isomer E6B, which results from reduction of both heavy-heavy chain disulfides and one heavy-light chain disulfide, while isomers with one heavy-heavy chain disulfide reduced were in the extreme minority. On the other hand, partial DTNB reoxidation yields almost the opposite result for E2 and E4 isomers, with predominantly isomers E2A and E4C, where one heavy-heavy chain disulfide is intact, and the same result for E6. We have observed qualitatively similar preferences of the isomer populations from partial reduction and partial reoxidiation of the humanized anti-Her2 IgG1 Herceptin (data not shown).

Previous investigations of mAb disulfide biochemistry did not demonstrate whether there was selective reduction of particular mAb interchain disulfides, in part because of the inability to fractionate the reduction reaction into subpopulations together with the low resolution of the analytical techniques employed. SDS−PAGE was used extensively (*26*−*28*), but this technique could not resolve and quantify the nine possible isomers present in a mAb reduction reaction. Figure 3 shows that the E4 mixtures prepared by partial DTT reduction and partial DTNB reoxidation are difficult to distinguish, while HIC-purified E4 prepared by these chemistries are readily distinguished. In the past, analytical ultracentrifugation was also used to characterize mAb interchain disulfide reduction using aminoethanethiol under acidic conditions, and these data were used to suggest that exclusively heavy-heavy disulfides can be cleaved under these conditions (*29*−*31*). These data are even lower resolution than SDS−PAGE and cannot provide molecular characterization of the generated species. Our data are in contrast to this report, since partial reduction of cAC10 by aminoethanethiol at pH 5 results in a mixture of E4B and E4C present in nearly a 1:1 ratio (Figure 5), rather than only E4C, which would result from exclusive heavy-heavy disulfide reduction. The analytical technologies used in the previous reports (*29*−*31*) were evidently not sensitive enough to support the conclusions drawn.

The isomeric populations that result from partial DTT reduction demonstrate that IgG1 heavy-heavy disulfide bond cleavage is a cooperative process. Very little of any of the isomers with one heavy-heavy disulfide bond intact are observed, even at very early time points during the reduction (Table 1). The E2 isomer formed in greater than 90% abundance (E2B) has one heavy-light disulfide bond cleaved, while the predominant E4 isomer (E4B) has both of the heavy-light chain disulfides cleaved.

The simulated partial reduction with equal rate constants for heavy-light and heavy-heavy disulfide reduction confirm that the reduction of cAC10 is not a random process. The drug loading distribution and isomer distribution are significantly different between the simulation and experimental data, suggesting that a more complex model with unequal rate constants is much more appropriate in describing the cAC10 reduction process. We are currently performing additional simulations with other models to determine the rate constants that describe cAC10 reduction. These simulations will enable us to determine the relative rate constants of reduction of the heavy-light versus heavy-heavy disulfides, as well as the rate constants of reduction of the first versus the second heavy-light and heavy-heavy disulfides. Simulations may also be able to explain the small observed differences between DTT and TCEP partial reduction, with these two reducing agents potentially having different absolute reducing strengths as well as differences in their rate constants for reduction of individual disulfides.

Inspection of X-ray crystal structures (PDB structures include 1HZH and 1IGT) (*20*, *32*, *33*) show the region around these heavy-heavy disulfides to be highly flexible, and electron density is often absent. These disulfide bonds may be responsible for any local structure, and release of one may open up this region, allowing the second to be more exposed to solvent and reducing agents. The cleavage of these disulfides is not expected to cause large changes in the overall protein structure (*20*).

The partial DTNB reoxidation process preferentially re-forms the heavy-light chain disulfides, as was seen previously for air reoxidation (*26*). The E6 isomer formed in greater than 90% abundance (E6B) has one heavy-light disulfide, and the predominant E4 isomer (E4C) has both heavy-light disulfides. Unlike DTT reduction, reformation of the heavy-heavy disulfides does not appear to be cooperative, in that the predominant E2 isomer has just one heavy-heavy disulfide. Reformation of heavy-heavy disulfides appears to be merely kinetically slower than the heavy-light disulfides. If cleavage of the heavy-heavy disulfides releases the local structure and the previously paired cysteines can move away from each other, the kinetics of heavy-heavy disulfide bond formation will be slow. The heavy-light disulfide is probably not responsible for local structure or relative positioning of the heavy and light chains, and the unpaired cysteines will remain in close proximity and proper orientation for disulfide bond formation.

The chemistries described herein enable the generation of highly site-specific conjugates. For cAC10-vcMMAE, the effect of the location of the drugs on biological activity is modest, with the only significant difference being the MTD values of E4 made by DTNB partial reoxidation being higher than E4 made by DTT partial reduction. It is likely that other biologically interesting molecules such as fluorophores and fluorescence resonance energy transfer reagents may benefit from site-specific conjugation, and this is an area that we are currently investigating. The ability to control the molecular composition in ADCs by chemical means complements recombinant strategies, and allows for the generation of well-defined ADCs with potent biological activities.

ACKNOWLEDGMENT

We thank Angela Merges, Sarah Hall, and Jamie Andreyka for technical assistance. This work was supported in part by Grant R44 CA088583-02A1 from the National Institutes of Health.

Supporting Information Available: The mechanism and equations used for the simulated reduction of cAC10. This material is available free of charge via the Internet at http://pubs.acs.org.

LITERATURE CITED

(1) Senter, P. D., and Springer, C. J. (2001) Selective activation of anticancer prodrugs by monoclonal antibody-enzyme conjugates. *Adv. Drug Delivery Rev. 53*, 247−64.

(2) Sharkey, R. M., and Goldenberg, D. M. (2005) Perspectives on cancer therapy with radiolabeled monoclonal antibodies. *J. Nucl. Med. 46 Suppl 1*, 115S−27S.

(3) Trail, P. A., King, H. D., and Dubowchik, G. M. (2003) Monoclonal antibody drug immunoconjugates for targeted treatment of cancer. *Cancer Immunol. Immunother. 52*, 328−37.

(4) Bohdiewicz, P. J. (1998) Indium-111 satumomab pendetide: the first FDA-approved monoclonal antibody for tumor imaging. *J. Nucl. Med. Technol. 26*, 155−63; quiz 170−1.

(5) Van de Wiele, C., Revets, H., and Mertens, N. (2004) Radioimmunoimaging. Advances and prospects. *Q. J. Nucl. Med. Mol. Imaging 48*, 317−25.

(6) Porstmann, T., and Kiessig, S. T. (1992) Enzyme immunoassay techniques. An overview. *J Immunol. Methods 150*, 5−21.

(7) Lichlyter, D. J., Grant, S. A., and Soykan, O. (2003) Development of a novel FRET immunosensor technique. *Biosens. Bioelectron. 19*, 219−26.

(8) Wisdom, G. B. (2005) Conjugation of antibodies to fluorescein or rhodamine. *Methods Mol. Biol. 295*, 131−4.

(9) Gudmundsson, B. M., Young, N. M., and Oomen, R. P. (1993) Characterisation of residues in antibody binding sites by chemical modification of surface-adsorbed protein combined with enzyme immunoassay. *J. Immunol. Methods 158*, 215−27.

(10) Wines, B. D., and Easterbrook-Smith, S. B. (1990) Carbodiimide cross-linking of human C1q and rabbit IgG. *Mol. Immunol*. *27*, 221−6.

(11) Casey, J. L., Coley, A. M., Tilley, L. M., and Foley, M. (2000) Green fluorescent antibodies: novel in vitro tools. *Protein Eng*. *13*, 445−52.

(12) Hayashi, N., Kipriyanov, S., Fuchs, P., Welschof, M., Dorsam, H., and Little, M. (1995) A single expression system for the display, purification and conjugation of single-chain antibodies. *Gene 160*, 129−30.

(13) Schneider, P. (2000) Production of recombinant TRAIL and TRAIL receptor: Fc chimeric proteins. *Methods Enzymol*. *322*, 325−45.

(14) Siemers, N. O., Kerr, D. E., Yarnold, S., Stebbins, M. R., Vrudhula, V. M., Hellstrom, I., Hellstrom, K. E., and Senter, P. D. (1997) Construction, expression, and activities of L49-sFv-beta-lactamase, a single-chain antibody fusion protein for anticancer prodrug activation. *Bioconjugate Chem. 8*, 510−9.

(15) Rodwell, J. D., Alvarez, V. L., Lee, C., Lopes, A. D., Goers, J. W., King, H. D., Powsner, H. J., and McKearn, T. J. (1986) Site-specific covalent modification of monoclonal antibodies: in vitro and in vivo evaluations. *Proc. Natl. Acad. Sci. U.S.A. 83*, 2632−6.

(16) Chang, I. N., Lin, J. N., Andrade, J. D., and Herron, J. N. (1995) Photoaffinity labeling of antibodies for applications in homogeneous fluoroimmunoassays. *Anal.Chem*. *67*, 959−66.

(17) Doronina, S. O., Toki, B. E., Torgov, M. Y., Mendelsohn, B. A., Cerveny, C. G., Chace, D. F., DeBlanc, R. L., Gearing, R. P., Bovee, T. D., Siegall, C. B., Francisco, J. A., Wahl, A. F., Meyer, D. L., and Senter, P. D. (2003) Development of potent monoclonal antibody auristatin conjugates for cancer therapy. *Nat. Biotechnol. 21*, 778−84.

(18) Trail, P. A., Willner, D., Lasch, S. J., Henderson, A. J., Hofstead, S., Casazza, A. M., Firestone, R. A., Hellstrom, I., and Hellstrom, K. E. (1993) Cure of xenografted human carcinomas by BR96-doxorubicin immunoconjugates. *Science 261*, 212−5.

(19) Francisco, J. A., Cerveny, C. G., Meyer, D. L., Mixan, B. J., Klussman, K., Chace, D. F., Rejniak, S. X., Gordon, K. A., DeBlanc, R., Toki, B. E., Law, C. L., Doronina, S. O., Siegall, C. B., Senter, P. D., and Wahl, A. F. (2003) cAC10-vcMMAE, an anti-CD30-monomethyl auristatin E conjugate with potent and selective antitumor activity. *Blood 102*, 1458−65.

(20) Saphire, E. O., Stanfield, R. L., Crispin, M. D., Parren, P. W., Rudd, P. M., Dwek, R. A., Burton, D. R., and Wilson, I. A. (2002) Contrasting IgG structures reveal extreme asymmetry and flexibility. *J. Mol. Biol. 319*, 9−18.

(21) Hamblett, K. J., Senter, P. D., Chace, D. F., Sun, M. M., Lenox, J., Cerveny, C. G., Kissler, K. M., Bernhardt, S. X., Kopcha, A. K., Zabinski, R. F., Meyer, D. L., and Francisco, J. A. (2004) Effects of drug loading on the antitumor activity of a monoclonal antibody drug conjugate. *Clin. Cancer Res. 10*, 7063−70.

(22) Wahl, A. F., Klussman, K., Thompson, J. D., Chen, J. H., Francisco, L. V., Risdon, G., Chace, D. F., Siegall, C. B., and Francisco, J. A. (2002) The anti-CD30 monoclonal antibody SGN-30 promotes growth arrest and DNA fragmentation in vitro and affects antitumor activity in models of Hodgkin's disease. *Cancer Res*. *62*, 3736−42.

(23) Mandy, W. J., and Nisonoff, A. (1963) Effect of Reduction of Several Disulfide Bonds on the Properties and Recombination of Univalent Fragments of Rabbit Antibody. *J. Biol. Chem. 238*, 206−213.

(24) Sanderson, R. J., Hering, M. A., James, S. F., Sun, M. M., Doronina, S. O., Siadak, A. W., Senter, P. D., and Wahl, A. F. (2005) In vivo drug-linker stability of an anti-CD30 dipeptide-linked auristatin immunoconjugate. *Clin. Cancer Res. 11*, 843−52.

(25) Olson, J. S. (1981) Numerical analysis of kinetic ligand binding data. *Methods Enzymol. 76*, 652−67.

(26) Sears, D. W., and Beychok, S. (1977) Acquisition of the covalent quaternary structure of an immunoglobulin G molecule. Theoretical reoxidation models. *Biochemistry 16*, 2026−31.

(27) Sears, D. W., Mohrer, J., and Beychok, S. (1977) Relative susceptibilities of the interchain disulfides of an immunoglobulin G molecule to reduction by dithiothreitol. *Biochemistry 16*, 2031−5.

(28) Virella, G., and Parkhouse, R. M. (1973) Sensitivity to reduction of human immunoglobulin G of different heavy chain subclasses. *Immunochemistry 10*, 213−7.

(29) Hermanson, G. (1996) *Bioconjugate Techniques*, Academic Press, San Diego.

(30) Kato, K., Hamaguchi, Y., Fukui, H., and Ishikawa, E. (1976) Enzyme-linked immunoassay. Conjugation of rabbit anti-(human immunoglobulin G) antibody with beta-D-galactosidase from Escherichia coli and its use for human immunoglobulin G assay. *Eur. J. Biochem*. *62*, 285−92.

(31) Palmer, J. L., Nisonoff, A., and Vanholde, K. E. (1963) Dissociation of Rabbit Gamma Globulin into Subunits by Reduction and Acidification. *Proc. Natl. Acad. Sci. U.S.A. 50*, 314−21.

(32) Harris, L. J., Larson, S. B., Hasel, K. W., and McPherson, A. (1997) Refined structure of an intact IgG2a monoclonal antibody. *Biochemistry 36*, 1581−97.

(33) Saphire, E. O., Parren, P. W., Pantophlet, R., Zwick, M. B., Morris, G. M., Rudd, P. M., Dwek, R. A., Stanfield, R. L., Burton, D. R., and Wilson, I. A. (2001) Crystal structure of a neutralizing human IGG against HIV-1: a template for vaccine design. *Science 293*, 1155−9.

BC050201Y

Site-Specific PEGylation of Engineered Cysteine Analogues of Recombinant Human Granulocyte-Macrophage Colony-Stimulating Factor

Daniel H. Doherty,[†] Mary S. Rosendahl,[†] Darin J. Smith,[†] Jennifer M. Hughes,[†] Elizabeth A. Chlipala,[‡] and George N. Cox*,[†]

Bolder BioTechnology, Inc., 4056 Youngfield Street, Wheat Ridge, Colorado 80033, and BolderPATH, Inc., Campus Box 347, University of Colorado, Boulder, Colorado 80309. Received June 16, 2005

Granulocyte macrophage colony-stimulating factor (GM-CSF) stimulates proliferation of hematopoietic cells of the macrophage and granulocyte lineages and is used clinically to treat neutropenia and other myeloid disorders. Because of its short circulating half-life, GM-CSF is administered to patients by daily injection. We describe here the engineering of highly potent, long-acting human GM-CSF proteins through site-specific modification of GM-CSF cysteine analogues with a cysteine-reactive poly(ethylene glycol) (PEG) reagent. Thirteen cysteine analogues of GM-CSF were constructed, primarily in nonhelical regions of the protein believed to lie away from the major receptor binding sites. The GM-CSF cysteine analogues were properly processed but insoluble following secretion into the *Escherichia coli* periplasm. The proteins were refolded and purified by column chromatography. Ten of the cysteine analogues could be modified with a 5-kDa maleimide PEG, and seven of the mono-PEGylated proteins were purified by ion-exchange column chromatography. Biological activities of the 13 cysteine analogues and 7 PEGylated cysteine analogues were comparable to that of wild-type GM-CSF in an in vitro cell proliferation assay using human TF-1 cells. One cysteine analogue was modified with larger 10-, 20-, and 40-kDa PEGs, with only minimal loss of in vitro bioactivity. Pharmacokinetic experiments in rats demonstrated that the PEGylated proteins had up to 47-fold longer circulating half-lives than wild-type GM-CSF. These data demonstrate the utility of site-specific PEGylation for creating highly potent, long-acting GM-CSF analogues and provide further evidence that the nonhelical regions of human GM-CSF examined are largely nonessential for biological activity of the protein.

INTRODUCTION

Granulocyte macrophage colony-stimulating factor (GM-CSF) stimulates the proliferation, differentiation, and functional activation of hematopoietic cells of the macrophage and granulocyte lineages. Recombinant human GM-CSF is used clinically to treat a variety of hematopoietic disorders, including reducing the severity of chemotherapy-induced neutropenia, accelerating hematopoietic recovery following bone marrow transplantation, and mobilizing blood progenitor cells for transplantation (*1*, *2*). Recombinant GM-CSF also has shown promise as a treatment for Crohn's disease and as an adjuvant therapy for melanoma (*3*, *4*). A limitation of current GM-CSF products is the fact that GM-CSF has a short circulating half-life (*1*, *2*) and must be administered to patients by daily injection for optimal effectiveness. Development of longer-acting forms of GM-CSF that require less frequent injections would be of significant benefit to patients and healthcare providers.

One method that has been used to prolong the circulating half-lives of protein therapeutics is to modify the protein with poly(ethylene glycol) (PEG) (*5*−*8*). Attachment of PEG to a protein increases the protein's effective size, thus reducing its clearance rate by the kidney and prolonging its circulating half-life. The most commonly used PEG reagents attach to primary and secondary amines on proteins, generally at lysine residues and/or at the N-terminal amino acid. This approach is not optimal for human GM-CSF because the protein contains six lysine residues in addition to the N-terminal amino acid. Five of these lysine residues are located in regions of the protein implicated in receptor binding (*9*, *10*). Site-directed mutagenesis studies showed that Lys72, Lys74, and Lys85 in Helix C and amino acids adjacent to these residues, Gly75 and Gln86, are required for optimal binding of GM-CSF to its receptor (*9*, *10*). The large number and critical locations of these lysine residues makes GM-CSF a poor target for modification with amine-reactive PEG reagents. Indeed, covalent modification of GM-CSF with an amine-reactive PEG reagent resulted in a heterogeneous mixture of mono- and multi-PEGylated GM-CSF variants that could not be separated from each other or from unmodified GM-CSF by conventional column chromatographic procedures (*11*). Additionally, partial loss of bioactivity was observed for the PEGylated GM-CSF mixture, but the effect was difficult to quantitate due to heterogeneity of the sample and inability to separate PEGylated protein from non PEGylated protein (*11*).

An alternative and potentially more selective method for PEGylating proteins covalently attaches PEG to cysteine residues using cysteine-reactive PEGs. At near-neutral pH, these PEG reagents selectively attach to the thiol groups of "free" cysteine residues, i.e., cysteine residues not involved in disulfide bonds. Most proteins, including GM-CSF, do not contain surface-exposed, free cysteine residues. By use of in vitro mutagenesis, it is

* Corresponding author. Tel: (303) 420-4420. Fax: (303) 420-4426. E-mail: jcox@bolderbio.com.
[†] Bolder BioTechnology, Inc.
[‡] BolderPATH, Inc.

10.1021/bc050172r CCC: $30.25 © 2005 American Chemical Society
Published on Web 09/07/2005

possible to introduce a non-native, free cysteine residue into a protein. The non-native cysteine residue can serve as the site for targeted modification of the protein with a cysteine-reactive PEG reagent, thus preserving biological activity of the modified protein (*12*). In this report, we describe the application of this technology to the rational design of highly potent, long acting human GM-CSF analogues.

EXPERIMENTAL PROCEDURES

Cloning of GM-CSF and Construction of GM-CSF Cysteine Analogues. A cDNA encoding human GM-CSF was cloned by the reverse transcriptase−polymerase chain reaction (PCR) method (*13*), using total RNA isolated from the human bladder carcinoma cell line 5637 (obtained from the American Type Culture Collection, Rockville, MD). The leader sequence of the *E. coli* heat-stable enterotoxin (STII) gene (*14*), preceded by an *Nde* I restriction site, was fused to the amino-terminal coding sequence of mature GM-CSF using PCR. At the same time, several changes in the GM-CSF gene were made to optimize the protein for expression in *E. coli*. A TAA stop codon, followed by an *Eco* RI restriction site, was added following the carboxy-terminal residue, E127, codons for prolines at positions 2, 6, 8, 12, 117, and 124 were all changed to CCG, and the codon for leucine at position 114 was changed to CTG. The STII-GM-CSF gene was cloned as a *Nde* I−*Eco* RI fragment into pUC18 (Sigma-Aldrich, Inc., St. Louis, MO), to create pBBT268, and its DNA sequence confirmed. The *Nde* I−*Eco* RI fragment of pBBT268 was subcloned subsequently into plasmid pBBT257, creating pBBT271. Plasmid pBBT257 was derived from the expression vector pCYB1 (New England BioLabs, Beverly, MA) by deleting the ampicillin-resistant gene of pCYB1 and replacing it with the gene for tetracycline resistance derived from plasmid pBR322 (*15*). In both pBBT257 and pCYB1, expression of the cloned gene is under the control of the *tac* promoter. Thirteen mutant GM-CSF genes were constructed by site-directed PCR-based mutagenesis (*16*, *17*) using pBBT268 as the DNA template. PCR products were digested with appropriate restriction endonucleases and cloned into pBBT268 vector DNA. Correct DNA sequences of all mutants were confirmed.

Expression and Purification of Wild-Type GM-CSF and GM-CSF Cysteine Analogues. Plasmids encoding wild-type GM-CSF and GM-CSF cysteine analogues were transformed into *E. coli* strain W3110. An overnight culture of each strain was inoculated at an optical density at 600 nm of ~0.05 in 400 mL of Luria Broth media containing 10 μg/mL tetracycline. When the culture reached an optical density of ~0.6, isopropyl-β-D-thiogalactopyranoside (IPTG) was added to a final concentration of 0.5 mM, and the induced culture was incubated overnight for about 16 h. The cells were pelleted by centrifugation and stored at −80 °C. The cell pellet was thawed and treated with 5 mL of bacterial protein extraction reagent (B-PER, Pierce Chemical Company, Rockford, IL) according to the manufacturer's protocols. Insoluble material was recovered by centrifugation and resuspended in B-PER. This mixture was treated with lysozyme (200 μg/mL) for 10 min to further disrupt the cell walls, and $MgCl_2$ (10 mM final concentration) and protease-free DNAse (2 μg/mL) were added. Insoluble GM-CSF was collected by centrifugation, resuspended in water, and recentrifuged. The insoluble pellet was dissolved in 10 mL of 8 M urea, 25 mM cysteine, and 20 mM Tris Base, stirred for 30 min at room temperature, and diluted into 100 mL of 20 mM Tris, 40 μM copper sulfate, 15% glycerol, pH 8.0. The refold mixture was held at 4 °C for 2 days, centrifuged, and loaded onto a 5-mL Q-Sepharose HiTrap column (Amersham Biosciences Corporation, Piscataway, NJ) equilibrated in 20 mM Tris, pH 8.0 (Buffer A). The bound proteins were eluted with a linear salt gradient from 0 to 35% Buffer B (1 M NaCl, 20 mM Tris, pH 8). Column fractions were analyzed by nonreducing sodium dodecyl sulfate polyacrylamide gel electrophoresis (SDS-PAGE), and fractions containing primarily GM-CSF were pooled. The Q-Sepharose pool was diluted with an equal volume of 30% ammonium sulfate and loaded onto a 1-mL Phenyl HP HiTrap column (Amersham Biosciences Corporation) previously equilibrated with 15% ammonium sulfate in 20 mM sodium phosphate, pH 7.5. GM-CSF was recovered from the column by elution with a reverse salt gradient (15% ammonium sulfate to 0% ammonium sulfate in 20 mM sodium phosphate, pH 7.5). Column fractions were analyzed by nonreducing SDS-PAGE and fractions containing GM-CSF, and no detectable contaminants were pooled.

PEGylation of GM-CSF Cysteine Analogues. Aliquots of 200−300 μg of the purified GM-CSF cysteine analogues were incubated with a 15-fold molar excess of Tris[2-carboxyethylphosphine]hydrochloride (TCEP, Pierce Chemical Company) and a 20-fold molar excess of a linear 5 kDa-maleimide-PEG (Nektar, Inc., Huntsville, AL). After 1.5 h at room temperature, the PEGylation mixture was diluted 20× with ice cold 20 mM Tris, pH 8.0, and loaded onto a 1-mL Q-Sepharose HiTrap column (Amersham Biosciences Corporation) equilibrated in 20 mM Tris, pH 8.0. Bound proteins were eluted as described above. Column fractions were analyzed by nonreducing SDS-PAGE, and fractions containing predominantly the mono-PEGylated GM-CSF cysteine analogue were pooled and stored at −80 °C. This procedure was scaled up to prepare the A3C analogue modified with linear 10- and 20-kDa maleimide PEGs and a branched 40-kDa maleimide PEG (Nektar, Inc.).

Biochemical Methods. N-Terminal protein sequencing was performed by Macromolecular Resources (Colorado State University, Fort Collins, CO) using an Edman degradation procedure. Protein samples were analyzed by SDS-PAGE on precast Tris−glycine polyacrylamide gels (Invitrogen Corporation, Carlsbad, CA) and stained with Coomassie Blue. 2-Mercaptoethanol was added to a final concentration of 1−5% (V/V) in sample buffer to reduce the proteins. Protein concentrations were determined using a Bradford protein assay kit (Bio-Rad Laboratories, Richmond, CA) using bovine serum albumin as the protein standard. Endotoxin levels of the proteins were measured using a chromogenic Limulus Amebocyte Lysate kit (QCL-1000, BioWhittaker, Walkersville, MD). Western blots were performed using standard methods. The primary antibody was polyclonal goat antihuman GM-CSF antisera (R&D Systems, Inc., Minneapolis, MN), and the secondary antibody was alkaline phosphatase-conjugated rabbit antigoat immunoglobulin antisera (Pierce Chemical Company). Western blots were developed using a NBT/BCIP staining kit (Promega Corporation, Madison, WI).

In Vitro Bioactivity Assays. The human TF-1 cell line was obtained from the American Type Culture Collection. The cells were maintained in RPMI 1640 media supplemented with 10% FBS, 50 units/mL penicillin, 50 μg/mL streptomycin, and 2 ng/mL recombinant human GM-CSF (*E. coli* derived; R&D Systems). For bioassays, the TF-1 cells were washed and resuspended at a concentration of 1×10^5/ml in RPMI 1640 media

containing 10% FBS, 50 units/mL penicillin, and 50 μg/mL streptomycin (assay media). Fifty microliters (5×10^3 cells) of the cell suspension was aliquotted per test well of a flat-bottom 96-well tissue culture plate. Serial dilutions of the protein samples to be tested were prepared in assay media. Serial dilutions of a commercial recombinant human GM-CSF standard (*E. coli* expressed; R&D Systems) were analyzed in parallel. Fifty microliters of the diluted protein samples were added to the test wells and the plates incubated at 37 °C in a humidified 5% CO_2 tissue culture incubator. Protein samples were assayed in triplicate wells. After 3 days, 20 μL of CellTiter 96 AQueous One Solution (Promega Corporation) was added to each well and the plates incubated at 37 °C in the tissue culture incubator for 1−4 h. Absorbance of the wells was read at 490 nm using a microplate reader.

Pharmacokinetic Experiments. Animal experiments were performed with the approval of BolderPATH's Institutional Animal Care and Use Committee. Groups of three male Sprague Dawley rats (Harlan Sprague Dawley, Inc., Indianapolis, IN), weighing 340−370 g each, received a single intravenous injection (lateral tail vein) of Leukine (sargramostim, a recombinant yeast-derived human GM-CSF containing a R23L amino acid substitution, Schering AG), wild-type *E. coli* expressed GM-CSF prepared by us, or the GM-CSF A3C cysteine analogue modified with 10-, 20-, or 40-kDa maleimide PEG, each at a dose of 100 μg protein/kg. At selected time points, blood samples (0.4 mL) were drawn from the rats into EDTA anticoagulant tubes. The blood samples were centrifuged and the plasma samples stored at −80 °C. Blood samples were drawn at 0.25, 1, 2, 4, 10, 24, 48, 72, 96, and 120 h after injection. A predose sample was drawn 1 day prior to injection of the test compounds. Plasma levels of the test proteins were quantitated using human GM-CSF enzyme-linked immunosorbent assay (ELISA) kits (R & D Systems, Inc.). Serial dilutions of plasma samples from one animal in each test group were analyzed in the in vitro bioassay to identify dilutions that fell within the linear range of the ELISA (7.8 to 500 pg/mL). Duplicate samples of appropriate dilutions of plasma samples from all rats were then analyzed in the ELISA. A subcutaneous pharmacokinetic experiment was performed in the same manner except that the protein samples were injected subcutaneously into the lateral sides of the rats. Blood samples were drawn at 0.16, 0.5, 1, 2, 4, 10, 24, 48, 72, 96, and 120 h after injection. Pharmacokinetic parameters were analyzed using the WinNonlin software package (Pharsight, Inc., MountainView, CA).

RESULTS

Expression of GM-CSF in *E. coli* Using the STII Signal Sequence. Human GM-CSF was engineered to be secreted to the *E. coli* periplasm by fusing the mature coding region of GM-CSF to the *E. coli* enterotoxin STII signal sequence. The protein was cloned under control of the *tac* promoter and expression of the protein induced by addition of IPTG to the cultures. SDS-PAGE analysis of the overnight induced cultures showed expression of a new 14-kDa protein, which is consistent with the mass of mature GM-CSF. These data suggested that the STII leader peptide had been removed, which was confirmed by the N-terminal sequencing studies presented below. Although GM-CSF appeared to be properly processed and secreted, the recombinant protein was largely insoluble. The insoluble protein was refolded using the procedure described in Experimental Procedures and purified from the refold mixture by Q-Sepharose and Phenyl-Sepharose column chromatography. N-Terminal sequencing of purified GM-CSF yielded the sequence APARSPS, which matches the first seven amino acids of mature human GM-CSF (*18*, *19*), and indicates that the N-terminus is correctly processed. Purified GM-CSF comigrated with an *E. coli* expressed human GM-CSF standard under reducing and nonreducing conditions (Figure 1). Western blots were used for this analysis because the commercial GM-CSF standard is formulated with a protein carrier. Both recombinant GM-CSF proteins exhibited a mobility shift to a higher apparent molecular weight under reducing conditions, presumably due to reduction of the two native intramolecular disulfide bonds, C54−C96 and C88−C121 (*20*). Bioactivities of the proteins were compared in an in vitro cell proliferation assay using human TF-1 cells. Our purified GM-CSF and the GM-CSF standard stimulated proliferation of human TF-1 cells to the same extent and had similar mean EC_{50} values of 105 and 97 pg/mL, respectively (Table 1).

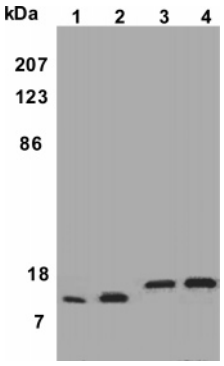

Figure 1. SDS-PAGE analysis of purified wild-type GM-CSF. Western blot of a wild-type GM-CSF standard (lanes 1 and 3; R & D Systems, Inc.) and our purified wild-type GM-CSF (lanes 2 and 4) following nonreducing (lanes 1 and 2) and reducing (lanes 3 and 4) SDS-PAGE. Positions of molecular weight standards are shown to the left.

Table 1. In Vitro Bioactivities of GM-CSF and GM-CSF Cysteine Analogues

GM-CSF protein	added cysteine location[a]	EC_{50} (pg/mL)[b]
GM-CSF[c]		97 ± 5
GM-CSF[d]		105 ± 8
*−1C	N-terminus	111 ± 5
A1C	N-terminus	80 ± 0
A3C	preceding helix A	108 ± 3
S5C	preceding helix A	125 ± 6
S7C	preceding helix A	106 ± 6
N27C	helix A	134 ± 30
S69C	B-C loop	103 ± 10
E93C	C-D loop	103 ± 14
T94C	C-D loop	120 ± 4
T102C	C-D loop	114 ± 3
V125C	following helix D	110 ± 0
Q126C	following helix D	126 ± 9
*128C	C-terminus	124 ± 3

[a] Based on the GM-CSF structure in ref 20. [b] Mean ± SD for at least 4 assays per protein in the TF-1 cell proliferation assay. [c] Wild-type GM-CSF standard (*E. coli* derived, R&D Systems, Inc.). [d] Wild-type GM-CSF prepared by us.

Expression and In Vitro Bioactivities of GM-CSF Cysteine Analogues. Human GM-CSF has a compact globular structure, comprising four α-helices joined by loops (*10*, *20*, *21*). The four α-helices are termed A−D beginning from the N-terminus of the protein. The loop regions are referred to by the helices they join, e.g., the A−B loop joins helices A and B. We constructed 13 GM-CSF cysteine analogues, primarily in the nonhelical

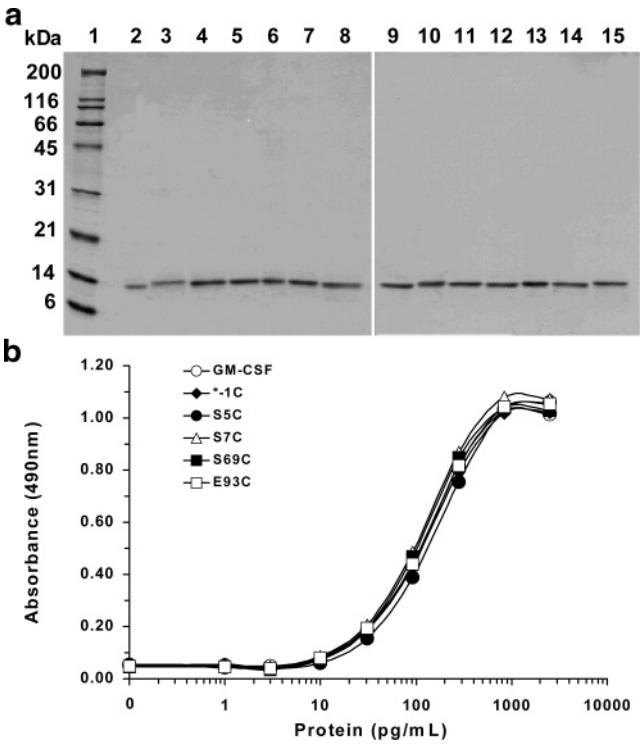

Figure 2. SDS-PAGE analysis and in vitro bioactivities of purified wild-type GM-CSF and GM-CSF cysteine analogues. Panel A shows nonreducing SDS-PAGE analysis of column pools of the purified GM-CSF cysteine analogues. Lane 1, molecular weight standards; Lane 2, wild-type GM-CSF; Lane 3, *−1C; Lane 4, A1C; Lane 5, A3C; Lane 6, S5C, Lane 7, S7C; Lane 8, N27C; Lane 9, S69C; Lane 10, E93C; Lane 11, T94C; Lane 12, T102C; Lane 13, V125C; Lane 14, Q126C; Lane 15, *128C. Proteins were stained with Coomassie Blue. Panel B shows dose−response curves for our wild-type GM-CSF and representative GM-CSF cysteine analogues for stimulating proliferation of TF-1 cells. Data are means of triplicate wells ± standard deviations (SD) from representative experiments. SDs were generally less than 5% of the means.

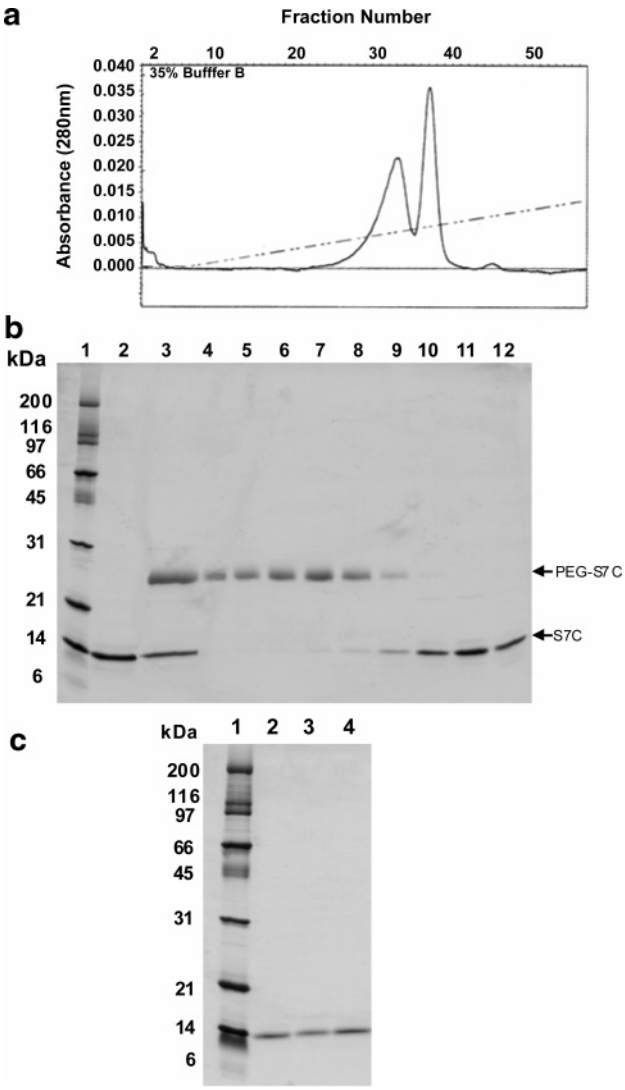

Figure 3. Purification of the PEGylated GM-CSF S7C protein and inability of wild-type GM-CSF to react with maleimide-PEG. Panel A shows Q-Sepharose column chromatography of the S7C PEGylation reaction products. Panel B shows nonreducing SDS-PAGE analysis of the Q-sepharose column fractions. Lane 1, molecular weight standards; Lane 2, S7C; Lane 3, S7C PEGylation reaction products; Lanes 4−12 represent Q-Sepharose column fractions 30−38. Fractions 30−34 (Lanes 4−8) contain predominantly PEGylated S7C. Fractions 36−38 (Lanes 10−12) contain unreacted S7C. Panel C is nonreducing SDS-PAGE analysis of wild-type GM-CSF PEGylation reaction products. Lane 1, molecular weight standards; Lane 2, wild-type GM-CSF; Lane 3, GM-CSF + 5-kDa maleimide−PEG; Lane 4, GM-CSF + 5-kDa maleimide−PEG + TCEP.

regions of the protein, which lie away from the identified receptor binding domains. Five cysteine analogues were constructed in the amino terminal region preceding helix A [*−1C (the addition of a cysteine residue preceding the natural amino terminus), A1C, A3C, S5C, and S7C]; one cysteine analogue was constructed in the B−C loop [S69C]; three cysteine analogues were constructed in the C−D loop [E93C, T94C, and T102C]; and three cysteine analogues were constructed in the carboxy-terminal region following helix D [V125C, Q126C, and *128C (the addition of a cysteine residue to the natural carboxy-terminus)]. We also constructed one cysteine analogue at an N-linked glycosylation site (N27C), which is the last amino acid in helix A. The GM-CSF cysteine analogues were expressed in *E. coli* using the STII signal sequence. Expression studies indicated that the cysteine analogues appeared to be correctly processed but largely insoluble. The cysteine analogues were refolded and purified using the protocols described for wild-type GM-CSF. Recoveries of the purified GM-CSF cysteine analogues ranged from 0.4 to 2.2 mg/400 mL of culture compared to 2.6 mg/400 mL of culture for wild-type GM-CSF. The cysteine analogues were recovered predominantly as monomers that comigrated with wild-type GM-CSF under reducing and nonreducing SDS-PAGE conditions. Nonreducing SDS-PAGE analysis of the 13 purified cysteine analogues is shown in Figure 2A. Mean EC_{50} values of the 13 cysteine analogues ranged from 80 to 134 pg/mL in the TF-1 cell proliferation assay and were similar to the EC_{50} of wild-type GM-CSF (Table 1). Dose−response curves for representative cysteine analogues are shown in Figure 2B.

Preparation and In Vitro Characterization of PEGylated GM-CSF Cysteine Analogues. The 13 purified GM-CSF cysteine analogues were reacted with a 5-kDa maleimide PEG under partial reducing conditions, as described in Experimental Procedures. These conditions yielded significant amounts of mono-PEGylated protein for 10 of the cysteine analogues. No di- or tri-PEGylated proteins were detected for any of the cysteine analogues. PEGylated GM-CSF cysteine analogues were purified from non-PEGylated protein by Q-Sepharose column chromatography (Figure 3A). Figure 3B, lane 3, shows nonreducing SDS-PAGE analysis of the PEGylation reaction for a representative cysteine ana-

Table 2. PEGylation Efficiencies and In Vitro Bioactivities of PEGylated GM-CSF Cysteine Analogues

GM-CSF analog	PEG size	PEGylation efficiency (%)[a]	EC_{50} (pg/mL)[b]
*−1C	5 kDa	45, 55	96 ± 5
A1C	5 kDa	55	115 ± 4
A3C	5 kDa	62	106 ± 3
A3C	10 kDa	70	78 ± 3
A3C	20 kDa	75	113 ± 5
A3C	40 kDa	70, 70	300 ± 50
S5C	5 kDa	76	80 ± 11
S7C	5 kDa	50, 70, 89	123 ± 15
S69C	5 kDa	71	88 ± 6
E93C	5 kDa	62	86 ± 5

[a] Percent PEGylated protein estimated by anion-exchange column chromatography of PEGylation reactions. Numbers represent results from individual PEGylation reactions. [b] Mean ± SD of at least 4 assays for each protein in the TF-1 cell proliferation assay.

logue, S7C. The only visible PEGylated species is the PEG-S7C monomer, which migrates with an apparent molecular mass of 26 kDa. Fractionation of the S7C PEGylation reaction mixture by Q-Sepharose column chromatography yielded two major peaks. SDS-PAGE analysis of the column fractions indicated that the early eluting peak was mono-PEGylated S7C, and the later eluting peak was unmodified S7C protein (Figure 3B). Fractions enriched for the mono-PEGylated S7C protein were pooled. The other GM-CSF cysteine analogues were PEGylated and purified by the same protocol. PEGylation efficiencies for the cysteine analogues were estimated from the peak areas of the Q-Sepharose column chromatograms and ranged from 11 (T102C) to 89% (S7C), with most analogues being in the 40−70% range (Table 2). No PEGylated products were observed for the three cysteine analogues near the C-terminus of the protein, V125C, Q126C, or *128C using these conditions. Wild-type GM-CSF did not PEGylate under the conditions used to PEGylate the cysteine analogues (Figure 3C), which strongly suggests that the site of PEGylation in the cysteine analogues is the newly introduced cysteine residue and not one of the four native cysteine residues.

Nonreducing SDS-PAGE analysis of the 10 purified PEGylated cysteine analogues is shown in Figure 4A. The PEGylated proteins displayed similar apparent molecular masses (26 kDa) by nonreducing SDS-PAGE, except for the PEG-E93C and PEG-T94C analogues, which displayed slightly smaller apparent molecular masses. The reason for this difference is unknown, although it may be significant that these analogues are adjacent residues in the C−D loop. Sufficient quantities of seven cysteine analogues (*−1C, A1C, A3C, S5C, S7C, S69C, and E93C) modified with a 5-kDa PEG were purified for accurate protein concentration and bioactivity measurements. Mean EC_{50} values for the PEG−GM−CSF cysteine analogues ranged from 80 to 123 pg/mL in the TF-1 cell proliferation assay and were similar to the EC_{50} of wild-type GM-CSF (Table 2). Dose−response curves for representative PEGylated GM-CSF cysteine analogues are shown in Figure 4.

The A3C protein was PEGylated with larger 10- and 20-kDa maleimide PEGs and a 40-kDa branched maleimide PEG and the PEGylated proteins purified by Q-Sepharose column chromatography as described above. SDS-PAGE analysis of the purified PEG-A3C proteins is shown in Figure 5A. Bioactivity experiments yielded mean EC_{50} values of 78, 113, and 300 pg/mL for the 10-, 20-, and 40-kDa PEG−A3C proteins in the TF-1 cell proliferation assay (Figure 5B and Table 2).

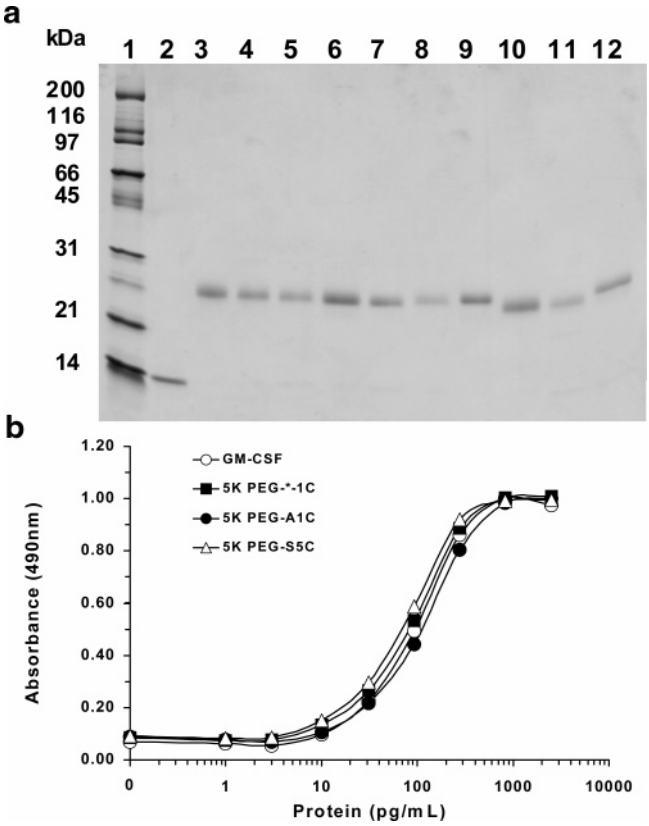

Figure 4. SDS-PAGE analysis and in vitro bioactivities of purified 5-kDa maleimide PEG−GM-CSF cysteine analogues. Panel A shows nonreducing SDS-PAGE analysis of column pools of purified PEG−GM-CSF cysteine analogues. Lane 1, molecular weight standards; Lane 2, wild-type GM-CSF; Lane 3, 5-kDa PEG−*-1C; Lane 4, 5-kDa PEG−A1C; Lane 5, 5-kDa PEG−A3C; Lane 6, 5 -kDa PEG−S5C; Lane 7, 5-kDa PEG−S7C; Lane 8, 5-kDa PEG−N27C; Lane 9, 5-kDa PEG−S69C; Lane 10, 5-kDa PEG−E93C; Lane 11, 5-kDa PEG−T94C; Lane 12, 5-kDa PEG−T102C. Proteins were stained with Coomassie Blue. Panel B shows dose−response curves for 5-kDA PEG−GM-CSF cysteine analogues and our wild-type GM-CSF for stimulating proliferation of TF-1 cells. Data are means of triplicate wells ± SD from representative experiments. SDs were generally less than 5% of the means.

Pharmacokinetic Experiments With PEGylated A3C Proteins. Circulating half-lives of the A3C protein modified with 10- and 20-kDa PEGs were determined by ELISA following intravenous administration to rats (Figure 6A). A commercial yeast-derived GM-CSF analogue (Leukine) and our *E. coli* derived wild-type GM-CSF were analyzed in parallel. Blood levels of the proteins were measured from 0.25 to 120 h after injection. Both Leukine and wild-type GM-CSF cleared rapidly from the rats and were undetectable 24 h after injection. Terminal half-lives for Leukine and wild-type GM-CSF were 0.9 and 1 h, respectively. In contrast, the PEGylated A3C proteins possessed significantly longer circulating half-lives. Both the initial distribution phase and the terminal half-life phase were longer for the PEGylated A3C proteins than for the wild-type GM-CSF proteins. Terminal half-lives for 10- and 20-kDa PEG−A3C proteins were 19 and 22 h, respectively. In a separate experiment, the terminal half-life of the 40-kDa PEG−A3C was determined to be 37 h following intravenous administration to rats (data not shown).

Half-lives of Leukine and the 10-, 20-, and 40-kDa PEG−A3C proteins also were determined following subcutaneous administration to rats. Blood levels of the proteins were measured from 0.16 to 120 h after injection

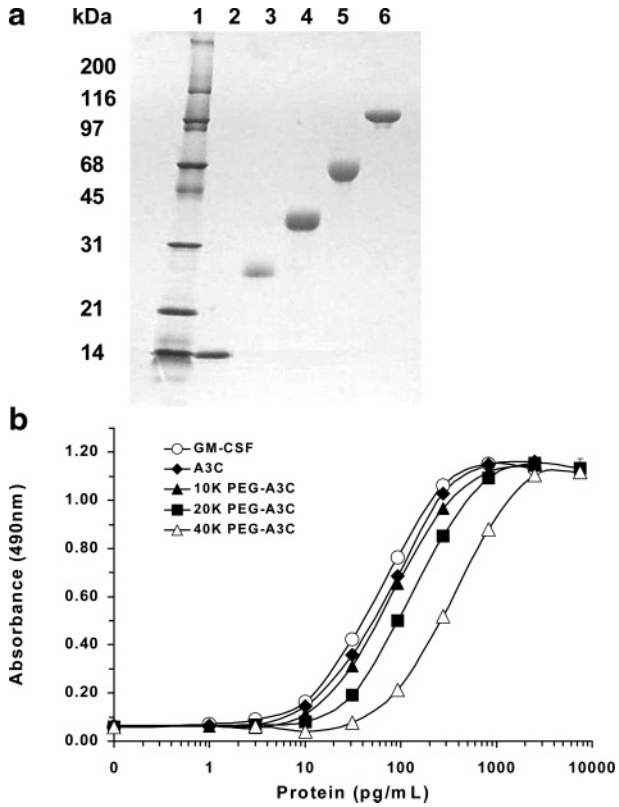

Figure 5. SDS-PAGE analysis and in vitro bioactivities of the GM-CSF A3C protein modified with different-sized PEGs. Panel A shows nonreducing SDS-PAGE analysis of the purified proteins. Lane 1, molecular weight standards; Lane 2, wild-type GM-CSF; Lanes 3−6 are column pools of the A3C protein modified with 5-, 10-, 20-, and 40-kDa maleimide−PEGs, respectively. Panel B shows dose−response curves for the 10-, 20-, and 40-kDa PEG−A3C proteins for stimulating proliferation of TF-1 cells. SDs were generally less than 5% of the means.

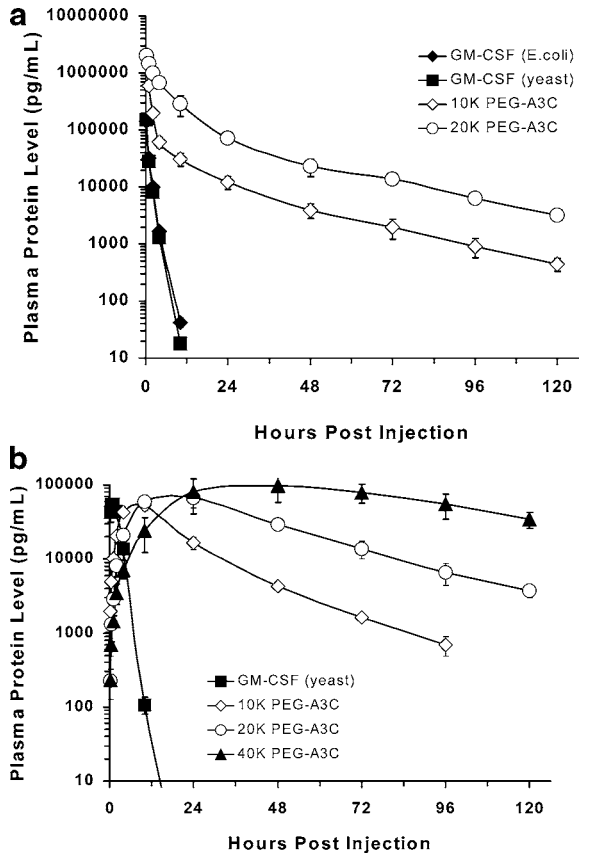

Figure 6. Circulating plasma levels of Leukine, *E. coli* derived wild-type GM-CSF and the GM-CSF−A3C protein modified with different-sized PEGs following (A) intravenous or (B) subcutaneous administration in rats. Data are means ± SD for three rats per group and were measured using human GM-CSF ELISAs. SDs were generally less than 25% of the means. The 120-h time point samples for the 10-kDa PEG−A3C protein in the subcutaneous study shown in (B) were lost and could not be analyzed.

and are shown in Figure 6B. Leukine reached maximum blood levels between 30 and 60 min after injection and decreased by greater than 10 000-fold to undetectable levels by 24 h after injection. The terminal half-life was 1 h. In contrast, blood levels of the 10-, 20-, and 40-kDa PEG−A3C proteins reached maximum levels at 10, 24, and 48 h after injection, respectively, indicating that the PEGylated proteins are absorbed more slowly than Leukine from the injection site. Terminal half-lives for the proteins were 14 h (10-kDa PEG−A3C), 23 h (20-kDa PEG−A3C), and 47 h (40-kDa PEG−A3C).

DISCUSSION

We found that wild-type human GM-CSF and human GM-CSF cysteine analogues can be secreted efficiently into the *E. coli* periplasm using the *E. coli* STII signal sequence. Although the STII signal sequence is correctly processed, the secreted proteins are insoluble and must be refolded into a biologically active form. Refolded GM-CSF comigrates with intracellular expressed *E. coli* GM-CSF and has a comparable specific activity in an in vitro cell proliferation assay using human TF-1 cells. Similar results were obtained using the bacterial ompA signal sequence to secrete human GM-CSF into the *E. coli* periplasm (*22*, *23*).

To identify sites in GM-CSF where a cysteine residue can be introduced and PEGylated without significantly affecting biological activity of the protein, we constructed a series of cysteine analogues in regions of the protein believed to lie away from the major receptor binding sites, which have been localized to helices A, C, and D (*9*, *10*, *24*−*27*). The 13 GM-CSF cysteine analogues analyzed possessed in vitro biological activities comparable to wild-type GM-CSF. The large number of highly active GM-CSF cysteine analogues identified was somewhat unexpected but probably biased by our choice of mutation sites. These data provide support for the notion that the regions of GM-CSF chosen for mutagenesis (the region preceding helix A, the B−C loop, the C−D loop, the region following helix D, and the N27 glycosylation site at the C-terminal end of helix A) are largely nonessential for proper in vitro biological activity of GM-CSF. The nonessential nature of these regions was explored further by attaching a large polymer, PEG, to the proteins at the cysteine residues introduced into these regions. All of the cysteine analogues, except those analogues located near the C-terminus of the protein, reacted with a maleimide PEG using our standard reaction conditions, yielding monoPEGylated proteins. Seven of the mono-PEGylated proteins were purified and their in vitro biological activities found to be similar to that of wild-type GM-CSF. These data strongly suggest that the amino acids analyzed (*−1, A1, A3, S5, S7, S69, and E93) and the regions in which they are located (the region preceding helix A, the B−C loop, and the C−D loop) are largely nonessential for *in vitro* biological activity of GM-CSF. Most of the in vitro bioactivity measurements for the GM-CSF cysteine analogues and PEGylated GM-CSF cysteine analogues were obtained from single preparations of the proteins. It remains to be determined

whether the minor differences observed in in vitro bioactivities of the proteins are due to intrinsic differences in bioactivities of the proteins or to other variables associated with purification, PEGylation, and quantitation of the proteins.

The three cysteine analogues introduced near the C-terminus of the protein, V125C, Q126C, or *128C, did not PEGylate using our standard PEGylation conditions. On the basis of the published structure of GM-CSF (*20*, *21*), these residues appear to be surface exposed and should be accessible to react with the PEG reagents. The C-terminal region of GM-CSF contains a short loop held together by a disulfide bond between residues C88 and C121 (*20*). It is possible that this disulfide loop, or another feature of this region, alters the local structure of the C-terminal region in a way that makes these residues unreactive with the PEG reagent. Other reaction conditions or use of other types of cysteine-reactive PEG reagents may permit modification of these residues. Studies with human growth hormone revealed that only selected surface-exposed lysine residues are modified by amine-reactive PEG reagents (*28*). These data, and those described here, indicate that surface accessibility is only one factor determining whether a particular amino acid residue will react with a PEG reagent.

With the A3C analogue, we explored the effect of different-sized PEGs on in vitro biological activity and circulating half-life of the protein. We found that modification of the A3C protein with linear 5-, 10-, and 20-kDa PEG reagents did not substantially affect in vitro biological activity of the protein, as measured by EC_{50} values in the TF-1 cell proliferation assay. Only when the protein was modified with a large, 40-kDa branched maleimide PEG did we detect an obvious decrease in in vitro bioactivity, but even this decrease was moderate (3-fold). Although this result is based upon a single preparation of the 40-kDA PEG−A3C protein, it is consistent with results by us (*29* and unpublished results) and others (*8*) showing greater loss of in in vitro bioactivity when proteins are modified with 40-kDa branched PEGs than with smaller, linear PEGs. Pharmacokinetic experiments demonstrated that the PEGylated GM-CSF (A3C) proteins have up to 47-fold longer circulating half-lives than unmodified GM-CSF proteins in rats. Circulating half-lives of the proteins correlated with the size of the PEG molecule, similar to what has been reported for other PEGylated proteins (*6*). Human GM-CSF is inactive in rodents due to a failure to bind rodent GM-CSF receptors (*19*). Since receptor-mediated endocytosis is one mechanism for promoting in vivo clearance of hematopoietic factors (*30*), the pharmacokinetic parameters obtained for the PEG-A3C protein in rats probably reflect primarily clearance of the protein by kidney filtration. The failure of human GM-CSF to function in rodents precluded us from measuring biological activities of the PEG-A3C proteins in these experiments. In studies to be reported elsewhere, we find that a site-specific PEGylated mouse GM-CSF homologue of human GM-CSF (A3C) is much more potent than mouse GM-CSF at stimulating granulopoiesis in rats (Lee, Rosendahl, Hughes, Cox, and Doherty, manuscript in preparation). Other researchers reported that a PEGylated murine GM-CSF protein was more effective than unPEGylated murine GM-CSF at expanding and stimulating differentiation of dendritic cells in mice (*31*, *32*).

The PEG−GM-CSF cysteine analogues described here have significantly different structural and biological properties than previously described nonspecific, amine-PEGylated GM-CSF proteins (*11*, *33*). Amine-PEGylated GM-CSF comprises a heterogeneous mixture of different molecular weight PEG−GM-CSF species modified at multiple amine groups and containing different numbers of PEG molecules. The various amine-PEGylated GM-CSF species could not be purified from each other or from nonPEGylated GM-CSF by conventional chromatography procedures, which prevented specific activity measurements of the various isoforms from being determined. An amine-PEGylated murine GM-CSF protein in which PEG is preferentially attached to the N-terminus of the protein has been described (*31*, *32*), but in vitro bioactivity and physical properties of the protein have not been reported. By contrast, each of the PEG−GM-CSF cysteine analogues described here is homogeneously modified at a single unique residue and can be readily purified from nonPEGylated GM-CSF by ion-exchange chromatography and possesses a specific activity in in vitro bioassays similar to wild-type GM-CSF. The high potency and long circulating half-lives of these site-specific PEGylated GM-CSF analogues warrant further investigation of their potential utility as human therapeutics.

ACKNOWLEDGMENT

This research was supported by Grant CA84850 from the National Cancer Institute to D.D. The publication's contents are solely the responsibility of the authors and do not necessarily represent the official views of the National Cancer Institute. We thank Sharon Carlson for preparing the figures and Stephen Eisenberg and Stacie Froelich for comments on the manuscript.

LITERATURE CITED

(1) Cebon, J. S., and Lieschke, G. J. (1994) Granulocyte-macrophage colony-stimulating factor for cancer treatment. *Oncology 51*, 177−188.

(2) Armitage, J. O. (1998) Emerging applications of recombinant human granulocyte-macrophage colony-stimulating factor. *Blood 92*, 4491−4507.

(3) Dieckgraefe, B. K., and Korzenik, J. R. (2002) Treatment of active Crohn's disease with recombinant human granulocyte-macrophage colony-stimulating factor. *Lancet 360*, 1478−1480.

(4) Spitler, L. E., Grossbard, M. L., Ernstoff, M. S., Silver, G., Jacobs, M., Hayes, F. A., and Soong, S. J. (2000) Adjuvant therapy of stage III and IV malignant melanoma using granulocyte-macrophage colony-stimulating factor. *J. Clin. Oncol. 18*, 1603−1605.

(5) Abuchowski, A., Kazo, G. M., Verhoest, C. R., Van Es, T., Kafkewitz, D., Nucci, M. L., Viau, A. T., and Davis, F. F. (1984) Cancer therapy with chemically modified enzymes. I. Antitumor proterties of poly(ethylene glycol)-asparaginase conjugates. *Cancer Biochem. Biophys. 7*, 175−186.

(6) Knauf, M., Bell, D., Hirtzer, P., Luo, Z., Young, J., and Katre, N. V (1988) Relationship of effective molecular size to systemic clearance in rats of recombinant interleukin-2 chemically modified with water-soluble polymers. *J. Biol. Chem. 263*, 15064−15070.

(7) Molineux, G., Kinstler, O., Briddell, B., Hartley, C., McElroy, P., Kerzic, P., Sutherland, W., Stoney, G., Kern, B., Fletcher, F. A., Cohen, A., Korach, E., Ulich, T., McNiece, I., Lockbaum, P., Miller-Messana, M. A., Gardner, S., Hunt, T., and Schwab, G. (1999) A new form of filgrastim with sustained duration in vivo and enhanced ability to mobilize PBPC in both mice and humans. *Exp. Hematol*. 27, 1724−1734.

(8) Bailon, P., Palleroni, A., Schaffer, C. A., Spence, C. L., Fung, W.-J., Porter, J. E., Ehrlich, G. K., Pan, W., Xu, Z.-X., Modi, M. W., Farid, A., and Berthold, W. (2001) Rational design of a potent, long-acting form of interferon: a 40 kDa branched poly(ethylene glycol)-conjugated interferon α2a for the treatment of hepatitis C. *Bioconjugate Chem. 12*, 195−202.

(9) Meropol, N. J., Altmann, S. W., Shanafelt, A. B., Kastelein, R. A., Johnson, G. D., and Prystowsky, M. B. (1992) Requirement of hydrophilic amino-terminal residues for granulocyte-macrophage colony-stimulating factor bioactivity and receptor binding. *J. Biol. Chem*. *267*, 14266−14269.

(10) Rozwarski, D. A., Diederichs, K., Hecht, R., Boone, T., and Karplus, P. A. (1996) Refined crystal structure and mutagenesis of human granulocyte-macrophage colony-stimulating factor. *Proteins 26*, 304−313.

(11) Malik, F., Delgado, C., Knusli, C., Fisher, D., and Francis, G. E. (1992) Poly(ethylene glycol) PEG)-modified granulocyte-macrophage colony-stimulating factor (GM-CSF) with conserved biological activity. *Exp. Hematol*. *20*, 1028−1035.

(12) Goodson, R. J., and Katre, N. V. (1990) Site-directed pegylation of recombinant interleukin-2 at its glycosylation site. *Biotechnology 8*, 343−346.

(13) Kawasaki, E. S. (1990) Amplification of RNA. *PCR Protocols: A Guide to Methods and Applications* (Innis, M. A., Gelfand, D. H., Sninsky, J. J., White, T. J., Eds.). pp 21−17. Chapter 3, Academic Press, San Diego, CA.

(14) Picken, R. N., Mazaitis, A. J., Maas, W. K., Rey, M., and Heyneker, H. (1983) Nucleotide sequence of the gene for heat-stable enterotoxin II of *Escherichia coli*. *Infect. Immun*. *42*, 269−275.

(15) Bolivar, F., Rodriguez, R. L., Greene, P. J., Betlach, M. C., Heyneker, H. L., Boyer, H. W., Crosa, J. H., and Falkow, S. (1977) Construction and characterization of new cloning vehicles II. A multipurpose cloning system. *Gene 2*, 95−113.

(16) Higuchi, R. (1990) Recombinant PCR. In *PCR Protocols: A Guide to Methods and Applications* (Innis, M. A., Gelfand, D. H, Sninsky, J. J., and White, T. J. Eds.). pp 177−183. Chapter 22, Academic Press, San Diego, CA.

(17) Horton, R. M. (1993) In Vitro Recombination and mutagnesis of DNA. SOIng together tailor-made genes. *Methods in Molecular Biology, Vol. 15: PCR Protocols: Current Methods and Applications* (White, B. A., Ed.). pp 251−266, Chapter 25, Humana Press, Totawa, NJ.

(18) Cantrell, M. A., Anderson, D., Cerretti, D. P., Price, V., McKereghan, K., Tushinski, R. J., Mochizuki, D. Y., Larsen, A., Grabstein, K., Gillis, S., and Cosman, D. (1985) Cloning, sequence and expression of a human granulocyte/macrophage colony-stimulating factor. *Proc. Natl. Acad. Sci. U.S.A.* 82, 6250−6254.

(19) Lee, F., Yokota, T., Otsuka, T., Giemmell, L., Larson, N., Luh, J., Arai, K.-I., and Rennick, D. (1985) Isolation of cDNA for a human granulocyte-macrophage colony-stimulating factor by functional expression in mammalian cells. *Proc. Natl. Acad. Sci. U.S.A. 82*, 4360−4364.

(20) Walter, M. R., Cook, W. J., Ealick, S. E., Nagabhushan, T. L., Trotta, P. T., and Bugg, C. E. (1992) Three-dimensional structure of recombinant human granulocyte-macrophage colony-stimulating factor. *J. Mol. Biol. 224*, 1075−1085.

(21) Diederichs, K., Boone, T., and Karplus, A. (1991) Novel fold and putative receptor binding site of granulocyte-macrophage colony-simulating factor. *Science 254*, 1779−1782.

(22) Libby, R. T., Braedt, G., Kronheim, S. R., March, C. J., Urdal, D. L., Chiaverotti, T. A., Tushinski, R. J., Mochizuki, D. Y., Hopp, T. P., and Cosman, D. (1987) Expression and purification of native human granulocyte-macrophage colony-stimulating factor from an *Escherichia coli* secretion vector. *DNA 6*, 221−229.

(23) Greenberg, R., Lundell, D., Alroy, Y., Bonitz, S., Condon, R., Fossetta J., Frommer, B., Gewain, K., Katz, M., Leibowitz, P. J., Narula, S. K., Kastelein, R., and Van Kimmenade, A. (1988) Expression of biologically active, mature human granulocyte-macrophage colony-stimulating factor with an *E. coli* secretory expression system. *Curr. Microbiol. 17*, 321−332.

(24) Clark-Lewis, I., Lopez, A. F., To, L. B., Vadas, M. A., Schrader, J. W., Hood, L. E., and Kent, S. B. (1988) Structure−function studies of human granulocyte-macrophage colony-stimulating factor. *J. Immunol*. *141*, 881−889.

(25) Shanafelt, A. B., and Kastelein, R. A. (1989) Identification of critical regions in mouse granulocyte-macrophage colony-stimulating factor by scanning deletion analysis. *Proc. Natl. Acad. Sci. U.S.A. 86*, 4872−4876.

(26) Kanamura, Y., Cannistra, S. A., Brown, C. B., Nakamura, M., Seelig, G. F., Prosise, W. W., Hawkins, J. C., Kaushansky, K., and Griffin, J. D. (1991) Identification of functionally distinct domains of human granulocyte-macrophage colony-stimulating factor using monoclonal antibodies. *Blood 77*, 1033−1043.

(27) Brown, C. B., Pihl, C. E., and Kaushansky, K. (1994) Mapping of granulocyte-macrophage colony-stimulating factor domains interacting with the human granulocyte-macrophage colony-stimulating factor receptor alpha subunit. *Eur. J. Biochem. 225*, 873−880.

(28) Clark, R., Olson, K., Fuh, G., Marian, M., Mortensen, D., Teshima, G., Chang, S., Chu, H., Mukku, V., Canova- Davis, E., Somers, T., Cronin, M., Winkler, M., and Wells, J. A. (1996) Long-acting growth hormones produced by conjugation with poly(ethylene glycol). *J. Biol. Chem*. *271*, 21969−21977.

(29) Rosendahl, M. S., Doherty, D. H., Smith, D. J., Carlson, S. J., Chlipala, E. A., and Cox, G. N. (2005) A long-acting, highly potent interferon alpha-2 conjugate created using site-specific PEGylation. *Bioconjugate Chem. 16*, 200−207.

(30) Kuwabara, T., Kato, Y., Kobayashi, S., Suzuki, H., and Sugiyama, Y. (1994) Nonlinear pharmacokinetics of a recombinant human granulocyte colony-stimulating factor derivative (nartograstim): species differences among rats, monkeys and humans. *JPET 271*, 1535−1543.

(31) Daro, E., Pulendran, B., Brasel, K., Teepe, M., Pettit, D., Lynch, D. H., Vremec, D., Robb, L., Shortman, K., McKenna, H. J., Maliszewski, C. R., and Maraskovsky, E. (2000) Poly-(ethylene glycol)-modified GM-CSF expands CD11b^{high} CD11c^{high} but not CD11b^{low} CD11c^{high} murine dendritic cells in vivo: a comparative analysis with Flt3 ligand. *J. Immunol. 165*, 49−58.

(32) Daro, E., Butz, E., Smith, J., Teepe, M., Maliszewski, C. R., and McKenna, H. J. (2002) Comparison of the functional properties of murine dendritic cells generated in vivo with Flt3 ligand, GM-CSF and Flt3 ligand plus GM-CSF. *Cytokine 17*, 119−130.

(33) Knusli, C., Delgado, C., Malik, F., Domine, M., Tejedor, M. C., Irvine, A. E., Fisher, D., and Francis, G. E. (1992) Poly-(ethylene glycol) (PEG) modification of granulocyte-macrophage colony- stimulating factor (GM-CSF) enhances neutrophil priming but not colony stimulating activity. *Brit. J. Haematol*. *82*, 654−663.

BC050172R

Glycomimetics as Decorating Motifs for Oligonucleotides: Solid-Phase Synthesis, Stability, and Hybridization Properties of Carbopeptoid–Oligonucleotide Conjugates

Jennifer D'Onofrio, Marcella de Champdoré, Lorenzo De Napoli, Daniela Montesarchio,* and Giovanni Di Fabio

Dipartimento di Chimica Organica e Biochimica, Università degli Studi di Napoli "Federico II", Complesso Universitario di Monte S. Angelo, via Cynthia, 4, I-80126 Napoli, Italy. Received June 6, 2005

The online solid-phase synthesis of oligonucleotides conjugated at the 3′ end with [1–6]-linked oligosaccharide mimics having the O-glycosidic linkages replaced by amide bonds is here described. The assembly of the carbohydrate domain has been carried out by exploiting classical solid phase peptide synthetic protocols, starting from solid supports functionalized with 1-azido sugars, in association with suitably protected 1-azido uronic acids of glucose and lactose, chosen as model addition monomers. After the insertion of a flexible linker, elongation of the oligodeoxyribonucleotide (ODN) chain was performed by standard automated phosphoramidite protocols. 3′-Glycoconjugated 18-mers exhibited an increased enzymatic stability with respect to the same unmodified ODN sequence. UV thermal denaturation experiments showed that the presence of the oligosaccharide tail at the 3′ end of the oligonucleotides did not negatively interfere with their duplex formation abilities.

INTRODUCTION

The development of efficient therapeutic agents based on oligonucleotide molecules has been largely hampered by their reduced bioavailability, mainly due to the characteristic polyanionic nature. Poor intracellular delivery, limited access to the specific target, and low resistance to nucleases are the major obstacles to the in vivo efficacy of synthetic, nonmodified oligodeoxyribonucleotides (ODNs) and therefore to their use as gene expression regulators in antisense (*1*), antigene (*2*), or aptamer (*3*) strategies. The low biostability in cells has emerged as the most relevant limit to in vivo applications of synthetic ODNs containing only 3′–5′ phosphodiester linkages. Many research efforts have been devoted, in the past decade, to overcome these drawbacks (*4*–*7*). Oligonucleotide analogues having the 3′ end masked with protecting residues generally show a consistently increased in vivo half life, not being recognized by 3′ exonucleases, by far the most abundant nucleases in cells. Therefore 3′ conjugation with suitable appendages, imparting specific, desirable physicochemical properties, is usually considered as a necessary prerequisite for ODNs to exert their functions within the cell. In addition to conferring enhanced enzymatic resistance, an ideal conjugating molecule should be designed to improve the cellular uptake and avoid endosomal accumulation of ODNs. In this frame, oligosaccharides offer several advantages. First of all, their fundamental role in cell-to-cell communication is largely accepted, as well as their recognition properties by specific surface membrane receptors (lectins) (*8*–*11*). Second, it is possible to largely modulate their properties, by a priori determining composition, length, and stereochemistry of these biopolymers. An enormous progress has been recently made in oligosaccharide synthesis, so that efficient protocols, even in the solid phase, are available to synthesize tailored oligosaccharidic structures, by sequentially adding the chosen scaffolds under strict regio- and stereocontrol (*12*–*15*). Still, further optimization of the existing chemistry is needed before the construction of any saccharidic skeleton reaches the same reliability and efficiency currently achieved in the solid-phase synthesis of peptides and oligonucleotides, so that a complete automation of the synthetic process can be accomplished. The picture is more complicated if the target molecules are oligosaccharide–oligonucleotide hybrids (*16*). In fact, in addition to the intrinsic difficulties in generating the desired *O*-glycosidic linkages in the carbohydrate domain, the still unsolved, nontrivial problems related to the compatibility between the two chemistries do not allow a general and simple online synthesis. For example, in an online synthetic protocol involving first the assembly of the oligonucleotide chain, the successive glycosidation procedure for the direct insertion of saccharide monomers at the 5′-OH end of the ODN can cause non-negligible depurination, thus leading to failure sequences (*17*).

Because of the flourishing interest in glycobiology, glycomimetics have emerged as a field in rapid evolution (*18*, *19*). In fact, by selecting suitable mimics, a wide number of more stable and easy-to-handle oligosaccharidic surrogates can be efficiently prepared. In principle, many synthetic problems can thus be escaped while still maintaining the carbohydrate scaffolds, putatively responsible for the biological activity, in the required presentation of the crucial stereocenters.

In our ongoing studies on the solid-phase synthesis of modified and/or conjugated oligonucleotides, we recently reported a straightforward protocol for the preparation of ODNs conjugated with oligosaccharide mimics having phosphodiester bonds as the interglycosidic linkages (*20*, *21*). Particularly, glucose–phosphate or sucrose–phosphate moieties, chosen as model compounds, have been inserted at both ends of oligonucleotides. This strategy is based on the usage of ad hoc functionalized solid

* To whom correspondence may be addressed. Phone: +39-081-674126/27/41. Fax: +39-081-674393. E-mail: montesar@unina.it.

10.1021/bc0501606 CCC: $30.25 © 2005 American Chemical Society
Published on Web 09/08/2005

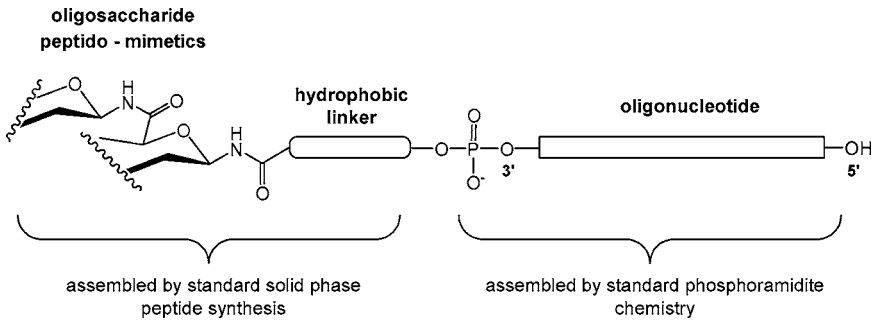

Figure 1. General structure of the synthesized carbopeptoid−oligonucleotide conjugates.

supports and appropriate phosphoramidite derivatives of the mono- or disaccharide compound, which can be incorporated in the growing chain at the last step of automated oligonucleotide syntheses. Thus it is possible to exploit efficient and high fidelity reactions, based on standard phosphoramidite chemistry, to generate chemically and enzymatically stable phosphodiester linkages tethering one or more saccharide residues at both ends of the oligonucleotide backbone.

With the aim of exploring different types of glycomimetics, fully compatible with the oligonucleotide chemistry and, more in general, with solid-phase synthetic methods, we here describe the online solid-phase assembly of oligonucleotide hybrids conjugated at the 3′ end with oligosaccharide mimics in which the *O*-glycosidic linkages are replaced by amide bonds (Figure 1). These glycomimetics, for which Nicolaou and co-workers introduced the term "carbopeptoids" (*22*), can be assembled by exploiting easy and high-yielding coupling procedures, well optimized in solution (*23*−*25*), and solid-phase peptide synthesis (*26*−*28*). Oligomers based on such structural motifs can adopt well-defined secondary structures, stabilized by intramolecular hydrogen bonds in solution (*29*), and therefore result attractive foldamers, of interest for their potential selective recognition properties.

MATERIALS AND METHODS

All reagents were of the highest commercially available quality and were used as received. 1,3-Propanedithiol was distilled prior use. Tentagel-NH_2 resin (0.29 meq/g) was purchased from NovaBiochem. The solid support functionalizations were carried out in a short glass column (5 cm length, 1 cm i.d.) equipped with a sintered glass filter, a stopcock, and a cap. The oligonucleotides were assembled on an Expedite PerSeptive Biosystems DNA synthesizer, using commercially available 3′-*O*-(2-cyanoethyl)-*N*,*N*-diisopropylphosphoramidite 2′-deoxyribonucleosides as building blocks.

The following abbreviations were used throughout the text: acetic anhydride (Ac_2O); dichloroacetic acid (DCA); dichloromethane (DCM); diisopropylcarbodiimide (DIC); diisopropylethylamine (DIPEA); *N*,*N*-dimethylaminopyridine (DMAP); *N*,*N*-dimethylformamide (DMF); 4,4′-dimethoxytriphenylmethyl (DMT); *O*-(7-azabenzotriazol-1-yl)-N,N,N′,N′-tetramethyluronium hexafluorophosphate (HATU); 1-hydroxybenzotriazole (HOBt); oligodeoxyribonucleotide (ODN); *p*-toluensulfonic acid (PTSA); pyridine (Py); triethylamine (TEA); trifluoroacetic acid (TFA); triethylammonium bicarbonate (TEAB); *tert*-butyldimethylsilyl (TBDMS); trimethylsilyl azide ($TMSN_3$).

High-performance liquid chromatography (HPLC) analyses and purifications were performed on a Beckman System Gold instrument equipped with a UV detector module 166 and a Shimadzu Chromatopac C-R6A integrator. By HPLC analysis on a Partisphere Whatman RP18 analytical column (125 × 4.0 mm, 5 μm), eluted with a linear gradient from 0 to 100% in 60 min of CH_3CN in TEAB buffer (0.1 M, pH 7.0), flow = 0.8 mL/min, the isolated oligomers **I**−**III** resulted to be more than 98% pure. NMR spectra were recorded on Bruker WM-400, Varian Gemini 300, Varian Gemini 200, and Varian Inova 500 spectrometers. All chemical shifts are expressed in ppm with respect to the residual solvent signal. Peak assignments have been carried out on the basis of H−H correlation spectroscopy and HSQC experiments. For the electrospray ionization spectroscopy mass spectrometry (ESI MS) analyses, a Waters Micromass ZQ instrument, equipped with an electrospray source, was used in the positive and/or negative mode. Matrix-assisted laser desorption ionization time-of-flight (MALDI TOF) mass spectrometric analyses were performed on a PerSeptive Biosystems Voyager-De Pro MALDI mass spectrometer in the linear mode using a picolinic/3-hydroxypicolinic acids mixture as the matrix. UV measurements and thermal denaturation experiments (detection at λ = 260 nm) were carried out on a Jasco V-530 UV spectrophotometer equipped with a Jasco ETC-505T temperature controller unit.

Synthesis of Glucose-Based Building Blocks 5 and 8. α-*1-Azido-4,6-benzyliden-*D*-glucopyranose (***2***).* α-Bromo-2,3,4,6-tetra-O-acetyl-D-glucose (1.0 g, 2.40 mmol), dissolved in 7 mL of anhydrous DMF, was treated with 470 mg (7.23 mmol) of sodium azide at 50 °C for 2 h. After 2 h, the reaction mixture was concentrated under reduced pressure and purified by silica gel chromatography (eluent system: acetone in CH_2Cl_2 from 0 to 3%), affording 857 mg of β-1-azido-2,3,4,6-tetra-O-acetyl-D-glucose (2.30 mmol, 95%).

The obtained compound (857 mg, 2.30 mmol) was then treated with 2 mL of NH_3/MeOH 7 N at 50 °C for 18 h. The mixture was concentrated under reduced pressure and then redissolved in 7 mL of anhydrous DMF and treated with 20 mg (0.11 mmol) of PTSA and 689 μL (4.60 mmol) of α,α-dimethoxytoluene at 50 °C for 6 h. The reaction mixture was then concentrated under reduced pressure and purified by silica gel chromatography (eluent system: acetone in CH_2Cl_2 from 5 to 10%), thus affording 685 mg (1.81 mmol, 80%) of **2** as a pure compound.

^{1}H NMR (500 MHz, CD_3OD): δ 7.50−7.33 (5H, complex signals, aromatic protons); 5.57 (1H, s, PhC*H*); 4.64 (1H, d, J = 9.0 Hz, H-1); 4.30 (1H, m, H-6_a); 3.79 (1H, t, J = 10.5 and 10.0 Hz, H-6_b); 3.67 (1H, t, J = 8.5 and 9.5 Hz, H-3); 3.55 (1H, m, H-5); 3.49 (1H, t, J = 9.0 and 9.5 Hz, H-4); 3.31 (1H, t, J = 9.0 and 9.5 Hz, H-2).

^{13}C NMR (125 MHz, CD_3OD): δ 139.49, 130.45, 129.53, and 128.00 (aromatic carbons); 103.41 (Ph*C*H); 92.96 (C-1β); 82.33 (C-4); 76.03 (C-2); 75.17 (C-3); 70.17 (C-5); 69.89 (C-6).

ESI-MS calculated for $C_{13}H_{15}N_3O_5$: 293.27. Found (positive ions): 316.40 ($M + Na^+$); 332.51 ($M + K^+$).

*β-1-Azido-2,3-di-O-acetyl-D-glucopyranose (***3***).* Compound **2** (685 mg, 1.81 mmol) was treated with 2 mL of Ac_2O in 3 mL of anhydrous pyridine at room temperature (rt). After 1 h, the reaction mixture was taken to dryness and the crude was treated with 5 mL of the system TFA/H_2O/DCM (1:0.5:10, v/v/v) at 0 °C for 3 h. The reaction was quenched by addition of a few drops of pyridine, concentrated under reduced pressure, and purified by silica gel chromatography (eluent system: CH_3OH in $CHCl_3$ from 1 to 5%), affording 477 mg (1.65 mmol, 90%) of **3** as a pure compound.

^{1}H NMR (500 MHz, CD_3OD): δ 5.09 (1H, t, J = 9.5 and 9.0 Hz, H-3); 4.81 (1H, d, J = 8.5 Hz, H-1); 4.75 (1H, t, J = 9.5 and 9.0 Hz, H-2); 3.92−3.72 (2H, m, H_2-6); 3.61 (1H, t, J = 9.5 and 9.5 Hz, H-4); 3.53 (1H, m, H-5); 2.04 and 2.03 (3H each, s's, 2 × COCH_3).

^{13}C NMR (125 MHz, CD_3OD): δ 172.54 and 171.68 (2 *C*O); 89.46 (C-1β); 80.50 (C-5); 77.22 (C-3); 73.19 (C-2); 69.51 (C-4); 62.48 (C-6); 21.28 and 21.05 (CO*C*H$_3$).

ESI-MS calculated for $C_{10}H_{15}N_3O_7$: 289.24. Found (positive ions): 312.16 (M + Na^+); 328.16 (M + K^+).

*β-1-Azido-2,3-di-O-acetyl-6-O−(4,4′-dimethoxytriphenylmethyl)-D-glucopyranose (***4***).* Compound **3** (477 mg, 1.65 mmol), dissolved in 4 mL of anhydrous pyridine, was treated with 670 mg (1.98 mmol) of DMTCl and 10 mg (0.08 mmol) of DMAP at 25 °C for 18 h. The reaction was quenched by addition of methanol. The resulting mixture was concentrated under reduced pressure and purified by silica gel chromatography (eluent system: ethyl acetate in benzene/Py 1:0.05, v/v, from 5 to 15%), which furnished 827 mg (1.40 mmol, 85%) of **4** as a pure compound.

^{1}H NMR (500 MHz, $CDCl_3$): δ 7.45−6.84 (13H, complex signals, aromatic protons); 5.06 (1H, t, J = 9.0 and 10.0 Hz, H-3); 4.91 (1H, t, J = 9.0 and 9.5 Hz, H-2); 4.60 (1H, d, J = 8.5 Hz, H-1); 3.84 (1H, t, J = 10.0 and 9.0 Hz, H-4); 3.82 (6H, s, OCH_3); 3.56 (1H, m, H-5); 3.45 (2H, m, H_2-6); 2.09 and 2.08 (3H each, s's, 2 × COCH_3).

^{13}C NMR (125 MHz, $CDCl_3$): δ 170.83 and 169.44 (2 *C*O); 158.50, 144.19, 135.29, 129.90, 129.86, 127.87, 126.86, and 113.17 (aromatic carbons); 87.47 (C-1β); 86.68 (quaternary carbon of DMT group); 76.22 (C-5); 74.98 (C-3); 70.75 (C-2); 70.17 (C-4); 63.21 (C-6); 55.08 (O*C*H$_3$); 20.66 and 20.51 (CO*C*H$_3$).

ESI-MS calculated for $C_{31}H_{33}N_3O_7$: 591.61. Found (positive ions): 614.15 (M + Na^+); 630.31 (M + K^+).

*β-1-Azido-2,3-di-O-acetyl-6-O−(4,4′-dimethoxytriphenylmethyl)-D-glucopyranose-4-O-succinic acid (***5***).* Compound **4** (827 mg, 1.40 mmol), dissolved in 4 mL of anhydrous pyridine, was treated with 630 mg (6.30 mmol) of succinic anhydride and 10 mg (0.074 mmol) of DMAP at 25 °C for 18 h. The reaction was quenched by addition of water and concentrated under reduced pressure. The residue was then taken up in 100 mL of $CHCl_3$, washed twice with water, and purified by silica gel chromatography (eluent system: CH_3OH in $CHCl_3$/Py 1:0.05, v/v, from 2 to 10%) affording 870 mg of **5** as a pure compound (1.26 mmol, 90%).

^{1}H NMR (500 MHz, $CDCl_3$): δ 7.45−6.82 (13H, complex signals, aromatic protons); 5.30 (1H, t, J = 10.0 and 10.0 Hz, H-4); 5.19 (1H, t, J = 10.0 and 10.0 Hz, H-3); 5.01 (1H, t, J = 9.0 and 9.0 Hz, H-2); 4.65 (1H, d, J = 8.5 Hz, H-1); 3.77 (6H, s, OCH_3); 3.69 (1H, m, H-5); 3.33−3.09 (2H, m, H_2-6); 2.49−2.38 (4H, m, CH_2 succinic group); 2.07 and 1.97 (3H each, s's, 2 × COCH_3).

^{13}C NMR (125 MHz, $CDCl_3$): δ 170.27 and 170.23 (2 *C*O); 158.39, 144.34, 135.64, 129.25, 128.21, 127.75, 126.72, and 113.03 (aromatic carbons); 87.36 (C-1β); 86.02 (quaternary carbon of DMT group); 75.51 (C-5); 72.57 (C-3); 70.94 (C-2); 68.18 (C-4); 61.42 (C-6); 55.05 (O*C*H$_3$); 28.69 and 28.61 (*C*H$_2$ succinic group); 20.44 and 20.38 (CO*C*H$_3$).

ESI-MS calculated for $C_{35}H_{37}N_3O_{12}$: 691.68. Found (negative ions): 690.38 (M − H)$^-$.

*β-1-Azido-2,3,4-tri-O-acetyl-6-O-tert-butyldimethylsilyl-D-glucopyranose (***7***).* 1-Azido-β-D-glucopyranose (390 mg, 1.9 mmol), dissolved in 5 mL of anhydrous DMF, was treated with 422 mg (2.8 mmol) of TBDMSCl and 258 mg (3.8 mmol) of imidazole at rt for 18 h. The reaction was quenched by addition of water at 0 °C, and the resulting mixture concentrated under reduced pressure. The residue was taken up in 100 mL of $CHCl_3$ and washed twice with 5% $NaHCO_3$ and then with water. The crude was purified by silica gel chromatography (eluent system: 5% CH_3OH in $CHCl_3$), affording 488 mg (1.6 mmol, 85%) of a pure compound. This was directly treated with 2 mL of Ac_2O in 3 mL of anhydrous pyridine at rt for 3 h. The reaction was quenched by addition of a few drops of CH_3OH and the mixture concentrated under reduced pressure. The residue afforded 690 mg (1.60 mmol) of **7** as a pure compound.

^{1}H NMR (400 MHz, $CDCl_3$): δ 5.17 (1H, t, J = 9.6 and 9.6 Hz, H-3); 5.06 (1H, t, J = 9.6 and 9.6 Hz, H-4); 4.89 (1H, t, J = 9.2 and 9.2 Hz, H-2); 4.55 (1H, d, J = 8.8 Hz, H-1); 3.76−3.66 (2H, m, H-6); 3.60 (1H, m, H-5); 2.03, 1.99 and 1.97 (3H each, s's, 3 × COCH_3); 0.86 {9H, s, [(CH_3)$_3$C]Si}; 0.04 and 0.028 [3H each, s's, Si(CH_3)$_2$].

^{13}C NMR (100 MHz, $CDCl_3$): δ 170.07, 169.07, and 169.00 (3 *C*O); 87.55 (C-1β); 76.78 (C-5); 72.87 (C-3); 70.71 (C-2); 68.20 (C-4); 61.93 (C-6); 25.63 {[(*C*H$_3$)$_3$C]Si}; 20.42 (CO*C*H$_3$); 18.17 [(CH$_3$)$_3$*C*]; −5.54 [Si(*C*H$_3$)$_2$].

ESI-MS calculated for $C_{18}H_{31}N_3O_8Si$: 445.54. Found (positive ions): 468.15 (M + Na^+); 484.25 (M + K^+).

*β-1-Azido-2,3,4-tri-O-acetyl-β-D-glucuronic acid (***8***).* Compound **7** (690 mg, 1.60 mmol) was treated with 3 mL of Jones reagent (5 g CrO_3/15 mL H_2O/5 mL H_2SO_4) at −15 °C for 15 min and then slowly taken to rt and left for additional 3 h under stirring. The reaction was quenched by addition of ethanol, neutralized by addition of 5% $NaHCO_3$ solution, and then washed once with $CHCl_3$. The aqueous phase was brought to pH = 2 with 3 M HCl and washed twice with $CHCl_3$. The organic layers were collected and concentrated under reduced pressure to give 497 mg (1.44 mmol, 90%) of **8** as a pure compound.

^{1}H NMR (300 MHz, $CDCl_3$): δ 5.30−5.25 (2H, overlapped signals, H-3 and H-4); 4.97 (1H, t, J = 8.6 and 9.4 Hz, H-2); 4.75 (1H, d, J = 8.8 Hz, H-1); 4.17 (1H, m, H-5); 2.08, 2.05, and 2.03 (3H each, s's, 3 × COCH_3).

^{13}C NMR (75 MHz, $CDCl_3$): δ 170.25, 169.74, 169.34, and 169.12 (3 *C*O and *C*OOH); 87.63 (C-1β); 73.25 (C-5); 71.76 (C-2); 70.16 (C-3); 68.63 (C-4); 20.29 (CO*C*H$_3$).

ESI-MS calculated for $C_{12}H_{15}N_3O_9$: 345.26. Found (negative ions): 344.18 (M − H)$^-$.

Synthesis of Lactose-Based Building Blocks 13 and 16. *β-1-Azido-lactose heptaacetate (***10***).* Lactose octaacetate (1.0 g, 1.47 mmol) was treated with 85 μL (0.73 mmol) of $SnCl_4$ and 483 μL (3.67 mmol) of trimethylsilyl azide in 20 mL of anhydrous CH_2Cl_2 and 1 mL of molecular sieves of 4 Å under nitrogen atmosphere for 18 h at rt. The reaction mixture was washed with 1 M $KHSO_4$ and then with water; the organic layers were collected and dried over anhydrous $MgSO_4$, affording 879 mg (1.32 mmol, 90%) of **10** as a pure compound.

^{1}H NMR (500 MHz, $CDCl_3$): δ 5.33 (1H, m, H-4 Gal); 5.19 (1H, t, J = 9.0 and 9.0 Hz, H-3 Glc); 5.08 (1H, t, J = 8.5 and 9.5 Hz, H-2 Gal); 4.94 (1H, dd, J = 3.5 and 10.5 Hz, H-3 Gal); 4.84 (1H, t, J = 9.5 and 9.5 Hz, H-2 Glc); 4.61 (1H, d, J = 9.0 Hz, H-1 Glc); 4.47 (1H, d, J =

7.5 Hz, H-1 Gal); 4.12−4.04 (4H, overlapped signals, H_2-6 Glc and H_2-6 Gal); 3.86 (1H, t, J = 7.0 and 7.0 Hz, H-5 Gal); 3.80 (1H, t, J = 9.5 and 9.5 Hz, H-4 Glc); 3.69 (1H, m, H-5 Glc); 2.08, 2.05, 2.04, 1.98, 1.97, 1.95, and 1.87 (3 H each, s's, 7 x $COCH_3$).

^{13}C NMR (125 MHz, $CDCl_3$): δ 170.13, 169.94, 169.86, 169.45, 169.31, and 168.89 (*C*O); 100.93 (C-1β Gal); 87.53 (C-1β Glc); 75.61 (C-4 Glc); 74.63 (C-5 Glc); 72.36 (C-3 Glc); 70.82 (C-5 Gal); 70.75 (C-3 Gal); 70.58 (C-2 Glc); 68.89 (C-2 Gal); 66.43 (C-4 Gal); 61.56 (C-6 Gal); 60.62 (C-6 Glc); 20.62, 20.55, 20.44, and 20.32 (CO*C*H_3).

ESI-MS calculated for $C_{26}H_{35}N_3O_{17}$: 661.57. Found (positive ions): 684.17 ($M + Na^+$); 700.14 ($M + K^+$).

*4,6-Benzyliden-2,3-di-O-acetyl-β-D-Galp(1→4)-1-azido-2,3,6-tri-O-acetyl-β-D-Glcp (***11***).* Compound **10** (879 mg, 1.32 mmol) was treated with 6 mL of NH_3/CH_3OH for 18 h at 50 °C. The mixture was concentrated under reduced pressure, redissolved in 7 mL of DMF, and then treated with 12 mg (0.06 mmol) of PTSA and 237 μL (1.58 mmol) of α,α-dimethoxytoluene at 50 °C for 6 h. The reaction mixture was diluted with AcOEt and washed twice with water. The organic phase was then taken to dryness and acetylated by treatment with 3:2 Py/acetic anhydride for 3 h at rt. The reaction mixture was concentrated under reduced pressure and purified by silica gel chromatography (eluent system: acetone in CH_2Cl_2 from 1 to 10%), affording 612 mg (0.92 mmol, 70%) of **11** as a pure compound.

^{1}H NMR (500 MHz, $CDCl_3$): δ 7.44−7.37 (5H, complex system, aromatic protons); 5.46 (1H, s, PhC*H*); 5.25−5.20 (2H, overlapped signals, H-2 Gal and H-3 Glc); 4.90−4.87 (2H, overlapped signals, H-3 Gal and H-2 Glc); 4.61 (1H, d, J = 9.0 Hz, H-1 Glc); 4.53 (1H, d, J = 12.0 Hz, H-6$_a$ Glc); 4.48 (1H, d, J = 8.5 Hz, H-1 Gal); 4.33 (1H, d, J = 3.5 Hz, H-4 Gal); 4.29 (1H, d, J = 11.0 Hz, H-6$_a$ Gal); 4.13 (1H, dd, J = 5.0 and 12.5 Hz, H-6$_b$ Glc); 4.05 (1H, d, J = 13.0 Hz, H-6$_b$ Gal); 3.81 (1H, t, J = 9.5 and 9.5 Hz, H-4 Glc); 3.71 (1H, m, H-5 Glc); 3.46 (1H, bs, H-5 Gal); 2.12, 2.10, 2.06, 2.05, and 2.03 (3H each, s's, 5 × $COCH_3$).

^{13}C NMR (125 MHz, $CDCl_3$): δ 170.59, 170.14, 169.42, 168.77, and 160.85 (*C*O); 137.26, 129.12, 128.14, and 126.34 (aromatic carbons); 101.23 (Ph*C*H); 100.94 (C-1β Gal); 87.74 (C-1β Glc); 75.33 (C-4 Glc and C-5 Glc); 74.93 (C-4 Gal); 72.97 (C-3 Glc); 71.91 (C-2 Glc); 70.74 (C-3 Gal); 68.83 (C-2 Gal); 68.30 (C-6 Glc); 66.41 (C-5 Gal); 61.60 (C-6 Gal); 20.69 and 20.47 (CO*C*H_3).

ESI-MS calculated for $C_{29}H_{35}N_3O_{15}$: 665.60. Found (positive ions): 688.28 ($M + Na^+$); 704.21 ($M + K^+$).

*2,3-Di-O-acetyl-β-D-Galp(1→4)-1-azido-2,3,6-tri-O-acetyl-β-D-Glcp (***12***).* Compound **11** (612 mg, 0.92 mmol) was treated with 5 mL of the system TFA/H_2O/DCM (1:0.5:10, v/v/v) at 0 °C for 3 h. The reaction was quenched by addition of pyridine, concentrated under reduced pressure, and purified by silica gel chromatography (eluent system: CH_3OH in $CHCl_3$ from 1 to 10%), affording 479 mg (0.83 mmol, 90%) of **12** as a pure compound.

^{1}H NMR (500 MHz, CD_3OD): δ 5.21 (1H, t, J = 9.5 and 9.5 Hz, H-3 Glc); 5.14 (1H, m, H-2 Gal); 4.87−4.81 (3H, overlapped signals, H-3 Gal, H-2 Glc, and H-1 Glc); 4.56 (1H, d, J = 7.5 Hz, H-1 Gal); 4.54−4.18 (2H, AB part of an ABX system, H_2-6 Glc); 4.06 (1H, d, J = 2.5 Hz, H-4 Gal); 3.92 (1H, t, J = 9.0 and 9.0 Hz, H-4 Glc); 3.86 (1H, m, H-5 Glc); 3.74 (2H, m, H_2-6 Gal); 3.62 (1H, t, J = 6.5 and 6.5 Hz, H-5 Gal); 2.12, 2.09, 2.08, 2.07, and 2.04 (3H each, s's, 5 × CO*C*H_3).

^{13}C NMR (125 MHz, CD_3OD): δ 172.83 and 171.81 (*C*O); 102.98 (C-1β Gal); 89.15 (C-1β Glc); 77.56 (C-4 Glc); 76.97 (C-5 Gal); 76.68 (C-5 Glc); 75.96 (C-3 Gal); 74.72 (C-3 Glc); 72.92 (C-2 Glc); 71.69 (C-2 Gal); 68.01 (C-4 Gal); 63.99 (C-6 Glc); 62.17 (C-6 Gal); 21.60, 21.29, 21.16, and 20.99 (CO*C*H_3).

ESI-MS calculated for $C_{22}H_{31}N_3O_{15}$: 577.49. Found (positive ions): 600.15 ($M + Na^+$); 616.31 ($M + K^+$).

*2,3-Di-O-acetyl-6-O−(4,4′-dimethoxytriphenylmethyl)-4-O-succinyl-β-D-Galp(1→4)-1-azido-2,3,6-tri-O-acetyl-β-D-Glcp (***13***).* Compound **12** (479 mg, 0.83 mmol), dissolved in 4 mL of anhydrous pyridine, was treated with 337 mg (0.99 mmol) of DMTCl and 5 mg (0.04 mmol) of DMAP at 25 °C for 18 h. The reaction was quenched by addition of methanol and the resulting mixture concentrated under reduced pressure. Purification by silica gel chromatography (eluent system: $CHCl_3$/Py 1:0.05, v/v) afforded 624 mg (0.71 mmol, 85%) of a pure compound, which was then dissolved in 4 mL of anhydrous Py and treated with 319 mg (3.19 mmol) of succinic anhydride and 5 mg (0.035 mmol) of DMAP at 25 °C for 18 h. The reaction was quenched by addition of water and concentrated under reduced pressure. The residue, taken up in 100 mL of $CHCl_3$, was washed twice with water, concentrated under reduced pressure, and purified by silica gel chromatography (eluent system: CH_3OH in $CHCl_3$/Py 1:0.05, v/v, from 2% to 10%), affording 617 mg of **13** as a pure compound (0.6 mmol, 89%).

^{1}H NMR (500 MHz, C_6D_6): δ 7.69−6.74 (13H, complex signals, aromatic protons); 6.17 (1H, d, J = 3.5 Hz, H-4 Gal); 5.62 (1H, m, H-2 Gal); 5.41 (1H, dd, J = 3.0 and 10.5 Hz, H-3 Gal); 5.33 (1H, t, J = 9.0 and 9.5 Hz, H-3 Glc); 5.12 (1H, t, J = 9.5 and 9.0 Hz, H-2 Glc); 4.50 (1H, d, J = 10.5 Hz, H-6$_a$ Glc); 4.40 (1H, d, J = 8.0 Hz, H-1 Gal); 4.14 (1H, partially overlapped signals, H-6$_b$ Glc); 4.12 (1H, d, J = 8.5 Hz, H-1 Glc); 3.78 (1H, m, H-6$_a$ Gal); 3.69 (1H, m, H-5 Gal); 3.48 (1H, m, H-6$_b$ Gal); 3.44 (4H, overlapped signals, OC*H*$_3$ DMT group and H-4 Glc); 3.27 (1H, m, H-5 Glc); 2.64−2.21 (4H, m, C*H*$_2$ succinic group); 2.06, 1.98, 1.91, 1.81, and 1.78 (3H each, s's, 5 × CO*CH*$_3$).

^{13}C NMR (125 MHz, C_6D_6): δ 174.23 (*C*OOH); 171.66, 170.13, 170.05, and 169.10 (*C*O); 159.35, 149.46, 144.70, 135.91, 130.72, 130.62, 130.41, 113.65, 128.75, 127.34, and 123.69 (aromatic carbons); 101.71 (C-1β Gal); 87.66 (C-1β Glc); 87.09 (quaternary carbon of DMT group); 76.57 (C-4 Glc); 75.02 (C-5 Glc); 73.11 (C-3 Glc); 72.44 (C-5 Gal); 71.80 (C-3 Gal); 71.18 (C-2 Glc); 70.01 (C-2 Gal); 67.46 (C-4 Gal); 62.40 (C-6 Glc); 60.93 (C-6 Gal); 54.80 (O*C*H$_3$ DMT group); 29.24 and 29.20 (C*H*$_2$ succinic group); 20.85, 20.47, 20.36, 20.20, and 20.10 (CO*C*H_3).

ESI-MS calculated for $C_{47}H_{53}N_3O_{20}$: 979.93. Found (negative ions): 978.50 $(M - H)^-$.

*2,3,4-Tri-O-acetyl-6-O-tert-butyldimethylsilyl-β-D-Galp-(1→4)-1-azido-2,3,6-tri-O-acetyl-β-D-Glcp (***15***).* Compound **12** (381 mg, 0.66 mmol), dissolved in 5 mL of DMF, was treated with 149 mg (0.99 mmol) of TBDMSCl and 90 mg (1.32 mmol) of imidazole at rt for 18 h. The reaction mixture was quenched by addition of water at 0 °C and concentrated under reduced pressure. The crude was taken up in 100 mL of $CHCl_3$ and washed twice with 5% $NaHCO_3$ and then with water. Purification by silica gel chromatography (eluent system: 2% CH_3OH in $CHCl_3$) afforded 366 mg (0.53 mmol, 80%) of a pure compound, which was directly acetylated by treatment with 3:2 Py/acetic anhydride at rt for 3 h. The reaction mixture was then diluted with $CHCl_3$ and washed twice with water; the organic layer was concentrated under reduced pressure, affording 388 mg (0.53 mmol) of **15** as a pure compound.

^{1}H NMR (500 MHz, $CDCl_3$): δ 5.41 (1H, d, J = 3.0 Hz, H-4 Gal); 5.17 (1H, t, J = 9.5 and 9.0 Hz, H-3 Glc); 5.05 (1H, m, H-2 Gal); 4.95 (1H, dd, J = 3.5 and 10.0 Hz, H-3 Glc); 4.82 (1H, t, J = 9.5 and 9.0 Hz, H-2 Glc); 4.59 (1H,

d, J = 8.5 Hz, H-1 Glc); 4.49 (1H, d, J = 12.0 Hz, H-6_a Glc); 4.43 (1H, d, J = 8.0 Hz, H-1 Gal); 4.07 (1H, dd, J = 4.5 and 12.0 Hz, H-6_b Glc); 3.80 (1H, t, J = 10.0 and 9.0 Hz, H-4 Glc); 3.69−3.61 (3H, overlapped signals, H-5 Glc, H-6_a Gal and H-5 Gal), 3.52 (1H, t, J = 7.5 and 8.0 Hz, H-6_b Gal); 2.10, 2.09, 20.4, 2.01, 2.00, and 1.93 (3H each, s's, 6 × COCH_3); 0.83 {9H, s, [(CH_3)$_3$C]Si}; −0.004 and −0.02 [3H each, s's, (CH_3)Si].

^{13}C NMR (125 MHz, $CDCl_3$): δ 170.08, 169.86, 169.66, 169.30, and 168.97 (*C*O); 100.82 (C-1β Gal); 87.50 (C-1β Glc); 75.21 (C-4 Glc); 74.57 and 73.41 (C-5 Glc and C-5 Gal); 72.42 (C-3 Glc); 71.06 (C-3 Gal); 70.79 (C-2 Glc); 69.26 (C-2 Gal); 66.35 (C-4 Gal); 61.53 (C-6 Glc); 59.88 (C-6 Gal); 25.47 {[(*C*H$_3$)$_3$C]Si}; 20.59, 20.45, 20.40, and 20.34 (CO*C*H$_3$); 17.88 (quaternary carbon of TBDMS group); −5.86 and −5.91 [(*C*H$_3$)$_2$Si].

ESI-MS calculated for $C_{30}H_{47}N_3O_{16}Si$: 733.79. Found (positive ions): 756.36 (M + Na^+); 772.32 (M + K^+).

*β-1-Azido-2,2′,3,3′,4′,6-hexa-O-acetyl-lacturonic Acid (***16***).* Compound **15** (388 mg, 0.53 mmol) was treated with 3 mL of Jones reagent (5 g CrO_3/15 mL H_2O/5 mL H_2SO_4) at −15 °C for 15 min, then slowly taken to rt and left for an additional 3 h under stirring. The reaction was quenched by addition of ethanol, neutralized by addition of 5% $NaHCO_3$ solution, and then washed once with $CHCl_3$. The aqueous phase was brought to pH = 2 with 3 M HCl and washed twice with $CHCl_3$. The organic layers were collected and concentrated under reduced pressure to give 298 mg (0.47 mmol, 90%) of **16** as a pure compound.

^{1}H NMR (500 MHz, $CDCl_3$): δ 5.68 (1H, d, J = 1.5 Hz, H-4 Gal); 5.26 (1H, t, J = 9.5 and 9.0 Hz, H-3 Glc); 5.12−5.05 (2H, overlapped signals, H-2 Gal and H-3 Gal); 4.84 (1H, t, J = 8.5 and 10.0 Hz, H-2 Glc); 4.68 (1H, d, J = 9.0 and 9.0 Hz, H-1 Glc); 4.58 (1H, d, J = 8.0 Hz, H-1 Gal); 4.50−4.47 (2H, overlapped signals, H-6_a Glc and H-5 Gal); 4.16 (1H, m, H-6_b Glc); 3.85−3.73 (2H, overlapped signals, H-4 Glc and H-5 Glc); 2.12, 2.11, 2.09, 2.08, 2.07, and 2.06 (3H each, s's, 6 × COCH_3).

^{13}C NMR (50 MHz, $CDCl_3$): δ 172.72, 172.39, 171.92, 171.48, 171.30, and 171.12 (*C*O and *C*OOH); 101.89 (C-1β Gal); 88.67 (C-1β Glc); 77.21 (C-5 Glc); 76.04 (C-5 Gal); 74.48 (C-2 Glc and C-3 Gal); 72.73 and 72.55 (C-2 Gal and C-3 Glc); 70.77 and 70.66 (C-4 Gal and C-4 Glc); 20.64, 20.57, and 20.48 (CO*C*H$_3$).

ESI-MS calculated for $C_{24}H_{31}N_3O_{17}$: 633.51. Found (negative ions): 632.18 (M − H)$^-$.

6-(4,4′-Dimethoxytriphenylmethoxy)hexanoic Acid Linker. Ethyl 6-hydroxyhexanoate (500 μL, 3.0 mmol), dissolved in 4 mL of anhydrous pyridine, was treated with 1.0 g (3.0 mmol) of DMTCl and 190 mg (1.5 mmol) of DMAP for 4 h at rt. The reaction mixture was quenched by addition of CH_3OH and concentrated under reduced pressure. The crude was taken up in 100 mL of $CHCl_3$ and washed twice with water. The obtained residue was dissolved in 4 mL of ethanol and treated with 25 mL of NaOH 6 M for 6 h at rt. The reaction mixture was diluted with $CHCl_3$ and washed twice with water. Purification by silica gel chromatography (eluent system: acetone in CH_2Cl_2/Py 1:0.05, v/v) afforded 1.0 g (2.25 mmol, 75%) of the desired 6-(4,4′-dimethoxytriphenylmethoxy)hexanoic acid as a pure compound.

^{1}H NMR (200 MHz, $CDCl_3$): δ 7.42−6.88 (13H, complex signals, aromatic protons); 3.86 (3H, s, OCH_3); 3.12 (2H, t, J = 4.4 and 4.2 Hz, CH_2 ϵ); 2.42 (2H, t, J = 4.8 and 5.2 Hz, CH_2 α); 1.69 (4H, overlapped signals, CH_2 β and CH_2 δ); 1.50 (2H, m, CH_2 γ).

^{13}C NMR (50 MHz, $CDCl_3$): δ 179.79 (*C*OOH); 158.20, 145.28, 136.55, 129.92, 128.07, 127.67, 126.54, and 112.89 (aromatic carbons); 85.59 (quaternary carbon of DMT group); 63.02 (*C*H$_2$ ϵ); 55.12 (OCH_3); 34.01 (*C*H$_2$ α); 29.68 (*C*H$_2$ β); 25.79 (*C*H$_2$ γ); 24.55 (*C*H$_2$ δ).

ESI-MS calculated for $C_{27}H_{30}O_5$: 434.52. Found (negative ions): 433.18 (M − H)$^-$.

Solid Support Functionalization: Synthesis of 18, 20, and 22. In a typical experiment, 300 mg of Tentagel−NH_2 (0.29 meq/g, 0.09 mmol) were reacted with 0.90 mmol of **5** or **13**, 130 μL (0.90 mmol) of DIC, 117 mg (0.90 mmol) of HOBt, and 150 μL (0.90 mmol) of DIEA in 500 μL of anhydrous DMF at rt for 12 h. After exhaustive washings with DCM, CH_3OH, and Et_2O, the support was dried under reduced pressure. DMT tests performed on dried and weighed samples of resulting supports **6** or **14** allowed to determine the incorporation yields of derivative **5** or **13**, respectively, onto the Tentagel resin, which resulted to be in the range 0.20−0.23 meq/g. DMT protecting group was removed by 1% DCA in DCM treatment, followed by a standard treatment with acetic anhydride in pyridine (2:3, v/v) to block the liberated 6-OH moiety. The resulting support (50 mg, 0.0095 mmol) was then treated with 24 μL (0.24 mmol) of 1,3-propanedithiol and 33 μL (0.24 mmol) of triethylamine in 300 μL of DMF under nitrogen atmosphere for 2 h at rt. After 2 h, the support was washed several times with anhydrous DMF and coupled with carboxylic acid **8** or **16** (0.095 mmol), 16 μL (0.095 mmol) of DIEA, 37 mg (0.095 mmol) of HATU, and 35 mg (0.095 mmol) of HOBt in 300 μL of DMF for 1.5 h at rt. The successive step required the treatment of the obtained supports (**17**, **19**, and **21**) with 24 μL (0.24 mmol) of 1,3-propanedithiol and 33 μL (0.24 mmol) of triethylamine in 300 μL of DMF under nitrogen atmosphere for 2 h at rt. After 2 h, the support was washed several times with anhydrous DMF and coupled with the 6-(4,4′-dimethoxytriphenylmethoxy)-hexanoic acid linker (0.095 mmol), 16 μL (0.095 mmol) of DIEA, 37 mg (0.095 mmol) of HATU, and 35 mg (0.095 mmol) of HOBt in 300 μL of DMF for 1.5 h at rt. DMT tests performed on dried and weighed samples of resulting supports **18**, **20**, and **22** allowed the determination of the support functionalization, which was always in the range 0.12−0.14 meq/g.

Synthesis of 3′-Glycoconjugates I, II, and III. ODN chain assembly was carried out on 50 mg (6.5 μmol) of supports **18**, **20**, or **22** on an automated DNA synthesizer following a standard phosphoramidite protocol with final DMT removal (*30*). The sequence d($^{5'}$GCGTGCCTCC-TCACTGGC$^{3'}$) was assembled, observing in all cases coupling yields always greater than 98%, as evaluated by DMT test. The oligomers were detached from the support and deprotected by an overnight concentrated aq ammonia treatment at 55 °C. The supernatant was filtered and the support washed with H_2O. The combined filtrates and washings were concentrated under reduced pressure, redissolved in H_2O, and analyzed and purified by HPLC on a Nucleogel SAX column (Macherey-Nagel, 1000−8/46); buffer A, 20 mM KH_2PO_4 aq solution, pH 7.0, containing 20% (v/v) CH_3CN; buffer B, 1 M KCl, 20 mM KH_2PO_4 aq solution, pH 7.0, containing 20% (v/v) CH_3CN; a linear gradient from 0 to 100% B in 30 min, flow rate 0.8 mL/min, was used. The isolated oligomers, having the following retention times: **I** = 21.37 min, **II** = 20.90 min, and **III** = 17.13 min, respectively, were collected and successively desalted by gel filtration on a Sephadex G25 column eluted with H_2O. HPLC profile of crude **III** is showed in Figure 2. By HPLC analysis on a Nucleosil 100−5 C18 analytical column (4.6 × 250 mm, 7 μm), the isolated oligomers resulted to be more than 98% pure (see Materials and Methods for conditions).

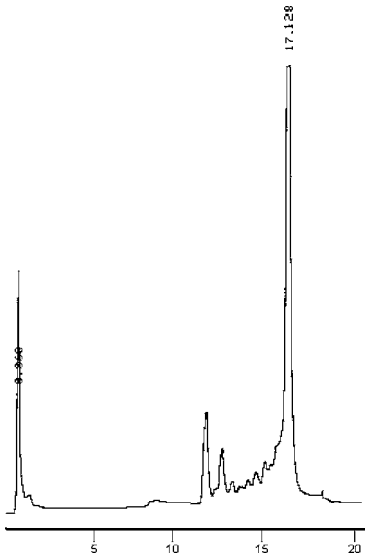

Figure 2. HPLC profile of crude oligonucleotide 3′-glycoconjugate **III** (conditions: Nucleogel SAX column; linear gradient from 0 to 100% B in 30 min; buffer A, 20 mM KH_2PO_4 aq solution, pH 7.0, containing 20% (v/v) CH_3CN; buffer B, 1 M KCl, 20 mM KH_2PO_4 aq. solution, pH 7.0, containing 20% (v/v) CH_3CN; flow rate 0.8 mL/min).

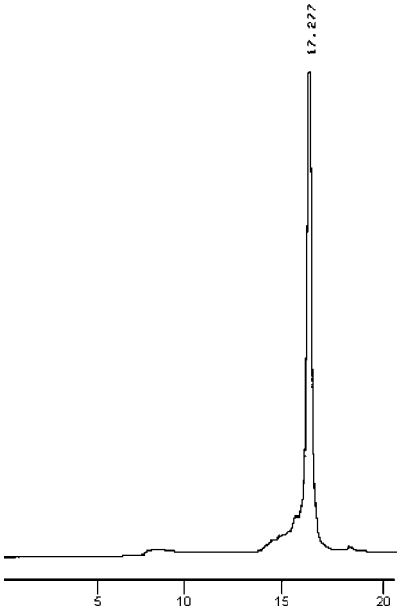

Figure 3. HPLC profile of purified oligonucleotide 3′-glycoconjugate **III** (conditions as reported in Figure 2) taken 20 days at pH 5.0.

Compound **I** MALDI TOF-MS: calculated mass for $C_{190}H_{251}N_{64}O_{123}P_{18}$, 5954.06; found, *m/z* 5952.57 $(M - H)^-$.

Compound **II** MALDI TOF-MS: calculated mass for $C_{196}H_{261}N_{64}O_{128}P_{18}$, 6116.11; found, *m/z* 6113.62 $(M - H)^-$.

Compound **III** MALDI TOF-MS: calculated mass for $C_{202}H_{271}N_{64}O_{133}P_{18}$, 6278.17; found, *m/z* 6276.56 $(M - H)^-$.

Enzymatic Experiments. Glycoconjugate **III** (5.0 optical density units,OD) was incubated at 37 °C with 1.0 mL of bovine fetal serum. Small aliquots of the mixture were taken at defined time intervals, kept at 85 °C for 5 min, equilibrated at rt, and analyzed by HPLC on an analytical anion exchange column. A parallel experiment, carried out on 5.0 OD of unmodified ODN sequence d($^{5'}$GCGTGCCTCCTCACTGGC$^{3'}$), showed that the peak corresponding to the intact ODN was not apparent after 2 h, with the natural oligonucleotide completely digested to a complex mixture of 3′- and 5′-mononucleotides within 3 h. On the contrary, the peak corresponding to intact glycoconjugate **III** was not detected only after 6 h (Figure 3).

Scheme 1. Synthesis of 6 and 8

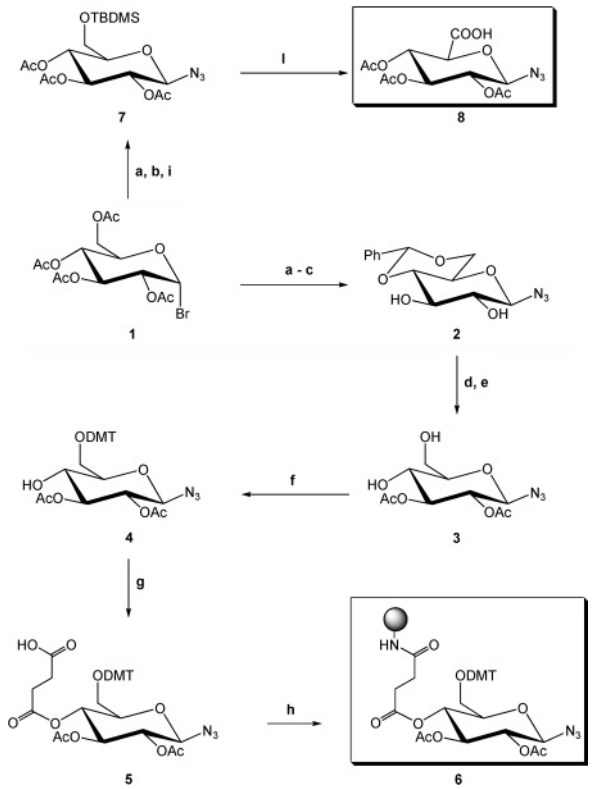

(a) NaN_3, DMF, 50 °C, 2 h, 95%; (b) 7M NH_3/CH_3OH, 50 °C, overnight, quant.; (c) PTSA, α,α-dimethoxytoluene 50 °C, 6 h, 80%; (d) Ac_2O/pyridine (2:3, v/v), rt, 30 min., quant.; (e) TFA/H_2O/DCM (1:0.5:10, v/v), 0 °C, 3 h, 90%; (f) DMTCl, DMAP, pyridine, rt, overnight, 85%; (g) succinic anhydride, DMAP, pyridine, rt, overnight, 90%; (h) Tentagel NH_2, DIPEA, DIC, HOBt, pyridine, rt, 48 h, 74%; (i) TBDMSCl, imidazole, DMF, rt, overnight, 85%; (l) Jones reagent, acetone, −15 °C to rt, 3 h, 90%.

Thermal Denaturation Experiments. The concentration of the synthesized ODNs was determined spectrophotometrically at $\lambda = 260$ nm and at 85 °C, using the molar extinction coefficient calculated for the unstacked oligonucleotide using the following extinction coefficients: 15400 (A); 11700 (G); 7300 (C); 8800 (T) cm^{-1} M^{-1} (*31*). In all cases, the contribution of the saccharidic residues to the absorbance at $\lambda = 260$ nm was considered negligible. A 100 mM NaCl, 10 mM NaH_2PO_4, aq solution at pH = 7.0 was used for the melting experiments. Melting curves were recorded using a concentration of approximately 1 μM for each strand in 1 mL of the tested solution in Teflon stoppered quartz cuvettes of 1 cm optical path length. The resulting solutions were then allowed to heat at 80 °C for 15 min, then slowly cooled and kept at 5 °C for 30 min. After thermal equilibration at 10 °C, UV absorption at $\lambda = 260$ nm was monitored as a function of the temperature, increased at a rate of 0.5 °C/min, typically in the range 20−80 °C. The melting temperatures, determined as the maxima of the first derivative of absorbance vs temperature plots, are the average values of three independent melting experiments. For all the studied cases, both the modified duplexes and the unmodified one, within the experimental error evaluated as ±0.5 °C, exhibited a melting temperature value of 60 °C.

Scheme 2. Synthesis of 14 and 16

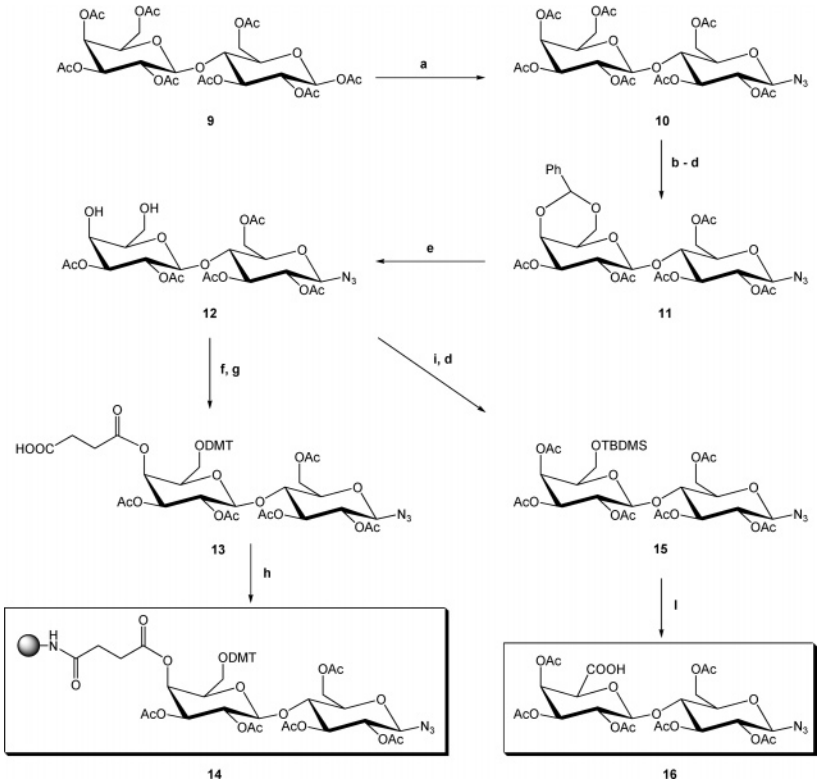

(a) $SnCl_4$, $TMSN_3$, DCM, molecular sieves, rt, 18 h, 90%; (b) 7M NH_3/CH_3OH, 50 °C, overnight, quant.; (c) PTSA, α,α-dimethoxytoluene, 50 °C, 5 h, 70%; (d) Ac_2O/pyridine (2:3, v/v), rt, 3 h, quant.; (e) TFA/H_2O/DCM (1:0.5:10, v/v), 0 °C, 3 h, 90%; (f) DMTCl, DMAP, pyridine, rt, overnight, 85%; (g) succinic anhydride, DMAP, pyridine, rt, overnight, 90%; (h) Tentagel NH_2, DIPEA, DIC, HOBt, pyridine, rt, 48 h, 70%; (i) TBDMSCl, imidazole, DMF, rt, overnight, 80%; (l) Jones reagent, acetone, −15 °C, 15 min, then rt, 3 h, 90%.

RESULTS AND DISCUSSION

In the here reported oligonucleotide hybrids, the saccharidic portion is composed of glucose- or lactose-based building blocks, chosen as model addition monomers, β-1,6-linked through amide bonds generated between the 1-amino function of the first sugar residue and the 6-COOH group of a suitably protected uronic acid derivative. The functionalization of the solid supports with the first sugar moiety and the synthesis of the building blocks are reported in Schemes 1 and 2, for glucose- and lactose-based molecules, respectively. In all cases, due to the intrinsic chemical instability of aminal functions, the building blocks are generated in the form of 1-azido derivatives. The azido group (*32*), as a masked form of a primary amine, offers several advantages: (i) it can be easily introduced; (ii) proved to be completely stable to the required chemical manipulations; and (iii) can be rapidly and in very high yields reduced to a primary amine in the solid phase immediately prior to the coupling with the selected uronic acid.

In the case of glucose derivatives, as described in Scheme 1, the β-azido group was classically inserted with an efficiency of 95% by reacting commercially available α-bromo-2,3,4,6-tetra-O-acetyl-D-glucose **1** with NaN_3 in DMF. After a methanolic ammonia treatment, β-1-azido-D-glucose, without isolation, was reacted with α,α-dimethoxytoluene in the presence of *p*-toluensulfonic acid to produce 4,6-protected derivative **2** in 80% yields. Treatment with acetic anhydride in pyridine, followed by benzylidene removal, gave compound **3** in 90% yields (for the two steps), which was then converted into derivative **4**, protected at the primary 6-OH position with the 4,4′-dimethoxytrityl group, in 85% yields. The successive reaction with succinic anhydride yielded intermediate **5** in 90% yields, which was then incorporated in the Tentagel amino solid support in the presence of DIC as

Scheme 3. Synthesis of Conjugate I

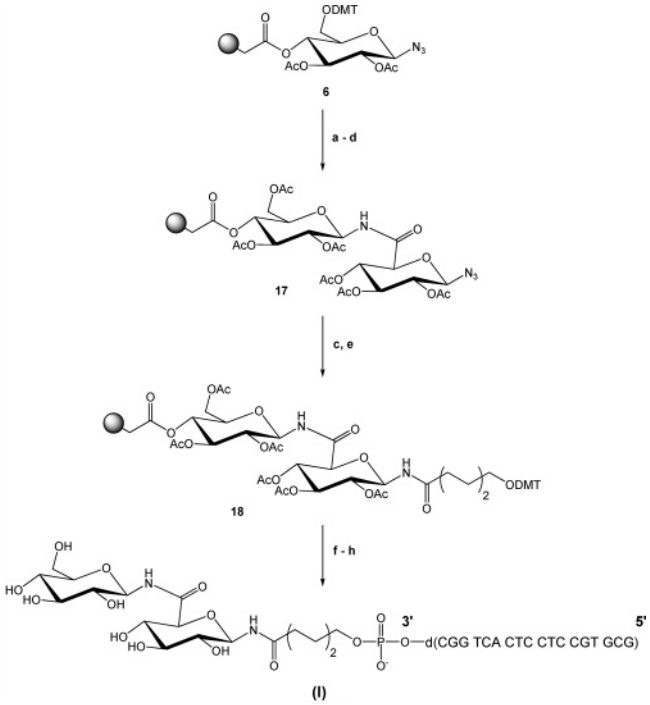

(a) 1% DCA in DCM, rt, 10 min; (b) Ac_2O/pyridine (1:1, v/v), rt, 30 min; (c) 1,3-propanedithiol, TEA, molecular sieves, DMF, rt, 2 h; (d) coupling with **8**, HATU, HOBt, DIPEA, DMF, rt, 1.5 h; (e) coupling with DMTO$(CH_2)_5$COOH, HATU, HOBt, DIPEA, DMF, rt, 1.5 h; (f) automated ODN chain assembly; (g) final DMT removal; (h) aq. NH_3, 50 °C, 6 h.

Scheme 4. Synthesis of Conjugates II and III

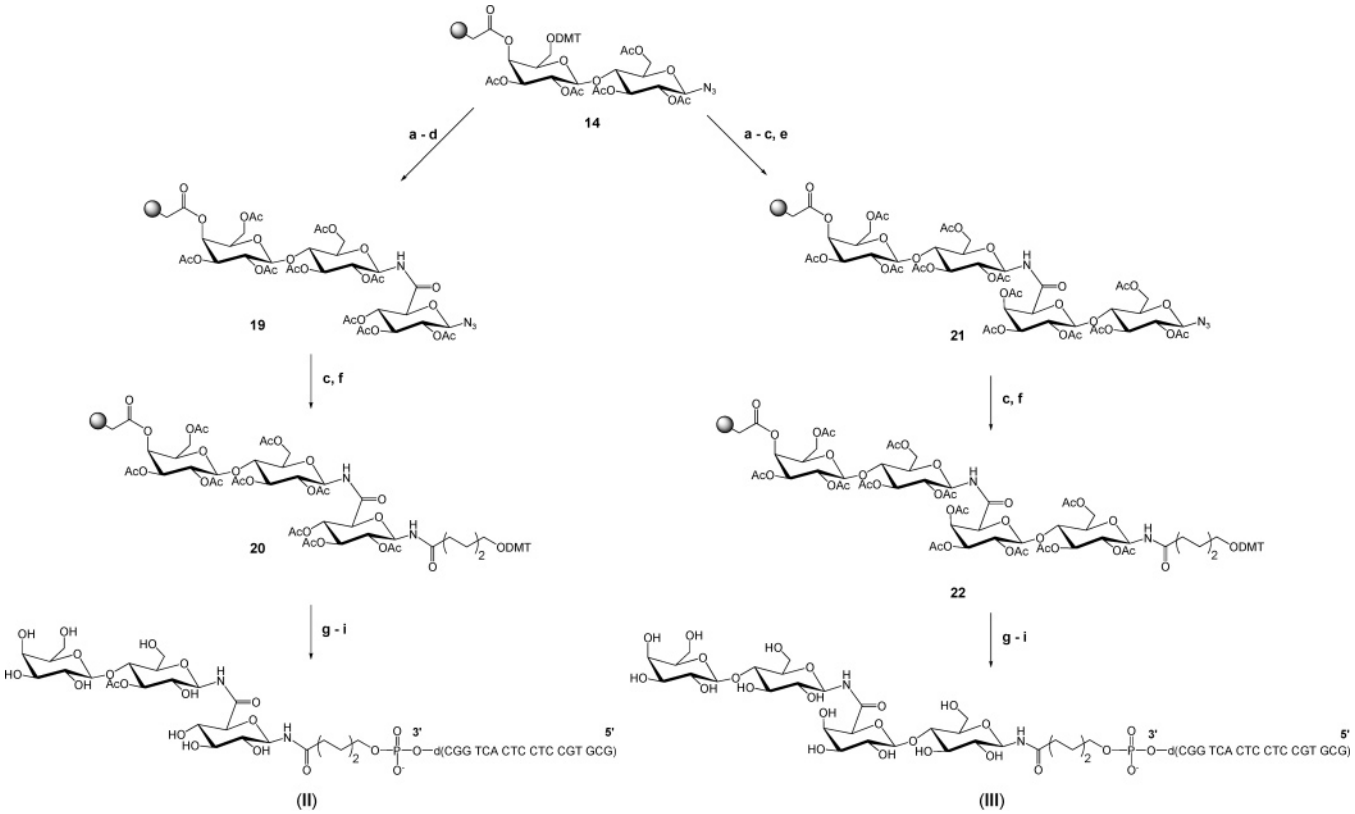

(a) 1% DCA in DCM, rt, 10 min; (b) Ac_2O/pyridine (1:1, v/v), rt, 30 min; (c) 1,3-propanedithiol, TEA, molecular sieves, DMF, rt, 2 h; (d) coupling with **8**, HATU, HOBt, DIPEA, DMF, rt, 1.5 h; (e) coupling with **16**, HATU, HOBt, DIPEA, DMF, rt, 1.5 h; (f) coupling with DMTO$(CH_2)_5$COOH, HATU, HOBt, DIPEA, DMF, rt, 1.5 h; (g) automated ODN chain assembly; (h) final DMT removal; (i) aq NH_3, 50 °C, 6 h.

the carboxyl activator, leading to **6**. Typically, functionalizations with the first glucose residue were in the range 0.20−0.23 meq/g, as evaluated by quantitative DMT test on weighed samples of dry resin **6**, corresponding to an average 74% incorporation yield.

The synthesis of building block **8** was achieved starting from **1**, which was first subjected, in a one-pot reaction, to NaN_3 treatment, then to deacetylation, followed by TBDMSCl addition (81% overall yields for the three steps). The obtained derivative was successively acetylated, leading to **7** in almost quantitative yields, which was then converted, by treatment with the Jones reagent, into **8** (90% yields for the two steps). Addition of sulfuric acid in pyridine caused both the TBDMS removal and the oxidation of the liberated hydroxyl group to carboxylic acid. Building block **8** had already been reported by Toth et al. (*27*), obtained from glucuronic acid in a two-step process with 73% overall yields. This synthon was exploited in the solid-phase synthesis, through standard Fmoc chemistry, of new glycosylated enkephalin analogues, containing one or two glucuronic acid residues connected at the C-terminus of the pentapeptide skeleton through amide bonds. In our strategy, compound **8** was obtained through five easy conversions, requiring only two chromatographic purifications, starting from **1** in 73% overall yield. This route, though longer, was preferred over the already published procedure, not involving the use of the aggressive and highly hygroscopic reagent tin (IV) chloride and therefore resulting in a more reproducible reaction system. **8** could be also directly obtained by oxidation of 1-azido-2,3,4-tri-O-acetyl-6-O-(4,4′-dimethoxytriphenylmethyl)-β-D-glucopyranose, but this procedure always gave an unclean reaction mixture.

To demonstrate that the here described procedure is not restricted only to monosaccharides but in principle can be easily extended to any preformed oligosaccharide, a similar protocol was developed for the synthesis of support **14**, functionalized with a β-1-azido lactose residue and the related lacturonic acid derivative **16**, to be used as the addition building block. Peracetylated lactose **9**, selected as the starting material, was first reacted with tin(IV) chloride and $TMSN_3$ in DCM, thus giving the corresponding β-1-azido derivative **10** in 90% yields. Deacetylation, followed by insertion of the benzylidene protecting group on the 4,6-OH functions of the galactose residue and then acetic anhydride treatment afforded **11** (70% yields for the three steps). TFA treatment to remove the benzylidene group yielded compound **12** with 90% yields, which was successively dimethoxytritylated on the primary hydroxyl (85% yields) and then succinylated at the free 4-OH function in 90% yields. Derivative **13** was then reacted with the Tentagel amino solid support in the presence of DIC as the condensing reagent, to afford functionalized support **14** with a typical loading of 0.20 meq/g (by DMT test).

1-Azido uronic acid **16** was synthesized from **12** in three steps, involving only one-column chromatography, and 72% overall yields. Reaction with TBDMSCl and imidazole in DMF gave a mixture of two regioisomers silylated, respectively, on the 6 and 4 positions, in 80% yields. This mixture was reacted as such with acetic anhydride in pyridine; under these conditions, the spontaneous migration of the TBDMS group from the 4- to the 6-OH position was observed, being **15** the sole obtained derivative. This compound was then treated with the Jones reagent, which afforded target compound

16 in 90% yield. In all the studied reactions, the azido group was found to be completely stable.

With the two functionalized solid supports **6** and **14** and the protected 1-azido uronic acids **8** and **16** as building blocks, the assembly of the glycomimetic domain was carried out in the solid phase, essentially following a previously reported protocol (*27*). The elongation cycle of the saccharidic portion required the following steps, based on simple and standard chemistry: (i) reduction of the 1-azido function by addition of 1,3-propanedithiol and Et_3N in DMF (*33*); (ii) coupling with the uronic acid building block **8** or **16** (10 equiv) in the presence of HATU (10 equiv), HOBt (10 equiv), and DIPEA (15 equiv) in DMF; (iii) capping by standard acetic anhydride treatment in pyridine (Schemes 3 and 4). Successively, a flexible 6-hydroxyhexanoic acid linker, protected at the hydroxy function as DMT−ether, was introduced in the solid support by exploiting the same coupling procedure described above. By quantitative DMT test on dried samples of supports **18**, **20**, and **22**, the loading of the linker was in the range 0.12−0.14 meq/g, thus indicating 65% overall yields for the whole synthetic cycle starting from **6** or **14**, with an average yield for each coupling cycle (reduction of the azide followed by amide bond formation) estimated to be not inferior to 80%. Assembly of the ODN chain could then be achieved starting from functionalized solid supports **18**, **20**, and **22** on an automated DNA synthesizer by exploiting standard phosphoramidite chemistry. Three 18-mers of sequence d(5′GCGTGCCTC-CTCACTGGC3′), differing in their saccharidic domains, were synthesized (**I**, **II**, and **III**). In all cases, DMT tests monitoring the efficiency of the ODN assembly indicated, for each coupling cycle, yields not inferior to 98%.

This ODN sequence was selected as a relevant target in antisense experiments, being complementary to a tract of mRNA of protein kinase A type 1 (PKA1), subunit RIα, which is overexpressed in the majority of human cancers. As potential therapeutic agents against neoplasia, several modifications of this sequence are currently under clinical trial (*34*, *35*).

Once completed the ODN chain assembly, detachment from the solid support and deprotection of the 3′-conjugated oligomers were achieved by treatment with concentrated aq ammonia. Purification of the detached material was carried out by HPLC on an anionic exchange Nucleogel column; HPLC profile of crude **III** is showed in Figure 2. The collected peaks were then desalted by gel filtration chromatography on a Sephadex G25 column eluted with H_2O. The isolated products were checked for purity by HPLC on an analytical RP18 column, showing all of them to be more than 98% pure. The synthesized ODNs **I**−**III** were characterized by mass analysis; in particular, MALDI-TOF MS spectra of each ODN conjugate showed a single peak in agreement with the expected molecular weight.

In a typical experiment, starting from 50 mg of support **6** or **14**, ca. 3 mg for each purified glycoconjugate **I**−**III** could be obtained, as evaluated by UV quantitation.

Samples of the functionalized supports **17**, **19**, and **21** were treated with aq ammonia and, in all cases, ^{1}H NMR analysis of the crude detached materials showed the coupling constants of the anomeric protons exclusively in the range 7.7−8.8 Hz, consistent with a β configuration, which indicates that the reducing thiol treatment on the 1-azido function, generally accepted as following a radicalic mechanism, does not affect the stereochemistry of the anomeric position.

The effect of the 3′-glycoconjugation on the chemical stability of the ODN was studied by incubating samples

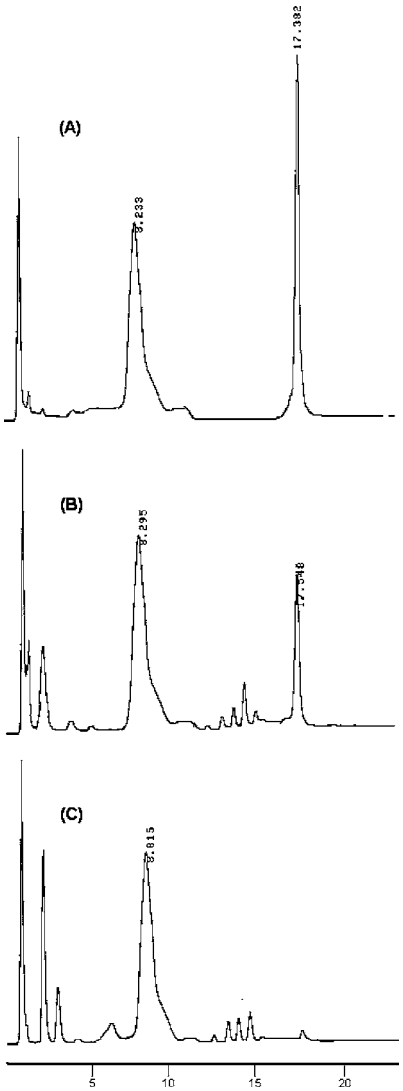

Figure 4. HPLC profiles of purified oligonucleotide 3′-glycoconjugate **III** (conditions as reported in Figure 2) treated with bovine fetal serum: panel A, aliquot of the mixture taken after 15 min; panel B, aliquot of the mixture taken after 3 h; panel C, aliquot of the mixture taken after 6 h.

of 1.0 OD of purified hybrids **I**−**III** at 37 °C with 1.0 mL of a phosphate buffer [20 mM KH_2PO_4 aq solution, containing 20% (v/v) CH_3CN] at pH values ranging from 5.0 to 9.0. In all cases, no degradation was observed even after 20 d, as judged by HPLC analysis of the treated oligomers on an analytical anionic exchange column (Figure 3). The stability of the synthesized glycoconjugates was investigated also in biological media: 3′-glycoconjugate **III** (1 OD) was incubated at 37 °C with 1 mL of bovine fetal serum and the mixture analyzed by HPLC. Total disappearance of the peak corresponding to the intact glycoconjugate was observed after 6 h (Figure 4), while the unconjugated 18-mer d(5′GCGTG-CCTCCTCACTGGC3′), treated in the same conditions for comparison, was completely degraded to a complex mixture of 3′- and 5′-mononucleotides in 3 h.

To investigate the binding affinities of the synthesized glycoconjugates with complementary DNA sequences, the UV thermal denaturation analysis of the duplex structures was carried out. Duplex formation was achieved by hybridizing oligomers **I**−**III** with equimolar amounts of the unmodified complementary 22-mer d(5′TTGCCAG-TGAGGAGGCACGCAT3′), dissolved in a 100 mM NaCl, 10 mM NaH_2PO_4, aq solution at pH = 7.0 at a final

concentration of approximately 1 μM per each strand. The melting curves of the duplexes under investigation registered at $\lambda = 260$ nm were in all cases superimposable to the one obtained in the same buffer conditions for the natural one ($T_m = 60$ °C), indicating that the recognition properties of oligonucleotide sequences were not modified upon 3′-conjugation with the here described glycomimetics.

CONCLUSIONS

We have synthesized, exploiting an online solid-phase procedure, new oligonucleotide hybrids, conjugated at the 3′-end of the chain with saccharide mimics having the O-glycosidic linkages replaced with stable 1,6-amide bonds. The key intermediate in our synthetic protocol is a suitably protected 1-azido uronic acid derivative of glucose or lactose (**8** or **16**, respectively), chosen as building blocks, in connection with the usage of Tentagel solid supports ad hoc functionalized with the first 1-azido sugar residue (**6** or **14**). To elongate the saccharidic domain, the azido function is in situ reduced to a primary amine just before the coupling step, performed on the solid support following a typical solid phase peptide synthetic protocol. After insertion of the flexible linker 6-hydroxyhexanoic acid, the oligonucleotide chain assembly was carried out by standard phosphoramidite chemistry. By exploitation of a completely automated synthetic process, three oligosaccharide−oligonucleotide hybrids were prepared and characterized by MALDI-TOF spectrometry. The presence of the saccharidic domain at the 3′-end of antisense 18-mer sequences significantly enhanced the stability of the oligonucleotides in bovine fetal serum, not negatively interfering with their ability to form stable duplexes with complementary DNA strands, as evaluated by UV thermal denaturation studies.

ACKNOWLEDGMENT

We thank MIUR (PRIN) and Regione Campania (Legge 5) for grants in support of this investigation and Centro di Metodologie Chimico-Fisiche (CIMCF), Università di Napoli "Federico II", for the NMR and MS facilities. The valuable contribution of Dr. Antonia De Capua in the initial part of the work is gratefully acknowledged.

LITERATURE CITED

(1) Dias, N. and Stein, C. A. (2002) Antisense Oligonucleotides: basic concepts and mechanisms. *Mol. Cancer Ther. 1*, 347−355.

(2) Thuong, N. T. and Hélène, C. (1993) Stereospecific detection and modification of double helix DNA by oligonucleotides. *Angew. Chem., Int. Ed. Engl. 32*, 666−690.

(3) Famulok, M., Mayer, G., and Blind, M. (2000) Nucleic acid aptamers - from selection in vitro to applications in vivo. *Acc. Chem. Res. 33*, 591−599.

(4) Goodchild, J. (1990) Conjugates of oligonucleotides and modified oligonucleotides: a review of their synthesis and properties. *Bioconjugate Chem. 1* (3), 165−87.

(5) Beaucage, S. L., and Iyer, R. P. (1993) The synthesis of modified oligonucleotides by the phosphoramidite approach and their applications. *Tetrahedron 49* (28), 6123−94.

(6) *Carbohydrate Modifications in Antisense Research*; Sanghvi, Y. S., Dan Cook, P., Eds., ACS Symposium Series: Washington, USA, 1994.

(7) Leumann, C. J. (2002) DNA analogues: from supramolecular principles to biological properties. *Bioorg. Med. Chem. 10*, 841−854.

(8) Gabius, H.-J., Siebert, H.-C., Andre, S., Jimenez-Barbero, J., and Ruediger, H. (2004) Chemical biology of the sugar code. *Chem. Bio. Chem. 5* (6), 740−764.

(9) *Carbohydrates in Chemistry and Biology, Part II: Biology of Saccharides, Volume 4: Lectins and Saccharide Biology*; Ernst, B., Hart, G. W., and Sinay, P., Eds., 2000, pp 529, Wiley-VCH, Weinheim, Germany.

(10) Lis, H., and Sharon, N. (1998) Lectins: carbohydrate-specific proteins that mediate cellular recognition. *Chem. Rev. 98*, 637−674.

(11) Dwek, R. A. (1996) Glycobiology: toward understanding the function of sugars. *Chem. Rev. 96*, 683−720.

(12) Davis, B. J. (2000) Recent developments in oligosaccharide synthesis. *J. Chem. Soc., Perkin Trans. 1*, 2137−2160.

(13) Seeberger, P. H., and Haase, W. (2000) Solid-phase oligosaccharide synthesis and combinatorial carbohydrate libraries. *Chem. Rev. 100*, 4349−4394.

(14) Seeberger, P. H. (2003) Automated carbohydrate synthesis to drive chemical glycomics. *J. Chem. Soc*., *Chem. Commun*. *10*, 1115−1121.

(15) Palmacci, E. R., Plante, O. J., Hewitt, M. C., and Seeberger, P. H. (2003) Automated synthesis of oligosaccharides. *Helv. Chim. Acta*, *86* (12), 3975−3990.

(16) Zatsepina, T. S. and Oretskaya, T. S. (2004) Synthesis and applications of oligonucleotide-carbohydrate conjugates. *Chem. Biodiversity 1*, 1401−1417.

(17) Adinolfi, M., De Napoli, L., Di Fabio, G., Guariniello, L., Iadonisi, A., Messere, A., Montesarchio, D., and Piccialli, G. (2001) Solid-phase synthesis of glyco-oligonucleotide conjugates. *Synlett 6*, 745−748.

(18) Barchi, J. J., Jr. (2000) Emerging roles of carbohydrates and glycomimetics in anticancer drug design. *Curr. Pharm. Design 6* (4), 485−501.

(19) Gruner, S. A. W., Locardi, E., Lohof, E., and Kessler, H. (2002) Carbohydrate-based mimetics in drug design: sugar amino acids and carbohydrate scaffolds. *Chem. Rev. 102*, 491−514.

(20) Adinolfi, M., De Napoli, L., Di Fabio, G., Iadonisi, A., Montesarchio, D., and Piccialli, G. (2002) Solid-phase synthesis of oligonucleotides tethered to oligo-glucose phosphate tails. *Tetrahedron 58*, 6697−6704.

(21) Adinolfi, M., De Napoli, L., Di Fabio, G., Iadonisi, A., and Montesarchio, D. (2004) Modulating the activity of oligonucleotides by carbohydrate conjugation: solid-phase synthesis of sucrose-oligonucleotide hybrids. *Org. Biomol. Chem. 2*, 1879−1886.

(22) Nicolaou, K. C., Florke, H., Egan, H., Egan, M. G., Barth, T., and Estevez, V. A. (1995) Carbonucleotoids and carbopeptoids: new carbohydrate oligomers.*Tetrahedron Lett. 36*, 1775−1778.

(23) Suhara, Y., Hildreth, J. E. K., and Ichikawa, Y. (1996) Synthesis of a new carbohydrate mimetics: "carbopeptoid" containing a C-1 carboxylate and C-2 amino group. *Tetrahedron Lett. 37*, 1575−1578.

(24) Suhara, Y., Izumi, M., Ichikawa, M., Penno, M. B. and Ichikawa, Y. (1997) Peptide-sugar hybrids: like peptide, like oligosaccharide. *Tetrahedron Lett. 38*, 7167−7170.

(25) Smith, M. D., Long, D. D., Marquess, D. G., Claridge, T. D. W., and Fleet, G. W. J. (1998) Synthesis of oligomers of tetrahydrofuran amino acids: furanose carbopeptoids. *Chem. Commun*. *18*, 2039−2040.

(26) Muller, C., Kitas E., and Wessel, H. P. (1995) Novel oligosaccharide mimetics by solid-phase synthesis. *Chem. Commun*. *23*, 2425−2426.

(27) Drouillat, B., Kellam, B., Dekany, G., Starr, M. S., and Toth, I. (1997) Solid-phase synthesis of C-terminal carbohydrate modified enkephalins. *Bioorg. Med. Chem. Lett*. *7*, 2247−2250.

(28) Long, D. D., Smith, M. D., Marquess, D. G., Claridge, T. D. W., and Fleet, G. W. J. (1998) A solid-phase approach to oligomers of carbohydrate amino acids: secondary structure in a trimeric furanose carbopeptoid. *Tetrahedron Lett*. *39*, 9293−9296.

(29) Smith, M. D., Claridge, T. D. W., Tranter, G. E., Sansom, M. S. P., and Fleet, G. W. J. (1998) Secondary structure in oligomers of carbohydrate amino acids. *Chem. Commun*. *18*, 2041−2042.

(30) *Oligonucleotides and Analogues: a Practical Approach*; Eckstein, F., Ed., IRL Press, Oxford, 1991.

(31) *Handbook of Biochemistry and Molecular Biology*, Volume I, Nucleic Acids, Fasman, G. D., Ed., 3rd ed., CRC Press, 1975; p 589.
(32) Gyorgydeak, Z., Szilagyi, L., and Paulsen, H. (1993) Synthesis, structure, and reactions of glycosyl azides. *J. Carbohydrate Chem. 12*, 139−163.
(33) Bayley, H., Standring, D. N., and Knowles, J. R. (1978) Propane-1,3-dithiol: a selective reagent for the efficient reduction of alkyl and aryl azides to amines. *Tetrahedron Lett. 39*, 3633−3634.
(34) Tortora, G., Bianco, R., Damiano, V., Fontanini, G., De Placido, S., Bianco, R., and Ciardiello, F. (2000) Oral antisense that targets protein kinase A cooperates with taxol and inhibits tumor growth, angiogenesis, and growth factor production. *Clin. Cancer Res. 6*, 2506−2512.
(35) Tortora, G., Caputo, R., Damiano, V., Fontanini, G., Melisi, D., Veneziani, B. M., Zunino, F., Bianco, A. R., and Ciardiello, F. (2001) Oral administration of a novel taxane, an antisense oligonucleotide targeting protein kinase A, and the epidermal growth factor receptor inhibitor Iressa causes cooperative antitumor and antiangiogenic activity. *Clin. Cancer Res*. *7* (*12*), 4156−4163.

BC0501606

TECHNICAL NOTES

Free Nonimmobilized Ligands as a Tool for Purification of Proteins

Guy Patchornik[†,*] and Amnon Albeck[§]

Affisink Biotechnology Ltd., 11 Hamaccabee St. Kiryat-Ono 55572, Israel, and The Julius Spokojny Bioorganic Chemistry Laboratory, Department of Chemistry, Bar-Ilan University, Ramat-Gan 52900, Israel.
Received March 28, 2005; Revised Manuscript Received July 11, 2005

Purification of proteins on a large scale is a complex multistep process, and alternative economic strategies are required. This study presents a novel approach (Affinity Sinking, AS) for purification of native proteins utilizing nonimmobilized modified ligands. The nonimmobilized state of the ligand circumvents the need for immobilizing ligands to polymeric supports. Therefore, purification from large volumes can be accomplished without the use of industrial-scale affinity columns. The mechanism of product capture is formation and precipitation of a specific [target-protein/modified-ligand] complex by using a soluble interconnecting entity that generates an insoluble [target-protein/modified-ligand/interconnecting entity] sediment containing the target protein. Rabbit IgG and two glycoproteins were purified accordingly, utilizing free avidin (as the interconnecting entity) and either desthiobiotinylated-protein A (DB-ProA) or desthiobiotinylated-concanavalin A (DB-ConA) as the modified ligand. The recovery yields for the IgG and the two glycoproteins were 80−86% and 70−75%, respectively. Target proteins are eluted from the generated pellet nearly without disrupting the [modified-ligand/interconnecting entity] macro-complex, thus enabling a practical procedure of recovering target proteins. Leaching of the DB-ProA ligand under eluting conditions (pH 3) was found to be lower than 1%. The two modified ligands, DB-ProA and DB-ConA, were regenerated without any chromatographic procedure in 80% and 85%-89% yield, respectively. The advantage of excluding the polymeric component from the purification process and obtaining highly purified proteins has been demonstrated, and it implies that other contaminants (e.g. endotoxins, prions, host DNA) could be excluded as well, thereby reducing the number of purification steps in a typical downstream process.

INTRODUCTION

There is a continuing search for alternative purification strategies capable of capturing minute amounts of target proteins from complex cell culture supernatants, plant extracts, or milk of transgenic animals containing excessive amounts of impurities (e.g. immunogenes, pyrogens, DNA, and perhaps endotoxins) (*1*, *2*). The scope of purification techniques is limited by the inherent tendency of proteins to denature in the presence of organic solvents, high temperature, or extreme pH. Therefore, low concentration of the target proteins, their fragility, and the need to cope with large amounts of complex media may have led to the fact that the least well engineered part in bioproduction processes are the purification steps (*3*), typically resulting in 50−80% of the total production cost (*4*, *5*). The largest purification factor within the multistep purification process is achieved by affinity chromatography (AC),[1] exploiting the high specific binding interaction between a ligand immobilized to a polymeric support and a protein of interest (Figure 1, A) (*6*, *7*). AC, perhaps the most widely used affinity technique at large-scale (*8*), has been used successfully in a number of biotech downstream processes, namely in the area of mammalian cell culture products (*9*).

Like any purification approach, AC suffers from several limitations at industrial scale. These include (a) careful control over column loading which generally results in formation of large volumes of dilute eluent, requiring concentration before further processing; (b) high operation and maintenance costs due to the high pressure involved and the special requirement for affinity media; (c) column fouling which prevents the use of AC during early product isolation when process streams are too crude; (d) capacity and flow rate limitations with an upper limit of 2−10 kg/day productivity for each production line; (e) limited adsorbent lifetime due to the growth of microorganisms that frequently either lead to breakdown of the column matrix or contaminate the product with unknown bacteria and their byproducts, or may even result in possible digestion of the product by the bacterial extracellular proteases; (f) implementation of harsh sanitizing protocols raise the concern of ligand degradation that may contaminate the product and decrease the capacity of the column. Therefore, a wide array of alternative affinity purification approaches has

* Corresponding author. E-mail: guy@affisink.com, Tel: 972-8-9302575, Fax: 972-8-9302565.
† Affisink Biotechnology Ltd.
§ Bar-Ilan University.

[1]Abbreviations: AC, affinity chromatography; AML, affinity macroligand; AP, Affinity precipitation; AS, affinity sinking; ConA, concanavalin A; DB, desthiobiotin; DB-ConA, desthiobiotinylated concanavalin A; DB-ProA, desthiobiotinylated protein A; EDTA, ethylenediaminetetraacetic acid; HPLC, high-pressure liquid chromatography; PAGE, poly acrylamide gel electrophoresis; SDS, sodium dodecyl sulfate.

10.1021/bc050096s CCC: $30.25 © 2005 American Chemical Society
Published on Web 08/27/2005

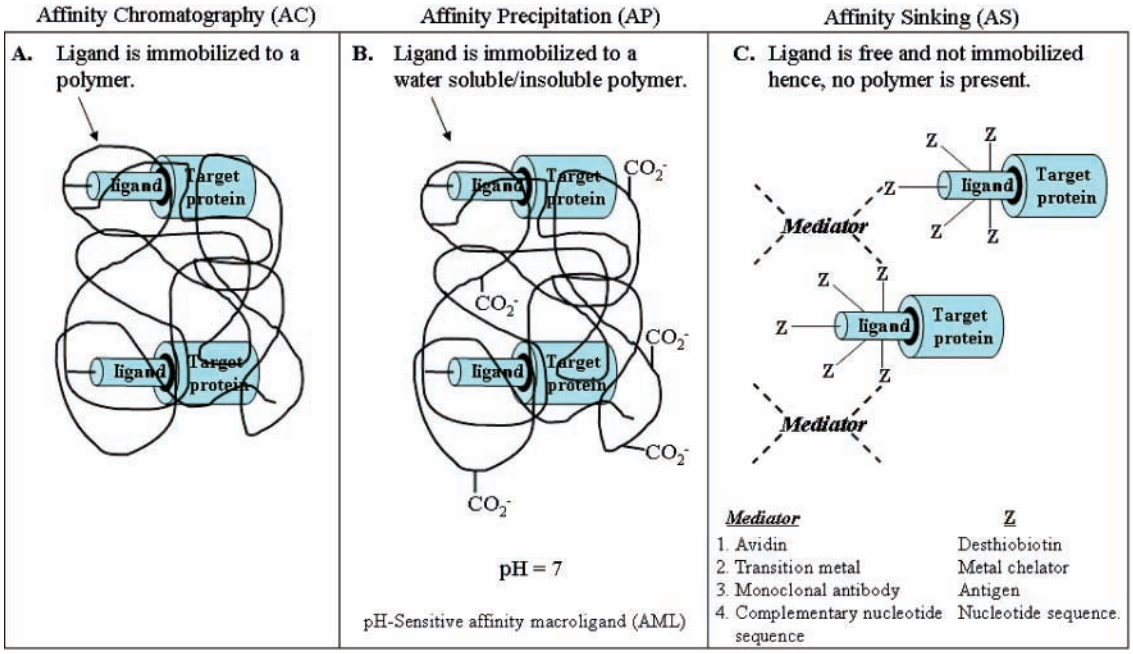

Figure 1. Comparison of the basic chemical architecture of AC, AP and AS. A. Ligands in AC are immobilized to insoluble polymeric matrixes. B. Ligands in AP are immobilized to water soluble polymers which would change reversibly to water insoluble upon a physiochemical change such as low pH. C. Ligands in AS are not immobilized but modified with a complexing entity enabling their precipitation upon addition of an appropriate mediator. Thus, no polymeric entity is present within the precipitation process and ligands are free in the medium.

been developed with the objective of meeting the unique difficulties addressed by large-scale purification (*10*−*15*).

Affinity precipitation (AP) (secondary effect), first introduced by Schneider et al. (*16*), has been postulated to become the purification technique with the highest large-scale potential (*4*, *17*−*19*). In AP, a water soluble polymer is conjugated with a specific ligand, generating an affinity macroligand (AML) (Figure 1, B). The AML forms a complex with the target molecule, which precipitates upon a critical physiochemical change in pH, temperature, or ionic strength. The target protein could then either be eluted directly from the [AML−target protein] complex or from the dissolved state of the complex under conditions which decrease the binding affinity between the AML and the target protein. The AML itself (without the target protein) is then precipitated again, leaving the target protein in the supernatant (*20*). The unique combination of specificity and precipitation features being utilized in all AP approaches has not yet led to an established downstream processing technique due to several difficulties: (a) steric hindrances induced by high molecular weight AML, limiting the access of the target molecule; (b) resolubilization of precipitated polymers was slow; (c) nonspecific adsorption and entrapment of impurities during precipitation was almost unavoidable, requiring up to three successive precipitation-resolubilization steps (*1*, *19*, *21*−*23*).

This state of affairs prompted us to develop the present specific precipitation approach, affinity sinking (AS), lacking any polymeric component and with ligands that are free in solution. Specific precipitation is obtained within two successive steps: first, the nonimmobilized modified ligand and the target protein are incubated to allow specific binding. This generates a [modified ligand−target protein] soluble complex. The latter complex is specifically precipitated by addition of an appropriate interconnecting entity (the mediator) such as free avidin that presumably forms macro networks with lower solubility properties (Figure 1, C). The approach was performed with two distinct ligands: (a) Protein A: a 42 kDa factor produced by *Staphylococcus aureus*, which specifically binds the constant region of a wide range of antibodies from various classes and therefore is extensively utilized for purification of immunoglobulins (*24*). (b) Concanavalin A: a lectin that exhibits distinct sugar specificities toward α-D-mannopyranosides, α-D-glucopyranosides, or α-*N*-acetyl-D-glucosaminides (*25*) and specifically binds glycoproteins. Both ligands were modified with desthiobiotin *N*-hydroxysuccinimidyl ester (desthiobiotin-NHS) and used for purification of rabbit IgG, porcine thyroglobulin, and glucose oxidase.

EXPERIMENTAL PROCEDURES

Materials. For SDS−PAGE, Precision plus protein standards and Gel Filtration Chromatography Standards were from Bio-Rad. All other reagents were of analytical grade. Tris (ultrapure) was from Bio-Lab, Jerusalem. Avidin, biotin, methyl α-D-glucopyranoside, concanavalin A Type IV, and EDTA were from Sigma. Porcine thyroglobulin and glucose oxidase were from GALAB Technologies GmbH, Germany. Desthiobiotin *N*-hydroxysuccinimidyl ester was from Berry & Associates, Dexter, MI. Recombinant protein A was from BioVision, Inc. (Palo Alto, CA). Rabbit IgG was from Sigma, Glucose oxidase kit was from Megazyme, Ireland.

Protein Analysis. Protein content was estimated by the method of Bradford (*26*), using bovine serum albumin as a standard.

Electrophoresis and Densitometry. Samples were loaded onto a 10% bis-Tris SDS-poly-acrylamide gel (1 mm thickness) according to Laemmli (*27*) and developed for 1 h at constant 120 V. All gels were stained with Coomassie Brilliant Blue R250, and the intensity of bands was measured by densitometry using the Scion Image program. These measurements were used for quantification of the recovery yields of the target proteins and their purity.

Preparation of Desthiobiotinylated Protein A (DB-ProA) and Desthiobiotinylated Concanavalin A (DB-ConA). Recombinant protein A or concanavalin A (ConA) were modified with desthiobiotin *N*-hydroxysuccinimidyl ester according to Bayer et al. (*28*), with a molar ratio of 4.4:1 between the desthiobiotin reagent and ConA, while protein A was modified accordingly with a molar ratio of 20:1.

Precipitation and Elution of Rabbit IgG. Precipitation was carried out at 4 °C in a medium containing: 50 mM sodium phosphate at pH 8, 0.23 mg/mL of DB-Pro A, 0.6 mg/mL rabbit IgG, and cell lysate in a total volume of 50 μL. A freshly prepared avidin solution (1.5 mg/mL final concentration) was added, and a precipitate was formed. This was followed by a short spin at 14000 rpm and removal of the supernatant. The pellet was resuspended once with 200 μL of 50 mM sodium phosphate buffer pH 8 and the supernatant discarded. To elute rabbit IgG, the pellet was further resuspended with 0.1 M sodium citrate pH 3, 0.9 M urea at 4°C for 10 min in a total volume of 50 μL with gentle agitation. After an additional spin, the supernatant was neutralized with 1 N NaOH and applied to the gel.

Regeneration of DB-ProA. Recovery of DB-Pro A was achieved by incubating the pellets in 0.1 M sodium citrate pH 3 and 5 mM of biotin at 4 °C for 10 min. A spin at 14000 rpm was performed and the supernatant was neutralized with 1 N NaOH and applied to the gel.

Precipitation of Porcine Thyroglobulin and Glucose Oxidase. Precipitations were carried out at 4 °C in a medium containing 20 mM Tris buffer pH 7.2, 3.3 mg/mL of DB-Con A, 2.2 mg/mL porcine thyroglobulin or 1.4 mg/mL glucose oxidase, and a mixture of native proteins (Biorad Gel Filtration Chromatography Standards), in a total volume of 30 μL. A freshly prepared avidin solution (3.3 mg/mL, final concentration) was then added, and a precipitate was formed. A short spin at 14 000 rpm allowed removal of the supernatant which contained the vast majority of the impurities, while the pellet was further washed by resuspending it once in 200 μL of 20 mM Tris buffer pH 7.2, and the supernatant discarded.

Elution of Porcine Thyroglobulin and Glucose Oxidase from the Pellets. Washed pellets were incubated at 4 °C for 2−5 min in a medium containing 0.1 M $NaHCO_3$ pH 7.8, 0.2 M methyl α-D-glucopyranoside (*29*), and 5 mM EDTA in a total volume of 30 μL with gentle agitation. After a short sedimentation at 14000 rpm, the supernatant of the pellet was applied to the gel.

Regeneration of DB-Con A. Recovery of DB-ConA was identical to that described above for DB-ProA.

Catalytic Activity of Glucose Oxidase. The catalytic activity of the purified glucose oxidase was studied with the glucose oxidase assay kit.

Generation of *E. coli* Lysate. BL21 bacteria harboring a pACYCDuet vector (Novagen) were grown in 4.5 L of LB medium for 2 h at 37 °C. Protein expression was induced by the addition of 0.05 mM IPTG, and the bacteria continued to grow for an additional 4 h at 15 °C. The bacteria were lysed by freeze thawing in lysis buffer (Tris 50 mM pH 8, 0.1 M NaCl, 20 mM imidazole, protease inhibitor cocktail, lysozyme, and Dnase) followed by sonication. The bacterial lysate was then centrifuged by ultracentrifugation at 40000 rpm, and the supernatant was applied to a Ni column at 4 °C. (The lysate is the flow-through from this Ni capture).

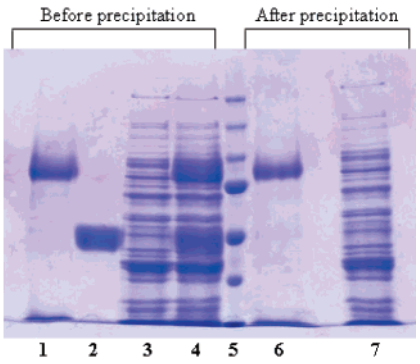

Figure 2. Purification of rabbit IgG from cell lysate, utilizing desthiobiotinylated protein A (DB-ProA) and free avidin. Lane 1 rabbit IgG; lane 2 DB-ProA; lane 3 bacterial cell lysate; lane 4 mixture of rabbit IgG, DB-ProA, and cell lysate; lane 5 Biorad prestained protein markers; lane 6 recovered IgG; lane 7 content of supernatant after specific precipitation of the IgG from the cell lysate.

RESULTS

Specific Precipitation and Elution of Target Proteins. *Rabbit IgG.* To demonstrate the selectively of the approach, rabbit IgG was purified from bacterial cell lysate. Thus, a medium containing whole cell lysate, DB-ProA, and rabbit IgG was prepared (Figure 2, lane 4). Upon addition of avidin, a precipitate was generated and the resulting pellet was washed once with 200 μL of fresh buffer. The washed pellet was further incubated under eluting conditions (0.1 M sodium citrate at pH 3, 4 °C, for 15 min), and the supernatant of the resuspended pellet was applied to the gel after being neutralized to pH 7. The recovery yield of the IgG was 85% (Figure 2, lane 6). Comparing the total amount of impurities (Figure 2, lane 3) with the amount of impurities present in the supernatant after the addition of avidin (Figure 2, lane 7) indicates that 95% were excluded from the pellet, prior to the washing step. Since no DB-ProA was observed by Coomassie staining in the eluted IgG (lane 6), the degree of leached DB-ProA was assessed by silver staining to be below 1%.

Porcine Thyroglobulin and Glucose Oxidase. Similar results, of target protein purification in high yield and high purity, were obtained for porcine thyroglobulin and glucose oxidase. In this case, the ligand was DB-ConA. The recovery yields of porcine thyroglobulin and glucose oxidase were 70−75% and the purity above 95% (by densitometry). Glucose oxidase and porcine thyroglobulin were not precipitated in the presence of native concanavalin A and avidin. The modified ligand (DB-ConA) was regenerated in 86%.

The purification data of the three target proteins are summarized in Table 1.

The Effect of Increased Background Contamination on the Purification Process. To study the effect of increased background contamination on the yield and purity of the purification process, identical amounts of rabbit IgG, avidin, and DB-ProA were added to increasing concentrations of either BSA (Figure 3, A) or cell lysate (Figure 3, B). All pellets were washed once with identical volumes of fresh buffer (200 μL) regardless of their contamination background and the IgG was eluted. The eluted IgG solutions exhibited similar purity and yield (Figure 3, A, lanes 2P−5P; B, lanes 3P-5P) whether BSA or the cell lysate served as the background contamination. Similar results were obtained with DB-ConA and the glycoproteins porcine thyroglobulin and glucose oxidase (data not shown).

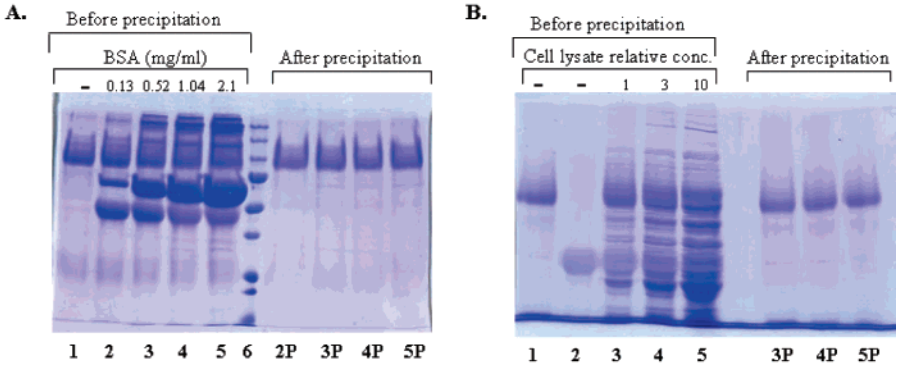

Figure 3. The effect of increased background contamination on the precipitation process. A. Lane 1 rabbit IgG; lanes 2−5 constant concentration of rabbit IgG and DB-ProA in the presence of increased BSA concentration; lane 6 Biorad prestained protein standards; lanes 2P−5P recovered IgG from pellets generated in lanes 2−5, respectively. B. Lane 1 rabbit IgG; lane 2 DB-ProA; lanes 3−5 constant concentration of rabbit IgG and DB-ProA in the presence of increased cell lysate concentration; lanes 3P−5P recovered IgG from pellets generated in lanes 3−5, respectively.

Table 1. Recovery Yields and Purity of the Target Proteins and the Modified Ligands

target protein	desthiobiotinylated ligand	recovery yield of target protein, %	purity of target protein, %	recovery yield of desthiobiotinylated ligand, %
rabbit IgG	protein A	80−86	97	80
thyroglobulin	concanavalin A	70−75	95	85−89
glucose oxidase	concanavalin A	70−75	95	85−89

Catalytic Activity of Recovered Glucose Oxidase. The purified glucose oxidase was assayed for its catalytic activity and was found to be 98 ± 3% active. This result emphasizes the mildness and lack of denaturation by the process.

DISCUSSION

It has been argued that the ideal strategy for large-scale purification of proteins would utilize a highly specific precipitation process rather than a chromatographic methodology (*4*, *19*). Therefore, we aimed at developing a simple precipitation approach (which we call affinity sinking, AS) that would lead to highly purified proteins while eliminating the need for sophisticated instrumentation (e.g. HPLC).

To the best of our knowledge, all known chromatographic and precipitation techniques require ligands covalently bound to various polymeric supports, while AS uses ligands at their free nonimmobilized state. The use of free ligands would circumvent the need for immobilizing ligands to polymers and would exclude polymers from the purification process. Figure 1 illustrates the differences in chemical architecture of well-established approaches (e.g. affinity chromatography, affinity precipitation) with that of AS. In AS, precipitation of the target protein requires two water soluble entities: a modified ligand and an interconnecting entity. The modified ligands used in this study were desthiobiotinylated protein A (DB-ProA) and desthiobiotinylated concanavalin A (DB-ConA). Incubation of the modified ligand with the target protein and addition of the interconnecting entity (free avidin) generated a precipitate, composed primarily of the [modified ligand−target protein−avidin] multicomplex (Figure 1, C). The target protein is then eluted from the generated sediment (i.e. pellet) under conditions that essentially do not dissociate the [modified ligand−avidin] multicomplex.

Since antibody purification is a major scientific and industrial need, we tested the ability of the approach to specifically capture and purify rabbit IgG from cell lysate, utilizing DB-ProA as the ligand (Figures 2 and 3). The high purity (97%) and yield (80−86%) of the recovered IgG demonstrates the feasibility of the approach. The majority of impurities are excluded from the pellet already in the precipitation step (Figure 2, lane 7), prior to the washing step. This emphasizes the advantage of the present purification approach, which lack any polymeric matrix onto which impurities would probably have been adsorbed nonspecifically.

Similar precipitation and recovery behavior was observed with a desthiobiotinylated concanavalin A derivative (DB-ConA), used for the capture of glucose oxidase and porcine thyroglobulin (Table 1). These consistent results with two distinct ligands indicate that other ligands may be similarly utilized and lead to highly purified proteins with good recovery yields. Native protein A or concanavalin A lacking bound desthiobiotin (DB) did not lead to precipitation of the target proteins (data not shown). The use of nonimmobilized ligands may raise the concern of ligand leaching. Nevertheless, leaching was not observed by Coomassie staining (Figure 2 lane 6; Figure 3, A, lanes 2P−5P, B, lanes 3P−5P). Therefore, gels were visualized by silver staining and the degree of leached DB-ProA was found to be less than 1% (data not shown). Since these values were obtained under highly acidic conditions (pH 3), one would expect lower levels of leaching under milder eluting conditions. These observations suggest that target proteins can be eluted directly from the generated precipitates, while keeping the [modified ligand−avidin] multicomplex intact in the precipitate. This feature may be advantageous for large-scale protein purification, where obtaining a relatively pure protein in high concentration by direct elution of the target protein from the pellet is a major advantage (*2*).

Furthermore, since all ligands according to AS are modified with a complexing entity (e.g. desthiobiotin, metal chelator), removal of minute amounts (<1%) of leached ligand can be accomplished by passing the sample containing primarily the eluted protein through an appropriate affinity column that would remove traces of leached modified ligand rather than the target protein. For example, a desthiobiotinylated-ligand could be re-

moved from a solution containing the target protein by an avidin column.

Generally, as background contamination increases, greater volumes of buffer are needed to remove impurities that bind nonspecifically to the polymeric matrix. Since no polymer matrix is present in AS, we postulated that a major increase in the contamination background would not affect the purity of the eluted protein. Thus, to demonstrate such a phenomenon, all pellets must be washed with minimum and identical volume of buffer, regardless of their background contamination. The results in Figure 3 (A, lanes 2P−5P; B, lanes 3P−5P) support our speculation and show that a 10- or 16-fold increase in the contamination background has no significant effect on either the purity or the yield of the target protein. Moreover, when pellets were not washed after their generation and the IgG was eluted, high purity was obtained, thus providing additional supporting data to the "nonstickiness" nature of the precipitates (data not shown). These results may imply that other contaminants (e.g. endotoxins, viruses, host DNA) could be excluded within the precipitation step, thereby reducing the number of purification steps in the downstream process.

In the preferred scenario, where the target protein has been eluted from the pellet, regeneration of the modified ligand could be accomplished by a simple dialysis procedure (which is supported by our experimental results). Since desthiobiotin has a lower association constant for biotin binding proteins ($K_a \sim 5 \times 10^{13}$ M^{-1} for streptavidin) than biotin ($K_a \sim 1 \times 10^{15}$ M^{-1}), the pellet will dissociate upon addition of biotin (*30*, *31*). Dialysis will remove excess of unbound biotin, leaving the modified ligand (DB-ProA or DB-ConA) and the [avidin-$(biotin)_4$] complex in the dialysis container. This mixture (devoid of free biotin) could be used directly in the next batch, since the free [avidin-$(biotin)_4$] complex is blocked (essentially irreversibly) with four biotins, cannot participate in network formation, and thus can be considered as an additional contaminant which will be excluded together with all impurities of the next cycle. This procedure was performed for the regeneration of both DB-ProA and DB-ConA (Table 1).

The nonimmobilized state of the modified ligand might possess additional theoretical advantages which include higher yields of purified product due to anticipated (a) faster and more efficient binding to the target protein in homogeneous solutions where no additional steric hindrances are imposed by the polymeric matrix. The nonimmobilized ligand is expected to be more available for binding, while in its immobilized state may also interact with the polymeric matrix making itself less available for binding (*1*); (b) the measured affinity of the modified ligand should represent its affinity upon use, enabling easier judgment as to the most appropriate modified ligand derivative to be utilized in a particular purification process. It has been argued that once a ligand is immobilized its affinity may be reduced by up to a factor of 1000 (*32*). Such a concern is not relevant to the present approach since no ligand immobilization is required; (c) the amount of added modified ligand to the medium is (theoretically) not limited, whereas affinity columns are characterized by their specific capacity. Therefore, more protein can be purified per batch. Additional benefits deriving from the nonimmobilized state may result in (a) higher purity of the end product due to the absence of a polymeric matrix onto which impurities can adsorb; (b) implementation of harsh sanitizing procedures without risking ligand functionality (i.e. the modified ligand can be removed from any instrumentation prior to sanitation); (c) the dramatic volume reduction within a single precipitation step would enable further purification manipulations with lab-scale machinery.

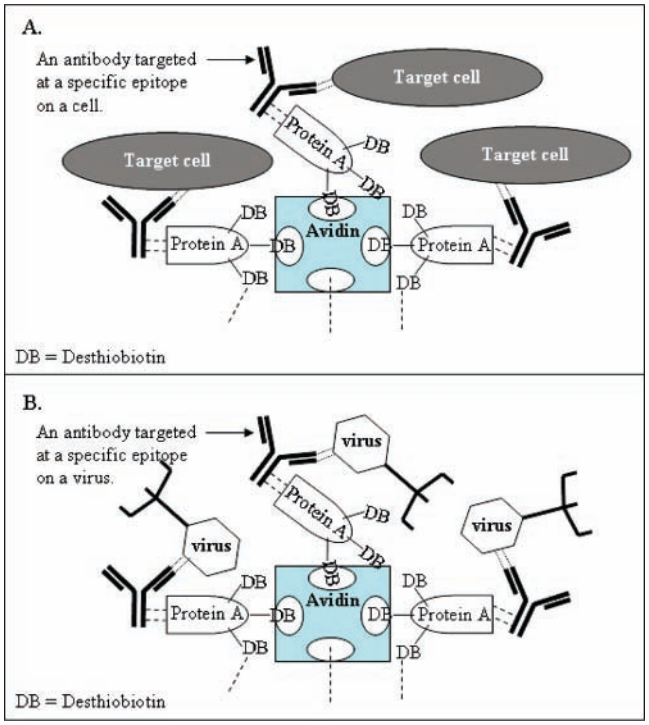

Figure 4. Schematic illustration of positive or negative cell selection (A) and virus depletion (B), utilizing a core complex composed of [DB-ProA−avidin].

A fundamental difference exists between AS and immunoprecipitation. In the latter, antibody−antigen complexes are removed from solution in the presence of an insoluble form of an antibody binding protein such as protein A or an immobilized second antibody, while in AS all components (i.e. the modified ligand and the interconnecting entity) are water soluble and are not immobilized.

Essentially, our approach does not introduce a new chemical principle but rather a different chemical architecture which could utilize any ligand, provided that specificity and affinity are preserved after ligand modification. The possibility of generating equivalent precipitates utilizing other types of modified ligands (e.g. ligand−chelator, ligand−antigen, ligand−nucleotide sequence) (Figure 1, C) emphasizes the wide scope of the presented approach. Furthermore, the [DB-ProA−avidin] complex may serve as a "core complex" for additional applications such as (a) positive/negative cell selection: target cells could be purified (or depleted) with the above "core complex" and an antibody targeted at an epitope on the target cell (Figure 4, A); (b) depletion of viruses could be performed with an antibody targeted at the virus (Figure 4, B).

CONCLUSIONS

This work presents a novel approach for simple and fast, high-yield and high-purity protein purification. It is based on nonimmobilized ligands, circumventing the use of polymeric supports. The new approach may provide an alternative route to obtain highly purified, concentrated protein preparations for crystallization trials. Its economical value for the bioseparation of therapeutics can only be assessed at industrial scales where the cost of regeneration and degree of leaching would be evaluated

together with the postulated advantages and simplicity of the process.

ACKNOWLEDGMENT

We are greatly indebted to Prof. E. Goldberg, Tufts University, for invaluable comments on the manuscript. We thank Prof. K. A. Jacobson, National Institutes of Health, for helpful suggestions.

LITERATURE CITED

(1) Mattiasson, B., Kumar, A., and Galaev, I. Yu. (1998) Affinity precipitation of proteins: design criteria for an efficient polymer. *J. Mol. Recognit. 11*, 211−216.
(2) Freitag, R. (1998) Reversible water-soluble affinity macroligands for bioseparation. *Curr. Trends Polym. Sci. 3*, 63−79.
(3) Freitag, R., and Horvath, C. (1996) Chromatography in the downstream processing of biotechnological products. *Adv. Biochem. Bioeng. 53*, 17−59.
(4) Labrou, N., and Clonis, Y. D. (1994) The affinity technology in downstream processing. *J. Biotechnol. 36*, 95−119.
(5) Lowe, C. R., Lowe, A. R., and Gupta, G. (2001) New developments in affinity chromatography with potential application in the production of biopharmaceuticals. *J. Biochem. Biophys. Methods 49*, 561−574.
(6) Cuatrecasas, P., Wilchek, M., and Anfinsen, C. B. (1968) Selective enzyme purification by affinity chromatography. *Proc. Natl. Acad. Sci. U.S.A. 61*, 636−643.
(7) Cuatrecasas, P., and Wilchek, M. (1968) Single step purification of avidin from egg white by affinity chromatography by biocytin-Sepharose columns. *Biochem. Biophys. Res. Commun. 33*, 235−239.
(8) Clonis, Y. D. (1991) Preparative dye-ligand chromatography. In *HPLC of Proteins Peptides and Polynucleotides* (Hearn, M., Ed.) pp 453−468, VCH, New York.
(9) Dyr, J. E., and Suttnar, J. (1997) Separation used for purification of recombinant proteins. *J. Chromatogr*. B *699*, 383−401.
(10) Ohlson, S., Hansson, L., Larsson, P.-O., and Mosbach, K. (1978) High performance liquid affinity chromatography (HPLAC) and its application to the separation of enzymes and antigens. *FEBS Lett. 93*, 5−9.
(11) Mattiasson, B., and Olson, U, (1986) General chromatographic procedure based on the use of heterobifunctional affinity ligands. *J. Chromatogr. 370*, 21−28.
(12) Afeyan, N., Gordonni, N., Mazsaroff, I., Varady, L., Fulton, S., Yang, Y. B., and Regnier, F. (1990) Flow through particles for the high performance liquid chromatographic separation of biomolecules: perfusion chromatography. *J. Chromatogr. 519*, 1−29.
(13) Teichberg, V. I. (1990) Affinity repulsion chromatography. *J. Chromatogr. 510*, 49−57.
(14) Slinerland, R., and Scouten, W. (1990) Centrifugal affinity chromatography. *J. Chromatogr. 510*, 205−211.
(15) Nilsson, J., Ståhl, S., Lundeberg, J., Uhlén, M., and Nygren, P. Å. (1997) Affinity Fusion Strategies for Detection, Purification, and Immobilization of Recombinant Proteins. *Protein Expression Purif. 11*, 1−16.
(16) Schneider, M., Guillot, C., and Lamy, B. (1981) The affinity precipitation technique. *Ann. N.Y. Acad. Sci. 369*, 257−263.
(17) Pearson, J., Clonis, Y. D., and Lowe, C. R. (1989) Preparative affinity precipitation of l-lactate dehydrogenase. *J. Biotechnol. 11*, 267−274.
(18) Gupta, M. N., and Mattiasson, B. (1994). Affinity precipitation. In *Highly Selective Separations in Biotechnology* (Street, G., Ed.) pp 7−33, Chapman and Hall, London.
(19) Hilbrig, F., and Freitag, R. (2003) Protein purification by affinity precipitation. *J. Chromatogr. B 790*, 79−90.
(20) Galaev, I. Yu., Gupta, M. N., and Mattiasson, B. (1996) Use smart polymers for Bioseparation. *CHEMTECH* 19−26.
(21) Galaev, I. Y., and Mattiasson, B. (1993) Affinity thermoprecipitation: the critical role of polymer in ligand-protein interactions. Presented at the 6th European Congress on Biotechnology, Florence, 13−17 June, 1993, Italy, Vol. I, MO099.
(22) Vaidya, A. A., Lele, B. S., Kulkarni, M. G., and Mashelkar, R. A. (1999) Enhancing ligand-protein binding affinity thermoprecipitation: elucidation of spacer effects. *Biothechnol. Bioeng. 64*, 418−425.
(23) Garret-Flaudy, F., and Freitag, R. (2001) Use of the avidin (imino) biotinsystem as a general approach to affinity precipitation. *Biotechnol. Bioeng. 71*, 223−234.
(24) Graille, M., Stura, E. A., Corper, A. L., Sutton, B. J., Taussig, M. J., Charbonnier, J. B., and Silverman, G. J. (2000) Crystal structure of a Staphylococcus aureus protein A domain complexed with the Fab fragment of a human IgM antibody: structural basis for recognition of B-cell receptors and superantigen activity. *Proc. Natl. Acad. Sci. U.S.A. 97*, 5399−404.
(25) Sharon, N., and Lis, H. (1972) Cell-Agglutinating and Sugar Specific Proteins. *Science 177*, 949−959.
(26) Bradford, M. M., (1976) A rapid sensitive method for the quantitation of micrograms quantities of protein utilizing the principle of protein-dye binding. *Anal. Biochem. 72*, 248−254.
(27) Laemmli, U. K. (1970) Cleavage of structural proteins during the assembly of the head of bacteriophage T4. *Nature 227*, 680−685.
(28) Bayer, E. D., Wilchek, M., and Skutelsky, E. (1976) Affinity cytochemistry: the localization of lectin and antibody receptors on erythrocytes via the avidin−biotin complex. *FEBS Lett. 68*, 240−244.
(29) Goldstein, I., Hollerman, C., and Smith E. (1965) Protein−Carbohydrate Interaction. II Inhibition Studies on the Interaction of Concanavalin A with Polysaccharides. *Biochemistry 4*, 876−883.
(30) Müller, W., Ringsdorf, H., Rump, E., Wildburg, G., Zhang, X., Angermaier, L., Knoll, W., Liley, M., and Spinke, J. (1993) Attempts to mimic docking processes of the immune system: recognition-induced formation of protein multilayers. *Science 262*, 1706−1708.
(31) Hirsch, J. D., Eslamizar, L., Filanoski, B. J., Malekzadeh, N., Haugland, R. P., Beechem, J. M., and Haugland, R. P. (2002) Easily reversible desthiobiotin binding to streptavidin, avidin, and other biotin-binding proteins: uses for protein labeling detection and isolation. *Anal. Biochem. 308* (2), 343−357.
(32) Kumar, A., and Gupta, M. N. (1994) Affinity precipitation of trypsin with soybean trypsin inhibitor linked Eudragit S-100. *J. Biotechnol. 37*, 185−189.

BC050096S

Bioactive Thin Film of Acidic Fibroblast Growth Factor Fabricated by Layer-by-Layer Assembly

Zhengwei Mao, Lie Ma, Jie Zhou, Changyou Gao,* and Jiacong Shen

Department of Polymer Science and Engineering, Zhejiang University, Hangzhou 310027, China.
Received October 10, 2004; Revised Manuscript Received June 24, 2005

A new class of bioactive thin films using growth factors as building blocks has been fabricated via layer-by-layer assembly (LBL) technique. Acid fibroblast growth factor (aFGF) in the presence of heparin was used as negatively charged polyelectrolytes, while poly(ethyleneimine) (PEI) was chosen as a positively charged counterpart. The self-deposition process and surface morphology of the resultant multilayers were monitored and detected by UV−vis absorbance spectra, advanced contact angle measurements, and scanning force microscopy (SFM) observations. Cell culture was performed to assess the efficiency of the growth factors. The fibroblasts proliferated faster on the surface assembled with five bilayers of (aFGF/heparin)/PEI with apparent higher cytoviability than on those surfaces modified by one bilayer of (aFGF/heparin)/PEI, five bilayers of aFGF/PEI, or five bilayers of heparin/PEI, and tissue culture polystyrene. Enhanced secretion of collagen type I and interleukin 6 (IL-6) by the fibroblasts seeded on the five bilayers of (aFGF/heparin)/PEI was also verified by immunohistochemical examination. The bioactivity of the (aFGF/heparin)/PEI multilayers could be largely preserved when stored at −20 °C.

INTRODUCTION

The field of tissue engineering exploits living cells in a variety of ways to restore, maintain, or enhance tissues and organs (*1*). New developments in biomaterials, innovative cell culture technique, and newly discovered growth factors open novel avenues to engineering living tissues in vitro for fundamental research and clinical applications (*2*). Many kinds of polymers, e.g. poly(lactide) (PLA)[1] and poly(lactide-*co*-glycotide) (PLGA), have been widely used in medical fields because of manipulable properties such as biodegradability and good mechanical properties (*3*). Yet their drawbacks such as poor cytocompatibility lead to inefficiency in constructing a bioactive interface with living cells.

Layer-by-layer assembly (LBL) technique, which is based on the alternating physiosorption of oppositely charged polyelectrolytes, has been extended from fundamental studies to practical applications, in particular surface modification of biomaterials. Sequential adsorptions of anionic and cationic polyelectrolytes allow the construction of multilayer films on most types of substratum. The method has many important advantages over other techniques; for example, the assembly is based on spontaneous adsorptions and can proceed under mild conditions without involvement of harmful organic solvent, and the assembled molecular films exhibit a much larger thermal and mechanical stability and can be prepared up to hundreds of layers (*4*). Moreover, the method is valid whatever the shape and the inner structure of substratum. By this technique, many charged biopolymers including a lot of extracellular matrix (ECM) and extracellular matrix-like molecules have been incorporated for the purpose of ameliorating biocompatibility of polymers (*5*−*7*).

Growth factors, which are generally soluble signaling proteins, play an important role in tissue regeneration and differentiation. Acidic fibroblast growth factor (aFGF) is a paradigm of a group of nine closely related, multifunctional proteins known as the fibroblast growth factor family (FGFs). FGFs induce mitosis, migration, and differentiation in most mesoderm and neuroectoderm-derived cells, influence angiogenesis, and regulate various biological responses (*8*−*10*). For instance, T. Imaizumi et al. find that 1 ng/mL of human recombinant basic fibroblast growth factor (bFGF, another paradigm of FGFs) in collagen gel can accelerate the proliferation of fibroblasts and decrease the contraction of collagen fibers induced by the fibroblasts (*11*). Owing to their powerful bioactivity, the FGFs are being tested to treat surgical, burn, and periodontal tissue wounds, gastric ulcers, segmental bony defects, and ligament and spinal cord injury (*12*). Toshi Fujisato et al. observed that the composite of chondrocytes and the collagen scaffold impregnated with bFGF is very promising for cartilage reconstruction (*13*). Ichiro Ono reports that administration of bFGF at the time of wound closure significantly increases the breaking strength after a full thickness incisional wound operation (*14*).

But unfortunately, successful use of growth factors for human tissue regeneration has been notoriously difficult, since they typically have half-lives only on the order of

* E-mail: cygao@mail.hz.zj.cn, Tel: +86-571-87951108, Fax: +86-571-87951948.

[1]Abbreviations: LBL, layer-by-layer; aFGF, acid fibroblast growth factor; PEI, poly(ethyleneimine); SFM, scanning force microscopy; PLA, poly(lactide); PLGA, poly(lactide-*co*-glycotide); ECM, extracellular matrix; FGFs, fibroblast growth factor family; bFGF, basic fibroblast growth factor; HMDA, hexamethylenediamine; EDAC, 1-ethyl-3-(3-dimethylaminopropyl)-carbodiimide; NHS, *N*-hydroxysuccinimide; FCS, fetal calf serum; DMEM, Dulbecco eagle's minimum essential medium; TCPS, tissue culture polystyrene; MTT, methylthiazoletetrazolium; CLSM, confocal laser scanning microscopy; FDA, fluorescein diacetate; IL, interleukin; PDGF, platelet-derived growth factor; NGF, tumor necrosis factor; TGF, transforming growth factor.

10.1021/bc049755b CCC: $30.25 © 2005 American Chemical Society
Published on Web 08/25/2005

minutes (*15*−*17*) and may cause uncontrolled cell growth when overdosed, as that which occurs in carcinoma (*18*, *19*). To prolong the lives of growth factors and decrease their side effects, alot of controlled release systems for growth factors including microspheres, hydrogels, and matrixes have been widely explored in tissue engineering. Katsuya Kawai et al. reported that bFGF incorporated in gelatin microspheres is gradually released in artificial dermis, which exhibits a remarkably enhanced angiogenic effect to that of free bFGF (*20*). Xanthe M. Lam et al. encapsulated insulin-like growth factor-I in PLGA microspheres. The growth factor maintains its bioactivity and can be sustained release for up to 14 days in vivo (*21*).

The heparin family is nearly ubiquitous in animal tissues as heparan sulfate proteoglycans on cell surfaces and in ECM. They possess a linear anionic polysaccharide chain and are typically heterogeneously sulfated on alternating L-iduronic acid and D-glucosamino sugars. Recently, Ram Sasisekharan et al. reported that the activation and protection of FGFs requires heparin-like molecules (*22*). Heparin and aFGF can form a complex in solution even at ultralow concentrations (~pmol/L). Both the life and bioactivity of aFGF are improved in the complex. J. Feijen et al. immobilized heparin on collagen matrixes for the loading of bFGF. The incorporated bFGF exhibited sustained release over a prolonged period of time (*23*). Yoshihiro Ito et al. built micropattern-immobilized heparin for guiding cell growth. After treatment in FGF solution, they found that mouse fibroblasts have enhanced bioactivity on the heparin-immobilized regions (*24*).

Herein, we intend to extend the LBL technique to build a new class of bioactive thin films by using growth factors as building blocks. aFGF with the protection of heparin is used as a negatively charged polyelectrolyte, while poly(ethyleneimine) (PEI) is chosen as the positively charged counterpart. Culture of fibroblasts in vitro demonstrates that the activity of aFGF in multilayers is largely preserved in the presence of heparin. This would provide a new strategy to immobilize cell growth factors in a more controllable manner, for example, the amount, stability, and durability of the growth factors. Because the charge interaction is nonspecific and not restricted to the macroscopic shape of the substratum, this method can also be extended to tissue regeneration scaffolds with porous and/or irregular inner structure.

EXPERIMENTAL SECTION

Materials. Acidic fibroblast growth factor (aFGF, M_w =16 000, 3 mg/mL, in phosphate buffer solution) was kindly donated by Wanxing Bio-Pharmaceutical Co., Ltd. China. Poly(ethyleneimine) (PEI, M_w = 750 000, 50 wt %) and heparin (sodium salt) were purchased from Sigma-Aldrich. All the chemicals were used as received. Triple distilled water was used throughout the experiments.

aFGF (0.2 mg/mL) and PEI (1 mg/mL) were labeled with 1 mg/mL fluorescein isothiocyanate (FITC, Sigma) at 4 °C for 48 h, followed by dialysis with water for 4 weeks. To label the heparin molecules with FITC, hexamethylenediamine (HMDA) was first coupled to introduce active amino groups. For this to occur, 1 mg/mL heparin was reacted with 1 mg/mL HMDA (heparin: HMDA = 1:100 mol) in 20 mM/10 mM 1-ethyl-3-(3-dimethylaminopropyl)carbodiimide (EDAC) and *N*-hydroxysuccinimide (NHS) solution for 24 h, followed by dialysis with water for 1 week to obtain aminolyzed heparin, which was then labeled with FITC similarly to that of PEI.

Multilayer Preparation. Multilayer thin films were deposited on a tissue culture polystyrene (TCPS) (Nunc, Denmark) sheet. The sheet was incubated in PEI solution (1 mg/mL with 0.15 M NaCl) for 20 min to adsorb a layer of PEI and then rinsed with phosphate buffer (PBS) three times. In the next step, the surface charge of the sheet was reversed by the adsorption of a layer of aFGF/heparin mixture (aFGF 0.2 mg/mL and heparin 0.4 mg/mL in PBS), followed by rinsing with PBS three times. Repeating this cycle produced self-organized multilayer films.

Characterization of the Multilayers. UV−vis spectra were measured on a UV−visible spectrophotometer (CARY 100 BIO, America). Water contact angle was measured at room temperature using a sessile drop technique on a DSA10-MK2 contact angle measuring system from Krüss. Advancing contact angle was measured to reveal the surface wettability. Before the measurement, all the samples were dried at 25 °C under reduced pressure overnight and then were equilibrated in ambient air for 1 day. The scanning force microscopy (SFM) image was obtained on a scanning probe microscope (SPA400, Seiko) in a dynamic mode.

Human Fibroblasts Culture. The human fibroblasts were isolated from foreskins (*25*) and routinely cultured on TCPS. The cells of 5−10 passages were then seeded on the TCPS wells assembled previously with (aFGF/heparin)/PEI multilayers, heparin/PEI multilayers, and aFGF/PEI multilayers as well as on the blank TCPS. The fibroblasts were incubated in a culture medium consisting of 10% (v/v) fetal calf serum (FCS, Sijiqing Biotech.Co., China) and 90% (v/v) DMEM (Gibcobrl Co.) supplemented with 100 units/mL of penicillin and 100 μg/mL of streptomycin in humidified air containing 5% CO_2 at 37 °C. The culture medium was changed every 2 days. The cell numbers were averaged from three parallel measurements by trypsinization of the fibroblasts and counting the cell number under a hemocytometer at every 2 days, respectively. The cell viability was measured using methylthiazoletetrazolium (MTT) method according to refs (*26*, *27*). The absorbance that has a proportional relationship with the number of living cells and cell viability is recorded at a wavelength of 570 nm. To observe the cell morphology under confocal laser scanning microscopy (CLSM, Bio-Rad 2100), the fibroblasts were stained with 5 μg/mL fluorescein diacetate (FDA, Aldrich) solution in the incubator for 15 min after being cultured for 8 days. Each value was averaged from three parallel experiments and expressed as mean±standard deviation.

Measurement of Secreted Collagen Type I. After being cultured for 10 days, the fibroblasts were fixed with 4% paraformaldehyde/PBS solution for 30 min at room temperature, followed by five washings with PBS. Then they were challenged with rabbit polyclonal antibodies against human type I collagen (The immunoreagents were purchased from Zhongshan Golden Bridge Co., Ltd., Beijing, China) overnight at 4 °C. After washing with PBS, poly-HRP anti-mouse/rabbit IgG detection system was used to stain collagen type I (brown color). After rinsing with PBS, the specimens were observed under a microscope. Negative controls of the same specimen were incubated with rabbit normal serum or directly reacted with poly-HRP anti-mouse/rabbit IgG detection system in the absence of primary antibody, and then they were processed as outlined above (*28*). No positive immunoreactivity was found in these negative controls.

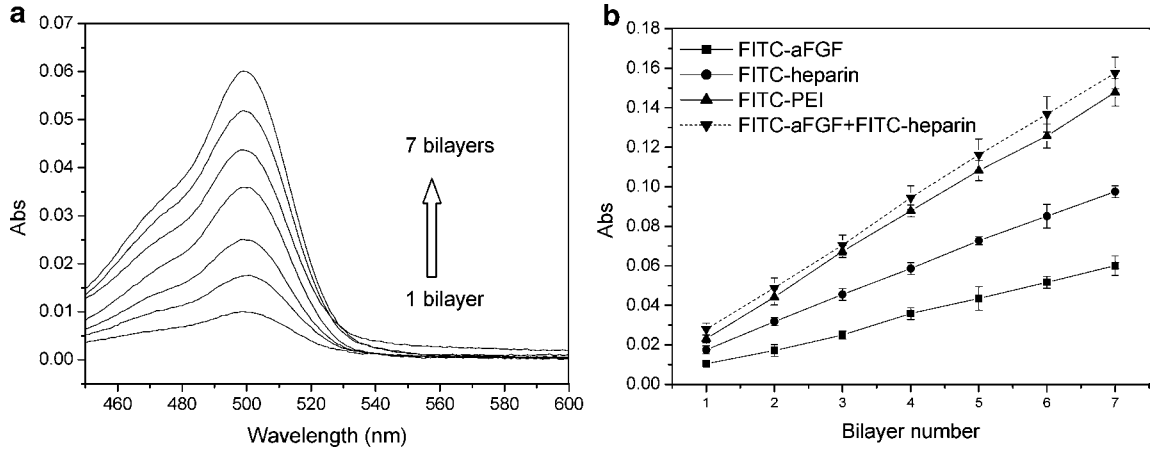

Figure 1. (a) UV−vis spectra of FITC-aFGF to show the layer growth process of (aFGF/heparin)/PEI multilayers. (b) Absorbance maximum at 490 nm to show the linear increase of layer thickness. The multilayers were deposited directly onto TCPS surfaces. For detail, see the text.

Measurement of Released Interleukin 6. Secretion of the interleukin 6 (IL-6) was measured in the supernatant of the cultured fibroblasts by IL-6 enzyme linked immunosorbent assay (ELISA, The Fourth Military Medical University, Xi'an, China). Spectrophotometric readings were performed at 405 nm. For detail measuring process, see refs 29 and 30. Final results were obtained by comparison with a standard curve constructed using dilutions of standard human IL-6. Each value was averaged from three parallel experiments.

The Stability of the Multilayers. Multilayer thin films deposited on the TCPS sheet were incubated in PBS at 37 °C. The normalized maximum absorbance at 490 nm was plotted as a function of incubation time to approximately depict the reservation of the building blocks. Each value was averaged from three parallel experiments.

Evaluation of Multilayer Activity after Storage. Five bilayers of (aFGF/heparin)/PEI were built on TCPS and then were incubated in culture medium at 37 °C for 24 h or 48 h, or stored at −20 °C for 3 months. Fibroblast cultures were similarly performed and evaluated as described above. Each value was averaged from three parallel experiments.

RESULTS AND DISCUSSION

Monitoring the LBL Deposition Process. In each LBL assembly, one of the normal aFGF, heparin, or PEI was substituted by a FITC-labeled counterpart for the purpose of monitoring layer growth by UV−vis spectroscopy. Total of three kinds of multilayer films were assembled with only one labeling component in each film. The spectra of all the multilayers exhibit a maximum absorbance at 490 nm arising from the fluorescein groups (Figure 1a). The maximum absorbance of all the labeled components increased linearly along with the increase of layer number (Figure 1b), demonstrating the homogeneous growth of the layer thickness or the total amount of the building blocks. Interestingly, the slopes of each component are different, with PEI being the sharpest and aFGF being the flattest. This would mean that the ratio of heparin to aFGF in the multilayers increased along with the layer number, e.g. more heparin will be incorporated into the multilayers compared with aFGF. However, this would not mean that the relative amount of PEI in each layer is larger than that of the negative components, since it equilibrates with both negative building blocks. Theoretically, the total absorbance of the negative layer can be derived from the summary of the corresponding value of heparin and aFGF, since the multilayers are assembled under identical conditions. The summarized values (dashed line in Figure 1b) indeed exhibit the same slope as that of the polycation, demonstrating the steady increase of both positive and negative layer thickness. The reason the relative mass of heparin increased faster than aFGF is not very clear at present. One possible reason is that the stronger charge property of heparin arises from its sulfate groups.

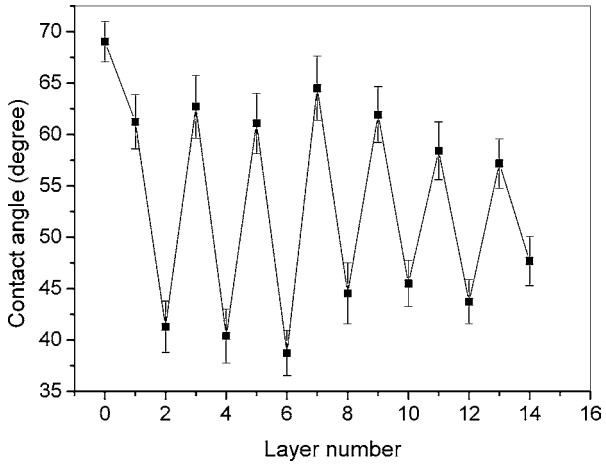

Figure 2. Advancing contact angle as a function of the layer number of (aFGF/heparin)/PEI multilayers. Odd numbers represent films with PEI as the outermost layer, whereas even number films have aFGF/heparin as the outermost layer.

The surface wettability of the sequentially layered PEI and aFGF/heparin as a function of layer number (Figure 2) also confirmed the occurrence of LBL assembly. The measurement of contact angle has been widely employed to diagnose the surface chemistry of synthesized surfaces such as a self-assembled monolayer. The surface wettability measured by an advancing contact angle is controlled primarily by the outermost layer if the layer is uniform (*31*, *32*). Thus, it is possible to monitor the deposition process by determining how surface wettability changes in a LBL manner. In the present case, samples with an odd number of layers have PEI as the outermost layer, whereas samples with an even number of layers have aFGF/heparin as the outermost layer. The advancing contact angle of the raw TCPS sheet was determined to be 69.1°. Figure 2 shows that the contact angles of the (aFGF/heparin)/PEI multilayers displayed

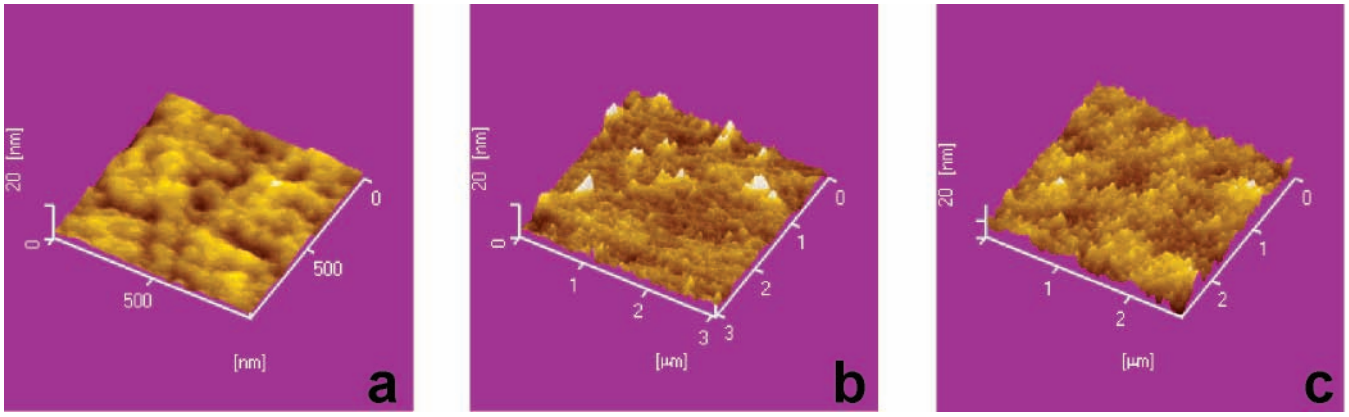

Figure 3. SFM images of (a) the TCPS surface, (b) deposited by one bilayer of (aFGF/heparin)/PEI and (c) by five bilayers of (aFGF/heparin)/PEI.

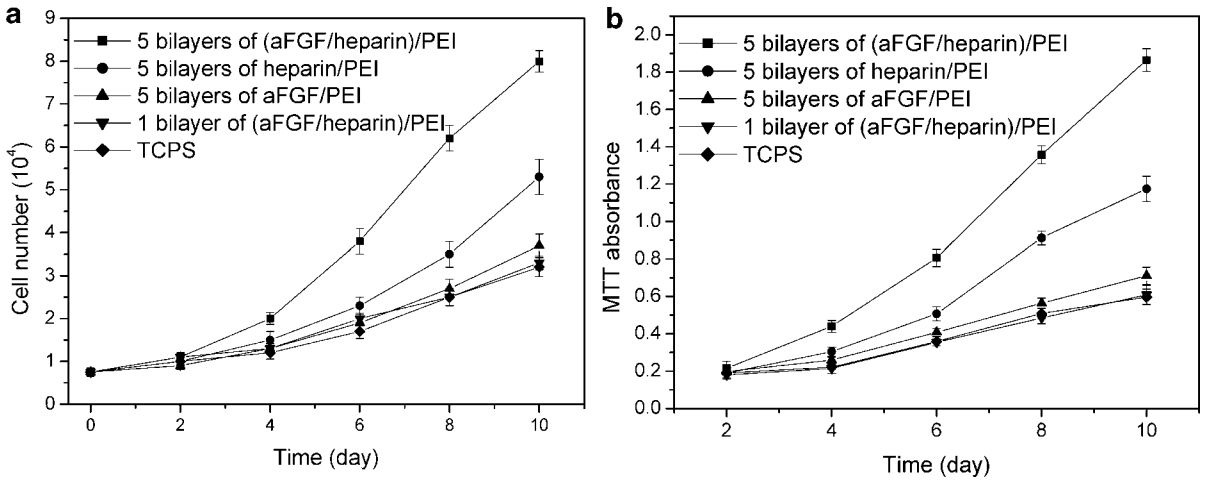

Figure 4. (a) Fibroblast proliferation and (b) cell viability seeded on multilayers (PEI being the outmost layers) or TCPS control.

a distinct oscillation as the outermost layer changed from PEI to aFGF/heparin, demonstrating the increased hydrophilicity of samples having aFGF/heparin as the outermost layer than that with PEI. However, the same outermost layer did not present the same contact angle. There was some fluctuation in a range of about 3−7°. This might be caused by the layer interpenetration between neighboring PEI and aFGF/heparin layers where the segments of the underlying layer are able to influence the surface hydrophilicity (*32*). It is worth noting that a more hydrophobic surface was found when heparin was partially substituted by aFGF, since a contact angle of 42° was measured for (aFGF/heparin)/PEI multilayers (the outmost layer is aFGF/heparin) and 28° for PEI/heparin multilayers (the outmost layer is heparin), respectively (*33*). This should be caused by the fact that aFGF is comparatively more hydrophobic than heparin.

It is known that the surface morphology of biomaterials also has a big influence on cell attachment, proliferation, and function in addition to the surface chemistry. Figure 3 shows that there exist minimal fluctuations on both the TCPS and the multilayer surface, which are in the range of nanometers as revealed by the roughness (RMS) measurements. The RMS increased from 1.38 nm (TCPS) to 1.90 nm (one bilayer) and to 4.52 nm (five bilayers). Some aggregates appeared on the first bilayer (Figure 3b), while some holes in a range of nanometers could be visualized after deposition of five bilayers (Figure 3c). This would mean that defects were formed either during layer assembly or drying process, or both. Yet compared with the fluctuation of the original TCPS, the alteration of the surface morphology after multilayer deposition is rather minimal. It is worth noting that these images measured in the dry state could only reflect the surface morphology to some extent, since multilayer swelling cannot be avoided in hydrated state, e.g. in the cell culture medium.

Cell Response to the (aFGF/Heparin)/PEI Multilayers. The aFGF built in the multilayers provides the possibility of promoting the mitosis of cells and inducing a series of signal pathways. Exemplified here with human fibroblasts, the cell culture results indeed showed a more positive cell response to the aFGF-assembled films in the presence of heparin (Figure 4). Both the cell proliferation ratio and the viability were substantially improved on the surface assembled with five bilayers of (aFGF/heparin)/PEI (with PEI being the outmost layer if not otherwise indicated), especially at longer culture time, while the multilayers composed of five bilayers of heparin/PEI exhibited somewhat improvement of cell proliferation and viability. On the other hand, during all the culture time no significant difference was found between the surfaces modified with five bilayers of aFGF/PEI, one bilayer (aFGF/heparin)/PEI, and an unmodified one, i.e., TCPS control.

The results that no difference was found between the aFGF/PEI and TCPS control would mean that the aFGF had lost its effect upon being assembled into the multilayers, which most possibly caused by the denaturation of aFGF or tight bonding (see below). Therefore, a strategy to ensure its bioactivity should be adopted during the LBL assembly process. We used here the heparin as a co-building block with aFGF. In the presence of heparin (*22*−*24*), the aFGF could actually act on the

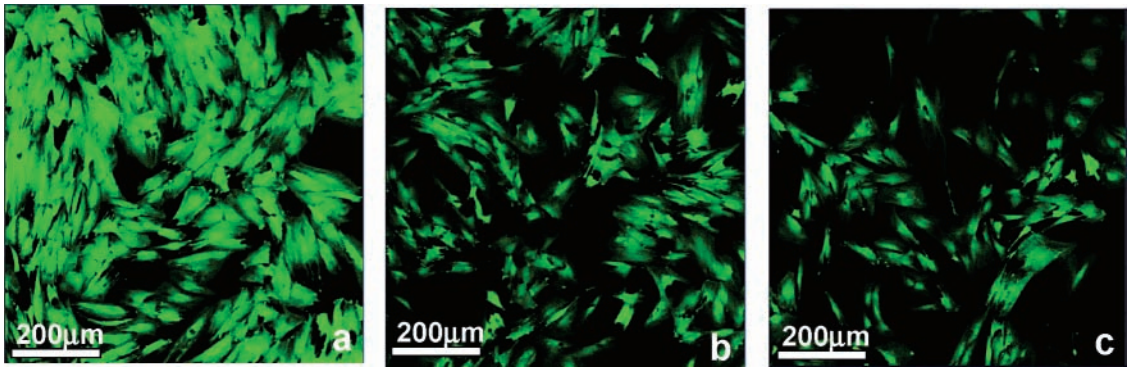

Figure 5. The morphology of fibroblasts observed under CLSM after being cultured for 8 days and stained with FDA. (a) Deposited by five bilayers of (aFGF/heparin)/PEI, (b) deposited by five bilayers of heparin/PEI, and (c) TCPS control.

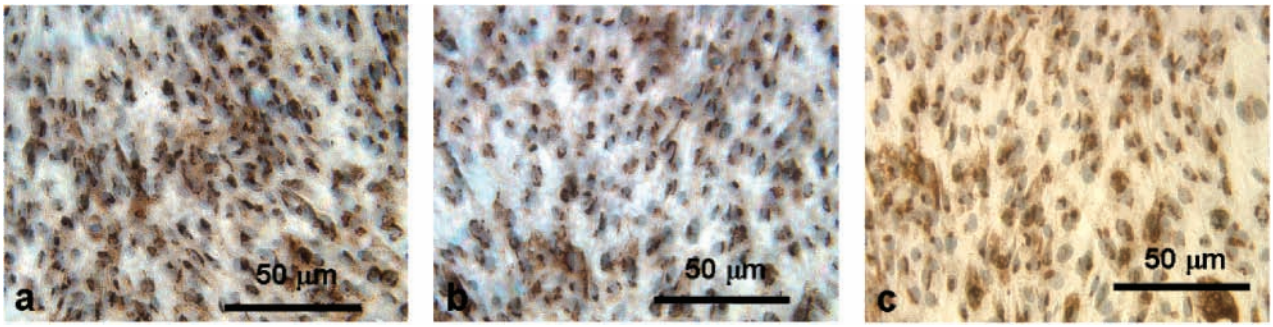

Figure 6. The immunohistorical stain of collagen type I secreted by fibroblasts after cultured for 8 days. (a) Deposited by five bilayers of (aFGF/heparin)/PEI, (b) deposited by five bilayers of heparin/PEI, and (c) TCPS control.

fibroblasts as shown in Figure 4. It is worth noting that PEI has similar ability to support cell attachment and growth as TCPS since no difference was observed for PEI-covered TCPS and TCPS control in our results (data not shown).

At the first 2 days, the fibroblasts cultured on five bilayers of (aFGF/heparin)/PEI did not show apparent difference with others in terms of cell number and viability. This may attribute to the facts that it takes 12 to 20 h for the fibroblasts to attach and spread on the culture substrate, and the main function of aFGF is inducing cell mitosis rather than cell attachment and spread. At longer culture time, the aFGF can then act on the fibroblasts to yield a higher proliferation ratio and viability than others. The fibroblasts cultured on five bilayers of (aFGF/heparin)/PEI for 10 days eventually reached 2.5 times the cell number and 3.1 times the MTT absorbance than that of TCPS control, respectively.

However, aFGF in only one bilayer of (aFGF/heparin)/PEI had not shown an effect on acceleration of fibroblast growth. This is attributed to the minimal amount of aFGF that existed on the material surface, leading to no obvious effect on the cells.

The fibroblasts cultured on the heparin/PEI multilayers also presented a higher proliferation ratio and viability. Heparin is also a kind of active factor which can stimulate cell proliferation at low concentration (*9*).

Observed under CLSM after culturing for 8 days, all the fibroblasts were spread well with their typical shapes. The cells on the five bilayers of (aFGF/heparin)/PEI displayed the highest density, and most of them reached confluence (Figure 5). Hence, one can conclude that the fibroblasts presented a larger number, higher viability, and normal morphology on the surface modified with five bilayers of (aFGF/heparin)/PEI than those on the heparin/PEI multilayers and TCPS control.

A regulated synthesis of interstitial collagens, the most abundant being type I collagen, is important during development and wound healing but also in a number of pathological conditions. Studies on these diseases as well as various in vitro models have shown that collagen synthesis and deposition are influenced by cytokines, growth factors, and mechanical tension (*34*, *35*). aFGF is one of the important regulatory factors for collagen synthesis in cultured fibroblasts. In the present case, human collagen type I (brown color, Figure 6) secreted by fibroblasts on all the substrates existed in the extracelluar matrix, in the cytoplasm, and in the nucleus. However, fibroblasts on the five bilayers of (aFGF/heparin)/PEI obviously secreted the greatest extent of collagen type I (Figure 6a), proving that aFGF built in the multilayers in the presence of heparin can stimulate the synthesis of collagen type I in fibroblasts.

aFGF not only induces fibroblast proliferation and influences collagen synthesis, but also acts as a multifunctional regulator of other water soluble factors such as interleukins (ILs), platelet-derived growth factor (PDGF), tumor necrosis factors (TNFs), and transforming growth factors (TGFs), etc. (*36*). Interleukin 6 (IL-6) which can be produced by human fibroblasts is a molecule that has both proinflammatory and antiinflammatory function, a modulator of bone resorption, a promoter of hematopoiesis, and an inducer of plasma cell development (*37*). Figure 7 shows that at first 4 days, fibroblasts on the surface covered by five bilayers of (aFGF/heparin)/PEI produced 2.9 times IL-6 of others. This value decreased to 1.3 at a still longer culture time. This is attributed to the limited life of aFGF which is only a few days in vitro/in vivo even stabilized by heparin. Although heparin can accelerate cell proliferation, very similar IL-6 secretion level was determined on both surfaces of heparin/PEI multilayers and unmodified TCPS, implying that heparin cannot stimulate the synthesis of IL-6 in human fibroblasts.

The (Bio)stability of the Multilayers. The stability of the multilayers in the culture conditions takes an

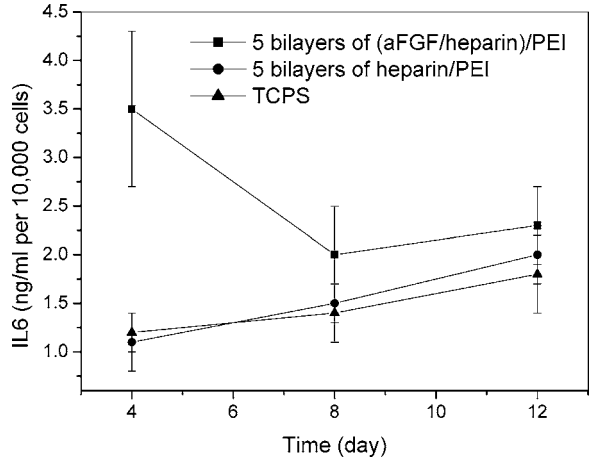

Figure 7. The IL-6 secretion of fibroblasts cultured on TCPS assembled with five bilayers of (aFGF/heparin)/PEI, five bilayers of heparin/PEI, or TCPS control.

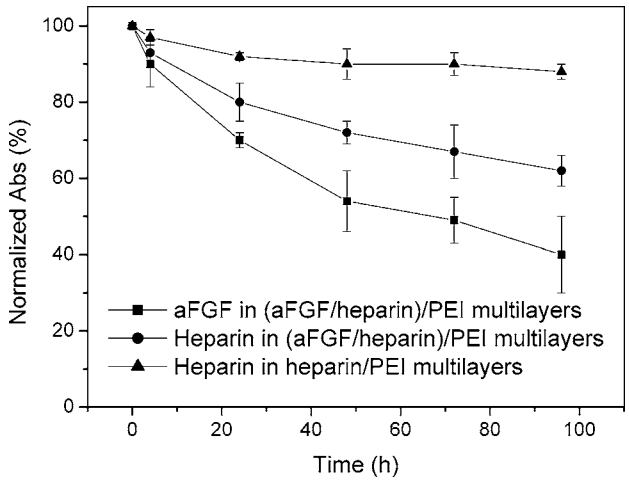

Figure 8. The normalized Abs as a function of incubation time in PBS at 37 °C.

important role in retaining their function. The multilayers were incubated in PBS at 37 °C to mimic the culture conditions. Figure 8 shows that the absorbance of the multilayers was reduced gradually as a function of incubation time, revealing that aFGF and heparin were released into the solution. For example, approximately 46% aFGF and 28% heparin had been released from the (aFGF/heparin)/PEI multilayers after incubated for 48 h, respectively. By contrast, heparin in heparin/PEI multilayers was rather stable. This proved that the structure of the (aFGF/heparin)/PEI multilayers was largely destroyed in a few days. As PEI/heparin multilayers were stable over several weeks (*33*), the damage of the (aFGF/heparin)/PEI multilayers must be caused by the introduction of aFGF. Therefore, this instability should be reasonably caused by the weak binding strength of PEI and aFGF/heparin complex. Consequently, the multilayers may swell in the buffer to enable the release of the building blocks, noting that hydrolysis of the biomacromolecules might also have partial contribution.

Hence, suitable storage is of practical importance since the materials may not be used immediately in many cases. Several storage conditions were determined with respect to bioactivity reservation. Figure 9 shows that stored at −20 °C even for 3 months the fibroblasts on the multilayers still behaved like those on the freshly made substrate, although a limited decrease in proliferation ratio and viability was detected. This result indicates that −20 °C is a suitable storage condition to keep the activity of the thin films. However, when the multilayers were incubated in vitro for 24 h, the activity largely decreased. A still longer incubation, e.g. for 48 h, had deteriorated the bioactivity dramatically, whose value was even lower than freshly made heparin/PEI multilayers. Besides the partial dissociation of the bioactive components from the multilayers, the denaturing of the native factors may also be one important reason.

CONCLUSIONS

We show here that the bioactive aFGF has been successfully deposited onto the TCPS sheet surface in the presence of heparin via a layer-by-layer manner. The aFGF built in the multilayers obviously enhances fibroblast proliferation and viability and regulates the secretion of collagen type I and IL-6. The bioactivity of the multilayers can be largely preserved when stored at −20 °C even for 3 months, while being diminished in vitro after a few days. In conclusion, herein a practical and simple technique has been provided to immobilize bioactive growth factors on a material surface with preserved bioactivity.

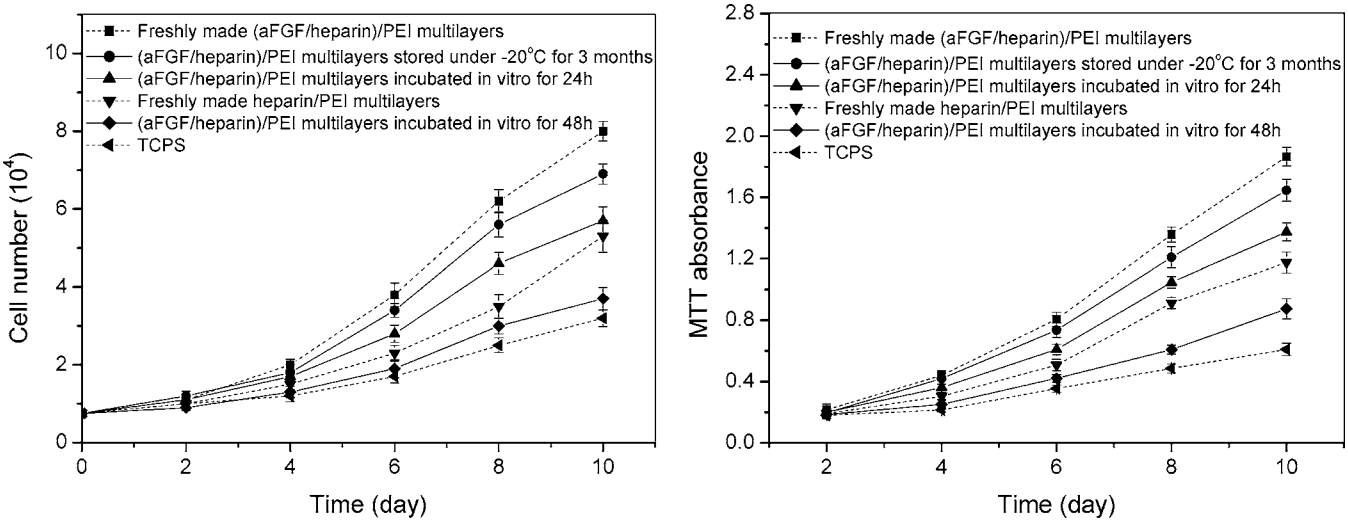

Figure 9. (a) Fibroblast proliferation and (b) cell viability seeded on five bilayers of (aFGF/heparin)/PEI, which were stored at different conditions previously.

ACKNOWLEDGMENT

We thank Prof. H. Möhwald, Prof. M. Grunze, and W. J. Tong for their stimulating discussion. This work was financially supported by the Science and Technology Program of Zhejiang Province (2004C21022), the Natural Science Foundation of China (20434030, 90206006), and the National Science Fund for Distinguished Young Scholars (50425311).

LITERATURE CITED

(1) Griffith, L. G., and Naughton, G. (2002) Tissue engineering-current challenges and expanding opportunities. *Science 295*, 1009−1014.
(2) Sittinger, M., Perka, C., Schutz, O., Haupl, T., and Burmester, G. R. (1999) Joint cartilage regeneration by tissue engineering. *Z. Rheumatol. 8*, 130−135.
(3) Seal, B. L., Otero, T. C., and Panitch, A. (2001) Polymeric biomaterials for tissue and organ regeneration. *Mater. Sci. Eng. R. 34*, 147−230.
(4) Chen W., McCarthy T. J. (1997) Layer-by-layer deposition: A tool for polymer surface modification.*Macromolecules 30*, 78−86.
(5) Zhu, Y. B., Gao, C. Y. He, T., Liu, X. Y., and Shen, J. C. (2003) Layer-by-layer assembly to modify poly(L-lactic acid) surface toward improving its cytocompatibility to human endothelial cells. *Biomacromolecules 4*, 446−452.
(6) Elbert, D. L., Herbert, C. B., and Hubbell, J. A. (1999) Thin polymer layers formed by polyelectrolyte multilayer techniques on biological surfaces. *Langmuir 15*, 5355−5362.
(7) Grant, G. G. S., Koktysh, D. S., Yun, B., Matts, R. L., and Kotov, N. A. (2001) Layer-by-layer assembly of collagen thin films: controlled thickness and biocompatibility. *Biomed. Microdevices 3*, 301−310.
(8) Bartletl, P. F., Brooker, G. J., and Faux, C. H. (1998) Regulation of neural stem cell differentiation in the forebrain. *Immunol. Cell. Biol. 76*, 414−418.
(9) Rcsengart, T. K., Budenbender, K. T., and Duenas, M. (1997) Therapeutic angiogenesis: a comparative study of the angiogenic potential of acidic fibroblast growth factor and hepain. *J. Vasc. Surg. 26*, 302−312.
(10) Szabo, S., and Sandor, Z. (1996) Basic fibroblast growth factor and PDGF in GI disease. *Gastroenterol. Clin. N. 10*, 97−112.
(11) Imaizumi, T., Jean-Louis, F., Dubertret, M. L., Bailly, C., and Cicurel, L. (1996) Effect of human basic fibroblast growth factor on fibroblast proliferation, cell volume, collagen lattice contraction: in comparison with acidic type. *J. Dermatol. Sci. 11*, 134−141.
(12) Yoneda, A., Asada, M., Oda, Y., Suzuki, M., and Imamura, T. (2000) Engineering of an FGF-proteoglycan fusion protein with heparin-independent, mitogenic activity. *Nature Biotechnol. 18*, 641−644.
(13) Fujisato, T., Sajiki, T., Qiang, L., and Ikada, Y. (1996) Effect of basic fibroblast growth factor on cartilage regeneration in chondrocyte-seeded collagen sponge scaffold. *Biomaterials 17*, 155−162.
(14) Ono, I. (2002) The effect of basic fibroblast growth factor (bFGF) on the breaking strength of acute incisional wounds. *J. Dermatol. Sci. 29*, 104−113.
(15) Kim, D. C., Sugiyama, Y., Satoh, H., Fuwa, T., Iga, T., and Hanano, M. (1988) Kinetic analysis of in vivo receptor-dependent binding of human epidermal growth factor by rat tissues. *J. Pharm. Sci. 77*, 200−207.
(16) Konturek, S. J., Pawlik, W., Mysh, W., Gustaw, P., Sendur, R., Mikos, E., and Bielanski, W. (1990) Comparison of organ uptake and disappearance half time of human epidermal growth factor and insulin. *Regul. Pept. 30*, 137−148.
(17) Edelman, E. R., Nugent, M. A., and Karnovsky, M. J. (1993) Perivascular and intravenous administration of basic fibroblast growth factor: vascular and solid organ deposition. *Proc. Natl. Acad. Sci. U.S.A. 90*, 1513−1517.
(18) Aaronson, S. A. (1991) Growth factors and cancer. *Science* 1146−1153.
(19) Kliln, J. G., Berns, P. M., Schmitz, P. I., and Foekens, J. A. (1992) The clinical significance of epidermal growth factor receptor(EGF−R) in human breast cancer: a review on 5232 patients. *Endocr. Rev. 13*, 3−17.
(20) Kawai, K., Suzuki, S., Tabata, Y., Ikada, Y., and Nishimura, Y. (2000) Accelerated tissue regeneration through incorporation of basic fibroblast growth factor-impregnated gelatin microspheres into artificial dermis. *Biomaterials 21*, 489−499.
(21) Lam, X. M., Duenas, E. T., Daugherty, A. L., Levin, N., and Cleland, J. L. (2000) Sustained release of recombinant human insulin-like growth factor-I for treatment of diabetes. *J. Controlled Release 67*, 281−292.
(22) Sasisekharan, R., Ernst, S., and Venkataraman, G. (1997) On the regulation of fibroblast growth factor activity by heparin-like glycosaminoglycans. *Angiogenesis 1*, 45−54.
(23) Wissink, M. J. B., Beernink, R., Pieper, J. S., Poot, A. A., Engbers, G. H. M., Beugeling, T., van Aken, W. G., and Feijen, J. (2001) Binding and release of basic fibroblast growth factor from heparinized collagen matrices. *Biomaterials 22*, 2291−2299.
(24) Park, Y. S., and Ito, Y. (2000) Micropattern-immobilization of heparin to regulate cell growth with fibroblast growth factor. *Cytotechnology 33*, 117−122.
(25) Ma, L., Gao, C. Y., Mao, Z. W., Zhou, J., and Shen, J. C. (2004) Enhanced biological stability of collagen porous scaffolds by using amino acids as novel cross-linking bridges. *Biomaterials 25*, 2997−3004.
(26) Liu, Y. Y., Yoshikoshi, A., Wang, B. C., and Sakanishi, A. (2003). Influence of ultrasonic stimulation on the growth and proliferation of *Oryza sativa* Nipponbare callus cells. *Colloid Surfaces B 27* (4), 287−293.
(27) Melo, P. D., Duran, N., and Haun, M. (2000). Cytotoxicity of prodigiosin and benznidazole on V79 cells. *Toxicol. Lett. 116* (3), 237−242.
(28) Ishizeki, K., Kubo, M., Yamamoto, H., and Nawa, T. (1998) Immunocytochemical expression of type I and type II collagens by rat Meckel's chondrocytes in culture during phenotypic transformation. *Arch. Oral Biol. 43*, 117−126.
(29) Arroyo, C. M., Burman, D. L., Sweeney, R. E., Broomfield, C. A., Ross, M. C., and Hackley, B. E. (2004) Neutralization effects of interleukin-6 (IL-6) antibodies on sulfur mustard (HD)-induced IL-6 secretion on human epidermal keratinocytes. *Environ. Toxicol. Phar. 17*, 87−94.
(30) Andoh, A., Takaya, H., Makino, J., Sato, H., Bamba, S., Araki, Y., Hata, K., Shimada, M., Okuno, T., Fujiyama, Y., and Bamba, T. (2001) Cooperation of interleukin-17 and interferon-gamma on chemokine secretion in human fetal intestinal epithelial cells. *Clin. Exp. Immunol. 125*, 56−63.
(31) Hsieh, M. C., Farris, R. J., and McCarthy, T. J. (1997) Surface "priming" for layer-by-layer deposition: Polyelectrolyte multilayer formation on allylamine plasma-modified poly(tetrafluoroethylene). *Macromolecules 30*, 8453−8458.
(32) Yoo, D., Shiratori, S. S., and Rubner, M. F. (1998) Controlling bilayer composition and surface wettability of sequentially adsorbed multilayers of weak polyelectrolytes. *Macromolecules 31*, 4309−4318.
(33) Tan, Q. G., Ji, J., Barbosa, M. A., Fonseca, C., and Shen, J. C. (2003) Constructing thromboresistant surface on biomedical stainless steel via layer-by-layer deposition anticoagulant. *Biomaterials 24*, 4699−4705.
(34) Nugent, A. W., and Iozzo, V. R. (2000) Fibroblast growth factor-2. *Int. J. Biochem. Cell B. 32*, 115−120.
(35) Ivarsson, M., McWhirter, A., Borg, T. K., and Rubin, K. (1998) Type I collagen synthesis in cultured human fibroblasts: Regulation by cell spreading, platelet-derived growth factor and interactions with collagen fibers. *Matrix Biol. 16*, 409−425.
(36) Bodo, M., Carinci, F., Baroni, T., Becchetti, E., Giaammarioli, M., Bellucci, C., Pezzetti, F., Evangelisti, R., and Carinci, P. (1996) Effects of interleukins on crouzon fibroblast phenotype in vitro. Release of cytokines and IL-6 mRNA expression. *Cytokine 8*, 772−783.
(37) Barton, B. E. (1997) IL-6: Insights into novel biological activities. *Clin. Immunol. Immunopathol. 85*, 16−20.

BC049755B

An Efficient Synthesis of a Heterobifunctional Coupling Agent

Rajarathnam E. Reddy,* Yon-Yih Chen, Donald D. Johnson, Gangamani S. Beligere, Sushil D. Rege, You Pan, and John K. Thottathil

Core R&D Chemistry Group (Department 09MD, Building AP20), Diagnostics Division, Abbott Laboratories, 100 Abbott Park Road, Abbott Park, Illinois 60064-6016. Received October 18, 2004; Revised Manuscript Received June 8, 2005

An efficient synthesis of 4-[(2,5-dioxo-2,5-dihydro-1*H*-pyrrol-1-yl)methyl]-*N*-(6-{[6-({6-[(2,5-dioxopyrrolidin-1-yl)oxy]-6-oxohexyl}amino)-6-oxohexyl]amino}-6-oxohexyl)cyclohexanecarboxamide (**12**), a heterobifunctional coupling agent, was developed, which is critical for chemoselective conjugation of proteins and enzymes. The synthesis involved seven steps starting from 6-{[(benzyloxy)carbonyl]-amino}hexanoic acid (**1**), and multigram quantities of coupling agent (**12**) were prepared using this protocol in excellent overall yield and 99.6% purity by reversed phase HPLC. The new method is suitable for the synthesis of coupling agent **12**, consistently with purity >99%, and is useful for the preparation of other analogous coupling agents.

INTRODUCTION

Recent advances in the field of bioconjugate chemistry have spurred the construction of biomolecules based on chemoselective coupling for a variety of applications (*1*−*3*). The native physical properties of the protein and enzyme components are typically preserved in the resulting conjugate, when the coupling is carried out under the selective conditions (*3*−*6*). Use of such well-defined conjugates for applications in biology and medical fields is critical for implementation of quality control as well as for reliable interpretation of biological results (*7*). Heterobifunctional coupling agents containing reactive groups, such as succinimidyl ester and maleimide, are important for cross-coupling of proteins and enzymes. The succinimidyl active ester can be chemoselectively reacted with an amine on one protein, and the resulting adduct can then be conjugated to the second unit, e.g., protein or enzyme, containing a thiol via the maleimide group present in linking agent. This controlled conjugation process is quite selective when compared to other groups, e.g., iodoacetyl group, and can be carried out at physiological pH.

Bieniarz and co-workers (*8*) have described the synthesis of four heterobifunctional reagents with varying lengths, e.g., 9, 16, 23, and 30 atoms long, and their application for the preparation of alkaline phosphatase conjugates, in a α-fetoprotein assay. They observed that the antibody−alkaline phosphatase conjugate prepared using the coupling agent with 30-atom long **12** gave 300% enhancement in the signal, when compared to the conjugate prepared with the corresponding 9-atom long analogue. The observed differences in performance of the conjugates was attributed to the improved antibody binding and lowered steric hindrance to the complementarity-determined region of the antibody, when a 30-atom long coupling agent (**12**) was used (*8*). Subsequently, the coupling agent **12** was found to be critical in the preparation of antibody−alkaline phosphatase conjugates for applications in the development of clinical assays, such as thyroid stimulating hormone (TSH) (*9*), prostate specific antigen (PSA) (*10*), troponin-1 (*11*), and progesterone (*12*), as well as in the preparation of thermally stabilized immunoconjugates (*13*).

However, the synthetic protocol described for the preparation of heterobifunctional coupling agent **12** is not practical and produced the material in very low overall yield (0.16−2.5%) (*8*). In addition, the quality of coupling agent **12** was varied significantly from batch to batch, ranging from 89 to 98% purity, as determined by analytical reversed phased HPLC method. We needed gram quantities of a good and consistent quality of coupling agent **12**, to prepare protein−enzyme conjugates, useful for diagnostic and medical applications. In this paper, we describe an efficient and convenient method for the preparation of heterobifunctional coupling agent **12**.

EXPERIMENTAL SECTION

General Methods and Materials. ^{1}H and ^{13}C NMR spectra were recorded on a Varian Mercury Plus 400 spectrometer with an Oxford AS400 magnet. The chemical shifts (δ) were reported in ppm relative to TMS, and coupling constants (J) were reported in hertz. Electrospray ionization mass spectrometry (ESI-MS) was carried out on a Perkin-Elmer (Norwalk, CT) Sciex API 100 benchtop system employing a Turbo Ionspray ion source. All chemicals were purchased either from Aldrich Chemical Co. (Milwaukee, WI) or NovaBiochem (San Diego, CA). Analytical reversed phase (RP) HPLC was performed using a Waters (Milford, MA) NovaPak (C18, 60 Å, 4 μm, 3.9 × 150 mm) reversed phase (RP) column (solvents ratio v/v reported). The final product, coupling agent **12**, was analyzed using an Akzonobel (Ferry, NY) kromasil reversed phased (RP) column (5.0 μm, 100 Å, 4.6 × 250 mm) (solvents ratio v/v reported). Melting points were recorded in open capillary tubes on an Electrothermal melting point apparatus and were uncorrected. Infrared spectra (IR) and elemental analysis were carried out by Roberson Microlit Laboratories, Inc. (Madison, NJ). IUPAC names of all compounds were obtained using the ACD/Ilab Web service version 3.5 at http://www.acdlabs.com/ilab.

* Corresponding author. Phone: 847-938-0409. Fax: 847-938-5188. E-mail: rajarathnam.reddy@abbott.com.

10.1021/bc040259x CCC: $30.25 © 2005 American Chemical Society
Published on Web 08/06/2005

Methyl 6-[(6-{[(Benzyloxy)carbonyl]amino}hexanoyl)amino]hexanoate (3). An oven-dried 2.0 L three-neck round-bottom flask was equipped with a mechanical stirrer and nitrogen inlet/outlet. To this flask were added 6-{[(benzyloxy)carbonyl]amino}hexanoic acid (**1**, 75.0 g, 282.7 mmol, 1.0 equiv) and methyl 6-aminohexanoate hydrochloride (**2**, 51.4 g, 282.7 mmol, 1.0 equiv) followed by anhydrous dichloromethane (1.1 L) at room temperature under nitrogen atmosphere. To the resulting suspension were added sequentially 1-hydroxybenzotriazole (HOBt, 45.8 g, 339.2 mmol, 1.2 equiv), diisopropylethylamine (DIEA, 123.1 mL, 706.8 mmol, 2.5 equiv), and 1-(3-dimethylaminopropyl)-3-ethylcarbodiimide hydrochloride (EDAC, 65.0 g, 339.2 mmol, 1.2 equiv), and the mixture was stirred at room temperature (21−23 °C) for 5−6 h. After completion of the reaction, as determined by the analysis of an aliquot by using HPLC, the reaction mixture was transferred into a separatory funnel and diluted with dichloromethane (1.0 L). The mixture was washed vigorously with 1.0 N hydrochloric acid (4 × 1.0 L), followed by 1.0 N sodium hydroxide (4 × 1.0 L) and finally with 3.5 M sodium chloride solution (2 × 1.0 L). The organic layer was dried with anhydrous $MgSO_4$ and filtered, and the solvent was removed on a rotary evaporator. The resulting solid material was dried on a vacuum pump at room temperature for 24 h to afford 105.5 g of ester **3** as a colorless (white) powder in 95% yield. Mp: 74−75 °C [Lit. (*15*) 73−74 °C]; Analytical reversed phase (RP) HPLC: MeCN:water:0.5% aqueous trifluoroacetic acid/35:55:10/1.0 mL/min at 215 nm, t_R: 7.4 min, 98%; IR (KBr): 3347, 3310, 2949, 1730, 1684, 1635, 1533, 1271, 1175, 734, 724 cm^{-1}; ^1H NMR ($CDCl_3$): δ 7.37−7.29 (m, 5 H), 5.58 (br s, 1 H), 5.09 (s, 2 H), 4.88 (br s, 1 H), 3.67 (s, 3 H), 3.26−3.16 (m, 4 H), 2.31 (t, 2 H, J = 7.2 Hz), 2.15 (t, 2 H, J = 7.6 Hz), 1.69−1.59 (m, 4 H), 1.55−1.46 (m, 4 H), 1.38−1.29 (m, 4 H); ^{13}C NMR ($CDCl_3$): δ 174.4, 173.1, 156.8, 137.0, 128.8, 128.4, 66.9, 51.8, 41.1, 39.5, 36.9, 34.2, 30.0, 29.6, 26.7, 26.6, 25.5, 24.8; ESI-MS (*m/z*): 393.3 $(M + H)^+$, 410.3 $(M + NH_4)^+$, 786.0 $(2 \times M + H)^+$, 802.5 $(2 \times M + NH_4)^+$; Elemental analysis: Calcd for $C_{21}H_{32}N_2O_5$, C, 64.26; H 8.22; N, 7.14, Found: C, 64.20; H, 8.48; N, 7.26.

Methyl 6-[(6-Aminohexanoyl)amino]hexanoate Hydrochloride (4). In a dry 2.0 L hydrogention flask equipped with a stir bar was dissolved methyl 6-[(6-{-[(benzyloxy)carbonyl]amino}hexanoyl)amino]hexanoate (**3**, 102.2 g, 260.0 mmol, 1.0 equiv) in anhydrous methanol (675 mL). To this solution were added 1.25 M hydrochloric acid in methanol (625 mL, 780.0 mmol, 3.0 equiv) and 10% palladium on activated carbon (10.4 g, wet, Degussa type E101 NE/W), and the mixture was stirred under hydrogen atmosphere (20−30 psi) at room temperature (21−23 °C). The reaction flask was re-filled with hydrogen gas periodically, and the progress of the reaction was monitored by HPLC for consumption of starting material **3**. After 5 h, an additional amount of Pd/C catalyst (2.6 g) was added, and the hydrogenation was continued for an additional 2 h. After completion of the reaction, as determined by the analysis of an aliquot by using HPLC, the mixture was filtered using a funnel containing a Celite bed (about 4−5 mm thickness). The filter cake was washed with an additional amount of methanol (50 mL), and the combined filtrates were evaporated on a rotary evaporator (bath temp: 35−40 °C). The residue was redissolved in methanol (200 mL) and toluene (400 mL), and the residual amount of water, which originated from the catalyst, was removed azeotropically on a rotary evaporator. The redissolving/azeotropic concentration was repeated two more times, and the resulting white solid was dried under vacuum at room temperature (21−23 °C) for 24 h to afford 81.2 g of methyl 6-[(6-aminohexanoyl)amino]hexanoate hydrochloride (**4**) as colorless gummy material in quantitative yield. IR (KBr): 3299, 2949, 1724, 1635, 1545, 1256, 1197, 1167, 978, 885, 732 cm^{-1}; ^1H NMR (CD_3OD): δ 3.68 (s, 3 H), 3.25 (t, 2 H, J = 7.2 Hz), 2.97 (t, 2 H, J = 8.0 Hz), 2.37 (t, 2 H, J = 7.2 Hz), 2.36−2.30 (m, 2 H), 1.76−1.62 (m, 6 H), 1.61−1.52 (m, 2 H), 1.50−1.42 (m, 2 H, 1.42−1.34 (m, 2 H); ^{13}C NMR (CD_3OD): δ 177.1, 176.7, 41.4, 41.3, 37.1, 35.5, 30.7, 29.1, 28.3, 27.8, 27.2, 26.5; ESI-MS (*m/z*): 259.2 $(M + H)^+$, 517.8 $(2 \times M + H)^+$.

Methyl 3,10,17-Trioxo-1-phenyl-2-oxa-4,11,18-triazatetracosan-24-oate (5). An oven-dried 2.0 L three-neck round-bottom flask was equipped with a mechanical stirrer and nitrogen inlet/outlet. To this flask was added 6-{[(benzyloxy)carbonyl]amino}hexanoic acid (**1**, Z-ϵ-Ahx-OH, 72.0 g, 271.3 mmol, 1.0 equiv) followed by a solution of methyl 6-[(6-aminohexanoyl)amino]hexanoate hydrochloride (**4**, 22.1 g, 75 mmol, 1.0 equiv) in anhydrous dichloromethane (1.2 L) at room temperature under nitrogen atmosphere. To the resulting suspension were added sequentially 1-hydroxybenzotriazole (HOBt, 44.0 g, 325.6 mmol, 1.2 equiv), diisopropyl ethylamine (DIPA, 118.2 mL, 678.4 mmol, 2.5 equiv), and 1-(3-dimethylaminopropyl)-3-ethylcarbodiimide hydrochloride (EDAC, 62.4 g, 325.6 mmol, 1.2 equiv). The resulting pale yellow clear solution was stirred at room temperature (21−23 °C) for 5−6 h. After completion of the reaction as determined by the analysis of an aliquot by using HPLC, the reaction mixture was transferred into a separatory funnel and diluted with a mixture of 5% methanol in dichloromethane (1.5 L). The mixture was washed vigorously with 1 N hydrochloric acid (3 × 1.0 L), followed by 1 N sodium hydroxide (4 × 1.0 L) and finally with 3.5 M sodium chloride solution (1 × 1.0 L). The organic layer was dried with anhydrous $MgSO_4$ and filtered, and the solvent was removed on a rotary evaporator. The resulting material was dried under vacuum for 60 h to afford 128.7 g of ester **5** as a colorless (white) powder in 94% yield. Mp: 121−24 °C [Lit. (*15*) 124−25 °C], IR (KBr): 3327, 2944, 2866, 1732, 1687, 1633, 1533, 1269, 733 cm^{-1}; Analytical reversed phase (RP) HPLC: MeCN:water:0.5% aqueous trifluoroacetic acid/35:55:10/1.0 mL/min at 215 nm, t_R: 5.85 min, 94−98.5%, ^1H NMR ($CDCl_3$): δ 7.38−7.28 (m, 5 H), 5.76 (m, 2 H), 5.08 (s, 2 H, 4.97 (m, 1 H), 3.66 (s, 3 H), 3.26−3.16 (m, 6 H), 2.31 (t, 2 H, J = 7.2 Hz), 2.15 (t, 4 H, J = 7.2 Hz), 1.68−1.58 (m, 6 H), 1.58−1.46 (m, 6 H), 1.38−1.28 (m, 6 H); ^{13}C NMR ($CDCl_3$): δ 174.4, 173.2, 156.8, 137.0, 128.8, 128.4, 128.3, 66.9, 51.8, 41.2, 39.5, 39.4, 36.8, 36.7, 34.2, 30.0, 29.6, 29.5, 26.7, 26.6, 26.5, 25.6, 25.4, 24.8; ESI-MS (*m/z*): 506.3 $(M + H)^+$, 523.8 $(M + NH_4)^+$, 1029.1 $(2 \times M + NH_4)^+$; Elemental analysis: Calcd for $C_{27}H_{43}N_3O_6$, C, 64.13, H; 8.57, N, 8.31, Found: C, 63.84, H, 8.57, N, 8.24.

3,10,17-Trioxo-1-phenyl-2-oxa-4,11,18-triazatetracosan-24-oic Acid (6). In a 3.0 L three-neck round-bottom flask equipped with mechanical stirrer was suspended the methyl 3,10,17-trioxo-1-phenyl-2-oxa-4,-11,18-triazatetracosan-24-oate (**5**, 125.0 g, 247.2 mmol, 1.0 equiv) in tetrahydrofuran (THF, 1.5 L). In a separate 1.0 L beaker, lithium hydroxide monohydrate (20.8 g, 494.4 mmol, 2.0 equiv) was dissolved in water (0.75 L), and the solution was added to the ester (**5**)−THF suspension at room temperature (21−23 °C). After the addition was complete, the white suspension slowly dissolved and a clear solution formed in about 10 min. The reaction mixture was stirred for an additional 2 h, and after completion of the reaction, as determined by the analysis

of an aliquot by using HPLC, the mixture was concentrated on a rotary evaporator to about 1.5 L final volume. The mixture was then diluted with water (750 mL), and the suspension was acidified to pH ~3.5 with 6.0 N hydrochloric acid (85 mL), while the mixture was continuously stirred. The resulting precipitate was filtered, and the solid was washed three times with water (3 × 1.5 L). The material was transferred into crystallizing dish and dried in an oven at 45−50 °C under vacuum for 14 h. The crude acid (110.0 g) was crystallized from ethanol (700 mL) and ethyl acetate (1.6 L). The resulting white solid material was filtered and dried under vacuum at room temperature over 18−24 h to afford 100.3 g of acid **6** as a colorless (white) powder in 83% yield. Mp: 136−37 °C [Lit. (*16*) 133−34 °C]; Analytical reversed phase (RP) HPLC: MeCN:water:0.5% aqueous trifluoroacetic acid/25:75:10/1.0 mL/min at 215 nm, t_R: 5.28 min, 99.9%; IR (KBr): 3533, 3140, 2250, 1578, 1460, 1392, 1253, 1180, 1126, 1033, 851 cm^{-1}; ^1H NMR (CD_3OD): δ 7.95 (dist t, 2 H), 7.39−7.28 (m, 5 H), 7.01 (dist t, 1 H), 5.09 (s, 2 H), 3.22−3.12 (m, 6 H), 2.32 (t, 2 H, J = 7.6 Hz), 2.20 (t, 4 H, J = 7.6 Hz), 1.68−1.60 (m, 6 H), 1.57−1.48 (m, 6 H), 1.43−1.34 (m, 6 H); ^{13}C NMR (CD_3OD): δ 178.3, 176.9, 176.8, 139.4, 130.3, 129.8, 129.6, 68.2, 42.5, 41.0, 41.1, 37.9, 37.8, 35.7, 31.5, 31.0, 28.4, 28.3, 28.2, 27.6, 27.5, 26.6, ESI-MS (*m/z*): 492.3 $(M + H)^+$, 509.3 $(M + NH_4)^+$; Elemental analysis: Calcd, $C_{26}H_{41}N_3O_6$, C, 63.52, H, 8.41, N, 8.55, Found, C, 63.54, H, 8.54, N, 8.54.

6-({6-[(6-Aminohexanoyl)amino]hexanoyl}amino)-hexanoic Acid (7). In a 2.0 L dry hydrogenation flask equipped with a stir bar was suspended the 3,10,17-trioxo-1-phenyl-2-oxa-4,11,18-triazatetracosan-24-oic acid (**6**, 50.0 g, 101.7 mmol) in methanol (900 mL). The mixture was gently heated to about 55 °C to dissolve the material, and then water (450 mL) was added. To the resulting clear solution was added 10% palladium on activated carbon (5.0 g, wet, Degussa type E101 NE/W) while the solution was still warm, and the mixture was stirred under hydrogen atmosphere (20−30 psi) for 2 h. The flask was refilled with hydrogen periodically, and the progress of the reaction was monitored by HPLC for the consumption of starting material, acid **6**. An additional amount of catalyst (2.5 g) was added, and the hydrogenation was continued for an additional 2 h. After completion of the reaction, as determined by the analysis of an aliquot by using HPLC (total time: 4 h), the mixture was then filtered over a Celite bed. The filter cake was washed with an additional methanol (100 mL), and the combined filtrates were evaporated on a rotary evaporator. The resulting solid was transferred into a crystallizing dish and dried in oven at 45−50 °C under vacuum for 36 h to afford 36.5 g of 6-({6-[(6-aminohexanoyl)-amino]hexanoyl}amino)hexanoic acid (Tri-ACA-peptide**,** **6**) as a colorless (white) powder in 99% yield. Mp: 218−20 °C [Lit. (*16*) 203−204 °C]; IR (KBr): 3366, 3026, 2886, 1846, 1488, 1444, 1340, 1289, 1230, 1184, 1111, 985, 940 cm^{-1}; ^1H NMR (D_2O + CD_3OD): δ 3.19 (t, 4 H, J = 6.8 Hz), 3.01 (t, 2 H, J = 7.6 Hz), 2.26 (t, 2 H, J = 7.6 Hz), 2.25 (t, 2 H, J = 6.8 Hz), 2.20 (t, 2 H, J = 7.2 Hz), 1.74−1.49 (m, 12 H), 1.45−1.29 (m, 6 H); ^{13}C NMR (D_2O + CD_3-OD): δ 185.0, 177.0, 177.8, 40.8, 40.7, 40.6, 40.0, 37.1, 37.0, 29.6, 29.5, 28.0, 27.6, 27.0, 26.9, 26.6, 26.5, 26.4; ESI-MS (*m/z*): 358.2 $(M + H)^+$, 715.9 $(2 \times M + H)^+$; Elemental analysis: Calcd for $C_{18}H_{35}N_3O_4$, C, 60.48, H, 9.87, N, 11.75, Found: C, 59.89, H, 9.81, N, 11.58.

Pentafluorophenyl 4-[(2,5-Dioxo-2,5-dihydro-1*H*-pyrrol-1-yl)methyl]cyclohexanecarboxylate (FMCC, 10). In a dry three-neck 2.0 L round-bottom flask equipped with mechanical stirrer and a nitrogen inlet, the powdered maleic anhydride (31.2 g, 318.1 mmol, 1.0 equiv) was dissolved in acetonitrile (500 mL) under nitrogen atmosphere. To this clear solution was added *trans*-4-(aminomethyl)cyclohexanecarboxylic acid (**8**, 50.0 g, 318.1 mmol, 1.0 equiv) at room temperature (21−23 °C). After the reaction mixture was stirred for 6 h, the resulting suspension was cooled to 2−5 °C with an ice bath. To this cold mixturewas added quickly diisopropylethylamine (DIEA, 150.0 mL, 858.9 mmol, 2.7 equiv) followed by pentafluorophenyl trifluoroacetate (**9**, 132.7 mL, 795.5 mmol, 2.5 equiv) slowly using an additional funnel over 20−25 min period. During this period, the temperature of the reaction mixture was maintained below 10 °C. After the addition was complete, the resulting pale brown color reaction mixture was stirred for 1.5 h at low temperature (<10 °C) and the cooling bath was removed. The reaction mixture was then allowed warm to room temperature, and the stirring was continued overnight, for 18 h. The resulting thick brown suspension was diluted with water (2.0 L) and extracted with dichloromethane (3 × 2.0 L). The combined dichloromethane extracts were washed with water (1 × 2.0 L), dried with anhydrous $MgSO_4$, and filtered. The solvent was removed using a rotary evaporator (bath temp: 35−40 °C), and the residue was dried on vacuum pump (0.1−0.3 mm/Hg) at room temperature for 5 h. The resulting solid (202 g) was crystallized from ethyl acetate (750 mL) and hexanes (200 mL) to afford 55.4 g of FMCC (**10**). The mother liquor was concentrated and recrystallized from ethyl acetate (500 mL) and hexanes (150 mL) to afford an additional 10.0 g of FMCC (**8**). Crops 1 and 2 were combined to give 65.3 g of FMCC (**8**) as a colorless crystalline solid in 51% yield. Mp: 157−59 °C [Lit. (*17*) 157−58 °C], Analytical reversed (RP) HPLC: Gradient: MeCN:water:1.0% aqueous trifluoroacetic acid/10:80:10 to 90:0:10 ratio from 0 to 15 min/1.0 mL/min at 220 nm, t_R: 10.61 min, 99.2%, ^1H NMR ($CDCl_3$): δ 6.68 (s, 2 H), 3.37 (d, 2 H, J = 7.2 Hz), 2.62−2.53 (m, 1 H), 2.15 (d, 2 H, J = 11.2 Hz), 1.84−1.66 (m, 3 H), 1.58−1.46 (m, 2 H), 1.16−1.10 (m, 2 H); ^{13}C NMR ($CDCl_3$): δ 171.5, 170.9, 134.0, 43.4, 42.4, 36.2, 29.4, 28.0; ESI-MS (*m/z*): 404.3 $(M + H)^+$, 422.3 $(M + NH_4)^+$; Elemental analysis: Calcd for $C_{18}H_{14}F_5NO_4$, C, 53,61, H, 3.50, N, 3.47, F, 23.55; Found: C, 53.64, H, 3.40, N, 3.42, F, 23.71.

6-{[6-({6-[({4-[(2,5-Dioxo-2,5-dihydro-1*H*-pyrrol-1-yl)methyl]cyclohexyl}carbonyl)amino]hexanoyl}-amino)hexanoyl]amino}hexanoic Acid (11). In a dry, 2.0 L three-neck round-bottom flask equipped with mechanical stirrer was added the 6-({6-[(6-aminohexanoyl)amino] hexanoyl}amino)hexanoic acid (tri-ACA-peptide, **7**, 64.0 g, 179.03 mmol, 1.0 equiv) followed by anhydrous-degassed DMF [1.5 L, which was stirred under vacuum (0.1−0.3 mm/Hg) for 30 min] at room temperature. To this suspension was added FMCC (**10**, 72.2 g, 179.03 mmol, 1.0 equiv), and the mixture was gently heated to 55 °C under nitrogen atmosphere for 7 h. During this period, the suspension gradually dissolved, and the mixture became a pale yellow clear solution. After completion of the reaction, as determined by the analysis of an aliquot by using HPLC, the mixture was concentrated on a rotary evaporator (bath temp: 50−55 °C) and the resulting material was further dried on a vacuum pump (0.1−0.5 mm/Hg) for 18 h. The resulting solid (239 g) was suspended in acetonitrile (1.5 L), stirred for 10 min, and filtered. The washing−filtration process with acetonitrile was repeated two more times (2 × 1.5 L), and the resulting solid was dried in oven at 45−50 °C under vacuum for 3 h. After being dried, the resulting crude product (97.7 g) was dissolved in a mixture of

Scheme 1. Synthesis of 6-({6-[(6-Aminohexanoyl)amino]hexanoyl}amino)hexanoic Acid (7)

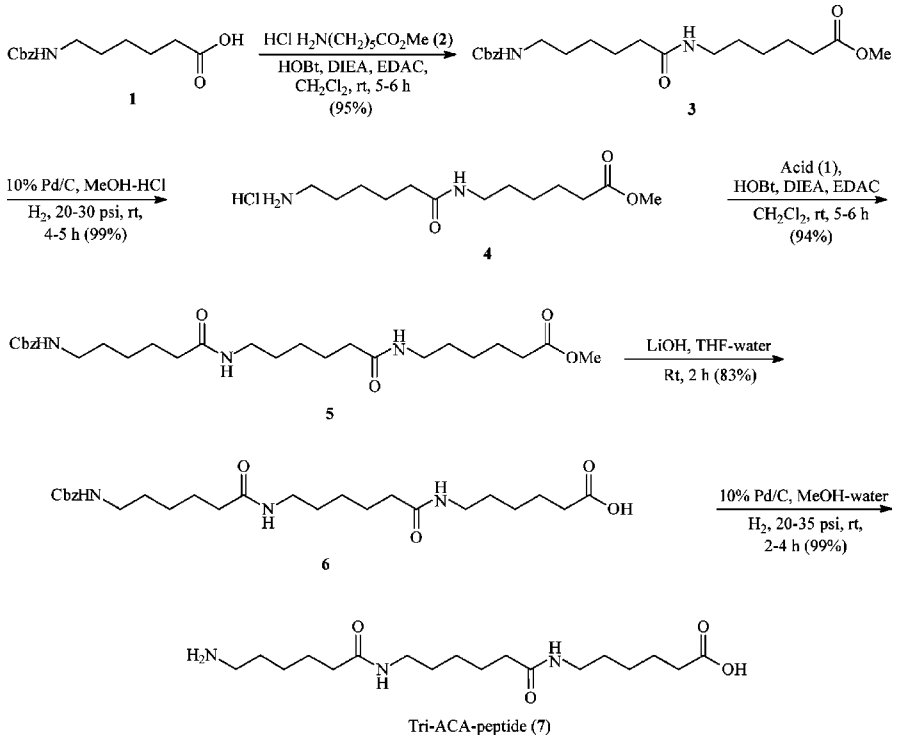

ethanol (1.4 L) and water (1.4 L) and treated with preactivated carbon (9.6 g) at 70−75 °C. The carbon was removed by filtration, and the crystallized solid was filtered and dried in oven at 45−50 °C under vacuum for 48 h to afford 81.7 g of acid **11** as a colorless powder in 79% yield. Mp: 170−72 °C, IR (KBr): 3533, 3342, 3144, 1759, 1586, 1457, 1381, 1183, 1085, 1028, 978, 880 cm^{-1}; Analytical reversed phase (RP) HPLC: MeCN:water:0.5% aqueous trifluoroacetic acid/25:65:10/1.0 mL/min at 215 nm, t_R: 4.79 min, 98.9%, ^1H NMR (DMSO-d_6): δ 7.75 (t, 1 H, J = 5.2 Hz), 7.73 (t, 1 H, J = 5.2 Hz), 7.66 (t, 1 H, J = 5.6 Hz), 7.04 (s, 2 H), 3.27 (d, 2 H, J = 7.2 Hz), 3.06−2.98 (m, 6 H), 2.22 (t, 2 H, J = 7.6 Hz), 2.08−2.02 (m, 4 H), 2.00 (dist t, 1 H), 1.75−1.60 (m, 5 H), 1.58−1.42 (m, 8 H), 1.42−1.33 (m, 6 H), 1.32−1.18 (m, 6 H), 0.98−0.86 (m, 2 H); ^{13}C NMR (DMSO-d_6): δ 175.6, 175.5, 172.7, 172.2, 135.3, 44.7, 44.0, 39.2, 39.2, 39.1, 37.1, 36.3, 34.5, 30.4, 29.9, 29.8, 29.8, 29.5, 27.1, 27.0, 26.9, 26.0, 25.1; ESI-MS (*m/z*): 577.9 $(M + H)^+$, 594.9 $(M + NH_4)^+$, 1171.2 $(2 \times M + NH_4)^+$; Elemental analysis: Calcd for $C_{30}H_{48}N_4O_7$, C, 62.48, H, 8.39, N, 9.71; Found, C, 62.33, H, 8.49, N, 9.64.

4-[(2,5-Dioxo-2,5-dihydro-1*H*-pyrrol-1-yl)methyl]-*N*-(6-{[6-({6-[(2,5-dioxopyrrolidin-1-yl)oxy]-6-oxohexyl}amino)-6-oxohexyl]amino}-6-oxohexyl)cyclohexanecarboxamide (12). In a dry three-neck 2.0 L round-bottom flask equipped with a mechanical stirrer and nitrogen inlet was added the acid (**11**, 70.0 g, 121.4 mmol, 1.0 equiv) followed by anhydrous-degassed DMF [1.2 L, which was stirred under vacuum (0.1−0.3 mm/Hg) for 30 min] at room temperature. To this suspension were added sequentially *N*-hydroxysuccinimide (NHS, 27.9 g, 242.8 mmol, 2.0 equiv) and 1-(3-dimethylaminopropyl)-3-ethylcarbodiimide hydrochloride (EDAC, 46.6 g, 242.8 mmol, 2.0 equiv). After the addition was complete, the reaction mixture was stirred overnight at room temperature (21−23 °C) under nitrogen atmosphere. After 18 h, the mixture was heated to 55 °C for 3 h under nitrogen atmosphere. After completion of the reaction, as determined by the analysis of an aliquot by using HPLC, the reaction mixture was concentrated on a rotary evaporator (bath temp: 50−55 °C) using a vacuum. The resulting solid material was further dried overnight under vacuum, and 173.6 g of solid residue was obtained. This material was suspended in acetonitrile (1.4 L) and stirred for about 10 min. The white suspension was filtered, and the washing with acetonitrile (1.4 L) was repeated. After filtering the material, the trituration−filtration process was carried out using water (2 × 1.4 L) and finally again with acetonitrile (1.4 L). The solid material (127.5 g) was then transferred into a crystallizing dish and dried in an oven at 45−50 °C under vacuum for 14 h to give 67.1 g of coupling agent **12** with 97−98% purity by HPLC. Crystallization of a 60 g portion of this material from absolute ethanol (1.5 L) and acetonitrile (900 mL) gave 51.4 g of material, which was recrystallized from ethanol (1.28 L) and acetonitrile (765 mL). After filtration and drying the solid in oven at 45−50 °C under vacuum for 24 h, 47.0 g of coupling agent **12** was obtained as a colorless powder in 58% yield. Mp: 189−92 °C [Lit. (*8*) 170−73 °C, Analytical reversed phase (RP) HPLC (Kromasil column): Gradient solvent system (MeCN:water:1.0% aqueous trifluoroacetic acid/10:80:10 to 40:50:10 in 30 min) with flow rate of 1.0 mL/min at 220 nm, t_R: 19.28 min, 99.6%; IR (KBr): 3459, 3081, 1777, 1556, 1434, 1391, 1300, 1247, 1211, 1119, 998, 927, 865; ^1H NMR (DMSO-d_6): δ 7.75 (t, 1 H, J = 5.6 Hz), 7.73 (t, 1 H, J = 6.0 Hz), 7.66 (t, 1 H, J = 5.6 Hz), 7.05 (s, 2 H), 3.27 (d, 2 H, J = 6.8 Hz), 3.08−2.98 (m, 6 H), 2.85 (s, 4 H), 2.69 (t, 2 H, J = 7.2 Hz), 2.08−2.02 (m, 4 H), 2.00 (dist t, 1 H), 1.75 − 1.61 (m, 5 H), 1.58−1.44 (m, 8 H), 1.44−1.32 (m, 6 H), 1.32−1.18 (m, 6 H), 0.98−0.86 (m, 2 H); ^{13}C NMR (DMSO-d_6): δ 175.4, 172.5, 172.4, 172.0, 170.9, 169.6, 135.1, 44.5, 43.8, 39.0, 38.9, 38.8, 36.8, 36.1, 30.8, 30.1, 29.7, 29.6, 29.3, 29.2, 26.8, 26.7, 26.1, 25.7, 24.6; ESI-MS (*m/z*): 674.9 $(M + H)^+$, 691.4 $(M + NH_4)^+$; Elemental analysis: Calcd for, $C_{34}H_{51}N_5O_9$, C, 60.61, H, 7.63, N, 10.39; Found, C, 60.60, H, 7.62, N, 10.38.

Scheme 2. Completion of the Synthesis of Coupling Agent 12

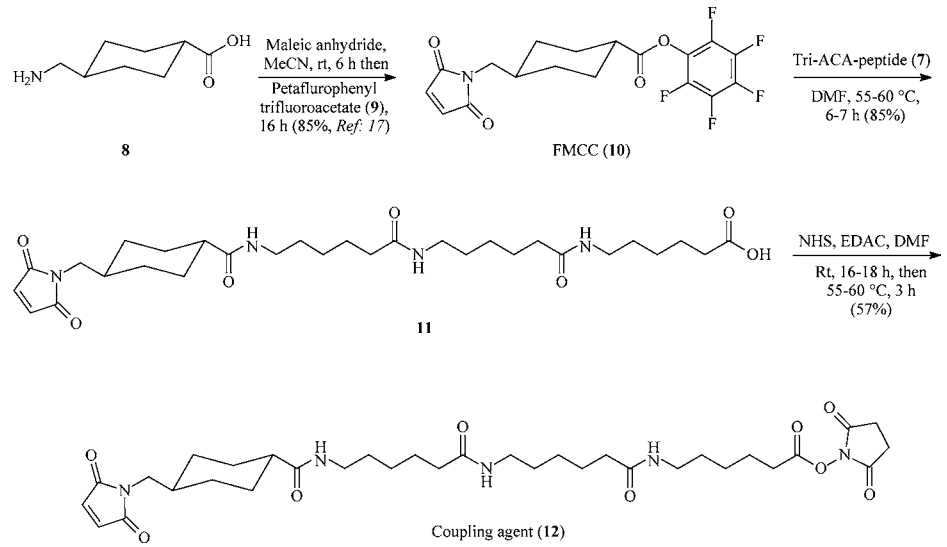

RESULTS AND DISCUSSION

Our strategy for the synthesis of the coupling agent **12** is based on a convergent approach, in which the tri-ACA-peptide **7** was assembled first, and then the cyclohexane-unit-containing maleimide group was introduced in the final stages. This strategy was envisioned not only for advantages of the convergent approach during scale-up, but also to avoid the formation of byproducts based on the reaction of maleimide group, from early stages of synthesis, as observed with the reported procedure (*8*). Accordingly, 6-{[(benzyloxy)carbonyl]amino}hexanoic acid (**1**) was coupled (Scheme 1) with methyl 6-aminohexanoate (**2**) in the presence of HOBt and EDAC in dichloromethane to afford methyl ester **3** (*14*−*15*) in 95% yield and 98% purity by HPLC. The next step in the synthesis was to remove the Cbz group in **3** by hydrogenolysis using 10% Pd/C, which was carried out in the presence of hydrochloric acid to prevent the formation any self-condensation products. The hydrogenation reaction was worked-up by filtration to give methyl 6-[(6-aminohexanoyl)amino]hexanoate (**4**) as its hydrochloride salt in quantitative yield. The hydrochloride salt **4** was then subjected to a second coupling reaction with acid **1** in the presence of HOBt and EDAC in dichloromethane to afford the ester **5** (*15*), which was also isolated by extractive workup in 94% yield. The methyl ester in **5** was then hydrolyzed using lithium hydroxide in methanol−water, and the resulting crude product was crystallized from ethanol−ethyl acetate to afford the acid **6** in 83% yield and 99.9% purity by HPLC. Subsequent hydrogenation of acid **6** in the presence of 10% Pd/C in a mixture of methanol−water gave the desired tri-ACA-peptide **7** (*16*) in quantitative yield, as a colorless solid. In the absence of water during hydrogenation, the tri-ACA-peptide **7** was precipitated in methanol and 2−3% of starting material **6** was still present, even after carrying out the reaction at higher pressure (50−60 psi) and for longer period (14−18 h).

The cyclohexanecarboxylic acid unit containing a maleimide group, FMCC (**10**), was synthesized on a 65 g scale by modifying the procedure reported by Adamczyk and Johnson (*17*). The reaction was carried out in acetonitrile solvent, which facilitated the aqueous extractive workup on a large scale, and the product **10** was isolated by crystallization. With FMCC (**10**) in hand, its coupling (Scheme 2) with the tri-ACA-peptide **7** was carried out in anhydrous DMF at 55 °C for 7 h. The crude product was crystallized from ethanol−water to afford the desired acid **11** in 79% yield and 99.4% purity. The acid **11** was then converted into the corresponding succinimidyl ester **12** by treatment with *N*-hydroxysuccinimide and EDAC in anhydrous DMF. The crude product **12**, which was isolated by removal of DMF and subsequent washing with acetonitrile and water, had 97−98% purity by HPLC consistently from different batch size reactions. The crude product **12**, with 97−98% purity, was further crystallized from a mixture of ethanol−acetonitrile to afford to the desired coupling agent **12** in 58% and 99.6% purity, as a colorless powder. The only impurity present in the crystallized coupling agent **12** was identified to be the acid **9**, in approximately 0.4% by HPLC (Figure 1).

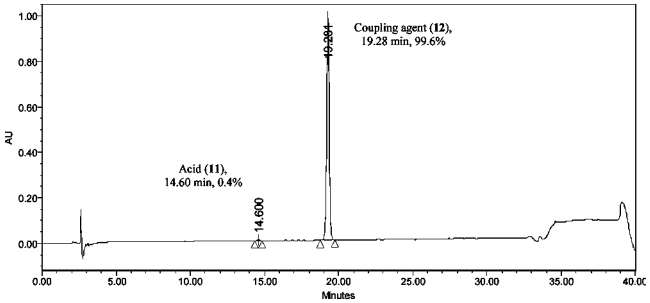

Figure 1. Analytical HPLC of heterobifunctional coupling agent **12**.

In summary, an efficient method for the preparation of a heterobifunctional coupling agent **12** was developed and the product was isolated in excellent over all yield (32%) and quality (99.6% purity). The method is suitable for synthesis of multigram quantities (47 g) of coupling agent **12** with consistent purity, >99% by HPLC, and can be useful for preparation of other analogous coupling agents, which are critical for bioconjugation.

ACKNOWLEDGMENT

We thank Dr. Phillip G. Mattingly of Abbott Laboratories for on-line literature search.

LITERATURE CITED

(1) Aslam, M., and Dent, A. H. (1999) *Bioconjugation: Protein coupling techniques for the biomedical sciences*, Macmillan Publishers, Houndsmills, England.

(2) Hermanson, G. T. (1996) *Bioconjugate Techniques*, Academic Press, New York.
(3) Sasay, M. A. (2003) Monoclonal antibody conjugation via chemical modification. *Biopharm. Int*. December, 32−39
(4) Brinkley, M. (1992) A brief survey of methods for preparing protein conjugates with dyes, haptens, and cross-linking reagents. *Bioconjugate Chem*. *3*, 2−13.
(5) Koppel, G. A. (1990) Recent advances with monoclonal antibody drug targeting for the treatment of human cancer. *Bioconjugate Chem*. *1*, 13−23.
(6) Means, G. E., and Feeney, R. E. (1990) Chemical modifications of proteins: History and applications. *Bioconjugate Chem*. *1*, 2−12.
(7) Henry, C. (1996) FDA, reform and the well-characterized biologic. *Anal. Chem*. *68*, 674A−677A.
(8) Bieniarz, C.; Husain, M., Barnes, G., King, C. A., and Welch, C. J. (1996) Extended length heterobifunctional coupling agents for protein conjugations. *Bioconjugate Chem*. *7*, 88−95.
(9) Bogacz, J. P., Novotny, M., Lewis, C. A., Peters, T., Sramek, L., Chacko, M., Sequeira, A., Jacob, J., and Wilson, D. H, (1997) Development of an automated random/continues access microparticle enzyme immunoassay (MEIA) for the determination of hTSH with 3rd generation sensitivity on the Abbott AxSYM automated immunoassay system. *Clin. Chem*. *43*, S189.
(10) Dewell, B., Jacobson, L., Friese, J., Rapp, J., Miceli, C., Loewen, N., Lauren, L., Salle, J., Slota, J., Seguado, O., and Weigand, R. (1997) Development of the Abbott AxSYM free PSA assay: Performance characteristics and preliminary clinical evaluation. *Anticancer Res*. *17*, 3037−3038.
(11) Qiu, K. Y., Bouma, S. R., Sumerdon, G. A., Biegalski, T. T., Gardiner, M. E., Munoz, J. J., and Peters, T. L. (2003) Development of a second generation troponin I assay for the Abbott AxSYM(R) immunoassay system. *Clin*. *Chem*. *49*, A62.
(12) Wilson, D. H., Groskopf, W., Hsu, S., Caplan, D., Langner, T., Baumann, M., DeManno, D., Williams, G., Paytte, D., Dagel, C., Lynch, D., and Manderino, G. (1998) Rapid, automated assay for progesterone on the Abbott AxSym analyzer. *Clin. Chem*. *44*, 86−91.
(13) Bieniarz, C., Young, D. F., and Cornwell, M. J. (1998) Thermally stabilized immunoconjugates: Conjugation of antibodies to alkaline phosphatase stabilized with polymeric cross-linkers. *Bioconjugate Chem*. *9*, 399−402.
(14) Zahn, H., and Determann, H. (1957) Nonakis-, decakis-, undecakis-, und dodecakis- ϵ-aminocapronsäure. *Chem. Ber*. *90*, 1963−1970.
(15) Cairns-Smith, A. G., and Pettigrew, R. (1969) Synthesis of nylon-like oligoamides. *J. Chem Soc*. 1606−1609.
(16) Zhan, H., and Hildebrand, D. (1957) Zur kenntnis der linearen oligamide der ϵ-amino-capronsäure. *Chem. Ber*. *90*, 320−329.
(17) Adamczyk, M., and Johnson, D. (1993) Synthesis of pentafluorophenyl-4-(*N*-maleimidomethyl)cyclohexane-1-carboxylate (FMCC). *Org. Prep. Proced. Int*. *25*, 592−594.

BC040259X

Preparation of ^{18}F-Human Serum Albumin: A Simple and Efficient Protein Labeling Method with ^{18}F Using a Hydrazone-Formation Method

Young Soo Chang,[†,‡,§] Jae Min Jeong,[†,‡,*] Yun-Sang Lee,[†] Hyung Woo Kim,[†] Ganesha B. Rai,[†] Seung Jin Lee,[§] Dong Soo Lee,[†] June-Key Chung,[†,‡] and Myung Chul Lee[†]

Department of Nuclear Medicine, Seoul National University College of Medicine, Seoul, Korea, Cancer Research Institute, Seoul National University College of Medicine, Seoul, Korea, and Department of Pharmacy, Ewha Womans University, Seoul, Korea. Received March 21, 2005; Revised Manuscript Received July 16, 2005

^{18}F-labeling of proteins and peptides is important for positron emission tomography (PET). Although there are many methods for the labeling of proteins with ^{18}F, most of these are characterized by complicated procedures or low yields. Here, we report a novel and simple method which includes the preparation of [^{18}F]fluorobenzaldehyde ([^{18}F]FBA) and successive conjugation with hydrazinonicotinic acid−human serum albumin conjugate (HYNIC−HSA) via hydrazone formation. HYNIC−HSA, which can also be used for labeling with ^{99m}Tc, was prepared via reaction with *N*-hydroxysuccinimide (NHS) or tetrafluorophenyl (TFP) esters of HYNIC with HSA. No-carrier-added [^{18}F]FBA was prepared by the nucleophilic substitution of [^{18}F]fluoride to 4-trimethylammonium benzaldehyde triflate in the presence of tetrabutylammonium bicarbonate. [^{18}F]FBA was purified by passing ion exchange cartridges (IC-H and QMA) and was adsorbed to a C_{18} Sep-Pak cartridge. The adsorbed [^{18}F]FBA was then eluted with 50% ethanol. HYNIC−HSA was added to the solution and conjugated with [^{18}F]FBA via hydrazone formation. ^{18}F-HSA was purified with a PD10 column. Biodistribution of ^{18}F-HSA, ^{99m}Tc-HSA, and [^{18}F]FBA in mice were investigated at 10, 20, and 60 min after intravenous injection. The number of conjugated HYNIC molecules per HSA ranged from 5.2 to 23.2 depending on the reaction conditions. The labeling efficiency of ^{18}F-FBA was 67 ± 15.7%. The radiochemical purity after purification was over 99%. The conjugation efficiency of HYNIC−HSA with [^{18}F]FBA was between 25% and 90%. The conjugation efficiency was observed to increase with increases in the number of conjugated HYNIC, the HYNIC−HSA concentration, or temperature. ^{18}F-HSA exhibited a biodistribution pattern similar to that of ^{99m}Tc-HSA while [^{18}F]FBA showed much lower blood activity than that of ^{18}F-HSA and ^{99m}Tc-HSA. We concluded that ^{18}F-HSA was successfully labeled using a novel method which involves hydrazone formation between [^{18}F]FBA and HYNIC−HSA. This method can be applied to the ^{18}F-labeling of other proteins or peptides.

INTRODUCTION

The application of bioactive proteins labeled with radionuclides for diagnostic imaging has emerged as a useful and interesting field in nuclear medicine (*1*−*4*). In particular, ^{18}F-labeled proteins or peptides bear a great deal of clinical and research potential due primarily to their favorable nuclear characteristics with regard to positron emission tomography (PET) that has high resolution and sensitivity (*5*−*7*).

Specially designed synthons are essential for the ^{18}F labeling of proteins or peptides because the biomolecules cannot be directly labeled by nucleophilic [^{18}F]-fluorination. A variety of ^{18}F-labeled synthons have been developed and successfully applied to a host of peptides and proteins for ^{18}F labeling (*8*−*12*). With a few exceptions (*8*), the most effective procedures for the synthesis of ^{18}F-labeled synthons are all multistep procedures. Among these synthons, *N*-succinimidyl 4-[^{18}F]fluorobenzoate ([^{18}F]SFB) remains the most widely applied agent for many bioactive molecules with regard to in vivo stability and radiolabeling yields. However, [^{18}F]SFB can be obtained via a time-consuming three-step synthesis method (*5*, *6*). Therefore, it is necessary to develop simpler and more efficient ^{18}F labeling methods with proteins or peptides for clinical routine use.

Here, we report a novel and simple method for the preparation of ^{18}F-labeled proteins. In this paper, we evaluated the efficacy of this method using human serum albumin (HSA) as a test protein. The resulting product, ^{18}F-HSA, might be used in blood pool imaging. The whole procedure is shown in Scheme 1. First, hydrazinonicotinic acid (HYNIC) was conjugated with HSA yielding HYNIC−HSA. [^{18}F]fluorobenzaldehyde ([^{18}F]FBA) was then prepared via the nucleophilic substitution of [^{18}F]fluoride. Finally, [^{18}F]FBA was conjugated to HYNIC−HSA via hydrazone formation. HYNIC−HSA might be used not only for ^{18}F-labeling but also for ^{99m}Tc-labeling.

EXPERIMENTAL PROCEDURES

Materials and Instrumentations. NMR spectroscopy was conducted with a Gemini 300 NMR spectrometer obtained from the Varian Company. Mass spectra

* Corresponding author: Jae Min Jeong, Ph.D., Department of Nuclear Medicine, Seoul National University Hospital, 28 Yungun-dong, Jongro-gu, Seoul 110-744, Korea. Tel: 82-2-2072-3805. Fax: 82-2-745-7690. E-mail address: jmjng@snu.ac.kr.

† Department of Nuclear Medicine, Seoul National University College of Medicine.

‡ Cancer Research Institute, Seoul National University College of Medicine.

§ Ewha Womans University.

10.1021/bc050086r CCC: $30.25 © 2005 American Chemical Society
Published on Web 08/25/2005

Scheme 1. Synthesis of ^{18}F-Labeled HSA via Formation of Hydrazone

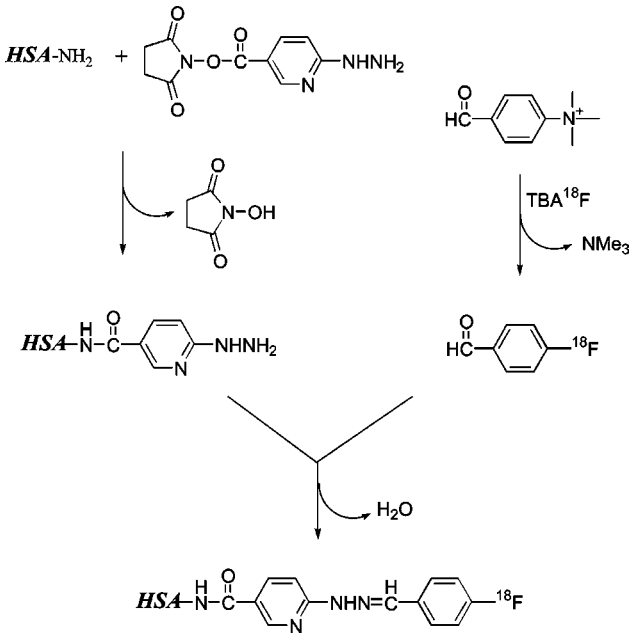

were obtained with a Applied Biosystems/MDS Sciex API 3000 LC/MS/MS System. A DU650 Spectrophotometer (Beckman Coulter) was used for absorbance measurements. A NaI well counter (Packard, Canberra Co.) and dose calibrator (Atomlab 100, Medical Systems Inc.) were used to measure the low and high levels of radioactivity, respectively. A Bio-Scan System 2000 imaging scanner was used to perform the Radio-TLC scan. For TLC, we purchased aluminum-backed silica gel 60 F_{254} from the E. Merck Company (Germany) and ITLC-SG plates from the Gelman Company. PD10 size-exclusion columns were from Amersham Biosciences (Sweden), C_{18} and QMA Sep-Pak cartridges were obtained from Waters (Milford, MA), IC-H Maxi-Clean cartridges were purchased from Alltech (Deerfield, IL), and BCA kit for the protein assay was from Pierce (Rockford, IL). [^{18}F]Fluoride was produced by the ^{18}O (p, n) ^{18}F reaction on ^{18}O-enriched (95%) water using a 13 MeV proton beam generated by a TR-13 cyclotron (Ebco Technologies, Vancouver, Canada). The ^{99}Mo/^{99m}Tc-generator was purchased from the DuPont Company. HSA kit for ^{99m}Tc-labeling was obtained from Daiichi Radioisotope Laboratories, LTD (Japan). All other reagents and solvents, if not specified, were purchased from Aldrich, Sigma, or Fluka and were used with no further purification.

Synthesis of HYNIC and 4-*N*,*N*,*N*-Trimethylammonium Benzaldehyde Triflate. *N*-Hydroxysuccinimide ester of hydrazinonicotinic acid (NHS−HYNIC) and tetrafluorophenyl ester of hydrazinonicotinic acid (TFP−HYNIC) compounds were synthesized according to previously reported methods (*14*, *15*). 4-*N*,*N*,*N*-Trimethylammonium benzaldehyde triflate was also synthesized according to a method published in the literature (*16*). Briefly, *N*,*N*-dimethylalininobenzaldehyde (100 mg, 0.44 mmol) was added to an evacuated and argon-purged 25 mL sidearm flask with a stirring bar. Methylene chloride (7 mL) was added to the flask with stirring, which produced a clear slightly greenish-yellow solution. Methyl trifluoromethanesulfonate (53.75 μL, 0.475 mmol) was then added, which resulted in an immediate color change to intense yellow. After stirring overnight, the crude product was obtained by addition of diethyl ether as a white powder (0.14 g). Recrystallizaiton from methylene chloride/diethyl ether produced a fine white crystalline powder. mp 105−107 °C; ^{1}H NMR (DMSO-d_6) δ: 3.64 (s, 9H, 3CH_3), 8.18 (q, 4H, J = 6.8 Hz, aromatic), 10.1 (s, 1H, CHO); ^{13}C NMR (DMSO-d_6) δ: 55.3, 120.7, 129.9, 135.8, 150.1, 191.2; ESI-MS (*m*/*z*): 165.1 [M + H]$^+$.

Preparation of HYNIC−HSA. HYNIC−HSA was prepared by reacting HSA with various amounts of NHS−HYNIC or TFP−HYNIC, according to the published method with some modifications (*17*). To 1 mL of 2% HSA solution in 0.05 M phosphate buffer (pH 7.5) we added 20 μL of NHS−HYNIC or TFP−HYNIC solution in dimethyl sulfoxide (DMSO). The molar ratios of HYNIC to HSA varied ranging from 8:1 to 32:1. After incubation for 2 h at room temperature, the unreacted HYNIC was removed with a PD10 size-exclusion column. HYNIC−HSA was eluted with 0.05 M phosphate buffer (pH 7.5). The protein concentration of purified HYNIC−HSA was determined using a BCA protein assay kit. The amount of conjugated HYNIC was determined by measuring optical density at 385 nm after conjugation with 0.5 mM *p*-nitrobenzaldehyde (extinction coefficient: 2.53 $\times$ 10^4 L mol^{-1} cm^{-1}) for 5 h at room temperature thereby forming hydrazone (*15*, *18*).

Preparation of [^{18}F]FBA. An aqueous solution of [^{18}F]fluoride in ^{18}O-enriched water was captured on a QMA light Sep-Pak cartridge which had been preconditioned with 5 mL of 0.5 M potassium bicarbonate and washed with 10 mL of deionized water. The [^{18}F]fluoride on the cartridge was eluted with 1 mL of 2.3% tetrabutylammonium bicarbonate in 83.8% acetonitrile. Azeotropic distillation was conducted twice, each at 90 °C after addition of 1 mL acetonitrile under a gentle stream of argon gas.

[^{18}F]FBA was prepared via the nucleophilic substitution of [^{18}F]fluoride to 4-*N*,*N*,*N*-trimethylaminebenzaldehyde triflate (*16*). To the above dried [^{18}F]fluoride in tetrabutylammonium bicarbonate (16 mg, 52.7 μmol) was added 5 mg of 4-*N*,*N*,*N*-trimethylammonium benzaldehyde triflate in DMSO (0.5 mL) and reacted for 6 min at 100 °C. The reaction mixture was diluted with deionized water and passed through a set of ion exchange cartridges (two IC-H Maxi-Clean cartridges for cation exchanger and a QMA Sep-Pak cartridge for anion exchanger) to remove ionic components. The labeled product was then adsorbed to a C_{18} Sep-Pak light cartridge. The adsorbed [^{18}F]FBA was eluted with 50% ethanol. Labeling efficiency was measured by a thin-layer chromatography with a Radio-TLC scanning (silica gel TLC/ethyl acetate:hexane = 1:3; R_f values: [^{18}F]fluoride ion = 0.0 and [^{18}F]FBA = 0.7).

Preparation of ^{18}F-HSA. HYNIC−HSA was conjugated with [^{18}F]FBA via hydrazone formation (Scheme 1). Purified [^{18}F]FBA solution (0.3 mL) was added to the HYNIC−HSA solution (the concentration of HSA was 3 mg/1.2 mL 0.05 M phosphate buffer (pH 7.5)), and the solution was incubated for 30 min at room temperature, 50 °C or 60 °C. The labeled ^{18}F-HSA was then purified with a PD10 column. Radiochemical purity was verified using ITLC-SG and normal saline or acetone. (ITLC−SG/normal saline; R_f values: ^{18}F-HSA = 0.0 and [^{18}F]FBA = 1.0; ITLC−SG/acetone; R_f values: ^{18}F-HSA = 0.0 and [^{18}F]FBA = 1.0).

Stability Test of ^{18}F-HSA. The labeled and purified ^{18}F-HSA was then stored at room temperature, and the radiochemical purity was determined by chromatography as described in the Preparation of ^{18}F-HSA section. The radiochemical purity was determined at 10 min, 30 min, 1 h, 2 h, 3 h, 4 h, 5 h, and 6 h.

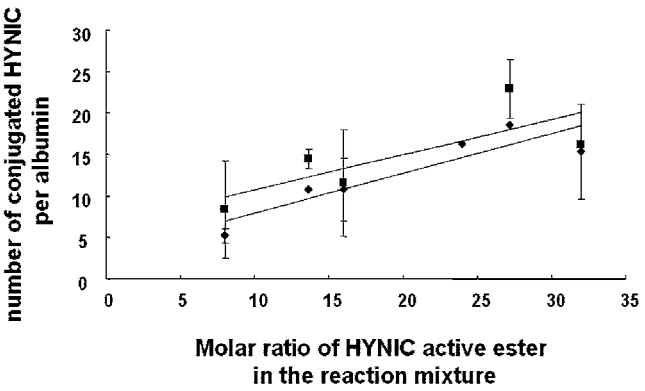

Figure 1. Conjugation of HYNIC to albumin as a function of the molar ratio of active HYNIC ester and HSA; NHS−HYNIC (◆) or TFP−HYNIC (■). Protein concentration of HYNIC−HSA was determined using a BCA protein assay kit, and the amount of conjugated HYNIC was determined by measuring OD385 after conjugation with *p*-nitrobenzaldehyde (extinction coefficient: 2.53×10^4 L mol^{-1} cm^{-1}).

Preparation of ^{99m}Tc-HSA. ^{99m}Tc-HSA was prepared and tested according to the protocols provided by the supplier.

Biodistribution Study in Mice. All animal studies were conducted in compliance with the local regulations. Male ICR mice (n = 3 or 4/group, 28 ± 1.9 g) were injected with 37 kBq (100 μL) of ^{18}F-HSA, ^{99m}Tc-HSA, or [^{18}F]FBA through the tail vein. The mice were subsequently sacrificed by cervical dislocation after 10, 20, and 60 min, respectively. The weight and radioactivity of the blood, muscle, fat, heart, lung, liver, spleen, stomach, intestine, kidney, brain, and bone from the sacrificed mice were then measured with electronic balance and gamma scintillation counter, respectively. Results were expressed as a percentage of injected dose per gram of tissue (% ID/g).

RESULTS

Preparation of HYNIC−HSA. The reaction of HSA with NHS−HYNIC or TFP−HYNIC resulted in the introduction of a number of hydrazinonicotinyl sidechains. The amount of conjugated HYNIC increased with increases in the molar ratio of the active ester of HYNIC to HSA (Figure 1). The amount ranged from 5.2 to 23.2 according to the reaction conditions utilized. When TFP−HYNIC was used, the amount of conjugated HYNIC molecules per HSA was slightly higher than that observed when NHS−HYNIC was used, but this difference was not significant (Figure 1).

Preparation of [^{18}F]FBA. [^{18}F]FBA was synthesized via the nucleophilic substitution of [^{18}F]fluoride to *N*,*N*,*N*-trimethylammonium benzaldehyde in the presence of tetrabutylammonium bicarbonate. The labeling efficiency of [^{18}F]FBA was about 67 ± 15.7%. The radiochemical purity of [^{18}F]FBA after purification was more than 99%.

Preparation of ^{18}F-HSA. HYNIC−HSA was conjugated with the purified [^{18}F]FBA via hydrazone formation, and the labeling efficiency was verified by an ITLC-SG chromatogram. As the HYNIC−HSA concentration increased, the radiochemical yield also increased (Figure 2). The conjugation yield of HYNIC−HSA with [^{18}F]FBA ranged from 25% to 90%. The more highly hydrazinonicotinylated HYNIC−HSA exhibited a higher conjugation yield. The radiochemical yield of the control HSA was less than 10% (Figure 3). The reaction temperature also influenced the radiochemical yield. This was determined to increase at higher temperatures (Figure 4).

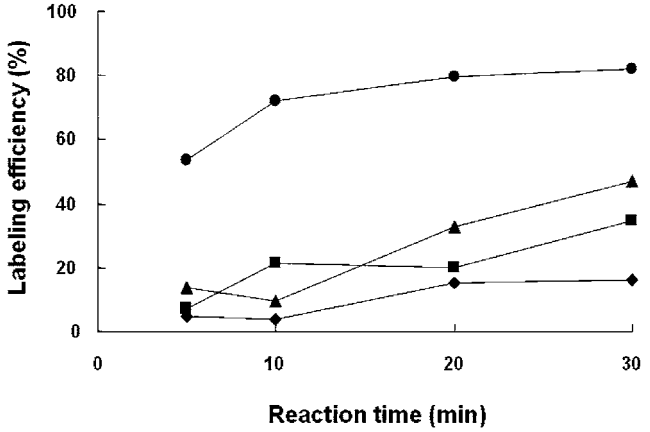

Figure 2. Conjugation efficiency of HYNIC−HSA with [^{18}F]-FBA as a function of time. The protein concentrations are 3 mg/1.5 mL (●), 2 mg/1.5 mL (▲), 1 mg/1.5 mL (■), and 0.5 mg/1.5 mL (◆).

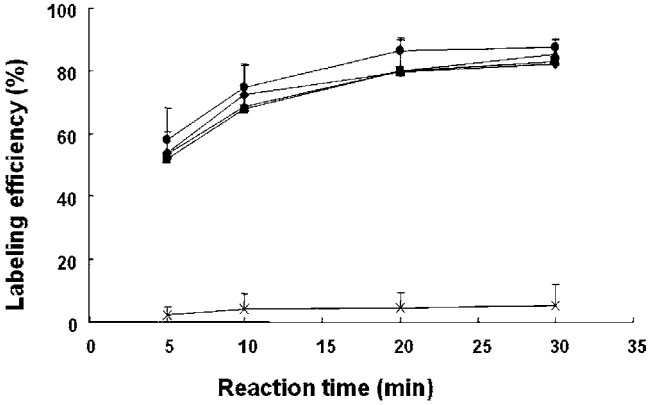

Figure 3. Conjugation efficiency of HYNIC−HSA with [^{18}F]-FBA as a function of time. The number of conjugated HYNIC per HSA on used HYNIC−HSA are 0 as a control (*), 5 (◆), 12 (■), and 23 (●).

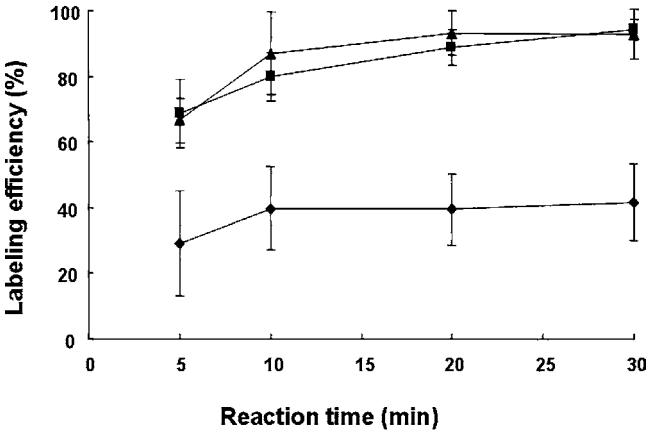

Figure 4. The effects of reaction temperature on conjugation efficiency of HYNIC−HSA with [^{18}F]FBA. The reaction temperatures are room temperature (◆), 50 °C (■), and 60 °C (▲).

Stability Test of ^{18}F-HSA. ^{18}F-HSA was very stable for 6 h both in 0.05 M phosphate buffer (pH = 7.4) at room temperature and in human serum at 37 °C (Figure 5).

Biodistribution Study in Mice. Biodistribution experiments using ^{18}F-HSA, ^{99m}Tc-HSA and [^{18}F]FBA were performed on normal mice (Figure 6). ^{18}F-HSA and ^{99m}Tc-HSA exhibited similar blood activities, while [^{18}F]FBA exhibited much lower blood activity. The bone

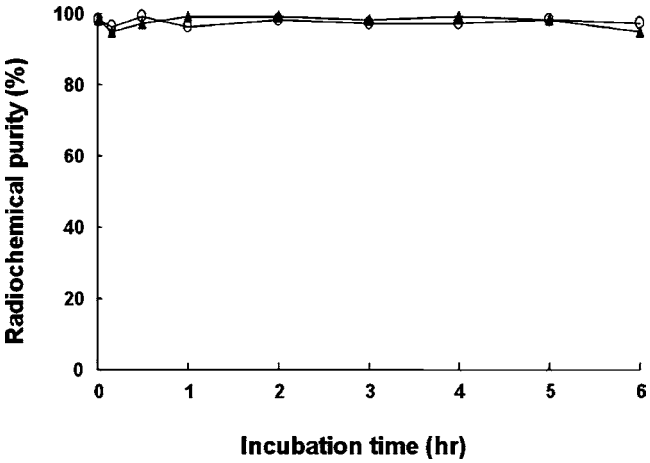

Figure 5. Stability test of ^{18}F-HSA in 0.05 M phosphate buffer (pH = 7.4) at room temperature (○) and in human serum at 37 °C (▲).

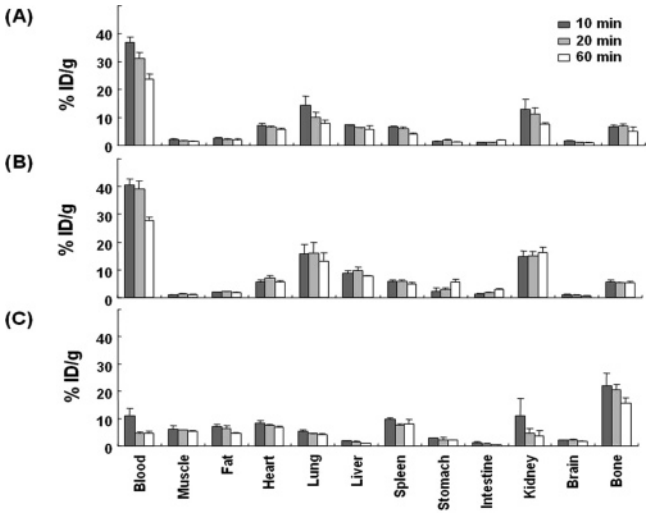

Figure 6. Biodistribution of (A) ^{18}F-HSA, (B) ^{99m}Tc-HSA, and (C) [^{18}F]FBA. The labeled agents were injected through the tail veins of mice.

uptake of ^{18}F-HSA was not increasing by time, which indicated that defluorination did not occur from ^{18}F-HSA in vivo. In the other organs, ^{18}F uptake was similar to or less than those observed with ^{99m}Tc-HSA.

DISCUSSION

HYNIC is a famous bifunctional chelating agent, which is used for the labeling of proteins with ^{99m}Tc (*1*, *2*, *13*, *15*, *17*). A variety of functional groups, including active esters, isothiocyanates, maleimides, hydrazides, and α-haloamides, have been developed in order to conjugate bifunctional chelating agents to proteins (*2*). Hydrazides have been demonstrated to react with aldehyde groups via the formation of stable hydrazone bonds with high yields. Thus, the hydrazone formation reaction for the coupling of aldehyde and/or hydrazide-containing proteins and/or bifunctional chelating agents has been applied to the preparation of protein−protein or protein−bifunctional chelating agent conjugates (*18*, *19*).

To determine the number of conjugated HYNIC per HYNIC-conjugated proteins, *p*-nitrobenzaldehyde is used, as it reacts with HYNIC−protein quantitatively with generation of a specific hydrazone, which exhibits a characteristic absorption at 385 nm. Actually, the protocols of this experiment are inspired from the quantification method used for HYNIC-protein. We used [^{18}F]FBA instead of *p*-nitrobenzaldehyde in this novel and simple method for the labeling of proteins or peptides with ^{18}F. This method proved to significantly reduce radiolabeling steps and reaction time relative to the other reported methods (*5*, *8*).

[^{18}F]FBA is a famous synthon which is used for the synthesis and ^{18}F-labeling of a variety of radiopharmaceuticals (*16*, *20*). In general, either *N*,*N*,*N*-trimethylammonium benzaldehyde or nitrobenzaldehyde can be used as a precursor for the synthesis of [^{18}F]FBA. We used *N*,*N*,*N*-trimethylammonium benzaldehyde because the positively charged quaternary ammonium can easily be removed from the neutral hydrophobic product using a combination of ion exchange and reverse phase cartridges. In this manner, [^{18}F]FBA can be produced in a no-carrier-added state which provides high specific activity.

Tetrabutylammonium bicarbonate, rather than crown ether such as Kryptofix 2.2.2, was used as a base to activate [^{18}F]fluoride in a nucleophilic substitution reaction in order to facilitate the next purification step in this experiment. Crown ether is difficult to remove as both it and [^{18}F]FBA are hydrophobic whereas the tetrabutylammonium ion can easily be removed by ion exchange cartridges together with precursor.

The prepared ^{18}F-HSA exhibited a high labeling efficiency and stability. Biodistribution studies in mice revealed that introduction of the HYNIC into HSA had no significant effects on the biological properties of HSA or on its in vivo stability as compared to ^{99m}Tc-HSA a verified and commercialized blood pool imaging agent.

A recent report reveals a chemoselective formation of oxime between unprotected aminooxy-functionalized peptides and [^{18}F]FBA with a high yield (*21*). They asserted that this method allowed for the fast and straightforward large-scale production of ^{18}F-labeled peptides for clinical routine PET application. Their method and our HYNIC method have a mechanism in common—namely, that some ammonia derivatives including hydroxylamine, hydrazine, phenylhydrazine, or semicarbazide form stable conjugates with either aldehydes or ketones. In our lab, the application of the HYNIC method proved to be more favorable than the oxime method as HYNIC has been already verified with regard to its application as a bifunctional chelating agent for the labeling of proteins or peptides with ^{99m}Tc. In addition, HYNIC−protein can be applied directly not only for ^{18}F labeling but also for ^{99m}Tc labeling.

There are some ^{18}F-labeling synthons those react with thiols (*22*) or contain thiols (*23*). Although these thiol-related synthons show high labeling efficiencies, highly reactive and unstable thiols can be a cause of problems in storage or preparation.

Our biodistribution study confirmed that ^{18}F-HSA labeled by this technique can be used for blood pool imaging, as it exhibited biodistribution pattern similar to that seen with ^{99m}Tc-HSA, which is an approved blood pool imaging agent, in the majority of the organs. [^{18}F]FBA, a small hydrophobic molecule, exhibited a very different biodistribution pattern as expected.

CONCLUSION

We developed a novel and simple method for the preparation of ^{18}F-HSA using a hydrazone formation mechanism between [^{18}F]FBA and HYNIC−HSA. The generated ^{18}F-HSA exhibited excellent in vitro and in vivo properties as a blood-pool imaging agent. This method

might prove quite applicable to the labeling of other proteins with ^{18}F as well.

ACKNOWLEDGMENT

This study was supported by a grant from the KOSEF.

Supporting Information Available: ^{1}H NMR spectrum of *N*,*N*,*N*-trimethylammonium benzaldehyde, ^{13}C NMR spectrum of *N*,*N*,*N*-trimethylammmonium benzaldehyde, mass spectrum of *N*,*N*,*N*-trimethylammonium benzaldehyde, UV spectrum of *p*-nitrobenzaldehyde, UV spectrum of HSA-HYNIC, UV spectrum of HSA-HYNIC + *p*-nitrobenzaldehyde, and UV spectrum of HSA + *p*-nitrobenzaldehyde. This material is available free of charge via the Internet at http://pubs.acs.org.

LITERATURE CITED

(1) Fichna, J., and Janecka, A. (2003) Synthesis of target-specific radiolabeled peptides for diagnostic imaging. *Bioconjugate Chem. 14*, 3−17.

(2) Weiner, R. E., and Thakur, M. L. (2002) Radiolabeled peptides in the diagnosis and therapy of oncological diseases. *Appl. Radiat. Isot. 57*, 749−763.

(3) Wilbur, D. S. (1992) Radiohalogenation of proteins: an overview of radionuclides, labeling methods, and reagents for conjugate labeling. *Bioconjugate Chem. 3*, 433−470.

(4) Jeong, J. M., Hong, M. K., Lee, J., Son, M., So, Y., Lee, D. S., Chung, J.-K., and Lee, M. C. (2004) ^{99m}Tc-Neolactosylated human serum albumin for imaging the hepatic asialoglycoprotein receptor. *Bioconjugate Chem. 15*, 850−855.

(5) Okarvi, S. M. (2001) Recent progress in fluorine-18 labeled peptide radiopharmaceuticals. *Eur. J. Nucl. Med. 28*, 929−938.

(6) Kilbourn, M. R., Dence, C. S., Welch, M. J., and Mathias, C. J. (1987) Fluorine-18 labeling of proteins. *J. Nucl. Med. 28*, 462−470.

(7) Varagnolo, L., Stokkel, M. P. M., Mazzi, U., and Pauwels, E. K. J. (2000) ^{18}F-labeled radiopharmaceuticals for PET in oncology, excluding FDG. *Nucl. Med. Biol. 27*, 103−112.

(8) Wester, H. J., Hamacher, K., and Stocklin, G. (1996) A comparative Study of N. C.A Fluorine-18 labeling of proteins via acylation and photochemical conjugation. *Nucl. Med. Biol. 23*, 365−372.

(9) Vries, E. F. J., Vroegh, J., Elsinga. P. H., and Vaalburg, W. (2003) Evaluation of fluorine-18-labeled alkylating agents as potential synthons for the labeling of oligonucleotides. *Appl. Radiat. Isot. 58*, 469−476.

(10) Vaidyanathan, G., and Zalutsky, M. R. (1992) Labeling proteins with fluorine-18 Using *N*-succinimidyl 4-[^{18}F]fluorobenzoate. *Nucl. Med. Biol. 19*, 275−281.

(11) Downer, J. B., McCarthy, T. J., Edwards, W. B., Anderson, C. J., and Welch, M. J. (1997) Reactivity of *p*-[^{18}F]Fluorophenacyl bromide for radiolabeling of proteins and peptides. *Appl. Radiat. Isot. 48*, 907−916.

(12) Iwata, R., Pascali, C., Bogni, A., Horvath, G., Kovacs, Z., Yanai, K., and Ido, T. (2000) A new, convenient method for the preparation of 4-[^{18}F]fluorobenzyl halides. *Appl. Radiat. Isot. 52*, 87−92.

(13) Abrams, M. J., Juweid, M., TenKate, C. I., Schwartz, D. A., Hauser, M. M., Gaul, F. E., Fuccello, A. J., Rubin, R. H., Strauss, H. W., and Fischman, A. J. (1990) Technetium-99m-human polyclonal IgG radiolabeled via the hydrazino nicotinamide derivative for imaging focal sites of infection in rats. *J. Nucl. Med. 31*, 2022−2028.

(14) Ono, M., Arano, Y., Mukai, T., Uehara, T., Fujioka, Y., Ogawa, K., Uehara, T., Saga, T., Konishi, J., and Saji, H. (2001) ^{99m}Tc-HYNIC-derivatized ternary ligand complexes for ^{99m}Tc-labeled polypeptides with low *in vivo* protein binding. *Nucl. Med. Biol. 28*, 215−224.

(15) Schwartz, D. A., Abrams, M. J., Hauser, M. M., Gaul, F. E., Larsen, S. K., Rauh, D., and Zubieta, J. A. (1991) Preparation of hydrazine-modified proteins and their use for the synthesis of ^{99m}Tc-protein conjugates. *Bioconjugate Chem. 2*, 333−338.

(16) Haka, M. S., Kilbourn, M. R., Watkins, G. L., and Toorongian, S. A. (1989) Aryltrimethylammonium trifluoromethanesulfonates as precursors to aryl [^{18}F]fluorides: imporved synthesis of [^{18}F]GBR-13119. *J. Labelled Compd. Radiopharm. 27*, 823−838.

(17) Verbeke, K., Hjelstuen, O., Debrock, E., Cleynhens, B., Roo, M., and Verbruggen, A. (1995) Comparative evaluation of ^{99}Tc^{m}-Hynic-HSA and ^{99}Tc^{m}-MAG3-HSA as possible blood pool agents. *Nucl. Med. Commun. 16*, 942−957.

(18) King, T. P., Zhao, S. W., and Lam T. (1986) Preparation of protein conjugates via intermolecular hydrazone linkage. *Biochemistry 25*, 5774−5779.

(19) Jeong, J. M., Lee, J., Paik, C. H., Kim, D. K., Lee, D. S., Chung, J.-K., and Lee, M. C. (2004) Site-specific ^{99m}Tc-labeling of antibody using dihydrazinophthalazine (DHZ) conjugation to Fc region of heavy chain. *Arch. Pharm. Res. 27*, 961−967.

(20) Choe, Y. S., Oh, S. J., Shim, I., Naruto, S., Chi, D. Y., Kim, S. E., Lee, K. H., Choi, Y., and Kim, B. T. (2000) Syntheses and biological evaluation of ^{18}F-labeled-3-(1-benzyl-piperidin-4-yl)-1-(1-methyl-1H-indol-3-yl)propan-1-ones for In vivo mapping of acetylcholinesterase. *Nucl. Med. Biol. 27*, 263−267.

(21) Poethko, T., Schottelius, M., Thumshirn, G., Hersel, U., Herz, M., Henriksen, G., Kessler, H., Schwaiger, M., and Wester, H. J. (2004) Two-step methodology for high-yield routine radiohalogenation of peptides: ^{18}F-labeled RGD and octerotide analogs. *J. Nucl. Med. 45*, 892−902.

(22) Toyokuni, T., Walsh, J. C., Dominguez, A., Phelps, M. E., Barrio, J. R., Gambhir, S. S., and Satyamurthy, N. (2003) Synthesis of a new heterobifunctional linker, *N*-[4-(aminooxy)-butyl]maleimide, for facile access to a thiol-reactive ^{18}F-labeling agent. *Bioconjugate Chem. 14*, 1253−1259.

(23) Glaser, M., Karlsen, H., Solbakken, M., Arukwe, J., Brady, F., Luthra, S. K., and Cuthbertson, A. (2004) ^{18}F-Fluorothiols: a new approach to label peptides chemiselectively as potential tracers for positron emission tomography. *Bioconjugate Chem. 15*, 1447−1453.

BC050086R

CORRECTIONS

Volume 16, Number 4, June/July, 2005.

Elena V. Batrakova, Serguei V. Vinogradov, Sandra M. Robinson, Michael L. Niehoff, William A. Banks, and Alexander V. Kabanov*

POLYPEPTIDE POINT MODIFICATIONS WITH FATTY ACID AND AMPHIPHILIC BLOCK COPOLYMERS FOR ENHANCED BRAIN DELIVERY

Page 798. The revised version of Figure 5 is presented below.

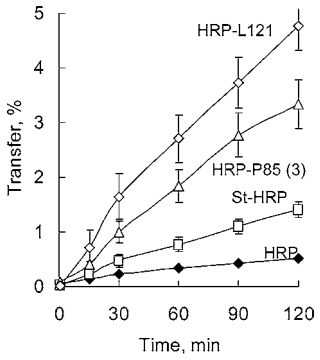

Figure 5. Apical to basolateral transport of HRP, St-HRP, HRP-P85(3), and HRP-L121 in BBMEC monolayers. Data are mean ± SEM (n = 4). At 30 min and later time points, the differences between modified-HRP and HRP groups are significant.

BC050240+

10.1021/bc050240+
Published on Web 09/02/2005

10.1021/bc050240+ CCC: $30.25 © 2005 American Chemical Society
Published on Web 09/02/2005

NOVEMBER/DECEMBER 2005
Volume 16, Number 6

© Copyright 2005 by the American Chemical Society

Bioconjugate Chemistry

COMMUNICATIONS

Lipid Phase Control of DNA Delivery

Rumiana Koynova,*,† Li Wang, Yury Tarahovsky,‡ and Robert C. MacDonald

Biochemistry, Molecular & Cell Biology, Northwestern University, Evanston, Illinois 60208. Received July 27, 2005; Revised Manuscript Received October 5, 2005

Cationic lipids form nanoscale complexes (lipoplexes) with polyanionic DNA and can be utilized to deliver DNA to cells for transfection. Here we report the correlation between delivery efficiency of these DNA carriers and the mesomorphic phases they form when interacting with anionic membrane lipids. Specifically, formulations that are particularly effective DNA carriers form phases of highest negative interfacial curvature when mixed with anionic lipids, whereas less effective formulations form phases of lower curvature. Structural evolution of the carrier lipid/DNA complexes upon interaction with cellular lipids is hence suggested as a controlling factor in lipid-mediated DNA delivery. A strategy for optimizing lipofection is deduced. The behavior of a highly effective lipoplex formulation, DOTAP/DOPE, is found to conform to this "efficiency formula".

Efficient delivery of genetic material into biological systems is needed for tasks of utmost importance in laboratory and clinic, such as gene transfection and gene silencing. Synthetic cationic lipids can be used as DNA carriers and are now considered the most promising nonviral gene carriers (*1*). They form complexes (lipoplexes) with polyanionic DNA. Understanding the mechanism of lipid-mediated DNA delivery (lipofection) is of paramount significance for their effective application, as well as for rational design and synthesis of novel cationic lipid compounds that are promising for superior gene delivery. Here we advance the concept that the controlling factor in lipofection is the structural evolution of lipoplexes upon interaction with cellular (anionic) lipids.

The unbinding of DNA from a cationic lipid carrier when the lipoplex gets inside the cell has been identified as one of the key steps in lipofection. According to the current understanding, the unbinding is a result of charge neutralization by cellular anionic lipids; indeed, experiments have revealed that addition of negatively charged liposomes to lipoplexes results in dissociation of DNA from the lipid (*2*−*6*). A set of significant recent findings suggest that the structure of cationic lipid carriers changes dramatically upon interaction with cellular lipids, and furthermore that such changes may critically affect the delivery efficiency.

Hydrated lipids are known for their ability to form an impressive variety of polymorphic and mesomorphic phases, lamellar and nonlamellar, brought about by the optimization of the hydrophobic effect in conjunction with various intra- and intermolecular interactions and geometric packing constraints (*7, 8*). These phases are generally differentiated by the curvature of their lipid−water interface. The lipid phase state is a key physical

* Corresponding author. E-mail: r-tenchova@northwestern.edu.
† Associate member of the Institute of Biophysics, Bulgarian Academy of Sciences.
‡ Current address: Institute of Theoretical and Experimental Biophysics, 142290, Pushchino, Russia.

10.1021/bc050226x CCC: $30.25 © 2005 American Chemical Society
Published on Web 10/20/2005

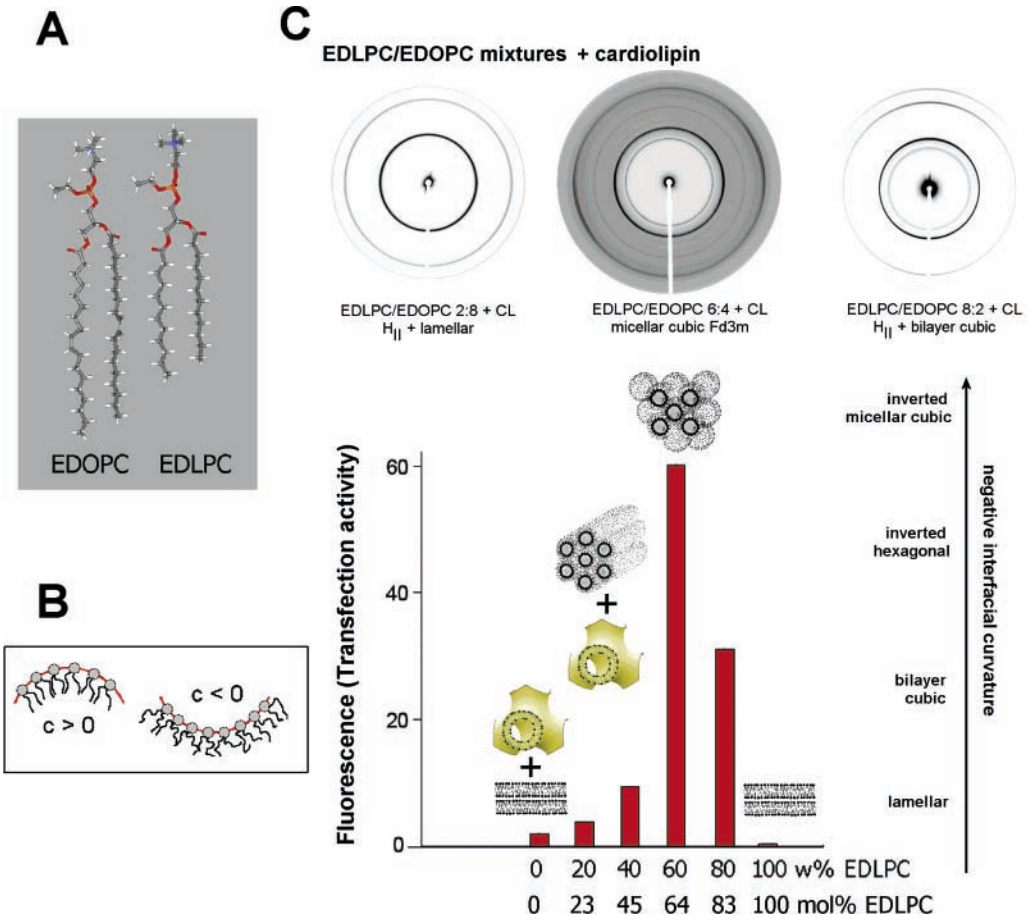

Figure 1. A. Molecular structures of the cationic phospholipids dioleoyl- and dilauroyl-*O*-ethylphosphatidylcholine. B. Illustration of lipid monolayers with positive (left) and negative (right) curvature. C. Correlation between the transfection efficiency (red bars) of ethyldilauroylphosphatidylcholine (EDLPC)/ethyldioleoylphosphatidylcholine (EDOPC) lipoplexes, as reported in ref 19 (quantified by expression of β-galactosidase in human umbilical artery endothelial cells) and the phase structure of their mixtures with the anionic lipid cardiolipin (CL). Cartoons of the phases are arranged vertically to give a qualitative notion about the increase of the interfacial curvature. Top row: diffraction patterns of mixtures of EDLPC/EDOPC lipoplex dispersions of different compositions with CL dispersions. The charge ratio of the cationic/anionic lipids in the samples is 1:1. Similar patterns were recorded also for mixtures of EDLPC/EDOPC with the anionic phosphatidylglycerol.

attribute because it mediates virtually all properties of lipid dispersions. Correlations between the mesomorphic phase state of the lipoplexes (lamellar vs inverted hexagonal) and their DNA delivery activity have been sought, but so far there is no clear consensus as to whether the hexagonal phase per se is beneficial for transfection (*9*−*14*).

It was recently reported that mixtures of cationic lipids with anionic lipids of the type found in cell membranes are unusually prone to form nonlamellar phases, even when the pure components form only the lamellar phase: even small amounts of anionic lipid added to certain cationic lipids generate virtually the entire panoply of possible lipid arrays (*15*−*17*). Since escape of DNA from the lipoplexes must involve neutralization of cationic lipid by cellular anionic lipids, most likely by fusion of cell membranes with lipoplexes, a wide variety of nonlamellar arrays can potentially appear in treated cells. Could the efficiency of transfection depend on which of those phases is preferred? This now seems very likely: in a previous study on this topic we demonstrated that DNA release measured after treating lipoplexes with anionic membrane lipids varies widely for the different cationic and anionic lipid combinations and, remarkably, showed an unambiguous correlation between the DNA unbinding and the phases formed by the mixtures of the anionic lipids with the cationic lipid of the lipoplexes (*18*). Specifically, the higher the negative interfacial curvature (polar/nonpolar interface curved toward the water, see Figure 1B) of the phase assumed by the cationic/anionic lipid mixture, the faster and more complete the release of DNA. We thus hypothesized that the structural evolution of lipoplexes upon interaction with cellular (anionic) lipids is a controlling factor in lipid-mediated DNA delivery. To test this suggestion, we compared the lipofection efficiency of certain lipoplexes with their phase behavior in mixtures with several anionic membrane lipids.

In our study we used lipoplex formulations comprising mixtures of the dilauroyl and dioleoyl derivatives of cationic ethylphosphatidylcholine (*2*), EDLPC/EDOPC (Figure 1A). It was discovered recently that delivery efficiency of such lipoplex formulations could be strongly modulated by merely varying the ratio of the two components (*19*). For example, the EDLPC/EDOPC mixture delivered DNA into cells more than 30-fold more efficiently at certain intermediate compositions than either compound separately (*19*). Given this astonishing synergy, we applied synchrotron X-ray diffraction to study the structural correlates of the lipoplex formulations and their mixtures with anionic lipids. The widely explored lipid transfection formulation, DOTAP/DOPE 1:1 (both from Avanti Polar Lipids) was also examined.

EDLPC/EDOPC cationic lipid dispersions were prepared by mixing lipids as chloroform solutions, with

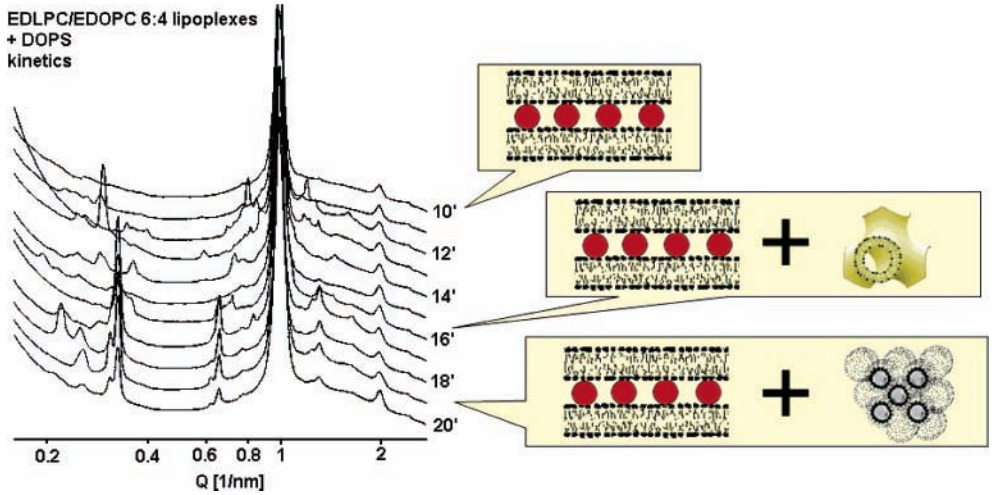

Figure 2. Kinetics of phase changes in the EDLPC/EDOPC lipoplexes of the highest activity (6:4 wt ratio (*19*)), upon addition of the anionic lipid DOPS, in the time interval 10 min to 30 min after the addition: bilayer cubic *Pn*3*m* phase forms initially in parallel to the lamellar phase; later, micellar cubic *Fd*3*m* could be distinguished. The charge ratio of the cationic/anionic lipids in the sample is 1:1.

subsequent chloroform evaporation under vacuum and overnight hydration in PBS (*17*). Lipoplexes were prepared by adding aqueous solution of herring sperm DNA (Invitrogen, Carlsbad, CA) to the cationic lipid dispersion at isoelectric ratio, vortexing, and overnight equilibration (*17, 20*). Anionic lipid dispersions were prepared from dioleoylphosphatidylserine (DOPS), dioleoylphosphatidylglycerol (DOPG), or tetraoleoylcardiolipin (CL) (Avanti Polar Lipids), as described in ref 18, and added to the lipoplexes. These mixed dispersions were then equilibrated for 1−2 days, filled into glass capillaries, and flame-sealed. For kinetic measurements, lipoplexes and anionic lipid dispersions were mixed and immediately mounted on the X-ray beamline for measurement. Small-angle X-ray diffraction (SAXD) measurements were performed at Argonne National Laboratory, Advanced Photon Source, BioCAT (beamline 18-ID) and DND-CAT (beamline 5-IDD), using 12 keV X-rays. A Linkam thermal stage (Linkam Sci Instruments, Surrey, England) provided temperature control. Linear heating scans were performed at rates of 0.8−2 °C/min. Exposure times were typically ∼0.5−1 s.

Both the lipid dispersions and the lipid/DNA complexes of the EDLPC/EDOPC mixture arrange into lamellar arrays at all compositions; the same is valid for the anionic lipid dispersions (not illustrated). When anionic lipids interact with the lipoplexes however, precisely those lipoplex compositions that exhibit particularly high transfection efficiency, EDLPC/EDOPC 60:40 w/w, formed the inverted micellar cubic phase, *Fd*3*m*, while either components and mixtures of other compositions all formed phases of lower curvature (Figure 1C), as revealed by our small-angle X-ray diffraction data. The micellar cubic phase exhibits even higher interfacial curvature than the more familiar inverted hexagonal phase (*8*). In the case of the anionic lipid cardiolipin (CL), in a sample of 1:1 cationic/anionic lipid charge ratio, this phase is identified by 11 diffraction maxima with reciprocal spacings fitting the ratio: $\sqrt{8}$: $\sqrt{11}$: $\sqrt{12}$: $\sqrt{16}$: $\sqrt{24}$: $\sqrt{32}$: $\sqrt{35}$: $\sqrt{36}$: $\sqrt{48}$: $\sqrt{51}$: $\sqrt{56}$, characteristic for the cubic aspect #15 (*21*). The anionic lipid dioleoylphosphatidylglycerol similarly formed micellar cubic phase when mixed with the most efficient EDLPC/EDOPC 6:4 formulation (not illustrated). Another anionic membrane lipid, phosphatidylserine, was found to form the micellar cubic phase transiently when mixed extempore with the EDLPC/EDOPC 6:4 formulation, as revealed by our kinetic synchrotron X-ray experiments (Figure 2). The pure cationic lipid components (EDLPC, EDOPC) and their mixtures of other, less effective compositions, formed phases of lower curvature: inverted hexagonal, bilayer cubic, and/or coexisting lamellar (Figure 1C).

Thus, transfection outcome appears to corellate with the propensity of the cationic/anionic lipid mixture to evolve into highly curved mesomorphic structure when they interact. According to our earlier study, DNA unbinding after treating lipoplexes with anionic lipids also unambiguously correlated with the disposition of the cationic/anionic lipid mixtures to form assemblies of highly curved topologies (*18*). The propensity of lipid bilayers to form nonlamellar phases has been described by the concept of bilayer "frustration" brought about by the imbalance of forces in the bilayer and which imposes a nonzero intrinsic curvature of the two opposing monolayers (*8, 22, 23*). In terms of this concept, those cationic lipid formulations, which tend to easily transform into curved nonlamellar arrays when mixed with anionic lipid, presumably retain higher degree of "frustration". The stored curvature elastic energy in a "frustrated" bilayer seems to be comparable to the cationic lipid-DNA binding energy: the same magnitude of $\sim 1-2k_BT$ has been estimated for both the binding free energy of lipoplexes (*24*−*26*) and the curvature elastic energy stored in a flat DOPE-dominated membrane (*27, 28*). The release of stored curvature elastic energy upon lamellar−nonlamellar phase transition and the balance between these energy terms could therefore play a significant role in lipoplex−membrane interactions and DNA unbinding energetics. This result corroborates our hypothesis that structural evolution of lipoplexes upon interaction with cellular lipids is the controlling factor in lipid-mediated DNA delivery. Here we recall that, for effective delivery, DNA must be retained until the lipoplex is inside the cell; thus, initial lamellar lipoplex structures are likely responsible for the successful import of DNA into cells.

Juxtaposing our results, a strategy for optimizing lipofection can be deduced: lamellar lipoplex formulations with compositions close to the lamellar−nonlamellar phase boundary, which could easily undergo phase transition upon mixing with cellular anionic lipids (Figure 3), are predicted to be especially efficient because they would be equally successful in transporting DNA into

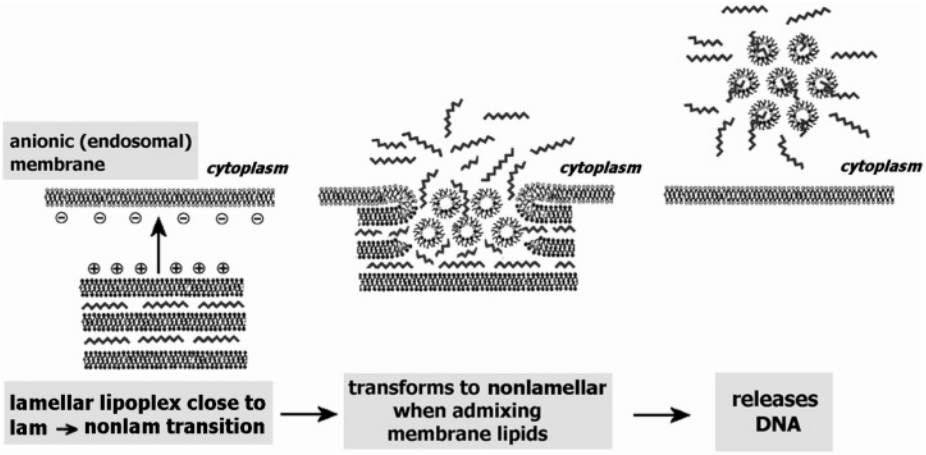

Figure 3. Hypothetical scheme for efficiency of DNA delivery: Lamellar lipoplexes residing close to the lamellar−nonlamellar phase transition form nonlamellar structures upon contacting the cellular lipids and thus exhibit optimum delivery efficiency (alternatively, lipoplexes retaining their lamellar structure after contacting the endosomal membrane may not efficiently release DNA; on the other hand, nonlamellar lipoplexes may release DNA prematurely).

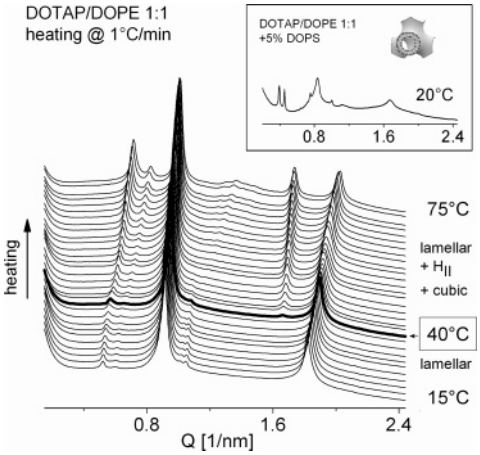

Figure 4. Small-angle X-ray diffraction patterns of DOTAP/DOPE (1:1 mol/mol) dispersion recorded during heating at 1 °C/min (exposure time 1 s): at low temperatures, the sample forms lamellar phase (with minor traces of cubic). Upon heating, hexagonal phase starts to form at ∼39−40 °C, which coexists with the lamellar phase. Inset: Upon addition of 5% of the anionic membrane lipid DOPS, cubic phase dominates in the dispersion at room and physiological temperatures.

cells (since lamellar phase optimally protects DNA (*18*)) and in releasing it subsequently.

Indeed, our X-ray diffraction experiments have now provided explicit support for this "efficiency formula": we found that one of the very effective and widely explored lipid transfection formulations, DOTAP/DOPE 1:1 (mol/mol), exhibits precisely this behavior: Samples prepared at low (below physiological) temperature form the lamellar phase, whereas upon heating, lamellar → inverted hexagonal phase transition begins just above physiological temperature, at ∼39−40 °C (Figure 4). Addition of a minor proportion (≤5%) of the anionic lipid phosphatidylserine was enough to convert the lipoplex structure into a predominantly cubic bicontinuous *Pn*3*m* phase at physiological temperature (Figure 4, inset). Thus, after uptake into the cell, these lipoplexes would very easily be converted into nonlamellar arrays that allow the DNA release, which is the likely reason for their effectiveness. Therefore, rational design of cationic lipid formulations residing close to the lamellar−nonlamellar phase transition may bring about superior delivery efficiency, especially if that phase transition is facilitated by acquisition of minor amounts of anionic lipids and/or elevation of the temperature to 37 °C.

ACKNOWLEDGMENT

Supported by NIH Grants GM52329 and GM57305. Synchrotron X-ray measurements were performed at BioCAT and DND-CAT at APS, Argonne National Laboratory. BioCAT is NIH-supported, Grant RR08630. DND-CAT is supported by E.I. DuPont de Nemours & Co., The Dow Chemical Company, NSF Grant DMR-9304725, and the State of Illinois through the Department of Commerce and the Board of Higher Education Grant IBHE HECA NWU 96. Use of APS was supported by the U.S. DOE, Basic Energy Sciences, Office of Energy Research, Contract No. W-31-102-Eng-38.

LITERATURE CITED

(1) Felgner, P. L., and Ringold, G. M. (1989) Cationic liposome-mediated transfection. *Nature 337*, 387−388.

(2) MacDonald, R. C., Ashley, G. W., Shida, M. M., Rakhmanova, V. A., Tarahovsky, Y. S., Pantazatos, D. P., Kennedy, M. T., Pozharski, E. V., Baker, K. A., Jones, R. D., Rosenzweig, H. S., Choi, K. L., Qiu, R. Z., and McIntosh, T. J. (1999) Physical and biological properties of cationic triesters of phosphatidylcholine. *Biophys. J. 77*, 2612−2629.

(3) Xu, Y. H., and Szoka, F. C. (1996) Mechanism of DNA release from cationic liposome/DNA complexes used in cell transfection. *Biochemistry 35*, 5616−5623.

(4) Zelphati, O., and Szoka, F. C. (1996) Mechanism of oligonucleotide release from cationic liposomes. *Proc. Natl. Acad. Sci. U.S.A. 93*, 11493−11498.

(5) Tarahovsky, Y., Koynova, R., and MacDonald, R. C. (2004) Efficiency of anionic lipids to release DNA from lipoplexes correlates with the interfacial curvature of the mesomorphic phases of cationic/anionic lipid mixtures. *Biophys. J. 86*, 37A.

(6) Ashley, G. W., Shida, M. M., Qiu, R., Lahiri, M. K., Levisay, P. C., Jones, R. D., Baker, K. A., and MacDonald, R. C. (1996) Phosphatidylcholinium compounds: A new class of cationic phospholipids with transfection activin and unusual physical properties (Abstract). *Biophys. J. 70*, A88.

(7) Luzzati, V., and Tardieu, A. (1974) Lipid Phases − Structure and Structural Transitions. *Annu. Rev. Phys. Chem. 25*, 79−94.

(8) Seddon, J. M., and Templer, R. H. (1995) In *Handbook of Biological Physics.* (Lipowsky, R., and Sackmann, E., Eds.) pp 97−160, Elsevier Science, Amsterdam.

(9) Koltover, I., Salditt, T., Radler, J. O., and Safinya, C. R. (1998) An inverted hexagonal phase of cationic liposome-DNA complexes related to DNA release and delivery. *Science 281*, 78−81.

(10) Smisterova, J., Wagenaar, A., Stuart, M. C. A., Polushkin, E., ten Brinke, G., Hulst, R., Engberts, J. B. F. N., and Hoekstra, D. (2001) Molecular shape of the cationic lipid controls the structure of cationic lipid/dioleylphosphatidylethanolamine-DNA complexes and the efficiency of gene delivery. *J. Biol. Chem. 276*, 47615−47622.

(11) Rakhmanova, V. A., McIntosh, T. J., and MacDonald, R. C. (2000) Effects of dioleoylphosphatidylethanolamine on the activity and structure of O-alkyl phosphatidylcholine-DNA transfection complexes. *Cell. Mol. Biol. Lett. 5*, 51−65.

(12) Simberg, D., Danino, D., Talmon, Y., Minsky, A., Ferrari, M. E., Wheeler, C. J., and Barenholz, Y. (2001) Phase behavior, DNA ordering, and size instability of cationic lipoplexes − Relevance to optimal transfection activity. *J. Biol. Chem. 276*, 47453−47459.

(13) Congiu, A., Pozzi, D., Esposito, C., Castellano, C., and Mossa, G. (2004) Correlation between structure and transfection efficiency: a study of DC−Chol-DOPE/DNA complexes. *Colloids Surfaces B: Biointerfaces 36*, 43−48.

(14) Ross, P. C., Hensen, M. L., Supabphol, R., and Hui, S. W. (1998) Multilamellar cationic liposomes are efficient vectors for in vitro gene transfer in serum. *J. Liposome Res. 8*, 499−520.

(15) Tarahovsky, Y. S., Arsenault, A. L., MacDonald, R. C., McIntosh, T. J., and Epand, R. M. (2000) Electrostatic control of phospholipid polymorphism. *Biophys. J. 79*, 3193−3200.

(16) Lewis, R. N. A. H., and McElhaney, R. N. (2000) Surface charge markedly attenuates the nonlamellar phase-forming propensities of lipid bilayer membranes: Calorimetric and P-31-nuclear magnetic resonance studies of mixtures of cationic, anionic, and zwitterionic lipids. *Biophys. J. 79*, 1455−1464.

(17) Koynova, R., and MacDonald, R. C. (2003) Mixtures of cationic lipid O-ethylphosphatidylcholine with membrane lipids and DNA: Phase diagrams. *Biophys. J. 85*, 2449−2465.

(18) Tarahovsky, Y. S., Koynova, R., and MacDonald, R. C. (2004) DNA release from lipoplexes by anionic lipids: Correlation with lipid mesomorphism, interfacial curvature, and membrane fusion. *Biophys. J. 87*, 1054−1064.

(19) Wang, L., and MacDonald, R. C. (2004) New strategy for transfection: mixtures of medium-chain and long-chain cationic lipids synergistically enhance transfection. *Gene Ther. 11*, 1358−1362.

(20) Koynova, R., and MacDonald, R. C. (2004) Columnar DNA superlattices in lamellar *o*-ethylphosphatidylcholine lipoplexes: Mechanism of the gel-liquid crystalline lipid phase transition. *Nano Lett. 4*, 1475−1479.

(21) Kasper, J. S., and Lonsdale, K. (1985) *International Tables for X-ray Crystallography,* Riedel Publishing Company, Dordrecht, The Netherlands.

(22) Gruner, S. M. (1985) Intrinsic curvature hypothesis for biomembrane lipid-composition − A role for nonbilayer lipids. *Proc. Natl. Acad. Sci. U.S.A. 82*, 3665−3669.

(23) Anderson, D. M., Gruner, S. M., and Leibler, S. (1988) Geometrical aspects of the frustration in the cubic phases of lyotropic liquid-crystals. *Proc. Natl. Acad. Sci. U.S.A. 85*, 5364−5368.

(24) Bruinsma, R. (1998) Electrostatics of DNA cationic lipid complexes: isoelectric instability. *Eur. Phys. J. B 4*, 75−88.

(25) Pozharski, E., and MacDonald, R. C. (2002) Thermodynamics of cationic lipid-DNA complex formation as studied by isothermal titration calorimetry. *Biophys. J. 83*, 556−565.

(26) Pozharski, E., and MacDonald, R. C. (2003) Lipoplex thermodynamics: Determination of DNA-cationic lipoid interaction energies. *Biophys. J. 85*, 3969−3978.

(27) Attard, G. S., Templer, R. H., Smith, W. S., Hunt, A. N., and Jackowski, S. (2000) Modulation of CTP: phosphocholine cytidylyltransferase by membrane curvature elastic stress. *Proc. Natl. Acad. Sci. U.S.A. 97*, 9032−9036.

(28) Botelho, A. V., Gibson, N. J., Thurmond, R. L., Wang, Y., and Brown, M. F. (2002) Conformational energetics of rhodopsin modulated by nonlamellar-forming lipids. *Biochemistry 41*, 6354−6368.

BC050226X

Polyketal Nanoparticles: A New pH-Sensitive Biodegradable Drug Delivery Vehicle

Michael J. Heffernan and Niren Murthy*

The Wallace H. Coulter Department of Biomedical Engineering, Georgia Institute of Technology, Atlanta, Georgia 30332. Received June 20, 2005; Revised Manuscript Received August 17, 2005

In this report, we present an acid-sensitive drug delivery vehicle, termed polyketal nanoparticles, which are designed to target therapeutics to the acidic environments of tumors, inflammatory tissues, and phagosomes. The polyketal nanoparticles are formulated from poly(1,4-phenyleneacetone dimethylene ketal) (PPADK), a new hydrophobic polymer which contains ketal linkages in its backbone. The polyketal nanoparticles undergo acid-catalyzed hydrolysis into low molecular weight hydrophilic compounds and should therefore release encapsulated therapeutics at an accelerated rate in acidic environments. Importantly, the polyketal nanoparticles do not generate acidic degradation products after hydrolysis, as with polyester-based biomaterials. Dexamethasone-loaded nanoparticles, 200−600 nm in diameter, were fabricated with PPADK via an emulsion procedure using chloroform and water. The hydrolysis half-life of PPADK was measured to be 102 h at pH 7.4 and 35 h at pH 5.0. PPADK was synthesized by a new polymerization strategy based on the acetal exchange reaction. This new delivery system should find numerous applications in the field of drug delivery because of its ease of synthesis and excellent degradation properties.

Drug delivery vehicles based on polyesters and polyanhydrides have been widely used for the sustained release of therapeutics because of their excellent biocompatibility profiles and slow hydrolysis rates (*1*−*4*). However, numerous medical applications, such as targeting the acidic environment of lysosomes and tumors, require drug delivery systems that undergo rapid, pH-sensitive degradation (*5*, *6*). The majority of degradable polymers used for drug delivery cannot fulfill this requirement because they are composed of ester linkages, which degrade by base-catalyzed hydrolysis at physiological pH values. Recently, pH-sensitive hydrophobic microparticles based on poly(ortho esters) and poly(β-amino esters) have been successfully used for intracellular drug delivery and tumor targeting, thus demonstrating the potential of acid-sensitive biomaterials for drug delivery (*7*−*10*). Consequently, there is great interest in developing new strategies for the synthesis of pH-sensitive biodegradable polymers.

In this communication, we present an acid-sensitive hydrophobic nanoparticle based on a new polymer, poly(1,4-phenyleneacetone dimethylene ketal) (PPADK), which complements existing biodegradable nanoparticle technologies. This polymer has ketal linkages in its backbone and degrades via acid-catalyzed hydrolysis into low molecular weight compounds that can be easily excreted. PPADK forms micro- and nanoparticles, via an emulsion procedure, and can be used for the delivery of hydrophobic drugs and potentially proteins. In contrast to polyester-based biomaterials (*11*), the hydrolysis of polyketal nanoparticles does not generate acidic degradation products. Also, PPADK decomposes on a time scale that is faster than PLGA, but slower than poly(ortho esters) and poly(β-amino esters), and therefore provides the drug delivery community with a greater ability to tailor drug release kinetics to a particular application.

* Corresponding author. Telephone 404-385-5145, fax 404-894-4243, e-mail: niren.murthy@bme.gatech.edu.

PPADK was synthesized via a new polymerization strategy based on the acetal exchange reaction. The acetal exchange reaction (*12*) is generally used to introduce protecting groups onto low molecular weight alcohols (*13*). However, we demonstrate here that the acetal exchange reaction can be used to generate acid labile polymers through the step growth polymerization of 1,4-benzenedimethanol and 2,2-dimethoxypropane (Scheme 1). This polymerization begins with an equilibrium reaction between 1,4-benzenedimethanol and 2,2-dimethoxypropane, generating dimers and trimers, which can further combine to form polymers. The formation of polymers is favored by distilling off the methanol byproduct formed during the polymerization reaction.

A representative polymerization of 2,2-dimethoxypropane and 1,4-benzenedimethanol gave PPADK with a 48% yield.[1] Figure 1A shows the GPC trace from one batch in which M_w = 4000 was obtained, corresponding to a degree of polymerization of 22.5 repeating units, with a polydispersity index of 1.54. The ^{1}H NMR spectrum

[1] The polymerization was carried out in a 25 mL two-necked flask connected to a short-path distilling head. 1,4-Benzenedimethanol (1.0 g, 7.3 mmol, Aldrich) dissolved in 10 mL of warm ethyl acetate was added to 10 mL of distilled benzene kept at 100 °C. Recrystallized *p*-toluenesulfonic acid (5.5 mg, 0.029 mmol, Aldrich) dissolved in 550 μL of ethyl acetate was then added. After allowing the ethyl acetate to distill off, distilled 2,2-dimethoxypropane (900 μL, 7.4 mmol, Aldrich) was added to initiate the reaction. Five additional doses of 2,2-dimethoxypropane were added via a metering funnel, with each dose consisting of 2 mL of benzene plus 300 to 500 μL of 2,2-dimethoxypropane. Each dose was added over a 30 to 40 min period with a 30 min interval in between. The total duration of the reaction was 7 h. The reaction was stopped with the addition of 100 μL of triethylamine and was precipitated in cold hexanes. The crude product was vacuum filtered, rinsed with ether and hexanes, and vacuum-dried to yield 600 mg of white solid product (48% yield). The recovered polymer was analyzed by GPC and ^{1}H NMR.

10.1021/bc050176w CCC: $30.25 © 2005 American Chemical Society
Published on Web 10/05/2005

Scheme 1. Synthesis of the Polyketal, Poly(1,4-phenyleneacetone dimethylene ketal) (PPADK), via the Acetal Exchange Reaction[a]

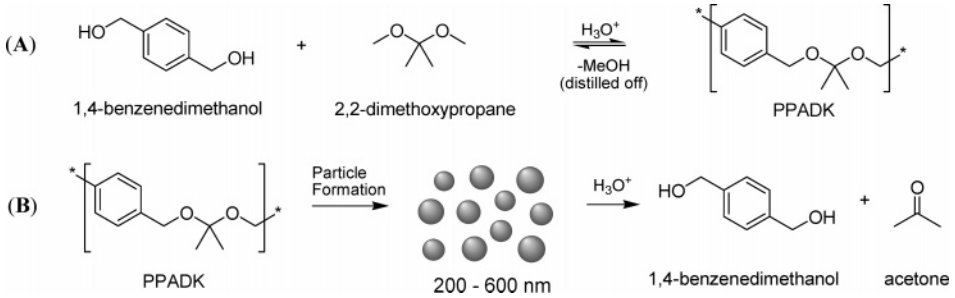

[a] (A) Stepwise polymerization based on the acetal exchange reaction between 1,4-benzenedimethanol and 2,2-dimethoxypropane to produce PPADK. (B) Formation of drug-loaded nanoparticles by the solvent evaporation method. Particles exhibit pH-sensitive degradation into low molecular weight excretable compounds.

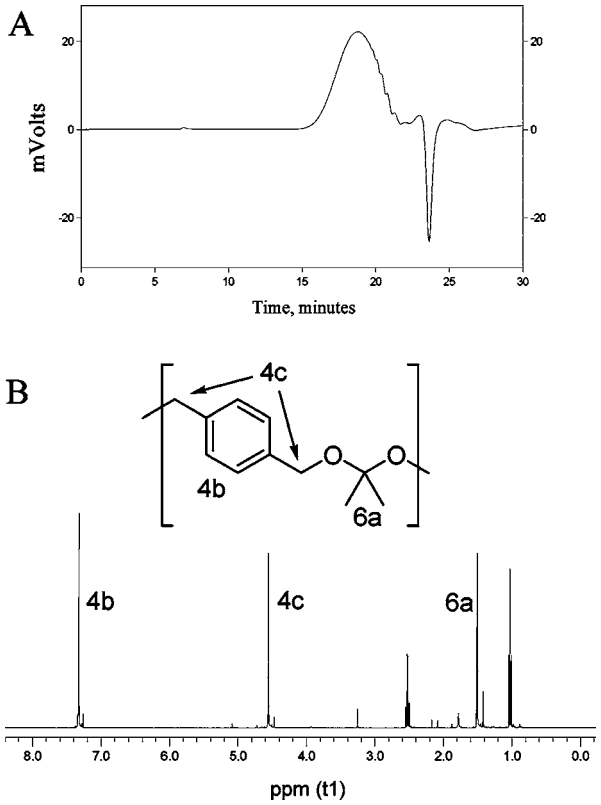

Figure 1. (A) GPC trace of PPADK in THF (Shimadzu SCL-10A). $M_w = 4000$, $M_w/M_n = 1.54$ based on a polystyrene standard (Polymer Laboratories, Inc.) (1060 M_w, 20.8 min; 2970 M_w, 19.0 min; 10,680 M_w, 16.5 min). *Y*-axis indicates relative absorbance at 262 nm. (B) ^{1}H NMR spectrum of PPADK in $CDCl_3$ (Varian Mercury Vx 400); repeating unit peaks at 7.3 ppm (4b), 4.5 ppm (4c), and 1.5 ppm (6a). Peaks at 2.5 and 1.0 are due to triethylamine added to prevent ketal hydrolysis.

(Figure 1B) confirms that the repeating unit of PPADK contains a ketal group ('6a'). Together, the GPC and ^{1}H NMR data provide evidence for the successful synthesis of PPADK.

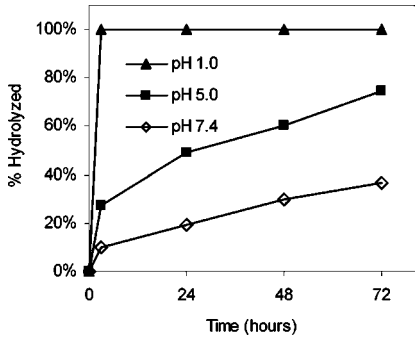

Figure 2. Hydrolysis kinetics of PPADK (finely ground powder) at pH 1.0, 5.0, and 7.4 (37 °C). Exponential decay half-lives are 102 h (pH 7.4) and 35 h (pH 5.0). The pH 1.0 control batch was completely hydrolyzed before the first time point.

The hydrolysis kinetics of PPADK was measured at pH values corresponding to lysosomes (pH 5.0) and the bloodstream (pH 7.4). The hydrolysis rates were measured by grinding PPADK into a fine powder and adding it to deuterated solutions at pH 7.4 (phosphate buffer), pH 5.0 (acetate buffer), and pH 1.0 (DCl).[2] Exponential decay half-lives were calculated to be 102 h at pH 7.4 and 35 h at pH 5.0, representing a 3-fold rate increase from pH 7.4 to 5.0 (Figure 2). The pH sensitivity of PPADK is significantly less than the 250-fold increase from pH 7.4 to 5.0 reported by Kwon et al. (*14*) for a water-soluble ketal. We hypothesize that the lower pH sensitivity of PPADK is due to its water insolubility, which limits the diffusion of water and creates another rate-limiting step that is pH-independent.

[2] The suspensions were stirred at 37 °C, and data points were taken at 3, 24, 48, and 72 h. Each suspension was centrifuged for 4 min at 1800*g*, and the supernatant was analyzed by ^{1}H NMR. The spectra contained peaks for 1,4-benzenedimethanol (7.24 and 4.47 ppm) and acetone (2.05 ppm). The average of the two 1,4-benzenedimethanol peak integrals was used to determine the relative degree of hydrolysis. The percent hydrolysis was calculated as the 1,4-benzenedimethanol peak average of the pH 7.4 or 5.0 sample divided by the 1,4-benzenedimethanol peak average of the pH 1.0 control batch.

[3] DLS samples were prepared by diluting the particle suspension in 10 mL of pH 9 buffer and allowing the larger particles to settle out. An aliquot from the liquid portion of each vial was then diluted for DLS particle sizing (Brookhaven 90Plus particle sizer). An SEM sample was made with the 0.2:1 ratio of PVA: PPADK by centrifuging the nanoparticle suspension for 10 min (5000*g*, 4 °C), washing with distilled water, and lyophilizing the recovered pellet.

[4] Control batches were prepared with PPADK/PVA only and Dex only. To measure Dex encapsulation, each particle batch was resuspended in pH 9 buffer, and an aliquot was then further diluted. A portion was filtered through a 0.1 μm Supor membrane Acrodisc syringe filter (Pall Corp.), and the 242 nm absorbance of the filtrate was recorded with a Shimadzu UV-1700 spectrophotometer. The encapsulation efficiency was calculated as $(A_{Dex} - A_{DexPoly})/(A_{Dex} - A_{Poly})$, where A is the absorbance at 242 nm and the subscripts 'Poly', 'Dex', and 'DexPoly' refer to the 'PPADK only', 'Dex only', and 'Dex + PPADK' samples, respectively. These calculations resulted in a Dex encapsulation efficiency of 43% to 53% for various samples.

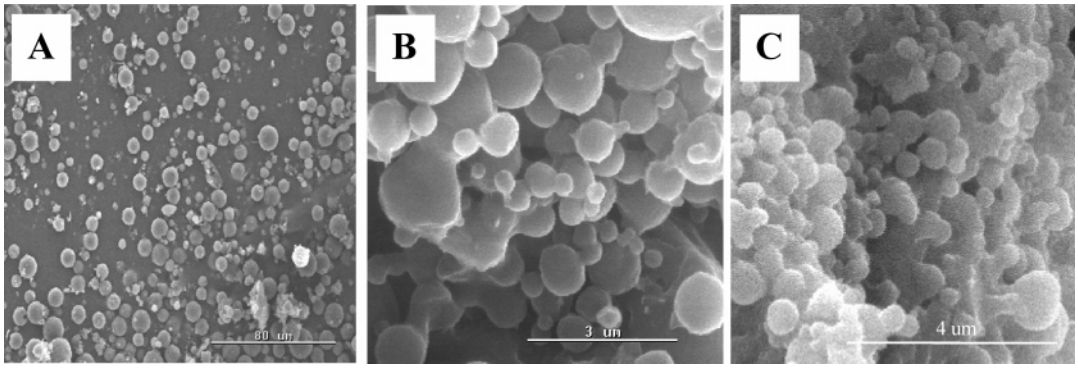

Figure 3. SEM images of particles made with PPADK. (A,B) Microparticles using 0.2:1 ratio of PVA to PPADK. (C) Dexamethasone-loaded nanoparticles made using 1:1 PVA:PPADK. Scale bars are (A) 80 μm, (B) 3 μm, and (C) 4 μm. SEM images were generated with a Hitachi S4100 by Dr. Lisa Detter-Hoskin of the Georgia Tech Research Institute, Atlanta, GA.

Micro- and nanoparticles were synthesized with PPADK using an oil-in-water emulsion method (*15*). Briefly, 50 mg of PPADK dissolved in 1 mL of $CHCl_3$ (with 0.1% triethylamine) was added to 5 mL of pH 9 buffer (10 mM $NaHCO_3$) containing various amounts of poly(vinyl alcohol) (PVA, 31−50 kDa, Aldrich) as the emulsifier. The oil−water mixture was shaken briefly and then sonicated for 2 to 3 min at 40 W (Branson Sonifier 250) to form a fine oil/water emulsion. The emulsion was stirred under N_2 flow for at least 3 h to evaporate the solvent and produce a nanoparticle suspension.

Particle sizes were analyzed by dynamic light scattering (DLS) and SEM.[3] As expected, the particle size was sensitive to the ratio of PVA to PPADK. The DLS particle diameters were 520, 290, and 280 nm for samples containing 0.2:1, 0.8:1, and 2:1 mass ratios of PVA:PPADK, respectively. The SEM images of the 0.2:1 batch (Figures 3A and 3B) confirm that PPADK does form micron-sized particles, with particle size distribution ranging from 0.5 to 30 μm in diameter.

The antiinflammatory drug dexamethasone (Dex, Sigma) was encapsulated into nanoparticles made with PPADK. Dex-loaded particles were formulated using the same procedure as that described above, except that the oil phase contained a 5 mg/mL concentration of Dex and the mass ratio of PVA:PPADK was 1:1. SEM images of these particles demonstrate that they are 200−600 nm in diameter (Figure 3C). Particle sizing by DLS indicated an effective diameter of 250 nm for the Dex-loaded particle batches. The Dex encapsulation efficiency ranged between 43 and 53%.[4]

In summary, we have developed a new pH-sensitive biodegradable polymer for drug delivery, synthesized via the acetal exchange reaction between 2,2-dimethoxypropane and 1,4-benzenedimethanol. This polymer is unique in that it contains ketal linkages in the polymer backbone, allowing for acid-catalyzed hydrolysis into low molecular weight, water soluble compounds. Dexamethasone-loaded nanoparticles were fabricated in the 200 to 600 nm range, which is suitable for applications involving phagocytosis by macrophages. The relative ease of polymer synthesis and particle formation, as well as its rapid pH-sensitive degradation into low molecular weight excretable compounds, suggest that this new polyketal will find numerous applications in the field of drug delivery.

ACKNOWLEDGMENT

M.J.H. is supported by a National Science Foundation Graduate Research Fellowship. We acknowledge the Georgia Tech/Emory Center for the Engineering of Living Tissues (funded by NSF-EEC-9731643) and NIH UO1 HL80711-01.

LITERATURE CITED

(1) Anderson, J. M., and Shive, M. S. (1997) Biodegradation and biocompatibility of PLA and PLGA microspheres. *Adv. Drug Delivery Rev. 28,* 5−24.
(2) Jain, R. A. (2000) The manufacturing techniques of various drug loaded biodegradable poly(lactide-*co*-glycolide) (PLGA) devices. *Biomaterials 21*, 2475−2490.
(3) Mathiowitz, E., Saltzman, W. M., Domb, A., Dor, Ph., and Langer, R. (1988) Polyanhydride microspheres as drug carriers. II. Microencapsulation by solvent removal. *J. Appl. Polym. Sci. 35*, 755−774.
(4) Berkland, C., Kipper, M. J., Narasimhan, B., Kim, K., and Pack, D. W. (2004) Microsphere size, precipitation kinetics and drug distribution control drug release from biodegradable polyanhydride microspheres. *J. Controlled Release 94*, 129−141.
(5) Stubbs, M., McSheehy, P. M. J., Griffiths, J. R., and Bashford, C. L. (2000) Causes and consequences of tumour acidity and implications for treatment. *Mol. Med. Today 6*, 15−19.
(6) Leroux, J.-C. (2004) pH-responsive carriers for enhancing the cytoplasmic delivery of macromolecular drugs. *Adv. Drug Delivery Rev. 56*, 925−926.
(7) Heller, J., and Barr, J. (2004) Poly(ortho esters) − From concept to reality. *Biomacromolecules 5*, 1625−1632.
(8) Heller, J., Barr, J., Ng, S. Y., Abdellauoi, K. S., and Gurny, R. (2002) Poly(ortho esters): synthesis, characterization, properties and uses. *Adv. Drug Delivery Rev. 54*, 1015−1039.
(9) Berry, D., Lynn, D. M., Sasisekharan, R., and Langer, R. (2004) Poly(β-amino ester)s promote cellular uptake of heparin and cancer cell death. *Chem. Biol. 11*, 487−498.
(10) Potineni, A., Lynn, D. M., Langer, R., and Amiji, M. M. (2003) Poly(ethylene oxide)-modified poly(β-amino ester) nanoparticles as a pH-sensitive biodegradable system for paclitaxel delivery. *J. Controlled Release 86*, 223−234.
(11) Fu, K., Pack, D. W., Klibanov, A. M., and Langer, R. (2000) Visual evidence of acidic environment within degrading poly(lactic-*co*-glycolic acid) (PLGA) microspheres. *Pharm. Res. 17*, 100−106.
(12) Lorette, N. B., and Howard, W. L. (1960) Preparation of ketals from 2,2-dimethoxypropane. *J. Org. Chem. 25*, 521−525.
(13) Greene, T. W., and Wuts, P. G. M. (1999) *Protective Groups in Organic Synthesis*, pp 201−230, Wiley-Interscience, New York.
(14) Kwon, Y. J., Standley, S. M., Goodwin, A. P., Gillies, E. R., and Fréchet, J. M. J. (2005) Directed antigen presentation using polymeric microparticulate carriers degradable at lysosomal pH for controlled immune responses. *Mol. Pharm. 2*, 83−91.
(15) Panyam, J., Williams, D., Dash, A., Leslie-Pelecky, D., and Labhasetwar, V. (2004) Solid-state solubility influences encapsulation and release of hydrophobic drugs from PLGA/PLA nanoparticles. *J. Pharm. Sci.* 93, 1804−1814.

BC050176W

Magnetic Resonance Imaging of Self-Assembled Biomaterial Scaffolds

Steve R. Bull,[†] Mustafa O. Guler,[†] Rafael E. Bras,[⊥] Palamadai N. Venkatasubramanian,[∥] Samuel I. Stupp,[†,⊥,#] and Thomas J. Meade*[,†,‡,§,#]

Departments of Chemistry, Biochemistry and Molecular and Cell Biology, and Neurobiology and Physiology, Center for Basic MR Research, Department of Radiology, Northwestern Healthcare Research Institute, Materials Science & Engineering, and the Feinberg School of Medicine, Northwestern University, Evanston, Illinois 60208. Received May 27, 2005; Revised Manuscript Received August 25, 2005

Current interest in biomaterials for tissue engineering and drug delivery applications have spurred research into self-assembling peptide amphiphiles (PAs). Nanofiber networks formed from self-assembling PAs can be used as biomaterial scaffolds with the advantage of specificity by the incorporation of peptide-epitopes. Imaging the materials noninvasively will give information as to their fate in vivo. We report here the synthesis and in vitro MR images of self-assembling peptide amphiphile contrast agents (PACAs) that form nanofibers. At 400 MHz using a 0.1 mM Gd(III) conjugate of the PA we observed a T_1 three times that of a control gel. The PA derivative was doped into various epitope bearing PA solutions and upon gelling resulted in a homogeneous biomaterial as imaged by MRI.

INTRODUCTION

Current interest in human tissue repair has prompted the development of biomaterial scaffolds where the goal is to envelop cells in an environment mimicking extracellular matrix and mediate processes such as cell proliferation and differentiation (*1*−*4*). Tissue repair in mature organisms can be crippled because many of the molecular cues present in early development are absent. Peptide sequences (epitopes) can be used to influence specific cell matrix interactions leading to tissue formation (*5*). Therefore, providing a synthetic scaffold with epitopes affords the possibility of in vivo tissue regeneration (*4, 5*).

Nanofiber networks derived from self-assembling peptide amphiphiles (PAs) have been used to mimic bone extracellular matrix and provide a scaffold to direct the differentiation of neural progenitor cells in vitro (*6, 7*). PA molecules contain a peptide sequence at one terminus that is hydrophilic relative to the hydrophobic alkyl segment (Figure 1). The PA's charge and amphiphilic nature allows for solubility and promotes self-assembly in aqueous media into long cylindrical structures that are nanometers in diameter and up to microns in length (*6*−*11*). These supramolecular structures can form fibrous strands because of hydrogen bond formation between the amino acids of adjacent PA molecules. In our case, the β-sheet-forming sequence of LLLAAA together with the hydrophobic alkyl tail's collapse is thought to be the driving force in extended structures, rather than spherical micelles (9−*11*). The high aspect ratio nanofibers form a three-dimensional network trapping water, to create a self-supporting gel that is 99% water by mass (*6, 11*). Since the hydrophilic portion of the PA contains charged amino acids and are accessible to the aqueous environment, the self-assembled nanofibers can present a high density of epitopes on the periphery (*6, 10, 11*) of the nanofibers to interact with cells trapped within (*7*). To understand the scaffolds properties in vivo, it is necessary to elucidate the structural degradation and migration of the self-assembled materials postimplantation (*12*−*16*).

Magnetic resonance imaging (MRI) is a noninvasive technique for in vivo imaging and is an ideal tool for fate mapping of tissue scaffolds at near cellular resolution (*15, 17, 18*). We have chosen this modality to image self-assembled gels that integrate into their structure PA molecules conjugated to Gd(III) contrast agents (PACAs). Recently, we reported on the synthesis and characterization of PACA derivatives of PA molecules that were capable of self-assembling into nanofibers or spherical micelles (*19*). Here, we report on the synthesis and in vitro images of two PACA derivatives mixed with a variety of epitope bearing PA biomaterials. A number of reports have described the use of MRI to track implants in vivo (*12, 14, 15, 20*−*23*); however, to our knowledge this is the first demonstration that self-assembled biomaterials conjugated with MR contrast agents can be imaged.

MATERIALS AND METHODS

Preparation of 1−3. Amino acids were purchased from NovaBiochem. All other reagents were purchased from Sigma-Aldrich and used without further purification unless otherwise stated. The branched PAs **1**, **2** (*19*), **3** were prepared by 9-fluorenylmethoxycarbonyl (Fmoc) solid-phase peptide synthesis (SPPS) on a 0.1 mmol scale. **1** was prepared by SPPS, and branching of the peptide

* To whom correspondence should be addressed. Phone: (847) 491-2481. Fax: (847) 491-3832. E-mail: tmeade@northwestern.edu.
[†] Department of Chemistry.
[‡] Department of Biochemistry and Molecular and Cell Biology.
[§] Department of Neurobiology and Physiology.
[∥] Center for Basic MR Research.
[⊥] Materials Science & Engineering.
[#] Feinberg School of Medicine.

10.1021/bc050153h CCC: $30.25 © 2005 American Chemical Society
Published on Web 10/05/2005

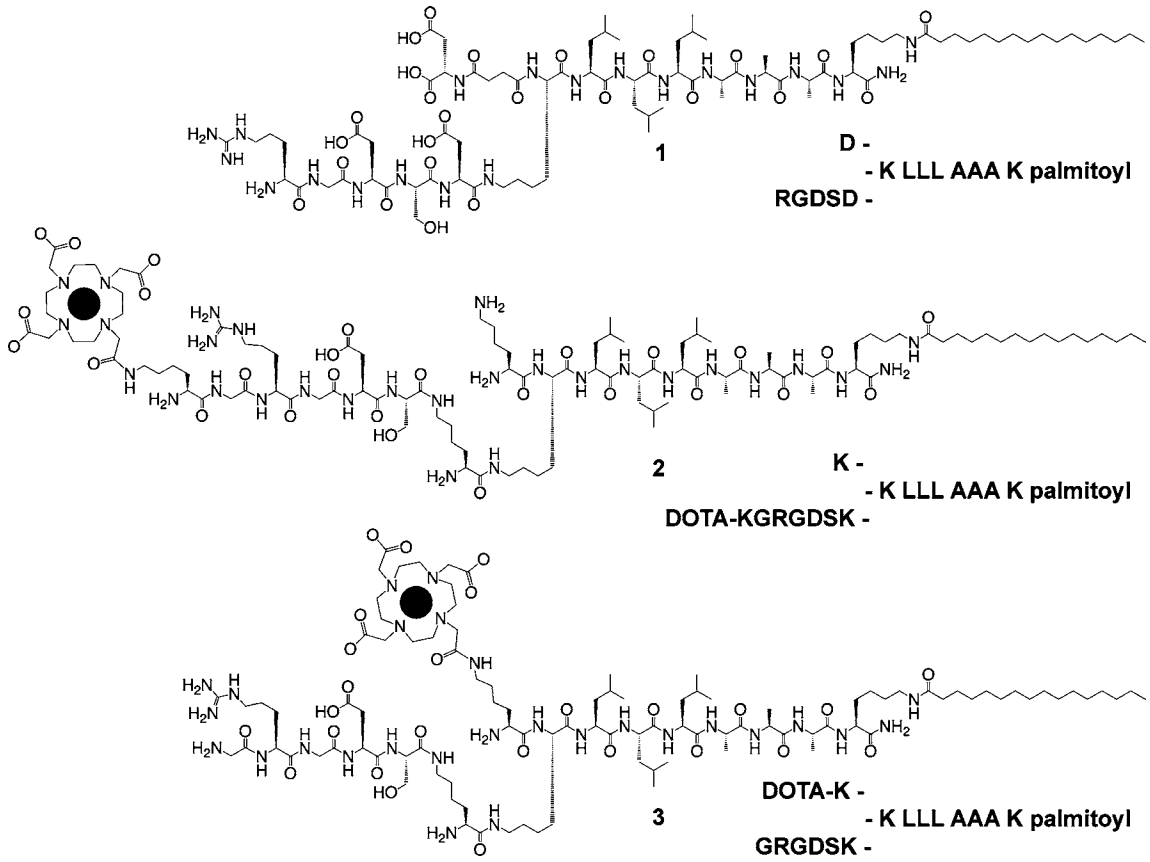

Figure 1. Structures of the PA molecules with the black circles representing the Gd(III) ion. **1** is an example of a filler PA and does not contain the Gd(III) chelate. **2** and **3** are the PACA molecules used in this study containing Gd(III). The basic structure of the PA contains three sections: a headgroup, body, and an alkyl tail. The headgroup is composed of an epitope for specific cell interaction and is presented on the outside of the supramolecular fibers. The body is structural in function by use of the hydrogen bond formation between molecules and is the driving force for fiber formation. The palmitoyl tail of the PA is used to drive self-assembly by initiating a hydrophobic collapse in an aqueous environment.

headgroup was achieved using orthogonal protecting group chemistry for the amines at the α and ϵ positions of the lysine residue (*19, 24*). Fmoc-Lys(Mtt)-OH (Mtt: 4-methyltrityl) was coupled to MBHA Rink Amide resin, followed by cleavage of the Mtt protecting group on the ϵ-amine to couple palmitic acid without affecting Fmoc protection with a 5% TFA in DMF solution for 5 min. This was followed by Fmoc removal on the α-amine to grow the LLLAAA peptide segment of the PA using 30% piperidine/DMF solution for 10 min. The branching point was introduced at a lysine dendron using Fmoc-Lys(Mtt)-OH. To grow the first arm of the PA, Fmoc on the α-amine was removed before Mtt. L-Aspartic acid di-*tert*-butyl ester hemiscucinate residue was coupled to the first branch. Mtt on the ϵ-amine of the lysine residue was removed, and bioactive peptide sequence RGDS was grown. Aspartic acid residue before the RGDS was coupled to increase solubility of the molecule in water. **1** was cleaved from the resin in 95:2.5:2.5 TFA:TIS:H_2O. Excess TFA was evaporated under reduced pressure and crude PA solutions were triturated using cold ether. MALDI-TOF mass spectroscopy 1810.40 (calcd 1810.14)

2 and **3** were synthesized using orthogonal protection group chemistry for the amines at the α and ϵ positions of the lysine residue. Fmoc-Lys(Mtt)-OH was coupled to MBHA Rink Amide resin, followed by cleavage of the Mtt protecting group on the ϵ-amine for palmitic acid coupling without affecting the Fmoc protection. This was followed by Fmoc removal on the α-amine to extend the peptide segment of the PA. The branching point in the PAs was introduced at a lysine dendron using Fmoc-Lys(Mtt)-OH. To extend the first arm of PAs, Fmoc on the α-amine was removed before Mtt. For molecule **2**, Boc-Lys(Boc)-OH was coupled at the end of the first branch. Both α and ϵ-amine positions of the lysine were blocked with Boc protection as it is more stable under the cleavage conditions employed for the removal of Fmoc and Mtt. For **3**, Boc-Lys(Fmoc)-OH was coupled as the first branch. Fmoc was deprotected and tris-*tert*-butyl-protected 1,4,7,10-tetraazacyclododecane-1,4,7,10 tetraacetic acid (DOTA) (purchased from Macrocyclics) was coupled at the end of the first branch. Mtt was removed, and the other branch was grown using Boc-Lys(Fmoc)-OH. The peptide sequence RGDS (important in cell adhesion) was coupled to the ϵ-amine in order to combine bioactivity and MR functionality. For **2**, the DOTA moiety was coupled on SPPS to the N-terminus of the peptide sequence by using a *tert*-butyl ester-protected DOTA molecule. **2** and **3** were cleaved from the resin in 95:2.5:2.5 TFA:TIS:H_2O. Excess TFA was evaporated under reduced pressure, and crude PA solutions were triturated using cold ether. **2** and **3** were dried under vacuum and characterized by MALDI-MS with a single peak found at 2308.66 (calcd 2308.87) and 2180.02 (calcd 2179.69), respectively. The final product was obtained by the addition of $GdCl_3$ with stirring at pH 6.5 for 72 h and purified by dialysis in deionized water (1000MWC Spectrum Laboratories Inc.). Samples were then lyophilized into a white powder. MALDI-MS showed peaks at 2464.40 (calcd 2463.09) and 2336.08 (calcd 2335.61) corresponding to **2** and **3** M + H, respectively.

Inductively Coupled Plasma Mass Spectrometry. Inductively coupled plasma mass spectrometry (ICP-MS) was performed on a Thermo Jarrell Ash Atomscan Model

25 Sequential ICP Spectrometer. Samples were prepared by taking an aliquot of **2** and **3** from the stock solution used for relaxivity and T_1 measurements and placed in 600 μL of neat nitric acid. Five milliliters of deionized water was added, and the solution was ultrasonicated for 3 min. The volume was brought up to 9990 μL with deionized water, and 10 μL of an indium standard was added to bring the total volume to 10 mL.

Relaxivity Measurements. Relaxivity measurements were performed on **2** and **3** by reconstituting the samples in deionized water to form stock solutions, and the relaxivity experiments were performed on a Bruker mq60 NMR Analyzer (Bruker Canada, Milton, Ont., Canada) in pH 7.41 (*25*) buffer at 37 °C. Four samples were prepared of each **2** and **3** at concentrations of about 0.005, 0.01, 0.015, 0.02 mM (actual concentrations of Gd(III) were calculated from ICP-MS). Measurements were performed in quadruplicate and plotted as $1/T_1$ vs mM Gd(III). The slope of this line provides the molar relaxivity.

T_1 Measurements. T_1 measurements were performed on a 9.4 T Oxford superconducting magnet (Bruker). The samples were prepared by making a 4 wt % solution of **1** in water. This solution was then aliquoted into four separate 3-dram vials. The appropriate amount of Gd(III)-containing molecules in aqueous solution was added to each vial to bring the concentration of Gd(III) to 0.1 mM (*26*). Excess water was added to bring the total volume to 250 μL. These solutions were ultrasonicated for 30 s and transferred to 5 mm NMR tubes. Fifty microliters of 0.1 M calcium carbonate buffer was added to each tube to increase the pH and induce gelation. Four sample tubes were bound together using Parafilm wax and inserted into the magnet. Images were acquired using a spin−echo pulse sequence with TR of 152, 200, 400, 750, 1000, 1400, 1800, 2500, 4000, 10 000 ms, TE 12 ms, slice thickness of 1 mm (eight slices taken), and FOV of 2 cm.

Circular Dichroism. Circular dichroism (CD) was performed on a Jasco J-715 CD spectrophotometer using a 2 mm quartz cuvette. Samples were prepared from the stock solution in water to a final concentration of 3.33×10^{-6} M at a pH of 7.4 in PBS buffer. Five spectra from 190 to 260 nm were averaged together.

AFM. AFM preparation was from the same stock solutions of **1**−**3** (0.005 mM) that were used to determine relaxivity, diluted 1:10 with deionized water. Samples were prepared by drop casting 5 μL of the diluted solutions onto freshly cleaved mica substrates. Samples were allowed to rest for 2 min before excess solution was wicked away. After drying in air, AFM was performed with a Digital Instruments MultiMode III SPM with a Quadrex extender and Olympus AC240TS cantilevers in tapping mode. Height measurements were taken on 149 straight fiber segments using the cross-sectional averaging tool included in Digital Instruments Nanoscope III acquisition analysis software.

RESULTS

Description of 1−3 and Molar Relaxivity. The Gd(III) chelator is a DOTA derivative selected because of its high binding constant for lanthanides and synthetic versatility (*27*). **1** (filler PA) is a self-assembling PA that forms self-supporting gels and is similar in sequence to **2** and **3** but does not contain the Gd(III) chelator and thus was used as a standard to compare to the MR images of the gels with Gd(III). Gels of **1** and **2**, or **1** and **3**, were prepared to demonstrate the minimal concentration of peptide amphiphile contrast agent (PACA) needed to obtain good MR contrast, leaving the remaining PA molecules free to present different epitopes on the nanofibers. Varying the position of the tethered DOTA derivative on the PAs induces changes in the molecule's relaxivity (efficiency) and imaging utility (*19*). The PACA derivatives described contain the RGD peptide sequence, a well-known epitope in integrin-binding domains of extracellular proteins that is critical for adhesion of many types of cells to the extracellular matrix (*28*). We have observed that positioning the chelate close to the hydrophobic end of the molecule results in a higher relaxivity (*19*). **2** and **3** differ in the position of the Gd(III) chelator, that results in a change in relaxivity in the self-assembled state from 14.7 mM^{-1} s^{-1} (*19*) to 21.5 mM^{-1} s^{-1}, respectively (*26*) in a buffer solution at pH 7.41 (*25*). The difference in relaxivity between **2** and **3** is likely due to a difference in the rotational correlation time, τ_r, arising from decreased internal flexibility and increased steric hindrance of the chelator in **3** as compared to **2** (*18, 29*).

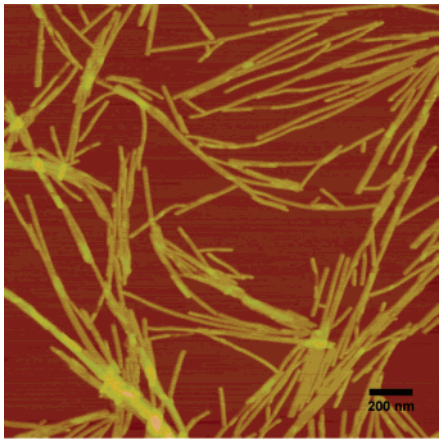

Figure 2. AFM micrograph of nanofibers formed from **3**. This image depicts the supramolecular assembly of the PACAs into fibers. These high aspect fibers then form a network trapping water and creating a gel. The fiber heights correspond to 6.0 ± 0.1 nm.

Supramolecular Properties of Nanofibers. Transmission electron microscopy (TEM) and atomic force microscopy (AFM) reveal the supramolecular structural aggregates from **1** (*30*), **2** (*19*), and **3** (Figure 2). Both **2** and **3** self-assemble into fibers at pH greater than 7.0 and **1**−**3** form uniform nanofibers microns in length. The fiber diameter of structures formed by **3** was calculated from AFM height measurements to be 6.0 ± 0.1 nm with 95% confidence. A self-supporting gel is formed upon mixing **2** or **3** with **1**, followed by ultrasonication and buffer addition. Circular dichroism (CD) spectroscopy was used to probe the hydrogen bonding interaction in the supramolecular polymer to compare with the structural observations in dried films obtained by TEM and AFM. The minima of **2** and **3** without Gd(III) reveal a peak at 212 nm, signifying a β-sheet like hydrogen bonding character (*31*), which supports fiber formation in the samples seen by AFM and TEM. These shifts in spectra from ideal β-sheets are thought to be from the change in hydrogen bonding caused by both the chelator and the branching motif used in synthesis.

Utility of PACAs. We found that mixing PACAs **2** or **3** with filler PA **1** could be successfully imaged by MR (Figure 3). The gels are homogeneous in image intensity throughout the samples, which implies uniform mixing of the PACA molecules within the filler PA at MR resolution. If heterogeneous mixing of PAs occur on a

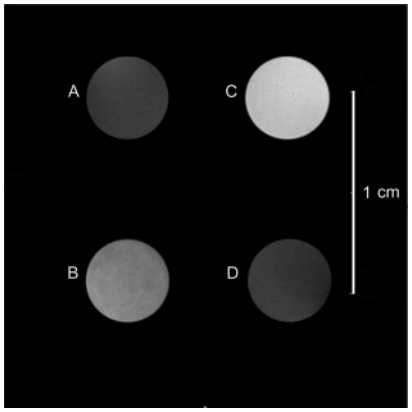

Figure 3. MR images of the phantom gels formed from **1**, **1** and **2**, **1** and **3**, and a Gd(III) DTPA standard corresponding to A, B, C, and D, respectively. The contrast arising from **3** is the greatest due to a change in τ_r of the Gd(III) chelator (*33*).

large enough scale, domains of bright and dark intensity would be observed (*30*). Figure 3 shows the difference in observed contrast between **1** (without Gd(III)), **2** mixed with **1**, **3** mixed with **1**, and a standard small molecule MR contrast agent diethylenetriaminepentaacetate (DTPA) doped into **1** (0.1 mM Gd(III)) (*26, 32*). The T_1 of these gels were measured at 3.03 ± 0.05 s, 1.89 ± 0.06 s, 1.08 ± 0.06 s, and 2.81 ± 0.05 s, respectively, the faster T_1's resulting in higher contrast. This clearly demonstrates the utility of using a contrast agent with a high relaxivity for imaging biomaterials.

Mixing of 3 with Various Epitope-Bearing PAs. A PACA that is able to mix homogeneously with a variety of different epitope containing PAs is important for biomaterial specificity. Using a PACA that universally mixes with other PAs simplifies the in vivo tests for fate mapping of different gels and allows for differing bioactivity without synthesizing a new PACA for every material. We tested the ubiquitous nature of **3**, owing to its higher relaxivity, with differing types of PA. We used a variety of PAs similar and different in structure and sequence (Figure 4) (*30*). The filler PAs were chosen based on their structure, epitopes, and sequence terminus (either C-terminus or N-terminus). Figure 4, **h**–**j**, are all linear PAs synthesized C- to N-terminus with an IKVAV

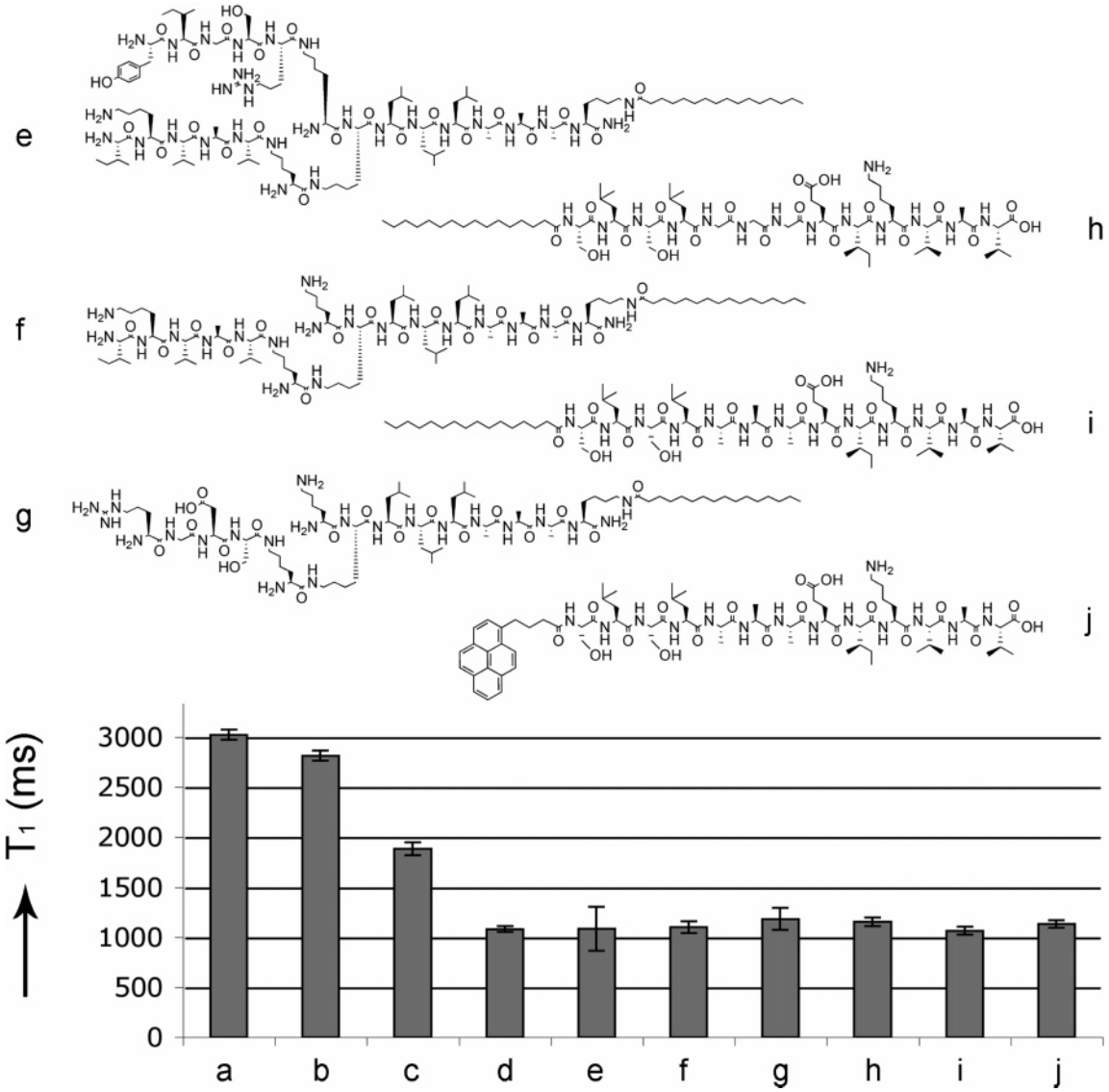

Figure 4. Results of T_1 study of PA gels and mixed PA gels. The concentration of Gd(III) is 0.1 mM in all samples except a and the concentration of filler PA is 1 wt % in each case (all samples form self-supporting gels). a corresponds to **1** alone and is used as a standard, b refers to **1** mixed with DTPA, c refers to **1** mixed with **2**, d refers to **1** mixed with **3**, e through j are mixed with **3** and their structures are depicted above. Error bars represent one standard deviation.

epitope (*7*) used for neuronal stem cell differentiation. **e** and **f** are branched PAs containing the IKVAV epitope, and **e** contains the YIGSR epitope as well also for use in neuronal stem cell differentiation. **g** is branched and contains the RGD epitope for cell adhesion. All samples formed aqueous self-supporting gels at 1 wt % and were imaged in a 400 MHz magnet. All of the gels imaged were of homogeneous signal intensity, and the T_1's of the gels were all similar values when doped with equal amounts of **3** (Figure 4). This finding shows the robustness and consistency of **3** and its ability to be used in differently structured and epitope presenting biomaterials.

DISCUSSION

The ability to noninvasively image gels formed by scaffolds of PA nanofibers doped with self-assembling PACA molecules provides a means for in vivo fate mapping of these new biomaterials. Our study compared two PACA molecules differing in the position of the Gd(III) chelator and used a variety of mixed systems to elucidate the minimal amount of PACA needed to achieve a homogeneous and significant signal intensity throughout the gel. We discovered that placing the Gd(III) closer to the hydrophobic region of the self-assembling molecules provides an increase in relaxivity and that **3** can be used with a variety of different PA gels. Further studies will explore the possibility of noninvasive three-dimensional imaging of the degradation and or migration of these PA bioactive gels in vivo are underway.

ACKNOWLEDGMENT

This work was supported by the U. S. Department of Energy (DOE) under award no. DE-FG02-00ER45810, the National Institutes of Health (NIH) under award no. 7R01 AI47003-4, T32 GM008449, and R01 EB003806-01. This work made use of the Keck Biophysics Facility, the EPIC and NIFTI facility of NUANCE Center and the Analytical Services Laboratory at Northwestern University. We thank K. MacRenaris for his assistance with ICP analysis, B. Messmore and J. Hulvat for helpful discussions and K. Niece for materials.

Supporting Information Available: Experimental details. This material is available free of charge via the Internet at http://pubs.acs.org.

LITERATURE CITED

(1) Lee, K. Y., and Mooney, D. J. (2001) Hydrogels for tissue engineering. *Chem. Rev. 101*, 1869−1879.

(2) Zhang, S. (2003) Fabrication of novel biomaterials through molecular self-assembly. *Nat. Biotechnol. 21*, 1171−1178.

(3) Langer, R., and Tirrell, D. A. (2004) Designing materials for biology and medicine. *Nature 428*, 487−492.

(4) Kisiday, J., Jin, M., Kurz, B., Hung, H., Semino, C., Zhang, S., and Grodzinsky, A. J. (2002) Self-assembling peptide hydrogel fosters chondrocyte extracellular matrix production and cell division: Implications for cartilage tissue repair. *Proc. Natl. Acad. Sci. U.S.A. 99*, 9996−10001.

(5) Holmes, T. C. (2002) Novel peptide-based biomaterial scaffolds for tissue engineering. *Trends Biotechnol. 20*, 16−21.

(6) Hartgerink, J. D., Beniash, E., and Stupp, S. I. (2001) Self-assembly and mineralization of peptide-amphiphile nanofibers. *Science (Washington, DC) 294*, 1684−1688.

(7) Silva, G. A., Czeisler, C., Niece, K. L., Beniash, E., Harrington, D. A., Kessler, J. A., and Stupp, S. I. (2004) Selective Differentiation of Neural Progenitor Cells by High-Epitope Density Nanofibers. *Science 303*, 1352−1355.

(8) Niece, K. L., Hartgerink, J. D., Donners, J., and Stupp, S. I. (2003) Self-assembly combining two bioactive peptide-amphiphile molecules into nanofibers by electrostatic attraction. *J. Am. Chem. Soc. 125*, 7146−7147.

(9) Hartgerink, J. D., Beniash, E., and Stupp, S. I. (2002) Peptide-amphiphile nanofibers: a versatile scaffold for the preparation of self-assembling materials. *Proc. Natl. Acad. Sci. U.S.A. 99*, 5133−5138.

(10) Behanna, H. A., Donners, J., Gordon, A. C., and Stupp, S. I. (2005) Coassembly of amphiphiles with opposite peptide polarities into nanofibers. *J. Am. Chem. Soc. 127*, 1193−1200.

(11) Guler, M. O., Soukasene, S., Hulvat, J. F., and Stupp, S. I. (2005) Presentation and recognition of biotin on nanofibers formed by branched peptide amphiphiles. *Nano Lett. 5*, 249−252.

(12) Weissleder, R., Poss, K., Wilkinson, R., Zhou, C., and Bogdanov, A. (1995) Quantitation of Slow Drug-Release from an Implantable and Degradable Gentamicin Conjugate by in-Vivo Magnetic-Resonance-Imaging. *Antimicrob. Agents Chemother. 39*, 839−845.

(13) Kohn, J. (2004) New approaches to biomaterials design. *Nat. Mater. 3*, 745−747.

(14) Mader, K., Cremmilleux, Y., Domb, A. J., Dunn, J. F., and Swartz, H. M. (1997) In vitro in vivo comparison of drug release and polymer erosion from biodegradable P(FAD-SA) polyanhydrides − A noninvasive approach by the combined use of electron paramagnetic resonance spectroscopy and nuclear magnetic resonance imaging. *Pharm. Res. 14*, 820−826.

(15) Mader, K., Bacic, G., Domb, A., Elmalak, O., Langer, R., and Swartz, H. M. (1997) Noninvasive in vivo monitoring of drug release and polymer erosion from biodegradable polymers by EPR spectroscopy and NMR imaging. *J. Pharm. Sci. 86*, 126−134.

(16) Melia, C. D., Rajabi-Siahboomi, A. R., and Bowtell, R. W. (1998) Magnetic resonance imaging of controlled release pharmaceutical dosage forms. *Pharm. Sci. Technol. Today 1*, 32−39.

(17) Aime, S., Botta, M., Garino, E., Crich, S. G., Giovenzana, G., Pagliarin, R., Palmisano, G., and Sisti, M. (2000) Noncovalent conjugates between cationic polyamino acids and GdIII chelates: a route for seeking accumulation of MRI-contrast agents at tumor targeting sites. *Chem. Eur. J. 6*, 2609−2617.

(18) Meade, T. J., Taylor, A. K., and Bull, S. R. (2003) New magnetic resonance contrast agents as biochemical reporters. *Curr. Opin. Neurobiol. 13*, 597−602.

(19) Bull, S. R., Guler, M. O., Bras, R. E., Meade, T. J., and Stupp, S. I. (2005) Self-Assemble Peptide Amphiphile Nanofibers Conjugated to MRI Contrast Agents. *Nano Lett. 5*, 1−4.

(20) Stroman, P. W., Dorvil, J. C., Marois, Y., Poddevin, N., and Guidoin, R. (1999) In vivo time course studies of the tissue responses to resorbable polylactic acid implants by means of MRI. *Magn. Reson. Med. 42*, 210−214.

(21) Traore, A. S., Woerly, S., Doan, V. D., Marois, Y., and Guidoin, R. (2000) In vivo magnetic resonance imaging and relaxometry study of a porous hydrogel implanted in the trapezius muscle of rabbits. *Tissue Eng. 6*, 265−278.

(22) Guidoin, R., Langevin, F., Basle, M. F., Alarcone, C., Legrand, A. P., Zhang, Z., Basse-Cathalinat, B., Franconi, J. M., Douville, Y., and Baquey, C. (2004) Can magnetic resonance imaging be the key technique to visualize and investigate endovascular biomaterials? *Artif. Cells Blood Substit. Immobil. Biotechnol. 32*, 105−127.

(23) Pihlajamaki, H., Kinnunen, J., and Bostman, O. (1997) In vivo monitoring of the degradation process of bioresorbable polymeric implants using magnetic resonance imaging. *Biomaterials 18*, 1311−1315.

(24) Aletras, A., Barlos, K., Gatos, D., Koutsogianni, S., and Mamos, P. (1995) Preparation of the very acid-sensitive Fmoc-Lys(Mtt)-OH. Application in the synthesis of side-chain to side-chain cyclic peptides and oligolysine cores suitable for the solid-phase assembly of MAPs and TASPs. *Int. J. Pept. Protein Res. 45*, 488−96.

(25) 10mM 3-(N-morpholino)propane sulfonic acid (MOPS), 100 mM sodium chloride, 20 mM sodium bicarbonate, and 4 mM sodium phosphate monobasic.

(26) Normalized to ICP measurements of Gd(III) concentration.
(27) Caravan, P., Ellison, J. J., McMurry, T. J., and Lauffer, R. B. (1999) Gadolinium(III) Chelates as MRI Contrast Agents: Structure, Dynamics, and Applications. *Chem. Rev. 99*, 2293−2352.
(28) Pierschbacher, M. D., and Ruoslahti, E. (1984) Cell Attachment Activity of Fibronectin Can Be Duplicated by Small Synthetic Fragments of the Molecule. *Nature 309*, 30−33.
(29) Toth, E., Helm, L., and Merbach, A. E. (2002) Relaxivity of MRI contrast agents. *Top. Curr. Chem. 221*, 61−101.
(30) See Supporting Information
(31) Greenfield, N., and Fasman, G. D. (1969) Computed Circular Dichroism Spectra for Evaluation of Protein Conformation. *Biochemistry 8*, 4108−4116.
(32) The gels were made using a 0.75 wt % of filler PA. The PACA molecule was mixed into this solution before gelling as was the DTPA.
(33) Images were acquired using a spin−echo pulse sequence with TR 750 ms, TE 12 ms, slice thickness of 1 mm, FOV of 2 cm, at 9.4 T on an Oxford superconducting magnet and Bruker software.

BC050153H

Transition from a Normal to Inverted Cylinder for an Amidine-Bearing Lipid/pDNA Complex and Its Excellent Transfection

Kazunori Koiwai,[†] Kenji Tokuhisa,[‡] Ryouji Karinaga,[‡] Yasuya Kudo,[‡] Shota Kusuki,[‡] Yoichi Takeda,[‡] and Kazuo Sakurai*,[‡]

Terumo Corporation R & D Center, 1500 Inokuchi, Nakai-machi, Ashigarakami-gun Kanagawa, 259-0151, Japan, and Department of Chemical Processes & Environments, The University of Kitakyushu, 1-1 Hibikino, Wakamatu-ku, Kitakyushu, Fukuoka 808-0135, Japan. Received June 10, 2005; Revised Manuscript Received August 23, 2005

A cationic lipid (TRX) having an amidine headgroup was synthesized, and a lipoplex (i.e., plasmid DNA+lipid complex) was prepared from the mixture of TRX and two other neutral colipids. Small-angle X-ray scattering showed that the addition of DNA induced a structural transition from normal to inverted hexagonally packed cylinders. Transmission electron microscopy showed a threadlike micelle was transformed to a spherical micelle about 50−200 nm in diameter by adding DNA. A combination of these results leads to the conclusion that the complexed DNA is hexagonally packed (or condensed) into spherical aggregates. The size and morphology are believed suitable for endocytosis uptake or vesicle fusion. The complex made from pDNA (pEGFP-C1) and TRX was transfected to Hep G2. Flow cytometry and confocal microscopy showed that the present system expressed green fluorescence protein (GFP) more than a conventional transfection reagent. Additionally, TRX was less cytotoxic than other transfection reagents. This paper presents the attractive possibility of the amidine group for a transfection device.

A lipoplex is an ionic complex made from cationic surfactants and pDNA and well-known for excellent performance in the transfection of bound DNA (*1*). It is involved in almost 20% of current clinical trials of gene therapy (*2*). In the lipoplex formulations, the cation-to-anion ratio is carefully adjusted so that the resultant lipoplex is positively charged overall, and this positive charge can induce cellular uptake. The cation also plays a crucial role in condensing DNA into a compact form. Of all the amines, tertiary amines are the most efficient in both transfection and condensation (*1*, *3*). However, cytotoxicity of the amines has been pointed out as a drawback.

Most lipoplex formulations require inclusion of a significant amount of a neutral colipid. Recent studies showed that the addition of colipids can control the morphology of the complex, which is strongly correlated to transfection efficiency. Small-angle X-ray scattering (SAXS) revealed that the inverted hexagonal phase, in which the cylinders consisting of DNA coated with a lipid monolayer are arranged on a hexagonal lattice, is more transfectant than the lamella phase where DNAs are sandwiched between cationic bilayers (*4*−*6*). Interestingly, the addition of pDNA to the lamella phase induces transition to the inverted hexagonal phase. The excellent transfection can be related to the fact that inverted hexagonal structures are often observed in the region where membranes fuse (*1*, *7*).

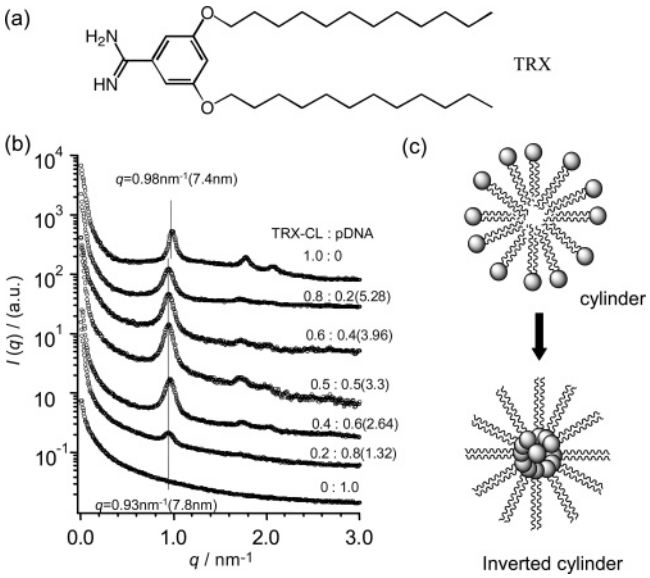

Figure 1. Chemical structure of TRX (a), SAXS profiles when TRX-CL was mixed with pDNA (pEGFP−C1) (b), and a schematic illustration for the morphological changes upon mixing TRX-CL and pDNA (c).

Recently, Aoyama et al. (*8*) reported a micellar glycocluster nanoparticle that can condense DNA into approximately 50 nm diameter spheres and showed excellent transfection. Their particle size seems to perfectly match the desirable dimension for transfection. Meanwhile, Engberts et al. (*9*), who synthesized a sugar-based cationic gemini surfactant, showed that their lipoplex

* Corresponding author: sakurai@env.kitakyu-u.ac.jp. Fax: +81-93-695-3390. Phone: +81 93-695-3298.
[†] Terumo Corporation.
[‡] The University of Kitakyushu.

10.1021/bc050164a CCC: $30.25 © 2005 American Chemical Society
Published on Web 10/22/2005

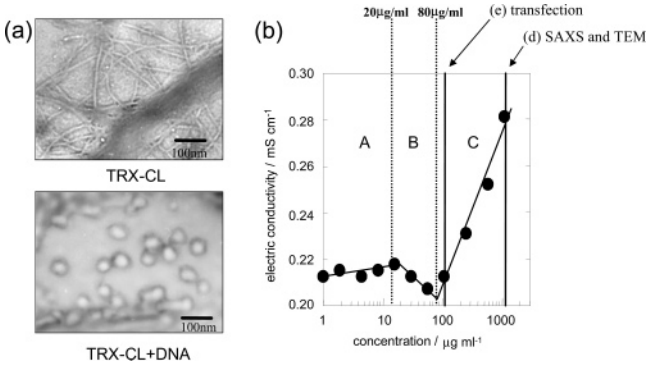

Figure 2. Comparison of TEM images between TRX-CL and TRX-CL+ pDNA where bar size is 100 nm (a) and the concentration dependence of the electric conductivity to relate the micelle structural changes (b). The concentration in b is defined by the total weight of TRX-CL+ pDNA. The transfection and SAXS and TEM were carried out at the concentrations indicated by e and d, respectively.

undergoes a pH-induced structural transition and interpreted the excellent transfection based on this transition. On the other hand, amidine has drawn attention as an alternative headgroup (*10*−*13*); however, the transfection efficiency has not been improved so much. Here, we report a novel gemini-type cationic surfactant (US Patent 6,228,391, 2001) having an amidine headgroup (denoted by TRX; the chemical structure is shown in Figure 1a) to show an excellent transfection and low cytotoxicity. In fact, the present report shows that the transfection efficiency and the cytotoxicity of TRX are much better than those of conventional transfection reagents. The major difference between TRX and the previous amidine derivative lies in the chemical structure of amidine, i.e., the amidine of TRX is protonated, while the previous one is alkylated. Therefore, TRX is considered to have a greater affinity for the phosphoric acid of DNA than the previous one.

Figure 1b presents SAXS profiles when TRX was mixed with pDNA (pCAG-luc, pEGFP-C1, 4731 base pairs) (*14*) in the presence of the colipids (DOPE and DLPC). Before the addition of the DNA to the lipid mixtures (denoted by TRX-CL), SAXS profiles show three distinctive peaks at $q = 0.98$, 1.74, and 2.02 nm^{-1}. The relation of these peaks satisfies the radio of $1:\sqrt{3}:2$, indicating the presence of hexagonally packed cylinders. After addition of DNA, the first peak position shifted to the lower q of 0.93 nm^{-1} and further addition did not change the peak position at all. It is clearly shown that the hexagonal cylinder still exists in the TRX-CL and DNA mixtures, although the unit cell length becomes longer than that of TRX-CL itself by about 3%. This increment of the unit cell length can be interpreted by the assumption that DNA molecules are included into the cylinder. Once DNA is included in the lipid cylinder, cationic TRX should form ion pairs with anionic DNA. Although further investigation is necessary to reach a definite conclusion, the changes in Figure 1b suggest the structural transition from a cylinder to an inverted cylinder. This feature is quite different from the results of Cherezov et al. (*10*−*12*) and Safinya and Koltover (*4*−*6*), in which the transitions of lamellae to inverted cylinders were observed by addition of DNA. This difference, especially from the previous amidine system, can be ascribed to the presence of the aromatic group attaching the headgroup, because this bulky headgroup may bend the bilayer surface to make the cylinder more thermodynamically favorable than lamellae.

The morphologies of TRX-CL and TRX-CL+DNA (1:1) were observed with transmission electron microscopy (TEM) (Figure 2a). Rodlike images and their bundles

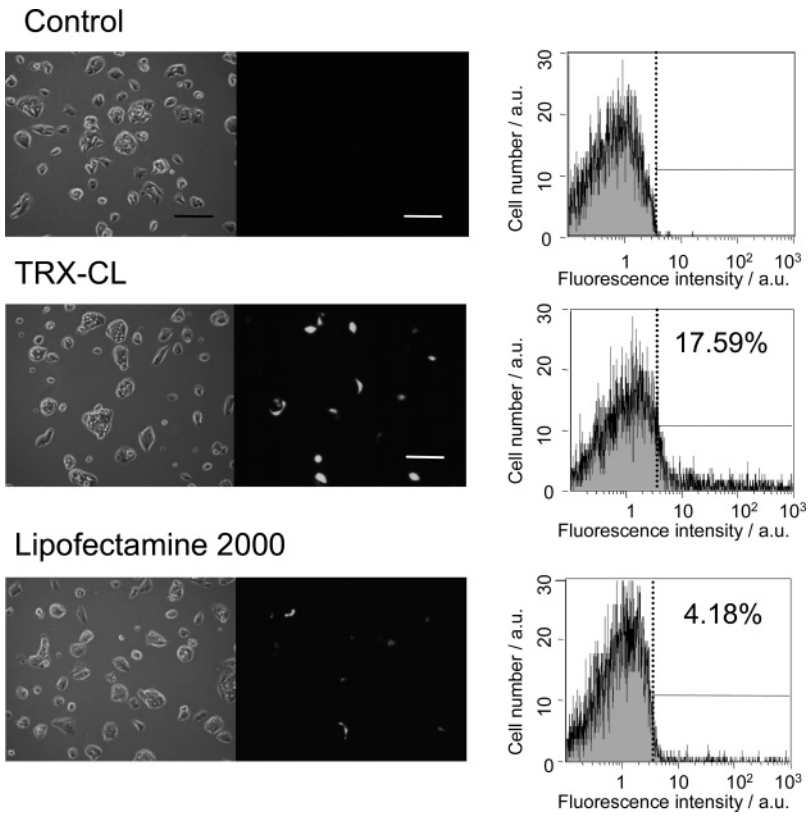

Figure 3. Comparison of the fluorescence microscopic images and the number of the cell distribution expressing GFP between TRX-CL and Lipofectamine 2000.

were observed in TRX-CL, which are quite similar to the image of other hexagonally packed molecules such as organogelators (*15*) or rodlike micelles. Once DNA was added, the morphology was completely different as presented in Figure 2a. Here, globular particles are observed and their diameters are about 50−200 nm, which can be interpreted as the amidine groups of TRX binding to the phosphoric groups of pDNA to lead to compaction of the DNA. Judging from the size, there are only a few DNA molecules present in one particle. The radius of gyrations obtained from SAXS was consistent with the TEM results. According to the literatures (*16*), this particle size seemed ideal for cellular uptake through an endocytosis pathway. Presence of such a small particle is one of the characteristics of the TRX system. Combining the SAXS and TEM results, we conclude that DNA molecules are condensed in the globular particle, and inside the particle the hexagonally packed inverted cylinders are formed as illustrated in Figure 1c. There seem to be discrepancies in size between SAXS and TEM; 50 nm from TEM and 50−200 nm from SAXS. We are in the middle of clarifying the size of the particles with dynamic light scattering and further SAXS and TEM measurements.

Figure 2b presents the relation between the concentration of TRX-CL+DNA and the electric conductivity of the solution. There appears to be three different regimes, denoted by A, B, and C. The range A should be the homogeneous solution and the range C, where we carried out TEM and SAXS, can be characterized by the inverted hexagonal cylinders phase. At this moment, however, we do not know what is happening in the range B. When we carried out the in vitro transfection experiment, the concentration indicated by e was used. The TRX-CL+DNA complex at e should have the same morphology as that of d where TEM and SAXS was done, because the concentrations of d and e were in the same regime of C. The complex made from pEGFP-C1 and TRX-CL was transfected to Hep G2. After 72 h, the cells were observed with fluorescence microscopy, and the number of the cells that expressed green fluorescent protein (GFP) was counted with a flow-cytometer (FCM) (Figure 3). The same experiments were carried out for Lipofectamine 2000. In the microscopic images, it seems that TRX-CL+pEGFP−C1 has more green cells (i.e., expressing GFP) than Lipofectamine 2000+pEGFP−C1. FCM indicates that 17.59% in the total cells are transfected in TRX-CL+pEGFP−C1, while 4.18% for Lipofectamine 2000. On the basis of the doubling time of Hep G2 being about 30 h, about 81% of the cells seemed to be transfected in the initial stage. Furthermore, when we examined the carrier concentration dependence of proliferation, comparing TRX-CL with Lipofectamine 2000, the results clearly showed that TRX-CL was less cytotoxic than Lipofectamine 2000 (see Supporting Information).

In summary, a new cationic lipid bearing an amidine headgroup is presented as a new transfection reagent, showing structural transition from a cylinder to inverted cylinder upon mixing with pDNA and showing excellent transfection ability as well as less cytotoxicity.

ACKNOWLEDGMENT

This work is finically supported by SORST of JST and a Grant-in-Aid for Scientific Research (No. 16350068 and 16655048). SAXS was performed at SPring-8 BL40B2 (2004A0425-NL2b-np and 2004B0135-NL2b-np).

Supporting Information Available: Synthesis of TRX and its characterization with NMR and mass spectroscopy, the lipoplex formulation, experimental details of SAXS, the Guinier plot by which we evaluated R_g (radius of gyration), comparison of cytotoxicity between TRX-CL and Lipofectamine2000, and experimental details of the transfection assay with flow cytometry and microscopy. This material is available free of charge via the Internet at http://pubs.acs.org.

LITERATURE CITED

(1) Huang, L., Hung, M. C., and Wagner, E. (1999) *Nonviral Vectors for Gene Therapy*, p 91, Academic Press, London, UK.
(2) Barenholz, Y. (2001) Liposome application: problems and prospects. *Curr. Opin. Colloid Interface Sci. 6*, 66−77.
(3) Farhood, H., Serbina, N., and Huang, L. (1995) The role of dioleoyl phosphatidylethanolamine in cationic liposome mediated gene transfer. *Biochim. Biophys. Acta 1235*, 289−295.
(4) Koltover, I., Salditt, T., Radler, J. O., and Safinya, C. R. (1998) An inverted hexagonal phase of cationic liposome-DNA complexes related to DNA release and delivery. *Science 281*, 78−81.
(5) Koltover, I., Salditt, T., and Safinya, C. R. (1999) Phase diagram, stability, and overcharging of lamellar cationic lipid-DNA self-assembled complexes. *Biophys. J. 77*, 915−924.
(6) Koltover, I., Wagner, K., and Safinya, C. R. (2000) DNA condensation in two dimensions. *Proc. Natl. Acad. Sci. U.S.A. 97*, 14046−14051.
(7) Lin, A. J., Slack, N. L., Ahmad, A., Koltover, I., George, C. X., Samuel, C. E., and Safinya, C. R. (2000) Structure and structure−function studies of lipid/plasmid DNA complexes. *J. Drug. Target. 8*, 13−27.
(8) Aoyama, Y., Kanamori, T., Nakai, T., Sasaki, T., Horiuchi, S., Sando, S., and Niidome, T. (2003) Artificial viruses and their application to gene delivery. Size-controlled gene coating with glycocluster nanoparticles. *J. Am. Chem. Soc. 125*, 3455−3457.
(9) Johnsson, M., Wagenaar, A., and Engberts, J. B. (2003) Sugar-based gemini surfactant with a vesicle-to-micelle transition at acidic pH and a reversible vesicle flocculation near neutral pH. *J. Am. Chem. Soc. 125*, 757−760.
(10) Cherezov, V., Qiu, H., Pector, V., Vandenbranden, M., Ruysschaert, J. M., and Caffrey, M. (2002) Biophysical and transfection studies of the diC(14)-amidine/DNA complex. *Biophys. J. 82*, 3105−3117.
(11) Ruysschaert, J. M. (2002) Biophysical and transfection properties of DNA-DiC14-amidine complexes. *Cell. Mol. Biol. Lett. 7*, 249−50.
(12) Ruysschaert, J. M., el Ouahabi, A., Willeaume, V., Huez, G., Fuks, R., Vandenbranden, M., and Di Stefano, P. (1994) A novel cationic amphiphile for transfection of mammalian cells. *Biochem. Biophys. Res. Commun. 203*, 1622−1628.
(13) Arjen, M., Funhoff, C., van Nostrum, F., Lok, M. C., Fretz, M. M., Daan, J., Crommelin, A., and Hennink, W. E. (2004) Poly(3-guanidinopropyl methacrylate): a novel cationic polymer for gene delivery. *Bioconjugate Chem. 15*, 1212−1220.
(14) Miyazaki, J., Takaki, S., and Araki, K. (1989) Expression vector system based on the chicken beta-actin promoter directs efficient production of interleukin-5. *Gene 79*, 269−277.
(15) Sakurai, K., and Jeonhwan, Y. (2003) Supramolecular Structure of a Sugar-Appended Organogelator Explored with Synchrotron X-ray Small-Angle Scattering. *Langmuir 19*, 8211−8217.
(16) Seymour, L., Schacht, E., and Duncan, R. (1991) The effect of size of polystyrene particles on their retention within the rat peritoneal compartment, and on their interaction with rat peritoneal macrophages in vitro. *Cell Biol. Int Rep. 15*, 277−286.

BC050164A

A Site-Specific Bifunctional Protein Labeling System for Affinity and Fluorescent Analysis

Thomas S. Shute,[†] Masayuki Matsushita,[‡] Tobin J. Dickerson,[‡] James J. La Clair,[†] Kim D. Janda,*[,‡] and Michael D. Burkart*[,†]

Department of Chemistry and Biochemistry, University of California, San Diego, 9500 Gilman Drive, La Jolla, California 92093-0358, and The Skaggs Institute for Chemical Biology and Departments of Chemistry and Immunology, The Scripps Research Institute, 10550 North Torrey Pines Road, La Jolla, California 92038.
Received July 20, 2005; Revised Manuscript Received August 22, 2005

Most covalent protein labeling schemes require a choice between visual and affinity properties, requiring the use of multiple fusion systems where both attributes are needed. While not disruptive at the single experiment level, this detail becomes critical when addressing high-throughput experimentation. Here we develop a uniform site-specific protein tag for use in both fluorescent and affinity screening. Covalent protein tagging with a stilbene reporter via promiscuous phosphopantetheinyltransferase (PPTase) modification enables a switchable, antibody-elicited fluorescent response in solution or on affinity resin. For demonstration purposes, VibB, a natural fusion protein harboring a carrier protein domain, was labeled with a stilbene tag through PPTase modification with a stilbene-labeled coenzyme A analogue. Analysis of the resulting stilbene-tagged VibB was accomplished by fluorescent and Western blot analysis with anti-stilbene monoclonal antibody EP2-19G2. The illustration of this method for general application to fusion protein analysis offers a dual role in assisting both solution-based fluorescent analysis and surface-based affinity detection and purification.

Site-specific protein labeling plays a major role in contemporary biomolecular research as a means to manipulate or visualize individual proteins. Tagged proteins are commonly generated for expression profiling, isolation, and cellular localization of targeted protein entities (*1*−*3*). In choosing an appropriate labeling system, function-specific properties are currently selected from a small list of available reporters, few of which serve more than one purpose. Of the established systems, labels such as histidine-fusion (*4*, *5*) and biotin-ligation (*6*) do not offer access to both optical and affinity applications. While systems such as dye and anti-dye antibody combinations (i.e., BODIPY and anti-BODIPY) provide dual functionality, these systems fail to correlate antibody binding with the generation of a fluorescent signal (*7*). Although several antibody-dye pairs undergo a net quenching of fluorescence upon binding (*8*, *9*), this loss of signal cannot be directly associated with a binding event, as such responses can arise from a number of external factors. To avoid this problem, additional control and regulatory elements, such as those common to immunofluorescent staining or fluorescent in situ hybridization (FISH) methods, are often favored for quantitative analyses (*10*−*12*). A practical solution arises through dye−antibody interactions that fluoresce upon binding. The combination of a site-specific vehicle for probe attachment and affinity-specific fluorometric gain presents an enhanced affinity tool with practical utility for molecular and cellular studies.

Posttranslational modification of carrier protein domains by a phosphopantetheinyltransferase (PPTase) provides a robust entry for site-specific transfer of both affinity and fluorescent probes (*13*). This technique has been shown to be viable with fusion proteins for both in vitro and in vivo analyses (*14*−*17*). While this technique tolerates an array of reporter species (*13*), we reasoned that the chosen reporter system should provide access to both affinity manipulation and optical analysis. An elegant choice for such a ligand was demonstrated with stilbene in its functional use with stilbene-binding antibodies (*18*−*21*). Here, a stilbene hapten becomes a visible fluorophore as it binds to a complementary monoclonal antibody (mAb).

Carrier protein-PPTase modification tools are derived from posttranslational modification of carrier proteins found in fatty acid, polyketide, and nonribosomal peptide biosynthetic pathways (*22*−*24*). As illustrated in Scheme 1, *apo*-carrier proteins (CP) may be labeled using reporter-modified coenzyme A (CoA) derivative **1** and a PPTase to yield the *crypto*-carrier protein (**1-CP**) bearing a stilbene-probe covalently tethered via a 4′-phosphopantetheine linkage (*13*). The scope of this technique is guided by the specificity of enzymatic transformation and the ability to chemically synthesize CoA derivatives (*25*−*27*). We reasoned that the application of a stilbene probe to this labeling scheme could provide an affinity tool with switchable optical response, and as such, sought to create a stilbene-tagged CoA derivative in order to develop this technique.

The synthesis of maleimide-terminal stilbene **6** was considered a key element of our strategy. In this con-

* Corresponding author. E-mail: mburkart@ucsd.edu; Fax 858-822-2182 or kdjanda@scripps.edu; Fax: 858-784-2595.

[†] Department of Chemistry and Biochemistry, University of California, San Diego.

[‡] The Skaggs Institute for Chemical Biology and Department of Chemistry, The Scripps Research Institute.

10.1021/bc050213j CCC: $30.25 © 2005 American Chemical Society
Published on Web 09/23/2005

Scheme 1. Labeling of VibB, a Carrier Protein Fusion (CP) by CoA Analogue 1 and a PPTase Provides a Site-Specific-Labeled Protein 1-CP[a]

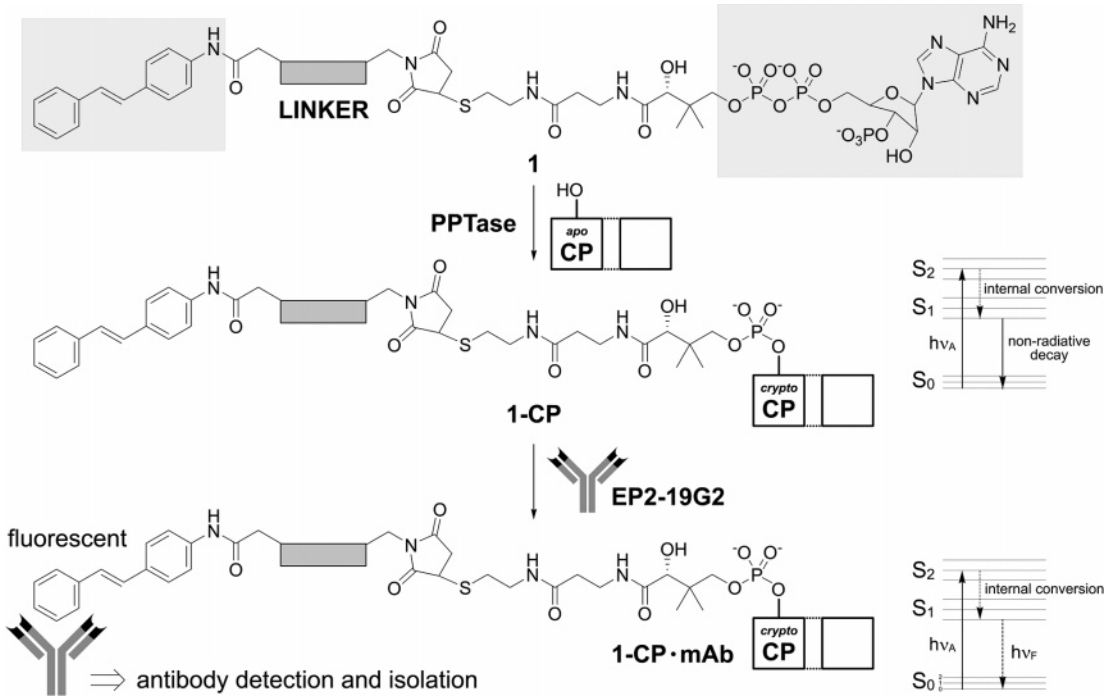

[a] Analysis of this *crypto*-state carrier protein **1-CP** can be done either by fluorescence or affinity methods using EP2-19G2, a stilbene-selective monoclonal antibody (mAb). Binding of EP2-19G2 to **1-CP** yields a fluorescent state.

Scheme 2. Synthesis of a Stilbene-Tagged Coenzyme A Analogue 1[a]

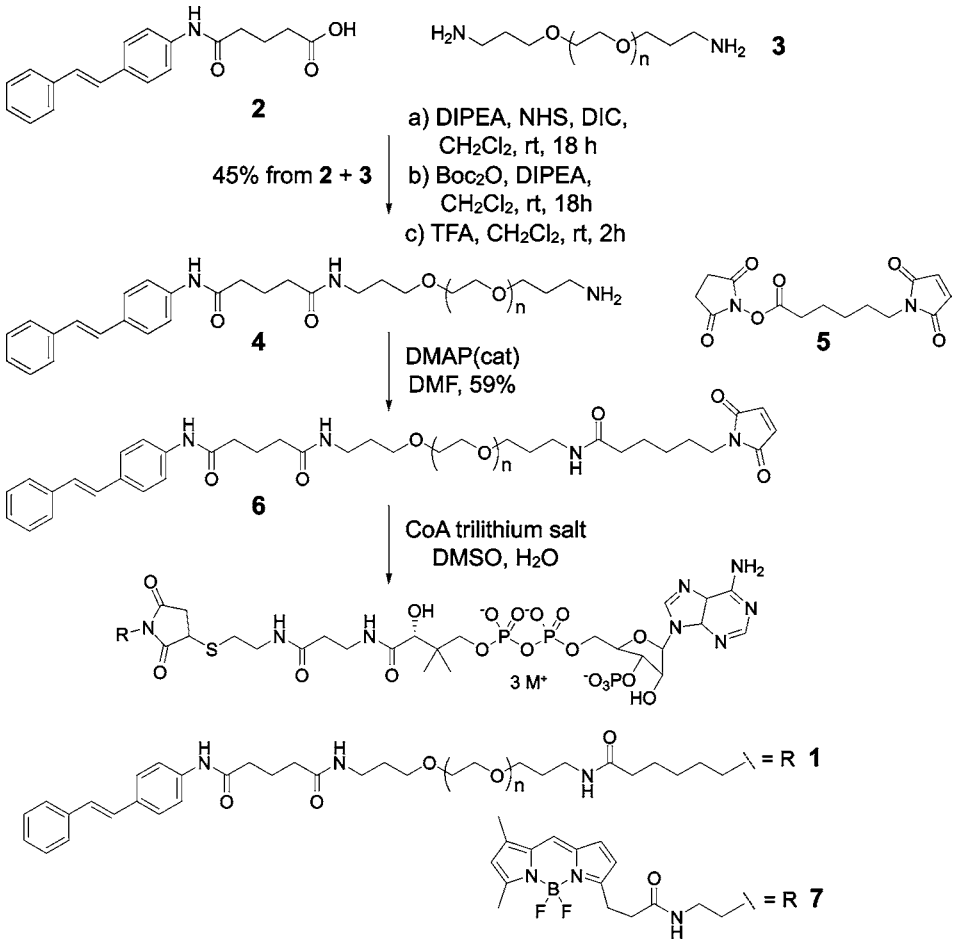

[a] Boc = *tert*-butoxycarbonyl, CoA = coenzyme A, DIPEA = *N,N*-diisopropylethylamine, DMF = *N,N*-dimethylformamide, NHS = *N*-hydroxysuccinimide, DIC = *N,N′*-diisopropylcarbodiimide, TFA = trifluoroacetic acid. n = 16−32, with an average of 25.

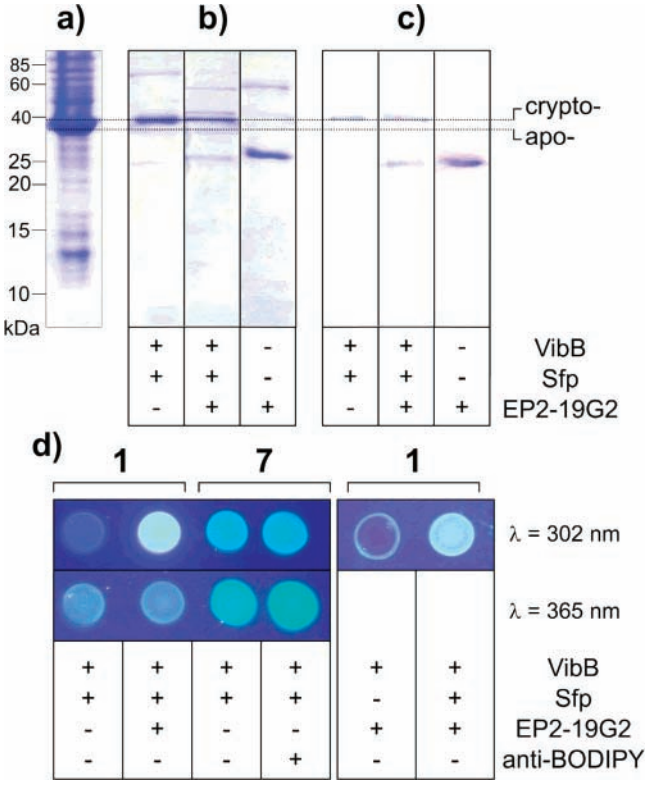

Figure 1. Fluorescent and affinity analysis of *crypto*-carrier protein (**1-CP**). (a) Coomassie stained gel depicting crude *E. coli* lysate containing overexpressed *apo*-VibB. (b) Affinity purification from crude *E. coli* lysate using EP2-19G2 appended to agarose beads. (left) Prepurified stilbene-*crypto*-VibB as positive control. (center) Eluate from EP2-19G2-bound agarose beads after exposure to a reaction containing crude cell lysate with recombinant VibB, Sfp, and **1**. (right) Eluate from affinity resin with no VibB. (c) Western blot of identical gels from b depicting the purification of VibB from lysate. Nitrocellulose was incubated with EP2-19G2 and followed by anti-mouse antibody reporter. The band at ~25 kDa in the center and right lanes was due to decomposition of mAb EP2-19G2. (d) Droplet analysis. (Left) Prepurified stilbene-*crypto*-VibB treated with either CoA analogue **1** or **7** after exposure to a Sfp. mAb EP2-19G2, mAb anti-BODIPY, or water was added to the spots, and UV light was irradiated from below. Droplets were ~2 mm in diameter. (top right) Droplets with *apo*-VibB or stilbene-*crypto*-VibB and mAb EP2-19G2.

struct, the appendage of a long PEG-spacer (16−32 ethylene glycol units) provides a linkage with maximum distance of 8.6 ± 2.8 nm, thereby allowing simultaneous analyses to be conducted on both native and denatured proteins (*27*). The synthetic route involved the conversion diamino PEG **3** (*18*) to the stilbene-labeled CoA analogue **1**. The synthesis began with the coupling of **2** to **3** by activation with *N*-hydroxysuccinimide and diisopropylcarbodiimide to give crude **4** in 60% yield (Scheme 2). To purify **4**, the resulting product was *N*-protected as its *tert*-butyl carbamate and purified by silica gel chromatography. Subsequent deprotection and precipitation yielded stilbene-PEG amine **4**. Selective functionalization of the terminal amine of **4** with *N*-succinimidyl-6-maleimidohexanoate **5** provided maleimide-derivatized stilbene **6**. Incubation of CoA with **6** followed by a rapid DEAE cellulose purification with an ammonium formate gradient (50 mM to 500 mM) offered pure stilbene-CoA **1**.

Stilbene-CoA **1** was incubated with purified recombinant vibriobactin synthase carrier protein domain (VibB), from *Vibrio cholerae*, and purified recombinant surfactin PPTase (Sfp), from *Bacillus subtilis*, as modifying enzymes. The reaction was separated via SDS−PAGE and electroblotted onto nitrocellulose. The resulting blot was incubated with anti-stilbene monoclonal antibody (mAb) EP2-19G2, followed with anti-mouse-alkaline phosphatase secondary antibody and developed with 5-bromo-4-chloro-3-indolyl phosphate/nitro blue tetrazolium (BCIP/NBT). The appearance of a band of an apparent molecular weight of 36 kDa indicated a gel shift of 2.5 kDA relative to *apo*-VibB (Figure 1c). This may be compared to the Coomassie stain of the same gel (Figure 1b), where stilbene-linked *crypto*-VibB runs at 36 kDa, while *apo*-VibB runs at 33.5 kDa (Figure 1a).

Stilbene-labeled molecules have been shown to fluoresce when bound to mAb EP2-19G2 (*18*−*21*). To verify the use of this protein modification scheme for both affinity and visualization applications, we quantified the fluorescence generated by antibody binding with stilbene-tagged protein **1-CP** in solution. Purified *apo*-VibB was modified by Sfp and stilbene-CoA **1**. The labeled protein, stilbene-*crypto*-VibB, was purified via size-exclusion chromatography and concentrated to 11 μM via spin concentration, mixed with mAb EP2-19G2 (1.67 μM), and fluorescence intensity was analyzed at the optimal wavelengths for mAb EP2-19G2 ($\lambda_{ex} = 327$ nm, $\lambda_{em} = 410$ nm) (*18*−*21*). Titration of mAb EP2-19G2 against stilbene-labeled *crypto*-VibB verified that maximal fluorescence arose from a 1:1 dependence of antibody binding sites to labeled protein.

To demonstrate cooperative affinity and fluorescence properties of the stilbene label, we also isolated labeled protein by affinity chromatography. Heterologously expressed *apo*-VibB was stilbene-tagged in vitro and purified from crude cell lysate using immobilized anti-stilbene mAb. The crude solution of *apo*-VibB from recombinant *Escherichia coli* lysate was incubated with **1** and recombinant Sfp. The resulting crude solution of stilbene-*crypto*-VibB **1-CP** was applied to agarose resin conjugated with mAb EP2-19G2. The progress of binding by stilbene-tagged *crypto*-VibB **1-CP** was readily visualized by the confinement of blue fluorescence to the agarose bead pellet. The affinity resin was then washed to remove unmodified cellular proteins. Conjugate **1-CP** was removed from the beads by heat denaturation in SDS buffer. The presence and purity of **1-CP** in the eluted fraction was confirmed by polyacrylamide gel electrophoresis and Western blotting (Figure 1c,d).

Droplet experiments were performed to demonstrate switchable fluorescence in solution. Two 20 μL droplets containing prepurified stilbene-*crypto*-VibB **1-CP** were placed on a transparent surface, and 2 μL of mAb EP2-19G2 (11.5 mg/mL) were added to one of the droplets. Similarly, two droplets of purified BODIPY-*crypto*-VibB, generated by incubation of BODIPY-CoA **7** with recombinant Sfp and recombinant *E. coli* lysate and purified by nickel chromatography (*13*), were placed on the surface, and 2 μL of anti-BODIPY monoclonal antibody (11 mg/mL) were added to one droplet. The droplets were visualized by UV illumination at $\lambda_{ex} = 302$ nm and $\lambda_{ex} = 365$ nm (Figure 1d). **1-CP** shows evident fluorescent gain at $\lambda_{ex} = 302$ nm in the presence of mAb EP2-19G2, indicating the switchable visualization as a result of antibody binding to the stilbene reporter. BODIPY-*crypto*-VibB (*13*) shows no change upon antibody addition with excitation at either wavelength. No fluorescence quenching was visualized as a result of anti-BODIPY mAb binding to BODIPY-labeled protein. As a control, mAb EP2-19G2 was added to each of two additional droplets, one with *apo*-VibB and the other with stilbene-*crypto*-VibB **1-CP** (Figure 1d, right). Fluorescence is seen at $\lambda = 302$ nm only in the stilbene-tagged protein,

demonstrating a modulated fluorescence gain through stilbene-tagged proteins in solution by selective binding of anti-stilbene mAb.

Using this stilbene-fusion/antibody technique, individual proteins may be screened in solution in a high-throughput format, analyzed by conventional SDS–PAGE and Western blotting techniques, and purified using immobilized antibodies. Fluorescence gain may be evaluated by a number of bioanalytical methods, including fluorescence spectroscopy, fluorescence microscopy, and biochemical methods such as immunoprecipitation and affinity chromatography. The combination of fluorescence and affinity methods presents a uniform reporter, and its application to carrier protein modification schemes provides a streamlined tagging-system for in vivo and in vitro protein analysis. Adaptation to carrier protein fusion systems provides a general tool for protein analysis.

ACKNOWLEDGMENT

Funding was provided by the University of California, San Diego, Department of Chemistry and Biochemistry, The Skaggs Institute for Chemical Biology (TSRI), and NSF CAREER award under Grant No. 0347681.

Supporting Information Available: Experimental details including procedure for the synthesis of synthesis of stilbene-linked CoA EP2–PEG1500-NH2 (**4**), methods for conjugation of carrier protein domains, and protocols for droplet and western blot analysis.This material is available free of charge via the Internet at http://pubs.acs.org.

LITERATURE CITED

(1) Chen, I., Howarth, M., Lin, W., and Ting A. Y. (2005) Site-specific labeling of cell surface proteins with biophysical probes using biotin ligase. *Nat. Methods. 2*, 99–104.
(2) Hu, Y., Huang, X., Chen, G. Y., and Yao, S. Q. (2004) Recent advances in gel-based proteome profiling techniques. *Mol. Biotechnol. 28*, 63–76.
(3) Miyawaki, A., Sawano, A., and Kogure, T. (2003) Lighting up cells: labeling proteins with fluorophores. *Nat. Cell Biol., Suppl.*, S1–S7.
(4) Porath, J. (1992) Immobilized metal ion affinity chromatography. *Protein Expr. Purif. 3*, 263–281.
(5) Larive, C. K., Lunte, S. M., Zhong, M., Perkins, M. D., Wilson, G. S., Gokulrangan, G., Williams, T., Afroz, F., Schoneich, C., Derrick, T. S., Middaugh, C. R., and Bogdanowich-Knipp, S. (1999) Separation and analysis of peptides and proteins. *Anal. Chem. 71*, 389R–423R.
(6) Cull, M. G., and Schatz, P. J. (2000) Biotinylation of proteins in vivo and in vitro using small peptide tags. *Methods Enzymol. 326*, 430–440.
(7) Adams, S. R., Campbell, R. E., Gross, L. A., Martin, B. R., Walkup, G. K., Yao, Y., Llopis, J., and Tsien, R. Y. (2002) New biarsenical ligands and tetracysteine motifs for protein labeling in vitro and in vivo: synthesis and biological applications. *J. Am. Chem. Soc. 124*, 6063–6076.
(8) Watt, R. M., and Voss, E. W., Jr. (1977) Mechanism of quenching of fluorescein by anti-fluorescein IgG antibodies. *Immunochemistry 14*, 533–551.
(9) Lukacs, G. L., Rotstein, O. D., and Grinstein, S. (1991) Determinants of the phagosomal pH in macrophages. In situ assessment of vacuolar H(+)-ATPase activity, counterion conductance, and H+ "leak". *J. Biol. Chem. 266*, 24540–24548.
(10) Jain, K. K. (2004) Current status of fluorescent in-situ hybridisation. *Med. Device Technol. 15*, 14–17.
(11) Heng, H. H., Spyropoulos, B., and Moens, P. B. (1997) FISH technology in chromosome and genome research. *Bioessays 19*, 75–84.
(12) Brelje, T. C., Wessendorf, M. W., and Sorenson, R. L. (2002) Multicolor laser scanning confocal immunofluorescence microscopy: practical application and limitations. *Methods Cell Biol. 70*, 165–244.
(13) La Clair, J. J., Foley, T. L., Schegg, T. R., Regan, C. M., and Burkart, M. D. (2004) Manipulation of carrier proteins in antibiotic biosynthesis. *Chem. Biol. 11*, 195–201.
(14) Yin, J., Liu, F., Li, X., and Walsh, C. T. (2004) Labeling proteins with small molecules by site-specific posttranslational modification. *J. Am. Chem. Soc. 126*, 7754–7755.
(15) George, N., Pick, H., Vogel, H., Johnsson, N., and Johnsson, K. (2004) Specific labeling of cell surface proteins with chemically diverse compounds. *J. Am. Chem. Soc. 126*, 8896–8897.
(16) Johnsson, N., George, N., and Johnsson K. (2005) Protein chemistry on the surface of living cells. *Chembiochem 6*, 47–52.
(17) Yin, J., Liu, F., Schinke, M., Daly, C., and Walsh, C. T. Phagemid encoded small molecules for high throughput screening of chemical libraries. *J. Am. Chem. Soc. 126*, 13570–13571.
(18) Simeonov, A., Matsushita, M., Juban, E. A., Thompson, E. H., Hoffman, T. Z., Beuscher, A. E., 4th, Taylor, M. J., Wirsching, P., Rettig, W., McCusker, J. K., Stevens, R. C., Millar, D. P., Schultz, P. G., Lerner, R. A., and Janda, K. D. (2000) Blue-fluorescent antibodies. *Science 290*, 307–313.
(19) Kaufmann, G. F., Meijler, M. M., Sun, C., Chen, D. W., Kujawa, D. P., Mee, J. M., Hoffman, T. Z., Wirsching, P., Lerner, R. A., and Janda, K. D. (2005) Enzymatic incorporation of an antibody-activated blue fluorophore into DNA. *Angew. Chem., Int. Ed. 44*, 2144–2148.
(20) Chen, D. W., Beuscher, A. E., 4th, Stevens, R. C., Wirsching, P., Lerner, R. A., and Janda, K. D. (2001) Preparation of stilbene-tethered nonnatural nucleosides for use with blue-fluorescent antibodies. *J. Org. Chem. 66*, 1725–1732.
(21) Matsushita, M., Yoshida, K., Yamamoto, N., Wirsching, P., Lerner, R. A., and Janda, K. D. (2003) High-throughput screening by using a blue-fluorescent antibody sensor. *Angew. Chem., Int. Ed. 42*, 5984–5987.
(22) Gehring, A. M., Lambalot, R. H., Vogel, K. W., Drueckhammer, D. G., and Walsh, C. T. (1997) Ability of Streptomyces spp. acyl carrier proteins and coenzyme A analogues to serve as substrates in vitro for E. coli holo-ACP synthase. *Chem. Biol. 4*, 17–24.
(23) Belshaw, P. J., Walsh, C. T., and Stachelhaus, T. (1999) Aminoacyl-CoAs as probes of condensation domain selectivity in nonribosomal peptide synthesis. *Science 284*, 486-489.
(24) Sieber, S. A., Tao, J., Walsh, C. T., Marahiel, MA. (2004) Peptidyl thiophenols as substrates for nonribosomal peptide cyclases. *Angew. Chem., Int. Ed. 43*, 493–498.
(25) Mandel, A. L., La Clair, J. J., and Burkart, M. D. (2004) Modular synthesis of pantetheine and phosphopantetheine. *Org. Lett. 6*, 4801–4803.
(26) Mishra, P. K., and Drueckhammer, D. G. (2000) Coenzyme A Analogues and Derivatives: Synthesis and Applications as Mechanistic Probes of Coenzyme A Ester-Utilizing Enzymes. *Chem. Rev. 100*, 3283–3310.
(27) Weimer, B. C., Walsh, M. K., and Wang X. (2000) Influence of a poly-ethylene glycol spacer on antigen capture by immobilized antibodies. *J. Biochem. Biophys. Methods 45*, 211–219.

BC050213J

Controlled Recovery of the Transcription of Nanoparticle-Bound DNA by Intracellular Concentrations of Glutathione

Gang Han, Nandini S. Chari,[§] Ayush Verma, Rui Hong, Craig T. Martin, and Vincent M. Rotello*

Department of Chemistry, University of Massachusetts, Amherst, Massachusetts 01003. Received June 16, 2005

Positively charged trimethylammonium-functionalized mixed monolayer protected clusters (MMPCs) bind DNA through complementary electrostatic interactions, resulting in complete inhibition of DNA transcription of T7 RNA polymerase. DNA was released from the nanoparticle by intracellular concentrations of glutathione, resulting in efficient transcription. The restoration of RNA production was dose-dependent in terms of GSH, with considerable control of the release process possible through variation in monolayer structure. This work presents a new approach to controlled release of DNA, with potential applications in the creation of transfection vectors and gene regulation systems.

Synthetic DNA-binding scaffolds are of great interests in bioorganic (*1*, *2*), biomedical (*3*), and materials chemistry (*4*, *5)* owing to numerous applications as DNA sensors (*6*), transcription regulators (*7*), nonviral transfection vectors (*8*), and biomaterials (*9*). These receptors offer the opportunity to directly regulate and control cellular activity by inhibiting or promoting DNA transcription based on either intercalative, major/minor groove binding, or complementary electrostatic interaction (*7*). Additionally, such nonviral gene transfection vectors based on these synthetic DNA-binding scaffolds have been widely used owing to their facile production and the reduced risk of cytotoxicity and immune and inflammatory responses (*10*).

Controlled release of functional DNA is required for efficient regulation of DNA transcription. The temporal and spatial control of DNA and corresponding RNA products is critical to the modulation of gene expression and is a fundamental issue in designing anticancer drugs (*11*) and potential therapeutic materials. Although some synthetic systems such as cisplatin (*12*) and polyamides (*13*) have been designed to bind with DNA to block the recognition between DNA and transcription factor proteins, controlled transcription has not been extensively studied. Additionally, while photoinduced transcription recovery of caged oligonucleotides has been reported (*14*), the tunable transcription of DNA using intracellular components provides new directions for the design of bioactive systems.

In addition to regulation, tunability is also essential in designing synthetic gene delivery systems: the process of unpackaging of DNA is a complicated process and vectors must be stable in the extracellular environments and then selectively unpackaged for transcription (*15*). Although a series of DNA trigger release mechanisms have been explored, which include either external means (e.g. photochemical (*16*)) or through differential cellular environment (e.g. pH (*17*) or the level of enzyme (*18*)), new release mechanisms may provide a means for overcoming current hurdles in gene therapy (*19*).

* To whom correspondence should be addressed. E-mail: rotello@chem.umass.edu.

[§] Present address: Department of Chemistry and Biochemistry, University of Texas, Austin, TX 78712.

We reasoned a unique mechanism of release MMPC bound DNA would involve glutathione (GSH), a tripeptide which is involved in many important physiological functions, in particular the control of the redox environment in cells (*20*). The large concentration differential of intracellular glutathione (e.g. ~2 mM in erythrocytes (*21*)) compared to extracelluar level (e.g. 2 μM in red blood plasma (*22*)) provides a unique opportunity for mediation of DNA release. Additionally, the wide range of the intracellular levels of glutathione (from ~500 μM to 10 mM, e.g. 10 mM in liver cells (*23*)) provides a potential control over both in vitro and in vivo gene delivery applications.

Recently, we have demonstrated that cationically modified mixed monolayer protected gold clusters (MMPCs) interact electrostatically with DNA, providing an effective tool for gene delivery in mammalian cells (*24,* 25). MMPCs show much higher transfection efficiency than polyethyleneimine (PEI), a widely used synthetic transfection agent. One potential mechanism for unpackaging DNA from MMPCs in our system is GSH incorporation onto the particle surface (*26*). The cationic particles would lose their electrostatic affinity for the DNA backbone resulting in release of DNA. Previously, we have shown that GSH can release and reactivate the enzyme bound to MMPCs by place-exchange reaction (*27*). Here, we report that MMPC−DNA complexes are dissociated by GSH to release DNA (Figure 1). Further, we demonstrate that DNA transcription inhibited by DNA−MMPC complexes (*28*) is rescued by addition of reduced glutathione (GSH) at intracellular concentrations. The recovery of DNA transcription is found to be dependent on the chain length of the MMPC monolayer: enhanced recoveries of transcription were observed using a MMPC featuring a shorter chain length relative to MMPCs with a longer monolayer.

An ethidium bromide (EtBr) fluorescence assay was performed to investigate the release of DNA 37mer from the nanoparticles by GSH (*30*). At a ratio of MMPC:DNA of 4:1, EtBr was completely quenched, demonstrating complete complexation of the DNA by MMPC. GSH was then added into preincubated (5 min) DNA−MMPC solutions to give final concentrations corresponding to extracellular and intracellular GSH levels. The intensity

10.1021/bc050173j CCC: $30.25 © 2005 American Chemical Society
Published on Web 09/30/2005

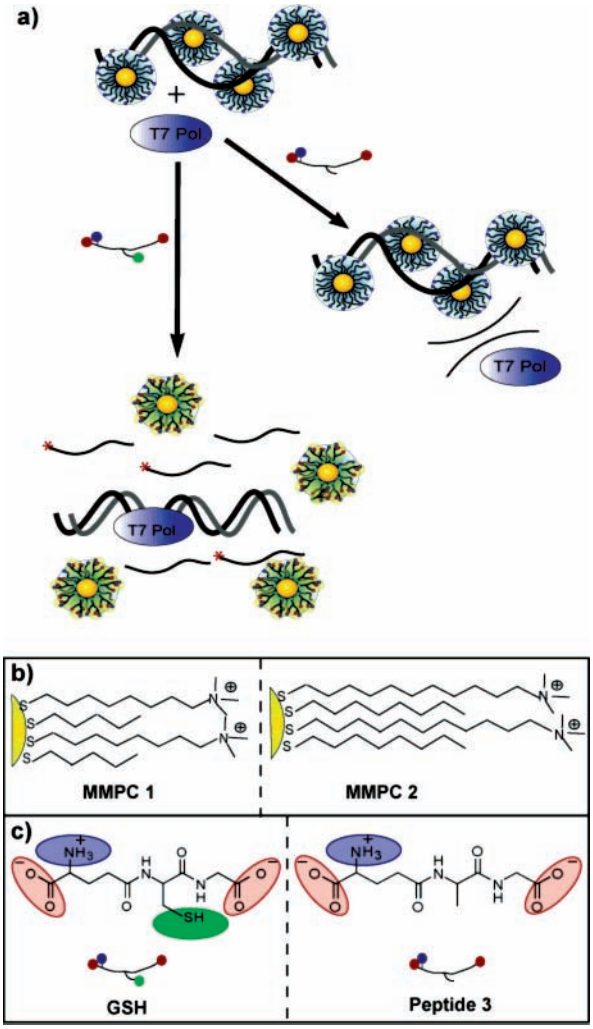

Figure 1. (a) Schematic representation of GSH-mediated reactivated of DNA transcription. (b) Structures of MMPC scaffolds. (c) Reduced glutathione and control peptide **3**.

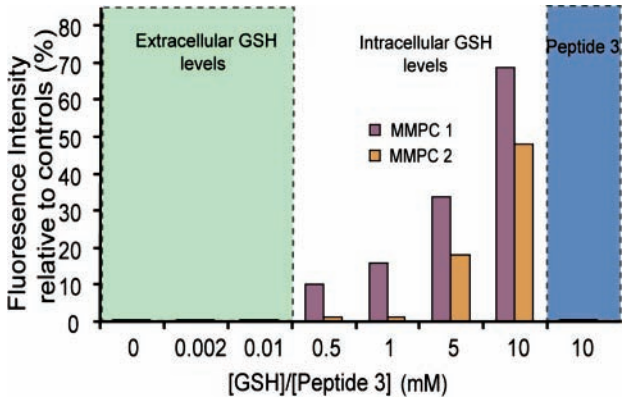

Figure 2. EtBr dye release obtained by addition of GSH and peptide **3** to MMPC/37mer DNA complexes followed by 1 h incubation at 37 °C. Normalized fluorescence intensities are relative to control experiments with corresponding concentrations of GSH or peptide **3** in absence of MMPCs (λ_{em} 595 nm).

of fluorescence was monitored after 1 h of incubation at 37 °C (Figure 2). No fluorescence recovery was observed at extracellular concentrations of GSH for both MMPCs. However, fluorescence for both MMPC **1** and **2** increased in a dose-dependent fashion with increasing GSH concentration. Significantly, enhanced fluorescence recovery was observed with the shorter chain MMPC **1** relative to MMPC **2**, consistent with the increased accessibility of the core of MMPC **1** with concomitantly faster place exchange (*29*). No fluorescence recovery was observed with peptide **3** (*30*), demonstrating that thiol−gold interaction is the operative mechanism for DNA release (*31*). Overall, these results indicate that the DNA−MMPC complexes are stable and intact in the extracellular GSH concentrations but are rapidly disrupted at intracellular GSH concentrations.

In our dye release studies we demonstrated that GSH has the ability to mediate unloading DNA from DNA−MMPC complexes. To determine the reversal of MMPC inhibition DNA transcription, premixed (5 min) DNA−MMPC (molar ratio DNA:MMPC = 1:4) solutions were incubated with different concentrations of GSH (from extracellular to intracellular levels) and peptide **3** for 1 h at 37 °C. The incubation was followed by addition of the T7 RNA polymerase (1:1 enzyme:DNA, 0.2 μM) and excess nucleotide triphosphates (including ^{32}P-labeled GTP for isotopic detection). The mixture was incubated for 5 min before being quenched with 15 mmol of EDTA in 95% formamide. The 20mer runoff RNA transcripts were quantified to determine the extent of reactions, with the transcription levels attained in the absence of MMPCs at corresponding GSH and peptide **3** concentrations set to 100% transcription (Figure 3b). No 20mer RNA transcripts were observed at extracellular concentrations of GSH for both of MMPCs. However, transcription was observed at intracellular GSH levels, reaching ~100% recovery for MMPC **1** and 83% recovery for MMPC **2** (10mM). A higher level of selectivity was also observed at intermediate GSH concentrations between MMPC **1** and **2** at typical intracellular concentrations (2−5 mM). Significantly higher levels of transcription recovery were observed relative to the fluorescence release experiments described above. In our previous studies it was shown that partially complexed DNA was efficiently transcribed; the present results are consistent with partial removal of MMPCs from the DNA strand. As expected, control experiments with peptide **3** resulted in a negligible DNA transcription level.

Our hypothesis for the glutathione-mediated release of DNA is that place exchange of the cationic residues of the nanoparticles with anionic GSH diminishes the overall positive charge of the particles. This decrease in charge would then be expected to reduce/or eliminate the affinity of the particles for DNA. This hypothesis was validated through zeta potential measurement (Figure 4). In these studies, MMPC **1** and **2** (0.8 μM) were incubated with 10 mM of GSH and peptide **3** separately for 1 h at 37 °C in PBS buffer (pH 7.8). Upon addition of GSH, the zeta potential of MMPC **1** decreased significantly from 26 ± 1 mV to 2 ± 4 mV. Interestingly, MMPC **2** showed a smaller but still significant decrease from 25 ± 2 mV to 17 ± 3 mV, indicating that the binding process is quite sensitive to particle charge. As expected, no significant change of the zeta potentials were observed with addition of peptide **3**. These data directly reflected the thiol-mediated incorporation of GSH onto gold surface, resulting in proportional positive charge attenuation of monolayer depending on the monolayer chain length.

Taken together, these results demonstrate the following processes: the original cationic MMPCs electrostatically bind the DNA with high affinity, forming supramolecular DNA−MMPC complexes that block the interaction between T7 polymerase and DNA. Anionic glutathione then place-exchanges onto the gold core, diminishing or eliminating the cationic charge of the MMPCs. An important aspect of this research is that recovery of transcription proceeds with greater efficacy than EtBr

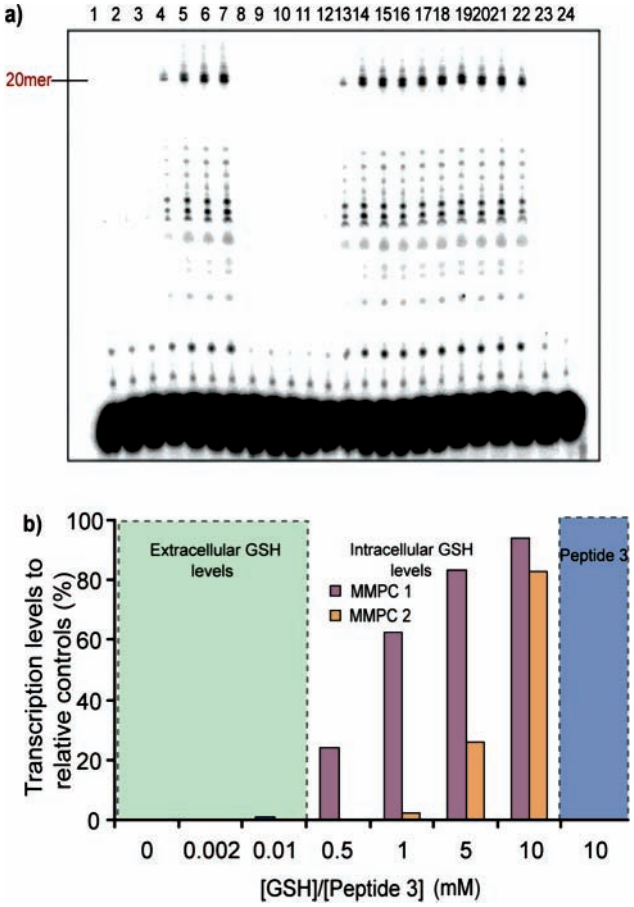

Figure 3. (a) Acrylamide gel electrophoresis of RNA products produced in the T7 RNA polymerase transcription assay. Lanes 1−7: Transcription recoveries in the presence of MMPC **1** by preincubation at 37 °C for 1 h with an increasing amount of GSH from extracellular concentrations (1) 0 μM, (2) 2 μM, (3) 10 μM to intracellular concentrations (4) 500 μM, (5) 1 mM, (6) 5 mM, and (7) 10 mM. Lanes 8−14: Transcription recoveries in the presence of MMPC **2** with (8) 0 μM, (9) 2 μM, (10) 10 μM, (11) 500 μM, (12) 1 mM, (13), 5 mM and (14) 10 mM GSH. Lanes 15−21: Control assays in absence of MMPCs with GSH (15) 0 μM, (16) 2 μM, (17)10 μM, (18) 500 μM, (19) 1 mM, (20) 5 mM, and (21) 10 mM. Lanes 22−24: Control assays with 10 mM peptide **3** and (22) no MMPCs, (23) MMPC **1**, (24) MMPC **2**. (b) The amount of 20mer runoff RNA detected relative to that produced in the absence of MMPCs at varying concentrations of GSH and peptide **3**.

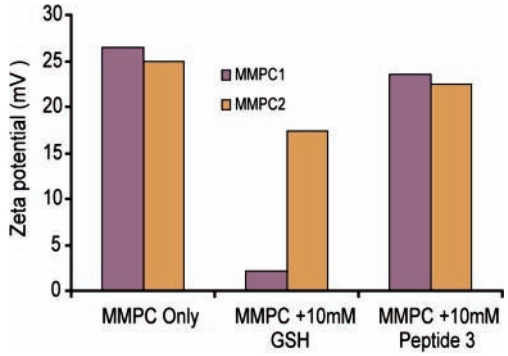

Figure 4. Zeta potential values of MMPCs upon addition of 10 mM GSH/peptide **3** followed by 1 h incubation at 37 °C.

release. The higher level of transcription recovery can be explained by the fact that transcription requires only the ability of the T7 RNA polymerase to anchor to the DNA. Once anchored, the polymerase can displace the nanoparticles from the DNA surface during the course of transcription. (Figure 5). In the case of EtBr displacement, however, there is a direct competition between the still partially cationic particles and the EtBr for DNA binding.

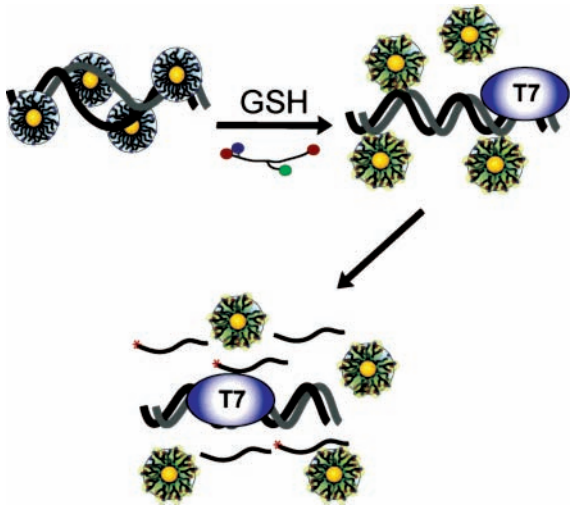

Figure 5. Proposed mechanism of GSH-triggered transcription recovery.

In summary, we have demonstrated glutathione-controlled DNA transcription. DNA−MMPC complexes are stable at extracellular GSH concentrations and labile at intracellular GSH levels, resulting in DNA release and transcription. The release of DNA and recoveries of DNA transcription can be tuned through the choice of monolayer coverage and intracellular GSH levels. This release mechanism provides potential strategies for the creation of MMPC-based DNA delivery vectors featuring new and unique properties.

ACKNOWLEDGMENT

Support for this research from the NIH (EB 004503 (VR) and GM55002 (C.T.M.)). We thank Prof. Jochen Weiss for assistance with zeta potential determination.

Supporting Information Available: Experimental details. This material is available free of charge via the Internet at http://pubs.acs.org.

LITERATURE CITED

(1) Cao, Y. W. C., Jin, R. C., and Mirkin, C. A. (2002) Nanoparticles with Raman spectroscopic fingerprints for DNA and RNA detection. *Science 297*, 1536−1540.

(2) Sissi, C., Rossi, P., Felluga, F., Formaggio, F., Palumbo, M., Tecilla, P., Toniolo, C., and Scrimin, P. (2001) Dinuclear Zn^{2+} complexes of synthetic heptapeptides as artificial nucleases. *J. Am. Chem. Soc. 123*, 3169−3170.

(3) Dervan, P. B. (2001) Molecular recognition of DNA by small molecules. *Bioorg. Med. Chem. 9*, 2215−2235.

(4) Seeman, N. C. (2003) DNA in a material world. *Nature 421*, 427−431.

(5) Verma, A., and Rotello, V. M. (2005) Surface recognition of biomacromolecules using nanoparticle receptors. *Chem. Commun*. 303−312.

(6) Nam, J. M., Stoeva, S. I., and Mirkin, C. A. (2004) Bio-barcode-based DNA detection with PCR-like sensitivity. *J. Am. Chem. Soc. 126*, 5932−5933.

(7) Gniazdowski, M., Denny, W. A., Nelson, S. M., and Czyz, M. (2003) Transcription factors as targets for DNA-interacting drugs. *Curr. Med. Chem. 10*, 909−924.

(8) Demeneix, B., Hassani, Z., and Behr, J. P. (2004) Towards multifunctional synthetic vectors. *Curr. Gene Ther. 4*, 445−455.

(9) Becerril, H. A., Stoltenberg, R. M., Wheeler, D. R., Davis, R. C., Harb, J. N., and Woolley, A. T. (2005) DNA-templated three-branched nanostructures for nanoelectronic devices. *J. Am. Chem. Soc. 127*, 2828−2829.
(10) Liu, Y. M., Wenning, L., Lynch, M., and Reineke, T. M. (2004) New poly(D-glucaramidoamine)s induce DNA nanoparticle formation and efficient gene delivery into mammalian cells. *J. Am. Chem. Soc. 126*, 7422−7423.
(11) Gershon, D. (1990) Human Gene-Therapy − Anticancer Trials Surprise Approval. *Nature 346*, 497−497.
(12) Ohndorf, U. M., Rould, M. A., He, Q., Pabo, C. O., and Lippard, S. J. (1999) Basis for recognition of cisplatin-modified DNA by high-mobility-group proteins. *Nature 399*, 708−712.
(13) Gottesfeld, J. M., and Barbas, C. F. (2003) RNA as a transcriptional activator. *Chem. Biol. 10*, 584−585.
(14) Krock, L., and Heckel, A. (2005) Photoinduced transcription by using temporarily mismatched caged oligonucleotides. *Angew. Chem., Int. Ed. 44*, 471−473.
(15) Wiethoff, C. M., and Middaugh, C. R. (2003) Barriers to nonviral gene delivery. *J. Pharm. Sci. 92*, 203-217.
(16) Nagasaki, T., Taniguchi, A., and Tamagaki, S. (2003) Photoenhancement of transfection efficiency using novel cationic lipids having a photocleavable spacer. *Bioconjugate Chem. 14*, 513−516.
(17) Venugopalan, P., Jain, S., Sankar, S., Singh, P., Rawat, A., and Vyas, S. P. (2002) pH-Sensitive liposomes: mechanism of triggered release to drug and gene delivery prospects. *Pharmazie. 57*, 659−671.
(18) Gopin, A., Rader, C., and Shabat, D. (2004) New chemical adaptor unit designed to release a drug from a tumor targeting device by enzymatic triggering. *Bioorg. Med. Chem. 12*, 1853−1858.
(19) Luo, D., and Saltzman, W. M. (2000) Enhancement of transfection by physical concentration of DNA at the cell surface. *Nat. Biotechnol. 18*, 893−895.
(20) Meister, A.; Anderson, M. E. *Annu. Rev. Biochem.* **1983**, *52*, 711−760.
(21) Hassan, S. S. M., and Rechnitz, G. A. (1982) Determination Of Glutathione And Glutathione-Reductase With A Silver Sulfide Membrane-Electrode. *Anal. Chem. 54*, 1972−1976.
(22) Jones, D. P., Carlson, J. L., Samiec, P. S., Sternberg, P., Mody, V. C., Reed, R. L., and Brown, L. A. S. (1998) Glutathione measurement in human plasma Evaluation of sample collection, storage and derivatization conditions for analysis of dansyl derivatives by HPLC. *Clin. Chim. Acta 275*, 175−184.
(23) Anderson, M. E. (1998) Glutathione: an overview of biosynthesis and modulation. *Chem.-Biol. Interact. 112*, 1−14.
(24) Sandhu, K. K., McIntosh, C. M., Simard, J. M., Smith, S. W., and Rotello, V. M. (2002) Gold nanoparticle-mediated Transfection of mammalian cells. *Bioconjugate Chem. 13*, 3−6.
(25) Goodman, C. M., McCusker, C. D., Yilmaz, T., and Rotello, V. M. (2004) Toxicity of gold nanoparticles functionalized with cationic and anionic side chains. *Bioconjugate Chem. 15*, 897−900.
(26) Schaaff, T. G., Knight, G., Shafigullin, M. N., Borkman, R. F., and Whetten, R. L. (1998) Isolation and selected properties of a 10.4 kDa Gold: Glutathione cluster compound. *J. Phys. Chem. B. 102*, 10643−10646.
(27) Verma, A., Simard, J. M., Worrall, J. W. E., and Rotello, V. M. (2004) Tunable reactivation of nanoparticle-inhibited beta-galactosidase by glutathione at intracellular concentrations. *J. Am. Chem. Soc. 126*, 13987−13991.
(28) McIntosh, C. M., Esposito, E. A., Boal, A. K., Simard, J. M., Martin, C. T., and Rotello, V. M. (2001) Inhibition of DNA transcription using cationic mixed monolayer protected gold clusters. *J. Am. Chem. Soc. 123*, 7626−7629.
(29) Ingram, R. S., Hostetler, M. J., and Murray, R. W. (1997) Poly-hetero-omega-functionalized alkanethiolate-stabilized gold cluster compounds. *J. Am. Chem. Soc. 119*, 9175−9178.
(30) Kwon, D. S., Lin, C. H., Chen, S. J., Coward, J. K., Walsh, C. T., and Bollinger, J. M. (1997) Dissection of glutathionylspermidine synthetase/amidase from *Escherichia coli* into autonomously folding and functional synthetase and amidase domains. *J. Biol. Chem. 272*, 2429−2436.
(31) Wang, Z. X., Kanaras, A. G., Bates, A. D., Cosstick, R., and Brust, M. (2004) Enzymatic DNA processing on gold nanoparticles. *J. Mater. Chem. 14*, 578−580.

BC050173J

ARTICLES

A Hydrophilic Azobenzene-Bearing Amino Acid for Photochemical Control of a Restriction Enzyme *Bam*HI

Koji Nakayama, Masayuki Endo, and Tetsuro Majima*

The Institute of Scientific and Industrial Research, Osaka University, 8-1 Mihogaoka, Ibaraki, Osaka 567-0047, Japan. Received November 15, 2004; Revised Manuscript Received August 12, 2005

A novel hydrophilic and negatively charged azobenzene-bearing amino acid, 4′-carboxyphenylazophenylalanine (azoAla **1**), has been designed and synthesized for investigation of the photochemical regulation of the enzyme activity. The properties of photoisomerization and thermal stability of the cis-isomer were similar to those of a commonly used phenylazophenylalanine (azoAla **2**). For photochemical control of the enzyme, these two azobenzene-bearing amino acids were incorporated into the specific position at the dimer interface of a restriction enzyme *Bam*HI. These *trans*-azobenzene derivatives in the *Bam*HI suppressed the enzymatic activity, and the following photoirradiation at 366 nm induced the recovery of its activity. Although the activities of both azoAla-*Bam*HI mutants were same level after a long time irradiation, the recovery of the activity of azoAla **1**-*Bam*HI was faster than that of azoAla **2**-*Bam*HI with a short time irradiation. This result suggests that the negatively charged carboxylate group introduced into an azobenzene moiety affects the behavior of azoAla in the protein scaffold during the trans−cis photoisomerization.

INTRODUCTION

The artificial and selective activation of an enzyme is one of the most important issues for the investigation of the specific biological phenomena in living cells. Caged compounds such as *o*-nitrobenzyl derivatives are widely used for regulation of the enzymatic activity by introduction of these compounds into an enzyme, which are then uncaged with photoirradiation for activation (*1*−*7*). These caged molecules unavoidably release the reactive nitroso derivatives after photoirradiation, which may cause a negative side-effect in the cells. In contrast, photochromic molecules, which change their conformations by photoirradiation, do not produce a side-product (*8*−*15*). When a photochromic moiety is incorporated into polymers and biomolecules, the mechanical movement of the photochromic molecules by irradiation at specific wavelengths can induce structural changes, which produces novel physical and biochemical properties (*8*−*15*). From this point of view, the use of photochromic molecules is a better choice for control of the activity of enzymes and the subsequent expression of biological phenomena.

The most commonly used and reliable photochemical switches for the functionalization of polymers and biomolecules are azobenzene derivatives, which have excellent features; i.e., the simplest chemical structure, rapid photoisomerization in both the trans−cis directions, a large structural motion, and a thermally stable cis isomer (*16*, *17*). However, for incorporation of phenylazophenylalanine into the proteins and enzymes, the hydrophobic property of the azobenzene moiety may cause the exclusion of water in the solvent-accessible surface of the proteins, which may result in a negative effect such as an unexpected missfolding of the proteins around the incorporated sites. One of the simplest solutions for water-accessibility is the introduction of a hydrophilic property into an azobenzene derivative.

In this report, we synthesized a negatively charged 4′-carboxyphenylazophenylalanine moiety and incorporated it into the dimer interface of a restriction enzyme *Bam*HI. In the previous study, we controlled the activity of *Bam*HI, which is activated through the dimer formation (*18*−*21*), by arranging the specific amino acids involved in the dimer interface by introducing the photoremovable *o*-nitroveratryl groups (*22*). At this dimer interface, side chains of four amino acids, K132, H133, E167, and E170, consist of a salt bridge network to maintain the conformation of the *Bam*HI dimer in the active form (Figure 1) (*18*−*21*). Especially, K132 in the dimer interface is the key position for the activity, since the K132 on the α-helix faces two glutamate side chains (E167 and E170) on the counterpart α-helix. We previously discovered that phenylazophenylalanine (azoAla **2**) incorporated into the 132 position can regulate the activity of *Bam*HI (*23*). For further investigation of relationship between the photochemical switching of azobenzene derivative and the expression of the enzymatic activity, we introduced a negatively charged 4′-carboxyphenylazophenylalanine (azoAla **1**) into the 132 position for changing the solvent-accessibility in the surface of *Bam*HI. We examined whether the negative charge affects the behavior of the azobenzene moiety during the trans−cis photoisomerization in the dimer interface, which may accompany local structural change around the azoAla residue for effective inactivation and photochemical activation of *Bam*HI.

* Corresponding author: majima@sanken.osaka-u.ac.jp; Phone: +81-6-6879-8495; Fax: +81-6-6879-8499.

10.1021/bc049724g CCC: $30.25 © 2005 American Chemical Society
Published on Web 09/14/2005

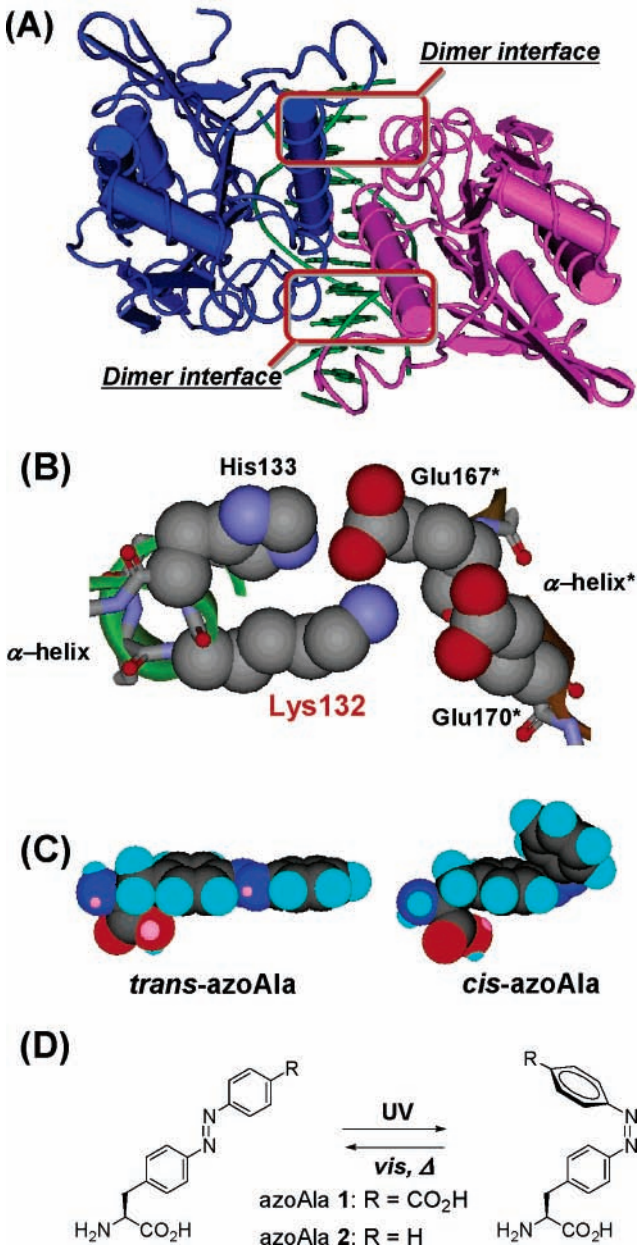

Figure 1. *Bam*HI dimer structures. (A) Side view of the *Bam*HI dimer−DNA complex (PDB 1BHM). (B) The detailed interaction of the amino acid side chains at the dimer interface. K132 and H133 are located on the same α-helix, and E167* and E170* are on the counterpart α-helix*. The asterisks represent the counterpart *Bam*HI monomer. (C) Minimized structure of the trans and cis form of azoAla **2**. (D) Photofunctionalized amino acid phenylazophenylalanine derivatives (azoAla **1** and **2**) employed in this experiment.

EXPERIMENTAL PROCEDURES

Materials. The reagents used in the experiment were purchased from the following companies: 4-nitrobenzoic acid methyl ester, N^{α}-*tert*-butoxycarbonyl-4-nitro-L-phenylalanine, *tert*-butyl hypochlorite, chloroacetonitrile, Wako Chemicals (Osaka, Japan); 4-nitrobenzoic acid methyl ester, Tokyo Kasei (Tokyo, Japan); restriction endonucleases, New England BioLabs (Beverly, MA); pET26b, Novagen (Madison, WI); *Pfu* DNA polymerase, Stratagene (LaJolla, CA); nucleoside triphosphates and L-[^{35}S]-methionine, Amersham Pharmacia Biotech (Piscataway, NJ); T4 RNA ligase, Takara Shuzo (Kyoto, Japan); T4 DNA ligase, T7 RNA polymerase, and RNase inhibitor, Toyobo (Osaka, Japan); RNeasy Project Mini Kit, Qiagen (Hilden, Germany); *E. coli* S30 Extract System, Promega (Madison, WI). Purification of the nucleotide derivatives was performed using a JASCO LC-2000Plus series HPLC system (Tokyo, Japan). Photoirradiation was carried out using an ultrahigh-pressure mercury lamp (Ushio USH-500D; 500 W) equipped with a monochromator (Ritsuoyo Kogaku MC-10N) which can control the specific wavelength within a 4 nm full-width at half-maximum. Visualization and quantification of the gels were performed using a Fujix BAS1000 imaging analyzer (Tokyo, Japan).

4-Nitrobenzoic Acid *tert*-Butyl Ester (3). *n*-Butyllithium (0.10 mol, 65 mL of 1.58 M hexane solution) was slowly added to a mixture of the 4-nitrobenzoic acid methyl ester (9.05 g, 50 mmol) and distilled *tert*-butyl alcohol (9.5 mL, 0.10 mol) in anhydrous THF (30 mL) at 0 °C under an argon atmosphere (*24*). The reaction mixture was warmed to room temperature and stirred at room temperature. After 18 h, diethyl ether (200 mL) and a saturated ammonium chloride aqueous solution (200 mL) were added to the mixture, and the organic layer was extracted and washed twice with a saturated sodium chloride aqueous solution and dried over anhydrous sodium sulfate. The resulting brown solid was purified by silica gel chromatography with toluene/hexane (1:1) to give compound **3** (3.48 g, 31%) as a yellow solid; ^{1}H NMR [270 MHz, $CDCl_3$ (TMS)]: δ 8.15 (d, 2H, J = 8.1 Hz), 7.96 (d, 2H, J = 8.1 Hz), 1.63 (s, 9H).

***tert*-Butyl 4-Hydroxylaminebenzoate (4).** Zinc powder (90%, 205 mg, 3.2 mmol) was slowly added to a mixture of **3** (352 mg, 1.6 mmol) and ammonium chloride (84.4 mg, 1.6 mmol) in MeOH/water (10:1, 20 mL) over a period of 5 min (*25*). The reaction mixture was stirred at room temperature for 3 h under an argon atmosphere. The insoluble precipitate was removed by filtration, and the filtrate was dried under reduced pressure. The resulting orange solid was diluted with methylene chloride (200 mL) and a saturated aqueous sodium bicarbonate solution, and the organic layer was washed twice with saturated aqueous sodium chloride. The organic layer was dried over anhydrous sodium sulfate, and the solvent was removed under reduced pressure. The orange solid was purified by silica gel chromatography with CH_2Cl_2/MeOH (100:2) to give compound **4** (220 mg, 67%) as a yellow solid. ^{1}H NMR [270 MHz, $CDCl_3$ (TMS)]: δ7.91 (d, 2H, J = 8.6 Hz), 6.97 (d, 2H, J = 8.6 Hz), 5.21 (s, 1H), 1.63 (s, 1H), 1.58 (s, 9H).

4-*tert*-Butoxycarbonyl-N^{α}-Boc-phenylazophenylalanine (5). *tert*-Butyl hypochlorite (114 mg, 1.05 mmol) was added to a solution of **4** (220 mg, 1.05 mmol) in THF (5 mL) at −78 °C (*26*). The reaction mixture was stirred under argon at −78 °C for 10 min and then allowed to react at −20 °C for 1 h. The reaction proceeded more than 90% based on TLC monitoring. The solvent was removed under reduced pressure at 10 °C, and the brown solid was dried under reduced pressure. The crude product was dissolved in 10 mL of 10% AcOH/MeOH. This solution was added to a 10% AcOH/MeOH solution (10 mL) of N^{α}-Boc-4-aminophenylalanine (263 mg, 0.94 mmol) under argon at 0 °C. The reaction mixture was allowed to react at room temperature for 2 h. After removal of the solvent under reduce pressure, the brown solid was dissolved in CH_2Cl_2 (200 mL), and then a saturated aqueous sodium bicarbonate solution was added. The organic layer was washed twice with a saturated aqueous sodium chloride solution and then dried over anhydrous sodium sulfate. The resulting orange solid was purified by silica gel column chromatography with CH_2Cl_2/MeOH (100:8) to give compound **5** (335 mg, 76%) as an orange solid. ^{1}H

NMR [270 MHz, $CDCl_3$(TMS)]: δ 8.15 (d, 2H, J = 8.1 Hz), 7.88, (dd, 4H, J = 8.1 Hz), 7.35 (d, 2H, J = 8.1 Hz), 5.04 (s, 1H), 4.64 (s, 1H), 3.22 (m, 2H), 1.62 (s, 9H), 1.41 (s, 9H).

4-*tert*-Butoxycarbonyl-N^{α}-Boc-phenylazophenylalanine Cyanomethyl Ester (6). Chloroacetonitrile (24 mg, 0.32 mmol) was added to a mixture of compound **5** (77 mg, 0.16 mmol) and triethylamine (24 mg, 0.24 mmol) in dry acetonitrile (20 mL). The reaction mixture was stirred at room temperature for 12 h under argon. After removal of the solvent under reduced pressure, the product was purified by silica gel column chromatography with CH_2Cl_2/MeOH (100:2) to give compound **6** (46 mg, 57%) as an orange solid. ^{1}H NMR [$CDCl_3$ (TMS)]: δ 8.13 (d, 2H, J = 8.1 Hz), 7.91, (dd, 4H, J = 8.1 Hz), 7.33 (d, 2H, J = 8.1 Hz), 5.00 (d, 2H, J = 7.8 Hz), 4.77 (dd, 2H, J = 15.8 Hz), 4.71 (s, 1H), 3.21 (m, 2H), 1.63 (s, 9H), 1.43 (s, 9H). FAB-MS (positive), *m/z* calcd for $C_{27}H_{33}N_4O_6$ 509.2 $[M+H]^+$, found 509.0.

4-*tert*-Butoxycarbonyl-N^{α}-Boc-phenylazophenylalanyl pdCpA (7). Compound **6** (1.25 μmol) was added to a dry DMF solution of pdCpA tetra-*n*-butylammonium salt (*27*) (20 μL, 0.25 μmol) in a microtube. The reaction mixture was incubated at room temperature for 3 h, and the reaction was monitored by a reversed-phase HPLC [linear gradient; 0−80% acetonitrile−50 mM ammonium acetate buffer (pH 4.8) over 30 min, flow rate 2 mL/min, Chemcobond C18 column (7.5 × 150 mm), detection at 260 nm]. After the reaction, the mixture was diluted with 50 mM ammonium acetate solution (pH 4.5, 1 mL), and the product was purified by HPLC. The retention time of compound **7** was 22.8 min. The product was concentrated under reduced pressure and then lyophilized. 67% yield. ESI-MS (negative), *m/z* calcd for $C_{40}H_{46}N_{11}O_{18}P_2$ 1030.3 $[M - H]^-$, found 1030.5.

Preparation of 4′-Carboxyphenylazophenylalanyl-tRNA$_{CCCG}$ (azoAla 1-tRNA$_{CCCG}$). Deprotection of compound **7** was performed in trifluoroacetic acid (20 μL) on ice for 10 min, and then the trifluoroacetic acid was removed by flowing nitrogen gas. The pellet was washed twice with ether and then dried under reduced pressure. The pellet was dissolved in DMSO to make a 0.5 mM solution and stored at −20 °C. The tRNA$_{CCCG}$ (-CA) was obtained according to a previous method (*22*, *23*). Ligation of aminoacyl-pdCpA to tRNA$_{CCCG}$(-CA) was carried out in a 20 μL solution containing 5 μg of tRNA$_{CCCG}$(-CA), 0.5 mM aminoacyl-pdCpA, 50 mM Tris-HCl (pH 7.5), 10 mM $MgCl_2$, 10 mM DTT, 1 mM ATP, 0.01% BSA, 10% DMSO, and T4 RNA ligase (40 units). The reaction mixture was incubated at 4 °C for 2 h, and then the reaction was quenched by the addition of 2 μL of sodium acetate (3 M, pH 5.2). The aminoacyl-tRNA$_{CCCG}$ was precipitated with ethanol, rinsed with 70% ethanol, and dried under reduced pressure. The aminoacyl-tRNA$_{CCCG}$ was dissolved in RNase-free water to a final concentration of 1 μg/μL.

In Vitro Translation of Wild-Type and azoAla-*Bam*HI. Preparation of a plasmid containing the *Bam*HI gene and its mutant was performed according to a previous method (*22*). The preparation of mRNA was carried out in a solution (50 μL) containing the template DNA (5 μg), T7 RNA polymease (147 units), RNase inhibitor (40 units), 2.5 mM NTP, 40 mM Tris-HCl (pH 7.5), 20 mM $MgCl_2$, and 5 mM DTT at 37 °C for 6 h, and then the mRNA was purified using an RNeasy Protect Mini Kit (Qiagen). The *E. coli* S30 Extract System (Promega) was employed for the in vitro protein synthesis following the reported method (*28*, *29*). The translation reaction was carried out in a 10 μL of reaction mixture containing mRNA (2 μg), aminoacyl-tRNA$_{CCCG}$ (1 μg), 0.10 mM amino acid mixture (lacking methionine and arginine), a 0.01 mM arginine, premix (4 μL), *E. coli* S30 extract (3 μL), and L-[^{35}S]-methionine (3 μCi) at 30 °C for 2 h. The wild-type *Bam*HI was prepared by the same method without aminoacyl-tRNA$_{CCCG}$. The reaction was quenched by the addition of a mixture containing 50 mM Tris-HCl (pH 6.8), 0.1 M DTT, 2% SDS, and 10% glycerol and loaded onto an 15% SDS-polyacrylamide gel for electrophoresis. The SDS−PAGE gels were visualized and quantified using an imaging analyzer. For the cold samples, the same procedure described above was employed by just replacing the [^{35}S]-methionine with 0.1 mM methionine, and the concentration was quantified by Western blotting using a hexahistidine antibody as the primary antibody. The generation of the full-length proteins was about 10 ng from a 10 μL scale synthesis of the in vitro translation system.

Photoirradiation to Phenylazophenylalanine Derivatives. The phenylazophenylalanine derivatives (azoAla) **1** and **2** were prepared by treatment of the N^{α}-Boc-phenylazophenylalanine and compound **5** with TFA, respectively. After removal of TFA under reduced pressure, the deprotected azoAla **1** and **2** were dissolved in DMSO. Photoirradiation was carried out using a 500 W ultrahigh-pressure mercury lamp equipped with a monochromator. Samples (1 mL) containing azoAla **1** or **2** (0.01 mM), 10 mM Tris-HCl (pH 8.0), and 10% DMSO were placed in a quartz cell with a 1 cm path length.

Photoirradiation and Measurements of the *Bam*HI Activities. Photoirradiation was carried out using the same instrument as described above. The trans to cis photoisomerization was carried out using the translation mixture prepared above by irradiation with 366 nm light on ice for 10 min. The translation mixtures (0.25 μL) before or after the photoirradiation were diluted by a reaction buffer containing 10 mM Tris-HCl (pH 8.0), 10 mM $MgCl_2$, 100 mM NaCl, 0.01% BSA, and 1 mM DTT, and then linearized pBR322 (6 nM) digested by *Nde*I was added. The reaction mixtures were incubated at 30 °C for 1 h. The reaction mixtures were loaded onto a 1.2% agarose gel in TBE buffer. The gels were visualized by ethidium bromide staining and quantified by the ImageJ program (NIH).

RESULTS AND DISCUSSION

Synthesis of 4′-Carboxyphenylazophenylalanine. The synthesis of the active ester of 4′-carboxyphenylazophenylalanine (azoAla **1**) was carried out according to Scheme 1. The transesterification of the 4-nitrobenzoic acid methyl ester to the *tert*-butyl ester was carried out by reaction with *n*-butyllithium and *tert*-butyl alcohol to give **3** (*24*). The reduction of the nitro group of **3** was carried out using Zn in ammonium hydroxide to produce **4** (*25*). For production of the azo group, compound **4** was oxidized to *tert*-butyl nitrosobenzoate using *tert*-butyl hypochlorite in THF at −20 °C (*26*), and the crude product was then coupled with N^{α}-Boc-4-aminophenylalanine in 10% AcOH/MeOH solution to yield **5**. The esterification of compound **5** with chloroacetonitrile gave the 4′-*tert*-butoxycarbonyl-N^{α}-Boc-phenylazophenylalanine cyanomethyl ester **6**. The active ester **6** was coupled with a nucleoside dimer 5′-phospho-2′-deoxycytidylyl-(3′-5′)-adenosine (pdCpA) tetrabutylammonium salt at room temperature for 3 h to give aminoacyl-pdCpA **7**.

Photochemical Properties of Phenylazophenylalanine Derivatives. To characterize the photochemical behaviors of the azoAla **1** and azoAla **2** monomers, the

Scheme 1[a]

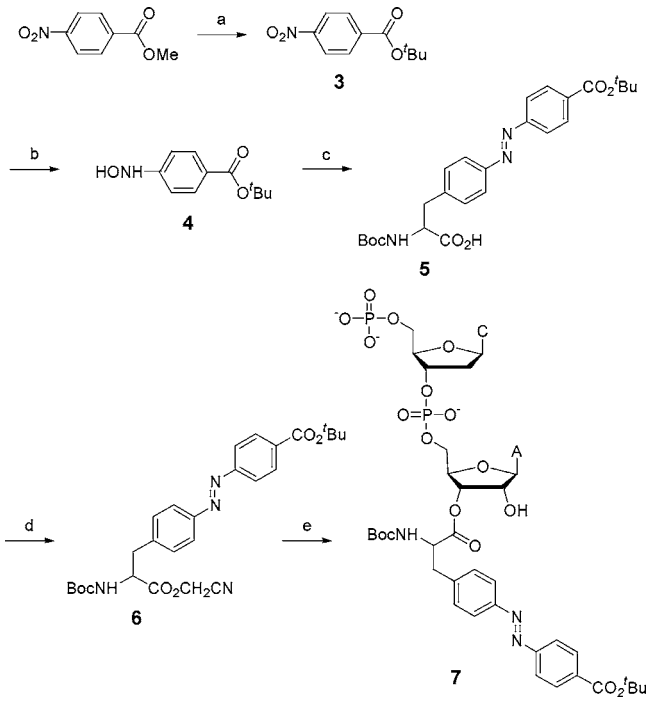

[a] Reagents and conditions: (a) *tert*-BuOH, *tert*-BuLi, THF, rt; (b) Zn, NH_4OH, MeOH, H_2O, rt; (c) i. *tert*-BuOCl, THF, −20 °C, ii. N^{α}-Boc-4-aminophenylalanine, AcOH, MeOH, rt; (d) chloroacetonitrile, CH_3CN, Et_3N, rt; (e) pdCpA tetra-*n*-butylammonium salt, DMF, rt.

absorption changes by photoirradiation were examined. 4′-*tert*-Butoxycarbonyl-N^{α}-Boc-azoAla **1** (compound **5**) and N^{α}-Boc-azoAla **2** were treated with TFA for deprotection. Due to the introduction of carboxylate to the 4′-position, azoAla **1** was solubilized in water at neutral pH, while azoAla **2** needed at least 10% DMSO for solubilization in water. The azoAla derivatives (0.01 mM) were dissolved in 10% DMSO and 10 mM Tris-HCl buffer (pH 8.0), and photoirradiation was carried out at 25 °C using a high-pressure mercury lamp equipped with a monochromator. Photoisomerization was monitored by a UV/vis spectrometer. The spectrum of the untreated azoAla **1** showed two major peaks at 242 and 334 nm, which are identified as the characteristic $\pi-\pi^*$, and at 432 nm as the characteristic $n-\pi^*$ absorption band of the trans isomer of the azobenzene derivatives, respectively (Figure 2A) (*16*, *17*).

By photoirradiation to azoAla **1** at 366 nm, the peak at 334 nm rapidly decreased and largely shifted to 310 nm, while the peak at 432 nm increased and shifted to 429 nm (Figure 2A). The reaction were completed within 20 min. When irradiation to this product (*cis*-azoAla **1**) was carried out using 436 nm light, the increasing peak at 310 nm shifted to 334 nm and the decreasing one at 429 nm shifted to 432 nm (Figure 2B). This behavior is also characteristic of the cis to trans isomerization of the azobenzene derivatives, indicating that the reversible trans−cis photoisomerization of azoAla **1** occurred under this condition. In the case of azoAla **2**, a similar photoisomerization was observed by the photoirradiation. The ratios of the cis isomers of azoAla **1** and **2** after the 20 min irradiation at 366 nm were 81% and 79% under this condition (quantified by HPLC), respectively.

The half-lives for the trans to cis and cis to trans isomerizations of the azoAla **1** and azoAla **2** monomers are summarized in Table 1. They show similar values, indicating that the substitution of the 4′-position by a carboxylate does not change the basic behavior of the photoisomerization as compared to the normally used azoAla **2**. *cis*-azoAla **1** showed a good thermal stability at 30 °C ($\tau_{1/2} = 27$ h) as similar to the *cis*-azoAla **2** ($\tau_{1/2} = 35$ h), meaning that most of the cis isomer is retained under the reaction conditions of the *Bam*HI with a DNA substrate (30 °C, 1 h) when these azoAla derivatives were incorporated into the enzyme. The photochemical properties of these azoAla derivatives indicate that these have substantial potentials for photochemical switches in the protein.

Preparation of Phenylazophenylalanyl-*Bam*HI. The incorporation of the modified amino acids was performed using a four-base codon−anticodon method according to a previously reported method (*28*, *29*). The protected azoAla **1**-pdCpA and azoAla **2**-pdCpA were treated with TFA followed by ligation onto a $tRNA_{CCCG}$-(-CA) using T4 RNA ligase to give azoAla **1**-$tRNA_{CCCG}$ and azoAla **2**-$tRNA_{CCCG}$.

The azoAla derivatives were incorporated into the specific positions of *Bam*HI. The introduction of the modified amino acids into the specific positions of *Bam*HI was carried out by employing the cell-free translation system with the mutant mRNA containing a four base codon and the synthesized aminoacyl-$tRNA_{CCCG}$. In vitro translation was carried out in a mixture containing the mutant mRNA, unnatural aminoacyl-$tRNA_{CCCG}$, *E. coli* S30 extract, and amino acid with [^{35}S]-methionine at 30 °C for 2 h. After the reaction, the mixtures were loaded onto a 18% SDS−PAGE, and the gel was visualized using an imaging analyzer (Figure 3). Wild-type *Bam*HI was expressed as a full-length form at 27 kDa (lane 1). For the translation with the mutant mRNA containing a four-base codon mutation, an incomplete length of *Bam*HI was observed in the absence of aminoacyl-$tRNA_{CCCG}$ (lane 2). In contrast, the full-length *Bam*HI was obtained in the presence of the specific aminoacyl-$tRNA_{CCCG}$ (lanes 3 and 4). The efficiencies of incorporation of azo-Ala **1** and azo-Ala **2** at position 132 were 40% and 36% quantified by the radioactivity of [^{35}S]-methionine, respectively. The incorporation efficiencies for both azoAla derivatives were similar, indicating that the steric hindrance and negative charge of the carboxyl group in the 4′-position did not affect the protein synthesis using this cell-free translation system. We employed these azoAla-*Bam*HI mutants for the investigation of the photochemical control of the enzymatic activities without further purification.

Photochemical Control of the Activity of Phenylazophenylalanine-Bearing *Bam*HI Mutants. To examine the properties of the azoAla functionalized *Bam*HI mutants, photoirradiation was performed at 0 °C for 10 min using a high-pressure mercury lamp (500 W) equipped with a monochromator for generating the 366 nm light. The photoirradiated enzymes were incubated with a substrate DNA to examine the activity. As shown in Figure 4, both azoAla **1** and azoAla **2** mutants suppressed the activities after the preparation of the protein without irradiation (lanes 3 and 5, respectively). In addition, the intrinsic activities were recovered (both 44% substrate cleaved) in the azoAla **1** and **2** mutants after photoirradiation (lanes 4 and 6, respectively). This sequence selectivity was similar to that of the wild-type *Bam*HI (lane 2). The results show that the activities of the azoAla **1** and azoAla **2** mutants can be regulated through the photoisomerization of the azobenzene moiety.

In the previous study, we identified that the key amino acid regulating the *Bam*HI activity is the K132 residue using the protection and deprotection of the ϵ-amino group with a photoremovable group (*22*). The result

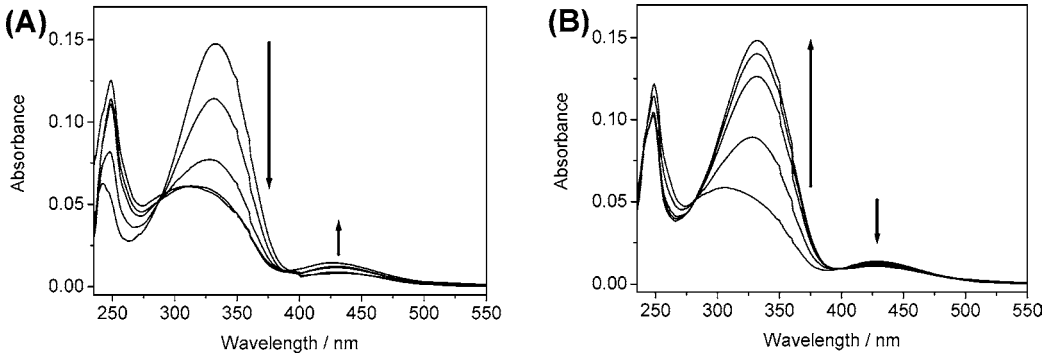

Figure 2. Absorption spectral changes of azoAla **1** with photoirradiation at 25 °C in pH 8.0 solution (water/DMSO = 9/1 v/v). (A) Trans to cis photoisomerization was carried out using 366 nm light for 0, 2, 5, 10, and 20 min. (B) Cis to trans isomerization was carried out. After the 20 min irradiation at 366 nm, the cis to trans photoisomerization was performed using 436 nm light for 0, 2, 5, 10, and 20 min.

Table 1. Photochemical Properties of Azobenzene Derivatives. Half-lives (min) of the Azobenzene Derivatives 1 and 2 at pH 8.0[a]

	photoisomerzation		thermal isomerization
azobenzene derivatives	trans to cis (366 nm)	cis to trans (436 nm)	cis to trans (30 °C)
1	5.5	11.3	1.6×10^3
2	5.8	7.3	2.1×10^3

[a] Detailed experimental conditions are described in the Experimental Section.

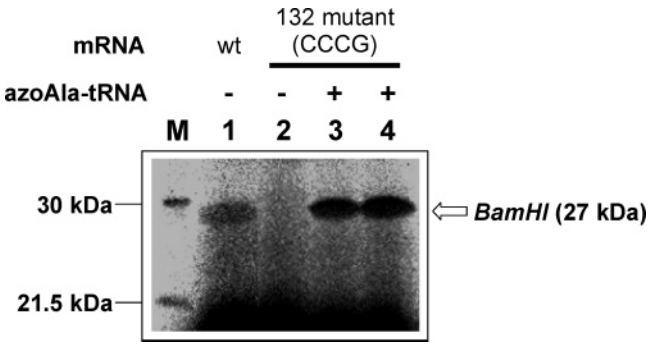

Figure 3. In vitro translation of azoAla-*Bam*HI mutants labeled with [^{35}S]-methionine. Lane 1, wild-type *Bam*HI; lane 2, translation with K132 mutant mRNA in the absence of aminoacyl-tRNA$_{CCCG}$; lane 3, translation with K132 mutant mRNA in the presence of azoAla **1**-tRNA$_{CCCG}$; lane 4, translation with K132 mutant mRNA in the presence of azoAla **2**-tRNA$_{CCCG}$.

obtained in this experiment indicates that both trans isomers of azoAlas **1** and **2** would induce a local structural change of the dimer interface to the inactive form. The *Bam*HI mutant having an *o*-nitroveratry group at the K132 position employed in the previous study showed activity, suggesting that the flexible *n*-butyl side chain of lysine would be excluded to outside of the dimer interface (*22*). The activities of azobenzene-bearing mutants after photoirradiation (366 nm, 10 min) were evaluated by kinetic parameters according to the previously reported method (*30*). Using the pBR322 restriction fragment as a substrate, kinetic parameters were obtained and summarized in Table 2. Although the *cis*-azoAla-*Bam*HI mutants showed lower activity than the wild-type, these mutants preserved the same level of the affinity and activity as compared to the H133A *Bam*HI mutant (*22*).

We tried the cis to trans photoisomerization using the cis forms of both azoAla-*Bam*HI mutants which were generated by irradiation with 366 nm light for 20 min. When these *cis*-azoAla-*Bam*HI mutants were irradiated

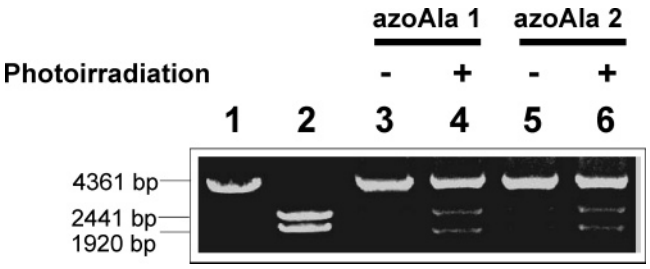

Figure 4. Cleavage of a substrate DNA (pBR322 digested by *Nde*I) with wild-type and photofunctionalized *Bam*HI mutants before and after photoirradiation at 366 nm. Lane 1, substrate DNA (4361 bp); lane 2, DNA fragments (1920 and 2441 bp) cleaved by wild-type *Bam*HI (New England BioLabs); lanes 3 and 4, DNA cleavage with azoAla **1**-*Bam*HI before (−) and after (+) photoirradiation, respectively; lanes 5 and 6, DNA cleavage with azoAla **2**-*Bam*HI before (−) and after (+) photoirradiation, respectively.

Table 2. Kinetic Parameters of *Bam*HI Mutants Containing Azobenzene Derivatives[a]

*Bam*HI mutants	K_M (nM)	V_{max} (nM min^{-1})	V_{max}/K_M (min^{-1})
1-*Bam*HI + *hν*	2.2	5.1×10^{-2}	2.3×10^{-2}
2-*Bam*HI + *hν*	2.9	7.2×10^{-2}	2.5×10^{-2}
Wild-type[b]	1.7	8.8×10^{-1}	5.2×10^{-1}
H133A[b]	2.3	6.5×10^{-2}	2.8×10^{-2}

[a] Detailed experimental conditions are described in the Experimental Section. [b] Data from ref 22.

with 436 nm, suppression of the DNA cleavage was not observed. In the previous study, the enzyme activity of Horseradish peroxidase was successfully controlled in switchable way using the site-selectively incorporated azophenylalanine (*12*). In this case, the phenylazophenylalanine introduced close to the substrate binding site effectively controls the binding and activity for the small substrate. In our case, once the cis forms of the azoAla derivatives are removed from the dimer interface for formation of the active dimer complex, the regenerated *trans*-azobenzene moieties would not be forced to change the conformation of the dimer to an inactive conformation.

Effect of the Carboxylate Group in the Azobenzene on the Recovery of the Activity. We examined the relationship between the recovery of the activities and irradiation time for the azoAla-*Bam*HI mutants during the trans to cis photoisomerization using 366 nm light. The irradiation time-dependent activitation of the enzyme was observed for both the azoAla **1** and azoAla **2** *Bam*HI mutants (Figure 5). During photoirradiation for 5 min, the activity of the enzymes gradually increased, and the trans to cis photoisomerization in both azoAla

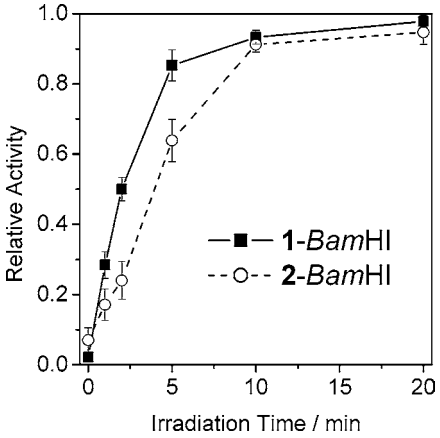

Figure 5. Recovery of the activity of the azoAla **1**-*Bam*HI and azoAla **2**-*Bam*HI mutants by photoirradiation (366 nm). Photoirradiation was carried out at 0 °C for 0, 1, 2, 5, 10, and 20 min, and then the samples were incubated with a substrate DNA at 30 °C for 1 h.

monomers was completed in 20 min. For an irradiation of more than 10 min, the activities reached the saturated level. Thus, the activity level of these azobenzene-functionalized enzymes can be regulated depending on the irradiation time within 10 min. The cis−trans thermal isomerization at 30 °C is slow enough to retain the cis form azoAla during the enzymatic reactions with substrates at 30 °C for 1 h (see Table 1). Therefore, the activity of the enzymes depends on the population of the active (cis isomer) and the inactive (trans isomer) *Bam*HI, namely the concentration of active *Bam*HI, can be purposely controlled by photoirradiation time.

Effect of the negatively charged carboxylate group on the azobenzene moiety for the activity was examined. As shown in Figure 5, we observed a faster recovery of the activity of azoAla **1**-*Bam*HI in shorter irradiation times (1−5 min) as compared to that of azoAla **2**-*Bam*HI. This means that the negatively charged azoAla **1** can rapidly produce the active *Bam*HI with correct dimer formation after photoirradiation. Since the properties of the photoisomerization between azoAla **1** and **2** were basically the same as the monomer level in solution (Table 1), the expression of the enzyme activity using the azoAla derivatives would be affected by the environment of the protein surface when the azoAla derivatives possessing different electrostatic properties were incorporated into the 132 position of the dimer interface.

In the present case, there are two possibilities for the regulation of the enzyme activity using the trans−cis photoisomerization of the azobenzene. One possibility is that the azobenzene moiety directly interferes the interaction between the two *Bam*HI monomers for the correct formation of the dimer. The short methylene chains of the azoAla residues constrain the orientations of the bulky *trans*-azobenzene moieties, which would cause the steric hindrance between the azobenzene moieties and the counterpart α-helix for consequent suppression of the activity. Recovery of the activities after the photoirradiation means the correct formation of the *Bam*HI dimer with the cis isomers. The compact *cis*-azobenzene moieties may reduce the steric interference in the dimer interface and exhibit the activity after the correct *Bam*HI dimer formation. The negatively charged carboxylate in the cis-isomer of the azoAla **1**-*Bam*HI would cause rapid dimer formation in the dimer interface as compared to the neutral azoAla **2**-*Bam*HI.

The other possibility is that the azobenzene moiety would change the local structure of the monomer around the azobenzene residue because of the interaction of the aromatic ring with the protein surface in order to avoid the water-accessible environment. The short methylene chains of the azoAla residues limit the movement of the *trans*-azobenzene moieties, and aromatic azobenzene may interact with the surface of *Bam*HI, which induces local structural changes for misalignment of the dimer structure and consequent suppression of the activity. Since the possible contact area of the *cis*-azobenzene moiety with the protein surface is smaller than that of the trans form, the cis isomer may weaken the interaction with the protein surface, and the *Bam*HI dimer forms an active one. Negative charge of the cis-isomer would work on the correct dimer formation in the environment on the surface of the *Bam*HI monomer. In these possibilities, the carboxylate group in the azobenzene affects the rapid expression of the activity in the protein scaffold as compared to the neutral azobenzene moiety without changing the potential of the activity of both *cis*-azoAla-*Bam*HI after a long time irradiation.

CONCLUSIONS

We designed and synthesized a novel hydrophilic and negatively charged azobenzene-bearing amino acid, 4′-carboxyphenylazophenylalanine, and investigated the photochemical regulation of *Bam*HI where the azobenzene derivatives were selectively incorporated. We found that the negative charge of the azobenzene moiety affects the initial activation of the enzyme in the trans−cis photoisomerization. The result suggests that these azobenzene derivatives may be a new tool for investigation of the environment such as solvent-accessibility, hydrophobicity, and electrostatic state in the protein.

ACKNOWLEDGMENT

This work has been partly supported by a Grant-in-Aid for Scientific Research (Project 17105005, Priority Area (417), 21st Century COE Research, and others) from the Ministry of Education, Culture, Sports, Science and Technology (MEXT) of the Japanese Government.

Supporting Information Available: Synthetic details. This material is available free of charge via the Internet at http://pubs.acs.org.

LITERATURE CITED

(1) (2005) Dynamic studies in biology: phototriggers, photoswitches and caged biomolecules (Goeldner, M., and Givens, R., Eds.) Wiley-VCH Verlag, Weinheim.

(2) Cornish, V. W., and Schultz, P. G. (1994) A new tool for studying protein structure and function. *Curr. Opin. Struct. Biol*. *4*, 601−607.

(3) Cook, S. N., Jack, W. E., Xiong, X., Danley, L. E., Ellman, J. A., Schultz, P. G., and Noren, C. J. (1995) Photochemically Initiated Protein Splicing. *Angew. Chem., Int. Ed. 34*, 1629−1630.

(4) Nowak, M. W., Kearney, P. C., Sampson, J. R., Saks, M. E., Labarca, C. G., Silverman, S. K., Zhong, W., Thorson, J., Abelson, J. N., Davidson, N., Schultz, P. G., Dougherty, D. A., and Lester, H. A. (1995) Nicotinic Receptor Binding Site Probed with Unnatural Amino Acids Incorporated in Intact Cells. *Science 268*, 439−442.

(5) Lodder, M., Golovine, S., Laikhter, A. L., Karginov, V. A., and Hecht, S. M. (1998) Misacylated Transfer RNAs Having a Chemically Removable Protecting Group. *J. Org. Chem*. *63*, 794−803.

(6) Pollitt, S. K., and Schultz, P. G. (1998) A Photochemical Switch for Controlling Protein−Protein Interactions. *Angew. Chem., Int. Ed. 37*, 2104−2107.

(7) Short, G. F., III, Lodder, M., Laikhter, A. L., Arslan, T., and Hecht, S. M. (1999) Caged HIV-1 Protease: Dimerization Is Independent of the Ionization State of the Active Site Aspartates. *J. Am. Chem. Soc. 121*, 478−479.

(8) Willner, I., and Rubin, S. Control of the Structure and Functions of Biomaterials by Light. (1996) *Angew. Chem., Int. Ed. Engl*. *35*, 367−385.

(9) Kumita, J. R., Smart, O. S., and Woolley, G. A. Photocontrol of helix content in a short peptide. (2000) *Proc. Natl. Acad. Sci. U. S. A.. 97*, 3803−3808.

(10) James, D. A., Burns, D. C., and Woolley, G. A. (2001) Kinetic characterization of ribonuclease S mutants containing photoisomerizable phenylazophenylalanine residues. *Protein Eng*. *14*, 983−991.

(11) Pieroni, O., Fissi, A., Angelini, N., and Lenci, F. (2001) Photoresponsive Polypeptides. *Acc. Chem. Res*. *34*, 9−17.

(12) Muranaka, N., Hohsaka, T., and Sisido, M. (2002) Photoswitching of peroxidase activity by position-specific incorporation of a photoisomerizable non-natural amino acid into horseradish peroxidase. *FEBS Lett*. *510*, 10−12.

(13) Dugave, C., and Demange, L. (2003) Cis−Trans Isomerization of Organic Molecules and Biomolecules: Implications and Applications. *Chem. Rev*. *103*, 2475−2532.

(14) Asanuma, H., Ito, T., Yoshida, T., Liang, X., and Komiyama, M. (1999) Photoregulation of the Formation and Dissociation of a DNA Duplex by Using the cis−trans Isomerization of Azobenzene. *Angew. Chem. Int. Ed*. *38*, 2393−2395.

(15) Liang, X., Asanuma, H., and Komiyama, M. (2002) Photoregulation of DNA triplex formation by azobenzene. *J. Am. Chem. Soc*. *124*, 1877−1883.

(16) Anzai, J., and Osa, T. (1994) Photosensitive artificial members based on azobenzene and spirobenzopyran derivatives. *Tetrahedron 50*, 4039−4070.

(17) Tamai, N., and Miyasaka, H. (2000) Untrafast Dynamics of Photochromic System. *Chem. Rev*. *100*, 1875−1890.

(18) Newman, M., Strzelecka, T., Dorner, L. F., Schildkraut, I., and Aggarwal, A. K. (1994) Structure of restriction endonuclease BamHI and its relationship to EcoRI. *Nature 368*, 660−664.

(19) Newman, M., Strzelecka, T., Dorner, L. F., Schildkraut, I., and Aggarwal, A. K. (1994) Structure of restriction endonuclease bamhi phased at 1.95 A resolution by MAD analysis. *Structure 2*, 439−452.

(20) Newman, M., Strzelecka, T., Dorner, L. F., Schildkraut, I., and Aggarwal, A. K. (1995) Structure of Bam HI endonuclease bound to DNA: partial folding and unfolding on DNA binding. *Science 269*, 656−663.

(21) Viadiu, H., and Aggarwal, A. K. (2000) Structure of BamHI bound to nonspecific DNA: a model for DNA sliding. *Mol. Cell*. *5*, 889−895.

(22) Endo, M., Nakayama, K., and Majima, T. (2004) Design and synthesis of photochemically controllable restriction endonuclease BamHI by manipulating the salt-bridge network in the dimer interface. *J. Org. Chem*. *69*, 4292−4298.

(23) Nakayama, K., Endo, M., and Majima, T. (2004) Photochemical regulation of the activity of an endonuclease BamHI using an azobenzene moiety incorporated site-selectively into the dimer interface. *Chem. Commun*. 2386−2387.

(24) Stanton, M. G., and Gagne, M. R. (1997) The Remarkable Catalytic Activity of Alkali-Metal Alkoxide Clusters in the Ester Interchange Reaction. *J. Am. Chem. Soc. 119*, 5075−5076.

(25) Huntress, E. H., Lesslie, T. E., and Hearon, W. M. (1956) A New Route to 1-Aryl Pyrroles. *J. Am. Chem. Soc*. *78*, 419−423.

(26) Davey, M. H., Lee, V. Y., Miller, R. D., and Marks, T. J. (1999) Synthesis of Aryl Nitroso Derivatives by *tert*-Butyl Hypochlorite Oxidation in Homogeneous Media. Intermediates for the Preparation of High-Hyperpolarizability Chromophore Skeletons. *J. Org. Chem*. *64*, 4976−4979.

(27) Nowak, M. W., Gallivan, J. P., Silverman, S. K., Labarca, C. G., Dougherty, D. A., and Lester, H. A. (1998) In Vitro Incorporation of Unnatural Amino Acids into Ion Channels in Xenopus Oocyte Expression System. *Methods Enzymol*. *293*, 504−529.

(28) Hohsaka, T., Ashizuka, Y., Murakami, H., and Sisido, M. (1996) Incorporation of Nonnatural Amino Acids into Streptavidin through In Vitro Frame-Shift Suppression. *J. Am. Chem. Soc*. *118*, 9778−9779.

(29) Hohsaka, T., Kajihara, D., Ashizuka, Y., Murakami, H., and Sisido, M. (1999) Efficient Incorporation of Nonnatural Amino Acids with Large Aromatic Groups into Streptavidin in in Vitro Protein Synthesizing Systems. *J. Am. Chem. Soc*. *121*, 34−40.

(30) Hinsch, B., and Kula, M. (1981) Reaction kinetics of some important site-specific endonucleases. *Nucleic Acids Res*. *9*, 3159−3174.

BC049724G

Temperature Sensitization of Liposomes by Use of Thermosensitive Block Copolymers Synthesized by Living Cationic Polymerization: Effect of Copolymer Chain Length

Kenji Kono,*,† Taishi Murakami,† Tomohide Yoshida,‡ Yasuhiro Haba,† Shokyoku Kanaoka,‡ Toru Takagishi,† and Sadahito Aoshima‡

Department of Applied Chemistry, Graduate School of Engineering, Osaka Prefecture University, 1-1, Gakuen-cho, Sakai, Osaka 599-8531, Japan, and Department of Macromolecular Science, Graduate School of Science, Osaka University, Toyonaka, Osaka 560-0043, Japan. Received January 10, 2005; Revised Manuscript Received September 25, 2005

We prepared block copolymers of (2-ethoxy)ethoxyethyl vinyl ether (EOEOVE) and octadecyl vinyl ether (ODVE) with the number average molecular weights of 6900, 9300, and 16 700 by living cationic polymerization. The poly(EOEOVE) block acts as a temperature-sensitive moiety, and the poly(ODVE) block acts as an anchor moiety. We also investigated the effect of chain length of the copolymer poly(EOEOVE) block on the ability to sensitize liposomes. The copolymers underwent a coil−globule transition at ∼36 °C in the presence of a membrane of egg yolk phosphatidylcholine (EYPC), detected using differential scanning calorimetry (DSC). Liposomes encapsulating calcein, a water-soluble fluorescent dye, were prepared from mixtures of dioleoylphosphatidylethanolamine, EYPC, and the copolymers. While the copolymer-modified liposomes released little calcein below 30 °C, release was enhanced above 35 °C, indicating that dehydrated copolymer chains destabilized the liposome membrane. In addition, copolymers with a longer poly(EOEOVE) block induced a more drastic enhancement of contents release in a narrow temperature region near the transition temperature of the poly(EOEOVE) block. As a result, the copolymer with an average molecular weight of 16 700 generated highly sensitive liposomes that produced rapid and dramatic release of the contents in response to temperature.

1. INTRODUCTION

Liposomes are highly attractive materials for drug delivery because of their biocompatibility, ability to encapsulate both hydrophilic and hydrophobic drugs, and size controllability (*1*). Therefore, studies to modify their functions have been conducted to increase their usefulness. While various functional liposomes have been developed, temperature-sensitive liposomes have received much attention (*2*−*4*). Temperature-sensitive liposomes have been produced by modifying liposomes with thermosensitive polymers according to methods by Kono et al. (*5*, *6*) and other groups (*7*−*10*).

The water solubility and conformation of thermosensitive polymers change at a specific temperature, called the lower critical solution temperature (LCST). These changes in water solubility and conformation provide temperature-sensitive properties to liposomes (*6*). Poly(*N*-isopropylacrylamide) [poly(NIPAM)] and copolymers of NIPAM, prepared via free radical polymerization, have been used for temperature-sensitization of liposomes (*5*−*7*, *9*, *11*−*13*). Highly hydrated polymer chains conjugated to the liposome surface increase the stability of liposomes below the LCST (*13*, *14*). In contrast, above the LCST, dehydrated polymer chains interact with the liposome membrane and induce release of the liposome contents (*6*). However, polymers and copolymers produced by this technique can have disadvantages, such as lack of control over molecular weight, high polydispersity, and limited freedom in choosing the architecture of the polymer chain, although efforts have been made recently to synthesize homopolymer and block copolymers of NIPAM with a defined structure by atom transfer polymerization (*15*) or reversible addition−fragmentation chain transfer polymerization (*16*−*18*).

Living cationic polymerization is an attractive technique for the synthesis of thermosensitive polymers with precisely controlled molecular architecture and molecular weight. In fact, a variety of thermosensitive polymers and block copolymers with controlled molecular structures have been prepared using this polymerization system (*19*−*21*). Aoshima et al. have shown that living cationic polymerization of 2-(2-ethoxy)ethoxyethyl vinyl ether (EOEOVE) gives a thermosensitive polymer, which allows control of molecular weight and a low polydispersity (*19*).

In this study, synthesis of block copolymers of EOEOVE and octadecyl vinyl ether (ODVE) for the sensitization of liposomes was examined (Figure 1). The poly(EOEOVE) block behaves as a thermosensitive moiety, whereas the poly(ODVE) block acts as an anchor for fixing the copolymer chain onto a liposomal membrane through hydrophobic interaction between its octadecyl chains and the liposome membrane. Temperature-sensitive content release or related behaviors were investigated for liposomes modified with the block copolymers having a poly(EOEOVE) block of varying chain lengths. The effect of chain length of the thermosensitive block

* To whom correspondence should be addressed. Phone: +81-72-254-9330. Fax: +81-72-254-9330. E-mail: kono@chem.osakafu-u.ac.jp.

† Osaka Prefecture University.

‡ Osaka University.

10.1021/bc050004z CCC: $30.25 © 2005 American Chemical Society
Published on Web 11/01/2005

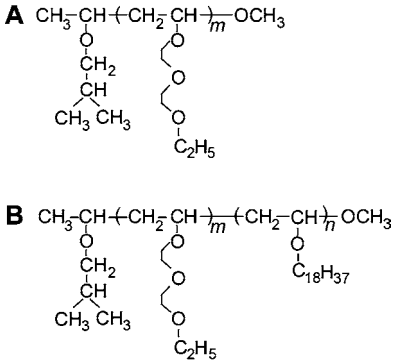

Figure 1. Structures of poly(EOEOVE) (A) and copoly(EOEOVE-*b*-ODVE) (B).

on the ability of block copolymers to sensitize liposomes is described.

2. EXPERIMENTAL SECTION

2.1. Materials. Egg yolk phosphatidylcholine (EYPC) and dioleoylphosphatidylethanolamine (DOPE) were kindly donated by Nippon Oil and Fats Co. (Tokyo, Japan). Octadecyl vinyl ether (ODVE) was obtained from BASF (Germany). 2-(2-Ethoxy)ethoxyethyl vinyl ether (EOEOVE) was purchased from Maruzen Petrochemical (Tokyo, Japan). Calcein, pyrenecarboxaldehyde (PyCHO) 1,6-diphenyl-1,3,5-hexatriene (DPH), and 8-anilino-1-naphthalenesulfonic acid (ANS) were obtained from Sigma-Aldrich Japan (Tokyo, Japan). $Et_{1.5}AlCl_{1.5}$ (1.0 M solution in toluene) and toluene were obtained from Wako Pure Chemical Industries (Osaka, Japan). Ethyl acetate was supplied from Nacalai Tesque (Kyoto, Japan). ODVE was distilled over calcium hydride under reduced pressure (150 °C/3 mmHg). EOEOVE was washed with 10% aqueous sodium hydroxide and then with water, dried overnight over potassium hydroxide pellets, and distilled twice over metallic sodium before use. Ethyl acetate was distilled at least twice over calcium hydride. Toluene as a polymerization solvent was washed by the usual method and distilled at least twice over calcium hydride and then metallic sodium just before use. Cationogen, 1-isobutylethyl acetate (IBEA) ($CH_3CH(OiBu)OCOCH_3$), was prepared from isobutyl vinyl ether (IBVE) and acetic acid and was distilled over calcium hydride under reduced pressure (*22*). All monomers, the $Et_{1.5}AlCl_{1.5}$ solution, and IBEA were stored in a brown ampule under dry nitrogen.

2.2. Polymerization Procedures. Polymerization was carried out at 0 °C under a dry nitrogen atmosphere in a glass tube equipped with a three-way stopcock baked at 240 °C for 10 min before use. The reaction was initiated by the addition of $Et_{1.5}AlCl_{1.5}$ solution in toluene into a mixture of a monomer, an added base, and the cationogen IBEA in toluene at 0 °C by a dry medical syringe. For block copolymerization, a typical example is as follows. EOEOVE (0.13 M, 0.11 mL) was first polymerized in the presence of $CH_3COOC_2H_5$ (1.0 M, 0.5 mL) as an added base ($[IBEA]_0 = 4.0$ mM; $[Et_{1.5}AlCl_{1.5}]_0 = 20$ mM in toluene). After 2.5 h, the second monomer, ODVE (0.04 M in toluene, 5.0 mL), was added to the reaction mixture at a given conversion of EOEOVE. After 2 h, ODVE had been consumed quantitatively (total 4.5 h). When the polymerization was finished, it was quenched with methanol containing a small amount of aqueous ammonia. The quenched reaction mixture was diluted with dichloromethane and then sequentially washed with dilute hydrochloric acid and with water to remove the initiator residues. The product polymer was recovered from the organic layer by evaporation of the solvent under reduced pressure and vacuum-dried overnight. Poly(NIPAM)s with different molecular weights were obtained by polymerization of NIPAM in tetrahydrofran using azobisisobutyronitrile as a free radical initiator as previously reported (*5*, *12*) and subsequent fractional precipitation by adding diethyl ether into poly(NIPAM) dissolved in tetrahydrofran.

2.3. Liposome Preparation. The liposomes were prepared as previously reported (*23*, *24*). A mixture of DOPE and EYPC (7:3, mol/mol) (4.4 mg) and varying amounts of the copolymer were dissolved in chloroform, and the solvent was removed by evaporation. The obtained thin lipid/copolymer-mixed membrane was further dried under vacuum overnight and dispersed in 0.75 mL of an aqueous calcein solution (63 mM, pH 7.4) or in 10 mM Tris-HCl-buffered solution containing 140 mM NaCl and 1 mM EDTA solution (pH 7.4). The obtained liposome suspension was extruded through a polycarbonate membrane with a pore diameter of 100 nm in an ice-cooled water bath. The free calcein and free copolymer were removed by gel permeation chromatography (GPC) on a Sepharose 4B column at 4 °C using a 10 mM Tris-HCl-buffered solution containing 140 mM NaCl and 1 mM EDTA solution (pH 7.4). The liposomes suspensions were kept at 5 °C until the measurements were made.

2.4. Calcein Release from Liposome. The release measurements were performed according to the method previously reported (*23*, *24*). An aliquot of dispersion of the calcein-loaded liposomes was added into 2 mL of 10 mM Tris-HCl, 140 mM NaCl, and 1 mM EDTA solution (pH 7.4) in a quartz cell (final concentration of the lipids, 10 μM) at a given temperature, and the fluorescence intensity of the solution was monitored using a spectrofluorometer (Shimadzu RF-5000). The excitation and monitoring wavelengths were 490 and 520 nm, respectively. The percent release of calcein from the liposomes was defined as

$$\%\ \text{release} = \frac{F^t - F^i}{F^f - F^i} \times 100$$

where F^i and F^t mean the initial and intermediary fluorescence intensities of the liposome suspension, respectively. F^f is the fluorescent intensity of the liposome suspension after the addition of Triton X-100 (final concentration of 0.15%).

2.5. Estimation of the Amount of Copolymer Bound to Liposome. The amount of the copolymer bound to the liposome was estimated using high-performance liquid chromatography as previously reported (*12*, *13*). The liposomes bearing the copolymer were dried under vacuum and then dissolved in methanol/water (7:3, v/v). The solution was filtered through a poly(tetrafluoroethylene) membrane with a pore size of 0.25 μm. The filtrate (20 μL) was injected into a KB-8501 column (Showa Denko), and the amount of the copolymer was evaluated using a refractive index detector (Jasco, RI-930). Also, the lipid amount was determined by the method of Bartlett (*25*).

2.6. Fluorescence Measurements. Emission spectra of PyCHO were obtained on a spectrofluorometer with excitation at 365.5 nm. Fluorescence polarization (P) of DPH and ANS was measured as reported previously (*26*). Fluorescence polarization of DPH and ANS was measured as reported previously (*24*, *27*). ANS and DPH were excited at 395 and 360 nm, respectively, and the fluorescence intensities of ANS and DPH were monitored at

467 and 428 nm, respectively. The P value was evaluated using

$$P = \frac{I_p - I_v}{I_p + I_v}$$

where I_p and I_v represent the intensities of parallel polarized fluorescence and vertically polarized fluorescence, respectively.

2.7. Retention of Fluorescein Isothiocyanate (FITC)−Dextran in Liposomes. The liposomes containing FITC−dextran was prepared by suspending a dry membrane of EYPC (10 mg) or a mixture (9 mg) of DOPE and EYPC (7/3, mol/mol) in a solution of FITC−dextran (6 mg) dissolved in 10 mM Tris-HCl and 140 mM NaCl solution (1.5 mL, pH 7.4) at varying temperatures for 30 min. Then, the liposomes were applied to a Sepharose 4B column to remove FITC−dextran released from the liposomes during the incubation. The percent of FITC−dextran remaining after the incubation was calculated from

$$\text{FITC−dextran remaining (\%)} = \frac{F^0 - F^t}{F^0} \times 100$$

where F^0 and F^t mean the fluorescence intensities of FITC-dextran-loaded liposomes per liposomal lipid before and after 30 min of incubation and subsequent GPC using a Sepharose 4B column, respectively. The excitation and monitoring wavelengths of FITC−dextran were 490 and 520 nm, respectively.

2.8. Other Methods. The molecular weight distribution of poly(EOEOVE) and poly(EOEOVE-*block*-ODVE) was measured by size exclusion chromatography (SEC) in chloroform at 40 °C on three polystyrene gel columns [TSK gel G-2000HXL (molecular range of 1×10^2 to 1×10^4 (PSt)), 3000HXL (6×10^3 to 6×10^4), and 4000HXL (1×10^4 to 4×10^5); 7.8 mm i.d. × 300 mm; flow rate, 1.0 mL/min] connected to a Tosoh DP-8020 dual pump and a RI-8020 refractive detector. The number-average molecular weight (M_n), the weight-average molecular weight (M_w), and the polydispersity index (M_w/M_n) were calculated from SEC curves on the basis of a polystyrene calibration. M_n and M_w of poly(NIPAM)s were determined using SEC on a system equipped with a Shodex KF-805L and KD-803 column (Showa Denko) with differential refractive index detection (Jasco, RI-930) using DMF as an eluent and poly(ethylene glycol) as the standard. ^{1}H NMR and ^{13}C NMR spectra were recorded on a JEOL JNM-EX270 (270 MHz). Differential scanning calorimetry (DSC) was performed with a DSC 120 microcalorimeter (Seiko Electronics). The size of liposomes was evaluated by dynamic light scattering using a Nicomp 380 ZLS instrument (Particle Sizing Systems).

3. RESULTS AND DISCUSSION

3.1. Characterization of Polymers and Copolymers. Three types of poly(EOEOVE) with different molecular weights were prepared by controlling the molar ratio of monomer EOEOVE to initiator IBEA for the polymerization (Figure 1). Polymerization at EOEOVE/IBEA (mol/mol) ratios of 32, 60, and 120 gave polymers with average molecular weights of 5300, 8300, and 15 800, respectively, within narrow molecular weight distributions (Table 1). The degree of polymerization for these polymers was estimated to be 33, 52, and 99, respectively. We also prepared three poly(EOEOVE)s with an oligo(ODVE) block, which acts as an anchor for fixing the polymer chain onto a liposomal membrane, through sequential living copolymerization of EOEOVE and ODVE (Table 1). When the poly(EOEOVE) segments of the block copolymers and homopolymers of EOEOVE were prepared at the same monomer/initiator ratio, they contained essentially the same number of EOEOVE units in the polymer and copolymer chains. In addition, these block copolymers contained approximately the same number of ODVE units (four or five) at the terminal moiety of the copolymer chain. We have already shown that two dodecyl groups fix chains of NIPAM copolymers stably onto liposome membranes (*23*, *24*). Therefore, highly hydrophobic octadecyl groups of the ODVE block at the terminal moiety of the copolymer should fix the copolymer chain onto the liposome surface tightly through hydrophobic interactions.

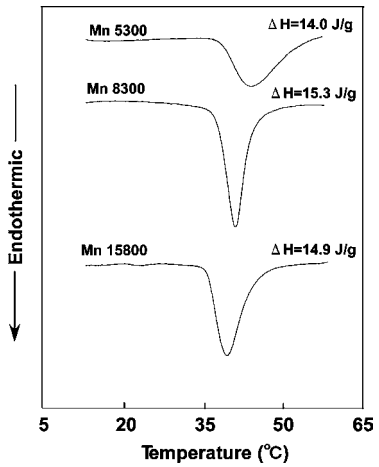

Figure 2. Microcalorimetric endotherms for poly(EOEOVE)s with M_n of 5300, 8300, and 15 800 in water.

Table 1. Preparation of Poly(EOEOVE) and Poly(EOEOVE-*b*-ODVE)

feed		composition				
EOEOVE (mol/L)	ODVE (mol/L)	EOEOVE (%)	ODVE (%)	M_w	M_n	M_w/M_n
0.13	0	33	0	6000	5300	1.14
0.24	0	52	0	9500	8300	1.15
0.48	0	99	0	18300	15800	1.16
0.13	0.04	31	5	7800	6900	1.13
0.24	0.04	52	4	10800	9300	1.16
0.48	0.04	99	4	19000	16700	1.14

An endotherm is associated with the LCST of thermosensitive polymers, such as poly(NIPAM) and poly(vinyl methyl ether) (*28*, *29*), mainly because of the destruction of water around the hydrophobic groups upon a coil-to-globule transition of the polymer chain at the LCST (*30*). Therefore, we conducted microcalorimetric analyses to estimate the LCST of poly(EOEOVE) and to determine the influence of polymer chain length (Figure 2). Despite differences in molecular weight, these polymers showed similar endotherms of 14−15 J/g for the conformational transition, indicating that the destruction of water associated with the polymers occurred with a similar efficiency. However, the molecular weight affected the transition temperature of the polymers. The polymers with molecular weights of 5300, 8300, and 15 800 exhibited endotherms centered at 45, 41, and 40 °C, respectively. Apparently, the polymer with a higher molecular weight underwent a transition at a lower temperature. It is likely that a longer polymer chain enhances dehydration through efficient intramolecular interactions in addition to intermolecular interactions, resulting in a transition in a lower temperature region.

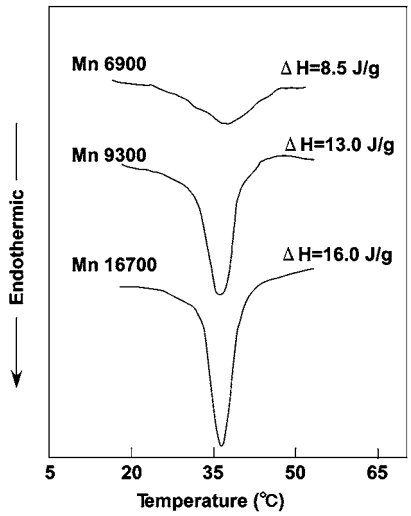

Figure 3. Microcalorimetric endotherms for copoly(EOEOVE−ODVE) with M_n of 6900, 9300 and 16 700 in the presence of EYPC in water. Copolymer/lipid (w/w) ratio was 1/1.

A microcalorimetric analysis was also performed for mixtures of EYPC and copoly(EOEOVE-*b*-ODVE) suspended in water to obtain information about the transition of poly(EOEOVE) chains fixed onto the lipid membrane (Figure 3). As shown in Figure 3, these copolymers on the surface of the lipid membrane showed endotherms in approximately the same temperature region of 36−39 °C, irrespective of the difference in poly(EOEOVE) chain length. In comparison with the transition in aqueous solution, it is apparent that the poly(EOEOVE) chain undergoes a phase transition at a lower temperature. The hydrophobic environment of the lipid membrane periphery may enhance dehydration of the polymer chain, enabling the polymer chain to undergo a transition at a low temperature. In addition, a comparison of endotherms for transitions of these copolymers with the EYPC membrane revealed that the copolymer with a higher molecular weight underwent the transition in a narrow temperature region with a large transition enthalpy, indicating that the longer polymer chain undergoes more efficient transition on the lipid membrane.

3.2. Characterization of Copolymer-Modified Liposomes. We used a mixture of DOPE and EYPC (7:3, mol/mol) as the liposomal lipids because inclusion of DOPE into EYPC liposomes modified with NIPAM copolymers improved their temperature sensitivity (*31*). The liposomes were prepared from mixtures of the lipids and block copolymers. The copolymer/DOPE/EYPC liposomes were extruded through a polycarbonate membrane with a pore size of 100 nm and purified by GPC using a Sepharose 4B column. The amounts of copolymers fixed onto the liposomes are listed in Table 2. Irrespective of poly(EOEOVE) chain length, generally more than 90% of the copolymer added for preparation of the liposome was retained in the liposome after purification by GPC, indicating that four or five octadecyl groups connected to the terminal moiety of the copolymer chain could fix the poly(EOEOVE) chains, although a slightly lower fixation efficiency was observed for liposomes prepared using the copolymer with an M_n of 16 700 and copolymer/lipid ratio of 1.5. The mean diameters of the copolymer-modified liposomes also are listed in Table 2, which possess slightly larger diameters than the pore size of the filter membrane used for the preparation of the liposomes. Since the liposomes containing the copolymer with higher M_n tend to have larger diameters, the chain length of the copolymer may increase the apparent size of the liposomes by assuming an extended conformation on the liposome surface.

Table 2. Characterization of Copoly(EOEOVE−ODVE)-Modified Liposomes[a]

M_n of copolymer	copolymer added (mg/mg lipid)	copolymer fixed (mg/mg lipid)	mean diameter (nm)
6900	0.5	0.44	132
	1.0	0.93	126
	1.5	1.36	132
9300	0.5	0.49	142
	1.0	0.96	139
	1.5	1.47	131
16700	0.5	0.40	157
	1.0	0.89	157
	1.5	1.25	151

[a] Measurements were performed at 20 °C.

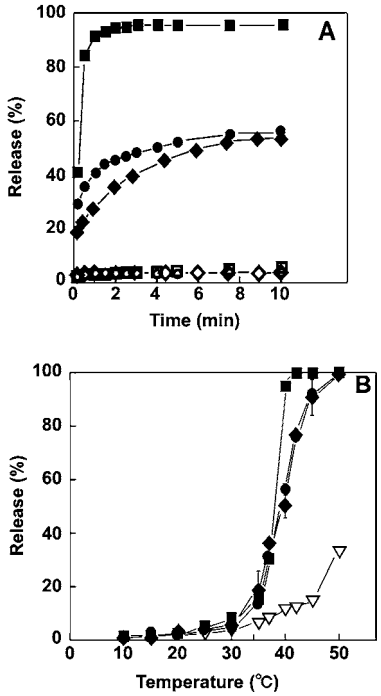

Figure 4. Release of calcein from the copolymer-modified DOPE/EYPC (7/3, mol/mol) liposomes: (A) profiles of calcein release from DOPE/EYPC (7/3, mol/mol) liposomes modified with copoly(EOEOVE-*b*-ODVE) with M_n of 6900 (diamonds), 9300 (circles), and 16 700 (squares) in 10 mM Tris-HCl, 140 mM NaCl, and 1 mM EDTA at 40 °C (solid symbols) and 25 °C (open symbols); (B) percent release of calcein from DOPE/EYPC (7/3, mol/mol) liposomes modified with copoly(EOEOVE-*b*-ODVE) with M_n of 6900 (diamonds), 9300 (circles), and 16 700 (squares) or unmodified DOPE/EYPC (7/3, mol/mol) liposome (triangles) after 10 min of incubation as a function of the incubation temperature. The liposomes were prepared from a copolymer/lipid (0.5/1, w/w) mixture.

3.3. Calcein Release from Copolymer-Modified Liposomes. To estimate first the ability of these block copolymers to sensitize the liposome to temperature and then to understand the effect of chain length of the copolymer on their ability for temperature sensitization of the liposome, we examined the content release behavior of liposomes modified with copoly(EOEOVE-*b*-ODVE) of varying molecular weights. Calcein (formula weight, 622.5) was used as a permeant because this water-soluble dye exhibits considerable self-quenching when entrapped in a liposome at high concentration but fluoresces when released into the outer phase (*31*). Figure 4A shows calcein release profiles from EYPC/DOPE liposomes modified with copolymers at 25 and 40 °C. As shown in Figure 4A, the liposomes did not release calcein at 25

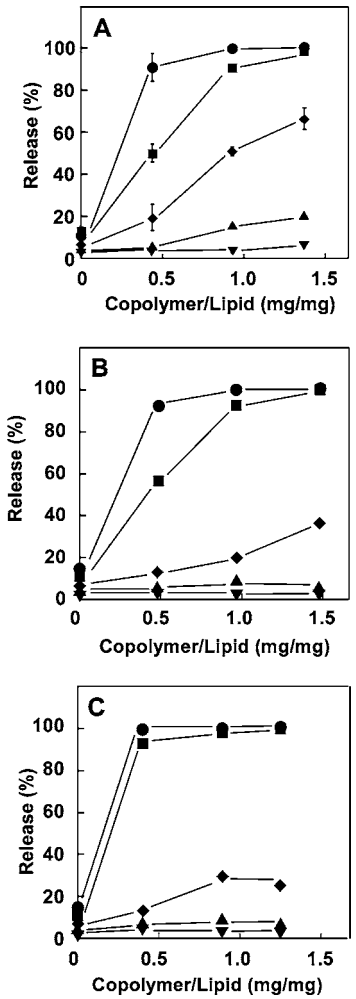

Figure 5. Percent release of calcein from DOPE/EYPC (7/3, mol/mol) liposomes after 10 min of incubation at 25 (▼), 30 (▲), 35 (◆), 40 (■), and 45 (●) as a function of content of copoly(EOEOVE-*b*-ODVE)s with M_n of 6900 (A), 9300 (B), and 16 700 (C).

°C; however, strong release was induced at 40 °C. As shown earlier, the poly(EOEOVE) segment of the copolymer changes its nature from hydrophilic to hydrophobic near 36 °C (Figure 3). Thus, these results imply that a hydrated chain of poly(EOEOVE) does not destabilize the liposomal membrane, but a dehydrated chain interacts with the membrane, enhancing permeation of calcein through the membrane. In addition, liposomes modified with copolymers of higher M_n exhibited more significant content release at 40 °C, indicating that the ability of the poly(EOEOVE) chain to sensitize liposomes increases with chain length. It is noteworthy that the copolymer with a M_n of 16 700 conferred a high degree of temperature sensitivity to liposomes, which achieved complete content release within 1 min.

As shown in Figure 4A, significant release was induced within the first 1 or 2 min. However, the release gradually slowed and approached a constant value after 10 min. The extent of content release after 10 min at varying temperatures was plotted as a function of incubation temperature (Figure 4B). The content release was clearly enhanced above 36 °C, where dehydration of poly(EOEOVE) presumably occurred on the lipid membrane, indicating that the change of the polymer chain from hydrophilic to hydrophobic triggered content release.

Figure 5 depicts the effect of copolymer content of the liposome membrane on calcein release behavior of the liposomes. No remarkable difference in calcein release was observed in liposomes modified with copolymers of different M_n below 30 °C or at 45 °C. These results suggest that highly hydrated or well-dehydrated polymer chains interact with membranes in a similar manner, irrespective of the difference in chain length. In contrast, a significant difference was observed in calcein release at 35 and 40 °C among these copolymer-modified liposomes. The copolymer with an M_n of 6900 possessed significant ability to enhance release at 35 °C, whereas the copolymer with an M_n of 16 700 exhibited a much lower ability to enhance release at the same temperature. In contrast, at 40 °C the copolymer with a high M_n achieved complete release even at a copolymer/lipid ratio of 0.5, whereas the copolymer with a low M_n induced only 50% release at the same copolymer/lipid ratio. As seen in Figure 3, dehydration of the poly(EOEOVE) segment was not complete at these temperatures. For the short chain of poly(EOEOVE), dehydrated segments of the polymer chain may interact with and destabilize the liposome membrane, although the degree of dehydration might be limited at 35 °C. However, for the longer polymer chain, because of its higher conformational freedom, dehydrated segments could associate with each other, resulting in weak interaction with the membrane. In contrast, at 40 °C, the longer polymer chain enables its dehydration more efficiently because of its larger freedom of conformation, resulting in a stronger interaction with the liposome and more significant release of calcein.

3.4. Interaction of Copolymers with Liposome Membrane. The influence of the copolymer on membrane fluidity of the liposome was investigated to obtain information about interactions with the lipid membrane using the fluorescent probes ANS and DPH. These fluorescent molecules are used widely to estimate membrane fluidity and provide information about the surface (ANS) and hydrophobic region (DPH) of the membrane (*32*). The inverse polarization of fluorescence probes (1/*P*) indicated the membrane fluidity (*32*).

For simplicity, EYPC was used as the liposomal lipid for estimation of membrane fluidity. Figure 6A depicts the temperature dependence of membrane fluidity of the liposomes as monitored by ANS. For unmodified liposomes, membrane fluidity increased with temperature. Similarly, the membrane fluidity of liposomes modified with the copolymer with an M_n of 6900 increased with temperature; no change in the temperature dependence of membrane fluidity was observed near the transition temperature. For liposomes modified with copolymers with M_n of 9300 and 16 700, the membrane fluidity increased monotonically up to 40 °C; this increase in membrane fluidity was slightly suppressed near 40 °C. Since this temperature is close to that at which significant enhancement of content release occurred, it is likely that the dehydrated chains of poly(EOEOVE) interact with the lipid membrane and suppress mobility of the lipid molecules. Because suppression was observed only with copolymers of higher molecular weights, the interaction of the copolymer with the membrane may increase with chain length of the poly(EOEOVE) segment. However, a previous study showed more significant suppression of the EYPC membrane upon modification with NIPAM copolymers (*24*, *27*); thus, the interaction of poly(EOEOVE) with the membrane may be relatively weak.

A similar tendency was seen for membrane fluidity as monitored by DPH (Figure 6B). Membrane fluidity of the unmodified EYPC liposome increased monotonically with temperature, whereas increase in membrane fluidity was

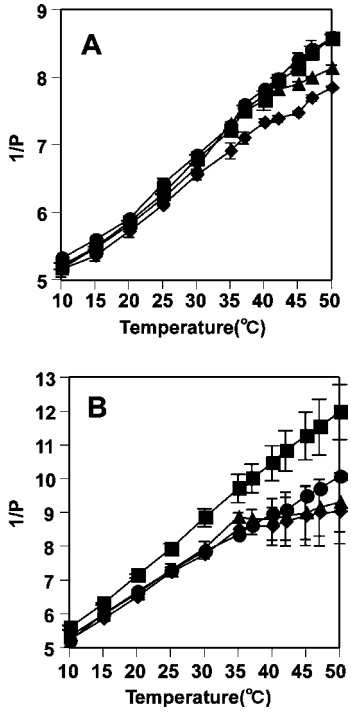

Figure 6. Temperature dependence of membrane fluidity (1/*P*) of EYPC liposomes modified with copoly(EOEOVE-*b*-ODVE)s with M_n of 6900 (●), 9300 (▲), and 16 700 (◆), and unmodified EYPC liposome (■) in 10 mM Tris-HCl and 140 mM NaCl solution (pH7.4) as monitored by ANS (A) and DPH (B). The concentrations of EYPC, ANS, and DPH were 0.4 mM, 4.4 μM, and 0.44 μM, respectively. Copolymer/lipid (w/w) ratio of the liposomes was 0.5/1.

suppressed above 37 °C for membranes having poly(EOEOVE) chains. More significant suppression was observed for membranes modified with copolymers of higher M_n. As mentioned earlier, copolymer chains with higher M_n underwent conformational transition more efficiently than did copolymers with a low M_n. Therefore, the longer chains of poly(EOEOVE) could form a more hydrophobic domain upon the transition and interact more strongly with the membrane. A comparison between membrane fluidities monitored by ANS and DPH showed that the latter indicated more pronounced suppression by the copolymers, implying that the copolymers interact with the hydrophobic region of the membrane more strongly than with the peripheral region of the membrane.

3.5. Retention of Dextran in Copolymer-Modified Liposomes. We examined the effect of temperature on retention of dextran in copolymer-modified liposomes to obtain information about the mechanism of content release induced by the copolymers. The copolymer-modified EYPC or DOPE/EYPC (7/3, mol/mol) liposome containing FITC−dextran with an average molecular weight of 4400 was incubated for 30 min at varied temperatures. Figure 7 shows the percent FITC−dextran remaining in the liposomes after a 30 min incubation as a function of incubation temperature. For copolymer-modified EYPC liposomes, more than 75% of the content was retained in the liposomes even at 50 °C, where the poly(EOEOVE) chain becomes fully dehydrated, indicating that the polymer chain causes only limited defects in the EYPC membrane. In contrast, for copolymer-modified liposomes containing DOPE, only a small portion of the contents remained after incubation above the transition temperature of poly(EOEOVE). Considering that a large molecule with an average molecular weight

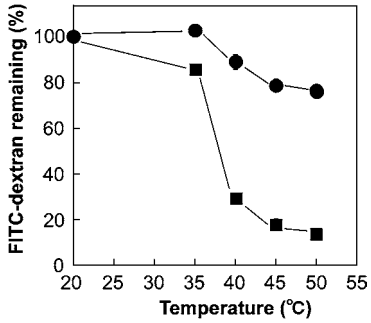

Figure 7. Retention of FITC−dextran from copoly(EOEOVE-*b*-ODVE) (M_n of 16 700) modified EYPC (●) and DOPE/EYPC (7/3, mol/mol) (■) liposomes after 30 min of incubation as a function of incubation temperature. Copolymer/lipid (w/w) ratio was 0.5/1.

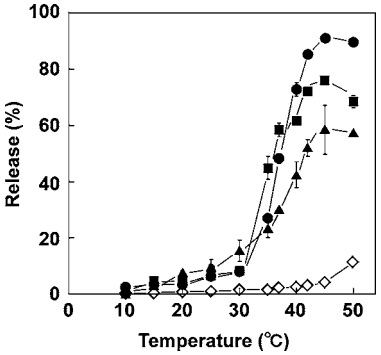

Figure 8. Percent release of calcein from EYPC liposomes modified with copoly(EOEOVE-*b*-ODVE) with M_n of 6900 (triangles), 9300 (squares), and 16 700 (circles) or unmodified EYPC liposome (diamonds) after 10 min of incubation in 10 mM Tris-HCl, 140 mM NaCl, and 1 mM EDTA as a function of the incubation temperature. The liposomes were prepared from a copolymer/lipid (1.5/1, w/w) mixture.

of 4400 was released effectively to the outer phase, it is likely that disintegration of the liposome was induced by the dehydrated polymer chain in the DOPE-containing liposome. It is well-known that EYPC forms a stable bilayer membrane under physiological condition, whereas DOPE has a tendency to form a hexagonal II structure (*33*, *34*). Therefore, it is likely that the interaction with the dehydrated chain of poly(EOEOVE) did not induce a significant defect in the stable bilayer membrane of EYPC but enhanced the transition of the DOPE-containing membrane from a lamellar to a nonlamellar phase, resulting in rupture of the liposome.

3.6. Sensitization of EYPC Liposomes by Copolymer-Modified Liposomes. It has been shown that the interaction between poly(NIPAM) and phosphatidylcholine membranes is not strong enough to induce significant release from the liposomes (*5*, *6*, *35*). Inclusion of DOPE has been shown to improve temperature-sensitive release properties of poly(NIPAM)-modified liposomes (*27*). At the same time, however, the stability of the liposomes decreases because DOPE has a high tendency to form a nonbilayer structure. Therefore, it is highly desired to provide highly temperature-sensitive properties to stable phosphatidylcholine liposomes. Thus, we examined the ability of these copolymers to sensitize EYPC liposomes. As is seen in Figure 8, EYPC liposomes modified with poly(EOEOVE-*b*-ODVE) enhanced release of calcein above 35 °C, indicating that these polymers have an ability to sensitize liposomes with a stable phosphatidylcholine membrane to temperature. In addition, the extent of enhancement of the contents release became more significant for the liposomes modified with the copolymer

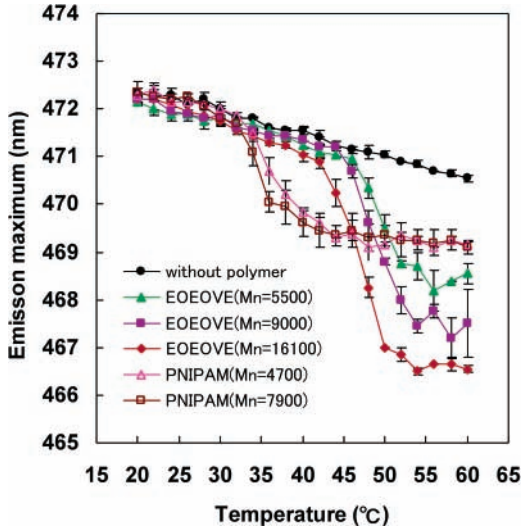

Figure 9. Emission maxima for PyCHO in the absence or presence of poly(NIPAM) or poly(EOEOVE) with varying molecular weights in water. The concentrations of PyCHO and the copolymers were 1 μM and 0.2 mg/mL, respectively. Poly(NIPAM)s with M_n of 4700 and M_w of 10 000 and with M_n of 7900 and M_w 23 000 were used. Poly(EOEOVE)s with M_n of 5500 and M_w of 6300, M_n of 9000 and M_w of 10 400, and M_n of 16100 and M_w of 18 400 were used.

of a higher molecular weight. In particular, the liposomes having a copolymer with a molecular weight of 16 700 exhibited a sharp and intensive contents release around the polymer transition temperature. This result clearly indicates that the poly(EOEOVE-*b*-ODVE) is very useful for obtaining stable phosphatidylcholine liposomes with temperature-sensitive properties.

The poly(EOEOVE-*b*-ODVE) was shown to be able to sensitize EYPC liposomes. This implies that poly(EOEOVE) forms a more hydrophobic domain than poly(NIPAM) does after their conformational transition because the contents release from the liposomes would be induced mainly by hydrophobic interaction between the liposome membrane and the dehydrated polymer chains. To confirm it, we further examined the hydrophobicity of domains formed by these polymers above the transition temperature using PyCHO. This molecule is known to change the wavelength of the emission maximum (λ_{max}) of the fluorescence, depending on polarity of the solvent (*26*). By using this property of PyCHO, Schild and Tirrell detected collapse of the backbone of the homopolymer and copolymers of NIPAM (*26*).

Two poly(NIPAM)s with M_n of 4700 and M_w of 10 000 and with M_n of 7900 and M_w of 23 000 were compared with three poly(EOEOVE)s with M_n of 5500 and M_w of 6300, M_n of 9000 and M_w of 10 400, and M_n of 16 100 and M_w of 18 400. As is seen in Figure 9, λ_{max} of PyCHO dissolved in an aqueous solution slightly decreased with increasing temperature in the absence of the polymer. In contrast, in the presence of the polymers, a marked blue shift above the LCST was observed around 35 °C for poly(NIPAM)s and at 44−46 °C for poly(EOEOVE)s, indicating that these polymers formed hydrophobic domains at these temperatures. As judged from the extent of emission blue shift, hydrophobicity of domains formed by poly(NIPAM)s is hardly affected by their molecular weights. In contrast, hydrophobicity of domains formed by poly(EOEOVE) increased with increasing molecular weight. This is consistent with the fact that the liposomes having longer chains of poly(EOEOVE) exhibited more intensive contents release (Figures 4 and 8) because polymer chains with greater hydrophobicity could destabilize liposome membrane more strongly and cause more intensive permeation of the contents through the membrane. In addition, when the extent of blue shift is compared between poly(NIPAM) and poly(EOEOVE), apparently the latter showed a more significant blue shift. For example, the poly(EOEOVE) with M_n of 5500 exhibited a larger blue shift than poly(NIPAM) with M_n of 7900. This result indicates that poly(EOEOVE) is more potent for sensitization of liposomes to temperature than poly(NIPAM), which has been used for the same purpose.

4. CONCLUSIONS

We synthesized three types of copoly(EOEOVE-*b*-ODVE) with varying chain lengths of poly(EOEOVE) segments, which become hydrophilic or hydrophobic depending on the local temperature, via living cationic polymerization. We also investigated the influence of chain length of the poly(EOEOVE) segments on their ability to sensitize liposomes. Irrespective of poly(EOEOVE) chain length, the copolymers on the surface of the liposomes enhanced the release of calcein entrapped in the EYPC/DOPE liposomes above 35°C, which corresponds to the transition temperature of the poly(EOEOVE) segment of the copolymer on the lipid membrane. However, a longer chain possessed a greater ability to enhance content release within a narrow temperature region near the transition temperature. Thus, the copolymer with an M_n of 16 700, which is the highest molecular weight among the copolymers prepared in this study, produced sharp and rapid control of content release at the transition temperature of the poly(EOEOVE) segment. NIPAM copolymers have been used for the sensitization of liposomes (*6*−*9*). However, we have shown that poly(EOEOVE-*b*-ODVE) can also be used to sensitize liposomes to temperature. Because the copolymers used in this study were prepared by living cationic polymerization, they have the advantage of allowing control of the molecular architecture. In addition, the thermosensitive moiety of poly(EOEOVE-*b*-ODVE) shares a common structural unit with poly(ethylene glycol), which is a widely used, biocompatible polymer. In addition, it is suggested that the block copolymers have greater ability to sensitize stable liposomes than poly(NIPAM). The localized hyperthermia can be achieved by the use of microwave or radiofrequency energy or phased array ultrasound; energy focused on the tumor results in an increase in local temperature (*36*). Therefore, when coupled with local hyperthermia, these liposomes are expected to deliver anticancer drugs specifically to the target tumor. We are currently studying heat-induced control of delivery of anticancer drugs, such as doxorubicin, using the copolymer-modified liposomes and evaluating their usefulness as a site-specific delivery system of anticancer drugs.

LITERATURE CITED

(1) Lian, T., and Ho, R. J. Y. (2001) Trends and developments in liposome drug delivery systems. *J. Pharm. Sci. 90*, 667−680.

(2) Yatvin, M. B., Weinstein, J. N., Dennis, W. H., and Blumenthal, R. (1978) Design of liposomes for enhanced local release of drugs by hyperthermia. *Science 202*, 1290−1293.

(3) Huang S. K., Stauffer, P. R., Hong, K., Guo, J. W. H., Phillips, T. L., Huang, A., and Papahadjopoulos, D. (1994) Liposomes and hyperthermia in mice: increased tumor uptake and therapeutic efficacy of doxorubicin in sterically stabilized liposomes. *Cancer Res. 54*, 2186−2191.

(4) Needham, D., and Dewhirst, M. W. (2001) The development of a new temperature-sensitive drug delivery system for the treatment of solid tumors. *Adv. Drug Delivery Rev. 53*, 285−305.

(5) Kono, K., Hayashi, H., and Takagishi, T. (1994) Temperature-sensitive liposomes: liposomes bearing poly(*N*-isopropylacrylamide). *J. Controlled Release 30*, 69−75.
(6) Kono, K. (2001) Thermosensitive polymer-modified liposomes. *Adv. Drug Delivery Rev. 53*, 307−319.
(7) Kitano, H., Maeda, Y., Takeuchi, S., Ieda, K., and Aizu, Y. (1994) Liposomes containing amphiphilic poly-(*N*-isopropylacrylamides) prepared by using a lipophilic radical initiator. *Langmuir 10*, 403−406.
(8) Wu, X. S., Hoffman, A. S., and Yager, P. (1991) Conjugation of phosphatidylethanolamine to poly(*N*-isopropylacrylamide) for potential use in liposomal drug delivery systems. *Polymer 33*, 4659−4662.
(9) Polozova, A., and Winnik, F. M. (1997) Mechanism of the interaction of hydrophobically-modified poly-(*N*-isopropylacrylamides) and liposomes. *Biochim. Biophys. Acta 1326*, 213−224.
(10) Chandaroy, P., Sen, A., and Hui, S. W. (2001) Temperature-controlled content release from liposomes encapsulating Pluronic F127. *J. Controlled Release 76*, 27−37.
(11) Ringsdorf, H., Sackmann, E., Simon, J., and Winnik, F. M. (1993) Interactions of liposomes hydrophobically-modified poly(*N*-isopropylacrylamides): an attempt to model the cytoskeleton. *Biochim. Biophys. Acta 1153*, 335−344.
(12) Hayashi, H., Kono, K., and Takagishi, T. (1999) Temperature sensitization of liposomes using copolymers of *N*-isopropylacrylamide. *Bioconjugate Chem. 10*, 412−418.
(13) Hayashi, H., Kono, K., and Takagishi, T. (1998) Temperature-dependent associating property of liposomes modified with a thermosensitive polymer. *Bioconjugate Chem*. *9*, 382−389
(14) Hayashi, H., Kono, K., and Takagishi, T. (1996) Temperature-controlled release property of phospholipid vesicles bearing a thermo-sensitive polymer. *Biochim. Biophys. Acta 1280*, 127−134.
(15) Masci, G., Giacomelli, L., and Crescenzi, V. (2004) Atom transfer radical polymerization of *N*-isopropylacrylamide. *Macromol. Rapid Commun. 25*, 559−564.
(16) Ray, B., Isobe, Y., Morioka, K., Habaue, S., Okamoto, Y., Kamigaito, M., and Sawamoto, M. (2003) Synthesis of isotactic poly(*N*-isopripylacrylamide) by RAFT polymerization in the presence of Lewis acid. *Macromolecules 36*, 543−545.
(17) Convertine, A. J., Ayres, N., Scales, C. W., Lowe, A. B., and McCormick, C. L. (2004) Facile, controlled, room-temperature RAFT polymerization of N-isopropylacrylamide. *Biomacromolecules 5*, 1177−1180.
(18) Yusa, S., Shimada, Y., Mitsukami, Y., Yamamoto, T., and Morishima, Y. (2004) Heat-induced association and dissociation behavior of amphiphilic diblock copolymers synthesized via reversible addition−fragmentation chain transfer radical polymerization. *Macromolecules 37*, 7507−7513.
(19) Aoshima, S., Oda, H., and Kobayashi, E. (1992) Synthesis of thermally-induced phase separating polymer with well-defined polymer structure by living cationic polymerization. I. Synthesis of poly(vinyl ether)s with oxyethylene units in the pendant and its phase separation behavior in aqueous solution. *J. Polym. Sci., Part* A: *Polym. Chem. 30*, 2407−2413.
(20) Aoshima, S., and Sugihara, S. (2000) Syntheses of stimuli-responsive block copolymers of vinyl ethers with side oxyethylene groups by living cationic polymerization and their thermosensitive physical gelation. *J. Polym. Sci.*: *Part A: Polym. Chem. 38*, 3962−3965.
(21) Aoshima, S., and Hashimoto, K. (2001) Stimuli-responsive block copolymers with polyalcohol segments: syntheses via living cationic polymerization of vinyl ethers with a silyloxyl group and their thermoreversible physical gelation. *J. Polym. Sci.: Part A: Polym. Chem. 39*, 746−750.
(22) Aoshima, S.; Higashimura, T. (1986) Living cationic polymerization of vinyl monomers by organoaluminum halides. 1. Etalsl2/ester initiating systems for living polymerization of vinyl ethers. *Polym. Bull. 15*, 417−423.
(23) Kono, K., Nakai, R., Morimoto, K., and Takagishi, T. (1999) Thermosensitive polymer-modified liposomes that release contents around physiological temperature. *Biochim. Biophys. Acta 1416*, 239−250.
(24) Yoshino, K., Kadowaki, A., Takagishi, T., and Kono, K. (2004) Temperature-sensitization of liposomes by use of *N*-isopropylacrylamide copolymers with varying transition endotherms. *Bioconjugate Chem. 15*, 1102−1109.
(25) Bartlett, G. R. (1959) Phosphrus assay in column chromatography. *J. Biol. Chem. 234*, 466−468.
(26) Schild, H., and Tirrell, D. A. (1991) Microheterogeneous solutions of amphiphilic copolymers of *N*-isopropylacrylamide. *Langmuir 7*, 1319−1324.
(27) Kono, K., Henmi, A., Yamashita, H., Hayashi, H., and Takagishi, T. (1999) Improvement of temperature-sensitivity of poly(*N*-isopropylacrylamide)-modified liposomes, *J. Controlled Release 59*, 63−75.
(28) Heskins, M., and Guillet, J. E. (1968) Solution properties of poly(*N*-isopropylacrylamide). *J. Macromol. Sci., Chem., A2*, 1441−1455.
(29) Schild, H. G., and Tirrell, D. A. (1990) Microcalorimetric detection of lower critical solution temperatures in aqueous polymer solutions. *J. Phys. Chem. 94*, 4352−4356.
(30) Feil, H., Bae, Y. H., Feijen, J., and Kim, S. W. Effect of comonomer hydrophilicity and ionization on the lower critical solution temperature of *N*-isopropylacrylamide copolymers. *Macromolecules 26*, 2496−2500.
(31) Allen, T. M. (1983) Calcein as a tool in liposome methodology. In *Liposome Technology, Vol. III. Targeted Drug Delivery and Biological Interaction* (Gregoriadis, G., Ed.) pp 177−182, CRC Press: Boca Raton, FL.
(32) Ohtoyo, T., Shimagaki, M., Otoda, K., Kimura, S., and Imanishi, Y. (1988) Change in membrane fluidity induced by lectin-mediated phase separation of the membrane and agglutination of phospholipids vesicles containing glycopeptides. *Biochemistry 27*, 6458−6463.
(33) Cullis, P. R., and De Kruiff, B. (1979) Lipid polymorphism and the functional roles of lipids in biological membranes. *Biochim. Biophys. Acta 559*, 399−420.
(34) Litzinger, D. C., and Huang, L. (1992) Phosphatidylethanolamine liposomes: drug delivery, gene transfer and immunodiagnostic applications. *Biochim. Biophys. Acta 1113*, 201−227.
(35) Kim, J.-C., Bae, S. K., and Kim, J.-D. (1997) Temperature-sensitivity of liposomal lipid bilayers mixed with poly(*N*-isopropylacrylamide-*co*-acrylic acid). *J. Biochem. (Tokyo) 121*, 15−19.
(36) Mills J. K., and Needham, D. (2004) The materials engineering of temperature-sensitive liposomes. *Methods Enzymol*. *387*, 82−113.

BC050004Z

Structural Characterization and Buffering Capacity in Relation to the Transfection Efficiency of Biodegradable Polyurethane

S-ja Tseng,[†,‡] Shiue-cheng Tang,[‡] Min-da Shau,*[,†] Yi-fang Zeng,[†] Jong-yuh Cherng,[§] and Mei-fen Shih[⊥]

Department of Applied Chemistry, and Department of Pharmacy, Chia-Nan University of Pharmacy and Science, 60 Erh-Jen Rd., Sec 1, Jen-Te, Taiwan, R.O.C., Department of Chemical Engineering, National Tsing-Hua University, Hsinchu 300, Taiwan, R.O.C., and Department of Chemistry and Biochemistry, National Chung Cheng University, 168 University Rd., Min-Hsiung Chia-Yi, Taiwan, R.O.C. Received January 11, 2005; Revised Manuscript Received October 13, 2005

Inefficient release of polymer/DNA complexes from endocytic vesicles into the cytoplasm and the cytotoxic nature of cationic polymers are two of the primary causes of poor gene delivery. EG−polyurethane [poly(ethylene glycol)−PU, **Poly 1**], EGDM−polyurethane [poly(ethylene glycol), 2-(dimethylamino)ethylamine−PU, **Poly 2**], and MDEADM−polyurethane [*N*-methyldiethanolamine, 2-(dimethylamino)ethylamine−PU, **Poly 3**] were designed in this study to overcome these obstacles. The structural characteristics of polyurethanes and physicochemical properties of their formed complexes with DNA were determined to correlate their transfection efficiency. The results revealed that **Poly 2** and **Poly 3** could bind with plasmid DNA and yield positively charged complexes with a size required for transfection. **Poly 3** showed the best in buffering capacity and its formed complexes with DNA could transfect COS-7 cells better than those of **Poly 2** and **Poly 1**. This study reveals that the amine groups in the polymeric structure and the buffer capacity of a polymeric transfectant would affect its potential in DNA delivery. Also the size and binding properties of DNA and polymeric transfectants can be in correlation to the transfection efficiency of resulting DNA/polymer complexes.

INTRODUCTION

Gene therapy (the introduction of an extraneous gene into a cell with the aim of replacing a lost cellular utility or introducing a new functionality) requires a gene delivery system that is efficient and has no or low cytotoxic side effects. Several polycations have been proposed for the delivery of DNA into mammalian cells (*1*−*8*). These polycations not only can condense DNA into structures small enough to enter cells through endocytosis but also afford protection from nuclease degradation. It has been demonstrated that the presence of polycations mediates transfection, but they were also associated with a considerable degree of cytotoxicity (*5*, *7*, *9*). As a result, the successful design of polycations for a gene vector application generally requires a balance between transfection efficiency and short-term or long-term cytotoxicity.

Polyurethane is a class of biodegradable polymer with urethane linkages in the backbone. It has been studied as a biomaterial in tissue engineering (*10*−*12*). Recently, we have first demonstrated that cationic polyurethane can introduce DNA into cells (*13*). Besides the evaluation of the buffer capacity of transfectants for better transfection efficiency, we also systemically investigated the correlations between the structure of polymers, the physicochemical characteristics of polymer/DNA complexes, and their transfection efficiency. To study these crucial factors of polymers and complexes efficient for gene delivery, for example, size distribution of polyurethane/plasmid DNA complexes and structural effect of polyurethane, three polymers with different structures of the polyurethane (e.g., tertiary amine groups in side chain or backbone) were prepared in this article. This insight of correlation can shed light on the preferred in vitro properties of DNA−polymer particles to achieve optimum transfection efficiency.

EXPERIMENTAL PROCEDURES

Materials. *N*-Methyldiethanolamine (MDEA), glutaraldehyde, 2-dimethylaminoethylamine (DMAE), and poly(ethylene glycol) (PEG, M_w = 200), which were vacuum-dried before use, were obtained from Fluka. L-Lysine methyl ester diisocyanate (LDI) was from Kyowa Hakko Kogyo co. (Japan). Polyethylenimine (branched PEI, M_w = 25 000), poly(L-lysine) (PLL, M_w = 25 600), ethidium bromide, bovine serum albumin, 5-bromo-4-chloro-3-indoyl-β-galacto-pyranoside (X-Gal), Triton X-100, dibutyltin dilaurate, and *N*-[2-hydroxyethyl] piperazine-*N*′-[2-ethaneslfonic acid] (HEPES) were purchased from Sigma co. (USA). *N*-Methyl dibenzopyrazine methyl sulfate (electron-coupling reagent) and sodium (2,3-bis-(2-methoxy-4-nitro-5-sulfophenyl)-2*H*-tetrazolium-5-carboxanilide) (XTT) were purchased from Roche co. (USA). *Kpn*I was purchased from Promega co. (USA). Solvent *N*,*N*-dimethylformamide (DMF, Tedia co., USA) was dried over calcium hydride and distilled just before use.

Polymer Characterization. The structures of polymers were characterized by nuclear magnetic resonance (NMR, Bruker AMX-400 spectrometer) and Fourier transform infrared (FT-IR, Mattson Galerxy Series 5000 spectroscopy). All of the chemical shifts in ^{1}H NMR and ^{13}C NMR spectra were reported in parts per million (ppm). A 99.8% pure DMSO-d_6 was used as the solvent to characterize polymers. IR spectra were recorded on a

* Corresponding author. Tel +886-6.2664911, ext 245. Fax +886-6.2667319. E-mail address: minda.shau@msa.hinet.net.
† Department of Applied Chemistry, Chia-Nan University of Pharmacy and Science.
‡ National Tsing-Hua University.
§ National Chung Cheng University.
⊥ Department of Pharmacy, Chia-Nan University of Pharmacy and Science.

10.1021/bc050005r CCC: $30.25 © 2005 American Chemical Society
Published on Web 11/01/2005

spectrometer as KBr pellets. The molecular weights of polymers were determined by high-performance liquid chromatography/gel permeation chromatography analysis (GPC, Waters model LC-2410). THF was used as the eluent and polystyrene as the reference. The weight- and number-average molecular weights (M_w and M_n, respectively) were calibrated with standard polystyrene samples. The sample concentration in the THF was 8.0 mg/mL, and the flow rate was 1.0 mL/min.

Preparation of pCMV-βgal and Cell Culture. The plasmid pCMV-LacZ (pCMV-βgal), which contained a CMV promoter to drive the β-galactosidase (LacZ) gene expression, was used (*7*, *9*, *13*, *14*). The plasmid DNA was amplified in *Escherichia coli* (DH5α strain) and purified by column chromatography (Qiagen Plasmid Mega kit, Germany). The purified plasmid DNA was dissolved in tris(hydroxymethyl) methylamine−ethyldiaminetetraacetic acid (Tris-EDTA) buffer (pH 8.0) and determined by the ratio of UV absorbance at 260 nm. Agarose gel electrophoresis analysis using restriction enzymes showed that the plasmid was in supercoiled form. The same analysis further indicated that a size of 7.8 kb of DNA was visible by using a restriction enzyme.

The cell line COS-7 (SV 40 virus transformed African green monkey cell line, ATCC CRL-1651) was cultured in Dulbecco's modified Eagle's medium (DMEM, Gibco-BRL Co., Ltd.) with 4 mM L-glutamine adjusted to 10% fetal serum albumin, 1.5 g/L sodium bicarbonate, and 4.5 g/L glucose at 37 °C in a humidified atmosphere of 5% CO_2.

Polymer Synthesis. The LDI and MDEA or PEG with a NCO/OH molar ratio of 1.1/1 were mixed in anhydrous DMF solvent within the three-necked reaction flask under dry nitrogen purge and then heated to 70 °C to react for 6 h with 0.5 wt % dibutyltin dilaurate included as a catalyst. And then an excess amount of methanol was slowly added into the reaction mixture until no unreacted isocyanate groups were detected. The **Poly 1** was precipitated in ethyl ether and then dried at 40 °C under vacuum. **Poly 2** and **Poly 3** were synthesized using the aminolysis reaction (*13*). The polymers were characterized by FT-IR, ^{1}H NMR, and ^{13}C NMR.

*EG−Polyurethane (**Poly 1**).* ^{1}H NMR(400 MHz, DMSO-d_6, ppm) δ: 1.3−1.8 (6H, −CH_2CH_2CH_2−), 2.9 (2H, −CH_2NHCOO−), 3.1 (1H, −C*H*NHCOO−), 3.3 (3H, −NHCOOCH_3), 3.6 (−CH_2− of PEG), 4.05 (3H, −COOCH_3), 5.2 (1H, −CH$_2$N*H*COO−), 5.5 (1H, −CHN*H*COO−). ^{13}C NMR (400 MHz, DMSO-d_6, ppm) δ: 22.3, 29.1, 31.4 (−*C*H$_2$*C*H$_2$*C*H$_2$−), 40.5 (−*C*H$_2$NHCOO−), 52.4 (−NHCOO*C*H$_3$), 56.3 (−*C*HNHCOO−), 60.9(−COO*C*H$_3$), 63.6−70.1 (−*C*H$_2$− of PEG), 156.6 (−CH$_2$NH*C*OO−), 158.1 (−CHNH*C*OO−), 173.8 (−*C*OOCH$_3$). *EGDM−Polyurethane (**Poly 2**).* ^{1}H NMR(400 MHz, DMSO-d_6, ppm) δ: 1.3−1.8 (6H, −CH_2CH_2CH_2−), 2 (6H, −N(CH_3)$_2$), 2.5 (2H, −CH$_2$CH_2N(CH$_3$)$_2$), 2.9 (2H, −CH_2NHCOO−), 3.1 (1H, −C*H*NHCOO−), 3.3 (3H, −NHCOOCH_3), 3.5 (2H, −CH_2-NHCO−), 3.6 (−CH_2- of PEG), 5.2 (1H, −CH$_2$N*H*COO−), 5.5 (1H, −CHN*H*COO−), 7.0 (1H, −N*H*CO−). ^{13}C NMR (400 MHz, DMSO-d_6, ppm) δ: 22.3, 29.1, 31.4 (−*C*H$_2$*C*H$_2$-*C*H$_2$−), 38.9 (−*C*H$_2$NHCO−), 40.5 (−*C*H$_2$NHCOO−), 45.8 (−N(*C*H$_3$)$_2$), 52.4 (−NHCOO*C*H$_3$), 56.1 (−CH$_2$*C*H$_2$N(CH$_3$)$_2$), 56.3 (-*C*HNHCOO−), 63.6−70.1 (−*C*H$_2$− of PEG), 156.6 (−CH$_2$NH*C*OO−), 158.1 (−CHNH*C*OO−), 162.8 (−NH*C*O−).

*MDEADM−Polyurethane (**Poly 3**).* ^{1}H NMR(400 MHz, DMSO-d_6, ppm) δ: 1.3−1.8 (6H, −CH_2CH_2CH_2−), 2 (6H, −N(CH_3)$_2$), 2.3 (3H, −CH$_2$CH$_2$N(CH_3)CH$_2$CH$_2$−), 2.5−2.8 (2H, −CH$_2$CH_2N(CH$_3$)$_2$; 4H, −CH$_2$CH_2N(CH$_3$)CH_2CH$_2$−), 2.9 (2H, −CH_2NHCOO−), 3.1 (1H, −C*H*NHCOO−), 3.3 (3H, −NHCOOCH_3), 3.5 (2H, −CH_2NHCO−), 4.1 (4H, −CH_2CH$_2$N(CH$_3$)CH$_2$CH_2−), 5.2 (1H, −CH$_2$N*H*COO−), 5.5 (1H, −CHN*H*COO−), 7.0 (1H, −N*H*CO−). ^{13}C NMR (400 MHz, DMSO-d_6, ppm) δ: 22.3, 29.1, 31.4 (−*C*H$_2$*C*H$_2$-*C*H$_2$−), 38.9 (−*C*H$_2$NHCO−), 40.5 (−*C*H$_2$NHCOO−), 44.1 (−CH$_2$CH$_2$N(*C*H$_3$)CH$_2$CH$_2$−), 45.8 (−N(*C*H$_3$)$_2$), 52.4 (−NHCOO*C*H$_3$), 56.1 (−CH$_2$*C*H$_2$N(CH$_3$)$_2$), 56.3 (−*C*HNHCOO−), 56.8 (−CH$_2$*C*H$_2$N(CH$_3$)*C*H$_2$CH$_2$−), 59.1 (−*C*H$_2$CH$_2$-N(CH$_3$)CH$_2$*C*H$_2$−), 156.6 (−CH$_2$NH*C*OO−), 158.1 (−CHNH*C*OO−), 162.8 (−NH*C*O−).

Acid−Base Titration. Acid−base titration was used to evaluate the buffering capacity of synthesized cationic polyurethanes. In this assay, 10 mg of polymer was dissolved in 10 mL of 150 mM NaCl, and then 100 μL of 1 N NaOH was added to the solution to adjust the pH to the alkaline range at 11.6. HCl (0.1 N) was used as the titratant to lower the pH to acidic conditions at around 2−2.5. Titration increment size = 100 μL.

Preparation and Characterization of Polymer/Plasmid DNA Complexes. *Formation of Polymer/Plasmid DNA Complexes.* **Poly 1**, **2**, and **3** (10 mg/mL) were dissolved in the 20 mM HEPES buffer (pH 7.4), and serial dilutions were made in which the mass ratio of polymer/DNA (w/w) was from 1/2 to 300/1.

Particle Size, ζ-Potential, and Atomic Force Microscopy (AFM) Measurements of Polymer/Plasmid DNA Complexes. The particle sizes and surface charges of the polymer/DNA complexes were determined by dynamic light scattering (Nicomp 380 system, USA) at 25 °C using a 5-mW He−Ne laser (λ = 633 nm) as the incident beam at a scattering angle of 90° and electrophoretic mobility with a ζ-potential system (Nicomp Instrument, USA) at 25 °C. The image of the **Poly 3**/DNA complexes coated on the ruby mica surface was observed on a nanoscope II (Digital Instruments, Santa Barbara, CA) as described previously (*13*).

Stability of the Polymer/DNA Complexes in the Presence of Bovine Serum Albumin. The stability studies of the complexes in the presence of bovine serum albumin were evaluated by agarose gel retardation. The complexes were prepared at a mass ratio of 150/1 for 30 min, and bovine serum albumin was added into the solution of complexes to make final albumin concentrations of 5, 25, and 50 mg/mL. The DNA released from complexes was determined after 12 h at room temperature and 37 °C.

DNA Gel Retardation and Restriction Endonuclease Protection Assay. The polymer/DNA complexes were loaded into a 0.7% agarose gel containing ethidium bromide (0.3 μg/mL) in a tris−acetate−EDTA (TAE) buffer and electrophoresed at 100 V for 45 min. After electrophoresis, the DNA bands were visualized by UV-irradiation. The MDEA−PU/DNA polyplexes at ratios of 1/1, 5/1, and 50/1 (w/w) were incubated with *Kpn*I at a concentration of 10 U/μL at 37 °C for 90 min in the provided reaction buffer. After the restriction endonuclease digests, samples were analyzed by 0.7% agarose gel electrophoresis in the same manner as described above.

Transfection Studies and β-Galactosidase Assay. The COS-7 cells were used to evaluate the transfection efficiency of the polymer/DNA complexes. The cells were seeded in a 96-well plate (1.0×10^4 cells per well) in complete DMEM and incubated for 24 h before transfection. The polymer/DNA complexes (volume 200 μL) then were added to the cells. The DNA concentration was kept constant at 5 μg/mL (1.0 μg/well), and the amounts of polymer/DNA were expressed as mass ratios. After 1 h at 37 °C, the transfection mixture was removed and replaced with complete DMEM for an additional 48 h.

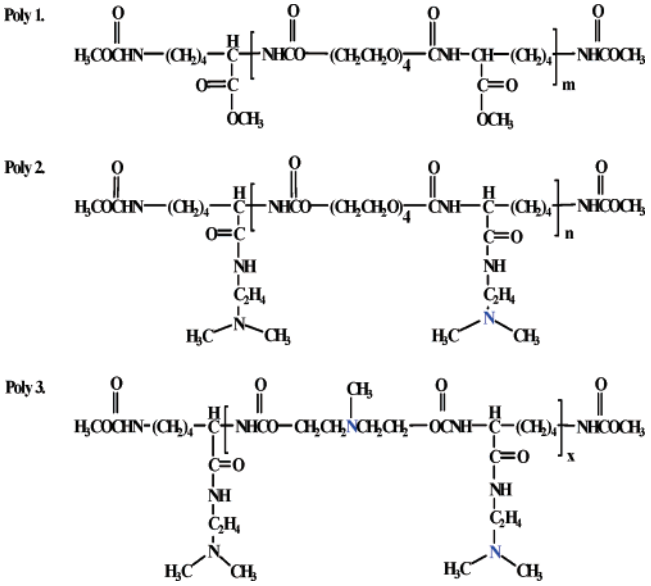

Figure 1. The structures of **Poly 1** (EG−polyurethane; EG−PU), **Poly 2** (EGDM−polyurethane; EGDM−PU), and **Poly 3** (MDEADM−polyurethane; MDEADM−PU).

Then a series of tests were performed for reporter gene expression (β-galactosidase) by histochemical staining with X-Gal, essentially as described previously (*7*, *9*, *13*, *15*).

Determination of the Cytotoxic Effect of Polymers and Polymer/DNA Complexes. Cytotoxicity of **Poly 1**, **Poly 2**, and **Poly 3** in comparison with a commonly used gene carrier, PEI, was evaluated using the XTT assay (*7*, *9*, *13*, 16). In a 96-well plate, COS-7 cells were cultured in complete DMEM then seeded at a density of 1.0×10^4 cells/well. The cells were incubated at 37 °C and 5% CO_2 in humidified atmosphere for 24 h. Subsequently, the cells were incubated for 1 h in 200 mL of FBS-free DMEM containing a polymer only (**Poly 1**, **Poly 2**, **Poly 3**, and PEI) or complexes at various concentrations. The cells incubated in DMEM were only for a negative control. After 1 h, the cells were washed with 200 μL of PBS solution and replaced by complete DMEM. After 48 h incubation, 50 μL of XTT labeling mixture was added to each well and incubated at 37 °C for 1 h. Results were expressed as the relatively cell viability (%) with respect to control wells containing culture medium cells.

RESULTS AND DISCUSSION

Structural Characterizations of Polymers. The structures of EG−polyurethane, EGDM−polyurethane, and MDEADM−polyurethane (**Poly 1**, **Poly 2**, and **Poly 3**, respectively) were shown in Figure 1. The resulting polyurethane (**Poly 3**) with tertiary amines ($-CH_2CH_2N(CH_3)CH_2CH_2-$) and ($-N(CH_3)_2$) in the backbone and side chain was isolated in up to 90% yield with weight average molecular weight of 37 000 and a polydispersity of 1.8 relative to polystyrene standards in THF. **Poly 2**, with tertiary amines ($-N(CH_3)_2$) in the side chain, and **Poly 1** showed that the weight-averaged molecular weights were 35 000 and 39 000 with a polydispersity of 1.7 and 1.8, respectively. The structures of **Poly 1**, **Poly 2**, and **Poly 3** were confirmed by FT-IR, ^{1}H NMR, and ^{13}C NMR. From the FT-IR spectra, the peaks at 1720 cm^{-1} (C=O stretching, urethane), 1651 cm^{-1} (C=O stretching, amide), 1553 cm^{-1} (N−H bending, amide), and 3320 cm^{-1} (N−H stretching, urethane) represent the absorptions of urethane links in **Poly 1**, **Poly 2**, and **Poly 3** (data not shown). In the ^{1}H NMR spectra of **Poly 1**, **Poly 2**, and **Poly 3**, two distinct peaks at 5.9 and 5.2 ppm were assigned to the NH protons derived from the α- and ϵ-amine groups of L-lysine respectively (*13*). Chemical shifts of 2.0 and 7.0 ppm, observed in the **Poly 2** and **Poly 3**, derived from the methyl and amide protons of the pendant group, respectively. In ^{13}C NMR spectra, there was an accompanied disappearance of chemical shift at 173.8 ppm, which represented the ester carbon of the pendent group in the **Poly 1**. The FT-IR, ^{1}H NMR, and ^{13}C NMR characterizations of the synthesized polymers provided clear evidence that **Poly 1**, **Poly 2**, and **Poly 3** had been successfully synthesized.

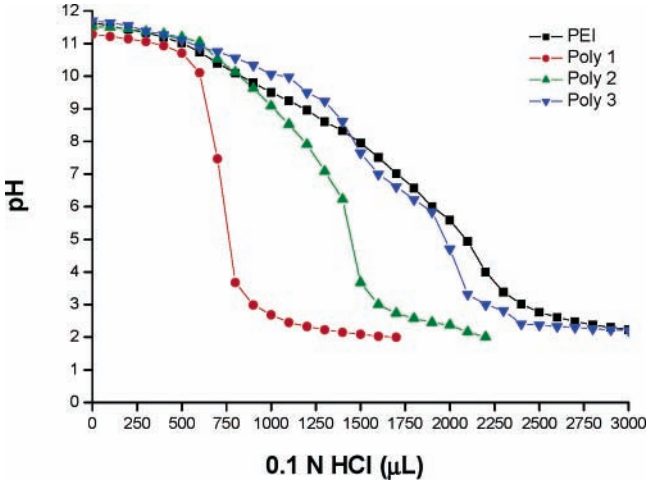

Figure 2. Acid−base titration profile of various polymers with 0.1 N HCl solution.

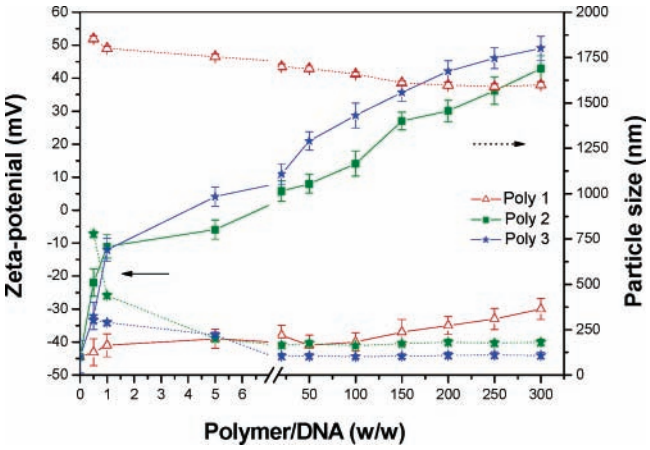

Figure 3. Sizes and ζ-potentials of polymer/pCMV-βgal complexes prepared at different mass ratios. Results are presented as mean ± SD (n = 3).

Buffering Capacity of Polymers. Titration studies were performed to determine the buffering capacities of the various polymers within the endosomal/lysosomal compartments of the cell (Figure 2). All of the polycation solutions had pH 11.5−11.8 after addition of 100 μL of 1.0 N NaOH. PEI showed the best buffering capacity with a wide pH range. **Poly 1**, containing no amine group in the structure, demonstrated a poor buffering range from pH 11.5 and 10. The buffering properties of the polymers were improved through the incorporation of tertiary amine groups into the backbone or side chain. **Poly 2**, bearing tertiary amines in the side chain, and **Poly 3**, with tertiary amines in the backbone and side chain, showed buffering capacities from pH 11.5−7.0 and 11.7−

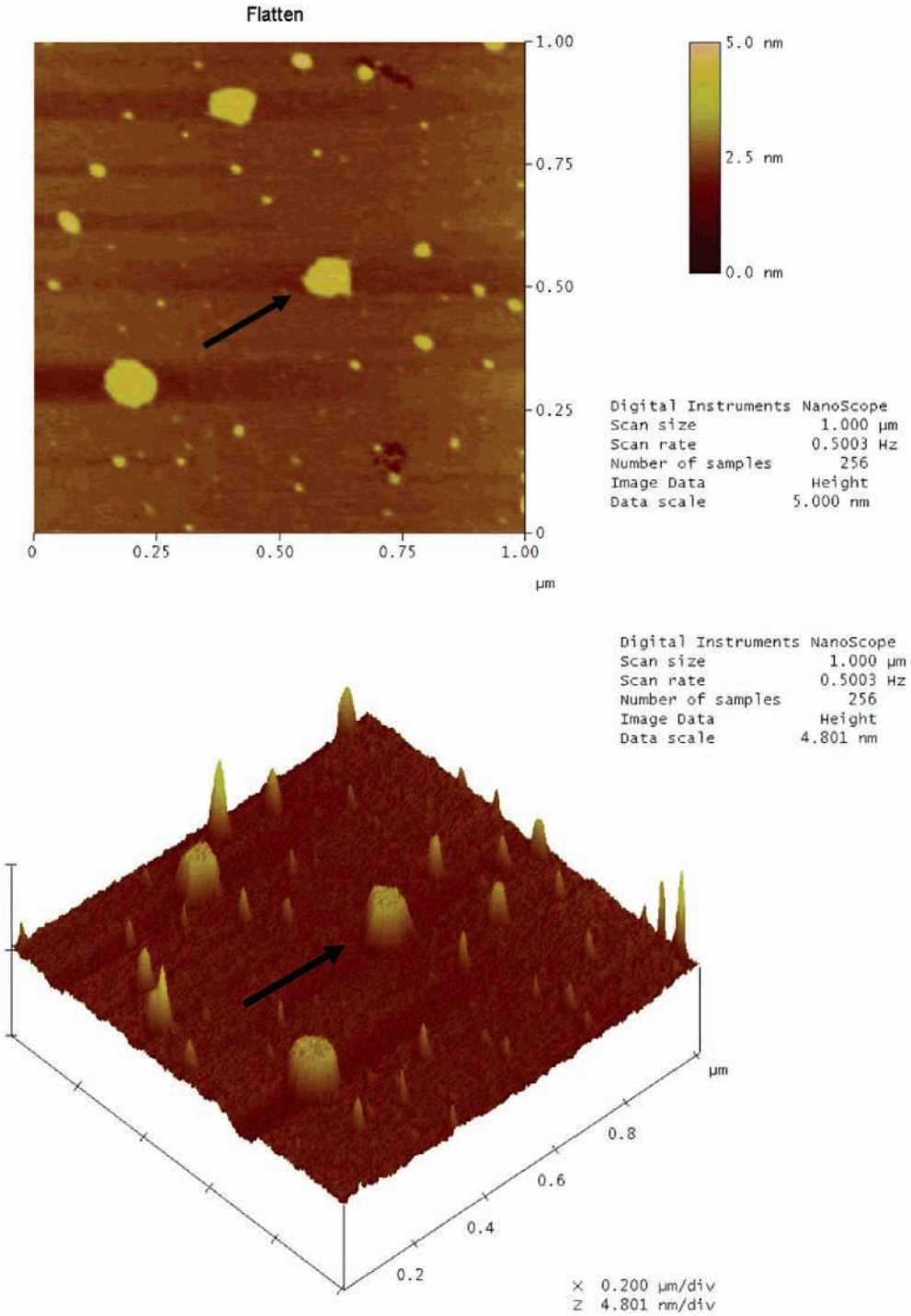

Figure 4. The AFM images of **Poly 3**/pCMV-βgal complexes (w/w), 150/1. The height of the AFM image is represented by a graded brown−yellow scale with the yellow color indicating a height more than 10 nm above the ruby mica. The x and y dimensions are scaled as shown.

5.0, respectively. It was found that **Poly 3** possessed excellent properties in DNA condensing and buffering abilities.

Self-Assembly of Polymer with Plasmid DNA and Restriction Endonuclease Protection Assay of Polymer/DNA Complexes. Figure 3 shows the size and ζ-potential of the **Poly 1**/DNA complexes, **Poly 2**/DNA complexes, and **Poly 3**/DNA complexes at various mass ratios ranging from 1/2 to 300/1. The results show that the average diameter (100−110 nm) of the **Poly 3**/DNA complexes and the average diameter (170−180 nm) of the **Poly 2**/DNA complexes fall within the general size required for cellular endocytosis (<0.2 μm). The DNA condensing ability of **Poly 1** was very weak as the average diameter (1550−1750 nm) of **Poly 1**/DNA complexes was formed because the backbone and side chain present no tertiary amines. The results demonstrated that tertiary amines in only the side chain of **Poly 2** were sufficient to condensed DNA into complexes and that introduction of tertiary amines in the backbone and side chain of **Poly 3** provided even better electrostatic interactions between **Poly 3** and DNA. Figure 4 shows the atomic force microscopy (AFM) images of **Poly 3**/DNA complexes at mass ratios of 150/1. The ζ-potential of the resulting complexes was changed from a negative charge to a positive charge when the amounts of **Poly 2** and

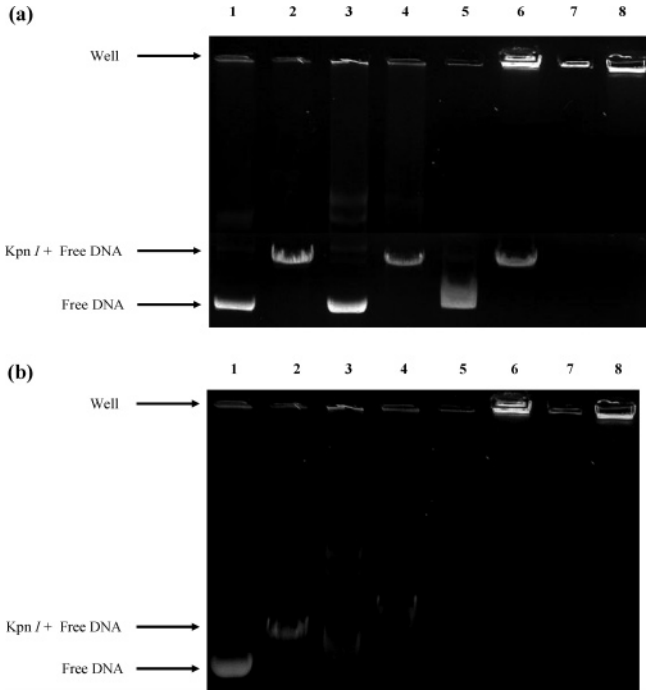

Figure 5. DNA gel retardation and restriction endonuclease protection assay of **Poly 2** (a) and **Poly 3** (b). Lanes: (1) 400 ng of pCMV-βgal; (2) 400 ng of pCMV-βgal treated with *Kpn*I; (3) polymer/pCMV-βgal (w/w), 1/1; (4) polymer/pCMV-βgal (w/w), 1/1, treated with *Kpn*I; (5) polymer/pCMV-βgal (w/w), 5/1; (6) polymer/pCMV-βgal (w/w), 5/1, treated with *Kpn*I; (7) polymer/pCMV-βgal (w/w), 50/1; (8) polymer/pCMV-βgal (w/w), 50/1, treated with *Kpn*I.

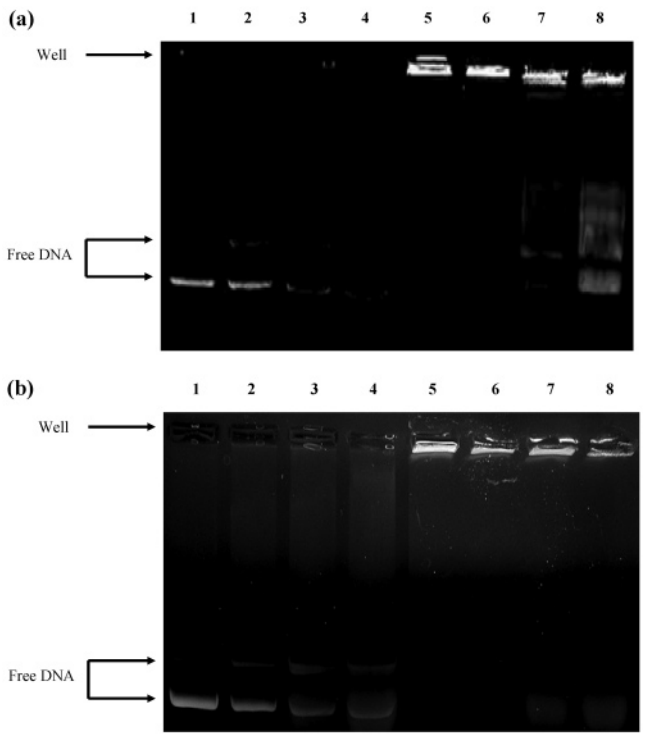

Figure 6. Stability of complexes based on **Poly 2** (a) and **Poly 3** (b) after 12 h incubation with albumin at 37 °C. The polymer/DNA complexes were prepared at mass ratio of 150/1, incubated with serum albumin, and analyzed on a 0.7% (w/v) agarose gel for 45 min at 100 V. Lanes: (1) 625 ng of pCMV-βgal; (2) 625 ng of pCMV-βgal treated with 5 mg/mL BSA; (3) 625 ng of pCMV-βgal treated with 25 mg/mL BSA; (4) 625 ng of pCMV-βgal treated with 50 mg/mL BSA; (5) polymer/pCMV-βgal (w/w), 150/1; (6) polymer/pCMV-βgal (w/w), 150/1, treated with 5 mg/mL BSA; (7) polymer/pCMV-βgal (w/w), 150/1, treated with 25 mg/mL BSA; (8) polymer/pCMV-βgal (w/w), 150/1, treated with 50 mg/mL BSA.

Poly 3 were increased. From particle size characterization and ζ-potential analysis, it was found that these properties varied with the number of amino groups in the polyurethanes and that the tertiary amine moieties within the backbone enhanced the electrostatic interaction between DNA and cationic polymers.

The ability of the polycation to interact electrostatically with DNA was indicated by a reduction in DNA electrophoretic mobility. In addition, the relative ability of the polymers to retain DNA within the complex was indicated by the formation of a DNA streak in the gel. This streak is caused by separation of the DNA and the polycation during electrophoresis induced by the electrophoretic force. Figure 5 shows that all polycations can condense DNA into nanosized complexes and afford protection from nuclease degradation (endonuclease *Kpn*I). At the low mass ratio 5/1 of **Poly 3**/DNA, plasmid DNA was totally retained, as indicated in lane 5 (Figure 5b). Plasmid DNA was partially retained in the presence of **Poly 2** at a mass ratio of 1/1 and 5/1 (lane 3 and 5) and totally retained at a mass ratio of 50/1 (lane 7 of Figure 5a). **Poly 1** was not completely bound with DNA at all mass ratios (data not shown). The higher efficiency of **Poly 3** in DNA complexation relative to **Poly 2** may be due to the further introduction of tertiary amines into the backbone of **Poly 3**.

The plasmid DNA (or polymer/DNA) was incubated with the restriction endonuclease *Kpn*I, which can cleave the plasmid DNA in the CMV-promoter region, at a concentration of 10 U/μL. Pure linear DNA was observed when the plasmid DNA was treated with *Kpn*I, in Figure 5a lane 2. **Poly 2** was unable to protect the plasmid DNA from enzyme degradation at the lower mass rations of 1/1 and 5/1 (shown in lanes 4 and 6 of Figure 5a). However, it was found that the plasmid DNA was completely protected against *Kpn*I at the higher mass ratios of **Poly 2**/DNA (shown in lanes 7 and 8 of Figure 5a). **Poly 3** showed excellent protective ability for DNA (shown in lane 6 of Figure 5) due to the existence of tertiary amino groups in the backbone and side chain.

Stability of the Polymer/DNA Complexes in the Presence of Bovine Serum Albumin. The interaction of bovine serum albumin with the complexes was investigated by means of agarose gel electrophoresis. The naked DNA and complexes were prepared at a mass ratio of 150/1, and subsequently bovine serum albumin was added to a final concentration of 5, 25, and 50 mg/mL. The DNA release was assessed after 12 h. It is clear that DNA was released through the interaction of albumin with the **Poly 2**/DNA complexes in lanes 7 and 8 (Figure 6a). Although **Poly 2** could self-assemble DNA into complexes, the electrostatic force between **Poly 2** and DNA was not stable toward bovine serum albumin. In lanes 5−8 (Figure 6b), the formation of stronger electrostatic complexes was suggested between the **Poly 3** and DNA. The **Poly 3**/DNA complexes were then more stable toward bovine serum albumin.

Cellular Delivery of Plasmid DNA via Polymer/DNA Complexes. The well-studied COS-7 cell line was transfected in vitro (*7*, *9*, *16*) with polymer/DNA complexes. The transfection efficiency of polymer/DNA complexes was assessed by an indication of β-galactosidase expression. Transfection with **Poly 1** was not observed because the particle size (1550−1750 nm) was large and the buffering capacity was low. The numbers of transfected cells showed a bell-shaped trend for the **Poly 2**/DNA and **Poly 3**/DNA (w/w) ratios above 100/1 (w/w)

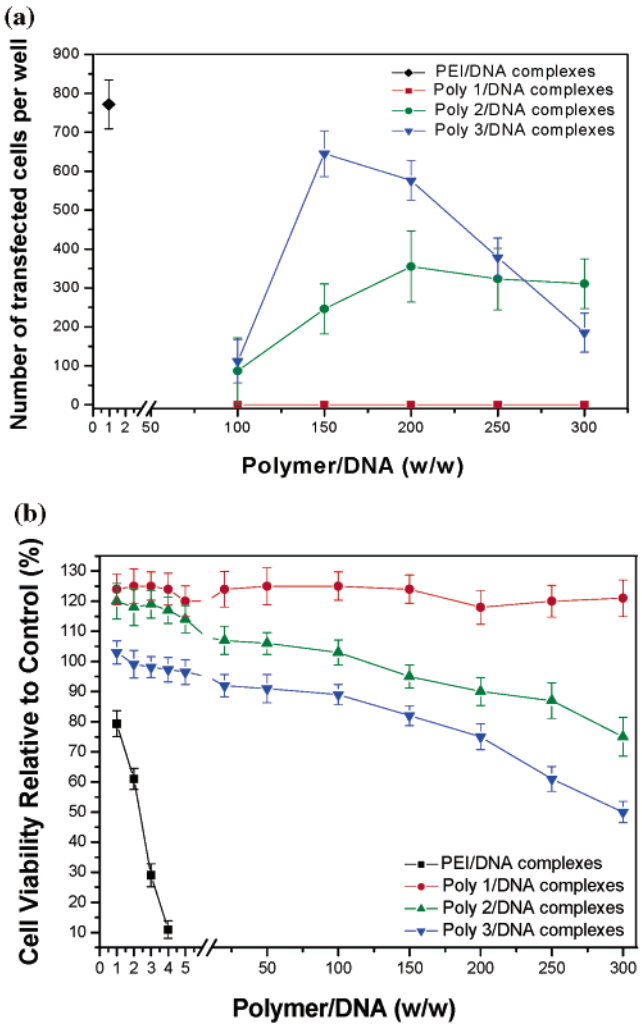

Figure 7. (a) Effect of polymer concentration on the number of transfected cells. Transfection was performed in COS-7 cells for 1 h at a 1 μg of DNA per well in DMEM, and then cells were incubated for an additional 48 h in fresh media with 5% FBS. Results are presented as mean ± SD ($n = 3$). (b) Cytotoxicity of polymer/pCMV-βgal complexes in COS-7 cells. Results are presented as mean ± SD ($n = 3$).

as observed previously for other polycation-based transfection systems (*7*, *13*, *17*). The highest transfection efficiency of **Poly 3**/DNA was reached at a mass ratio of 150/1, and **Poly 3** displays the highest gene delivery efficacy (equivalent to branched PEI made with the optimal transfection efficiency at a mass ratio of 1/1 (*18*), shown in Figure 7a). In addition, it was demonstrated that the transfection efficiency of **Poly 3** was greater than that of **Poly 2**. This may be due in part to the particle size and "proton sponge" hypothesis (*5*, *8*, *19*). Although **Poly 2** with tertiary amines in the side chain has been shown to effectively condense plasmid DNA into complexes (170−180 nm), mostly the amine groups of **Poly 2** have already been protonated under pH 11.5−7.0. This result suggests that endosomal buffering effect could be limited from the **Poly 2**/DNA complexes when the pH in the activated endosome drops to 5. And the size of **Poly 3**/DNA complexes (100−110 nm) and **Poly 3** buffering capacity between pH 11.7 and 5.0, due to introduction of tertiary amines in the backbone and side chain, are capable of buffering the endosomal pH and increasing the endosomal release of the **Poly 3**/DNA complexes.

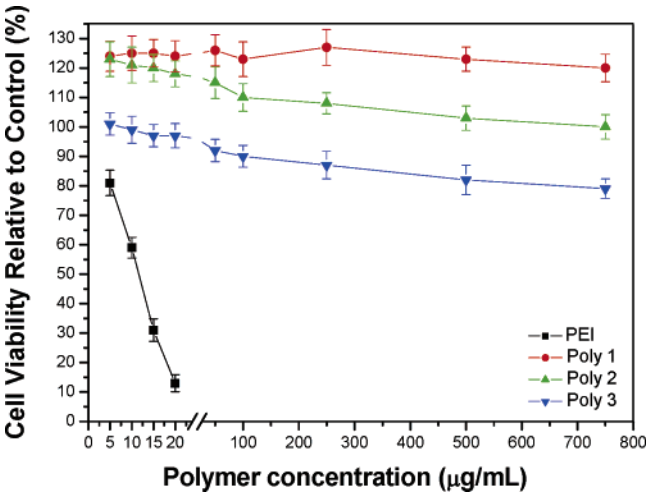

Figure 8. Cytotoxicity of polymers in COS-7 cells.

Relative cell viability in the presence of **Poly 1**/DNA, **Poly 2**/DNA, and **Poly 3**/DNA complexes in comparison with PEI/DNA complexes was shown in Figure 7b. It was found that the cell viability in the presence of PEI/DNA complexes rapidly decreased with an increase of polymer concentration, whereas cell viability in the presence of **Poly 1**/DNA, **Poly 2**/DNA, and **Poly 3**/DNA complexes was slightly changed with an increase of polymer concentration, indicating much less toxicity than PEI.

Cytotoxicity of Polymers. To determine the cytotoxicity of **Poly 1**, **Poly 2**, and **Poly 3** in comparison with PEI, we performed an XTT assay using the COS-7 cell line. Cells were incubated with increasing amounts of **Poly 1**, **Poly 2**, and **Poly 3** (ranging from 5 to 750 μg/mL) or PEI (ranging from 5 to 20 μg/mL). The results show that **Poly 1**, **Poly 2**, and **Poly 3** exhibited substantially lower toxicity on COS-7 cells than PEI in Figure 8. The IC_{50} [defined as the concentration resulting in 50% inhibitory activity (cell death)] for the PEI was around 15 μg/mL, whereas **Poly 1**, **Poly 2**, and **Poly 3** showed more than 80% viable cells even at a higher dose (750 μg/mL) with no significant change in cell morphology and proliferation relative to controls. We infer that the polyurethanes can provide better cytotoxicity profiles than presently used gene carrier (PEI) due to the introduction of amino groups and urethane units in the polycation backbone alternately to reduce the high charge density of the polycation.

CONCLUSION

It was found that the positive charge on pendent amine groups or within the backbone of the polymer can condense DNA to form DNA−polycation complexes due to the electrostatic force between the DNA and the polycation. Stronger electrostatic interaction between DNA and cationic polymer could make nanosized DNA/polymer complexes and resist endonuclease and albumin degradations, resulting a better bioactivity in transfection efficiency. Besides the existence of positive charges in polymer being crucial, optimal buffering capacity was needed for the release of DNA/polymer complexes from endosomes. Having a high transfection efficiency and low cytotoxicity, the new biodegradable polyurethane is an interesting candidate for a nonviral gene delivery system.

ACKNOWLEDGMENT

The authors acknowledge with gratitude financial support from the National Science Council of the Republic of China through Grant No. NSC 91-2216-E-041-003.

LITERATURE CITED

(1) Zauner, W., Ogris, M., and Wagner, E. (1998) Polylysine-based transfection systems utilizing receptor-mediated delivery. *Adv. Drug Delivery Rev. 30*, 97−113.
(2) Woolfert, M. A., Schacht, E. H., Toncheva, V., Ulbrich, K., Nazarova, O., andn Seymour, L. W. (1996) Characterization of Vector for Gene Formed by Self-Assembly of DNA With Synthetic Block Co−Polymers. *Hum. Gene Ther. 7*, 2123−2133.
(3) Pouton, C. W., Lucas, P., Thomas, B. J., Uduehi, A. N., Milroy, D. A., and Moss, S. H. (1998) Polycation−DNA complexes for gene delivery: a comparison of the biopharmaceutical properties of cationic polypeptides and cationic lipids. *J. Controlled Release 53*, 289−299.
(4) Haensler, J., and Szoka, F. C. (1993) Polyamidoamine Cascade Polymers Mediate Efficient Transfection of Cells in Culture. *Bioconjugate Chem. 4*, 372−379.
(5) Boussif, O., Lezoualch, F., Zanta, M. A., Mergny, M. D., Scherman, D., Demeneix, B., and Behr, J. P. (1995) A Versatile Vector for Gene and Oligonucleotide Transfer into Cells in Culture and in-Vivo − Polyethylenimine. *Proc. Natl. Acad. Sci. U.S.A. 92*, 7297−7301.
(6) Godbey, W. T., Wu, K. K., and Mikos, A. G. (1999) Poly-(ethylenimine) and its role in gene delivery. *J. Controlled Release 60*, 149−160.
(7) Cherng, J. Y., vandeWetering, P., Talsma, H., Crommelin, D. J. A., and Hennink, W. E. (1996) Effect of size and serum proteins on transfection efficiency of poly((2-dimethylamino)-ethyl methacrylate)-plasmid nanoparticles. *Pharm. Res. 13*, 1038−1042.
(8) Zanta, M. A., Boussif, O., Adib, A., and Behr, J. P. (1997) In vitro gene delivery to hepatocytes with galactosylated polyethylenimine. *Bioconjugate Chem. 8*, 839−844.
(9) vandeWetering, P., Cherng, J. Y., Talsma, H., and Hennink, W. E. (1997) Relation between transfection efficiency and cytotoxicity of poly(2-(dimethylamino)ethyl methacrylate)/plasmid complexes. *J. Controlled Release 49*, 59−69.
(10) Zhou, C. R., and Yi, Z. J. (1999) Blood-compatibility of polyurethane/liquid crystal composite membranes. *Biomaterials 20*, 2093−2099.
(11) Guan, J. J., Fujimoto, K. L., Sacks, M. S., and Wagner, W. R. (2005) Preparation and characterization of highly porous, biodegradable polyurethane scaffolds for soft tissue applications. *Biomaterials 26*, 3961−3971.
(12) Zhang, J. Y., Beckman, E. J., Piesco, N. P., and Agarwal, S. (2000) A new peptide-based urethane polymer: synthesis, biodegradation, and potential to support cell growth in vitro. *Biomaterials 21*, 1247−1258.
(13) Yang, T. F., Chin, W., Cherng, J., and Shau, M. (2004) Synthesis of novel biodegradable cationic polymer: *N*,*N*-diethylethylenediamine polyurethane as a gene carrier. *Biomacromolecules 5*, 1926−1932.
(14) van de Wetering, P., Moret, E. E., Schuurmans-Nieuwenbroek, N. M. E., van Steenbergen, M. J., and Hennink, W. E. (1999) Structure−activity relationships of water-soluble cationic methacrylate/methacrylamide polymers for nonviral gene delivery. *Bioconjugate Chem. 10*, 589−597.
(15) Lim, K., and Chae, C. B. (1989) A Simple Assay for DNA Transfection by Incubation of the Cells in Cultured Dishes with Substrates for Beta-Galactosidase. *Biotechniques 7*, 576−579.
(16) Scudiero, D. A., Shoemaker, R. H., Paull, K. D., Monks, A., Tierney, S., Nofziger, T. H., Currens, M. J., Seniff, D., and Boyd, M. R. (1988) Evaluation of a Soluble Tetrazolium Formazan Assay for Cell-Growth and Drug Sensitivity in Culture Using Human and Other Tumor-Cell Lines. *Cancer Res. 48*, 4827−4833.
(17) Gebhart, C. L., and Kabanov, A. V. (2001) Evaluation of polyplexes as gene transfer agents. *J. Controlled Release 73*, 401−416.
(18) Putnam, D., Zelikin, A. N., Izumrudov, V. A., and Langer, R. (2003) Polyhistidine-PEG: DNA nanocomposites for gene delivery. *Biomaterials 24*, 4425−4433.
(19) Behr, J. P. (1997) The proton sponge: A trick to enter cells the viruses did not exploit. *Chimia 51*, 34−36.

BC050005R

Fluorescent Kabiramides: New Probes to Quantify Actin in Vitro and in Vivo

Chutima Petchprayoon,[†] Khanit Suwanborirux,*[,†] Junichi Tanaka,[‡] Yuling Yan,[§] Tomoyo Sakata,[⊥] and Gerard Marriott*[,⊥]

Bioactive Marine Natural Products Chemistry Research Unit (BMNCU), Department of Pharmacognosy, Faculty of Pharmaceutical Sciences, Chulalongkorn University, Pathumwan, Bangkok 10330, Thailand, Department of Chemistry, Biology, and Marine Science, University of the Ryukyus, Nishihara, Okinawa 903-0213, Japan, Department of Mechanical Engineering, University of Hawaii at Monoa, Honolulu, Hawaii 96822, and Department of Physiology, University of Wisconsin, 1300 University Avenue, Madison, Wisconsin 53706. Received January 12, 2005; Revised Manuscript Received August 7, 2005

We present the design, synthesis, and biochemical and spectroscopic characterization of five functional fluorescent conjugates of kabiramide C (KabC), a small molecule biomimetic of gelsolin. The tetramethylrhodamine (TMR), rhodol green (RG), IC5, dapoxyl (DAP), and fluorescein diester (FDE) conjugates of KabC bind specifically to actin at the barbed end in a 1:1 complex. These probes are shown to function in an indistinguishable manner to the unmodified KabC. Various modalities of the fluorescence emission of these KabC probes, including fluorescence anisotropy and fluorescence resonance energy transfer, are used for the development of assays for the rapid determination of G-actin concentration in solution. The TMR−KabC and FDE−KabC probes are cell permeable and provide unique imaging information on the distribution and dynamics of actin filament within living cells.

INTRODUCTION

Cell protrusion is characterized by fluctuations in the concentrations and activities of, and/or interactions between, membrane receptors, Rac1, Ca^{2+}, PIP_2, cofilin, and actin filament barbed-end capping protein—these dynamic events are usually confined to lamellipodia and are coupled to the rapid and polarized polymerization of actin filaments in the vicinity of the activated membrane receptor (*1*−*2*). A major challenge in cell motility research is to develop innovative approaches and techniques that permit the study of the temporal and spatial regulation of these events within the lamellipodium. The critical concentration for the in vitro polymerization of pure G-actin is ∼100 nM, yet as much as 50% of the ∼200 μM concentration of actin within an eukaryotic cell exists as G-actin (*2*). The large amount of unpolymerized G-actin results from the sequestering activity of monomer binding proteins that include thymosin β4 and profilin, which reduce the free concentration of G-actin to ∼100 nM; filament capping proteins such as tropomodulin (pointed-end) (*3*) and gelsolin, capping protein (CP), and CapG (fast growing, barbed-end) also block actin polymerization from existing filaments (*4*−*6*). However, during cell protrusion, a rise in membrane-associated PIP_2 dissociates barbed-end capping proteins from these filaments and is accompanied by an explosive polarization of actin facilitated by the nucleating proteins ARP2/3-WASP and formins (*2*, *7*−*11*).

Given the central role of the barbed-end in regulating actin filament polymerization, a better understanding of cell protrusion will require knowledge of molecular events at the barbed-end of the filament and how they are regulated within cells. These are challenging studies since the protomer at the barbed-end of an actin filament accounts for only 1 in 10^4 of actin monomers within a 10 μM solution of pure F-actin (average filament length of 2.5 μm) or 1 in 10^6 of all protomers in a typical cell. While certain actin-directed probes such as GFP−actin (*12*) and TMR−phalloidin (*13*) are useful in quantifying total actin and the average rate of actin filament dynamics in a cell, they do not provide specific information on molecular events at the barbed-end. Furthermore, the linkage of large, aromatic, charged fluorescent probes such as TMR−maleimide to Cys-374 of actin can impair or inhibit polymerization (*25*). We have recently shown that a family of actin-targeted trisoxazole macrolides typified by kabiramide C (KabC) (*14*, *15*) function in vitro and in living cells as small molecule biomimetics of the barbed-end capping proteins, gelsolin, and CapG (*15*). Since correct regulation of the barbed-end of the actin filament is essential to many cellular processes, it is no wonder that KabC and related macrolides exhibit potent cytotoxic effects (*15*). We argue that the binding specificity of KabC-related drugs to the cleft between subdomans 1 and 3 of actin (the barbed-end) provides an opportunity to develop a new class of optical probes that serve as an indicator of molecular events associated with actin polymerization. Here, we describe the preparation and characterization of several new fluorescent KabC probes and show that they bind to G-actin with high specificity—this interaction can be quantified using a variety of changes in the fluorescence emission of the probe (quantum yield, polarization, lifetime, and Foerster resonance energy transfer). Finally, we show using confocal imaging

* To whom correspondence should be addressed. G.M.: e-mail, GM@physiology.wisc.edu; tel, (608) 262-6309; fax, (608) 265-5512. K.S.: e-mail, skhanit@chula.ac.th; tel, (662) 218-8363; fax, (662) 254-5195.

[†] Chulalongkorn University.

[‡] University of the Ryukyus.

[§] University of Hawaii at Monoa.

[⊥] University of Wisconsin.

10.1021/bc050006j CCC: $30.25 © 2005 American Chemical Society
Published on Web 09/13/2005

of living cells that the tetramethylrhodamine− and the fluorescein diester−KabC derivatives (TMR−KabC and FDE−KabC, respectively) are cell permeable and can be used to image and quantify actin filament dynamics in living cells.

EXPERIMENTAL PROCEDURES

Instrumentation. ESI mass spectra were carried out on a Micromass LCT for exact mass measurement**.** Absorption spectra were recorded using a Shimadzu 1601PC instrument. An SLM-Aminco AB2 fluorometer was used to record emission and excitation spectra of fluorescent dyes and their conjugates. Fluorescence emission spectra were recorded using excitation and emission polarizers aligned at 0 and 54°, respectively, and corrected for the instrument response (*16*). Fluorescence resonance energy transfer (FRET) between 6-proprionyl-2-dimethylaminonaphthalene (Prodan) labeled to G-actin to the bound fluorescent KabC probes was performed by exciting Prodan at 385 nm and recording the emission from the complexes between 400 and 650 nm for rhodol green and for TMR and 400−750 nm for *N*-ethyl-*N*′-[5-(*N*″-succininmidyloxycarbonyl)pentyl]-3,3,3′,3′-tetramethyl-2,2′-indodicarbocyanine chloride (IC5, a de-sulfated derivative of the better known Cy5). Fluorescence anisotropy (FA) was measured according to Heidecker et al. (*17*). All spectra were recorded at room temperature.

Syntheses. 5-(and-6)-Carboxytetramethylrhodamine, succinimidyl ester (C-1171), dapoxyl carboxylic acid, succinimidyl ester (D-10161), and rhodol green carboxylic acid, succinimidyl ester (mixed isomer, R-6108) were purchased from Molecular Probes. *N*-Ethyl-*N*′-[5-(*N*″-succininmidyloxycarbonyl)pentyl]-3,3,3′,3′-tetramethyl-2,2′-indodicarbocyanine chloride (IC5−OSu) was purchased from Dojindo, and 5(6)-carboxyfluorescein diacetate *N*-succinimidyl ester was purchased from Fluka. Dichlorometane (CH_2Cl_2) was dried over CaH_2, and dimethyl sulfoxide (DMSO) was opened immediately before use. 7-(4-Aminomethyl-1*H*-1,2,3-triazol-1-yl)kabiramide C (AMT−KabC) was synthesized from KabC as described in Petchprayoon et al. (*18*). Silica gel 60 F_{254} thin-layer chromatography (TLC) plates were purchased from Merck (250 μm thick), and C_{18}-silica gel F_{254} TLC plates were purchased from Fisher Scientific (Analtech UNIPLATES; 250 μm thick).

Synthesis of the Tetramethylrhodamine Derivative of 7-(4-Aminomethyl-1*H*-1,2,3-triazol-1-yl)kabiramide C (TMR−KabC). To a solution of AMT−KabC (1 mg, 0.98 μmol) in dry CH_2Cl_2 (100 μL), a solution of 5-(and-6)-carboxytetramethylrhodamine, succinimidyl ester (0.6 mg, 1.14 μmol) in DMSO (100 μL) was added. The reaction mixture was stirred at room temperature in the dark under N_2 atmosphere. After 8 h, the mixture was concentrated and isolated by silica gel TLC (CH_2Cl_2/MeOH = 20:3) and C_{18}-silica gel TLC (MeOH/H_2O = 7:3) to give TMR−KabC. ESIMS *m/z*: $[M + Na]^+$ 1456.6838 (calcd for $C_{76}H_{95}N_{11}O_{17}Na$, 1456.6805).

Synthesis of the Rhodol Green Derivative of 7-(4-Aminomethyl-1*H*-1,2,3-triazol-1-yl)kabiramide C (RG−KabC). To a solution of AMT−KabC(1 mg, 0.98 μmol) in dry CH_2Cl_2 (100 μL), a solution of rhodol green carboxylic acid, succinimidyl ester (0.5 mg, 1.06 μmol) in DMSO (100 μL) was added. The mixture was stirred at room temperature in the dark under N_2 atmosphere for 8 h. The mixture was concentrated and purified by silica gel TLC (CH_2Cl_2/MeOH = 8:2) to give RG−KabC. ESIMS *m/z*: $[M + Na]^+$ 1401.6028 (calcd for $C_{72}H_{86}N_{10}O_{18}Na$, 1456.6019).

Synthesis of the IC5 Derivative of 7-(4-Aminomethyl-1*H*-1,2,3-triazol-1-yl)kabiramide C (IC5−KabC). To a solution of AMT−KabC(1 mg, 0.98 μmol) in dry CH_2Cl_2 (100 μL), a solution of IC5−OSu (0.7 mg, 1.11 μmol) in DMSO (70 μL) was added and stirred at room temperature in the dark under N_2 atmosphere. After being stirred for 8 h, the mixture was concentrated and purified by silica gel TLC (CH_2Cl_2/MeOH = 10:1) to give IC5−KabC. ESIMS *m/z*: $[M + H]^+$ 1501.8665 (calcd for $C_{84}H_{115}N_{11}O_{14}$, 1501.8619).

Synthesis of the Dapoxyl Derivative of 7-(4-Aminomethyl-1*H*-1,2,3-triazol-1-yl)kabiramide C (DAP−KabC). To a solution of AMT−KabC(1 mg, 0.98 μmol) in dry CH_2Cl_2 (100 μL), a solution of dapoxyl carboxylic acid, succinimidyl ester (0.5 mg, 1.23 μmol) in DMSO (100 μL) was added and stirred at room temperature in the dark under N_2 atmosphere. After 8 h, the mixture was concentrated and purified by silica gel TLC (CH_2Cl_2/MeOH = 10:1) to give DAP−KabC. ESIMS *m/z*: $[M + Na]^+$ 1334.6503 (calcd for $C_{69}H_{89}N_{11}O_{15}Na$, 1334.6437).

Synthesis of the Fluorescein Diester Derivative of 7-(4-Aminomethyl-1*H*-1,2,3-triazol-1-yl)kabiramide C (FDE−KabC). To a solution of AMT−KabC(1 mg, 0.98 μmol) in dry CH_2Cl_2 (100 μL), a solution of 5(6)-carboxyfluorescein diacetate *N*-succinimidyl ester (0.8 mg, 1.44 μmol) in dry CH_2Cl_2 (100 μL) was added and stirred at room temperature in the dark under N_2 atmosphere. After 8 h, the mixture was purified by silica gel TLC (CH_2Cl_2/MeOH = 20:1) to give FDE−KabC. ESIMS *m/z*: $[M + Na]^+$ 1486.6056 (calcd for $C_{76}H_{89}N_9O_{21}Na$, 1486.6071).

G-Actin. G-actin was prepared from rabbit skeletal muscle using a standard protocol developed in the principal investigator's laboratory (*16*). The purity and activity of actin was analyzed using SDS−PAGE, polymerization assays, and a motility assay (*17*).

Prodan−Actin. Rabbit muscle G-actin was labeled with the thiol reactive, environmentally sensitive probe, acrylodan (Molecular Probes, Eugene, OR), according to our earlier publication (*16*). Briefly G-actin was dialyzed at 20 μM against dialysis buffer (DB, 2 mM Tris, 0.2 mM $CaCl_2$, and 0.2 mM ATP, pH 8.0) overnight and further treated with a 2-fold excess of acrylodan freshly prepared to 20 mM in DMF. The reaction was left in the dark for 1 h at 20 °C and then dialyzed overnight at 4 °C against DB containing 1 mM DTT (G-buffer). The labeled conjugate was polymerized for 90 min at 20 °C by adding $MgCl_2$ and KCl to 2 mM and 0.1 M, respectively, and centrifuged at 4 °C for 90 min at 100 000*g* in a Beckman ultracentrifuge. The pelleted fluorescent actin conjugate was resuspended in G-buffer and dialyzed against 0.5 L G-buffer as described above. Prodan-labeled G-actin was recovered from the supernatant fraction following a 100 000*g* spin at 4 °C. Absorption spectroscopic analysis routinely showed that the labeling ratio of Prodan/actin monomer was 1. The emission maximum of Prodan−actin shifted during the polymerization of G-actin from 496 to 465 nm and was accompanied by an 8-fold increase in intensity at 465 nm (*16*). Prodan−actin behaved as unlabeled actin in all functional assays tested (*16*, *19*).

Live Cell Imaging of TMR−KabC and FDE−KabC. Live cell imaging of barbed-end dynamics using TMR−KabC and FDE−KabC was performed using a Zeiss 510 confocal microscope. NIH 3T3 cells (a gift from Dr. Anna Huttenlocher, UW-Madison) shown on a 24 mm acid-washed coverslip housed in a sample chamber (*12*) were incubated with 100 nM FDE−KabC or TMR−KabC for 10 min at 37 °C. Following exchange of the cell

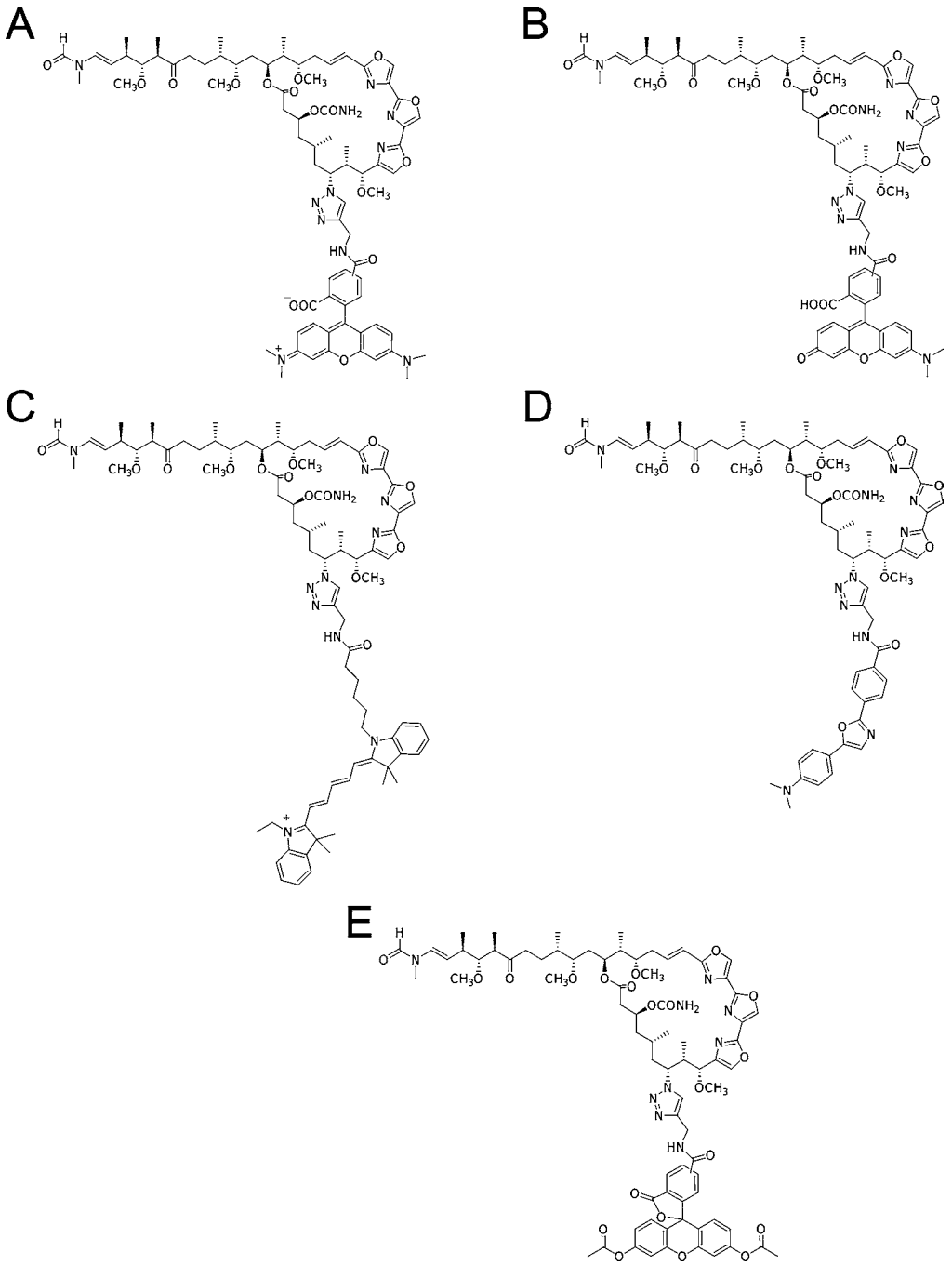

Figure 1. Chemical structures of the five fluorescent KabC probes studied in this work, TMR−KabC (A), RG−KabC (B), IC5−KabC (C), DAP−KabC (D), and FDE−KabC (E).

medium, the cells were imaged using the appropriate excitation and emission wavelengths according to Choidas et al. (*12*).

RESULTS AND DISCUSSION

Design of Fluorescent KabC Probes. Previous analyses of the structural and binding properties of KabC suggested that bulky groups linked to the terminal aldehyde of the tail region of KabC would interfere with its binding to the cleft between subdomains 1 and 3 of G-actin (*15*, *20*). Correspondingly, a 2,5-dimethylamino-naphthalenehydrazide-linked KabC derivative was found to be inactive when tested in our cytotoxicity assay (data not shown) (*15*). This result agrees with a finding by Wada et al. (*21*) who showed that biotin attached to the aldehyde group of mycalolide failed to stain actin within living cells.

On the basis of our previous studies (*15*, *20*), we reasoned that optical probes introduced into KabC via the 7-hydroxyl would face the solvent and therefore not interfere with KabC binding to G-actin. After considering several different approaches for the preparation of C-7-directed optical probes, we elected to synthesize the key intermediate, 7-(4-aminomethyl-1*H*-1,2,3-triazol-1-yl)-kabiramide C (AMT−KabC) from KabC (*18*). The long linker between the C-7 of KabC and the optical probe minimizes effects of the bulky probe on actin binding. Furthermore, the introduction of a terminal amino group on KabC allows for the facile synthesis of optical and capture group derivatives using commercially available carboxy-activated fluorescence probes that include the succinimidyl esters of tetramethylrhodamine (TMR), rhodol green (RG), IC5, fluorescein diester (FDE), and dapoxyl (DAP). The structures of the fluorescent KabC

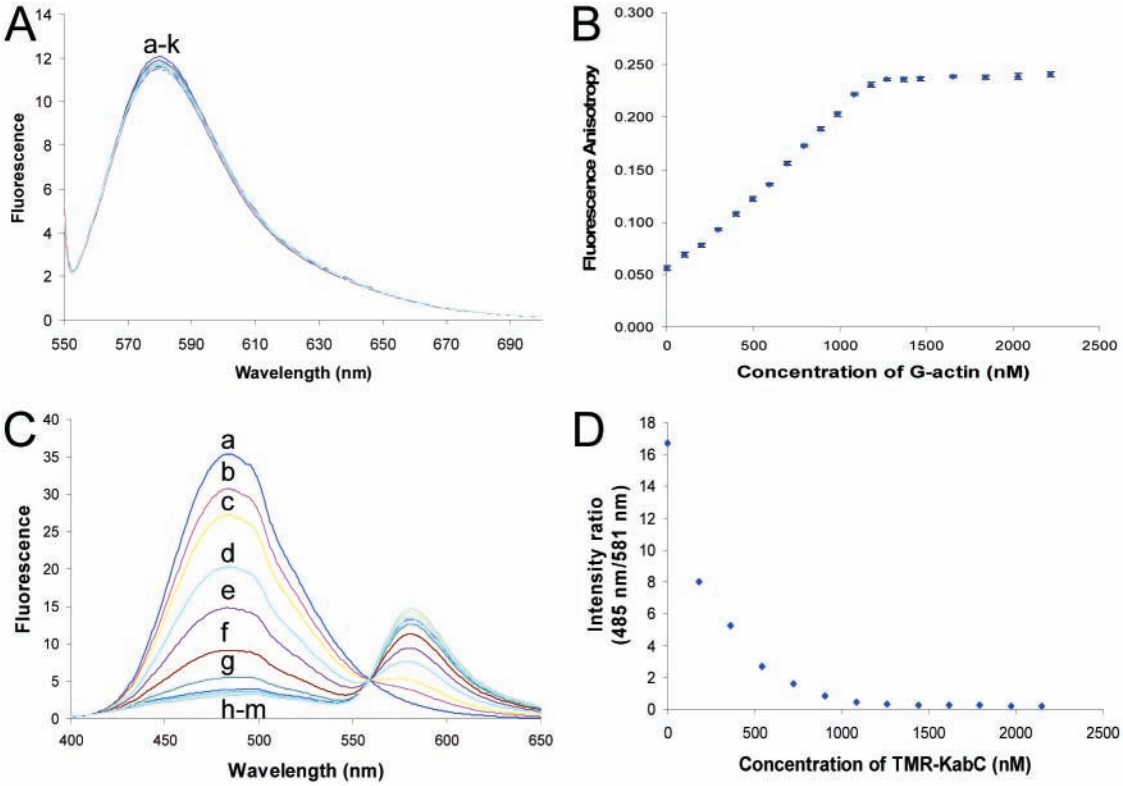

Figure 2. Spectroscopic and actin-binding properties of the TMR−KabC probe. (A) Fluorescence emission spectra of 1 μM TMR−KabC in G-buffer as a function of unlabeled G-actin concentrations: (a) 0 nM, (b) 144 nM, (c) 286 nM, (d) 423 nM, (e) 564 nM, (f) 700 nM, (g) 835 nM, (h) 968 nM, (i) 1099 nM, (j) 1228 nM, and (k) 1356 nM. Excitation wavelength was 546 nm (±4 nm bandwidth), and emission was collected over 550−700 nm (±4 nm bandwidth). (B) Fluorescence anisotropy values of 1 μM TMR−KabC in G-buffer as a function of unlabeled G-actin concentrations. Excitation wavelength was 546 nm (±4 nm bandwidth) and emission was collected over 575−585 nm (±4 nm bandwidth) for the four measurements of polarized emission. (C) Fluorescence emission spectra of 1 μM Prodan−G-actin in G-buffer as a function of TMR−KabC concentrations: (a) 0 nM, (b) 182 nM, (c) 364 nM, (d) 545 nM, (e) 725 nM, (f) 905 nM, (g) 1084 nM, (h) 1263 nM, (i) 1441 nM, (j) 1618 nM, (k) 1800 nM, (l) 1971 nM, and (m) 2147 nM. Excitation wavelength was 385 nm (±4 nm bandwidth), and emission was collected over 400−650 nm (±4 nm bandwidth). (D) Fluorescence intensity ratio of Prodan−G-actin (485 nm, 1 μM) to TMR−KabC (581 nm) as a function of TMR−KabC concentrations. The binding of TMR−KabC was monitored using the fluorescence intensity decrease in Prodan resulting from KabC-mediated quenching of Prodan fluorescence, and the donor quenching and TMR-sensitized emission due to FRET.

probes shown in Figure 1 were determined by their exact molecular weights obtained from ESI mass spectral analyses. The interactions of the fluorescent KabC probes and G-actin were characterized using spectroscopic and binding assays as described in the following sections for each probe.

Characterization of Fluorescent KabC Probes. *TMR*−KabC. Neither the fluorescence quantum yield nor the average emission energy of the TMR group of TMR−KabC changes upon binding to unlabeled G-actin (Figure 2A). This result suggests that the molecular environment of the TMR group is similar in both the free and bound states and that the linker is sufficiently constrained by the triazole ring to prevent interactions between the polar TMR group with the protein. However, the binding of TMR−KabC to G-actin substantially increases the hydrodynamic volume of the bound TMR−KabC compared to free TMR−KabC. This change is accurately quantified by measuring the steady-state FA (*22*) of free TMR−KabC and increasing amount of unlabeled G-actin (Figure 2B). The FA values increase linearly under the stoichiometric binding condition, and analysis of the FA data shows that TMR−KabC binds to G-actin in a 1:1 complex (Figure 2B) (*15*). Further support for this conclusion is provided in a FRET study of the interaction between TMR−KabC and Prodan (Cys-374)-labeled G-actin shown in Figure 2C. Excitation of Prodan on G-actin generates a strong fluorescence centered at 496 nm that decreases significantly upon adding increasing amounts of TMR−KabC, which is caused by KabC-mediated quenching as was previously reported (*15*) and by FRET from Prodan to TMR−KabC, which is also seen by the sensitization of TMR fluorescence. The increase in TMR-sensitized fluorescence emission and decrease in Prodan fluorescence as a function of added TMR−KabC provide a signal to analyze the stoichiometry of the complex; thus, the plateau region of the titration occurs at a KabC−TMR concentration of 1 mM, which is the same as that of Prodan−actin and suggests that, over the concentration range studied, TMR−KabC binds stoichiometrically to G-actin in a 1:1 complex (Figure 2D).

The fact that the quantum yield of the TMR emission, and by implication the lifetime of excited state, is constant in the free and bound states was exploited in the development of a simple and quantitative FA-based assay for G-actin. Thus, the change in FA value of TMR−KabC is directly related to the fractions of the probe in a sample that exist in the free state (r of 0.056 ± 0.002) and the G-actin-bound state (r of 0.236 ± 0.002) according to the equation $r = F_f r_f + F_b r_b$, where $F_f + F_b = 1$, r is the observed FA value, F_f and F_b are fractions of free and bound fluorescent ligand, and r_f and r_b are FA of free and bound fluorescent ligand, respectively. The relatively low FA value (0.236 ± 0.002) found for TMR−KabC in the G-actin complex suggests that the TMR group experiences a considerable degree of local motion. Furthermore, the FA value is unchanged when the TMR−KabC−G-actin complex is added at a substoichiometric level to a

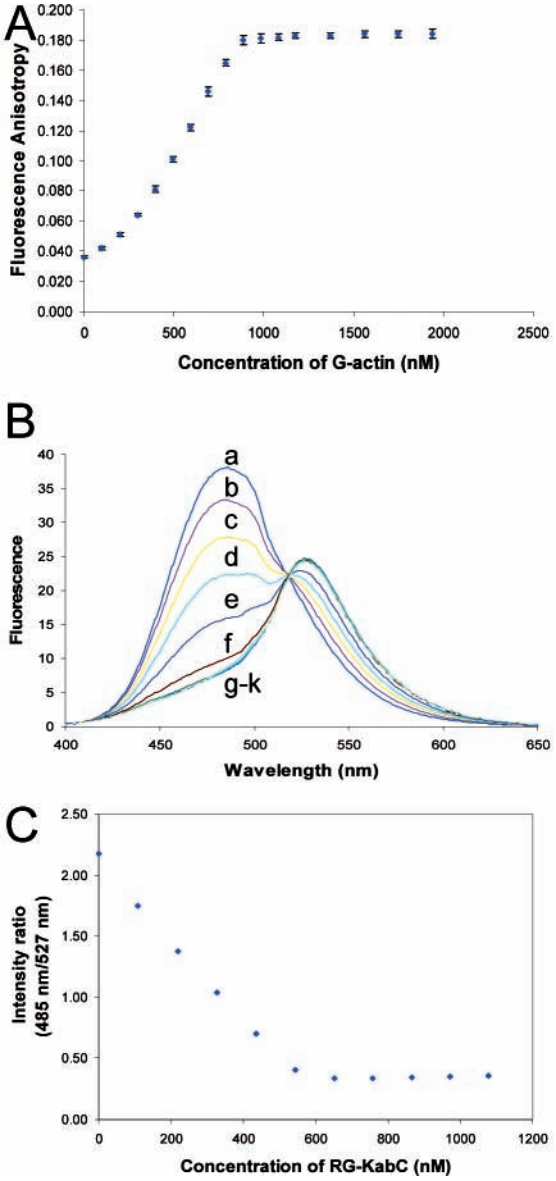

Figure 3. Spectroscopic and actin-binding properties of the RG−KabC probe. (A) Fluorescence anisotropy values of 1 μM RG−KabC as a function of unlabeled G-actin concentrations. Excitation wavelength was 499 nm (±4 nm bandwidth), and emission was collected over 520−530 nm (±4 nm bandwidth) for the four measurements of polarized emission. (B) Fluorescence emission spectra of 1 μM Prodan−G-actin in G-buffer as a function of RG−KabC concentrations: (a) 0 nM, (b) 109 nM, (c) 218 nM, (d) 327 nM, (e) 435 nM, (f) 543 nM, (g) 651 nM, (h) 758 nM, (i) 865 nM, (j) 971 nM, and (k) 1071 nM. Excitation wavelength was 385 nm (±4 nm bandwidth), and emission was collected over 400−650 nm (±4 nm bandwidth). (C) Fluorescence intensity ratio of Prodan−G-actin (485 nm, 1 μM) to RG−KabC (527 nm) as a function of RG−KabC concentrations. The binding of RG−KabC was monitored using the fluorescence intensity decrease in Prodan resulting from KabC-mediated quenching of Prodan fluorescence, and the donor quenching and RG-sensitized emission due to FRET.

polymerizing solution of actin, where it forms TMR−KabC-capped, barbed-ends (*15*). These results support our view that the TMR probe in KabC complex with both G- and F-actin is fully exposed to the solvent where it experiences considerable rotational freedom.

RG−KabC. The rhodol green derivative of KabC exhibits an excitation spectrum centered at 488 nm and emission at 517 nm. The fluorescence spectrum of RG−KabC does not change upon binding to G-actin, which suggests that the molecular environments of the probe

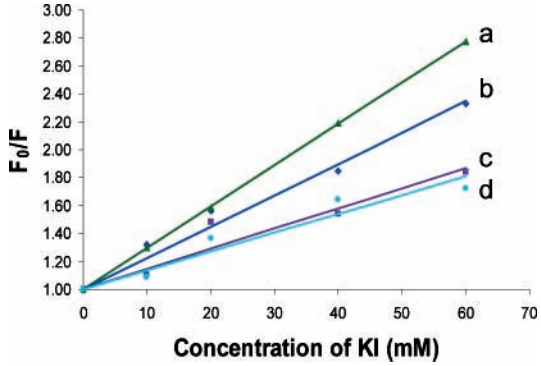

Figure 4. Stern−Volmer plot of iodide quenching behaviors of TMR−KabC, RG−KabC, and G-actin complexes in G-buffer as a function of potassium iodide concentrations: (a) TMR−KabC, (b) RG−KabC, (c) TMR−KabC−G-actin complex, and (d) RG−KabC−G-actin complex.

in the free and bound states are similar. The FA value of RG−KabC changes from a value of 0.036 ± 0.001 in the free state to 0.180 ± 0.003 when bound to G-actin (Figure 3A). As we saw with TMR−KabC, this anisotropy value suggests that the probe exhibits considerable rotational freedom when bound to G-actin and confirms our suggestion that the short linker between the C-7 of KabC and the probe prevents the RG group from interacting with the protein. The similarity of the molecular environments for the RG−KabC within G-actin and capped to the (+)-end of actin filaments is implied from the unchanged FA value of RG−KabC in these two preparations. The higher degree of spectral overlap between Prodan emission on G-actin and the absorption spectrum of RG−KabC results in an efficient FRET process (Figure 3B,C), which can be used to determine properties of the interaction including the formation of a 1:1 complex.

Iodide Quenching of TMR−KabC and RG−KabC. To learn more about the molecular environment of the RG and TMR groups in their G-actin complexes, we performed a potassium iodide-mediated collision quenching study. The IC5 probe was found to be irreversibly quenched by KI, presumably by iodination, and was not included in these studies. The quenching curves for free and bound RG− and TMR−KabC show two quenching modes with the faster rate accounting for the greater degree of quenching (Figure 4). Analysis of the rapid quenching mode was achieved by restricting the linear regression of fluorescence quenching data to 60 mM KI (Figure 4). Free KabC probes were found to exhibit collision molar quenching constants of 29.6 M^{-1} (R^2 of 0.999) for TMR−KabC and 22.5 M^{-1} (R^2 of 0.976) for RG−KabC. These corresponding values for TMR−KabC and RG−KabC bound to G-actin are 13.5 M^{-1} (R^2 of 0.929) and 14.5 M^{-1} (R^2 of 0.914), respectively. Given a fluorescence lifetime for both TMR−KabC and RG−KabC of 4 ns (*17*), we calculate that the unbound probes are quenched at 7.4×10^9 M^{-1} s^{-1} and 5.6×10^9 M^{-1} s^{-1}, respectively, which are very close to the diffusion-controlled rate of 8×10^9 M^{-1} s^{-1} (*16*). Since the lifetimes of the TMR−KabC and RG−KabC probes do not change on binding to G-actin, the quenching rate constants calculated for the bound probes are very similar at 3.38×10^9 M^{-1} s^{-1} and 3.63×10^9 M^{-1} s^{-1}, respectively. The analysis of these quenching data supports the conclusion reached from the spectral and FA analyses showing that the TMR−KabC and RG−KabC probes are fully exposed to the solvent and experience a considerable degree of rotational freedom.

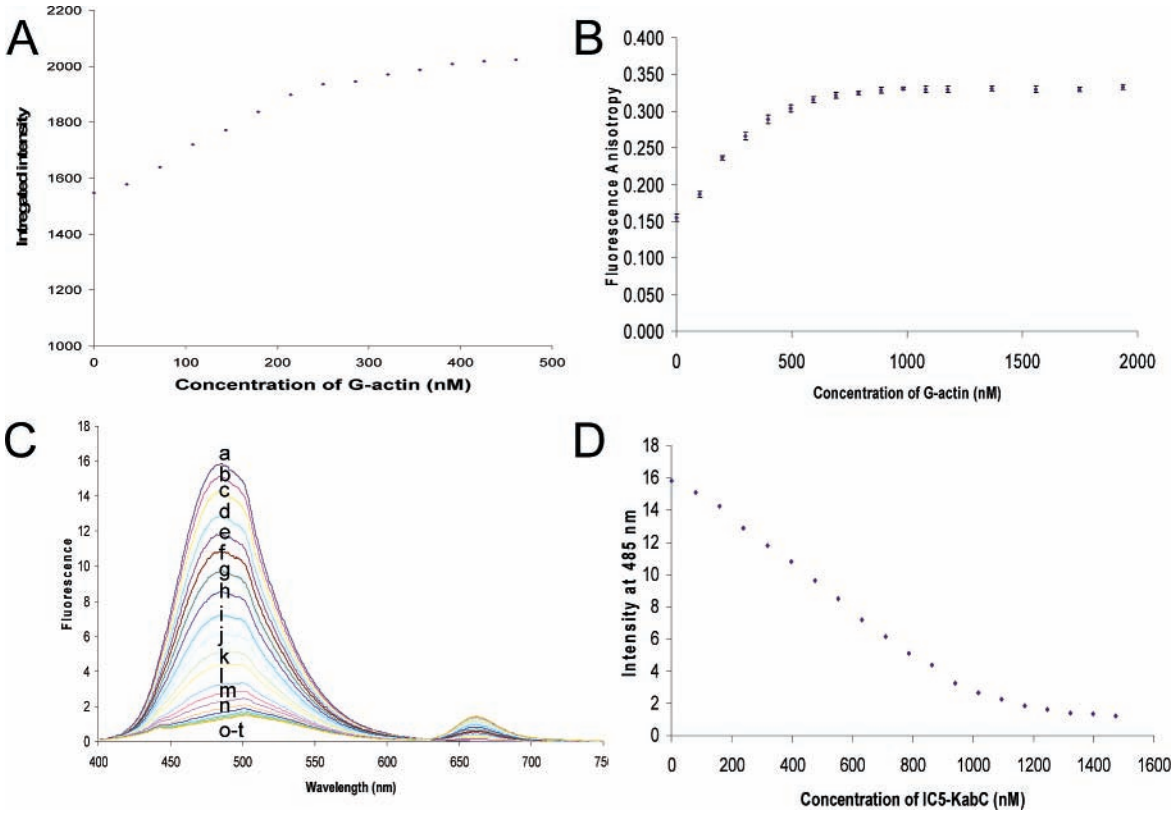

Figure 5. Spectroscopic and actin-binding properties of the IC5−KabC probe. (A) Fluorescence intensity of IC5−KabC binding to G-actin. The binding of IC5−KabC was monitored using the increase in the integrated emission intensity of IC5−KabC (200 nM, in G-buffer) upon binding to actin as a function of G-actin concentrations. (B) Fluorescence anisotropy values of 1 μM IC5−KabC in G-buffer as a function of unlabeled G-actin concentrations. Excitation wavelength was 630 nm (±4 nm bandwidth), and emission was collected over 655−665 nm (±4 nm bandwidth) for the four measurements of polarized emission. (C) Fluorescence emission spectra of 1 μM Prodan−G-actin in G-buffer as a function of IC5−KabC concentrations: (a) 0 nM, (b) 80 nM, (c) 160 nM, (d) 239 nM, (e) 318 nM, (f) 397 nM, (g) 475 nM, (h) 554 nM, (i) 632 nM, (j) 709 nM, (k) 787 nM, (l) 864 nM, (m) 941 nM, (n) 1018 nM, (o) 1095 nM, (p) 1171 nM, (q) 1247 nM, (r) 1323 nM, (s) 1398 nM, and (t) 1473 nM. Excitation wavelength was 385 nm (±4 nm bandwidth), and emission was collected over 400−750 nm (±4 nm bandwidth). (D) Fluorescence intensity of 1 μM Prodan−G-actin at 485 nm as a function of IC5−KabC concentrations. The binding of IC5−KabC is detected mainly from the decrease in Prodan fluorescence resulting from KabC-mediated quenching of Prodan fluorescence and donor quenching due to FRET to IC5.

IC5−KabC. The relative fluorescence quantum yield of IC5−KabC increases ~20% upon binding to G-actin and does not involve any significant spectral shift (Figure 5A). As expected, the binding of IC5−KabC to G-actin substantially increases the hydrodynamic volume sensed by the IC5 probe compared to free IC5−KabC. Steady-state FA measurements of IC5−KabC increase from 0.155 ± 0.005 in the free state to 0.331 ± 0.002 when stoichiometrically bound to G-actin (Figure 5B). Both the integrated fluorescence intensity of the emission spectrum and the FA value increase linearly with increasing G-actin concentration—analysis of these data shows that IC5−KabC binds stoichiometrically (1:1) to G-actin. This result was confirmed from a FRET-based analysis of Prodan−actin emission at 485 nm as a function of IC5−KabC concentration (Figure 5C,D). The FA value of IC5−KabC in the complex (0.331) does not change in the presence of a large excess of the (+)-end binding protein, CapG (data not shown), which suggest that the complex has a long complex lifetime to prevent competition binding from CapG. Since the FA value for IC5−KabC bound to the terminal protomer at the (+)-end of an actin filament does not increase compared to the G-actin complex, we ascribe the small difference in the FA of the IC5−KabC−G-actin complex (0.331) to the limiting anisotropy (0.4) in terms of a low amplitude local motion of the IC5−KabC within the complex.

The high value of the steady-state FA measured for IC5−KabC compared to the RG− and TMR−KabC probes on actin is expected (a) if the lifetime of IC5−KabC in the G-actin complex was short compared to the RG−KabC- and TMR−KabC-bound probes or (b) if the longer link between the IC5 group and the C-7 of KabC allows the IC5 probe to double-back and engage in interactions with the protein surface that restrict local motion. Since the relative quantum yield of IC5−KabC emission is already high, then the fluorescence lifetime would if anything increase on binding to G-actin; on the basis of this argument, it is possible to rule out the first possibility. On the other hand, the emission spectrum of the IC5 probe (*23*) is slightly red-shifted in the G-actin complex compared to the free probe, which is evidence that the probe engages in different interactions in the G-actin complex compared to water. Taken together, we propose that the very high FA value measured for IC5−KabC-bound G-actin results from a significant reduction in local motion of the probe that is brought about by interactions between the IC5 probe and the G-actin.

DAP−KabC. Dapoxyl group has been reported to be sensitive to changes in its molecular environment, and accordingly, the relative fluorescence quantum yield of DAP−KabC decreased upon binding to G-actin (Figure 6A). These data were used to confirm that the KabC probe binds to G-actin in a 1:1 complex. While the fluorescence of the DAP probe is severely quenched in the complex, we expect that the bound probe may prove to be sensitive to the presence of ternary protein and

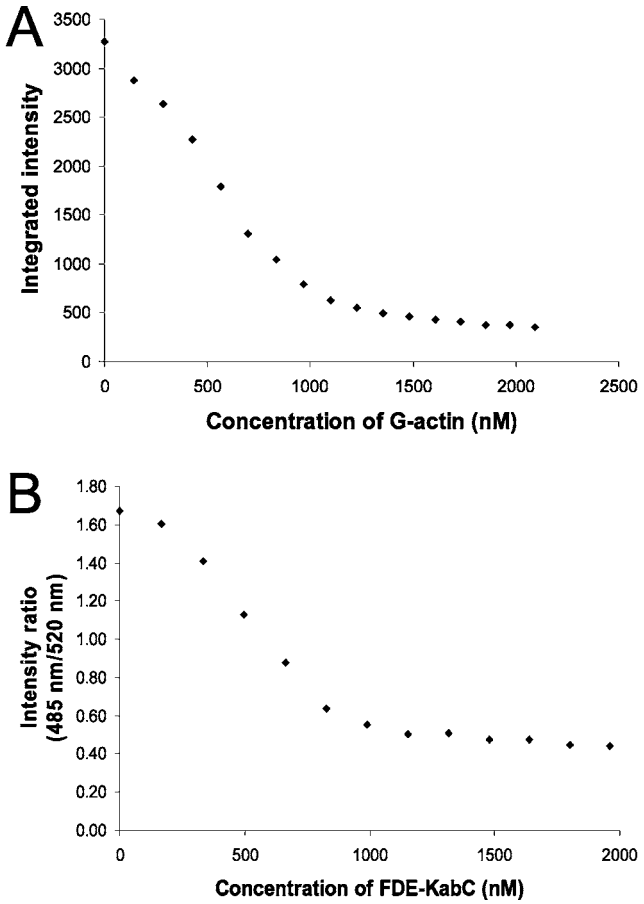

Figure 6. Spectroscopic and actin-binding properties of DAP−and FDE−KabC probes. (A) Fluorescence intensity of DAP−KabC binding to G-actin. The binding of DAP−KabC (1 μM, in G-buffer) was monitored using the decrease in the integrated emission intensity of DAP−KabC upon binding to actin as a function of G-actin concentrations. (B) Fluorescence intensity ratio of Prodan−G-actin (485 nm, 1 μM) to FDE−KabC (520 nm) as a function of FDE−KabC concentrations. The binding of FDE−KabC is monitored using the fluorescence intensity decrease in Prodan resulting from KabC-mediated quenching of Prodan fluorescence, and the donor quenching and FDE-sensitized emission due to FRET.

ligand interactions within G-actin or the terminal actin protomer at the (+)-end of the filament.

FDE−KabC. The binding of the nonfluorescent FDE−KabC probe to G-actin was confirmed by monitoring of Prodan−actin/FDE−KabC emission ratio at 485/520 nm as a function of FDE−KabC concentrations. Excitation of the Prodan fluorophore in G-actin leads to a strong emission centered at 496 nm that decreases upon the addition of increasing amount of FDE−KabC due to KabC-mediated quenching of Prodan fluorescence and the donor quenching and FDE-sensitized emission due to FRET. Analysis of these data confirms that the FDE−KabC probe binds to G-actin in a 1:1 complex (Figure 6B).

Imaging of the Fluorescent KabC Probes in Living Cells. Having shown that all of the fluorescent KabC derivatives bind in vitro to the barbed-end of actin in a tight, long-lived, and stoichiometric complex, we next sought to use TMR−KabC and FDE−KabC as optical probes in a confocal fluorescence image microscopy to image sites within living cells that are undergoing actin filament dynamics, i.e., uncapping of barbed-ends. The FDE−KabC optical probe has three key features that make it suitable for in vivo imaging studies: (1) the probe readily permeates the plasma membrane of living cells; (2) the fluorescein is nonfluorescent until one or both

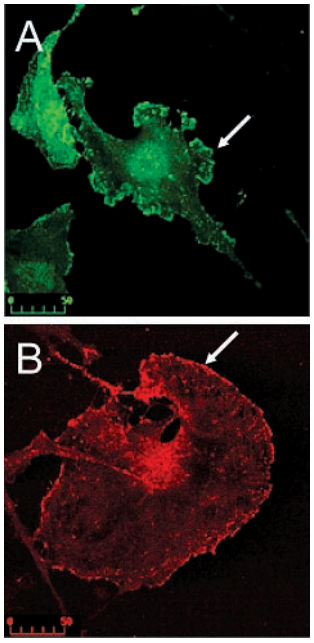

Figure 7. The confocal images of FDE−KabC−G-actin (A) and TMR−KabC−G-actin (B) in actin filament at protrusion site (arrow) of live NIH 3T3 cells.

acetate groups are hydrolyzed by intracellular esterases; and (3) once cleaved, the FDE−KabC probe remains trapped within the cell. Cells treated with medium containing 100 nM FDE−KabC display robust fluorescence within a few minutes. Confocal imaging of FDE−KabC within live NIH-3T3 cells shows two categories of staining. The first is a diffuse fluorescence that associates with FDE−KabC−G-actin existing in complex with G-actin-sequestering proteins such as thymosin β4 (*19*); the second is a far more intense fluorescence of FDE−KabC−G-actin in actin filament and is found at the cell cortex, especially at sites of cell protrusion (Figure 7A). The brilliantly fluorescent TMR−KabC also crosses the plasma membrane where it becomes trapped within the cytoplasm. After washing cells with fresh medium, fluorescence imaging also shows that the distribution of the entrapped probe is similar to that described for FDE−KabC (Figure 7B). The red-shifted excitation and emission spectra of the TMR probe together with its increased photostability generate images that are of higher contrast than FDE−KabC.

SUMMARY

We have previously shown that KabC acts as a functional, unregulated biomimetic of gelsolin and CapG, which bind to the (+)-end of the actin filament. In this study, we demonstrate the design, synthesis, and spectroscopic, functional, and biochemical characterization of five new fluorescent derivatives of KabC. We introduced a rigid triazole linker group terminated with a primary amine to facilitate the synthesis of a diverse range of fluorescence probes using commercially available succinimidyl esters. The probes were characterized by exact molecular weight obtained from ESIMS. All fluorescent KabC probes formed a high stable, 1:1 complex with G-actin. The fluorescent KabC probes are truly unique among the commonly used optical probes for actin (*25*) in that the irreversible binding can be used to titrate actin that is present in complex mixtures.

The specific binding of the five fluorescent KabC probes to G-actin provides an unparalleled opportunity to study

the structural and structural dynamic properties of actin in the critical region between subdomains 1 and 3 and to map molecular events around this critical region. The rapid rate of iodide quenching of TMR−KabC and RG−KabC fluorescence in the G-actin complex supports the conclusion of the FA and spectral data that the KabC probes experience considerable rotational freedom in the G-actin complex and are exposed to solvent molecules. On the other hand, spectroscopic characterization of the IC5−KabC complex with G-actin shows that the longer linker in the probe allows the IC5 group to associate with the surface of actin as seen in the restriction of the rotational freedom of the probe causing the slightly red-shifted emission spectrum in the complex.

The fluorescence property of each KabC probe was largely unaffected following the polymerization of G-actin to F-actin. The extremely tight molecular complex between the fluorescent KabC and G-actin, together with the fact that this complex can only associate with actin filaments at the (+)-end in an unregulated manner, fulfills a major objective of this study, which was to design probes that can map and quantify molecular events at the (+)-end of the filament. The family of fluorescent, membrane permeable, unregulated (+)-end KabC-based capping probes described herein, as well as KabC probes based on quantum dots (*26*), will provide the necessary contrast to map molecular events occurring at the (+)-end of actin filaments in motile cells and should be useful to advance our understanding of the regulation of actin filament dynamics in cell protrusion (*2*, *10*, *11*).

ACKNOWLEDGMENT

This research was financially supported by setup funds from the UW-Madison and NIH R01 HL069970-01 awarded to G.M. and by the Thailand Research Fund for the 2001 Golden Jubilee Ph.D. Program Scholarship (PHD/0115/2544) to C.P. and K.S. BMNCU was supported by Centers of Excellence from Chulalongkorn University.

LITERATURE CITED

(1) Schleicher, M., and Noegel, A. A. (1992) Dynamics of the *Dictyostelium* cytoskeleton during chemotaxis. *New Biol. 4*, 461−472.

(2) Pollard, T. D. (2003) The cytoskeleton, cellular motility and the reductionist agenda. *Nature 422*, 741−745.

(3) Weber, A., Pennise, C. R., and Fowler, V. M. (1999) Tropomodulin increases the critical concentration of barbed end-capped actin filaments by converting ADP·P_i-actin to ADP-actin at all pointed ends. *J. Biol. Chem. 274*, 34637−34645.

(4) Allen, P. G. (2003) Actin filament uncapping localizes to ruffling lamellae and rocketing vesicles. *Nat. Cell Biol. 5*, 972−979.

(5) Cooper, J. A., and Schafer, D. A. (2000) Control of actin assembly and disassembly at filament ends. *Curr. Opin. Cell Biol. 12*, 97−103.

(6) Mejillano, M. R., Kojima, S., Applewhite, D. A., Gertler, F. B., Svitkina, T. M., and Borisy, G. G. (2004) Lamellipodial versus filopodial mode of the actin nanomachinery: pivotal role of the filament barbed end. *Cell 118*, 363−373.

(7) Barkalow, K., Witke, W., Kwaiatkowski, D. J., and Hartwig, J. H. (1996) Coordinated regulation of platelet actin filament barbed ends by gelsolin and capping protein. *J. Cell Biol. 134*, 389−399.

(8) Botelho, R. J., Teruel, M., Dierckman, R., Anderson, R., Wells, A., York, J. D., Meyer, T., and Grinstein, S. (2000) Localized biphasic changes in phosphatidylinositol-4,5-bisphosphate at sites of phagocytosis. *J. Cell Biol. 151*, 1353−1368.

(9) Rozelle, A. L., Machesky, L. M., Yamamoto, M., Driessens, M. H. E., Insall, R. H., Roth, M. G., Luby-Phelps, K., Marriott, G., Hall, A., and Yin, H. L. (2000) Phosphatidylinositol 4,5-bisphosphate induces actin-based movement of raft-enriched vesicles through WASP−Arp2/3. *Curr. Biol. 10*, 311−320.

(10) Pollard, T. D., and Borisy, G. G. (2003) Cellular motility driven by assembly and disassembly of actin filaments. *Cell 112*, 453−465.

(11) Svitkina, T. M., Bulanova, E. A., Chaga, O. Y., Vignjevic, D. M., Kojima, S., Vasiliev, J. M., and Borisy, G. G. (2003) Mechanism of filopodia initiation by reorganization of a dendritic network. *J. Cell Biol. 160*, 409−421.

(12) Choidas, A., Jungbluth, A., Sechi, A., Murphy, J., Ullrich, A., and Marriott, G. (1998) The suitability and application of a GFP-actin fusion protein for long-term imaging of the organization and dynamics of the cytoskeleton in mammalian cells. *Eur. J. Cell Biol. 77*, 81−90.

(13) Faulstich, H., Zobeley, S., Rinnerthaler, G., and Small, J. V. (1988) Fluorescent phallotoxins as probes for filamentous actin. *J. Muscle Res. Cell Motil. 9*, 370−383.

(14) Matsunaga, S., Fusetani, N., Hashimoto, K., Koseki, K., and Noma, M. (1986) Kabiramide C, a novel antifungal macrolide from nudibranch eggmasses. *J. Am. Chem. Soc. 108*, 847−849.

(15) Tanaka, J., Yan, Y., Choi, J., Bai, J., Klenchin, V. A., Rayment, I., and Marriott, G. (2003) Biomolecular mimicry in the actin cytoskeleton: mechanisms underlying the cytotoxity of kabiramide C and related macrolides. *Proc. Natl. Acad. Sci. U.S.A. 100*, 13851−13856.

(16) Marriott, G., Zechel, K., and Jovin, T. M. (1988) Spectroscopic and functional characterization of an environmentally sensitive fluorescent actin conjugate. *Biochemistry 27*, 6214−6220.

(17) Heidecker, M., Yan-Marriott, Y., and Marriott, G, (1995) Proximity relationships and structural dynamics of the phalloidin binding site of actin filaments in solution and on single actin filaments on heavy meromyosin. *Biochemistry 34*, 11017−11025.

(18) Petchprayoon, C., Suwanborirux, K., Miller, R., Sakata, T., and Marriott, G. (2005) Synthesis and characterization of 7-(4-aminomethyl-1*H*-1,2,3-triazol-1-yl) analogue of kabiramide C. *J. Nat. Prod. 68*, 157−161.

(19) Roy, P., Rajfur, Z., Jones, D., Marriott, G., Loew, L., and Jacobson, K. (2001) Local photorelease of caged thymosin β4 in locomoting keratocytes causes cell turning. *J. Cell Biol. 153*, 1035−1047.

(20) Klenchin, V. A., Allingham, J., King, R., Tanaka, J., Marriott, G., and Rayment, I. (2003) Trisoxazole macrolide toxins mimic the binding of actin-capping proteins to actin. *Nat. Struct. Biol. 10*, 1058−1063.

(21) Wada, S., Matsunaga, S., Saito, S., Fusetani, N., and Watabe, S. (1998) Actin-binding specificity of marine macrolide toxins, mycalolide B and kabiramide D. *J. Biochem. 123*, 946−952.

(22) Yan, Y., and Marriott, G. (2003) Analysis of protein interactions using fluorescence technologies. *Curr. Opin. Chem. Biol. 7*, 635−640.

(23) Mujumdar, R. B., Ernst, L. A., Mujumdar, S. R., Lewis, C. J., and Waggoner, A. S. (1993) Cyanin dye labeling reagents: sulfoindocyanine succinimidyl esters. *Bioconjugate Chem. 4*, 105−111.

(24) Forscher, P., and Smith, S. J. (1988) Actions of cytochalasins on the organization of actin filaments and microtubules in a neuronal growth cone. *J. Cell Biol. 107*, 1505−1516.

(25) Kuhn, J. R., and Pollard, T. (2005). Real-time measurements of actin filament polymerization by total internal reflection fluorescence microscopy. *Biophys. J. 88*, 1387−1402.

(26) Mansson, A., Sundberg, M., Balaz, M., Bunk, R., Nicholls, I. A., Omling, P., Tagerud, S., and Montelius, L. (2004) In vitro sliding of actin filaments labeled with single quantum dots. *Biochem. Biophys. Res. Commun. 314*, 529−534.

BC050006J

Biophysical and Transfection Studies of an Amine-Modified Poly(vinyl alcohol) for Gene Delivery

Matthias Wittmar,[†] James S. Ellis,[§] Frank Morell,[†] Florian Unger,[†] Jeanette Christine Schumacher,[†] Clive J. Roberts,[§] Saul J. B. Tendler,[§] Martyn C. Davies,[§] and Thomas Kissel*[,†]

Philipps University Marburg, Department of Pharmaceutics and Biopharmacy, Ketzerbach 63, D-35032 Marburg, Germany, and Laboratory of Biophysics and Surface Analysis, School of Pharmacy, The University of Nottingham, Nottingham, NG7 2RD, UK. Received March 31, 2005; Revised Manuscript Received October 4, 2005

Novel, multifunctional polymers remain an attractive objective for drug delivery, especially for hydrophilic macromolecular drugs candidates such as peptides, proteins, RNA, and DNA. To facilitate intracellular delivery of DNA, new amine-modified poly(vinyl alcohol)s (PVAs) were synthesized by a two-step process using carbonyl diimidazole activated diamines to produce PVAs with different degrees of amine substitution. The resulting polymers were characterized using NMR, thermogravimetric analysis (TGA), and gelpermation chromatography (GPC). Atomic force microscopy (AFM), dynamic light scattering photon correlation spectroscopy (PCS), and zeta-potential were used to investigate polyplexes of DNA with PVA copolymers. These studies suggest an influence of the polycation structure on the morphology of condensed DNA in polyplexes. Significant differences were observed by changing both the degrees of amine substitution and the structure of the PVA backbone, demonstrating that both electrostatic and hydrophobic interactions affect DNA condensation. DNA condensation measured by an ethidium bromide intercalation assay showed a higher degree of condensation with pDNA with increasing degrees of amine substitution and more hydrophobic functional groups. These findings are in line with transfection experiments, in which a good uptake of these polymer DNA complexes was noted, unfortunately, with little endosomal escape. Co-administration of chloroquine resulted in increased endosomal escape and higher transfection efficiencies, due to disruption of the endosomal membrane. In this study, the structural requirements for DNA complexation and condensation were characterized to provide a basis for rational design of nonviral gene delivery systems.

INTRODUCTION

Delivery of hydrophilic molecules such as proteins and DNA is generally considered as the Achilles heel for their therapeutic application (*1*−*3*). These molecules are rapidly degraded by enzymes found under in vivo conditions both intracellularly at the site of application as well as in the general circulation, causing low bioavailabilities and requiring frequent injections (*4*−*6*). Because of their size and lability, uptake through the epithelium of the gastrointestinal tract is low and thus necessitates parenteral administration (*7*, *8*). To overcome these problems, carrier systems are necessary to allow efficient, safe, and convenient delivery to patients (*9*−*20*).

In this context, nanoscale carriers such as nanoparticles and nanocomplexes have reached increasing attention, since they can be administered by various routes, including the intravenous and intranasal routes (*9*, *21*, *22*). Controlled and sustained release of these drug candidates can be accomplished using microspheres and implants from biodegradable polymers (*1*, *14*, *20*, *23*). The classic copolyesters of lactic and glycolic acid (PLGA) are not ideal for protein and DNA delivery since inactivation and uncontrolled release is a consequence of poor compatibility between lipophilic polymers and hydrophilic drug candidates (*7*, *24*−*27*). This is especially the case for DNA, where the complexation capabilities and protecting abilities of the carrier substance are very important. We hypothesized that comblike polyesters consisting of both lipophilic and hydrophilic components could be beneficial for drug delivery.

We selected PVA with a molecular weight of 15 000 g/mol, which is considered biocompatible and can be eliminated from the body by renal excretion (*28*−*30*). To this polymer backbone, amine groups were covalently coupled in a polymer-analogous reaction using carbonyl diimidazole (CDI) to introduce cationic charges under physiological conditions (*31*−*33*). This modification was thought to affect colloidal stability of carrier systems by imparting positive surface charges on one hand (*34*) and increasing the protein or DNA loading by electrostatic interactions on the other hand (*35*, *36*). As the secondary and tertiary amino-groups functions possess lower cytotoxicity, diamines, and PVA were coupled via the hydrolytically stable urethane bond (*38*). The resulting PVA could be used in different ratios to complex DNA.

EXPERIMENTAL SECTION

Materials. Diethylaminoethylamine (*purum*, >98%), Diethylaminopropylamine (*purum*, >98%), Dimethylaminopropylamine (*purum*, >98%), PVA (MW 15000; degree of polymerization 300 (P = 300); degree of hydrolysis 86−89%), CDI (*purum*, ∼97%), *N*-methyl pyrrolidone (NMP) (absolute), dimethylacetamide (DMAc) (for HPLC, 99.8% and 1,3-dimethyl-3,4,5,6-tetrahydro-2(1H)-pyrimidinone

* To whom correspondence should be addressed. Tel.: ++49-6421-2825881. Fax: +49−6421−2827016. E-mail: kissel@staff.uni-marburg.de.

[†] Philipps University Marburg.

[§] The University of Nottingham.

10.1021/bc0500995 CCC: $30.25 © 2005 American Chemical Society
Published on Web 10/29/2005

Table 1. Backbone Polymers: Synthesis and Molar Mass

polymer	feeding[a]	M_n[b] g/mol	M_n[c] g/mol	M_w[c] g/mol	M_n/M_w[c]
DMAPA(7)	12.00/1.20/0.07/*4*	15320	9895	11710	1.2
DMAPA(13)	12.00/2.39/0.17/*4*	15890	12070	14460	1.2
DMAPA(21)	12.00/4.81/0.31/*4*	16750	11770	13690	1.2
DMAPA(32)	12.00/11.99/0.79/*4*	17880	12170	14410	1.2
DMAPA(69)	11.00/23.09/1.51/*4*	22420	15590	20060	1.3
DMAPA(105)	4.50/15.00/0.85/*4*	20880	n.d.	n.d.	n.d.
DMAEA(55)	7.00/14.35/0.85/*4*	27400	n.d.	n.d.	n.d.
DEAEA(70)	10.00/22.48/1.37/*4*	23630	29580	32780	1.1
DEAPA(68)	10.00/23.12/1.32/*4*	23910	33590	67790	2.0
DMABA(99)	2.67/9.04/0.55/*3.75*	27560			
DMAHA(81)	2.48/2.75/0.15/*3.75*	28000			

[a] Feed (mass/g): m(PVA)/m(amine-CI)/m(DMPU)/days of reaction. [b] Calculated by ^{1}H NMR depending on the degree of polymerization of PVA (P = 300). [c] Measured by GPC-MALLS.

(DMPU) (*puriss.*, absolute, over molecular sieve) were purchased from Fluka GmbH (Germany) and used as received. Lithium bromide (extra pure) (Merck) was used as received. Tetrahydrofuran (THF) (BASF, Germany) was dried over sodium and distilled under nitrogen before use. All other chemicals were used as received without further purification.

Synthesis of Amine Carbonylimidazoles. A total of 90 mL of dry THF was distilled under nitrogen into a rigorously dried 100 mL round-bottomed flask equipped with gas inlet, a septum cap, and a magnetic stir bar. Then, 16.72 g (0.10 mol) of CDI was dissolved, and the diamine (at a 1:1 molar ratio) was injected by syringe, while the temperature in the flask was monitored to ensure that it did not exceed 55 °C (*31*).

After stirring of the sample for 16 h at room temperature, the resulting imidazole/amine-carbonylimidazole solution was isolated by evaporation of THF. The resulting oily, slight yellow mixture was used without further purification after the amount of amine-CI was quantitated by ^{1}H NMR spectroscopy. Yields: >90%.

Synthesis of Amine-Modified PVAs. Poly(vinyl (dialkylamino)alkylcarbamate-*co*-vinyl acetate-*co*-vinyl alcohol): A 250 mL round-bottomed flask with gas inlet and magnetic stirring bar was rigorously dried and filled with PVA and anhydrous NMP. During heating to 80 °C, the PVA was dissolved. After complete dissolution (dialkylamino)alkyl)-1H-imidazole-1-carboxamide was added, and finally DMPU was injected. The mixture was heated to 80 °C under stirring for 4.5 days (Table 1).

The resulting amine-modified PVA was purified by ultrafiltration using an YM1 membrane (cut off 1000 g/mol, Millipore). During filtration, the solvent was substituted by demineralized water. After filtration of 2.5 L water, the volume in the cell was reduced to 50 to 100 mL. The solution was frozen at −20 °C and dried by lyophilization (Edward Freeze Dryer Modulyo, standard conditions). The polymers were milled and stored until use at 40 °C in a vacuum to minimize water uptake during storage. The polymers are obtained as slightly yellowish hygroscopic powders. Yields: ∼83%.

Nomenclature. The source-based IUPAC nomenclature for these polymers lead to the designation: poly(vinyl 3-(alkylamino)alkylcarbamate-*co*-vinyl acetate-*co*-vinyl alcohol). As an abbreviation the short form of the amine followed by a number in brackets was used. (e.g., DEAPA(x) = 3-diethylaminopropylamine; while x the number displays the modified vinyl alcohol monomers in the chain, for example, DMAPA(13), etc.)

Sample Characterization. ^{1}H and ^{13}C NMR spectroscopic data were collected using a JEOL Eclipse+ 500 and a Joel GX 400 D at a frequency of 500 respective 400 MHz for ^{1}H NMR and 126 respective 101 MHz for ^{13}C NMR at 50 °C in DMSO-d_6 (euriso-top, <0.02% HDO+D_2O). A 40−50 mg sample was used for each measurement. ^{1}H NMR was performed with 64 scans. The ^{13}C NMR was performed with 4096 scans.

Table 2. TGA Measurements Degradation Caused by Amine Substitution

polymer	amine substitution[a]	mass loss[b]/%	calc mass loss[c]/%
DMAPA(7)	2.3	4.8	7.6
DMAPA(13)	4.4	11.8	14.1
DMAPA(21)	7.1	20.0	21.9
DMAPA(32)	10.8	36.9	31.1
DMAPA(69)	23.0	60.7	53.1
DMAPA(105)	33.2	78.2	65.9
DMAEA(55)	18.4	48.7	41.7
DMABA(99)	32.2	79.9	67.2
DMAH(81)	27.0	71.2	62.1
DEAEA(70)	23.3	54.8	55.1
DEAPA(68)	22.7	58.5	57.0

[a] Degree of amine substitution/% calculated form ^{1}H NMR measurements. [b] Mass loss during the first degradation step. [c] Mass loss calculated from NMR data.

The amine substitution (AS) was evaluated by calculating the ratio between the integral of the CH_3 end group of the amine and the integral of the methylene protons of PVA on the basis of the degree of polymerization. $(100/(I_{PVA}/2))(I_{amine}/3) = DS$; DS*3 = AS.

Fourier transform-infrared spectroscopy (FT-IR) was performed on a Nicolet 510P FTIR spectrometer (range between 4000 and 400 cm^{-1}, resolution: 2 cm^{-1}). All powder samples were compressed into KBr pellets.

CHN analysis was performed with a Hewlett-Packard autoanalyser 185.

Gelpermation chromatography in combination with a multi-angle-laser-light scattering detector (GPC-MALLS) was employed for the determination of absolute molecular weights and weight distributions using a Duratec DDG-75 degasser, a Merck-Hitachi L-6000 pump and an AS-2000A autosampler, a Merck T-6300 Column Thermostat, a Wyatt DAWN Eos multiangle-laser-light-scattering detector (normalized with PSS (Polymer Standard Service, Mainz) PMMA 200k standard). The separation was performed using an Optilab DSP together with a PSS SDV linear M (8 × 300, 5μ) column with a precolumn of the same type (8 × 50, 5μ). The measurements were performed at 60 °C column temperature at a flow rate of 0.5 mL min^{-1} using dimethylacetamide (DMAc) and 2.5 g lithium bromide /L (LiBr) as eluent. The molecular weights of the samples were determined using the Wyatt software Astra V4.73. To calculate the molecular weights total mass recovery was used (third-order fit).

Differential scanning calorimetry (DSC) was performed on a Perkin-Elmer DSC7 calibrated against indium and gallium. Using ca. 5 mg of polymer the sample was scanned between −10 and 200 °C at a heating rate of 10 °C/min. Glass transition temperatures were calculated from the second run.

Thermogravimetric Analysis (TGA). About 5 mg of polymer was used for thermogravimetric analysis in a TGA7 (Perkin-Elmer) (under nitrogen, heating rate of 20 °C/min, run 30−600 °C) (Table 2).

DNA. The plasmid DNA pBR322 (4363 bp) (Sigma-Aldrich, Poole, Dorset, UK) was diluted to a stock solution of 10 μg mL^{-1} w/v in deionized water (resistivity of about 18.2 MΩ cm) obtained from an ELGA purification system (Maxima USF ELGA, High Wycombe, UK) and 10% phosphate buffered saline (PBS) (Sigma-Aldrich PLC);

Table 3. AFM: Grain Sizes and Mean Ring Volume.

polymer	N/P ratio	mean grain size ($nm^2 \times 10^3$)[a]	mean ring volume ($nm^3 \times 10^3 \pm SD$)[a,b]	hydrodynamic diameter ($nm \pm SD$)[c]	ζ-potential ($mV \pm SD$)[c]
DMAPA(69)	12	15 ± 9	424 ± 512	302.5 ± 10.4	n.d.
	6	6 ± 2	496 ± 512	326.8 ± 3.2	n.d.
DMAEA(55)	12	17 ± 18	234 ± 68	859.2 ± 66.7	38.7 ± 2.1
	6	1 ± 11	130 ± 42	247.5 ± 2.4	37.3 ± 2.4
DEAPA(68)	12	35 ± 51	279 ± 73	221.5 ± 1.8	33.4 ± 7.7
	6	35 ± 12	496 ± 376	213.5 ± 7.2	22.4 ± 5.77
DEAEA(70)	12	28 ± 47	199 ± 201	247.5 ± 2.4	39.0 ± 0.6
	6	36 ± 52	378 ± 303	200.9 ± 3.4	−16.4 ± 9.0

[a] Data from atomic force microscopy. [b] Ring volume calculation cited in ref *61*. [c] PCS and ζ-potential measurements, sizes at N/P 10 and N/P 3.

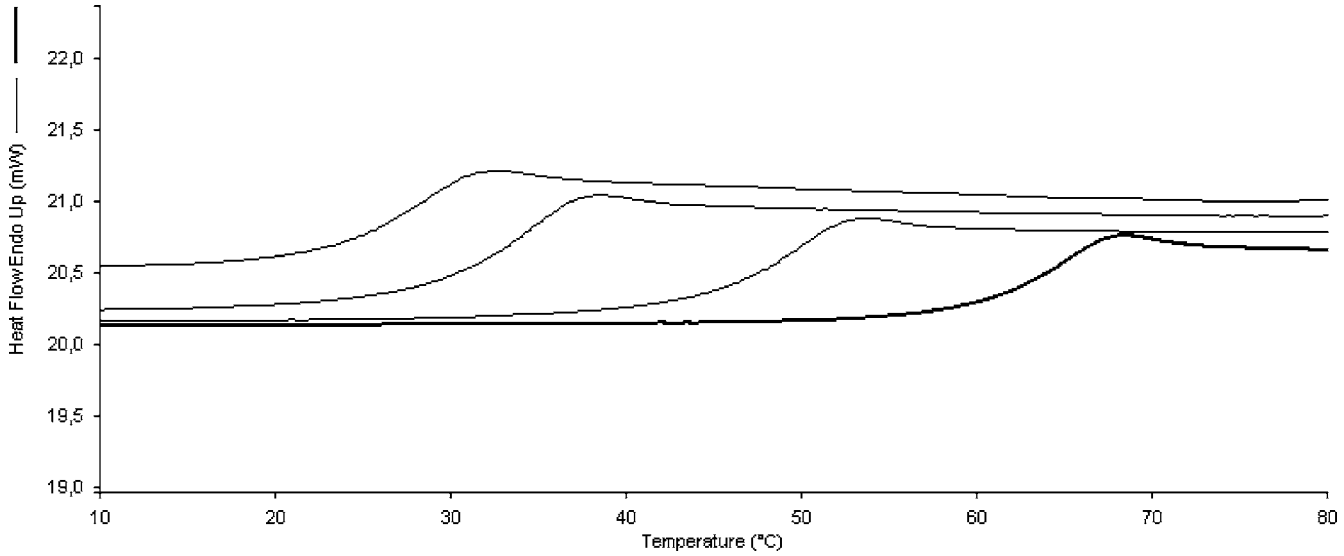

Figure 1. Downshift of the glass transition temperature caused by water uptake: from right to left: M(21): bottled under anhydrous conditions, under environment conditions, pan closed after 5 min and after 10 min under environment conditions.

these stocks were further diluted with deionized water to give a concentration of 1 μg mL^{-1} DNA in 1% PBS (pH 5.5).

Atomic Force Microscopy (AFM) Instrumentation. A Multimode AFM (Veeco Instruments, Santa Barbara, CA) operating with a NanoScope IIIa controller with a size E scanner was used throughout this study. For imaging in liquid, silicon nitride, oxide sharpened, triangular cantilevers (Veeco Instruments) were selected, operating at resonant frequencies of approximately 8 kHz. All imaging was conducted in tapping mode at 512 × 512 pixel resolution, with scan speeds of approximately 3.05 Hz. We chose optimal set-points to reduce sample distortion. Post-imaging analysis, unless otherwise indicated, was carried out on either NanoScope IIIa software, version 5.12b48 or SPIP version 3.0.0 (Image Metrology, Lyngby, Denmark). The background slope was removed from image data using a first- or second-order polynomial function, and some images were subjected to a median filter of 3 × 3. All lateral cross-sectional measurements acquired from AFM images were taken at half-maximum height (*39*).

Grain size analysis was conducted using the Nanoscope Software. Using such software, the average (mean) surface area (nm^2) was calculated for each selected condensate. To reduce the effect of noise and substrate defects on the analysis, height thresholds were optimized. First, a height threshold was chosen such that unwanted pixels were removed and second, each individual particle was selected, giving either its grain size (projected two-dimensional area) or the mean grain size of particles of similar dimension, followed by the standard deviation (Table 3).

Scheme 1. Synthesis of Amine-Substituted PVA

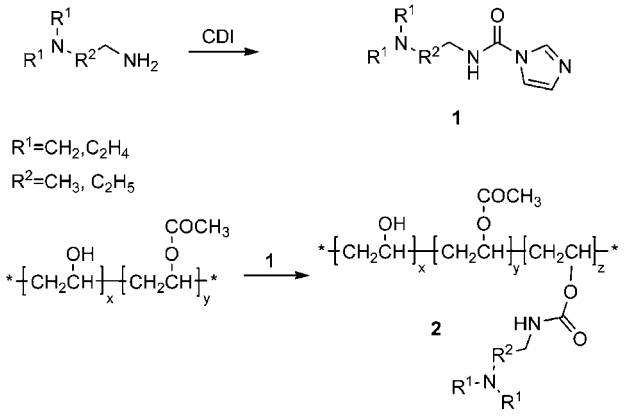

In Vitro Cytotoxicity Using (3-(4,5-Dimethylthiazol-2-yl)-2,5-diphenyl Tetrazolium Bromide (MTT) Assay. L929 mouse fibroblasts were grown in Dulbecco's modified Eagle's medium (DMEM) (Gibco, Eggenstein, Germany) supplemented with 10% fetal calf serum (Cytogen, Sinn, Germany) and 2 mM glutamine.

In vitro cytotoxicity of the polymers was evaluated using the MTT assay as described previously (*13*). L929 were seeded into 96-well microtiter plates (Nunclon, Nunc, Germany) at a density of 8000 cells/well. After 24 h, the culture medium was replaced with 100 μL/well of

serial dilutions of polymer stock solutions in DMEM (n = 7). After an incubation period of 24 h, MTT (Sigma-Aldrich, Germany) was dissolved in phosphate buffered saline at 5 mg/mL and 20 μL was added to each well reaching a final concentration of 0.5 mg of MTT/mL. After an incubation time of 4 h, unreacted dye was removed by aspiration and the purple formazan product was dissolved in 200 μL/well dimethyl sulfoxide and quantitated by a plate reader (Titertek Plus MS 212, ICN, Germany) at wavelengths of 570 and 690 nm. The relative cell viability [%] related to control wells containing cell culture medium without polymer was calculated by [A] test/[A] control × 100. Poly(ethylene imine) 25 kDa (BASF, Germany) was used as a positive control.

Transfection. Transfection experiments were carried out as reported earlier (*40*). In brief, polymer (in isotonic NaCl solution) was mixed in the intended ratio with 4 μg of pCMV-Luc (c = 5 μg/ μL) in 100 μL of isotonic NaCl solution resulting a final volume of 200 μL.

NIH/3T3 mouse fibroblasts were seeded onto 12-well plates, 50 000/well (n = 3). After 24 h medium (DMEM with 10% FKS) was exchanged against polymer/DNA complex solution and chloroquine (10.32 μL, 10 μg/μL, final concentration 100 μmol/L (*41*). After 4 h, the medium was changed, and after 44 h cells were washed and lysed. (Growth conditions: 8.5% CO_2, 90% rel. humidity, 37 °C.) *For assays of luciferase activity:* 20 μL of cell lysis medium was mixed with 100 μL of luciferase assay reagent (Promega) and measured in a luminometer (calibration: 8.33 × 10^5 RLU = 1 ng/mL Luciferase).

Confocal Laser Scanning Microscopy (CLSM). Labeling: 10 mg of polymer was dissolved in $NaHCO_3$ buffer (pH 9.0) and 0.26 mg of (5-(4,6-dichlorotriazinyl)-aminofluoresceine (5-DTAF) in DMSO (c = 0.01 mg/μL) was added. The mixture was heated to 70 °C. The conjugate was purified by size exclusion chromatography on a PD-10 column (SEC-column, cutoff 10 kDa, Amersham Biosciences, Sweden) and subsequently freeze-dried.

Preparation of Polyplexes. Labeled polymer was mixed with YOYO1-DNA (*42*) at a N/P ratio of 20 and incubated in chamber-slides with 20 000 NIH/3T3 cells for 4 h. Then PBS buffer was used to wash the cells. The cells were fixed with formalin and stained with 4′,6-diamidine-2-phenylindol (DAPI). Images were recorded using confocal laser scanning microscopy (CLSM) (Zeiss Axiovert 100 M coupled to Zeiss LSM 510 scanning device).

RESULTS AND DISCUSSION

Different diamines were used to synthesize amine-modified PVA with different degrees of substitution ranging between 0.02 and 0.35. PVA with a molar mass of 15 000 g/mol (M_n) (P = 300, degree of hydrolysis 87−89%) was used as starting material. CDI chemistry was used to modify PVA with tyramine (*32*). Here we present a modified way to couple amines to PVA. To avoid cross-linking, we used substituted diamines such as N^1,N^1-diethylpropane-1,3-diamine activated with CDI (Scheme 1) (*31*). The amines were injected into solution/suspension of CDI in THF to prevent disubstitution. The resulting amine-carbonylimidazole (amine-CI) is less reactive than CDI. No further purification of the resulting amine-CI/imidazole mixture was necessary, and ^{1}H NMR spectroscopy was used to determine the concentration of amine-CI in the reaction mixture. On the basis of these calculations, amine-modified PVAs with degrees of amine substitution of 0.02, 0.04, 0.11, 0.23, and 0.35 were synthesized (Table 1). Substitution was determined by setting the signals of PVA at δ = 1.87−1.17 ppm

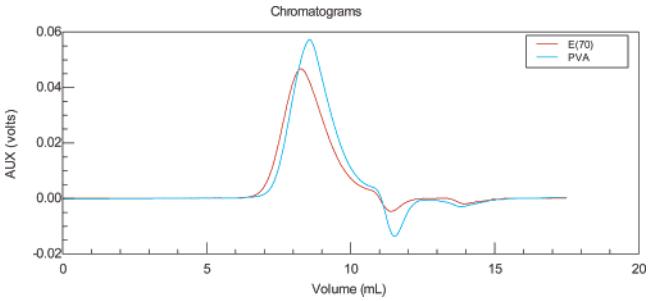

Figure 2. GPC: elugram of E(70) in comparison to unmodified PVA.

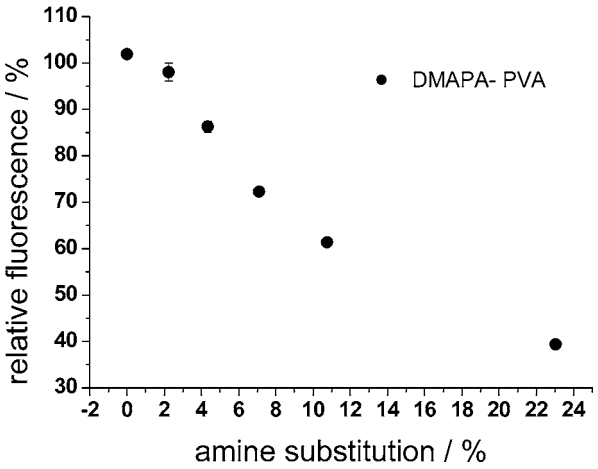

Figure 3. Ethidium bromide assay of DMAPA(x) (x = 0.0, 2.3, 4.4, 7.1, 10.8, 23.0) and salmon testis DNA at the same N/P ratio.

(methylene protons) into relation to a clearly separated signal of the amine substitution, e.g., at δ = 0.95 ppm for DEAPA modification. On the basis of the known degree of polymerization of PVA, the stoichiometric amount of substituted hydroxyl groups could be calculated. To achieve higher degrees of amine substitution, it is necessary to use an excess of amine-CI (Table 1). The resulting amine-modified PVAs are water soluble. Their hygroscopic properties increase with increasing amine substitution as demonstrated by a shift of the glass transition temperature (T_g) shown in Figure 1.

The postulated structure of the amine-modified PVA was in accordance with NMR and FT-IR spectra and was confirmed by CHN elemental analysis. These results are in good agreement with NMR and TGA data (Table 2). NMR, FT-IR, and CHN data are presented as Supporting Information. Previously, we have confirmed the covalent attachment of amines to PVA backbone using two-dimensional NMR spectroscopy. Mainly isotactic triads of the precursor PVA react with the amine reactant and form a polymer with an average block length of nine vinyl alcohol monomer groups between each amine-modified monomer region for polymer DMAPA (*32*). Further, the three-dimensional structure and the tacticity of amine-modified PVA was verified (*43*). GPC measurements demonstrate a monomodal distribution of molecular weights in good correspondence to values calculated from NMR measurements (Table 1, Figure 2).

Because of their amino functions which were protonated under physiological conditions these polymers formed complexes with DNA through electrostatic interactions (*44*, *45*). We hypothesized that polyplex formation could influenced by the degree of amine substitution as well as by the type of the amine function (*46*). The tertiary amino function was substituted dimethyl or

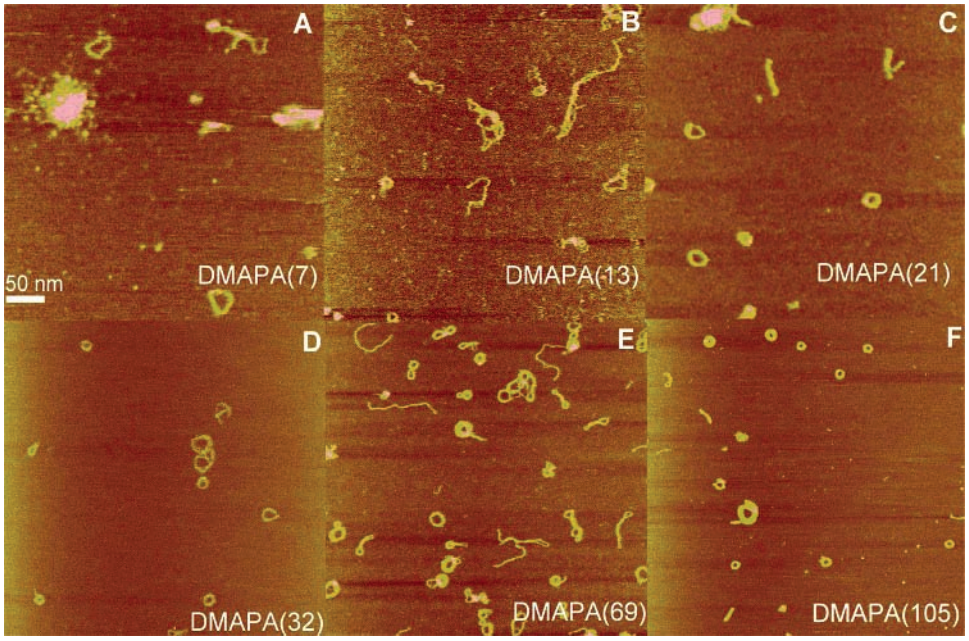

Figure 4. (A−F) Changes in the morphology of the DNA/polymer complexes due to different amine substitution of DMAPA-modified PVA (N/P ratio 12).

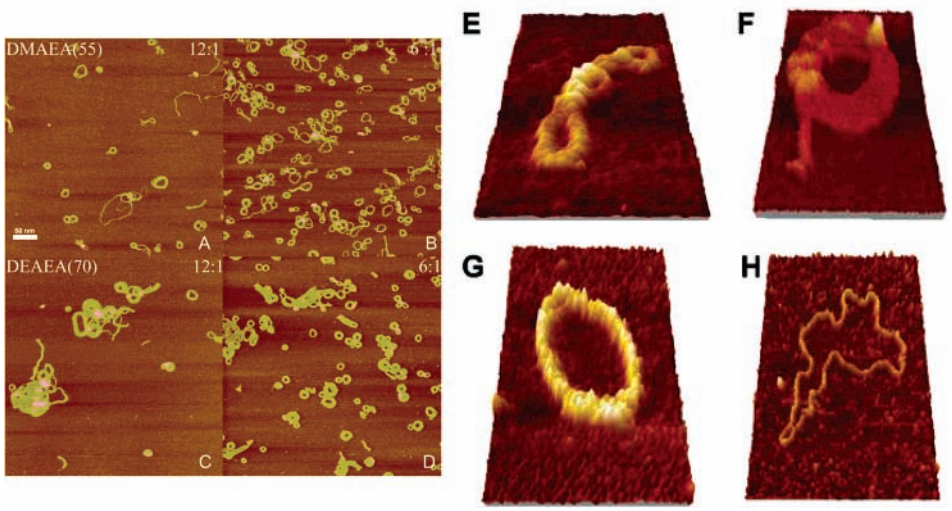

Figure 5. Panels A−D depict various AFM topographical images of both DMAEA(55) and DEAEA(70) highlighting different morphologies of DNA with 12:1 ratios, compared to 6:1 ratios (A, B, C and D, respectively). These data suggest a 6:1 ratio of DMAEA forms partially condensed toroids and plectonomics, whereas 6:1 DEAEA forms complete toroids. $Z = 10$ nm; (E−G) highlights different morphologies of the DNA/polymer complexes which are compared to naked DNA (H).

diethyl moieties, and different spacer length were realized for coupling to PVA backbone. Both factors are thought to contribute to polyplex size and structure.

To test this hypothesis, we investigated polyplex formation with DNA using DMAPA−PVA with different degrees of amine substitutions. Polyplex formation was monitored by an ethidium bromide exclusion assay at constant N/P ratios (Figure 3). Higher degrees of amine substitution resulted in decreased fluorescence intensities, compatible with an increasing complexation and condensation of DNA as a function of the degree of substitution. Obviously, increasing amine densities lead to an increase in charge density and hence to stronger complexation at a constant N/P ratio. There was no significant difference between diethyl and dimethylamine-modified PVA showing similar complexation behavior (data not shown). Therefore, condensation and complexation of the DNA seem to be mainly dominated by charge density and not by the chemical structure of charge carrying groups.

The interaction between DNA and the polymers was directly observed using AFM, which provides useful information on polyplex size, morphology, and mechanisms of condensation (*39*, *47*−*50*). Differences in the morphology of the polyplexes formed by different polymers are recognizable. Figures 4 and 5A−D depict the changing of morphology of condensed DNA with increasing amine substitution and at different N/P ratios. The complexes formed between DNA and DMAPA(7) are very diffuse and not clearly defined (Figure 4A). Increasing the amine substitution leads to further refinement of morphology (Figure 4B−F), where these diffuse particles are transformed into toroids, plectonomic rods, and other highly condensed morphologies (Figure 5, right E−G). These shapes are totally different from noncondensed DNA (Figure 5, right H), and they highlight the PVA/

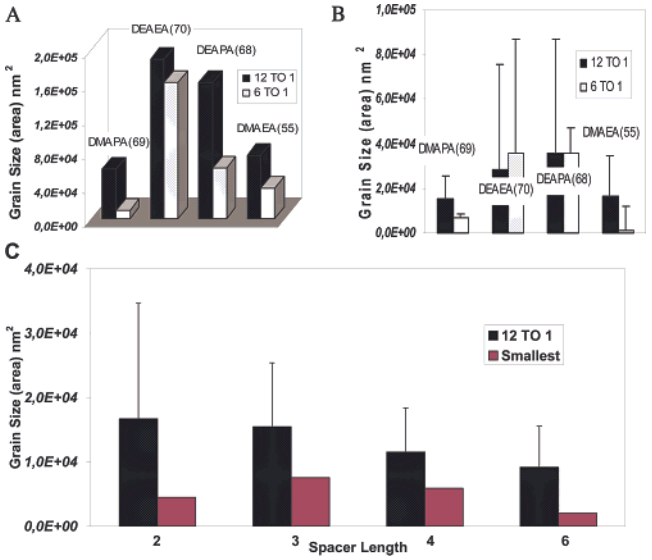

Figure 6. (A) Max grain sizes for each polymer (nm^2) both 6:1 and 12:1; (B) mean particle size for each polymer + S/D; (C) mean particle size for each polymer + S/D.

DNA interaction very clearly. Previous publications suggest distinct pathways for the formation of these morphologies; starting with neutralization of 89−90% of the charge of naked DNA (*45*), where toroid formation is concerned, the formation of a nucleus or "static loop" precedes charge neutralization, where the dimensions of this static loop directly affect the diameter of the toroid formed (*51*, *52*). AFM has identified possible mechanisms for the formation of ringlike and flowerlike DNA (*49*) and have identified possible intermediary structures that may be precursors to the final product of condensation (*53*, *54*).

Many factors are believed govern the morphology and dimension of condensed DNA, including hydrophobicity (*55*, *56*), polymer charge, and solution pH (*57*). With such knowledge of DNA condensation, an ideal nonviral gene delivery candidate is yet to be synthesized. To this end, we investigated possible structure activity relationships of different amine-modified PVAs to investigate how they affect DNA condensation and transfection.

Our data suggest that the elongation of spacer length leads to a reduction in the mean grain size of particles (Figure 6). As the tertiary amine groups of the amine-PVA are largely responsible for the binding of polymer to DNA and subsequent condensation of DNA, it is reasonable to believe that the distance between the amine functionalities and the polymer backbone has the ability to affect these interactions. It would be expected that a long flexible spacer results in easily accessible amino functionality and hence a better adaptation to DNA. Finally, less polymer is necessary to complex the DNA, and because of the better compatibility between both components smaller particles are formed. Consistent with this view is that a polymer having shorter spacers (such as ethyl) form larger mean particles than those of hexyl spacer type (Figure 6, Table 3). Further, AFM image

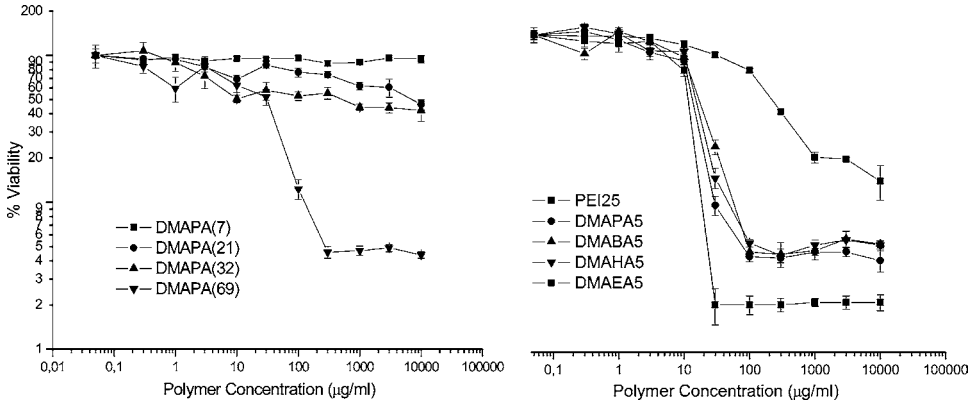

Figure 7. MTT test on L929 mouse fibroblasts: amine-modified PVA with degrees of substitution smaller than 0.2 are nontoxic (left); higher DS results in toxicity at polymer concentrations above 10 μL/mL (right).

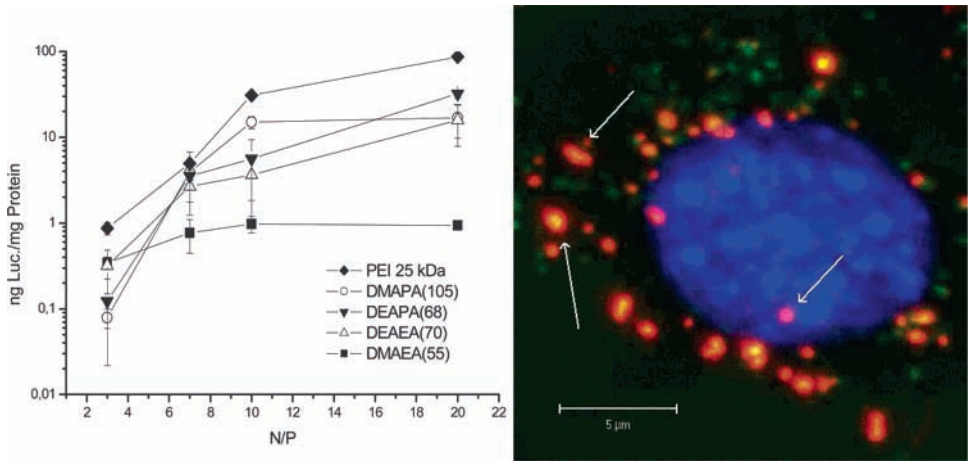

Figure 8. (Left) Transfection abilities of amine-modified PVA in the presence of chloroquin: higher degrees of amine substitution results in higher transfection abilities of the polymer; (right) the CLSM image indicates endosomes filled with PVA/DNA complexes (orange) in the nucleus plane within a NIH/3T3 cell (nucleus (DAPI, blue), polymer (FITC, green), DNA (YOYO1-DNA, red) (scale: 5 μm).

analysis demonstrated the influence of the amino protecting group where, independent of the N/P ratio, the methyl protecting groups enable amine-modified PVA to form smaller polymer/DNA particles than ethyl-protected ones (Figure 6). This effect could be a result of better accessibility to methyl protected amino groups due to lower steric hindrance. The effect of amino protecting groups on particle size seems to be more significant than that of the spacer length on particle size. These data suggest that optimal condensation would be achieved with a higher degree of amine substitution, a smaller amino-protecting group, and a longer spacer.

In MTT tests amine-modified polymers with degrees of substitutions (DS) smaller than 0.2 (20%) are nontoxic. Any increase in the DS above 0.2 results in an increased toxicity at polymer concentrations > 10 μg/mL (Figure 7). This toxicity seems to be independent of the amine type and is only dependent on DS. Apparently, charge density is the decisive factor in determining toxicity, which does not appear to be affected by the means in which it is introduced to the cell. Toxicity is therefore unspecific and a function of charge and not of structure (*58*).

Investigation of the transfection abilities of these polymers are shown in Figure 8. Increasing DS of amine leads to an overall better transfection in comparison to lower-substituted polymers. Increasing the N/P ratio leads to increasing transfection in the presence of chloroquine. Without addition of chloroquine, there is no detectable transfection. In contrast, CLSM images demonstrate an uptake of polymer/DNA particles into the cell but no release into the cytoplasm. The particles stay intact in the endosomes but they cannot leave them without the addition of chloroquine. Positive charges of polymers enable particles formed by these substances and DNA to enter cells. Indeed, this uptake process is only a part of the whole transfection mechanism. It is necessary that something enables the particles to leave the endosomes and to reach the cytoplasm and lastly the nucleus. In the literature, it is discussed that polymers such as poly(ethylene imine) (PEI) open the endosomes by a so-called proton sponge effect (*40*). This effect is based on the buffering capacity of the polymer. Because of its high density of amino groups, PEI has a huge buffer capacity and leads to an increasing influx of protons and water into the endosomes. This process finally results in a breakdown of the vesicles and release of its content into the cytoplasm. The low amine density in the synthesized PVA results in insufficient proton buffering. As a result, polyplexes are not released from the endosomes, resulting in very poor transfection. This result is not unexpected and in line with transfection efficiencies observed with other polycations such as poly-L-lysine (*59*). Further modifications of the PVA backbone using PLGA grafting have led to surprisingly efficient gene delivery systems reported elsewhere (*60*).

In conclusion, this study underscores the necessity to establish more detailed structural-activity relationships between polycations as demonstrated here for the amine-modified PVA structure and DNA morphology. Such a relationship was highlighted using PCS, AFM, and zeta-potential. Our transfection data demonstrate that the rate-limiting step for gene expression seems to be associated with endosomal escape of PVA−DNA polyplexes. The addition of chloroquine appears to circumvent this process and achieves superior luciferase expression. The results of this study clarifies that an effective transfection device needs more functionality than simply positive charges. It must also be able to leave the endosomes without addition of further substances. As demonstrated by Oster et al., the grafting of these PVA will lead to transfection efficiencies even higher than with PEI/DNA complexes (*60*).

ACKNOWLEDGMENT

We gratefully acknowledge financial support of this work by the Deutsche Forschungsgemeinschaft (DFG). We thank Wyatt Technology Europe GmbH and Dr. A. Theisen. James Ellis would like to thank the BBSRC for funding and Professor X. Chen for his help and advice.

Supporting Information Available: NMR data of amine-carbonylimidazole; CHN analysis and NMR data of amine-modified poly(vinyl alcohol); figure of FT-IR and ^{1}H-NMR of amine-modified PVA assignment. This material is available free of charge via the Internet at http://pubs.acs.org.

LITERATURE CITED

(1) Lengsfeld, C. S., Manning, M. C., and Randolph, T. W. (2002) Encapsulating DNA within biodegradable polymeric microparticles. *Curr. Pharm. Biotechnol. 3*, 227−235.

(2) Gulati, M., Grover, M., Singh, S., and Singh, M. (1998) Lipophilic drug derivatives in liposomes. *Int. J. Pharm. 165*, 129−168.

(3) Drin, G., Rousselle, C., Scherrmann, J.-M., Rees, A. R., and Temsamani, J. (2002) Peptide delivery to the brain via adsorptive-mediated endocytosis: advances with SynB vectors. *AAPS Pharm. Sci. 4*, 26.

(4) Evans, R. K., Zheng Xu, Bohannon, K. E., Wang, B., Bruner, M. W., and Volkin, D. B. (2000) Evaluation of degradation pathways for plasmid DNA in pharmaceutical formulations via accelerated stability studies. *J. Pharm. Sci. 89*, 76−87.

(5) Uchida, T., Yagi, A., Oda, Y., Nakada, Y., and Goto, S. (1996) Instability of bovine insulin in poly(lactide-co-glycolide) (PLGA) microspheres. *Chem. Pharm. Bull. (Tokyo) 44*, 235−236.

(6) Pillai, O., and Panchagnula, R. (2001) Insulin therapies − past, present and future. *Drug Discovery Today 6*, 1056−1061.

(7) van de Weert, M., Hennink, W. E., and Jiskoot, W. (2000) Protein instability in poly(lactic-co-glycolic acid) microparticles. *Pharm. Res. 17*, 1159−1167.

(8) Fasano, A. (1998) Innovative strategies for the oral delivery of drugs and peptides. *Trends Biotechnol. 16*, 152−157.

(9) Akiyoshi, K., Kobayashi, S., Shichibe, S., Mix, D., Baudys, M., Kim, S. W., and Sunamoto, J. (1998) Self-assembled hydrogel nanoparticle of cholesterol-bearing pullulan as a carrier of protein drugs: Complexation and stabilization of insulin. *J. Controlled Release 54*, 313−320.

(10) Bernkop-Schnurch, A., Scholler, S., and Biebel, R. G. (2000) Development of controlled drug release systems based on thiolated polymers. *J. Controlled Release 66*, 39−48.

(11) Brazel, C. S., and Peppas, N. A. (2000) Modeling of drug release from swellable polymers. *Eur. J. Pharm. Biopharm. 49*, 47−58.

(12) Breitenbach, A., Li, Y. X., and Kissel, T. (2000) Branched biodegradable polyesters for parenteral drug delivery systems. *J. Controlled Release 64*, 167−178.

(13) Fischer, D., Bieber, T., Li, Y., Elsasser, H. P., and Kissel, T. (1999) A novel non-viral vector for DNA delivery based on low molecular weight, branched polyethylenimine: effect of molecular weight on transfection efficiency and cytotoxicity. *Pharm. Res. 16*, 1273−1279.

(14) Higaki, M., Azechi, Y., Takase, T., Igarashi, R., Nagahara, S., Sano, A., Fujioka, K., Nakagawa, N., Aizawa, C., and Mizushima, Y. (2001) Collagen minipellet as a controlled release delivery system for tetanus and diphtheria toxoid. *Vaccine 19*, 3091−3096.

(15) Jones, D. H., Corris, S., McDonald, S., Clegg, J. C., and Farrar, G. H. (1997) Poly(DL-lactide-co-glycolide)-encapsulated

plasmid DNA elicits systemic and mucosal antibody responses to encoded protein after oral administration. *Vaccine 15*, 814−817.

(16) Mi, F. L., Lin, Y. M., Wu, Y. B., Shyu, S. S., and Tsai, Y. H. (2002) Chitin/PLGA blend microspheres as a biodegradable drug-delivery system: phase-separation, degradation and release behavior. *Biomaterials 23*, 3257−3267.

(17) Maruyama, A., Ishihara, T., Kim, J.-S., Kim, S. W., and Akaike, T. (1997) Nanoparticle DNA Carrier with Poly(L-lysine) Grafted Polysaccharide Copolymer and Poly(D,L-lactic acid). *Bioconjugate Chem. 8*, 735−742.

(18) Walter, E., Dreher, D., Kok, M., Thiele, L., Kiama, S. G., Gehr, P., and Merkle, H. P. (2001) Hydrophilic poly(DL-lactide-co-glycolide) microspheres for the delivery of DNA to human-derived macrophages and dendritic cells. *J. Controlled Release 76*, 149−168.

(19) Walter, E., Moelling, K., Pavlovic, J., and Merkle, H. P. (1999) Microencapsulation of DNA using poly(DL-lactide-co-glycolide): stability issues and release characteristics. *J. Controlled Release 61*, 361−374.

(20) Witt, C., and Kissel, T. (2001) Morphological characterization of microspheres, films and implants prepared from poly(lactide-co-glycolide) and ABA triblock copolymers: is the erosion controlled by degradation, swelling or diffusion? *Eur. J. Pharm. Biopharm. 51*, 171−181.

(21) Fernandez-Urrusuno, R., Calvo, P., Remunan-Lopez, C., Vila-Jato, J. L., and Alonso, M. J. (1999) Enhancement of nasal absorption of insulin using chitosan nanoparticles. *Pharm. Res. 16*, 1576−1581.

(22) Couvreur, P., Barratt, G., Fattal, E., Legrand, P., and Vauthier, C. (2002) Nanocapsule technology: a review. *Crit. Rev. Ther. Drug Carrier Syst. 19*, 99−134.

(23) Okada, H., and Toguchi, H. *Biodegradable Microspheres in Drug Delivery*; 1st ed.; Bergell House Inc.: New York, 1995; Vol. 12.

(24) Crotts, G., and Park, T. G. (1998) Protein delivery from poly(lactic-co-glycolic acid) biodegradable microspheres: release kinetics and stability issues. *J. Microencapsul. 15*, 699−713.

(25) Yamaguchi, Y., Takenaga, M., Kitagawa, A., Ogawa, Y., Mizushima, Y., and R. Igarashi, R. (2002) Insulin-loaded biodegradable PLGA microcapsules: initial burst release controlled by hydrophilic additives. *J. Controlled Release 81*, 235−249.

(26) Pistel, K. F., Bittner, B., Koll, H., Winter, G., and Kissel, T. (1999) Biodegradable recombinant human erythropoietin loaded microspheres prepared from linear and star-branched block copolymers: Influence of encapsulation technique and polymer composition on particle characteristics. *J. Controlled Release 59*, 309−325.

(27) Cleland, J. L., Mac, A., Boyd, B., Yang, J., Duenas, E. T., Yeung, D., Brooks, D., Hsu, C., Chu, H., Mukku, V., and Jones, A. J. (1997) The stability of recombinant human growth hormone in poly(lactic-co-glycolic acid) (PLGA) microspheres. *Pharm. Res. 14*, 420−425.

(28) Emo Chiellini, Corti, A., D'Antone, S., and Solaro, R. (2003) Biodegradation of poly (vinyl alcohol) based materials. *Prog. Polym. Sci. 28*, 963−1014.

(29) Matsumura, S., Tomizawa, N., Toki, A., Nishikawa, K., and Toshima, K. (1999) Novel poly(vinyl alcohol)-degrading enzyme and the degradation mechanism. *Macromolecules 32*, 7753−7761.

(30) Petersen, H., Merdan, T., Kunath, K., Fischer, D., and Kissel, T. (2002) Poly(ethylenimine-co-L-lactamide-co-succinamide): a biodegradable polyethylenimine derivative with an advantageous pH-dependent hydrolytic degradation for gene delivery. *Bioconjugate Chem. 13*, 812−821.

(31) van Dijk-Wolthuis, W. N. E., Tsang, S. K. Y., Kettenes-van den Bosch, J. J., and Hennink, W. E. (1997) A new class of polymerizable dextrans with hydrolyzable groups: hydroxyethyl methacrylated dextran with an without oligolactate spacer. *Polymer 25*, 6235−6242.

(32) Yamaoka, T., Tabata, Y., and Ikada, Y. (1995) Fate of water-soluble polymers administered via different routes. *J. Pharm. Sci. 84*, 349−354.

(33) Tabata, Y., Murakami, Y., and Ikada, Y. (1998) Tumor accumulation of pol(vinyl alcohol) of different sizes after intravenous injection. *J. Controlled Release 50*, 123−133.

(34) Blessing, T., Remy, J.-S., and Behr, J.-P. (1998) Template oligomerization of DNA-bound cations produces calibrated nanometric particles. *J. Am. Chem. Soc. 120*, 8519−8520.

(35) Nakamae, K., Nizuka, T., Miyata, T., Furukawa, M., Nishino, T., Kato, K., Inoue, T., Hoffman, A. S., and Kanzaki, Y. (1997) Lysozyme loading and release from hydrogels carrying pendant phosphate groups. *J. Biomater. Sci., Polym. Ed. 9*, 43−53.

(36) Jung, T., Kamm, W., Breitenbach, A., Klebe, G., and Kissel, T. (2002) Loading of tetanus toxoid to biodegradable nanoparticles from branched poly(sulfobutyl-poly(vinyl alcohol))-g-(lactide-co-glycolide) nanoparticles by protein adsorption: a mechanistic study. *Pharm. Res. 19*, 1105−1113.

(37) Reference withdrawn by author in proof.

(38) Vinogradov, S. V., Bronich, T. K., and Kabanov, A. V. (1998) *Bioconjugate Chem. 9*, 805−812.

(39) Golan, R., Pietrasanta, L. I., Hsieh, W., and Hansma, H. G. (1999) DNA Toroids: Stages in Condensation. *Biochemistry 38*, 14069−14076.

(40) Merdan, T., Kunath, K., Fischer, D., Kopecek, J., and Kissel, T. (2002) Intracellular processing of poly(ethylene imine)/ribozyme complexes can be observed in living cells by using confocal laser scanning microscopy and inhibitor experiments. *Pharm. Res. 19*, 140−146.

(41) Wolfert, M. A., Dash, P R., Nazarova, O., Oupicky, D., Seymour, L W., Smart, S., Strohalm, J., and Ulbrich, K. (1999) Polyelectrolyte vectors for gene delivery: influence of cationic polymer on biophysical properties of complexes formed with DNA. *Bioconjugate Chem. 10*, 993−1004.

(42) Ogris, M., Steinlein, P., Carotta, S., Brunner, S., and Wagner, E (2001) DNA/polyethylenimine transfection particles: influence of ligands, polymer size, and PEGylation on internalization and gene expression. *AAPS Pharm. Sci. 3*, E21.

(43) Xie, X., Wittmar, M., and Kissel, T. (2004) A two-dimensional NMR study of poly(vinyl dialkylaminoalkylcarbamate-co-vinyl acetate-co-vinyl alcohol). *Macromolecules 37*, 4598−4606.

(44) Bloomfield, V. A. (1998) DNA condensation by multivalent cations. *Biopolymers 53*, 329−341.

(45) He, S. Q., Arscott, P. G., and Bloomfield, V. A. (2000) Condensation of DNA by multivalent cations: Experiment studies of condensation kinetics. *Biopolymers 53*, 329−341.

(46) Kunath, K., von Harpe, A., Fischer, D., Petersen, H., Bickel, U., Voigt, K., and Kissel, T. (2003) Low-molecular-weight polyethylenimine as a nonviral vector for DNA delivery: comparison of physicochemical properties, transfection efficiency and in vivo distribution with high-molecular-weight polyethylenimine. *J. Controlled Release 89*, 113−125.

(47) Ellis, J. S., Abdelhady, H. G., Allen, S., Davies, M. C., Roberts, C. J., Tendler, S. J. B., and Williams, P. M. (2004) Direct atomic force microscopy observation of monovalent ion induced binding of DNA to mica. *J. Microsc. 215*, 297−301.

(48) Hansma, H. G., and Pietrasanta, L. (1998) Atomic force microscopy and other scanning probe microscopies. *Curr. Opin. Chem. Biol. 2*, 579−584.

(49) Martin, A., Stolnik, S., Davies, M. C., Laughton, C. A., Roberts, C. J., Tendler, S. J. B., and Williams, P. M. (2000) Observation of DNA-Polymer condensate formation in real-time at the molecular level. *FEBS Lett. 480*, 106−112.

(50) Abdelhady, H. G., Allen, S., Davies, M. C., Roberts, C. J., Tendler, S. J. B., and Williams, P. M. (2003) Direct real-time molecular scale visualisation of the degradation of condensed DNA complexes exposed to DNase I. *Nucleic Acids Res. 31*, 4001−4005.

(51) Shen, M. R., Downing, K. H., Balhorn, R., and Hud, N. V. (2000) Nucleation of DNA condensation by static loops: Formation of DNA toroids with reduced dimensions. *J. Am. Chem. Soc. 122*, 4833−4834.

(52) Conwell, C. C., Vilfan, I. D., and Hud, N. V. (2003) Controlling the size of nanoscale toroidal DNA condensates with static curvature and ionic strength. *Proc. Natl. Acad. Sci. U.S.A. 100*, 9296−9301.

(53) Liu, F., Song, Y., and Liu, D. (1999) Hydrodynamics-based transfection in animals by systemic administration of plasmid DNA. *Gene Ther. 6*, 1258−1266.
(54) Liu, K. (2003) Breakthroughs in cancer gene therapy. *Semin. Oncol. Nursing 19*, 217−226.
(55) Bloomfield, V. A. (1996) DNA condensation. *Curr. Opin. Struct. Biol. 6*, 334−341.
(56) Deng, H., and Bloomfield, V. A. (1999) Structural effects of cobalt-amine compounds on DNA condensation. *Biophys. J. 77*, 1556−1561.
(57) Rungsardthong, U., Ehtezazi, T., Bailey, L., Armes, S. P., Garnett, M. C.; Stolnik, S. (2003) Effect of polymer ionization on the interaction with DNA in nonviral gene delivery systems. *Biomacromolecules 4*, 683−690.
(58) Fischer, D., Li, Y., Ahlemeyer, B., Krieglstein, J., and Kissel, T. (2003) In vitro cytotoxicity testing of polycations: Influence of polymer structure on cell viability and hemolysis. *Biomaterials 24*, 1121−1131.
(59) Merdan, T., Kopecek, J., and Kissel, T. (2002) Prospects for cationic polymers in gene and oligonucleotide therapy against cancer. *Adv. Drug Delivery Rev. 54*, 715−758.
(60) Oster, C. G., Wittmar, M., Unger, F., Barbu-Tudoran, L., Schaper, A. K., and Kissel, T. (2004) Effective biodegradable DNA nanocarrier systems of newly synthesized amphiphilic, amine-modified graft polyesters. *Pharm. Res. 21*, 927−931.
(61) Rackstraw, B. J., Martin, A. L., Stolnik, S., Roberts, C. J., Garnett, M. C., Davies, M. C., and Tendler, S. J. B. (2001) Microscopic investigations into PEG-cationic polymer-induced DNA condensation. *Langmuir 17*, 3185−3193.

BC0500995

Cell Transduction Pathways of Transportans

Kärt Padari,[†,‡] Pille Säälik,[†] Mats Hansen,[§] Kaida Koppel,[†] Raivo Raid,[‡] Ülo Langel,[§] and Margus Pooga*[,†,‡]

Estonian Biocenter, 23 Riia Street, 51010 Tartu, Estonia, Institute of Zoology and Hydrobiology, University of Tartu, 46 Vanemuise Street, 51014 Tartu, Estonia, and Department of Neurochemistry and Neurotoxicology, Arrhenius Laboratories, Stockholm University, S-10691 Stockholm, Sweden. Received April 25, 2005; Revised Manuscript Received September 8, 2005

Attempts to unravel the cell translocation mechanism of a growing number of cell-penetrating peptides (CPP) have revealed molecular determinants essential for internalization ability. The peptide sequence and the charge have been proposed to be the major factors in determining the membrane interaction mode and subsequent internalization pathway. Recent research in this field has shifted to search and design of novel CPPs with predefined vectorial properties and elucidation of the mechanism of cell entry of CPPs with high cargo delivery efficiency. Here we present a map of interaction modes with cell surface and intracellular traffic of transportan and its analogue TP10 complexed with fluorescently labeled avidin or streptavidin−gold conjugates. The protein cargo complexed with either peptide is transduced into HeLa and Bowes cells mostly in the endocytic vesicles with heterogeneous morphology and size as demonstrated by transmission electron microscopy (TEM) and confocal laser scanning fluorescence microscopy. Most of the induced vesicles are large, with 0.5−2 μm diameter, probably macropinosomes, but the complexes are present also in smaller vesicles, suggesting involvement of different pathways. Later the majority of complexes are translocated from the cell periphery into vesicles of perinuclear region and partly to lysosomes. A fraction of transportan−streptavidin complexes is present also freely in cytoplasm, both in the close vicinity of plasma membrane and more centrally, suggesting the escape from endosomal vesicles, since vesicles with discontinuous membrane were also detected by TEM. The cell-translocation process of transportan−protein complexes is temperature dependent and strongly inhibited at 8−10 °C and blocked at 4 °C when only interaction with the plasma membrane takes place.

INTRODUCTION

One of the major bottlenecks in introduction of oligonucleotide and peptide or protein-based drugs is the poor uptake of hydrophilic compounds by cells. For a decade, great expectations to overcome this obstacle were connected with cell-penetrating peptides (CPP) (also called protein transduction domains, membrane translocating sequences, or Trojan peptides), a class of 10−30 amino acid long peptides. Cationic and hydrophilic CPPs of natural and synthetic origin were first suggested to cross cellular membrane in a receptor- and temperature-independent mode (*1*−*3*). The model of direct passage of CPPs across the plasma membrane, however, has been displaced by the more cell-centered concept of mainly endocytic uptake. Evidence that the cellular uptake of CPPs and their cargoes is highly dependent on physical parameters such as temperature (*4*−*7*), charge of the peptide (*8*−*10*), and experimental conditions (*4*, *11*, *12*) has been accumulated rapidly during the past years. Taking into consideration that more than 200 peptide sequences have shown cellular delivery properties and the number is still growing, one has to assume that the details of internalization mechanisms might vary. The rapidly growing number of examples of successful CPP-mediated cargo delivery (*13*) demonstrates the potential and development in the field of application of peptidic delivery vectors for biotechnological applications. The detailed knowledge about the internalization mechanism and intracellular trafficking of CPPs and their cargoes is still of fundamental significance. Efforts to define the intracellular pathway used by different CPP−protein complexes and fusion proteins have provided controversial results. It has been shown that Tat−GFP fusion proteins are taken up by HeLa and Jurkat cell lines via lipid raft-dependent caveolar endocytosis (*14*, *15*). On the other hand, rapid internalization by lipid raft-dependent macropinocytosis without the involvement of caveolar marker protein caveolin has been demonstrated for Tat−Cre fusion protein in mouse lymphocytes (*16*). Recently, Nakase and co-workers demonstrated that the uptake of penetratin is not mediated by macropinocytosis in HeLa cells (*7*). On the other hand, slightly improved oligoarginine uptake was observed when coapplied to HeLa cells with epidermal growth factor (*7*) suggesting a macropinocytic mechanism. Macropinocytosis is an actin-mediated endocytic process initiated usually by growth factors and characterized by the membrane ruffles and outgrowth of protrusions, which collapse and fuse with the plasma membrane generating large endocytic vesicles (*17*). Macropinosomes might be dissimilar, it has been reported about the different translocation speed of Adenovirus type 2 virus (Ad2)-containing and EGF-induced macropinosomes and the shorter lifetime of former (*18*). The same group also observed the increase of Ad2 uptake by clathrin-mediated endocytosis and the reduction of viral escape from endosomes as a response

* To whom correspondence should be addressed. Tel: (372-7) 375 023, Fax: (372-7) 420 286. E-mail: mpooga@ebc.ee.
[†] Estonian Biocenter.
[‡] University of Tartu.
[§] Stockholm University.

10.1021/bc050125z CCC: $30.25 © 2005 American Chemical Society
Published on Web 10/22/2005

to the inhibition of macropinocytosis (*18*). It is not clear yet, whether the CPP-containing vesicular structures are of the same character/type as adenovirus- or EGF-induced macropinosomes and if the CPPs switch between the endocytic routes. The CPP-containing vesicular structures could be disrupted leading to the initiation of escape and the increased functional activity of delivered proteins as demonstrated by including membrane destabilizing sequences into fusion protein or exposing cells to multifunctional peptides containing both a CPP and the membrane disrupting motif (*16*, *19*). The polyarginine−peptide conjugates labeled with the fluorescent dye molecule are released from vesicular structures upon irradiation at an appropriate wavelength (*20*). Although it might provide a potentially useful technique for increasing the efficiency of CPP-mediated delivery of active cargoes, the mechanism of photo-destabilization of vesicular membranes is not well understood and the putative toxic effects of this method are not evaluated yet. Therefore, application of CPPs with intrinsic membrane-destabilizing properties is still of interest. One of the potential membrane-interacting peptides is transportan, a 27 amino acid long chimeric peptide (*21*), the C-terminal part of which has helical structure both in the aqueous environment and in the presence of lipid vesicles (*10*) and interacts with phospholipids using the hydrophobic face of the α-helix (*22*). Transportan has been demonstrated to be an efficient carrier for PNA (*23*), fluorophore-labeled peptide (*24*), and protein (*12*). One possibility to explain the high delivery efficiency of MAP (*24*) and transportan is the more efficient escape from vesicular structures as compared to penetratin and Tat peptide due to stronger interaction with membrane lipids. Therefore, the more detailed analysis of internalization and cellular trafficking of transportan are of interest. Since transportan modulates the activity of membranous G-proteins at high concentration (*21*), an analogue TP10, with no effect on the activity of GTPases, was designed (*25*). The cellular uptake and fate of CPPs and their cargoes has been mainly studied by using fluorescence or activity-based methods. The vesicular structures mediating the cell entry of CPPs are specified either by looking for colocalization with the respective marker proteins or by specifically inhibiting a certain type of endocytic process. Visualization on ultrastructural level might be helpful in characterizing the sites of initial interaction of CPPs with the plasma membrane or membrane-bound extracellular structures, changes of membrane morphology, size and shape of vesicular structures hiding CPPs, etc. Therefore, we used a preembedding labeling procedure and transmission electron microscopy (TEM) to visualize protein cellular delivery by transportan and TP10. The cellular uptake and trafficking of biotin−CPP complexes with colloidal-gold-labeled streptavidin was characterized after fixation and embedding of cells by TEM. The results obtained by electron microscopy in fixed cells were compared with confocal laser scanning microscopy (CLSM) data in living cells using analogous experimental setup, i.e., by using the complexes of biotin−CPP with fluorescently labeled avidin.

MATERIALS AND METHODS

Peptide Synthesis. Transportan (GWTLNSAGYLLGKINLKALAALAKKIL-amide) and TP10 (AGYLLGKINLKALAALAKKIL-amide) were synthesized stepwise on a 0.1 mmol scale on an automated peptide synthesizer (Applied Biosystems Model 431A) using the *t*-Boc solid-phase peptide synthesis strategy. *tert*-Butyloxycarbonyl amino acids were coupled as hydroxybenzotriazole esters to a *p*-methylbenzylhydrylamine resin (Neosystem, Strasbourg, France) to obtain C-terminally amidated peptides. Biotin was coupled to the side-chain of Lys^{13} or Lys^{7} in transportan and transportan 10, respectively, as previously described (*12*). The final cleavage and purification of peptides was performed, as described (*12*). The molecular weights of biotinylated peptides were determined by MALDI-TOF mass spectroscopy (Voyager STR).

Cell Cultures. The human breast cancer cell line HeLa (ATCC CCL-2) and the human Bowes melanoma cells (ATCC CRL-9607) were cultivated in a humidified atmosphere containing 5% CO_2 at 37 °C in Iscove's Modified Dulbecco's Medium (IMDM) or in Dulbecco's Modified Eagle's Medium (DMEM), respectively. Culture medium was supplemented with 10% fetal calf serum (FCS), 100 IU/mL penicillin, and 100 μg/mL streptomycin.

Delivery of Streptavidin−Gold into Cultured Cells by Biotinyl−Transportan and Biotin−TP10. The cells used for experiments were grown for 2 days on round Thermanox tissue culture coverslips (diam 13 mm, Electron Microscopy Science, Fort Washington, PA) in 24-well plates to 80−100% confluence. The stock solution of biotin−transportan (1 mM) was treated with 10 mg/mL L-leucine in a minimal volume for 5 min at room temperature in order to dissociate the multimers of peptide. The biotinylated transportan or TP10 was complexed with streptavidin−gold (d 10 nm, Amersham Pharmacia Biotech, UK) for 3 min, diluted with the respective culture medium and applied to cells. Cells were incubated with the complexes of 25 or 5 μM biotin−transportan or -TP10 and streptavidin−gold (1:50 dilution) at 10, 20, or 37 °C for 20 min to 72 h depending on the experiment.

Labeling of Transferrin with Colloidal Gold. The colloidal gold solution of particles with 20 nm diameter was prepared, and absorption of transferrin was performed essentially as described earlier by Bendayan (*26*). Briefly, the gold sol was prepared by adding 1.5 mL of 1% sodium citrate solution to 100 mL of boiling solution of 0.01% $HAuCl_4$ dropwise over 5 min and boiling the mixture for 5 min. The resulting gold colloid was coated with 2.5 mg transferrin (Sigma, dissolved in 2 mL of water) at room temperature for 30 min. Transferrin−gold was stabilized with 1 mg/mL PVP40, 0.5 mg/mL PEG20000, and 0.5 mg/mL BSA and harvested by centrifugation at 10000*g* for 1 h at 4 °C. The residual free protein and aggregated material was removed by centrifugation at 5000 rpm for 45 min in discontinuous gradient of 10, 30, and 50% glycerol in PBS in a SW41 rotor. The most intensely colored fraction of transferrin−gold with homogeneous particle size was collected and stabilized for storage with 2% PVP (poly(vinylpyrrolidone)), 0.2 mg/mL PEG and 0.05% NaN_3.

Comparative Uptake of Transferrin and Transportan−Streptavidin Complexes by HeLa Cells. HeLa cells were grown on Thermanox coverslips in 24-well plates as described above. The nearly confluent cell layer was washed twice with serum-free IMDM and incubated in serum-free culture medium for 1 h in order to upregulate the transferrin receptors on plasma membrane (*27*). The starved cells were incubated with complexes of 25 or 5 μM biotin−TP and 1:50 dilution of streptavidin−gold (10 nm) along with the transferrin−gold complex (20 nm) at 1:50 dilution in serum-free IMDM in CO_2 incubator at 37 °C for 30 min. In some experiments cells were first incubated with TP−streptavidin complexes for 30 min, and then the solution

containing complexes was removed and replaced with the culture medium with gold-labeled transferrin and incubated for an additional 30 min. An analogous experiment with reversed order, first transferrin followed by TP−streptavidin complexes, was also carried out.

Electron Microscopy. Cells were fixed for transmission electron microscopy with 3% glutaraldehyde in 0.1 M sodium cacodylate-HCl buffer (pH 7.3) containing 0.05 M sucrose for 1−2 h. After being rinsed with cacodylate buffer, the cells were postfixed with 1.5% osmium tetraoxide in the same buffer containing 0.7% potassium ferrocyanate at 4 °C for 30 min and dehydrated in ethanol series from 50% up to 96%. Cells on Thermanox coverslips were embedded in epoxy resin, and the material was cut into ultrathin sections of 40−60 nm by using the Reichert Om U2 ultramicrotome. The sections were collected on grids and stained with 2% uranyl acetate in 50% ethanol and lead citrate according to instruction (*28*). Microtomed sections on the grids were examined and the images recorded by using a JEM-100S (JEOL, Japan) electron microscope. The scanned electron microphotos were analyzed and processed with Adobe Photoshop version 7.0 software.

Fluorescence Microscopy Experiments with Live Cells. HeLa cells (8×10^3) were seeded onto eight-well chambered coverglasses (Nalge Nunc International, Rochester, NY) 2 days before uptake experiments. The glasses were coated with collagen−fibronectin solution (10 μg/mL fibronectin, 30 μg/mL collagen, 0.01% bovine serum albumin, 100 IU/mL penicillin, and 100 μg/mL streptomycin in DMEM) for 30 min before seeding the cells. Cells were incubated with the complexes of 0.15 μM Alexa Fluor (AF) 488 labeled avidin (Molecular Probes, Leiden, Netherlands) and 0.5 or 1 μM biotin−CPP in serum free IMDM for 1 h at 37 °C. The incubation solution was supplemented with 25 μg/mL transferrin (labeled with AF 594, Molecular Probes) or 150 nM Lyso Tracker Red DND-99 (Molecular Probes) depending on experiment. For visualizing the Golgi apparatus, the cells were incubated with 0.5 μM BODIPY-TR-C_5 ceramide complex with BSA (prepared according to manufacturer's instructions, Molecular Probes) in serum free IMDM for 30 min before applying peptide−avidin complexes into the same medium. After 1 h incubation, the medium with CPP−avidin complexes and the markers of cellular organelles was removed and the cells were rinsed with PBS (containing 1 mM of $CaCl_2$ and 0.5 mM $MgCl_2$) followed by a brief rinse with 0.05% trypan blue in PBS and two additional washing steps with PBS. Cells were covered with calcium and magnesium-supplemented PBS, and the serial images from live cells were recorded using the laser confocal scanning microscope MRC-1024 with excitation at 488 and 568 nm (Bio-Rad Laboratories, Hercules, CA). To avoid cross-talk between the channels, emission signals were collected independently. Obtained images were processed with Adobe Photoshop version 6.0 software.

Fluorescence Microscopy Experiments with Fixed Cells. HeLa cells (2×10^4) were seeded 2 days before experiment on round glass coverslips into 24-well plate. Incubation with peptide−protein complexes was performed in serum-containing (10% FCS) medium. For the pulse-chase study, the medium with complexes was replaced after 1 h by media containing no complexes for 4 or 24 h according to the experiment. Before applying fresh media, the cells were rinsed twice in PBS to completely remove the nonassociated complexes. Cells were fixed for 20 min in 4% paraformaldehyde on ice, followed by 5 min permeabilization in 0.1% Triton X-100 in PBS. Nonspecific binding sites were blocked with 10% (w/v) nonfat dry milk solution in PBS for 30 min. Lysosomes were visualized with 1:50 (hybridoma supernatant) solution of LAMP2 primary antibody and 10 μg/mL AF 594-labeled goat anti-mouse secondary antibody. For revealing the actin fibers, cells were stained with 30 nM Texas Red-labeled phalloidin. Images were recorded using the laser confocal scanning microscope or Olympus BX61 microscope equipped with CCD camera DX70.

RESULTS

Association of Transportan−Streptavidin Complexes with the Cell Surface. To characterize the cellular delivery of proteins by transportan peptides, we followed the uptake of noncovalent complexes of biotin−transportan (or biotin−TP10) with streptavidin−gold by electron microscopy. The complexes between the biotin−CPP and gold-labeled streptavidin form quickly and were assembled by coincubating the respective components before applying to cells. The association of transportan− and TP10−protein complexes with the cell surface was examined in HeLa and human Bowes melanoma cells, which slightly differ in morphology. The surface of HeLa cells was usually more structured, possessing protrusions, long filopodia, and smaller microvillar extensions, whereas Bowes cells had a rather smooth plasma membrane with fewer protrusions and long extensions spread only between adjacent cells. The peptide−protein complexes associated quickly with the surface of the cells, already upon a 5−10 min incubation and were detectable by electron microscopy between the cells mostly as elongated structures of 0.4−2 μm on the electron dense background (Figure 1A−C). The initial interaction of transportan−streptavidin complexes induced formation of a small pit in the plasma membrane (Figure 1A). The aggregates were more typical for the complexes with transportan rather than with TP10. Formation of big peptide−protein aggregates was reduced by hindering the multimerization of transportan during formation of complexes with gold-labeled streptavidin by using leucine. The cells incubated with such "dissociated" complexes at 3 μM peptide concentration resembled the complexes of TP10 and showed significantly lower degree of aggregation (Figure 1D). The smaller aggregates but not the extensive agglomerates still formed, and the complexes were distributed more diffusely on the protrusions of cells. The peptide−protein complexes preferentially associated with filopodia and extensions of plasma membrane in HeLa cells. A smaller fraction of complexes associated with the flat areas, and most of these seemed to be in close contact with the lipids of the plasma membrane.

Transportan−Avidin Complexes Associate with Membrane Protrusions and Actin Cytoskeleton. The nature of membrane protrusions involved in the transportan-mediated protein internalization was further assessed by confocal microscopy in cells with visualized actin. Staining of actin cytoskeleton with Texas Red-labeled phalloidin revealed highly structured morphology of HeLa cells' plasma membrane with numerous protrusions. The protrusions were most abundant between the neighboring cells and oriented parallel bridging the cells, whereas thinner and more heterogeneous microspikes were observed in other regions of cellular membrane (Figure 2A). Transportan−avidin complexes docked to the intercellular membrane protrusions starting from 5 min incubation (data not shown). After 1 h incubation, the complexes were detected as punctate structures abundantly decorating the actin-filament-containing mem-

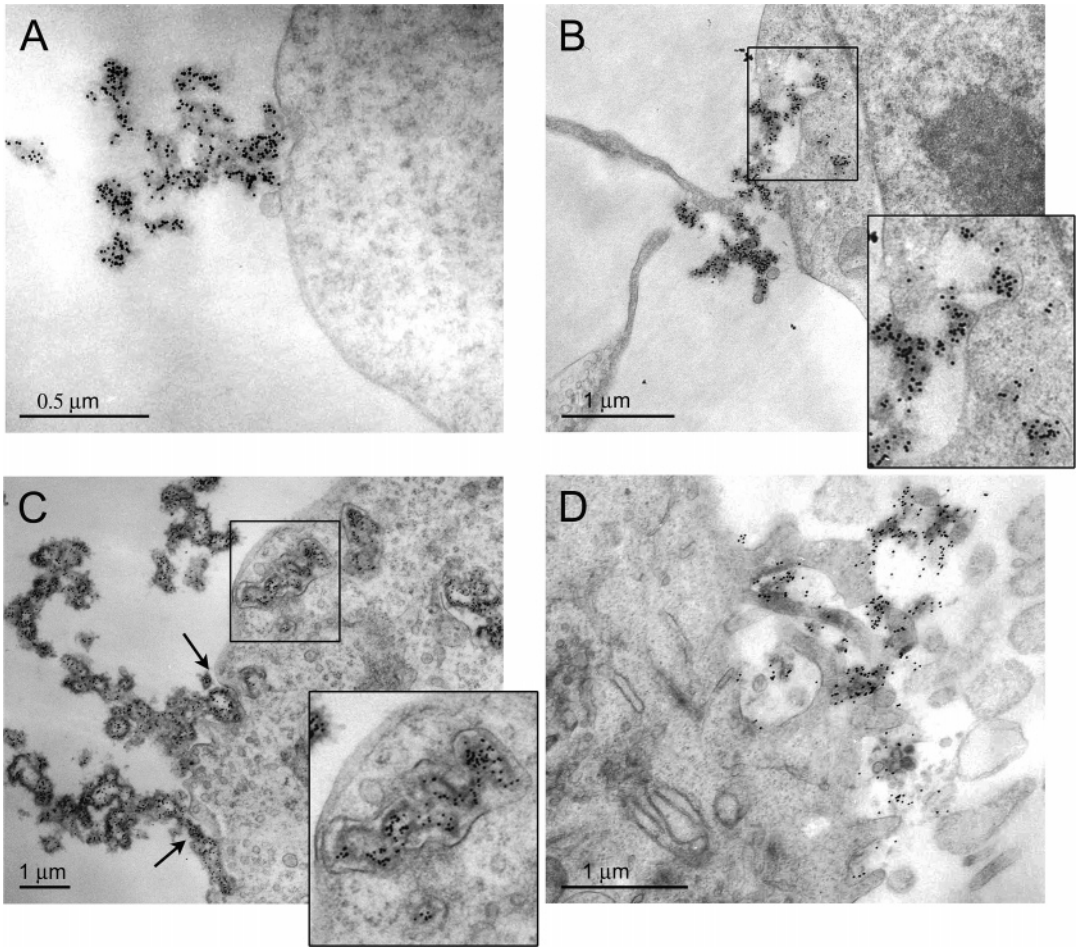

Figure 1. Interaction of CPP−protein agglomerates at the plasma membrane of cells. Human Bowes melanoma cells incubated with the complexes of gold-labeled streptavidin (10 nm, dilution 1:50) and 5 μM biotin−transportan for 30 min (A, B) or 2 h (C). HeLa cells (D) incubated for 1 h with the complexes of streptavidin−gold (10 nm, 1:50) and 2.5 μM biotin−transportan, treated with leucine (10 mg/mL) before complexing with protein−gold.

brane protrusions. The colocalization of peptide−protein complexes with actin fibers was detected also in the cortical cytoplasm of cells where actin filaments were packed less densely (Figure 2A). This suggests that intracellular translocation of peptide−avidin complexes might at least partially be mediated by actin cytoskeleton.

Morphology of the Plasma Membrane Changes upon Internalization of Transportan−Streptavidin Complexes. Streptavidin−gold complexes with transportan or TP10 entered the cells by using at least two morphologically clearly distinguishable mechanisms. First, docking of larger CPP−protein aggregates induced morphological changes in the plasma membrane leading to the formation of membrane invaginations (Figure 1B−D). Later the complexes shifted deeper into the cytoplasm, being finally fully engulfed by the cell into endocytic vacuoles (arrows in Figure 1C and enlarged sections of Figure 1B and C). The membrane bound aggregates seemed to repulse or force the indentation of plasma membrane. Various cell surface extensions were frequently involved in the translocation process as demonstrated in Figure 1B and D. The second mode of internalization was characteristic for smaller complexes containing few or a single gold particle, which did not induce detectable changes in the membrane morphology upon interaction with the plasma membrane (arrows in Figure 3A and the enlarged section of Figure 3A and B). Later the complexes with a single gold particle were also detectable in cortical cytoplasm, and changes in morphology of plasma membrane were not observed (Figure 3C). The second mode was not the major cell entry mechanism of streptavidin−gold complexes and was more characteristic for TP10 than transportan complexes and at the lower concentrations of peptide. It has to be mentioned that despite the differences in HeLa and Bowes cells morphology, both internalization modes were observed in both cell lines.

Distribution of Protein Delivered into Cells by Transportans. Streptavidin−gold complexes with transportan or TP10 were detectable in the cortical cytoplasm of Bowes and HeLa cells already after 10 min of incubation with complexes at 37 °C. Later in 1−2 h, transportan−streptavidin complexes spread over the cytoplasm, including the perinuclear region. The cell-transduced peptide−protein aggregates resided mainly in vesicular structures of irregular shape and varying diameter of 0.5−2.0 μm, which primarily seemed to depend on the size of internalized aggregate (Figure 4). The gold particles localized mostly in large vacuoles of 0.5−1.0 μm and in the multivesicular relatively spherical structures of 200−300 nm in diameter (large arrows in Figure 4A and B), the latter resembling the structures of endosomal−lysosomal pathway. Some complexes were present in long tubulovesicular structures, which were more typical for Bowes cells (Figure 4C and small arrow in Figure 4A). The complexes containing vesicles in HeLa cells were more homogeneous and spherical with maximal diameter of 0.3−0.5 μm. A small fraction of peptide−protein complexes was also present in small caveosome-

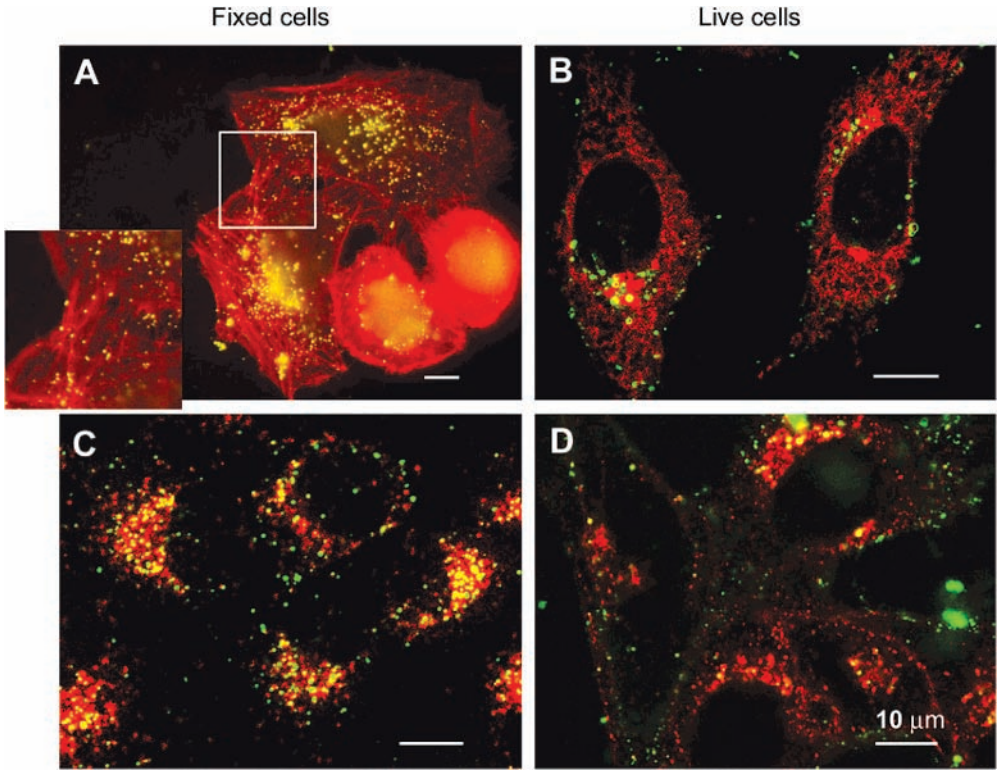

Figure 2. Localization of peptide−avidin complexes in relation to the actin cytoskeleton and organelles. Complexes of 1 μM (A) or 0.5 μM (B−D) biotinylated transportan with 0.15 μM AF 488-labeled avidin in HeLa cells after 1 h incubation (green). Actin fibers were stained with 30 nM phalloidin−Texas Red (A). Coincubation of cells with TP−avidin complexes with 0.5 μM BODIPY-TR-C_5 ceramide (B) or 50 μg/mL AF 594-labeled transferrin (D) was performed to reveal Golgi apparatus, and endosomes, respectively. Pulse-chase study: cells were incubated for 1 h with TP−avidin complexes, followed by a 24 h chase period. Lysosomes were visualized by staining with LAMP2 antibody and AF 594-labeled anti mouse antibody (red) (C). Colocalized structures are visible as yellow. Fluorescence microphoto of HeLa cells (A) and confocal sections at the equatorial level of nuclei (B−D).

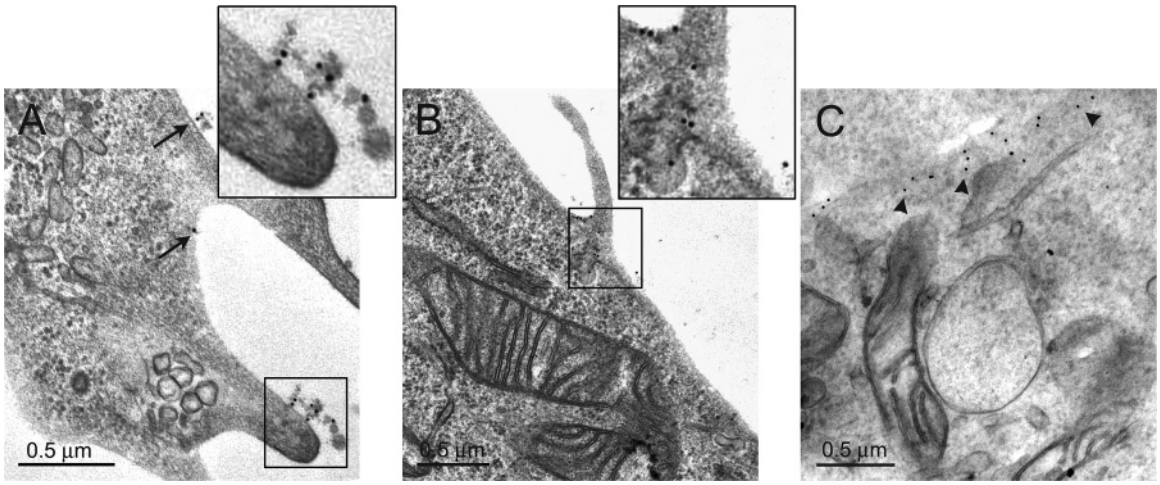

Figure 3. Nonaggregated CPP−protein complexes associate directly with the plasma membrane. HeLa cells incubated for 1 h with streptavidin−gold (10 nm, 1:50) complexed with 2.5 μM biotin−transportan (A, B) or biotin−TP10 (C) in the presence of leucine.

like vesicles of about 100 nm diameter or less (arrowhead in Figure 4A). Most of the complexes containing vesicles in HeLa cells were intact and surrounded by a continuous membrane. However, some of the vesicles that contained peptide−protein complexes had a discontinuous membrane, and the electron density of the vesicle content was undistinguishable from that of cytosol (arrows in Figure 4C). Moreover, considerable part of gold particles was spread apparently free in cytosol, often in the close proximity of vesicles with discontinuous membrane as indicated by the arrowheads in the enlarged section of Figure 4C. One might assume that the membrane was destabilized by transportan or TP10, and some vesicles were broken enabling the escape of complexes into cytosol.

Data obtained by electron microscopy were complemented by analogous experiments using the confocal laser scanning microscopy for analyzing the localization of biotinylated transportan complexed with AF 488-labeled avidin. After 1 h incubation, the transportan−avidin complexes localized in living cells in a punctate manner mostly at the cellular membrane or in the cortical cytoplasm but also in the perinuclear area (Figure 2B−D). However, fluorescent punctate structures

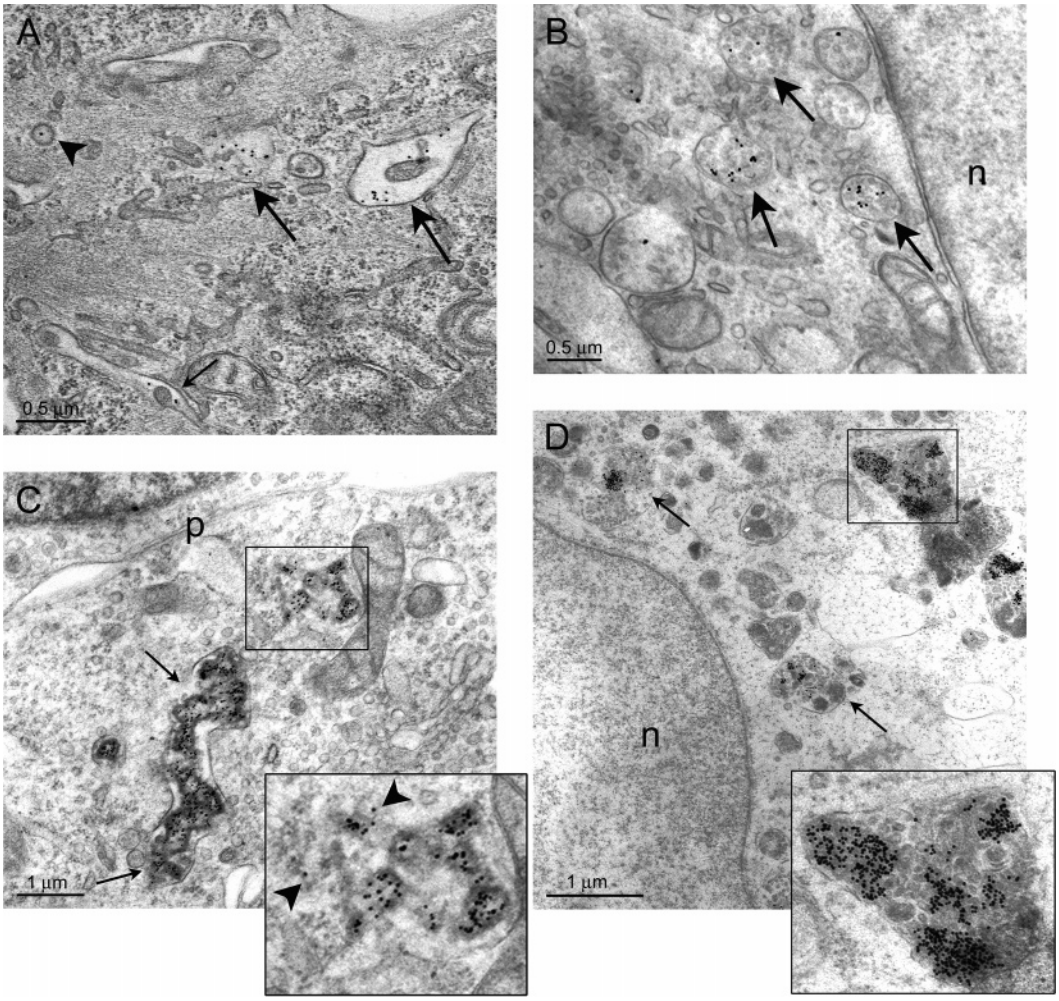

Figure 4. Localization of CPP−protein complexes in the cells after incubation at 37 °C. HeLa cells (A, B) incubated for 1 h with streptavidin−gold (10 nm, 1:50) complexed with 3 μM biotin−transportan (A) or 2.5 μM biotin−TP10 (B) in the presence of leucine. Bowes cells (C, D) incubated with the complexes of streptavidin−gold (10 nm, 1:50) and 5 μM biotin−transportan for 2 h (C) and 72 h (D). p = plasma membrane; n = nucleus.

were different—spherical aggregates with the higher diameter concentrated to the perinuclear area into one or two centers, whereas smaller dots were distributed in the cortical cytoplasm (Figure 2A−D). Some big fluorescent aggregates were attached to the cellular membrane, and very few were occasionally moving freely in the extracellular media. Large aggregates probably resulted from the multimerization of the peptide and the assembly of the formed complexes into bigger agglomerates, which was observed also at higher peptide concentrations in electron microscopy experiments (Figure 1A−C). Some agglomerates were not in contact with the cells, and their presence in the media after many washing steps suggests that initially membrane-bound aggregates could detach during treatment/visualization.

CPP−Protein Complexes Accumulated in the Perinuclear Area of Cells upon Extended Incubation at 37 °C. To find out whether the cell-transduced protein is later mainly directed to the cellular degradative pathway or remains in the cytoplasm, we extended the incubation of Bowes cells with transportan−streptavidin complexes to 2 days or longer. After 20−72 h, peptide−protein complexes were concentrated in structures resembling late endosomes and lysosomes as observed by electron microscopy (enlarged section and arrows in Figure 4D). However, some gold particles were still scattered diffusely in the cytoplasm. Upon extended incubation of the cells with the complexes, the amount of gold particles was significantly increased, especially in the perinuclear region, confirming the continuous uptake for more than 4 h (*12*). Our data indicated that some complexes of CPP−protein retained intactness for at least several hours before accumulation to the degradative organelles after 20 h. The intracellular trafficking of peptide−protein complexes in relation to structures of the degradative pathway was studied by visualizing the plasma membrane and Golgi complex with BODIPY TR C_5-labeled ceramide and acidic intracellular vesicles, including lysosomes, with Lyso Tracker Red DND-99. Fluorescent ceramide derivative inserts into the plasma membrane of live cells and is preferentially targeted to the Golgi apparatus. After incubating HeLa cells with TR−ceramide, the whole cell cytoplasm exhibited reticular staining reminiscent with the endoplasmic reticulum. Labeled ceramide concentrated also into one or two perinuclear centers probably in Golgi apparatus (Figure 2B). The transportan−avidin complexes showed, after translocation into the HeLa cells, a partial colocalization with TR−ceramide in perinuclear areas (Figure 2B). Specific accumulation of transportan−avidin complexes in the reticular structures of cytoplasm was not observed. Lyso Tracker intensely stained the perinuclear area of the HeLa cells and some cortically localized vesicles, but the entire cell area fluoresced weakly red probably due to nonspecific interaction with other membranous structures. Localization of transportan−avidin complexes

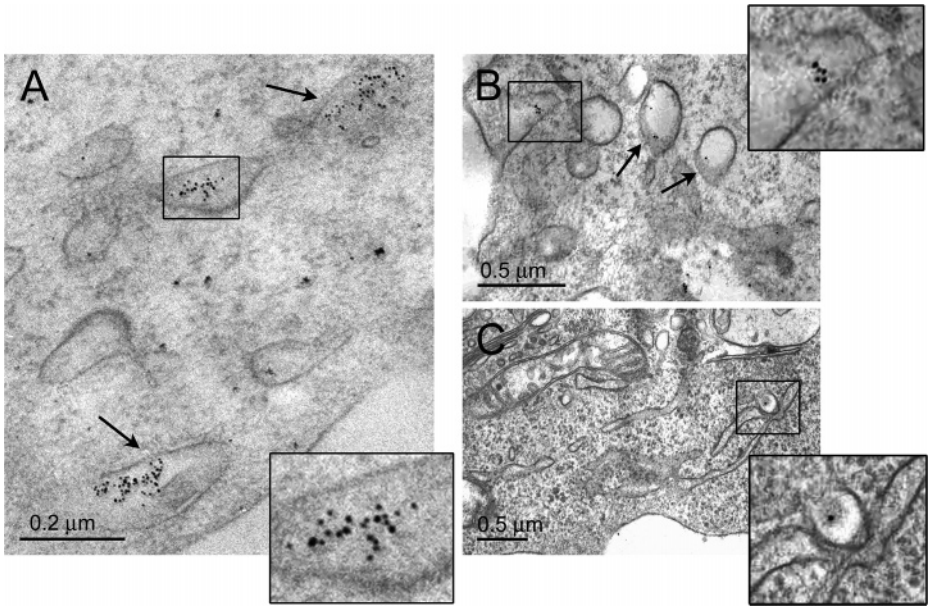

Figure 5. Interaction of CPP−protein complexes with plasma membrane of cells and internalization at 10 °C. Bowes (A) or HeLa (B, C) cells were incubated with complexes of 5 μM biotin−transportan (A, B) or 3 μM biotin−TP10 (C) with 5 nm (A) or 10 nm (B, C) streptavidin−gold (1:50) for 1 h at 10 °C.

taken up by the cells and Lyso Tracker overlapped partially only in large vesicles of the perinuclear area (data not shown). A more specific staining of lysosomes in HeLa cells was achieved with antibody specific to lysosome-associated membrane protein-2 (LAMP2). For enlightening the intracellular targeting of peptide−protein complexes in time, we performed pulse-chase experiments by growing the cells for 4 or 24 h in culture media after a 1 h pulse with complexes of transportan and avidin. After a 4-h chase, the fraction of complexes in lysosomes was not substantial (data not shown). However, after a 24-h chase, the amount of complexes inside the HeLa cells had markedly increased, suggesting the continuing accumulation of internalized complexes (Figure 2C) corroborating the data obtained by electron microscopy. Colocalization of transportan−avidin complexes with lysosomes was detected mostly in the perinuclear region including some very big vesicular structures. However, even after a 24 h chase, a fraction of complexes-containing vesicles retained their localization distinct from the degradative organelles marked by LAMP2 antibody (Figure 2C).

Translocation of CPP−Streptavidin Complexes into HeLa and Bowes Cells Is Not Blocked at 10 °C. The pinocytosis and receptor-mediated endocytosis are the potential cellular uptake mechanisms of large molecular structures. Endocytosis occurs usually within minutes to several hours and is cellular-energy-dependent. In general, if the temperature is lowered below 18 °C, endocytosis is considered to be blocked, and also the flexibility and the fluidity of plasma membrane is drastically reduced (*29*) and the membrane traffic is slowed (*30*). We evaluated whether peptide−protein complexes could enter the cultured cells at the endocytosis abolishing temperatures, e.g. 8−10 °C. After incubation of Bowes or HeLa cells with complexes of biotin−transportan and streptavidin−gold for 1 h at 10 °C, the gold particles were clearly detectable attached at the plasma membrane but also in the vesicular structures of cortical cytoplasm. The amount of internalized complexes at 10 °C was markedly lower compared to the complexes visible at the physiological conditions but still clearly detectable by electron microscopy. As demonstrated in Figure 5, transportan−streptavidin complexes resided mainly in rather small spherical vesicles of 0.2−0.3 μm diameter (arrows in Figure 5A and B) and localized at the plasma membrane of cells (enlarged section of Figure 5B). TP10−protein complexes were mostly localized randomly as single particles near the plasma membrane or very rarely in vesicles in the peripheral cytoplasm (enlarged section of Figure 5C). In addition, no big agglomerates of peptide−protein complexes formed nor were large cell surface invaginations observed at 8−10 °C. Thus, under the conditions of cellular energy deficiency, the cellular uptake of biotin−transportan complexes with streptavidin−gold was not completely abolished, but the formation of very big vesicular structures and their further translocation toward the cell center were strongly inhibited, as the complexes were detected only in the cortical cytoplasm. On the contrary, at 20 °C, the transportan−streptavidin complexes were distributed in the cells in vesicular structures analogously as observed at the physiological temperature. Still, the amount of complexes in cells was lower, and the large membrane invaginations so typical to physiological temperature were almost missing (data not shown).

Cellular Uptake of Transportan−Streptavidin Complexes Is Abolished at 4 °C and Lower Temperature. Although the internalization of CPP−protein complexes was diminished at 8 °C, we assessed whether transportan or TP10 could transduce streptavidin−gold into cells at 0−4 °C also. After incubation of the cells with transportan−streptavidin complexes on ice for 1 h, only a negligible amount of gold particles had associated with the plasma membrane. Association of transportan−streptavidin complexes with the plasma membrane was rather rare, and no complexes were detected in the cells. The absence of uptake at 4 °C suggests the prevalence of energy-dependent processes in the internalization of peptide−protein complexes. However, some complexes of streptavidin−gold with transportan or TP10 translocated into cells even at 10 °C support the ideas about uptake pathways that are active at low temperatures (*31*) also.

Cellular Uptake of Transportan−Streptavidin Complexes in Parallel with Transferrin. Our results indicate that CPP−protein complexes are taken up by

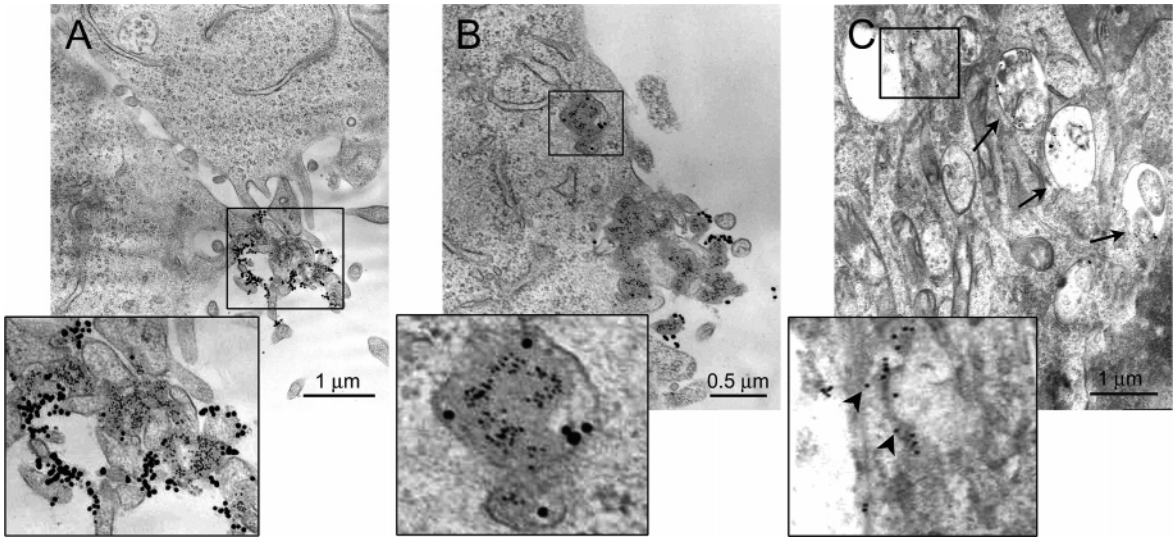

Figure 6. Colocalization of transferrin and CPP−protein complexes in HeLa cells. Cells were incubated in serum free culture medium containing the complexes of streptavidin−gold (10 nm, 1:50) with 5 μM (A, B) or 2.5 μM (C) biotin−transportan, and 20 nm gold-labeled transferrin (1:50) at 37 °C for 1 h.

the cells mainly via temperature-dependent endocytic pathways that originate from the cell membrane invaginations and result in the formation of cellular vesicles of different shape and size. Transferrin, an iron-transport protein, is known to be internalized via clathrin-coated pits and vesicles (*32*). To assess whether this endocytic pathway is involved in the internalization of transportan−streptavidin complexes, we tested the putative colocalization of internalized complexes with transferrin. Prior to the addition of the peptide−protein complexes, HeLa cells were first incubated with serum-free culture medium for 30 min to induce the targeting of transferrin receptors to the plasma membrane (*27*). Transferrin, tagged with colloidal gold, induced the formation of clathrin-coated pits and the respective vesicles and in addition associated with the terminals of microvilli and filopodia. Cells incubated with the peptide−streptavidin complexes labeled with a 10 nm gold particle along with a 20 nm gold particle-tagged transferrin in serum-free medium for 30 min revealed no specific colocalization of these proteins. Still, in some areas at the plasma membrane and cellular vesicles, location of transferrin and transportan−streptavidin complexes overlapped. Complexes of streptavidin with TP10 showed less colocalization with transferrin than transportan complexes. The ultrastructural analysis, however, revealed that if transportan−protein complexes and transferrin were used at high concentrations (respectively 5 μM biotin−transportan and 1:25 transferrin−gold), colocalization on the plasma membrane was prevailing. As shown in Figure 6A and B, transferrin associated mainly with the regions of plasma membrane where peptide−protein complexes had concentrated—preferentially at the protrusions and also on smooth areas. Inside the cell, both the peptide−protein complexes and transferrin molecules were usually confined to the same big vacuoles of 0.5−1 μm diameter in the cortical and perinuclear cytoplasm (enlarged section of Figure 6B and arrows in Figure 6C). Some peptide−protein complexes localized in cytoplasm/cells without transferrin as indicated by arrowheads on the enlarged section of Figure 6C. Distribution of peptide−protein complexes in the cells coincubated with the gold-labeled transferrin was very similar to that observed in cells treated with the complexes only, whereas the localization of transferrin at the plasma membrane and inside the cells was radically altered by coincubation with transportan−streptavidin complexes. The colocalization of CPP−protein complexes with transferrin was observed mainly at higher concentrations. Surprisingly, a considerably lower number of transferrin−gold particles associated with the cells incubated with transferrin only as compared to the cells coincubated with transportan−streptavidin complexes (data not shown). In addition to peptide-streptavidin complexes, transportan also induced increased association of transferrin with the plasma membrane and subsequent uptake. In principle the cationic transportan might associate at high concentration with anionic transferrin and increase association with the plasma membrane and the uptake of transferrin by cells.

To exclude the putative association of transportan with transferrin in solution or at the plasma membrane, we incubated cells with these consecutively. Cells were first incubated with TP−streptavidin complexes for 30 min, washed several times, and then incubated with transferrin−gold complexes for an additional 30 min. An analogous experiment with reversed order of incubations was also performed. Under these conditions, no noticeable colocalization was detected between transferrin and transportan−protein complexes (data not shown). In the cells, transferrin and peptide−protein complexes localized mainly to different vesicular compartments, whereas a fraction of both was colocalizing in a certain type of vesicular structures, probably in late endosomes. This suggests that transportan−streptavidin complexes are taken up to large vesicular structures and that this pathway does not overlap with the well-characterized clathrin-mediated endocytic pathway of the transferrin receptor. However, during later targeting, the structures containing peptide−protein complexes may fuse with multivesicular bodies on their way to lysosomes.

The involvement of receptor-mediated endocytosis in the internalization of peptide−avidin complexes was proven by confocal microscopy as well, following their cellular uptake in the culture medium containing AF 594-labeled transferrin. After 1-h incubation, transferrin had concentrated in a punctate manner in the cytoplasm of cells with more intense signal in the vesicular structures of perinuclear area (Figure 2D). Structures containing transportan−avidin complexes rarely overlapped with

the transferrin-positive vesicles in the cortical cytoplasm and were usually less abundant, whereas in larger perinuclear vesicles the colocalization with transferrin was more common but still not prevailing (Figure 2D).

DISCUSSION

The power of cell-penetrating peptides to transduce various payloads of very different nature and size into living cells in culture and in animal models has found rapidly growing application (*13*). Despite intense studies during the past decade, the cell entry mechanism of "Trojan peptides" has remained elusive (*33*), though several cellular pathways have been demonstrated to be involved in the uptake of CPPs (*4*, *14*−*16*, *31*, *34*−*37*). We characterized the uptake and cellular whereabouts of proteins complexed with delivery peptides transportan and TP10 by transmission electron microscopy and confocal fluorescence microscopy. Electron microscopy reveals that the complexes of gold-labeled streptavidin with biotin−transportans are mostly detectable as elongated agglomerates on the electron-dense background associating with the plasma membrane of the cells frequently at the cell surface extensions, microspikes and filopodia. Since large aggregates of peptide−protein complexes formed only at higher peptide concentration (5 μM) and were more typical for transportan rather than TP10−protein complexes, the aggregation might be caused by multimerization in solution (*21*). Complexation of biotin−transportan at 0.5−1 μM concentration with avidin did not induce formation of aggregates as observed by fluorescence microscopy, whereas by increasing the peptide concentration the size of cell-associating assemblages also increased. Peptide−protein complexes associated with the cellular surface were mostly on the electron dense background, which was not present when the complexes were assembled in solution in the absence of the cells. Therefore, the electron dense material is obviously of cellular origin and may represent exoplasmic membrane proteins or cell surface proteoglycans. Considering the role of proteoglycans in cell−cell and cell−matrix interactions (*38*, *39*), in peptide-mediated cellular transduction (*35*, *40*, *41*) and strong interaction of cationic CPPs with heparan sulfates (*42*), the interaction of transportan−protein complexes with the cell surface proteoglycans is highly probable.

The mechanisms used by CPPs to translocate into mammalian cells may vary in different cells and between peptides; so far endocytosis via clathrin-coated pits (*34*, *43*) and via lipid rafts (*14*, *40*) have been suggested. In parallel, macropinocytosis has been proposed as a route for CPPs translocation (*7*, *16*). Macropinocytosis is a lipid raft-mediated, clathrin- or caveolae-independent endocytic process (*44*), which starts with the induction of actin-dependent lamellipodia and membrane ruffling leading internalization of extracellular material into the macropinosomes of 1 μm or greater. The results obtained by electron microscopy reveal that transportan−streptavidin complexes associated with the extensions of cell surface and induced invaginations of the plasma membrane are reminiscent of the changes preceding the macropinocytosis of some pathogenic bacteria (*45*, *46*). The vacuoles formed in the cytoplasm could fuse with lysosomes or release their content into the cytosol (*17*). Our results demonstrate that the cell-transduced gold-tagged streptavidin localized mainly in intracellular vesicular structures with different size (0.5−2 μm) and in Bowes cells the vesicular membrane was not always intact (*47*). On the basis of these considerations, it seems probable that transportan-mediated cellular uptake of protein molecules proceeds at least partially by macropinocytosis and transportan is able to destabilize the macropinosomes.

The peptide−protein complexes marked by gold particles were also found in vesicles characteristic to receptor-mediated endocytic pathway, e.g. multivesicular bodies and endosomal-lysosomal structures suggesting the involvement of clathrin-dependent endocytosis. In most animal cells, the clathrin-dependent pathway guarantees the uptake of specific macromolecules, nutrients, and ions from the extracellular fluid (*48*). Transferrin, a typical marker of clathrin-dependent endocytosis, and transportan−protein complexes colocalized partially on the plasma membrane of the HeLa cells and later in the endocytic vacuoles. Colocalization of transportan−streptavidin complexes and transferrin was more characteristic at higher concentrations of substances and less obvious at lower concentration. The results of confocal laser scanning microscopy confirmed that vesicular structures containing transportan−avidin complexes rarely overlapped with transferrin-AF 594 positive vesicles, suggesting that a small fraction of transportan−protein complexes was cointernalized with transferrin or targeted into the same vesicles intracellularly. At high concentrations weak electrostatic interaction of cationic transportan complexes with anionic transferrin might be envisaged, leading to the increase of transferrin uptake and altering its intracellular distribution.

Different endocytic pathways target the ingested material to specific cellular destinations: degradative organelles, the plasma membrane, ER, Golgi apparatus. The destination of the protein molecules translocated into cells by CPPs is of primary importance both from the view of mechanisms and application. Neither electron- nor fluorescence microscopy revealed accumulation of transportan−protein complexes to endoplasmic reticulum or Golgi apparatus, though some colocalization with the respective markers was detected by fluorescence microscopy in perinuclear area. On the contrary, part of transportan−protein complexes was targeted to late endosomes and lysosomal structures, especially after 20 h or later. However, a substantial amount of labeled complexes was detectable in the cytoplasm or vesicles of nondegradative character after 24 or even 48 h of incubation.

Caveolae-mediated endocytosis which starts from cholesterol and sphingolipid rich membrane rafts has been proposed for the cellular translocation of Tat fusion proteins (*14*, *15*). Electron microscopy revealed that streptavidin complexed with transportans was occasionally present also in caveosome-like structures, mainly in the cortical cytoplasm. This internalization mechanism is not prevailing since by confocal fluorescence microscopy we did not observe the accumulation of peptide−protein complexes to the Golgi apparatus, but it suggests that complexes can use different endocytic pathways simultaneously.

Apparently all endocytic pathways have been shown to be used to gain access into eukaryotic cells by viruses (*49*). Cell-entry of peptide−protein complexes has several features similar to internalization of Simian Virus 40 (SV40). We detected peptide−protein complexes in vesicles of different size and morphology with little overlap with clathrin-coated vesicles, indicating other transduction modes; for example, SV40 is known to enter cells dynaminII-independently (*50*) and the recruitment of caveolae seems not to be obligatory (*51*). Moreover, like the infectivity of SV40, internalization of transportan/TP10−(strept)avidin complexes can be blocked by actin depo-

lymerization and depletion of cholesterol from the plasma membrane (Säälik and Padari, unpublished data). It has to be assessed if the same or different inducible actin- and cholesterol-dependent endocytic processes lead to internalization of some viruses, bacteria, and peptide−cargo complexes and which receptors are involved, if any.

In parallel to translocation into cells in membrane-surrounded vesicles, transportan−streptavidin complexes with a single gold particle were detectable in the cortical cytoplasm of cells in the close proximity of the intact plasma membrane, suggesting direct passage across the membrane. The amount of complexes that seemingly directly crossed the plasma membrane was very small compared to that in vesicles and was higher for TP10 rather than transportan complexes. The presence of transportan−streptavidin complexes with a single (or few) gold particle in the cortical cytoplasm could be caused by redistribution of complexes from the cell surface into cells upon fixation (*4*, *11*) or an embedding procedure. Neither can we exclude that those complexes are encompassed by the membrane, which remains undetectable by electron microscopy, in analogy with SV40 particles internalization within the vesicles devoid of the visible coat (*51*), which were found when studying a novel clathrin-, caveolae-, and dynaminII-independent cholesterol-sensitive endocytic pathway (*51*, *52*). On the other hand, we cannot completely ignore the possibility that a small fraction of transportan−protein complexes translocates into cells by inducing a pore-like structure in the plasma membrane hypothesized for complexes of carrier peptides MPG and Pep-1 with cargo molecules (*36*) or the nondefined mechanism observed in studies of Seelig and collaborators (*31*). Presence of oligoarginine both in cytoplasmic and vesicular fraction after fractionation of CHO cell material (*53*, *54*) and the activity of biological cargo delivered into cells by transportan and/or TP10 (*55*, *56*) supports the cytoplasmic localization of peptide−protein complexes observed in our experiments. The translocation mode has been also suggested to depend on the size of the particle as proposed by Morris and co-workers (*57*) which could be the case for transportan/TP10-streptavidin complexes of different size. However, until now this hypothesis has not found unambiguous affirmation.

The contribution of endocytosis in the cellular uptake process of CPPs is often estimated after blocking this pathway by lowering temperature, which has sometimes led to the contradicting results. Cellular translocation of gold-tagged streptavidin−transportan complexes was highly temperature/energy-dependent. Lowering temperature to endocytosis-permissive 20 °C markedly reduced amount of internalized complexes. Minimal uptake of transportan−streptavidin complexes was detected also at endocytosis nonpermissive 8−10 °C but not at 0−4 °C. Unexpectedly, the internalization detected at 8−10 °C was mainly vesicular and cortical; the vesicles had not translocated markedly toward perinuclear region in 1 h. It has been demonstrated earlier that FITC-labeled avidin complexes with biotin−Tat and biotin−penetratin cannot enter CHO cells at 0−4 °C (*41*). Very recently, transduction of Cy3-tagged streptavidin into HEK293 cells after complexing with biotin−maurocalcine, a 33 amino acid long scorpion toxin (*58*), was shown, but only after fixation of cells. Our results are in line with the suggestion of mainly endocytic uptake of CPP−protein complexes (*41*). Reduction of uptake at 20 °C and ceasing at 0−4 °C suggests that the decrease in fluidity of the membrane has also considerable effect on the internalization of CPPs and their constructs as proposed earlier for penetratin peptide (*29*). The reduced association of CPP−avidin/streptavidin complexes with cell surface structures at 0−4 °C observed by Console and collaborators (*41*) and by us might be also partly ascribed to the increased rigidity of the plasma membrane.

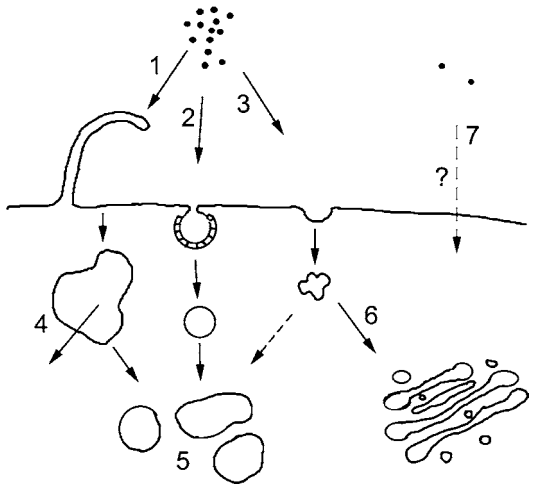

Figure 7. Internalization and intracellular routing of CPP−protein complexes. Internalization via macropinosomes (1), clathrin-coated vesicles (2) and caveosomes (3) leading to different cellular compartments: escape from macropinosomes (4), targeting to lysosomes (5) and partial direction to Golgi complex (6). Putative translocation of peptide−protein complexes across plasma membrane without induction of vesicular structures (7).

Summing up, as we schematically represent in Figure 7, complexes of transportan and TP10 with protein can translocate into cells by different mechanisms in parallel, mainly by endocytic processes using diverse vesicles and probably also by translocation without inducing the membrane invagination and vesicle formation. The latter mode could be more common for CPPs alone than detected here for constructs with proteins. The morphology and size of formed vesicles suggests that macropincytosis is the main mechanism of transportan−protein complexes' uptake by Bowes and HeLa cells. It seems also that the size (degree of concentration) of complexes on the cell surface influences the size of the forming vesicle, the mode of internalization and further cellular targeting.

ACKNOWLEDGMENT

This work was supported by grants from European Community (QLK3-CT-2002-01989), Estonian Science Foundation (ESF 5588 and 5995), the Swedish Institute Visby Program, Swedish Royal Academy of Sciences, and Swedish Research Councils NT and Med.

LITERATURE CITED

(1) Derossi, D., Joliot, A. H., Chassaing, G., and Prochiantz, A. (1994) The third helix of the Antennapedia homeodomain translocates through biological membranes. *J. Biol. Chem*. *269*, 10444−50.

(2) Futaki, S., Goto, S., and Sugiura, Y. (2003) Membrane permeability commonly shared among arginine-rich peptides. *J. Mol. Recognit*. *16*, 260−4.

(3) Vives, E., Brodin, P., and Lebleu, B. (1997) A truncated HIV-1 Tat protein basic domain rapidly translocates through the plasma membrane and accumulates in the cell nucleus. *J. Biol. Chem*. *272*, 16010−7.

(4) Richard, J. P., Melikov, K., Vives, E., Ramos, C., Verbeure, B., Gait, M. J., Chernomordik, L. V., and Lebleu, B. (2003) Cell-penetrating peptides. A reevaluation of the mechanism of cellular uptake. *J. Biol. Chem*. *278*, 585−90.

(5) Thorén, P. E., Persson, D., Esbjorner, E. K., Goksör, M., Lincoln, P., and Nordén, B. (2004) Membrane binding and translocation of cell-penetrating peptides. *Biochemistry 43*, 3471−89.

(6) Christiaens, B., Grooten, J., Reusens, M., Joliot, A., Goethals, M., Vandekerckhove, J., Prochiantz, A., and Rosseneu, M. (2004) Membrane interaction and cellular internalization of penetratin peptides. *Eur. J. Biochem. 271*, 1187−97.

(7) Nakase, I., Niwa, M., Takeuchi, T., Sonomura, K., Kawabata, N., Koike, Y., Takehashi, M., Tanaka, S., Ueda, K., Simpson, J. C., Jones, A. T., Sugiura, Y., and Futaki, S. (2004) Cellular uptake of arginine-rich peptides: roles for macropinocytosis and actin rearrangement. *Mol. Ther. 10*, 1011−22.

(8) Persson, D., Thorén, P. E., Herner, M., Lincoln, P., and Nordén, B. (2003) Application of a novel analysis to measure the binding of the membrane-translocating peptide penetratin to negatively charged liposomes. *Biochemistry 42*, 421−9.

(9) Terrone, D., Sang, S. L., Roudaia, L., and Silvius, J. R. (2003) Penetratin and related cell-penetrating cationic peptides can translocate across lipid bilayers in the presence of a transbilayer potential. *Biochemistry 42*, 13787−99.

(10) Magzoub, M., Kilk, K., Eriksson, L. E., Langel, Ü., and Gräslund, A. (2001) Interaction and structure induction of cell-penetrating peptides in the presence of phospholipid vesicles. *Biochim. Biophys. Acta 1512*, 77−89.

(11) Lundberg, M., and Johansson, M. (2002) Positively charged DNA-binding proteins cause apparent cell membrane translocation. *Biochem. Biophys. Res. Commun. 291*, 367−71.

(12) Säälik, P., Elmquist, A., Hansen, M., Padari, K., Saar, K., Viht, K., Langel, Ü., and Pooga, M. (2004) Protein cargo delivery properties of cell-penetrating peptides. A comparative study. *Bioconjugate Chem. 15*, 1246−53.

(13) Dietz, G. P., and Bähr, M. (2004) Delivery of bioactive molecules into the cell: the Trojan horse approach. *Mol. Cell Neurosci. 27*, 85−131.

(14) Fittipaldi, A., Ferrari, A., Zoppe, M., Arcangeli, C., Pellegrini, V., Beltram, F., and Giacca, M. (2003) Cell membrane lipid rafts mediate caveolar endocytosis of HIV-1 Tat fusion proteins. *J. Biol. Chem. 278*, 34141−9.

(15) Ferrari, A., Pellegrini, V., Arcangeli, C., Fittipaldi, A., Giacca, M., and Beltram, F. (2003) Caveolae-mediated internalization of extracellular HIV-1 tat fusion proteins visualized in real time. *Mol Ther 8*, 284−94.

(16) Wadia, J. S., Stan, R. V., and Dowdy, S. F. (2004) Transducible TAT-HA fusogenic peptide enhances escape of TAT-fusion proteins after lipid raft macropinocytosis. *Nat. Med. 10*, 310−5.

(17) Conner, S. D.. and Schmid, S. L. (2003) Regulated portals of entry into the cell. *Nature 422*, 37−44.

(18) Meier, O., Boucke, K., Hammer, S. V., Keller, S., Stidwill, R. P., Hemmi, S., and Greber, U. F. (2002) Adenovirus triggers macropinocytosis and endosomal leakage together with its clathrin-mediated uptake. *J. Cell Biol. 158*, 1119−31.

(19) Michiue, H., Tomizawa, K., Wei, F. Y., Matsushita, M., Lu, Y. F., Ichikawa, T., Tamiya, T., Date, I., and Matsui, H. (2005) The NH2 Terminus of Influenza Virus Hemagglutinin-2 Subunit Peptides Enhances the Antitumor Potency of Polyarginine-mediated p53 Protein Transduction. *J. Biol. Chem. 280*, 8285−8289.

(20) Maiolo, J. R.r., Ottinger, E. A., and Ferrer, M. (2004) Specific redistribution of cell-penetrating peptides from endosomes to the cytoplasm and nucleus upon laser illumination. *J. Am. Chem. Soc. 126*, 15376−7.

(21) Pooga, M., Hällbrink, M., Zorko, M., and Langel, Ü. (1998) Cell penetration by transportan. *FASEB J. 12*, 67−77.

(22) Barany-Wallje, E., Andersson, A., Gräslund, A., and Mäler, L. (2004) NMR solution structure and position of transportan in neutral phospholipid bicelles. *FEBS Lett. 567*, 265−9.

(23) Pooga, M., Soomets, U., Hällbrink, M., Valkna, A., Saar, K., Rezaei, K., Kahl, U., Hao, J. X., Xu, X. J., Wiesenfeld-Hallin, Z., Hökfelt, T., Bartfai, T., and Langel, Ü. (1998) Cell penetrating PNA constructs regulate galanin receptor levels and modify pain transmission in vivo. *Nat. Biotechnol. 16*, 857−61.

(24) Hällbrink, M., Florén, A., Elmquist, A., Pooga, M., Bartfai, T., and Langel, Ü. (2001) Cargo delivery kinetics of cell-penetrating peptides. *Biochim. Biophys. Acta 1515*, 101−9.

(25) Soomets, U., Lindgren, M., Gallet, X., Hällbrink, M., Elmquist, A., Balaspiri, L., Zorko, M., Pooga, M., Brasseur, R., Langel, Ü., Prochiantz, A., and Brakenhielm, E. (2000) Deletion analogues of transportan. *Biochim. Biophys. Acta 1467*, 165−76.

(26) Bendayan, M. (1984) Protein A-Gold Electron Microscopic Immunocytochemistry, Applications and Limitations. *J. Electron. Microsc. Technique 1*, 243−270.

(27) Chitambar, C. R., and Zivkovic-Gilgenbach, Z. (1990) Influence of cellular iron status on the release of soluble transferrin receptor from human promyelocytic leukemic HL60 cells. *J. Lab. Clin. Med. 116*, 345−53.

(28) Venable, J. H., and Coggeshall, R. (1965) A Simplified Lead Citrate Stain for Use in Electron Microscopy. *J. Cell Biol.* 25.

(29) Letoha, T., Gaal, S., Somlai, C., Czajlik, A., Perczel, A., and Penke, B. (2003) Membrane translocation of penetratin and its derivatives in different cell lines. *J. Mol. Recognit. 16*, 272−9.

(30) Haylett, T., and Thilo, L. (1991) Endosome-lysosome fusion at low temperature. *J. Biol. Chem. 266*, 8322−7.

(31) Ziegler, A., Nervi, P., Dürrenberger, M., and Seelig, J. (2005) The cationic cell-penetrating peptide CPP(TAT) derived from the HIV-1 protein TAT is rapidly transported into living fibroblasts: optical, biophysical, and metabolic evidence. *Biochemistry 44*, 138−48.

(32) Schmid, S. L., McNiven, M. A., and De Camilli, P. (1998) Dynamin and its partners: a progress report. *Curr. Opin. Cell Biol. 10*, 504−12.

(33) Torchilin, V. P. (2005) Fluorescence microscopy to follow the targeting of liposomes and micelles to cells and their intracellular fate. *Adv Drug Delivery Rev. 57*, 95−109.

(34) Richard, J. P. M., K. Brooks, H. Prevot, P. Lebleu, B. Chernomordik, L. V. (2005) Cellular uptake of unconjugated TAT peptide involves clathrin-dependent endocytosis and heparan sulfate receptors. *J. Biol. Chem. 280*, 15300−6.

(35) Tyagi, M., Rusnati, M., Presta, M., and Giacca, M. (2001) Internalization of HIV-1 tat requires cell surface heparan sulfate proteoglycans. *J. Biol. Chem. 276*, 3254−61.

(36) Deshayes, S., Heitz, A., Morris, M. C., Charnet, P., Divita, G., and Heitz, F. (2004) Insight into the mechanism of internalization of the cell-penetrating carrier peptide Pep-1 through conformational analysis. *Biochemistry 43*, 1449−57.

(37) Potocky, T. B., Menon, A. K., and Gellman, S. H. (2003) Cytoplasmic and nuclear delivery of a TAT-derived peptide and a beta-peptide after endocytic uptake into HeLa cells. *J. Biol. Chem. 278*, 50188−94.

(38) Gallo, R. L., Ono, M., Povsic, T., Page, C., Eriksson, E., Klagsbrun, M., and Bernfield, M. (1994) Syndecans, cell surface heparan sulfate proteoglycans, are induced by a proline-rich antimicrobial peptide from wounds. *Proc. Natl. Acad. Sci. U.S.A. 91*, 11035−9.

(39) Belting, M. (2003) Heparan sulfate proteoglycan as a plasma membrane carrier. *Trends Biochem. Sci. 28*, 145−51.

(40) Sandgren, S., Wittrup, A., Cheng, F., Jonsson, M., Eklund, E., Busch, S., and Belting, M. (2004) The human antimicrobial peptide LL-37 transfers extracellular DNA plasmid to the nuclear compartment of mammalian cells via lipid rafts and proteoglycan-dependent endocytosis. *J. Biol. Chem. 279*, 17951−6.

(41) Console, S., Marty, C., Garcia-Echeverria, C., Schwendener, R., and Ballmer-Hofer, K. (2003) Antennapedia and HIV transactivator of transcription (TAT) "protein transduction domains" promote endocytosis of high molecular weight cargo upon binding to cell surface glycosaminoglycans. *J. Biol. Chem. 278*, 35109−14.

(42) Gonçalves, E., Kitas, E., and Seelig, J. (2005) Binding of oligoarginine to membrane lipids and heparan sulfate: struc-

tural and thermodynamic characterization of a cell-penetrating Peptide. *Biochemistry 44*, 2692−702.
(43) Vendeville, A., Rayne, F., Bonhoure, A., Bettache, N., Montcourrier, P., and Beaumelle, B. (2004) HIV-1 Tat enters T cells using coated pits before translocating from acidified endosomes and eliciting biological responses. *Mol. Biol. Cell 15*, 2347−60.
(44) Swanson, J. A. and Watts, C. (1995) Macropinocytosis. *Trends Cell Biol. 5*, 424−8.
(45) Ammendolia, M. G., Bertuccini, L., Minelli, F., Meschini, S., and Baldassarri, L. (2004) A Sphingomonas bacterium interacting with epithelial cells. *Res. Microb. 155*, 636−46.
(46) Garcia-Perez, B. E., Mondragon-Flores, R., and Luna-Herrera, J. (2003) Internalization of Mycobacterium tuberculosis by macropinocytosis in non-phagocytic cells. *Microb. Pathog. 35*, 49−55.
(47) Pooga, M., Kut, C., Kihlmark, M., Hällbrink, M., Fernaeus, S., Raid, R., Land, T., Hallberg, E., Bartfai, T., and Langel, Ü. (2001) Cellular translocation of proteins by transportan. *FASEB J. 15*, 1451−3.
(48) Lamaze, C. and Schmid, S. L. (1995) The emergence of clathrin-independent pinocytic pathways. *Curr. Opin. Cell Biol. 7*, 573−80.
(49) Pelkmans, L. and Helenius, A. (2003) Insider information: what viruses tell us about endocytosis. *Curr. Opin. Cell Biol. 15*, 414−22.
(50) Pelkmans, L., Puntener, D., Helenius, A., and Kartenbeck, J. (2002) Local actin polymerization and dynamin recruitment in SV40-induced internalization of caveolae. *Science 296*, 535−9.
(51) Damm, E. M., Pelkmans, L., Kartenbeck, J., Mezzacasa, A., Kurzchalia, T., and Helenius, A. (2005) Clathrin- and caveolin-1-independent endocytosis: entry of simian virus 40 into cells devoid of caveolae. *J. Cell Biol. 168*, 477−88.
(52) Kirkham, M., Fujita, A., Chadda, R., Nixon, S. J., Kurzchalia, T. V., Sharma, D. K., Pagano, R. E., Hancock, J. F., Mayor, S., and Parton, R. G. (2005) Ultrastructural identification of uncoated caveolin-independent early endocytic vehicles. *J. Cell Biol*. 168, 465−76.
(53) Zaro, J. L. and Shen, W. C. (2003) Quantitative comparison of membrane transduction and endocytosis of oligopeptides. *Biochem. Biophys. Res. Commun*. *307*, 241−7.
(54) Zaro, J. L. and Shen, W. C. (2005) Evidence that membrane transduction of oligoarginine does not require vesicle formation. *Exp. Cell Res. 307*, 164−73.
(55) Kaushik, N., Basu, A., Palumbo, P., Myers, R. L., and Pandey, V. N. (2002) Anti-TAR polyamide nucleotide analog conjugated with a membrane-permeating peptide inhibits human immunodeficiency virus type 1 production. *J. Virol*. *76*, 3881−91.
(56) Fisher, L., Soomets, U., Cortes Toro, V., Chilton, L., Jiang, Y., Langel, Ü., and Iverfeldt, K. (2004) Cellular delivery of a double-stranded oligonucleotide NFkappaB decoy by hybridization to complementary PNA linked to a cell-penetrating peptide. *Gene Ther*. *11*, 1264−72.
(57) Morris, M. C., Depollier, J., Mery, J., Heitz, F., and Divita, G. (2001) A peptide carrier for the delivery of biologically active proteins into mammalian cells. *Nat. Biotechnol*. *19*, 1173−6.
(58) Esteve, E., Mabrouk, K., Dupuis, A., Smida-Rezgui, S., Altafaj, X., Grunwald, D., Platel, J. C., Andreotti, N., Marty, I., Sabatier, J. M., Ronjat, M., and De Waard, M. (2005) Transduction of the scorpion toxin Maurocalcine into cells-Evidence that the toxin crosses the plasma membrane. *J. Biol. Chem*. *280*, 12833−9.

BC050125Z

In Vitro Lipofection with Novel Asymmetric Series of 1,2-Dialkoylamidopropane-Based Cytofectins Containing Single Symmetric Bis-(2-dimethylaminoethane) Polar Headgroups

Michalakis Savva,* Pensung Chen, Ahmad Aljaberi, Bilge Selvi, and Michael Spelios

Division of Pharmaceutical Sciences, Arnold & Marie Schwartz College of Pharmacy and Health Sciences, Long Island University, 75 Dekalb Avenue, Brooklyn, New York 11201. Received May 11, 2005; Revised Manuscript Received August 31, 2005

Novel *N*,*N*′-diacyl-1,2-diaminopropyl-3-carbamoyl[bis-(2-dimethylaminoethane)] bivalent cationic lipids were synthesized and evaluated for in vitro transfection activity against a murine melanoma cell line. In the absence of the helper lipid DOPE (1,2-dioleoyl-sn-glycero-3-phosphoethanolamine), only the dioleoyl derivative **22** (1,2lb5) elicited transfection activity. The transfection activity of this lipid was reduced when formulated with DOPE. Contrary to that, the dimyristoyl derivative **19** (1,2lb2) mediated no activity when used alone but induced the highest levels of marker gene expression in the presence of DOPE. In an effort to correlate the transfection activity with cationic lipid structures, the physicochemical properties of cationic lipids in isolation and of lipoplexes were studied with surface tensiometry, photon correlation spectroscopy, gel electrophoresis mobility shift assay, and fluorescence techniques. In regard to the lipoplex properties, gel electrophoresis mobility shift assay and EtBr exclusion fluorescence assay revealed that the 1,2lb5 was the only lipid to associate and condense plasmid DNA, respectively. Photon correlation spectroscopy analysis found that 1,2lb5/DNA complexes were of relatively small size compared to all other lipoplexes. With respect to the properties of isolated lipids, Langmuir monolayer studies and fluorescence anisotropy on cationic lipid dispersions verified high two-plane elasticity and increased fluidity of the transfection competent dioleoyl derivative 1,-2lb5, respectively. The results indicate that high transfection activity is mediated by cationic lipids characterized by an expanded mean molecular area, high molecular elasticity, and increased fluidity.

INTRODUCTION

Gene delivery reagents comprising a variety of recombinant replication deficient viruses (*1*, *2*), positively charged synthetic polymers and peptides and cationic lipids (*3*−*5*), are currently being used to treat genetic diseases (*6*) and a wide variety of cancers (*7*). These delivery systems have their pluses and minuses. Viral vectors unambiguously induce much higher transgene expression levels than their nonviral rivals. Their in vivo application, however, is severely compromised by the innate immunity and by the more refined adaptive immunity, as provided by the natural killer cells, biochemicals and cellular proteins of the patient, and neutralizing antibodies, respectively. On the other hand, cationic lipids are a particularly attractive alternative to the viral vectors because they do not induce any humoral responses. Moreover, it is possible to design and synthesize a wide variety of cationic lipids that, depending on their structural features, promote gene expression by affecting one or more of the essential requirements for transfection, i.e., efficient compaction of plasmid DNA, lipoplex internalization, fusion of the internalized lipoplex with lysosome membrane, and translocation of the plasmid DNA to the nucleus. Unfortunately, the transfection activity of nonviral vectors is currently very low to permit disease treatment. Thus, for gene therapy to become common medicine therapeutics, current vehicles have to be improved significantly. Nevertheless, despite the present lack of clinical success of gene therapy, the promise that it holds to eradicate the cause of a disease rather than to treat the symptoms of it has kept the drive for discovering efficient cationic transfection lipids active, for more than 17 years.

Toward this effort, we have recently launched a systematic investigation of the transfection potency of a series of positively charged lipids containing primary and tertiary amine groups attached to the 2-position of the 1,3-diamino-2-propanol backbone, whereas the acyl chains were linked to the backbone at the 1- and 3-positions via amide bonds (*8*, *9*). Herein, we report on the synthesis and transfection activity of novel cationic lipids of the 1,2-diamino-3-propanol series, in which the polar headgroup bis-(2-dimethylaminoethane) is attached via a carbamate spacer at the 3-position of the 1,2-diaminopropan-3-ol, whereas the hydrophobic alkyl chains are bonded to the nitrogen atoms at the 1- and 2-position of the diaminopropanol backbone through acyl linkers. The physicochemical properties of the cationic lipids in isolation were investigated in an effort to correlate structures with transfection activity.

MATERIALS AND METHODS

Materials. Bis-(2-chloroethyl)amine hydrochloride, 98%, 2,3-diaminopropionic acid monohydrochloride 98%, lauroyl chloride 98%, myristoyl chloride 97%, palmitoyl chloride 98%, stearoyl chloride 99%, oleoyl chloride technical grade (∼85%), 4-nitrophenyl chloroformate 97%, hydrogen chloride gas anhydrous 99+%, lithium borohydride 2.0 M solution in THF, tetrahydrofuran (THF) anhydrous 99.9%, triethylamine 99.5% (TEA), ethyl alcohol 99.5%, *N*,*N*-dimethylformamide (DMF) 99%,

* To whom correspondence should be addressed. Phone: 718-488-1471. Fax: 718-780-4586. E-mail: msavva@liu.edu.

10.1021/bc050138c CCC: $30.25 © 2005 American Chemical Society
Published on Web 11/01/2005

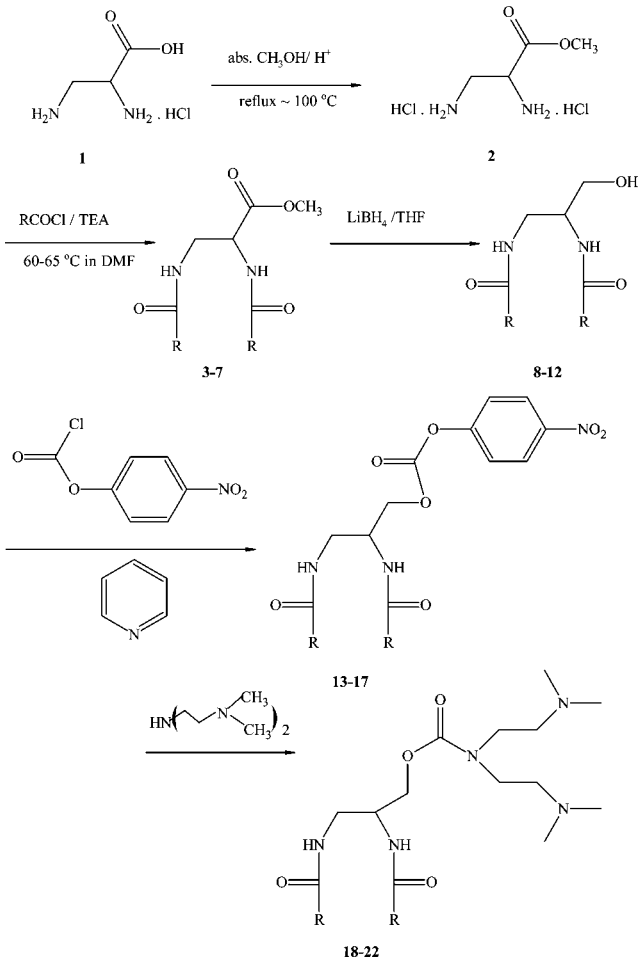

Figure 1. Synthetic scheme for the preparation of 1,2-dialkoylamidopropane-based lipids: R = $C_{11}H_{23}$ (**18**, 1,2lb1), $C_{13}H_{27}$ (**19**, 1,2lb2), $C_{15}H_{31}$ (**20**, 1,2lb3), $C_{17}H_{35}$ (**21**, 1,2lb4), $C_{17}H_{33}$ (**22**, 1,-2lb5).

and pyridine 99+% were purchased from Aldrich. Dimethylamine 40% was purchased from ACROS ORGANICS. Methanol (anhydrous) and all other reagents used were from VWR. All tissue culture reagents were purchased from Life Technologies Inc. (Rockville, MD), unless otherwise specified.

Synthesis. The synthesis of the bivalent cationic lipids is summarized in Figure 1. Mobile phase systems v/v for thin layer chromatography (TLC) (A) $CH_3OH/CHCl_3$ (1:1), (B) $CH_3OH/CHCl_3$ (1:4), (C) $CH_3OH/CHCl_3$ (1:9), (D) $CH_3OHCHCl_3$ (1: 20), (E) $CH_3OH/CHCl_3/NH_4OH$ (1:2:0.15).

Bis-(2-(dimethylamino)ethyl)amine. Solid bis-(2-chloroethyl)amine hydrochloride (17.85 g, 0.10 mol) was dissolved in a 500 mL round-bottom flask with addition of 152 mL of dimethylamine (54 g, 1.20 mol). After a 72 h of rigorous stirring at room temperature, the mixture was made alkaline with 6 M NaOH (100 mL) and further saturated with anhydrous potassium carbonate. Upon alkalization an oily liquid separates on the upper layer. The mixture was stirred for one-half hour and then transferred to a 500 mL separation funnel where the crude product was extracted with 4 × 150 mL of ethyl ether (ninhydrin test of the organic phase turns negative). The extracts were collected and dried ($MgSO_4$) overnight. $MgSO_4$ was removed by suction filtration and the organic solvent was eliminated under diminished pressure at 45 °C to give a total of 5.0 g of colorless oil (yield 31%). Further purification of the triamine was performed by chromatography with 50% recovery (*10*). MS (FAB and ES) *m/z* 160.2 $[M + H]^+$; ^1H NMR (400 MHz, $CDCl_3$, 20 °C, TMS) δ 2.60−2.63 (t, 4H, J = 6.2 Hz, $NCH_2CH_2N(CH_3)_2$), 2.31−2.34 (t, 4H, J = 6.2 Hz, $CH_2N(CH_3)_2$), 2.13 (s, 12H, $N(CH_3)_2$); ^{13}C NMR (100 MHz, $CDCl_3$, 20 °C, TMS) δ 59.21 ($2CH_2$), 47.48 ($2CH_2$), 45.60 ($4CH_3$).

Methyl 2,3-Diaminopropionate Dihydrochloride (2). 2,3-Diaminopropionic acid monohydrochloride (2.0 g, 14.2 mmol) was pulverized and transferred to a 500 mL round-bottom flask containing 50 mL of anhydrous methanol. Bound water was removed by evaporating the solvent several times at low pressure at 75 °C. The dry powder was finally dissolved in fresh anhydrous methanol (100 mL) saturated with anhydrous hydrogen chloride gas. The mixture was refluxed at 85−90 °C for 17 h. Methanol was eliminated under diminished pressure to give 2.85 g as a yellowish crystal of 86−90% purity, depending on the batch, as determined by ^1H NMR. R_f = 0.86 (A). ^1H NMR (400 MHz, D_2O, 20 °C, TMS) δ 4.26−4.34 (t, 1H, $CH_2CH(NH_2)CO$), 3.66 (s, 3H, $COOCH_3$), 3.22−3.44 (m, 2H, CH_2CH).

Methyl 2,3-Dilauroylamidopropionate (3). Methyl 2,3-dilauroylamidopropionate was synthesized using a procedure similar to that described by Sunamoto and coworkers (*11*). Briefly, to a 100 mL anhydrous DMF solution of methyl 2,3-diaminopropionate dihydrochloride (1.36 g, 7.11 mmol) in a 250 mL round-bottom flask was added 10.0 mL of TEA (71.1 mmol) immediately followed by dropwise addition of 7.0 mL of lauroyl chloride (28.4 mmol). The mixture was stirred at 60 °C for 6 h. DMF was evaporated with the aid of a rotary evaporator at 90 °C under reduced pressure, and the crude material was transferred with 100 mL of $CHCl_3$ to a 500 mL separation funnel where it was washed once with HCl and once with Na_2CO_3. The organic phase was collected in a 250 mL round-bottom flask, and the $CHCl_3$ was removed under reduced pressure with the aid of a rotary evaporator. The dried crude was dissolved in a minimum amount of hot methanol and left overnight for crystallization. The product was collected by suction filtration as a white crystalline powder (2.1 g, 61.3%). R_f = 0.76 (C). ^1H NMR (400 MHz, $CDCl_3$, 20 °C, TMS) δ 6.89 (d, 1H, *H*NCH), 6.25 (t, 1H, $HNCH_2$), 4.57 (m, 1H, $CHCOOCH_3$), 3.72 (s, 3H, $COOCH_3$), 3.60 (t, 2H, $HNCH_2CH$), 2.11−2.21 (m, 4H, $COCH_2$), 1.58 (m, 4H, $COCH_2CH_2$), 1.21 (b, 32H, $(CH_2)_8CH_3$), 0.82−0.85 (t, 6H, CH_3).

2,3-Dilauroylamidopropan-3-ol (8). To a 100 mL solution of methyl 2,3-dilauroylamidopropionate (3.52 g, 7.29 mmol) in absolute ethanol in a 250 mL round-bottom flask was added 10.9 mL (21.87 mmol) of 2.0 M lithium borohydride solution in THF. Hydrogenation was performed in a dry N_2 gas environment at 50−60 °C for 3 h and then at 23 °C for an additional 12 h. Ethanol was removed, and the crude material was taken with 100 mL of chloroform, transferred to a 500 mL separation funnel, and washed once with 100 mL of 1.0 N HCl and once with Na_2CO_3. The organic phase was concentrated to an oil of high viscosity, which was applied to a silica gel column (3.2 cm × 30 cm). Elution was performed with 100 mL of $CHCl_3$ and 1%, 1.5%, 2%, 2.5%, 3%, 10%, 20%, and 50% MeOH/$CHCl_3$. Fractions between 2% and 20% were pooled and concentrated to give a total of 2.94 g of 2,3-dilauroylamidopropanol as a white powder (89% yield). R_f = 0.27 (D). ^1H NMR (400 MHz, $CDCl_3$, 20 °C, TMS) δ 6.25−6.50 (b, 2H, $HNCH_2HNCH$), 3.60−3.90 (m, 2H, $HNCH_2CH$), 3.40−3.55 (m, 2H, $CH(NH)CH_2OH$), 3.20−3.30 (m, 1H, C*H*), 2.12−2.22 (m, 4H, $COCH_2$), 1.59

(b, 4H, $COCH_2CH_2$), 1.23 (b, 32H, $(CH_2)_8CH_3$), 0.83−0.86 (t, 6H, CH_3).

2,3-Dilauroylamidopropane-1-(*p*-nitrophenyl) Carbonate (13). 2,3-Dilauroylamidopropanol (2.94 g, 6.47 mmol) was suspended with continuous stirring in 100 mL of anhydrous THF in a 250 mL capacity round-bottom flask. The mixture was kept at 25 °C with the aid of an oil bath. To the suspension was added 4-nitrophenyl chloroformate (1.30 g, 6.47 mmol) followed by a dropwise addition of pyridine (0.52 mL, 6.47 mmol). The reaction was stopped after 5 h. THF was removed under diminished pressure, and the crude was transferred with 100 mL of chloroform to a 500 mL separation funnel and washed once with 100 mL of 1.0 N HCl and once with 100 mL of Na_2CO_3. The organic phase was concentrated to a viscous oil with the aid of a rotary evaporator and purified by chromatography on a silica gel column, eluting with 100 mL of 1%, 2%, 3%, 4%, 5%, 20%, 50% MeOH/$CHCl_3$. Fractions between 3% and 20% were pooled and dried to give a total of 3.9 g (6.28 mmol, 97% yield) of 2,3-dilauroylamidopropane-1-(*p*-nitrophenyl) carbonate as a white crystalline material. R_f = 0.49 (D). ^{1}HNMR (400 MHz, $CDCl_3$, 20 °C, TMS) δ 8.27−8.24, 7.37−7.23 (two d, each J = 9.1 Hz, 4H, C_6H_4), 6.64 (d, 1H, *H*NCH), 6.02 (t, 1H, *H*NCH_2), 4.18−4.40 (m, 3H, NHC*HCH*$_2$OCOO), 3.42−3.57 (m, 2H, HNC*H*$_2$CH), 2.14−2.20 (m, 4H, $COCH_2$), 1.57−1.79 (m, 4H, $COCH_2CH_2$), 1.0−1.24 (bs, 32H, $(CH_2)_8CH_3$), 0.82−0.90 (t, 6H, CH_3).

1,2-Dilauroylamidopropane-3-[bis-(2-dimethylaminoethane)] Carbamate (18, 1,2lb1). To a solution of 2,3-dilauroylamidopropane-1-(*p*-nitrophenyl) carbonate (3.9 g, 6.28 mmol) in 100 mL of chloroform was added bis-(2-dimethylaminoethyl)amine (1.7 mL, 9.42 mmol). The mixture was stirred at room temperature for 17 h. The reaction mixture was then transferred to a 500 mL separation funnel where it was washed once with 100 mL of 1.0 N Na_2CO_3. The organic phase was concentrated to an oil, which was chromatographed on a silica gel column, eluting with 100 mL of 2%, 4%, 200 mL of 5%, 100 mL of 7%, 10%, and 200 mL of 15%, 20%, 25%, 30%, 35%, 40% MeOH/$CHCl_3$. Fractions between 15% and 40% were pooled and dried to obtain a total 2.95 g (73%). R_f = 0.46 (E). Anal. Calcd for $C_{36}H_{73}N_5O_4$ (MW 639): C, 67.56; H, 11.50; N, 10.94. Found: C, 66.97; H, 11.77; N, 10.90. MS (ESI) *m/z* 662.5 $[M + Na]^+$; ^{1}H NMR (400 MHz, $CDCl_3$, 20 °C, TMS) δ 7.15 (d, 1H, *H*NCH), 6.70 (t, 1H, *H*NCH_2), 4.13 (m, 3H, NHC*HCH*$_2$OCO), 3.20−3.50 (m, 6H, NHC*H*$_2$CH(NH)CH_2OCON$(CH_2)_2$−), 2.35−2.42 (m, 4H, $CH_2N(CH_3)_2$), 2.19−2.20 (d, 12H, $N(CH_3)_2$), 2.05−2.18 (m, 4H, $COCH_2$), 1.45−1.60 (m, 4H, $COCH_2CH_2$), 1.187 (b, 32H, $(CH_2)_8CH_3$), 0.80−0.90 (t, 6H, CH_3); ^{13}C NMR (100 MHz, $CDCl_3$, 20 °C) δ 176.04 (NHCO), 175.34 (NHCO), 157.47 (OCO), 65.30, 58.63, 46.83, 37.75, 32.96, 30.68, 30.41, 27.35, 23.73, 15.17.

Methyl 2,3-Dimyristoylamidopropionate (4). Methyl 2,3-dimyristoylamidopropionate was crystallized from methanol analogously to compound **3** to afford a total of 1.3 g as white crystals (68%). R_f = 0.89 (B), R_f = 0.82 (C). ^{1}H NMR (400 MHz, $CDCl_3$, 20 °C, TMS) δ 6.77 (d, 1H, *H*NCH), 6.15 (t, 1H, *H*NCH_2), 4.55 (m, 1H, C*H*COO), 3.72 (s, 3H, $COOCH_3$), 3.60 (t, 2H, HNCH_2), 2.11−2.21 (m, 4H, $COCH_2$), 1.56 (m, 4H, $COCH_2CH_2$), 1.22 (b, 40H, $(CH_2)_{10}CH_3$), 0.82−0.85 (t, 6H, $(CH_2)_{10}CH_3$); ^{13}C NMR (100 MHz, $CDCl_3$, 20 °C) δ 175.77 (NHCO), 174.95 (NHCO), 171.82 (COO), 54.72, 51.74, 46.64, 37.60, 37.48, 32.93, 30.68, 30.38, 26.55, 26.71, 23.70, 15.11.

2,3-Dimyristoylamidopropanol (9). This compound was prepared similarly to compound **8** with lithium borohydride at 60 °C for 5 h and gave the product as a white powder (2.23 g, 99%). R_f = 0.27 (D). ^{1}H NMR (400 MHz, $CDCl_3$, 20 °C, TMS) δ 6.44−6.55 (m, 2H, *H*NCH_2-*H*NCH), 3.40−3.90 (m, 4H, HNCH_2CH(NH)CH_2OH), 3.20−3.30 (m, 1H, $HNCH_2CH$), 2.13−2.21 (m, 4H, $COCH_2$), 1.56 (m, 4H, $COCH_2CH_2$), 1.21 (b, 40H, $(CH_2)_{10}$-CH_3), 0.82−0.85 (t, 6H, CH_3).

2,3-Dimyristoylamidopropane-1-(*p*-nitrophenyl) Carbonate (14). Compound **14** was prepared analogously to **13** and purified by silica gel column chromatography (70−230, 3.2 cm × 30 cm), eluting with 100 mL of 1%, 1.5%, 2%, 2.5%, 3%, 3.5%, 4%, 5%, 40% MeOH/$CHCl_3$. The 2−4% fractions were pooled to give 1.16 g (1.7 mmol, 79.5%) of the product as a white solid. R_f = 0.71 (D). ^{1}H NMR (400 MHz, $CDCl_3$, 20 °C, TMS) δ 8.26−8.23, 7.36−7.34 (two d, each J = 9.1 Hz, 4H, C_6H_4), 6.77 (d, 1H, *H*NCH), 6.25 (t, 1H, *H*NCH_2), 4.20−4.38 (m, 3H, NHC*HCH*$_2$OCOO), 3.30−3.60 (m, 2H, HNC*H*$_2$CH), 2.16−2.18 (m, 4H, $COCH_2$), 1.56 (m, 4H, $COCH_2CH_2$), 1.20 (b, 40H, $(CH_2)_{10}CH_3$), 0.81−0.85 (t, 6H, CH_3).

1,2-Dimyristoylamidopropane-3-[bis-(2-dimethylaminoethane)] Carbamate (19, 1,2lb2). 19 was prepared analogously to **18** on a 1.5 mmol scale to give upon purification the product as a white solid (0.6 g, 0.87 mmol, 57%). R_f = 0.76 (E). Anal. Calcd for $C_{40}H_{81}N_5O_4$ (MW 695): C, 69.02; H, 11.73; N, 10.06. Found: C, 68.74; H, 11.99; N, 9.98. MS (FAB) *m/z* 697.1 $[M + H]^+$. ^{1}H NMR (400 MHz, $CDCl_3$, 20 °C, TMS) δ 7.15 (d, 1H, *H*NCH) 6.70 (t, 1H, *H*NCH_2), 4.13 (m, 3H, *CH*(NH)*CH*$_2$OCO), 3.24−3.46 (m, 6H, NHCH_2CH(NH)CH_2OCON$(CH_2)_2$), 2.36−2.47 (m, 4H, $CH_2N(CH_3)_2$), 2.21−2.23 (d, 12H, $N(CH_3)_2$), 2.12 (m, 4H, $COCH_2$), 1.56−1.58 (m, 4H, $COCH_2CH_2$), 1.24 (b, 40H, $(CH_2)_{10}CH_3$), 0.80−0.90 (t, 6H, CH_3); ^{13}C NMR (100 MHz, $CDCl_3$, 20 °C) δ 176.16 (NHCO), 175.34 (NHCO), 157.35 (OCO), 65.76, 58.63, 46.83, 46.37, 46.25, 37.69, 32.96, 30.71, 30.41, 27.05, 23.73, 15.20.

Methyl 2,3-Dipalmitoylamidopropionate (5). This compound was prepared similarly to **4** and gave the product as white crystals (2.9 g, 4.9 mmol, 68%). R_f = 0.76 (C). ^{1}H NMR (400 MHz, $CDCl_3$, 20 °C, TMS) δ 6.80 (d, 1H, *H*NCH), 6.18 (t, 1H, *H*NCH_2), 4.58 (m, 1H, C*H*$COOCH_3$), 3.73 (s, 3H, $COOCH_3$), 3.61 (m, 2H, HNCH_2-CH), 2.14−2.20 (m, 4H, $COCH_2$), 1.57−1.58 (m, 4H, $COCH_2CH_2$), 1.24 (b, 48H, $(CH_2)_{12}CH_3$), 0.83−0.86 (t, 6H, $(CH_2)_{12}CH_3$).

2,3-Dipalmitoylamidopropan-3-ol (10). Compound **10** was prepared analogously to **9** on a 4.9 mmol scale and gave the product, after chromatography ($CHCl_3$/MeOH), as a white powder (2.5 g, 89%). R_f = 0.37 (D). ^{1}H NMR (400 MHz, $CDCl_3$, 20 °C, TMS) δ 6.24−6.36 (b, 2H, *H*NCH_2*H*NCH), 3.40−3.90 (m, 4H, HNCH_2CH(NH)-CH_2OH), 3.20−3.30 (m, 1H, $HNCH_2CH$), 2.15−2.19 (m, 4H, $COCH_2$), 1.58−1.59 (m, 4H, $COCH_2CH_2$), 1.23 (b, 48H, $(CH_2)_{12}CH_3$), 0.84−0.87 (t, 6H, CH_3).

2,3-Dipalmitoylamidopropane-1-(*p*-nitrophenyl) Carbonate (15). This compound was prepared similarly to **14** and was recovered as a white powder (2.3 g, 3.1 mmol, 72%). R_f = 0.71 (D). ^{1}H NMR (400 MHz, $CDCl_3$, 20 °C, TMS) δ 8.27−8.25, 7.38−7.36 (two d, each J = 9.1 Hz, 4H, C_6H_4), 6.69 (m, 1H, −*H*NCH−), 6.13 (m, 1H, *H*NCH_2), 4.23−4.36 (m, 3H, NHC*HCH*$_2$OCOO), 3.38−3.59 (m, 2H, HNCH_2CH), 2.15−2.20 (m, 4H, $COCH_2$), 1.57−1.58 (m, 4H, $COCH_2CH_2$), 1.24 (b, 48H, $(CH_2)_{12}$-CH_3), 0.82−0.86 (t, 6H, CH_3),

1,2-Dipalmitoylamidopropane-3-[bis-(2-dimethylaminoethane)] Carbamate (20, 1,2lb3). 20 was prepared similarly to **19** as a white sticky powder (1.9 g, 2.5 mmol, 58%). R_f = 0.52 (E). Anal. Calcd for $C_{44}H_{89}N_5O_4$ (MW 751): C, 70.26; H, 11.92; N, 9.31. Found: C, 70.14;

H, 11.97; N, 9.32. MS (ESI) *m*/z 774.7 $[M + Na]^+$; ^{1}H NMR (400 MHz, $CDCl_3$, 20 °C, TMS) δ 7.15 (d, 1H, OC*H*NCH) 6.70 (t, 1H, OC*H*NCH$_2$CH), 4.13 (m, 3H, NHC*HCH*$_2$OCO), 3.20−3.50 (m, 6H, C*H*$_2$CHCH$_2$OCON-(C*H*$_2$)$_2$), 2.40−2.50 (m, 4H, C*H*$_2$N(CH$_3$)$_2$), 2.22−2.25 (d, 12H, N(C*H*$_3$)$_2$), 2.10−2.20 (m, 4H, COC*H*$_2$), 1.45−1.60 (m, 4H, COCH$_2$C*H*$_2$), 1.21 (b, 48H, (C*H*$_2$)$_{12}$CH$_3$), 0.82−0.86 (t, 6H, (CH$_2$)$_{12}$C*H*$_3$); ^{13}C NMR (100 MHz, $CDCl_3$, 20 °C) δ 176.04 (NHCO), 175.34 (NHCO), 157.44 (OCO), 65.67, 58.61, 46.83, 46.58, 37.72, 32.96, 30.74, 30.41, 26.74, 23.73, 15.20.

Methyl 2,3-Distearoylamidopropionate (6). Compound **6** was prepared analogously to **3** on a 6.6 mmol scale to give upon crystallization from methanol the product **6** as a brownish powder (2.4 g, 3.7 mmol, 56%). R_f = 0.92 (A), R_f = 0.68 (C). ^{1}H NMR (400 MHz, $CDCl_3$, 20 °C, TMS) δ 6.78 (d, 1H, *H*NCH), 6.08 (s, 1H, *H*NCH$_2$), 4.58 (m, 1H, C*H*COOCH$_3$), 3.72 (s, 3H, COOC*H*$_3$), 3.60 (m, 2H, HNC*H*$_2$), 2.13−2.19 (m, 4H, COC*H*$_2$), 1.56−1.68 (m, 4H, COCH$_2$C*H*$_2$), 1.20 (b, 56H, (C*H*$_2$)$_{14}$CH$_3$), 0.82−0.85 (t, 6H, (CH$_2$)$_{14}$C*H*$_3$).

2,3-Distearoylamidopropanol (11). Compound **11** was prepared by reducing **6** with lithium borohydride in anhydrous THF at 50−60 °C for 25 h. The crude was worked up similarly to **8** to give the product **11** as white crystals (1.0 g, 1.6 mmol, 47%). R_f = 0.5 (D). ^{1}H NMR (400 MHz, $CDCl_3$, 20 °C, TMS) δ 6.40 (m, 2H, *H*NCH$_2$-(*H*N)CH), 3.20−3.90 (m, 5H, HNC*H*$_2$C*H*(NH)C*H*$_2$OH), 2.15−2.19 (m, 4H, COC*H*$_2$), 1.59 (m, 4H, COCH$_2$C*H*$_2$), 1.23 (b, 56H, (C*H*$_2$)$_{14}$CH$_3$), 0.85 (t, 6H, C*H*$_3$).

2,3-Distearoylamidopropane-1-(*p*-nitrophenyl) Carbonate (16). This compound was prepared similarly to **13** with *p*-nitrophenylchloroformate and gave the product as white solid (1.2 g, 1.6 mmol, 96%). R_f = 0.63 (D). ^{1}HNMR (400 MHz, $CDCl_3$, 20°C, TMS) δ 8.25−8.23, 7.37−7.35 (two d, each J = 9.1 Hz, 4H, C_6H_4), 6.64 (s, 1H, *H*NCH), 6.02 (s, 1H, *H*NCH$_2$CH), 4.08−4.40 (m, 3H, NHC*HCH*$_2$OCOO), 3.42−3.75 (m, 2H, HNC*H*$_2$CH), 2.20 (m, 4H, COC*H*$_2$), 1.58−1.59 (m, 4H, COCH$_2$C*H*$_2$), 1.23 (b, 56H, (C*H*$_2$)$_{14}$CH$_3$), 0.84−0.87 (t, 6H, C*H*$_3$).

1,2-Distearoylamidopropane-3-[bis-(2-dimethylaminoethane)] Carbamate (21, 1,2lb4). 21 was prepared similarly to **20** with bis-(2-dimethylaminoethyl) amine and gave the product as a half-white sticky solid (0.6 g, 0.7 mmol, 48%). R_f = 0.48 (E). Anal. Calcd for $C_{48}H_{97}N_5O_4$ (MW 807): C, 71.32; H, 12.09; N, 8.66. Found: C, 71.38; H, 11.92; N, 8.18. MS (ESI) *m/z* 830.7 $[M + Na]^+$; ^{1}H NMR (400 MHz, $CDCl_3$, 20°C, TMS) δ 7.00 (d, 1H, *H*NCH), 6.67 (t, 1H, *H*NCH$_2$CH), 4.13 (m, 3H, NHC*HCH*$_2$OCON), 3.33 (m, 6H, C*H*$_2$CHCH$_2$OCON-(C*H*$_2$)$_2$−), 2.10−2.40 (m, 20H, C*H*$_2$N(C*H*$_3$)$_2$, COC*H*$_2$-CH$_2$(CH$_2$)$_{14}$CH$_3$), 1.55−1.57 (m, 4H, COCH$_2$C*H*$_2$), 1.22 (s, 56H, (C*H*$_2$)$_{14}$CH$_3$), 0.84 (t, 6H, C*H*$_3$).

Methyl 2,3-Dioleoylamidopropionate (7). Compound **7** was prepared as a brown oil (impure mixture) analogously to compound **6** on a 6.8 mmol scale. R_f = 0.94 (A). ^{1}H NMR (400 MHz, $CDCl_3$, 20 °C, TMS) δ 6.80 (b, 1H, *H*NCH), 6.18 (b, 1H, *H*NCH$_2$), 5.3 (m, 4H, C*H*=C*H*), 3.5−4.7 (m, 6H, HNC*H*$_2$HNC*H*COOC*H*$_3$), 1.4−2.4 (b, 16H, COC*H*$_2$C*H*$_2$(CH$_2$)$_4$C*H*$_2$CH=CHC*H*$_2$(CH$_2$)$_6$CH$_3$), 1.24 (b, 40H, CH$_2$(C*H*$_2$)$_4$CH$_2$CH=CHCH$_2$(C*H*$_2$)$_6$CH$_3$), 0.83−0.86 (t, 6H, (CH$_2$)$_6$C*H*$_3$).

2,3-Dioleoylamidopropan-3-ol (12). Compound **12** was prepared analogously to **11** on a 1.8 mmol scale to give upon purification (column chromatography, $CHCl_3$/MeOH) the product as a yellow solid (0.49 g, 0.8 mmol, 44%). R_f = 0.5 (D). ^{1}H NMR (400 MHz, $CDCl_3$, 20 °C, TMS) δ 7.33 (s, 1H, *H*NCH), 6.80 (s, 1H, *H*NCH$_2$CH), 5.27 (m, 4H, C*H*=C*H*), 3.20−3.80 (m, 5H, HNC*H*$_2$(HN)-C*H*CH$_2$OH), 2.14 (m, 4H, COC*H*$_2$), 1.95 (m, 8H, C*H*$_2$CH=CHC*H*$_2$), 1.56 (m, 4H, COCH$_2$C*H*$_2$) 1.23 (b, 40H, COCH$_2$-(C*H*$_2$)$_4$CH$_2$CH=CHCH$_2$(C*H*$_2$)$_6$CH$_3$), 0.8−0.83 (t, 6H, (CH$_2$)$_6$-CH$_3$).

2,3-Dioleoylamidopropane-1-(p-nitrophenyl) Carbonate (17). Compound **17** was prepared analogously to **16** on a 5.8 mmol scale to give upon purification (column chromatography, $CHCl_3$/MeOH) the product as a yellow-brown oil (2.9 g, 3.7 mmol, 63%). R_f = 0.73 (D). ^{1}H NMR (400 MHz, $CDCl_3$, 20°C, TMS) δ 8.25−8.23, 7.37−7.35 (two d, each J = 9.1 Hz, 4H, C_6H_4), 7.0 (b, 1H, *H*NCH), 6.82 (b, 1H, *H*NCH$_2$CH), 5.31 (m, 4H, C*H*=C*H*), 4.18−4.40 (m, 3H, NHC*HCH*$_2$OCOO), 3.22−3.57 (m, 2H, HNC*H*$_2$CH), 2.17 (m, 4H, COC*H*$_2$), 1.97 (m, 8H, C*H*$_2$CH=CHC*H*$_2$), 1.55 (m, 4H, COCH$_2$C*H*$_2$), 1.23 (b, 40H, COCH$_2$-(C*H*$_2$)$_4$CH$_2$CH=CHCH$_2$(C*H*$_2$)$_6$CH$_3$), 0.82−0.86 (t, 6H, (CH$_2$)$_6$C*H*$_3$).

2,3-Dioleoylamidopropane-1-[bis-(2-dimethylaminoethane)] Carbamate (22, 1,2lb5). 22 was prepared similarly to **21** with bis-(2-dimethylaminoethyl)amine and gave the product as a yellow oil (0.9 g, 1.1 mmol, 35%). R_f = 0.5 (E). Anal. Calcd for $C_{48}H_{93}N_5O_4$ (MW 803): C, 71.68; H, 11.65; N, 8.71. Found: C, 71.03; H, 11.85; N, 7.73. MS (ESI) *m/z* 826.7 $[M + Na]^+$; ^{1}H NMR (400 MHz, $CDCl_3$, 20°C, TMS) δ 7.3 (b, 1H, *H*NCH), 6.89 (b, 1H, *H*NCH$_2$), 5.28 (m, 4H, C*H*=C*H*), 4.16 (m, 3H, HNC*HCH*$_2$OCO), 3.39 (m, 6H, HNC*H*$_2$(HN)CHCH$_2$OCON-(C*H*$_2$−)$_2$), 1.97−2.42 (m, 28H, COC*H*$_2$; C*H*$_2$CH=CHC*H*$_2$, C*H*$_2$N(C*H*$_3$)$_2$), 1.21−1.55 (m, 44H, COCH$_2$C*H*$_2$(CH$_2$)$_4$CH$_2$-CH=CHCH$_2$(CH$_2$)$_6$), 0.80−0.83 (t, 6H, CH$_2$C*H*$_3$); ^{13}C NMR (100 MHz, $CDCl_3$, 20 °C) δ 175.40 (NHCO), 174.10 (NHCO), 157.38 (OCO), 130.86−129.50 (C=C), 58.24, 46.852, 37.69, 32.96, 30.80, 30.38, 28.25, 26.80, 23.76, 15.17.

Lipoplex Formation. Solutions of cationic lipids in chloroform were prepared on a weight to volume basis. Aliquots of cationic lipids, DOPE, and cholesterol were transferred with the aid of graduated glass syringes to 12 mm × 75 mm borosilicate glass tubes (pyrex, Corning Inc., NY) in appropriate amounts to provide the relative lipid concentrations desired upon reconstitution with 1 mL of 40 mM Tris buffer, pH 7.1. Bulk organic solvent was removed with a stream of nitrogen gas, and residual solvent was removed under high vacuum (0.40 mmHg) for 4−5 h. The dried lipids were hydrated with 40 mM Tris buffer, pH 7.1, for 30−45 min at 50−60 °C with occasional vortexing. Lipid dispersions were further diluted in serum-free RPMI media (0.3 μmol/mL) and mixed with pUC19-CMV-β-gal plasmid DNA (0.2 μg/mL), as described elsewhere (*8*). Lipoplexes were added to the cells within 1 h after mixing.

Transfection Assays. Approximately 50 000 B16F0 cells (CRL-6322, ATCC, Rockville, MD) in 0.5 mL of 10% FBS/90% RPMI, supplemented with 100 units/mL penicillin, 100 μg/mL streptomycin, 4 mM L-glutamine, and 1 mM sodium pyruvate were seeded into each well of 48-well plates and cultured overnight in a 5% CO_2 incubator at 37 °C. After 12−14 h, the medium was removed, and 250 μL of the lipoplexes in serum-free RPMI was added. Lipoplexes were aspirated after 3 h, and 0.5 mL of 10% FBS/90% RPMI was added to each well. After a total of 48 h, the medium was removed and 150 μL of lysis buffer (0.1% Triton X-100 in 0.1 M Tris and 2 mM EDTA, pH 8) was added to lyse the cells. The cell lysate was centrifuged, and an amount of 120 μL was collected and assayed for β-galactosidase activity using a microplate colorimetric assay that employed the substrate *o*-nitrophenyl-β-D-galactopyranoside (*12*).

Cytotoxicity Assay. B16F0 cells were subjected to lipoplex formulations and further incubated for 44 h, as described above in the in vitro transfection studies. MTT was dissolved in PBS at 5 mg/mL and filtered through a 0.22 μm membrane to remove insoluble material. The 50 μL of MTT solution was added into each well, and the cells were incubated for 4 h at 37 °C in 5% CO_2. The medium was then flicked out, the cells were washed once with cold PBS, and 250 μL of DMSO was added to each well. The cells were subsequently shaken for 30 min at room temperature using an orbital shaker to ensure complete dissolution of the formazan crystals. The emerged deep-purple color was measured at 630 nm with a multiwell scanning spectrophotometer (El_x 800 UV, Bio-Tek Instruments, Inc.).

Agarose Gel Electrophoresis. Agarose powder (400 mg) was added to 50 mL of TAE buffer (0.8% dispersion) in an Erlenmeyer flask. The mixture was boiled for a minute until it became clear. To the solution, 2.5 μL (10 mg/mL) of ethidium bromide (dye) was added. The solution was allowed to cool to 50−60 °C, then poured into the electrophoresis apparatus and allowed to solidify. The lipoplexes were prepared as 0.5, 1.0, 2.0, 4.0, 6.0, and 8.0 +/− charge ratios. Calculations were based on a nucleotide average molecular weight of 330 g/mol. The ratio for cationic lipids mixed with neutral lipids was kept constant at cationic lipid/ DOPE/cholesterol 3:2:1 mol/ mol.

A fixed quantity of DNA of 0.2 μg was added to each microfuge. Aliquots of cationic liposomes were then added to provide the desired +/− charge ratio. The total volume was brought to 8 μL by addition of appropriate buffer. The microfuges were briefly centrifuged (10−20 s), and they were allowed to stand at room temperature for at least 15 min. The complexes were then loaded into the wells of the gel sequentially with proper mixing. Naked DNA was loaded on the outermost lanes as a control experiment. After loading the complexes in the wells, the gel tank was filled with TAE buffer, pH 7.4, to a few millimeters above the gel surface and the lipoplexes were subjected to an electrophoretic field of 5 V/cm for 25−30 min. Migration of naked DNA and lipoplexes was noted with the aid of a BioRad minitransluminator.

Particle Size Determination. Size determination was carried out using a 90° fixed scattering angle nanoparticle analyzer (Nicomp 370, PCS Inc., CA). All measurements were performed at room temperature with a 5 min run time. Particle size measurements were done using buffers of pH 7.2 and pH 8.0, 40 mM Tris buffer. All buffers were filtered using 0.22 μm filters. Lipid dispersions were prepared as described under the Lipoplex Formation section and subsequently diluted with a dust-free buffer to a final concentration of 1.5 mM in borosilicate tubes, 12 mm × 75 mm (KIMAX 51, VWR). Lipoplexes were prepared at a cationic lipid-to-DNA molar ratio of 1:1 (+/− ratio of 2) from 0.3 mM lipid dispersions. Lipoplexes were always freshly prepared by simply adding DNA to the lipid dispersions with gentle agitation. Preparation and manipulation of the liposomes were performed in a dust-free environment. "Equilibration time" was set to 2 min and "run time" to 10 min. Mean particle size and standard deviation reported are the cumulative average and cumulative standard deviation of five consecutive scans as calculated from intensity-weighted Gaussian analysis (C370, version 12.4). Despite the high polydispersity index of some samples, individual scans were highly reproducible.

Ethidium Bromide Displacement Assay. The studies were performed on a Cary Eclipse spectrofluorometer at an excitation wavelength of 515 nm (band-pass = 5 nm, linear reciprocal dispersion D^{-1} = 2 nm/mm, slit width = 2.5 mm) and an emission wavelength of 595−605 nm (band-pass = 10 nm, D^{-1} = 2 nm/mm, slit width = 5 mm). The amount of DNA added was set to 22.5 μg, and ethidium bromide was added in aliquots in order to identify the concentration that gave the maximum signal-to-noise ratio. In a typical titration experiment, ethidium bromide (0.8 μg, 1.01 μM) was added to the quartz cuvette that contained a small magnetic stirrer and diluted to 3 mL with appropriate buffer. Addition of 22.5 μg (67.5 nmol, by nucleotide equivalent) of plasmid DNA with continuous gentle stirring yielded a 27−29 times increase in fluorescence intensity. Cationic lipids (1.5 mM) were then added in aliquots (4.5 μL) under continuous stirring at ambient temperature, and fluorescence was monitored continuously until the reading became stable. To minimize the effects of light source fluctuation and to provide a more accurate measurement, the light intensity emitted by the sample was always ratioed with the reference signal from the excitation light source. Processing of the fluorescence values as described before (*13, 14*) provided the relative ethidium bromide displacement from the plasmid DNA. The binding profiles of cationic reagents to plasmid DNA were modeled as parabolas on a domain and range [0, +∞) and [0, −∞), respectively, with the aid of PSI-Plot (version 7, Polysoftware International, NY). Vertical shifting of the curves yielded parabolas of the form $y = ax^b$, the slopes of which can easily be compared. Instantaneous rates (dF/dr, where r stands for charge ratio) were calculated either by taking the first derivative of the best fit parabolic equation or from the experimental data for 0.2 charge ratio intervals, using $dF/dc = (F_n - F_{n-1})/0.2$. The two methods correlated well. The cumulative average rates were calculated from the experimental data for 0.2 charge ratio intervals using $\Delta F/\Delta c = (F_{in} - F_{final})/\Delta c$.

Monolayers Studies. The studies were conducted on a KSV Minitrough, Langmuir-type film balance equipped with symmetric barriers (KSV Instruments Ltd., Helsinki, Finland) and thermostated with the aid of a circulating water bath (VWR brand, model 1162, PolyScience, IL). Stock solutions of pure cationic lipids were prepared by dissolving lipids in chloroform at concentrations less than 0.5 mg/mL. The buffer (40 mM Tris, pH 7.2) was prepared with HPLC grade water, the surface tension of which was 72.0−72.8 dynes/cm. All experiments were performed in an open-air vibration-free environment. Prior to each experiment, the platinum plate was rinsed with ethanol and burned with a strong flame for 1 min and the barrier and trough were washed with soap and rinsed with distilled water. The proper volume of buffer was poured into the trough, and the platinum plate was adjusted at one-third of its height immersed in the buffer. The balance and barrier position were zeroed before any addition of the lipid. The 10−25 μL of the lipid dissolved in chloroform were applied through a microsyringe drop by drop on the surface of the buffer. After the chloroform was evaporated (15−20 min), the barriers were closed at constant speed of 9.99 mm/min. The data were collected using the proprietary KSV software (WinLB, version 1.61) and were plotted as surface pressure (mN/m) against mean molecular area (Å^2/molecule). The apparatus was validated using DPPC as a standard (*15*).

The data were subsequently imported into an Excel spreadsheet, and the compressibility modulus was cal-

culated from the first derivative of the monolayer force−area isotherms using

$$K = -A(\partial\Pi/\partial A)_T$$

where K is the isothermal compressibility modulus of the monolayer and where A is the area per molecule at the corresponding surface pressure Π. Values of the compressibility moduli at monolayer collapse pressure were calculated from the plots of the compressibility modulus as a function of the mean molecular area.

Fluorescence Polarization Studies. Fluorescence anisotropies of lipid dispersions were measured using a Cary Eclipse spectrofluorometer (Varian Inc., Victoria, Australia) equipped with motorized polarizers. The slit widths of both excitation and emission were 5 nm. Samples of lipid doped DPH dispersions (0.5 mM lipid, lipid/DPH molar ratio of 100:1) in a standard 1 cm × 1 cm square fluorescence cuvette were placed in a thermoelectric temperature-controlled four-window cuvette holder with a magnetic stirrer (temperature control precision of ±0.02 °C) and illuminated with a beam at 351 nm. The fluorescence intensities (λ_{max} = 430 nm) of the emitted light polarized parallel (I_h) and perpendicular (I_v) to the excited light were recorded at different temperatures. Anisotropy values at each temperature were calculated by the Eclipse software according to the equation

$$r = \frac{I_v - GI_h}{I_v + 2GI_h}$$

where G is the instrumental grating factor that corrects for the anisotropy introduced by the optical components of the detection system. A 5 min equilibration time was left between each temperature. The anisotropy−temperature curves were fitted to

$$r = A - \frac{B}{1 + e^{-C(T-D)}}$$

where A, B, C, and D are constant parameters to be determined. The parameter D represents the gel to liquid crystalline phase transition temperature, T_m. Nonlinear fitting of the experimental data was done in an iterative fashion using the Prostat (Poly Software Intenational, version 3, New York). Initial parameters for A and B were r_{max} and $r_{max} - r_{min}$, respectively, where r_{max} is the maximum anisotropy or average of the upper third and r_{min} represents the minimum anisotropy value or the average of the lower third of the anisotropy values of data points. The initial value of D (or T_m) is the average of the temperature values of the crossover area. Best fit parameters were assessed within a 95% confidence interval.

RESULTS

Biological Results. To establish the effect of varying the alkyl chain length on transfection efficiency, the ability of cationic lipids to mediate DNA transfection in the absence and presence of helper lipids DOPE and cholesterol was evaluated in B16F0 cells. Figure 2 illustrates the transfection properties of lipoplexes at cationic lipid-to-DNA charge ratios ranging from 1 to 4. As shown in Figure 2A, only the dioleoyl derivative, 1,-2lb5, mediated efficient transfection that increased with increasing charge ratio. At charge ratio 8:1 the transfection activity of cationic lipids decreased dramatically

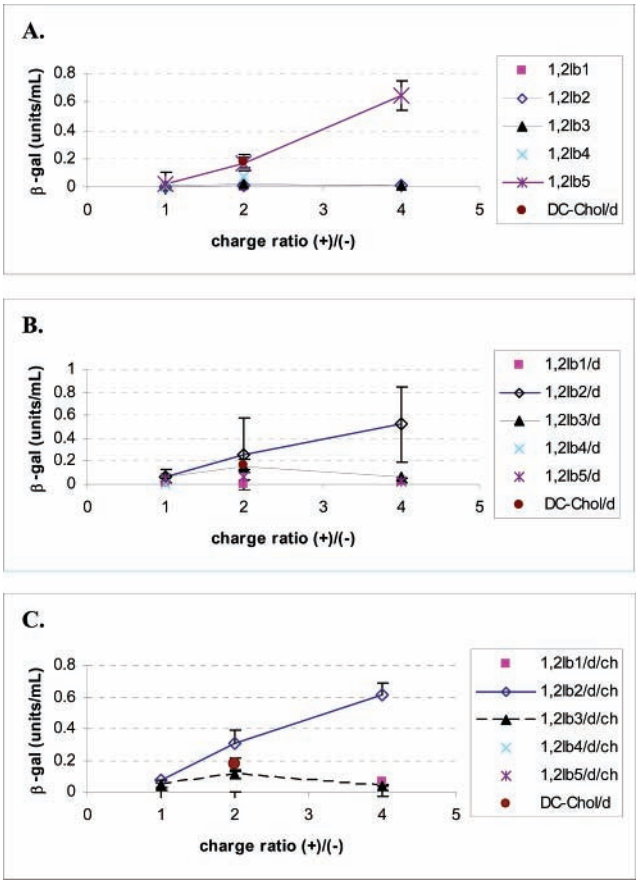

Figure 2. Transfection activity of cationic lipids in B16F0 cells: (A) 1,2lb lipoplexes; (B) 1,2lb/d lipoplexes; (C) 1,2lb/d/ch lipoplexes. The *o*-nitrophenol formation was converted to units, using a standard curve obtained with commercial β-galactosidase. The data presented are the average of values obtained from seven wells (n = 7) of two independent experiments performed at different times.

because of toxicity (not shown). Also, it is noted that the transfection potency of complexes containing 1,2lb5 at 2:1 +/− charge ratio is comparable to the potency of complexes containing the commercially available cationic lipid DC-chol, and it is much greater at higher charge ratios. Surprisingly, the activity of the 1,2lb5 is greatly diminished in the presence of helper lipids (Figure 2B,C). Contrary to that, the dimyristoyl derivative 1,2lb2 induced high levels of β-galactosidase when used with DOPE and DOPE/cholesterol (Figure 2). Lipoplexes made by the dilauroyl derivative 1,2lb1 and the distearoyl analogue 1,2lb4 were devoid of activity at all charge ratios and compositions. The dipalmitoyl derivative 1,-2lb3 mediated low levels of gene expression at all +/− ratios when it was combined with DOPE and DOPE and cholesterol (Figure 2B,C).

The cytotoxicity of the cationic lipids alone or in combination with DOPE and DOPE and cholesterol was tested by the MTT reduction method. All lipoplex formulations were well tolerated with cell survival greater than 75% at all different charge ratios (not shown).

Physicochemical Properties. Agarose Gel Electrophoresis. Since DNA condensation is considered a requirement for efficient in vitro internalization of lipoplexes by the cells, techniques that provide information about lipid−DNA interaction are useful tools to provide insight about the mechanism of transfection. One such technique is agarose gel electrophoresis, in which lipoplexes are subjected to an electric field and the electrostatic and hydrophobic interactions of cationic

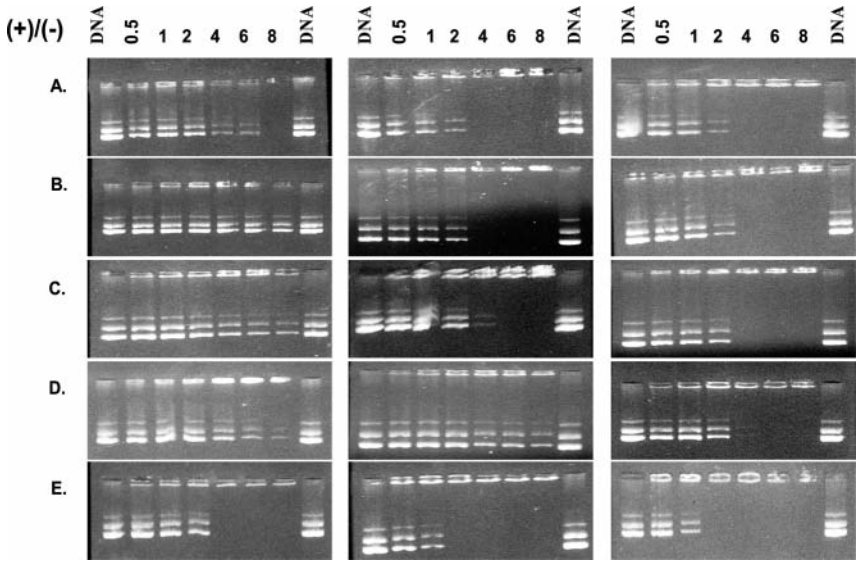

Figure 3. Gel retardation assay (from left to right): (A) 1,2lb1, 1,2lb1/d, 1,2lb1/d/ch; (B) 1,2lb2, 1,2lb2/d, 1,2lb2/d/ch; (C) 1,2lb3, 1,2lb3/d, 1,2lb3/d/ch; (D) 1,2lb4, 1,2lb4/d, 1,2lb4/d/ch; (E) 1,2lb5, 1,2lb5/d, 1,2lb5/d/ch. All gels were repeated at least once. Details of the assay are as described in Materials and Methods.

lipids with DNA can be evaluated from the migration pattern of the plasmid DNA. Electrophoretic migration of molecules is dependent on both molecular charge and size. Thus, retardation of plasmid DNA on agarose gel can occur because of its encapsulation by cationic lipids or because of charge neutralization and compaction to small particles. Plasmid DNA compaction by cationic lipids is ordinarily accompanied by ethidium bromide exclusion yielding DNA bands of reduced intensity. This is the basis for differentiating compacted DNA from encapsulated DNA that has precipitated in the slots of the gel.

Figure 3 illustrates the effect of bivalent cationic lipids on plasmid DNA electrophoretic migration. In the absence of helper lipids only the dioleoyl derivative 1,2lb5 promoted complete DNA retardation at charge ratios relevant to those used in the transfection experiments (Figure 3E, left lane). The results suggest that lack of activity of lipoplexes composed of saturated cationic lipids is due to their extremely weak interaction with the plasmid DNA. Moreover, the complete retardation of plasmid DNA promoted by 1,2lb5 at charge ratios of >2 suggests that the higher levels of gene expression observed at the highest charge ratio (Figure 2A) is due to a larger population of DNA associated with the lipid or due to a greater degree of plasmid condensation induced by the cationic lipid.

The presence of DOPE in the formulations greatly facilitated association of plasmid DNA with the cationic lipids. The sole exception was the distearoyl derivative 1,2lb4, where DOPE had no effect (Figure 3D, middle lane). The binding profiles of 1,2lb1/d and 1,2lb2/d were similar with a full retention of the plasmid in the slots of the gel occurring at +/− ratio of ≥4. The results are in agreement with the high transfection activity of the 1,2lb2/d and 1,2lb2/d/ch, but they contradict the lack of activity of the 1,2lb1 formulated with DOPE and DOPE and cholesterol. The binding efficiency of the dipalmitoyl derivative 1,2lb3 also increases when formulated with helper lipids (Figure 3C), and the transfection activity of these lipoplexes increases accordingly (Figure 2C). In contrast, although plasmid DNA migration is inhibited by the 1,2lb4/d/ch (Figure 3D, right lane), its transfection activity is practically zero. A similar contradiction between the gel electrophoresis and transfection activity occurred with the 1,2lb5/d and 1,2lb5/d/ch. Although the binding efficiency of the cationic lipids to the DNA is increased compared to the 1,2lb5 alone, their transfection activity is reduced (Figure 2B,C).

Ethidium Bromide Displacement Assay. Another approach used to characterize lipid−DNA complexes is the EtBr displacement assay. The distinct fluorescence enhancement of intercalated EtBr allows accurate spectrofluorometric quantification of its exclusion from the double helix of plasmid DNA by cationic lipids. This method is used to determine the exact charge ratio at which cationic lipids fully displace EtBr from plasmid DNA.

Figure 4A shows that none of the cationic lipids totally displaces EtBr at charge ratios ranging from 0.5 to 2 at physiological pH and ambient temperature. In fact, the only lipid that was appreciably bound to DNA is the 1,2lb5. At a charge ratio of 2, this lipid had accomplished 66% EtBr exclusion. Fitting the experimental data into a parabolic equation as described in the methods section suggested that complete exclusion of EtBr by the 1,2lb5 analogue takes place at a +/− charge ratio equal to 2.7. This is in agreement with the agarose gel electrophoresis results that indicated that complete retention of plasmid DNA in the slots occurred at charge ratios greater than 2. Binding of cationic lipids bearing a tertiary amine as the polar headgroup was also dependent on the pH of the media. Figure 4B signifies the cooperative nature of DNA binding of the 1,2lb5 at both pH values; i.e., the binding rate increases with charge ratio exponentially. As expected, DNA binding of the lipid at pH 7.2 was more effective than at pH 8.0. Paradoxically, binding cooperativity at pH 8 was higher as signified by the higher curvature of the neutralization curve (Figure 4B) and the higher slope of the average binding rate in the +/− range of 0.2−1.2 (Figure 4C). Specifically, at a +/− charge ratio of 0.2, the lipid quenched 4.2% of the total fluorescence at pH 7.2 as opposed to only 0.87% fluorescence quenching at pH 8.0. The average rate difference at the two pH values was 4.9. At a +/− ratio equal to 2, the lipid quenched 66.4% of the total fluorescence at pH 7.2 as opposed to 43.0% fluorescence quenching at pH 8.0, thus reducing the rate difference between the two pH values to 1.5. To explain the higher curvature of the plasmid DNA binding curve at pH 8, one has to account for the

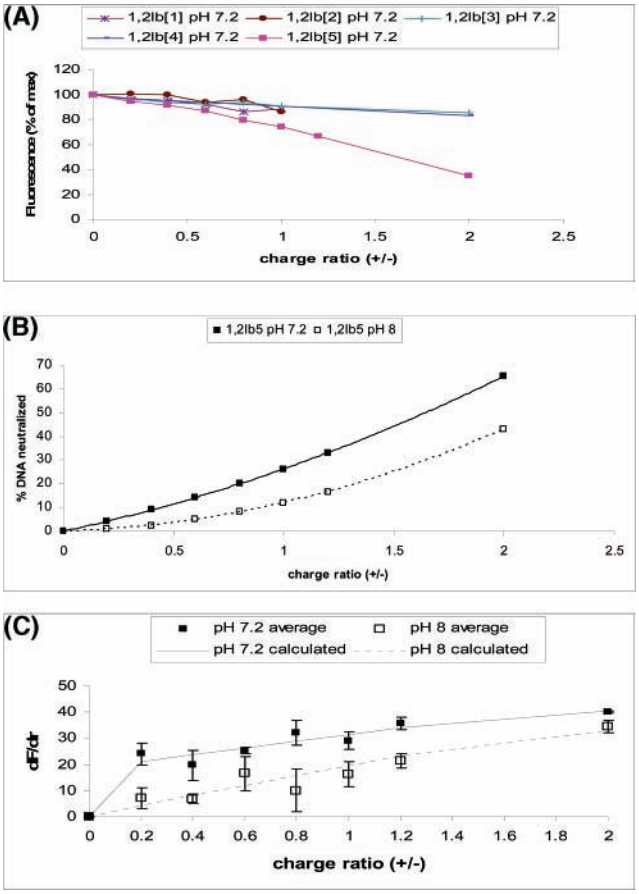

Figure 4. (A, B) Titration of plasmid DNA with cationic lipids in the presence of ethidium bromide. Fluorescence is reported relative to the fluorescence in the absence of cationic lipids, after subtracting the baseline of ethidium bromide alone, for each of the buffer conditions examined. (C) The noncumulative average rates d*F*/d*r* were calculated from the data shown in (B), as described in Methods.

forces responsible for EtBr exclusion. The main two forces that play a major role in plasmid DNA condensation by cationic lipids are the electrostatic and hydrophobic ones. Electrostatic forces are long range and are responsible for the initial approach of the cationic lipids to the DNA. Neutralization of the negative charges of the double helix causes its collapse and its compaction to a random coil configuration identified in our case with EtBr displacement. The collapse of the double helix is accompanied by a reduction of the water of hydration; a condition that encourages the cationic lipids to surround the plasmid DNA in greater numbers and pack tighter around it, thus facilitating further dehydration and compaction of the DNA. It appears that the electrostatic interactions are weaker at pH 8 than at pH 7.2, whereas dehydration-mediated DNA condensation due to hydrophobic attractive interactions plays a bigger role at pH 8.

Dynamic Light Scattering. Hydration of cationic lipids in Tris buffer, pH 7.2, resulted in liposome formation of quite heterogeneous size, as indicated by the large coefficient of variation (Table 1). The size of liposomes made by 1,2lb1 and 1,2lb2 was above 1 μm, whereas dispersions made of the 1,2lb3 and 1,2lb4 had an average particle size of 0.5 μm. Upon addition of DNA, the diameter of all the complexes composed of saturated cationic lipids increased, with the only exception being the complex made of the dioleoyl derivative 1,2lb5. The results of the particle size distribution suggest that, in agreement with the gel electrophoresis and the EtBr displacement assay, saturated cationic lipids failed to electrostatically interact and effectively condense the plasmid DNA. In addition, the results verify the dependence of DNA binding on the pH. The very big particle size of the 1,2lb5−DNA complex measured at pH 8, as opposed to the compact particle of the complex at pH 7.2, validates the results obtained from the EtBr displacement assay and suggests that at pH 8, the lipid is loosely associated with plasmid DNA mainly through hydrophobic forces.

Table 1. Summary of Particle Size Distribution of Lipid Dispersions and Lipoplexes at a +/− Charge Ratio Equal to 2

	pH	mean diameter ± SD (nm)	coefficient of variation	macroscopic appearance
		Particle Size Distribution of Cationic Lipid Dispersions[a]		
1,2lb1	7.2	5698 ± 5800	1.018	turbid
1,2lb2	7.2	990 ± 704	0.712	turbid
1,2lb3	7.2	488 ± 352	0.723	slightly turbid/ aggregates
1,2lb4	7.2	326 ± 215	0.663	slightly turbid
1,2lb5	7.2	429 ± 330	0.771	clear solution
1,2lb5	8.0	573 ± 295	0.516	clear solution
		Particle Size Distribution of Lipid−DNA Complexes[b]		
1,2lb1	7.2	3363 ± 3869	1.151	clear solution
1,2lb2	7.2	1620 ± 1211	0.748	aggregates
1,2lb3	7.2	3561 ± 3349	0.941	clear solution
1,2lb4	7.2	980 ± 881	0.899	clear solution
1,2lb5	7.2	368 ± 160	0.436	clear solution
1,2lb5	8.0	15096 ± 22201	1.471	clear solution

[a] All of the lipid concentrations are 1.5 mM. [b] All of the lipid concentrations are 0.1 mM.

Monolayer Studies. Studies performed on spread monolayer at the air−water interface enabled investigation of surface properties of the novel cationic lipids. Cationic lipids 12lb1 and 1,2lb5 exist at liquid-expanded phases at both 23 and 37 °C, exhibiting almost identical monolayer collapse areas and pressures at corresponding temperatures (Figure 5 and Table 2). Contrary to the 1,-2lb1 and 1,2lb5, 1,2lb2 monolayers were at a liquid condensed state at high compressions at 23 °C while monolayers of this lipid displayed an all-liquid expanded behavior at 37 °C, as indicated by the absence of a phase transition in the force−area isotherm of the 1,2lb monolayers and its larger mean molecular area at 37 °C (Table 2).

Monolayers composed of the 1,2lb3 derivative were at liquid expanded states at low surface pressures and at liquid condensed phases at high surface pressures, at both temperatures. The distearoyl derivative 1,2lb4 displayed only liquid-condensed behavior at 23 °C as concluded by the relatively small molecular area at monolayer collapse, the high value of the compressibility modulus *K*, and the absence of any discontinuities in the Π−*A* isotherm. Isotherms of this cationic lipid at 37 °C displayed two discontinuities at two different surface pressures and mean molecular areas. The first discontinuity was centered at the mean molecular area and surface pressure of approximately 93 Å^2 and 10 mN/m, respectively, while the second one occurred at smaller molecular dimensions (63 Å^2) and higher compression forces (18 mN/m). Although the exact nature of these two transitions is not known, it is possible that the lower pressure transition is related to the merging of several lipid islets (2D micelles on the interface) into a more uniform surface, whereas the discontinuity that occurred at higher pressure represents an L_1-to-L_2 phase transition. Nevertheless, the small average cross-sectional molecular areas (Table 2) of this lipid at monolayer

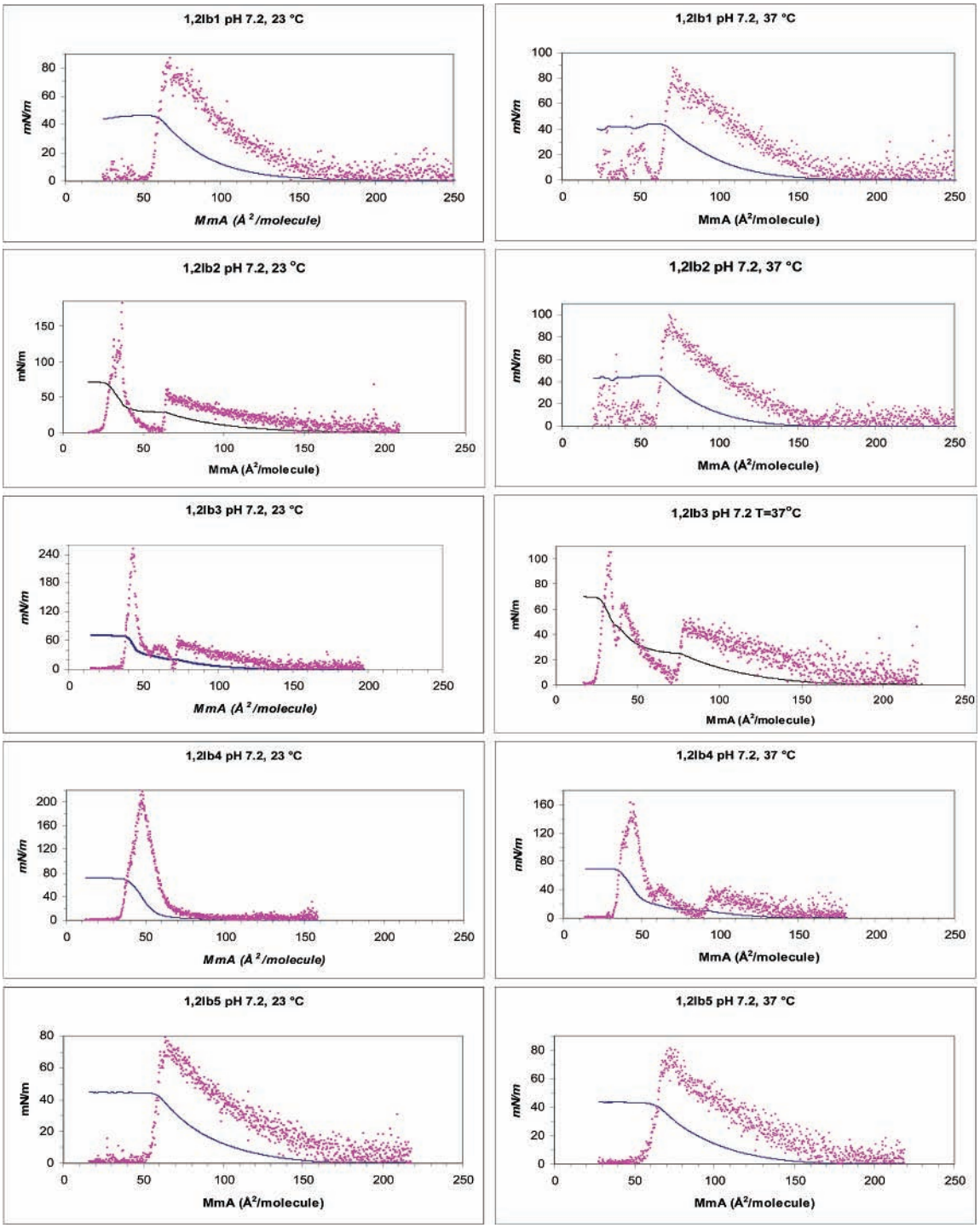

Figure 5. Representative compression isotherms of 1,2lb cationic lipids spread on 40 mM Tris buffer, pH 7.2, at 23 °C (left) and 37 °C (right). Line represents the Π−*A* isotherm, while dots represent calculated *K*−*A* isotherm.

collapse argue in favor of a compact assembly of the 1,-2lb4 at both temperatures.

Fluorescence Anisotropy Studies. As shown in Figure 6, the nature and length of the acyl chain affected the dependence of fluorescence anisotropy of cationic lipid/DPH dispersions on the temperature profoundly. All lipids exhibited one or more inflections in their profile with the exception of dioleoyl derivative 1,2lb5, suggesting that this monounsaturated derivative existed at the liquid crystalline state within the temperature range studied in agreement with the monolayer studies (Figures 5 and 6). For the DPPC, a phase transition temperature of 41.3 °C was obtained that agrees well with literature values (*16*). Not surprisingly, the phase transition of DPPC was strikingly sharp compared to the much broader phase transitions of the other saturated cationic lipids. Specifically, the temperature span of the DPPC phase transition was only 1 °C, compared to approximately 18, 38, 44, and 36 °C for 1,2lb1, 1,2lb2, 1,2lb3, and 1,2lb4, respectively. The larger temperature span of the transition signifies the uncooperative nature of the phase transition of cationic lipids compared to the highly cooperative gel-to-liquid crystalline phase transition of DPPC.

As shown in Table 3, the midpoint of the phase transition temperature for 1,2lb1 was found to be equal

Table 2. Monolayer Parameters of 1,2lb Series[a]

	mean molecular area (Å^2)		Πc (mN/m)		K (mN/m)		dΠ/dA		phase state[c]	
	23 °C	37 °C	23 °C	37 °C	23 °C	37 °C	23 °C	37 °C	23 °C	37 °C
1,2lb1 (n = 4)	63.08 (2.96)	69.71 (0.93)	39.66 (1.71)	38.13 (0.28)	88.44 (4.32)	86.30 (5.04)	1.34 (0.12)	1.22 (0.06)	L_1	L_1
1,2lb2 (n = 4)	39.5 (1.64) 68.6[b] (4.08)	63.59 (1.96)	59.05 (2.7) 28.25[b] (0.37)	40.64 (0.71)	121.3 (36.9)	HV	3.7 (1.0)	HV 28.25[b] (0.37)	M	L_1
1,2lb3 (n = 3)	43.48 (0.80) 91.9[b] (1.00)	40.62 (2.32) 79.4[b] (1.9)	60.77 (2.77) 12.97[b] (0.67)	57.14 (1.41) 23.45[b] (0.10)	239.49 (41.31)	92.25 (18.45)	3.62 (0.34)	2.85 (0.50)	M	M
1,2lb4 (n = 4)	47.54 (0.90)	42.84 (1.06) 63.11[b] (2.43) 92.82[b] (1.15)	41.35 (2.09)	46.04 (1.98) 17.13[b] (0.74) 9.59[b] (0.27)	211.00 (8.04)	154.13 (15.39)	4.43 (0.27)	3.59 (0.27)	L_2	M
1,2lb5 (n = 3)	64.16 (0.94)	69.00 (2.06)	38.72 (0.74)	37.42 (0.99)	84.62 (7.33)	77.82 (3.10)	1.31 (0.12)	1.08 (0.04)	L_1	L_1

[a] Measured in 40 mM Tris buffer, pH 7.2. [b] Phase transition denoted by a maximum in the dΠ/dA plot as a function of mean molecular area. [c] M denotes mixture of liquid-expanded and liquid-condensed states. L_1 denotes liquid-expanded state. L_2 denotes liquid-condensed state. HV denotes high variability.

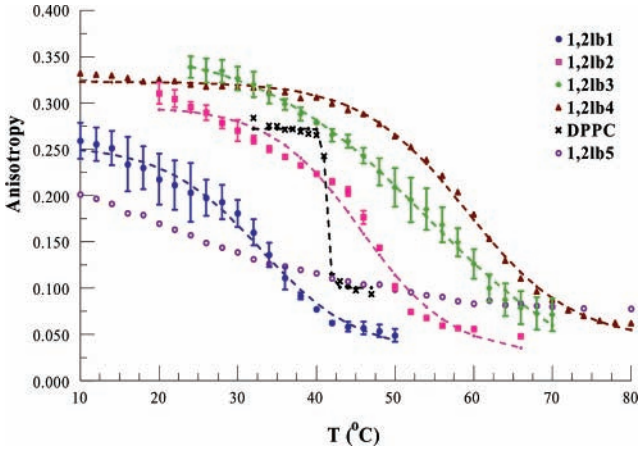

Figure 6. Fluorescence anisotropy (r) against temperature plots for cationic lipid dispersions at pH 7.2. Broken lines are the curve fits of the experimental data (symbols).

Table 3. Phase Transition Parameters of 1,2lb Lipids As Determined by Fluorescence Anisotropy

lipid	T_m (°C)	coefficient of determination[a]	T_{onset} (°C)[b]
1,2lb1	32.9	0.989	30
1,2lb2	46.5	0.983	44
1,2lb3	54.3	0.997	46
1,2lb4	59.1	0.998	48
1,2lb5	<4	ND	
DPPC	41.3	0.996	40

[a] Goodness-of-fit statistics for T_m were assessed within a 95% confidence interval. [b] Onset transition temperature values were determined from Figure 7.

to 32.9 °C. However, as shown in Figure 5, compression isotherms of 1,2lb1 indicated an all-liquid expanded state of this lipid at 23 °C. Similar to the 1,2lb1, the compression isotherm of 1,2lb2 monolayers indicated the liquid expanded state of this lipid at 37 °C, contrary to the anisotropy experiments that indicated a fluid phase of this lipid existing above 44 °C. This monolayer−bilayer inconsistency of the short-chain derivatives appeared to start breaking down with the dipalmitoyl derivative 1,-2lb3.

In view of this inconsistency between the 2D and 3D experiments and the wide onset−offset temperature range of the phase transitions of the cationic lipids, an attempt was made to determine the onset 3D phase transition temperatures of cationic lipids from the derivative profile of the anisotropy temperature plot (Figure 7). The values tabulated in Table 3 are not very different from the corresponding transition midpoints and reinforce the very different behavior of the saturated cationic lipids observed in 2D monolayers as opposed to their 3D bilayers assemblies.

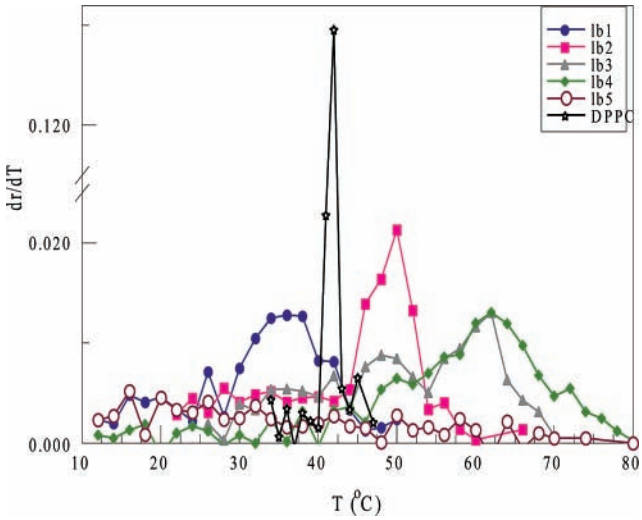

Figure 7. Derivative data of fluorescence anisotropy (r) against temperature plots for cationic lipid dispersions at pH 7.2.

DISCUSSION

The transfection activity of *N*,*N*′-diacyl-1,2-diaminopropyl-3-carbamoyl(dimethylaminoethane) amphiphilic monovalent derivatives was recently correlated with a low compressibility modulus recovered from monolayer studies (*12*). Assessment of the interfacial compressibility moduli (K) as a function of cross-sectional area has provided valuable insights into lipid in-plane elastic interactions in the past (*17*−*19*). As shown in Table 2, the liquid-condensed states of saturated cationic lipids with the exception of the 1,2lb1 were characterized with high K values at 23 °C. In sharp contrast, monolayers of the transfection potent dioleoyl derivative 1,2lb5 exhibited the lowest compressibility modulus, 84.6 mN/m, at 23 °C. Low values of the compressibility modulus are indicative of a more compressible packing state of lipid molecules with enhanced in-plane elasticity and larger mean cross-sectional average area. Interestingly, the only lipid that mediated high levels of gene expression in the absence of helper lipids was the 1,2lb5. The larger mean molecular area of 1,2lb5 allows efficient protonation of the amine headgroup and plasmid DNA charge neutralization, thus initiating the process of compaction. Increased hydration and elasticity of the 1,2lb5 help the lipid navigate through, pack nicely, and dehydrate the plasmid DNA in a cooperative fashion, thus leading to small stable lipoplex particles (Table 1).

Using the Henderson−Hasselbach equation, one could calculate the apparent pK_a of the cationic lipid under the assumption that complete neutralization of the "visible" negative charges of the plasmid DNA occurs somewhere

within the range of 80−100% of fluorescence quenching. The percent of maximum fluorescence values, at pH 7.2 and pH 8, at the lowest charge ratio where the contribution to the displacement of EtBr due to any other forces other than electrostatic ones was minimum (Figure 4 B), was applied to the equation. Interestingly, the apparent average pK_a was calculated to be in the range 6.63−6.75, which is significantly lower than the pK_a of the isolated triamine (pK_{a1} = 8.959, pK_{a2} = 9.592) (*20*). The difference between the apparent pK_a of the lipids and those of the free amine is obviously due to reduced hydration and due to the spatial dispersion of the charge of one molecule to the immediate neighbors promoted by the tight packing of the hydrophobic long acyl chains. Nevertheless, according to the calculation above, the amine polar headgroup of the 1,2lb5 is only 20−25% protonated at pH 7.2, thus implying that DNA charge neutralization would occur with 4−5 excess amount of 1,2lb5 cationic lipid. However, as mentioned in the Results section, complete EtBr exclusion from plasmid DNA occurs at a +/− charge ratio of 2.7. These two results suggest that a minimum of 32.5% contribution to DNA condensation is due to the cooperative hydrophobic forces of the acyl chains of the cationic lipid. Furthermore, the results indicate that association of plasmid DNA with the cationic lipid is extremely important, since maximum transfection activity occurred at +/− ratios high enough (+/− ratio of 4/1) to ensure association of the whole DNA population with the lipid.

It was furthermore shown that the presence of DOPE consistently reduced the transfection activity of the 1,-2lb5 (Figure 2). Although its presence increased the binding efficacy of the cationic lipid to the DNA (Figure 3), EtBr exclusion assay indicated that this increased association did not lead to increased compaction (Figure 4A). DOPE has been shown before to adversely affect the in vivo performance of cationic lipids (*21*, *22*) but never the in vitro transfection activity, especially in the absence of serum proteins. The values of the compressibility modulus of the 1,2lb1 at 23 and 37 °C were also low: 88.4 and 86.3 mN/m, respectively. Nonetheless, lipoplexes composed of 1,2lb1 failed to induce marker gene expression. A possible reason for the lack of activity of the dilauroyl derivative 1,2lb1 can be found in the early work of Minsky and co-workers (*23*). They have suggested that fatty acid chains of 12 carbons are not long enough to create the hydrophobic environment required for efficient dehydration and compaction of plasmid DNA. Another reason could be that the shorter double-chained dilauroyl derivative does not cause sufficient cell membrane perturbation to enable the DNA to gain access to the cytoplasm (*24*).

Unlike the 1,2lb5, the transfection activity of the dimyristoyl derivative 1,2lb2 has increased tremendously in the presence of DOPE. This increase was correlated with an enhanced association of this lipid with plasmid DNA in the presence of DOPE, as verified by gel electrophoresis (Figure 3) and EtBr exclusion assay (Figure 4A). Perhaps the presence of DOPE increased the hydration and fluid properties of 1,2lb2 vesicles, thus increasing its binding to plasmid DNA and cell surfaces.

The discontinuity present in the compression isotherm, the small mean molecular area, and the high surface pressure of 1,2lb2 at monolayer collapse suggest that this lipid exists at a liquid condensed state at 23 °C (Figure 5). The large "lift off" areas (150−220 Å^2), however, imply that this lipid exists at an extremely expanded spread state at low compressions, contrary to the corresponding *N*,*N*′-dimyristoyl-1,2-diaminopropyl-3-carbamoyl(dimethylaminoethane) monovalent derivative (*12*). In fact, all 1,2lb derivatives had large "lift off" areas compared to their monovalent counterparts (*12*). It appears that the presence of the branched symmetric diamine imposes steric hindrance and prevents close lipid apposition at low surface pressures. At high compressions, the headgroup steric barrier is overcome; thus, all monovalent and bivalent analogues but the shorter chain 1,2lb1 (R = 12C) have similar mean molecular dimensions at monolayer collapse.

The increased two-plane elasticity of the transfection incompetent 1,2lb1 derivative prompted investigation of the physical properties of cationic lipids in bilayer assemblies. Surprisingly, fluorescence anisotropy studies demonstrated that vesicles made of saturated shorter chain 1,2lb derivatives, i.e., 1,2lb1 and 1,2lb2, behave very differently from the corresponding monolayer surfaces (Figure 6, Table 3). Extreme caution needs to be exercised when correlating the liquid expanded properties measured in lipid monolayers with fluid properties of lipid dispersion.

In summary, it has been shown repeatedly in the past that the exterior of lipoplexes is predominantly composed of cationic lipid alone (*25, 26*). There have been many attempts in the past to relate physicochemical properties of cationic lipids in isolation with transfection potency in an effort to derive meaningful structure−activity relationships (*27*). Several of the physicochemical properties that were found to play a role in the transfection activity are gel-to-liquid crystalline phase transition below 37 °C (*28*−*31*), induction of the nonbilayer H_{II} structure (*32*), and extent of lipid hydration (*33*). These parameters contain indirect information about physical properties such as hydrogen bonding and surface activity that may be relevant to the transfection activity mediated by one kind of lipid structure but not by another. For example, the transfection potency of glycerol backbone monovalent cationic lipids appears to be related to their main phase transition temperature but that does not necessarily apply to polyvalent cationic lipids (*34*). The results of this investigation indicated a correlation between the transfection activity of these bivalent cationic lipids and high two-dimensional elasticity and fluidity of corresponding cationic lipid vesicles.

LITERATURE CITED

(1) Wang, D., Fischer, H., Zhang, L., Fan, P., Ding, R. X., and Dong, J. (1999) Efficient CFTR expression from AAV vectors packaged with promoters—the second generation. *Gene Ther. 6*, 667−675.

(2) Lowenstein, R. P. (2002) Immunology of viral-vector-mediated gene transfer into the brain: an evolutionary and developmental perspective. *Trends Immunol. 23*, 23−30.

(3) Nishikawa, M., and Huang, L. (2001) Nonviral vectors in the new millennium: delivery barriers in gene transfer. *Hum. Gene Ther. 20*, 861−870.

(4) Pedroso de Lima, M. C., Simoes, S., Pires, P., Fanesa, H., and Duzgunes, N. (2001) Cationic lipid−DNA complexes in gene delivery: from biophysics to biological applications. *Adv. Drug Delivery Rev. 47*, 277−294.

(5) Maurer, N., Fenske, D. B., and Cullis, P. R. (2001) Developments in liposomal drug delivery systems. *Expert Opin. Biol. Ther. 1*, 1−25.

(6) Ziady, A. G., Davis, P. B., and Konstan, M. W. (2003) Nonviral gene transfer therapy for cystic fibrosis. *Expert Opin. Biol. Ther. 3*, 449−458.

(7) Rochlitz, C. F. (2001) Gene therapy of cancer. *Swiss Med. Wkly 131*, 4−9.

(8) Sheikh, M., Feig, J., Savva, M. (2003) In vitro lipofection with novel series of symmetric 1,3-dialkoylamidopropane-

based cationic surfactants containing single primary and tertiary amine polar head groups. *Chem. Phys. Lipids 124*, 49−61.
(9) Savva, M., Aljaberi, A., Feig, J., Stolz, B. D. (2005) Correlation of the physicochemical properties of symmetric 1,3-dialkoylamidopropane-based cationic lipids containing single primary and tertiary amine polar head groups with in vitro transfection activity. *Colloids Surf., B 43*, 43−56.
(10) Kupchan, S. M., Bondensson, G., and Davies, A. P. (1971) Tumor inhibitors. 70. Structure−cytotoxicity relationships among *N*-acyltriamines related to solapalmitine. *J. Med. Chem. 15*, 65−68.
(11) Sunamoto, J., Goto, M., Iwamoto, K., Kondo, H., Sato, T. (1990) Synthesis and characterization of 1,2-dimyristoylamido-1,2-deoxyphosphatidylcholine as an artificial boundary lipid. *Biochim. Biophys. Acta 1024*, 209−219.
(12) Aljaberi, A., Chen, P., and Savva, M. (2005) Synthesis, in vitro transfection activity and physicochemical characterization of novel *N*,*N*′-diacyl-1,2-diaminopropyl-3-carbamoyl-(dimethylaminoethane) amphiphilic derivatives. *Chem. Phys. Lipids 133*, 135−149.
(13) Xu, Y., and Szoka, F. C., Jr. (1996) Mechanism of DNA release from cationic liposome/DNA complexes used in cell transfection. *Biochemistry 35*, 5616−5623.
(14) Sorgi, F. L., Bhattacharaya, S., Huang, L. (1997) Protamine enhances lipid-mediated gene transfer. *Gene Ther. 4*, 961−968.
(15) Ramstedt, B., and Slotte, J. P. (1999) Interaction of cholesterol with sphingomyelins and acyl-chain-matched phosphatidylcholines: a comparative study of the effect of the chain length. *Biophys. J. 76*, 908−915.
(16) Savva, M., and Huang, L. (1999) Effect of peg homopolymer and grafted amphiphilic peg-palmityl on the thermotropic phase behavior of 1,2-dipalmitoyl-sn-glycero-3-phosphocholine bilayer. *J. Lipid Res. 9*, 357−366.
(17) Smaby, J. M., Kulkarni, V. S., Momsen, M., and Brown, R. E. (1996) The interfacial elastic packing interactions of galactosylceramides, sphingomyelins, and phosphatidylcholines. *Biophys. J. 70*, 868−877.
(18) Li, X.-M., Smaby, J. M., Momsen, M. M., Brockman, H. L., and Brown, R. E. (2000) Sphingomyelin interfacial behavior: the impact of changing acyl chain composition. *Biophys. J. 78*, 1921−1931.
(19) Holopainen, J. M., Brockman, H. L., Brown, R. E., and Kinnunen, P. K. J. (2001) Interfacial interactions of ceramide with dimyristoylphosphatidylcholine: impact of the *N*-acyl chain. *Biophys. J. 80*, 765−775.
(20) Yperman, J., Mullens, J., Françols, J.-P., and Van Poucke, L. C. (1982) Calorimetric and potentiometric investigation of diethylenetriamine and its *N*-methyl-substituted derivatives in aqueous solution. *J. Phys. Chem. 86*, 298−303.
(21) Sakurai, F., Nishioka, T., Saito, H., Baba, T., Okuda, A., Matsumoto, O., Taga, T., Yamashita, F., Takakura, Y., Hashida, M. (2001) Interaction between DNA−cationic liposome complexes and erythrocytes is an important factor in systemic gene transfer via the intravenous route in mice: the role of the neutral helper lipid. *Gene Ther. 8*, 677−686.
(22) Laxmi, A. A., Vijayalakshmi, P., Kaimal, T. N. B., Chaudhuri, A., Ramadas, Y., and Rao, N. M. (2001) Novel non-glycerol-based cytofectins with lactic acid-derived head groups. *Biochem. Biophys. Res. Commun. 289*, 1063−1066.
(23) Ghirlando, R., Wachtel, E. J., Arad, T., and Minsky, A. (1992) DNA packaging induced by micellar aggregates: a novel in vitro DNA condensation system. *Biochemistry 31*, 7110−7119.
(24) Mui, B., Ahkong, Q. F., Chow, L., Hope, M. J. (2000) Membrane perturbation and the mechanism of lipid-mediated transfer of DNA into cells. *Biochim. Biophys. Acta 1467*, 281−292.
(25) Oberle, V., Bakowsky, U., Zuhom, S. I., and Hoekstra, D. (2000) Lipoplex formation under equilibrium conditions reveals a three-step mechanism. *Biophys. J. 79*, 1447−1454.
(26) Hubner, S., Battersby, B. J., Grimm, R., and Cevc, G. (1999) Lipid−DNA complex formation: reorganization and rupture of lipid vesicles in the presence of DNA as observed by cryoelectron microscopy. *Biophys. J. 76*, 3158−3166.
(27) Niculescu-Duvaz, D., Heyes, J., and Springer, C. J. (2003) Structure−activity relationship in cationic lipid mediated gene transfection. *Curr. Med. Chem. 10*, 1233−1261.
(28) Felgner, P. L., Gadek, T. R., Holm, M., Roman, R., Chan, H. W., Wenz, M., Northrop, J. P., Ringold, G. M., Danielsen, M. (1987) Lipofection: a highly efficient, lipid-mediated DNA-transfection procedure. *Proc. Natl. Acad. Sci. U.S.A. 84*, 7413−7417.
(29) Leventis, R., Silvius, J. R. (1990) Interactions of mammalian cells with lipid dispersions containing novel metabolizable cationic amphiphiles. *Biochim. Biophys. Acta 1023*, 124−132.
(30) Akao, T., Osaki, T., Ito, A., Kunitake, T. (1991) Correlation between physicochemical characteristics of synthetic cationic amphiphiles and their DNA transfection ability. *Bull. Chem. Soc. Jpn. 64*, 3677−3681.
(31) Wang, J., Guo, X., Xu, Y., Barron, L., and Szoka, F. C., Jr. (1998) Synthesis and characterization of long alkyl acyl carnitine esters. Potentially biodegradable cationic lipids for use in gene delivery. *J. Med. Chem. 41*, 2207−2215.
(32) Gaucheron, J., Wong, T., Wong, K. F., Maurer, N., and Cullis, P. R. (2002) Synthesis and properties of novel tetraalkyl cationic lipids. *Bioconjugate Chem. 13*, 671−675.
(33) Bennett, M. J., Aberle, A. M., Balsubramaniam, R. P., Malone, J. G., Malone, R. W., and Nantz, M. H. (1997) Cationic lipid-mediated gene delivery to murine lung: correlation of lipid hydration with in vivo transfection activity. *J. Med. Chem. 40*, 4069−4078.
(34) Pitard, B., Aguerre, O., Airiau, M., Lachages, A.-M., Boukhnikachvilli, T., Byk, G., Dubertret, C., Herviou, C., Scherman, D., Mayaux, J.-F., and Crouzet, J. (1997) Virus-sized self-assembling lamellar complexes between plasmid DNA and cationic micelles promote gene transfer. *Proc. Natl. Acad. Sci. U.S.A. 94*, 14412−14417.

BC050138C

Preparation and Evaluation of Thiol-Modified Gelatin Nanoparticles for Intracellular DNA Delivery in Response to Glutathione

Sushma Kommareddy and Mansoor Amiji*

Department of Pharmaceutical Sciences, School of Pharmacy, Northeastern University, 110 Mugar Life Sciences Building, Boston, Massachusetts 02115. Received May 20, 2005; Revised Manuscript Received August 18, 2005

To enhance the intracellular delivery potential of plasmid DNA using nonviral vectors, we have developed thiolated gelatin nanoparticles that can release the payload in the highly reducing environment, such as in response to glutathione. Thiolated gelatin was synthesized by covalent modification of the primary amino groups of Type B gelatin using 2-iminothiolane (Traut's reagent). The degree of thiolation of the polymers ranged from 0 to 43.71 mmol of reduced sulfhydryl (SH) groups when the amount of 2-iminothiolane was increased up to 100 mg per gram of the biopolymer. Cytotoxicity evaluations carried out by the formazan (MTS) assay showed that the thiolated gelatin prepared with 20 mg and 40 mg of 2-iminothiolane (SHGel-20 and SHGel-40) per gram of gelatin had comparable cell viability profile to that of the unmodified gelatin. In vitro release studies of fluorescein isothiocyanate (FITC)-labeled dextran (mol wt. 70 000 Da), when encapsulated in gelatin and thiolated gelatin nanoparticles (150−250 nm in diameter), was found to be affected by the presence of glutathione (GSH) in the medium. The presence of GSH was found to enhance the release by about 40% in case of thiolated gelatin and about 20% in gelatin nanoparticles under similar conditions of temperature and GSH concentrations. Qualitative and quantitative analysis of transfection in NIH-3T3 murine fibroblast cells by the nanoparticles carrying plasmid DNA encoding for enhanced green fluorescent protein (EGFP-N1) was done by fluorescence confocal microscopy and fluorescence-activated cell sorting (FACS). Qualitative results showed highly efficient expression of GFP that remained stable for up to 96 h. Quantitative results from FACS showed that the thiolated gelatin nanoparticles (SHGel-20) were significantly more effective in transfecting NIH-3T3 cells than other carrier systems examined. The results of this study show that thiolated gelatin nanoparticles would serve as a biocompatible intracellular delivery system that can release the payload in a highly reducing environment.

INTRODUCTION

In recent years, there has been an enormous interest in ex vivo and in vivo gene therapy approaches, which necessitates the formulation of DNA into vectors for targeting a specific population of cells either locally or systemically. The gene delivery to target cells can be achieved by either viral or nonviral methods (*1*−*6*). Viral vectors, although efficient in transfection, are plagued by issues of integration with the host genome, self-replication, recombination potential, and immunogenicity. There are several reported incidents of insertional mutagenesis with viral vector administration in humans leading to serious safety concerns (*7*−*9*). Viral vectors are also relatively expensive to manufacture and have difficulties in bypassing the immune defense mechanism.

The nonviral vectors for gene delivery applications are increasingly popular owing to several advantages, such as ease of production and administration and lack of immunogenicity and mutagenesis. An ideal vector used in gene therapy needs to be inert while in circulation and release its payload at the target site resulting in an efficient transfection of the cells. The vector used should have sufficiently small size and stability, minimal aggregation in blood, and the ability to efficiently target cells. Once in the cell, the system should disassemble and release intact DNA in the supercoiled state for nuclear uptake and transcription. Cationic lipids and biodegradable polymers have been synthesized to condense DNA and promote efficient intracellular delivery (*10*). However, the design of an ideal vector is still a limiting step, and various strategies are needed for achieving effective nonviral gene therapy (*11*).

Polymeric nanoparticles offer an attractive alternative for intracellular gene delivery because of their high surface-to-volume ratio and their ability to encapsulate DNA without a precondensing step (*12*). In addition, these colloidal carriers are stable and can be prepared and modified with relative ease. Tissue- and cell-targeted polymeric nanocarriers can be obtained by attaching specific ligands such as antibodies or lectins in order to achieve site-specific delivery, and the surface can be modified with hydrophilic polymers, such as poly(ethylene glycol) (PEG), resulting in long circulating properties in the systemic circulation. Due to the small size these nanoparticles can be used to achieve tumor targeting by the enhanced permeability and retention (EPR) effect (*13*−*15*).

For the past several years, our group has been engaged in exploring the use of gelatin and modified gelatin-based nanoparticles for intracellular drug and gene delivery. The nanoparticulate carriers of gelatin have been used for efficient intracellular delivery of the encapsulated payload. Kaul and Amiji (*16*, *17*) have shown that Type-B gelatin and PEG-modified gelatin nanoparticles loaded with TMR-dextran, as a model hydrophilic macromolecule, can be used for cell trafficking (BT-20 cells). Also, from the trafficking experiments, using colloidal gold-

* Corresponding author: Tel. (617) 373−3137. Fax (617) 373-8886. E-mail: m.amiji@neu.edu.

10.1021/bc050146t CCC: $30.25 © 2005 American Chemical Society
Published on Web 09/28/2005

encapsulated gelatin nanoparticles, it was evident that nanoparticles were efficiently taken up by the cells through nonspecific endocytosis and accumulated in the perinuclear region. Furthermore, it was reported that plasmid-encapsulated gelatin and PEG-modified gelatin nanoparticles were internalized in NIH-3T3 fibroblast cells within the first 6 h of incubation, and the transfection results are quantified by flow cytometry at different time points up to 96 h (*18*). Kaul and Amiji also showed the biodistribution and tumor targeting results of gelatin and PEG-modified gelatin nanoparticles, labeled with iodine-125, upon intravenous administration in mice bearing Lewis lung carcinoma (LLC) (*19*). From the radioactivity in plasma, tumor mass, and various organs collected, it was evident that the majority of PEGylated nanoparticles were present either in the blood pool or taken up by the tumor mass and liver. The plasma and the tumor half-lives, the mean residence time, and the area-under-the-curve of the PEGylated gelatin nanoparticles were significantly higher than those for the gelatin nanoparticles. The results of this study showed that PEGylated gelatin nanoparticles do possess long circulating properties and can preferentially distribute in the tumor mass after systemic delivery (*19*). Last, it has been shown that the in vivo transgene expression in LLC tumor bearing C57BL/6J mice administered with plasmid DNA encoding β-galactosidase (pCMV-β) encapsulated in gelatin and PEG-modified gelatin nanoparticles. Qualitative and quantitative analysis has shown a significantly greater transfection efficiency with the use of PEG-modified gelatin nanoparticles following systemic administration (*20*).

It is the unique physical, chemical, and biological properties of the gelatin and its modified derivatives that make this system suitable for systemic gene delivery and other therapeutic applications (*16*, *18*, *19*, *21*−*26*). Despite numerous advantages of gelatin, it is still sometimes necessary to chemically modify the biopolymer so that it remains stable during blood circulation which can lead to efficient expression at the target site. Based on the fact that the free thiol groups can form disulfide bonds within the polymer, the added thiol groups can be used in strengthening the tertiary and quaternary protein structure. The disulfide bonds also stabilize the nanoparticles, and when they are broken, the polymer unfolds, releasing the encapsulated payload. This mechanism is environment-sensitive and is enhanced by the presence of glutathione (GSH) or other redox enzymes that are present in high concentrations in the hypoxic regions, such as the tumor cells. The cells generally contain majority of the glutathione in the cytosol and at concentrations ranging from 1 to 11 mM, while the extracellular concentration is about 1000-fold less (*27*−*29*).

On the basis of the differences in the intracellular and extracellular GSH concentrations, we hypothesize that thiolated gelatin nanoparticles will provide a unique platform for intracellular DNA delivery in response to GSH levels. In the present study, therefore, we describe the synthesis of thiolated gelatin and preparation of nanoparticulate systems for intracellular plasmid DNA delivery. Transgene expression efficiencies, using enhanced green fluorescent protein (EGFP-N1) plasmid, were examined by qualitative and quantitative analysis.

EXPERMENTAL PROCEDURES

Materials. Type-B gelatin (225 bloomstrength) with 100−115 mmol of carboxylic acid per 100 g of protein, an isoelectric point of 4.7−5.2, and an average molecular weight 40 000−50000 Da was purchased from Sigma-Aldrich (St Louis, MO). 2-Iminothiolane (Traut's reagent) and 5,5′- dithiobis(2-nitrobenzoic acid) (Ellman's reagent) were purchased from Pierce Biotechnology Inc., (Rockford, IL). CellTiter 96 AQ_{ueous} one solution cell proliferation assay was obtained from Promega Corporation (Madison, WI). Ethyl alcohol, absolute, 200 proof, 99.5% ACS reagent, was obtained from Acros Chemicals (Pittsburgh, PA). Glyoxal 40% w/v and glycine were purchased from Fisher Scientific (Fair Lawn, NJ). Poly(ethyleneimine) (PEI, M_n = 10 000 Da) and fluorescein isothiocyanate (FITC) dextran with a molecular weight 70 000 Da and degree of substitution of 0.004 mol of FITC per mole of dextran were obtained from Sigma as well. The NIH-3T3, mouse embryonic fibroblast cell line, was obtained from American Type Culture Collection (ATCC, Rockville, MD) and maintained in Dulbecco's modified Eagle medium (DMEM) with 4 mM L-glutamine, 1.5 g/L sodium bicarbonate, and 4.5 g/L glucose and supplemented with 10% fetal bovine serum and 1% each of penicillin−streptomycin, HEPES buffer, and sodium pyruvate. General purpose serum-free medium (UltraCulture) was obtained from BioWhittaker (Walkersville, MD). Lipofectin lipid transfection reagent was obtained from Invitrogen (Carlsbad, CA). All aqueous solutions and reagents were prepared in deionized distilled water from Nanopure II (Barnstead/Thermolyne, Dubuque, IA).

Synthesis and Purification of Thiolated Gelatin. Thiolated gelatin was synthesized by covalent modification of the primary amino groups of gelatin by the addition of sulfhydryl moieties, and the chemistry involved in thiolation is shown in Figure 1. For the synthesis, 1 g of gelatin was dissolved in 100 mL of deionized water and then incubated with varying amount of 2-iminothiolane hydrochloride, 20 mg (SHGel-20), 40 mg (SHGel-40), and 100 mg (SHGel-100) at room temperature for 15 h (*30*). Any unreacted 2-iminothiolane was removed by repeated dialysis against 5 mM HCl followed by 1 mM HCl solution for 24 h each. The purified thiolated gelatin was dried in vacuo and stored at −80 °C for further use.

Determination of the Degree of Thiolation. To determine the degree of thiolation, the control gelatin and thiolated gelatin derivatives were dissolved in 0.1 M sodium phosphate buffer (pH 8.0) containing 1 mM EDTA. The colorimetric reaction was carried out by mixing 500 μL of the sample solutions with 100 μL of Ellman's reagent (4 mg/mL) and 5 mL of buffer. After 15 min of reaction at room temperature, the absorbance of the solution was measured at 412 nm by Shimadzu UV160U spectrophotometer (Columbia, MD) (*31*). The degree of thiolation was calculated by extrapolating the results obtained to that of the standard curve of cysteine and expressed in terms of millimoles of free sulfhydryl groups per gram of gelatin.

Preparation of Nanoparticles. Nanoparticles of the control gelatin and thiolated gelatin derivatives were prepared by desolvation using ethanol under controlled conditions of temperature and pH as previously described (*16*). Briefly, a 1% (w/v) solution in water was prepared by dissolving 200 mg of the control or thiolated gelatin in a temperature controlled water bath at 37 °C. The pH of the resulting solution was adjusted to 7.0 with 0.2 M sodium hydroxide. Nanoparticles were formed when the solvent composition was changed from 100% water to 75 vol % hydro-alcoholic solution, upon gradual addition of ethanol, under continuous stirring conditions. The formed nanoparticles were further cross-linked with 0.1 mL of

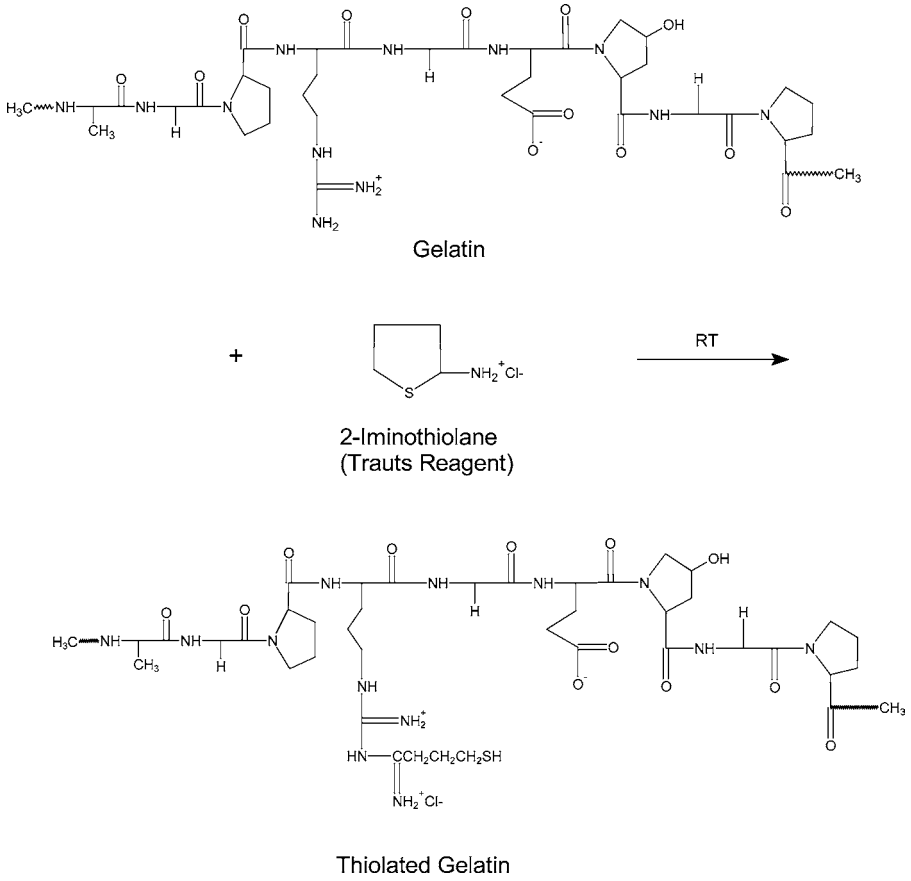

Figure 1. Schematic illustration of the synthesis of thiolated gelatin by reacting Type-B gelatin with 2-iminothiolane (Traut's Reagent).

40% (v/v) aqueous solution of glyoxal for desired time interval, and any unreacted aldehyde was quenched with 0.2 M glycine solution. The particles obtained were centrifuged either before or after cross-linking at 16 000 rpm for 30 min. The nanoparticles were washed twice with deionized distilled water and lyophilized.

Characterization of Nanoparticles. *Particle Size Analysis.* The resulting non-cross-linked and cross-linked systems of the control and thiolated gelatin nanoparticles were analyzed for mean particle size by ZetaPALS, 90Plus (Brookhaven Instruments Corporation, Holtsville, NY). The colloidal suspension of the nanoparticles was diluted with deionized distilled water, and the particle size analysis was carried out at a scattering angle of 90° and a temperature of 25 °C.

Scanning Electron Microscopy. The gelatin and thiolated gelatin nanoparticles were separated from suspension by centrifugation at 16 000 rpm for 30 min and lyophilized. The freeze-dried nanoparticles were mounted on an aluminum sample mount and sputter-coated with gold−palladium to enhance conductivity and minimize the buildup of charges. The samples were then observed for surface morphology under a Hitachi 4800 field emission scanning electron microscope.

Surface Charge Measurements. Zeta potential (ξ) measurements of the control and thiolated gelatin nanoparticles (both non-cross-linked and cross-linked systems) in suspension in deionized water were performed using a ZetaPALS (Brookhaven Instruments Corporation, Holtsville, NY). The nanoparticles were dispersed in deionized water and the zeta potential values measured at the default parameters of dielectric constant, refractive index, and viscosity of water.

Cell Viability Studies with Thiolated Gelatin. The NIH-3T3 murine fibroblast cells were grown in 96-well plates at an initial seeding density of 10 000 cells per well in 150 μL of supplemented DMEM. The cells were allowed to grow for 24 h, and the growth medium was replaced by serum free media containing gelatin and thiolated gelatins in aqueous solutions at a concentrations ranging from 0 to 200 μg/mL along with negative control (serum free media alone). PEI, a known cytotoxic cationic polymer, was used as a positive control. The cells were treated with the control and test materials for 6 h and then replaced by 20 μL of MTS along with 100 μL of culture media per well. The cells were incubated for ~2 h along with the reagent at 37 °C in a 5% CO_2 incubator, and the absorbance of the purple colored formazan product formed was measured at 490 nm with a Biotek SynergyHT plate reader (Winooski, VT). The percent viability of the cells was expressed as the ratio of absorbance of the polymer-treated cells relative to those in serum alone multiplied by 100 and plotted as a function of the polymer concentration.

Glutathione-Responsive In Vitro Release Studies. FITC-dextran of molecular weight 70 000 Da with a degree of substitution of 0.004 mol of FITC per mole of dextran was used as a model of hydrophilic macromolecular drugs. A 1.0% (w/v) solution of gelatin and thiolated gelatins (SHGel-20 and SHGel-40) in water were prepared and adjusted to pH 7.0, followed by addition of FITC-dextran at a concentration of 1.0% (w/w) to the polymer. Using this solution FITC-dextran loaded nanoparticles were prepared by desolvation process as described above. The free FITC-dextran was separated from the loaded by a series of centrifugation

and washing steps, and the loading efficiency in the nanoparticulate formulations was determined by dissolving the nanoparticles in PBS containing protease (0.2 mg/mL) at 37 °C. The resulting solution was filtered through a 0.22 μm filter, and the fluorescence intensity was measured at 490 nm excitation and 520 nm emission wavelengths, using a Biotek SynergyHT plate reader (Winooski, VT). The efficiency of FITC-dextran loading in the nanoparticle formulations was determined using a standard curve of FITC-dextran in protease-containing PBS.

The in vitro release of FITC-dextran from the nanoparticles was performed in varying concentrations of glutathione (GSH) in PBS at 37 °C and compared with the release in PBS alone. The study was carried out in PBS and 0.1, 1.0, and 5.0 mM GSH containing PBS at 37 °C. Twenty milligrams of the FITC-dextran-loaded control gelatin and thiolated gelatin nanoparticulate samples were weighed into microcentrifuge tubes with 1.5 mL of the buffer solutions. The samples were placed in a temperature-controlled bath, and 0.5 mL of the supernatant was removed at specified intervals following centrifugation at 10 000 rpm for 5 min. Sink conditions were maintained by replacing an equal volume of the release medium each time. The fluorescence intensity of the released FITC-dextran in the samples was measured using a plate reader, and the percentage of dye released was calculated from calibration curves constructed in PBS containing various concentrations of glutathione. The release studies were repeated for both cross-linked and non-cross-linked systems.

Preparation and Characterization of Plasmid DNA-Encapsulated Nanoparticles. Nanoparticles encapsulating plasmid DNA expressing enhanced green fluorescent protein (EGFP-N1) were prepared by desolvation using ethanol under controlled conditions of temperature and pH as previously described. The pH of the 1% (w/v) solution of control gelatin or thiolated gelatin (SHGel-20, SHGel-40, and SHGel-100) was adjusted to 7.0, and 1 mL of the plasmid DNA at a concentration of 1 mg/mL was added. The nanoparticles encapsulated with plasmid DNA were formed by controlled precipitation of the aqueous gelatin solution with ethanol under continuous stirring. The nanoparticles were centrifuged at 16 000 rpm for 30 min either before or after cross-linking and were analyzed for mean particle size, size distribution, and zeta potential by ZetaPALS (Brookhaven Instruments Corporation, Holtsville, NY).

DNA Encapsulation Efficiency. The pDNA-loaded nanoparticles were separated from the free pDNA by a series of centrifugation and washing steps. The loading efficiency of pDNA in the nanoparticle formulations was determined by dissolving the nanoparticle sample in protease (0.2 mg/mL)-containing PBS at 37 °C. The pDNA concentrations were estimated in solution using the PicoGreen dsDNA reagent (Molecular Probes, Eugene, OR), a one step, sensitive, fluorescent, quantitation kit for double-stranded DNA (dsDNA). The reagent was incubated with the samples for 5 min, and the fluorescence intensity was measured at 480 nm excitation and 520 nm emission wavelengths, using a Bio-Tek plate reader.

Stability of Encapsulated Plasmid DNA. The stability of the encapsulated plasmid DNA was confirmed by running the extracted DNA on precast gels. The nanoparticles were digested using protease containing PBS, diluted, and mixed with 5-fold diluted loading buffer (1×). The samples were then loaded onto 1.2% agarose gels (E-Gel, Invitrogen, Carlsbad, CA) prestained with ethidium bromide at a concentration of 100 ng/well in a 15 μL volume per well. Naked plasmid DNA and DNA encapsulated in gelatin nanoparticles were used as control and the gel was run at 65 V for 30 min using a Biorad model 200/2 power supply, and the bands were visualized using KODAK Gel logic 100 imaging system (Scientific Imaging, New Haven, CT). The process was repeated for both cross-linked and non-cross-linked nanoparticles.

In Vitro Transfection Studies. *Qualitative Analysis of Transfection.* NIH-3T3 cells, murine fibroblast cells, were grown in six-well cell culture plates containing a Corning's circular glass cover-slip with 2×10^5 cells seeded per well. The cells were grown to semi-confluence in an incubator at 37 °C and 5% CO_2 atmosphere. The plasmid DNA encapsulated non-cross-linked and cross-linked nanoparticles prepared from control gelatin, and thiolated gelatins were dispersed in serum-free medium. Twenty micrograms of EGFP-N1 plasmid DNA complexed with 20 μL of Lipofectin, a cationic lipid transfection reagent, was used as a positive control and untreated cells were used as a negative control. After filtration, the DNA-containing nanoparticle suspension was added at a concentration equivalent to 20 μg of plasmid DNA per well and incubated with the cells at 37 °C for a period of 6 h. The media was removed from each well and replaced with the DMEM. The cover slips were washed three times with sterile PBS at time intervals of 12, 24, 48, and 96 h postincubation and mounted on to microscopic slides containing a drop of fluorescence-free mounting medium (Fluoromount-G, Southern Biotech Associates, Birmingham, AL). The expression of GFP in the cells was observed by a fluorescence microscope. Differential interference contrast (DIC) and fluorescence images acquired using Olympus BX61 microscope and the digital images were processed with Adobe Photoshop software.

Quantitative Analysis of Transfection. NIH3T3 cells were grown to semi-confluence in a six-well cell culture plate and transfected with EGFP-N1 plasmid DNA encapsulated non-cross-linked and cross-linked systems of gelatin, SHGel-20, and SHGel-40 nanoparticles and compared with the Lipofectin−plasmid DNA transfected cells and cells treated with serum free media alone. The nanoparticles carrying pDNA and the Lipofectin−DNA mixture were dispersed in serum free media and added to each of the six wells at a concentration of 20 μg of plasmid DNA per well. The cells are allowed to incubate for a period of 6 h at 37 °C in a 5% CO_2 incubator and then replaced by fresh growth medium. The adherent cells are trypsinized at 12, 24, and 48, and 96 h postincubation, centrifuged, and resuspended in 0.5 mL of DMEM before fixing with 100 μL of 4% formalin buffer solution. The fluorescence of the GFP produced in the transfected a cell was detected by a Beckman Coulter (Epics/Altra) (FACS) equipped with an argon 488 laser. The FL1 channel was used to detect the cells expressing GFP fluorescence, and the results obtained were analyzed using Expo 32 software.

RESULTS AND DISCUSSION

Synthesis and Characterization of Thiolated Gelatin. The degree of thiolation was calculated by determining the number of free sulfhydryl groups using Ellman's reagent. The results obtained were extrapolated to that of the standard curve of cysteine and expressed in terms of millimoles of free sulfhydryl groups per gram of the polymer and are shown in Table 1. There was an increase

Table 1. Characterization of the Control and Thiolated Gelatin Nanoparticles

amount of iminothiolane (mg) per gram of gelatin	degree of thiolation (mM/g gelatin)	mean diameter of nanoparticles (nm)		zeta potential (mV)	
		non-cross-linked	cross-linked	non-cross-linked	cross-linked
0 mg (gelatin)	0	151.3 ± 53.8[a]	230 ± 11.5	−8.86 ± 0.78	−8.45 ± 0.45
20 mg (SHGel-20)	6.08 ± 0.7[b]	156.6 ± 60.7	244 ± 6.8	−9.09 ± 0.81	−9.36 ± 0.64
40 mg (SHGel-40)	16.41 ± 0.14	165.3 ± 45.0	232.8 ± 6.4	−9.83 ± 0.74	−11.88 ± 0.72
100 mg (SHGel-100)	43.71 ± 0.35	150.9 ± 58.4	253.7 ± 8.9	−11.97 ± 1.20	−12.98 ± 0.77

[a] Mean ± SE (n = 8). [b] Mean ± SD (n = 4).

in the degree of thiolation with increasing amounts of iminothiolane, with SHGel-20 containing 6.08 mmol/g followed by SHGel-40 (16.4 mmol/g) and SHGel-100 (43.7 mmol/g). The increasing amounts of iminothiolane resulted in an increase in thiolation at the free amino groups present on gelatin.

Preparation and Characterization of the Control and Thiolated Gelatin Nanoparticles. The nanoparticles prepared by desolvation were characterized for particle size and zeta potential. The average size and surface charge of the particles prepared from thiolated gelatins with different degrees of thiolation are listed in Table 1. The mean particle size for both non-cross-linked control and thiolated gelatin nanoparticles was found to be around 150 nm and that of cross-linked nanoparticles at 200 nm. The net charge on the gelatin nanoparticles was found to be negative, and there was no significant difference in the values between the cross-linked and non-cross-linked nanoparticles. The control gelatin nanoparticles were found to have a zeta potential value of −8.86 mV as compared to the −11.97 mV for the thiolated gelatin (SHGel-100) nanoparticles. The slight difference in zeta potential values between control and thiolated gelatin nanoparticles could be due to the fact that a hydrochloride salt of 2-iminothiolane was used. The surface presence of chloride ions would result in the nanoparticles having a greater negative zeta potential value with increasing amount of 2-iminothiolane used. The net negative charge on the surface adds to the stability of these colloidal particles. On the basis of these results, we find that the solvent exchange method can still be used to make nanoparticles from thiolated gelatin with different degrees of thiolation. Also, from these studies, we find that there was no significant difference in the particle size of the formed nanoparticles between gelatin and thiolated gelatin. Cross-linking of the nanoparticles did increase the size, probably due to disulfide bridging of two or more nanoparticles. Lastly, the surface charge on nanoparticles was also not affected by the degree of thiolation.

SEM images shown in Figure 2 reveal the surface morphology and spherical shape of the control and thiolated gelatin nanoparticles. The actual diameter of the nanoparticles observed by SEM was around 200 nm and was found to be similar to the values obtained by measurements based on light scattering. From the studies of Jain and co-workers, it is known that molecular size is one of the key determinants of vascular transport in tumors and that tumor vessels are permeable and have pores with a cutoff size of around 400−600 nm. Therefore, the thiolated gelatin nanoparticles with a mean particle size of around 200 nm would be effective in delivering DNA to solid tumors in vivo.

The in vitro toxicity studies of the control and thiolated gelatins were conducted by MTS assay with NIH3T3 cells. The percent viability of the polymer-treated cells was compared with PEI (mol wt 10 kDa), a known cytotoxic DNA-condensing gene carrier, as a positive control. The results of the cell viability profile as seen in

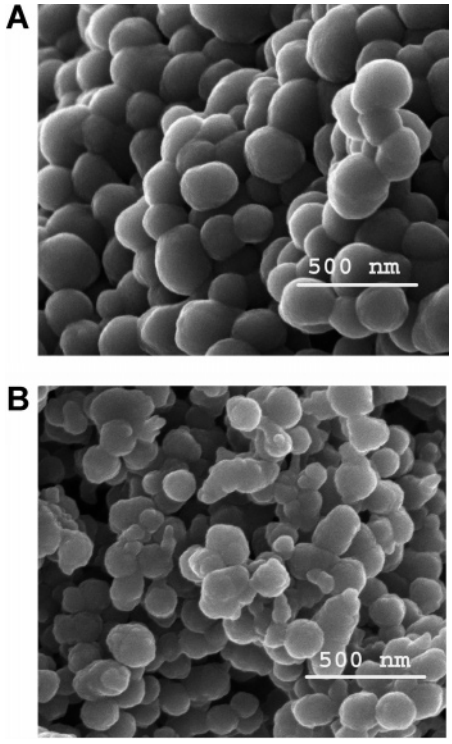

Figure 2. Scanning electron micrographs of non-cross-linked gelatin (A) and thiolated gelatin nanoparticles prepared by reacting 20 mg of 2-iminothiolane per gram of gelatin (SHGel-20) (B).

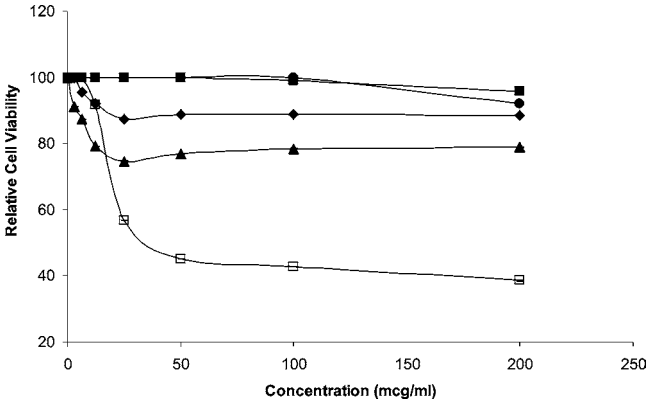

Figure 3. Cytotoxicity profiles of the control gelatin (■), and thiolated gelatin prepared with 20 mg of 2-iminothiolane (SHGel-20) (●), 40 mg of 2-iminothiolane (SHGel-40) (◆), and 100 mg of 2-iminothiolane (SHGel-100) (▲) per gram of gelatin. Poly(ethyleneimine) (mol wt 10 000 Da) (□) was used as a positive control. The relative cell viability was determined in NIH-3T3 murine fibroblast cells by the MTS assay and plotted against the polymer concentration in aqueous solution at 37 °C.

Figure 3 indicate that gelatin was highly biocompatible and nontoxic showing 100% viability at all concentrations tested. At the highest concentration of 200 μg/mL, SHGel-20 showed 92% viability, SHGel-40 showed 88%, and SHGel-100 showed 79% relative cell viability. Increase in the amount of 2-iminothiolane used in thiolation did

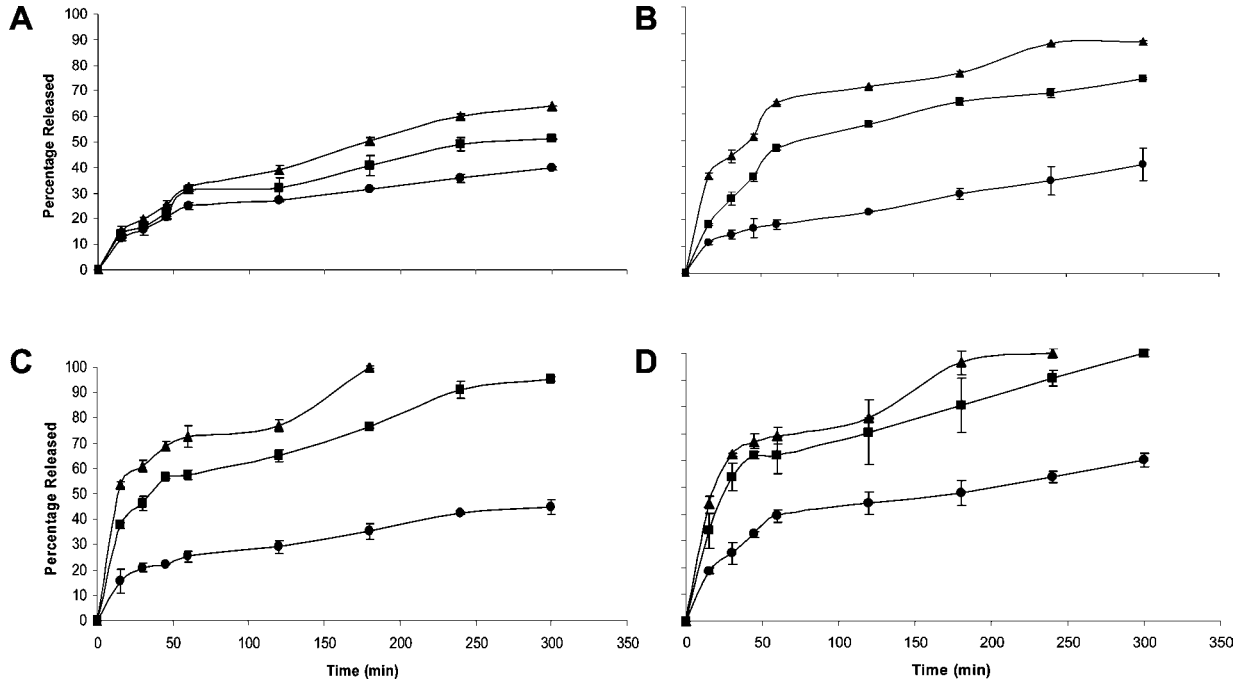

Figure 4. Release profile of fluorescein isothiocyanate-labeled dextran (mol wt 70 000 Da) from non-cross-linked nanoparticles of control gelatin (●) and thiolated gelatin prepared with 20 mg of 2-iminothiolane (SHGel-20) (■) and 40 mg of 2-iminothiolane (SHGel-40) (▲) in phosphate-buffered saline (PBS, pH 7.4) (A) and in the presence of increasing glutathione (GSH) concentrations: 0.1 mM GSH (B), 1.0 mM GSH (C), and 5.0 mM GSH (D) containing PBS at 37 °C.

result in an increase in the cytotoxicity that has been observed from the relative cell viability profiles. Based on these cytotoxicity results, further studies were carried out with SHGel-20 and SHGel-40 nanoparticles only.

In Vitro Release of FITC-Dextran in Response to Glutathione. Fluorescein isothiocyanate-conjugated dextran (FITC-dextran) was used as a model for hydrophilic macromolecular drugs, as it can be encapsulated into nanoparticles by a simple process, impermeable to cellular membranes unless taken up by endocytosis and can be easily visualized under a florescence microscope. In addition, unlike other fluorophores such as rhodamine, the fluorescence of FITC is not affected by the presence of high glutathione concentration in solution. The loading efficiency was determined using FITC-dextran at a concentration of 1.0% w/w to that of the polymer. The non-cross-linked systems had a loading efficiency of 86.7% in case of nanoparticles prepared from gelatin followed by SHGel-20 and SHGel-40 with a loading efficiency of 91.9% and 99.7%, respectively. A similar trend was observed in loading efficiencies of cross-linked systems with gelatin nanoparticles having 84.6% followed by SHGel-20 with 86.1% and SHGel-40 with 99.6%.

The in vitro release of FITC-dextran from the nanoparticles was performed in the presence of varying concentrations of GSH, which was included in the release medium to evaluate its nonenzymatic reducing action on the thiolated gelatin nanoparticles versus control gelatin nanoparticles. Also, we were interested in determining differences in the release behavior between non-cross-linked and cross-linked systems. As seen in Figures 4 and 5, the release of FITC-dextran from the non-cross-linked nanoparticles was significantly greater than from the cross-linked nanoparticles both in the presence and absence of glutathione in the release medium. The release from the thiolated gelatin nanoparticles was found to be faster in the presence of 5 mM GSH than in 1.0 mM GSH or 0.1 mM GSH containing PBS or PBS alone. In 5 mM GSH-containing PBS, the SHGel-20 nanoparticles released 100% of the payload content from the non-cross-linked and 73.6% from the cross-linked system within 5 h. Similar results were obtained from SHGel-40 were 100% and 74% of FITC-dextran released from non-cross-linked and cross-linked nanoparticles in a span of 4 h, with cross-linked nanoparticles releasing up to 87.8% of their payload in 5 h. The presence of GSH was found to enhance the release by about 40% in case of thiolated gelatin and 20% in the case of gelatin nanoparticles. The predominant difference in the release characteristics can be attributed to the nonenzymatic reducing properties of GSH which cleaves off the disulfide bonds leaving the free thiol groups. Thus, the disulfide bonds formed within the thiolated gelatins could be used for achieving rapid release system in a highly reducing environment.

Plasmid DNA Encapsulation in the Control and Thiolated Gelatin Nanoparticles. Nanoparticles encapsulating plasmid DNA expressing green fluorescent protein (pEGFP-N1) were prepared by desolvation using ethanol under controlled conditions of temperature and pH. The particles formed were harvested either before or after cross-linking and were characterized for particle size and zeta potential. Both the cross-linked and non-cross-linked nanoparticles encapsulated with plasmid DNA were found to have mean particle size similar to that of the empty nanoparticles, with non-cross-linked control and thiolated gelatin nanoparticles around 150 nm and that of cross-linked nanoparticles at 200 nm. The zeta potential of the plasmid DNA encapsulated nanoparticles had values ranging from −9.01 for gelatin to −11.78. The net charge was found to be negative, and there was no significant difference in the values between the cross-linked and non-cross-linked nanoparticles as well as between the empty and DNA containing nanoparticles, indicating the encapsulation rather than adsorption of DNA on the surface of the particles.

The loading capacity and efficiency of plasmid DNA in the nanoparticle formulations was determined using a standard curve of DNA in protease-containing PBS. The results as seen in Figure 6 indicate that cross-linking of gelatin does not affect the loading capacity of the nano-

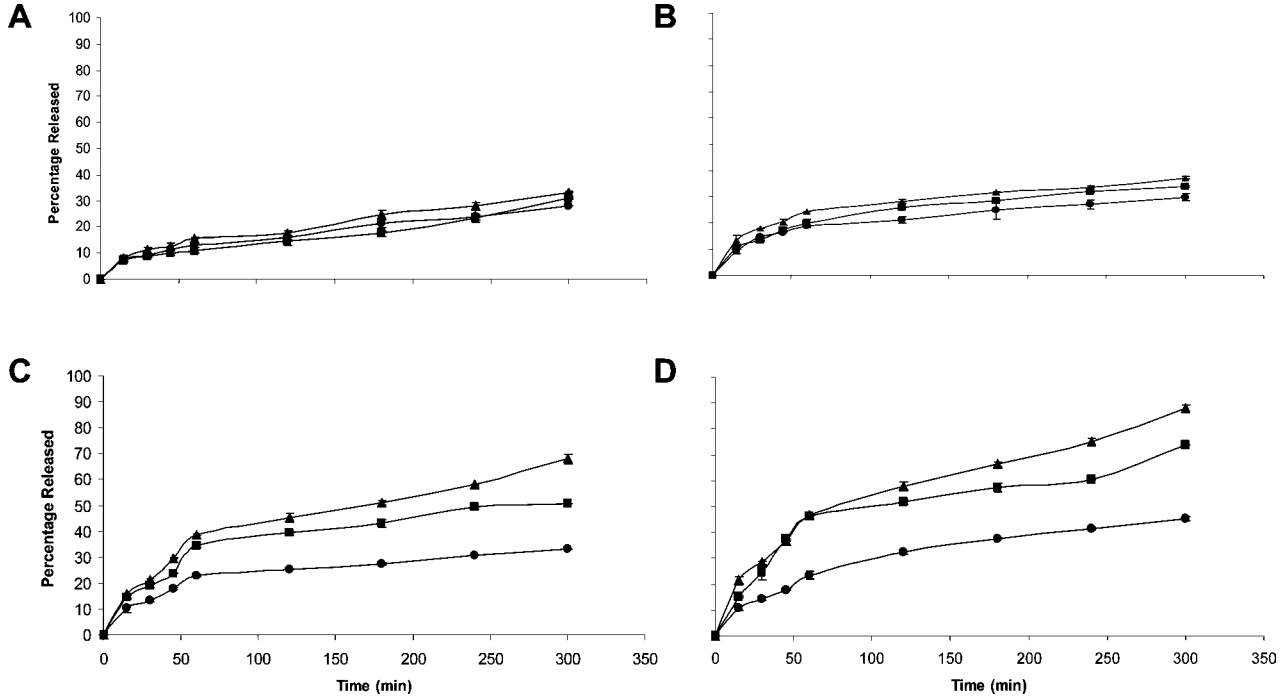

Figure 5. Release profile of fluorescein isothiocyanate-labeled dextran (mol wt 70 000 Da) from cross-linked nanoparticles of control gelatin (●) and thiolated gelatin prepared with 20 mg of 2-iminothiolane (SHGel-20) (■) and 40 mg of 2-iminothiolane (SHGel-40) (▲) in phosphate-buffered saline (PBS, pH 7.4) (A) increasing glutathione (GSH) concentrations: 0.1 mM GSH (B), 1.0 mM GSH (C), and 5.0 mM GSH (D) containing PBS at 37 °C.

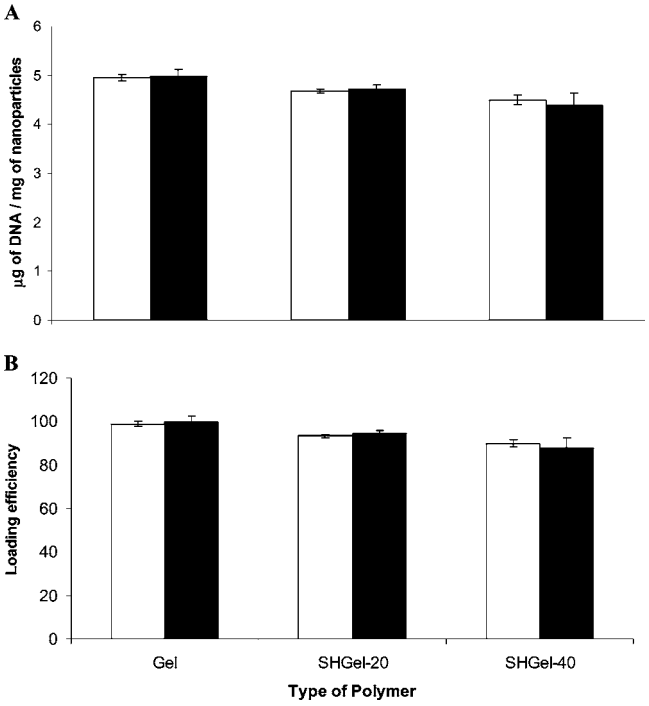

Figure 6. The encapsulation of plasmid DNA encoding for enhanced green fluorescent protein (EGFP-N1) in control gelatin and thiolated gelatin nanoparticles. Loading studies of pDNA (pEGFP-N1) from non-cross-linked (□) and cross-linked (■) nanoparticles prepared using control gelatin and thiolated gelatin prepared with 20 mg of 2-iminothiolane (SHGel-20) and 40 mg of 2-iminothiolane (SHGel-40) per gram of gelatin. The DNA encapsulation was expressed in terms of capacity as μg of DNA loaded per mg of nanoparticles (A) and efficiency as percent encapsulated (B). DNA encapsulation was determined by digesting the nanoparticles in the presence of 0.2 mg/mL protease-containing in phosphate buffered saline at 37 °C.

particulate systems. The gelatin nanoparticles had a loading efficiency of 99% as compared to SHGel-20, which had the loading efficiency of 94%, and SHGel-40, which had the loading efficiency of 90%. The slight decrease in DNA loading with an increase in the degree of thiolation could be explained by the fact that DNA is negatively charged, and with increase in the negative charge of the thiolated gelatin there was a slight decrease in encapsulation efficiency which could be attributed to electrostatic repulsion.

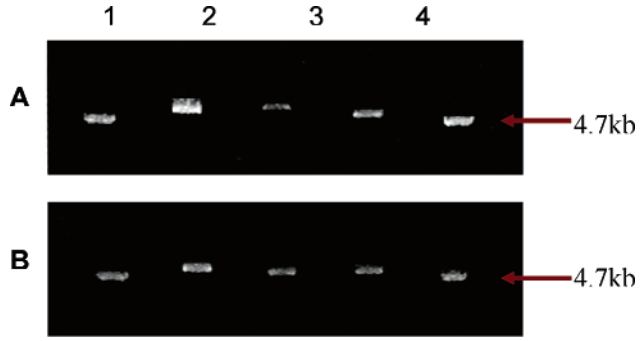

Figure 7. Stability of encapsulated plasmid DNA encoding for enhanced green fluorescent protein (EGFP-N1) by agarose gel electrophoresis. Gel electrophoresis of DNA encapsulated in non-cross-linked (A) and cross-linked (B) nanoparticles. Lane 1 and 5 represent naked plasmid DNA (pEGFP-N1) as a control, lane 2 is DNA band from control gelatin nanoparticles, lane 3 is DNA band from thiolated gelatin nanoparticles prepared with 20 mg of 2-iminothiolane (SHGel-20), and lane 4 is DNA band from thiolated gelatin nanoparticles prepared with 40 mg of 2-iminothiolane (SHGel-40) per gram of gelatin. For the nanoparticle systems, the encapsulated plasmid was extracted by digesting the matrix in 0.2 mg/mL protease-containing phosphate-buffered saline (pH 7.4) at 37 °C.

Stability of Encapsulated Plasmid DNA. The effect of thiolated gelatin and process parameters on the stability of DNA was detected by gel electrophoresis. The results, as seen in Figure 7, show that the plasmid DNA encapsulated in SHGel-20 and SHGel-40 are stable and are comparable to that encapsulated in gelatin nanopar-

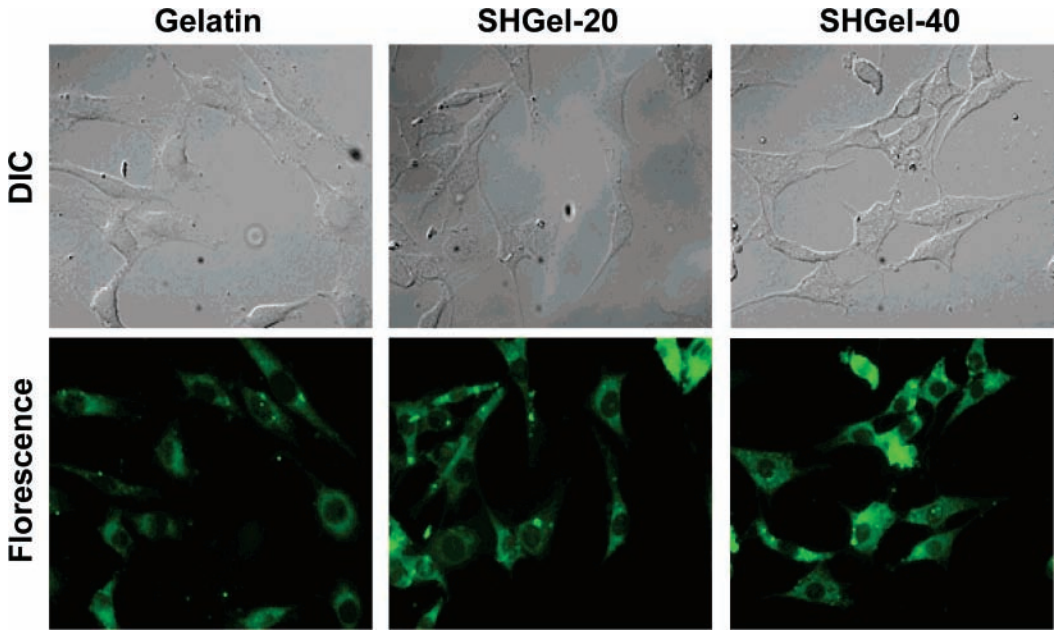

Figure 8. Qualitative evaluation of enhanced green fluorescent protein (EGFP-N1) transgene expression in NIH-3T3 murine fibroblast cells with non-cross-linked control gelatin and thiolated gelatin nanoparticles prepared with 20 mg of 2-iminothiolane (SHGel-20) and 40 mg of 2-iminothiolane (SHGel-40) per gram of gelatin. Differential interference contrast (DIC) and fluorescence confocal images of the cells were obtained after 96 h upon incubation of DNA-containing nanoparticles with the cells in culture at 37 °C.

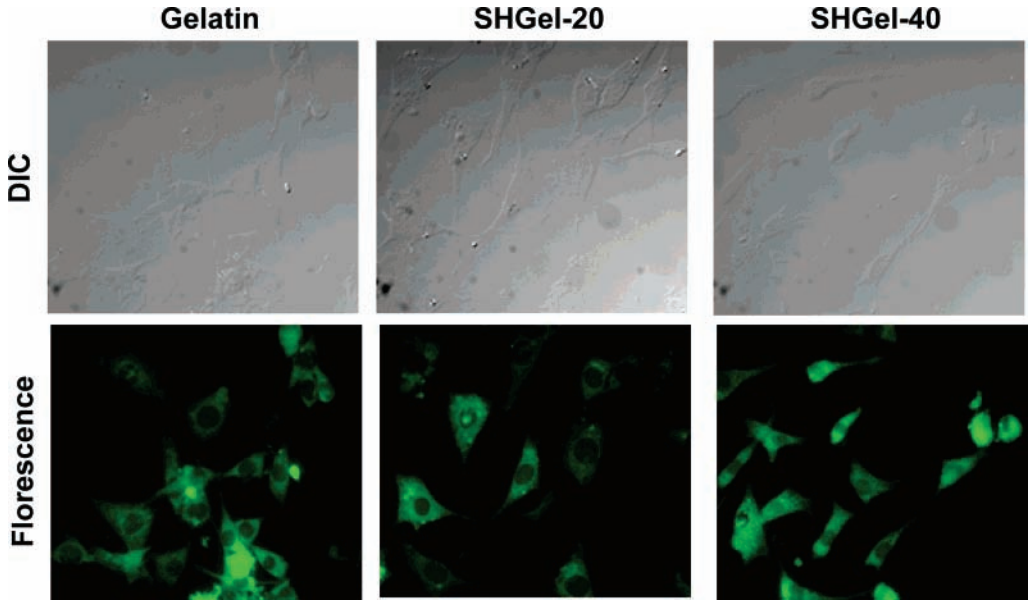

Figure 9. Qualitative evaluation of enhanced green fluorescent protein (EGFP-N1) transgene expression in NIH-3T3 murine fibroblast cells with cross-linked control gelatin and thiolated gelatin nanoparticles prepared with 20 mg of 2-iminothiolane (SHGel-20) and 40 mg of 2-iminothiolane (SHGel-40) per gram of gelatin. Differential interference contrast (DIC) and fluorescence confocal images of the cells were obtained after 96 h upon incubation of DNA-containing nanoparticles with the cells in culture at 37 °C.

ticles and naked plasmid DNA. The processes of cross-linking and protease digestion did not have any detectable effect on the DNA encapsulated and the polymers have a protective action on the plasmid.

Qualitative and Quantitative Transgene Expression Studies. The qualitative analysis of GFP expression upon transfection in NIH3T3 cells was evaluated by florescence microscopy. The Figures 8 and 9 show the DIC and fluorescence images of cells transfected with cross-linked and non-cross-linked nanoparticles prepared from the control gelatin and thiolated gelatins. The images show that the polymeric nanoparticles carrying the plasmid DNA were able to transfect the cells and the protein expression was seen as early as 6 h (data not shown) and was stable for as long as 96 h posttransfection. The fluorescence images show that these nanoparticles protect the plasmid DNA during its transport which are later taken up by the cells through the endosomal pathway and released into the cytosol. The released DNA molecules would then diffuse into the nucleus through the nuclear pores and bring about transfection of the transgene. From the results it can also be noted that cross-linking and thiolation did not affect the ability of transfection of these plasmid DNA carrying nanoparticles.

The quantitative analysis of transfection efficiency was carried out by flow cytometry. The transfection results at various time points for gelatin and the two thiolated gelatins were compared in non-cross-linked and cross-linked systems by plotting percentage of transfected cells

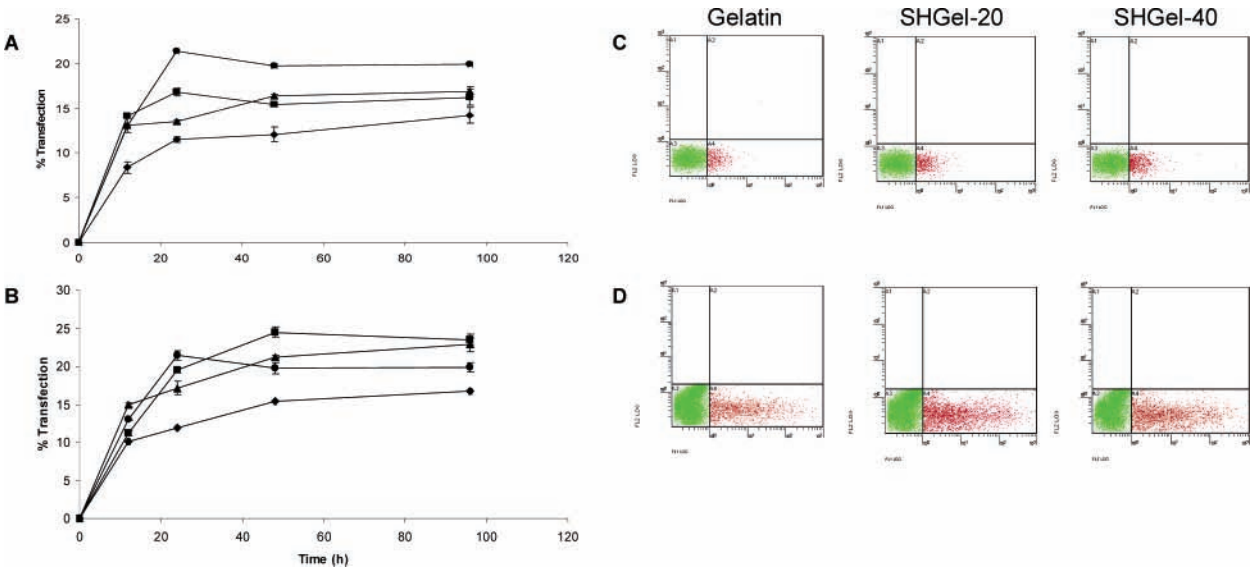

Figure 10. Quantitative evaluation of enhanced green fluorescent protein (EGFP-N1) transgene expression in NIH-3T3 murine fibroblast cells as a function of time as measured by flow cytometric analysis. Percent cell transfection with non-cross-linked (A) and cross-linked (B) nanoparticles encapsulated with EGFP-N1 plasmid DNA were prepared from control gelatin (◆), and thiolated gelatin prepared with 20 mg of 2-iminothiolane (SHGel-20) (■) and 40 mg of 2-iminothiolane (SHGel-40) (▲) per gram of gelatin. The flow cytometric scatter plots were obtained at 96 h posttransfection using non-cross-linked (C) and cross-linked nanoparticle systems (D). Plasmid DNA-complexed with Lipofectin, a commercially available cationic lipid transfection reagent was used as a control.

as a function of time as seen in the Figures 10A and 10B. The corresponding scatter plots of the transfected and normal cells at 96 h time point were represented in the form of pixels in regions A1 to A4 in Figures 10C and 10D. The transfected cells were expressed as a percentage of the total cells present in quadrants A3 and A4. Among the non-cross-linked systems the two thiolated gelatins showed better transfection than the gelatin nanoparticles but lower than the Lipofectin−pDNA-treated cells. Upon cross-linking, the SHGel-20 nanoparticles showed better transfection properties than either SHGel-40 or Lipofectin−pDNA. The results can be explained by the fact that cross-linking resulted in a stable particle, which probably provided stability to the payload in the cells by protecting it until the DNA reached the perinuclear region. In the case of SHGel-40 nanoparticles, the polymer would probably be slightly more cytotoxic than the SHGel-20 and showed lesser transfection efficiency due to its effect on cell viability. When incubated for longer periods of time the protein expressed is cytotoxic to the cells resulting in apoptosis or cell death, which led to a decrease in the percentage of transfected cells.

CONCLUSIONS

Gelatin was thiolated successfully using the 2-iminothiolane reagent, and the thiolated biopolymer was used to prepare nanoparticles by desolvation method. A well-characterized nanoparticulate system with a size of about 200 nm and negative surface charge was achieved. The in vitro release studies resulted in a significantly greater release of encapsulated macromolecular payload (FITC-dextran) from the non-cross-linked as compared to the cross-linked nanoparticles both in the presence and absence of GSH. The release from thiolated gelatin nanoparticles was enhanced in the presence of GSH-containing PBS than PBS alone. Both the non-cross-linked and cross-linked thiolated and control gelatin nanoparticles carrying the EGFP-N1 transgene were internalized by the NIH-3T3 cells, and the expression of the green fluorescent protein was observed as early as 6 h after transfection. Upon quantitative analysis, the cross-linked nanoparticles prepared from thiolated gelatin, namely the SHGel-20, was found to have greater transfection efficiency than the other nanocarriers as well as Lipofectin−pDNA complexes. The results of the study indicate that the thiolation resulted in faster release of their payload in the cells and cross-linking resulted in a particle that remains stable during its transport, and hence these cross-linked, thiolated gelatin nanoparticles could be used for rapid delivery of drugs and genes in vitro. Further, these particles can be used as vectors for systemic delivery of DNA in order to target tissues with a highly reducing environment.

ACKNOWLEDGMENT

This study was supported by a grant RO1-CA095522 from the National Cancer Institute of the National Institutes of Health. The flow cytometry studies were performed at the Forsyth Dental Institute (Boston, MA). We deeply appreciate the assistance of Dr. Jean Eastcott with the flow cytometric experiments and results interpretation.

LITERATURE CITED

(1) Lundstrom, K. (2004) Gene therapy applications of viral vectors. *Technol Cancer Res Treat. 3*, 467−477.

(2) Oga, M., Takenaga, K., Sato, Y., Nakajima, H., Koshikawa, N., Osato, K., and Sakiyama, S. (2003) Inhibition of metastatic brain tumor growth by intramuscular administration of the endostatin gene. *Int. J. Oncol. 23*, 73−79.

(3) Templeton, N. S., Lasic, D. D., Frederik, P. M., Strey, H. H., Roberts, D. D., and Pavlakis, G. N. (1997) Improved DNA: liposome complexes for increased systemic delivery and gene expression. *Nat. Biotechnol. 15*, 647−652.

(4) Chen, Q. R., Kumar, D., Stass, S. A., and Mixson, A. J. (1999) Liposomes complexed to plasmids encoding Angiostatin and endostatin inhibit breast cancer in nude mice. *Cancer Res. 59*, 3308−3312.

(5) Cusi, M. G., Terrosi, C., Savellini, G. G., Di Genova, G., Zurbriggen, R., and Correale, P. (2004) Efficient delivery of DNA to dendritic cells mediated by influenza virosomes. *Vaccine 22*, 735−739.

(6) Alvarez, D., Harder, G., Fattouh, R., Sun, J., Goncharova, S., Stampfli, M. R., Coyle, A. J., Bramson, J. L., and Jordana, M. (2005) Cutaneous antigen priming via gene gun leads to skin-selective Th2 immune-inflammatory responses. *J. Immunol. 174*, 1664−1674.

(7) Lehrman, S. (1999) Virus treatment questioned after gene therapy death. *Nature 401*, 517−518.

(8) Marshall, E. (2003) Gene therapy. Second child in French trial is found to have leukemia. *Science 299*, 320.

(9) Thomas, K. A. (1996) Vascular endothelial growth factor, a potent and selective angiogenic agent. *J. Biol. Chem. 271*, 603−606.

(10) Pack, D. W., Putnam, D., and Langer, R. (2000) Design of imidazole-containing endosomolytic biopolymers for gene delivery. *Biotechnol. Bioeng. 67*, 217−223.

(11) Blessing, T., Remy, J. S., and Behr, J. P. (1998) Monomolecular collapse of plasmid DNA into stable virus-like particles. *Proc. Natl. Acad. Sci. U.S.A. 95*, 1427−1431.

(12) Gebrekidan, S., Woo, B. H., and DeLuca, P. P. (2000) Formulation and in vitro transfection efficiency of poly (D, L-lactide-*co*-glycolide) microspheres containing plasmid DNA for gene delivery. *AAPS PharmSciTech. 1*.

(13) Maeda, H., and Matsumura, Y. (1989) Tumoritropic and lymphotropic principles of macromolecular drugs. *Crit. Rev. Ther. Drug Carrier Syst. 6*, 193−210.

(14) Maeda, H. (2001) SMANCS and polymer-conjugated macromolecular drugs: advantages in cancer chemotherapy. *Adv. Drug Delivery Rev. 46*, 169−185.

(15) Matsumura, Y., and Maeda, H. (1986) A new concept for macromolecular therapeutics in cancer chemotherapy: mechanism of tumoritropic accumulation of proteins and the antitumor agent smancs. *Cancer Res. 46*, 6387−6392.

(16) Kaul, G., and Amiji, M. (2002) Long-circulating poly(ethylene glycol)-modified gelatin nanoparticles for intracellular delivery. *Pharm. Res. 19*, 1062−1068.

(17) Kaul, G., Lee-Parsons, C., and Amiji, M. (2003) Poly(ethylene glycol)-modified gelatin nanoparticles for intracellular delivery. *Pharm. Eng. 23*, 1−5.

(18) Kaul, G., and Amiji, M. (2004) Cellular interactions and in vitro DNA transfection studies with poly(ethylene glycol)-modified gelatin nanoparticles. *J. Pharm. Sci. 94*, 184−198.

(19) Kaul, G., and Amiji, M. (2004) Biodistribution and Targeting Potential of Poly(ethylene glycol)-modified Gelatin Nanoparticles in Subcutaneous Murine Tumor Model. *J. Drug Target. 12*, 585−591.

(20) Kaul, G., and Amiji, M. (2005) Tumor-targeted delivery of plasmid DNA using poly(ethylene glycol)-modified gelatin nanoparticles: In vitro and in vivo studies. *Pharm. Res. 22*, 951−961.

(21) Zwiorek, K., Kloeckner, J., Wagner, E., and Coester, C. (2004). In vitro gene transfection with surface modified gelatin nanoparticles. In *2004 International Conference on MEMS and NANO and Smart Systems,* pp 60−63, IEEE Computer Society, Banff, Alberta, Canada.

(22) Li, J. K., Wang, N., and Wu, X. S. (1997) A novel biodegradable system based on gelatin nanoparticles and poly(lactic-*co*-glycolic acid) microspheres for protein and peptide drug delivery. *J. Pharm. Sci. 86*, 891−895.

(23) Vandervoort, J., and Ludwig, A. (2004) Preparation and evaluation of drug-loaded gelatin nanoparticles for topical ophthalmic use. *Eur. J. Pharm. Biopharm. 57*, 251−261.

(24) Cascone, M. G., Lazzeri, L., Carmignani, C., and Zhu, Z. (2002) Gelatin nanoparticles produced by a simple W/O emulsion as delivery system for methotrexate. *J Mater. Sci. Mater. Med. 13*, 523−526.

(25) Leo, E., Arletti, R., Forni, F., and Cameroni, R. (1997) General and cardiac toxicity of doxorubicin-loaded gelatin nanoparticles. *Farmaco 52*, 385−388.

(26) Leo, E., Cameroni, R., and Forni, F. (1999) Dynamic dialysis for the drug release evaluation from doxorubicin-gelatin nanoparticle conjugates. *Int. J. Pharm. 180*, 23−30.

(27) Schafer, F. Q., and Buettner, G. R. (2001) Redox environment of the cell as viewed through the redox state of the glutathione disulfide/glutathione couple. *Free Radic. Biol. Med. 30*, 1191−1212.

(28) Bulmus, V., Woodward, M., Lin, L., Murthy, N., Stayton, P., and Hoffman, A. (2003) A new pH-responsive and glutathione-reactive, endosomal membrane-disruptive polymeric carrier for intracellular delivery of biomolecular drugs. *J. Controlled Release 93*, 105−120.

(29) Miyata, K., Kakizawa, Y., Nishiyama, N., Harada, A., Yamasaki, Y., Koyama, H., and Kataoka, K. (2004) Block catiomer polyplexes with regulated densities of charge and disulfide cross-linking directed to enhance gene expression. *J. Am. Chem. Soc. 126*, 2355−2361.

(30) King, T. P., Li, Y., and Kochoumian, L. (1978) Preparation of protein conjugates via intermolecular disulfide bond formation. *Biochemistry 17*, 1499−1506.

(31) Riddles, P. W., Blakeley, R. L., and Zerner, B. (1979) Ellman's reagent: 5,5′-dithiobis(2-nitrobenzoic acid) − a reexamination. *Anal. Biochem 94*, 75−81.

BC050146T

Near-Infrared Fluorescent RGD Peptides for Optical Imaging of Integrin $\alpha_v\beta_3$ Expression in Living Mice

Zhen Cheng,[†] Yun Wu,[†] Zhengming Xiong,[†,‡] Sanjiv Sam Gambhir,[†] and Xiaoyuan Chen*[,†]

Molecular Imaging Program at Stanford (MIPS), Department of Radiology and Bio-X Program, Stanford University, California, California, 94305-5344, and Department of Pediatrics, Tongji Medical College, Huazhong University of Science and Technology & Tongji Hospital, Wuhan, China, 430030. Received June 14, 2005; Revised Manuscript Received August 25, 2005

Near-infrared fluorescence optical imaging is a powerful technique for studying diseases at the molecular level in preclinical models. We recently reported that monomeric RGD peptide c(RGDyK) conjugated to the NIR fluorescent dye specifically targets integrin receptor both in cell culture and in living subjects. In this report, Cy5.5-conjugated mono-, di-, and tetrameric RGD peptides were evaluated in a subcutaneous U87MG glioblastoma xenograft model in order to investigate the effect of multimerization of RGD peptide on integrin avidity and tumor targeting efficacy. The binding affinities of Cy5.5-conjugated RGD monomer, dimer, and tetramer for $\alpha_v\beta_3$ integrin expressed on U87MG cell surface were determined to be 42.9 ± 1.2, 27.5 ± 1.2, and 12.1 ± 1.3 nmol/L, respectively. All three peptide−dye conjugates had integrin specific uptake both in vitro and in vivo. The subcutaneous U87MG tumor can be clearly visualized with each of these three fluorescent probes. Among them, tetramer displayed highest tumor uptake and tumor-to-normal tissue ratio from 0.5 to 4 h postinjection. Tumor-to-normal tissue ratio for Cy5.5-conjugated RGD monomer, dimer, and tetramer were found to be 3.18 ± 0.16, 2.98 ± 0.05, and 3.63 ± 0.09, respectively, at 4 h postinjection. These results suggest that Cy5.5-conjugated monomeric, dimeric, and tetrameric RGD peptides are all suitable for integrin expression imaging. The multmerization of RGD peptide results in moderate improvement of imaging characteristics of the tetramer, compared to that of the monomer and dimeric counterparts.

INTRODUCTION

Near-infrared fluorescence (NIRF)[1] optical imaging is emerging as a powerful technology for studying diseases at molecular level in small animal models (*1*−*5*). Water and biological tissues have minimal absorbance and autofluorescence in the NIR window (650−900 nm), thus allowing efficient photon penetration into, and out of tissue with low intra-tissue scattering. Recent advances in the field of molecular imaging have demonstrated that this technology can be used for monitoring the biological activity of a wide variety of molecular targets such as intracellular enzymes (*6*−*10*), cell surface receptors (*11*−*16*), and antigens (*17*−*18*), as well as other targets (*19*−*20*), providing a unique opportunity to achieve insight into the biological events involved with these molecules of interest. Moreover, NIR optical imaging technology is a highly sensitive imaging modality, which does not require use of ionizing radiation or radioactive materials (*1*−*5*). It is expected that NIR optical imaging will make a significant impact in disease detection and staging, drug development, and treatment assessment.

The cell adhesion molecule integrin $\alpha_v\beta_3$ is a very important factor involved in angiogenesis and metastasis in many tumor types (*20*−*22*). It is found that $\alpha_v\beta_3$ is significantly up-regulated in activated endothelial cells and fast-growing solid tumor cells, compared to its minimum expression in quiescent blood vessels and most normal tissues (*22*, *23*). The ability to noninvasively image the integrin $\alpha_v\beta_3$ expression in living subjects would render a novel approach to diagnose tumor and its metastasis and to help to better understand tumor biology of angiogenesis, as well as to greatly facilitate the development of integrin targeted therapy. For this purpose, numerous molecular probes have been developed for imaging integrin expression using different modalities such as magnetic resonance imaging (*24*), ultrasound (*25*−*27*), optical imaging (*28*−*30*), positron emission tomography (PET) (*31*−*40*), and single-photon emission computed tomography (SPECT) (*41*−*44*).

We reported recently that NIRF dye Cy5.5-labeled monomeric arginine-glycine-aspartic acid (RGD) peptide c(RGDyK) specifically targets integrin $\alpha_v\beta_3$ both in cell culture and in living subjects (*28*). Cy5.5-c(RGDyK), however, had only moderate integrin binding affinity and thus might provide suboptimal tumor targeting efficacy. We and others found that dimeric and multimeric RGD peptides, consisting of multiple cyclic RGD monomer appropriately linked together, have significantly higher integrin avidity than the monomeric counterpart, presumably due to the polyvalency effect (*35*−*37*, *43*, *44*). It was hypothesized that the receptor binding of one RGD cyclic peptide moiety will significantly enhance the "local concentration" of the other RGD peptide moieties in the vicinity of the receptor, which may lead to a faster rate of receptor binding or a slower rate of dissociation of the oligomer from the integrin $\alpha_v\beta_3$ receptor. In this report, we evaluate the effect that multimerization of RGD

* To whom correspondence should be addressed. Phone: (650)725-0950, Fax: (650)736-7925, E-mail: shawchen@stanford.edu.
† Stanford University.
‡ Huazhong University of Science and Technology & Tongji Hospital.

[1] Abbreviations used: NIRF, near-infrared fluorescence; RGD, arginine-glycine-aspartic acid; HPLC, high-performance liquid chromatography; PET, positron emission tomography; SPECT, single-photon emission computed tomography; pi, postinjection.

10.1021/bc0501698 CCC: $30.25 © 2005 American Chemical Society
Published on Web 10/29/2005

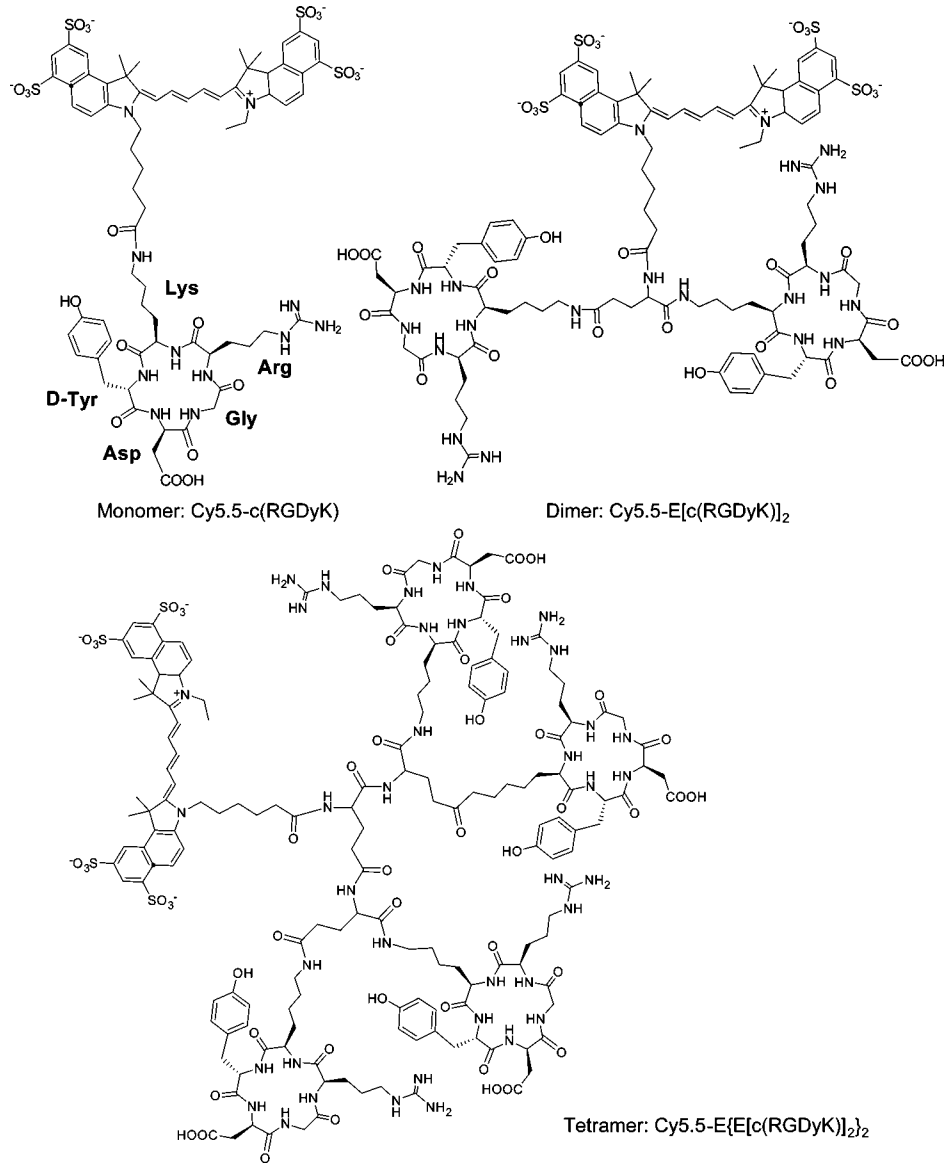

Figure 1. Schematic structures of Cy5.5-conjugated RGD monomer Cy5.5-c(RGDyK), dimer Cy5.5-E[c(RGDyK)]$_2$, and tetramer Cy5.5-E{E[c(RGDyK)]$_2$}$_2$.

peptide has on integrin binding affinity and tumor targeting efficacy in three novel NIRF probes: Cy5.5-labeled monomer c(RGDyK), dimer E[c(RGDyK)]$_2$, and tetramer E{E[c(RGDyK)]$_2$}$_2$ (structures are shown in Figure 1).

MATERIALS AND METHODS

General. All commercially available chemical reagents were used without further purification. 9-Fluorenylmethoxycarbonyl (Fmoc) amino acids and 2-chlorotrityl chloride resin were purchased from Novabiochem (San Diego, CA). Arginine and lysine were protected by the 2,2,4,6,7-pentamethyldihydrobenzofuran-5-sulfonyl (Pbf) and *tert*-butoxycarbonyl (Boc) groups, respectively, while D-tyrosine and aspartic acid were protected as a *tert*-butyl ester. Cy5.5 monofunctional *N*-hydroxysuccinimide (NHS) ester (Cy5.5-NHS) and ^{125}I-echistatin labeled by the lactoperoxidase method to a specific activity of 2000 Ci/mmol were purchased from Amersham Biosciences (Piscataway, NJ). Echistatin was purchased from Sigma (St. Louis, MO). The purification of the crude product was carried out on a semipreparative reversed-phase high-performance liquid chromatography (HPLC) system equipped with a 170U 4-Channel UV−Vis absorbance detector (Dionex Summit HPLC system, Dionex Corporation, Sunnyvale, CA) using a Vydac protein and peptide column (218TP510, 5 μm 250 × 10 mm). The flow was 5 mL/min, with the mobile phase starting from 95% solvent A (0.1% TFA in water) and 5% solvent B (0.1% TFA in acetonitrile) (0−3 min) to 35% solvent A and 65% solvent B at 33 min. The analytical HPLC method was performed with the same gradient system, but with a Vydac 218TP54 column (5 μm, 250 × 4.6 mm) and flow rate of 1 mL/min.

Peptide Synthesis. Monomeric cyclic RGD peptide c(RGDyK) (MW = 617.6) was synthesized via solution cyclization of the fully protected linear pentapeptide H-Gly-Asp(OtBu)-D-Tyr(OtBu)-Lys(Boc)-Arg(Pbf)-OH, followed by trifluoroacetic acid (TFA) deprotection (*45*). Dimeric RGD peptide, E[c(RGDyK)]$_2$, was prepared according to the literature method (*37*). The tetrameric RGD peptide E{E[c(RGDyK)]$_2$}$_2$ was obtained by coupling Boc-protected glutamic acid activated ester Boc-E(OSu)$_2$ with RGD dimer E[c(RGDyK)]$_2$ in the presence of diisopropylethylamine (DIPEA) (pH = 8.5−9) followed by semipreparative HPLC purification (*46*).

Cy5.5-RGD Conjugates Synthesis. Appropriate RGD peptide (monomer, dimer, or tetramer) (5 μmol) was dissolved in 1 mL of 0.1 M sodium borate ($Na_2B_4O_7$) buffer (pH = 8.3) and then mixed with 1.2 equiv of Cy5.5-NHS (6.7 mg, 6 μmol) in H_2O (1 mL). The reaction mixture (pH = 8.1) was incubated in the dark at 4 °C overnight and then quenched by adding 200 μL of 5% acetic acid (HOAc). The crude product was purified by a semipreparative reversed-phase HPLC and characterized by an analytical HPLC and matrix-assisted laser desorption/ionization time-of-flight mass spectrometry (MALDI-TOF-MS). α-Cyano-4-hydroxycinnamic acid (α-CHCA, prepared as 10 g/L in 33.3% CH_3CN: 33.3% EtOH: 33.3% H_2O: 0.1% TFA) was used as solid matrix. Fractions containing RGD-Cy5.5 conjugates were collected, lyophilized, redissolved in saline at a concentration of 1 mg/mL, and stored in the dark at −20 °C until use.

U87MG Glioblastoma Xenograft Model. U87MG human glioblastoma cell line was obtained from American Type Culture Collection (Manassas, VA) and was maintained at 37 °C in a humidified atmosphere containing 5% CO_2 in Iscove's modified Dulbecco's medium and 5% fetal bovine serum (Life Technologies, Inc., Grand island, NY). Animal procedures were performed according to a protocol approved by the Stanford University Administrative Panels on Laboratory Animal Care (APLAC). Female athymic nude mice (*nu*/*nu*), obtained from Charles River Laboratories, Inc. (Cambridge, MA) at 4−6 weeks of age, were injected subcutaneously in the right foreleg with 5×10^6 U87MG glioblastoma cells suspended in 100 μL of phosphate-buffered saline (PBS). The tumor bearing mice were subjected to in vivo imaging studies when the tumors reached 0.4−0.6 cm in diameter (14−21 d after implant).

Receptor Binding Assay. The $\alpha_v\beta_3$ receptor binding assay was performed to determine binding affinities of NIR fluorescent RGD conjugates. Briefly, 2×10^5 U87MG cells/well in a 96-well plate were incubated with ^{125}I-echistatin (0.06 nM) in the binding buffer [25 mM 2-amino-2-(hydroxymethyl)-1,3-propanediol, hydrochloride (Tris-HCl), pH 7.4, 150 mM NaCl, 1 mM $CaCl_2$, 0.5 mM $MgCl_2$ and 1 mM $MnCl_2$, 0.1% bovine serum albumin (BSA)] in the presence of different concentrations of Cy5.5-RGD conjugates at room temperature for 3 h. After incubation, the plate was washed three times with binding buffer, and the radioactivity was solubilized with 2 N NaOH followed by γ-counting. Nonspecific binding of ^{125}I-echistatin to $\alpha_v\beta_3$ was determined in the presence of 100 nM echistatin. The IC_{50} values were calculated by nonlinear regression analysis using the GraphPad Prism computer-fitting program (GraphPad Software, Inc., San Diego, CA). Each data point is a result of the average of triplicate wells.

Fluorescence Microscopic Studies. For fluorescence microscopic studies, 1×10^4 cells were cultured on 35 mm MatTek glass bottom culture dishes (cat. no.: P35G-0-14-C, Ashland, MA). After 24 h, the cells were washed with PBS and then incubated at 37 °C with appropriate Cy5.5-RGD conjugate (10 nM) for 30 min. Integrin specificity of the RGD-Cy5.5 conjugates in cell culture was verified by incubating U87MG cells with or without blocking dose of the nonfluorescent monomeric RGD peptide c(RGDyK) (10 μmol/L). After the incubation period, cells were washed three times with ice-cold PBS. The fluorescence signal of the cells was recorded using an Axiovert 200M fluorescence microscope (Carl Zeiss MicroImaging, Inc., Thornwood, NY) equipped with a Cy5.5 filter set (Exciter, HQ 650/20 nm; Emitter, HQ 675/35 nm). An AttoArc HBO 100W microscopic illuminator was used as a light source for fluorescence excitation. Images were taken using a thermoelectrically cooled charge-coupled device (CCD) (Micromax, model RTE/CCD-576, Princeton Instruments Inc., Trenton, NJ) and analyzed using MetaMorph Software version 6.2r4 (Molecular Devices Corporation, Downingtown, PA).

In Vivo Optical Imaging of Tumors. In vivo fluorescence imaging was performed with an IVIS 200 small animal imaging system (Xenogen, Alameda, CA). A Cy5.5 filter set was used for acquiring Cy5.5-conjugated RGD monomer, dimer, and tetramer fluorescence in vivo. Identical illumination settings (lamp voltage, filters, f/stop, field of views, binning) were used for acquiring all images, and fluorescence emission was normalized to photons per second per centimeter squared per steradian (p/s/cm^2/sr). Images were acquired and analyzed using Living Image 2.5 software (Xenogen, Alameda, CA). For the control experiment, mice ($n = 3$ for each probe) were injected via tail vein with 500 pmol Cy5.5-RGD (monomer, dimer, or tetramer) and subjected to optical imaging at various time points postinjection (pi). For the blocking experiment, mice ($n = 3$ for each probe also) were injected with the mixture of 10 mg/kg of c(RGDyK) and 500 pmol Cy5.5-conjugated RGD peptides. All NIRF images were acquired using 1 s exposure time (f/stop = 4). The mice in the control experiment were euthanized at 24 h pi. The tumor and major tissues and organs were dissected, wet weighted, and placed on black papers. The fluorescence images were acquired, and total fluorescence flux (p/s/cm^2/sr) for each sample was obtained. Aliquots with known amount of the injectates were also put on the black papers and imaged together with the samples. The results were presented as the percentage injected dose per gram (%ID/g). Values were quoted as mean ± standard deviation (SD) for a group of three animals.

Data Processing and Statistics. All the data are given as means ± SD of n independent measurements. Statistical analysis was performed using a Student's t-test. Statistical significance was assigned for P values < 0.05. For determining tumor contrast, mean fluorescence intensities of the tumor area (T) at the right foreleg of the animal and of the area (N) at the right flank (normal tissue) were calculated by the region-of-interest (ROI) function of Living Image software integrated with Igor (Wavemetrics, Lake Oswego, OR). Dividing T by N yielded the contrast between tumor tissue and normal tissue.

RESULTS

Conjugation and Purification of Cy5.5-RGD Conjugates. The synthesis of Cy5.5-RGD conjugates was achieved through conjugation of Cy5.5-NHS ester with the ϵ-amino group of the lysine residue (in the case of monomer) or glutamate amine (in the case of dimer and tetramer) of the RGD peptides. The desired products were purified by semipreparative HPLC. The purity of Cy5.5-labeled peptides were over 95% from analytical HPLC analysis. The retention times on analytical HPLC for monomer, dimer, and tetramer are found to be: 15.5, 15.8, and 16.2 min, respectively. The yields of Cy5.5-RGD conjugates were typically over 70%. The purified RGD-Cy5.5 conjugates were characterized by MALDI-TOF-MS. Cy5.5-c(RGDyK) (monomer): $m/z = 1518.4$ for $[M + H]^+$ ($C_{68}H_{83}N_{11}O_{21}S_4$, Calculated MW= 1518.7); Cy5.5-E[c(RGDyK)]$_2$ (dimer): $m/z = 2249.0$ for $[M + H]^+$ ($C_{100}H_{129}N_{21}O_{31}S_4$,calculated MW= 2249.5); Cy5.5-E{E[c(RGDfK]$_2$}$_2$ (tetramer): $m/z = 3711.8$ for $[M + H]^+$ ($C_{165}H_{222}N_{40}O_{51}S_4$, calculated MW = 3710.02); The absorption and fluores-

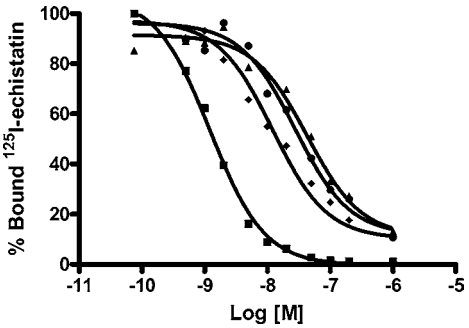

Figure 2. Competitive integrin receptor assay of unlabeled echistatin (■), monomer Cy5.5-c(RGDyK) (▲), dimer Cy5.5-E[c(RGDyK)]$_2$ (●), and tetramer Cy5.5-E{E[c(RGDyK)]$_2$}$_2$ (◆) to U87MG human glioma cells. All experiments were done in triplicate. The IC_{50} values for echistatin, Cy5.5-monomer, dimer, and tetramer were determined to be 1.2 ± 0.1, 12.1 ± 1.3, 27.5 ± 1.2, and 42.9 ± 1.2 nmol/L, respectively.

cence emission characteristics of Cy5.5-RGD conjugates were identical to those of free Cy5.5, as apparent from the spectrums measured in H_2O (data not shown).

Integrin Binding Characteristics in Vitro. The receptor binding affinity study of Cy5.5-RGD conjugates for integrin $\alpha_v\beta_3$ was carried out using $\alpha_v\beta_3$ positive U87MG cells. We compared the receptor binding affinity of the three probes by performing competitive displacement studies with ^{125}I-echistatin as radioligand (Figure 2). All the peptides inhibited the binding of ^{125}I-echistatin to U87MG cells in a dose dependent manner. The IC_{50} values for echistatin, Cy5.5-E{E[c(RGDyK)]$_2$}$_2$, Cy5.5-E[c(RGDyK)]$_2$, and Cy5.5-c(RGDyK) were 1.2 ± 0.1, 12.1 ± 1.3, 27.5 ± 1.2, and 42.9 ± 1.2 nmol/L, respectively.

To demonstrate the $\alpha_v\beta_3$ integrin specificity and subcellular localization of the Cy5.5-RGD conjugates, cyanine dye-labeled RGD peptides were incubated with U87MG tumor cells and images taken with a fluorescent microscope. Receptor-mediated endocytosis of the fluorescent dye was observed for all three RGD peptide conjugates (Figure 3 A−C) after 30 min of incubation at 37 °C as indicated by the appearance of fluorescence in the perinuclear region. Integrin receptor specificity of the Cy5.5-RGD conjugates was further demonstrated by the absence of the cell associated fluorecscence in the presence of a blocking dose of monomeric RGD peptide c(RGDyK) (1 μmol/L) (Figure 3D−F).

Imaging of U87MG Tumor in Vivo. Whole-body imaging of subcutaneous U87MG tumor xenografted mice was accomplished by using tungsten−halogen lamp light source to excite the probe at 610−665 nm wavelength and monitoring the distribution of the imaging agents with IVIS200 system equipped with a cooled charged-coupled device (CCD) camera. Figure 4A shows typical NIRF images of athymic nude mice bearing subcutaneous U87MG glioblastoma tumor after intravenous (iv) injection of 500 pmol of Cy5.5-RGD monomer, dimer, and tetramer, respectively. For all three probes, the subcutaneous U87MG tumor could be clearly visualized from the surrounding background tissue from 30 min to 24 h pi. Quantification analysis of these images was performed using software Living Image2.5. The fluorescence intensities in the tumor and the normal tissues as a function of time for monomer, dimer, and tetramer are depicted in Figure 4B−D, respectively. Monomer, dimer, and tetramer all exhibited fast tumor targeting character in vivo. The tumor uptake reached a maximum at 30 min pi and slowly washed out over time. Most importantly, at early time points (from 0.5 to 4 h) pi, both tetramer and dimer had significantly higher accumulation in tumor than monomer ($P < 0.05$). Tetramer also showed higher tumor uptake than dimer, although the difference is not significant ($P > 0.05$). The differences in tumor uptakes among the three probes were minimal at 24 h pi. The fluorescence intensity ratio between the tumor and normal tissue (*T*/*N*) for Cy5.5-conjugated RGD peptides were calculated and shown in Figure 4E. The tetramer shows significantly higher *T*/*N* value than both monomer and dimer at early time points (0.5, 1, 2, and 4 h) ($P < 0.05$). For example, *T*/*N* ratio for tetramer, dimer, and monomer are found to be 3.63 ± 0.09, 2.98 ± 0.05, and 3.18 ± 0.16, respectively, at 4 h pi, while the difference diminished at 24 h time point ($P > 0.05$). No significant difference in *T*/*N* is observed between dimeric and monomeric peptide probes ($P > 0.05$ for all time

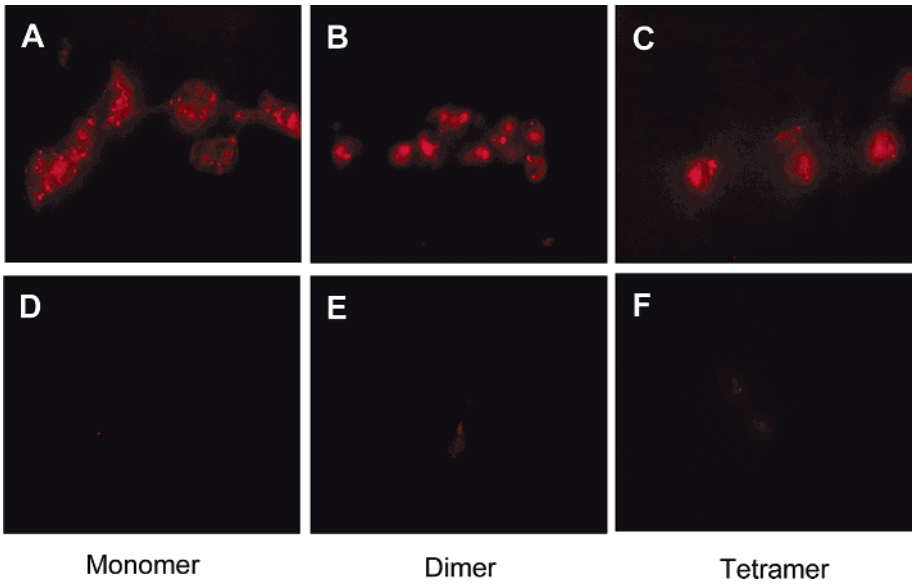

Figure 3. Specific binding and endocytosis of the Cy5.5-labeled cyclic RGD peptides. NIRF images of U87MG were obtained after the cells were incubated for 30 min at 37 °C in the presence of 10 nmol/L monomer Cy5.5-c(RGDyK), dimer Cy5.5-E[c(RGDyK)]$_2$, tetramer Cy5.5-E{E[c(RGDyK)]$_2$}$_2$ with (D, E, F) or without (A, B, C) blocking dose of nonfluorescent RGD peptide c(RGDyK) (10 μmol/L). Complete blocking of NIR fluorescence of U87MG cells demonstrating high $\alpha_v\beta_3$ integrin specificity of these NIR dye-labeled RGD peptides.

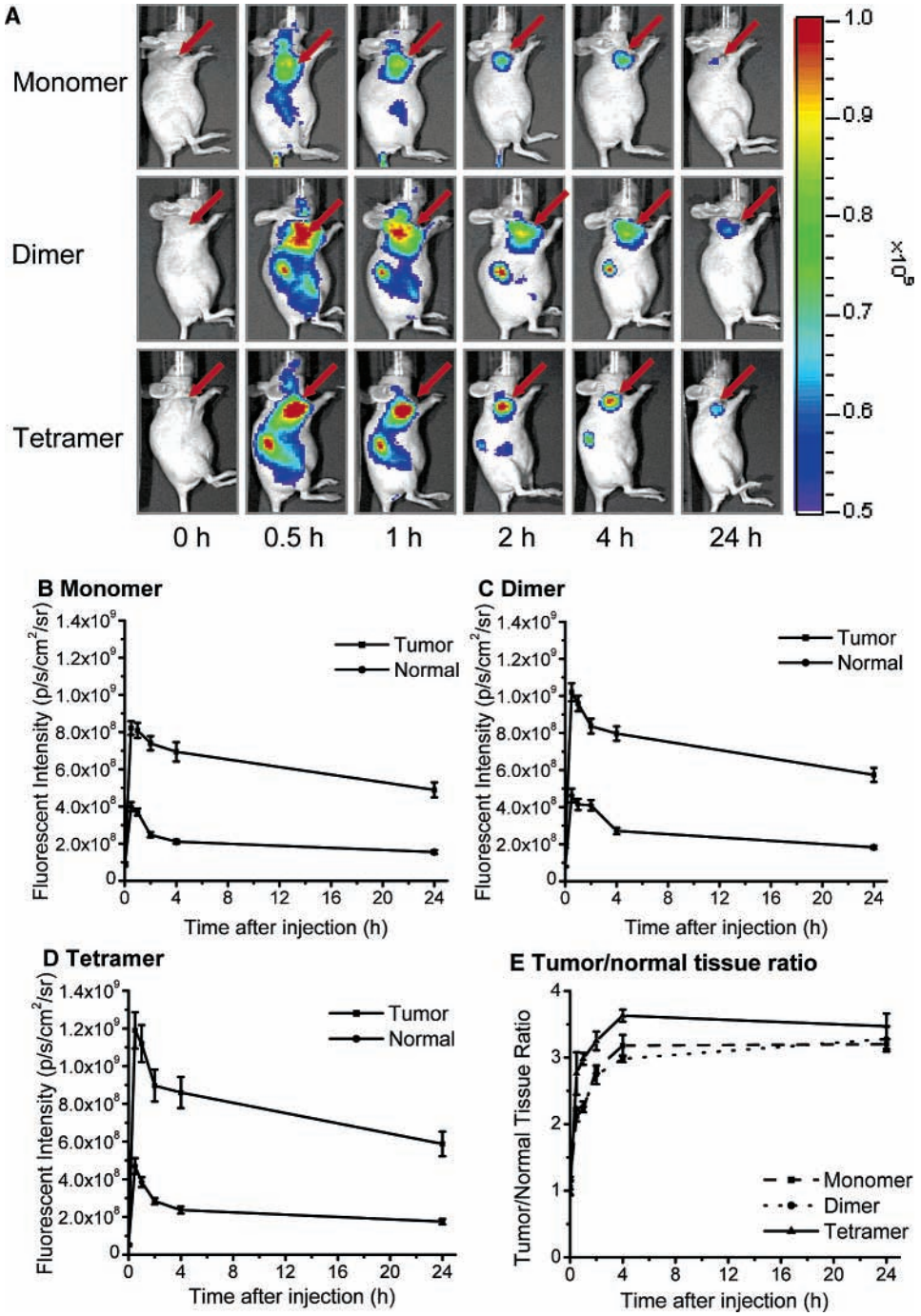

Figure 4. (A) In vivo fluorescence imaging of athymic nude mice bearing subcutaneous U87MG glioblastoma xenografts after intravenous injection of 500 pmol Cy5.5-RGD monomer, dimer, or tetramer. The location of the tumor was indicated by an arrow. Fluorescence signal from Cy5.5 was pseudo-colored red. The tetramer and dimer displayer higher tumor uptake and tumor/normal contrast than that of monomer from 0.5 to 4 h pi. (B−D) In vivo targeting characters of Cy5.5-RGD monomer, dimer, and tetramer, respectively. Both tetramer and dimer had significantly higher accumulation in tumor than monomer ($P < 0.05$) at early time points (from 0.5 to 4 h) pi. But the differences in tumor uptakes among the three probes were minimal at 24 h pi. (E) Tumor contrast (tumor-to-normal tissue ratio) as a function of time post-administration of Cy5.5-RGD monomer (■), dimer (●), and tetramer (▲). The fluorescence intensity for the region of interest was recorded as photons per second per centimeter squared per steradian (p/s/cm²/sr). The tumor contrast of Cy5.5-RGD-tetramer from 0.5 to 4 h postinjection is significantly higher than that of Cy5.5-RGD-dimer and monomer ($P < 0.05$).

points examined in this experiment). Kidneys were clearly visualized for dimeric and tetarmeric peptides, indicating that dimer and tetramer have significantly higher renal activity accumulation than the monomer.

Receptor specificities of these probes were validated by a blocking experiment. Unlabeled monomeric RGD peptide, c(RGDyK), successfully reduced tumor contrast for all three tracers (Figure 5). Tumor contrast as quantified by ROI analysis of noninvasive optical imaging indicated that the *T*/*N* was reduced from 2.22 ± 0.04 to 1.27 ± 0.05 for monomer, 2.26 ± 0.27 to 1.28 ± 0.02 for dimer, and 2.98 ± 0.09 to 1.09 ± 0.18 for tetramer, respectively.

To further characterize the distribution of RGD peptide−dye conjugates in U87MG in vivo, the tumor-bearing mice were sacrificed right after noninvasive imaging at 24 h pi. Tumors and other normal organs and tissues were removed and subjected to IVIS200 imaging

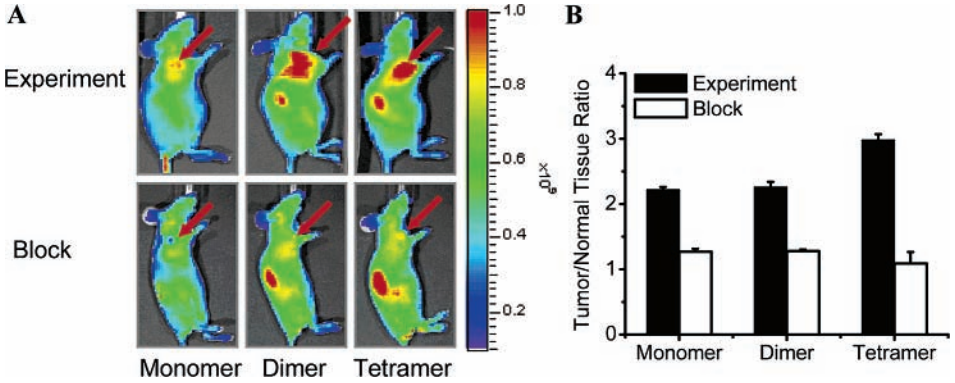

Figure 5. Representative NIRF images of mice bearing subcutaneous U87MG tumor on the right foreleg demonstrating blocking of Cy5.5-RGD conjugates (500 pmol) uptake in the tumors by coinjection with 10 mg/kg of c(RGDyK). Pseudo-color fluorescence images of tumor-bearing mice were acquired 1 h after intravenous injection of Cy5.5-RGD conjugates (experiment) or Cy5.5-RGD conjugates + c(RGDyK) (block). (B) Tumor contrast (tumor-to-normal tissue ratio) calculated from region of interest measurement at 1 h postadministration of Cy5.5-RGD conjugates.

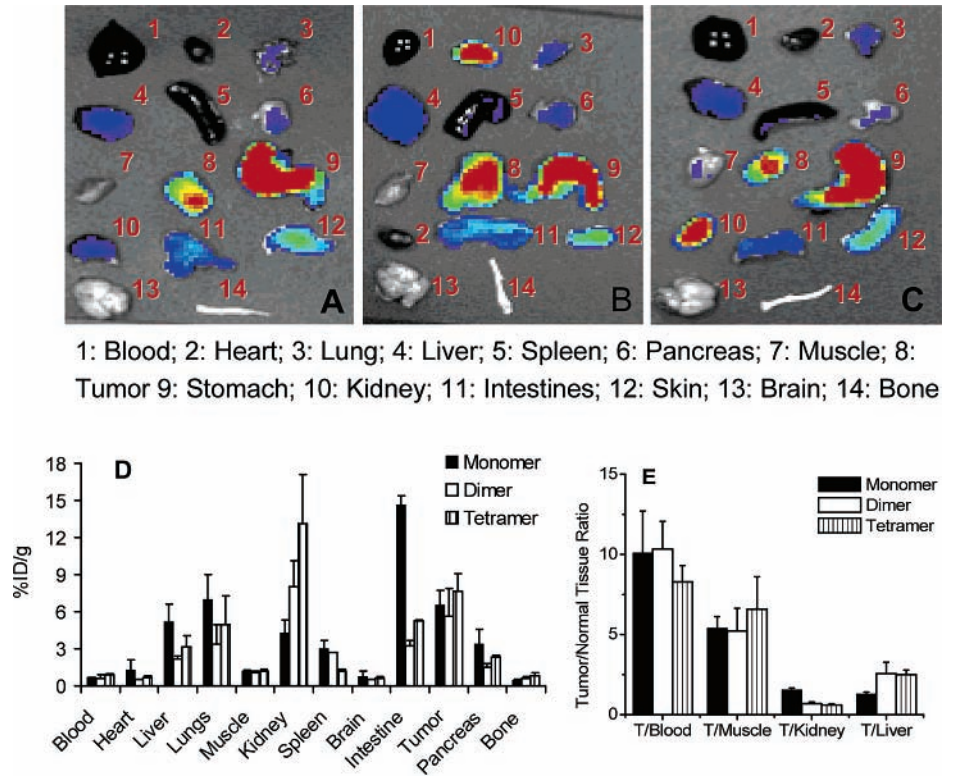

Figure 6. Representative images of dissected organs of mice bearing U87MG tumor sacrificed 24 h after intravenous injection of Cy5.5-RGD monomer (A), dimer (B), and tetramer (C) at a dose of 500 pmol per mouse. (D) Biodistribution of the probes at 24 h postinjection. (E) Tumor-to-normal organ ratios.

(Figure 6). The total fluorescence of the whole organ was obtained, and %ID/g was calculated for each organ. The biodistribution of the probes at 24 h pi is shown in the Figure 6B. Tumor-to-blood, tumor-to-muscle, tumor-to-kidney, and tumor-to-liver ratios are illustrated in Figure 6C. The renal uptake for tetramer and dimer are much higher than monomer, consistent with the imaging data obtained in living mice. The tumor accumulation and tumor/muscle and tumor/blood ratios for monomer are similar to that of dimer and tetramer. This corroborated the noninvasive imaging data obtained in living mice.

DISCUSSION

NIRF imaging, which uses neither ionizing radiation nor radioactive materials, is emerging as a complement to nuclear imaging methods. A relatively low-cost, safe, and easy-to-use NIRF imaging system has been proven to be a very powerful tool for noninvasive imaging diseases in preclinical models such as rodents (*3*). Furthermore, NIRF imaging may provide both surgical anatomy and functional/molecular information when exogenous fluorescent probes are used; thus, it has a potential in the clinical setting by allowing easy visualization and guidance in surgery (*47*). We are very interested in applying this NIRF imaging technique for studying an important molecular target integrin $\alpha_v\beta_3$, so we can better understand tumor angiogenesis and eventually develop methods for integrin-directed tumor therapy. To achieve this goal, a highly specific and sensitive NIRF agent needs to be developed first.

We have previously demonstrated that Cy5.5-labeled monomeric RGD peptide c(RGDyK) targets integrin $\alpha_v\beta_3$-expressed tumor in vivo (*28*). However, this agent only provides moderate tumor contrast in a highly integrin

positive U87MG tumor model. Cell receptor binding assay using ^{125}I-echistatin as radioligand indicated that the IC_{50} value for c(RGDyK) was approximately 50 nM. Because the cyclic pentatpeptide c(RGDyK) has already been optimized for receptor−ligand interactions (*48*), it is very unlikely that one can significantly improve receptor avidity of monomeric RGD peptide by fine-tuning of the peptide configuration. An alternative is to apply the concept of multivalency or multimerization and to develop oligomeric RGD peptide probes. In principle, the introduction of a homogeneous multimeric RGD peptide system is expected to improve integrin targeting by cooperative receptor interactions and receptor shielding to endogenous competition. We and others have previously reported that suitably labeled dimeric RGD peptide tracers had incremental improvement on tumor targeting efficiency and pharmacokinetics, compared to the monomeric RGD peptide analogues (*35*−*37*, *43*, *44*). We hypothesize that multimerization to introduce tetrameric RGD peptides might further increase the receptor binding affinity. In this study, we designed a new Cy5.5-labeled tetrameric RGD peptide with repeating c(RGDyK) units connected through glutamate linkers (Figure 1). As expected, integrin affinity followed the order of tetramer > dimer > monomer. Fluorescence microscope imaging studies also confirmed the effectiveness of all three probes for integrin positive U87MG cell staining and receptor mediated endocytosis.

We recently radiolabeled DOTA-conjugated RGD monomer, dimer, and tetramer with ^{64}Cu and compared their tumor targeting efficacy and in vivo kinetics (*33*, *37*, *46*). Tetrameric RGD peptide tracer had almost twice as much tumor uptake than the corresponding dimer. The dimer also had significantly higher tumor uptake than the monomeric counterpart. Renal and hepatic activity accumulation of tetramer was also somewhat higher than that of dimer and monomer. In agreement with these data, we observed significant ($P < 0.05$) increase of tumor fluorescence intensity for Cy5.5-conjugated tetramer and dimer, compared to the monomic analogue at early time points (from 0.5 to 4 h) pi (Figure 4). However, between tetramer and dimer, no significant difference in tumor accumulation is observed. Another important finding in this research is that tetramer demonstrated the highest *T/N* contrast from 0.5 to 4 h pi (Figure 4). This attribute is apparent from the high tumor uptake and relatively low normal tissue uptake. The monomer displayed low uptake in the tumor, but it was quickly cleared from normal tissue. This results in a moderate *T/N* contrast. For the dimer, although it showed a higher tumor uptake thanthat of the monomer, the relatively high uptake in normal tissue reduced its *T/N* contrast. We did not observe significant differences in the magnitude of tumor uptake or *T/N* contrast at 24 h after administration of the NIRF probes by which most of the tumor uptake has been cleared. Moreover, the tumor uptake of NIRF RGD peptides could be specifically inhibited by the unlabeled c(RGDyK) (Figure 5). This demonstrates that Cy5.5-conjugated monomeric, dimeric, and tetrameric RGD peptides are all specific agents for NIR fluorescence imaging of integrin expression. Overall, these data suggest that based on the highest tumor uptake and contrast at early time points pi, the tetramer appears to be the best integrin $\alpha_v\beta_3$ targeting agent among these three compounds. However, only moderate improvement was achieved through multimerization of the peptide strategy. Compared to the monomer, the tetramer only shows 1.20−1.45-fold increase in tumor accumulation and 1.08−1.30-fold increase in *T/N* ratio at different time points postinjection.

The small animal optical imaging studies above also highlight the importance of evaluation of polyvalency effects of the contrast agents in vivo. Initially we expected that higher tumor uptake, retention, and *T/N* ratio would be achieved for Cy5.5-labeled RGD multimers due to their increased binding affinities. However, although it was found that the absolute tumor uptake of Cy5.5-labeled RGD probes was generally enhanced with increasing number of RGDs in each probe, multimerization of RGD also changes the molecular size, overall molecular charge, and hydrophilicity of the resulting peptides, thus altering their in vivo pharmacokinetics and clearance from nontarget tissues. These results are consistent with the data reported in the literature (*43*, *46*). In both reports, the multlimeric RGD peptides showed significantly higher IC_{50} values in vitro and the magnitude of tumor uptake in vivo; however, the improvement of tumor-to-background ratio is marginal. Apparently, for applying the strategy of peptide multmerization extensively and efficiently, more studies are needed to investigate what the essential effects are required to improve the biodistribution and achieve greater targeting selectivity.

Fluorescence intensities of the dissected tumors and normal organs and tissues agreed well with the aforementioned in vivo observations, except that the ex vivo tumor-to-muscle ratio was substantially higher than that observed noninvasively, which might be attributed to the minimal loss of excitation and emission of light density without the need of penetration in and out of skin in addition to the scatter caused by the skin. Quantification analysis verified there were no significant differences in tumor/blood and tumor/muscle ratios for these NIRF probes at 24 h pi. Furthermore, both dimer and tetramer had much lower tumor-to-kidney ratios than the monomer, likely reflecting the more net positive charge character of the dimer and tetramer than the monomer. The membranes of the renal tabular cells contain negatively charged sites to which the positively charged groups (such as guanidines in the RGD sequence) are expected to bind. There is no significant difference in liver uptake of the three probes.

To further optimize the NIRF RGD probes, it also should carefully choose fluorescent labels itself. The emission maximum of Cy5.5 at 694 nm is at the lower limit of NIRF window. It is expected that fluorescent dyes with more red-absorbing character may provide deeper tissue penetration and thus a closer reflection of an actual distribution of the probe in vivo. Another major problem with Cy5.5 dye is the very small Stokes shift (20 nm). Development of fluorescent dyes with a large Stokes shift would provide better fluorescence detection sensitivity by eliminating the interference with the excitation source, minimizing the rejection of excitation light by the emission filter, and reducing the error by excitation light and scattered light. A good alternative to the fluorescent dyes would be quantum dots (QDs) as fluorescent biolabeling reagents. In comparison with organic fluorophores, QDs have unique optical and electronic properties, such as size- and composition-tunable fluorescence emission from visible to NIR wavelengths, a large absorption coefficient across a wide spectral range, and very high level of brightness and photostability (*49*). Because of their broad excitation profiles and narrow, symmetric emission spectra, high-quality QDs are suited for optical multiplexing. Whether conjugation of RGD peptides with novel reporter components such as fluorescent dyes with a large Stokes

shift or QDs could generate better NIRF imaging agents for integrin $\alpha_v\beta_3$ requires further investigation.

Initially we also expected that NIRF imaging using Cy5.5-labeled RGD peptides might provide the opportunity for rapid and cost-effective structure−activity studies to screen newly developed ligands, rather than the more costly radionuclide-based imaging studies such as SPECT and PET. However, this hypothesis oversimplifies the complex effect that a fairly bulky Cy 5.5 label has on the pharmacokinetics of a probe. The in vivo behavior is the combination of many factors, including, but not limited, to the receptor affinity and specificity, molecular size, overall molecular charge, hydrophilicity, and metabolic stability. Cy5.5 is a rather large chromophore with a molecular weight of ca. 1000. Tumor contrast obtained with a Cy5.5-RGD conjugate may not truly reflect the same RGD peptide labeled with a radionuclide. Additional studies to evaluate the impact of cyanine dye structure on the receptor targeting properties of RGD peptide in vivo is needed to elucidate the discrepancy between NIRF imaging and radionuclide imaging.

CONCLUSION

Cy5.5-RGD monomer, dimer, and tetramer all exhibit specific uptake in the U87MG glioblastoma both in vitro and in vivo. Among these three probes, Cy5.5-RGD tetramer displays the highest tumor uptake and tumor-to-background ratio up to 4 h postinjection and as such appears to be the most promising probe for integrin receptor NIRF imaging. However, the improvement of imaging character of tetramer is only moderate, compared to that of monomer. More research is needed to further optimize such probes.

ACKNOWLEDGMENT

This work was supported, in part, by the National Institute of Biomedical Imaging and Bioengineering (NIBIB) Grant R21 EB001785, Department of Defense (DOD) Breast Cancer Research Program (BCRP) Concept Award DAMD17-03-1-0752, DOD BCRP IDEA Award W81XWH-04-1-0697, DOD Prostate Cancer Research Program (PCRP) New Investigator Award (NIA) DAMD-1717-03-1-0143, American Lung Association California (ALAC), the Society of Nuclear Medicine Education and Research Foundation, National Cancer Institute (NCI) Small Animal Imaging Resource Program (SAIRP) grant R24 CA93862, and NCI *In Vivo* Cellular Molecular Imaging Center (ICMIC) grant P50 CA114747.

LITERATURE CITED

(1) Massoud, T. F., and Gambhir, S. S. (2003) Molecular imaging in living subjects: seeing fundamental biological processes in a new light. *Genes Dev. 17*, 545−80.

(2) Sevick-Muraca, E. M., Houston, J. P., and Gurfinkel, M. (2002) Fluorescence-enhanced, near infrared diagnostic imaging with contrast agents. *Curr. Opin. Chem. Biol. 6*, 642−50.

(3) Ntziachristos, V., Bremer, C., and Weissleder, R. (2003) Fluorescence imaging with near- infrared light: new technological advances that enable in vivo molecular imaging. *Eur. Radiol. 13*, 195−208.

(4) Tung, C. H. (2004) Fluorescent peptide probes for in vivo diagnostic imaging. *Biopolymers 76*, 391−403.

(5) Weissleder, R., and Mahmood, U. (2001) Molecular imaging. *Radiology 219*, 316−33.

(6) Weissleder, R., Tung, C. H., Mahmood, U., and Bogdanov, A., Jr. (1999) In vivo imaging of tumors with protease-activated near-infrared fluorescent probes. *Nat. Biotechnol. 17*, 375−8.

(7) Tung, C. H., Mahmood, U., Bredow, S., and Weissleder, R. (2000) In vivo imaging of proteolytic enzyme activity using a novel molecular reporter. *Cancer Res. 60*, 4953−8.

(8) Tung, C. H., Zeng, Q., Shah, K., Kim, D. E., Schellingerhout, D., and Weissleder, R. (2004) In Vivo Imaging of β-Galactosidase Activity Using Far Red Fluorescent Switch. *Cancer Res. 64*, 1579−83.

(9) Wunder, A., Tung, C. H., Muller-Ladner, U., Weissleder, R., and Mahmood, U. (2004) In vivo imaging of protease activity in arthritis: a novel approach for monitoring treatment response. *Arthritis Rheum. 50*, 2459−65.

(10) Mahmood U., and Weissleder, R. (2003) Near-Infrared Optical Imaging of Proteases in Cancer. *Mol. Cancer Ther. 2*, 489−496.

(11) Ke, S., Wen, X., Gurfinkel, M., Charnsangavej, C., Wallace, S., Sevick-Muraca, E. M., and Li, C. (2003) Near-infrared optical imaging of epidermal growth factor receptor in breast cancer xenografts. *Cancer Res. 63*, 7870−5.

(12) Moon, W. K., Lin, Y., O'Loughlin, T., Tang, Y., Kim, D. E, Weissleder, R., and Tung, C. H. (2003) Enhanced tumor detection using a folate receptor-targeted near-infrared fluorochrome conjugate. *Bioconjugate Chem. 14*, 539−45.

(13) Licha, K., Hessenius, C., Becker, A., Henklein, P., Bauer, M., Wisniewski, S., Wiedenmann, and B., Semmler, W. (2001) Synthesis, characterization, and biological properties of cyanine-labeled somatostatin analogues as receptor-targeted fluorescent probes. *Bioconjugate Chem. 12*, 44−50.

(14) Achilefu, S., Jimenez, H. N., Dorshow, R. B., Bugaj, J. E., Webb, E. G., Wilhelm, R. R., Rajagopalan, R., Johler, J., and Erion, J. L. (2002) Synthesis, in vitro receptor binding, and in vivo evaluation of fluorescein and carbocyanine peptide-based optical contrast agents. *J. Med. Chem. 45*, 2003−15.

(15) Achilefu, S., Dorshow, R. B., Bugaj, J. E., and Rajagopalan, R. (2000) Novel receptor-targeted fluorescent contrast agents for in vivo tumor imaging. *Invest. Radiol. 35*, 479−85.

(16) Bugaj, J. E., Achilefu, S., Dorshow, R. B., and Rajagopalan, R. (2001) Novel fluorescent contrast agents for optical imaging of in vivo tumors based on a receptor- targeted dye-peptide conjugate platform. *J. Biomed. Opt. 6*, 122−133.

(17) Moore, A., Medarova, Z., Potthast, A., and Dai, G. (2004) In vivo targeting of underglycosylated MUC-1 tumor antigen using a multimodal imaging probe. *Cancer Res. 64*, 1821−7.

(18) Ballou, B., Fisher, G. W., Hakala, T. R., and Farkas, D. L. (1997) Tumor detection and visualization using cyanine fluorochrome-labeled antibodies. *Biotechnol. Prog. 13*, 649−58.

(19) Zaheer, A., Lenkinski, R. E., Mahmood, A., Jones, A. G., Cantley, L. C, and Frangioni, J. V. (2001) In vivo near-infrared fluorescence imaging of osteoblastic activity. *Nat. Biotechnol. 19*, 1148−54.

(20) Ntziachristos, V., Schellenberger, E. A., Ripoll, J., Yessayan, D., Graves, E., Bogdanov, A., Jr., Josephson, L., and Weissleder R. (2004) Visualization of antitumor treatment by means of fluorescence molecular tomography with an annexin V−Cy5.5 conjugate. *Proc. Natl. Acad. Sci. U.S.A. 101*, 12294−9.

(21) Jin, H., and Varner. J. (2004) Integrins: roles in cancer development and as treatment targets. *Br. J. Cancer 90*, 561−5.

(22) Cairns, R. A., Khokha, R., and Hill, R. P. (2003) Molecular mechanisms of tumor invasion and metastasis: an integrated view. *Curr. Mol. Med. 3*, 659−71.

(23) Felding-Habermann, B. (2003) Integrin adhesion receptors in tumor metastasis. *Clin. Exp. Metastasis 20*, 203−13.

(24) Schmieder, A. H., Winter, P. M., Caruthers, S. D., Harris, T. D., Williams, T. A., Allen, J. S., Lacy, E. K., Zhang, H., Scott, M. J., Hu, G., Robertson, J. D, Wickline, S. A., and Lanza, G. M. (2005) Molecular MR imaging of melanoma angiogenesis with $\alpha_v\beta_3$-targeted paramagnetic nanoparticles. *Magn. Reson. Med. 53*, 621−7.

(25) Ellegala, D. B., Leong-Poi, H., Carpenter, J. E., Klibanov, A. L., Kaul, S., Shaffrey, M. E., Sklenar, J., and Lindner, J. R. (2003) Imaging tumor angiogenesis with contrast ultrasound and microbubbles targeted to $\alpha_v\beta_3$. *Circulation 108*, 336−41.

(26) Leong-Poi, H., Christiansen, J., Klibanov, A. L., Kaul, S., and Lindner, J. R. (2003) Noninvasive assessment of angiogenesis by ultrasound and microbubbles targeted to $\alpha_v\beta_3$-integrins. *Circulation 107*, 455−60.

(27) Dayton, P. A., Pearson, D., Clark, J., Simon, S., Schumann, P. A., Zutshi, R., Matsunaga, T. O., and Ferrara, K. W. (2004) Ultrasonic analysis of peptide- and antibody-targeted microbubble contrast agents for molecular imaging of $\alpha_v\beta_3$-expressing cells. *Mol. Imaging 3*, 125−34.

(28) Chen, X., Conti, P. S., and Moats, R. A. (2004) In vivo near-infrared fluorescence imaging of integrin $\alpha_v\beta_3$ in brain tumor xenografts. *Cancer Res. 64*, 8009−14.

(29) Wang, W., Ke, S., Wu, Q., Charnsangavej, C., Gurfinkel, M., Gelovani, J. G., Abbruzzese, J. L., Sevick-Muraca, E. M., and Li, C. (2004) Near-infrared optical imaging of integrin $\alpha_v\beta_3$ in human tumor xenografts. *Mol. Imaging 3*, 343−51.

(30) Achilefu, S., Bloch, S., Markiewicz, M. A., Zhong, T., Ye, Y., Dorshow, R. B., Chance, B., and Liang, K. (2005) Synergistic effects of light-emitting probes and peptides for targeting and monitoring integrin expression. *Proc. Natl. Acad. Sci. U.S.A. 102*, 7976−81.

(31) Chen, X., Park, R., Shahinian, A. H., Tohme, M., Khankaldyyan, V., Bozorgzadeh, M. H., Bading, J. R., Moats, R., Laug, W. E., and Conti, P. S. (2004) ^{18}F-labeled RGD peptide: initial evaluation for imaging brain tumor angiogenesis. *Nucl. Med. Biol. 31*, 179−89.

(32) Chen, X., Hou, Y., Tohme, M., Park, R., Khankaldyyan, V., Gonzales-Gomez, I., Bading, J. R., Laug, W. E., and Conti, P. S. (2004) Pegylated Arg-Gly-Asp peptide: ^{64}Cu labeling and PET imaging of brain tumor $\alpha_v\beta_3$ -integrin expression. *J. Nucl. Med. 45*, 1776−83.

(33) Chen, X., Park, R., Tohme, M., Shahinian, A. H., Bading, J. R., and Conti, P. S. (2004) MicroPET and autoradiographic imaging of breast cancer α_v-integrin expression using ^{18}F- and ^{64}Cu-labeled RGD peptide. *Bioconjug. Chem. 15*, 41−9.

(34) Chen, X., Park, R., Hou, Y., Khankaldyyan, V., Gonzales-Gomez, I., Tohme, M., Bading, J. R., Laug, W. E., and Conti, P. S. (2004) MicroPET imaging of brain tumor angiogenesis with ^{18}F-labeled PEGylated RGD peptide. *Eur. J. Nucl. Med. Mol. Imaging 31*, 1081−9.

(35) Chen, X., Sievers, E., Hou, Y., Park, R., Tohme, M., Bart, R., Bremner, R., Bading, J. R., and Conti, P. S. (2005) Integrin $\alpha_v\beta_3$ -targeted imaging of lung cancer *Neoplasia 7*, 271−9.

(36) Chen, X., Tohme, M., Park, R., Hou, Y., Bading, J. R., and Conti, P. S. (2004) Micro-PET imaging of $\alpha_v\beta_3$ -integrin expression with ^{18}F-labeled dimeric RGD peptide. *Mol. Imaging 3*, 96−104.

(37) Chen, X., Liu, S., Hou, Y., Tohme, M., Park, R., Bading, J. R., and Conti, P. S. (2004) MicroPET imaging of breast cancer α_v-integrin expression with ^{64}Cu-labeled dimeric RGD peptides. *Mol. Imaging Biol. 6*, 350−9.

(38) Haubner, R., Kuhnast, B., Mang, C., Weber, W. A., Kessler, H., Wester, H. J., and Schwaiger, M. (2004) [^{18}F]Galacto-RGD: synthesis, radiolabeling, metabolic stability, and radiation dose estimates. *Bioconjugate Chem. 15*, 61−9.

(39) Haubner, R., Wester, H. J., Weber, W. A., Mang, C., Ziegler, S. I., Goodman, S. L., Senekowitsch-Schmidtke, R., Kessler, H., and Schwaiger, M. (2001) Noninvasive imaging of $\alpha_v\beta_3$ integrin expression using ^{18}F-labeled RGD-containing glycopeptide and positron emission tomography. *Cancer Res. 61*, 1781−5.

(40) Haubner, R., Weber, W. A., Beer, A. J., Vabuliene, E., Reim, D., Sarbia, M., Becker, K. F., Goebel, M., Hein, R., Wester, H. J., Kessler, H., and Schwaiger, M. (2005) Noninvasive Visualization of the Activated $\alpha_v\beta_3$ Integrin in Cancer Patients by Positron Emission Tomography and [^{18}F]Galacto-RGD. *PLoS Med. 2*, 0244−51.

(41) Sadeghi, M. M., Krassilnikova, S., Zhang, J., Gharaei, A. A., Fassaei, H. R., Esmailzadeh, L., Kooshkabadi, A., Edwards, S., Yalamanchili, P., Harris, T. D., Sinusas, A. J., Zaret, B. L., and Bender, J. R. (2004) Detection of injury-induced vascular remodeling by targeting activated $\alpha_v\beta_3$ integrin in vivo. *Circulation 110*, 84−90.

(42) Meoli, D. F., Sadeghi, M. M., Krassilnikova, S., Bourke, B. N., Giordano, F. J., Dione, D. P., Su, H., Edwards, D. S., Liu, S., Harris, T. D., Madri, J. A., Zaret, B. L., and Sinusas, A. J. (2004) Noninvasive imaging of myocardial angiogenesis following experimental myocardial infarction. *J. Clin. Invest. 113*, 1684−91.

(43) Janssen, M., Oyen, W. J., Massuger, L. F., Frielink, C., Dijkgraaf, I., Edwards, D. S., Radjopadhye, M., Corstens, F. H., and Boerman, O. C.(2002) Comparison of a Monomeric and dimeric radiolabeled RGD-peptide for tumor targeting. *Cancer Biother. Radiopharm. 17*, 641−6.

(44) Janssen, M. L., Oyen, W. J., Dijkgraaf, I., Massuger, L. F., Frielink, C., Edwards, D. S., Rajopadhye, M., Boonstra, H., Corstens, F. H., and Boerman, O. C. (2002) Tumor targeting with radiolabeled $\alpha_v\beta_3$ integrin binding peptides in a nude mouse model. *Cancer Res. 62*, 6146−51.

(45) Chen, X., Park, R., Shahinian, A. H., Bading, J. R., and Conti, P. S. (2004) Pharmacokinetics and tumor retention of ^{125}I-labeled RGD peptide are improved by PEGylation. *Nucl. Med. Biol. 31*, 11−9.

(46) Wu, Y., Zhang, X., Xiong, Z., Cheng, Z., Fisher, D. R., Liu, S., Gambhir, S. S., and Chen, X. (2005) MicroPET Imaging of Glioma α_v-Integrin Expression Using ^{64}Cu Labeled Tetrameric RGD Peptide. *J. Nucl. Med. 46*, 1707−18.

(47) Nakayama, A., del Monte, F., Hajjar, R. J., and Frangioni, J. V. (2002) Functional near-infrared fluorescence imaging for cardiac surgery and targeted gene therapy. *Mol. Imaging 1*, 365−77.

(48) Xiong, J. P., Stehle, T., Zhang, R., Joachimiak, A., Frech, M., Goodman, S. L., and Arnaout, M. A. (2002) Crystal structure of the extracellular segment of integrin $\alpha_v\beta_3$ in complex with an Arg-Gly-Asp ligand. *Science 296*, 151−5.

(49) Gao, X., and Nie, S. (2005) Quantum dot-encoded beads. *Methods Mol. Biol. 303*, 61−72.

BC0501698

Uptake of Branched Polypeptides with Poly[L-Lys] Backbone by Bone-Marrow Culture-Derived Murine Macrophages: The Role of the Class A Scavenger Receptor

Rita Szabó,[†,⊥] Leanne Peiser,[||,⊥] Annette Plüddemann,[‡,⊥] Szilvia Bösze,[†] Sigrid Heinsbroek,[‡] Siamon Gordon,[‡] and Ferenc Hudecz*[,†,§]

Research Group of Peptide Chemistry at Eötvös L. University, Hungarian Academy of Sciences, Budapest 112, POB 32, H-1518 Hungary, Sir William Dunn School of Pathology, Oxford University, Oxford, OX1 3RE, UK, Department of Organic Chemistry, Eötvös L. University, Budapest 112, POB 32, H-1518 Hungary, and Department of Genome Sciences, University of Washington, HSB K-116, Box 357710, 1959 NE Pacific Street, Seattle, Washington 98195. Received June 14, 2005; Revised Manuscript Received August 18, 2005

Selective delivery of antiparasitic or antibacterial drugs into infected macrophages could be a promising approach for improved therapies. Methotrexate conjugate with branched chain polypeptides exhibited pronounced anti-*Leishmania* activity in vitro and in vivo as reported here earlier. To identify structural requirements for efficient uptake of branched polypeptides, we have studied murine bone marrow culture-derived macrophages (BMMϕ) from 129/ICR mice. We report on the translocation characteristics of structurally closely related compounds labeled with 5(6)-carboxyfluorescein. We found that this process is dependent on experimental conditions (e.g. polypeptide concentration, incubation time, and temperature). Using specific inhibitors as well as macrophages from wild-type and class-A scavenger receptor knockout (SR-A −/−) mice, we demonstrated that SR-A was involved in the endocytosis of some polypeptides depending on their charge. Uptake could be blocked by unlabeled polypeptide, by SR-A inhibitors, and by specific anti-SR-A monoclonal antibody. The polyanionic polypeptide poly[Lys(Succ-Glu$_{1.0}$-DL-Ala$_{3.8}$)] (SuccEAK) with high charge density translocated more efficiently than poly[Lys(Ac-Glu$_{1.0}$-DL-Ala$_{3.8}$)] (AcEAK), which had a lower anionic charge density. On the basis of experimental data presented, SuccEAK can be considered as a potential candidate for the design of a macromolecular carrier for specific drug delivery of bioactive entities into macrophages via SR-A.

INTRODUCTION

A number of intracellular pathogens including *Mycobacterium tuberculosis* (*1*) and the unicellular parasite *Leishmania* (*2*) are capable of surviving intracellularly in macrophages within phagosomes. Macrophage-selective delivery of antibacterial or antiparasitic drugs by endocytosis via specific receptors could be an attractive strategy for more efficient therapies. This approach would require the development of therapeutic macrophage receptor-specific carriers of macromolecular nature. Scavenger receptors play a crucial role in the uptake of bacteria (*3*, *4*), apoptotic cells, and modified lipoproteins (*5*). Scavenger receptors are structurally varied transmembrane proteins binding mainly polyanions with diverse chemical composition (e.g. sulfated polysaccharides, poly(I) and poly(G)) (*6*). Reports published earlier described successful introduction of antimycobacterial *p*-aminosalicylic acid (*7*) and phthalocyanine derivatives (*8*) into macrophages or macrophage cell lines by using maleylated BSA (mal-BSA). The conjugate of *p*-aminosalicylic acid was taken up by peritoneal macrophages infected in culture by *M. tuberculosis* and was 100 times more effective in killing the intracellular organisms (*7*). J774 macrophages treated with the conjugate of phthalocyanine derivatives with mal-BSA exhibited phototoxicity higher than in nonphagocytic EMT-6 cells (*8*). Mukhopadhyay et al. found that daunomycin coupled to mal-BSA entered daunomycin resistant J774A.1 cells (*9*) in vitro. When injected into mice, the daunomycin−mal-BSA conjugate was cleared rapidly from the circulation and accumulated in the macrophage-rich tissues, liver, lung, and spleen (*10*). The same group described also that the conjugate of methotrexate and mal-BSA delivered the drug into *Leishmania donovani*-infected macrophages (*11*). Also, Prasad and colleagues coupled antisense oligonucleotide to a 10-mer poly(G) and introduced this into the J774E macrophage cell line (*12*).

Very few systematic studies have been reported on structural and functional factors required for delivery/targeting of bioactive entities by macromolecules. To this end we have initiated systematic structure−function studies for rational selection of polypeptides as synthetic macromolecular carriers. For this we prepared several groups of branched chain polypeptides with the general formula of poly[Lys(X$_i$−DL-Ala$_m$)] (XAK) (Figure 1), where $i \cong 1$, $m \cong 3-4$, and X represents an additional optically active amino acid residue (*13*, *14*). These polypeptides characterized by chemical (primary structure, conformation) and biological (in vitro cytotoxicity, biodegradation, immunoreactivity, and biodistribution) properties (*13*−

* Corresponding author. Fax: 36-1-372-2620, tel: 36-1-372 2828, e-mail: hudecz@szerves.chem.elte.hu.

† Research Group of Peptide Chemistry at Eötvös L. University.

‡ Oxford University.

§ Department of Organic Chemistry, Eötvös L. University.

|| University of Washington.

⊥ R.S., L.P., and A.P. contributed equally to this study.

10.1021/bc050168f CCC: $30.25 © 2005 American Chemical Society
Published on Web 10/22/2005

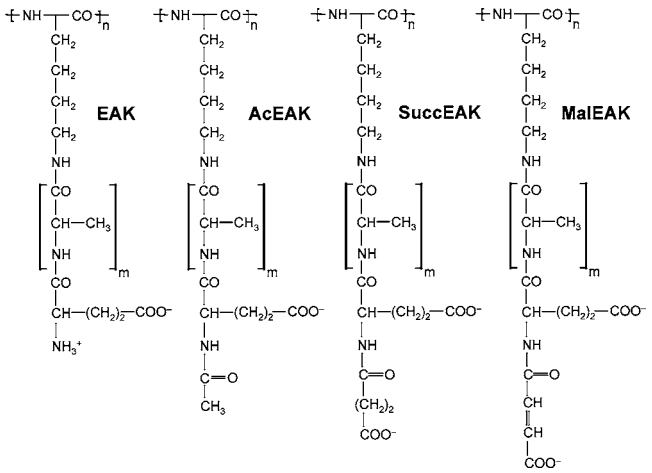

Figure 1. Chemical structure of the amphoteric EAK and its polyanionic derivatives.

15) had a marked effect on phospholipid model membranes depending on their side chain structure (*16*−*18*).

Recently we prepared several highly active bioconjugates in which an antitumor agent (*19*), radionucleide (*20*), or epitope peptide (*21*) was covalently attached to selected branched polypeptides.The coupling of an acid labile derivative of daunomycin to poly[Lys(Glu_i−DL-Ala_m)] (EAK) resulted in compensation of the immunosuppressive effect of the drug, and this conjugate in vivo was very effective in mice bearing L1210 leukemia producing 66−100% long-term (>60 days) survivors (*22*). Recently, a pronounced anti−*Leishmania donovani* effect of methotrexate (MTX) branched polypeptide conjugates was observed in vitro and in vivo (*23*). We demonstrated that the leishmanicidal activity was carrier dependent and the covalent bond between the carrier and MTX is essential. On the basis of in vitro observations, we postulated that the MTX conjugate exhibited an effect through uptake by macrophages, which was different from that of the free drug.

The aim of this work was to analyze the uptake of structurally related branched polypeptides by murine bone marrow culture-derived macrophages (BMMϕ) from 129/ICR mice. We found that polypeptides labeled with 5(6)-carboxyfluorescein are taken up and that the process was dependent on experimental conditions (e.g. polypeptide concentration, incubation time, and temperature). Furthermore, comparing polypeptide uptake by wild-type and class A macrophage scavenger receptor (SR-A)-deficient macrophages, we demonstrated that SR-A played a crucial role in the uptake of some of the polypeptides tested. SR-A-dependent recognition and endocytosis of the polypeptides was dependent on their charge properties. Taken together, our data indicate that the polypeptide poly[Lys(Succ-$Glu_{1.0}$-DL-$Ala_{3.8}$)] (SuccEAK) could be a potential candidate for the design of a macromolecular carrier for specific drug delivery of bioactive entities into macrophages via SR-A.

EXPERIMENTAL PROCEDURES

Abbreviations. Abbreviations of amino acids and their derivatives follow the revised recommendation of the IUPAC−IUB Committee on Biochemical Nomenclature entitled "Nomenclature and Symbolism for Amino Acids and Peptides" (recommendations of 1983). Nomenclature of branched chain polypeptides was used in accordance with the recommended nomenclature of graft polymers (*24*). For the sake of brevity, codes of branched chain polypeptides were constructed by us using the one-letter codes of amino acids. All amino acids are L configuration unless otherwise stated. The other abbreviations in this paper are the following: Z: benzyloxycarbonyl, Boc: *tert*-butyloxycarbonyl, Pcp: pentachlorophenyl, NCA: *N*-carboxy anhydride, HOBt: 1-hydroxybenzotriazole, DMF: *N,N*-dimethylformamide, DMSO: dimethyl sulfoxide, TEA: triethylamine, DCM: dichloromethane, NMM: 4-methylmorpholine, TEA: triethylamine, TFA: trifluoracetic acid PBS: phosphate-buffered saline, Ac: acetyl, Succ: succinyl, Mal: maleyl, CF: 5(6)-carboxyfluorescein, DiI: 1,1′-dioctadecyl-1−3,3,3′,3′-tetramethylindocarbocyanine perchlorate, LDL: low-density lipoprotein.

Branched Chain Polypeptides. *Reagents and Solvents.* Amino acids used for this study, HCl, trifluoracetic acid, acetic acid anhydride, and succinic anhydride, were purchased from REANAL (Budapest, Hungary). Benzyloxycarbonyl chloride, pentachlorophenol, *N,N′*-dicyclohexylcarbodiimide, HOBt, TEA, DMSO, and NMM were from Fluka (Buchs, Switzerland). Acetonitrile was from Merck (Darmstadt, Germany). 5(6)-Carboxyfluorescein succinimide ester was obtained from Sigma-Aldrich (Budapest, Hungary).

Synthesis of Poly[Lys]·HBr. The synthesis was carried out from N^{α}-carboxy-N^{ϵ}-benzyloxycarbonyl-lysine anhydride under conditions to obtain an average degree of polymerization of approximately 100 (monomer: diethylamine initiator molar ratio = 50:1), as reported previously (*25*). Protecting groups were cleaved by HBr in glacial acetic acid (35%, m/V) and poly[Lys]·HBr was precipitated using diethyl ether. The polypeptide was purified by dialysis against distilled water using visking casing and was isolated by freeze-drying. The average relative molar masses (M_w, M_z) were determined by sedimentation equilibrium using a short column technique at 25 °C (MOM 3180 type analytical ultracentrifuge, Hungary). The number average of the relative molar mass (M_n), the polydispersity factor (M_z/M_w), and the average degree of polymerization (DP_n) values were calculated from data described earlier (*26*).

Synthesis of Poly[Lys(X_i-DL-Ala_m)] (XAK) Type Polypeptides and the Polyanionic Derivatives of Poly[Lys(Glu_i-DL-Ala_m)], (EAK). Poly[Lys(DL-Ala_m)] (AK) (*27*) and poly[Lys(X_i-DL-Ala_m)] (XAK) polypeptides, where X = Glu or Ser, were prepared as described earlier (*28*). Briefly, AK polypeptide was synthesized by grafting short oligomeric DL-Ala chains to the $^{\epsilon}NH_2$ group of lysine residues using *N*-carboxy-DL-Ala-anhydride. The terminal amino acids (X) were coupled to the $^{\alpha}NH_2$-groups of the side chains as Z−X-OPcp, where X = Glu or Ser. The reaction was performed by an in situ active ester method using an equivalent amount of HOBt dissolved in DMF as activating reagent. The pH of the solution was adjusted to 8.0 by adding NMM. Stirring was continued at room-temperature overnight. Z-protecting groups were removed with HBr using acetic acid containing 35% HBr. The polypeptides were purified by dialysis against distilled water for 2 days using a Visking tube (cutoff = 12000−14000 Da) and isolated by freeze-drying.

Poly[Lys(AcGlu$_i$-DL-Ala_m)] (AcEAK) was prepared by acetylation of poly[Lys(Glu_i-DL-Ala_m)] (EAK) as follows. 85 mg (159 μmol) of EAK was dissolved in 2 mL of distilled water and diluted with 10 mL of DMF under cooling at 0 °C. 27 μL (198 μmol) of TEA was added to this solution to neutralize the polymer. Five equivalents of freshly prepared imidazolyl-acetate was used for the acetylation (*29*), and then the product was dialyzed against distilled water followed by freeze-drying.

Poly[Lys(Succ-Glu_i-DL-Ala_m)] (SuccEAK) was prepared by succinylation and poly[Lys(Mal-Glu_i-DL-Ala_m)] (MalEAK) by maleylation of poly[Lys(Glu_i-DL-Ala_m)],(EAK) as follows. 10 mg (18.5 μmol) EAK) was dissolved in 2 mL of 0.1 M carbonate buffer (pH = 9.2). 220 μL (220 mmol) of succinic anhydride or 219 μL (220 mmol) maleic anhydride, respectively, was dissolved in DMSO (c = 100 mg/mL) and was added to this solution with continuous stirring for 30 min at RT (*30*). The pH was maintained between 9.0 and 9.2 with 0.1 M NaOH. The reaction was continued for 4 h followed by dialysis against distilled water for 2 days and then freeze-drying.

Amino Acid Analysis. The amino acid composition of the polymeric polypeptides was determined by amino acid analysis using a Beckman 6300 analyzer (Fullerton, CA). Prior to analysis, the samples were hydrolyzed in 6 M HCl in sealed and evacuated tubes at 105 °C for 24 h.

Labeling of Branched Polypeptides with 5(6)-Carboxyfluorescein. 10 mg (6×10^{-7} to 1.9×10^{-7} mol) amounts of polypeptides were dissolved in 2 mL of Na_2CO_3 buffer (0.1 M; pH 9.4). The amino-reactive dye 5(6)-carboxyfluorescein succinimide ester (5(6)-CF-SE) was dissolved in DMF (c = 10 mg/mL, 0.21 mM) and was added to the polypeptide solution in 20 μL aliquots. The reaction was continued for 1 h at room temperature with continuous stirring. The product was purified on a PD10 Sephadex G25 column using distilled water as eluent. The samples were then freeze-dried and they were resolved in PBS (0.1 M, pH 7.4) before use.

Determination of 5(6)-Carboxyfluorescein Content of Conjugates. Labeled polypeptide samples and 5(6)-carboxyfluorescein succinimide ester were hydrolyzed in 6 M HCl in sealed and evacuated tubes at 110 °C for 24 h. HCl was removed, and the hydrolysate was dissolved in DMSO. The hydrolyzed samples (20 μL) were analyzed by RP-HPLC using reversed phase Eurospher C_{18} column (3.9 × 250 mm; packed with spherical 5 μm silica with 100 Å pore size [Knauer, Bad Homburg, Germany] and gradient elution consisted of 0.1% TFA in water [eluent A] and 0.1% TFA in acetonitrile/water = 80/20 v/v [eluent B]). During chromatography the eluent B content was between 25 and 45%, in 20 min, 45−99%, in 10 min. The flow rate was 1 mL/min at room temperature. The average sample concentration applied was 0.65 μg/mL. Peaks were detected at λ_{ex} = 419 nm and λ_{em} = 519 nm using a fluorescence detector (Shimadzu, Japan). A calibration curve was constructed using 5(6)-carcoxyfluorescein in the 4.8×10^{-5} M to 1.2×10^{-5} M concentration range.

Functional Studies. *Reagents.* 1,1′-Dioctadecyl-1−3,3,3′,3′-tetramethylindocarbocyanine perchlorate (DiI)-labeled acetylated LDL (DiI-AcLDL) was obtained from Autogen Bioclear, and poly(I) from Signa (Reading, UK). OptiMEM medium and all other culture media were from Invitrogen (Paisley, United Kingdom). Rat anti-mouse SR-A antibody 2F8 was prepared at the Sir William Dunn School of Pathology, Oxford, as described previously (*33*). CAMPATH rat anti-mouse IgG, an isotype-control for 2F8, was a kind gift from H. Waldmann, Sir William Dunn School of Pathology, Oxford. Cy3-labeled donkey anti-rat IgG was from Jackson ImmunoResearch (Soham, UK), and rabbit and goat sera were from Sigma. Fluorescent Mounting Medium was from DakoCytomation (Glostrup, Denmark). Plastic products were purchased from Becton Dickinson Labware (Oxford, UK).

Animals. Mice deficient in SR-AI and II (SR-A −/−) were produced as previously described (*31*). SR-A −/− and SR-A +/+ control 129/ICR mice of the same sex were used at 8−12 weeks of age. All animals were handled in accordance with guidelines issued by the Home Office, United Kingdom.

Cell Isolation and Culture. BMMϕ were obtained and cultured by standard procedures described previously (4). The cells were maintained in 15 cm bacteriologic plastic (BP) Petri dishes containing RPMI 1640 with 50 IU/mL penicillin G, 50 μg/mL streptomycin, 2 mM glutamine (PSG), 10% fetal calf serum (FCS), and 15% (vol/vol) L-cell conditioned medium (LCM) as a source of macrophage colony-stimulating factor (*32*). The macrophages were harvested with PBS (0.1 M, pH 7.4) containing 10 mM EDTA and 4 mg/mL lidocaine·HCl and plated onto six-well BP plates (Greiner, Gloucester, United Kingdom). The cells were maintained in the six-well plate for further 24 h at 37 °C. The bone marrow from the femurs and tibias of one mouse gave $(1-5) \times 10^7$ Mϕ after 7 days in culture.

Cytotoxicity Assay. Prior to the experiment, cells were washed three times with PBS. Each polypeptide was added in OptiMEM at a concentration of 1 μg/mL or 20 μg/mL. BMMϕ were incubated with the polypeptide solution for 1 h and then harvested with lidocaine/EDTA. The number of living cells was determined by counting the cells in a Neubauer haemocytometer after staining with 0.4% trypan blue dissolved in PBS. The statistical significance of data was determined by Student's t test at the 95% confidence level.

Flow Cytometry Analysis of Cellular Uptake. Polypeptides labeled with 5(6)-CF dissolved in OptiMEM were used. Before adding CF-labeled polypeptides, the cells were washed three times with PBS. The CF-labeled polypeptides were incubated with the cells for 1 h at 37 °C or 4 °C. For the inhibition experiments poly(I) at 50 μg/mL (4) or 2F8 at 15 μg/mL was used (*33*). Prior to the addition of polypeptides, cells were preincubated for 30 min with inhibitor which was also maintained throughout the experiment. In some experiments unlabeled polypeptides were added at 10 times excess of labeled molecule concentration. The increase in macrophage fluorescence following incubation with labeled molecules was analyzed by flow cytometry. Data were analyzed with CellQuest 3.0 software. The mean fluorescence of untreated control cells was subtracted from the mean fluorescence obtained with treated samples under all different assay conditions applied. Statistical analysis of data was performed using Student's t test at the 95% confidence level.

Analysis of the Cellular Uptake by Confocal Microscopy. Wild-type 129/ICR BMMϕ were plated on sterile glass coverslips in 24-well tissue-culture dishes in RPMI 1640 medium supplemented PSG; 10% FCS; and 15% (vol/vol) LCM at 5×10^4 macrophages per well 24 h prior to the experiment. The cells were washed three times with PBS. CF-labeled polypeptides were incubated with the cells for 5, 15, 30, and 60 min at 37 °C. Cells were fixed with 4% formaldehyde/PBS for 15 min at room temperature then permeabilized using a blocking buffer containing 1% (m/V) BSA, 0.25% (m/V) saponin, and 1% goat and 1% rabbit serum. The cells were incubated with 2F8 (c = 10 μg/mL) or with an isotype-matched control antibody (CAMPATH 1G) in parallel for 1 h at room temperature followed by washing three times with blocking buffer. After incubation with Cy3 labeled anti-rat IgG antibody for 1 h in the dark, the coverslips were mounted on glass microscopy slides using DakoCytomation Fluorescent Mounting Medium. Cells were analyzed in a BIO RAD Radiance 2000 confocal microscope (λ_{ex} = 488 nm).

Table 1. Characteristics of Polylysine Based Branched Chain Polymeric Polypeptides with Poly[Lys(X_i-DL-Ala_m)] Formula

polypeptide	code[a]	amino acid composition[b] Lys	Ala (m)	X (i)	$\overline{DP_n}$[c]	$\overline{M_w}$[d] ± 5%	CF [%][e]
poly[Lys]	-	1.00	-	-	130	16700	-
poly[Lys(Glu_i-DL-Ala_m)]	EAK	1.00	3.80	1.00	60	31600	2.91
poly[Lys(Ac-Glu_i-DL-Ala_m)]	AcEAK	1.00	3.80	1.00	60	34500	0.46
poly[Lys(Succ-Glu_i-DL-Ala_m)]	SuccEAK	1.00	3.80	1.00	60	37900	0.53
poly[Lys(Succ-Glu_i-DL-Ala_m)]	MalEAK	1.00	3.80	1.00	60	37800	0.72

[a] Code of branched chain polymeric polypeptides, based on one-letter symbol of amino acids. [b] Amino acid composition was determined by amino acid analysis as after hydrolysis in 6 M HCl at 105 °C for 24 h. [c] Number of average degree of polymerization determined by sedimentation equilibrium measurements. [d] Average molecular mass of polymers; calculated from the average degree of polymerization (DP_n) of poly[Lys] and of the side chain composition. [e] Average degree of substitution for 5(6)-carboxyfluorescein (CF) was determined by reverse phase HPLC after hydrolysis of the samples in 6 M HCl at 105 °C for 24 h.

RESULTS

Branched Polypeptides. Branched polypeptides with the general formula poly[Lys(X_i-DL-Ala_m)], ($m \cong 4$, $i \cong 1$), which were used for these studies have short oligo-(DL-Ala) side chains and Glu at the *N*-terminal of the branches. The terminal amino acid X was coupled to the $^{\alpha}NH_2$ groups of the terminal alanine by an in situ active ester method (*28*). EAK bearing $^{\alpha}NH_2$ and also free carboxyl groups at the end of the branches possess an amphoteric character. The three additional polypeptides that were also included in our studies were the polyanionic derivatives of poly[Lys($Glu_{1.0}$-DL-$Ala_{3.8}$)] (EAK) prepared by acetylation, succinylation or maleylation of the $^{\alpha}NH_2$ groups of the terminal glutamic acid residues (Figure 1). Poly[Lys($AcGlu_{1.0}$-DL-$Ala_{3.8}$)] (AcEAK) side chains contain only one negative charge per monomer unit under conditions used for the present studies. The charge density of the succinylated (poly[Lys($SuccGlu_{1.0}$-DL-$Ala_{3.8}$)], SuccEAK) and maleylated (poly[Lys($MalGlu_{1.0}$-DL-$Ala_{3.8}$)], MalEAK) polypeptides were higher, since two negative charges were present per unit. Thus, we investigated this group of structurally related polypeptides built on a polylysine backbone with systematically altered chemical properties (charge, conformation (*13*, *30*)). The polypeptides were characterized according to their relative average molar mass, determined by sedimentation equilibrium analysis (*26*), and the composition of their side chain. The chemical characteristics of the polypeptides are shown in Table 1.

Cytotoxic Effect of Polypeptides on BMMϕ. The cytotoxicity of polypeptides labeled with CF was studied on BMMϕ cells from wild-type mice at two different concentrations (1 μg/mL and 20 μg/mL). The cytotoxicity of the polypeptides was determined by counting live cells by trypane blue exclusion. Polylysine was included as a control. Results are expressed as a percentage of untreated cells and summarized in Figure 2. We found that after 1 h incubation none of the polypeptides had a significant toxic effect on the macrophages at 1 μg/mL concentration. At 20 μg/mL poly[Lys] proved to be highly toxic, but no cytotoxic effect of the other polypeptides was observed.

Uptake of polypeptides by BMMϕ. We studied the endocytosis of polypeptides by BMMϕ from wild-type mice under different conditions. The effects of polypeptide concentration, incubation time, and temperature on uptake were analyzed. Furthermore we investigated the influence of unlabeled polypeptides on the internalization of CF-polypeptides in inhibition assays.

Influence of the Polypeptide Concentration on the Uptake. BMMϕ from wild-type mice were incubated with varying concentrations (0.1−100 μg/mL) of the CF-labeled polypeptides, and the rate of uptake was detected by flow cytometry. The amphoteric EAK and polyanionic AcEAK were internalized only at 100 μg/mL concentration. In the case of polyanionic SuccEAK, uptake was proportional with the increasing concentration in the concentration range tested, while MalEAK was taken up effectively only at 50 and 100 μg/mL (Figure 3).

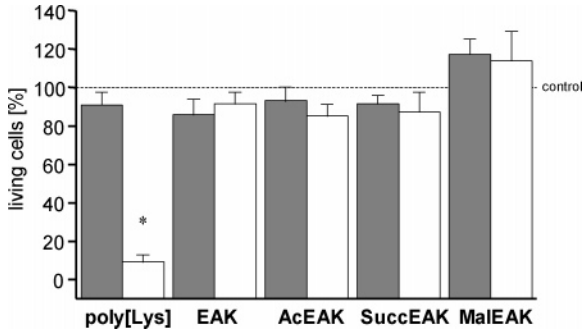

Figure 2. The effect of the branched CF-polypeptides on the survival of BMMϕ. Columns represent the number of living cells as a percentage of untreated control ± SD. Polylysine ($\overline{DP_n}$ = 130, $\overline{M_w}$ = 17000) was used as control polypeptide. ■: c = 1 μg/mL, □: c = 20 μg/mL. Statistical analysis of data was performed by Student's t test; *: p<0.05. Poly[L-Lys] (M_w = 17000, DP_n = 130) was used as control.

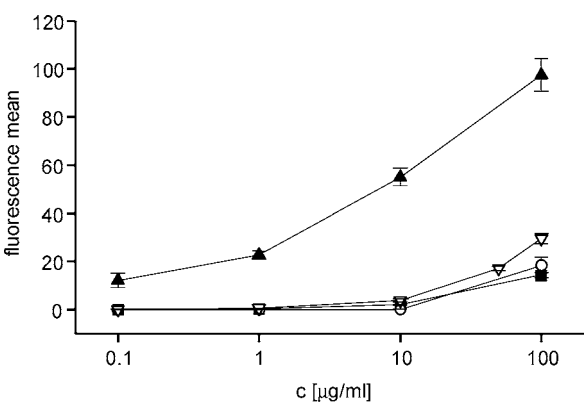

Figure 3. Concentration dependence of the uptake of the CF-polypeptides by BMMϕ after 60 min incubation with the polypeptides. Symbols represent the average of mean fluorescence values of a representative experiment of three independent assays ± SD after subtracting the control. ■: CF-EAK, ○: CF-AcEAK, ▲: CF-SuccEAK, ▽: CF-MalEAK.

Time Dependence. Time dependence of uptake was examined by flow cytometry after 1, 5, 10, 20, 30, 45, and 60 min incubation with the polypeptides (Figure 4). The internalization of the polyanionic polypeptides by the cells was in direct proportion to the duration of incubation. The uptake of neither the scavenger receptor ligand DiI-AcLDL (c = 5 μg/mL) used as positive control (6, 34) nor the CF-polypeptides was saturable during the 1 h

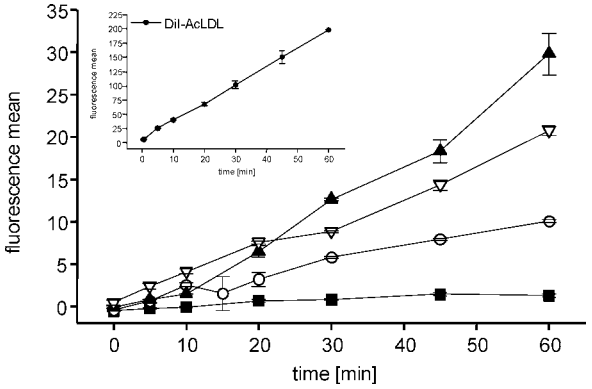

Figure 4. Time dependence of the endocytosis of polypeptides. Symbols represent the average of mean fluorescence values of a representative experiment of three independent assays ± SD after subtracting the control. ■: CF-EAK, c =100 μg/mL; ○: CF-AcEAK, c = 100 μg/mL; ▲: CF-SuccEAK, c = 50 μg/mL; ▽: CF-MalEAK, c = 100 μg/mL. Insert: time dependence of the uptake of DiI-AcLDL (c = 5 μg/mL) under the same conditions.

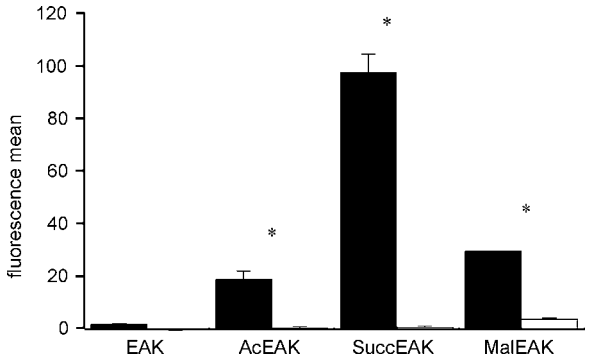

Figure 5. Uptake of polypeptides by 129/ICR BMMϕ at 4 °C and 37 °C after 1 h. Columns represent the average of mean fluorescence values of a representative experiment of three independent assays ± SD after subtracting the control. ■: 37 °C μg/mL, □: 4 °C. Statistical analysis of data was performed by Student's t test; *: $p < 0.05$.

study period, and the polyanionic polypeptides were taken up continuously by the BMMϕ during this time (Figure 4).

Temperature Dependence. The uptake of the polypeptides was also investigated at 4 °C versus 37 °C by flow cytometry. The results are summarized in Figure 5. In the case of the amphoteric EAK no significant uptake could be observed at 37 °C or 4 °C. Two polyanionic polypeptides, AcEAK and SuccEAK, were internalized only at 37 °C. In the case of MalEAK a significant difference could be observed between the uptake at 4 °C or at 37 °C.

The Effect of Pretreatment with Unlabeled Polypeptides. In this experiment the endocytosis of CF-SuccEAK was examined at the lowest concentration that could be easily detected. Macrophages were pretreated with unlabeled polypeptides at a concentration 10 times higher than the labeled polypeptide for 30 min prior to the incubation of the cells with the respective CF-polypeptides. The polyanionic polypeptides, AcEAK and SuccEAK, significantly inhibited the uptake of the labeled SuccEAK into the macrophages (Figure 6). Pretreatment of the macrophages with c = 10 μg/mL unlabeled SuccEAK inhibited the uptake of CF-SuccEAK (c = 1 μg/mL) to the control levels. After 60 min incubation with the labeled polypeptide, mean fluorescence was 1.43 ± 0.15 in the presence and 10.77 ± 0.65 in the absence of the unlabeled SuccEAK, p < 0.01. To a

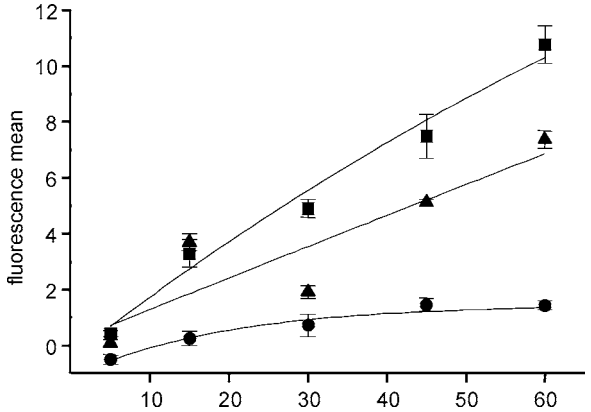

Figure 6. Effect of pretreatment with unlabeled polypeptides of similar chemical character. Symbols represent the average of mean fluorescence values of a representative experiment of three independent assays ± SD after subtracting the control. ■: uptake of CF-SuccEAK, c = 1 μg/mL; ●: uptake of CF-SuccEAK pretreated with unlabeled SuccEAK, c = 10 μg/mL, ▲: uptake of CF-SuccEAK pretreated with unlabeled AcEAK, c = 10 μg/mL.

lesser extent, unlabeled AcEAK also elicited a statistically significant inhibition of the internalization of CF-SuccEAK (mean fluorescence [%] = 7.36 ± 0.31 in the presence of AcEAK, $p < 0.01$).

The Role of the Scavenger Receptor in the Uptake of Polyanionic Polypeptides. To clarify the potential involvement of the SR-A, we examined the uptake of the polypeptides by BMMϕ from SRA −/− mice. In these studies in order to block the receptor we utilized a known general SR-A ligand, poly(I), and a specific anti-SR-A monoclonal antibody, 2F8.

Uptake of Polypeptides by Wild-Type and SR-A −/− Macrophages. The uptake of polyanionic polypeptides CF-AcEAK, CF-SuccEAK, and CF-MalEAK was tested. The scavenger receptor ligand DiI-AcLDL was used as a positive control (*34*), and the amphoteric CF-EAK polypeptide as negative control. The three polyanionic polypeptides were internalized by wild-type macrophages, but to a lower extent compared with DiI-AcLDL (Figures7 and 8). The uptake of CF-SuccEAK, with higher negative charge density, by wild-type BMMϕ was greater than CF-AcEAK having less negative charges and CF-MalEAK containing a double bond in its anionic end-group. In all cases we observed that the internalization of these polypeptides was significantly diminished in SR-A −/− cells (Figure 7). In the case of CF-SuccEAK (c = 50 μg/mL) we detected a thirteen-fold difference between the fluorescence intensities of the internalized polypeptide by the wild-type and SRA −/− BMMϕ (mean fluorescence = 52.49 ± 1.34 and 3.77 ± 0.01 respectively, $p < 0.001$). With CF-AcEAK (c = 100 μg/mL) a statistically significant difference could be demonstrated between the uptake of the wild-type and of the SR-A −/− macrophages, a 8-fold decrease in the uptake could be observed (mean fluorescence = 10.195 ± 1.43 for the wild-type and 1.235 ± 0.26 for the SRA −/− cells, $p < 0.001$) (Figure 8).

Blocking of Scavenger Receptor-A with Poly(I) and MAb 2F8. Next, wild-type and SR-A −/− BMMϕ were pretreated with the scavenger receptor ligand poly(I) (c = 50 μg/mL) (*4*, *6*) or the SR-A specific monoclonal antibody 2F8 (at c = 15 μg/mL) for 30 min before the addition of the polypeptides. Data are presented in Figure 8. We observed that the presence of these SR-A scavenger receptor ligands significantly reduced the uptake of the

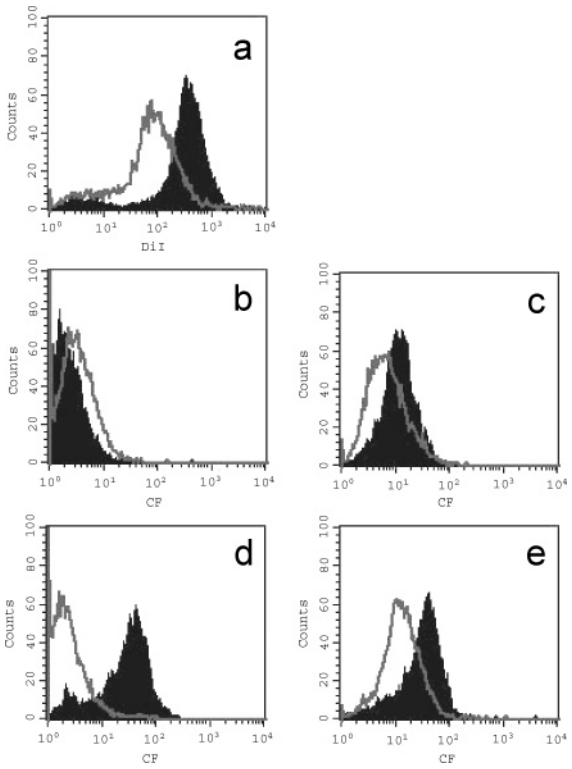

Figure 7. Uptake of polyanionic polypeptides by wild-type and SR-A −/− BMMϕ. Cells were fixed with 2% formaldehyde. Diagrams were recorded by measurig 10000 cells. Data were analyzed by CellQuest 3.0. a. Filled diagrams represent wild-type macrophages, while open lines represent *SR-A* −/− cells. (a) DiI-AcLDL, $c = 5$ μg/mL, (b) CF-EAK, $c = 100$ μg/mL, (c) CF-AcEAK: $c = 100$ μg/mL, (d) CF-SuccEAK, $c = 50$ μg/mL, (e) CF-MalEAK, $c = 50$ μg/mL.

polyanionic polypeptides and of DiI-AcLDL used as positive control.

Colocalization of SR-A and CF-polypeptides in the Cells. The time-dependence of the uptake of CF-SuccEAK and its colocalization with SR-A were further investigated by confocal microscopy. We detected SR-A in cells, using 2F8- and Cy3-labeled anti-rat IgG secondary antibody. We found that CF-SuccEAK was internalized by the cells. Vesicles containing the polypeptide were observed in the cytoplasm (Figure 9). We detected colocalization of CF-SuccEAK (green) and SR-A (red) within 5 min of incubation.

DISCUSSION

Class A scavenger receptors are membrane glycoproteins that are present mainly on cells of the macrophage lineage (*35*). Therefore these receptors are potential targets for macrophage-specific delivery of macromolecules and their drug or epitope conjugates. The scavenger receptor ligands described in the literature are polyanionic compounds with diverse chemical structure and composition (e.g. sulfated polysaccharides such as fucoidin, AcLDL, maleylated proteins, poly(I), and poly(G) (*6*).

The present studies are the first attempt at systematic examination of the interaction between SR-A-bearing cells and a chemically related polypeptide family with different charge and structure. Our previous results with these polypeptides imply that chemical structure, the charge and length of the side chains, have a pronounced effect on various biological and physicochemical properties (*16*, *17*). Results presented in this paper indicate that the uptake of branched polypeptides by murine BMMϕ depends on the composition of the branches, indicating the importance of both charge and the structure of the terminal amino acid derivative. As assessed by the fluorescence intensity of CF-labeled polypeptides, we found a significant difference between the rate of uptake of the polyanionic polypeptides. Although both SuccEAK and MalEAK contain two carboxyl groups at the end of the side chain, whereas AcEAK possesses only one in the terminal glutamic acid, SuccEAK was internalized by BMMϕ to a greater extent than MalEAK. This observation could be explained by the presence of a C−C double bond in MalEAK, which is in conjugation with the C−O double bond influencing the charged state of the terminal carboxyl group.

To analyze the mechanism of uptake we performed inhibition studies with the polypeptide internalized most efficiently. The translocation of CF-SuccEAK was investigated in the presence of unlabeled SuccEAK and also AcEAK. The results of this study showed that unlabeled SuccEAK markedly inhibited the internalization of the CF-labeled polypeptide compound, but AcEAK exhibited only a partial inhibitory effect. These data suggest that AcEAK and SuccEAK share the same receptor, but AcEAK binds with lower affinity or that there are multiple receptors for SuccEAK some of which are shared.

To clarify if SR-A was involved in the endocytosis, we investigated the uptake of the polyanionic polypeptides on wild-type and SR-A −/− BMMϕ. Results show that SR-A −/− macrophages internalize these compounds at a substantially lower level compared with wild-type cells. Blocking of the SR-A with receptor antagonist, poly(I), or with an anti-SR-A monoclonal antibody, resulted in a clear reduction in uptake. In addition, confocal microscopic studies provided independent evidence of colocalization of CF-SuccEAK with SR-A soon after internalization into cells. Taken together, these results suggest that CF-SuccEAK is taken up by SR-A-mediated endocytosis and indicate that the receptor recognizes polyanionic polypeptides and has an important role in their uptake.

It is known that not all polyanionic molecules are able to bind SR-A due to the presence of an undetermined structural requirement for recognition by the receptor. Using our systematic modification of polylysine, we were able to demonstrate that we could enhance binding to SR-A. Thus, the use this approach provides us a powerful new tool to study SR-A binding in further detailby structural manipulation of the polylysine to enhance or reduce binding to the receptor and by modeling how the changes alter the charge distribution and spatial arrangement.

We showed that SuccEAK had higher accumulation in macrophages compared to AcEAK. Interestingly, our previous data on the blood clearance and biodistribution of branched polypeptides showed that AcEAK had prolonged blood survival in Balb/c mice, while SuccEAK was cleared rapidly from the circulation (*36*). This difference in the blood clearance, which was not due to enzymatic degradation, could be related to the difference of macrophage uptake between AcEAK and SuccEAK. Thus, the enhanced uptake by macrophages, mainly through SR-A, could contribute to the rapid clearance of SuccEAK.

Several previous papers have reported on the uptake of modified proteins and conjugates by macrophages. Majumdar et al. demonstrated that the binding of PAS-MalBSA labeled with ^{125}I to peritoneal macrophages was saturable, indicating a limited number of binding sites. Addition of unlabeled conjugate to medium of the macrophages eliminated binding of the labeled compound.

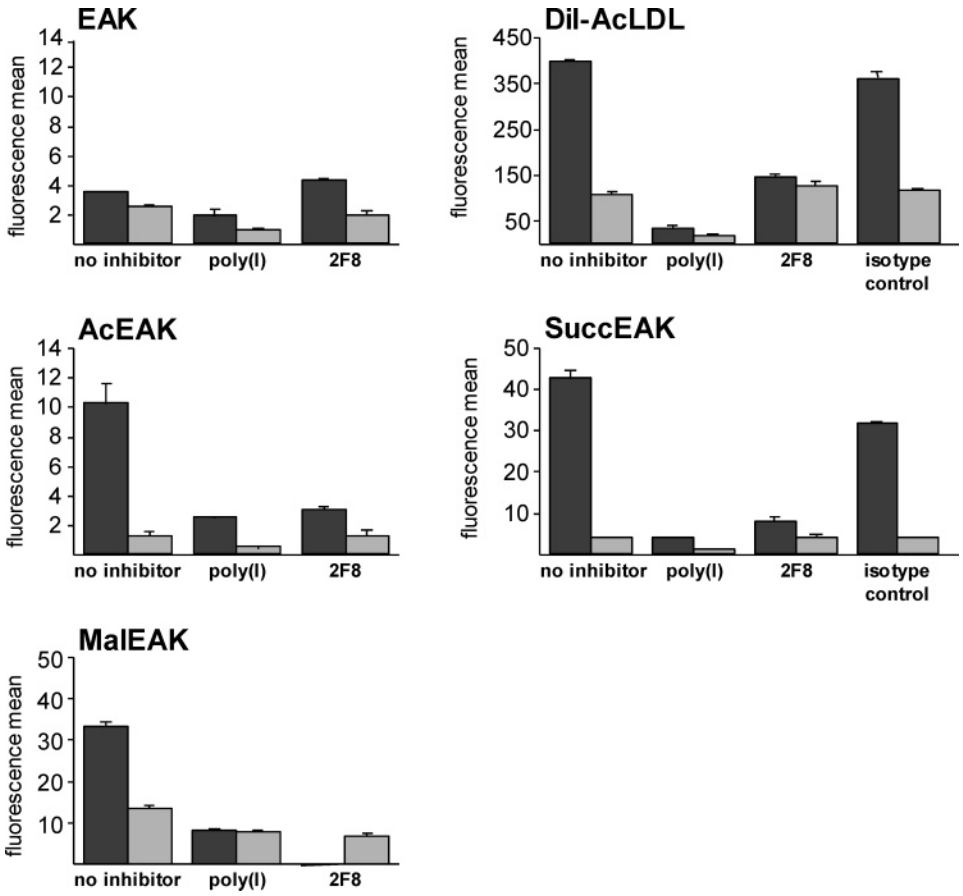

Figure 8. Uptake of polyanionic polypeptides by wild-type and SR-A −/− BMMϕ, CF-AcEAK: $c = 100$ μg/mL. CF-SuccEAK, $c = 50$ μg/mL,MalEAK, $c = 50$ μg/mL DiI-AcLDL, $c = 5$ μg/mL. Columns represent the average of mean fluorescence values of a representative experiment of three independent assays ± SD after subtracting the control. ■: 129/ICR, gray: SR-A −/−.

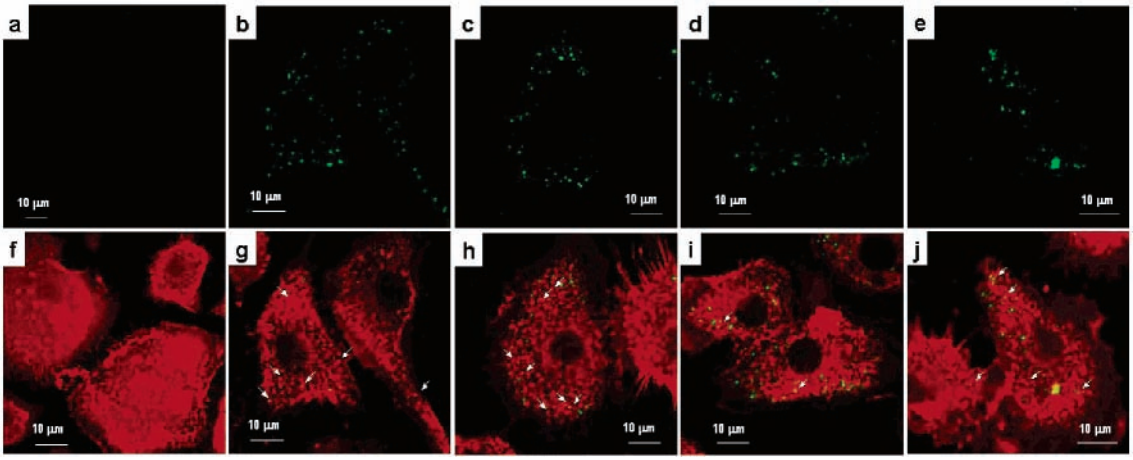

Figure 9. Colocalization of SR-A (red) and CF-SuccEAK (green). SR-A was detected by the SR-A specific monoclonal antibody 2F8 and a Cy3-labeled secondary antibody. The cells were analyzed by confocal microscopy ($\lambda_{ex} = 488$ nm). (a) isotype control of 2F8, (b) CF-SuccEAK 5 min, (c) CF-SuccEAK 15 min, (d) CF-SuccEAK 30 min, (e) CF-SuccEAK 60 min, (f) control cells not reated with polypeptide, SR-A detected by 2F8 and a Cy3 labeled secondary antibody, (g) CF-SuccEAK 5 min and SR-A: merge, (h) CF-SuccEAK 15 min and SR-A: merge, (i) CF-SuccEAK 30 min and SR-A: merge, (j) CF-SuccEAK 60 min and SR-A: merge. Arrows show examples of colocalization.

The authors also demonstrated the uptake of the conjugate at 37 °C, which was followed by its lysosomal degradation (*7*). Brasseur et al. described the specific uptake of phthalocyanine-malBSA conjugates followed by photoinactivation of J774 macrophages. The receptor binding was demonstrated by competition assay between labeled and nonlabeled conjugates (*8*). These studies showed no direct evidence of the involvement of scavenger receptors in the processes described. Similarly, the articles of Mukhopadhyay et al. contained no experimental data on the involvement of scavenger receptors in the uptake and cytotoxicity of daunomycin or methotrexate conjugates with mal-BSA (*9*−*12*). Recognition of a 10-mer poly(G)-tethered antisense oligonucleotide by scavenger receptors was assessed by a competition assay. In this the degradation of ^{125}I-labeled mal-BSA by J774E

cells in the presence or absence of different polyanionic molecules as competitors exhibited the characteristic scavenger receptor profile (*12*).

To the best of our knowledge this is the first report to show that systematic chemical modification of polylysine-based polypeptides greatly influences the rate and mechanism of uptake by BMMϕ. We also demonstrated for the first time that the internalization of polyanionic synthetic polypeptides, especially SuccEAK, could be considered a SR-A mediated process. Thus, this polypeptide seems to be appropriate as a macromolecular carrier for specific drug delivery into macrophages and they can become the basis for development of further carrier molecules and bioconjugates.

ACKNOWLEDGMENT

Experimental work summarized in this paper was supported by grants from the British-Hungarian Intergovernmental Program (2/2003), from the Hungarian Research Fund (OTKA No. T-045679), and from the Hungarian Ministry of Education (Medichem 2, NKFP). Work in the laboratory of S.G. was supported by a grant from the Medical Research Council, UK. The authors thank Dr. Hedvig Medzihradszky-Schweiger for the amino acid analyses.

LITERATURE CITED

(1) Hostetter, J., Steadham, E., Haynes, J., Bailey, T., and Cheville, N. (2003) Phagosomal maturation and intracellular survival of *Mycobacterium avium* subspecies paratuberculosis in J774 cells. *Comput. Immun. Microbiol. Infect. Dis. 26*, 269−283.

(2) Bogdan, C., and Röllinghoff, M. (1998) The immune response to *Leishmania*: mechanisms of parasite control and evasion. *Int. J. Parasitol. 28*, 121−134.

(3) Peiser, L., M. de Winther, P. J., Makepeace, K., Hollinshead, M., Coull, P., Plested, J., Kodama, T., Moxon, E. R., and Gordon, S. (2002) The class A macrophage scavenger receptor is a major pattern recognition receptor for *Neisseria meningitidis* which is independent of lipopolysaccharide and not required for secretory responses. *Infect. Immun. 70*, 5346−5354.

(4) Peiser, L., Gough, P. J., Kodama, T., and Gordon, S. (2000) Macrophage class A scavenger receptor-mediated phagocytosis of *Escherichia coli*: Role of cell heterogeneity, microbial strain, and culture conditions *in vitro*. *Infect. Immun. 68*, 1953−1963.

(5) Sambrano, G. R., Parthasarathy, S., and Steinberg, D. (1994) Recognition of oxidatively damaged erythrocytes by a macrophage receptor with specificity for oxidized low-density lipoprotein. *Proc. Natl. Acad. Sci. U.S.A. 91*, 3265−3269.

(6) Krieger, M., and Herz, J. (1994) Structures and function of multiligand lipoprotein receptors − macrophage scavenger receptors and LDL receptor-related protein (LRP). *Annu. Rev. Biochem. 63*, 601−637.

(7) Majumdar, S., and Basu, S. K. (1991) Killing of *Mycobacterium tuberculosis* by receptor-mediated drug delivery. *Antimicrob. Agents. Chemother. 35*, 135−140.

(8) Brasseur, N., Langlois, R., La Madeleine, C., Ouellet, R., and Van Lier, J. E. (1999) Receptor-mediated targeting of phthalocyanines to macrophages via covalent coupling to native or maleylated bovine serum albumin. *Photochem. Photobiol. 69*, 345−352.

(9) Mukhopadhyay, A., Mukhopadhyay, B., and Basu, S. K. (1995) Circumvention of multidrug resistance in neoplastic cells through scavenger receptor mediated drug delivery. *FEBS Lett. 376*, 95−98.

(10) Mukhopadhyay, B., Mukhopadhyay, A., and Basu, S. K. (1993) Enhancement of tumouricidal activity of daunomycin by receptor-mediated delivery. In vivo studies. *Biochem. Pharmacol. 46*, 912−924.

(11) Mukhopadhyay, A., and Basu, S. K. (1990) Enhanced intracellular delivery of methotrexate by a receptor mediated process. *Biotechnol. Appl. Biochem. 12*, 529−36.

(12) Prasad, V., Hashim, S., Mukhopadhyay, A., Basu, S. K., and Roy, R. P. (1999) Oligonucleotides tethered to a short poly(G)uanylic acid stretch are targeted to macrophages: Enhanced antiviral activity of a vesicular stomatitis virus-specific antisense oligonucleotide. *Antimicrob. Agents Chemother. 43*, 2689−2696.

(13) Hudecz, F. (1995) Design of synthetic branched-chain polypeptides as carriers for bioactive molecules. *Anti-Cancer Drugs 6*, 171−193.

(14) Mezö, G., Kajtár, J., Nagy, I. B., Szekerke M., and Hudecz, F. (1997) Carrier design: synthesis and conformational studies of poly(l-lysine) based branched polypeptides with hydroxyl groups in the side chains. *Biopolymers 42*, 713−730.

(15) Hudecz, F., Pimm, M. V., Rajnavölgyi, É., Mezö, G., Fabra, A., Gaál, D., Kovács, A. L., Horváth, A., and Szekerke, M. (1999) Carrier design: new generation of polycationic branched polypeptides containing OH groups with prolonged blood survival and diminished in vitro cytotoxicity. *Bioconjugate Chem. 10*, 781−790.

(16) Nagy, I. B., Haro, I., Alsina, M. A., Reig, F. and Hudecz, F. (1998) Interaction of branched chain polymeric polypeptides with phospholipid model membranes. *Biopolymers 46*, 169−179.

(17) Nagy, I. B., Hudecz, F., Alsina, M. A., and Reig, F. (2003) Physicochemical characterisation of branched chain polymeric polypeptide carriers based on a poly-Lysine backbone. *Biopolymers 70*, 323−335.

(18) Szabó, R., Hudecz F., and Reig F. (2003) Interfacial interactions between poly[L-Lysine] based branched polypeptides and phospholipids model membranes. *J. Colloid Interface Sci. 267*, 18−24.

(19) Hudecz, F., Kóczán, Gy., and Reményi, J. (2002) Peptide or protein based delivery and targeting. In Molecular pathomechanisms and new trends in drug research (Keri, Gy., and Toth, I., Eds.) pp 553−578, Harwood Academic Publishers, Taylor and Francis Group, London.

(20) Perkins, A. C., Frier, M., Pimm, M. V., and Hudecz, F. (1998) Tc^{99m}-branched chain polypeptide (BCP): a potential synthetic radiopharmaceutical. *J. Labelled Compd. 41*, 631−638.

(21) Hudecz, F. (2001) Manipulation of epitope fuction by modification of peptide structure: A minireview. *Biologicals 29*, 197−207.

(22) Gaál, D., and Hudecz, F. (1998) Low toxicity and high antitumour activity of daunomycin by conjugation to immunpotential amphoteric branched polypeptide. *Eur. J. Cancer 34*, 155−161.

(23) Kóczán, Gy., Ghoose, A. C., Mookerjee, A., and Hudecz, F. (2002) Methotrexate conjugate with branched polypeptide influences *Leishmania donovani* infection in vitro and in experimental animals. *Bioconjugate Chem. 13*, 518−524.

(24) IUPAC−IUB Commission on Biomedical Nomenclature. (1984) *Eur. J. Biochem. 138*, 9−37.

(25) Hudecz, F., and Szekerke, M. (1980) Investigation of drug−protein interactions and the drug-carrier concept by the use of branched polypeptides as model systems. Synthesis and characterization of the model peptides. *Collect. Czech. Chem. Commun. 45*, 933−940.

(26) Hudecz, F., Kutassi-Kovács, S., and Kajtár J. (1984) GPC, CD and sedimentation analysis of polylysine and branched chain poly-Lys-poly-L-Ala polypeptides. *Colloid Polym. Sci. 262*, 208−212.

(27) Hudecz, F., Votavova, H., Gaál, D., Sponar, J., Kajtár, J., Blaha, K., and Szekerke M. (1985) Branched polypeptides with a poly(l-lysine) backbone: synthesis, conformation, and immunomodulation. In *Polymeric Materials in Medication* (Gebelein, Ch. G., and Carraher, Ch. E., Eds.) pp 265−289, Plenum Press, New York.

(28) Mezö, G., Kajtár, J., Hudecz, F., and Szekerke, M. (1993) Carrier design: Conformational studies of amino acid (X) and oligopeptide (X-DL-Ala_m) substituted poli(l-lysine). *Biopolymers 33*, 873−885.

(29) Mezö, G, Mezö, I., Pimm, M. V., Kajtár, J., Seprödi, J., Teplán, I., Kovács, M., Vincze, B., Pályi, I., Idei, M., Szekerke, M., and Hudecz, F. (1996) Synthesis, conformation, biodistribution, and hormone-related *in vitro* antitumor activity of a gonadotropin-releasing hormone antagonist-branched polypeptide conjugate. *Bioconjugate Chem. 7*, 642−650.

(30) Hudecz, F., Kojima, Y., Miyamoto, Y., Kajtár, J., and Maeda, H. (1994) The effect of charge on the biodistribution of synthetic branched polypeptides in tumour bearing mice. *J. Controlled Release 28*, 301−302.

(31) Suzuki, H., Kurihara, Y., Takeya, M., Kamada, N., Kataoka, M., Jishage, K., Ueda, O., Sakaguchi, H., Higashi, T., Suzuki, T., Takashima, Y., Kawabe, Y., Cyn-shi, O., Wada, Y., Honda, M., Kurihara, H., Aburatani, H., Doi, T., Matsumoto, A., Azuma, S., Noda, T., Toyoda, Y., Itakura, H., Yazaki, Y., and Kodama, T. (1997) A role for macrophage scavenger receptors in atherosclerosis and susceptibility to infection. *Nature 386*, 292−296.

(32) Hume, D. A., and Gordon, S. (1983) Optimal conditions for proliferation of bone marrow-derived mouse macrophages in culture: the roles of CSF-1, serum, Ca21, and adherence. *J. Cell. Physiol. 117*, 189−194.

(33) Fraser, I., Hughes, D. A., and Gordon, S. (1993) Divalent cation-independent macrophage adhesion inhibited by monoclonal antibody to murine scavenger receptor. *Nature 364*, 343−346.

(34) Voyta, J. C. Via, D. P., Butterfield, C. E., and Zetter, B. R. (1984) Identification and isolation of endothelial cells based on their increased uptake of acetylated-low-density lipoprotein. *J. Biol. Chem. 99*, 2034−2040.

(35) Naito, M., Kodama, T., Matsumoto, A., Doi, T., and Takahashi, K. (1991) Tissue distribution, intracellular localization, and in vitro expression of bovine macrophage scavenger receptors. *Am. J. Pathol. 139*, 1411−1423.

(36) Pimm, M. V., Gribben, S. J., Bogdán K., and Hudecz, F. (1995) The effect of charge on the biodistribution in mice of branched polypeptides with a poly(l-lysine) backbone labeled with ^{125}I, ^{111}In or ^{51}Cr. *J. Controlled Release 37*, 161−172.

BC050168F

Combined Physical and Chemical Immobilization of Glucose Oxidase in Alginate Microspheres Improves Stability of Encapsulation and Activity

Huiguang Zhu,*,† Rohit Srivastava,† J. Quincy Brown,† and Michael J. McShane†,‡,§

Institute for Micromanufacturing and Biomedical Engineering Program, Louisiana Tech University, 911 Hergot Avenue, Ruston, Louisiana 71272. Received June 16, 2005; Revised Manuscript Received September 13, 2005

Chemical sensors utilizing immobilized enzymes and proteins are important for monitoring chemical processes and biological systems. In this study, calcium-cross-linked alginate hydrogel microspheres were fabricated as enzyme carriers by an emulsification technique. Glucose oxidase (GOx) was encapsulated in alginate microspheres using three different methods: physical entrapment (emulsion), chemical conjugation (conjugation), and a combination of physical entrapment and chemical conjugation (emulsion−conjugation). Nano-organized coatings were applied on alginate/GOx microspheres using the layer-by-layer self-assembly technique in order to stabilize the hydrogel/enzyme system under biological environment. The encapsulation of GOx and formation of nanofilm coating on alginate microspheres were verified with FTIR spectral analysis, ζ-potential analysis, and confocal laser scanning microscopy. To compare both the immobilization properties of enzyme encapsulation techniques and the influence of nanofilms with uncoated microspheres, the relationship between enzyme loading, release, and effective GOx activity (enzyme activity per unit protein loading) were studied over a period of four weeks. The results produced four key findings: (1) the emulsion−conjugation technique improved the stability of GOx in alginate microspheres compared to the emulsion technique, reducing the GOx leaching from microsphere from 50% to 17%; (2) the polyelectrolyte nanofilm coatings increased the GOx stability over time, but also reduced the effective GOx activity; (3) the effective GOx activity for the emulsion−conjugation technique (about 3.5×10^{-5} AU μg^{-1} s^{-1}) was higher than that for other methods, and did not change significantly over four weeks; and (4) the GOx concentration, when compared after one week for microspheres with three bilayers of poly(allylamine hydrochloride)/sodium poly(styrene sulfonate) ({PAH/PSS}) coating, was highest for the emulsion−conjugation technique. As a result, the comparison of these three techniques showed the emulsion−conjugation technique to be a potentially effective and practical way to fabricate alginate/GOx microspheres for implantable glucose biosensor application.

INTRODUCTION

Chemical sensors utilizing immobilized enzymes and proteins are important for monitoring of chemical processes and biological systems. They have been widely used for the processing of a variety of products from food to environmental control, and even for biomedical applications (*1*−*3*). The main goal behind enzyme immobilization is to entrap the protein in a semipermeable support material, which prevents the enzyme from leaching while allowing its substrate(s) to pass at an appropriate rate (*4*). Some essential features of the immobilization matrix are nondegradability and compatibility with the enzymes. Because of the three-dimensional structure of enzymes that determines their specific function, it is critical that the encapsulation matrix and procedures have minimal effect upon the structure and function of the proteins.

In search of suitable matrices for enzyme immobilization, polysaccharides such as alginate and chitosan (*5*−*8*) have been found to be among the top candidates due to their biocompatibility and processability. Ionically cross-linked alginate encapsulation has been reported as suitable for many biological components including cells (*9*−*18*), owing to the relatively inert aqueous environment within the matrix, the mild room temperature encapsulation process, and high gel porosity allowing high diffusion rates of macromolecules (*19*, *20*). Chemical immobilization, in which the enzyme is covalently linked to the hydrogel matrix, has been employed to stably entrap the enzyme, but this approach often results in significant loss of enzymatic activity (*21*). In contrast, simple one-step coating procedures have been applied to decrease enzyme leaching (*22*−*25*).

The layer-by-layer (LbL) self-assembly technique enables polyelectrolytes of opposite charge to be deposited onto charged templates, forming a stable multilayer with each component layer being 1−10 nm thick (*26*, *27*). These nanofilm coatings applied to negatively charged alginate matrix provide a protective shell for encapsulated biomolecules and prolong the life span of alginate microspheres in a biological environment. Multilayer coatings involving chitosan/alginate, poly(lysine)/alginate, and other polyelectrolyte coatings have been used as barrier membranes for alginate microspheres to slow release of the encapsulated macromolecule (*28*−*33*).

* Corresponding author. Tel: (318) 257-5127. Fax: (318) 257-5104. E-mail: hzhu@latech.edu.
† Institute for Micromanufacturing.
‡ Biomedical Engineering Program.
§ Tel: (318) 257-5100. Fax: (318) 257-5104. E-mail: mcshane@latech.edu.

10.1021/bc050171z CCC: $30.25 © 2005 American Chemical Society
Published on Web 10/26/2005

Recent work in our lab has shown that the application of self-assembled ultrathin film coatings can reduce leaching of macromolecules from alginate microspheres (*34*, *35*). Diffusion of the enzyme from the gel matrix depends upon porosity of the gel and concentration gradients, as well as the permeability of the thin-film coatings to the enzyme. The nanofilm coatings also slow down the decomposition of alginate microspheres in PBS buffer or biological environments relative to bare alginate microspheres without coatings, which make the structures useful for long-term biomedical applications. Coimmobilization of glucose oxidase and an oxygen-quenched fluorescent compound (such as ruthenium or porphyrin compound) within alginate hydrogel microspheres coated with specialized biocompatible ultrathin films has been proposed as an approach to realize optical glucose microsensor systems (*3*). The nanofilms provide stabilization of the hydrogel spheres in addition to a transport barrier. These ratiometric sensors respond to glucose transients via local oxygen changes, which can be transduced by the fluorescence intensity of the oxygen quenched fluorescent compound.

The work described here is a comparison of glucose oxidase encapsulation in alginate microspheres using three different encapsulation techniques, with the integration of the LbL self-assembly nanofilm coating to stablize alginate/enzyme microspheres, with an effort to maximize the enzyme loading in alginate hydrogel microspheres while retaining its catalytic activity. In this work, alginate microspheres with a diameter of $<10\ \mu$m were used, due to their intended application as implantable glucose sensors for diabetic monitoring (*3*). To compare the immobilization properties of enzyme encapsulation techniques and the influence of nanofilm thickness for coated and uncoated microspheres, the relationship between enzyme loading, release, and effective activity was studied over a period of four weeks. These fundamental results should provide useful information for further investigations, including testing of enzymatic sensors in in vitro and in vivo studies, toward practical implantable biosensors.

EXPERIMENTAL PROCEDURES

Materials. Sodium alginate (low viscosity, 250 cps, MW 12−80k) and anhydrous calcium chloride were obtained from Aldrich. Sorbitan trioleate (SPAN 85) and polyoxyethylene sorbitan trioleate (TWEEN 85) were purchased from Sigma. OmniSolv 2,2,4-trimethylpentane (isooctane) was purchased from EMD Chemicals Inc. 1,6-Diaminohexane, *N*-(3-dimethylaminopropyl)-*N*′-ethylcarbodiimide hydrochloride (EDC), and *N*-hydroxysulfosuccinimide sodium salt (NHSS) were obtained from Fluka. Sodium poly(styrene sulfonate) (PSS, MW ∼70 000), poly(allylamine hydrochloride) (PAH, MW ∼70 000) were obtained from Aldrich. Glucose oxidase (GOx, from *Aspergillus niger* type VII, lyophilized powder, 198 000 units/g solid (without added oxygen)) was obtained from Sigma. Peroxidase (Sigma), *o*-dianisidine (Aldrich), and β-D-glucose (Sigma) were used for the GOx activity test. Fluorescein isothiocyanate (FITC, isomer I) and rhodamine B isothiocyanate (RITC) were obtained from Sigma. For confocal fluorescence microscopy, PAH was labeled with FITC in pH 8.5 sodium bicarbonate buffer and precipitated in acetone. GOx was labeled with RITC or FITC in pH 8.5 sodium bicarbonate buffer and purified through a Sephadex G-25M column (Amersham Pharmacia Biotech AB). All chemicals were reagent grade and used as received.

Synthesis of FITC-Alginate Derivative. Sodium alginate (120 mg) was mixed with EDC/NHSS (50 mg/30 mg) for the activation of carbonyl groups on alginate in pH 5.0 sodium acetic buffer for 30 min, followed by addition of 1,6-diaminohexane (60 mg) for another 4 h. The mixture was precipitated in 2-propanol to remove unreacted diamine. The alginate-amine derivative was reacted with FITC (0.5 mg) in pH 8.5 sodium bicarbonate solution for 4 h and precipitated in acetone to remove unreacted FITC. The resulting FITC-alginate derivative was dissolved in DI water, and absorbance was measured with a UV−vis spectrometer (Lambda 45, PerkinElmer), and then the labeled alginate was mixed with 50 g of 3 wt % unlabeled sodium alginate solution and made into microspheres using the following process.

Fabrication of Alginate Hydrogel Microspheres. Alginate hydrogel microspheres were prepared by an emulsification method (*36*−*38*). Briefly, 50 g of 3 wt % sodium alginate aqueous solution was dispersed in 75 g of isooctane containing 1.7 g of SPAN 85 using an ultrasonicator (Cole Palmer, CPX-750) at 60% power for 5 min. A solution containing 0.9 g of TWEEN 85 in 5 g of isooctane was then added to the emulsion and ultrasonicated at the same power for another 5 min to achieve stable water/oil emulsion droplets. After this, 20 mL of aqueous solution containing 10 wt % of calcium chloride was added to allow formation of ionic cross-links while stirring for 20 min. The microspheres were then rinsed three times with DI water by successive centrifugation cycles and stored in DI water at room temperature. FITC-alginate derivative was added into alginate solution to facilitate the confocal microscopy (Leica TCS SP2) investigation. The number and size distribution of alginate microspheres were measured with a Coulter counter (Beckman Coulter Z Series).

Conjugation of GOx to Alginate Microspheres. GOx was first mixed with alginate solution followed by alginate cross-linking by calcium ions, as described above, in which case the GOx was physically entrapped in alginate microspheres. This GOx encapsulation method is named the "emulsion technique" in this study and is a commonly used technique for materials encapsulation in alginate hydrogel microspheres. However, there is severe limitation for this technique, as the entrapped molecules can easily leach out from the hydrogel microspheres after fabrication, causing substantial loss of the enzyme from the matrix.

Two conjugation methods were used to improve the stability of GOx in alginate microspheres. For the first method, alginate microspheres (200 μL, without enzyme) were incubated in 1 mL of pH 5.0 buffer for 30 min, and then 2.0 mg of EDC and 1.2 mg of NHSS were added to activate the alginate microspheres for another 30 min. The activated alginate microspheres were centrifuged and rinsed with DI water to remove unreacted EDC and NHSS. Next, 1 mL of GOx solution (5 mg/mL in DI water) was added to react with alginate microspheres for another 4 h. The microspheres were centrifuged and triple rinsed with DI water to remove unreacted GOx, followed by slowly adding 200 μL of 1 M $CaCl_2$ to strengthen the alginate hydrogel microspheres and avoid de-cross-linking during the following LbL assembly procedure. In this case, GOx will only react with activated alginate. This GOx encapsulation method is named the "conjugation technique" in this study. For the second method, alginate microspheres already containing GOx (from the emulsion step) were also reacted with EDC/NHSS in pH 5.0 buffer for 4 h, which is named the "emulsion−conjugation" technique. In this case, GOx

should react with not only alginate but also the enzyme itself, since enzyme contains both amine groups and carboxylic acid groups. Fourier transform infrared spectroscopy (Nexus 470 FTIR) was used to analyze the unmodified alginate microspheres and alginate/GOx microspheres. Confocal micrographs were taken with a Leica TCS SP2 equipped with a 63× oil-immersion objective, using the 488/514 nm lines of an Ar/Kr laser for FITC/RITC excitation, respectively.

Layer-by-Layer Assembly of PAH/PSS Nanofilm Coating on Alginate Microspheres. The PSS and PAH solutions used for alternating adsorption of {PAH/PSS} multilayers on alginate (or alginate/GOx) microspheres were prepared at a concentration of 2 mg/mL in DI water containing 0.1 M $CaCl_2$. For deposition of each coating, 1 mL of polyelectrolyte solution was added to a microcentrifuge tube containing 100 μL of microsphere suspension. Adsorption was allowed to proceed for 20 min, after which the suspension was centrifuged at 3000 rpm to separate the spheres from remaining unadsorbed polyelectrolyte. The microspheres were then triple-rinsed with DI water by successive centrifugation cycles. The process was repeated for the oppositely charged polyelectrolyte, and then alternated until a total of three bilayers of {PAH/PSS} films were obtained. The assembly of polyelectrolyte layers on alginate microspheres was monitored by electrophoretic mobility measurements (ZetaPlus ζ-potential analyzer, Brookhaven Instrument Corp.).

Enzyme Stability in Alginate/GOx Microspheres. For wet storage loss experiments, alginate/FITC-GOx microspheres prepared by the emulsion, conjugation, and emulsion−conjugation techniques, with zero (uncoated alginate) and three bilayers of {PAH/PSS} coatings, were suspended in individual cuvettes containing 1.5 mL of 0.01 M PBS buffer at pH 7.4, which were stored at room temperature, covered and in the dark. Leaching analysis was performed by removing the supernatant by centrifugation and recording the fluorescence from the supernatant with a scanning spectrometer (Photon Technologies Inc, QM-1), allowing determination of the relative supernatant enzyme concentration by comparison to a standard FITC-dextran emission (7 μM in 2 mL of PBS buffer) at each point of time. This supernatant was then placed back with the sphere suspension. The relative fluorescence resulting from leaching through different coatings was then used to compare final total enzyme lost from the microspheres with each coating.

Enzyme Activity in Alginate/GOx Microspheres. Glucose oxidase activity was monitored through a colorimetric assay, based on the oxidation of *o*-dianisidine through a peroxidase-coupled system.

$$\beta\text{-D-glucose} + O_2 + H_2O \xrightarrow{\text{glucose oxidase}} \text{D-gluconic acid} + H_2O_2$$

$$H_2O_2 + o\text{-dianisidine (reduced)} \xrightarrow{\text{peroxidase}} o\text{-dianisidine (oxidized)} + H_2O$$

The GOx activity assay comprised 2.4 mL of *o*-dianisidine solution (0.21 mM in 0.01 M PBS buffer pH 7.4), 0.5 mL of β-D(+)-glucose solution (100 mg/mL in 0.01 M PBS buffer), and 0.1 mL of peroxidase solution (60 purpurogallin units/mL in DI water). During continuous stirring with a magnetic bar at 25 °C (Peltier temperature controlled cell holder, Quantum Northwest), a 100 μL aliquot of GOx-loaded alginate microspheres suspended in DI water (approximately 10^6 spheres) was added to the assay and the absorbance at 500 nm was monitored as a function of time, resulting in a catalytic profile of the encapsulated GOx. The experiment was repeated for the different alginate/GOx microspheres (different preparation techniques, bare and three bilayer coating spheres) after a period of 0, 1, and 4 weeks, and the results were compared by calculating the slopes of the activity curves. In each case, the experiments were performed in triplicate, and results were normalized to the mass of glucose oxidase present in the spheres, as determined using the Lowry assay. The effective GOx activity (AU μg^{-1} s^{-1}, enzyme activity per unit protein loading) is expressed as total GOx activity (absorbance units/second) divided by the mass of GOx (micrograms) encapsulated in alginate microspheres.

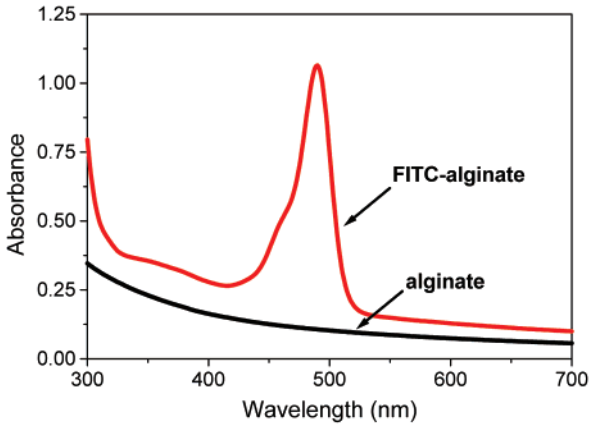

Figure 1. UV−vis absorbance spectrum of alginate and FITC-alginate derivative.

RESULTS AND DISCUSSION

Synthesis of FITC-Alginate Derivative. Figure 1 contains the UV−vis absorbance spectrum of unmodified alginate and FITC-labeled alginate. The unmodified alginate material does not display any characteristic absorbance between 300 and 700 nm. However, the FITC-alginate derivative possessed strong absorbance at 488 nm, which corresponds to the absorbance of FITC and verifies the successful synthesis of the FITC-alginate derivative. For quantitative analysis of FITC-alginate derivative, a series of solutions of known concentration of FITC were measured with UV−vis spectroscopy, which gives the relationship between FITC absorbance and concentration. The FITC content was calculated to be 1.7 wt % in FITC-alginate derivative. The FITC-labeled alginate was therefore mixed with alginate and made into microspheres for confocal imaging.

Characterization of Alginate Microspheres. The emulsion technique used for fabrication of alginate hydrogel microspheres is illustrated in Figure 2a. Calcium ions were used to cross-link the alginate microspheres while in the emulsion. By adjusting the ultrasonicator power, ratio of surfactant, or concentration of alginate solution, different sizes (1−200 μm) of alginate microspheres can be obtained. Figure 2b is an image of typical alginate microspheres obtained by confocal microscopy, with FITC-labeled alginate showing green fluorescence. Coulter counter measurements revealed that the process resulted in a typical alginate microsphere mean diameter of 4.25 ± 0.49 μm (N > 5000 spheres counted). The microspheres were found to be stable in DI water after removal of the surfactant, and the microspheres exhibited the expected negative surface charge, which therefore

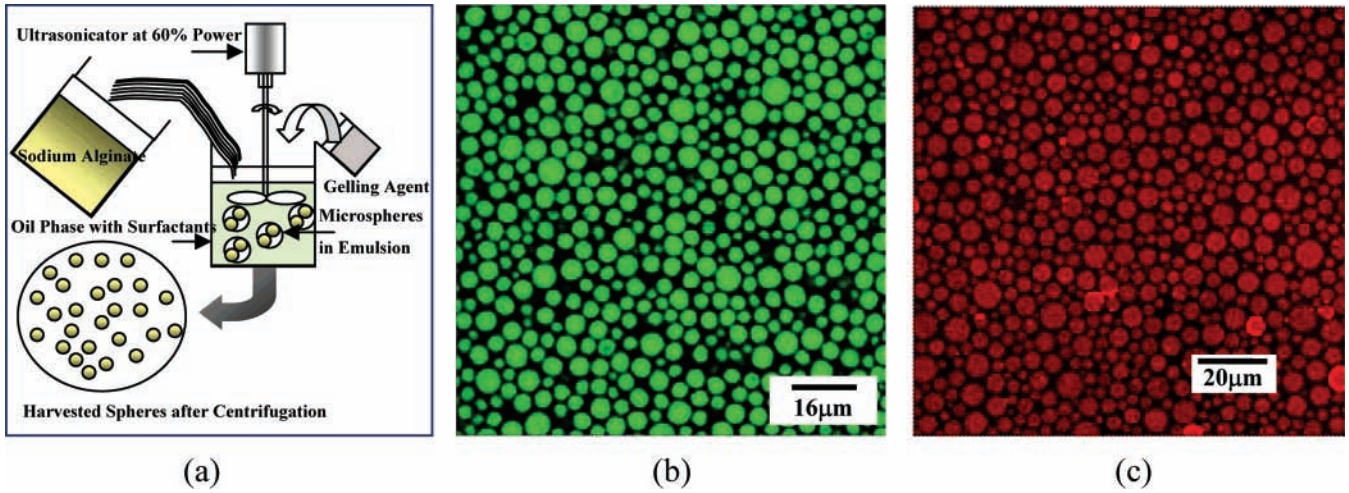

Figure 2. (a) Emulsion technique for the production of alginate microspheres. (b) Confocal images of alginate microspheres, alginate labeled with FITC. (c) Confocal images of alginate microspheres with physically embedded GOx, where GOx was labeled with RITC.

Scheme 1. Schematic Diagram of Enzyme Conjugated to Alginate Microspheres and Then Coated with Polyelectrolyte Multilayer Nanofilm

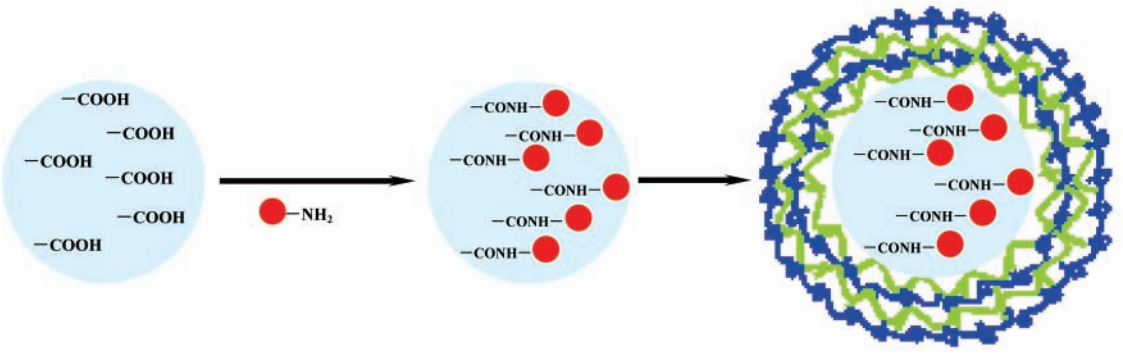

could be used for polyelectrolyte LbL assembly to provide protective shells. It was also found, as illustrated in Figure 2c, that the RITC-labeled GOx was uniformly distributed in the alginate hydrogel microspheres made by the emulsion technique.

Conjugation of Enzyme to Alginate Microspheres. Alginates are linear chains of 1,4′-linked residues of β-D-mannuronic acid (β-DMA) and α-L-guluronic acid (α-LGA). A key property of sodium alginate is the formation of ionically cross-linked gel in the presence of multivalent cations. Thus, when sodium alginate is exposed to $CaCl_2$ solution, the carboxylic acid groups on polyguluronate units from different alginate molecules form a cross-linked structure with calcium ions called an "egg-box" junction with interstices in which the cations may pack and be coordinated. Because the carboxylic acid groups will not be depleted during the ionic-cross-linking procedure, the residual carboxylates in alginate microspheres could be activated by EDC/NHSS and bind to amine-containing molecules such as enzymes. Under biological conditions, the calcium-cross-linked structure may be replaced and de-cross-linked slowly by monovalent cations such as sodium ions and therefore are not stable for long-term application (*39*); however, polyelectrolyte coatings can provide protective shells and improve the stability of the alginate microspheres to some extent. A schematic diagram of enzyme conjugated to alginate microspheres and subsequent coating with polyelectrolytes is shown in Scheme 1.

Since alginate and GOx (pI = 4) exhibit the same negative charge around neutral pH, it is difficult for GOx to be stable within alginate microspheres when only physical entanglement between alginate and GOx exists. Similary, it is also difficult for free GOx to diffuse into alginate microspheres and interact with alginate. To improve the stability of GOx in alginate microspheres for long-term applications, two different conjugation techniques were applied, which are called the "conjugation technique" and the "emulsion−conjugation technique". To verify conjugation-made alginate/GOx microspheres, alginate microspheres were mixed with GOx solution for 4 h, without adding EDC/NHSS. Both treated alginate microspheres and bare microspheres were triple rinsed with DI water before FT-IR measurement (Figure 3). The spectrum of alginate microspheres mixed with GOx solution was exactly the same as that of alginate microspheres, with strong absorbance at 1600 cm^{-1} contributed by carbonyl groups. This result shows that GOx cannot become entrapped in alginate microspheres by simply mixing GOx with the spheres after fabrication. In contrast, the spectrum for conjugation-made alginate/GOx microspheres possesses two shoulders beside the 1600 cm^{-1} carbonyl peak, related to amide I (1750 cm^{-1}) and amide II (1550 cm^{-1}) bonds. The amide signal may be contributed by amide bonds on the enzyme or amide bonds formed between carboxylic acid groups on alginate and amine groups on enzyme; in either case, this result demonstrates that the GOx could be chemically conjugated to alginate microspheres by using EDC/NHSS activation process.

The LbL assembly of polyelectrolyte layers on alginate (or alginate/GOx) microspheres was monitored by electrophoretic mobility measurements. Three bilayers of {PAH/PSS} were deposited on alginate microspheres and

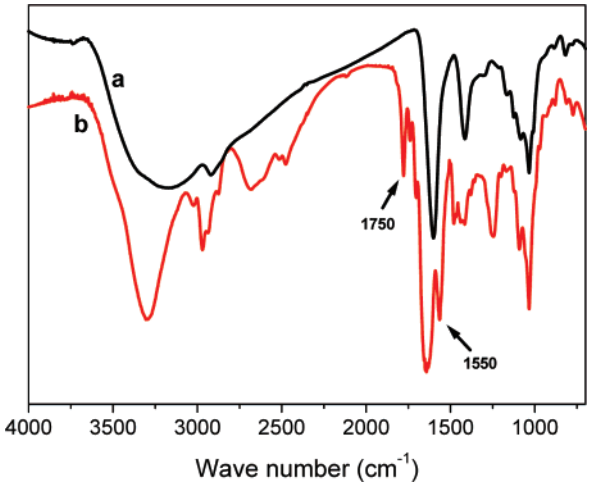

Figure 3. FTIR spectrum of (a) alginate microspheres and (b) conjugation-made alginate/GOx microspheres.

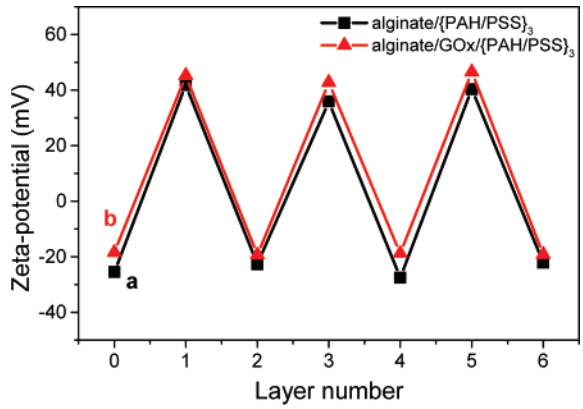

Figure 4. ζ-Potential measurements for deposition of {PAH/PSS}$_3$ on (a) alginate microspheres and (b) alginate/GOx microspheres. The first measurement (layer 0) is the surface potential of uncoated alginate microspheres.

GOx-encapsulated alginate microspheres. It was found that there was no significant difference between alginate cores and alginate cores with encapsulated GOx. The surface potential of the microspheres was observed to change regularly from −25 mV for alginate (or alginate/GOx) and PSS to +40 mV for PAH (Figure 4), indicating the formation of the desired {PAH/PSS}$_3$ wall architecture. This result shows that the alginate microspheres still have strong negative surface charge after calcium gelation, which makes polyelectrolyte nanofilm deposition onto alginate microspheres straightforward. The polyelectrolyte multilayer wall may serve multiple purposes, including providing a protective shell for encapsulated biomolecules and stabilizing alginate microspheres against dissolution in a biological environment, as well as a necessary barrier to control substrate mass transport in the development of enzymatic glucose sensors (*3*, *40*).

Confocal microscopy was used to image conjugated alginate/GOx microspheres, and coating of {PAH/PSS} on microspheres (Figure 5), which clearly shows that the GOx was uniformly distributed in the alginate microspheres, no matter whether the conjugation (Figure 5a) or the emulsion−conjugation (Figure 5b) technique was used. RITC-labeled GOx solution was also mixed with bare alginate microspheres, however they exhibit no RITC fluorescence under confocal microscopy after rinsing with DI water. Three bilayers of {FITC-PAH/PSS} were coated on emulsion−conjugation-made alginate/GOx microspheres, as illustrated in Figure 5c, which shows that the GOx was still uniformly distributed in alginate microspheres after coating with polyelectrolytes. It should be noted that the GOx cannot be conjugated into alginate microspheres once they have been coated with polyelectrolytes, although GOx is able to penetrate through the {PAH/PSS} multilayer wall (data not shown); this is because most of the GOx becomes entrapped in the polyelectrolyte wall, rather than diffusing into the sphere and reacting with alginate.

Enzyme Stability in Alginate/GOx Microspheres. Fluorescence spectroscopy was employed to investigate and compare the stability of GOx in alginate microspheres made by the emulsion, conjugation, and emulsion−conjugation techniques, with 0 and 3 bilayers of {PAH/PSS} nanofilm coating. The result of the leaching study (Figure 6) showed the percentage of GOx leached out from alginate microspheres over one week. It can be seen that the emulsion-made alginate/GOx microspheres leach approximately 50% of the standard concentration in 1 week. This may be attributed to relatively large pores in alginate hydrogel microspheres, which allow large and small molecules to pass through, and charge repulsion between alginate and GOx in pH 7.4 PBS buffer. As expected, three bilayers {PAH/PSS} of nanofilm decreased the GOx leaching substantially, from 50.0% to 17.8%.

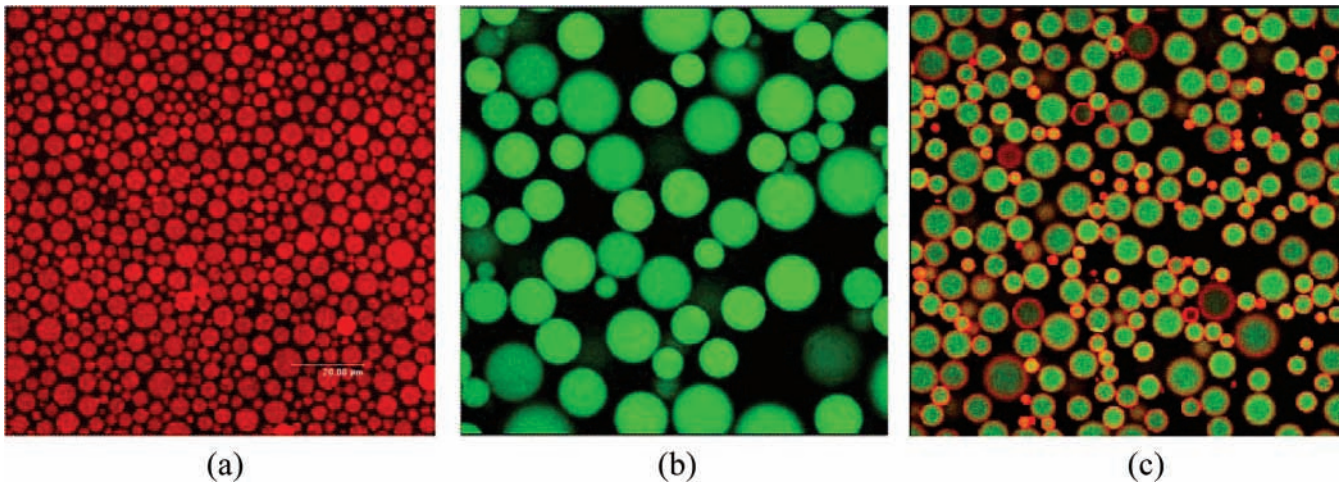

Figure 5. Confocal images of alginate/GOx microspheres. (a) Conjugation-made alginate/GOx microspheres, GOx labeled with RITC. (b) Emulsion−conjugation-made alginate/GOx microspheres, GOx labeled with FITC. (c) Emulsion−conjugation-made alginate/GOx microspheres with 3 bilayers of {PAH/PSS}, GOx labeled with FITC and PAH labeled with RITC.

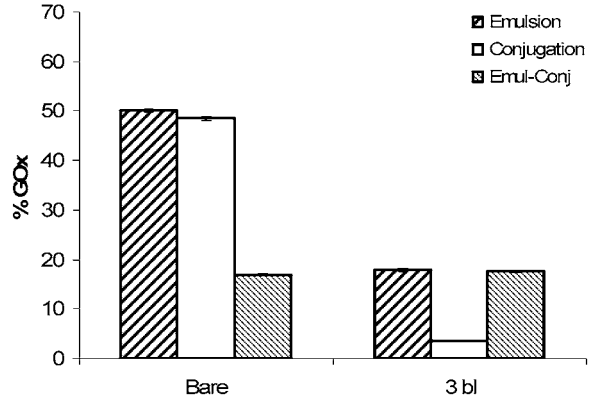

Figure 6. GOx stability in alginate-templated microspheres one week after fabrication.

Unexpectedly, the GOx in conjugation-made alginate/GOx microspheres was found to be unstable in PBS buffer (48.5% leaching), although GOx has been verified to chemically conjugate to alginate. The reason for this may be that the cross-linked alginate hydrogel was decomposed via ion-exchange since PBS buffer contains many monovalent cations (Na^+, K^+) and polyvalent anions (PO_4^{3-}). The calcium ions on alginate hydrogel microspheres may be replaced by those monovalent cations and form insoluble calcium phosphate. Alginate−GOx conjugate, rather than GOx, was therefore leached from the alginate microspheres. For bare alginate microspheres without polyelectrolyte coating, the microspheres will be decomposed and eventually disappear over 2−3 months in PBS buffer. The polyelectrolyte nanofilm coatings were proved to prevent the alginate hydrogels from decomposing substantially, as seen from the leaching result of conjugation-made alginate/GOx microspheres with three bilayers of {PAH/PSS} (3.5% leaching).

The emulsion−conjugation technique also improved the stability of GOx in alginate microspheres. The leaching data for uncoated and three bilayers of {PAH/PSS} alginate microspheres indicated 16.9% and 17.6% loss, respectively. Compared with the conjugation technique, the emulsion−conjugation technique increased the GOx stability for uncoated microspheres, which is especially important since most of the enzyme leaching occurs in the first few hours after the fabrication of alginate microspheres, and substantial loss even occurs during the polyelectrolyte coating process.

Enzyme Activity in Alginate/GOx Microspheres. Since the primary function of enzymes is catalysis, it is ideal to preserve as much activity as possible when encapsulated in alginate microspheres. To determine the effect, if any, of different encapsulation techniques and nanofilm assembly on activity of encapsulated enzyme, the activity of the alginate/GOx microspheres was studied over four weeks of wet storage (0.01 M PBS buffer, room temperature). Figure 7 contains a summary of the experimental results to determine the effect of three different encapsulation techniques and nanofilms on the effective catalytic activity per unit mass of encapsulated GOx (determined by Lowry assay).

For the emulsion technique (Figure 7a), the results show that uncoated alginate microspheres exhibited an 80% reduction in initial activity after one week, with no further notable reduction in activity after four weeks. Coating of {PAH/PSS} nanofilm was observed to reduce the GOx activity from 3.5×10^{-5} to 2.7×10^{-5} AU μg^{-1} s^{-1}; however, reduction of enzyme activity over time for nanofilm coated microspheres was decreased substantially. As seen from Figure 7a, the GOx activity for uncoated microspheres at 4 weeks is about 0.75×10^{-5} AU μg^{-1} s^{-1}, while the GOx activity for the three bilayers of {PAH/PSS} coated microspheres at 4 weeks remains 2.0×10^{-5} AU μg^{-1} s^{-1}.

Table 1. Enzyme Concentration in Alginate/GOx Microspheres

	uncoated spheres (mM)		$\{PAH/PSS\}_3$-coated spheres (mM)	
	0 week	1 week	0 week	1 week
emulsion	66.7	33.4	61.5	50.4
conjugation	3.38	1.69	0.45	0.43
emulsion−conjugation	86.0	68.8	70.1	58.2

For the conjugation technique (Figure 7b), the enzyme activity test results show that increasing nanofilm thickness leads to increased enzyme activity after one week, with the enzyme activity also increasing over time. These unexpected results may arise from two possible explanations: The first is that the total enzyme activity before normalization (division by enzyme mass) is much lower (about 60 times lower than uncoated microspheres at 0 week) than the activity from the emulsion technique. According to our observations, low activity due to low enzyme concentration will still result in relatively high normalized enzyme activity, with larger standard deviation, using the peroxidase assay. A second reason for increasing enzyme activity may be the decomposition of alginate microspheres, in which case the GOx or alginate−GOx conjugates should regain activity as the steric barrier from the cross-linked hydrogel is reduced, providing greater access of substrate to enzyme. A combination of these reasons may cause the result shown in Figure 7b, which needs further studies in the future.

For the emulsion−conjugation technique (Figure 7c), increasing the nanofilm thickness generally decreased the enzyme activity. Furthermore, the enzyme activity also decreased over time. These results are similar with those of the emulsion technique. However, the overall effect on effective activity of nanofilm thickness and time is slight, relative to the emulsion technique. As a result, the enzyme activity of alginate/GOx with three bilayers of {PAH/PSS} made by the emulsion−conjugation technique is almost double that made by the emulsion technique.

All the above results showed the effective GOx activity (GOx activity per unit mass of encapsulated enzyme). It is also important to know the total GOx amount left in alginate microspheres, which is related with enzyme stability. The total enzyme activity could therefore be calculated from the effective GOx activity and amount in the alginate microsphere, which is responsible for the function of glucose biosensor. Table 1 presents the enzyme concentration (determined by Lowry assay) in the alginate/GOx microspheres over 1 week. The GOx is found to be stable in conjugation-made alginate/GOx microspheres, although the enzyme concentration is very low; therefore, the conjugation technique may not be practically useful for large enzymes such as GOx to be encapsulated for biosensors. However, it should be useful to encapsulate small molecules with amine groups (such as peptides) in microspheres where other techniques are difficult to achieve and only a small amount of molecules is needed for encapsulation in this case. The GOx is also stable in the microspheres coated with three bilayers of nanofilm, however, most of the GOx leaching took place before the microspheres were coated with polyelectrolytes. The "emulsion−conjugation" technique greatly

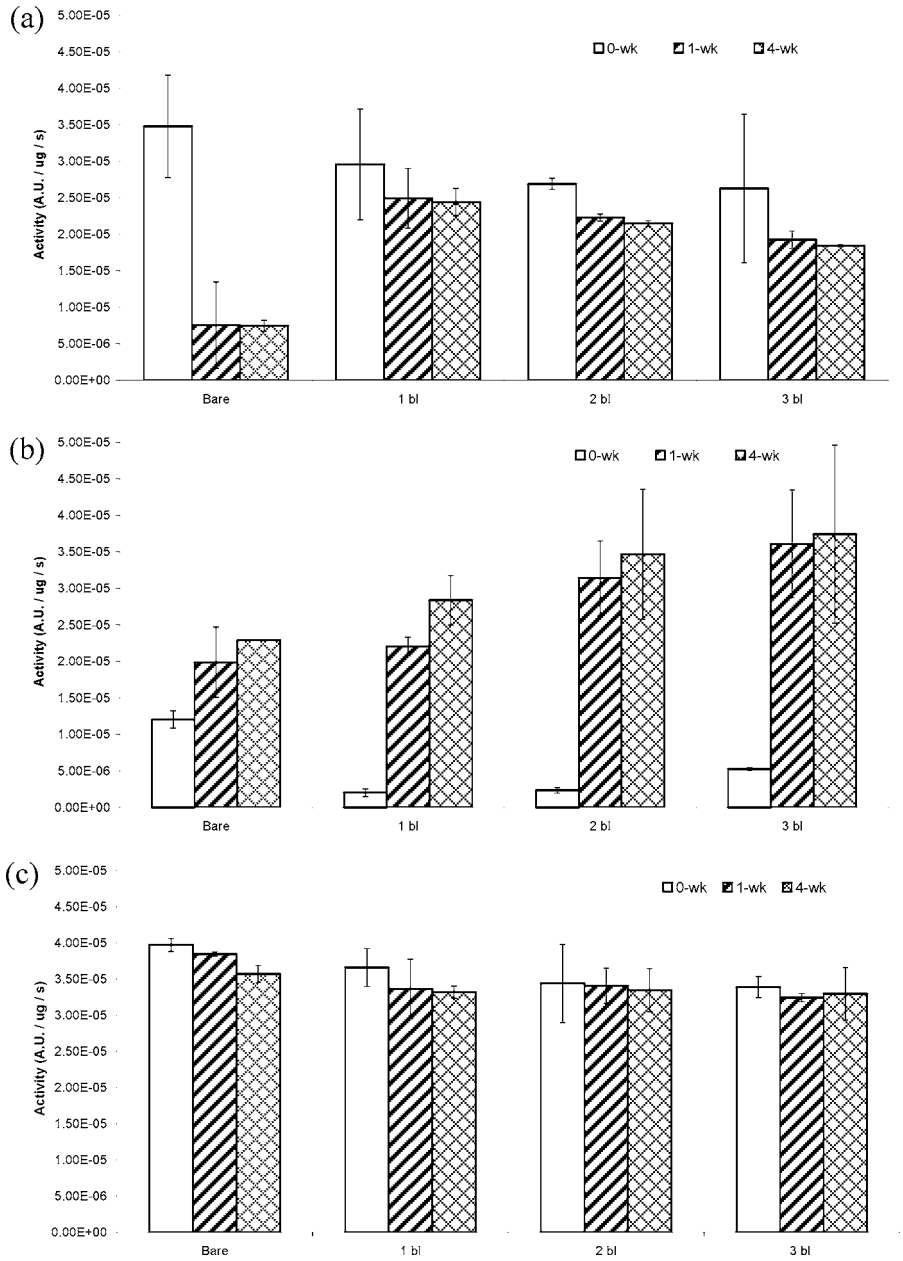

Figure 7. Enzyme activity of alginate/GOx microspheres over time. (a) Emulsion technique. (b) Conjugation technique. (c) Emulsion–conjugation technique.

improved the GOx stability right after the alginate microsphere fabrication. High concentration of GOx and enzyme activity were retained after nanofilm assembly on microspheres. Among the three techniques investigated in our study, emulsion–conjugation was shown to be the most efficient and practical way for GOx encapsulation in alginate microspheres.

CONCLUSIONS

Glucose oxidase (GOx) was successfully encapsulated into calcium-cross-linked alginate hydrogel microspheres via three different techniques, the emulsion, conjugation, and emulsion–conjugation techniques, to be used as implantable glucose biosensors. FTIR, ζ-potential analyzer, and confocal microscopy were used to verify the encapsulation of GOx and formation of nanofilm coating on alginate microspheres. The stability and effective activity of GOx were also investigated to compare these three techniques, with and without polyelectrolyte multilayer nanofilms over 4 weeks. GOx concentration in alginate microspheres was also given to compare the total enzyme activity over time for these three techniques. Of these, the emulsion–conjugation technique was shown to be a practical and effective way to fabricate GOx-encapsulating alginate microspheres for future use as implantable glucose biosensors.

ACKNOWLEDGMENT

This work was supported by NIH (R01 EB00739) and the National Science Foundation (NIRT 0210298).

LITERATURE CITED

(1) Liang, J. F., Li, Y. T., and Yang, V. C. (2000) Biomedical Application of Immobilized Enzymes. *J. Pharm. Sci. 89*, 979–990.

(2) McShane, M. J. (2002) Potential for glucose monitoring with nanoengineered fluorescent biosensors. *Diabetes Technol. Ther. 4*, 533–538.

(3) Brown, J. Q., Srivastava, R., and McShane, M. J. (2005) Encapsulation of glucose oxidase and an oxygen-quenched

fluorophore in polyelectrolyte-coated calcium alginate microspheres as optical glucose sensor systems. *Biosens. Bioelectron. 21*, 212−216.
(4) Amiji, M., and Taqieddin, E. (2004) Enzyme immobilization in novel alginate-chitosan core shell microcapsules. *Biomaterials 25*, 1937−1945.
(5) Gregor, J. E., Fenton, E., Brokenshire, G., Brink, P. V. D., and Sullivan, B. O. (1996) Interactions of Calcium and Aluminum ions with Alginate. *Water Res. 30* (6), 1319−1324.
(6) Heng, P. W. S., and Chan, L. W. (2002) Effect of aldehydes and methods of cross-linking on properties of calcium alginate microspheres prepared by emulsification. *Biomaterials 23*, 1319−1326.
(7) Heng, P. W. S., Chan, L. W., and Jin, Y. (2002) Cross-linking mechanisms of calcium and zinc in production of alginate microspheres. *Int. J. Pharm. 242*, 255−258.
(8) Heng, P. W. S., Chan, L. W., and Lee, H. Y. (2002) Production of alginate microspheres by internal gelation using an emulsification method. *Int. J. Pharm. 242*, 259−262.
(9) Chang, T. M. S. (1964) Semipermeable microcapsules. *Science 146*, 524−525.
(10) Blandino, A., Macias, M., and Cantero, D. (2001) Immobilization of glucose oxidase within calcium alginate gel capsules. *Proc. Biochem. 36*, 601−606.
(11) DeGroot, A. R., and Neufeld, R. J. (2001) Encapsulation of urease in alginate beads and protection from a-chymotrypsin with chitosan membranes. *Enzyme Microb. Technol. 29*, 321−327.
(12) Hussain, Q., Iqbal, J., and Saleemuddin, M. (1985) Entrapment of Concavilin A-Glycoenzyme complexes in Calcium Alginate Gels. *Biotechnol. Bioeng. 27*, 1102−1107.
(13) Bregni, C., Degrossi, G., Garcia, R., Lamas, M. C., Firenstein, R., and Aquino, M. D. (2000) Alginate microspheres of Bacillus subtilis. *Ars. Pharm. 41* (3), 245−248.
(14) Goosen, M. F. A., Al-Hajry, H. A., Al-Maskry, S. A., Al-Kharousi, L. M., El-Mardi, O., and Shayya, W. H. (1999) Electrostatic Encapsulation and Growth of Plant Cell Cultures in Alginate. *Biotechnol. Prog. 15*, 768−774.
(15) Kierstan, M., and Bucke, C. (1977) The immobilization of Microbial Cells, Subcellular Organelles, and Enzymes in Calcium Alginate Gels. *Biotechnol. Bioeng. 19*, 387−397.
(16) Lanza, R. P., and Chick, W. L. (1997) Transplantation of encapsulated cells and tissues. *Surgery 121* (1), 1−9.
(17) Neufeld, R. J., and Quong, D. (1998) DNA Protection from Extracapsular Nucleases, within Chitosan- or Poly-L-Lysine Coated Alginate Beads. *Biotechnol. Bioeng. 60*, 124−134.
(18) Skjak-Braek, G., and Smidsrod, O. (1990) Alginate as immobilization matrix for cells. *TIBTECH 8*, 71−77.
(19) Okano, T., Kikuchi, A., Kawabuchi, M., Sugihara, M., and Sakurai, Y. (1997) Pulsed Dextran release from calcium-alginate gel beads. *J. Controlled Release 47*, 21−29.
(20) Skjak-Braek, G., Strand, B. L., Gaserod, O., Kulseng, B., and Espevik, T. (2002) Alginate-polylysine-alginate microcapsules: effect of size reduction on capsule properties. *J. Microencapsulation 19* (5), 615−630.
(21) Ghanem, A., and Ghaly, A. (2004) Immobilization of glucose oxidase in chitosan gel beads. *J. Appl. Polym. Sci. 91*, 861−866.
(22) Amsden, B., and Turner, N. (1999) Diffusion Characteristics of Calcium Alginate Gels. *Biotechnol. Bioeng. 65*, 605−610.
(23) Liu, L., Liu, S., Ng, S. Y., Froix, M., Ohno, T., and Heller, J. (1997) Controlled release of interleukin-2 for tumour immunotherapy using alginate/chitosan porous microspheres. *J. Controlled Release 43*, 65−74.
(24) Skjak-Braek, G., Gaserod, O., and Sanned, A. (1999) Microcapsules of alginate-chitosan II. A study of capsule stability and permeability. *Biomaterials 20*, 773−783.
(25) Skjak-Braek, G., Thu, B., Bruheim, P., Espevik, T., Smidsrod, O., and Soon-Shiong, P. (1996) Alginate polycation microcapsules I. Interaction between alginate and polycation. *Biomaterials 17* (10), 1031−1040.
(26) Decher, G., Hong, J. D., and Schmitt, J. (1992) Buildup of ultrathin multilayer films by a self-assembly process: III. Consecutively alternating adsorption of anionic and cationic polyelectrolytes on charged surfaces. *Thin Solid Films 210*, 831−835.
(27) Möhwald, H., Sukhorukov, G. B., Donath, E., Davis, S., Lichtenfield, H., Caruso, F., and Popov, V. I. (1998) Stepwise Polyelectrolyte Assembly on Particle Surfaces: a Novel Approach to Colloid Design. *Polym. Adv. Technol. 9*, 759−767.
(28) Lee, C., and Chu, I. (1997) Characterization of modified alginate-poly-l-lyisne microcapsules. *Artif. Organs 21* (9), 1002−1009.
(29) Robitaille, R., Pariseau, J.-F., Leblond, F. A., Lamoureux, M., Lepage, Y., and Halle, J.-P. (1999) Studies on small (<350μm) alginate-poly-l-lysine mirocapsules III. Biocompatibility of smaller versus standard microcapsules. *J. Biomed. Mater. Res. 44*, 116−120.
(30) de Vos, P., Hoogmoed, C. G., and Busscher, H. J. (2002) Chemistry and biocompatibility of alginate-PLL capsules for immunoprotection of mammalian cells. *J. Biomed. Mater. Res. 60*, 252−259.
(31) Gaumann, A., Laudes, M., Jacob, B., Pommersheim, R., Laue, C., Vogt, W., and Schrezenmier, J. (2000) Effect of media composition on long term in vitro stability of barium alginate and polyacrylic acid multilayers. *Biomaterials 21*, 1911−1917.
(32) Rilling, P., Walter, T., Pommersheim, R., and Vogt, W. (1997) Encapsulation of cytochrome C by multilayer microcapsules. A model for improved enzyme immobilization. *J. Membr. Sci. 129*, 283−287.
(33) Schneider, S., Feilen, P. J., Slotty, V., Kampfner, D., Preuss, S., Berger, S., Beyer, J., and Pommersheim, R. (2001) Multilayer capsules: a promising microencapsulation system for transplantation of pancreatic islets. *Biomaterials 22*, 1961−1970.
(34) Srivastava, R., Brown, J. Q., Zhu, H., and McShane, M. J. (2005) Stabilization of Glucose Oxidase in Alginate Microspheres with Photoreactive Diazoresin Nanofilm Coatings. *Biotechnol. Bioeng. 91*, 124−131.
(35) Srivastava, R., Brown, J. Q., Zhu, H., and McShane, M. J. (2005) Stable Encapsulation of Active Enzyme by Application of Multilayer Nanofilm Coatings to Alginate Microspheres. *Macromol. Biosci. 5* (8), 717−727.
(36) Wan, L. S. C., Heng, P. W. S., and Chan, L. W. (1992) Drug encapsulation in alginate microspheres by emulsification. *J. Microencapsulation 9* (3), 309−316.
(37) Srivastava, R., and McShane, M. J. (2005) Application of Self-Assembled Ultrathin Film Coatings to Stabilize Macromolecule Encapsulation in Alginate Microspheres. *J. Microencapsulation 22* (4), 397−411.
(38) Zhu, H., Srivastava R., and McShane, M. J. (2005) Spontaneous Loading of Positively-Charged Macromolecules into Alginate-Templated Polyelectrolyte Multilayer Microcapsules. *Biomacromolecules 6*, 2221−2228.
(39) Kikuchi, A., Kawabuchi, M., Sugihara, M., Sakurai, Y., and Okano, T. (1997) Pulsed dextran release from calcium-alginate gel beads. *J. Controlled Release 47* (1), 21−29.
(40) Brown, J. Q., and McShane, M. J. (2005) Modeling of spherical fluorescent glucose microsensor systems: Design of enzymatic smart tattoos. *Biosens. Bioelectron*., in press.

BC050171Z

Tumor Necrosis Factor (TNF)-Functionalized Nanostructured Particles for the Stimulation of Membrane TNF-Specific Cell Responses

Susanne Bryde,[⊥] Ingo Grunwald,[‖,⊥] Angela Hammer,[†] Anja Krippner-Heidenreich,[†] Thomas Schiestel,[†] Herwig Brunner,[†,§] Günter E. M. Tovar,[†,§] Klaus Pfizenmaier,[†] and Peter Scheurich*[,†]

Institute of Cell Biology and Immunology, University of Stuttgart, Allmandring 31, D-70569 Stuttgart, Germany, Fraunhofer Institute for Interfacial Engineering & Biotechnology, Nobelstrasse 12, D-70569 Stuttgart, Germany, and Institute for Interfacial Engineering, University of Stuttgart, Nobelstrasse 12, D-70569 Stuttgart, Germany. Received June 24, 2005; Revised Manuscript Received September 22, 2005

Most members of the tumor necrosis factor (TNF) ligand family occur in both a membrane-bound and a soluble form, which can possess differential bioactivities. The aim of this work was the construction of a synthetic−biological hybrid system consisting of chemically nanostructured core−shell particles with a diameter of 100 nm, 1 μm, or 10 μm and the cytokine TNF to obtain a tool that mimics the bioactivity of naturally occurring membrane-bound TNF. Synthetic core−shell nanoparticles consisting of an inorganic silica core and an ultrathin organic shell bearing a maleimide group at the shell surface which allowed for a covalent and site-directed coupling of CysHisTNF mutants were prepared. The TNF mutants were modified at the N-terminus by PCR cloning by introducing a His-Tag for purification and a free cysteine group for reaction with the particle-attached maleimide group. The resulting nanostructured hybrid particles initiated strong TNF receptor type 2 specific responses, otherwise only seen for the membrane-bound form of TNF, but not the soluble cytokine, thus clearly demonstrating new and membrane TNF-like properties of the bioconjugated soluble TNF.

INTRODUCTION

Nano- to micrometer-sized particles made of inorganic and organic materials have been used in the past for different biological applications. Micrometer-sized particles for example were used to bind biological targets from biological samples, as has been published for cell sorting (Bildirici and Rickwood, 2001; Kruger et al., 2000) or protein enrichment and purification (Hurst et al., 1999). Furthermore, particles were functionalized with peptides for promoting cellular uptake of the bioconjugated particles (Becker et al., 2004), as a DNA carrier (Maruyama et al., 1997), for drug delivery (Lockman et al., 2002), or for mammalian cell transformation (Sandhu et al., 2002). In addition, fluorescent-labeled particles decorated with affinity ligands such as antibodies were successfully used for cell imaging (Willard, 2003; Gao et al., 2005). Particles exposing streptavidin on their surface to allow coating of the particles with biotin-conjugated proteins were shown to represent a valuable tool for spatially restricted receptor-selective stimulation of cells (Verveer et al., 2000).

In multicellular organisms, receptor ligands are often presented at the surface of cells. Such cell membrane-bound ligands bind highly specific to their corresponding interaction partners, based on molecular recognition processes. This type of intercellular communication is essential to sustain homeostasis in all higher organisms. The inflammatory cytokine tumor necrosis factor (TNF, also termed TNFα) is the representative member of a large homologous protein ligand family, mirrored by a respective family of cell surface membrane receptor proteins (Locksley et al., 2001; Aggarwal, 2003). TNF is crucially involved in inflammatory responses to elicit effective innate immune responses but is also a key player in many pathological situations such as septic shock, rheumatoid arthritis, and neurodegenerative diseases, e.g. multiple sclerosis (Grell and Scheurich, 1999; Wajant et al., 2003). In addition, TNF is capable of inducing apoptosis and is a promising candidate for new strategies in cancer therapy under conditions where systemic side effects can be avoided, as demonstrated in isolated limb perfusion (Eggermont and ten Hagen, 2001). Most studies with TNF have been performed with the soluble cytokine (sTNF). However, typical for the members of the TNF ligand family, TNF is a genuine type 2 transmembrane protein (memTNF) and initially expressed at the cell membrane. From this membrane-bound protein sTNF is subsequently derived from proteolytic processing by the metalloproteinase TACE (tumor necrosis factor alpha-converting enzyme) (Black et al., 1997). Both memTNF and sTNF bind to two different cell membrane receptors, termed TNFR1 (CD120a) and TNFR2 (CD120b) (Locksley et al., 2001). Whereas TNFR1 is ubiquitously expressed in all tissues, TNFR2 is highly

* To whom correspondence should be addressed. Phone: +49 711 685 6987; Fax: +49 711 685 7484; E-mail: peter.scheurich@izi.uni-stuttgart.de.

† Institute of Cell Biology and Immunology, University of Stuttgart.

‡ Fraunhofer Institute for Interfacial Engineering & Biotechnology.

§ Institute for Interfacial Engineering, University of Stuttgart.

‖ Present address: Fraunhofer Institute for Manufacturing and Advanced Materials, Bonding Technology and Surfaces Department, Wiener Str. 12, D-28359 Bremen, Germany.

⊥ These authors contributed equally to this work.

10.1021/bc0501810 CCC: $30.25 © 2005 American Chemical Society
Published on Web 10/27/2005

Scheme 1. TNF-α Signaling Capabilities[a]

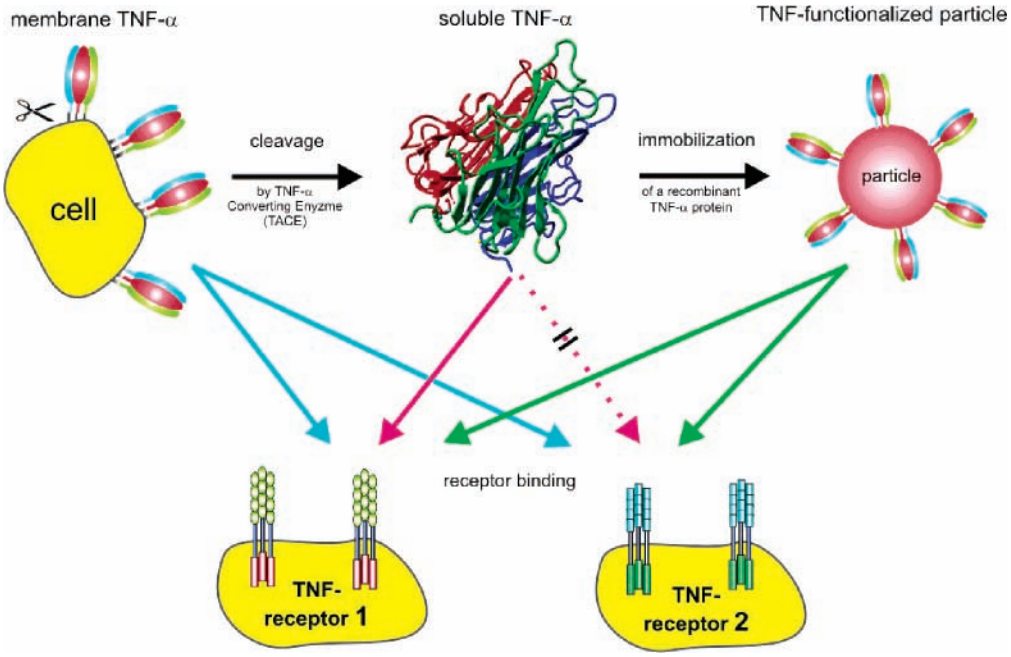

[a] TNF is a transmembrane protein (membrane or memTNF) and initially expressed at the cell surface. From this membrane-bound form the soluble TNF (sTNF) is proteolytically derived by action of the metalloproteinase TACE (tumor necrosis factor alpha-converting enzyme). Both memTNF and sTNF bind to two different cell membrane receptors, termed TNF receptor (TNFR) 1 and 2. Membrane TNF strongly activates both receptors, whereas sTNF is capable to only stimulate TNFR1 but not TNFR2. Functionalized particles with a recombinant TNF protein bind to and strongly activate both receptors, thus mimicking the action of memTNF.

regulated in expression and mainly found in immune cells and endothelial cells but also in neuronal tissue.

The two TNF forms possess differential capabilities for the induction of larger signaling complexes. Whereas sTNF binding enforces receptor trimerization only, cell-associated memTNF might subsequently cause the formation of larger complexes by induction of capping of the membrane-bound ligand molecules and the receptors at the respective interacting cellular sites.

In light of these data, it is very likely that the physiological role of TNFR2 is largely underestimated, simply because sTNF has been used in by far the most studies. Accordingly, there is a need for a memTNF-adequate stimulus that can be easily applied in experimental systems in vitro but also in animal model systems in vivo. To overcome the lack of an appropriate memTNF-like stimulating reagent, we have here constructed silica-based particles covalently coupled with mutated functional TNF derivatives (here also termed as muteins), forming bioactive homotrimers at the particle surface (Scheme 1). These novel particles are able to initiate memTNF-resembling cellular responses.

EXPERIMENTAL PROCEDURES

Particle Synthesis and Characterization. Nano- and microparticles of three different mean particle sizes (100 nm, 1 μm, and 10 μm) and consisting of silica were used as core material for organic modification. The smaller sized silica particles (100 nm and 1 μm) were synthesized following the method of Stober (Stober et al., 1968) as described elsewhere (Schiestel et al., 2004). Briefly, to obtain particles with a mean particle diameter of 100 nm, a mixture of 1.37 mL ammonia (25 wt. %, SAF, Taufkirchen, Germany), 2 mL of H_2O, and 500 mg of tetraethoxysilane (TEOS; ABCR, Karlsruhe, Germany) in 40 mL of ethanol (HPLC-grade, SAF, Taufkirchen, Germany) were stirred for 24 h at room temperature (RT). Afterward they were separated by centrifugation (13000 rpm, 15 min) and suspended in 10 mL of ultrapure water, then put into dialysis until conductance was below 1.3 μS/cm. Particle sizes and ζ-potentials were routinely monitored by photocorrelation spectroscopy and microelectrophoresis using a Zetasizer 3000 HSA (Malvern Instruments, Herrenberg, Germany). ζ-Potentials of the 100 nm and 1 μm particles were determined at pH 4.7 in acetate buffer. The ζ-potential of 10 μm particles was not determined by microelectrophoresis due to instability toward sedimentation during the measurements. To generate particles with a mean diameter of 1 μm, a mixture of 1.44 g of ammonia, 1.04 g of TEOS, and 10 mL of ethanol were stirred for 3.5 h at RT. The resulting particles were washed with 100% ethanol and suspended in 10 mL of 100% ethanol prior to any further modification. The 10 μm particles were purchased from Kisker (Steinfurt, Germany) and washed in the particular solvent before use.

Preparation of Fluorescent Shell. An ultrathin fluorescent shell for confocal microscopy studies was covalently attached to the 100 nm, 1 μm, and 10 μm particles according to the following method. *N*-Hydroxysuccinimide ester Alexa dye 546 or 568 (MoBiTec, Göttingen, Germany) (500 μg) was incubated for 3 h at RT with 111 μg of (3-aminopropyl)triethoxysilane (ABCR, Karlsruhe, Germany) in 64 μL of ethanol. An amount of 50 mg of silica particles in 1.6 mL of 100% ethanol, 3.3 μL (3.05 mg) of TEOS, and 167 μL of ammonia were added, and the mixture was stirred for 20 h at RT. To avoid photobleaching, all steps involving fluorescence markers were performed in the dark. The resulting particles were washed five times with 100% ethanol and once with acetate-buffered solution (pH 4.7) and suspended in acetate buffer.

Particle Surface Modification. An amount of 100 mg of silica particles (in acetate buffer) was stirred with 100 μL of ammonia, 6.8 mg of TEOS, and 20.4 mg of APS for 24 h at room temperature. The resulting particles

were washed intensively and suspended in water. An amount of 1 mg of APS-modified particles was suspended in PP72 (183 μL of 10 mM phosphate buffer pH 7.2), 817 μL of a 3.06 mM sulfosuccinimidyl-4-(*N*-maleimidomethyl)cyclohexane-1-carboxylate (SMCC; Perbio Science, Bonn, Germany) solution in PP72 was added, and the reaction mixture was shaken for 1 h. All steps were performed under sterile conditions. The resulting particles were collected by centrifugation at 4 °C, washed with 1 mL of ice-cold PP72, suspended in 1 mL of ice-cold PP72, and then immediately used for protein coupling reactions.

Construction and Purification of CysHisTNF and Derived Muteins. Expression constructs optimized for bacterial codon usage of a histidine-tagged soluble TNF (HisTNF) was originally obtained from Philippe Holliger, Cambridge, UK. The CysHisTNF expression construct, pQE5 CysHisTNF, was produced by site-directed mutagenesis introducing the coding sequence of a cysteine residue as well as a factor Xa cleavage site (IEGR) and a His tag. This generated an N-terminal sequence tag (MGELIEGR**C**AGGSGHHHHHHGSDGAS) fused to serine 79 of human TNF. Receptor specific TNF muteins (CysHisTNF143N/145R and CysHisTNF32W/86T) were also generated by site-directed mutagenesis using pQe5CysHisTNF as template. All constructs generated by PCR were verified by sequencing. For the production of CysHisTNF, *E.coli* XL1 blue cells transformed with CysHisTNF expression constructs were grown overnight. The following day the cultures were diluted 1:10, grown to a density of $OD_{600\ nm}$ 0.5−0.7, and then induced by 1 mM IPTG for 6 h at 30 °C. Cells were washed in phosphate-buffered saline (PBS) and centrifuged, and the pellet was frozen at −20 °C. The cell pellet was resuspended in PBS (3 mL PBS/g pellet), cells were lysed by sonification on ice, and the cell debris was pelleted at 12000 g for 15 min at 4 °C.

CysHisTNF was purified using a HiTrap column (1 mL; Pharmacia) following the instructions of the manufacturer. Briefly, the column was connected to a peristaltic pump with a flow rate of 1 mL/min and equilibrated with 10 mL of buffer 1 (20 mM NaH_2PO_4 pH 7.4, 0.5 mM NaCl, 10 mM imidazole), and then the supernatant was loaded and the column was washed with 10 mL of buffer 2 (20 mM NaH_2PO_4 pH 7.4, 0.5 mM NaCl, 30 mM imidazole) followed by elution of CysHisTNF using 7 mL of buffer 3 (20 mM NaH_2PO_4 pH 7.4, 0.5 mM NaCl, 500 mM imidazol). Fractions of 500 μL were collected and analyzed for their CysHisTNF content by Coomassie gel analysis as described in Grunwald et al. (2003). Positive fractions were pooled and dialyzed against PBS at 4 °C. Protein concentration was determined by Bradford method (BioRad, Germany) and the protein stored at 4 °C.

TNF-Coupling to Core−Shell Particles. Similar to wildtype TNF, CysHisTNF exists in its bioactive form as a noncovalently linked homotrimer, with each monomer carrying a free Cysteine residue near its N-terminus, all three located close together. Accordingly, CysHisTNF tends to form disulfide bridges, one type linking two of its monomers and a second type bridging two CysHisTNF homotrimers. To reduce these cysteine bridges, CysHisTNF or its derivatives were pretreated with 10 mM dithiothreitol (DTT) overnight at 4 °C. DTT was removed by dialysis for 3 h against PBS, and the solution was sterilized by filtration. DTT-treated CysHisTNF showed the same bioactivity as the native protein, indicating that the reduction of the N-terminal cysteines does not influence the disulfide bridges within the TNF monomers (data not shown).

Nanostructured particles with a diameter of 100 nm, 1 μm, or 10 μm and bearing a sulfoSMCC-shell (1 mg beads/mL) were incubated with 25 μg (1 μm, 100 nm beads) of CysHisTNF in PBS or 50 μg (10 μm beads) of CysHisTNF in PBS for 1 h at RT in vials which were constantly being rolled. Control beads were prepared by addition of 200 mM β-mercaptoethanol to 1 mg of beads in PBS. Labeled beads were centrifuged at 14000 g for 10 min at 4 °C. The supernatant with surplus CysHisTNF was discarded, and the beads were washed twice (centrifugation step between the washings) with sterile cell culture medium to remove unligated CysHisTNF. The final preparation was resuspended in 200 μL of culture medium and stored at 4 °C, protected from light. Bioactivity of the particles was determined in a cytotoxicity assay as described.

Cell Lines. HeLa cells stably transfected with human TNFR2 (HeLa80) or immortalized mouse fibroblasts (MF) from TNFR1/TNFR2 double knockout mice stably transfected with TNFR1-Fas or TNFR2-Fas expression plasmids (MF TNFR1-Fas, MF TNFR2-Fas) have been described elsewhere (Weiss et al., 1997; Krippner-Heidenreich et al., 2002). The human rhabdomyosarcoma cell line KYM-1 was supplied by M. Sekiguchi (University of Tokyo, Tokyo, Japan), and the human HeLa cell line was obtained from the American Type Culture Collection. HeLa cells, KYM-1 cells, and the immortalized mouse fibroblasts MF TNFR1-Fas and MF TNFR2-Fas were grown in RPMI 1640 medium supplemented with 5% (v/v) heat-inactivated fetal calf serum and 2 mM L-glutamine. The expression of the receptor fusion proteins TNFR1-Fas and TNFR2-Fas in fibroblasts was controlled routinely by FACS analysis (Krippner-Heidenreich et al., 2002).

Transient Transfection and Live Imaging by Confocal Laser Scanning Microscopy. Cells were harvested and transiently transfected with 6 μg of pFADD-EGFP or pTNFR2-EGFP expression plasmids by electroporation. An amount of 10^6 cells per 800 μL of culture medium was electroporated at 250 V and 1800 μF in a 0.4 cm cuvette (Peqbio Easyject Plus, Peqlab). An amount of 3×10^5 cells was seeded immediately after electroporation into 3.5 cm coated glass bottom dishes (Mattek Corp., Ashland, MA) and cultured for 24 h before stimulation. Cells were then treated with CysHisTNF-labeled particles of different sizes. Images were taken at the indicated time points using a TCS SL confocal laser scanning microscope (Leica).

Cytotoxicity Assays. Mouse fibroblasts or KYM-1 cells (1×10^4 cells/well) were grown in 96-well plates overnight. Cells were then treated as indicated and cultivated overnight. The next day cells were washed three times with PBS followed by crystal violet staining (20% methanol, 0.5% crystal violet) for 15 min. The wells were washed with H_2O and air-dried. The dye was resolved with methanol for 15 min, and optical density at 550 nm was determined with an ELISA plate reader (SPECTRAmax 340PC, Molecular Devices Corp., Sunnyvale, CA).

RESULTS

Functionality of Organically Activated Core−Shell Particles. Core−shell nanoparticles and microparticles were prepared consisting of an inorganic core and an organic shell bearing both fluorescent markers and functional surface groups suitable for the coupling of TNF muteins. The inorganic core of the particles consisted of silica prepared via sol−gel chemistry (Scheme

Scheme 2. Synthesis, Modification and Assembling of the TNF-Functionalized Particles[a]

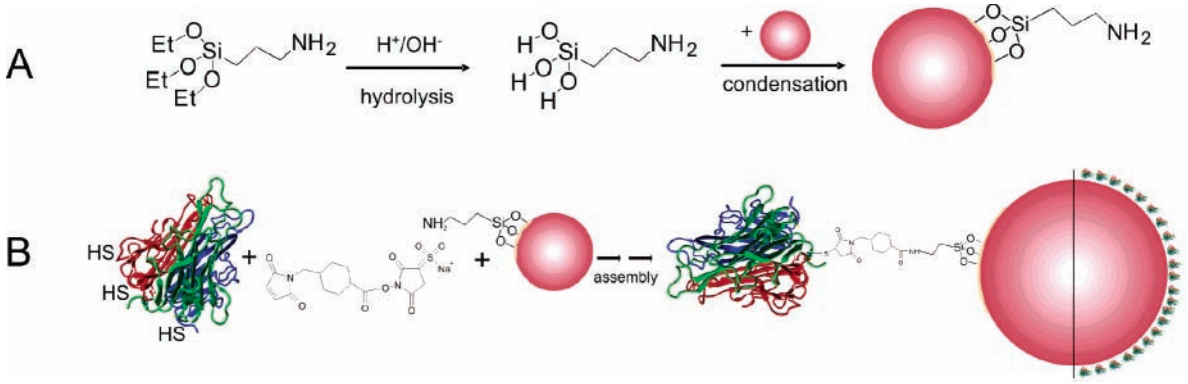

[a] Core particles are generated in a reaction mixture containing tetraethoxysilane, ammonia, water, and ethanol. Subsequently the silica particles are surface-modified using APS, ammonia, and TEOS (A). The particles are then surface activated using the heterobifunctional cross-linker SMCC (B) which is coupled to the amino groups of the modified particles. The maleimide group of the cross-linker then reacts with the free sulfhydryl groups of the TNF molecule, generating stable thioether bonds. The schemes are not drawn at the same scale (calculated sizes are: SMCC ~ 0.13 nm, TNF ~5.5 × 4.4 nm and nanoparticle ~ 100 nm) with the exception of the right part of the functionalized particle in B.

2A) and showed a negative ζ-potential of −(13.9 ± 1.6) mV for the 100 nm particles and −(13.7 ± 3.3) mV for the 1 μm particles. The ζ-potential was shifted toward highly positive values during the preparation of the organic shell consisting of APS (Scheme 2B) and fluorescent markers and resulting values of (40.1 ± 4.2) mV for the 100 nm particles and (43.2 ± 6.5) for the 1 μm particles. The colloidal stability of the core−shell particles was high enough that in this case the ζ-potential of the 10 μm particles was detectable by microelectrophoresis, rendering a value of ~52.3 mV. The organic shell was further modified by the bifunctional organic cross-linker SMCC, bearing one chemical group for reaction with the particles' amino surface and a maleimido group as second functional group for formation of a shell surface suitable for later protein coupling reactions to the shell surface. The shell modification by SMCC led to a slightly negative ζ-potential with −(3.4 ± 6.0) mV for the 100 nm particles.

Functionality of TNF-Coupled Nanoparticles. For covalent binding on the activated silica particles, CysHisTNF was used, a TNF mutein containing a His tag for purification purposes and a cysteine residue near its N-terminus (Scheme 2B). Under nonreducing conditions CysHisTNF rapidly forms covalently linked dimers (calculated M_r 39 × 10^3; Figure 1A, lane 1). To obtain reduced CysHisTNF, the TNF mutein was treated with DTT overnight and subsequently dialyzed against PBS (Figure 1A, lane 2). This protein shows a slightly higher apparent molecular weight as compared to soluble human TNF, in accordance with the added CysHis tag (Figure 1A, lane 3).

Mouse fibroblasts derived from TNFR1 and TNFR2 double knockout animals stably expressing TNF receptor/Fas chimeras rapidly develop apoptosis when adequately stimulated. The TNFR1-Fas chimera positive cells respond to both sTNF and memTNF, whereas the TNFR2-Fas chimera only responds to the membrane-bound form of the ligand (Krippner-Heidenreich et al., 2002). TNFR2-Fas positive cells were used for an initial characterization of the bioactivity of TNF-coated particles. Soluble CysHisTNF was inactive on these cells over a wide dose range and induced only at high concentrations a weak cytotoxic effect (Figure 1B), presumably caused by the presence of a minor proportion of higher molecular weight aggregates, e.g. hexamers comprised of three covalently linked dimers (data not shown). In the presence of the TNFR2-specific antibody 80M2, however, known to develop a membrane TNF-like activity when combined with soluble TNF (Grell et al., 1993; Grell et al., 1995), a strong cytotoxic activity toward TNFR2-Fas positive cells was observed (Figure 1B). These data demonstrate that CysHisTNF bioactivity resembles wildtype sTNF, i.e., the introduction of the N-terminal tags did not significantly affect sTNF's function. When coupled to beads, the parental TNFR1/TNFR2 knockout fibroblasts were fully unresponsive to treatment with CysHisTNF positive particles, similar to unconjugated control beads (Figure 1C). However, when TNFR2-Fas-expressing mouse fibroblasts were used, CysHisTNF beads induced a strong and dose-dependent cytotoxic effect, whereas control beads were ineffective (Figure 1D). These results demonstrate a memTNF-like bioactivity of CysHisTNF positive beads.

Receptor Selectivity of Beads Coated with CysHisTNF Mutants. Various mutants of human TNF have been produced that exert a pronounced selectivity for one of the two TNF receptors (Van, X et al., 1993; Loetscher et al., 1993). A high selectivity for TNFR1 and TNFR2, respectively, can be obtained by exchange of only two amino acids, leading to the TNF mutants TNF32W/86T (TNFR1 selective) and TNF143N/145R (TNFR2 selective), that have been characterized quite extensively in the past (Beyaert and Fiers, 1994). CysHis-variants of these two TNF muteins were constructed, produced, and coupled to activated beads. CysHisTNF32W/86T shows a bioactivity on TNFR1-Fas chimeric receptors comparable to wild-type TNF but is inactive on TNFR2. CysHisTNF143N/145R possesses a mild memTNF-like bioactivity on TNFR2-Fas molecules while inactive on TNFR1-Fas (Krippner-Heidenreich et al., 2002). As expected, a marked receptor selectivity could be observed when applied to cells expressing TNFR1-Fas or TNFR2-Fas receptor chimera. Similar to control beads, CysHisTNF143N/145R positive beads induced no cytotoxic response in TNFR1-Fas-expressing mouse fibroblasts, whereas CysHisTNF32W/86T positive beads were strongly cytotoxic (Figure 2A). Vice versa, the TNFR2-Fas chimera expressing cells were responsive to treatment with CysHisTNF143N/145R positive beads only (Figure 2B).

Stability of CysHisTNF-Labeled Beads. To test for the stability of generated TNF-beads, CysHisTNF-coupled particles of 10 μm diameter were produced washed and their cytotoxic activity was quantified using

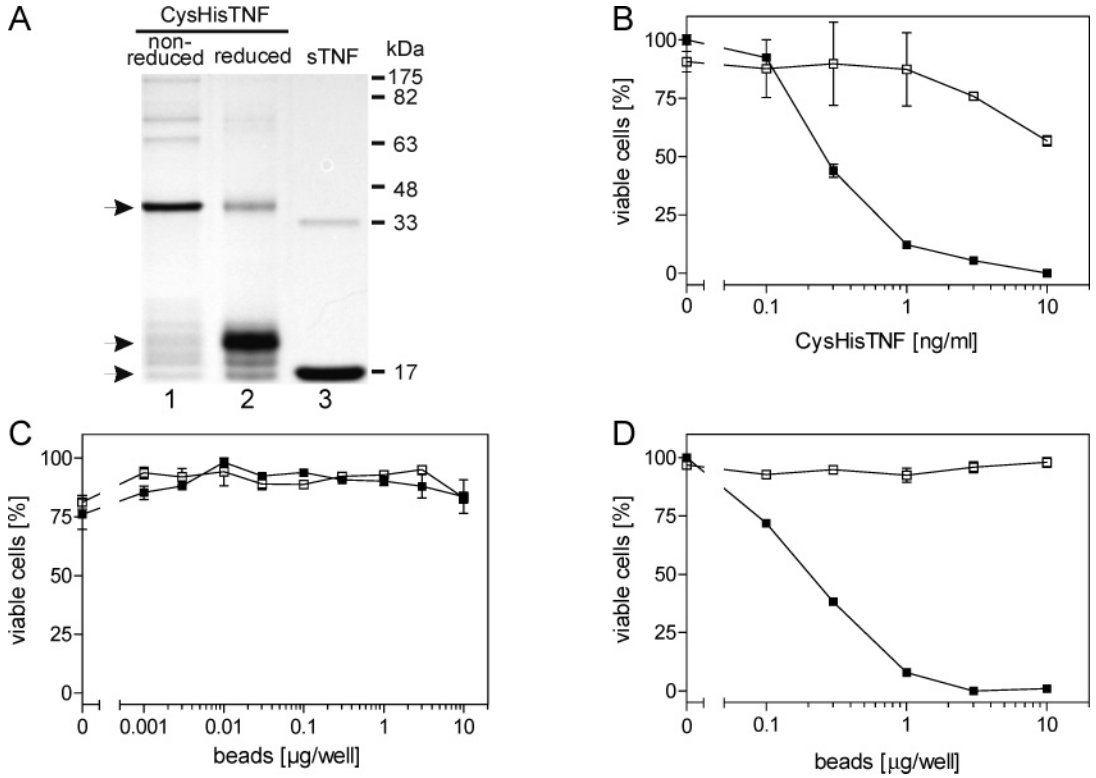

Figure 1. Characterization and bioactivity of soluble CysHisTNF and CysHisTNF coupled beads. CysHisTNF was incubated overnight with 10 mM DTT to reduce covalently linked dimers and dialyzed for 3 h against PBS. A**.** An amount of 5 μg of protein per lane was analyzed using a 15% nonreducing SDS−PAGE. Lane 1: CysHisTNF before DTT treatment, lane 2: CysHisTNF treated with DTT, lane 3: wild-type soluble TNF. The arrows at the left indicate dimeric CysHisTNF, monomeric CysHisTNF, and wild-type sTNF monomers, respectively. Numbers at the right indicate molecular weight markers. B, C, and D. Cell viability was determined in a standard cytotoxicity assay using crystal violet staining. Results are expressed as mean values of duplicates, representative results from three independent experiments are shown. B. TNFR2-Fas expressing mouse fibroblasts were stimulated with soluble CysHisTNF alone (□) or after preincubation with the mAb 80M2 (■; 1 μg/mL). C and D. DTT-treated CysHisTNF was coupled onto activated 1 μm beads. TNF-coated particles (■) and uncoated beads (□) as a negative control were used to stimulate TNFR1/TNFR2 double knockout mouse fibroblasts (C) or TNFR2-Fas expressing cells (D).

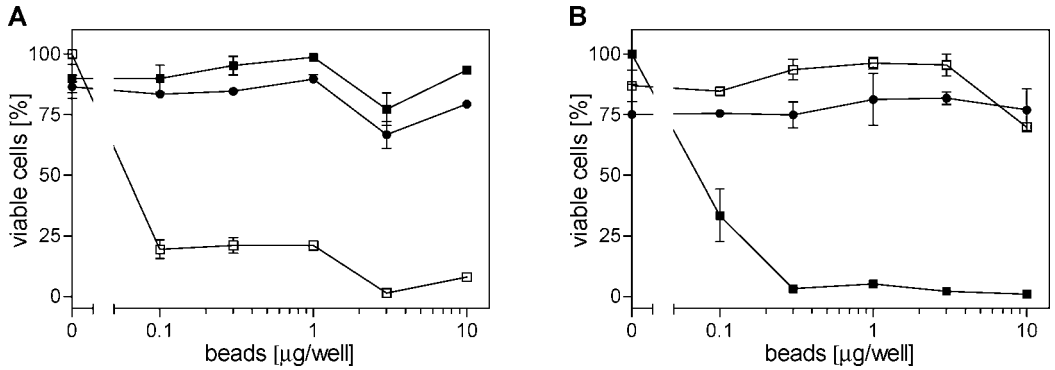

Figure 2. Receptor selectivity of beads coated with CysHisTNF mutants. The TNF derived muteins CysHisTNF32W/86T (□) and CysHisTNF143N/145R (■) were pretreated with DTT to reduce covalently linked dimers, dialyzed, and coupled onto activated beads. Bioactivity and receptor-selectivity were determined using TNFR1-Fas (A) and TNFR2-Fas (B) chimera expressing mouse fibroblasts in comparison to TNF negative control beads (●). Cell viability was quantified using crystal violet staining. Mean values of duplicates are shown.

the rhabdomyosarcoma cell line KYM-1 (Figure 3A). An aliquot was stored at a concentration of 5 μg particels/μL in fetal calf serum containing cell culture medium for five weeks at 4 °C. Thereafter, the beads were washed once to remove unbound CysHisTNF, and their bioactivity was tested in a cytotoxicity assay (Figure 3B). Whereas control beads induced no significant cytotoxic effect in both experiments, the CysHisTNF positive beads induced a strong cytotoxic effect with half-maximum efficiency at a concentration of about 0.5 μg/well, indicating no significant loss of bioactivity during the storage period of five weeks (Figures 3, A and B).

Specific Bioactivity of CysHisTNF-Labeled Beads. The LD_{50} value of CysHisTNF coated beads of 1 μm size was found to be in the order of 0.2 μg beads/well (1.0 μg/mL) in a standard cytotoxicity assay using TNFR2-Fas positive mouse fibroblasts (Figure 1D). From these values it can be calculated that about 2×10^5 particles induced half-maximum apoptosis in a single well containing 20000 cells, or 10 beads per cell (1 mg of beads with 1 μm size equals to 9.55×10^8 particles). This method to assess the bioactivity of the beads might be inadequate, however, since the particles might come into contact with their target cells only statistically. More reliable informa-

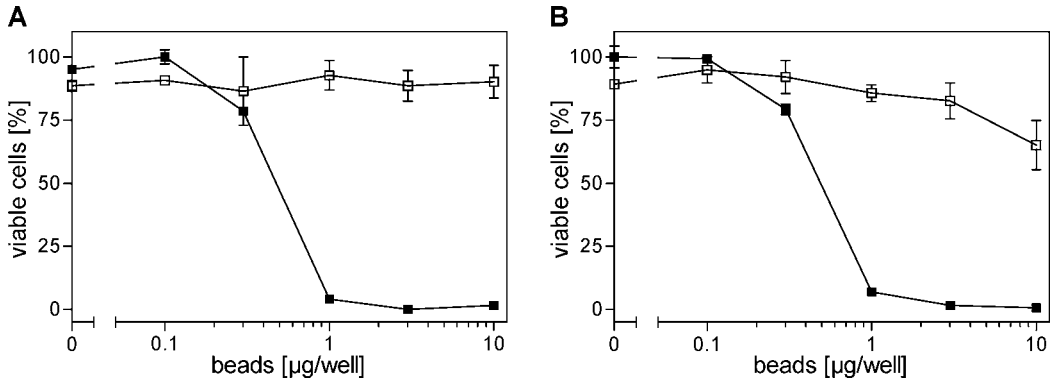

Figure 3. The bioactivity of TNF-coated particles remains stable upon storage at 4 °C. CysHisTNF-coupled beads (■) were stored at a concentration of 5 μg particles/μL for five weeks in FCS-containing culture medium. Subsequently they were washed, resuspended in fresh culture medium, and tested on KYM-1 cells in a standard cytotoxicity assay in comparison to control beads negative for TNF (□). A. Freshly prepared particles. B. Beads after storage for 5 weeks at 4 °C in RPMI/FCS 5%. Results are expressed as the mean values of duplicates.

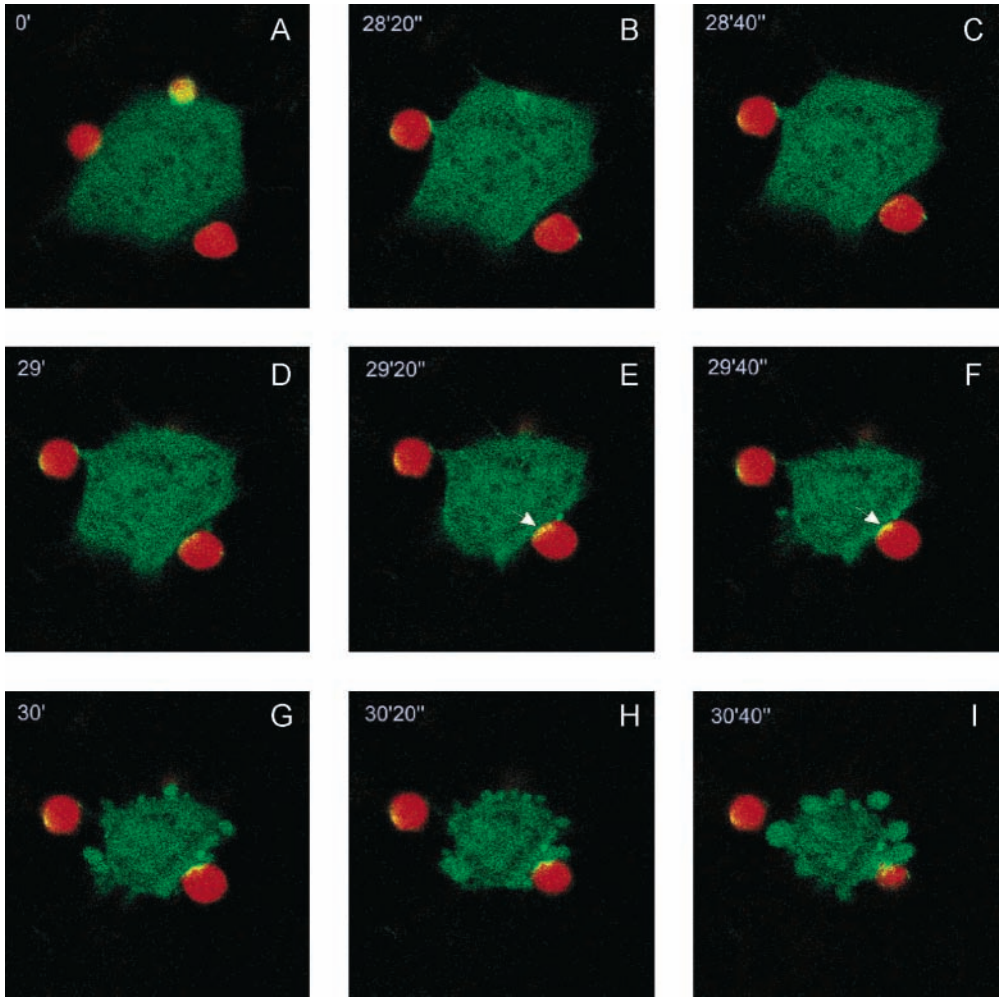

Figure 4. Induction of apoptosis in TNFR2-Fas positive mouse fibroblasts.Alexa-Fluor-568 stained beads of 10 μm diameter had been coated with CysHisTNF. 10^6 TNFR2-Fas mouse fibroblasts were transiently transfected with human pEGFP−FADD and grown overnight in glass bottom culture dishes. An amount of 100 μg of beads was added to the cells, and a particular cell was chosen for further observation ($t = 0$) using a confocal laser scanning microscope. Images were taken every 10 s over a time period of 40 min (A−I). The white arrows indicate FADD recruitment. Note that the development of the apoptotic phenotype takes place within only about 2 min after a lag time of about 29 min (F−I).

tion regarding the potency of TNF-coupled beads could be obtained from data at the single cell level. Large CysHisTNF-coated particles of 10 μm diameter, prelabeled with Alexa-Fluor-568-dye, were used for live cell imaging experiments using confocal microscopy. These beads were added to TNFR2-Fas positive mouse fibroblasts overexpressing human FADD (Fas-associated death domain protein)-EGFP. The cells were then observed regarding their contact with one or more beads. In Figure 4, a single TNFR2-Fas-expressing mouse fibroblast is shown to undergo apoptosis after stimulation by three 10 μm CysHisTNF beads. As a receptor-proximal event, FADD-EGFP recruitment into the death-inducing signaling complex (DISC) was evident from induced membrane

colocalization with beads (yellow color; see white arrows). Cell shrinking, the first optically visible sign of cell death, was observed after 29 min. Blebbing and fragmentation of the cell into smaller vesicles followed rapidly within the next 2 min (Figure 4).

To perform statistical analyses, we used particles of 1 μm diameter. TNFR2-Fas positive mouse fibroblasts expressing human FADD-EGFP were treated with 25 μg of red fluorescent beads that had been coupled with CysHisTNF. After an incubation time of 5 min, single cells were identified with beads in contact and observed for the next 30 min. Twenty-seven cells from nine different sample preparations were observed to develop apoptosis. These cells had been in contact, in average, with six beads (6.3 ± 3.2, $n = 27$; data not shown). Approximately 600 cells from six different dishes were subsequently counted to determine the total percentage of apoptotic cells (66%). Accordingly, at a beads dose close to the LD_{50} value, the apoptotic cells had been in contact, on average, with six beads. This value is very similar to that determined in dose−response assays applying serial dilution of beads, where the observed LD_{50} value of 0.2 μg/well corresponds to 10 beads/cell (Figure 1D).

Within a size ranging from 100 nm to 10 μm in diameter, the beads had been estimated to bind on average 4.5 μg of CysHisTNF per mg of carrier material (3.2−5.5 μg/mg beads; $n = 11$; data not shown). These results indicate some limiting factor in the coupling procedure independent of the surface size of the beads, which varies by a factor of hundred within the used size range. Accordingly, a single particle of 1 μm diameter has bound about 50000 molecules of TNF (trimers) at the surface, a number which is in good agreement with the specific binding capacity calculated earlier (Schiestel et al., 2004). We estimated from microscopical analyses that one-third of the particle surface would be in direct contact with the cell, i.e., capable to engage receptors. From these estimations, it follows that, with an average of six beads contacting the cell surface at a LD_{50} dose, about 100000 TNF molecules are available for signaling. However, the receptor number available at the contact site of the cell is much lower. We assume that the 45000 TNFR2-Fas molecules expressed per cell are homogeneously distributed at the cell surface, as indicated from confocal microscopy data (Krippner-Heidenreich et al., 2002). The cellular contact site with the six beads covers about 5.6 μm^2, or about 0.6% of the cell surface (with an estimated available cell surface of about 900 μm^2), i.e., only about 270 receptor molecules would be directly targeted. Although the number of engaged receptors might increase somewhat due to lateral diffusion of more molecules into the contact site, these data indicate that particle-mediated activation of less than 1000 receptors is sufficient to kill a cell. These estimations indicate a very high memTNF-like potential of the carrier coupled CysHisTNF.

DISCUSSION

Most of the members of the TNF-ligand superfamily exist in two bioactive forms: a membrane-bound form and its soluble counterpart, processed from the membrane-bound TNF by metalloproteases and/or produced by alternative splicing (Black et al., 1997; Grell and Scheurich, 1999). Both soluble and membrane-bound TNF do bind and stimulate TNFR1. Although TNFR2 also binds sTNF and memTNF, only the latter is capable to strongly activate this receptor (Grell et al., 1995). Therefore, the investigation of TNFR2 signaling pathways has long been hampered by the lack of adequate memTNF-mimicking tools. In this work, we have produced nano- and microparticles with directedly and covalently coupled TNF derivatives at their surface (Scheme 1). As core particles, silica-based beads have been used that can be easily activated for covalent coupling (Schiestel et al., 2004). Silica particles of various sizes were coated with CysHisTNF, exposing a free SH-group in their N-terminal cysteine residue to generate a memTNF equivalent. In average, about 5 μg of CysHisTNF could be coupled per mg of beads, independent of its size ranging between 0.1 μm and 10 μm. This indicates a decreasing density of the coupled TNF molecules with decreasing particle size. In any case the resulting particles contained a much higher density of CysHisTNF molecules on their surface as compared to a typical receptor density of a TNF responsive cell (approximately 16000 molecules of CysHisTNF per μm^2 on a 1 μm particle versus an about 100 fold lower cellular receptor density).

Beside covalent coupling, some adsorption of CysHisTNF was also observed in our experiments, although the particles had been intensively washed to remove unligated CysHisTNF. This was estimated to be 10% or less of the covalently coupled material, as calculated from control experiments with wild-type TNF (data not shown). CysHisTNF-coated beads could be stored at 4 °C for several weeks without significant loss in bioactivity, although small amounts of bioactive, soluble TNF was detectable in supernatants of pelleted particles. This minor leakiness of the conjugated particles can be explained by a slow release of passively adsorbed material and/or by reversible dissociation of TNF trimers that are covalently linked to the particle surface by only one or two of its monomers, rather than all three monomers of the homotrimer (Scheme 1, Figure 3, and data not shown).

The oriented presentation of CysHisTNF at the surface of the beads, with its N-terminus forming a covalent bond with sulfoSMCC, permits the formation of biologically active trimers possessing a bioactivity comparable to the membrane-expressed ligand. This could be demonstrated by the effective induction of apoptosis in cells expressing wild-type TNF receptors (Figure 3) as well as TNFR2-Fas chimera (Figure 4), the latter being responsive to membrane-bound TNF only but fully resistant to soluble TNF (Krippner-Heidenreich et al., 2002). Induction of apoptosis was preceded by recruitment of FADD to the membrane-bound receptor chimeras (Figure 4), further supporting the formation of a functional death inducing signaling complex. Similarly, in cells expressing wild-type TNFR2 molecules, stimulation of the cells with CysHisTNF positive beads induced receptor clustering, recruitment of TRAF2-EGFP, and translocation of p65/relA into the nucleus (data not shown).

Cells from various human tissues have been shown to typically express between 300 and a few thousand endogenous TNF receptors (Scheurich et al., 1986; Kull, Jr. et al., 1985). Accordingly, the receptor density at the cell surface is rather low, provided that TNF receptors are distributed homogeneously, which is supported for TNFR2 by confocal microscopy analyses of ectopically expressed TNFR2-EGFP and of TNFR2-Fas chimeric receptors (Krippner-Heidenreich et al., 2002). In the case of the TNFR2-Fas chimera we could estimate the efficiency of the beads in comparison to the most efficient tool for TNFR2 stimulation so far available, the combination of sTNF with the TNFR2 specific mAb 80M2 (Grell et al., 1993; Grell et al., 1995). A comparable cytotoxic activity (50 and 66% of maximum apoptosis) could be

obtained with about 6500 sTNF molecules per cell in the presence of the mAb 80M2 or 6 CysHisTNF positive 1 μm beads. These beads present a large number of TNF molecules (about 100000 per particle) but are likely to interact with only a few hundred cellular receptor molecules. Accordingly, particle-coupled TNF proved to be superior in bioactivity when compared to sTNF plus 80M2 by approximately 1 order of magnitude.

Human TNF-derived muteins with high receptor selectivity have been described (Van, X et al., 1993; Loetscher et al., 1993). We were questioning whether receptor selectivity would be preserved after coupling of the respective receptor-selective CysHisTNF mutants to the beads or whether subtype specificity would be overcome by a positive cooperativity of the surface-bound ligands in terms of an increased avidity. The results shown in Figure 2, however, clearly show that receptor selectivity remains preserved, and therefore TNFR2-selective, strongly activating agonists can be produced on the basis of nano/microparticles covalently coupled with the TNFR2-selective mutein CysHisTNF143N/145R.

In summary, we have generated TNF-functionalized particles capable to efficiently stimulate TNFR2, thus mimicking the action of membrane-bound TNF. Moreover, these tools can be used for selective and spatially restricted activation of either of the two TNF receptors and allows live imaging of receptor proximal events and apoptosis events. Future areas of application for similar but biodegradable (nano)particles might include the in vivo usage of particles carrying more than a single effector/targeting protein for therapeutic treatment.

ACKNOWLEDGMENT

We thank I.-W. von Broen (Knoll AG, Ludwigshafen, Germany) for recombinant TNF, D. Männel (University of Regensburg, Germany) for murine fibroblasts, M. Lenardo (NIH, Bethesda) for pFADD-EGFP, H. Wajant (University of Würzburg, Germany) for pTRAF2-EGFP, and A. Strasser (The Walter and Eliza Hall Institute, Melbourne, Australia) for pEF PGKpuro. We thank Eva Behrle, Nadja Reinhardt, Alexander Ganser, Gudrun Zimmermann, and Syliva Willi for technical assistance. This work was supported by the Bundesministerium für Bildung und Forschung (BMBF), grant 0312003B, and in part by Deutsche Forschungsgemeinschaft, Sonderforschungsbereich 495, project A4.

LITERATURE CITED

(1) Aggarwal, B. B. (2003) Signaling pathways of the TNF superfamily: a double-edged sword. *Nat. Rev. Immunol. 3*, 745−756.

(2) Becker, M. L., Remsen, E. E., Pan, D., and Wooley, K. L. (2004) Peptide-derivatized shell-cross-linked nanoparticles. 1. Synthesis and characterization. *Bioconjugate Chem. 15*, 699−709.

(3) Beyaert, R., and Fiers, W. (1994) Molecular mechanisms of tumor necrosis factor-induced cytotoxicity. What we do understand and what we do not. *FEBS Lett. 340*, 9−16.

(4) Bildirici, L., and Rickwood, D. (2001) An investigation into the suitability of silica beads for cell separations based on density perturbation. *J. Immunol. Methods 252*, 57−62.

(5) Black, R. A., Rauch, C. T., Kozlosky, C. J., Peschon, J. J., Slack, J. L., Wolfson, M. F., Castner, B. J., Stocking, K. L., Reddy, P., Srinivasan, S., and et al. (1997) A metalloproteinase disintegrin that releases tumour-necrosis factor- alpha from cells. *Nature 385*, 729−733.

(6) Eggermont, A. M., and ten Hagen, T. L. (2001) Isolated limb perfusion for extremity soft-tissue sarcomas, in-transit metastases, and other unresectable tumors: credits, debits, and future perspectives. *Curr. Oncol. Rep. 3*, 359−367.

(7) Gao, X. H., Yang, L. L., Petros, J. A., Marshal, F. F., Simons, J. W., and Nie, S. M. (2005) In vivo molecular and cellular imaging with quantum dots. *Curr. Opin. Biotechnol. 16*, 63−72.

(8) Grell, M., and Scheurich, P. (1999) Tumor Necrosis Factors. In *Nature Encyclopedia of Life Sciences,* Nature Publishing Group, London.

(9) Grell, M., Douni, E., Wajant, H., Lohden, M., Clauss, M., Maxeiner, B., Georgopoulos, S., Lesslauer, W., Kollias, G., Pfizenmaier, K., and Scheurich, P. (1995) The transmembrane form of tumor necrosis factor is the prime activating ligand of the 80 kDa tumor necrosis factor receptor. *Cell 83*, 793−802.

(10) Grell, M., Scheurich, P., Meager, A., and Pfizenmaier, K. (1993) TR60 and TR80 tumor necrosis factor (TNF)-receptors can independently mediate cytolysis. *Lymphokine Cytokine Res. 12*, 143−148.

(11) Grunwald, I., Rupprecht, I., Schuster, G., and Kloppstech, K. (2003) Identification of guttation fluid proteins: the presence of pathogenesis-related proteins in noninfected barley plants. *Physiol. Plant. 119*, 192−202.

(12) Hurst, G. B., Buchanan, M. V., Foote, L. J., and Kennel, S. J. (1999) Analysis for TNF-alpha using solid-phase affinity capture with radiolabel and MALDI-MS detection. *Anal. Chem. 71*, 4727−4733.

(13) Krippner-Heidenreich, A., Tubing, F., Bryde, S., Willi, S., Zimmermann, G., and Scheurich, P. (2002) Control of receptor-induced signaling complex formation by the kinetics of ligand/receptor interaction. *J. Biol. Chem. 277*, 44155−44163.

(14) Kruger, W., Datta, C., Badbaran, A., Togel, F., Gutensohn, K., Carrero, I., Kroger, N., Janicke, F., and Zander, A. R. (2000) Immunomagnetic tumor cell selection—implications for the detection of disseminated cancer cells. *Transfusion 40*, 1489−1493.

(15) Kull, F. C., Jr., Jacobs, S., and Cuatrecasas, P. (1985) Cellular receptor for 125I-labeled tumor necrosis factor: specific binding, affinity labeling, and relationship to sensitivity. *Proc. Natl. Acad. Sci. U.S.A. 82*, 5756−5760.

(16) Lockman, P. R., Mumper, R. J., Khan, M. A., and Allen, D. D. (2002) Nanoparticle technology for drug delivery across the blood-brain barrier. *Drug Dev. Ind. Pharm. 28*, 1−13.

(17) Locksley, R. M., Killeen, N., and Lenardo, M. J. (2001) The TNF and TNF receptor superfamilies: integrating mammalian biology. *Cell 104*, 487−501.

(18) Loetscher, H., Stueber, D., Banner, D., Mackay, F., and Lesslauer, W. (1993) Human tumor necrosis factor alpha (TNF alpha) mutants with exclusive specificity for the 55-kDa or 75-kDa TNF receptors. *J. Biol. Chem. 268*, 26350−26357.

(19) Maruyama, A., Ishihara, T., Kim, J. S., Kim, S. W., and Akaike, T. (1997) Nanoparticle DNA carrier with poly(L-lysine) grafted polysaccharide copolymer and poly(D,L-lactic acid) 162. *Bioconjugate Chem. 8*, 735−742.

(20) Sandhu, K. K., McIntosh, C. M., Simard, J. M., Smith, S. W., and Rotello, V. M. (2002) Gold nanoparticle-mediated transfection of mammalian cells. *Bioconjugate Chem. 13*, 3−6.

(21) Scheurich, P., Ucer, U., Kronke, M., and Pfizenmaier, K. (1986) Quantification and characterization of high-affinity membrane receptors for tumor necrosis factor on human leukemic cell lines. *Int. J. Cancer 38*, 127−133.

(22) Schiestel, T., Brunner, H., and Tovar, G. E. (2004) Controlled surface functionalization of silica nanospheres by covalent conjugation reactions and preparation of high-density streptavidin nanoparticles. *J. Nanosci. Nanotechnol. 4*, 504−511.

(23) Stober, W., Fink, A., and Bohn, E. (1968) Controlled Growth of Monodisperse Silica Spheres in Micron Size Range. *J. Colloid Interface Sci. 26*, 62−72.

(24) Van, O., X., Vandenabeele, P., Everaerdt, B., Loetscher, H., Gentz, R., Brockhaus, M., Lesslauer, W., Tavernier, J., Brouckaert, P., and Fiers, W. (1993) Human TNF mutants with selective activity on the p55 receptor. *Nature 361*, 266−269.

(25) Verveer, P. J., Wouters, F. S., Reynolds, A. R., and Bastiaens, P. I. (2000) Quantitative imaging of lateral ErbB1

receptor signal propagation in the plasma membrane. *Science 290*, 1567−1570.
(26) Wajant, H., Pfizenmaier, K., and Scheurich, P. (2003) Tumor necrosis factor signaling. *Cell Death Differ. 10*, 45−65.
(27) Weiss, T., Grell, M., Hessabi, B., Bourteele, S., Muller, G., Scheurich, P., and Wajant, H. (1997) Enhancement of TNF receptor p60-mediated cytotoxicity by TNF receptor p80: requirement of the TNF receptor-associated factor-2 binding site. *J. Immunol. 158*, 2398−2404.
(28) Willard, D. M. (2003) Nanoparticles in bioanalytics. *Anal. Bioanal. Chem. 376*, 284−286.

BC0501810

Preparation and Characterization of a DOTA−Lysine−Biotin Conjugate as an Effector Molecule for Pretargeted Radionuclide Therapy

James Hainsworth,[†] Peter Harrison,[‡] and Stephen J. Mather*,[†]

Cancer Research UK, Nuclear Medicine Group, St. Bartholomew's Hospital, London, and Bioventix Ltd., 7 Romans Business Park, East Street, Farnham, Surrey GU9 7SX. Received June 28, 2005; Revised Manuscript Received September 5, 2005

Pretargeted radionuclide therapy depends on the establishment of a high concentration of secondary binding sites at a tumor to which low-molecular weight radiolabeled effector molecules can be directed. This study describes the simple synthesis of an effector molecule and its subsequent characterization to determine the extent to which it complied with the ideal requirements of such a compound. (ϵ)-DOTA−(α)-biotinamidolysine (DLB) was synthesized in high yield and purity using conventional SPPS methodology. High radiochemical purities were obtained when labeled with several potentially useful radionuclides. The radiolabeled analogue bound to streptavidin efficiently with a stoichiometry similar to that of native biotin and showed high stability in serum and upon challenge with acid conditions. Biodistribution studies in normal animals showed a rapid rate of clearance from the blood and low retention of radioactivity by normal tissues. This design of effector molecule therefore shows promise for further pretargeted radionuclide therapy studies.

INTRODUCTION

Despite the recent successes in the application of targeted radionuclide therapy for treatment of lymphoma, the relative lack of success of RIT[1] in the treatment of solid tumors has led many researchers to look for alternative strategies, one of the most promising of which is pretargeted radionuclide therapy (for a recent review see ref 1). This involves the preadministration of an antibody conjugate to establish secondary binding sites on the tumor which can then be more efficiently targeted by low molecular weight radiolabeled effector molecules. To prevent these effector molecules from interacting with molecules of antibody conjugate still circulating in the blood, it may be necessary to inject a clearing agent between the first and last reagents in order to reduce the amount of circulating antibody conjugate.

The most widely explored system to date is that based on the biotin−(strept)avidin interaction. Thus the first administration might be that of an antibody−streptavidin conjugate or fusion protein, a suitable clearing agent would be a macromolecular biotin conjugate which remains confined to the vasculature, and the final effector molecule might be a small radiolabeled biotin analogue which is able to diffuse rapidly into the extravascular space surrounding the tumor and bind to the pretargeted antibody−streptavidin conjugate.

It has become clear in recent years that each stage of this targeting regimen needs to be optimized. Not only the reagents themselves but the doses used and the timing between the different stages have all been extensively studied in order to increase the efficacy of the treatment as a whole. This publication is concerned with developments in the design of the last stage in the process, the radiolabeled effector molecule (EM).

The ideal EM should maximize the delivery of a therapeutic radionuclide to the tumor and minimize its uptake by nontarget organs in the body. To achieve this it should have (a) a high affinity for streptavidin, (b) a high stability in vivo, and (c) a favorable pharmacokinetic profile which ensures that it is cleared rapidly from the blood and excreted through the kidneys without any significant retention by organs of excretion and metabolism such as the kidneys and liver. Supplementary benefits include the ability to radiolabel with a range of potentially useful radionuclides and a simple and efficient synthetic route.

The most successful therapies have been achieved using biotin-based EMs which have been labeled with metallic radioisotopes, most commonly yttrium-90. This is achieved by conjugating a chelating agent such as diethylenetraminepentaacetic acid (DTPA) or tetraazacyclododecanetetraacetic acid (DOTA) to biotin. Both bifunctional chelators have the ability to complex a variety of potentially useful metallic radionuclides including those of yttrium, indium, gallium, and lutetium, but DOTA is generally preferred because higher stability metal complexes can be obtained (*2, 3*). In the first DTPA−biotin conjugates to be employed for pretargeting purposes, one of the carboxylic acid groups of DTPA was condensed with the ϵ-amino group of biocytin as shown in Figure 1A (*4*). However, a significant disadvantage of this design is the fact that the amido bond so formed can

* To whom correspondence should be addressed. Phone: +44 207 601 7153. Fax: +44 207 601 7143. E-mail: Stephen.mather@cancer.org.uk.

[†] St. Bartholomew's Hospital.

[‡] Bioventix Ltd.

[1] Abbreviations: DLB, (ϵ)-DOTA−(α)-biotinamidolysine; DOTA, tetraazacyclododecanetetraacetic acid; DTPA, diethylenetraminepentaacetic acid; EM, effector molecule; Fmoc, 9-fluorenylmethoxycarbonyl; HOBT, hydroxybenzotriazole; MTT, 4-methyltrityl; NMP, *N*-methylpyrrolidone; pi, postinjection; RIT, radioimmunotherapy; SPSS, solid-phase peptide synthesis; TFA, trifluoroacetic acid, TIS, triisopropylsilane.

10.1021/bc050188h CCC: $30.25 © 2005 American Chemical Society
Published on Web 10/22/2005

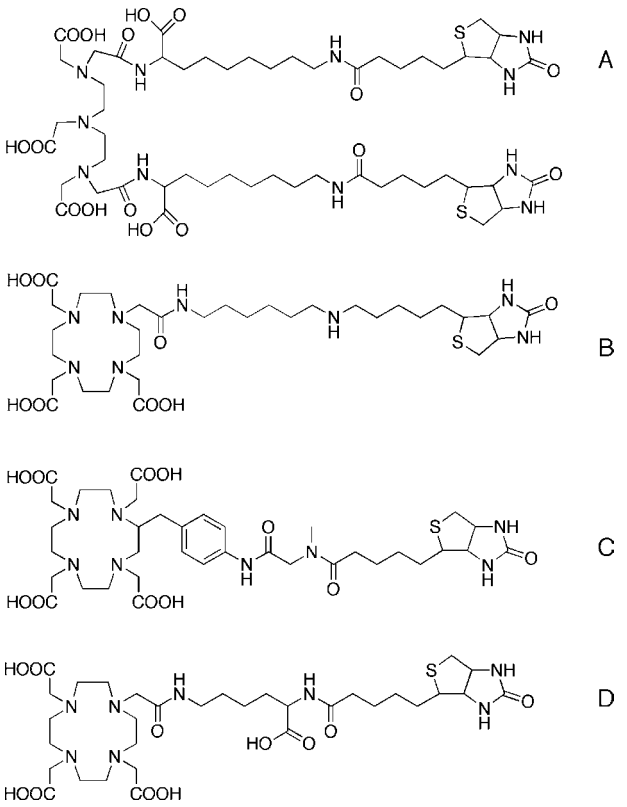

Figure 1. Structure of biotin-based effector molecules. A: DTPA α,ω-bis(biocytinamide). B: DOTA−N-linked-*N*-methylglycyl-biotin. C: Reduced biotinamidohexylamine DOTA. D: (ϵ) DOTA−(α) biotinamidolysine, DOTA

be cleaved by biotinidase, a ubiquitous enzyme present in mammalian serum (*5*) . A number of strategies have been formulated to overcome this problem including the use of reduced or sterically hindered amide bonds to render the linkage stable to biotinidase. Examples are shown in Figures 1B (*6*) and 1C (*7*). A second possible route of instability relates to dissociation of the metal core from the complex in vivo. It is important that the radionuclide remains firmly bound in the complex to ensure that it is not scavenged by other metabolic pathways in the body which would result in an increased radiation dose to normal tissues. The main question in relation to DOTA conjugate design is whether to attach the DOTA chelate to biotin via one of the four pendant carboxylic acid groups or to engineer a point of attachment into one of the ethylene backbones in the molecule. The former approach has the advantage of simpler and easier synthesis but the latter the advantage of potentially greater stability.

For reasons discussed below, we were interested in preparing DOTA conjugates of L-biotin [the mirror image of naturally occurring D-biotin] for use in a novel pretargeting strategy. The synthesis of L-biotin is a complex, six-step procedure, and the material is therefore in limited supply. We therefore wished to develop a simple but efficient route to the preparation of a DOTA−L-biotin conjugate which retained all of the prerequisite properties discussed above. Our preferred design for this molecule is shown in Figure 1D. This molecule has the advantage that it can be prepared using conventional solid-phase peptide synthetic (SPSS) procedures, in high yield. A full characterization of the properties of this EM and the extent to which they complied with our list of requirements was performed.

EXPERIMENTAL PROCEDURES.

Chemicals and Reagents. All reagents were purchased from Sigma-Aldrich unless otherwise indicated**.** Indium chloride ($^{111}InCl_3$) was sourced from Mallinckrodt Medical b.v (Petten, Netherlands), yttrium chloride ($^{90}YCl_3$) from MDS Nordion (Fleurus, Belgium), lutetium chloride ($^{177}LuCl_3$) from Perkin-Elmer Life Sciences, Inc. (Boston, Massachusetts), and cobalt chloride ($^{57}CoCl_2$) from ICN (Basingstoke, Hamps, UK).

Reverse-Phase Chromatography. HPLC analysis was performed using a Beckman 126 solvent-module pump system with a Beckman 168 diode array detector and a sodium iodide flow through radiochemical detector attached to a Raytest gamma radioactivity monitor. Preparative HPLC was performed using a an Agilent Zorbax 300SB-C8 preparative column (21.2 mm × 25 cm) while for analysis a Galaxy Jupiter 5μ C_{18} column, 300 Å; 4.6 × 250 mm i.d. was used (Phenomenex, Cheshire, England). Data collection was handled by a PC running System Gold Nouveau (Beckman, High Wycombe, England). A mobile phase system comprising water and acetonitrile containing 0.05% TFA was used at a flow-rate of 1 mL per minute.

(ϵ) DOTA−(α)-Biotinamidolysine (DLB) Synthesis. Classical SPPS methods were used to synthesize the conjugate as described in Scheme 1. Ninhydrin assays were performed at each stage to check completion of the reactions. The starting point was an Fmoc-Lys(MTT)-Wang resin (Novabiochem). Briefly, after removal of the Fmoc protection with 20% piperidine, biotinylation on the α-amino group was performed overnight using a 4-fold molar excess of HOBT activated D- or L-biotin. The ϵ-MTT protection was removed with 1% TFA, 5% TIS in dichloromethane, and DOTA conjugation to the lysine side chain was performed overnight by addition of a 4-fold molar excess of HOBT-activated DOTA-tris(*tert*-butyl) ester (Macrocyclics, TX). Cleavage from the resin and removal of the *tert*-butyl protection was performed with 2.5% TIS, 2.5% water in TFA. The resin was removed by filtration, the DLB precipitated in cold diethyl ether, washed, redissolved in water, and lyophilized. The crude product was purified by reverse-phase HPLC using a C_8 column. The samples were analyzed by reverse-phase HPLC to check their purity, and matrix-assisted laser desorption/ionization time-of-flight (MALDI-TOF) mass spectrometry (Lasermat 2000, Finnigan-Mat, Thermo Electron Corp) was used to verify their molecular mass.

Radiolabeling of DOTA−Biotin Conjugates. The DLB was labeled with indium-111, yttrium-90, and lutetium-177 using the same reaction conditions. Typically, a volume of 10 μL (7 MBq) of the radionuclide was added to an equal volume of 2 M ammonium acetate, pH 5.4, in a 2 mL polypropylene vial. This was followed by 5 μL of a 1 mg/mL solution of DLB in water. The volume was made up to 100 μL with water, and the reaction vial was sealed, heated in a boiling bath for 30 min, and finally quenched with 10 μL of 50 mM EDTA before further analysis. Sodium ascorbate was added to ^{90}Y-labeled solutions at a final concentration of 100 μg/mL to prevent radiolysis.

Assay of DOTA−Lysine Biotin. Because of inaccuracies in weighing small amounts and to compensate for the presence of residual water, the concentration of DLB was confirmed by labeling a sample with $^{57}CoCl_3$ of a known specific activity (*8*). A range of concentrations was labeled with ^{57}Co, quenched with EDTA, and analyzed by ITLC (Pall Life Sciences, Portsmouth, UK) using 10 mM EDTA in 0.1 M ammonium acetate as mobile

Scheme 1. Solid-Phase Synthesis of DLB[a]

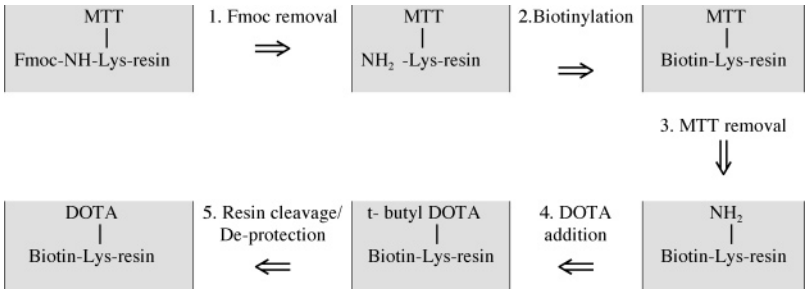

[a] Step 1: A volume of 3 mL of 20% piperidine/DMF was mixed with 50 mg of peptidyl resin and incubated for 1 h at room temperature. The reacted sample was centrifuged at 6500 rpm for 1 min, and the supernatant was discarded and replaced with a further 3 mL of 20% piperidine/DMF to ensure complete reaction for another 1 h. The supernatant was discarded, and the pellet evaporated to dryness in a Savant SpeedVac Plus. The resin was washed three times with 1 mL of dimethylformamide and twice with 1 mL of dichloromethane before drying in the SpeedVac. Step 2: The deprotected lysine resin beads were preswollen with 250 μL of NMP, and the excess supernatant was removed. A 4:1 molar excess of biotin (0.12 mmol) to lysine was dissolved in 1 mL of DMSO and 400 μL of NMP. Then 200 μL of 1 M HOBT in NMP was added to the D-biotin solution and left for 3 min. A volume of 200 μL of diisopropylcarbodiimide activator (1 M in NMP) was added to the D-biotin solution and reacted for 30 min. The activated D-biotin solution was then added to the resin and mixed overnight on a 4RT-rocking table (Luckham, Ltd., Burgess Hill, UK). The next day the beads were washed three times with 1.5 mL of NMP. A volume of 500 μL of DCM was used to shrink and dry the beads. Step 3: The resin was washed four times for 3 min with 2 mL of a solution containing 1% TFA, 5% TIS, and 94% DCM. Initially the solution became a fluorescent yellow color, indicating the presence of MTT (3-(4,5-dimethylthiazol-2-yl)-2,5-diphenyl-2*H*-tetrazolium bromide) in solution. Washing was continued until the wash solution became colorless again. The beads were then washed in DCM. Step 4: The resin beads were preswollen with 200 μL of NMP. A mass of 115 μg (0.2 mmols) (6× excess) of DOTA-tris(*tert*-butyl ester) (Macrocyclics, Dallas, TX) was dissolved in 700 μL of DMF, and a 200 μL aliquot of 1 M HOBT in NMP was added and mixed for 3 min. A volume of 50 μL of diisopropylcarbodiimide (1 M in NMP) was added and incubated for 30 min at room temperature. The "Activated DOTA" was added to the swollen resin and gently mixed overnight. The resin beads were then washed five times with DMF and twice with DCM. Step 5: A 1 mL aliquot of a cleavage solution containing 2.5% water, 2.5% TIS, and 95% TFA was added to the resin, and the suspension was slowly filtered through a microtube filter over a period of 2 h. The solute was precipitated with 1 mL of cold diethyl ether and centrifuged for 1 min and the supernatant discarded. The pellet was washed with a second 1 mL of ether, the supernatant discarded, and the compound dried in the SpeedVac. The resultant solid was weighed in a microfuge tube on a Sartorius analytical balance (Goettingen, Germany) and then redissolved in water for preparative HPLC purification.

phase. Under these conditions, DLB-bound ^{57}Co has an $R_f = 0$ while unbound ^{57}Co has an $R_f = 1$. A graph of bound cobalt concentration vs estimated DLB concentration was drawn and the gradient determined by linear correlation from which the true concentration of the DLB was calculated.

Streptavidin Binding of Labeled DOTA−Biotin Conjugates. ^{111}In-labeled DLB was incubated with a series of dilutions of streptavidin (ICN, MP Biomedicals, Irvine CA) ranging from 0.2 pM to 2 μM corresponding to DLB:streptavidin ratios of 10^{-5} to 100:1. The reaction mixtures were incubated for 30 min at 37 °C, and samples were taken and analyzed using Sephadex G-50 spin columns (Amersham Biosciences, Amersham UK) to determine the degree of streptavidin binding.

Serum Stability. To asses the stability of DLB to biotinidase and other serum proteases, 50 μL of ^{111}In-labeled DLB (containing 1 μg of labeled EM) was diluted 10-fold in fresh human serum and incubated with gentle mixing at 37 °C for up to 24 h. Samples were taken at 0, 1, 2, 6, and 24 h, serum proteins were precipitated with an equal volume of acetonitrile, and the supernatant was analyzed by reverse-phase HPLC.

Stability of DOTA−Metal Complexes. The stability of the ^{111}In- and ^{90}Y-DLB complexes were compared with those of the unconjugated DOTA and DTPA radiometal complexes by assessing their resistance to competition by hydrogen ions. The complexes were prepared and diluted with a 10-fold excess of 0.1 M glycine·HCl buffers ranging in pH from 0.5 to 5. After incubation at room temperature for 30 min, the solutions were neutralized by addition of phosphate buffer and analyzed by ITLC using 10% aqueous ammonium hydroxide:methanol (1:1) as mobile phase. Under these conditions, any complexed radioisotope has an $R_f = 1$ while that which has been lost from the complex has an $R_f = 0$.

Biodistribution of ^{111}In-Labeled DLB. The biodistribution of labeled DOTA−biotin conjugate was determined after intravenous administration to normal mice. Twelve normal adult balb/c mice were injected with 35 ng of conjugate labeled with 70 kBq of ^{111}In. Two, six, and twenty-four hours after injection, groups of four mice were killed, and a sample of their blood, a sample of muscle, a femur, both kidneys, the liver, the complete intestine, and the spleen were transferred to preweighed tubes and counted in a suitably calibrated gamma counter together with a series of dilutions of the injected material in order to allow the percentage of the injected dose in each sample to be calculated.

RESULTS

Synthesis of the DOTA−lysine−biotin (DLB) proceeded without difficulty. A practical yield of around 80% was obtained. Although our synthesis was performed manually starting with only 50 mg (0.03 mmol) of loaded resin, no difficulty in scaling the synthesis up to the levels normally performed by automated peptide synthesizers would be expected. The DLB produced was pure as assessed by analytical HPLC (see Figure 2 upper trace) and showed the expected mass of 759 on MS (see Figure 3). Radiolabeling of the effector molecule consistently produced complexes with radiochemical purities greater than 99% as assessed by RP-HPLC (see Figure 2 lower trace). The complexes remained stable in aqueous solution for at least 48 h provided that (in the case of ^{90}Y-labeled DLB) sodium ascorbate was added to prevent radiolysis.

To perform an accurate assessment of the properties of the radiolabeled DLB solution, in particular the stoichiometry of its binding to streptavidin, an accurate assessment of its concentration was required. Since only very small amounts of the DLB were required for each assay, very small quantities were weighed out on most

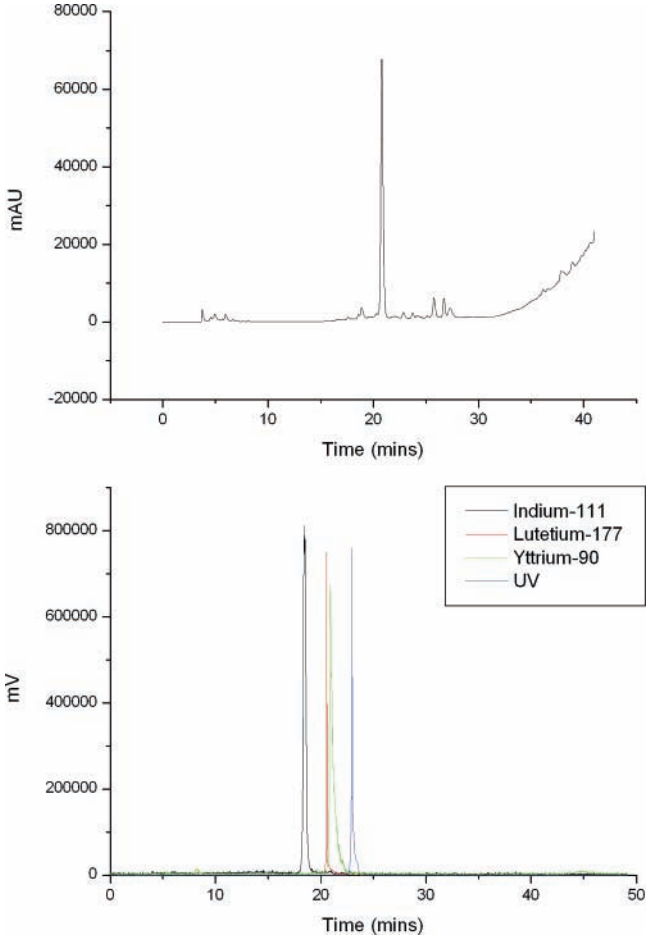

Figure 2. Reverse phase HPLC analysis of DLB. Upper trace UV detection of unlabeled compound. Lower trace radioactive detection of DLB labeled with ^{111}In, ^{90}Y, and ^{177}Lu.

occasions, and, in the knowledge that many peptides are hygroscopic, it was considered likely that this could lead to inaccuracies in the estimated concentrations of the DLB solutions prepared. An accurate assessment was therefore performed by titrating the DLB solution with a known concentration of $^{57}CoCl_3$ solution and plotting the concentration of bound ^{57}Co against the estimated DLB concentration. An example is shown in Figure 4. If the estimated concentration of DLB was correct, then the slope of the line would be 1. In this example the slope is 0.64, indicating that the real concentration of DLB was 1/0.64 or 1.56 times greater than that estimated.

Using a precisely known concentration of ^{111}In-DLB, a titration was performed with a range of streptavidin solutions and the extent of streptavidin binding measured by size-exclusion spin columns. The results show a sigmoidal pattern of binding as seen in Figure 5. With a large molar excess of streptavidin, up to 99% of the ^{111}In-DLB was protein bound. At a DLB:streptavidin ratio of 4:1 (the expected stoichiometric ratio of biotin binding), about 93% of the DLB is protein bound.

A high level of stability of the effector molecule in vivo is required. Two main routes of instability are likely: degradation by serum proteases such as biotinidase and transchelation of the radiometal from the DOTA complex. The first route of degradation was studied by incubating the labeled DLB in fresh human serum for up to 72 h and analyzing the mixture by reverse-phase HPLC. The rate of breakdown was compared with that of ^{111}In-DTPA α,ω-bis(biocytinamide) which is a known biotinidase substrate. No significant breakdown of the ^{111}In-DLB was observed over a 72 h incubation period. This contrasted with a loss of 46% of ^{111}In DTPA α,ω-bis(biocytinamide) in 24 h and a ~100% loss in 72 h. The level of serum protein binding of ^{111}In-DLB after 24 h incubation was found by size-exclusion spin column analysis to be 5%.

Although the high stability of the ^{111}In- and ^{90}Y-DOTA complexes are well documented, it is possible that the removal of one of the pendant carboxylic acid side chains may sufficiently reduce the stability to permit transchelation of the radiolabel in vivo. The stability of ^{111}In- and ^{90}Y-labeled DLB were therefore compared with that of ^{111}In- and ^{90}Y-labeled DOTA as well as ^{111}In- and ^{90}Y-labeled DTPA and ^{111}In- and ^{90}Y-labeled DTPA α,ω-bis(biocytinamide) using a modification of the approach described by Stimmel et al. (*9*). This was performed by diluting the complexes with an excess of glycine·HCl buffers of pH ranging from 0.5 to 5. Under low pH conditions, the high concentration of hydrogen ions would be expected to compete more effectively with the metal, and any loss in stability would result in a more rapid rate of transchelation than that which would be observed at higher pH. The results are shown in Figure 6. It can be seen that at least down to pH 0.5, no difference in stability between ^{111}In- and ^{90}Y-labeled DLB and DOTA complexes can be seen, indicating that the loss of one carboxylate arm has no profound effect upon the rate of loss of metal from the complex. By contrast the DTPA complexes and especially the DTPA α,ω-bis(biocytinamide) complexes (in which two carboxylate groups are used for conjugation) show a much greater rate of metal loss.

The biodistribution of ^{111}In-labeled DLB conjugates was studied in normal mice 2, 6, and 24 h after intravenous administration. The results are shown in Table 1. These show a rapid rate of clearance from the blood with very low retention in all tissues except kidney and bone where values ranged from 1 to 2% per gram.

DISCUSSION

Our aim in this exercise was to develop a simple efficient synthesis of a biotin-based effector molecule which provides high, reproducible labeling efficiency, high stability in a biological environment, effective interaction with its streptavidin target, and low nonspecific retention by normal organs and tissues in vivo. The results show that these aims have been largely achieved. The design of our DOTA–lysine–biotin was based on the results of a number of previous pivotal publications. In 1987 Hnatowich and co-workers (*4*) based their initial pretargeting studies on a DTPA–biocytin analogue. Although this firmly established the proof of principle, this effector molecule suffered from a number of shortcomings. The same group subsequently described the preparation of a DOTA–biotin analogue (*10*) and Chinol later showed that DOTA was a superior chelator for this purpose (*11*). The realization that a simple biocytin conjugate was a substrate for biotinidase led to the development of a number of more stable designs (*6, 7*). Wilbur et al. have explored in detail the effects of different substitutions on biotinidase stability (*12, 13*). In particular they showed that substitutions alpha to the biotinamide bond inhibited the activity of the enzyme through steric hindrance (*14*). Wilbur et al. have also studied the effect of different lengths of spacer between the radionuclide and the biotin. Because of their desire to radiolabel with halogens, they developed a series of ether-containing linkers to maintain the hydrophilicity of the molecule. Since DOTA itself confers a high degree of hydrophilicity on the structure,

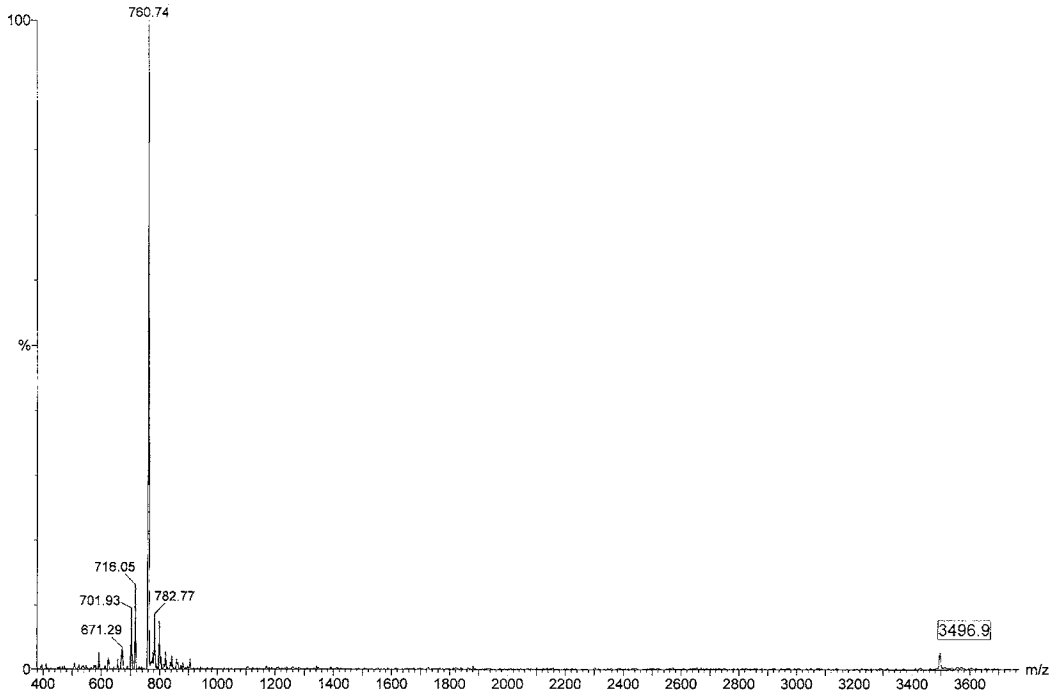

Figure 3. DLB matrix-assisted laser desorption/ionization time-of-flight (MALDI-TOF) mass spectrometric analysis of DLB. M + H^+ of 760 corresponds to the expected mass of DLB of 759.

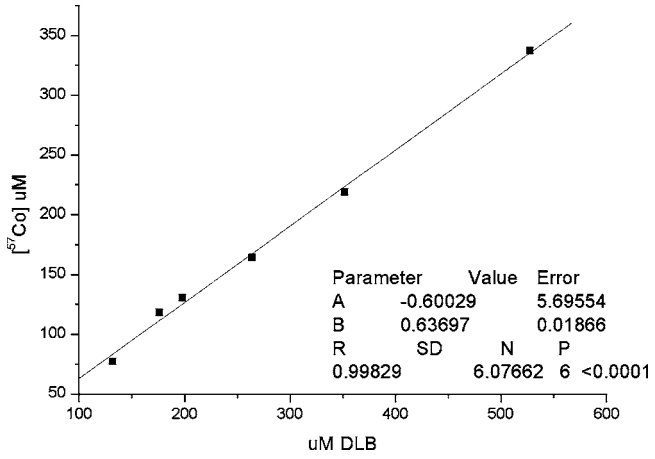

Figure 4. ^{57}Co titration to determine accurate concentration of DLB. A range of concentrations was labeled with ^{57}Co, quenched with EDTA, and analyzed by ITLC. A graph of bound cobalt concentration vs estimated DLB concentration was drawn and the gradient determined by linear correlation from which the true concentration of the DLB was calculated.

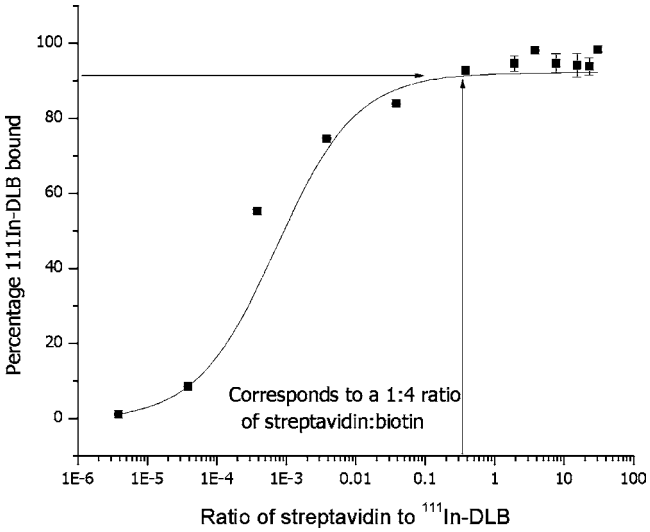

Figure 5. Binding of ^{111}In-DLB to streptavidin. ^{111}In-labeled DLB was incubated with a series of dilutions of streptavidin. After 30 min at 37 °C, samples were taken and analyzed using Sephadex G-50 spin columns to determine the degree of streptavidin binding.

we were not so constrained. For that reason we chose to use lysine as a linker since this would allow us to use standard SPPS chemistry to prepare the effector molecule. By substituting the biotin at the α- rather than the more usual ϵ-amino group of the lysine we ensured that the terminal carboxylate of the peptide provided the necessary steric hindrance of the biotinamide bond (see Figure 1D).

No difficulties were encountered in the synthesis of the effector molecule in acceptable yields. As well as preparing the DOTA−L-lysine−D-biotin described above we also prepared DOTA−L-lysine−L-biotin and achieved similar yields and purities. L-Biotin does not bind to streptavidin, but the rationale for our interest in this compound stems from a desire to combine the advantages of the streptavidin−biotin pretargeting system with those of the bispecific antibody approach (*15*). The streptavidin−biotin system has two significant drawbacks. The first is that streptavidin itself can be highly immunogenic (*16*), and this limits the number of potential administrations that can be made. The second drawback is the likelihood that endogenous biotin present in the blood will compete with the radiolabeled biotin for the limited number of binding sites on the pretargeted streptavidin conjugate (*17*). As effector molecules based on the D-isomer of biotin have many ideal properties (high specific activity, low toxicity, favorable stability, rapid renal excretion), it is expected that compounds based on the L-isomer would retain these advantages. We have therefore raised high affinity antibodies to L-biotin that do not cross-react with D-biotin and would, therefore, not be affected by endogenous biotin in the blood. The work presented in this publication stems from a desire to be able to perform studies directly comparing the two approaches in our laboratory. One of

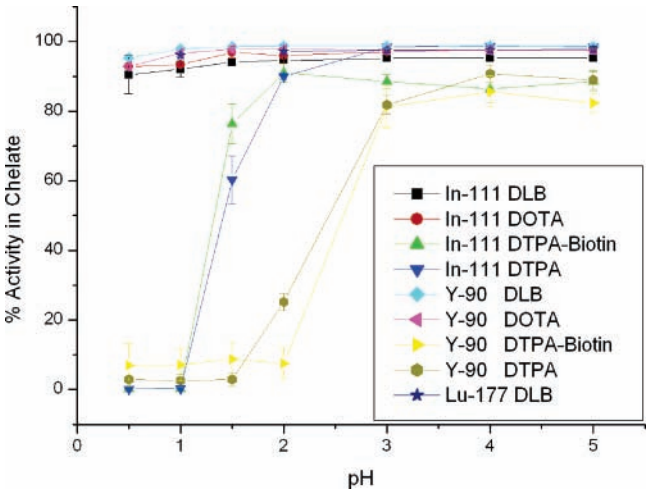

Figure 6. Dissociation of radiometal complexes under challenge at varying pH. The stability of the ^{111}In- and ^{90}Y-DLB complexes were compared with those of the unconjugated DOTA and DTPA radiometal complexes by assessing their resistance to competition by hydrogen ions. The complexes were prepared and diluted with a 10-fold excess of 0.1M glycine·HCl buffers at pH ranging from 0.5 to 5. After 30 min, the solutions were analyzed by ITLC to determine the proportion of intact complex remaining.

Table 1. Biodistribution of ^{111}In-DLB in Normal balb/c Mice

	% of injected dose/g tissue (SD) at time point (h)		
tissue	2	6	24
BLOOD	0.09 (0.02)	0.08 (0.02)	0.02 (0)
MUSCLE	0.21 (0.13)	0.41 (0.31)	0.11 (0.07)
BONE	1.31 (0.52)	1.39 (0.91)	0.1 (0.03)
KIDNEY	1.76 (0.27)	1.93 (0.38)	1.19 (0.26)
LIVER	0.29 (0.19)	0.22 (0.11)	0.13 (0.03)
GUT	0.61 (0.51)	0.61 (0.14)	0.27 (0.17)
SPLEEN	0.22 (0.17)	0.24 (0.09)	0.3 (0.32)

the difficulties in exploiting L-biotin as an effector molecule is its difficult synthesis. We obtained the material from an expensive commercial custom synthesis (CMS Chemical, Abingdon, UK) which synthesized the compound from L-mannose according to the method of Ohrui (*18*). Although our DLB synthesis was performed manually on a small scale in order to limit the amount of the expensive L-biotin required, no difficulty in scaling the synthesis up to the levels normally performed by automated peptide synthesizers would be expected. It would also be possible to prepare the corresponding D-lysine analogues (*19*) if desired.

High levels of purity of the DLB and its radiolabeled counterparts were achieved. The molecule was able to bind efficiently to streptavidin in solution with a stoichiometry similar to that of native biotin indicating that the lysine spacer did not significantly inhibit this interaction.

In vitro measures of stability were encouraging. HPLC analysis of the radiolabeled effector molecule after incubation in serum for up to 3 days indicated no loss in purity over this time, indicating that the α-amino-linked molecule was not cleaved by serum proteases such as biotinidase. This is in contrast to the radiolabeled DTPA–ϵ-amino-linked control biotin analogue which was completely degraded over the same time period. However, it is possible that a proportion of this loss can be attributed to transchelation from the DTPA to transferrin present in the serum.

The stability of the radiometal–DOTA complexes were studied by comparing their rate of acid-assisted dissociation in a modification of the method described by Stimmel et al. (*9*). While Stimmel studied the dissociation of various chelates at pH 2 over a period of several days, we chose to study the effect of a range of pH (0.5–5) at a single time of 30 min. The results show that while the yttrium–DTPA complexes start to show dissociation at pH 3, the yttrium–DOTA complexes show no significant dissociation even at pH 0.5. As expected the indium–DTPA complexes are rather more stable than their yttrium counterparts while the indium–DOTA complexes are as stable as the yttrium analogues under the conditions studied. Although it has been shown that DOTA lacking one of the *N*-acetate side chains has a lower thermodynamic stability constant than DOTA itself (*20*), the most important issue in radiopharmaceutical design is that of kinetic stability since the great majority of the yttrium-90 will either clear from the body or decay within a few days. These results suggest that, from a practical point of view, the convenience of using the SPSS-friendly commercially available reagent DOTA-tris(*tert*-butyl) ester is not outweighed by a large decrease in the kinetic stability of the complex and taken together with the serum stability study indicate that this effector molecule would have a suitable stability profile for pretargeting studies.

The final stage of the characterization of the DOTA–lysine–biotin was to study its biodistribution in normal animals. The dose of compound chosen for this study (1.4 μg/kg) was within the range of those chosen for clinical pretargeting studies – 0.7 to 30 μg/kg (*21–23*). The ideal effector molecule would show no significant retention by any normal tissues or organs. With the exception of the bone and kidney, all tissues showed a retention of 0.5% or less. Bone showed an initially quite high value of around 1% but declined to only 0.1% by 24 h while kidney uptake varied between 1 and 2%. With the exception of the high initial bone uptake, these results are similar to those published from similar studies of alternative effector molecules. Goodwin et al. (*24*) showed very similar results with a DOTA–C-linked-isothiocyanatobenzylbiotin analogue in most tissues but only around 0.1% bone uptake at 2 h pi, while Sharkey et al. (*25*) showed similar results but a rapidly clearing kidney retention with DOTA–N-linked (D)-ϵ-lysine–biotin. The biodistribution of a DOTA–N-linked-*N*-methylglycyl-biotin (*26*) is presented in graphical form only but appears to follow a similar pattern of biodistribution.

In conclusion we consider that the design and simple synthetic method described above is suitable for the preparation of radiolabeled effector molecules for pretargeted radionuclide therapy.

ACKNOWLEDGMENT

We gratefully acknowledge the financial support of Cancer Research UK and the UK EPSRC, the facilities of the Barts Foundation for Research, and the technical assistance of Mrs. Sandra Peak, Mrs. Nicola O'Reilly, Dr. Maria Stalteri, and Mr. David Ellison.

LITERATURE CITED

(1) Boerman, O. C., van Schaijk, F. G., Oyen, W. J., and Corstens, F. H. (2003) Pretargeted radioimmunotherapy of cancer: progress step by step. *J Nucl Med 44*, 400–11.

(2) Moi, M. K., Meares, C. F., and Denardo, S. J. (1988) The Peptide Way to Macrocyclic Bifunctional Chelating Agents: Synthesis of 2-(*p*-Nitrobenzyl)-1,4,7,10-tetraazacyclododecane-*N*,*N*′,*N*″,*N*‴-tetraacetic Acid and Study of Its Yttrium(III) Complex. *J. Am. Chem. Soc. 110*, 6266–6267.

(3) Cox, J. P. L., Jankowski, K. J., Kataky, R., Parker, D., Beeley, N. R. A., Boyce, B. A., Eaton, M. A. W., Millar, K., Millican, A. T., Harrison, A., and Walker, C. (1989) Synthesis of a Kinetically Stable Y-90 Labeled Macrocycle Antibody Conjugate. *J. Chem. Soc., Chem. Commun.* 797−798.

(4) Hnatowich, D. J., Virzi, F., and Rusckowski, M. (1987) Investigations of avidin and biotin for imaging applications. *J. Nucl. Med. 28*, 1294−302.

(5) Hymes, J., and Wolf, B. (1996) Biotinidase and its roles in biotin metabolism. *Clin. Chim. Acta 255*, 1−11.

(6) Axworthy, D. B., Theodore, L. J., Gustavson, L. M., and Reno, J. M. (1997) United States Patent 5,608,060.

(7) Sabatino, G., Chinol, M., Paganelli, G., Papi, S., Chelli, M., Leone, G., Papini, A. M., De Luca, A., and Ginanneschi, M. (2003) A new biotin derivative−DOTA conjugate as a candidate for pretargeted diagnosis and therapy of tumors. *J. Med. Chem. 46*, 3170−3.

(8) Meares, C. F., McCall, M. J., Reardan, D. T., Goodwin, D. A., Diamanti, C. I., and McTigue, M. (1984) Conjugation of antibodies with bifunctional chelating agents: isothiocyanate and bromoacetamide reagents, methods of analysis, and subsequent addition of metal ions. *Anal. Biochem. 142*, 68−78.

(9) Stimmel, J. B., Stockstill, M. E., and Kull, F. C. J. (1995) Yttrium-90 chelation properties of tetraazatetraacetic acid macrocycles, diethylenetriaminepentaacetic acid analogues, and a novel terpyridine acyclic chelator. *Bioconjugate Chem. 6*, 219−225.

(10) Wu, C., Virzi, F., and Hnatowich, D. J. (1992) Investigations of N-linked macrocycles for 111In and 90Y labeling of proteins. *Int. J. Radiat. Appl. Instrum. B 19*, 239−44.

(11) Chinol, M., Paganelli, G., Sudati, F., Meares, C., and Fazio, F. (1997) Biodistribution in tumour-bearing mice of two 90Y-labeled biotins using three-step tumour targeting. *Nucl. Med. Commun. 18*, 176−82.

(12) Wilbur, D. S., Hamlin, D. K., Pathare, P. M., and Weerawarna, S. A. (1997) Biotin reagents for antibody pretargeting. Synthesis, radioiodination, and in vitro evaluation of water soluble, biotinidase resistant biotin derivatives. *Bioconjugate Chem. 8*, 572−84.

(13) Wilbur, D. S., Hamlin, D. K., Chyan, M. K., Kegley, B. B., and Pathare, P. M. (2001) Biotin reagents for antibody pretargeting. 5. Additional studies of biotin conjugate design to provide biotinidase stability. *Bioconjugate Chem. 12*, 616−23.

(14) Wilbur, D. S., Hamlin, D. K., Chyan, M. K., Kegley, B. B., Quinn, J., and Vessella, R. L. (2004) Biotin reagents in antibody pretargeting. 6. Synthesis and in vivo evaluation of astatinated and radioiodinated aryl- and nido-carboranyl−biotin derivatives. *Bioconjugate Chem. 15*, 601−16.

(15) Gruaz-Guyon, A., Raguin, O., and Barbet, J. (2005) Recent advances in pretargeted radioimmunotherapy. *Curr. Med. Chem. 12*, 319−38.

(16) Knox, S. J., Goris, M. L., Tempero, M., Weiden, P. L., Gentner, L., Breitz, H., Adams, G. P., Axworthy, D., Gaffigan, S., Bryan, K., Fisher, D. R., D., C., Horak, I. D., and Weiner, L. M. (2000) Phase II trial of yttrium-90-DOTA-biotin pretargeted by NR-LU-10 antibody/streptavidin in patients with metastatic colon cancer. *Clin. Cancer Res. 6*, 406−414.

(17) Hamblett, K. J., Kegley, B. B., Hamlin, D. K., Chyan, M. K., Hyre, D. E., Press, O. W., Wilbur, D. S., and Stayton, P. S. (2002) A streptavidin−biotin binding system that minimizes blocking by endogenous biotin. *Bioconjugate Chem 13*, 588−98.

(18) Ohrui, H., and Emoto, S. (1975) Stereospecific Synthesis Of (+)-Biotin. *Tetrahedron Lett.* 2765−2766.

(19) Karacay, H., Sharkey, R. M., Govindan, S. V., McBride, W. J., Goldenberg, D. M., Hansen, H. J., and Griffiths, G. L. (1997) Development of a streptavidin-anti-carcinoembryonic antigen antibody, radiolabeled biotin pretargeting method for radioimmunotherapy of colorectal cancer. Reagent development. *Bioconjugate Chem. 8*, 585−94.

(20) Kumar, K., Chang, C. A., Francesconi, L. C., Dischino, D. D., Malley, M. F., Gougoutas, J. Z., and Tweedle, M. F. (1994) Synthesis, Stability, and Structure of Gadolinium(Iii) and Yttrium(Iii) Macrocyclic Poly(Amino Carboxylates). *Inorg. Chem. 33*, 3567−3575.

(21) Breitz, H. B., Weiden, P. L., Beaumier, P. L., Axworthy, D. B., Seiler, C., Su, F. M., Graves, S., Bryan, K., and Reno, J. M. (2000) Clinical optimization of pretargeted radioimmunotherapy with antibody-streptavidin conjugate and 90Y-DOTA-biotin. *J. Nucl. Med. 41*, 131−40.

(22) Grana, C., Chinol, M., Robertson, C., Mazzetta, C., Bartolomei, M., De Cicco, C., Fiorenza, M., Gatti, M., Caliceti, P., and Paganelli, G. (2002) Pretargeted adjuvant radioimmunotherapy with yttrium-90-biotin in malignant glioma patients: a pilot study. *Br. J. Cancer 86*, 207−12.

(23) Paganelli, G., Grana, C., Chinol, M., Cremonesi, M., De Cicco, C., De Braud, F., Robertson, C., Zurrida, S., Casadio, C., Zoboli, S., Siccardi, A. G., and Veronesi, U. (1999) Antibody-guided three-step therapy for high grade glioma with yttrium-90 biotin. *Eur. J. Nucl. Med. 26*, 348−357.

(24) Goodwin, D. A., Meares, C. F., and Osen, M. (1998) Biological properties of biotin-chelate conjugates for pretargeted diagnosis and therapy with the avidin/biotin system. *J. Nucl. Med. 39*, 1813−8.

(25) Sharkey, R. M., Karacay, H., Griffiths, G. L., Behr, T. M., Blumenthal, R. D., Mattes, M. J., Hansen, H. J., and Goldenberg, D. M. (1997) Development of a streptavidin-anti-carcinoembryonic antigen antibody, radiolabeled biotin pretargeting method for radioimmunotherapy of colorectal cancer. Studies in a human colon cancer xenograft model. *Bioconjugate Chem. 8*, 595−604.

(26) Axworthy, D. B., Reno, J. M., Hylarides, M. D., Mallett, R. W., Theodore, L. J., Gustavson, L. M., Su, F., Hobson, L. J., Beaumier, P. L., and Fritzberg, A. R. (2000) Cure of human carcinoma xenografts by a single dose of pretargeted yttrium-90 with negligible toxicity. *Proc. Natl. Acad. Sci. U.S.A. 97*, 1802−7.

Phosphoinositide-Containing Polymerized Liposomes: Stable Membrane-Mimetic Vesicles for Protein−Lipid Binding Analysis

Colin G. Ferguson,*,† Robyn D. James,† Cleve S. Bigman,† Donnie A. Shepard,† Yasmina Abdiche,‡ Phinikoula S. Katsamba,‡ David G. Myszka,‡ and Glenn D. Prestwich†,§

Echelon Biosciences Inc., 675 Arapeen Drive, Suite 302, Salt Lake City, Utah 84108, Center for Biomolecular Interaction Analysis, University of Utah, 50 North Medical Drive, Salt Lake City, Utah 84132, and Department of Medicinal Chemistry, University of Utah, 419 Wakara Way, Suite 205, Salt Lake City, Utah 84108. Received July 6, 2005; Revised Manuscript Received September 2, 2005

Stable phosphoinositide (PIP_n)-containing liposomes were prepared using polydiacetylene photochemistry. Tethered pentacosadiynyl inositol polyphosphate ($InsP_n$) analogues of Ins(1,3,4)P_3, Ins(1,4,5)P_3, and Ins(1,3,4,5)P_4 were synthesized, incorporated into vesicles made up of diyne-phosphatidylcholine and -phosphatidylethanolamine, and polymerized by UV irradiation. The polymerized liposome nanoparticles showed markedly increased stability over conventional PIP_n-containing vesicles as a result of the covalent conjugated ene-yne network in the acyl chains. The polymerized liposomes were specifically recognized by PIP_n binding PH domains in liposome overlay assays and amplified luminescent proximity homogeneous assays. Moreover, the biotin moiety allowed attachment of the nanoparticles to a streptavidin-coated sensor chips in surface plasmon resonance (SPR) sensor. The PIP_n headgroups displayed on SPR sensors showed higher affinities for PH domains and PIP_n monoclonal antibodies than did monomeric PIP_n-analogues with biotinylated acyl chains.

INTRODUCTION

Phosphatidylinositol polyphosphates (PIP_ns) are important second messengers for a diverse array of cellular functions (*1*, *2*). These charged lipids are minor components of cellular membranes and are biosynthesized by the interplay of kinases (*3*), lipases, and phosphatases (*4*). PIP_ns are essential elements in tyrosine kinase growth factor receptor and G-protein receptor signaling pathways (*5*). Furthermore, they have important roles in membrane traffic (*6*), including endocytosis, exocytosis, Golgi vesicle movement and protein trafficking (*7*), in cell adhesion and migration, in remodeling of the actin cytoskeleton, and in mitogenesis and oncogenesis (*8*, *9*). Activation of cellular signaling pathways often results from specific PIP_n production in response to stimuli.

The common mechanism employed by PIP_ns appears to be localized signal generation and the spatially localized recruitment of effector proteins (*1*, *10*). Recruitment generally occurs through a specific PIP_n binding domain on the protein. For example, pleckstrin homology (PH) domains bind to PIP_ns with varying affinities and specificities and are present in over 110 proteins (*11*, *12*). Other domains include PX and FYVE, both of which predominantly bind PI(3)P (*13*, *14*), and the COOH-terminal domain of the tubby protein which binds to PI(4,5)P_2 (*15*). Finally, the first known PIP_n-binding nuclear receptor ING2, a putative tumor suppressor protein that promotes p53 acetylation, predominantly binds to the rare species, PI(5)P by a plant homeodomain (PHD) zinc finger (*16*). The association of ING2 with chromatin is modulated by phosphoinositides and it was shown that ING2-dependent p53 acetylation and transactivation requires an intact PIP_n-binding domain.

An example of the importance of PIP_n binding domains is that of the PH domains of PDK1 and Akt (protein kinase B) and their involvement in the PI-3 kinase pathway and cancer. Both PDK1 and Akt are sequestered to the membrane by binding to PI(3,4,5)P_3 and Akt possibly undergoes a conformational change thought to make it susceptible to activation through phosphorylation on Ser^{473} by PDK1 (*17*). Activated Akt then inhibits apoptosis by phosphorylating a critical serine residue (Ser^{136}) which suppresses pro-apoptic activity of BAD leading to subsequent cell death (*18*). Rationally designed PI analogues have been prepared that act as specific Akt PH domain inhibitors with low μM activities and increasing apoptosis 20−30 times in cancer cells with high Akt activity and 4−5 times in those with low activity (*19*, *20*). Results such as these demonstrate the importance of PIP_n-protein interactions in disease and suggest that small molecule modulators of these processes are an attractive new avenue for therapeutics (*21*, *22*).

Presentation of the PIP_n ligand in liposomes has been a common technique employed to mimic the cell membrane for binding studies. For example, binding between the effector domain of the myristoylated alanine-rich C kinase substrate (MARCKS) and PI(4,5)P_2 has been measured using sucrose laden vesicles (*23*) and vesicles containing spin labeled (*24*) and fluorescently labeled PI(4,5)P_2 analogues (*25*). PIP_n-containing liposomes have found extensive use in surface plasmon resonance (SPR) measurements of the PHD finger of ING2 (*16*), mammalian PH domains (*26*), and a recent genome-wide analysis of yeast PH domains (*27*). However, liposomes have some drawbacks, in particular, their instability and short lifetime. After 24−48 h at 4 °C, the carefully

* To whom correspondence should be addressed. Tel: (801) 588-0455. Fax: (801) 588-0497. E-mail: cferguson@echelon-inc.com.

† Echelon Biosciences Inc.

‡ Center for Biomolecular Interaction Analysis, University of Utah.

§ Department of Medicinal Chemistry, University of Utah.

10.1021/bc050197q CCC: $30.25 © 2005 American Chemical Society
Published on Web 10/22/2005

prepared unilamellar liposomes begin to fuse and form an irregular mixture of sizes. Thus, new batches need to be frequently prepared leading to potential inconsistencies and difficulties in experimental reproducibility. To make more robust liposomes capable of providing in highly reproducible data we report herein the preparation of stable, polymerized, PIP_n-containing liposomes. These new nanoparticles show properties similar to those of conventional liposomes and monomeric PIP_ns in three binding assays: liposome overlays, the amplified luminescence proximity homogeneous assay (ALPHA), and SPR.

EXPERIMENTAL PROCEDURES

General. Thin-layer chromatography was performed on 0.25 mm precoated glass plates (Merck silica gel $60F_{254}$) with detection by phosphomolybdic acid (5% in EtOH). Flash column chromatography (FCC) used Merck silica gel 60 (230−400 mesh). ^1H, ^{13}C, and ^{31}P NMR spectra were recorded on a Varian INOVA 400 instrument. Coupling constants are recorded in Hz and chemical shifts in ppm. Mass spectra were measured at the University of Utah Medicinal Chemistry Department using matrix-assisted laser desorption ionization (MALDI). Bis-10,12-tricosadiynoyl-phosphatidylcholine and -phosphatidyletheanolamine (diyne-PC and diyne-PE) were purchased from Avanti Polar Lipids (Alabaster, AB). Biotin-X, succinimide ester was purchased from Invitrogen (Eugene, OR). All other reagents were purchased from Aldrich or Acros and used without further purification. *N*-Succinimidyl-10,12-pentacosadiynoate was prepared from 10,12-pentacosadiynoic acid (GFS Chemicals Inc) as previously described (*28*). Aminopropyl-Ins(1,3,4)-P_3, −Ins(1,4,5)P_3, and −Ins(1,3,4,5)P_4 were synthesized according to established protocols (*29*−*31*). DiC_8-PIP_ns, acyl-biotinylated PIP_ns, and anti-PIP_n mAbs were from Echelon. PH domain GST fusions were prepared at Echelon except for Akt-PH (Upstate Biotech).

1-*O*-(10,12-Pentacosadiynylaminopropyl-1-phospho)-*myo*-inositol-4,5-diphosphate (triethylammonium salt) (1a). A solution of *N*-succinimidyl-10,12-pentacosadiynoate (7.0 mg, 14.8 mmol) in DMF (0.6 mL) was added to a solution of (3-aminopropyl-1-phospho)-*myo*-inositol-4,5-diphosphate, sodium salt (5.8 mg, 9.8 mmol) in TEAB (0.5 M, 0.6 mL, pH 7.8). THF (∼10 drops) was added to the suspension to dissolve solids, and the reaction was stirred in the dark for 16 h. The reaction mixture was dried in vacuo, and the solid residue was washed with acetone (5 × 1.5 mL). The product was dissolved in water, passed through a short column (4 × 40 mm) of DOWEX 50 × 8−100 (triethylammonium form) to convert the product from the sodium salt, then lyophilized. Yield: 10.6 mg (77%). ^1H NMR (400 mHz, D_2O, free acid) δ 0.79 (m, 3H), 1.20 (m, 26H), 1.43 (m, 4H), 1.72 (m, 2H), 1.88 (quin, J = 6.0 Hz, 2H), 2.10 (m, 6H), 3.04 (t, J = 7.2 Hz, 2H), 3.58 (dd, J = 9.6, 2.8 Hz, 1H), 3.77−3.98 (m, 5H), 4.10−4.17 (m, 2H). ^{31}P NMR (D_2O, 162 MHz) δ 0.61, 3.20, 3.66 (1:1:1). MALDI-TOF MS: 832.0 $(M - H)^-$ (free acid).

1-*O*-(10,12-Pentacosadiynylaminopropyl-1-phospho)-*myo*-inositol-3,4-diphosphate (triethylammonium salt) (1b). The same procedure was followed as for **1a**. ^1H NMR (400 MHz, CD_3OD, 3-$TEAH^+$ salt) δ 0.89 (t, J = 6.4 Hz, 3H), 1.28 (m, 24H), 1.30 (t, J = 7.6 Hz, 27H), 1.50 (quin, J = 6.8 Hz, 4H), 1.59 (m, 2H), 1.79 (quin, J = 5.6 Hz, 2H), 2.15−2.21 (m, 2H), 2.23 (t, J = 8.0 Hz, 4H), 3.19 (quart, J = 7.6 Hz, 18H), 3.47 (t, J = 8.4 Hz, 1H), 3.86 (t, J = 9.2 Hz, 1H), 3.95 (m, 3H), 1.38 (m, 4H), 4.10 (t, J = 9.2 Hz, 1H), 4.41 (quart, J = 8.8 Hz, 1H). ^{31}P NMR (162 MHz, CD_3OD) δ 1.50, 1.79, 2.87 (1:1:1). MALDI-TOF MS: 832.1 $(M - H)^-$ (free acid).

1-*O*-(10,12-Pentacosadiynylaminopropyl-1-phospho)-*myo*-inositol-3,4,5-trisphosphate (triethylammonium salt) (1c). The same procedure was followed as for **1a**. ^1H NMR (400 MHz, CD_3OD) δ 0.89 (J = 6.8 Hz, t, 3H), 1.28 (m, 26 H), 1.30 (J = 6.8 Hz, t, 45H), 1.49 (J = 7.2 Hz, quin, 4H), 1.79 (m, 2H), 2.19 (J = 8.0 Hz, t, 2H), 1.58 (m, 2H), 2.23 (J = 6.8 Hz, t, 4H), 3.19 (J = 7.2 Hz, quart, 30H), 3.91−4.19 (m, 5H), 4.41 (m, 2H), 4.56 (m, 1H). ^{31}P NMR (162 MHz, CD_3OD) δ 1.33, 1.87, 2.20 (2:1:1). MALDI-TOF MS: 912.2 $(M - H)^-$ (free acid).

Biotin-diyne-PE. NEt_3 (10 μL, 72 μmol) was added to a solution of Biotin-X, succinimde ester (11.6 mg, 25 μmol) and diyne-PE (17.7 mg, 20 μmol) in chloroform (2 mL), and the reaction was stirred at room temperature for 2 h. The solution was evaporated to half the volume and purified by flash column chromatography (70:20:4 $CHCl_3$:MeOH:concentrated NH_4OH). Yield: 22.8 mg (95%). ^1H NMR (400 MHz, $CDCl_3$) δ 0.87 (t, J = 6.8 Hz, 6H), 1.22−1.76 (m, 70H), 2.20 (m, 4H), 2.23 (t, J = 7.2 Hz, 8H), 2.28 (q, J = 7.2 Hz, 4H), 2.75 (d, J = 12.8 Hz, 1H), 2.89 (dd, J = 12.8, 4.8 Hz, 1H), 3.01−3.12 (m, 3H), 3.14 (q, J = 4.4 Hz, 1H), 3.21 (q, J = 6 Hz, 2H), 3.46 (d, J = 4.0 Hz, 2H), 3.92−4.06 (m, 5H), 4.26−4.39 (m, 2H), 4.51 (dd, J = 4.8 Hz, 1H), 5.21 (m, 1H), 6.73 (bs, 1H), 6.94 (bs, 1H), 7.39 (bs, 1H). ^{13}C NMR (101 MHz $CDCl_3$) δ 8.79, 14.32, 19.42, 22.89, 25.03, 25.07, 25.37, 25.74, 26.52, 27.96, 28.06, 28.55, 28.57, 29.02, 29.08, 29.16, 29.31, 29.34, 29.51, 29.69, 29.77, 32.10, 32.68, 34.25, 34.43, 35.71, 36.34, 39.41, 40.85, 45.90, 55.97, 60.49, 62.10, 64.21, 65.18, 65.44, 65.54, 173.62, 173.63, 173.72, 173.97. ^{31}P NMR (162 MHz, $CDCl_3$) δ 0.88. MALDI-TOF MS: 1209.3 $(M - H)^-$ (free acid).

Polymerized Liposome Preparation The following details a typical preparation of polymerized liposomes. Lipid constituents 1,2-bis(10,12-tricosadiynoyl-*sn*-glycero-3-phosphatidylcholine (diyne-PC), 1,2-bis(10,12-tricosadiynoyl-*sn*-glycero-3-phosphatidylethanolamine (diyne-PE) (Avanti Polar Lipids,), $InsP_n$-diyne, and biotin-diyne-PE) were dissolved in $CHCl_3$/MeOH (9:1) and dried to a film on a rotary evaporator then dried further under high vacuum for 2 h. The proportions were typically 65:24:10:1 or 65:29:5:1 diyne-PC:diyne-PE:$InsP_n$-diyne:biotin-diyne-PE [mol %]. Deionized water was added to give a 1 mM (total lipid) suspension. The mixture was heated to 70 °C and probe sonicated (Fisher Scientific 60 Sonic Dismembrator, setting 8) for 30 min, forming a clear solution. The solution was cooled to 4 °C for 2 h and then polymerized by UV irradiation (254 nm) at the same temperature using a handheld lamp. The faintly red solutions were filtered through 0.45 μm cellulose acetate syringe filters to remove any insoluble aggregates. Liposome solutions were stored at 4 °C in amber vials with 0.02% sodium azide to prevent bacterial growth.

Liposome Overlay Assays. Aliquots of the desired protein solutions were spotted on a piece of nitrocellulose membrane (Hybond-C, Amersham Life Sciences) by hand and the membrane was allowed to dry for 5 min. The membrane was blocked for 2 h in blocking buffer (PBS (10 mM sodium phosphate, 138 mM NaCl, 2.7 mM KCl, pH 7.4), 3% BSA) at room temperature. The membrane was incubated in the polymerized liposome solution (5 μg/mL in PBS, 3% BSA) for 1 h at room temperature. The membrane was washed (4 × 10 min) in blocking buffer, then incubated in streptavidin-horseradish peroxidase (1:50 000) (Biosource International) in blocking buffer for 30−60 min at room temperature. Finally, the

membrane was washed with blocking buffer (5 × 10 min), and then visualized with enhanced chemiluminescence (ECL, Amersham plc). Exposure times varied from 5 s to 2 min.

Far Western/Liposome Overlay. Samples of PLCδ1-, Grp1-, LL5α-, and FAPP−PH domains (5, 1, or 0.1 μg) were dissolved in 13.3 μL of Laemilli buffer (Bio Rad Laboratories Inc.) then diluted to 20 μL with water. The samples were applied to the lanes of a 12% polyacrylamide gel, electrophoresed for 1.25 h at 100 V, and then electrotransferred to nitrocellulose in tris/glycine/SDS buffer at 300 mA for 70 min. The membrane was washed with PBS (2 × 5 min) and then subsequently treated with 6, 3, 1, and 0.1 M guanidine buffers (25 mM NaCl, 10% glycerol, 1 mM DTT) for 1 h each to renature the proteins followed by incubating with the blocking buffer overnight at 4 °C. The membrane was treated with 3 μg/mL PI-(4,5)P_2 liposomes in blocking buffer for 1 h, and the subsequent steps were identical to those described above for the overlay assay.

Alphascreen Assays. Alphascreen assays were performed on a Fusion instrument (Perkin-Elmer, Inc.) using standard settings and the recommended buffer (50 mM Tris pH 7.5, 150 mM NaCl, 0.1% Tween-20, 0.1% BSA). In a 384-well microplate was added 10 μL of buffer followed by 5 μL each of the GST-PH domain ([PLCδ1-PH] = 7.5 nM, [Akt-PH] = 92 nM, [Grp1-PH] = 8.4 nM final concentrated) and liposomes (0.01−10 uM PIP_n ligand). A solution of anti-GST acceptor beads and streptavidin donor beads (5 μL, 5 μg/mL) were added, the plate was gently shaken, stored for 2 h in the dark, and read on the Fusion instrument. For competition experiments, solutions of diC_8-PIP_ns (Echelon Biosciences Inc.) or biotin-free liposomes at varying concentrations were incubated with PLCδ1-PH (7.52 nM final concentrated) in buffer (10 μL) for 1 h in a 384-well microplate followed by addition of liposomes (0.20 μM final concentrated) and acceptor and donor beads (5 μL, 5 μg/mL). The plate was incubated in the dark for another hour and the luminescence was measured. Data were graphed and analyzed (nonlinear regression) using GraphPad Prism version 4.00 for Windows (GraphPad Software).

Surface Plasmon Resonance. Interaction analysis was conducted at 20 °C using a Biacore 2000 biosensor (Biacore AB) equipped with a CM5 sensor chip. Streptavidin was immobilized onto the sensor surface (CM5) at 23 °C using a standard three step amine-coupling approach in HBS running buffer (10 mM HEPES pH 7.4, 150 mM NaCl). First, all flow cells were activated by injecting a freshly mixed solution of 50 mM NHS in 200 mM EDC for 7 min. Second, streptavidin (ImmunoPure grade, Pierce Biotechnology, Inc.) was reconstituted in 10 mM sodium acetate at pH 5.0 to ~1 mg/mL and injected for 7 min. Finally, excess activated esters were blocked by treating them with 1 M sodium ethanolamine at pH 8.5, using a 7-min pulse. Liposome solutions (100 nM in HBS) and biotin-PIP_ns (200−250 nM in HBS) were diluted 10-fold in HBS running buffer and injected across individual flow cells at a flow rates of 5 or 10 μL/min until the desired loading was obtained. Fresh ligand surfaces were post-conditioned by injecting three 30 s pulses of 5 mM NaOH at 100 μL/min. Unmodified streptavidin flow cells served as reference and control surfaces. Antibodies were diluted into HBS running buffer supplemented with 0.5 mg/mL BSA and injected at 100 μL/min. The surfaces were regenerated with a single 15 s pulse of 10 mM H_3PO_4. PH domain samples were diluted into modified running buffer (10 mM HEPES pH 7.4, 150 mM NaCl, 2% v/v glycerol, and 0.1 or 0.5 mg/mL BSA (for PLCδ1-PH and Grp1-PH, respectively)) and injected at 30 or 100 μL/min (for PLCδ1-PH and Grp1-PH respectively) across all surfaces. A single pulse of 5 mM NaOH was used to regenerate the surfaces. Binding responses were referenced by subtracting the response generated across an unmodified streptavidin flow cell, and double referenced by subtracting an average buffer response (from at least two blank injections). The kinetic parameters were obtained by fitting globally to a mass transport model ($[A_0] = [A]$, $[A] + [B] = [AB]$, where A_0 = injected analyte, A = analyte concentration at surface, B = immobilized ligand, AB = bound complex).

RESULTS AND DISCUSSION

Polymerized liposomes (vesicles) offer an attractive method of presenting multiple ligands in a stable membrane mimetic system. In a highly ordered state, diacetlyenes can be polymerized by UV light (254 nm) to form a conjugated enyne system (Figure 1A). Thus, when diacetylene amphiphiles are formed into vesicles and irradiated, polymerized vesicles are created (*32*). Poly(diacetylene) (PDA) liposomes are not disrupted by organic solvents or osmotic shock and show no evidence of fusion into larger aggregates over time (*32*, *33*).

Polymerizable inositol polyphosphate ($InsP_n$)-diynes (**1a**−**c**) were synthesized from the aminopropyl analogues of Ins(1,4,5)P_3, Ins(1,3,4)P_3, and Ins(1,3,4,5)P_4 via the *N*-hydroxysuccinimide ester of 10,12-pentacosadiynoic acid as shown in Figure 1B. $InsP_n$s rather than acyl-labeled PIP_ns were chosen for two reasons. First, using a simple aminopropyl linker shortens the synthesis facilitates handling of the required headgroup. Since the headgroup will be anchored to the membrane through the diyne acyl group, incorporating the diacylglycerol seemed unnecessary. Second, $InsP_n$ probes have demonstrated effectiveness in mimicking a biologically relevant context (*21*). For instance, Ins(1,4,5)P_3- and Ins(1,3,4,5)-P_4-tethered resins have been used in affinity purification of PI(4,5)P_2 and PI(3,4,5)P_3 binding proteins with equal to or greater efficacy than PI(4,5)P_2 or PI(3,4,5)P_3 resins (*21*, *34*). Similar results have been observed for photolabeling proteins with PIP_n vs $InsP_n$ probes (*21*, *35*). To act as a detection tag, biotin-diyne-PE was synthesized from commercially available diyne-PE by condensation with the active ester of biotin-X (Figure 1C). Sonication of aqueous dispersions of the lipids at 70 °C gave liposomes, appearing as clear or slightly opaque solutions at concentrations of 1 mM (total lipid). The PIP_n component constituted 1−10 mol % of the total lipids. Irradiation of the cooled solutions at 254 nm polymerized the acyl chains resulting in a faintly red color. Liposome suspensions up to 5 mM total lipid could be prepared but at that point, the viscosity increased dramatically when polymerized. For the remainder of this report, the polymerized liposomes will often be referred to simply as liposomes unless otherwise indicated.

PI(4,5)P_2 and PI(3,4,5)P_3 liposomes were analyzed using a liposome overlay assay with immobilized PIP_n-binding proteins. In this assay, the polymerized liposomes are incubated with proteins bound on a membrane and binding interactions are detected via the biotin tag (a scheme of the steps is shown in Figure 2A). First, solutions of GST fusions of the PH domains of PLCδ1, Grp1, LL5α, DAPP, and/or FAPP were spotted on nitrocellulose in varying amounts (0.021−21 pmol). Next, the membranes were incubated with a solution of polymerized liposomes in PBS containing 3% BSA (to prevent nonspecific binding to nitrocellulose), followed by treat-

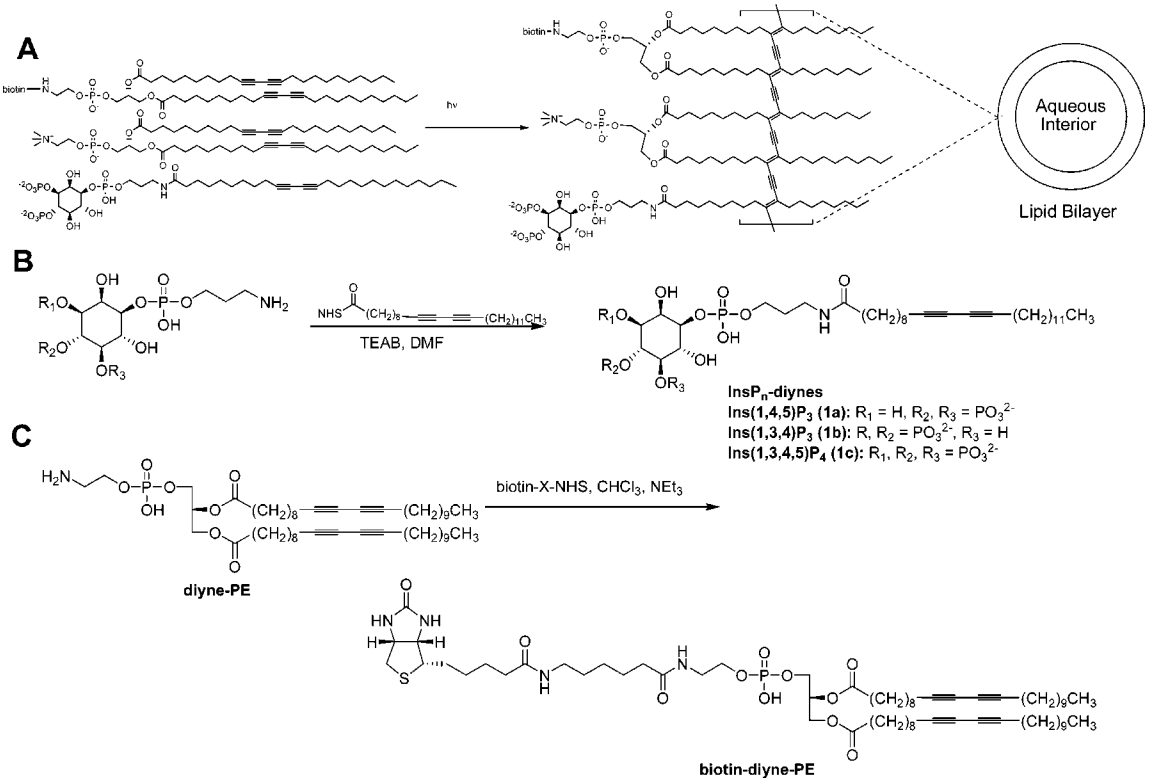

Figure 1. (A) Schematic representation of the polymerization of monomeric lipids in the outer layer of a liposome, (B) synthesis of InsP$_n$-diynes, and (C) synthesis of diyne-PE-biotin.

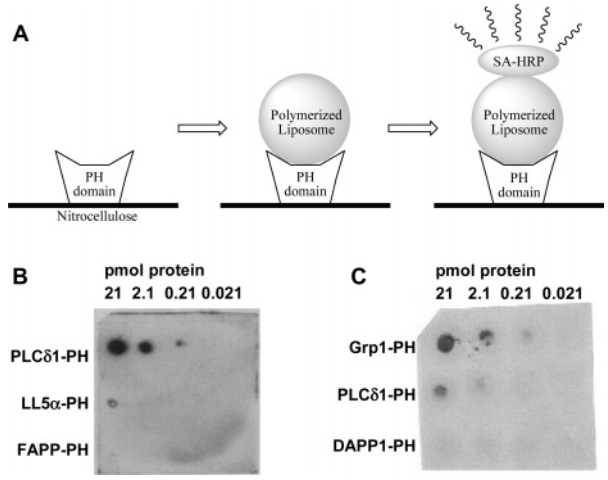

Figure 2. Detection of nitrocellulose immobilized PH domains by polymerized liposomes in liposome overlay assays. (A) Schematic of steps in the liposome overlay assay. (B) PLCδ1-PH was selectively recognized by PI(4,5)P$_2$ liposomes. (C) Grp1-PH was selectively detected by PI(3,4,5)P$_3$ liposomes.

ment with streptavidin−horseradish peroxidase (SA-HRP) and chemiluminescent detection. As shown in Figure 2B, PLCδ1-PH was detected preferentially by the PI(4,5)P$_2$ liposomes down to 0.21 pmol (10 ng) while FAPP-PH which binds PI(4)P was not detected. LL5α-PH is a promiscuous PIP$_n$ binder and was recognized at 21 pmol, which is consistent with its weaker affinity for all PIP$_n$s. PI(3,4,5)P$_3$ liposomes bound preferentially to Grp1-PH down to 0.21 pmol (10 ng) but did show some cross reactivity with PLCδ1-PH (Figure 2B). Importantly, binding was not observed using liposomes prepared without Ins(1,4,5)P$_3$-diyne clearly demonstrating that the observed interactions are due to the PIP$_n$ headgroups (data not shown). Similar experiments with conventional liposomes showed essentially identical specificity but

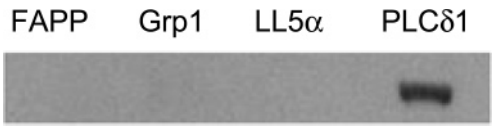

Figure 3. Detection of electrophoresed PH domains by polymerized liposomes. PH domain proteins were electrophoresed and electrotransferred to nitrocellulose and PLCδ1-PH (5 μg) was selectively recognized by PI(4,5)P$_2$ liposomes in a liposome overlay assay.

approximately 10-fold greater sensitivity than polymerized liposomes (data not shown). Nonetheless, the anticipated benefit of the polymerized liposomes was their stability compared with conventional liposomes. Thus, no appreciable differences in specificity or detection limits were observed between freshly prepared PI(4,5)P$_2$ polymerized liposomes and an older batch that had been stored at 4 °C for six months.

The polymerized liposomes could also be used to specifically detect electrophoretically separated proteins in a fashion analogous to a Western blot. PH domains were separated on SDS−PAGE, electrotransferred onto nitrocellulose, and partially renatured in guanidinium hydrochloride, and then the membrane was treated as described above for the overlay experiments. As shown in Figure 3, PLCδ1-PH (5 μg) was selectively detected using PI(4,5)P$_2$ liposomes compared with FAPP−PH and Grp1-PH; however, LL5α-PH was not detected likely due to lower affinity. As little as 1 μg of protein could be detected, and this sensitivity was increased when DTT was replaced with a glutathione redox pair at the expense of an increase in background. The detection limit was not as low as the overlays described above which we attribute to incomplete renaturation of the PH domains. In a related application, Elkin et al. employed the polymerized liposomes in liposome pull-down assays to confirm the PIP$_n$ binding specificity of the PHD finger containing RAG2 (*36*). RAG2 is essential for generating

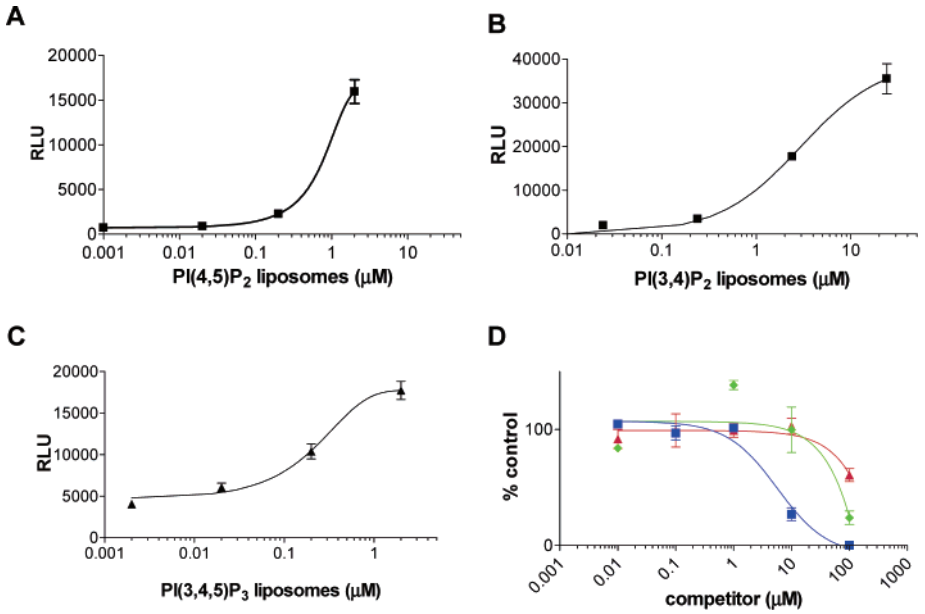

Figure 4. Alphascreen binding and competition assays for liposome-PH domain interactions. Dose-dependent binding was demostrated for: (A) $PI(4,5)P_2$ liposomes and PLCδ1-PH (7.5 nM), (B) $PI(3,4)P_2$ liposomes and Akt-PH (92 nM), and (C) $PI(3,4,5)P_3$ liposomes and Grp1-PH (8.4 nM). X-axes represent the concentration of PIP_n ligand in the assay well. (D) Competition of PIP_ns with $PI(4,5)P_2$ liposomes for binding to PLCδ1-PH. DiC_8−$PI(4,5)P_2$ (■) preferentially competed compared with diC_8-$PI(3,4)P_2$ (▲) and diC_8-$PI(3,4,5)P_3$ (◆). RLU = Relative light units.

effective immune responses by catalyzing V(D)J recombination, and it is suggested that mutations in the PIP_n-binding PHD finger alter the recombination activity leading to immunodeficiency. Additional control experiments in the report demonstrated the proteins PLCδ1-PH [$PI(4,5)P_2$], ING2-PHD [PI(5)P], p40-PX [PI(3)P], and FAPP1-PH [PI(4)P] specifically bound their known PIP_n partners [in brackets].

The second technique used to analyze the binding characteristics of polymerized liposomes was ALPHA, a bead-based platform developed by Packard Biosciences for detecting biological interactions. The AlphaScreen system uses photosensitive donor beads, which convert ambient oxygen to singlet oxygen when irradiated at 680 nm. When the donor bead comes in close proximity to an acceptor bead, through a binding event, chemiluminescent receptor and fluorescent acceptor molecules in the acceptor bead are activated by the diffusion of singlet oxygen. The resulting emission shift from 580 to 620 nm can be measured as a luminescent signal. The pairing of acyl labeled biotin-PIP_ns and PH domains in this format have been demonstrated and implemented in assays for PI 3-kinase and PTEN (*22*, *37*) suggesting that this technique would be suitable for validating the utility of the polymerized liposomes. The first experiment was designed to determine if binding occurred in this format and optimize a ratio of lipid to protein. A solution of GST-PLCδ1-PH in assay buffer was incubated with increasing amounts of $PI(4,5)P_2$-containing polymerized liposomes. Streptavidin-coated donor and anti-GST-coated acceptor beads were added and allowed to incubate for 120 min, followed by measurement of the luminescence output. Increasing luminescence was observed with increasing amount of $PI(4,5)P_2$-containing nanoparticles indicating dose-dependent binding to PLCδ1-PH (Figure 4A). The concentration on the *X*-axis represents the concentration of $PI(4,5)P_2$ ligand in the assay well. In addition, $PI(3,4)P_2$- and $PI(3,4,5)P_3$-containing polymerized liposomes bound to Akt-PH and Grp1-PH domains respectively in a dose-dependent manner (Figures 4B and 4C). At higher liposome concentrations, the luminescence dropped off, likely due to saturation of the donor beads and competition by unbound vesicles.

A second experiment examined the ability of small soluble PIP_ns to compete with liposomes for protein binding. As observed in Figure 4D, diC_8-$PI(4,5)P_2$ preferentially competed with $PI(4,5)P_2$ liposomes compared with diC_8-$PI(3,4)P_2$ and $PI(3,4,5)P_3$ for binding to PLCδ1-PH. Similarly, $PI(4,5)P_2$ liposomes, prepared without diyne-PE-biotin, caused a decrease in luminescence by competing with biotinylated-$PI(4,5)P_2$ liposomes while nonbiotinylated $PI(3,4)P_2$ liposomes could not compete at concentrations up to 500 pmol/well confirming specificity (data not shown). Both experiments show that $PI(4,5)P_2$ liposomes are selectively recognized in solution by PLCδ1-PH.

The final technique employed SPR to analyze the polymerized liposomes. SPR measurements of PIP_n-protein interactions have typically used two methods of immobilizing lipids to chip surfaces to mimic membranes: (i) trapping liposomes onto a hydrophobic dextran surface (e.g. L1 chip from Biacore), or (ii) collapsing liposomes to form a lipid monolayer on the chip (e.g. HPA chip from Biacore). Initial experiments with $PI(4,5)P_2$-polymerized liposomes used a hydrophobic L1 chip for direct capture of vesicles. Although the vesicles were captured and protein binding was observed, the results were not reproducible, but some clues as to optimum running and regeneration conditions were elucidated.

In contrast, streptavidin-coated sensor chips gave outstanding results with the biotinylated nanoparticles. Thus, the biotinylated polymerized liposomes were compared with acyl-biotinylated PIP_ns for binding to PIP_n-specific monoclonal antibodies (mAbs) and PH domains. Two anti-PIP_n mAbs, an anti-$PI(3,4)P_2$ IgG and anti-$PI(4,5)P_2$ IgM, were analyzed against their respective cognate ligands. As shown in Figure 5A−D the anti-$PI(3,4)P_2$ IgG bound to both $PI(3,4)P_2$ surfaces as did the anti $PI(4,5)P_2$ IgM to the $PI(4,5)P_2$ surfaces. The responses for the liposomes are concentration-dependent and reproducible for both cases. Binding was undetectable over an unmodified streptavidin control surface

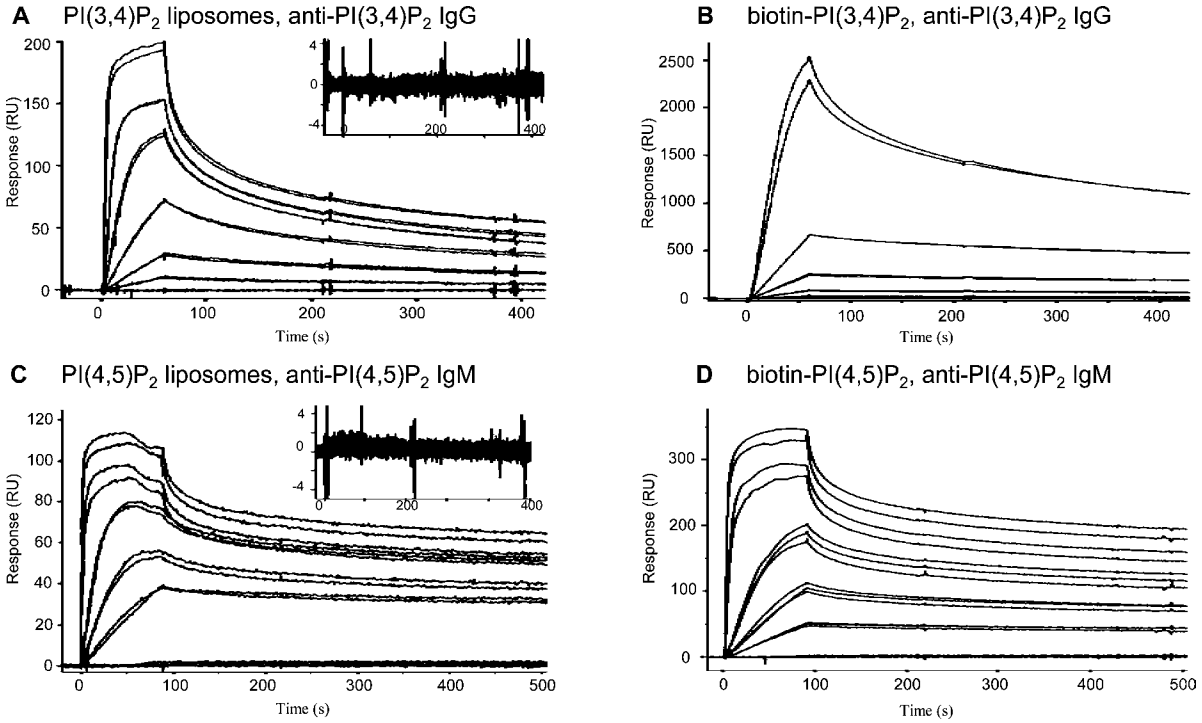

Figure 5. Sensorgrams comparing anti-PIP_n mAbs binding to polymerized liposome and biotin-PIP_n surfaces. Binding of anti-PI(3,4)P_2 IgG (0.3, 0.8, 2.4, 7.3, 22, and 66 nM) to (A) PI(3,4)P_2-liposome and (B) biotin-PI(3,4)P_2-coated streptavidin chips at 20 °C (100 μL/min). Anti-PI(4,5)P_2 IgM (0.8, 2.5, 7.4, 22.4, 66.6, and 200 nM) binding to (C) PI(4,5)P_2 liposome and (D) biotin-PI(4,5)P_2 at 20 °C (100 μL/min). The insets in parts A and C show the lack of binding to control surfaces. Surfaces were regenerated with single pulses of 10 mM H_3PO_4 (15 s.).

(insets, Figures 5A and C), demonstrating that the binding signals detected over the biotin PIP_n and liposome surfaces are specific to the PIP_n surfaces (0.5 mg/mL BSA was included in the running buffer to minimize nonspecific binding to unmodified sensor chip surfaces). Kinetically, the interactions are limited by mass transport as described by the linear slopes during the association phase. The shapes appear slightly different between the PI(3,4)P_2-containing polymerized liposome vs biotin-PI(3,4)P_2 surfaces due to mass transport. The biotin-PIP_n surface has a much higher capacity and is therefore limited more by mass transport. The bivalent nature of the mAbs contributes to avidity effects making it challenging to determine binding rate constants. No binding was detected when anti-PI(3,4,5)P_3 IgM was injected over the PI(4,5)P_2 surfaces at 200 nM indicating specific interactions between the anti-PI(4,5)P_2 mAb and the PI(4,5)P_2 liposomes (data not shown).

PH domain binding was analyzed under slightly modified conditions, 2% glycerol was included in the running buffer which helped stabilize the protein in addition to BSA. High-resolution data were collected across similar capacity PI(4,5)P_2-liposome and biotin-PI(4,5)P_2 surfaces by randomly injecting PLCδ1-PH ranging in concentration from 200 to 3.1 nM in duplicate at 30 μL/min (Figure 6A and B). After each run, the sensor chips were regenerated with single pulse of 5 mM NaOH. Binding responses were concentration dependent and reproducible. At concentrations above 100 nM, protein appeared to saturate all binding sites on the liposome surface, but not the biotin-PI(4,5)P_2 surface. The reactions were analyzed globally using a mass transport model, which provided a reasonable fit to the measured data. As shown in Table 1A, PLCδ1-PH bound with a sixteen-fold higher affinity to the liposome surface than to the biotin-PI(4,5)-P_2 surface. The on-rates (k_a) for the two surfaces were fairly similar but the off-rate (k_d) was 8.5-fold slower for the liposome surface. The slower off-rates could be due to hydrophobic interactions between proteins and the bilayer interior and/or an avidity effect of close proximity of multiple headgroups on the vesicle surface.

Table 1. Kinetic Studies into the Binding of (A) PLCδ1-PH and (B) Grp1-PH to Monomeric PIP_ns and Polymerized Liposomes by SPR[a]

	k_a (M^{-1} s^{-1})	k_d (s^{-1})	K_D(nM)
	(A) PLCδ1-PH		
PI(4,5)P_2 liposomes	1.2×10^6	7.9×10^{-3}	6.6
Biotin-PI(4,5)P_2	8.9×10^5	9.3×10^{-2}	104
	(B) Grp1-PH		
PI(3,4,5)P_3 liposomes	3.9×10^5	9.5×10^{-4}	2.5
Biotin-PI(3,4,5)P_3	1.7×10^5	2.1×10^{-3}	12

[a] The kinetic parameters were obtained by fitting globally to a mass transport model. This gave the association rate constant (k_a) and the dissociation rate constant (k_d) which yielded the equilibrium dissociation constant (K_D).

Grp1-PH was assayed under essentially identical conditions, except that BSA was increased to 0.5 mg/mL and the flow rate was increased to 100 μL/min (Figure 6C and D). Data were fit globally using a mass transport model (Table 1B) and revealed that Grp1-PH bound biotin-PI(3,4,5)P_3 probe with a 5-fold lower affinity (K_D = 12 nM) than the PI(3,4,5)P_3 liposome surface (K_D = 2.5 nM). As with the PLCδ1-PH/PI(4,5)P_2 interactions, the liposome surfaces interacted more strongly with the protein. However, the on- and off-rates were both approximately 2.3-fold faster and slower respectively for the liposome surface, both contributing equally to the increase in affinity. The improved binding to the liposome surfaces for both proteins could be due to hydrophobic interactions between proteins and the bilayer interior and/or an avidity effect of close proximity of multiple headgroups on the vesicle surface, both of which would be missing from the acyl-linked surfaces.

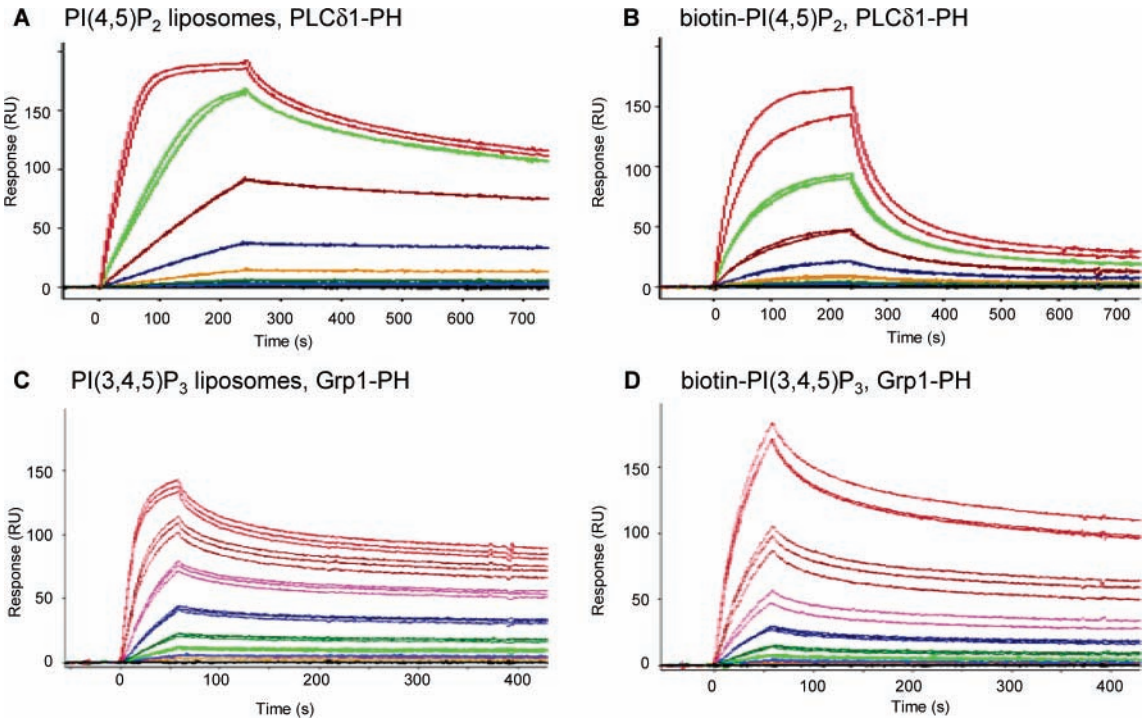

Figure 6. Sensorgrams comparing PH domain binding to polymerized liposome and biotin-PIP$_n$ surfaces. PLCδ1-PH (0, 3.1, 6.3, 12.5, 25, 50, 100, 200 nM) binding to (A) PI(4,5)P_2-liposome and (B) biotin-PI(4,5)P_2-coated streptavidin chips at 20 °C (30 μL/min). Grp1-PH (1.4, 2.7, 5.4, 10.9, 21.8, 43.5, 87, 173 nM) binding to (C) PI(3,4,5)P_3-liposome and (D) biotin-PI(3,4,5)P_3-coated streptavidin chips at 20 °C (100 μL/min). Surfaces were regenerated with pulses of 5 mM NaOH.

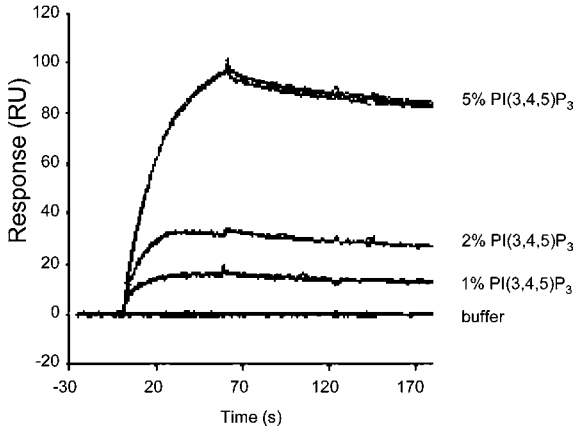

Figure 7. Grp1-PH binding to varying mol % PI(3,4,5)P_3-liposome surfaces by surface plasmon resonance. The overlay plot of 173 nM Grp1-PH injected across three polymerized liposome surfaces (1, 2, and 5% PIP_3) at 20 °C (100 μL/min) shows increasing signal comparable to the increasing PI(3,4,5)-P_3 composition in the liposomes. Probe surfaces were regenerated with a single 30-s pulse of 25 mM NaOH.

To examine the effect of varying ligand concentrations within the vesicles, additional liposomes were prepared with 1, 2, and 5 mol % PI(3,4,5)P_3 and analyzed (for the previous experiment, the PI(3,4,5)P_3 proportion in the vesicles was 10 mol %). As expected, the binding capacity increased with mol % PI(3,4,5)P_3 (Figure 7). Of these probes, results with the 5% preparation were superior as these polymerized liposomes afforded surfaces that were the easiest to regenerate between runs. The affinities of the two other preparations were judged to be comparable but did not regenerate as well, requiring a 5-fold increase in NaOH to 25 mM. For all of the SPR experiments conducted, the data deviated from the simulated data, most notably in the dissociation phase. This suggested that, as expected for a multivalent ligand, the mechanism was complex and that simple bimolecular models were not applicable.

Finally, to investigate the selectivity of PI(3,4,5)P_3 liposomes for Grp1-PH, competition studies were undertaken using water soluble diC_8-PI(3,4,5)P_3 and diC_8-PI-(4,5)P_2. The competitors at varying concentrations were preincubated with the protein and then passed over the PI(3,4,5)P_3-liposome chip surface. As shown in Figure 8, increasing diC_8-PI(3,4,5)P_3 competed with the liposome surface to bind Grp1-PH causing a decrease in response with almost complete competition at 87 nM. DiC_8−PI-(4,5)P_2 did not effectively compete until much higher concentrations, with essentially complete competition at 21 μM. This demonstrates the strong selective affinity of Grp1-PH for the PI(3,4,5)P_3-liposome surface as it is only interrupted by the presence of an analogue of the natural ligand.

In this report, we describe the preparation of stable polymerized PIP$_n$-containing vesicles. InsP_n ligands containing a pentacosadiynyl acyl chain were synthesized for Ins(1,4,5)P_2, Ins(1,3,4)P_2, and Ins(1,3,4,5)P_4, and a diyne-PE-biotin was prepared as a detection tag. Vesicles were prepared and polymerized at 254 nm and were validated in a number of formats. Liposome overlay assays using PI(4,5)P_2- and PI(3,4,5)P_3-polymerized liposomes showed selectivity comparable to that of conventional liposomes when binding to nitrocellulose-immobilized PH domains. In addition, PLCδ1-PH that had been electrophoretically separated and electrotransferred was recognized specifically by PI(4,5)P_2 liposomes in the presence of other PH domains. Polymerized liposomes were applicable the ALPHA assays, binding was observed between PI(4,5)P_2/PLCδ1-PH, PI(3,4)P_2/Akt-PH, and PI-(3,4,5)P_3/Grp1-PH. The interaction of PI(4,5)P_2/PLCδ1-PH was specifically disrupted by soluble PI(4,5)P_2. Finally, the interactions of with anti-PIP$_n$ mAbs and PLCδ1-PH and Grp1-PH were validated using SPR. The polymerized liposome nanoparticles proved to be robust

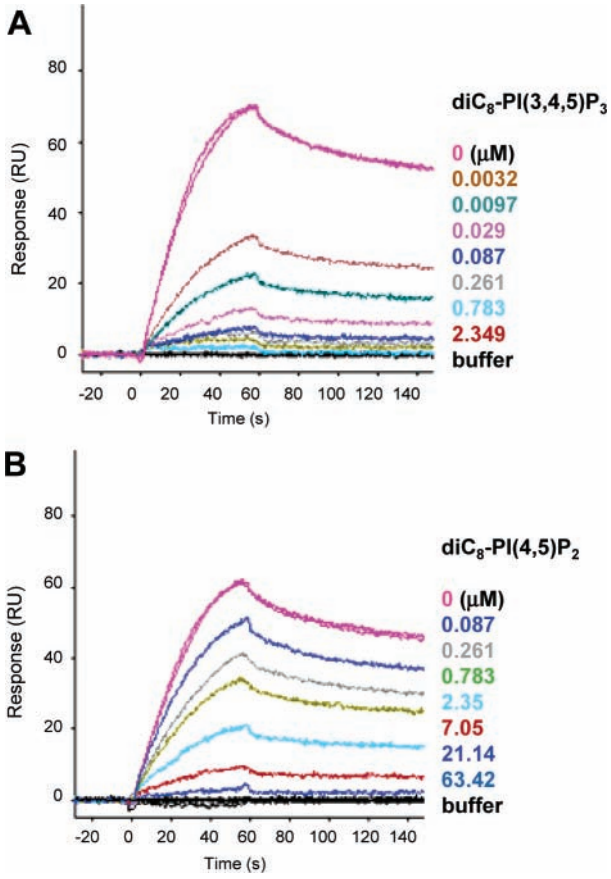

Figure 8. Sensorgrams of Grp1-PH binding to $PI(3,4,5)P_3$-liposome surfaces in the presence of water soluble PIP_ns. Grp1-PH (87 nM) was incubated with varying concentrations of competitors: (A) diC_8-$PI(3,4,5)P_3$ and (B) diC_8-$PI(4,5)P_2$ and injected over $PI(3,4,5)P_3$-liposome-coated surfaces at 20 °C (100 μL/min). Probe surfaces were regenerated with a single 30 s pulse of 5 mM NaOH. DiC_8-$PI(3,4,5)P_3$ competed at approximately 250-fold lower concentration than diC_8-$PI(4,5)P_2$.

coatings for streptavidin-coated chips and bound the PH domain proteins more strongly than the corresponding monomeric PIP_n ligands. Polymerized PIP_n-containing liposomes are thus appropriate, convenient, and biologically informative tools for studying protein lipid interactions.

ACKNOWLEDGMENT

The work in this paper was supported by a grant (R43 GM685683 to C.G.F.) from the National Institutes of Health. Additional help provided by Dr. Randy Booth (UUtah) and Ms. Heather Hudson (Echelon) were greatly appreciated

LITERATURE CITED

(1) Martin, T. F. J. (1998) Phosphoinositide lipids as signaling molecules: Common themes for signal transduction, cytoskeletal regulation, and membrane trafficking. *Annu. Rev. Cell Developmental Biol. 14*, 231−264.

(2) Czech, M. P. (2000) PIP2 and PIP3: Complex roles at the cell surface. *Cell 100*, 603−606.

(3) Anderson, R. A., Boronenkov, I. V., Doughman, S. D., Kunz, J., and Loijens, J. C. (1999) Phosphatidylinositol phosphate kinases, a multifaceted family of signaling enzymes. *J. Biol. Chem. 274*, 9907−9910.

(4) Majerus, P. W., Kisseleva, M. V., and Norris, F. A. (1999) The role of phosphatases in inositol signaling reactions. *J. Biol. Chem. 274*, 10669−10672.

(5) Toker, A. (1998) The synthesis and cellular roles of phosphatidylinositol 4,5-bisphosphate. *Curr. Opin. Cell. Biol. 10*, 254−261.

(6) Corvera, S., DArrigo, A., and Stenmark, H. (1999) Phosphoinositides in membrane traffic. *Curr. Opin. Cell. Biol. 11*, 460−465.

(7) Odorizzi, G., Babst, M., and Emr, S. D. (2000) Phosphoinositide signaling and the regulation of membrane trafficking in yeast. *Trends. Biochem. Sci. 25*, 229−235.

(8) Vanhaesebroeck, B., Leevers, S. J., Ahmadi, K., Timms, J., Katso, R., Driscoll, P. C., Woscholski, R., Parker, P. J., and Waterfield, M. D. (2001) Synthesis and function of 3-phosphorylated inositol lipids. *Annu. Rev. Biochem. 70*, 535−602.

(9) Rameh, L., and Cantley, L. (1999) The role of phosphoinositide 3-kinase lipid products in cell function. *J. Biol. Chem. 274*, 8347−8350.

(10) Varnai, P., Lin, X., Lee, S. B., Tuymetova, G., Bondeva, T., Spat, A., Rhee, S. G., Hajnoczky, G., and Balla, T. (2002) Inositol lipid binding and membrane localization of isolated pleckstrin homology (PH) domains − studies on the PH domains of phospholipase C delta(1) and p130. *J. Biol. Chem. 277*, 27412−27422.

(11) Lemmon, M. A. (1999) Structural basis for high-affinity phosphoinositide binding by pleckstrin homology domains. *Biochem. Soc. Trans. 27*, 617−24.

(12) Rebecchi, M. J., and Scarlata, S. (1998) Pleckstrin homology domains: a common fold with diverse functions. *Annu. Rev. Biophys. Biomol. Struct. 27*, 503−28.

(13) Sato, T. K., Overduin, M., and Emr, S. (2001) Location, location, location: membrane targeting directed by PX domains. *Science 294*, 1881−1885.

(14) Misra, S., Miller, G. J., and Hurley, J. H. (2001) Recognizing Phosphatidylinositol 3-Phosphate. *Cell 107*, 559−562.

(15) Santagata, S., Boggon, T., Baird, C., Gomez, C., Zhao, J., Shan, W., Myszka, D., and Shapiro, L. (2001) G-protein signaling through tubby proteins. *Science 292*, 2041−2045.

(16) Gozani, O., Karuman, P., Jones, D. R., Field, S. J., Baird, C. L., Cha, J., Villasenor, J., Mehrotra, B., Zhu, H., Chen, J., Rao, V. R., Brugge, J. S., Ferguson, C. G., Myszka, D. G., Divecha, N., Cantley, L. C., Prestwich, G. D., and Yuan, J. (2003) The PHD finger of the chromatin-associated protein ING2 functions as a nuclear phosphoinositide receptor. *Cell 114*, 99−111.

(17) Milburn, C. C., Deak, M., Kelly, S. M., Price, N. C., Alessi, D. R., and Aalten, D. M. F. V. (2003) Binding of phosphatidylinositol 3,4,5-trisphosphate to the pleckstrin homology domain of protein kinase B induces a conformational change. *Biochem. J. 275*, 531−538.

(18) Datta, S. R., Dudek, H., Tao, X., Masters, S., Fu, H., Gotoh, Y., and Greenberg, M. E. (1997) Akt phosphorylation of BAD couples survival signals to the cell-intrinsic death machinery. *Cell 91*, 231−241.

(19) Meuillet, E. J., Mahadevan, D., Vankayalapati, H., Berggren, M., Williams, R., Coon, A., Kozikowski, A. P., and Powis, G. (2003) Specific Inhibition of the Akt1 Pleckstrin Homology Domain by D-3-Deoxy-Phosphatidyl-myo-Inositol Analogues. *Mol. Cancer Ther. 2*, 289−399.

(20) Castillo, S. S., Brognard, J., Petukhov, P. A., Zhang, C., Tsurutani, J., Granville, C. A., Li, M., Jung, M., West, K. A., Gills, J. G., Kozikowski, A. P., and Dennis, P. A. (2004) Preferential Inhibition of Akt and Killing of Akt-Dependent Cancer Cells by Rationally Designed Phosphatidylinositol Ether Lipid Analogues. *Cancer. Res. 64*, 2782−2792.

(21) Prestwich, G. D. (2004) Phosphoinositide signaling: from affinity probes to pharmaceutical targets. *Chem. Biol. 11*, 619−637.

(22) Drees, B. E., Mills, G. B., Rommel, C., and Prestwich, G. D. (2004) Therapeutic potential of phosphoinositide 3-kinase inhibitors. *Expert Opin. Ther. Pat.*, in press.

(23) Glaser, M., Wanaski, S., Buser, C. A., Boguslavsky, V., Rashidzada, W., Morris, A., Rebecchi, M., Scarlata, S. F., Runnels, L. W., Prestwich, G. D., Chen, J., Aderem, A., Ahn, J., and McLaughlin, S. (1996) Myristoylated alanine-rich C kinase substrate (MARCKS) produces reversible inhibition

of phospholipase C by sequestering phosphatidylinositol 4,5-bisphosphate in lateral domains. *J. Biol. Chem. 271*, 26187−26193.

(24) Rauch, M., Ferguson, C., Prestwich, G. D., and Cafiso, D. (2002) MARCKS sequesters spin-labeled phsophatidylinositol-4,5-bisphosphate in lipid bilayers. *J. Biol. Chem. 277*, 14068−14076.

(25) Gambhir, A., Hangyas-Mihalyne, G., Zaitseva, I., Cafiso, D. S., Wang, J., Murray, D., Pentyala, S. N., Smith, S. O., and McLaughlin, S. (2004) Electrostatic sequestration of PIP2 on phospholipid membranes by basic/aromatic regions of proteins. *Biophys. J. 86*, 2188−2207.

(26) Dowler, S., Currie, R. A., Campbell, D., Deak, M., Kular, G., Downes, C. P., and Alessi, D. R. (2000) Identification of pleckstrin-homology-containing proteins with novel phosphoinositide-binding specificities. *Biochem. J. 351*, 19−31.

(27) Yu, J. W., Mendrola, J. M., Audhya, A., Singh, S., Keleti, D., DeWald, D. B., Murray, D., Emr, S. D., and Lemmon, M. A. (2004) Genome-wide analysis of membrane targeting by S. cerevisiae pleckstrin homology domains. *Mol. Cell 13*, 677−688.

(28) Spevak, W., Nagy, J. O., Charych, D. H., Schaefer, M. E., Gilbert, J. H., and Bednarski, M. D. (1993) Polymerized liposomes containing *C*-glycosides of sialic acid: potent inhibitors of influenza virus in vitro infectivity. *J. Am. Chem. Soc. 115*, 1146−1147.

(29) Estevez, V. A., and Prestwich, G. (1991) Synthesis of Enantiomerically Pure, P-1-Tethered inositol tetrakis(phosphate) Affinity labels via a Ferrier Rearrangement. *J. Am. Chem. Soc. 113*, 9885−9887.

(30) Dorman, G., Chen, J., and Prestwich, G. D. (1995) Synthesis of D-myo-P-1-(O-aminopropyl)-inositol-1,4,5-trisphosphate affinity probes from alpha-D-glucose. *Tetrahedron Lett. 36*, 8719−8722.

(31) Thum, O., Chen, J., and Prestwich, G. D. (1996) Synthesis of a photoaffinity analogue of phosphatidylinositol 3,4-bisphosphate, an effector in the phosphoinositide 3-kinase signaling pathway. *Tetrahedron Lett. 37*, 9017−9020.

(32) Okada, S., Peng, S., Spevak, W., and Charych, D. (1998) Color and chromism of polydiacetylene vesicles. *Acc. Chem. Res. 31*, 229−239.

(33) Hub, H.-H., Hupfer, B., Koch, H., and Ringsdorf, H. (1980) Polymerizable phospholipid analogues − new stable biomembrane and cell models. *Angew. Chem., Int. Ed. Engl. 19*, 938−940.

(34) Chaudhary, A., Dorman, G., and Prestwich, G. D. (1994) Synthesis of p-5 tethered inositol-1,2,6-trisphosphate, an affinity reagent for alpha-trinositol receptors. *Tetrahedron Lett. 35*, 7521−7524.

(35) Chaudhary, A., Gu, Q. M., Thum, O., Profit, A. A., Qi, Y., Jeyakumar, L., Fleischer, S., and Prestwich, G. D. (1998) Specific interaction of Golgi coatomer protein alpha-COP with phosphatidylinositol 3,4,5-trisphosphate. *J. Biol. Chem. 273*, 8344−8350.

(36) Elkin, S. K., Ivanov, D., Ewalt, M., Ferguson, C. G., Hyberts, S. G., Sun, Z.-Y. J., Prestwich, G. D., Yuan, J., Wagner, G., Oettinger, M. A., and Gozani, O. (2005) A PHD Finger Motif in the C-terminus of RAG2 Modulates Recombination Activity. *J. Biol. Chem. 280*, 28701−28710.

(37) Gray, A., Olsson, H., Batty, I. H., Priganica, L., and Downes, C. P. (2003) Nonradioactive methods for the assay of phosphoinositide 3-kinases and phosphoinositide phosphatases and selective selection of signaling lipids in cell and tissue extracts. *Anal. Biochem. 313*, 234−245.

BC050197Q

Fabrication and Application of Enzyme-Incorporated Peptide Nanotubes

Lingtao Yu, Ipsita A. Banerjee, Xueyun Gao, Nurxat Nuraje, and Hiroshi Matsui*

Department of Chemistry and Biochemistry at Hunter College and the Graduate Center, The City University of New York, New York, New York 10021. Received July 8, 2005; Revised Manuscript Received August 23, 2005

Enzyme engineering is a fast-growing field in the pharmaceutical and food markets. For those applications, various substrates have been examined to immobilize and stabilize enzymes. In this report, we examined peptide nanotubes as supports for enzymes. When a model enzyme, *Candida rugosa* lipase, was encapsulated in peptide nanotubes, the catalytic activity of nanotube-bound lipases was increased 33% as compared to free-standing lipases at room temperature. At an elevated temperature, 65 °C, the activity of lipases inside the nanotubes was 70% higher than free-standing lipases. The activity enhancement of lipases in the peptide nanotubes is likely induced by the conformation change of lipases to the open form (the enzymatically active structure) as lipases are adsorbed on the inner surfaces of peptide nanotubes.

INTRODUCTION

Enzymes are versatile biocatalysts that control specific chemical reactions effectively in vivo and in vitro (*1*−*3*). To make enzymes cost-effective, long-lived, and highly active, supports, such as sol−gels (*4, 5*), polymer membranes (*6*), silica (*7, 8*), and zeolites (*9, 10*), have been utilized to immobilize enzymes. While there are supports that enhance enzymatic activity, lifetime, and thermal stability (*4, 6, 10, 11*), some supports also decrease the lifetime and the activity of enzymes (*8, 12*). Nanometer-scale materials have potential to serve as superior enzyme supports due to their large surface-to-volume ratios in comparison with traditional macroscale materials while the reduction of substrate size may induce the deactivation and the desorption of enzymes in the processes of enzymatic reactions (*12*). Recently, the catalytic activity and the thermal stability of enzymes were reported to be enhanced when they were immobilized on magnetic nanoparticle supports (*11, 13*). To evaluate the effectiveness of nanoscale enzymatic supports, more studies in various types of nanosupports are desirable.

In this report, we explored a new nanoscale support, peptide nanotube, to immobilize enzymes inside the nanotubes. Peptide nanotubes have an advantage to immobilize enzymes on the nanotube surfaces with a simple incubation process via hydrogen bonding between amide groups of the nanotube and the complementary functional groups of proteins (*14, 15*). It is also advantageous that the adsorption of enzymes can be limited inside the peptide nanotubes via capillary effect (*16*). Previously, the coating location of peptides and nanocrystals, inside or outside the nanotubes, was controlled by optimizing concentrations of adsorbents and functionalities of nanotube surfaces (*16, 17*). In this report, a *Candida rugosa* lipase was chosen as a model enzyme to test the peptide nanotube support because the *Candida rugosa* lipase has previously shown enhancement of the enzymatic activity on other supports (*11, 13*). The enzymatic activity of *Candida rugosa* lipases inside the peptide nanotube was enhanced not only at room temperature but also at elevated temperatures as compared to free-standing lipases.

EXPERIMENTAL PROCEDURES

First, 10 mM of bis(*N*-α-amido-glycylglycine)-1,7-heptane dicarboxylate, bolaamphiphile peptide, was self-assembled into peptide nanotubes in a pH 4.5 citric acid/NaOH solution. Methods for the bolaamphiphile peptide synthesis and the nanotube self-assembly are described elsewhere (*18, 19*). After the peptide nanotubes were washed with deionized water several times, 200 μL of nanotubes in a phosphate buffer solution (pH = 7.4) was mixed with 1−20 μL of *Candida rugosa* lipase solutions, respectively. The enzyme in the peptide nanotube was protected during the incubation time of a week by keeping the sample in a refrigerator at 4 °C. After these samples were washed twice with centrifugation for 3 h to remove excess lipases in the supernatant solutions, the immobilization of lipases inside the peptide nanotubes was confirmed by transmission electron microscopy (TEM, JEOL 1200EX) at 100 kV acceleration voltage. The TEM samples were prepared by dropping 10 μL of the sample solution on carbon membrane 300 mesh copper grids and then the samples were dried completely in air. The loaded amount of lipase inside the nanotubes was determined by the colorimetric protein assay with a Bio-Rad reagent. After lipases and peptide nanotubes in the solution were separated by centrifugation, the lipase concentration in the supernatant was determined by the assay. The amount of lipases bound in the nanotubes was calculated by subtracting the lipase concentration in the supernatant from the initial lipase concentration. In this measurement, bovine serum albumin was applied as a standard. The resulting nanotubes, whose lipase loadings were determined by the assay, were used to study their activities and thermal stabilities after washing these nanotubes. To study the activities of those peptide nanotubes, 30 μL of *p*-nitrophenyl butyrate solution (13.8 mg/mL in 2-propanol) was added to 200 μL of the lipase−nanotube solution, and the mixture was balanced to 1

* To whom correspondence should be addressed. E-mail: hmatsui@hunter.cuny.edu. Tel: 212-650-3918, Fax: 212-772-5332.

10.1021/bc050199a CCC: $30.25 © 2005 American Chemical Society
Published on Web 10/21/2005

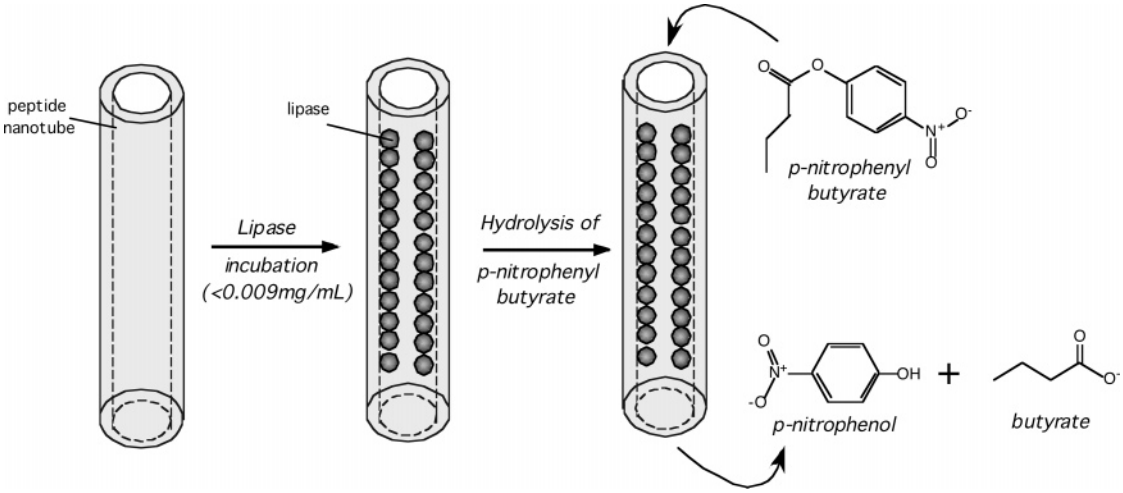

Figure 1. Illustration of lipase nanotube fabrication and its enzymatic application.

mL by a pH 7.4 buffer solution. The hydrolysis rates of *p*-nitrophenyl butyrate solutions were monitored by the product concentration, [*p*-nitrophenol], by means of UV−vis spectroscopy (Varian Cary 300 Bio). These processes are summarized in Figure 1. The thermal stability of lipases was also investigated at various reaction temperatures from 25 °C to 75 °C. In this thermal experiment, 6 μL of lipase solution was mixed with 200 μL of the nanotube solution at 4 °C for one week. After the resulting solution was diluted to 1 mL by a pH 7.4 buffer solution, the thermal stability of lipases were examined. Fluorescence studies of free-standing lipases and nanotube-bound lipases were carried out with a Jobin Ybin-SPEX, FL3-11 fluorometer. The excitation wavelength was 310 nm, and the bandwidth was 3 nm for both excitation and emission. This protocol allowed us to observe the tryptophan peak shift around 339 nm.

RESULTS AND DISCUSSION

A model enzyme, *Candida rugosa* lipase, was encapsulated within peptide nanotubes and its catalytic activity in hydrolysis of *p*-nitrophenyl butyrate was examined, as shown in Figure 1. The peptide nanotube was synthesized with the previously published method (*18, 19*). We used the peptide nanotube with the inner diameter of 160 nm, large enough to introduce substrates and lipases inside the nanotube while the ideal porous diameter of nanotube for lipase incorporation is not completely investigated yet.

After lipases were incubated in the nanotube solutions for one week, the inner wall of the nanotube was coated by lipases, as shown in Figure 2. Figure 2a shows TEM image of the peptide nanotube without incorporating lipases. Figure 2b is TEM image of the nanotube with 0.002 mg/mL of lipases. As shown in this TEM image, lipases appeared as darker areas in the nanotube because they were crystallized inside when the samples were dried on TEM grids (*20*). Figure 2c is TEM image of the lipase nanotube with 0.006 mg/mL of lipases. This TEM image shows that the inner wall of nanotube was fully coated by lipases. When the lipase concentration exceeded 0.009 mg/mL, the lipases were coated outside the nanotubes because the saturation of lipase binding on the inner wall induced the outside coating with the excess lipases. While we do not have direct evidence to explain this inside-coating mechanism, various nanoparticles were observed to coat inside the peptide nanotubes at lower nanoparticle concentrations via capillary effect (*16, 21*) and the trend of lipase incorporation at the lower

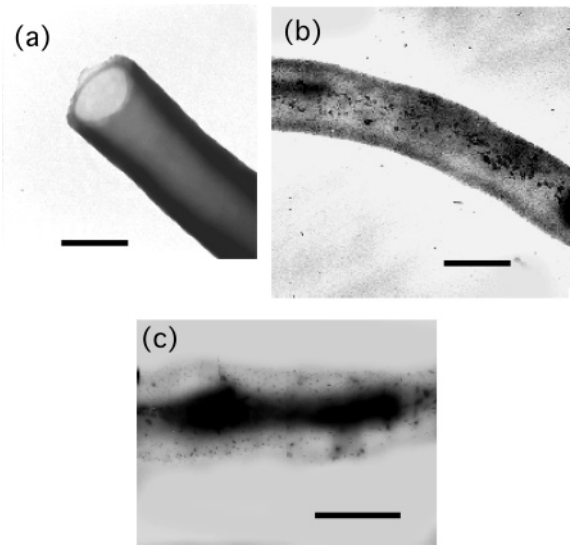

Figure 2. TEM images of peptide nanotubes incorporating *Candida rugosa* lipase at (a) [lipase] = 0 mg/mL (b) [lipase] = 0.002 mg/mL (c) [lipase] = 0.006 mg/mL. Scale bar = 200 nm.

concentrations is consistent with these previous outcomes. Another possible mechanism is the hydrophobic interaction between the nanotubes and the lipases. In general, the hydrophobic nonpolar residues of lipase spread on the outer shell while the enzymatic active sites are clustered (*9, 22, 23*), and then lipases aggregate on hydrophobic surfaces (*24, 25*). Therefore, the incorporation of lipases in the peptide nanotubes may also be due to the hydrophobicity of the inner surface of the peptide nanotube.

Enzymatic activities of lipases immobilized inside the peptide nanotubes were studied by monitoring the hydrolysis rate of *p*-nitrophenyl butyrate via the concentration change of a product, *p*-nitrophenol (Figure 1). To obtain their activities, the initial slopes of *p*-nitrophenol concentration changes over the reaction time were used. Figure 3 shows that the hydrolysis rate of lipases inside the peptide nanotubes increased linearly as a function of the lipase concentration. This feature indicates that the peptide nanotube support could maintain the enzymatic function of lipase, and the binding inside the nanotube did not hinder the catalytic reaction (*26*). Since the peptide nanotube itself has amino groups that may react with the resulting esters to affect the observed hydrolysis rates, the extent of the *p*-nitrophenyl ester

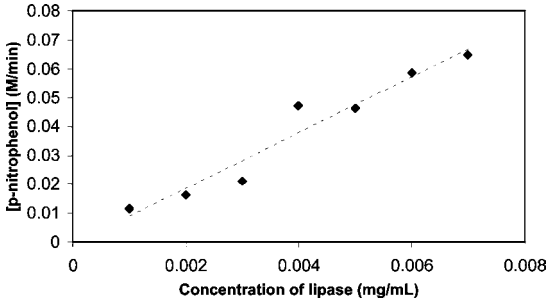

Figure 3. Hydrolysis rate of lipid catalyzed by lipases inside the nanotubes. A dotted line is a fit for experimental data points.

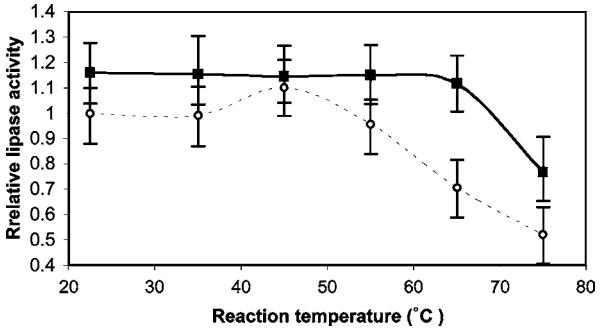

Figure 4. Thermal stability of lipases. The solid line and ■ represent lipases inside the nanotubes and the dotted line and ○ represent free-standing lipases.

hydrolysis by the neat peptide nanotubes without the enzyme was examined. This control experiment showed that the product concentration was 10^3 times lower as compared to the one by the peptide nanotubes with the enzyme, which means that the peptide nanotube itself cannot hydrolyze *p*-nitrophenyl ester efficiently. Since the product formation by the neat peptide nanotubes was negligible, the observed hydrolysis rates in Figure 3 are solely contributed by the lipases in the nanotubes.

The thermal stabilities of lipases (0.006 mg/mL) inside the nanotubes and free-standing lipases were compared in the temperature range, 25 °C to 75 °C, as shown in Figure 4. In this figure, the activity of the lipase was obtained by its initial slope of the *p*-nitrophenol concentration change over the reaction time, and the lipase activities were normalized by the hydrolysis rate of free-standing lipase at 22 °C. In the temperature range of 25−50 °C, the yield of *p*-nitrophenol by the nanotube-bound lipases is 33% higher than the one by the free-standing lipases. In the higher temperature range, the nanotube-bound lipases still maintained its activity up to 65 °C (a solid line in Figure 4); however the free-standing lipases lost their activity rapidly (a dotted line in Figure 4). As a result, the activity of nanotube-bound lipases was observed to be 70% higher as compared to the activity of free-standing lipases at 65 °C. The similar magnitude of the activity enhancement of nanotube-bound lipases was still observable at 75 °C. The drop of the activity for the lipases in the nanotubes at 75 °C (Figure 4) was not caused by the destruction of the peptide nanotube because the nanotube structure was observed to be rigid up to 200 °C (*18*). It is also unlikely that the activity decrease was caused by the lipase desorption since no lipases were released from the nanotubes in all temperature range during the activity measurement.

This outcome indicates that the noncovalent binding between the inner nanotube surfaces and lipases is strong enough to hold lipases during the enzymatic reaction even in the elevated temperatures. The increase of lipase

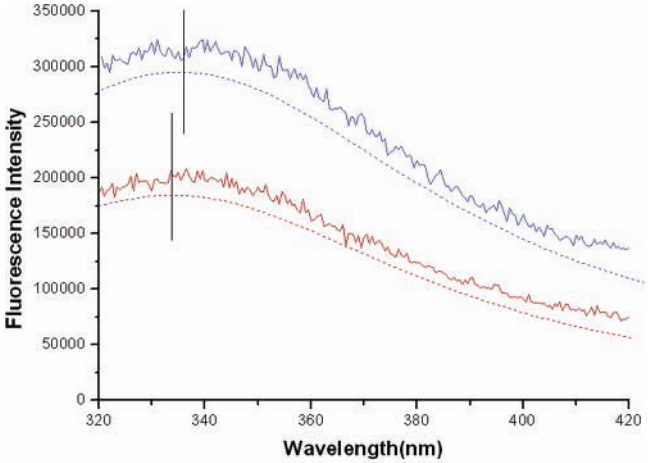

Figure 5. Fluorescence spectra of lipases bound the inside wall of peptide nanotubes (a blue line) and free-standing lipases (a red line). Dotted lines are the Lorentzian fits for these spectra and the computed peak positions by these fittings are also marked in this plot.

activity is also likely contributed by the conformation change of lipases, which exposes the catalytic active sites of lipases as lipase molecules are attached on the peptide nanotubes. For example, when lipases were attached on an oil−water interface, their catalytic activity was enhanced dramatically because lipases could undergo the conformation change from a closed form (i.e., enzymatically inactive) to a more open form (i.e., enzymatically active) (*27*). This type of conformation change has been detected by monitoring intrinsic fluorescence intensity of tryptophan in lipases (*28, 29*). When lipases were unfolded to the open conformation, the hydrophobic pockets of lipases were exposed, which increased the fluorescence intensity of tryptophan. If the activity of lipases on the peptide nanotubes is increased with the same mechanism via the conformation change induced by the nanotube−water interface, the increase of the Trp fluorescence intensity of nanotube-bound lipases should be observed as compared to free-standing lipases. Figure 5 shows the fluorescence intensity change of lipases before and after adding the peptide nanotube solution. The exact peak positions of these spectra was determined by the Lorenztian fits, as shown in dotted lines in Figure 5. Indeed, the increase of the tryptophan fluorescence intensity at 339 nm (blue) was observed after lipases bound the nanotubes, which is consistent with the enhancement mechanism observed in the lipase system at the oil−water interface. The red-shift of the tryptophan peak from 333 nm (a peak of the red line in Figure 5) to 339 nm (a peak of the blue line in Figure 5) after the nanotube solution was added to lipases, is also consistent with the red-shift of the tryptophan's fluorescence spectra in polar environments. When we added the substrate to a solution of the peptide nanotubes without lipase and measured the amount of substrate remaining in solution by UV−vis absorption, the resulting substrate concentration was identical to the initial concentration of the substrate. Since there is no partitioning of substrates in the nanotubes over 24 h, the observed enhancement of lipase activity in the peptide nanotubes is not due to simply local increase of the substrate concentration inside the nanotube. The conformation change of lipases may also indicate that the inner surface of the peptide nanotube facilitates lipases on the nanotube surfaces in the favorable orientation to maximize the contact with the substrate, *p*-nitrophenyl butyrate (*9, 23*).

In conclusion, peptide nanotubes were applied as supports for enzymes. We encapsulated a model enzyme inside peptide nanotubes, and the catalytic activity of nanotube-bound lipases was 33% higher as compared to free-standing lipases at room temperature. It was remarkable that the peptide nanotubes behaved as even better enzyme supports at higher temperature. At the elevated temperature, 65 °C, the activity of lipases inside the nanotubes was 70% higher as compared to free-standing lipases. The activity enhancement of lipases in the peptide nanotubes is likely induced by the conformation change of lipases to the open form (the enzymatically active structure) as lipases are adsorbed on the inner surfaces of peptide nanotubes. The stable binding between the nanotubes and lipases may also contribute to maintain the open (enzymatically active) form of lipases, which keeps the high catalytic activity at elevated temperature. It is advantageous to apply these peptide nanotubes as enzyme supports because the nanotubes can immobilize enzymes on the surfaces with a simple procedure and provide an appropriate environment for the active conformation of lipases (*15, 17*). The peptide nanotube can also be decorated by magnetic materials, which is beneficial to develop recyclable sensors and high-throughput catalysts (*21*).

ACKNOWLEDGMENT

This work was supported by the U.S. Department of Energy (DE-FG-02-01ER45935) and the National Science Foundation-CAREER (EIA-0133493). Hunter College Chemistry infrastructure is supported by the National Institutes of Health, the RCMI program (G12-RR-03037). We thank Professor K. Fath and Dr. A. Tsiola at the Core Facilities for imaging, Cellular and Molecular Biology at Queens College-CUNY, for the use of transmission electron microscope.

LITERATURE CITED

(1) Liu, J. J., and Wong, C. H. (2002) Aldolase-Catalyzed Asymmetric Synthesis of Novel Pyranose Synthons as a New Entry to Heterocycles and Epothilones. *Angew. Chem., Int. Ed. Engl. 41*, 1404−1407.

(2) Fugantic, C., Grasselli, P., Spreafico, F., Zirotti, C., and Casati, P. (1984) Synthesis of the enantiomeric forms of.alpha.- and.beta.-alkoxy carbonyl compounds from the (2S,3R)-2,3-diol prepared in fermenting bakers' yeast from.alpha.-methylcinnamaldehyde. *J. Org. Chem. 49*, 543−546.

(3) Bednarski, M. D., Simon, E. S., Bischofberger, N., Fessner, W.-D., Kim, M. J., Lees, W., Saito, T., Waldmann, H., and Whitesides, G. M. (1989) Rabbit muscle aldolase as a catalyst in organic synthesis. *J. Am. Chem. Soc. 111*, 627−635.

(4) Hsu, A. F., Foglia, T. A., and Shen, S. (2000) Immobilization of Pseudomonas cepacia lipase in a phyllosilicate sol−gel matrix: effectiveness as a biocatalyst. Biotechnol. *Appl. Biochem. 31*, 179−183.

(5) Reetz, M. T., Zonta, A., Vijayakrishnan, V., and Schimossek, K. (1998) Entrapment of Lipases in Hydrophobic Magnetite-containing Sol−Gel Materials: Magnetic Separation of Heterogeneous Biocatalysts. *J. Mol. Catal. A: Chem. 134*, 251−258.

(6) de Oliveira, P. C., Alves, G. M., and de Castro, H. F. (2000) Immobilisation studies and catalytic properties of microbial lipase onto styrene-divinylbenzene copolymer. *Biochem. Eng. J. 5*, 63−71.

(7) Cao, L. Q., Bornscheuer, U. T., and Schmid, R. D. (1999) Lipase-catalyzed solid-phase synthesis of sugar esters. Influence of immobilization on productivity and stability of the enzyme. *J. Mol. Catal. B: Enzym. 6*, 279−285.

(8) Letant, S. E., Hart, B. R., Kane, S. R., Hadi, M. Z., Shields, S. J., and Reynolds, J. G. (2004) Enzyme Immobilization on Porous Silicon Surfaces. *Adv. Mater. 16*, 689−692.

(9) Dumitriu, E., Secundo, F., Patarin, J., and Fechete, L. (2003) Preparation and properties of lipase immobilized on MCM-36 support. *J. Mol. Catal. B: Enzy. 22*, 119−133.

(10) Seetharam, G., and Saville, B. A. (2002) L-DOPA production from tyrosinase immobilized on zeolite. *Enzym. Microb. Technol. 31*, 747−753.

(11) Huang, S. H., Liao, M. H., and Chen, D. H. (2003) Direct Binding and Characterization of Lipase onto Magnetic Nanoparticles. *Biotechnol. Prog. 19*, 1095−1100.

(12) Dyal, A., Loos, K., Noto, M., Chang, S. W., Spagnoli, C., Shafi, K. V. P. M., Ulman, A., Cowman, M., and Gross, R. A. (2003) Activity of *Candida rugosa* Lipase Immobilized on γ-Fe2O3 Magnetic Nanoparticles. *J. Am. Chem. Soc. 125*, 1684−1685.

(13) Phadtare, S., Kumar, A., Vinod, V. P., Dash, C., Palaskar, D. V., Rao, M., Shukla, P. G., Sivaram, S., and Sastry, M. (2003) Direct Assembly of Gold Nanoparticle "Shells" on Polyurethane Microsphere "Cores" and Their Application as Enzyme Immobilization Templates. *Chem. Mater. 15*, 1944−1949.

(14) Douberly, G. J., Pan, S., Walters, D., and Matsui, H. (2001) Fabrication of Protein Tubules: Immobilization of Proteins on Peptide Tubules. *J. Phys. Chem. B. 105*, 7612−7616.

(15) Matsui, H., Porrata, P., and Douberly, G. E. J. (2001) Protein Tubule Immobilization on Self-Assembled Monolayers on Au Substrates. *Nano Lett. 1*, 461−463.

(16) Djalali, R., Chen, Y.-f., and Matsui, H. (2003) Au Nanocrystal Growth on Nanotubes Controlled by Conformations and Charges of Sequenced Peptide Templates. *J. Am. Chem. Soc. 125*, 5873−5879.

(17) Banerjee, I. A., Yu, L., and Matsui, H. (2003) Location-Specific Biological Functionalization on Nanotubes: Attachment of Proteins at the Ends of Nanotubes Using Au Nanocrystal Masks. *Nano* Lett. *3*, 283−287.

(18) Matsui, H., and Gologan, B. (2000) Crystalline Glycylglycine Bolaamphiphile Tubules and Their pH-Sensitive Structural Transformation. *J. Phys. Chem. B. 104*, 3383−3386.

(19) Kogiso, M., Ohnishi, S., Yase, K., Masuda, M., and Shimizu, T. (1998) Dicarboxylic Oligopeptide Bolaamphiphiles: Proton-Triggered Self-Assembly of Microtubes with Loose Solid Surfaces. *Langmuir 14*, 4978−4986.

(20) Caruso, F., Trau, D., Mohwald, H., and Renneberg, R. (2000) Enzyme Encapsulation in Layer-by-Layer Engineered Polymer Multilayer Capsules. *Langmuir 16*, 1485−1488.

(21) Yu, L., Banerjee, I. A., Shima, M., Rajan, K., and Matsui, H. (2004) Size-Controlled Ni Nanocrystal Growth on Peptide Nanotubes and Their Magnetic Properties. *Adv. Mater. 16,* 709−712.

(22) Fojan, P., Jonson, P. H., Petersen, M. T. N., and Petersen, S. B. (2000) What distinguishes an esterase from a lipase: A novel structural approach. *Biochimie 82*, 1033−1041.

(23) Fernandez-Lafuente, R., Armisen, P., Sabuquillo, P., Fernandez-Lorente, G., and Guisan, J. M. (1998) Immobilization of lipases by selective adsorption on hydrophobic supports. *Chem. Phys. Lipids 93*, 185−197.

(24) Sugiura, M., and Isobe, M. (1975) Studies on the mechanism of the lipase reaction II. Comparative studies on the adsorption of lipases and various proteins at the air−water interface. *Biochim. Biophys.* A *397*, 412−417.

(25) Sugiura, M., and Isobe, M. (1975) Studies on the mechanism of lipase reaction. I. Inhibition of lipase activity by emulsion of organic solvents. *Chem. Pharm. Bull. 23*, 1221−1225.

(26) Tinoco, I. J., Sauer, K., and Wang, J. C. (1995) *Physical Chemistry−Principles and Applications in Biological Sciences*, 3rd ed., Simon & Schuster Co. Publishers, Englewood Cliffs, NJ.

(27) Lopez-Amaya, C. I., and Marangoni, A. G. (2003) Binding parameters for the interaction between *Candida rugosa* lipase and DPPC liposomes. *Colloids Surfaces B 32*, 263−274.

(28) Jutila, A., Zhu, K., Patkar, S. A., Vind, J., Svendsen, A., and Kinnunen, P. K. J. (2000) Detergent-Induced Conformational Changes of Humicola lanuginosa Lipase Studied by Fluorescence Spectroscopy. *Biophys. J. 78*, 1634−1642.

(29) Acharya, P., and Rao, N. M. (2003) Stability Studies on a Lipase from Bacillus subtilis in Guanidinium Chloride. *J. Protein Chem. 22*, 51−60.

BC050199A

Surface Modification To Reduce Nonspecific Binding of Quantum Dots in Live Cell Assays

Elizabeth L. Bentzen,[†,§] Ian D. Tomlinson,[†,§] John Mason,[‡] Paul Gresch,[‡] Michael R. Warnement,[†] David Wright,[†] Elaine Sanders-Bush,[†] Randy Blakely,[‡] and Sandra J. Rosenthal*[,†]

Department of Chemistry, Vanderbilt University, Station B, 351822, Nashville, Tennessee 37235-1822, and Department of Pharmacology, Vanderbilt School of Medicine, Vanderbilt University, Nashville, Tennessee 37235-1822. Received July 8, 2005; Revised Manuscript Received September 7, 2005

Nonspecific binding is a frequently encountered problem with fluorescent labeling of tissue cultures when labeled with quantum dots. In these studies various cell lines were examined for nonspecific binding. Evidence suggests that nonspecific binding is related to cell type and may be significantly reduced by functionalizing quantum dots with poly(ethylene glycol) ligands (PEG). The length of PEG required to give a significant reduction in nonspecific binding may be as short as 12−14 ethylene glycol units.

INTRODUCTION

Fluorescence is a tool widely employed in biological assays. Current organic dyes suffer from many limitations including narrow excitation spectra, broad emission spectra, and photobleaching. Fluorescent semiconducting nanocrystals, also known as quantum dots, are beginning to find their way into the tool box of many biologists, chemists, and biochemists. Quantum dots are an attractive alternative to the traditional organic dyes due to their broad excitation spectra, narrow emission spectra, and photostability which allows for multiplexed experiments (*1*−*10*). During the synthesis of quantum dots, the size and composition can be varied in order to obtain emission wavelengths from blue to near-IR (*1*, *3*, *4*). Additionally, through the judicious choice of an appropriate excitation source, multiple color quantum dots may be excited simultaneously.

Typically prepared CdSe/ZnS quantum dots are limited for biological uses because they are soluble only in nonpolar solvents making them incompatible with biological systems (*5*). This is overcome by an additional polymer shell consisting of amphiphilic poly (acrylic acid) (AMP) (*6*). The AMP coating can subsequently be conjugated, through a 1-ethyl-3-(3-dimethylaminopropyl)carbodiimide (EDC) coupling (*7*) reaction, to biological molecules. Though the AMP-coated quantum dots are compatible with biological assays, studies are still needed to refine this functionalization strategy. Additional studies are also needed to investigate their stability in biological conditions, such as highly concentrated electrolyte solutions, and to minimize background fluorescence due to nonspecific binding.

Currently, quantum dots are being explored as biological imaging agents in vitro (*11*, *12*) and in vivo (*13*, *14*). A number of groups have attached small molecules (*15*−*18*), peptides (*19*), proteins (*20*), antibodies (*21*−*24*), and DNA (*25*) to quantum dots and imaged their binding. It has been reported that the carboxyl groups on the surface of quantum dots lead to nonspecific binding to oligonucleotides (*25*), and we have observed nonspecific binding of mercaptoacetic acid-conjugated quantum dots to human epithelial kidney cells (HEK). While other studies have optimized labeling using quantum dots for their own particular applications, presented here are generalized strategies to reduce nonspecific binding of quantum dots through PEG functionalization of the quantum dot surface that can be utilized in a variety of applications.

To advance studies of conjugated quantum dots for live cell applications, it is necessary to address the issue of nonspecific binding. It has been previously reported that quantum dots conjugated to methoxy-terminated PEG^{5000} (5000 g molecular wt) reduces nonspecific binding in mouse animal models (*26*). We assessed the degree of nonspecific binding of AMP-coated quantum dots (AMP dots) to cell surfaces of six different cell lines. We report that cell type is an important factor in the degree of nonspecific binding that is exhibited with quantum dots. The optimal conjugation conditions of PEG to AMP dots were investigated to ensure maximum fluorescence quantum yield after conjugation. The effect of ligand coverage of the quantum dot and PEG lengths required to sufficiently reduce background fluorescence caused by nonspecific binding of quantum dots was also evaluated in live cell assays.

MATERIALS AND METHODS

Reagents. Poly(ethylene glycol) (PEG) 2000 monomethyl ether, 550 monomethyl ether, and 350 mono methyl ether were obtained from Fluka. Tosyl chloride, *N*-hydroxysuccinamide (NHS), and 1-ethyl-3-(3-dimethylaminopropyl)carbodiimide (EDC), tetraethylene glycol, and methyl iodide were obtained from Aldrich. Potassium hydroxide was purchased from EM Science, Potassium phthalimide was obtained from Lancaster, and hydrazine hydrate was purchased from VWR. Borate buffer was obtained from Polysciences Inc (Warrington PA 18976); Sephadex G-50 was obtained from Amersham Biosciences (AB SE 751 84 Uppsala Sweden). All reagents were used as supplied without further purification.

* To whom correspondence should be addressed. E-mail: sandra.j.rosenthal@vanderbilt.edu. Phone: 615-322-2633. Fax: 615-343-1234.
[†] Department of Chemistry.
[‡] Department of Pharmacology.
[§] These authors contributed equally to this work.

10.1021/bc0502006 CCC: $30.25 © 2005 American Chemical Society
Published on Web 11/01/2005

Scheme 1. Synthetic Route for Creating Methoxy-Terminated Amino PEGs

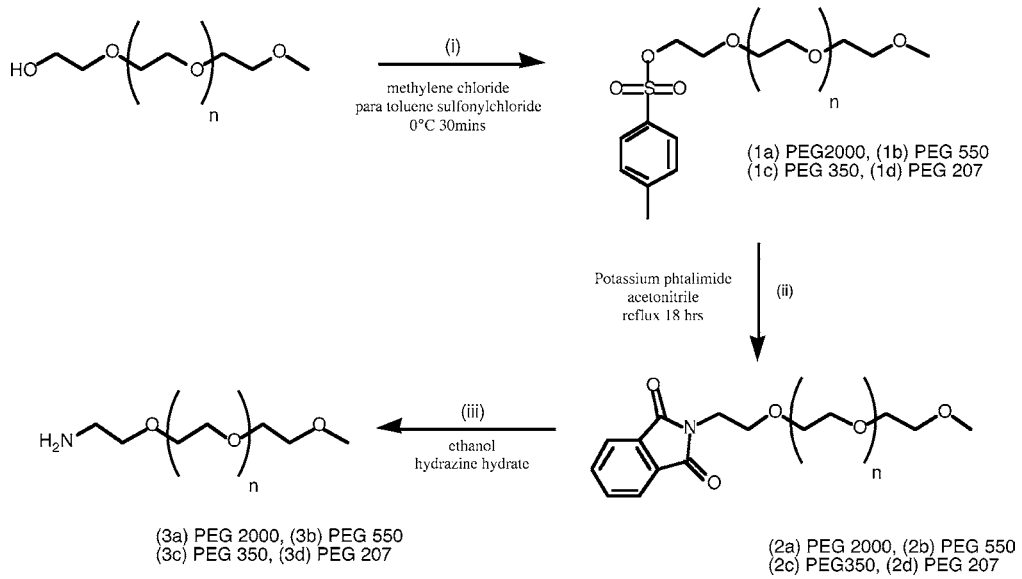

Quantum Dots. Amphiphilic poly(acrylic acid) polymer-coated quantum dots (AMP dots) were a gift from the Quantum Dot Corporation (Hayward, CA 94545). Core shell cadmium selenide/zinc sulfide quantum dots emitting at 605 nm were used in this study. Concentrations of quantum dots were measured using a Carey 50 UV−visible spectrophotometer. Their absorbance at 600 nm was measured, and the concentration was calculated based upon an extinction coefficient of 650 000.[1]

Spectroscopic Characterization. The PEG intermediates and the final product were characterized by NMR and MALDI mass spectroscopy. All NMR data was obtained using $CDCl_3$ as a solvent unless otherwise stated and analyses were performed using a Brucker 300 MHz instrument. Chemical shifts were measured relative to TMS, and coupling constants are measured in Hz.

Mass Spectroscopy. MALDI-TOF mass spectra were recorded on an Applied Biosystems Voyager mass spectrometer equipped with a 337 nm nitrogen laser. For each spectrum, 30 to 64 scans were averaged using an acceleration voltage of 25 kV. Samples were prepared, using a standard DBA matrix. A PEG standard prepared in the same manner as the other samples was used for mass calibration of the instrument.

PEG Synthesis. Four methoxy terminated amino PEGs were used in this study. These were methoxy-terminated amino PEG 2000, 550, 350 and the methoxy-terminated amino PEG derived from tetra PEG (PEG 207). The synthetic route used to synthesize these compounds is shown in Scheme 1. The mono methoxy PEG derivative of tetra PEG was synthesized as described by Masci (*27*).

Initially the PEG mono methyl ether was converted to a tosylate using the method described by Kegstra (*28*) resulting in tosylates **1a**−**d**. The tosylate was displaced using potassium phthalimide by refluxing in acetonitrile for 18 h resulting in **2a**−**d**. These were subsequently converted to the amino PEG derivative by stirring in ethanol with hydrazine hydrate giving **3a**−**d**. Compounds **1a**−**d**, **2a**−**d**, **3a**−**d** were characterized by NMR. Compounds **3a**−**d** were further characterized by MALDI mass spectroscopy.

The tosylates of the four PEG lengths were prepared as follows:

Mono Tosyl Poly(ethylene glycol) 2000 Mono Methyl Ether (1a). PEG 2000 monomethyl ether (20 g) was dissolved in methylene chloride (200 mL) and cooled to 0 °C in an ice/acetone bath. *p*-Toluenesulfonyl chloride (2 g, 0.01 mol) was added, and the mixture was stirred at 0 °C for 30 min. Freshly powdered potassium hydroxide (4.5 g, 0.08 mol) was added, and the mixture was stirred at 0 °C for 6 h (*28*). After warming to room temperature, the solution was washed with water (2 × 20 mL) and dried over magnesium sulfate. The methylene chloride was removed under reduced pressure, and the product was purified by washing with hexanes (5 × 200 mL). This yielded 18 g of the product as a waxy solid. ^{1}H NMR ($CDCl_3$) δ 2.42 (3H), 3.39 (3H), 3.60 (*n*H), 3.82−3.86 (2H), 4.10−4.14 (2H), 7.31 (2ArH), 7.75 (2 ArH).

Mono Tosyl Poly(ethylene glycol) 550 Mono Methyl Ether (1b). An amount of 22 g of PEG 550 mono methyl ether gave 26 g of crude mono tosyl poly(ethylene glycol) 550 mono methyl ether, and this was purified by column chromatography on silica gel eluted with methylene chloride then methylene chloride/methanol (5%), giving 24 g of the product as a colorless oil. ^{1}H NMR ($CDCl_3$) δ 2.40 (3H), 3.33 (3H), 3.60 (*n*H), 4.10−4.12 (2H), 7.29 (2ArH), 7.76 (2 ArH).

Mono Tosyl Poly(ethylene glycol) 350 Mono Methyl Ether (1c). An amount of 14 g of mono methyl PEG 350 gave 18 g of crude tosylate which was purified using column chromatography on silica gel eluted with methylene chloride and then a methylene chloride (98%)/methanol (2%) mixture, resulting in 17.3 g of the product as colorless oil. ^{1}H NMR ($CDCl_3$) δ 2.37 (3H), 3.28 (3H), 3.46 (*n*H), 4.05 (2H), 7.27 (2ArH), 7.70 (2ArH).

Toluene-4-sulfonic Acid 2-{2-[2-(2-Methoxyethoxy)-ethoxy]ethoxy}ethyl Ester (1d). An amount of 10.4 g of 2-{2-[2-(2-methoxyethoxy)ethoxy]ethoxy}ethanol gave 9.5 g of tosylate after column chromatography on silica gel eluted with methylene chloride 98%/methanol 2%. Mass spectroscopy indicated that this material was contaminated with 1-methoxy-2-{2-[2-(2-methoxyethoxy)-ethoxy]ethoxy}ethane (**I**). Attempts to remove this contaminant using column chromatography failed, and the product was used without further purification in the next synthetic step. ^{1}H NMR ($CDCl_3$) δ 2.27 (3H), 3.17 (*n*H), 3.47 (*n*H), 3.96 (2H), 7.19 (2ArH), 7.61 (2ArH).

Mono Phthalimido Poly(ethylene glycol) 2000 Monomethyl Ether (2a). Mono tosyl PEG 2000 mono

[1] Brucez, M. Private communication.

methyl ether (18 g) was dissolved in acetonitrile (200 mL) and heated at reflux with stirring for 18 h. The mixture was cooled and evaporated and dissolved in methylene chloride (200 mL). The organic solution was washed with water (2 × 50 mL) and dried over magnesium sulfate. After filtration and evaporation under reduced pressure, the product was purified by washing the crude product with hexanes (5 × 200 mL). This gave 7.7 g of the product as a colorless wax. ^{1}H NMR ($CDCl_3$) δ 3.36 (3H), 3.52 (*n*H), 3.68 (2H), 3.82 (2H), 7.69 (2ArH), 7.79 (2ArH).

Mono Phthalimido Poly(ethylene glycol) 550 Monomethyl Ether (2b). The phthalimide was prepared as previously described for the phthalimide of mono methyl PEG 2000. Thus, 20 g of tosylate gave 15 g of crude phthalimide which was purified using column chromatography on silica gel eluted with a gradient system running from methylene chloride to 95% methylene chloride/5% methanol. This gave 14 g of the purified phthalimide as a yellow oil. ^{1}H NMR ($CDCl_3$) δ 3.20 (3H), 3.48 (*n*H), 3.56 (2H), 3.71 (2H), 7.57 (2ArH), 7.66 (2ArH).

Mono Phthalimido Poly(ethylene glycol) 350 Monomethyl Ether (2c). An amount of 17.3 g of tosylate gave 8.7 g of phthalimide, after purification on silica gel eluted with a gradient system eluted with a solvent system from methylene chloride to methylene chloride (98%)/methanol (2%). ^{1}H NMR ($CDCl_3$) δ 3.30 (3H), 3.46 (*n*H), 3.66 (2H), 3.82 (2H), 7.65 (2ArH), 7.76 (2ArH).

2-(2-{2-[2-(2-Methoxyethoxy)ethoxy]ethoxy}ethyl)-isoindole-1,3-dione (2d). An amount of 9.5 g of tosylate gave 3.9 g of phthalimide, after purification on silica gel eluted with a gradient system eluted with a solvent system from methylene chloride to methylene chloride (98%)/methanol (2%). Mass and NMR spectroscopy indicated that this material was contaminated with 1-methoxy-2-{2-[2-(2-methoxyethoxy)ethoxy]ethoxy}ethane (**I**) and was used without further purification.^{1}H NMR ($CDCl_3$) 2.22 (*n*H), 3.45 (*n*H), 3.75 (2H), 7.57 (2ArH), 7.68 (2ArH).

Mono Amino Poly(ethylene glycol) 2000 Monomethyl Ether (3a). Mono phthalimido PEG 2000 monomethyl ether (7.7 g) was dissolved in ethanol (200 mL), and hydrazine mono hydrate (10 mL) was added. The mixture was stirred at room temperature for 18 h and then evaporated under reduced pressure. The crude product was dissolved in methylene chloride and stirred for 18 h at room temperature. The solution was filtered and washed with water (2 × 50 mL) and dried over magnesium sulfate. After filtration and evaporation, the product was purified by washing with hexanes (5 × 200 mL). This gave the product as a colorless wax (5.9 g). ^{1}H NMR ($CDCl_3$) δ 3.32 (3H), 3.56 (nH), 3.69 (NH_2).

Mono Amino Poly(ethylene glycol) 550 Monomethyl Ether (3b). Mono amino poly(ethylene glycol) 550 monomethyl ether was prepared as previously described for mono amino poly(ethylene glycol) 2000 monomethyl ether. Thus 10 g of phthalimide resulted in 7.5 g of the desired product as colorless oil. ^{1}H NMR ($CDCl_3$) δ 2.73 (2H), 3.32 (3H), 3.44 (*n*H).

Mono Amino Poly(ethylene glycol) 350 Monomethyl Ether (3c). Mono amino poly(ethylene glycol) 350 monomethyl ether was prepared as previously described for mono amino poly(ethylene glycol) 2000 monomethyl ether. Thus 8.7 g of phthalimide resulted in 7.5 g of the desired product as a colorless oil. ^{1}H NMR ($CDCl_3$) δ 2.81 (2H), 3.09 (3H), 3.36 (*n*H).

2-{2-[2-(2-Methoxyethoxy)ethoxy]ethoxy}ethylamine (3d). 2-{2-[2-(2-Methoxyethoxy)ethoxy]ethoxy}-ethylamine (mono amino poly(ethylene glycol) 207 monomethyl ether) was prepared as previously described for mono amino poly(ethylene glycol) 2000 monomethyl ether. Thus, 3.9 g of phthalimide resulted in 1.0 g of the desired product as colorless oil after distillation under reduced pressure at 1 mmHg (bp 115−125 °C). NMR and mass spectroscopy of this material indicated that it was a mixture of the desired product (70%) and 1-methoxy-2-{2-[2-(2-methoxyethoxy)ethoxy]ethoxy}ethane (**I**) (30%). As 1-methoxy-2-{2-[2-(2-methoxyethoxy)ethoxy]ethoxy}-ethane is inert it was decided to couple this material to AMP dots without further purification. ^{1}H NMR ($CDCl_3$) δ 1.3 (NH_2), 2.71 (2H), 3.22 (*n*H), 3.40 (*n*H).

Coupling PEG Ligands to AMP Dots. During the course of our studies, we tried several different coupling methodologies using different ratios of EDC, NHS, and AMP dots. We observed that the best methodology used a ratio of 2000 PEGs, 1500 EDCs, 1500 NHS, and 1 dot. Thus, in a typical ligand exchange, 0.1 mL of a 8.9 μM solution of AMP dots was placed in a vial equipped with a stir bar. Mono methyl PEG 2000 amine (3.6 mg, 1.8 μM) was dissolved in borate buffer (0.3 mL) at pH 8.4, and this was added to the solution of the AMP dots. This mixture was stirred for 10 min at room temperature, and then N-hydroxysuccinamide (0.15 mg, 1.3μM) dissolved in borate buffer (0.1 mL) was added. The mixture was stirred for a further 10 min at room temperature, and then 1-[3-(dimethylamino)propyl]-3-ethylcarbodiimide hydrochloride (0.25 mg, 1.3 μM) was added. The solution was stirred at room temperature for 2 h, and the pegylated dots were purified via size exclusion chromatography using sephadex (G50).

Gel Electrophoresis. Conjugation was confirmed by gel electrophoresis. Gels were 1% agarose in Tris-EDTA acetate (TEA) buffer. Gels were run at 80 V for 80 min with TEA buffer as the running buffer. Gel images were taken on an AlphaImager 2000 imaging station (Alpha Innotech Corp.).

Quantification of PEG on the Surface. The number of PEG molecules coupled to each quantum dot was determined by using the fluorescamine assay. An excess of fluorescamine (3 mg/mL) in acetone was added to each reaction mixture and vortexed for 15 min at room temperature. The fluorescence at 480 nm was measured and compared to the fluorescence produced by the same reaction mixture without EDC. The ratio of the fluorescence of these two reactions is the percentage of PEG still in solution, unconjugated to the quantum dots. This is subtracted by the amount of initial PEG and then divided by the number of quantum dots used in the reaction to give the number of PEG molecules conjugated to each quantum dot (equation given in Supporting Information).

Cell Cultures. Several cell lines were chosen to compare the nonspecific binding of AMP dots to PEG conjugated AMP dots (PEG dots). These cell types were as follows: mouse fibroblasts (3T3); African green monkey kidney cells (COS7); Chinese hamster ovary (CHO), a gift from Dr. Tad Inagami (Vanderbilt University, Nashville, TN); human epithelial kidney (HEK); porcine renal epithelial (LLC); human epithelial larynx carcinoma (HEp-2). Approximately 5000 cells/well of 3T3 cells were plated in black/clear bottom 96-well plates and grown to confluency in DMEM (Gibco) containing 9% bovine serum, 5 units/mL penicillin, and 5 μg/mL streptomycin media. Approximately 10−15 000 cells/well of COS7, CHO, HEK, and LLC cells were plated in black/clear bottom 96-well plates and grown to confluency in DMEM containing 10% fetal bovine serum, 2 mM glutamine, 100 units/mL penicillin, and 100 mg/mL streptomycin media. Approximately 10 000 cells/well of

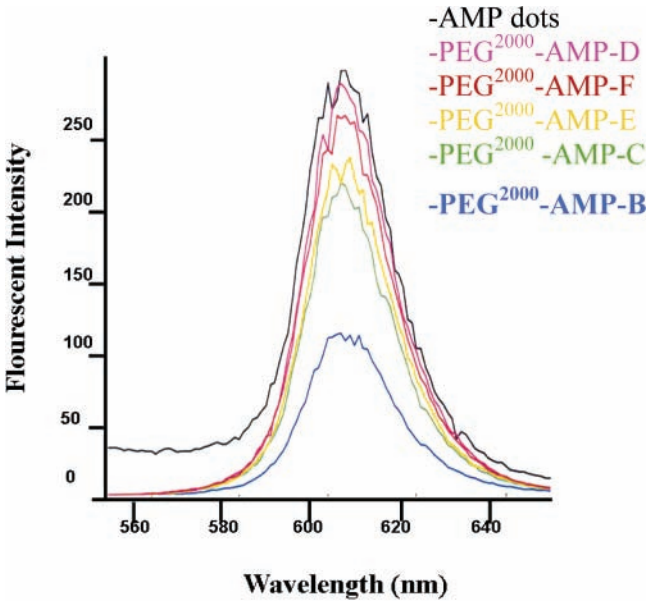

Figure 1. Fluorescent spectra used to determine relative quantum yield of PEGylated AMPdots with varied ratios of PEG:NHS:EDC. PEG^{2000}-AMP-D (purple) and PEG^{2000}-AMP-F (red) are 2000 equivalents of PEG to 1500 equivalents of NHS and EDC (separate reactions). PEG^{2000}-AMP-E (yellow) is 2000 equivlaents of PEG, NHS and EDC. PEG^{2000}-AMP-C (green) is 2000 equivalents of PEG to 1000 equivalents of NHS and EDC. PEG^{2000}-AMP-B (blue) is 1000 equivalents of PEG to 3000 equivalents of NHS and EDC.

HEp-2 cells were plated in black/clear bottom 96-well plates and grown to confluency in OPTI-MEM containing 2% fetal bovine serum, 200 mM glutamine, 250 μg/mL of amphotericin-B, and 10 mg/mL gentamicin media. All cells were incubated at 37 °C with 5% CO_2.

Microscopy. Images of labeled cells were taken using a Nikon Diaphot epifluorescent microscope equipped with phase/fluorescent/camera and a Quixell automated micromanipulator on a Nikon D100 digital camera.

Quantification of Nonspecific Binding. The nonspecific binding of the AMP dots and PEG dots to each cell type was quantified by fluorescence measurements of cell cultures grown in 96-well plates. Concentrations of PEG and AMP dots ranging from 1 nM to 50 nM were tested against each cell type by incubating three wells with each concentration for 30 min and then washing with excess KRH buffer. The fluorescent intensity of each well was measured using a BIO-TEK Synergy HT plate reader (excitation 250 nm/10, emission filter 590 nm/35, top optic position with a vertical offset of 1 mm and sensitivity = 88.)

RESULTS AND DISCUSSION

Conjugating PEG to the surface of the AMP dots was employed to reduce nonspecific binding in live cell assays. Previous studies indicated that the quantum efficiencies of the 605 nm AMP dots were affected by the conjugation chemistry (data not shown). Ratios of methoxy terminated amino PEG^{2000}, NHS, and EDC were varied to determine the optimal conditions for coupling PEG to the surface of AMP dots without compromising the probe's quantum yield. The relative quantum yields of 50 nM solutions of each of the PEG dots were determined by comparison of their emission intensity at 605 nm. The ratio 2000:1500:1500 of PEG/NHS/EDC equivalents per quantum dot (purple and red) (Figure 1) exhibited the least amount of quenching after conjugation. An excess of NHS and EDC (blue) displayed less than half of the original fluorescent emission, while lower ratios resulted in nonoptimal PEG coupling. The pH of the reactions was monitored to determine if the decrease in fluorescent intensity was due to etching of the quantum dot surface by hydrochloric acid liberated from EDC hydrolysis. Etching of the surface from HCl does not appear to be the cause of decreased fluorescence since the borate buffer maintained a pH of 8.5−8.2 throughout the 2 h coupling. All subsequent conjugations of PEG to AMP dots were carried at the 2000:1500:1500 ratio of PEG/NHS/EDC equivalents per quantum dot.

Six common cell lines, 3T3, LLC, COS7, CHO, HEp-2, and HEK, were chosen in order to determine the degree of nonspecific binding of AMP dots in live cell assays. Each cell line was incubated with 50 nM AMP dots for 30 min, washed, and imaged. While all cell lines showed some degree of nonspecific binding, the amount varied with each cell line (Figure 2: A1−F1). HEK cells (Figure 2: C1) displayed the most nonspecific binding while 3T3 cells exhibited the least (Figure 2:E1). The reduction of nonspecific binding was evaluated in parallel experiments by incubating the cell lines with 50 nM PEG functionalized AMP dots. PEG-conjugated quantum dots significantly reduced the nonspecific binding with all the selected cell types. Controls indicated that there was no binding of the AMP dots or the PEG conjugated quantum dots to the surface of the 96-well microtiter plates used for cells seeding, therefore, all binding was attributed to the cell surfaces. In cell lines that did not exhibit much nonspecific binding initially, like 3T3, there was a reduction of 18% when using 50 nM PEG dots. In cell lines like HEK, where there were very significant amounts of nonspecific binding PEG dots reduced nonspecific binding by as much as 90% at working concentrations of 50 nM (Supporting Information). While nonspecific bind-

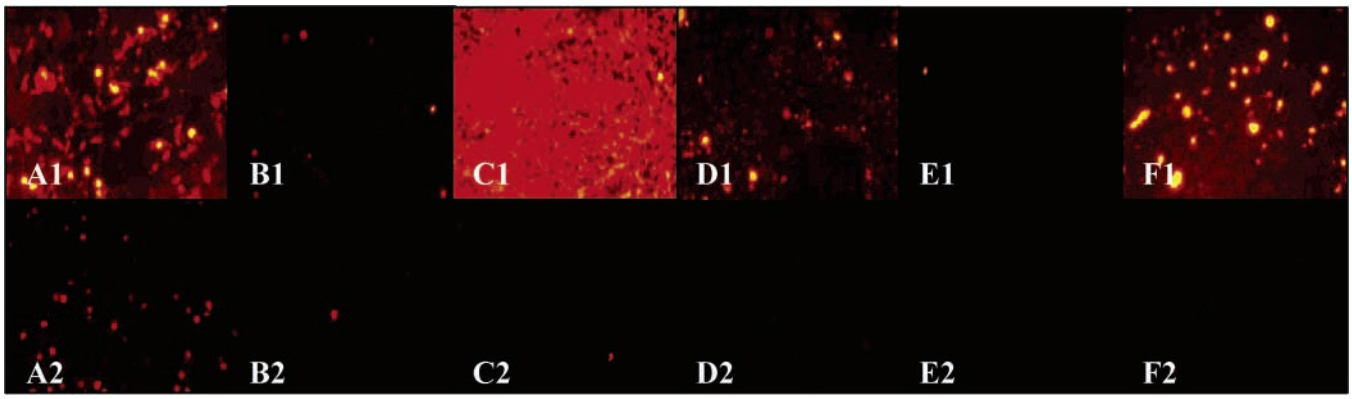

Figure 2. Comparison of the nonspecific binding of 50 nM AMP dots (A1−F1) to PEGylated AMP dots (A2−F2). The comparison was done in six different cell lines: HEp-2 (A), LLC (B), HEK (C), COS7 (D), 3T3 (E), and CHO (F).

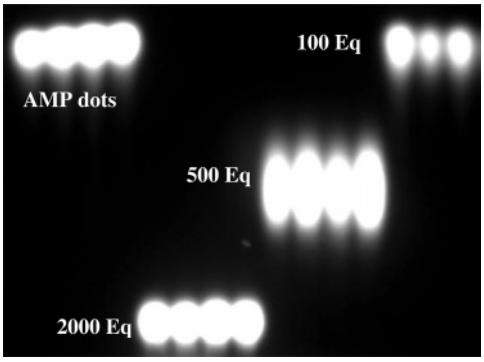

Figure 3. Electrophoretic gels (1% agarose) of AMP dots and PEGylated AMP dots. The gel was run at 80 V for 80 min. The gel indicates that the conjugation was successful and that the AMP dots have been PEGylated with different equivalents of PEG^{2000}. As expected, the more equivalents of PEG used the less electrophoretic movement.

ing is clearly related to the surface chemistry of the cells, the nature of the interaction that causes nonspecific binding likely arises from a variety of different interactions.

It is possible to envision hydrophobic interactions occurring between tri-*n*-octylphosphine oxide (TOPO) on the surface of the quantum dot and lipids in cellular membranes. These hydrophobic interactions might occur from an incomplete coverage of the core/shell with the AMP coating. Different cell types express a variety of proteins or lipids on their surfaces that allow for interaction with exposed hydrophobic regions of the quantum dots. This variation of proteins and lipids expressed in a cell type dependent manner would give rise to some cell lines displaying larger amounts of nonspecific binding than others.

Another possibility for nonspecific binding is the electrostatic interactions between the surfaces of cells and the carboxylic acids on the surfaces of the AMP-coated quantum dots. PEG reduces the ability of the quantum dots to form these interactions with the surface of the cell or proteins expressed in the extra cellular matrix, resulting in a reduction of nonspecific binding. Consequently, PEG functionalization yields an essentially passivated surface that minimizes cellular interaction. Further surface modifications of quantum dots with PEG will change the electrical double layer surrounding the quantum dots and this may also reduce the nonspecific binding. PEG is able to solvate cations in a manner similar to crown ethers (*27*). It is possible that cations surrounding the quantum dot are solvated by the PEGs on the surface of the quantum dot. Thus these cations may be less able to form interactions such as salt bridges between negatively charged groups on the cell surface and the quantum dot.

Since HEK cells exhibited the most nonspecific binding and 3T3 cells the least, these cells lines were selected as the subjects for focused study of the effects of both the coverage and length of the PEG modulator on nonspecific cellular binding. The effect of ligand coverage was studied by coupling 2000, 500, and 100 equivalents of PEG^{2000} to AMP dots. Quantitation of the number of PEGs coupled to the surface was determined by a fluorescamine difference assay. The fluorescamine assay produces a fluorescent species when it reacts with primary amines thereby giving you the amount of amino PEGs that still have primary amines (*26*). Controls for Qdot interference and issues of solvent incompatibilities (i.e. presence of acetone) showed no interference. Assay results indicated approximately 380, 106, and 11 PEG modulators per quantum dot in the 2000, 500, and 100 equivalent reactions, respectively (Supporting Information). In the 2000 equivalent reaction it is expected that all surface accessible carboxyl groups of the AMP coating on the quantum dot are funtionalized. Subsequent characterization with gel electrophoresis (Figure 3) confirmed the coupling reaction and was consistent with the fluorescamine quantitation.

Quantum dots with 380 PEG^{2000} displayed little to no nonspecific binding (Figure 4). Very little increase in nonspecific binding to HEK and 3T3 cells was observed with quantum dots which had about 106 PEG^{2000}. However, when only 11 PEG^{2000} were coupled to the quantum dot, the nonspecific binding to HEK cells increased. Nevertheless, even though the surface has very few PEG molecules on it, it is still apparent that the nonspecific binding is reduced by about 50%. These results suggest that it may not be necessary to functionalize every site on the surface of the quantum dot with PEG to reduce nonspecific binding but the more complete functionalization of the AMP surface the better the reduction of nonspecific binding. There was little effect on the nonspecific binding of the quantum dots with only 11 PEG to the 3T3 cells, which had originally shown the least nonspecific binding to the AMPdots.

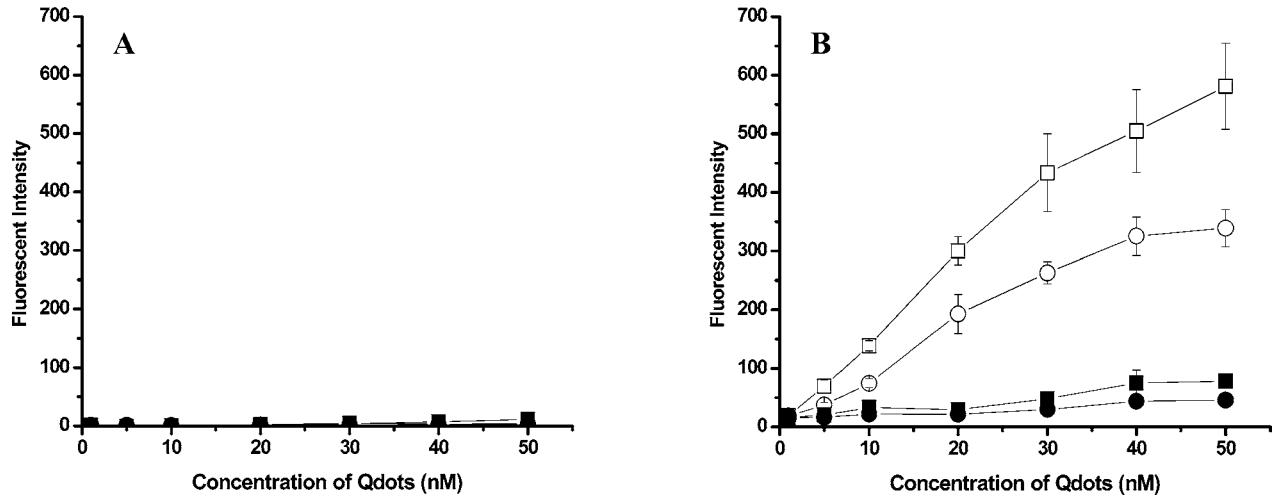

Figure 4. Graphs of the fluorescent intensity of AMP dots (□) and AMP dots PEGylated with 100 equivalent of PEG^{2000} (○), 500 equivalents of PEG^{2000} (■), and 2000 equivalents of PEG^{2000} (●) for 3T3 (A) and HEK (B).

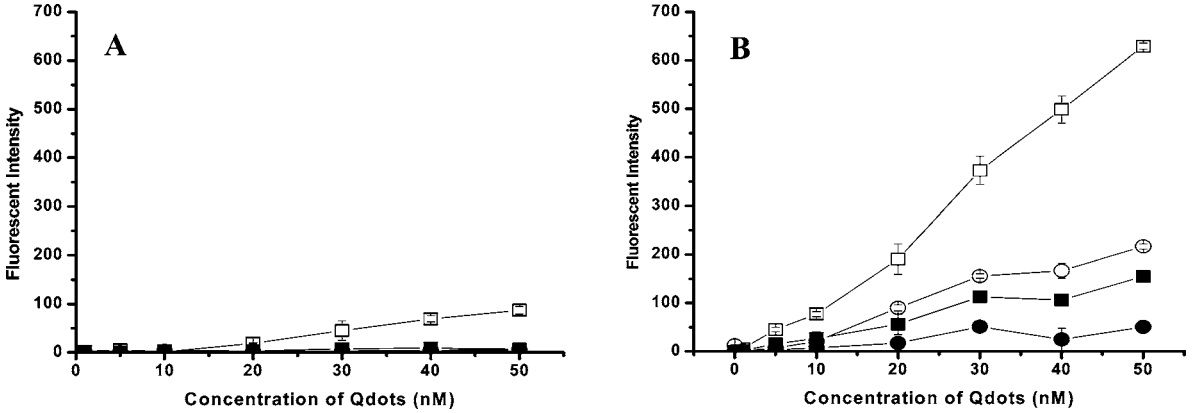

Figure 5. Graphs of the fluorescent intensity of AMP dots (□) and AMP dots PEGylated with 2000 equivalents of PEG^{350} (○), PEG^{550} (■), and PEG^{2000} (●) for 3T3 (A) and HEK (B).

The effect of PEG length was determined by comparing the amount of nonspecific binding AMPdots functionalized with PEG^{2000}, PEG^{550}, and PEG^{350} with uniform coverage (Figure 5). To ensure that nonspecific binding in these assays was a product of PEG length, all conjugations were done with 2000 equivalents of PEG as described above so that all surface available carboxyl groups were utilized. It has been observed by Ballou (*26*) et al. that when methoxy amino PEG^{5000} was attached to AMP dots only 100 PEGs were observed to bind, but when PEG^{750} was attached, 300 PEGs were observed to bind. Electrophoretic gels indicate that the mobility of PEG conjugated to quantum dots appear to behave as a function of the PEG length (Supporting Information). Consequently, with lengths shorter than PEG^{2000}, steric hindrance does not appear to affect PEG conjugation but may be a factor in the reduced number of conjugations with longer PEGs.

The length of the PEG chain does not seem to be important until it is shorter than about 14 units, and even PEG^{350} was able to eliminate most nonspecific binding. All lengths of PEG dots used reduced the nonspecific binding in both HEK cells and 3T3 cells. In the 3T3 cells, which had originally shown the least nonspecific binding to the AMP dots, length of the PEG had no effect on nonspecific binding. However, nonspecific binding of PEG dots to HEK cells did increase with decreasing PEG length (Figure 5). In HEK cells, the PEG^{2000} eliminated the nonspecific binding over the concentration range investigated by approximately 90%. While the PEG^{550} and PEG^{350} did show an increase in nonspecific binding, they still provide a significant reduction of 70% and 60%, respectively, over most concentrations examined. For most biological assays the working concentration of quantum dots will be around 10 nM, where the nonspecific binding for all lengths is very low.

CONCLUSIONS

The nonspecific binding of AMP dots to cell surfaces is dependent upon the cell type. In our study, HEK cells exhibited the most nonspecific binding at concentrations of 50 nM. When AMP dots are conjugated to methoxy amino PEG^{2000}, the nonspecific binding at 50 nM concentrations is greatly reduced. The PEG may be shortened to approximately 12−14 units without increasing nonspecific binding. While it may not be necessary to coat the entire quantum dot surface with PEG to reduce nonspecific binding, complete coverage of the AMP surface on the dots is optimal.

While PEG coated dots do not provide a biologically interesting probe, this study shows that a small number of PEGs are sufficient to reduce nonspecific binding. A coligand strategy could be implemented utilizing some of the available conjugation sites for PEG while other sites may be filled with ligands of biological relevance. Another strategy would be to fill available conjugation sites with customized ligands consisting of a PEG linker arm attached to a biologically relevant moiety.

ACKNOWLEDGMENT

We would like to thank Quantum Dot Corporation for supplying the core/shell nanocrystals used in this study. We would like to thank David Hercules and Matthew Vergne for doing the MALDI mass spectrometry studies used in this work, and Marcus Voeler and Brian O. Bachman for providing the equipment to run and study agarose gels. This work was supported by the NIH under grant RO1 EB003728.

Supporting Information Available: Experimental details. This material is available free of charge via the Internet at http://pubs.acs.org.

LITERATURE CITED

(1) Alivisatos, A. P. (1996) Perspectives on the physical chemistry of semiconductor nanocrystals. *J. Phys. Chem. 100*, 13226−13239.

(2) Schmelz, O., Mews, A., Basché, T., Herrmann, A., and Müllen, K. (2001) Supramolecular complexes from CdSe nanocrystals and organic fluorophors. *Langmuir 17*, 2861−2865.

(3) Peng, Z. A., and Peng, X. (2001) Formation of high-quality CdTe, CdSe, and CdS nanocrystals using CdO as precursor. *J. Am. Chem. Soc. 123*, 183−184.

(4) Hines, M. A., and Guyot-Sinnest, P. (1996) Synthesis and characterization of strongly luminescing ZnS-capped CdSe nanocrystals. *J. Phys. Chem. 100*, 468−471.

(5) Dabbousi, B. O., Rodriguez-Viejo, Mikulec, F. V., Heine, J. R., Mattoussi, H., Ober, R., Jensen K. F., and Bawendi, M. G. (1997) (CdSe)ZnS Core−Shell Quantum Dots: Synthesis and Optical and Structural Characterization of a Size Series of Highly Luminescent Materials. *J. Phys. Chem. B 101*, 9463−9475.

(6) Peng X., Schlamp, M. C., Kadavanich, A. V., and Alivisatos, A. P. (1997) Epitaxial growth of highly luminescent CdSe/CdS core/shell nanocrystals with photostability and electronic accessibility *J. Am. Chem. Soc. 119*, 7019−7029.

(7) Michalet, X., Pinaud, F., Lacoste, T. D., Dahan, M., Bruchez, M. P., Alivisatos, A. P., and Weiss, S. (2001) Properties of fluorescent semiconductor nanocrystals and their application to biological labeling. *Single Mol. 2*, 261−276.

(8) Bruchez, M., Moronne, M., Gin, P., Weiss, S., and Alivisatos, A. P. (1998) Semiconductor nanocrystals as fluorescent biological labels. *Science 281*, 2013−2016.

(9) Chan, W. C. W., and Nie, S. (1998) Quantum dot bioconjugates for ultrasensitive nonisotopic detection. *Science 281*, 2016−2018.
(10) Klarreich, E. (2001) Biologists join the dots. *Nature 413*, 450−452.
(11) Chan, W. C. W., Maxwell D. J., Gao, X., Bailey, R. E., Han, M., and Nie, S. (2002) Luminescent quantum dots for multiplexed biological detection and imaging. *Curr. Opin. Biotechnol. 13*, 40−46.
(12) Watson, A., Wu, X., and Bruchez, M. (2003) Lighting up cells with quantum dots. *BioTechniques 34*, 296−303.
(13) Åkerman, M. E., Chan, W. C. W., Laakkonen, P., Bhatia, S. N., and Ruoslahti, E. (2002) Nanocrystal targeting in vivo. *Proc. Natl. Acad. Sci. U.S.A. 99*, 12617−12621.
(14) Dubertret, B., Skourides, P., Norris, D. J., Noireaux, V., Brivanlou, A. H., and Libchaber, A. (2002) In vivo imaging of quantum dots encapsulated in phospholipid micelles. *Science 298*, 1759−1762.
(15) Rosenthal, S. J., Tomlinson, I. D., Adkins, E. M., Schroeter, S., Adams, S., Swafford, L., Mcbride, J., Wang, Y., DeFelice, L. J., and Blakely, R. D. (2002) Targeting cell surface receptors with ligand-conjugated nanocrystals. *J. Am. Chem. Soc. 124*, 4586−4594.
(16) Tomlinson, I. D., Kippeny, T., Swafford, L., Siddiqui, N. H., and Rosenthal, S. J. (2002) Novel poly(ethylene glycol) derivatives of melatonin and serotonin. Ligands for conjugation to fluorescent cadmium selenide/zinc sulfide core shells and nanocrystals. *J. Chem. Res.* 527−539.
(17) Tomlinson I. D., Grey, J. L., and Rosenthal, S. J. (2002*)* A synthesis of 6-(2,5-dimethoxy-4-(2-aminopropyl)phenyl)hexylthiol. A ligand for conjugation with fluorescent cadmium selenide/zinc sulfide core/shell nanocrystals and biological imaging. *Molecules 7*, 777−790.
(18) Tomlinson I. D., Mason, J., Burton, J. N., Blakely, R., and Rosenthal, S. J. (2003) The design and synthesis of novel derivatives of the dopamine uptake inhibitors GBR 12909 and GBR 12935. High-affinity dopaminergic ligands for conjugation with highly fluorescent cadmium selenide/zinc sulfide core/shell nanocrystals. *Tetrahedron 59*, 8035−8047.
(19) Tomlinson, I. D., Mason, J., Blakely, R. D., and Rosenthal, S. J. (2005) Peptide-conjugated quantum dots: Imaging the angiotensin type 1 receptor in living cells. *NanoBiotechnology Protocols (Methods in Molecular Biology)*Rosenthal, S. J., and Wright, D., Eds.) pp 51−60, Humana Press, Totowa, NJ.
(20) Chunyang, Z., Hui, M., Nie, S., Yao, D., Lei, J., and Dieyan, C. (2000) Quantum dot-labeled trichosanthin. *The Analyst 125*, 1029−1031.
(21) Goldman, E. R., Balighian, E. D., Mattoussi, H., Kuno, M. K., Mauro, J. M., Tran, P. T., and Anderson, G. P. (2002) Avidin: A Natural Bridge for Quantum Dot-Antibody Conjugates. *J. Am. Chem. Soc. 124*, 6378−6382.
(22) Bentzen, E. L., House, F., Utley, T. J., Crowe, J. E., Jr., and Wright, D. W. (2005) Progression of Respiratory Syncytial Virus Infection Monitored by Fluorescent Quantum Dot Probes. *Nano Lett. 5*, 591−595.
(23) Jaiswal, J. K., Mattoussi, H., Mauro, J. M., and Simon, S. M. (2003) Long-term multiple color imaging of live cells using quantum dot bioconjugates. *Nat. Biotechnol.. 21*, 47−51.
(24) Wu, X., Liu, H., Lui, J., Haley, K. N., Treadway, J. A., Larson, P. J., Ge, N., Peale, F., and Bruchez, M. P. (2003) Immunofluorescent labeling of cancer marker Her2 and other cellular targets with semiconductor quantum dots. *Nat. Biotechnol. 21*, 41−46.
(25) Gerion, D., Parak, W. J., Williams, S. C., Zanchet, D., Micheel, C. M., and Alivisatos, A. P. (2002**)** Sorting Fluorescent Nanocrystals with DNA. *J. Am. Chem. Soc. 124*, 7070−7074.
(26) Ballou B., Lagerholm B. C., Ernst L. A., Bruchez M. P., and Waggoner A. S. (2004) Noninvasive imaging of quantum dots in mice. *Bioconjugate Chem. 15*, 79−86.
(27) Ercolani G., Mandolini L., and Masci B., (1981) Template effects. 3. The quantitative determination of the catalytic effects of alkali and alkaline earth cations in the formation of benzo-18-crown-6 in methanol solution. *J. Am. Chem. Soc. 103*, 7484−7489.
(28) Keegstra, E. M. D., Zwikker, J. W., Roest, M. R., and Jenneskens, L. W. (1992) A highly selective synthesis of monodisperse oligo(ethylene glycols). *J. Org. Chem. 57*, 6678−6680.

BC0502006

Synthesis and Cellular Studies of Porphyrin−Cobaltacarborane Conjugates

Erhong Hao, Timothy J. Jensen, Brandy H. Courtney, and M. Graça H. Vicente*

Department of Chemistry, Louisiana State University, Baton Rouge LA, 70803. Received July 15, 2005; Revised Manuscript Received August 25, 2005

The total syntheses of five new porphyrin−cobaltacarborane conjugates (**1**−**5**) have been achieved in 88−98% yields in a single-step reaction between a nucleophilic *meso*-pyridyl-containing porphyrin and zwitterionic cobaltacarborane [3,3′-Co(8-$C_4H_8O_2$-1,2-$C_2B_9H_{10}$)(1′,2′-$C_2B_9H_{11}$)]. These unique zwitterionic compounds have one to four cobaltabisdicarbollide anions conjugated to the porphyrin macrocycle via $(CH_2CH_2O)_2$ chains. The X-ray structure of one of these conjugates (**1**) is presented and discussed. The cellular uptake, cytotoxicity, and subcellular localization of cobaltacarboraneporphyrins **1**−**5** were investigated in human HEp2 cells. The number and distribution of cobaltacarborane residues linked to the porphyrin macrocycle has a significant effect on the cellular uptake of the conjugates.

INTRODUCTION

Boron neutron capture therapy (BNCT), a binary modality for cancer treatment based on the ability of ^{10}B nuclides to capture low-energy neutrons with subsequent production of high linear energy transfer particles ($^4He^{2+}$ and $^7Li^{3+}$), has attracted much interest in the past decades because it can selectively target and destroy malignant cells in the presence of normal cells (*1*−*3*). The success of BNCT depends on the availability of nontoxic boron-containing compounds that can selectively target and accumulate in tumors with high tumor:normal tissues and tumor:blood boron concentration ratios. Among all BNCT agents reported to date, porphyrins are particularly promising due to their known ability to selectively incorporate into tumor cells in high amounts and their subsequent persistence within tumors (*3*−*5*). Furthermore, porphyrins are highly fluorescent, thus enabling tumor diagnosis and facilitating treatment planning. The timely discovery of borane clusters in the late 1950s (*6*) has made possible the syntheses of porphyrins with high percentages of boron by weight, able to deliver therapeutic concentrations of boron (∼20 μg ^{10}B/g tumor) to target tumors. Several porphyrins carrying multiple boron clusters have been synthesized and evaluated in both cellular and animal studies (*4*, *5*, *7*−*10*), but to date there is still limited availability of boron-containing porphyrins because of lengthy synthetic routes and overall low reaction yields. Consequently, there is a lack of structure/activity relationships conducted for this type of compound that could allow the identification of the best candidates for application in BNCT (*11*). Such studies have been much more extensively reported in the development of porphyrins for application in the photodynamic therapy (PDT) of tumors, another binary therapy that uses red light for the activation of a tumor-localized photosensitizer (*4*, *12*, *13*). These studies show that the uptake of porphyrins by tumors is highly dependent upon their physicochemical properties, such as structural features (nature of peripheral side chains), charge and charge distribution, hydrophobic character, and aggregation state.

Metallacarboranes, first reported in 1965 (*14*), belong to the large family of metallocene-type complexes. Among these, the cobaltabisdicarbollide anion [3,3′-Co(1,2-$C_2B_9H_{11}$)$_2$]$^-$ was among the first to be synthesized, and its chemistry has been extensively investigated (*15*, *16*). In the 1980s Spryshkova et al. showed that the potassium salt of [3,3′-Co(1,2-$C_2B_9H_{11}$)$_2$]$^-$ had low toxicity (LD_{50} = 0.08750 mg/kg) in tumor-bearing rats (*17*, *18*). This property, along with the remarkable thermal, kinetic, and photochemical stabilities of cobaltacarborane and some of its derivatives, has led to their investigation as radiotherapeutic (*19*, *20*) and as BNCT agents (*21*−*23*). The bisdicarbollide complexes contain a larger number of boron atoms than the carboranes and the *closo*-dodecaborate anions and are water-soluble in the form of sodium or potassium salts while still maintaining hydrophobic character needed for crossing cellular membranes. Since the discovery of a convenient synthesis of the zwitterionic [3,3′-Co(8-$C_4H_8O_2$-1,2-$C_2B_9H_{10}$)(1′,2′-$C_2B_9H_{11}$)] (*24*, *25*), several new cobaltacarborane-substituted molecules have been reported (*26*−*30*). The dioxane ring of [3,3′-Co(8-$C_4H_8O_2$-1,2-$C_2B_9H_{10}$)(1′,2′-$C_2B_9H_{11}$)] readily undergoes a ring-opening reaction in the presence of a variety of nucleophilic reagents, including halide and hydroxide anions (*26*), phthalimide ions and amines (*27*), phenolate ions and phosphines (*28*), pyrrolyl salts (*29*), and pyridine and phenol (*30*). Using this methodology, a nucleoside−cobaltacarborane conjugate was recently synthesized and found to have low cytotoxicity toward Vero and A549 cells (IC_{50} > 80 μM), using an MTT-based assay (*23*).

With the aim to investigate structure/activity relationships in porphyrin−carborane conjugates, we report herein the synthesis and in vitro evaluation of a series of five conjugates (**1**−**5**) containing one to four cobaltabisdicarbollide anions linked to the porphyrin macrocycle via $(CH_2CH_2O)_2$ chains. An efficient one-step ring-opening reaction between cobaltacarborane **6** and five pyridylporphyrins (**7**−**11**) afforded the target conjugates

* Corresponding author. Phone: (225) 578 7405. Fax: (225) 578 3458. E-mail: vicente@lsu.edu.

10.1021/bc0502098 CCC: $30.25 © 2005 American Chemical Society
Published on Web 11/01/2005

Chart 1. Structures of Porphyrin−Cobaltacarborane Conjugates 2−5

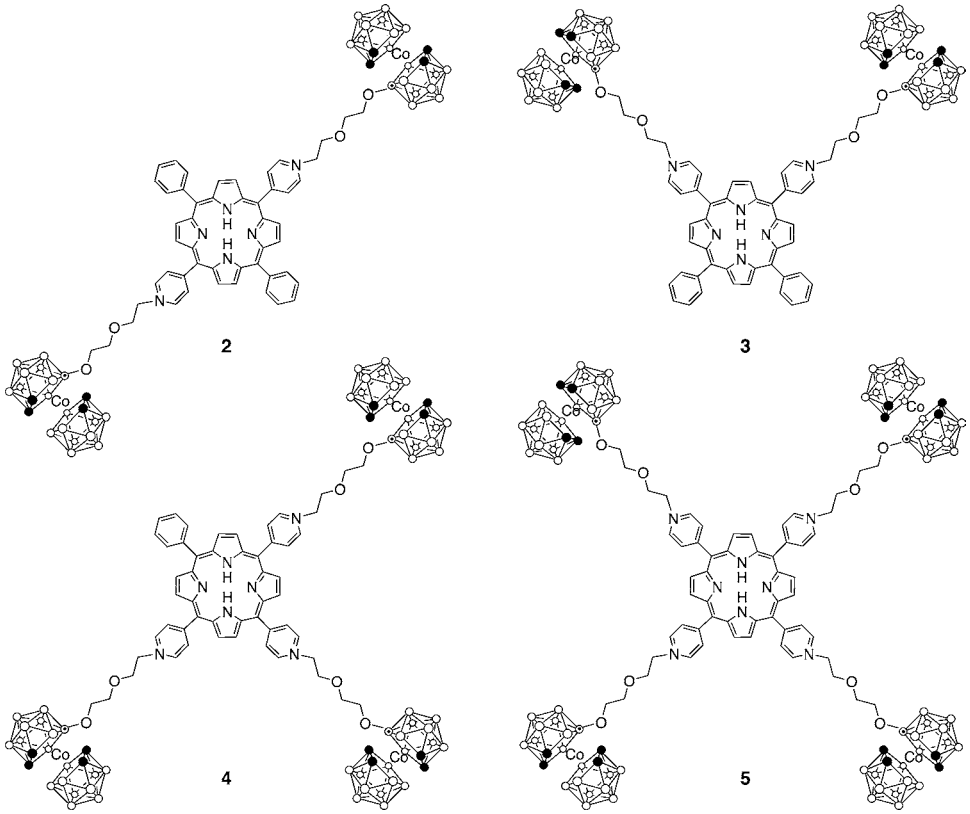

in 88−98% yields. We have previously shown that this reaction also proceeds with phenol-substituted porphyrins as the nucleophilic species (*30*). Since cobaltacarborane−porphyrins contain twice as many boron atoms as *nido*-carboranylporphyrins while still bearing a delocalized negative charge, we anticipate that the conjugates reported herein will be very promising boron carriers for BNCT.

EXPERIMENTAL PROCEDURES

Syntheses. All reactions were monitored by TLC using 0.25 mm silica gel plates with or without UV indicator (Merck 60F-254). Silica gel from Sorbent Technologies 32−63 μm was used for flash column chromatography. ^{1}H and ^{13}C NMR were obtained on either a DPX-250 or a ARX-300 Bruker spectrometer. Chemical shifts (δ) are given in ppm relative to acetone-d_6 (2.05 ppm, ^{1}H; 207.07 ppm, ^{13}C) unless otherwise indicated. Electronic absorption spectra were measured on a Perkin-Elmer Lambda 35 UV−Vis spectrophotometer, and fluorescence spectra were measured on a Perkin-Elmer LS55 spectrometer. Mass spectra were obtained on an Applied Biosystems QSTAR XL. All solvents were purchased from Fisher Scientific (HPLC grade) and used without further purification. Zwitterionic [3,3′-Co(8-$C_4H_8O_2$-1,2-$C_2B_9H_{11}$)(1′,2′-$C_2B_9H_{11}$)] (**6**) was prepared from the cesium salt of cobaltabisdicarbollide, obtained from Katchem Ltd (Czech Republic), as described in the literature (*25*). The 5-(4′-pyridyl)-10,15,20-triphenylporphyrin (**7**), *trans*-5,15-di-(4′-pyridyl)-10,20-diphenylporphyrin (**8**), *cis*-5,10-di(4′-pyridyl)-15,20-diphenylporphyrin (**9**), and 5,10,15-tri(4′-pyridyl)-20-phenylporphyrin (**10**) were prepared according to the literature (*31*). 5,10,15,20-Tetra(4′-pyridyl)porphyrin (**11**) was obtained from Sigma-Aldrich and recrystallized from chloroform/methanol before use.

General Procedure for Conjugate Synthesis. Cobaltacarborane **6** and the 4-pyridylporphyrin were dissolved into a 1:1 (v/v) mixture of chloroform and acetonitrile (Scheme 1). The reaction was stirred at 60 °C under an argon atmosphere until the reaction was complete (monitored by TLC and ^{1}H NMR). The reaction mixture was cooled to room temperature and the solvent evaporated under vacuum. The remaining residue was washed with diethyl ether (3 × 5 mL) and with methanol (3 × 5 mL). Finally, the product was dried overnight under vacuum to afford the targeted conjugate.

5-(4′-Cobaltacarboranepyridyl)-10,15,20-triphenylporphyrin (1). Porphyrin **7** (61.6 mg, 0.10 mmol) and compound **6** (61.5 mg, 0.15 mmol) were heated in 40 mL of chloroform/acetonitrile 1:1 for 12 h. The title conjugate was obtained in 98.4% yield (101.0 mg) as a purple solid. UV−Vis (acetone) λ_{max} (ϵ/M^{-1} cm^{-1}) 418 (157 600), 515 (10 100), 551(5300), 590 (3400), 646 (2600). ^{1}H NMR (acetone-d_6): δ 9.73 (d, 2H, J = 6.7 Hz, *o*-PyrH), 9.10−9.07 (m, 4H, β-H), 9.00 (d, 2H, J = 4.8 Hz, *m*-PyrH), 8.90 (s, 4H, β-H), 8.28−8.24 (m, 6H, *o*-PhH), 7.86−7.76 (m, 9H, *m,p*-PhH), 5.34−5.30 (m, 2H, NCH_2), 4.51−4.42 (m, 2H, OCH_2), 4.06−4.03 (m, 4H, OCH_2), 3.84−3.82 (br s, 4H, carborane-H), 1.6−3.0 (br, 17H, BH), −2.74 (s, 2H, NH). ^{13}C NMR (acetone-d_6): δ 160.1, 144.8, 142.2, 135.1, 133.6, 128.9, 127.7, 123.0, 122.1, 113.3, 73.0, 69.7, 61.8, 52.5, 46.9. HRMS (MALDI-TOF) *m/z* 1026.5713, calculated for $C_{51}B_{18}H_{58}N_5O_2Co$ 1026.5739.

***trans*-5,15-Di(4′-cobaltacarboranepyridyl)-10,20-diphenylporphyrin (2).** Porphyrin **8** (16.0 mg, 0.026 mmol) and compound **6** (43 mg, 0.10 mmol) were heated in 40 mL of chloroform/acetonitrile 1:1 for 2 days, affording 34.1 mg (91.1%) of the title conjugate. UV−Vis (acetone) λ_{max} (ϵ/M^{-1} cm^{-1}) 422 (129 400), 516 (8400), 554 (5200), 590 (3400), 651 (2800). ^{1}H NMR (acetone-d_6): δ 9.76 (d, 4H, J = 6.7 Hz, *o*-PyrH), 9.13−9.09 (m, 8H, β-H), 9.04 (d, 4H, J = 4.9 Hz, *m*-PyrH), 8.29−8.26 (m, 4H, *o*-PhH), 7.91−7.83 (m, 6H, *m,p*-PhH), 5.34−5.32 (br m, 4H, NCH_2), 4.44−4.42 (br m, 4H, OCH_2), 4.06 (br s, 4H,

Scheme 1 [a]

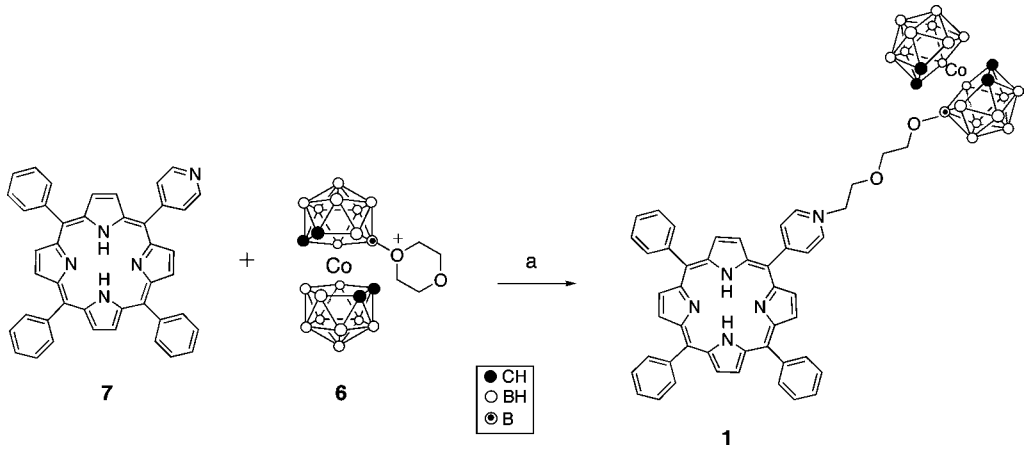

7 6 1

[a] Conditions: (a) $CHCl_3/CH_3CN$ 1:1, 60 °C, 12 h (98.4%).

OCH_2), 4.02 (br s, 4H, OCH_2), 3.87−3.83 (m, 8H, carborane-H), 1.6−3.0 (br, 34H, BH), −2.80 (s, 2H, NH). ^{13}C NMR (acetone-d_6): δ 160.0, 145.3, 142.2, 135.5, 133.8, 129.5, 128.2, 123.2, 115.5, 73.7, 70.4, 62.6, 53.1, 47.6. HRMS (MALDI-TOF) *m/z* 1438.9027, calculated for $C_{58}B_{36}H_{86}N_6O_4Co_2$ 1438.8987.

***cis*-5,10-Di(4′-cobaltacarboranepyridyl)-15,20-diphenylporphyrin (3).** Porphyrin **9** (16.0 mg, 0.026 mmol) and compound **6** (43 mg, 0.10 mmol) were heated in 40 mL of chloroform/acetonitrile 1:1 for 2 days, affording 33.5 mg (91.0%) of the title conjugate. UV−Vis (acetone) λ_{max} (ϵ/M^{-1} cm^{-1}) 423 (141 000), 518 (10 600), 553 (5000), 590 (4000), 645 (1600). ^1H NMR (acetone-d_6): δ 9.75 (d, 4H, J = 6.7 Hz, *o*-PyrH), 9.18 (s, 2H, *m*-PyrH), 9.11 (d, 6H, J = 6.7 Hz, β-H), 9.04 (d, 2H, J = 4.9 Hz, β-H), 8.92 (s, 2H, *m*-PyrH), 8.27−8.23 (m, 4H, *o*-PhH), 7.85−7.82 (m, 6H, *m,p*-PhH), 5.33−5.31 (br m, 4H, NCH_2), 4.50−4.48 (br m, 4H, OCH_2), 4.09−4.03 (m, 8H, OCH_2), 3.86−3.81 (m, 8H, carborane-H), 1.6−3.0 (br, 34H, BH), −2.75 (s, 2H, NH). ^{13}C NMR (acetone-d_6): δ 159.9, 145.3, 142.1, 135.4, 133.8, 129.4, 128.0, 124.2, 114.6, 73.6, 70.3, 70.2, 62.5, 53.0, 47.5. HRMS (MALDI-TOF) *m/z* 1438.8960, calculated for $C_{58}B_{36}H_{86}N_6O_4Co_2$ 1438.8987.

5,10,15-Tri(4′-cobaltacarboranepyridyl)-20-phenylporphyrin (4). Porphyrin **10** (31.0 mg, 0.05 mmol) and compound **6** (100.3 mg, 0.24 mmol) were heated in 40 mL of chloroform/acetonitrile 1:1 for 2 days to afford 83.0 mg (90.0%) of the title conjugate. UV−Vis (acetone) λ_{max} (ϵ/M^{-1} cm^{-1}) 425 (168 000), 516 (12 600), 553 (5600), 591 (4300), 647 (1900). ^1H NMR (acetone-d_6): δ 9.79−9.75 (m, 6H, *o*-PyrH), 9.21−9.19 (m, 6H, *m*-PyrH), 9.14−9.11 (m, 6H, β-H), 9.07 (d, 2H, J = 5.8 Hz, β-H), 8.29−8.25 (m, 2H, *o*-PhH), 7.91−7.86 (m, 3H, *m,p*-PhH), 5.34 (br s, 6H, NCH_2), 4.43 (br s, 6H, OCH_2), 4.04 (s, 6H, OCH_2), 3.99 (s, 6H, OCH_2), 3.84 (s, 12H, carborane-H), 1.6−3.0 (br, 51H, BH), −2.83 (s, 2H, NH). ^{13}C NMR (acetone-d_6): δ 159.2, 145.2, 142.1, 135.2, 133.5, 129.4, 127.9, 124.2, 116.1, 73.4, 70.0, 62.3, 52.7, 47.3. HRMS (MALDI-TOF) *m/z* 1850.2320, calculated for $C_{65}B_{54}H_{114}N_7O_6Co_3$ 1850.2263.

5,10,15,20-Tetra(4′-cobaltacarboranepyridyl)porphyrin (5). Porphyrin **11** (17.0 mg, 0.027 mmol) and compound **6** (62.0 mg, 0.15 mmol) were heated in 40 mL of chloroform/acetonitrile 1:1 for 3 days, affording 53.3 mg (87.7%) of the title conjugate. UV−Vis (acetone) λ_{max} (ϵ/M^{-1} cm^{-1}) 427 (210 000), 517 (15 600), 553 (5880), 590 (5630), 645 (1500). ^1H NMR (acetone-d_6): δ 9.80 (d, 8H, J = 6.3 Hz, *o*-PyrH), 9.26 (s, 8H, β-H), 9.15 (d, 8H, J = 6.3 Hz, *m*-PyrH), 5.36 (br s, 8H, NCH_2), 4.43 (br s, 8H, OCH_2), 4.05 (br s, 8H, OCH_2), 4.00 (br s, 8H, OCH_2), 3.86−3.84 (m, 16H, carborane-H), 1.6−3.0 (br, 68H, BH), −2.89 (s, 2H, NH). ^{13}C NMR (acetone-d_6): δ 159.4, 145.9, 134.1, 117.4, 74.0, 70.6, 70.5, 62.9, 53.3, 47.9. HRMS (MALDI-TOF) *m/z* 2262.5566, calculated for $C_{72}H_{142}N_8O_8B_{72}Co_4$ 2262.5509.

Molecular Structure. The crystal structure of porphyrin−cobaltacarborane conjugate **1** was determined using data collected at T = 110 K with Mo Kα radiation on a Nonius KappaCCD diffractometer. Crystal data: $C_{51}H_{58}B_{18}CoN_5O_2$, triclinic space group $P\bar{1}$, a = 6.941(5), b = 10.982(7), c = 35.48(3) Å, α = 89.46(2), β = 86.86(3), γ = 75.03(4)°, V = 2609(3) Å^3, Z = 2, R = 0.125 ($F^2 > 2\sigma$), Rw = 0.359 (all F^2) for 7181 unique data and 324 refined parameters. Due to the limited quality of the crystal, anisotropic refinement was not possible, except for the Co atom. Disorder was present in the chain connecting the porphyrin to the cobaltacarborane, and two atoms were modeled as pairs of half-populated sites. The N−H hydrogen atoms could not be located.

Cell Culture. Human HEp2 cells were obtained from the ATCC and maintained in a 50:50 mixture of DMEM: Advanced MEM (Gibco) supplemented with 5% FBS (Gibco). Phosphate buffered saline (PBS), FBS and trypsin were purchased from Gibco. All conjugate solutions were filter sterilized using a 0.22 μm Pal syringe filter.

Cellular Uptake. HEp2 cells were seeded at 10 000 cells per well in a Costar 96 well plate and incubated overnight. Solutions of the conjugates 10 mM in DMSO (Sigma) were prepared and further diluted to 1 mM by adding Cremophor EL (Fluka) to give final concentrations of 90% DMSO and 10% Cremophor EL. These solutions were then diluted 50-fold into medium and filter-sterilized to give 2× stock solutions. Equal volumes of conjugate stocks were added to the wells containing cells, giving a final concentration of 10 μM, and incubated for 0, 1, 2, 4, 8, and 24 h. The conjugate uptake was stopped by removing the loading medium and washing the cells with 200 μL of PBS. The cells were solubilized in 0.25% Triton X-100 (Calbiochem) in PBS. Conjugate concentration was determined by measuring the conjugate fluorescence using a BMG FLUOstar Optima plate reader at 410/650 nm excitation/emission. Cell counts were performed using the CyQuant cell proliferation assay reagent (Molecular Probes) as described by the manufacturer.

Dark Cytotoxicity. Cells were plated in 96-well plates and incubated overnight. Conjugate was added to

a final concentration of 10 μM as described above and incubated overnight. The conjugate was then removed and replaced with medium containing Cell Titer Blue (Promega) viability reagent. The cytotoxicity was assayed as per the manufacturer's instructions. The controls consist of cells not treated with either conjugate or vehicle, but incubated under the same conditions to provide a 100% viable reference point. Cells were also treated with 0.2% saponin overnight to provide a 100% dead control, and with vehicle alone (0.9%DMSO/0.1% Cremophor EL) to test residual toxic effects of the delivery vehicle.

Microscopy. Cells were trypsinized and plated on LabTek 2 chamber coverslips (Nunc) and allowed to attach overnight. Lipofectamine liposomes were used as a delivery vehicle. The conjugate stocks were first prepared in DMSO to a concentration of 1 mM, and 1 μL of this stock was mixed with 5 μL of Lipofectamine (Invitrogen), vortexed, and incubated for 15 min. Serum free AMEM (100 μL) was then added, and the mixture was vortexed and incubated for 30 min at room temperature. During this incubation, the cells were washed once with serum free AMEM. The liposome complex was then diluted with 900 μL of serum free AMEM and the mixture transferred to the cells and incubated for 4 h. At the end of the incubation period, 1 mL of medium containing 2 $\times$ FBS was added, and the cells were incubated overnight. The cells were then washed five times with medium supplemented with 50 mM HEPES pH 7.4 and viewed using a Zeiss Axiovert 200M inverted microscope fitted with standard FITC and Texas Red fluorescent filter sets (Chroma). For the colocalization experiments, LysoSensor Green and MitoTracker Green (Molecular Probes) were diluted into medium to a final concentration of 50 nM (LysoSensor Green) and 250 nM (MitoTracker Green). The cells were incubated concurrently with conjugate for 30 min before being washed and viewed by microscopy as described above.

RESULTS

Synthesis and Characterization. Cobaltacarborane **6** was prepared from the reaction of cobaltabisdicarbollide anion $[Co(C_2B_9H_{11})_2]^-$ with 1,4-dioxane in the presence of $BF_3{\cdot}Et_2O$, according to the literature procedure (*25*). Pyridylporphyrins **7**−**11**, synthesized using an Adler-Longo mixed condensation in boiling propionic acid (*31*), were used as the nucleophilic species in the dioxane ring-opening of **6**. Conjugates **1**−**5** were prepared in 88−98% yield in a single-step reaction between the corresponding 4-pyridylphenylporphyrin and an excess of cobaltacarborane **6**, in a mixture of chloroform and acetonitrile at 60 °C (*30*). At higher temperatures (e.g. at 80 °C or in refluxing chloroform) small amounts of green byproducts were also obtained, due to substitution reactions at the porphyrin core (*32*). The targeted conjugates were isolated in pure form upon washing the resulting reaction residues with ethyl ether to remove the excess of compound **6**, without need of chromatography. The molecular structure of conjugate **1** is shown in Figure 1. The porphyrin core is reasonably planar, having mean deviation of 24 atoms from their best plane of only 0.07 Å and maximum deviation 0.18(2) Å. The two dicarbollide moieties coordinate the Co atom with their five-membered rings parallel. The Co atom is equidistant from the two five-membered rings, having a perpendicular distance of 1.463(2) Å to the untethered dicarbollide and 1.464(2) Å to the tethered one. The centroid−Co−centroid angle is 178.3(1)°.

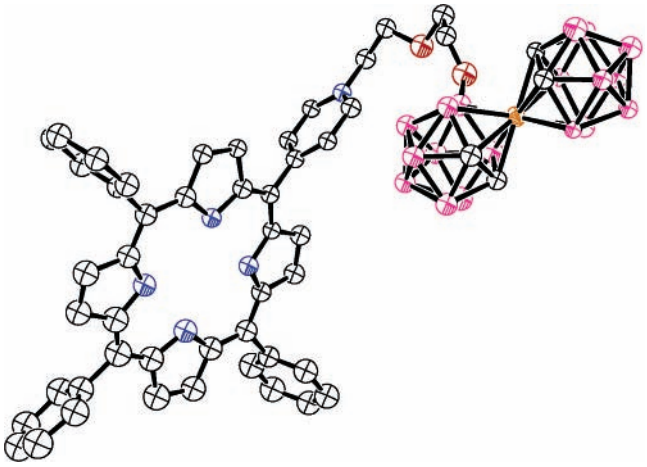

Figure 1. Molecular structure of porphyrin−cobaltacarborane **1**.

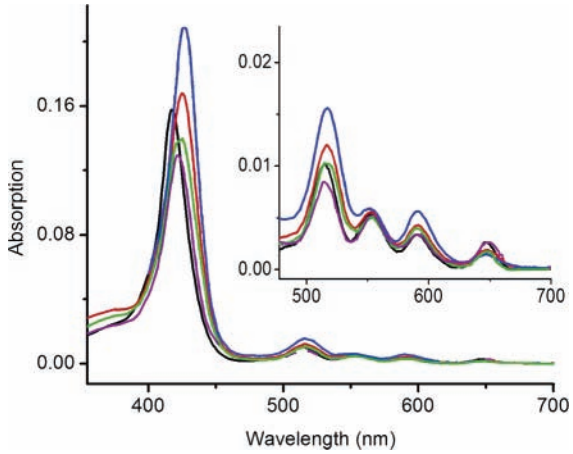

Figure 2. Optical spectra of conjugates **1** (black), **2** (purple), **3** (green), **4** (red), and **5** (blue) at 1 μM in acetone solution.

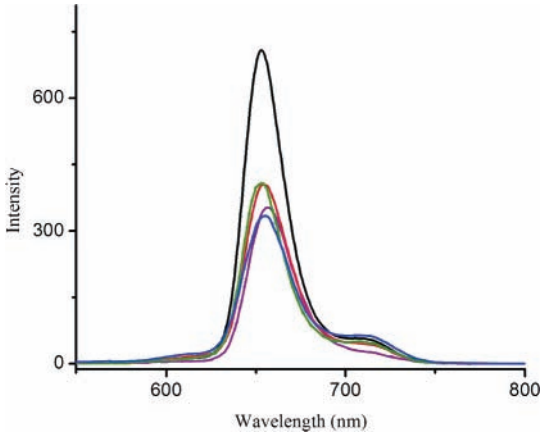

Figure 3. Fluoresence emission spectra of conjugates **1** (black), **2** (purple), **3** (green), **4** (red), and **5** (blue) at 1 μM in acetone solution upon excitation at 416 nm at room temperature.

The zwiterionic porphyrin conjugates **1**−**5** are soluble in polar aprotic solvents, such as acetonitrile, acetone, ethyl acetate, THF, DMF, and DMSO but are not soluble in methanol or water. Their observed low extinction coefficients in acetone solution compared with the corresponding starting porphyrins (Figure 2) indicates the formation of small aggregates even at micromolar concentrations and may explain their poor solubility in protic solvents. Interestingly, 2−3 nm red-shifts of the conjugate Soret bands were observed with increasing number

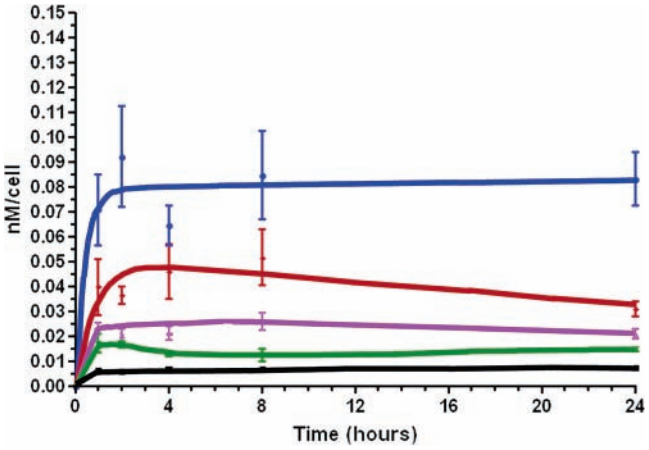

Figure 4. Time-dependent uptake of conjugates **1** (black), **2** (purple), **3** (green), **4** (red), and **5** (blue) at 10 μM by HEp2 cells.

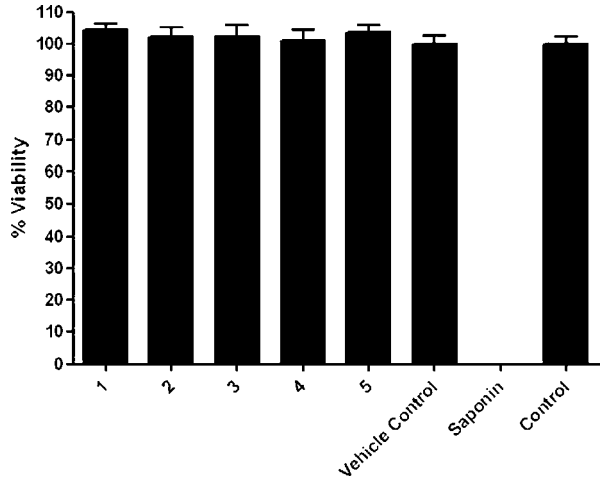

Figure 5. Dark cytotoxicity of conjugates **1**–**5** and controls toward HEp2 cells using the Cell Titer Blue assay.

of cobaltacarborane moieties linked to the porphyrin macrocycle; for example, the Soret bands of conjugates **1** and **5** appear at 418 and 427 nm, respectively. The fluorescence spectra of conjugates **1**–**5** (Figure 3) all display emissions at ~653 nm in acetone solution, upon excitation at 512 nm. The most intense fluorescence band was observed for conjugate **1**, containing only one cobaltacarborane substituent on the porphyrin macrocycle.

Cellular Studies. The time-dependent uptake of conjugates **1**–**5** was evaluated in HEp2 cells at a concentration of 10 μM (Figure 4). Since the conjugates were poorly soluble in water, DMSO and Cremophore EL were used as the delivery vehicles (0.9%DMSO/0.1% Cremophor EL). At 10 μM concentration all conjugates were found to be nontoxic to the cells, as evaluated using the Cell Titer Blue assay (Figure 5). Higher concentrations were not investigated due to the poor solubility of the conjugates in aqueous solutions. At the low concentration used, the DMSO/Cremophor EL vehicle was nontoxic to cells (Figure 5, vehicle control), while 0.2% saponin provided 100% cell death, and the control cells (in the absence of both conjugate and vehicle) showed 100% cell viability (Figure 5). The cellular uptake of conjugates **1**–**5** significantly increased with the number of cobaltacarborane moieties linked to the porphyrin macrocycle, as shown in Figure 4. Conjugate **5**, bearing four cobaltacarboranes, accumulated the most within cells, approximately 16 times more than **1**, bearing only one cobaltacarborane, at all time points. Conjugate **3**, with two cobaltacarboranes linked to adjacent *meso*-pyridyl rings, was taken up by HEp2 cells to a significantly higher extent (~25%) than **2**, bearing two cobaltacarboranes linked to opposite pyridyls. The uptake kinetics were similar for all conjugates, proceeding rapidly in the first 1–2 h after which a plateau was reached.

The intracellular localization of conjugates **1**–**5** in HEp2 cells was investigated by fluorescence microscopy, using Lipofectamine liposomes as the delivery vehicle (Figure 6). In the absence of liposomes the fluorescent signal for the conjugates was too weak to be clearly detected above the background autofluorescence, due to their poor water solubility. Using liposomes as the delivery vehicle, we observed a very punctate fluorescence for all conjugates, as seen in Figure 6, indicating that they all localize within vesicles. Colocalization experiments with LysoSensor Green and Mitotracker Green, as seen in Figure 7 for conjugate **3** (similar figures are available for conjugates **1**, **2**, **4**, and **5** in the Supporting Information), indicate that some of the conjugates' fluorescence correlates with the cell lysosomes.

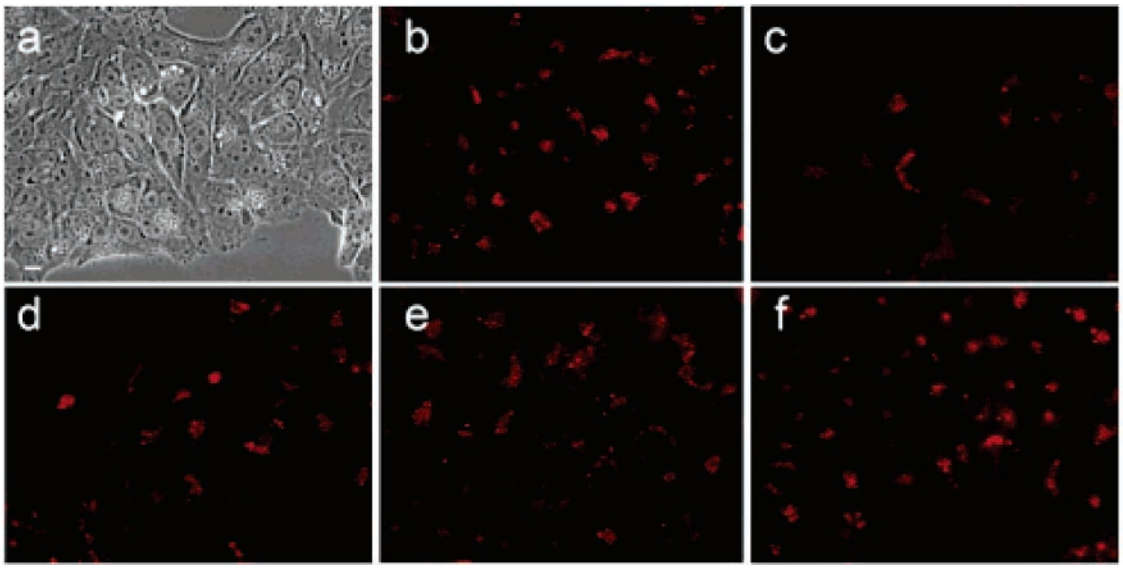

Figure 6. Subcellular localization of conjugates **1**–**5** in HEp2 cells at 1 μM in liposomes for 18 h. (a) Phase contrast, (b) **1** fluorescence, (c) **2** fluorescence, (d) **3** fluorescence, (e) **4** fluorescence, (f) **5** fluorescence. Scale bar: 10 μm.

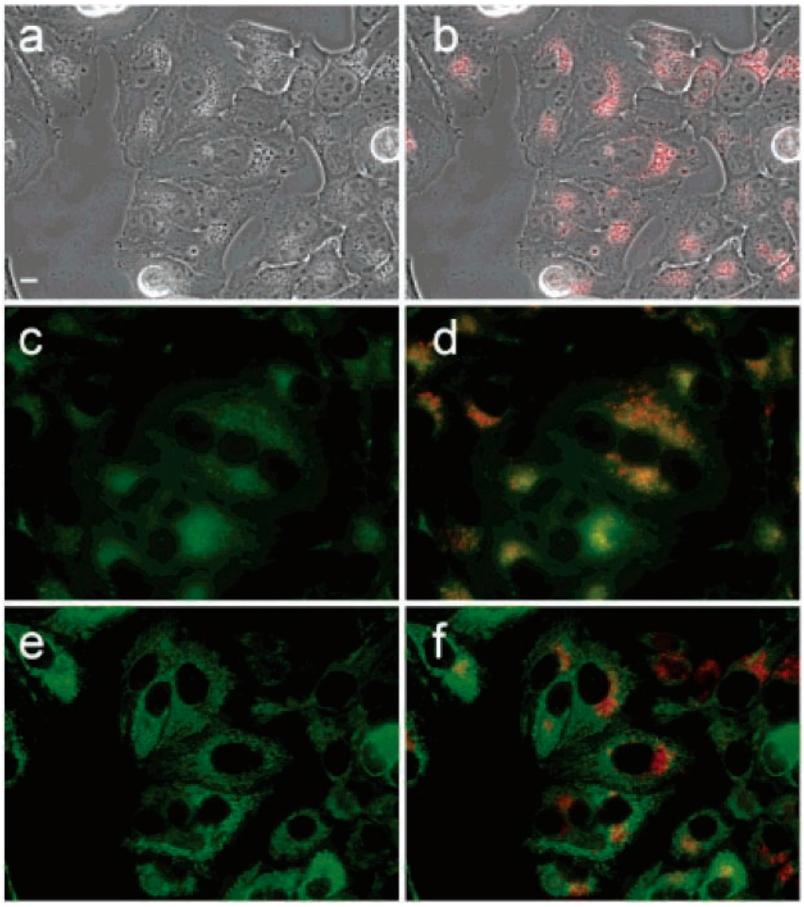

Figure 7. Subcellular localization of conjugate **3** in HEp2 cells at 1 μM in liposomes, for 18 h. (a) Phase contrast, (b) overlay of **3** fluorescence and phase contrast, (c) LysoSensor Green fluorescence, (e) MitoTracker Green fluorescence, (d), (f) overlays of organelle tracers with **3** fluorescence. Scale bar: 10 μm.

DISCUSSION

Cobaltacarborane−porphyrin conjugates **1**−**5** were synthesized in 88−98% yields in a single-step reaction between cobaltacarborane **6** and pyridylporphyrins **7**−**11**. This methodology allows the easy and expeditious preparation of the target porphyrin conjugates, in gram amounts. N-Alkylated pyridylporphyrins, in particular *meso*-tetra(*N*-methylpyridyl)porphyrin, have been extensively studied as DNA and RNA binding probes (*33*−*37*) and as antibacterial and antiviral agents (*38*−*41*). The biological activity of this type of compound depends on the size and distribution of the macrocycle periphery groups, the molecule charge and its distribution, and on the nature of the centrally chelated metal ion and associated axial ligand(s) (*42*). The new zwiterionic porphyrin conjugates **1**−**5** bearing one to four *N*-cobaltacarboranepyridyl moieties were synthesized in order to study their biological activity and to correlate their structure and charge distribution with their cellular uptake and preferential sites of intracellular localization. All conjugates display absorption spectra characteristic of porphyrin macrocycles (Figure 2) and fluorescence emissions in the red region of the optical spectrum (Figure 3).

The cellular uptake of all conjugates in the presence of a DMSO/Cremophor EL delivery vehicle was studied in HEp2 cells at a concentration of 10 μM. The amount of conjugate accumulated by cells depended significantly on the number of cobaltacarborane residues linked to the porphyrin macrocycle, and on its distribution about the ring (conjugates **2** and **3**). Compound **5**, bearing four cobaltacarboranes, accumulated the most within cells, while conjugate **1**, bearing a single cobaltacarborane, accumulated the least (Figure 4). Although conjugate **1**, with only one positive and one negative charges, is expected to be more hydrophobic than **5**, which bears four positive and four negative charges, the latter showed decreased solubility in polar solvents and increased tendency for aggregation, as indicated by its lower emission intensity of all conjugates studied (Figure 3). Porphyrin aggregates are potentially taken up to a higher extent by cells in culture, via an endocytic pathway (*43*). We have previously observed that free-base carboranylporphyrins accumulated within cells to a higher extent than their Zn(II) counterparts, as a result of their higher tendency for forming aggregates and consequently higher hydrophobicity (*10*, *44*). We have also observed that a porphyrin bearing eight *nido*-carborane groups was taken up by T98G cells to a lower extent than a related tetra(*nido*-carboranyl)porphyrin, although in this case the overall molecule charge changed from −8 to −4 and the octa-anionic porphyrin was more hydrophilic than the tetra-anionic derivative (*10*). On the other hand, the overall molecule charge for all conjugates **1**−**5** is zero, and their tendency for aggregation likely increases with the number of charges. The charge distribution about the porphyrin ring was also found to affect cellular uptake; conjugate **3**, bearing two cobaltacarboranes on adjacent pyridyl rings, accumulated to a higher extent within cells compared with **2**, bearing the charges and substituents on opposite pyridyl rings. It is expected that conjugate **3**, with two distinctive charged/hydrophobic moieties, will have different aggregation behavior from **2**. In agreement with these results, we have recently discovered that two

(*N*-trimethylaminophenyl)porphyrins, bearing two positive charges on either adjacent or opposite *meso*-phenyl rings, display different photodynamic efficacy, possibly as a result of their different interactions with biological substrates (*45*).

All porphyrin−cobaltacarborane conjugates localized into vesicles within HEp2 cells, when delivered by Lipofectamine liposomes (Figure 6). Colocalization experiments showed that these vesicles correlated to some extent with the cell lysosomes (Figure 7). Our group and others have previously observed that carboranylporphyrins preferentially localize in the cell lysosomes (*10*, *44*, *46*). However, the use of liposomes as delivery vehicle could potentially alter the subcellular distribution of porphyrin sensitizers, as we have recently reported (*47*, *48*). This could in part explain the vesicle localization observed in this study for conjugates **1**−**5** and its partial correlation with the cell lysosomes.

ACKNOWLEDGMENT

The authors thank Dr. Frank Fronczek for assistance with the molecular structure determination and Dr. Martha Sibrian-Vazquez for assistance with HPLC. This work was supported by the National Institutes of Health, grant number R01 CA098902.

Supporting Information Available: Additional spectroscopic data including HRMS and NMR spectra for all conjugates synthesized, HPLC conditions, and subcellular localization figures for conjugates **1**, **2**, **4**, and **5** is available free of charge via Internet at http://pubs.acs.org. Crystallographic data (excluding structure factors) for the structure in this paper have been deposited with the Cambridge Crystallographic Data Centre as supplementary publication no. CCDC 272582. Copies of the data can be obtained, free of charge, on application to CCDC, 12 Union Road, Cambridge, CB2 1EZ, UK, (fax: +44-(0)1223-336033 or e-mail: deposit@ccdc.cam.ac.uk).

LITERATURE CITED

(1) Soloway, A. H., Tjarks, W., Barnum, B. A., Rong, F. G., Barth, R. F., Codogni, I. M., and Wilson, J. G. (1998) The chemistry of neutron capture therapy. *Chem. Rev. 98*, 1515−1562.

(2) Hawthorne, M. F. (1993) The role of chemistry in the development of boron neutron capture therapy of cancer. *Angew. Chem., Int. Ed. Engl. 32*, 950−984.

(3) Barth, R. F., Coderre, J. A., Vicente, M. G. H., and Blue, T. E. (2005) Boron neutron capture therapy of cancer: Current status and future prospects. *Clin. Cancer Res. 11*, 3987−4002.

(4) Vicente, M. G. H. (2001) Porphyrin-based sensitizers in the detection and treatment of cancer: Recent progress. *Curr. Med. Chem. Anti-Cancer Agents 1*, 175−194.

(5) Bregadze, V. I., Sivaev, I. B., Gabel, D., and Wohrle, D. (2001) Polyhedral boron derivatives of porphyrins and phthalocyanines. *J. Porphyrins Phthalocyanines 5*, 767−781.

(6) Hawthorne, M. F., and Pitochelli, A. R. (1959) The reaction of bis-acetonitrile decarborane with amines. *J. Am. Chem. Soc. 81*, 5519−5519.

(7) Miura, M., Morris, G. M., Micca, P. L., Lombardo, D. T., Youngs, K. M., Kalef-Ezra, J. A., Hoch, D. A., Slatkin, D. N., Ma, R., and Coderre, J. A. (2001) Boron neutron capture therapy of a murine mammary carcinoma using a lipophilic carboranyltetraphenylporphyrin. *Radiat. Res. 155*, 603−610.

(8) Vicente, M. G. H., Wickramasinghe, A., Nurco, D. J., Wang, H. J. H., Nawrocky, M. M., Makar, M. S., and Miura, M. (2003) Syntheses, toxicity and biodistribution of two 5,15-di-[3,5-(*nido*-carboranylmethyl)phenyl]porphyrin in EMT-6 tumor bearing mice. *Bioorg. Med. Chem. 11*, 3101−3108.

(9) Ozawa, T., Santos, R. A., Lambom, K. R., Bauer, W. F., Koo, M.-S., Kahl, S. B., and Deen, D. F. (2004) In vivo evaluation of the boronated porphyrin TABP-1 in U-87 MG intracerebral human glioblastoma xenografts. *Mol. Pharm. 1*, 368−374.

(10) Gottumukkala, V., Luguya, R., Fronczek, F. R., and Vicente, M. G. H. (2005) Synthesis and cellular studies of an octaanionic 5,10,15,20-tetra[3,5-(*nido*-carboranylmethyl)phenyl]-porphyrin (H_2OCP) for application in BNCT. *Bioorg. Med. Chem. 13*, 1633−1640.

(11) For an example see: Miura, M., Micca, P. L., Fisher, C. D., Gordon, C. R., Heinrichs, J. C., and Slatkin, D. N. (1998) Evaluation of carborane-containing porphyrins as tumour targeting agents for boron neutron capture therapy. *Br. J. Radiol. 71*, 773−781.

(12) Dougherty, T. J., Gomer, C. J., Henderson, B. W., Jori, G., Kessel, D., Korbelik, M., Moan, J., and Peng, Q. (1998) Photodynamic therapy. *J. Natl. Cancer Inst. 90*, 889−905.

(13) Pandey, R. K., and Zheng, G. (2000). Porphyrins as photosensitizers in photodynamic therapy. *The Porphyrin Handbook*, *Volume 6: Applications: past, present and future* (Kadish, K. M., Smith, K. M., and Guilard, R., Eds.) pp 157−230, Chapter 43, Academic Press, New York.

(14) Hawthorne, M. F., Young, D. C., and Wegner, P. A. (1965) Carbametallic boron hydride derivatives. I. Apparent analogues of ferrocene and ferricinium ion. *J. Am. Chem. Soc. 87*, 1818−1819.

(15) Sivaev, I. B., and Bregadze, V. I. (1999) Chemistry of cobalt bis(dicarbollides). A review. *Collect. Czech. Chem. Commun. 64*, 783−805.

(16) Sivaev, I. B., and Bregadze, V. I. (2000) Chemistry of nickel and iron bis(dicarbollides). A review. *J. Organomet. Chem. 614−615*, 27−36.

(17) Spryshkova, R. A., Brattsev, V. A., Sherman, T. L., and Stanko, V. I. (1981) Accumulation of carborane-series compounds in animal tissues during neutron-capture therapy. *Med. Radiologiya 26*, 7, 51−55.

(18) Spryshkova, R. A., Karaseva, L. I., Brattsev, V. A., and Serebriakov, N. G. (1981) Toxicity of functional derivatives of polyhedral carboranes. *Med. Radiologiya 26*, 6, 62−64.

(19) Hawthorne, M. F., Varadavajan, A., Knobler, C. B. Chakrabarti, S., Paxton, R. J., Beatty, B. G., and Curtis, F. L. (1990) Radiometallacarboranes as tumor imaging reagents. *J. Am. Chem. Soc. 112*, 5365−5366.

(20) Hawthorne, M. F., and Maderna, A. (1999) Applications of radiolabeled boron clusters to the diagnosis and treatment of cancer. *Chem. Rev. 99*, 3421−3434.

(21) Sivaev, I. B., Bregadze, V. I., and Kuznetsov, N. T. (2002) Derivatives of the closo-dodecaborate anion and their application in medicine. *Russ. Chem. Bull. 51*, 1362−1374.

(22) Valliant, J. F., Guenther, K. J., King, A. S., Morel, P., Schaffer, P., Sogbein, O. O., and Stephenson, K. A. (2002) The medicinal chemistry of carboranes. *Coord. Chem. Rev. 232*, 173−230.

(23) Olejniczak, A. B., Plesek, J., Kriz, O., and Lesnikowski, Z. J. (2003) A Nucleoside conjugate containing a metallacarborane group and its incorporation into a DNA oligonucleotide. *Angew. Chem., Int. Ed. 42*, 5740−5743.

(24) Plesek, J., Hermanek, S., Franken, A., Cisarova, I., and Nachtigal, C. (1997) Dimethyl sulfate induced nucleophilic substitution of the [bis(1,2-dicarbollido)-3-cobalt(1-)]ate ion. Syntheses, properties and structures of its 8,8′-mu-sulfato, 8-phenyl and 8-dioxane derivatives. *Collect. Czech. Chem. Commun. 62*, 47−56.

(25) Teixidor, F., Pedrajas, J., Rojo, I., Vinas, C., Kivekas, R., Sillanpaa, R., Sivaev, I., Bregadze, V., and Sjoberg, S. (2003) Chameleonic capacity of $[3,3'\text{-Co}(1,2\text{-}C_2B_9H_{11})_2]^-$ in coordination. Generation of the highly uncommon S(thioether)-Na bond. *Organometallics 22*, 3414−3423.

(26) Peymann, T., Kuck, K., and Gabel, D. (1997) Ring opening of tetrahydropyran attached to undecahydro-*closo*-dodecaborate(1−) by nucleophiles. *Inorg. Chem. 36*, 5138−5139.

(27) Sivaev, I. B., Starikova, Z. A., Sjoberg, S., and Bregadze, V. I. (2002) Synthesis of functional derivatives of the $[3,3'\text{-Co}(1,2\text{-}C_2B_9H_{11})_2]^-$ anion. *J. Organomet. Chem. 649*, 1−8.

(28) Plesek, J., Gruner, B., Hermanek, S., Baca, J., Marecek, V., Janchenova, J., Lhotsky, A., Holub, K., Selucky, P., Rais, J., Cisarova, I., and Caslavsky, J. (2002) Synthesis of functionalized cobaltacarboranes based on the *closo*-$[(1,2\text{-}C_2B_9H_{11})_2$-

3,3′-Co]$^-$ ion bearing polydentate ligands for separation of M^{3+} cations from nuclear waste solutions. Electrochemical and liquid−liquid extraction study of selective transfer of M^{3+} metal cations to an organic phase. Molecular structure of the *closo*-[(8-(2-CH_3O-C_6H_4-O)-(CH_2CH_2O)(2)-1,2-$C_2B_9H_{10}$)-(1′,2′-$C_2B_9H_{11}$)-3,3′-Co]Na determined by X-ray diffraction analysis. *Polyhedron 21*, 975−986.

(29) Llop, J., Masalles, C., Vinas, C., Teixidor, F., Sillanpaa, R., and Kivekas, R. (2003) The [3,3′-Co(1,2-$C_2B_9H_{11})_2$]$^-$ anion as a platform for new materials: Synthesis of its functionalized monosubstituted derivatives incorporating synthons for conducting organic polymers. *J. Chem. Soc., Dalton Trans.* 556−561.

(30) Hao, E., and Vicente, M. G. H. (2005) Expeditious synthesis of porphyrin-cobaltacarborane conjugates. *Chem. Commun.* 1306−1308.

(31) (a) Fleischer, E. B., and Shachter, A. M. (1991) Coordination oligomers and a coordination polymer of zinc tetraarylporphyrins. *Inorg. Chem. 30*, 3763−3769. (b) Alessio, E., Macchi, M., Heath, S. L., and Marzilli, L. G. (1997) Ordered supramolecular porphyrin arrays from a building block approach utilizing pyridylporphyrins and peripheral ruthenium complexes and identification of a new type of mixed-metal building block. *Inorg. Chem. 36,* 5614−5623.

(32) Hao, E., Fronczek, F. R., Courtney, B. H., and Vicente, M. G. H. Manuscript in preparation.

(33) Marzilli, L. G. (1990) Medical aspects of DNA-porphyrin interactions. *New J. Chem. 14*, 409−420.

(34) Fiel, R. J. (1989) Porphyrin-nucleic-acid interactions—a review. *J. Biomol. Struct. Dyn. 6*, 1259−1274.

(35) Bustamante, C., Gurrieri, S., Pasternack, R. F., Purrello, R., and Rizzarelli, E. (1994) Interaction of water-soluble porphyrins with single- and double-stranded polyribonucleotides. *Biopolymers 34*, 1099−1104.

(36) Duarte, V., Sixou, S., Favre, G., Pratviel, G., and Meunier, B. (1997) Oxidative damage on RNA mediated by cationic metalloporphyrin-antisense oligonucleotides conjugates. *J. Chem. Soc., Dalton Trans.* 4113−4118.

(37) For a recent reference see: Keating, L. R., and Szalai, V. A. (2004) Parallel-stranded guanine quadruples interactions with a copper cationic porphyrin. *Biochemistry 43*, 15891−15900.

(38) Li, H., Fedorova, O. S., Grachev, A. N., Trumble, W. R., Bohach, G. A., and Czuchajowski, L. (1997) A series of meso-tris(*N*-methyl-pyridiniumyl)-(4-alkylamidophenyl)porphyrins: Synthesis, interaction with DNA and antibacterial activity. *Biochim. Biophys. Acta 1354*, 252−260.

(39) Reddi, E., Ceccon, M., Valduga, G., Jori, G., Bommer, J. C., Elisei, F., Latterini, L., and Mazzucato, U. (2002) Photophysical properties and antibacterial activity of meso-substituted cationic porphyrins, *Photochem. Photobiol. 75*, 462−470.

(40) Casteel, M. J., Jayaraj, K., Gold, A., Ball, L. M., and Sobsey, M. D. (2004) Photoinactivation of hepatitis A virus by synthetic porphyrins. *Photochem. Photobiol. 80*, 294−300.

(41) Lazzeri, D., Rovera, M., Pascual, L., and Durantini, E. N. (2004) Photodynamic studies and photoinactivation of *Escherichia coli* using meso-substituted cationic porphyrin derivatives with asymmetric charge distribution. *Photochem. Photobiol. 80*, 286−293.

(42) (a) Sari, M. A., Battioni, J. P., Dupré, D., Mansuy, D., and Le Pecq, J. B. (1990) Interaction of cationic porphyrins with DNA: Importance of the number and position of the charges and minimum structural requirements for intercalation. *Biochemistry 29*, 4205−4215. (b) Croke, D. T., Perrouault, L., Sari, M. A., Battioni, J. P., Mansuy, D., Helene, C., and Le Doan, T. (1993) Structure−activity relationships for DNA photocleavage by cationic porphyrins. *J. Photochem. Photobiol. B: Biol. 18*, 41−50.

(43) Osterloh, J., and Vicente, M. G. H. (2002) Mechanisms of porphyrinoid localization in tumors. *J. Porphyrins Phthalocyanines 6*, 305−324.

(44) Vicente, M. G. H., Edwards, B. F., Shetty, S. J., Hou, Y., and Boggan, J. E. (2002) Synthesis and preliminary biological studies of four tetra(*nido*-carboranylmethylphenyl)porphyrins. *Bioorg. Med. Chem. 10*, 481−492.

(45) Kessel, D., Luguya, R., and Vicente, M. G. H. (2003) Localization and photodynamic efficacy of two cationic porphyrins varying in charge distribution. *Photochem. Photobiol. 78*, 431−435.

(46) Nguyen, T., Brownell, G. L., Holden, S. A., Kahl, S., Miura, M., and Teicher, B. A. (1993) Subcellular distribution of various boron compounds and implications of their efficacy in boron neutron capture therapy by Monte Carlo simulations. *Radiat. Res. 133*, 33−40.

(47) Liu, W., Jensen, T. J., Fronczek, F. R., Hammer, R. P., Smith, K. M., and Vicente, M. G. H. (2005) Synthesis and in vitro studies of nonaggregated water-soluble phthalocyanines. *J. Med. Chem. 48*, 1033−1041.

(48) Sibrian-Vazquez, M., Jensen, T. J., Fronczek, F. R., Hammer, R. P., and Vicente, M. G. H. (2005) Synthesis and characterization of positively charged porphyrin−peptide conjugates. *Bioconjugate Chem. 16*, 852−863.

BC0502098

Development and Brain Delivery of Chitosan−PEG Nanoparticles Functionalized with the Monoclonal Antibody OX26

Yeşim Aktaş,[†,⊥] Muge Yemisci,[⊗] Karine Andrieux,[⊥] R. Neslihan Gürsoy,[†] Maria Jose Alonso,[§] Eduardo Fernandez-Megia,[#] Ramón Novoa-Carballal,[#] Emilio Quiñoá,[#] Ricardo Riguera,[#] Mustafa F. Sargon,[∥] H. Hamdi Çelik,[∥] Ayhan S. Demir,[‡] A. Atilla Hıncal,[†] Turgay Dalkara,[⊗] Yılmaz Çapan,[†] and Patrick Couvreur[⊥,*]

Department of Pharmaceutical Technology, Faculty of Pharmacy, Hacettepe University, 06100 Ankara, Turkey, Physico-Chimie, Pharmacotechnie, Biopharmacie, Faculté de Pharmacie, Université Paris Sud, UMR CNRS 8612, 92296 Chatenay Malabry, France, Department of Neurology, Faculty of Medicine, and Institute of Neurological Sciences and Psychiatry, Hacettepe University, 06100 Ankara, Turkey, Departament of Pharmaceutical Technology, Faculty of Pharmacy, University of Santiago de Compostela, 15782 Santiago de Compostela, Spain, Departamento de Química Orgánica, Facultad de Química, and Unidad de RMN de Biomoleculas asociada al CSIC, Universidad de Santiago de Compostela, Avda. de las Ciencias S.N. 15782 Santiago de Compostela, Spain, Department of Anatomy, Faculty of Medicine, Hacettepe University, 06100 Ankara, Turkey, and Department of Chemistry, Faculty of Arts and Sciences, Middle East Technical University, 06531 Ankara, Turkey. Received July 21, 2005; Revised Manuscript Received September 16, 2005

The inhibition of the caspase-3 enzyme is reported to increase neuronal cell survival following cerebral ischemia. The peptide Z-DEVD-FMK is a specific caspase inhibitor, which significantly reduces vulnerability to the neuronal cell death. However, this molecule is unable to cross the blood−brain barrier (BBB) and to diffuse into the brain tissue. Thus, the development of an effective delivery system is needed to provide sufficient drug concentration into the brain to prevent cell death. Using the avidin (SA)−biotin (BIO) technology, we describe here the design of chitosan (CS) nanospheres conjugated with poly(ethylene glycol) (PEG) bearing the OX26 monoclonal antibody whose affinity for the transferrin receptor (TfR) may trigger receptor-mediated transport across the BBB. These functionalized CS−PEG−BIO−SA/OX26 nanoparticles (NPs) were characterized for their particle size, zeta potential, drug loading capacity, and release properties. Fluorescently labeled CS−PEG−BIO−SA/OX26 nanoparticles were administered systemically to mice in order to evaluate their efficacy for brain translocation. The results showed that an important amount of nanoparticles were located in the brain, outside of the intravascular compartment. These findings, which were also confirmed by electron microscopic examination of the brain tissue indicate that this novel targeted nanoparticulate drug delivery system was able to translocate into the brain tissue after iv administration. Consequently, these novel nanoparticles are promising carriers for the transport of the anticaspase peptide Z-DEVD-FMK into the brain.

INTRODUCTION

The blood−brain barrier (BBB) is a diffusion barrier essential for the normal function of the central nervous system. The BBB endothelial cells differ from endothelial cells in the rest of the body by the absence of fenestrations, more extensive tight junctions (TJs), and sparse pinocytic vesicular transport. Endothelial cell tight junctions limit the paracellular flux of hydrophilic molecules across the BBB (*1*). In fact, only nonionic, lipophilic, and low molecular weight molecules can diffuse freely through the endothelial membrane and may passively cross the BBB. On the other hand, a large number of drugs that possess a favorable lipophilicity, which normally should enable an easy transport across these cells, are rapidly pumped back into the bloodstream by effective efflux pump systems (*2*, *3*). These efflux pump systems include multiple organic anion transporter (MOAT) and especially P-glycoprotein (P-gp) sometimes referred to as multidrug resistance protein (mdr). Other essential compounds such as amino acids, hexoses, neuropeptides, and proteins need specific carriers or transporter systems to permeate the brain (*2*). Consequently, very few molecules may be transported efficiently into the brain which may compromise the efficient treatment of neurological and psychiatric disorders.

Vector-mediated drug delivery to the brain employs the chimeric peptide technology, wherein the drug is conjugated to a molecular carrier of protein nature (i.e. cationized albumin or OX26 monoclonal antibody). Although this approach has been found useful for the brain delivery of a vasoconstrictive intestinal peptide analogue (VIP), the amount of drug transported with the aid of this technology remains generally limited since the ratio

* Corresponding author. Tel:+33 1 46 83 53 96. Fax:+33 1 46 61 93 34. E-mail: patrick.couvreur@cep.u-psud.fr.
[†] Department of Pharmaceutical Technology, Faculty of Pharmacy, Hacettepe University.
[⊥] Université Paris Sud.
[⊗] Department of Neurology, Faculty of Medicine, and Institute of Neurological Sciences and Psychiatry, Hacettepe University.
[§] Departament of Pharmaceutical Technology, University of Santiago de Compostela.
[#] Departamento de Química Orgánica, University of Santiago de Compostela.
[∥] Department of Anatomy, Hacettepe University.
[‡] Middle East Technical University.

10.1021/bc050217o CCC: $30.25 © 2005 American Chemical Society
Published on Web 10/20/2005

of drug to carrier protein is usually not above 1:1. This is the reason, poly(ethylene glycol) or span 80-coated polymeric nanoparticles have been proposed as an interesting alternative for targeted brain delivery (*3*). It is hypothesized that with such types of hydrophilic coatings, the natural blood opsonization process of the particles is reduced; hence, a relative avoidance of the recognition by macrophages in the liver and spleen is conferred. This steric repulsion augments particle blood half-life and therefore extravasation to nonreticuloendothelial system organs, including the brain, especially when brain pathologies occur together with an increase in the endothelial permeability (*4*, *5*).

Transferrin receptor (TfR), which is highly concentrated in brain capillary endothelium, may trigger receptor-mediated transport across the BBB since it undergoes trancytosis through the BBB (*6*, *7*). Because the circulating concentration of transferrin is manyfold greater than the dissociation (K_D) of the BBB transferrin receptor (*8*), it appears more efficient to use the OX26 mouse monoclonal antibody to the rat transferrin receptor to target the brain. Transferrin itself is limited as a brain drug transport vector since the transferrin receptors are almost saturated under physiologic conditions due to high endogenous plasma concentrations of transferrin. However, the antibodies that bind to the TfR have been shown to selectively target BBB endothelium due to the high levels of TfR expressed by these cells. Therefore, these antibodies are potential carriers for the delivery of therapeutic agents to the central nervous systems. With a mouse monoclonal antibody against the rat TfR, OX26, a high abundance of transferrin receptors at the brain microvascular endothelium has been detected. The OX26 monoclonal antibody against the rat TfR is likely to be a candidate in the delivery of therapeutic agents to the brain (*9*).

Chitosan (CS) is obtained from the deacetylation of chitin, a naturally occurring and abundantly available biocompatible polysaccharide which is obtained from crabs. However, applications of chitin are limited compared to CS, since it is chemically inert (*10*). CS, on the otherhand is a cationic polysaccharide in neutral or basic pH conditions and contains free amino groups which can go undergo protonation, thus making it soluble in water. CS is biocompatible with living tissues since it does not cause allergic reactions and rejection. It is degraded into nontoxic amino sugars under fermentation. The biocompatibility and nontoxic properties of chitosan make this polymer a good candidate for pharmaceutical applications such as targeted drug delivery. The primary amine groups render special properties that make CS very useful in pharmaceutical applications. Compared to many other natural polymers, CS has a positive charge and is mucoadhesive (*11*). Therefore, CS has been used for widespread applications such as colon targeted drug delivery, mucosal delivery, cancer theraphy, gene delivery, topical delivery, and ocular delivery (*12*−*17*). Another advantage of this type of NPs is that due to the hydrophilic nature of chitosan, it can be prepared under exceptionally mild conditions (*18*, *19*), thus being particularly attractive for the association of delicate compounds such as peptides and proteins.

It has been reported that, in focal as well as global brain ischemia, the caspase-3 enzyme is induced and its pro form is activated in ischemic neurons. Caspase-3 activation precedes and its regional distribution correlates with cell death. Furthermore, caspase-3 inhibitors increase cell survival after ischemia which strongly supports a cell death effector role for the caspase-3 protease in ischemic brain injury. Similarly, knocking out the caspase-3 gene confers resistance to brain ischemia. Thus, inhibition of caspase-3-like protease activity is of great interest and may have therapeutic significance in the treatment of stroke and related neurological disorders (*20*). Supporting this view, Ma et al. (*21*) showed that the combined administration of subthreshold doses of basic fibroblast growth factor (bFGF) and caspase inhibitors reduced infarct volume as well as neurological deficit after focal ischemia.

Scheme 1. The Schematic View of Novel Drug Delivery System for Brain Delivery of Chitosan−PEG Nanoparticles Functionalized with the Monoclonal Antibody OX26

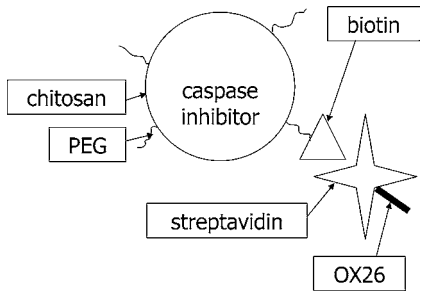

On the basis of these considerations, we describe here a new nanotechnology for the brain delivery of the caspase inhibitor peptide Z-DEVD-FMK. This technology consists of PEG-overcoated chitosan (CS) nanoparticles conjugated with the monoclonal antibody OX26, using the avidin−biotin approach. These addressed CS nanoparticles combine (i) the ability of cationic CS to interact with the negative charges of the brain endothelium and (ii) the affinity of OX26 for the transferrin receptor to trigger receptor-mediated transport across the BBB (Scheme 1).

EXPERIMENTAL SECTION

Materials. The CS Protasan Cl 113 (Mw < 150 kD, deacetylation degree: 75−90%) and the caspase inhibitor peptide Z-DEVD-FMK were purchased from FMC Biopolymers (Norway) and Enzyme Systems (Livermore, CA), respectively. Pentasodium tripolyphosphate (TPP), streptavidin−FITC, trifluoroacetic acid (TFA), maleimidobenzoyl *N*-hydroxy-
succinimide ester (MBS), and Traut's Reagent (2-iminothiolane) were purchased from Sigma-Aldrich (St. Louis, MO). Antihuman CD71 (OX26) was received from Cymbus Biotechnology (Hants, UK). Acetonitrile was purchased from Carlo Erba Reagenti (Italy). All other reagents used were of analytical or pharmaceutical grade.

Synthesis of Chitosan-PEG (CS−PEG). Chitosan·HCl [80 mg, 0.40 mmol, degree of acetylation 13.7%, M_w 113650, (Protasan UP CL113)] was dissolved in H_2O (11.5 mL). MeO-PEG-CH_2CO_2H (14.2 mg, 2.77 μmol, M_n 5114 by MALDI-TOF) and NHS (1.63 mg, 0.014 mmol) were added to the solution. Then, EDC (21.7 mg, 0.113 mmol) was added gradually due to its instability. The resulting solution was stirred at room temperature for 22 h and then ultrafiltered (Amicon, YM30), and lyophilized to give chitosan-PEG (CS−PEG) as a white foam [74 mg, degree of substitution (DS) 0.56% determined by ^{1}H NMR]. ^{1}H NMR (500 MHz, D_2O) δ (ppm): 2.07 (s, 41.1 H, $COCH_3$), 3.10−3.30 (m, 84 H, H2 from $GluNH_2$), 3.30−4.30 (m, 778 H, H2 from GluNHAc; H3, H4, H5, H6 from $GluNH_2$ and GluNHAc; CH_3O, CH_2O from PEG), 4.55−4.70 (m, H1 from GluNHAc) 4.80−4.95 (m, H1 from $GluNH_2$).

Synthesis of Chitosan−PEG−Biotin (CS−PEG−BIO). The copolymer made of chitosan and PEG−biotin

(CS−PEG−BIO) was synthesized in two steps from a heterobifunctional PEG as described below.

Synthesis of HO_2C−PEG-Biotin. [$HO_2C(CH_2)_3CONH$-$(CH_2CH_2O)_nCH_2CH_2CONH(CH_2CH_2O)_2CH_2CH_2NHCO$−biotin]: $FmocHN(CH_2CH_2O)_nCH_2CH_2CONHS$ ($M_n = 3837$, M_w=3890 determined by MALDI-TOF, Nektar) was treated with $H_2N(CH_2CH_2O)_2CH_2CH_2NHCO$−biotin in $CHCl_3$. The resulting product was subjected to Fmoc deprotection and reaction with glutaric anhydride to give the desired HO_2C−PEG−biotin in 76% combined yield ($M_n = 4009$, $M_w = 4030$ by MALDI-TOF). ^{1}H NMR (400 MHz, CD_3Cl, 333 K) δ (ppm): 1.35−1.55 (m, 2H, CH_2), 1.57−1.90 (m, 4H, CH_2), 1.95 (q, $J = 6.9$ Hz, 2H, CH_2), 2.15 (t, $J = 6.7$ Hz, 2H, CH_2CONH), 2.22 (t, $J = 7.1$ Hz, 2H, CH_2CO), 2.32 (t, $J = 6.8$ Hz, 2H, CH_2CO), 2.41 (t, $J = 5.5$ Hz, 2H, CH_2CONH), 2.75 (d, $J = 12.8$ Hz, 1H, CH_2), 2.93 (dd, $J = 4.9$ Hz, $J = 12.8$ Hz, 1H, CH_2), 3.00−3.20 (m, 1H, CH), 3.25−3.90 (m, 325H,CH_2O, CH_2NH), 4.25−4.35 (m, 1H, CH), 4.35−4.50 (m, 1H, CH), 4.67 (br s, 1H, NH), 6.16 (br s, 2H, NH), 6.64 (br s, 1H, NH).

Synthesis of Chitosan−PEG−Biotin. CS−PEG−BIO was synthesized as described above for CS−PEG (under the title of Synthesis of Chitosan−PEG (CS−PEG)) from chitosan·HCl [53.3 mg, 0.27 mmol (Protasan UP CL113)], HO_2C-PEG−biotin (7.8 mg, 1.94 μmol), NHS (1.0 mg, 8.59 μmol), and EDC (14.4 mg, 0.075 mmol). The desired CS−PEG−BIO was obtained as a white foam (60.8 mg, DS 0.55% determined by ^{1}H NMR). ^{1}H NMR (500 MHz, D_2O) δ (ppm): 2.07 (s, 41.1 H, $COCH_3$), 3.10−3.30 (m, 87 H, H2 from $GluNH_2$), 3.30−4.30 (m, 691 H, H2 from GluNHAc; H3, H4, H5, H6 from $GluNH_2$ and GluNHAc; CH_3O, CH_2O from PEG), 4.62 (m, H1 from GluNHAc) 4.91 (m, H1 from $GluNH_2$).

Preparation of Chitosan and Surface-Modified Chitosan Nanoparticles. CS, CS−PEG, or CS−PEG−BIO nanoparticles were prepared by the ionic gelation of TPP and CS, CS−PEG, or CS−PEG−BIO according to the procedure previously developed by P. Calvo et al. for the preparation of CS nanoparticles (*18*, *19*).

Preliminary experiments were performed in order to identify the optimal concentrations of CS and TPP for NP formation. Practically, CS nanoparticles were formed upon dropwise addition of 1 mL TPP aqueous solution (0.4 mg/mL) to 1 mL of CS aqueous solution (1.75 mg/mL). Likewise, CS−PEG and CS−PEG−BIO (1 mg/mL each) nanoparticles were prepared by dropwise addition of 0.4 mL TPP aqueous solution (0.84 mg/mL) to 1 mL of each of the corresponding aqueous polymer solutions. These solutions were then stirred under magnetic stirring at medium speed and room temperature.

Z-DEVD-FMK-loaded nanoparticles were obtained according to the same procedure, and the ratio of polymer/TPP remaining unchanged. Z-DEVD-FMK was incorporated in the polymer solution before the addition of the TPP. The initial concentration of the peptide in the NP suspension was 800 ng/mL. Although the previous study (*22*) showed that the optimum loading concentration was 400 ng/mL, the 800 ng/mL concentration was used in the present study since the released amount would be higher compared to the former loading concentration.

The resulting mixtures were broadly characterized as either a clear solution, an opalescent suspension displaying a tyndall effect (NPs), or aggregates. Nanoparticles were isolated by ultracentrifugation (10 000 rpm, 4 °C, 60 min in the presence of 10 μL of glycerol) and then resuspended in water by manual shaking.

Preparation of the Streptavidin/OX26 Conjugate (SA/OX26). The SA/OX26 conjugates were prepared according to the procedure described by Yoshikawa and Pardridge (*23*). Briefly, 1 mg of streptavidin−FITC (SA−FITC) was dissolved in 100 μL of borate buffer containing 0.1 M EDTA (0.1 M) and 5 μL of 2-iminothiolane (4 mg/mL). After stirring for 90 min at room-temperature nonthiolated streptavidin was removed by dialysis in 0.05 M phosphate buffer (pH 6.5). Then, 100 μL of OX26 solution was added to 100 μL of SA−FITC solution. After stirring for 30 min, nonreacted OX26 was discarded by dialysis.

Preparation of OX26-Conjugated Nanoparticles (CS−PEG-BIO−SA/OX26). 10 μL of SA/OX26 conjugate was added to 1 mg of lyophilized CS−PEG−BIO NP previously resuspended in deionized water (100 μL); this suspension was incubated for 30 min. The CS−PEG−BIO−SA/OX26 nanoparticles obtained were lyophilized for further use.

Characterization of Nanoparticles. Measurements of particle size and zeta potential of the NPs were performed in triplicate by photon correlation spectroscopy and laser doppler anemometry, respectively, using a Zetasizer Nanosystems 3000 HS (Malvern Instruments, UK). The size measurements were carried out at 25 °C at a 90° scattering angle and recorded for 180 s for each measurement. After staining with 1% (w/v) phosphotungstic acid, the morphological characterization of the CS NPs was done using a transmission electron microscope (TEM; CM12 Philips).

Quantitative Analysis of Z-DEVD-FMK. Z-DEVD-FMK was analyzed by reversed-phase (RP) HPLC utilizing a Hewlett-Packard Agilent 1100 apparatus with HP CHEMSTATION software and a C18 RP column (250 × 4.6 mm; particle size 5 μm; Waters Assoc.). Water:acetonitrile (80:20) containing 0.1% TFA was used as the mobile phase with a flow rate of 1 mL/min. Column effluent was monitored by UV absorption at 215 nm. Total run time was 6 min and the injection volume was 50 μL. The retention time of the peptide was 2.8 min. A calibration curve was constructed using standard Z-DEVD-FMK solutions prepared in the incubation medium. The calibration curve was linear between 25 and 150 ng/mL ($y = 2.6309x - 20.542$, $R^2 = 0.9975$). The limit of detection was 10 ng/mL. Peptide solution was found to be stable both at room temperature and at 4 °C for 1 day.

Evaluation of the Peptide Association Efficiency. The NPs loaded with Z-DEVD-FMK anticaspase peptide were subjected to ultracentrifugation (10 000 rpm at 4 °C for 1 h). Then, the amount of free peptide was measured in the clear supernatant by RP-HPLC as described above (under the title of Quantitative Analysis of Z-DEVD-FMK). The peptide loading capacity (LC) and the association efficiency (AE) of the nanoparticle were calculated according to the following equations:

$$\%\ \mathrm{LC} = 100 \times (\text{total peptide amount} - \text{free peptide amount})/\text{nanoparticle weight}$$

$$\%\ \mathrm{AE} = 100 \times (\text{total peptide amount} - \text{free peptide amount})/\text{total peptide amount}$$

Evaluation of in Vitro Z-DEVD-FMK Release. The NPs were collected by centrifugation at 10 000 rpm for 1 h on a glycerol bed, and an aliquot of NPs (1 mg) was then resuspended and incubated in 1 mL of PBS (pH 7.4) at 37 °C under light agitation. At varying time points, supernatants were isolated by centrifugation at 10 000 rpm for 20 min, and the amount of Z-DEVD-FMK released was measured by RP-HPLC as described earlier. All measurements were performed in triplicate.

The stability of the peptide in the release medium was checked by a 24 h stability assay. Practically, peptide solutions in PBS with three concentrations (25, 50, and 150 ng/mL) were prepared, each solution being divided into three equal portions. The first portion was immediately analyzed, while the remaining two portions were kept at room temperature and at 4 °C prior to HPLC analysis.

In Vivo Brain Uptake of the CS−PEG−BIO−OX26/SA Nanoparticles. Swiss albino mice weighing 30−33 g were housed under diurnal lighting conditions (12 h darkness and 12 h light) and fasted overnight but allowed free access to water before the experiment. Animal housing, care and application of experimental procedures were all done in accordance with institutional guidelines. Mice ($n = 9$) were anesthetized intraperitoneally (ip) with 50 mg/kg ketamin (Ketalar, Parke-Davis) and 10 mg/kg xylasine (Rompun, Bayer). Body temperature was monitored with a rectal probe and maintained at 37.0 ± 0.2 °C by a homeothermic blanket.

FITC-labeled NPs were detected with fluorescence microscopy (Nikon Eclipse E600, λ_{Ex} 450−490 nm). In preliminary experiments, to observe the appearance of FITC-labeled NPs, microscopic slides prepared from nanoparticle containing suspensions (1 mg in 200 μL of saline) were examined under the microscope. Later, the NPs (1 mg in 200 μL of saline) were injected intracerebrally with a microsyringe to the right frontal cortex, and mice were immediately sacrificed and decapitated ($n = 2$). NPs not conjugated to OX26 were administered as control ($n = 4$). Coronal cryosections of 20 μm thickness obtained from 2 mm posterior of the frontal pole and coverslipped with mounting medium containing Hoechst-33258 to counterstain the nuclei were examined. After determining how FITC-labeled nanospheres appeared in the brain, coronal sections obtained by the same method were examined from mice brains administered with the same nanoparticle suspensions via the tail vein. Mice were sacrificed and decapitated one ($n = 2$) and two ($n = 4$) hours after the iv injection of the NPs.

Histological specimens (1 mm^3) were obtained from the frontal cortex, striatum, and the occipital cortex of both hemispheres for examination under transmission electron microscope. They were fixed in 2.5% gluteraldehyde for 24 h, washed in phosphate buffer (pH 7.4), postfixed in 1% osmium tetroxide in phosphate buffer (pH 7.4), and dehydrated in increasing concentrations of alcohol for TEM examination. Then the tissues were washed with propylene oxide and embedded in epoxy-resin embedding media. Semithin sections about 2 μm in thickness and ultrathin sections about 60 nm in thickness were cut with a glass knife on a LKB−Nova (Sweden) ultramicrotome. Semithin sections were stained with methylene blue and examined by a Nikon Optiphot (Japan) light microscope. After trimming procedure of these semithin sections, ultrathin sections were taken, collected on copper grids, stained with uranyl acetate and lead citrate, and examined with a JEOL JEM 1200 EX (Japan) transmission electron microscope.

RESULTS AND DISCUSSION

Characterization of Chitosan−PEG, PEG−Biotin, and Chitosan−PEG−Biotin. In Figure 1A the ^{1}H NMR spectrum of the starting CS is depicted. In the ^{1}H NMR spectra of CS−PEG and CS−PEG−BIO (Figures 1B and 1C), the presence of PEG is clearly established by the big intense signal at 3.7 ppm. Also, the differences in the spectra between unfunctionalized PEG and PEG−biotin (Figures 1D and 1E) demonstrate the attachment of biotin to PEG. Noteworthy is that the signal corresponding to biotin in the CS−PEG−BIO ^{1}H NMR spectrum (Figure 1C) could not be observed due to the very low proportion of PEG−BIO in this polymer (DS 0.56%). We can also confirm the formation of PEG−BIO prior to the synthesis of CS−PEG−BIO from the molecular weight of PEG−BIO as shown in Figure 2A. Thus, the presence of a signal at 3.7 ppm in the ^{1}H NMR spectrum of CS−PEG−BIO (Figure 1C) indicates with no doubt the efficient linkage of PEG−BIO to CS.

Nanoparticle Preparation and Characterization. The formation of the Z-DEVD-FMK-loaded CS, CS−PEG, CS−PEG−BIO NPs occurred spontaneously upon incorporation of the counteranion TPP into the corresponding CS, CS−PEG, and CS−PEG−BIO polymer solutions. Nanoparticle construction resulted from the ionic interactions between the negative TPP and the positively charged amino groups of CS. The ratio of CS/TPP was established according to the preliminary studies. Confirmation of the conjugates CS−PEG and CS−PEG−BIO was made by utilizing MALDI-TOF and NMR analyses. However the MALDI-TOF analysis of the CS−PEG−BIO/SA−OX26 could not be achieved due to the high molecular weight of the final product.

TEM images of blank CS and PEG-CS NPs are shown in Figures 3A and 3B, respectively. The particles showed a dense and generally spherical structure. It can be seen that the hydrodynamic diameter of the particles measured by light scattering (PCS) is higher than the size estimated from microscopy (TEM) as observed in the previous study of our group (*22*). This may be attributed to the high swelling capacity of the CS NPs. It is worth mentioning that the NPs studied by TEM were dried samples whereas NPs studied by light scattering were aqueous suspensions. In the latter case the NPs were swollen in aqueous medium while in the former case there was a shrinkage of the NPs. This situation may have led to a difference in particle size obtained by light scattering and by TEM. As shown in Table 1, blank CS NPs displayed a zeta potential of +28.4 mV. The addition of the negatively charged Z-DEVD-FMK resulted in a significant lowering of the zeta potential values of the NPs. It was observed that the size of PEG-CS NPs was smaller as compared to CS NPs. This may be explained by the colloid stabilization exerted by the PEG. On the other hand, when the NPs were surface-modified with either PEG−BIO or PEG−BIO−SA/OX26, an important increase in size was observed. This may be attributed to an increase in the hydrophobicity of the surface of the NPs leading to some aggregation due to presence of bulky groups on the surface. Confirmation of the conjugates CS−PEG and CS−PEG−BIO was made by utilizing Maldi-TOF and NMR analyses. However the Maldi-TOF analysis of the CS−PEG−BIO/SA−OX26 could not be achieved due to the high molecular weight of the final product.

Z-DEVD-FMK Encapsulation. Results in Table 1 show the significant increase in the Z-DEVD-FMK encapsulation efficiency for the conjugated NPs as compared with the nonconjugated CS NPs. There are several factors which could affect the encapsulation of the peptide in the CS NPs, such as CS/TPP ratio, auxiliary molecules, and interaction between the peptide and CS (*24*). In this study, the % AE and % LC could be correlated with the surface modification of the CS. However, the association efficiency of the peptide Z-DEVD-FMK in CS NPs was

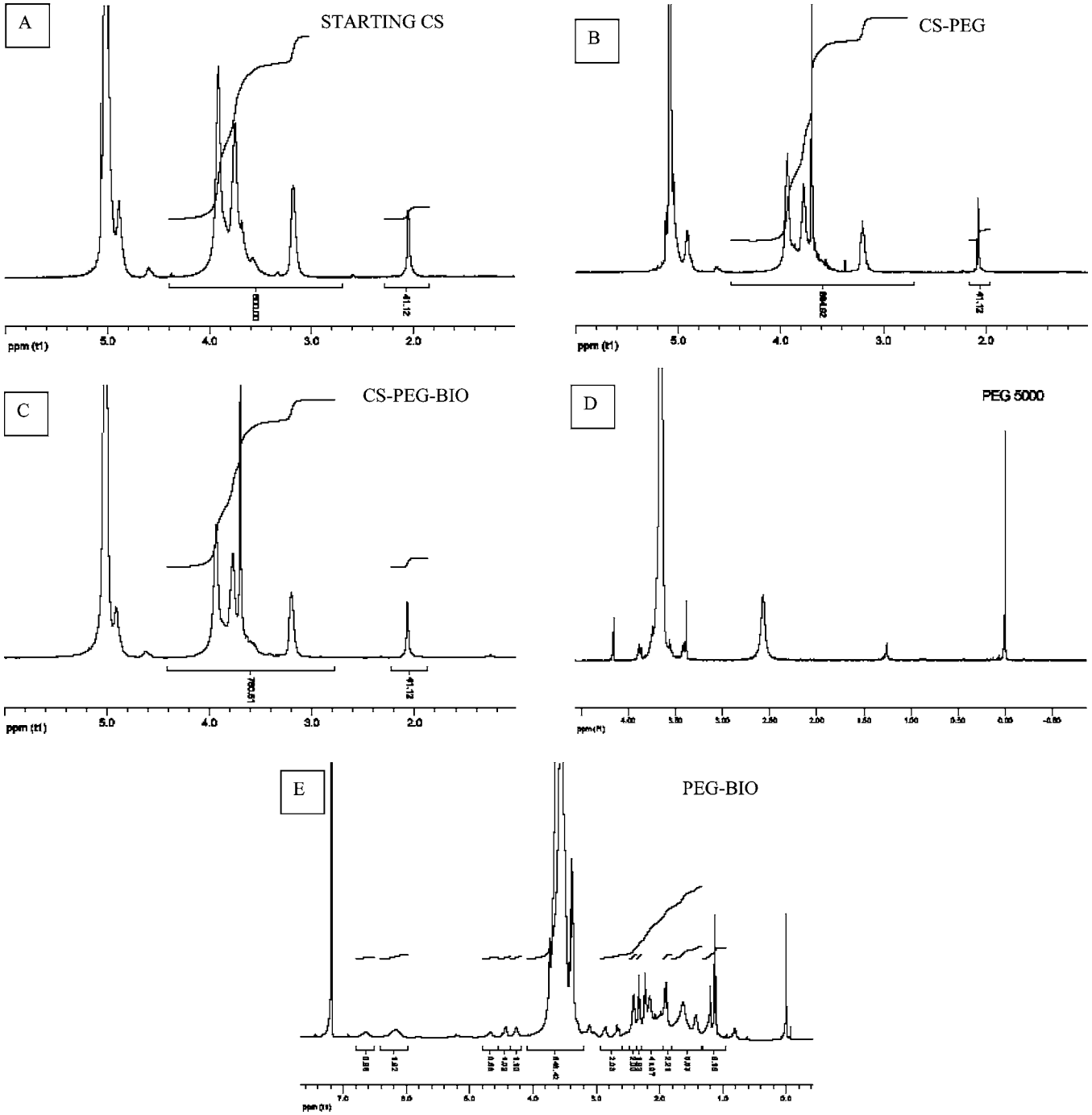

Figure 1. ^{1}H NMR spectra of (A) CS; (B) CS−PEG; (C) CS−PEG−BIO; (D) PEG; (E) PEG−BIO. The identification of the conjugates were determined on the basis of the presence of PEG which gave a signal at 3.7 ppm.

surprisingly low if we take into account the anionic structure of the peptide and its expected tendency to interact with the positively charged chitosan molecules. In fact, the association efficiency reported until now for acidic peptides and proteins such as insulin (*25*), BSA (*19*), and tetanus toxoid (*26*) has always been higher than 30%. It was additionally surprising that CS−PEG NPs exhibited a higher encapsulation efficiency (248 ng per mg nanoparticle) than CS NPs. Further modification of the nanocarrier with BIO and BIO−SA−OX26 led to minor reductions in the amount of peptide associated (188 ng per mg nanoparticle). The fact that the PEGylation of the polymer leads to an increase in the association of the peptide to the NPs suggests that the ionic interaction between the acidic peptide and the positively charged molecules is not the main force involved in the association process. However, more experiments are needed in order to fully clarify the association mechanism of the peptide to the different nanocarriers.

In Vitro Release of Z-DEVD-FMK from Nanoparticles. Figure 4 shows the release profiles in PBS of Z-DEVD-FMK from the different types of CS NPs. A fast initial release (25−45% in 60 min) suggests that some of the peptide could be located onto the surface of the NPs. Release rate constants of different NP types are given in Table 2. For the CS, CS−PEG, and CS−PEG−BIO NPs, similar release profiles were observed despite different peptide loadings. Interestingly, whereas the burst release of Z-DEVD-FMK from CS−PEG−BIO−SA−OX26 NPs was reduced, likely due to the steric

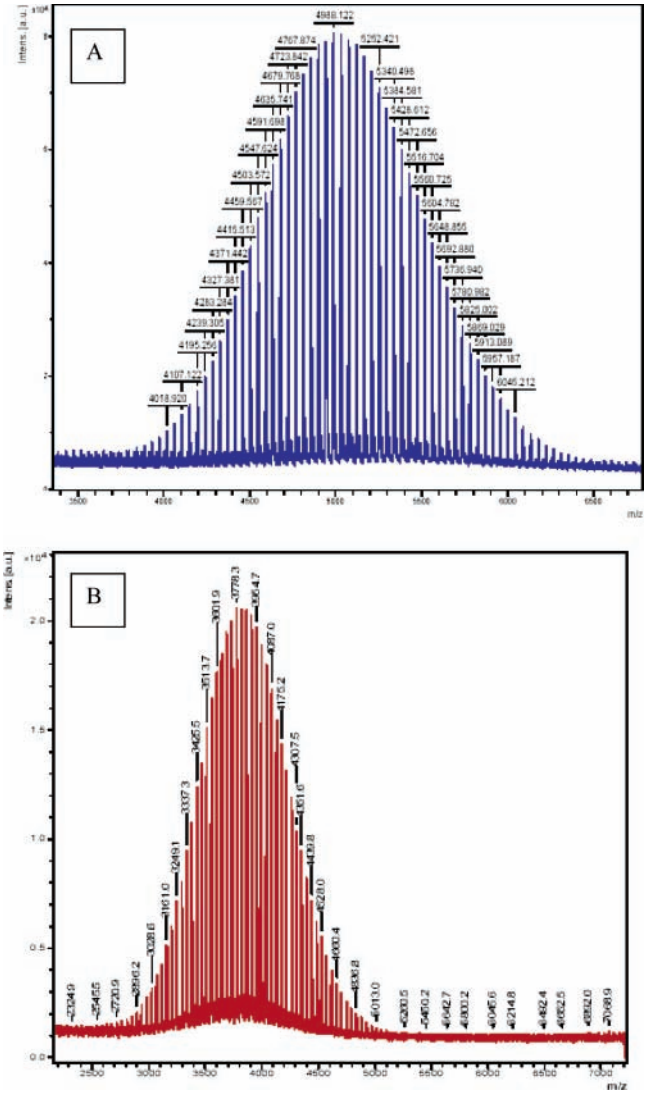

Figure 2. MALDI-TOF mass spectra of (A) PEG−BIO; (B) PEG. The solvent was CH_3Cl for both compounds. The resulting product; PEG−BIO had a combined yield of 76% (M_n = 4009, M_w = 4030).

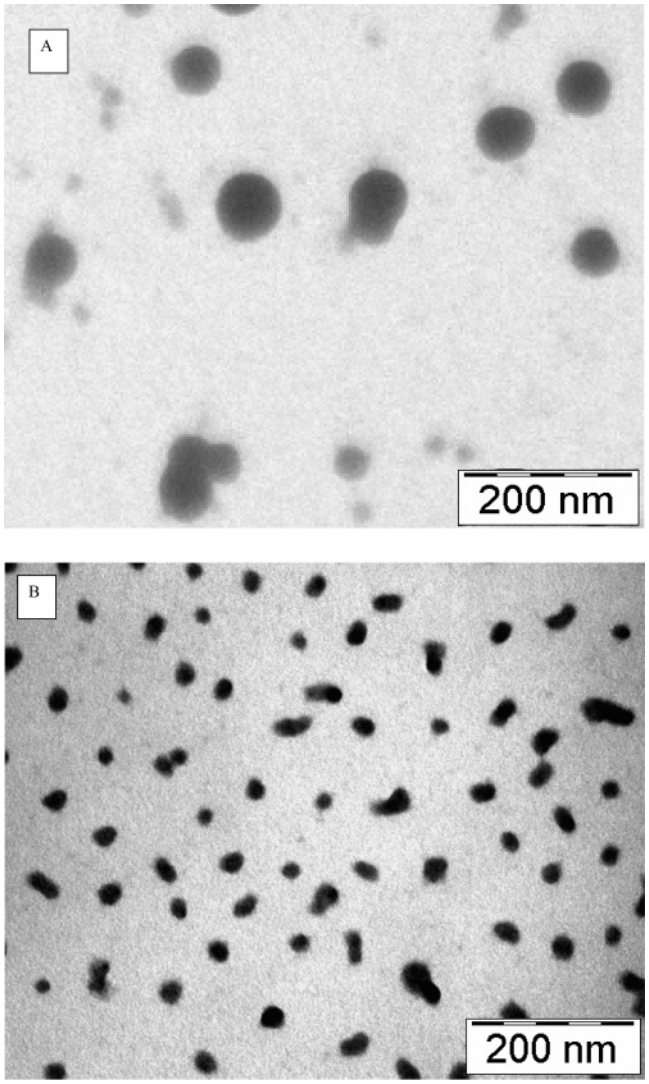

Figure 3. Transmission electron micrographs of photographs of blank (A) CS nanoparticles; (B) PEG−CS nanoparticles.

hindrance induced by the SA/OX26 molecules at the surface of the NPs, CS−PEG−BIO−SA−OX26 NPs exhibited then a much faster second phase release than the other NPs. Thus, surface modification of the CS NPs was observed to have a dramatic impact on the release profile of the peptide. It appears that conjugation of OX26 not only leads to an increase in particle size but also facilitates the faster release of the peptide from the NPs. Although unexpected, this release profile observed with OX26-decorated NPs was very reproducible as confirmed in separate independent experiments. The hypothesis that the OX26 monoclonal antibody may account for a more regular leakage of Z-DEVD-FMK from the nanoparticle will deserve further investigation. Finally, the total amount of the peptide released at the end of 24 h is much higher with CS−PEG−BIO−SA/OX26 NPs (80 ng/mL) than with the others (35−40 ng/mL). This could be an advantage for the intervention to prevent brain ischemia within the very first few hours of brain damage. Additionally, it was calculated that 80 ng of the peptide would be available upon the injection of only 1 mg of the CS−PEG−BIO−SA/OX26 NPs, which is in the range of the therapeutic dose (*27*). In other words, the therapeutic dose of the peptide could be achieved utilizing this technology.

In Vivo Evaluation of the Brain Uptake of CS−PEG−BIO−OX26/SA Nanoparticles. FITC-labeled NPs either OX26-not bearing (Figure 5A) or bearing (Figure 5B) were microscopically detected discretely or as small aggregates in saline solution. The suspensions of OX26-

Table 1. Physicochemical Properties of Different Types of Chitosan NPs

NP type	particle size (nm)	zeta potential (mV)	% AE[a]	% LC[b]	% Z-DEVD-FMK theoretical loading	encapsulated amount (ng)
CS-blank	339.03 ± 5.67	+28.39 ± 0.18	-	-	-	-
CS	383.43 ± 4.60	+20.25 ± 4.60	7.87 ± 0.77	$0.011 \pm 0.014 \times 10^{-3}$	74.4×10^{-3}	112.96
CS−PEG	149.73 ± 1.85	+16.06 ± 3.43	31.13 ± 1.61	$0.025 \pm 0.013 \times 10^{-3}$	83.8×10^{-3}	248.99
CS−PEG-BIO	590.47 ± 2.17	+17.38 ± 4.94	23.52 ± 1.03	$0.019 \pm 0.022 \times 10^{-3}$	83.8×10^{-3}	188.17
CS−PEG-BIO-SA/OX26	636. 69 ± 2.26	+18.23 ± 4.06	23.52 ± 1.03	$0.019 \pm 0.022 \times 10^{-3}$	83.8×10^{-3}	188.17

[a] Association efficiency. [b] Loading capacity.

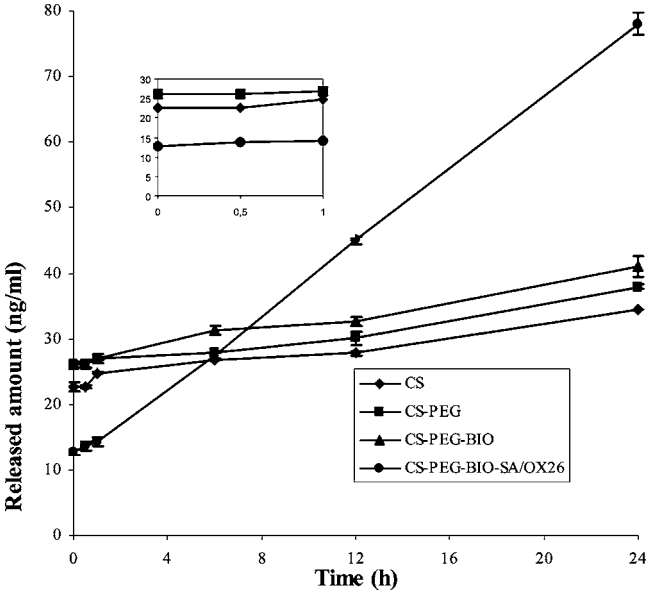

Figure 4. Release profiles of various kinds of chitosan nanoparticles: (◆: CS; ■: CS−PEG; ▲: CS−PEG−BIO; ●: CS−PEG−BIO−SA/OX26) suspended in PBS at 37 °C. Inset demonstrates the release profiles for the same formulations during the 0−1 h time period. The data points of CS−PEG and CS−PEG−BIO are superimposed.

Table 2. Release Rate Constants ± (SD) of Different Types of Chitosan NPs

NP type	release rate constant (ng·mL·h^{-1})
CS−PEG−BIO−SA/OX26	2.7460 ± 0.0213
CS−PEG−BIO	0.6098 ± 0.0118
CS−PEG	0.4755 ± 0.0090
CS	0.4639 ± 0.0103

free NPs were injected intravenously to mice; the mice were then decapitated and the brains were removed. The brains were checked under a fluorescent microscope. As expected, no fluorescent NP was observed in the brain (Figure 5C). When mice were injected OX26-bearing formulation intravenously (iv), the horizontal sections showed the fluorescent particles scattered all over the hemispheres and were identified again as the same fine, spherical particles, sometimes forming aggregates (Figure 5D). When the vascular lumen was identified with oval-shaped endothelial nuclei linings on both sides (Hoechst staining), no particles were observed inside the lumen of the vessels, most of them being located outside of the intravascular space (Figure 5E). When mice were injected intracerebrally to the right frontal cortex, microscopic observations of horizontal sections have shown that the green fluorescent particles were localized close to the injection site and were identified as fine, spherical particles sometimes forming aggregates as they did in the saline solution (Figure 5F). It is important to note that the appearance of OX26-free formulation administered to the mice brain did not differ from the control brain (Figure 5G). The results indicate that the OX26-conjugated NPs could penetrate into the brain whereas the OX26-free NPs could not, since only the FITC-labeled CS−PEG−BIO/SA−OX26 NPs could be observed under the fluorescence microscope whereas FITC-labeled CS−PEG/SA NPs could not.

In the transmission electron microscopic examination of the ultrathin serial sections, CS−PEG−BIO−OX26/SA NPs having a diameter of approximately 200 nm were observed in the lumen of the blood vessels together with erythrocytes (Figure 6A) and also in the brain interstitium (Figure 6B). The NPs seen in the lumen of the blood vessels were located very close to the endothelial layer. Additionally they were forming groups inside the lumen of the vessels. In the ultrastructural examination of the perivascular tissue, an edema was observed around the blood vessels. On the other hand, the NPs which were observed in the brain interstitium were sparsely distributed inside the tissue. However, in the ultrastructural examination of the control specimens, netiher NPs nor ultrastrcutural changes were observed (Figure 6C). On the contrary CS−PEG−BIO nanospheres could not be observed in the brain of the corresponding animals. These

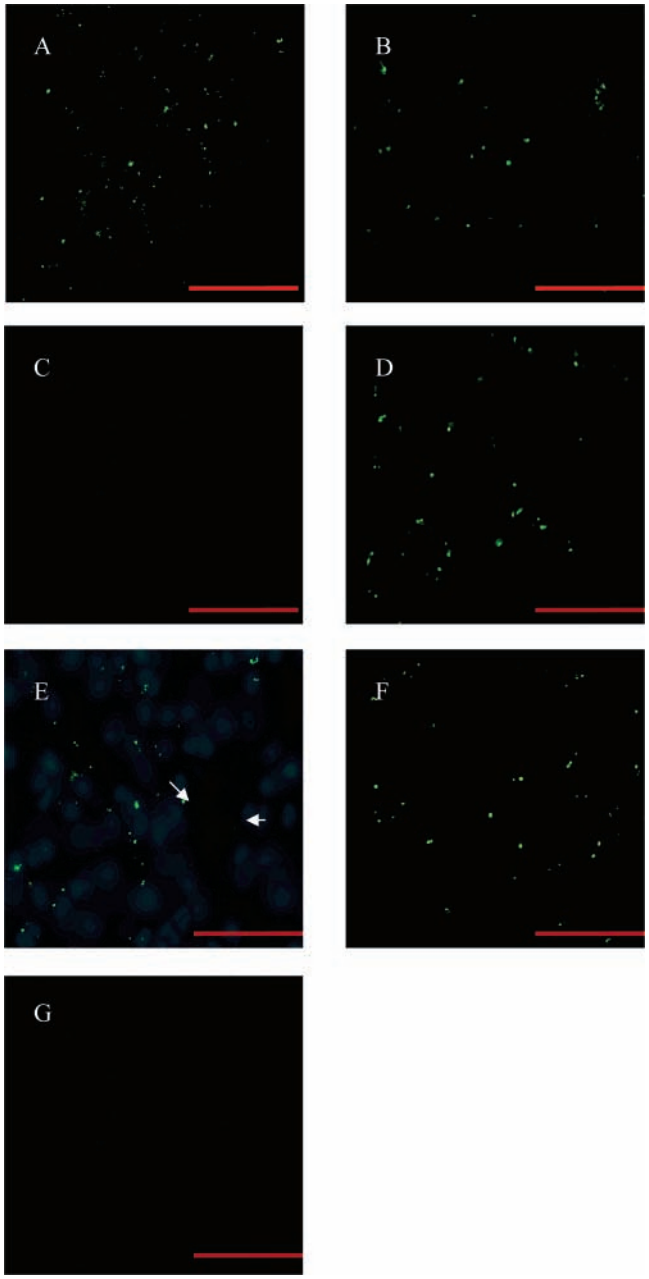

Figure 5. Fluorescence micrographs of CS−PEG−BIO−SA NPs in saline (A); CS−PEG−BIO−SA/OX26 NPs in saline (B); 2 h after intravenous injection of CS−PEG−BIO−SA NPs magnification 40 nm (C); 2 h after intravenous injection of CS−PEG−BIO−SA/OX26 NPs, magnification 40 nm (D); the same microscopic field in D combined with Hoechst 33258 staining, magnification 40 nm (arrows indicate the borders of the vascular compartment) (E); intracerebral injection of CS−PEG−BIO−SA/OX26 NPs (F); mouse brain which did not receive any formulation (G).

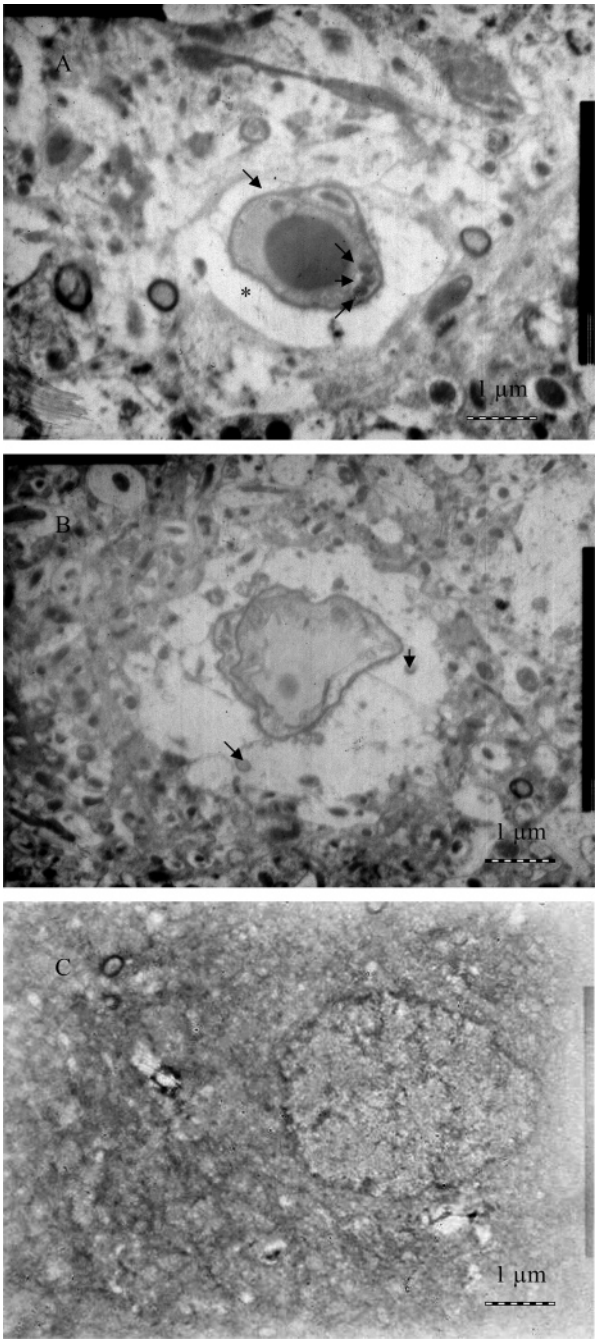

Figure 6. Transmission electron micrographs showing (A): the perivascular edema (*) and nanoparticles (arrows) in the endothelium of a brain vessel (original magnification ×7500); (B) nanoparticles in the brain interstitium (original magnification ×5000); (C) the control specimen showing the blood vessels and the brain interstitum (original magnification ×7500).

results showed that the OX26 adressed NPs have the capability to translocate into the brain tissue.

CONCLUSION

In this study, the design of OX26 functionalized chitosan-PEG NPs has been successfully achieved, using the avidin−biotin system. This novel nanocarrier showed a capacity for the association of the peptide Z-DEVD-FMK. In addition, it was shown that the functionalization of the NPs with the OX26 antibody was critical for facilitating their translocation into the brain tissue after iv administration. Since therapeutic doses of the anti-caspase peptide Z-DEVD-FMK may be transported and released utilizing this technology, experiments are underway in order to investigate the pharmacological activity of Z-DEVD-FMK-loaded NPs on experimental models of brain ischemia.

ACKNOWLEDGMENT

Yeşim Aktaş has been supported by Ambassade de France for her stages in France and Spain.

LITERATURE CITED

(1) Ballabh, P., Braun, A., and Nedergaard, M. (2004) Blood-brain barrier: An overview, structure, regulation and clinical implication. *Neurobiol. Dis. 16*, 1−13.

(2) Begly, D. (1996) The blood-brain-barrier: Principles for targeting peptides and drugs to the central nervous system. *J. Pharm. Pharmacol. 48*, 136−146.

(3) Kreuter, J. (2001) Nanoparticulate systems for brain delivery of drugs. *Adv. Drug Delivery Rev. 23*, 65−81.

(4) Brigger, I., Morizet, J., Aubert, G., Chacun, H., Terrier-Lacombe, M. J., and Couvreur, P. (2002) Poly(ethylene glycol)-coated hexadecylcyanoacrylate nanospheres display a combined effect for brain tumor targeting. *J. Pharmacol. Exp. Ther. 303*, 928−936.

(5) Calvo, P., Gouritin, B., Villaroya, H., Eclancher, F., Giannavola, C., Klein, C., Andreux, J.-P., Couvreur, P. (2002) Quantification and localization of PEGylated polycyanoacrylate nanoparticles in brain and spinal cord during experimental allergic encephalomyelitis in the rat. *Eur. J. Neurosci. 15*, 1317−1326.

(6) Jefferies, W. A., Brandon, M. R., Hunt, S. V., Williams, A. F., Gatter, K. C., and Mason, D. Y. (1984) Transferrin receptor on endothelium of brain capillaries. *Nature 312*, 162−163.

(7) Pardridge, W. M., Buciak, J. L., and Friden, P. M. (1991) Selective transport of an anti-transferrin receptor antibody through the blood-brain barrier in vivo. *J. Pharmacol. Exp. Ther. 1*, 66−70.

(8) Pardridge, W. M., Eisenberg, J., and Yang, J. (1987) Human blood-brain barrier transferrin receptor. *Metabolism. 9*, 892−895.

(9) Qian, Z. M., Li, H., Sun, H., and Ho, K. (2002) Targeted Drug Delivery via the Transferrin Receptor-Mediated Endocytosis Pathway. *Pharmacol. Rev. 4*, 561−587.

(10) Muzzarelli, R. A. A., Jeuniauk, C., and Gooday, G. W. (1986) *Chitin in Nature and Technology*, Plenum, New York.

(11) Berscht, P. C., Nies, B., Liebendorfer, A., and Kreuter, J. (1994) Incorporation of basic fibroblast growth factor into methylpyrrolidinone chitosan fleeces and determination of the in vitro release characteristics. *Biomaterials 15*, 593−600.

(12) Ritger, P. L., and Peppas, N. A. (1987) A simple equation for description of solute release. II. Fickian and anomalous release from swellable devices. *J. Controlled Release 5*, 37−42.

(13) Artursson, P., Lindmark, T., Davis, S. S., and lllum, L. (1994) Effect of chitosan on the permeability of monolayers of intestinal epithelial cells (CACO-2). *Pharm. Res. 11*, 1358−1361.

(14) Tokumitsu, H., Ichikawa, H., and Fukumori, Y. (1999) Chitosan-gadopentetic acid complex nanoparticles for gadolinium neutron capture therapy of cancer: preparation by novel emulsion-droplet coalescence technique and characterization. *Pharm. Res. 16*, 1830−1835.

(15) Cui, Z., and Mumper, R. J. (2001) Chitosan-based nanoparticles for topical genetic immunization. *J. Controlled Release 75*, 409−419.

(16) Conti, B., Giunchedi, P., Genta, I., and Conte, U. (2000) The preparation and in vivo evaluation of the wound-healing properties of chitosan microspheres. *STP Pharma. Sci. 10*, 101−104.

(17) De Campos, A. M., Sanchez, A., and Alonso, M. J. (2001) Chitosan nanoparticles: a new vehicle for the improvement of the delivery of drugs to the ocular surface. Application to cyclosporin A. *Int. J. Pharm. 224*, 159−168.

(18) Calvo, P., Remunan-Lopez, C., Vila-Jato, J. L., and Alonso, M. J. (1997) Novel hydrophilic chitosan-poly(ethylene oxide) nanoparticles as protein carriers. *J. Appl. Pol. Sci. 63*, 125−132.

(19) Calvo, P., Remunan-Lopez, C., Vila-Jato, J. L., and Alonso, M. J. (1997) Chitosan and Chitosan/ethylene oxide-propylene oxide block copolymer nanoparticles as novel carriers for poly-(ethylene oxide) nanoparticles as proteins and vaccines. *Pharm. Res. 14*, 1431−1436.

(20) Chen, J., Nagayama, T., Jin, K., Stetler, R. A., Zhu, R. L., Graham, S. H., and Simon, R. P. (1998) Induction of caspase-3-like protease may mediate delayed neuronal death in the hippocampus after transient cerebral ischemia. *J. Neurosci. 18*, 4914−4928.

(21) Ma, J., Qiu, J., Hirt, L., Dalkara, T., and Moskowitz, M. A. (2001) Synergistic protective effect of caspase inhibitors and bFGF against brain injury induced by transient focal ischemia. *Br. J. Pharmacol. 133*, 345−350.

(22) Aktaş, Y., Andrieux, K., Alonso, M. J., Calvo, P., Gürsoy, R. N., Couvreur, P., and Çapan, Y. (2005) Preparation and in vitro evaluation of Z-DEVD-FMK loaded chitosan nanoparticles. *Int. J. Pharm. 298*, 378−383.

(23) Yoshikawa, T., and Pardridge, W. M. (1992) Biotin delivery to brain with a covalent conjugate of avidin and a monoclonal antibody to the transferrin receptor. *J. Pharmacol. Exp. Ther. 263*, 897−903.

(24) Janes, K. A., Calvo, P., and Alonso, M. J. (2001) Polysaccharide colloidal nanoparticles as delivery systems for macromolecules. *Adv. Drug. Delivery Rev. 47*, 83−97.

(25) Fernandez-Urrusuno, R., Calvo, P., Remunan-Lopez, C., Vila-Jato, J. L., and Alonso, M. J. (1999) Enhancement of nasal absorption of insulin using chitosan nanoparticles. *Pharm. Res. 12*, 1385−1387.

(26) Vila, A., Sánchez, A., Janes, K., Behrens, I., Kissel, T., Vila Jato, J. L., and Alonso, M. J. (2004) Low molecular weight chitosan nanoparticles as new carriers for nasal vaccine delivery in mice. *Eur. J. Pharm. Biopharm. 57*, 123−131.

(27) Pardridge, W. M. (1995) Vector-mediated peptide drug delivery to the brain. *Adv. Drug. Delivery Rev. 15*, 109−146.

BC050217O

Synthesis and Evaluation of Hydrolyzable Hyaluronan-Tethered Bupivacaine Delivery Systems

Diego A. Gianolio,[§] Michael Philbrook,[§] Luis Z. Avila,[§] Hollace MacGregor,[§] Su X. Duan,[§] Richard Bernasconi,[‡] Marina Slavsky,[‡] Sandra Dethlefsen,[§] Peter K. Jarrett,[§] and Robert J. Miller[§,*]

Biomaterials Science & Engineering, and Drug Discovery, Genzyme Corporation, 500 Kendall Street, Cambridge, Massachusetts 02142. Received August 5, 2005; Revised Manuscript Received October 6, 2005

Local anesthetics are useful for reducing acute pain, but their short duration precludes them from use in solely managing postoperative pain. To prolong the duration of local anesthesia, we conjugated bupivacaine to native hyaluronan (HA) and divinyl sulfone cross-linked Hylan A (Hylan B particles) using a hydrolyzable linker incorporating an imide. Bupivacaine was prepared for conjugation to HA by forming the acryl imide derivative. Separately, the carboxyl group of HA was reacted with nipsylethylamine (NEA) using carbodiimide-mediated coupling to provide HA-NEA that was subsequently reduced with tris(2-carboxyethylphosphine) hydrochloride to yield HA carrying a free sulfhydryl (HA-SH). The HA−bupivacaine conjugate was assembled by reacting HA-SH with acrylbupivacaine. Characterization of the conjugates showed 22% degree of modification by 1 mol of carboxyl. In vitro release studies comparing bupivacaine admixed in HA with bupivacaine conjugated to HA showed half-lives of 0.4 ± 0.1 h, and 16.9 ± 0.2 h, respectively, and the bupivacaine was released chemically unaltered as confirmed by LC-MS. In vivo studies to assess the duration of anesthetic activity were performed in a rat sciatic nerve blockade model. For these studies, bupivacaine was conjugated to Hylan B following a similar procedure, and the degree of modification obtained was 14%. Free bupivacaine (3 and 16 mg/kg) and free bupivacaine (3 mg/kg) admixed with Hylan B particles showed nerve block over 4, 9, and 6 h, respectively. Free bupivacaine (3 mg/kg) admixed with bupivacaine (13 mg/kg) conjugated to Hylan B particles showed a four to 5-fold longer impairment of motor function over the free bupivacaine formulations with a total block time of 19 h. Bupivacaine conjugated to Hylan B particles has the potential to prolong the duration of local anesthesia.

INTRODUCTION

Minimizing postoperative surgical recovery periods has become one of the major goals of hospitals to contain and reduce health care costs (*1*−*3*). Optimized local and regional anesthesia regimens improve postoperative rehabilitation by modulating the postoperative stress response thereby improving pulmonary and gastrointestinal function and facilitating postoperative rehabilitation. In treatments such as total knee arthroplasty, accelerating the postoperative convalescence time has been shown to benefit the functional operation outcome while minimizing postoperative complications (*4*). Given the increasing number of older patients with higher comorbidity, this is of particular therapeutic importance as well as considerable economic implications (*5*).

Continuous techniques of regional anesthesia such as indwelling catheters, continuous infusions and repeated, fractional dosing are used to provide several days of effective postoperative analgesia. While these drug delivery approaches have proven their utility at accelerating postoperative recovery and preventing postoperative adverse outcomes, they are often cumbersome, prone to complications, time-consuming, and costly. For example, epidural catheters require the need for subcutaneous tunneling and fixation of the catheter, bacterial filters, frequent changes of tubing, catheter site protection and monitoring to prevent infection, and training for caretakers (*6*). External drug delivery devices and fractional dosing regimens are further challenged by the pharmacokinetic profiles of analgesics, as most widely used anesthetic agents are hydrophilic, small molecules that are rapidly distributed and eliminated from the administration site. For example, local infiltration of bupivacaine shows rapid distribution and elimination with peak systemic levels occurring in 30 to 40 min, followed by a decline to insignificant levels during the next 3 to 6 h (*7*). Therefore, there exists a clinical need for a long-acting local anesthetic that can be simply administered to the patient prior to discharge and can provide 1 to 3 days of local pain management (*8*).

In recent years, several studies investigated approaches to prolong the duration of local anesthetics. Lipids and liposomes (*9*−*11*), microspheres (*12*−*14*), polymeric implants (*15*, *16*), sodium channel toxins (*17*, *18*), butamben formulations (*19*), and new molecules that target sodium channel subtypes (*20*) are all examples of formulations that have shown modest extension of anesthetic duration. Of these, the most promising demonstration of long-term motor blockade was achieved using microspheres combining bupivacaine and an antiinflammatory steroid that showed nerve blockade lasting 2 to 7 days, depending on the species, dosing, and site of administration (*21*).

Hyaluronan (HA) is a naturally occurring linear polysaccharide of alternating β-1,3-D-glucuronic acid and β-1,4-*N*-acetyl-D-glucosamine units found in the extracellular matrix and synovial fluid (*22*). HA is hydrophilic and

* Corresponding author. Tel: + 617-252-7524. Fax: + 617-591-5509. E-mail: Bob.Miller@genzyme.com.
[§] Biomaterials Science & Engineering.
[‡] Drug Discovery.

10.1021/bc050239a CCC: $30.25 © 2005 American Chemical Society
Published on Web 11/01/2005

forms gels of varying viscosity depending on its molecular weight and concentration. HA that is free of contaminating proteins and nucleotide is nonimmunogenic and therefore an ideal candidate for surgical applications that involve sensitive areas, including nerves and muscles. In addition, HA can be modified using a variety of cross-linkers generating novel copolymeric materials and can be used also for tissue engineering (*23*). As an example, cross-linkers may contain disulfide bonds that can be reduced by dithiothreitol to yield thiol-modified HA that in turn can be reacted with poly(ethylene glycol) diacrylate and other thiol-modified polymers to generate copolymers capable of controlled release of basic fibroblast growth factor (*24*, *25*).

Particular interest has been devoted to HA as a potential delivery vehicle for bupivacaine. Prolongation of bupivacaine's effect by viscous HA formulations was observed in rabbits with the duration of action and pharmacological effects being dependent directly on viscosity (*26*). During these studies it was stated that the influences of ionic interactions between bupivacaine free base and HA were difficult to assess since viscosity masked the electrostatic feature. HA derivatives (i.e., cross-linked) were also used to prolong the duration of action of bupivacaine. In a recent study an in situ cross-linked HA derivative was tested in rats as a vehicle for bupivacaine. Although cross-linked HA appeared to be a safe and effective means for delivery, the curing process used in this method imposed a need for a rapid injection technique to avoid needle blockage during administration (*27*).

The aim of this study is to investigate the release rate and efficacy of bupivacaine tethered via a reversible covalent bond to HA. We hypothesized that a reversible covalent bond may be more effective in maintaining the drug in the carrier for a longer period of time. We used a cross-linked form of HA that did not require an in situ curing process. It is known that HA cross-linked with divinyl sulfone (DVS) to form the derivative, Hylan B, shows longer residence time at the injection site compared to un-cross-linked HA (*28*). Thus, bupivacaine was conjugated via a linker containing a hydrolytically labile bond (i.e. imide) to HA. Moreover, a sulfide bond was included in the proximity of the imide to favor the hydrolysis rate in a fashion similar to the one observed when conjugating the drug paclitaxel to poly(ethylene glycol) (*29*).

This report describes a method to prepare the tethered bupivacaine to HA and Hylan B particles. This HA–bupivacaine conjugate had a significantly slower release rate compared to free bupivacaine in an infinite sink in vitro release system. The HA–bupivacaine conjugate was compared against free bupivacaine, and bupivacaine–hylan B particles admixture formulations in a rat model using the sciatic nerve blockade of motor function.

EXPERIMENTAL PROCEDURES

Materials and Methods. Low molecular weight HA (130 kDa) was prepared by gamma-irradiation of bacterially fermented HA (*30*). HA cross-linked with DVS (Hylan B particles) was prepared following a method in the literature (*31*). Anhydrous solvents and starting materials were purchased from Sigma-Aldrich Co. and used without further purification. ^{1}H and ^{13}C NMR spectra were obtained on a Varian spectrometer (400 MHz) against tetramethylsilane (δ = 0.0 ppm). Mass spectra and high-resolution mass spectra (HRMS) were obtained on a Applied Biosystems Qstar XL spectrometer with Turbolonspray source. Thin-layer chromatography (TLC) was performed on Silica Gel 60 F_{254} precoated on aluminum sheets (EM Separation Technology) using CH_3OH:CH_2Cl_2 (1:19). Dialyses were performed using either membrane tubing (7 kDa MWCO, Spectrum) or tangential flow cassette (10 kDa MWCO, Pierce). Phosphate-buffered saline (PBS) contained 137 mM NaCl, 2.7 mM KCl, 10 mM phosphate buffer, pH = 7.3–7.5, and was purchased as a 10-fold concentrate (EMD Chemicals, Inc.) and diluted to a working concentration with deionized water. UV/visible measurements were obtained using a Varian Cary 50 Probe spectrometer. The molecular weight and degree of modification of HA conjugates were determined using size exclusion chromatography and multiangle laser light scattering (SEC-MALLS) analyzer (model DAWN-EOS, Wyatt Technology). A SEC-MALLS analyzer was connected to refractive index and UV/visible (model UVIS-205, Perkin-Elmer) detectors. Separation was performed using a size exclusion column (300 Å, 7.5 × 300 mm, Macrosphere, Alltech), and the mobile phase was a 0.05 M Na_2SO_4 solution. HA degree of modification was defined as the molar percentage of conjugated repeating dimeric units in HA. The quantitation of bupivacaine rate of release in vitro was determined by high performance liquid chromatography using a C18 reverse-phase column (100 Å, 4.6 × 150 mm, Waters Symmetry) and mobile phase consisting of 55% 10 mM Na_2HPO_4 in 0.1% H_2PO_4 and 45% acetonitrile (pH 2.9–3.0). The purity of bupivacaine released in vitro was determined by high performance liquid chromatography (HPLC model Waters 2690) connected to a UV/visible detector (model Waters 2487) reading at 210 nm and a mass spectrometer (model Waters ZQ-2000) with positive ion electrospray interface. The column used for the separation was a C8 reverse-phase (100 Å, 4.6 × 250 mm, Ace 5, Mac-Mod Analytical). The separation was performed at a column temperature of 25 °C ± 2 °C. Mobile Phase A = 0.1% HCOOH + 0.01% trifluoroacetic acid (TFA) in water. B = 0.1% HCOOH + 0.01% TFA 60% CH_3CN 20% CH_3OH 20% H_2O. Flow rate: 1 mL/min split to 0.2 mL/min after the UV/visible detector into the mass spectrometer. A linear gradient was used: 5–100% B over 10 min, followed by 100% B for 5 min.

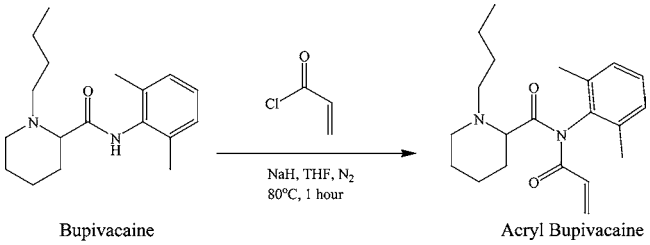

Figure 1. Synthesis of acrylbupivacaine.

Synthesis of Acryl Bupivacaine (Figure 1). Bupivacaine (**1**, 500 mg, 1.74 mmol) was placed in a 100-mL round-bottom flask and dried by azeotropic removal of water with toluene under reduced pressure. Anhydrous THF (5 mL) was added under a nitrogen atmosphere. A suspension of 60% NaH in mineral oil (140 mg, 3.48 mmol) was added, gradually allowing for venting. The resulting mixture was allowed to stir for 30 min at room temperature. Acryloyl chloride (157 μL, 1.92 mmol) was subsequently added. The reaction flask was equipped with a condenser and placed in an oil bath, and the reaction mixture was allowed to stir under reflux for 1 h under nitrogen. After completion of the reaction, as monitored by TLC, the mixture was allowed to cool to

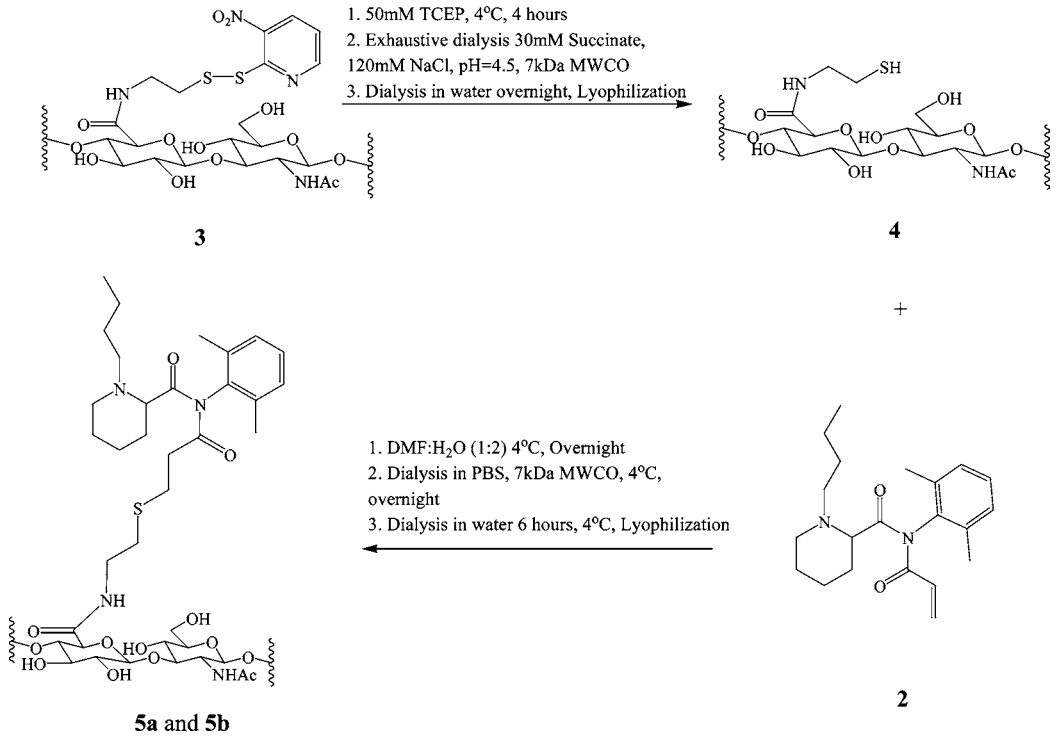

Figure 2. Synthesis of HA conjugates. **5a** HA−bupivacaine 130 kDa MW, 22% degree of modification. **5b** Hylan B−bupivacaine particles, 14% degree of modification.

room temperature and the reaction quenched by addition of MeOH (1 mL). The solvents were removed under reduced pressure, and the crude product was dissolved in dichloromethane (50 mL), transferred into a separatory funnel and washed with water (100 mL). The organic phase was collected, dried with Na_2SO_4, and concentrated under reduced pressure. An aliquot was further purified by chromatography over silica using 5% MeOH in dichloromethane. The product acryl bupivacaine (**2**, 162 mg) was obtained as a white solid after removal of solvent under reduced pressure. R_f (methanol/dichloromethane, 1/19): 0.43. ^{1}H NMR (DMSO-d_6): δ = 0.83 (t, 3Hs, J = 7.6 Hz, CH_3 alkyl), 1.2−1.3 (m, 3Hs, CH_2), 1.4−1.5 (m, 5Hs, CH_2), 1.7−1.8 (m, 2Hs, CH_2), 1.9 (s, 3Hs, CH_3 aromatic), 2.0 (s, 3Hs, CH_3 aromatic), 2.3−2.4 (m, 2Hs, CH_2), 5.7 (d, 1H, J = 10.0 Hz, acryl), 5.8 (dd, 1H, J = 10.0, 16.0 Hz, acryl), 6.3 (d, 1H, J = 16.0 Hz, acryl), 7.1−7.3 (m, 3Hs, aromatic) ppm; ^{13}C NMR (DMSO-d_6): δ = 14.3, 14.5, 18.0, 18.6, 20.6, 21.6, 25.6, 28.7, 29.5, 49.5, 55.4, 63.2, 129.0, 129.5, 132.2, 136.4, 136.5, 136.9, 137.2, 167.2, 167.3 ppm HRMS calculated for $C_{21}H_{31}N_2O_2$ (M + H^+): 343.2386; found: 343.2386.

Synthesis of HA-NEA. 3-Nitro-2-pyridinesulfenylethylamine (NEA) was prepared according to a published procedure (*32*, *33*). To a solution of HA (1.5 g, 3.74 mmol, 130 kDa MW) in water (375 mL) was added 1-hydroxybenzotriazole (1.0 g, 7.48 mmol) followed by NEA (1.5 g, 5.61 mmol). The pH of the reaction mixture was adjusted to 4.5 using 2 N HCl. Subsequently, 1-ethyl-3-(3-dimethylaminopropyl)carbodiimide hydrochloride (2.15 g, 11.22 mmol) was added, and the reaction was allowed to stir at room temperature for 2 h. The resulting HA carrying NEA (**3**) was purified by exhaustive dialysis using a 7 kDa MWCO membrane against PBS, followed by dialysis against water overnight. HA-NEA was recovered by lyophilization as yellow foam (95% yield). Molecular weight and degree of modification of carboxy-modified HA-NEA were determined by SEC-MALLS analysis with detection at 350 nm.

Synthesis of HA-SH (Figure 2). Compound **3** (1.0 g, 2.5 mmol, 130 kDa MW, and 22% degree of modification) was treated with a 50 mM tris(2-carboxyethylphosphine) hydrochloride (TCEP) solution (250 mL) at 4 °C for 4 h. The resulting HA carrying free sulfhydryl (**4**) was purified by exhaustive dialysis using a 7 kDa MWCO membrane against 30 mM succinate buffer containing 120 mM NaCl (pH = 4.5) followed by dialysis against water overnight. HA-SH was recovered by lyophilization as off-white foam (90% yield). Free sulfhydryl group was quantitated colorimetrically using Ellman's reagent (*34*, *35*).

Synthesis of HA−Bupivacaine (Figure 2). A solution of compound **4** (50 mg, 0.130 mmol of HA, 0.032 mmol of free SH) in water (10 mL) was pH adjusted to 8.0 using triethanolamine and the solution cooled using an ice−water bath. A solution of compound **2** (14 mg, 0.038 mmol) in dimethylformamide (DMF, 130 μL) was added to the solution of **4**. Additional DMF (5 mL) was added to maximize the solubility of both compounds **2** and **4**. The solution was stirred at 4 °C overnight. The consumption of the free sulfhydryl groups was monitored colorimetrically (Ellman's reagent). At the end of the reaction, the mixture was transferred into a 7 kDa MWCO membrane and dialyzed at 4 °C against PBS overnight, followed by dialysis against water for 6 h. The retentate was lyophilized to give a white solid product (40 mg, 80% yield). The results of the SEC-MALLS and UV/visible spectroscopy were consistent with the HA−bupivacaine conjugate, **5a**.

Synthesis of Hylan B−Bupivacaine (Figure 2). Bupivacaine was conjugated to Hylan B following a similar procedure to the one described above for compound **5a**. The synthesis was performed starting from sterile Hylan B particles and operating under aseptic conditions. Hylan B particles (378 mL, 5.3 mg/mL in 0.9% NaCl solution) were functionalized with NEA and reduced to the free sulfhydryl form. Degree of modification was 14% as determined colorimetrically using Ellman's reagent (*34*, *35*). Hylan B particles carrying free sulfhy-

Table 1. Scoring Method for the Rat Sciatic Nerve Blockade Study

score	observations
2	completely blocked rats dragged their leg and failed to grasp the bars upon elevation of the hindquarters
1	partially blocked rats walked gathering the forepart of the foot, keeping it sideways, and had limited ability to grasp the bars
0	normal rats were able to walk and grasp normally

dryl group were reacted with **2**. The Hylan B−bupivacaine conjugate particles (**5b**) were transferred into a 7 kDa MWCO membrane and dialyzed at 4 °C against PBS overnight, followed by dialysis against water for 6 h. The retentate was lyophilized to give a white solid product (1.9 g, 94% yield). Degree of modification was 14% as determined by UV/visible spectroscopy with detection at 260 nm, using bupivacaine as a standard.

Release Rate of Bupivacaine In Vitro. The release rate of bupivacaine in vitro (infinite sink) from the compound **5a** was compared to an admixture of free bupivacaine in a HA solution. To prepare the test sample, compound **5a** was dissolved at 5% w/w in distilled water. The admixed control sample was prepared by dissolving one part bupivacaine hydrochloride in 99 parts of a 5% aqueous solution of HA (MW 130 kDa). Aliquots (approximately 1 to 1.5 g) of each solution were weighed in triplicate into tangential flow cassettes (10 kDa MWCO, Pierce). The cassettes were then placed individually in 0.1 M PBS (250 mL) at 37 °C with stirring. The composition of the receptor phase over time was analyzed by HPLC.

In Vivo Studies, Sciatic Blockade Technique, and Evaluation. Female Sprague Dawley rats weighing 250 to 300 g were acclimated with free access to food and water for a minimum of 5 days prior to the procedure. Three days prior to each experiment, rats were acclimated to stainless steel cages with mesh flooring. Anesthesia was induced with 2−3% isoflurane in 100% oxygen in a sealed chamber. The skin of the dorsal thigh was shaved, and 200 μL of either a control solution or test formulation was injected into the perineural space of the sciatic nerve. Animals were allowed to recover and were returned to their cages. Immediately following recovery, all animals were observed for the onset of motor block. Motor block was defined as loss of local motor function, exhibited by foot dragging, curling of toes, weight bearing on the lateral margin of the foot, and inability to grab the bars of the cage. The extent of nerve blockade was assessed by monitoring the rats over time using a three-point scoring system (Table 1).

The approximate time to onset was recorded. Animals were evaluated every hour until motor block was observed. If no evidence of motor block was observed for more than three consecutive hours, animals were considered unaffected. The experimenter was blinded as to which formulation was injected.

Histology. One week after injection, the animals were sacrificed and the sciatic nerves and surrounding tissues were removed, fixed in formalin, and processed for histology by hematoxylin and eosin staining. Slides containing the tissue sections were examined by a board certified pathologist and blinded to the treatment, and microscopic findings were graded according to the intensity and extent of change.

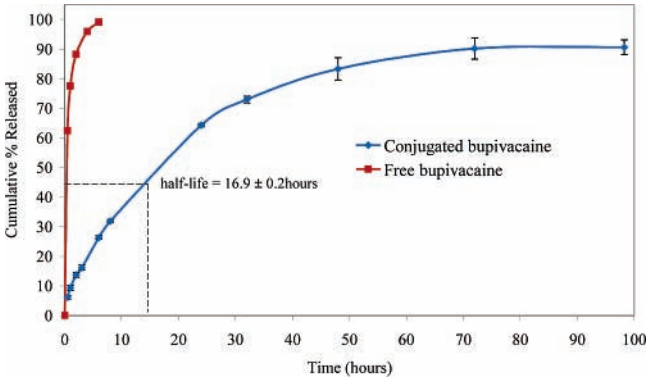

Figure 3. Release profiles of free and conjugated bupivacaine (**5a**) into receptor phase.

RESULTS AND DISCUSSION

Bupivacaine lacks reactive sites (e.g. primary amine, hydroxyl group) for mild chemical modification; however, it possesses an amide bond that could potentially be a site for acylation after deprotonation to give an imide conjugate. The hydrolysis of the imide bond in the resulting HA−bupivacaine conjugate (**5a**) may either regenerate authentic bupivacaine or produce an undesirable side-product depending on which of the two imide bonds undergoes hydrolytic cleavage. With this possibility in mind, we designed the synthesis of the linker to include a sulfide group in proximity to one of the imide functional groups to favor the hydrolysis toward the regeneration of bupivacaine (*29*). Using this approach described in Figures 1 and 2, bupivacaine was conjugated to HA (**5a**) with a 22% degree of modification and an overall yield of 80%. To avoid premature hydrolysis and consequent loss of bupivacaine from the conjugate, PBS and water used for dialysis were chilled to 4 °C before use and maintained in the cold room (4 ± 2 °C) during workup.

The in vitro release rate of bupivacaine from compound **5a** was compared to a physical admixture of bupivacaine in HA (MW 130 kDa). Figure 3 shows the release profiles obtained from this experiment. Bupivacaine hydrochloride admixed to HA quickly eluted into the receptor phase, with half of the drug eluting within 1 h and 100% of the drug eluting within 6 h. In contrast, the HA−bupivacaine conjugate (**5a**) showed more prolonged delivery with half the drug eluting within 17 h and 100% of the drug eluting within 2−3 days. The release profile follows approximately first-order kinetics consistent with the expected pseudo-first-order hydrolysis reaction.

LC-MS analysis of the hydrolysis solution from compound **5a** showed that 95% of the molecules in the receptor phase were authentic bupivacaine (Figure 4). The remaining peaks present in the chromatogram were attributed to impurities generated during the preparation of the conjugate and were also observed in the control samples without bupivacaine.

This result agrees with our initial design hypothesis that the thioether moiety on the methylene β to the acyl group would render this imide bond more susceptible to hydrolysis relative to the other imide bond (Figure 5). The preferential acceleration of the hydrolysis of this bond is due perhaps to a combination of favorable factors. One possible factor is the stabilization of the tetrahedral intermediate by the overlap of low lying empty d orbitals of the sulfur atom with the nonbonded electrons on one of the two oxygen atoms. Another contributing factor that may influence the carbonyl cleavage site is the steric hindrance of the substituents around the two tetrahedral transition states. In particular, inspection of the putative

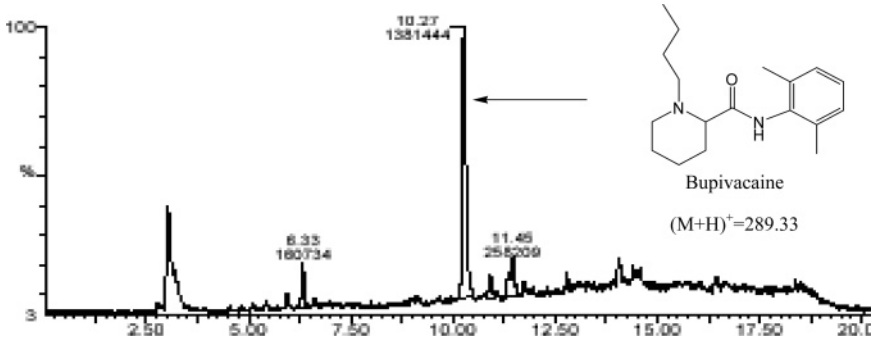

Figure 4. LC-MS analysis of the hydrolysis solution in the receptor phase.

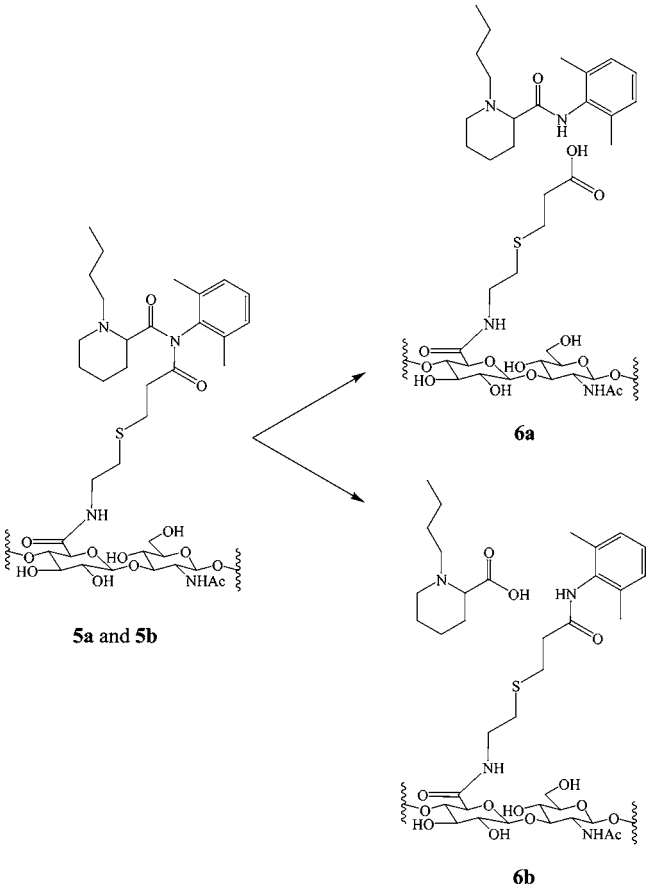

Figure 5. **6a**, major product of hydrolysis observed. **6b**, side product.

tetrahedral intermediate for the hydrolysis of the two carbonyls shows that the tetrahedral intermediate that gives free bupivacaine is less sterically hindered and therefore more stable. This greater stability would lead to a higher equilibrium concentration and in turn faster subsequent hydrolysis rate. These explanations work synergistically to favor the desired hydrolysis.

Unmodified HA has a short residence time at most placement sites in the body due to its rapid uptake and degradation by cells (*36*). To create an HA-based drug carrier that can persist for several days at the placement site we used the insoluble divinyl sulfone (DVS) cross-linked HA. This HA derivative is used in several approved HA products and has a well-established safety profile (*37*, *38*). Thus we conjugated bupivacaine to DVS cross-linked HA, Hylan B particles (*31*), using the same synthetic approach described for the soluble HA conjugate described above to give the bupivacaine conjugate (**5b**) with a 14% degree of modification and an overall yield of 94%.

Table 2. Amounts of Free Bupivacaine and Bupivacaine from the Conjugate 5b Injected in Each Rat

	free bupivacaine (mg/kg)	conjugated bupivacaine[a] (mg/kg)	N^b
saline	3	0	5
Hylan B particles admixture	3	0	10
Hylan B conjugate particles	3	13	9
saline	16	0	9

[a] Hylan B−bupivacaine particles (**5b**) 14% degree of modification. [b] N = number of animals for each group.

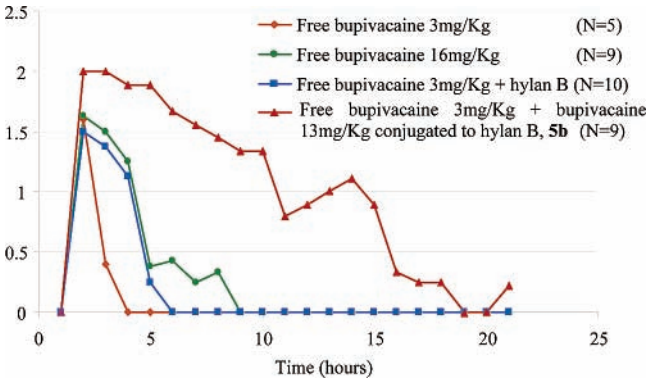

Figure 6. Nerve blockade scores as a function of time. Scoring methods shown in Table 1. N = number of animals for each group. Values are means.

In vivo studies were conducted using an adaptation of the rat sciatic nerve model (*39*). The duration of efficacy of bupivacaine conjugate (**5b**) relative to bupivacaine free in solution was assessed in vivo by injecting the conjugate in the proximity of the rat sciatic nerve and by observing the loss and recovery of motor function over time. Control rats were injected with either a 0.5% solution of bupivacaine in saline or an admixture of bupivacaine and Hylan B particles. Table 2 summarizes the amounts of free and conjugated bupivacaine injected per kilogram of animal for each of the controls and test samples.

Rats injected with bupivacaine next to the sciatic nerve generally lost their ability to ambulate as a consequence of the nerve blockage. They dragged the injected leg, gathered the forepart of the foot, and lost their grasping ability.

The onset time for each rat generally showed nerve blockage within the first 15 min. Figure 6 shows that the duration of motor loss for the bupivacaine control or bupivacaine admixed with Hylan B particles was about 5 h for either sample. This observation is consistent with published findings with similar formulations in the same rat model (*40*). This result shows that the presence of an insoluble HA gel did not significantly affect the loss of motor function in this model.

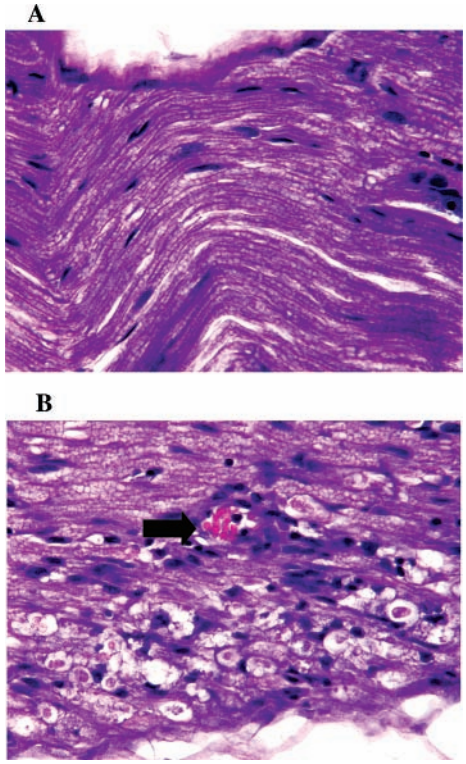

Figure 7. (A) Representative histology of a **5b** treated animal and (B) tissue taken from one of the nine treated animals showing extensive regions of vacuolation indicative of dilated axon sheaths. Axon/myelin debris from degenerating axons within the dilated spaces are indicated by the arrow.

Rats injected with a combination of 13 mg/kg of conjugated bupivacaine and 3 mg/kg of free bupivacaine showed a 4- to 5-fold longer impairment of motor function compared to those animals injected with free bupivacaine and free bupivacaine in Hylan B particles.

Histological evaluation of each of the injection sites revealed minimal to mild epineurial inflammation with fibroplasia in each of the treatment groups (Figure 7A). The incidence and severity appeared to be somewhat increased in the Hylan B−bupivacaine conjugate particle-treated nerves relative to their respective untreated controls. Axonal degeneration characterized by locally extensive regions of dilated axon sheets filled with axon/myelin debris and associated with inflammatory cell infiltrates and Schwann cell hypertrophy was observed in one of the nine animals (Figure 7B).

CONCLUSION

Tethering bupivacaine to HA sustained release in vitro and extended the duration of effect in a sciatic nerve blockage model in vivo. Although nerve blockage was significantly extended by conjugation, there was asymptomatic moderate nerve degeneration in one of the nine animals injected with compound **5b**. The extension of motor block with compound **5b** is very encouraging, although the axonal degeneration observed in one of the nine animals suggests further evaluation before it is used perineurally. This may not be a concern for local anesthesia at the incision line following surgery. Some degree of inflammation and myotoxicity was also reported for other controlled-release formulations for similar applications (*12*, *27*). This study identifies an additional utility of HA as a drug carrier and deserves further investigation.

LITERATURE CITED

(1) Michaloliakou, C., Chung, F., and Sharma, S. (1996) Preoperative multimodal analgesia facilitates recovery after ambulatory laparoscopic cholecystectomy. *Anesth. Analg. 82*, 44−51.
(2) Kehlet, H., and Mogensen, T. (1999) Hospital stay of 2 days after open sigmoidectomy with a multimodal rehabilitation programme. *Br. J. Surg. 86*, 227−30.
(3) Collier, P. E. (1995) Are one-day admissions for carotid endarterectomy feasible? *Am. J. Surg. 170*, 140−3.
(4) Capdevila, X., Barthelet, Y., Biboulet, P., Ryckwaert, Y., Rubenovitch, J., and d'Athis, F. (1999) Effects of perioperative analgesic technique on the surgical outcome and duration of rehabilitation after major knee surgery. *Anesthesiology 91*, 8−15.
(5) Rasche, S., and Koch, T. (2004) Regional anaesthesia versus general anaesthesia−pathophysiology and clinical implications. *Anaesthesiol. Reanim. 29*, 30−8.
(6) Mercadante, S. (1999) Neuraxial techniques for cancer pain: an opinion about unresolved therapeutic dilemmas. *Reg. Anesth. Pain. Med. 24*, 74−83.
(7) *Physicians' Desk Reference* (2004) Thomson: Montvale, NJ.
(8) Grant, S. A. (2002) The Holy Grail: Long-acting local anaesthetics and liposomes. *Clin. Anaesthesiol. 16*, 345−52.
(9) Dollo, G., Le Corre, P., Chevanne, F., and Le Verge, R. (2004) Bupivacaine containing dry emulsion can prolong epidural anesthetic effects in rabbits. *Eur. J. Pharm. Sci. 22*, 63−70.
(10) Mowat, J. J., Mok, M. J., MacLeod, B. A., and Madden, T. D. (1996) Liposomal bupivacaine. Extended duration nerve blockade using large unilamellar vesicles that exhibit a proton gradient. *Anesthesiology 85*, 635−43.
(11) Malinovsky, J. M., Le Corre, P., Meunier, J. F., Chevanne, F., Pinaud, M., Leverge, R., and Legros, F. (1999) A dose−response study of epidural liposomal bupivacaine in rabbits. *J. Controlled Release 60*, 111−9.
(12) Kohane, D. S., Smith, S. E., Louis, D. N., Colombo, G., Ghoroghchian, P., Hunfeld, N. G., Berde, C. B., and Langer, R. (2003) Prolonged duration local anesthesia from tetrodotoxin-enhanced local anesthetic microspheres. *Pain 104*, 415−21.
(13) Montanari, L., Cilurzo, F., Selmin, F., Conti, B., Genta, I., Poletti, G., Orsini, F., and Valvo, L. (2003) Poly(lactide-*co*-glycolide) microspheres containing bupivacaine: comparison between gamma and beta irradiation effects. *J. Controlled Release 90*, 281−90.
(14) Drager, C., Benziger, D., Gao, F., and Berde, C. B. (1998) Prolonged intercostal nerve blockade in sheep using controlled-release of bupivacaine and dexamethasone from polymer microspheres. *Anesthesiology 89*, 969−79.
(15) Hasirci, V., Bonney, I., Goudas, L. C., Shuster, L., Carr, D. B., and Wise, D. L. (2003) Antihyperalgesic effect of simultaneously released hydromorphone and bupivacaine from polymer fibers in the rat chronic constriction injury model. *Life Sci. 73*, 3323−37.
(16) Park, E. S., Maniar, M., and Shah, J. C. (1998) Biodegradable polyanhydride devices of cefazolin sodium, bupivacaine, and taxol for local drug delivery: preparation, and kinetics and mechanism of in vitro release. *J. Controlled Release 52*, 179−89.
(17) Kohane, D. S., Yieh, J., Lu, N. T., Langer, R., Strichartz, G. R., and Berde, C. B. (1998) A reexamination of tetrodotoxin for prolonged duration local anesthesia. *Anesthesiology 89*, 119−31.
(18) Kohane, D. S., Lu, N. T., Gokgol-Kline, A. C., Shubina, M., Kuang, Y., Hall, S., Strichartz, G. R., and Berde, C. B. (2000) The local anesthetic properties and toxicity of saxitonin homologues for rat sciatic nerve block in vivo. *Reg. Anesth. Pain Med. 25*, 52−9.
(19) Shulman, M., Harris, J. E., Lubenow, T. R., Nath, H. A., and Ivankovich, A. D. (2000) Comparison of epidural butamben to celiac plexus neurolytic block for the treatment of the pain of pancreatic cancer. *Clin. J. Pain 16*, 304−9.
(20) Porreca, F., Lai, J., Bian, D., Wegert, S., Ossipov, M. H., Eglen, R. M., Kassotakis, L., Novakovic, S., Rabert, D. K., Sangameswaran, L., and Hunter, J. C. (1999) A comparison

of the potential role of the tetrodotoxin-insensitive sodium channels, PN3/SNS and NaN/SNS2, in rat models of chronic pain. *Proc. Natl. Acad. Sci. U.S.A. 96*, 7640−4.
(21) Castillo, J., Curley, J., Hotz, J., Uezono, M., Tigner, J., Chasin, M., Wilder, R., Langer, R., and Berde, C. (1996) Glucocorticoids prolong rat sciatic nerve blockade in vivo from bupivacaine microspheres. *Anesthesiology 85*, 1157−66.
(22) Patti, A. M., Gabriele, A., Vulcano, A., Ramieri, M. T., and Della Rocca, C. (2001) Effect of hyaluronic acid on human chondrocyte cell lines from articular cartilage. *Tissue Cell 33*, 294−300.
(23) Prestwich, G. D., Marecak, D. M., Marecek, J. F., Vercruysse, K. P., and Ziebell, M. R. (1998) Controlled chemical modification of hyaluronic acid: synthesis, applications, and biodegradation of hydrazide derivatives. *J. Controlled Release 53*, 93−103.
(24) Cai, S., Liu, Y., Zheng Shu, X., and Prestwich, G. D. (2005) Injectable glycosaminoglycan hydrogels for controlled release of human basic fibroblast growth factor. *Biomaterials 26*, 6054−67.
(25) Shu, X. Z., Liu, Y., Luo, Y., Roberts, M. C., and Prestwich, G. D. (2002) Disulfide cross-linked hyaluronan hydrogels. *Biomacromolecules 3*, 1304−11.
(26) Dollo, G., Malinovsky, J. M., Peron, A., Chevanne, F., Pinaud, M., Le Verge, R., and Le Corre, P. (2004) Prolongation of epidural bupivacaine effects with hyaluronic acid in rabbits. *Int. J. Pharm. 272*, 109−19.
(27) Jia, X., Colombo, G., Padera, R., Langer, R., and Kohane, D. S. (2004) Prolongation of sciatic nerve blockade by in situ cross-linked hyaluronic acid. *Biomaterials 25*, 4797−804.
(28) Larsen, N. E., Leshchiner, E. A., Pollak, C., Balazs, E. A., and Piacquadio, D. (1995) Evaluation of Hylan B (Hylan gel) as soft tissue dermal implants. *Mater. Res. Soc. Symp. Proc. 394*, 193−7.
(29) Schoenmakers, R. G., van de Wetering, P., Elbert, D. L., and Hubbell, J. A. (2004) The effect of the linker on the hydrolysis rate of drug-linked ester bonds. *J. Controlled Release 95*, 291−300.
(30) Miller, R. J., and Shiedlin, A. U.S. Patent 6,383,344, 2002.
(31) Balazs, E., and Leshchiner, A. U.S. Patent 4,605,691, 1986.
(32) Calias, P., and Miller, R. U.S. Patent 6,749,865, 2004.
(33) Vyas, D. M., Benigni, D., Rose, W. C., Bradner, W. T., and Doyle, T. W. (1989) Synthesis and in vivo antitumor activity of novel mitomycin A disulfide analogs. *J Antibiot. (Tokyo) 42*, 1199−201.
(34) Ellman, G. L. (1959) Tissue sulfhydryl groups. *Arch. Biochem. Biophys. 82*, 70−7.
(35) Riddles, P. W., Blakeley, R. L., and Zerner, B. (1983) Reassessment of Ellman's reagent. *Methods Enzymol. 91*, 49−60.
(36) Vercruysse, K. P., and Prestwich, G. D. (1998) Hyaluronate derivatives in drug delivery. *Crit. Rev. Ther. Drug Carrier. Syst. 15*, 513−55.
(37) Piacquadio, D., Larsen, N. E., Denlinger, J. L., and Balazs, E. (1998) Hylan B gel (Hylaform) as a soft tissue augmentation material. *Basic Clin. Dermatol. 15*, 269−91.
(38) Larsen, N. E., Pollak, C. T., Reiner, K., Leshchiner, E., and Balazs, E. A. (1993) Hylan gel biomaterial: dermal and immunologic compatibility. *J. Biomed. Mater. Res. 27*, 1129−34.
(39) Hu, D., Hu, R., and Berde, C. B. (1997) Neurologic evaluation of infant and adult rats before and after sciatic nerve blockade. *Anesthesiology 86*, 957−65.
(40) Gerner, P., Mujtaba, M., Sinnott, C. J., and Wang, G. K. (2001) Amitriptyline versus bupivacaine in rat sciatic nerve blockade. *Anesthesiology 94*, 661−7.

BC050239A

SialylTn-mAb17-1A Carbohydrate–Protein Conjugate Vaccine: Effect of Coupling Density and Presentation of SialylTn

Ralf Kircheis,* Petra Vondru, Andreas Nechansky, Renate Ohler, Hans Loibner, Gottfried Himmler, and Geert C. Mudde

igeneon AG, Immunotherapy of Cancer, Vienna, Austria. Received June 1, 2005

Carbohydrate antigens resulting from aberrant glycosylation of tumor cells, such as SialylTn, represent attractive targets for cancer vaccination. However, T-cell-independent carbohydrate antigens are poorly immunogenic and fail to induce memory and IgG class switch. Clustered expression patterns of some carbohydrates on the cell surface add further complexity to the design of carbohydrate-based vaccines. We describe here a vaccine consisting of SialylTn carbohydrate epitopes coupled to a highly immunogenic carrier molecule, mAb17-1A, adsorbed on alhydrogel and coformulated with a strong adjuvant, QS-21. The SialylTn–mAb17-1A conjugate vaccine was administered in Rhesus monkeys, and the immune responses against mAb17-1A, SialylTn, ovine submaxillary mucin, and tumor cells were analyzed. The data demonstrate that the density of carbohydrate epitopes on the carrier is an essential parameter for induction of anti-carbohydrate specific memory IgG immune responses. Furthermore, the influence of different types of presentation of SialylTn (monomeric vs trimers vs clustered via a branched polyethylenimine linker) on antibody titers and specificity was studied. High-density coupling of SialylTn epitopes to mAb17-1A induced the strongest immune response against synthetic SialylTn and showed also the highest reactivity against natural targets, such as OSM and tumor cells.

INTRODUCTION

Accumulating data indicate that tumor-recognizing antibodies and immune effector cells may play a deciding role for the long-term benefit of cancer therapy. Elimination of circulating tumor cells and eradication of micrometastases which remain after surgery or radiotherapy are considered primary targets for immune cancer therapy. Therefore, identification and selection of the appropriate target antigen(s) on the tumor cells is essential for therapy efficacy. Cell surface-exposed carbohydrate and mucin antigens resulting from aberrant glycosylation of tumor cells may provide attractive targets. In animal models (*1*–*3*) as well as cancer patients the presence of natural or vaccine-induced antibodies against carbohydrates such as GM_2 and SialylTn was found to correlate with prolonged survival (*4*–*6*). The mucin-derived SialylTn is expressed in more than 80% of cancers of breast, colorectal, prostate, and ovarian origin showing no or very limited expression on the corresponding normal tissues (*7*–*9*). SialylTn expression by various epithelial cancers correlates with a more aggressive phenotype and poor prognosis (*10*, *11*). Recent data indicate that mucin-derived O-glycosylated truncated carbohydrates, such as the monosaccharide Tn or the disaccharides TF or SialylTn, are predominantly expressed as molecular clusters on the surface of tumor cells (*9*, *12*–*17*). The exact pattern of these clusters is still under debate; clustering in trimers has been suggested as one favorable pattern for antibody recognition found on ovine submaxillary mucin (OSM) and on the surface of some tumor cells (*14*–*17*). However, it is rather likely that in different tumors slightly different predominant expression patterns exist, and coexpression of monomeric and clustered forms (*13*–*15*) as well as heteroclusters consisting of different types of carbohydrates are likely (*18*).

Our strategy consists of coupling tumor-associated carbohydrate epitopes to a highly immunogenic murine antibody with intrinsic antitumor activity (*19*) in order to (i) use an immunogenic carrier protein to increase the immunogenicity of the carbohydrate antigen and (ii) to benefit from the antitumor immune response induced by the carrier molecule itself (*20*, *21*). IGN402 is a first candidate of this type of conjugate vaccine consisting of SialylTn carbohydrate epitopes chemically coupled to mAb17-1A. The murine 17-1A antibody, a monoclonal antibody recognizing EpCAM (*19*–*21*), adsorbed on aluminum hydroxide has been used as vaccine antigen in the cancer vaccine candidate IGN101 and has recently been reported to prolong survival in metastatic colorectal cancer patients (*22*). Recently we have shown that the SialylTn carbohydrate conjugate vaccine IGN402, coformulated with QS-21 adjuvant, can induce an IgG response against the SialylTn moiety (*23*).

In the present study we investigated the effect of the SialylTn coupling density on the immune response. Furthermore, different types of presentation of SialylTn (monomeric vs trimers vs clustered via a branched polyethylenimine linker) were studied. High-density coupling of SialylTn epitopes to mAb17-1A induced the strongest immune response against synthetic SialylTn as well as against natural targets such as OSM and tumor cells. IGN402 may provide an attractive prototype for further development toward multi-epitope vaccines with multiple carbohydrate epitopes coupled to an immunogenic murine antibody.

* Correspondence: Ralf Kircheis, igeneon AG, Immunotherapy of Cancer, Brunnerstrasse 69/3, A-1230 Vienna, Austria. Tel.: +43-1-90 250 205. Fax: +43-1-90 250 901. E-mail: ralf.kircheis@igeneon.com.

10.1021/bc050157m CCC: $30.25 © 2005 American Chemical Society
Published on Web 11/01/2005

EXPERIMENTAL PROCEDURES

Coupling of SialylTn Carbohydrate to mAb17-1A at Different Ratios. The SialylTn carbohydrate antigen was coupled to the murine monoclonal antibody 17-1A (mIgG2a) at different molar ratios (i.e. 4.5:1; 18:1; and 36:1) to produce SialylTn−mAb17-1A carbohydrate−protein conjugate vaccines with low, medium, and high SialylTn density, respectively. Coupling was performed by reacting 4.5, 18, or 36 mol of nitrophenylated spacered SialylTn, Neu5Acα2-6GalNAcα-O$(CH_2)_3$ NHCO$(CH_2)_4$-COO-(*p*-$NO_2C_6H_4$) (mw 819 g/mol, Lectinity, Finland), to 1 mol of mAb17-1A. Briefly, 70 mg of mAb17-1A was dialyzed twice against coupling buffer (0.1 M $NaPO_4$, 0.15 M NaCl, pH 8.5) using a Slide-A-Lyzer dialysis cassette MWCO 10K (Pierce). Concentration of mAb17-1A was determined by size exclusion chromatography (SEC) on a Zorbax GF-250. Dialyzed mAb17-1A was diluted to a final concentration of 4 mg/mL and stored on ice. The following amounts were transferred to 15 mL vials (Falcon): 3.5 mL for IGN402 'high SialylTn', 4.6 mL for IGN402 'medium SialylTn', and 4.6 mL for IGN402 'low SialylTn'. In parallel, 5 mg of SialylTn-O$(CH_2)_4$NHCOO-pNp was dissolved in 250 μL of DMF, giving a final concentration of 20 mg/mL. SialylTn (dissolved in DMF) was added to ice cold mAb17-1A as follows: 22 μL to IGN402 (low), 90 μL to IGN402 (medium), and 138 μL to IGN402 (high). The reaction mixture was rotated at +4 °C. After 53 h, the reaction was stopped by dialyzing the reaction mixtures against formulation buffer (1 mM $NaPO_4$, 0.86% NaCl, pH 6) using Slide-A-Lyzer dialysis cassette 3.5K (Pierce) at 4 °C. For comparison, uncoupled mAb17-1A was treated in parallel.

To get a very high carbohydrate density, SialylTn was coupled to mAb17-1A at a molar ratio of 100:1. Briefly, 20 mg of nitrophenylated spacer SialylTn, Neu5Acα2-6GalNAcα-O$(CH_2)_3$NHCO$(CH_2)_4$COO-(*p*-$NO_2C_6H_4$), was dissolved in 500 μL of DMF, and 423 μL of this solution was added to ice cold, dialyzed mAb17-1A (31 mg in 7.75 mL of coupling buffer). The reaction mixture was incubated 74 h under rotation at +4 °C. The coupling product was dialyzed twice against formulation buffer.

Coupling of SialylTn Carbohydrate Trimers to mAb17-1A. The SialylTn carbohydrate antigen trimers attached to one linker molecule having a nitrophenyl group, [Neu5Acα2-6GalNAcα-O$(CH_2)_3$NHCO$(CH_2)_4$CO-Gly_3-$NHCH_2$-]$_3$ [(*p*-$NO_2C_6H_4$)O-CO$(CH_2)_4$CO-Gly_3-$NHCH_2$-)]$_1$C (mw 3105 g/mol, Lectinity, Finland), was coupled to the mAb17-1A at a molar ratio of 33:1 (calculation based on trimers). Five milligrams of [Neu5Acα2-6GalNAcα-O$(CH_2)_3$NHCO$(CH_2)_4$CO-Gly_3-$NHCH_2$-]$_3$[(*p*-$NO_2C_6H_4$)O-CO$(CH_2)_4$CO-Gly_3-$NHCH_2$-)]$_1$C was dissolved in 300 μL of DMF and added to 8.1 mg of ice cold, dialyzed mAb17-1A. The reaction mixture was incubated 72 h under rotation at +4 °C. The coupling product was dialyzed twice against formulation buffer.

Mimicing SialylTn Clusters on mAb17-1A by Using a Branched PEI Linker. The coupling procedure consisted of coupling the branched polyethylenimine (PEI) linker molecule to mAb17-1A, followed by the coupling of nitrophenylated spacer SialylTn to the mAb17-1A−PEI conjugate

Coupling of Branched PEI Linker to mAb17-1A. Branched PEI (25 kDa, Aldrich) was coupled to mAb17-1A via the heterobifunctional cross-linker SPDP (*N*-succinimidyl 3-(2-pyridyldithio)propionate, Pierce, Rockford, IL). Briefly, mAb17-1A (2.7 mg, 10 mg/mL) and PEI (4.9 mg, 1 mg/ml) were dialyzed against PBS using Slide-A-Lyzer dialysis cassettes. Concentration was measured using SEC and ninhydrin assay for mAb17-1A and PEI, respectively.

Coupling of SPDP to mAb17-1A and PEI, Respectively. mAb17-1A (26 mg, 10 mg/mL in PBS) was coupled with 65 μL of SPDP (20 mM in DMSO) for 60 min at RT. PEI (4.2 mg, 1 mg/mL in PBS) was coupled with 65 μL of SPDP (20 mM in DMSO) for 60 min at RT. The SPDP conjugates were dialyzed against PBS. PEI−SPDP (4.2 mg in 2.1 mL PBS) was reduced with 55 mg of DTT for 30 min at RT. The reduced PEI−SPDP was dialyed against PBS.

Reaction of mAb17-1A−SPDP with Reduced PEI−SPDP. Reduced PEI−SPDP (3.95 mg) and mAb17-1A−SPDP (24.4 mg) were reacted at a molar ratio of 1:1 for 24 h at +4 °C. The reaction mixture was dialyzed against PBS using SpectraPor Float-A-Lyzer (MWCO 60 kDa). The mAb17-1−PEI coupling product was confirmed by LDS−PAGE, WesternBlot, BioRAD protein assay, and ninhydrin assay.

Coupling of SialylTn to mAb17-1A−PEI. Ten milligrams of nitrophenylated spacered SialylTn, Neu5Acα2-6GalNAcα-O$(CH_2)_3$NHCO $(CH_2)_4$COO-(*p*-$NO_2C_6H_4$), were dissolved in 200 μL of DMF, and added to ice cold mAb17-1A−PEI conjugate (18 mg/7.2 mL). The reaction mixture was incubated 75 h under rotation at +4 °C. The coupling product was dialyzed twice against formulation buffer.

Analysis of Final Coupling Products. *Size Exclusion Chromatography.* Concentrations of SialylTn−mAb17-1A coupling products were quantified by size exclusion chromatography (SEC) on a ZORBAX GF-250 column in a Dionex system and on a TSKgel G3000SW column in a HP1100 system.

IEF, LDS−PAGE, and Western Blots. SialylTn−mAb17-1A coupling products were analyzed by SERVALYT PRECOTES horizontal flatbed IEF electrophoresis pH 3−10 (SERVA) followed by Coomassie blue staining (Invitrogen) and by lithium dodecyl sulfate polyacrylamide gel electrophoresis (LDS−PAGE, NuPAGE Electrophoresis System, Bis-Tris-Gel, 4−12%) under both nonreducing and reducing conditions (50 mM DTT, 1,4-dithiothretiol) followed by SilverXpress staining (Invitrogen).

For Western blot analysis, samples following LDS−PAGE were transferred (25 V, 1.1 W, 1.5 h) to Immobilon membranes (PVDF 0.45 μm, Millipore). Membranes were blocked with 3% skim milk and stained with rabbit anti-mouse IgG (H+L)−HRP (1:1000, Zymed) or alternatively with anti-SialylTn CD175s (IgG1) (10 μg/mL, DAKO) and rat anti-mouse IgG1−HRP (1:1000, Becton Dickinson).

Quantification of Sialic Acid by the Resorcinol Assay. Amount of sialic acid in the coupling products was quantified by the resorcinol-HCl reaction in the presence of $CuSO_4$, and spectrophotometric measurement of absorbance at 562 nm. Briefly, 0.15 mL of samples and 0.15 mL of resorcinol reagent (2% resorcinol, 2.5 mM $CuSO_4$, HCl (37%)) were mixed in tightly closed glass vials and incubated at 100 °C for 1 h. The optical density (OD) of the developing color was measured by adsorption at 562 nm (Spectrophotometer Ultrospec II, LKB Biochrom). As a standard, a 'SialylTn mix' (consisting of sialic acid (i.e. *N*-acetylneuraminic acid) and GalNAc at a molar ratio 1:1), 1.25−25 μg/mL, was used for calibration.

Quantification of Sialic Acid by HPLC. Quantification of amount of sialic acid in the coupling products was performed by HPLC analysis and fluorescence detection of DMB derivatives of sialic acid (DMB = 1,2-diamino-4,5-methylenedioxybenzyl). Briefly, samples were treated with 2 M acetic acid at 80 °C for 3 h and derivatized with DMB. Derivatized samples were analyzed by reversed

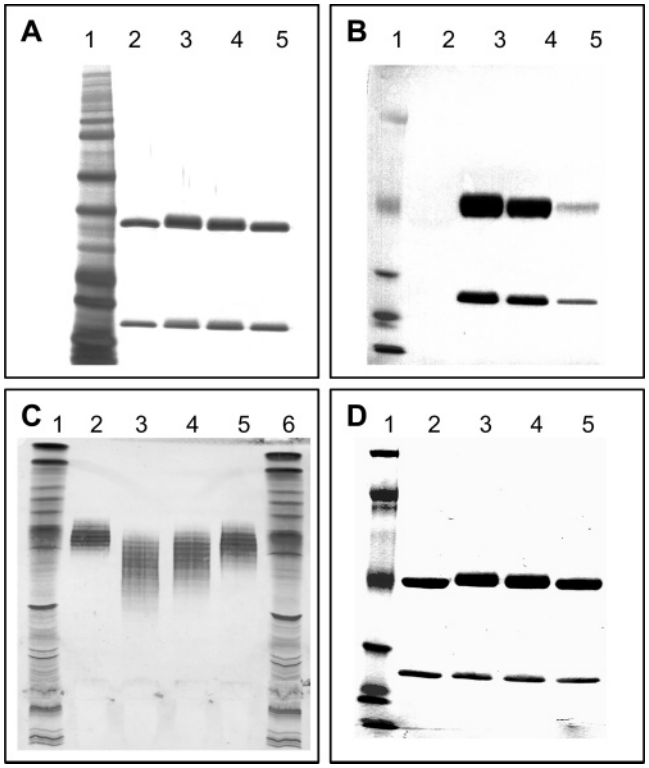

Figure 1. Characterization of SialylTn−mAb17-1A coupling products with high, medium, or low SialylTn density by IEF, LDS−PAGE, and Western Blots. Unconjugated mAb17-1A (lane 2) and SialylTn−mAb17-1A conjugates with high (lane 3), medium (lane 4), and low SialylTn density (lane 5) were subjected to LDS−PAGE under reducing conditions followed by silver staining (A), or blotted and stained with anti-SiaTn CD175s (mIgG1) and rat-anti-mouse IgG1−HRP (B) or rabbit-anti-mouse IgG (H+L)−HRP (D), or subjected to IEF−PAGE and stained by Coomassie blue (C). Heavy and light chains of mAb17-1A or conjugated SialylTn−mAb17-1A under reducing conditions (A, B, D) can be seen.

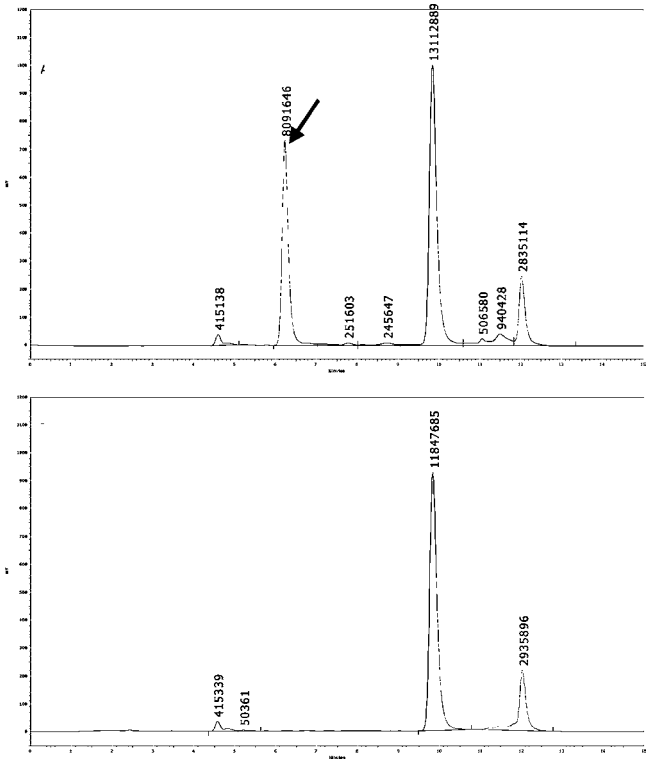

Figure 2. Quantification of sialic acid by reverse phase HPLC. Quantification of amount of sialic acid in the coupling products was performed by HPLC analysis and fluorescence detection of DMB derivatives of sialic scid. Derivatized samples were injected into reversed phase HPLC with fluorescence detection. Quantification was done by measuring the peak area of *N*-acetylneuraminic acid (NANA). HPLC profile of SialylTn−mAb17-1A conjugate (upper panel) and nonconjugated mAb17-1A (lower panel) are shown. The arrowhead points to the peak corresponding to NANA in the sample. Synthetic NANA (Sigma), 1.25−25 μg/mL, was used for calibration.

phase HPLC with fluorescence detection. Quantification was done by the peak area of *N*-acetylneuraminic acid. Synthetic *N*-acetylneuraminic acid (Sigma), 1.25−25 μg/mL, was used for calibration.

IGN402 Vaccine Formulations. SialylTn−mAb17-1A conjugate (500 μg) was adsorbed on 1.67 mg of aluminum hydroxide in 0.5 mL of formulation buffer (1 mM $NaPO_4$, 0.86% NaCl, pH 6) and coformulated with 100 μg of QS-21 adjuvant (Antigenics Inc., Lexington, MA).

LAL Assay and Pyrogenicity Test in Rabbits. Amounts of endotoxin in the vaccine formulations were estimated by Limulus Amebocyte Lysate−Endochrome Assay (Charles River Endosafe). None of the final vaccine formulations contained detectable amounts of endotoxin.

Furthermore, the final vaccine formulations were subjected to pyrogenicity test by iv application in rabbits. The formulations used for this study were negative regarding pyrogenicity testing.

Rhesus Monkey Immunization Study. Safety, tolerability, and immunogenicity of multiple subcutaneous injections of IGN402 were evaluated in a vaccination study in Rhesus monkeys. All animal studies were performed under controlled and documented conditions in accordance with animal health care standards at Biotest Ltd., Konarovice, Czech Republic. Each SialylTn−mAb17-1A conjugate was tested in groups each consisting of four Rhesus monkeys (sex and age matched). In a first comparative study animals were vaccinated with four initial immunizations on days (d) 1, 15, 29, and 57. Blood samples were taken before (d −15, −11, −6) and after immunization (d 15, 22, 29, 36, 57; 71 and 85).

In a second Rhesus monkey study, four animals per group were vaccinated with four initial immunizations on days (d) 1, 21, 49, and 76. Blood samples were taken before (d −13 and −6) and after immunization (d 27, 49, 52, 70, 79, and 91). All immunizations were well tolerated by the animals with no signs of systemic or local toxicity related to immunization. One animal (no. 83 from the SialylTn[tri]−mAb17-1A group), however, had to be euthanized during the course of the study because of moribund conditions. The pathological and histopathological examinations of the animal showed pathologies in blood coagulation (thrombus in liver vein, embolus in lungs) most probably not related to the vaccination.

ELISA for Immune Reactivity against mAb17-1A. Presera and immune sera were analyzed regarding the induced immune response against mAb17-1A by ELISA. Briefly, ELISA plates (F96 Maxisorp, NUNC) were coated with 10 μg/mL mAb17-1A. ELISA plates were blocked with 2% HSA in PBS (1 h, 37 °C), and samples were prediluted in PBS with 0.5% HSA and were incubated for 1.5 h at 37 °C. A positive control serum with known reactivity against mAb17-1A was tested in parallel and used for normalization between different ELISA plates. For detection, plates were incubated with a sheep anti-human IgG-(γ-chain)−HRP conjugate (1:2000, Chemicon) for 30 min at 37 °C. Staining with substrate OPD (10 mg OPD dissolved in 25 mL + 10 μL 30% H_2O_2) was stopped by adding 50 μL of H_2SO_4 (30%) and measured

Table 1. Molar Ratios of SialylTn to mAb17-1A[a]

coupling product	molar ratio SialylTn to mAb17-1A	
	resorcinol	HPLC (NANA)
mAb17-1A	–	–
SiaTn-mAb17-1A (high)	16.2 (0.5)	12.9
SiaTn-mAb17-1A (medium)	9.1 (0.4)	7.1
SiaTn-mAb17-1A (low)	2.8 (0.1)	1.9

[a] Quantification of sialic acid in the different SialylTn−mAb17-1A coupling products were estimated by the resorcinol assay. The resorcinol assay is based on the resorcinol-HCl reaction in the presence of $CuSO_4$ and spectrophotometric measurement of absorbance at OD562 nm. Mean and standard deviation (SD) are shown.

at 492/620 nm. The titer was defined as reciprocal serum dilution yielding an absorbance of OD = 1.0 on a titration curve. Curve fitting was done using GraphPad Prism program version 4.0.

SialylTn−PAA ELISA. Preserum and immune sera were analyzed concerning the immune response against the synthetic SialylTn carbohydrate antigen (coupled to polyacrylamide) by SialylTn−PAA ELISA. Briefly, ELISA plates (F96 Maxisorp, NUNC) were coated 10 μg/mL SialylTn−PAA (Lectinity). ELISA plates were blocked with PBS containing 2% HSA for 1 h at 37 °C. Serum samples were prediluted in PBS containing 0.5% HSA and 5% glucose and incubated for 2 h at 37 °C. A positive control serum with known reactivity against SialylTn was used for normalization between different ELISA plates. For detection, plates were incubated with mouse anti-human IgM−HRP conjugate (1:2000, SB, Southern Biotechnology) or sheep anti-human IgG-(γ-chain)−HRP conjugate (1:2000, Chemicon), respectively, for 30 min at 37 °C. Staining with substrate OPD (10 mg OPD dissolved in 25 mL + 10 μL of 30% H_2O_2) was stopped by adding 50 μL of H_2SO_4 (30%) and measured at 492/620 nm. Titers were defined as the reciprocal of serum dilutions yielding an absorbance of OD = 1.0 and OD = 0.5 for IgM and IgG, respectively. Curve fitting was done using GraphPad Prism program version 4.0.

Ovine Submaxillary Mucin (OSM) ELISA. Presera and immune sera were analyzed regarding the immune response to OSM which is a natural substrate highly expressing SialylTn. Briefly, ELISA plates (F96 Maxisorp, NUNC) were coated with 10 μg/mL OSM (Accurate Chemical, Westbury, NY). ELISA plates were blocked with 2% HSA for 1 h at 37 °C, followed next by a washing step. Samples were prediluted in PBS with 0.5% HSA and incubated for 2 h at 37 °C. A positive control serum with known reactivity against OSM was tested in parallel and used for normalization between different ELISA plates. For detection, plates were incubated with mouse anti-human IgM−HRP conjugate (1:2000, SB, Southern Biotechnology) or sheep anti-human IgG-(γ-chain)−HRP conjugate (1:2000, Chemicon), respectively, for 30 min at 37 °C. Staining with substrate OPD (10 mg OPD dissolved in 25 mL + 10 μL of 30% H_2O_2) was stopped by adding 50 μL of H_2SO_4 (30%) and measured at 492/620 nm. Titers were defined as reciprocal of serum dilutions yielding an absorbance of OD = 1.0 and OD = 0.5 for IgM and IgG, respectively. Curve fitting was done using GraphPad Prism program version 4.0.

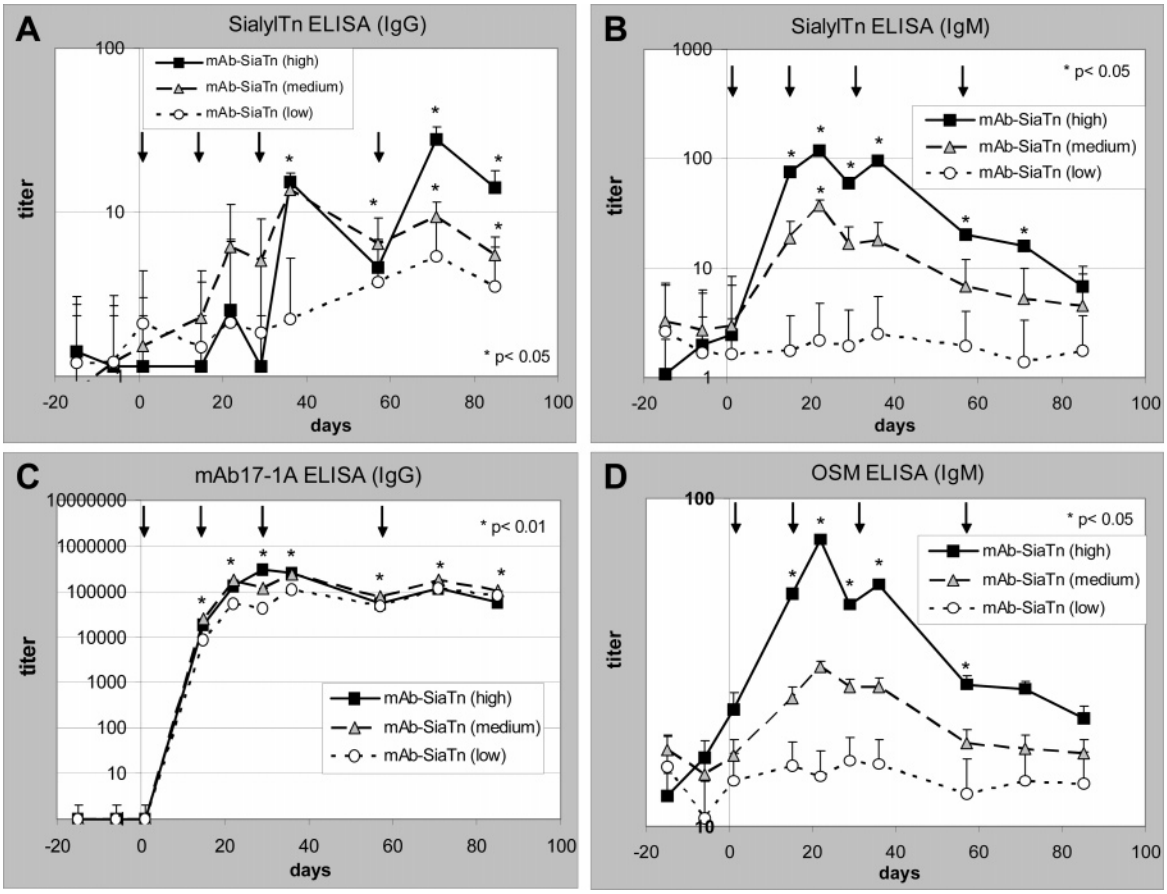

Figure 3. Effect of SialylTn coupling density on immune responses induced against SialylTn, mAb17-1A, and OSM. Rhesus monkeys were immunized with SialylTn−mAb17-1A plus QS-21 vaccines containing high, medium, or low SialylTn coupling density. Preserum and immune sera at a time kinetic were analyzed for immune response against mAb17-1A carrier protein and SialylTn carbohydrate antigen and ovine submaxillary mucin by ELISA. Antibody titers (geomean and Scatter factor) against SialylTn (IgG) (A), IgM (B), mAb17-1A (IgG) (C), and OSM (IgM) (D) are shown. Statistics: *p < 0.05 vs preserum (one-tailed, paired t-test).

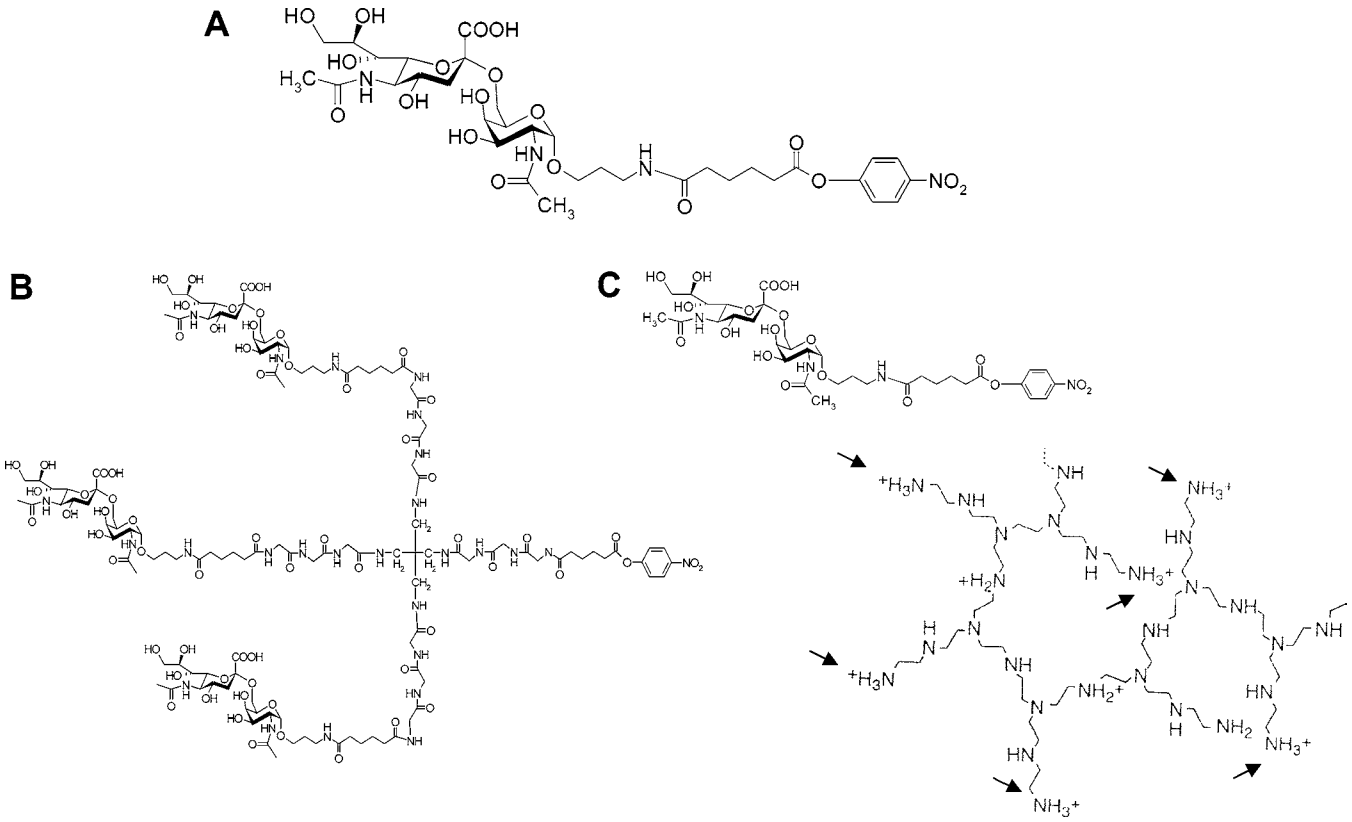

Figure 4. Different presentation of SialylTn epitope: monomeric; trimers; clustered via branched linker. The following SialylTn−mAb17-1A variants with different presentations of SialylTn were designed and tested in a Rhesus monkey study: monomeric presentation of SialylTn (A) at high and very high coupling ratios (33:1 and 100:1, respectively); SialylTn presentation as trimers (ratio 33 [tri]:1) (B); clustered presentation of SialylTn on mAb17-1A−PEI (SialylTn coupling ratio 100:1) (C).

Immune Response against Tumor Cells (FACS analysis). Binding of immune sera to tumor cells was measured by cell surface staining using a FACScan (Becton Dickinson). OVCAR-3 human ovary adenocarcinoma cells (ATCC, HTB-161) were incubated with serum (diluted 1:40 in PBS with 2% FCS) for 2 h on ice. For detection, a goat $F(ab')_2$ anti-human IgG (H+L)−PE conjugate (1:100, Immunotech, Marseille, France) was used. Mean fluoresence intensities (MFI) values obtained for binding of preserum were compared to binding of the corresponding immune serum. For better comparison, the binding of preserum of each individual animal was set at 10% positive cells.

Antibody-Dependent Cellular Cytotoxicity, ADCC. Preserum and immune serum was tested for ADCC against SialylTn positive OVCAR-3 cells. Human PBMCs were used as effector cells and incubated with the ^{51}Cr-labeled target cells at different E:T ratios, i.e., 60:1 and 20:1 for 14 h. ^{51}Cr -release was measured by a γ-counter.

RESULTS

Effect of SialylTn Coupling Density on Immune Responses Induced against mAb17-1A, SialylTn, and OSM. Nitrophenyl-activated SialylTn carbohydrates were coupled to mAb17-1A at three different molar ratios of SialylTn to mAb17-1A (4.5:1; 18:1; and 36:1) resulting in three SialylTn−mAb17-1A conjugate vaccines with low, medium, and high SialylTn density, respectively. SialylTn−mAb17-1A coupling products analyzed by LDS−PAGE under reducing conditions followed by Silver staining are shown in Figure 1A. LDS−PAGE showed an increase in the molecular weight of the heavy chains (50 kDa) and the light chains (25 kDa) in the coupling products (lanes 3−5, compared to uncoupled mAb17-1A, lane 2) indicating that SialylTn has been coupled to both heavy and light chains of mAb17-1A. Western blot analysis of the SialylTn−mAb17-1A coupling products with either anti-SialylTn CD175s (mIgG1)) and rat anti-mouse IgG1−HRP (Figure 1B) or alternatively with rabbit anti-mouse IgG (H+L)−HRP (Figure 1D) demonstrated that SialylTn was detectable in the SialylTn−mAb17-1A coupling products but not in the mAb17-1A (Figure 1B vs 1D). The amount of SialylTn detectable in the coupling product correlated with the coupling ratio (lane 3: high, lane 4: medium, lane 5: low). Coupling of the negatively charged SialylTn to mAb17-1A resulted also in a shift of the isoelectric point (pI) in the coupling products as shown by IEF (Figure 1C). The pI shift correlated with the coupling SialylTn ratio (lane 3: high; lane 4: medium, lane 5: low SialylTn).

The molar ratios of SialylTn to mAb17-1A in the coupling products were quantified by Recorcinol assay or HPLC of N−Acetylneuraminic acid (NANA). In the resorcinol assay the amount of sialic acid (as part of SialylTn) in the coupling products is quantified by the resorcinol-HCl reaction. Molar ratios of SialylTn to mAb17-1A for the high, medium, and low ratio coupling product as determined by the resorcinol assay are shown in Table 1. Quantification of amount of sialic acid in the coupling products was also performed by reverse phase HPLC followed by fluorescence detection of DMB derivatives of sialic acid. Quantification is based on the peak area of *N*-acetylneuraminic acid (Figure 2). Molar ratios of SialylTn to mAb17-1A for the high, medium, and low ratio coupling product as determined by HPLC of NANA correlate well with those estimated by the resorcinol assay (Table 1).

The SialylTn−mAb17-1A coupling products (i.e. with final SialylTn to mAb17-1A ratios of 3:1, 9:1, and 16:1,

respectively, as determined by the resorcinol assay) were adsorbed on aluminum hydroxide (i.e. 500 μg coupling product coupled to 1.67 mg aluminum hydroxide) and coformulated with 100 μg QS-21 adjuvant. Addition of strong adjuvants, such as QS-21, was previously found to be essential for induction of switching carbohydrate specific IgM antibodies to the IgG isotype (*23*).

Rhesus monkeys, four animals per group, were immunized with SialylTn−mAb17-1A vaccines with high, medium, or low SialylTn coupling density, respectively. The time kinetics of the immune responses against mAb17-1A carrier protein, the SialylTn carbohydrate antigen, and OSM, a natural substrate with high SialylTn expression, were analyzed by ELISA (Figure 3, Panels A to D). The induced immune responses against SialylTn (Panel A: IgG, Panel B: IgM) and OSM (Panel D: IgM) were found to correlate with the density of coupled SialylTn. Highest responses against SialylTn (IgM, IgG) and OSM (IgM) were induced at the highest coupling density (i.e. 16:1), while only low IgG titers against OSM were found (data not shown). With the low SialylTn density (i.e. 3:1) vaccine formulation, generally only marginal reactivity against SialylTn and no reactivity with OSM were found. In contrast, all three vaccines induced comparable IgG responses against the mAb17-1A carrier protein (Panel C). The data demonstrate a clear correlation between SialylTn ligand density and the efficacy to induce an anti-carbohydrate immune response, with the highest tested density showing highest efficacy of immune response against SialylTn or OSM.

Mimic of Clustered Presentation of SialylTn. Recent data from the literature indicate that mucin-derived, truncated carbohydrates, such as Tn or SialylTn, are recognized by antibodies preferably as clusters on the surface of tumor cells rather than as single molecule epitopes (*12*−*17*). To address this issue, the following variants of vaccines with different presentations of SialylTn were designed: monomeric SialylTn (Figure 4A) coupled at a ratio of 33:1 (corresponding to the highest ratio of the previous experiment) was compared with a conjugate coupled at very high SialylTn to mAb17-1A ratio, i.e. 100:1. Furthermore, a trimer SialylTn with three SialylTn moieties attached to one linker, SialylTn[tri], was coupled to mAb17-1A at a ratio of 33:1 (trimer-to-carrier ratio) (Figure 4B). Finally SialylTn was coupled to a mAb17-1A−PEI conjugate at a coupling ratio of 100:1. The branched polyethylenimine linker molecule, PEI 25 kDa, is a polycation with a high density of primary amino groups, and coupling of SialylTn to the mAb17-1A−PEI conjugate aimed to mimic highly clustered SialylTn presentation (Figure 4C). SialylTn−mAb17-1A coupling products were analyzed using LDS−PAGE under reducing conditions (Figure 5A). An increase in molecular weight of the heavy and the light chains was found in all coupling products. The SialylTn[tri]−mAb17-1A conjugate (lane 5) showed a peculiar ladder pattern with several distinct bands for both heavy and light chains. Western blot analysis with anti-SialylTn CD175s (IgG1) and rat anti-mouse IgG1−HRP demonstrated that SialylTn was detectable in all coupling products, but not in mAb17-1A (Figure 5B). All coupling products showed a pI shift compared to mAb17-1A (lane 2) due to the coupling of negatively charged SialylTn. Different to all other coupling products, the SialylTn−PEI-mAb17-1A conjugate repeatedly showed a very peculiar IEF pattern (lane 6) which may be due to superimposing effects of the negatively charged SialylTn and the positively charged PEI (Figure 5C).

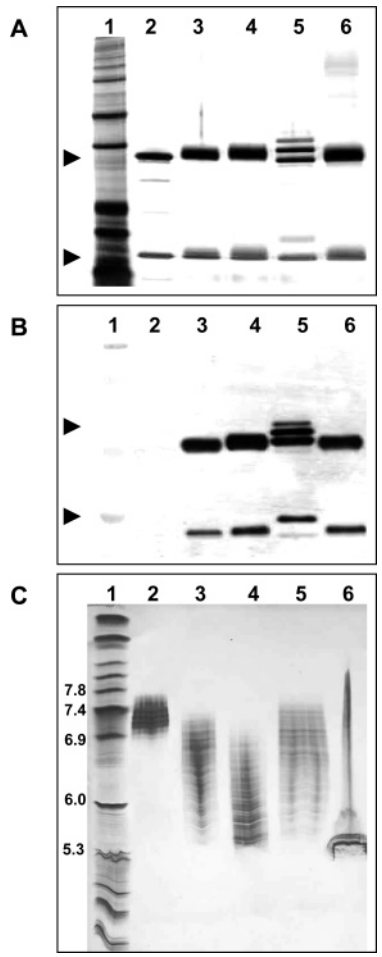

Figure 5. Characterization of different SialylTn−mAb17-1A coupling products by IEF, LDS−PAGE, and Western Blots. Unconjugated mAb17-1A (lane 2) and SialylTn−mAb17-1A conjugates, monomeric at coupling ratio 33:1 (lane 3), monomeric at coupling ratio 100:1 (lane 4), SialylTn[tri] at coupling ratio 33:1 (lane 5), and SialylTn−PEI-mAb17-1A (lane 6) were subjected to LDS−PAGE under reducing conditions followed by silver staining (A), or blotted and stained with anti-SiaTn CD175s (mIgG1) x rat-anti-mouse IgG1−HRP (B), or subjected to IEF−PAGE and stained by Coomassie blue (C). Heavy and light chains of mAb17-1A or conjugated SialylTn−mAb17-1A under reducing conditions (A, B) can be seen.

Table 2. Molar Ratio of SialylTn to mAb in Different Coupling Products[a]

coupling product	molar ratio SialylTn to mAb17-1A (resorcinol)
SialylTn-mAb17-1A 33:1	19
SialylTn-mAb17-1A 100:1	75
SialylTn-mAb17-1A 33[tri]:1	65
SialylTn-mAb17-1A 100:1	27

[a] Quantification of sialic acid in the different SialylTn−mAb17-1A coupling products were estimated by the resorcinol assay. The resorcinol assay is based on the resorcinol-HCl reaction in the presence of $CuSO_4$ and spectrophotometric measurement of absorbance at OD562 nm.

SialylTn to mAb17-1A ratios in the final coupling products were quantified by the resorcinol assay, and the following ratios (calculated on monomeric SialylTn) were estimated: 19:1, 75:1, 65:1, and 27:1 for the monomeric SialylTn−mAb17-1A (reacted at 33:1 and 100:1), SialylTn[tri]-mAb17-1A, and SialylTn−PEI-mAb17-1A, respectively (Table 2). While the molar SialylTn to mAb17-1A ratios in the 100:1 monomeric SialylTn−mAb17-1A (final ratio 75:1) and SialylTn[tri]−mAb17-1A (final ratio 65:1) showed, as expected, an approximately 3-fold higher

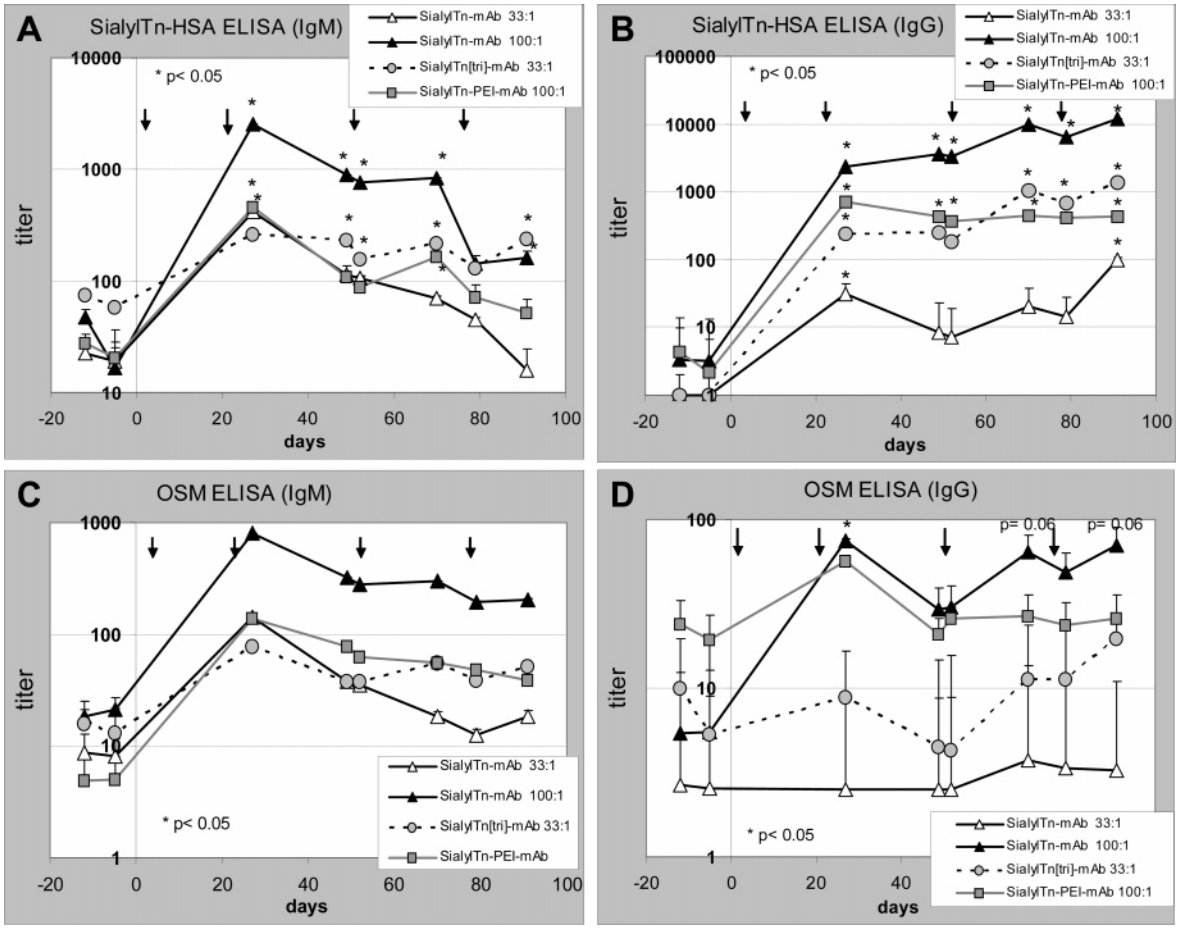

Figure 6. Effect of SialylTn coupling density and presentation on immune responses induced against synthetic SialylTn and ovine submaxillary mucin. Rhesus monkeys were immunized with the different SialylTn−mAb17-1A vaccines, adsorbed on alhydrogel, and coformulated with QS-21 adjuvant. Preserum and immune sera at a time kinetic were analyzed for immune response against SialylTn carbohydrate antigen and OSM by ELISA. Antibody titers (geomean and Scatter factor) against SialylTn (IgM) (A), IgG (B), and OSM (IgM) (C), (IgG) (D), are shown.

ratio compared to the 33:1 coupled conjugate (final ratio 19:1); a lower ratio (27:1) was measured in the SialylTn−PEI-mAb17-1A coupling product. The SialylTn−mAb17-1A conjugates were adsorbed on aluminum hydroxide, coformulated with QS-21 adjuvant and tested in a Rhesus monkey vaccination study. Presera and the corresponding immune sera were tested for reactivity against SialylTn−HSA and OSM by ELISA (Figure 6). The time kinetics for the immune responses against SialylTn (Panel A: IgM, Panel B: IgG) and OSM (Panel C: IgM, Panel D: IgG) are shown. Again, a strong correlation between density of coupled SialylTn and the immune responses against both synthetic SialylTn and OSM was found. Regarding induced titers, the high coupling product of monomeric SialylTn to mAb17-1A (coupling ratio at 100:1, i.e. final ratio 75:1) was found superior to all other coupling products. The SialylTn[[tri]−mAb17-1A and the SialylTn−PEI−mAb17-1A conjugates were significantly more efficient than the monomeric SialylTn (33:1, final 19:1), but were inferior when compared to the 75:1 monomeric coupling product. The superior efficacy of the high density coupling product was particularly dramatic concerning the response against OSM, a natural substrate with high SialylTn content (Figure 6C,D).

Immune Response against SialylTn Positive Tumor Cells. Finally, the immune response against the natural target, SialylTn positive tumor cells, was tested. Preserum and immune sera of Rhesus monkeys immunized with SialylTn−mAb17-1A plus QS-21 were analyzed for binding to SialylTn positive OVCAR-3 cells by FACS analysis. Histograms of IgG and IgM binding to OVCAR-3 cells are shown for the 75:1 high-density SialylTn−mAb17-1A vaccine (Figure 7A,B). A statistically significant increase in cell binding to OVCAR-3 cells (both IgG and IgM) was found for the high coupling product ($p < 0.05$, paired t-test). A less consistent reactivity was found with the other coupling products (data not shown).

Finally, presera and immune sera of animals immunized with the high-density SialylTn−mAb17-1A vaccine were tested for ADCC against SialylTn positive OVCAR-3 cells. Human PBMCs were used as effector cells and incubated with the target cells at two E:T ratios, i.e., 60:1 and 20:1. While different initial levels of lytic activity were found in the different animals, a clear increase in ADCC activity was found in the immune sera of all animals in comparison to the corresponding presera (Figure 7C).

DISCUSSION

A panel of synthetic cancer vaccine formulations based on SialylTn carbohydrate antigens chemically coupled to an immunogenic protein carrier molecule were designed and tested in Rhesus monkeys. Coupling of the SialylTn carbohydrate epitopes to mAb17-1A aims to increase the immunogenicity of the SialylTn carbohydrate antigen and to provide with the mAb17-1A carrier an additional antigen that is thought to mediate an immune response against epithelial cancer. The murine 17-1A antibody, a monoclonal antibody (mAb) recognizing the epithelial cell

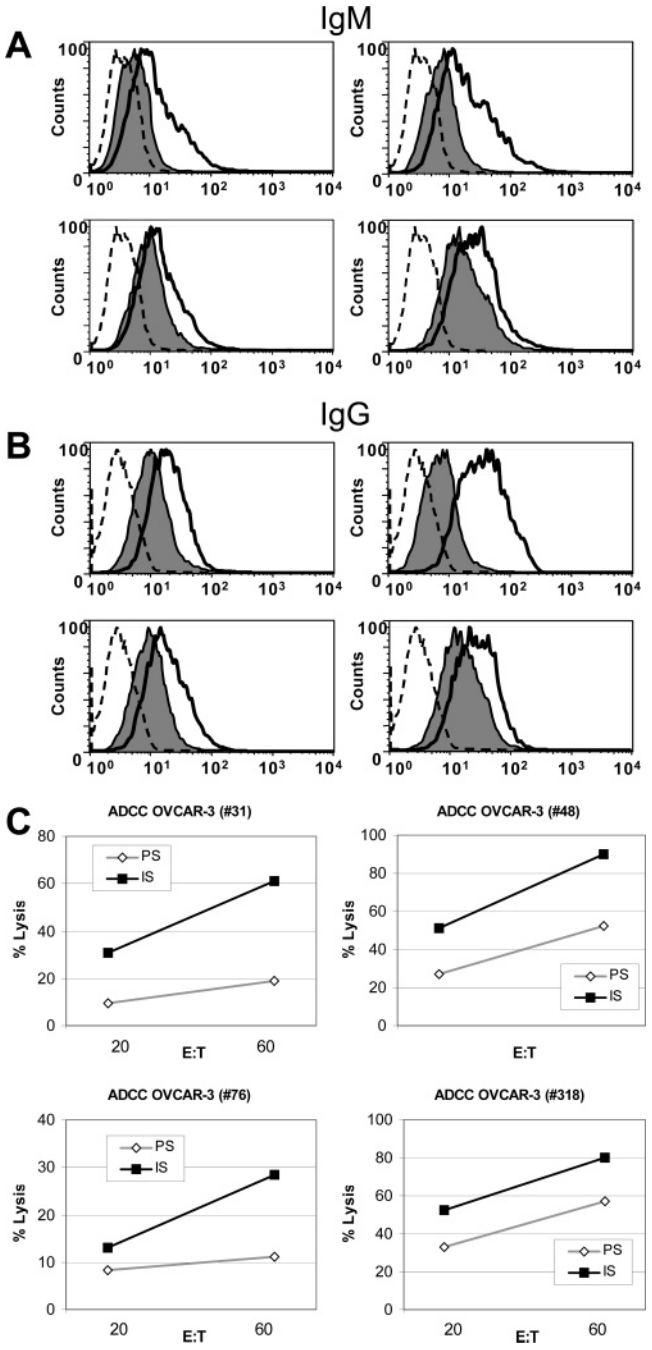

Figure 7. Rhesus monkeys were immunized with the SialylTn–mAb17-1A vaccines. Preserum (grey line filled) and immune sera (bold blank line) (both diluted 1:40 in PBS + 2% FCS) were analyzed for cell binding by FACS analysis (dotted line: unstained control). Cell binding to SialylTn positive OVCAR-3 tumor cells is shown for immunization with the high-density SialylTn coupling product (IgM (A), IgG (B)). Preserum and immune serum was tested for ADCC against SialylTn positive OVCAR-3 cells. Human PBMCs were used as effector cells and incubated with the ^{51}Cr-labeled target cells at E:T ratio of 60:1 and 20:1 for 14h. ^{51}Cr -release was measured using a γ-counter (C).

adhesion molecule (EpCAM), has been used for passive cancer therapy in patients with epithelial carcinomas (*19*) whereby part of the observed efficacy has been attributed to the induction of anti-idiotypic and anti-anti-idiotypic antibodies (*20*, *21*). In the cancer vaccine candidate IGN101 mAb17-1A adsorbed on aluminum hydroxide is being used as vaccine antigen to induce an immune response against epithelial cancer. IGN101 has demonstrated an excellent safety profile and has recently been shown to improve survival in metastatic colorectal cancer patients (*22*).

In the present study, we investigated the effect of various SialylTn coupling densities and different ways of carbohydrate presentation on the carrier molecule on the induced immune response. Recent data have indicated that the monosaccharide Tn or the disaccharide SialylTn are predominantly present as molecular clusters on the surface of tumor cells (*9*, *12*, *17*). Therefore, increasing the coupling density of SialylTn on the carrier molecule and mimicking various types of clustered presentation was tested in this study. Our results demonstrate that at least for this type of carbohydrate–protein conjugate vaccine, the coupling density of SialylTn is an essential parameter determining the efficacy of the induced immune response against the carbohydrate antigen. While only marginal anti-SialylTn responses were generated at a very low carbohydrate to mAb17-1A carrier ratio of 3:1, a ratio of ~16:1 resulted in significant anti-SialylTn IgG titers. At the highest coupling density achieved in this study of 75:1, the highest IgG titers against SialylTn were induced. In contrast, the immune response against mAb17-1A was not significantly affected by the SialylTn to mAb17-1A ratio. However, the magnitude of the immune response against OSM was again strongly dependent on the SialylTn coupling density in the vaccine. In particular IgG antibodies (indicative for an isotype switch from IgM to IgG) specific for OSM were found at significant levels only with high SialylTn coupling densities in the vaccine. Induction of a significant IgG response against OSM and tumor cells indicates that SialylTn in its natural presentation is also recognized by the induced immune response, although to a lesser degree than the synthetic SialylTn immunogen. Alternatively designed clustered presentation of SialylTn as trimers or on a branched PEI linker did not further improve the induced immune response against SialylTn, OSM, or tumor cells compared to the highest monomeric SialylTn coupling density. This result was somewhat unexpected as trimeric presentation of SialylTn on an immunogenic carrier has been shown by others to be a better mimic of the natural presentation (*9*, *12*, *17*). One explanation may be that the recognition of the trimer SialylTn in the present study is negatively influenced by the use of longer and more flexible linker molecules in the trimer conjugate, thus perhaps placing the three SialylTn moieties at an unfavorably large distance to each other for recognition. Furthermore, recent data indicate that it is not only the clustered carbohydrate but also the context with the peptide anchor which can affect the immune response (*16*, *17*). It is currently still under investigation whether the native mucin glycopeptide architecture (*16*) or rather the more immunogenic non-native carbohydrate–peptide linkage (*17*) would be better suited for induction of therapeutic efficacy in tumor patients. Finally, it is known that different tumor cell lines, depending on the growth conditions, but also primary tumors and metastatic cells can differ in their carbohydrate clusters. A trimeric cluster may be typical for certain cells; for others different types of clusters may prevail (*13*, *14*, *18*).

On the basis of its amino acid sequence, the mAb17-1A carrier, a murine monoclonal IgG2a antibody, contains a total of 98 lysine residues which present potential primary amino groups for coupling, depending on the accessibility. Lysines, due to their positive charge and extended, rather rigid structure, are generally surface exposed (*25*). To get insight in the three-dimensional distribution of the lysine residues within the murine

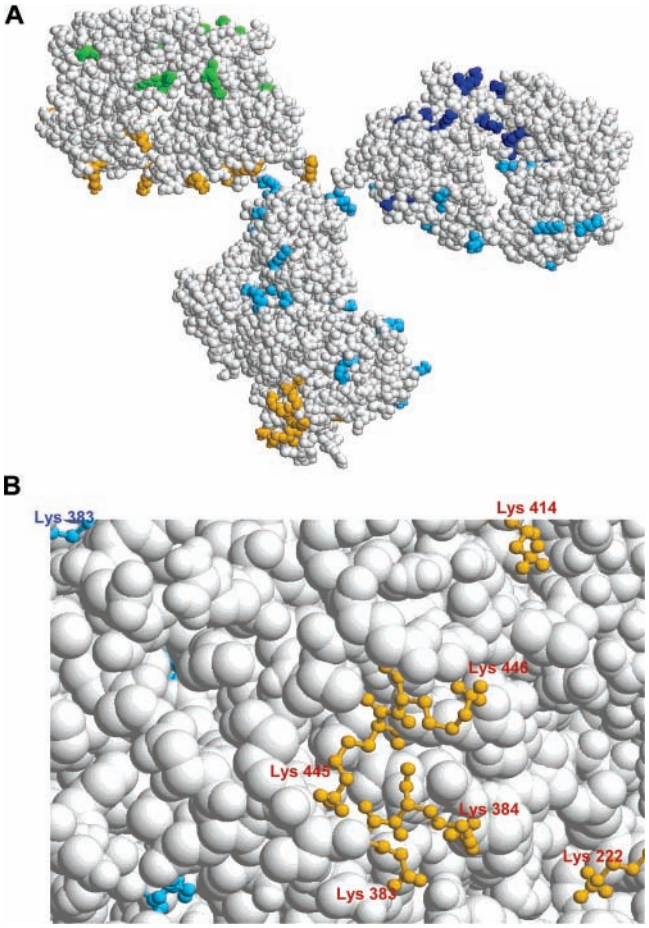

Figure 8. Spatial distribution of lysine residues in a 3D-model of muIgG2a The three-dimensional distribution of the lysine residues within the murine IgG2a molecule (anti-canine lymphoma mAb 321 (*26*)) was obtained from the Brookhaven Protein Data Bank (code: 1IGT), and for visualization the Rasmol computer software version 2.7.1.1 (ftp://ftp.dcs.ed.ac.uk/pub/rasmol) was used. The lysines, shown in yellow and light blue for the two heavy chains, and in green and dark blue for the two light chains, respectively, appear to be dispersed over the whole antibody molecule (Panel A: overview on the muIgG2a molecule in "space-fill" mode). Panel B: a cluster of four lysines is shown at higher magnification (lysines in ball-stick mode; all other amino acids in space-fill mode).

IgG2a molecule, the published structure of the anti-canine lymphoma mAb 321 (*26*) was chosen as a model system. Atomic coordinates for mAb 321 were obtained from the Brookhaven Protein Data Bank (code: 1IGT), and for visualization, the Rasmol computer software version 2.7.1.1 (ftp://ftp.dcs.ed.ac.uk/pub/rasmol) was used. According to this model (Figure 8, Panel A), the majority of these lysines (shown in yellow and light blue for the two heavy chains, and in green and dark blue for the two light chains, respectively) appear to be dispersed over the whole antibody molecule (shown in the "space-fill" mode). In contrast, some of them, especially in the Fc part of the molecule, are present in spatial proximity to other lysine residues thus forming clusters (Figure 8, Panel B). As the free amino groups on accessible lysine side chains are used for coupling of the sugar moieties to the protein carrier, clustered lysines may allow for a clustered coupling and subsequent presentation of carbohydrates. It should be stressed here that, although mAb321 (muIgG2a) serves only as a model for the mAb17-1A (muIgG2a) used as the carrier molecule in the present study, still, based on the high homology, we believe that this approach is justified. Alignment of the amino acid sequence of the heavy chain constant regions reveals 100% homology whereas for the variable regions the homology is, as expected, lower due to the unique complementary determining regions.

Coupling of carbohydrate epitopes to mAb17-1A may provide the advantage of creating different types of presentation for the carbohydrate epitopes, both monomeric as well as different kinds of clusters. Furthermore, the data of the present study demonstrate that it is feasible to design a synthetic cancer vaccine which is adjustable to a controlled and reproducible, large scale manufacturing process. The SialylTn−mAb17-1A conjugate vaccine may provide a prototype for development of vaccines with several different carbohydrate epitopes coupled to the same immunogenic carrier molecule. The need for high density coupling may limit the number of different types of carbohydrate epitopes which can be coupled to the carrier. However, immune recognition of clustered carbohydrates has been shown so far only for a selected group of carbohydrates such as Tn and SialylTn and is probably not typical for recognition of larger carbohydrates, such as GM2 and GloboH. Therefore, combining carbohydrate epitopes which are recognized as monomers with epitopes with clustered presentation on one carrier molecule should be feasible (*18*). Alternatively, using a mixture of different types of carbohydrate-carrier conjugates coformulated in one vaccine formulation might be another pragmatic solution for the generation of a sufficiently broad panel of tumor-associated carbohydrate recognizing IgG antibodies. Strategies for cancer vaccines which target multiple tumor antigens (*18*, *24*) can be expected to provide higher therapeutic efficacy and to minimize the risk for tumor escape, two key parameters for the successful treatment of cancer patients.

ACKNOWLEDGMENT

We thank Dr. C. R. Kensil from Antigenics Inc., Lexington, MA, for kindly providing the QS-21 adjuvant and for critical review of the manuscript.

LITERATURE CITED

(1) Fung, P. Y. S., Madej, M., Koganty, R. R., and Longenecker, B. M. (1990) Active specific immunotherapy of a murine mammary adenocarcinoma using a synthetic tumor-associated glycoconjugate. *Cancer Res. 50*, 4308−4314.
(2) Singhal, A., Fohn, M., and Hakomori, S−I. (1991) Induction of a α-N-acetylgalactosamine-O-serine/threonine (Tn) antigen-mediated cellular immune response for active immunotherapy in mice. *Cancer Res. 51*, 1406−1411.
(3) Zhang, S., Walberg, L. A., Helling, F., Ragupathi, G., Adluri, S., Lloyd, K. O., and Livingston P. O. (1996) Augmenting the immunogenicity of synthetic MUC-1 vaccines in mice. *Cancer Res. 55*, 3364−3368.
(4) Zhang, H., Zhang, S., Cheung, N. K., Ragupathi, G., and Livingston, P. O. (1998) Antibodies can eradicate cancer micrometastases. *Cancer Res. 58*, 2844−2849.
(5) Livingston, P. O., Wong, G. Y. C., Adluri, S., Tao, Y., Padavan, M., Parente, R., Hanlon, C., Helling, F., Ritter, G., Oettgen, H. F., and Old, L. J. (1994) Improved survival in AJCC stage III melanoma patients with GM2 antibodies: a randomized trial of adjuvant vaccination with GM2 ganglioside. *J. Clin. Oncol. 12*, 1036−1044.
(6) MacLean, G. D., Reddish, M. A., Koganty, R. R., and Longenecker, B. M. (1996) Antibodies against mucin-associated SialylTn epitopes correlate with survival of metastatic adenocarcinoma patients undergoing active specific immunotherapy with synthetic STn vaccine. *J. Immunother. 19*, 59−68.
(7) Itzkowitz, S. H., Yuan, M., Montgomery, C. K., Kjeldsen, T., Takahashi, H. K., Bigbee, W. L., and Kim, Y. S. (1989)

Expression of Tn, sialosyl-Tn, and T antigens in human colon cancer. *Cancer Res. 49*, 197−204.
(8) Zhang, S., Zhang, S. H., Cordon-Cardo, C., Reuter, V. E., Singgal, A. K., Lloyd, K. O., and Livingston, P. O. (1997) Selection of tumor antigens as targets for immune attack using immunohistochemistry. II. Blood group-related antigens. *Int. J. Cancer. 73*, 50−56.
(9) Zhang, S., Walberg, L. A., Ogata, S., Itzkowitz, S. H., Koganty, R. R., Reddish, M., Gandhi, S. S., Longenecker, B. M., Lloyd, K. O., and Livingston, P. O. (1995) Immune sera and monoclonal antibodies define two configurations for the sialylTn tumor antigen. *Cancer Res. 55*, 3364−3368.
(10) Itzkowitz, S. H., Bloom, E. J., Kokal, W. A., Modin, G., Hakomori, S., and Kim, Y. S. (1990) Sialosyl-Tn: a novel mucin antigen associated with prognosis in colorectal cancer patients. *Cancer 66*, 1960−1966.
(11) Werther, J. L., Rivera-MacMurray, S., Bruckner, H., Tatematsu, M., and Itzkowitz, S. H. (1994) Mucin-associated sialosyl-Tn antigen expression in gastric cancer correlates with an adverse outcome. *Br. J. Cancer 69*, 613−616.
(12) Nakada, H., Numata, Y., Inoue, M., Tanaka, N., Kitagawa, H., Funakoshi, I., Fukui, S., and Yamashina, I. (1991) Elucidation of an essential structure recognized by an anti-GalNAcα-Ser(Thr) monoclonal antibody (MLS 128). *J. Biol. Chem. 266*, 12402−12405.
(13) Tanaka, N., Nakada, H., Inoue, M., and Yamashina, I. (1999) Binding characteristics of an anti-Siaα2-6GalNAcα-Ser/Thr (sialylTn) monoclonal antibody (MLS132). *Eur. J. Biochem. 263*, 27−32.
(14) Ragupathi, G., Howard, L., Capello, S., Koganthy, R. R., Qiu, D., Longenecker, B. M., Reddish, M. A., Lloyd, K. O., and Livingston, P. O. (1999) Vaccines prepared with SialylTn and SialylTn trimers using the 4-(4-maleimidomethyl)cyclohexane-1-carboxyl hydrazide linker group result in optimal antibody titers against ovine submaxillary mucin and SialylTn-positive tumor cells. *Cancer Immunol. Immunother. 48*, 1−8.
(15) Kagan, E., Ragupathi, G., Yi, S. S., Reis, C. A., Gildersleeve, J., Kahne, D., Clausen, H., Danishefsky, S. J., and Livingston, P. O. (2005) Comparison of antigen constructs and carrier molecules for augmenting the immunogenicity of the monosaccharide epithelial cancer antigen Tn. *Cancer Immunol Immunother. 54*, 424−430.
(16) Lo-Man, R., Vichier-Guerre, S., Bay, S., Deriaud, E., Cantacuzene, D., and Leclerc, C. (2001) Anti-tumor immunity provided by a synthetic multiple antigenic glycopeptide displaying a tri-Tn glycotope. *J. Immunol. 166*, 2849−2854.
(17) Lo-Man, R., Vichier-Guerre, S., Perraut, R., Deriaud, E., Huteau, V., BenMohamed, L., Diop, O. M., Livingston, P. O., Bay, S., and Leclerc, C. (2004) A fully synthetic therapeutic vaccine candidate targeting carcinoma-associated Tn carbohydrate antigen induces tumor-specific antibodies in nonhuman primates. *Cancer Res. 64*, 4987−4994.
(18) Ragupathi, G., Coltart, D. M., Williams, L. J., Koide, F., Kagan, E., Allen, J., Harris, C., Glunz, P. W., Livingston, P. O., and Danishefsky, S. J. (2002) On the power of chemical synthesis: Immunological evaluation of models for multiantigenic carbohydrate-based cancer vaccines. *Proc. Natl. Acad. Sci U.S.A. 99*, 13699−13704.
(19) Riethmuller, G., Schneider-Gadicke, E., Schlimok, G., Schmiegel, W., Raab, R., Hoffken, K., Gruber, R., Pichlmaier, H., Hirsche, H., and Pichlmayr, R. et al. (1994) Randomized trial of monoclonal antibody for adjuvant therapy of resected Dukes' C colorectal carcinoma. German Cancer Aid 17-1A Study group. *Lancet 343*, 1172−1174.
(20) Fagerberg, J., Ragnhammar, P., Liljefors, M., Hjelm, A. L., Mellstedt, H., and Frodin, J. E. (1996) Humoral anti-idiotypic and anti-anti-idiotypic immune response in cancer patients treated with monoclonal antibody 17-1A. *Cancer Immunol. Immunother. 42*, 81−87.
(21) Fagerberg, J., Frodin, J. E., Wigzell, H., and Mellstedt, H. (1993) Induction of an immune network cascade in cancer patients treated with monoclonal antibodies (ab1). I. May induction of ab1-reactive T cells and anti-anti-idiotypic antibodies (ab3) lead to tumor regression after mAb therapy? *Cancer Immunol. Immunother. 37*, 264−270.
(22) Settaf, A., Salzberg, M., Groiss, F., Eller, N., Schuster, M., Himmler, G., Kundi, M., Eckert, H., and Loibner, H. (2004) A randomized placebo-controlled Phase II study with the cancer vaccine IGN101 in patients with epithelial cancers. Presented at the iSBTc 19th Annual Meeting, San Franscisco, Nov 4−7.
(23) Kircheis, R., Vondru, P., Zinöcker, I., Häring, D., Nechansky, A., Loibner, H., Himmler, G., and Mudde, G. C. Immunization of Rhesus monkeys with the conjugate vaccine IGN402 induces an IgG immune response against carbohydrate and protein antigens, and cancer cells. *Vaccine*, submitted
(24) Ragupathi, G., Koide, F., Santhyan, N., Kagan, E., Spassova, M., Bornmann, W., Gregor, P., Reis, C. A., Clausen, H., Danishefsky, S. J., and Livingston, P. O. (2003) A preclinical study comparing approaches for augmenting the immunogenicity of a heptavalent KLH-conjugate vaccine against epithelial cancer. *Cancer Immunol Immunother. 52*, 608−616.
(25) Janin, J., and Wodak, S. (1997) Conformation of amino acid side-chains in proteins. *J. Mol. Biol. 125*, 357−386.
(26) Harris, L. J., Larson, S. B., Hasel, K. W., and McPherson, A. (1997) Refined structure of an intact IgG2a monoclonal antibody. *Biochemistry 36*, 1581−1597.

BC050157M

Novel Thermosensitive 5-Fluorouracil–Cyclotriphosphazene Conjugates: Synthesis, Thermosensitivity, Degradability, and in Vitro Antitumor Activity

Yong Woo Cho,† Jeong-Ryel Lee, and Soo-Chang Song*

Division of Life Science, Korea Institute of Science and Technology, Seoul 130-650, Korea. Received December 22, 2004; Revised Manuscript Received August 18, 2005

A novel thermosensitive macromolecular prodrug of 5-fluorouracil (5-FU) was synthesized using cyclotriphosphazene, and its thermosensitivity, degradability, and in vitro antitumor activity were studied. A series of α-substituted glycine derivatives of 5-FU containing carboxylic groups were prepared, and cyclotriphosphazenes with amino groups were synthesized via the stepwise substitution of hexachlorocyclotriphosphazene $(NPCl_2)_3$ with methoxy-poly(ethylene glycol) (MPEG) or alkoxy ethylene oxide and lysine ethyl ester (LysOEt). The coupling reaction of the two derivatives, and their subsequent deprotection, yielded a thermosenstive 5-FU–cyclotriphosphazene conjugate, which exhibited a unique octopus-shaped molecular structure, in which the three hydrophilic PEG groups (or alkoxy ethylene oxides) were oriented in one direction, opposing the other three hydrophobic groups containing 5-FU, with respect to the trimer ring plane. This conjugate exhibited a reversible and thermosensitive phase transition in an aqueous medium, from soluble to insoluble states. The lower critical solution temperature (LCST) of the conjugate was controlled by substitution with different hydrophilic/hydrophobic side groups, and a few of the conjugates displayed LCSTs which were just below body temperature. This, of course, implies possible applications for local drug delivery by direct intratumoral injection. The conjugate exhibited gradual degradation at 37 °C in both neutral and acidic buffer solutions, and high temperature significantly facilitated its hydrolytic degradation. All of the conjugates displayed dose-dependent cytotoxicity against the leukemia L1210 cell line and exhibited more pronounced cytotoxic effects than did 5-FU.

INTRODUCTION

One of the limitations inherent in current cancer chemotherapy is the lack of specificity with regard to anticancer drugs. Most anticancer drugs exert prohibitively cytotoxic effects on normal cells. The systemic administration of a chemotherapeutic agent results in its spread throughout the body, leading to serious side effects from nonspecific toxicity. A common approach to localize a chemotherapeutic agent into tumor tissues is the target-specific drug delivery with polymer–drug conjugates bearing specific ligands capable of being recognized by the target cells or with particulate drug carriers passively accumulated in tumor tissues by the enhanced permeability and retention (EPR) effect (*1*–*6*). Since Ringsdorf's landmark work (*7*) in 1975 introduced the concept of targetable polymer–drug conjugates, a number of polymer–drug conjugates have been developed (*1*), some of which are now being tested clinically (*8*, *9*). Much effort has been devoted to the search for specific ligands and their conjugation with appropriate polymeric carriers (*1*, *2*, *10*–*14*).

Another promising approach for the localization of a chemotherapeutic agent is the injectable drug delivery system, which utilizes a thermosensitive polymer which undergoes a phase transition from a soluble to an insoluble state at around body temperature. Typical biodegradable and thermosensitive polymers for such an injectable drug delivery system include triblock copolymers of poly(ethylene glycol) and poly[(D,L-lactide)-*co*-glycolide] (PEG–PLGA–PEG) (*15*–*17*), chitosan (*18*–*21*), and poly(organophosphazenes) (*22*–*25*) with PEG and amino acid ester side groups. These polymers are readily soluble in water at room temperature, and their aqueous solutions undergo a phase transition to gel or insoluble precipitate under increased temperatures. The local administration of these systems could be performed by simple intratumoral injection of the aqueous solution, thereby circumventing the necessity of surgery.

Our group has reported a series of biodegradable and thermosensitive poly(organophosphazenes) (*22*–*25*) and cyclotriphosphazenes (*26*, *27*) bearing PEG and amino acid esters as side groups. Temperature-triggered intermolecular associations between the hydrophobic amino acid ester side groups result in the thermosensitive phase transitions of the aqueous polymer solutions. At lower temperatures, these polymers are readily soluble in water and are fully hydrated. As the temperature rises, however, the hydrogen bonds between the water molecules and the polymers weaken gradually, and the hydrophobic associations of the side groups become more pronounced, thereby resulting in the formation of hydrogels or precipitate. The thermosensitive phase transitions of these polymer solutions are completely reversible. The gels or precipitates formed at high temperatures rehydrate when cooled, reverting to the original soluble state.

In recent years, our group has also developed biodegradable and thermosensitive polymer–platinum(II) conjugates via the complexation of cisplatin with cyclotriphosphazenes, through chelate-type coordination bonds

* Corresponding author. Tel: +82-2-958-5123. Fax: +82-2-958-5089. e-mail: scsong@kist.re.kr.

† Present address: Asan Institute for Life Sciences, University of Ulsan College of Medicine, Seoul 138-736, Korea.

10.1021/bc049697u CCC: $30.25 © 2005 American Chemical Society
Published on Web 11/01/2005

(*28*). The conjugates exhibited thermosensitivity at lower critical solution temperatures (LCST), during which phase transitions from solution to precipitate occurred (sol-to-prep). Our thermosensitive conjugates evidenced outstanding antitumor activity, both in vitro and in vivo, against the murine leukemia L1210 cell line. This study prompted us to develop a series of thermosensitive anticancer drug conjugates, such as 5-fluorouracil(5-FU)-cyclotriphosphazene conjugates and doxorubicin−poly(organophosphazene) conjugates. We herein report our development of a series of biodegradable and thermosensitive 5-FU−cyclotriphosphazene conjugates with variable LCSTs. A series of α-substituted glycine derivatives of 5-FU with carboxylic groups were prepared, in addition to a group of functionalized cyclotriphosphazenes with amino groups. Their coupling reaction yielded a set of 5-FU−cyclotriphosphazene conjugates with a unique, octopoidal molecular structure. Thereafter, the conjugates were assessed in terms of thermosensitivity, biodegradability, and in vitro antitumor activity.

EXPERIMENTAL SECTION

Materials. Hexachlorocyclotriphosphazene (Aldrich) was used without further purification. Dicylohexylcarbodimide (DCC), *N*-hydroxysuccinimide (NHS), $Pb(OAc)_4$, 5-FU, and different amino acid derivatives from Acros were used as received. Methoxy-poly(ethylene glycol) (MPEG), 2-(2-methoxyethoxy)ethanol (MEE), 2-(2-ethoxyethoxy)ethanol (EEE), and 2-(2-buthoxyethoxy)ethanol (BEE) were azeotropically dried with benzene, followed by vacuum-drying, and then stored over molecular sieve 4A. Tetrahydrofuran (THF), ethyl acetate (EA), triethylamine (TEA), and dimethyl formamide (DMF) were freshly distilled prior to use.

Instruments. Proton-decoupled ^{31}P NMR spectra were recorded with a Varian Gemini-300 spectrometer, operating at 121.4 MHz, and using triphenyl phosphate as an external standard. ^1H NMR spectra were recorded with the same spectrometer, but operating at 300 MHz in Fourier transform mode. Elementary analysis was performed with a Fisons 1108 CHNS Microanalyzer and a Polyscan 61E ICP. HPLC was performed on a C18 column (3.9 × 300 mm) at 25 °C. Pure methanol was used as a mobile phase, with a flow rate of 1.0 mL/min.

Synthesis of α-Substituted Glycine Derivatives of 5-FU. Different α-substituted glycine derivatives of 5-FU were prepared through slight modifications of the protocol described by Putman and Kopeček (*29*).

***N*-(Carbobenzyloxy)-L-leucyl-2-(5-fluorouracil-1-yl)-l,d-glycine (L-1).** ^1H NMR (DMSO-d_6), δ (ppm): 0.9 (m, 6H, leucyl CH_3), 1.4 (br m, 2H, leucyl CH_2), 1.6 (br m, 1H, leucyl CH), 4.2 (q, 1H, leucyl α-CH), 5.0 (s, 2H, benzylic CH_2), 6.3 (d, 1H, glycyl CH), 7.3 (s, 5H, aromatic H), 8.0 (overlapping d, 1H, pyrimidine CH).

***N*-(Carbobenzyloxy)-l-alanyl-2-(5-fluorouracil-1-yl)-l,d-glycine (L-2).** ^1H NMR (DMSO-d_6), δ (ppm): 1.2 (overlapping d, 3H, diastereomeric alanyl CH_3), 4.2 (q, 1H, alanyl CH), 5.0 (s, 2H, benzylic CH_2), 6.3 (m, 1H, glycyl CH), 7.3 (s, 5H, aromatic H), 8.0 (overlapping d, 1H, pyrimidine CH).

***N*-(Carbobenzyloxy)-l-phenylalanyl-2-(5-fluorouracil-1-yl)-l,d-glycine (L-3).** ^1H NMR (DMSO-d_6), δ (ppm): 3.1 (m, 2H, d, phenyl alanyl CH_2), 4.4 (br m, 1H, phenylalanyl CH), 5.0 (s, 2H, benzylic CH_2), 6.2 (d, 1H, glycyl CH), 7.3 (br m,10H, aromatic H), 8.0 (overlapping d, 1H, pyrimidine CH).

***N*-(Carbobenzyloxy)-l-valinyl-2-(5-fluorouracil-1-yl)-l,d glycine (L-4).** ^1H NMR (DMSO-d_6), δ (ppm): 0.8 (m, 6H, valinyl CH_3), 2.0 (m, 1H, valinyl CH), 4.0 (br m, 1H, valinyl α-CH), 5.0 (s, 2H, benzylic CH_2), 6.2 (d, 1H, glycyl CH), 7.3 (br m, 10H, aromatic H), 8.0 (overlapping d, 1H, pyrimidine CH).

***N*-(Carbobenzyloxy)-l-glycyl-2-(5-fluorouracil-1-yl)-l,d glycine (L-5).** ^1H NMR (DMSO-d_6), δ (ppm): 3.8 (s, 2H, glycyl CH_2), 5.0 (s, 2H, benzylic CH_2), 6.2 (d, 1H, glycyl CH), 7.3 (s, 5H, aromatic H), 8.0 (overlapping d, 1H, pyrimidine CH).

Synthesis of Cyclotriphophazenes with Amino Groups. $N_3P_3(MPEG350)_3(LysOEt)_3$. A sodium salt of methoxy-poly(ethylene glycol) ($M_w = 350$, MPEG350) was prepared by the reaction of MPEG350 (7.05 g, 20.1 mmol) with 1.5 equiv of sodium metal in THF (230 mL) at refluxing temperature, for 24 h. After filtration for the removal of excess sodium, the solution was cooled to −60 °C in a dry ice−acetone bath and added to a solution of hexachlorocyclotriphosphazene (2.00 g, 5.75 mmol) in THF. The reaction was stirred for 5 h at −60 °C. Meanwhile, L-lysine ethyl ester dihydrochloride (12.8 g, 51.8 mmol) was suspended in anhydrous THF (150 mL) containing TEA (28.7 mL, 207 mmol). The trimer solution was added to the L-lysine ethyl ester solution, which was then stirred for 24 h at room temperature. The reaction mixture was filtered, and the filtrate was concentrated under reduced pressure. The filtrate was then poured into a large amount of hexane, to obtain precipitates. The polymer was further purified by LCST separation, as described below. The other polymers were prepared in a similar manner, using different substituents and molar ratios. Yield: 6.45 g (60%). ^1H NMR (D_2O), δ (ppm): 1.3 (t, 3H, ester CH_3), 1.4 (br m, 2H, lysine γ CH_2), 1.6 (br m, 2H, lysine β CH_2), 1.7 (br m, 2H, lysine δ CH_2), 2.9 (br m, 2H, lysine ϵ CH_2), 3.4 (s, 3H, methoxy CH_3), 3.6 (t, 1H, lysine α CH_2), 3.7 (br m, 26H, MPEG CH_2), 4.1 (m, 2H, MPEG CH_2), 4.2 (q, 2H, ester CH_2). ^{31}P NMR (D_2O), δ (ppm): 42.42.

LCST Separation (27). Trifluoroethanol was used as an LCST-lowering agent. Trifluoroethanol was slowly added to a trimer solution (5 w/v %) in water, until the solution became turbid. The turbid solution was moved to an ice bath, yielding a transparent solution, and it was then incubated in a water bath, with agitation, for 15 min at the desired temperatures (20−30 °C). The reprecipitated trimer was then centrifugally separated and freeze-dried.

$N_3P_3(MEE)_3(LysOEt)_3$. Yield: 73%. ^1H NMR (D_2O), δ (ppm): 1.3 (t, 3H, ester CH_3), 1.4 (br m, 2H, lysine γ CH_2), 1.6 (br m, 2H, lysine β CH_2), 1.7 (br m, 2H, lysine δ CH_2), 2.9 (br m, 2H, lysine ϵ CH_2), 3.4 (s, 3H, methoxy CH_3), 3.6 (t, 1H, lysine α CH), 3.7 (br m, 6H, MEE CH_2), 4.1 (m, 2H, MEE CH_2), 4.2 (q, 2H, ester CH_2). ^{31}P NMR (D_2O), δ (ppm): 42.47.

$N_3P_3(EEE)_3(LysOEt)_3$. Yield: 57%. ^1H NMR (D_2O), δ (ppm): 1.2 (t, 3H, EEE CH_3), 1.3 (t, 3H, ester CH_3), 1.4 (br m, 2H, lysine γ CH_2), 1.6 (br m, 2H, lysine β CH_2), 1.7 (br m, 2H, lysine δ CH_2), 2.9 (br m, 2H, lysine ϵ CH_2), 3.6 (t, 1H, lysine α CH), 3.7 (br m, 8H, EEE CH_2), 4.1 (m, 2H, EEE CH_2), 4.2 (q, 2H, ester CH_2). ^{31}P NMR (D_2O), δ (ppm): 42.46.

$N_3P_3(BEE)_3(LysOEt)_3$. Yield: 48%. ^1H NMR (D_2O), δ (ppm): 1.2 (t, 3H, BEE CH_3), 1.3 (t, 3H, ester CH_3), 1.4 (br m, 2H, lysine γ CH_2), 1.6 (m, 4H, buthoxy CH_2), 1.6 (br m, 2H, lysine β CH_2), 1.7 (br m, 2H, lysine δ CH_2), 2.9 (br m, 2H, lysine ϵ CH_2), 3.5 (t, 2H, buthoxy CH_2), 3.6 (t, 1H, lysine α CH), 3.7 (br m, 4H, BEE CH_2), 4.1 (m, 2H, BEE CH_2), 4.2 (q, 2H, ester CH_2). ^{31}P NMR (D_2O), δ (ppm): 44.68.

Synthesis of 5-Fluorouracil/Cyclotriphophazenes Conjugates. N_3P_3(MPEG350)$_3$(Leu-Gly(5-Fu)-Lys)$_3$ (conjugate 1). DCC (0.219 g, 10.6 mmol) and NHS (0.122 g, 10.6 mmol) were added to a solution of L-1 (0.477 g, 10.6 mmol) dissolved in dry THF (30 mL) and stirred for 24 h. N_3P_3(MPEG350)$_3$(LysOEt)$_3$ (0.500 g, 0.294 mmol) in $CHCl_3$ (30 mL) was added dropwise to the reaction mixture and stirred for 4 h. The reaction was monitored using ninhydrin. The solvents were evaporated under reduced pressure, and the resulting product was purified by LCST separation. The obtained polymer, N_3P_3(MPEG350)$_3$(CBZ-Leu-Gly(5-Fu)-Lys)$_3$ (0.640 g, 0.213 mmol), was then dissolved in 15 mL of methanol and added to a suspension of 10% Pd/C (0.192 g) in 1 mL of dry methanol. The reaction mixture was stirred at room temperature for 4 h, under H_2 gas. After completion of the reaction, the catalyst was removed by filtration through a 0.45 μm membrane filter. The organic filtrate was evaporated under reduced pressure. The resulting polymer was dissolved in a small amount of water and then freeze-dried. The other polymers were prepared in a similar manner, using different substituents. Yield: 0.530 g (67%). ^{1}H NMR (D_2O), δ (ppm): 1.0 (6H, CH_3), 1.3 (3H, CH_3), 1.5∼1.9 (9H, CH, CH_2), 3.0 (2H, CH_2), 3.35 (3H, CH_3), 3.6 (27H, CH_2, CH), 4.0∼4.2 (4H, CH_2), 4.3∼4.5 (1H, CH), 6.4 (1H, CH), 8.2 (1H, CH). ^{31}P NMR (D_2O, ppm): 43.65. HPLC: 99.82%. Elem. anal. (%) calcd: C (46.6), H (7.06), N (10.9). Found: C (46.7), H (7.38), N (10.8).

N_3P_3(MPEG350)$_3$(Phe-Gly(5-Fu)-Lys)$_3$ (conjugate 2). 10.6 mmol of L-3 and 0.294 mmol of N_3P_3(MPEG350)$_3$-(LysOEt)$_3$. Yield: 62%. ^{1}H NMR (D_2O), δ (ppm): 1.2 (3H, CH_3), 1.5∼1.9 (6H, CH_2), 2.9 (2H, CH_2), 3.2 (2H, CH_2), 3.3 (3H, CH_3), 3.65 (27H, CH_2, CH), 4.1 (2H, CH_2), 4.2 (2H, CH_2), 4.4 (1H, CH), 6.4 (1H, CH), 7.3 (5H, CH), 7.6∼7.8 (1H, CH). ^{31}P NMR (D_2O, ppm): 43.76. HPLC: 99.71%. Elem. anal. (%) calcd: C (49.2), H (7.02), N (10.5). Found: C (49.0), H (7.00), N (9.62).

N_3P_3(MEE)$_3$(Leu-Gly(5-Fu)-Lys)$_3$ (conjugate 3). 17.8 mmol of L-1 and 0.495 mmol of N_3P_3(MEE)$_3$(LysOEt)$_3$ Yield: 44%. ^{1}H NMR (D_2O, ppm): 0.9 (6H, CH_3), 1.2 (3H, CH_3), 1.4∼1.9 (9H, CH_2, CH), 2.85 (2H, CH_2), 3.35 (3H, CH_3), 3.7 (7H, CH_2, CH), 4.0 (2H, CH_2), 4.2 (2H, CH_2), 4.4 (1H, CH), 4.5 (1H, CH), 6.5 (1H, CH), 7.8 (1H, CH). ^{31}P NMR (D_2O, ppm): 42.30. HPLC: 99.95%. Elem. anal. (%) calcd: C (45.5), H (7.00), N (14.9). Found: C (45.6), H (6.86), N (14.6).

N_3P_3(MEE)$_3$(Phe-Gly(5-Fu)-Lys)$_3$ (conjugate 4). 17.8 mmol of L-3 and 0.495 mmol of N_3P_3(MEE)$_3$(LysOEt)$_3$. Yield: 52%. ^{1}H NMR (D_2O, ppm): 1.2 (3H, CH_3), 1.5∼1.9 (6H, CH_2), 2.9 (2H, CH_2), 3.2 (2H, CH_2), 3.3 (3H, CH_3), 3.7 (7H, CH_2, CH), 4.1 (2H, CH_2), 4.2 (2H, CH_2), 4.4 (1H, CH), 6.4 (1H, CH), 7.3 (5H, CH), 7.6∼7.8 (1H, CH). ^{31}P NMR (D_2O, ppm): 42.37. HPLC: 99.99%. Elem. anal. (%) calcd: C (46.5), H (6.56), N (13.6). Found: C (46.5), H (5.98), N (13.1).

N_3P_3(MEE)$_3$(Ala-Gly(5-Fu)-Lys)$_3$ (conjugate 5). 17.8 mmol of L-2 and 0.495 mmol of N_3P_3(MEE)$_3$(LysOEt)$_3$. Yield: 40%. ^{1}H NMR (D_2O, ppm): 1.2 (3H, CH_3), 1.5 (3H, CH_3), 1.4∼1.9 (6H, CH_2), 2.85 (2H, CH_2), 3.35 (3H, CH_3), 3.65 (7H, CH_2, CH), 4.0 (2H, CH_2), 4.2 (2H, CH_2), 4.4 (1H, CH), 4.5 (1H, CH), 6.5 (1H, CH), 7.9 (1H, CH). ^{31}P NMR (D_2O, ppm): 42.35. HPLC: 99.99%. Elem. anal. (%) calcd: C (40.1), H (6.79), N (14.9). Found: C (39.8), H (6.16), N (14.4).

N_3P_3(EEE)$_3$(Leu-Gly(5-Fu)-Lys)$_3$ (conjugate 6). 17.1 mmol of L-1 and 0.474 mmol of N_3P_3(EEE)$_3$(LysOEt)$_3$. Yield: 43%. ^{1}H NMR (D_2O, ppm): 0.9 (6H, CH_3), 1.2∼1.3 (6H, CH_3), 1.5∼1.9 (9H, CH, CH_2), 2.9 (2H, CH_2), 3.5 (9H, CH, CH_2), 4.0 (2H, CH_2), 4.2 (2H, CH_2), 4.4 (1H, CH), 6.5 (1H, CH), 7.9 (1H, CH). ^{31}P NMR (D_2O, ppm): 42.18. HPLC: 99.96%. Elem. anal. (%) calcd: C (44.0), H (7.35), N (13.8). Found: C (43.9), H (6.83), N (13.2).

N_3P_3(EEE)$_3$(Val-Gly(5-Fu)-Lys)$_3$ (conjugate 7). 17.1 mmol of L-4 and 0.474 mmol of N_3P_3(EEE)$_3$(LysOEt)$_3$. Yield: 52%. ^{1}H NMR (D_2O, ppm): 0.9∼1.0 (6H, CH_3), 1.2∼1.3 (6H, CH_3), 1.5∼1.9 (7H, CH, CH_2), 2.9 (2H, CH_2), 3.7 (9H, CH, CH_2), 4.0 (2H, CH_2), 4.2 (2H, CH_2), 4.4 (1H, CH), 6.5 (1H, CH), 7.8∼7.9 (1H, CH). ^{31}P NMR (D_2O, ppm): 42.18. HPLC: 99.94%. Elem. anal. (%) calcd: C (46.4), H (6.91), N (15.1). Found: C (46.1), H (6.87), N (14.2).

N_3P_3(BEE)$_3$(Ala-Gly(5-Fu)-Lys)$_3$ (conjugate 8). 15.8 mmol of L-2 and 0.439 mmol of N_3P_3(BEE)$_3$(LysOEt)$_3$. Yield: 36%. ^{1}H NMR (D_2O, ppm): 0.9 (3H, CH_3), 1.2 (3H, CH_3), 1.5 (3H, CH_3), 1.3∼1.9 (10H, CH_2), 2.9 (2H, CH_2), 3.5 (2H, CH_2), 3.7 (7H, CH_2, CH), 4.0 (2H, CH_2), 4.2 (2H, CH_2), 4.4 (1H, CH), 6.5 (1H, CH), 7.9 (1H, CH). ^{31}P NMR (D_2O, ppm): 42.12. HPLC: 98.85%. Elem. anal. (%) calcd: C (44.3), H (7.10), N (14.5). Found: C (44.4), H (6.68), N (13.9).

N_3P_3(BEE)$_3$(Gly-Gly(5-Fu)-Lys)$_3$ (conjugate 9). 15.8 mmol of L-5 and 0.439 mmol of N_3P_3(BEE)$_3$(LysOEt)$_3$. Yield: 45%. ^{1}H NMR (D_2O, ppm): 0.9 (3H, CH_3), 1.2 (3H, CH_3), 1.3∼1.9 (10H, CH_2), 2.85 (2H, CH_2), 3.5 (2H, CH_2), 3.7 (6H, CH_2), 3.9 (2H, CH_2), 4.0 (2H, CH_2), 4.2 (2H, CH_2), 4.4 (1H, CH), 6.5 (1H, CH), 7.9 (1H, CH). ^{31}P NMR (D_2O, ppm): 42.25. HPLC: 99.86%. Elem. anal. (%) calcd: C (43.4), H (6.95), N (14.8). Found: C (43.8), H (6.57), N (14.4).

Measurement of LCST. The phase transition of the aqueous solution of a conjugate was detected visually, in a closed glass tube immersed in an oil bath. The LCST was identified as the temperature at which the solution became turbid.

In Vitro Hydrolytic Degradation. The time-dependent degradation of 5-FU–cyclotriphosphazene conjugates was assessed in different pH buffer solutions at different temperatures. The conjugates (50 mg) were dissolved in 1 mL of 0.5 M concentrations of different buffer solutions (pH 5 acetate buffer, pH 7.4 tris buffer, and pH 10 carbonate buffer), which were incubated in a water bath at different temperatures. The hydrolytic degradation behaviors were determined by ^{31}P NMR spectroscopy.

In Vitro Antitumor Activity. The in vitro antitumor activity of 5-FU–cyclotriphosphazene conjugates was assessed using leukemia L1210 cells, which were maintained in RPMI 1640 medium supplemented with 10% fetal bovine serum. Cell suspensions containing 1×10^5 cells/mL in culture medium were distributed onto a 24-well plate and incubated with the conjugates in a 5% CO_2 atmosphere at 37 °C for 24, 48, or 72 h. The number of viable cells was determined by means of MTT [3-(4,5-dimethylthiazole-2-yl)-2,5-diphenyltetrazolium bromide] enzyme assay, using a microplate reader (SOFTmax PRO, Molecular Device Corp.), and the concentration of the conjugate exhibiting 50% inhibition of cell growth (ED_{50}) was determined.

RESULTS AND DISCUSSION

Synthesis of 5-FU–Cyclotriphosphazene Conjugates. The 5-FU–cyclotriphosphazene conjugates were synthesized by the following stepwise reactions, syntheses of α-substituted glycine derivatives of 5-FU, and cyclotriphosphazenes with functional groups, and their conjugations. α-Substituted glycine derivatives of 5-FU were prepared for coupling with cyclotriphosphazenes

Scheme 1. Synthetic Pathway to 5-FU Derivatives[a]

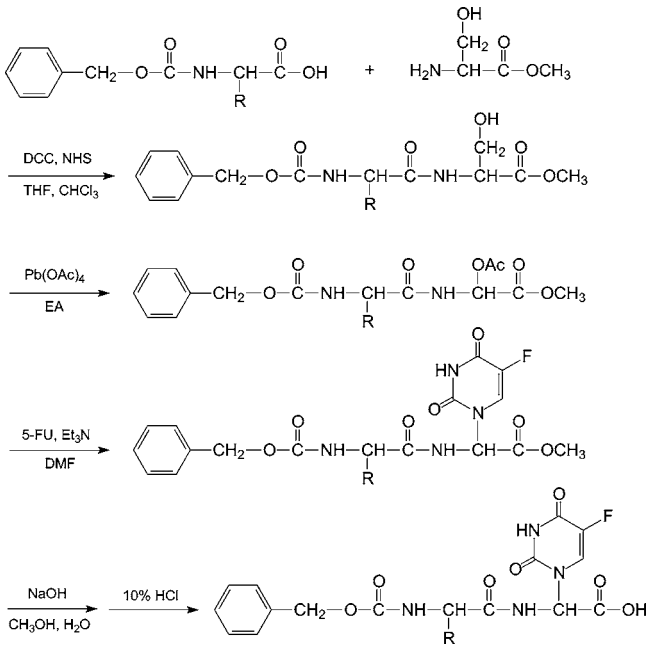

[a] R is $CH_2CH(CH_3)_2$ for L-1, CH_3 for L-2, $CH_2C_6H_5$ for L-3, $CH(CH_3)_2$ for L-4, and H for L-5.

with amino groups via a slightly modified version of the protocol described by Putman and Kopeček (*29*), as shown in Scheme 1. An excellent description of the synthesis and release of 5-FU from the derivative is given in the literature. Substitution at the α-carbon of glycine with the secondary amine of 5-FU results in an intrinsically unstable glycine derivative, which undergoes spontaneous decomposition into the α-substitutent and a glyoxylate. However, the acylation of the glycyl derivative through peptide bond formation stabilizes the α-substituted glycine derivative. Free 5-FU can then be liberated by peptide bond cleavage through enzymatically catalyzed hydrolysis by aminopeptidases.

The synthesis of thermosensitive cyclotriphosphazenes has been previously reported by our group (*26*, *27*). Themosensitive cyclotriphosphazenes are synthesized by the stepwise substitution of hexachlorocyclotriphosphazene $(NPCl_2)_3$ with alkoxy-poly(ethylene glycol) (APEG) and amino acid esters (AAEs). The initial substitution of the chlorotrimer with 3 mol of sodium salt of APEG follows a cis-nongeminal pathway. Successive substitution with AAE yields trimeric derivatives, which exhibit a unique, octopoidal molecular configuration, in which the three hydrophilic APEG groups are oriented in one direction, opposing the other three hydrophobic AAE groups, with respect to the trimer ring plane (*26*). In our present study, the intermediate $N_3P_3(MPEG350)_3(LysOEt)_3$ was synthesized for conjugation with 5-FU by the stepwise substitution of hexachlorocyclotriphosphazene $(NPCl_2)_3$ with methoxy-poly(ethylene glycol) (MPEG) and lysine ethyl ester (LysOEt). Then, the intermediate $N_3P_3(MPEG350)_3(LysOEt)_3$ with amino groups was coupled with an α-substituted glycine derivative of 5-FU with a carboxylic group. All the compounds were fully characterized by means of elementary analysis and H NMR spectroscopy. For the structural characterization of cyclotriphosphazene derivatives, the substitution reactions were monitored by P NMR spectrospcopy (data not shown). P NMR spectroscopy is one of the most powerful tools for the structural study of cyclotriphosphagene derivatives since most critical structural information is available from the chemical shifts and spin−spin coupling data of their ^{31}P NMR spectra. In general, when hexachlorocyclotriphosphazene $(NPCl_2)_3$ is substituted by 3 mol of a substituent, three isomers (geminal 2,2,4; nongeminal *cis*-2,4,6; nongeminal *trans*-2,4,6) may be formed (*26*, *27*). Unreacted hexachlorocyclotriphosphazene exhibits a sharp singlet of ^{31}P resonance, but the addition of MPEG to the chlorotrimer resulted in a mixture of partially substituted products, including mono-, di-, and trisubstituted products. More MPEG was added to the reaction mixture until the peak due to the trisubstituted product became predominant, coupled with

Scheme 2. Synthetic Pathway to 5-FU−Cyclotriphosphazene Conjugates[a]

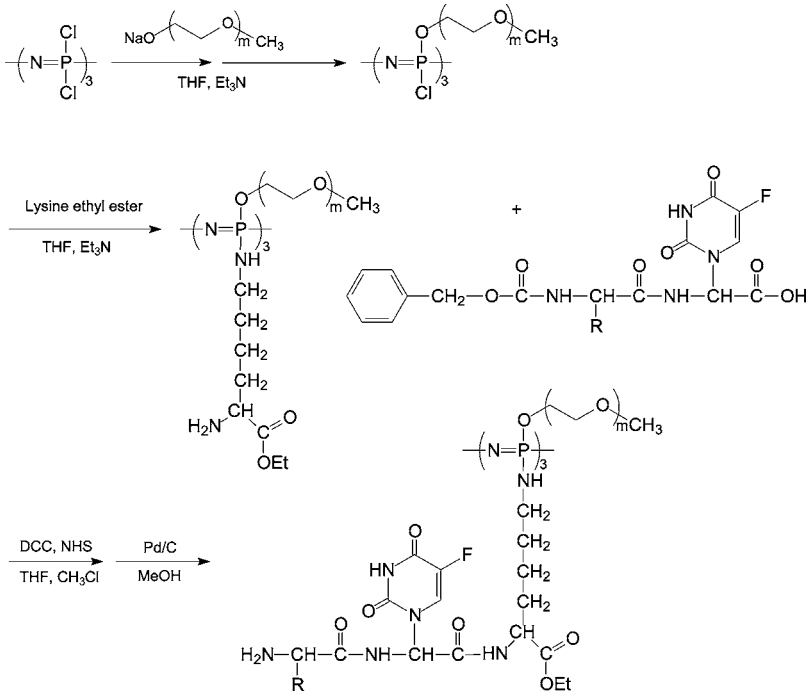

[a] R is $CH_2CH(CH_3)_2$ for L-1, CH_3 for L-2, $CH_2C_6H_5$ for L-3, $CH(CH_3)_2$ for L-4, and H for L-5.

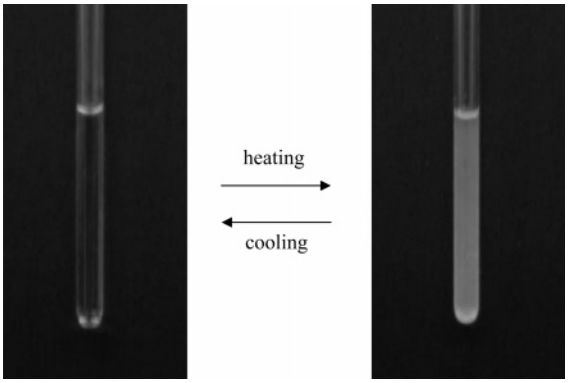

Figure 1. The thermosensitive phase transition of a 5-FU–cyclotriphosphazene conjugate from a soluble to an insoluble state in an aqueous medium. (A) Below LCST. (B) Above LCST.

the disappearance of the peaks due to the partially substituted isomers. The major single peak became complex upon the addition of LysOEt. However, as the reaction progressed, the side peaks disappeared, finally culminating after 24 h in a singlet peak. This sharp singlet ^{31}P resonance clearly indicates that the final product, $N_3P_3(MPEG350)_3(LysOEt)_3$, is a cis-nongeminal isomer. After purification by LCST separation, its isomeric purity was over 99.0%, as determined by HPLC.

The conjugation of α-substituted glycine derivatives of 5-FU to cyclotriphosphazene with amino groups was carried out via coupling reaction, using DCC and NHS. A carboxylic group in a 5-FU derivative is activated to form an ester intermediate, which subsequently reacts with a primary amino group in cyclotriphosphazene, via reaction with NHS, to form an amide bond. After the coupling reaction, the deprotection of an amino group of 5-FU derivative residues from a benzyloxycarbonyl group was carried out by catalytic hydrogenolysis. The chemical structure of the final 5-FU–cyclotriphosphazene conjugate was verified via ^{1}H NMR and ^{31}P NMR spectroscopy in conjunction with elemental analysis. In ^{1}H NMR spectra, the 5-FU signals in the final conjugates were clearly observed at 7.6–8.2 ppm. In ^{31}P NMR spectra, all of the 5-FU–cyclotriphosphazene conjugates exhibited sharp singlet ^{31}P resonances at 40∼45 ppm, and their isomeric purities were over 99%, as determined by HPLC.

Thermosensitivity of 5-FU–Cyclotriphosphazene Conjugates. The thermosensitive behavior of cyclotriphosphazenes with hydrophilic ethylene oxide chains and hydrophobic amino acid esters was previously commented on by our group (*26*, *27*). The cyclotriphosphazene exhibited a reversible and thermosensitive phase transition in an aqueous medium, from a soluble to an insoluble state.

The present 5-FU conjugates also exhibited a reversible and thermosensitive sol-to-prep transition in aqueous media, as shown in Figure 1. The phase transition with LCST is illustrated in Figure 2, and the LCSTs of the conjugates were listed in Table 1. Below LCST, the 5-FU–cyclotriphosphazene conjugate is readily soluble in aqueous media. Water molecules form hydrogen bonds with the fully extended side chains of the conjugates. As the temperature rises, however, the hydrogen bonds gradually degenerate and the hydrophobic groups are exposed, leading to physical association between the hydrophobic groups of the amino acid esters. As the temperature increases further, water molecules surrounding hydrophilic ethylene oxide chains are also excluded, leading to precipitation of the conjugate from the solution. This thermosensitive phase transition process is completely reversible, in that the polymer solutions precipitate upon warming and then are able to revert upon cooling to the original sol state. The rates of the phase transitions, both sol-to-prep and prep-to-sol, are fairly fast. A transparent solution in water became turbid in less than 10 s at 10 °C above LCST, and the turbid solution reverted to transparency in less than 10 s at 10 °C below LCST.

The LCST was greatly affected by the hydrophobic–hydrophilic balance of the conjugate. More hydrophobic

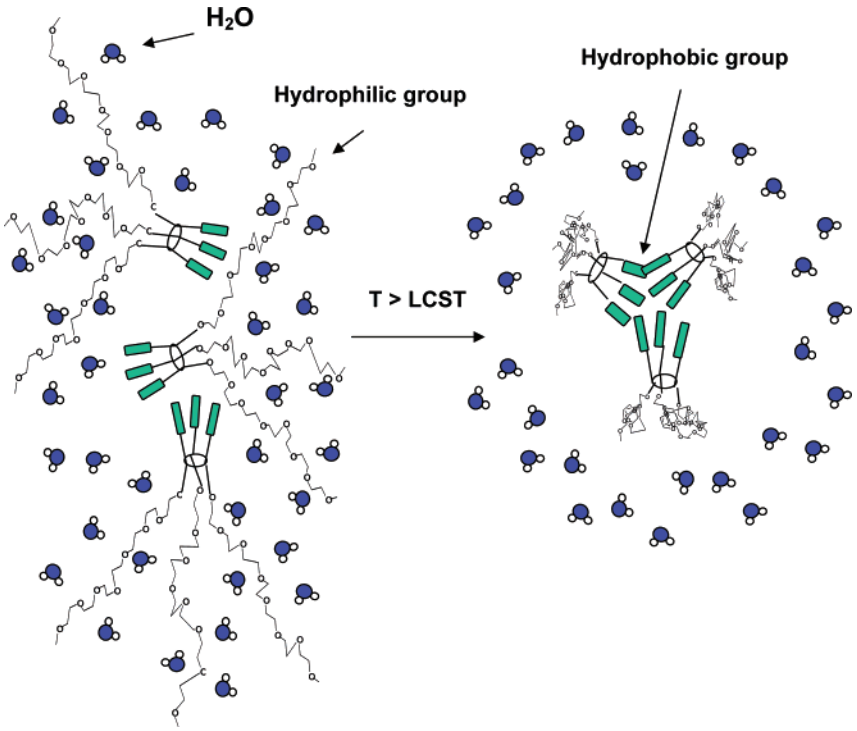

Figure 2. Schematic representation for the clouding of an aqueous solution of a 5-FU–cyclotriphosphazene conjugate with a unique octopoidal molecular structure.

Table 1. LCSTs and in Vitro Antitumor Activities of 5-FU−Cyclotriphophazene Conjugates

conjugate	compound formula[a]	LCST (°C)		ED_{50}[b]	
		H_2O	PBS	μg/mL	μM
1	$N_3P_3(MPEG350)_3(Leu\text{-}Gly(5\text{-}Fu)\text{-}Lys)_3$	>100	>100	4.2	1.6
2	$N_3P_3(MPEG350)_3(Phe\text{-}Gly(5\text{-}Fu)\text{-}Lys)_3$	56	47	7.3	2.6
3	$N_3P_3(MEE)_3(Leu\text{-}Gly(5\text{-}Fu)\text{-}Lys)_3$	27	28	1.7	0.9
4	$N_3P_3(MEE)_3(Phe\text{-}Gly(5\text{-}Fu)\text{-}Lys)_3$	11	9	7.5	3.5
5	$N_3P_3(MEE)_3(Ala\text{-}Gly(5\text{-}Fu)\text{-}Lys)_3$	>100	>100	2.0	1.0
6	$N_3P_3(EEE)_3(Leu\text{-}Gly(5\text{-}Fu)\text{-}Lys)_3$	17	17	4.0	2.1
7	$N_3P_3(EEE)_3(Val\text{-}Gly(5\text{-}Fu)\text{-}Lys)_3$	15	13	7.0	3.3
8	$N_3P_3(BEE)_3(Ala\text{-}Gly(5\text{-}Fu)\text{-}Lys)_3$	14	12	3.7	1.9
9	$N_3P_3(BEE)_3(Gly\text{-}Gly(5\text{-}Fu)\text{-}Lys)_3$	19	18	5.4	2.9
5-FU		-	-	0.3	4.6

[a] MPEG: methoxy poly(ethylene glycol), MEE: 2-(2-methoxyethoxy)ethanol, EEE: 2-(2-ethoxyethoxy)ethanol, BEE: 2-(2-buthoxyethoxy)ethanol. [b] The concentration of the conjugate exhibiting 50% inhibition of cell growth.

tripeptide side groups resulted in lower LCST values. Comparing conjugates **1** and **2**, the LCST of the conjugate containing phenylalanine ($CH_2C_5H_5$) was 56 °C, while no LCST was observed in the conjugate containing leucine [$CH_2CH(CH_3)_2$]. The LCST could be also lowered by increasing the alkyl chain lengths of the alkoxy groups, due to increases in hydrophobicity. The LCSTs of conjugates **3** (methoxy) and **6** (ethoxy) were 27 and 17 °C, respectively. On the contrary, the conjugates with longer ethylene oxide chains (conjugates **1** and **2**) exhibited high LCSTs due to their high hydrophilicity. These results are consistent with previous studies of poly(organophosphazenes) or cyclotriphosphazenes with PEG and amino acid esters as side groups (*22*, *26*, *27*). The attached 5-FU did not significantly affect the thermosensitive behavior of cyclotriphosphazene. Considering over 20 different naturally occurring amino acids with different hydrophobicities, the LCST of a 5-FU−cyclotriphosphazene conjugate could be readily manipulated by substitution with different amino acid side groups. Among the present 5-FU−cyclotriphosphazene conjugates, conjugate **3** exhibited an LCST which was just slightly below body temperature. Therefore, it would appear to have great potential with regard to direct drug delivery to a tumor site. Upon intratumoral injection and subsequent warming to body temperature, the drug−polymer conjugate will precipitate from solution, hopefully functioning as a depot for the sustained release of 5-FU into tumor tissues.

Hydrolytic Degradation of 5-FU−Cyclotriphosphazene Conjugates. The in vitro hydrolytic degradation behaviors of 5-FU−cyclotriphosphazene conjugates were assessed under varying conditions of pH and temperature. The hydrolysis of the conjugate was monitored by ^{31}P NMR spectroscopy for 20 days (data not shown). The conjugate was relatively stable in a basic buffer solution. However, the conjugate demonstrated gradual degradation in neutral and acidic buffer solutions, and high temperature greatly facilitated its hydrolytic degradation. The conjugate before hydrolytic degradation exhibited a sharp singlet ^{31}P resonance. After 10 days incubation in neutral and basic buffer solutions, the small peaks appeared around the main peak, implying the ring opening of the cyclotriphosphazene conjugate due to hydrolytic degradation. The main resonance upfield-shifted with increasing incubation time, and the ring cleavage-associated peaks became more pronounced, suggesting gradual hydrolytic degradation in neutral and acidic buffer solutions. These results are inconsistent with those of the previous study (*27*), in that the hydrolysis of cyclotriphosphazene with MPEG and amino acid ester was faster in a basic solution than in acidic or neutral solutions. Two possible mechanisms underlying the hydrolytic degradation of cyclotriphosphazene derivatives have been proposed by Allcock and colleagues (*30*). One is the protonation of the nitrogen atom in the skeleton or in the side group, resulting in ring cleavage. The other is carboxylic acid-catalyzed degradation. The initial step in this process is the hydrolysis of a pendant ester group, with a consequent protonation of the nitrogen atom in the skeleton or in the side group. It appears that the present cyclotriphosphazene derivatives underwent hydrolytic degradation through the first pathway, whereas the cyclotriphosphazenes (*27*) with MPEG and amino acid esters were hydrolyzed via the second pathway.

In Vitro Antitumor Activity of 5-FU−Cyclotriphosphazene Conjugates. The in vitro cytotoxicity of 5-FU−cyclotriphosphazene conjugates was assessed by MTT assay, with regard to its action against the murine leukemia L1210 cell line. Table 1 lists the ED_{50} values, representing the concentration of the conjugate necessary to inhibit 50% of tumor cell growth. All of the conjugates displayed dose-dependent cytotoxicity against the tumor cell line, and all exhibited more pronounced cytotoxicity than did 5-FU, implying that the macromolecular prodrug of 5-FU should retain its antitumor activity, even after derivatization. However, the effect of thermosensitivity with the LCST of the prodrug on antitumor activity could not be definitively determined in the in vitro study. The in vivo study using tumor-bearing mice is still underway, and its results will be reported soon.

CONCLUSIONS

Novel macromolecular prodrugs of 5-FU were synthesized and assessed with regard to their ability to undergo thermosensitive phase transition from a soluble to an insoluble state. The LCSTs of these compounds appeared to be dependent on the hydrophilic−hydrophobic balance of the 5-FU−cyclotriphosphazene conjugate. More hydrophobic side groups resulted in lower LCST values. The LCST of the conjugate could be readily manipulated by the application of different ethylene oxide chains and amino acids with different hydrophobicities. The conjugate was gradually degraded in neutral and acidic buffer solutions, but relatively stable in a basic buffer solution. The conjugate exhibited effective antitumor activity against the murine leukemia L1210 cell line. This thermosensitive, polymeric drug delivery system is a very appealing option for a future drug delivery system, in which, by a simple injection rather than a surgical operation, a depot for drug release may be created.

ACKNOWLEDGMENT

This research was financially supported by the Ministry of Science and Technology in Korea.

LITERATURE CITED

(1) Duncan, R. (2003) The dawning era of polymer therapeutics. *Nature Rev. Drug Discovery 2*, 347−360.
(2) Marcucci, F., and Lefoulon, F. (2004) Active Targeting with particulate drug carriers in tumor therapy: fundamentals and recent progress. *Drug Discovery Today 9*, 219−228.
(3) Iwai, K., Maeda, H., and Konno, T. (1984) Use of oily contrast medium for selective drug targeting to tomour: Enhanced therapeutic effect and X-ray imaging. *Cancer Res. 44*, 2114−2121.
(4) Matsumura, Y., and Maeda, H. (1986) A new concept for macromolecular therapeutics in cancer chemotherapy: mechanism of thmoritropic accumulation of proteins and antitumor agent smancs. *Cancer Res. 46*, 6387−6392.
(5) Omelyaneko, V., Kopecekova, P., Gentry, C., and Kopecek, J. (1998) Targetable HPMA copolymer adriamycin conjugates. Recognition, internalization, and subcellular fate. *J. Controlled Release 53*, 25−37.
(6) Son, Y. J., Jang, J.-S., Cho, Y. W., Chung, H., Park, R.-W., Kwon, I. C., Kim, I.-S., Park, J. Y., Seo, S. B., Park, C. R., and Jeong, S. Y. (2003) Biodistribution and anti-tumor efficacy of doxorubicin loaded glycol-chitosan nanoaggregates by EPR effect. *J. Controlled Release 91*, 135−145.
(7) Ringdorf, H. (1975) Structure and properties of pharmacologically active polymers. *J. Polym. Sci.: Polym. Symp. 51*, 135−153.
(8) Vasey, P. A., Kaye, S. B., Morrison, R., Twelves, C., Wilson, P., Duncan, R., Thomson, A. H., Murray, L. S., Hilditch, T. E., Murray, T., Burtles, S., Fraier, D., Frigerio, E., and Cassidy, J. (1999) Phase I clinical and pharmacokinetic study of PK1 [N-(2-hydroxypropyl)methacrylamide copolymer doxorubicin]: First member of a new class of chemotherapeutic agents-drug-polymer conjugates. *Clin. Cancer Res. 5*, 83−94.
(9) Seymour, L. W., Ferry, D. R., Anderson, D., Hesslewood, S., Julyan, P. J., Poyner, R., Doran, J., Young, A. M., Burtles, S., and Kerr, D. J. (2002) Hepatic drug targeting: Phase I evaluation of polymer-bound doxorubicin. *J. Clin. Oncol. 20*, 1668−1676.
(10) Laakkonen, P., Porkka, K., Hoffman, J. A., and Ruoslahti, E. (2002) A tumor-homing peptide with a targeting specificity related to lymphatic vessels. *Nature Med. 8*, 751−755.
(11) David, A., Kopeckova, P., Rubinstein, A., and Kopecek, J. (2001) Enhanced biorecognition and internalization of HPMA copolymers containing multiple or multivalent carbohydrate side-chains by human hepatocarcinoma cells. *Bioconjugate Chem. 12*, 890−899.
(12) Dube, D., Francis, M., Leroux, J.-C., and Winnik, F. M. (2002) Preparation and tumor cell uptake of poly(N-isopropylacrylamide) folate conjugates. *Bioconjugate Chem. 13*, 685−692.
(13) Olivier, V., Meisen, I., Meckelein, B., Hirst, T. R., Peter-Katalinic, J., Schmidt, M. A., and Frey, A. (2003) Influence of targeting ligand flexibility on receptor binding of particulate drug delivery systems. *Bioconjugate Chem. 14*, 1203−1208.
(14) Pastorino, F., Brignole, C., Marimpietri, D., Sapra, P., Moase, E. H., Allen, T. M., and Ponzoni, M. (2003) Doxorubicin-loaded Fab′ fragments of anti-disaloganglioside immunoliposomes selectively inhibit the growth and dissemination of human neuroblastoma in nude mice. *Cancer Res. 63*, 86−92.
(15) Jeong, B., Bae, Y. H., Lee, D. S., and Kim, S. W. (1997) Biodegradable block copolymers as injectable drug-delivery systems. *Nature 388*, 860−862.
(16) Jeong, B., Kim, S. W., and Bae, Y. H. (2002) Thermosensitive sol−gel reversible hydrogels. *Adv. Drug Delivery Rev. 54*, 37−51.
(17) Jeong, B., Choi, Y. K., Bae, Y. H., Zentner, G., and Kim, S. W. (1999) New biodegradable polymers for injectable drug delivery systems. *J. Controlled Release 62*, 109−114.
(18) Ruel-Gapriepy, E., Chenite, A., Chaput, C., Guirguis, S., and Leroux, J.-C. (2000) Characterization of thermosensitive chitosan gels for the sustained delivery of drugs. *Int. J. Pharm. 203*, 89−98.
(19) Molinaro, G., Leroux, J.-C., Damas, J., and Adam, A. (2002) Biocompatibility of thermosensitive chitosan-based hydrogels: an in vivo experimental approach to injectable biomaterials. *Biomaterials 23*, 2717−2722.
(20) Ruel-Gapriepy, E., Leclair, G., Hildgen, P., Gupta, A., and Leroux, J.-C. (2002) Thermosensitive chitosan-based hydrogel containing liposomes for the delivery of hydrophilic molecules. *J. Controlled Release 82*, 373−383.
(21) Ruel-Gapriepy, E., Shive, M., Bichara, A., Berrada, M., Garrec, D. L., Chenite, A., and Leroux, J.-C. (2004) A thermosensitive chitosan-based hydrogel for the local delivery of paclitaxel. *Eur. J. Pharm. Biopharm. 57*, 53−63.
(22) Song, S.-C., Lee, S. B., Jin, J.-I., and Sohn, Y. S. (1999) A new class of biodegradable thermosensitive polymers. I. Synthesis and characterization of poly(organophosphazenes) with methoxy-poly(ethylene glycol) and amino acid esters as side groups. *Macromolecules 32*, 2188−2193.
(23) Lee, S. B., Song, S.-C., Jin, J.-I., and Sohn, Y. S. (1999) A new class of biodegradable thermosensitive poymers. 2. Hydrolytic properties and salt effect on the lower critical solution temperature of poly(organophosphazenes) with methoxypoly(ethylene glycol) and amino acid esters as side groups. *Macromolecules 32*, 7820−7827.
(24) Lee, B. H., Lee, Y. M., Sohn, Y. S., and Song, S.-C. (2002) A thermosensitive poly(organophosphazene) gel. *Macromolecules 35*, 3876−3879.
(25) Lee, B. H., and Song, S.-C. (2004) Synthesis and characterization of biodegradable thermosensitive poly(organophosphazene) gels. *Macromolecules 37*, 4533−4537.
(26) Lee, S. B., Song, S.-C., Jin, J.-I., and Sohn, Y. S. (2000) Thermosensitive cyclotriphosphazenes. *J. Am. Chem. Soc. 122*, 8315−8316.
(27) Lee, S. B., Song, S.-C., Jin, J.-I., and Sohn, Y. S. (2001) Structural and thermosensitive properties of cyclotriphosphazenes with poly(ethylene glycol) and amino acid esters as side groups. *Macromolecules 34*, 7565−7569.
(28) Song, S.-C., Lee, S. B., Lee, B. H., Ha, H.-W., Lee, K. T., and Sohn, Y. S. (2003) Synthesis and antitumor activity of novel thermosensitive platinum(II)-cyclotriphosphazene conjugates. *J. Controlled Release. 90*, 303−311.
(29) Putman, D., and Kopecek, J. (1995) Enantioselective release of 5-fluorouracil from N−(2-hydroxypropyl)methacrylamide-based copolymers via lysosomal enzymes. *Bioconjugate Chem. 6*, 483−492.
(30) Allcock, H. R., Fuller, T. J., and Matsumura, K. (1982) Hydrolysis pathways for aminophosphazenes. *Inorg. Chem. 21*, 515−521.

BC049697U

"Clickable" Agarose for Affinity Chromatography

Sreenivas Punna, Eiton Kaltgrad, and M. G. Finn*

Department of Chemistry and The Skaggs Institute for Chemical Biology, The Scripps Research Institute, 10550 North Torrey Pines Road, La Jolla, California 92037. Received August 8, 2005; Revised Manuscript Received August 12, 2005

Successful purification of biological molecules by affinity chromatography requires the attachment of desired ligands to biocompatible chromatographic supports. The Cu(I)-catalyzed cycloaddition of azides and alkynes—the premier example of "click chemistry"—is an efficient way to make covalent connections among diverse molecules and materials. Both azide and alkyne units are highly selective in their reactivity, being inert to most chemical functionalities and stable to wide ranges of solvent, temperature, and pH. We show that agarose beads bearing alkyne and azide groups can be easily made and are practical precursors to functionalized agarose materials for affinity chromatography.

INTRODUCTION

Biological processes depend on specific interactions between molecules, such as between antibodies and antigens, carbohydrates and lectins, and enzymes and inhibitors. Affinity chromatography (*1*) exploits these various interactions for the analysis and purification of mixtures of biomolecules. One of the members of the interacting pair is immobilized on an insoluble support and is used to "fish out" the complementary agent from a solution passed through or over the column. In many cases, affinity chromatography is a crucial step in the isolation of desired species, for example, providing the only practical means for the separation of tagged or functional proteins from cellular extracts.

Beaded agarose bearing functional groups such as amine ($-NH_2$), carboxylic acid ($-COOH$), aldehyde ($-CHO$), thiol ($-SH$), and hydroxyl ($-OH$) is the support of choice for most ligands of interest (*2*) due to its inexpensive and biocompatible nature. For selective immobilization, a ligand should possess a functional group for attachment to the support that is not essential to its binding property. Ligands can be immobilized in ways detrimental to their intended function when more than one of the attachment units is present in a ligand or when other reactive functional groups on the ligand compete in the immobilization chemistry. A matched pair of groups which is selective in reacting with each other while being unreactive to other functional groups in the molecule would therefore be highly useful in the preparation of functional agarose beads. Organic azides and terminal alkynes fit this description, being inert to most chemical functionalities and stable to wide ranges of solvent, temperature, and pH. While their uncatalyzed [3+2] dipolar cycloaddition is typically very slow at room temeperature (*3*), Cu(I) catalysts accelerate the reaction to a great degree (*4*, *5*). Here we report the first use of azides, alkynes, and their "click reaction" (*6*) for the convenient immobilization of ligands on agarose for affinity chromatography and related purposes.

* To whom correspondence should be addressed. E-mail: mgfinn@scripps.edu.

EXPERIMENTAL PROCEDURES

General. ^1H and ^{13}C NMR spectra were recorded on Bruker DRX-500, AMX-400, or Varian Mercury 200 spectrometers, using $CDCl_3$ or CD_3OD as solvents. Mass spectra were obtained on an Agilent 1100 LC/MS spectrometer (model G1946A). Melting points were measured in a Mel-Temp II capillary melting point apparatus and are uncorrected. Infrared spectra were recorded on a MIDAC EM200 instrument with horizontal attenuated total reflectance accessory from Pike Instruments or in KBr pellets. Column chromatography was performed on EM Science silica gel (40−63 μm mesh). TLC analysis was facilitated by the use of phosphomolybdic acid or $KMnO_4/H_2O$ stains in addition to UV light with fluorescent-indicating plates. Anhydrous sodium sulfate was used for drying solutions. Carboxy Link coupling gel (50% aqueous slurry, 16 μmol of amine groups per milliliter), biotin-PEG-amine, and avidin-HABA complex were purchased from Pierce. All other commercially available reagents were purchased from Acros or Aldrich. Compounds **6** and **7**, kindly provided by Mr. Warren G. Lewis, have been previously described (*5*). Reactions requiring anhydrous conditions were performed under nitrogen.

5-Azidopentanoic Acid 4-Nitrophenyl Ester (2). 1-(3-Dimethylaminopropyl)-3-ethylcarbodimide hydrochloride (EDCI·HCl, 703.8 mg, 3.67 mmol) was added to a solution of *p*-nitrophenol (510.5 mg, 3.67 mmol) and 5-azidopentanoic acid (500 mg, 3.49 mmol) in CH_2Cl_2 (25 mL) at room temperature and stirred overnight, followed by the addition of water and excess EtOAc. The separated organic phase was washed with H_2O and brine solution, dried over Na_2SO_4, and evaporated. The crude product was purified by silica gel column chromatography (1:4 EtOAc/hexane) to give **2** (514 mg) as a pale yellow oil in 52% yield. ^1H NMR ($CDCl_3$) δ 1.62−1.92 (m, 4H), 2.60 (t, J = 6.6 Hz, 2H, $-CH_2N_3$), 3.34 (t, J = 6.6 Hz, 2H), 7.25 (d, J = 9.2 Hz, 2H), 8.23 (d, J = 8.8 Hz, 2H); ^{13}C NMR ($CDCl_3$) δ 22.1, 28.4, 33.9, 51.2, 60.6, 122.6, 125.4, 145.5, 155.5, 170.8; IR (thin film, cm^{-1}): 2946, 2100 (azide), 1768, 1593, 1534, 1345, 1211, 1130, 910, 865, 748; ESMS *m/z* (relative intensity) 287 $(M + Na)^+$ (75), 237 (100), 223 (70).

10.1021/bc0501496 CCC: $30.25 © 2005 American Chemical Society
Published on Web 09/13/2005

Scheme 1

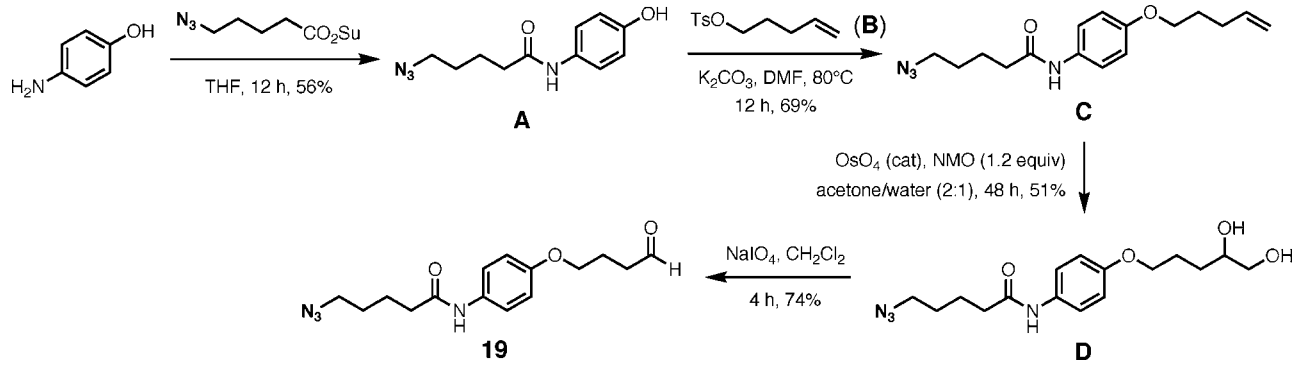

Agarose Azide and Alkyne Beads (4 and 5). CarboxyLink gel (8 mL, maximum of 64 μmol of amine groups) was transferred to a disposable frit, allowed to settle for 30 min, and equilibrated with 5 column volumes of pH 4.7 MES buffer (0.1 M). To the gel was added *p*-nitrophenyl ester **2** (143.4 mg, 64 mmol, 16 μmol/mL) dissolved in DMF with 5% of the MES buffer (8.4 mL), and the capped fritted tube was rotated gently at room temperature for 2 days. Phosphate buffer (600 μL, pH 7, 1.5 M) was added to the reaction mixture, which was then drained into a clean scintillation vial and the absorbance at 412 nm was measured directly. An agarose sample lacking the amine group was used in a control experiment to correct for residual hydrolysis of **2**, which was negligible under these conditions. The amount of attached azide was assumed to be equivalent to the amount of released *p*-nitrophenol, which was determined with the aid of an extinction coefficient measured by the addition of authentic *p*-nitrophenol to the same mixture of DMF, pH 4.7 MES, and pH 7 phosphate (ϵ = 432 M^{-1} cm^{-1}). Agarose **5** was prepared and analyzed by the same procedure, using *p*-nitrophenyl ester **3**.

Fluorescein-alkyne (8). To fluorescein NHS ester (97 mg, 0.205 mmol) in THF (30 mL) was added propargylamine (32 μL, 0.451 mmol), and the reaction was stirred under nitrogen atmosphere at room temperature overnight. After the sample was filtered to remove a small amount of insoluble material, the solvent was evaporated and the residue was washed with CH_2Cl_2 and then Et_2O to afford **8** as a yellow solid in quantitative yield (87 mg). ESMS *m/z* (relative intensity) 414 (M^+, base peak).

Typical Immobilization Procedure. Stock solutions (50 mM) of the following reagents were prepared: 2,6-lutidine (DMF), 2,2′-bipyridine (DMF), CuBr (DMF), and sodium ascorbate (water). A slurry of agarose-azide/alkyne beads (1.0 equiv) in DMF in a disposable frit was treated with the molecule to be attached bearing the complementary (alkyne or azide) group (4.0 equiv), followed by 2,6-lutidine (8.0 equiv), 2,2′-bipyridine (8.0 equiv), cuprous bromide (4.0 equiv), and finally sodium ascorbate (8.0 equiv). The resulting suspension was bubbled with a gentle flow of nitrogen for 1 min, capped, and rotated at room temperature for 12−18 h. The reaction mixture was drained and washed sequentially with approximately 5 column volumes each of DMF, H_2O, MeOH, 0.1 M aq EDTA, H_2O, and DMF.

Biotin-PEG-alkyne (12). To a solution of biotin-PEG-amine (**11**, 33 mg, 0.079 mmol) in CH_2Cl_2 (5 mL) was added 4-pentynoic acid (7.4 mg, 0.045 mmol) followed by 1-(3-dimethylaminopropyl)-3-ethylcarbodimide hydrochloride (EDCI·HCl; 704 mg, 3.67 mmol). The mixture was stirred at room temperature overnight and was then partitioned between EtOAc (10 mL) and water. The organic layer was dried (Na_2SO_4) and evaporated to give compound **12** (9 mg) as a colorless syrup. A further 11 mg was recovered from the aqueous layer by stirring in the presence of additional EtOAc and excess NaCl (overall yield 51%). ^{1}H NMR ($CDCl_3$) δ 1.49−1.55 (m, 2H), 1.86−1.88 (m, 4H), 2.25−2.85 (m, 2H), 2.36 (s, 1H), 2.49−2.60 (m, 6H), 2.75−2.85 (m, 2H), 2.92−3.02 (m, 2H), 3.25−3.30 (m, 1H), 3.40 (m, 2H), 3.41−3.50 (m, 4H), 3.58−3.64 (m, 4H), 3.67−3.70 (m, 2H), 4.35−4.40 (m, 1H), 4.55−4.60 (m, 1H), 8.20 (br s, 1H), 8.4 (br s, 1H);^{13}C NMR ($CDCl_3$) δ 14.7, 25.8, 28.5, 28.7, 34.9, 35.7, 40.0, 56.03, 60.64, 62.4, 68.9, 69.5, 70.2, 70.27, 70.6, 74.4, 82.5, 175.2, 177.7, 178.05; IR (film, cm^{-1}): 3287 (CCH), 3084, 2864, 2114 (alkyne), 1629, 1553, 1265, 1140, 951, 879, 726; ESMS *m/z* (relative intensity) 521 $(M+Na)^+$ (100), 499 $(M+1)^+$ (25), 375 (60).

HIV-Protease Peptide Alkyne (15). Standard Fmoc-based solid phase peptide synthesis techniques were employed (*7*), starting with Wang resin bearing the C-terminal amino acid (Fmoc-Phe-OH, 0.77 mmol/g). Fmoc deprotection was accomplished with two treatments of 20% piperidine in DMF, and amino acid coupling was typically performed with 5.5 equiv of Fmoc-amino acid, 5.0 equiv of HBTU, and excess *i*Pr_2NEt. Fmoc-propargylglycine (CSPS Chemicals, San Diego) was installed as the final (*N*-terminal) amino acid, using DIC/HOBt (5.0 equiv) in CH_2Cl_2. The crude peptide containing the N-terminal Fmoc protecting group was obtained by treating the resulting resin with 94/2.5/2.5/1 CF_3CO_2H/H_2O/1,2-ethanedithiol/SiH(*i*Pr)$_3$ mixture for 3 h at room temperature. The desired peptide was identified by MALDI-MS of fractions from analytical HPLC of the crude product, and then purified by preparative HPLC. The final purified product (peptide G*QCTLNF, where G* = propargylglycine) was obtained in approximately 9% yield, calculated from the weight of the isolated material relative to the amount of amino acid on the starting resin.

After attachment of **15** to **4** by the above procedure, the resulting beads (**16**) were treated with 20% piperidine (4 mL) at room temperature for 10 min. The solution was drained, and the absorbance at 300 nm was measured against a blank composed of 20% piperidine in DMF. Using the measured fluorene molar extinction coefficient of 7800 M^{-1} cm^{-1} determined under identical conditions, the attached peptide concentration was found to be 0.71 μmol/mL, representing approximately 39% conversion of the available azides on the resin (measured as above at 1.84 μmol/mL). Attachment of Fmoc-propargylglycine alone proceeded in 63% yield by the same assay. A contributing factor to the relatively poor attachment of the peptide is its poor solubility, even in DMF, causing it to aggregate and precipitate slowly during the reaction.

4-Azido-*N*-[4-(4-oxobutoxy)phenyl]butyramide (19, Scheme 1). To the *N*-hydroxysuccinimide (Su) ester of

Scheme 2

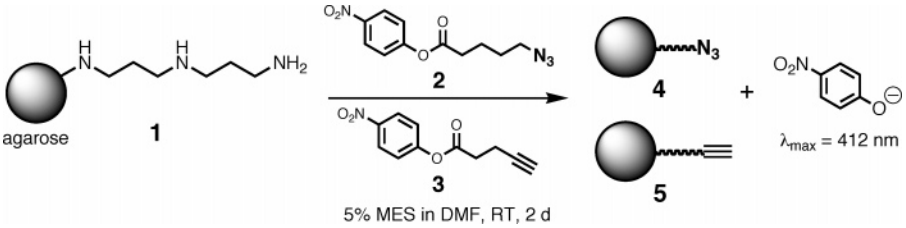

4-azidobutyric acid (2.2 g, 18.32 mmol) in THF (20 mL) was added *p*-aminophenol (1.0 g, 18.32 mmol), and the mixture was stirred overnight at room temperature. The solvent was evaporated and the resulting residue was partitioned between equal volumes of 1 M HCl and EtOAc. The aqueous layer was extracted twice more with EtOAc and the combined organic layers were washed with 1 N HCl, H_2O (2×), brine, dried, and evaporated. The crude product (designated as compound **A**) was purified by column chromatography (1:3 EtOAc/hexanes) to give a brown solid (1.19 g, 57% yield). mp 67−69 °C; ^{1}H NMR ($CDCl_3$) δ 1.50−1.57 (m, 2H), 1.63−1.71 (m, 2H), 2.26 (t, J = 7.5 Hz, 2H), 6.68 (d, J = 8.0 Hz, 2H), 7.19 (dd, J = 8.5, 3.5 Hz), 8.37 (s, 1H); ^{13}C NMR (CD_3OD) δ 24.3, 29.6, 37.2, 52.3, 116.3, 123.6, 131.7, 155.5, 173.9; IR (KBr, cm^{-1}): 2959, 2465, 2096 (azide), 1665, 1449, 1238, 839; ESMS *m/z* (relative intensity) 257 $(M + Na)^+$ (22), 235 $(M+H)^+$ (100).

To a solution of 4-pentene-1-ol (3.0 g, 35 mmol), Et_3N (14.5 mL, 105 mmol), and DMAP (425 mg, 3.5 mmol) in THF (50 mL) was added *p*-TsCl (6.64 g, 34.88 mmol), and the reaction was stirred for 6 h at room temperature. The resulting mixture was filtered through a sintered funnel, the solid was washed with additional THF, and the combined solution was evaporated. The crude product was purified by column chromatography (silica gel, 1:4 EtOAc/hexanes) to obtain the desired tosylate **B** (Scheme 1) as a colorless liquid (6.6 g, 79% yield). ^{1}H NMR ($CDCl_3$) δ 1.58−1.72 (m, 2H), 1.92−2.08 (m, 2H), 2.36 (s, 3H), 3.96 (t, J = 6.4 Hz, 2H), 4.80−4.94 (m, 2H), 5.50−5.73 (m, 1H), 7.27 (d, J = 8.0 Hz, 2H), 7.70 (d, J = 7.8 Hz); ^{13}C NMR ($CDCl_3$) δ 13.9, 21.3, 27.7, 29.1, 69.6, 115.5, 127.6, 132.8, 136.4, 144.6; IR (thin film, cm^{-1}): 3075 (olefin), 2981, 1926, 1643, 1598, 1449, 1346, 1185, 920, 825, 749; ESMS *m/z* (relative intensity) 241 $(M + H)^+$ (10).) This material (720 mg, 3.00 mmol) was combined with compound **A** (702 mg, 3.00 mmol) and K_2CO_3 (1.24 g, 9.0 mmol) in DMF (5.0 mL), and the mixture was stirred at 80 °C for 12 h. Saturated aqueous NH_4Cl solution (25 mL) and EtOAc (25 mL) were added, and the organic layer was separated and washed with additional NH_4Cl solution, water, and brine. The solution was dried and evaporated, and the residue was purified by column chromatography (silica gel, 1:4 EtOAc/hexanes) to give the ether-amide intermediate **C** (627 mg, 69% yield) as a red solid. mp 60−62 °C; ^{1}H NMR ($CDCl_3$) δ 1.63−1.69 (m, 2H), 1.75−1.82 (m, 2H), 1.82−1.89 (m, 2H), 2.22 (q, J = 7.0 Hz, 2H), 2.35 (t, J = 7 Hz, 2H), 3.30 (t, J = 6.5 Hz, 2H, $-CH_2N_3$), 3.93 (t, J = 6 Hz), 4.98−5.08 (m, 2H), 5.84 (m, 1H), 6.83 (d, J = 10.0 Hz), 7.37 (d, J = 8.5 Hz, 2H), 7.41 (br s, 1H); ^{13}C NMR ($CDCl_3$) δ 22.3, 27.9, 29.6, 36.2, 50.7, 66.9, 114.3, 115.0, 121.4, 130.3, 137.3, 155.4, 170.15; IR (KBr, cm^{-1}): 2950, 2100 (azide), 1650, 1310, 1250, 820, 760; ESMS *m/z* (relative intensity) 303 $(M + H)^+$ (100).

To a cooled (ice bath) solution of olefin **C** (500 mg, 1.65 mmol) in 2:1 acetone/water (6 mL) was added a small crystal of OsO_4. After 5 min, *N*-methylmorpholine *N*-oxide (193.3 mg, 1.65 mmol) was added, and the mixture was stirred at room temperature for 2 days. EtOAc and brine were added, and the aqueous layer was further extracted with EtOAc (2 × 25 mL). The crude product obtained from the combined organic layers was purified by column chromatography (silica gel, EtOAc) to give the desired diol (**D**, Scheme 1, 248 mg, 51% yield) as a white solid. Approximately 65 mg of the starting material was also recovered. mp 82−84 °C; ^{1}H NMR ($CDCl_3$) δ 1.50−1.90 (m, 8H), 2.34 (t, J = 7.0 Hz, 2H), 2.70 (br s, −OH), 3.29 (t, J = 5.5 Hz, 2H, $-CH_2N_3$), 3.40−3.44 (m, 1H), 3.60−3.85 (m, 2H), 3.92 (s, 2H), 6.79 (d, J = 9.5 Hz), 7.36 (dd, t, J = 7.0, 5.0 Hz, 2H), 8.32 (br s, 1H); ^{13}C NMR ($CDCl_3$) δ 23.9, 26.5, 29.3, 30.8, 36.9, 52.0, 67.2, 69.0, 72.8, 115.4, 122.9, 132.6, 157.1, 173.6; IR (thin film, cm^{-1}): 2945, 2869, 2132 (azide), 1661, 1490, 1301, 1238, 1018, 830; ESMS *m/z* (relative intensity) 337 $(M + H)^+$ (100).

To a solution of diol **D** (100 mg, 0.297 mmol) in CH_2Cl_2 (5 mL + 2 drops of MeOH) was added saturated aqueous $NaHCO_3$ (0.5 mL) followed by $NaIO_4$ (127 mg, 0.60 mmol). After the sample was stirred at room temperature for 4 h, anhydrous Na_2SO_4 (approximately 1 g) and CH_2Cl_2 (25 mL) were added and the mixture was stirred for a further 30 min. Filtration, washing of the solid with CH_2Cl_2, and evaporation of the combined organic solutions provided compound **19** (67 mg, 74% yield) as a thick colorless syrup. ^{1}H NMR ($CDCl_3$) δ 1.60−1.70 (m, 2H), 1.74−1.85 (m, 2H), 2.08−2.15 (m, 2H), 2.34 (t, J = 6.4 Hz, 2H), 2.65 (t, J = 5.8 Hz, 2H), 3.28 (t, J = 5.6 Hz, 2H, $-CH_2N_3$), 3.95 (t, J = 5.4 Hz, 2H), 6.8 (d, J = 10.8 Hz, 2H, ArH), 7.38 (d, J = 10.8 Hz, 2H, ArH), 7.74 (s, 1H), 9.8 (s, 1H, −CHO); ^{13}C NMR ($CDCl_3$) δ 21.3, 22.0, 27.6, 35.8, 39.9, 50.4, 66.2, 113.9, 121.2, 130.6, 154.7, 170.3, 201.4; IR (film, cm^{-1}): 2949, 2877, 2096 (azide), 1727, 1664 (C=O), 1301, 1233, 959, 833, 743; ESMS *m/z* (relative intensity) 305 $(M+1)^+$ (85).

Test of Affinity Chromatography Function with Aldehyde 19. Functionalized agarose **20**, prepared in the standard manner from **19**, was poured into a column (Amersham Tricom, 5 mm × 50 mm; 1 mL volume; cat#18−1163−09). At pH 7, the column was found to retain the catalytic antibody 84G3 originally obtained by Barbas and co-workers (*8*, *9*) and not an unrelated antibody; details can be found in Figure 5.

RESULTS AND DISCUSSION

Commercially available Carboxy-Link agarose (**1**), which bears addressable amine groups, was treated with the *p*-nitrophenyl ester of 5-azidopentanoic acid (**2**) and 5-pentynoic acid (**3**) to give azide- and alkyne-functionalized beads **4** and **5**, respectively (Scheme 2). The degree of acylation was determined by measurement of the concentration of released *p*-nitrophenol. Loadings of between 3.3 and 4.6 μmol/mL of gel were typical, representing approximately 20−30% of the available amine groups according to the commercial specifications of the gel. However, the standard Kaiser (ninhydrin) test (*10*) gave a positive signal for **1** and negative signals for **4** and **5**, suggesting that most or all of the accessible amine groups of **1** were acylated by **2** and **3**.

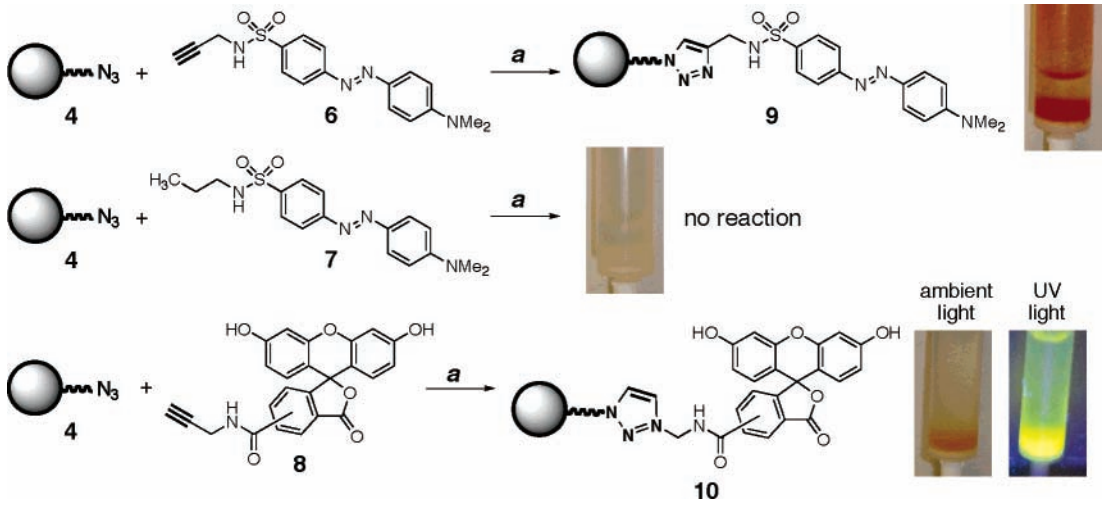

Figure 1. CuAAC coupling of dye reagents to agarose azide and alkyne; a, standard Cu·bipy-mediated coupling conditions (see Experimental Procedures), followed by a wash procedure including 0.l M EDTA to remove Cu ions.

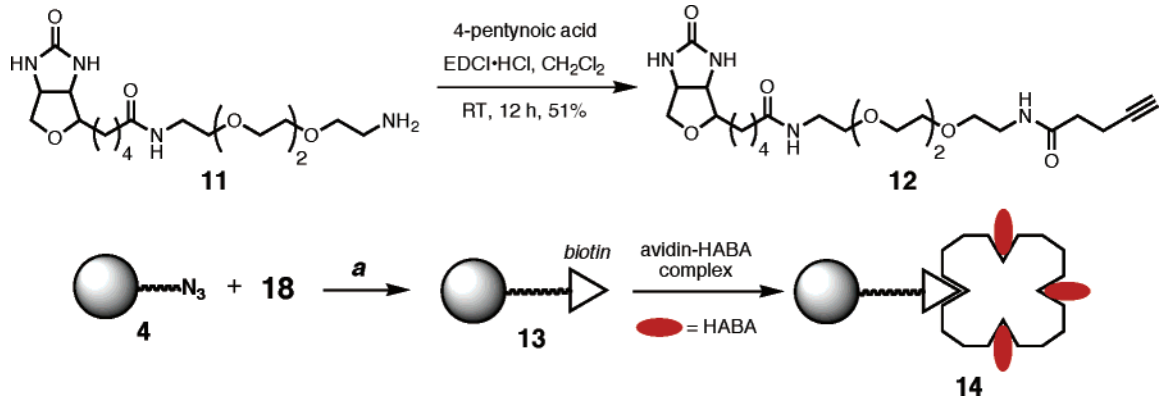

Figure 2. Biotinylation of agarose azide; a, standard Cu·bipy-mediated coupling conditions (see Experimental Procedures), followed by a wash procedure including 0.l M EDTA to remove Cu ions.

To test the feasibility of resin attachment by the Cu-mediated azide-alkyne cycloaddition (CuAAC) reaction, agarose-azide beads **4** were treated with a dabsyl-alkyne derivative (**6**) and the corresponding dye with an *n*-propyl group in place of the alkyne (**7**), in the presence of cuprous bromide, 2,2′-bipyridine as accelerating ligand (*5*), sodium ascorbate to maintain a reducing environment, and 2,6-lutidine as mild base (Figure 1). The dye was successfully attached with **6**, as indicated by the production of an intense and permanent red color in the resulting beads (**9**). Use of the control **7** or omission of Cu(I) from the reaction of **6** gave colorless beads. In addition, no dye could be washed from **9** even upon extensive treatment with DMF; these observations show that the dye does not adsorb to the resin. Similarly, **4** was treated with fluorescein alkyne **8** under CuAAC conditions to give yellow beads that were strongly fluorescent under ultraviolet light. The same successful results were obtained with agarose-alkyne **5** and the complementary azide-substituted dabsyl compound (data not shown).

Biotinylated supports are a mainstay of protein immobilization and therefore of experimental biochemistry. The CuAAC reaction provides a convenient addition to the many methods already in use for constructing such materials. Biotin alkyne **12** was prepared from commercially available biotin-PEG-amine **12** and 4-pentynoic acid (Figure 2). Immobilization on agarose azide beads gave **13**, which was treated with a red solution of avidin-HABA (HABA = 2-(4′-hydroxyphenyl)azobenzoic acid) complex. Tight avidin−biotin interaction gave the resulting beads a persistent red color (**14**), whereas a mixture of avidin-HABA with agarose-azide **4** resulted in no such binding.

The immobilization of peptides is a common application of activated agarose supports. To demonstrate the ease and convenience of clickable agarose in this endeavor, we prepared a derivative of the C-terminal sequence of HIV protease (QCTLNF), which contains primary amide, carboxylic acid, thiol, and alcohol functional groups which would otherwise complicate the choice of attachment stragtegy. An extra alkyne-containing amino acid was used to end the standard solid-phase peptide synthesis sequence, and the final oligopeptide was cleaved from the resin retaining its N-terminal Fmoc protecting group (compound **15**, Figure 3). Purification by reversed-phase chromatography was followed by reaction with agarose azide **4** by the method described above. Fmoc deprotection of **16** with piperidine revealed the amine-terminated immobilized peptide **17** and showed by quantitation of the released fluorene chromophore a capture of 39% of the azide groups installed on the agarose support. The resulting peptide concentration is more than enough to be useful for applications such as aptamer selection and binding studies, which are currently underway.

Affinity purification of enzymes and antibodies by reversible interaction with a binding site or reactive tag is enabled by attachment of the complementary group to the solid support with a chemically compatible linker. An example is shown in Figure 4. Certain monoclonal antibodies generated against diketone **20** (Figure 5) have been shown to possess crucial active-site lysine residues

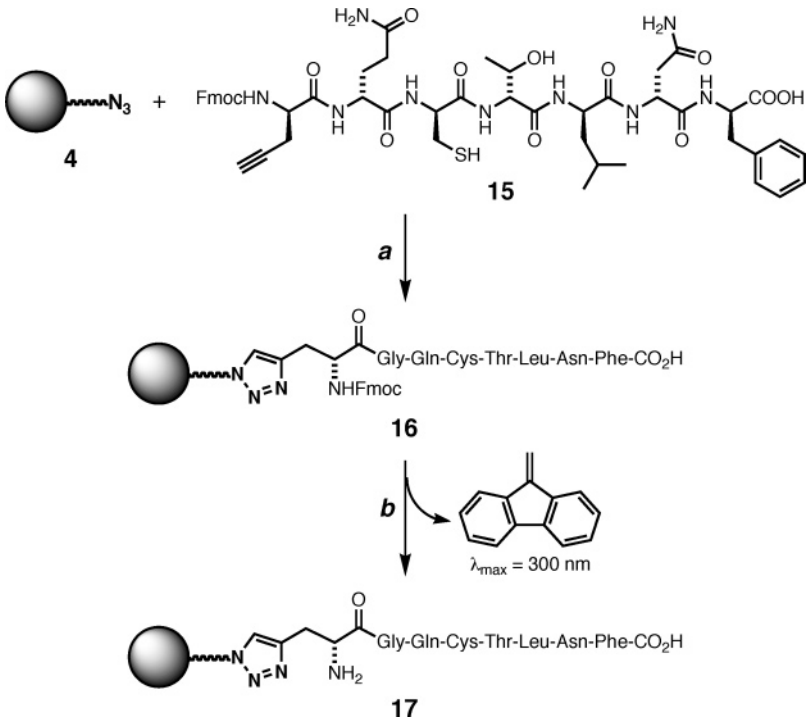

Figure 3. Peptide immobilization on agarose azide; a, standard Cu·bipy-mediated coupling conditions (see Experimental Procedures), followed by a wash procedure including 0.l M EDTA to remove Cu ions; b, 20% piperidine in DMF, RT, 10 min.

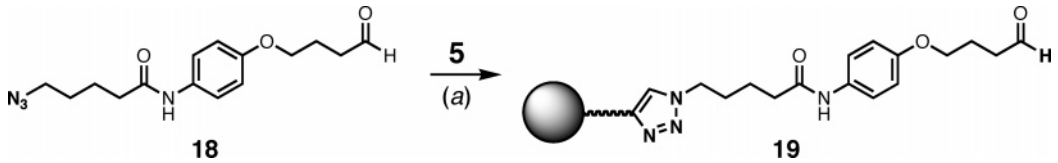

Figure 4. Aliphatic aldehyde immobilization on agarose azide; a, standard Cu·bipy-mediated coupling conditions (see Experimental Procedures), followed by a wash procedure including 0.l M EDTA to remove Cu ions.

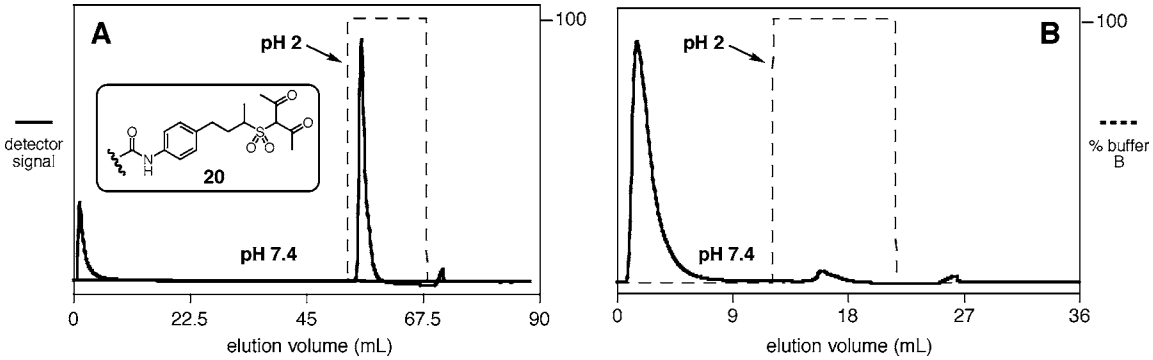

Figure 5. Elution profiles on a column of agarose **19** of (A) antibody 84G3 and (B) IgY isolated from chicken eggs obtained prior to an immunization. A greater wash volume at pH 7.4 was used in A, but the patterns were reproducible. The antibody isolated from chromatograph A was found to be catalytically active in a standard retro-aldol reaction. The structure of the hapten used to generate 84G3 (**20**) is shown.

which catalyze asymmetric aldol and retro-aldol reactions by the formation of enamine intermediates from aldehyde substrates (*8*, *11*). It was envisioned that an immobilized aldehyde could be used to purify such antibodies by virtue of reversible imine formation. The attachment of such an aldehyde to agarose by standard amide or ether bond-forming methods would usually require protection/deprotection steps, which are avoided by the use of the CuAAC process. Thus, azidoaldehyde **18** was ligated without difficulty to agarose-alkyne **5** by the standard protocol to give **19**. The presence of the aldehyde group was confirmed by treatment of agarose **19** with *p*-nitrophenylhydrazine to give a yellow color consistent with the formation of the corresponding hydrazone. As shown in Figure 5, agarose **19** did indeed bind an antibody raised against **20**, but not an unrelated polyclonal antibody.

The results described here illustrate the convenient use of a single pair of functionalized agarose materials, azide **4** and alkyne **5**, for the attachment of a chemically diverse set of functional molecules. While we produced **4** and **5** for this study from a commercial "specialty" agarose-amine, it should be possible to access similar materials from agarose itself and much less expensive reagents; such large-scale production of clickable agarose materials is underway in our laboratory. Given the established applicability of the CuAAC reaction to a widely diverse set of building blocks in organic, materials, and biological chemistry, we believe that there are few limitations to

the nature of structures that can be married to soluble or insoluble supports in this manner for a wide variety of applications.

ACKNOWLEDGMENT

We thank the Skaggs Institute for Chemical Biology and the National Institutes of Health (GM48870) for support of this work, Dr. Sayam Sen Gupta for helpful discussions, and Dr. Diane Kubitz for a sample of antibody 84G3.

LITERATURE CITED

(1) Wilchek, M., Miron, T., and Kohn, J. (1984) Affinity-chromatography. *Methods Enzymol. 104*, 3−55, Part C.; Scouten, W. H. (1981) *Affinity Chromatography*, John Wiley & Sons, New York.

(2) Janson, J.-C., and Ryden, L. (1998) in *Protein Purification*, pp 375−442, John Wiley & Sons, New York.

(3) Huisgen, R. (1984) 1,3-Dipolar cycloaddition − introduction, survey, mechanism, in *1,3-Dipolar Cycloaddition Chemistry* (Padwa, A., Ed.) pp 1−176, Wiley, New York.

(4) (a) Rostovtsev, V. V., Green, L. G., Fokin, V. V., and Sharpless, K. B. (2002) A stepwise Huisgen cycloaddition process: Copper(I)-catalyzed regioselective ligation of azides and terminal alkynes. *Angew. Chem., Int. Ed. 41*, 2596−2599. (b) Tornøe, C. W., Christensen, C., and Meldal, M. (2002) Peptidotriazoles on solid phase: [1,2,3]-triazoles by regiospecific copper(I)-catalyzed 1,3-dipolar cycloadditions of terminal alkynes to azides. *J. Org. Chem. 67*, 3057−3062. (c) Wang, Q., Chan, T. R., Hilgraf, R., Fokin, V. V., Sharpless, K. B., and Finn, M. G. (2003) Bioconjugation by copper(I)-catalyzed azide-alkyne [3+2] cycloaddition. *J. Am. Chem. Soc. 125*, 3192−3193. (d) Rodionov, V. O., Fokin, V. V., and Finn, M. G. (2005) Mechanism of the ligand-free Cu^{I}-catalyzed azide-alkyne cycloaddition reaction. *Angew. Chem., Int. Ed. 44*, 2210−2215.

(5) Lewis, W. G., Magallon, F. G., Fokin, V. V., and Finn, M. G. (2004) Discovery and characterization of catalysts for azide-alkyne cycloaddition by fluorescence quenching. *J. Am. Chem. Soc. 126*, 9152−9153.

(6) Kolb, H. C., Finn, M. G., and Sharpless, K. B. (2001) Click chemistry: Diverse chemical function from a few good reactions. *Angew. Chem., Int. Ed. 40*, 2004−2021.

(7) Chan, W. C. W., and White, P. D. (2000) *Fmoc Solid-Phase Peptide Synthesis: A Practical Approach*, Oxford University Press, New York.

(8) Zhong, G., Lerner, R. A., and Barbas, C. F. I. (1999) Broadening the aldolase catalytic antibody repertoire by combining reactive immunization and transition state theory: new enantio- and diastereoselectivities. *Angew. Chem., Int. Ed. 38*, 3738−3741.

(9) Turner, J. M., Bui, T., Lerner, R. A., Barbas, C. F. I., and List, B. (2000) An efficient benchtop system for multigram-scale kinetic resolutions using aldolase antibodies. *Chem. Eur. J. 6*, 2772−2774.

(10) Kaiser, E., Colescott, R. L., Bossinger, C. D., and Cook, P. I. (1970) Color test for detection of free terminal amino groups in the solid-phase synthesis of peptides. *Anal. Biochem. 34*, 595−598.

(11) Wagner, J., Lerner, R. A., and Barbas, C. F. I. (1995) Efficient aldolase catalytic antibodies that use the enamine mechanism of natural enzymes. *Science 270*, 1797−1800.

BC0501496

"Clickable" Agarose for Affinity Chromatography

Sreenivas Punna, Eiton Kaltgrad, and M. G. Finn*

Department of Chemistry and The Skaggs Institute for Chemical Biology, The Scripps Research Institute, 10550 North Torrey Pines Road, La Jolla, California 92037. Received August 8, 2005; Revised Manuscript Received August 12, 2005

Successful purification of biological molecules by affinity chromatography requires the attachment of desired ligands to biocompatible chromatographic supports. The Cu(I)-catalyzed cycloaddition of azides and alkynes—the premier example of "click chemistry"—is an efficient way to make covalent connections among diverse molecules and materials. Both azide and alkyne units are highly selective in their reactivity, being inert to most chemical functionalities and stable to wide ranges of solvent, temperature, and pH. We show that agarose beads bearing alkyne and azide groups can be easily made and are practical precursors to functionalized agarose materials for affinity chromatography.

INTRODUCTION

Biological processes depend on specific interactions between molecules, such as between antibodies and antigens, carbohydrates and lectins, and enzymes and inhibitors. Affinity chromatography (*1*) exploits these various interactions for the analysis and purification of mixtures of biomolecules. One of the members of the interacting pair is immobilized on an insoluble support and is used to "fish out" the complementary agent from a solution passed through or over the column. In many cases, affinity chromatography is a crucial step in the isolation of desired species, for example, providing the only practical means for the separation of tagged or functional proteins from cellular extracts.

Beaded agarose bearing functional groups such as amine ($-NH_2$), carboxylic acid ($-COOH$), aldehyde ($-CHO$), thiol ($-SH$), and hydroxyl ($-OH$) is the support of choice for most ligands of interest (*2*) due to its inexpensive and biocompatible nature. For selective immobilization, a ligand should possess a functional group for attachment to the support that is not essential to its binding property. Ligands can be immobilized in ways detrimental to their intended function when more than one of the attachment units is present in a ligand or when other reactive functional groups on the ligand compete in the immobilization chemistry. A matched pair of groups which is selective in reacting with each other while being unreactive to other functional groups in the molecule would therefore be highly useful in the preparation of functional agarose beads. Organic azides and terminal alkynes fit this description, being inert to most chemical functionalities and stable to wide ranges of solvent, temperature, and pH. While their uncatalyzed [3+2] dipolar cycloaddition is typically very slow at room temeperature (*3*), Cu(I) catalysts accelerate the reaction to a great degree (*4*, *5*). Here we report the first use of azides, alkynes, and their "click reaction" (*6*) for the convenient immobilization of ligands on agarose for affinity chromatography and related purposes.

* To whom correspondence should be addressed. E-mail: mgfinn@scripps.edu.

EXPERIMENTAL PROCEDURES

General. ^1H and ^{13}C NMR spectra were recorded on Bruker DRX-500, AMX-400, or Varian Mercury 200 spectrometers, using $CDCl_3$ or CD_3OD as solvents. Mass spectra were obtained on an Agilent 1100 LC/MS spectrometer (model G1946A). Melting points were measured in a Mel-Temp II capillary melting point apparatus and are uncorrected. Infrared spectra were recorded on a MIDAC EM200 instrument with horizontal attenuated total reflectance accessory from Pike Instruments or in KBr pellets. Column chromatography was performed on EM Science silica gel (40−63 μm mesh). TLC analysis was facilitated by the use of phosphomolybdic acid or $KMnO_4/H_2O$ stains in addition to UV light with fluorescent-indicating plates. Anhydrous sodium sulfate was used for drying solutions. Carboxy Link coupling gel (50% aqueous slurry, 16 μmol of amine groups per milliliter), biotin-PEG-amine, and avidin-HABA complex were purchased from Pierce. All other commercially available reagents were purchased from Acros or Aldrich. Compounds **6** and **7**, kindly provided by Mr. Warren G. Lewis, have been previously described (*5*). Reactions requiring anhydrous conditions were performed under nitrogen.

5-Azidopentanoic Acid 4-Nitrophenyl Ester (2). 1-(3-Dimethylaminopropyl)-3-ethylcarbodimide hydrochloride (EDCI·HCl, 703.8 mg, 3.67 mmol) was added to a solution of *p*-nitrophenol (510.5 mg, 3.67 mmol) and 5-azidopentanoic acid (500 mg, 3.49 mmol) in CH_2Cl_2 (25 mL) at room temperature and stirred overnight, followed by the addition of water and excess EtOAc. The separated organic phase was washed with H_2O and brine solution, dried over Na_2SO_4, and evaporated. The crude product was purified by silica gel column chromatography (1:4 EtOAc/hexane) to give **2** (514 mg) as a pale yellow oil in 52% yield. ^1H NMR ($CDCl_3$) δ 1.62−1.92 (m, 4H), 2.60 (t, J = 6.6 Hz, 2H, $-CH_2N_3$), 3.34 (t, J = 6.6 Hz, 2H), 7.25 (d, J = 9.2 Hz, 2H), 8.23 (d, J = 8.8 Hz, 2H); ^{13}C NMR ($CDCl_3$) δ 22.1, 28.4, 33.9, 51.2, 60.6, 122.6, 125.4, 145.5, 155.5, 170.8; IR (thin film, cm^{-1}): 2946, 2100 (azide), 1768, 1593, 1534, 1345, 1211, 1130, 910, 865, 748; ESMS *m/z* (relative intensity) 287 $(M + Na)^+$ (75), 237 (100), 223 (70).

10.1021/bc0501496 CCC: $30.25 © 2005 American Chemical Society
Published on Web 09/13/2005

Scheme 1

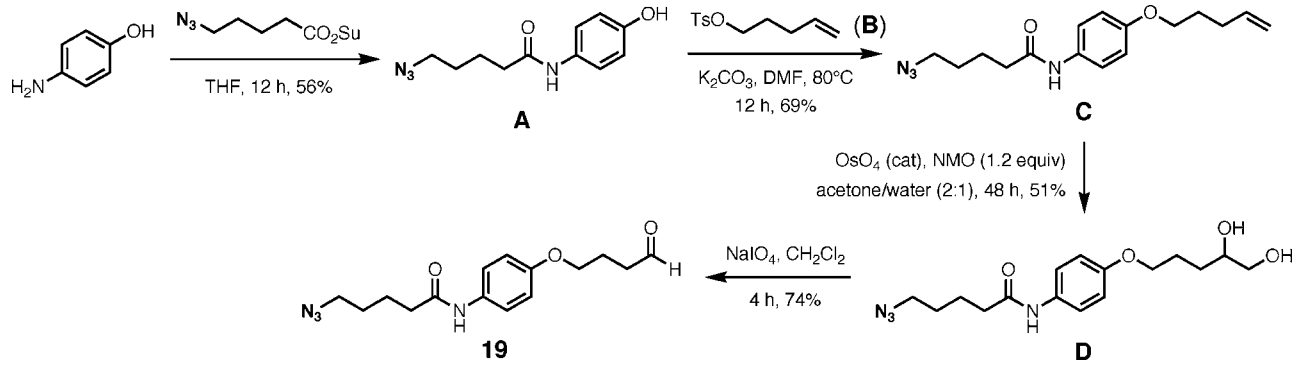

Agarose Azide and Alkyne Beads (4 and 5). CarboxyLink gel (8 mL, maximum of 64 μmol of amine groups) was transferred to a disposable frit, allowed to settle for 30 min, and equilibrated with 5 column volumes of pH 4.7 MES buffer (0.1 M). To the gel was added *p*-nitrophenyl ester **2** (143.4 mg, 64 mmol, 16 μmol/mL) dissolved in DMF with 5% of the MES buffer (8.4 mL), and the capped fritted tube was rotated gently at room temperature for 2 days. Phosphate buffer (600 μL, pH 7, 1.5 M) was added to the reaction mixture, which was then drained into a clean scintillation vial and the absorbance at 412 nm was measured directly. An agarose sample lacking the amine group was used in a control experiment to correct for residual hydrolysis of **2**, which was negligible under these conditions. The amount of attached azide was assumed to be equivalent to the amount of released *p*-nitrophenol, which was determined with the aid of an extinction coefficient measured by the addition of authentic *p*-nitrophenol to the same mixture of DMF, pH 4.7 MES, and pH 7 phosphate (ϵ = 432 M^{-1} cm^{-1}). Agarose **5** was prepared and analyzed by the same procedure, using *p*-nitrophenyl ester **3**.

Fluorescein-alkyne (8). To fluorescein NHS ester (97 mg, 0.205 mmol) in THF (30 mL) was added propargylamine (32 μL, 0.451 mmol), and the reaction was stirred under nitrogen atmosphere at room temperature overnight. After the sample was filtered to remove a small amount of insoluble material, the solvent was evaporated and the residue was washed with CH_2Cl_2 and then Et_2O to afford **8** as a yellow solid in quantitative yield (87 mg). ESMS *m/z* (relative intensity) 414 (M^+, base peak).

Typical Immobilization Procedure. Stock solutions (50 mM) of the following reagents were prepared: 2,6-lutidine (DMF), 2,2′-bipyridine (DMF), CuBr (DMF), and sodium ascorbate (water). A slurry of agarose-azide/alkyne beads (1.0 equiv) in DMF in a disposable frit was treated with the molecule to be attached bearing the complementary (alkyne or azide) group (4.0 equiv), followed by 2,6-lutidine (8.0 equiv), 2,2′-bipyridine (8.0 equiv), cuprous bromide (4.0 equiv), and finally sodium ascorbate (8.0 equiv). The resulting suspension was bubbled with a gentle flow of nitrogen for 1 min, capped, and rotated at room temperature for 12−18 h. The reaction mixture was drained and washed sequentially with approximately 5 column volumes each of DMF, H_2O, MeOH, 0.1 M aq EDTA, H_2O, and DMF.

Biotin-PEG-alkyne (12). To a solution of biotin-PEG-amine (**11**, 33 mg, 0.079 mmol) in CH_2Cl_2 (5 mL) was added 4-pentynoic acid (7.4 mg, 0.045 mmol) followed by 1-(3-dimethylaminopropyl)-3-ethylcarbodimide hydrochloride (EDCI·HCl; 704 mg, 3.67 mmol). The mixture was stirred at room temperature overnight and was then partitioned between EtOAc (10 mL) and water. The organic layer was dried (Na_2SO_4) and evaporated to give compound **12** (9 mg) as a colorless syrup. A further 11 mg was recovered from the aqueous layer by stirring in the presence of additional EtOAc and excess NaCl (overall yield 51%). ^{1}H NMR ($CDCl_3$) δ 1.49−1.55 (m, 2H), 1.86−1.88 (m, 4H), 2.25−2.85 (m, 2H), 2.36 (s, 1H), 2.49−2.60 (m, 6H), 2.75−2.85 (m, 2H), 2.92−3.02 (m, 2H), 3.25−3.30 (m, 1H), 3.40 (m, 2H), 3.41−3.50 (m, 4H), 3.58−3.64 (m, 4H), 3.67−3.70 (m, 2H), 4.35−4.40 (m, 1H), 4.55−4.60 (m, 1H), 8.20 (br s, 1H), 8.4 (br s, 1H);^{13}C NMR ($CDCl_3$) δ 14.7, 25.8, 28.5, 28.7, 34.9, 35.7, 40.0, 56.03, 60.64, 62.4, 68.9, 69.5, 70.2, 70.27, 70.6, 74.4, 82.5, 175.2, 177.7, 178.05; IR (film, cm^{-1}): 3287 (CCH), 3084, 2864, 2114 (alkyne), 1629, 1553, 1265, 1140, 951, 879, 726; ESMS *m/z* (relative intensity) 521 $(M+Na)^+$ (100), 499 $(M+1)^+$ (25), 375 (60).

HIV-Protease Peptide Alkyne (15). Standard Fmoc-based solid phase peptide synthesis techniques were employed (*7*), starting with Wang resin bearing the C-terminal amino acid (Fmoc-Phe-OH, 0.77 mmol/g). Fmoc deprotection was accomplished with two treatments of 20% piperidine in DMF, and amino acid coupling was typically performed with 5.5 equiv of Fmoc-amino acid, 5.0 equiv of HBTU, and excess *i*Pr_2NEt. Fmoc-propargylglycine (CSPS Chemicals, San Diego) was installed as the final (*N*-terminal) amino acid, using DIC/HOBt (5.0 equiv) in CH_2Cl_2. The crude peptide containing the N-terminal Fmoc protecting group was obtained by treating the resulting resin with 94/2.5/2.5/1 CF_3CO_2H/H_2O/1,2-ethanedithiol/SiH(*i*Pr)$_3$ mixture for 3 h at room temperature. The desired peptide was identified by MALDI-MS of fractions from analytical HPLC of the crude product, and then purified by preparative HPLC. The final purified product (peptide G*QCTLNF, where G* = propargylglycine) was obtained in approximately 9% yield, calculated from the weight of the isolated material relative to the amount of amino acid on the starting resin.

After attachment of **15** to **4** by the above procedure, the resulting beads (**16**) were treated with 20% piperidine (4 mL) at room temperature for 10 min. The solution was drained, and the absorbance at 300 nm was measured against a blank composed of 20% piperidine in DMF. Using the measured fluorene molar extinction coefficient of 7800 M^{-1} cm^{-1} determined under identical conditions, the attached peptide concentration was found to be 0.71 μmol/mL, representing approximately 39% conversion of the available azides on the resin (measured as above at 1.84 μmol/mL). Attachment of Fmoc-propargylglycine alone proceeded in 63% yield by the same assay. A contributing factor to the relatively poor attachment of the peptide is its poor solubility, even in DMF, causing it to aggregate and precipitate slowly during the reaction.

4-Azido-*N*-[4-(4-oxobutoxy)phenyl]butyramide (19, Scheme 1). To the *N*-hydroxysuccinimide (Su) ester of

Scheme 2

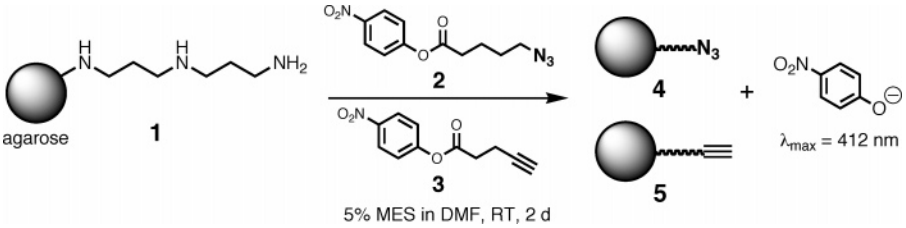

4-azidobutyric acid (2.2 g, 18.32 mmol) in THF (20 mL) was added *p*-aminophenol (1.0 g, 18.32 mmol), and the mixture was stirred overnight at room temperature. The solvent was evaporated and the resulting residue was partitioned between equal volumes of 1 M HCl and EtOAc. The aqueous layer was extracted twice more with EtOAc and the combined organic layers were washed with 1 N HCl, H_2O (2×), brine, dried, and evaporated. The crude product (designated as compound **A**) was purified by column chromatography (1:3 EtOAc/hexanes) to give a brown solid (1.19 g, 57% yield). mp 67−69 °C; ^{1}H NMR ($CDCl_3$) δ 1.50−1.57 (m, 2H), 1.63−1.71 (m, 2H), 2.26 (t, J = 7.5 Hz, 2H), 6.68 (d, J = 8.0 Hz, 2H), 7.19 (dd, J = 8.5, 3.5 Hz), 8.37 (s, 1H); ^{13}C NMR (CD_3OD) δ 24.3, 29.6, 37.2, 52.3, 116.3, 123.6, 131.7, 155.5, 173.9; IR (KBr, cm^{-1}): 2959, 2465, 2096 (azide), 1665, 1449, 1238, 839; ESMS *m/z* (relative intensity) 257 $(M + Na)^+$ (22), 235 $(M+H)^+$ (100).

To a solution of 4-pentene-1-ol (3.0 g, 35 mmol), Et_3N (14.5 mL, 105 mmol), and DMAP (425 mg, 3.5 mmol) in THF (50 mL) was added *p*-TsCl (6.64 g, 34.88 mmol), and the reaction was stirred for 6 h at room temperature. The resulting mixture was filtered through a sintered funnel, the solid was washed with additional THF, and the combined solution was evaporated. The crude product was purified by column chromatography (silica gel, 1:4 EtOAc/hexanes) to obtain the desired tosylate **B** (Scheme 1) as a colorless liquid (6.6 g, 79% yield). ^{1}H NMR ($CDCl_3$) δ 1.58−1.72 (m, 2H), 1.92−2.08 (m, 2H), 2.36 (s, 3H), 3.96 (t, J = 6.4 Hz, 2H), 4.80−4.94 (m, 2H), 5.50−5.73 (m, 1H), 7.27 (d, J = 8.0 Hz, 2H), 7.70 (d, J = 7.8 Hz); ^{13}C NMR ($CDCl_3$) δ 13.9, 21.3, 27.7, 29.1, 69.6, 115.5, 127.6, 132.8, 136.4, 144.6; IR (thin film, cm^{-1}): 3075 (olefin), 2981, 1926, 1643, 1598, 1449, 1346, 1185, 920, 825, 749; ESMS *m/z* (relative intensity) 241 $(M + H)^+$ (10).) This material (720 mg, 3.00 mmol) was combined with compound **A** (702 mg, 3.00 mmol) and K_2CO_3 (1.24 g, 9.0 mmol) in DMF (5.0 mL), and the mixture was stirred at 80 °C for 12 h. Saturated aqueous NH_4Cl solution (25 mL) and EtOAc (25 mL) were added, and the organic layer was separated and washed with additional NH_4Cl solution, water, and brine. The solution was dried and evaporated, and the residue was purified by column chromatography (silica gel, 1:4 EtOAc/hexanes) to give the ether-amide intermediate **C** (627 mg, 69% yield) as a red solid. mp 60−62 °C; ^{1}H NMR ($CDCl_3$) δ 1.63−1.69 (m, 2H), 1.75−1.82 (m, 2H), 1.82−1.89 (m, 2H), 2.22 (q, J = 7.0 Hz, 2H), 2.35 (t, J = 7 Hz, 2H), 3.30 (t, J = 6.5 Hz, 2H, $-CH_2N_3$), 3.93 (t, J = 6 Hz), 4.98−5.08 (m, 2H), 5.84 (m, 1H), 6.83 (d, J = 10.0 Hz), 7.37 (d, J = 8.5 Hz, 2H), 7.41 (br s, 1H); ^{13}C NMR ($CDCl_3$) δ 22.3, 27.9, 29.6, 36.2, 50.7, 66.9, 114.3, 115.0, 121.4, 130.3, 137.3, 155.4, 170.15; IR (KBr, cm^{-1}): 2950, 2100 (azide), 1650, 1310, 1250, 820, 760; ESMS *m/z* (relative intensity) 303 $(M + H)^+$ (100).

To a cooled (ice bath) solution of olefin **C** (500 mg, 1.65 mmol) in 2:1 acetone/water (6 mL) was added a small crystal of OsO_4. After 5 min, *N*-methylmorpholine *N*-oxide (193.3 mg, 1.65 mmol) was added, and the mixture was stirred at room temperature for 2 days. EtOAc and brine were added, and the aqueous layer was further extracted with EtOAc (2 × 25 mL). The crude product obtained from the combined organic layers was purified by column chromatography (silica gel, EtOAc) to give the desired diol (**D**, Scheme 1, 248 mg, 51% yield) as a white solid. Approximately 65 mg of the starting material was also recovered. mp 82−84 °C; ^{1}H NMR ($CDCl_3$) δ 1.50−1.90 (m, 8H), 2.34 (t, J = 7.0 Hz, 2H), 2.70 (br s, −OH), 3.29 (t, J = 5.5 Hz, 2H, $-CH_2N_3$), 3.40−3.44 (m, 1H), 3.60−3.85 (m, 2H), 3.92 (s, 2H), 6.79 (d, J = 9.5 Hz), 7.36 (dd, t, J = 7.0, 5.0 Hz, 2H), 8.32 (br s, 1H); ^{13}C NMR ($CDCl_3$) δ 23.9, 26.5, 29.3, 30.8, 36.9, 52.0, 67.2, 69.0, 72.8, 115.4, 122.9, 132.6, 157.1, 173.6; IR (thin film, cm^{-1}): 2945, 2869, 2132 (azide), 1661, 1490, 1301, 1238, 1018, 830; ESMS *m/z* (relative intensity) 337 $(M + H)^+$ (100).

To a solution of diol **D** (100 mg, 0.297 mmol) in CH_2Cl_2 (5 mL + 2 drops of MeOH) was added saturated aqueous $NaHCO_3$ (0.5 mL) followed by $NaIO_4$ (127 mg, 0.60 mmol). After the sample was stirred at room temperature for 4 h, anhydrous Na_2SO_4 (approximately 1 g) and CH_2Cl_2 (25 mL) were added and the mixture was stirred for a further 30 min. Filtration, washing of the solid with CH_2Cl_2, and evaporation of the combined organic solutions provided compound **19** (67 mg, 74% yield) as a thick colorless syrup. ^{1}H NMR ($CDCl_3$) δ 1.60−1.70 (m, 2H), 1.74−1.85 (m, 2H), 2.08−2.15 (m, 2H), 2.34 (t, J = 6.4 Hz, 2H), 2.65 (t, J = 5.8 Hz, 2H), 3.28 (t, J = 5.6 Hz, 2H, $-CH_2N_3$), 3.95 (t, J = 5.4 Hz, 2H), 6.8 (d, J = 10.8 Hz, 2H, ArH), 7.38 (d, J = 10.8 Hz, 2H, ArH), 7.74 (s, 1H), 9.8 (s, 1H, −CHO); ^{13}C NMR ($CDCl_3$) δ 21.3, 22.0, 27.6, 35.8, 39.9, 50.4, 66.2, 113.9, 121.2, 130.6, 154.7, 170.3, 201.4; IR (film, cm^{-1}): 2949, 2877, 2096 (azide), 1727, 1664 (C=O), 1301, 1233, 959, 833, 743; ESMS *m/z* (relative intensity) 305 $(M+1)^+$ (85).

Test of Affinity Chromatography Function with Aldehyde 19. Functionalized agarose **20**, prepared in the standard manner from **19**, was poured into a column (Amersham Tricom, 5 mm × 50 mm; 1 mL volume; cat#18−1163−09). At pH 7, the column was found to retain the catalytic antibody 84G3 originally obtained by Barbas and co-workers (*8*, *9*) and not an unrelated antibody; details can be found in Figure 5.

RESULTS AND DISCUSSION

Commercially available Carboxy-Link agarose (**1**), which bears addressable amine groups, was treated with the *p*-nitrophenyl ester of 5-azidopentanoic acid (**2**) and 5-pentynoic acid (**3**) to give azide- and alkyne-functionalized beads **4** and **5**, respectively (Scheme 2). The degree of acylation was determined by measurement of the concentration of released *p*-nitrophenol. Loadings of between 3.3 and 4.6 μmol/mL of gel were typical, representing approximately 20−30% of the available amine groups according to the commercial specifications of the gel. However, the standard Kaiser (ninhydrin) test (*10*) gave a positive signal for **1** and negative signals for **4** and **5**, suggesting that most or all of the accessible amine groups of **1** were acylated by **2** and **3**.

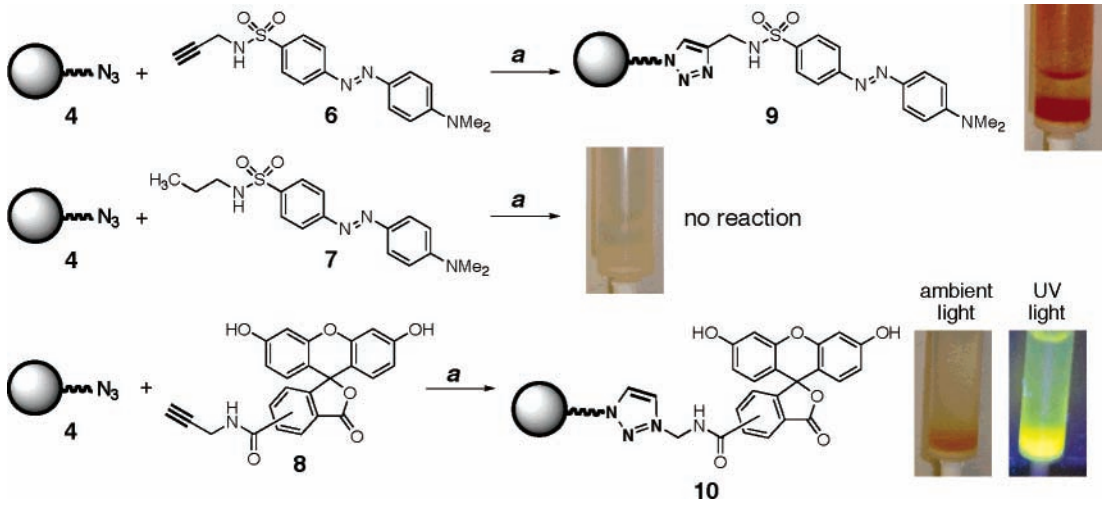

Figure 1. CuAAC coupling of dye reagents to agarose azide and alkyne; a, standard Cu·bipy-mediated coupling conditions (see Experimental Procedures), followed by a wash procedure including 0.l M EDTA to remove Cu ions.

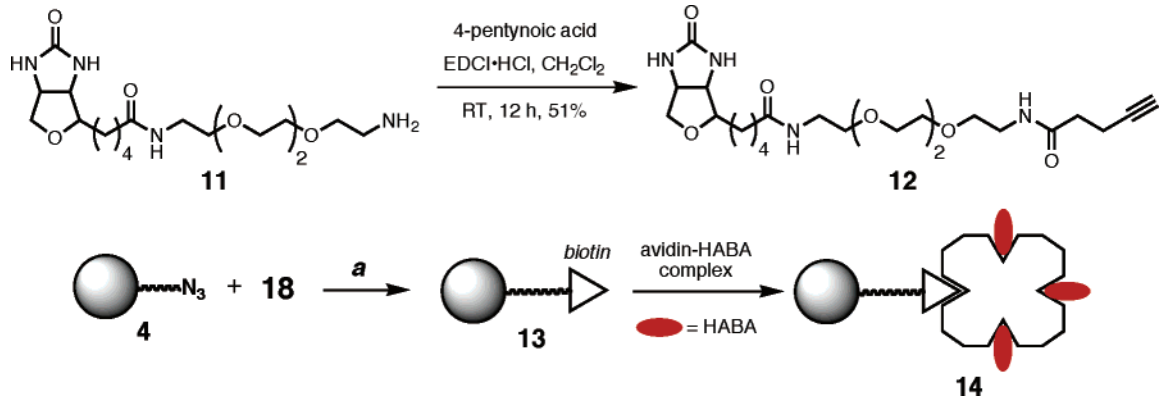

Figure 2. Biotinylation of agarose azide; a, standard Cu·bipy-mediated coupling conditions (see Experimental Procedures), followed by a wash procedure including 0.l M EDTA to remove Cu ions.

To test the feasibility of resin attachment by the Cu-mediated azide-alkyne cycloaddition (CuAAC) reaction, agarose-azide beads **4** were treated with a dabsyl-alkyne derivative (**6**) and the corresponding dye with an *n*-propyl group in place of the alkyne (**7**), in the presence of cuprous bromide, 2,2′-bipyridine as accelerating ligand (*5*), sodium ascorbate to maintain a reducing environment, and 2,6-lutidine as mild base (Figure 1). The dye was successfully attached with **6**, as indicated by the production of an intense and permanent red color in the resulting beads (**9**). Use of the control **7** or omission of Cu(I) from the reaction of **6** gave colorless beads. In addition, no dye could be washed from **9** even upon extensive treatment with DMF; these observations show that the dye does not adsorb to the resin. Similarly, **4** was treated with fluorescein alkyne **8** under CuAAC conditions to give yellow beads that were strongly fluorescent under ultraviolet light. The same successful results were obtained with agarose-alkyne **5** and the complementary azide-substituted dabsyl compound (data not shown).

Biotinylated supports are a mainstay of protein immobilization and therefore of experimental biochemistry. The CuAAC reaction provides a convenient addition to the many methods already in use for constructing such materials. Biotin alkyne **12** was prepared from commercially available biotin-PEG-amine **12** and 4-pentynoic acid (Figure 2). Immobilization on agarose azide beads gave **13**, which was treated with a red solution of avidin-HABA (HABA = 2-(4′-hydroxyphenyl)azobenzoic acid) complex. Tight avidin−biotin interaction gave the resulting beads a persistent red color (**14**), whereas a mixture of avidin-HABA with agarose-azide **4** resulted in no such binding.

The immobilization of peptides is a common application of activated agarose supports. To demonstrate the ease and convenience of clickable agarose in this endeavor, we prepared a derivative of the C-terminal sequence of HIV protease (QCTLNF), which contains primary amide, carboxylic acid, thiol, and alcohol functional groups which would otherwise complicate the choice of attachment stragtegy. An extra alkyne-containing amino acid was used to end the standard solid-phase peptide synthesis sequence, and the final oligopeptide was cleaved from the resin retaining its N-terminal Fmoc protecting group (compound **15**, Figure 3). Purification by reversed-phase chromatography was followed by reaction with agarose azide **4** by the method described above. Fmoc deprotection of **16** with piperidine revealed the amine-terminated immobilized peptide **17** and showed by quantitation of the released fluorene chromophore a capture of 39% of the azide groups installed on the agarose support. The resulting peptide concentration is more than enough to be useful for applications such as aptamer selection and binding studies, which are currently underway.

Affinity purification of enzymes and antibodies by reversible interaction with a binding site or reactive tag is enabled by attachment of the complementary group to the solid support with a chemically compatible linker. An example is shown in Figure 4. Certain monoclonal antibodies generated against diketone **20** (Figure 5) have been shown to possess crucial active-site lysine residues

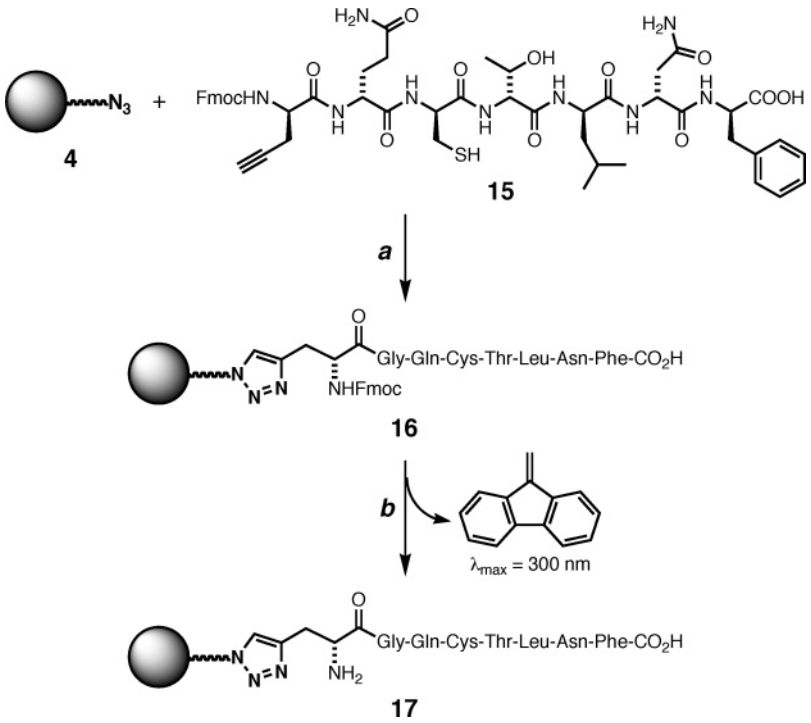

Figure 3. Peptide immobilization on agarose azide; a, standard Cu·bipy-mediated coupling conditions (see Experimental Procedures), followed by a wash procedure including 0.l M EDTA to remove Cu ions; b, 20% piperidine in DMF, RT, 10 min.

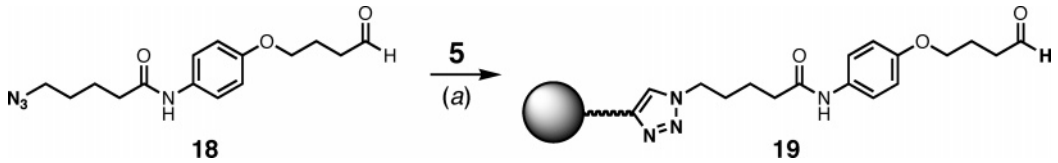

Figure 4. Aliphatic aldehyde immobilization on agarose azide; a, standard Cu·bipy-mediated coupling conditions (see Experimental Procedures), followed by a wash procedure including 0.l M EDTA to remove Cu ions.

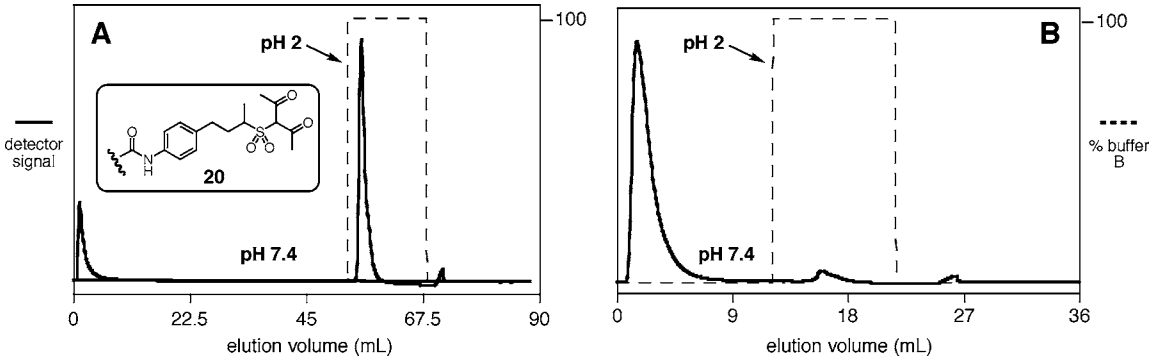

Figure 5. Elution profiles on a column of agarose **19** of (A) antibody 84G3 and (B) IgY isolated from chicken eggs obtained prior to an immunization. A greater wash volume at pH 7.4 was used in A, but the patterns were reproducible. The antibody isolated from chromatograph A was found to be catalytically active in a standard retro-aldol reaction. The structure of the hapten used to generate 84G3 (**20**) is shown.

which catalyze asymmetric aldol and retro-aldol reactions by the formation of enamine intermediates from aldehyde substrates (*8*, *11*). It was envisioned that an immobilized aldehyde could be used to purify such antibodies by virtue of reversible imine formation. The attachment of such an aldehyde to agarose by standard amide or ether bond-forming methods would usually require protection/deprotection steps, which are avoided by the use of the CuAAC process. Thus, azidoaldehyde **18** was ligated without difficulty to agarose-alkyne **5** by the standard protocol to give **19**. The presence of the aldehyde group was confirmed by treatment of agarose **19** with *p*-nitrophenylhydrazine to give a yellow color consistent with the formation of the corresponding hydrazone. As shown in Figure 5, agarose **19** did indeed bind an antibody raised against **20**, but not an unrelated polyclonal antibody.

The results described here illustrate the convenient use of a single pair of functionalized agarose materials, azide **4** and alkyne **5**, for the attachment of a chemically diverse set of functional molecules. While we produced **4** and **5** for this study from a commercial "specialty" agarose-amine, it should be possible to access similar materials from agarose itself and much less expensive reagents; such large-scale production of clickable agarose materials is underway in our laboratory. Given the established applicability of the CuAAC reaction to a widely diverse set of building blocks in organic, materials, and biological chemistry, we believe that there are few limitations to

the nature of structures that can be married to soluble or insoluble supports in this manner for a wide variety of applications.

ACKNOWLEDGMENT

We thank the Skaggs Institute for Chemical Biology and the National Institutes of Health (GM48870) for support of this work, Dr. Sayam Sen Gupta for helpful discussions, and Dr. Diane Kubitz for a sample of antibody 84G3.

LITERATURE CITED

(1) Wilchek, M., Miron, T., and Kohn, J. (1984) Affinity-chromatography. *Methods Enzymol. 104*, 3−55, Part C.; Scouten, W. H. (1981) *Affinity Chromatography*, John Wiley & Sons, New York.

(2) Janson, J.-C., and Ryden, L. (1998) in *Protein Purification*, pp 375−442, John Wiley & Sons, New York.

(3) Huisgen, R. (1984) 1,3-Dipolar cycloaddition − introduction, survey, mechanism, in *1,3-Dipolar Cycloaddition Chemistry* (Padwa, A., Ed.) pp 1−176, Wiley, New York.

(4) (a) Rostovtsev, V. V., Green, L. G., Fokin, V. V., and Sharpless, K. B. (2002) A stepwise Huisgen cycloaddition process: Copper(I)-catalyzed regioselective ligation of azides and terminal alkynes. *Angew. Chem., Int. Ed. 41*, 2596−2599. (b) Tornøe, C. W., Christensen, C., and Meldal, M. (2002) Peptidotriazoles on solid phase: [1,2,3]-triazoles by regiospecific copper(I)-catalyzed 1,3-dipolar cycloadditions of terminal alkynes to azides. *J. Org. Chem. 67*, 3057−3062. (c) Wang, Q., Chan, T. R., Hilgraf, R., Fokin, V. V., Sharpless, K. B., and Finn, M. G. (2003) Bioconjugation by copper(I)-catalyzed azide-alkyne [3+2] cycloaddition. *J. Am. Chem. Soc. 125*, 3192−3193. (d) Rodionov, V. O., Fokin, V. V., and Finn, M. G. (2005) Mechanism of the ligand-free Cu^{I}-catalyzed azide-alkyne cycloaddition reaction. *Angew. Chem., Int. Ed. 44*, 2210−2215.

(5) Lewis, W. G., Magallon, F. G., Fokin, V. V., and Finn, M. G. (2004) Discovery and characterization of catalysts for azide-alkyne cycloaddition by fluorescence quenching. *J. Am. Chem. Soc. 126*, 9152−9153.

(6) Kolb, H. C., Finn, M. G., and Sharpless, K. B. (2001) Click chemistry: Diverse chemical function from a few good reactions. *Angew. Chem., Int. Ed. 40*, 2004−2021.

(7) Chan, W. C. W., and White, P. D. (2000) *Fmoc Solid-Phase Peptide Synthesis: A Practical Approach*, Oxford University Press, New York.

(8) Zhong, G., Lerner, R. A., and Barbas, C. F. I. (1999) Broadening the aldolase catalytic antibody repertoire by combining reactive immunization and transition state theory: new enantio- and diastereoselectivities. *Angew. Chem., Int. Ed. 38*, 3738−3741.

(9) Turner, J. M., Bui, T., Lerner, R. A., Barbas, C. F. I., and List, B. (2000) An efficient benchtop system for multigram-scale kinetic resolutions using aldolase antibodies. *Chem. Eur. J. 6*, 2772−2774.

(10) Kaiser, E., Colescott, R. L., Bossinger, C. D., and Cook, P. I. (1970) Color test for detection of free terminal amino groups in the solid-phase synthesis of peptides. *Anal. Biochem. 34*, 595−598.

(11) Wagner, J., Lerner, R. A., and Barbas, C. F. I. (1995) Efficient aldolase catalytic antibodies that use the enamine mechanism of natural enzymes. *Science 270*, 1797−1800.

BC0501496

A Peptide Sequence Controls the Physical Properties of Nanoparticles Formed by Peptide–Polymer Conjugates That Respond to a Protein Kinase A Signal

Tatsuhiko Sonoda,[†] Takashi Nogami,[†] Jun Oishi,[†] Masaharu Murata,[†] Takuro Niidome,[†] and Yoshiki Katayama*[,†,‡]

Department of Applied Chemistry, Faculty of Engineering, Kyushu University, Hakozaki, Higashi-ku, Fukuoka 812-8581, Japan, and CREST, Japan Science and Technology Agency, Japan. Received December 3, 2004; Revised Manuscript Received August 19, 2005

We previously reported that poly(*N*-isopropylacrylamide) grafted with Peptide 1 (-GLRRASLG) and poly(ethylene glycol) changed its physical properties in response to an intracellular protein phosphorylation signal, protein kinase A (PKA) (Katayama, Y. et al. (2001) *Macromolecules 34*, 905). In this study, we investigated the effect of changing peptide structure on the lower critical solution temperature (LCST) of peptide–polymer conjugates, before and after phosphorylation with PKA. For Peptide 2 (Ac-LRRASL-), which has a formal net charge of +2 at physiological pH, the LCST of the conjugate decreased on phosphorylation. In contrast, the LCSTs of the conjugates with Peptide 3 (-ALRRASLE) and Peptide 4 (Ac-DWDALRRASL-), which have neutral net charges, were greatly increased. This suggests that the LCST of the polymer was mainly governed by two factors: the change in hydration around the polymer chain and the interpeptide electrostatic repulsion, resulting from phosphorylation. These polymers have potential for use as drug capsules that respond to cellular conditions.

INTRODUCTION

The intracellular signal transduction system plays an important role in regulating various cellular events such as cellular proliferation (*1*), hormone secretion (*2*), gene transcription (*3*), and cell differentiation (*4*). Control of these events is mainly achieved by the regulation of a protein's activation or inactivation as caused by a conformational change of the protein. Protein phosphorylation is one of the most versatile ways of changing protein conformation. Incorporation of a phosphate group into a target protein leads to the following three effects: (i) enhancement of hydration around the phosphorylation site, (ii) introduction of anionic charges, and (iii) introduction of an additional hydrogen bonding site. Such protein phosphorylation is catalyzed by protein kinases. A living cell possesses nearly 800 kinds of protein kinases to regulate cellular events. Of those protein kinases, cyclic AMP-dependent protein kinase (PKA) is one of the most important enzymes (*5*–*7*). Its extraordinary continuous activation is related to various diseases such as colon cancer (*8*), melanoma (*9*), and prostate cancer (*10*). In a previous paper, we reported that two types of thermo-responsive polymer, NIPAM–PEP and NIPAM–PEPEP, responding to protein kinase A (PKA) (*11*). In this paper, we termed them NIPAM–PEP1 and NIPAM–PEPEP1, respectively. NIPAM–PEP1 is synthesized by copolymerization of *N*-isopropylacrylamide and a methacryloyl derivative of a PKA substrate peptide (GLRRASLG). NIPAM–PEPEP1 is another type of copolymer, which has some extra poly(ethylene glycol) (PEG) units. These polymers possessed lower critical solution temperatures (LCSTs), and we found that their LCSTs increased with the phosphorylation, by PKA, of incorporated peptides. This was due to enhancement of the hydration around the polymer backbone by introduced phosphate groups. The phosphorylation caused an increase in the temperature at which NIPAM–PEP1 is isolated from its aqueous solution and caused disintegration of the polymer micelle which was formed by NIPAM–PEPEP1 above its LCST (Figure 1a). This type of material, especially the 'nanoparticle' formed by NIPAM–PEPEP1, is potentially useful as a drug capsule which releases drugs in response to PKA levels in cells. However, the increase in the LCST in these polymers after phosphorylation was still insufficient. In the present work, we developed new polyNIPAM–peptide conjugate derivatives that have a greater response to PKA activity than NIPAM–PEP1 and NIPAM–PEPEP1, by changing the peptide sequence in the polymer. We also clarified that the formal net charge of the polymer before and after PKA phosphorylation and the extent of hydration around the ionic parts of the peptide are the key factors controlling the response of the NIPAM–peptide conjugate to the PKA signal.

EXPERIMENTAL PROCEDURES

Materials. Fmoc-amino acids were purchased from Calbiochem-Novabiochem AG (Laufelfingen, Switzerland) and Watanabe Chemical Ind., Ltd. (Hiroshima, Japan). DMF for peptide synthesis and acetonitrile and trifluoroacetic acid (TFA) for HPLC (HPLC grade) were obtained from Kanto Chemical Co., Ltd. (Tokyo, Japan). α-Methoxy-ω-aminopoly(ethylene oxide) was kindly donated by Nippon Oil & Fats Co. Ltd. (Tokyo, Japan). PKA C-subunit was purchased from Promega Co. Ltd. (Madison, WI).

Synthesis of Peptide Monomers and Poly(ethylene glycol) Macromonomer. Substrate peptide monomer 1 (Peptide 1: CH_2=C(CH_3)CO-GLRRASLG) was

* Corresponding author. Tel: +81–92–642–3608, Fax: +81–92–642–3606, e-mail: ykatatcm@mbox.nc.kyushu-u.ac.jp.
† Department of Applied Chemistry.
‡ CREST.

10.1021/bc049710a CCC: $30.25 © 2005 American Chemical Society
Published on Web 09/24/2005

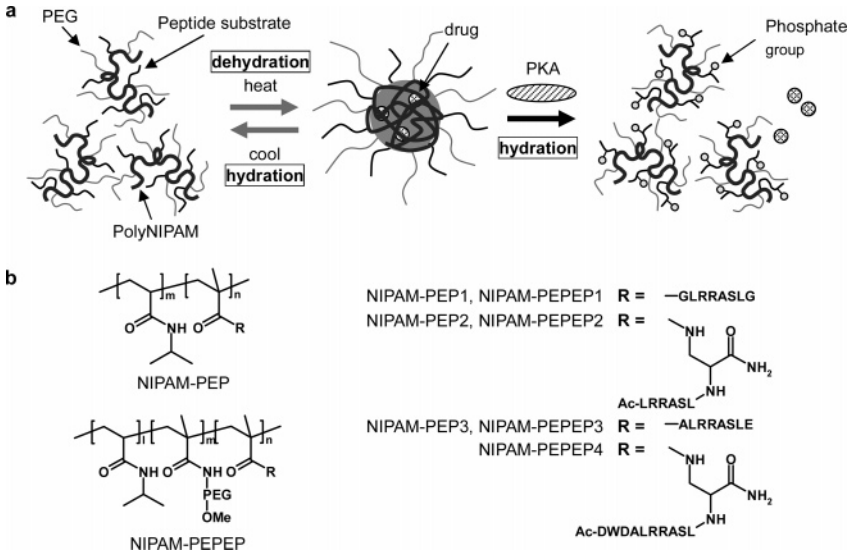

Figure 1. Schematic outline of the disintegration in NIPAM–PEPEP derivatives (a) and chemical structures of PKA-responding polymers (b).

synthesized by an automatic peptide synthesizer by Fmoc chemistry using the corresponding Fmoc amino acids and *N*-methacryloyl-L-glycine, as reported previously.[11] Substrate peptide monomer 2 and 4 (Peptide 2: CH_3CO-LRRASL-Dpr($COC(CH_3)=CH_2$)-NH_2, Peptide 4: CH_3CO-DWDALRRASL-Dpr($COC(CH_3)=CH_2$)-NH_2) were prepared in a manner similar to that for Peptide 1, using the corresponding Fmoc amino acids and N^{α}-Fmoc-N^{β}-1-(4,4-dimethyl-2,6-dioxocyclohex-1-ylidene)-3-methylbuthyl-L-diaminopropionic acid (Fmoc-Dpr(ivDde)-OH) as the residue to incorporate the vinyl group. Vinylation of the peptide was accomplished by selective deprotection of ivDde from Dpr, by incubating the peptide-loaded resin for 5 min with DMF/2% hydrazine and subsequently coupling it with the *N*-methacryloyloxysuccinimide in DMF. Substrate peptide monomer 3 (Peptide 3: $CH_2=C(CH_3)CO$-ALRRASLE) was also synthesized in a manner similar to that of Peptide 1, using *N*-methacryloyl-L-alanine as an N-terminus amino acid. The obtained peptides were purified by reverse-phase high performance liquid chromatography (HPLC) using a mobile phase of acetonitrile/water containing 0.1% TFA (20% v/v to 27.5–50% v/v) and then lyophilized. The *N*-methacryloyl-PEG was prepared by stirring a mixture of *N*-methacryloyloxysuccinimide (90 mg, 0.5 mmol) and α-methoxy-ω-aminopoly(ethylene oxide) (600 mg, MW 12 000) in chloroform (5 mL) overnight at room temperature. The obtained *N*-methacryloyl-PEG was purified by column chromatography on Sephadex LH-20 using methanol as the eluting solvent.

Preparation of NIPAM–PEPs and NIPAM–PEPEPs. NIPAM–PEP1–3 were synthesized by radical copolymerization of *N*-isopropylacrylamide and the corresponding substrate peptide monomer, in distilled water at 25 °C for 1.5 h under a nitrogen atmosphere, using ammonium persulfate (2.8 mM) and *N*,*N*,*N*′,*N*′-tetramethylethylenediamine (5.78 mM) as the redox initiator couple. The total monomer concentration was 72.3 mM. The NIPAM–PEPs were purified by dialysis using a semipermeable membrane bag (with a molecular weight cutoff of 10 000) against water for 1–3 days, followed by lyophilizing. NIPAM–PEPEP1–4 were synthesized similarly to the NIPAM–PEPs, using *N*-methacryloyl-PEG, the appropriate substrate peptide monomer and *N*-isopropylacrylamide. In this case, a semipermeable membrane bag with a molecular weight cutoff of 50 000 was used for the dialysis. The chemical structures of these conjugates are shown in Figure 1b. The mole fractions of each peptide and PEG unit are shown in Table 1. This information was obtained by elemental analysis and ^1H NMR.

Table 1. Mole Fraction of Each Peptide and PEG Unit in NIPAM–PEPs and NIPAM–PEPEPs

	mole fraction (mol %)				
	peptide		PEG		
	in feed	observed	in feed	observed	yield (%)
NIPAM–PEP1	1.9	1.3	-	-	67
NIPAM–PEP2	1.5	1.0	-	-	77
NIPAM–PEP3	1.5	1.1	-	-	72
NIPAM–PEPEP1	1.9	1.6	0.2	0.3	49
NIPAM–PEPEP2	1.5	1.2	0.2	0.3	66
NIPAM–PEPEP3	3.0	2.7	0.2	0.2	42
NIPAM–PEPEP4	2.0	1.0	0.2	0.3	39

Table 2. LCST Change on Phosphorylation by PKA in NIPAM–PEPs

	LCST (°C)		
	before phosphorylation	after phosphorylation	ΔT (°C)
NIPAM–PEP1	38.2	41.8	3.6
NIPAM–PEP2	>42.5	37.5	> −5
NIPAM–PEP3	38.0	46.5	8.5

Gel Permeation Chromatography (GPC) Analysis. GPC of NIPAM–PEPs and NIPAM–PEPEPs was performed using a Viscotek model 300 TDA system equipped with refractive index, viscosity, and light scattering detectors operating at 25 °C. TSKgel α - M columns (TOSOH Co. Ltd., Tokyo, Japan) were used, with DMF containing 10 mM LiBr as the eluent. The flow rate was 0.8 mL/min.

Light Transmittance Measurement. Light transmittance was measured using a UV-2550 UV–Visible spectrophotometer (Shimadzu Co. Ltd., Kyoto, Japan). 50 mM MOPS buffer solution (pH 7.0) containing 0.3 mg/mL NIPAM–PEP1–3, 0.2 mM ATP, and 10 mM $MgCl_2$ was prepared to a final volume of 500 μL. The light transmittance of each solution at 500 nm was monitored from 30 °C to 45–55 °C at a heating rate of 0.5 °C/min. For the experiment using the phosphorylated NIPAM–PEP, 25 U PKA C-subunit was added to the above solution 2 h before the measurements.

Fluorescence Measurement. Fluorescence spectra were measured using a RF-5300PC spectrofluorophotometer (Shimadzu Co. Ltd., Kyoto, Japan). Dansyl-aniline (final concentration 20 μM) was dissolved in 50 mM MOPS buffer solution (pH 7.0) containing 10 mM $MgCl_2$ and 0.2 mM ATP in the presence of 0.3 mg/mL NIPAM−PEPEP1−4. Fluorescence spectra were then measured at an excitation wavelength of 340 nm at various temperatures. For the experiment using phosphorylated NIPAM−PEPEPs, 25 U PKA C-subunit was added to the above solution 2 h before the fluorescence measurements. Measurement of the release of dansyl-aniline encapsulated in the nanoparticle formed by NIPAM−PEPEP4 was also performed under similar conditions, except for the use of PBS(−) instead of MOPS buffer solution.

Laser Light Scattering. A modified commercial LLS spectrometer (DLS-7000, Ohtsuka Electronics Co. Ltd., Osaka, Japan) and an argon laser (output power ca. 20 mW at $\lambda = 488$ nm) were used. The incident light beam was vertically polarized with respect to the scattering plane. NIPAM−PEPEP2 (final concentration 0.3 mg/mL) was dissolved in 50 mM MOPS buffer (pH 7.0) containing 10 mM $MgCl_2$ and 0.2 mM ATP. This solution was filtered before DLS measurement.

RESULTS AND DISCUSSION

GPC Analysis of Polymers. The average molecular weights of the polymers were evaluated using GPC. The results suggested that all NIPAM−PEPs and NIPAM−PEPEPs had similar molecular weights in the range 270 000−300 000.

Effect of Phosphorylation on Physical Properties of NIPAM−PEPs. In our previous report (*11*), we showed that the LCST of NIPAM−PEP1 was raised in response to phosphorylation by PKA (Figure 2a). To construct a polymer-peptide conjugate which shows a larger difference than NIPAM−PEP1 in the LCST as a result of PKA treatment, we designed two types of substrate peptides for PKA. Peptide 2 has a methacryloyl group at the carboxyl terminus. It means that a serine residue of the phosphorylation site is located closer to the polymer backbone than that in NIPAM−PEP1 (Figure 1b). It is expected that the enhancement of the hydration around the polymer backbone is greater than for NIPAM−PEP1. We evaluated the effect of NIPAM−PEP2 phosphorylation by PKA on the LCST of this polymer (Figure 2b). Surprisingly, light transmittance of NIPAM−PEP2 was 80% even at 45 °C; that is, this polymer was water-soluble over the full range of temperatures we tested, while phosphorylated NIPAM−PEP2 had a LCST of 37 °C. This result indicates that the LCST in NIPAM−PEP2 was lowered on the introduction of phosphate groups into the polymer, contrary to our expectation. The major reason the effects of phosphorylation in the two polymers were entirely different can be found in the net charge of the peptide in both polymers at neutral pH. In the case of NIPAM−PEP1, the net charge of Peptide 1 is considered to be +1, and this changes to −1 after the phosphorylation. In this case, the interpeptide electrostatic repulsion is scarcely changed, and the LCST of NIPAM−PEP1 was increased due to the enhancement of the hydration around the polymer chain by the phosphorylation. On the other hand, the net charge of Peptide 2 in NIPAM−PEP2 is +2 at pH 7. In this case, the interpeptide electrostatic repulsion will be larger than for Peptide 1. Such repulsion would completely disappear as a result of the neutralization of the charges on Peptide 2 on modification with the phosphate group. Thus, the LCST of NIPAM−PEP2 decreased, even though the effect of the enhanced hydration resulting from phosphorylation could be greater in NIPAM−PEP2 than that in NIPAM−PEP1. These results suggest that the change in water solubility of the NIPAM−peptide conjugate is mainly governed by the change in the net charge of the peptide on phosphorylation.

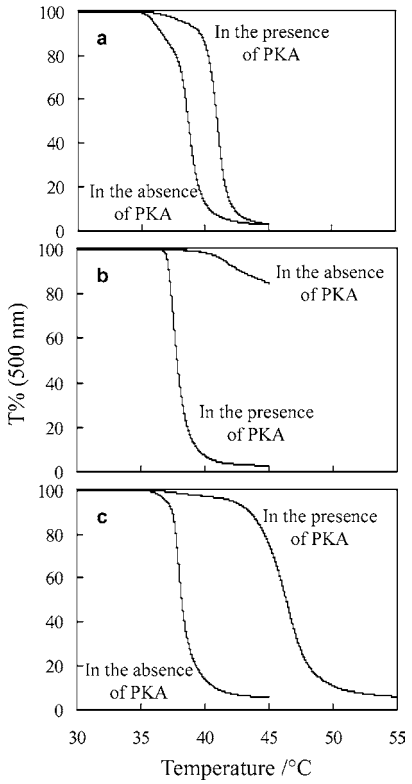

Figure 2. Temperature dependence of the light transmittance of the NIPAM−PEP solution before and after phosphorylation with activated PKA. The experiment was performed in 50 mM MOPS buffer (pH 7.0) containing 0.3 mg/mL each of NIPAM−PEP, 0.2 mM ATP, and 10 mM $MgCl_2$. In the case of phosphorylated NIPAM−PEP, light transmittance was measured after 2 h of incubation of the solution with PKA C-subunit (25 U). (a) NIPAM−PEP1, (b) NIPAM−PEP2, (c) NIPAM−PEP3.

We designed another substrate peptide for PKA, Peptide 3, and synthesized NIPAM−PEP3 (Figure 1b). The light transmittance of the NIPAM−PEP3 solution indicates that the LCST of NIPAM−PEP3 increased as a result of phosphorylation by PKA to a greater degree than in the case of NIPAM−PEP1 (Figure 2c). The LCST of NIPAM−PEP3 was increased from 38 °C to 46 °C by phosphorylation. The net charge of Peptide 3 changes from 0 to −2 on phosphorylation by PKA. It was expected that the physical properties of NIPAM−PEP3 would change a large amount as a result of phosphorylation, because the phosphotransfer into Peptide 3 causes great enhancement of the hydration around the polymer backbone and the electrostatic repulsion between the peptides. It is reasonable to suppose that the change in the physical properties of the conjugates due to phosphorylation is mainly governed by the change in the formal net charge on the pendant peptide.

Modification of NIPAM−PEPs with PEG Chain. As described in our previous paper (*11*), NIPAM−PEP1 containing a PEG chain (NIPAM−PEPEP1) forms polymer micelles above the LCST without precipitation. We synthesized NIPAM−PEPEP2 and NIPAM−PEPEP3 by radical copolymerization in a manner similar to that for

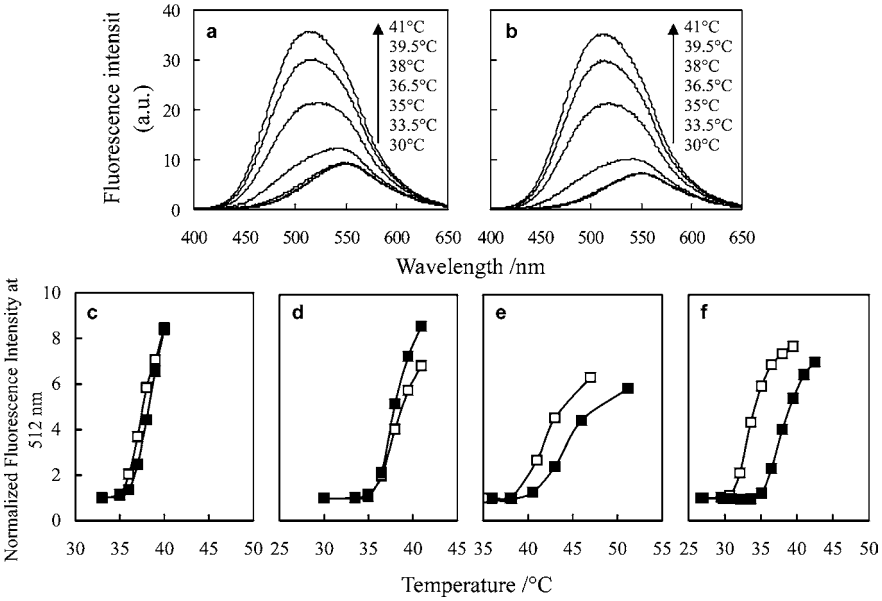

Figure 3. Temperature dependence of fluorescence spectra of dansyl aniline with NIPAM−PEPEP2 before (a) and after (b) phosphorylation, and the change in the fluorescence intensity of dansyl aniline at 512 nm in the presence of NIPAM−PEPEPs (c−f). Closed and open squares indicate the phosphorylated and unphosphorylated polymer, respectively. (c) NIPAM−PEPEP1, (d) NIPAM−PEPEP2, (e) NIPAM−PEPEP3, (f) NIPAM−PEPEP4. Dansyl aniline (20 μM final concentration) was dissolved in 50 mM MOPS (pH 7.0) containing 0.3 mg/mL of NIPAM−PEPEP2, 0.2 mM ATP and 10 mM $MgCl_2$. Phosphorylation was performed by the addition of 12.5 U of PKA C-subunit.

the preparation of NIPAM−PEPEP1 (Figure 1b) (*11*). To study the effect of phosphorylation on their physical properties, the fluorescence intensity of dansyl aniline, which has a fluorescence spectrum that is sensitive to the polarity of its environment, was monitored at various temperatures in the presence of the phosphorylated or unphosphorylated NIPAM−PEPEPs (Figure 3a,b). The dye tends to be encapsulated into the hydrophobic core of the NIPAM−PEPEPs polymer micelles above their LCSTs. In the case of the phosphorylated and unphosphorylated NIPAM−PEPEP2, the fluorescence intensity started to increase at the same temperature (36 °C) regardless of the phosphorylation (Figure 3c). This means that the phosphorylation of NIPAM−PEPEP2 did not affect the temperature at which particle formation began. However, the hydrophobicity of the polymer micelle core increased with phosphorylation, because the increase in the fluorescence intensity of the dansyl aniline at 512 nm is larger in the presence of the phosphorylated polymer than in the presence of the unphosphorylated polymer.

The size distribution of NIPAM−PEPEP2 micelles was evaluated at 38 °C, before and after treatment with PKA (Figure 4). The average diameter of the unphosphorylated micelles was 86.7 nm. After addition of PKA, the particle size was decreased within 6 min, simultaneous to the increase in the fluorescence intensity of the dansyl aniline. These results indicate that the collapse of the polyNIPAM chain in NIPAM−PEPEP2 accelerated as a result of the phosphorylation due to disappearance of the interpeptide electrostatic repulsion on phosphorylation.

A similar fluorescent measurement was performed for NIPAM−PEPEP3 (Figure 3c). Here, the temperature at which the polymer micelle was formed increased more remarkably on phosphorylation than for NIPAM−PEPEP1. This result indicates that the polymer micelle of NIPAM−PEPEP3 disintegrated in the presence of PKA much more readily than the polymer micelle of NIPAM−PEPEP1. Thus, the change in the net charge of the pendant peptide and the extent of the hydration around

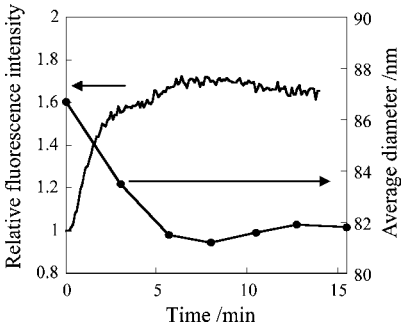

Figure 4. Time course of the change in the average hydrodynamic radius (circles) of the NIPAM−PEPEP2 particle, and of the fluorescence intensity at 512 nm (solid line) of dansyl aniline after PKA addition. The NIPAM−PEPEP2 (0.3 mg/mL) was dissolved in 50 mM MOPS (pH 7.0) containing 0.2 mM ATP and 10 mM $MgCl_2$, and dansyl aniline was added to a final concentration of 20 μM only in the fluorescence measurement. The light scattering intensity was monitored at 37 °C with a 90° detection angle. The change in the fluorescence intensity at 512 nm was estimated as the ratio of the intensity at each time to that at 0 min.

the polymer chain are key factors in the NIPAM−PEPEP-type conjugates.

In this experiment, unphosphorylated NIPAM−PEPEP3 began to form polymer micelles at 38 °C. This temperature was higher than that for NIPAM−PEPEP1 (35 °C). It is likely that a larger quantity of hydrophilic substrate peptides was introduced in NIPAM−PEPEP3 (2.7 mol %) than in NIPAM−PEPEP1 (1.6 mol %).

Further Sophisticated Peptides. These findings encouraged us to design NIPAM−PEPEP-type conjugates which provide a greater response than NIPAM−PEPEP1−3. We designed and synthesized NIPAM−PEPEP4 as an ideal material that exhibited sufficient response to PKA activity (Figure 1b). The net charge of the pendant Peptide 4 is the same as that of Peptide 3, so that the change in the net charge of the peptide should be able to increase the LCST. In addition, a serine residue as a phosphorylation site is located closer to the polymer main

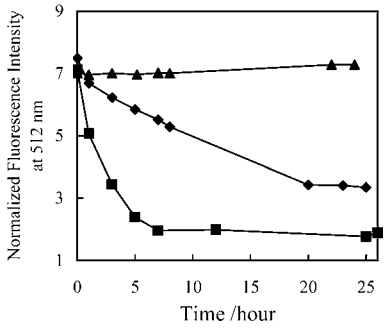

Figure 5. Time course of the release of dansyl aniline encapsulated in nanoparticles of NIPAM−PEPEP4 at 34 °C. Dansyl aniline (20 μM final concentration) was dissolved in PBS(−) (pH 7.2) containing 0.3 mg/mL of NIPAM−PEPEP4, 0.2 mM ATP and 10 mM $MgCl_2$. The fluorescence intensity at 512 nm was then monitored in the absence (triangles) or presence (diamonds: 60 U, squares: 300 U) of PKA.

chain than in Peptide 3. It was expected that the enhancement of the hydration on PKA phosphorylation could be greater than that for NIPAM−PEPEP3. Figure 3c shows the fluorescence measurement results for NIPAM−PEPEP4. The temperature at which polymer micelles were formed increased by ca. 5 °C on phosphorylation by PKA. This was the greatest change of all the peptide-polymer conjugates developed. Although it is not clear the reason LCST of NIPAM−PEPEP4 was lower than that of other NIPAM−PEPEPs, the increase of the hydrophobicity of the peptide side chains introduced in NIPAM−PEPEP4 may contribute to the phenomenon. This polymer will be more suitable than other NIPAM−PEPEPs in the use at physiological temperatures.

Next, the potential of NIPAM−PEPEP4 as a drug capsule responding to a PKA signal was investigated. The fluorescence of dansyl aniline encapsulated in NIPAM−PEPEP4 stayed at its initial level for over 25 h at 34 °C, indicating that the fluorescence dye did not leak from the micelles into the solvent, while leakage of the dye from the micelles was observed in the presence of PKA (Figure 5). When 300 U PKA was added, the fluorescence intensity at 512 nm reached a minimum at 5 h. Addition of 60 U PKA showed a more gradual release of the dansyl aniline. NIPAM−PEPEP4 will be applicable for use in drug capsules to achieve the selective release of drugs in response to cellular conditions, because PKA activation occurs in various diseases.

CONCLUSION

In this work we reported on the physical properties of polyNIPAM−peptide conjugates containing a new type of PKA substrate peptide. The assembly of our designed PKA-responding polymers could be regulated by phosphorylation at temperatures above their LCSTs. The synthesized polymers all responded differently to phosphorylation by PKA. This difference can be accomplished by making a small change in the substrate peptide sequence. In the case of the polymers containing Peptide 1 and Peptide 3, an increase in the LCST was observed on phosphorylation by PKA. On the other hand, the LCST for Peptide 2 was lowered on phosphorylation. Our findings suggest that two major factors contribute to determining the direction and degree of the change in the LCST resulting from phosphorylation of the polymer−peptide conjugates reported here. One factor is the enhancement of the hydration around the polymer-chain backbone, and the other is a change in the formal net charge of the peptide due to the introduction of the anionic charge of the phosphate group on its serine residue. By controlling these two factors, we succeeded in designing a new material, NIPAM−PEPEP4, that forms a polymer micelle-type capsule that disintegrated with a much greater response to PKA phosphorylation than other materials. We recently reported an artificial gene regulation system for the new concept of gene delivery and termed this system D-RECS, which stands for drug-delivery system responding to cellular signals.[12] The polymer micelle formed by NIPAM−PEPEP4 will be another tool for use in D-RECS.

ACKNOWLEDGMENT

This work was financially supported by CREST, the Japan Science and Technology Agency, and a grant-in-aid for Scientific Research from the Ministry of Education, Science, Sports, and Culture, and also the Ministry of Health, Labor and Welfare, in Japan.

LITERATURE CITED

(1) Roger, P. P., Christophe, D., Dumont, J. E., and Pirson, I. (1997) The dog thyroid primary culture system − a model of the regulation of function, growth and differentiation expression by cAMP and other well-defined signaling cascades. *Eur. J. Endocrinol. 137*, 579−598.

(2) McCusker, R. H., and Clemmons, D. R. (1998) Role for cyclic adenosine monophosphate in modulating insulin-like growth factor binding protein secretion by muscle cells. *J. Cell. Physiol. 174*, 293−300.

(3) Montminy, M. (1997) Transcriptional regulation by cyclic AMP. *Annu. Rev. Biochem. 66*, 807−822.

(4) Bertolotto, C., Abbe, P., Hemesath, T. J., Bille, K., Ficher, D. E., Ortonne, J. P., and Ballotti, R. (1998) Microphthalmia gene product as a signal transducer in cAMP-induced differentiation of melanocytes. *J. Cell Biol. 142*, 827−835.

(5) Nguyen, P. V., and Kandel, E. R. (1996) A macromolecular synthesis-dependent late phase of long-term potentiation requiring cAMP in the medial perforant pathway of rat hippocampal slices. *J. Neurosci. 16*, 3189−3198.

(6) Harada, H., Becknell, B., Wilm, M., Mann, M., Huang, L. J. S., Taylor S. S., Scott, J. D., and Korsmeyer, S. J. (1999) Phosphorylation and inactivation of BAD by mitochondria-anchored protein kinase A. *Mol. Cell 3*, 413−422.

(7) Fladmark, K. E., Gjertsen, B. T., Doskeland, S. O., and Vintermyr, O. K. (1997) FAS/APO-1(CD95)-induced apoptosis of primary hepatocytes is inhibited by cAMP. *Biochem. Biophys. Res. Commun. 232*, 20−25.

(8) Kim, S. H., Forman, A. P., Mathews, M. B., and Gunnery, S. (2000) Human breast cancer cells contain elevated levels and activity of the protein kinase, PKR. *Oncogene 19*, 3086−3094.

(9) Nabel, G. J., Nabel, E. G., Yang, Z. Y., Fox, B. A., Plautz, G. E., Gao, X., Huang, L., Shu, S., Gordon, D., and Chang, A. E. (1993) Direct gene transfer with DNA liposome complexes in melanoma − expression biologic activity and lack of toxicity in humans. *Proc. Natl. Acad. Sci. U.S.A. 90*, 11307−11311.

(10) Page, C., Huang, M., Jin, X., Cho, K., Lilja, J., Reynolds, R. K., and Lin, J. (2000) Elevated phosphorylation of AKT and Stat3 in prostate, breast, and cervical cancer cells. *Int. J. Oncol. 17*, 23−28.

(11) Katayama, Y., Sonoda, T., and Maeda, M. (2001) A polymer micelle responding to the protein kinase A signal. *Macromolecules 34*, 8569−8573.

(12) Katayama, Y., Fujii, K., Ito, E., Sakakihara, S., Sonoda, S., Murata, M., and Maeda, M. (2002) Intracellular signal-responsive artificial gene regulation for novel gene delivery. *Biomacromolecules 3*, 905−909.

BC049710A

Evaluation of ((4-Hydroxyphenyl)ethyl)maleimide for Site-Specific Radiobromination of Anti-HER2 Affibody

Eskender Mume,[†] Anna Orlova,[‡] Barbro Larsson,[‡] Ann-Sofie Nilsson,[‡] Fredrik Y. Nilsson,[‡] Stefan Sjöberg,[†] and Vladimir Tolmachev*[,§]

Department of Chemistry, Organic Chemistry, Uppsala University, Uppsala, Sweden, Affibody AB, Bromma, Sweden, and Unit of Biomedical Radiation Sciences, Rudbecklaboratoriet, Uppsala University, S-751 85, Uppsala, Sweden. Received February 28, 2005; Revised Manuscript Received August 7, 2005

Affibody molecules are a new class of small phage-display selected proteins using a scaffold domain of the bacterial receptor protein A. They can be selected for specific binding to a large variety of protein targets. An affibody molecule binding with high affinity to a tumor antigen HER2 was recently developed for radionuclide diagnostics and therapy in vivo. The use of the positron-emitting nuclide ^{76}Br ($T_{1/2}$ = 16.2 h) could improve the sensitivity of detection of HER2-expressing tumors. A site-specific radiobromination of a cysteine-containing variant of the anti-HER2 affibody, $(Z_{HER2:4})_2$-Cys, using ((4-hydroxyphenyl)ethyl)maleimide (HPEM), was evaluated in this study. It was found that HPEM can be radiobrominated with an efficiency of 83 ± 0.4% and thereafter coupled to freshly reduced affibody with a yield of 65.3 ± 3.9%. A "one-pot" labeling enabled the radiochemical purity of the conjugate to exceed 97%. The label was stable against challenge with large excess of nonlabeled bromide and in a high molar strength solution. In vitro cell tests demonstrated that radiobrominated affibody binds specifically to the HER2-expressing cell-line, SK-OV-3. Biodistribution studies in nude mice bearing SK-OV-3 xenografts have shown tumor accumulation of 4.8 ± 2.2% IA/g and good tumor-to-normal tissue ratios.

INTRODUCTION

Radionuclide tumor targeting uses molecular recognition of tumor-associated structures for the selective delivery of diagnostic or therapeutic nuclides to tumor sites. Molecular recognition has mainly been associated with the use of monoclonal antibodies and their products or of peptide receptor ligands and their analogues. During last years, nonpeptide small molecular weight ligands for receptors and enzymes attracted attention as potential targeting agents as well. Development in this area has enabled the production of targeting molecules with excellent specificity and high binding affinity. Still, each approach has its disadvantages. Monoclonal antibodies are relatively bulky proteins, and this bulkiness limits blood clearance rate, extravasation, and tumor penetration. The use of receptor ligands is restricted in terms of target selection to receptors that are overexpressed in tumors. Sometimes, receptor ligands possess strong agonistic action, and efforts should be made in order to develop antagonistic analogues or provide high specific radioactivity of targeting conjugates.

A possible alternative in creating new targeting vectors is to use phage display technology (*1*). One variant of phage display proteins, termed affibody molecules (*2*, *3*), uses the domain scaffold of the immunoglobulin-binding Staphylococcal receptor protein A. This 58-amino acid-long cysteine-free protein provides a robust framework, independent of disulfide bonds for its folding. The small size (about 7 kDa in monomeric and about 15 kDa in dimeric form) of affibody molecules enables fast blood clearance and good tumor penetration. Randomization of 13 solvent-accessible surface residues of the protein A domain was used to create a library containing about 10^9 members, enabling the isolation of high-affinity ligands for virtually any tumor-associated protein target. The selection of the affibody $Z_{HER2:4}$, which binds with high specificity and affinity of 50 nM to the HER2/neu receptor, was recently reported by Wikman and co-workers (*4*). Dimerization of $Z_{HER2:4}$ enabled to obtain affinity of 3 nM (*22*). This HER2/neu receptor is often overexpressed in a number of carcinomas, such as breast, ovarian, and urinary bladder cancer (*5*−*7*). The prognostic and predictive values of HER2/neu receptor overexpression are well documented (*6*, *8*, *9*), and HER2 imaging can provide important information that can influence patient management. Preliminary biodistribution and imaging data for $Z_{HER2:4}$ derivatives labeled with ^{125}I (*10*) confirmed the utility of affibody molecules for tumor diagnostics.

It is reasonable to assume that the use of positron-emitting labels may improve quality of targeted diagnostics due to the better sensitivity and resolution of positron emission tomography (PET) in comparison to those of other radionuclide imaging modalities (*11*). A possible candidate radionuclide for labeling affibody molecules is ^{76}Br. Its half-life of 16.2 h matches the fast kinetics of affibody molecules well, and it can easily be produced using cyclotrons available at PET centers (*12*).

When a radionuclide is to be selected as a label, its labeling chemistry should be carefully considered. Though the radiobromination of proteins or peptides is not as

* To whom correspondence should be addressed. Phone: + 46 18 471 34 14, FAX: + 45 18 471 34 32, e-mail: Vladimir.Tolmachev@bms.uu.se.

[†] Department of Chemistry, Organic Chemistry, Uppsala University.

[‡] Affibody AB.

[§] Unit of Biomedical Radiation Sciences, Rudbecklaboratoriet, Uppsala University.

10.1021/bc050056o CCC: $30.25 © 2005 American Chemical Society
Published on Web 10/27/2005

Scheme 1. Labeling of HPEM and Conjugation of the Labeled Product, 2, to His_6-$(Z_{HER2:4})_2$-Cys[a]

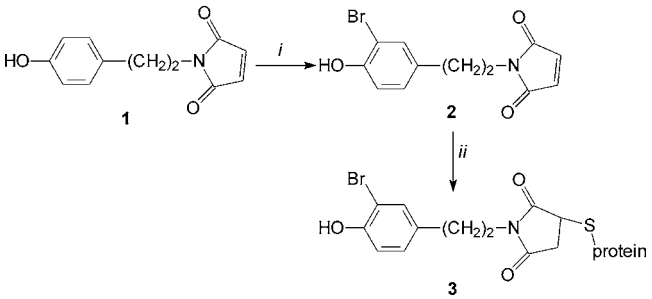

[a] Reagents and conditions: (i) $^{76}Br^-$, Chloramine-T, MeOH/HOAc, RT; (ii) His_6-$(Z_{HER2:4})_2$-Cys, pH 6.

well-studied as is radioiodination, some experience has been amassed pertaining to bromine-75, bromine-76, and bromine-77. Radiobromine can be attached to proteins either *directly* to tyrosine residues, using peroxidases (*13*−*15*) and Chloramine-T (*16*) as oxidants, or *indirectly* by labeling several precursors and subsequent coupling to the ϵ-amino groups of lysine residues (*17*−*21*). However, both lysines and tyrosines can appear in the binding regions of the selected affibody candidates, and their modification may therefore reduce the binding affinity. In fact, direct radioiodination of $Z_{HER2:4}$ led to loss of HER2 binding (*22*), while some labeling methods directed to lysines decreased such binding. For this reason, it would be useful to develop a method for conjugating radiobromine to affibody molecules in a site-specific manner.

The approach used in this study exploits the fact that cysteine residues have been excluded from the affibody selection library. This allows us to introduce, using genetic engineering, a unique cysteine residue at C-terminal of the selected affibody molecules and to use the thiol group for the coupling of a radiobrominated precursor. As a model, a dimeric cysteine-containing variant of $Z_{HER2:4}$, $(Z_{HER2:4})_2$-Cys, was created for this study. A maleimide derivative of tyramine, ((4-hydroxyphenyl)ethyl)maleimide (HPEM) (*1*) (see Scheme 1), was selected as a bifunctional linker for attaching radiobromine to the cysteine-containing affibody. Use of this compound for the radioiodination of radioimmunoconjugates was reported in an abstract (*23*), but no details concerning synthesis or characterization were provided.

The present study explores the labeling chemistry of the indirect site-specific radiobromination of cysteine-containing affibody molecules using HPEM and evaluates the tumor-targeting properties of cysteine-containing $(Z_{HER2:4})_2$-Cys, both in vitro and in vivo.

EXPERIMENTAL PROCEDURES

Material. Organic solvents were purchased from Merck (Darmstadt, Germany), and Chloramine-T (CAT) and sodium metabisulfite from Sigma Chemical Company (St. Louis, MO); all chemicals were of analytical grade or higher. Acetate buffer (0.1 M, pH 5) was prepared using sodium acetate and acetic acid (Merck, Darmstadt, Germany). Phosphate-buffered saline (PBS, 5 mM, pH 7.4) was prepared from $Na_2HPO_4 \cdot 10H_2O$, $NaH_2PO_4 \cdot H_2O$, and NaCl, all of analytical grade (Merck, Darmstadt, Germany). High-quality Milli-Q water (resistance > 18 MΩ/cm) was used in preparing solutions and buffers. Solutions of CAT, sodium metabisulfite, and ((4-hydroxyphenyl)ethyl)maleimide were prepared immediately before use. Merck silica gel 60 (230−400 mesh) was used for column chromatography. Thin-layer chromatography

Scheme 2. Synthesis of HPEM, 1, and the Chromatography Standard, 8[a]

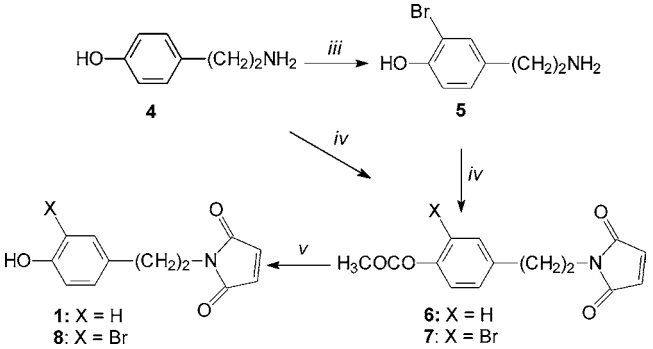

[a] Reagents and conditions: (iii) Br_2, AcOH, RT; (iv) maleic anhydride, acetic anhydride, KOAc, THF; (v) Amberlyst-15, MeOH.

(TLC) was performed using Merck Silica 60 F_{254} gel, and compounds were visualized with UV (254 nm) or by developing the plates with ninhydrin/acetic acid (0.4/4 w/w% in *n*-butanol) followed by heating. Tetrahydrofuran (THF) was dried according to standard methods.

Instrumentation. Radioactivity measurements were carried out with an ultrapure germanium detector (ORTEC, Oak Ridge, TN) connected to a 8192-channel, PC-based multichannel analyzer (The Nucleus Inc., Oak Ridge, TN). The detector was calibrated for energy and efficiency with a standard ^{152}Eu source. Dead-time losses were always below 10% during measurements. Alternatively, the radioactivity was measured with the automatic 1480 WIZARD 3" Gamma Counter (Wallac) equipped with 3-in. NaI(Tl) well detector using a measurement protocol with an energy window of 300−2047 keV. The ^1H and ^{13}C spectra were recorded in $CDCl_3$ (7.26 ppm ^1H, 77.0 ppm ^{13}C) on a Varian Unity 400 spectrometer operating at 400 and 100.6 MHz, respectively, or on a Varian Unity 500 spectrometer operating at 500 and 125 MHz, respectively. Melting points were determined on a Buchi capillary melting point apparatus and are uncorrected. High-resolution mass spectroscopy (HRMS) was conducted at the Organisch Chemisches Institut der Universitaet Muenster, Germany, for compounds **1**−**7** and on a Thermoquest GCQ GC/MS instrument, using the electron impact (EI), direct inlet mode for compound **8**. High-performance liquid chromatography (HPLC) was conducted with a Gilson Model 322 pump and UV/VIS-152 detector. HPLC chromatography was carried out using an ODS C-18 HPLC column 150 × 20 mm ID, 5 μm at a flow rate of 5 mL/min. Spectrophotometer analysis of the HPLC effluent was performed by means of UV detection at 254 nm. Distribution of radioactivity along the TLC and instant thin-layer chromatography (ITLC) strips was measured using the Cyclone Storage Phosphor System and analyzed with the OptiQuant image analysis software. Size-exclusion chromatography was performed on disposable NAP-5 columns (Amersham Pharmacia Biotech AB, Uppsala; Sweden) according to the manufacturer's instructions.

Synthesis of HPEM (1) and of the Chromatography Standard, 1-[2-(3-Bromo-4-hydroxyphenyl)-ethyl]-1*H*-pyrrole-2,5-dione (8) (Scheme 2). *4-(2-Aminoethyl)-2-bromophenol (**5**).* A solution (0.7 M) of bromine in carbon tetrachloride (1.51 g, 9.46 mmol) was added dropwise to a stirred solution of tyramine (0.649 g, 4.73 mmol) in 15 mL acetic acid over 13 min. Analysis by means of nuclear magnetic resonance (NMR) indicated that the tyramine was fully consumed after 20 min at RT. The solvent was evaporated, and the residue was

dissolved in 0.5 g K_2CO_3/MeOH and stirred for 10 min; thereafter the salt was filtered off and the mixture was concentrated under a vacuum. The crude product was filtered through a short plug of silica to afford a white solid of bromide **5** along with a dibromide, (4-(2-aminoethyl)-2,6-dibromophenol). This was further purified by RP-HPLC, holding 100% (0.05% formic acid in water) for 5 min, followed by a gradient of 100% (0.05% formic acid in water)/0% acetonitrile (0.05% formic acid in acetonitrile), changing to 100% acetonitrile (0.05% formic acid in acetonitrile) over 35 min, to give 0.394 g of compound **5** as white crystals, mp = 152−155 °C, in 41% yield. ^{1}H NMR (CD_3OD): δ 7.39 (d, 1H, benz), 7.07 (dd, 1H, benz), 6.87 (d, 1H, benz), 3.10 (t, 2H, NCH_2), 2.84 (t, 2H, CH_2); ^{13}C NMR (CD_3OD): δ 153.5, 133.1, 129.1, 128.8, 116.4, 109.9, 40.7, 32.2. HRMS(*m/z*): calcd for [$C_8H_{10}BrNO$ + H^+], 216.0019; found, 215.9988.

*4-[2-(2,5-Dioxo-2,5-dihydro-1H-pyrrol-1-yl)ethyl]phenyl Acetate (**6**).* Maleic anhydride (0.452 g, 4.63 mmol) was added to a stirred solution of tyramine (0.529 g, 3.86 mmol) in 50 mL of dry THF at 40 °C. The solution mixture was stirred overnight at 40 °C under an argon atmosphere. The solvent was then evaporated under reduced pressure. Acetic anhydride (125 mL) and potassium acetate (1.47 g, 15.3 mmol) were added to the white solid residue, and the mixture was stirred at 90 °C for 1 h. After this, the black reaction mixture was stirred at RT overnight. The solvent was evaporated under reduced pressure, and the residue was dissolved in CH_2Cl_2 and then washed three times with water and once with saturated $NaHCO_3$. The organic phase was dried over anhydrous Na_2SO_4 and filtered, and then the solvent was removed under reduced pressure. The resulting crude product was purified by flash chromatography (10:1%, CH_2Cl_2:Et_2O as the mobile phase) to afford 0.660 g of **6** as white crystals, mp = 96−97 °C, in 66% yield. ^{1}H NMR ($CDCl_3$): 7.21 (2H, m, AA′ part of AA′XX′, benz), 7.01 (2H, m, XX′ part of AA′XX′, benz), 6.66 (s, 2H, CH=CH-), 3.75 (t, 2H, NCH_2), 2.90 (t, 2H, CH_2), 2.28 (s, 3H, $COCH_3$); ^{13}C NMR ($CDCl_3$): δ 170.7, 169.6, 149.7, 135.6, 134.3, 130.0, 121.9, 39.2, 34.1, 21.3. HRMS(*m/z*): calcd for [$C_{14}H_{13}NO_4$ + Na^+], 282.0737; found, 282.0711.

*2-Bromo-4-[2-(2,5-dioxo-2,5-dihydro-1H-pyrrol-1-yl)ethyl]phenyl Acetate (**7**).* Compound **7** was synthesized using the same procedure as for compound **6**, except that 4-(2-aminoethyl)-2-bromophenol (0.135 g, 0.63 mmol) replaced tyramine and a temperature of 60 °C and a reaction time of 11 h were used. The crude product was purified using flash chromatography using neat $CHCl_3$ as a mobile phase to produce **7** with some impurities; this was then further purified using RP-HPLC, holding 100% (0.05% formic acid in water) for 5 min, followed by a gradient of 100% (0.05% formic acid in water)/0% acetonitrile (0.05% formic acid in acetonitrile), changing to 100% acetonitrile (0.05% formic acid in acetonitrile) over 60 min, to provide 0.098 g of **7**, as a white solid, in 46% yield. ^{1}H NMR ($CDCl_3$): δ 7.47 (d, 1H, benz), 7.18 (dd, 1H, benz), 7.05 (d, 1H, benz), 6.68 (s, 2H, CH=CH), 3.74 (t, 2H, NCH_2), 2.88 (t, 2H, CH_2), 2.34 (s, 3H, $COCH_3$); ^{13}C NMR ($CDCl_3$): δ 170.7, 168.8, 147.2, 137.6, 134.3, 133.8, 129.1, 123.9, 116.4, 38.9, 33.9, 21.0. HRMS(*m/z*): calcd for [$C_{14}H_{12}BrNO_4$ + Na^+], 359.9842; found, 359.9834.

*1-[2-(4-Hydroxyphenyl)ethyl]-1H-pyrrole-2,5-dione (**1**).* Amberlyst-15 (0.400 g) was added to a stirred solution of compound **6** (0.300 g, 1.16 mmol) in MeOH (30 mL), and the mixture was stirred at 55 °C for 4 h. The starting material was fully consumed according to TLC. The catalyst was filtered off and washed with MeOH/CH_2Cl_2 (2 × 3 mL). The filtrate was concentrated under reduced pressure. The resulting crude product was purified using flash chromatography with a dichloromethane−diethyl ether gradient (100% CH_2Cl_2:0% Et_2O to 90% CH_2Cl_2: 10% Et_2O) as a mobile phase to give 0.244 g of **1** as white crystals, mp = 144−145 °C, in 97% yield. ^{1}H NMR ($CDCl_3$): 7.05 (2H, m, AA′ part of AA′XX′, benz), 6.75 (2H, m, XX′ part of AA′XX′, benz), 6.65 (s, 2H, CH=CH), 3.72 (t, 2H, NCH_2), 2.82 (t, 2H, CH_2); ^{13}C NMR ($CDCl_3$): δ 170.9, 154.5, 134.3, 130.3, 130.2, 115.6, 39.5, 33.8. HRMS-(*m/z*): calcd for [$C_{12}H_{11}NO_3$ + Na^+], 240.0631; found, 240.0613.

*1-[2-(3-Bromo-4-hydroxyphenyl)ethyl]-1H-pyrrole-2,5-dione (**8**).* Compound **8** was synthesized using the same procedure as was used for compound **1**, except that compound **7** (34 mg, 0.10 mmol) was used as the starting material. The crude product was purified by means of flash chromatography using neat $CHCl_3$ as a mobile phase to give 26 mg of compound **8**, as a white solid, in 87% yield. ^{1}H NMR ($CDCl_3$): δ 7.32 (d, 1H, benz), 7.10 (dd, 1H, benz), 6.95 (d, 1H, benz), 6.69 (s, 2H, CH=CH), 3.73 (t, 2H, NCH_2), 2.83 (t, 2H, CH_2); ^{13}C NMR ($CDCl_3$): δ 170.7, 151.2, 134.3, 132.3, 131.7, 129.8, 116.3, 39.2, 33.6. MS(*m/z*): calcd for [$C_{12}H_{10}BrNO_3$ + H^+], 295.99; found, 294.52.

Production of $(Z_{HER2:4})_2$-Cys. The selection of a novel affibody ligand, denoted $Z_{HER2:4}$, binding to HER2, was previously described (*10*). The dimeric form of $Z_{HER2:4}$, from now on called $(Z_{HER2})_2$, was constructed by subcloning the gene fragment encoding the Z_{HER2} protein (*10*) into the expression vector pAY81-Z_{HER2}. The fragment was then digested with *Xho*I (ER0691, Fermentas, Vilnius, Lithuania) and *Sal*I (ER0641, Fermentas) and ligated into the pAY81-Z_{HER2} vector, previously restricted with *Sal*I to form pAY321 (*22*). In the present study, a C-terminal cysteine was introduced to form the clone pAY393 (pAY243-$(Z_{HER2})_2$-Cys) in the following way. A PCR product of the affibody molecule was generated from plasmid pAY321 (pAY81-$(Z_{HER2})_2$) with forward primer AFFI-77 (5′gccgctcgaggtagacaacaaattcaacaaag), introducing a *Xho*I restriction site, and reverse primer AFFI-223 (5′gatctgctgcagttagcatttcggcgcctgagcatcatttag), introducing a C-terminal cysteine and a *Pst*I restriction site downstream. Using as template a dimer consisting of two repetitive monomers, the PCR generated a monomeric and a dimeric version of the affibody molecule corresponding to Z_{HER2}. The dimer band was extracted from a preparative agarose gel using the QIAquick gel extraction kit (QIAGEN GmbH, Germany).

The affibody fragment, $(Z_{HER2})_2$-Cys, and the expression vector, pAY243, were digested using *Xho*I and *Pst*I, purified with the QIAquick PCR purification kit (QIAGEN GmbH, Germany), subsequently ligated with T4 DNA ligase, and transformed into the *Escherichia coli* strain BL21(DE3). The cells were plated on TBAB plates supplemented with 50 μg/mL kanamycin, and positive clones containing the introduced $(Z_{HER2})_2$-Cys fragment were verified by means of DNA sequencing on an ABI PRISM 3100 Genetic Analyzer (Applied Biosystems, Foster City, CA). *Escherichia coli* strain RRI$\Delta M15$[10] was used as bacterial host during the cloning procedure. The resulting vector, pAY393 (pAY243-$(Z_{HER2})_2$-Cys), encodes the bivalent affibody, $(Z_{HER2})_2$, fused to a C-terminal cysteine for thiol coupling and an N-terminal hexahistidyl (His_6) tag, allowing purification by immobilized metal ion affinity chromatography (IMAC).

The bivalent affibody protein was expressed as an His_6-tagged fusion protein in *E. coli* strain BL21(DE3) and recovered by means of IMAC purification on a TALON Metal Affinity Resin (8901-2, BD Biosciences, CA) column

under denaturing conditions, as described earlier (*22*). Renaturation of the purified fusion protein, the bivalent affibody, was performed by gel filtration using PD-10 columns, equilibrated with PBS (10 mM phosphate, 154 mM NaCl, pH 7.1), according to the manufacturer's protocol (Amersham Biosciences, Uppsala, Sweden). Protein concentration was calculated from absorbance measurements made at 280 nm using the extinction coefficient (30440 M^{-1} cm^{-1}). The purified protein was further analyzed by SDS−PAGE on a Tris-Glycine 16% homogeneous gel, using a Novex system (Novex, CA).

Radiobromine Production. A mixture of bromine radioisotopes was used for the radiobromination study. These nuclides were produced by irradiating copper(II) selenide of natural isotopic composition with 40-MeV protons. Radioactivity measurements of the irradiated targets and produced radiobromine were carried out using gamma-spectroscopy, as it was described in the Instrumentation section. The proton bombardment induces the bromine isotopes ^{77}Br, ^{76}Br, and ^{82}Br, as well as a number of radioisotopes of copper, zinc, selenium, and arsenic, in the target material. Radiobromine was separated from the target by dry distillation coupled with on-line thermochromatography purification (*12*) and was obtained as a no-carrier-added bromide solution in 200−400 μL of ultrapure Milli-Q water. No radioactive nuclides other than bromine isotopes were found in the product. Typical production batch contained 290 MBq ^{77}Br, 228 MBq ^{76}Br, and 6 MBq ^{82}Br at the end of separation. Measurements of specific radioactivity were not performed for this preparation. Earlier, we produced ^{76}Br using the same technique. The specific activity of the product was about 40 times lower than theoretical value, 200 GBq/μmol (*24*). Presence of fairly long-lived ^{77}Br ($T_{1/2}$ = 57 h) enabled the use of the radioactivity of a single batch for up to several days after radionuclide production.

Radiobromination of ((4-Hydroxyphenyl)ethyl)-maleimide (HPEM). The precursor molecule was radiobrominated using CAT as oxidant. An initial series of experiments was performed using 0.1% acetic acid in water, 1% acetic acid in methanol, and 5% acetic acid in methanol as reaction media. Typically, 3 μL of radiobromide were mixed with 10 μL of solvents and 5 μL of HPEM solution in methanol (varying concentrations), and CAT was added in 10 μL of water (varying concentrations). The reaction proceeded for a predetermined time and then was quenched by a double excess of sodium metabisulfite in 10 μL of water. Since the use of 5% acetic acid in methanol provided the best yields, this solvent was selected for further experiments. Labeling-yield dependence on the amount of added CAT and HPEM, and on reaction time, was determined by varying one parameter at a time. Typical reaction conditions were as follows: 5 μL of HPEM solution in 5% acetic acid in methanol was mixed with 3 μL of ^{76,77}Br in Milli-Q water in an Eppendorf tube (1.5 mL). To this mixture was added 10 μL of CAT solution in 5% acetic acid in methanol. The HPEM amount varied between 0.031 and 20 μg (0.144 and 92 nmol), and the CAT amount varied between 0 and 80 μg (283 nmol). The tube was agitated throughout the reaction time, which ranged from 5 to 20 min. The reaction was terminated by adding 10 μL of sodium metabisulfite solution in water, given in double molar excess to CAT. All experiments were made at least in duplicate.

Varying CAT Amount. When the amount of CAT was varied, the amount of added HPEM remained constant at 5 μg and the reaction time was 5 min.

Varying ((4-Hydroxyphenyl)ethyl)maleimide Amount. When the amount of HPEM was varied the amount of added CAT remained constant at 40 μg and the reaction time was 15 min. Blank experiments were performed, when 5% acetic acid in methanol was used instead of HPEM.

Varying Reaction Time. When the reaction time was varied the amount of added HPEM remained constant at 5 μg and the amount of added CAT was 40 μg.

Silica gel 60 F_{254} TLC plates (20 × 100 mm, elution path 80 mm, E. Merck, Darmstadt, Germany) were used for analysis. Neat acetonitrile was used for elution. For the analysis, 1−2 μL of the reaction mixture was applied on a TLC plate, which was then left to evaporate spontaneously before being developed in freshly prepared eluent.

Conjugation of Radiobrominated ((4-Hydroxyphenyl)ethyl)maleimide to His_6-$(Z_{HER2:4})_2$-Cys. Before labeling, affibody solution was treated with dithiothreitol (DTT, E. Merck, Darmstadt, Germany) in order to reduce spontaneously formed disulfide bonds. Typically, 0.5 mL of stock affibody solution (1 mg/mL in citrate-phosphate buffer, pH 4.5) was mixed with 10 μL of DTT (1 M solution in water, freshly prepared) and incubated for 40 min at 37 °C. Thereafter, the mixture was applied to NAP-5 size-exclusion columns, preequilibrated, and eluted with well-degassed 0.1 M acetate buffer, pH 6.0; the first 900 μL of the high-molecular-weight (HMW) fraction were used for labeling. Reduced affibody was used for labeling within 10−15 min after reduction.

((4-Hydroxyphenyl)ethyl)maleimide was radiobrominated for conjugation as previously described. A small sample (0.5 μL) of the reaction mixture was taken for radio-TLC analysis. $(Z_{HER2:4})_2$-Cys was added in an equimolar amount to HPEM, and the mixture was incubated at RT. At predetermined times (10 and 30 min), aliquots were taken, and the overall labeling yield was determined by size-exclusion chromatography as the ratio of radioactivity in the HMW fraction to the sum of the radioactivity in the HMW fraction, in the low-molecular-weight fraction (LMW) and on the column. Conjugation yield was calculated by correcting overall labeling yield for the yield of HPEM radiobromination. All experiments were performed in duplicate. Radiochemical purity of the labeled affibody was controlled using the ITLC SG strip (Pall Life Sciences, New York, NY) eluted with 70% acetone in water.

To verify that the labeling was associated with HPEM, blank experiments were performed in duplicate. In this case, 5% acetic acid in methanol was used instead of the HPEM solution, but all manipulations were the same as in the case of HPEM labeling.

To verify that coupling of radiobrominated ((4-hydroxyphenyl)ethyl)maleimide is directed to SH-group of cysteine, a control experiment was performed using subclone $(Z_{HER2:4})_2$, which does not contained cysteine. All other manipulations were the same as for $(Z_{HER2:4})_2$-Cys.

Stability Test. The in vitro stability of radiobromine binding to $(Z_{HER2:4})_2$-Cys was assessed by using 8 M urea to achieve high ion strength and 1 M NaBr to challenge with an excess of nonradioactive bromine. The labeling was performed according to the method described above. To Eppendorf tubes (1.5 mL) containing 1 mL of each of the stability test solutions was added 100 μL of radiobrominated $(Z_{HER2:4})_2$-Cys. The tubes were shaken vigorously for 15 s. The NaBr and urea solutions were kept at RT for 1.5 h of gentle agitation, and a fraction of 100 μL was taken for analysis. The samples were analyzed using size-exclusion chromatography, and the portion of

radioactivity in the LMW fraction was assumed to have resulted from release of the label. All tests were performed in duplicate.

Binding Specificity of Labeled Conjugates to HER2-Expressing Cells. Binding specificity of the obtained conjugates was tested on HER2-expressing SK-OV-3 ovarian cancer cells. Labeled conjugate was added to two groups of Petri dishes (3−4 dishes, ∅ 3.5 cm, 2−5 × 10^5 cells per dish). One group of dishes in each experiment was presaturated with a 1000-fold excess of nonlabeled affibody 10 min before the labeled affibody was added. Cells were incubated with labeled conjugate for 2 h at 37 °C; the incubation media was then collected. Cell dishes were washed 6 times with cold serum-free medium and then treated with 0.5 mL of trypsin-EDTA solution (0.05% trypsin, 0.02% EDTA in buffer, Flow Irvine, UK) for 10 min at 37 °C. When cells were detached, 1 mL of complete medium was added to every dish and the cells were resuspended. Of this cell suspension, 0.5 mL was used for cell counting and 1 mL for radioactivity measurements, along with 1 mL of the corresponding incubation medium.

Biodistribution Studies. The animal study was approved by the local Ethics Committee for Animal Research. Female outbreed BALB/c nu/nu mice (10−12 weeks old at arrival) were acclimatized for one week at the Rudbeck Laboratory animal facility before subcutaneous (sc) injection of ∼5 × 10^6 SK-OV-3 cells in the left hind leg. Xenografts were allowed to become established for two months.

Groups of four animals were used for the biodistribution study. All mice were subcutaneously injected with ∼50 μL (approximately 100 kBq, 0.8 μg) of radiolabeled affibody. After 4 h, the mice were anesthetized and sacrificed by heart puncture. Blood was collected using heparinized syringes (heparin 5000 IE/mL, from Leo Pharma, Köpenhamn, Denmark), while organs (heart, lung, liver, spleen, pancreas, kidney, stomach, muscle, and brain) and tumors were excised, and their radioactivity content was measured. Percent of injected dose per gram tissue (%IA/g) was calculated by dividing the radioactivity in a tissue by the average radioactivity in three control syringes, minus the radioactivity left in the syringe after injection and divided by the organ weight.

Since results of biodistibution study have demonstrated unusually low uptake of radioactivity in kidneys, a control experiment was performed with no-cysteine-containing clone $(Z_{HER2:4})_2$, which has been indirectly radiobrominated using *N*-succinimidyl 4-bromobenzoate (PBrB-$(Z_{HER2:4})_2$). Labeling was done according to Höglund and co-workers (*18*). Study protocol was the same as for HPEM-labeled affibody, but no-tumor-bearing nude mice were used in this study.

RESULTS

The synthesis of HPEM (**1**) and the chromatography standard 1-[2-(3-bromo-4-hydroxyphenyl)ethyl]-1*H*-pyrrole-2,5-dione (**8**) was carried out as outlined in Scheme 2 (see Material and Methods). Electrophilic bromination of commercially available tyramine (**4**) with bromine in carbon tetrachloride in the presence of acetic acid gave bromide, **5**, along with the dibromide, (4-(2-aminoethyl)-2,6-dibromophenol). Compound **5** (yield 41%) was isolated by reverse phase (RP). Tyramine (**4**) and 4-(2-aminoethyl)-2-bromophenol) (**5**) were reacted with maleic anhydride in dry tetrahydrofurane (THF) above room temperature (RT). The crude product was purified using column chromatography to give a 66% yield of compound

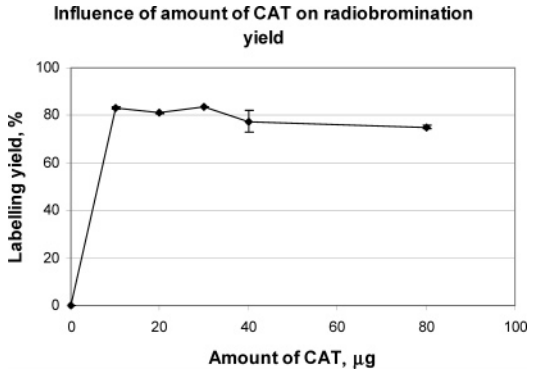

Figure 1. Dependence of bromination yield on amount of CAT. Other conditions: HPEM 5 μg; reaction time 5 min.

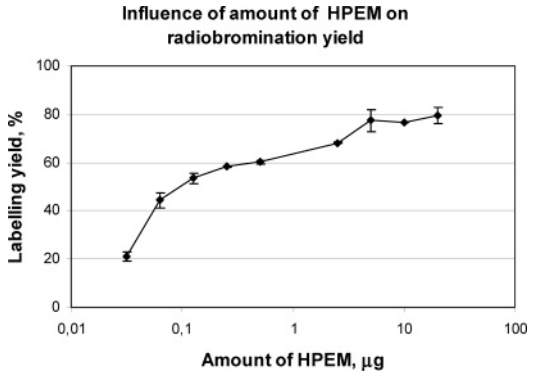

Figure 2. Dependence of bromination yield on amount of HPEM. Note the logarithmic scale. Other conditions: CAT 40 μg; reaction time 15 min.

6. Compound **7** (yield 46%) was isolated using RP-HPLC. The aryl acetates, **6** and **7**, were converted to the corresponding phenols, **1** and **8**, respectively, by means of methanolysis in the presence of Amberlyst-15, using the methodology developed by Das and co-workers (*25*). After completion of the reaction, Amberlyst-15 was easily removed from the reaction mixture by filtration to give a high yield of the parent phenols.

The following solutions were evaluated as reaction media for radiobromination of HPEM: 0.1% acetic acid in water, 1% acetic acid in methanol, and 5% acetic acid in methanol. The use of 0.1% acetic acid in water provided yields of about 40%, and increasing either amount of oxidant or reaction time resulted in no increase of labeling yield. The use of acidified methanol solutions enabled us to obtain, while using the same reactant concentration, yields of about 60% using 1% acetic acid in methanol and of about 70% using 5% acetic acid in methanol. Further experiments were performed using 5% acetic acid in methanol as a solvent.

Influence of oxidant amount on HPEM radiobromination efficiency is shown in Figure 1. The use of 10 μg of CAT provided a maximum labeling efficiency of 83 ± 0.4% when 5 μg of HPEM was radiobrominated for 5 min. Increasing the amount of oxidant to 40 μg did not increase yield. Further increase of CAT even decreased the yield somewhat (Figure 1), presumably due to the overoxidation of radiobromine.

Dependence of radiobromination yield on amount of substrate showed two distinct segments (Figure 2). Up to approximately 5 μg of HPEM, labeling yield increased proportionally to the amount of substrate. Thereafter, even a 4-fold increase in the amount of HPEM caused no significant improvement in labeling yield. An important feature of this is that the ascendant part of the curve

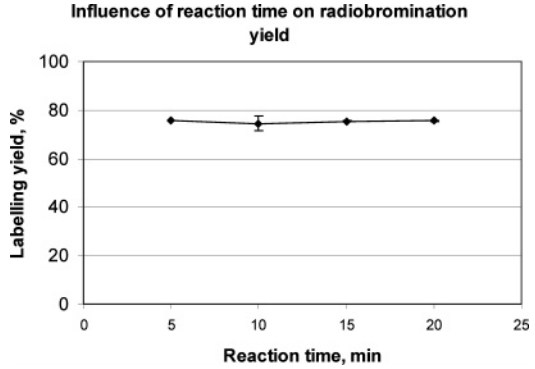

Figure 3. Dependence of bromination yield on reaction time. Other conditions: CAT 40 μg; HPEM 5 μg.

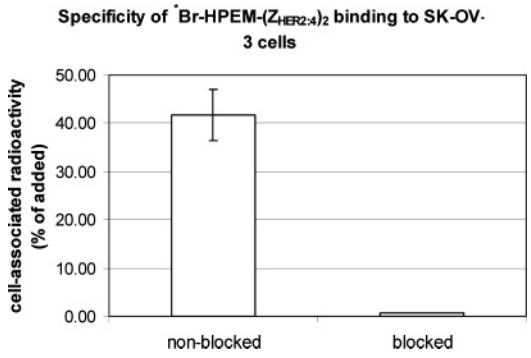

Figure 4. Antigen binding test. The test was performed on the ovarian cancer cell line, SK-OV-3. For presaturation of antigens, a 1000-fold molar excess of nonradioactive affibody was added. Cells were incubated with radiobrominated $(Z_{HER2:4})_2$ for 2 h and then washed six times. Data are presented as mean values from three dishes and maximum errors.

is rather shallow, with yields exceeding 50% even with the use of sub-microgram amounts of substrate. No peak corresponding to brominated HPEM was observed when neat 5% acetic acid in methanol was added to the reaction mixture instead of to the HPEM solution. This blank experiment confirms our interpretation of the radio-TLC data.

Electrophilic radiobromination of HPEM seems to be a rather rapid reaction at RT (Figure 3). For 5 μg of HPEM, the maximum yield of 75.9% was obtained in 5 min. Prolongation of reaction time did not increase the yield.

Coupling to the affibody molecule was performed without intermediate purification of radiobrominated HPEM. Freshly prepared reduced His_6-$(Z_{HER2:4})_2$-Cys in acetate buffer, pH 6.0, was added to the reaction mixture and incubated at RT. With approximately equimolar amounts of HPEM and His_6-$(Z_{HER2:4})_2$-Cys, conjugation yield was 29.3 ± 2.4% after 10 min of incubation and 65.3 ± 3.9% after 30 min. According to ITLC analysis, the radiochemical purity of the conjugate was >97%. Blank experiments, where no HPEM was added into the reaction mixture, or no-cysteine-containing affibody variant His_6-$(Z_{HER2:4})_2$ was used, did not show any labeling. It can be concluded that labeling was HPEM-mediated and cysteine-specific.

Stability of the label was tested by challenge with a high concentration of cold sodium bromide and by exposure to a high molar strength solution (8 M urea). After separating the test mixture on a NAP-5 size-exclusion column, radioactivity in the LMW fraction was 3.8 ± 0.9% for the sodium bromide test and 2.2 ± 0.35% for the urea test. Given the results of the ITLC testing (radiochemical purity of 98%), we can conclude that radiobromine was stably attached to affibody.

To ensure that the HER2 binding capacity of the affibody was retained after labeling, the labeled affibody was incubated with SK-OV-3 cells, which express HER2/neu antigen (as described in Experimental Procedures). The data concerning the cell-binding test are given in Figure 4. It was found that 41.6 ± 5.3% and 0.64 ± 0.02% of added radioactivity was bound to the nonblocked and blocked cells, respectively ($p < 0.001$). The results of the test demonstrated the specific binding of the antibody to antigen-expressing cells, since it can be displaced by nonradioactive antibody.

Biodistribution of radiobrominated affibody dimer in nude mice with grafted HER2-expressing SK-OV-3 tumors was performed at 4 h postinjection (pi). Radioactivity uptake in the tumors was 4.88 ± 1.59% IA/g. The blood level of radioactivity was low at 0.54 ± 0.03% IA/g. Radioactivity accumulation in other organs and tissues was also low, typically <1% IA/g, which resulted in a high tumor-to-normal organ ratio. Interestingly, radioactivity uptake in the kidney was low at 1.04 ± 0.17% IA; this is unusual for small proteins, which undergo renal excretion. The renal uptake in this study was much lower than renal uptake of $(Z_{HER2:4})_2$, which was radioiodinated using *N*-succinimidyl 4-iodobenzoate (*10*). A biodistribution study on non-tumor-bearing nude mice was performed to confirm that the use of HPEM reduced renal uptake also in comparison with the use *N*-succinimidyl 4-bromobenzoate. It was shown that the use site-specific HPEM-mediated labeling reduced kidney uptake from 7.43 ± 1.64% IA/g to 1.04 ± 0.17% IA/g. Significant difference in radioactivity concentration was observed in blood and liver, which were, in case of HPEM labeling, 1.5- and 5.9-fold higher, respectively.

Table 1. Biodistribution of *Br-HPEM-His_6-$(Z_{HER2:4})_2$-cys and *Br-benzoyl-His_6-$(Z_{HER2:4})_2$ in Nude Mice, 4 h pi[a,b]

	HPEM-$(Z_{HER2:4})_2$-Cys	PBrB-$(Z_{HER2:4})_2$	*p* value
blood	0.54 ± 0.03	0.34 ± 0.05	0.0004
heart	0.44 ± 0.11	0.30 ± 0.18	
lung	0.56 ± 0.07	0.45 ± 0.10	
liver	1.32 ± 0.31	0.22 ± 0.03	0.0004
spleen	0.36 ± 0.06	0.29 ± 0.04	
pancreas	0.27 ± 0.09	0.27 ± 0.10	
kidney	1.04 ± 0.17	7.43 ± 1.64	0.0003
stomach	0.76 ± 0.69	0.39 ± 0.06	
tumor	4.88 ± 1.59	no tumors	
muscle	0.17 ± 0.05	0.20 ± 0.09	
brain	0.14 ± 0.04	0.11 ± 0.02	

[a] Biodistribution of *Br-HPEM-His_6-$(Z_{her2:4})_2$-cys was performed on BALB/c nu/nu mice bearing SK-OV-3 xenograft. Average tumor weight was 0.029 ± 0.12 g. Biodistribution of *Br-PBrB-His_6-$(Z_{HER2:4})_2$ was performed on tumor-free animals of the same strain. [b] Each data point represents an average from four animals, ± standard deviation, and expressed as percent of injected radioactivity per gram of organ or tissue.

DISCUSSION

The site-specific labeling of tumor-targeting proteins is an attractive approach, as it provides well-defined conjugates. With this approach, a label can be placed some distance from the binding site of the affibody molecule, thus not interfering with recognition of the target structure. Introducing a cysteine appends a unique reactive thiol group to the affibody molecule, enabling such site-specific labeling. However, a linker molecule is required for the attachment of radiohalogen to cysteine-containing affibody. Such a linker molecule should be bifunctional, i.e., contain one part that can be easily and

stably radiohalogenated, and another part that can be quickly and stably attached to the SH group.

Wilbur's excellent review of protein radiohalogenation methods (*26*) indicates that the two most promising thiol-reactive groups are maleimides and acyl halides. The same review suggests two major ways to attach radiohalogens to organic compounds: to use molecules containing a strongly activated aromatic ring, or to exploit organometallic intermediates. Though no thiol-reactive radiobrominating agents have been reported so far, information concerning radioiodinating analogues was very helpful due to the close chemical similarity of these two heavy halogens. Of a number of candidates, ((4-hydroxyphenyl)ethyl)maleimide (HPEM) was especially attractive for two reasons. First, its synthesis seemed to be straightforward. Second, our previous experience with the direct radiobromination (*16*) of antibodies suggested that the activated aromatic ring could be efficiently radiobrominated.

An important aspect of electrophilic radiohalogenation of activated aromatic rings is that high labeling yields may be obtained using rather small amounts of substrate. This factor is decisive when choosing a radiolabeling strategy. Indirect radiohalogenation of proteins includes two major steps: labeling the pendant group, and attaching it to proteins. Often, a radiolabeled pendant group is purified from nonlabeled precursor and other components of the first-step reaction mixture (see, e.g., refs 18, 27, 28). In this case, the labeled pendant group can be obtained free of nonlabeled precursor, which would otherwise compete for the same binding groups in a protein molecule. For this reason, the amount of protein to be labeled can be decreased, and a higher specific radioactivity of radiolabeled conjugate can be obtained. On the other hand, introducing an extra step, and, in most cases, subsequently changing the solvent after purification, increases the probability of operator error. This decreases the overall reliability of the labeling procedure, a factor that might be important in mass producing the conjugate.

An alternative is the "one-pot" procedure, in which no intermediate purification is performed and conjugation of the labeled pendant group is carried out in the same vial as is the labeling (*19*−*21*, *29*). This labeling procedure is simpler and reduces the risk of human error. However, a nonseparated, nonlabeled precursor would require more protein substrate in order to obtain the same degree of modification. It may be that overall labeling efficiency should be sacrificed to a certain extent in order to obtain a more robust procedure and a product of higher specific radioactivity. In fact, in this study 2.3 nmol (0.5 μg) of HPEM was labeled at 60% efficiency, while labeling reproducibility was very good. In comparison, the same molar amount of *N*-succinimidyl *p*-trimethylstannyl-bromobenzoate was labeled under similar conditions at an average efficiency of 47%, and with rather large labeling yield variation (*18*). Under optimal conditions, the radiobromination yield of HPEM (83%) was similar to the radioiodination yield of trialkylstannyl derivatives of maleimide-conjugated aromatic rings (*29*, *30*).

The coupling of maleimide to free thiol in this study was efficient, with maximum coupling yield obtained within 30 min. The coupling efficiency of 65.3 ± 3.9% was in the same range as the efficiency reported for radioiodinated maleimides or acyl halides (*30*−*32*). Though increasing the cysteine-to-maleimide ratio may increase coupling efficiency, this would undesirably reduce specific radioactivity. Blank experiments confirmed that the labeling was HPEM-mediated and cysteine-specific. Both bromide challenge and exposure to a high-ion-strength solution failed to cause dissociation of radiobromine from the affibody molecule, thus confirming that the attachment is mediated by stable covalent bonds.

As expected, the site-specific labeling of the affibody molecule preserved its ability to bind HER2, which was demonstrated in vitro. Biodistribution of radiobrominated $(Z_{HER2:4})_2$-Cys showed its ability to accumulate in HER2-expressing SK-OV-3 xenografts. The combination of quick extravasation and good tumor binding with fast clearance from blood and normal organs provided high tumor-to-normal tissue ratios. For example, the radioactivity concentration in tumors 4 h pi exceeded the radioactivity concentration in blood, liver, and muscle by 9.1 ± 2.9, 3.7 ± 0.8, and 31 ± 10 times, respectively. Such high tumor-to-normal tissue ratios in combination with the high registration efficiency of PET may enable the highly sensitive detection of HER2 expression in small tumors, if positron-emitting nuclide ^{76}Br is used. An interesting finding was the low accumulation of radioactivity in kidneys. In our previous studies, when [^{125}I] *N*-succinimidyl 4-iodobenzoate was used for labeling of $(Z_{HER2:4})_2$, kidney uptake 4 h pi was found to be appreciably higher (*10*). Much higher kidney uptake is typical, for example, of radioiodinated scFv, which has a similar molecular weight and also undergoes renal excretion (*33*). To investigate if reduction of the kidney accumulation is dependent on the linker molecule, or on radionuclide, a biodistribution of cysteine-free variant $(Z_{HER2:4})_2$ labeled using *N*-succinimidyl 4-bromobenzoate was performed. The results have demonstrated that the use of HPEM reduced kidney accumulation more than 7-fold. It should be noted that at the same time, a significant increase of radioactivity concentration in blood and liver, in the case of HPEM labeling, was observed. Though high renal accumulation of radioactivity is generally not considered to be a major problem in diagnostics, it creates serious problems in therapeutic applications. Therefore, further investigation of the use of HPEM to reduce kidney uptake when using small proteins labeled with ^{131}I for therapy is warranted.

As Srivastava and co-workers have indicated (*23*), the same method can be applied, after some reoptimization of labeling chemistry, in radioiodinating affibody molecules. This opens up the possibility of the site-specific labeling of affibody molecules with ^{123}I for SPECT, with ^{124}I for PET, and with ^{131}I for therapy. In this way, a variety of labels with different emissions and half-lives are made available, and adjustment of such properties for a given clinical application is possible. A limitation of HPEM labeling is that it cannot be applied in attaching the promising alpha-emitting therapeutic nuclide ^{211}At to thiol-containing proteins; this is because the astatine−carbon bond in activated aromatic rings is weak and undergoes spontaneous dissociation (*34*).

In conclusion, the indirect radiobromination of anti-HER2 affibody using HPEM provides site-specific stable labeling at a level of efficiency similar to that of the thiol-specific radioiodination of targeting proteins. The radiobrominated affibody molecule preserves its capacity to bind HER2 both in vitro and in vivo. Importantly, HPEM-radiobrominated His_6-$(Z_{HER2:4})_2$-Cys provides for low accumulation of radioactivity in kidneys. This is promising for the development of positron-emitting anti-HER2 conjugates labeled with ^{76}Br. This method may also be used for the site-specific radiobromination of other affibody molecules, of various genetically engineered peptides or proteins, and of Fab′ fragments.

ACKNOWLEDGMENT

This work was financially supported by grants from the Swedish Cancer Society (Cancerfonden) and from Affibody AB (Bromma, Sweden). The authors are grateful to Prof. Jörgen Carlsson (Division of Biomedical Radiation Sciences, Uppsala University) and Prof. Stefan Ståhl (Department of Biotechnology, AlbaNova University Center, Kungliga Tekniska Högskolan—KTH, Stockholm, Sweden) for initiating research into tumor targeting using anti-HER2 affibody molecules in our laboratories; their efforts have provided much inspiration for this study. The authors also thank the personnel of the Svedberg Laboratory, Uppsala, Sweden, and especially Mr. Lars Einarsson for technical support in radiobromine production.

LITERATURE CITED

(1) Landon, L. A., and Deutscher, S. L. (2003) Combinatorial discovery of tumor targeting peptides using phage display. *J. Cell. Biochem. 90*, 509−517.

(2) Nord, K., Gunneriusson, E., Ringdahl, J., Ståhl, S., Uhlén, M. and Nygren, P-Å. (1997) Binding proteins selected from combinatorial libraries of an alpha-helical bacterial receptor domain. *Nat. Biotechnol. 15*, 772−777.

(3) Gunneriusson, E., Nord, K., Uhlen, M., and Nygren, P. (1999) Affinity maturation of a Taq DNA polymerase specific Affibody by helix shuffling. *Protein Eng. 12*, 873−878.

(4) Wikman, M., Steffen, A. C., Gunnieriusson, E., Tolmachev, V., Adams, G. P., Carlsson, J., and Ståhl, S. (2004) Selection and characterisation of HER2/neu-binding Affibody ligands. *Protein Eng. Des. Select. 17*, 455−462.

(5) Carlsson, J., Nordgren, H., Sjostrom, J., Wester, K., Villman, K., Bengtsson, N. O., Ostenstad, B., Lundqvist, H., and Blomqvist, C. (2004) HER2 expression in breast cancer primary tumours and corresponding metastases. Original data and literature review. *Br. J. Cancer 90*, 2344−2348.

(6) Hogdall, E. V., Christensen, L., Kjaer, S. K., Blaakaer, J., Bock, J. E., Glud, E., Norgaard-Pedersen, B., and Hogdall, C. K. (2003) Distribution of HER-2 overexpression in ovarian carcinoma tissue and its prognostic value in patients with ovarian carcinoma: from the Danish MALOVA Ovarian Cancer Study. *Cancer 98*, 66−73.

(7) Wester, K., Sjostrom, A., de la Torre, M., Carlsson, J., and Malmstrom, P. U. (2002) HER-2 − a possible target for therapy of metastatic urinary bladder carcinoma. *Acta Oncol. 41*, 282−288.

(8) Sjögren, S., Inganas, M., Lindgren, A., Holmberg, L., and Bergh, J. (1998) Prognostic and predictive value of c-erbB-2 overexpression in primary breast cancer, alone and in combination with other prognostic markers. *J. Clin. Oncol. 16*, 462−469.

(9) Masood, S., and Bui, M. M. (2002) Prognostic and predictive value of HER2/neu oncogene in breast cancer. *Microsc. Res. Technol. 59*, 102−108.

(10) Wikman, M. Ph.D. Thesis, 2005. Rational and combinatorial protein engineering for vaccine delivery and drug targeting. School of Biotechnology, Royal Institute of Technology, Albanova University Center, Stockholm, Sweden. ISBN 91-7178-003-3.

(11) Lundqvist, H., and Tolmachev, V. (2002) Targeting peptides and positron emission tomography. *Biopolymers 66*, 381−392.

(12) Tolmachev, V., Lövqvist, A., Einarsson, L., Schultz, J., and Lundqvist, H. (1998) Production of ^{76}Br by a low-energy cyclotron. *Appl. Radiat. Isot. 49*, 1537−1540.

(13) Knight, L. C., Krohn, K. A., Welch, M. J., Spomer, B., and Hager, L. P. ^{77}Br: A new protein label. *Radiopharmaceuticals.* (Subramanian, G., Ed.) pp 149−154. Society of Nuclear Medicine, New York.

(14) McElvany, C. D., Barnes, J. W., and Welch, M. J. (1980) Characterization of bromine-77-labeled proteins prepared using myeloperoxidase. *Int. J. Appl. Radiat. Isot. 31*, 679−688.

(15) Lovqvist, A., Sundin, A., Ahlstrom, H., Carlsson, J., and Lundqvist, H. (1995) ^{76}Br-labeled monoclonal anti-CEA antibodies for radioimmuno positron emission tomography. *Nucl. Med. Biol. 22*, 125−131.

(16) Sundin, J., Tolmachev, V., Koziorowski, J., Carlsson, J., Lundqvist, H., Welt, S., Larson, S., and Sundin, A. (1999) High-yield direct ^{76}Br-bromination of monoclonal antibodies using the Chloramine-T. *Nucl. Med. Biol. 26*, 923−929.

(17) Wilbur, D. S., and Hylarides, M. D. (1991) Radiolabeling of a monoclonal antibody with *N*-succinimidyl *para*-[^{77}Br]-bromobenzoate. *Int. J. Radiat. Appl. Instrum. B. 18*, 363−365.

(18) Höglund, J,Tolmachev, V., Orlova, A., Lundqvist, H., and Sundin, A. (2000) Optimized indirect ^{76}Br-bromination of antibodies using *N*-succinimidyl para-[^{76}Br]bromobenzoate for radioimmuno PET. *Nucl. Med. Biol. 27*, 837−843.

(19) Bruskin, A., Sivaev, I., Persson, M., Lundqvist, H., Sjöberg, S., and Tolmachev, V. (2004) Radiobromination of monoclonal antibody using isothiocyanato derivative of *closo*-dodecaborate ([^{76}Br]Bromo-DABI). *Nucl. Med. Biol. 31*, 205−211.

(20) Winberg, K. J., Persson, M., Malmström, P. U., Sjöberg, S., and Tolmachev, V. (2004) Radiobromination of anti-HER2/neu/erbB-2monoclonal antibody using the *p*-isothiocyanatobenzene derivative of the [^{76}Br]undecahydro-bromo-7,8-dicarba-*nido*-undecaborate(1-) ion. *Nucl. Med. Biol. 31,* 425−422.

(21) Mume, E., Orlova, A., Malmström, P. U., Lundqvist, H., Sjoberg, S., and Tolmachev, V.(2005) Radiobromination of humanized anti-HER2 monoclonal antibody trastuzumab using N-succinimidyl 5-bromo-3-pyridinecarboxylate, a potential label for immunoPET. *Nucl. Med. Biol. 32,* 613−622.

(22) Steffen, A.-C., Wikman, M., Tolmachev, V., Adams, G. P., Nilsson, F., Ståhl, S., and Carlsson, J. (2005) In vitro characterization of a bivalent anti-HER-2 Affibody with potential for radionuclide based diagnostics. *Cancer Biother Radiopharm. 20*, 239−248.

(23) Srivastava, P. C., Allred, J. F., Lambert, C. R., and Kennel, S. J. (1990) No-carrier-added preparation of a new radioiodinated maleimide as a potentially attractive radioimmunoconjugator with low in vivo deiodination. *J. Nucl. Med. 31*, 906 (abstract).

(24) Forngren, B. H., Yngve, U., Forngren, T., and Langstrom, B. (2000) Determination of specific radioactivity for ^{76}Br-labeled compounds measuring the ratio between ^{76}Br and ^{79}Br using packed capillary liquid chromatography mass spectrometry. *Nucl. Med. Biol. 27,* 851−853.

(25) Das, B., Banerjee, J., Ramu, R., Pal, R., Ravindranath, N., and Ramesh, C. (2003) Efficient, selective deprotection of aromatic acetates catalysed by Amberlyst-15 or iodine. *Tetrahedron Lett. 44*, 5465−5468.

(26) Wilbur, D. S. (1992) Radiohalogenation of proteins: an overview of radionuclides, labeling methods, and reagents for conjugate labeling. *Bioconjugate Chem. 3,* 433−470.

(27) Zalutsky, M. R., and Narula, A. S. (1988) Radiohalogenation of a monoclonal antibody using an *N*-succinimidyl 3-(tri-*n*-butylstannyl)benzoate intermediate. *Cancer Res. 48,* 1446−1450.

(28) Garg, S., Garg, P. K., and Zalutsky, M, R. (1991) *N*-Succinimidyl 5-(Trialkylstannyl) −3-pyridinecarboxylates: A New Class of Reagents for Protein Radioiodination, *Bioconjugate Chem. 2*, 50−56.

(29) Hylarides, M. D., Wilbur, D. S., Reed, M. W., Hadley, S. W., Schroeder, J. R., and Grant, L. M. (1991) Preparation and in vivo evaluation of an *N*− *(p*-[^{125}1]I∼dophenethyl)maleimide-antibody conjugate *Bioconjugate Chem. 2*, 435−440.

(30) Khawli, L. A., van den Abbeele, A. D., and Kassis, A. I. (1992) *N*-(m-[^{125}I]Iodophenyl) maleimide: an agent for high yield radiolabeling of antibodies. *Nucl. Med. Biol. 19*, 289−295.

(31) Wilbur, D. S., Hylarides, M. D., Hadley, S. W., Schroeder, J., and Fritzberg, A. R. (1989) A general approach to radiohalogenation of proteins. Radiohalogenation of organometallic intermediates containing protein reactive substituents. *J. Labelled Compd. Radiopharm. 26*, 316−318.

(32) Holowka, D. (1981) *N*-chloroacetyl-[^{125}I]iodotyramine: an alkylating agent with high specific activity. *Anal. Biochem. 117*, 390−397.

(33) Kobayashi, H., Han, E. S., Kim, I. S., Le, N., Rajagopal, V., Kreitman, R. J., Pastan, I., Paik, C. H., and Carrasquillo, J. A. (1998) Similarities in the biodistribution of iodine-labeled anti-Tac single-chain disulfide-stabilized Fv fragment and anti-Tac disulfide-stabilized Fv fragment. *Nucl. Med. Biol. 25*, 378−393.

(34) Visser, G. W. M., Diemer, E. L., Vos, C. M., and Kaspersen, F. M. (1981) The nature of the astatine-protein bond. *Int. J. Appl. Radiat. Isot. 32*, 905.

BC050056O

Hydrophobic Transmembrane-Peptide Lipid Conjugations Enhance Membrane Binding and Functional Activity in T-Cells

Marina Ali,† Michael Amon,† Veronika Bender, and Nicholas Manolios*

Rheumatology Department, Westmead Hospital, Westmead, NSW Australia 2145. Received April 26, 2005; Revised Manuscript Received August 22, 2005

Application of different delivery methods for therapeutic peptides has gained much attention in recent years. In this paper we conjugated a transmembrane hydrophobic peptide (core peptide; CP) derived from the T-cell antigen receptor α-chain sequence with either one (LP1), two (LP2), or three (LP3) palmitic acids through a Tris linkage. The effect of these lipopeptides (LPs) were compared to CP's activity both in vitro and in model membrane binding experiments using surface plasmon resonance. The influence of charged amino acids, arginine and lysine, within the CP sequence was examined by synthesizing analogues where arginine and lysine were replaced by the neutral amino acid alanine and these analogues were subsequently Tris-lipid conjugated with either one (XP1), two (XP2), or three (XP3) palmitic acids through a Tris linkage. The results indicated that the amount of irreversible binding for LPs were all greater than that of the underivatized CP in model membranes. None of the LPs could be dissociated from the liposome membranes, even after prolonged washing. Binding results for the neutral conjugates showed that only the XP1 bound to model membranes. This binding was 20% as efficient compared to LP1. In biological assays it was found that LP1 and XP1 were toxic to cells. LP3 inhibited IL-2 production more effectively than CP. Control lipopeptides (XP2, XP3) did not inhibit IL-2 production. These results demonstrate that the number of lipids conjugated to peptide, and the charged amino acids of CP, are both essential factors for peptide function and activity that can be enhanced by lipidation.

INTRODUCTION

The T cell receptor (TCR)[1] serves a critical function in the immune system and represents one of the most complex receptor structures in biology. The ability to inhibit pathogenic T-cells by blocking the TCR represents a novel means to treating autoimmune conditions such as rheumatoid arthritis, psoriasis, and lupus at a very early phase in disease progression. This opens the door to more selective treatment options than are currently available with the multipotent cytokine related drugs.

We have previously identified and subsequently shown in vitro that a nonapeptide derived from the TCR-α transmembrane region was able to inhibit IL-2 production in T-cells following antigen recognition. This hydrophobic transmembrane peptide (core peptide, CP) contains two positively charged amino acids, which are critical for receptor assembly (*1*, *2*). Extending these studies in vivo, CP given subcutaneously or intraperitoneally significantly reduced the induction of T-cell mediated inflammation in animal models with adjuvant-induced arthritis, allergic encephalomyelitis, and delayed type contact hypersensitivity (*3*, *4*). In preliminary studies by Gollner et al. (*5*), when CP was tested in humans it was noted that CP was effective in the treatment of autoimmune skin conditions. More recently, Mahnke et al. (*6*) have genetically engineered dendritic cells to secrete this peptide and thereby reduce inflammation in the T-cell dependent, experimental allergic encephalomyelitis animal disease model. The therapeutic effect was demonstrated to be antigen specific.

To increase CP's bioavailability we undertook to conjugate lipids to CP using the previously reported 2-amino-2-(hydroxymethyl)-1,3 propanediol (Tris) technology (*7*). The advantages of using Tris technology for such a linking function are, first, the hydroxy methyl groups in Tris are all symmetrically arranged around a central carbon atom, thereby removing the problems of stereoisomerization. Second, with the molecule of interest coupled to the amino group of Tris, all three hydroxymethyl groups are available for coupling to lipophilic groups. Peptides have been coupled to Tris by the formation of an amide bond between the amino group of Tris and the carboxyl group of the peptide.

Tris technology was used by Wells et al. (*8*) to prepare fatty acid conjugates of the analgesic morphine, nonsteroidal antiinflammatory drug indomethacin, antiviral drug 3′-azido-3′-deoxythymidine (AZT), and antineoplastic drugs methotrexate and chlorambucil. In their studies they demonstrated that biological properties such as cellular uptake, delivery profiles, skin retention, and toxicity of these conjugates could be altered.

Tris-lipidation may also provide a useful way of manipulating the pharmacokinetic properties of drugs. Lockett et al. (*9*) demonstrated that Tris-lipidated con-

* To whom correspondence should be addressed. Tel: 612-98458099. Fax: 612−98458317. E-mail: nickm@westgate.wh.usyd.edu.au.

† Both authors contributed equally to this work.

[1] Abbreviations: AZT, 3′-azido-3′-deoxythymidine; Boc, *tert*-butyloxycarbonyl; CP, core peptide; DMAP, (dimethylamino)-pyridine; DMPC, dimyristoyl phosphatidyl choline; DMPG, dimyristoyl phosphatidyl glycerol; GTP, Gly-Tris-palmitate; HEPES, *N*-2-hydroxyethylpiperazine-*N*′-2-ethanesulfonic acid; HPLC, high performance liquid chromatography; P3, tripalmitate; Pmc, 2,2,5,7,8-pentamethylchroman-6-sulfonyl; SPR, surface plasmon resonance; SUV, small unilamellar vesicles; TCR, T cell receptor; TFA, trifluoroactic acid; TLC, thin layer chromatography; TPTU, *O*-(1,2-dihydro-2-oxo-1-pyridyl)-*N*,*N*,*N*′,*N*′-tetramethyluronium tetrafluoroborate; Tris, 2-amino-2-(hydroxymethyl)-1,3-propanediol; Z, benzyloxycarbonyl.

10.1021/bc050127j CCC: $30.25 © 2005 American Chemical Society
Published on Web 10/22/2005

jugates of the widely used cytotoxic and antiinflammatory drug methotrexate, using a mouse melanoma model, displayed improved potency in the local treatment of tumors and reduced systemic toxicity when compared with the unconjugated drug. They also showed that Tris-lipidated cationic peptides could efficiently deliver (transfect) DNA into cells in culture.

To determine the effect of Tris-lipidation on a drug's cytoxicity in multidrug resistant cells, Davey et al. (*10*) also investigated the effect and cytotoxicity of various Gly-Tris-Palmitate (GTP1, GTP2, and GTP3) derivatives of the cancer chemotherapeutic drugs chlorambucil and methotrexate, and of the anti-HIV drug AZT in comparison to parent drugs.

In this study CP was C-terminally attached to the amino group of the Tris molecule, and the hydroxyl group of the Tris was attached to long chain fatty acyl molecules in order to produce lipopeptides. The effect of lipopeptides on modulation of T-cell function was examined in vitro by measuring IL-2 production and it was found that the biological activity of certain lipopeptides increased compared to the parent peptide. We therefore decided to investigate some of the aspects of the mode of action of these compounds using surface plasmon resonance (SPR). The biophysical findings were then correlated with the biological effects of these lipopeptides on T-cell IL-2 production reflecting T-cell activation. To examine the importance of amino acid charge (arginine, lysine) within the lipopeptide's sequence (LP1, LP2, and LP3) a set of neutral analogues were synthesized by replacing arginine and lysine with alanine (XP1, XP2, XP3). The biological and biophysical properties of these lipopeptides are reported in this paper.

EXPERIMENTAL PROCEDURES

Materials. Phospholipids dimyristoyl phoshatidyl choline (DMPC), dimyristoyl phosphatidyl glycerol (DMPG), and *N*-octyl β-D-glucopyranoside were purchased from Sigma (St. Louis, MO). Pioneer sensor L1 chips were purchased from Biacore (Uppsala, Sweden).

Peptides. Protected peptides with greater than 80% purity were purchased from Auspep with an amino acid analysis and HPLC data supplied (Melbourne, Australia). The lysine residue and the N-terminal amino group of CP (GLRILLLKV) was *tert*-butyloxycarbonyl (Boc)-protected, and the arginine residue was protected with 2,2,5,7,8-pentamethylchroman-6-sulfonyl (Pmc). In the control peptide (GLAILLLAV) the lysine and arginine residues of CP were replaced with alanine and the N-terminal amino group was Boc protected.

High Performance Liquid Chromatography (HPLC). Analytical HPLC was carried out on a Millipore Waters HPLC equipment, comprising of a 6000A series solvent delivery system. The separations were performed on a NovapakC18 reverse phase column (100 × 8 mm). Elution was carried out at a flow rate of 2 mL/min. Detection was at 260 nm using a Waters Lambda Max Spectrophotometer, Model 480. The lipopeptide conjugates were analyzed on a C18 column with a linear gradient from 40% water: 50% acetonitrile: 10% THF to 50% acetonitrile: 50% THF containing 0.1% TFA over 5 min. at a flow rate of 2 mL/min.

Preparative HPLC. Briefly, separations were carried out on a Millipore Waters DeltaPrep 4000 HPLC using PrepPak C4 or C18 reverse phase columns (Prep Nova-Pak HR 40 × 100 mm) with flow rates of 20 mL/min, or Prep-Pak C4 semipreparative cartridges 25 × 10 mm with an extension cartridge of the same size. Flow rates for these conditions were 6 mL/min. Elution was with linear gradients using the same eluent buffer systems as for the analytical HPLC.

Thin Layer Chromatography (TLC). These were performed on Alufolien Kieselgel 60 F_{254} plates (Riedel-de Haen) of 0.2 mm thickness in petroleum ether:ethyl ether:acetic acid (50:50:1 and 70:30:1), methanol:chloroform (1:9), and in ethyl acetate:hexane (60:40). Visualization of spots was under UV light, 5% solution of ninhydrin in butan-1-ol, 2′,7′-dichlorofluorescein (TCI, Japan) in ethanol, and 10% phosphomolybdate in ethanol.

Synthesis of Lipopeptides. All lipid conjugates were synthesized as per the method published by Whittaker et al. (*7*). Briefly, benzyloxycarbonyl (Z)-protected gly-Tris mono-, di-, and tripalmitates (ZGTP1, ZGTP2, and ZGTP3, respectively) were synthesized by reacting Z-gly-Tris (6.4 mmol) with palmitic acid (12.8 mmol) in the presence of DCC (12.8 mmol) and catalytic amounts of (dimethylamino)pyridine (DMAP). The purity of Z-gly-Tris was confirmed by comparison of its ^{1}H NMR spectrum to previously published data (*11*). The mixture of ZGTP1, ZGTP2, and ZGTP3 were separated on a silica column using gradient elution with ethyl acetate and hexane (20% to 80% ethyl acetate) and further purified by HPLC on a C4 column using THF/acetonitrile system to give chromatographically pure compounds with single peaks on analytical HPLC. These compounds coeluted with previously described samples of ZGTP1, ZGTP2, and ZGTP3, respectively (*11*). After removal of the Z group by hydrogenation each GTP1, GTP2, and GTP3 (1 equiv) were coupled to protected CP (1 equivalent) or the control peptide (1 equiv) in the presence of 4 equiv of *O*-(1,2-dihydro-2-oxo-1-pyridyl)-*N*,*N*,*N*′,*N*′-tetramethyluronium tetrafluoroborate (TPTU) at apparent pH 9. Lipopeptides were purified by preparative HPLC to give the mono-, di-, and tripalmitates in 55%, 31%, and 74% yields, respectively. Analytical HPLC showed single peaks at t_R 7.92 for monopalmitate, 8.8 for dipalmitate, and 9.8 for tripalmitate derivatives. After appropriate purity was demonstrated by HPLC using solvent systems described above, the protecting groups were then removed using trifluoroacetic acid (TFA) and scavenger mixture. TLC was used to confirm the presence of a single spot, which visualized with ninhydrin, dichlorofluorescein, and the phosphomolybdate spray. The resulting lipopeptides shown in Figure 1 were recovered by repeated lyophylization from tertiary butanol and characterized by Perkin-Elmer AP365 LC-MS-MS with an electrospray source.

Lipopeptides were dissolved in dimethyl sulfoxide (DMSO) as 10 mM, 5 mM, 2 mM, and 1 mM stock solutions and diluted with the *N*-2-hydroxyethylpiperazine-*N*′-2-ethanesulfonic acid (HEPES)-buffered saline (HBS-N) running buffer prior to the SPR studies and with culture media for the bioassays to give concentrations of 50 μM, 25 μM, 10 μM, and 5 μM as required.

Antigen Activation Assay. IL-2 assays were carried out using 2B4.11 hybridoma cells as previously described by Manolios et al. (*3*). Briefly, 2B4.11 hybridoma (5×10^4cells) and LK35.2 (5×10^4) were incubated with pigeon cytochrome C (50 μM) in 96-well microtiter plates for 24 h in the presence and absence of peptides. An aliquot of each supernatant (100 μL) was removed and serial 2-fold dilutions prepared using RPMI medium. Diluted supernatant was then incubated with CTLL-2 cells (2×10^4) for 18 h in microtiter plates. [^{3}H]-Thymidine (0.5 μCi) was added for 6 h, and the CTLL cells were collected onto glass fiber filter paper using a cell harvester (TiterTek, Packard Bioscience). [^{3}H]-

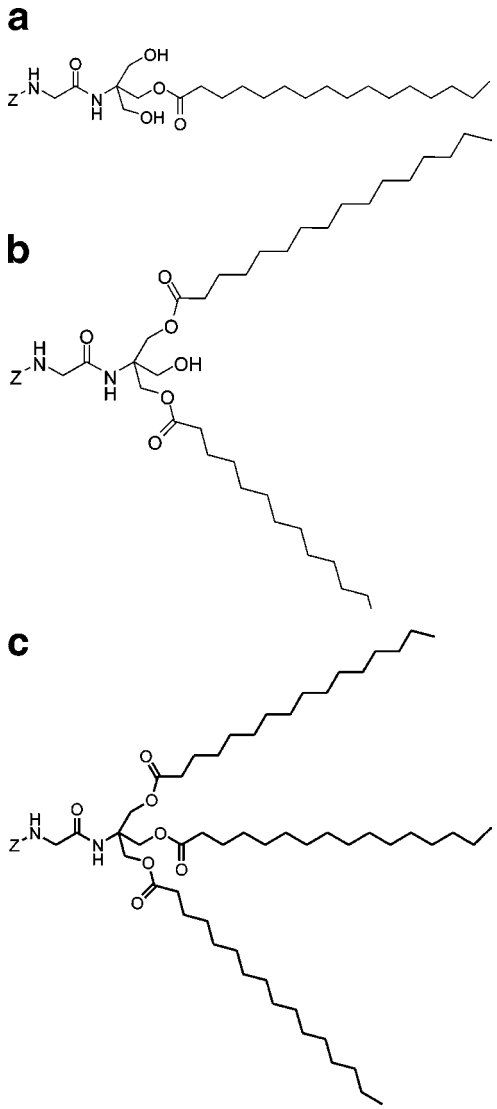

Figure 1. Structure of peptide conjugates with mono-, di-, and tripalmitate (a, b, and c) where Z = GLRILLLKV or GLAILLLAV.

Thymidine uptake was measured by scintillation counting (Packard Bioscience) and compared to standard curves to determine the amount of IL-2 produced. All lipopeptides and CP were tested at 50 μM, 25 μM, 10 μM, and 5 μM in 0.5% DMSO. IL2 production results were analyzed and expressed in terms of the concentration resulting in 50% IL2 production relative to a control of 0.5% DMSO (IC-50). All errors presented is standard error of the mean (SEM).

Cell Proliferation and Viability Assays. Mouse T-cell hybridoma 2B4.11 cells (1×10^5) were cultured in microtiter wells in the presence of lipopeptides at various concentrations. After 20 h, 30 μL of the 50 μM culture was removed and assessed for viability by trypan blue exclusion. The remaining cells in culture were pulsed with 0.5 μCi [^{3}H] thymidine for 5 h, harvested, and quantitated for [^{3}H]-thymidine uptake as per the antigen presentation assay described above. Proliferation results were analyzed and expressed in terms of the concentration resulting in 50% cell proliferation relative to a control of 0.5% DMSO (IC-50).

Preparation of Small Unilamellar Vesicles (SUV). Model membranes composed of zwitterionic and anionic phospholipids and their mixtures were produced. Briefly, DMPC was dissolved in dry chloroform and DMPG in chloroform:methanol (2:1) to give 10 mg/mL solutions.

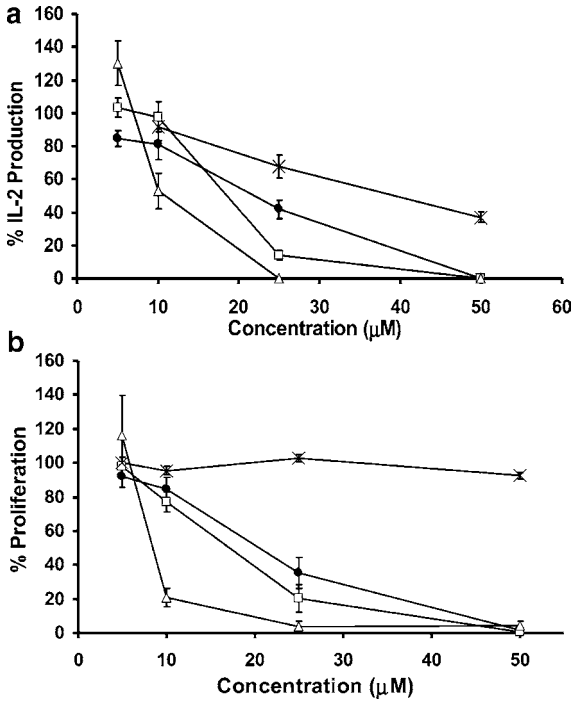

Figure 2. IL-2 production and cell proliferation dose curves of the monopalmitate conjugations. LP1 (filled circles), XP1 (open squares), unconjugated GTP1 (open triangles), and unconjugated CP (×). % IL-2 production (a) and % proliferation (b) are calculated relative to a control of 0.5% DMSO set to 100%. Each graph represents the mean ± SEM of three sets of triplicate experiments.

These were mixed in appropriate proportions before being evaporated under reduced pressure and the resulting lipid films dried overnight in vacuo. Lipids were then hydrated by resuspending in HEPES buffer for 60 min at 34 °C to give 0.5 mM concentration in respect of phospholipids. The solution was then sonicated in an ultrasonic bath for 20 min. Eight cycles of freeze/thawing was followed by extrusion through polycarbonate filters, first 100 nm (21 times) then 50 nm (21 times) pore diameter, using a Liposofast apparatus (Avestin,-Ottawa,Canada) and SUV were used immediately.

Binding Analysis by Surface Plasmon Resonance. SPR was carried out on a BIAcore 2000 instrument using Pioneer Sensor Chip L1 and HBS-N (Biacore, Upssala, Sweden) as running buffer. The chip surface was cleaned with 40 mM octyl glycoside (30 μL, 10 μL/min) followed by running buffer (100 μL, 10 μL/min). Liposomes (SUV) were injected (100 μL, 5 μL/min) giving a response of approximately 8000 RU. 10 mM NaOH (40 μL, 10 μL/min) removed any multilamellar vesicles from the surface, which was followed by 10 mM glycine pH 2.2 (10 μL, 10 μL/min) before injecting the peptide/lipopeptide of interest (100 μL, 5 μL/min). After peptide injection, the dissociation phase was commenced by replacing the peptide solution with elution buffer (5 μL/min) for 1200 s. Complete regeneration of the sensor chip was difficult. All SPR experiments were run at 25 °C, and all analyses were performed using the BIAevaluation software (Biacore, Upssala, Sweden).

RESULTS

IL 2 and Proliferation Assays. The monopalmitate conjugations demonstrated a greatly increased ability to inhibit IL-2 production in the antigen presentation model (Figure 2a). The monopalmitate conjugated CP (LP1) resulted in an IC-50 value of 21.92 μM, the control

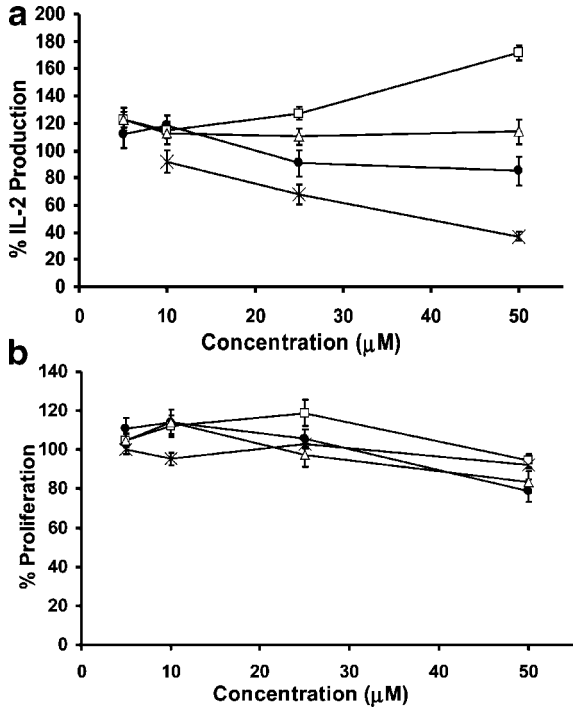

Figure 3. IL-2 production and cell proliferation dose curves of the dipalmitate conjugations. LP2 (filled circles), XP2 (open squares), unconjugated GTP2 (open triangles) and unconjugated CP (×). % IL-2 production (a) and % proliferation (b) are calculated relative to a control of 0.5% DMSO set to 100%. Each graph represents the mean ± SEM of three sets of triplicate experiments.

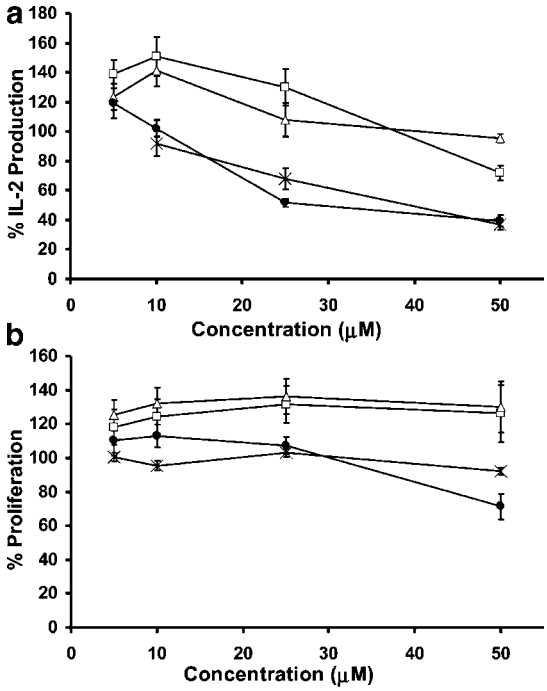

Figure 4. IL-2 production and cell proliferation dose curves of the tripalmitate conjugations. LP3 (filled circles), XP3 (open squares), unconjugated GTP3 (open triangles), and unconjugated CP (×). % IL-2 production (a) and % proliferation (b) are calculated relative to a control of 0.5% DMSO set to 100%. Each graph represents the mean ± SEM of three sets of triplicate experiments.

peptide conjugation (XP1) resulted in an IC-50 of 18.57 μM, and the building block of the monopalmitate Tris-conjugates, GTP1, resulted in an IC-50 value of 10.85 μM. The parent peptide displayed an IC-50 value of 39.52 μM in the IL2 assay. The proliferation results shown in Figure 2b mirror the IL-2 data. The IC-50 values calculated from Figure 2b showed that all monopalmitate conjugations increased CP's cytotoxicity. The IC-50 value of GTP1 was found to be 8.47 μM, 17.15 μM for XP1, and 20.50 μM for LP1, whereas that of CP was greater than 50 μM.

Each of the dipalmitate conjugations tested resulted in a marked increase in all IC-50 values to greater than 50 μM, meaning that the activity of the unconjugated CP had been effectively lost (Figure 3a and b).

The tripalmitate conjugations gave more interesting results (Figure 4a and b). LP3 resulted in an IC-50 value of 28.23 μM for the IL-2 production experiments, whereas each of the other tripalmitate conjugations resulted in IC-50 values above 50 μM. The corresponding IC-50 values for the proliferation experiments, were all well above the 50 μM mark. IC-50 values for all conjugations tested in the antigen presentation assay and the cell proliferation assay are summarized in Table 1.

Viability. Cell viability was performed by trypan blue exclusion to determine if the observed changes in proliferation were due to possible cytotoxic effects of each conjugation. When the effect of CP, control peptide, and their lipidated derivatives were examined on cell viability by trypan blue exclusion, both LP1 and XP1 were found to be toxic to cells (Figure 5), with viability at 14.72% ± 9.89 for LP1, and 8.92% ± 3.04 for XP1 at 50 μM. The di- and tripalmitate conjugates showed minimal toxicity, resulting in 90.06% ± 4.31 and 93.64% ± 2.85 viability, respectively. The control peptide's di- and tripalmitate conjugates also appeared nontoxic at 50 μM, presenting

Table 1. IC-50 Values for IL-2 Production and Cell Proliferation Assays[a]

	IC-50, μM	
conjugation	IL-2 production	proliferation
CP	39.52	>50
LP1	21.92	20.50
XP1	18.57	17.15
GTP1	10.85	8.47
LP2	>50	>50
XP2	>50	>50
GTP2	>50	>50
LP3	28.23	>50
XP3	>50	>50
GTP3	>50	>50

[a] IC-50 values are calculated from Figures 2−4. IC-50 is taken as the value in which the amount of IL-2 produced (or cell proliferation) is equal to 50% of that obtained in control experiments of 0.5% DMSO.

at 99.40% ± 1.61 and 100.93% ± 1.96 cell viability relative to control. The parent peptide, CP, resulted in 97.14% ± 1.96 cell viability.

Surface Plasmon Resonance Measurements of Lipopeptide Binding to Model Membranes. Membrane binding behavior of CP and the lipidated derivatives was examined on immobilized liposomes consisting of mixtures of DMPC:DMPG and are shown in Figure 6. Figure 6a shows the comparative binding sensorgrams of CP and lipopeptides to model membranes where the zwitterionic to anionic phospholipid ratio (DMPC:DMPG) is 70:30. The sensorgram revealed that LP1 and LP2 exhibit stronger binding to this model membranes than LP3 and the underivatized CP, with LP1 showing close to a 10-fold increase in irreversible binding. None of the lipopeptides could be dissociated from the liposomes even after extended washing with running buffer.

Figure 6b shows comparative binding of lipopeptides to membranes prepared from DMPC:DMPG mixtures in

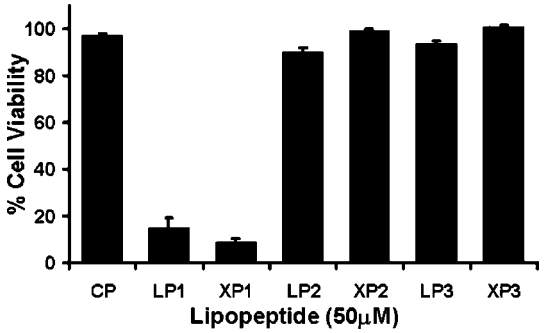

Figure 5. Viability of 2B4 cells (1×10^5) following overnight incubation with CP, LP, and XP series. Viability was assessed by trypan blue exclusion at a peptide or lipopeptide concentration of 50 μM. Results are shown relative to control (0.5% DMSO).

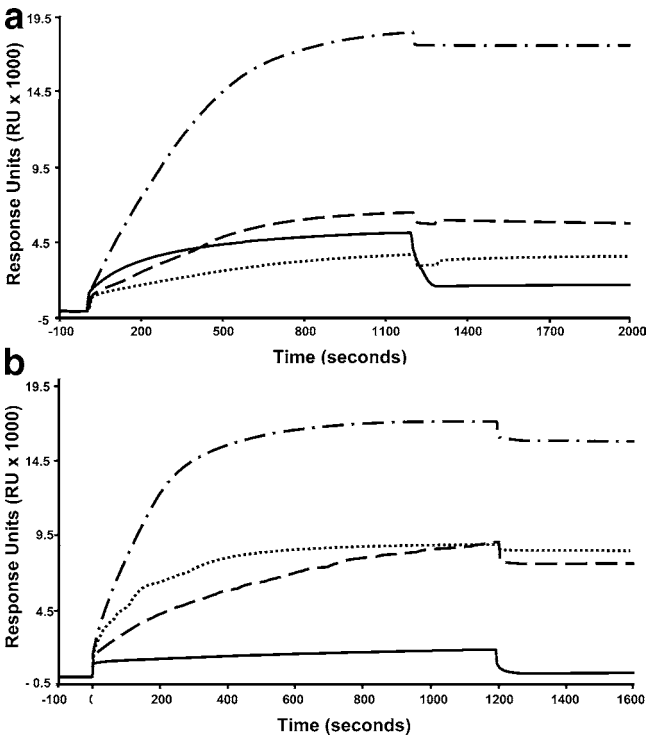

Figure 6. Sensorgrams showing the binding of CP (—), LP1 (— · —), LP2 (- — -), and LP3 (···) to (a) DMPC:DMPG 70:30 and (b) DMPC:DMPG 50:50 liposomes immobilized on an L1 sensor chip. Concentration for both CP and lipopeptides were 50 μM. Binding is expressed as the difference in signal between points before sample injection and after the dissociation phase.

the proportion of 50:50. Lipopeptides bound irreversibly to these liposomes as well. Under these conditions, LP1 continued to exhibit strong binding to liposomes, close to 15000 response units (RU) while LP2 and LP3 showed binding in the vicinity of 8000 RU.

In control lipopeptides, where CP's positively charged amino acids arginine and lysine were replaced with alanine, sensorgrams showing the binding of these lipopeptides to model membranes composed of 50:50 DMPC:DMPG revealed a dramatic loss of binding with both the di- and tripalmitate conjugates (XP2 and XP3 respectively). This was not so for the neutral monopalmitate conjugate (XP1), which was shown to bind, but to a lesser degree, when compared to that shown by the monopalmitate of CP-lipopeptide (Figure 7). Figure 8 graphically summarizes these results showing the relative binding of all lipopeptides to a 50:50 DMPC:DMPG liposome bilayer.

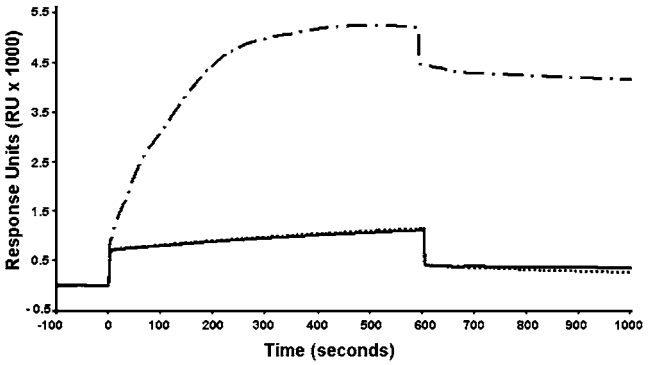

Figure 7. Sensorgram showing the binding of XP1 (— · —), XP2 (—), and XP3 (···) to DMPC:DMPG 50:50 liposomes immobilized on an L1 sensor chip. Lipopeptide concentration was 50 μM. Binding was expressed as the difference in signal between points before sample injection and after the dissociation phase.

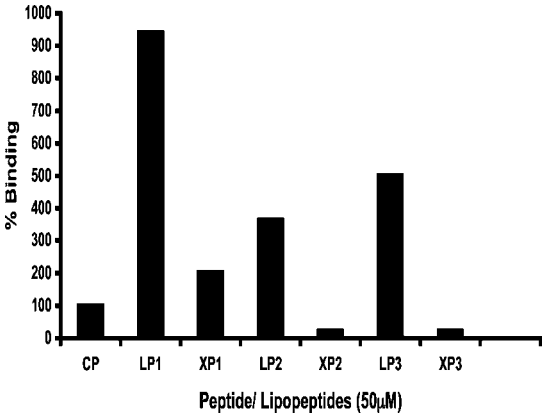

Figure 8. Bar graph representation of data shown in Figure 6b and Figure 7 showing comparative binding of CP and lipopeptide analogues to DMPC:DMPG 50:50 liposomes immobilized onto L1 sensor chip. Peptide concentrations were all the same at 50 μM.

DISCUSSION

The Tris-lipidation method makes use of the observation that the three hydroxyl groups of the Tris molecule may be acylated while the amino group provides a convenient attachment site for the formation of a covalent linkage of amino acids/peptides to the molecule (*7*). The structural similarity of the Tris molecule to glycerol enables fatty acyl groups to be attached to mimic naturally occurring mono-, di-, and triglycerides. The central carbon atom in the multifunctional Tris molecule is symmetrical and lends itself to derivatization without structural isomerization. Both synthesis and purification are less difficult than those of the glycerol derivatives and the three hydroxyl groups are all equal in reactivity. In contrast to glycerol, Tris enables the formation of triacyl derivatives of lipopeptides.

Earlier work involving Tris conjugation (*7*–*10*, *12*) has given interesting and important results concerning the design and potential therapeutic application of this system. In one study, one, two, or three palmitic acid groups were conjugated to three different drugs, chlorambucil, AZT, and methotrexate, whereupon the cytotoxicity of each compound was compared in various multidrug resistant cell lines(*10*). In general, Davey et al. (*10*) noted a trend in which the cytoxicity of each conjugated compound decreased with increasing numbers of palmitic acid groups. Furthermore, it was noted that the same type of conjugation (mono-, di-, or tripalmitate) could

result in different toxicity trends depending on the nature of the parent molecule. A monopalmitate conjugation of either chlorambucil or AZT both resulted in an increase in cytotoxicity relative to the parent compound, while the same conjugation to methotrexate resulted in a drop in cytotoxicity relative to the unconjugated methotrexate-(*10*). Overall, this paper demonstrated that conjugating various numbers of palmitates using Tris technology not only has the potential to dramatically alter a drug's performance in vitro, but that the parent drug itself remains an important component as it continues to exert a strong and directing influence on the behavior of the overall conjugate.

In the present study, a known immunosuppressant (CP) has been conjugated using Tris-lipidation with one, two, or three palmitic acid groups to try and increase the cellular uptake of CP and thereby increase its bioavailability. Each conjugate was then tested for its ability to inhibit T-cell activation in an antigen presentation model, results of which were then correlated with toxicity and membrane binding data using cell culture based assays and surface plasmon resonance.

Surface plasmon resonance (SPR) is a proven technique used to study interactions between peptides and lipopeptides with phospholipid membranes (*13*−*16*). The advantages of using SPR to study peptide−membrane interactions is that it not only allows real-time monitoring of a peptide binding and dissociating from model membranes, but it overcomes the need to use labeled peptides and/or cumbersome separation procedures employed in other techniques. Recently, CP and several sequence analogues have been analyzed using SPR and the antigen presentation assay described herein. A remarkable correlation was observed between each peptide's ability to bind to model membranes and their ability to inhibit T cell activation (*15*). In that study, it was noted that replacement of one or both of CP's basic residues with acidic residues led to a loss of peptide binding to both DMPC and DMPG model membrane systems. In addition, by changing the position of the charged amino acids in the sequence, the number of hydrophobic amino acids between the charged residues, and substitution of one or both basic residues to neutral amino acids, were found to negatively affect binding. Each loss of peptide−membrane binding was mirrored by a corresponding loss of activity in the antigen presentation assay thereby adding further evidence to CP's reliance not only on the presence of it's two positively charged residues, but also on their specific location.

To determine if CP's reliance on it's two positively charged residues behaves in the context of Tris-lipidation as it did in the nonlipidated peptide experiments of Bender et al. (*15*), a control peptide was synthesized in which CP's arginine and lysine residues have been switched to the neutral alanine residue.

In the antigen presentation assay, the monopalmitate conjugation of CP resulted in the highest degree of IL-2 inhibition with an IC-50 value of 21.92 μM. Comparing this value to that obtained from the proliferation experiments, 20.50 μM, it would appear that LP1 exerted its inhibitory effect in the antigen presentation assay through cytotoxicity. This was confirmed through viability experiments, which resulted in 14.72% ± 4.42 cell viability at 50 μM. XP1 followed a similar trend as that of LP1, in which the IC-50 value for the IL-2 production approximated that of the proliferation experiments. This suggests that the monopalmitate conjugations acted nonspecifically. The results of monopalmitate building block GTP1 confirmed this, as it was roughly twice as toxic as the LP1 conjugation, with IC-50 values of 10.85 μM for IL-2 production, and 8.47 μM for cell proliferation.

The di-palmitate conjugations (LP2, XP2, and GTP2) all presented with IC-50 values above 50 μM, whereas upon analysis of the tripalmitate conjugations, a significant difference was observed. The IC-50 value for LP3 in the IL-2 assay was 28.23 μM, whereas that of the proliferation assay was greater than 50 μM. Besides the parent CP this is the only compound which shows a significant difference between the IC-50 values obtained from the IL-2 production and cell proliferation curves. This suggests that LP3 is acting on the T-cells in a mechanism that does not affect cell proliferation, as further confirmed by the viability results (93.64% ± 1.27 viability at 50 μM). The XP3 and GTP3 conjugations presented with IC-50 values for both the IL-2 and proliferation assays above 50 μM.

Table 1 highlights these results, and the utility of Tris-lipidation as a means to alter a peptide's activity by regulating its lipophilicity. In accordance with what was observed by others (*10*), Table 1 and Figure 5 show that all of the monopalmitate conjugations were more toxic than their di- or tripalmitate counterparts. Figure 5 further suggests that the toxicity of CP is not largely affected by Tris conjugation with two or three palmitate groups. T-cells treated with CP display a viability of 97%, which only drops by 7% to 90% when treated with LP2, or by 3% to 94% when treated with LP3. This again agrees with work presented by Davey et al. who have found toxicity to decrease with increasing lipophilicity in this Tris-lipidation system (*10*).

Comparing the results of the CP conjugations to those of the XP peptide, the only difference lies in the results for the tripalmitate conjugation. XP1 behaves similar to LP1, and appears to be cytotoxic, which as discussed earlier, is likely nonspecific and due to the cytotoxicity of the GTP1 starting complex. As with LP2, XP2 is not active in any of the biological assays used. The tripalmitate conjugate, XP3, remains inactive in the IL-2 assay, proliferation assay, and the viability assay, whereas LP3 is active in the IL-2 assay with an IC-50 value of 28.23 μM. Since the main difference between CP and XP is that CP has its two basic charges, arginine and lysine, switched to the neutral alanine in the XP peptide, these results suggest that the charges present in CP are still important for activity. These results are in agreement with those found by Bender et al. (*15*) discussed earlier, where it was observed that altering CP's charges renders the peptide biologically inactive in the antigen stimulation model.

The general trend of decreasing toxicity noted with increasing lipophilicity may be the result of a notable decrease in solubility when more lipids are conjugated to an already hydrophobic peptide. It is also possible, as has been discussed by other groups using this system (*8*−*10*), that the structure of the resulting lipopeptides likely alters the degradative steps these peptides undergo when delivered in their unconjugated forms. It is possible that the degradation products of the monopalmitate conjugations result in a compound that is more toxic to cells than that which may be produced by the degradation of the di- and tripalmitate conjugations. However, it is interesting to note the results of the tripalmitate conjugation of CP, which, despite its poor solubility, LP3 was more active than the unconjugated CP in the IL-2 assay, while displaying the smallest effect on cell viability of all the CP conjugations (Figure 5). This combines to suggest that despite poor solubility, LP3 has succeeded in improving CP's immunomodulatory behavior.

Variable CP lipidation was performed in this study to help CP bind more effectively to a cell's membrane, thereby increasing its bioavailability within the cell membrane and decreasing its effective dosage. Covalent attachment of lipids such as palmitic, myristic, and prenyl groups to proteins and peptides and the role of the lipid group in partitioning the lipopeptides to membranes has been the subject of several excellent reviews (*17*, *18*). Myristic acid is generally found in amide linkage to the N-terminal group of certain proteins and peptides while in nature palmitic acid is more often found in a thioester linkage to a Cys side chain (*19*). The properties of a family of synthetic lipopeptides with agonist properties were described by Gras-Masse (*18*).

In one study using fluorescently labeled Tris conjugated peptides, Bender et al. (*20*) have shown that Tris conjugates are capable of passing through a cell's membrane, but also that conjugations containing only one lipid group enter cells much more rapidly than their di- or trilipidated counterparts. We have previously labeled LP1, LP2, and LP3 conjugates with fluorescein isothiocyanate to study their ability to enter cells (*3*). These conjugates were added to COS cells and/or the murine cytochrome *c*-specific T-cell hybridoma, 2B4, and their intracellular localization was determined by confocal microscopy. It was found that lipopeptides crossed cell membranes and localized within the cellular cytoplasm, reaching as far as the endoplasmic reticulum. The extent of cellular penetration was found to be influenced by lipid moieties attached. LP1 showed the most ability to permeate the fibroblasts and T cell reaching the nucleus. These observations have led us to consider this as a potential reason for the toxicity observed in all of the monopalmitate conjugations observed in this study. It is possible that LP1 and XP1 are cytotoxic because they are binding to such a high degree, causing lysis as shown in Table 1 and Figure 5. It is also possible that the degree of self-association is an important consideration in this matter. Cameron et al. (*12*) have shown with the help of transmission electron microscopy that the transfection ability of their Tris conjugations depended upon their ability to self-associate into membranous structures (*12*). What might be occurring is differential self-association and differential membrane preference between each of the lipidated compounds.

To confirm that Tris-lipidation improves a peptide's ability to bind to lipid membranes and to explore differential membrane preference between each of the lipid conjugations synthesized herein, each Tris compound was examined using surface plasmon resonance in order to quantify the amount of lipopeptide that binds to various lipid membrane bilayers. The results in Figure 6 indicate that all of the lipopeptide derivatives of CP, bind very strongly to both model membranes tested, DMPC:DMPG 70:30 (6a) and 50:50 (6b). Although the di- and tripalmitate conjugations of CP demonstrated a preference for membranes consisting of a higher anionic proportion (DMPC:DMPG = 50:50), the monopalmitate conjugate LP1 bound to both 70:30 and 50:50 membranes at roughly the same level. The most interesting finding in these SPR studies was the lack of dissociation of all three bound lipopeptides from the model membranes. None of the lipopeptides could be removed from the liposome surfaces at the concentration examined (50 μM), even after extensive washing with elution buffer. This indicates that at this stage, the lipopeptides might be irreversibly bound to membranes, presumably through strong hydrophobic forces/interactions.

The binding of the XP conjugations to liposomes consisting of DMPC:DMPG at a 50:50 ratio (Figure 7) show that, as is the case with the CP series, the monopalmitate conjugation results in the highest level of membrane binding. The CP conjugation, LP1, exhibited more than a 10-fold increase in irreversible binding when compared to CP (Figure 8), adding weight that this high affinity for lipid membranes is a factor in the cytotoxicity observed in the biological studies. In a study of N-terminally lipid conjugated magainin analogues (*21*) self-association of these constructs in solutions and in membranes were demonstrated and a direct correlation between oligomerization of the lipopeptides in solution and potent antifungal activity were found.

We have shown previously (*15*) that CP displays association to, and dissociation from, both zwitterionic and anionic liposomes. CP, like several other cationic hydrophobic peptide sequences reported (*22*−*25*), binds to liposomes with a rapid initial association. However, the dissociation was found to be slower and the signal does not return to baseline even after extensive washing with buffer, indicating that some of the peptide bound irreversibly to both membranes. We reported earlier (*15*) that while some binding by various CP neutral analogues was exhibited to the zwitterionic DMPC membranes, binding to the anionic DMPG was completely abolished. The above results showing that the neutral XP1, XP2, and XP3 bind poorly to membranes, whereas the di-basic CP conjugations LP1, LP2, and LP3, bind much stronger, indicate that lipid conjugation alone is not sufficient to alter this requirement.

In an investigation to deliver reporter genes into various cultured cells Cameron et al. (*12*) studied tri-lysine-Ala-Tris -mono, -di- and -tripalmitate (K_3 ATP_1, K_3 ATP_2, and K_3 ATP_3). These compounds differed in their level of palmitoylation similar to the lipopeptides in our study. Cameron et al. found that although the dipalmitate derivative of tri-lysine-Ala-Tris compound gave the highest transfection levels under optimal conditions compared to the tripalmitate (P3) compound in at least two cell types, this effect was limited to a narrow lipid:DNA ratio and concentration range whereas the P3 compound was quite effective over a broad range. It was therefore the P3 construct chosen to be the prototype molecule in their transfection studies. In our studies of the CP-lipopeptides, we found the dipalmitate derivative the least efficient in inhibiting IL-2 levels in T-cell function following antigen recognition as well as poorly binding to the model membrane mixtures in our SPR studies. Unlike the above transfection agent K3ATP3, where the headgroup carries four positive charges, LP3 has two positively charged amino acids giving a total of three positive charges including the amino terminus of the peptide of this molecule.

This study has given important insights into the types of modifications Tris-lipidation can have on peptide drugs, as well as the importance of the inherent properties found in the unconjugated peptide itself. We have examined the biological and biophysical outcomes of conjugating a peptide with known immunomodulating effects to one, two, or three palmitoyl groups via the Tris-lipidation strategy. In this study, we have found that monopalmitate conjugation results in a compound with greatly increased cytotoxicity and a 10-fold increase in membrane binding potential relative to the parent compound. Di- and tripalmitate conjugations resulted in minimal toxicity and greater binding potential with LP3, demonstrating an improved biological activity in the T-cell activation assay. The importance of the peptide in

each conjugation was further examined by removing the two essential basic residues of CP, replacing them with alanine, and then analyzing their biological and biophysical properties as well (XP series). This alteration effectively removed all biological activity and greatly reduced the membrane binding potential of each conjugation tested. These data combine to show that although Tris-lipidation has the potential to dramatically alter this peptide's function, the peptide's inherent properties still remain a deciding factor in the conjugate's overall activity.

ACKNOWLEDGMENT

We express our sincere appreciation to Dr. Eve Diefenbach for her expert advice on SPR analysis and Mr Jim Keegan from the University of Technology Sydney for the LC-MS-MS data acquisition. M. Amon and Dr. M Ali were supported by the Barbara Cameron Memorial Scholarship Sydney University, and a Grant-in-Aid from the Arthritis Foundation of Australia, respectively. A grant-in-aid from the Rebecca Cooper Medical Research Foundation is appreciated.

LITERATURE CITED

(1) Manolios, N., Letourneur, F., Bonifacino, J. S., and Klausner, R. D. (1991) Pairwise, cooperative and inhibitory interactions describe the assembly and probable structure of the T cell antigen receptor. *EMBO J. 10*, 1643−1651.

(2) Manolios, N., Bonifacino, J. S., and Klausner, R. D. (1990) Transmembrane helical interactions and the assembly of the T cell receptor complex. *Science 249*, 274−77.

(3) Manolios, N., Collier, S., Taylor, J., Pollard, J., Harrison, L., and Bender, V. (1997) T-cell antigen receptor transmembrane peptides modulate T-cell function and T cell-mediated disease. *Nature Med. 3*, 84−88.

(4) Manolios, N., Huynh, N., and Collier, S. (2002) Peptides in the treatment of inflammatory skin disease. *Aust. J. Dermatol. 43*, 226−7.

(5) Gollner, G. P., Muller, G., Alt, R., Knop, J., and Enk, A. H. (2000) Therapeutic application of T cell receptor mimic peptides or cDNA in the treatment of T cell-mediated skin diseases. *Gene Ther. 7*, 1000−1004.

(6) Mahnke, K., Qian, Y., Knop, J., and Enk, A. H. (2003) Dendritic cells, engineered to secrete a T-cell receptor mimic peptide, induce antigen-specific immunosuppression in vivo. *Nature Biotechnol. 21*, 903−908.

(7) Whittaker, R. G., Hayes, P. J., and Bender, V. (1993) A gentle method of linking Tris to amino acids and peptides. *Pept. Res. 6*, 125−128.

(8) Wells, X., Bender, V., Francis, C., He−Williams, H. M., Manthey, M. K., Moghaddam, M. J., Reilly, W. G., and Whittaker, R. G. (1999) Tris and the Ready Production of Drug-Fatty Acyl Conjugates. *Drug Development Res. 46*, 302−308.

(9) Lockett, T., Reilly, W., Manthey, M., Wells, X., Cameron, F., Moghaddam, M., Johnston, J., Smith, K., Francis, C., Yang, Q., and Whittaker, R. G. (2000) Tris lipidation: a chemically flexible technology for modifying the delivery of drugs and genes. *Clin. Exp. Pharmacol. Physiol. 27*, 563−567.

(10) Davey, R. A., Davey, M. W., Cullen, K. V., Wells, X. E., Francis, C. L., Williams, H.-M., Yang, Q., Moghaddam, M. J., Widmer, F., and Whittaker, R. G. (2002) The use of Tris-Lipidation to modify drug cytotoxicity in multidrug resistant cells expressing P-glycoprotein or MRP1. *Br. J. Pharmacol. 137*, 1280−1286.

(11) Whittaker, R. G., Hayes, P. J., and Bender, V. (1993) A gentle method for linking Tris to amino acids and peptides. *Pept. Res. 6*, 125−128.

(12) Cameron, F. H., Moghaddam, M. J., Bender, V. J., Whittaker, R. G., Mott, M., and Lockett, T. J. (1999) A transfection compound series based on a versatile tris linkage. *Biochim. Biophys. Acta 1417*, 37−50.

(13) Peters, C., Wolf, A., Wagner, M., Kuhlmann, J., and Waldmann, H. (2004) The cholesterol membrane anchor of the Hedgehog protein confers stable membrane association to lipid-modified protein. *Proc. Natl. Acad. Sci. U.S.A. 101*, 8531−8536.

(14) Schelhaas, M., Nagele, E., Kuder, N., Bader, B., Kuhlmann, J., Wittinghofer, A., and Waldmann, H. (1999) Chemoenzymatic synthesis of biotinylated Ras peptides and their use in membrane binding studies of lipidated model proteins by surface plasmon resonance. *Chem.-A Eur. J. 5*, 1239−1252.

(15) Bender, V., Ali, M., Amon, M., Diefenbach, E., and Manolios, N. (2004) T-cell antigen receptor peptide − lipid membrane interactions using surface plasmon resonance. *J. Biol. Chem. 279*, 54002−54007.

(16) Mozsolits, H., and Aguilar, M. I. (2002) Surface plasmon resonance spectroscopy: An emerging tool for the study of peptide-membrane interactions. *Biopolym. (Pept. Sci.) 66*, 3−18.

(17) Waldmann, H. (2003) At the Crossroads of Chemistry and Biology. *Bioorg. Med. Chem. 11*, 3045−3051.

(18) Gras-Masse, H. (2003) Lipid vector for the delivery of peptides towards intracellular pharmacological targets. *J. Mol. Recognit. 16*, 234−239.

(19) Epand, R. M. (1997) Biophysical Studies of Lipopeptide-Membrane Interactions. *Biopolymers 43*, 15−24.

(20) Bender, V. J., Cameron, F. H., Hendry, P., Lockett, T. J., and Whittaker, R. G. (1994) Delivery studies using peptide-fatty acid conjugates. In *Peptides. Chemistry, Structure and Biology*; pp 327−328, Leiden, ESCOM.

(21) Avrahami, D., and Shai, Y. (2002) Conjugation of a magainin analogue with lipophilic acids controls hydrophobicity, solution assembly, and cell selectivity. *Biochemistry 41*, 2254−2263.

(22) Mozsolits, H., Wirth, H. J., Werkmeister, J., and Aguilar, M. I. (2001) Analysis of antimicrobial peptide interactions with hybrid bilayer membrane systems using surface plasmon resonance. *Biochim. Biophys. Acta 1512*, 64−76.

(23) Mozsolits, H., Unabia, S., Ahmad, A., Morton, C. J., Thomas, W. J., and Aguilar, M. I. (2002) Electrostatic and hydrophobic forces tether the proximal region of the angiotensin II receptor (AT_{1A}) carboxyl terminus to anionic lipids. *Biochemistry 41*, 7830−7840.

(24) Shai, Y. (1999) Mechanism of the binding, insertion and destabilization of phospholipid bilayer membranes by α-helical antimicrobial and cell nonselective membrane-lytic peptides. *Biochim. Biophys. Acta 1462*, 55−70.

(25) Wang, W., Smith, D. K., Moulding, K., and Chen, H. M. (1998) The dependence of membrane permeability by the antibacterial peptide cecropin B and its analogues, CB-1 and CB-3, on liposomes of different composition. *J. Biol. Chem. 273*, 27438−27448.

BC050127J

2,2-Bis(ethoxycarbonyl)- and 2-(Alkylaminocarbonyl)-2-cyano-Substituted 3-(Pivaloyloxy)propyl Groups as Biodegradable Phosphate Protections of Oligonucleotides

Päivi Poijärvi,* Petri Heinonen, Pasi Virta, and Harri Lönnberg

Department of Chemistry, University of Turku, FIN-20014 Turku, Finland. Received May 18, 2005; Revised Manuscript Received August 22, 2005

Oligonucleotides bearing biodegradable phosphate protecting groups have been synthesized on a solid support. For this purpose, two dimeric building blocks, viz. 5′-*O*-(4,4′-dimethoxytrityl)-(R_P,S_P)-O^P-[2,2-bis(ethoxycarbonyl)-3-(pivaloyloxy)propyl]-*P*-thiothymidylyl-(3′,5′)-thymidine 3′-[*O*-(2-cyanoethyl)-*N*,*N*-diisopropylphosphoramidite] (**1**) and 5′-*O*-(4,4′-dimethoxytrityl)-(R_P,S_P)-O^P-[2-cyano-2-(2-phenylethylaminocarbonyl)-3-(pivaloyloxy)propyl]thymidylyl-(3′,5′)-thymidine 3′-(*H*-phosphonate) (**2**), were prepared. Phosphoramidite **1** was incorporated into an phosphorothioate oligothymidylate sequence on a base-labile hydroquinone-*O*,*O*′-diacetic acid linker (Q-linker) and on a photolabile 4-alkoxy-5-methoxy-2-nitrobenzyl carbonate linker (**11**). *H*-Phosphonate **2** was, in turn, incorporated into an oligothymidylate sequence only on the photolabile linker. Kinetics of the removal of the protecting groups by porcine liver esterase and subsequent retro aldol condensation/phosphate elimination were then studied. While the pro-oligonucleotide that contained only one phosphate protection gave the deprotected phosphorothioate oligonucleotide in a quantitative yield, the enzymatic step was markedly decelerated upon increasing the number of protection groups, and hence chain cleavage started to compete.

INTRODUCTION

Antisense oligonucleotides have long been studied as potential chemotherapeutic agents, with which gene expression could be inhibited in a highly selective manner (*1*−*4*). Unfortunately, oligonucleotides as polyanions exhibit only poor cellular uptake. Temporary masking of the negative charges with biodegradable phosphate protections has been suggested to enhance the cytoplasmic transfection (*5*, *6*). A similar approach has given promising results with monomeric nucleotides. The 5′-monophosphates of numerous nucleoside analogues have been protected as bis[(pivaloyloxy)methyl] (*7*), bis{[(isopropoxy)carbonyloxy]methyl} (*8*), bis[2-(acylthio)ethyl] (*9*), [2-(acylthio)ethyl] aryl (*10*), and cyclosaligenyl (*11-15*) triesters, and as cyclic (*16*) or acyclic O,N-disubstituted phosphoramidates (*17-19*). However, at oligonucleotide level only two biodegradable protecting groups have been tested so far, viz. the *S*-acyl-2-thioethyl (*20*−*24*) and acyloxymethyl (*25*) groups. The cellular uptake of *S*-acyl-2-thioethyl protected pro-oligonucleotides (*26*, *27*) and their complete release in cell extracts (*28*) have been verified.

We have recently reported on two novel biodegradable groups that are expected to find applications as temporary protections of internucleosidic phosphorothioate linkages (*29*). Studies with thymidylyl-(3′,5′)-thymidine phosphorothioate bearing an *S*-[2,2-bis(ethoxycarbonyl)-3-(pivaloyloxy)propyl] or *O*-[2-cyano-2-(2-phenylethylaminocarbonyl)-3-(pivaloyloxy)propyl] protection have shown that the pivalic acid ester undergoes a carboxyesterase-mediated hydrolysis and the remaining 2,2-disubstituted 3-hydroxypropyl group is readily cleaved by retro aldol condensation and concomitant phosphate elimination (*30*, *31*). We now report on solid-supported synthesis of oligothymidylates and their phosphorothioate analogues bearing internucleosidic *O*-[2,2-bis(ethoxycarbonyl)-3-(pivaloyloxy)propyl] or *O*-[2-cyano-2-(2-phenylethylaminocarbonyl)-3-(pivaloyloxy)propyl] protections and on partial success of the removal of these groups by treatment with porcine liver carboxyesterase.

EXPERIMENTAL SECTION

General Methods and Materials. The ^{1}H and ^{31}P NMR spectra were recorded at 400, 500, or 600 MHz. The chemical shifts are given in ppm referenced to internal $SiMe_4$ and external ortophosphoric acid. The mass spectra were recorded by ESI and MALDI ionization.

High-Performance Liquid Chromatography (HPLC). The pro-oligonucleotides prepared were analyzed and purified on an analytical Butyl Hypersil C-4 column (4.6 × 150 mm, 5 μm) using a linear gradient elution from A to B in 40 min (flow rate 1 mL min^{-1}, buffer A = 10 mmol L^{-1} TEAA, buffer B = buffer A containing 65% MeCN).

5′-*O*-(4,4′-Dimethoxytrityl)-(R_P,S_P)-O^P-[2,2-bis(ethoxycarbonyl)-3-(pivaloyloxy)propyl]-*P*-thiothymidylyl-(3′,5′)-thymidine 3′-[*O*-(2-cyanoethyl)-(*N*,*N*-diisopropyl)]phosphoramidite (1). To a solution of 5′-*O*-(4,4′-dimethoxytrityl)thymidine 3′-(*N*,*N*,*N*′,*N*′-tetramethylphosphorodiamidite (*29*) (**3**, 2.50 g, 4.59 mmol) in MeCN (10 mL) were added 0.9 equiv of 3′-*O*-(levulinyl)-thymidine (**4**, 1.25 g, 3.76 mmol) and 1.5 equiv of tetrazole (15 mL, 6.89 mmol), and the mixture was agitated for 24 h at room temperature. 2,2-Bis(ethoxycarbonyl)-3-hydroxypropyl pivalate (*29*) (**5a**, 1.12 g, 3.76 mmol) and tetrazole dissolved in MeCN (0.45 mol L^{-1}, 15 mL, 6.75 mmol) were added, and the agitation was continued for 24 h. The phosphite triester was not isolated, but

* To whom correspondence should be addressed. E-mail: paipoi@utu.fi.

10.1021/bc050143g CCC: $30.25 © 2005 American Chemical Society
Published on Web 09/28/2005

sulfurization with S_8 (0.60 g, 18.78 mmol) was carried out by allowing the reaction to proceed for 20 h. The reaction was quenched by water (20 mL), a CH_2Cl_2/H_2O workup was performed, the organic phase was dried (Na_2SO_4), and the solvent was evaporated. The residue was purified by column chromatography (silica gel, MeOH/CH_2Cl_2 1:9, *v/v* containing 0.1% Et_3N) to yield 2.68 g (51%) of **6a**. ^{1}H NMR ($CDCl_3$, 600 MHz): 7.57 (m, 1H, *H*6); 7.24−7.41 (m, 10H, 9H of ODMTr, 1H, *H*6); 6.83−6.87 (m, 6H, 4H, of ODMTr, 2H of *H*1′); 5.42 (m, 1H, *H*3′ of the 3′-linked Thy); 4.43−4.61 (m, 5H, *H*′5′, *H*″5′ of the 5′-linked Thy, *H*4′ of the 3′-linked Thy, C*H*$_2$O); 4.12−4.37 (m, 10H, *H*′5′, *H*″5′ of the 3′-linked Thy, *H*4′ of the 5′-linked Thy, C*H*$_2$OPiv, 2 × C*H*$_2$CH$_3$, *H*3′ of the 5′-linked Thy); 3.80 (m, 6H, (*Me*O)$_2$Tr); 3.41−3.52 (m, 2H, COC*H*$_2$); 2.93−3.13 (m, 2H, C*H*$_2$CO); 2.10−2.67 (m, 4H, 2 × *H*′2′, 2 × *H*″2′); 2.19 (s, 3H, COC*H*$_3$); 1.95 (s, 3H, 5-C*H*$_3$); 1.24 (t, 6H, CH$_2$C*H*$_3$); 1.16 (s, 3H, 5-C*H*$_3$); 1.13 (s, 9H, COC(C*H*$_3$)$_3$). ^{31}P NMR ($CDCl_3$, 600 MHz): 67.45, 67.65. MS (ESI) $[M + H]^+$ calcd 1249.0, obsd 1249.6, $[M + Na]^+$ calcd 1271.0, obsd 1271.9.

The levulinyl group was removed by hydrazinium acetate treatment. Accordingly, a solution of **6a** (0.76 g, 0.61 mmol) in 0.5 mol L^{-1} $NH_2NH_2 \cdot H_2O$ Py/AcOH (4:1, *v/v*, 5 mL) was stirred at 0 °C for 1.5 h and at room temperature for 11 h. The reaction was quenched with aq NaH_2PO_4 solution (0.1 mol L^{-1}, 20 mL). The mixture was extracted with CH_2Cl_2, washed with water and dried with Na_2SO_4. The solvent was removed under reduced pressure and the residue was chromatographed on a silica gel column eluting with MeOH/CH_2Cl_2 1:9, *v/v* containing 0.2% Et_3N to obtain **7a** in 77% yield (0.54 g). ^{1}H NMR ($CDCl_3$, 500 MHz): 7.59 (d, $J = 1.0$ Hz, 1H, *H*6); 7.21−7.40 (m, 10H, 9H of ODMTr, 1H, *H*6); 6.83−6.86 (m, 4H, ODMTr); 6.30−6.35 (m, 2H, *H*1′); 5.31 (m, 1H, *H*3′ of the 3′-linked Thy); 4.42−4.57 (m, 5H, *H*′5′,*H*″5′ of the 5′-linked Thy, *H*4′ of the 3′-linked Thy, C*H*$_2$O); 4.12−4.31 (m, 9H, *H*′5′, *H*″5′ of the 3′-linked Thy, *H*4′ of the 5′-linked Thy, C*H*$_2$OPiv, 2 × C*H*$_2$CH$_3$); 4.04 (m, 1H, O*H* of the 5′-linked Thy); 3.79 (m, 6H, (*Me*O)$_2$Tr); 3.44 (m, 1H, *H*3′ of the 5′-linked Thy); 2.11−2.68 (m, 4H, 2 × *H*′2′, 2 × *H*″2′); 1.93 (s, 3H, 5-C*H*$_3$); 1.43 (s, 3H, 5-C*H*$_3$); 1.16 (t, $J = 5.8$ Hz, 6H, CH$_2$C*H*$_3$); 1.13 (s, 9H, COC(C*H*$_3$)$_3$). ^{31}P NMR ($CDCl_3$, 500 MHz): 67.14, 67.64. MS (ESI) $[M + H]^+$ calcd 1151.0, obsd 1151.8, $[M + Na]^+$ calcd 1172.9, obsd 1173.8, $[M + K]^+$ calcd 1189.1, obsd 1189.9.

Dinucleoside triester **7a** was then converted into a phosphoramidite building block (**1**). The phosphitylation was carried out with 2-cyanoethyl-*N*,*N*,*N*′,*N*′-tetraisopropylphosphorodiamidite. 5′-*O*-Protected dinucleoside (0.25 g, 0.22 mmol) was dissolved in 1 mL of dry MeCN, and 90 μL of the diamidite (0.28 mmol) and tetrazole dissolved in MeCN (0.45 mol L^{-1}, 490 μL, 0.22 mmol) were slowly added. The mixture was stirred 3 h at room temperature and evaporated to dryness. The reaction mixture was partitioned between 25 mL $NaHCO_3$ and 25 mL CH_2Cl_2. The organic layer was separated, washed with $NaHCO_3$, and dried with Na_2SO_4, and the solvent was evaporated to obtain **1** as white powder. ^{1}H NMR ($CDCl_3$, 500 MHz): 7.56 (m, 1H, *H*6); 7.24−7.42 (m, 10H, 9H of ODMTr, 1H, *H*6); 6.86 (d, 4H, ODMTr); 6.41 (m, 1H, *H*1′); 6.29 (m, 1H, *H*1′); 5.42 (m, 1H, *H*3′ of the 3′-linked Thy); 4.42−4.63 (m, 5H, *H*′5′,*H*′5′ of the 5′-linked Thy, *H*4′ of the 3′-linked Thy, C*H*$_2$O); 4.12−4.40 (m, 10H, *H*′5′,*H*′5′ of the 3′-linked Thy, *H*4′ of the 5′-linked Thy C*H*$_2$OPiv, 2 × C*H*$_2$CH$_3$, *H*3′ of the 5′-linked Thy); 3.81 (m, 6H, (*Me*O)$_2$Tr); 3.38−3.58 (m, 4H, C*H*$_2$C*H*$_2$CN); 2.76−2.79 (m, 1H, C*H*N); 2.64−2.70 (m, 1H, C*H*N); 2.53−2.60 (m, 1H, *H*′2′); 2.25−2.51 (m, 2H, *H*′2′,*H*″2′); 2.14−2.29 (m, 1H, *H*″2′); 1.93 (m, 3H, 5-CH$_3$); 1.40 (m, 3H, 5-CH$_3$); 1.23−1.32 (t and m, 18H, 2 × CH$_2$C*H*$_3$, 4 × C*H*$_3$CH); 1.17, 1.14 (2s, 9H, COC(C*H*$_3$)$_3$). ^{31}P NMR ($CDCl_3$, 500 MHz): 68.03, 67.83, 67.77, 67.56 (4 s); 149.7, 149.6, 149.3, 149.1 (4 s, phosphoramidite). MS (ESI) $[M + H]^+$ calcd 1285.2, obsd 1285.5.

5′-*O*-(4,4′-Dimethoxytrityl)-(R_P,S_P)-*O*^{P}-[2-cyano-2-(2-phenylethylaminocarbonyl)-3-(pivaloyloxy)propyl]thymidylyl-(3′,5′)-thymidine 3′-(*H*-phosphonate) (2). 5′-*O*-(4,4′-Dimethoxytrityl)thymidine 3′-(*N*,*N*,*N*′,*N*′-tetramethylphosphorodiamidite (*29*) (**3**, 2.00 g, 3.02 mmol), 0.9 equiv of 3′-*O*-(levulinyl)thymidine (**4**, 0.93 g, 2.72 mmol) and 1.5 equiv of tetrazole dissolved in MeCN (0.45 mol L^{-1}, 10 mL, 4.53 mmol) were dissolved in dry MeCN (10 mL). After overnight stirring at room temperature, 2-cyano-3-hydroxy-2-pivaloyloxymethyl-*N*-(2-phenylethyl)propanamide (**5b**) (*29*) (0.89 g, 2.67 mmol) and tetrazole dissolved in MeCN (0.45 mol L^{-1}, 10 mL, 4.53 mmol) were added and the agitation was continued for 25 h. Oxidation with I_2 (2.07 g, 8.15 mmol in THF/H_2O/lutidine 4:2:1, *v/v/v*) was carried out in situ by allowing the reaction proceed for 21 h. The reaction was quenched by 5% aqueous $NaHSO_3$ solution (20 mL), a CH_2Cl_2/aq 5% $NaHSO_3$ workup was performed, the organic phase was dried (Na_2SO_4), and the solvent was evaporated. The residue was chromatographed on a silica gel column (MeOH/CH_2Cl_2 1:99 → 20:80, *v/v* containing 0.1% Et_3N) giving 5′-*O*-(4,4′-dimethoxytrityl)-3′-*O*-levulinyl-(R_P,S_P)-*O*^{P}-[2-cyano-2-(2-phenylethylaminocarbonyl)-3-(pivaloyloxy)propyl]thymidylyl-(3′,5′)-thymidine (**6b**) in a 56% yield (1.9 g). ^{1}H NMR (DMSO-d_6, 400 MHz): 8.61 (m, 1H, CON*H*); 7.09−7.54 (m, 14H, 9H of ODMTr, 5H of *Ph*); 7.01 (s, 1H, *H*6); 6.99 (s, 1H, *H*6); 6.83−6.88 (m, 4H, ODMTr); 6.16−6.28 (m, 2H, *H*1′); 5.17 (m, 1H, *H*3′ of the 3′-linked Thy); 4.35−4.62 (m, 4H, *H*′5′, *H*″5′ of the 3′-linked Thy and C*H*$_2$O); 4.21−4.27 (m, 3H, *H*3′ of the 5′-linked Thy and C*H*$_2$NH); 4.13 (m, 1H, *H*4′ of the 3′-linked Thy); 3.72 [s, 6H, (*Me*O)$_2$Tr]; 3.69 (s, 2H, C*H*$_2$OPiv); 3.20−3.34 (m, 5 H, *H*4′ *H*′5′, *H*″5′ of the 5′-linked Thy, C*H*$_2$-Ph); 2.70 (m, 2H, *H*′2′, *H*″2′ of the 3′-linked Thy); 2.23−2.34 (m, 2H, *H*′2′, *H*″2′ of the 5′-linked Thy); 1.74 (s, 3H, 5-C*H*$_3$); 1.42 (m, 3H, 5-C*H*$_3$); 1.12 (s, 9H, COC(C*H*$_3$)$_3$). ^{31}P NMR (DMSO-d_6, 161.8 MHz): −3.16, −3.09, −2.73, −2.68 (4 s). MS (ESI) $[M - H]^-$ calcd 1260.5, obsd 1260.6; (MALDI) $[M + Na]^+$, calcd 1283.5, obsd 1288.6.

The levulinyl group was removed by dissolving **6b** (1.90 g, 1.51 mmol) in 0.5 mol L^{-1} $NH_2NH_2 \cdot H_2O$ in Py/AcOH (4:1, *v/v*, 10 mL). The mixture was stirred at 0 °C for 1.5 h and at room temperature for 1 h. The reaction was quenched with aq NaH_2PO_4 solution (0.1 mol L^{-1}, 20 mL), and the mixture was subjected to CH_2Cl_2/H_2O workup. The organic phase was dried with Na_2SO_4, and the solvent was removed under reduced pressure. Purification by silica gel chromatography (MeOH/CH_2Cl_2 1:99 → 10:90, *v/v* containing 0.1% Et_3N) afforded 5′-*O*-(4,4′-dimethoxytrityl)-(R_P,S_P)-*O*^{P}-[2-cyano-2-(2-phenylethylaminocarbonyl)-3-(pivaloyloxy)propyl]thymidylyl-(3′,5′)-thymidine (**7b**) in an 85% yield (1.49 g). ^{1}H NMR (DMSO-d_6, 400 MHz): 8.56−8.62 (m, 3H, CON*H*, 2 N1*H*); 7.07−7.54 (m, 14H, 9H of ODMTr, 5H of *Ph*); 7.02 (s, 1H, *H*6); 7.00 (s, 1H, *H*6); 6.83−6.89 (m, 4H, ODMTr); 6.13−6.27 (m, 2H, *H*1′); 5.13 (m, 1H, *H*3′ of the 3′-linked Thy); 4.35−4.48 (m, 4H, *H*′5′,*H*″5′ of the 3′-linked Thy and C*H*$_2$O); 4.19 (m, 3H, *H*3′ of the 5′-linked Thy and C*H*$_2$NH); 3.92 (m, 1H, *H*4′ of the 3′-linked Thy); 3.72 (s, 6H, (*Me*O)$_2$Tr); 3.69 (s, 2H, C*H*$_2$OPiv); 3.17−3.31 (m, 5H, *H*4′, *H*′5′, *H*″5′ of the 5′-linked Thy, C*H*$_2$Ph); 2.69 (m, 2H, *H*′2′, *H*″2′ of the 3′-linked Thy); 2.04−2.09 (m, 2H, *H*′2′, *H*″2′ of the 5′-linked Thy); 1.73 (s, 3H, 5-C*H*$_3$); 1.42 (m, 3H, 5-C*H*$_3$);

1.12 (s, 9H, COC(CH_3)$_3$). ^{31}P NMR (DMSO-d_6, 161.8 Hz): −3.10, −3.01, −2.61, −2.56 (4 s). MS (ESI) [M − H]$^-$ calcd 1162.5, obsd 1162.5; (MALDI) [M + Na]$^+$ calcd 1285.5, obsd 1282.9.

7b was converted to its 3′-(*H*-phosphonate) as follows (*32*). The 5′-*O*-protected dinucleoside phosphoriester (**7b**, 1.49 g, 1.28 mmol) was dissolved in 6.4 mL of 2 mol L^{-1} solution of H_3PO_3 in pyridine (12.8 mmol), and 864 μL of pivaloyl chloride (7.04 mmol) was slowly added. The mixture was stirred overnight at room temperature and after completion quenched with aq TEAB (2 mol L^{-1}, 1 mL). The reaction mixture was partitioned between 75 mL CH_2Cl_2 and 50 mL of 2 mol L^{-1} TEAB. The organic layer was separated and dried with Na_2SO_4, and the solvent was evaporated to obtain the product as white foam. The crude product mixture was purified by silica gel chromatography using MeOH/CH_2Cl_2 (1:9, *v*/*v*, containing 0.2% Et_3N) to elute the product (**2**) in a 44% yield (0.74 g). ^{1}H NMR (acetone-d_6, 500 MHz): 7.24−7.60 (m, 16H, 9H of ODMTr, 5H of *Ph*, 2 *H*6); 6.90 (s, 4H, ODMTr); 6.35 (m, 2H, *H*1′); 5.36 (m, 1H, *H*3′ of the 3′-linked Thy); 4.51 (m, 10H, *H*3′ of the 5′-linked Thy, CH_2-NH, *H*′5′, *H*″5′ of the 3′-linked Thy, CH_2O, *H*4′ of the 3′-linked Thy, *H*′5′, *H*″5′ of the 5′-linked Thy); 3.77 (s, 6H, (*Me*O)$_2$Tr); 3.50 (m, 5H, CH_2OPiv, *H*4′ of the 5′-linked Thy, *H*′2′, *H*″2′ of the 3′-linked Thy); 2.44 − 2.62 (m, CH_2-Ph, *H*′2′, *H*″2′ of the 5′-linked Thy); 1.80 (s, 3H, 5-CH_3); 1.42 (m, 3H, 5-CH_3); 1.19 (s, 9H, COC(CH_3)$_3$). ^{31}P NMR (Acetone-d_6, 161.8 Hz): 0.14 (average, set of signals caused by 3 diastereomeric centers, *H*-phosphonate), −3.04 (average, set of signals caused by 3 diastereomeric centers). MS (MALDI) [M + Na]$^+$ calcd 1226.1, obsd 1222.7.

Synthesis of 2,2-Bis(ethoxycarbonyl)-3-(pivaloyloxy)propyl-Protected Oligodeoxyribonucleotide Phosphorothioates on a CPG-Q-Thymidine Support. The oligonucleotide phosphorothioates bearing one or two 2,2-bis(ethoxycarbonyl)-3-(pivaloyloxy)propyl groups were assembled on an Applied Biosystems 3400 DNA synthesizer on a 1.0 μmol scale using 500 Å CPG-Q-thymidine support and phosphoramidite chemistry. The phosphoramidite building block **1** was used as a 0.15 mol L^{-1} solution, the coupling time being 600 s. For thymidine 3′-phosphoramidite the coupling time was 60 s. Based on the DMTr-cation report of the synthesizer, 95, 96, and 97% average coupling efficiencies were obtained for pro-oligonucleotides **8**, **9**, and **10**, respectively. The internucleosidic phosphorothioate linkages were generated using 3*H*-1,2-benzodithiole-3-one-1,1-dioxide (*33*) as an oxidant (0.1 mol L^{-1} in MeCN, 420 s). The removal of the 2-cyanoethyl phosphate protecting groups was carried out by DBU treatment (1.5% in dry MeCN, 30 min), and the cleavage of oligonucleotides (**8**, **9** and **10**) from the support was performed using K_2CO_3 (0.05 mol L^{-1}, MeOH, rt, 1 min). Finally, the desired sequences were purified by RP HPLC (Butyl Hypersil, 150 × 4.6 mm, 5μm) with gradient solvent system (from A to B in 40 min, A: 10 mmol L^{-1} TEAA, B:10 mmol L^{-1} TEAA, 65% MeCN, flow rate 1 mL/min) and identified by ESI-MS. Observed masses (**8**): *m/z* 1384.37 [M − 2H]$^{2-}$, 922.28 [M − 3H]$^{3-}$, 691.45 [M − 4H]$^{4-}$ calculated masses: 1384.66, 922.77, 691.82, respectively. Observed masses (**9**): *m/z* 2007.12 [M − 2H]$^{2-}$, 1338.73 [M − 3H]$^{3-}$, 1003.33 [M − 4H]$^{4-}$ 802.84 [M − 5H]$^{5-}$ calculated mass: *m/z* 2007.61, 1338.07, 1003.30, 802.44, respectively. Observed masses (**10**): *m/z* 1444.64 [M − 3H]$^{3-}$, 1083.25 [M − 4H]$^{4-}$, 866.74 [M − 5H]$^{5-}$, 721.80 [M − 6H]$^{6-}$, 618.55 [M − 7H]$^{7-}$, 541.12 [M − 8H]$^{8-}$ calculated mass: *m/z* 1444.97, 1083.47, 866.58, 721.98, 618.70, 541.23, respectively.

Pro-oligodeoxyribonucleotide Synthesis on Photolabile Support 11. Commercially available Tentagel resin (Novabiochem, 250 mg, 0.07 mmol) bearing a photolabile 5-(4-hydroxymethyl-6-methoxy-3-nitrophenoxy)butanoyl linker (*34-38*) was suspended in CH_2Cl_2 (2 mL), and 10 equiv of *N*-methylmorpholine (77 μL) and *p*-nitrophenyl chloroformate (10 equiv, 141 mg, 0.70 mmol) were added at 0 °C. The suspension was shaken overnight, and the resin was then washed on filter with CH_2Cl_2 and Et_2O and finally dried under diminished pressure for 30 min. To a suspension of the activated support in DMF (2 mL) were added 10 equiv of 5′-*O*-(4,4′-dimethoxytrityl)thymidine (385 mg, 0.70 mmol) and 2 equiv of DMAP (1.4 mmol, 17 mg), and the mixture was shaken overnight. The resin was washed on the filter with DMF, CH_2Cl_2, and MeOH. The unreacted, active carbonate groups were deactivated with MeOH (1 mL) in DMF (2 mL) in the presence of catalytic amount of DMAP. Since this treatment reduces also the loading by cleaving the carbonate bonds, no longer than 45 min reaction time at RT was used. After this deactivation, the remained OH-groups of the support were finally capped by treating the support with a mixture of Ac_2O, lutidine, *N*-methylimidazole, and THF (5:5:8:132, *v*/*v*/*v*/*v*) for 15 min. The support was washed on filter with DMF, CH_2Cl_2, and MeOH and dried under vacuum. A loading of 170 μmol g^{-1}, determined by the standard dimethoxytrityl cation assay (*39*), was obtained.

The protected oligonucleotide **12** was assembled on an Applied Biosystems 392 DNA synthesizer in a 1.0 μmol scale using support **11** and the *H*-phosphonate chemistry. The *H*-phosphonate protocol was generated for the Applied Biosystems 392 DNA synthesizer on the basis of previous reports (*40*,*41*). The *H*-phosphonate building block (**2**) was used as a 50 mmol L^{-1} solution in dry Py/MeCN (1:3, *v*/*v*), the coupling time being 240−300 s. The monomeric thymidine 3′-(*H*-phosphonate) was used as a 30 mmol L^{-1} solution in dry Py/MeCN (1:3, *v*/*v*), the coupling time being 30−60 s. Pivaloyl chloride was used as an activator (120 mmol L^{-1} Py/MeCN 1:3, *v*/*v* solution). Despite the prolonged coupling time used for **2**, the coupling yield of this block remained surprisingly low, below 80%. The support-bound material was treated with I_2 (0.1 M, Py/H_2O, 98:2, *v*/*v*) at RT for 30 min, washed with MeCN and MeOH, and dried on the filter. The supports were exposed to light at 20 °C (Hg-lamp, 250 W) for 26 h to release the desired pro-oligonucleotide (MeOH/H_2O, 1:9, *v*/*v*, 2 mL). After the solvent evaporation, the product mixture was dissolved in water and purified by RP HPLC (Butyl Hypersil, 150 × 4.6 mm, 5 μm) using gradient elution (from A to B in 40 min, A: 10 mmol L^{-1} TEAA, B:10 mmol L^{-1} TEAA, 65% MeCN, flow rate = 1 mL/min). Fractions were identified with ESI-MS and the desired sequence was further purified to yield **12** as a diastereomeric mixture. Observed masses (**12**): *m/z* 1499.64 [M − 2H]$^{2-}$, 999.77 [M − 3H]$^{3-}$, 749.83 [M − 4H]$^{4-}$, 599.86 [M − 5H]$^{5-}$ calculated masses: *m/z* 1499.04, 999.02, 749.01, 599.01, respectively.

The synthesis of **8** was also carried out on support **11** applying the phosphoramidite chemistry and similar methods as described above for the synthesis on the Q-linker. Observed masses (**8**): *m/z* 1384.96 [M − 2H]$^{2-}$, 922.30 [M − 3H]$^{3-}$, 691.73 [M − 4H]$^{4-}$ calculated masses: *m/z* 1384.66, 922.77, 691.82, respectively.

Enzymatic Hydrolysis. The pivaloyl groups were removed from oligonucleotides **8**, **9**, **10**, and **12** with porcine liver esterase (PLE, Sigma) in HEPES buffer

Chart 1. Synthesized Building Blocks 1 and 2

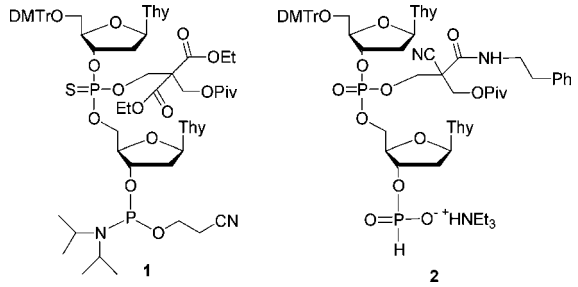

(0.01/0.01 mol L^{-1}) at pH 7.5, $t = 25$ °C, $I = 0.1$ mol L^{-1} (NaCl). To start the enzymatic cleavage, 0.33 mg of the PLE enzyme as an aqueous solution (1.5 μL, 4.8 units) was dissolved in 300 μL of the HEPES buffer and 3 OD (90 μg, 38 nmol) of the protected oligonucleotide was added. Aliquots of 20 μL were withdrawn at appropriate intervals, made acidic (pH 2) with aqueous hydrochloride, and cooled on an ice-bath. The samples were analyzed immediately by HPLC on a Butyl Hypersil column eluted with triethylammonium acetate buffer (0.01 mol L^{-1}, pH = 7.0) containing MeCN (0−65%, *v*/*v*).

RESULTS AND DISCUSSION

Synthesis of the Building Blocks. Chart 1 shows the two building blocks used to assemble the pro-oligonucleotides. The phosphoramidite building block **1** was obtained by replacing the dimethylamino ligands from tris(dimethylamino)phosphine one after another with 5′-*O*-(4,4′-dimethoxytrityl)thymidine (**3**), 3′-*O*-levulinylthymidine (**4**), and 2,2-bis(ethoxycarbonyl)-3-hydroxypropyl pivalate **5a** (*29*), using MeCN as a solvent and tetrazole as an activator (Scheme 1). The resulting phosphite ester was sulfurized with S_8 to phosphoromonothioate **6a** and the 3′-levulinyl protection was removed to obtain **7a**. The exposed 3′-hydroxy function was finally phosphitylated with 2-cyanoethyl *N*,*N*,*N*′,*N*′-tetraisopropylphosphorodiamidite to obtain **1**.

Building block **2** was prepared in an analogous manner (Scheme 1). 2-Cyano-3-hydroxy-2-(pivaloyloxymethyl)-*N*-(2-phenylethyl)propanamide (**5b**) (*29*) was used to create the biodegradable moiety. Oxidation with I_2 gave phosphotriester **6b**, which after removal of the levulinyl protection (**7b**) was converted by a standard procedure to *H*-phosphonate triethylammonium salt **2**. Reverse phase HPLC analysis showed the presence of two isomers, in all likehood the R_P and S_P stereoisomers of the phosphate triester.

Synthesis of Oligodeoxyribonucleotides Bearing 2,2-Bis(ethoxycarbonyl)-3-(pivaloyloxy)propyl Groups (8, 9, 10). The internucleosidic phosphotriester groups of 2,2-bis(ethoxycarbonyl)-3-(pivaloyloxy)propyl protected oligonucleotides, as well as the ester linkages of the protecting group itself, may be expected to be susceptible to nucleophiles (*29*). For this reason, these oligonucleotides were assembled on a hydroquinone-*O*,*O*′-diacetic acid linker (Q-linker) that is considerably more base labile than the conventional succinyl linker (*42*). The 2-cyanoethyl protections were removed from the phosphate groups by weakly nucleophilic DBU in an inert solvent (*22*) instead of ammonolysis.

A T_6-sequence containing the dimeric phosphotriester block **1** at the 5′-end of the chain was first assembled on a CPG-Q-thymidine support to test the coupling efficiency of **1** and the applicability of the developed protocol. The standard phosphoramidite protocol for phosphorothioates was applied, except that prolonged coupling times, 60s and 600s, were used for the thymidine 3′-phosphoramidite and the dimeric building block **1**, respectively. Additionally, a 0.1 mol L^{-1} solution of 3*H*-1,2-benzodithiol-3-one 1,1-dioxide and a waiting step of 420 s were used for sulfurization. On the basis of the DMTr-cation report given by the synthesizer, an acceptable 95% coupling efficiency was obtained. The cyanoethyl groups were removed by 30 min treatment with 1.5% DBU in dry acetonitrile (*22*). Standard potassium carbonate treatment (0.05 mol L^{-1} K_2CO_3 in methanol, 1 min) released the pro-oligonucleotide **8** (Figure 1). No signs of hydrolysis or degradation products were observed during either of these treatments. The crude pro-oligonucleotide **8** was purified by RP HPLC (see Figure 1 and Table 1).

Longer T-sequences (**9**, **10** Figure 2) containing two building blocks **1** either in the central part of the chain (**9**) or close to the ends of chain (**10**), were then synthesized in a similar manner on a CPG-Q-thymidine support. The average coupling yields were 96% (**9**) and 97% (**10**). The crude pro-oligonucleotides **9** and **10** were purified by RP HPLC (see Figure 2 and Table 1). The authenticity of pro-oligonucleotides **8**, **9** and **10** was verified by ESI-MS.

Scheme 1[a]

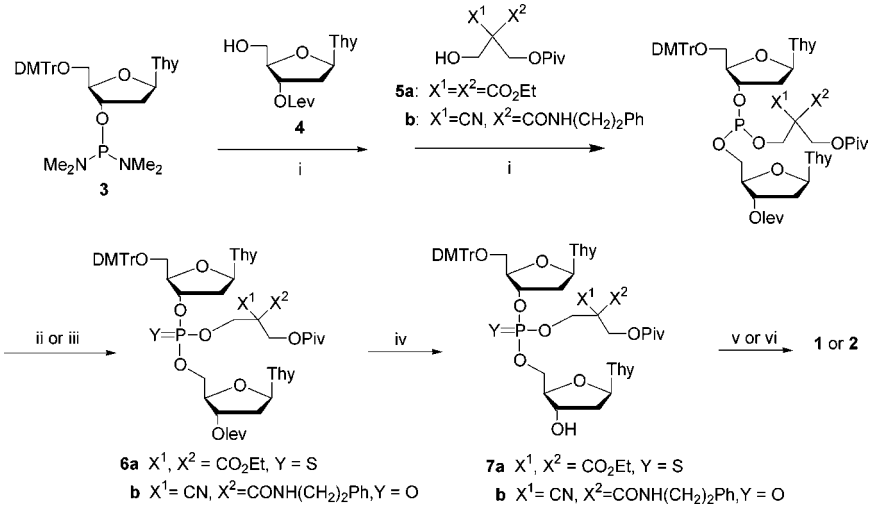

[a] Reagents and conditions: (i) TetH, MeCN, (ii) S_8 (iii) I_2, THF, H_2O, lutidine, (iv) 0.5 mol L^{-1} $N_2H_2{\cdot}H_2O$ Py/AcOH, (v) 2-cyanoethyl *N*,*N*,*N*′,*N*′-tetraisopropylphosphorodiamidite, TetH, MeCN, (vi) H_3PO_3, PivCl, Py.

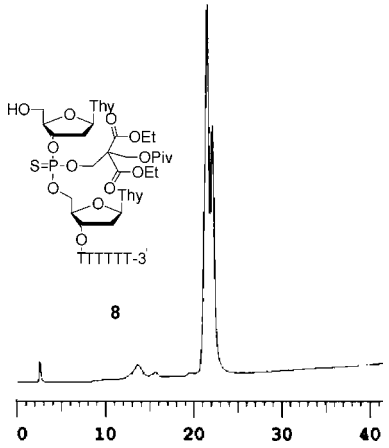

Figure 1. RP HPLC profile of the pro-oligonucleotide **8** at 260 nm. For detailed chromatographic conditions, see Experimental Section.

Table 1. Properties of Pro-oligonucleotides

pro-oligonucleotide	retention time/min[a]	yield/% [b]
8	21.1	79
9	23.3	67
10	22.7	70
12	23.7	19

[a] RP HPLC; for detailed chromatographic conditions, see Experimental Section. [b] Percentage of the pro-oligonucleotide in the crude reaction mixture on the basis of the HPLC peak areas.

The synthesis of pro-oligonucleotide **8** was also attempted on the Tentagel-immobilized photolabile linker (**11** Chart 2) described below. The overall yield of the synthesis was 67%, and the sulfurization was not complete. Accordingly, the CPG-Q-support turned out to be superior to the **11** for the present purpose.

Synthesis of the Oligodeoxyribonucleotides Bearing 2-Cyano-2-(2-phenylethylaminocarbonyl)-3-(pivaloyloxy)propyl Groups. It has been shown previously (*29*) that *O*-[2-cyano-2-(2-phenylethylaminocarbonyl)-3-pivaloyloxypropyl] group is readily cleaved from internucleosidic phosphorothioate linkage under basic conditions. At pH 12, the half-life of this reaction is about 5 min. The cleavage proceeds by retention of configuration around the phosphorus atom, probably by formation of a β-lactam by intramolecular attack of the deprotonated amide nitrogen on the phosphate bound carbon. To avoid basic conditions, oligonucleotide **12** bearing this protecting group was assembled on photolabile linker **11** (Chart 2) by the *H*-phosphonate chemistry. A prolonged coupling time (240−300 s) was used for building block **2**. An 8-mer sequence containing two phosphotriester blocks (**12**, Figure 3) was assembled. The concentration of the dimeric building block (**2**) was 50 mmol L^{-1} and that of the activator 120 mmol L^{-1}. The oxidation was performed by 30 min treatment with 0.1 mol L^{-1} I_2 in Py/H_2O (98:2, *v*/*v*) solution. The resin suspended in MeOH/H_2O solution (1:9, *v*/*v*, 2 mL) was then exposed to the light filtered with a Pyrex glass for 26 h at 20 °C (Hg-lamp, 250 W) to release the crude pro-oligonucleotide. The cleavage was monitored by analyzing the aliquots of the solution by reversed-phase HPLC. No sign of photodimer formation between thymidine residues was observed. RP HPLC analysis of the crude product mixture showed the desired sequence to be the main product. The crude pro-oligonucleotide **12** was purified by RP HPLC (see Figure 3 and Table 1) and it was identified by ESI-MS.

Chart 2. Photolabile Support 11

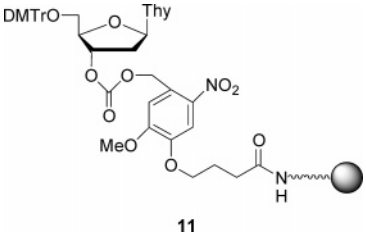

Enzymatic Hydrolysis of the Pro-oligonucleotides. The pro-oligonucleotides prepared (**8**, **9**, **10**, **12**) were treated with porcine liver esterase (PLE) to demonstrate that both 2,2-bis(ethoxycarbonyl)-3-(pivaloyloxy)propyl and 2-(phenylethylaminocarbonyl)-2-cyano-3-pivaloyloxypropyl protecting groups could really be removed by a reaction trigged by enzymatic hydrolysis of the pivalic ester moiety and that the desired T-sequence is released. During the enzymatic hydrolysis of **8**, accumulation of an intermediate was observed by HPLC analysis. In all likehood this intermediate is the oligo-

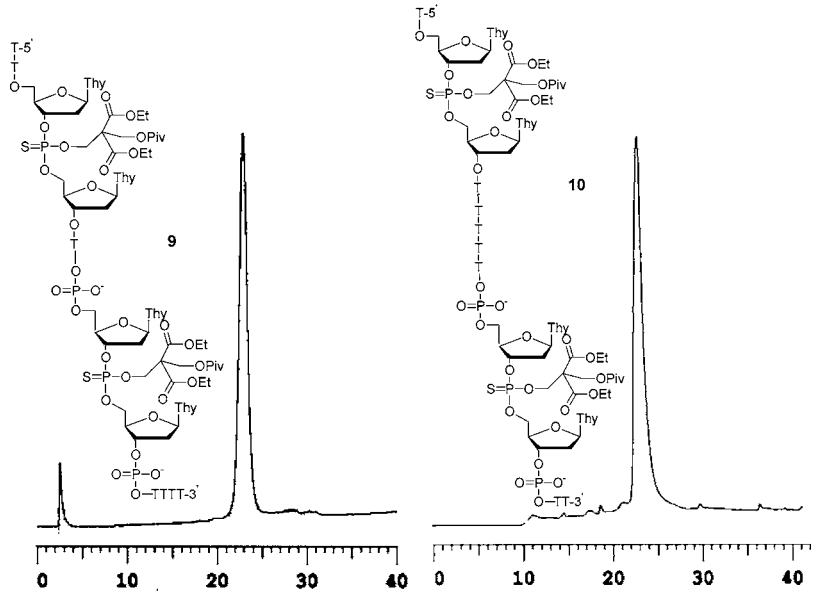

Figure 2. RP HPLC profile of the pro-oligonucleotides **9** and **10** at 260 nm. For detailed chromatographic conditions, see Experimental Section.

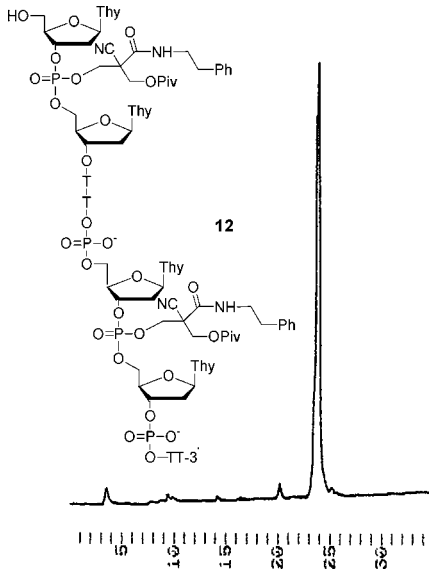

Figure 3. RP HPLC profile of the purified pro-oligonucleotide **12** at 260 nm. For detailed chromatographic conditions, see Experimental Section.

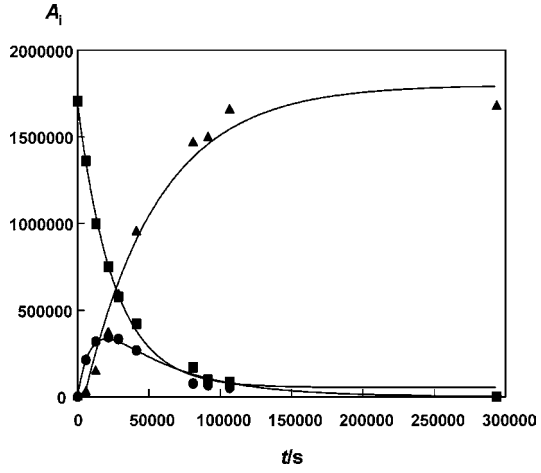

Figure 4. Time-dependent product distribution for the PLE-trigged deprotection of pro-oligonucleotide **8.** A_i is the peak area in the HPLC chromatogram for the enzymatic hydrolysis of **8** in 0.02 mol L^{-1} HEPES buffer at pH 7.5 and 25 °C. The ionic strength was adjusted to 0.1 mol L^{-1} with NaCl. [Notation: **8** (■), intermediate (●) and T_8 (▲)].

nucleotide triester having the pivaloyloxy group hydrolyzed to a hydroxyl function. The data obtained from the enzymatic hydrolysis of **8** is given as an illustrative example in Figure 4. The situation is very similar to the previously reported PLE-triggered deprotection of thymidylyl-(3′,5′)-thymidine phosphorothioate bearing the same protecting group on the sulfur atom (*29*). The intermediate was finally converted quantitatively to T_8-phosphorothioate, which was identified by ESI-MS analysis and spiking with an authentic sample. The rate of the PLE-triggered deprotection was relatively slow; a complete release of phosphorothioate was observed in 30 h.

Pro-oligonucleotide **9** bearing two biodegradable 2,2-bis(ethoxycarbonyl)-3-(pivaloyloxy)propyl groups was also subjected to carboxyesterase-mediated hydrolysis, and again HPLC analysis revealed accumulation of an intermediate. However, the deprotection was found to be much slower than with **8**. Consequently, a prolonged treatment with PLE resulted in partial degradation of the phosphorothioate backbone concurrent with release of the deprotected oligomer. Since the distance between the two

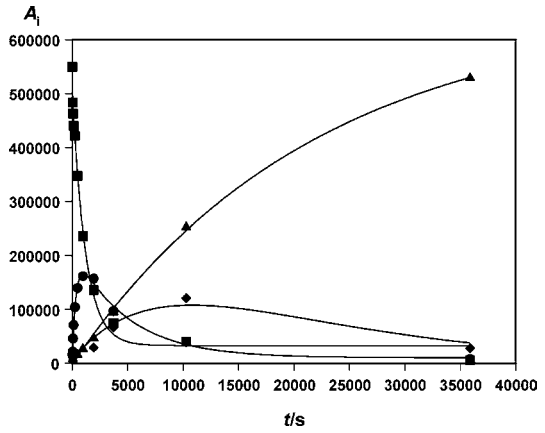

Figure 5. Time-dependent product distribution of the PLE-triggered deprotection of pro-oligonucleotide **12**. A_i is the peak area in the HPLC chromatogram for the enzymatic hydrolysis of **12** in 0.02 mol L^{-1} HEPES buffer at pH 7.5 and 25 °C. The ionic strength was adjusted to 0.1 mol L^{-1} with NaCl. [Notation: **12** (■), intermediates (● and ◆) and thymidine (▲)].

protecting groups could play a role, a 12-mer bearing two 2,2-bis(ethoxycarbonyl)-3-(pivaloyloxy)propyl groups (**10**) apart from each other was prepared and subjected to PLE triggered hydrolysis. The deprotection was now faster than with **9** and accumulation of the desired full-length phosphorothioate could be verified by spiking. However, also with this pro-oligonucleotide the chain cleavage to a marked extent competed with the removal of the phosphate protections.

Pro-oligonucleotide **12**, bearing two 2-cyano-2-(2-phenylethylaminocarbonyl)-3-(pivaloyloxy)propyl groups initially behaved similarly: intermediates exhibiting HPLC signals at a shorter retention time than the starting material appeared (Figure 5). These intermediates were, however, finally converted not to T_8, as expected, but to thymidine. In other words, the enzyme employed quite readily cleaved the phosphodiester bonds, although it did not cleave phophorothioate linkages of **8**. When the PLE-mediated hydrolysis of unmodified T_8 in water was followed with RP HPLC, it turned out that within 1 day T_8 was completely hydrolyzed to thymidine.

CONCLUDING REMARKS

Pro-oligonucleotides containing two different biodegradable protecting groups have been prepared, and their carboxyesterase-mediated hydrolysis has been studied. Both protecting groups contain a pivalic ester moiety in their structure. Hydrolysis of this ester linkage by porcine liver esterase (PLE) triggers a retroaldol condensation/phosphate elimination reaction that releases the oligonucleotide. Treatment of a pro-oligonucleotide bearing one 2,2-bis(ethoxycarbonyl)-3-pivaloyloxypropyl group (**8**) with porcine liver esterase released the phosphorothioate T_8 in an intact form. Presence of more than one such protection (**9**, **10**), however, markedly retarded the enzymatic deprotection, and hence the phosphorothioate backbone was partially degraded concurrent with release of the deprotected oligomer. In vivo experiments are needed to find out whether the situation is the same with intracellular esterases. Oligonucleotides bearing the 2-cyano-2-(2-phenylethylaminocarbonyl)-3-pivaloyloxypropyl groups were not phosphorothioates, and hence enzymatic hydrolysis to thymidine took place concurrent with the cleavage of the protecting groups. The attractive feature of the present protecting groups is that they allow temporary attachment of conjugate groups to the oligonucleotide backbone, since the ethoxy and 2-phenylethyl-

amino groups in their structure may in all likelihood be replaced by other conjugate groups. Hence, both of these groups appear as viable candidates for biodegradable linkers through which various conjugate groups facilitating the cellular uptake could be attached.

ACKNOWLEDGMENT

We thank Dr. Harri Hakala for the skilful assistance in MS analyses.

LITERATURE CITED

(1) Crooke, S. T. (2004) Progress in antisense technology. *Annu. Rev. Med. 55*, 61−95.

(2) Cook, P. D. (2001) *Antisense Drug Technology* (Crooke, S. T., Ed.) pp 29−56 Marcel Dekker, New York.

(3) Agrawal, S., and Kandimalla, E. R. (2001) Antisense and/or immunostimulatory oligonucleotide therapeutics. *Curr. Cancer Drug Targets 1*, 197−209.

(4) Dean, N. M., and Bennett, C. F. (2003) Antisense oligonucleotide-based therapeutics for cancer. *Oncogene 22*, 9087−9096.

(5) Morvan, F., Vasseur, J.-J., Vives, E., Rayner, B., and Imbach, J.-L. (2000) *Pharmaceutical Aspects of Oligonucleotides* (Couvreur, P., and Malvy, C., Eds.) pp 79−97, Taylor & Francis, London, U.K.

(6) Schultz, C. (2003) Prodrugs of biologically active phosphate esters. *Bioorg. Med. Chem. 11*, 885−898.

(7) Farquhar, D., Khan, S., Srivastva, D. N., and Saunders, P. P. (1994) Synthesis and antitumor evaluation of bis[(pivaloyloxy)methyl] 2′-deoxy-5-fluorouridine 5′-monophosphate (FdUMP): a strategy to introduce nucleotides into cells. *J. Med. Chem. 37*, 3902−3909.

(8) Fridland, A., Robbins, B. L., Srinivas, R. V., Arimilli, M., Kim, C., and Bischofberger, N. (1997) Antiretroviral activity and metabolism of bis(POC)PMPA, an oral bioavailable prodrug of PMPA. *Antiviral Res. 34*, A49, 27.

(9) Bazzanini, R., Manfredini, S., Durini, E., Gröschel, B., Cinatl, J., Balzarini, J., DeClercq, E., Imbach, J.-L., Périgaud C., and Gosselin, G. (1999) Prodrugs of Ara-CMP and Ara-AMP with a S-acyl-2-thioethyl (SATE) biolabile phosphate protecting group: synthesis and biological evaluation. *Nucleosides Nucleotides 18*, 971−972.

(10) Schlienger, N., Peyrottes, S., Kassem, T., Imbach, J.-L., Gosselin, G., Aubertin, A.-M., and Périgaud, C. (2000) S−Acyl-2-thioethyl aryl phosphotriester derivatives as mononucleotide prodrugs. *J. Med. Chem. 43*, 4570−4574.

(11) Lorey, M., Meier, C., De Clercq, E., and Balzarini (1997) New synthesis and antitumor activity of cycloSal-derivatives of 5-fluoro-2′-deoxyuridinemonophosphate. *Nucleosides Nucleotides 16*, 789−792.

(12) Meier, C., Lorey, M., De Clercq, E., and Balzarini, J. (1997) Cyclic saligenyl phosphotriester of 2′, 3′-dideoxy-2′, 3′-didehydrothymidine (d4T) − a new pro-nucleotide approach. *Bioorg. Med. Chem. Lett. 7*, 99−104.

(13) Meier, C., De Clercq, E., and Balzarini, J. (1998) Nucleotide delivery from cycloSaligenyl-3′-azido-3′-deoxythymidine monophosphates (cycloSal-AZTMP). *Eur. J. Org. Chem.* 837−846.

(14) Meier, C., Knispel, T., De Clercq, E., and Balzarini, J. (1999) CycloSal-pronucleotides of 2′, 3′-dideoxy-2′, 3′-didehydroadenosine: synthesis and antiviral evaluation of a highly efficient nucleotide delivery system. *J. Med. Chem. 42*, 1604−1614.

(15) Meier, C., Knispel, T., Marquez, V. E., Siddiqui, M. A., De Clercq, E., and Balzarini, J. (1999) CycloSal-pronucleotides of 2′-fluoro-ara- and 2′-fluoro-ribo-2′,3′-dideoxyadenosine as a strategy to bypass a metabolic blockade. *J. Med. Chem. 42*, 1615−1624.

(16) Lorey, M., and Meier, C. (1999) A new cyclic phosphoramidate d4T prodrug approach, cycloAmb-d4T-phosphoramidates. *Nucleosides Nucleotides 18*, 947−948.

(17) Egron, D., Périgaud, C., Gosselin, G., Aubertin, A.-M., and Imbach, J.-L. (1999) Synthesis and anti-HIV activity of some S-acyl-2-thioethyl (SATE) phosphoramidate derivatives of 3′-azido-2′,3′-dideoxythymidine. *Nucleosides Nucleotides 18*, 981−982.

(18) Meyers, C. L. F., Hong, L., Joswig, C., and Borch, R. F. (2000) Synthesis and biological activity of novel 5-fluoro-2′-deoxyuridine phosphoramidate prodrugs. *J. Med. Chem. 43*, 4313−4318.

(19) Tobias, S. C., and Borch, R. F. (2001) Synthesis and biological studies of novel nucleoside phosphoramidate prodrugs. *J. Med. Chem. 44*, 4475−4480.

(20) Tosquellas, G., Barber, I.; Morvan, F., Rayner, B., and Imbach, J.-L. (1996) The prooligonucleotide approach. III: synthesis and bioreversibility of a chimeric phosphorodithioate prooligonucleotide. *Bioorg. Med. Chem. Lett. 6*, 457−462.

(21) Tosquellas, G., Alvarez, K., Dell'Aquila, C., Morvan, F., Vasseur, J.-J., Imbach, J.-L., and Rayner, B. (1998) The prooligonucleotide approach: solid-phase synthesis and preliminary evaluation of model pro-dodecathymidylates. *Nucleic Acids Res. 26*, 2069−2074.

(22) Tosquellas, G., Bologna, J.-C., Morvan, F., Rayner, B., and Imbach, J.-L. (1998) First synthesis of alternating SATE-phosphotriester/phosphodiester prooligonucleotides on solid support. *Bioorg. Med. Chem. Lett. 8*, 2913−2918.

(23) Bologna, J.-C., Morvan, F., and Imbach, J.-L. (1999) The prooligonucleotide approach: synthesis of mixed phosphodiester and SATE phosphotriester prooligonucleotides using H-phosphonate and phosphoramidite chemistries. *Eur. J. Org. Chem.* 2353−2358.

(24) Alvarez, K., Vasseur, J.-J., Beltran, T., and Imbach, J.-L. (1999) Photocleavable protecting groups as nucleobase protections allowed solid-phase synthesis of base-sensitive SATE-prooligonucleotides. *J. Org. Chem. 64*, 6319−6328.

(25) Iyer, R. P., Yu, D., and Agrawal, S. (1995) Prodrugs of oligonucleotides: the acyloxyalkyl esters of oligodeoxyribonucleoside phosphorothioates. *Bioorg. Chem. 23*, 1−21.

(26) Morvan, F., Bologna, J. C., Vivès, E., and Imbach, J.-L. (2001) Cellular uptake and intracellular quantification of fluorescent labeled T_{20} Me-SATE prooligonucleotides. *Nucleosides, Nucleotides Nucleic Acids 20*, 1165−1168.

(27) Bologna, J.-C., Vivès, E., Imbach, J.-L., and Morvan, F. (2002) Uptake and quantification of intracellular concentration of lipophilic pro-oligonucleotides in HeLa cells. *Antisense Nucleic Acid Drug Dev. 12*, 33−41.

(28) Morvan, F., Brès, J.-C., Lefebvre, I., Vasseur, J.-J., Pompon, A., and Imbach, J.-L. (2001) Kinetics study of the biotransformation of an oligonucleotide prodrug in cells extract by matrix-assisted laser desorption/ionization time-of-flight mass spectrometry. *Nucleosides, Nucleotides Nucleic Acids 20*, 1159−1163.

(29) Poijärvi, P., Oivanen, M., and Lönnberg, H. (2004) Towards oligonucleotide pro-drugs: 2,2-bis(ethoxycarbonyl) and 2-(alkylaminocarbonyl)-2-cyano substituted 3-(pivaloyloxy)propyl groups as biodegradable protecting groups for internucleosidic phosphoromonothioates linkages. *Lett. Org. Chem. 1*, 183−188.

(30) Poijärvi, P., Mäki, E., Tomperi, J., Ora, M., Oivanen, M., and Lönnberg, H. (2002) Towards nucleotide prodrugs derived from 2,2-bis(hydroxymethyl)malonate and its congeners: hydrolytic cleavage of 2-cyano-2-(hydroxymethyl)-3-methoxy-3-oxopropyl and 3-(alkylamino)-2-cyano-2-(hydroxymethyl)-3-oxopropyl protections from the internucleosidic phosphodiester and phosphorothioate linkages. *Helv. Chim. Acta 85*, 1869−1876.

(31) Ora, M., Mäki, E., Poijärvi, P., Neuvonen, K., Oivanen, M., and Lönnberg, H. (2001) Hydrolytic stability of nucleoside phosphotriesters derived from bis(hydroxymethyl)-1,3-dicarbonyl compounds and their congeners: towards a novel prodrug strategy for antisense oligonucleotides. *J. Chem. Soc., Perkin Trans. 2* 881−885.

(32) Stawinski, J., and Strömberg, R. (2001) *Current Protocols in Nucleic Acid Chemistry* (Beaucage, S. L., Bergstrom, D. E., Glick, G. D., Jones, R. A., Harkins, E. W., Eds.) pp 2.6.1−2.6.15, John Wiley & Sons, Inc., New York.

(33) Iyer, R. P., Egan, W., Regan, J. B., and Beaucage, S. L. (1990) 3*H*-1,2-Benzodithiole-3-one 1,1-dioxide as an improved

sulfurizing reagent in the solid-phase synthesis of oligodeoxyribonucleoside phosphorothioates. *J. Am. Chem. Soc. 112*, 1253−1254.

(34) Dressman, B. A., Spangle, L. A., and Kaldor, S. W. (1996) Solid-phase synthesis of hydantoins using a carbamate linker and a novel cyclization/cleavage step. *Tetrahedron Lett. 37*, 937−940.

(35) Alsina, J., Chiva, C., Ortiz, M., Rabanal, F., Giralt, E., and Albericio, F. (1997) Active carbonate resins for solid-phase synthesis through the anchoring of a hydroxyl function. Synthesis of cyclic and alcohol peptides. *Tetrahedron Lett. 38*, 883−886.

(36) Albericio, F., Giralt, E., and Eritja, R. (1991) NPE-resin, a new approach to the solid-phase synthesis of protected peptides and oligonucleotides II. Synthesis of protected peptides. *Tetrahedron Lett. 32*, 1515−1518.

(37) Eritja, R., Robles, J., Fernandez-Forner, D., Albericio, F., Giralt, E., and Pedroso, E. (1991) NPE-resin, a new approach to the solid-phase synthesis of protected peptides and oligonucleotides I. Synthesis of the supports and their application to oligonucleotide synthesis. *Tetrahedron Lett. 32*, 1511−1514.

(38) Zhu, S., Shi, S., Gerritz, S. W., and Sofia, M. J. (2003) Attachment of unreactive amines to the solid support: synthesis of phenyl-substituted anilines, 2-aminopyridines, and 2-aminopyrimidines. *J. Comb. Chem. 5*, 205−207.

(39) Atkinson, T., and Smith, M. (1984) *Oligonucleotide Synthesis: A Practical Approach* (Gait, M. J., Ed.) p 48, IRL Press, Oxford, U.K.

(40) Garegg, P. J., Lindh, I., Regberg, T., Stawinski, J., and Strömberg, R. (1986) Nucleoside H-phosphonates. III. Chemical synthesis of oligodeoxyribonucleotides by the hydrogenphosphonate approach. *Tetrahedron Lett. 27*, 4051−4054.

(41) Garegg, P. J., Lindh, I., Regberg, T., Stawinski, J., and Strömberg, R. (1986) Nucleoside H-phosphonates. IV. Automated solid-phase synthesis of oligodeoxyribonucleotides by the hydrogenphosphonate approach. *Tetrahedron Lett. 27,* 4055−4058.

(42) Pon, R. T., and Yu, S. (1997) Hydroquinone-*O*,*O*′-diacetic acid ('Q-linker') as a replacement for succinyl and oxalyl linker arms in solid-phase oligonucleotide synthesis. *Nucleic Acids Res. 25*, 3629−3635.

BC050143G

Accelerated Bioorthogonal Conjugation: A Practical Method for the Ligation of Diverse Functional Molecules to a Polyvalent Virus Scaffold

Sayam Sen Gupta,[†] Jane Kuzelka,[†] Pratik Singh,[‡] Warren G. Lewis,[†] Marianne Manchester,[‡] and M. G. Finn*,[†]

Department of Chemistry and The Skaggs Institute for Chemical Biology, and Department of Cell Biology, The Scripps Research Institute, 10550 North Torrey Pines Road, La Jolla, California 92037. Received May 23, 2005; Revised Manuscript Received August 12, 2005

Covalent bond formation to proteins is made difficult by their multiple unprotected functional groups and normally low concentrations. A water-soluble sulfonated bathophenanthroline ligand (**2**) was used to promote a highly efficient Cu^{I}-mediated azide−alkyne cycloaddition (CuAAC) reaction for the chemoselective attachment of biologically relevant molecules to cowpea mosaic virus (CPMV). The ligated substrates included complex sugars, peptides, poly(ethylene oxide) polymers, and the iron carrier protein transferrin, with routine success even for cases that were previously resistant to azide−alkyne coupling using the conventional ligand tris(triazolyl)amine (**1**). The use of 4−6 equiv of substrate was sufficient to achieve loadings of 60−115 molecules/virion in yields of 60−85%. Although it is sensitive to oxygen, the reliably efficient performance of the Cu·**2** system makes it a useful tool for demanding bioconjugation applications.

INTRODUCTION

Chemoselective ligation, a process whereby unprotected molecular fragments couple through uniquely complementary reactive functional groups, is a powerful technique for bioconjugation (*1*, *2*). The azide group in particular has emerged as a very useful chemical handle for this purpose, participating in the Staudinger ligation with phosphines (*1*) as well as the [3 + 2] cycloaddition reaction with strained (*3*) and terminal (*4*) alkynes. Under the influence of copper(I) catalysis (*4*), the latter process has permitted the selective modification of virus particles (*5*, *6*), enzymes (*7*), cells (*8*), and proteins from complex tissue lysates (*9*). The unreactive nature of both azides and alkynes with the functional groups of biomolecules, as well as their small size and therefore unobtrusive presence when appended to enzymatic substrates, makes improved methods for their ligation of interest for a wide range of biomolecular applications.

The successful execution of the Cu-catalyzed azide−alkyne cycloaddition (CuAAC) reaction at mild temperatures and low concentrations requires the presence of a copper-binding ligand. The ligand must accelerate the reaction, maintain the +1 oxidation state of the metal, and preserve the integrity of the biological scaffold by sequestering the copper ions away from proteins and polynucleotides. To this end, tris(triazolyl)amine ligand (**1**) (*10*) has been utilized for the conjugation of a variety of molecules to protein surfaces. Although **1** strongly accelerates the CuAAC process when the reaction is homogeneous, the ligand is not very soluble in water, and there have been some indications that proteins may be damaged if insufficient amounts of the ligand are available in solution (*3*). Most importantly, the reaction in water in the presence of **1** is too slow to eliminate the need for large excesses of substrate, on the same order of concentrations as are needed for the more conventional reactions of cysteine residues with maleimides. In other words, bioconjugation reactions catalyzed by Cu·**1** are too demanding of precious or expensive coupling partners to be routinely useful for preparative applications.

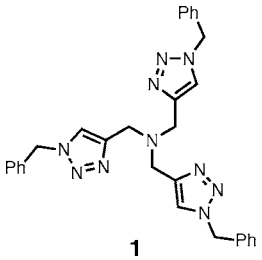

1

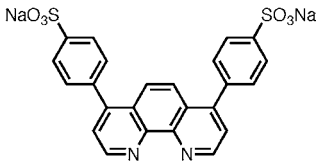

2

For several years, we have developed the use of icosahedral virus particles as chemical building blocks for studying the role of polyvalency in diagnostic and therapeutic applications (*11*, *12*). As a prototypical scaffold, we have employed cowpea mosaic virus (CPMV), which is a stable and crystallographically characterized particle available in large quantities. The range of target functions is broad, requiring the attachment of such structures as carbohydrates, peptides, organic polymers, and proteins. A single common attachment methodology would greatly assist synthetic access to diverse particles. However, the aforementioned deficiencies of the Cu·**1** system constrained our initial efforts to obtain such materials in relatively large amounts. We describe here an improved procedure for the CuAAC process that makes it a truly general method for polyvalent scaffold decoration and, by extension, for the creation of functionalized surfaces of almost any kind. Importantly, this

* To whom correspondence should be addressed. E-mail: mgfinn@scripps.edu.

[†] Department of Chemistry and The Skaggs Institute for Chemical Biology, The Scripps Research Institute.

[‡] Department of Cell Biology, The Scripps Research Institute.

10.1021/bc050147l CCC: $30.25 © 2005 American Chemical Society
Published on Web 09/13/2005

system permits the chemoselective bioconjugation of molecules that were hitherto unreactive to azide−alkyne coupling.

EXPERIMENTAL PROCEDURES

Materials. Fluorescein-PEG-NHS-3400 (NHS = *N*-hydroxysuccinimide) was obtained from Nektar (Huntsville, AL). The water-soluble sulfonated bathophenanthroline ligand **2** was purchased from GFS. Human holotransferrinn (98%) was supplied by Sigma. The resins Fmoc-Phe-Wang (0.77 mmol/g, 100−200 mesh) and Fmoc-Lys(Boc)-Wang (0.12 mmol/g, 100−200 mesh), as well as other Fmoc-protected amino acids were purchased from Chem-Impex International. Compounds **5** (*13*), **6** (*13*), and $[Cu(MeCN)_4](OTf)$ (*14*) were prepared as previously described; **7a** and **8a** were provided by the Consortium for Functional Glycomics at The Scripps Research Institute. CPMV−alkyne and −azide conjugates **3** and **4** were prepared as previously described (*13*) using purified NHS esters of the acid-bearing linkers. Fmoc-L-propargylglycine was purchased from CSPS (San Diego, CA). All other chemical reagents were obtained from commercial suppliers and used as received, unless indicated otherwise.

Instrumentation. Air-sensitive manipulations were performed under nitrogen in a Vacuum Atmospheres glovebox. Preparative HPLC was performed with a Dynamax/Rainin Preppy SD-1 instrument and a Vydac protein and peptide reverse phase column, eluting with a gradient solvent mixture (solvent A = H_2O/0.1% TFA; solvent B = CH_3CN/0.1% TFA). MALDI-TOF analyses were performed by the Mass Spectrometry Facility at The Scripps Research Institute. FPLC analyses were performed on an AKTA Explorer (Amersham Pharmacia Biotech) equipped with a Superose-6 size exclusion column. Samples for transmission electron microscopy (TEM) were obtained by deposition of 20 μL sample aliquots onto 100-mesh carbon-coated copper grids, followed by staining with 20 μL of 2% uranyl acetate. Images were obtained using a Philips CM100 electron microscope.

Modification of CPMV with NHS Esters. Reagents were introduced into a solution of CPMV, such that the final mixture contained ≤20% DMSO. Unless otherwise specified, the buffer used was 0.1 M phosphate, pH 7.0. Purification of derivatized virus (>1 mg) was performed by ultracentrifugation over a 10−40% sucrose gradient, pelleting of the recovered virus, and dissolution of the resulting material in Tris buffer (0.1 M, pH 8). Mass recoveries of derivatized viruses were typically 60−80%; all such samples were composed of >95% intact particles as determined by analytical size-exclusion FPLC. Virus concentrations were measured by absorbance at 260 nm; virus at 0.10 mg/mL gives a standard absorbance of 0.80. Fluorescein concentrations were obtained by measurement of absorbance at 495 nm, applying an extinction coefficient of 70 000 M^{-1} cm^{-1}. Each data point is the average of values obtained from three independent parallel reactions; loading values (the number of substrate molecules attached to the virus) are subject to an experimental error of ±10%. The average molecular weight of the CPMV virion is 5.6×10^6 g/mol.

Compounds 7b and 8b. To a solution of **7a** (10 mg, 12.4 μmol) in H_2O (1 mL) was added **9** (70 mg, 0.125 mmol) in THF (1 mL). *t*-BuOH (1 mL) was added, followed by sodium ascorbate (0.5 M in H_2O, 72 μL, 36 μmol) and $CuSO_4$ (0.5 M in H_2O, 24 μL, 12 μmol). The reaction mixture was stirred in a closed vial for 48 h at room temperature, followed by removal of the volatile solvents by rotary evaporation and addition of 5 mL of H_2O. Excess **9** was largely removed by extraction with EtOAc. The reaction was monitored by TLC (R_f = 0.6 in 8:3:3:2 EtOAc/MeOH/AcOH/H_2O,) as well as by disappearance of the azide peak (2100 cm^{-1}) using FT-IR spectroscopy. The aqueous phase was concentrated by evaporation and residual **9** was removed by column chromatography (Sephadex G-15, 95:5 H_2O/BuOH), giving a yellow solid (11 mg, 65% yield) upon lyophilization of the collected fraction. MALDI-TOF: $[M + H]^+ = 1361$, $[M + Na]^+ = 1383$, $[M + K]^+ = 1399$. Compound **8b** was synthesized in 55% yield from **8a** using the same procedure. MALDI-TOF: $[M + Na]^+ = 1472$, $[M + K]^+ = 1488$.

Compound 9. A mixture of fluorescein amine (1.57 g, 4.54 mmol) and sodium bicarbonate (1.57 g, 1.87 mmol) in dry THF (30 Ml) was cooled in an ice bath and stirred under N_2 for 15 min. 3,5-Bis-prop-2-ynyloxy-benzoyl chloride (1.15 g, 4.99 mmol) in dry THF (30 mL) was added dropwise and the mixture was stirred overnight at room temperature. The solid bicarbonate was removed by filtration, and the solvent was evaporated to give **4** as an orange solid, which was purified by column chromatography (silica gel, 95:5 EtOAc/MeOH). ^1H NMR (CD_3OD, δ) 8.4 (s, 1H), 8.2 (d, 2H), 7.3 (m, 3H), 6.8−7 (m, 3H), 6.6−6.8 (m, 4H), 4.8 (d, 4H) (s, 6 H), 3.1 (t, 2H). ESI-MS *m/z* = 560.1 (MH^+); UV−vis (0.1 M phosphate, pH 7) λ_{max} 494 nm, ϵ = 64 000.

Peptides 10 and 11. Compound **10** was prepared by standard techniques of solid-phase Fmoc peptide synthesis using 0.2 mmol of Fmoc-Phe-Wang resin. Coupling of Fmoc-L-propargylglycine was performed as reported elsewhere (*15*). Conjugation of fluorescein to the N-terminus of the peptide chain was accomplished by addition of a DMF/*i*Pr_2Net (2:1 v/v) solution containing 5(6)-carboxyfluorescein (414 mg, 1.1 mmol) and HBTU (417 mg, 1.1 mmol) to the drained resin. The mixture was agitated overnight and purified by reverse phase HPLC after cleavage from the resin. MALDI-TOF: $[M + H]^+ = 1579$. Peptide **11** was obtained from the analogous procedure using 0.1 mmol of Fmoc-Lys(Boc)-Wang resin. MALDI-TOF: $[M + H]^+ = 1571$, $[M + Na]^+ = 1593$.

Polymer 12. A toluene solution of 3-azido-1-propylamine (0.66 M, 334 μL, 0.22 mmol) was added to a solution of fluorescein-PEG-NHS-3400 (150 mg, 0.044 mmol) in dry CH_2Cl_2 (5 mL). The mixture was stirred overnight, followed by removal of the solvents under reduced pressure. H_2O (10 mL) was added and the solution was extracted with EtOAc to remove the excess azide compound. The aqueous solution was lyophilized to afford **12** as a yellow powder (135 mg, 90% yield).

Polymer 13. To a solution of fluorescein-PEG-NHS-3400 (150 mg, 0.044 mmol) in dry CH_2Cl_2 (5 mL) was added propargylamine (12.1 mg, 0.22 mmol). The mixture was stirred overnight and worked up as described for **12**. Compound **13** was isolated as a yellow powder (135 mg, 90% yield).

Transferrin−Alkyne Conjugate 14. To human holotransferrin (50 mg, 0.625 μmol) in phosphate buffer (0.1 M, pH 7, 2 mL) was added *N*-(*N*-(prop-2-ynyl)hexanamidyl)maleimide (3.9 mg, 9.1 μmol) in DMSO (500 μL), and the mixture was incubated overnight at room temperature. Purification through a G-15 Sephadex coloumn followed by dialysis and lyophilization afforded **14** as a pink powder (30 mg).

Modification of CPMV by CuAAC Reaction. CPMV conjugate **3** or **4** (1 mg as a 2 mg/mL solution) was incubated with complementary azide or alkyne compound (concentrations given in Table 1) in Tris buffer (0.1 M, pH 8, 0.5 mL) containing **2** (3 mM) and $[Cu(MeCN)_4](OTf)$

Scheme 1

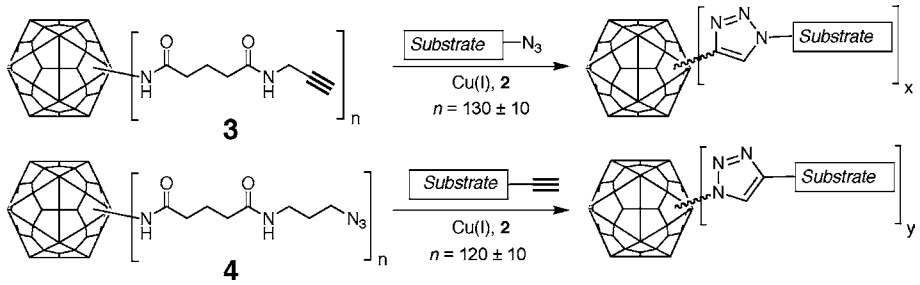

Table 1. Azide−Alkyne Cycloaddition on CPMV[a] with Various Substrates

entry	substrate	CPMV derivative	[substrate] (μM)	loading	yield (%)
1	7b	4	200	115	85
2	8b	4	200	105	85
3	10	4	120	60	85
4	11	4	250	115	80
5	12	3	500	60	60
6	13	4	250	90	75
7	14	4	260	*b*	*b*

[a] 2 mg/mL; 47 μM in alkyne for **3**, 43 μM in azide for **4**. [b] not determined.

(1 mM) for 12 h at room temperature with rigorous exclusion of dioxygen. CPMV−**12**, CPMV−**13**, and CPMV−**14** conjugates were purified by sucrose gradients and pelleting as described above. All other CPMV conjugates were purified by size exclusion chromatography using Bio-Spin disposable chromatography columns filled with Bio-Gel P-100 as described elsewhere (*16*).

RESULTS AND DISCUSSION

Optimization of Reaction Conditions. Our recent discovery of sulfonated bathophenanthroline **2** as a highly efficient ligand in a fluorescence quenching catalysis assay (*17*) prompted us to further investigate **2** for the coupling of compounds to suitably derivatized CPMV particles. The viral capsids were labeled with alkynes (**3**) or azides (**4**) at surface-exposed lysine residues using standard NHS ester chemistry (Scheme 1) (*5*). Initial experiments were performed using functionalized fluorescein dyes as substrates because the success of the bioconjugation could be readily monitored using UV−vis spectroscopy. Thus, fluorescein derivatives **5** and **6** (Figure 1) (*5*) were condensed with **3** and **4**, respectively, in the presence of Cu·**2** in Tris buffer (pH 8) under inert atmosphere, to give CPMV−dye conjugates with good loading in a concentration-dependent fashion. In all cases, the reaction yield (the percent of virus recovered after purification of protein away from small molecules) and purity (intact virus particles vs disassembled viral protein) was high. Thus, >85% of the protein was recovered in each case, and size-exclusion FPLC indicated that >95% of the virons were intact particles (*18*). SDS−PAGE analysis visualized under ultraviolet light revealed two dye-labeled bands corresponding to the small and large subunits of CPMV, indicating that both subunits of the virus were chemically modified (data not shown). No attachment was found to occur in the absence of Cu^{I}, ruling out nonspecific adsorption of dye to virus. It should also be noted that the use of phosphate buffer diminishes the effectiveness of the reaction, while HEPES buffer is at least as good or better than Tris.

The dependence of the observed loading (dye attachments per virion) on substrate concentration is shown in Figure 2. Upon treatment of 2 mg/mL **4** (0.36 μM in virus particles) with 200 μM **6**, corresponding to a 5-fold molar excess with respect to azide groups on **4**, the CPMV particles were found to be fully labeled (in other words, all of the attached azide groups converted to triazoles, approximately 110 per particle). Similar results were obtained with **3** + **5**. In contrast, the use of ligand **1** under otherwise identical conditions required a 5 mM concentration of **6** (250 equiv) to achieve such dye loadings. Furthermore, the reaction of opposite "polarity" (**3** + **5**) mediated by Cu·**1** was significantly worse than **4** + **6**.

The same results with each ligand were obtained using $[Cu(MeCN)_4](OTf)$, $[Cu(MeCN)_4](PF_6)$, or CuBr as the source of Cu^{I}. The optimal copper concentration was found to be 1 mM; lower concentrations significantly decreased the coupling efficiency. The ligand-to-metal ratio is also important. A 3:1 ratio of **2** to Cu^{I} afforded the best results; a lower ratio resulted in significant degradation of the viral capsid, whereas a larger excess of ligand slowed the reaction to provide incomplete labeling. The efficiency of the Cu·**2** mediated AAC process thereby far exceeds that of standard NHS and maleimide coupling reactions with lysine and cysteine side chains, respectively. For example, the addition of a 10-fold excess of fluorescein NHS ester to CPMV under similar conditions results in the attachment of approximately 20 dyes to each capsid (*19*), and fluorescein maleimide deposits between 10 and 25 dye molecules on CPMV mutants bearing surface cysteine residues, depending on the local environment of the sulfhydryl groups (*20*). While the linker used to attach azides and alkynes to CPMV may make these groups more accessible than the lysine or cysteine side chains of native and mutant forms of the particle, we believe that the differences will be small given the highly solvent-exposed nature of many of the surface peptide residues.

Preparation of CPMV−Carbohydrate Conjugates. With the optimal reaction conditions thus established, biologically relevant substrates were attached to the CPMV capsid as shown in Figure 1 and Table 1. Carbohydrate **7a** binds the protein galectin-4, an early marker of breast cancer cells (*21*). Sialyl Lewis X, an azide derivative of which is **8a**, is overexpressed on cancer cells and also plays a role in inflammation (*22*). We envisioned that the attachment of these two compounds to the surface of a virus particle could be useful for drug targeting, as well as for the elusive goal of antibody production against carbohydrate epitopes (*23*). To allow for ready quantitation of the attachment of these nonfluorescent compounds, the azides were subjected to a CuAAC reaction with fluorescein dialkyne reagent **9** to provide dye−alkyne derivatives **7b** and **8b**. Using the Cu·**2** system, **7b** and **8b** were then successfully grafted to virus−azide **4** with loadings of 115 and 105 per virion, respectively. Only 4 equiv of **7b** or **8b** per azide group on **2** was necessary to reach this level of loading at a virus

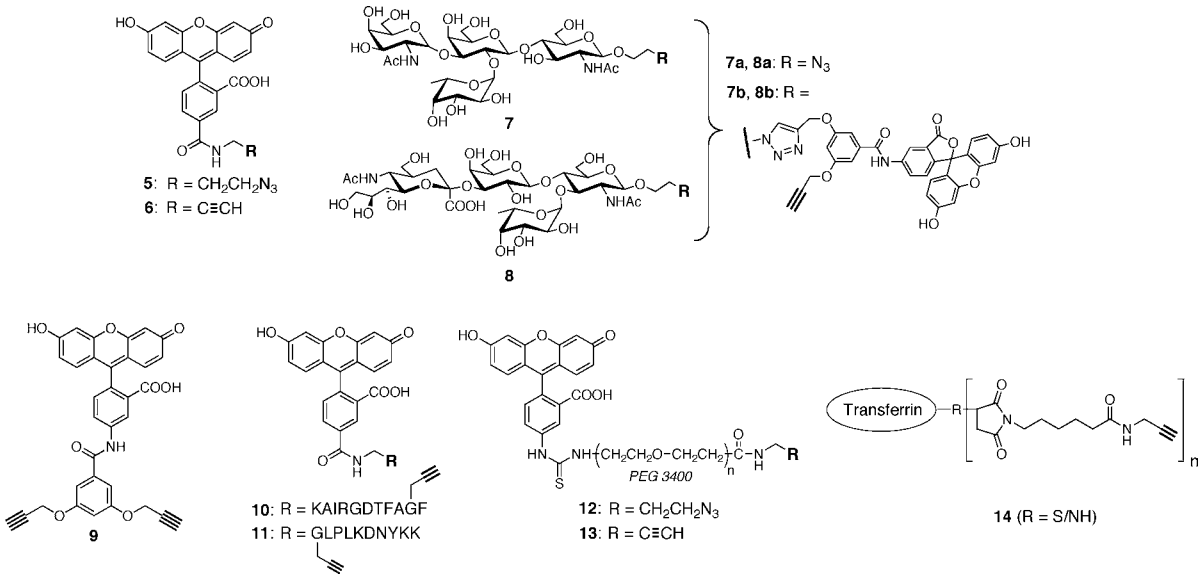

Figure 1. Substrates used in CuAAC attachment to CPMV.

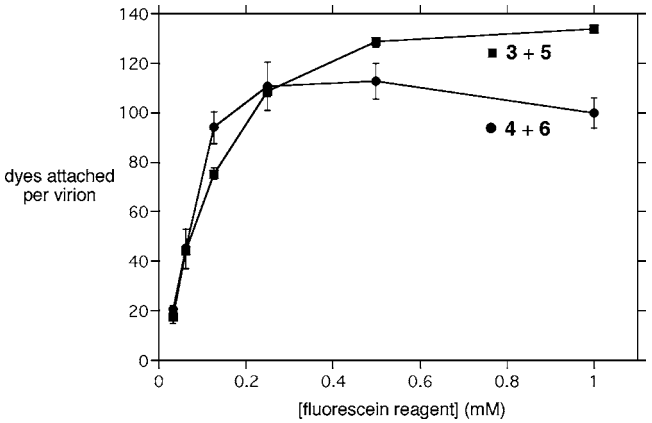

Figure 2. Dependence of dye loading on reagent concentration. Conditions used: 2 mg/mL **3** or **4**, complementary fluorescein derivatives **5** or **6**, 1 mM $[Cu(MeCN)_4](Otf)$, 3 mM **2**, Tris-HCl buffer (pH 8), r.t., 14 h.

concentration of 1−2 mg/mL. The integrity of polyvalently displayed **7** and the retention of the activity of the carbohydrate was verified by the formation of a gel upon the addition of CPMV−$(\mathbf{7b})_{115}$ to dimeric galectin-4 (*18*). The use of **7a** and **8a** with particle **3** under similar conditions likewise gave intact derivatized virions in high yield with the ability to efficiently crosslink a solution of galectin-4. We assume in these cases that the loading of small molecules lacking the fluorescein tag is approximately the same as for their fluorescent counterparts since we have established with extensive studies that the nature of the substrate has little effect on the efficiency of the CuAAC reaction.

This facile attachment of complex, unprotected sugars to proteins by CuAAC ligation represents a significant advancement over existing methodologies employing a bifunctional linker on the carbohydrate for standard bioconjugation reactions. Typically, squarates (*24*) and maleiimide-hydrazide or maleiimide-NHS ester linkers have been employed for this purpose (*23*, *25*), and the additional synthetic steps required to functionalize the sugars in the appropriate fashion result in poor overall coupling yields. In contrast, azides can be readily incorporated into the carbohydrate scaffold early in the synthesis and rarely interfere in subsequent synthetic steps.

Attachment of Peptides to CPMV. Although the genetic incorporation of peptide loops into selected regions of the CPMV capsid structure is well established (*26*), the production of such chimeras suffers from restrictions in terms of size, position, and sequence. Given the great importance of cyclic and linear peptides to a wide variety of targets in biochemistry, molecular recognition, and drug development, robust methods for the attachment of natural and nonnatural oligopeptides to polyvalent scaffolds are of interest. To demonstrate the virtues of the CuAAC reaction in this regard, we chose peptides containing carboxylic acid or amine side chain functional groups and which would therefore require protection/deprotection strategies to be incorporated in standard peptide coupling procedures. To date, the decoration of full proteins with functional peptides has been accomplished predominantly with native chemical ligation (*27*) or maleimide-cysteine reactions. Both of these strategies require the presence of accessible cysteine residues in the protein, the former at the N-terminus (*28*).

We tested the Cu·**2** system with two functional peptides. The arginine-glycine-aspartate (RGD) sequence of **10** is derived from an adenovirus serotype that binds α_v integrins, extracellular matrix receptors that are overexpressed on many cancer cells (*29*). The amino acid sequence of **11** comes from a portion of the protective antigen (PA) of anthrax toxin, a moiety that binds edema factor (EF) and lethal factor (LF) and permits cell entry of the toxin (*30*). Peptide **10** was successfully attached to **4** with a loading of 60 peptides per viral particle using only a 6-fold excess of substrate and standard Cu·**2** conditions. Significantly, no peptide attachment was obtained when ligand **1** was employed with up to 5 mM substrate present. The attachment of **11** afforded a loading of 115 peptides/virion, and SDS−PAGE analysis by UV irradiation indicated that both small and large subunits of CPMV were modified with the PA peptide (data not shown). The ready incorporation of alkyne groups into synthetic peptides (*15*) permits the Cu·**2**-mediated AAC reaction to serve as a general strategy for the attachment of peptides to biomolecular scaffolds.

Preparation of Virus−Polymer Constructs. CPMV was previously derivatized with poly(ethylene oxide) (PEG) using an NHS ester derivative to give well-controlled loadings of the polymer on the outer coat-

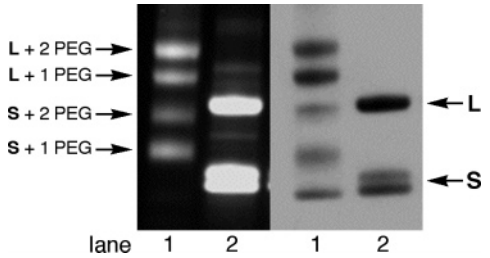

Figure 3. SDS−PAGE of CPMV−(**13**)$_{90}$ (lane 1) and CPMV−(**5**)$_{110}$ (lane 2). On the right (light background) is shown the gel visualized after SimplyBlue staining; the two extra bands corresponding to each subunit arise from modification by 1 or 2 PEG-3400 moieties. On the left (dark background) is the gel illuminated by UV light prior to protein staining. Because PEG-3400 is labeled with fluorescein, only the modified subunits are visible in lane 1. The two small-subunit bands appearing in lane 2 arise from incomplete C-terminal peptide cleavage in vivo and are unrelated to the present experiments.

protein assembly (*12*). Compared with wild-type CPMV, the PEGylated particle showed altered physical properties and a reduced immunogenic response in mice. Lysine reactivity with activated ester derivatives of PEG allowed us to reach a maximum of only 30 attached PEG molecules per virion. Attempts to boost the loading past this value required such high concentrations of PEG reagents that the virus particle precipitated before the reaction could occur. The enhanced activity of the Cu·**2** catalyst allowed us to improve on this prior result. Thus, fluorescein end-functionalized PEG reagents **12** and **13** were coupled to their complementary CPMV alkyne and azide scaffolds to give loadings of 60 and 90 PEG chains per virion, respectively, using easily accessible concentrations in which the virus particles were stable (Table 1). The resulting particles were again less dense on sucrose gradient sedimentation and larger as indicated by size-exclusion FPLC (*18*). Figure 3 shows the denaturing gel of CPMV−(**13**)$_{90}$ and CPMV−(**5**)$_{110}$ visualized by UV irradiation and protein staining. In both cases, both large (L) and small (S) subunits of the CPMV coat protein were labeled, as expected. The PEG conjugate CPMV−**13** gave rise to two higher molecular weight bands for each subunit, corresponding to single and double labeling of the subunits by the polymer. Protein staining of this conjugate also revealed the presence of a small proportion of unmodified subunits.

Attachment of the Transferrin Protein. As a final example of the ability of Cu·**2** to efficiently promote the AAC reaction, the coupling of a large protein to the outer surface of CPMV was performed. Receptors for transferrin (Tfn), an iron carrier protein in vertebrates, are overexpressed on a variety of cancer cells. Polyvalent assemblies of Tfn on such scaffolds as liposomes and iron oxide nanoparticles have therefore been prepared for cancer cell targeting (*31*). The display of multiple copies of Tfn on CPMV could similarly afford a particle that binds tightly and selectively to receptor-bearing cells.

Human holo-transferrin, an 80 kDa bilobed glycoprotein, was incubated at high concentration (20 mg/mL) with 15 equiv of a maleimide-alkyne linker at pH 7 to afford the alkyne-derivatized protein **14**, with attachments made at one or more accessible cysteines (and perhaps, to a lesser extent, lysine) residues. The successful conjugation of alkyne to Tfn was verified by the

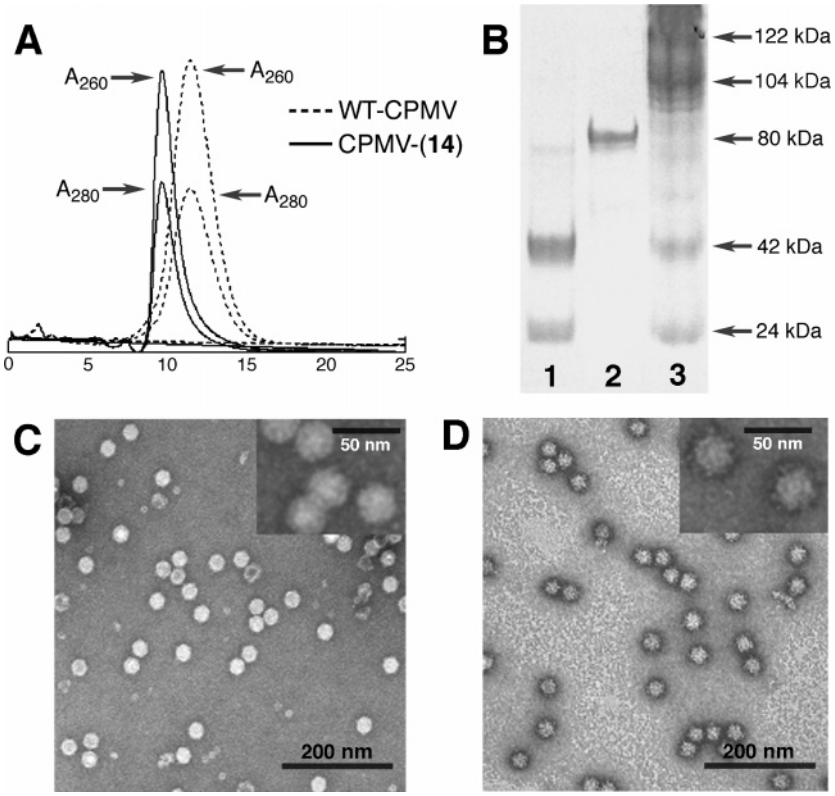

Figure 4. (A) Size-exclusion FPLC of wild-type CPMV and CPMV−(**14**)$_n$. Protein from disassembled particles would appear at longer retention times than the peaks observed here, and the A_{260}/A_{280} ratios are characteristic of intact, RNA-containing capsids for both samples. The more rapid elution of CPMV−(**14**)$_n$ indicates a substantial size increase in the particle, as 10 mL is approximately the void volume of the column. (B) SimplyBlue-stained gel (4−12% bis-tris) of wild-type CPMV (subunits at 42 and 24 kDa) (lane 1), Tfn (80 kDa) (lane 2), and CPMV−(**14**)$_n$ (lane 3). Note the appearance of two strong bands of approximately 102 and 122 kDa in the lane 3, corresponding to the CPMV subunits conjugated with Tfn. (C) Negative-stained TEM of wild-type CPMV. (D) Negative-stained TEM of CPMV−(**14**)$_n$. Automated measurement of the particles showed the average diameters to be 30 ± 1 nm for wild-type and 46 ± 5 nm for CPMV−(**14**)$_n$.

reaction of **14** with the fluorescein derivative **5** under CuAAC conditions. Analysis by SDS−PAGE confirmed that all of the Tfn was covalently labeled with at least one fluorescein molecule (data not shown).

The CPMV−Tfn conjugate CPMV−(**14**)$_n$ was then prepared by reaction of **4** with **14** using Cu·**2**. Examination of the product by FPLC, SDS−PAGE, TEM (Figure 4), and Western immunoblotting (*18*) indicated that a significant number of Tfn molecules were arrayed on the particle. Importantly, the virus−protein conjugates were isolated as individual particles, with no evidence of aggregation that might be expected if Tfn species bearing more than one alkyne were to couple to polyvalent CPMV azides. In negative-stained electron microscopy, individual CPMV−(**14**)$_n$ particles were larger than wild-type CPMV by approximately 16 nm in diameter, and displayed a clear knobby appearance contrasting with the smooth hexagonal shape of the wild-type virion. These observations confirm that Tfn molecules were covalently attached evenly over the CPMV surface. Preliminary measurements show the attached Tfn molecules to be active in binding the target receptor.

A recent report employing thiol-maleimide chemistry for the attachment of proteins (up to 22 kDa) to CPMV required the use of a 50-fold excess of protein with respect to the viral asymmetric unit, as well as subsequent chromatographic purification of the desired conjugate (*32*). We have obtained many similar results for NHS ester-lysine as well as thiol-electrophile reactions. In contrast, protein conjugation is achieved by the CuAAC reaction with efficiencies comparable to those of native chemical ligation (NCL) (*27*). Here, only a 6-fold excess of Tfn was required, and the relatively small amount of Tfn employed allowed for simple purification by sucrose gradients and pelleting. While NCL reactions are typically conducted with nearly equimolar ratios of coupling reagents, the concentrations of thioester and *N*-terminal cysteine reaction partners are typically much higher (0.1−1 mM) than the CPMV azides and alkynes used here (*33*). The Cu·**2**-mediated AAC protocol is therefore an excellent alternative for the coupling of suitably functionalized proteins (*34*).

In summary, we have developed a highly efficient azide−alkyne cycloaddition protocol using a simple copper(I) salt and sulfonated bathophenanthroline (**2**) for chemoselective ligation. This catalytic system permits the attachment of complex carbohydrates, peptides, polymers, and proteins to biomacromolecules in yields and substrate loadings far superior to those possible with previously established procedures. Advantages to the Cu·**2**-mediated AAC method include the use of modest excesses of the desired coupling partners and simple purification. The unfortunate tendency of copper ions to speed the hydrolytic cleavage of peptides and polynucleotides is largely controlled by the use of enough ligand to restrict access to the metal center. We anticipate that the improved CuAAC reaction will be particularly beneficial to those wishing to join substrates that are expensive or available in only small quantities and for biological molecules in which azides or alkynes are incorporated by biosynthetic procedures (*6*, *35*). The single drawback to this system is the requirement that the reaction be performed under inert atmosphere; ligands designed to solve this problem are currently being developed.

ACKNOWLEDGMENT

This work was supported by the NIH (EB00432 and N01-CO-27181), The David and Lucille Packard Foundation Interdisciplinary Science Award program, and The Skaggs Institute for Chemical Biology; S.S. and W.G.L. are Skaggs Postdoctoral and Predoctoral Fellows, respectively. We thank Dr. Wendy Ochoa for obtaining the TEM images, Dr. Ola Blixt for generous gifts of **7a** and **8a**, and Mr. Eiton Kaltgrad for assistance with the preparation of **7b** and **8b**.

Supporting Information Available: Size-exclusion FPLC of CPMV conjugates, reaction of CPMV-**8b** with dimeric galectin-4, Western blots of CPMV−(**14**)$_n$. This material is available free of charge via the Internet at http://pubs.acs.org.

LITERATURE CITED

(1) (a) Lemieux, G. A., and Bertozzi, C. R. (1998) Chemoselective ligation reactions with proteins, oligosaccharides and cells. *Trends Biotechnol. 16*, 506−513. (b) Prescher, J. A., and Bertozzi, C. R. Chemistry in living systems. *Nature Chem. Biol. 1*, 13-21. (c) Van Swieten, P. F., Leeuwenburgh, M. A., Kessler, B. M., and Overkleeft, H. S. (2005) Bioorthogonal organic chemistry in living cells: novel strategies for labeling biomolecules. *Org. Biomol. Chem. 3*, 20−27. (d) Rademann, J. (2004) Organic protein chemistry: drug discovery through the chemical modification of proteins. *Angew. Chem., Int. Ed. 43*, 4554−4556.

(2) Link, A. J., Mock, M. L., and Tirrell, D. A. (2003) Non-canonical amino acids in protein engineering. *Curr. Opin. Biotechnol. 14*, 603−609.

(3) Agard, N. J., Prescher, J. A., and Bertozzi, C. R. (2004) A strain-promoted [3+2] azide-alkyne cycloaddition for covalent modification of biomolecules in living systems. *J. Am. Chem. Soc. 126,* 15046−15047.

(4) (a) Rostovtsev, V. V., Green, L. G., Fokin, V. V., and Sharpless, K. B. (2002) A stepwise huisgen cycloaddition process: Copper(I)-catalyzed regioselective "ligation" of azides and terminal alkynes. *Angew. Chem., Int. Ed. 41*, 2596−2599. (b) Tornøe, C. W., Christensen, C., and Meldal, M. (2002) Peptidotriazoles on solid phase: [1,2,3]-triazoles by regiospecific copper(I)-catalyzed 1,3-dipolar cycloadditions of terminal alkynes to azides. *J. Org. Chem. 67*, 3057−3062.

(5) Wang, Q., Chan, T. R., Hilgraf, R., Fokin, V. V., Sharpless, K. B., and Finn, M. G. (2003) Bioconjugation by copper(I)-catalyzed azide-alkyne [3 + 2] cycloaddition. *J. Am. Chem. Soc. 125*, 3192−3193.

(6) Tian, F., Tsao, M.-L., and Schultz, P. G. (2004) A phage display system with unnatural amino acids. *J. Am. Chem. Soc. 126*, 15962−15963.

(7) (a) Deiters, A., Cropp, T. A., Summerer, D., Mukherji, M., and Schultz, P. G. (2004) Site-specific pegylation of proteins containing unnatural amino acids. *Bioorg. Med. Chem. Lett.* 14, 5743−5745. (b) Deiters, A., Cropp, T. A., Mukherji, M., Chin, J. W., Anderson, J. C., and Schultz, P. G. (2003) Adding amino acids with novel reactivity to the genetic code of *Saccharomyces cerevisiae*. *J. Am. Chem. Soc. 125*, 11782−11783.

(8) Link, A. J., Vink, M. K. S., and Tirrell, D. A. (2004) Presentation and detection of azide functionality in bacterial cell surface proteins. *J. Am. Chem. Soc. 126*, 10598−10602.

(9) (a) Speers, A. E., and Cravatt, B. F. (2004) Profiling enzyme activities in vivo using click chemistry methods. *Chem. Biol. 11*, 535−546. (b) Speers, A. E., Adam, G. C., and Cravatt, B. F. (2003) Activity-based protein profiling in vivo using a copper(I)-catalyzed azide-alkyne [3 + 2] cycloaddition. *J. Am. Chem. Soc. 125*, 4686−4687.

(10) Chan, T. R., Hilgraf, R., Sharpless, K. B., and Fokin, V. V. (2004) Polytriazoles as copper(I)-stabilizing ligands in catalysis. *Org. Lett. 6*, 2853−2855.

(11) (a) Wang, Q., Lin, T., Tang, L., Johnson, J. E., and Finn, M. G. (2002) Icosahedral virus particles as addressable nanoscale building blocks. *Angew. Chem., Int. Ed. 41*, 459−462. (b) Wang, Q., Raja, K. S., Janda, K. D., Lin, T., and Finn, M. G. (2003) Blue fluorescent antibodies as reporters of steric accessibility in virus conjugates. *Bioconjugate Chem. 14*, 38−

43. (c) Raja, K. S., Wang, Q., and Finn, M. G. (2003) Icosahedral virus particles as polyvalent carbohydrate display platforms. *ChemBioChem 4*, 1348−1351. (d) Smith, J. C., Lee, K.-B., Wang, Q., Finn, M. G., Johnson, J. E., Mrksich, M., and Mirkin, C. A. (2003) Nanopatterning the chemospecific immobilization of cowpea mosaic virus capsid. *Nano Lett. 3*, 883−886.

(12) Raja, K. S., Wang, Q., Gonzalez, M. J., Manchester, M., Johnson, J. E., and Finn, M. G. (2003) Hybrid virus-polymer materials. 1. Synthesis and properties of PEG-decorated cowpea mosaic virus. *Biomacromolecules 4*, 472−476.

(13) Wang, Q., Chan, T. R., Hilgraf, R., Fokin, V. V., Sharpless, K. B., and Finn, M. G. (2003) Bioconjugation by copper(I)-catalyzed azide-alkyne [3+2] cycloaddition. *J. Am. Chem. Soc. 125*, 3192−3193.

(14) Kubas, G. J. (1979) Copper(I) complexes. *Inorg. Synth. 19*, 90−92.

(15) Punna, S., Kuzelka, J., Wang, Q., and Finn, M. G. (2005) Head-to-tail peptide cyclodimerization by copper-catalyzed azide-alkyne cycloaddition. *Angew. Chem., Int. Ed. 44*, 2215−2220.

(16) Wang, Q., Kaltgrad, E., Lin, T., Johnson, J. E., and Finn, M. G. (2002) Natural supramolecular building blocks: Wild-type cowpea mosaic virus. *Chem. Biol. 9*, 805−811.

(17) Lewis, W. G., Magallon, F. G., Fokin, V. V., and Finn, M. G. (2004) Discovery and characterization of catalysts for azide-alkyne cycloaddition by fluorescence quenching. *J. Am. Chem. Soc. 126*, 9152−9153.

(18) See Supporting Information.

(19) Wang, Q., Kaltgrad, E., Lin, T., Johnson John, E., and Finn, M. G. (2002) Natural supramolecular building blocks. Wild-type cowpea mosaic virus. *Chem. Biol. 9*, 805−811.

(20) Strable, E., and Finn, M. G., unpublished work.

(21) (a) Blixt, O., Head, S., Mondala, T., Scanlan, C., Huflejt, M. E., Alvarez, R., Bryan, M. C., Fazio, F., Calarese, D., Stevens, J., Razi, N., Stevens, D. J., Skehel, J. J., Die, I. v., Burton, D. R., Wilson, I. A., Cummings, R., Bovin, N., Wong, C.-H., and Paulson, J. C. (2004) Printed covalent glycan array for ligand profiling of diverse glycan binding proteins. *Proc. Natl. Acad. Sci. U.S.A. 101*, 17033−17038. (b) Huflejt, M. E., and Leffler, H. (2004) Galectin-4 in normal tissues and cancer. *Glycoconjugate J. 20*, 247−255.

(22) Ohyama, C., Tsuboi, S., and Fukuda, M. (1999) Dual roles of sialyl lewis x oligosaccharides in tumor metastasis and rejection by natural killer cells. *EMBO J. 18*, 1516−1525.

(23) Seitz, O. (2000) Glycopeptide synthesis and the effects of glycosylation on protein structure and activity. *ChemBioChem 1*, 214−246.

(24) (a) Zhang, J., Yergey, A., Kowalak, J., and Kovac, P. (1998) Studies towards neoglycoconjugates from the monosaccharide determinant of *Vibrio cholerae*, serotype Ogawa using the diethyl squarate reagent. *Carbohydr. Res. 313*, 15−20. (b) Hossany, R. B., Johnson, M. A., Eniade, A. A., and Pinto, B. M. (2004) Synthesis and immunochemical characterization of protein conjugates of carbohydrate and carbohydrate-mimetic peptides as experimental vaccines. *Bioorg. Med. Chem. 12*, 3743−3754.

(25) Allen, J. R., Allen, J. G., Zhang, X.-F., Williams, L. J., Zatorski, A., Ragupathi, G., Livingston, P. O., and Danishefsky, S. J. (2000) A second generation synthesis of the MBR1 (globo-H) breast tumor antigen: new application of the *n*-pentenyl glycoside method for achieving complex carbohydrate protein linkages. *Chem. Eur. J. 6*, 1366−1375.

(26) (a) Taylor, K. M., Porta, C., Lin, T., Johnson, J. E., Barker, P. J., and Lomonossoff, G. P. (1999) Position-dependent processing of peptides presented on the surface of cowpea mosaic virus. *Biol. Chem. 280*, 387−392. (b) Taylor, K. M., Lin, T., Porta, C., Mosser, A., Giesing, H., Lomonossoff, G. P., and Johnson, J. E. (2000) Influence of 3-dimensional structure on the immunogenicity of a peptide expressed on the surface of a plant virus. *J. Mol. Recognit. 13*, 71−82. (c) Chatterji, A., Burns, L. L., Taylor, S. S., Lomonossoff, G. P., Johnson, J. E., Lin, T., and Porta, C. (2002) Cowpea mosaic virus: From the presentation of antigenic peptides to the display of active biomaterials. *Intervirology 45*, 362−370.

(27) (a) Dawson, P. E., Muir, T. W., Clark-Lewis, I., and Kent, S. B. H. (1994) Synthesis of proteins by native chemical ligation. *Science 266*, 776−779. (b) Dawson, P. E., and Kent, S. B. H. (2000) Synthesis of native proteins by chemical ligation. *Annu. Rev. Biochem. 69*, 923−960.

(28) Recently, palladium-catalyzed C−C coupling was employed to attach small molecules to short peptides, but extension to a biological scaffold has not been reported: Dibowski, H., and Schmidtchen, F. P. (1998) *Angew. Chem., Int. Ed. 37*, 476−478.

(29) Nemerow, G. R., and Stewart, P. L. (1999) Role of av integrins in adenovirus cell entry and gene delivery. *Microbiol. Mol. Biol. Rev. 63*, 725−734.

(30) (a) Mogridge, J., Cunningham, K., Lacy, D. B., Mourez, M., and Collier, R. J. (2002) The lethal and edema factors of anthrax toxin bind only to oligomeric forms of the protective antigen. *Proc. Natl. Acad. Sci. U.S.A. 99*, 7045−7048. (b) Cunningham, K., Lacy, D. B., Mogridge, J., and Collier, R. J. (2002) Mapping the lethal factor and edema factor binding sites on oligomeric anthrax protective antigen. *Proc. Natl. Acad. Sci. U.S.A. 99*, 7049−7053. (c) Bradley, K. A., Mogridge, J., Mourez, M., Collier, R. J., and Young, J. A. T. (2001) Identification of the cellular receptor for anthrax toxin. *Nature 414*, 225−229.

(31) (a) Högemann-Savellano, D., Bos, E., Blondet, C., Sato, F., Abe, T., Josephson, L., Weissleder, R., Gaudet, J., Sgroi, D., Peters, P. J., and Basilion, J. P. (2003) The transferrin receptor: a potential molecular imaging marker for human cancer. *Neoplasia 5*, 495−506. (b) Ryschich, E., Huszty, G., Knaebel, H. P., Hartel, M., Buchler, M. W., and Schmidt, J. (2004) Transferrin receptor is a marker of malignant phenotype in human pancreatic cancer and in neuroendocrine carcinoma of the pancreas. *Eur. J. Cancer 40*, 1418−1422. (c) Derycke, A. S. L., Kamuhabwa, A., Gijsens, A., Roskams, T., De Vos, D., Kasran, A., Huwyler, J., Missiaen, L., and de Witte, P. A. M. (2004) Transferrin-conjugated liposome targeting of photosensitizer ALPCS4 to rat bladder carcinoma cells. *J. Nat. Cancer Inst. 96*, 1620−1630.

(32) Chatterji, A., Ochoa, W., Shamieh, L., Salakian, S. P., Wong, S. M., Clinton, G., Ghosh, P., Lin, T., and Johnson, J. E. (2004) Chemical conjugation of heterologous proteins on the surface of cowpea mosaic virus. *Bioconjugate Chem. 15*, 807−813.

(33) See the following four samples of the vast literature reporting the use of NCL reactions for preparative purposes. (a) Dawson, P. E., Churchill, M. J., Ghadiri, M. R., and Kent, S. B. H. (1997) Modulation of reactivity in native chemical ligation through the use of thiol additives. *J. Am. Chem. Soc. 119*, 4325−4329. (b) Xu, R., Ayers, B., Cowburn, D., and Muir, T. W. (1999) Chemical ligation of folded recombinant proteins: segmental isotopic labeling of domains for NMR studies. *Proc. Nat. Acad. Sci. U.S.A. 96*, 388−393. (c) Offer, J., Boddy, C. N. C., and Dawson, P. E. (2002) Extending synthetic access to proteins with a removable acyl transfer auxiliary. *J. Am. Chem. Soc. 124*, 4642−4646. (d) Bang, D., and Kent, S. B. H. (2005) His_6 tag-assisted chemical protein synthesis. *Proc. Nat. Acad. Sci. U.S.A. 102*, 5014−5019.

(34) Native chemical ligation and azide-alkyne cycloaddition reactions have been combined in the synthesis of lipoprotein analogues: Bausinger, R., Zumbusch, A., Bertsch, U., and Moroder, L. (2005) Toward semisynthetic lipoproteins by convergent strategies based on click and ligation chemistry. *ChemBioChem 6*, 625−628.

(35) (a) Wang, L., and Schultz, P. G. (2001) A general approach for the generation of orthogonal trnas. *Chem. Biol. 8*, 883−890. (b) Deiters, A., Cropp, T. A., Mukherji, M., Chin, J. W., Anderson, J. C., and Schultz, P. G. (2003) Adding amino acids with novel reactivity to the genetic code of *Saccharomyces cerevisiae*. *J. Am. Chem. Soc. 125*, 11782−11783. (c) Feng, T., Tsao, M. L., and Schultz, P. G. (2004) A phage display system with unnatural amino acids. *J. Am. Chem. Soc. 126*, 15962−15963. (d) Kwon, I., Kirshenbaum, K., and Tirrell, D. A. (2003) Breaking the degeneracy of the genetic code. *J. Am. Chem. Soc. 125*, 7512−7513. (e) Link, A. J., and Tirrell, D. A. (2003) Cell surface labeling of *Escherichia coli* via copper-(I)-catalyzed [3+2] cycloaddition. *J. Am. Chem. Soc. 125*,

11164−11165. (f) Saxon, E. and Bertozzi, C. R. (2000) Cell surfaceengineering by a modified Staudinger reaction. *Science 287*, 2007−2010. (g) Hang, H. C., Yu, C., Kato, D. L., and Bertozzi, C. R. (2003) A metabolic labeling approach toward proteomic analysis of mucin-type O-linked glycosylation. *Proc. Natl. Acad. Sci. U.S.A. 100*, 14846−14851.

BC050147L

Effect of Coligands on Biodistribution Characteristics of Ternary Ligand ^{99m}Tc Complexes of a HYNIC-Conjugated Cyclic RGDfK Dimer

Shuang Liu,*,† Wen-Yuan Hsieh,† Young-Seung Kim,† and Sulma I. Mohammed‡

Department of Industrial and Physical Pharmacy, School of Pharmacy, Purdue University, 575 Stadium Mall Drive, West Lafayette, Indiana 47907, and Veterinary Pathobiology, Veterinary School of Medicine, Purdue Cancer Center Drug Discovery Shared Resource, Purdue University, West Lafayette, Indiana 47907
Received June 13, 2005; Revised Manuscript Received September 16, 2005

This report describes biodistribution characteristics of three ternary ligand complexes [^{99m}Tc(SQ168)-(tricine)(L)] (SQ168 = [2-[[[5-[carboonyl]-2-pyridinyl]hydrazono]methyl]-benzenesulfonic acid]-Glu-(cyclo{Lys-Arg-Gly-Asp-D-Phe})-cyclo{Lys-Arg-Gly-Asp-D-Phe}; L = TPPTS (trisodium triphenylphosphine-3,3′,3″-trisulfonate), ISONIC (isonicotinic acid) and PDA (2,5-pyridinedicarboxylic acid)) in athymic nude mice bearing MDA-MB-435 human breast cancer xenografts. Ternary ligand complexes [^{99m}Tc(SQ168)(tricine)(L)] (L = TPPTS, ISONIC and PDA) were prepared and were analyzed by a reversed HPLC method. Surprisingly, coligands have little impact on log *P* values of their ternary ligand ^{99m}Tc complexes even though HPLC retention times suggest that [^{99m}Tc(SQ168)(tricine)(PDA)] and [^{99m}Tc(SQ168)(tricine)(ISONIC)] are more hydrophilic than [^{99m}Tc(SQ168)(tricine)(TPPTS)]. The results from biodistribution studies indicated that excretion kinetics of the ^{99m}Tc-labeled cyclic RGDfK dimer can be modified by the choice of coligand. The fact that all three radiotracers show high tumor uptake during the 2 h study period suggests that the coligand has minimal effect on the tumor targeting capability of the ^{99m}Tc-labeled cyclic RGDfK dimer. Results from the blocking experiment suggest that the tumor localization of the ^{99m}Tc-labeled cyclic RGDfK dimer is integrin $\alpha_v\beta_3$-mediated. On the basis of their liver uptake and tumor/liver ratios, we believe that PDA has the advantage over TPPTS and ISONIC for the ^{99m}Tc-labeling of HYNIC−biomolecule conjugates.

INTRODUCTION

For the last several years, we have been using cyclic RGD peptide dimers, such as E[c(RGDfK)]$_2$, for development of the integrin $\alpha_v\beta_3$-targeted diagnostic (^{64}Cu, ^{99m}Tc and ^{111}In) and therapeutic (^{90}Y and ^{177}Lu) radiopharmaceuticals (*1*−*10*). For the ^{99m}Tc-labeling, we have been using 6-hydrazinonicotinic acid (HYNIC) as the bifunctional coupling agent, and tricine and a water-soluble phosphine or pyridine analogue as coligands to prepare ternary ligand complexes [^{99m}Tc(HYNIC−BM)-(tricine)(L)] (Figure 1: BM = biomolecule; L = TPPDS, TPPMS, ISONIC, NIC, PA, PDA and PSA) (*11*−*21*). In these complexes, the ^{99m}Tc chelate (HYNIC, tricine and L) contributes greatly to their overall molecular weight and charge. It was reported that the use of different phosphine coligands caused a significant change in both distribution patterns and excretion routes of the ^{99m}Tc-labeled GPIIb/IIIa receptor antagonist (*12*). Similar coligand effects have also been observed for a variety of binary and ternary ligand ^{99m}Tc complexes of HYNIC-conjugated small biomolecules, including chemotactic peptides (*22*, *23*), somatostatin analogues (*24*−*26*), antisense DNA (*27*), interleukin-8 (*28*) and cholecystokinin (CCK8) peptides (29). It was found that the combination of tricine with NIC reduced the protein binding of the ^{99m}Tc-labeled HYNIC-conjugates (*30*−*32*). The complex [^{99m}Tc(HYNIC−IL-8)(tricine)(NIC)] (IL-8 = interleukin-8) was shown to have the highest abscess uptake (~6.5 ± 1.3% ID/g at 6 h postinjection) and abscess/muscle ratio (248 ± 69) while the use of TPPTS as coligand resulted in the complex [^{99m}Tc(HYNIC−IL-8)(tricine)(TPPTS)] with a significant reduction of receptor binding affinity, low abscess uptake (1.1 ± 0.1% ID/g at 6 h postinjection), and high liver uptake (0.28 ± 0.01% ID/g at 6 h postinjection) (*29*). It was also found that the combination of tricine with NIC gave the best ^{99m}Tc-labeling efficiency, tumor uptake and excretion characteristics for the ^{99m}Tc-labeled cholecystokinin (CCK8) peptides (*29*).

In our previous communication (*1*), we reported the ^{99m}Tc-labeled cyclic RGDfK peptide dimer (Figure 2: SQ168 = [2-[[[5-[carboonyl]-2-pyridinyl]hydrazono]methyl]benzenesulfonic acid]-Glu(cyclo{Lys-Arg-Gly-Asp-D-Phe})-cyclo{Lys-Arg-Gly-Asp-D-Phe}). We prepared [^{99m}Tc(SQ168)(tricine)(TPPTS)] and its ^{99}Tc analogue, [^{99}Tc(SQ168)(tricine)(TPPTS)] using tricine and TPPTS as coligands. We found that [^{99m}Tc(SQ168)(tricine)-(TPPTS)] was stable and exists in solution as two detectable diastereomers. [^{99}Tc(SQ168)(tricine)(TPPTS)] has the integrin $\alpha_v\beta_3$ binding affinity comparable to that of SQ168 in an in vitro assay, suggesting that attachment of the Tc chelate had minimal effect on the integrin $\alpha_v\beta_3$ binding affinity (*1*).

As an extension of our previous studies, we evaluated the biodistribution characteristics of three ternary ligand complexes [^{99m}Tc(SQ168)(tricine)(L)] (L = TPPTS, ISONIC, and PDA) in athymic nude mice bearing the MDA-MB-435 human breast cancer xenografts. The objective of this study is to explore the impact of coligands (TPPTS, ISONIC and PDA) on the tumor uptake, excretion

* To whom correspondence should be addressed. Phone: 765-494-0236; fax 765-496-3367; e-mail: lius@pharmacy.purdue.edu.
† Department of Industrial and Physical Pharmacy.
‡ Veterinary Pathobiology.

10.1021/bc0501653 CCC: $30.25 © 2005 American Chemical Society
Published on Web 10/25/2005

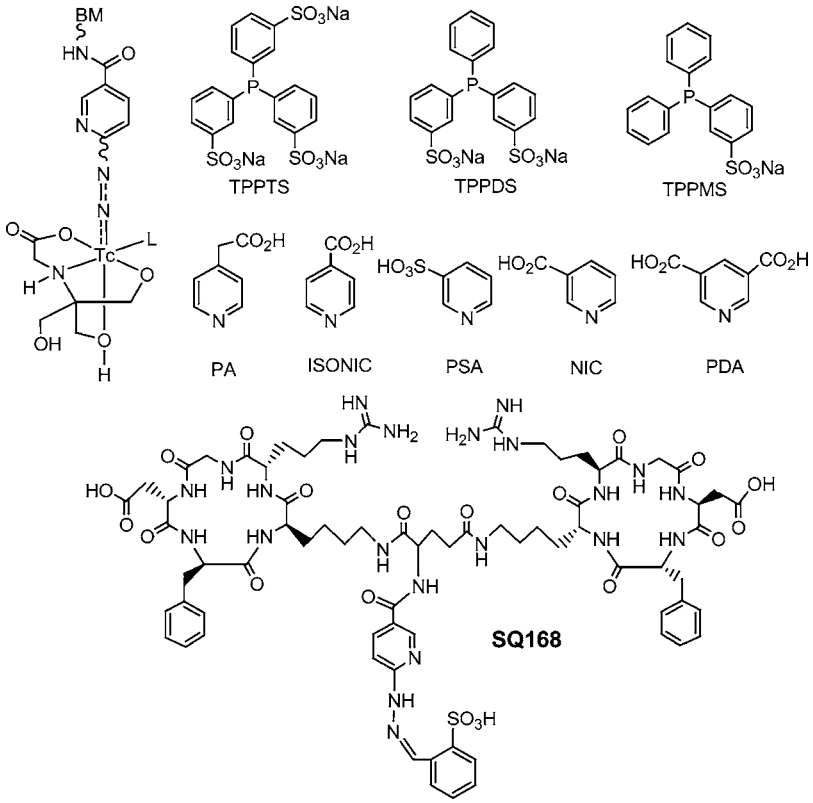

Figure 1. Structures of coligands and their ternary ligand complexes [^{99m}Tc(HYNIC−BM)(tricine)(L)] (BM = biomolecule; L = TPPTS, TPPDS, TPPMS, ISONIC, NIC, PA, PDA and PSA). SQ168 is a HYNIC-conjugated cyclic RGDfK dimer.

kinetics and metabolic fate of the ^{99m}Tc-labeled cyclic RGDfK dimer. Results from biodistribution studies will allow us to select an optimal coligand (TPPTS, ISONIC or PDA) for the ^{99m}Tc-labeling of cyclic RGDfK dimer or other HYNIC-conjugated biomolecules.

EXPERIMENTAL SECTION

Materials. Dicyclcohexylcarbodiimide (DCC), *N*-hydroxysuccinimide (NHS), isonicotinic acid (ISONIC), 1,5-pyridinedicarboxylic acid (PDA), succinic acid, trisodium triphenylphosphine-3,3′,3″-trisulfonate (TPPTS), and tricine were purchased from Aldrich Chemical Co. The cyclic pentapeptide, cyclo(RGDfK), was prepared according to the literature method (*33*). Na^{99m}TcO$_4$ was obtained from a commercial DuPont Pharma ^{99}Mo/^{99m}Tc generator, N. Billerica, MA.

Instruments and Methods. The NMR (^{1}H and ^{13}C) data were obtained using a Bruker ARX 300 MHz FT NMR spectrometer, and chemical shifts as δ are reported in ppm relative to TMS. Mass spectral data were collected on a Finnigan LCQ classic mass spectrometer, School of Pharmacy, Purdue University. The semi-prep HPLC method (Method 1) used a LabAlliance semi-prep HPLC system equipped with a UV/vis detector (λ = 254 nm) and Zorbax C$_{18}$ semi-prep column (9.4 mm × 250 mm, 100 Å pore size) for peptide purification. The flow rate was 2.5 mL/min. The mobile phase was isocratic with 90% solvent A (0.1% acetic acid in water) and 10% solvent B (0.1% acetic acid in acetonitrile) at 0−5 min, followed by a gradient mobile phase going from 90% solvent A and 10% solvent B at 5 min to 60% solvent A and 40% solvent B at 20 min. The radio-HPLC method (Method 2) used the LabAlliance HPLC system equipped with a β-ram IN-US detector and Zorbax C$_{18}$ column (4.6 mm × 250 mm, 300 Å pore size). The flow rate was 1 mL/min. The mobile phase was isocratic with 90% solvent A (25 mM ammonium acetate buffer, pH = 5.0) and 10% solvent B (acetonitrile) at 0−2 min, followed by a gradient mobile phase going from 10% solvent B at 2 min to 15% solvent B at 5 min and to 20% solvent B at 20 min.

Synthesis of Boc-Glu(OSu)$_2$. To a solution of the Boc-protected glutamic acid (0.247 g, 1.0 mmol) in 5 mL *N*,*N*-dimethylforamide (DMF) were added *N*-hydroxysuccinimide (0.253 g, 2.2 mmol) and DCC (0.453 g, 2.2 mmol). The mixture was stirred at room temperature for 10 h. After filtration, the filtrate was evaporated to dryness to give crude product, which was then taken up in 3 mL of methylene chloride. The insoluble solid was filtered off. The filtrate was concentrated to about 1 mL. The solution was added dropwise into 30 mL of diethyl ether. The desired product was precipitated as white solid, which was dried in vacuo. The yield was 0.27 g (∼61%). ^{1}H NMR (in CDCl$_3$): 5.23 (br s, 1H, NH), 4.82 (m, 1H, CH), 2.85 (m, 8H, succinimide group), 2.44−2.25 (m, 2H, CH$_2$CO), 1.52 (m, 2H, *CH*$_2$CH$_2$CO), 1.46 (s, 9H, *t*-Bu).

Synthesis of Cyclic RGDfK Peptide Dimer E[c(RGDfK)]$_2$. Boc-Glu(OSu)$_2$ (24.7 mg, 100 μmol) and c(RGDfK) (124 mg, 205 μmol) were dissolved in dry DMF (2 mL). Upon addition of triethylamine (1 mmol), the reaction mixture was stirred at room-temperature overnight. The mixture was diluted with 3 mL of 0.5 M ammonium acetate buffer (pH = 5.0), and the resulting solution was filtered with a Millex-LG syringe driven filter unit to remove any precipitate or particles. The product was separated by HPLC (Method 1). Collections of the fraction at 15 min were combined. Lyophilization of the solution gave a white powder. The yield was ∼75%. ES-MS for Boc-E[c(RGDfK)]$_2$: *m/z* = 1419 for [M + H]$^+$ (C$_{64}$H$_{95}$N$_{19}$O$_{18}$) and 710.3 for [M + 2H]$^{2+}$. Boc-E[c(RGDfK)]$_2$ (50 mg) was dissolved in anhydrous TFA (1.0 mL), and was stirred at room temperature for 5 min. Excess

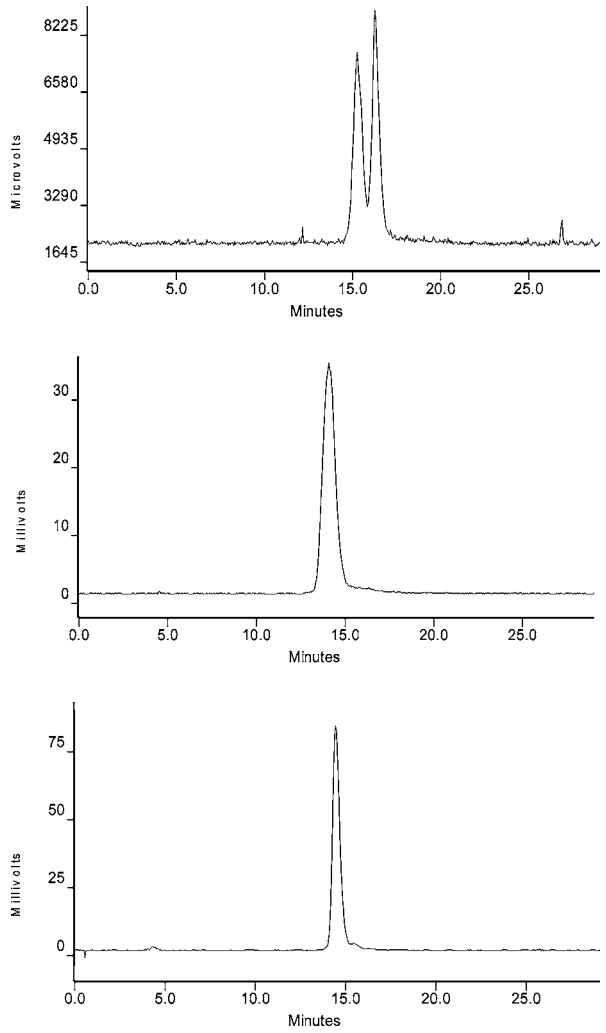

Figure 2. Radio-HPLC chromatograms of [^{99m}Tc(SQ168)-(tricine)(TPPTS)] (top) and [^{99m}Tc(SQ168)(tricine)(ISONIC)] (middle) and [^{99m}Tc(SQ168)(tricine)(PDA)] (bottom) using Method 2.

TFA was removed under reduced pressure and the residue was purified by HPLC (Method 1). Collections of the fraction at ~12 min were combined, and the combined solution was then lyophilized give a white powder. The yield was 28 mg (~60%) with the purity > 95% by HPLC (Method 1). ES-MS for E[c(RGDfK)]$_2$: m/z = 1319.5 for $[M + H]^+$ ($C_{59}H_{87}N_{19}O_{16}$).

Synthesis of HYNIC-E[c(RGDfK)]$_2$ (SQ168). HYNIC-OSu was prepared according to literature method (*34*). HYNIC-OSu (4.17 mg, 10 μmol) and E[c(RGDfK)]$_2$ (14.0 mg, 10.6 μmol) were dissolved in a mixture of DMF and water (50:50 = v:v). The pH was adjusted to 8.5−9.0 with 0.1 N NaOH. The reaction mixture was allowed to incubate overnight at room temperature. The product was purified by HPLC (Method 1). The peak of interest at ~14 min was collected. The collected fractions were combined. Lyophilization of the solution gave a pale yellow powder. The yield was 11 mg (~65%) with the purity > 95% by HPLC (Method 1). The HPLC retention time was 14.5 min (Method 1). ES-MS for HYNIC-E[c(RGDfK)]$_2$ (SQ168): m/z = 1621.7 for $[M + H]^+$ ($C_{72}H_{97}N_{22}O_{20}S$).

Synthesis of [^{99m}Tc(SQ168)(tricine)(TPPTS)]. To a vial filled with 1.0 mL of a solution containing 5 mg of TPPTS, 6.5 mg of tricine, 40 mg of mannitol, 38.5 mg of disodium succinate hexahydrate, and 12.7 mg of succinic acid (pH = 4.8) were added 0.2 mL of SQ168 solution (100 μg/mL in water) and 0.3 mL of Na[^{99m}TcO$_4$] solution (30 mCi/mL) in saline. The vial was heated at 100 °C for 10−25 min in a lead-shielded water bath. After heating, the vial was placed back into the lead pig and allowed to stand at room temperature for ~10 min. A sample of the resulting solution was analyzed by the radio-HPLC. The radiochemical purity (RCP) was >95%. The HPLC retention time was ~15.5 min (Method 2).

Synthesis of [^{99m}Tc(SQ168)(tricine)(ISONIC)]. To a clean vial filled with 1.0 mL of a solution containing 15 mg of ISONIC, 20 mg of tricine, 38.5 mg of disodium succinate hexahydrate, and 12.7 mg of succinic acid (pH = 4.8) were added 0.2 mL of SQ168 solution (100 μg/mL in water) and 0.3 mL of Na[^{99m}TcO$_4$] solution (30−60 mCi/mL) in saline. The vial was sealed and heated at 100 °C for 15 min. A sample of the resulting solution was analyzed by radio-HPLC. The RCP was >95%. The HPLC retention time was ~15.5 min (Method 2). The solution stability of [^{99m}Tc(SQ168)(tricine)(ISONIC)] was monitored by radio-HPLC for 24 h.

Synthesis of [^{99m}Tc(SQ168)(tricine)(PDA)]. To a clean vial filled with 1.0 mL of solution containing 15 mg of PDA, 20 mg of tricine, 38.5 mg of disodium succinate hexahydrate, and 12.7 mg of succinic acid (pH = 4.8) were added 0.2 mL of SQ168 solution (100 μg/mL in water) and 0.3 mL of Na[^{99m}TcO$_4$] solution (30−60 mCi/mL) in saline. The vial was sealed and heated at 100 °C for 15 min. A sample of the resulting solution was analyzed by radio-HPLC. The RCP was >95%. The HPLC retention time was ~15.5 min (Method 2). The solution stability of [^{99m}Tc(SQ168)(tricine)(PDA)] was monitored by radio-HPLC for 24 h.

Doses Preparation for Animal Studies. Doses for animal studies were prepared by dissolving the HPLC-purified ternary ligand complex [^{99m}Tc(SQ168)(tricine)-(L)] (L = TPPTS, ISONIC and PDA) in saline to give a concentration of ~10 μCi/mL. For the blocking experiment, E[c(RGDfK)]$_2$ was used as the blocking agent. Doses were prepared by dissolving E[c(RGDfK)]$_2$ in the solution containing [^{99m}Tc(SQ168)(tricine)(ISONIC)] (~10 μCi/mL) to give a final concentration of 7.5 mg/mL. Each tumor-bearing mouse was injected with 0.1 mL of solution, which corresponds to a dose of 30 mg/kg.

Determination of Log *P* Values. Log *P* values of complexes [^{99m}Tc(SQ168)(tricine)(L)] (L = TPPTS, ISONIC and PDA) were determined using the following procedure: the ternary ligand complex [^{99m}Tc(SQ168)-(tricine)(L)] (L = TPPTS, ISONIC and PDA) was prepared and purified by HPLC. Volatiles were removed under reduced pressure, and the residue was dissolved in a mixture of equal volume (3 mL:3 mL) of *n*-octanol and 25 mM phosphate buffer (pH = 7.4). After vertex mixing for at least 20 min, samples (in triplets) from *n*-octanol and aqueous layers were counted in a gamma counter (Beckman Gama 8000). Partition coefficients were calculated using the following equation: P = (activity concentration in *n*-octanol)/(activity concentration in aqueous layer). The log P value was measured three different times and reported as an average of three different measurements.

Animal Studies. Biodistribution and imaging studies were performed according to the literature procedures (*3*). These studies were carried out using the athymic nude mice bearing the MDA-MB-435 human breast cancer xenografts in compliance NIH animal experiment guidelines (*Principles of Laboratory Animal Care*, NIH Publication No. 86-23, revised 1985). The animal protocol for the animal studies has been approved by the Purdue University Animal Care and Use Committee (PACUC).

Table 1. Biodistribution Data of [^{99m}Tc(SQ168)(tricine)(TPPTS)] in Athymic Nude Mice Bearing MDA-MB-435 Human Breast Cancer Xenografts[a]

organ	5 min	30 min	60 min	120 min
tumor	3.50 ± 0.18	3.59 ± 0.24	3.38 ± 0.40	3.82 ± 0.29
blood	2.70 ± 0.12	1.66 ± 0.15	1.60 ± 0.36	0.52 ± 0.06
heart	2.75 ± 0.18	2.40 ± 0.72	2.49 ± 0.35	2.08 ± 0.21
lungs	4.83 ± 0.18	4.79 ± 0.61	4.19 ± 0.30	2.83 ± 0.38
liver	4.75 ± 0.21	4.30 ± 0.28	4.12 ± 0.47	3.11 ± 0.18
spleen	4.44 ± 0.23	3.53 ± 0.25	2.74 ± 0.29	2.39 ± 0.45
kidney	24.15 ± 1.23	21.36 ± 3.68	15.89 ± 2.89	14.33 ± 2.39
brain	0.19 ± 0.01	0.21 ± 0.11	0.18 ± 0.02	0.17 ± 0.03
muscle	2.61 ± 0.09	2.60 ± 0.77	1.43 ± 0.37	1.37 ± 0.17
eyes	1.84 ± 0.27	1.63 ± 0.13	1.65 ± 0.12	1.39 ± 0.13
intestine	8.26 ± 1.32	6.20 ± 0.42	6.00 ± 0.80	4.93 ± 0.20

[a] The organ uptake is expressed %ID/g. Each data point represents an average of biodistribution data in four animals.

Tumor-Bearing Mice. Female athymic nu/nu mice were purchased from Harlan (Indianapolis, IN) at 4−5 weeks of age. The mice were orthotopically implanted with 5×10^6 cells of MDA-MB-435 estrogen receptor-negative human breast cancer cells into the mammary fat pad. Tumor cells were grown at 37 °C in Minimal Essential Medium (Alpha Modification) containing 3.7 g of sodium bicarbonate/L and 10% fetal bovine serum v/v, in a humidified atmosphere of 5% carbon dioxide. Four weeks after inoculation, animals were used for biodistribution studies.

Biodistribution. Sixteen tumor-bearing mice (20−25 g) were anesthetized with ip injection of ketamine (40−100 mg/kg) and xylazine (2−5 mg/kg). Once the animal was in the surgical plane of anesthesia, as noted by lack of pain response, the radiotracer (∼1 μCi) dissolved in 0.1 mL of saline was administered via the tail vein. Four animals were sacrificed by exsanguinations and opening of thoracic cavity at 5, 30, 60, and 120 min postinjection. Organs were excised, washed with saline, weighed, and counted on a gamma counter. Organs of interest included tumor, blood, brain, eyes, spleen, lungs, liver, kidneys, muscle and intestine. The organ uptake was calculated as a percentage of the injected dose per organ (%ID/organ) and a percentage of the injected dose per gram of wet tissue (%ID/g). For the blocking experiment, four tumor-bearing mice (20−25 g) were used, and each animal was administered with 0.1 mL of saline solution containing ∼1 μCi of the test agent and 750 μg (∼ 30 mg/kg) of E[c(RGDfK)]$_2$, a known integrin $\alpha_v\beta_3$ antagonist. At 1 h postinjection, all four animals were sacrificed for organ biodistribution using the same procedure above. The results were compared to those obtained in animals without the coinjection of E[c(RGDfK)]$_2$. Biodistribution data were analyzed using the one-way ANOVA test, and the level of significance was set at $p = 0.05$ (Tables 1−3).

Metabolism. Each tumor-bearing mouse was administered with the radiotracer at a dose of 100 μCi/mice. The urine samples were collected at 2 h postinjection by manual void and were mixed with equal volume of acetonitrile. The mixture was centrifuged at 8000 rpm. The supernatant was collected and filtered through a 0.20 μm Millex-LG syringe driven filter unit. The filtrate was analyzed by radio-HPLC. The feces samples were collected at ∼120 min postinjection. The sample was suspended in a mixture of 50% acetonitrile aqueous solution, and the resulting mixture was vertexed for 5−10 min. After centrifugation, the supernatant was collected and passed through a 0.20 μm Millex-LG syringe driven filter unit. The filtrate was analyzed by radio-HPLC.

RESULTS AND DISCUSSION

Synthesis and HPLC Analysis. Synthesis of SQ168 was straightforward by conjugation of the Boc-protected bis(*N*-hydroxysuccinmide) glutamic acid ester with 2 equiv of c(RGDfK), followed by TFA deprotection of the Boc-protecting group and conjugation with HYNIC-OSu in a mixture of water and DMF. SQ168 was purified before being used for the ^{99m}Tc-labeling. Ternary ligand ^{99m}Tc complexes [^{99m}Tc(SQ168)(tricine)(L)] (L = TPPTS, ISONIC and PDA) were prepared according to literature methods (*1*, *13*) and were analyzed using a reversed phase radio-HPLC method (Method 2). Figure 2 shows their typical HPLC chromatograms. Using this method, the HPLC retention times were 16.5, 14.0 and 14.5 min for [^{99m}Tc(SQ168)(tricine)(TPPTS)], [^{99m}Tc(SQ168)(tricine)(ISONIC)] and [^{99m}Tc(SQ168)(tricine)(PDA)], respectively. It seems that [^{99m}Tc(SQ168)(tricine)(ISONIC)] and [^{99m}Tc(SQ168)(tricine)(PDA)] are more hydrophilic than [^{99m}Tc(SQ168)(tricine)(TPPTS)] according to their HPLC retention times.

To further explore the impact of coligands on lipophilicity of their ternary ligand complexes [^{99m}Tc(SQ168)(tricine)(L)] (L = TPPTS, ISONIC and PDA), we also determined their distribution coefficients in a mixture of *n*-octanol and 25 mM phosphate buffer (pH = 7.4). The log *P* values are −2.66 ± 0.25, −2.70 ± 0.24 and −2.62 ± 0.17 for [^{99m}Tc(SQ168)(tricine)(TPPTS)], [^{99m}Tc(SQ168)(tricine)(ISONIC)] and [^{99m}Tc(SQ168)(tricine)(PDA)], respectively. Surprisingly, there is no significant difference in log *P* values of three radiotracers within the experimental error, even though their HPLC retention times suggest that [^{99m}Tc(SQ168)(tricine)(ISONIC)] and [^{99m}Tc(SQ168)(tricine)(PDA)] might be more hydrophilic than [^{99m}Tc(SQ168)(tricine)(TPPTS)]. This is probably related to the low pH value of the HPLC mobile phase. Complexes [^{99m}Tc(SQ168)(tricine)(L)] (L = TPPTS, ISONIC and PDA) may have different degrees of protonation in the HPLC mobile phase (pH = 5.0 in the 25 mM

Table 2. Biodistribution Data of [^{99m}Tc(SQ168)(tricine)(ISONIC)] in Athymic Nude Mice Bearing MDA-MB-435 Human Breast Cancer Xenografts[a]

organ	5 min	30 min	60 min	120 min	60 min/block
tumor	3.71 ± 0.16	3.98 ± 0.50	3.44 ± 0.28	2.96 ± 0.16	0.77 ± 0.07
blood	3.02 ± 0.51	1.61 ± 0.06	0.74 ± 0.20	0.56 ± 0.09	1.58 ± 0.16
heart	2.32 ± 0.20	1.90 ± 0.23	1.34 ± 0.25	1.15 ± 0.45	0.87 ± 0.09
lungs	5.37 ± 0.40	3.64 ± 0.74	2.69 ± 0.31	1.72 ± 0.25	1.31 ± 0.21
liver	5.11 ± 0.24	3.41 ± 0.38	2.35 ± 0.46	2.76 ± 0.27	0.72 ± 0.05
spleen	2.75 ± 0.33	2.50 ± 0.66	2.06 ± 0.25	2.00 ± 0.25	0.52 ± 0.09
kidney	20.73 ± 3.82	11.57 ± 1.13	8.38 ± 0.55	6.11 ± 1.68	5.86 ± 1.08
brain	0.24 ± 0.05	0.21 ± 0.02	0.16 ± 0.02	0.11 ± 0.03	0.12 ± 0.09
muscle	3.32 ± 1.21	2.26 ± 0.31	2.15 ± 0.36	0.94 ± 0.35	0.92 ± 0.39
eyes	4.41 ± 0.52	1.46 ± 0.10	0.91 ± 0.20	0.76 ± 0.24	0.55 ± 0.30
intestine	6.96 ± 1.49	4.80 ± 0.16	3.53 ± 0.52	3.23 ± 0.87	0.64 ± 0.11

[a] The organ uptake is expressed %ID/g. Each data point represents an average of biodistribution data in four animals.

Table 3. Biodistribution Data of [^{99m}Tc(SQ168)(tricine)(PDA)] in the Athymic Nude Mice Bearing the MDA-MB-435 Human Breast Cancer Xenografts[a]

organ	5 min	30 min	60 min	120 min
tumor	3.51 ± 0.49	3.69 ± 0.25	4.77 ± 0.19	4.35 ± 0.33
blood	2.62 ± 0.30	2.01 ± 0.09	0.85 ± 0.24	0.39 ± 0.10
heart	2.79 ± 0.33	2.62 ± 0.43	1.51 ± 0.24	1.39 ± 0.17
lungs	3.63 ± 0.16	4.43 ± 0.48	3.62 ± 0.56	2.65 ± 0.01
liver	3.28 ± 0.27	3.61 ± 0.38	3.12 ± 0.50	1.99 ± 0.20
spleen	2.43 ± 0.39	2.87 ± 0.17	2.08 ± 0.48	1.58 ± 1.23
kidney	27.56 ± 3.61	19.25 ± 4.98	9.78 ± 0.82	8.44 ± 0.45
brain	0.24 ± 0.05	0.23 ± 0.01	0.19 ± 0.04	0.14 ± 0.01
muscle	1.00 ± 0.13	1.97 ± 0.45	1.65 ± 0.38	1.39 ± 0.15
eyes	1.22 ± 0.36	1.35 ± 0.50	1.45 ± 0.50	1.09 ± 0.14
intestine	4.63 ± 0.64	5.59 ± 0.76	4.52 ± 0.35	3.54 ± 0.22

[a] The organ uptake is expressed %ID/g. Each data point represents an average of biodistribution data in four animals.

succinate buffer) as compared to pH 7.4 for the log *P* value determination

It is interesting to note that [^{99m}Tc(SQ168)(tricine)(TPPTS)] always shows two peaks due to its two diastereomers, which are formed because of chiral centers on the Tc chelate and the RGDfK dimer (*1*). However, ternary ligand complexes [^{99m}Tc(SQ168)(tricine)(ISONIC)] and [^{99m}Tc(SQ168)(tricine)(PDA)] show only one radiometric peak under the same chromatographic conditions (Figure 2). Attempts to separate diastereomers of [^{99m}Tc(SQ168)(tricine)(ISONIC)] and [^{99m}Tc(SQ168)(tricine)(PDA)] were not successful most likely due to the fact that the size of Tc chelate becomes much smaller with ISONIC and PDA as coligands, and two diastereomers are more difficult to separate than those of [^{99m}Tc(SQ168)(tricine)(TPPTS)].

Solution Stability. The solution stability of [^{99m}Tc(SQ168)(tricine)(TPPTS)] has been described in our previous report (*1*). [^{99m}Tc(SQ168)(tricine)(TPPTS)] is stable for at least 12 h even in the presence of cysteine. The solution stability of [^{99m}Tc(SQ168)(tricine)(ISONIC)] and [^{99m}Tc(SQ168)(tricine)(PDA)] was monitored by radio-HPLC after purification. It was found that both of them remained stable in the ammonium acetate buffer (pH = 5) for more than 12 h, which is completely consistent with the results obtained from our previous report (*13*) and their in vivo stability in tumor bearing mice as described in this study.

Choice of Animal Model. To evaluate the impact of coligands on biological properties (tumor uptake and excretion kinetics), we performed the biodistribution studies on complexes [^{99m}Tc(SQ168)(tricine)(L)] (L = TPPTS, ISONIC and PDA) using athymic nude mice bearing the MDA-MB-435 human breast cancer xenografts. The orthotopically growing tumors in the axillary mammary fat pad give rise to spontaneous metastasis that resemble the clinical behavior of the original human tumor (*35*, *36*). This animal model has been used for evaluation of radiolabeled RGD peptides (*3*, *37*).

Biodistribution Characteristics. For biodistribution studies, all three radiotracers were purified by HPLC to remove excess "unlabeled" SQ168 that may compete with the radiotracer in binding to the integrin $\alpha_v\beta_3$ expressed in both tumor and normal tissues. The biodistribution data for ternary ligand complexes [^{99m}Tc(SQ168)(tricine)(L)] (L = TPPTS, ISONIC and PDA) are summarized in Tables 1−3. Figure 3 shows the direct comparison of their organ uptake and excretion kinetics of from blood, liver and kidneys at 5, 30, 60 and 120 min postinjection. The T/B ratios in several selected organs are illustrated in Figure 4.

In general, all three radiotracers displayed a rapid clearance via the renal route. Their blood clearance

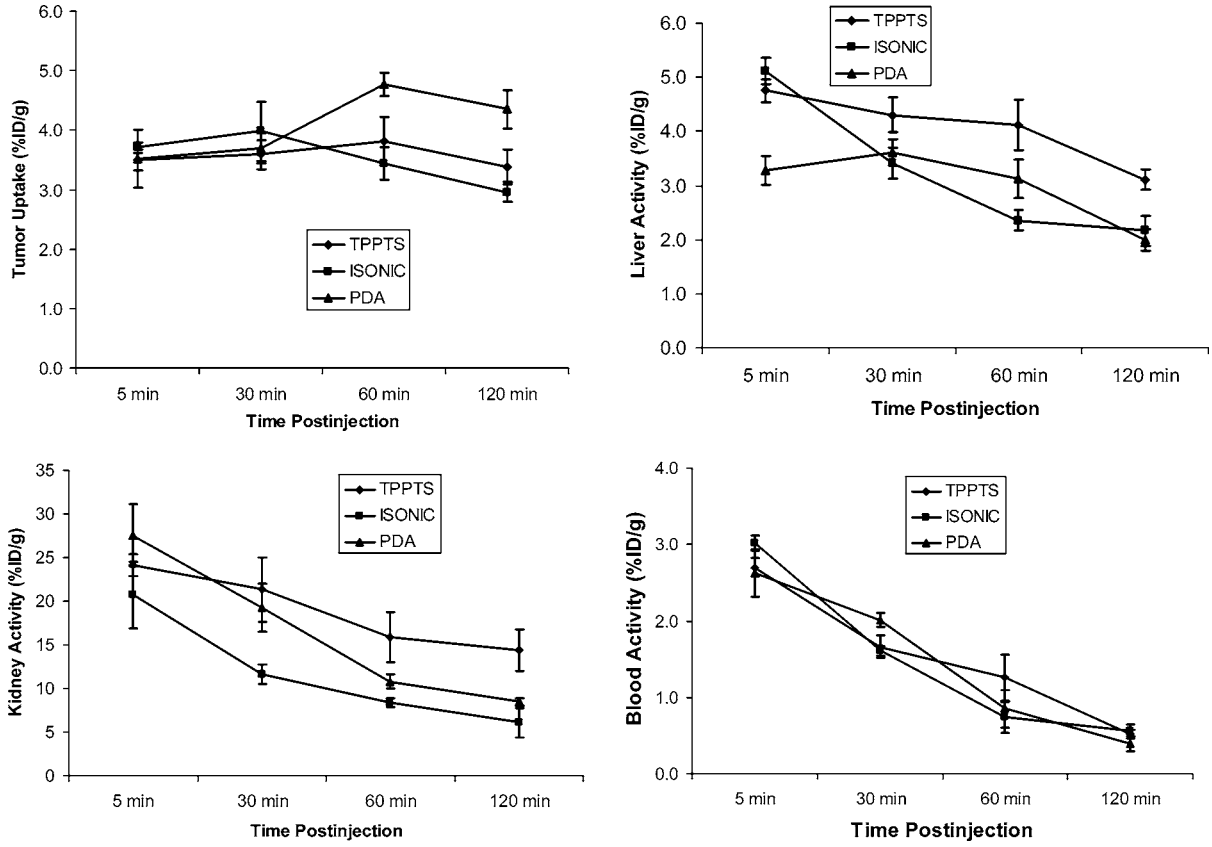

Figure 3. Comparison of excretion kinetics between [^{99m}Tc(SQ168)(tricine)(TPPTS)] (■), [^{99m}Tc(SQ168)(tricine)(ISONIC)] (◆), and [^{99m}Tc(SQ168)(tricine)(PDA)] (▲) in nude mice bearing the MDA-MB-435 human breast cancer xenografts.

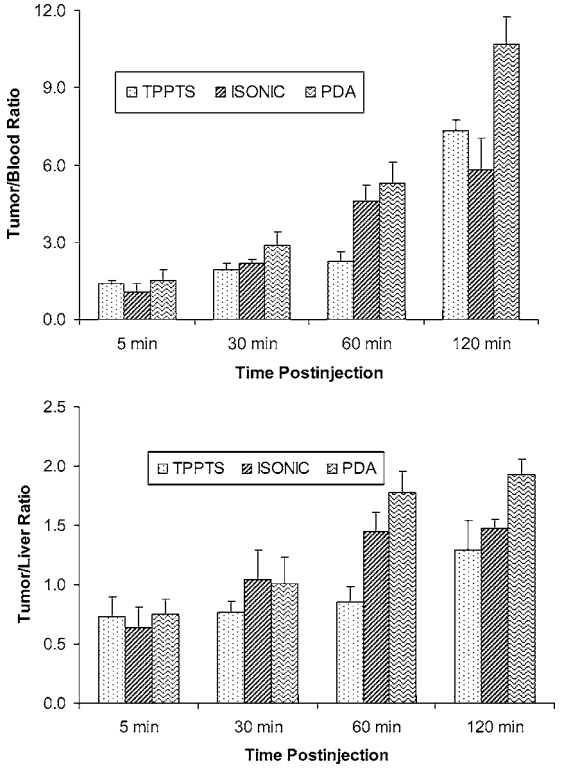

Figure 4. The tumor/background ratios for [^{99m}Tc(SQ168)(tricine)(TPPTS)], [^{99m}Tc(SQ168)(tricine)(ISONIC)], and [^{99m}Tc(SQ168)(tricine)(PDA)] in athymic nude mice bearing MDA-MB-435 human breast cancer xenografts.

curves were almost identical (Figure 3), suggesting that coligands have little impact on their protein binding capability. The tumor uptake of [^{99m}Tc(SQ168)(tricine)(L)] (L = TPPTS, ISONIC and PDA) was comparable at 5−30 min postinjection. While the tumor uptake of [^{99m}Tc(SQ168)(tricine)(TPPTS)] remained relatively unchanged over 2 h, the complex [^{99m}Tc(SQ168)(tricine)(ISONIC)] showed a slow washout between 60 and 120 min postinjection (Figure 3). In contrast, the tumor uptake of [^{99m}Tc(SQ168)(tricine)(PDA)] peaked at 60 min postinjection (4.77 ± 0.19%ID/g), and remained relatively unchanged at 120 min postinjection (4.35 ± 0.33%ID/g). As a result, there was a significant increase in the tumor/blood ratio during 2 h study period (Figure 4). The initial kidney uptake of all three radiotracers was high; but it was significantly lower than that reported for a ^{99m}Tc-labeled cyclic RGDfK peptide monomer (*39*). [^{99m}Tc(SQ168)(tricine)(TPPTS)] was cleared very slowly from kidneys. The kidney clearance of [^{99m}Tc(SQ168)(tricine)(ISONIC)] and [^{99m}Tc(SQ168)(tricine)(PDA)] is much faster. The liver uptake of [^{99m}Tc(SQ168)(tricine)(TPPTS)] was high (4.75 ± 0.21% ID/g at 5 min postinjection), and the liver clearance was slow. [^{99m}Tc(SQ168)(tricine)(ISONIC)] also showed a higher initial liver uptake (5.41 ± 0.24%ID/g at 5 min postinjection), but it cleared faster from the liver than [^{99m}Tc(SQ168)(tricine)(TPPTS)]. [^{99m}Tc(SQ168)(tricine)(PDA)] had a lower liver uptake than [^{99m}Tc(SQ168)(tricine)(TPPTS)] at all four time points. As a result, it has a better tumor/liver ratio than [^{99m}Tc(SQ168)(tricine)(TPPTS)] at 120 postinjection (Figure 4).

Excess E[c(RGDfK)]$_2$ on Biodistribution Characteristics. The blocking experiment by coinjecting a known receptor ligand is often used to demonstrate the tumor-specificity of a radiotracer (*3*, *38*). In this study, we used E[c(RGDfK)]$_2$ (~30 mg/kg corresponding to ~750 μg/mouse), the IC$_{50}$ value of which was 15.1 ± 1.1 nM against ^{125}I-echistatin binding to integrin $\alpha_v\beta_3$ on U87MG tumor cells (*38*), as the blocking agent. We used such as a high dose to make sure that integrin $\alpha_v\beta_3$ is almost completely blocked. Figure 5 shows a comparison of organ uptake for [^{99m}Tc(SQ168))(tricine)(NIC)] at 60 min postinjection with/without the excess E[c(RGDfK)]$_2$. Obviously, coinjection of excess E[c(RGDfK)]$_2$ resulted in a significant reduction in the uptake of [^{99m}Tc(SQ168))(tricine)(NIC)] in tumor, lungs, liver, spleen, and intestine. The muscle and kidney uptake was also inhibited (to a much lesser degree) by the presence of excess E[c(RGDfK)]$_2$. The blood activity in the presence of excess E[c(RGDfK)]$_2$ was higher than that without E[c(RGDfK)]$_2$. This is probably caused by the saturation effect of E[c(RGDfK)]$_2$ in distribution and transport mechanism. Similar results were obtained for [^{99m}Tc(SQ168)(tricine)(TPPTS)] and ^{111}In-DOTA-E[c(RGDfK)]$_2$ in the BALB/c mice bearing ovarian carcinoma (*2*), and for ^{64}Cu-DOTA-E[c(RGDfK)]$_2$ in the nude mice bearing the MDA-MB-435 human breast cancer xenografts (*3*).

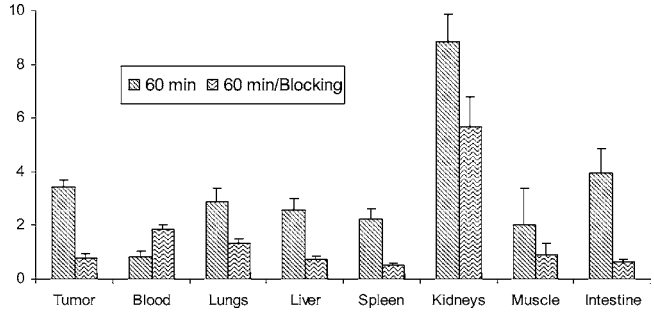

Figure 5. Comparison of the organ uptake (%ID/g) for [^{99m}Tc(SQ168)(tricine)(ISONIC)] at 60 min postinjection in the absence/presence of excess cyclic RGDfK dimer, E[c(RGDfK)]$_2$. Biodistribution was performed in nude mice bearing the MDA-MB-435 human breast cancer xenografts. Each data point represents an average of biodistribution data in four animals.

It is very important to note that the athymic tumor-bearing mice used in this study were all at their rapidly growing stage. Recently, the integrin $\alpha_v\beta_3$ expression in microvessels of lungs and, to a lesser extent, the liver of the rat has also been documented (*40*). It is not surprising to see a high uptake in nontumor organs (such as liver, lungs, spleen, and kidneys) when small rodent tumor-bearing animals are used to evaluate biodistribution patterns of the integrin $\alpha_v\beta_3$-targeted radiotracers. Thus, caution must be taken when using the biodistribution data obtained from small animals to predict the radiotracer distribution patterns in humans.

Metabolic Properties. The in vivo distribution characteristics of a radiolabeled small biomolecule are determined by the size and type of the targeting biomolecule, the metal chelate (radiometal plus bifunctional chelator), and the overall molecular charge, lipophilicity, and protein binding affinity. Radiolabeled small peptides (such as cyclic RGD peptide monomers, dimers and tetramers) often accumulate in kidneys. Extensive metabolic degradation has been observed for the ^{99m}Tc-labeled cyclic RGDfK monomer (*39*) and the ^{64}Cu-labeled cyclic RGDfK tetramer in both kidneys and urine samples (*38*). Since all three complexes [^{99m}Tc(SQ168)(tricine)(L)] (L = TPPTS, ISONIC and PDA) are excreted mainly from the renal system, we analyzed urine samples from tumor-bearing mice. To our surprise, [^{99m}Tc(SQ168)(tricine)(TPPTS)] shows a significant metabolism at 30 min postinjection while [^{99m}Tc(SQ168)(tricine)(PDA)] remains intact over 120 min postinjection (Figure 6). The complex [^{99m}Tc(SQ168))(tricine)(ISONIC)] has a very similar meta-

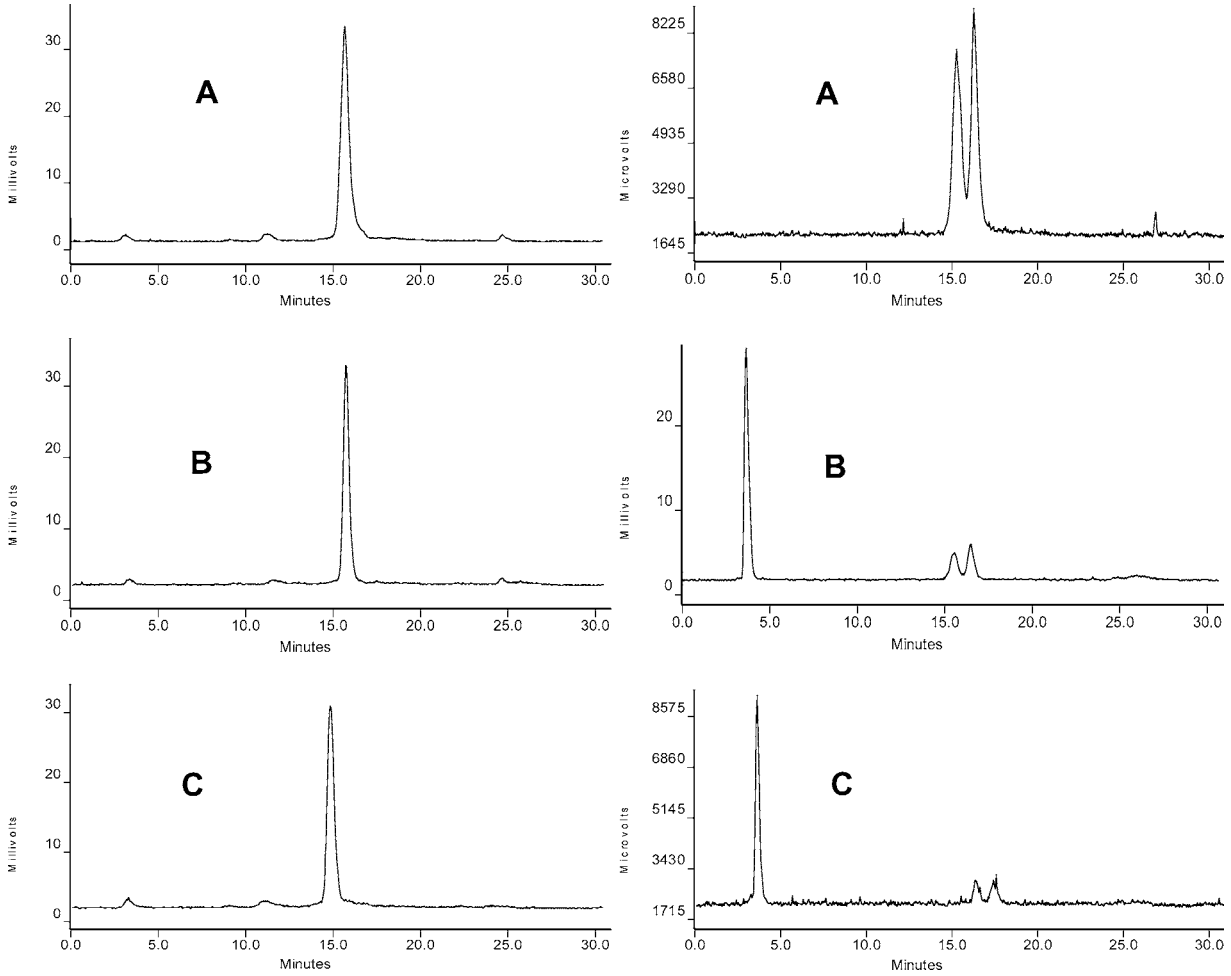

Figure 6. Radio-HPLC chromatograms of [^{99m}Tc(SQ168)(tricine)(PDA)] (left) and [^{99m}Tc(SQ168)(tricine)(TPPTS)] (right) in the kit matrix before injection (A), in the urine at 30 min postinjection (B), and in the urine at 120 min postinjection (C). The metabolic pattern of [^{99m}Tc(SQ168)(tricine)(ISONIC)] in the urine is similar to [^{99m}Tc(SQ168)(tricine)(TPPTS)]. Each tumor-bearing mouse was administered with ~100 μCi of radiotracer. Two tumor-bearing mice were used for each radiotracer.

bolic pattern to that of [^{99m}Tc(SQ168))(tricine)(TPPTS)]. We tried to extract the radioactivity from the feces samples, but the activity level was so low that we were unable to detect either intact ternary ligand ^{99m}Tc complexes or their metabolites. It has been suggested that extensive metabolic degradation is caused by the cyclic RGDfK peptide (*39*). Since all three radiotracers used in this study share the same HYNIC-conjugated cyclic RGDfK dimer, the difference in their metabolic fate is likely related to the coligand and the Tc chelate. At this moment, we cannot explain the different metabolic fate of these three radiotracers according to chemical stability of the Tc chelate. It is also important to note that these data are very preliminary (two tumor-bearing mice for each radiotracer), and more detailed metabolic studies are still in progress. Results from these studies will be reported as a separate account.

Coligand Effect. Since HYNIC can occupy only one coordination site, glucoheptonate and tricine are often used as coligands to complete the Tc coordination sphere. The choice of coligands allows easy modification of biological properties of the ^{99m}Tc-labeled biomolecules. Fischman and co-workers have been using the ^{99m}Tc-labeled fMLFK−HYNIC to image acute infection (*22*, *23*, *41*, *42*). Different biodistribution properties were observed for binary ligand complexes [^{99m}Tc(fMLFK−HYNIC)(L)$_2$] (L = glucoheptonate, mannitol, and glucamine) (*22*). Although the biological data from animal and clinical studies show that the binary ligand complexes [^{99m}Tc-(HYNIC−BM)(L)$_2$] (BM = chemotactic peptides, somatostatin analogues, DNA oligonucleotides, and a folate receptor antagonist; L = tricine and EDDA) are able to localize at the disease site (*43*−*47*), it would be still difficult to develop them for routine clinical use due to their solution instability and the presence of multiple species in solution (*11*, *14*).

To solve the problem, we have developed several ternary ligand systems (Figure 1) that form complexes [^{99m}Tc(HYNIC−BM)(tricine)(L)] (L = TPPTS, TPPDS, TPPMS, ISONIC, NIC, PA, PDA and PSA) with extremely high solution stability (*1*, *11*, *13*). The effect of coligands on biological properties has been reported for the ^{99m}Tc-labeled HYNIC−BM conjugates, including a glycoprotein IIB/IIIa receptor antagonist (*12*), somatostatin analogues (*24*−*26*), interleukin-8 (*28*), and cholecystokinin (CCK8) peptides (*29*). It is very important to note that the coligand effect is largely dependent on the targeting biomolecule. For the ^{99m}Tc-labeled HYNIC−IL-8 conjugate, the use of TPPTS coligand results in the complex [^{99m}Tc(HYNIC−IL-8)(tricine)(TPPTS)] that has the significantly reduced in vitro receptor binding affinity, low abscess uptake, and high liver uptake (*28*). The best coligands for the ^{99m}Tc-labeled HYNIC−IL-8 and CCK8 peptides are NIC and ISONIC (*28*, *29*). For the ^{99m}Tc-labeled cyclic RGDfK dimer, changing the coligand had a minimal effect on their lipophilicity and tumor-targeting capability, which is consistent with that fact that [^{99}Tc(SQ168)(tricine)(TPPTS)] has almost the same

integrin $\alpha_v\beta_3$ binding affinity as the "unlabeled" SQ168 in an in vitro assay (*1*). Thus, caution must be taken when comparing the coligand effect for different HYNIC−biomolecule conjugates.

One of the factors in selecting an optimal coligand (L) is the liver and tumor/liver ratio uptake of the radiotracer. Despite its faster liver clearance (Figure 3), the tumor/liver ratio of [^{99m}Tc(SQ168)(tricine)(ISONIC)] was comparable to that of [^{99m}Tc(SQ168)(tricine)(TPPTS)] due to its slow tumor washout. The complex [^{99m}Tc(SQ168)-(tricine)(PDA)] has a lower liver uptake than [^{99m}Tc(SQ168)(tricine)(TPPTS)] at all four time points and has a better tumor/liver ratio than [^{99m}Tc(SQ168)(tricine)-(TPPTS)] at >60 min postinjection (Figure 4). From this viewpoint, PDA has the advantage over TPPTS and ISONIC. However, for other ^{99m}Tc-labeled HYNIC-conjugated biomolecules, the choice of coligand should be confirmed according to their distribution characteristics.

CONCLUSION

In this report, we described biodistribution characteristics of ternary ligand complexes [^{99m}Tc(SQ168)(tricine)-(L)] (L = TPPTS, ISONIC and PDA) in athymic nude mice bearing the MDA-MB-435 human breast cancer xenografts. The key finding of this study is that the excretion kinetics of the ^{99m}Tc-labeled RGDfK dimer can be modified by the choice of coligand. The fact that all three radiotracers show relatively high tumor uptake during a 2 h study period suggests that changing the coligand has minimal effect on the integrin $\alpha_v\beta_3$ targeting capability of the ^{99m}Tc-labeled RGDfK dimer. On the basis of the liver uptake and tumor/liver ratio of ternary ligand complexes [^{99m}Tc(SQ168)(tricine)(L)], we believe that PDA has the advantage over TPPTS and ISONIC for the ^{99m}Tc-labeling of HYNIC-biomolecule conjugates.

ACKNOWLEDGMENT

Authors would like to thank Lee Ann Grote, Carol Dowell and Cheryl Anderson from the Department of Veterinary Clinical Sciences, Purdue University, for their assistance with biodistribution studies. This work is supported, in part, by Purdue University, Bristol-Myers Squibb Medical Imaging Inc., and research grants R21 EB003419 (S.L.) from National Institute of Biomedical Imaging and Bioengineering (NIBIB) and BCTR0503947 (S.L.) from Susan G. Komen Breast Cancer Foundation.

Supporting Information Available: Additional experimental details. This material is available free of charge via the Internet at http://pubs.acs.org.

LITERATURE CITED

(1) Liu, S., Edwards, D. S., Ziegler, M. C., Harris, A. R., Hemingway, S. J., and Barrett, J. A. (2001) ^{99m}Tc-Labeling of a hydrazinonicotinamide-conjugated vitronectin receptor antagonist useful for imaging tumor. *Bioconjugate Chem. 12*, 624−629.

(2) Janssen, M. L., Oyen, W. J. G., Dijkgraaf, I., Massuger, L. F., Frielink, C., Edwards, D. S., Rajopadyhe, M., Boonstra, H., Corsten, F. H., and Boerman, O. C. (2002) Tumor targeting with radiolabeled $\alpha_v\beta_3$ integrin binding peptides in a nude mouse model. *Cancer Res. 62*, 6146−6151.

(3) Chen, X. Y., Liu, S., Hou, Y., Tohme, M., Park, R., Bading, J. R., and Conti, P. S. (2004) MicroPET imaging of breast cancer α_v-integrin expression with ^{64}Cu-labeled dimeric RGD peptides. *Mol. Imag. Biol. 6*, 350−359.

(4) Liu, S., Cheung, E., Rajopadyhe, M., Ziegler, M. C., and Edwards, D. S. (2001) ^{90}Y- and ^{177}Lu-labeling of a DOTA-conjugated vitronectin receptor antagonist useful for tumor therapy. *Bioconjugate Chem. 12*, 559−568.

(5) Janssen, M. L., Frielink, C., Dijkgraaf, I., Oyen, W. J., Edwards, D. S., Liu, S., Rajopadhye, M., Massuger, L. F., Corstens, F. H., and Boerman, O. C. (2004) Improved tumor targeting of radiolabeled RGD-peptides using rapid dose fractionation. *Cancer Biother. Radiopharm. 19*, 399−404.

(6) Liu, S., and Edwards, D. S. (2001) Stabilization of ^{90}Y-labeled DOTA-biomolecule conjugates using gentisic acid and ascorbic acid. *Bioconjugate Chem. 12*, 554−558.

(7) Liu, S., and Edwards, D. S. (2001) Synthesis and characterization of two ^{111}In labeled DTPA-peptide conjugates. *Bioconjugate Chem. 12*, 630−634.

(8) Liu, S., and Edwards, D. S. (2002) Fundamentals of receptor-based diagnostic metalloradiopharmaceuticals. *Topics Curr. Chem. 222*, 259−278.

(9) Liu, S., Robinson, S. R., and Edwards, D. S. (2003) Integrin $\alpha_v\beta_3$ directed radiopharmaceuticals for tumor imaging. *Drugs Future 28*, 551−564.

(10) Liu, S., Robinson, S. R., and Edwards, D. S. (2005) Radiolabeled integrin $\alpha_v\beta_3$ antagonists as radiopharmaceuticals for tumor radiotherapy. *Topics Curr. Chem. 252*, 193-216.

(11) Edwards, D. S., Liu, S., Barrett, J. A., Harris, A. R., Looby, R. J., Ziegler, M. C., Heminway, S. J., and Carroll, T. R. (1997) A new and versatile ternary ligand system for technetium radiopharmaceuticals: water soluble phosphines and tricine as coligands in labeling a hydrazino nicotinamide-modified cyclic glycoprotein IIb/IIIa receptor antagonist with ^{99m}Tc. *Bioconjugate Chem. 8*, 146−154.

(12) Barrett, J. A., Crocker, A. C., Damphousse, D. J., Heminway, S. J., Liu, S., Edwards, D. S., Lazewatsky, J. L., Kagan, M., Mazaika, T. J., and Carroll, T. R. (1997) Biological evaluation of thrombus imaging agents utilizing water soluble phosphines and tricine as coligands when used to label a hydrazinonicotinamide-modified cyclic glycoprotein IIb/IIIa receptor antagonist with ^{99m}Tc. *Bioconjugate Chem. 8*, 155−160.

(13) Liu, S., Edwards, D. S., and Harris, A. R. (1998) A novel ternary ligand system for ^{99m}Tc-labeling of hydrazinonicotinamide-modified biologically active molecules using imine-N containing heterocycles as coligands. *Bioconjugate Chem. 9*, 583−595.

(14) Edwards, D. S., Liu, S., Ziegler, M. C., Harris, A. R., Crocker, A. C., Heminway, S. J., Barrett, J. A., Bridger, G. J., Abrams, M. J., and Higgins, J. D. (1999) RP463: A stabilized technetium-99m complex of a hydrazino nicotinamide derivatized chemotactic peptide for infection imaging. *Bioconjugate Chem. 10*, 884−891.

(15) Brouwers, A. H., Laverman, P., Boerman, O. C., Oyen, W. J. G., Barrett, J. A., Harris, T. D., Edwards, D. S., and Corstens, F. H. M. (2000) A ^{99}Tc^{m}-labeled leukotriene B4 receptor antagonist for scintigraphic detection of infection in rabbits. *Nucl. Med. Commun. 21*, 1043−1050.

(16) Liu, S., Edwards, D. S., Williams, N. E., and Harris, A. R. (2002) ^{99m}Tc-labeling of a hydrazinonictotinamide-conjugated LTB_4 receptor antagonist useful for imaging infection and inflammation. *Bioconjugate Chem. 13*, 881−886.

(17) van Eerd, J. E. M., Oyen, W. J. G., Harris, T. D., Rennen, H. J. J. M., Edwards, D. S.; Liu, S., Ellars, C. E., Corstens, F. H. M., and Boerman, O. C. (2003) A bivalent leukotriene B4 antagonist for scintigraphic imaging of infectious foci. *J. Nucl. Med. 44*, 1087−1091.

(18) Liu, S., Edwards, D. S., Harris, A. R., Ziegler, M. C., Poirier, M. J., Ewels, B. A., DiLuzio, W. R., and Hui, P. (2001) Towards developing a non-$SnCl_2$ formulation for RP444: a new radiopharmaceutical for thrombus imaging. *J. Pharm. Sci. 90*, 114−123.

(19) Liu, S., Edwards, D. S., Harris, A. R., Heminway, S. J., and Barrett, J. A. (1999) Technetium complexes of a hydrazinonicotinamide-conjugated cyclic peptide and 2-hydrazinopyridine: Synthesis and characterization. *Inorg. Chem. 38*, 1326−1335.

(20) Liu, S., Ziegler, M. C., and Edwards, D. S. (2000) Radio-LC-MS for the characterization of ^{99m}Tc-labeled bioconjugates. *Bioconjugate Chem. 11*, 113−117.

(21) Liu, S. (2005) 6-Hydrazinonicotinamide derivatives as bifunctional coupling agents for ^{99m}Tc-labeling of small biomolecules. *Topics Curr. Chem. 252*, 117−153.
(22) Babich, J. W., and Fischman, A. J. (1995) Effect of "coligand" on the biodistribution of ^{99m}Tc-labeled hydrazino nicotinic acid derivatized chemotactic peptides. *Nucl. Med. Biol. 22*, 25−30.
(23) Babich, J. W., Coco, W. G., Barrow, S. A., Fischman, A. J., Femia, F. J., and Zubieta, J. (2000) ^{99m}Tc-labeled chemotactic peptides: influence of coligand on distribution of molecular species and infection imaging properties. Synthesis and structural characterization of model complexes with the {Re(η^2-HNNC$_5$H$_4$N)(η^1-NNC$_5$H$_4$N)} core. *Inorg. Chim. Acta 309*, 123−136.
(24) Decristoforo, C., and Mather, S. J. (1999) Preparation, ^{99m}Tc-labeling, and in vitro characterization of HYNIC and N$_3$S modified RC-160 and [Tyr3]octreotide. *Bioconjugate Chem. 10*, 431−438.
(25) Decristoforo, C., and Mather, S. J. (1999) Technetium-99m somatostatin analogues: effect of labelling methods and peptide sequence. *Eur. J. Nucl. Med. 26*, 869−876.
(26) Decristoforo, C., and Mather, S. J. (1999) ^{99m}Tc-labeled peptide-HYNIC conjugates: effect of lipophilicity and stability on biodistribution. *Nucl. Med. Biol. 26*, 389−396.
(27) Zhang, Y.-M., Liu, N., Zhu, Z.-H., Rusckowski, M., and Hnatowich, D. J. (2000) Influence of different chelators (HYNIC, MAG$_3$ and DTPA) on tumor cell accumulation and mouse biodistribution of technetium-99m labeled antisense DNA. *Eur. J. Nucl. Med. 27*, 1700−1707.
(28) Rennen, H. J. J. M., van Eerd, J. E., Oyen, W. J. G., Corstens, F. H. M., Edwards, D. S., and Boerman, O. C. (2002) Effects of coligand variation on the in vivo characteristics of Tc-99m-labeled interleukin-8 in detection of infection. *Bioconjugate Chem. 13*, 370−377.
(29) Laverman, P., Béhé, M., Oyen, W. J. G., Willems, P. H. G. M., Corstens, F. H. M., Behr, T. M., and Boerman, O. C. (2004) Two technetium-99m-labeled cholecystokinin-8 (CCK8) peptides for scintigraphic imaging of CCK receptors. *Bioconjugate Chem. 15*, 561−568.
(30) Ono, M., Arano, Y., Mukai, T., Uehara, T., Fujioka, Y., Ogawa, K., Namba, S., Nakayama, M., Saga, T., Konishi, J., Horiuchi, K., Yokoyama, A., and Saji, H. (2001) Plasma protein binding of ^{99m}Tc-labeled hydrazine nicotinamide derivatized polypeptides and peptides. *Nucl. Med. Biol. 28*, 155−164.
(31) Ono, M., Arano, Y., Mukai, T., Fujioka, Y., Ogawa, K., Uehara, T., Saga, T., Konishi, J., and Saji, H. (2001) ^{99m}Tc−HYNIC-derivatized ternary ligand complexes for ^{99m}Tc-labeled polypeptides with low in vivo protein binding. *Nucl. Med. Biol. 28*, 215−224.
(32) Ono, M., Arano, Y., Mukai, T., Saga, T., Fujioka, Y., Ogawa, K., Kawashima, H., Konishi, J., and Saji, H. (2002) Control of radioactivity pharmacokinetics of ^{99m}Tc−HYNIC-labeled polypeptides derived with ternary ligand complexes. *Bioconjugate Chem. 13*, 491−501.
(33) Haubner, R., Gratias, R., Diefenbach, B., Goodman, S. L., Jonczyk, A., and Kessler, H. (1996) Structural and functional aspect of RGD-containing cyclic pentapeptides as highly potent and selective integrin $\alpha_v\beta_3$ antagonists. *J. Am. Chem. Soc. 118*, 7461−7472.
(34) Harris, T. D., Sworin, M., Williams, N., Rajopadhye, M., Damphousse, P. R., Glowacka, D., Poirier, M. J., and Yu, K. (1999) Synthesis of stable hydrazones of a hydrazinonicotinyl-modified peptide for the preparation of ^{99m}Tc-labeled radiopharmaceuticals. *Bioconjugate Chem. 10*, 808−814.
(35) Hoffman, R. M. (2002) Green fluorescent protein imaging of tumor growth, metastasis, and angiogenesis in mouse models. *The Lancet Oncol. 3*, 546−556.
(36) Yang, M., Baranov, E., Li, X. M., Wang, J. W., Jiang P., Li, L., Moossa, A. R., Penman, S., and Hoffman, R. M. (2001) Whole-body and intravital optical imaging of angiogenesis in orthotopically implanted tumors. *Proc. Natl. Acad. Sci. U.S.A. 98*, 2616−2621.
(37) Chen, X.-Y., Park, R., Tohme, M., Shahinian, A. H., Bading, J. R., and Conti, P. S. (2004) MicroPET and autoradiographic imaging of breast cancer α_v-integrin expression using ^{18}F- and ^{64}Cu-labeled RGD peptide. *Bioconjugate Chem. 15*, 41−49.
(38) Wu, Y., Zhang, X.-Z., Xiong, Z.-M., Cheng, Z., Fisher, D. R., Liu, S., and Chen, X.-Y. (2005) MicroPET imaging of glioma α_v-integrin expression using ^{64}Cu-labeled tetrameric RGD peptide. *J. Nucl. Med. 46*, 1707−1718.
(39) Haubner, R., Bruchertseifer, F., Bock, M., Schwaiger, M., Wester, H.-J. (2004) Synthesis and biological evaluation of ^{99m}Tc-labeled cyclic RGD peptide for imaging integrin $\alpha_v\beta_3$ expression. *Nuklearmedizin 43*, 26−32.
(40) Singh, B., Fu, C. Z., and Bhattacharya, J. (2000) Vascular expression of the $\alpha_v\beta_3$-integrin in lung and other organs. *Am. J. Physiol. Lung Cell. Mol. Physiol. 278*, L217-L226.
(41) Babich, J. W., Solomon, H., Pike, M. C., Kroon, D., Graham, W., Abrams, M. J., Tompkins, R. G., Rubin, R. H., and Fischman, A. J. (1993) Technetium-99m labeled hydrazino nicotinamide derivatized chemotactic peptide analogs for imaging focal sites of bacterial infection. *J. Nucl. Med. 34*, 1964−1974.
(42) Babich, J. W., Graham, W., Barrow, S. A., and Fischman, A. J. (1995) Comparison of the infection imaging properties of a ^{99m}Tc labeled chemotactic peptide with ^{111}In IgG. *Nucl. Med. Biol. 22*, 643−648.
(43) Decristoforo, C., Melendez-Alafort, L., Sosabowski, J. K., and Mather, S. J. (2000) ^{99m}Tc−HYNIC-[Tyr^3]-octreotide for imaging somatostatin-receptor-positive tumors: preclinical evaluation and comparison with ^{111}In-Octreotide. *J. Nucl. Med. 41*, 1114−119.
(44) Bangard, M., Béhé, M., Guhlke, S., Otte, R., Bender, H., Maecke, H. R., and Biersack, H. J. (2000) Detection of somatostatin receptor-positive tumors using the new ^{99m}Tc-tricine-HYNIC-D-Phe^1-Tyr^3-octreotide: first results in patients and comparison with ^{111}In-DTPA-D-Phe^1-octreotide. *Eur. J. Nucl. Med. 27*, 628−637.
(45) Decristoforo, C., Mather, S. J., Cholewinski, W., Donnemiller, E., Riccabona, G., and Moncayo, R. (2000) ^{99m}Tc-EDDA/HYNIC-TOC: a new ^{99m}Tc-labeled radiopharmaceutical for imaging somatostatin receptor-positive tumors: first clinical results and intrapatient comparison with ^{111}In-labeled octreotide derivatives. *Eur. J. Nucl. Med. 27*, 1318−1325.
(46) Hnatowich, D. J., Winnard P. Jr., Virzi, F., Fogarasi, M., Santo, T., Smith, C. L., Cantor, C. R., and Rusckowski, M. (1995) Technetium-99m labeling of DNA oligonucleotides. *J. Nucl. Med. 36*, 2306−2314.
(47) Guo, W. J., Hinkle, G. H., and Lee, R. J. (1999) ^{99m}Tc−HYNIC-folate: a novel receptor-based targeted radiopharmaceutical for tumor imaging. *J. Nucl. Med. 40*, 1563−1569.

BC0501653

Hemostatic Effects of Phospholipid Vesicles Carrying Fibrinogen γ Chain Dodecapeptide in Vitro and in Vivo

Yosuke Okamura,[†,§] Ippei Maekawa,[†] Yuji Teramura,[†] Hitomi Maruyama,[‡] Makoto Handa,[§] Yasuo Ikeda,[‡] and Shinji Takeoka*[,†]

Graduate School of Science and Engineering, Waseda University, Tokyo, 169-8555, Japan, Department of Internal Medicine, School of Medicine, Keio University, Tokyo, 160-8582, Japan, and Department of Transfusion Medicine & Cell Therapy, School of Medicine, Keio University, Tokyo, 160-8582, Japan. Received June 21, 2005; Revised Manuscript Received September 15, 2005

We studied prototypes of platelet substitutes that bear on their surface a dodecapeptide, HHLGGAKQAGDV (H12). The peptide is a fibrinogen γ chain carboxy-terminal sequence (γ400−411) and recognizes specifically the active form of glycoprotein (GP) IIb/IIIa on the surface of activated platelets. We conjugated H12 to the end of poly(ethylene glycol) chains on the surface of a phospholipid vesicle with an average diameter of 220 nm to prepare H12−PEG−vesicles. The half-life of the H12−PEG−vesicles was significantly prolonged by PEG modification, and the ability of H12 on the surface of the vesicle to recognize GPIIb/IIIa was maintained even though the surface was modified with PEG chains. The H12−PEG−veiscles enhanced the in vitro thrombus formation of platelets that were adhering to a collagen-immobilized plate, when thrombocytopenia-imitation blood was passed over the plate. Based on the flow cytometric analyses of PAC-1 binding and P-selectin expression, the H12−PEG−vesicles were shown not to cause platelet activation. Furthermore, the H12−PEG−vesicles dose-dependently shortened the tail bleeding time of thrombocytopenic rats. It was confirmed that the H12−PEG−vesicles had a hemostatic effect and may be a suitable candidate for an alternative to human platelet concentrates transfused into thrombocytopenic patients.

INTRODUCTION

Platelet transfusion plays an important role in prophylactic therapy for patients with thrombocytopenia caused by hematologic malignancies or intensive chemotherapy for solid tumors or as a result of surgical procedures and radiotherapy. However, due to the short storage life of platelets (3 days in Japan), the shortage has become a serious concern in an aging society. Furthermore, the risk of viral and bacterial infections accompanied by transfusion is also a serious issue. To solve these problems, various platelet substitutes (*1*) have been developed, such as, solubilized platelet membrane protein-conjugated liposomes (Plateletsome) (*2*), infusible platelet membranes (IPM) (*3*), fibrinogen-coated albumin microcapsules (Synthocyte) (*4*), fibrinogen-bonded red blood cells (*5*), liposomes bearing fibrinogen (*6*), and arginine-glycine-aspartic acid (RGD) peptide-bound red blood cells (Thromboerythrocyte) (*7*). These platelet substitutes consist of materials derived from blood components.

We have developed platelet substitutes using polymerized albumin particles (polyAlb) (*8*−*11*) and phospholipid vesicles (*12*−*15*) as biocompatible and biodegradable carriers and shown that those carriers carrying recombinant fragments of platelet membrane proteins (rGPIbα (*16*, *17*) and rGPIa/IIa complex (*18*, *19*)) specifically interact with a surface that mimics the site of bleeding injury, such as von Willebrand factor (VWF) and collagen immobilized on a surface under flow conditions in vitro. Moreover, we demonstrated that rGPIa/IIa-conjugated polyAlb reduced the tail bleeding time of thrombocytopenic mice (*8*). These carriers have the ability to induce platelet hemostasis; however, they cannot recruit flowing platelets to induce platelet aggregation.

When platelets are made to adhere to collagen immobilized on a surface and activated, the conformation of GPIIb/IIIa which exists on the platelet membrane changes from a silent form to an activated form (*20*−*22*). The activated form acts as a receptor for fibrinogen and VWF (*23*−*25*), which is followed by platelet aggregation (*26*, *27*). This is because fibrinogen contains three putative platelet interaction sites, namely, a tetrapeptide containing RGD sequences such as RGDF and RGDS at α95−98 and α572−575, respectively, and a dodecapeptide (HHLGGAKQAGDV, H12) at a γ chain carboxy-terminal segment (γ400−411) (*28*).

To study the usefulness of fibrinogen as a recognition site of platelet substitutes, we prepared fibrinogen-conjugated polyAlb, and we confirmed that the polyAlb enhanced adhesion of the flowing platelets to an activated platelet-immobilized surface in vitro (*9*). However, fibrinogen is derived from human blood and when isolated in solution tends to precipitate at 4 °C within a few hours (*29*).

Recently, we have focused on the stable dodecapeptide, H12, instead of fibrinogen (*28*, *30*−*33*). Based on our results obtained from flow cytometric analyses of agglutination, H12-conjugated latex beads showed minimal interaction with nonactivated platelets in comparison

* To whom correspondence should be addressed. E-mail: takeoka@waseda.jp. Tel: +813-5286-3217. Fax: +813-5286-3217.
† Graduate School of Science and Engineering, Waseda University.
§ Department of Transfusion Medicine & Cell Therapy, School of Medicine, Keio University.
‡ Department of Internal Medicine, School of Medicine, Keio University.

10.1021/bc050178g CCC: $30.25 © 2005 American Chemical Society
Published on Web 11/01/2005

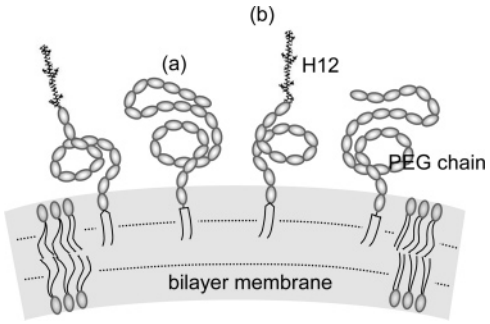

Figure 1. The structure of H12−PEG−vesicles: (a) PEG−DSPE (PEG 5.0 kDa) and (b) H12−PEG−Glu2C18 (PEG: 3.1 kDa, H12: 1.3 kDa) are incorporated into the bilayer membrane.

with RGD-conjugated latex beads (*34*). Furthermore, the H12-conjugated latex beads enhanced in vitro thrombus formation on the collagen-immobilized plate when thrombocytopenia-imitation blood was passed over the plate (*34*).

Phospholipid vesicles have been extensively studied as carriers for biologically important substances such as drugs, hemoglobin, enzymes, hormones, and DNA. In particular, recognition proteins such as antibodies and various ligands have been conjugated to the surface of vesicles to bind and interact with tissue epitopes or specific cells. Recently, it was reported that H12-liposomes enhanced platelet aggregation and specifically adhered to the platelets activated on the collagen surface in a state of rest (*35*). On the other hand, poly(ethylene glycol) (PEG) modification of the surface of the vesicles has been widely used to prolong the half-life or to stabilize their dispersion states (*36*−*40*). We previously reported that PEG modification of the vesicles was effective in preventing intervesicular access and aggregation as determined using a capillary viscosimeter and optical microscopy. Also, subcutaneous microvascular studies showed that PEG conjugates significantly improved microcirculation (flow rate, functional capillary density, and vessel diameter) (*38*, *39*).

In this study, we prepared phospholipid vesicles carrying both H12 and PEG chains to enhance the biocompatibility as a platelet substitute and to enhance the stabilization of the vesicles in vitro and in vivo, as noted above. Our purpose was to produce a platelet substitute for the indication of prophylactic transfusion. However, the excluded volume effect of the neighboring PEG chains might shield the recognition ability of H12. Therefore, we conjugated H12 to the end of the PEG chain by using PEG−lipids and prepared the PEG-modified vesicles carrying H12 (H12−PEG−vesicles, Figure 1). Then we studied the recognition ability toward platelets activated on collagen immobilized on a surface when thrombocytopenia-imitation blood was passed over the surface. Furthermore, we intravenously administered the H12−PEG−vesicles into thrombocytopenic rats and measured the tail bleeding time for evaluation of the hemostatic ability of the vesicles.

MATERIALS AND METHODS

Materials. All reagents were used without further purification. L-Glutamic acid, *p*-toluenesulfonic acid monohydrate (*p*-Tos), stearyl alcohol, and *N*,*N*′-dicyclohexylcarbodiimide were purchased from Kanto Chemical (Tokyo). 1,2-Distearoyl-*sn*-glycero-3-phosphatidylethanolamine-*N*-[monomethoxy poly(ethylene glycol)] (5000) (PEG−DSPE, M_w = 5.1 kDa), and α-maleimidyl-ω-hydroxy succinimidyl poly(ethylene glycol) (MAL−PEG−NHS, M_w = 3.5 kDa) were purchased from NOF (Tokyo). 1,2-Dipalmitoyl-*sn*-glycero-3-phosphatidylcholine (DPPC) and cholesterol were purchased from Nippon Fine Chemical (Osaka). 1,5-Dihexadecyl-*N*-succinyl-L-glutamate (DHSG) was synthesized in our laboratory (*41*, *42*). A fibrinogen γ chain dodecapeptide (C-HHLGGAKQAGDV, Cys-H12) was synthesized with a solid-phase synthesizer by BEX (Tokyo). 3,3′-Dihexyloxacarbocyanine iodide ($DiOC_6$), which is a platelet fluorescent dye, and dioctadecyloxacarbocyanine perchlorate ($DiOC_{18}$), which is a vesicle fluorescent dye, were purchased from Molecular Probes (Eugene, OR). Collagen I-A (Cellmatrix) was purchased from Nitta Gelatine (Osaka). D-Phe-Pro-Arg-chloromethyl ketone (PPACK) was purchased from Calbiochem (San Diego, CA). FITC-labeled PAC-1, which is anti-GPIIb/IIIa antibody, and FITC-labeled anti-P-selectin (CD62P) antibody were obtained from Becton Dickinson (San Jose, CA) and BD-Pharmingen (San Diego, CA), respectively. Both busulfan and poly(ethylene glycol) (average molecular weight 400) were purchased from Sigma-Aldrich (St Louis, MO).

Scheme 1. Syntheses of H12−PEG-Glu2C18 (PEG 3.1 kDa, H12 1.3 kDa)

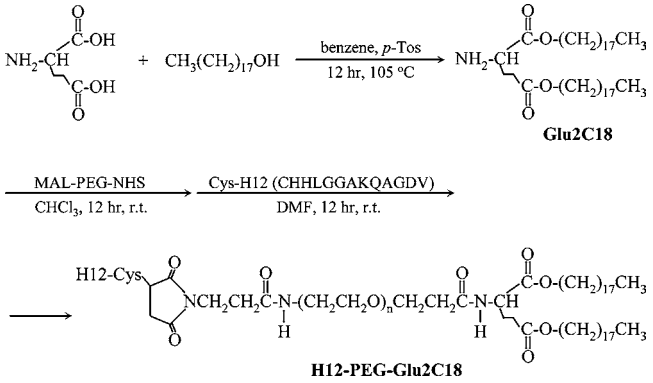

Synthesis of H12−PEG−Glu2C18. The syntheses were performed according to Scheme 1. L-Glutamic acid (2.96 g, 20 mmol) and *p*-Tos (4.56 g, 24 mmol) were dissolved in benzene and refluxed for 1 h at 105 °C. Stearyl alcohol was added to the solution, and the solution was refluxed for 12 h at 105 °C. The crude product was washed with an aqueous solution of saturated Na_2CO_3 and then distilled water. After recrystallization from methanol at 4 °C, 1,5-distearoyl-L-glutamate (Glu2C18) was obtained (9.5 g, yield 80%). Glu2C18 (115 mg, 176 μmol) and MAL−PEG−NHS (300 mg, 88 μmol) were dissolved in chloroform and stirred for 12 h at room temperature (rt). The crude product was purified by reprecipitation from diethyl ether. After recrystallization from ethanol, the MAL−PEG−Glu2C18 was obtained as a white solid (265 mg, yield 64%). MAL−PEG−Glu2C18 (100 mg, 25 μmol) and Cys-H12 (33 mg, 25 μmol) were reacted in *N*,*N*-dimethylformamide (DMF) for 12 h at rt. The crude product was purified by reprecipitation from diethyl ether and extracted with distilled water. The H12−PEG−Glu2C18 was obtained as a white solid (63 mg, 12 μmol, 47%).

Physicochemical Properties of H12−PEG−Glu2C18. TLC (silica gel, chloroform/methanol = 4/1, v/v): R_f 0.17. IR (film; cm^{-1}): 1736($\nu_{C=O}$, ester). ^1H NMR ($CDCl_3$, 500 MHz, δ ppm): 0.89 (t, 6H, $-CH_3$), 1.26 (br, 60H, $-CH_2-$), 1.63 (m, 4H, $-COOCH_2\mathbf{CH}_2-$), 2.00 (m, 2H, $-\mathbf{CH}_2CHCON-$), 2.46 (m, 2H, $-CH_2COO-$), 4.08 (m, 4H, $-COOCH_2-$), 3.63 (br, 360H, PEG).

Preparation of H12−PEG−vesicles. DPPC (100 mg, 136 μmol), cholesterol (52.7 mg, 136 μmol), DHSG (18.9

mg, 27.2 μmol), PEG−DSPE (5.2 mg, 0.90 μmol), and H12−PEG−Glu2C18 (0, 0.47, 1.57, 4.7, or 9.4 mg; 0, 0.090, 0.30, 0.90, or 1.8 μmol, respectively) were dissolved in benzene and then freeze-dried. The resulting white powder was hydrated with distilled water and extruded with membrane filters (pore sizes 3.00, 0.80, 0.65, 0.30, or 0.22 μm, FM filter, Fuji Film, Tokyo). The vesicles were washed with phosphate-buffered saline (PBS, pH 7.4) by suspension and centrifugation (100 000*g*, 30 min, 4 °C, twice). The particle diameter was analyzed by a dynamic light scattering method (N4 PLUS, Beckman-Coulter, Fullerton, FL). We prepared PEG−vesicles or vesicles using lipids in the absence of H12−PEG−Glu2C18 or H12−PEG−Glu2C18 and PEG−DSPE, respectively.

Measurement of the Stability of H12−PEG−vesicles. For the measurement of the incorporation ratio of H12−PEG−Glu2C18 to the vesicle, the H12−PEG−vesicles dispersion was freeze-dried to dissolve in $CDCl_3$. The peak area ratio (R_1) of the choline methyl proton of DPPC (3.37 ppm) to the methylene proton of the PEG chain in H12−PEG−Glu2C18 (3.64 ppm) was measured by ^{1}H NMR spectroscopy (JNM-Lambda 500, JEOL, Tokyo) to determine the incorporation ratio of the H12−PEG−Glu2C18. To study the change of the incorporated PEG lipids in the vesicles, the 30-fold diluted sample dispersion ([lipid] = 0.58 M in PBS, pH 7.4) was incubated at 37 °C, and R_1 was calculated from the ^{1}H NMR spectrum as described above. The peak area ratio before the incubation was defined as R_0. The incorporation ratio was calculated from a percentage of R_1 to R_0.

Preparation of Collagen Immobilized on a Surface. Collagen I-A (3.0 mg/mL) was suspended in PBS at 4 °C (30 μg/mL), and glass plates (diameter 24 mm, thickness 0.5 mm) were immersed into the collagen suspension at 4 °C for 8 h. The glass plates were carefully rinsed with PBS and immersed in a bovine serum albumin solution (20 mg/mL) at rt for 2 h before perfusion studies were performed, as described below.

Preparation of Platelets Immobilized on a Surface. Blood withdrawn from three healthy volunteers was mixed with a 10% volume of 3.8% (w/v) sodium citrate. Platelet-rich plasma (PRP) was prepared by centrifugation (100*g*, 15 min, 22 °C). The PRP was mixed with a 15% volume of acid−citrate−dextrose composed of 2.2% (w/v) sodium citrate, 0.8% (w/v) citric acid, and 2.2% (w/v) glucose (ACD) containing 1 μM prostaglandin E_1 (PGE_1, Sigma, St. Louis, MO). The suspension was centrifuged (2200*g*, 10 min, 22 °C), and the plasma was replaced with a Ringer's−citrate−dextrose solution (RCD solution, composition 0.76% (w/v) citric acid, 0.090% (w/v) glucose, 0.043% (w/v) $MgCl_2$, 0.038% (w/v) KCl, 0.60% (w/v) NaCl, pH 6.5) containing 1 μM PGE_1. After the pellets were resuspended in the RCD solution, the suspension was centrifuged (2200*g*, 10 min, 22 °C), and the concentrated platelets were resuspended at $2.0 \times 10^5/\mu$L in a Hepes−Tyrode buffer (H−T buffer, pH 7.4). The platelet counts were determined using an automated hematology analyzer (K-4500, Sysmex, Kobe, Japan). A collagen-coated glass plate was immersed into the platelet suspension for 1 h at 37 °C and carefully rinsed with PBS.

Measurement of Interaction of the H12−PEG−vesicles with Platelets Immobilized on a Glass Plate using Reconstituted Blood. Blood containing a 10% volume of 3.8% (w/v) sodium citrate was centrifuged (100*g*, 15 min, 22 °C) to replace PRP with an equal volume of a 0.9% (w/v) NaCl solution containing 10% (v/v) ACD (10% ACD−saline). The red blood cell suspension was centrifuged (2200*g*, 10 min, 22 °C) and washed with 10% ACD−saline three times to remove the buffy coat and plasma completely. After the final centrifugation, the red blood cells were resuspended in a H−T buffer to adjust the hematocrit (Hct) to 50%. The residual platelet counts were determined to be $(5.0 \pm 2.0) \times 10^3/\mu$L.

A solution of $DiOC_{18}$ in DMSO (10 mM, 50 μL) was added to the H12−PEG−vesicle suspension (20 mg/mL, 5 mL), and the suspension was incubated at rt for 30 min. The free $DiOC_{18}$ was separated by washing with PBS and centrifugation at 100 000*g* for 30 min at 4 °C twice, and the $DiOC_{18}$-labeled H12−PEG−vesicles were collected.

The reconstituted blood and the $DiOC_{18}$-labeled H12−PEG−vesicle mixtures were placed in a recirculating chamber mounted on an epifluorescent microscope (ECLIPS TE300, Nikon, Tokyo) equipped with a CCD camera, and the interaction of the H12−PEG−vesicles with the platelets immobilized on the surface was observed. All perfusion studies were performed at 37 °C. Single-frame images of the H12−PEG−vesicles on the plates were obtained with an image processor, Argus-50 (Hamamatsu Photonics, Hamamatsu).

Measurement of the Dynamic Interaction of Platelets in Thrombocytopenia-Imitation Blood with a Collagen-Coated Surface in the Presence of the H12−PEG−vesicles. Blood containing PPACK (40 μM), a thrombin inhibitor, was filtered with a leukocyte removal filter (NEO1J, Nihon Poll, Tokyo), which can remove both leukocytes and platelets from whole blood. The residual platelet count in the blood was $(6.0 \pm 2.0) \times 10^3/\mu$L. The platelet count was adjusted to $5.0 \times 10^4/\mu$L with PRP. This blood preparation was termed thrombocytopenia-imitation blood.

Platelets in the blood were labeled with $DiOC_6$ (final concentration, 2 μM), and the H12−PEG−vesicles were added to the blood for 5 min at 37 °C ([lipid] = 0.89 mM). The blood was placed in a recirculating chamber mounted on an epifluorescent microscope as described above, and the interaction of platelets with the collagen immobilized on the surface was observed. The surface coverage of the platelets that adhered on the plate was calculated with an image processor, Argus-20 (Hamamatsu Photonics).

Measurement of PAC-1 Binding and P-Selectin Expression of Resting Platelets in the Presence of the H12−PEG−vesicles Using Flow Cytometry. H12−PEG−vesicles or PEG−vesicles (final lipid concentration 0.82 μM) were added to PRP ([platelet] = $5.0 \times 10^4/\mu$L), and the mixtures were stirred at 37 °C for 30 min. Before and after stirring, FITC-labeled anti-P-selectin antibody (approximately 0.5 μg) was added to the mixture, incubated at 37 °C for 10 min, and then fixed with formaldehyde (final concentration 1.5% (v/v)). Alternatively, FITC-labeled PAC-1 (approximately 0.5 μg) was added to the mixture of platelets and samples and stirred at 37 °C for 10 min, followed by fixing with formaldehyde. As a positive control, ADP-stimulated platelets (final concentration of ADP; 20 or 100 μM) were prepared from PRP. The platelets were gated according to their characteristic forward versus side scatter, and 20 000 platelets were analyzed using a FACSCalibur flow cytometer (Nihon Becton Dickinson, Tokyo). PAC-1 binding or P-selectin expression was quantified as a fraction of the fluorescent-positive platelets. Each experiment was performed at least three times.

Measurement of Tail Bleeding Time and Half-Life of H12−PEG−vesicles Using Thrombocytopenic Rats. All animal studies were approved by the Animal Subject Committee of Keio University School of Medicine and performed according to NIH guidelines for the care

and use of laboratory animals. Experiments were carried out using male Wistar rats (230−250 g, CLEA Japan, Tokyo). A busulfan solution was prepared at a final concentration of 5 mg/mL in poly(ethylene glycol) (average molecular weight 400) (*11*, *43*, *44*). Rats were anesthetized with diethyl ether and injected on day 0 and day 3 with 10 mg/kg on each dosing day to produce a total dosage of 20 mg/kg of busulfan. On day 10, thrombocytopenic rats were anesthetized with sevofrane, and the sample suspension was infused into the tail vein. The samples were the H12−PEG−vesicles and the PEG−vesicles at a dose of 4 mL/kg; saline was used for control. Five minutes after administration, a template-guided incision (Quikheel, Becton-Dickinson, San Jose, CA) 2.5 mm in length and 1.0 mm in depth was made 1 cm from the tip of the tail. The tail was immersed in a 50 mL cylinder of saline, and the time taken for bleeding to stop was measured. In addition, blood was sampled from ether-anesthetized rats 5 min before and 30 min after sample injection by inserting a 25-gauge needle into the tail vein, and the cell counts were determined using an automated hematology analyzer (K-4500).

Half-life was measured from the β-phase of the clearance curve as follows: the $DiOC_{18}$-labeled H12−PEG−vesicles, PEG−vesicles, or vesicles were infused into the tail vein of thrombocytopenic rats at a dose of 40 mg/kg (equivalent lipid concentration). Following this, 400 μL of blood was collected from the tail vein of the rats at time intervals and centrifuged (2200*g*, 10 min, 22 °C), and 200 μL of plasma containing vesicles was collected. The plasma was mixed with deca(oxyethylene) dodecyl ether ($C_{12}E_{10}$) and was heated at 42 °C for 2 min to enhance the solubilization of the vesicles. The fluorescent intensity was then measured (E_x = 485 nm, E_m = 500 nm), and the half-life was calculated using a spectrofluorometer (FP-750, JASCO, Tokyo).

Statistical Analysis. Statistical significance of the results for H12−PEG−vesicles group vs the PEG−vesicles group was tested with Tukey−Kramer tests (Figure 4). A P value of less than 0.05 was considered to be statistically significant. Statistical analyses were performed using Stat View software (SAS Institute).

RESULTS

Characterization of H12−PEG−vesicles. L-Glutamic acid was selected as a connector to synthesize PEG−lipid derivatives as shown in Scheme 1. Each of the two carboxyl groups of the glutamic acid were bonded to a stearyl alcohol molecule by an ester bond to produce a hydrophobic moiety. The product, Glu2C18, was obtained after reprecipitation and recrystallization with a yield of 80%. MAL−PEG−Glu2C18 was obtained from the reaction of MAL−PEG−NHS and Glu2C18 with a yield of 64%. Cys-H12, where cysteine was introduced at the N terminal end of H12, was reacted with MAL−PEG−Glu2C18 in DMF to obtain H12−PEG−Glu2C18. In the ^{1}H NMR spectrum of H12−PEG−Glu2C18, the peak (δ = 6.70 ppm) that was attributed to the maleimide group of MAL−PEG−Glu2C18 disappeared, indicating the bonding of the thiol group of the cysteine with the maleimide group of MAL−PEG−Glu2C18 (yield 47%).

Next, we prepared H12−PEG−vesicles (220 ± 70 nm), DPPC/cholesterol/DHSG = 5/5/1, by molar ratio (Figure 1), which were modified with PEG−DSPE (0.3 mol %) and H12−PEG−Glu2C18 (from 0.03 to 0.6 mol %). The molecular weights of the PEG chain of the PEG−DSPE and H12−PEG−Glu2C18 were 5.0 and 3.1 kDa, respectively. The incorporated ratio (R_1/R_0) of the H12−PEG−Glu2C18 (0.3 and 0.6 mol %) was measured after incubation at 37 °C in a 30-fold dilution to analyze the stability of the lipids in the vesicle. From the ^{1}H NMR analyses, the R_1/R_0 of the H12−PEG−Glu2C18 did not change after the incubation for 12 h at 37 °C. The endotoxin concentration in the H12−PEG−vesicle suspension ([lipid] = 53.5 mM) was below 0.2 EU/mL. Furthermore, the half-life of H12−PEG−vesicles was estimated to be 200 ± 23 min from the β-phase of the clearance curve. In the cases of the control PEG−vesicles and the bare vesicles, the half-life was calculated to be 268 ± 2 min and 29 ± 1 min, respectively.

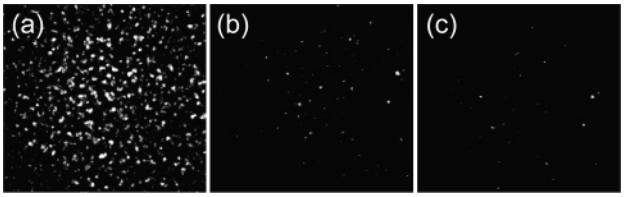

Figure 2. Specific adhesion of H12−PEG−vesicles in the reconstituted blood (Hct. 50%, platelet counts = (5.0 ± 2.0) × $10^3/\mu$L) to platelets activated on the collagen surface at a shear rate of 150 s^{-1}: (a) H12−PEG−vesicles; (b) H12−PEG−vesicles in the presence of PAC-1; (c) PEG−vesicles. Images a−c were obtained after blood was circulated for 500 s ([lipid] = 0.89 M).

Interaction of the H12−PEG−vesicles with Platelets Immobilized on a Surface under Flow Conditions. $DiOC_{18}$-prelabeled H12−PEG−vesicles (modification ratio of H12 0.3 mol %) were mixed with the reconstituted blood, and the mixture was allowed to flow over the activated platelets that were adhering to the collagen surface at a shear rate of 150 s^{-1}. The vesicles adhered and accumulated on the surface in a time-dependent manner, whereas the control PEG−vesicles did not adhere (Figure 2). The adhesion of the H12−PEG−vesicles was suppressed in the presence of PAC-1, an inhibitor of GPIIb/IIIa of the activated platelets.

Platelet Adhesion to a Collagen-Coated Surface in Thrombocytopenia-Imitation Blood Containing the H12−PEG−vesicles. We prepared a thrombocytopenia-imitation blood and adjusted the platelet counts to 5.0 × $10^4/\mu$L. The platelets were labeled with a fluorescent reagent, $DiOC_6$, to observe the dynamic interactions of the platelets with the collagen-coated surface at a shear rate of 150 s^{-1}. In this case, vesicles were not labeled. In the presence of the control PEG−vesicles, the surface coverage of platelets gradually increased to 10.6% ± 1.3% after 300 s of flow (Figure 3A, filled triangle). The value was not appreciably different (9.1% ± 0.4%) in the absence of the PEG−vesicles (Figure 3A, filled circle). When the H12−PEG−vesicles (modification ratio of H12 0.3 mol %) were added to the blood in the same way, the initial adhesion rate was comparable to that obtained with the PEG−vesicles; however, the adhesion rate increased dramatically with time, and the surface coverage reached 17.2% ± 1.9% (Figure 3A, opened circle).

We carried out the same experiments using the H12−PEG−vesicles with various modification ratios of the H12−PEG−Glu2C18 from 0 to 0.6 mol % (Figure 3B). The surface coverage of the PEG−vesicles and the H12−PEG−vesicles having the modification ratio of 0.1 mol % was 8.8% ± 1.8% and 9.5% ± 4.2% after 300 s of flow, respectively. When the H12-modification ratio was higher than 0.3 mol %, the surface coverage increased significantly to 17.2% ± 1.9% and then saturated.

PAC-1 Binding to and P-Selectin Expression of Platelets in the Presence of the H12−PEG−vesicles.

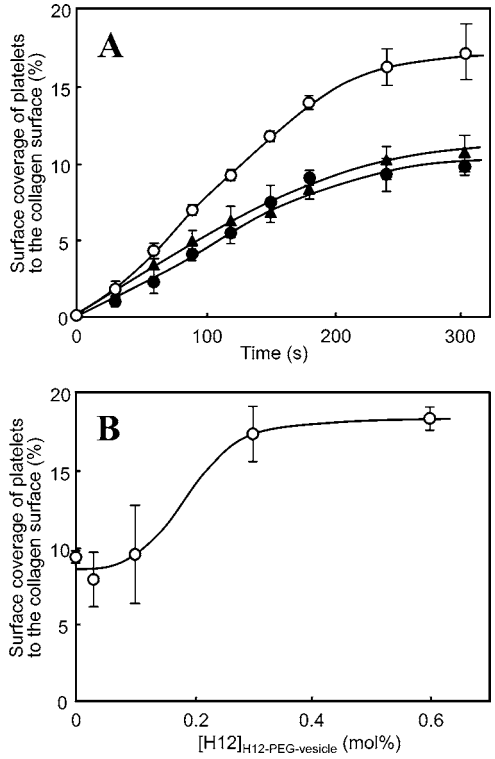

Figure 3. (A) Time course studies of surface coverage of platelets in the thrombocytopenic-imitation blood on the collagen surface after addition of (○) H12−PEG−vesicles, (●) PEG−vesicles, and (▲) PBS and (B) comparison between surface coverage of platelets and modification ratio of H12 on the surface of vesicles (shear rate 150 s^{-1}, [platelets] = $5.0 \times 10^4/\mu$L, [lipid] = 0.89 M, $N = 3$). The surface coverage was measured after 300 s.

Table 1. Binding Ratios of PAC-1 and Anti-P-selectin Antibody to the Resting Platelets in the Presence of H12−PEG−vesicles ($N = 3$)

stirring time (min)	PAC-1 binding (%)		P-selectin expression (%)	
	0	10	0	10
PBS	0.37 ± 0.12	3.77 ± 0.89	0.35 ± 0.11	2.52 ± 0.52
PEG−vesicles	0.52 ± 0.11	3.35 ± 0.32	0.50 ± 0.09	2.27 ± 0.54
H12−PEG−vesicles ([H12] = 0.3 mol %)	0.34 ± 0.16	3.72 ± 0.53	0.40 ± 0.10	2.43 ± 0.21
	89.80 ± 10.90[a]		33.42 ± 6.87[b]	

[a] ADP = 100 μM. [b] ADP = 20 μM.

We measured the ratios of PAC-1 binding to platelets and the P-selectin expression of platelets in the presence of the H12−PEG−vesicles (modification ratio of H12 0.3 mol %) (Table 1). In the ADP-stimulated and the resting platelets, the PAC-1 binding ratio was 89.8% ± 10.9%, and 0.37% ± 0.12%, respectively. When the resting platelets were stirred for 10 min at 37 °C, the ratio increased slightly to 3.77% ± 0.89%. Before and after mixing with the H12−PEG−vesicles, the ratio was 0.34% ± 0.16% and 3.72% ± 0.53%, respectively. In the case of the PEG−vesicles, the values (before 0.52% ± 0.11%, after 3.35% ± 0.32%) were approximately the same as those of the H12−PEG−vesicles.

On the other hand, the P-selectin expression ratios before and after mixing with the H12−PEG−vesicles were 0.40% ± 0.10% and 2.43% ± 0.21%, respectively, whereas in the PEG−vesicles, the values did not change (before 0.50% ± 0.09%, after 2.27% ± 0.54%). The positive and negative controls were 33.42% ± 6.87% and 0.35% ± 0.11%, respectively.

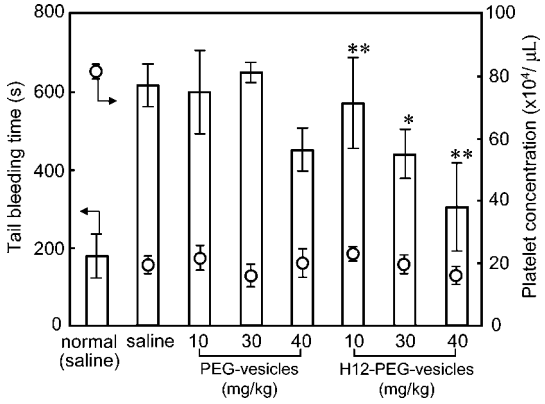

Figure 4. Effects of the administration of H12−PEG−vesicles on tail bleeding time. The administered amount of H12−PEG−vesicles was 10, 30, or 40 mg/kg equivalent of lipid. ○ indicates the platelet concentration in the rats ($N = 6-10$); ∗ indicates $P < 0.05$ or ∗∗ indicates not significant for H12−PEG−vesicles vs PEG−vesicles group at the same dose.

Measurement of the Tail Bleeding Time of Thrombocytopenic Rats in the Presence of the H12−PEG−vesicles. Thrombocytopenic rats were prepared by administering busulfan at a total dose of 20 mg/kg as described in our previous study (*11*). The tail bleeding times of normal rats ([platelet] = $(8.1 \pm 0.9) \times 10^5/\mu$L) and thrombocytopenic rats ([platelet] = $(2.0 \pm 0.3) \times 10^5/\mu$L) were 178 ± 56 and 618 ± 51 s, respectively (Figure 4). The bleeding time of the thrombocytopenic rats was about 3.5 times longer than that of the normal rats. Intravenous administration of the H12−PEG−vesicles at a dose of 10 mg/kg slightly reduced the bleeding time to 573 ± 127 s in comparison with those of a saline group (618 ± 51 s) or a control PEG−vesicle group at the same dose of the H12−PEG−vesicles (598 ± 115 s). At doses of 30 and 40 mg/kg, we confirmed a dose-dependent reduction of the bleeding time as shown in Figure 4; the time decreased significantly to 441 ± 66 and 335 ± 96 s, respectively. By comparison, the bleeding times of the control PEG−vesicles groups at doses of 30 and 40 mg/kg were 662 ± 21 and 432 ± 22 s, respectively. At the dose of 30 mg/kg, H12−PEG−vesicles significantly reduced the bleeding time in comparison with controls, whereas the H12−PEG−vesicles tended to reduce the bleeding time at the dose of 40 mg/kg.

DISCUSSION

We previously showed that fibrinogen-related dodecapeptide (H12) did not interact with the nonactivated platelets and did not cause platelet activation by using H12-latex beads (*34*). This indicated that H12 is a promising candidate as a key material of platelet substitutes. In this paper, we prepared H12−vesicles modified with PEG to obtain information about the possibility of constructing biocompatible and biodegradable particles with hemostatic ability in thrombocytopenic conditions. On the other hand, PEG-conjugated phosphatidylethanolamines (PEG−phospholipids) have been widely used for modification of the surface of vesicles to prolong the blood circulation time or to stabilize their dispersion states (*40*−*44*). Furthermore, PEG−phospholipids in which the terminus has an active group such as maleimido and pyridyl disulfide groups were also utilized to conjugate receptor proteins or ligands. We are proposing the use of amino acid-based lipids instead of phospholipid because various modifications are possible by simple syntheses. In this study, we used the PEG-conjugated amino acid-based lipid, as in our previous studies (*41*,

42). L-Glutamic acid was used as a connector between the PEG chain and two hydrophobic chains, in this case, stearyl alcohol (Glu2C18). The length of the alkyl chain is important because shorter alkyl chains should result in the dissociation of the PEG−lipid from the surface of the vesicle. The amino group of Glu2C18 reacted with the NHS group of MAL−PEG−NHS to produce MAL−PEG−Glu2C18 with a yield of 64%. The low yield is understandable because the NHS group was degraded before or during the reaction by hydrolysis. H12−PEG−Glu2C18 was thus obtained in a relatively high yield via an addition reaction between the maleimido and the mercapto groups of H12.

Next, we prepared vesicles consisting of DPPC/cholesterol/DHSG/PEG−DSPE at a molar ratio of 5/5/1/0.033. The vesicles with this composition were confirmed to be very stable in the state of aqueous dispersion and had excellent blood compatibility with an adequate blood circulation time (*41*). In the case of the PEG modification ratio of 0.3 mol %, the PEG chain is considered to take a so-called mushroom structure on the surface of the vesicle (*45*). For example, if 0.3 mol % of PEG−DSPE (M_w 5.0 kDa) and 0.3 mol % of H12−PEG−Glu2C18 (M_w of PEG chain 3.4 kDa) were incorporated in the surface of the vesicle, the excluded volume of the PEG chains would be estimated from the globular polymer chain as a radius of 6.2 and 4.9 nm, respectively, and the linear dodecapeptide (ca. 4.5 nm) was conjugated to the end of the PEG chain. This means that the H12 should locate on the more outer side more than the neighboring PEG chains, and therefore, the H12 has a possibility to be recognized by the platelets activated on the collagen plate.

The H12−PEG−Glu2C18 was incorporated into the bilayer membrane of the H12−PEG−vesicles in an equilibrium state. We have to determine whether the PEG−lipid tends to dissociate from the vesicular surface after dilution of the H12−PEG−vesicle suspension. We measured the incorporated ratio of H12−PEG−Glu2C18 (0.3 and 0.6 mol %) after incubation at 37 °C in a 30-fold dilution to analyze the stability of the lipids incorporated in the vesicles. From the ^{1}H NMR analyses, the incorporated ratio of the H12−PEG−Glu2C18 did not change. This indicated that the H12−PEG−Glu2C18 with the molecular weight of 4.4 kDa could be tethered to the vesicular surface with two stearoyl chains of Glu2C18. Therefore, the H12−PEG−vesicles would circulate stably in vivo without dissociation of the PEG−lipids. Furthermore, we confirmed that the half-life of the H12−PEG−vesicles was approximately 7-fold longer than that of the bare vesicles due to the effect of PEG modification, indicating that the H12−PEG−vesicles were useful for prophylactic transfusion. We are now studying the prolongation of the hemostatic effects at 180 min and longer after the intravenous administration of the H12−PEG−vesicles.

We prepared the immobilized-platelet surface and reconstituted blood to determine whether the H12−PEG−vesicles specifically bind to the immobilized platelets. In our previous studies, the flowing platelets specifically tethered and adhered to the platelets immobilized on the collagen plate, and the adhesion was suppressed in the presence of PAC-1 (*46*), soluble RGD, or soluble H12, which are GPIIb/IIIa antibodies or inhibitors, indicating that the immobilized-platelet plate should have GPIIb/IIIa exposed on the surface (*9*, *47*) (data not shown). Especially, PAC-1 recognizes an epitope on the GPIIb/IIIa complex of activated platelets at or near the platelet fibrinogen receptor (*46*). In reconstituted blood flowing over the immobilized-platelet plate, the H12−PEG−vesicles adhered and accumulated on the surface, whereas the control PEG−vesicles did not adhere as shown in Figure 2. When PAC-1 was added to the blood containing the H12−PEG−vesicles, the adhesion of the H12−PEG−vesicles was completely inhibited, indicating that the H12−PEG−vesicles were specifically bound to the activated GPIIb/IIIa on the surface of the platelets even with PEG modification. This was supported by the results showing that the number of the adherent H12−PEG−vesicles increased with increasing H12-modification ratio to the vesicle from 0.03 to 0.6 mol % (data not shown).

To determine whether the H12−PEG−vesicles have an ability to reinforce thrombus formation under thrombocytopenic conditions, we prepared a thrombocytopenic blood and adjusted the number of platelets to $5.0 \times 10^4/\mu$L (one-fifth of normal). When the thrombocytopenic blood flowed over the collagen surface, the control PEG−vesicles did not influence the surface coverage of platelets as shown in Figure 3A (filled circle). In the case of the H12−PEG−vesicles having 0.3 mol % H12, the enhancement of the platelet thrombus formation was confirmed as shown in Figure 3A (opened circle). These results suggest that the H12−PEG−vesicles cross-link the activated platelets to enhance the platelet aggregation. In the initial 30 s, the adhesion rate of platelets in the presence of the H12−PEG−vesicles was similar to that of the PEG−vesicles, and then the surface coverage increased dramatically with time in the case of the H12−PEG−vesicles. Furthermore, we confirmed that the H12−PEG−vesicles labeled with rhodamine were involved in the platelet thrombus labeled with $DiOC_6$ by a double-stain method (data not shown). The above results suggest that (1) the adhesion of the H12−PEG−vesicles could be initiated by the activated platelets, which had already adhered on the surface of the immobilized-collagen plate, (2) the H12−PEG−vesicles adhering to the surface of the platelet could act as binding sites for the activated platelets, and (3) the H12−PEG−vesicles could accelerate the formation of the thrombus of the remaining flowing platelets in the thrombocytopenic blood.

Figure 3B summarized the results of the surface coverage of platelets after 300 s in the presence of the H12−PEG−vesicles in which the modification ratio of H12 is from 0 to 0.6 mol % in thrombocytopenic blood. From 0 to 0.1 mol %, the constant surface coverage in the region of the modification ratios suggests that the recognition ability of the H12−PEG−vesicles to the GPIIb/IIIa on the activated platelets was very low because of the low modification density of H12. Surprisingly, the surface coverage increased significantly when the modification ratio was raised above 0.3 mol %. This indicated that the H12−PEG−vesicles had the ability to cross-link the activated platelets. Therefore, we adopted the H12 modification ratio of 0.3 mol %.

Before in vivo studies, we used platelet-activation markers, PAC-1 or anti-P-selectin antibody (*48*), to determine whether the H12−PEG−vesicles caused the activation of platelets. P-selectin is a membrane glycoprotein existing in the α granules of platelets and Weibel−Palade bodies of vascular endothelial cells, and following cellular activation, it becomes surface-expressed by exocytosis (*48*). When a mixture of platelets and the control PEG−vesicles was stirred with PAC-1 or anti-P-selectin antibody, the binding ratios of both antibodies to the platelets were slightly increased after stirring as shown in Table 1. These phenomena were also observed in the absence of the control PEG−vesicles or in the

presence of H12−PEG−vesicles as shown in Table 1. This suggested that the increase was caused by stirring and was within the error limit in comparison with that of PAC-1 binding and P-selectin expression to ADP-stimulated platelets. We concluded that the H12−PEG−vesicles did not activate platelets and did not interact with the nonactivated platelets under flow and that the adhesion of the H12−PEG−vesicles was induced by the platelets activated by the collagen surface. Therefore, H12−PEG−vesicles have the potential to be a candidate for platelet substitutes.

Next, we evaluated the hemostatic ability of the H12−PEG−vesicles using thrombocytopenic rats. In our previous studies, we succeeded in preparing thrombocytopenic rats by busulfan administration and getting the extinction curve of platelets reproducibly (*11*). From the data of hematologic indices, where the platelet counts were sufficiently decreased and the erythrocyte and leukocyte counts were maintained, we determined that the appropriate total dosage of busulfan for the rats (8 weeks) was 20 mg/kg. The incision of the tail was to be made on Day 10 after busulfan infusion. We also confirmed that the bleeding time correlated with their platelet concentration, indicating that the tail bleeding time was an effective evaluation parameter for measuring the hemostatic capability of the platelet substitutes.

As shown in Figure 4, the bleeding time of the thrombocytopenic rats was significantly extended in comparison with that of normal rats 5 min after the intravenous administration of saline, and we determined that it was possible to evaluate the hemostatic effect of the H12−PEG−vesicles in vivo using thrombocytopenic rats. The circulating H12−PEG−vesicles at the dose of 30 mg/kg significantly reduced the bleeding time of the thrombocytopenic rats, whereas at a lower concentration of 10 mg/kg, the hemostatic effect did not reach a significant level. At a higher concentration of 40 mg/kg, however, the bleeding time was significantly reduced in comparison with that of the saline group but not with the control PEG−vesicles group (40 mg/kg). This suggested that the PEG−vesicles themselves possessed a hemostatic activity at the higher concentration, because the PEG−vesicles having negative charge at pH 7.4 might nonspecifically bind to site of bleeding injury.

We estimated that the hemostatic ability of the H12−PEG−vesicles at a dose of 30 mg/kg (approximately 2.0×10^{12} particles) would correspond to 1/500th of the hemostatic ability in particle base, which was based on the bleeding time of the thrombocytopenic rats and platelet concentration. Furthermore, we confirmed that hematologic indices such as the platelet and leukocyte counts did not change before and after the administration of the H12−PEG−vesicles.

In conclusion, we demonstrated that the H12−PEG−vesicles did not interact with nonactivated platelets, and the vesicles were shown to preferentially interact with an activated platelet surface via GPIIb/IIIa receptors and to facilitate platelet accumulation at sites of hemostasis. Furthermore, the H12−PEG−vesicles could reduce the tail bleeding time of thrombocytopenic rats. Thus, the H12−PEG−vesicles may be a suitable candidate for an alternative to human platelet concentrates infused into thrombocytopenic patients.

ACKNOWLEDGMENT

The authors thank Drs. M. Murata and K. Yokoyama at Keio University for useful discussion about the functional evaluation of H12 peptide. This work was supported in part by Health and Labor Sciences Research Grants (Research on Pharmaceutical and Medical Safety, S.T., M.H., and Y.I.), Ministry of Health, Labor and Welfare, Japan, and grants-in-aid from the JSPS, Japan (No. 15300171, S.T.), Ministry of Education, Culture, Sports, Science and Technology (Leading Project for Biosimulation, M.H.), 21COE "Practical Nano-Chemistry", and "Consolidated Research Institute for Advanced Science and Medical Care" from MEXT (S.T.), Japan. Y.O. was the recipient of a Research Fellowship from the JSPS for Young Scientists.

LITERATURE CITED

(1) Blajchman, M. A. (2003) Substitutes and alternatives to platelet transfusions in thrombocytopenic patients. *J. Thromb. Haemostasis 1*, 1637−1641.

(2) Rybak, M., and Renzulli, L. A. (1993) A liposome based platelet substitutes, the plateletsome, with hemostatic efficacy. *Biomater. Artif. Cells Immobilization Biotechnol. 21*, 108−118.

(3) Graham, S. S., Gonchoroff, N. J., and Miller, J. L. (2001) Infusible platelet membranes retain partial functionality of the platelet GPIb/IX/V receptor complex. *Am. J. Clin. Pathol. 115*, 144−147.

(4) Levi, M., Friedrich, P. W., Middleton, S., De Groot, P. G., Wu, Y. P., Harris, R., Biemond, B. J., Heijien, F. G., Levin, J., and Ten Cate, J. W. (1999) Fibrinogen-coated albumin microcapsules reduce bleeding in severely thrombocytopenic rabbits. *Nat. Med. 5*, 107−111.

(5) Agam, G., and Livine, A. A. (1992) Erythrocytes with covalently bound fibrinogen as a cellular replacement for the treatment of thrombocytopenia. *Eur. J. Clin. Invest. 22*, 105−112.

(6) Casals, E., Verdaguer, A., Tonda, R., Galan, A., Escolar, G., and Estelrich, J. (2003) Atomic force microscopy of liposomes bearing fibrinogen. *Bioconjugate Chem. 14*, 593−600.

(7) Coller, B. S., Springer, K. T., Beer, J. H., Mohandas, N., Scudder, L. E., Norton, K. J., and West, S. M. (1992) Thromboerythrocytes. In vitro studies of a potential autologous, semi-artificial alternative to platelet transfusion. *J. Clin. Invest. 89*, 546−555.

(8) Teramura, Y., Okamura, Y., Takeoka, S., Tsuchiyama, H., Narumi, H., Kainoh, M., Handa, M., Ikeda, Y., and Tsuchida, E. (2003) Hemostatic effects of polymerized albumin particles bearing rGPIa/IIa in thrombocytopenic mice. *Biochem. Biophys. Res. Commun. 306*, 256−260.

(9) Takeoka, S., Teramura, Y., Okamura, Y., Handa, M., Ikeda, Y., and Tsuchida, E. (2001) Fibrinogen-conjugated albumin polymers and their interaction with platelets under flow conditions. *Biomacromolecules 2*, 1192−1197.

(10) Takeoka, S., Teramura, Y., Ohkawa, H., Ikeda, Y., and Tsuchida, E. (2000) Conjugation of von Willebrand factor-binding domain of platelet glycoprotein Ibα to size-controlled albumin microsheres. *Biomacromolecules 1*, 290−295.

(11) Okamura, Y., Takeoka, S., Teramura, Y., Maruyama, H., Tsuchida, E., Handa, M., and Ikeda, Y. (2005) Hemostatic effects of fibrinogen-γ chain dodecapeptide-conjugated polymerized albumin particles *in vitro* and *in vivo*. *Transfusion 45*, 1221−1228.

(12) Takeoka, S., Teramura, Y., Okamura, Y., Tsuchida, E., Handa, M., and Ikeda, Y. (2002) Rolling properties of rGPIbα-conjugated phospholipid vesicles with different membrane flexibilities on vWf surface under flow conditions. *Biochem. Biophys. Res. Commun. 296*, 765−770.

(13) Kitaguchi, T., Murata, M., Iijima, K., Kamide, K., Imagawa, T., and Ikeda, Y. (1999) Characterization of liposomes carrying von Willebrand factor-binding domain of platelet glycoprotein Ibα: A potential substitute for platelet transfusion. *Biochem. Biophys. Res. Commun. 261*, 784−789.

(14) Nishiya, T., Murata, M., Handa, M., and Ikeda, Y. (2000) Targetting of liposomes carrying recombinant fragments of platelet membrane glycoprotein Ibα to immobilized von Willebrand factor under flow conditions. *Biochem. Biophys. Res. Commun. 270*, 755−760.

(15) Nishiya, T., Kainoh, M., Murata, M., Handa, M., and Ikeda, Y. (2002) Reconstitution of adhesive properties of human platelets in liposomes carrying both recombinant glycoproteins Ia/IIa and Ibα under flow conditions: specific synergy of receptor−ligand interactions. *Blood 100*, 136−142.
(16) Murata, M., Ware, J., and Ruggeri, Z. M. (1991) Site-directed mutagenesis of a soluble recombinant fragment of platelet glycoprotein Ibα demonstrating negatively charged residues involved in von Willebrand factor binding. *J. Biol. Chem. 266*, 15474−15480.
(17) Marchese, P., Saldivar, E., Ware, J., and Ruggeri, Z. M. (1999) Adhesive properties of the isolated amino-terminal domain of platelet glycoprotein Ibα in a flow field. *Proc. Natl. Acad. Sci. U.S.A. 96*, 7837−7842.
(18) Sixma, J. J., van Zanten, G. H., Huizinga, E. G., van der Plas, R. M., Verkley, M., Wu, Y. P., Gros, P., and de Groot, P. G. (1997) Platelet adhesion to collagen: An update. *Thromb. Haemostasis 78*, 434−438.
(19) Santro, S. A., and Zutter, M. M. (1995) The α2β1integrin: A collagen receptor on platelets and other cells. *Thromb. Haemostasis 74*, 813−821.
(20) Takagi, J., Petre, B. M., Walz, T., and Springer, T. A. (2002) Global comformational rearrangements in integrin extracellular domains in outside-in and inside-out signaling. *Cell 110*, 599−611.
(21) Xiao, T., Takagi, J., Coller, B. S., Wang, J. H., and Springer, T. A. (2004) Structual basis for allostery in integrins and binding to fibrinogen-mimetic therapeutics. *Nature 432*, 59−67.
(22) Shattil, S. J., Hoxie, J. A., Cunningham, M., and Brass, L. F. (1985) Changes in the platelet membrane glycoprotein IIb-IIIa complex during platelet activation. *J. Biol. Chem. 260*, 11107−11114.
(23) Marguerie, G. A., Plow, E. F., and Edgington, T. S. (1979) Human platelets possess an inducible and saturable receptor specific for fibrinogen. *J. Biol. Chem. 254*, 5357−5363.
(24) Ruggeri, Z. M., De Marco, L., and Gatti, L. (1983) Platelets have more than one binding site for von Willebrand factor. *J. Clin. Invest. 72*, 1−12.
(25) Mustard, J. F., Packham, M. A., and Kinlough-Rathbone, R. L. (1978) Fibrinogen and ADP-induced platelet aggregation. *Blood 52*, 453−466.
(26) De Marco, L., Girolami, A., and Zimmerman, T. S. (1986) Von Willebrand factor interaction with the glycoprotein IIb/IIIa complex. *J. Clin. Invest. 77*, 1272−1277.
(27) Hawiger, J., Kloczewiak, M., Bednarek, M. A., and Timmons, S. (1989) Platelet receptor recognition domains on the α chain of human fibrinogen: structure−function analysis. *Biochemistry 28*, 2909−2914.
(28) Kloczewiak, M., Timmons, S., and Hawiger, J. (1982) Localization of a site interacting with human platelet receptor on carboxy-terminal segment of human fibrinogen γ chain. *Biochem. Biophys. Res. Commun. 107*, 181−187.
(29) Wertheimer, E., Shapiro, B., and Fodor-Salomonowicz, I. (1944) Stability of fibrinogen in normal and pathological plasma. *Br. J. Exp. Pathol. 25*, 121−125.
(30) Kloczewiak, M., Timmons, S., Lukas, T. J., and Hawiger, J. (1984) Platelet receptor recognition site on human fibrinogen. Synthesis and structure−function relationship of peptides corresponding to the carboxy-terminal segment of the γ chain. *Biochemistry 23*, 1767−1774.
(31) Kloczewiak, M., Timmons, S., Bednarek, M. A., Sakon, M., and Hawiger, J. (1989) Platelet receptor recognition domain on the γ chain of human fibrinogen and its synthetic peptide analogues. *Biochemistry 28*, 2915−2919.
(32) Lam, S. C., Plow, E. F., Smith, M. A., Andrieux, A., Ryckwaert, J. J., Marguerie, G., and Ginsberg, M. H. (1987) Evidence that arginyl-glycyl-aspartate peptides and γ chain peptides share a common binding site on platelets. *J. Biol. Chem. 262*, 110−115.
(33) Hallahan, D. E., Geng, L., Cmelak, A. J., Chakravathy, A. B., Martin, W., Scarfone, C., and Gonzalez, A. (2001) Targeting drug delivery to radiation-induced neoantigens in tumor microvasculature. *J. Controlled Release 74*, 183−191.
(34) Takeoka, S., Okamura, Y., Teramura, Y., Watanabe, N., Suziki, H., Tsuchida, E., Handa, M., and Ikeda, Y. (2003) Function of fibrinogen γ-chain dodecapeptide-conjugated latex beads under flow. *Biochem. Biophys. Res. Commun. 312*, 773−779.
(35) Nishiya, T., and Toma, C. (2004) Interaction of platelets with liposomes containing dodecapeptide sequence from fibrinogen. *Thromb. Haemostasis 91*, 1158−1167.
(36) Klibanov, A. L., Maruyama, K., Torchilin, V. P., and Huang, L. (1990) Amphipathic poly(ethylene glycol)s effectively prolong the circulation time of liposomes. *FEBS Lett. 268*, 235−237.
(37) Zalipsky, S. (1995) Functionalized poly(ethylene glycol) for preparation of biologically relevant conjugates. *Bioconjugate Chem. 6*, 150−165.
(38) Sakai, H., Takeoka, S., Park, S. I., Kose, T., Nishide, H., Izumi, Y., Yoshizu, A., Kobayashi, K., and Tsuchida, E. (1997) Surface modification of vHemoglobin vesicles with poly (ethylene glycol) and effects on aggregation, viscosity, and blood flow during 90% exchange transfusion in anesthetized rats. *Bioconjugate Chem. 8*, 23−30.
(39) Sakai, H., Tsai, A. G., Kerger, H., Park, S. I., Takeoka, S., Nishide, H., Tsuchida, E., and Intaglietta, M. (1998) Subcutaneous microvascular responses to hemodilution with a red cell substitutes consisting of poly(ethylene glycol)-modified vesicles encapsulating hemoglobin. *J. Biomed. Mater. Res. 40*, 66−78.
(40) Sou, K., Endo, T., Takeoka, S., and Tsuchida, E. (2000) Poly(ethylene glycol)-modification of the phospholipid vesicles by using the spontaneous incorporation of poly(ethylene glycol)-lipid into the vesicles. *Bioconjugate Chem. 11*, 372−379.
(41) Sou, K., Naito, Y., Endo, T., Takeoka, S., and Tsuchida, E. (2003) Effective encapsulation of proteins into size-controlled phospholipid vesicles using freeze−thawing and extrusion. *Bioconjugate Chem. 19*, 1547−1552.
(42) Takeoka, S., Mori, K., Ohkawa, H., Sou, K., and Tsuchida, E. (2000) Synthesis and assembly of poly(ethylene glycol)-lipids with mono-, di-, tetraacyl chains and a poly(ethylene glycol) chain of various molecular weights. *J. Am. Chem. Soc. 122*, 7927−7935.
(43) Yang, C., Li, Y. C., and Kuter, D. J. (1999) The physiological response of thrombopoietin (c-Mpl ligand) to thrombocytopenia in the rat. *Br. J. Haematol. 105*, 478−485.
(44) Stenberg, P. E., Barrie, R. J., Pestina, T. I., Steward, S. A., Arnold, J. T., Murti, A. K., Hutson, N. K., and Jackson, C. A. (1998) Prolonged bleeding time with defective platelet filopodia formation in the wistar furth rat. *Blood 91*, 1599−1608.
(45) Hristova, K., and Needham, D. (1995) Phase Behavior of a Lipid/Polymer−Lipid Mixture in Aqueous Medium. *Macromolecules 28*, 991−1002.
(46) Taub, R., Gould, R. J., Garsky, V. M., Ciccarone, T. M., Hoxie, J., Friedman, P. A., and Shattil, S. J. (1989) A monoclonal antibody aganst the platelet fibrinogen reseptor contains a sequence that mimics a receptor recognition domein receptor. *J. Biol. Chem. 264*, 259−265.
(47) Kulkarni, S., Dopheide, S. M., Yap, C. L., Ravanat, C., Freund, M., Mangin, P., Heel, K. A., Street, A., Harper, I. S., Lanza, F., and Jackson, S. P. (2000) A revised model of platelet aggregation. *J. Clin. Invest. 105*, 783−791.
(48) Lasky, L. A. (1992) Selectin: interpreters of cell-specific carbohydrate information during inflamation. *Science 258*, 964−969.

BC050178G

Carbohydrate-Bearing 3-Hydroxy-4-pyridinonato Complexes of Gallium(III) and Indium(III)

David E. Green,[†,‡,§] Cara L. Ferreira,[†,‡] Robert V. Stick,[⊥] Brian O. Patrick,[†] Michael J. Adam,[‡] and Chris Orvig*[,†]

Medicinal Inorganic Chemistry Group, Department of Chemistry, University of British Columbia, Vancouver, BC, V6T 1Z1, Canada, TRIUMF, 4004 Westbrook Mall, Vancouver, B.C., V6T 2A3, Canada, and Chemistry M313, School of Biomedical and Chemical Sciences, University of Western Australia, Crawley WA 6009, Australia. Received June 23, 2005; Revised Manuscript Received August 23, 2005

Gallium and indium complexes with pendant carbohydrates have been prepared and examined for their potential as radiopharmaceuticals. Carbohydrate-bearing 3-hydroxy-4-pyridinone ligand precursors and their tris(ligand)gallium(III) and -indium(III) complexes were synthesized and characterized by mass spectrometry, elemental analysis, and ^{1}H and ^{13}C NMR spectroscopy, and in the case of one intermediate, by X-ray crystallography. With three equivalents of ligand, neutral complexes formed with the bidentate hydroxypyridinone moiety complexing the gallium(III) and indium(III) metal centers.

INTRODUCTION

Isotopes of gallium and indium have been used in diagnostic nuclear medicine for decades (*1*–*5*). The gamma-emitting isotopes ^{67}Ga ($t_{1/2}$ = 78 h, γ = 93, 185, 300 keV) and ^{111}In ($t_{1/2}$ = 68 h, γ = 245, 172 keV) are the most common radionuclides of gallium and indium used in nuclear medicine. Another promising gallium radionuclide with the ideal characteristics for generator technology is the positron-emitting ^{68}Ga ($t_{1/2}$ = 68 min) produced from a $^{68}Ge/^{68}Ga$ couple. Advantages of this radionuclide are that the long half-life of ^{68}Ge ($t_{1/2}$ = 280 d) gives the generator a life of at least one year and ^{68}Ga has a short half-life and can also be used for quantitative PET imaging; an on-site cyclotron is not required for production.

Currently, gallium citrate is the most used gallium radiopharmaceutical for diagnostic imaging; however, the coordinating citrate ligands are readily displaced by transferrin which complexes the gallium(III) ions, thus facilitating the biodistribution of the isotope ^{67}Ga (*6*, *7*). For a metal complex to remain intact it must be kinetically and thermodynamically stable in comparison to other biological chelators. A high stability constant for a metal complex indicates its thermodynamic stability and is one criterion considered for radiopharmaceutical evaluation. Chelators such as 8-hydroxyquinoline (Chart 1) are used to form gallium and indium complexes with high stability constants that are used in radiopharmaceutical applications (*6*). More recent efforts include the use of a pendant peptide linked to DTPA (pentetreotide, Chart 1). This is a bifunctional chelate approach: the DTPA portion of the molecule chelates the gallium or indium metal center, and the peptide portion helps to direct the metal complex to somatostatin receptors in vivo (*8*).

Chart 1. Selected Relevant Compounds That Form Gallium and Indium Complexes

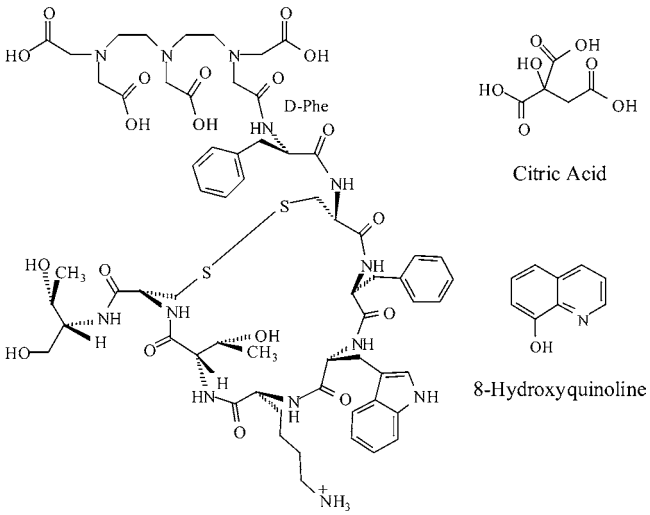

Recently FDA-approved, this ^{111}In radiopharmaceutical (OctreoScan) is being used for diagnostic imaging.

To expand further the types of gallium and indium radiopharmaceuticals, metal complexes stable under in vivo conditions are needed. 3-Hydroxy-4-pyridinones also have high stability constants with gallium(III) and indium(III) ions (*9*–*11*). These ligands form neutral tris(ligand)gallium(III) and indium(III) complexes that predominate from pH 4.5 to 9 and have high thermodynamic stabilities (log β_3 ~36–38 for Ga(III) and ~31–33 for In(III)). The pyridinone moiety also has a number of sites where it can be functionalized with the addition of biomolecules such as carbohydrates.

In this work, we report carbohydrate-bearing pyridinone complexes of gallium and indium. Several novel

* Corresponding author. E-mail: orvig@chem.ubc.ca.
[†] University of British Columbia.
[‡] TRIUMF.
[⊥] University of Western Australia.
[§] Present Address: Medical Biophysics, B.C. Cancer Research Centre, 675 West 10th Avenue, Vancouver, BC, V5Z 4E6, Canada

10.1021/bc0501808 CCC: $30.25 © 2005 American Chemical Society
Published on Web 10/04/2005

Scheme 1. Synthesis of HOG6GP[a]

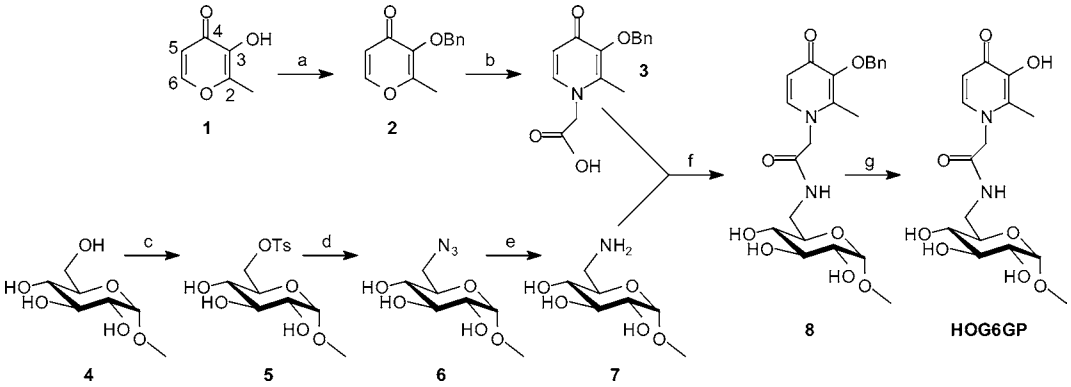

[a] (a) BnCl, NaOH, MeOH/H_2O, 71%; (b) sodium glycinate, MeOH/H_2O, 48%; (c) TsCl, pyridine, 30%; (d) NaN_3, acetone, 97%; (e) Pd black, 60 atm. H_2, MeOH, 73%; (f) DCC/NHS, DMF, 76%; (g) 10% Pd/C, 1 atm H_2, MeOH/H_2O, 53%.

Scheme 2. Synthesis of HOGBAP[a]

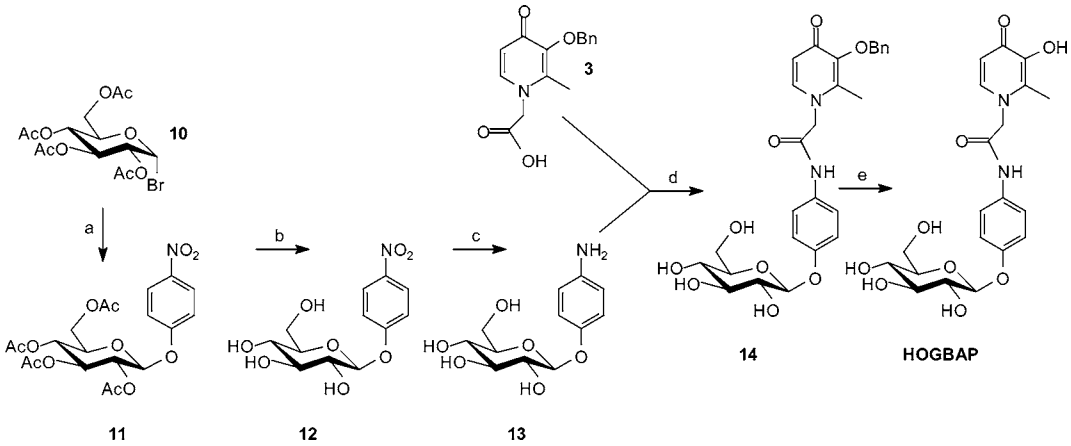

[a] (a) 4-Nitrophenol, Ag_2CO_3, MeCN, 68%; (b) NaOMe, MeOH/dichloromethane, 99%; (c) 10% Pd/C, H_2, MeOH/H_2O, 87%; (d) DCC/NHS, DMF, 71%; (e) 10% Pd/C, 1 atm H_2, MeOH/H_2O, 59%.

3-hydroxy-4-pyridinone ligands bearing pendant glucose derivatives are described as well as an improved synthesis of the previously published Feralex-G (*12*). The glucose-bearing ligands will likely direct the metal complexes in vivo, as carbohydrates have extensive transport and metabolic pathways. The corresponding radioactive gallium or indium complexes may have applications in diagnostic nuclear medicine (^{67}Ga, ^{68}Ga, ^{111}In) and radiotherapy (^{111}In) related to metabolic glucose imaging such as tumor, myocardial, or brain imaging or perhaps in imaging of glucose transport receptors. Several studies of carbohydrate pendant metal complexes using the SPECT radioisotope ^{99m}Tc have been reported (*13*−*16*), but none with gallium or indium radioisotopes.

RESULTS AND DISCUSSION

Ligand Preparations. The conditions for pyridinone synthesis from the corresponding pyranone often require heating for extended periods of time in slightly acidic or rather basic conditions. Larger amino substituents typically hinder pyridinone formation resulting in very low or no yields. For these reasons the strategy was to form the pyridinone-linker system first using relatively smaller amines and then couple this linker to the glucose moiety. The linkers include the carboxylic acid substituent as in **3** and a phenolic substituent as in **17**. The point of glucose attachment was chosen to give some variety in structure that was relatively straightforward to synthesize.

All six ligand precursors **HOG6GP**, **HOG2GP**, **HOGBAP**, **HOGBPP**, **HAG6GP**, and **HAGBAP** were prepared by various routes from maltol (**1**). The hydroxyl group of maltol was benzyl-protected using benzyl chloride to produce **2**. Glycine was reacted with **2** under basic conditions to produce the corresponding pyridinone **3**. DCC was used to activate the carboxylic acid group of **3** as the NHS ester, which was then reacted in situ with amines **7**, **13**, and glucosamine to produce the amide-coupled compounds **8** (Scheme 1), **14** (Scheme 2), and **19**, respectively. Debenzylation of **8**, **14**, and **19** was accomplished by hydrogenolysis using 10% Pd/C to produce **HOG6GP**, **HOGBAP**, and **HOG2GP (Feralex-G)**, respectively.

Amine **7** (Scheme 1) was prepared starting from methyl α-D-glucopyranoside (**4**) that was tosylated to produce **5** and further reacted with sodium azide, according to literature preparations (*17*), to afford **6**. Hydrogenation of the azide was accomplished at 60 atm using palladium black as a catalyst producing amine **7**.

Amine **13** (Scheme 2) was prepared from 2,3,4,6-tetra-*O*-acetyl-α-D-glucopyranosyl bromide (**10**); Koenigs−Knorr conditions (*18*) with silver carbonate were used to convert **10** to 4-nitrophenyl 2,3,4,6-tetra-*O*-acetyl-β-D-glucopyranoside (**11**). Deacetylation with sodium methoxide produced 4-nitrophenyl β-D-glucopyranoside (**12**), and the nitro group was hydrogenated with 10% Pd/C as a catalyst to produce the amine **13** that was recrystallized as the hydrochloride.

The synthesis of **HOGBPP** is shown in Scheme 3. 4-Aminophenol was reacted with benzyl-protected maltol **2** under slightly acidic conditions to produce 3-benzyloxy-

Scheme 3. Synthesis of HOGBPP[a]

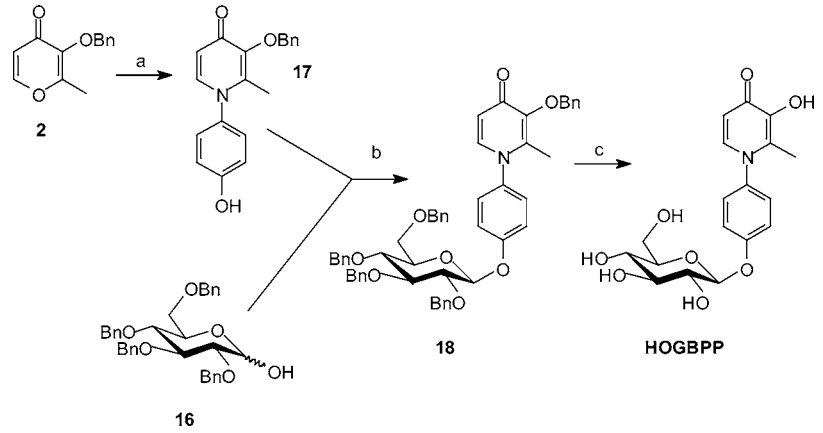

[a] (a) 4-Aminophenol, H_2O/MeOH, 29%; (b) ADDP, Bu_3P, dichloromethane, 66%; (c) 10% Pd/C, 1 atm H_2, MeOH/H_2O, 86%.

Scheme 4. Synthesis of HAG6GP[a]

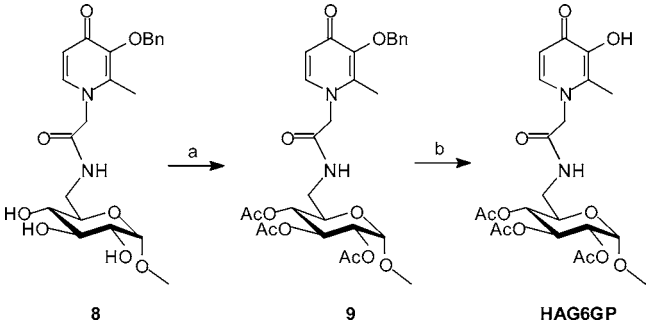

[a] (a) Ac_2O, pyridine, 77%; (b); 10% Pd/C, 1 atm H_2, MeOH/H_2O, 71%.

Scheme 5. Synthesis of HAGBAP[a]

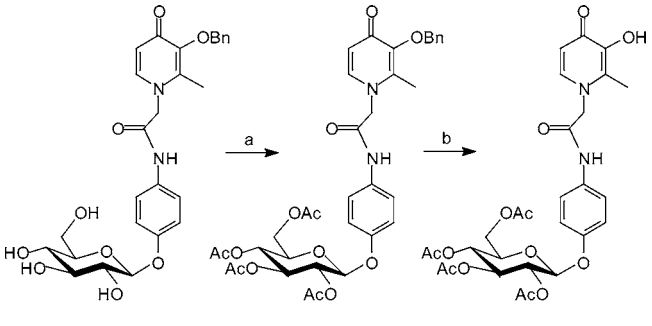

[a] (a) Ac_2O, pyridine, 74%; (b); 10% Pd/C, 1 atm H_2, MeOH/H_2O, 71%.

1-(4-hydroxyphenyl)-2-methyl-4(1*H*)-pyridinone (**17**). ADDP and tributylphosphine were used to couple the phenolic moiety of **17** to 2,3,4,6-tetra-*O*-benzyl-D-glucopyranose (**16**) under Mitsunobu conditions (*19*) which produced the β-glucoside (**18**) after column chromatography. Debenzylation of **18** with H_2 and 10% Pd/C afforded **HOGBPP**.

The syntheses of **HAG6GP** and **HAGBAP** are shown in Schemes 4 and 5, respectively. Compounds **8** and **14** were acetylated using acetic anhydride in pyridine to produce **9** and **15**, respectively. Debenzylation of **9** and **15** with H_2 and 10% Pd/C afforded **HAG6GP** and **HAGBAP**, respectively.

A synthesis of **HOG2GP**, also known as Feralex-G, has been previously reported. In the literature preparation, the nonbenzylated analogue of **3**, 1-carboxymethyl-2-methyl-4(1*H*)-pyridinone, is coupled to glucosamine (*12*). Although the reported synthesis gives good yields, purification of the product posed difficulties. Easier purification was afforded by preparing the benzyloxy-protected **HOG2GP** (**19**). The greater lipophilicity of **19** facilitated its silica gel purification, and a protected pyridinone also prevented adventitious metal chelation from the silica. Debenzylation of **19** with H_2 and 10% Pd/C afforded high purity **HOG2GP** (Scheme 6).

Scheme 6. Synthesis of HOG2GP[a]

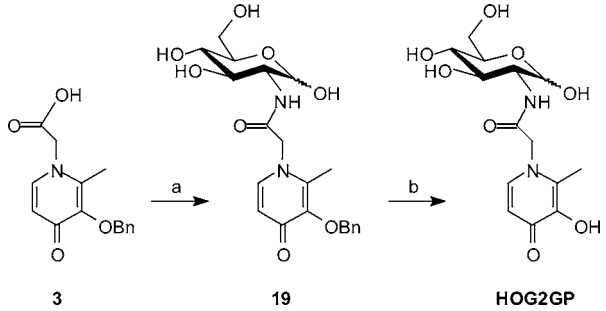

[a] (a) Glucosamine hydrochloride, DCC, NHS, DMF, 80 °C, 54% (b) 10% Pd/C, 1 atm H_2, MeOH/H_2O, 100%.

All ligands were thoroughly characterized by elemental analysis and mass spectrometry, and complete ^1H and ^{13}C NMR spectral assignments were made using 2D techniques. The ^1H NMR spectrum of **HOG2GP** has been previously reported, but only for the α anomer (*12*). As a hemiacetal, **HOG2GP** can mutarotate and is present as a 7:3 α:β ratio in water (at RT). The other five ligands were designed as single anomers.

Tris(3-oxy-4-pyridinato)gallium(III) and -indium-(III) Complexes. The neutral gallium(III) and indium-(III) complexes were prepared by addition of gallium or indium nitrate solutions to solutions containing the precursor ligands. The acidic solutions containing the reaction mixtures were adjusted to neutral pH with sodium hydroxide, and subsequent column purification (G10) or precipitate collection yielded the metal complexes (Scheme 7).

Elemental analyses of all the metal complexes were consistent with the calculated values. All metal complexes included 1 to 5 waters of hydration that were not eliminated after drying for at least 48 h in a vacuum desiccator at RT. These waters are consistent with other gallium and indium pyridinone complexes with 0.5−5.5 waters of hydration often being reported (*9*), although up to 12 waters of hydration have been reported in some solid-state structures (*20*, *21*). Drying some gallium and indium pyridinone complexes at 85 °C in vacuo for 24 h failed to remove all waters of hydration from these complexes (*9*). The mass spectra (+ESI) for the metal

Scheme 7. Synthesis of ML_3 Complexes[a]

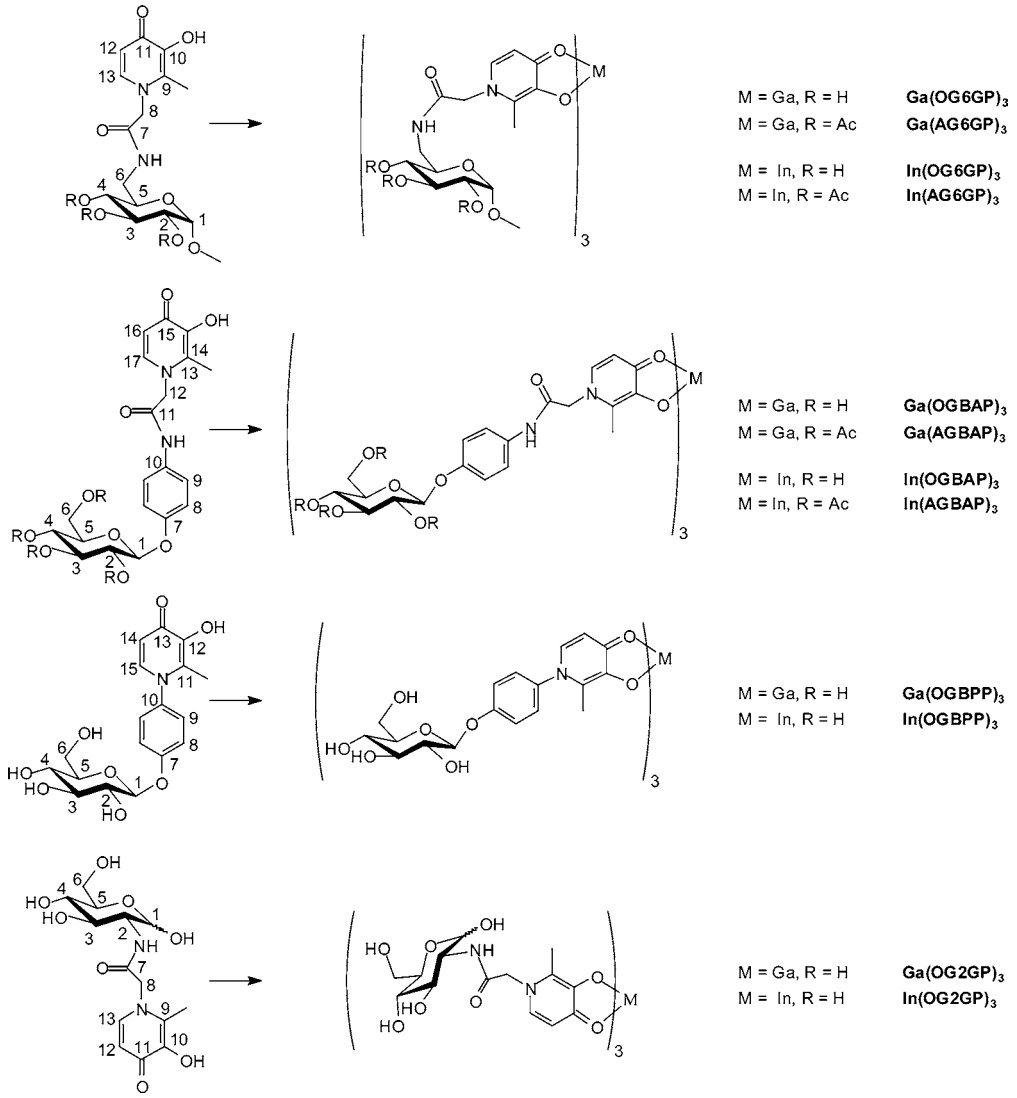

[a] **Ga(OG6GP)$_3$** (95%)[b], **In(OG6GP)$_3$** (89%)[c], **Ga(AG6GP)$_3$** (83%)[c], **In(AG6GP)$_3$** (86%)[d], **Ga(OGBAP)$_3$** (95%)[b], **In(OGBAP)$_3$** (91%)[c], **Ga(AGBAP)$_3$** (90%)[c], **In(AGBAP)$_3$** (93%)[d], **Ga(OGBPP)$_3$** (88%)[b], **In(OGBPP)$_3$** (91%)[c], **Ga(OG2GP)$_3$** (91%)[b], and **In(OG2GP)$_3$** (70%)[c]. [b]$Ga(NO_3)_3{\cdot}9H_2O$, H_2O; [c]$In(NO_3)_3{\cdot}3H_2O$, H_2O; [d]$Ga(NO_3)_3{\cdot}9H_2O$, H_2O:EtOH; [e]$In(NO_3)_3{\cdot}3H_2O$, H_2O:EtOH.

Scheme 8. Synthesis of Ga(hpp)$_3$[a]

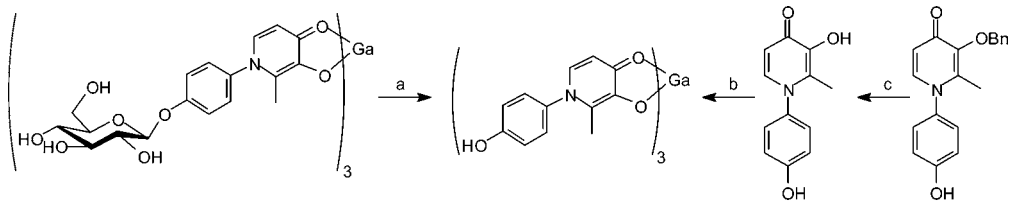

[a] (a) Abg, sodium phosphate buffer; (b) $Ga(NO_3)_3{\cdot}9H_2O$, DMF, 86%; (c) 10% Pd/C, 1 atm H_2, MeOH/DMF/H_2O, 35%.

complexes revealed protonated, sodiated, or sometimes potassiated parent molecules. These parent ions had the expected fragmentation patterns and isotopic distributions.

^{1}H and ^{13}C NMR Spectra. ^{1}H NMR spectra indicated that the pyridinone ring protons had the most prominent changes in chemical shift upon metal complexation. The largest coordination induced shift (CIS) was observed for H5, (see Table 1 for pyridinone ring numbering) where metal complexation resulted in downfield shifts of 0.11−0.19 ppm for the complexes studied. These are close to the 0.19−0.32 ppm downfield shifts observed for other (crystallographically characterized) gallium and indium pyridinone complexes in $CDCl_3$ and $(CD_3)_2SO$ (*9*). Significant shifts were also observed in this work for H6 with upfield shifts from 0.04 to 0.11 ppm.

Gallium(III) and indium(III) ions have the potential to coordinate alkoxy groups from citric acid (*22*, *23*) or gluconic acid (*24*). The overlap of the glucose protons in some of the ^{1}H NMR spectra in this work (3.4−3.7 ppm) made it difficult to ascertain whether there were any interactions between the hydroxyl groups of glucose and the gallium or indium metal centers. ^{13}C NMR spectra were obtained and assigned using 2D techniques to aid

Table 1. ^{13}C NMR Coordination Induced Shifts ($\Delta\delta$) for Selected Tris(3-oxy-4-pyridinato)gallium and -indium Complexes versus the Free Ligands[a]

Atom Numbers		Δδ vs **HOG6GP** for **Ga(OG6GP)$_3$, In(OG6GP)$_3$**	Δδ vs **HOGBAP** for **Ga(OG6GP)$_3$, In(OG6GP)$_3$**	Δδ vs **HOGBPP** for **Ga(OGBPP)$_3$, In(OGBPP)$_3$**	Δδ vs **HOG2GP** for **Ga(OG2GP)$_3$, In(OG2GP)$_3$**
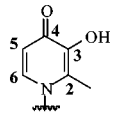	2 (pyridinone)	-0.16, +1.60	+0.25, +2.34	-0.29, +1.31	+0.54, +2.28
	3	+6.48, +6.77	+7.77, +8.26	+6.51, +6.76	+6.22, +6.19
	4	-2.34, -1.81	-1.12, -0.45	-1.22, -0.71	-0.88, -0.96
	5	-4.09, -2.54	-4.27, -2.47	-4.11, -2.53	-3.6, -1.95
	6	-3.39, -3.97	-4.44, -4.92	-3.41, -4.02	-2.71, -3.5
	2-*C*H$_3$	+0.70, +0.88	+0.76, +0.83	+0.76, +0.92	+1.00, +1.19
	1 (glucose)	-0.07, -0.04	-0.03, +0.04	+0.01, +0.06	+0.08, +0.10
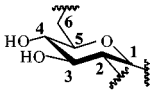	2	-0.06, -0.04	-0.01, +0.05	0.00, +0.02	+0.07, +0.08
	3	-0.04, -0.03	-0.03, +0.02	-0.01, +0.03	-0.04, -0.04
	4	-0.04, -0.01	-0.05, +0.05	+0.01, +0.04	+0.04, +0.06
	5	-0.02, -0.01	-0.05, 0.00	-0.02, +0.01	+0.13, +0.13
	6	-0.03, -0.01	-0.07, +0.04	+0.01, +0.03	+0.02, +0.02

[a] Only the pyridinone and glucose moieties are considered. A positive/negative value indicates a downfield/upfield shift for the metal complexes compared to the free ligand.

in determining whether any glucose−metal direct interactions take place. Also, a comparison of the pyridinone ^{13}C NMR region upon complexation to gallium and indium has not been previously undertaken (to our knowledge). The ^{13}C NMR coordination induced shifts for **HOG6GP**, **HOGBAP**, and **HOGBPP** are listed in Table 1. There are very small chemical shift differences for the glucose carbon atoms (all less than 0.1 ppm shifts), indicating clearly that the hydroxyl groups of glucose do not coordinate to the gallium or indium metal centers; one would expect more dramatic shifts if the glucose hydroxyl groups coordinated gallium or indium. When gluconic acid complexes gallium(III), the C2−C4 hydroxyl groups deprotonate/coordinate to gallium and the resulting ^{13}C NMR shifts for C2−C4 range from −0.3 ppm (upfield shift) to +0.6 ppm (downfield shift) in 9:1 H_2O:D_2O (*23*−*25*). Citrate complexation of gallium at neutral pH results in a 1.1 ppm upfield ^{13}C CIS for the tertiary hydroxyl group that deprotonates/coordinates gallium(III).

While there are small changes in the glucose ^{13}C NMR chemical shifts, all of the pyridinone ring carbon atoms shift by −5 ppm to +8 ppm, indicating that the pyridinone moiety is complexing gallium and indium. A representative ^{13}C NMR spectrum is shown in Figure 1. The largest CIS occurs for the pyridinone C3 atom, where a downfield shift of 6.5−8.3 ppm occurs upon formation of the gallium or indium complex. Each indium complex has a slightly larger downfield CIS for C3 (∼0.3−0.5 ppm) compared to that for the corresponding gallium complex. In contrast, upfield shifts are observed for the C4 pyridinone carbonyl ranging from ∼0.4 to 2.3 ppm. Each gallium complex has a slightly larger CIS for C4 (∼0.5−0.7 ppm) compared to the corresponding indium complex. The C5 and C6 atoms have upfield shifts from 2.5 to 4.9 ppm after metal complexation, while only the indium complexes show a consistent downfield CIS of 1.3−2.3 ppm for the C2 atom.

So far, attempts to recrystallize the metal complexes or the precursor ligands have failed to produce X-ray quality crystals. Vapor diffusion of alcohols into water or slow evaporation of water or MeCN were the most common methods employed. Sugars are notoriously difficult to crystallize; however, X-ray quality crystals of a benzylated pyridinone-glucose compound (**8**) were grown by slow evaporation of a 3:1 ethyl acetate:methanol solution (Figure 2). The bond lengths and angles (Table 2) are typical for pyridinones. The torsional angles indicate the near-planarity of the pyridinone ring, and the first carbon atom of the N2-substituent (C9) is also close to the plane of the pyridinone ring, both characteristics of other pyridinone structures. The α-anomer of glucose is also displayed in the structure of **8** which concurs with the coupling constant and chemical shift in the ^{1}H NMR spectrum (Supporting Information). Intermolecular hydrogen bonds form a tight net in the unit cell (Supporting Information). The amide H-atom (H26) is 1.931(19) Å from O2 of the glucose ring, the amide O-atom (O6) is 1.83(2) Å from H23, and the pyridinone carbonyl O-atom (O7) is 1.81(3) Å from H24.

Typically, aromatic- or alkyl-substituted pyridinone ligands and their complexes have low water solubility. The solubility of the complexes is usually less of an issue in radiopharmaceutical chemistry due to the low concentrations of the tracers; however, the ligand solubility may influence the efficiency of radiolabeling. Interestingly, the presence of the attached carbohydrates increases the solubility of both the ligands and the complexes compared to those of other pyridinone-based ligands. The water solubilities of **Ga(OG6GP)$_3$, In(OG6GP)$_3$, Ga(OGBPP)$_3$, In(OGBPP)$_3$, Ga(OG2GP)$_3$, In(OG2GP)$_3$, Ga(AG6GP)$_3$**, and **In(AG6GP)$_3$** were all greater than 10 mM at RT. **Ga(OGBAP)$_3$** and **In(OGBAP)$_3$** have water solubilities of ∼2.5−3 mM at RT while **Ga(AGBAP)$_3$** and **In(AGBAP)$_3$** have quite low water solubilities (<0.5 mM). Mixtures of water and EtOH improve the solubilities of **Ga(AGBAP)$_3$** and **In(AGBAP)$_3$**, and depending on the study, EtOH content may be acceptable for injection.

Enzymatic Cleavage. The glycoside linkage has the potential to be cleaved in vivo by a number of β-glycosidases, some of which are found naturally occurring in

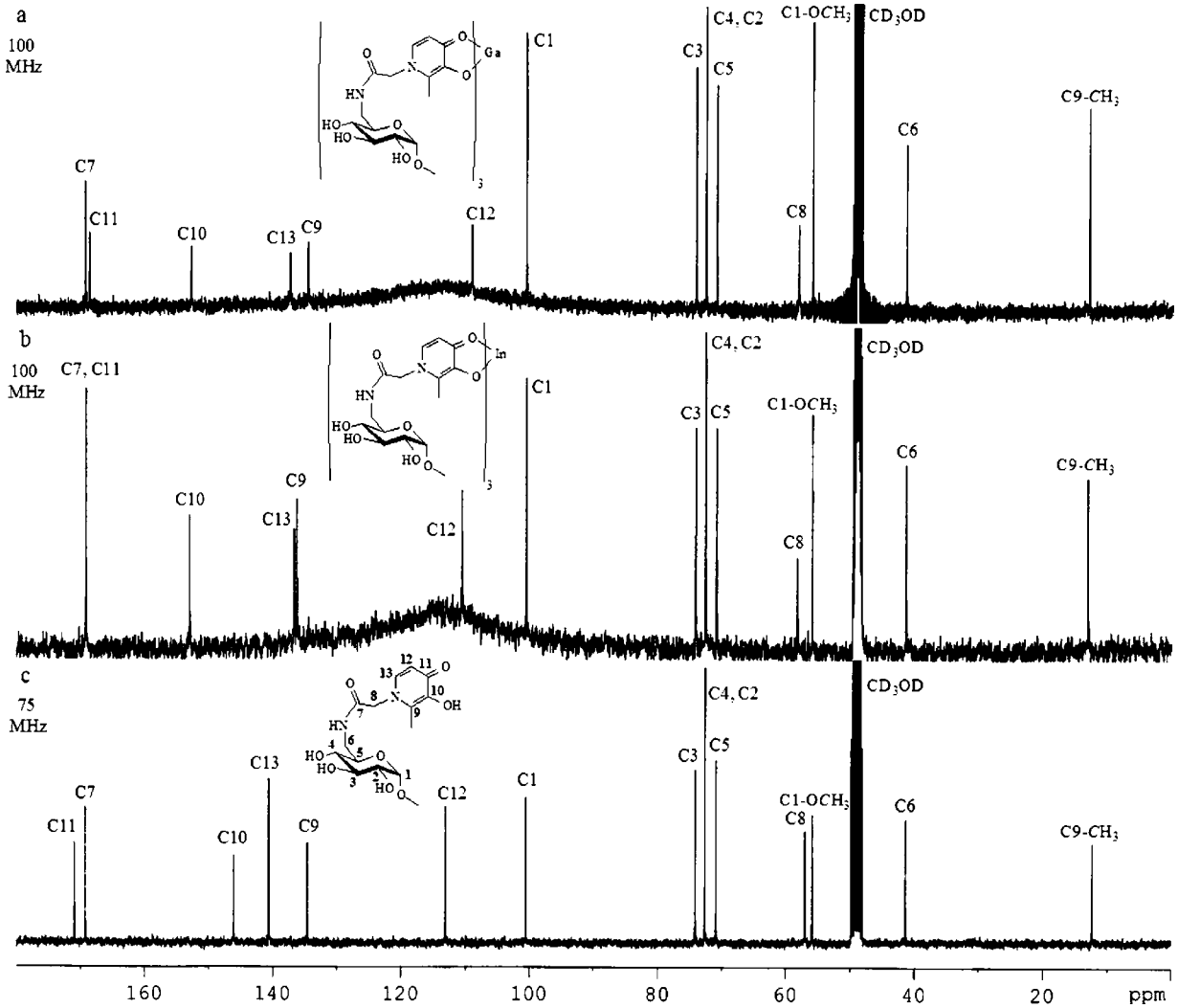

Figure 1. ^{13}C NMR spectra in 1:1 $CD_3OD:D_2O$ for (a) **Ga(OG6GP)$_3$** (100 MHz), (b) **In(OG6GP)$_3$** (100 MHz), and (c) **HOG6GP** (75 MHz).

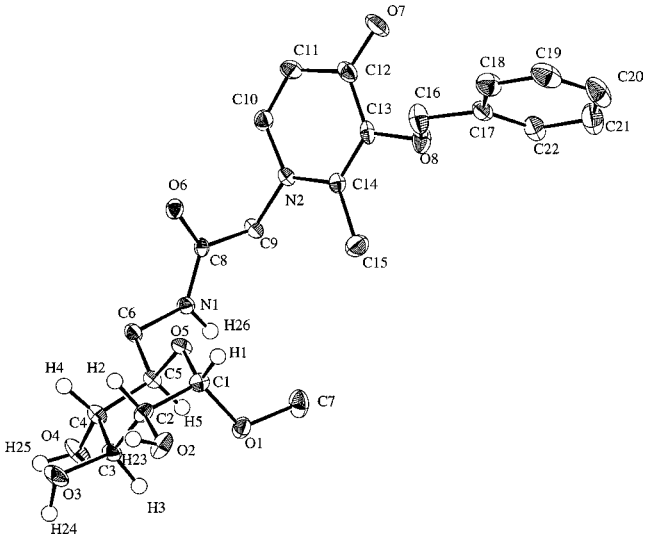

Figure 2. ORTEP diagram of **8** (with some H-atoms omitted for clarity) showing 50% thermal probability ellipsoids.

Table 2. Selected Bond Lengths (Å) and Angles (deg) in 8

O(7)−C(12)	1.257(2)	O(7)−C(12)−C(11)	123.1(2)
O(8)−C(13)	1.376(2)	O(7)−C(12)−C(13)	122.9(2)
O(6)−C(8)	1.242(2)	O(8)−C(13)−C(12)	118.6(1)
N(1)−C(6)	1.454(2)	C(13)−O(8)−C(16)	113.3(1)
N(1)−C(8)	1.327(2)	C(10)−C(11)−C(12)	121.5(2)
N(2)−C(9)	1.463(2)	C(11)−C(12)−C(13)	114.0(1)
N(2)−C(10)	1.363(2)	C(12)−C(13)−C(14)	122.7(2)
N(2)−C(14)	1.375(2)	N(2)−C(9)−C(8)	111.2(1)
C(10)−C(11)	1.349(3)	N(2)−C(10)−C(11)	122.1(2)
C(11)−C(12)	1.424(3)	N(2)−C(14)−C(13)	119.1(2)
C(12)−C(13)	1.445(2)	N(1)−C(6)−C(5)	112.0(1)
C(13)−C(14)	1.369(2)	O(6)−C(8)−N(1)	125.3(2)

the brain (*26*, *27*). Cleavage of the β-glucosides to produce pyridinone complexes without the attached carbohydrates may allow accumulation of activity in target sites, such as the brain. One of the metal complexes that contained β-glucose linkages (**Ga(OGBPP)$_3$**) was randomly chosen as a substrate for a broad-specificity β-glucosidase, Abg (*28*). After addition of Abg to a buffered solution containing **Ga(OGBPP)$_3$**, a white precipitate formed within a few minutes at RT. The mass spectrum of this precipitate is identical to that of an authentic sample of **Ga(hpp)$_3$** indicating that three β-glucose molecules were cleaved to produce **Ga(hpp)$_3$**. If **Ga(OGBPP)$_3$** were to come in contact with a similar specificity β-glucosidase enzyme in vivo, this suggests that the β-glucose linkages would be cleaved.

EXPERIMENTAL PROCEDURES

Materials. All solvents were purchased from Fisher except anhydrous pyridine which was purchased from Aldrich. MeOH, MeCN, and ethyl acetate solvents were

HPLC grade, and all other solvents were ACS grade or higher. Dry DMF was obtained by stirring over 4 Å molecular sieves followed by distillation. Other anhydrous solvents were dried according to standard procedures (*29*). All chemicals were from Aldrich unless otherwise stated. 3-Hydroxy-2-methyl-4-pyranone (maltol, **1**) was obtained from Pfizer (New York). H_2 and N_2 gases were from Praxair. Palladium black was obtained from Alfa Aesar. *Agrobacterium sp.* β-glucosidase (Abg) (*28*) was generously provided by Prof. S. G. Withers (UBC).

Methods. All pH measurements were made using an Accumet 950 pH/ion Meter with a Metrohm Porotrode micro-combination glass electrode. A Parr series 4750 (200 mL) split ring high-pressure reactor was used for higher pressure hydrogenations. A thick-walled glass insert (test tube shaped) was made (UBC Chemistry Glass Shop) that inserted into the Parr apparatus and held 100 mL of solvent when full. Vacuum desiccators contained phosphorus pentoxide as a desiccant.

NMR spectral data are contained in the Supporting Information. NMR spectra of samples were recorded on Bruker Avance 300, Avance 400, or AMX 500 instruments at room temperature (RT). NMR spectra were calibrated with the deuterated solvent, and in the case where mixtures were used, CD_3OD was chosen as the reference. Two-dimensional NMR techniques such as COSY, HMQC, and HMBC were used to aid in the characterization of all the final products and a number of intermediates. Mass spectra were obtained with either a Kratos Concept II H32Q instrument (Cs^+-LSIMS) or a Macromass LCT (electrospray ionization, ESI). Microanalyses for C, H, and N were done in this department (Mr. P. Borda or Mr. M. Lakha) or by Delta Microanalytical Services (Delta, BC).

X-ray data for **8** were collected and processed (*30*) using a Rigaku/ADSC CCD diffractometer and are shown in the Supporting Information. The X-ray structure was solved using direct methods (*31*) and expanded using Fourier techniques (*32*). The non-hydrogen atoms were refined anisotropically. Some hydrogen atoms were refined isotropically, the rest were included in fixed positions. All calculations were performed using the teXan crystallographic software package (*33*).

Synthesis. *3-Benzyloxy-2-methyl-4-pyranone (**2**) (benzyl maltol).* This compound was prepared in a manner similar to a previously published procedure (*34*) with some modifications. Maltol (**1**) (151.3 g, 1.2 mol) was dissolved in 1 L of MeOH and 120 mL of 10.5 M NaOH (50.4 g, 1.26 mol) was added. Benzyl chloride (160 mL, 1.39 mol) was added, and the reaction mixture was refluxed for 6 h. Then additional benzyl chloride (40 mL, 0.35 mmol) and NaOH (2.5 g, 0.062 mmol) (predissolved in 10 mL water) were added to the reaction mixture which was refluxed for an additional 12 h. The bright yellow solution containing white precipitate was reduced using a rotary evaporator (50 °C), then redissolved in 700 mL of water and 350 mL of dichloromethane. The water layer was discarded, and the dichloromethane was washed with 3 × 250 mL of 5% NaOH and 100 mL of water. The organic layer was dried (Na_2SO_4) and filtered, and the solution was removed using a rotary evaporator (40 °C), which produced a yellow oil. The oil was recrystallized in the freezer from 500 mL of EtOH. The crystals formed were filtered out and washed with a minimum of cold EtOH to remove the smell of benzyl chloride. The volume of the filtrate was reduced to ~200 mL using a rotary evaporator, and the product was crystallized as above with the addition of seed crystals. A third recrystallization from the mother liquor was also performed; all the crystals were combined and dried under vacuum 24 h to produce a white solid (183.0 g, 71% yield). Mp 52−54 °C.

*3-Benzyloxy-1-(carboxymethyl)-2-methyl-4(1H)-pyridinone (**3**).* Sodium glycinate (58.2 g, 600 mmol) and benzyl maltol (**2**) (86.5 g, 400 mmol) were dissolved in water and MeOH (125 mL each). After 36 h of reflux the volume of the red-brown solution was reduced to ~100 mL using a rotary evaporator (50 °C). An additional 200 mL of water was added, the solution was heated to dissolve all the material and cooled, and unreacted benzyl maltol was extracted with 4 × 100 mL dichloromethane. The water layer was stirred, and the pH was adjusted from 10.2 to 2.2 by adding 2 M HCl. A fine light yellow precipitate started to form at pH ~5. After being cooled on ice, the precipitate was filtered and rinsed with 2 × 30 mL cold water. The light yellow solid was dried 30 h on the vacuum line and weighed (108.5 g). This solid was recrystallized by refluxing in 83:17 MeOH:water (21 mL/g solid), then cooling. The yellow crystalline solid was filtered, rinsed with 2 × 30 mL cold water, and dried at least 48 h in the vacuum desiccator (52.32 g, 48% yield based on **2**). Anal. ($C_{15}H_{15}NO_4$) C, H, N. MS (+LSIMS): *m/z* 274 $[M + H]^+$.

*Methyl 6-O-Tosyl-α-D-glucopyranoside (**5**).* This compound was prepared using a previously published procedure (*17*) starting from methyl α-D-glucopyranoside (**4**) (Sigma) (30% yield).

*Methyl 6-Azido-6-deoxy-α-D-glucopyranoside (**6**).* This compound was prepared from **5** using a previously published procedure (*35*). After the solvent was removed, a light yellow syrup was produced that was dried 24 h in a vacuum desiccator (97% yield).

*Methyl 6-Amino-6-deoxy-α-D-glucopyranoside (**7**).* Palladium black has been used previously for azide reductions on carbohydrates (*36*). Compound **6** (2.92 g, 13.3 mmol) was dissolved in 50 mL of MeOH and transferred to a Parr reactor with glass insert. Palladium black (142 mg, 1.33 mmol) was wetted with ~0.5 mL of water and added to the reactor using ~5 mL of MeOH. A stir bar was added, and the reaction mixture was stirred rapidly. The reactor was sealed and pressurized to 60 atm with H_2 gas and stirred for 20 h. The reaction mixture was filtered through a medium frit, and the filtrate was removed using a rotary evaporator, which produced a viscous oil. A tacky white solid formed from the oil after drying 48 h in the vacuum desiccator. After the product was cooled in the freezer, the white solid was scraped into a vial (1.412 g, 73% yield) and used without further purification. The remaining oil was dissolved in water, the pH was adjusted to ~5 using 2 M HCl solution, and the solvent was removed using a rotary evaporator. This was recrystallized in a freezer from a minimum amount of hot MeOH producing the hydrochloride which was characterized. MS (+LSIMS): *m/z* 194 $[M + H]^+$.

*3-Benzyloxy-1-{[((2R,3S,4S,5R,6S)-3,4,5-trihydroxy-6-methoxy-tetrahydropyran-2-yl-methyl)carbamoyl]methyl}-2-methyl-4(1H)-pyridinone (**8**).* The reaction used was typical of activated ester reactions in the literature (*37*) and was done under dry conditions using Schlenk line techniques. *N*-Hydroxysuccinimide (NHS) (575 mg, 5.0 mmol) and compound **3** (1.4 g, 5.0 mmol) were dissolved in 65 mL of dry DMF. In a separate vessel dicyclohexylcarbodiimide (DCC) (1.08 g, 5.25 mmol) was dissolved in 10 mL of DMF. The DCC solution was added to the other stirring reaction mixture via cannula. This reaction mixture was left to stir for 24 h at RT under positive N_2 pressure. The activated ester that formed was filtered into a flask containing **7** (1.01 g, 5.25 mmol). The filtrate

dissolved **7**, and the solution was stirred under N_2 for 4 h at RT. The reaction mixture was rotovaporated to dryness (55 °C, ~30 min). Purification was done by silica chromatography using 3:1 ethyl acetate:MeOH. The solid obtained was dried in a vacuum desiccator 48 h to yield a white product (1.70 g, 76% based on **3**). X-ray quality crystals were grown from slow evaporation in ~3:1 ethyl acetate:MeOH. Anal. ($C_{22}H_{28}N_2O_8$) C, H, N. MS (+LSIMS): *m/z* 449 $[M + H]^+$.

*1-{[((2R,3S,4S,5R,6S)-3,4,5-Triacetoxy-6-methoxy-tetrahydropyran-2-yl-methyl)carbamoyl]methyl}-3-benzyloxy-2-methyl-4(1H)-pyridinone Hemihydrate (**9**·0.5H_2O).* This reaction was done under dry conditions using Schlenk line techniques. Compound **8** (448 mg, 1.00 mmol), dry pyridine (12 mL), and 1.7 mL of acetic anhydride (18 mmol, 6 equiv per OH) were left to stir under a positive N_2 pressure for 8 h at RT. The reaction mixture was evaporated at reduced pressure on the vacuum line while being stirred for 17 h. The solid was redissolved in a minimum of hot 1:1 EtOH:water and recrystallized. After cooling the reaction flask on ice, the precipitate was filtered, rinsed with 2 × 3 mL of cold water, and dried in a vacuum desiccator at least 48 h to yield a white solid (447 mg, 77% yield). Anal. ($C_{28}H_{35}N_2O_{11.5}$) C, H, N. MS (+ESI): *m/z* 597 $[M + Na]^+$, 575 $[M + H]^+$.

*4-Nitrophenyl 2,3,4,6-Tetra-O-acetyl-β-*D*-glucopyranoside (**11**).* This compound was prepared in a manner similar to other previously published Koenigs−Knorr procedures (*18*) with a number of modifications. 4-Nitrophenol (2.78 g, 20.0 mmol), silver carbonate (5.51 g, 20.0 mmol), activated 4 Å molecular sieves (~10 g), 100 mL of dry MeCN, and 2,6-dimethylpyridine (2.5 mL, 21.0 mmol) were combined. In a separate vessel 4.112 g (10.0 mmol) of 2,3,4,6-tetra-*O*-acetyl-α-D-glucopyranosyl bromide (**10**) (Aldrich) was dissolved in 40 mL of dry MeCN, and the solution was transferred to the reaction mixture via a cannula. The reaction mixture was stirred for 1 h at RT in the dark, filtered through Celite, and rinsed with 30 mL of dichloromethane. The solvents were removed using a rotary evaporator (40 °C), producing an oil that was placed on the vacuum line for 2 h. The resulting syrup was dissolved with 150 mL of dichloromethane and washed with water (100 mL), 5% NaOH (3 × 100 mL), 5% HCl (100 mL), and water (2 × 100 mL). The organic layer was dried and filtered, and the solvent was removed from the filtrate using a rotary evaporator (40 °C). The product was recrystallized from a minimum of hot ethyl acetate/hexanes, filtered, and dried 16 h on the vacuum line to produce a white solid (3.20 g, 68% yield).

*4-Nitrophenyl β-*D*-Glucopyranoside (**12**).* This deacetylation was typical of other deacetylations in the literature (*38*). The reaction was done under dry conditions. Compound **11** (22.5 g, 48.0 mmol) was dissolved in dry MeOH (~500 mL) and dry dichloromethane (~200 mL). Sodium methoxide (260 mg, 4.8 mmol) was added, and the reaction mixture was stirred for 3 h at RT. The dichloromethane was removed using a rotary evaporator (35 °C), an additional 100 mL of MeOH was added, and the solution was heated to dissolve any precipitate. Upon cooling (~30−40 °C), strongly acidic cation-exchange resin (Rexyn 101, Fisher) was added (5 g of resin was activated with 6 M HCl and rinsed with water until the solution was neutral in pH). The resin was stirred for 30 min and filtered out through a Buchner funnel, and the filtrate was recrystallized at RT for a few hours before it was placed in the freezer. The precipitate was filtered, washed with cold MeOH, and dried 24 h on the vacuum line (12.3 g). A second crop of crystals was obtained from a minimum amount of hot MeOH as above (1.96 g), and these products were combined (14.3 g, 99% yield). MS (+LSIMS): *m/z* 302 $[M + H]^+$.

*4-Aminophenyl β-*D*-Glucopyranoside, Hydrochloride (**13**).* This hydrogenation setup is similar to that described for **HOG6GP**. In a flask compound **12** (9.64 g, 32.0 mmol) was dissolved in 150 mL of MeOH and 220 mL of water. The 10% Pd/C (3.405 g, 3.2 mmol Pd) was wetted and rinsed into the flask with water (~30 mL). About 5 drops of 0.5 M HCl were added, and the adaptor was opened to the balloon containing hydrogen gas. After 3 h, 2 mL of 2 M HCl solution was added to the reaction mixture. An additional 2 mL of 2 M HCl solution was added after 6 h, the hydrogen balloon was refilled, and the reaction mixture was left to stir an additional 18 h. The reaction mixture was suction filtered through a medium frit, and the Pd/C was rinsed with 10 mL of water. To the light yellow filtrate was added 2 M HCl solution with stirring until the pH meter read ~4. The solvent was removed using a rotary evaporator (45 °C, ~2 h) and placed on the vacuum line for 24 h. The precipitate was recrystallized from a minimum amount of hot MeOH, filtered, and rinsed with cold MeOH (2 × 15 mL) to give a white solid. The mother liquor was reduced to a minimum amount using a rotary evaporator, and the remaining residue was recrystallized a second time as above. The white solids were combined and dried in a vacuum desiccator at least 48 h before weighing to determine the yield (8.55 g, 87% yield). MS (+LSIMS): *m/z* 272 $[M + H]^+$.

*3-Benzyloxy-1-{[4-(β-*D*-glucopyranosyloxy)phenylcarbamoyl]methyl}-2-methyl-4(1H)-pyridinone (**14**).* This was prepared in a similar fashion as **8** with the following changes: 1.91 g (7.0 mmol) **3**, 0.80 g NHS, 1.47 g DCC (9.1 mmol), and 2.80 g (9.1 mmol) **13**·HCl were used with 250 mL round-bottom flasks. Dry DMF (~140 mL) dissolved the NHS and **8**. The DCC was dissolved in ~15 mL of dry DMF, and a minimum amount of dry DMF was used to dissolve **13**·HCl (250 mL round-bottom flask with septum), followed by the addition of triethylamine (1.9 mL, 9.1 mmol) just prior to Schlenk filtering of the activated ester. After 12 h at 50 °C, the DMF was removed using a rotary evaporator (55 °C, ~1.5 h), taken up in a minimum amount of warm MeOH, filtered, and purified on a silica column run in 4:1 ethyl acetate: MeOH. A small amount of product coeluted with a slight red-brown color. These fractions were recrystallized from hot EtOH to afford a white product. The white solids were combined and dried in a vacuum desiccator at least 48 h (2.63 g, 71% based on **3**). Anal. ($C_{27}H_{30}N_2O_9$) C, H, N. MS (+LSIMS): *m/z* 527 $[M + H]^+$.

*1-{[4-(2,3,4,6-Tetra-O-acetyl-β-*D*-glucopyranosyloxy)-phenylcarbamoyl]methyl}-3-benzyloxy-2-methyl-4(1H)-pyridinone Hemihydrate (**15**·0.5 H_2O).* This reaction was carried out in a similar fashion as for **9** with the following changes: **14** (0.71 g, 1.34 mmol) was dissolved in 15 mL of dry pyridine, and acetic anhydride (2.0 mL, 21 mmol) was used. After 12 h stirring at RT, the reaction mixture was evaporated to dryness using a rotary evaporator (50 °C, <30 min) and dried 12 h on the vacuum line. After recrystallization and filtration, the product was dried in a vacuum desiccator at least 48 h to obtain a white solid (699 mg, 74% yield). Anal. ($C_{35}H_{39}N_2O_{13.5}$) C, H, N. MS (+ESI): *m/z* 717 $[M + Na]^+$, 695 $[M + H]^+$.

*3-Benzyloxy-1-(4-hydroxyphenyl)-2-methyl-4(1H)-pyridinone (**17**).* To a 2 L round-bottom flask were added 4-aminophenol (49.11 g, 450 mmol), benzyl maltol (**2**) (64.9 g, 300 mmol), 1.2 L of water, and 250 mL of MeOH. The reaction mixture was stirred and heated in an oil bath at 90 °C for 72 h. The solution was filtered hot and rinsed with cold water and MeOH (25 mL each), yielding

a white precipitate which was dried in a vacuum desiccator for 16 h (13.2 g). The warm filtrate was left at RT to cool and allow for further precipitation. The precipitate was filtered and dried for 3 h in a vacuum desiccator (22.4 g). The precipitate was refluxed in 50 mL of MeOH, and a red-brown solution was decanted. This was repeated four more times, with the last decant having a slight yellow color. The remaining solid was recrystallized from refluxing MeOH (~800 mL) followed by cooling in the freezer for 16 h. The crystals were dried in a vacuum desiccator 24 h to produce a white solid (13.7 g). The ^{1}H NMR spectra and TLC in 9:1 ethyl acetate:MeOH looked identical for the precipitated and recrystallized products; they were combined (26.9 g, 29% yield). Mp 240−242 °C. Anal. ($C_{19}H_{17}NO_3$) C, H, N. MS (+LSIMS): *m/z* 308 [M + H]$^+$.

*1-[4-(2,3,4,6-Tetra-O-benzyl-β-*D*-glucopyranosyloxy)-phenyl]-3-benzyloxy-2-methyl-4(1H)-pyridinone (**18**).* This reaction was typical of Mitsunobu reactions in the literature (*19*) and was done under dry conditions using Schlenk line techniques. 2,3,4,6-Tetra-*O*-benzyl-D-glucopyranose (**16**, Aldrich) (5.41 g, 10.0 mmol) and **17** (3.69 g, 12.0 mmol) were combined in 240 mL of dry dichloromethane. Tributylphosphine (3.74 mL, 15.0 mmol) was added via a syringe, and the reaction mixture was stirred for 5 min. Separately, azodicarboxylic acid dipiperidide (ADDP) (3.79 g, 15 mmol) was dissolved with 20 mL of dichloromethane and transferred to the reaction mixture via a syringe, followed by rinsing with 10 mL of dichloromethane. The reaction mixture was light orange in color. All material dissolved after ~1 h. The flask was stirred for 10 h at RT. The dichloromethane was removed using a rotary evaporator (45 °C), and the reaction mixture was redissolved in hot ethyl acetate (~120 mL) and then cooled in the freezer. A white solid recrystallized (ADDP byproduct), was filtered with a course frit, and was rinsed with 2 × 10 mL of cold ethyl acetate. The ethyl acetate filtrate was removed using a rotary evaporator (45 °C) to form an orange-brown oil. The oil was purified on a silica column eluting with ethyl acetate. A bright yellow band elutes just ahead of the product. The product was dried in vacuo 48 h to produce a yellow viscous oil (6.01 g, 66% yield). MS (+LSIMS): *m/z* 830 [M + H]$^+$.

*3-Benzyloxy-1-{[((2R/S,3R,4R,5S)-6-hydroxymethyl-2,4,5-trihydroxy-tetrahydropyran-3-yl)carbamoyl]methyl}-2-methyl-4(1H)-pyridinone (**19**).* Prepared in a similar manner to that of **8**, this reaction was done under dry conditions using Schlenk line techniques. To a 100 mL flask were added **3** (769 mg, 2.8 mmol), glucosamine hydrochloride (728 mg, 3.4 mmol), DCC (744 mg, 3.6 mmol), and NHS (377 mg, 3.3 mmol). DMF (10 mL) was added via a syringe and the mixture stirred into a slurry. Diisopropylethylamine (1.3 mL, 7.5 mmol) was added to the stirring mixture, and the reaction was heated at 80 °C for 16 h. The solvent and excess base were removed on a rotary evaporator, and the resulting dark residue was redissolved in water. Insoluble impurities were removed by filtration, and the filtrate was reduced to a thick orange syrup, which was purified by silica chromatography eluting with 2:2:1 ethyl acetate:CH_3CN:MeOH. Fractions containing the product were recrystallized in MeOH to give a white solid (675 mg, 54%). Anal. ($C_{21}H_{26}N_2O_8$) C, H, N. MS (+ESI): *m/z* 457 [M + Na]$^+$, 435 [M + H]$^+$.

*3-Hydroxy-1-{[((2R,3S,4S,5R,6S)-3,4,5-trihydroxy-6-methoxy-tetrahydropyran-2-yl-methyl)carbamoyl]methyl}-2-methyl-4(1H)-pyridinone (**HOG6GP**).* **8** (1.34 g, 3.0 mmol) was dissolved in MeOH (60 mL) with stirring in a round-bottom flask. Water (40 mL) was added to prevent the product from precipitating when formed. 10% Pd/C (319 mg, 0.3 mmol Pd) was wetted with water (5 mL) and poured into the flask. An 11 L latex balloon was filled with H_2 gas and fitted to a stopcocked adaptor which was opened to the round-bottom flask. After stirring at RT for 12 h, the H_2 atmosphere was removed. The solution was suction filtered through a medium frit, the Pd/C was washed with 10 mL of water, and the filtrate was syringed through a nylon filter (25 mm, 0.2 μm) to remove fine Pd/C. This light orange solution was reduced in volume using a rotary evaporator (50 °C, <30 min) and recrystallized by adding 3 mL of water and 4 mL of methanol, heating until dissolved, and cooling at RT. The precipitate was cooled on ice, filtered out, and rinsed with 2 × 3 mL of cold MeOH to produce a white solid and a red-orange colored filtrate. The solid was dried in a vacuum desiccator at least 48 h (568 mg, 53%). Anal. ($C_{15}H_{22}N_2O_8$) C, H, N. MS (+LSIMS): *m/z* 359 [LH + H]$^+$; (+ESI): *m/z* 359 [LH + H]$^+$.

*Tris(1-{[((2R,3S,4S,5R,6S)-3,4,5-trihydroxy-6-methoxy-tetrahydropyran-2-yl-methyl)carbamoyl]methyl}-2-methyl-3-oxy-4(1H)-pyridinonato)gallium(III) Tetrahydrate (**Ga(OG6GP)$_3$·4H$_2$O**).* Gallium nitrate nonahydrate (41.8 mg, 0.1 mmol) was dissolved in 3 mL of water. This solution was added dropwise to a stirring solution of **HOG6GP** (358 mg, 0.315 mmol) in 4 mL of water. The initial pH of the reaction mixture was 1.6. A 1% NaOH solution was added dropwise to the reaction mixture until the pH was 7.0, and the solvent was then removed using a rotoevaporation (50 °C, <30 min) to produce an off-white precipitate. The precipitate was redissolved in 3 mL of water and applied on a Sephadex G10 size exclusion column; the column was eluted with deionized water. Silica TLC of the fractions was conducted (1:1 ethyl acetate:MeOH) to determine the presence of product. Salts remained white on a charred TLC plate, and the ligand had a higher R_f value than did the metal complex. The fractions containing the desired compound were combined, and the solvent was removed using a rotary evaporator (50 °C, <30 min) to produce an off-white solid. The solid was dried in a vacuum desiccator at least 48 h (115.6 mg, 95%). Anal. ($C_{45}H_{71}N_6O_{28}Ga$) C, H, N. MS (+ESI): *m/z* 1163/1165 [$^{69/71}GaL_3Na$]$^+$ 1141/1143 [$^{69/71}GaL_3H$]$^+$ (with similar isotopic distribution as that calculated for $C_{45}H_{64}GaN_6O_{24}$), 783/785 [$^{69/71}GaL_2$]$^+$, 381 [LH + Na]$^+$, 359 [LH + H]$^+$; (+LSIMS): *m/z* 783/785 [$^{69/71}GaL_2$]$^+$, 359 [LH + H]$^+$.

*Tris(1-{[((2R,3S,4S,5R,6S)-3,4,5-trihydroxy-6-methoxy-tetrahydropyran-2-yl-methyl)carbamoyl]methyl}-2-methyl-3-oxy-4(1H)-pyridinonato)indium(III) Hydrate (**In(OG6GP)$_3$·H$_2$O**).* This reaction was carried out in a similar fashion as for the analogous gallium complex except that indium nitrate trihydrate was used (35.5 mg, 0.1 mmol). The off white solid obtained was dried in a vacuum desiccator for 48 h (108 mg, 89% yield). Anal. ($C_{45}H_{65}InN_6O_{25}$) C, H, N. MS (+ESI): *m/z* 1225 [$^{115}InL_3$ + K]$^+$ (with similar isotopic distribution as that calculated for $C_{45}H_{63}N_6O_{24}KIn$), 1209 [$^{115}InL_3$ + Na]$^+$, 867 [$^{115}InL_2K(-H)$]$^+$, 851 [$^{115}InL_2Na(-H)$]$^+$, 829 [$^{115}InL_2$]$^+$, 397 [LH + K]$^+$, 381 [LH + Na]$^+$.

*1-{[4-(β-*D*-Glucopyranosyloxy)phenylcarbamoyl]methyl}-3-hydroxy-2-methyl-4(1H)-pyridinone Hemihydrate (**HOGBAP·0.5H$_2$O**).* This reaction was carried out in a similar fashion as for **HOG6GP** with the following changes: the starting material (**14**, 790 mg, 1.5 mmol) was dissolved in MeOH (40 mL) followed by the addition of water (20 mL) and 10% Pd/C (160 mg, 0.15 mmol). After the solvent was removed using a rotary evaporator,

a minimum amount of 2:1 MeOH:water (~10−15 mL) was added to redissolve the product under reflux and was left to recrystallize at RT. The product obtained from recrystallization was dried in a vacuum desiccator (394.8 mg, 59%). Anal. ($C_{20}H_{25}N_2O_{9.5}$) C, H, N. MS (+ESI): *m/z* 475 $[LH + K]^+$, 459 $[LH + Na]^+$.

*Tris(1-{[4-(β-*D*-glucopyranosyloxy)phenylcarbamoyl]-methyl}-2-methyl-3-oxy-4(1H)-pyridinonato)gallium(III) Dihydrate (**Ga(OGBAP)$_3$·2H$_2$O**).* To a 100 mL flask were added **HOGBAP**·0.5H_2O (122.4 mg, 0.315 mmol) and water (15 mL). A solution of 1% HCl was added dropwise with stirring until the pH was 1.0, at which time all the ligand dissolved. Gallium nitrate nonahydrate (42 mg, 0.1 mmol) was dissolved in 3 mL of water and added dropwise to the solution in the flask; this solution was clear and colorless (pH 1.4). 1% NaOH solution was added dropwise with stirring. At pH ~ 4 a white precipitate formed and was redissolved upon warming (~50 °C). Continued addition of 1% NaOH to the cooling solution (until pH ~ 6.5) resulted in more precipitate formation. The pH was adjusted to 7.0 after cooling to RT, and the solution was left to stir for 15 min. The precipitate was filtered and washed with cold water (5 mL). The filtrate was reduced to a few mL using a rotary evaporator (50 °C, <30 min). Purification was done on a Sephadex G10 column. TLC of the fractions (1:1 ethyl acetate:MeOH) was used to verify product fractions as described above. ^{1}H NMR spectra were identical for both the precipitated and column purified product. The product was dried in a vacuum desiccator at least 48 h to yield precipitate: 56.6 mg; column: 60.2 mg (116.8 mg combined, 83% yield). Anal. ($C_{60}H_{73}GaN_6O_{29}$) C, H, N. MS (+ESI): *m/z* 1397/1399 $[^{69/71}GaL_3 + Na]^+$ (consistent isotopic distribution), 961/963 $[^{69/71}GaL_2 + Na(-H)]^+$, 939/941 $[^{69/71}GaL_2]^+$, 777/779 $[^{69/71}GaL_2(-C_6H_{10}O_5$ for one glucose molecule$)]^+$, 459 $[LH + Na]^+$.

*Tris(1-{[4-(β-*D*-glucopyranosyloxy)phenylcarbamoyl]-methyl}-2-methyl-3-oxy-4(1H)-pyridinonato)indium(III) Pentahydrate (**In(OGBAP)$_3$·5H$_2$O**).* This reaction was carried out in a similar fashion as for the analogous gallium complex except that indium nitrate trihydrate was used (35.5 mg, 0.1 mmol). The product was dried in a vacuum desiccator at least 48 h to yield precipitate: 61.1 mg; column: 68.2 (129.3 mg combined, 86% yield). Anal. ($C_{60}H_{79}InN_6O_{32}$) C, H, N. MS (+ESI): *m/z* 1443 $[^{115}InL_3 + Na]^+$ (consistent isotopic distribution), 1007 $[^{115}InL_2 + Na(-H)]^+$, 985 $[^{115}InL_2]^+$, 823 $[^{115}InL_2-(-C_6H_{10}O_5$ for 1 glucose molecule$)]^+$, 661 $[^{115}InL_2-(-C_{12}H_{20}O_{10}$ for two glucose molecules$)]^+$, 459 $[LH + Na]^+$.

*1-[4-(β-*D*-Glucopyranosyloxy)phenyl]-3-hydroxy-2-methyl-4(1H)-pyridinone Hydrate (**HOGBPP·H$_2$O**).* This reaction was carried out in a similar fashion as for **HOG6GP** with the following changes: **18** (1.66 g, 2.0 mmol) was dissolved with MeOH (40 mL). The 10% Pd/C (2.13 g, 2.0 mmol Pd) was wetted with water (10 mL) and rinsed with MeOH (~10 mL). The reaction was stirred vigorously under H_2 gas at RT for 24 h. Following filtering and filtrate solvent removal with a rotary evaporator, the product was dissolved in 50 mL of water and washed with 3 × 15 mL of dichloromethane. The water was removed using a rotovaporator (50 °C) to produce an off-white solid, which was dried in a vacuum desiccator at least 48 h (652 mg, 86%). Anal. ($C_{18}H_{23}NO_9$) C, H, N. MS (+ESI): *m/z* 402 $[LH + Na]^+$; (+LSIMS): *m/z* 380 $[LH + H]^+$.

*Tris{1-[4-(β-*D*-glucopyranosyloxy)phenyl]-2-methyl-3-oxy-4(1H)-pyridinonato}gallium(III) Dihydrate (**Ga(OGBPP)$_3$·2H$_2$O**).* This reaction was carried out in a similar fashion as for **Ga(OG6GP)$_3$** with substitution of the ligand (**HOGBPP**·H_2O, 125 mg, 0.315 mmol) and the pH after addition of the gallium nitrate solution was 1.4. After drying in the vacuum desiccator at least 48 h, an off-white solid was produced (117 mg, 95% yield). Anal. ($C_{54}H_{64}GaN_3O_{26}$) C, H, N. MS (+ESI): *m/z* 1226/1228 $[^{69/71}GaL_3 + Na]^+$ (consistent isotopic distribution), 825/827 $[^{69/71}GaL_2]^+$, 402 $[LH + Na]^+$.

*Tris{1-[4-(β-*D*-glucopyranosyloxy)phenyl]-2-methyl-3-oxy-4(1H)-pyridinonato}indium(III) Tetrahydrate (**In(OGBPP)$_3$·4H$_2$O**).* This reaction was carried out in a similar fashion as for the analogous gallium complex, with the exception that indium nitrate trihydrate was used (35.5 mg, 0.1 mmol) and the pH after its addition to the ligand was 1.8. After drying in the vacuum desiccator at least 48 h, an off-white solid was obtained (120 mg, 91% yield). Anal. ($C_{54}H_{68}InN_3O_{28}$) C, H, N. MS (+ESI): *m/z* 1272 $[^{115}InL_3 + Na]^+$ (consistent isotopic distribution), 871 $[^{115}InL_2]^+$, 402 $[LH + Na]^+$.

*1-{[((2R,3S,4S,5R,6S)-3,4,5-Triacetoxy-6-methoxy-tetrahydropyran-2-yl-methyl)carbamoyl]methyl}-3-hydroxy-2-methyl-4(1H)-pyridinone Hydrate (**HAG6GP·H$_2$O**).* This reaction was carried out in a similar fashion as for **HOG6GP** with the following changes: **9**·0.5H_2O (950 mg, 1.63 mmol) was dissolved in MeOH (40 mL), 10% Pd/C (175 mg, 0.164 mmol) was used (wetted with 5 mL of H_2O, rinsed with 5 mL of MeOH), and the reaction was stopped after 20 h at RT. The filtered Pd/C was rinsed with 3 × 10 mL of MeOH taking care not to completely dry the Pd/C in the frit. After filtering through a 0.2 μm filter, the filtrate solvent was removed using a rotary evaporator (40 °C, <30 min). The solid was redissolved in a minimum amount of hot 1:1 water:EtOH and recrystallized at RT. Filtering the precipitate and rinsing with 2 × 3 mL of cold ethanol produced a white solid and an orange filtrate. The product was dried in a vacuum desiccator for at least 48 h (321 mg, 71%). Anal. ($C_{21}H_{30}N_2O_{12}$) C, H, N. MS (+ESI): *m/z* 507 $[LH + Na]^+$, 485 $[LH + H]^+$.

*Tris(1-{[((2R,3S,4S,5R,6S)-3,4,5-triacetoxy-6-methoxy-tetrahydropyran-2-yl-methyl)carbamoyl]methyl}-2-methyl-3-oxy-4(1H)-pyridinonato)gallium(III) Hydrate (**Ga(AG6GP)$_3$·H$_2$O**).* This reaction was carried out in a similar fashion as for **Ga(OG6GP)$_3$** with the following changes: **HAG6GP**·H_2O (157 mg, 0.315 mmol) was dissolved in 4 mL of 1:1 EtOH:water. Gallium nitrate nonahydrate (41.8 mg, 0.1 mmol) was dissolved in 2 mL of 1:1 H_2O:EtOH and added dropwise to the solution containing the ligand. The initial pH was 2.4 for this reaction mixture, and a 1% NaOH solution was added dropwise until the pH was 7.0. The solvent was removed using a rotary evaporator at 50 °C (<30 min) to produce a white precipitate. The precipitate was purified on a Sephadex G10 size exclusion column run in 1:1 EtOH:water. The relevant fractions were combined, and the solvent was removed using a rotary evaporator (50 °C, <30 min). The resulting solid was dried in a vacuum desiccator at least 48 h (139 mg, 90%). Anal. ($C_{63}H_{83}GaN_6O_{34}$) C, H, N. MS (+ESI): *m/z* 1541/1543 $[^{69/71}GaL_3 + Na]^+$ (consistent isotopic distribution), 1035/1037 $[^{69/71}GaL_2]^+$, 507 $[LH + Na]^+$, 485 $[LH + H]^+$.

*Tris(1-{[((2R,3S,4S,5R,6S)-3,4,5-triacetoxy-6-methoxy-tetrahydropyran-2-yl-methyl)carbamoyl]methyl}-2-methyl-3-oxy-4(1H)-pyridinonato)indium(III) Tetrahydrate (**In(AG6GP)$_3$·4H$_2$O**).* This reaction was carried out in a similar fashion as for the analogous gallium complex, with the exception that indium nitrate trihydrate was used (35.5 mg, 0.1 mmol). After drying in the vacuum desiccator at least 48 h, a white solid was produced (172

mg, 93% yield). Anal. ($C_{63}H_{89}InN_6O_{37}$) C, H, N. MS (+ESI): *m/z* 1587 $[^{115}InL_3 + Na]^+$ (consistent isotopic distribution), 1081 $[^{115}InL_2]^+$, 507 $[LH + Na]^+$, 485 $[LH + H]^+$.

*1-{[4-(2,3,4,6-Tetra-O-acetyl-β-*D*-glucopyranosyloxy)-phenylcarbamoyl]methyl}-3-hydroxy-2-methyl-4(1H)-pyridinone Hydrate (**HAGBAP·**H_2O).* This reaction was carried out in a similar fashion as for **HAG6GP** with the following changes: **11** (507 mg, 0.71 mmol) and 10% Pd/C (76 mg, 0.071 mmol) were used, and the reaction was stopped after 24 h at RT. The product was recrystallized from hot 1:1 MeOH:water (10 mL). After filtering out a white solid, an orange filtrate remained. The white solid was dried (321 mg, 71%). Anal. ($C_{28}H_{32}N_2O_{13}$) C, H, N. MS (+ESI): *m/z* 627 $[LH + Na]^+$, 605 $[LH + H]^+$.

*Tris(1-{[4-(2,3,4,6-tetra-O-acetyl-β-*D*-glucopyranosyloxy)phenylcarbamoyl]methyl}-2-methyl-3-oxy-4(1H)-pyridinonato)gallium(III) Tetrahydrate (**Ga(AGBAP)$_3$·**$4H_2O$).* This reaction was carried out in a similar fashion as for **Ga(AG6GP)$_3$** with the following changes: **HAGBAP·**$1H_2O$ (196 mg, 0.315 mmol) was dissolved in 1:1 EtOH:water (10 mL). After the addition of gallium nitrate, the pH was 2.2. When dropwise addition of 1% NaOH produced a precipitate, the reaction mixture was heated to ~40 °C. As the reaction mixture cooled, 1% NaOH solution was added until pH 7 and more precipitate formed. The solution was cooled on ice 15 min, and the precipitate was filtered and rinsed with 5 mL of cold water. The solid was dried in a vacuum desiccator at least 48 h (172 mg, 88%). Anal. ($C_{84}H_{101}GaN_6O_{43}$) C, H, N. MS (+ESI): *m/z* 1879/81 $[^{69/71}GaL_3 + H]^+$ (consistent isotopic distribution), 1275/1277 $[^{69/71}GaL_2]^+$, 605 $[LH + H]^+$.

*Tris(1-{[4-(2,3,4,6-tetra-O-acetyl-β-*D*-glucopyranosyloxy)phenylcarbamoyl]methyl}-2-methyl-3-oxy-4(1H)-pyridinonato)indium(III) Dihydrate (**In(AGBAP)$_3$·**$2H_2O$).* This reaction was carried out in a similar fashion as for the analogous gallium complex, with the exception that indium nitrate trihydrate was used (35.5 mg, 0.1 mmol). After drying, a white solid was produced (178 mg, 91% yield). Anal. ($C_{84}H_{97}InN_6O_{41}$) C, H, N. MS (+ESI): *m/z* 1947 $[^{115}InL_3 + Na]^+$ (consistent isotopic distribution), 1925 $[^{115}InL_3 + H]^+$, 1321 $[^{115}InL_2]^+$, 627 $[LH + Na]^+$, 605 $[LH + H]^+$.

*3-Hydroxy-1-{[((2R/S,3R,4R,5S)-6-hydroxymethyl-2,4,5-trihydroxy-tetrahydropyran-3-yl)carbamoyl]methyl}-2-methyl-4(1H)-pyridinone Hydrate (**HOG2GP·**H_2O or **Feralex-G·**H_2O).* This reaction was carried out in a similar fashion as for **HOG6GP** with the following changes: the starting material **19** (450 mg, 1.0 mmol) was dissolved in MeOH (30 mL) and water (30 mL), and 10% Pd/C (115 mg, 0.11 mmol) was used. The solvent was removed on a rotary evaporator (40 °C) to give a quantitative yield of white crystalline product (358 mg, 100%). Anal. ($C_{14}H_{22}N_2O_9$) C, H, N. MS (+ESI): *m/z* 345 $[LH + H]^+$.

*Tris({[((2R/S,3R,4R,5S)-6-hydroxymethyl-2,4,5-trihydroxy-tetrahydropyran-3-yl)carbamoyl]methyl}-2-methyl-3-oxy-4(1H)-pyridinonato)gallium(III) Pentahydrate (**Ga(OG2GP)$_3$·**$5H_2O$).* Gallium nitrate hexahydrate (11 mg, 0.03 mmol) was dissolved in 3 mL of water and added to **HOG2GP** (32 mg, 0.093 mmol) dissolved in 3 mL of water. The pH of the resulting solution was adjusted to 7 with 0.1 M NaOH. The solution volume was reduced on a rotary evaporator (30 °C) and the residue purified on a Sephadex G10 column. Precipitation with acetone from a minimal amount of water gave a white solid, which was dried 48 h in a vacuum desiccator (30 mg, 91% yield). Anal. ($C_{42}H_{67}Ga\ N_6O_{29}$) C, H, N. MS (+ESI): *m/z* 755 $[GaL_2]^+$.

*Tris({[((2R/S,3R,4R,5S)-6-hydroxymethyl-2,4,5-trihydroxy-tetrahydropyran-3-yl)carbamoyl]methyl}-2-methyl-3-oxy-4(1H)-pyridinonato)indium(III) Tetrahydrate (**In(OG2GP)$_3$·**$4H_2O$).* This reaction was carried out in a similar fashion as for the analogous gallium complex except indium nitrate trihydrate was used (20 mg, 0.045 mmol) and 59 mg of **HOG2GP** (0.17 mmol). The product was a white solid (45 mg, 70% yield). Anal. ($C_{42}H_{65}InN_6O_{28}$) C, H, N. MS (+ESI): *m/z* 801 $[InL_2]^+$.

*3-Hydroxy-1-(4-hydroxyphenyl)-2-methyl-4(1H)-pyridinone (**Hhpp**).* This reaction was carried out in a similar fashion as for **HOG6GP** with the following changes: the starting material **17** (1.53 g, 5.0 mmol) was dissolved in MeOH (50 mL) and DMF (50 mL). The 10% Pd/C (532 mg, 0.50 mmol Pd) was wetted and transferred to the flask using ~10 mL of water. The reaction was stopped after 12 h at RT. The filtered Pd/C was rinsed with 3 × 10 mL of warm MeOH (taking care not to completely dry the Pd/C) and 3 × 10 mL of warm DMF (~60 °C). The solvent of the light pink-orange filtrate was removed using a rotary evaporator (50 °C, ~1.5 h) and the residue dried in vacuo for 2 h. The resulting light pink solid was dissolved in a minimum of hot MeOH, ~25% more MeOH was added, and a fine precipitate formed on cooling. The precipitate was filtered and rinsed with 2 × 3 mL of cold MeOH to produce a white solid and orange filtrate. A second crop of white precipitate was obtained from the orange filtrate. The precipitates were combined and dried in a vacuum desiccator for at least 48 h (381 mg, 35%). Anal. ($C_{12}H_{11}NO_3$) C, H, N. MS (+ESI): *m/z* 218 $[LH + H]^+$.

Tris(1-(4-hydroxyphenyl)-2-methyl-3-oxy-4(1H)-pyridinonato)gallium(III) Sesquihydrate (Ga(hpp)$_3$·1.5H_2O). Method A: Synthesis from Hhpp. Gallium nitrate nonahydrate (208.9 mg, 0.50 mmol) was dissolved in DMF (5 mL). This solution was added dropwise to a stirring solution of **Hhpp** (330 mg, 1.52 mmol) at RT in 40 mL of DMF. A 1.0% NaOH solution (6.2 mL) was added dropwise to the reaction mixture, and the solvent was removed using a rotary evaporator at 55 °C. After drying on the vacuum line for 16 h, the precipitate was transferred to a medium frit, stirred with warm water, and filtered (3 × 20 mL). The resulting white precipitate was dried in a vacuum desiccator for at least 48 h (319.2 mg, 86%). Anal. ($C_{36}H_{33}GaN_3O_{10.5}$) C, H, N. MS (+ESI): *m/z* 718/720 $[^{69/71}GaL_3 + H]^+$ (consistent isotopic distribution), 501/503 $[^{69/71}GaL_2]^+$, 218 $[LH + H]^+$.

Method B: Enzymatic Cleavage of Ga(OGBPP)$_3$. To a 1 mL Eppendorf tube were added 30 μL of 50 mM solution of **Ga(OGBPP)$_3$** and 65 μL of 75 mM sodium phosphate buffer (pH 6.8). The solution was mixed briefly (vortex mixer) and 5 μL of a buffered solution containing 3.98 mg/mL of Abg was added to start the reaction. A white precipitate formed within a few minutes. After 30 min at RT, the reaction mixture (with some white precipitate) was spotted on a TLC plate (dried at RT between spotting). TLC in 1:1 ethyl acetate:MeOH was run ~45 min. after addition of enzyme. The TLC indicated a new spot with the same R_f value (0.55) as the **Ga(hpp)$_3$** precipitate from Method A. After ~1 h, the white precipitate was filtered. TLC of the supernatant and filtered precipitate indicated that free glucose ($R_f = 0.35$) was present in the supernatant. The precipitate was dried 2 h in a vacuum desiccator producing ~1 mg of a white solid. MS (+ESI): *m/z* 740/742 $[^{69/71}Ga(hpp)_3 + Na]^+$ (consistent isotopic distribution), 501/503 $[^{69/71}Ga(hpp)_2]^+$, 218 $[Hhpp + H]^+$.

CONCLUSIONS

A number of glucose-bearing tris(pyridinonato)gallium and indium complexes were synthesized and characterized by mass spectrometry and ^{1}H and ^{13}C NMR spectroscopy. With three equivalents of ligand, neutral complexes formed, with the pyridinone moiety complexing the gallium and indium metal centers. There are no indications that the glucose moiety coordinates to, or interacts with, the gallium or indium metal centers. How the glucose moieties interact in vivo will dictate the biodistribution of the metal complexes and their potential for use in diagnostic nuclear medicine. Labeling studies with suitable gallium isotopes are now in progress.

ACKNOWLEDGMENT

We thank the Natural Sciences and Engineering Research Council (NSERC) of Canada for support and Ryan Moslin and Sherwin Sattarzadeh for technical/experimental assistance.

Supporting Information Available: ^{1}H NMR and ^{13}C NMR spectral assignments for all compounds and selected NMR spectra. This material is available free of charge via the Internet at http://pubs.acs.org/BC.

LITERATURE CITED

(1) Bruner, H. D., Hayes, R. L., and Perkinson, J. D. (1953) A study of gallium-72. Summary and conclusions. X. Preliminary data on gallium-67. *Radiology 61*, 602−613.

(2) van der Werff, J. T. (1954) Clinical investigations on the use of radioactive gallium (Ga-66 and Ga-67) in bone diseases. *Acta Radiol. 41*, 343−347.

(3) Hayes, R. L. (1966) Radioisotopes of gallium. *U. S. At. Energy Comm., Symp. Ser. 6*, 603−618.

(4) Goodwin, D. A., Stern, H. S., and Wagner, H. N., Jr. (1967) Indium-113m labeled iron hydroxide particles for lung scanning. *J. Nucl. Med. 8*, 346.

(5) Pal, J., Gacs, J., Torko, J., and Farkas, G. (1967) Clinical experiences in use of In-115m. *Strahlentherapie* [Sonderb] *65*, 63−69.

(6) Anderson, C. J., and Welch, M. J. (1999) Radiometal labeled agents (non-technetium) for diagnostic imaging. *Chem. Rev. 99*, 2219−2234.

(7) Luttropp, C. A., Jackson, J. A., Jones, B. J., Sohn, M. H., Lynch, R. E., and Morton, K. A. (1998) Uptake of gallium-67 in transfected cells and tumors absent or enriched in the transferrin receptor. *J. Nucl. Med. 39*, 1405−1411.

(8) de Jong, M., Breeman, W. A. P., Bakker, W. H., Kooij, P. P. M., Bernard, B. F., Hofland, L. J., Visser, T. J., Srinivasan, A., Schmidt, M. A., Erion, J. L., Bugaj, J. E., Macke, H. R., and Krenning, E. P. (1998) Comparison of In-111-labeled somatostatin analogues for tumor scintigraphy and radionuclide therapy. *Cancer Res. 58*, 437−441.

(9) Zhang, Z., Rettig, S. J., and Orvig, C. (1991) Lipophilic coordination compounds: aluminum, gallium, and indium complexes of 1-aryl-3-hydroxy-2-methyl-4-pyridinones. *Inorg. Chem. 30*, 509−515.

(10) Clevette, D. J., Lyster, D. M., Nelson, W. O., Rihela, T., Webb, G. A., and Orvig, C. (1990) Solution chemistry of gallium and indium 3-hydroxy-4-pyridinone complexes in vitro and in vivo. *Inorg. Chem. 29*, 667−672.

(11) Clevette, D. J., and Orvig, C. (1990) Comparison of ligands of differing denticity and basicity for the *in vivo* chelation of aluminium and gallium. *Polyhedron 9*, 151−161.

(12) Kruck, T. P. A., and Burrow, T. E. (2002) Synthesis of feralex a novel aluminum/iron chelating compound. *J. Inorg. Biochem. 88*, 19−24.

(13) Bayly, S. R., Fisher, C. L., Storr, T., Adam, M. J., and Orvig, C. (2004) Carbohydrate conjugates for molecular imaging and radiotherapy: ^{99m}Tc(I) and ^{186}Re(I) tricarbonyl complexes of *N*-(2′-hydroxybenzyl)-2-amino-2-deoxy-D-glucose. *Bioconjugate Chem. 15*, 923−926.

(14) Storr, T., Obata, M., Fisher, C. L., Bayly, S. R., Green, D. E., Brudziñska, I., Mikata, Y., Patrick, B. O., Adam, M. J., Yano, S., and Orvig, C. (2005) Novel carbohydrate-appended metal complexes for potential use in molecular imaging. *Chem. Eur. J. 11*, 195−203.

(15) Petrig, J., Schibli, R., Dumas, C., Alberto, R., and Schubiger, P. A. (2001) Derivatization of glucose and 2-deoxyglucose for transition metal complexation: substitution reactions with organometallic ^{99m}Tc and Re precursors and fundamental NMR investigations. *Chem. Eur. J. 7*, 1868−1873.

(16) Yang, D. J., Kim, C. G., Schechter, N. R., Azhdarinia, A., Yu, D. F., Oh, C. S., Bryant, J. L., Won, J. J., Kim, E. E., and Podoloff, D. A. (2003)Imaging with ^{99m}Tc ECDG targeted at the multifunctional glucose transport system: feasibility study with rodents. *Radiology 226*, 465−473.

(17) Cramer, F. D. (1962) *Methods In Carbohydrate Chemistry* (Whistler, R. L., Wolfrom, M. L., Eds.) Vol. I, pp 244−245, Academic Press, New York.

(18) Conchie, J., and Levvy, G. A. (1963) *Methods In Carbohydrate Chemistry* (Whistler, R. L., Wolfrom, M. L., Eds.) Vol. II, pp 335−337, Academic Press, New York.

(19) Tsunoda, T., Yamamiya, Y., and Ito, S. (1993) 1,1′-(Azodicarbonyl)dipiperidine-tributylphosphine, a new reagent system for mitsunobu reaction. *Tetrahedron Lett. 34*, 1639−1642.

(20) Nelson, W. O., Rettig, S. J., and Orvig, C. (1989) Aluminum and gallium complexes of 1-ethyl-3-hydroxy-2-methyl-4-pyridinone: a new exoclathrate matrix. *Inorg. Chem. 28*, 3153−3157.

(21) Matsuba, C. A., Nelson, W. O., Rettig, S. J., and Orvig, C. (1988) Neutral water-soluble indium complexes of 3-hydroxy-4-pyrones and 3-hydroxy-4-pyridinones. *Inorg. Chem. 27*, 3935−3939.

(22) Chang, C. H. F., Pitner, T. P., Lenkinski, R. E., and Glickson, J. D. (1977) Carbon-13 Fourier transform nuclear magnetic resonance study of gallium citrate in aqueous solution. *Inorg. Chem. 99*, 5858−5863.

(23) Hawkes, G. E., O'Brien, P., Salacinski, H., Motevalli, M., and Abrahams, I. (2001) Solid and solution state NMR spectra and the structure of the gallium citrate complex $(NH4)_3[Ga(C_6H_5O_7)_2]\cdot 4H_2O$. *Eur. J. Inorg. Chem.*, 1005−1011.

(24) Escandar, G. M., Olivieri, A. C., Gonzalez-Sierra, M., Frutos, A. A., and Sala, L. F. (1995) Complexation of aluminum(III), gallium(III) and indium(III) ions with D-gluconic and lactobionic acids − a potentiometric and nuclear magnetic resonance spectroscopic study (Correction, Addition). *J. Chem. Soc.-Dalton Trans.*, 1393−1393.

(25) Escandar, G. M., Olivieri, A. C., Gonzalez-Sierra, M., Frutos, A. A., and Sala, L. F. (1995) Complexation of aluminum(III), gallium(III) and indium(III) ions with D-gluconic and lactobionic acids − a potentiometric and nuclear magnetic resonance spectroscopic study. *J. Chem. Soc., Dalton Trans.* 799−804.

(26) Pardridge, W. M., Boado, R. J., and Farrell, C. R. (1990) Brain-type glucose transporter (Glut-1) is selectively localized to the blood-brain-barrier − studies with quantitative western blotting and in situ hybridization. *J. Biol. Chem. 265*, 18035−18040.

(27) Heidren, M., Boermans, H., Friedrich, L., and Siegfried, M. (2001) Molecular cloning and expression of human bile acid β-glucosidase. *J. Biol. Chem. 276*, 37929−37933.

(28) Kempton, J. B., and Withers, S. G. (1992) Mechanism of Agrobacterium β-glucosidase − kinetic studies. *Biochemistry 31*, 9961−9969.

(29) Perrin, D. D., Armarego, W. L. F., and Perrin, D. R. (1980) *Purification of laboratory chemicals*, Permagon Press, Oxford.

(30) Molecular Structure Corporation (2001) d*Trek Area Detector Software. 3200 Research Forest Drive, The Woodlands, TX, 77381.

(31) Altomare, A., Burla, M. C., Camalli, M., Cascarano, G. L., Giacovazzo, C., Guagliardi, A., Moliterni, A. G. G., Polidori, G., and Spagna, R. (1999) SIR97: a new tool for crystal structure determination and refinement. *J. Appl. Crystallogr. 32*, 115−119.

(32) Beurskens, P. T., Admiraal, G., Beurskens, G., Bosman, W. P., de Gelder, R., Israel, R., and Smits, J. M. M. *The DIRDIF-94 Program System*, University of Nijmegen, The Netherlands, 1994.

(33) Molecular Structure Corporation (1992−1997) teXsan Single-Crystal Structure Analysis Software. 3200 Research Forest Dr., The Woodlands, TX, 77381.

(34) Harris, R. L. N. (1976) Potential wool growth inhibitors. Improved syntheses of mimosine and related 4(1*H*)-pyridones. *Aust. J. Chem. 29*, 1329−1334.

(35) Cramer, F. D. (1963) *Methods In Carbohydrate Chemistry* (Whistler, R. L., Wolfrom, M. L., Eds.) Vol. II, pp 242−246, Academic Press, New York.

(36) Matsuda, K., Tsuchiya, T., Torii, T., and Umezawa, S. (1986) Synthesis of 6-amino-6-deoxy-L-idopyranosides. *Bull. Chem. Soc. Jpn. 59*, 1397−1401.

(37) Rosowsky, A., Yu, C.-S., Uren, J., Lazarus, H., and Wick, M. (1981) Methotrexate analogues. 13. Chemical and pharmacological studies on amide, hydrazide, and hydroxamic acid derivatives of the glutamate side chain. *J. Med. Chem. 24*, 559−567.

(38) Thompson, A., Wolfrom, M. L., and Pacou, E. (1963) *Methods In Carbohydrate Chemistry* (Whistler, R. L., Wolfrom, M. L., Eds.) Vol. II, pp 215−220, Academic Press, New York.

BC0501808

In Vitro System To Estimate Renal Brush Border Enzyme-Mediated Cleavage of Peptide Linkages for Designing Radiolabeled Antibody Fragments of Low Renal Radioactivity Levels

Yasushi Fujioka,[†] Satoshi Satake,[‡] Tomoya Uehara,[‡] Takahiro Mukai,[†] Hiromichi Akizawa,[‡] Kazuma Ogawa,[†] Hideo Saji,[†] Keigo Endo,[§] and Yasushi Arano[‡,*]

Graduate School of Pharmaceutical Sciences, Kyoto University, Yoshida-shimoadachi-cho, Sakyo-ku, Kyoto 606-8501, Graduate School of Medicine, Gunma University, 3-39-22 Showa-machi, Maebashi 371-8511, and Graduate School of Pharmaceutical Sciences, Chiba University, 1-8-1 Inohana, Chuo-ku, Chiba 260-8675, Japan. Received July 20, 2005; Revised Manuscript Received September 5, 2005

Renal localization of radiolabeled antibody fragments presents a problem in targeted imaging and radiotherapy. We recently reported that Fab fragments labeled with 3′-[^{131}I]iodohippuryl N^{ϵ}-maleoyl-L-lysine (HML) demonstrated markedly low renal radioactivity levels from early postinjection in mice. Previous studies suggested that low renal radioactivity levels were attributable to cleavage of the glycyl-lysine sequence in HML by the action of renal brush border enzymes, followed by urinary excretion of the resulting *m*-iodohippuric acid. In this study, an in vitro system using brush border membrane vesicles (BBMVs) isolated from the rat kidney cortex was developed to estimate renal brush border enzyme(s)-mediated cleavage of the peptide linkage. Low molecular weight HML derivatives, 3′-[^{125}I]iodohippuryl L-lysine (HL), 3′-[^{125}I]iodohippuryl N^{ϵ}-*tert*-butoxycarbonyl-L-lysine (HBL), and their D-amino acid counterparts, were synthesized and incubated in BBMVs. Both [^{125}I]HL and [^{125}I]HBL generated *m*-[^{125}I]iodohippuric acid after incubation in BBMVs at 37 °C while the latter liberated significantly higher amounts of the metabolite. [^{125}I]D-HL and [^{125}I]D-HBL failed to release the metabolite under similar conditions. The liberation of *m*-[^{125}I]iodohippric acid from [^{125}I]HL was significantly facilitated or completely inhibited by the addition of an activator or an inhibitor for carboxypeptidase M. The release of *m*-[^{125}I]iodohippuric acid from [^{125}I]HBL increased by the addition of the activator, whereas the inhibitor partially inhibited the release of the metabolite from [^{125}I]-HBL. The BBMV-mediated release of *m*-[^{125}I]iodohippuric acid from [^{125}I]HBL was not impaired by the addition of inhibitors for neutral endopeptidase or renal dipeptidase. These findings showed that the glycyl-L-lysine sequence in HML would be recognized and cleaved by metalloenzymes and nonmetalloenzymes on the renal brush border even when iodine was incorporated into a benzene ring and the N^{ϵ}-amine residue of lysine was chemically modified, which supported the hypothesis that low renal radioactivity levels of HML-conjugated Fab fragments would be attributed to the release of *m*-iodohippuric acid by renal brush border enzymes. This study suggested that this in vitro system using BBMVs would be useful to estimate radiolabeling reagents of antibody fragments or peptides designed to reduce renal radioactivity with a variety of radionuclides.

INTRODUCTION

Recent clinical studies of ^{90}Y- and ^{131}I-labeled intact antibodies against CD20 demonstrated significant response rates in patients with chemotherapy-refractory non-Hodgkin's lymphoma (*1*). Although the ^{90}Y-labeled antibodies caused myelosuppresion as a result of long circulation times, this could be reduced by using antibody fragments in place of intact antibodies, due to the faster clearance of antibody fragments from the systemic circulation. The uniform intratumor distribution of antibody fragments would also be advantageous to increase the therapeutic efficacy (*2*). However, radiolabeled antibody fragments showed high and persistent localization of radioactivity in the kidneys from early postinjection onward, which causes therapeutic limitations (*3*−*6*).

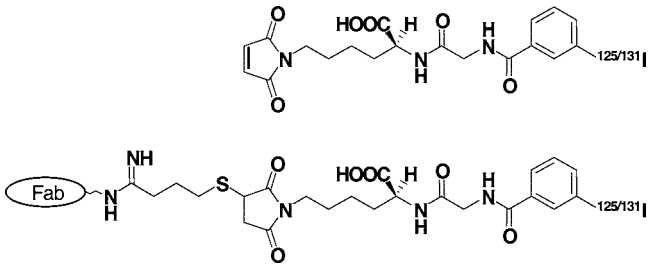

Figure 1. Chemical structures of [$^{125/131}$I]HML and [$^{125/131}$I]-HML-conjugated Fab fragments.

To circumvent this problem, we recently developed a radioiodination reagent, 3′-iodohippuryl N^{ϵ}-maleoyl-L-lysine (HML, Figure 1) based on the hypothesis that glycyl-lysine linkage in HML would be cleaved by brush border enzyme(s) present on the lumen of the renal tubule while the antibody fragments are taken up by renal cells (*7*). In tumor-bearing nude mice, [^{131}I]HML-conjugated Fab fragments (Figure 1) significantly reduced renal radioactivity levels from early postinjection onward without impairing radioactivity levels in the

* Corresponding author. Tel.: 81-43-226-2896; fax: 81-43-226-2897; e-mail: arano@mail.p.chiba-u.ac.jp.
[†] Kyoto University.
[‡] Chiba University.
[§] Gunma University.

10.1021/bc050211z CCC: $30.25 © 2005 American Chemical Society
Published on Web 11/01/2005

tumor (*7*, *8*). A follow-up in vivo study showed that cleavage of the glycyl-lysine sequence in [$^{125/131}$I]HML-conjugated Fab fragments occurred at the membrane fractions of renal cells from an early postinjection time (*9*). These in vivo studies supported the validity of this chemical design to prepare radiolabeled antibody fragments of low renal radioactivity levels. However, it remains uncertain whether a renal enzyme(s) on the brush border membrane was responsible for cleavage of the glycyl-lysine sequence in HML-conjugated antibody fragments. In addition, since the ability of HML to release *m*-iodohippuric acid was only estimated by biodistribution studies after conjugation with antibody fragments, an in vitro experimental system is highly warranted to estimate the release of *m*-iodohippuric acid prior to conjugation with antibody fragments. Such an experimental system would provide an insight into better understanding the mechanism of releasing *m*-iodohippuric acid from HML-conjugated antibody fragments. Such an in vitro system would also be useful to develop new radiolabeling reagents for antibody fragments or peptides with a variety of radionuclides.

Renal brush border membrane vesicles (BBMVs) have been used to investigate the transport mechanisms of drugs in the renal brush border membrane (*10*, *11*). BBMVs have a predominantly luminal side-out orientation with a variety of enzymes on their surface (*10*, *12*). Furthermore, enzymes in renal lysosomes can be separated from those on BBMVs during preparation (*12*). Such characteristics rendered BBMVs attractive as an in vitro system to estimate the radiolabeling reagents for antibody fragments or peptides of low renal radioactivity levels utilizing enzymes on renal brush border membrane.

In this study, 3′-[^{125}I]iodohippuryl L-lysine ([^{125}I]HL), 3′-[^{125}I]iodohippuryl N^{ϵ}-*tert*-butoxycarbonyl-L-lysine ([^{125}I]-HBL), and their D-lysine counterparts, 3′-[^{125}I]iodohippuryl D-lysine ([^{125}I]D-HL) and 3′-[^{125}I]iodohippuryl N^{ϵ}-*tert*-butoxycarbonyl-D-lysine ([^{125}I]D-HBL) were synthesized as HML derivatives, and the brush border enzyme-mediated release of *m*-[^{125}I]iodohippuric acid was investigated using BBMVs prepared from the rat kidney cortex. The BBMV-mediated release of *m*-[^{125}I]iodohippuric acid was also determined by the presence of an activator for carboxypeptidase M (CPM) or inhibitors of some enzymes on BBMVs. The findings in this study showed that the in vitro system using BBMVs would be useful to evaluate newly developed radiolabeling reagents designed to liberate radiometabolites by the action of renal brush border enzymes prior to conjugation to antibody fragments.

MATERIALS AND METHODS

Reagents and Chemicals. Na[^{125}I]I was purchased from Biomedicals, Inc. (California). Reversed phase high-performance liquid chromatography (RP-HPLC) was performed with a Cosmosil 5C_{18}-AR-300 column (4.6 × 150 mm, Nacalai Tesque, Kyoto, Japan) eluted at a flow rate of 1 mL/min with a gradient mobile phase starting from 100% water to 100% acetonitrile in 30 min (solvent system 1) or from 80% A (0.1% aqueous trifluoroacetic acid; TFA) and 20% B (acetonitrile with 0.1% TFA) to 20% A and 80% B in 30 min (solvent system 2). Size-exclusion high-performance liquid chromatography (SE-HPLC) was performed with a Cosmosil Diol-120 column (7.5 × 600 mm, Nacalai Tesque, Kyoto) eluted with 0.1 M phosphate buffer (pH 6.8) at a flow rate of 1 mL/min. Each eluent was collected with a fraction collector (Redi-Frac; Pharmacia Biotech, Tokyo) at 30-s intervals, and

Scheme 1[a]

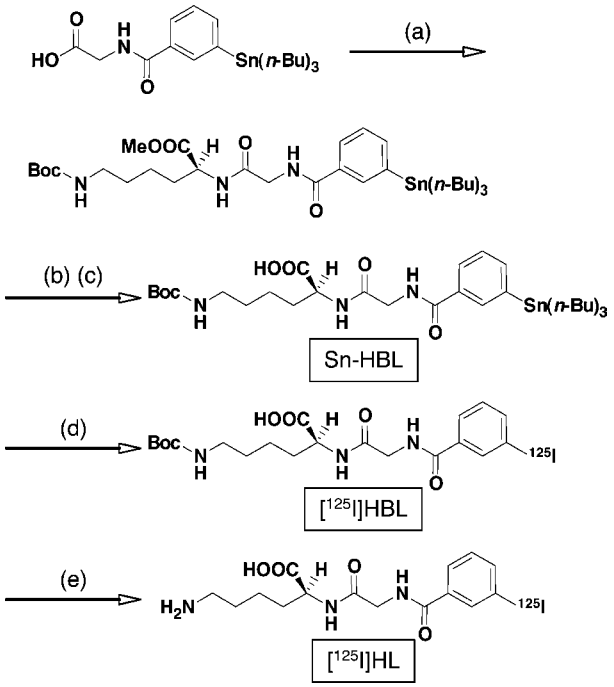

[a] Reagents: (a) 1-hydroxybenzotriazole, triethylamine, N^{ϵ}-*tert*-butoxycarbonyl-L-lysine methyl ester hydrochloride, 1-ethyl-3-(3-dimethylaminopropyl)-carbodiimide hydrochloride; (b) NaOH; (c) HCl; (d) *N*-chlorosuccinimide, Na[^{125}I]I; (e) TFA.

the radioactivity levels in each fraction (500 μL) were determined with an auto well counter (ARC-2000; Aloka, Tokyo). TLC analyses were performed with silica plates (Merck Art 5553) developed with a mixture of chloroform, methanol, and water (15:8:1) (solvent system 3) or a mixture of chloroform, methanol, and acetic acid (50:10:1) (solvent system 4). ^{1}H NMR spectra were recorded on a Bruker AC-200 spectrometer, and chemical shifts are reported in ppm downfield from an internal tetramethylsilane standard. Mass spectra were obtained with the JMS−HX/HX110 A model (JEOL Ltd., Tokyo), API III model (Perkin-Elmer Sciex Instruments, Canada), or LCMS-QP8000α model (Shimadzu, Kyoto). Sn-HML was synthesized according to the procedure of Wakisaka et al. (*13*). DL-2-Mercaptomethyl-3-guanidinoethylthiopropanoic acid (MGTA), phosphoramidon, and tienam were purchased from Calbiochem (La Jolla, CA), Peptide Institute (Osaka, Japan) and Banyu Pharmaceutical Co., Ltd. (Tokyo), respectively. L-γ-Glutamyl-*p*-nitroanilde, L-leucine-*p*-nitroanilide, *p*-nitrophenyl-β-D-galactopyranoside, and glycyl-D-phenylalanine were obtained from Wako Pure Chemical Industries Ltd. (Osaka), ICN Pharmaceutical Inc. (Costa Mesa, CA), Nacalai Tesque, and Bachem AG (Bubendorf, Switzerland), respectively. Other reagents were of reagent grade.

Synthesis of 3′-(Tri-*n*-butylstannyl)hippuryl N^{ϵ}-*tert*-Butoxycarbonyl-L-lysine (Sn-HBL). 3-(Tri-*n*-butylstannyl)hippuric acid was synthesized as described previously (*13*). 3-(Tri-*n*-butylstannyl)hippuric acid (300 mg, 0.64 mmol), 1-hydroxybenzotriazole (118 mg, 0.77 mmol), triethylamine (143 mg, 1.41 mmol), and N^{ϵ}-*tert*-butoxycarbonyl-L-lysine methyl ester hydrochloride (190 mg, 0.64 mmol) were dissolved in dry chloroform (10 mL) (Scheme 1). After the mixture was cooled to 0 °C, a solution of 1-ethyl-3-(3-dimethylaminopropyl)-carbodiimide hydrochloride (147 mg, 0.77 mmol) in 3 mL of dry chloroform was added to the solution. After being stirred for 12 h at 0 °C, the reaction mixture was washed with

5% aqueous citrate (10 mL × 3), saturated $NaHCO_3$ (10 mL × 3), and saturated NaCl (10 mL × 3) successively before drying over anhydrous calcium sulfate. The organic layer was removed in vacuo to produce 3′-(tri-*n*-butylstannyl)hippuryl N^{ϵ}-*tert*-butoxycarbonyl-L-lysine methyl ester (250 mg, 55%) as a colorless oil. ^{1}H NMR ($CDCl_3$): δ 0.85−1.94 (33H, m, $SnBu_3$, $(CH_2)_3$), 1.42 (9H, s, Boc), 3.10 (2H, q, NHCH_2), 3.74 (3H, s, $COOCH_3$), 4.19 (2H, d, NHCH_2), 4.62 (1H, q, NHC*H*), 7.39 (1H, t, aromatic), 7.60 (1H, d, aromatic), 7.70 (1H, d, aromatic), 7.90 (1H, t, aromatic). Electro spray ionization mass spectra (ESI-MS) calcd for $C_{33}H_{58}N_3O_6Sn$ (MH^+): *m/z* 712. Found: 712.

3′-(Tri-*n*-butylstannyl)hippuryl N^{ϵ}-*tert*-butoxycarbonyl-L-lysine methyl ester (250 mg, 0.35 mmol) in methanol (10 mL) was added to a solution of 1 N NaOH (2 mL), and the mixed solution was refluxed with stirring for 1 h. After removal of methanol in vacuo, the solution was neutralized with 1 N HCl at 0 °C before extraction with ethyl acetate (10 mL). The organic layer was dried over anhydrous calcium sulfate before removing the solvent in vacuo to produce 3′-(tri-*n*-butylstannyl)hippuryl N^{ϵ}-*tert*-butoxycarbonyl-L-lysine (138 mg, 56%) as a colorless oil. ^{1}H NMR ($CDCl_3$): δ 0.85−1.82 (33H, m, $SnBu_3$, $(CH_2)_3$), 1.42 (9H, s, Boc), 3.08 (2H, q, NHCH_2), 4.25 (2H, d, NHCH_2), 4.55 (1H, q, NHC*H*), 7.31 (1H, t, aromatic), 7.58 (1H, d, aromatic), 7.72 (1H, d, aromatic), 7.91 (1H, t, aromatic). Fast atom bombardment mass spectra (FAB-MS) calcd for $C_{32}H_{55}N_3O_6Sn$ (MH^+): *m/z* 698. Found: 698.

Synthesis of 3′-(Tri-*n*-butylstannyl)hippuryl N^{ϵ}-*tert*-Butoxycarbonyl-D-lysine (D-Sn-HBL). This compound was synthesized by the reaction of N^{ϵ}-*tert*-butoxycarbonyl-D-lysine methyl ester hydrochloride with 3-(tri-*n*-butylstannyl)hippuric acid as described above. ^{1}H NMR ($CDCl_3$): δ 0.85−1.88 (33H, m, $SnBu_3$, $(CH_2)_3$), 1.42 (9H, s, Boc), 3.01 (2H, q, NHCH_2), 4.26 (2H, d, NHCH_2), 4.50 (1H, q, NHC*H*), 7.32 (1H, t, aromatic), 7.57 (1H, d, aromatic), 7.66 (1H, d, aromatic), 7.85 (1H, t, aromatic). ESI-MS calcd for $C_{32}H_{55}N_3O_6Sn$ (MH^+): *m/z* 698. Found: 698.

Synthesis of 3′-Iodohippuryl N^{ϵ}-*tert*-Butoxycarbonyl-L-lysine (HBL). 3-Iodohippuric acid was synthesized as described previously (*13*). A mixture of 3-iodohippuric acid (305 mg, 1.00 mmol), 1-hydroxybenzotriazole (184 mg, 1.20 mmol), triethylamine (223 mg, 2.20 mmol), and N^{ϵ}-*tert*-butoxycarbonyl-L-lysine methyl ester hydrochloride (297 mg, 1.00 mmol) dissolved in dry acetonitrile (10 mL) was cooled to 0 °C. A solution of 1-ethyl-3-(3-dimethylaminopropyl)-carbodiimide hydrochloride (230 mg, 1.20 mmol) in 10 mL of acetonitrile was added, and the reaction mixture was stirred for 7 h at 0 °C. After removal of the solvent in vacuo, the residue was dissolved in ethyl acetate (10 mL) and the organic phase was washed with 5% aqueous citrate (10 mL × 3), saturated $NaHCO_3$ (10 mL × 3), and saturated NaCl (10 mL × 3) successively. After the solvent was dried over anhydrous calcium sulfate, the organic layer was removed in vacuo to produce 3′-iodohippuryl N^{ϵ}-*tert*-butoxycarbonyl-L-lysine methyl ester (443 mg, 81%) as a colorless oil. ^{1}H NMR ($CDCl_3$): δ 1.12−1.95 (6H, m, $(CH_2)_3$), 1.42 (9H, s, Boc), 3.10 (2H, q, NHCH_2), 3.75 (3H, s, $COOCH_3$), 4.19 (2H, d, NHCH_2), 4.60 (1H, q, NHC*H*), 7.18 (1H, t, aromatic), 7.78 (1H, d, aromatic), 7.85 (1H, d, aromatic), 8.17 (1H, t, aromatic). FAB-MS calcd for $C_{21}H_{30}N_3O_6I$ (MH^+): *m/z* 548. Found: 548. Anal. ($C_{21}H_{30}N_3O_6I$) C, H, N.

3′-Iodohippuryl N^{ϵ}-*tert*-butoxycarbonyl-L-lysine methyl ester (425 mg, 0.78 mmol) was added to a mixture of 1 N NaOH (1.55 mL) and methanol (10 mL), and the solution was refluxed with stirring for 1 h. After removal of methanol in vacuo, the solution was neutralized with 1 N HCl at 0 °C before extraction with ethyl acetate (10 mL). The organic layer was dried over anhydrous calcium sulfate before removing the solvent in vacuo to produce 3′-iodohippuryl N^{ϵ}-*tert*-butoxycarbonyl-L-lysine (290 mg, 70%) as a colorless oil. ^{1}H NMR (CD_3OD): δ 1.12−1.99 (6H, m, $(CH_2)_3$), 1.42 (9H, s, Boc), 3.02 (2H, q, NHCH_2), 4.05 (2H, d, NHCH_2), 4.41 (1H, q, NHC*H*), 7.25 (1H, t, aromatic), 7.84 (1H, d, aromatic), 7.89 (1H, d, aromatic), 8.22 (1H, t, aromatic). ESI-MS calcd for $C_{20}H_{28}N_3O_6I$ (MH^+): *m/z* 534. Found: 534. Anal. ($C_{20}H_{28}N_3O_6I \cdot 1/2H_2O \cdot 1/4CH_3COOC_2H_5$) C, H, N.

Synthesis of 3′-Iodohippuryl N^{ϵ}-*tert*-Butoxycarbonyl-D-lysine (D-HBL). D-HBL was synthesized by the reaction of N^{ϵ}-*tert*-butoxycarbonyl-D-lysine methyl ester hydrochloride with 3-iodohippuric acid as described above. ^{1}H NMR (CD_3OD): δ 0.88−1.98 (6H, m, $(CH_2)_3$), 1.42 (9H, s, Boc), 3.03 (2H, q, NHCH_2), 4.07 (2H, d, NHCH_2), 4.42 (1H, q, NHC*H*), 7.22 (1H, t, aromatic), 7.85 (1H, d, aromatic), 7.90 (1H, d, aromatic), 8.25 (1H, t, aromatic). ESI-MS calcd for $C_{20}H_{28}N_3O_6I$ (MH^+): *m/z* 534. Found: 534.

Synthesis of 3′-Iodohippuryl L-Lysine (HL). 3-Iodohippuric acid (450 mg, 1.48 mmol), 1-hydroxybenzotriazole (239 mg, 1.77 mmol), triethylamine (328 mg, 3.25 mmol), and N^{ϵ}-*tert*-butoxycarbonyl-L-lysine *tert*-butyl ester hydrochloride (500 mg, 1.48 mmol) were dissolved in dry acetonitrile (10 mL). After the mixture was cooled to 0 °C, a solution of 1-ethyl-3-(3-dimethylaminopropyl)-carbodiimide hydrochloride (339 mg, 1.77 mmol) in 15 mL of acetonitrile was added to the solution. After being stirred for 7 h at 0 °C, the solvent was removed in vacuo and the residue was dissolved in ethyl acetate (10 mL). The organic phase was washed with 5% aqueous citrate (10 mL × 3), saturated $NaHCO_3$ (10 mL × 3), and saturated NaCl (10 mL × 3) successively. After the solvent was dried over anhydrous calcium sulfate, the organic layer was removed in vacuo to produce 3′-iodohippuryl N^{ϵ}-*tert*-butoxycarbonyl-L-lysine *tert*-butyl ester (679 mg, 78%) as a colorless oil. ^{1}H NMR ($CDCl_3$): δ 1.26−2.04 (6H, m, $(CH_2)_3$), 1.44 (9H, s, *t*-Bu), 1.47 (9H, s, Boc), 3.13 (2H, q, NHCH_2), 4.17 (2H, d, NHCH_2CO), 4.50 (1H, q, NHC*H*), 7.18 (1H, t, aromatic), 7.79 (1H, d, aromatic), 7.85 (1H, d, aromatic), 8.18 (1H, t, aromatic). Electron Impact mass spectra (EI-MS) calcd for $C_{21}H_{30}N_3O_6I$: *m/z* 589. Found: 589. Anal. ($C_{24}H_{36}N_3O_6I$) C, H, N.

3′-Iodohippuryl N^{ϵ}-*tert*-butoxycarbonyl-L-lysine *tert*-butyl ester (180 mg, 0.31 mmol) was dissolved in TFA (15 mL) containing anisole (66 μL) and stirred for 1 h at room temperature. After removal of TFA in vacuo, the residue was treated with ether to precipitate 3′-iodohippuryl L-lysine (102 mg, 59%) as a white crystal. ^{1}H NMR (DMSO-d_6): δ 1.05−2.04 (6H, m, $(CH_2)_3$), 3.44 (2H, q, NHCH_2), 4.04 (2H, d, NHCH_2CO), 4.22 (1H, q, NHC*H*), 7.30 (1H, t, aromatic), 7.91 (1H, d, aromatic), 8.08 (1H, d, aromatic), 8.29 (1H, t, aromatic). EI-MS calcd for $C_{15}H_{20}N_3O_4I$: *m/z* 433. Found: 433. Anal. ($C_{15}H_{20}N_3O_4I \cdot 7/4CF_3COOH \cdot 1/2H_2O \cdot 1/2C_2H_5OC_2H_5$) C, H, N.

Synthesis of 3′-Iodohippuryl D-Lysine (D-HL). 3′-Iodohippuryl D-lysine was synthesized by the reaction of N^{ϵ}-*tert*-butoxycarbonyl-D-lysine *tert*-butyl ester hydrochloride with 3-iodohippuric acid as described above. ^{1}H NMR (CD_3OD): δ 1.05−2.02 (6H, m, $(CH_2)_3$), 3.28 (2H, q, NHCH_2), 4.09 (2H, d, NHCH_2CO), 4.49 (1H, q, NHC*H*), 7.22 (1H, t, aromatic), 7.85 (1H, d, aromatic), 7.91 (1H, d, aromatic), 8.23 (1H, t, aromatic). ESI-MS calcd for $C_{15}H_{21}N_3O_4I$ (MH^+): *m/z* 434. Found: 434.

Synthesis of [^{125}I]HL and [^{125}I]HBL. Sn-HBL was radioiodinated in the presence of *N*-chlorosuccinimide (NCS) as an oxidant. Sn-HBL was dissolved in dry methanol containing 1% acetic acid (0.5 mg/mL), and 44.6 μL of this solution was mixed with 9.9 μL of NCS in methanol (0.5 mg/mL) in a sealed vial, followed by the addition of Na[^{125}I]I (2 μL). After incubation for 25 min at room temperature, [^{125}I]HBL was purified by RP-HPLC (solvent system 1). The radiochemical yield and purity of [^{125}I]HBL were determined by RP-HPLC (solvent system 2) and TLC (solvent system 4), respectively.

[^{125}I]HL was prepared by treating RP-HPLC-purified [^{125}I]HBL with TFA (100 μL). After standing for 10 min at room temperature, [^{125}I]HL was purified by RP-HPLC (solvent system 1). The radiochemical yield and purity of [^{125}I]HL were determined by RP-HPLC (solvent system 2) and TLC (solvent system 3), respectively.

Synthesis of D-[^{125}I]HL and D-[^{125}I]HBL. D-[^{125}I]HL and D-[^{125}I]HBL were prepared from D-Sn-HBL as described above.

Preparation of BBMVs. BBMVs were isolated from the renal cortex of male Wistar rats according to the Mg/EGTA precipitation method reported previously (*11*). All steps were performed on ice or at 4 °C. The cortex was homogenized with a Polytron homogenizer (PT10-35, Kinematica GmbH Littau, Switzerland) at full speed for 2 min in an appropriate volume of 300 mM mannitol, 12 mM Tris-HCl (pH 7.1), and 5 mM ethylenebis(oxyethylenenitrilo)tetraacetic acid (EGTA), followed by the addition of the same buffer to make a 10% homogenate. After the mixture was diluted with distilled water (1:1), $MgCl_2$ was added to a final concentration of 10 mM, and the homogenate was allowed to stand for 15 min. The homogenate was centrifuged at 1900*g* for 15 min in a Hitachi High-Speed Refrigerated Centrifuge SCR 20B (rotor RPR20-2). The supernatant was centrifuged at 24 000*g* for 30 min. The pellet was resuspended in an appropriate volume of buffer composed of 150 mM mannitol, 6 mM Tris-HCl (pH 7.1), and 2.5 mM EGTA and homogenized in a Potter-Elvehjem homogenizer with a Teflon pestle at 1000 rpm (10 strokes). $MgCl_2$ was added to a final concentration of 10 mM, and the suspension was centrifuged at 1900*g* for 15 min. The supernatant was centrifuged at 24000*g* for 30 min. The final pellet (purified brush border membrane) was resuspended in a 0.1 M phosphate buffer (pH 7.0) by 10 passages through a fine needle (0.4 × 19 mm) attached to a plastic syringe. For incubation studies, the vesicles were diluted with 0.1 M phosphate buffer (pH 7.0) to give a final protein concentration of 10 mg/mL. The γ-glutamyltransferase, aminopeptidase, and renal dipeptidase activities on BBMVs, determined according to the procedures of Glossmann et al. (*14*), Kramers et al. (*15*), and Hooper et al. (*16*), using L-γ-glutamyl-*p*-nitroanilide, L-leucine-*p*-nitroanilide, and glycyl-D-phenylanaline as substrates, were found to be 5.22 μmol/min/mg protein, 893 and 6.22 nmol/min/mg protein, respectively. The β-galactosidase activity on BBMVs, determined accoroding to the procedure of Wallner et al. using *p*-nitrophenyl β-D-galactopyranoside (*17*), was not detectable, which indicated that BBMVs were free from cross-contamination by lysosomal enzymes.

Preparation of Cilastatin. One gram of tienam (a mixture of imipenem 0.5 g and sodium cilastatin 0.5 g) was stirred in 20 mL of ethanol for 3 min at room temperature. After filtration, the filtrate was removed *in* vacuo to produce 120 mg of cilastatin as a sodium salt. ^{1}H NMR (D_2O); δ 0.71−0.87 (2H, m, $(CH_3)_2C-CH_2$), 0.95−1.04 (6H, m, $C(CH_3)_2$) 1.38−1.55 (5H, m, $(CH_2)_2$, $(CH_3)C-CH$), 1.96 (2H, q, CH_2CH_2S), 2.47 (2H, t, SCH_2-CH), 2.85−2.96 (2H, m, $CHCH_2CH_2$), 3.75 (1H, q, CH-COOH), 6.31 (1H, t, $CCHCH_2$). FAB-MS calcd for $C_{16}H_{25}N_2NaO_5S$ $(MH)^+$: *m/z* 381. Found: 381.

In Vitro Studies. Synthetic substrates were incubated with BBMVs as follows: a solution of BBMVs (20 μL) was preincubated for 2 h at 4 °C, followed by the addition of each substrate solution (20 μL) in 0.1 M phosphate buffer (pH 7.0). After incubation for 3 and 6 h at 37 °C, samples were taken from the solution and analyzed immediately by TLC (solvent system 3 or 4). Each sample was also analyzed by RP-HPLC (solvent system 2) after ultrafiltration with a 10-kDa cutoff membrane (Microcon-10, Millipore). A solution of Co^{2+}, MGTA, and phosphoramidon or cilastatin in 0.1 M phosphate buffer (pH 7.0) was added to preincubating solution with a final concentration of 1 mM, and the release of [^{125}I]iodohippuric acid from [^{125}I]HL or [^{125}I]HBL was estimated by TLC and RP-HPLC as described above.

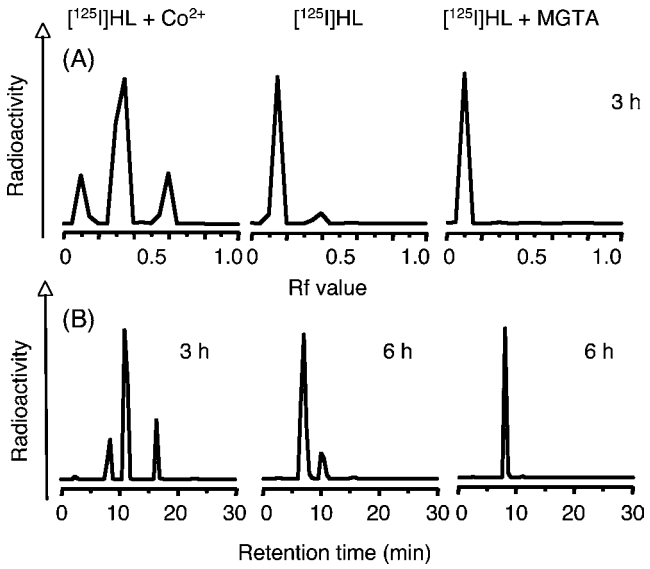

Figure 2. Radioactivity profiles of [^{125}I]HL after incubation in BBMVs (center panels) in the presence of 1 mM Co^{2+} (left panels) or 1 mM MGTA (right panels) at 37 °C as determined by (A) TLC (solvent system 3) or (B) RP-HPLC (solvent system 2). Under these conditions, *m*-iodohippuric acid and *m*-iodobenzoic acid had an R_f value of 0.35−0.40 and 0.60, and a retention time of 11 and 16 min, respectively.

RESULTS

Figure 2 shows TLC radiochromatograms of [^{125}I]HL after incubation in BBMV solution at 37 °C using solvent system 3. Under this condition, HL had an R_f value of 0.1, whereas *m*-iodohippuric acid and *m*-iodobenzoic acid had R_f values of 0.35−0.4 and 0.6, respectively. After 3 h incubation, a radioactivity peak at an R_f value of 0.35−0.4 was observed. On the other hand, this was not detected when [^{125}I]HL was incubated in BBMVs at 4 °C or in the absence of BBMVs at 37 °C (data not shown). The radioactivity peak at an R_f value of 0.35−0.4 significantly increased when [^{125}I]HL was incubated with BBMVs at 37 °C in the presence of Co^{2+}. A radioactivity peak at an R_f value of 0.6 was also observed; however, no radioactivity peak other than [^{125}I]HL was observed when [^{125}I]HL was incubated in BBMV solution at 37 °C in the presence of MGTA. Similar results were obtained when the reactions were analyzed by RP-HPLC as shown in Figure 2. Under these conditions (solvent system 2), HL and *m*-iodohippuric acid had a retention time of 7.5 and 11 min, respectively. Figure 3 summarizes the

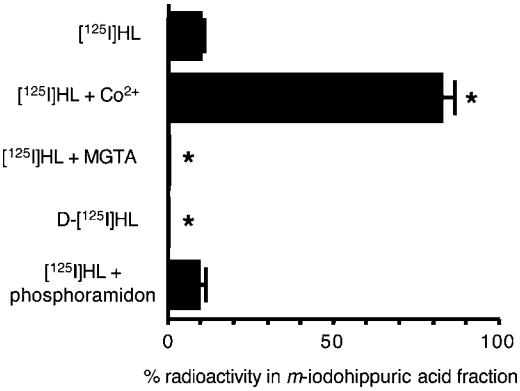

Figure 3. Liberation of *m*-[^{125}I]iodohippuric acid from [^{125}I]-HL after incubation in BBMVs at 37 °C for 3 h in the presence of an activator of CPM, or an inhibitor of CPM (MGTA), neutral endopeptidase (phosphoramidon), or dipeptidase (cilastatin), respectively. Columns and bars show the means and SD of three experiments. Significance was determined by unpaired Student's *t*-test [(*) $p < 0.01$ compared to [^{125}I]HL].

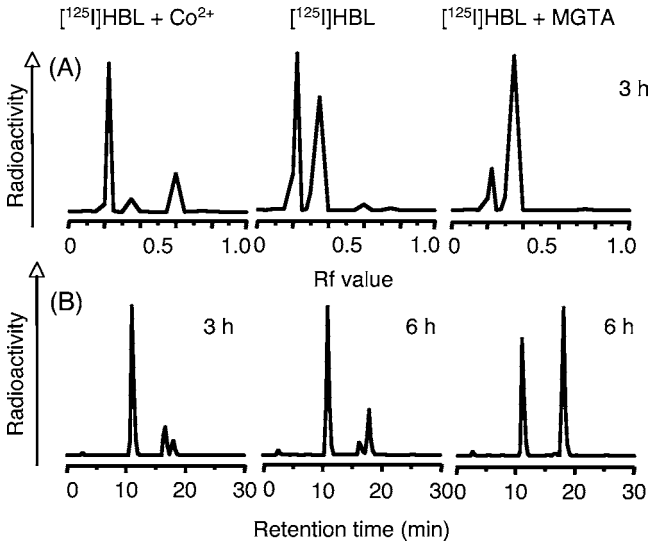

Figure 4. Radioactivity profiles of [^{125}I]HBL after incubation in BBMVs (center panels) or in the presence of 1 mM Co^{2+} (left panels) or 1 mM MGTA (right panels) at 37 °C, as determined by (A) TLC (solvent system 4) or (B) RP-HPLC (solvent system 2). Under these conditions, *m*-iodohippuric acid and *m*-iodobenzoic acid had an R_f value of 0.20 and 0.60 on TLC, and a retention time of 11 and 16 min, respectively.

amount of radioactivity in *m*-iodohippuric acid fractions after [^{125}I]HL incubation in the presence of BBMVs at 37 °C for 3 h, as determined by TLC. The addition of an inhibitor of neutral endopeptidase (phosphoramidon) had no effect on the generation of a radioactivity peak at an R_f value of 0.35−0.4. D-[^{125}I]HL remained unchanged when incubated in BBMV solution in the presence or absence of Co^{2+}.

TLC radiochromatograms of [^{125}I]HBL after incubation in BBMV solution at 37 °C are depicted in Figure 4. Under these conditions (solvent system 4), HBL, *m*-iodohippuric acid, and *m*-iodobenzoic acid had an R_f value of 0.35, 0.2, and 0.6, respectively. No radiometabolites were detected when [^{125}I]HBL was incubated in BBMVs at 4 °C or in the absence of BBMVs at 37 °C (data not shown). The radioactivity peak at an R_f value of 0.2 increased when [^{125}I]HBL was incubated in the presence of Co^{2+} (Figure 4). An additional radioactivity peak was observed at an R_f value of 0.6 in the presence of Co^{2+}. Contrary to [^{125}I]HL, [^{125}I]HBL generated a radioactivity peak at an R_f value of 0.2 when incubated in the presence

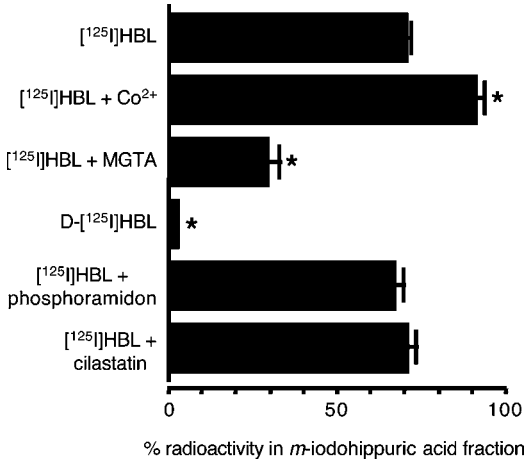

Figure 5. Liberation of *m*-[^{125}I]iodohippuric acid from [^{125}I]-HBL after incubation in BBMVs at 37 °C for 3 h in the presence or absence of an activator of CPM (Co^{2+}), or an inhibitor of CPM (MGTA), neutral endopeptidase (phosphoramidon) or dipeptidase (cilastatin), respectively. Columns and bars show the means and SD of three experiments. Significance was determined by unpaired Student's *t*-test [(*) $p < 0.01$ compared to [^{125}I]HBL].

of MGTA although the amount of the radioactivity at this R_f value was significantly reduced (Figure 5, right panel). Similar results were observed by RP-HPLC analyses where [^{125}I]HBL and *m*-[^{125}I]iodohippuric acid had a retention time of 18 and 11 min (solvent system 2), respectively (Figure 4). Figure 5 summarizes the amount of radioactivity in the *m*-[^{125}I]iodohippuric acid fraction after incubation of [^{125}I]HBL in BBMV solution at 37 °C for 3 h, when determined by TLC. [^{125}I]HBL generated a significantly higher amount of radioactivity in *m*-iodohippuric acid fractions than did [^{125}I]HL. The amount of radioactivity in *m*-iodohippuric acid fractions increased with the presence of Co^{2+}, as also observed with [^{125}I]-HL. However, radioactivity fractions were still observed when [^{125}I]HBL was incubated in the presence of MGTA. Both phosphoramidon and cilastatin had no effect on the generation of *m*-[^{125}I]iodohippuric acid from [^{125}I]HBL. D-[^{125}I]HBL hardly liberated any radiometabolites when incubated in BBMV solution at 37 °C in the presence or absence of Co^{2+}.

DISCUSSION

HML was designed based on the hypothesis that the glycyl-lysine sequence in HML would be recognized and cleaved by CPM on the renal brush border membrane during the internalization process of the antibody fragment, since it is well-known that glycyl-lysine is one of the substrates for CPM on the renal brush border membrane (*18*). Although hippuryl lysine is also recognized and cleaved by CPM (*18*), HML differs from hippuryl-lysine in that the former has an iodine atom at the meta-position of hippuric acid and the N^{ϵ}-amine residue of HML is converted to the maleoyl group, which is further converted to the succinimidyl group after conjugation to thiolated Fab fragments. The latter modification would significantly affect CPM recognition since the presence of a positive charge in the side-chain of the C-terminal lysine residue of glycyl-lysine prefers CPM recognition (*19*).

To estimate the effect of iodination at the meta-position of hippuric acid on CPM recognition, [^{125}I]HL was incubated in BBMVs in the presence or absence of Co^{2+} or MGTA, an activator and inhibitor of the enzyme, respectively (*18*, *20*). As summarized in Figure 3, the BBMV-

mediated release of *m*-[^{125}I]iodohippuric acid from [^{125}I]-HL showed temperature dependency. D-[^{125}I]HL was not recognized as a substrate for enzymes on BBMVs. Both Co^{2+} and MGTA were effective to facilitate and inhibit the hydrolysis reaction. These results suggested that CPM recognized the glycyl-lysine sequence of hippuryl-L-lysine when iodine was introduced at the meta-position of hippuric acid.

To investigate the effect of the modification of N^{ϵ}-amine residue of L-lysine on CPM recognition, [^{125}I]HBL was incubated in the presence of BBMVs. [^{125}I]HBL liberated much higher amounts of *m*-[^{125}I]hippuric acid than [^{125}I]-HL (Figures 3 and 5). The hydrolysis reaction of [^{125}I]-HBL also showed temperature dependency. D-[^{125}I]HBL was hardly recognized as a substrate by enzymes on BBMVs. Although the addition of Co^{2+} facilitated the hydrolysis reaction, MGTA acted as a partial inhibitor of the reaction (Figure 5). These studies implied that chemical modification of the N^{ϵ}-amine residue of HL made the resulting compound, HBL, a substrate for more than two enzymes on BBMVs at the expense of reduced specificity for CPM. Enzymes on the renal brush border membrane are classified into two types: transmembrane enzymes and glycophosphatidylinositol (GPI)-anchored enzymes. Since the N^{ϵ}-amine residue in [^{125}I]HBL was modified with the lipophilic Boc group, [^{125}I]HBL would gain access to not only GPI-anchored enzymes but also transmembrane enzymes on BBMVs, which may account for the significantly higher release of *m*-[^{125}I]iodohippuric acid from [^{125}I]HBL compared with [^{125}I]HL. Antibody fragments are internalized into renal cells through the brush border of renal tubules. Thus, the iodohippuryl-lysine moiety in HML-conjugated Fab fragments would also gain access to both types of enzymes during the internalization process. This suggested that a variety of enzymes on BBMVs were involved in the in vivo cleavage of the glycyl-lysine sequence in HML-conjugated Fab fragments.

To further investigate the enzymes responsible for the release of *m*-iodohippuric acid from HML-conjugated antibody fragments, [^{125}I]HBL was incubated in BBMVs in the presence of representative inhibitors for enzymes that cleave the C-terminal peptide sequence. The lack of inhibition of the BBMV-mediated release of *m*-[^{125}I]-iodohippuric acid from [^{125}I]HBL by phosphoramidon and cilastatin indicated that neither neutral endopeptidase nor renal dipeptidase catalyzed the hydrolysis reaction. The acceleration or partial inhibition of the BBMV-mediated hydrolysis of [^{125}I]HBL by the presence of Co^{2+} or MGTA showed that both metalloenzymes and non-metalloenzymes were involved in the release of *m*-[^{125}I]-iodohippric acid from [^{125}I]HBL and HML-conjugated Fab fragments. These results suggested the involvement of CPM in the hydrolysis of the glycyl-lysine sequence in HBL- and HML-conjugated antibody fragments although the N^{ϵ}-amine residues of the two compounds were chemically modified. However, since both activation by Co^{2+} and inhibition by MGTA are not specific to CPM but rather typical to a variety of metalloenzymes (*21*, *22*), further studies are required for confirmation.

In conclusion, the findings in this study suggested that N^{ϵ}-modified iodohippuryl-lysine would be recognized as a substrate by enzymes on the renal brush border membrane, which supported our hypothesis that low renal radioactivity levels of [^{125}I]HML-conjugated Fab would be attributable to enzyme-mediated hydrolysis during the internalization process of the conjugate into renal cells. Thus, this study showed that this in vitro system using renal BBMVs would constitute a useful approach to the development of radiolabeling reagents for antibody fragments and peptides based on the notion of the renal brush border enzyme-mediated release of radiometabolites for low renal radioactivity levels.

ACKNOWLEDGMENT

This study was supported in part by a Grant-in-Aid for Scientific Research (B) by the Ministry of Education, Culture, Sports, Science and Technology, Japan, and a Grant-in-Aid from the Fugaku Trust for Medicinal Research. The authors are also grateful to Mr. Takio Kobayashi for financial support.

LITERATURE CITED

(1) Marcus, R. (2005) Use of ^{90}Y-ibritumomab tiuxetan in non-Hodgkin's lymphoma. *Semin. Oncol. 32*, S36−S43.

(2) Yokota, T., Milenic, D. E., Whitlow, M., Wood, J. F., Hubert, S. L., and Schlom, J. (1993) Microautoradiographic analysis of the normal organ distribution of radioiodinated single-chain Fv and other Immunoglobulin forms. *Cancer Res. 53*, 3776−3783.

(3) Akizawa, H., and Arano, Y. (2002) Altering pharmacokinetics of radiolabeled antibodies by the interposition of metabolizable linkages. Metabolizable linkers and pharmacokinetics of monoclonal antibodies. *Q. J. Nucl. Med. 46*, 206−223.

(4) Behr, T. M., Behe, M., Stabin, M. G., Wehrmann, E., Apostolidis, C., Molinet, R., Strutz, F., Fayyazi, A., Wieland, E., Gratz, S., Koch, L., Goldenberg, D. M., and Becker, W. (1999) High-linear energy transfer (LET) alpha versus low-LET beta emitters in radioimmunotherapy of solid tumors: therapeutic efficacy and dose-limiting toxicity of ^{213}Bi− versus ^{90}Y-labeled CO17−1A Fab' fragments in a human colonic cancer model. *Cancer Res. 59*, 2635−2643.

(5) Lambert, B., Cybulla, M., Weiner, S. M., Van De Wiele, C., Ham, H., Dierckx, R. A., and Otte, A. (2004) Renal toxicity after radionuclide therapy. *Radiat. Res. 161*, 607−611.

(6) Olafsen, T., Cheung, C. W., Yazaki, P. J., Li, L., Sundaresan, G., Gambhir, S. S., Sherman, M. A., Williams, L. E., Shively, J. E., Raubitschek, A. A., and Wu, A. M. (2004) Covalent disulfide-linked anti-CEA diabody allows site-specific conjugation and radiolabeling for tumor targeting applications. *Protein Eng. Des. Sel. 17*, 21−27.

(7) Arano, Y., Fujioka, Y., Akizawa, H., Ono, M., Uehara, T., Wakisaka, K., Nakayama, M., Sakahara, H., Konishi, J., and Saji, H. (1999) Chemical design of radiolabeled antibody fragments for low renal radioactivity levels. *Cancer Res. 59*, 128−134.

(8) Nakamoto, Y., Sakahara, H., Saga, T., Sato, N., Zhao, S., Arano, Y., Fujioka, Y., Saji, H., and Konishi, J. (1999) A novel immunoscintigraphy technique using metabolizable linker with angiotensin II treatment. *Br. J. Cancer 79*, 1794−1799.

(9) Fujioka, Y., Arano, Y., Ono, M., Uehara, T., Ogawa, K., Namba, S., Saga, T., Nakamoto, Y., Mukai, T., Konishi, J., and Saji, H. (2001) Renal metabolism of 3′-iodohippuryl N$^{\epsilon}$-maleoyl-L-lysine (HML)-conjugated Fab fragments. *Bioconjugate Chem. 12*, 178−185.

(10) Inui, K., Saito, H., Takano, M., Okano, T., Kitazawa, S., and Hori, R. (1984) Enzyme activities and sodium-dependent active D-glucose trasport in apical membrane vesicles isolated from kidney epithelial cell line (LLC-PK1). *Biochim. Biophys. Acta 769*, 514−518.

(11) Hori, R., Tomita, Y., Katsura, T., Yasuhara, M., Inui, K., and Takano, M. (1993) Transport of bestatin in rat renal brush-border membrane vesicles. *Biochem. Pharmacol. 45*, 1763−1768.

(12) Biber, J., Stieger, B., Haase, W., and Murer, H. (1981) A high yield preparation for rat kidney brush border membranes different behaviour of lysosomal markers. *Biochim. Biophys. Acta 647*, 169−176.

(13) Wakisaka, K., Arano, Y., Uezono, T., Akizawa, H., Ono, M., Kawai, K., Ohmomo, Y., Nakayama, M., and Saji, H. (1997) A novel radioiodination reagent for protein radiopharmaceuticals with L-lysine as a plasma-stable metabolizable

linkage to liberate *m*-iodohippuric acid after lysosomal proteolysis. *J. Med. Chem. 40*, 2643−2652.
(14) Glossmann, H., and Neville, D. M. (1972) γ-Glutamyltransferase in kidney brush border membranes. *FEBS Lett. 19*, 340−344.
(15) Kramers, M. T., and Robinson, G. B. (1979) Studies on the structure of the rabbit kidney brush border. *Eur. J. Biochem. 99*, 345−351.
(16) Hooper, N. M., Low, M. G., and Turner, A. J. (1987) Renal dipeptidase is one of the membrane proteins released by phosphatidylinositol-specific phospholipase C. *Biochem. J. 244*, 465−469.
(17) Wallner, S. J., and Walker, J. E. (1975) Glycosidases in cell wall-degrading extracts of ripening tomato fruits. *Plant Physiol. 55*, 94−98.
(18) Skidgel, R. A., Davis, R. M., and Tan, F. (1989) Human carboxypeptidase M. *J. Biol. Chem. 264*, 2236−2241.
(19) Skidgel, R. A. (1988) Basic carboxypeptidases: Regulators of peptide hormone activity. *Trends Pharmcol. Sci. 91*, 299−304.
(20) Deddish, P. A., Skidgel, R. A., and Erdos, E. G. (1989) Enhanced Co^{2+} activation and inhibitor binding of carboxypeptidase M at low pH. Similarity to carboxypeptidase H (enkephalin convertase). *Biochem. J. 261*, 289−291.
(21) Patterson, E. K., Gatmaitan, J. S., and Hayman, S. (1975) The effect of Mn^{2+} and Co^{2+} on the activities of a zinc metallodipeptidase from a mouse ascites tumor. *Biochemistry 14*, 4261−4266.
(22) Salgado, H. C., Carretero, O. A., Scicli, A. G., and Murray, R. D. (1986) Effect of DL-2-mercaptomethyl-3-guanidinoethylthiopropanoic acid on the blood pressure response to vasoactive substances. *J. Pharmacol. Exp. Ther. 237*, 204−208.

BC050211Z

Site-Specific Cross-Linking of Proteins through Tyrosine Hexahistidine Tags

R. Scott Stayner, Dong-Joon Min,‡ Patrick F. Kiser, and Russell J. Stewart*

Department of Bioengineering, 20 South 2030 East, Room 506, University of Utah, Salt Lake City, Utah 84112.
Received August 12, 2005

The genetic addition of hexahistidine (H_6) tags is widely used to isolate recombinant proteins by immobilized metal-affinity chromatography (IMAC). Addition of a tyrosine residue to H_6 tags enabled proteins to be covalently cross-linked under mild conditions in a manner similar to the natural, site-specific cross-linking of tyrosines into dityrosine. A series of seven hexahistidine tags with tyrosines placed in various positions (H_6Y tags) were added to the amino terminus of the I28 immunoglobulin domain of the human cardiac titin. The H_6Y-tagged I28 dimerized in the presence of excess Ni^{2+} with a K_D of 200 μM. Treatment of Ni^{2+}-dimerized H_6Y-I28 with an oxidant, monoperoxyphthalic acid (MMPP) or sodium sulfite, resulted in covalent protein multimerization through chelated Ni^{2+}-catalyzed cross-linking of the Y residues engineered into the H_6 tag. The protein oligomerization was observed by sodium dodecyl sulfate polyacrylamide gel electrophoresis (SDS PAGE). The presence of dityrosine in the cross-linked proteins was confirmed by fluorescence emission at 410 nm. Proteins lacking the Y residue in the H_6 tag treated with the same oxidative conditions did not cross-link or exhibit dityrosine fluorescence, despite the presence of an endogenous Y residue. The method may have potential uses in other protein conjugation applications such as protein labeling and interfacial immobilization of proteins on artificial surfaces.

INTRODUCTION

The expanding use of recombinant proteins in several major industries feeds a growing need for new technologies for labeling, cross-linking, and interfacial immobilization of active proteins. Current protein conjugation and cross-linking methods have several major limitations. Most rely on diffusible reagents that react somewhat specifically with a particular class of nucleophilic functional group, such as the thiol of cysteines or primary amine of lysines. One problem with this approach is the lack of selectivity where all accessible groups of a particular class are modified. This can create multiple compounds, and if one of the targeted functional groups is in or near the active site, the target protein can be inactivated. For purposes of interfacial immobilization, this lack of selectivity can lead to random orientations and conjugation inefficiency. A further drawback of nonselectively modifying an entire class of functional groups is that specific protein modification cannot be carried out in a mixture with several other proteins. Therefore, relatively large quantities of purified protein are required for chemical modifications. All of these problems could be overcome with the development of a conjugation chemistry that utilizes nondiffusible, reactive groups at a genetically specified site on the target protein.

Looking to nature, one can find many examples of natural materials composed of highly cross-linked proteins and other biopolymers (*1*−*7*). The extensive covalent cross-linking gives these materials their impressive tensile strength, elasticity, tear resistance, toughness, and other critical material properties. A common natural strategy to cross-link biopolymers is the localized oxidation of specific amino acid side chains by metalloenzymes to form reactive intermediates that then spontaneously form cross-links within a restricted space. An example of this strategy is the oxidative deamination by lysyl oxidase of specific lysine residues that then condense with vicinal nucleophiles to covalently cross-link collagen and elastin (*8*, *9*). Another example is oxidative coupling of the phenolic moiety of two tyrosines, which is catalyzed by several structurally and mechanistically distinct categories of metalloenzymes, including peroxidases, tyrosinases, and laccases (*10*−*13*). Dityrosine protein linkages have been found in many structural proteins including elastin (*1*), silk, and plant cell wall extensin (*3*, *4*), and in hardened fertilization membranes of insect and sea urchin eggs (*7*).

Tyrosine residues are not a common target for site-specific chemical modification of proteins in vitro because they are generally unreactive under physiological pH. However, there have been reports of in vitro dityrosine cross-linking based on metal-catalyzed oxidation of tyrosine phenolic side chains that are reminiscent in some respects to the natural tyrosine cross-linking process described above (*14*−*17*). Peptidic complexes of Ni^{2+} in the presence of peracid oxidizing agents catalyze the formation of tyrosine free radicals that then react with proximal tyrosine residues to form dityrosine or isodityrosine cross-links (*9*, *14*−*17*). Brown and co-workers (*9*) found that Ni^{2+} complexed with the tripeptide GGH catalyzed the cross-linking of dimeric proteins in the presence of the relatively strong oxidant monoperoxyphthalic acid (MMPP) through natural tyrosine residues. Similarly, when GGH was genetically appended to the dimeric protein, ecotin, intermolecular cross-linking occurred between tyrosine residues in the presence of

* Corresponding author. Phone: (801) 581-8581. Fax: (801) 581-8966. E-mail: rstewart@eng.utah.edu.

‡ Current address: Division of Pediatric Hematology-Oncology, New York University School of Medicine, New York, NY 10016.

10.1021/bc050249b CCC: $30.25 © 2005 American Chemical Society
Published on Web 11/01/2005

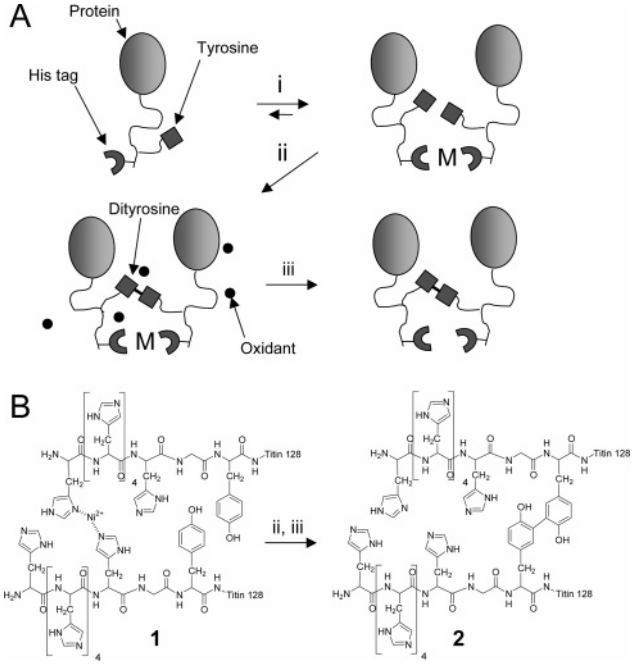

Figure 1. A. Schematic diagram of the protein cross-linking strategy. i. Formation of a ternary complex between Ni^{2+} and two His_6-tagged proteins. ii. Addition of an oxidant to trigger H_6Ni^{2+}-catalyzed dityrosine cross-linking. iii. Addition of ETDA to remove Ni^{2+}. B. Titin 128 model protein engineered with H_6-GY N Terminus **1**, the proposed structure of the cross-linked protein dimer **2** after oxidation and treatment with ETDA to remove complexed Ni^{2+}.

MMPP and Ni^{2+} (*8*). The tyrosine cross-linking efficiency was shown to be dependent on the distance between tyrosines in these experiments. In wild-type ecotin, in which natural tyrosines at the dimer interface are separated by 20 Å, the cross-linking efficiency was 15%. In ecotin genetically modified to move the tyrosines to within 5 Å of one another at the dimer interface, the cross-linking efficiency was 60%.

Similarly, the hexapeptide H_6, which is routinely used as a tag for purification of recombinant proteins by immobilized metal affinity chromatography (*18*, *19*), has also been shown to be redox active when complexed with Ni^{2+}. The dimer of H_6-tagged glutathione S-transferase (H_6GST) was covalently cross-linked by dityrosine formation in the presence of Ni^{2+} and MMPP (*14*). Proteins that do not naturally associate with H_6GST were not cross-linked, demonstrating that H_6-mediated cross-linking did not proceed through a highly diffusible reactant but instead was localized to the vicinity of the H_6 tag. Going further, the same research group demonstrated that, in the presence of MMPP and Ni^{2+}, H_6GST mediated the formation of dityrosine from free tyrosine, that the mutagenic removal of tyrosine residues from H_6GST decreased cross-linking efficiency, and that chemical addition of tyrosine-like residues, using the Bolton–Hunter reagent, increased cross-linking efficiency.

In this paper, we take this biomimetic strategy a step further by developing methods for site-specific dityrosine cross-linking of proteins that do not normally associate in solution. Using the I28 immunoglobulin domain from human cardiac titin as a model protein, we show that H_6-tagged I28 domains reversibly self-associate in solution in the presence of Ni^{2+} and that the complexed Ni^{2+} will catalyze the formation of dityrosine cross-links between Y residues strategically placed in or near the H_6 tag (Figure 1).

EXPERIMENTAL PROCEDURES

Preparation of the H_6(Y) Titin I28 Plasmids. The construction of the double H_6 tagged protein, H_6-titin I28–H_6 pET24a was previously published (*20*). The constructs containing the various H_6-tyr (H_6Y) tags (Table 1) were prepared by amplifying the I28 region with PCR primers, in separate reactions, that incorporated the DNA sequence of the H_6Y tag into the 5′ end of the PCR product along with *Nde*I and *Xho*I restriction sites for cloning. The PCR products were ligated into pET 26b (Novagen, Inc.) after digestion with *Nde*I and *Xho*I and transformed into DH5α. The constructs were verified by DNA sequencing.

Expression and Purification of H_6YI28 Proteins. For expression, the pET26b-I28 plasmids were transformed into *E. coli* strain BL21(DE3) (Novagen, Inc.) by electroporation (EPX Genetics, ECM 395). Single colonies from agar plates containing 50 μg/mL kanamycin were grown overnight at 37 °C in 5 mL LB media with 50 μg/mL kanamycin. LB cultures (500 mL) with 50 μg/mL kanamycin were then inoculated with the overnight cultures and grown at 37 °C until A_{600} was between 0.6 and 1.0 (about 2 h). Expression of the target protein was induced by adding isopropyl β-D-thiogalactoside (IPTG) to a final concentration of 0.1 mM followed by shaking for 4 h at 37 °C. The cells were then centrifuged (Beckman JA 10 rotor) at 4500 rpm for 15 min at 4 °C. The cell pellets were stored at −70 °C. Frozen pellets were resuspended in 5 mL of binding buffer (50 mM NaH_2PO_4, 500 mM NaCl, pH 7.5) per gram of pellet. Phenylmethanesulfonyl fluoride (PMSF) and Triton ×100 were added to concentrations of 1 mM and 0.1% v/v, respectively. The cell suspension was sonicated (Fisher 550 Sonic Dismembranator) at power level 4 on ice for 10 s followed by 1 min of cooling, which was repeated six times. The insoluble cell components were pelleted by centrifugation at 20 000 g (Beckman J2-HS Centrifuge, JA-17 rotor) for 45 min at 4 °C. The supernatant was mixed with 2 mL of Ni^{2+} nitrilotriacetic acid (NTA) agarose beads (Qiagen) equilibrated with binding buffer, allowed to settle in a column and drained by gravity. The collected flow-through was reapplied to the Ni–NTA column. The column was washed with several column bed volumes of the washing buffer (15 mM NaH_2PO_4, 500 mM NaCl, 60 mM imidazole, pH 7.5). H-tagged proteins were eluted into1 mL aliquots of the elution buffer (15 mM NaH_2PO_4, 500 mM NaCl, 300 mM imidazole, pH 7.5). The purity of the protein fractions was determined by sodium dodecyl sulfate polyacrylamide gel electrophoresis (SDS PAGE) using 15% polyacrylamide gels. Combined fractions were desalted into phosphate-buffered solution (PBS) (50 mM NaH_2PO_4, 150 mM NaCl, pH 7.5) on PD 10 sepharose columns (Pharmacia). After desalting, the proteins were aliquoted and stored at −70 °C. I28 proteins were concentrated using a 3000 MW cutoff centrifuge filter (Amicon). Protein concentrations were measured using a Coomasie protein assay (Biorad) with bovine serum albumin (BSA) as a standard. Each protein sample was concentrated so that the subsequent cross-linking reactions could be performed in a total volume of 20 μL, with a total protein concentration of 20 μM (4 nmol).

Sedimentation Equilibrium. Sedimentation equilibrium experiments were conducted in a Beckman Optima XL-A analytical ultracentrifuge, with an AnTi60 rotor at 20 °C, using six-channel, 12 mm thick, charcoal-epon centerpieces. Prior to the analysis, the protein samples were dialyzed against fresh PBS for 20 h. The three sample channels in each cell contained three

Table 1. Relative Fluorescence after Ni^{2+}/Sodium Sulfite Treatment

protein name	protein sequence	fluorescence, 410 nm (normalized)[a]
YH_6-I28	MNS**YH_6**GMA-titin I28	0
YGH_6-I28	MNS**YGH_6**GMA-titin I28	0
$YGYGH_6$-I28	MNS**$YGYGH_6$**GMA-titin I28	0
H_6GYG- I28	M**H_6GYG**-titin I28	0.4
H_6GYGYG-I28	M**H_6GYGYG**-titin I28	1
YGH_6GY-I28	MNS**YGH_6GY**A-titin I28	0.3
H_3GYGH_3-I28	MNS**H_3GYGH_3**GMA-titin I28	0
H_6-I28−H_6	MRGS**H_6**GMA-titin I28-**H_6**	0

titin I28 sequence: GSPLIFITPL SDVKVFEKDE AKFECEVSRE KTFRWLKGTQ EITGDDRFEL IKDGTKHSMV IKSAAFEDEA K**Y**MFEAEDKH TSGKLIIEGI LE

[a] The sequences of the H_6Y tags and the relative emission fluorescence at 410 nm of each of the proteins in the presence of Ni^{2+} after treatment with the Na_2SO_3. The complete sequence of I28 is shown in the bottom panel with the endogenous Y residue in bold.

different concentrations (1.4 μM, 4.3 μM, and 13 μM) of either the H_6GY-titin I28 protein without added nickel or that had been incubated overnight at 4 °C with 10-fold excess nickel(II) acetate. The reference channels contained PBS. Samples were centrifuged until sedimentation and chemical equilibrium were attained. Values of v-bar and the extinction coefficients for each protein were calculated from the amino acid sequence using the method of Laue (*21*). Various models describing the concentration distribution were fit to final absorbance versus radius data using nonlinear least squares techniques and the analysis program NONLIN (*22*, *23*). NONLIN performs simultaneous nonlinear least-squares fits to one or more sets of ultracentrifuge data.

Oxidative Cross-Linking of H_6Y-I28 Proteins. All cross-linking reactions were performed in PBS (50 mM NaH_2PO_4, 150 mM NaCl, pH 7.5). The nickel(II) acetate, monoperoxyphthalic acid (MMPP), and Na_2SO_3 stock solutions were prepared in DDI H_2O. To determine the effect of the position of Y on cross-linking efficiency, the series of H_6Y-I28 proteins (Table 1) were mixed in a final volume of 20 μL with nickel(II) acetate, 20 μM, and MMPP at final concentrations of 20, 200, or 200 μM. After addition of nickel(II) acetate, the solution was left on ice for 30 min, then warmed to room temperature before the addition of MMPP to initiate cross-linking. After 2 min, the cross-linking reaction was quenched by addition of 5 μL of 5× SDS−PAGE sample buffer (0. 25 M Tris pH 6.8, 1% SDS, 2% bromophenol blue, 50% glycerol, 10% β-mercaptoethanol). The samples were then analyzed using SDS PAGE. The extent of cross-linking of H_6GY-I28 as a function of oxidant and oxidant concentration was determined by cross-linking in 4 mM, 400 μM or 40 μM MMPP, or 40 mM, 4 mM, or 400 μM Na_2SO_3. The reactions were quenched by the addition of 5 μL of 5× sample buffer containing 10% β-mercaptoethanol. The samples were then analyzed by SDS PAGE.

Fluorescence Spectroscopy. The formation of dityrosine in the Ni^{2+}/Na_2SO_3 treated H_6GY-I28 proteins was verified using fluorescence spectroscopy. The cross-linking reactions were performed in a 1 mL quartz crystal cuvette at room temperature in a final volume of 400 μL PBS using 15 μM H6GY-I28 and 150 μM of nickel(II) acetate. With an excitation wavelength of 325 nm the fluorescence emission was scanned from 350 to 600 nm with an excitation slit width of 10 nm, emission slit width of 5 nm, and a scan speed of 500 nm/min on a Perkin-Elmer LS 55 fluorimeter. As a control, fluorescence emission was scanned in the absence of Ni^{2+}. To verify that the fluorescence of cross-linked H_6GY-I28 was due to dityrosine, the emission spectrum was compared to the emission spectrum of dityrosine produced by a laccase enzyme purified from pleurotus ostreatus, (Earthfax Development,7324 South Union Park Ave, Midvale, UT 84047, 938 units of activity/mg laccase). Laccase, at a final concentration of 0.3 mg/mL (281 U/mL) was reacted with 1.25 mM L-tyrosine in 600 μL PBS. Dityrosine formation catalyzed by the GGH/Ni^{2+} complex and Na_2SO_3 was also analyzed. L-Tyrosine (15 μM) in DDI H_2O was combined with a solution of GGH and Ni(II) acetate (150 μM each, DDI H_2O) such that the concentration of the GGH tripeptide and the Ni^{2+} concentration was 10 times that of the L-tyrosine concentration. The solution was allowed to sit at room temperature for 10 min, after which Na_2SO_3 was added for a final concentration of 1.5 mM. Dityrosine formation was followed using fluorescence spectroscopy. As a control, the preceding experiment was performed in the absence of the GGH tripeptide to demonstrate that Ni^{2+} and Na_2SO_3 alone are not sufficient to catalyze the reaction.

RESULTS

Self-Association of H_6-Tagged I28 Immunoglobulin Domains. It has been reported that a H_{10}-tagged fusion protein oligomerizes in the presence of Ni^{2+} (*24*). SDS PAGE analysis showed a ladder of proteins oligomerized into high molecular species that had a stoichiometry of three and six with respect to the monomeric protein. The oligomers were readily converted to the monomeric species by using excess EDTA to remove Ni^{2+} or by boiling.. Control experiments in which the protein was incubated in the buffer without added Ni^{2+} did not result in oligomerization. Enzymatic removal of the H_{10} tags from the fusion protein prevented oligomerization, indicating that oligomer formation involved Ni^{2+}/H_{10}-tag coordination complexes.

The titin I28 protein used in these experiments is an Ig domain found in cardiac titin (*26*). In muscle the physical properties of I28, and other Ig domains, help titin act as an elastic spring that keeps the sarcomere in register (*27*) by partially unfolding when the muscle is subjected to tensile stress (*28*). Previous SDS PAGE analysis of I28 have shown that the protein does not self-associate in vitro (*28*). To investigate if H_6- I28 dimerizes through the H_6 tags in the presence of Ni^{2+}, the native molecular weight of I28 was determined by equilibrium sedimentation in the absence and presence of Ni^{2+}. As titin Ig domains are not known to spontaneously associate in vivo (*27*) or in vitro (*29*) it was not unexpected that in the absence of Ni^{2+}, an H_6-I28 protein behaved as a 12.3 ± 1 kDa monomer (Figure 2A), which is consistent with the sequence derived molecular weight of 11.7 kDa. The H6GY-titin I28 protein in the presence of a 10-fold excess of Ni(II) acetate is weakly associated into a dimer with a dissociation constant of approximately 200 μM (Figure 2B).

Oxidative Cross-Linking through H_6Y-tags. The known redox activity of the H_6Ni^{2+} complex and the H_6-

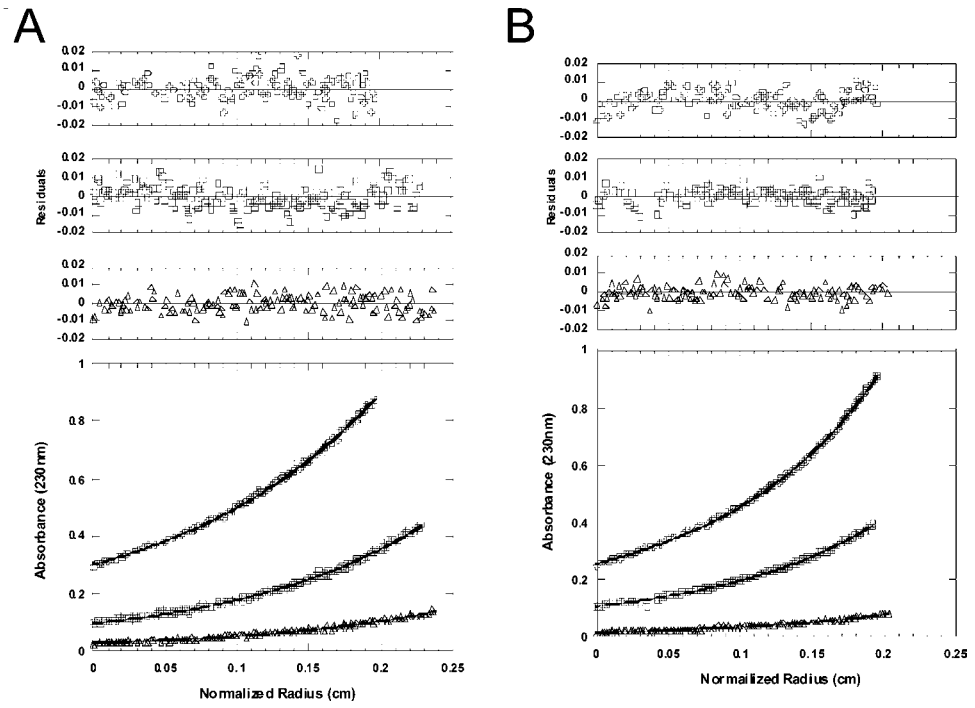

Figure 2. A. Sedimentation equilibrium of H6GY-titin I28 protein without Ni_2^+. The lower panels show experimental data points for three different loading concentrations of each protein with the corresponding calculated curve fit (solid line). The H_6GY-titin I28 protein is fit to a monomer model, MW = 12.3 ± 1 kDa. The upper panels show the residuals for these fits, which are small and random indicating a good fit to the monomer model. B. Sedimentation equilibrium data H_6GY-titin I28 protein with a 10-fold molar excess of Ni_2^+. The lower panels show experimental data points for three different loading concentrations of each protein with the corresponding calculated curve fit (solid line). In the presence of Ni_2^+, the H_6GY-titin I28 protein fit a monomer−dimer model with an equilibrium KD of approximately 200 μM. The upper panels show the residuals for these fits, which indicate a good fit to the monomer−dimer model.

Ni^{2+}-mediated self-association of I28 suggested that the ternary Ni^{2+} complex might catalyze site specific oxidative cross-linking of I28 if Y residues were placed near the H_6-tags (Figure 1). To investigate this possibility and to optimize Y placement, a series of H_6-I28 proteins were constructed that had Y residues strategically positioned within or adjacent to the H_6-tags (Table 1). Solutions of I28 in the presence of Ni^{2+} were treated with the oxidizing agent MMPP and the efficiency of I28 cross-linking was investigated by SDS−PAGE (Figure 3). The H_6Y-tags in which the Y residues were on the inside, or carboxyl end, of the H_6 tag (lanes 4 and 5) were covalently cross-linked into dimers predominantly, but also into trimers and higher molecular weight species. These multimers remained intact after vigorous boiling and in the presence of the reducing agent, β-mercaptoethanol, indicating that neither metal-mediated complexes nor disulfide bonds were responsible for the observed inter-protein cross-linking. The H_6-tags in which the Y residues are on the outside, or amino end, of the H_6 tag (lanes 1−3 and 6−7) underwent little cross-linking. In the absence of Ni^{2+} or MMPP, no cross-linking occurred. A control I28 protein that did not have a Y residue in the H_6 tag was not cross-linked in the presence of Ni^{2+} and MMPP although it does have a single endogenous Y residue (lane 8). These results demonstrate first that H_6-complexed Ni^{2+} will catalyze covalent cross-linking between HY-tagged I28, and second that the position of the Y residue relative to the H_6-tag has a profound effect on the covalent cross-linking efficiency.

Covalent cross-linking of H_6GY-I28 protein was also induced by sodium sulfite (Na_2SO_3) in the presence of Ni^{2+} (Figure 4). Although the precise mechanism of this process is unknown, XXH peptide/Ni^{2+} complexes in the presence of SO_3^- and dioxygen have been shown to

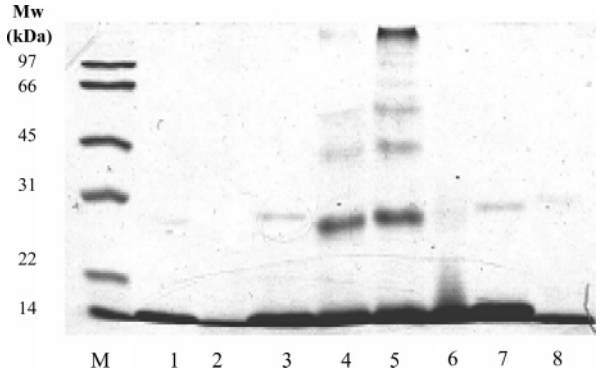

Figure 3. Protein cross-linking efficiency depends on the placement of the Y residue(s) near the H_6 tag. Proteins with the Y residue on the inside of the H_6 tag, lanes 4 (MH_6GY-titin I28) and 5 (MH_6GYGY-titin I28) showed efficient cross-linking when treated with MMPP. However, those versions of the protein in which Y residue(s) were placed within or on the amino side of the H_6 tag underwent little or no cross-linking when subjected to the same conditions: lanes 1 (YH_6-titin I28), 2 (YGH_6-titin I28), 3 (MNSYGYGH_6-titin I28), 6 (YGH_6GY−Titin I28), 7 (H_3GYGH_3−Titin I28). Lane M: molecular weight markers. Lane 8: no Y control protein (H_6-Titin I28-H_6).

generate sulfur oxyradicals, e.g. $SO_3^{\bullet-}$, $SO_5^{\bullet-}$, and $SO_4^{\bullet-}$ (*30*). The sulfite radical anion $SO_3^{\bullet-}$ is known to react rapidly with dioxygen to form the short-lived monoperoxysulfite radical anion $SO_5^{\bullet-}$ which can then dimerize to form the more stable sulfate radical anion $SO_4^{\bullet-}$ (for a detailed discussion of the metal-catalyzed redox chemistry of Na_2SO_3 see ref 30). Alternatively, an oxidized nickel metal complex (Ni^{3+}/Ni^{2+}) may also be acting as the phenolic oxidizing agent. One or more of these reactive intermediate species could then oxidize the Y

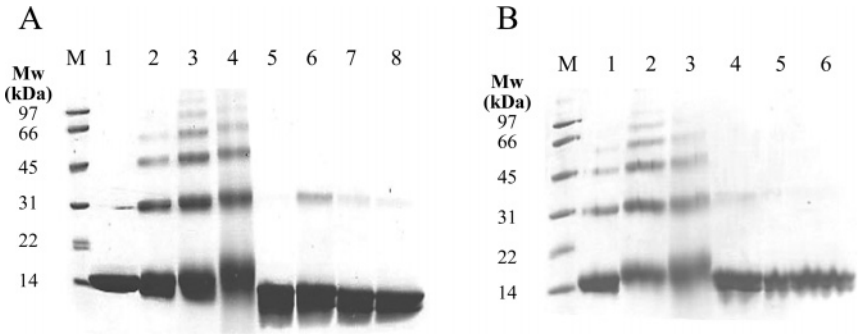

Figure 4. Effect of oxidant concentration on I28 cross-linking. (A). MMPP-induced cross-linking. Lanes 1−4: H_6GY-titin I28. Lanes 5−8: H_6-titin I28-H6 no Y control. The final concentration of MMPP was 0 in lanes 1 and 5, 40 μM in lanes 2 and 6, 400 μM in lanes 3 and 7, and 4 mM in lanes 4 and 8. (B) Na_2SO_3 induced cross-linking. Lanes 1−3: H_6GY-titin I28. Lanes 4−6: H_6-titin I28-H_6 control. The final concentration of Na_2SO_3 was 400 μM in lanes 1 and 4, 4 mM in lanes 2 and 5 with 40 mM in lanes 3 and 6. Lane M: molecular weight markers.

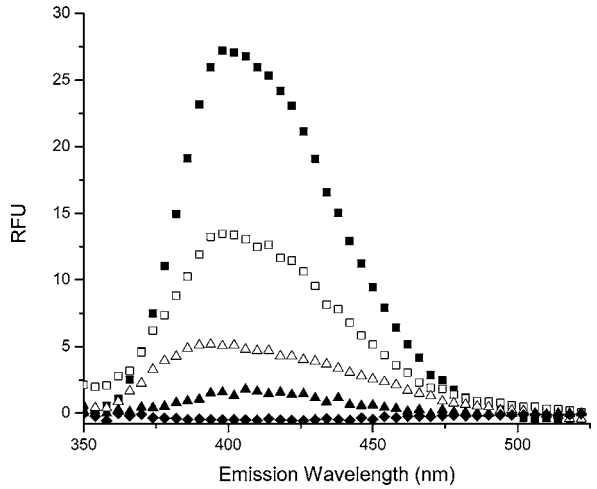

Figure 5. Dityrosine fluorescence. (■) L-Tyrosine and laccase enzyme. (□) H6GYG-titin I28 treated with Ni_2^+ and Na_2SO_3, (△) L-tyrosine treated with GGH/Ni_2^+/Na_2SO_3, (▲) H_6GYG-titin I28 treated with Na_2SO_3 (no Ni_2^+ control), (◆) L-tyrosine treated with Ni_2^+ and Na_2SO_3 (no ligand control).

phenol ring residue, resulting in the formation of a phenolic free radical species, which could then undergo oxidative cross-linking with an adjacent phenolic moiety. This scheme is thermodynamically possible as the one-electron redox potential of [(XXH)Ni^{2+}]-Ni^{3+}/Ni^{2+} (∼+800 mV) (*30*), $SO_3^{\bullet-}$/SO_3^{2-} (+390 mV) (*31*), $SO_5^{\bullet-}$/SO_5^{2-} (+840 mV) (*31*), and $SO_4^{\bullet-}$/SO_4^{2-} (+2900 mV) (*30*) are all potent enough oxidizing agents to oxidize phenolic residues (+300 mV) (*32*).

Dityrosine Formation. As further evidence that covalent cross-linking was occurring through the formation of dityrosine bonds, the cross-linked H_6Y-I28 proteins were analyzed by fluorescence spectroscopy. Dityrosine has an excitation maximum at 325 nm and a fluorescence maximum at 410 nm (*34*). Laccase is an enzyme that catalyzes the polymerization of phenol derivatives in nature, such as urushiol found in oriental lacquers (*35*). Laccase has been used to create dityrosine linkages in Y-containing peptides(*36*) and to polymerize free phenol, the functional group on tyrosine (*11*). Reaction of L-tyrosine with laccase to create an internal dityrosine standard resulted in a broad peak of fluorescence at about 400 nm (Figure 5). As an additional control, dityrosine was formed by reacting L-tyrosine with Ni^{2+} complexed by the tripeptide, GGH, which has been shown previously to generate dityrosine (*8*, *37*).

The oxidatively cross-linked H_6Y-tagged I28 proteins had fluorescence spectra similar to dityrosine formed from L-tyrosine with laccase. In the absence of oxidant or Ni^{2+} there was little or no fluorescence (Figure 5). These results confirm that the covalent cross-linking in the H_6Y-I28 proteins was due, at least in part, to the formation of dityrosine near the H-tags. Furthermore, the relative fluorescence intensity of the oxidatively cross-linked H_6Y-I28 proteins correlated with the degree of cross-linking observed by SDS−PAGE; the most cross-linked protein (Figure 3) had the highest fluorescence (Table 1).

DISCUSSION

The goal of this work was to develop an alternative method to modify proteins in a site-specific manner under mild conditions. Our approach was predicated on two previously reported observations. First, H-tagged proteins can associate through a ternary complex formed between the H-tags and Ni^{2+} (*24*). Second, H_6 complexed Ni^{2+} catalyzes oxidative covalent cross-linking of tyrosine residues into dityrosine (*9*, *14*, *16*). We reasoned that it should be possible to use H_6-tags to first form a metal-mediated complex between H_6-tagged proteins and that the metal complex could then be used to catalyze the localized cross-linking of tyrosine residues placed in the vicinity of the metal complex.

That H_6-tagged proteins associate in solution in the presence of Ni^{2+} was confirmed by sedimentation equilibrium analysis. H_6-tagged I28 existed in a monomer−dimer equilibrium in solution with a K_D of approximately 200 μM (Figure 2). The Ni^{2+}-mediated association through H_6-tags brings genetically placed Y residues into close proximity to one another and the catalytic Ni^{2+} H_6 complex. Addition of an oxidant generates reactive oxidative species, which then generate tyrosine free radicals that react with proximal tyrosines and other residues. By localizing two tyrosine residues in space by the ternary complex, we envisioned the possibility of observing enhanced rates of reaction as the local concentration of tyrosine could be higher than what could be obtained in solution. This rate enhancement affect has been recently observed in reactants tethered to DNA dimers (*38*, *39*). Additionally, the ternary metal complex prevents the reactive free radicals from diffusing away and thereby localizes the cross-linking reaction.

The position of the Y residue in the H_6-tag had a profound effect on the cross-linking efficiency of the reaction (Figure 3). Placement of the Y residue(s) on the carboxy side of the H_6 tag facilitates the cross-linking whereas the placement of Y residue(s) near the amino terminus resulted in little or no cross-linking. Although the mechanism that leads to this difference is not known,

it may be related to the half-life of the Y free radical generated in the reaction which can vary considerably depending on the local environment of the radical (*40*, *41*).

Our data indicates that the His-tagged proteins were dimerized via the formation of Y−Y cross-links, there is also evidence of side reactions. Metal-catalyzed oxidation has been reported to induce peptide bond cleavage in proteins (*42*−*44*), sometimes near Y residues (*45*, *46*). Mass spectrometry analysis after trypsin digestion of the H_6GY I28 proteins subjected to the oxidative treatment revealed the presence of small peptides conjugated to the H_6GY tag digest fragment (data not shown). Peptides containing Y residues generated by the cleavage of the protein near Y residue in the H_6 tag likely cross-linked with intact proteins, which accounts for the increased width of the monomer band in the SDS PAGE results (Figure 4). These same results, however, indicate that though the protein cleavage does occur the predominant product is protein cross-linking. It is conceivable that assay conditions such as oxidizing species, oxidant concentration, dioxygen concentration, and the reaction time could be optimized to enhance cross-linking while reducing protein cleavage.

The presence of dityrosine was detected by fluorescence spectroscopy in the cross-linked proteins (Figure 5). However, other residues in the H_6 tag region are likely to have reacted with the Y free radical. Of the residues vicinal to the Y in the H_6 tag, G is a likely candidate since it was shown previously to react with Y in proteins subjected to metal-catalyzed oxidation (*37*). The strong fluorescence observed indicates that the ladder of high molecular weight proteins observed in the SDS−PAGE studies is mainly due to the formation of Y−Y cross-linking; however, other Y-amino acid cross-links likely contributed to the oligomerization as well.

We demonstrated that the H_6 tag in conjunction with Ni^{2+} caused the protein to associate weakly into dimers. However, the association was transient and therefore only observable by sedimentation equilibrium studies. There are a number of residues that can participate in metal binding complexes: E, Y, H, R, K, D, M, C (*47*). Combinations of these residues in protein tags have the potential to yield stronger metallopeptide complexes than polyhistadine tags. For example, it has been reported that the HNRYGCGCC protein tag was shown to have a stronger metal binding capacity when compared to the common hexahistadine tag and yielded 20% more protein after purification during immobilized metal affinity chromatography (*48*). The focus of future research will be to develop methods to screen for additional peptides for the propensity to form metal-mediated complexes and catalyze oxidative dityrosine cross-linking triggered by low concentrations of a mild oxidant.

In conclusion, the metal-catalyzed oxidative cross-linking system described with further optimization to limit side reactions may circumvent some of the major limitations of conventional protein chemical modification methods. First, the conjugation site is preestablished as a ternary complex before functional groups are created by a mild oxidant. The conjugation site itself catalyzes the creation of the reactive species, which localizes covalent bond formation to the intended region. Therefore, the target functional group is not active in mild reaction conditions, unlike the C residues sometimes used in protein conjugation reactions (*49*, *50*), and the site limits random modifications that may damage or inactivate the target protein. Second, the conjugation site on the protein is genetically encoded in the form of a metal chelating peptide. Therefore, it is unnecessary to purify the target protein as a prerequisite for modification; it can be modified within a complex mixture of proteins. The implication for protein array applications is that recombinant proteins may be selectively captured onto a solid support from a crude lysate of cells expressing the protein. Purification and posttranslational chemical modification will be unnecessary.

ACKNOWLEDGMENT

This work was supported in part by NIH grant GM070826-01.

LITERATURE CITED

(1) LaBella, F. S., Keeley, F. W., Vivian, S., and Thornhill, D. P. (1967) Evidence for dityrosine in elastin. *Biochem. Biophys. Res. Commun. 26*, 748−753.

(2) Deleted in proof.

(3) Brady, J. D., Sadler, I. H., and Fry, S. C. (1998) Pulcherosine, an oxidatively coupled trimer of tyrosine in plant cell walls: its role in cross-link formation. *Phytochemistry 47*, 349−353.

(4) Waffenschmidt, S., Woessner, J. P., Beer, K., and Goodenough, U. W. (1993) Isodityrosine cross-linking mediates insolubilization of cell walls in Chlamydomonas. *Plant Cell 5*, 809−820.

(5) Vaccaro, E., and Waite, J. H. (2001) Yield and post-yield behavior of mussel byssal thread: a self-healing biomolecular material. *Biomacromolecules 2*, 906−911.

(6) Yamamoto, H., Tanisho, H., Ohara, S., and Nishida, A. (1992) Cross-linking and gel formation of water-soluble lysine polypeptides. An insolubilization model reaction for adhesive proteins. *Int. J. Biol. Macromol. 14*, 66−72.

(7) Foerder, C. A., and Shapiro, B. M. (1977) Release of ovoperoxidase from sea urchin eggs hardens the fertilization membrane with tyrosine cross-links. *Proc. Natl. Acad. Sci. U.S.A. 74*, 4214−4218.

(8) Brown, K. C., Yu, Z., Burlingame, A. L., and Craik, C. S. (1998) Determining protein−protein interactions by oxidative cross-linking of a glycine-glycine-histidine fusion protein. *Biochemistry 37*, 4397−4406.

(9) Brown, K. C., Yang, S. H., and Kodadek, T. (1995) Highly Specific Oxidative Cross-linking of Proteins Mediated by a Nickel−Peptide Complex. *Biochemistry 34*, 4733−4739.

(10) Oudgenoeg, G., Hilhorst, R., Piersma, S. R., Boeriu, C. G., Gruppen, H., Hessing, M., Voragen, A. G., and Laane, C. (2001) Peroxidase-mediated cross-linking of a tyrosine-containing peptide with ferulic acid. *J. Agric. Food Chem. 49*, 2503−2510.

(11) Uchida, H., Fukuda, T., Miyamoto, H., Kawabata, T., Suzuki, M., and Uwajima, T. (2001) Polymerization of bisphenol A by purified laccase from Trametes villosa. *Biochem. Biophys. Res. Commun. 287* (2), 355−8.

(12) Muzzarelli, R. A. A., Ilari, P., Xia, W., Pinotti, M., and Tomasetti, M. (1994) Tyrosinase-mediated quinone tanning of chitinous materials. *Carbohyd. Polym. 24*, 295−300.

(13) Obataya, E., Umemura, K., Norimoto, M., and Ohno, Y. (1999) Viscoelastic properties of Japanese lacquer film. *J. Appl. Polym. Sci. 73*, 1727−1732.

(14) Fancy, D. A., and Kodadek, T. (1998) A critical role for tyrosine residues in His6Ni-mediated protein crosslinking. *Biochem. Biophys. Res. Commun. 247*, 420−426.

(15) Fancy, D. A., Melcher, K., Johnston, S. A., and Kodadek, T. (1996) New chemistry for the study of multiprotein complexes: the six-histidine tag as a receptor for a protein crosslinking reagent. *Chem. Biol. 3*, 551−559.

(16) Fancy, D. A., and Kodadek, T. (1997) Site-directed oxidative protein crosslinking. *Tetrahedron 53*, 11953−11960.

(17) Gill, G., Richter-Rusli, A. A., Ghosh, M., Burrows, C. J., and Rokita, S. E. (1997) Nickel-dependent oxidative cross-linking of a protein. *Chem. Res. Toxicol. 10*, 302−309.

(18) Porath, J., Carlsson, J., Olsson, I., and Belfrage, G. (1975) Metal chelate affinity chromatography, a new approach to protein fractionation. *Nature (London) 258*, 598−599.
(19) Chaga, G. S. (2001) Twenty-five years of immobilized metal ion affinity chromatography: past, present and future. *J. Biochem. Biophysi. Methods 49*, 313−334.
(20) Chen, L. (2000) Doctoral Thesis, Department of Bioengineering, University of Utah, Salt Lake City, UT, p 86.
(21) Laue, T. M., Shah, B., Ridgeway, T. M., and Pelletier, S. L. (1992) Computer-aided interpretation of analytical sedimentation data for proteins. *Analytical Ultracentrifug. Biochem. Polym. Sci.* 90−125.
(22) Johnson, M. L., Correia, J. J., Yphantis, D. A., and Halvorson, H. R. (1981) Analysis of data from the analytical ultracentrifuge by nonlinear least-squares techniques. *Biophys. J. 36*, 575−588.
(23) Yphantis, D. A. (1964) Equilibrium Ultracentrifugation of Dilute Solutions. *Biochemistry 47*, 297−317.
(24) Sprules, T., Green, N., Featherstone, M., and Gehring, K. (1998) Nickel-induced oligomerization of proteins containing 10-histidine tags. *Biotechniques 25*, 20−22.
(25) Fraser, K. A., and Harding, M. M. (1967) Crystal and molecular structure of bis(histidino)-nickel(II) monohydrate. *J. Chem. Soc. [Sect.] A: Inorg., Phys., Theor.* 415−420.
(26) Skeie, G. O. (2000) Skeletal muscle titin: physiology and pathophysiology. *Cell. Mol. Life Sci. 57*, 1570−1576.
(27) Improta, S., Politou, A. S., and Pastore, A. (1996) Immunoglobulin-like modules from titin I-band: extensible components of muscle elasticity. *Structure (London) 4*, 323−337.
(28) Cieplak, M., Pastore, A., and Hoang, T. X. (2005) Mechanical properties of the domains of titin in a Go-like model. *J. Chem. Phys. 122*, 054906/1−054906/10.
(29) Freiburg, A., Trombitas, K., Hell, W., Cazorla, O., Fougerousse, F., Centner, T., Kolmerer, B., Witt, C., Beckmann, J. S., Gregorio, C. C., Granzier, H., and Labeit, S. (2000) Series of exon-skipping events in the elastic spring region of titin as the structural basis for myofibrillar elastic diversity. *Circ. Res. 86*, 1114−1121.
(30) Muller, J. G., Hickerson, R. P., Perez, R. J., and Burrows, C. J. (1997) DNA Damage from Sulfite Autoxidation Catalyzed by a Nickel(II) Peptide. *J. Am. Chem. Soc. 119*, 1501−1506.
(31) Neta, P., Huie, R. E., and Ross, A. B. (1988) Rate constants for reactions of inorganic radicals in aqueous solution. *J. Phys. Chem. Ref. Data 17*, 1027−284.
(32) Eickhoff, H., Jung, G., and Rieker, A. (2001) Oxidative phenol coupling − tyrosine dimers and libraries containing tyrosyl peptide dimers. *Tetrahedron 57*, 353−364.
(33) All redox potentials reported versus SCE.
(34) Dalle-Donne, I., Milzani, A., and Colombo, R. (2001) Fluorometric detection of dityrosine coupled with HPLC separation for determining actin oxidation. *Am. Biotechnol. Lab. 19*, 34−36.
(35) Uyama, H., and Kobayashi, S. (2002) Enzyme-catalyzed polymerization to functional polymers. *J. Mol. Catal. B Enzym. 19−20*, 117−127.
(36) Mattinen, M.-L., Kruus, K., Buchert, J., Nielsen Jacob, H., Andersen Henrik, J., and Steffensen Charlotte, L. (2005) Laccase-catalyzed polymerization of tyrosine-containing peptides. *FEBS J. 272*, 3640−50.
(37) Person, M. D., Brown, K. C., Mahrus, S., Craik, C. S., and Burlingame, A. L. (2001) Novel inter-protein cross-link identified in the GGH-ecotin D137Y dimer. *Protein Sci. 10*, 1549−1562.
(38) Li, X., and Liu, D. R. (2004) DNA-templated organic synthesis: Nature's strategy for controlling chemical reactivity applied to synthetic molecules. *Angew. Chem., Int. Ed. 43*, 4848−4870.
(39) Gartner, Z. J., Kanan, M. W., and Liu, D. R. (2002) Multistep small-molecule synthesis programmed by DNA templates. *J. Am. Chem. Soc. 124*, 10304−10306.
(40) Diner, B. A. (2001) Amino acid residues involved in the coordination and assembly of the manganese cluster of photosystem II. Proton-coupled electron transport of the redox-active tyrosines and its relationship to water oxidation. *Biochim. Biophys. Acta 1503*, 147−163.
(41) Debus, R. J. (2001) Amino acid residues that modulate the properties of tyrosine YZ and the manganese cluster in the water oxidizing complex of photosystem II. *Biochim. Biophys. Acta 1503*, 164−186.
(42) Bal, W., Liang, R., Lukszo, J., Lee, S.-H., Dizdaroglu, M., and Kasprzak, K. S. (2000) Ni(II) Specifically Cleaves the C−Terminal Tail of the Major Variant of Histone H2A and Forms an Oxidative Damage-Mediating Complex with the Cleaved-Off Octapeptide. *Chem. Res. Toxicol. 13*, 616−624.
(43) Goldshleger, R., Patchornik, G., Shimon, M. B., Tal, D. M., Post, R. L., and Karlish, S. J. (2001) Structural organization and energy transduction mechanism of Na+,K+-ATPase studied with transition metal-catalyzed oxidative cleavage. *J. Bioenerg. Biomembr. 33*, 387−399.
(44) Greiner, D. P., Miyake, R., Moran, J. K., Jones, A. D., Negishi, T., Ishihama, A., and Meares, C. F. (1997) Synthesis of the Protein Cutting Reagent Iron (*S*)-1-(*p*-Bromoacetamidobenzyl)ethylenediaminetetraacetate and Conjugation to Cysteine Side Chains. *Bioconjugate Chem. 8*, 44−48.
(45) Govindaraju, K., Ramasami, T., and Ramaswamy, D. (1989) Chymotrypsin-catalyzed hydrolysis of chromium(III) derivatives of insulin: evidence for stabilization of the protein through interactions with metal ions. *J. Inorg. Biochem. 35*, 127−135.
(46) Wright, A., Bubb, W. A., Hawkins, C. L., and Davies, M. J. (2002) Singlet Oxyge-mediated Protein Oxidation: Evidence for the Formation of Reactive Side Chain Peroxides on Tyrosine Residues{para}. *Photochem. Photobiol. 76*, 35−46.
(47) Arnold, F. H. (1991) Metal-affinity separations: a new dimension in protein processing. *Bio/Technology 9*, 151−156.
(48) Enzelberger, M. M., Minning, S., and Schmid, R. D. (2000) Designing new metal affinity peptides by random mutagenesis of a natural metal-binding site. *J. Chromatog., A 898*, 83−94.
(49) Goodson, R. J., and Katre, N. V. (1990) Site-directed PEGylation of recombinant interleukin-2 at its glycosylation site. *Bio/Technology 8*, 343−646.
(50) Veronese, F. M., and Morpurgo, M. (1999) Bioconjugation in pharmaceutical chemistry. *Farmaco 54*, 497−516.

BC050249B

TECHNICAL NOTES

Synthesis of Chemical Probes to Map Sulfenic Acid Modifications on Proteins

Leslie B. Poole,[†]* Bu-Bing Zeng,[‡,||] Sarah A. Knaggs,[‡] Mamudu Yakubu,[§] and S. Bruce King[‡,]*

Departments of Chemistry and Biochemistry, Wake Forest University, Winston-Salem, North Carolina 27109, and Department of Chemistry, Elizabeth City State University, Elizabeth City, North Carolina 27909 .
Received August 23, 2005

Cysteine sulfenic acids in proteins can be identified by their ability to form adducts with dimedone, but this reagent imparts no spectral or affinity tag for subsequent analyses of such tagged proteins. Given its similar reactivity toward cysteine sulfenic acids, 1,3-cyclohexadione was synthetically modified to an alcohol derivative and linked to fluorophores based on isatoic acid and 7-methoxycoumarin. The resulting compounds retain full reactivity and specificity toward cysteine sulfenic acids in proteins, allowing for incorporation of the fluorescent label into the protein and "tagging" it based on its sulfenic acid redox state. Control experiments using dimedone further show the specificity of the reaction of 1,3-diones with protein sulfenic acids in aqueous media. These new compounds provide the basis for an improved method for the detection of protein sulfenic acids.

INTRODUCTION

Interest in the identification of cysteine sulfenic acids in proteins by biochemists has grown substantially over the past decade as their biological roles in redox regulation and catalysis within an array of cellular proteins have become better defined (*1*, *2*). Despite their importance, only a limited set of tools to identify these species exist, and most of these are only applicable to in vitro studies of pure, isolated proteins (*3*, *4*). Chemical modification of cysteine sulfenic acids by dimedone (5,5-dimethyl-1,3-cyclohexanedione) provides a useful way to "tag" these species with a specific, irreversible alkylating agent, but the lack of any spectral or affinity label associated with dimedone requires that the detection of this tag be undertaken by mass spectrometry(*4*−*7*). A recently reported method involving biotin tagging of nascent cysteine thiols following cysteine sulfenic acid-specific reduction of cell extracts by sodium arsenite (*8*) has provided a new way to detect and isolate sulfenic acid proteins in a whole cell, proteomics format, although limitations of this method due in particular to cysteine sulfenic acid instability indicate that a rapid trapping and labeling method directed toward the unique chemistry of cysteine sulfenic acid would still be preferable.

To provide a new tool for identifying and isolating sulfenic acid-containing proteins and peptides, we designed and synthesized a functionalized derivative of 1,3-cyclohexadione (**3**, Scheme 1), a dimedone-like compound. Linkage of the alcohol functional group of this derivative to two different fluorophores, isatoic acid and 7-methoxycoumarin, yields fluorescent, sulfenic acid-reactive compounds (**6** and **7**, Scheme 3). Data presented herein confirm the utility of these reagents in specifically and rapidly labeling sulfenic acid groups in proteins. Further, the synthetic methods should be generally useful for linking other types of fluorescent or affinity tags to sulfenic acid-containing proteins for analysis and isolation.

Scheme 1

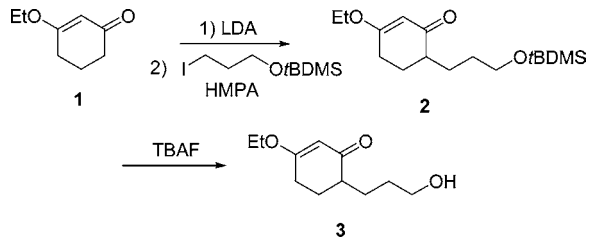

Scheme 2

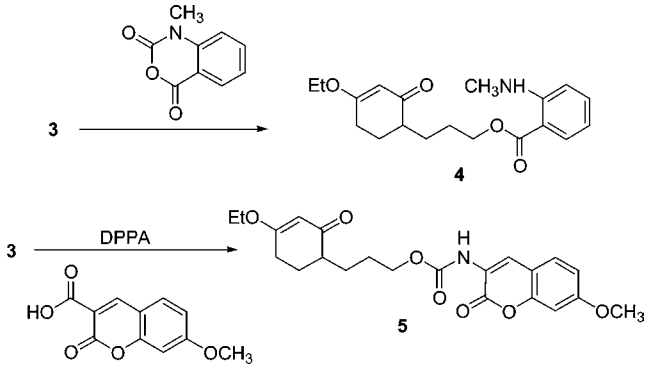

* Corresponding author. Phone: 336-758-5774; fax: 336-758-4656 (King); or phone: 336-716-6711; fax: 336-777-3242 (Poole). E-mail: kingsb@wfu.edu, lbpoole@wfubmc.edu.

[†] Department of Biochemistry, Wake Forest University School of Medicine.

[‡] Department of Chemistry, Wake Forest University.

[§] Elizabeth City State University.

[||] Present address: School of Pharmacy, East China University of Science and Technology, Shanghai, China, 200237.

10.1021/bc050257s CCC: $30.25 © 2005 American Chemical Society
Published on Web 11/01/2005

Scheme 3

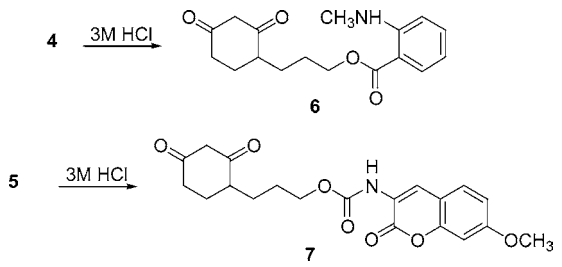

EXPERIMENTAL PROCEDURES

3-Ethoxy-6-(3-*tert*-butyldimethylsilyloxypropyl)-cyclohex-2-enone (2). To a lithium diisopropylamide (LDA) solution [prepared from diisopropylamine (3.82 mL, 27 mmol) and ^{n}BuLi (7.26 mL of a 2.5M solution in hexanes, 18 mmol) in tetrahydrofuran (THF, 12 mL)[1] at 0 °C] at −78 °C was added 3-ethoxy-2-cyclohexen-1-one (2.64 mL, 18 mmol) in THF (6 mL), dropwise, over 40 min. After stirring for an additional 30 min at −78 °C, hexamethyl phosphoramide (HMPA, 3.16 mL, 18 mmol) was added followed by the dropwise addition of 3-iodo-1-*tert*-butyldimethylsiloxypropane (5.45 g, 18 mmol) in THF (8 mL). The resultant mixture was allowed to warm to room temperature, stirred for 6 h, and then quenched by the addition of water (10 mL). The reaction mixture was then partitioned between dichloromethane (DCM, 100 mL) and sat. NH_4Cl (40 mL). The aqueous phase was extracted with DCM (3 × 50 mL), and the organic phases were combined and washed with brine (50 mL), dried over anhydrous $MgSO_4$, and reduced to dryness. The resultant syrup was purified by flash column chromatography (hexanes/EtOAc 8/2) to yield **2** as a pale yellow oil (2.92 g, 51.2%). R_f 0.21 (hexanes/EtOAc 8/2); ^{1}H NMR (300 MHz, $CDCl_3$) δ 5.26 (1H, s), 3.83 (2H, q, J = 7.0 Hz), 3.59 (1H, t, J = 6.5 Hz), 3.58 (H, t, J = 6.5 Hz), 2.38 (2H, t, J = 6.2 Hz), 2.20−1.99 (2H, m), 1.85−1.35 (5H, m), 1.31 (3H, t, J = 7.0 Hz), 0.84 (s, 9H), 0.00 (s, 6H); ^{13}C NMR (75 MHz, $CDCl_3$) δ 201.6, 176.7, 102.3, 64.2, 63.4, 45.0, 30.5, 28.0, 26.4, 26.0 (×2), 18.4, 14.2, −5.2.

3-Ethoxy-6-(3-hydroxypropyl)cyclohex-2-enone (3). To a solution of **2** in THF (20 mL) was added TBAF (23.2 mL of a 1.0 M solution in THF, 23.2 mmol) and NEt_3 (3.2 mL, 23.2 mmol). After stirring at room temperature for 2 h, the reaction was quenched by the addition of water (20 mL) and sat. NH_4Cl (20 mL). The mixture was extracted with DCM (3 × 80 mL), and the combined organic phases were dried over anhydrous $MgSO_4$ and reduced to dryness. The resultant syrup was purified by flash column chromatography with gradient elution (DCM/diethyl ether 1/1 to 3/7) to yield **3** as a pale yellow oil (1.85 g, 100%). R_f 0.37 (hexanes/EtOAc/MeOH 6/3/1); ^{1}H NMR (300 MHz, $CDCl_3$) δ 5.32 (1H, s), 3.89 (2H, q, J = 7.1 Hz), 3.64 (2H, t, J = 6.2 Hz), 2.44 (2H, 2d, J = 7.1 Hz), 2.24 (1H, m), 2.06 (1H, m), 1.92−1.49 (5H, m), 1.36 (3H, t, J = 7.1 Hz); ^{13}C NMR (75 MHz, $CDCl_3$) δ 202.0, 177.2, 102.3, 64.4, 62.6, 44.9, 30.3, 28.4, 26.8, 25.8, 14.3.

3-(4-Ethoxy-2-oxocyclohex-3-enyl)propyl 2-(methylamino)benzoate (4). Alcohol **3** (180 mg, 0.89 mmol), NEt_3 (0.56 mL), and catalytic DMAP were added to a solution of *N*-methylisatoic anhydride (220 mg, 0.89 mmol) in dry DMF (2.0 mL) at room temperature. After stirring overnight, the solution was warmed to 65 °C for 3 h. After cooling to room temperature, water was added and this mixture was extracted with ethyl acetate (5 × 50 mL). The combined organic layers were washed with brine, dried over Na_2SO_4, filtered, and evaporated to give the crude product, which was purified by flash column chromatography to afford 87.0 mg (45% yield) of **4** as a white solid: ^{1}H NMR (300 MHz, $CDCl_3$) δ 7.85 (1H, m), 7.33 (1H, m), 6.56 (2H, m), 5.27 (1H, s), 4.22 (2H, t, J = 5.2 Hz), 3.85 (2H, q, J = 7.0 Hz), 2.86 (3H, s), 2.39 (2H, t, J = 5.3 Hz), 2.04−1.41 (7H, m), 1.31 (3H, t, J = 7.0 Hz); ^{13}C NMR (75 MHz, $CDCl_3$) δ 201.1, 176.8, 168.7, 151.7, 134.7, 131.7, 115.0, 111.3, 110.6, 102.5, 101.9, 64.7, 64.5, 64.3, 44.9, 30.0, 28.2, 26.6, 26.5, 26.4, 14.3; ESI MS *m/z* 354 ($M^+ + Na^+$).

3-(4-Ethoxy-2-oxocyclohex-3-enyl)propyl-7-methoxy-2-oxo-2*H*-chromen-3-ylcarbamate (5). A solution of 7-methoxy-3-carboxycoumarin (335 mg, 1.5 mmol), NEt_3 (1.05 mL, 7.6 mmol), and DPPA (0.36 mL, 1.7 mmol) in benzene (15 mL) was stirred at 65 °C for 4 h. A solution of **3** (260 mg, 1.3 mmol) in benzene (2 mL) was then added and the mixture stirred at 65 °C for 16 h. Upon cooling, water (40 mL) was added and the mixture extracted with DCM (3 × 40 mL). The combined organic phases were washed with sat. $NaHCO_3$ (30 mL) and brine (30 mL), dried over anhydrous $MgSO_4$, and reduced to dryness. The resultant solid was purified by flash column chromatography (×2, gradient elution with DCM/EtOAC (8/2) to DCM/EtOAc/MeOH (8/1/1), and then DCM/MeOH (9/1)) to yield **5** as an off-white solid (270 mg, 49.5%). R_f 0.63 (hexanes/EtOAc 1/2); mp 131−134 °C; ^{1}H NMR (300 MHz, $CDCl_3$) δ 8.22 (1H, s), 7.34 (2H, m), 6.84 (1H, dd, J = 8.6 Hz, 2.4 Hz), 6.79 (1H, d, J = 2.4 Hz), 5.29 (1H, s), 4.18 (2H, t, J = 6.3 Hz), 3.85 (2H, 2q, J = 7.0 Hz), 3.82 (3H, s), 2.42 (2H, 2d, J = 7.1 Hz), 2.22 (1H, m), 2.08 (1H, dq, J = 14.2 Hz, 5.0 Hz), 1.94−1.85 (1H, m), 1.78−1.66 (3H, m), 1.52−1.42 (1H, m), 1.33 (3H, t, J = 7.0 Hz); ^{13}C NMR (75 MHz, $CDCl_3$) δ 201.0, 176.9, 161.1, 158.9, 153.6, 151.3, 128.4, 122.0, 121.9, 113.3, 113.2, 102.4, 100.8, 66.0, 64.4, 55.9, 44.9, 28.3, 26.6 (×2), 26.2, 14.3; ESI MS *m/z* 438 ($M^+ + Na^+$).

3-(2,4-Dioxocyclohexyl)propyl 2-(methylamino)-benzoate (DCP-MAB, compound 6). Compound **4** was stirred in a mixture of THF/3 N HCl (1/1) at room temperature for 3 h, and the mixture was concentrated. The crude product was washed with EtOAc/hexane/MeOH (1/2/0.5) to afford **6** as a white solid: ^{1}H NMR (300 MHz, $CDCl_3$) δ 7.83 (1H, m), 7.34 (1H, m), 6.55 (2H, m), 4.22 (2H, t, J = 6.3 Hz), 3.60 (2H, m), 2.84 (3H, s), 2.52−1.50 (9H, m); ^{13}C NMR (75 MHz, $CDCl_3$) δ 204.3, 203.8, 168.6, 151.6, 134.9, 131.7, 131.5, 115.2, 111.6, 110.5, 64.1, 58.4, 49.1, 39.9, 30.1, 26.4, 26.0, 24.7; ESI MS *m/z* 326 ($M^+ + Na^+$).

3-(2,4-Dioxocyclohexyl)propyl 7-Methoxy-2-oxo-2*H*-chromen-3-ylcarbamate (DCP-MCC, compound 7). Compound **5** (240 mg, 0.58 mmol) was stirred in a mixture of THF/DCM (3/1 v/v, 4 mL) and 3 N HCl (4 mL) for 1 h. The reaction mixture was diluted with water (10 mL) and extracted with DCM (3 × 30 mL). The combined organic phases were dried over anhydrous $MgSO_4$, and reduced to dryness to yield the crude product, which was purified by flash column chromatography (EtOAc/acetone 4/1) to yield **7** as an off-white solid (133 mg, 59.4%). R_f 0.62 (hexanes/EtOAc/MeOH 6/3/1); mp 154−156 °C; ^{1}H

[1]Abbreviations used: TBDMS, *tert*-butyldimethylsilyl; TBAF, tetra-*n*-butylammonium fluoride; amu, atomic mass units; THF, tetrahydrofuran; HMPA, hexamethylphosphoramide; DMAP, 4-(dimethylamino)pyridine; DPPA, diphenyl phosphorazidate; GSNO, *S*-nitrosoglutathione; NMR, nuclear magnetic resonance; LDA, lithium diisopropylamide; DCM, dichloromethane; ESI-MS, electrospray ionization mass spectrometry; NBD chloride, 7-chloro-4-nitrobenzo-2-oxa-1,3-diazole; DCP-MAB, 3-(2,4-dioxocyclohexyl)propyl 2-(methylamino)benzoate; DCP-MCC, 3-(2,4-dioxocyclohexyl)propyl 7-methoxy-2-oxo-2*H*-chromen-3-ylcarbamate.

NMR (300 MHz, $CDCl_3$) δ 8.25 (1H, s), 7.42 (1H, s), 7.39 (1H, d, J = 8.7 Hz), 6.88 (1H, dd, J = 8.6 Hz, 2.1 Hz), 6.83 (1H, d, J = 2.1 Hz), 4.23 (2H, t, J = 6.5 Hz), 3.86 (3H, s), 3.44 (2H, d, J = 5.1 Hz), 2.78−2.69 (1H, dt, J = 16.4 Hz, 4.4 Hz), 2.67−2.51 (2H, m), 2.24−2.15 (1H, dq, J = 14.1 Hz, 4.8 Hz), 2.03−1.95 (1H, m), 1.88−1.47 (6H, m); ^{13}C NMR (75 MHz, $CDCl_3$) δ 204.2, 203.8, 161.2, 158.9, 153.5, 151.3, 128.4, 122.0, 121.8, 113.3, 113.2, 100.9, 65.6, 58.5, 55.9, 49.1, 39.9, 26.6, 25.7, 24.8; ESI MS *m/z* 410 ($M^+ + Na^+$), 388 ($M^+ + H^+$); CHN calcd for $C_{20}H_{21}NO_7 \cdot 0.5H_2O$, C: 60.59, H: 5.61, N: 3.53, found C: 61.31, H: 5.56, N: 3.48.

Generation of Pure, Sulfenic Acid-Containing C165S AhpC. The C165S mutant of AhpC was expressed in bacteria and purified in the presence of 5 mM 1,4-dithiothreitol (added to all buffers) essentially as described previously (*9*). Purification of wild type AhpC was also carried out as previously described (*10*). For generation of the sulfenic acid form of C165S AhpC, thawed enzyme in 25 mM phosphate buffer at pH 7, containing 1 mM EDTA, was washed free of the dithiothreitol and transferred into fresh buffer using a PD-10 column (Amersham Biosciences), and pooled fractions were transferred to an anerobic cuvette. The protein solution (160 nmol in 0.60 mL) was made anaerobic by repeated cycles of argon and vacuum over about 30 min, then rapidly titrated with 11 mM hydrogen peroxide to give a maximal absorbance signal at ~367 nm for the sulfenate anion as described previously (*3*, *4*). In subsequent experiments, optimal sulfenic acid formation was observed by adding and mixing the hydrogen peroxide much more slowly (additions of about 0.05 equiv and thorough mixing every ~1 min) and quantitating the sulfenic acid formed using a freshly prepared 2-nitro-5-thiobenzoate (TNB) solution (0.28 mL) and a 60 μL aliquot of the protein removed anaerobically from the cuvette (*3*, *4*). Using this method, ~73% of the protein was converted to the sulfenic acid form after addition of 1.08 equiv of hydrogen peroxide. Protein was kept in the anaerobic cuvette at room temperature for several hours before conducting experiments with no loss in sulfenic acid content.

Labeling of Sulfenic Acid-Containing C165S AhpC for Spectral and Mass Spectrometric Analysis. The pure, oxidized enzyme (32 μL, 6 nmol each) from the anaerobic cuvette was added to argon-flushed 500 μL Eppendorf tubes containing the compound of choice (either dimethyl sulfoxide alone, or dimethyl sulfoxide into which dimedone, 1,3-cyclohexanedione, **6**, or **7** had been dissolved) to give a final concentration of 5 mM for the added reagent in final volumes of 50 μL, and the tubes were flushed again with argon before closing. Other redox forms of C165S AhpC or the wild-type enzyme were also tested for reactivity with one or more of these four compounds. Approximate 100 mM stock solutions of **6** or **7** in dimethyl sulfoxide were standardized using expected extinction coefficients of 5700 M^{-1} cm^{-1} at 353 nm or 25000 M^{-1} cm^{-1} at 334 nm, respectively, for the esterified isatoic acid conjugate or the methoxycoumarin conjugate in methanol (*11*). Samples were incubated at room temperature for 60 min, then transferred to Apollo ultrafiltration devices (30K cutoff, Orbital Biosciences, Topsfield, MA), washed with 5.5 mL of 10 mM ammonium bicarbonate and reconcentrated to about 50 μL, for a total of four washes (>10^8-fold dilution of the initial small molecule components).

Mass Spectrometric and Spectral Analyses of Adducts with the Sulfenic Acid-Containing Form of C165S AhpC. For mass spectrometric analyses, 60 μL of the ammonium bicarbonate buffer containing 1−2 nmol of labeled or unlabeled protein was submitted to the Mass Spectrometer Facility at Wake Forest University School of Medicine for infusion analysis on a Micromass Quattro II triple quadrupole mass spectrometer equipped with a Z-spray source. Just prior to analysis, samples were diluted 1:1 with acetonitrile and 1% formic acid was added. The data were processed and analyzed using MassLynx Version 3.5.

Labeled protein samples washed (with Apollo concentrators) into potassium phosphate or ammonium bicarbonate buffers were also analyzed for their UV−visible spectroscopic and fluorescence properties using a Beckman DU7500 diode array spectrophotometer or a SLM Aminco-Bowman Series 2 luminescence spectrophotometer, respectively. By comparison with the reported extinction coefficients for each of the free reagents in methanol (5700 M^{-1} cm^{-1} for esterified isatoic acid, and 25000 M^{-1} cm^{-1} for methoxycoumarin) (*11*), the free and presumably protein-bound reagents in neutral pH phosphate buffer exhibited average extinction coefficients of ~4500 and ~21800 M^{-1} cm^{-1}, respectively, for **6** and **7**. These measured values were subsequently used to standardize **6** and **7** and to estimate the labeled protein concentrations.

RESULTS AND DISCUSSION

Synthesis. As preliminary biochemical results revealed that 1,3-cyclohexadione reacts in a manner similar to dimedone, the protected version of 1,3-cyclohexadione, 3-ethoxy-2-cyclohexen-1-one (**1**, Scheme 1), was chosen as the initial starting material for the preparation of fluorescently labeled probes. Starting with **1**, which readily hydrolyzes to 1,3-cyclohexadione under acidic conditions, removes any synthetic complications from the highly acidic (pK_a = 5.15) (*12*) active methylene group of dimedone. Alkylation of the anion of commercially available 3-ethoxy-2-cyclohexen-1-one with *tert*-butyldimethylsilyl (TBDMS) (*13*)-protected 3-iodo-1-propanol yields **2** (51% yield, Scheme 1). Treatment of **2** with tetra-*n*-butylammonium fluoride (TBAF) removes the silyl group to give the alcohol (**3**, 100%, Scheme 1). The alcohol group of **3** provides an attachment site for the fluorescent groups.

Condensation of **3** with *N*-methylisatoic anhydride yields the protected 1,3-cyclohexadione derivative (**4**, 45%, Scheme 2). Heating 7-methoxycoumarin-3-carboxylic acid in the presence of diphenyl phosphorazidate (DPPA) and **3** gives the protected derivative (**5**, 50%, Scheme 2), presumably through the Curtius rearrangement of the acyl azide to the isocyanate followed by condensation of **3**. Treatment of **4** and **5** with aqueous HCl cleanly produces 3-(2,4-dioxocyclohexyl)propyl 2-(methylamino)benzoate (**6,** DCP-MAB, Scheme 3**)** and 3-(2,4-dioxocyclohexyl)propyl 7-methoxy-2-oxo-2*H*-chromen-3-ylcarbamate **(7**, DCP-MCC, Scheme 3) in 96 and 59% yield, respectively. Both the ester linkage of **6** and the carbamate linkage of **7** appear generally stable to these acidic deprotection conditions.

Reactivity of New Compounds toward Cysteine Sulfenic Acids in Proteins. To test for the reactivity of **6** and **7** toward protein sulfenic acids, a mutant, cysteine-dependent peroxidase enzyme was used in which the oxidized, sulfenic acid form of the cysteinyl redox center is stabilized, yet accessible (the C165S mutant of AhpC from *Salmonella typhimurium*, a peroxiredoxin) (*3, 9, 13*). Both compounds, dissolved initially in dimethyl sulfoxide and diluted 20-fold to a final concentration of 5 mM in aqueous, neutral pH buffer, gave covalent

Scheme 4

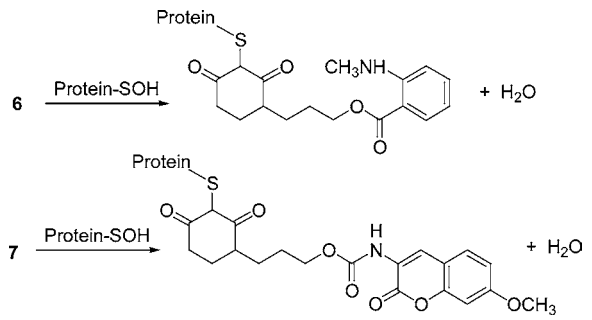

adducts with the sulfenic, but not sulfinic or sulfonic, acid forms of the peroxidase (Scheme 4).

The thiol group of the reduced protein and the oxidized, disulfide-bonded form of wild type AhpC were also unreactive toward these compounds, as confirmed by electrospray ionization mass spectrometry (ESI-MS) of the ammonium bicarbonate-washed proteins following incubations with the labeling agents (Figure 1 and data not shown). As illustrated in Figure 1 and summarized in Table 1, mass spectrometry results were completely consistent with the expected reactivity and products generated with the sulfenic acid-containing protein using dimedone, 1,3-cyclohexadione, and our two new labeling agents (**6** and **7**). Where sulfenic acid and hence adduct generation was substoichiometric due to the rapid addition of excess hydrogen peroxide (converting much of the enzyme to the sulfinic and perhaps sulfonic acid forms), additional peaks for thiol (unoxidized) and hyperoxidized (RSO_2^- and RSO_3^-) protein were observed (Figure 1). Under the conditions used, the sulfenic acid form of the protein either reacts with the reagent or is further oxidized during the workup or analysis of the sample and is therefore not observed. In a subsequent experiment where sulfenic acid formation was measured at ~73%, an equivalent amount of **6** or **7** (74 and 67%, respectively) was incorporated into the protein as observed by ESI-MS (Table 1).

The fluorescence properties of **7** ($\lambda_{ex,max} = 341$ nm and $\lambda_{em,max} = 414$ nm) were unchanged upon reaction with the cysteine sulfenic acid**,** while small shifts in both the excitation and emission wavelength maxima were observed upon adduct formation with **6**, the isatoic acid derivative (from $\lambda_{ex,max} = 353$ nm to $\lambda_{ex,max} = 357$ nm, and from $\lambda_{em,max} = 440$ nm to $\lambda_{em,max} = 430$ nm, Figure 2). This fluorescence difference may allow for the monitoring of the protein reaction with the fluorophore, although apparent bleaching of the fluorophore during measurements makes such experiments technically difficult. Protein adduct amounts assessed by ESI-MS analyses of the intact proteins indicate approximately equal labeling of the protein with the two reagents when 1:1 mixtures of the **6** and **7** are added, suggesting similar rates of reaction for these two compounds. While it is unlikely that all protein sulfenic acids react with these compounds at the same rate due in part to varying accessibility of the reactive group, it is probable that, under denaturing and anaerobic conditions, reaction rates will be similar to those with the model protein sulfenic acid.

Specificity of Dimedone and/or Fluorescent, Cyclohexadione-Derived Reagents toward Sulfenic Acids in Proteins. The known reactivity of the nucleophilic center of dimedone is toward cysteine sulfenic acids and aldehydes (*14, 15*). Amines have also been shown to condense with dimedone (*16*). As described above, control

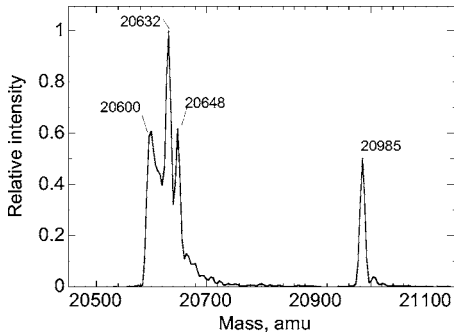

Figure 1. Electrospray ionization mass spectrometry analysis of adducts with the sulfenic acid form of C165S AhpC. The mutant of the bacterial peroxidase AhpC (C165S) containing only the peroxidatic cysteine (Cys46) but not the resolving cysteine (Cys165) that participates in disulfide bond formation was treated with hydrogen peroxide to yield the relatively stabilized sulfenic acid form of the protein under anaerobic conditions, then incubated with DCP-MCC (**7**) to yield the covalent protein adduct. The treated protein sample was concentrated and rediluted four times into 10 mM ammonium bicarbonate buffer using a 30K cutoff Apollo ultrafiltration device (>10^8-fold dilution of the initial small molecule components). Just prior to analysis, samples were diluted 1:1 with acetonitrile, made 1% in formic acid, and then infused at 5 μL/min. The capillary voltage was 3.5 kV; the cone voltage was ramped (30−120 V) and the spectrum scanned from *m/z* 600−1800 in 2.1 s. Eight to twenty scans were acquired for each sample. The data were processed using MassLynx 3.5 to generate the absolute molecular weight of the protein ± 2.1 Da. Shown are the transformed data that represent the relative abundance (shown as both the predicted and observed masses, see Table 1 for more detailed mass information) of four prominent species of C165S AhpC: the protein with the active site Cys46 in the thiol (20600 amu), sulfinic acid (20632 amu), or sulfonic acid (20648 amu) states, or in a covalent complex with **7** (20985 amu). In this case the initial method described in the Experimental Section (based on maximal A_{367} and rapid hydrogen peroxide addition) was used to generate the sulfenic acid form of C165S AhpC, resulting in approximately 1/5 of the protein being stabilized in this redox state at the time of reaction with **7**.

Table 1. Observed and Predicted Masses of Products Following Sulfenic Acid-Directed Labeling of Target Protein (C165S AhpC)

reagent	observed increase in mass of product compared with RSH form[a]	predicted additional mass of product[b]
1,3-cyclohexadione	109.2	110.1
DCP-MAB (**6**)	300.7	301.4
DCP-MCC (**7**)	384.5	385.4
dimedone	137.3	138.2

[a] Mass from electrospray ionization mass spectrometry on a Micromass Quattro II triple quadrapole mass spectrometer of the modified product from which was subtracted the mass for the oxidized sulfinic acid product (RSO_2^-) present in each sample, adjusted 32 amu for the two oxygen atoms. [b] Mass of labeling agent minus 2.016 for loss of hydrogens during adduct formation.

reactions of thiol, disulfide, or hyperoxidized forms of AhpC (wild type or C165S) demonstrated their lack of reactivity toward **6**, **7**, and dimedone based on the lack of ESI-MS-detectable adduct formation. To test for general cross-reactivity of these reagents with other oxidized sulfur-containing functional groups, we tested the reactivity of dimedone, as a model reagent, with a *S*-nitrosothiol and two sulfoxides. Dimedone fails to react with *S*-nitrosoglutathione (GSNO) as judged by absorbance spectroscopy over 1 h at room temperature. Nuclear magnetic resonance (NMR) and spectroscopic and chemical isolation experiments show that dimedone does not

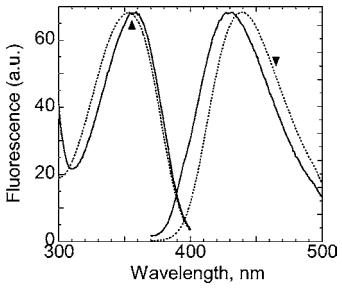

Figure 2. Fluorescence spectra of DCP-MAB (**6**) before (solid) and after (dotted) reaction with cysteine sulfenic acid-containing protein. Labeled C165S AhpC was prepared as described in the Experimental Section with the cysteine sulfenic acid form of the protein incubated anaerobically with 5 mM of **6** for 60 min, then washed free of the unreacted reagent and buffer components into a final buffer of 50 mM Tris-HCl at pH 8 using an Apollo concentrator. The absorbance at 347 nm of this sample was 0.14, and the fluorescence measurements were taken using a semi-microcuvette with the 0.4 mm cuvette width directed toward the excitation beam and the 1.0 mm internal width directed toward the emission detector at 90°. Emission scans (370 to 500 nm) were collected at an excitation wavelength of 353 or 357 nm, respectively, for the free and protein-bound **6**, and excitation scans (250 to 400 nm) were collected at an emission wavelength of 440 or 430 nm, respectively. Arrows indicate excitation and emission wavelengths used in attempts to monitor rates of reaction of cysteine sulfenic acid-containing C165S AhpC with **6**; technical problems were encountered with these measurements, and reproducible rates were not obtained.

react with aqueous solutions of either dimethyl sulfoxide or methionine sulfoxide (Supporting Information).

As reported, dimedone demonstrates reactivity with both aldehydes and amines (*15, 16*). Control reactions show that dimedone reacts with butyraldehyde in the presence of piperidine at 50 °C in aqueous ethanol but fails to react with the same aldehyde at room temperature in the absence of base. In addition, while dimedone condenses with benzylamine to form an imine in organic solvent, no reaction occurs in aqueous ethanol. The failure of **6** and **7** to react with either reduced or oxidized wild type or reduced C165S AhpC proteins also indicates that these compounds do not react with protein amine groups under these conditions. Taken together, these results demonstrate the relative specificity of the reaction of these compounds for sulfenic acids in proteins in aqueous buffers.

CONCLUSIONS

Functionalization of 1,3-cyclohexadione derivatives with an alcohol group and subsequent coupling to fluorophores has successfully generated two sulfenic acid-reactive compounds that specifically incorporate a fluorescent label into a sulfenic acid-containing model protein. Compounds such as these should prove useful in tagging protein sulfenic acids for their detection and isolation from complex protein mixtures in the future.

ACKNOWLEDGMENT

The authors thank Drs. Larry Daniel and Jacquelyn Fetrow for experimental and editorial guidance and acknowledge financial support from the American Heart Association Established Investigatorship program (to both L.B.P., 0140175N, and S.B.K., 0140020N), from the Cross Campus Collaborative Research Program at Wake Forest University (to S.B.K. and L.B.P.), and from the National Institutes of Health to L.B.P., with S.B.K. as coinvestigator (R21 CA112145). The Quattro II tandem mass spectrometer was purchased, updated, and supported in part with funds from National Science Foundation BIR-9414018, the North Carolina Biotechnology Center (9903IDG-1002), the Winston-Salem Foundation, and the Comprehensive Cancer Center of Wake Forest University. The NMR spectrometers used in this work were purchased with partial support from NSF (CHE-9708077) and the North Carolina Biotechnology Center (9703-IDG-1007).

Supporting Information Available: Experimental details and NMR data for compounds **2**−**7**. This material is available free of charge via the Internet at http://pubs.acs.org.

LITERATURE CITED

(1) Claiborne, A., Yeh, J. I., Mallett, T. C., Luba, J., Crane, E. J., III, Charrier, V., and Parsonage, D. (1999) Protein-sulfenic acids: diverse roles for an unlikely player in enzyme catalysis and redox regulation. *Biochemistry 38*, 15407−15416.

(2) Poole, L. B., Karplus, P. A., and Claiborne, A. (2004) Protein sulfenic acids in redox signaling. *Annu. Rev. Pharmacol. Toxicol. 44*, 325−347.

(3) Poole, L. B., and Ellis, H. R. (2002) Identification of cysteine sulfenic acid in AhpC of alkyl hydroperoxide reductase. *Methods Enzymol 348*, 122−136.

(4) Poole, L. B. (2003) Measurement of protein sulfenic acid content. In *Current Protocols in Toxicology* (Maines, M. D., Ed.) pp 17.12.11−17.12.20, John Wiley & Sons, Inc., New York.

(5) Allison, W. S. (1976) Formation and reactions of sulfenic acids in proteins, *Acc. Chem. Res. 9*, 293−299.

(6) Willett, W. S., and Copley, S. D. (1996) Identification and localization of a stable sulfenic acid in peroxide-treated tetrachlorohydroquinone dehalogenase using electrospray mass spectrometry. *Chem Biol 3*, 851−857.

(7) Detection of radioactively labeled dimedone has also been used in the past, although this material is no longer commercially available and is prohibitively expensive to synthesize.

(8) Saurin, A. T., Neubert, H., Brennan, J. P., and Eaton, P. (2004) Widespread sulfenic acid formation in tissues in response to hydrogen peroxide. *Proc. Natl. Acad. Sci. U.S.A 101*, 17982−17987.

(9) Ellis, H. R., and Poole, L. B. (1997) Roles for the two cysteine residues of AhpC in catalysis of peroxide reduction by alkyl hydroperoxide reductase from *Salmonella typhimurium*. *Biochemistry 36*, 13349−13356.

(10) Poole, L. B., and Ellis, H. R. (1996) Flavin-dependent alkyl hydroperoxide reductase from *Salmonella* typhimurium. 1. Purification and enzymatic activities of overexpressed AhpF and AhpC proteins. *Biochemistry 35*, 56−64.

(11) Haugland, R. P. (2002) *Handbook of fluorescent probes and research products*, 9th ed., Molecular Probes, Inc., Eugene, OR.

(12) *The Merck Index*, 12th ed.; Merck and Co., Inc.: Whitehouse Station, NJ, 1996; p 548.

(13) Ellis, H. R., and Poole, L. B. (1997) Novel application of 7-chloro-4-nitrobenzo-2-oxa-1,3-diazole to identify cysteine sulfenic acid in the AhpC component of alkyl hydroperoxide reductase. *Biochemistry 36*, 15013−15018.

(14) Benitez, L. V., and Allison, W. S. (1974) The inactivation of the acyl phosphatase activity catalyzed by the sulfenic acid form of glyceraldehyde 3-phosphate dehydrogenase by dimedone and olefins. *J. Biol. Chem. 249*, 6234−6243.

(15) Vogel, A. I. (2005) Investigation and characterisation of organic compounds. In *Vogel's Textbook of Practical Organic Chemistry* (Furniss, B. S., Hannaford, A. J., Smith, P. W. G., and Tatchell, A. R., Eds.) pp 1259−1260, Pearson, Singapore.

(16) Halpern, B., and James, L. B. (1964) Dimedone (5, 5-dimethylcyclohexane-1, 3-dione) as a protecting agent for amino groups in peptide synthesis. *Aust. J. Chem. 17*, 1282−1287.

BC050257S